JOURNAL

OF THE

PHYSICAL SOCIETY

OF JAPAN

Volume 13

1958

Published by the

PHYSICAL SOCIETY OF JAPAN

JOURNAL OF THE PHYSICAL SOCIETY OF JAPAN Vol. 13, No. 1, JANUARY, 1958

Angular Distribution of Photo-neutrons Produced by 17 Mev X-rays

By Tsunesaburo ASADA, Masayoshi MASUDA, Masayuki OKUMURA and Juzo Okuma

Department of Physics, Faculty of Science, University of Osaka

(Received August 19, 1957)

The angular distributions of photo-neutrons from lead, copper, aluminum and beryllium have been measured by using bremsstrahlung of maximum energy of 17 Mev from a betatron. The neutron detector is ZnS-paraffin-Lucite light guide button. The results are $1+(1.29\pm0.53)\sin^2\theta$, $1+(1.6\pm0.8)\sin^2\theta$, $1+(0.17\pm0.06)\sin^2\theta$, $1+(0.30\pm0.11)\sin^2\theta$ for beryllium, aluminum, copper, and lead.

§ 1. Introduction

The photonuclear processes can be conveniently divided into two mechanisms; i.e., evaporation and direct ejection.[1]

The former is the one in which the γ-rays are absorbed by a collective nuclear motion which results in general heating of the nucleus and subsequent decay which can be explained by the statistical model. The latter is the transition of a nucleon in the upper shell to an unfilled state by the electric dipole absorption of γ-rays.

The evaporation process results in the spherically symmetric distribution of ejected particles and in the direct process it is expected to be of the form $(a+b\sin^2\theta)$[1] where θ is the angle at which neutrons are emitted with respect to the incident γ-rays, a and b are constants.

In this paper, we report a measurement of the angular distribution of photo-neutrons in the energy range of "*off the giant resonance*" using the bremsstrahlung from the University of Osaka Betatron.

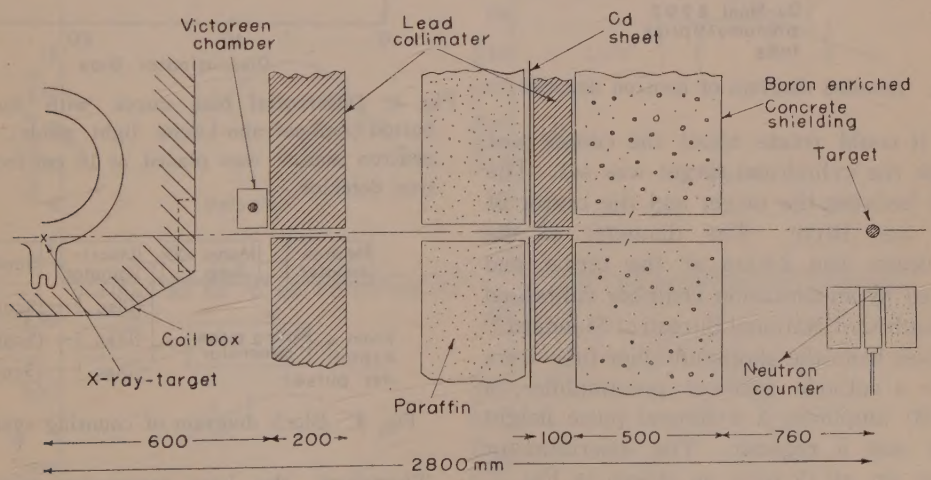

Fig. 1. Block diagram of experimental arrangement.

The results are compared with the earlier experiments[2,3,4] in lead, copper, and aluminum. A measurement of angular distribution of photo-neutrons from beryllium is also reported. Guth and Mullin[5] and Czyz[6] have calculated the angular distribution for the reaction $Be^9(\gamma n)Be^8$ assuming that the Be^9 nucleus consists of Be^8 core plus a valence neutron in $P_{3/2}$ ground state. They have obtained a distribution of the form $(a+b\sin^2\theta)$ arising from electric dipole transition to S and D state, with the ratio b/a depending on the respective

transition probabilities.

§ 2. Experimental Procedure

The arrangement of experimental instruments are shown in Fig. 1. The boron enriched concrete shielding has increased the signal to background ratio by factor of 10. The targets were cut in the shape of cylinder of $1''\phi \times 1''$. The neutrons were detected by a ZnS-paraffin-Lucite light guide button[7] mounted on Du-Mont 6292 photomultiplier tube as shown in Fig. 2. This counter was arranged

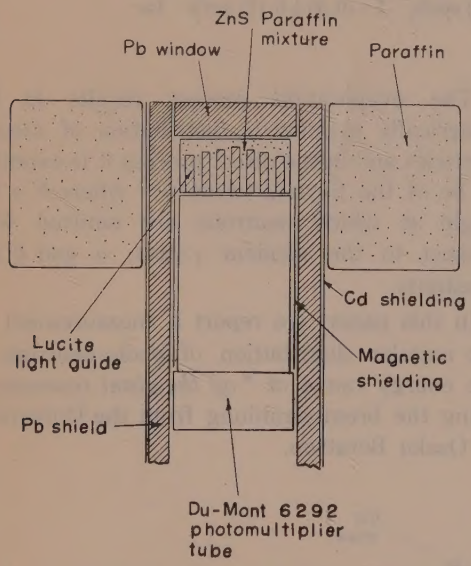

Fig. 2. Detailed diagram of neutron detector.

so that it could rotate about the center post on which the cylindrical target was set. The distance between the target and the center of counter was 16 cm. The diameter of the X-ray beam was 2.0 cm at the target and monitored by an ionization chamber calibrated by the method of National Bureau of Standard.[8] The pulses from the photomultiplier tube were fed into a cathode follower pre-amplifier, a Model-100 amplifier, a 4-channel pulse height analyzer and a register. The discriminator bias was set at 15 volts as shown in Fig. 3. This indicate the efficiency of 0.3 % for Rn-Be neutrons.

In measuring the photo-neutrons, one must contend with background noises of very large intensity which originate in the target placed in the center of the X-ray beam. It is possible to obtain the required discrimination between the X-rays and recoil protons from the fact that the specific ionization of recoil protons is much higher than that of secondary electrons. But the high intensity burst of X-rays causes high voltage scintillation pulses by the pile-up effect of electrons. It is difficult to distinguish the neutron pulses from these pile-up pulses.

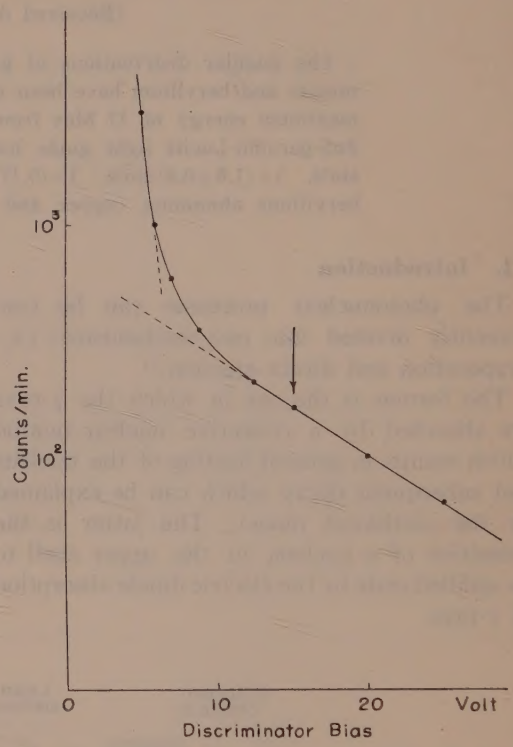

Fig. 3. Differential bias curve with Emmerich button (ZnS-parrafin-Lucite light guide). Rn-Be neutron source was placed at 16 cm from neutron detector.

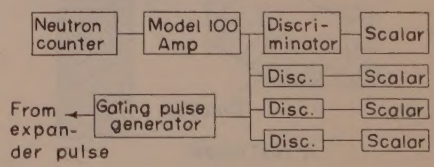

Fig. 4. Block diagram of counting system.

Therefore, the long expansion technique[9] was adopted for the betatron operation. The long expansion pulse of 80 μsec results in a long X-ray burst and reduces the pile-up difficulties in measuring the low yield neutrons in the large X-ray burst. In this point of view, we changed our integrator expander for a delayed expander for this experiment. Readings were taken at 40°, 50°, 70°, 90°, 110°,

130°, 140°. The pile-up difficulties made the readings for more forward angles impossible. Moreover, the forward reading with aluminum target was unobtainable due to its low neutron yield.

Also, the pile-up difficulties could be lessened by using a thick lead window in the detector. This result is shown in Fig. 5. The target was lead and a lead sheet was inserted between the detector and the target.

For example, the counting rate was 133 per 1.5 min. with lead window of 12 mm thickness, while 112 per 1.5 min. with 22 mm window when the lead target was bombarded by bremsstrahlung with maximum energy of 17 Mev.

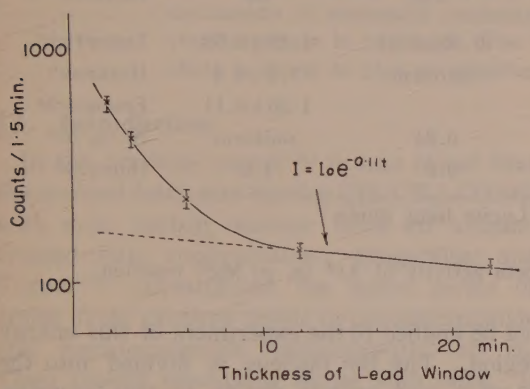

Fig. 5. The absorption curve of photo-neutrons with lead window inserted between the counter and the target. It is shown that the 12 mm window is sufficient to avoid the pile-up effect.

By the way, the counting rate for neutrons from the Rn-Be neutron source was 116 with 22 mm window when normalized at 12 mm window counting. This value was taken by placing the Rn-Be neutron source at the position of target without the bremsstrahlung bombardment. The both counting rate with 22 mm window agrees within the experimental error.

The similar procedures were followed in other targets and we can say with confidence that our results are free of the errorneous counts due to piled up electrons.

§ 3. Results and Discussion

The observed angular distributions for lead, copper, and aluminum have the shape of $(a+b\sin^2\theta)$, which are the same as reported by Johanson[2], Dixson[3] and Price.[4] This is shown in Fig. 6. The value of b/a was compared with the data of earlier experiments in Table I. Since these detectors are all fast neutron

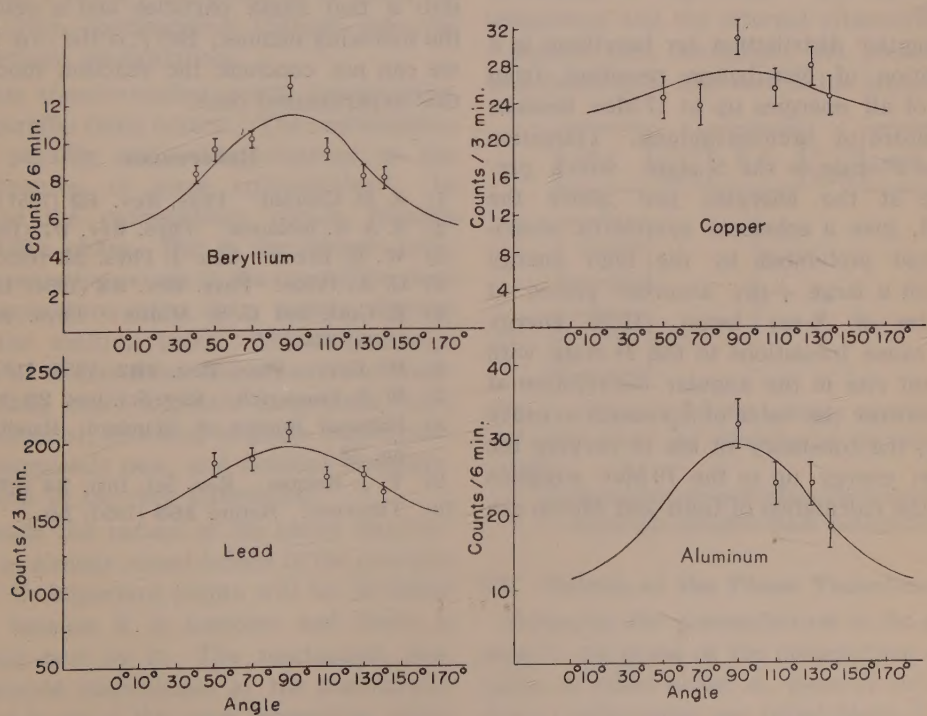

Fig. 6. The angular distributions of photo-neutrons as measured with Emmerich button type scintillation detector.

detectors, the detected neutrons are those of direct emission. Therefore, assuming these neutrons are due to the transitions from unknown upper shells, one can conjecture that the transitions from which shells are predominant by the relation $(l+2)/2l=b/a$, where l is the angular momentum of the state before nuclear excitation. However, because of large differences between the results of earlier experimenters, above conjecture is not reliable. The photo-neutrons of lead seems to originate in the transitions from lower state than in copper. But the large value of b/a of angular distribution of aluminum can not be explained satisfactorily by the theory. The theoretical value of b/a deduced by the Courant model can fit the experimental distribution only if the majority of the observed neutrons have an angular momentum of one in the nucleus before excitation. This seems unlikely in aluminum.

Table I. The values of b/a.

Energy		Target nucleus Al	Cu	Pb	Be	Detector
Present	(17 Mev)	1.6±0.8	0.17±0.06	0.30±0.11	1.29±0.53	Emmerich[a]
Dixon	(70 Mev)	0.36±0.29	0.23±0.15	uniform	1.2±0.4	Hornyak[b]
Halpern	(70 Mev)				1.26±0.11	Emmerich[a]
Price	(22 Mev)		0.33	0.84	uniform	Al (n, p)[c]
Johanson	(65 Mev)	1		0.8	1.5	Hornyak[b]

a) A scintillation detector with a ZnS-paraffin-Lucite light guide.
b) A scintillation detector with a ZnS-Lucite.
c) A fast neutron detector by measuring the beta activity of Al^{27} (n, p) Mg^{27} reaction.

The angular distribution for beryllium is a superposition of distribution resulting from photons of all energies up to 17 Mev because of the nature of bremsstrahlung. Transition from the P state to the S state, which predominate at the energies just above the threshold, give a spherical symmetric distribution and prohibited by the high energy filter with a large γ-ray absorber placed at the center of X-ray beam. High energy photons cause transitions to the D state with a resultant rise in the angular distribution at 90°. However the value of b/a seems to prove this fact, the constancy of b/a in varying the excitation energy up to the 70 Mev suggests us that the calculation of Guth and Mullin can not be applied to the experiment of this energy region. The Be^9 nucleus is divided into the neutron and proton clouds at this energies. The mechanism of photodisintegration which looks more is the one given by Titterton[10] that Be^9 may disintegrate by photon absortion into a two alpha particles and a neutron in the following manner, $Be^9(\gamma, \alpha)He^5 \rightarrow \alpha+n$, but we can not conclude the reaction mode with this experimental data.

References

1) E. D. Courant: Phys. Rev. **82** (1951) 703.
2) S. A. E. Johanson: Phys. Rev. **97** (1955) 434.
3) W. R. Dixon: Can. J. Phys. **33** (1956) 785.
4) G. A. Price: Phys. Rev. **93** (1954) 1269
5) E. Guth and C. S. Mullin: Phys. Rev. **76** (1949) 234.
6) W. Czyz: Phys. Rev. **102** (1956) 1184
7) W. S. Emmerich: Rev. Sci. Inst. **25** (1954) 69.
8) National Bureau of Standard, Handbook 55 pp. 33.
9) T. J. Keegan: Rev. Sci. Inst. **24** (1953) 472.
10) Titterton: Nature **165** (1950) 721.

JOURNAL OF THE PHYSICAL SOCIETY OF JAPAN Vol. 13, No. 1, JANUARY, 1958

The Phase Transformation of Solid Normal Hexadecanamide

By Tosio SAKURAI and Masaya YABE

Institute of Science and Technology, University of Tokyo

(Received September 4, 1957)

A phase transformation of normal hexadecanamide ($C_{15}H_{31}CONH_2$) in which the crossed hydrocarbon chain configuration changes into the parallel-chain one is investigated by means of X-rays, thermal analysis, infrared absorption and proton magnetic resonance absorption. Based upon the knowledge of the crystal structure and X-ray observation, a mechanism of successive reorientation of the hydrocarbon chain at this transformation is proposed. The twisting vibration of the hydrocarbon chain is found to play an important role for this transformation.

§ 1. Introduction

In the previous report[1)2)] it was found that the normal fatty acid amides $CH_3(CH_2)_nCONH_2$ with even carbon number have an unusual crossed-chain configuration. Lingafelter and Turner[3)4)] investigated the same series of amide from propane amide to tetradecanamide and hexadecanamide independently of us. Their results essentially agree with ours. It was also found[1)] that heptadecanamide and hexadecanamide have another phase with parallel-chain configuration, and hexadecanamide has a phase transformation at which the crossed-chain configuration changes into the parallel-chain configulation.

At this transformation point, reorientation of the paraffin chain occurs. The reorientation of the paraffin chain was observed at the transformation of some triglycerides[5)]. In this case the reorientation occurs through a liquid-like phase. But in the present case, the reorientation occurs in the crystalline state at a temperature more than twenty degrees below the melting point. Although a large number of works about the phase transformation of long chain aliphatic compounds have been published, this kind of phase transformation is completely new, and detailed investigation seems to be very interesting.

Although the nature of the phase transformation is already stated briefly in the previous report,[1)] its important points will be reviewed in § 2, because it is complex and there is something new in it. The mechanism how the molecule reorientates at the transformation point is one of the most interesting points of the present work. From the knowledge of the crystal structure and X-ray observation at the transformation point, it is shown that the hydrocarbon chain is brandished around the terminal amide group which forms the strong hydrogen bond network with surrounding molecules. The behavior of the hydrogen bond is investigated by infrared absorption. Thermal properties indicate that large entropy change occurs at the transformation point and internal vibration of the molecule plays an important role. Results of the proton magnetic resonance absorption are consistent with the above view and show the marked motional narrowing corresponding to the molecular reorientation and the internal vibrations.

Sample used throughout the present work was the same as that used in the previous ones.

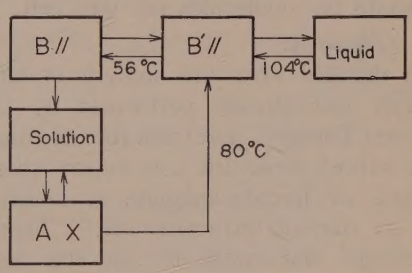

Fig. 1. Diagram of the phase transformation. Arrows show the direction of the transformation.
× represents crossed-chain configuration,
// represents parallel-chain configuration.

§ 2. Nature of the Phase Transformtion

Following the nomenclatures in the previous paper[1)], the phase of the crosed-chain configuration is called phase A, those of the parllel-chain configuration are called phase B and B'. The relation between these phases are shown in Fig. 1.

When hexadecanamide is crystallized from a solution at or near room temperature, phase A appears, and when it is cooled from its own melt phase B' appears. This phase transforms into another phase B on cooling at about 56°C. When phase A is heated, it changes into phase B' at about 80°C, but on cooling it never returns to phase A. Arrows in Fig. 1 show the direction of the transformation. × represents the crossed-chain configuration and // represents the parallel-chain one. Every attempt to reverse this process, namely from B' to A by slow cooling or maintaining the sample just above or just below the transformation temperature for a long time has failed. At room temperature, both phases A and B persist at least for three years.

Another phase named B'' appears in some special case. It resembles phase B and appears either on cooling from its own melt or heating phase A. But, as it comes out accidentally and the systematic investigation is therefore very difficult, the proplem of this phase is out of the main scope of this paper.

§ 3. Crystal Structures

Phase A is monoclinic and the space group is reported to be $P2_1/a$[1]. Phases B and B' are triclinic. Piezoelectric effect of phase B is absent, therefore the space group will be $P\bar{1}$.

Their unit cell dimensions were determined by a conventional single crystal rotation camera. The camera radius, about 35 mm, was calibrated by the diffraction lines of copper and calcite. Results are tabulated in Table I.

Table I. Unit cell dimensions

Phase	a	b	c	α	β	γ
A	9.790 Å	5.535 Å	32.43 Å	90°	104°4	90°
B	5.185	5.509	45.403	115.8	110.3	113.3
B' *	5.168	5.492	45.474	117.1	109.7	110.9

* Values for B' was determined at about 82°C.

The values for phase A are slightly refined than the previous ones. Phase A contains four molecules per unit cell and phases B and B' contain two molecules per unit cell.

3 a. *Phase A.*

The detailed structure analysis of tetradecanamide was already performed by Lingafelter and Turner[4], and from the investigation of the subcell structure it is known that the structure of hexadecanamide is nearly the same as that of tetracanamide.[1] Therefore no attempt was made to get the detailed structure.

The packing of the hydrocarbon chain is best understood from Fig. 2 of the previous paper[1]. If we consider a plane containing b axis and the chain axis (defined as the row plane by Lingafelter and Turner), molecular axis in one row plane are all parallel. But the chain axes of two neibouring row planes are almost perpendicular to each other. Therefore the crystal is composed of two kinds of row planes. If we name these planes S_1 and S_2 respectively, S_1 and S_2 planes are stacked alternately in the crystal. The plane of the zigzag chain is almost perpendicular to the row plane.

3 b. *Phase B.*

Small needle-shaped crystals of phase B were obtained by cooling the sample from its own melt. The needle axis was taken as b axis, and the intensity data of the b axis projection were obtained by Bouman type camera. Multiple-film method was used, and the photographic density was measured by the microphotometer. As the crystal used was very small, no absorption correction was applied and corrections for Lorentz and polarization factors were applied in the usual way.

In the present structure, two molecules are in the unit cell and are situated centtrosymmetrically. An approximate value of the distance between CH_2 groups in a molecule is easily obtained from the subcell structure. From Patterson synthesis the direction of the molecular axis is shown to deviate a few degrees from the c axis of the crystal. Therefore one main unknown parameter is the separation of two molecules. Thus by varing this parameter, several trials were made to

get the best agreement between observed and calculated structure factors of (00 l) reflections. After these parameters were determined approximately, the signs of structure factors were calculated, and a Fourier synthesis was performed. The result is shown in Fig. 2. Due to the effect of the large temperature factor, neighbouring CH_2 groups are not separated.

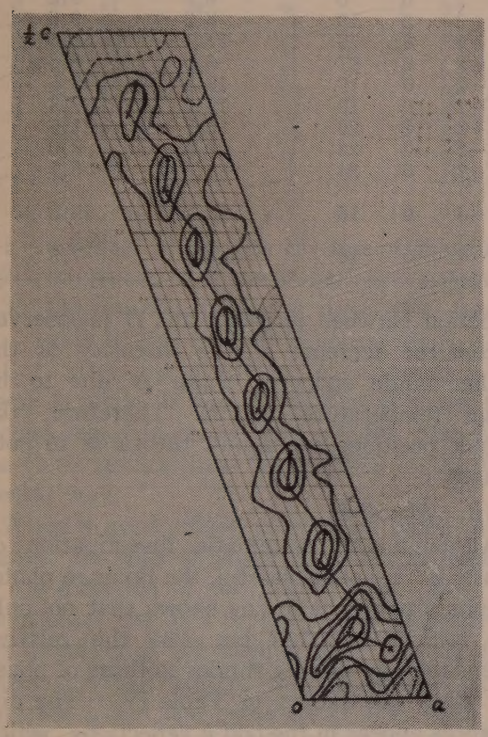

Fig. 2. Phase B. Projection along the b axis.

But it is clear that the chain axis is not quite straight but bends in this projection. This means that twisting of the molecule occurs. A similar case is reported by Sydow[6] for fase C' of n-hendecanoic acid. In that case, the helical twisting is observed, and the temperature factor reaches to 9.8 Å^2 at a temperature five degrees below the melting point.

Final atomic position and calculated and observed structure factors are tabulated in Table II and Table III. For the structure factor calculation, atomic structure factors for valence state[7] were used and CH_2 groups and NH_2 group were treated as single atoms having the structure factors $f=f_C+2f_H$ and $f=f_N+2f_H$ respectively. No significant difference occurs by exchanging the positions of the oxygen atom and the nitrogen atom. The temperature factor is taken to be 5.3 Å^2. The reliability index R is 30%.

Table II. Coordinate of atoms of phase B.

atom	x/a	z/c
N	0.20	0.024
O	0.80	0.040
C_1	0.60	0.051
C_2	0.69	0.070
C_3	0.59	0.106
C_4	0.68	0.126
C_5	0.57	0.162
C_6	0.66	0.183
C_7	0.54	0.216
C_8	0.63	0.239
C_9	0.50	0.272
C_{10}	0.60	0.295
C_{11}	0.45	0.329
C_{12}	0.54	0.353
C_{13}	0.40	0.385
C_{14}	0.48	0.412
C_{15}	0.35	0.439
C_{16}	0.41	0.467

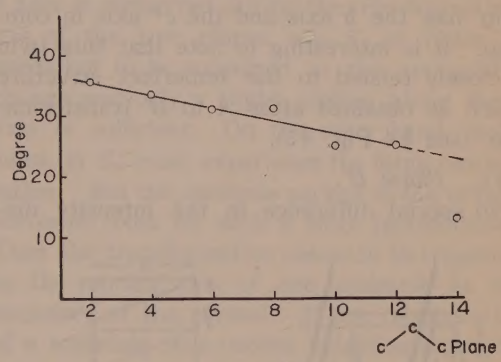

Fig. 3. Angle between C/C\C plane an ac plane.
nth C/C\C plane means the C_n/C_{n-1}\C_{n+1} plane.
C_n has the same meaning with that in Table II.

As the shape of the crystal is very fine needle, projections along other axes are very difficult to get. But, if the tetrahedral angle and the ordinary single bond length are assumed for the c/C\c bond, the angle between the c/C\c plane and ac plane can be calculated. This angle varies gradually for successive c/C\ plane as shown in Fig. 3. Thus

Table III. Observed and calculated structure factors of phase B.

Index			F_c	$\lvert F_0 \rvert$
0	0	1	12.3	strong
0	0	2	2.0	0
0	0	3	8.8	strong
0	0	4	−1.9	weak
0	0	5	6.7	12.1
0	0	6	−7.0	10.2
0	0	7	0.1	0
0	0	8	−10.0	13.1
0	0	9	−3.2	7.7
0	0	10	−10.9	14.7
0	0	11	−6.7	9.6
0	0	12	−10.4	13.7
0	0	13	−7.0	9.9
0	0	14	−8.1	10.5
0	0	15	−4.2	7.0
0	0	16	−6.2	7.0
0	0	17	4.8	5.4
0	0	18	4.8	9.3
1	0	6	8.5	4.5
1	0	4	23.3	10.5
1	0	2	37.1	30.0
1	0	0	−64.4	63.2
−1	0	8	4.8	4.8
−1	0	10	8.3	9.9
−1	0	12	8.5	11.2
−1	0	14	10.3	12.1
−1	0	16	26.0	15.3
−1	0	18	−16.4	12.8
2	0	2	−20.5	13.4
2	0	0	6.5	9.2
−2	0	10	8.2	9.6
−2	0	16	−27.1	30.6
−2	0	17	6.5	8.3
−2	0	18	19.8	19.5
−2	0	19	14.2	7.3
−2	0	20	5.7	11.5
−2	0	22	2.4	8.0
−2	0	24	−0.8	5.1
−3	0	16	21.2	15.3
−4	0	16	−8.4	7.3

the total twisting of the molecule reaches 12 degrees.

Twinned crystals are often obtained. This twin has the b axis and the c^* axis in common. It is interesting to note that this twin is closely related to the imperfect structure which is obtained after A to B' transformation. (see § 4 Fig. 4 c).

3 c. *Phase B'.*

No special difference in the intensity distribution between phases B and B' is observed except the decrease of the intensity of the higher angle spots of phase B' due to the large temperature factor. Therefore, the atomic positions are almost the same in both phases.

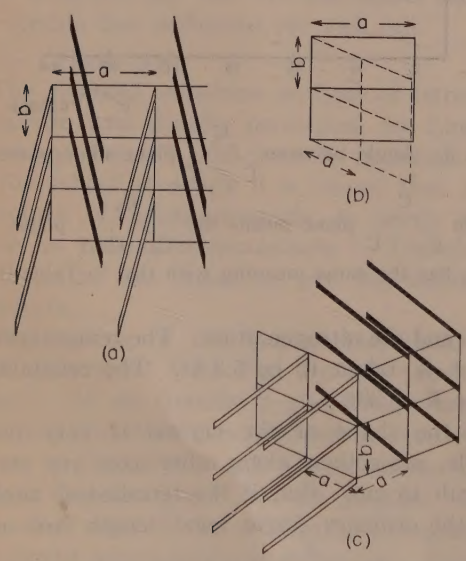

Fig. 4. (a) ab basal plane of phase A. (b) Relation between phase A and phase B'. (c) ab plane of phase B' after transformation. Black and white bars in (a) and (c) represents the projection of the hydiocarbon chain.

3 d. *Phase B''.*

Although the systematic investigation of phase B'' is not successful, the Bouman photographs around the b axis shows that not only the lattice constants but also the relative intensities are closely similar to those of phase B. They are shown in Table IV. The differences appear in the odd h reflections, which means that the molecular configuration is closely similar to that in phase B except that x coordinates of phase B'' shifts $\frac{1}{4}a$ compared with that of phase B. This phase might be the phase II' reported by Kurokawa[8]. But, as the powder pattern of phase B'' could not be obtained, direct comparison was impossible. The best indication of phase B'' is the appearance of the strong $(\bar{1}017)$ reflection, which is very weak in phase B.

§ 4. Mechanism of the Reorientation of the Molecule

At the A to B' transformation point, long molecule must be subjected to the large reorientation in the solid state. Three important results concerning this problem were already pointed out in the previous report[1]. Namely, when a single crystal of phase A is heated,

Table IV. Comparison of the observed intensities of phase B and B''.

Index			Intensity		Index			Intensity		Index			Intensity	
			B	B''				B	B''				B	B''
0	0	4	w	w	1	0	6	vw	vw	−1	0	15	0	m
0	0	5	m	m	1	0	5	0	w	−1	0	16	s	w
0	0	6	m	m	1	0	4	m	w	−1	0	17	vw	s
0	0	7	0	0	1	0	3	0	m	−1	0	18	m	0
0	0	8	m	m	1	0	2	s	m	−1	0	19	0	vw
0	0	9	w	w	1	0	1	0	vs					
0	0	10	m	m	1	0	0	vs	?	2	0	2	m	m
0	0	11	w	w	−1	0	7	0	m	2	0	0	w	w
0	0	12	m	m	−1	0	8	w	0	−2	0	10	w	w
0	0	13	w	w	−1	0	9	0	m	−2	0	16	s	s
0	0	14	m	m	−1	0	10	m	m	−2	0	18	m	m
0	0	15	vw	vw	−1	0	11	0	m	−2	0	20	w	w
0	0	16	vw	vw	−1	0	12	m	m					
0	0	17	vw	vw	−1	0	13	0	m	−3	0	16	m	0
0	0	18	w	w	−1	0	14	m	m	−3	0	17	0	m

1. it sprits into a few crystals of phase B',
2. the direction of the c^* axis is conserved,
3. the direction of the b axis (the needle axis of the crystal) is conserved.

But, after repeating such experiments with many crystals, it was found that although the second result is always correct, the first and the third results must be modified in the following way.

When a good single crystal of phase A is heated, the axis of phase B' is apt to appear in the direction of the needle axis. But, in some cases the axis or the [1 1 0] appears in the direction of the needle axis. Among the fifteen crystals tested, ten possesed b, four possesed a and one possesed [1 1 0] axes as the direction of the needle axis.

When the original crystal of phase A is imperfect, powder-like rings appear. In this case discrete (0 0 1) reflections are still observed. From these results following mechanism is suggested. As the c^* axis is conserved, *ab* basel plane is conserved and the reorientation occurs between these planes. The separation of these planes ((0 0 1) spacing) is 31.5 Å for phase A and 32.5 Å for phase B'. Therefore the molecule tilts from *ab* basal plane about 45° and 46° respectively. Fig. 4 a represents this *ab* basel plane of phase A. Bars represent the projection of the hydrocarbon chain. Chains represented by black bars are situated on the plane S_1 and those represented by white bars are on the plane S_2. Fig. 4 b represents *ab* plane of phase A and phase B' at the transformation point with the same origin and the same direction of the b axis. The lengths of these axes have the following relations. The b axis of both phases A and B' are almost the same, and $2\,a \sin\gamma$ of the phase B' is almost equal to the a axis of phase A. Therefore, when the b axis is conserved during the transformation, one of the row planes say S_1 of phase A needs not to be subjected to the appreciable change and only a slight gliding along the b axis is sufficient. On the other hand, molecules on S_2 must experience the large reorientation. But the molecule packed in the crystal leaves no room for such a large reorientation. Thus the transformation seems to be triggered by the reorientation of one molecule at the boundary of the crystal. If the reorientation of a molecule once occurs, neighbouring molecule on the same S_2 plane follows the first and the reoirentation propagates in the crystal. This model is consistent with the observation under the polarizing microscope[1]. The end group of a molecule on S_2 plane is linked to the molecules on S_1 by hydrogen bonds and the direction of this hydrogen bond network is conserved. Therefore the hydrocarbon chain is brandished around the end group.

The triggering occurs either in S_1 plane or in S_2 plane with equal probability. If both kinds of triggering occur at different parts of the same crystal, resultant phase split into several crystals with different directions of the a axis, as shown in Fig. 4 c. Bouman photographs shown in Fig. 5 of the previous paper clearly corresponds to this structure. This is the most common case. But if reorientation of the triggering molecule occurs

in some different way, succeeding molecules will follow the first and the resultant B' phase has different axial direction.

When the original crystal is not perfect, mainly composed of the layer like crystal packed in the same orientation, the direction of the axis of each layer after the transformation is controlled by each triggering molecule, thus the resultant crystal is composed of small crystallities with different orientations and the powder-like pattern appears.

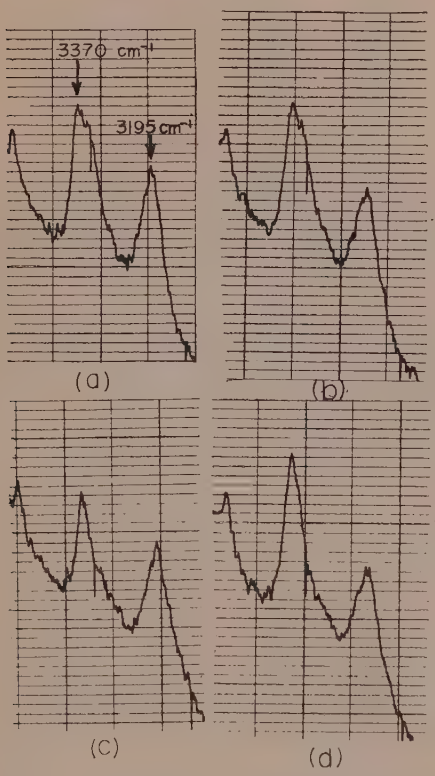

Fig. 5. Infra red absorption spectra.
(a) Phase A. 29°C. (b) Phase A. 73°C.
(c) Phase B. 35°C. (d) Phase B'. 94°C.

§ 5. Infrared Absorption

From the discussion in § 4, it is clear that the hydrogen bonds between terminal amide groups have an important role for the phase transformation. But in X-ray analysis it is not easy to deduce the exact form of the hydrogen bond. Therefore infrared spectrum of N–H stretching vibrations was examined. H–N–H bending vibration is very near to the C=O stretching vibration and it proved to be very difficult to separate them.

Absorption spectrum is recorded by commercial Parkin Elmer spectrometer. The sample is sandwitched between rock salt plates, and heaters are attached on both sides of the plates. The temperature is measured by the thermojunction inserted into a small hole drilled into the rock salt plate. The measured temperature seems to be slightly lower than the temperature of the sample itself. Therefore it is corrected by assigning the melting point of the sample to the temperature at which the abrupt change of the observed infrared spectrum occurs. Typical absorption curves are shown in Fig. 5. In Phase A small side peak appears in the 3370 cm^{-1} band, and in phase B' the 3195 cm^{-1} band broadens slightly. But in other respect, both the frequency and the intensity of the absorption band are nearly the same for all phases. The frequencies against the temperature is tabulated in Table V. At the melting point, this absorption band suddenly disappears.

Table V. Stretching vibrations of the N–H bond.

Phase	Temperature	1	2
A	29°C	3370 cm^{-1}	3195 cm^{-1}
A	73	3370	3195
B	35	3365	3195
B	47	3365	3195
B'	62	3365	3195
B'	82	3370	3195
B'	102	3370	3200

The relation between the stretching frequencies and the bond distances of the hydrogen bond is given by Nakamoto et. al.[9] From Fig. 1 of their paper, N–H..O distance of amide is evaluated to be 2.97 Å. This value agrees well with that obtained by Lingafetler and Turner[4] for tetradecanamide. Therefore it may be concluded that the hydrogen bond length is not changed during the phase transformation.

§ 6. Thermal Properties

6 a. *Differential thermal analysis.*

Differential thermal analysis was performed by the method developed by Vold[10]. In this method, the sample and the reference material, packed into cylindrical containers of the same shape are heated and cooled in the same furnace. The condition of the heat transfer is made as equal as possible for both sample

and reference material. The sample temperature and the temperature difference between the sample and the reference are measured. These temperatures are recorded against the time, and if the transformation is the first order, not only the transformation temperature but also the latent heat should be obtained. Whether the transformation is the first order or not, is determined from the shape of the curve. In the present case cetane was used as the reference material.

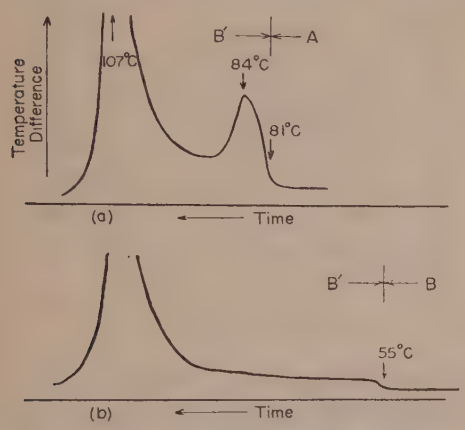

Fig. 6. Curves for differential thermal analysis.
(a) Virgin curve.
(b) Repeated curve.

A virgin curve shown in Fig. 6a indicates that the A to B' transformation is the first order. In cooling curve or reheating curve this latent heat disappeared completely, and only the small anomalous specific heat near 56°C which corresponds to the B to B' transformation was observed. In phase B' the temperature difference from reference material was observed. This means that the specific heat of phase B' is large compared with the other phases. These results are consistent with the specific heat measurement of the B to B' transformation[11].

From the average of the two independent observations using the different quantities of sample, the heat and the entropy of the transformation are obtained and listed in Table VI.

Table VI. Thermal data.

	latent heat	entropy change
A to B' transformation	4.0±0.3 kcal/mole	12.4±0.9 cal/deg. mole.
Melting	15.7±0.3	46.6±0.8

6 b. *Temperature factor.*

Temperature factor for phase A is taken to be 3.4 Å² (in the previous paper[1]) and that for phase B is 5.3 Å² both at room temperature.

By comparing the powder photographs at different temperatures it was immediately noticed that although the lines for phases A and B are not greatly affected by the temperature change, the intensities of higher angle lines of phase B' decrease rapidly on elevating the temperature. Therefore our main concern was directed towards phase B'.

Now the observed intensity $I(T)$ of the powder pattern at the temperature T will be expressed in the form

$$I(T)=I_0(T)\exp(-2B(T)\sin^2\theta(T)/\lambda^2)\ ,*$$

where $I_0(T)$ is the intensity for a structure with atoms at rest at their equilibrium positions at the temperature T. In the present case θ does not change appreciably with temperature. Therefore, when the intensities of the powder lines having the same index are compared at different temperatures, say T_1 and T_2, and if $I_0(T_1)$ and $I_0(T_2)$ is the same, the temperature factor difference can be deduced. The powder pattern changes gradually from phase B to B', and their intensity change can be followed throughout both phases. But, as the maximum attainable temperature difference is only about 40 degrees for each phase, an accurate result can not be expected.

Powder photographs were taken by ordinary powder camera with simple attachment to adjust the sample temperature. Multiple-film method was used and the photographic density of the film was measured visually and by the microphotometer. Exposure time for each temperature was kept constant, but owing to the fluctuation of the output of the X-ray source, resultant exposures could not be made quite the same. The correction was made in

* The current notation B is used for the temperature factor. Their may be no fear of confusion with phase B

the following way. When $\ln I(T_1)/I(T_2)$ are plotted against $\sin^2\theta$, and extrapolated to $\theta=0$, it must be zero if the exposure is the same. If it differs from 0, a suitable correction factor is applied.

After the correction was made, $\ln I$ was plotted against the temperature. In the present case, not only I_0 changes with temperature, but also the lattice constant change. Thherefore some lines overlap each other and some lines, overlapped at room temperature, separate into several lines on raising temperature. Data for these lines were omitted and those for very weak and very strong lines were omitted too. In this way among more than 35 lines observed in the powder photographs, only seven lines were selected. Logarithmic intensities of them were plotted against the temperature (Fig. 7). Even for these lines I_0 and the temperature factor B may change from line to line. However, Fig. 7 shows that $\ln I$ is linear against the temperature and have a knick near 60°C. The temperature factor difference between 60°C and 20°C for phase B and that between 100°C and 60°C for phase B' are obtained for each line (Table VII). The mean values are 0.7 and 4.2 respectively. As the temperature factor of phase B is 5.3 at room temperature, that of phase B' exceeds 10 at 100°C.

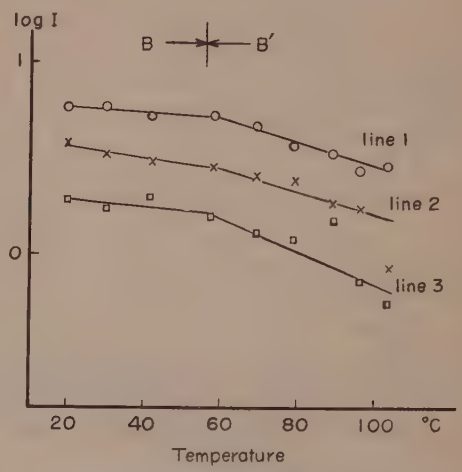

Fig. 7. Variation of the relative intensities of the powder pattern against the temperature.

Table VII. Temperature factor differences.

Line	Bragg angle at room temp.	$B(60°C)-B(20°C)$	$B(100°C)-B(60°C)$
1.	13.8 degree	0.8 A^2	2.9 A^2
2.	19.2	1.3	2.9
3.	20.3	0.6	4.3
4.	22.1	0.7	5.6
5.	23.6	0.8	5.5
6.	25,6	0.7	
7.	28.1	0.5	
	Mean	0.8	4.2

6 c. *Thermal expansion.*

Generally the thermal expansion of the crystal is closely related to the thermal vibrations of atoms in the crystal. Therefore from the results in §6b the large thermal expansion is expected for phase B'.

Lattice constants are measured for various temperatures. The volumes of the unit cell and the density are tabulated in Table VIII.

The mean volume expansion coefficients of phases A and B have the values of 5.8×10^{-4} and 5.1×10^{-4} respectively, as is usual for ordinary long chain compounds. On the other hand, the volume of the phase B' changes irregularly and expand more rapidly at higher temperatures.

Table VIII. Volume of the unit cell and the density.

Phase	Temperature	Volume of the unit cell	Calculated density
A	26°C	1702 A^3	0.997 g/cm³
A	80	1756	0.966
B	10	829	1.023
B	16	838	1.012
B	39	845	1.004
B	48	853	0.994
B'	62	849	0.999
B'	72	849	0.999
B'	82	860	0.986
B'	86	876	0.968

§ 7. Proton Magnetic Resonance Absorption

Preliminary measurements of the proton magnetic resonance absorption were kindly performed by H. Komatsu. The method is almost the same as that used for the study

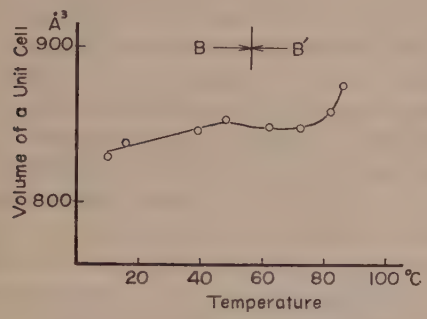

Fig. 8. Thermal expansion.

of normal alcohol[12]. The line width (the peak to peak distance of the derivative of the resonance curve) is plotted against the temperature (Fig. 9).

In phase A, when the temperature is raised, a small central peack appears, but the peak to peak distance of the main line does not change up to the transformation. At the transformation point, the broad absorption line almost disappears and only the sharp peak is observed. This seems to correspond to the reorientation of the molecule at the transformation. In phase B, the line breadth almost remains constant up to the B to B' transformation point and then decreases appreciably above the transformation point, showing larger degrees of freedom in phase B' compared with that in phase B. In phase B', the line breadth decreases gradually on raising the temperature. This corresponds to the large temperature factor shown in § 6 b. The second moment of phase A and B at the room temperature is 16 Gauss^2.

According to Andrew[13], the second moment of the normal paraffin with carbon number n is $(18.5+19.1/(n+1))+7.8$ in so far as the molecule can be assumed to be rigid. The term in the bracket is the intramolecular contribution, and the last term is that of the intermolecular contribution. In the present case, intermolecular contribution of the phase A will be less than the ordinary parallel-chain configuration. But the observed value is less than the intramolecular contribution. Therefore, even at the room temperature, considerable motional narrowing occurs. In order to get the intermolecular contribution, the low temperature study seems to be very desirable.

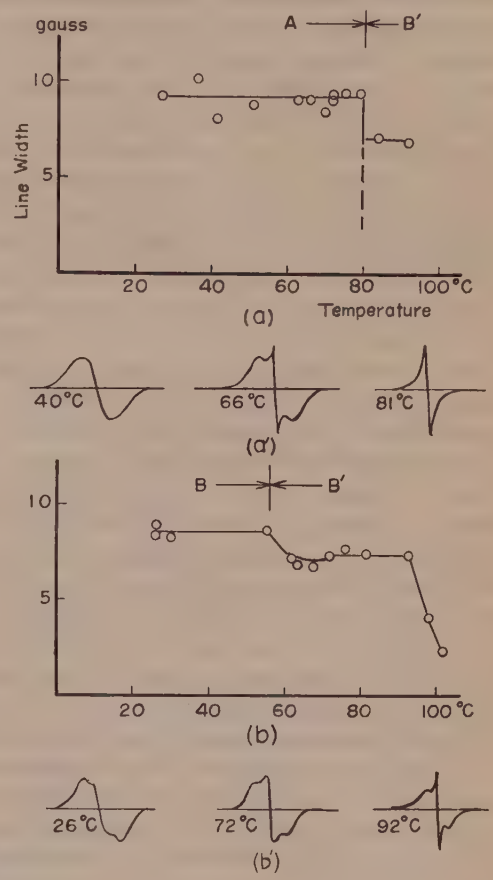

Fig. 9.
(a) Virgin curve.
(a′) Line shape of virgin curve.
(b) Repeated curve.
(b′) Line shape of repeated curve.

§ 8. Discussion of the Results

The fact that almost all the known crystal structures of the normal aliphatic compounds possess the parallel-chain configuration shows that the parallel-chain configuration has more stable van der Waals energy than that of the crossed-chain configulation. This point is already discussed by De Boer[14]. On the other hand, from the results of the infrared absorption, length and energy of hydrogen bond do not seem to differ for both phases. Where do the large latent heat and entropy change at A to B' transformation come from then?

One of the important contributions will be the thermal vibrations of the hydrocarbon

chain. As we saw in § 6 and § 7, thermal vibrations of the molecule increase remarkably in phase B'. Therefore, when phase A transforms to B', molecular vibrations are excited abruptly, and the large entropy change is observed. Thermal vibrations in the crystal consist of the vibrations of the molecule as a whole and the internal vibrations. In ordinary molecules, the contributions of the internal vibrations to the temperature factor are very small. But in the long chain molecules, some modes of internal vibrations extend to the very low frequencies and contribute remarkably to the total temperature factor. According to Pitzer[15], if the hydrocarbon chain takes plane zigzag form, the lowest frequency band of internal vibrations corresponds to the out-of-plane vibrations of CH_2 groups and is extending from 0 to 220cm^{-1}. These vibrations cause the twisting of the molecule. The force constant of these twisting vibrations will be largely affected by the surroundings of the molecule, because the twisting is caused by the rotation around the C–C single bond and intramolecular force resisting this rotation is very weak. Now in the crystal structure of phase B shown in § 3, twisting of the hydrocarbon chain is really observed at its equilibrium position. This means that intermolecular force to suppress the twisting is weak in this structure. Therefore, when temperature is raised, the twisting vibrations are excited and give the large temperature factor for phase B'.

The B to B' transformation has a special character that, at this transformation point, not the physical quantities themselves, but their temperature coefficients change. This phenomenon may have some relation to the melting of these normal aliphatic compounds. Internal vibrations of the molecule are affected by the packing of the molecule in the crystal. When the amplitude of thermal vibrations increases, the force packing the molecule at the equilibrium point will change, and when the amplitude becomes very large, the instability of the crystal lattice occurs. Explanation of the melting of the solid from this standpoint is already expressed by many authors[16][17] for ionic crystals. According to Lindemann the mean amplitude of vibrations at the melting point is 0.075 times the interatomic distance, and Thompson found that the instability occurs when the increase in interionic distance, as compared with that at 0°K, is between 6 and 7%. Although the binding force for the hydrocarbon chain is quite different from that for the ionic crystal, still it may be said that, when the amplitude of the thermal vibration reaches a certain extent, the melting occurs. When the way of packing is similar, the mode of internal vibration of the hydrocarbon chain having the same chain length will be similar for different compounds. Now, two molecules of amide are connected by the hydrogen bond and form a dimer. Therefore the chain length of the hexadecanamide roughly equals to 43 Å. Other aliphatic compounds with the same length, for example palmitic acid (dimer) or n-tetratriacontane, melts near 60°C. Therefore, the crystal should become unstable at this temperature if only the van der Waal forces are taken into account. The B to B' transformation really occurs near this temperature. But, in the case of amide, the melting does not occur because the strong end group interactions connect molecules. The increase of the atomic vibrations above this point is naturally understood, however. The real melting occurs by the breaking of the hydrogen bond. This corresponds to the sudden disappearance of the N–H stretching frequencies in the infrared absorption spectra and to the large latent heat of fusion and seems to be consistent with the fact that the melting point of the amide depends neither on the carbon number nor the crystal structure.

On the other hand, for phase A, the way of packing of the hydrocarbon chain is quite different, and similar effect to the B to B' transformation does not occur. Thus the large entropy change due to the twisting vibrations occurs when phase A transforms to phase B'.

§ 9. Acknowledgements

Authors express their sincere thanks to Prof. Y. Kakiuchi for his kind guidance, Prof. H. Kambe for his aid for the differential thermal analysis, Mr. H. Komatsu for his aid in proton magnetic resonance absorption measurements and Prof. K. Kuratani for his advice in the measurement of the infrared absorption.

References

1) T. Sakurai: J. Phys. Soc. Japan **10** (1955) 1040.
2) T. Sakurai and S. Kurokawa: Ann. Meeting of Chem. Soc. Japan (1956).
3) J. D. Turner and E. C. Lingafelter: Acta Cryst. **8** (1955) 549.
4) J. D. Turner and E. C. Lingafelter: ibid. **8** (1955) 551.
5) for ex. C. E. Clarkson and T. Malkin: J. Chem. Soc. (1934) 666.
6) E. von Sydow: Acta Cryst. **8** (1955) 810.
7) J. Berghuis, I. M. Haanappel, M. Potters, B. O. Loopsta, C. H. Macgillavry and A. L. Veenendaal: Acta Cryst. **8** (1955) 478.
8) S. Kurokawa: Bul. Chem. Soc. Japan **28** (1955) 660.
9) N. Nakamoto, M. Margoshes and R. E. Rundle: J. Amer. Chem. Soc. **177** (1955) 6480.
10) V. Vold: Anal. Chem. **21** (1949) 683.
11) T. Sakurai: J. Phys. Soc. Japan **6** (1951) 199.
12) H. Komatsu: J. Phys. Soc. Japan **11** (1956) 755.
13) E. R. Andrew: J. Chem. Phys. **18** (1950) 607.
14) J. H. De Boer: Ned. t. Natuurk. **15** (1949) 205.
15) K. S. Pitzer: J. Chem. Phys. **8** (1940) 711.
16) F. A. Lindemann: Phys. Zeit. **11** (1910) 609.
17) J. H. C. Thompson: Phil. Mag. **44** (1953) 131.

JOURNAL OF THE PHYSICAL SOCIETY OF JAPAN Vol. 13, No. 1, JANUARY, 1958

Variation of the Hall Coefficient of Mg-Cd Superlattice Alloys with Degree of Order

By Kiyoshi YONEMITSU and Takao SATO

Department of Physics Tokyo Metropolitan University Tokyo

(Received June 22, 1957)

Temperature dependence of Hall coefficient of three superlattice alloys of Mg–Cd system, Mg_3Cd, MgCd and $MgCd_3$, was measured to find the effect of order-disorder transformation upon it. At the transformation temperature, the Hall coefficient of these alloys showed a discontinuous increase in positive direction, while the electrical resistivity, which was measured simultaneously, decreased discontinuously at that temperature.

It is discussed that the change of Brillouin zone structure due to the order-disorder transformation of these alloys might be considered to be the origin of such a change of the Hall coefficient.

§ 1. Introduction

It was suggested by Slater[1] that electronic energy may play an important role in the order-disorder transformation of superlattice alloy, and from this point of view, qualitative discussion was made by Nicholas[2] about band structure of CuAu, CuPt, and Ag_3Mg. To proceed further along this line, it may be useful to know the information about the change of electronic structure when the order-disorder transformations of these alloys take place.

In 1938, Muto[3] has predicted that some change in Hall coefficient and magnetic susceptibility must be observed in the transformation. The prediction was proved to be true by Komar and Sidrov[4]. They measured the Hall coefficient of Cu_3Au at room temperature after quenching it from high temperature and found that a discontinuous change occurred when ordered state was formed. The same result has been obtained by present authors, who have measured Hall coefficient of Cu_3Au at varying temperatures. The authors are now trying to verify Muto's prediction about other superlattice alloys by the experiment of the Hall coefficient, and in this paper the results on three Mg–Cd superlattice alloys are presented.

§ 2. Preparation of Specimen, and Experimental Procedure

Purity of magnesium used in the present investigation was 99.97% and that of cadmium was 99.95%. They were alloyed in an iron crucible, and casted into a small plate 20 of

mm×10 mm×2 mm. They were homogenized in argon gas about 70 hrs at 300°C, and then polished by sand paper until they were 0.15 mm~0.5 mm in thickness. After the copper leads of 0.2 mm in diameter were spotwelded to the specimens, they were again annealed in argon atmosphere about 10 hrs to remove residual strain. The specimens were enclosed in quartz tubes with argon gas, then they were placed between the pole pieces of an electromagnet.

It is less difficult to measure the Hall coefficient of quenched specimen at room temperature than at higher temperatures, because of smaller parasitic thermoelectric potential due to the inhomogeneous temperature distribution in the specimen. The relaxation time of these alloys, however, are so short that the quenching method can not be used. Moreover, as they, especially Cd_3Mg, are easily corroded in the air, we were afraid that there were some damage by corrosion during the repetition of heating and quenching process.

Astabilized A.C. 100 volt source was used for the electric furnace, and the heater current was controlled by hand. The magnetic field strength given by an electromagnet was about 6 kG.

The circuit for measurement are shown in Fig. 1. The resistors R_1 and R_2 are con-

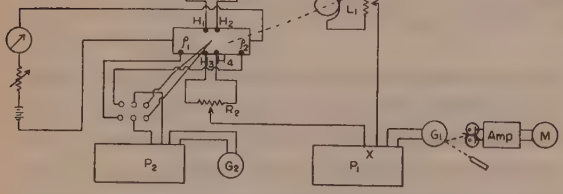

Fig. 1. Circuit for measurement of Hall potential
P_1, P_2: Potentiometer, G_1, G_2: Galvanometer,
H_1, H_2, H_3, H_4: Hall lead M: Output meter.

nected to two pairs of the Hall leads, which are denoted as H_1, H_2 and H_3, H_4 respectively in the figure, by which it was possible to balance the voltage drop in the specimen due to the primary current. Both the coil L, which is coupled with electromagnet magnetically, and resistor R_3 were used to compensate the e.m.f. which were induced in the secondary circuit by changing the strength of magnetic field. R_1, R_2 and R_3 were made of manganin wire, the resistance of which were about 3Ω, and each wire had a copper contact which were able to slide on them. The thermoelectric potential and the residual voltage drop that was not cancelled by R_1 and R_2, could be compensated by Yokogawa Low Potential Type Potentiometer P_1, which had resistance of 10Ω when measured from X terminals. The out-put was lead to galvanometer G_1 (Yokogawa G–3C type, voltage sensitivity is 3×10^{-7} V/mm), and its deflection was amplified by twin phototube P and electronic amplifier, and was read by an out-put meter M_1. The voltage sensitivity of this galvanometer-amplifier system was 1.5×10^{-8} volts per one division of out-put meter[5].

The leads which are denoted as ρ_1, ρ_2 in the figure, were for measurement of electrical resistivity, and the out-put potential from them and the potential of Alumel-Chromel thermocouple were read by potentiometer P_2 and galvanometer G_2. The primary current 1 amp. was given by a storage battery.

The measurement at every temperature was made with following procedure. At first the specimen was heated above the transformation temperature, then heater current was decreased a little. After the equilibrium temperature of the specimen had been reached, Hall potential and voltage drop were measured. The magnetic field was turned on and then off, and the difference of the potentials which were read at Hall leads in both cases, gave the Hall potential at that temperature. After a measurement had been done, the heater current was decreased again, and the same procedure was repeated. The cooling rate is given in Tables I, II and III.

§ 3. Results

The results of the measurement are given in Table I, II and III and Figs. 2, 3 and 4.

As the measurements were made at high temperatures, the temperature distribution in the furnace was easily disturbed, which caused the drift or fluctuation of parasitic thermoelectric potential to increase. In such cases, the measurement was repeated twice or three times, the results of which are shown in the columns that are denoted 1, 2 and 3 in the tables. The cooling rate is given in these tables, but in those temperature ranges where cooling rate is not shown in the tables, the

Table I (a). Temperature dependence of the Hall coefficient of Mg_3Cd

T°C	Hall coeff. × 10^4 e.m.u. 1	2	3
302	1.1	0.9	
290.2	0.7	0.6	
266	0.2	0.3	
228	1.4	0.8	
194	1.7		
191	2.0		
183	1.9		
181	2.0		
166	2.1	2.3	
159	2.5	2.9	
155	6.6	6.2	
150	8.9	9.1	
146	9.4	8.5	9.4
144	9.2		
143	9.1		
130	11.9		
139	11.3		
117	11.6		
113	11.6		
113	11.7		
90	13.1	12.8	
69	13.2	14.0	
53	13.8	13.2	
23.8	14.0	13.9	

Cooling rate; 194°C–158°C: 3 min/°C,
155°C–130°C: 6 min/°C,
117°C– : 2 min/°C

Table I (b). Temperature dependence of the Hall coefficient of Mg_3Cd (slowly cooled)

T°C	Hall coeff. × 10^4 e.m.u. 1	2	3	4	5
186	2.93				
184	2.5				
180	2.2				
169	2.9				
157	5.1	5.8	5.1	5.1	
155	8.4	8.4	9.8	8.8	8.9
144	12.0	11.4	11.5		
134	13.3	13.1			
109	14.7	14.7			
60	17.4	17.8			
35	17.9	19.2	18.3		

Cooling rate; 186°C–157°C: 5 min/°C,
157°C–144°C: 15 min/°C,
144°C–109°C: 16 min/°C,
60°C–R. T.: 8 min/°C.

specimens were cooled with rate of one degree per minute.

As can be seen from the tables and figures, the Hall coefficient of disordered $MgCd_3$ decreased considerably with increasing temperature. That is, Hall coefficient of $MgCd_3$ was 10.7×10^{-4} e.m.u. at just above the transfor-

Table II. Temperature dependence of the Hall coefficient of MgCd

T°C	Hall coeff. × 10^4 e.m.u. 1	2	3
307	0.0		
305	0.2		
304	0.2		
302	0.0		
301	0.3		
290	0.3		
288	0.1		
275	0.4		
274	0.5		
257	2.5		
254	7.3		
251	6.9		
250	6.7		
248	7.0		
247	7.0	7.0	
243	7.0		
239	6.8		
230	7.5		
229	7.4		
219	7.3		
208	7.6		
198	7.8		
194	7.6		
180	7.5		
166	7.5		
153	7.4		
141	7.6		
116	8.2		
112	7.9	7.6	
78	7.5	7.4	7.3
32	7.5	7.6	7.7

Cooling rate; 300°C–260°C: 4 min/°C,
260°C–230°C: 9 min/°C,
230°C–140°C: 5 min/°C.

Table III. Temperature dependence of the Hall coefficient of $MgCd_3$

T°C	Hall coeff. × 10^4 e.m.u. 1	2	3
208	3.0	4.1	4.2
246	4.9	4.8	
205	7.0	6.8	
147	9.4	8.9	
146	10.4		
95	11.0	10.8	
93	11.2		
88	10.8	10.5	
83	16.0	14.8	
79	14.8	14.3	
68	14.5	14.5	
50	14.4		
24	14.4	14.2	

Cooling rate; 100°C–88°C: 10 min/°C,
88°C–79°C: 7 min/°C,
79°C–68°C: 10 min/°C.

mation temperature, while it decreased to 4×10^{-4} e.m.u. at 300°C. As soon as the temperature is below the transformation temperature, and ordering formation sets in, then Hall coefficient increases abruptly. After the transformation finished perfectly, the Hall coefficient of Mg_3Cd increased still a little with descending temperature. On the other hand, the Hall coefficients of MgCd and $MgCd_3$ were nearly constant.

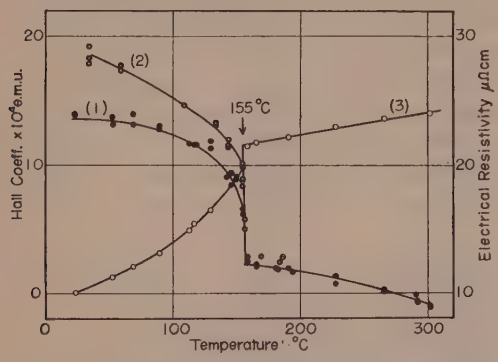

Fig. 2. Temperature dependence of Hall coefficient and electrical resistivity of Mg_3Cd.
(1) Hall coefficient.
(2) Hall coefficient (cooled very slowly).
(3) Electrical resistivity.

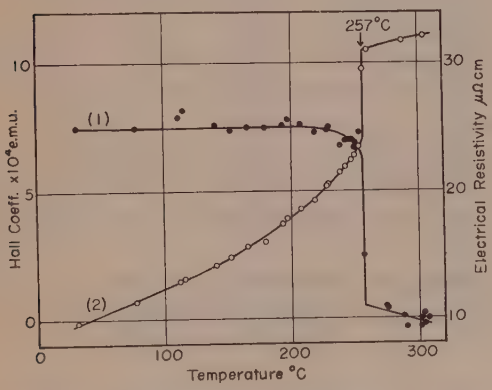

Fig. 3. Temperature dependence of Hall coefficient and electrical resistivity of MgCd.
(1) Hall coefficient.
(2) Electrical resistivity.

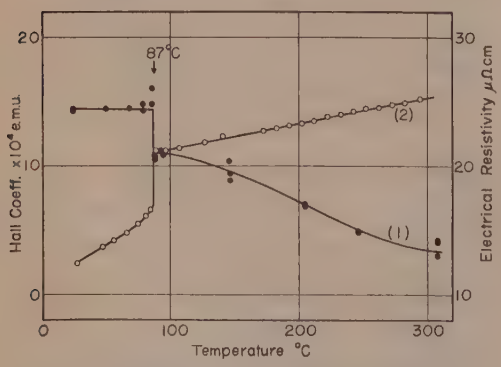

Fig. 4. Temperature dependence of Hall coefficient and electrical resistivity of $MgCd_3$.
(1) Hall coefficient.
(2) Electrical resistivity.

It also must be supplemented that there were considerable fluctuations in the absolute values of measured Hall coefficient of the specimens which had the same concentration, though their temperature-dependences, signs and transformation-temperature were not so different from one another.

§ 4. Discussions

As was described in the preceding section, there were some fluctuations in absolute values of the Hall coefficient, though its reason is not clear at present. The metals from which these specimens were made, the method of alloying of these metals to the specimen and their heat treatment were all the same, and yet such fluctuation appeared, so it may be thought that there might be some delicate and unknown factor which causes these fluctuations. Nevertheless, the sign and temperature dependence of the Hall coefficient were quite similar for all specimens, so that it may be reasonable to conclude that the Hall coefficients of the superlattice alloys of Mg–Cd system did change rather abruptly their magnitude toward positive direction during the transformation from the disordered to the ordered state.

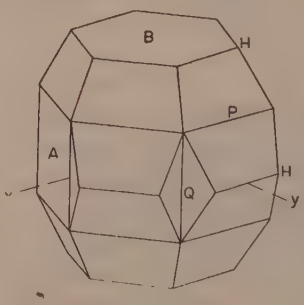

Fig. 5. The Brillouin zone of h.c.p. structure.

In the disordered state, these alloys have h.c.p. structure and there 1-st Brillouin zone is, as is shown by Fig. 5, surrounded by these surfaces such as {100} (surface A), {002} (surface B), and {101} (surface P) surfaces. In this zone

$$2-\frac{3}{4}\left(\frac{a}{c}\right)^2\left\{1-\frac{1}{4}\left(\frac{a}{c}\right)^2\right\}$$

electrons per atom are contained. If we add prisms which are surrounded by the surfaces such as {101}, {100}, we obtain the complete zone which can contains 2 electrons per atom. As the number of valence electrons of magnesium and cadmium are 2 per atom, the complete zone is nearly filled in the disordered state, and then there are some overlapping electrons in the next zone, the equal number of holes appearing in the complete zone.

The positions where the mentioned overlaps take place, can not always be decided geometrically by the distance from the position to the origin of the wave number space, for it is naturally expected that, when the Fermi surface approaches the zone boundary, the electronic behaviours can not be approximated by the free electron model, and thus the form of the Fermi surface will depart from sphere. We shall tentatively assume that the holes are present at the corners of the zone according to Reitz and Smith[6]. The positions where the overlaps take place are rather speculative at present, and we shall be contented with examining the effect of the superzone in the ordered state upon these speculative overlaps, such as Q-overlaps in the equatorial plane, P-overlaps on the slant faces, and the B-overlaps at the bottom.

The number of valence electrons per atom of Mg_3Cd and $MgCd_3$ and also two, so that it may be thought that, in the disordered state, the number of electrons in the higher zone are equal to that of holes is the lower zone. Therefore, the positive Hall coefficients of these alloys in the disordered state may be considered to indicate the predominance of hole-mobility over electron-one in this state.

The discontinuous change of the Hall coefficient during the order-disorder transformation, predicted by Muto and first observed for Cu_3Au superlattice alloy by Komar and Sidrov, was ascribed to the effect of the new reflection planes in the k-space, which appear in the ordered state and are responsible for the superzone, upon the behaviour of the electrons of the Fermi surface.

In order to understand quantitatively the reason why the change occurs towards the positive direction, however, it is necessary to know the details of the electronic structure such as the energy gaps at the zone boundaries, the form of the Fermi surface and the state density etc.. For example, if we adopt the two-band model, the Hall coefficient R may be expressed as

$$R=\frac{1}{ec}\frac{n_1\mu_1^2-n_2\mu_2^2}{(n_1\mu_1+n_2\mu_2)^2}$$

where n_1 and n_2 are the numbers of electrons and holes, and μ_1 and μ_2 are mobilities of electrons and holes, respectively. Without the knowledge of the variation of n and μ with the order-disorder transformation, we can hardly understand the reason why the Hall coefficient changes in the positive direction when the ordered state is formed. In the ordered state, as was already pointed out, we may reasonably assume that $n_1=n_2$, whereas, in the ordered state, this can no more be true, and, furthermore, μ's must be varied too, on account of the appearance of the superzone. In view of the above situation, it is difficult to derive a decisive conclusion about the theoretical basis of the measured changes of the Hall coefficient from the data at hand; at present we only know the observed data of the variation of the Hall caefficient and of the arrangement of atoms in the ordered and disordered state, determined by the x-ray analysis, from which the corresponding Brillouin zone (B.Z.) is constructed in an ordinary method.

In the following paragraphs, therefore, we will suggest a few situations, which may serve as interpretations of the above described change of the Hall coefficient due to the ordering formation, mainly refering to the change of n_1 and n_2.

(1) Mg_3Cd

The ordered structure of Mg_3Cd is also h.c.p., but as shown Table IV, the axial ratio becomes half times of that of the disordered states, and the unit cell contains 4 atoms. Therefore, new reflection planes, which are absent in the disordered states, appear in the k space in the ordered state. Among the resulting superzones, those which modifies the Fermi surface greatly and may give an important effect on the Hall coefficient, are shown in Fig. 6. In that figure, Q tetrahedra which appear at the position near the Q overlap, and pentahedra P which appear on the slant face P may play an important role in this case.

Table IV.

	disorder			order		
	a	c	c/a	a	c	c/a
Mg_3Cd	3.1792	5.1730	1.6271	6.26	5.07	0.81 *)
$MgCd_3$	3.0856	5.3247	1.726	6.2209	5.0348	0.8093**)
				orthorhombic		
				a_1	a_2	a_3
MgCd	3.1410	5.1512	1.640	3.2217	5.0051	5.2700***)

W. Hume-Rothery and G. V. Raynor: Proc. Roy. Soc. 174 (1940) 471 for disordered state.
*) U. Dehlinger: Zeit. f. anorg. allgem. Chemie 194 (1930) 223.
**) D. A. Edwards, W. E. Wallace and R. S. Craig: J. A. C. S. 74 (1956) 1253.
***) H. Steeple: Acta Cryst. 5 (1952) 247.

Tetrahedra Q are surrounded by those surfaces as $\{21\bar{1}\}$, $\{211\}$, $\{222\}$ and $\{200\}$, each contains

$$\frac{3}{4}\frac{1}{(c/a)}\left\{\frac{1}{2}\frac{1}{(c/a)}-\frac{2}{3}\left(\frac{c}{a}\right)\right\}^3$$

electrons per atom. In the case of Mg_3Cd, there are 9.3×10^{-4} electrons per atom, and this values seems to be too small to give any effect upon the Hall coefficient.

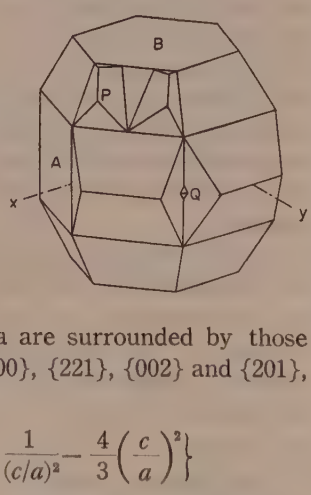

Fig. 6. The Brillouin zone of ordered Mg_3Cd and $MgCd_3$

P-type pentahedra are surrounded by those planes as $\{111\}$, $\{200\}$, $\{221\}$, $\{002\}$ and $\{201\}$, and can contain

$$\frac{1}{9}\left\{10+\frac{15}{8}\frac{1}{(c/a)^2}-\frac{4}{3}\left(\frac{c}{a}\right)^2\right\}$$

electrons per atom. Mg_3Cd has 1.2 electrons per atom in these pentahedra. If these are overlapping electrons at point P to the next zone, it is natural to think that they may be contained in the pentahedra. If this is true, the mean energy of the overlapping electrons must increase a little because the distance from the origin of the k space to the overlaps increase a little; it is probable that this can be cancelled by the depression of the energy levels by the newly appeared reflection planes. It is not unreasonable to consider that the contribution of these pentahedra is such that Hall coefficient increase in the positive direction in the ordered state, changing the mobility of overlapping electrons at P, although it is natural to think that some electrons in the pentahedra still contribute to the conduction as negative charges in the ordered state too and it is not clear how P-overlaps behave in the ordered state.

(2) $MgCd_3$

The crystal structure of disordered $MgCd_3$ is similar with that of disordered Mg_3Cd, but as can be seen from Table IV, its axial ratio is larger than that of Mg_3Cd. So that, in the case of disordered $MgCd_3$, we have electron's overlap at the bottom (B) of the B.Z., while there are no Q overlaps. In the ordered state, c/a decreases and becomes nearly equal with that of Mg_3Cd. Therefore, it is possible that a part or all of those electrons which overlap to the next zone at B in the disordered state,

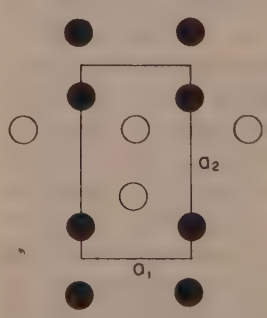

Fig. 7. Orthorhombic structure of MgCd (from Ref. (7))

can be contained in the first zone in the ordered state. This may be thought as a chief contribution to the increase of Hall coefficient in the ordered state though a little contribution from those holes in the tetrahedra

at point Q, which appears in the ordered state, can be expected.

(3) MgCd

The ordered structure of MgCd, which was determined by Steeple[7], is orthorhombic structure as in shown in Fig. 7. Its B.Z. which contains two electrons per atom is given by slightly distorting B.Z. of h.c.p. structure. In Fig. 8, the cross section of B.Z. of orthorhombic MgCd on the equatorial plane is shown

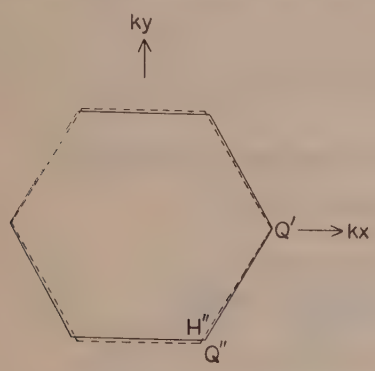

Fig. 8. Crossection of the Brillouin zone of ordered (broken line) and disordered (real line) of MgCd.

by broken line, while that of disordered MgCd is given by full line. From the figure, it can be seen that the B.Z. of the ordered MgCd is given by slightly contracting the B.Z. of disordered MgCd in the k_x direction, and expanding it in the k_y direction. This suggests that the Q overlaps in the [110] direction,

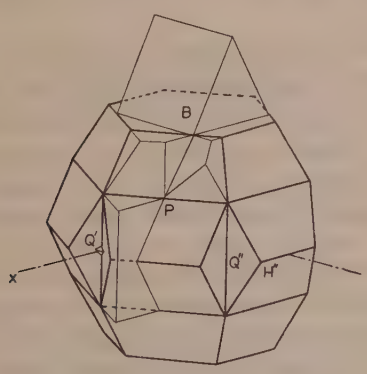

Fig. 9. The Brillouin zone of ordered MgCd.

which is denoted as Q', may increase, while the other Q overlaps, Q'', decrease; and H'' holes increase. Such situation will contribute to increase the absolute value of Hall coefficient in the ordered state.

As can be seen from Fig. 9, the Q tetrahedra in the ordered Mg_3Cd and $MgCd_3$ appear only at point Q' in the case of ordered MgCd. Q' tetrahedra are surrounded by those planes as $\{101\}$, $\{10\bar{1}\}$, $\{111\}$, $\{1\bar{1}1\}$, and have volume which can contain

$$\frac{1}{3}\left\{1+\left(\frac{a_1}{a_3}\right)^2\right\}\left(\frac{a_3}{a_2}-\frac{a_2}{a_3}\right)^2$$

electrons per atom, which is 4.7×10^{-3} electrons per atom in the case of MgCd. As in the case of Mg_3Cd and $MgCd_3$, this may be too small to affect the Hall coefficient.

It may be presumed that P overlaps are distorted in the complicated way as in the case of Mg_3Cd, while B overlaps are not affected appreciably by the order-disorder transformation.

It seems to be not so far from the truth to assume that the main cause of the increase in Hall coefficient in the ordered state of MgCd will come from the following facts that the number of overlapping electrons at point Q'' decrease while H'' holes increase, and, further, a part or all of the Q'' overlaps are contained in the Q' tetrahedra in the ordered state, may chiefly contribute to the increase of the Hall coefficient by ordering formation.

§ 5. Conclusion

1. The Hall coefficient of Mg–Cd system superlattice alloys increased towards positive direction by ordering formation. 2. At least, the change can be partly explained by band model, assuming the distortion of Fermi surface by the appearance of superzone in the ordered state.

It also seems to be an interesting problem that h.c.p. structure of disordered MgCd is distorted and becomes orthorhombic in the ordered state, which seems to be able to be explained by assuming a contribution of electronic energy to such distortion. It is also necessary to notice about the temperature dependence of these alloys in the disordered. state.

In order to proceed further, the following experiment must be necessary; to control the number of electrons by adding to these alloys the third elements which are mono-, tri-, and quadri-valent, and have nearly equal atomic size with magnesium and cadmium; to measure the anisotropy of Hall coefficient by single crystal.

Acknowledgements

The authors are indebted to Mr. S. Noguchi for helpful discussions and suggestions. Our thanks also to Mr. H. Nogami for his assistance at various stages in the data-taking.

References

1) J. C. Slater: Phys. Rev. **84** (1951) 179.
2) J. F. Nicholas: Proc. Phys. Soc. **21** (1950) 23.
3) T. Muto: Sci. Pap. Inst. Phys. Chem. Res. Tokyo **34** (1938) 377.
4) A. Komar and S. Sidrov: J. Phys. USSR **4** (1941) 552.
5) K. Yonemitsu and T. Sato: Oyo Butsuri **26** (1957) 153.
6) J. R. Reitz and C. S. Smith: Phys. Rev. **104** (1956) 1253.
7) H. Steeple: Acta Cryst. **5** (1952) 247.

JOURNAL OF THE PHYSICAL SOCIETY OF JAPAN Vol. 13, No. 1, JANUARY, 1958

Surface Photoconductivity of Cadmium Sulphide modified with Magnetic Field

By Shōji TANAKA and Taizō MASUMI

Department of Applied Physics, University of Tokyo, Tokyo, Japan

(Received April 13, 1957, Revised July 17, 1957)

An experiment on the changes of photocurrent in cadmium sulphide single crystals in magnetic field was performed. The results obtained are as follows; the changes of photocurrent by magnetic field are dependent on the strength of electric and magnetic fields which are parallel to the illuminated surface and are perpendicular to each other, and the changes are also dependent on the frequency of the alternating electric field, the wavelength of illuminating light and on the ambient atmosphere, while these changes are independent of the intensity of illuminating light. Some theoretical treatments based on the phenomenological theory of surface recombination are proposed with these experimental results, and they seem to give some informations about surface recombination of cadmium sulphide single crystals.

§ 1. Introduction

A large number of investigations on the surface recombination of electrons and holes in semiconductors have been reported already, especially in germanium, as related with some surface properties. Suhl effect, contact potential difference, surface conductance, noise, photoelectromagnetic effect, and field effect were studied in details. These phenomena suggest that the surface traps act as recombination centers of electrons and holes, and the effective carrier mobility in the space charge layer is slightly different from that of electrons in the volume.

The existence of surface photoconductivity in cadmium sulphide and zinc sulphide has been investigated by Bube[1], and it is found that the presence of water vapour decreases both the photosensitivity and time constant for exciting wavelength shorter than the absorption edge of CdS. On the assumption that the conductivity of surface region is less than that of the volume in the absence of water vapour, he explained these results presenting a model, where the presence of water vapour increases the conductivity of the surface, thereby increasing the recombination rate for electron-hole pairs generated at the surface. Liebson[2], and Tanaka and Aoki[3] emphasized also the influence of a change in barrier height on the photoconductivity and other properties. We have previously reported the change of surface-excited photocurrent of CdS in magnetic field[4]. Though Moss and Pincherle[5], Aigrain and Bulliard[6] have investigated the photoelectromagnetic effects in

germanium and lead sulphide and studied recombinations of electrons and holes in these semiconductors and Sommers et al.[7] observed the similar effect in CdS, the observed phenomena in our experiment seem to be different from the other effects mentioned above, and it may be preferable that they are considered as the effects of the surface recombination decreased or increased by magnetic field. These effect also might be closely related to the observation of surface life time by Bube[8]. We present here the general description and some physical considerations about the experiments of these phenomena.

§ 2. Experimental Method

The outline of the experimental arrangement is simple as shown in Fig. 1; a, b schematically. Samples used in this experiment are thin flakes of hexagonal cadmium sulphide single crystals produced by Frerichs' method,[9] which are about the size of 10 mm $\times$3 mm$\times$0.05 mm. Nearly all the samples are of pure type prepared without doping and treated neither physically nor chemically. The distance between the evaporated metal electrodes is 0.2 mm. The specimens are set on a blackened glass sheet by metal spring. For the measurement in vacuum, this glass

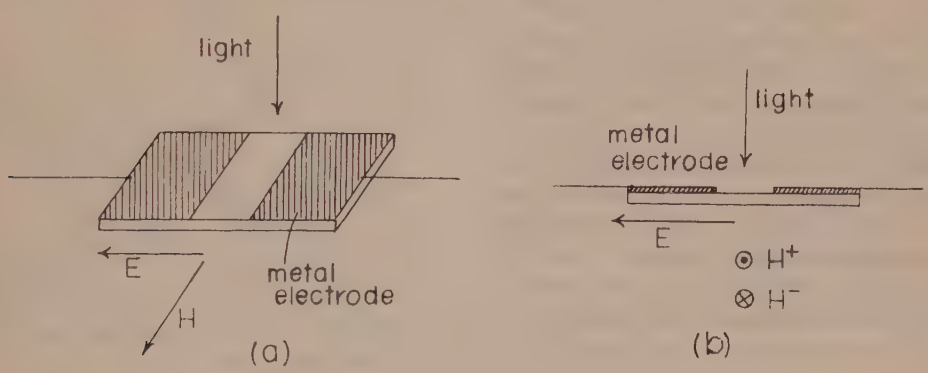

Fig. 1. Schematic experimental arrangement.

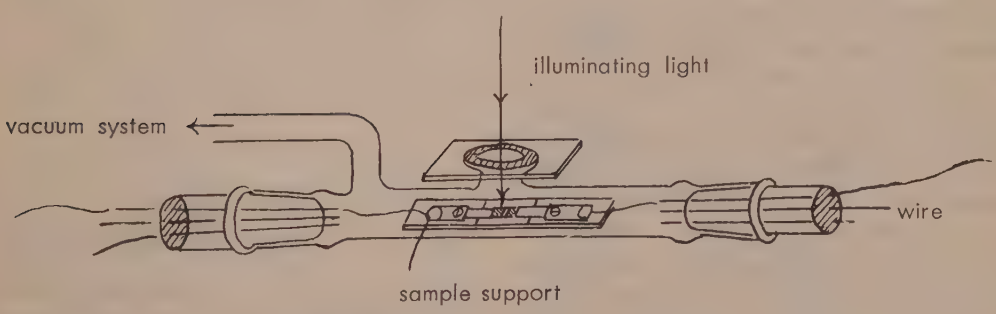

Fig. 2. Glass tube enclosing the sample.

sheet was enclosed in a glass tube as shown in Fig. 2 through the window of which one surface of the sample is illuminated by the focalized monochromatic lights of 436 mμ and 546 mμ in wavelength, the former wavelength lies in the strong absorption region and the latter in the long wavelength tail of the absorption edge of CdS at room temperature. It seems to be important that the homogeneity of the intensity of illumination should be kept constant all over the surface of the sample. As shown in the following section, absolute intensity of the illuminating light has little meaning, then, its measurement is replaced by that of the photocurrent under the constant electric field, and in this experiment the highest intensity corresponds to 70 μA in photocurrent at most in the electric field of about 8×10^3 volts/cm. The applied electric fields are static or alternative sinusoidal ones sufficiently stabilized, and their maximum magnitude is 10^4 volts/cm in static

field and 7.5×10^3 volts/cm in alternative field respectively, the frequency range of the latter extends from 25 cps to 5 kc/s. In the latter case, the alternating photocurrent are measured by reading the positive peak voltage across the connecting resistor. For the measurement of the changes of photocurrents in both cases, the low potential end of the sample is connected to ground through a low impeadance resistor, the voltage across which was measured with a difference amplifier. The magnetic field used in the present experiment is static one, the strength of which varies from 0 to 8×10^3 gauss. The effective field area is sufficiently large to ensure the homogeneity of field around the specimen.

Thus, as shown already in Fig. 1, a sample is illuminated on one surface by light at room temperature and the applied electric and magnetic field are set to be parallel to this surface and perpendicular to each other where the direction of magnetic field is taken to be parallel to that of c-axis in hexagonal cadmium sulphide single crystals. When the magnetic field is applied, the photocurrent of CdS single crystal increases or decreases according to the directions of the fields.

§ 3. Experimental Results

The experimental results were mainly represented as the ratio of the changes of photocurrent in a magnetic field $(\Delta I)_H$ to the magnitude of photocurrent I, i.e., $(\Delta I)_H/I$, and we have observed some dependences of $(\Delta I)_H/I$ upon the several variables; strength of applied electric and magnetic fields, intensity of iluminating light or photocurrent corresponding to it, frequency of alternative electric field, wavelength of illuminating light, and ambient atmosphere.

The photocurrents of CdS single crystal decrease or increase according to the positive or negative sign of the product of applied electric and magnetic fields ($\boldsymbol{E}\times\boldsymbol{H}$) in the coordinate system chosen in Fig. 1. The positive sign of the product of electric and magnetic fields ($\boldsymbol{E}\times\boldsymbol{H}$) such that the flowing current carriers in the crystals are deflected towards the illuminated surface reduces the photocurrent, and the inversion of magnetic field shows a quite equivalent effect to that of electric field.

At first, in order to observe the dependence of $(\Delta I)_H/I$ upon electric field, the field-photocurrent relation for static field was studied with constant illumination of blue light (436 mμ in wavelength) in air. Though the observed relations show slight differences with intensity

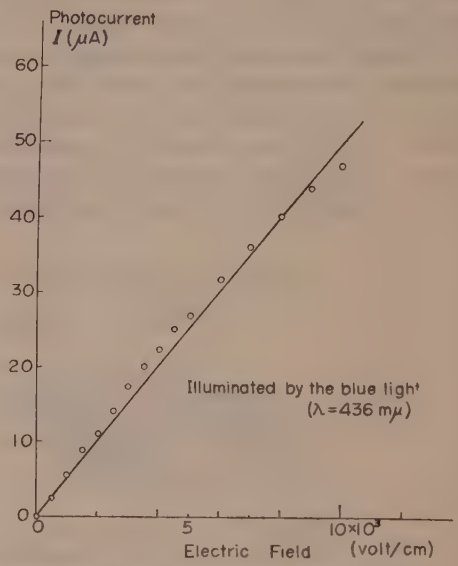

Fig. 3. The electric field-photocurrent relation for static field in air.

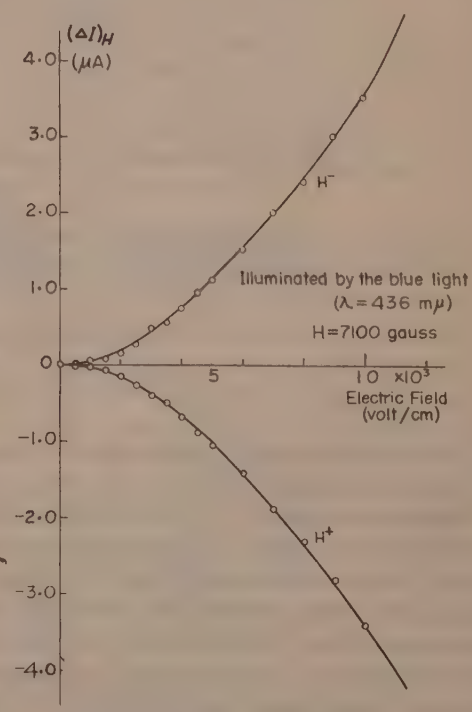

Fig. 4. Dependence of $(\Delta I)_H$ upon electric field (in air).

of illuminating light, they have, in general, considerably good linearites as shown in Fig. 3. The changes of photocurrent $(\Delta I)_H$ in a constant magnetic field (H=7100 gauss) under the same conditions have a parabolic dependence on the magnitude of electric field for the range from 0 to 10^4 volt/cm as presented in Fig. 4. Therefore, we obtain a linear relation between $(\Delta I)_H/I$ and applied electric field E as in Fig. 5. This is a fundamental relation throughout the present experimental results.

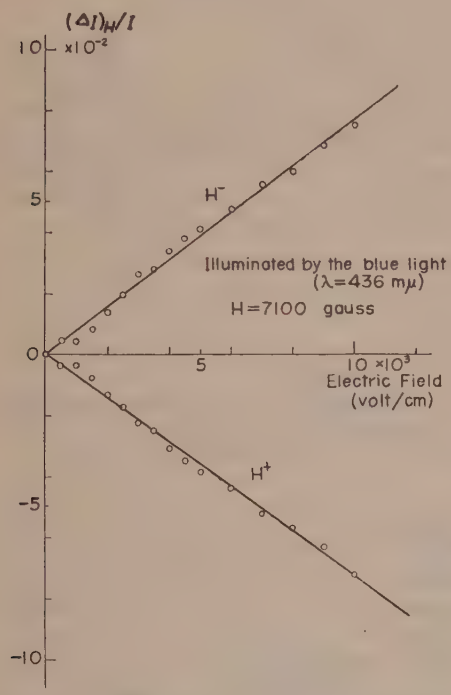

Fig. 5. Dependence of $(\Delta I)_H/I$ upon electric field (in air).

When the magnetic field strengths are varied under the same conditions with a fixed, the relative change of photocurrent $(\Delta I)_H/I$ increases or decreases proportional to the strength of the magntic field H as shown in Fig. 6, where the electric field is about 10^4 volts/cm, and the photocurrent of 45.9 μA. Furthermore, the observed result of similar dependence of $(\Delta I)_H/I$ on the intensity of illuminating light or on the equivalent photocurrent itself corresponding to the intensity are illustrated in Fig. 7 under the same conditions with a fixed electric and magnetic fields ($E=8\times10^3$ volts/cm, H=70000 gauss), and it is found that the changes of photocurrent are linear to I itself so $(\Delta I)_H/I$ are nearly independent on the intensity of illuminating light in the range of the present experiment in which the photocurrent is at most 71 μA with the electric field of about 8×10^3 volts/cm.

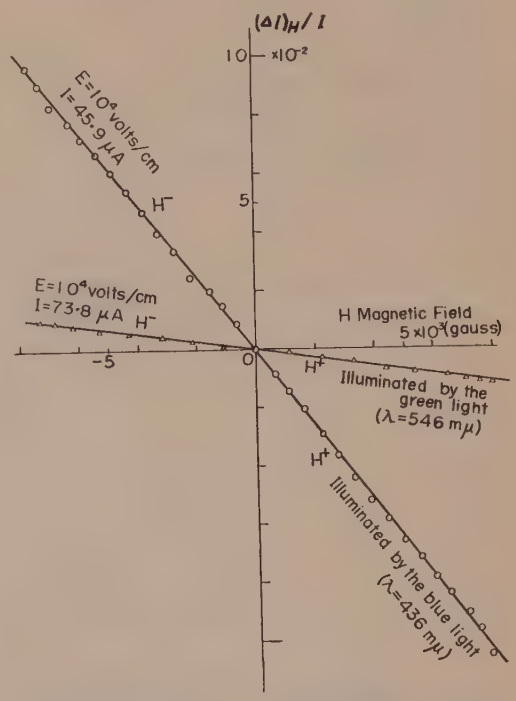

Fig. 6. Dependence of $(\Delta I)_H/I$ upon magnetic field (in air).

Therefore, putting together these results, the following expression may be probable for our observations

$$(\Delta I)_H/I=\mp CEH \tag{3.1}$$

where C is a constant dependent on some external and internal factors but independent of the intensity of illuminating light and its experimental value was observed to be 10^{-9} (cm/volt. gauss) in some samples. If the sample is illuminated by the green light (546 mμ in wavelength) longer than the absorption edge, the values of $(\Delta I)_H/I$ are smaller by a factor of ten at least under the same conditions as illustrated in Fig. 6 as an example, though the general features of the results seem to be similar to the case of the blue light.

These amounts of $(\Delta I)_H/I$, however, have considerable fluctuations from sample to sample, and the fluctuations might be caused

by some sensitive properties included in the constant C in the equation (3.1). Similar experiments carried out in vacuum of $10^{-2\sim3}$ mmHg for the blue light present a few informations relating to these considerations.

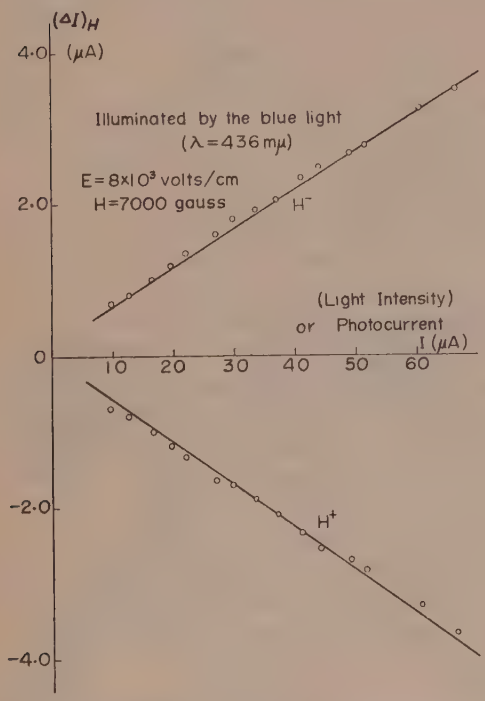

Fig. 7. Dependence of $(\Delta I)_H$ upon light intensity or photocurrent (in air).

As shown in Fig. 8, general tendencies of these phenomena are kept to be almost unchangeable from those of in air though the electric field dependence in Fig. 8 shows a slight deviation from the general relation in the high field region and the absolute value of C decreases to about three-fourth of the initial value in air. Besides, it is a very interesting fact that the photocurrents for the blue light differ between in air and in vacuum for the same conditions, and seems to suggest the existence of surface photoconductivity.

In the preceeding experiments, we used the static electric field, but the further experiment was performed under the application of sinusoidal alternating electric field and static magnetic field in order to indicate the relaxation effects, that are observed under relatively low frequencies. According to the measurement corresponding to the static case, the equation (3.1) are also maintained for a certain fixed frequency excepting that the electric field dependence of $(\Delta I)_H/I$ are slightly deviated at low field region (Fig. 9). To observe the relaxation effect, the dependence of $(\Delta I)_H/I$ on the frequency was studied

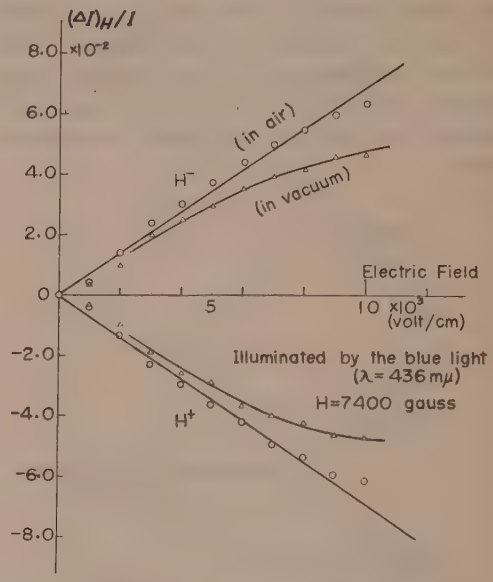

Fig. 8. Comparison of electric field dependences between in air and in vacuum.

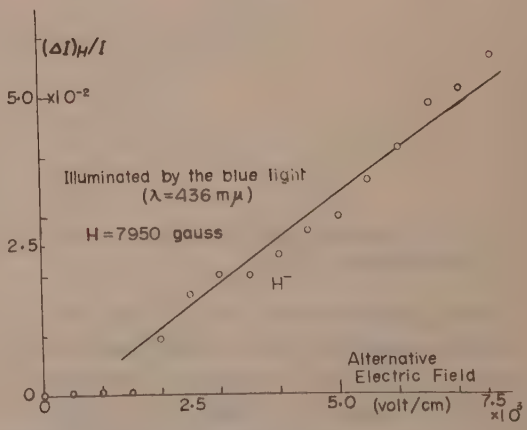

Fig. 9. Dependence of $(\Delta I)_H/I$ upon alternative electric field (in air) ($f=30$ cps).

keeping the amplitudes of the alternating fields at a fixed value, for example 7.5×10^3 and 5×10^3 volts/on respectively, over the frequency range from 25 cps to 5 Kc/sec. A typical example of the experimental results is illustrated in Fig. 10 and indicates that the relaxation effects for the alternating field of 7.5×10^3 volts/cm appear even below 300 cps,

and the effects of static magnetic fields are not observed in the frequency range above 2 kc/s, while the photocurrent is nearly independent of the frequency of the electric field in this region. For the smaller field strength of 5×10^3 volts/cm, the relaxation effect seems to appear in the lower frequency range than for the higher field strength, but this behaviours still involves some experimental ambiguities. These results, however, will present some knowledges on the relaxation effect.

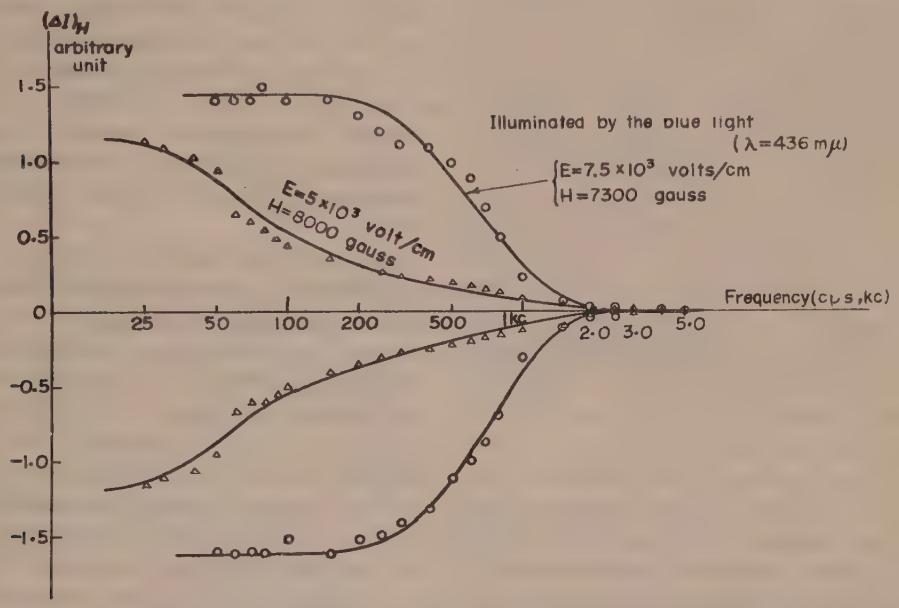

Fig. 10. Dependence of $(\Delta I)_H$ upon frequency of alternating electric field (in air).

In short, it may be concluded that the relative changes of photocurrent in a magnetic field $(\Delta I)_H/I$ generally depend on the electric and magnetic field strength proportionally and do not depend on the intensity of illuminating light under nearly all conditions. Then, in the range of our observation, the experimental expression of the equation (3.1) must be valid in nearly all cases, though the value of constant C varies with the frequency of electric field, the wavelength of illuminating light and the other external conditions such as humidity in air, etc. For example, the value of C is 1.25×10^{-9} (cm/volt. gauss) in static case for the blue light in air, and smaller by a factor of ten at least for the green light under the same condition. These complicated factors which have considerable fluctuations from sample to sample, may result from the some sensitive properties inherent to these phenomena.

§ 4. Discussions

It may be expected that there are several possible interpretations about the experimental results in the preceding section. Then, we describe here some qualitative discussions and present a detailed treatment in the following section.

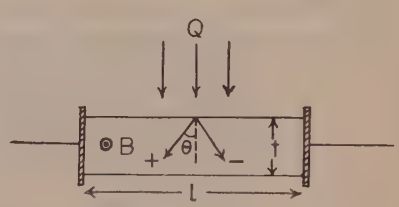

Fig. 11. Schematic figure of photoelectromagnetic effect.

In regard to these effects that rise from the behaviours of photoelectrons in a external magnetic field, the closely related phenomenon seems to be the photoelectromagnetic effect that are observed in germanium and lead sulphide. The photoelectromagnetic effect is understood as the phenomenon specified in Fig. 11 by Moss and Pincherle and others,[5),6)] and the short-circuited current in

this effect is expressed as follows,

$$(I_s)=\frac{\eta QeB}{l}\{\mu_e(D_e\tau)^{1/2}+\mu_h(D_h\tau)^{1/2}\} \quad (4.1)$$

where Q is the number of photons absorbed at the surface of the sample (quanta/sec), η quantum efficiency, l dimension of the sample, B magnetic flux, e electronic charge, μ_e, μ_h; D_e, D_h, mobilities and diffusion constants of electrons and holes, respectively, excited at the surface, τ life time. However, this short-circuited current may be produced when no external electric field is applied, and even if it were superposed on the photocurrent I, (I_s) would have the opposite signs to $(\Delta I)_H$ involved in the equation (3.1) for the same directions of magnetic field. These circumstances suggest that it is difficult to adopt the photoelectromagnetic effect for the explanation of the present experiment, although it was recently observed in insulating CdS crystal by Sommer et al.[7]

In any case, however, it is considered that the relative changes of photocurrent expressed by the equation (3.1) are due to the changes in total number of photoelectrons N or the changes in mobility μ_e due to the surface scattering. The quadratic dependence of $(\Delta I)_H$ upon the electric field with a fixed magnetic field and light intensity (Fig. 4) also suggests it to be probable that only the changes of N must be responsible for the change of photocurrent. Such considerations lead us to a following interpretation, based on the surface recombination of photoelectrons and holes at the illuminated surface.

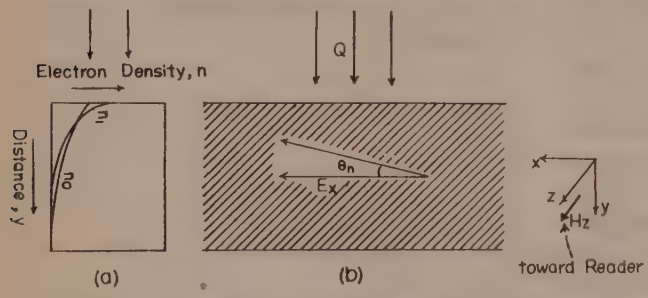

Fig. 12. Concentration of electrons near the surface.

Recombinatian of electrons and holes generally occurs in the volume and surface, and as bulk recombination is not always negligible, the change of N due to it might be an important factor in some cases. The experimental results expressed in section (3), however, show that the value of contant C in the equation (3.1) for the wavelength shorter than the fundamental absorption edge is much larger than that of the longer wavelength tail in absorption edge. Bube[8] also has shown an evidence that the free electron life time for surface excitation is smaller than the life time for volume excitation, because of a higher rate of recombination at the surface. These facts suggest a particular significance of surface recombination at the illuminated surface for the present experiment.

Surface recombination is primarily determined by the density of charge carriers at the surface, and then the change of this quantity seems to be exclusively responsible for the observed phenomena. If we take the coordinate system as shown in Fig. 12, x, the direction of electric field E; y, the direction perpendicular to the illuminated surface, z, that of magnetic field, the concertration of distributed carriers $n(y)$ is independent on x and z under the present condition. When we apply magnetic field H, $n(y)$ varies according to the transverse effective electric field $\mu EH/c$ due to the deflection of moving carriers and also does the concentration at the illuminated surface $n(0)$, Therefore, the rate of surface recombination must be modified which results the change of N, and also photocurrents themselves, although the surface recombination velocity has a fixed value. This interpretation seems to be considerably plausible, and the more detailed phenomenological treatment of these phenomena based on it will be proposed in the following section with regard to the exprimental results.

§ 5. Phenomenological Theory based on Surface Recombination

For the analytical consideration of the experimental results in the section (3), some equations must be introduced that are well-known as the "current" equation and others under a few assumptions. The definitions of the symbols used throughout this section are as follows;

n; concentration of photoelectrons (cm^{-3}),
τ_n; life time of excited electrons in bulk (sec),
s; surface recombination velocity (cm/sec),
e; positive charge of one hole, absolute value of electronic charge (coulomb),
κ; absorption coefficient of semiconductor (cm^{-1}),
Q; illumination intensity in quanta ($cm^{-2}\,sec^{-1}$),
D_n; diffusion constant of electron (cm^2/sec),
μ_n; mobility of electron (cm^2/volt sec),
$\boldsymbol{I}_n$; charge current flow by electrons (ampere),
$\boldsymbol{E}$; total electric field (volt/cm),
$\boldsymbol{E}_s$; electric field due to the spatial distribution of charg carriers themselves (volt/cm),
$\boldsymbol{E}_t$; transverse effective electric field produced by application of magnetic field (volt/cm),
v_t; transverse drift velocity of electron (cm/sec),
$\boldsymbol{H}$; magnetic field (gauss),
N; total number of electrons per unit surface area (cm^{-2}),
A; concentration of electrons at the illuminated surface (cm^{-3}),
α; parameter representing the distribution of electrons (cm^{-1}),
d; depth of specimens.

If we take such definitions and adopt some assumptions with them, we can show a trial treatment for the experimental results. The assumptions involved in this consideration are as follows. (1) The concentration of carriers is sufficiently small that the "current" equation based on the diffusion theory is valid and the electric field is also small enough, so that it does not introduce any non-linear term of $\boldsymbol{E}$ into the current equation. (2) The photoelctrons excited by photons are completely free from electron-traps in the volume except direct recombination with trapped holes, while all the positive holes are almost immobile, that is, they have small diffusion length nearly equal to zero. (3) The distributions of photoelectron density may be considered to have the following form in all region,

$$n(y)=Ae^{-\alpha y}-\frac{Q}{D_n\kappa}e^{-\kappa y}$$

that approximate to

$$n(y)=Ae^{-\alpha y}$$

with κ of sufficiently large value,[10] and the similar expressions are valid even in the presence of magnetic field.* (4) Surface recombination velocity s assumed to be dependent upon only the concentration of trarped holes at the illuminated surface and their capture cross section for electrons accepts no modification by magnetic field, because all positive holes are immobile and the change in surface barrier height is not emphasized. Furthermore, the absolute value of s is sufficiently large that the condition $s \gg v_t$ is valid, i.e., the modification of surface recombination of carriers by magnetic field is also small. (5) The generation of carriers excited by illumination must keep a balance with the recombination in bulk and surface in steady state, then, the expression

$$Q=\frac{N}{\tau_n}+sA$$

holds. (6) Mobility of photoelectron shows no change by magnetic field, so the changes of total number of electrons N are exclusively responsible for those of photocurrents, and the difference between Hall and drift mobility is also neglected.

The current equation for photolectrons assuming the small density of carriers (assumpt. (1)) is given by

$$\boldsymbol{I}_n=e\mu_n n\boldsymbol{E}+eD_n\nabla n \tag{5.1}$$

In the configuration of electron distribution in stationary state shown in the Fig. 12, this equation is induced to the following forms

$$\begin{aligned} I_{nx}&=e\mu_n nE_x \\ I_{ny}&=e\mu_n nE_y+eD_n\frac{dn}{dy} \\ I_{nz}&=0 \end{aligned} \tag{5.2}$$

where E_x is the externally applied field and E_y is

$$E_y=E_{sy}+E_{ty} \tag{5.3}$$

and

$$E_{ty}=\theta_n E_x=\frac{\mu_n E_x H_z}{c} \tag{5.4}$$

is the transverse effective electric field due to the magnetic field. But, here, we are

* Refining for more satisfactory form based on the diffusion theory of charge carriers will be discussed elsewhere.

particularly concerned with the y-component of them because of the importance of the changes of E_y and therefore the modification of $n(y)$ by magnetic field.

According to the assumption (3), $n(y)$ is expressed as follows

$$n(y)=Ae^{-\alpha y} \tag{5.5}$$

and α may be supposed to be enough large compared with $1/d$ so that the specimen depth d is equivalent to infinity for the specimen illuminated by the blue light.

(1) In the Absence of Magnetic Field (specified with suffix "0")

In the absence of magnetic field, the current equation and other expressions above, specified with suffix "0", are

$$I_{ny0}=e\mu_n n_0 E_{sy0}+eD_n\frac{dn_0}{dy} \tag{5.6}$$

$$n_0(y)=A_0\,e^{-\alpha_0 y} \tag{5.7}$$

Supposing the fixed surface recombination velocity s at the illuminated surface even in the absence of magnetic field, we have

$$I_{ny0}(0)=esn_0(0) \tag{5.8}$$

as the boundary condition at the illuminated surface. These equations are equivalent to

$$\mu_n E_{sy0}(0)-D_n\alpha_0=s \tag{5.9}$$

or

$$\alpha_0=\frac{\mu_n E_{sy0}(0)-s}{D_n} \tag{5.10}$$

where D_n may be also written using the Einstein relation

$$\mu_n=\frac{e}{kT}D_n \tag{5.11}$$

Furthermore, total number of photoelectrons per unit area of surface in xz-plane may be given as follows

$$N_0=\int_0^\infty n_0(y)dy=\frac{A_0}{\alpha_0} \tag{5.12}$$

by integrating the eq. (5.7) for the specimen illuminated by the blue light.

(2) In the Presence of Magnetic Field (specified with suffix "1")

The current equation of this case modified by the transverse electric field E_{ty} and other similar expressions with those in the case (1) are assumed to be valid even in the presence of magnetic field.

$$I_{ny1}=e\mu_n n_1(E_{sy1}+E_{ty})+eD_n\frac{dn_1}{dy} \tag{5.13}$$

$$n_1(y)=A_1e^{-\alpha_1 y} \tag{5.14}$$

If we suppose the same surface recombination velocity s with that in the case (1) in the presence of magnetic field (assumpt. (4)), the boundary condition in this case gives

$$I_{ny1}(0)=esn_1(0) \tag{5.15}$$

hence

$$\mu_n\{E_{sy1}(0)+E_{ty}\}-D_n\alpha_1=s \tag{5.16}$$

or

$$\alpha_1=\frac{\mu_n\{E_{sy1}(0)+E_{ty}\}-s}{D_n}=\frac{\mu_n E_{sy1}(0)-v_t-s}{D_n} \tag{5.17}$$

where

$$v_t=-\mu_n E_{ty}=-\mu_n\theta_n E_x=-\frac{\mu_n{}^2E_xH_z}{c} \tag{5.18}$$

is the transverse drift velocity of electron, and the total number of photoelectrons per unit surface area may be similarly given by

$$N_1=\int_0^\infty n_1(y)\,dy=\frac{A_1}{\alpha_1} \tag{5.19}$$

for the same specimen.

Then, we should consider a balance between the generation and the recombination of electrons in a stationarily illuminated state. Hence,

$$Q=\frac{N}{\tau_n}+sA \tag{5.20}$$

holds according to the assumpt. (5). As the specimen is illuminated under a constant intensity of light, we have the following expressions with the same Q and s, τ_n corresponding to the both cases.

$$Q=\frac{N_0}{\tau_n}+sA_0 \tag{5.21}$$

$$Q=\frac{N_1}{\tau_n}+sA_1\,. \tag{5.22}$$

Thus, these equations result in

$$N_1-N_0=\frac{A_1}{\alpha_1}-\frac{A_0}{\alpha_0}=s\tau_n(A_0-A_1) \tag{5.23}$$

or

$$\frac{A_1}{A_0}=\frac{1+s\tau_n\alpha_0}{1+s\tau_n\alpha_1}\cdot\left(\frac{\alpha_1}{\alpha_0}\right). \tag{5.24}$$

Suppose that there is no modification to the mobility μ_n of photoelectron by magnetic field (assumpt. (6)), the equation

$$\frac{(\Delta I_{nx})_H}{I_{nx}}=\frac{N_1-N_0}{N_0}=\frac{\dfrac{A_1}{\alpha_1}}{\dfrac{A_0}{\alpha_0}}-1 \tag{5.25}$$

is valid for the change of photocurrent $(\Delta I_{nx})_H/I_{nx}$, and, whereas the quantities A_1/A_0, α_1, α_0 are easily given from the eq. (5.10), (5.17), (5.24) and $\mu_n\{E_{sy_0}(0)-E_{sy_1}(0)\}$ may be considered to be much smaller than v_t, this leads to

$$\frac{(\Delta I_{nx})_H}{I_{nx}}=\frac{s\tau_n(\alpha_0-\alpha_1)}{1+s\tau_n\alpha_1}=\frac{s\tau_n v_t}{s\tau_n\{\mu_n E_{sy}(0)-v_t-s\}+D_n} \tag{5.26}$$

Furthermore, in the case to which we may impose some conditions based on the assumpt. (4) and neglect v_t and $D_n/s\tau_n$ in the denominator comparing with s, a more simplified form may be obtained

$$\frac{(\Delta I_{nx})_H}{I_{nx}}=\frac{v_t}{\mu_n E_{sy}(0)-s}=-\frac{\mu_n^2}{\mu_n E_{sy}(0)-s}\cdot E_x H_z \tag{5.27}$$

where c is the light velocity introduced in the eq. (5.18) for the absolute unit system of electric and magnetic fields while it takes the value of 10^8 for the practical unit system (volt/cm, gauss), and the sign of right side is determined from the combination E_x, H_z directions.

The eq. (5.27) is a suitable expression for a qualitative explanation of the present experiments, and the experiment conditions for the blue light ($\kappa\sim10^5$ cm^{-1}) with static electric field satisfy the adopted assumptions almost completely, while these are not the case for other cases. Then, finally, we can obtain the following relation comparing the eq. (5.27) with the eq. (3.1) in this case

$$s=\mu_n E_{sy}(0)-\frac{\mu_n^2}{Cc}. \tag{5.28}$$

The experimental value of C for the blue light with static electric field given in the section (3) being the order of 1.25×10^{-9} (cm/volt, gauss^{-1}) with one of samples, the value of s may be expressed as a function of μ_n

$$s=\mu_n E_{sy}(0)-10\mu_n^2 \tag{5.29}$$

involving the parameter $E_{sy}(0)$ that must be properly chosen from other physical considerations. Hence, these results seem to suggest us that the value of s is the order of $10^4\sim10^5$ (cm/sec) provided that $\mu_n=100\sim150$ (cm^2/volt·sec)[11] and $E_{sy}(0)=1200\sim2000$ (volt/cm).

The obtained value of surface recombination velocity s is relatively larger than the ordinary observed value in some semiconductors.[12),13)] The phenomenological treatment based on surface recombination in this section, however, is related to the so-called surface monolayer of illuminated surface, and compels us to consider that all the surface recombinations are due to this monolayer because of the importance of the boundary conditions in the treatment. The surface region effective to the recombination has a small but finite depth in fact and $n(y)$ is not always a satisfactory form. The treatment also involves some other assumptions, then, it is not improbable that s obtained from this treatment has such large values even if we properly select the arbitrariness in μ_n and $E_{sy}(0)$. For the green light, κ of which are much small, some of the assumptions become no longer valid and the treatment must be considerably modified.

The ambiguous points in this treatment lie in the following fact that we have neglected the changes in surface barrier height due to the surface states and the changes in effective carrier mobility by magnetic field. If we take account of the surface barrier height, the treatment will be slightly complicated. But, even in such case, the corresponding results would be scarecely modified from that of the present treatment, as the surface barrier due to the surface states would be lowered by the illumination of light[3)]. Though the second problem is also considerably important and some suggestions may be given by Schrieffer's theory[14)], we have no detailed informations about this problem.

Finally, if we may regard these effects as the small ones of second order because of the small magnitude of the effective transverse electric field due to the magnetic field, it may be concluded that the changes of photocurrents are able to be explained in the terms of surface recombination modified with magnetic field. In addition, the dependence of $(\Delta I)_H/I$ upon the frequency of the alternating electric field would give some contributions to the kinematic properties of surface recombination. But, further detailed treatment based on the concepts of imperfection and surface state will be necessary for the more obvious interpretation of these phenomena.

§ 6. Summary and Conclusions

The observed phenomena in the present

experiment show many kinds of behaviours of photoelectrons and holes in cadmium sulphide single crystals, but, though these phenomena are complicated with other, we can express the summarized conclusions as follows.

(1) The relative changes of photocurrents of cadmium sulphide single crystals in a magnetic field are experimentally characterized by the equation (3.1).

$$(\Delta I)_H/I = \mp CEH$$

and, for instance, the value of constant C for the blue light ($\lambda = 436\,\mathrm{m}\mu$) is the order of 10^{-9} (cm/volt. gauss^{-1}) for a sample and generally dependent on some sensitive properties of the illuminated surface.

Similar experiment for the alternative electric field presents some knowledges about the relaxation effect in these phenomena that rises in comparatively low frequency region.

(2) The phenomenological treatment of modified surface recombination in a magnetic field based on the diffusion theory of charge carriers seems to present a considerably plausible interpretation for the experimental results of surface-excited photoconductivity under several assumptions.

§ 7. Acknowledgments

The authors would like to express their sincere gratitudes to Professor Y. Suge and Professor T. Inui of Tokyo University for their continual encouragements and to Professor Y. Uemura of Tokyo University and Dr. H. Miyazawa of Matsuda Research Laboratory of Tokyo-Shibaura Electric Company for their suggestive discussions. They are also indebted to Dr. S. Iijima of the Electrotechnical Laboratory for his co-operative works.

References

1) R. H. Bube: Journ. Chem. Phys. **21** (1953) 1409.
2) S. H. Liebson: Journ. Electrochem. Soc. **101** (1954) 359.
3) S. Tanaka and M. Aoki: Ōyō Butsuri, **22** (1953) 311.
4) S. Tanaka, T. Masumi, and S. Iijima: Journ. Phys. Soc. Japan **11** (1956) 90.
5) T. S. Moss, L. Pincherle, and A. M. Woodwarth: Proc. Phys. Soc. **B 66** (1953) 743.
6) P. Aigrain, and H. Bulliard: Compt. Rend. **236** (1953) 595.
7) H. S. Sommers, R. E. Berry, and I. Sochard: Phys. Rev. **101** (1956) 987.
8) R. H. Bube: Phys. Rev. **101** (1956) 1668.
9) R. Frerichs: Phys. Rev. **72** (1947) 594.
10) H. B. De Vore: Phys. Rev. **102** (1956) 86.
11) F. A. Kroeger, H. J. Vink, and J. Volger: Physica **20** (1954) 1095.
12) B. H. Schultz: Physica **20** (1954) 1031.
13) H. K. Henisch, W. N. Reynolds, and P. M. Tipple: Physica **20** (1954) 1033.
14) J. R. Schrieffer: Phys. Rev. **97** (1955) 641.

JOURNAL OF THE PHYSICAL SOCIETY OF JAPAN Vol. 13, No. 1, JANUARY, 1958

Electron Spin Resonance of M centers in Potassium Chloride

By Hazimu KAWAMURA and Keiko ISHIWATARI

Department of Applied Physics, Osaka City University, Osaka

(Received August 7, 1957)

An experiment on the electron spin resonance of colored KCl containing F and M centers was performed at 9500 Mc/sec. Subtracting the contribution from the F centers from the observed resonance curve, we could estimate the shape of the resonance line due to M centers alone, which was found to be Gaussian with the half-breadth of 48 oersteds and g value of 2,000. This result was discussed on the LCAO model.

§ 1. Introduction

The spin resonance absorption of F center in alkali halide has been measured by several authors[1),2),3),7)], and it is found that the absorption line is rather broad, being Gaussian in shape and independent of temperature. Kip *et al.*[2)] have attributed this broadening to the hyperfine interaction between the F center electron and the nuclear magnetic moments of the neighboring ions. They could estimate the density of the electron cloud of F center at these nuclei from the observed line breadth. This interpretation was well confirmed when nineteen lines were separated for LiF and NaF by Lord[3)].

The next common and well studied center in colored alkali halide is M center. Seitz has proposed the model of M center as composed of two negative ion vacancies and one positive ion vacancy, with an electron being attached as shown in Fig. 1. The optical absorption peak for this center lies at 1.5 ev for KCl as shown in Fig. 3, while that of F center is found at 2.2 ev at room temperature. The electron cloud of M center may spread as that of F center and will have a broad and structureless line for electron spin resonance just as F center at least for KCl. Moreover the M center is always accompanied by F center, and hence we shall have the two broad lines superposed.

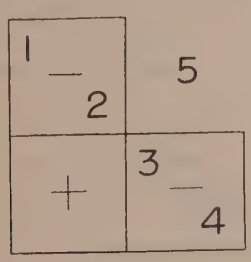

Fig. 1. Schematic model of M center. Squares are the positive or negative ion vacancies. Numbers show the position of K ions, 5 being in the plane of paper, 1 and 3 above, and 2 and 4 below it.

We have carried out an experiment with additively colored crystals of potassium chloride. The M centers were produced by irradiating the quenched crystal with F light. The density of M centers was about 0.4 times that of F centers, which was the highest attainable relative value for the former. The shape of the resonance line was found by subtracting the contribution from the F center.

Although the definite conclusion cannot be drawn from this broad line, it will nevertheless afford some criterions about the electronic structure of M center.

§ 2. Experiment

The spin resonance measurements were performed by an equipment as shown in Fig. 2. The frequency at which these experiments were made was about 9500 Mc/sec and the corresponding field was 3500 oerseds. The microwave source was 2K25 reflex klystron having the output power of 40 mW. The microwave power was fed to a rectangular cavity operated at TE 101 mode through the coaxial cable. The transmitted power was detected by a 1N23 crystal. The magnetic field was modulated at 455 Kc/sec, where the crystal noise is much less than at the conventional frequencies of some fifty cycles. But since the alternating magnetic field of such a high frequency is unable to penetrate into the cavity, a coil of few turns was wound directly around the specimen and set on the end surface of the cavity. The absorption signal

detected by the crystal was fed to three stage resonant amplifier operated at 455 Kc/sec and then detected by a phase sensitive lock-in detector.

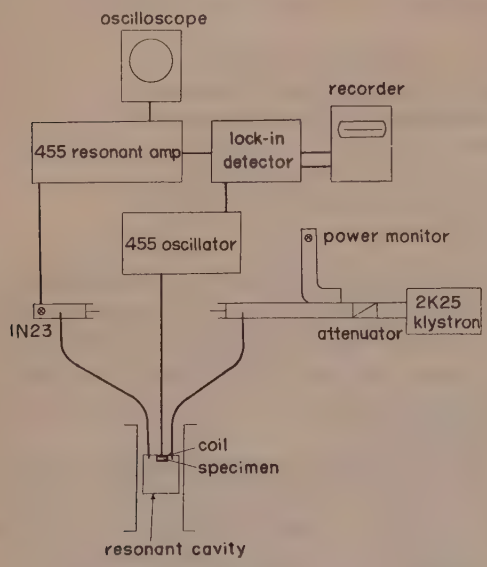

Fig. 2. Block diagram of electron spin resonance apparatus.

The specimens were the single crystals of potassium chloride which were additively colored at 580°C in potassium vapor. The small pieces of $8\times4\times2$ mm. cut from these crystals were heated at 500°C for one minute and then quenched on a copper block. The optical absorption spectrum of this specimen has a typical F absorption band as shown with curve 1 in Fig. 3. Assuming the oscillator strength to be 0.81, the density of the F centers is estimated to be $5.6\times10^{17}\,\mathrm{cm}^{-3}$. The

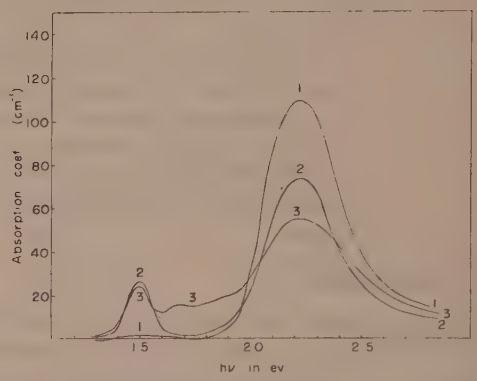

Fig. 3. Optical absoption spectra of colored KCl. Curve 1; quenched from 500°C. Curve 2; irradiated with sodium lamp for 5 minutes after quenching. Curve 3; irradiated for 30 minutes.

other specimens were then irradiated at room temperature with a sodium lamp whose line spectrum is at 2.1 ev and hence just within the F band. The M band grows as shown in curve 2 and 3 by this treatment. When the time of irradiation is as short as five minutes, we observe only M and F bands as shown by curve 2. If, however, the irradiation is continued half an hour, R_1 and R_2 bands come out between F and M bands as in curve 3. Since Okura* find the oscillator strength of M center to be about 0.42 times that of F center, the density of M centers of these specimens can be estimated as in Table I.

Table I.

Specimen	ΔH in oersteds		g	N_M/N_F	
	peak to peak	half breadth		optical	spin resonance
1	49.5	58.5	1.994	0	0
2	46		1.996	0.31	0.36
3	45		1.997	0.41	0.46
F	49.5	58.5	1.994		
M	40.5	47.5	2.000		

The spin resonance measurements were performed with these three specimens which we shall call 1, 2 and 3 in accordance with the numbering of the absorption curves in Fig. 3. An example of the resonance curve recorded on a chart is shown in Fig. 4. The sharp line

* H. Okura, to be published in this Journal. If the irradiation is not so heavy, the intensity of M band increases in proportion with the decreases of the F band. He estimates the ratio of the oscillator strength comparing the changes of the area of the absorption curves, assuming that the total density of F and M centers is constant.

superposed on the curve is the absorption due to diphenyl trinitrophenyl hydrazyl, an extremely small speck of which is attached on the modulating coil. The absolute values of g were determined referred to this line.

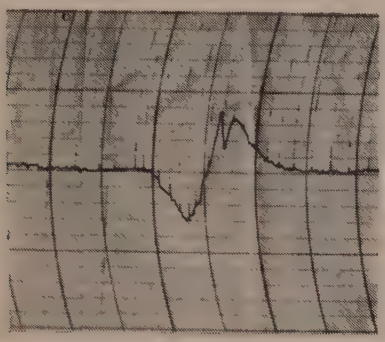

Fig. 4. Spin resonance absorption of specimen 2. Sharp line superposed is the absorption line due to diphenyl trinitrophenyl hydrazyl.

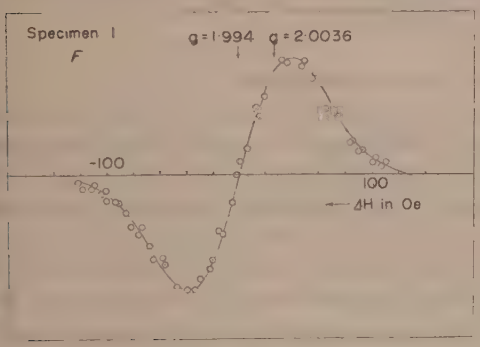

Fig. 5a. Spin resonance absorption of F centers. Solid curve is the theoretical Gaussian curve with half breadth of 58.5 oersteds. The arrow at g=2.0036 shows the position of the absorption line due to diphenyl trinitrophenyl hydrazyl.

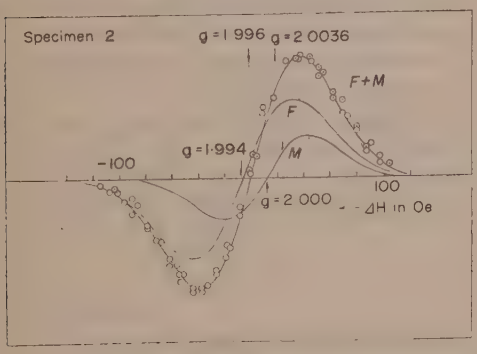

Fig. 5b. Spin resonance absorption of F and M centers of specimen 2. Experimental curve is decomposed into curves due to F and M centers.

Fig. 5a, b and c are the absorption curves for many runs reproduced from the recording charts. In Fig. 5a we show the plots for specimen 1, with the theoretical Gaussian curve having the half-breadth of 58.5 oersteds and the g value of 1.994 which are to be compared with 54 oersteds and 1.995 obtained by

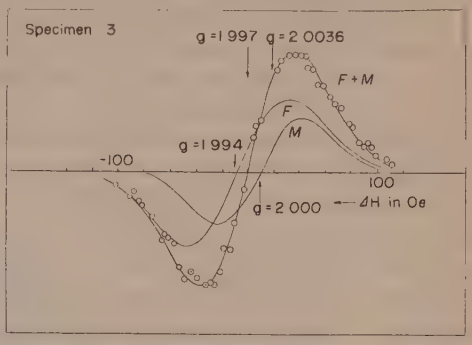

Fig. 5c. Spin resonance absorption of F and M centers of specimen 3. Experimental curve is decomposed into curves due to F and M centers.

Kip *et al.* The results for the specimens 2 and 3 are shown in Fig. 5b and 5c. Although the curve shapes are not so much different from that of specimen 1, the g values were 1.996 and 1.997 respectively which differ, beyond the experimental error, from that of pure F centers.

In the experiments shown in these figures, the magnetic field was applied along [100] direction. Almost the same curve with an identical g value was obtained for specimen 2, when the field was applied along [110] direction.

§ 3. Analysis of the Results

It may be expected that the curves in Fig. 5b and c are composed of the absorption curves due to F centers and M centers. Although R_2 centers have no effect upon spin resonance because of the pairing of the trapped electrons, R_1 centers in specimen 3 may give some contribution. But we shall neglect this effect in the following analysis, since its density is expected to be small enough. Since the shape and position of the curve for F centers is known from the above result, we can determine the absorption curve for M centers, adjusting so that the $\Delta H^2 \times D$ of these two curves have the appropriate ratio, where

ΔH is the peak to peak separation and D is the maximum deflection value of the derivative curve. $\Delta H^2 \times D$ is clearly proportional to the spin density of M or F centers. The ratio of these values which give the best fits of the curves are shown in the Table I. The fairly good coincidences with the optical data are seen. Thus we get the absorption curve for M centers alone as shown in these figures. The curve shape is Gaussian with the half-breadth of 48 oersteds and the g value 2,000.

In order to make the discussion to be concrete, we shall adopt the LCAO model[4),5)]. According to Inui, Uemura and Toyozawa[4)] we shall consider only the five nearest atomic orbitals of potassium as shown in Fig. 1. The ions 1 and 3 are above the plane of the paper and 2 and 4 are below it, all being equivalent. According to Kip *et al.* we shall assume that the line broadening is resulting from the hyperfine coupling between each orbital electron and the nuclear magnetic moment of the corresponding potassium. Now let the amplitude of s function at the position 5 be α and 1 to 4 be β. Since the nuclear spin of potassium is 3/2, it takes one of the four different values of magnetic moment along the direction of the magnetic field. If the magnetic moment of the nucleus at the position 5 takes one of these values, we may have the nearly Gaussian broadening due to the random orientation of the nuclear spin at four equivalent positions, the half-breadth* being $5.7\,\beta A/g\mu$, where A is the hyperfine constant for free potassium and μ is the Bohr magneton. Now we shall allow for the nuclear moment at the position 5 to change from $+3/2$ to $-3/2$. Then we may have a curve composed of the four lines with this broadening, each of which is separated by $\alpha^2 A/g\mu$. If this separation is sufficiently small, the resultant curve is nearly Gaussian. The borderline for this situation is at about $\alpha^2 A/g\mu \sim 1.5\beta^2 A/g\mu$. Since the larger value of α is favored from the theory, we shall assume tentatively that $\alpha^2 = 1.5\beta^2$. Then the half-breadth of the resultant curve becomes $7.1\,\beta^2 A/g\mu$. Comparing this with the observed value of 48 oersteds and taking $A = 0.0077\,\mathrm{cm}^{-1}$, we get $\beta^2 = 0.08$ and $\alpha^2 = 0.12$. The total of s part, therefore, amounts to 0.44. Among the residue the p function at the ion 5 may be largest since the polarizing field is farily large. Moreover the considerable mixing of p functions are expected in the atomic orbitals around the ions 1 to 4.

Although the anisotropy of g value is expected because of the anisotropic configuration of the atomic p orbitals, the absolute value of Δg is as small as 0.002 which corresponds to 3~4 oersteds, and, accordingly, it will affect little the above analysis.

While we are preparing this manuscript, we were informed of the paper of Lord[6)] concerning the spin reonance of M centers in LiF. He found that the line of M centers are rather broad and structureless in accord with our result.

§ 4. Acknowledgement

We should like to express our deepest thanks to Dr. Y. Uemura of the Tokyo University for his stimulating discussion and to Dr. J. M. Baker of the Clarendon Laboratory to whom we owe the detailed technique of spin resonance with high frequency modulation. We are also indebted to Mr. H. Okura and Mr. E. Otsuka for many details of the experiments and discussions.

References

1) C. A. Hutchison, Jr. and G. A. Noble: Phys. Rev. **87** (1952) 1125.
2) A. F. Kip, C. Kittel, R. A. Levy, and A. M. Portis: Phys. Rev. **91** (1953) 1066.
3) N. W. Lord: Phys. Rev. **105** (1957) 756.
4) T. Inui, Y. Uemura, and Y. Toyozawa: Prog. Theor. Phys. **8** (1952) 355.
5) T. Nagamiya, T. Kojima, and H. Kondo: Jour. Phys. Soc. Japan **9** (1954) 310.
6) N. W. Lord: Phys. Rev. **106** (1957) 1100.
7) G. Feher: Phys. Rev. **105** (1957) 1122.

* We defined the half-breadth by $1.18\,\Delta H$, ΔH being the peak to peak separation of the derivative curve. Since the absorption curve is not strictly Gaussian, $\Delta H/2$ is not equal to the square root of second-moment, and both are not strictly equal to the 2.35 times of true half-breadth.

JOURNAL OF THE PHYSICAL SOCIETY OF JAPAN Vol. 13, No. 1, JANUARY, 1958

Electrical Properties of $FeTiO_3$-Fe_2O_3 Solid Solution Series

By Yoshikazu ISHIKAWA

Institute of Science and Technology, University of Tokyo, Tokyo

(Received September 14, 1957)

D.C. electrical conductivity and Seebeck voltage of the synthesized solid solution $x\,FeTiO_3\cdot(1-x)\,Fe_2O_3$ of ilmenite ($FeTiO_3$) and hematite (Fe_2O_3) were measured for a composition range of $1\geqq x\geqq 0.33$. It was found that both conductivity and Seebeck voltage change continuously with the composition. At room temperature, the conduction is that of p type for $x>0.73$ and n type for $x<0.73$. Judging from these results, it was concluded that the valence state of Ti ions in the compound is tetravalent for the whole range of composition. Conductivity of all specimens obeys a simple Wilson's formula $\sigma=\sigma_0\exp(-E/2kT)$ over a temperature range from 200°K to 970°K with two or three activation energies for each specimen. No anomalous change of conductivity could be observed at the ferrimagnetic or antiferromagnetic Curie point. It was, therefore, expected that the conduction electrons do not correlate with the magnetic spins in these compounds. Conductivity and Seebeck voltage of both ordered (ferrimagnetic) and disordered (antiferromagnetic) specimens with the same composition were compared. It was found that change of the ion arrangement does not affect electrical properties of these componds.

§ 1. Introduction

It may safely be said that the conduction in the oxides of transition metals can be characterized by the extremely low mobility of its carriers. Owing to such a situation, the normal Hall voltage can not be observed for these compounds[1)2)] and the conduction mechanism can not be explained by the ordinary Bloch type approximation.

The stoichiometric oxides of transition metals are, ordinarily, poor conductors. Their conductivity, however, is enhanced greatly by presence of ions of a given element in more than one valence states which are distributed randomly over crystallographically equivalent lattice points. In this conduction, the carriers are usually holes (p type conduction) when small amounts of cations in a higher valence state are distributed among those of the host and the carriers are electrons when small amounts of cations in a lower valence state are distributed. Detailed discussions of such a conduction mechanism in these compounds have been reported in the papers of Verwey and de Boer.[3)4)]

In this paper, we shall report the electrical properties of the solid solution of $FeTiO_3$ and Fe_2O_3. This investigation has been carried out mainly for the purpose of understanding the peculiar magnetic properties of the solid solutions which have been reported in detail in the previous paper.[5)]*

In order to understand their magnetic properties, it is very important to know the valence states of ions contained in the compounds. There are two possible valence states for ilmenite. One is $Fe^{2+}Ti^{4+}O_3$ and the other is $Fe^{3+}Ti^{3+}O_3$. Though we have showed in I that the magnetic properties can be interpreted well by assuming the former state, it is still possible to interpret the saturation value of magnetization and the general feature of thermomagnetic curves by assuming the latter state, because the magnetic interactions of Ti^{3+} ions between themselves and with other ions are expected to be fairly smaller than those of Fe^{3+} ions. Hence we can not decide conclusively from only the magnetic study which of these two states is realized in the compound.

The electrical conduction of these compounds, however, must be greatly different in these two cases. When we assume the former state for $FeTiO_3$, Fe^{3+} ions in hematite are substituted by Fe^{2+} ions with increase of ilmenite content in the solid solution. Then

* This paper will be referred to as I hereafter in this paper.

there exist in the solid solutions a great number of pairs of Fe^{3+} and Fe^{2+} ions which increase the electrical conductivity of the solid solutions greatly. Furthermore, it is expected that the conduction is n type when the composition is near hematite and it changes into p type when the composition approaches to ilmenite.

On the other hand, when we assume another state, Fe ions in the solid solutions are always trivalent. Therefore, the compounds must be poor conductors when they are prepared stoichiometrically. The high conductivity of these compounds must be attributed, in this case, to the presence of pairs (Fe^{3+}, Fe^{2+}) and (Ti^{4+}, Ti^{3+}) which are produced by the deviation of the composion from the stoichiometrical value. Hence, in this case, the conduction is expected to be affected greatly by the atmosphere under which they are prepared and the continuous change of the electrical properties with their compositions can not be expected.

There are two other aims to investigate the electrical properties of these solid solutions. We have reported in I that the solid solution $x\ FeTiO_3\cdot(1-x)\ Fe_2O_3$ becomes strong ferrimagnetics in the composition range of $0.95 \geqq x \gtrsim 0.5$. It is, therefore, necessary to investigate whether the conduction electron has any correlation with the magnetic spins as have been found in the conducting oxides such as magnetite and mixed lanthnum and strontium manganites.[6]

Another aim is as follows. We have also reported in I and in another paper[7] that the magnetic properties of the solid solutions are affected greatly by heat treatments. For example, a specimen of $x=0.5$ can be changed from the antiferromagnetic state to the ferrimagnetic state by an appropriate heat treatment. We have interpreted this experimental fact as a kind of order-disorder transformation phenomenon, where Ti and Fe ions are assumed to be distributed at random in the antiferromagnetic state, while in order in the ferrimagnetic state.

If the ordered ions are responsible for the electrical conduction, such a change of the arrangement of ions would cause a great change in the conductivity. Hence we may obtain some knowledge on the ordered state by comparing the electrical conductivity and the Seebeck voltage of the ferrimagnetic specimen with those of the antiferromagnetic specimen.

§ 2. Preparation of Specimens

The methods for preparing specimens have been reported in detail in I and in another paper.[8] For the present purpose, a mixture of $FeTiO_3$ and Fe_2O_3 in a desired proportion was pressed into a parallelepiped of 4 mm × 4 mm × 20 mm dimension, by using a pressure of 5 ton per square centimeter, which was sealed into an evacuated quartz tube. Then, after sintering at 1200°C for more than 12 hours, it was quenched down to room temperature. The composition was determined by the X-ray and the chemical analysis as was reported in I.

In this method for preparation, the oxygen atmosphere under which the specimen is prepared is controled properly by the specimen itself which absorbs or ejects out the oxygen in the quartz tube. Accordingly, the specimens thus obtained have very different porosities with each other and the specimen of $x<0.33$ can not be sintered at all by this method. Hence we must restrict our measurement in a composition range of $x \geqq 0.33$. In Table I,

Table I. The porosity and magnetic property of the specimen

No.	$FeTiO_3$ mol %	Porosity (%)	Curie point	Magnetic property
1	100		55 (°K)	antiferromagnetic
2	95	12.0	63	ferrimagetic
3	80	16.5	224	ferrimagetic
4	67	8.0	394	ferrimagetic
5	51	10.8	483	antiferromagnetic
5′	(51)	10.8	530	ferrimagetic
6	47	21.0	529	antiferromagnetic
7	33	33.1	632	antiferromagnetic

we showed the porosity of the specimens used in the experiment which is defined as $P=\rho_b-\rho_x/\rho_x$ where ρ_b and ρ_x mean the bulk and X-ray density of the specimen.

In this table, the magnetic properties of the specimens are also presented. As we see in the table, all specimens have fairly high porosities. Hence the absolute value of the conductivity seems to have no meaning in this experiment.

§ 3. Experimental Results

The electrical conductivity was measured in air by a usual potential probe method over a temperature range from 800~700°K to 100°K. These specimens are not stable either in air or in high vacuum at temperatures higher than 800°K except a specimen No. 2 for which the measurement was carried out up to 1100°K.

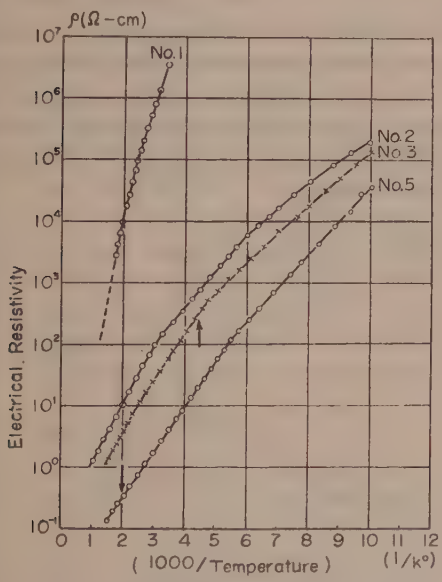

Fig. 1. D.C. resistivity vs. the reciprocal of temperature. Arrows indicate the Curie points of the specimens.

In Fig. 1, we showed the resistivity vs. the reciprocal of temperature curves of several specimens, all of which were found to obey a formula $\rho=\rho_0 \exp(E/2kT)$ having one or two breaks above 200°K. Arrows in the figure indicate the Curie temperatures of the specimens. We can find from the figure that even a slight break does not occur on $\log \rho$ vs. $1/T$ curves at the ferrimagnetic Curie point as well as the antiferromagnetic Curie point. The temperature at which the break occurs seems to depend rather on the degree of sintering, because the specimens with the same composition have different break points when they are prepared at different times. Other specimens which were omitted in this figure have similar temperature dependence.

In Fig. 2 the value of the resistivity at

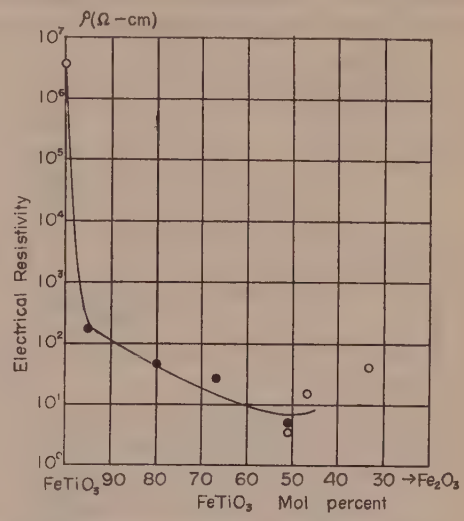

Fig. 2. D.C. resistivity at room temperature vs. the composition.
●.....ferrimagnetic specimens.
○.....antiferromagnetic specimens.

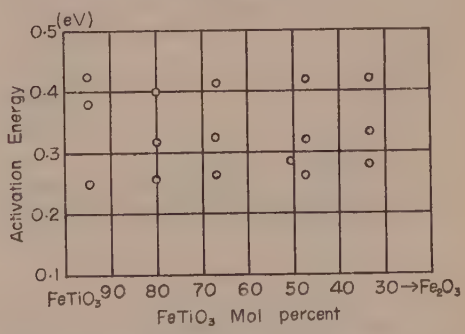

Fig. 3. Activation energies above 200°K obtained from Fig. 1 vs. the composition.

room temperature of these specimens are plotted against their compositions. As the resistivity is greatly affected by the porosity of the specimen, these values can not be plotted on a smooth line. It may, however, be concluded from this figure that the resistance decreases continuously with increase of the concentration of hematite in the solid solution. In Fig. 3 the activation energies obtained from Fig. 1 are plotted against the composition.

This quantity is also found to be strongly dependent on the porosity of the specimen. Nevertheless, it must be noticed that all specimens have nearly same activation energies.

The Seebeck voltage was measured with respect to a PtRh wire by the same method as was described in the previous paper.[8] The measurement was carried out in air over a temperature range from room temperature to 400°C and results are shown in Fig. 4.

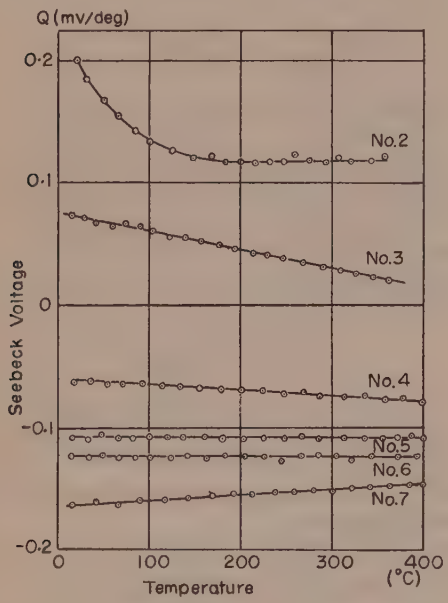

Fig. 4. Seebeck voltage vs. temperature.

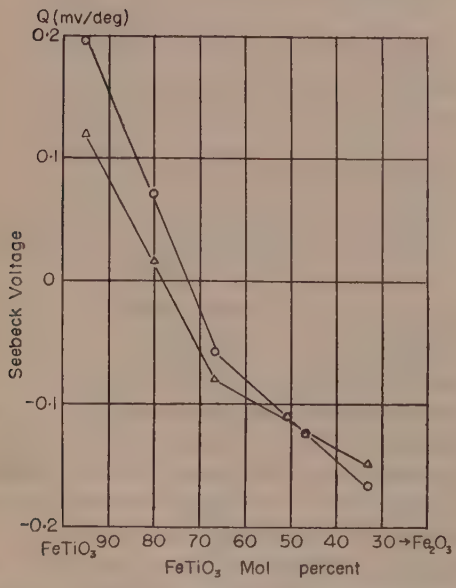

Fig. 5. Seebeck voltage vs. the composition.
○.....the value at room temperature.
△.....the value at 400 °C.

We can find in the figure that the Seebeck voltages of all specimens change linearly with temperature over this temperature range, and their slopes change continuously with the composition. In Fig. 5, the values of the Seebeck voltage at room temperature and at 400°C are plotted against the composition. Contrary to the case of the conductivity these values are expressed by smooth lines. This fact is expected naturally. Because, as the measurement of the Seebeck voltage does not involve the current flow, it value is expected to be independent on the porosity or the intergranular barrier. We can see from the figure that the Seebeck voltage change continuously with composition, and their signs are those of p type for $x>0.73$, and n type for $x<0.73$.

Effect of the heat treatment.

As we stated in the introduction, the specimen of $x=0.5$ can be changed from antiferromagnetic to ferrimagnetic by the appropriate heat treatment. In order to see how the heat treatment or the change of arrangement of ions affect the conductivity and the Seebeck voltage, we carried out the following experiment.

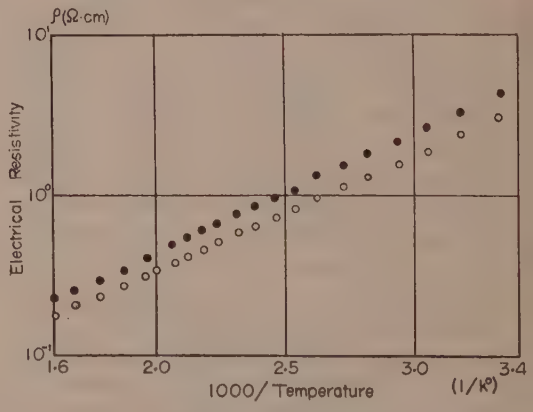

Fig. 6. D.C. resistivity of a specimen No. 5 vs. temperature.
○.....before the heat treatment (antiferromagnetic).
●.....after the heat treatment (ferrimagnetic).

We measured at first the conductivity and the Seebeck voltage of an antiferromagnetic specimen with $x=0.51$. This specimen was sealed again into evacuated quartz tube and was cooled very slowly from 800°C to room temperature, which was recently found the best way to establish the perfect ordering

between Fe and Ti ions.[9] After this heat treatment this specimen becomes strong ferrimagnetics.

In Figs. 6 and 7 the resistivity and the

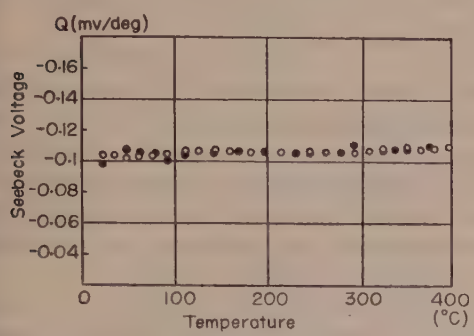

Fig. 7. Seebeck voltage of a specimen No. 5. vs. temperature.
○.....before the heat treatment (antiferromagnetic).
●.....after the heat treatment (ferrimagnetic).

Seebeck voltage measured for the specimen before and after the heat treatment are plotted against temperature. We found from these results that the Seebeck voltage does not change at all by the heat treatment. Though the resistivity increased a little after the heat treament, the difference may be due to other effects such as the slight change of the composition on the grain boundary by the heat treatment. Hence it may safely be said that the conductivity as well as the Seebeck voltage are not affected by the heat treatment.

§ 4. Discussion

As was stated in the previous section, the specimens used for the measurement are very porous. Then the effect of the porosity or the intergranular barrier on the conductivity must be considered first in discussion.

According to Henish[10], when the specimen contains the intergrain boundaries, the observed activation energy obtained from a $\log \rho$ vs. $1/T$ curve is not real one of this substance. He showed that the average activation energy obtained between temperature T_1 and T_2 can be expressed by

$$E_{0b}=E+2\bar{\phi}+S^2/2kT_1+S^2/2kT_2\,, \qquad (1)$$

where E is the true activation energy of the substance and $\bar{\phi}$ and S are the mean of the height of the intergranular barriers and the standard deviation from it respectively. He showed further that a standard deviation of as much as 10 per cent in the value of ϕ would not normally result in any detectable departure from the exponential form of the temperature dependence so long as the temperature range is not so wide.

His theory seems to be applicable to our case. We can see this by comparing the activation energy obtained from the measurement of the conductivity with that obtained from the Seebeck voltage.

For example, for the specimen No. 2, the carriers are expected to be only the holes. So the Seebeck voltage Q can be expressed by the following equation

$$QT=E_f=E/2\,, \qquad (2)$$

where E_f means the Fermi level measured from the filled valence band. The kinetic energy term in the Seebeck voltage was neglected following Morin's suggestion.[11] Then, the activation energy obtained from the Seebeck voltage turns to be the order of 0.12 ev at room temperature which is fairly smaller than the value 0.42 ev obtained from the conductivity. This difference must be attributed to the intergranular barriers as the equation shows.

Though we can not, thus, obtain the true activation energy from the experimental results, it may be concluded from Fig. 3. that the true activation energy also does not change greatly with the composition in this solid solution.

Next we consider the result of the Seebeck voltage. The Seebeck voltage Q of the specimen is expressed as following when two types of the carriers are contained in it.

$$QT=(Q_+\mu_+n_++Q_-\mu_-n_-)T/n_+\mu_++n_-\mu_-\,, \qquad (3)$$

where Q_+, μ_+ and n_+ mean the Seebeck voltage, the mobility and the concentration of holes and Q_-, μ_- and n_- are those of electrons.

When we assume that Ti ions are tetravalent in the solid solution, the concentration n_+ and n_- in the solid solution $x\mathrm{FeTiO_3}\cdot(1-x)\mathrm{Fe_2O_3}$ may be proportional to x and $2(1-x)$ respectively. Then, if we assume, as the first approximation, $Q_+=Q_-$ and $\mu_+=\mu_-$, the Seebeck voltage disappears at the concentration of $x=2/3$, and at this point its sign changes from that of n type to p type with increase of $FeTiO_3$ in the solid solution. Such a situation is nearly realized as we can see in Fig. 5.

On the other hand, when we assume that Ti ions in the solid solution are trivalent, their conduction must be attributed to the production of pairs (Ti^{3+}, Ti^{4+}) and (Fe^{2+}, Fe^{3+}) in the solid solution as was stated in the above paragraph. In this case, n_+ and n_- indicate the numbers of pairs (Ti^{3+}, Ti^{4+}) and (Fe^{2+}, Fe^{3+}) respectively, which do not depend on the concentration of ilmenite in the solid solution. Hence the change of the Seebeck voltage or the numbers of carriers with the composition can not be expected in this case. Furthermore, as we found from the experimental result that in the specimens for $x>0.73$ the conduction is p type, (Ti^{3+}, Ti^{4+}) conduction is expected to predominate over (Fe^{2+}, Fe^{3+}) conduction in these specimens, while in the specimens for $x<0.73$, the latter must be predominant. Accordingly, the activation energy of the specimen for $x>0.73$ must be different from that of the specimen for $x<0.73$, because (Ti^{3+}, Ti^{4+}) conduction is expected to have the different activation energy from that of (Fe^{2+}, Fe^{3+}) conduction.

Such situations are, however, not observed in the solid solution. Hence we can conclude, from these considerations, that nearly all of Ti ions in the solid solution are tetravalent and do not play any role on the magnetic coupling.

Of course, we can not decide completely from these experimental results whether a small amount of trivalent ions exist in the compound or not. It may, however, be said that the amount of trivalent Ti ions is, if existed, too small to affect the magnetic properties as well as the electrical properties.

The answer to the second problem is very evident. As we could not observe any anomalous change of the conductivity at the Curie point, the conduction electrons have little correlation with the magnetic spins.

In § 3, we found that the change of arrangement of ions does not affect the conductivity as well as the Seebeck voltage. This result suggests that Fe^{2+} and Fe^{3+} ions in the hexagonal layer are distributed at random even in the ordered specimen. Because if Fe^{3+} and Fe^{3+} ions are arranged in some ordered pattern, the electron transfer from Fe^{2+} to a neighbouring Fe^{3+} must need higher activation energy than in the case when they are distributed randomly. The simple consideration on the electrostatic energy of the several states of ion arrangements also supports this situation as was stated in I.

If (Ti^{3+}, Ti^{4+}) conduction plays important role in these compounds, it is expected that the ferromagnetic specimen in which Ti ions arrange in the ordered pattern must have higher resistance than the antiferromagnetic one. Hence, the result on the effect of the heat treatment also supports the conclusion which we have made above.

In view of the grain structure of these ceramic specimens, there seems to be nonsense in computing the mobility of the carriers from the experimental results apart from the difficulty that this is a case of mixed electron and hole conductions. Hence, the problem relating to the d-electron conduction in general was not treated in this paper.

Acknowledgement

The author wishes to express his hearty thanks to Prof. Shozo Sawada for his kind encouragement. His thanks are also due to Dr. Akimoto for his X-ray analysis and kind criticism, to Dr. Katsura for his chemical analysis and to Drs. Iida, Kurosawa and Kondho for their discussions.

References

1) F. J. Morin: Phys. Rev. **83** (1951) 1005.
2) J. Volger: Physica **20** (1954) 49.
3) J. H. de Boer and E. J. W. Verwey: Proc. Phys. Soc. Lond. **49** extra part (1937) 59.
4) E. J. W. Verwey: Semiconducting materials (1951) 151.
5) Y. Ishikawa and S. Akimoto: Journ. Phys. Soc. Japan **12** (1957) 1083.
6) J. H. Van Santen and G. H. Jonker: Physica **16** (1950) 599.
7) Y. Ishikawa and S. Akimoto: Journ. Phys. Soc. Japan **12** (1957) 834.
8) Y. Ishikawa and S. Sawada: Journ. Phys. Soc. Japan **11** (1951) 469.
9) Y. Ishikawa: Journ. Phys. Soc. Japan to be published.
10) H. K. Henish: Phil. Mag. **42** (1951) 734.
11) F. J. Morin: Phys. Rev. **93** (1954) 1195.

JOURNAL OF THE PHYSICAL SOCIETY OF JAPAN Vol. 13, No. 1, JANUARY, 1958

Absorption Coefficients of Fine Structures of X-ray Absorption Spectra at Various Absorber Thickness

By Kenjiro TSUSTUMI,* Masayoshi OBASHI,** and Masao SAWADA*

* *Department of Physics, Faculty of Science, Osaka University*
** *North College, Osaka University*

(Received June 15, 1957)

By using the North American Philips Diffraction Unit and Wide Range Goniometer modified to a tube spectrometer described by Coster and De Lang, the fine structures of X-ray K absorption spectra of copper in metallic copper, $CuCl_2 \cdot 2H_2O$, $CuSO_4 \cdot 5H_2O$ and cobalt in $CoCl_2 \cdot 6H_2O$ at various thickness were measured. The structures near the absorption edges are affected by the absorber thickness. The mass absorption coefficients of maximum absorption jumps become large with decreasing absorber thickness, and the small maximum and ninimum near the absorption edges also become indistinct with increasing absorber thickness. The wavelengths of these structures are slightly affected. This is due to the finite resolving power of the spectrometer and the tail of the spectral window as mentioned by Parratt. In the high energy regions from the absorption edges the absorption coefficients are not affected by the absorber thickness.

§ 1. Introduction

On the short wavelength side of the X-ray absorption edges, typical for a certain element, the absorption coefficient does not show a monotonic variation but fluctuates over a distance of several hundred volts from the main edge in the case of crystalline solids or polyatomic molecules in which the absorption element forms a constituent. This phenomenon, the so-called "fine structures of X-ray absorption edges", finds its explanation[1] in the scattering of a K photoelectron in the crystalline solid or in the polyatomic molecule that contains the absorbing atom. To date many investigations of these fine structures have been carried out but measurements have been confined almost exclusively to wavelengths of the fine structures. Moreover, there is only a few investigations[2] on the relation of the absorption coefficients of fine structures with the absorber thickness.

This is due to the fact that it is very difficult to measure the non-absorbed intensities at least when the photographic recording is being used in such a simple way as has mostly been done. Sandström[3] remarked at the Madison Conference on the applications of X-ray spectroscopy to solid state problems in October 1950 that under certain conditions nonreal details could be introduced into the absorption spectra, and in many ways a spectrum giving the variations with wavelength of the transmitted intensity was deficient as the details would depend on the thickness of the absorber. Recently Parratt[4] and others investigated the thickness effect in absorption spectra near absorption edges of chlorine in KCl, and found that the details of an observed absorption spectrum depended upon the thickness of the absorber, and they concluded that this was due to the role of the effective spectral window of the spectrometer.

Authors also found the same effect when we investigated the fine structures of X-ray K absorption spectra of various compounds[5] by using the North American Philips Diffraction Unit and Wide Range Goniometer modified to a tube spectrometer with the Geiger-Müller counter. Thus we investigate the relation of the absorption coefficients of the fine structures of X-ray K absorption spectra with the thickness of the absorber. As absorbers we choose metallic copper and $CuCl_2 \cdot 2H_2O$[6] and $CuSO_4 \cdot 5H_2O$[7] which are considered as a metallic and homopolar and ionic compounds respectively, and $CoCl_2 \cdot 6H_2O$ which contains the different absorbing element.

§ 2. Experiments

Preparation of Specimens. The copper foil was prepared by the electrolysis. The alkali electrolyte containing CuCN, NaCN, and

Na_2CO_3. The P_H of this electrolyte was 11.5. The electrolytic current densities were 0.1–0.2 amp./dm². When the stainless steel cathode was used, the electrodepositions were easily stripped from the cathode. Several foils were prepared and we chose the foil which had the proper thickness and had no hole. The thickness was determinded by weights and areas of the foils. The weight of foil which was used was 1.47 mg/cm². As $CuCl_2 \cdot 2H_2O$, $CuSO_4 \cdot 5H_2O$ and $CoCl_2 \cdot 6H_2O$ were very well solved into water, we solved these compounds into water and infiltrated in the filter papers which had been measured their weights and areas. Then after these papers were dried in the vacuum desiccator, the total weights and areas were measured. Thus, the weights of compounds were determinded. The weights of $CuCl_2 \cdot 2H_2O$, $CuSO_4 \cdot 5H_2O$ and $CoCl_2 \cdot 6H_2O$ were 2.30, 3.55 and 3.03 mg/cm² respectively.

Absorption Spectra. X-ray Diffraction Unit and Wide Range Goniometer of North American Philips Company Inc. (Norelco)[8] were used. This unit is mechanically so arranged as to maintain a 1:2 ratio of the rotational speed between the crystal holder of the centre of the spectrometer and the Geiger-Müller counter as required for Bragg reflections. We used this unit as a tube spectrometer described by Coster and De Lang.[9] The techniques of our modified method have been described in previous publications.[10] As we can directly measure the primary X-ray intensity and the transmission X-ray intensity in this case, this method is easily changed so as to enable the measurement of the absorption coefficient. The divergency of the slit system of this instrument was about 0.0004 radians. The first order reflections of the LiF was used. The X-ray tube with a Mo target was loaded with 10–20 mA. at 14 kV. for the copper edges and 12 kV. for the cobalt edge which were too low to excite the second order. The fine structures of absorption spectra of copper in Cu, $CuCl_2 \cdot 2H_2O$ and $CuSO_4 \cdot 5H_2O$, and of cobalt in $CoCl_2 \cdot 6H_2O$ at various thickness were recorded automatically on the strip-charts. Considering the time constants of the ratemeter and the recorder, the scanning speed of the Geiger-Müller tube 1/8 °/min was used in all cases. Several runs were recorded at various time constants 2–8 sec. Then the intensities of the large maximum and minimum points were also measured manually by fixed counting method.[8] As the absorbers we used the sheet of onefold to fourfold or fivefold of above mentioned specimens. The primary intensities were measured through only the same filter paper in the cases of compounds.

§ 3. Results and Discussions

Photos 1, 2, 3 and 4 are the reproductions of the curves of the fine structures of the X-ray K absorption spectra of copper in metallic copper, $CuCl_2 \cdot 2H_2O$ and $CuSO_4 \cdot 5H_2O$, and cobalt in $CoCl_2 \cdot 6H_2O$ respectively. Tables I, II, III and IV show the wavelength values of

Table I. Wavelength values of the fine structures of the X-ray K absorption spectrum of copper in metallic copper at various absorber thickness.

Amount	1.47 mg/cm²	1.47×2 mg/cm²	1.47×3 mg/cm²	1.47×4 mg/cm²	1.47×5 mg/cm²
	x.u.	x.u.	x.u.	x.u.	x.u.
K_1	1378.3	1378.3	1378.3	1378.3	1378.3
Q	1378.0	1377.9	1377.9	1377.8	1378.0
K_2	1377.0	—	—	—	—
A	1375.9	1375.9	—	—	—
α	1375.1	1375.4	—	—	—
B	1374.8	1374.9	1374.2	1374.9	1374.9
β	1373.7	1373.5	1373.4	1373.4	1373.4
C	1371.3	1371.3	1371.2	1371.1	1371.1
γ	1368.8	1368.8	1368.9	1368.9	1368.8
D	1368.2	1368.0	1368.3	1368.4	1368.2
δ	1367.3	1367.0	1367.3	1367.3	1367.3
E	1365.3	1364.6	1364.5	1364.3	1364.7
ε	1364.0	1363.4	1363.4	1363.4	1363.6
F	1363.4	1363.1	1363.1	1362.7	1363.1
ζ	1360.7	1360.7	1360.6	1360.6	1360.7
G	1359.1	1359.4	1359.4	1359.4	1359.4
η	1357.8	1357.6	1357.7	1357.8	1357.7
H	1356.0	1356.0	1356.0	1356.0	1355.9
θ	1355.4	1355.0	1355.5	1355.4	1355.2
I	1353.9	1354.1	1353.9	1354.0	1354.1
ι	1350.8	1351.1	1350.8	1350.8	1351.0
J	1349.5	1349.1	1349.1	1349.1	1349.2
κ	1348.1	1347.8	1348.1	1348.2	1348.3
K	1347.1	1347.1	1347.0	1346.9	1346.9
λ	1345.4	1345.6	1345.4	1345.4	1345.3
L	1343.5	1343.5	1343.4	1343.4	1343.7
μ	1338.7	1338.6	1338.5	1338.5	1338.5
M	1337.4	1337.5	1337.3	1337.4	1337.4
ν	1333.3	1333.2	1333.4	1333.4	1333.4
N	1331.1	1330.9	1331.0	1331.0	1331.0

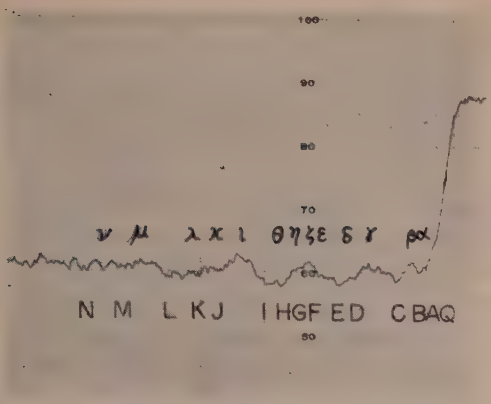

(a)

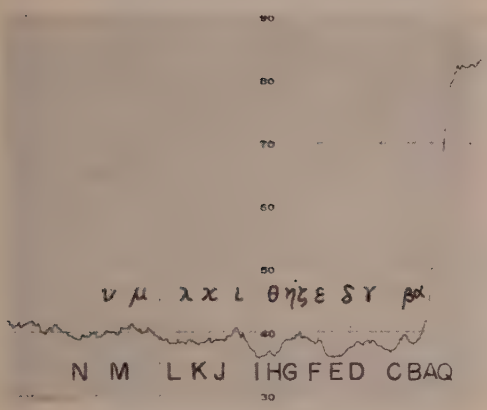

(b)

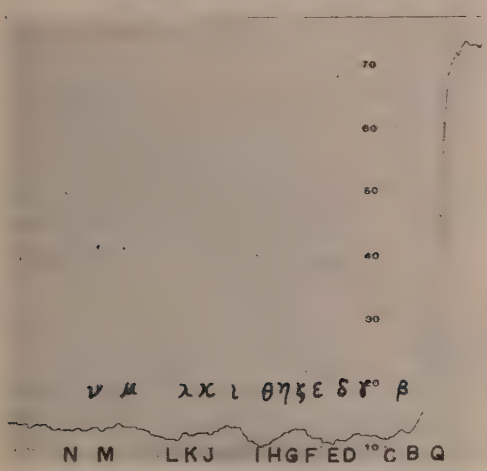

(c)

Photo. 1. X-ray K absorption spectra of copper in metallic copper.
a) at the onefold sheet
b) at the twofold sheet
c) at the fivefold sheet
(time constant of the rate-meter, 8 sec.)

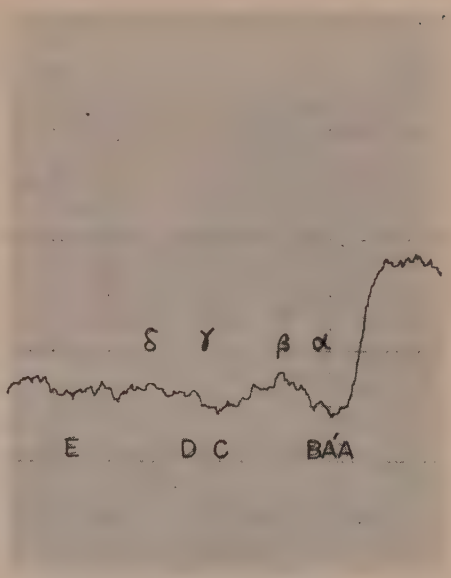

(a)

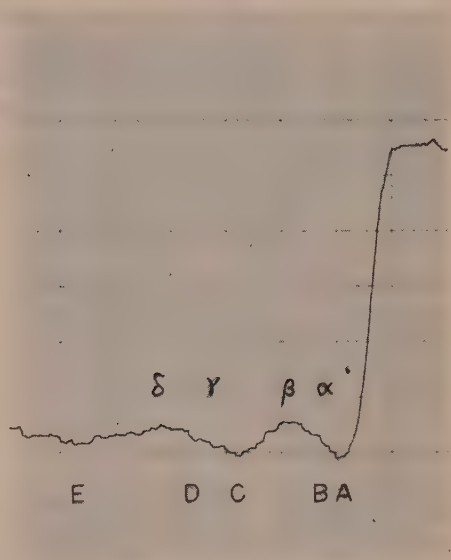

(b)

Photo. 2. X-ray K absorption spectra of copper in $CuCl_2 \cdot 2H_2O$.
a) at the onefold sheet
b) at the fourfold sheet
(time constant of the rate-meter, 8 sec.)

the fine structures of these absorption spectra at various absorber thickness, and Tables V, VI, VII and VIII show the mass absorption coefficients of these structures. Figs. 1, 2, 3 and 4 show the curves of the mass absorption coefficients at various thickness *vis* wave-lengths. It will be seen from these results that the fine structures only near the absorption

(a)

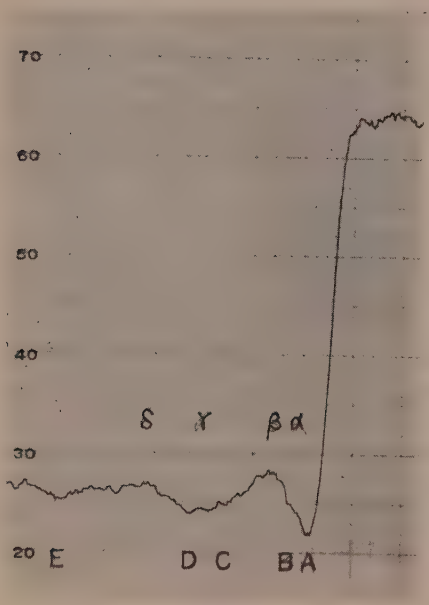

(b)

Photo. 3. X-ray K absorption spectra of copper in $CuSO_4 \cdot 5H_2O$.
a) at the onefold sheet
b) at the fourfold sheet
(time constant of the rate-meter, 8 sec.)

edges are affected by absorber thickness. The affected region is about 40 eV from the main edges. The maximum absorption jump A, small minimum α and small maximum B are especially affected in all cases. The absorption coefficients of maximum absorption jump

(a)

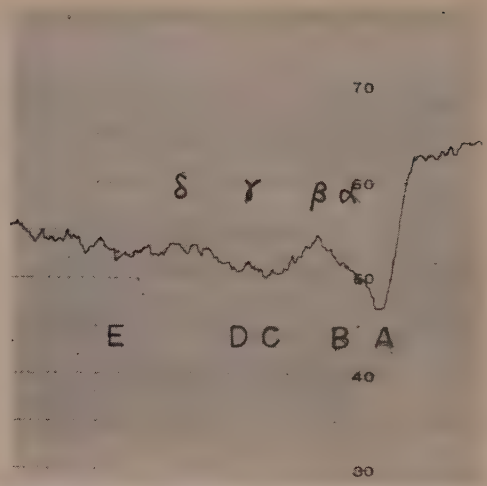

(b)

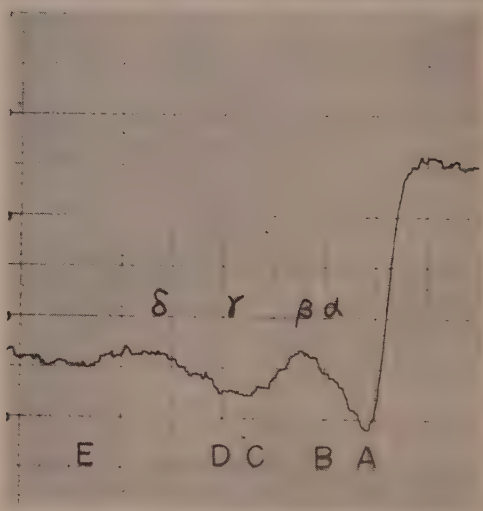

(c)

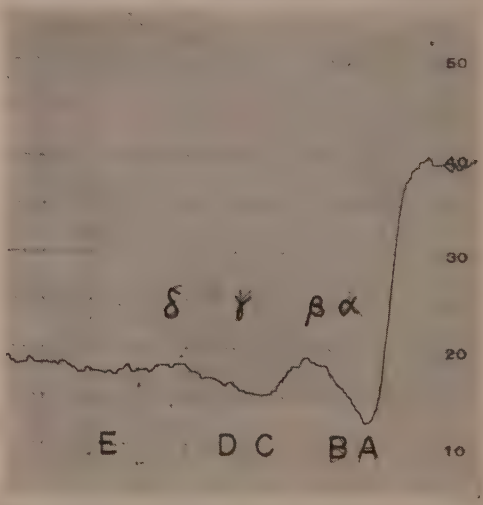

Photo. 4. X-ray K absorption spectra of cobalt in $CoCl_2 \cdot 6H_2O$.
a) at the onefold sheet
b) at the threefold sheet
c) at the fourfold sheet
(time constant of the rate-meter, 8 sec.)

Table II. Wavelength values of the fine structures of the X-ray K absorption spectrum of copper in $CuCl_2$–$2H_2O$ at various absorber thickness.

Amount	2.30 mg/cm²	2.30×2 mg/cm²	2.30×3 mg/cm²	2.30×4 mg/cm²
	x.u.	x.u.	x.u.	x.u.
K	1377.1	1377.1	1377.1	1377.1
A	1375.3	1375.0	1375.0	1375.0
A′	1374.4	—	—	—
α	1373.4	1374.0	1374.4	1374.4
B	1372.8	1373.1	1372.9	1372.9
β	1370.9	1370.9	1370.9	1370.9
C	1367.0	1367.0	1367.0	1366.9
γ	1364.8	1364.8	1364.8	1364.8
D	1363.2	1363.4	1363.4	1363.4
δ	1360.8	1360.8	1360.8	1360.8
E	1353.8	1353.8	1353.8	1353.9

Table III. Wavelength values of the fine structures of the X-ray K absorption spectrum of copper in $CuSO_4 \cdot 5H_2O$ at various absorber thickness.

Amount	3.55 mg/cm²	3.55×2 mg/cm²	3.55×3 mg/cm²	3.55×4 mg/cm²
	x.u.	x.u.	x.u.	x.u.
K	1376.9	1376.9	1376.9	1376.9
A	1374.9	1374.8	1374.8	1374.8
α	1373.4	1373.5	1373.9	1373.4
B	1372.5	1372.5	1373.0	1372.5
β	1371.3	1371.4	1371.3	1371.3
C	1368.3	1368.5	1368.3	1368.3
γ	1367.2	1367.0	1367.0	1367.0
D	1365.3	1365.1	1365.5	1365.1
δ	1360.8	1360.8	1360.8	1360.8
E	1354.0	1354.0	1353.7	1354.0

Table IV. Wavelength values of the fine structures of the X-ray K absorption spectrum of cobalt in $CoCl_2 \cdot 6H_2O$ at various absorber thickness.

Amount	3.03 mg/cm²	3.03×2 mg/cm²	3.03×3 mg/cm²	3.03×4 mg/cm²
	x.u.	x.u.	x.u.	x.u.
K	1604.4	1604.4	1604.2	1604.4
A	1602.5	1602.3	1602.3	1602.0
α	1599.9	1599.7	1599.3	1600.2
B	1599.3	1599.1	1598.6	1599.4
β	1596.5	1596.7	1596.7	1596.8
C	1593.4	1593.6	1593.2	1593.5
γ	1590.5	1590.5	1589.4	1589.8
D	1589.5	1589.7	1589.5	1589.5
δ	1585.6	1585.6	1585.5	1585.6
E	1580.2	1580.4	1580.0	1580.0

A become larger with decreasing absorber thickness, and the small minimum α and small maximum B become indistict with increasing absorber thickness. In general in the regions of 40 eV from the main edges the mass absorption coefficients of maxima become large with decreasing absorber thickness. In the case of metallic copper the initial absorption Q is also greatly affected by the absorber thickness, and this initial absorption become indistinct with increasing absorber thickness, so that the percentage of the maximum absorption jump A accounted for by the initial absorption Q is only true when the absorber thickness becomes infinitesimally thin.

The wavelength values of these structures in this region are slightly affected. These thickness effects are more apparent when the main absorption jump are large. In the high energy region from the main edge the fine structures are not affected by the absorber thickness. As the suitable thickness of the absorber for the absorption spectra we must choose the thinner absorber when the absorp-

Table V. Mass absorption coefficients of the fine structures of the X-ray K absorption spetrum of copper in metallic copper at various absorber thickness.

Amount	1.47 mg/cm²	1.47×2 mg/cm²	1.47×3 mg/cm²	1.47×4 mg/cm²	1.47×5 mg/cm²
at 1382 x.u.	cm²/g 37.6	cm²/g 37.6	cm²/g 36.6	cm²/g 37.2	cm²/g 37.0
Q	166	149	114	118	99
A	295	282	—	—	—
α	284	274	—	—	—
B	306	300	296	294	293
β	273	272	272	274	275
C	310	309	308	305	306
γ	284	283	286	286	288
D	296	296	296	294	294
E	321	320	316	317	318
F	306	305	306	305	303
ζ	268	270	267	272	271
η	284	284	286	286	285
I	313	314	313	313	313
ι	265	266	263	265	264
J	291	291	290	294	290
L	299	300	296	300	299
μ	265	266	263	265	264
ν	277	274	272	274	275
N	288	287	283	286	287

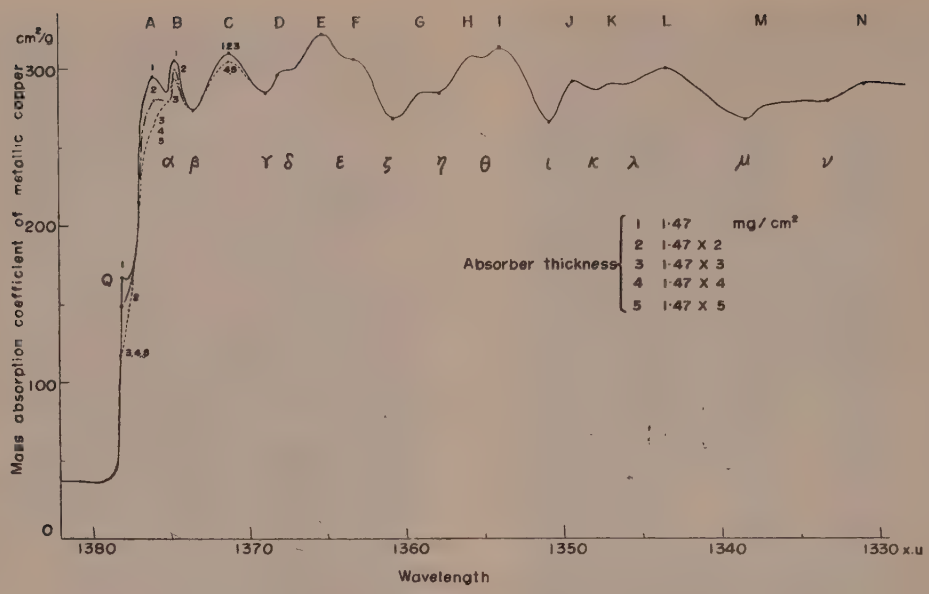

Fig. 1. Mass absorption coefficients of metallic copper *vis* wavelengths.

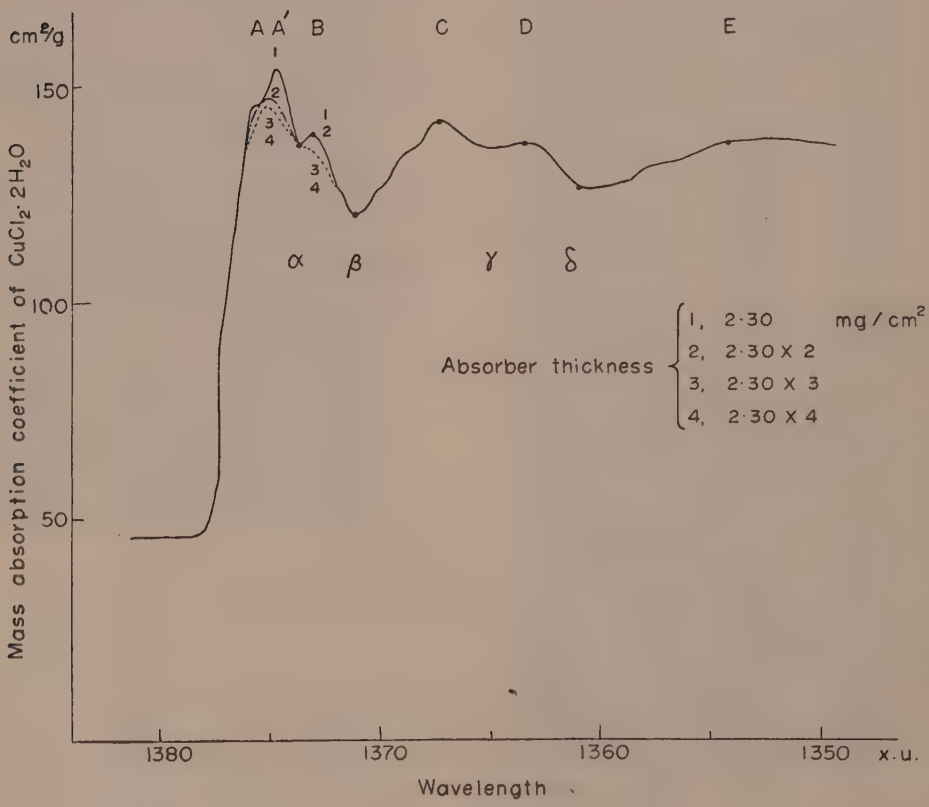

Fig. 2. Mass absorption coefficients of $CuCl_2 \cdot 2H_2O$ *vis* wavelengths.

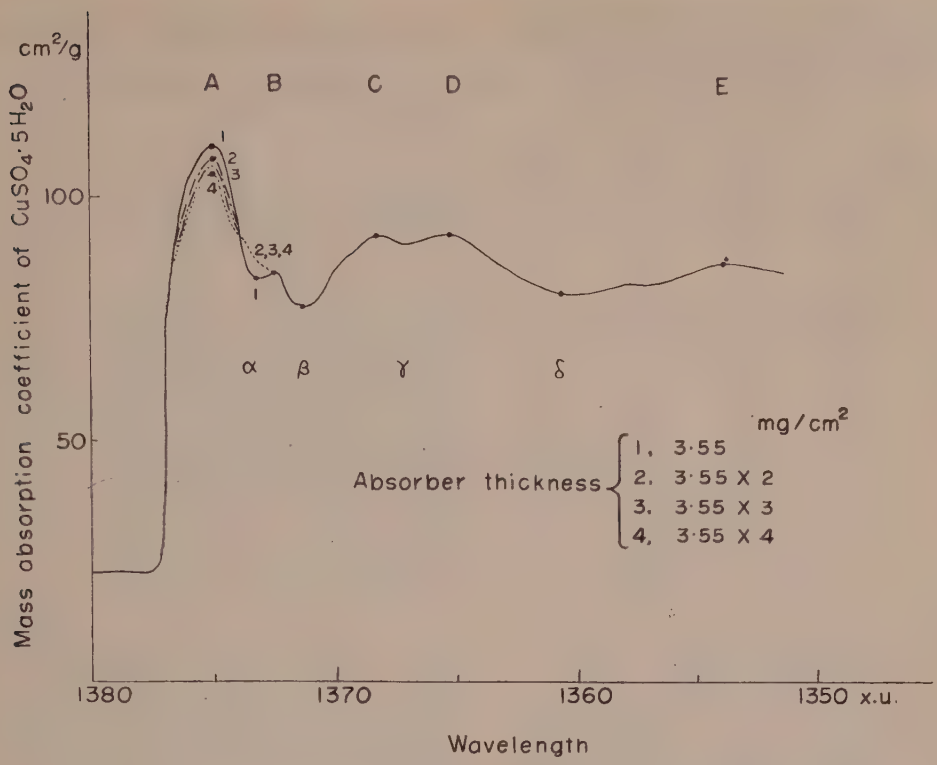

Fig. 3. Mass absorption coefficients of $CuSO_4 \cdot 5H_2O$ *vis* wavelengths.

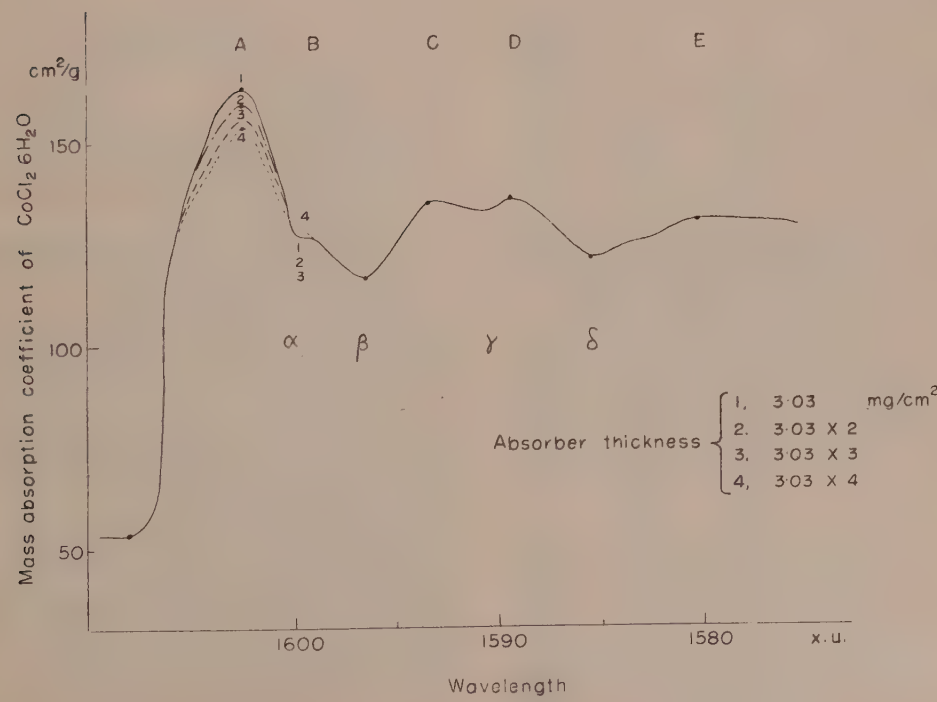

Fig. 4. Mass absorption coefficients of $CoCl_2 \cdot 6H_2O$ *vis* wavelengths.

Table VI. Mass absorption coefficients of the fine structures of the X-ray K absorption spectrum of copper in $CuCl_2 \cdot 2H_2O$ at various absorber thickness.

Amount	2.30 mg/cm²	2.30×2 mg/cm²	2.30×3 mg/cm²	2.30×4 cm/cm²
at 1382 x.u.	cm²/g 46	cm²/g 46	cm²/g 46	cm²/g 46
A	146	148	146	148
A′	154	—	—	—
α	136	136	135	135
B	139	139	—	—
β	120	121	121	121
C	142	141	141	141
D	137	136	137	137
δ	126	126	127	127
E	137	136	137	137

Table VII. Mass absorption coefficients of the fine structures of the X-ray K absorption spectrum of copper in $CuSO_4 \cdot 5H_2O$ at various absorber thickness.

Amount	3.55 mg/cm²	3.55×2 mg/cm²	3.55×3 mg/cm²	3.55×4 mg/cm²
at 1382 x.u.	cm²/g 22.5	cm²/g 22.4	cm²/g 22.8	cm²/g 22.5
A	111	108	107	106
α	84	—	—	—
B	85	85	85	85
β	78	78	78	79
C	93	93	93	93
D	93	93	93	93
δ	81	81	81	82
E	87	87	87	87

Table VIII. Mass absorption coefficients of the fine structures of the X-ray K absorption spectrum of cobalt in $CoCl_2 \cdot 6H_2O$ at various absorber thickness.

Amount	3.03 mg/cm²	3.03×2 mg/cm²	3.03×3 mg/cm²	3.03×4 mg/cm²
at 1610 x.u.	cm²/g 54.0	cm²/g 54.1	cm²/g 54.1	cm²/g 54.0
A	163	159	155	154
α	124	124	124	126
β	116	116	116	116
C	135	135	135	135
D	136	136	136	136
δ	121	122	122	122
E	130	129	130	129

tion spectra near the absorption edge are investigated and the relatively thicker absorber when the extended fine structures are investigated. It is evident that the thickness effect is not due to the bonding type of the substances in which absorbing element forms a constitute or the sort of the absorbing element. Perhaps it is true that the thickness effect is due to the spectral window of the spectrometer as pointed out by Parratt.[44] In our spectrometer the resolving power is not so high due to the slit divergency and the penetration of the X-rays in the reflecting crystal, and moreover the X-ray focal spot used as a slit is not strictly a rectangular shape and it has a very weak tail due to the scattering of bombarding electrons and fluorescent excitations. In the case of the single crystal spectrometer there is no difinition of the spectral window shape but in our tube spectrometer it is similar to that of the double spectrometer. The thickness effect is due to the finite resolving power of the spectrometer and the enormous asymmetry of the shape of absorption edge. This quite agrees with the conclusion mentioned by Parratt[4] and we will support their conclusion in our present experimental results.

References

1) R. de Kronig: Zs. f. Phys. **70** (1931) 317, **75** (1932) 191.
2) D. Coster and J. Veldkamp: Zs. f. Phys. **70** (1931) 306, Zs. f. Phys. **74** (1932) 191.
D. G. Doran and S. T. Stephenson: Phys. Rev. **105** (1957) 1156.
3) A. Sandström: A Conference on the Applications of X-ray Spectroscopy to Solid States Problems. 23-25 Oct., 1950.
4) L. G. Parratt, C. F. Hempstead and E. L. Jossem: Phys. Rev. **105** (1957) 1228.
5) K. Tsutsumi, A. Hayase and M. Sawada: Jour. Phys. Soc. Japan **12** (1957) 793.
6) D. Harker: Zs. f. Krist. **A93** (1936) 136.
7) C. A. Beevers and H. Lipson: Proc. Roy. Soc. **A146** (1934) 570.
8) Instruction Book for Installation and Operation of Norelco: North American Philips Comp. Inc. New York.
9) D. Coster and H. De Lang: Physica **13** (1947) 379.
10) K. Tsutsumi, A. Hayase and M. Sawada: Jour. Phys. Soc. Japan **12** (1957) 793.

JOURNAL OF THE PHYSICAL SOCIETY OF JAPAN Vol. 13, No. 1, JANUARY, 1958

Studies on the Radial Distribution Analysis in Diffraction Methods

II. Effect of Non-nuclear Scattering and Analysis of the Radial Distribution Curve* **

By Kinya KATADA

The Institute of Polytechnics, Osaka City University, Osaka

(Received August 20, 1957)

An improved procedure is described for determining the molecular structures from electron diffraction data of gases by the radial distribution method. By this procedure the structural data can be straightforwardly obtained from the radial distribution function derived from the observed intensity data without any assumption on the structure and disregard of the effect of non-nuclear scattering.

The radial distribution function derived here is the sum of the nuclear distribution function and the additional terms which have the same forms as the former. A method of the analysis of the radial distribution curve is developed by use of the moments of the distribution function.

In addition, Karle and Karle's procedure is discussed and errors involved there are estimated.

§ 1. Introduction

In the studies on the structures of gaseous molecules by electron diffraction the radial distribution method, which gives us directly much information on the structure, became more powerful in consequence of the advances of experimental techniques and procedures of analysis. The ingenious procedure proposed by Debye[2] in 1941 and realized by Karle and Karle[3] in 1949 made clear the structures of various molecules. It was shown that the sine transformation of

structure sensitive intensity=(observed total intensity/estimated background intensity)−1 (1)

gave the radial *nuclear* distribution approximately. In their procedure, of course, it is necessary to assume a structure model of the molecule in question, from which the intensity in the range of small scattering angle is calculated since the observed intensity data can not be used in that region. The validity of the approximation involved in their procedure, that is the disregard of the differences among the unitary scattering factors of constituent atoms in the range of moderate and large angles, has not been examined closely. It is, however, clear that a more rigorous treatment is now necessary for discussing details of the structure from the consideration of resent experimental accuracy. Recently Bartell, Brockway and Schwendeman[4] developed a refined procedure for analysis. They converted succesively the experimental intensity to an intensity without non-nuclear scattering, which was then used in computing the radial nuclear distribution function.

In this paper the author will present another improved procedure, by which the structural data can be straightforwardly obtained from the sine transformation of the experimental intensity function without any assumption on the structure and disregard of the effect of non-nuclear scattering. In § 2 a radial distribution function which is convenient for the practical use is derived by considering the modifying effect of the atomic scattering factor. In § 3 a method of the analysis of the radial distribution curve is described.

In addition, errors involved in the Karle and Karle's procedure are discussed in § 4.

§ 2. A Radial Distribution Function

The radial distribution function*** $rD(r)$ is

* This paper was read at the Annual Meeting of the Physical Society of Japan, Tokyo, October 1955.

** The first paper in the series was presented by T. Ino in this Journal. See reference 1.

*** In this paper, $rD(r)$ is called the "radial distribution function" for convenience and is mainly treated rather than $r^2D(r)$ or $D(r)$, because $r(D)r$ possesses more advantageous mathematical properties than $r^2D(r)$ or $D(r)$. See reference 5 or 6.

given by Fourier sine transformation of the structure sensitive intensity function $I(s)$; that is

$$\left.\begin{aligned} sI(s)&=\int_0^\infty 4\pi r D(r)\cdot\sin sr\,dr \\ \text{and}\quad 4\pi r D(r)&=(2/\pi)\int_0^\infty sI(s)\cdot\sin sr\,ds\,, \end{aligned}\right\} \quad (2)$$

where $s=(4\pi/\lambda)\cdot\sin(\theta/2)$, λ=wave-length of electrons, θ=scattering angle and r=distance occurring in the aggregation of atoms. $rD(r)$ may directly give us information on the structure, whose physical meanings are different according to the type of $I(s)$ used.

In this paper the same type of the structure sensitive intensity function as shown in Eq. (1) is adopted. If all atoms in the molecule are considered to be undergoing simple harmonic vibrations, the structure sensitive intensity function $I^\phi(s)$, which is directly derived from the observed data, may have the form[7]:

$$\begin{aligned} sI^\phi(s)&=\sum_{(ij)} si^\phi_{(ij)}(s) \\ &=\sum_{(ij)}\frac{2Z_iZ_j\phi_i(s)\phi_j(s)\exp(-l_{ij}^2s^2)\sin sr_{ij}}{r_{ij}\sum_i Z_i^2\phi_i^2(s)}\,, \end{aligned} \quad (3)$$

where $\phi_i(s)=(Z_i-F_i(s))/Z_i$ = unitary atomic scattering factor of i-th atom for electrons, Z_i=atomic number of i-th atom, $F_i(s)$=atomic scattering factor of i-th atom for X-rays, r_{ij} =equilibrium internuclear distance between i-th and j-th atoms, $2l_{ij}^2$=average of the square of the deviation of distance from its equilibrium value r_{ij}, and $\sum_{(ij)}$=summation taken over all atomic pairs in the molecule. In Eq. (3), the term of the inelastic scattering is omitted, since this part may not be essential to the discussion.* Let us define another structure sensitive intensity function $I^z(s)$ as follows:

$$\begin{aligned} sI^z(s)&=\sum_{(ij)} si^z_{(ij)}(s) \\ &=\sum_{(ij)}\frac{2Z_iZ_j\exp(-l_{ij}^2s^2)\sin sr_{ij}}{r_{ij}\sum_i Z_i^2}\,. \end{aligned} \quad (4)$$

This function may present the intensity without non-nuclear scattering. These two intensity functions $I^\phi(s)$ and $I^z(s)$ respectively produce two kinds of the radial distribution functions:

$$\begin{aligned} rD^\phi(r)&=\sum_{(ij)} rd^\phi_{(ij)}(r) \\ &=(1/2\pi^2)\sum_{(ij)}\int_0^\infty si^\phi_{(ij)}(s)\cdot\sin sr\,ds \end{aligned} \quad (5)$$

and

$$\begin{aligned} rD^z(r)&=\sum_{(ij)} rd(r)^z_{(ij)} \\ &=(1/2\pi^2)\sum_{(ij)}\int_0^\infty si^z_{(ij)}(s)\cdot\sin sr\,ds\,. \end{aligned} \quad (6)$$

It is not $rD^\phi(r)$ but $rD^z(r)$ that gives us directly the "radial nuclear distribution".

When the radial distribution function is computed by the transformation of experimental intensity function, the artificial temperature factor, $\exp(-a^2s^2)$, is often used in order to diminish the effect of terminating the intensity function. Thus, $\boldsymbol{rD}^\phi(r)$ is defined as

$$\begin{aligned} &\boldsymbol{rD}^\phi(r) \\ &\quad=(1/2\pi^2)\int_0^\infty \exp(-a^2s^2)\cdot sI^\phi(s)\sin sr\,ds\,. \end{aligned} \quad (7)$$

The following expression of $\boldsymbol{rD}^\phi(r)$ may be suitable for further calculations:

$$\begin{aligned} &\boldsymbol{rD}^\phi(r)=\sum_{(ij)}\boldsymbol{rd}^\phi_{(ij)}(r)=(1/2\pi^2) \\ &\quad\sum_{(ij)}\int_0^\infty\{m_0(s)+m_{ij}(s)\}\cdot si^z_{(ij)}(s)\sin sr\,ds\,, \end{aligned} \quad (8)$$

where

$$\left.\begin{aligned} m_0(s)&=\exp(-a^2s^2) \\ \text{and}\quad m_{ij}(s)&=\left[\frac{i^\phi_{(ij)}(s)}{i^z_{(ij)}(s)}-1\right]\cdot\exp(-a^2s^2) \\ &=\left[\frac{\phi_i(s)\phi_j(s)\sum_i Z_i^2}{\sum_i Z_i^2\phi_i^2(s)}-1\right]\cdot\exp(-a^2s^2). \end{aligned}\right\} \quad (9)$$

$m_0(s)$ and $m_{ij}(s)$ are called the "modification functions"[6]. The former does not depend on the kind of atomic pair**, but the latter is characteristic of atoms i and j and modifies the peak shape of the radial nuclear distribution curve in the different manner for each atomic pair.

As $m_{ij}(s)$ does not depend on the configuration of atoms, it may be possible to express it approximately in terms of an appropriate function in advance. For example, if $m_{ij}(s)$

* See the footnote * in p. 53.

** The modifying effect of $m_0(s)$ on the radial distribution function has been already studied by several investigators. For example, see reference 3 or 5.

is approximated as follows:

$$m_{(ij)}s=\sum_{k=1} A_{ij,k}\exp(-a_{ij,k}^2 s^2)\,, \qquad (10)$$

as done by Bartell *et al.*,[4] then, it follows from Eqs. (8), (10) and (4) that

$$rD^{\phi}(r)=\sum_{(ij)} rd_{(ij)}^{\phi}(r)=(8\pi^{3/2}\sum_i Z_i^2)^{-1}$$
$$\sum_{(ij)}[(2Z_iZ_j/r_{ij})\cdot\sum_{k=0} A_{ij,k}(a_{ij,k}^2+l_{ij}^2)^{-1/2}\cdot\{\exp[-(r-r_{ij})^2/4(a_{ij,k}^2+l_{ij}^2)]$$
$$-\exp[-(r+r_{ij})^2/4(a_{ij,k}^2+l_{ij}^2)]\}]\,, \qquad (11)$$

where $A_{ij,0}\equiv 1$ and $a_{ij,0}^2\equiv a^2$ (the coefficient in the artificial temperature factor). The component $k=0$ is the radial nuclear distribution function $rD^z(r)$ modified by the artificial temperature factor and the sum of components $k\neq 0$ is the additional term arising from the consideration of non-nuclear scattering. The area $\sigma_{(ij)}^{\phi}$ under the peak of $r^2d_{(ij)}^{\phi}(r)$ for each atomic pair is given as

$$\sigma_{(ij)}^{\phi}=(4\pi\sum_i Z_i^2)^{-1}\cdot(2Z_iZ_j)\cdot\sum_{k=0} A_{ij,k}\,, \qquad (12)$$

being equal to $\sum_{k=0} A_{ij,k}$ times $\sigma_{(ij)}^{z}$, the area under the peak of $r^2d_{(ij)}^{z}(r)$.

An example is presented below for carbon tetrachloride. $m_{CCl}(s)$ and $m_{ClCl}(s)$ are obtained from values of the atomic scattering factors $F_C(s)$ and $F_{Cl}(s)$ tabulated by Viervoll and Ögrim[8] and $a^2=(0.070/\pi^2)$Å^2, as shown

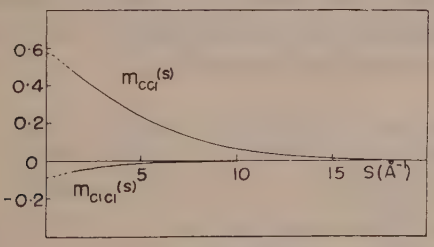

Fig. 1. Curves of the modification function $m_{ij}(s)$ for carbon tetrachloride.

in Fig. 1. By curve fittings the values of the coefficients in Eq. (10) are determined as follows* **:

$$\left.\begin{aligned} &A_{CCl,1}=0.30, \quad A_{ClCl,1}=-0.020,\\ &A_{CCl,2}=0.23, \quad A_{ClCl,2}=-0.015,\\ &A_{CCl,3}=0.14, \quad A_{ClCl,3}=-0.014,\\ &a_{CCl,1}^2=a_{ClCl,1}^2=(0.17/\pi^2)\text{Å}^2,\\ &a_{CCl,2}^2=a_{ClCl,2}^2=(0.42/\pi^2)\text{Å}^2,\\ &a_{CCl,3}^2=a_{ClCl,3}^2=(3.5/\pi^2)\text{Å}^2\,. \end{aligned}\right\} \qquad (13)$$

* The values of $A_{ij,k}$ and $a^2_{ij,k}$ vary slightly when the inelastic scattering is taken into account.

** It is the author's experience that $m_{ij}(s)$ can be satisfactorily expressed by two or, at most, three terms of Gaussian functions.

In Fig. 2 components of Eq. (11) are illustrated which are calculated by using $r_{CCl}=1.77$Å, $r_{ClCl}=2.88$Å (regular-tetrahedral structure), $l_{CCl}^2=l_{ClCl}^2=(0.030/\pi^2)$Å^2 and the values of $A_{ij,k}$ and $a_{ij,k}^2$ given above. It is shown that the contributions from the additional term

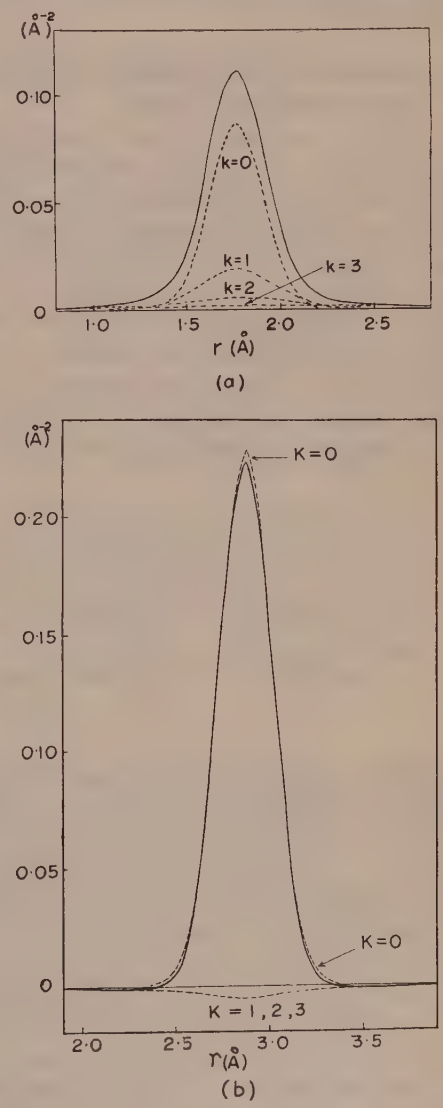

Fig. 2. $rd_{(ij)}^{\phi}(r)$ and their components (dushed line) for carbon tetrachloride: (a) $4\cdot rd_{(CCl)}^{\phi}(r)$ and (b) $6\cdot rd_{(ClCl)}^{\phi}(r)$.

(sum of the components $k=1$, 2 and 3) are considerably large for C-Cl pair but small and negative for Cl-Cl pair. These behaviours are characteristic of the constitution of the compound.

The radial distribution curve computed numerically from the experimental intensity data by Eq. (7) is expressed in terms of unknown parameters r_{ij}, l_{ij}^2 and Z_iZ_j by Eq. (11). Therefore, it is possible to determine these parameters by analysing the curve. The method of "trial and error" for the analysis usually used is applicable in this case, but the author will show another method in the next section.

§ 3. A Method of the Analysis of the Radial Distribution Curve

It is always necessary in the radial distribution method to analyse the obtained distribution curve. Some hunches of the radial distribution curve are composed of peaks for several distances, when the molecule possesses nearly equal equilibrium distances or the effective artificial temperature factor is used in order to diminish what is called the "diffraction effect". The direct method of resolution without any assumption on the structure is desirable. Investigators, however, decomposed the composite peaks with some introductory knowledge about the structure*. A procedure for the determination of unknown parameters r_{ij}, l_{ij}^2 *etc.*, or the decomposition of composite peaks into the components without any assumption on their approximate values is briefly described below.

The n-th "moment" of the radial distribution function $rD(r)$, defined by

$$\mu_n=\int_{-\infty}^{\infty} r^n\cdot rD(r)dr\,, \qquad (n=0,\ 1,\ 2,\cdots), \quad (14)$$

may be useful when the distribution function has the Gaussian form, because integral in Eq. (14) can be performed and an algebraic function is derived.

As $rD(r)$ is the odd function and the moments of even order vanish certainly, it is advantageous to omit the second term of $rD(r)$, the term $\exp[-(r+r_{ij})^2/4(a_{ij,k}^2+l_{ij}^2)]$. Then, for such a radial distribution function as shown in Eq. (11), moments are obtained as follows:

The moments of the lower order can be easily calculated by the usual numerical integration from the radial distribution function obtained experimentally. Thus, the unknown parameters may be determined by solving the above simultaneous equations.

$$\left.\begin{aligned}
\mu_0&=(4\pi\sum_i Z_i^2)^{-1}\sum_{(ij)}[(2Z_iZ_j\sum_{k=0}A_{ij,k})/r_{ij}]\,,\\
\mu_1&=(4\pi\sum_i Z_i^2)^{-1}\sum_{(ij)}[2Z_iZ_j\sum_{k=0}A_{ij,k}]\,,\\
\mu_2&=(4\pi\sum_i Z_i^2)^{-1}\sum_{(ij)}[(2Z_iZ_j\sum_{k=0}A_{ij,k})r_{ij}+4Z_iZ_j\sum_{k=0}A_{ij,k}(a_{ij,k}^2+l_{ij}^2)/r_{ij}]\,,\\
\mu_3&=(4\pi\sum_i Z_i^2)^{-1}\sum_{(ij)}[(2Z_iZ_j\sum_{k=0}A_{ij,k})r_{ij}^2+12Z_iZ_j\sum_{k=0}A_{ij,k}(a_{ij,k}^2+l_{ij}^2)]\,,\\
&\cdots\cdots\cdots\cdots\cdots\cdots
\end{aligned}\right\} \quad (15)$$

In order to examine the usefulness of this method an arbitrary model is set up as follows: $r_{AB}=1.50$Å, $l_{AB}^2=0.0010$Å^2, $Z_AZ_B=150$, $r_{CD}=1.70$Å, $l_{CD}^2=0.0030$Å^2 and $Z_CZ_D=300$. Fig. 3 shows the $rD^{\phi}(r)$ curve obtained from this model with the values of $A_{ij,k}$ and $a_{ij,k}^2$ given in the previous section. Now, the four moments μ_0, μ_2, μ_3 and μ_4 are calculated from this $rD^{\phi}(r)$ and the simultaneous equations are set up, regarding r_{AB}, l_{AB}^2, r_{CD} and l_{CD}^2 as unknown. The approximate values of them are obtained by solving the equations and the correct values of them are finally determined by the method of least squares in such a way that the best fit is obtained between the curve in Fig. 3 and that calculated by Eq. (11) with the obtained values. The final results are $r_{AB}=1.50_0$Å, $l_{AB}^2=0.0010_2$Å^2, $r_{CD}=1.70_0$Å and $l_{CD}^2=0.0030_6$ Å^2.

Another test is also carried out for the case where a peak in the radial distribution curve is not known to be single or composite. $rD^{\phi}(r)$ curve is drawn by the use of one kind of atomic pair ($r_{AB}=1.50$Å, $l_{AB}^2=0.0010$ Å^2 and $Z_AZ_B=150$). Even if this peak of

* For example, see reference 9.

$rD^{\phi}(r)$ is assumed to be a composite peak of two kinds of atomic pairs, (r_1, l_1^2 and $(ZZ)_1$) and (r_2, l_2^2 and $(ZZ)_2$), the procedure mentioned above leads to such results as $r_1=r_2=r_{AB}$, $l_1^2=l_2^2=l_{AB}^2$ and $(ZZ)_1+(ZZ)_2=Z_AZ_B$.

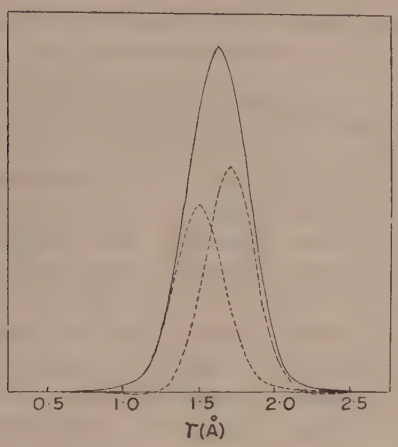

Fig. 3. The radial distribution curve $rD^{\phi}(r)$ obtained from an arbitrary model. Dushed line shows the individual peaks for each distance.

It may be worthwhile to note here that the procedure of solving the simultaneous equations when $rD^{\phi}(r)$ is taken as the radial distribution function in Eq. (14) is no more troublesome than that when $rD^{z}(r)$ is taken, because values of $A_{ij,k}$ and $a_{ij,k}^2$ are known.

§ 4. Errors due to the Partial Disregard of the Differences among the Unitary Scattering Factors of the Constituent Atoms

Since Karle and Karle's work[3], many investigators have analysed the molecular structures, assuming that $\phi_i(s)\approx\phi_j(s)$ in the range of moderate and large scattering angles ($s\geqq s_0$) and hence such a radial distribution function as

$$rD^{c}(r)=(1/2\pi^2)\left[\int_0^{s_0} sI^{z}(s)\cdot\sin sr\,ds + \int_{s_0}^{\infty} sI^{\phi}(s)\cdot\sin sr\,ds\right] \qquad (16)$$

is approximately equal to $rD^{z}(r)$. In this section the deviation of $rD^{c}(r)$ from $rD^{z}(r)$ will be estimated.

Let us consider carbon tetrachloride again, which has the same structure as shown in in § 2. From this model the intensity functions $I^{\phi}(s)$ and $I^{z}(s)$ are calculated and then three radial distribution functions $rD^{\phi}(r)$, $rD^{c}(r)$ and $rD^{z}(r)$ are obtained by means of the punched-card method[10] with $a^2=(0.070/\pi^2)$ Å^2. These are shown in Fig. 4 together with the differences among them. In the computation of $rD^{c}(r)$, $sI^{\phi}(s)$ is connected to $sI^{z}(s)$ at the point $s_0=\pi$Å^{-1}*. Fig. 4 shows that

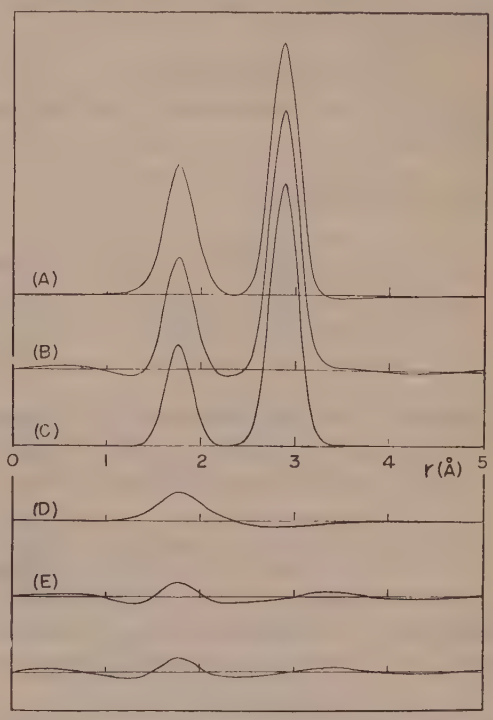

Fig. 4. Computed radial distribution curves and differences among them for carbon tetrachloride in the same longitudinal scale. Curve (A) is $rD^{\phi}(r)$, (B) $rD^{c}(r)$, (C) $rD^{z}(r)$, (D) $\Delta rD^{\phi}(r)=rD^{\phi}(r)-rD^{z}(r)$ and (E) $\Delta rD^{c}(r)=rD^{c}(r)-rD^{z}(r)$. The lowest curve is $\Delta rD^{c}(r)$ calculated from eq. (19).

both $rD^{\phi}(r)$ and $rD^{c}(r)$ deviate appreciably from $rD^{z}(r)$ and the areas under the peaks of $rD^{\phi}(r)$ and $rD^{c}(r)$, especially for C-Cl pair, are not equal to those of $rD^{z}(r)$**, but the positions of the maxima of the peaks agree satisfactorily with each other. Moreover, it is to be noted here that $rD^{c}(r)$ has ripple along the base line.

Now, the deviation $\Delta rD^{c}(r)=rD^{c}(r)-rD^{z}(r)$

* The manner of the connection in the vicinity of s_0 has little influence on the resultant $rD^{c}(r)$.

** From (13) the factors $\sum_{k=0} A_{ij,k}$ in (12) are 1.57 and 0.95 for C–Cl and Cl–Cl pairs, respectively.

is considered from such a standpoint as described in § 2. It followed that

$$\Delta rD^c(r)=\sum_{(ij)}\Delta rd^c_{(ij)}(r)$$
$$=(1/2\pi^2)\sum_{(ij)}\int_{s_0}^{\infty} m_{ij}(s)\cdot si^z_{(ij)}(s)\cdot\sin sr\,ds. \quad (17)$$

Therefore, $\Delta rd^c_{(ij)}(r)$ depends on the value of $m_{ij}(s)$ in the range $s\geqq s_0$. If $m_{ij}(s)$ in $s\geqq s_0$ is roughly fitted as

$$m_{ij}(s)=B_{ij}\exp(-b_{ij}s)\,, \quad (18)$$

then $\Delta rD^c(r)$ is approximately obtained as follows:

$$\Delta rD^c(r)=\sum_{(ij)}\Delta rd^c_{(ij)}(r)$$
$$=(4\pi^2\sum_i Z_i^2)^{-1}\sum_{(ij)}\Big[(2Z_iZ_j/r_{ij})\cdot B_{ij}\exp(-b_{ij}s_0)$$
$$\cdot\left\{\frac{b_{ij}\cos s_0(r-r_{ij})-(r-r_{ij})\cdot\sin s_0(r-r_{ij})}{b_{ij}^2+(r-r_{ij})^2}\right\}\Big]. \quad (19)$$

Maximum of the deviation $\Delta rd^c_{(ij)}(r)$ appears at the equilibrium distance r_{ij} and its value $\Delta r_{ij}d^c_{(ij)}(r_{ij})$ varies inverse-exponentially with s_0.

In practice, the ratio of $\Delta n_{ij}r_{ij}d^c_{(ij)}(r_{ij})$ or $\Delta r_{ij}D^c(r_{ij})$ to $n_{ij}r_{ij}d^z_{(ij)}(r_{ij})$ may be suitable for the estimation of error in the peak of atomic pair (ij), where n_{ij} is the number of atomic pairs having an equal equilibrium distance. It follows approximately that

$$\Delta r_{ij}d^c_{(ij)}(r_{ij})/r_{ij}d^z_{(ij)}(r_{ij})$$
$$=(2\pi^{-1/2})\cdot(aB_{ij}/b_{ij})\cdot\exp(-b_{ij}s_0)\,, \quad (20)$$

and such a relation as

$$\Delta r_{ij}D^c(r_{ij})\leqq(4\pi^2\sum_i Z_i^2)^{-1}\sum_{(i'j')}(2Z_{i'}Z_{j'}/r_{i'j'})$$
$$\cdot|B_{i'j'}|\exp(-b_{i'j'}s_0)\frac{b_{i'j'}+|r_{ij}-r_{i'j'}|}{b_{i'j'}^2+(r_{ij}-r_{i'j'})^2} \quad (21)$$

is useful for the approximate calculation of $\Delta r_{ij}D^c(r_{ij})/n_{ij}r_{ij}d^z_{(ij)}(r_{ij})$, because rough estimation of unknown $r_{i'j'}$ may be permissible. Of these two ratios, the latter is related to the case where the effect of neighbouring peaks is considered and must be adopted when some neighbouring peaks have the large deviations of $m_{ij}(s)$ from zero and the large scattering powers. These estimations of errors seem to be useful in choosing the value of s_0 for the compound in question in the case where $rD^c(r)$ is adopted in place of $rD^z(r)$.

For carbon tetrachloride, $B_{CCl}=0.86$, $B_{ClCl}=-0.065$ and $b_{CCl}=b_{ClCl}=(0.85/\pi)$Å and some results obtained from Eqs. (20) and (21) are listed in Table I. In the calculation of $\Delta r_{ij}D^c(r_{ij})/n_{ij}r_{ij}d^z_{(ij)}(r_{ij})$, values of $r_{i'j'}$ are roughly estimated as follows: $r_{CCl}=1.8$Å and $r=2.9_{ClCl}$Å. The lowest curve in Fig. 4 is the one obtained from Eq. (19) and agrees satisfactorily with the curve (E).

Table I. Some results obtained from Eqs. (20) and (21) for carbon tetrachloride.

s_0	$\Delta r_{ij}d^c_{(ij)}(r_{ij})/r_{ij}d^z_{(ij)}(r_{ij})$		$\Delta r_{ij}D^c(r_{ij})/n_{ij}r_{ij}d^z_{(ij)}(r_{ij})$	
	for C–Cl pair	for Cl–Cl pair	for C–Cl pair	for Cl–Cl pair
1.0πÅ^{-1}	13 %	−1 %	14 %	2.6%
1.5π	8.4	−0.6	2.0	1.7
2.0π	5.5	−0.4	5.9	1.1
2.5π	3.6	−0.3	3.8	0.7
3.0π	2.4	−0.2	2.5	0.5

§ 5. Discussion

There are many cases where the radial distribution function $rD^c(r)$ used by many investigators has the appreciable deviation from the correct nuclear distribution function $rD^z(r)$ as described in § 4. For example, the peak height for C-Cl pair of carbon tetrachloride varies by 15 ~ 10% of it when the calculated intensity function $I^z(s)$ is connected to the experimental one $I^\phi(s)$ at $s=3\sim5$Å^{-1}. In the "correlation" method the experimental intensity is usually compared with the calculated intensities with constant coefficients Z_i in place of $(Z_i-F_i(s))$. These procedures in which the differences among $\phi_i(s)$ of the constituent atoms are partially disregarded make uncertain the measurements of the mean square amplitude of vibration and the distances for atomic pairs with the weaker scattering powers. Therefore, the reliability of the results obtained in the past should be examined closely.

If the structural data obtained from such $rD^c(r)$ are correct or closely approximate, it may happen that some errors in the observed total intensity or in the estimated background intensity compensate for the deviation of $rD^c(r)$ from $rD^z(r)$. In the latter case it seems that an incorrect background intensity is intentionably determined in order to obtain such a structure sensitive intensity that gives $rD^z(r)$. If so, the consequent background line

should fluctuate, at least, in the case of carbon tetrachloride. Moreover, it is doubtful whether such conversion of $rD^c(r)$ into $rD^z(r)$ can be performed uniquely only by the criterion for the estimation of the background intensity given by Karle and Karle[11], because it is only a necessary condition that the nuclear distribution function must be non-negative everywhere.

Recently Bartell *et al.*[4] discussed on the uncertainty of the results due to neglect of the valiability of $m_{ij}(s)$ with s and developed a refined procedure which compensated for the interference arising from non-nuclear scattering. They converted successively $I^{\phi}(s)$ into $I^z(s)$, starting with values of r_{ij} and l_{ij}^2 obtained from $rD^c(r)$. Their procedure may be easy of access, but there remains the necessity of assuming a structure model and there may be some questions about the convergency of the successive approximation.

The Norwegian school[12] took into account the effect of non-nuclear scattering as it is. Consequently the radial distribution curve is intricate and its analysis becomes troublesome.

In the procedure described in this paper the interference effects arising from non-nuclear scattering are partially compensated by deviding the total scattered intensity by the background intensity as done by the American school, and the residual effects are taken into account with the consideration of the differences among the unitary scattering factors of the constituent atoms. Therefore, the comparably small additional terms are only supplemented to the radial nuclear distribution function. Furthermore, the additional term has the Gaussian form which is similar to the radial nuclear distribution function modified by the artificial temperature factor and hence the analysis of the distribution curve becomes little complicated.

Another advantage of the procedure is the fact that the observed intensity data can be used up to the range of smaller scattering angle. Therefore, no structure model need be assumed from which the intensity is calculated in that region. The assumption of the model is difficult in the case where the material has the complicated structure. The author prefers to abolish the presumption on the structure in the radial distribution method. In the neighborhood of the diffraction center, however, it is difficult not only to measure the diffracted intensity but also to estimate the background intensity. The extrapolation method which will be presented in the following paper may be easily adopted to make up the absence of the structure sensitive intensity in the range of very small angle.

The modification function $m_{ij}(s)$ can be obtained from the chemical constitution of the compound and the values of the atomic scattering factors without any knowledge about the atomic configuration. However, in the range of very small angle there remains some uncertainty in the values of the elastic and inelastic scattering factors and hence it may be difficult to obtain $m_{ij}(s)$ correctly in that region. However, the behaviour of $m_{ij}(s)$ in the inner-most region of s gives only very small and flat contribution over the wide range of r on the radial distribution function. Therefore, such an approximation as shown in (13) may be practical and the values of $\sigma_{(ij)}^{\phi}$ obtained with values of $A_{ij,k}$ in (13) agree satisfactorily with those of areas under the peaks of $r^2D^{\phi}(r)$ derived from $rD^{\phi}(r)$ in Fig. 4.

The advantage of the method of the analysis of the radial distribution curve described in § 3 is the fact that the structure data can be obtained by this method without any introductory knowledge about the structure. Therefore, the method is very powerful when the kind or number of atomic pairs coming in a composite peak is unknown. As the method is especially easily applicable to the decomposition of the peak composed of small number of components, it is desirable to devide the whole radial distribution curve into some parts mutually isolated if possible and apply it to each part. When the numerical integration is performed for lower order moments ($n \lesssim 4$), it is permissible to cut the integral range at the arbitrary points on the both feet of the peak.

At the end it is noteworthy that such a treatment as described here is able to be extended by some proper considerations to the cases of liquid and amorphous solid in which halo patterns are obtained by the diffraction of X-rays or electrons.

It is the author's pleasure to express his

sincere thanks to Prof. J. Kakinoki and Mr. T. Ino for their valuable criticisms. The author also wishes to thank the Osaka Municipal Office for making available to him a set of electrical accounting machines of the I.B.M. Corporation.

References

1) T. Ino: J. Phys. Soc. Japan **12** (1957) 495.
2) P. Debye: J. Chem. Phys. **9** (1941) 55.
3) I. L. Karle and J. Karle: J. Chem. Phys. **17** (1949) 1052.
4) L. S. Bartell, L. O. Brockway and R. H. Schwendeman: J. Chem. Phys. **23** (1955) 1854.
5) J. Waser and V. Schomaker: Revs. Mod. Phys. **25** (1953) 671.
6) H. Viervoll: Skrifter Norske Videnskaps Akad., Oslo, Mat. Naturv. Kl. No. 2 (1950).
7) For example, L. O. Brockway: Revs. Mod. Phys. **8** (1936) 231.
8) H. Viervoll and O. Ögrim: Acta Cryst. **2** (1949) 277.
9) I. L. Karle and J. Karle: J. Chem. Phys. **18** (1950) 963.
10) P. A. Shaffer Jr., V. Schomaker and L. Pauling: J. Chem. Phys. **14** (1946) 659.
11) J. Karle and I. L. Karle: J. Chem. Phys. **18** (1950) 957.
12) H. Viervoll: Acta Chem. Scand. **1** (1947) 120. O. Hassel and H. Viervoll: *ibid.* **1** (1947) 149.

JOURNAL OF THE PHYSICAL SOCIETY OF JAPAN Vol. 13, No. 1, JANUARY, 1958

Uniaxial Anisotropy in Iron-Cobalt Ferrites

By Shūichi IIDA, Hisashi SEKIZAWA, and Yoshimichi AIYAMA

Department of Physics, Faculty of Science, Tokyo University, Tokyo

(Received April 13, 1957)

The uniaxial anisotropy induced by the magnetic annealing in both single and poly-crystals of iron-cobalt ferrites has been studied experimentally. It is shown that the magnitudes of the uniaxial anisotropy depend essentially on the degree of oxidation of the specimens and become almost zero after deoxidizing heat treatments. Contrary to the conclusion by Bozorth *et al.*, the dependence of the magnitude of the uniaxial anisotropy on the direction of the annealing magnetic field is observed for a cobalt rich single crystal, showing a maximum along ⟨100⟩ and a minimum along ⟨110⟩ in (001) plane. Relaxation behaviour of the uniaxial anisotropy is studied by measuring directly the change of torque at high temperatures (240°C~350°C) with a polycrystalline cobalt ferrite. It has been found that the results can be described by a simple empirical formula, supporting that the magnetic annealing effect has no critical temperature. The variation of electrical conductivity with temperature has also no anomaly at the effective temperature range.

Considering all the experimental results obtained, we have reached the conclusion that the uniaxial anisotropy in these ferrites is due to the presence of directional short range order among various cations and cation vacancies in the spinel matrix. The nearest neighbour pair of a cobalt ion and a vacancy seems to play a principal role in this mechanism.

§ 1. Introduction

It is well known that certain ferromagnetic materials respond to heat treatment in a magnetic field. When they have been annealed in a magnetic field in a certain temperature range, they get a uniaxial anisotropy with a stable direction parallel to the annealing field. Iron-nickel alloys,[1] alnico V,[2] copper-cobalt alloys,[3] and magnetite[4] are typical examples. In the case of iron-nickel alloys the magnetic annealing effect is well accounted for by the mechanism of the directional short

range order and in the case of alnico V by the formation of oriented precipitates.

The magnetic annealing effect in the iron-cobalt ferrits was first found by Kato and Takei in 1933[5]. Since then, Kawai[6], Nakamura[7], Sugiura[8], Guillaud[9], Bozorth *et al.*[10] and H. J. Williams *et al.*[11] have made many interisting studies from various points of view. Especially Bozorth *et al.* have performed the study on single crystals of these ferrites and clarified various characteristics of this effect. But the conclusive theoretical interpretation does not seem to be given by them.

Since 1951, we have also been engaged in experimental studies of this problem and reached the conclusion that the uniaxial anisotropy originates in the directional local order among cobalt ions and cation vacancies in the ferrite crystal[12]. The present paper reports the principal parts of the studies concerning the uniaxial anisotropy of the iron-cobalt ferrites. The experimental study of the phase diagram of iron-cobalt-oxygen system was published already[13].

In § 2, the ways of the preparation of various specimens used are described. In § 3, the results of the experimental study for the uniaxial anisotropy constants of the polycrystalline specimens are described. It is shown that the magnitude of the constants depends strongly on the degree of oxidation of the specimens. Magnetostriction curves of these specimens at each degree of the oxidation are also shown. In § 4, the details of the magnetic study carried out on single crystals are presented. In § 5, the results of the study on the relaxation of the induced uniaxial anisotropy of cobalt ferrite are shown. In § 6, the experimental results on the variation of the electrical conductivity of the iron-cobalt ferrites with temperature are presented. In § 7, a possible mechanism of the uniaxial anisotropy in iron-cobalt ferrites is presented. Lastly in § 8, several of other mechanisms proposed for the uniaxial anisotropy of these ferrites are discussed together with the possibility of the presence of similar effects in other ferrites.

§ 2. Preparation of the Specimens

Both polycrystalline and single crystal specimens were used.

The polycrystalline specimens were prepared by the usual ceramic techniques: calcination, milling, pressing and firing. The starting oxides were prepared by "nitric acid method", i.e., dissolving the mixture of constituent metals in the desired proportion in conc. HNO_3, drying the solution with an infra-red ray lamp and heating at about 800°C in air to remove the nitrogen. The proposed compositions of metals were $r=0.000$, 0.083, 0.167, 0.250, 0.333, and 0.417, where r stands for the atomic ratio Co/(Fe+Co).

The firings, i.e., the heat treatments after the pressing, were made according to the phase diagram established by one of the authors[13]. The heat treatments were made in an air tight alumina tube. The phase diagram is reproduced in Fig. 1. In the figure, the region

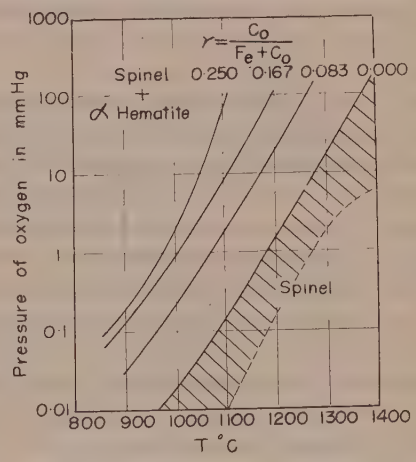

Fig. 1. Phase boundaries of Iron-Cobalt oxides with various metallic compositions. Each solid line indicates the boundary corresponding to each metallic composition, by which spinel phase field (lower) is separated from two phase field with hematite and spinel (upper).

Broken line indicates the partial pressure of CoO vapour decomposing from the spinel matrix. Below this critical pressure, active decomposition of CoO vapour from the spinel matrix occurs.

in which spinel phase is stable in common to all the compositions now studied is hatched. We prepared several sets of specimens with the various compositions mentioned and the firing was made to each set of specimens simultaneously. It was an annealing for thirty minutes at 1400°C in oxygen of about 50 mm Hg and the following slow cooling in the hatched region (during cooling the pressure

of oxygen was controlled). The firing by this program is refered as heat treatment "S", for convenience in the present report.

It is remarked that below 800°C the oxygen pressure required in this heat treatment becomes lower than the lowest limit obtainable with our apparatus. However, as concluded before and is confirmed again by various measurements in this report, a simple extrapolation of the phase diagram shown in Fig. 1 is considered to be still valid below 800°C. Actually the electric and magnetic properties of the specimens were found to be affected to some extent by a slight change in conditions of vacuum below 800°C.

Polycrystalline specimens used in torque measurements were discs of 14 mm in diameter and of 1 mm in thickness, and those used in electrical conductivity measurements were square rods of 4 mm×4 mm ×25 mm in size.

Single crystals used were grown from the melt in a platinum crucible in air. Measurements were made on two cobalt rich single crystals one of which had a mixing composition of $r=0.253$ and cut in a sphere of 2.75 mm in diameter and the other had a composition of $r=0.283$ according to chemical analysis and cut in a (001) disc of 6.00 mm in diameter and of 0.70 mm in thickness.

Preceding the measurements, heat treatments were also applied to these specimens according to the phase diagram.

§ 3. Uniaxial Anisotropy and Magnetostriction in Polycrystals

The magnitudes of the uniaxial anisotropy induced by the magnetic annealing were measured for the disc-shaped polycrystalline specimens by a torque-meter.

It was found by preliminary measurements that the uniaxial anisotropy constants induced by the magnetic annealing depend strongly upon the degree of oxidation of the specimens. Fig. 2 shows the results. Curves from (1) to (7) illustrate the variation of the uniaxial anisotropy constants of a set of specimens caused by applying various heat treatments in a vacuum successively. The magnetic field applied was about 4000 Oe and it was applied in each time perpendicular to the direction of the magnetic field applied in the preceding heat treatment so as to eliminate the influence of the preceding magnetic annealing.

The results show that the uniaxial anisotropy in these ferrites which is induced by the magnetic annealing decreases considerably by repeating heat treatments in a high vacuum and is almost zero in the most deoxidized state. It seems certain that the dependence of the magnitude of the uniaxial anisotropy on the rate of the cooling is not so distinctive.

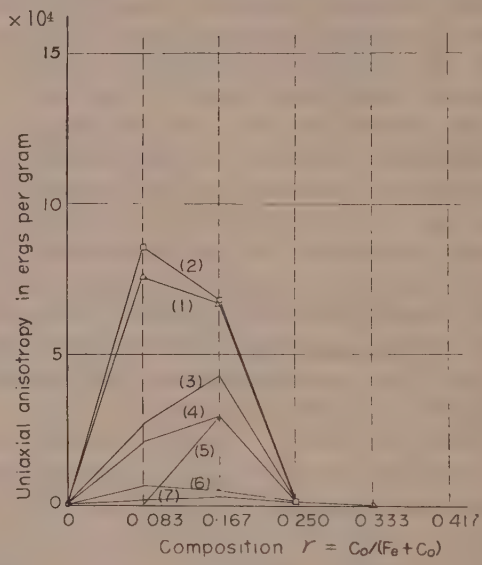

Fig. 2. Change of uniaxial anisotropy of an iron-cobalt ferrite series caused by applying various heat treatments in a vacuum successively. The heat treatments are as follows.

(1): The specimens after heat treatment "S" were heated up to 750°C in a vacuum and quenched from this temperature in a vacuum with an applied magnetic field.

(2): again heated up to 750°C in a vacuum, cooled slowly with an applied magnetic field.

(3), (4): heated up to 750°C in a vacuum, cooled to 260°C in (3), and from 750°C in (4).

(5): heated up to 250°C in a vacuum, and cooled with a magnetic field.

(6), (7): heated up to 750°C in a vacuum, kept 24 hours in (6), and 56 hours in (7), and cooled in a magnetic field.

It should be mentioned that the change in weight of the specimens after these heat treatments could not be detected (probably less than 0.5%) and x-ray study confirmed spinel structure of the specimens even in the most deoxidized state.

Then, starting from specimens in the most deoxidized state, the recovering process of the uniaxial anisotropy was observed. Another set

of specimens with a series of composition r, identical to the former, were annealed for five hours at 1000°C in a high vacuum and then cooled slowly with an applied magnetic field. The anisotropy constants measured after this treatment are shown by curve (0) in Fig. 3 (a). Then, seven oxidizing heat treatments were performed in succession on these specimens. The first six treatments were the annealings at 400°C for four hours in oxygen of various

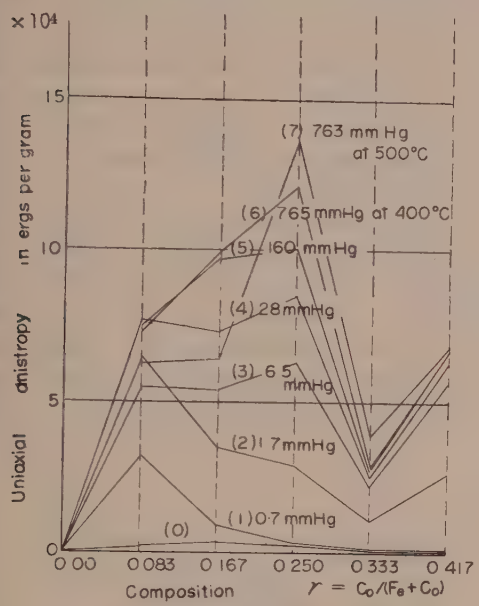

Fig. 3 (a) Change of the uniaxial anisotropy of an iron-cobalt ferrite series caused by applying the heat treatments in various oxidizing conditions. The heat treatments, applied successively, are in turn as follows.

(0): Specimens were annealed for five hours at 1000°C in a vacuum and cooled with an applied magnetic field.

(1), (2), ... (6): annealed for four hours at 400°C in oxygen at the pressure indicated in the figure, and cooled in a magnetic field.

(7): annealed at 500°C in oxygen at 763 mm Hg.

pressures. The results were shown in Fig. 3 (a) by curves (1) to (6). The pressures of the oxygen gas in the successive heat treatments are 0.7, 1.7, 6.4, 28, 160, and 765 mm Hg, respectively. The last heat treatment, corresponding to curve (7), was an annealing at 500°C in oxygen at 763 mm Hg. In these cases also, the directions of the applied magnetic field were always chosen to be perpendicular to that in the foregoing heat treatment. The results are replotted in Fig. 3 (b) against the pressure of oxygen atmosphere during the heat treatments.

From these measurements it is confirmed that the uniaxial anisotropy in these ferrites are essentially influenced by the degree of oxidization of the specimens and it increases almost monotonously as the degree of oxidation increases.

According to Fig. 1, the final equilibrium state of these specimens in every condition of the above heat treatments is undoubtedly a mixture of hematite and cobalt rich spinel (probably nearly stoichiometric cobalt ferrite). However, it should be pointed out that the oxidization of the ferrite containing divalent iron ions progresses at low temperatures frequently with little precipitation of α hematite but the increase of cation vacancies in the spinel matrix. Therefore, it is also certain that the oxidization in the above heat treatments progresses to some extent in the spinel matrix itself with the associated increase of the cation vacancies. The detailed discussion will be given in § 7.

Together with these measurements of the anisotropy constants, measurements of the magnetostriction of these specimens were carried out at each stage of oxidization by an optical lever method. The measurements were performed on both longitudinal and transverse magnetostriction in both settings at which the applied magnetic field is parallel and perpendicular to the direction of the annealing magnetic field. The results at typical four stages for each specimen are shown in Fig. 3 (c). The abscissa in Fig. 3 (c) does not indicate the effective field but the applied external magnetic field.

Here, the magnetizing characters of these specimens are discussed shortly. According to the measurements performed on single crystals by several authors, the variation of the three major constants K_1, λ_{100}, and λ_{111} with the composition in iron-cobalt ferrites are as follows: K_1 is about -1×10^5 in magnetite[4)10)], changes sign with slight addition of cobalt ferrite (below one percent)[14)], and increases steeply to about 4×10^6 in cobalt ferrite; λ_{100} is about -2×10^{-5} in magnetite, increases its absolute value steeply to -6×10^{-4} in cobalt ferrite; and λ_{111} is about 8×10^{-5} in magnetite, increases slowly to about 1×10^{-4} in cobalt

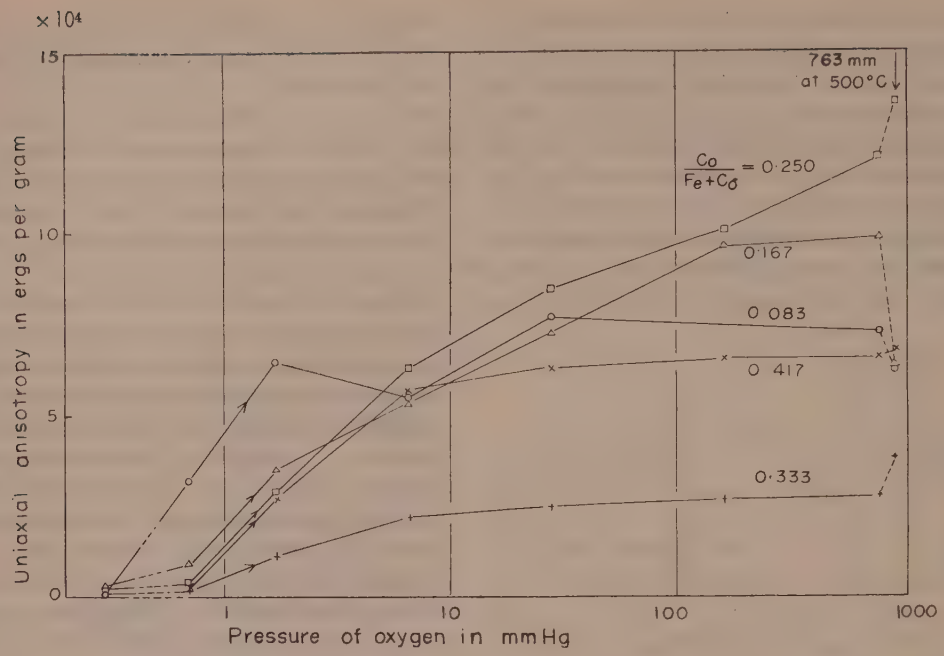

Fig. 3 (b). Change of the uniaxial anisotropy of an iron-cobalt ferrite serie with the pressure of oxygen at which specimens were annealed for four hours at 400°C successively. The points on the rightest side indicate the values after annealing at 500°C with the pressure of oxygen at 763 mm Hg.

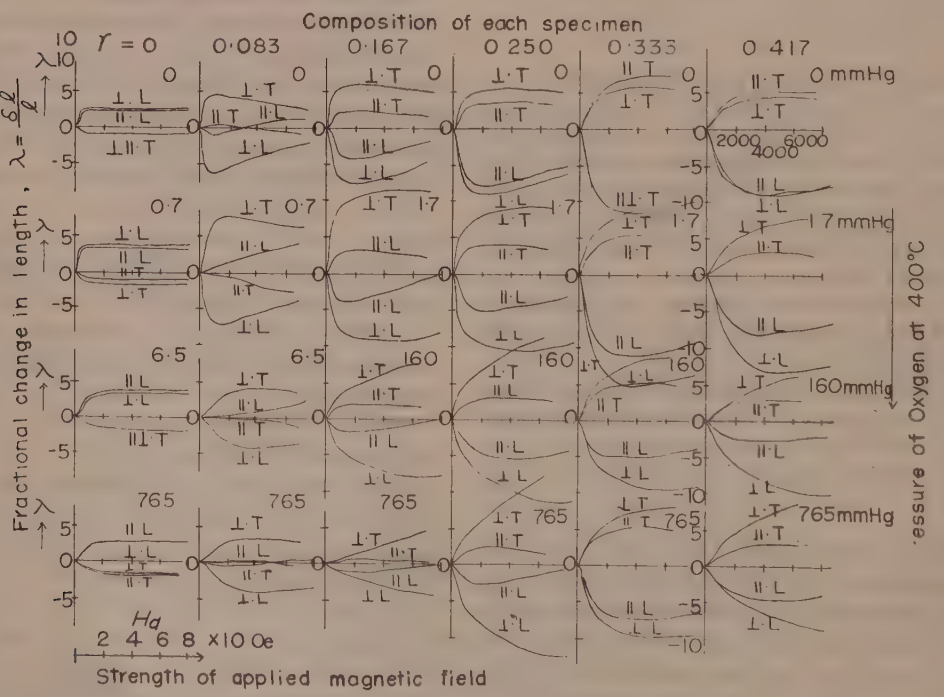

Fig. 3 (c). Change of magnetostriction curve of iron-cobalt ferrites caused by applying various heat treatments successively to the specimens. The notations ∥·L and ∥·T or ⊥·L and ⊥·T mean longitudinal and transverse magnetostrictions in each setting at which the applied magnetic field is parallel or perpendicular to the direction of annealing magnetic field. The pressure of oxygen in the preceding annealing at 400°C is indicated in each unit figure.

ferrite. All curves in Fig. 8 are explained well by these variations of the constants. The arge change of the magnetostriction curves rom $r=0$ to $r=0.083$ corresponds clearly to he change of the sign in K_1. All longitudinal nagnetostriction curves of the specimens conaining cobalt have positive slopes in high ield range. It indicates the presence of the positive magnetostriction constant λ_{111}. It should be pointed out that in spite of the fact hat large uniaxial anisotropy is present, the lirection of the magnetization of each domain seems to be aligned not so much parallel to he direction of the annealing magnetic field. This conclusion can be deduced from the fact hat the magnetostriction does not become so small in the setting at which the applied magnetic field is parallel to the annealing magnetic ield. From this view point, it should be also pointed out that the cubic anisotropy predominates especially in $r=0.333$, i. e., stoichiometric cobalt ferrite specimen.

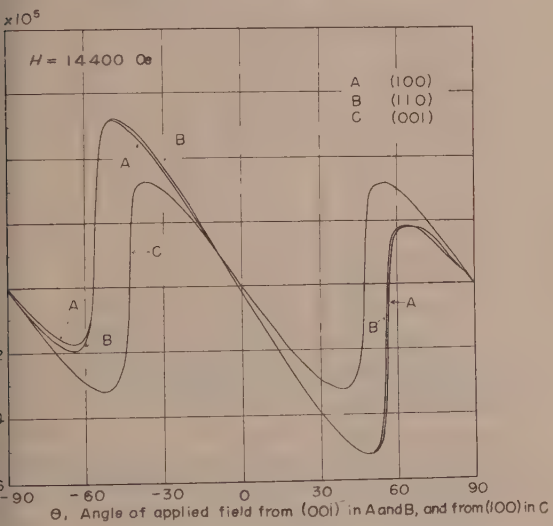

Fig. 4. Torque curves in (100), (110), and (001) planes of a spherical single crystal (Co/(Co+Fe)=0.253) after cooling in a magnetic field along [001].

4. Uniaxial Anisotropy in Single Crystals of Cobalt Ferrite

A spherical single crystal specimen with the proposed composition $r=0.253$ was heated up to 300°C in oxygen of about 1~2 mm Hg and cooled with a magnetic field of about 6000 Oe applied along [001] direction. The torque curves of this single crystal in (100), (110) and (001) planes are shown in Fig. 4. It shows clearly the presence of the uniaxial anisotropy with the easy direction along [001] superposed on the usual cubic crystal anisotropy.

Next the dependence of the magnitudes of the uniaxial anisotoropy on the direction of the annealing magnetic field was studied by using another single crystal of (001) disc, having a composition $r=0.283$. After the preparation, it was annealed for two days in air at about 750°C in order to get a sufficiently oxidized state. Then it was heated up to 400°C in air and cooled slowly with an applied magnetic field. The treatment was applied repeatedly with the annealing magnetic field along various crystal directions in the (001) plane. The torque curve for the specimen with the annealing magnetic field applied along [100] is shown in Fig. 5, together with the

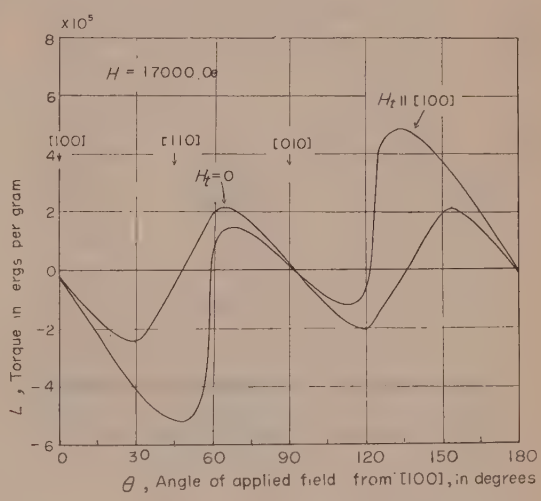

Fig. 5. Torque curves for a (001) disc of cobalt ferrite after cooling with and without a magnetic field along [100].

one without the annealing magnetic field. The torque curves with the anealing magnetic field applied along other directions than [100] were very complicated. The magnetic field of 17000 Oe applied at the torque measurements was not sufficient to obtain a saturated magnetization.

The influence of the higher order harmonics can be reduced in the magnetic energy curves which can be obtained from torque curves by integration. Several of these curves are shown in Fig. 6. The uniaxial anisotropy constants were calculated from these curves by using certain approximation techniques. The procedures are given in Appendix.

From these analysis it can be concluded that

an expression of the magnetocrystalline energy in (001) plane of the type:

$$E=K_1 \sin^2\theta \cos^2\theta + K_u \sin^2(\theta-\theta_T) \qquad (1)$$

is also applicable in this case, where θ is the angle of the direction of the magnetization from [100], and θ_T is the angle of the direction of the uniaxial anisotropy from [100]. It was found in every case that the direction of the uniaxial anisotropy coincided with that of the annealing magnetic field within several degrees.

The expression given above is the same as that proposed for cobalt-zinc ferrite by Bozorth *et al.*[10]. However, being different from their results, our value of K_u was dependent on the direction of the annealing magnetic field. (The value of K_1 was about 2×10^6 ergs/gr.*). The results are shown in Fig. 7. It is shown that ⟨100⟩ is the most effective direction for the magnetic annealing, while ⟨110⟩ the least effective in (001) plane. This variation of the magnitudes of the uniaxial anisotropy with the direction of the annealing magnetic field is smaller than that which is predicted by Néel's theory but larger than that which is calculated by Taniguchi. There are some ambiguities about the measurements along the directions near [110] in Fig. 7. The annealing magnetic field of about 7000 Oe is not sufficiently large to saturate the magnetization completely along these directions.

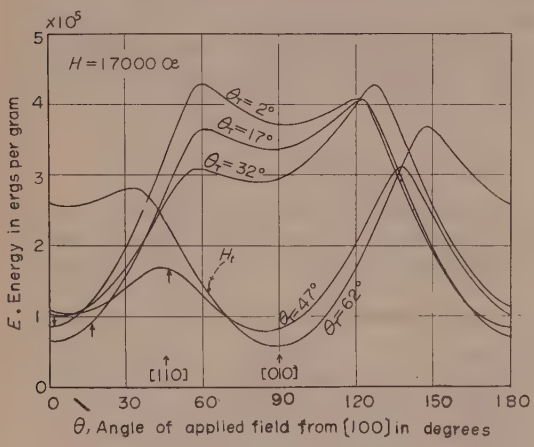

Fig. 6. Effect of magnetic anneal in various directions in (001) plane taken for a (001) disc of cobalt ferrite. Energy curves are illustrated and the direction of annealing magnetic fields is indicated by an arrow.

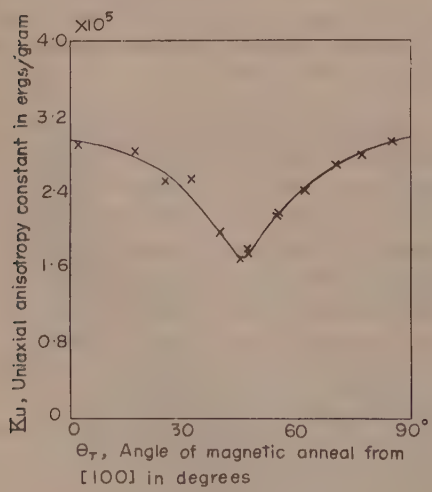

Fig. 7. Uniaxial anisotropy constant of cobalt ferrite plotted against the direction of annealing magnetic field in (001) plane.

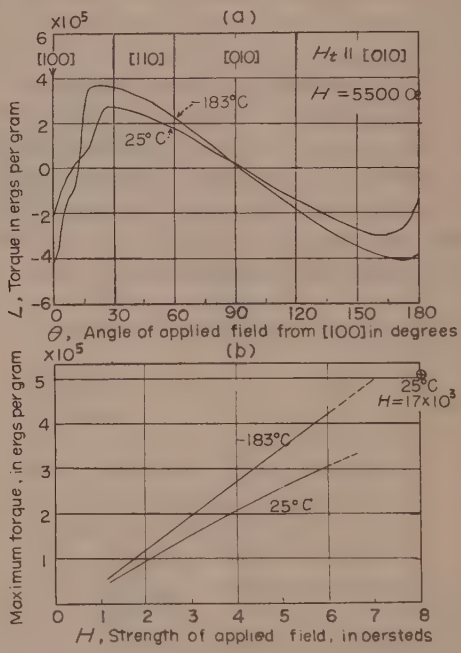

Fig. 8 (a), (b). Uniaxial anisotropy of a cobalt ferrite at liquid air temperature as compared with that at room temperature. (a) shows the torque curve in the (001) plane, and (b) shows the variation of maximum torque with the strength of applied magnetic field in the measurements.

The uniaxial anisotropy constant increases steeply as the temperature is lowered. Figs. 8 (a) and (b) show the results. Fig. 8 (a) shows the torque curves at 25°C and −183°C of the

* K_2 of about -1.5×10^6 ergs/gr was observed for a (111) disc specimen with $r=0.333$ made by flux method.

001) disc specimen after annealed with a magnetic field applied along [010]. Fig. 8 (b) shows the variation of the maximum value of the torque with the intensity of the applied magnetic field in these measurements. As can be seen, at −183°C, saturation of the magnetization has not been attained by the magnetic field applied.

Lastly, the specimen was annealed at 750°C for one day in a high vacuum and cooled with and without applied magnetic field along [100]. The results are shown in Fig. 9. In accordance with the result for the polycrystalline specimens, the magnitude of the uniaxial anisotropy reduced to almost zero by this vacuum treatment.

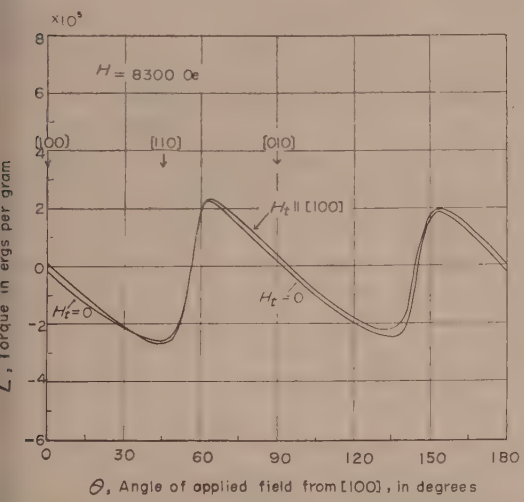

Fig. 9. Torque curves of a cobalt ferrite single crystal after annealing in a vacuum, showing a remarkable decrease of the magnetic annealing effect.

§ 5. Relaxation Character of the Uniaxial Anisotropy

It is well known that the magnetic annealing effect shows magnetic relaxation phenomenon in its effective temperature range[15]. Our experiments were performed on a disc-shaped polycrystalline cobalt ferrite by a torque-meter at high temperatures. The specimen was heated up in a furnace to 600°C in air, kept 30 minutes, and cooled down with an applied magnetic field of about 4000 Oe to a desired temperature. After maintaining for about 30 minutes at this temperature, the specimen was abruptly rotated by 45 degrees with its normal axis as the rotation axis. In this case a torque L_u must be exerted to the specimen in order to maintain the orientation of the specimen unchanged. This torque L_u was considered to be proportional to the uniaxial anisotropy $K_u(t)$ which should have been formed in the specimen during the preceding heat treatment along the direction of the applied magnetic field and should be decaying after the rotation. In these conditions, a new uniaxial anisotropy K_u' whould grow along the new direction of the applied magnetic field, but it should have no effect on the torque.

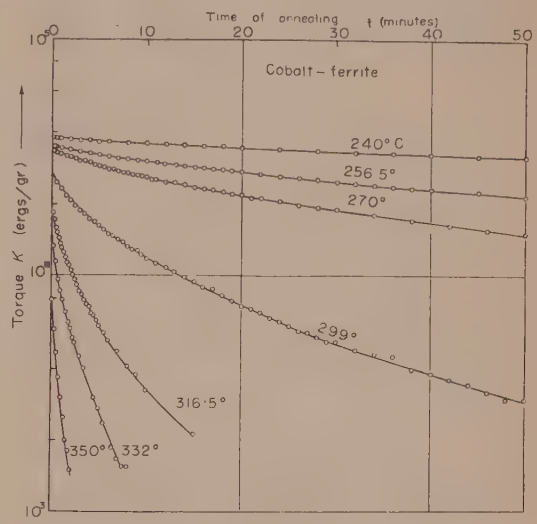

(a)

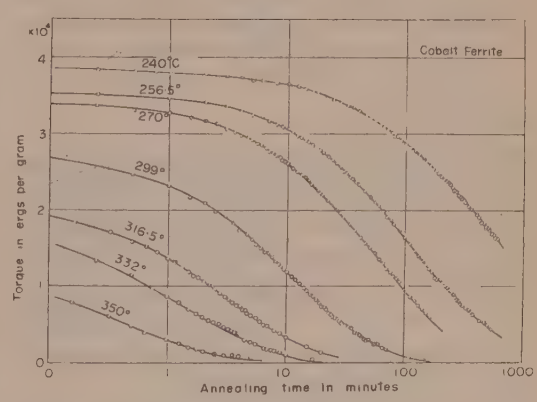

(b)

Fig. 10 (a), (b). Decaying of the torque of a cobalt ferrite disc with time of annealing in a magnetic field. The torque is due to the presence of the uniaxial anisotropy induced by the preceding cooling and annealing with an applied magnetic field along the direction different by 45 degrees from the direction of the magnetic field during measurements. Characters are illustrated by different scales in (a) and (b).

Fig. 10 (a) and (b) show the obtained results.

It has been found that these curves can be expressed accurately (within the experimental errors) by an empirical formura:

$$K_u(t)=K_0 \exp\{-t/(\tau+\alpha t^{1/2})\} \qquad (2)$$

with suitable values of K_0, τ, and α. The values of K_0, τ, and α are shown in Fig. 11.

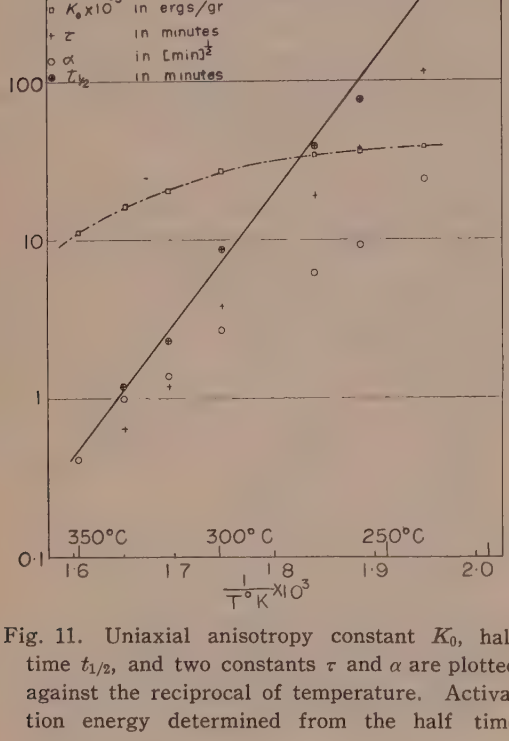

Fig. 11. Uniaxial anisotropy constant K_0, half time $t_{1/2}$, and two constants τ and α are plotted against the reciprocal of temperature. Activation energy determined from the half time curve is 1.6 eV.

In the figure, the annealing time $t_{1/2}$ at which the torque becomes one half of the initial value is also shown. We can see from these curves, in accordance with the conclusion in § 2, that there is no critical temperature for the phenomenon. The activation energy calculated from the inclination of the $\log t_{1/2}-1/T$ curve is 37000 cal/mole=1.6 ev.

Similar studies of the relaxation were also carried out by Sakamoto[16] (variation of the residual magnetization of a polycrystalline cobalt ferrite) and Bozorth *et al.*[10] (variation of the ratio of the first minimum torque to the first maximum torque of a cobalt-zinc ferrite single crystal). Both reported also that there was no critical temperature, giving the activation energies of 37500 cal/mole, and 21400 cal/mole, respectively.

§ 6. Electrical Conductivity in Polycrystals

In order to observe the variation of the electrical conductivity as a function of temperature, two sets of polycrystalline specimens with the identical series of compositions r were prepared. One set of specemens were those by the standard method, i.e., prepared by heat treatment "S". Another set of specimens were those which were considered to be in the most deoxidized state, i.e., heat-treated according to the program of heat treatment "S" and then annealed at 900° C for four hours in a high vacuum.

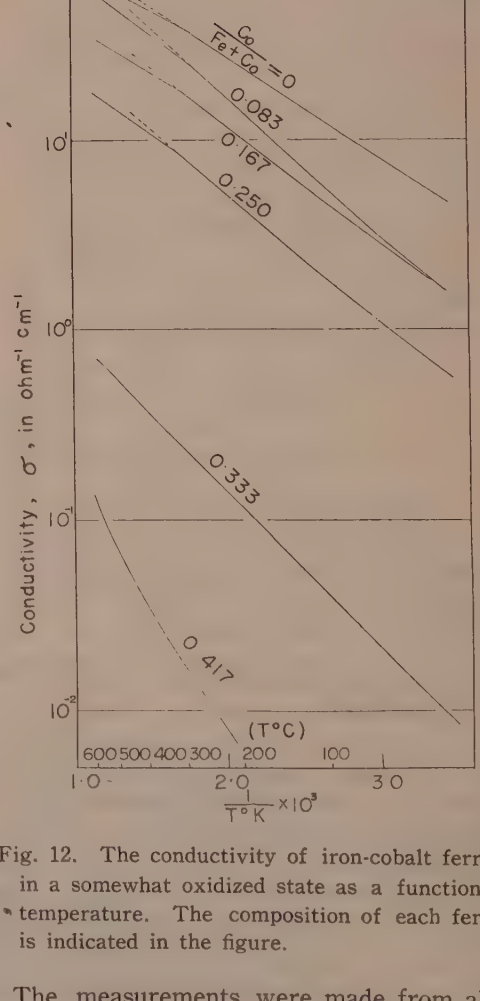

Fig. 12. The conductivity of iron-cobalt ferrites in a somewhat oxidized state as a function of temperature. The composition of each ferrite is indicated in the figure.

The measurements were made from about 700°C to liquid air temperature in a high vacuum. The results for the former set of specimens are shown in Fig. 12 and that for the latter in Figs. 13 (a) and (b).

As shown, no anomaly is observed at about

300°C for all the curves. This supports also that there is no phase change in this temperature range. The curves in Fig. 12 for the specimens with compositions $r=0.000$, 0.083, 0.167, and 0.250 have slight angles at about 300°C. The angles, however, are so slight that they will not indicate the presence of any structural change. The fact that the angle is present also in magnetite ($r=0$) suggests that it might be related to the rapid change of diffusion rates of cations in the ferrite matrix[13].

In Fig. 13 (b), the well-known low temperature transition of magnetite is seen at −160°C. Comparing with Verwey's data, it shows that this specimen is nearly stoichiometric[17]. The specimen of magnetite of the former set did not show any anomaly in this low temperature range.

§ 7. A Possible Mechanism of the Uniaxial Anisotropy

Various mechanisms were already proposed in order to explain the uniaxial anisotropy in iron-cobalt ferrites. Considering all the experimental results mentioned, however, we reached to another mechanism.

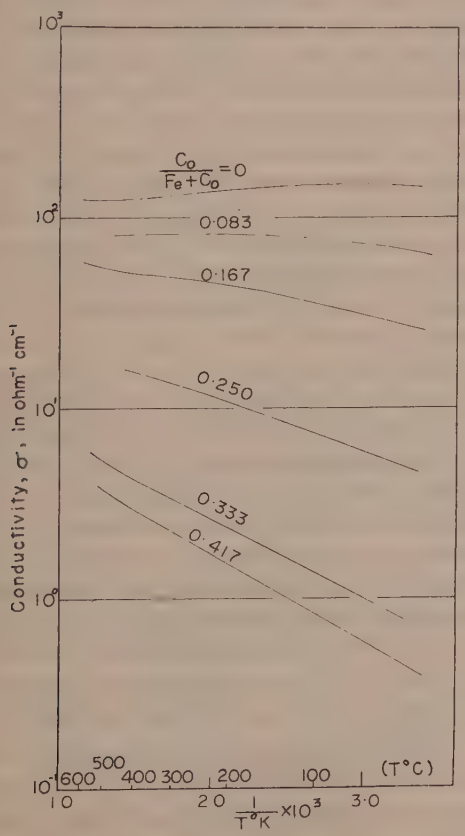

(a)

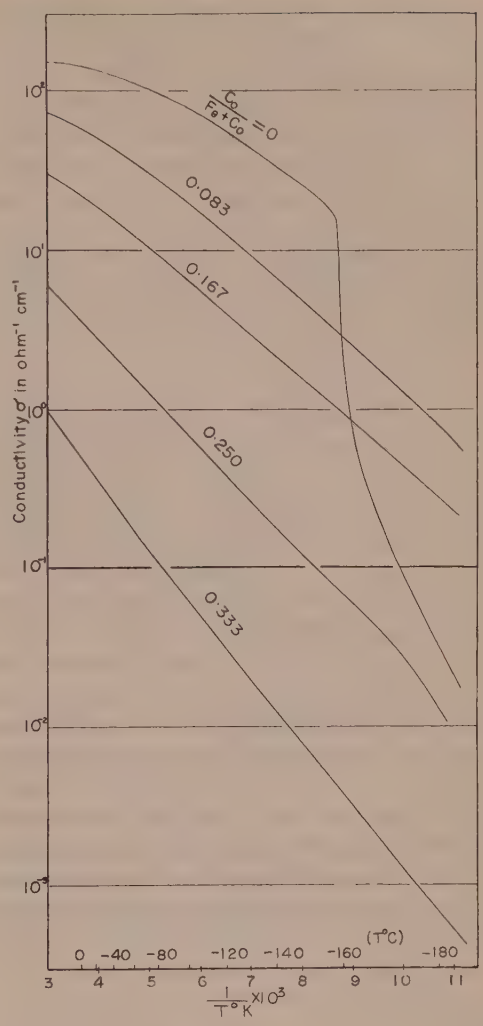

(b)

Fig. 13 (a), (b). The conductivity of iron-cobalt ferrites in a deoxidized state (probably near stoichimetric composition) as a function of temperature. At high temperatures in (a), and at low temperatures in (b).

Our propositions are as follows.

I. Below the Curie temperature, a certain degree of directional local ordering between the magnetic ions and cation vacancies is formed along the direction of the spontaneous magnetization in these ferrites.

II. Iron-cobalt ferrites have no phase changes in the temperature range from 400°C to room temperature. For the time duration of the order of our experiments, however, the diffusion rate of cations seems to decrease

remarkably below about 300°C and the cation configuration realized at that temperature is fixed fairly completely by the ordinary cooling.

Proposition I is deduced mainly from the magnetic data which show strong dependence of the magnitude of the uniaxial anisotropy on the degree of oxidation, and the relaxation experiments which show that the direction of the uniaxial anisotropy is reversibly changeable at high temperatures, regardless of the duration of the preceding annealing, i.e., there is no "over-aging effect".

On this model it is reasonable to assume that cation vacancies in these ferrites distort the crystalline fields at the neighbouring sites severely. Since it is known that a cobalt ion in these ionic crystals has a strongly anisotropic wave function coupled to its spin direction through spin-orbit coupling, the electronic energy of the Co^{++} ion neighbouring a vacancy may depend considerably on its spin direction refered to the direction of the pair of the Co^{++} ion and the vacancy. (It is well known that the lowest orbital energy level of a Co^{++} ion in a cubic crystalline field is a triplet, whereas that of a Fe^{+++} ion is a singlet[18].) Then, it follows that the pair energies of magnetic ions, especially of cobalt ion and a vacancy, are affected by the change in their spin direction, resulting in non uniform distribution of the number of the pairs refered to the spin direction (Fig. 14).

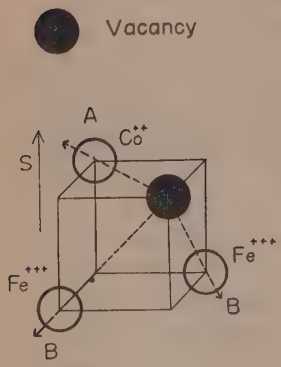

Fig. 14. Illustration of the directional order present between a cobalt ion, iron ions, and a cation vacancy. The smallest unit of cation arrangement on 16d sites in spinel is shown. Dotted arrows indicate the direction of the anisotropic crystalline field induced by the presence of a vacancy.

Accordingly, below the Curie temperature, where the magnetic moments in 16d sites are alligned parallel mutually, the directional short range ordering is expected to be formed along the direction of the magnetization. The directional order should increase as the temperature is lowered, as expected from Fig. 11, and would be fixed in the temperature range from 300°C to 200°C owing to the rapid decrease of the diffusion rate of cations. The uniaxial anisotropy at room temperature is thus formed by the presence of this directional ordering.

Even if the specimen is annealed without a magnetic field, each magnetic domain of the specimen has a uniaxial anisotropy along its spontanous magnetization but the total uniaxial anisotropy of the specimen is canceled out.

§ 8. Discussions on Other Mechanisms

Many mechanisms have been already presented for the origin of the uniaxial anisotropy in iron-cobalt ferrites. Bozorth *et al.* discussed these mechanisms in detail[10], pointing out certain difficulties involved in each of the mechanisms. Here, difficulties will be pointed out again from the stand point based on our experimental results.

The first mechanism[19], suggested by Néel, is the one which ascribes the uniaxial anisotropy to the directional order between cobalt ion and iron ion. It is a straightforward extension of the mechanism successful in explaining the magnetic annealing effect in metallic solid solutions. However, it has difficulties in explaining the observed strong dependence of the uniaxial anisotropy on the degree of oxidation. An assumption seems to be possible that the dependence is caused by the change of the diffusion rate of cations due to the change of the concentration of cation vacancies. But as can be seen from our various relaxation experiments (in § 3, and § 5), it is almost certain that we are dealing with the almost saturated value of the uniaxial anisotropy.

The second mechanism is the one which assumes the preferential growth of micro-precipitates of the second phase[20]. In this case two different mechanisms are considered: The one is based on the anisotropy induced by the change of magnetostatic energy with the direction of magnetization, and the other on the anisotropic surface energy due to the spin-orbit coupling of the magnetic ions as proposed by Néel[19]. The magnetostatic energy in this case, however, is estimated roughly by

$$E_u = \frac{1}{2}\Delta N \cdot (\Delta M_s)^2 \cdot v(1-v) \lesssim 10^5 \text{ ergs/cc} \quad (3)$$

where v is the total volume fraction of the precipitates. It is much smaller than that

observed experimentally ($\sim 10^6$ ergs/cc). It can not explain also the steep increase of the anisotropy at low temperatures. Therefore, the former mechanism by magnetostatic energy will not be applicable in this case. H. J. Williams *et al.*[11] stated recently that they had proved experimentally the existence of the second phase with spinel structure. However, their electron diffraction patterns of the second phase obtained for cobalt-zinc ferrites seem to involve some ambiguous points and they have not determined the composition of the second phase. The phenomenon of the torque reversal in single crystals of these ferrites, which they considered an evidence for the existence of the precipitates, should be regarded as a general property of single crystals which respond to magnetic annealing, as pointed out by Chikazumi and others[21].

According to the phase diagram in Fig. 1, it is probable that the relevant second phase is α hematite[22]. However, there are many experimental facts against the mechanism by precipitation of α hematite. Those are:

(1) Cobalt rich specimens ($r=0.333$ and 0.417) have also the uniaxial anisotropy of the same order of magnitude. It may be difficult to suppose the precipitates of α hematite existing in these specimens in the same order of amount as in the cobalt poor specimens.

(2) X-ray study has shown that the iron-cobalt ferrites are oxidized easily (and with appreciable decreases in lattice constants) without changing the crystal structure.

(3) The observation of the relaxation of the uniaxial anisotropy shows that the decaying down or growing up of the uniaxial anisotropy takes place fairly rapidly and the phenomenon has no critical temperature. At about 350°C, the change is finished almost within a minute. It will be difficult to assume that the shape of precipitates of α hematite is altered so rapidly at these temperatures. Relating to this consideration it should be also mentioned that in the experiments in § 3, the magnetic annealing effect does not decay down after the prolonged annealing.

The plastic deformation theory seems too poor to bear quantitative discussions. One more mechanism might be considered that some linear or planar imperfections such as dislocation lines or dislocated layers (analogous to the stacking fault in the extended dislocation) combine with the cobalt ions and make directional configurations. It should, however, be noticed that the density of such imperfections large enough to be effective for the uniaxial anisotropy must be much larger than that probably existing in the usual oxides.

Our mechanisms can account for all the experimental results well. Abovementioned fact (1) is explained by considering that the Co^{++} ions can be oxidized to Co^{+++} ions and accordingly vacancies must be also present in the cobalt rich specimens. The fact (2) is a convincing evidence for the existence of a considerable amount of cation vacancies. The fact (3) is quite natural in our mechanism, for the local order will easily change its directionality through several elementary processes of ionic migration.

It is added here that a suitable explanation can be given to the fact in Fig. 5 that the anisotoropy is rather small for pure cobalt ferrite. Namely, the composition might be especially favourable to make a certain short range order of iron and cobalt ions in the 16d sites in the meaning of the usual non-directional superstructure[23] and this tendency suppresses the growth of the directional local order between vacancies and cabalt ions; an analogous situation is seen in the case of Ni_3Fe.

Quite recently Oguchi[24] has performed a theoretical calculation of the uniaxial anisotropy in the case of our model. Assuming that the crystalline field on the 16d sites neighbouring a cation vacancy is orthorhombic, he has concluded that the energy of the cobalt ion at A position in Fig. 14 can be lower than that at B position by about 30 cm^{-1}. He gives a maximum of anisotropy along $\langle 100 \rangle$ direction and zero along $\langle 110 \rangle$ and $\langle 111 \rangle$. His result agrees in tendency with our experimental result shown in Fig. 12. The discrepancy should be mainly due to several simplified assumptions made by him.

Lastly, we will mention about the uniaxial anisotropy of other ferrites. According to our mechanism, every kind of other ferrites are expected to show the magnetic annealing effect to some extent after appropriate oxidation heat treatment, although the magnitude of the induced uniaxial anisotropy is to depend on both the manner of splitting of the orbital energy levels under the influence of the cry-

stalline field and the strength of the spin-orbit coupling of the metal ions concerned. We found that the iron-nickel ferrites show magnetic annealing effect which is also dependent on the degree of oxidation of the specimens[25]. This effect certainly exists also in iron-manganese ferrites, as infered from permeability measurements[26]. It can also be possible that Néel's mechanism, i.e., directional order without vacancy, is dominant in the case where the concentration of vacancies is very small.

Acknowledgments

We wish to express our hearty thanks to Prof. Seiji Kaya for his advice and constant encouragements. We also thank to Mr. Hiroshi Nakamura of the Mitsubishi Electric Mfg. Company for his kind communications of his data, to Mr. Takehiko Oguchi for permission to mention his unpublished results, and to Mr. Motoo Hori for his cooperation in the early stage of our study.

This research was financially supported by the Scientific Research Expenditure of the Ministry of Education.

Appendix Analysis of the Torque Curves

It is first assumed that the magnetic free energy of the (001) disc specimen in torque measurements is expressed as

$$E=K_1\sin^2\varphi\cos^2\varphi+K_u(\theta_T)\sin^2(\varphi-\theta_T)-HM\cos(\varphi-\theta) \qquad (1)$$

Here, φ, θ_T, θ are the angles of the directions of the magnetization M, of the annealing magnetic field and of the applied magnetic field H from [100] axis.

φ should be determined from the equation:

$$\frac{\partial E}{\partial\varphi}=0\,. \qquad (2)$$

The condition is rewritten as

$$\frac{K_u}{HM}\Big[\sin 2(\theta-\theta_T)\cos 2\varepsilon+2(\theta-\theta_T)\sin 2\varepsilon\Big]+\frac{K_1}{2HM}\Big[\sin 4\theta\cdot\cos 4\varepsilon+\cos 4\theta\cdot\sin 4\varepsilon\Big]+\sin\varepsilon=0 \qquad (3)$$

where

$$\varepsilon=\varphi-\theta\,. \qquad (4)$$

In our measurements, $K_u\approx1.5\times10^6$ ergs/cc, $K_1=2\times10^6$ ergs/cc and $HM\approx7\times10^6$ ergs/cc. So that

$$\frac{K_u}{HM}\approx0.21<1\,,\qquad \frac{K_1}{2HM}\approx0.14<1\,, \qquad (5)$$

Therefore, by expanding $\sin\varepsilon$ in the powers of $K_u/H\cdot M$ and $K_1/2\cdot H\cdot M$, we can obtain $\sin\varepsilon$ from Eq. (3) with successive approximation. Using this expression, the magnetic energy of the specimen is expressed as a function of θ.

$$\begin{aligned}E(\theta_T,\theta)=-\int L d\theta=&\frac{1}{2}K_u(\theta_T)+\frac{K_1}{8}\\&-\frac{K_u}{2}\cos 2(\theta-\theta_T)-\frac{K_1}{8}\cos 4\theta\\&-\frac{K_u}{2}\cdot\frac{K_1}{2HM}\cos 2(\theta+\theta_T)\\&+\frac{K_u}{2}\cdot\frac{K_u}{HM}\cos 4(\theta-\theta_T)\\&+\frac{K_u}{2}\cdot\frac{K_1}{2HM}\cos(6\theta-2\theta_T)\\&+\frac{K_1}{8}\cdot\frac{K_1}{2HM}\cos 8\theta+\cdots\end{aligned} \qquad (6)$$

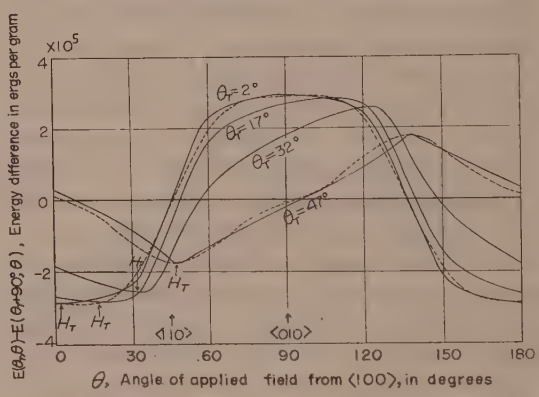

Fig. 15. Comparison of the experimental curves (full lines) and the calculated curves (dotted lines).

The expression can be simplified by taking the difference of the two curves in which the directions of the two annealing magnetic fields make a right angle. Namely,

$$\begin{aligned}&E(\theta_T,\theta)-E\Big(\theta_T+\frac{\pi}{2},\theta\Big)\\&=F(\theta_T,\theta)=-K_u\cos 2(\theta-\theta_T)\\&\quad-2K_u\cdot\frac{K_1}{2HM}\cdot 4\sin 4\theta\cdot\sin 2(\theta-\theta_T)\,.\end{aligned} \qquad (7)$$

Therefore,

$$F\Big(\theta_T,\theta_T+\frac{\pi}{2}\Big)-F(\theta_T,\theta_T)=2K_u\,. \qquad (8)$$

Basing upon these arguments, we performed

14 pairs of heat treatments in which every pair consists of two heat treatments with the applied magnetic fields at a right angle with each other. Some typical curves of $F(\theta_T, \theta)$ are shown in Fig. 15. The two dotted curves were drawn by calculating the right-hand side of Eq. (7), using the values of parameters K_u, and $K_1/2HM$ determined from the experimental curves. They fit fairly well with the experimental curves, showing the appropriateness of the procedure.

References

1) S. Kaya: Rev. Mod. Phys. **25** (1953) 49; S. Chikazumi: J. Phys. Soc. Japan **11** (1956) 551; S. Chikazumi and T. Oomura: J. Phys. Soc. Japan **10** (1955) 842.
2) R. D. Heidenreich and E. A. Nesbitt: J. Appl. Phys. **23** (1952) 352; E. A. Nesbitt and R. D. Heidenreich: J. Appl. Phys. **23** (1952) 366.
3) T. Mitui and S. Miyahara: J. Phys. Soc. Japan **10** (1955) 1023; S. Miyahara and T. Mitui: J. Phys. Soc. Japan **7** (1952) 536; S. Miyahara and T. Mitui: J. Fac. Sci. Hokkaido Univ. **4** (1953) 275.
4) C. A. Domenicali: Phys. Rev. **78** (1950) 458; H. J. Williams, R. M. Bororth and M. Goertz: Phys. Rev. **91** (1953) 1107; L. R. Bickford, Jr.: Rev. Mod. Phys. **25** (1953) 75.
5) Y. Kato and T. Takei: J. Inst. Elect. Engrs. Japan **53** (1933) 408; Y. Kato, T. Takei, N. Kawai and Aikawa: J. Chem. Japan **55** (1934) 584; T. Takei: Elect. Chem. Japan **5** (1937) 411; T. Takei, T. Yasuda, S. Ishihara: Electrotech. J. Japan **4** (1940) 75.
6) N. Kawai: Thesis to Tokyo Univ.
7) H. Nakamura: unpublished.
8) I. Sugiura: J. Appl. Phys. Japan **19** (1950) 198, 231; **20** (1951) 98.
9) C. Guillaud: Rev. Mod. Phys. **25** (1953) 64.
10) R. M. Bozorth, E. F. Tilden and A. J. Williams: Phys. Rev. **99** (1955) 1788.
11) H. J. Williams, R. D. Heidenreich and E. A. Nesbitt: J. Appl. Phys. **27** (1956) 885.
12) S. Iida, H. Sekizawa and Y. Aiyama: J. Phys. Soc. Japan **10** (1955) 907.
13) S. Iida: J. Phys. Soc. Japan **11** (1956) 846.
14) J. H. Epstein: M. I. T. Prog. Rep. **14** (1953) 46.
15) S. Chikazumi: J. Phys. Soc. Japan **5** (1950) 327; L. R. Bickford: Phys. Rev. **78** (1950) 449.
16) N. Sakamoto: unpublished.
17) E. J. W. Verwey and P. W. Haayman: Physica **8** (1941) 979; J. Martinet: C. R. **234** (1952) 2167.
18) B. Bleaney and K. W. H. Stevens: Repts. Prog. Phys. **16** (1953) 103.
19) L. Néel: J. Phys. Rad. **15** (1954) 225; S. Taniguchi and M. Yamamoto: Sci. Rep. Res. Inst. Tōhoku Univ. **A6** (1954) 330; S. Taniguchi: Sci. Rep. Res. Inst. Tōhoku Univ. **A7** (1955) 269.
20) L. Néel: C. R. **225** (1947) 109; L. A. Shubina and J. S. Shru: J. Tech. Phys. USSR **19** (1949) 88; C. Kittel, E. A. Nesbitt and W. Shockley: Phys. Rev. **77** (1950) 739.
21) S. Chikazumi: J. Phys. Soc. Japan **11** (1956) 718.
22) R. M. Bozorth: "*Ferromagnetism*" Van Nostrand, New York (1951) 422.
23) E. W. Gorter: Philips Res. Rep. **9** (1954) 295, 403.
24) T. Oguchi: unpublished.
25) Y. Aiyama, H. Sekizawa and S. Iida: J. Phys. Soc. Japan **12** (1957) 742.
26) S. Iida: unpublished.

JOURNAL OF THE PHYSICAL SOCIETY OF JAPAN Vol. 13, No. 1, JANUARY, 1958

Narrowing Effect in Nuclear Magnetic Double Resonance in Solids

By Yushiro SAITO

Department of Physics, Kobe University

(Received September 9, 1957)

Experiments on nuclear magnetic double resonance were performed in several ionic crystals of type AB where the resonance behavior of the A-spin was investigated under the irradiation of strong rf field resonating to the B-spin. At the strongest rf field experimented, narrowing of the line width was observed and this fact showed evidently that the local field at the position of A-spin originating from B-spin was averaged out to zero. By using this principle the origin of the anomalously broad line width in TlBr crystal was pursued. The experimental results supported our suggestion that the broad line width would be attributable to the indirect nuclear spin-spin coupling. The second moment of the line width in double resonance calculated by the use of rotating coordinate system was in agreement with the experimental value.

§ 1. Introduction

Recently the technique of the double resonance has been applied to various problems, especially the precise measurement of the h.f. coupling constant,[1] the determination of the molecular structures,[2] the analysis of the relaxation time,[3] the nuclear polarization,[3),4] the Maser[5] and so on.[6] But there have been few[7] of the n.m. double resonance experiments in *Solids*. In this paper we reported the experimental results of the n.m. double resonance in solids, discussed the condition for narrowing of the line width in a double resonance experiment, and analysed the origin of the anomalously broad line width in TlBr crystal.

In some of the thallium halide crystals, the observed line widths are much larger than the theoretical ones calculated by the direct dipolar couplings between nuclear magnetic moments. For example, the observed second moments of the Tl^{205} and the $Br^{79,81}$ resonances in TlBr crystal are both about ten times larger than the calculated ones. Yosida and Moriya[8] estimated the line width due to the indirect $\boldsymbol{I}\cdot\boldsymbol{I}$ coupling caused by the partially covalent bonding in ionic crystals. To get the coupling constant appropriate to the experimental line width, the theory needed a great degree of covalency between the thallium and the bromine atoms which was inconsistent with the chemical shift data of n.m. resonance[9] of the Br spin. Therefore, it was desired to analyse the contribution of each constituent magnetic isotope to the line width. The narrowing effect observed in our double resonance experiments is well fitted for this purpose as will be stated below.

Hereafter we will call it the "AB-experiment" where the former, "A" denotes the nucleus whose resonance behavior is under investigation with the weak rf field and the latter, "B", the nucleus irradiated by the strong rf field.

§ 2. Experiments and Results

The AB-experiment was performed by the use of permanent magnet of field strength either of 6200 gauss or of 3900 gauss. Keeping the frequency f_B constant, n.m. resonance of the A-spin was observed by sweeping the frequency f_A by a slow rotation of the axis of the variable condenser of the autodyne detector. Experimental diagram is shown schematically in Fig. 1. As the rf voltage applied to the coil B amounted to as much as 800 volts (effective value) we had to prevent the coil from heating up by blowing the air cooled by the freezing mixture (dry ice and ethyl alcoholsystem). For the measurements of the net effect of strong rf field resonating to the B-spin, the line width and the intensity of A-resonance in the just-resonant case, $f_B=f_B^0$, were compared with those in the completely off-resonant case, $f_B \gg f_B^0$ or $f_B \ll f_B^0$, alternately, in order to cancel the spurious effects

caused by the strong irradiating field.

In the case of $f_B = f_B^0$ and in some kinds of crystals having rather long relaxation time, as we increased the rf voltage of f_B, the intensity of A-resonance gradually decreased and finally disappeared from observation. We call this phenomenon "collapsing". As the field strength was further increased, the resonance line appeared again, but in this time with a narrowed line width. This narrowing effect was observed in *all* the crystals experimented and so, these two phenomena, collapsing and narrowing, are considered to be of different origins. Since the collapsing is not yet thoroughly interpreted, we here report only about the narrowing effect.

Consider the $Tl^{205}F^{19}$-experiment. While the rf field $2H_2 \cos \omega_2 t$ was irradiated to the F^{19} spin, the resonance line of the Tl^{205} spin was observed. The variation of the maximum slope separation $(\Delta H)_{ms}$ of Tl^{205} resonance with the strength of the rf field H_2 is shown in Fig. 2 and Photo. 1. In Fig. 2 the dotted line corresponds to the region where the collapsing was observed and hence the width could not be measured exactly. The intensity

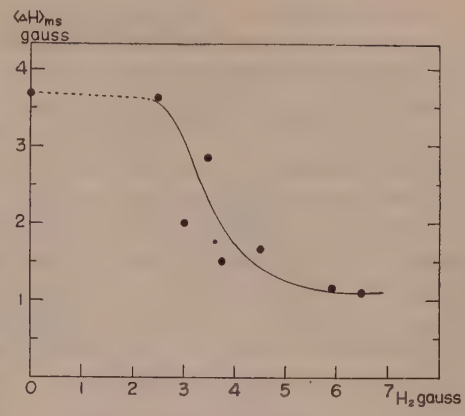

Fig. 2. Variation of the maximum slope separation $(\Delta H)_{ms}$ of Tl^{205} resonance with the strength of rf field H_2 irradiating to F^{19} spin in $Tl^{205}F^{19}$-experiment.

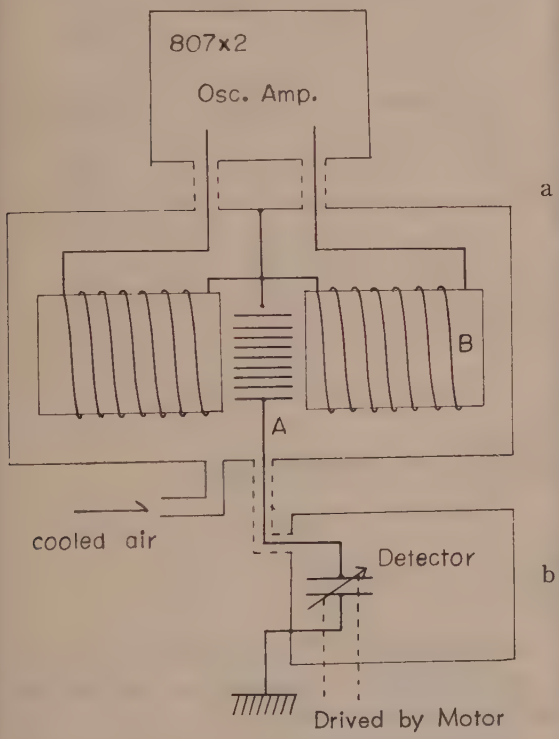

Fig. 1. Block diagram of the expermiental apparatus.

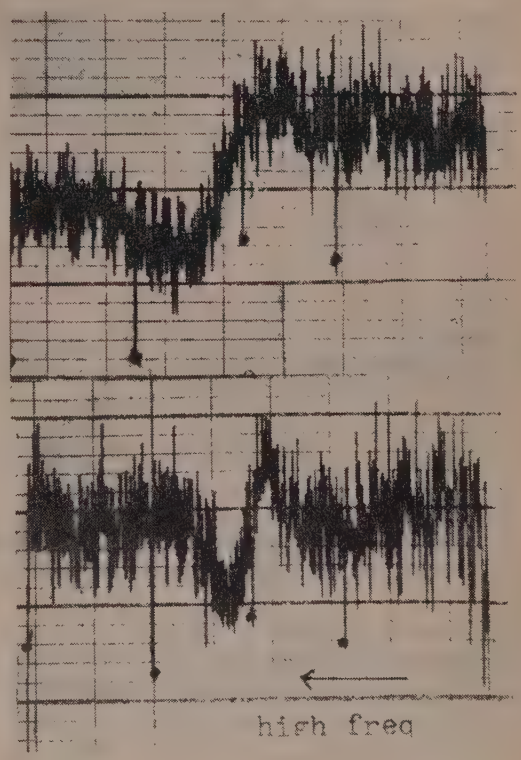

Photo. 1. Experimental recordings of the derivative of the n.m. double resonance absorption in $Tl^{205}F^{19}$-experiment. Vertical marks are separated each by 5 kc/sec.

a) off-resonant case, $f_F - f_F^0 \doteqdot 100$ kc/sec ($f_F^0 = 16.0$ Mc/sec.), which is the same as the case of single resonance.

b) just-resonant case, $f_F = f_F^0$, which shows the narrowed width compared to the case a).

(maximum deflection of the derivative curve) of the most narrowed resonance was unexpectedly approximately the same as that of the original broad resonance. But the intensity problem in the $Tl^{205}F^{19}$-experiment cannot be further discussed because of the simultaneous occurrence of the collapsing effect.

In Table I are listed the calculated second moments[11] contributed from each constituent isotope under the assumption of the direct dipolar coupling alone, and also the observed second moments in single and double resonances in TlF and TlBr crystals. The condition for narrowing will be discussed in Sec. 3 in terms of the relation of the strength of rf field to the line width. The line shape in single resonance in these crystals was nearly Gaussian. In the double resonance experiments, we had to use as small an amount of powder sample as possible in order to produce the large strength of rf field. Accordingly the resonance was inevitably of low S–N ratio, so that the second moment in double resonance experiment was forced to be estimated from the peak-to-peak separation of a derivative curve under the assumption of Gaussian shape. In the case of $Tl^{205}F^{19}$-experiment (the 3rd column in Table I), the narrowed width

Table I. Calculated second moments from constituent isotopes and experimental values in single and double resonances in TlF and TlB crystals.

crystal	TlF		TlBr	
observed nucles	F^{19}	Tl^{205}	$Br^{81,79}$	Tl^{205}
dipolar contribution from halogen nuclei	1.31 gauss^2	2.13 gauss^2	0.17 gauss^2 0.16 [2]	0.25 gauss^2
dipolar contribution from Tl^{205} nucleus	0.51	0.31	0.18	0.16
dioplar contribution from Tl^{203} nucleus	0.21	0.06	0.07	0.03
total $\langle \Delta H^2 \rangle_{cal}$	2.03	2.50	0.42 0.41 [2]	0.44
$\langle \Delta H^2 \rangle_{exp}$ in single resonance	2.6	3.1	10.2	20.4
$\langle \Delta H^2 \rangle_{exp}$ in double resonance[1]	1.7 ($F^{19}Tl^{205}$ – exp)	0.3 ($Tl^{205}F^{19}$ – exp)	3.7 ($Br^{81,79}Tl^{205}$ – exp)	
			7.4 ($Br^{81,79}Tl^{203}$ – exp)	

1) estimated from Gaussian-shape assumption.
2) upper figure being for Br^{81} and lower one for Br^{79}.

of 0.3 gauss^2 is almost in agreement with the difference between the calculated total width of 2.5 gauss^2 and the width of 2.1 gauss^2 from the F^{19} spin, or with the width of 0.4 gauss^2 from only Tl^{203} and Tl^{205} spins. This fact shows evidently that the field, existing at the location of the Tl spin and originating from the F spin, is averaged out to zero, and that the remaining local field is due to only Tl^{203} and Tl^{205} spins. And further referring to the 6th and 7th rows of this Table, we see that the second moments of Tl and Br resonances in TlBr crystal calculated from the above-mentioned dipolar assumption account for only a few per cent of the experimental values. The peak-to-peak separation reduced to about 60 per cent of original one in $Br^{79,81}$ Tl^{205}-experiment and to about 85 per cent in $Br^{79,81}$ Tl^{203}-experiment. The contribution of the Tl^{205} spin to the second moment of $Br^{79,81}$ resonance was proved, by our double resonance experiments, to be 64 per cent, and that of the Tl^{203} spin to be 28 per cent of total ones. Taking into account the magnetic moment ratios and abundances of these two isotopes, the experimental results confirmed that the broadening originated from the interaction between nuclear spins themselves and not from, say, pa-

ramagnetic impurities and so on.

§ 3. Discussion

Consider a crystal which includes three spin species A (S, g, $j=1, 2, \cdots N$), B' (S', g', $j'=1, 2, \cdots N'$) and C'' (S'', g'', $j''=1, 2, \cdots N''$) and a case when a strong rf field is impressed to B'-spin and a weak rf field for observation to A-spin. The total Hamiltonian of the system in Van Vleck's notation[12] is the sum of

$$\mathscr{H}=\mathscr{H}_z+\mathscr{H}_{\text{dip.+ex.}}+\mathscr{H}_{\text{strong rf}} \tag{1}$$

and

$$\mathscr{H}_{\text{det. rf}}$$

where

$$\mathscr{H}_z=g\beta H_0\sum_j S_{zj}+g'\beta H_0\sum_{k'} S'_{zk}+g''\beta H_0\sum_{l''} S''_{zl''} \tag{2}$$

$$\mathscr{H}_{\text{dip.+ex.}}=\sum_{j\neq k}\mathscr{H}_{jk}+\sum_{j'\neq k'}\mathscr{H}_{j'k'}+\sum_{j''\neq k''}\mathscr{H}_{j''k''}+\sum_{jk'}\mathscr{H}_{jk'}+\sum_{jl''}\mathscr{H}_{jl''}+\sum_{k'l''}\mathscr{H}_{k'l''} \tag{3}$$

$$\mathscr{H}_{jk}=\frac{1}{2}(A_{ik}\boldsymbol{S}_j\cdot\boldsymbol{S}_k+B_{jk}S_{zj}S_{zk})$$

etc. (between like spins) (4)

$$\mathscr{H}_{jk'}=C_{jk'}S_{zj}S'_{zk'}$$

etc. (between unlike spins) (5)

$$\mathscr{H}_{\text{strong rf}}=g'\beta\sum_{k'} S'_{xk'}2H_2\cos\omega_2 t \tag{6}$$

$$\mathscr{H}_{\text{det. rf}}=g\beta\sum_j S_{xj}2H_1\cos\omega_1 t\,. \tag{7}$$

In the above Hamiltonian, A_{jk} and $C_{jk'}$ correspond to the expressions (6) and (26) of Van Vleck's paper, respectively, that is, contain dipolar and exchange couplings.

Transform this Hamiltonian by the operator

$$R_{z\omega_2 t}=\exp\left[-i\omega_2 t\sum_j S_{zj}\right]\cdot\exp\left[-i\omega_2 t\sum_{k'} S'_{zk'}\right]\times\exp\left[-i\omega_2 t\sum_{l''} S''_{zl''}\right] \tag{8}$$

to the r-system[13] (rotated around the z-axis by an angle $\omega_2 t$) and then transform the B′ spin-coordinate alone by the operator

$$R_{y\theta}=\exp\left[-i\theta\sum_{k'} S'_{yk'}\right] \tag{9}$$

to the ρ-system (rotated around the y-axis by an angle $\theta=\tan^{-1}[\gamma H_2/(\omega_2-\omega_0')]$, which is the angle between the z-axis and the direction of the effective field for the B′spin, ω_0' being resonance frequency of the B′-spin). And we get:

$$\mathscr{H}^\rho=\mathscr{H}_z{}^\rho+\sum_{j\neq k}\mathscr{H}_{jk}+\sum_{j'\neq k'}\mathscr{H}^\rho_{j'k'}+\sum_{j''\neq k''}\mathscr{H}_{j''k''}+\sum_{jk'}\mathscr{H}^\rho_{jk'}+\sum_{k'l''}\mathscr{H}^\rho_{k'l''}+\sum_{jl''}\mathscr{H}_{jl''} \tag{10}$$

and

$$\mathscr{H}^\rho_{\text{det. rf}}=g\beta H_1\left[\sum_j S_{zj}\cos(\omega_1-\omega_2)t-\sum_j S_{yj}\sin(\omega_1-\omega_2)t\right] \tag{11}$$

where

$$\mathscr{H}^\rho_z=g\beta(H_0-\omega_2/\gamma)\sum_j S_{zj}+g'\beta[(H_0-\omega_2/\gamma')^2+H_2^2]^{1/2}\sum_{k'} S'_{zk'}+g''\beta(H_0-\omega_2/\gamma'')\sum_{l''} S''_{zl''} \tag{12}$$

$$\mathscr{H}^\rho_{j'k'}=\frac{1}{2}\Big[A_{j'k'}\boldsymbol{S}'_{j'}\cdot\boldsymbol{S}'_k+B_{j'k'}\cos^2\theta S'_{zj'}S'_{zk'}+\frac{1}{4}B_{j'k'}\sin^2\theta(S'^+_{j'}S'^+_{k'}+S'^-_{j'}S'^-_{k'}+S'^+_{j'}S'^-_{k'}+S^-_{j'}S^+_{k'})+\frac{1}{2}B_{j'k'}\sin\theta\cos\theta\{S'_{zj'}(S'^+_{k'}+S'^-_{k'})+S'_{zk'}(S'^+_{j'}+S'^-_{j'})\}\Big] \tag{13}$$

$$\mathscr{H}^\rho_{jk'}=C_{jk'}S_{zj}\left[S'_{zk'}\cos\theta+\frac{1}{2}(S'^+_{k'}+S'^-_{k'})\sin\theta\right] \tag{14}$$

$$\mathscr{H}^\rho_{k'l''}=C_{k'l''}S''_{zl''}\left[S'_{zk'}\cos\theta+\frac{1}{2}(S'^+_{k'}+S'^-_{k'})\sin\theta\right]. \tag{15}$$

Applying the Van Vleck's method to ρ-system, it follows that

$$h^2\langle\nu_\rho{}^2\rangle_{\text{Av}}=-\frac{T_r[U^\rho]^2}{T_r[\mathscr{H}^\rho_{\text{det. rf}}]^2}$$

and (16)

$$h^4\langle\nu_\rho{}^4\rangle_{\text{Av}}=\frac{T_r[\mathscr{H}^\rho U^\rho-U^\rho\mathscr{H}^\rho]^2}{T_r[\mathscr{H}^\rho_{\text{det. rf}}]^2},$$

where

$$U^\rho=\mathscr{H}^\rho\mathscr{H}^\rho_{\text{det. rf}}-\mathscr{H}^\rho_{\text{det. r}}\mathscr{H}^\rho\,. \tag{17}$$

In the above expression $\langle\nu_\rho{}^2\rangle_{\text{Av}}$ means the

mean square deviation of the frequency of A-resonance spectrum from the frequency of irradiating field $\omega_2/2\pi$.

Under the condition

$$g'\beta H_2 \gg g\beta H_{\rm loc} = \sum (A_{jk}, B_{jk}, C_{jk'}, C_{jl''}) , \quad (18)$$

where $2H_{\rm loc}$ means the peak-to-peak separation of A-resonance, the side bands resulted from the terms including $\mathbf{S}'_{k'}{}^{\pm}$ do not overlap the central one. Then by the use of the "truncated" Hamiltonian missing such terms as $\mathbf{S}_{zj}\cdot S'_{k'}{}^{\pm}$, the second moment in the ρ-system is obtained as follows:

$$h^2\langle \Delta\nu^2\rangle_{\rm Av} = \frac{1}{3} S(S+1)\sum_k B_{jk}^2 + \frac{1}{3} S'(S'+1) \sum_{k'} C_{jk'}^2 \cos^2\theta + \frac{1}{3} S''(S''+1) \sum_{l''} C_{jl''}^2 . \quad (19)$$

In the case of just-resonance, $f_{\rm B} = f_{\rm B}^{\circ}$, and of strong rf field $H_2 \gg (g/g')H_{\rm loc}$, we may put $\cos\theta = 0$ and then both dipolar and exchange couplings with B′-spin cease to contribute to the second and the fourth moments of A-resonance, whereas the contribution from A and C'' spins leaves unchanged. In the $Tl^{205}F^{19}$- and $F^{19}Tl^{205}$-experiments, the above results were confirmed quantitatively (Fig. 2, and Table I).

In our experiments, the necessary condition for narrowing, that is, the expression (18) was satisfactorily fulfilled as shown in Table II and the complete narrowing was experimentally ascertained.

Finally, consider the origin of the anomalously broad resonance width in TlBr-crystal. As seen from Table I, the total second moment of the Br single resonance and the narrowed moment of the $BrTl^{205}$-experiment are 10.2 gauss² and 3.7 gauss², respectively, and

Table II. The relation between the strength of irradiating field $2H_2 \cos\omega_2 t$ and the line width of observed spin.

experimental type	$Tl^{205}F^{19}$	$F^{19}Tl^{205}$	$Br^{79,81}Tl^{205}$	$Br^{79,81}Tl^{203}$	$Tl^{205}Br^{81}$
$H_{\rm loc}$ 1)	gauss 1.95	gauss 1.53	gauss 3.4	gauss 3.4	gauss 5.6
$(\gamma/\gamma')H_{\rm loc}$	1.3	2.3	1.6	1.6	12
H_2	7	15	10	10	

1) $2H_{\rm loc}$ means the maximum slope separation of the observed resonance.
2) The unprimed γ is the gyromagnetic ratio of the observed spin and the primed γ' is of the irrrdiated spin.

we may expect that the difference between them corresponds to the contribution from the Tl^{205} spin. We see from this Table that this differences, 6.5 gauss², is nearly equal to the moment in the $BrTl^{203}$-experiment, 7.4 gauss², which includes the contributions from Tl^{205} and Br nuclei. These experimental results show that the contributions to Br resonance width from Br spins or nuclear electric quadrupole coupling are negligibly small. Possible quantitative explanation of broad line widths will be given below.

When two atoms A and B are covalently bonded in a crystal through their s or p electrons, the exchange or dipolar coupling between electron and nucleus will produce an indirect spin-spin coupling between A and B nucleus. Generally, this coupling is expressed as a sum of the exchange type and the dipolar type;

$$\mathscr{H}_{\rm AB} = a\gamma_{\rm A}\gamma_{\rm B}\hbar^2 \boldsymbol{I}_{\rm A}\cdot\boldsymbol{I}_{\rm B} + b\gamma_{\rm A}\gamma_{\rm B}\hbar^2\{\boldsymbol{I}_{\rm A}\cdot\boldsymbol{I}_{\rm B} - 3(\boldsymbol{R}\cdot\boldsymbol{I}_{\rm A})(\boldsymbol{R}\cdot\boldsymbol{I}_{\rm B})\} \quad (20)$$

where $\boldsymbol{R}$ is a unit vector connecting A and B nucleus. Expressions of a and b are listed in Table III for s and p electronic wave functions belonging to A or B atom. Using $4p$-orbital of Br atom and $7s$-orbital of Tl atom, $\langle 1/r^3\rangle_p$ given by Barnes and Smith[14], h.f.s.-constant[15], and corrected excitation energy[5], we get the degree of covalency per bond of 33 per cent to interprete the experimental line width. The change of $7s$ of Tl to $6p$ orbital will give too weak a coupling to inter-

prete the width (Table IV). On the other hand, the chemical shift of Br-resonance is explained by the covalency per bond of 4.4 per cent[9] and that of Tl resonance by the covalency of 9.4 per cent.[16]

Table III. The coefficients a and b of the indirect exchange and the pseudo-pipolar couplings in the Expression (20).

electronic orbital A	electronic orbital B	a	b
s	s	$\frac{\beta^2}{\Delta E}\frac{128\pi^2}{9}\lvert\psi_A(0)^2\psi_B(0)^2\rvert$	0
s	p	0	$\frac{\beta^2}{\Delta E}\frac{32\pi}{15}\lvert\psi_A(0)\rvert^2\left\langle\frac{3}{r^3}\right\rangle_B$
s	p	$\frac{\beta^2}{\Delta E}\frac{16}{25}\left\langle\frac{1}{r^3}\right\rangle_A\left\langle\frac{1}{r_3}\right\rangle_B$	$\frac{\beta^2}{\Delta E}\frac{8}{25}\left\langle\frac{1}{r^3}\right\rangle_A\left\langle\frac{1}{r^3}\right\rangle_B$

Table IV. Numerical values of a and b.

electronic orbital Tl	electronic orbital Br	calc. (10^{23} cm^{-3})	exp. (10^{23} cm^{-3})	covalency (%)
$7s$	$4p$	$b=4.5$	$b=1.5$	33
$6p$	$4p$	$a=0.32$ $b=0.16$	$a=1.34$ $b=0.67$	420

The discrepancy between the covalency obtained from the chemical shift and that obtained from the line width of the Br-resonance may be partly due to (i) some amounts of s–p hybridization, because an s-part is ineffective to the chemical shift and a p-part to the line width, and (ii) the difference of $|\psi_{Tl}(0)|^2$ in solid state from that in atomic state. And moreover, from the analysis of the chemical shift of the Tl resonance we get much larger degree of covalency than that from the Br resonance, as mentioned above. This is interpreted by the presence of covalent bonding between Tl atoms which is consistent with the following conclusion resulted from the line width analysis: using the coupling constant between Tl and Br spins, the second moment of Tl resonance is calculated to be contributed from the Br spins by 50 per cent of its total value and by the remainder 50 per cent presumbly from remote Tl spins. On this problem the TlBr-experiment would give us the decisive evidence, but it was not performed because (i) much stronger rf field was required for the TlBr-experiment than for the BrTl-experiment to satisfy the necessary condition for narrowing (18), and (ii) only the transition $+\frac{1}{2}\leftrightarrow-\frac{1}{2}$ might be observed owing to the quadrupole coupling and so the Br nucleus in other spin states than $\pm\frac{1}{2}$ would not be effected by the rf field.

§ 4. Concluding Remarks

Here we reported only the case of just resonance $f_B=f_B^0$. When f_B was slightly deviated from the center of the resonance line, the line shape of A-resonance displayed a remarkable asymmetry. Interpretation is not yet done and we will postpone the discussion to a future time.

The author wishes to express his gratitude to Professor T. Kanda under whose direction this work was performed. He is grateful also to Assistant Professor Y. Masuda for his kind cooperation throughout this experiment and to Mr. A. Tsunekawa for his technical assistance. This work has been supported in part by the Scientific Research Expenditure of Ministry of Education.

References

1) N. W. Lord: Phys. Rev. **105** (1957) 756.
G. Feher: Phys. Rev. **105** (1957) 1122.
2) J. N. Shoolery: Discuss Farad. Soc. **19** (1955) 215.
3) W. G. Procter and W. Tantilla: Phys. Rev. **101** (1956) 1757.
W. G. Procter and W. A. Robinson: Phys. Rev. **104** (1956) 1344.
N. Bloembergen: Phys. Rev. **104** (1956) 1542.
4) T. R. Carver and C. P. Slichter: Phys. Rev. **102** (1956) 975.
H. G. Berjers, L. Van der Kint and J. S. Van Wieringen: Phys. Rev. **95** (1954) 1683.
5) J. P. Gordon, M. J. Zeiger and C. H. Townes: Phys. Rev. **99** (1955) 1264.
H. E. D. Scovil, G. Feher and H. Seidel: Phys. Rev. **105** (1957) 762.
6) A. L. Bloom and J. N. Shoolery: Phys. Rev. **97** (1955) 1261.
A. G. Redfield: Phys. Rev. **98** (1955) 1787.
W. A. Anderson: Phys. Rev. **102** (1956) 151.
S. H. Autler and C. H. Townes: Phys. Rev. **100** (1955) 703.
G. Feher: Phys. Rev. **103** (1951) 834.
7) L. R. Sarles and R. M. Cotts: Bull. Am.

Phys. Soc. II **1** (1956) 282.
B. Herzog and E. L. Hahn: Phys. Rev. **103** (1956) 148.
8) K. Yosida and T. Moriya: J. Phys. Soc. Japan **11** (1956) 33.
9) T. Kanda: J. Phys. Soc. Japan: **10** (1955) 85.
10) C. Kittel: Phys. Rev. **95** (1954) 589.
A. Abragam: Phys. Rev. **98** (1955) 1729.
F. Bloch: Phys. Rev. **102** (1956) 104.
11) H. S. Gutowsky and B. R. McGarvey: J. Chem. Phys. **20** (1952) 1472.
12) J. H. Van Vleck: Phys. Rev. **74** (1948) 1168.
13) A. G. Redfield: Phys. Rev. **98** (1955) 1787.
14) R. G. Barnes and W. V. Smith: Phys. Rev. **93** (1954) 95.
15) H. E. White: Introduction to Atomic Spectra (McGraw-Hill Book Company, Inc., New York, 1934) 1st ed. p. 363.
16) T. Kanda et al: the Annual Meeting of the Physical Society of Japan, Osaka, November, 1954.

JOURNAL OF THE PHYSICAL SOCIETY OF JAPAN Vol. 13, No. 1, JANUARY, 1958

Theory of Dilute Polymer Solutions (I)†
Chain Configuration and Light Scattering

By Hiromi YAMAKAWA* and Michio KURATA**

*Department of Textile Chemistry and **Department of Industrial Chemistry, Kyoto University, Kyoto, Japan

(Received October 2, 1957)

Statistical properties of a single polymer-chain in a continuous medium are studied on the basis of the pearl-necklace model. Proper account is taken of the spatial interference between segments and of the effect of a heat of interaction between solvent and polymer. The $2m$-th moment of the distribution function of the distance between k-th and l-th segments $\langle R_{kl}^{2m}\rangle$, the mean square distance between k-th segment and the molecular center of mass $\langle S_k^2\rangle$, and the mean square radius of gyration $\langle S^2\rangle$ are calculated by using Ursell-Mayer-Teramoto's method of expanding the chain phase integral. The results obtained are of non-Markoffian character at any temperature but the Flory point, and are qualitatively in consistency with the experimental data of lattice chain obtained by direct counting of its configurations. The angular distribution of scattered light is also calculated and a method is proposed to evaluate $\langle S^2\rangle$ by the dissymmetry method.

§ 1. Introduction

Whether the introduction of the long-range excluded volume effect into the polymer chain statistics changes the Markoffian character of the chain or not, proposes an interesting problem in both mathematical and statistical-mechanical senses, and has close relation to the various properties of the solution. According to Flory,[1] the mean square end-to-end distance $\langle R^2\rangle$ is given by

$$\langle R^2\rangle \propto M^{1+\varepsilon} \qquad (0<\varepsilon<0.2)\,,$$

where M is the molecular weight, and the polymer chain can never be regarded as the Markoffian. This is inevitably of importance for theoretical interpretation of the intrinsic viscosity[1),2)] and other physical properties.

A number of ways of approach, accordingly, has been presented by many researchers to the excluded volume effect. In 1951, Teramoto[3)] has developed the statistical theory of a chain polymer based on the Ursell-Mayer method of imperfect gas theory and justified the conclusion of Flory. Thereafter, Zimm and others[4)-7)] have reached the similar conclusion. On the other hand, Teramoto, Kurata and their coworkers[8)] have made clear by direct counting of the possible configuratiosn of lattice chains that the excluded volume effect gives the distribution function of the

† For the preliminary reports of this work see ref. 14.

end-to-end distance considerably different from a Gaussian type, and that the ratio of $\langle R^2 \rangle$ to the mean square radius of gyration $\langle S^2 \rangle$ exceeds the value 6 for Gaussian chain.

However, in most previous theories except the Flory's, the effect of a heat of interaction between solvent and polymer has not explicitly been taken into consideration and thereby some difficulties in the experimental verification have been raised. Accordingly, it would be interesting to discuss from a unified standpoint the various physical properties connected with the excluded volume effect taking account of the segment size as well as the dispersion energy (or heat of interaction) between segments.

In the present paper, the excluded volume effect is discussed for a single polymer chain present in dilute solution. We follow the outline of Teramoto's method,[3] and then calculate the $2m$-th moment of the distribution function of the distance between k-th and l-th segments $\langle R_{kl}^{2m} \rangle$, that of the end-to-end distance $\langle R^{2m} \rangle$, and the mean square radius of gyration $\langle S^2 \rangle$, etc. Our results qualitatively account for the experimental data for lattice chains obtained by Teramoto-Kurata.[8] The introduction of the effect of dispersion energy between segments makes it possible to discuss the Flory point in poor solvents and the influences of temperature and of solvents on the chain configurations. The present paper will be closed by the discussions on the excluded volume effect on the dissymmetry ratio in the light scattering.

§ 2. Model and Formulation

Suppose the polymer chain, in which $N+1$ spherical segments (with diameter b) are connected one after the other with a constant bond length a and are attached numbers $0, 1, 2, \cdots, N$ from one end to the other (pearl-necklace model). Their coordinates, according to McMillan-Mayer's symbolisms,[9] are represented by $(0), (1), (2), \cdots, (N)$, and the coordinate set and the number set of n segments are denoted by $\{n\}=(1), (2), \cdots, (n)$ and $[n]=1, 2, \cdots, n$, respectively.

For the sake of simplicity, the chain is assumed to be completely flexible; the short range interferences, for example, the hindrance to the free rotation about the single bonds, are neglected. However we take into consideration the short range forces like the van der Wall's forces between solvent molecules, between segments, and between solvent molecules and segments. Now if we adopt a continuous medium approximation, the potential $\phi(r_{ij})$ of mean force between segments may be assumed to be additive, where r_{ij} is the distance between segments i and j, being $r_{ij}=|(j)-(i)|$. Accordingly the potential energy of this system Φ may be written in the form,

$$\Phi\{N+1\}=\sum_{\substack{0\leq i<j\leq N\\ j-i\neq 1}} \phi(r_{ij}) \equiv \sum \phi_{ij} \,. \qquad (1)$$

Here the summation extends over all segment pairs except $j-i=1$ (chemical bond).

For this system the problem is formally the same as that of imperfect gases, namely the evaluation of the partition function

$$\Omega(R_{kl}, N, T)$$
$$=\iint_{|(i+1)-(i)|=a}\cdots\int \exp\left[-\sum \phi_{ij}/kT\right] d\{N-1\} \qquad (2)$$
$$=\iint_{|(i+1)-(i)|=a}\cdots\int \Big[1+\sum_{\substack{0\leq i<j\leq N\\ j-i\neq 1}} f_{ij} + \sum\sum f_{ij} f_{mn} + \cdots\Big] d\{N-1\} \qquad (2')$$

with

$$f_{ij}=\exp(-\phi_{ij}/kT)-1 \,, \qquad (3)$$

where the integration extends over all the possible configurations under the conditions of constant bond length a and of fixing segment k to origin and segment l to a point at distance R_{kl} from the origin; i.e. $R_{kl}\equiv r_{kl}=|(l)-(k)|$. The partition function Ω is a function of R_{kl}, N, temperature T, and segment numbers k and l, but abbreviated to $\Omega(R_{kl})$ hereafter.

Teramoto[3] has shown that, fixing both ends with the distance R $(\equiv R_{0N})$, the partition function $\Omega(R)$ can be expanded in ascending order μ of interaction between segments. His method can be easily extended to apply to $\Omega(R_{kl})$, and we obtain

$$\Omega(R_{kl})=\sum_{\mu=0}^{N} B_\mu(R_{kl}) \qquad (4)$$

with

$$B_0(R_{kl})=\iint_{|(i+1)-(i)|=a}\cdots\int d\{N-1\} \qquad (5)$$
$$=\iint \Omega_0(r_{0k}, k)\Omega_0(r_{kl}, l-k) \times \Omega_0(r_{lN}, N-l)\, d(0)\, d(N) \,, \qquad (5')$$

$$B_\mu(R_{kl})=\sum_{\kappa=\mu+1}^{2\mu}\mathscr{F}_\mu^\kappa(R_{kl}) \qquad (\mu\geq 1)\,, \tag{6}$$

$$\mathscr{F}_\mu^\kappa(R_{kl})=\sum_{\substack{\text{conf.}\\(\kappa_1,\kappa_2,\kappa_3=\text{const})}}\ \sum_{\kappa_1+\kappa_2+\kappa_3=\kappa} F_\mu(R_{kl},[\kappa])\,, \tag{7}$$

$$\begin{aligned}F_\mu(R_{kl},[\kappa])&\\ =\iint\cdots\int \sum_{\substack{ij\in[\kappa]\\ \text{cluster}\\ \text{number}=\kappa-\mu}}\prod & f_{ij}\Omega_{\kappa_1}(r_{0k},k,\{\kappa_1\})\\ &\times\Omega_{\kappa_2}(r_{kl},l-k,\{\kappa_2\})\\ &\times\Omega_{\kappa_3}(r_{lN},N-l,\{\kappa_3\})\,d\{\kappa+2\}\,,\end{aligned} \tag{8}$$

$$\Omega_\kappa(r,n,\{\kappa\})=\iint\cdots\int_{|(i+1)-(i)|=a} d\{n-1-\kappa\} \tag{9}$$

$$=\prod_{(i<j)\in[\kappa]}\Omega_0(r_{ij},j-i)\,, \tag{9'}$$

$$\Omega_0(r,n)=\iint\cdots\int_{|(i+1)-(i)|=a} d\{n-1\}\,, \tag{10}$$

where $\Omega_0(r,n)$ is the partition function of an ideal random flight chain composed of $n+1$ segments, fixing both ends with the distance r. $\Omega_\kappa(r,n,\{\kappa\})$ is the *partial* phase integral of this chain, and the integrations in Eq. (9) extend over the coordinates of all segments except some κ and both end ones. The integrations in Eq. (8) are performed over the coordinates of both end segments and of κ ones in the state of interaction (κ_1, κ_2 and κ_3 of them belong to the subchains $-1(0\sim k)$, $-2(k\sim l)$ and $-3(l\sim N)$ respectively). The sumation in Eq. (8) is carried out over all configurations in which these κ segments compose $\kappa-\mu$ clusters. The first summation sign in Eq. (7) denotes summation over all the ways, in which κ_1, κ_2 and κ_3 segments are selected from the subchains -1, -2 and -3 respectively, and the second, summation over κ_1, κ_2 and κ_3 under the condition $\kappa_1+\kappa_2+\kappa_3=\kappa$.

§ 3. Functional Forms of $\phi(r)$ and $\Omega_0(r,n)$

The potential $\phi(r)$, for convenience, is assumed to have the form*

$$\phi(r)=\begin{cases}\infty & ;\ r\leq b\\ -\varepsilon_0\exp\left(-\dfrac{3}{2\lambda^2}r^2\right) & ;\ r>b\end{cases} \tag{11}$$

where λ is a parameter which is assumed to be of the same order as a. $\phi(r)$ is shown in Fig. 1. In the case of $\varepsilon_0>0$, the force between segments becomes attractive in the range of $r>b$, and the segments have the tendency to condense. Therefore this corresponds to a poor solvent system. On the other hand, ε_0 is negative in a good solvent system. Substituting Eq. (11) into Eq. (3), the function $f(r)$ becomes

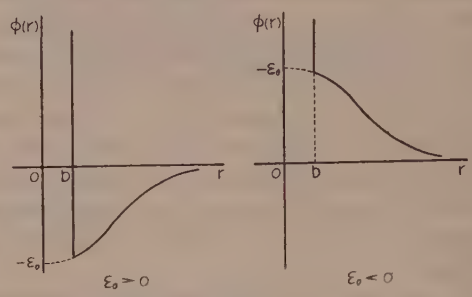

Fig. 1. Potential $\phi(r)$.

$$f(r)=\begin{cases}-1 & ;\ r\leq b\\ \dfrac{\varepsilon_0}{kT}\exp\left(-\dfrac{3}{2\lambda^2}r^2\right) & ;\ r>b\end{cases} \tag{12}$$

where all terms higher than the second of ε_0/kT were neglected. This neglection is justified by the experimental result that the heat of mixing is usually small in polymer solutions.

Next, if the chain, in which there exists no interaction, is approximated by a Gaussian chain, $\Omega_0(r,n)$ is given by

$$\Omega_0(r,n)=\frac{(4\pi a^2)^n}{(2\pi na^2/3)^{3/2}}\exp\left(-\frac{3}{2na^2}r^2\right) \qquad (n\geq 2)\,, \tag{13}$$

Here $(4\pi a^2)^n$ is the partition function of this chain which is allowed to have all the configurations without fixing both ends. We shall use Eqs. (12) and (13) in the further calculations.

§ 4. End-to-End Distance and Radius of Gyration

In this section, our primary aim is to calculate the mean square end-to-end distance $\langle R^2\rangle$ and the mean square radius of gyration $\langle S^2\rangle$, which characterize the statistical properties of a single polymer chain present in dilute solution. Before proceeding to this, it would be useful to derive the general expression for $\langle R_{kl}^{2m}\rangle$ from the partition function $\Omega(R_{kl})$, be-

* If we denote the depth of $\phi(r)$ at $r=b$ by ε, it may be rewritten as

$$\phi(r)=-\varepsilon\exp\left(\frac{3b^2}{2\lambda^2}\right)\exp\left(-\frac{3}{2\lambda^2}r^2\right)\ \text{for}\ r\geq b\,. \tag{11'}$$

cause this would not only give the expressions for $\langle R^2\rangle$ and $\langle S^2\rangle$, but also serve to calculate the angular distribution in the light scattering.

Considering the terms up to the order of interaction $\mu=1$,* the partition function $\Omega(R_{kl})$ simplifies to

$$\Omega(R_{kl})=B_0(R_{kl})+B_1(R_{kl})\ . \tag{14}$$

$B_0(R_{kl})$ can be easily obtained by Eqs. (5′) and (13), that is,

$$B_0(R_{kl})=\frac{(4\pi a^2)^N}{\{2\pi(l-k)a^2/3\}^{3/2}}\exp\left\{-\frac{3R_{kl}^2}{2(l-k)a^2}\right\}. \tag{15}$$

Using Eqs. (6) to (10) $B_1(R_{kl})$ may be written down as

$$\begin{aligned}B_1(R_{kl})=&\sum_{(1)}F_1(R_{kl},[200])+\sum_{(2)}F_1(R_{kl},[020])+\sum_{(3)}F_1(R_{kl},[002])\\&+\sum_{(4)}F_1(R_{kl},[110])+\sum_{(5)}F_1(R_{kl},[011])+\sum_{(6)}F_1(R_{kl},[101])\end{aligned} \tag{16}$$

with

$$\left.\begin{aligned}F_1(R_{kl},[200])=&\iiiint f_{ij}\Omega_0(r_{0i},i)\Omega_0(r_{ij},j-i)\Omega_0(r_{jk},k-j)\\&\times\Omega_0(r_{kl},l-k)\Omega_0(r_{lN},N-l)\,d(i)\,d(j)\,d(0)\,d(N)\ ,\\F_1(R_{kl},[020])=&\iiiint f_{ij}\Omega_0(r_{0k},k)\Omega_0(r_{ki},i-k)\Omega_0(r_{ij},j-i)\\&\times\Omega_0(r_{jl},l-j)\Omega_0(r_{lN},N-l)\,d(i)\,d(j)\,d(0)\,d(N)\ ,\\&\cdots\cdots\cdots\cdots\end{aligned}\right\} \tag{17}$$

The other integrals also can be easily presented. Each summation in Eq. (16) extends to the configurations corresponding to each cluster diagram illustrated in Fig. 2.

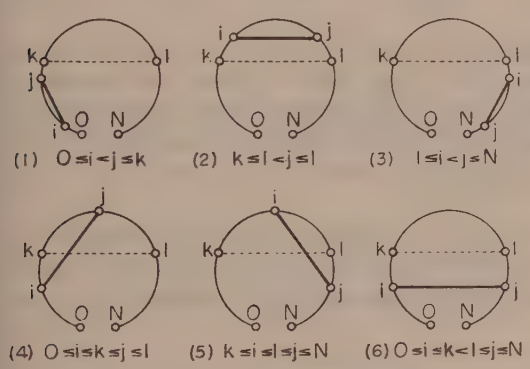

Fig. 2. Cluster Diagrams.

On performing the integrations in Eq. (17), the following approximation is introduced,

$$b\ll\lambda\leq a\ . \tag{18}$$

This is a necessary condition in order that the imperfect gas-like expansion could be applied: the first condition, $b\ll a$, indicates that the volume effect is sufficiently small, and the second condition, $\lambda\leq a$, means the mean force of segmental interaction to be short-ranged, as supposed from Eq. (11).

All the integrals in Eq. (17) can be evaluated by the Fourier and its inverse transformations.[3),11)] An example is taken of $F_1(R_{kl},[020])$ below. Integrating over (0) and (N), we obtain

$$F_1(R_{kl},[020])=(4\pi a^2)^{N+k-l}\iint f_{ij}\Omega_0(r_{ki},i-k)\Omega_0(r_{ij},j-i)\Omega_0(r_{jl},l-j)\,d(i)\,d(j)\ . \tag{19}$$

If the Fourier transform of this integral is denoted by $H_1(\boldsymbol{q},[020])$, the inverse transform F_1 is

$$F_1(R_{kl},[020])=\frac{(4\pi a^2)^{N+k-l}}{8\pi^3}\int\exp(-i\boldsymbol{q}\cdot\boldsymbol{R}_{kl})H_1(\boldsymbol{q},[020])\,d\boldsymbol{q} \tag{20}$$

with

* This corresponds to the single contact approximation of Zimm.[4),10)]

$$\left.\begin{aligned} H_1(\boldsymbol{q}, [020]) &= \alpha(\boldsymbol{q}, i-k)\beta(\boldsymbol{q}, j-i)\alpha(\boldsymbol{q}, l-j)\ , \\ \alpha(\boldsymbol{q}, i-k) &= \int \Omega_0(r_{kl}, i-k)\exp(i\boldsymbol{q}\cdot\boldsymbol{r}_{kl})\,d\boldsymbol{r}_{kl}\ , \\ \beta(\boldsymbol{q}, j-i) &= \int f(r_{ij})\Omega_0(r_{ij}, j-i)\exp(i\boldsymbol{q}\cdot\boldsymbol{r}_{ij})\,d\boldsymbol{r}_{ij}\ , \\ \alpha(\boldsymbol{q}, l-j) &= \int \Omega_0(r_{jl}, l-j)\exp(i\boldsymbol{q}\cdot\boldsymbol{r}_{jl})\,d\boldsymbol{r}_{jl}\ . \end{aligned}\right\} \tag{21}$$

After laborious calculations, $F_1(R_{kl}, [020])$ becomes

$$\begin{aligned} &F_1(R_{kl}, [020]) \\ &= -\frac{(4\pi a^2)^N}{(2\pi a^2/3)^{3/2}}\left(\frac{6}{\pi}\right)^{1/2}\frac{1}{(j-i)^{3/2}(l-k-j+i)^{3/2}}\left(\frac{b}{a}\right)^3\left[\exp\left\{-\frac{3R_{kl}^2}{2(l-k-j+i)a^2}\right\}-\left(\frac{\varepsilon_0}{kT}\right)\right. \\ &\times\left\{\left(\frac{\pi}{6}\right)^{1/2}\left[\frac{(j-i)(l-k-j+i)}{(j-i)(l-k-j+i)+(\lambda/a)^2(l-k)}\right]^{3/2}\left(\frac{\lambda}{b}\right)^3\exp\left[-\frac{3\{j-i+(\lambda/a)^2\}R_{kl}^2}{2\{(j-i)(l-k-j+i)+(\lambda/a)^2(l-k)\}a^2}\right]\right. \\ &\left.\left.\qquad -\exp\left[-\frac{3R_{kl}^2}{2(l-k-j+i)a^2}\right]\right\}\right] \end{aligned} \tag{22}$$

up to the terms of order $(b/a)^3$, the approximation (18) being taken into account. If we further neglect $(\lambda/a)^2$ compared to $j-i$ by the approximation (18), F_1 is simplified to

$$\begin{aligned} &F_1(R_{kl}, [020]) \\ &= -\frac{(4\pi a^2)^N}{(2\pi a^2/3)^{3/2}}\left(\frac{6}{\pi}\right)^{1/2}\frac{1}{(j-i)^{3/2}(l-k-j+i)^{3/2}}\left(\frac{b}{a}\right)^3\left(1-\frac{\Theta}{T}\right)\exp\left\{-\frac{3R_{kl}^2}{2(l-k-j+i)a^2}\right\} \end{aligned} \tag{23}$$

with

$$\Theta = \left\{\left(\frac{\pi}{6}\right)^{1/2}\left(\frac{\lambda}{b}\right)^3 - 1\right\}\left(\frac{\varepsilon_0}{k}\right). \tag{24}$$

Θ/T corresponds to the integral over the range $b \leq r_{ij} \leq \infty$ in $\beta(\boldsymbol{q}, j-i)$, namely the energetical part. This integral is split into two parts, 0 to ∞ and b to 0, which correspond to the first and second terms in Eq. (24) respectively. Θ has the dimension of temperature and it is expected from Eq. (18) to have the same sign as ε_0. If we would consider higher terms than the second of ε_0/kT in Eq. (12), $(1-\Theta/T)$ would be replaced by a power series of Θ/T in general.

If we would calculate the remaining F_1's in Eq. (16) by using the similar procedure as mentioned above and sum up them, $\Omega(R_{kl})$ could be evaluated. However, without deriving the explicit form of $\Omega(R_{kl})$,* we turn immediately to the derivation of $\langle R_{kl}^{2m}\rangle$. That is

$$\langle R_{kl}^{2m}\rangle = \frac{\int_0^\infty R_{kl}^{2m+2}\Omega(R_{kl})\,dR_{kl}}{\int_0^\infty R_{kl}^2\Omega(R_{kl})\,dR_{kl}} \tag{25}$$

$$= \frac{(2m+1)!}{6^m m!}(l-k)^m a^{2m}\left[1+\left(\frac{6}{\pi}\right)^{1/2}\left(\frac{b}{a}\right)^3\left(1-\frac{\Theta}{T}\right)D_m(N, k, l)\right] \tag{26}$$

where

$$\begin{aligned} D_m(N, k, l) &= \sum_{(2)}\left[1-\left(1-\frac{j-i}{l-k}\right)^m\right](j-i)^{-3/2}+\sum_{(4)}\left[1-\left\{1-\frac{(j-k)^2}{(l-k)(j-i)}\right\}^m\right](j-i)^{-3/2} \\ &+\sum_{(5)}\left[1-\left\{1-\frac{(l-i)^2}{(l-k)(j-i)}\right\}^m\right](j-i)^{-3/2}+\sum_{(6)}\left[1-\left(1-\frac{l-k}{j-i}\right)^m\right](j-i)^{-3/2}\ . \end{aligned} \tag{27}$$

* The implicit from of $\Omega(R_{kl})$ will be used to calculate the osmotic 2nd virial coefficient in the next paper.

Each summation in Eq. (27) denotes summation over i and j under the conditions specified in Fig. 2, and the configurations $-(1)$ and $-(3)$ are easily seen to make no contribution to $\langle R_{kl}^{2m}\rangle$. When the terms like $(\ )^m$ in Eq. (27) are expanded, and summations over i and j are replaced by integrations, D_m becomes

$$\begin{aligned} D_m(N,k,l)=&4\sum_{p=1}^{m}\frac{(-1)^{p+1}p}{(p^2-\frac{1}{4})(p+\frac{1}{2})}\binom{m}{p}(l-k)^{1/2}+\sum_{p=1}^{m}\frac{(-1)^{p+1}}{p+\frac{1}{2}}\binom{m}{p}\sum_{q=0}^{2p}\frac{(-1)^{q+1}}{p-q+\frac{1}{2}}\binom{2p}{q}\\ &\times(l-k)^{-p}[k^q(l^{p-q+1/2}-k^{p-q+1/2})+(N-l)^q\{(N-k)^{p-q+1/2}-(N-l)^{p-q+1/2}\}]\\ &+\sum_{p=1}^{m}\frac{(-1)^{p+1}}{p^2-\frac{1}{4}}\binom{m}{p}(l-k)^p\{N^{-p+1/2}-l^{-p+1/2}-(N-k)^{-p+1/2}\} \end{aligned} \tag{27'}$$

up to the terms of order $N^{1/2}$.

When $m=1$, $\langle R_{kl}^{2m}\rangle$ reduces to

$$\left.\begin{aligned} \langle R_{kl}^2\rangle&=(l-k)a^2\left[1+\left(\frac{6}{\pi}\right)^{1/2}\left(\frac{b}{a}\right)^3\left(1-\frac{\Theta}{T}\right)D_1(N,k,l)\right],\\ D_1(N,k,l)&=\frac{4}{3}\left[\frac{8}{3}(l-k)^{1/2}-4(N-k)^{1/2}-4l^{1/2}+\frac{l-k}{N^{1/2}}\right.\\ &\qquad\left.-\frac{8}{3(l-k)}\{(N-l)^{3/2}-(N-k)^{3/2}-l^{3/2}+k^{3/2}\}\right]. \end{aligned}\right\} \tag{28}$$

In the case of $k=0$ and $l=N$, we obtain for the $2m$-th moment of the distribution function of the end-to-end distance

$$\langle R^{2m}\rangle=\frac{(2m+1)!}{6^m m!}N^m a^{2m}\left[1+\left\{\sum_{p=1}^{m}\frac{(-1)^{p+1}}{p^2-\frac{1}{4}}\binom{m}{p}\right\}\xi\right], \tag{29}$$

where

$$\xi=\left(\frac{6}{\pi}\right)^{1/2}\left(\frac{b}{a}\right)^3\left(1-\frac{\Theta}{T}\right)N^{1/2}. \tag{30}$$

Eq. (29), when $m=1$, gives the mean square end-to-end distance,

$$\langle R^2\rangle=Na^2\left(1+\frac{4}{3}\xi\right). \tag{31}$$

We are now in a position to calculate the mean square radius of gyration $\langle S^2\rangle$. If we denote the distance between the molecular center of mass and segment k by S_k, $\langle S^2\rangle$ is given by

$$\langle S^2\rangle=\frac{1}{N}\sum_k\langle S_k^2\rangle=\frac{1}{N^2}\sum_{k<l}\langle R_{kl}^2\rangle. \tag{32}$$

Substituting from Eq. (28), and replacing summation by integration, we see that Eq. (32) becomes

$$\langle S^2\rangle=\frac{Na^2}{6}\left(1+\frac{134}{105}\xi\right). \tag{33}$$

In addition, $\langle S_k^2\rangle$ can be easily shown to have the expression,

$$\langle S_k^2\rangle=\frac{1}{N}\sum_{l=0}^{k-2}\langle R_{lk}^2\rangle+\frac{1}{N}\sum_{l=k+2}^{N}\langle R_{kl}^2\rangle-\langle S^2\rangle, \tag{34}$$

where $\langle R_{lk}^2\rangle$ is obtained by exchanging k for l and vice versa in Eq. (28). Thus we have

$$\left.\begin{aligned}\langle S_k^2\rangle &= a^2\left\{\frac{3k^2-3kN+N^2}{3N}+\frac{4}{3}D(N,k)\xi\right\},\\ D(N,k) &= \frac{6}{5N^{3/2}}\{k^{5/2}+(N-k)^{5/2}\}-\frac{8}{3N^{1/2}}\{k^{3/2}+(N-k)^{3/2}\}\\ &\quad+\frac{1}{3N^2}\{k^3+(N-k)^3\}+\frac{121}{84}N.\end{aligned}\right\} \tag{35}$$

Eqs. (28) and (35) will be used to calculate the intrinsic viscocity in the succeeding paper.

Eqs. (31) and (33) show that a polymer chain, owing to the repulsive interaction (volume effect), will expand more largely than a Gaussian case and, in good solvents, the energetical interactions between segments and solvents force the chain to expand more and more, whereas in poor solvents they work to shrink it. Therefore, when $T=\Theta$, the volume effect counteracts the energetical interaction so that the polymer chain apparently behaves like a Gaussian chain. Accordingly Θ defined by Eq. (24) is nothing but the Flory tempera ture[12] and becomes higher as ε_0 is large, namely in the poorer solvents.

In the above calculation, we have neglected all higher terms than the second corresponding to the order of interaction $\mu=2$. Otherwise, the higher terms than the second of ξ would generally occur in Eqs. (31) and (33). Accordingly, these equations would have the validity only in the case of $|\xi|\ll 1$, that is in the vicinity of the Θ temperature in poor solvents, and the range of ξ will be determined by comparison with experiments in the other paper.

§ 5. Statistical Properties of a Polymer Chain

Many studies have been proposed on the excluded volume effect of a polymer chain. Most of them have been dealing with the relationship between $\langle R^2\rangle$ and N, which has already been discussed out. Here our attentions are forcused on a few other statistical properties of a polymer chain in dilute solution which are easily deduced from the results obtained in the previous section.

(a) Suppose the Gaussian distribution function, the second moment of which is given by Eq. (31). We obtain for the $2m$-th moment of this function

$$\langle R^{2m}\rangle_G=\frac{(2m+1)!}{6^m m!}N^m a^{2m}\left(1+\frac{4}{3}m\xi\right). \tag{36}$$

Comparing Eq. (36) with Eq. (29), we know that $\langle R^{2m}\rangle_G>\langle R^{2m}\rangle$ when $m\geq 2$ and $\xi>0$: the Gaussian distribution function approaches zero slowly in the range of larger R than that corresponding to the maximum, while the distribution function of R for a real polymer chain increases gradually to a maximum, and then falls down to zero suddenly.

(b) Eqs. (31) and (33) lead us to

$$\frac{\langle R^2\rangle}{\langle S^2\rangle}=6\left(1+\frac{2}{35}\xi\right). \tag{37}$$

When $\xi>0$, the ratio $\langle R^2\rangle/\langle S^2\rangle$ is larger than the value 6 for the Gaussian chain, and increases with N.

These conclusions are in qualitative agreement with those obtained by Teramoto, Kurata and their coworkers[8] who directly counted the number of all possible configurations for the two-dimensional square lattice chains ($N\leq 20$) and the simple cubic lattice chains ($N\leq 8$).

§ 6. Light Scattering

Here we calculate the angular distribution $P(\theta)$ in the light scattering, using the same model as before, and propose a procedure to evaluate $\langle S^2\rangle$ by the dissymmetry method. $P(\theta)$ is expressed in the form,[13]

$$P(\theta)=\int_{-\infty}^{+\infty}\rho(R_{kl})\exp\left(\frac{2\pi i\boldsymbol{s}\cdot\boldsymbol{R}_{kl}}{\lambda'}\right)d\boldsymbol{R}_{kl}, \tag{38}$$

where λ' is the wave length in the medium, θ the scattering angle, ρ the radial distribution function for segments of the same polymer chain, $\boldsymbol{s}$ the vector difference between unit vectors in the directions of the incident and scattered lights, and the magnitude $\boldsymbol{s}$ is given by

$$s=|\boldsymbol{s}|=2\sin\frac{\theta}{2}. \tag{39}$$

The integration in Eq. (38) extends over all directions as well as magnitudes of $\boldsymbol{R}_{kl}$ at constant $\boldsymbol{s}$.

Now, using the partition function $\Omega(R_{kl})$, we may write $\rho(R_{kl})$ as

$$\rho(R_{kl})=\frac{2}{N^2}\sum_{k<l}C\,\Omega(R_{kl}), \tag{40}$$

where C is the normalization constant and

$$C^{-1}=\int_0^\infty 4\pi R_{kl}^2\,\Omega(R_{kl})\,dR_{kl}\,. \tag{41}$$

Inserting Eq. (40) in Eq. (38), $P(\theta)$ can be expanded in the form,

$$\left.\begin{aligned} P(\theta)&=1-\alpha_1\left(2\sin\frac{\theta}{2}\right)^2+\alpha_2\left(2\sin\frac{\theta}{2}\right)^4-\cdots+(-1)^m\alpha_m\left(2\sin\frac{\theta}{2}\right)^{2m}+\cdots\,,\\ \alpha_m&=\frac{2}{(2m+1)!\,N^2}\left(\frac{2\pi}{\lambda'}\right)^{2m}\sum_{k<l}\langle R_{kl}^{2m}\rangle\,. \end{aligned}\right\} \tag{42}$$

In particular, from Eq. (32) α_1 becomes

$$\alpha_1=\frac{4\pi^2}{3(\lambda')^2}\langle S^2\rangle\,. \tag{43}$$

Substituting Eq. (26) into α_m of Eq. (42), and replacing summation by integration over k and l, $P(\theta)$ can be finally rewritten as

$$P(\theta)=\frac{2}{u^2}(e^{-u}-1+u)+\xi\sum_{m=1}^{\infty}\frac{(-1)^m}{m!}C_m u^m\,, \tag{44}$$

where

$$u=\frac{8\pi^2}{3}\frac{Na^2}{(\lambda')^2}\sin^2\frac{\theta}{2}\,, \tag{45}$$

$$\begin{aligned} C_m=2\sum_{p=1}^{m}\frac{(-1)^{p+1}}{p^2-1/4}\binom{m}{p}\Bigg[&\frac{4p}{(m+3/2)(m+5/2)(p+1/2)}-\frac{m+2p+3/2}{(m+p+1)(m+p+2)(m+5/2)}\\ &+(2p-1)\sum_{q=0}^{2p}\frac{(-1)^{q+1}}{p-q-1/2}\binom{2p}{q}\Bigg\{\frac{1}{m+5/2}\sum_{s=0}^{m-p}\frac{(-1)^s}{q+s+1}\binom{m-p}{s}\\ &-\frac{1}{m-p+1}\sum_{t=0}^{m-p+1}\frac{(-1)^t}{p+t+3/2}\binom{m-p+1}{t}\Bigg\}\Bigg]\,. \end{aligned} \tag{46}$$

The numerical values of $C_m(m\leq 7)$ are shown in Table I, which were calculated by Eq. (46). Fig. 3 gives the $\sqrt{u}$ $-P(\theta)$ curves for various values of ξ, which were drawn taking accunt of the terms up to $m=7$ in Eq. (44) with the values of C_m in Table I. Similarly, the dissymmetry ratio z_{45} $(=P(45°)/P(135°))$ vs. $\sqrt{Na^2}/\lambda'$ is plotted in Fig. 4.

Table I. The Values of C_m.

m	1	2	3	4	5	6	7
C_m	0.4254	0.3889	0.3240	0.2699	0.2279	0.1953	0.173

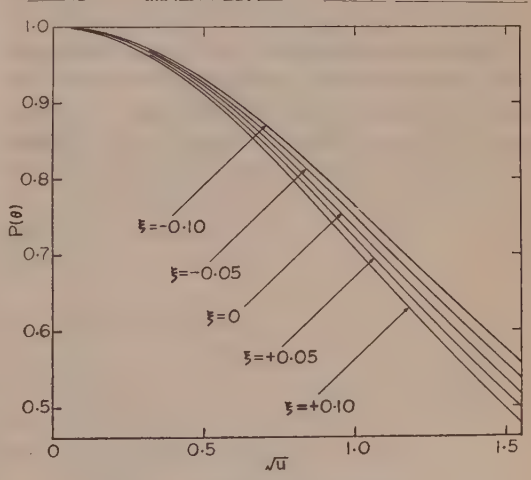

Fig. 3. Angular Distribution.

The angular variation method leads us to α_1 in Eq. (43) and hence $\langle S^2\rangle$ itself. On the other hand, in the dissymmetry method, Na^2 is customarily determined by using the curve for $\xi=0$ (Gaussian) in Fig. 4. Accordingly Na^2 obtained in such a way is not strictly equivalent to either $\langle R^2\rangle$ or $6\langle S^2\rangle$ at non-Flory temperatures. Following is our method to

determine $\langle S^2 \rangle$ by the dissymmetry method. We first read the value of Na^2 from the observed value of z_{45} at the Θ temperature and the curve for $\xi=0$ in Fig. 4; and next we determine ξ from the observed value of z_{45} at the other temperature and from the value of Na^2 obtained above, using Fig. 4. Inserting these values of Na^2 and ξ in Eq. (33), we obtain $\langle S^2 \rangle$. This method, however, is not applicable to a good solvent system, for the equations obtained here are derived only for small ξ.

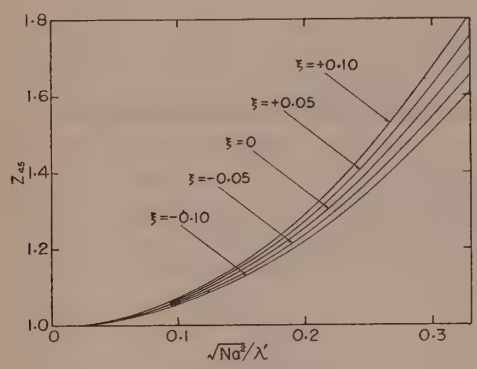

Fig. 4. Dissymmetry Ratio.

The agreement between the value of $\langle S^2 \rangle$ determined by this method and that by the angular variation method has to be checked experimentally. This is an interesting problem, but we will leave it untouched in the present paper.

In conclusion, we are greatly indebted to Professor Ichiro Sakurada of this University for his indispensable advice and constant encouragement during the course of this research. Thanks are tendered also to Prof. Akio Nakajima, Dr. Ei Teramoto, Dr. Misazo Yamamoto and Prof. Hiroshi Inagaki for their stimulating discussions, and to the Ministry of Education of the Japanese Government for a grant-in-aid. One of the authors (M. K.) wishes to express his sincere thanks also to Professor Mikio Tamura who gave him helpful discussions with ever increasing interest.

References

1) P. J. Flory: J. Chem. Phys. **17** (1949) 303.
2) K. Suzuki: Bull. Chem. Soc. Japan **22** (1939) 8.
3) E. Teramoto: Proceedings of the International Conference of Theoretical Physics, Kyoto and Tokyo, (1953) 410; Busseiron-Kenkyu (in Japanese) **39** (1951) 1, and the succeeding papers.
4) B. H. Zimm, W. H. Stockmayer and M. Fixman: J. Chem. Phys. **21** (1953) 1716.
5) N. Saito: J. Phys. Soc. Japan **9** (1954) 780.
6) M. Fixman: J. Chem. Phys. **23** (1955) 1656.
7) W. R. Krigbaum: J. Chem. Phys. **23** (1955) 2113.
8) E. Temamoto, M. Kurata, R. Chujo, C. Suzuki, K. Tani and T. Kajikawa: J. Phys. Soc. Japan **10** (1955) 953.
E. Teramoto and M. Kurata: Busseiron-Kenkyu (in Japanese) **80** (1955) 11.
9) W. G. McMillan and J. E. Mayer: J. Chem. Phys. **13** (1945) 276.
10) B. H. Zimm: J. Chem. Phys. **14** (1946) 164.
11) S. Chandrasekhar: Rev. Mod. Phys. **15** (1943) 1.
12) P. J. Flory and W. R. Krigbaum: J. Chem. Phys. **18** (1950) 1086.
13) B. H. Zimm: J. Chem. Phys. **16** (1948) 1093.
14) H. Yamakawa: Busseiron-Kenkyu (in Japanese) **96** (1956) 93; **104** (1957) 55.
H. Yamakawa and M. Kurata: ibid. **99** (1956) 62.

JOURNAL OF THE PHYSICAL SOCIETY OF JAPAN Vol. 13, No. 1, JANUARY, 1958

Theory of Dilute Polymer Solutions (II)*
Osmotic Pressure

By Hiromi YAMAKAWA

Department of Textile Chemistry, Kyoto University, Kyoto, Japan

(Received October 2, 1957)

A statistical-mechanical theory of dilute polymer solutions is developed following the solution theory of McMillan and Mayer, and the osmotic second virial coefficient A_2 is calculated taking account of the intra- and intermolecular interactions. The final expression for A_2 is expressed in terms of the molecular constants such as the molecular weight, segment size and bond length. The molecular weight dependence of A_2 is improved at least in the vicinity of the Flory point in comparison with the theories of Flory-Krigbaum and Isihara-Koyama.

§ 1. Introduction

According to the general theory of solutions developed by McMillan and Mayer,[1] the osmotic second virial coefficient A_2 can be expressed in terms of the reduced phase integrals of the solute molecules, namely one-body phase integrals at the infinite dilution. In the case of chain polymer solutions, however, the reduced phase integrals themselves are cumbersome owing to the *liquid-like* character, and the calculation of A_2 cannot be completed, in general, unless some approximations are made. For example, Flory and Krigbaum,[2] and recently Orofino and Flory[3] developed theories of polymer solutions by introducing the Gaussian approximation for the spatial distribution of segments about the molecular center of mass, and derived the expressions for A_2, which indicate a gradual decrease of A_2 with the molecular weight. This seems to be a good success of their theories, though there remains some phenomenological parameters uneliminated and the agreement with the experimental data is no more than semi-quantitative. Recently, Isihara and Koyama[4] improved the Flory and Krigbaum theory[2] with respect to the approximation for the radial distribution function for segments, but the Gaussian character of polymer chains is still assumed. In these theories, furthermore, n-segment distribution functions about the molecular center of mass are approximated by the products of one-segment distribution functions. Since the volume effect dominating A_2 introduces a non-Gaussian character into the chain behaviors as was shown in TPS I,** and since, by introducing the *factorization approximation* into the segment distribution function mentioned above, the effect of the spatial correlation between segments is almost ignored, we found it necessary to re-examine the theory of dilute polymer solutions with respect to these points.

In this paper, we are concerned with the calculation of the two-body phase integral of polymer chains. The method of expanding the one-body phase integral developed in TPS I can be conveniently extended to the present problem. The contributions to A_2 of the *intra*- and *inter*molecular interactions are able to be separated by proper introduction of a *partial* one-body phase integral. Although a similar approach to the problem has already been attempted by Zimm,[6] he has been neglected the influences of the intramolecular interactions. In the last section our excluded volume function ($\mathscr{F}$-function), which occurs in A_2, will be compared with those obtained by Flory-Krigbaum[2] and Isihara-Koyama,[4] and the difference among them will be discussed.

§ 2. Formulation

In this section, the formulation will be given in order to derive the theoretical expression for the second virial coefficient of the osmotic pressure of chain polymer solutions.

As in TPS I, we make use of the pearl-necklace model and the continuous medium approximation. Consider two polymer chains

* For the preliminary reports of this work see ref. 12.

** Part I of this series.[5] This paper will be cited as TPS I.

in dilute solutions; their segments are attached numbers $0_s, 1_s, 2_s, \cdots, N_s$ from one end to the other, where the subscript $s(=1$ or $2)$ indicates the distinction of two polymer chains. The coordinates of the segments, as before, are denoted by $(0_s), (1_s), \cdots, (N_s)$, and the coordinate set and the number set of n segments are represented by $\{n_s\}=(1_s)(2_s)\cdots(n_s)$ and $[n_s]=1_s, 2_s, \cdots, n_s$, respectively.

According to the solution theory of McMillan and Mayer,[1] the osmotic pressure π is expanded in powers of the concentration c (in g/cc) as follows,

$$\pi=RT\left(\frac{1}{M}c+A_2c^2+A_3c^3+\cdots\right) \qquad (1)$$

with

$$A_n=-\frac{(n-1)N_0^{n-1}}{M^n}B_n\,, \qquad (2)$$

where R is the gas constant, T the temperature, M the polymer molecular weight, A_n the n-th virial coefficient, N_0 Avogadro's number, and B_n the irreducible integral. In particular, B_2, equal to the cluster integral b_2, is given by

$$B_2=b_2=\frac{1}{2!\,V}\iint\cdots\int_V g_2(\{N_1+1_1+N_2+1_2\}, T) \times d\{N_1+1_1+N_2+1_2\}\,, \qquad (3)$$

where V is the volume of the system. g_2 is defined as

$$g_2\{N_1+1_1+N_2+1_1\}=F_2\{N_1+1_1+N_2+1_2\} -F_1\{N_1+1_1\}F_1\{N_2+1_2\}\,, \qquad (4)$$

where F_1 and F_2 are the one-body and two-body distribution functions of McMillan and Mayer, respectively. It must be noted here that F_1, F_2 and the related functions all refer to the state of infinite dilution of solute polymers and are functions of T, though the symbol T is omitted in Eq. (4) for simplicity's sake. Inserting Eq. (3) in Eq. (2), A_2 can be rewritten as

$$A_2=-\frac{N_0}{2VM^2}\iint\cdots\int_V g_2\{N_1+1_1+N_2+1_2\} \times d\{N_1+1_1+N_2+1_2\}\,. \qquad (5)$$

The distribution functions F_1 and F_2 are related to the potentials of mean force Φ_1 and Φ_2 respectively as follows,

$$\left.\begin{aligned} F_1\{N_s+1_s\}&=C\exp[-\Phi_1\{N_s+1_s\}/kT] \\ F_2\{N_1+1_1+N_2+1_2\}&=C'\exp[-\Phi_2\{N_1+1_1+N_2+1_2\}/kT]\,, \end{aligned}\right\} \qquad (6)$$

where C and C' are the normalization constants. In the continuous medium approximation, Φ_1 and Φ_2 are given by the sums of potentials $\phi(r_{i_s j_t})$ of segment pairs $(r_{i_s j_t}=|(j_t)-(i_s)|$; $s, t=1, 2)$:

$$\left.\begin{aligned} \Phi_1\{N_s+1_s\}&=\sum_{\substack{0\le j_s<j_s\le N\\ j_s i_s\ne 1}}\phi(r_{i_s j_s})\equiv\sum\phi(r_{i_1 i_2})\,, \\ \Phi_2\{N_1+1_1+N_2+1_2\}&=\Phi_1\{N_1+1_1\}+\Phi_1\{N_2+1_2\}+\sum_{i_1,i_2}\phi(r_{i_1 i_2})\,, \\ &\equiv\sum\phi_{i_1 j_1}+\sum\phi_{i_2 j_2}+\sum\phi_{i_1 i_2}\,. \end{aligned}\right\} \qquad (7)$$

g_2 is a correction term which would represent the amount by which the two-body distribution function F_2 deviates from the independent value given by the product of the one-body distribution functions F_1's, so that g_2 approaches zero as all $r_{i_1 i_2}$'s become infinite.* Accordingly, C' is equal to C^2 and g_2 can be rewritten as

$$\begin{aligned} g_2\{N_1+1_1+N_2+1_2\}&=C^2\exp(-\sum\phi_{i_1 j_1}/kT)\exp(-\sum\phi_{i_2 j_2}/kT)[\exp(-\sum\phi_{i_1,i_2}/kT)-1] \qquad (8) \\ &=C^2(1+\sum_{\substack{0\le i_1<j_1\le N\\ j_1-i_1\ne 1}}f_{i_1 j_1}+\sum\sum f_{i_1 j_1}f_{k_1 l_1}+\cdots) \\ &\quad\times(1+\sum_{\substack{0\le i_2<j_2\le N\\ j_2-i_2\ne 1}}f_{i_2 j_2}+\sum\sum f_{i_2 j_2}f_{k_2 l_2}+\cdots) \qquad (8') \\ &\quad\times(\sum_{i_1,i_2}f_{i_1 i_2}f_{j_1 j_2}+\cdots)\,, \end{aligned}$$

* The definition of g_2 is somewhat different from that of the correlation function $g_2(r)$ in the theory of liquids, which has the property: $\lim_{r\to\infty} g_2(r)=1$.

where

$$f_{i_s j_t}=\exp(-\phi_{i_s j_t}/kT)-1\,, \tag{9}$$

and C can be determined by the normalization condition of F_1. That is,

$$C^{-1}=\frac{1}{V}\iint\cdots\int_V \exp(-\sum\phi_{i_s j_s}/kT)d\{N_s+1_s\}\,. \tag{10}$$

We are now in a position to give the expansion form of A_2 from the standpoint of successive approximation. The situation is very complicated, because there exist the intra- and inter molecular interactions simultaneously. In the case of a single polymer chain, we defined the *order of interaction* by the difference between the number of segments in the state of interaction and the number of clusters. In the present paper, the order of interaction, for simplicity, is expressed by the number of *bonds* in a cluster diagram (See Fig. 1). This would not be the source of appreciable error in so far as the terms of considerably higher order are not concerned, since N is large enough.

We begin by introducing the *partial* one-body phase integral*

$$\Omega^{\kappa}\{\kappa_s\}=\iint\cdots\int_{|(i_s+1_s)-(i_s)|=a}[1+\sum_{\substack{0\leq i_s<j_s\leq N\\ j_s-i_s\neq 1}} f_{i_s j_s}+\cdots]d\{N_s+1_s-\kappa_s\}\,, \tag{11}$$

where the integration extends over all the coordinates of segments of the same chain except some κ segments under the conditions of constant bond length a. It is obvious that Ω^{κ}, when $\kappa=2$, results in $\Omega(R_{kl})$ discussed in TPS I. On performing the term-by-term integrations over the coordinates of segments except ones in the state of *inter*molecular interaction in Eq. (5), A_2, using $\Omega^{\kappa}\{\kappa_s\}$, can be rewritten as

$$A_2=-\frac{N_0}{2VM^2}(G_1+G_2+\cdots)\,, \tag{12}$$

where

$$G_{\kappa}=\sum_{\text{conf.}}G_{\kappa}([\kappa_1][\kappa_2])\,, \tag{13}$$

$$\left.\begin{aligned}
G_1([1_1][1_2])&=C^2\iint f_{i_1 i_2}\Omega^1(i_1)\Omega^1(i_2)d(i_1)d(i_2)\,,\\
G_2([2_1][2_2])&=C^2\iiiint(f_{i_1 i_2}f_{j_1 j_2}+f_{i_1 j_2}f_{j_1 i_2})\Omega^2(r_{i_1 j_1})\Omega^2(r_{i_2 j_2})d(i_1)d(j_1)d(i_2)d(j_2)\,,\\
&\cdots\cdots\cdots\cdots\cdots\cdots\\
G_{\kappa}([\kappa_1][\kappa_2])&=C^2\iint\cdots\int\sum\Pi\, f_{i_1 j_2}\Omega^{\kappa}\{\kappa_1\}\Omega^{\kappa}\{\kappa_2\}d\{\kappa_1+\kappa_2\}\,,\\
&\cdots\cdots\cdots\cdots\cdots\cdots
\end{aligned}\right\} \tag{14**}$$

The summation sign in Eq. (13) denotes summation over all the ways in which κ segments are selected from the chain 1 and the same number of segments from the chain 2. From Eq. (10), we obtain immediately

$$\Omega^1(i_1)=\Omega^1(i_2)=C^{-1}\,. \tag{15}$$

Hence, $G_1([1_1][1_2])$ simplifies to

$$G_1([1_1][1_2])=\iint f_{i_1 i_2}d(i_1)d(i_2)\,. \tag{16}$$

* In TPS I, the partial phase integral was used for an ideal (Gaussian) chain.

** Even if the symmetry numbers of the chains are taken into account in the integrand, they are cancelled out by those occurring in C^2; that is, A_2 is independent of the symmetry number.

In the following, we shall consider $G_\kappa([\kappa_1][\kappa_2])$ for $\kappa \geq 2$.

In general, the expansion terms of $\Omega^\kappa\{\kappa_s\}$ are arranged in ascending order of interaction as in the case of $\Omega(R_{kl})$:

$$\Omega^\kappa\{\kappa_s\} = \sum_{\nu_s=0}^{N} B^\kappa_{\nu_s}\{\kappa_s\}\,, \tag{17}$$

where ν_s is the order of *intra*molecular interaction. If we denote the orders of *inter*molecular and *overall* interactions by $\kappa-1$ and μ respectively, we must have the relation: $\mu+1=\kappa+\nu_1+\nu_2$ $(2\leq\kappa\leq\mu+1)$. Accordingly, if we consider in $G_\kappa([\kappa_1][\kappa_2])$ the terms up to the order μ of overall interaction, $G_\kappa([\kappa_1][\kappa_2])$ reduces to

$$G_{\kappa\mu}([\kappa_1][\kappa_2]) = (C_{\kappa\mu})^2 \iint\cdots\int \sum \Pi\, f_{i_1 j_2}[\sum_{0\leq\nu_1+\nu_2\leq\mu-\kappa+1} B^\kappa_{\nu_1}\{\kappa_1\} B^\kappa_{\nu_2}\{\kappa_2\}]d\{\kappa_1+\kappa_2\} \tag{18}$$

with

$$(C_{\kappa\mu})^{-1} = \iint\cdots\int \sum_{\nu_s=0}^{\mu-\kappa+1} B^\kappa_{\nu_s}\{\kappa_s\} d\{\kappa_s - 1_s\}\,. \tag{19}$$

There must be dropped some of the terms in $(C_{\kappa\mu})^{-2}$, which do not correspond to those in the integrand in Eq. (18). If we denote the sum of $G_{\kappa\mu}([\kappa_1][\kappa_2])$ over all the configurations by $G_{\kappa\mu}$, A_2 is finally given by

$$A_2 = -\frac{N_0}{2VM^2}(G_1 + \sum_{\kappa=2}^{\mu+1} G_{\kappa\mu}) \tag{20}$$

with the specified value of μ. The degree of approximation for A_2, of course, increases with increasing μ.

In order to perform the calculation of A_2 in the following section, we adopt the same forms of $f(r)$ and of the partition function of an ideal chain $\Omega_0(r, n)$ as in TPS I:

$$f(r) = \begin{cases} -1 & ;\ r \leq b \\ \dfrac{\varepsilon_0}{kT} \exp\left(-\dfrac{3}{2\lambda^2} r^2\right) & ;\ r > b \end{cases} \tag{21}$$

$$\Omega_0(r, n) = \frac{(4\pi a^2)^n}{(2\pi n a^2/3)^{3/2}} \exp\left(-\frac{3}{2na^2} r^2\right) \quad (n \geq 2)\,. \tag{22}$$

And the diameter of segment b, the bond length a and a parameter λ are assumed to satisfy the condition:

$$b \ll \lambda \leq a\,. \tag{23}$$

§ 3. Calculations of $G_{\kappa\mu}$

We shall concern ourselves with the case of $\mu=2$. Then, from Eq. (20), A_2 becomes

$$A_2 = -\frac{N_0}{2VM^2}(G_1 + G_{22} + G_{32})\,. \tag{24}$$

(i) *Calculation of* G_1

From Eqs. (13), (16) and (21) with the approximation (23), we obtain

$$G_1 = 4\pi V N^2 \int_0^\infty f(r) r^2 dr = -\frac{4\pi V}{3} N^2 b^3 \left(1 - \frac{\Theta}{T}\right) \tag{25}$$

with

$$\Theta = \left\{\left(\frac{\pi}{6}\right)^{1/2} \left(\frac{\lambda}{b}\right)^3 - 1\right\} \left(\frac{\varepsilon_0}{k}\right), \tag{26}$$

where Θ is the Flory temperature discussed in TPS I.

(ii) *Calculation of* G_{22}

Although the products of f's in the integrand of $G_{22}([2_1][2_2])$ are $f_{i_1 i_2} f_{j_1 j_2}$ and $f_{i_1 i_2} f_{j_1 j_2}$, it is easy to see that these make the same contribution to A_2. Hence, G_{22} can be written as

$$G_{22} = \sum_{i_1, j_1} \sum_{i_2, j_2} 2(C_{22})^2 \iiiint f(r_{i_1 i_2}) f(r_{j_1 j_2}) [B^2_{0_1}(r_{i_1 j_1}) B^2_{0_2}(r_{i_2 j_2}) + 2B^2_{1_1}(r_{i_1 j_1}) B^2_{0_2}(r_{i_2 j_2})] d(i_1)(d(j_1) d(i_2) d(j_2)\,. \tag{27}$$

$B^2_{0_1}(r_{i_1 j_1})$ and $B^2_{1_1}(r_{i_1 j_1})$ are given by the following equations, as have already been calculated in TPS I.

$$B^2_{0_1}(r_{i_1 j_1}) = (4\pi a^2)^{N-(j_1-i_1)} \Omega_0(r_{i_1 j_1}, j_1 - i_1)\,, \tag{28}$$

$$B^2_{1_1}(r_{i_1j_1})=\sum_{k_1,l_1}{}^{(2-1)}F_1(r_{i_1j_1},[200])+\sum_{k_1,l_1}{}^{(2-2)}F_1(r_{i_1j_1},[020])+\cdots+\sum_{k_1,l_1}{}^{(2-6)}F_1(r_{i_1j_1},[101]) \tag{29}$$

with

$$\left.\begin{aligned}
F_1(r_{i_1j_1},[200])&=-(4\pi a^2)^{N-(j_1-i_1)}\left(\frac{6}{\pi}\right)^{1/2}(l_1-k_1)^{-3/2}\left(\frac{b}{a}\right)^3\left(1-\frac{\Theta}{T}\right)\Omega_0(r_{i_1j_1},j_1-i_1)\,,\\
F_1(r_{i_1j_1},[020])&=-(4\pi a^2)^{N-(j_1-i_1-l_1+k_1)}\left(\frac{6}{\pi}\right)^{1/2}(l_1-k_1)^{-3/2}\left(\frac{b}{a}\right)^3\left(1-\frac{\Theta}{T}\right)\\
&\qquad\times\Omega_0(r_{i_1j_1},j_1-i_1-l_1+k_1)\,,\\
&\cdots\cdots\cdots\cdots\cdots\cdots\cdots\cdots
\end{aligned}\right\} \tag{30}$$

The first term in Eq. (27) corresponds to cluster diagram (2—0) illustrated in Fig. 1, and the functions F_1's correspond to cluster diagrams (2—1) to (2—6) respectively. The summation signs in Eq. (29) denote summations over k_1 and l_1, the ranges of which would be rather obvious from the cluster diagrams.

The integrations in Eq. (27) can be easily performed by the Fourier and inverse transformations:[5),7)]

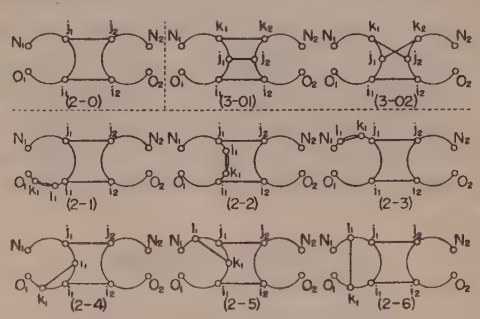

Fig. 1. Cluster Diagrams.

$$G_{22}=\sum_{i_1,j_1}\sum_{i_2,j_2}2V(C_{22})^2\int_0^\infty 4\pi\, r^2_{i_1i_2}f(r_{i_1j_2})F(r_{i_1i_2})dr_{i_1i_2}\,, \tag{31}$$

where

$$F(r_{i_1i_2})=\frac{1}{8\pi^3}\int\exp(-i\boldsymbol{q}\cdot\boldsymbol{r}_{i_1i_2})H(\boldsymbol{q})d\boldsymbol{q}\,, \tag{32}$$

$$\left.\begin{aligned}
H(\boldsymbol{q})&=\alpha(\boldsymbol{q})\beta(\boldsymbol{q})\gamma(\boldsymbol{q})\,,\\
\alpha(\boldsymbol{q})&=\int[B^2_{0_1}(r_{i_1j_1})+2B^2_{1_1}(r_{i_1j_1})]\exp(i\boldsymbol{q}\cdot\boldsymbol{r}_{i_1j_1})d\boldsymbol{r}_{i_1j_1}\,,\\
\beta(\boldsymbol{q})&=\int f(r_{j_1j_2})\exp(i\boldsymbol{q}\cdot\boldsymbol{r}_{j_1j_2})d\boldsymbol{r}_{j_1j_2}\,,\\
\gamma(\boldsymbol{q})&=\int B^2_{02}(r_{i_2i_2})\exp(i\boldsymbol{q}\cdot\boldsymbol{r}_{i_2j_2})d\boldsymbol{r}_{i_2j_2}\,,
\end{aligned}\right\} \tag{33}$$

$$(C_{22})^{-2}=(4\pi a^2)^{2N}\left[1-2\sum_{\substack{0\le k_1<l_1\le N\\ l_1-k_1\neq 1}}(l_1-k_1)^{-3/2}\left(\frac{6}{\pi}\right)^{1/2}\left(\frac{b}{a}\right)^3\left(1-\frac{\Theta}{T}\right)\right]. \tag{34}$$

The calculations eventually lead us to

$$G_{22}=-G_1\gamma_{20}\xi\left(1-\frac{\gamma_{21}}{\gamma_{20}}\xi\right), \tag{35}$$

where

$$\xi=\left(\frac{6}{\pi}\right)^{1/2}\left(\frac{b}{a}\right)^3\left(1-\frac{\Theta}{T}\right)N^{1/2}\,, \tag{36}$$

$$\frac{N^{3/2}}{2}\gamma_{20}=\sum_{(2-0)}(j_1-i_1+j_2-i_2)^{-3/2}\,, \tag{37}$$

$$\begin{aligned}\frac{N^3}{4}\gamma_{21}=&\sum_{(2-2)}(l_1-k_1)^{-3/2}[\{j_1-i_1+j_2-i_2-(l_1-k_1)\}^{-3/2}-(j_1-i_1+j_2-i_2)^{-3/2}]\\&+2\sum_{(2-4)}(l_1-k_1)^{-3/2}\left[\left\{j_1-i_1+j_2-i_2-\frac{(l_1-i_1)^2}{l_1-k_1}\right\}^{-3/2}-(j_1-i_1+j_2-i_2)^{-3/2}\right]\\&+\sum_{(2-6)}(l_1-k_1)^{-3/2}\left[\left\{j_1-i_1+j_2-i_2-\frac{(l_1-i_1)^2}{l_1-k_1}\right\}^{-3/2}-(j_1-i_1+j_2-i_2)^{-3/2}\right].\end{aligned} \tag{38}$$

Eq. (38) shows that clusters (2—1) and (2—3) make no contribution to A_2 and the contributions of clusters (2—4) and (2—5) are the same. Since we know that the intramolecular cluster corresponding to (2—2) makes main contribution to the mean radius of gyration of the polymer chain,[5] the second and third sums in Eq. (28), for simplicity, are neglected. Then, replacing summations by integrations, we obtain for the numerical values of γ_{20} and γ_{21},

$$\gamma_{20}=\frac{32}{15}(7-4\sqrt{2})=2.865\,, \tag{39}$$

$$\begin{aligned}\gamma_{21}&\simeq\frac{4}{N^3}\sum_{(2-2)}\cdots\\&=8\left\{\frac{304}{45}-\frac{11\sqrt{2}}{3}+3\,ln(1+\sqrt{2})-\pi\right\}=8.78\,.\end{aligned} \tag{40}$$

(iii) *Calculation of* G_{32}

There exist six products of f's in the integrand of G_{32}, which reduce to two $f_{i_1i_2}f_{j_1j_2}f_{k_1k_2}$'s and four $f_{i_1i_2}f_{j_1k_2}f_{k_1j_2}$'s Therefore, G_{32} can be written as

$$\begin{aligned}G_{32}=&\sum_{i_1j_1k_1}\sum_{i_2j_2k_2}2(C_{32})^2\iint\cdots\\&\times\int[f(r_{i_1i_2})f(r_{j_1j_2})f(r_{k_1k_2})\\&+2f(r_{i_1i_2})f(r_{j_1k_2})f(r_{k_1j_2})]B^3_{0_1}\{3_1\}B^3_{0_2}\{3_2\}\\&\times d(i_1)d(j_1)d(k_1)d(i_2)d(j_2)d(k_2)\end{aligned} \tag{41}$$

with

$$(C_{32})^2=(4\pi a^2)^{-2N}\,. \tag{42}$$

The first and second terms in Eq. (42) correspond to clusters (3—01) and (3—02) respectively. And $B^3_{0_s}\{3_s\}$ is given by

$$\begin{aligned}&B^3_{0_s}\{3_s\}\\&=(4\pi a^2)^{N-(i_s-k_s)}\Omega_0(r_{j_si_s},\,j_s-i_s)\Omega_0(r_{j_sk_s},\,k_s-j_s)\,.\end{aligned} \tag{43}$$

Since the integrations in Eq. (41) can be performed in like manner as in G_{22}, the method need not be reproduced. The result is

$$G_{32}=G_1\gamma_{30}\xi^2\,, \tag{44}$$

where

$$\begin{aligned}\frac{N^3}{2}\gamma_{30}=&\sum_{(3-01)}(k_1-j_1+k_2-j_2)^{-3/2}\\&\times(j_1-i_1+j_2-i_2)^{-3/2}\\&+2\sum_{(3-02)}\{(k_1-j_1+k_2-j_2)(j_1-i_1+j_2-i_2)\\&+(k_1-j_1)(k_2-j_2)\}^{-3/2}\,.\end{aligned} \tag{45}$$

Replacing summations by integrations, we obtain for the numerical value of γ_{30}

$$\gamma_{20}=8\left(\pi-\frac{8}{3}\right)+5.93=9.73\,. \tag{46}$$

§ 4. The Second Virial Coefficient and Comparison with Other Theories

From Eqs. (24), (25), (35) and (44), we obtain the final expression for the osmotic second virial coefficient,

$$A_2=\frac{2\pi N_0b^3}{3M_0^2}\left(1-\frac{\Theta}{T}\right)\mathscr{F}(\xi)\,, \tag{47}$$

where

$$M_0=\frac{M}{N}\,, \tag{48}$$

$$\mathscr{F}(\xi)=1-\gamma_{20}\left(1-\frac{\gamma_{21}}{\gamma_{20}}\right)\xi+\gamma_{30}\xi^2 \tag{49}$$

$$=1-\gamma_{20}\xi+(\gamma_{21}+\gamma_{30})\xi^2-\cdots \tag{49'}$$

up to the terms of order ξ^2. Here, γ_{20}, γ_{21} and γ_{30} have the positive values given by Eqs. (39), (40) and (46) respectively. But strictly speaking, γ_{21} would have somewhat larger value than the above one, owing to the neglection of the minor sums in Eq. (38).

Eq. (49′) shows that the influence of intramolecular interactions (represented by γ_{21} to the present approximation) would appear in higher terms than the second of ξ; in other words, the (intramolecular) excluded volume effect may be considered to have no influence on the second virial coefficient in the vicinity of the Θ temperature in poor solvents, but increases gradually with increasing temper-

ature and forces the second virial coefficient, which is the measure of the excluded volume of a pair of two polymer molecules, to become larger. In so far as we are concerned with the terms up to the first of ξ, Eq. (47) is essentially equivalent to Zimm's formula* derived without taking account of the intramolecular interactions.

From the general theory developed in § 2 and Eq. (49), we suggest that the excluded volume function $\mathscr{F}(\xi)$, if account is taken of the higher order interactions, may be expressed in the form,

$$\mathscr{F}(\xi)=1-\gamma_{20}\alpha_1(\xi)\xi+\gamma_{30}\alpha_2(\xi)\xi^2-\cdots \qquad (50)$$

$\alpha_1(\xi)$, $\alpha_2(\xi)$, etc. are the correction factors which would represent the influences of the intramolecular excluded voulme on the second virial coefficient. It is easy to see that all these functions decrease with increasing temperature in poor solvents, namely increasing ξ, and take the value of unity at $T=\Theta$.

According to the Flory-Krigbaum theory,[2] the function $\mathscr{F}$ is given by

$$\left.\begin{aligned}\mathscr{F}(X)&=1-\frac{X}{2!2^{3/2}}+\frac{X}{3!3^{3/2}}-\cdots,\\ X&=2(\alpha^2-1)=3^{3/2}\frac{\xi}{\alpha^3},\end{aligned}\right\} \qquad (51)^{**}$$

where α is a linear intramolecular deformation factor. Therefore, $\mathscr{F}$ may be rewritten as

$$\mathscr{F}(\xi)=1-0.919\frac{\xi}{\alpha^3}+0.866\frac{\xi^2}{\alpha^6}-\cdots$$

(the F. K. theory) (52)

Comparing Eq. (52) with Eq. (50), α^{-3}, α^{-6}, etc. are easily found to correspond to $\alpha_1(\xi)$, $\alpha_2(\xi)$, etc. respectively and to just similarly behave as these do. In our theory, if the partial one-body phase integral is assumed to have the form,

$$\Omega^{\kappa}\{\kappa_s\}=\prod_{\substack{0\leq i_s<j_s\leq N\\ i_s,j_s\in[\kappa_s]}}\Omega_0\left(\frac{r_{i_sj_s}}{\alpha},j_s-i_s\right), \qquad (53)$$

namely if the polymer chain is assumed to be a Gaussian one uniformly expanded by a factor α, it is easily shown that $\mathscr{F}$ can be expressed by

$$\mathscr{F}(\xi)=1-\gamma_{20}\frac{\xi}{\alpha^3}+\gamma_{30}\frac{\xi^2}{\alpha^6}-\cdots, \qquad (54)$$

which is equivalent to the Flory-Krigbaum equation (52) except the expansion coefficients. From Eq. (33) in TPS I (the mean radius of gyration) and from the values of γ_{20} and γ_{21}, it would be expected that if $\alpha_1(\xi)$ is written in the form α^{-n}, n is somewhat larger than 3. This descrepancy might be attributed to a non-Gaussian character of the chain.

On the other hand, according to the Isihara-Koyama theory,[4] the function $\mathscr{F}$ is given by

$$\mathscr{F}(\xi)=1-1.024\xi+1.134\xi^2-\cdots$$

(the I. K. theory) (55)***

The intramolecular excluded volume effect has been ignored in their theory, namely all $\alpha_n(\xi)\equiv 1$.

The essential difference between our theory and the F. K. or I. K. theory is that the expansion coefficients γ_{20}, γ_{30}, etc. in the former are considerably greater than the corresponding coefficients in the latter two. This could be interpreted as follows: in the F. K. and I. K. theories the important chain character of the connections of segments has seen lost owing to the introduction of their factorized distribution approximation into the distribution function for κ segments about the molecular center of mass, while in our theory the correlation between segments, namely the connections of segments, which seem to be closely related to the *liquid-like* behavior of the chain, have been explicitly taken into account, even when the approximation (55) is used. In the I. K. theory, slightly larger coefficients than in the F. K. theory have been obtained with taking account of the distinguishability between segments i and j.

In conclusion, it must be noticed that in the experimental verification our large expansion coefficients will improve the molecular

* See reference 6. His coefficient of ξ is half smaller than ours because of miss counting of clusters.

** According to the statistical theory of a single polymer chain present in dilute solutions developed by Flory,[8] α, using our parameter ξ, satisfies the relation:

$$\alpha^5-\alpha^3=(3^{3/2}2)\xi\,.$$

Recently Orofino and Flory[3] have improved the theory, in which a correctihn term, dependent on temperature and the polymer molecular weight, has been added on the right-hand side of the above equation.

*** The argument of $\mathscr{F}(X)$ in the I. K. theory is equal to $3^{3/2}\xi$.

weight dependence of the second virial coefficient at least in the vicinity of the Θ temperature since ξ is proportional to $M^{1/2}$. This dependence has been underestimated in the F. K. theory.[9),10),*]

The author wishes to express his hearty thanks to Professors Ichiro Sakurada and Akio Nakajima who gave him kind encouragement and helpful discussions. Thanks are tendered also to members of the Research Group on Polymer Science of this University, especially to Professors Michio Kurata and Ei Teramoto, for their advices and stimulating discussions.

References

1) W. G. McMillan and J. E. Mayer: J. Chem. Phys. **13** (1945) 276.
2) P. J. Flory and W. R. Krigbaum: J. Chem. Phys. **18** (1950) 1086.
3) T. A. Orofino and P. J. Flory: J. Chem. Phys. **26** (1957) 1067.
4) A. Ishihara and R. Koyama: J. Chem. Phys. **25** (1956) 712.
5) H. Yamakawa and M. Kurata: This journal **13** (1958) 78.
6) B. H. Zimm: J. Chem. Phys. **14** (1946) 164.
7) S. Chandrasekhar: Rev. Mod. Phys. **15** (1246) 164.
8) P. J. Flory: J. Chem. Phys. **17** (1949) 303.
9) P. J. Flory: *Principles of Polymer Chemistry* (Cornell Univ. Press, New York, 1953) pp. 536 and 537.
10) W. R. Krigbaum and P. J. Flory: J. Am. Chem. Soc. **75** (1953) 1775.
11) A. C. Albrecht: J. Chem. Phys. **27** (1957) 1002.
12) H. Yamakawa: Busseiron-Kenkyu (in Japanese) **97** (1956) 153; **98** (1956) 175; 2-2 (1957) 329.

* Work of a similar nature has recently been communicated by A. C. Albrecht.[11)]

JOURNAL OF THE PHYSICAL SOCIETY OF JAPAN Vol. 13, No. 1, JANUARY, 1958

Theory of Dilute Polymer Solutions (III) Intrinsic Viscosity

By Hiromi YAMAKAWA* and Michio KURATA**

**Department of Textile Chemistry and **Department of Industrial Chemistry, Kyoto University, Kyoto, Japan*

(Received October 2, 1957)

A theory of the intrinsic viscosity $[\eta]$ of chain polymer solutions is developed on the basis of the Kirkwood and Riseman scheme, taking some modifications concerning the excluded volume effect into account. If the volume effect is represented by the linear expansion factor α of the root mean square radius of gyration, it is concluded that $[\eta]$ is proportional to α^2 for the free-draining molecule and $\alpha^{2.43}$ for the non-free-draining molecule. This implies that the effective hydrodynamic radius of the polymer coil is not proportional to the statistical one in the limit, where the rigid sphere model is asymptotically valid; in other words, the more the polymer chain is expanded, the deeper the solvent molecules penetrate into the polymer coil.

§ 1. Introduction

Theories of the intrinsic viscosity $[\eta]$ of chain polymer solutions have been developed by Debye-Bueche (D.B.),[1)] Kirkwood-Riseman (K.R.),[2)] and Flory-Fox (F.F.).[3)] The D.B. and K.R. theories have the apparent difference in their mathematical analyses, but equivalent are the physical meanings involved by them: the molecular weight dependence of $[\eta]$ is uniquely related to the variation of the velocity gradient of fluids in the polymer coil, which is subjected to the hydrodynamic interactions between segments. Combining with Stokes' law, these theories render us the smaller diameter of the segment than that to be expected. This would take its rise in their

Gaussian model and none other. On the other hand, the F.F. theory is established on Einstein's rigid sphere model and attributes the molecular weight dependence of $[\eta]$ to the intramolecular deformation of the chain due to the thermodynamic interactions between segments.

If $[\eta]$, following Flory and Fox, is written in the form,

$$[\eta]=6^{3/2}\Phi\frac{(\langle S^2\rangle_0)^{3/2}}{M}\alpha^3 ,$$

α reduces to unity (Gaussian) and Φ depends on the molecular weight in the D.B. and K.R. theories, while Φ assumes its asymptotic value independent of the molecular weight and α varies with the molecular weight in the F.F. theory. Since, however, in deriving the above formula Flory and Fox have introduced the intuitive assumption that the effective hydrodynamic radius of the polymer coil is proportional to the statistical one, their theory is of empirical nature. In addition this assumption is not necessarily satisfied according to the recent experimental data.[4]

The K.R. theory seems to be superior to the D.B. theory in their model and formulations in so far as linear polymers are concerned. In the present paper, for this reason, we study the intrinsic viscosity of a chain polymer solution in the manner of Kirkwood and Riseman, taking into consideration the thermodynamic interactions between segments as well as the hydrodynamic ones. And we discuss the proportionality between the hydrodynamic and statistical radii.

§ 2. Model and Average Quantities

Although the pearl-necklace model and the continuous medium approximation are adopted[5] in this paper as before, for convenience, the segments are attached numbers $-n, \cdots, -1, 0, +1, \cdots, +n$ in place of $0, 1, 2, \cdots, N$. Thus we have the relation, $N=2n$.

If we denote the distance between segments i and j by R_{ij} $(j>i)$ and the distance between the molecular center of mass and segment i by S_i, we obtain the following expressions for various average quantities over chain configurations from Eqs. (28) and (35) in TPS I;*

$$\langle R_{ij}^2\rangle=(j-i)a^2+\xi\frac{4(j-i)a^2}{3\sqrt{2}\,n^{1/2}}\Big[\frac{8}{3}(j-i)^{1/2}-4(n-i)^{1/2}+4(n+j)^{1/2}+\frac{j-i}{\sqrt{2}\,n^{1/2}}$$
$$-\frac{8}{3(j-i)}\{(n+i)^{3/2}-(n-i)^{3/2}-(n+j)^{3/2}+(n-j)^{3/2}\}\Big], \tag{1}$$

$$\langle S_i^2\rangle=\frac{(3i^2+n^2)a^2}{6n}+\xi\frac{4a^2}{3\sqrt{2}\,n^{1/2}}\Big[\frac{3}{5n}\{(n+i)^{5/2}+(n-i)^{5/2}\}-\frac{8}{3}\{(n+i)^{3/2}+(n-i)^{3/2}\}$$
$$+\frac{1}{6\sqrt{2}\,n^{3/2}}\{(n+i)^3+(n-i)^3\}+\frac{121\sqrt{2}}{42}n^{3/2}\Big], \tag{2}$$

$$\langle S_i\cdot S_j\rangle=\frac{1}{12n}\{3(i+j^2)-6(j-i)n+2n^2\}a^2+\xi\frac{\sqrt{2}\,a^2}{3n^{1/2}}\Big[\frac{1}{6\sqrt{2}\,n^{3/2}}\{(n+i)^3+(n-i)^3+(n+j)^3+(n-j)^3\}$$
$$+\frac{3}{5n}\{(n+i)^{5/2}+(n-i)^{5/2}+(n+j)^{5/2}+(n-j)^{5/2}\}-\frac{1}{\sqrt{2}\,n^{1/2}}(j-i)^2-\frac{8}{3}(j-i)^{3/2}$$
$$-\frac{16}{3}(n-i)^{3/2}-\frac{16}{3}(n+j)^{3/2}+4(j-i)(n-i)^{1/2}+4(j-i)(n+j)^{1/2}+\frac{121\sqrt{2}}{21}n^{3/2}\Big], \tag{3}$$

with

$$\xi=\left(\frac{6}{\pi}\right)^{1/2}\left(\frac{b}{a}\right)^3\left(1-\frac{\Theta}{T}\right)N^{1/2} , \tag{4}$$

where b is the diameter of segment, a its constant bond length, and Θ the Flory temperature. When $T=\Theta$, Eqs. (1) to (3), which have their validity in the vicinity of the Θ temperature, reduce to the corresponding formulae used by Kirkwood and Riseman for the Gaussian chain.

$\langle 1/R_{ij}\rangle$ can be evaluated in the same way as $\langle R_{ij}^2\rangle$, using the partition function $\Omega(R_{ij})$ mentioned in TPS I, but the result is very complicated, as shown in Appendix I. As will

* Part I of this series[5] is cited as TPS I.

be discussed in the next section, this is closely related to the Oseen tensor, and becomes the kernel of the K.R. integral equation which determines the hydrodynamic interactions between segments. Now, therefore, if $\langle 1/R_{ij}\rangle$ is written as

$$\left\langle \frac{1}{R_{ij}} \right\rangle = \beta \left\langle \frac{1}{R_{ij}} \right\rangle_0 , \tag{5}$$

where the subscript 0 indicates a Gaussian chain, and if β is assumed to be independent of i and j in order to simplify the further calculations, then Eq. (5) can be immediately rewritten as

$$\beta = \frac{\dfrac{1}{2n^2} \sum_{i<j} \left\langle \dfrac{1}{R_{ij}} \right\rangle}{\dfrac{1}{2n^2} \sum_{i<j} \left\langle \dfrac{1}{R_{ij}} \right\rangle_0} . \tag{6}$$

Namely β is a correction factor which would represent the amount by which the average quantity of $\langle 1/R_{ij}\rangle$ over i and j deviates from that for the Gaussian chain. Since, however, it is almost impossible to evaluate the sum in the numerator of Eq. (6), the correction factor of $\langle 1/R_{ij}\rangle_0$ is assumed to be approximately equal to the inverse square root of that of $\langle R_{ij}^2\rangle$. Then β becomes

$$\left.\begin{aligned} \beta &= \frac{\dfrac{1}{2n^2} \sum_{i<j} \alpha_{ij}^{-1} \left\langle \dfrac{1}{R_{ij}} \right\rangle_0}{\dfrac{1}{2n^2} \sum_{i<j} \left\langle \dfrac{1}{R_{ij}} \right\rangle_0} , \\ \alpha_{ij} &= \left(\frac{\langle R_{ij}^2 \rangle}{\langle R_{ij}^2 \rangle_0} \right)^{1/2} . \end{aligned}\right\} \tag{6'}$$

Calculating the sums in Eq. (6′), eventually we obtain for $\langle 1/R_{ij}\rangle$

$$\left\langle \frac{1}{R_{ij}} \right\rangle = \left(\frac{6}{\pi} \right)^{1/2} \frac{1}{(j-i)^{1/2} a} \left\{ 1 - 2\left(\pi - \frac{44}{15} \right) \xi \right\} . \tag{7}$$

§ 3. Kirkwood-Riseman Integral Equation and Intrinsic Viscosity

According to Kirkwood and Riseman,[2] when a polymer chain is introduced into a continuous medium of solvent molecules in a state of stationary two-dimensional viscous flow between parallel plane boundaries, the force $\boldsymbol{F}_i$ of frictional resistance exerted on the fluid by segment i is given by

$$\boldsymbol{F}_i = -\frac{\zeta \dot{\varepsilon}}{2} [\boldsymbol{e}_x(\boldsymbol{S}_i \cdot \boldsymbol{e}_y) + \boldsymbol{e}_y(\boldsymbol{S}_i \cdot \boldsymbol{e}_x)] - \zeta \sum_{\substack{s=-n \\ \neq i}}^{+n} \boldsymbol{T}_{is} \cdot \boldsymbol{F}_s \quad (-n \leq i \leq +n) . \tag{8}$$

Here ζ is a friction constant characteristic of the fluid and the segment, $\dot{\varepsilon}$ is the velocity gradient, and $\boldsymbol{e}_x$, $\boldsymbol{e}_y$, $\boldsymbol{e}_z$ are unit vectors defining a coordinate system with origin at the molecular center of mass with $\boldsymbol{e}_x$ parallel to the stream lines of the unperturbed flow and $\boldsymbol{e}_y$ perpendicular to the plane boundaries. And the Oseen tensor $\boldsymbol{T}_{is}$ has the form,

$$\boldsymbol{T}_{is} = \frac{1}{8\pi\eta_0 R_{is}} \left(\boldsymbol{1} + \frac{\boldsymbol{R}_{is}\boldsymbol{R}_{is}}{\boldsymbol{R}_{is}^2} \right) , \tag{9}$$

where η_0 is the viscosity coefficient of the solvent fluid.

Following the analyses of Burgers and Kirkwood-Riseman, the expression for the intrinsic viscosity is

$$[\eta] = \lim_{c \to 0} \frac{\eta - \eta_0}{\eta_0 c} \tag{10}$$

$$= -\frac{N_0}{100 M \eta_0 \dot{\varepsilon}} \sum_{i=-n}^{+n} \langle (\boldsymbol{S}_i \cdot \boldsymbol{e}_x)(\boldsymbol{F}_i \cdot \boldsymbol{e}_y) \rangle , \tag{11}$$

where η is the viscosity coefficient of the solution, c the concentration in grams per 100 ml, $M\,(=NM_0)$ the molecular weight, and N_0 Avogadro's number.

If we define φ_{ij} by the relation,

$$\langle (\boldsymbol{S}_j \cdot \boldsymbol{e}_x)(\boldsymbol{F}_i \cdot \boldsymbol{e}_y) \rangle = -\frac{na^2 \zeta \dot{\varepsilon}}{9} \varphi_{ij} , \tag{12}$$

then from Eqs. (11) and (12), $[\eta]$ may be expressed in the form,

$$\left.\begin{aligned} [\eta] &= \frac{N_0 \zeta a^2 M}{3600 \eta_0 M_0^2} F , \\ F &= \frac{1}{n} \sum_{i=-n}^{+n} \varphi_{ii} . \end{aligned}\right\} \tag{13}$$

For large n, the sum defining F may be replaced by the integral

$$\left.\begin{aligned} F &= \int_{-1}^{+1} \varphi(x, x) dx , \\ \varphi_{ij} &= \varphi(x, y) , \quad x = \frac{i}{n} , \quad y = \frac{j}{n} . \end{aligned}\right\} \tag{14}$$

Now, according to Kirkwood and Riseman, ignoring the fluctuation of $\boldsymbol{T}_{is}$ and approximating it by $\langle \boldsymbol{T}_{is}\rangle$, we obtain

$$\begin{aligned} \langle \boldsymbol{T}_{is} \rangle &= \frac{\boldsymbol{1}}{6\pi\eta_0} \left\langle \frac{1}{R_{is}} \right\rangle \\ &= \frac{\boldsymbol{1}}{(6\pi^3)^{1/2} a \eta_0} \frac{1}{|i-s|^{1/2}} \left\{ 1 - 2\left(\pi - \frac{44}{15} \right) \xi \right\} , \end{aligned} \tag{15}$$

and then φ_{ij} could be determined as the solutions of the following simultaneous equation,

$$\varphi_{ij}=f_{ij}-\frac{\lambda}{n^{1/2}}\left\{1-2\left(\pi-\frac{44}{15}\right)\xi\right\}\sum_{\substack{s=-n\\ \neq i}}^{+n}\frac{\varphi_{sj}}{|i-s|^{1/2}}$$

$$(-n\leq i\leq +n\,,\quad -n\leq j\leq +n) \tag{16}$$

with

$$f_{ij}=\frac{3}{2na^2}\langle \boldsymbol{S}_i\cdot\boldsymbol{S}_j\rangle\,, \tag{17}$$

$$\lambda=\frac{\zeta}{(12\pi^3)^{1/2}a\eta_0}\left(\frac{M}{M_0}\right)^{1/2}. \tag{18}$$

For large n, Eq. (16) reduces to the integral equation,

$$\varphi(x,\,y)=f(x,\,y)-\lambda\left\{1-2\left(\pi-\frac{44}{15}\right)\xi\right\}\int_{-1}^{+1}\frac{\varphi(t,\,y)}{|x-t|^{1/2}}dt\,, \tag{19}$$

where

$$\left.\begin{aligned}
&f(x,\,y)=f^0(x,\,y)+\xi f^1(x,\,y)\,,\\
&f^0(x,\,y)=\frac{1}{8}\{3(x^2+y^2)-6|x-y|+2\}\,,\\
&f^1(x,\,y)=\begin{cases}u(x,\,y); & y\geq x\\ u(y,\,x); & y<x\,,\end{cases}\\
&u(x,\,y)=\frac{1}{12}\{(1+x)^3+(1-\chi)^3+(1+y)^3+(1-y)^3\}+\frac{3\sqrt{2}}{10}\{(1+x)^{5/2}+(1-x)^{5/2}\\
&\qquad+(1+y)^{5/2}+(1-y)^{5/2}\}-\frac{1}{2}(x-y)^2-\frac{4\sqrt{2}}{3}(y-x)^{3/2}-\frac{8\sqrt{2}}{3}(1-x)^{3/2}\\
&\qquad-\frac{8\sqrt{2}}{3}(1+y)^{3/2}+2\sqrt{2}\,(y-x)(1-\chi)^{1/2}+2\sqrt{2}\,(y-x)(1+y)^{1/2}+\frac{121}{21}\,.
\end{aligned}\right\} \tag{20}$$

If Eq. (19) is solved with respect to $\varphi(x,\,y)$, $[\eta]$ is obtained by Eq. (13) and (14). Although, when $\xi=0$, Eq. (19) is nothing but the K.R. integral equation for Gaussian chain, it is clear that the integral equation (19) is of the same type as the K.R.'s whenever ξ is equal to zero or not. But, as has been pointed out by Zimm[6] and Kirkwood,[7),8)] the integral equation of this type can not analytically be solved.

If $\varphi(x,\,y)$ and $f(x,\,y)$ are expanded in Fourier series of the forms

$$\left.\begin{aligned}
\varphi(x,\,y)&=\sum_{k=-\infty}^{+\infty}\varphi_k(y)e^{i\pi kx}\,,\\
f(x,\,y)&=\sum_{k=-\infty}^{+\infty}f_k(y)e^{i\pi kx}\,,
\end{aligned}\right\} \tag{21}$$

respectively, then Eq. (19) is transformed into the following set of linear equations for the Fourier coefficients,

$$\varphi_k(y)+\lambda\left\{1-2\left(\pi-\frac{44}{15}\right)\xi\right\}\sum_{l=-\infty}^{+\infty}a_{kl}\varphi_l(y)=f_k(y)\,.$$

$$(k=0,\,\pm1,\,\pm2,\,\cdots) \tag{22}$$

When the matrix elements a_{kl} are approximated by the values which are asymptotically valid for large k and l, a_{kl} becomes

$$a_{kl}=\begin{cases}\dfrac{8\sqrt{2}}{3}\quad;\quad k=l=0\\[2ex] \left(\dfrac{2}{|k|}\right)^{1/2}\delta_{kl}\,;\quad k\neq 0\,.\end{cases} \tag{23}$$

With the approximation (23), inserting the solutions of Eq. (22) in Eq. (21), we find

$$\varphi(x,\,y)=\frac{f_0(y)}{1+\dfrac{8\sqrt{2}}{3}\lambda\left\{1-2\left(\pi-\dfrac{44}{15}\right)\xi\right\}}+\sum_{\substack{k=-\infty\\ \neq 0}}^{+\infty}\frac{f_k(y)}{1+\lambda\left\{1-2\left(\pi-\dfrac{44}{15}\right)\xi\right\}\left(\dfrac{2}{|k|}\right)^{1/2}}e^{i\pi kx}\,. \tag{24}$$

Since it can be easily shown that $f_0(y)\equiv 0$, $\varphi(x,\,y)$ given by Eq. (24), when $\xi=0$, reduces to the approximate solution obtained by Kirkwood and Riseman.[2)] Adopting the approximate solution (24), we obtain, after laborious calculations,

$$F(x)=\frac{6}{\pi^2}\sum_{k=1}^{\infty}\frac{1}{k^2}\,\frac{1}{1+\left\{1-2\left(\pi-\dfrac{44}{15}\right)\xi\right\}\chi/k^{1/2}}\times\left[1+\frac{2}{3}\xi\left\{1+2\pi^{1/2}\frac{C(2\pi k)}{(\pi k)^{1/2}}+\frac{3}{2}\pi^{1/2}\frac{S(2\pi k)}{(\pi k)^{3/2}}\right\}\right], \tag{25}$$

where

$$\left.\begin{aligned}
x&=\sqrt{2}\,\lambda=\lambda_0N^{1/2}\,,\\
\lambda_0&=\frac{\zeta}{(6\pi^3)^{1/2}a\eta_0}\,,
\end{aligned}\right\} \tag{26}$$

and Fresnel's integrals $C(y)$ and $S(y)$ are defined as

$$\left.\begin{aligned} C(y)&=\int_0^y \frac{\cos t}{(2\pi t)^{1/2}}dt\,,\\ S(y)&=\int_0^y \frac{\sin t}{(2\pi t)^{1/2}}dt\,. \end{aligned}\right\} \tag{27}$$

The higher terms of ξ than the second have to be neglected in the expansion of $F(\chi)$ in powers of ξ, as for various average quantities discussed in § 2. $[\eta]$ can then be expressed in the form,

$$[\eta]=\frac{N_0\zeta a^2}{3600\eta_0 M_0}NF_0(\lambda_0 N^{1/2})\left[1+\frac{F_1(\lambda_0 N^{1/2})}{F_0(\lambda_0 N^{1/2})}\xi\right], \tag{28}$$

where

$$F_0(x)=\frac{6}{\pi^2}\sum_{k=1}^{\infty}\frac{1}{k^2}\frac{1}{1+x/k^{1/2}}\,, \tag{29}$$

$$\left.\begin{aligned} F_1(x)&=F_1{}^1(x)+F_1{}^2(x)\,,\\ F_1{}^1(x)&=\frac{4}{\pi^2}\sum_{k=1}^{\infty}\frac{1}{k^2}\frac{1}{1+x/k^{1/2}}\\ &\quad\times\left[1+2\pi^{1/2}\frac{C(2\pi k)}{(\pi k)^{1/2}}+\frac{3}{2}\pi^{1/2}\frac{S(2\pi k)}{(\pi k)^{3/2}}\right],\\ F_1{}^2(x)&=\frac{12}{\pi^2}\left(\pi-\frac{44}{15}\right)\sum_{k=1}^{\infty}\frac{1}{k^{5/2}}\frac{x}{(1+x/k^{1/2})^2}\,. \end{aligned}\right\} \tag{30}$$

$F_1{}^1(x)$ and $F_1{}^2(x)$ are associated with correction terms which would represent the amounts by which $\langle \boldsymbol{S}_i\cdot\boldsymbol{S}_j\rangle$ and $\langle 1/R_{ij}\rangle$ deviate from those for a Gaussian chain, respectively. Although the functions $F_0(x)$ and $F_1(x)$ obtained above are not rigorously correct, the hydrodynamic behavior of a Gaussian chain could be completely understood throughout $F_0(x)$ given by Eq. (29), as has been discussed by Kirkwood and others.[8] According to Kirkwood and Riseman,[2] $xF_0(x)\to 1.588$ as $x\to\infty$, but its correct asymptotic value is 1.259.[9] Therefore, it must be only remarked that some corrections for the values of $F_0(x)$ and $F_1(x)$ obtained above are required. However, the coefficient of ξ, $F_1(x)/F_0(x)$ seems to be correct, because such corrections in the numerator and denominator might be cancelled out one another.

$F_1(x)/F_0(x)$ has the numerical value 1.276 (=134/105) in the limit for $\chi=0$, as shown in Appendix II. The results of the numerical calculations for $F_1(x)/F_0(x)$ are summarized in Table I with the asymptotic value 1.551 for $x=\infty$. Remembering that the mean square radius of gyration of a polymer chain is given by

$$\langle S^2\rangle=\frac{Na^2}{6}\left(1+\frac{134}{105}\xi\right), \tag{31}$$

Table I. Numerical Values of Viscosity Function.

x	$xF_0(x)$*	$\frac{F_1{}^1(x)}{F_0(x)}$	$\frac{F_1{}^2(x)}{F_0(x)}$	$\frac{F_1(x)}{F_0(x)}$	$\gamma(x)$
0	0	1.276	0	1.276	1.00
0.5	0.358	1.26	0.11	1.37	1.07
1.0	0.564	1.25	0.16	1.41	1.10
2.0	0.800	1.23	0.22	1.45	1.13
3.0	0,936	1.21	0.25	1.46	1.14
4.0	1.024	1.21	0.27	1.48	1.16
5.0	1.090	1.20	0.28	1.48	1.16
10.0	1.260	1.18	0.32	1.50	1.17
20.0	1.400	1.16	0.34	1.50	1.17
50.0	(1.486)	1.15	0.37	1.52	1.19
100.0	(1.528)	1.14	0.38	1.52	1.19
∞	1.588	1.135	0.416	1.551	1.215

* From Kirkwood and Riseman.

and defining the linear intramolecular deformation α as

$$\alpha^2\equiv\frac{\langle S^2\rangle}{\langle S^2\rangle_0}=1+\frac{134}{105}\xi\,, \tag{32}$$

we obtain the following expressions for the intrinsic viscosity in the two interesting extreme cases:

(i) in the limit for $\lambda_0 N^{1/2}\to 0$,

$$[\eta]=\frac{N_0\zeta}{600\eta_0 M_0}\langle S^2\rangle_0\left(1+\frac{134}{105}\xi\right) \tag{33}$$

$$=\frac{N_0\zeta}{600\eta_0 M_0}\langle S^2\rangle_0\alpha^2 \tag{33'}$$

(ii) in the limit for $\lambda_0 N^{1/2}\to\infty$,

$$[\eta]=\frac{\pi^{3/2}N_0}{100}[\chi F_0(x)]_{x\to\infty}\frac{(\langle S^2\rangle_0)^{3/2}}{M}(1+1.551\xi) \tag{34}$$

$$=\frac{\pi^{3/2}N_0}{100}[xF_0(x)]_{x\to\infty}\frac{(\langle S^2\rangle_0)^{3/2}}{M}\alpha^{2.43}\,. \tag{34'}$$

In general, $[\eta]$ is proportional to $\alpha^{2\gamma}$, where $\gamma\simeq 105F_1(x)/134F_0(x)$ in the vicinity of the Θ temperature. γ varies monotonically from 1 to 1.215 as x increases from 0 to ∞. The values of γ for various values of x are also given in Table I.

§ 4. Comparison with the Flory-Fox Theory and Discussions

As is well known, according to the empirical theory of Flory and Fox,[3] the intrinsic viscosity is given by

$$[\eta]=6^{3/2}\Phi\frac{(\langle S^2\rangle_0)^{3/2}}{M}\alpha^3\,, \tag{35}$$

where Φ is a universal constant for any polymer-solvent pair, independent of temperature

and the polymer molecular weight. Eq. (35) has been derived, based on the Einstein rigid sphere model, by introducing the assumption that the effective hydrodynamic radius of the polymer coil is proportional to the statistical one. But, in the following, it will be shown what assumptions lead us to Eq. (35) in terms of the K.R. theory.

If $\langle \boldsymbol{S}_i \cdot \boldsymbol{S}_j \rangle$ and $\langle 1/R_{ij} \rangle$ are assumed to be expressed in the forms,

$$\langle \boldsymbol{S}_i \cdot \boldsymbol{S}_j \rangle = \alpha^2 \langle \boldsymbol{S}_i \cdot \boldsymbol{S}_j \rangle_0 , \tag{36}$$

$$\left\langle \frac{1}{R_{ij}} \right\rangle = \alpha^{-1} \left\langle \frac{1}{R_{ij}} \right\rangle_0 \tag{37}$$

respectively, where α is defined by Eq. (32), then the integral equation for $\varphi(x, y)$ becomes

$$\varphi(x, y) = \alpha^2 f^0(x, y) - \frac{\lambda}{\alpha} \int_{-1}^{+1} \frac{\varphi(t, y)}{|x-t|^{1/2}} dt , \tag{38}$$

and it leads us to

$$F(x) = \frac{6}{\pi^2} \sum_{k=1}^{\infty} \frac{1}{k^2} \frac{\alpha^2}{1 + x/\alpha k^{1/2}} . \tag{39}$$

Here, consider the limit for $x \to \infty$, and $[\eta]$ results in

$$[\eta] = \frac{\pi^{3/2} N_0}{100} [x F_0(x)]_{x=\infty} \frac{(\langle S^2 \rangle_0)^{3/2}}{M} \alpha^3 , \tag{40}$$

which is equivalent to the F.F. formula (35).

The only difference between our formula (34′) and F.F.'s (35) or (40) is the exponent of α in the limit for $x \to \infty$. When the coefficients of ξ are compared, the asymptotic values of $F_1^1(x)/F_0(x)$ and $F_1^2(x)/F_0(x)$ are 1.135 and 0.416* respectively in the former, and 1.276 (=134/105) and 0.638 (=67/105) in the latter. It follows, therefore, that the numerical values of $F_1^1(x)/F_0(x)$ become smaller without averaging the correction factor of $\langle \boldsymbol{S}_i \cdot \boldsymbol{S}_j \rangle_0$. And the difference between the asymptotic values of $F_1^2(x)/F_0(x)$ in either theory arises from that between Eqs. (7) and (37). When averaged in such a way as mentioned in § 2, the correction factor of $\langle \boldsymbol{S}_i \cdot \boldsymbol{S}_j \rangle_0$ proves to be α^2, whereas that of $\langle 1/R_{ij} \rangle$ not to be α^{-1}. Accordingly, in view of the averaging, Eq. (37) might be unreasonable.

It may be concluded that the exponent of α in the expression for the intrinsic viscosity is smaller than three, according to our theory, in the limit where Einstein's rigid sphere model is asymptotically valid, though the detailed discussions could not be given because of many approximations involved. This implies that the effective hydrodynamic radius is, there, not proportional to the satistical one. If we denote the hydrodynamic radius by S_H, from Eq. (34′) we obtain

$$S_H \propto (\langle S^2 \rangle_0)^{1/2} \alpha^{0.81} . \tag{41}$$

On the other hand, the statistical radius is proportional to the first power of α. So the degree of expansion of the former is lower than that of the latter. This situation may be interpreted as follows. For the root mean square distance $(\langle S_i^2 \rangle)^{1/2}$ between segment i and the molecular center of mass, Eq. (35) in TPS I gives

$$(\langle S_i^2 \rangle)^{1/2} = \begin{cases} \dfrac{1}{\sqrt{3}} N^{1/2} a (1 + 0.61\xi) \text{ for } i = \pm n , \\ \dfrac{1}{2\sqrt{3}} N^{1/2} a (1 + 0.50\xi) \text{ for } i = 0 . \end{cases} \tag{42}$$

Hence,

$$\left(\frac{\langle S_{\pm n}^2 \rangle}{\langle S_0^2 \rangle} \right)^{1/2} = 2(1 + 0.11\xi) . \tag{42′}$$

These equations indicate that the excluded volume effect has the larger influence on the segments near the ends than on the intermediate segments; those are located, on the average, in the *skin* part of the polymer coil and these in the *core* part. Accordingly, the expansion of polymer chain does not occur *uniformly* in the inside of the coil, but mainly in the *skin* part. Therefore, the more the polymer chain is expanded owing to the thermodynamic interaction between segments, the deeper the solvent molecules penetrate into the coil.

When Eq. (34) is rewritten in the form that $[\eta]$ is proportional to α^3 as in Eq. (35), Φ may be expressed as

$$\Phi = \frac{(\pi/6)^{3/2} \Lambda_0}{100} [x F_0(x)]_{x=\infty} (1 - 0.363\xi) . \tag{43}$$

Eq. (43) shows that Flory's universal constant Φ decreases with increasing temperature, namely increasing ξ, in the poor solvent system ($\Theta > 0$).

Finally we discuss the molecular weight dependence of the intrinsic viscosity. From Eq. (28), it is easy to see that the molecular weight dependence of $[\eta]$ is attributed only to

* Without such averaging as in Eq. (5), it would be expected that this value becomes somewhat smaller.

$NF_0(\lambda_0 N^{1/2})$ at the Θ temperature. This matter has already been discussed out by Kirkwood and Riseman. But ξ makes contribution to the molecular weight dependence at other temperatures, and Flory's considerations may be supported.

In conclusion, we are indebted to Professors Ichiro Sakurada and Akio Nakajima of Kyoto University for their stimulating discussions and kind encouragement. Thanks are tendered also to Dr. Misazo Yamamoto for his indispensable advice, and to the Ministry of Education for a grant-in-aid.

Appendix I. $\left\langle \frac{1}{R_{ij}} \right\rangle$

$$\left\langle \frac{1}{R_{ij}} \right\rangle = \left(\frac{6}{\pi}\right)^{1/2} \frac{1}{(j-i)^{1/2}a} - \xi \left(\frac{3}{\pi}\right)^{1/2} \frac{1}{(j-i)^{1/2}n^{1/2}a} \Bigg[\left\{ 4 \sum_{p=1}^{\infty} \frac{C_p p}{(p+1/2)(p^2-1/4)} \right\} (j-i)^{1/2}$$
$$+ \sum_{p=1}^{\infty} \left(\frac{C_p}{p+1/2} \right) \sum_{q=0}^{2p} \frac{(-1)^{q+1}}{p-q+1/2} \binom{2p}{q} (j-i)^{-p}$$
$$\times \{ (n+i)^q (n+j)^{p-q+1/2} - (n+i)^{p+1/2} + (n-i)^{p-q+1/2} (n-j)^q - (n-j)^{p+1/2} \}$$
$$+ \sum_{p=1}^{\infty} \left(\frac{C_p}{p^2-1/4} \right) (j-i)^p \{ (2n)^{-p+1/2} - (n-i)^{-p+1/2} - (n+j)^{-p+1/2} \} \Bigg],$$

where

$$C_p \equiv \frac{(2p)!}{2^{2p}(p!)^2}.$$

Appendix II. $\lim_{x \to 0} \frac{F_1(x)}{F_0(x)}$

From tables of the Riemann ζ-function, we have

$$\zeta(2) = \sum_{k=1}^{\infty} \frac{1}{k^2} = \frac{\pi^2}{6}. \qquad \text{(A.II.1)}$$

If we consider the functions $(1+x)^{3/2} + (1-x)^{3/2}$ and $(1+x)^{5/2} + (1-x)^{5/2}$ for $-1 \leq x \leq +1$, and expand them in Fourier series, putting $x=1$ with taking account of Eq. (A.II.1) respectively, then we obtain

$$\left.\begin{aligned} &\pi^{1/2} \sum_{k=1}^{\infty} \frac{C(2\pi k)}{(\pi k)^{5/2}} = \frac{1}{15}, \\ \text{and} \quad &\pi^{1/2} \sum_{k=1}^{\infty} \frac{S(2\pi k)}{(\pi k)^{7/2}} = \frac{4}{315}. \end{aligned}\right\} \qquad \text{(A.II.2)}$$

By using Eqs. (A.II.1) and (A.II.2), we have

$$\lim_{x \to 0} F_0(x) = \frac{6}{\pi^2} \sum_{k=1}^{\infty} \frac{1}{k^2} = 1,$$

$$\lim_{x \to 0} F_0(x) = \frac{4}{\pi^2} \sum_{k=1}^{\infty} \frac{1}{k^2} \left[1 + 2\pi^{1/2} \frac{C(2\pi k)}{(\pi k)^{1/2}} + \frac{3}{2} \pi^{1/2} \frac{S(2\pi k)}{(\pi k)^{3/2}} \right] = \frac{134}{105}.$$

Hence,

$$\lim_{x \to 0} \frac{F_1(x)}{F_0(x)} = \frac{134}{105}.$$

References

1) P. Debye and A. M. Bueche: J. Chem. Phys. **16** (1948) 573.
2) J. G. Kirkwood and J. Riseman: J. Chem. Phys. **16** (1948) 565.
3) P. J. Flory and T. G. Fox: J. Am. Chem. Soc. **73** (1951) 1904.
4) W. R. Krigbaum and D. K. Carpenter: J. Phys. Chem. **59** (1955) 1166.
5) H. Yamakawa and M. Kurata: This journal **13** (1958) 78.
6) B. H. Zimm: J. Chem. Phys. **24** (1956) 269.
7) J. G. Kirkwood and J. Riseman: J. Chem. Phys. **22** (1954) 1626.
8) J. G. Kirkwood, R. W. Zwanzig and R. J. Plock: J. Chem. Phys. **23** (1955) 213.
9) P. L. Auer and C. S. Gardner: J. Chem. Phys. **23** (1955) 1545 and 1546.

JOURNAL OF THE PHYSICAL SOCIETY OF JAPAN Vol. 13, No. 1, JANUARY, 1958

Quadrupole Moment of Nb^{93} and Test of the Hyperfine Structure Formulas

By Kiyoshi MURAKAWA

Institute of Science and Technology, University of Tokyo, Komaba-machi, Meguro-ku, Tokyo

(Received October 5, 1957)

The hyperfine structure (hfs) of the spectrum of Nb I was studied by means of a liquid air-cooled hollow cathode discharge tube and a Fabry-Pérot etalon. The quadrupole moment of Nb^{93} was deduced to be -0.29 barn and -0.20 barn (1 barn $=10^{-24}$ cm^2) from the levels $4d^35s^2\ {}^4F_{3/2}$ and $4d^45s\ {}^6D_{3/2}$ respectively, in which no shielding correction is included. Assuming that the shielding correction in this case is zero, we get $Q(Nb^{93})=-0.2_5\pm0.1_5$ barn.

The interval factors of the levels $4d^35s^2\ {}^4F_{3/2,\ 5/2,\ 7/2,\ 9/2}$ and $4d^45s\ {}^6D_{3/2,\ 5/2,\ 7/2,\ 9/2}$ were measured and compared with hfs formulas, and a small but definite discrepancy was detected.

§ 1. Introduction

The hyperfine structure (hfs) of the spectrum of Nb I was first measured by Ballard[1] (referred to as B), and the nuclear spin of Nb^{93} was determined to be 9/2. Further measurement was made by Meeks and Fisher[2] (referred to as MF); they studied the interval factors of some levels of Nb I and compared them with their calculations. They expressed the interval factor of the level ${}^6D_J$ of the configuration d^4s (which was assumed to be of LS-coupling) in the form

$$A({}^6D_J)=c(J)a(s)+c'(J)a(d^4)+c''(J)b(d^4)\,,$$

in which $a(s)$ is the coupling coefficient of the s electron, and $a(d^4)$ and $b(d^4)$ are (according to their definitions) the orbital and spin parts, respectively, of the coupling coefficient for the d^4 electron group.

In order to calculate the quadrupole moment, the wave-functions must be reviewed more critically, and such an investigation was carried out by the author some years ago[3]. The present report will treat the problem more thoroughly and will show that the present hfs theory is somewhat inadequate for reproducing observed interval factors.

§ 2. Experimental Procedure

The spectrum of Nb I was obtained by a liquid-air cooled hollow cathode discharge tube that was described previously[4]. In order to resolve the hfs, a Fabry-Pérot etalon was used. Some important lines were accompanied by close lying lines. The most remarkable of them is given in Table I, in which the wavelength was taken from Meggers and King[5]. In the case of the present investigation also such lines appeared on the plate,

Table I. Group of close lying lines.

Main line	Close lying lines
λ5665.63 (120)	5664.70(100), 5666.86(9)
λ5271.526(60c)	5269.910(6), 5272.48(5)
λ4648.949(100)	4649.255(40), 4649.622(2)
λ4523.409(200)	4522.545(6), 4523.727 (5), 4524.127 (20)
λ4195.096(80)	4195.515(4), 4195.660(15)

and an example is reproduced in Fig. 1. In the case of λ4523, it is almost certain that more lines than given by Meggers and King lie close to the main line. It was therefore necessary to use thin spacers in the measurement of the hfs of these lines.

The result of measurement is shown schematically in Figs. 2—11, in which Figs. 2, 3, 4 and 5 can be used for the determination of $Q(Nb^{93})$. The other figures are used only for the determination of interval factors.

§ 3. Calculation of the Quadrupole Moment

The term analysis of the spectrum of Nb I was published by Meggers and Scribner[6], and their term notation will be employed here. (The multiplet $d^3s^2\,{}^4F$—$d^3sp\,{}^4G$ was classified in the present work on the basis of the

hfs.) Of the even terms of Nb I, $4d^45s^6D$, ^4D and $4d^35s^2\,^4F$ are known. For examining the quadrupole effect the levels $4d^35s^2\,^4F_{3/2}$ and $4d^45s\,^6D_{3/2}$ seem to be the most suited.

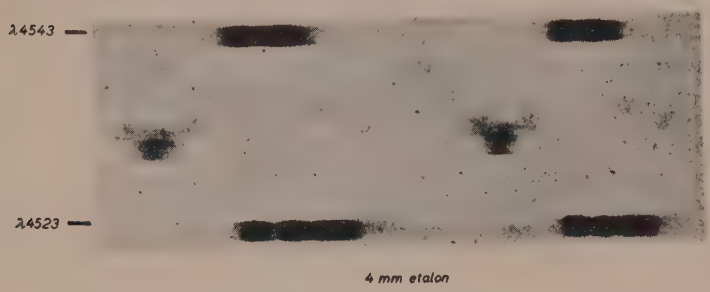

Fig. 1. Enlargement of interference patterns of Nb I.

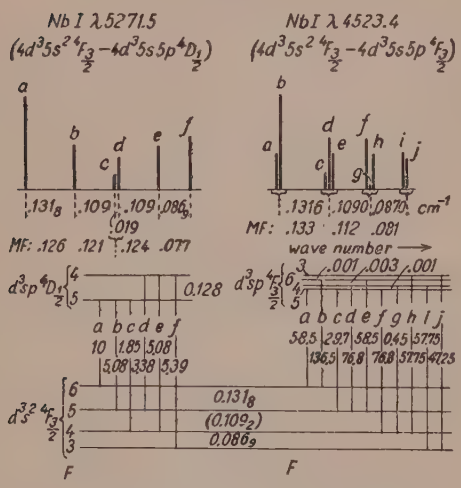

Fig. 2. Hfs of Nb I λ5271.5 and λ4523.4.

The hfs of the level $4d^35s^2\,^4F_{3/2}$ can be obtained from the line λ5271.5 as shown in Fig. 2. As shown in Table I, two lines lie close, so the measurement of the hfs was somewhat difficult. The accuracy of the measurement is, however, just sufficient for determining the order of magnitude and sign of Q. The hfs of the level $4d^35s^2\,^4F_{3/2}$ (see Fig. 2) can be represented by the interval factor $A=0.02187\,\mathrm{cm}^{-1}$ and the quadrupole coupling constant $B=0.0031\times10^{-3}\,\mathrm{cm}^{-1}$.

We can calculate $Q(\mathrm{Nb}^{93})$ from $B(d^3\,^4F_{3/2})$. In the case of Nb I, $d^3s^2\,^4F$ lies higher than d^4s^6D, so we will have to take the interaction between the configurations d^3s^2 and d^4s into account. Since only the terms $d^3s^2\,^4F$, d^4s^6D and ^4D are known, it is not possible to determine the interaction accurately, but the following consideration would be sufficient for a one-digit calculation.

We shall make the assumption that the configurations d^3s^2 and d^4s are of good LS-coupling. Let ζ_d denote the spin-orbit interaction parameter of the $4d$-electron. We shall use the same notations as Condon and Shortley[7] for the other parameters. We get $\zeta_d=475$ and 438 from $d^3s^2\,^4F$ and $d^4s\,^6D$ respectively, the mean value being $\zeta_d=450$. From the multiplet structure of d^4s^6D and ^4D, we get $G_2=1692$. The parameters F_2, F_4 and H_2 cannot be deduced from the data published by Meggers and Scribner[6], so we shall assume that F_2, F_4 and H_2 for Nb I are the same as those for Mo I, namely $F_2=759$, $F_4=54.2$ and $H_2=(1/35)R^2(dd,\ ds)=357.3$, as given by Trees and Harvey[8] for Mo I.

Center of gravity (c.g.) of d^4s^6D lies at 634.44, where the ground level $d^4s\,^6D_{1/2}$ is taken as the origin. That of $d^3s^2\,^4F$ lies at 2120.7. Under the above-mentioned assumption for F_2 and F_4, we get

$$d^4s\,^4F^a=13320\,,$$
$$d^4s\,^4F^b=27912\,.$$

Each of these two wave-functions can be expressed as a linear combination of the wave-functions $d^4(^3{}_2F)s$ and $d^4(^3{}_4F)s$ defined by Racah[9]. Putting

$$d^4s^4F=c_1[d^4(^3{}_2F)s^4F]+c_2[d^4(^3{}_4F)s^4F]\,,$$

we get

$$c_1=-0.4516,\quad c_2=0.8922\quad \text{for } d^4s\,^4F^a$$
$$c_1=0.8922,\quad c_2=0.4516\quad \text{for } d^4s\,^4F^b.$$

The wave-function $d^4(^3{}_4F)s\,^4F$ contained in $d^4s\,^4F^a$ and $d^4s\,^4F^b$ perturbs the wave-function $d^3s^2\,^4F$. We thus get

$$d^3s^2\,^4F'=K_1[d^3s^2\,^4F]+K_2[d^4(^3{}_4F)s\,^4F]\,,$$
$$K_1^2=0.952,\ K_2^2=0.048\,,$$

where the prime on the left hand side denotes the actual wave-function.

We shall put $\omega=3\cos^2\theta-1$ for brevity. Then we have

$$(d^3s^2\,^4F_{3/2}'|\omega/r^3|d^3s^2\,^4F_{3/2}')$$
$$=K_1^2(d^3s^2\,^4F_{3/2}|\omega/r^3|d^3s^2\,^4F_{3/2})$$
$$+K_2^2(d^4(^3{}_4F)s\,^4F_{3/2}|\omega/r^3|d^4(^3{}_4F)s\,^4F_{3/2}).$$

In this expression, we omit M for brevity,

since $M=J$. In the case of Nb I we have

$$K_1^2(d^3s^2\,{}^4F_{3/2}|\omega/r^3|d^3s^2\,{}^4F_{3/2})=0.1306\,\langle r^{-3}\rangle,$$

$$K_2^2(d^4({}^3{}_4F)s\,{}^4F_{3/2}|\omega/r^3|d^4({}^3{}_4F)s\,{}^4F_{3/2})$$
$$=-0.01207\,\langle r^{-3}\rangle.$$

We shall show later that the effective charge on the d-electron obtained from the hfs of various levels is to some extent ambiguous, but $Z_d{}^*=23.5$ that was obtained earlier[3)] would be a sufficient approximation for the present purpose. Putting this value and $I=9/2$, $J=3/2$ and the above-mentioned value of B and $({}^4F_{3/2}{}'|\omega/r^3|{}^4F_{3/2}{}')$ in the usual formula we get

$$Q'(\mathrm{Nb}^{93})=-0.29\ \text{barn}\qquad \text{from } d^3s^2\,{}^4F_{3/2},$$

where the prime means that no shielding correction is included, and 1 barn$=10^{-24}$ cm^2.

In the hfs of λ4523.4 (see Fig. 2) the hfs of the upper level is not resolved. Since the quadrupole effect of this level is expected to be somewhat larger than that of $d^3s^2\,{}^4F_{3/2}$, no attempt has been made to calculate Q from the hfs of λ4523.4.

The hfs of λ4648.9 is shown in Fig. 3. The

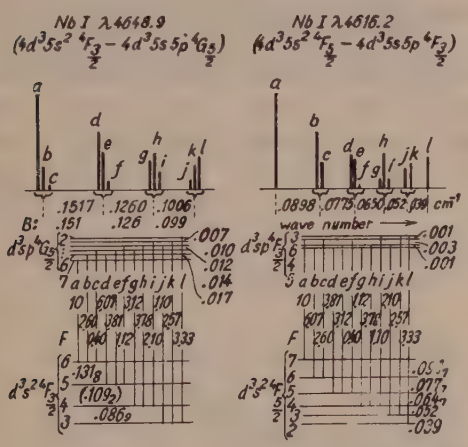

Fig. 3. Hfs of Nb I λ4648.9 and λ4616.2.

hfs of the upper level $d^3sp\,{}^4G_{5/2}$ is not resolved. Let A, B and A', B' denote the interval factor and the quadrupole coupling constant of the lower and the upper level respectively. Then we get from the hfs of λ4648.9:

$$A-(7/5)A'=0.02523,$$
$$B-(28/15)B'=0.0016\times10^{-3}.$$

Since $A=0.02187$, we get $A'=-0.00240$. A simple calculation shows that B' should be far smaller than B, so $(28/15)B'$ can be neglected. Then we get $B=0.0016\times10^{-3}$. This is to be compared with $B=0.0031\times10^{-3}$ obtained from λ5271.5. The discrepancy lies within the experimental uncertainty, and has no physical meaning.

From the hfs of λ4523.4 (Fig. 2) and λ4616.2 (Fig. 3) we can eliminate $B(d^3sp\,{}^4F_{3/2})$, and get $B(d^3s^2\,{}^4F_{5/2})$. This procedure is,

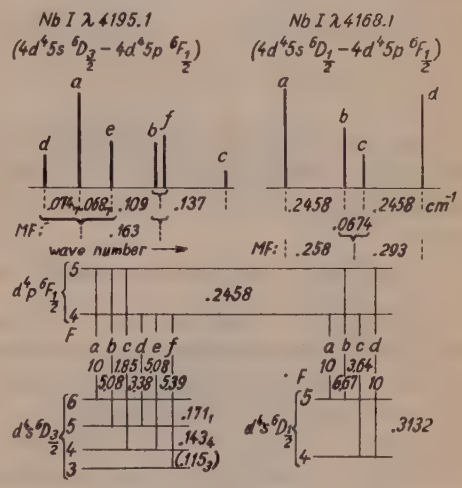

Fig. 4. Hfs of Nb I λ4195.1 and λ4168.1.

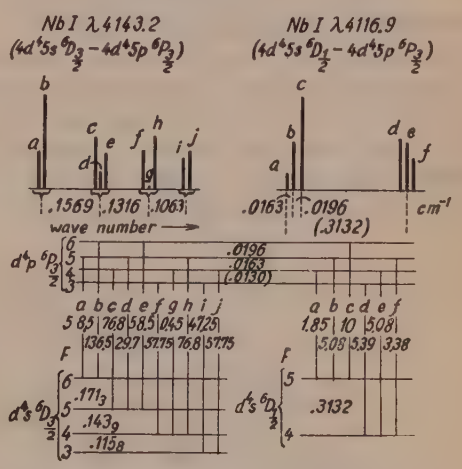

Fig. 5. Hfs of Nb I λ4143.2 and λ4116.9.

however, not so accurate, so no detailed calculation will be given here. But it is easy to show that Q' calculated in this way is in satisfactory agreement with Q' obtained from the level $d^3s^2\,{}^4F_{3/2}$.

The hfs of λ4195.1 is shown in Fig. 4. At least two lines lie close, and the measurement is difficult. The hfs of λ4143.2 (Fig.

5) was measured, assuming that the hfs of the upper level is not resolved. On the other hand the measurement of the hfs of $\lambda 4116.9$ which has the common upper level shows that the quadrupole effect in the upper level is negligible. We get, therefore, from the hfs of $\lambda 4143.2$ that $B(d^4s\,{}^6D_{3/2}) = -0.0052 \times 10^{-3}\,\mathrm{cm}^{-1}$.

The following formula was deduced previously[10]:

$$(d^4s\,{}^6D_{3/2}|\omega/r^3|d^4s\,{}^6D_{3/2}) = -\frac{2}{4375}(584\,R_2' - 91\,R_2'' + 132\,S_2)\langle r^{-3}\rangle.$$

Putting $\zeta_d = 450$, $Z_d^* = 23.5$, $J = 3/2$, $I = 9/2$ and the above-mentioned value of B and the matrix element of ω/r^3 in the usual formula, we get

$$Q'(\mathrm{Nb}^{93}) = -0.20 \text{ barn} \quad \text{from } d^4s\,{}^6D_{3/2}.$$

According to the calculations of Sternheimer[11], the atomic core shields or antishields the nuclear quadrupole coupling, so that the quadrupole moment Q' deduced from the hfs of atomic spectra must be multiplied by the factor $1+\Delta$, namely the true quadrupole moment Q is given by

$$Q = (1+\Delta)Q'.$$

(Sternheimer's $1/(1-R)$ is our $1+\Delta$).

Concerning the deep d-electrons, Sternheimer obtained positive Δ for the state $3d^94s^2$ of Cu I and negative Δ for the state $5d^4$ of W I. One would be probably permitted to assume that for the states $4d^35s^2\,{}^4F$ and $4d^45s\,{}^6D$ the shielding correction Δ would be small, based on the interpolation between Cu I and W I. We shall, therefore, assume that $\Delta = 0$ for the above-mentioned states, till an accurate calculation is available. Then the true quadrupole moment Q is given by

$$Q(\mathrm{Nb}^{93}) = -0.2_5 \pm 0.1_5 \text{ barn}.$$

Cotts and Knight[12] had previously observed nuclear resonance of Nb^{93} in $\mathrm{KNbO_3}$ and found definite evidence of the existence of a quadrupole moment in Nb^{93}. Speck and Jenkins[13] studied the hfs of Nb I $\lambda 5271$, and obtained $A = (21.7 \pm 0.1) \times 10^{-3}\,\mathrm{cm}^{-1}$ and $B = (-0.0044 \pm 0.0027) \times 10^{-3}\,\mathrm{cm}^{-1}$ for the level $4d^35s^2\,{}^4F_{3/2}$, and deduced $Q(\mathrm{Nb}^{93}) = -0.4 \pm 0.3$ barn. It is, however, difficult to see in what way a negative value of Q results from a negative vaule of $B(d^3s^2\,{}^4F_{3/2})$.

§ 4. Test of the Hyperfine Structure Formulas

From the hfs shown in Figs. 6, 7, 8 and 9 we can deduce the interval factors of $d^3s^2\,{}^4F_{7/2}$

Table II. Hfs of Nb I

$4d^35s^2$	A (cm^{-1}) K.M.*	A (cm^{-1}) MF**	$4d^45s$	A (cm^{-1}) K.M.*	A (cm^{-1}) MF**
${}^4F_{9/2}$	0.0092	0.005	${}^6D_{9/2}$	0.0226	0.021
${}^4F_{7/2}$	0.0099	0.004	${}^6D_{7/2}$	0.0226	0.022
${}^4F_{5/2}$	0.0129	0.013	${}^6D_{5/2}$	0.0241	0.024
${}^4F_{3/2}$	0.02187	0.021	${}^6D_{3/2}$	0.02871	0.028
			${}^6D_{1/2}$	0.06264	0.060

* Our value.

** Value given in ref. 2.

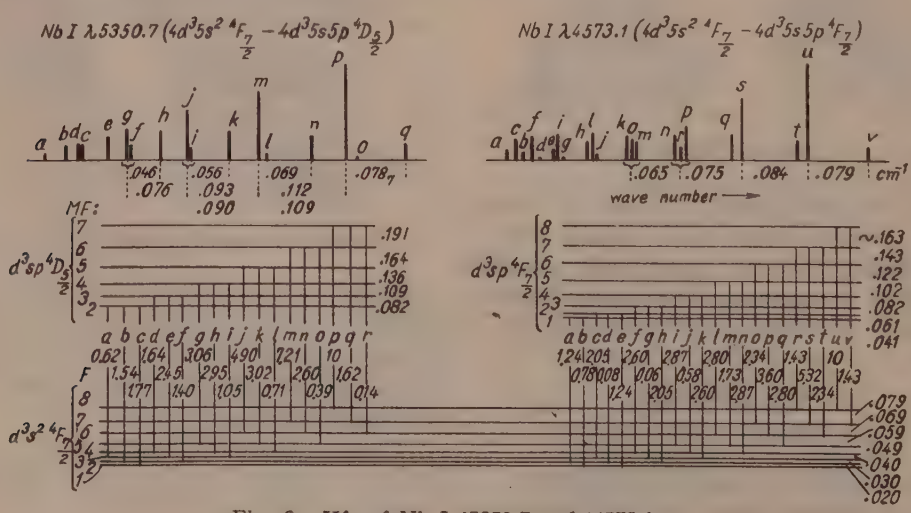

Fig. 6. Hfs of Nb I $\lambda 5350.7$ and $\lambda 4573.1$.

and $^4F_{9/2}$, and, together with those of $^4F_{3/2}$ and $^4F_{5/2}$, they are listed in Table II. From the hfs shown in Figs. 10 and 11 the interval factors of $d^4s\,^6D_{5/2}$, $^6D_{7/2}$ and $^6D_{9/2}$ were deduced and listed in Table II. The off-diagonal components in λ4139.7 were extremely difficult to measure, so the measured interval factor $A(d^4s\,^6D_{9/2})$ can claim no great accuracy.

The term $d^3s^2\,^4F$ will be treated at first. The following formulas (for *LS*-coupling) were deduced previously[3]):

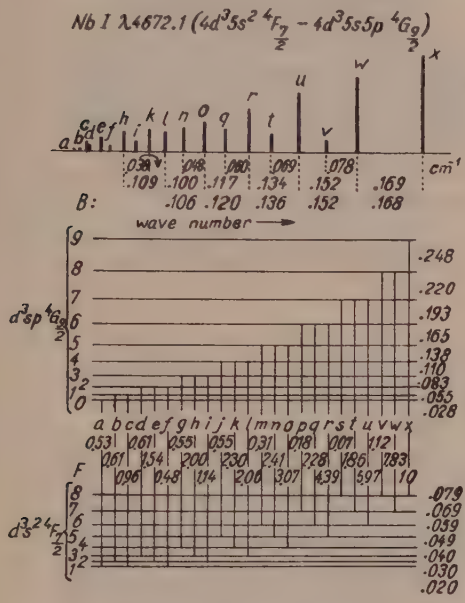

Fig. 7. Hfs of Nb I λ4672.1.

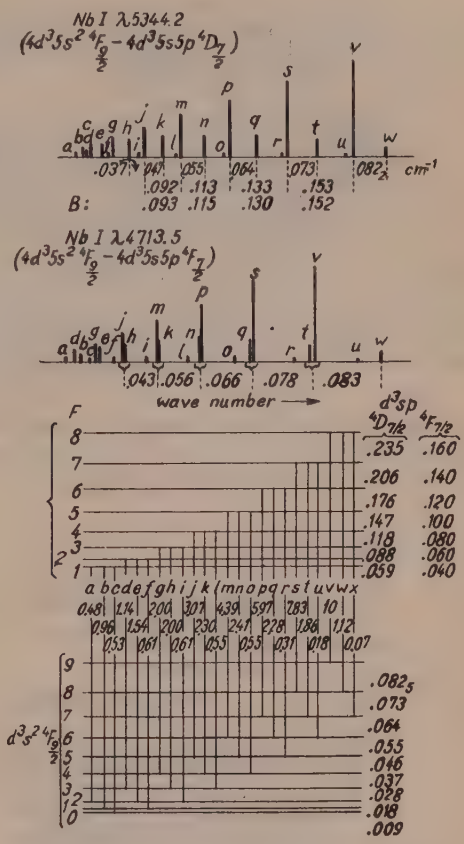

Fig. 8. Hfs of Nb I λ5344.2 and λ4713.5.

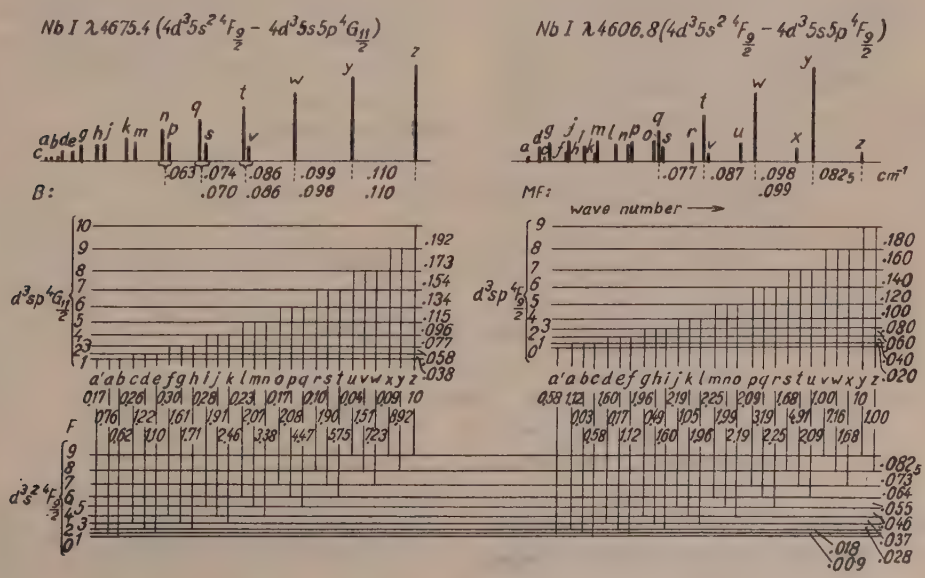

Fig. 9. Hfs of Nb I λ4675.4 and λ4606.8.

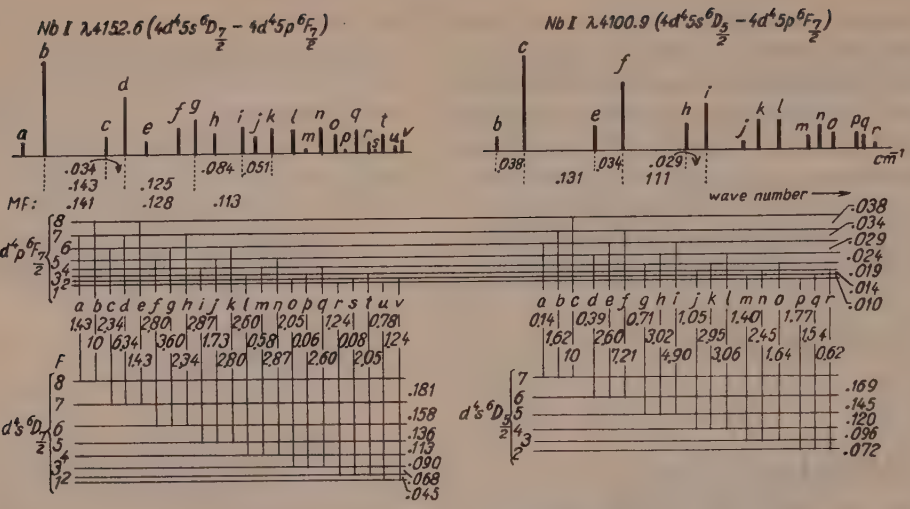

Fig. 10. Hfs of Nb I λ4152.6 and λ4100.9.

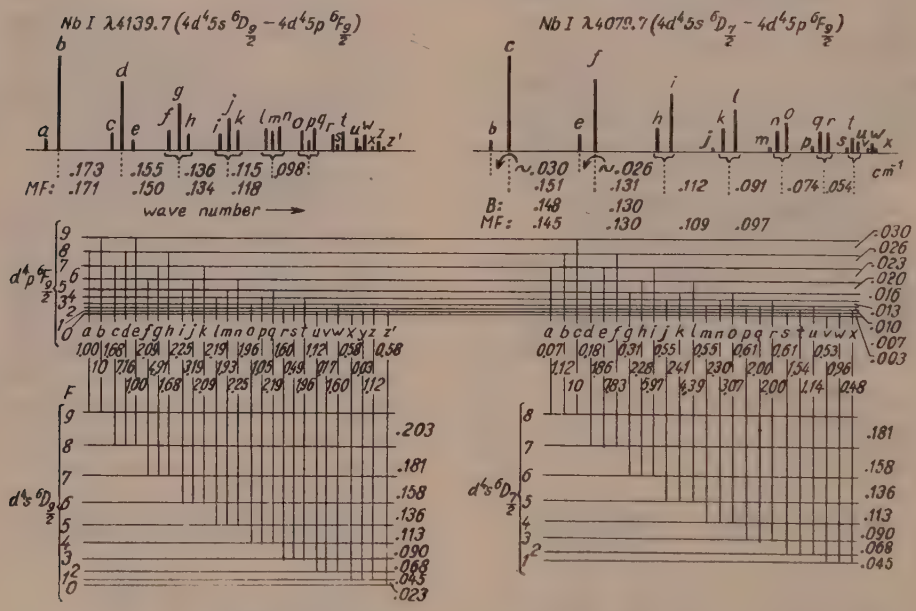

Fig. 11. Hfs of Nb I λ4139.7 and λ4079.7.

$$
\left.
\begin{aligned}
A(d^3\,{}^4F_{9/2}) &= \frac{1}{9}(8a_d' + a_d'' + 8a_d'''),\\
A(d^3\,{}^4F_{7/2}) &= \frac{1}{315}(281a_d' + 34a_d'' + 128a_d'''),\\
A(d^3\,{}^4F_{5/2}) &= \frac{1}{875}(712a_d' + 163a_d'' - 424a_d'''),\\
A(d^3\,{}^4F_{3/2}) &= \frac{1}{125}(59a_d' + 66a_d'' - 368a_d'''),\\
a_d' &= a(d_{5/2}),\quad a_d'' = a(d_{3/2}),\quad a_d''' = a(d_{5/2,3/2}).
\end{aligned}
\right\}
\tag{1}
$$

In the previous work[3)] the following theoretical formulas were assumed to be valid:

$$
a_d' = \frac{48}{35}\langle 1/r^3\rangle F_2'\ 1.585\left(\frac{\mu}{I}\right)\times 10^{-3}\ \mathrm{cm}^{-1},
\tag{2}
$$

$$a_d'' = \frac{48}{15}\langle 1/r^3\rangle F_2'' \, 1.585\left(\frac{\mu}{I}\right)\times 10^{-3}\,\mathrm{cm}^{-1}, \tag{3}$$

$$a_d''' = -\frac{1}{5}\langle 1/r^3\rangle G_2 \, 1.585\left(\frac{\mu}{I}\right)\times 10^{-3}\,\mathrm{cm}^{-1}, \tag{4}$$

$$a_d' = \frac{3}{7}\,\frac{F_2'}{F_2''}\,a_d''\,. \tag{5}$$

In the work concerning the hfs of $3d^94s^2\,{}^2D_{5/2,3/2}$ of Cu I[14], the author found that the formula (5) obtained by eliminating $\langle r^{-3}\rangle$ from (2) and (3) is not in agreement with the empirical facts. We shall, therefore, abandon the relations (2), (3), (4) and (5) in treating the term $d^3s^2\,{}^4F$ of Nb I and consider a_d', a_d'' and a_d''' in (1) as independent variables. Inserting the values of $A(d^3\,{}^4F_J)$ given in Table II into the formulas (1) and solving the simultaneous equations, we get

$$a_d' = 0.0088, \quad a_d'' = 0.0247, \quad a_d''' = -0.0016$$

In the case of $d^9s^2\,{}^2D_{5/2,3/2}$ of Cu I, the formula (5) was found to be invalid; a_d' was found to be too small to satisfy the relation (5). In the case of $d^3\,{}^4F$ of Nb I also, the discrepancy shows the same tendency.

On the other hand the relation between a_d'' and a_d''' is obtained from (3) and (4), and is given by

$$a_d''' = -\frac{1}{16}\,\frac{G_2}{F_2''}\,a_d''\,. \tag{6}$$

This relation seems to be satisfied by $d^3\,{}^4F$ of Nb I within experimental error or at least approximately.

We now turn our attention to the term $d^4s\,{}^6D$ of Nb I. The interval factors (in LS-coupling case) are given by:

$$\left.\begin{aligned}
A(d^4s\,{}^6D_{9/2}) &= \frac{1}{9}\,a(s) + \frac{1}{45}(38\,a_d' + 2\,a_d'' + 64\,a_d'''),\\
A(d^4s\,{}^6D_{7/2}) &= \frac{37}{315}\,a(s) + \frac{1}{1575}(1613\,a_d' - 223\,a_d'' + 1864\,a_d'''),\\
A(d^4s\,{}^6D_{5/2}) &= \frac{23}{175}\,a(s) + \frac{2}{875}(509\,a_d' - 129\,a_d'' + 512\,a_d'''),\\
A(d^4s\,{}^6D_{3/2}) &= \frac{13}{75}\,a(s) + \frac{1}{375}(473\,a_d' - 163\,a_d'' + 664\,a_d'''),\\
A(d^4s\,{}^6D_{1/2}) &= \frac{7}{15}\,a(s) + \frac{1}{75}(98\,a_d' - 58\,a_d'' + 544\,a_d''').
\end{aligned}\right\} \tag{7}$$

If we assume the relations (2), (3) and (4), then it can easily be shown that the observed values of $A(d^4s\,{}^6D_J)$ cannot be fitted in the formulas (7) unambiguously. We shall, therefore, try to abandon the relations (2), (3) and (4) and solve the equations (7) by considering $a(s)$, a_d', a_d'' and a_d''' as independent variables and putting the observed values of $A(d^4s\,{}^6D_J)$ given in Table II into (7). It can easily be shown that the rank of the matrix of the equations (7) is 3, whereas we have four independent variables $a(s)$, a_d', a_d'' and a_d'''. The four variables are, therefore, linearly dependent. For example, we get

$$a_d'' + a_d''' = 0.0120.$$

If we assume the relation (6), then we get $a_d''=0.0128$, which value is so different from that obtained from the term $d^3s^2\,{}^4F$ that it can hardly be accepted.

If we consider all of the relations (2), (3), (4) and (7) as approximate, then we get

$$a(s) = 0.161, \quad a_d' = 0.0083,$$
$$a_d'' = 0.0232, \quad a_d''' = -0.0015.$$

This is to be compared with the previous approximation[3] $a_d''=0.0222$, $a(s)=0.172$ (misprinted as 0.217).

From the above discussions we can conclude that the hfs formulas (2), (3) and (4) for the d-electrons do not have a rigorous validity. The inaccuracy of the hfs formulas for the d-electrons in the case of Nb I is, however, not so serious as in the case of V I[15], and we shall consider the effective charge on the d-electrons of Nb I $Z_d^*=23.5$ that was deduced previously[3] as being sufficient for a one- or two-digit discussion of Q.

The hfs of $4d^45s\,{}^6D_{9/2}$, ${}^6D_{7/2}$ and ${}^6D_{5/2}$ that are published in the present paper are still preliminary. The author hopes to be able to

improve the experimental set-up and to increase the accuracy of measurement of these hfs in the future.

The kindness of Professor S. Makishima (Department of Applied Chemistry) of eliminating iron from the niobium sample that was used in the present experiment is greatly appreciated.

Note added in proof. The small discrepancy between hfs theory and experiment in the Nb I levels containing d-electrons has been, in the meantime, solved. For example the mixing of $4d^3 5s6s$ in $4d^3 5s^2$ can account for the observed interval factors of $4d^3 5s^2\,{}^4F$.

References

1) S. S. Ballard: Phys. Rev. **46** (1934) 806.
2) W. W. Meeks and R. A. Fisher: Phys. Rev. **72** (1947) 451.
3) K. Murakawa: Phys. Rev. **98** (1955) 1285.
4) K. Murakawa: J. Phys. Soc. Japan **9** (19 391.
5) W. F. Meggers and A. S. King: J. Resear Natl. Bur. Standards **16** (1936) 385.
6) W. F. Meggers and B. F. Scribner: J. search Natl. Bur. Standards **14** (1935) 629.
7) E. U. Condon and G. H. Shortley: *The Theo of Atomic Spectra*, Cambridge Univers Press, London (1951).
8) R. E. Trees and M. M. Harvey: J. Resear Natl. Bur. Standards **49** (1952) 397.
9) G. Racah: Phys. Rev. **63** (1943) 367.
10) K. Murakawa and T. Kamei: Phys. Rev. **1** (1957) 671.
11) R. M. Sternheimer: Phys. Rev. **95** (1954) 7
12) R. M. Cotts and W. D. Knight: Phys. Re **93** (1954) 940.
13) D. R. Speck and F. A. Jenkins: Phys. Re **98** (1955) 282.
14) K. Murakawa: J. Phys. Soc. Japan **11** (19 774.
15) K. Murakawa: J. Phys. Soc. Japan **11** (19 422.

JOURNAL OF THE PHYSICAL SOCIETY OF JAPAN Vol. 13, No. 1, JANUARY, 1958

Note on the Information Capacity of a Coloured Picture

By Hiroshi SATŌ

University of Electro-communications

(Received September 20, 1957)

The information capacity of a coloured picture is obtained taking into account the restriction inherent to the human perception of colour. Calculations are made concerning a one-dimensional picture, and the result is used as an upper bound for the capacity of a two-dimensional picture.

§ 1. Introduction

The information capacity[1),2)] of a coloured picture will be larger than that of a monochrome picture as colour enhances infermation. By adopting the usual trichromatic theory of colour perception, the information capacity will increase to a value three times as large as that of a monochrome picture. Meanwhile, by the recent advances in colour television researches it is found that we need trichrome only for the part of the picture where the brightness changes slowly, while for the part where the brightness changes rapidly from place to place the use of a monochrome is sufficient for preception. This roughness in colour preception is utilized in the transmission of colour television as a principle of "mixed highs". Thus now, the increase the information by addition of colour is su posed to be very small.

Seki[3)] tried to obtain the information cap city of a coloured picture by dividing it to very large number of small picture elemer in which all the chromatic property can regarded as uniform. In this paper, we sol this problem in the case of a one-dimensior picture that has an almost rigorous solutic and use the result to estimate the capaci of a two-dimensional picture.

In § 2, 3, the information capacity of a or dimensional picture is obtained and the meth is criticized in § 4. In § 5, it is shown th the result of the one-dimensional case can used as an upper bound for the capacity o

wo-dimensional picture.

2. Formulation of a One-dimensional Problem

A one-dimensional picture consists of a very arge number N of picture elements in each f which the chromatic properties can be rearded as uniform and each of which can take ome definite number of chromatic states. In rder to obtain the information capacity taking nto account the roughness of our colour perception, it is more convenient to consider a icture as composed of groups of picture elenents rather than of picture elements themelves. A group of picture elements is a successive sequence of picture elements and every icture elements in the same groups should ake the same chromatic states simultaneously. A number of picture elements in a group called the length of the group, and a group f length l is assumed to take b_l different hromatic states. When a picture is composed f $m_1, m_2, \cdots, m_l, \cdots, m_N$ groups of length , 2, $\cdots$, l, $\cdots$, N respectively, the following elation holds:

$$\sum_{l=1}^{N} l m_l = N . \tag{1}$$

If we write the total number of groups in picture as M,

$$\sum_{l=1}^{N} m_l = M . \tag{2}$$

'or a given set of number of groups $m_1, m_2, \cdots, m_N$ which satisfies Eq. (1), the number f ways in which these groups can be arnged is

$$\frac{M!}{\prod_l m_l!} , \tag{3}$$

nd for every arrangements the number of ifferent possible pictures is

$$\prod_l (b_l)^{m_l} , \tag{4}$$

ince the groups of length l can take b_l diferent states. Therefore for a given $m_1, m_2, \cdots, m_N$, the number of different possible picures P is the product of (3) and (4),

$$P = \frac{M!}{\prod m_l!} \prod (b_l)^{m_l} , \tag{5}$$

where M is defined in Eq. (2). In order to btain the total number of different possible ictures P_0, we have only to sum (5) over all ossible sets of numbers $m_1, m_2, \cdots, m_N$ which satisfies Eq. (1),

$$P_0 = \sum P . \tag{6}$$

(This is not quite correct as will be discussed in § 4.) The information capacity of this one-dimensional picture is then.

$$C = \log P_0 . \tag{7}$$

(All throughout this paper we use natural logarithm for the sake of convinience.) We shall next evaluate this by the usual method of maximum term evaluation, since N is very large. According to that method, we have only to take the logarithm of the maximum term of the right-hand side of Eq. (6) to obtain

$$C = \log P_0 \simeq \log P_{\max} \tag{8}$$

so that the expression (5) should be maximized by changing the variables $m_1, m_2, \cdots, m_N$ under the subsidiary condion (1). For the sake of convinience we introduce new variables p_l defined by

$$p_l = \frac{m_l}{M} , \quad l = 1, 2, \cdots, N \tag{9}$$

in place of m_l, then Eqs. (1), (2) are reduced to

$$M \sum_l l p_l = N , \tag{1'}$$

$$\sum_l p_l = 1 , \tag{2'}$$

and the logarithm of the expression (5) becomes by means of Stirling's formula

$$\log P \simeq M \sum_l p_l (\log b_l - \log p_l) , \tag{10}$$

retaining important terms only. Our problem is now to optimize the expressions (10) changing variables $M, p_1, p_2, \cdots, p_N$ under the subsidiary conditions (1′), (2′). After multiplying to the left-hand sides of (1′) and (2′) by $-\beta$ and α, adding them to (10) and putting the differential coefficients to zero, we obtain

$$\sum_l p_l (\log b_l - \log p_l - \beta l) = 0 , \tag{11}$$

$$M(\log b_l - \log p_l - 1 - \beta l) + \alpha = 0 ,$$
$$l = 1, 2, \cdots, N . \tag{12}$$

From Eqs. (11) and (12) we can easily show

$$\alpha = M$$

and

$$p_l = b_l e^{-\beta l} ; \quad l = 1, 2, \cdots, N , \tag{13}$$

so that Eqs. (1′) and (2′) take the following forms

$$M \sum_l l b_l e^{-\beta l} = N , \tag{1''}$$

$$\sum_l b_l e^{-\beta l}=1 . \qquad (2'')$$

When we assume an appropriate form for $\boldsymbol{b}_l$, as is actually done in the next section, we can first get β from (2″), and then $\boldsymbol{p}_l$ and M from (13) and (1″). Further, the capacity is obtained by putting (13) into (10) and taking Eq. (1″) into account as follows:

$$C=\beta N . \qquad (14)$$

Therefore, in order to obtain the information capacity per picture element, the only thing to do is to solve β from Eq. (2).

Letting $x=e^{-\beta}$, Eq. (2) can be written as

$$\sum_l b_l x^l=1 , \qquad (2''')$$

which we call the characteristic equation.

§ 3. Calculation of the Capacity of a One-dimensional Picture

We assume here that the number of levels of each colour components are the same as is usually admitted as a first approximation in the colour television case. It is further assumed that only monochrome is used for the groups whose lengths are less than $\boldsymbol{l}_1$, dichrome for those whose lengths are between $\boldsymbol{l}_1$ and $\boldsymbol{l}_2-1$, and trichrome for those whose lengths are above $\boldsymbol{l}_2$. Then the numbers of possible states of groups can be written

$$\begin{aligned} b_l &= L , & \text{for } 1 \leq l < l_1 \\ &= L^2 , & \text{for } l_1 \leq l < l_2 \\ &= L^3 , & \text{for } l_2 \leq l \end{aligned} \qquad (15)$$

where L is the number of levels of each colour components and the distance between successive levels are taken as small as possible so far as they can be distinguished by human perception.

The characteristic equation in this case can be written as

$$x^{l_2}+\frac{1}{L}x^{l_1}+\frac{L+1}{L^2(L-1)}x-\frac{1}{L^2(L-1)}=0 , \qquad (16)$$

after a little manipulation letting N tend to infinity. For numerical calculation, we take here that L is of the order of 10^2, then it is shown that for the case $\boldsymbol{l}_2 > \boldsymbol{l}_1 \geq 3$ the ratio of increment of the capacity to the capacity of an overall monochrome picture is less than one percent. Therefore we omit such cases and calculate next two cases. The results are shown in Table I. Here $\beta_0=\log L$ means the information capacity of an overall monochrome picture, $\boldsymbol{r}$ is the ratio of increment the capacity to the capacity of a monochrom picture defined by $\boldsymbol{r}=(\beta-\beta_0)/\beta_0$. Needless say that for very large $\boldsymbol{l}_1$, $\boldsymbol{l}_2$ the capacity almost equal to β_0 since in this case trichrom or dichrome is not used for the most part the picture.

In case we do not use dichrome, $\boldsymbol{b}_l$ can b written as follows:

$$\begin{aligned} b_l &= L , & \text{for } 1 \leq l < l_2 \\ &= L^3 , & \text{for } l_2 \leq l \end{aligned} \qquad (15$$

and the characteristic equation is

$$x^{l_2}+\frac{1}{L(L+1)}x-\frac{1}{L(L^2-1)}=0 . \qquad (16$$

The results are tabulated in Table II. Aga calculations are made in cases when the rat of increment is above one percent.

Table I. Increment of the capacity when mon chrome, dichrome and trichrome are used.

	x	$\beta-\beta_0$	r for $L=100$
$l_1=2,\ l_2=3$	$0.54/L$	0.59	0.13
$l_1=2,\ l_2\geq 4$	$0.62/L$	0.48	0.10

Table II. Increment of the capacity when mon chrome and trichrome are used.

	x	$\beta-\beta_0$	r for $L=1$
$l_2=2$	$L^{-\frac{3}{2}}(1-L^{-\frac{1}{2}})$	$\frac{1}{2}\log L+\frac{1}{2}L^{-\frac{1}{2}}$	0.51
$l_2=3$	$0.68/L$	0.38	0.08

§ 4. Critique of the Method

In order to check the validity of our metho we first consider the case when all pictu elements can take trichrome freely. Sin every elements can take L states indepen ently, the capacity of the picture should be

$$C=N\log L^3 . \qquad (1$$

If we apply our method to this problem, t number of possible states of a group of leng $\boldsymbol{l}$ is

$$b_l=L^3 , \qquad \text{for all } l$$

and from (2″) we obtain

$$\beta=\log(L^3+1) ,$$

and

$$C=N\log(L^3+1) . \qquad (1$$

This result is a little different from the e

pected value (17), although the difference is very small when L is very large. This comes from the fact that by our method some pictures are counted more than once. In the above example, we can get the correct result (17) from one term in the right-hand side of (6) that corresponds to $m_1=N$, $m_2=m_3=\cdots=m_N=0$. In this example all other terms are redundant.

Similar criticism holds in the general case. In the right-hand side of Eq. (6), among the possible pictures which are composed of the groups $l_1, l_2, \cdots, l_{s-1}, l_s, l_{s+1}, \cdots, l_m$, those pictures whose s'th and $s+1$'th groups take the same chromatic state are counted again in the division into the groups $l_1, l_2, \cdots, l_{s-1}, l_s', l_{s+2}, \cdots, l_M$, where $l_s'=l_s+l_{s+1}$. In this way our method gives a larger value as the capacity, but as is seen from the result of the above example, the error would be so small (of the order of $1/L^3$ in β) that we can safely neglect this error.

§ 5. Two-dimensional Pictures

As it seems difficult to solve the two-dimensional problem in the same line of thought as in the one-dimensional case, we will here utilize the previous result to obtain the upper bound of the capacity of a two-dimensional picture.

Let the two-dimensional picture consist of picture elements arranged in rectangular way N horizontally N' vertically. We assume that the picture is composed of rectangular groups of picture elements the number of possible states of which are determined by their horizontal length l just the same way as Eq. (15). So the vertical length of the group is quite irrelevant in determining the number of states. We restrict the property of the two-dimensional picture as above, but it seems that it is not too severe a restriction. For example, such a sort of pictures that are composed of squares are involved in the above defined class of pictures.

Let the information capacity per picture element of such a two-dimensional picture be β_2, and that of the corresponding one-dimensional picture be β_1, and we can get the following relation:

$$NN'\beta_2 \leq NN'\beta_1 , \tag{19}$$

or

$$\beta_2 \leq \beta_1 . \tag{19'}$$

The above relation is derived from the following consideration. The right-hand side of Eq. (19) represents the capacity of such a two-dimensional picture that is an independent vertical collection of N' horizontal one-dimensional pictures, while the left-hand side represents a true capacity of our two-dimensional picture that has a statistical correlation not only in a horizontal direction but also in a vertical one. Therefore, Eq. (19) is the result of Shannon's wellknown inequality[1]. Or we may as well interprete it as follows. All the pictures considered in the left-hand side are involved in the right-hand side.

We can easily obtain the lower bound because for the monochrome picture every b_l are bounded by those of the coloured picture,

$$NN' \log L \leq NN'\beta_2 , \tag{20}$$

or

$$\log L \leq \beta_2 . \tag{20'}$$

In conclusion we have the result as follows:

$$\log L \leq \beta_2 \leq \beta_1 ,$$

or if we write the ratio of increment of the capacity to the capacity of the monochrome picture r_1, r_2 in one- and two-dimensional cases, we obtain

$$0 \leq r_2 \leq r_1 , \tag{21}$$

where r_1 is calculated in § 4 to be 0.13 and 0.10 for the cases $l_1=2$, $l_2=3$ and $l_1=2$, $l_2 \geq 4$ respectively.

References

1) C. E. Shannon and W. Weaver: "The Mathematical Theory of Communication"; Univ. of Illinois Press, Urbana, Ill., 1949.
2) L. Brillouin: "Science and Information Theory", Academic Press Inc., New York, 1656.
3) H. Seki: Journal of the Colour Television Engineering Institute (in Japanese) Vol. 8, No. 6 (1954) p. 15.

Short Notes

This section is intended to secure prompt publication of important discoveries in physics. The reports should not exceed 800 words in length. A figure of size 7 cm × 7 cm will be counted as 150 words.

J. PHYS. SOC. JAPAN **13** (1958) 112

Electron Collection and Electron Sheath

By Takayoshi OKUDA and Kenzo YAMAMOTO

Faculty of Engineering, University of Nagoya, Nagoya

(Received October 15, 1957)

In this paper, we deal with an anomalous electron collection made by positive probe, the mechanism of which is to drain off electrons, independent of electron sheath.

So far we have considered either the electron collection limited by the sheath area or the electron collection determined by the orbital motion, both are also applicable to ion collection made by negative probe.

There is the question now, "What is the relation between electron sheath and electron collection?" For our answer, we must measure the radius of the electron sheath. This can be done by using the variable-length probe method, which is described in the other paper[1] in connection with measuring radius of ion sheath. With ion sheath in high density plasma, there is good agreement between the measured radius and the theoretical radius when an appropriate space charge equation is used.

Table I. The measured and the evaluated sheath radius in Ar plasma of discharge current of 50 mA. r_p=0.075 cm.

p (mm Hg)	V (V)	sheath radius (cm)		
		a_1	a_2	a_3
0.003	4	0.077	0.150	—
〃	10	0.082	0.245	—
0.02	4	0.076	0.172	—
〃	10	0.081	0.233	—
0.2	4	0.094	0.146	0.165
〃	10	0.101	0.183	0.212
1.0	4	0.096	0.187	0.141
〃	10	0.097	0.198	0.155

In the same way, we measure the radius of the electron sheath in various conditions in Ar discharge plasma. In Table I we give the measured radius a_1 as well as the evaluated radii, a_2 and a_3 corresponding respectively to space charge equations in practical units:

$$i_e = 14.66.10^{-6} \frac{l}{r_p} \frac{V^{3/2}}{\beta^2} \qquad (1)$$

$$i_e = 55.5.10^{-14} \frac{l}{r_p^2} \frac{K_0}{p} \frac{V^2}{\Phi_c^2} \qquad (2)$$

where i_e is electron current (A), l length of cylindrical probe (cm), r_p radius of probe (cm), V positive probe voltage (V), p pressure (mm Hg), K_0 mobility of electron at 1 mm Hg (cm².mm Hg/V.sec) (K_0=3.17.10⁵ for Ar), and β^2, Φ_c geometrical factors of function of a/r_p.

By Langmuir's theory, our experimental condition is the sheath area limited because $r_p \gg a - r_p$. In Table I we see that the measured radius is always smaller than the theoretical radius. Furthermore, anomalous behavior of the radius is readily found by plotting the measured radius against the positive voltage, as shown in Fig. 1. From this

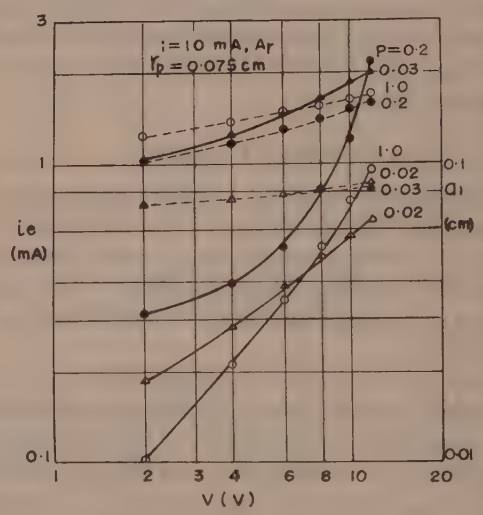

Fig. 1. Plots of electron current vs. positive probe voltage (solid line) and sheath radius vs. positive probe voltage (dotted line).

figure we can confirm that there is little expansion of the electron sheath and that there is no relation between the plot of the sheath radius vs. the positive probe voltage and the plot of the electron current vs. the positive probe voltage. Should the collection meachanism be the sheath area limited, both slopes would be the same.

In low pressure where Eq. (1) is valid, the theoretical slope must be 0.72 ~ 0.15 at random electron current densities of 0.1~100 mA/cm², and at 1 mm Hg where Eq. (2) is valid, theoretical slope must be 0.48~0.15 at random electron current densities of 0.1~100 mA/cm². Fig. 1 shows the steep rise of the electron current with increasing positive probe voltage, far exceeding the theoretical expectation.

All these experimental results support the reasonable conclusion that electron collection is not caused by sheath area limited mechanism, but that it is a drainage mechanism which can be regarded as an increase of plasma density occuring close to the boundary of the sheath-plasma.

Reference

1) T. Okuda and K. Yamamoto: J. Phys. Soc. Japan, will be published.

J. Phys. Soc. Japan **13** (1958) 113

Afterglow of Pure and Mixed Gases

By Susumu Takeda

Department of Electrical Engineering, Faculty of Engineering, Yokohama National University

(Received Nobember 2, 1957)

The most interesting and remarkable fact in the actual counting tube is known to be that the maximum counting speed can very much increased by adding some amount of Hydrogen to the rare gas used[1]. In order to investigate the mechanism of the deionization of the discharge tube, the decay of electron density was studied here by the microwave method[2]. In the present experiment DC pulse is added to ignite a post discharge.

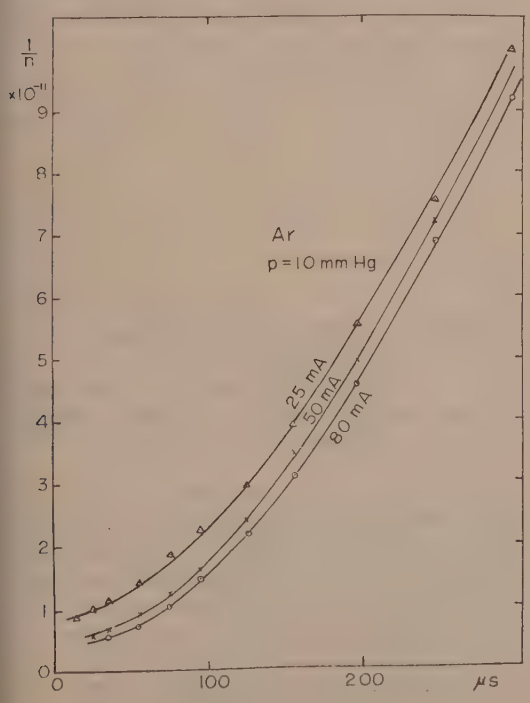

Fig. 1.

Fig. 1 shows the relation of $1/n$ and t for various peak currents in Argon, showing no constant slope for $t<300\,\mu s$. When a small amount of Hydrogen is added, these become quite linear as shown in Fig. 2 and 3 for different peak currents and pulse widths respectively, because metastable ions of puer gas that will ionize and apparently decrease the decay in the early period would be broken by Hydrogen molecules.

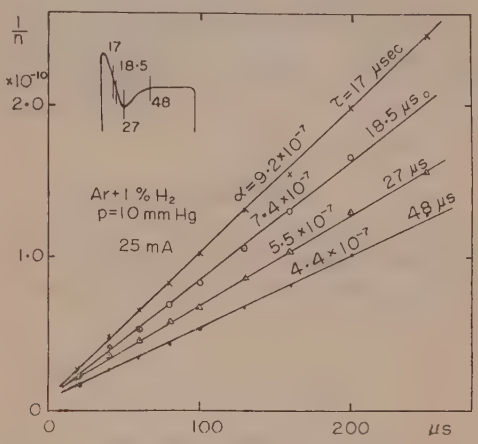

Fig. 2.

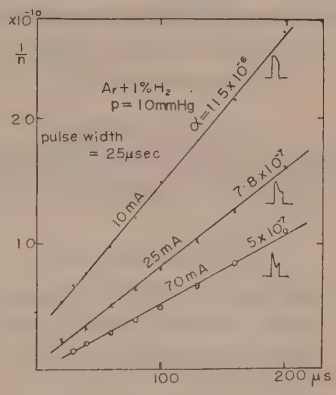

Fig. 3.

The difference of slopes in each line in both figures is supposed to be due to the different content of Hydrogen ion. The small current gives a similiar effect as short width as expected from the wave form of the voltage as shown in these figures.

Judging from the voltage form in pure Argon and Hydrogen, the time of growth of Argon, ions may be longer than that of Hydrogen ions, and it can be supposed that the latter density would be larger in the shorter pulse or the smaller current in such a mixed gas.

The conclusions are follows,

(1) In the rare gases as Argon where the recombination predominates over diffusion the decay in the early period of afterglow is slower than that deter-

mined by their recombination coefficients.

(2) When mixed with Hydrogen, only a small amount of Hydrogen affects very much and makes $1/n$ linear even in the early period.

(3) $1/n$ have different slopes for various currents and pulse widths. The reason will be that the amount of positive ions of Hydrogen is different respectively.

The author sincerely appreciates Prof. K. Honda of Tokyo University, Mr. K. Takatsu who is a member of Electric Communication Laboratory and Mr. K. Ogawa of Matsuda Research Laboratory of Tokyo Shibauro Electric Company. He also thanks Mr. Y. Ishikawa of our university for his technical assistance.

References

1) S. Watanabe and M. Iwasaki: Electric Engineering Conference in Japan **594** (1954)
2) M. A. Biondi and S. C. Brown: Phys. Rev. **75** (1949) 1700

J. PHYS. SOC. JAPAN **13** (1958) 114

Dielectric Properties of Lead Titanate and Its Solid Solutions at Low Temperature under Strong Electric Field

Shoichiro NOMURA
Institute of Science and Technology, University of Tokyo, Tokyo, Japan
and
Jinzo KOBAYASHI
Department of Applied Physics, Waseda University, Tokyo, Japan

(Received December 5, 1957)

Lead titanate $PbTiO_3$ is well known to be ferroelectric at room temperature. X-ray and dielectric studies have revealed that it transforms into another phase at low temperature[1),2)]. However, the low temperature transition of $PbTiO_3$ is very sluggish, a retardation always occurs when a transformation point is passed. This may be the principal reason why this transition was masked in some investigations by others on $PbTiO_3$. Even when we could recognize the transformation to occur, it was difficult to determine the transition temperature exactly because of its Sluggish nature.

With this in view we studied the polarization vs. temperature characteristics of $PbTiO_3$ and its solid solutions at low temperature by applying strong a.c. field, and found that their transformations were markedly affected by the applied field. Some results on these natures are reported here briefly.

We used disk-shaped ceramics as the specimens ca 2.3 cm in diameter and 0.08 cm thick; electrode being dried silver paste. Temperature dependencie of the maximum polarization P_{max} were measure by using Sawyer-Tower circuit and an oscilloscope Fig. 1 shows P_{max} vs. temperature relations fo $PbTiO_3$ which were obtained from D–E loops fo several different field strengths, the frequency use being 50 cycle/sec. We can obviously recogniz that an anomaly occurs on each curve and thes transition points stand out and shift to the lowe temperature side by increasing the applied fiel strength.

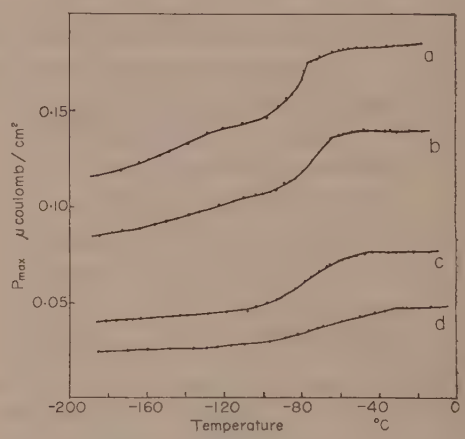

Fig. 1. Maximum polarization vs. temperature curves for $PbTiO_3$. Field strengths are (a) 15.7 KV/cm, (b) 11.7 KV/cm, (c) 5.8 KV/cm and (d) 3.5 KV/cm.

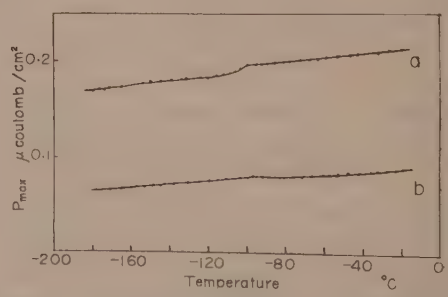

Fig. 2. Maximum polarization vs. temperature curves for $Pb(0.8Ti \cdot 0.2Sn)O_3$ Field strengths are (a) 11.5 KV/cm and (b) 4.6 KV/cm.

Similar results were obtained for $PbTiO_3$ soli solutions series. One of them, $Pb(0.8\,Ti \cdot 0.2\,Sn)O$ for example, is shown in Fig. 2. The effect of th applied field on the transition temperatures is show in Fig. 3. It is noted that the falling rates of th transition point are very large and reach $-3.$ $\times 10^{-3}$ °C/volt/cm for $PbTiO_3$ and $-1.9 \times 10^{-}$ °C/volt/cm for $Pb(0.8\,Ti \cdot 0.2\,Sn)O_3$. Then th transition temperature for the normal states can b

obtained by extraporating these curves to zero field; $-30°C$ for $PbTiO_3$ and $-80°C$ for $Pb(0.8\,Ti \cdot 0.2\,Sn)O_3$ respectively. If we compare the present results on $PbTiO_3$ with the former measurement of dielectric constant[2], it is obvious that there exist some discrepancies between them. In our recent experiments, however, we obtained dielectric constant vs. temperature curves, showing the characteristics similar to (d) in Fig. 1, which corresponds to a weak applied field. Therefore we may suppose that some of the discrepancies were brought about by the sluggish nature of the phase transformation.

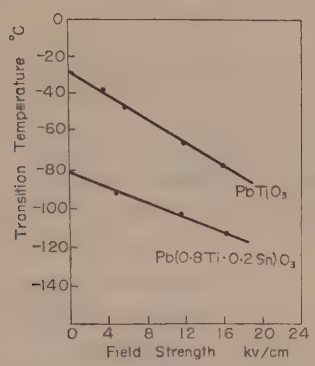

Fig. 3. Transition temperatures as a function of field strength.

It is concluded that several measurements under strong electric fields are effective to determine the exact transition point in such materials, $PbTiO_3$ and its solid solutions that have sluggish transformations.

The details of our results will be reported shortly.

References

1) J. Kobayashi and R. Ueda: Phys. Rev. **99** (1955) 1900.
2) J. Kobayashi, S. Okamoto and Ueda: Phys. Rev. **103** (1956) 830.

Erratum

Molecular Sound Velocity of Aqueous Sugar Solutions

Otohiko NOMOTO and Tadashi KISHIMOTO

J. Phys. Soc. Japan **12** (1957) 311

The words "sugars" and "saccharides" in this paper must be replaced by "sugars and polyhydric alcohols", and "sugar solutions" by "solutions of sugars and polyhydric alcohols", because erythrite and mannite are polyhydric alcohols.

Errata (Addenda)

to

Application of the Thin-Wing-Expansion Method to the Flow of a Compressible Fluid past a Symmetrical Circular Arc Aerofoil

By Saburô ASAKA

J. Phys. Soc. Japan, Vol. 10, No. **6**, pp. 482–492 (1955)
Errata, ibid. Vol. 10, No. **7**, p. 593 (1955)

In equation (5.10) on page 487,

eleventh line from the bottom	$(4/3\pi^3)\{2(1+\cdots\cdots$
should be	$(4/3\pi^3)\{4(1+\cdots\cdots$
seventh line from the bottom	$\cdots\cdots+6\nu^2\}[\cdots\cdots$
should be	$\cdots\cdots+16\nu^2\}[\cdots\cdots$

The author is indebted to Dr. John R. Spreiter for pointing out these errors. They are mistakes in printing and the numerial results in § 6 are not affected by these errors.

PROGRESS OF THEORETICAL PHYSICS

CONTENTS

Progress of Theoretical Physics Vol. 18, No. 5, November 1957

Some Considerations on the High-Energy Electron-Proton Scattering and the Nucleon Mass Difference..... Kichiro HIIDA and Makoto SAWAMURA..451
On the Lattice Model of Liquid Helium proposed by Matsubara and Matsuda. ..... Tohru MORITA..462
Pion-Nucleon Scattering and the Structure of the Pion ..... Shigeru MACHIDA..467
Pairing Energy of Nuclear Particles .....Morikazu NOMOTO..483
Analysis of Neutron-Electron Interaction in the Relativistic Perturbation Theory .....Kin-ichi ISHIDA..493
Deuteron Production by Nucleons Bombarding Atomic Nuclei ..... Ken KIKUCHI..503
Band Theory of Superexchange Interaction ..... Jun KONDO..541
Letters to the Editor:
On the Spin-Lattice Relaxation Process in Ferromagnets..... ..... F. TERASAKI and I. MANNARI..552
The Artificial Satellite and the Relativistic Red Shift ..... A. DAS..554
Efficiency of Acceleration of Relativistic Particles in the Crab Nebula ..... S. HAYAKAWA and Y. TERASHIMA..555
Contents of Journ. of the Phys. Soc. of Japan, Vol. 12, No. 9 558

Price $ 1.25 per copy
$ 15.00 per year (postage inclusive)
Annual dues for foreign members (individual subscribers)
$ 12.00 (postage inclusive)
" for foreign members of the Physical Society of Japan
$ 10.00 (postage inclusive)

Application for members, subscriptions and orders for back numbers should be sent, directly or through book-dealers, to

The Publication Office
in
Yukawa Hall, Kyoto University, Kyoto, Japan

JOURNAL OF THE PHYSICAL SOCIETY OF JAPAN Vol. 13, No. 2, FEBRUARY, 1958

Directional Correlations of Gamma Rays in Te^{124}

By Takeo HAYASHI

Department of Physics, Saikyo University, Kyoto

(Received August 30, 1957)

The directional correlations of the 2.11–0.605 Mev and 1.71–0.605 Mev gamma-gamma cascades in Te^{124} have been measured by using a coincidence spectrometer newly designed. Both of the correlation functions are compatible with the sequence 3 (D, Q) 2 (Q) 0, where quadrupole admixture in the first radiation is expected to be very small. The false coincidences occurring in this type of circuit are also described in some details.

§ 1. Introduction

In early studies the spins and parities of the excited states in Te^{124} were assigned indirectly on the basis of the informations about the spin and parity of the ground state in Sb^{124} as well as the degree of forbiddenness of the beta transitions from this ground state to the concerned excited states in Te^{124}. In those days, however, the informations concerning the first beta ray spectrum of Sb^{124} had many inconsistencies[1,2,3,4], so that no spin and parity assignment could be obtained for this state. In the following years the internal conversion coefficient for the 0.605 Mev gamma ray in Te^{124} was measured by Metzger[5]. The result of his measurement, in conjunction with an empirical rule[6] proposed just then concering the first excited states of even-even nuclei, seemed to show that the 0.605 Mev state should be 2^+. Based upon these informations Morita and Yamada[7] have shown that the directional correlation[8,9] between the 2.317 Mev beta ray and the 0.605 Mev gamma ray can be explained theoretically by assigning 3^- to the ground state in Sb^{124}, and this led to the spin and parity assignments for the excited states in Te^{124} by taking account of *ft* values for the concerned transitions.

Now this situation has stimulated the direct determination of the spins of the excited states in Te^{124} by the measurement of the angular correlations between the cascade gamma rays. In the early experiments[9,10,11], however, no appreciable anisotropy could be observed before Kraushaar and Goldhaber[12] investigated the 1.71–0.605 Mev cascade and found that the form of the correlation function agreed with that of a 3–2–0 cascade. They also reported that the first radiation may be mainly dipole with a small admixture of quadrupole. But, since they measured, by the use of integral discrimination in their pulse height analysis, all the gamma rays above 0.1 Mev in one channel and 0.7 Mev in the other respectively, their results contained, besides the main contribution from the 1.71–0.605 Mev cascade, unknown part due to the 2.11–0.605 Mev transitions. Such an ambiguity was removed by Metzger[13] who measured the 2.11–0.605 Mev angular correlation separately from the contribution due to the 1.71–0.605 Mev cascade. However, he reported his result only briefly, probably because of weak intensity of the 2.11 Mev gamma ray. Moreover, the assignment of 3^- to both of the 2.72 Mev and 2.32 Mev levels seems to cast some questions on the 3^- assignment to the ground state in Sb^{124}, since the *ft* values of the beta disintegrations between the concerned states are much greater than the expected value for the 3^-–3^- transition. Under these circumstances, therefore, it seems worth while to study the 2.11–0.605 Mev angular correlation more precisely and to reinvestigate, at the same time, the 1.71–0.605 Mev cascade subject to the correction for the contribution from the ascertained 2.11–0.605 Mev cascade.

§ 2. Methods and Apparatus

The RCA 5819 photomultiplier tubes mounted with thallium-activated sodium iodide crystals of $1\frac{1}{2}$ in.$\phi \times 1$ in. were used as detectors. The source material obtained from Radiochemical Centre in England was $SbCl_3$ in 5 N HCl, and since about two months had elapsed after its production when the

present work was started, the contribution from the impurity of Sb^{122} in the source material need not be considered. For the purpose of avoiding extranuclear interaction the source was used in liquid form. It was prepared by dropping the solution into the 1 mm diameter hole of a glass source container with thin wall thickness and by sealing the top of the hole in order to avoid the evaporation of the solvent. The distance between the source and the front face of each crystal was 5 cm. Since the slightest asymmetry in the source position would seriously change the observed correlation, care was taken for the setting of the source, and small setting correction was made to the raw experimental data. The protection against the spurious coincidence counts due to the radiations scattered in the other crystal was not necessary, because the discriminator windows were placed outside the shifted energies due to the Compton scattering. The energetic beta rays were slowed down with thin absorbing materials and were excluded in a similar manner.

A block diagram of the electronic circuits is shown in Fig. 1. This coincidence spectrometer is, in its basic idea, similar to that of

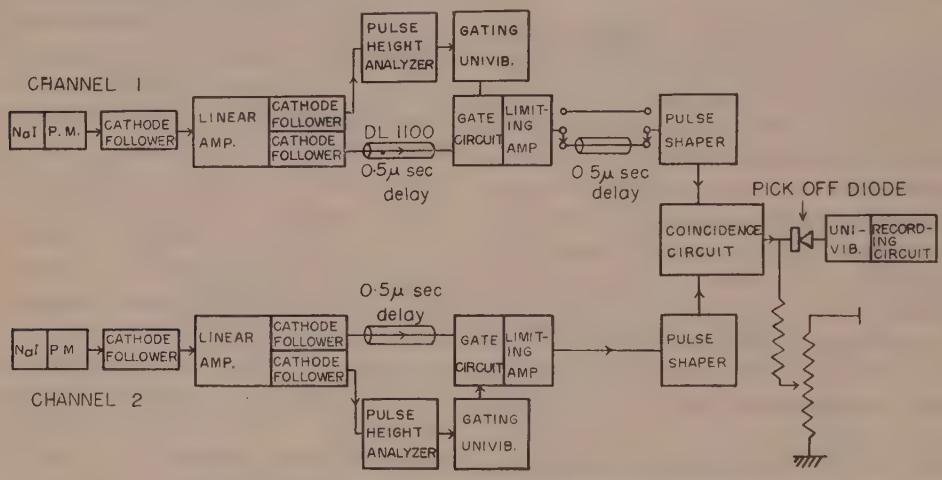

Fig. 1. Block diagram of the coincidence spectrometer.

Stanford and Pieper[14], but was newly designed by the present author. In the coincidence counting with pulse height discrimieation we cannot achieve high resolving power with good coincidence efficiency as far as we apply output pulses from a pulse height analyzer directly to a coincidence circuit, even when the output pulses are shaped into narrow ones by a pulse shaping circuit and are then fed to the coincidence circuit. The cause of this defect is that the process of pulse height selection imposes a time delay upon the pluse output. Moreover, this delay depends on the height and shape of the pulses at the input of the pulse height analyzer and it spreads over the order of magnitude of the pulse rise time. Therefore, the coincidence pulse at a photomultiplier output is not always in strict coincidence at the input of the coincidence circuit. In our circuit, however, this difficulty is avoided as follows. The pulse from the linear amplifier is divided into two parts, the one part of which is, when the gate in Fig. 1 is opened, applied to the mixing tube of the coincidence circuit through the limiting amplifier and the pulse shaper without suffering any time delay caused by the process of pulse height analysis. While the other part is fed to the pulse height analyzer, and when the pulse has a desirable height, its output pulse, after having been properly shaped through the gating univibrator, opens the gate circuit. Since the gate should have been opened precisely just before the one part of the pulse come to the gate, a delay-line having suitable time delay must be placed between the linear amplifier and the gate circuit in order to compensate the delay-time spent in the pulse height analyzer. In view of the pulse height attenuation and the slow-down of the pulse leading edge in the delay-line, however, it is desirable

that the length of the delay-line should be as short as possible. Since the conventional pulse height analyzer has a rather long delay-time (1 μ sec or more)[15,16], some devises were applied to the pulse height analyzer itself in order to minimize the time delay as short as 0.3 μ sec without deteriorating reliability and rapidity in its anticoincidence operation. With this improvement the delay-time in the delay-line could be made as short as 0.5 μ sec, while in the circuit of Stanford and Pieper the required delay amounted to about 3 μ sec. Thus the present measurements were performed in good efficiency with the resolving time of 6×10^{-8} sec. The measured rise times of the linear amplifier and window amplifier in the pulse height analyzer were 0.08 μ sec and 0.06 μ sec respectively. A delay-line placed between the limiting amplifier and the pulse shaper was used for measuring accidentals. It may be mentioned here that our coincidence spectrometer can also be used as two independent single channel pulse height analyzers by changing the grid voltage of the mixing tube in the coincidence circuit. Further details of this circuit are described elsewhere[17].

§ 3. Measurements and Results

The measurement of the gamma ray spectrum was carried out by means of the pulse height analyzer described above. The result obtained is shown in Fig. 2. According

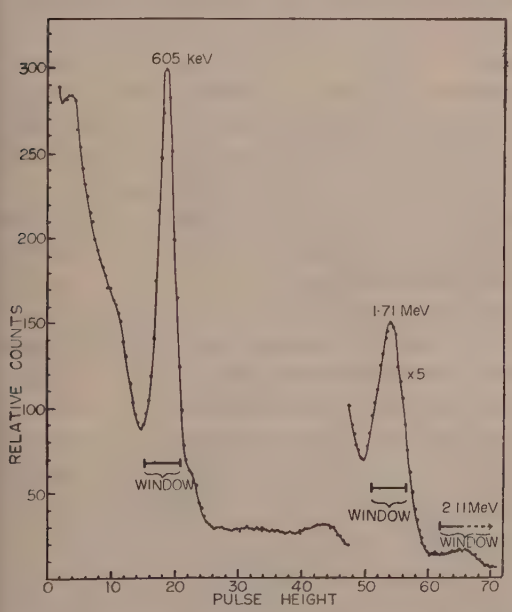

Fig. 2. Gamma ray spectrum of antimony trichloride source. The brackets represent the positions of the windows of the pulse height analyzers for the present experiment.

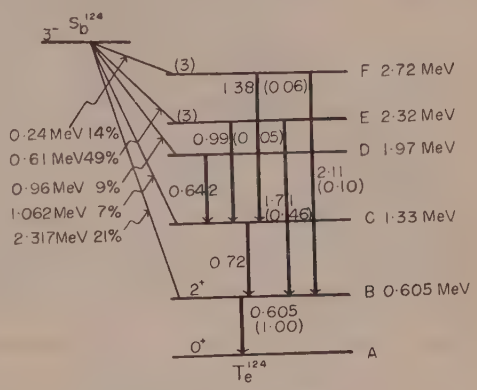

Fig. 3. Proposed decay scheme for Te^{124} as given by Lazar.

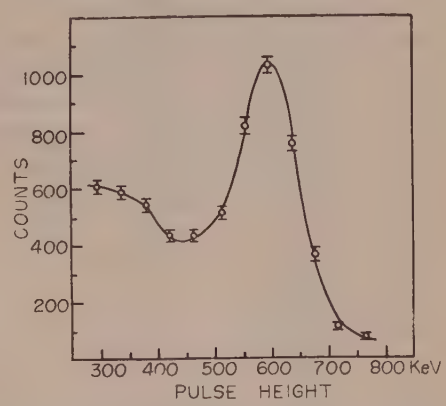

Fig. 4 (A). Coincidence spectrum of the 2.11 Mev gamma ray in Te^{124}.

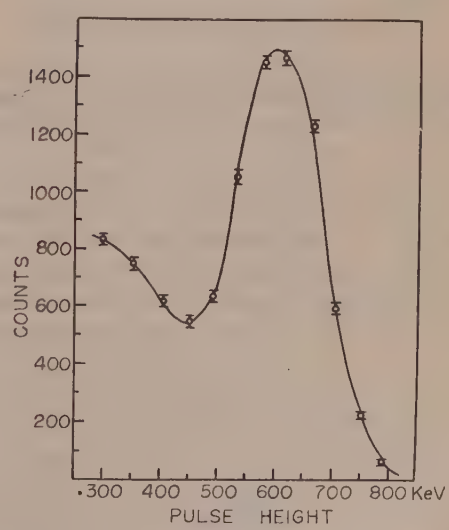

Fig. 4 (B). Coincidence spectrum of the 1.71 Mev gamma ray in Te^{124}.

to the decay scheme proposed by Lazar[18] (Fig. 3) the 2.11 and 1.71 Mev gamma rays should be in coincidence only with the 0.605 Mev gamma ray. This was ascertained by measuring the coincidence spectra of both gamma rays. The results are shown in Fig. 4 (A) and (B). These spectra indicate that both of the 2.11 and 1.71 Mev gamma rays are coincident only with the 0.605 Mev gamma ray and the scheme of Kern et al.[19] insisting that the 2.11 Mev transition should go to the ground level seems to be doubtful.

The directional correlations of the 2.11–0.605 Mev cascade and the 1.71–0.605 Mev cascade were then measured. The windows of the pulse height analyzers were placed, as shown in Fig. 2, so as to include only the full-energy pulse spectrum peak of the gamma ray. The true coincidence counts were about 20/min for the 2.11–0.605 Mev cascade and 200/min for the 1.71–0.605 Mev cascade respectively. The result for the 2.11–0.605 Mev cascade is shown, with its statistical errors, in Fig. 5. Since the 2.11 Mev gamma

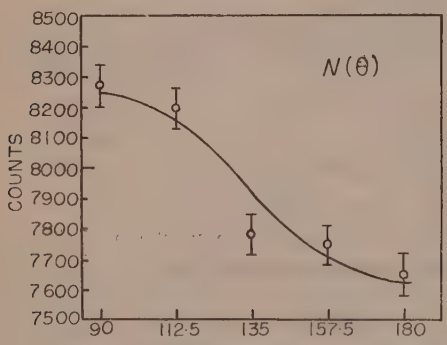

Fig. 5. Directional correlation of the 2.11–0.605 Mev cascade in Te^{124}. The solid curve represents $N(\theta)=(8035\pm104)-(417\pm73)P_2(\cos\theta)$.

ray is of the highest energy emitted from the source, the measurement of the angular correlation of this cascade is a clean one and needs no consideration of the interference due to the other cascade except for the false coincidence event which will be described in § 4. The most fitted theoretical curve as corrected for the finite geometry[20] is drawn by a solid line. It corresponds to the curve for a 3–2–0 (D, Q–Q) ($\delta=-0.025$), where δ is the ratio of the reduced matrix element of the quadrupole radiation to that of the dipole radiation. The normalized correlation function obtained for this cascade can be expressed as

$$W(\theta)=1-(0.052\pm0.006)P_2(\cos\theta),$$

where the term of $P_4(\cos\theta)$ has been neglected due to the smallness of the value of δ^2 and only the interference term of the dipole and quadruple radiations has been included in the coefficient of $P_2(\cos\theta)$. The result of the 1.71–0.605 Mev cascade is shown in Fig. 6. The most fitted curve in this case is also

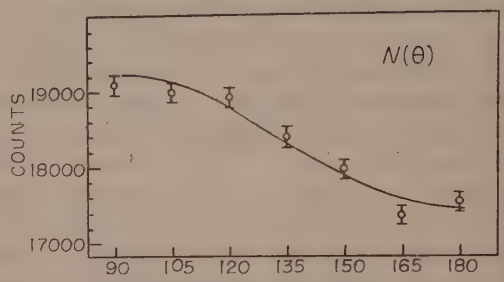

Fig. 6. Directional correlation of the 1.71–0.605 Mev cascade in Te^{124}. The solid curve represents $N(\theta)=(18600\pm160)-(1183\pm103)P_2(\cos\theta)$.

the one for a 3–2–0 (D, Q–Q), in which δ is estimated to be -0.010. The correlation formula for this case is given as

$$W(\theta)=1-(0.064\pm0.004)P_2(\cos\theta),$$

where the term of $P_4(\cos\theta)$ has been neglected by the same reason as in the former case. The interference effect of the Compton component of the 2.11 Mev gamma ray having energy of about 1.71 Mev upon the angular correlation of the 1.71–0.605 Mev cascade could be neglected because of similar correlation functions for both cascades and the weak intensity of the 2.11 Mev gamma ray. The present results are in agreement with those obtained by Metzger[13] as well as by Kraushaar and Goldhaber[12].

Recently, Dzhelepov et al.[21] have found a a few kinds of gamma rays in Te^{124} other than those as reported by Lazar[18]. Among them the 1.330 Mev gamma ray seems to correspond to the crossover transition between the levels A and C in Lazar's scheme. While, from the viewpoint of its energy value, the 1.370 Mev gamma ray should be emitted in the D–B or F–C transition and if it is emitted in the F–C transition, the 1.330 Mev gamma ray must be in coincidence with the 1.370 Mev gamma ray. Thus a measurement of the coincidence event between the two gamma rays was carried out. However,

no appreciable coincidence count could be found which would be expected from the gamma ray intensity given by Dzhelepov et al. This result tells us that, unlike Lazar's scheme, at least the main part of the 1.36 Mev gamma ray as reported by him should be emitted in the D–B transition.

§ 4. Estimation of False Coincidence Counts

Next we shall discuss the false coincidence counts which will occur in the coincidence spectrometer of our type. As described in § 2, the true coincidence counts are obtained by subtraction of the counts measured by delaying the pulse in one channel with respect to the other from those measured without the time delay. Some question is remained whether this operation gives us true data or not. Consideration on this matter is especially necessary for the coincidence measurement of a weak cascade subject to the disturbance of strong cascades. The trouble peculiar to the circuits of our type is caused at the gate or the slow coincidence circuit shown in Fig. 1. It will occur as described below.

Now, the output pulse of the gating univibrator and that of the linear amplifier described in § 2 are shown schematically in Fig. 7 (A) and (B) respectively. When the amplitude of the output pulse from the linear amplifier falls within the upper and lower levels of the window in the pulse heigt analyzer—hereafter this kind of pulse is called the selected pulse—the two pulses should be in coincidence as shown in Fig. 7 (C). However, as shown in Fig. 7 (D) and (E), it will possibly happen that another pulses, which precede or succeed the selected pulses, are fed to the gate circuit within the time interval less than the resolving time of this circuit. Among such chance coincidence events the one occurred as shown in Fig. 7 (E) has no effect upon the true counts because of the large dead time of the scaling circuit. Accordingly in the fast coincidence circuit placed in succession to the gate circuit too, the occurrences of another coincidence events are expected between the above-mentioned gate output pulses which are fed to this circuit. Possible cases of these expected coincidence events including the true and chance coincidences are summarized in Fig. 8

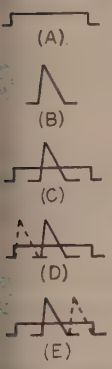

Fig. 7. Occurrence of the false coincidence in the gate circuit.
(A) The pulse from the gating univibrator.
(B) The pulse from the linear amplifier.
(C) Simple coincidence between the pulses given in (A) and (B).
(D) Chance coincidence caused by another preceding pulse.
(E) Chance coincidence caused by another succeeding pulse.

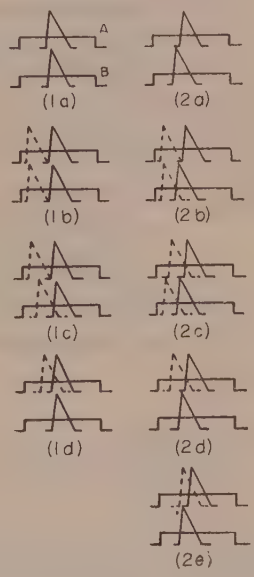

Fig. 8. Possible cases of coincidences between the pulses in channel 1 and 2. Detailed explanation is given in Table I.

and Table I. The changes of these coincidence rates when one channel is delayed by 0.5 μ sec with respect to the other are also shown in Table I. The total counting rate measured by adjusting in such a way that both channels should have no delay with each other is represented as N_{total}. Since this rate is composed of all cases in (1) and (2) of Table I, it can be written as

$$N_{\text{total}}=N_{1a}+N_{1b}+N_{1c}+N_{1d}+N_{2a}+N_{2b}+N_{2c}+N_{2d}+N_{2e}. \quad (4.1)$$

While the chance coincidence rate N_{chance} measured as described above is given by

$$N_{\text{chance}}=N_{2a}+N_{2c}+N_{2d}\,, \quad (4.2)$$

so that the counting rate which is regarded

Table I.

Possible cases of coincidence			Assumed counting rate	Counting rate when one channel is delayed with respect to the other
(1) Cases in which the selected pulses are in true coincidence	a	Simple true coincidence.	N_{1a}	0
	b	The selected pulses A and B are preceded by other coincidence pulses.	N_{1b}	0
	c	The selected pulses are preceded by another pulse pair which is in chance coincidence within $2\tau_f$.	N_{1c}	0
	d	Preceding A (or B) another pluse in chance coincidence with B (or A) is fed.	N_{1d}	0
(2) Cases in which the selected pluses are in chance coincidence	a	Simple chance coincidence.	N_{2a}	N_{2a}
	b	The selected pulses are preceded by other coincidence pulses.	N_{2b}	0
	c	The selected pulses are preceded by other pulses which are in chance coincidence with each other.	N_{2c}	N_{2c}
	d	Preceding A (or B) another pulse which is in chance coincidence with B (or A) is fed.	N_{2d}	N_{2d}
	e	Preceding A (or B) another pulse which is in coincidence B (or A) is fed.	N_{2e}	0

nominally as the true coincidence can be represented as

$$N_{\text{true}}=N_{\text{total}}-N_{\text{chance}}$$
$$=(N_{1a}+N_{1b}+N_{1c}+N_{1d})+N_{2b}+N_{2e}. \tag{4.3}$$

Before going into further theoretical consideration, notations for some quantities to be used and their definitions will be given.

N_{t1}, N_{t2}: total rates of pulses which come out from the linear amplifier in channel 1 and 2 respectively;

N_{s1}, N_{s2}: rates of the selected pulses in channel 1 and 2 respectively;

N_{ns1}, N_{ns2}: rates of non-selected pulses, or of pulses whose amplitudes fall outside of the given window position in channel 1 and 2 respectively;

n_{s1}, n_{s2}: rates of the selected pulses which belong to N_{s1} and N_{s2} respectively and are not in coincidence with the pulses in the other channel;

$c_{s1,\,s2}$: rate of the selected pulses whic belong to N_{s1} in channel 1 and t N_{s2} in channel 2 and are in coinc dence with each other;

$c_{s1,\,ns2}$: rate of pulses which belong to N in channel 1 and to N_{ns2} in channe 2 and are in coincidence with eac other;

$c_{ns1,\,s2}$: rate of pulses which belong to N_n in channel 1 and to N_{s2} in channe 2;

n_{ns1}, n_{ns2}: rates of pulses which belong to N_n and N_{ns2} respectively and are n in coincidence with the pulses the other channel;

$c_{ns1,\,ns2}$: rate of pulses which belong to N_n and N_{ns2} and are in coinciden with each other;

$2\tau_s$: resolving time of the gate (slc coincidence) circuit;

$2\tau_f$: resolving time of the fast coinciden circuit.

It will immediately be seen that the follo ing relations can hold:

$$\left.\begin{aligned} N_{t1}&=N_{s1}+N_{ns1}\,, & N_{t2}&=N_{s2}+N_{ns2}\,,\\ N_{s1}&=n_{s1}+c_{s1,\,s2}+c_{s1,\,ns2}\,, & N_{s2}&=n_{s2}+c_{s1,\,s2}+c_{ns1,\,s2}\,,\\ N_{ns1}&=n_{ns1}+c_{ns1,\,ns2}+c_{s2,\,ns1}\,, & N_{ns2}&=n_{ns2}+c_{ns1,\,ns2}+c_{s1,\,ns1}\,, \end{aligned}\right\} \tag{4}$$

and in ordinary cases

$$n_{s1} \gg \begin{cases} c_{s1,\,s2}\,, \\ c_{s1,\,ns2}\,; \end{cases} \quad n_{s2} \gg \begin{cases} c_{s1,\,s2}\,, \\ c_{ns1,\,s2}\,; \end{cases} \quad n_{ns1} \gg \begin{cases} c_{ns1,\,ns2}\,, \\ c_{ns1,\,s2}\,; \end{cases} \quad n_{ns2} \gg \begin{cases} c_{ns1,\,ns2}\,, \\ c_{s1,\,ns2}\,. \end{cases} \tag{4.5}$$

Making use of these notations the counting rates of the output pulses in the gate circuits are given by

$$\left.\begin{aligned} &N_{s1}(1-\tau_s N_{ns1})+\tau_s N_{ns1}N_{s1} \quad \text{(for channel 1)}\,, \\ \text{and} \\ &N_{s2}(1-\tau_s N_{ns2})+\tau_s N_{ns2}N_{s2} \quad \text{(for channel 2)}\,, \end{aligned}\right\} \tag{4.6}$$

respectively. Here the correction for the suppression[22),23)] of the pulses due to the dead time in the pulse height analyzer has been neglected. The first quantity in (4.6) gives the rate of the pulses which come out from the gate circuit without receiving any chance coincidence event, while the second corresponds to that of the pulses which are in chance coincidences with N_{ns1} and N_{ns2} pulses. The factor 2 in front of τ_s has been omitted, since in this case it is sufficient to consider only the case of Fig. 7 (D).

Now it is expected in the fast coincidence output that the following cases, together with the corresponding counting rates, should occur between the two pulses expressed in (4.6).

$$\left.\begin{aligned} &\text{Case (1):} \quad c_{s1,\,s2}\{(1-\tau_s n_{ns1})(1-\tau_s n_{ns2})-\tau_s(c_{ns1,\,ns2}+c_{ns1,\,s2}+c_{s1,\,ns2})\}; \\ &\text{Case (2):} \quad c_{s1,\,s2}\,[\tau_f\{n_{ns1}(1-\tau_s n_{ns2})+n_{ns2}(1-\tau_s n_{ns1})\} \\ &\qquad +2\tau_s\tau_f n_{ns1}n_{ns2}+\tau_s'(c_{ns1,\,ns2}+c_{ns1,\,s2}+c_{s1,\,ns2})]; \\ &\text{Case (3):} \quad 2\tau_f(n_{s1}+c_{s1,\,ns2})(1-\tau_s N_{ns1})(n_{s2}+c_{s2,\,ns1})(1-\tau_s N_{ns2}); \\ &\text{Case (4):} \quad \{c_{s1,\,ns2}(1-\tau_s N_{ns1})\tau_s'(n_{s2}+c_{ns1,\,s2})+c_{ns1,\,s2}(1-\tau_s N_{ns2})\tau_s'(n_{s1}+c_{s1,\,ns2})\} \\ &\qquad +\{2\tau_f n_{s1}(1-\tau_s N_{ns2})\tau_s(n_{s2}+c_{ns1,\,ns2}+c_{s1,\,ns2})(n_{s2}+c_{ns1,\,s2}) \\ &\qquad +2\tau_f n_{s2}(1-\tau_s N_{ns2})\tau_s(n_{ns1}+c_{ns1}+c_{s1,\,ns2})(n_{s1}+c_{s1.\,ns2})\}; \\ &\text{Case (5):} \\ &\qquad 2\tau_f\tau_s^2(n_{ns1}+c_{ns1,\,ns2}+c_{ns1,\,s2})(n_{s1}+c_{s1,\,ns2})(n_{ns2}+c_{ns1,\,s2}+c_{s1,\,ns2})(n_{s2}+c_{ns1,\,s2}); \\ &\text{Case (6):} \quad \tau_s' c_{ns1,\,ns2}(n_{s1}+c_{s1,\,ns2})(n_{s2}+c_{ns1,\,s2})\,. \end{aligned}\right\} \tag{4.7}$$

It is to be noticed that in some terms of the formulas for cases (2), (4) and (6) the notation τ_s' has been used instead of τ_s*.

In the above formulas (4.7), (1) gives the rate of the true coincidence pluse which comes out without suffering any chance coincidence event. While (2) means the rate of the chance coincidence events which will occur between the true coincidence pulses and the other kinds of pulses and then be recorded as output pulses. All of the true coincidence pulses lost due to the chance coincidence events are not always restored by the process (2), namely (1)+(2) is expected to be a little less than $c_{s1,\,s2}$. And (1) corresponds to N_{1a} of Table I and the first, second and third term of (2) represent N_{1d}, N_{1c} and N_{1b} respectively. The formula (3) gives mainly the chance coincidence rate between the selected but non-coincident pulses, while (4), (5) and (6) indicate the fast coincidence events between the chance coincidence output pulses of the gate circuits themselves. The formulas (3), (5), (6) and the first and second term of (4) correspond to N_{2a}, N_{2c}, N_{2b}, N_{2e} and N_{2d} of Table I respectively. Other terms of smaller

* As described in § 4 some portion of $c_{s1,\,s2}$ is lost in the gate circuit due to the chance coincidence with the pulses belonging, for instance, to $c_{ns1,\,ns2}$ by the rate of $\tau_s c_{s1,\,s2} c_{ns1,\,ns2}$. Now $c_{ns1,\,ns2}$ as well as $c_{s1,\,s2}$ are the coincidence counts, so that all of $\tau_s c_{s1,\,s2} c_{ns1,\,ns2}$ should be restored if the gates of both channels were opened simultaneously without suffering any variable time delay caused by the process of the pulse height selection. But since the gates for both channels are not always opened simultaneously or at least within the time difference corresponding to the magnitude of the resolving time of the fast coincidence circuit, some portion of the lost pulses cannot be restored. Therefore, by using the quantity $\tau_s'(0<\tau_s'<\tau_s)$ the restored portion can be expressed effectively, for instance, as $\tau_s' c_{s2,\,s2} c_{ns1,\,ns2}$, while the lost portion being $\tau_s c_{s1,\,s2} c_{ns1,\,ns2}$. This situtation will be the same for $c_{ns1,\,s2}$ and $c_{s1,\,ns2}$.

order, including, for instance, the correction for γ proposed by Westcott et al.[22], have been omitted in the above formulas.

In applying above considerations to the error estimation of our data on the directional correlations, it seems necessary to discuss, first of all, the effect of the false counts upon the term $(N_{1a}+N_{1b}+N_{1c}+N_{1d})$ in (4.3). Using (1) and (2) of (4.7) this term can be written as

$$\begin{aligned}&(N_{1a}+N_{1b}+N_{1c}+N_{1d})\\&\quad=N_0\{1+XP_2(\cos\theta)\}\\&\qquad\times[A+B\{1+YP_2(\cos\theta)+ZP_4(\cos\theta)\}]\,.\end{aligned}\tag{4.8}$$

Here $N_0\{1+YP_2(\cos\theta)\}$, being equal to $c_{s1,\,s2}$, expresses the true angular correlation, A represents the sum of all the factors in (1) and (2) of (4.7) except for those including $(c_{ns1,\,ns2}+c_{ns1,\,s2}+c_{s1,\,ns2})$, and $B\{1+YP_2(\cos\theta)+ZP_4(\cos\theta)\}$ is the sum of the factors including $(c_{ns1,\,ns2}+c_{ns1,\,s2}+c_{s1,\,ns2})$ and expresses the angular correlation of $(c_{ns1,\,ns2}+c_{ns1,\,s2}+c_{s1,\,ns2})$. Thus, to a first approximation $(N_{1a}+N_{1b}+N_{1c}+N_{1d})$ becomes

$$N_0A\left\{1+\left(X+\frac{B}{A}Y\right)P_2(\cos\theta)+\frac{B}{A}ZP_4(\cos\theta)\right\},\tag{4.9}$$

whose angular correlation differs from the true value by $(B/A)YP_2(\cos\theta)$ and $(B/A)ZP_4(\cos\theta)$.

Now applying to the formula (4.9) the practical values in the 2.11–0.605 Mev correlation measurement, such as $\tau_f=3\times10^{-8}$ sec, $\tau_s=5\times10^{-7}$ sec, $N_{t1}\fallingdotseq N_{t2}\fallingdotseq10^6$/min, $c_{s1,\,s2}=20$/min and other values as calculated from these by considering the spectrum shape, intensity ratios, detecting efficiencies and so forth, (B/A) was estimated to be less than 1/3000. Thus assuming $X\fallingdotseq Y$ and $Z\ll X,\,Y$ in this case*, it was concluded that for the 2.11–0.605 Mev cascade the true correlation would not be changed by more than 0.03% on account of the contribution from the false coincidence events described above. Secondly, similar estimation was made for N_{2b} and N_{2c} in (4.3). The results show that N_{2b} and N_{2c} should be less than 0.04% and 0.65% of $c_{s1,\,s2}$ respectively. Since more than half of N_{2b} and N_{2c} are contributed from the 1.71–0.605 Mev coincidence and its $W(\theta)$ is nearly the same as that of the 2.11–0.605 Mev cascade, the effect of these terms upon the correlation coefficient will become more trivial. For the 1.71–0.605 Mev correlation the above effects are expected to have smaller values because of the strong intensity of the measured cascade. Thus it is concluded that the correction for the abovementioned effect is unnecessary in the present correlation measurements. However, it may be noted that this is not always the case in other experiments.

* In the present experiment the disturbing cascade is mainly consist of the 1.71–0.605 Mev cascade and its directional correlation is similar to that of the 2.11–0.605 Mev cascade.

§ 5. Discussions

A few assignments other than the 3–2–0 could be fitted with the experimental data. However, none of them could meet the other requirements. As to the two assignments proposed by Kraushaar and Goldhaber[12], we could also fit the data with the 2–1–0 (D, Q–D) combination, in which the mixing ratios were assumed to be −1.97 or 0.17 for the 2.11–0.605 Mev cascade and −1.94 or −0.19 for the 1.71–0.605 Mev cascade. The 1–1–0 (D, Q–D) in which $\delta=-7.72$ or −0.13 for the 2.11–0.605 Mev cascade and $\delta=-8.00$ or −0.13 for the 1.71–0.605 Mev cascade could be fitted with data. But, in the latter case some difference from the value of Kraushaar and Goldhaber was found in the mixing ratio. Moreover, a 3–1–0 (Q–D) combination nearly fits the data and a better agreement will be expected by small admixture of different multipoles having the same parity to both or either of the two radiations. However, the assignment of spin 1 to the 0.605 Mev level is not consistent with the results of the internal conversion measurements as well as with the usual assumption about even-even nuclei.

We have no definite information about the parities of both radiations except for an attempt of Tomlinson for the 1.71 Mev gamma ray cited by Metzger[13]. However, combining his result with the empirical rule[24,25] concerning the lowest excited states of odd spin in even-even nuclei and other theoretical considerations[26], it may be concluded that the main component of the 1.71 Mev gamma ray is the electric dipole rather than the magnetic

dipole. Thus, it will be seen that 3^- should be assigned to the 2.32 Mev level. Further experiment to determine the parity is necessary for the 2.11 Mev gamma ray.

The theoretical foundations for assigning spin 3 to both of the 2.72 and 2.32 Mev states seem to be rather difficult. In the single particle aspects[27,28] it may be expected that, as the configurations of the last two protons and neutrons, the following ones:

$$\{(g_{7/2})^2(0)\}_P\{(h_{11/2})^2(0)\}_N(0),$$
$$\{(g_{7/2})^2(2)\}_P\{(h_{11/2})^2(0)\}_N(2),$$
$$\{(g_{7/2})^2(0)\}_P\{(h_{11/2})^2(2)\}_N(2),$$
$$\{(g_{7/2})^2(2)\}_P\{(h_{11/2})^2(2)\}_N(0,\ 2 \text{ or } 4),$$
$$\{(g_{7/2})^1(h_{11/2})^1(3)\}_P\{(h_{11/2})^2(0)\}_N(3) \quad \text{and}$$
$$\{(d_{5/2})^1(h_{11/2})^1(3)\}_P\{(h_{11/2})^2(0)\}_N(3)$$

are reasonable for the levels A, B, C, D, E and F in Fig. 3 respectively. Confining our discussions to the levels measured by the present author, the dipole transition from the 2.32 Mev level can be explained by the above configurations. But the same transition from the higher 3 level will become the two particle transition and then should be forbidden in these configurations. This situation becomes worse when the beta decays from Sb^{124} too are taken into consideration. However, as pointed out by Crayson and Nordheim[29], the $d_{5/2}$ proton configuration must in this region ($Z=50-55$) be mixed with $g_{11/2}$ orbits, while on the neutron side ($N=69-80$) there is the irregular fill-in of the $h_{11/2}$ orbits and the reappearance holes in the $g_{7/2}$ and $d_{5/2}$ shells. These will mix the configurations strongly and some of the difficulties described above may be dissolved by considering the configurational mixings for the concerned states.

Acknowledgement

The author expresses his hearty gratitude to Professor K. Kimura of Kyoto University for his sustained interest and encouragement throughout the present work. He is also deeply indebted to his colleagues, Messrs. M. Kawamura and A. Aoki, who have been in cooperation during the whole experiments.

This work was partly supported by a grant-in-aid for scientific research of the Ministry of Education.

References

1) D. R. Hutchinson and M. L. Wiedenbeck: Phys. Rev. **88** (1952) 699.
2) L. M. Langer, R. J. D. Moffat and H. C. Price, Jr.: Phys. Rev. **79** (1950) 808.
3) S. Nakamura, M. Umezawa and H. Takebe: Phys. Rev. **83** (1951) 1273.
4) L. M. Langer, N. H. Lazar and R. J. D. Moffat: Phys. Rev. **91** (1953) 338.
5) F. R. Metzger: Phys. Rev. **86** (1952) 435.
6) G. Scharff-Goldhaber: Phys. Rev. **90** (1953) 587.
7) M. Morita and Y. Yamada: Prog. Theor. Phys. **10** (1953) 641.
8) E. K. Darby and W. Opechowski: Phys. Rev. **83** (1951) 676.
9) D. T. Stevenson and M. Deutsch: Phys. Rev. **83** (1951) 1202.
10) R. M. Kloepper, E. S. Lennox and M. L. Wiedenbeck: Phys. Rev. **88** (1952) 695.
11) J. R. Beyster and M. L. Wiedenbeck: Phys. Rev. **79** (1950) 169.
12) J. J. Kraushaar and M. Goldhaber: Phys. Rev. **89** (1953) 1081.
13) F. R. Metzger: Phys. Rev. **90** (1953) 328.
14) G. S. Stanford and G. E. Pieper: Rev. Sci. Instr. **26** (1955) 847.
15) A. B. Van Rennes: Nucleonics **10** (1952) 25.
16) C. W. Johnstone: Nucleonics **11** (1953) 36.
17) T. Hayashi, M. Kawamura and A. Aoki: Soc. Rep. Saikyo Univ. **2** (1957) A199.
18) N. H. Lazar: Phys. Rev. **95** (1955) 292.
19) B. D. Kern, D. J. Zaffarans and A. C. G. Mitchel: Phys. Rev. **91** (1948) 1142.
20) M. E. Rose: Phys. Rev. **91** (1953) 610.
21) B. S. Dzhelepov, N. N. Zhukovsky, V, G. Nedovesov, I. F. Uchevatkin and V. G. Chumin: Nucl. Phys. **2** (1956/1957) 408.
22) C. H. Westcott, J. S. Greenberg and J. S. Greenberg and J. S. Kirkaldy: Canadian J. Phys. **31** (1953) 859.
23) P. T. Porter, M. S. Freedman, T. B. Novey and F. Wagner, Jr.: ANL-5525 (1956) 29.
24) H. Morinaga: Phys. Rev. **103** (1956) 503.
25) M. J. Glaubman: Phys. Rev. **90** (1953) 1000.
26) I. Talmi: Phys. Rev. **90** (1953) 1001.
27) N. Zeldes: Nucl. Phys. **2** (1956/1957) 1.
28) P. F. A. Klinkenberg: Revs. Modern Phys. **24** (1952) 63.
29) W. C. Crayson and L. W. Nordheim: Phys. Rev. **102** (1956) 1093.

JOURNAL OF THE PHYSICAL SOCIETY OF JAPAN Vol. 13, No. 2, FEBRUARY, 1958

Excitation Curves of the $N^{14}(d, n)O^{15}$ Reaction

By Susumu MORITA

Department of Physics, Faculty of Science, Kyushu University, Fukuoka, Japan

(Received October 30, 1957)

The excitation curves of the $N^{14}(d, n)O^{15}$ reaction were measured with a thin plastic scintillator and a pulse height analyser in the energy range of deuterons from 1.00 to 2.15 MeV. Three excitation functions were obtained at the directions of 0, 90 and 165 degrees (lab. system) with respect to the incident deuterons.

The curves obtained at 0 and 165 degrees show remarkable peaks at the deuteron energies, $E_d=1.6$ and 1.9 MeV, respectively, while the curve obtained at 90 degrees is nearly flat.

§ 1. Introduction

In our previous work,[1] the angular distribution of neutrons from the $N^{14}(d, n)O^{15}$ reaction leading to O^{15} ground state was measured in the angular range of 0 to 165 degrees (lab. system) with the deuterons of energy of 1.96 MeV. The results show the forward peak at 30 degrees, which can be fitted well by the stripping theory, and a remarkable increase of the neutron yield in the backward direction was found, the intensity of neutrons at 165 degrees reaching 2.3 times that of the forward peak.

As it seemed to us that these results gave an important information for the analysis of deuteron induced reaction, we were interested to extend the investigation on this reaction to the measurements of the excitation function and of the variation of angular distribution of neutrons with the deuteron energy.

In the present work, the excitation curves of this direction were measured in the energy range of deuterons from 1.00 to 2.15 MeV, and in the reaction of 0, 90 and 165 degrees (lab. system) with respect to the incident deuterons.

§ 2. Experimental Procedure

The experimental arrangement, except the neutron detector, was reported in detail in the previous work.[1] The energy of the deuteron beam, accelerated by the Van de Graaff Generator at the Kyushu University, was calibrated by the resonances of the $F^{19}(p, \alpha\gamma)O^{16}$ reaction and the energy spread of the beam was estimated to be less than 0.5 percent. The deuterons entered into the target chamber through a nickel foil of 1.3 mg /cm^2 in thickness. The chamber was 2.0 cm in depth and was filled with nitrogen gas of pressure of 20.0 cmHg. The energy loss of the deuterons in the nickel foil and the nitrogen gas was evaluated to be about 250 KeV for the deuteron energy of 2 MeV, based on the data obtained by S. K. Allison and S. D. Warshaw.[2]

A plastic scintillator, made by National Radiac Co., of 10 mm in diameter and 1 mm in thickness and a EMI 6097 photomultiplier tube was used as the neutron detector and the pulses from the photomultiplier tube were fed to a linear amplifier and were analysed by a twenty channel pulse height analyser.

In the case of $N^{14}(d, n)O^{15}$ reaction with deuterons of about 2 MeV, it was expected that the reaction would be accompanied with the rather intense gamma-rays of about 5 MeV due to the process leading to the first excited state of O^{15}. But allowing for the response curves and their range-energy relations in the scintillator for proton and electron, we hoped to be able to make the maximum pulse height for recoil proton much larger than that for the gamma-rays by choosing a suitable thickness for the scintillator.

The pulse height distributions for $N^{14}(d,n)O^{15}$ reaction were measured with plastic scintillators of 10 mm in diameter and of 1, 2 and 3 mm in thickness, respectively, and the results obtained are shown in Fig. 1, in which the angles show the directions relative to the incident deuteron. From these results, the plastic scintillator of 1 mm in thickness was selected as the most suitable one.

The pulse height distributions from the recoil protons in this plastic scintillator due to the neutrons from the $N^{14}(d, n)O^{15}$ reaction leading to the O^{15} ground state and those from the $D(d, n)He^3$ reaction are shown in Fig. 2

together with the pulse height distribution due to the gamma-ray of 6 MeV from the $F^{19}(p, \alpha\gamma)O^{16}$ reaction.

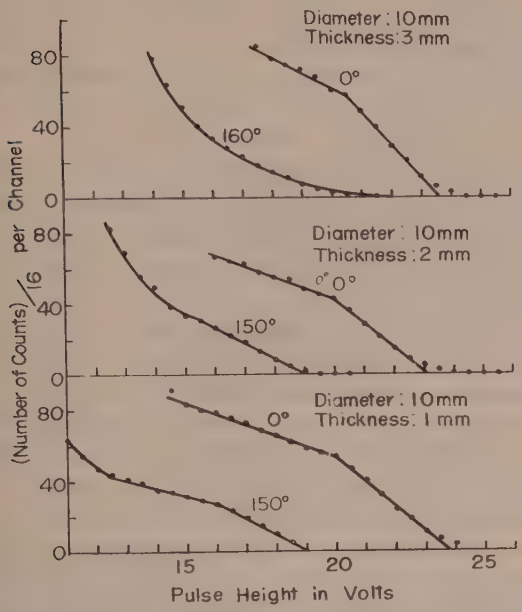

Fig. 1. Pulse height spectra of recoil protons from the $N^{14}(d, n)O^{15}$ reaction, measured with plastic scintillators of 10 mm in diameter and 1, 2 and 3 mm in thickness.

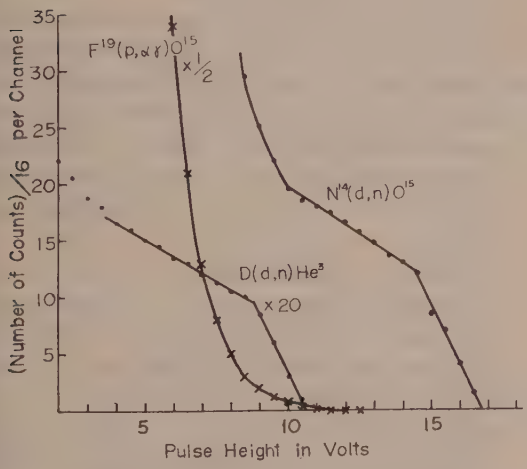

Fig. 2. Pulse height spectra of recoil protons from the neutrons of the $N^{14}(d, n)O^{15}$ and those of the $D(d, n)He^3$ reaction. The pulse height spectrum due to the gamma-ray of 6 MeV from the $F^{19}(p, \alpha\gamma)O^{16}$ reaction is also shown.

In Figs. 1 and 2, the flat portion of the pulse height distribution corresponds to the recoil protons, as is expected, and the steep rise in the lower energy region in the case of $N^{14}(d, n)O^{15}$ reaction shows the presence of the gamma-ray of 5 MeV.

The rather gentle slopes at the high energy end would be attributed to the end effect of the thin plastic scintillator, that is, a proton may escape from the crystal before giving up its full energy. The corrections for the end effect were calculated[3] and one of the corrected pulse height distribution is shown in Fig. 3. In this figure, the pulse height distribution is integrated and the number of pulses above a height S is plotted against S. It should be noted that the linearity of the plot is improved in the corrected curve. The extrapolation of the straight portion gives the pulse height corresponding to the end point and thus allows conversion to an energy spectrum. Thus, the pulse height distributions were replotted against the energy values of protons and then, we took the total counts in the pulse height distribution larger than 80 percent of the maximum energy as a measure

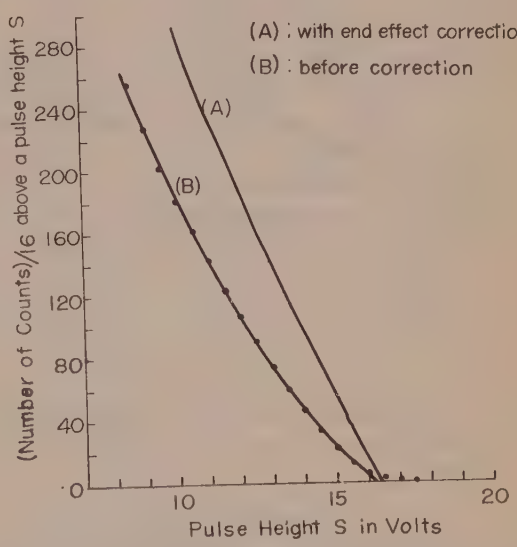

Fig. 3. Integrated recoil proton energy spectrum for neutrons from the $N^{14}(d, n)O^{15}$ reaction. The curve (A) shows the result of the end effect correction.

of the neutron intensity. These counts were corrected for the variation of (n, p) scattering cross section with the energy of the neutron.

The amount of stray neutrons was estimated to be less than a few percent of that of the direct neutrons, by inserting an iron absorber of 10 cm thickness between the target and detector.

The distances between the target and detector were 5.3 cm in the observation at 0 and 90 degrees and 16.5 cm in the case of 165 degrees.

§ 3. Results and Discussion

The excitation functions obtained at 0, 90 and 165 degrees (lab. system) with respect to the direction of incident deuteron are shown as curves (A), (B) and (C), respectively, in Fig. 4. The value of the absolute cross section, shown in the ordinate, was referred to the previous work[1] and is thought to have an uncertainty of about twenty percent. The errors in the ordinate of each experimental points are statistical ones and those in the abscissa were estimated from the energy loss of deuteron beam in the target gas.

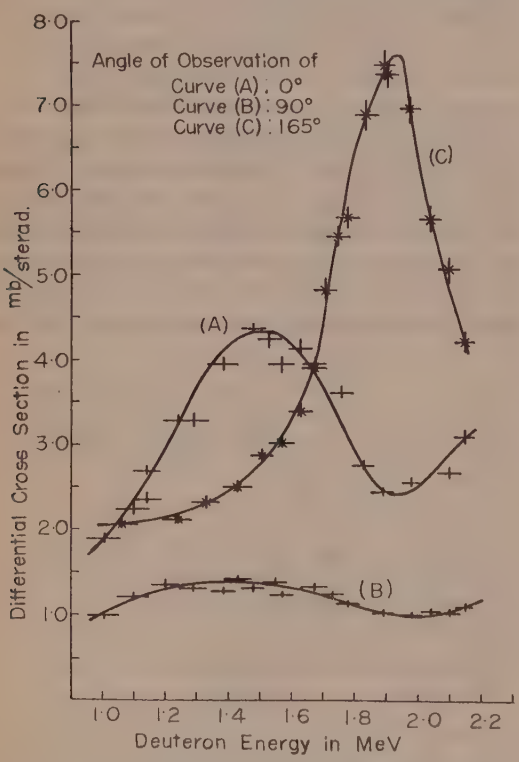

Fig. 4. Excitation curves of the $N^{14}(d, n)O^{15}$ reaction obtained at angles of 0, 90 and 165 degrees.

In our previous result[1] obtained with deuterons of 1.96 MeV, the ratio of the neutron intensity at 0, 90 and 165 degrees was evaluated as 1:0.5:3.4 and the value of this ratio in the present work, is obtained as 1:0.4:3.1 from Fig. 4. These ratios are in good agreement with each other despite the difference in the methods of neutron detection.

It is to be noted that the curves (A), (B) and (C) show quite different behaviour; that is, the excitation curves obtained at 0 and 165 degrees show remarkable peaks at 1.6 and 1.9 MeV, respectively, while the curve (B) obtained at 90 degrees is nearly flat and similar to the curve (A) in its general tendency. Moreover, the curve (A) shows minimum at 1.9 MeV, where the curve (C) reaches the maximum. It was found from these facts that the remarkable increase in neutron intensity in the backward direction, obtained in the previous work, will disappear with a small change in the energy of deuterons and the angular distribution of neutrons will be sensitive to the deuteron energy.

It will be worthwhile to investigate the change of angular distribution with deuteron energy in more detail.

The author wishes to express his cordial thanks to Prof. I. Nonaka, Mr. N. Kawai and all other staffs of the nuclear laboratory of Kyushu University for their support and discussions throughout this work. This work has been supported by the Scientific Research Expenditure of the Ministry of Education.

References

1) I. Nonaka, S. Morita, N. Kawai, T. Ishimatsu, K. Takeshita, Y. Nakajima and N. Takano: J. Phys. Soc. Japan **12** (1957) 841.
2) S. K. Allison and S. D. Warshaw: Rev. Mod. Phys. **25** (1953) 779.
3) National Nuclear Energy Series, Manhattan Proj. Tech. Sect. Div. V, Vol. 2 by B. Rossi and H. H. Staub.

JOURNAL OF THE PHYSICAL SOCIETY OF JAPAN Vol. 13, No. 2, FEBRUARY, 1958

$Co^{59}(n, \alpha)Mn^{56}$ and $Mn^{55}(n, \alpha)V^{52}$ Reactions Induced by 14.8-Mev Neutrons

By Isao KUMABE, Eiko TAKEKOSHI*, Hiroshi OGATA, Yoshikazu TSUNEOKA and Shinpei ŌKI

Department of Physics, Faculty of Science, University of Kyoto

(Received November 1, 1957)

The angular and energy distributions of alpha particles resulting from $Co^{59}(n, \alpha)Mn^{56}$ and $Mn^{55}(n, \alpha)V^{52}$ reactions induced by 14.8-Mev neutrons were measured with Ilford C2 nuclear plates.

As in the case of $Al^{27}(n, \alpha)Na^{24}$ reaction, the angular distributions for the entire energy region are approximately 90° symmetrical and concave upward, and the energy distributions show that the alpha particles with energies below the Coulomb barrier are more emitted than has been expected. The curves on a semilog plot of the relative level density calculated from the energy distributions of the alpha particles cannot fit a straight line.

The total (n, α) cross sections of cobalt and manganese are 84 mb±15% and 96 mb±15% respectively. The results are compared with the predictions of the statistical theory of nuclear reactions.

§ 1. Introduction

Paul and Clarke[1] carried out an extensive survey of (n, p), (n, α) and $(n, 2n)$ reactions at 14.5 Mev. They have shown that the $(n, 2n)$ reaction cross sections are approximately in agreement with the evaporation theory. However, the cross sections of (n, p) and (n, α) reactions for heavy elements have had orders of magnitude larger than expected. They suggested the existence of the direct process in these cases. Experimental data of the angular and energy distributions on (n, α) reactions may give reliable information on these problems.

In the past few years several attempts[2] have been made to measure the dependence of the density of energy levels on excitation energy, which can be determined from reaction and inelastic scattering experiments in which particles are emitted from the compound nucleus produced by bombardment with energetic particles. However, these experimental results have been accompanied by ambiguities owing to the presence of non-compound-nucleus processes. On the other hand, data on (n, α) reactions have been considered to give more reliable information on the level density, since it seems improbable that alpha particles are emitted by direct interactions.

In the previous paper[3], we have reported the angular and energy distributions of the alpha particles from the $Al^{27}(n, \alpha)Na^{24}$ reaction induced by 14.8-Mev neutrons. It has been found that the angular distribution of particles for the entire energy region is concave upward and approximately 90° symmetrical, and the curve on a semilog plot of the relative level density calculated from the energy distribution of alpha particles fits a straight line with a temperature of about

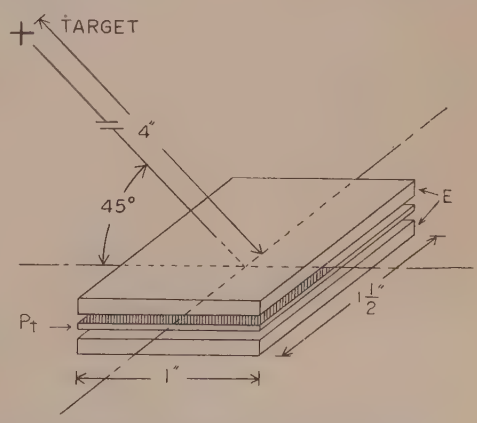

Fig. 1. Experimental arrangement.
E: Ilford C2 nuclear plates
Pt: platinum foil
Target of cobalt or manganese was attached onto the shaded regions of both surfaces of the platinum foil.

* Now at Atomic Energy Research Establishment of Japan.

1.45 Mev.

In this paper the measurements extended to the target nuclei of cobalt and manganese are reported.

§ 2. Experimental Procedure

The experimental arrangement is shown schematically in Fig. 1. The experimental method was described in detail in the previous paper[3] cited above. Targets of cobalt and manganese were respectively electroplated and vacuum evaporated onto platinum foil of thickness 60 mg/cm². Target thickness used was 3.7 mg/cm² for cobalt and 3.3 mg/cm² for manganese respectively.

§ 3. Results

The angular distributions in the center of mass system of the alpha particles from $Co^{59}(n, \alpha)Mn^{56}$ and $Mn^{55}(n, \alpha)V^{52}$ reactions for the entire energy region are shown in Fig. 2, and the energy distributions are shown in Fig. 3. The corrections for stopped alpha particles and energy loss in the target materials were carried out in the same way as in the case of aluminium[3].

It is assumed that the relation between the measured alpha particle energy distributions and the energy level densities of the residual nucleus is provided by the following formula[4];

$$n(\mathcal{E})d\mathcal{E} = \text{const}\, \mathcal{E}\sigma_c(\mathcal{E})\omega(\mathcal{E}_r)d\mathcal{E}\,,$$

where $n(\mathcal{E})d\mathcal{E}$ = number of alpha particles emitted with energy between $\mathcal{E}$ and $\mathcal{E}+d\mathcal{E}$, $\sigma_c(\mathcal{E})$[5] is the cross section, including the effects of barrier penetration for a nuclear radius of $1.5\times10^{-13}\,A^{1/3}$ cm, for the formation of the compound nucleus in the same state of excitation by the reverse reaction, in which particles of energy $\mathcal{E}$ strike the excited residual nucleus, and $\omega(\mathcal{E}_r)$ is the density of energy level of the residual nucleus at excitation $\mathcal{E}_r = \mathcal{E}_{max} - \mathcal{E}$, $\mathcal{E}_{max}$ being the maximum energy which the emitted particle may have.

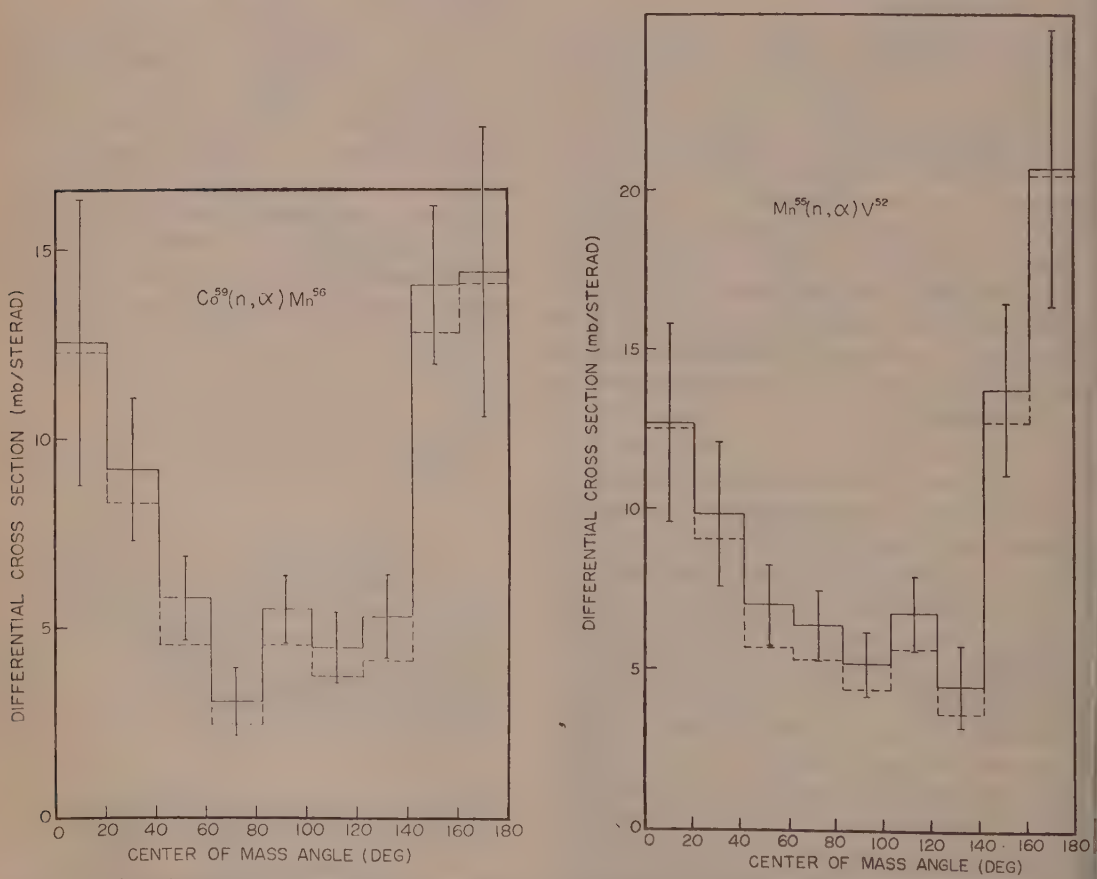

Fig. 2. Angular distributions of alpha particles from $Co^{59}(n, \alpha)Mn^{56}$ and $Mn^{55}(n, \alpha)V^{52}$ reactions. The dashed lines show the observed angular distributions, while the solid lines show the corrected angular distributions.

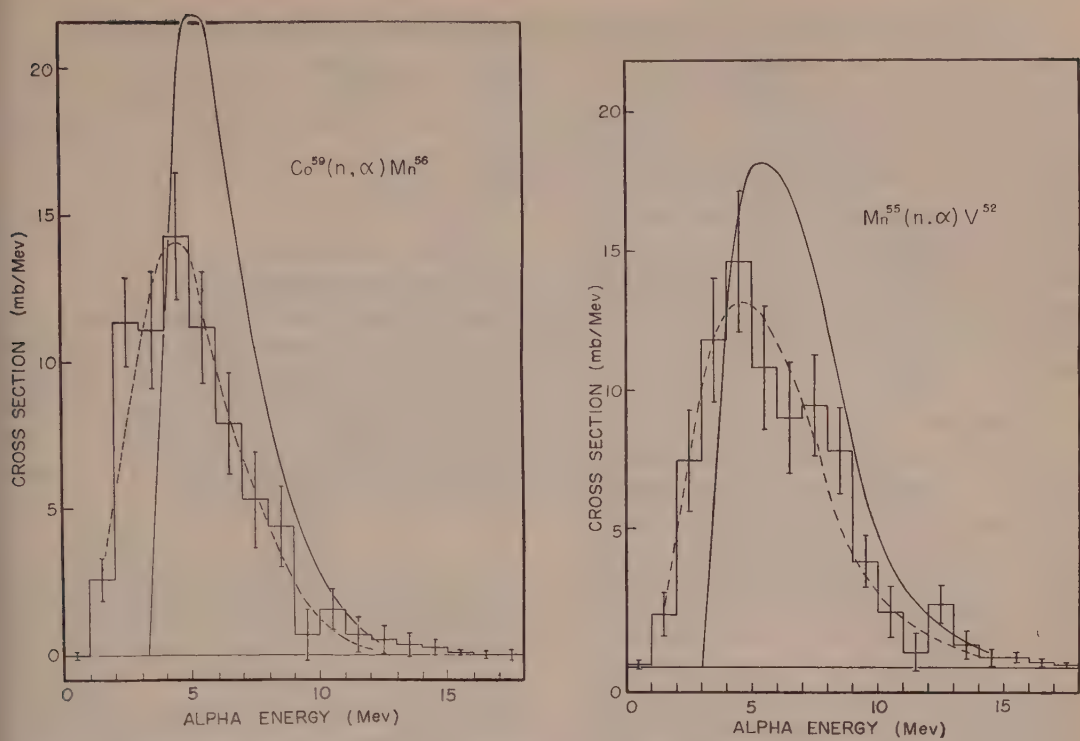

Fig. 3. Energy distributions of alpha particles from $Co^{59}(n, \alpha)Mn^{56}$ and $Mn^{55}(n, \alpha)V^{52}$ reactions. The histograms and dashed curves show the observed energy distributions, while the solid curves show the corrected energy distributions.

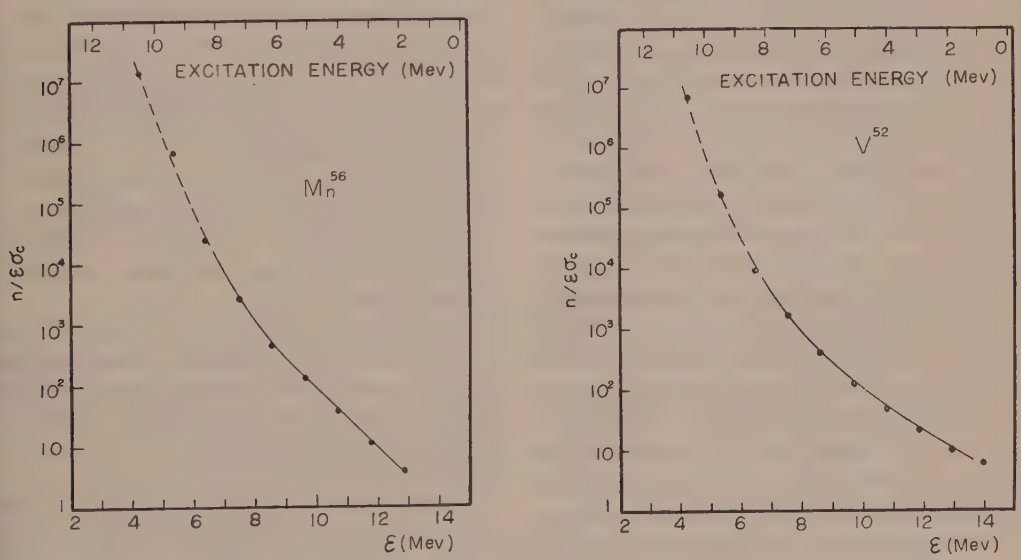

Fig. 4. The relative level densities $\omega = n/\varepsilon\sigma_c$ of Mn^{56} and V^{52}.

Fig. 4 shows the results presented by plotting the measured energy spectra divided by $\varepsilon\sigma_c(\varepsilon)$[5]. The data cannot fit a straight line. It is found that the curves are both concave upward, and for Mn the nuclear temperature is about 0.85 Mev at the high energy side ($13 > \varepsilon > 9$ Mev) and about 0.55 Mev at the low energy side ($9 > \varepsilon > 7$ Mev) and for V about 1.0 Mev at the high energy side ($12 > \varepsilon > 9$ Mev) and about 0.65 Mev at the low energy side ($9 > \varepsilon > 7$ Mev). The temperatures at the further low energy side (< 7 Mev for Mn and < 7 Mev for V) are not included in the present discussion because

of the large contribution of the second alpha particles from $(n, n\alpha)$ events.

The total (n, α) cross sections of Co and Mn are 84 and 96 mb respectively, which are fairly large as compared with that obtained by other authors[1),6)] with activation method. However, it must be noted that the cross sections obtained by us contain large yield from the $(n, \alpha n)$ and the $(n, n\alpha)$ reactions. Combined systematic and statistical uncertainties are estimated to be roughly 15% in the total cross sections.

§ 4. Discussion

As in the case of aluminium[3)], the angular distributions for the entire energy region are approximately 90° symmetrical and concave upward, and the energy distributions show that the alpha particles with energies below the Coulomb barrier are more emitted than has been expected.

The approximate 90° symmetry of the angular distributions of the alpha particles indicates the fact that most of the reactions probably occur through the formation of the compound nucleus, although the fairly large deviation from isotropy cannot be explained with the statistical theory of nuclear reactions[7)]. However, this may be explained by introducting a kind of selection rule for the emission of the alpha particles such as the isotopic spin selection rule.

Fig. 3 shows that the low energy alpha particles are more emitted than has been expected from the conventional statistical theory with the usual potential. It is considered that this may be explained by introducing a diffuse nuclear potential such as used by K. Kikuchi[8)] in his recent paper, which can be expected to give considerably larger yield at the low energy side than the usual square-well potential. Indeed he has shown that our previous results[3)] which give somewhat lower temperature than others' can be explained with the temperature of 2 Mev by introducing a diffuse potential.

It may be considered that the (n, α) cross sections larger than expected from the evaporation theory are not due to the non-compound processes but the large penetrabilities, which are explained by introducing a diffuse potential. But these problems should be discussed in more detail in future. Further investigation on other elements is now in progress.

§ 5. Acknowledgments

The authers wish to thank Professor K. Kimura for many useful discussions and suggestions throughout the course of the present work. Thanks are also due to Mr. M. Kurachi and Mr. B. Ikeo for their helps in preparing the targets. This work has been supported by the Scientific Research Expenditure of Ministry of Education.

References

1) E. B. Paul and R. L. Clarke: Can. J. Phys. **31** (1953) 267.
2) E. R. Graves and L. Rosen: Phys. Rev. **89** (1953) 343.
B. G. Whitmore and G. E. Dennis: Phys. Rev. **84** (1951) 296.
P. C. Gugelot: Phys. Rev. **81** (1951) 51.
D. M. Thomson: Proc. Phys. Soc. (London) A**69** (1956) 447.
P. C. Gugelot: Phys. Rev. **93** (1954) 425.
R. M. Eisberg and G. Igo: Phys. Rev. **93** (1954) 1039.
R. Britten: Phys. Rev. **88** (1952) 283.
R. M. Eisberg, G. Igo and H. E. Wegner: Phys. Rev. **100** (1955) 1309.
"*Statistical Aspects of the Nucleus*," Brookhaven National Laboratory Report BNL-331, 1955 (unpublished).
D. L. Allan: Proc. Phys. Soc. (London) A**70** (1957) 195.
3) I. Kumabe, E. Takekoshi, H. Ogata, Y. Tsuneoka and S. Ōki: Phys. Rev. **106** (1957) 155.
4) V. F. Weisskopf: Phys. Rev. **52** (1937) 295.
5) J. M. Blatt ane V. F. Weisskopf: *Theoretical Nuclear Physics* (John Wiley and Sons, Inc., New York, 1952), p. 353.
6) D. J. Hughes and J. A. Harvey: *Neutron Cross Sections* (McGraw-Hill Book Company, Inc., New York, 1955).
7) W. Hauser and H. Feshbach: Phys. Rev. **87** (1952) 366.
8) K. Kikuchi: Prog. Theor. Phys. **17** (1957) 643.

JOURNAS OF THE PHYSICAL SOCIETY OF JAPAN Vol. 13, No. 2, FEBRUARY, 1958

The Thermoelectric, Galvanomagnetic and Thermomagnetic Effects of Monovalent Metals

By Mikio TSUJI

General Education Department, Kyushu University, Fukuoka

(Received October 11, 1957)

A Theory of the thermoelectric effects and transverse galvano- and thermomagnetic effects of monovalent metals is described on a model of general spherical energy band. Boltzmann's equation is solved by a variational method, and whence we get a formula of thermoelectric power which shows the possibility of positive thermoelectric power at high temperatures but not at low temperatures. The effect of the Umklapp processes on the time of relaxation at high temperatures is also investigated. Our simple model can derive the negative Ettingshausen and Ettingshausen-Nernst coefficients of noble metals at high temperatures.

§ 1. Introduction

In the theory of transport phenomena of metals, an assumption is usually made that the conduction electrons can be treated as quasi-free. The theory based on this simple assumption gives fairly good agreement with experiment for the electrical conductivity of monovalent metals, but rather poor agreement for the thermal conductivity of noble metals at low temperatures[1]. Especially for the thermoelectric, thermomagnetic and magneto-resistance effects, the assumption of quasi-free electrons gives a large discrepancy between the theory and experiments. For example the magneto-resistance effect is much larger than the results given by the theory based on the spherical energy surface model. For the magneto-resistance effect the anisotropy of band structure is essentially important[2]. For the thermoelectric phenomena, the theory based on the free electron model gives a negative value of thermoelectric power, but the experiments show that the thermoelectric powers of noble metals and lithium are positive in sign, and those of rubidium and caesium change their signs from negative to positive as temperature decreases.

Jones[3] showed that the positive sign of thermoelectric power can be interpreted in terms of departures of the electronic energy-level structure from that postulated for quasi-free electrons. In his treatment, the anisotropy of the band structure is not essential, but a large increase of the density of states near the Fermi surface which is brought about by the anisotropy is essential for the occurrence of positive sign. Thus, the sign of thermoelectric power seems to be determined from the behavior of state density curve near the Fermi level, which should in turn be obtained from the electronic band structure of metals. But, the full determination of the electronic band structure is very complicated, and at present the theory does not give so reliable informations about the detailed nature of energy near the Fermi level.

Hence, we assume in the first approximation a spherical energy surface which is in a certain sence an averaged surface of real energy surface and is more general than that of quasi-free electrons. The same idea was suggested by Klemens[4] in his paper on the thermoelectric power of monovalent metals at high temperatures, in which he showed that the thermoelectric power of potassium is not anomalous, contrary to the result of MacDonald and Roy[5]. Klemens[1] has also investigated the thermal conductivities of monovalent metals on the same model and concluded that the thermal conductivities of noble metals at low temperatures are not interpreted by the spherical energy band model. The thermoelectric power of metals at low temperatures has never been studied on the model, and hence it seems to be worth while to study the behavior of the thermoelectric power of metals at all temperatures by using the model of the spherical energy surface.

In § 2 a transport equation for the conduction electrons which have a general spherical energy-level structure is set up by assuming

that the distribution function of lattice waves can be replaced by its thermal equilibrium value. Since the effect of non-equilibrium lattice distribution gives a negative contribution to the thermoelectric power[6], the assumption of the thermal equilibrium of lattice may be allowed for the purpose of a qualitative investigation of the possibility of the positive sign of the thermoelectric power. The 'Umklapp processes' are also disregarded on the derivation of the transport equation. An approximate solution of the transport equation by the variational method of Kohler[7] is given and the results are discussed. It is shown that there is a possibility of positive sign of the thermoelectric power at high temperatures, but no possibility for pure metals at low temperatures on the model of spherical energy surface. Hence the model is not appropriate to interpret the thermoelectric powers of metals at low temperatures. There is a reason, however, that we believe the model may be a good approximation at high temperatures at least semi quantitatively.

Therefore we further study on the case of high temperatures after § 3. At high temperatures, the effect of the non-equilibrium distribution of lattice waves may be disregarded, but the effect of Umklapp processes (we shall call them U-processes) may become important. The effect of U-processes on the electric and thermal conductivities were calculated by Bardeen[8] and Ziman[9], but their effect on the thermoelectric power has never been studied. In § 3 the effect of U-processes on the time of relaxation at high temperatures is considered.

By using the results obtained in § 3, the thermoelectric powers at high temperatures are calculated and the effects of impurities on the thermoelectric powers are discussed in § 4. It is shown that the U-processes give a positive contribution to the thermoelectric power.

In § 5 the transverse galvano- and thermomagnetic effects are calculated. An interpretation is given of the observation that the Ettingshausen, and Ettingshausen-Nernst coefficients of noble metals are negative. This had never been interpreted theoretically. A relation between thermoelectric power and Ettingshausen coefficient is derived. The relation shows fairly good agreement with experiments. The effects of impurity on the Ettingshausen and Ettingshausen-Nernst effects are also considered.

Our results obtained in § 2 are also applicable to the calculation of the influence of exchange and correlation of electrons on the transport phenomena of metals. In the appendix, we calculate the effects by using Bohm and Pines' curve and correct the errors in the calculation of Barrier[10].

§ 2. General Theory based on Spherical Energy Surphace Model

2.1. *The Transport Equation*

Assuming that the energy $E(\boldsymbol{k})$ of an electron depends only on the absolute value of wave vector $\boldsymbol{k}$, we expand $E(\boldsymbol{k})$ at the Fermi surface as

$$E(\boldsymbol{k})=\zeta+\alpha(k-k_0)+\tfrac{1}{2}\beta(k-k_0)^2+\cdots \qquad (1)$$

where $k=|\boldsymbol{k}|$, k_0 is the value of k at the Fermi surface, ζ is the Fermi level, and α and β are constants independent of k. The frequency $\nu(q)$ of a lattice wave is assumed to be related to the lattice wave vector $\boldsymbol{q}$ by $\nu(q)=u_0q/2\pi$, where u_0 is the (constant) velocity of sound, and the vector $\boldsymbol{q}$ is assumed to lie inside a sphere of radius

$$q_0=\left(\frac{3}{4\pi}\right)^{1/3}\frac{2\pi}{a},$$

where a is the lattice constant.

When the electric field $\boldsymbol{F}$ and the temperature gradient grad T are in the x direction, the appropriate form of the electron distribution function $f(\boldsymbol{k})$ is

$$f(\boldsymbol{k})=f_0(E)-k_xc(\eta)\frac{\partial f_0}{\partial E}, \qquad (2)$$

where $\eta=(E-\zeta)/\kappa T$, f_0 is the Fermi function $1/(e^\eta+1)$ and κ is the Boltzmann constant. The rate of change of f due to the field is given by

$$\left[\frac{\partial f}{\partial t}\right]_F=\frac{k_x}{\hbar k}\frac{dE}{dk}\frac{\partial f_0}{\partial E}\left(eF+T\frac{\partial}{\partial x}\frac{\zeta}{T}+\frac{E}{T}\frac{\partial T}{\partial x}\right), \qquad (3)$$

where $-e$ is the charge of an electron. For the scattering of electrons by the impurity atoms and the lattice defects, a time of relaxation τ exists, and is given by[11]

$$\frac{1}{\tau}=\frac{1}{\hbar}\frac{dE}{dk}N_iQ, \qquad (4)$$

where N_i is the number of impurity atoms per unit volume and Q is the scattering cross section of an impurity atom. Hence the rate

of change of f due to the impurity scattering is given by

$$\left[\frac{\partial f}{\partial t}\right]_1 = -\frac{f-f_0}{\tau} = \frac{k_x}{\hbar}\frac{dE}{dk}\frac{\partial f_0}{\partial E} N_i Q c(\eta) . \tag{5}$$

Assuming the scattering potential to be

$$V(r) = \frac{ze^2}{r}\exp(-r/r_0) ,$$

Barrie[12] has calculated the scattering cross section Q and has obtain

$$Q = 2\pi z^2 e^4 k^{-2}\left(\frac{dE}{dk}\right)^{-2}\left\{\ln(1+4k^2r_0^2) - \frac{4k^2r_0^2}{4k^2r_0^2+1}\right\} , \tag{6}$$

where $z+1$ is the valency of impurity atoms. If we expand the term in the bracket in a power series of η, we have

$$Q = k^{-2}\left(\frac{dE}{dk}\right)^{-2} P\{1+\gamma_1\kappa T\eta+\gamma_2(\kappa T\eta)^2+\cdots\} , \tag{7}$$

where P is a constant independent of k. Actually it is sufficient for our purpose to retain the right side of (7) up to the second term.

If we disregard the 'Umklapp processes' and assume that the lattice waves are in thermal equilibrium, the term due to the lattice scattering in the first approximation may be written in the form[13),14)]

$$\left[\frac{\partial f}{\partial t}\right]_2 = k_x\frac{\partial f_0}{\partial E}\frac{3\pi C^2}{2Mu_0}\left(\frac{dE}{dk}\right)^{-1}\left(\frac{T}{\Theta}\right)^3$$
$$\times\int_{-\Theta/T}^{\Theta/T}\left[c(\eta)-c(\eta+z)\left\{1+\frac{\kappa Tz}{k\,dE/dk}-\frac{q_0^2}{2k^2}\left(\frac{T}{\Theta}\right)^2 z^2\right\}\right]\frac{e^\eta+1}{e^{\eta+z}+1}\frac{1}{|1-e^{-z}|}z^2\,dz , \tag{8}$$

where M is the mass of lattice ion, Θ is the Debye characteristic temperature and C is the interaction constant between electrons and lattice waves used by Wilson[15] and is equal to 2/3 of the interaction constant used by Sommerfeld and Bethe[13]. Eq. (8) is sufficiently good approximation to obtain the leading terms of the electrical and thermal conductivities, but not to obtain the thermoelectric powers at low temperatures.

Eq. (8) is obtained, for example, from Eq. (9.33.7) of Wilson's text[15], by using the approximation that

$$\frac{1}{\pi\hbar}\Omega(E_{k+q}-E_k\pm h\nu_q) = \delta(E_{k+q}-E_k\pm h\nu_q)$$
$$= \delta\left\{\frac{dE}{dk}\left(q\cos\theta+\frac{q^2}{2k}\right)\pm h\nu_q\right\} = \frac{1}{q\,dE/dk}\,\delta\left\{\left(\cos\theta+\frac{q}{2k}\right)\pm\frac{h\nu_q}{q\,dE/dk}\right\} , \tag{9}$$

and by integrating over the orientation of $\boldsymbol{q}$, where θ is the angle between $\boldsymbol{k}$ and $\boldsymbol{q}$.

In the higher approximation required, (9) must be replaced by

$$\delta\left\{\frac{dE}{dk}\left(q\cos\theta+\frac{q^2}{2k}\right)+\frac{1}{2}\left(\frac{d^2E}{dk^2}-\frac{1}{k}\frac{dE}{dk}\right)q^2\left(\cos\theta+\frac{q}{2k}\right)^2\pm h\nu_q\right\} . \tag{10}$$

Now to simplify (10), we use the following theorem: If the two real roots of $ax^2+bx+c=0$ are x_1 and x_2, then

$$\delta(ax^2+bx+c) = \frac{1}{|a(x_1-x_2)|}\delta(x-x_1)+\frac{1}{|a(x_1-x_2)|}\delta(x-x_2) . \tag{11}$$

If the region of integration over x does not include x_2, the second term of right side of (11) may be omitted. By using (11) and the relation $h\nu_q/q(dE/dk)\ll 1$, (10) may be rewritten as

$$\delta(E_{k+q}-E_k\pm h\nu_q) = \frac{1}{q\,dE/dk}\left\{1\pm\frac{\dfrac{d^2E}{dk^2}-\dfrac{1}{k}\dfrac{dE}{dk}}{(dE/dk)^2}h\nu_q\right\}\delta\left(\cos\theta+\frac{q}{2k}\pm\frac{h\nu_q}{q\,dE/dk}\right) . \tag{12}$$

Then (8) is replaced by

$$\left[\frac{\partial f}{\partial t}\right]_2 = k_x \frac{\partial f_0}{\partial E}\frac{3\pi C^2}{2Mu_0}\left(\frac{dE}{dk}\right)^{-1}\left(\frac{T}{\Theta}\right)^3\int_{-\Theta/T}^{\Theta/T}\left\{1-\frac{\frac{d^2E}{dk^2}-\frac{1}{k}\frac{dE}{dk}}{(dE/dk)^2}\kappa Tz\right\}$$
$$\times\left[c(\eta)-c(\eta+z)\left\{1+\frac{\kappa Tz}{k\,dE/dk}-\frac{q_0^2}{2k^2}\left(\frac{T}{\Theta}\right)^2 z^2\right\}\right]\frac{e^\eta+1}{e^{\eta+z}+1}\frac{z^2\,dz}{|1-e^{-z}|}\,. \tag{13}$$

From (3), (5), (7) and (13), we may write the equation for the steady state of the electron distribution in the form

$$\frac{1}{k}\frac{dE}{dk}\left(eF+T\frac{\partial}{\partial x}\frac{\zeta}{T}+\frac{E}{T}\frac{\partial T}{\partial x}\right)=\mathscr{L}(c)\,, \tag{14}$$

where

$$\mathscr{L}(c)=-N_iP(1+\gamma_1\kappa T\eta+\cdots)k^{-2}\left(\frac{dE}{dk}\right)^{-1}c(\eta)$$
$$-\Lambda^{-1}\left(\frac{dE}{dk}\right)^{-1}\left(\frac{T}{\Theta}\right)^3\int_{-\Theta/T}^{\Theta/T}\left\{1-\frac{\frac{d^2E}{dk^2}-\frac{1}{k}\frac{dE}{dk}}{(dE/dk)^2}kTz\right\}$$
$$\times\left[c(\eta)-c(\eta+z)\left\{1+\frac{\kappa Tz}{k\,dE/dk}-\frac{q^2}{2k^2}\left(\frac{T}{\Theta}\right)^2 z^2\right\}\right]\frac{e^\eta+1}{e^{\eta+z}+1}\frac{z^2\,dz}{|1-e^{-z}|}\,, \tag{15}$$

and Λ denotes $4Mu_0/(3hC^2)$. To solve Eq. (14), we put

$$c(\eta)=\left(eF+T\frac{\partial}{\partial x}\frac{\zeta}{T}\right)c^{(1)}(\eta)+\frac{1}{T}\frac{\partial T}{\partial x}c^{(2)}(\eta)\,, \tag{16}$$

then $c^{(1)}$ and $c^{(2)}$ are the solutions of

$$E^{n-1}\frac{1}{k}\frac{dE}{dk}=\mathscr{L}(c^{(n)})\qquad(n=1,2)\,. \tag{17}$$

The electric and heat current densities are given by

$$J=K_{11}\left(e^2F+eT\frac{\partial}{\partial x}\frac{\zeta}{T}\right)+K_{12}\frac{e}{T}\frac{\partial T}{\partial x}\,, \tag{18}$$

$$w=K_{21}\left(-eF-T\frac{\partial}{\partial x}\frac{\zeta}{T}\right)-K_{22}\frac{1}{T}\frac{\partial T}{\partial x}\,, \tag{19}$$

where

$$K_{mn}=\frac{1}{3\pi^2\hbar}\int_{-\infty}^{\infty}E^{m-1}k^3c^{(n)}(\eta)\frac{\partial f_0}{\partial\eta}\,d\eta\,. \tag{20}$$

2.2. *Solution of the Transport Equation*

To solve the integral equation (17), we use the variation principle of Kohler[7]. The principle applied to the case of spherical energy band can be stated as follows:

The solution of (17) is such as to make the integral

$$(c^{(n)},c^{(n)})=\int_{-\infty}^{\infty}k^4\left(\frac{dE}{dk}\right)^{-1}c^{(n)}\mathscr{L}(c^{(n)})\frac{\partial f_0}{\partial\eta}d\eta \tag{21}$$

a maximum, subject to the subsidiary condition

$$\int_{-\infty}^{\infty}k^4\left(\frac{dE}{dk}\right)^{-1}c^{(n)}\mathscr{L}(c^{(n)})\frac{\partial f_0}{\partial\eta}\,d\eta=\int_{-\infty}^{\infty}E^{n-1}k^3c^{(n)}\frac{\partial f_0}{\partial\eta}\,d\eta\,. \tag{22}$$

Now we put $c^{(n)}(\eta)$ in the form

$$c^{(n)}(\eta)=\sum_{r=0}^{1} c_r^{(n)}\eta^r\,, \tag{23}$$

and put

$$\alpha_r^{(n)}=\int_{-\infty}^{\infty} E^{n-1}k^3\eta^r\frac{\partial f_0}{\partial\eta}\,d\eta\,, \tag{24}$$

$$d_{rs}=(\eta^r,\eta^s)=\int_{-\infty}^{\infty} k^4\left(\frac{dE}{dk}\right)^{-1}\eta^r\mathscr{L}(\eta^s)\frac{\partial f_0}{\partial\eta}\,d\eta\,. \tag{25}$$

Then

$$(c^{(n)},c^{(n)})=\sum_{r=0}^{1}\sum_{s=0}^{1} d_{rs}c_r^{(n)}c_s^{(n)}$$

must be a maximum, subject to the condition

$$\sum_{r=0}^{1}\sum_{s=0}^{1} d_{rs}c_r^{(n)}c_s^{(n)}-\sum_{r=0}^{1}\alpha_r^{(n)}c_r^{(n)}=0\,.$$

The current densities are given by (18) and (19), and now (20) becomes

$$K_{mn}=\frac{1}{3\pi^2\hbar}\sum_{r=0}^{1}\alpha_r^{(m)}c_r^{(n)}\,.$$

By the symmetry relation $d_{01}=d_{10}$, we can easily show the reciprocal relation

$$K_{21}=K_{12}\,. \tag{26}$$

The solutions of the variational problem are easily obtained by the usual method[16], and we obtain the leading terms of the conductivities and thermoelectric power as follows:

$$\sigma=\frac{e^2}{3\pi^2\hbar}\frac{(\alpha_0^{(1)})^2}{d_{00}}\,,$$

$$\kappa_T=\frac{1}{3\pi^2\hbar T}\frac{(\alpha_0^{(1)}\alpha_1^{(2)}-\alpha_1^{(1)}\alpha_0^{(2)})^2}{(\alpha_0^{(1)})^2 d_{11}}\,,$$

$$S=-\frac{\kappa}{e}\,\frac{\alpha_1^{(1)}\alpha_0^{(1)}d_{11}-\{\alpha_2^{(1)}\alpha_0^{(1)}+(\alpha_1^{(1)})^2\}d_{01}+\alpha_2^{(1)}\alpha_1^{(1)}d_{00}}{(\alpha_0^{(1)})^2 d_{11}}\,.$$

To calculate $\alpha_r^{(n)}$ and d_{rs}, we use the expansion

$$k=k_0\left(1+\frac{1}{\alpha k_0}\kappa T\eta-\cdots\right),$$

$$\frac{dE}{dk}=\alpha\left(1+\frac{\beta}{\alpha^2}\kappa T\eta-\cdots\right)$$

in (24) and (25).

The final results are

$$\frac{1}{\sigma}=\frac{1}{\sigma_i}+\frac{1}{\sigma_0}\,, \tag{27}$$

$$\frac{1}{\sigma_i}=\rho_i=\frac{3\pi^2\hbar}{e^2k_0^4\alpha^2}N_iP\,, \tag{28}$$

$$\frac{1}{\sigma_0}=\rho_0=\frac{3\pi^2\hbar q_0^2\Lambda^{-1}}{e^2k_0^4\alpha^2}\left(\frac{T}{\Theta}\right)^5 J_5\left(\frac{\Theta}{T}\right), \tag{29}$$

$$\frac{1}{\kappa_T}=\frac{1}{\kappa_i}+\frac{1}{\kappa_0}, \tag{30}$$

$$\frac{1}{\kappa_i}=\frac{9\hbar N_i P}{\kappa^2 T\alpha^2 k_0^4}, \tag{31}$$

$$\frac{1}{\kappa_0}=\frac{27\hbar\Lambda^{-1}}{\pi^2\kappa^2k_0^2\alpha^2}\left(\frac{T}{\Theta}\right)^3\left[J_5+\left(\frac{T}{\Theta}\right)^2\frac{q_0^2}{k_0^2}\left\{\frac{1}{3}\pi^2J_5-\frac{1}{6}J_7\right\}\right], \tag{32}$$

$$S=-\frac{\pi^2\kappa^2T}{3e}$$
$$\times\frac{\frac{\pi^2N_iP}{3}\left(\frac{4}{\alpha k_0}+\frac{2\beta}{\alpha^2}-\gamma_1\right)+\frac{1}{\Lambda}\left(\frac{T}{\Theta}\right)^3\left[\frac{2}{\alpha k_0}k_0^2J_5+\left(\frac{T}{\Theta}\right)^2q_0^2\left\{\frac{4}{3}\pi^2\left(\frac{1}{\alpha k_0}+\frac{\beta}{2\alpha^2}\right)J_5-\frac{1}{6}\left(\frac{5}{\alpha k_0}-\frac{2\beta}{\alpha^2}\right)J_7\right\}\right]}{\frac{\pi^2N_iP}{3}+\frac{1}{\Lambda}\left(\frac{T}{\Theta}\right)^3\left\{k_0^2J_5+\left(\frac{T}{\Theta}\right)^2q_0^2\left(\frac{\pi^2}{3}J_5-\frac{1}{6}J_7\right)\right\}}, \tag{33}$$

where

$$J_n\left(\frac{\Theta}{T}\right)=\int_0^{\Theta/T}\frac{z^n\,dz}{(e^z-1)(1-e^{-z})},$$

and ρ denotes the electrical resistivity and suffices i and 0 denote residual and ideal parts respectively. Using (28) and (29), Eq. (33) can be rewritten in the form

$$S=-\frac{\pi^2\kappa^2T}{3e}\,\frac{\rho_i\left(\frac{4}{\alpha k_0}+\frac{2\beta}{\alpha^2}-\gamma_1\right)+\rho_0\left\{\left(\frac{4}{\alpha k_0}+\frac{2\beta}{\alpha^2}\right)-\frac{1}{2\pi^2}\left(\frac{5}{\alpha k_0}-\frac{2\beta}{\alpha^2}\right)\frac{J_7}{J_5}+\frac{6}{\pi^2}\frac{k_0^2}{q_0^2}\frac{1}{\alpha k_0}\left(\frac{\Theta}{T}\right)^2\right\}}{\rho_i+\rho_0\left\{1-\frac{J_7}{2\pi^2J_5}+\frac{3}{\pi^2}\frac{k_0^2}{q_0^2}\left(\frac{\Theta}{T}\right)^2\right\}}. \tag{34}$$

Now, in the case that $\rho_i\gg\rho_0$, the Boltzmann equation can be solved by successive approximation, and then thermoelectric power is obtained as a power series of ρ_0/ρ_i. If we expand (34) in a power series of ρ_0/ρ_i, and retain up to the second term, the coefficient of the term of J_7/J_5 differs from that of the solution obtained by successive approximation. This is due to the fact that we restricted the function $c^{(n)}(\eta)$ to the form such as (23). However the terms of J_7/J_5 give practically negligible contribution to the numerical results, and so we neglect those terms in (34). Then (34) becomes

$$S=-\frac{\pi^2}{3e}\kappa^2T\,\frac{\rho_i\left(\frac{4}{\alpha k_0}+\frac{2\beta}{\alpha^2}-\gamma_1\right)+\rho_0\left\{\frac{4}{\alpha k_0}+\frac{2\beta}{\alpha^2}+\frac{6}{\pi^2}\frac{k_0^2}{q_0^2}\frac{1}{\alpha k_0}\left(\frac{\Theta}{T}\right)^2\right\}}{\rho_i+\rho_0\left\{1+\frac{3}{\pi^2}\frac{k_0^2}{q_0^2}\left(\frac{\Theta}{T}\right)^2\right\}}. \tag{35}$$

2.3. *Discussion about the Results of the Simple Theory*

Eq. (29) agrees with that obtained by Bloch as an interpolation formula[13], and (32) agrees with that obtained by Klemens[13]. From Eqs. (27) through (32) we see that the electrical conductivity and the thermal conductivity depend only on α^2 and not on β. These equations will be obtained from corresponding formulae for the quasi-free electrons by replacing the effective mass m^* by $\hbar^2k_0/\alpha$, and vice versa. Therefore our model does not give essentially different results from quasi-free electron model.

On the other hand for the thermoelectric power, we obtain a remarkable result (35) which is not deduced from that of free electron model by the simple replacement of m^*. For pure metals (35) reduces to

$$S_0=-\frac{\pi^2}{3e}\left(\frac{4}{\alpha k_0}+\frac{2\beta}{\alpha^2}\right)\kappa^2 T \tag{36}$$

at high temperatures ($T\gg\Theta$), and to

$$S_0=-\frac{2\pi^2\kappa^2 T}{3e\alpha k_0}\,, \tag{37}$$

at low temperatures ($T\ll\Theta$).

For the free electron limit ($\beta=\alpha/k_0$, $\alpha k_0=2\zeta$), (36) and (37) reduce to the well known formulae[15]. Eq. (37) shows that the sign of the thermoelectric powers of pure metals at low temperatures is always negative contrary to the experimental results for noble metals, Li, Cs and Rb[17]. On the other hand, (36) shows that at high temperatures

$$S_0<0 \quad \text{if} \quad \beta+2\alpha/k_0 \;>0\,, \tag{38a}$$

and

$$S_0>0 \quad \text{if} \quad \beta+2\alpha/k_0 \;<0\,. \tag{38b}$$

Experimentally, noble metals and Li have positive thermoelectric powers at high temperatures. Therefore, for these metals the condition (38b) should hold.

Now, near the center of the Brilloin zone (energy minimum point), the energy band shape may well be approximated by the quasi-free electron model and hence $d^2E/dk^2=2(dE/dk)/k=\hbar^2/m_1^*$ (>0). On the other hand near the energy maximum point on the zone boundary, the band shape may well be approximated by the positive hole model with $d^2E/dk^2=-\hbar^2/m_2^*$ (<0), and $2(dE/dk)/k\simeq 0$. Here m_1^* and m_2^* are the effective masses in each region. Therefore, if the Fermi surface goes from the center to the boundary of the zone, the value of β changes its sign from positive to negative and then its absolute value becomes larger than $2\alpha/k_0$. In the monovalent metals, the Fermi surface lies rather near the zone boundary, so that it may be reasonable to assume that $\beta<0$ and $|\beta|>2\alpha/k_0$ for noble metals.

The fact that noble metals should have larger negative values of β than those of alkali metals (except lithium) may be interpreted by the fact that the distance between the Fermi surface and the zone boundary is smaller for the face centered cubic structure than for the body centered cubic structure.

Our simple model is not appropriate to interpret the thermoelectric power at low temperatures, but it is expected that the thermoelectric power at high temperatures may be interpreted by our simple model. The reason is as follows.

For the general case of anisotropic energy band, the rate of change of distribution function $f(k)$ by the lattice scattering is written in the form[15],

$$\left[\frac{\partial f}{\partial t}\right]_2=-\frac{1}{\kappa T}\int V(\boldsymbol{k},\boldsymbol{k}')\{\Phi(\boldsymbol{k})-\Phi(\boldsymbol{k}')\}\,d\boldsymbol{k}'\,, \tag{39}$$

where

$$\Phi=-(f-f_0)/(\partial f_0/\partial E)\,. \tag{40}$$

At low temperatures, the wave numbers of effective phonons are small compared to those of electrons, and so only the states $\boldsymbol{k}'$ on the Fermi surface near the state $\boldsymbol{k}$ contribute to the integration of (39). Therefore $(\partial f/\partial t)_2$ depends strongly on the behavior of the energy band near the state $\boldsymbol{k}$, and hence the anisotropy of band structure gives large effects at low temperatures. On the contrary, at high temperatures, the wave numbers of effective phonons are large, and all states $\boldsymbol{k}'$ on the Fermi surface contribute to the integration (39), so that $(\partial f/\partial t)_2$ depends on the behavior of the energy band on the whole states near the Fermi surface. Hence the anisotropy may be averaged out to a certain extent. Accordingly the averaged spherical energy model may be a good approximation at high temperatures at least semi quantitatively.

§ 3. Effects of Umklapp Processes

In the preceding section, we neglected the Umklapp processes, but at high temperatures they play important role for the transport of electrons. Therefore we consider the effects at high temperatures in this section. Using the interaction parameters $C^2(q)$ calculated by Bardeen[8], Ziman[9] has considered the effects of the U-processes on the electrical and thermal conductivities of monovalent metals. But the effects of U-processes on the thermoelectric powers have never been calculated. Here we will show that the effect of the U-processes on the thermoelectric power is considerably important.

If we use Zieman's method to calculate the time of relaxation of pure metals at high temperatures, we have

$$\frac{1}{\tau(k)}=\frac{\Delta}{4\pi^2 M\,dE/dk}\int_0^{2k}C^2(q)\frac{\kappa T q}{h}\left\langle\frac{1}{\nu_p^2}\right\rangle\frac{q^4}{2k^2}\,dq\,, \tag{41}$$

where Δ is the volume of a unit cell and $\boldsymbol{q}=\boldsymbol{k}-\boldsymbol{k}'$. ν_p is given by

$$\nu_p/\nu_0 \equiv n(u, \psi)$$

$$= \begin{cases} u/u_0 & \text{for} \quad 0 \leq u \leq u_0 \quad (42a) \\ (u^2+b^2-2ub\cos\psi)^{1/2}/u_0 & \text{for} \quad u_0 < u \leq 1\,, \quad (42b) \end{cases}$$

where ν_0 is the maximum frequency of lattice wave, $u=q/2k=\sin(\phi/2)$, $u_0=q_0/2k$, $b=g_1/2k$, $\boldsymbol{g}_1$ being a reciprocal lattice vector (see Fig. 1), and ϕ and ψ are the angles shown in Fig. 1. For the U-processes ($u_0<u\leq 1$), $\langle 1/\nu_p^2\rangle$ means the averaged value of $1/\nu_p^2$ with the orientation of $\boldsymbol{q}$ relative to the reciprocal lattice:

$$\langle 1/\nu_p^2\rangle = \int_0^{\psi_0} \frac{1}{\nu_p^2}\sin\psi\, d\psi \Big/ \int_0^{\psi_0}\sin\psi\, d\psi\,.$$

The interaction parameter $C^2(q)$ calculated by Bardeen is written in the form,

$$C^2(q)=\zeta^2 G^2(\bar{u})\,, \tag{43}$$

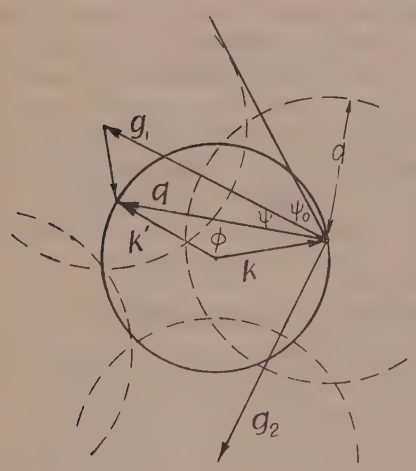

Fig. 1. Geometry of the scattering process. (See Ziman's paper[9].)

where $\bar{u}=q/2k_0=2^{-2/3}$, and the function $G^2(\bar{u})$ is identical with $G^2(u)$ given in (27) of Ziman's paper if we replace u by $\bar{u}$. (For the calculation of the electrical and thermal conductivities only, it is not necessary to discriminate u and $\bar{u}$.) Eq. (41) is evaluated in the same manner as Ziman's, and becomes

$$\frac{1}{\tau(k)}=\frac{1}{\tau_0}k^{-2}\left(\frac{dE}{dk}\right)^{-1}\left(\frac{T}{\Theta}\right)^5 \times\int_0^{\Theta/T}\left\{G^2\left(\frac{T}{\Theta}\bar{u}_0 x\right)+\Gamma^2\left(\frac{T}{\Theta}u_0 x\right)\right\}x^3\,dx\,, \tag{44}$$

where $\bar{u}_0=q_0/2k_0$,

$$\frac{1}{\tau_0}\equiv\frac{\Delta\zeta^2 q_0^6}{8\pi^2 M\nu_0}\,, \tag{45}$$

and

$$\Gamma^2(y)\equiv\frac{6}{y^4 b}\int_{b-y}^{1} u^4 G^2\left(\frac{k}{k_0}u\right)du\,. \tag{46}$$

Ziman's expression for the electrical resistivity at high temperatures is easily obtained from (44) by putting $k=k_0$ ($u=u_0$).

For the calculations of the thermoelectric power, Ettingshausen and Ettingshausen-Nernst coefficients, we have to obtain the values of $\{(1/\tau)(d\tau/dE)\}_{E=\zeta}$ which is easily calculated from (44) as follows:

$$\left(\frac{1}{\tau}\frac{d\tau}{dE}\right)_{E=\zeta}=\frac{2}{\alpha k_0}+\frac{\beta}{\alpha^2}-\frac{\lambda}{\alpha k_0}\,, \tag{47}$$

$$\lambda=\frac{6G^2(1)\bar{b}^{-1}\log\bar{u}_0/(\bar{b}-1)}{\int_0^{\bar{u}_0}\{G^2(y)+\Gamma^2(y)\}y^3\,dy}\,, \tag{48}$$

where $\bar{b}=g_1/2k_0$ (=1.138 for b.c.c. structures). Ziman calculated the numerical values of $G^2(y)$ and $\Gamma^2(y)$ for sodium and showed in Figs. 2 and 5 of his paper. We have graphically evaluated the integral in the denominator of (48) from Ziman's Fig. 5, and have recalculated $G(1)$ in the numerator (since it is difficult to read $G(1)$ from Ziman's Fig. 2). Thus we have obtained the numerical value of λ for sodium,

$$\lambda=1.8\,. \tag{49}$$

Bardeen used the quasi-free electron approximation in his calculation of $C(q)$, so that the numerical value of λ given in (49) is not very accurate. Since it is not easy to evaluate the numerical values of λ for all monovalent metals with sufficient accuracy, hereafter we regard λ as a parameter. Considering the value given in (49), we may assume that the numerical values of λ are generally positive and order of magnitude of unity.

§ 4. Thermoelectric Power

The relaxation time τ in the case when both thermal and impurity scatterings exist is given by

$$\frac{1}{\tau}=\frac{1}{\tau_i}+\frac{1}{\tau_0} \tag{50}$$

where τ_0 is the relaxation time due to the lattice scattering obtained in the preceeding section (Eq. (44)), and τ_i is that due to the impurity scattering and, from (10), τ_i is given by

$$\frac{1}{\tau_i}=\frac{N_iP}{\hbar}k^{-2}\left(\frac{dE}{dk}\right)^{-1}\{1+\gamma_1(E-\zeta)+\cdots\}\,. \tag{51}$$

The thermoelectric power at high temperatures is easily obtained from Mott's formula[11] as

$$S=-\frac{\pi^2\kappa^2T}{3e}\frac{\left\{\frac{d}{dE}\left(k^2\frac{dE}{dk}\tau\right)\right\}_{E=\zeta}}{k_0^2\alpha\tau}=-\frac{\pi^2\kappa^2T}{3e}\left(\frac{2}{\alpha k_0}+\frac{\beta}{\alpha^2}+\frac{1}{\tau}\frac{d\tau}{dE}\right). \tag{52}$$

Eq. (52) was also derived by Klemens[4]. From (51) we have

$$\left(\frac{1}{\tau_i}\frac{d\tau_i}{dE}\right)_{E=\zeta}=\frac{2}{\alpha k_0}+\frac{\beta}{\alpha^2}-\gamma_1\,. \tag{53}$$

Inserting (50) with (47) and (53) into (52), we have

$$S=-\frac{\pi^2\kappa^2T}{3e}\frac{\rho_i\left(\frac{4}{\alpha k_0}+\frac{2\beta}{\alpha^2}-\gamma_1\right)+\rho_0\left(\frac{4}{\alpha k_0}+\frac{2\beta}{\alpha^2}-\frac{\lambda}{\alpha k_0}\right)}{\rho_i+\rho_0}\,. \tag{54}$$

If we put $\lambda=0$, (54) reduces to high temperature approximation of (35). Now we will discuss two special cases.

4.1. *Pure Metals*

From (54) with $\rho_i=0$, we get the thermoelectric power for the pure metals as

$$S_0=-\frac{\pi^2\kappa^2T}{3e}\left(\frac{4-\lambda}{\alpha k_0}+\frac{2\beta}{\alpha^2}\right) \tag{55a}$$

or

$$=-0.0244T\left(\frac{4-\lambda}{\alpha k_0}+\frac{2\beta}{\alpha^2}\right), \tag{55b}$$

in which S_0 is in μV/deg. and αk_0 and α^2/β are in electron-volts. About the sign of the thermoelectric powers, from (55), we have

$$S_0<0 \quad \text{if} \quad \beta+\frac{\alpha}{k_0}(2-\lambda)>0\,, \tag{56a}$$

and

$$S_0>0 \quad \text{if} \quad \beta+\frac{\alpha}{k_0}(2-\lambda)<0\,. \tag{56b}$$

The condition (56b) for the occurrence of positive thermoelectric power is less stringent than the condition (39b) where the U-processes are neglected.

In (55) the value of αk_0 can be obtained from the data of electronic specific heat. The electronic specific heat C_e per mole of a metal is given by[18]

$$C_e=\gamma T=\frac{V}{3}\kappa^2k_0^2\alpha^{-1}T\,, \tag{57}$$

where V is the molar volume. From (57) we easily obtain

$$\alpha k_0=\pi^2N_0\kappa^2/\gamma\,,$$

where N_0 is the Avogadro number. Inserting the numerical values for the constants, we have

$$\alpha k_0=1.69\times10^{-3}/\gamma\,, \tag{58}$$

in which αk_0 is in electron-volts and γ in cal/mole-deg^2. But, since (55) includes further two unknown parameters β and λ, we can not determine these parameters from the experiments on the thermoelectric powers only.

If we neglect, tentatively, the U-processes ($\lambda=0$), the value of β/α^2 and β are obtained from (55). Table I shows the results these obtained for noble metals from the measurements of Otters[19] on the thermoelectric power and those of Corak et al.[20] on the electronic specific heats. If the U-processes were taken into account, the values of β/α^2 should become larger than those given in Table I. (Absolute values of β/α^2 should become smaller.)

For alkali metals, since the electronic specific heats have never been measured except for sodium, we make a crude approximation that αk_0 in (55) may be replaced by $2\zeta\simeq\hbar k_0^2/m^*$. Using the experimental values[21] of S_0 at 0°C and the calculated values[22] of m^*, we can obtain a rough estimation of the values of β/α^2. The results are shown in Table II.

Table I.

Metals	S_0 at 400°C.	$S_0/0.0244T$	αk_0	β/α^2
	(μV/deg.)	(eV^{-1})	(eV)	(eV^{-1})
Cu	3.85	0.23	10.3	−0.31
Ag	4.1	0.25	11.6	−0.30
Au	3.25	0.20	9.5	−0.31

For sodium, if we use the electronic specific heats $\gamma T=4.3\times10^{-4}T$ cal/mole-deg.[23], we ob-

Table II.

Metals	S_0 at 0°C (μV/deg.)	$S_0/0.0244T$ (eV^{-1})	αk_0 (eV)	β/α^2 (eV^{-1})
Li	10.0	1.50	6.76	−1.05
Na	− 5.3	−0.80	6.44	0.09
K	−12.5	−1.87	4.40	0.48
Rb	− 8.1	−1.21	4.12	0.12
Cs	− 1.2	−0.18	3.70	−0.45

tain $\alpha k_0=3.9$ eV and $\beta/\alpha^2=-0.11$ (eV)$^{-1}$. It has been believed that the band structures of sodium and potassium are very well approximated by the free electron model. However, a recent calculation on the electronic energy states of potassium[24] shows that there are considerable deviations from the free electron model, and therefore it is not surprising that sodium might have a very small or even a negative value of β.*

4.2. *Effect of Impurity*

Eq. (54) holds for any concentration of impurity atom. But when the valency of impurity atoms differs from unity and the concentration is large, the total number of the conduction electrons changes and so the Fermi level shifts. Therefore the change of the values of α and β must be taken into account. Here we consider only the initial change of the thermoelectric power when the concentration of impurity atoms is small. In this case, the change of the thermoelectric powers is mostly due to the impurity scattering of electrons and the change of the values of α and β may be neglected.

Let p be the fraction of the impurity atoms in a metal. We define the initial increase of the resistivity by

$$\xi_i=\left(\frac{\partial\rho_i}{\partial p}\right)_{p=0},$$

and then from (54) the initial increase of the thermoelectric power by the impurities is obtained as follows,

$$\left(\frac{\partial S}{\partial p}\right)_{p=0}=\xi_i\frac{\pi^2\kappa^2T}{3e}\frac{\gamma_1-\lambda/\alpha k_0}{\rho_0}. \tag{59}$$

Therefore we have

$$\left(\frac{\partial S}{\partial p}\right)_{p=0}>0, \quad \text{if} \quad \gamma_1>-\lambda/\alpha k_0 \tag{60a}$$

$$\left(\frac{\partial S}{\partial p}\right)_{p=0}<0, \quad \text{if} \quad \gamma_1<-\lambda/\alpha k_0. \tag{60b}$$

The experiments on noble metals show that generally (60b) seems to hold, but in the cases of Mn as the impurity in noble metals and possibly Ti and Cr in Cu, the relation (60a) seems to hold[25].

Domenicali and Otter[26] calculated the initial increases of the thermoelectric powers of impure metals by using the quasi-free electron model. They expanded the scattering cross section Q in the form

$$Q=Q_0(1+\alpha_1\kappa T\eta+\cdots). \tag{61}$$

Comparing (61) with (7), we have

$$\alpha_1=-\frac{2}{\alpha k_0}-\frac{2\beta}{\alpha^2}+\gamma_1. \tag{62}$$

Domenicali and Otter's results (their Eq. (22)) may be written in our notations in the form

$$\left(\frac{\partial S}{\partial p}\right)_{p=0}=\frac{\xi_i}{\rho_0}\left\{\frac{\pi^2\kappa^2T}{3e}\left(\frac{1}{2\zeta}+\alpha_1\right)-S_0\right\}. \tag{63}$$

Eq. (59) may also be rewritten in the corresponding form

$$\left(\frac{\partial S}{\partial p}\right)_{p=0}=\frac{\xi_i}{\rho_0}\left\{\frac{\pi^2\kappa^2T}{3e}\left(\gamma_1-\frac{4}{\alpha k_0}-\frac{2\beta}{\alpha^2}\right)-S_0\right\}$$
$$=\frac{\xi_i}{\rho_0}\left\{\frac{\pi^2\kappa^2T}{3e}\left(\alpha_1-\frac{2}{\alpha k_0}\right)-S_0\right\}, \tag{64}$$

and in the case of quasi-free electrons, (64) reduces to

$$\left(\frac{\partial S}{\partial p}\right)_{p=0}=\frac{\xi_i}{\rho_0}\left\{\frac{\pi^2\kappa^2T}{3e}\left(\alpha_1-\frac{1}{\zeta}\right)-S_0\right\}. \tag{65}$$

Eq. (63) does not agree with (65). This is due to the fact that Domenicali and Otter assumed erroneously the number of electrons n_0 to be independent of energy E in their Eq. (3). Using (63), Otter[19] analysed his experimental results on the thermoelectric power and electrical resistivity of dilute alloys of Mn, Pd and Pt in Cu, Ag and Au, and obtained the values of α_1. Since (63) is not correct, we have recalculated α_1 from (64). If we compare (64) with Eq. (2) of Otter's paper, it is seen that $\alpha_1-\alpha_c$ of Otter's must be replaced by $\alpha_1-2/\alpha k_0-3eS_0/\pi^2\kappa^2T$. Therefore if we use the values of αk_0 determined from the electronic specific heats and the observed values of S_0/T, we can obtain the correct values of α_1 from the values of α_1 and α_c given in Table I and Fig. 7 of Otter's paper. Table III (except for the last two rows) shows the results thus obtained.

* Recently L. M. Roberts (Proc. Phys. Soc. B **70** (1957), 744) has measured the electronic specific heats of Li and Na. If we use his values of γ, the values of αk_0 in Table II become 4.06 and 5.15 for Li and Na respectively, and the values of β/α^2 become −1.24 and 0.01 for Li and Na respectively.

Table III. Estimation of the values of α_1.

Solvent	Solute	Temperature (°C)	Otter's values of $\alpha_1-\alpha_c$ (eV^{-1})	$2/\alpha k_0$ (eV^{-1})	$S_0/0.0244T$ (eV^{-1})	Correct values of α_1 (eV^{-1})
Cu	Pd	400	−0.64	0.19	0.23	−0.22
〃	Pt	〃	−1.04	〃	〃	−0.62
〃	Mn	300	0.04	〃	〃	0.46
Ag	Pd	400	−1.28	0.17	0.25	−0.86
〃	Pt	〃	−1.10	〃	〃	−0.68
〃	Mn	300	0.15	〃	〃	0.57
Au	Pd	400	−1.76	0.21	0.20	−1.35
〃	Pt	〃	−1.81	〃	〃	−1.40
〃	Mn	300	0.02	〃	〃	0.43
Cu	Si		−0.34	0.19	0.23	0.08
〃	Zn		−0.27	〃	〃	0.15

Domenicali and Otter[25] analysed the thermoelectric powers of Cu–Si alloy and Cu–Zn alloy by using their Eq. (17). Using their values of α_1 and α_c, we can also obtain the correct values of α_1. The results are shown on the last two lows of Table III.

If we use Barrie's calculation (6), the theoretical value of α_1 is given by (62), and here γ_1 is easily calculated from (6) as

$$\gamma_1=\frac{\mu}{\alpha k_0},$$

where

$$\mu=\frac{32k_0^4r_0^4}{(1+4k_0^2r_0^2)^2\ln(1+4k_0^2r_0^2)-4k_0^2r_0^2(1+4k_0^2r_0^2)},$$

and the value of μ changes from 4 to 0 when k_0r_0 changes from 0 to infinity. Therefore the values of γ_1 of noble metals should be in the range between 0.4 and 0 $(eV)^{-1}$ and, if we use the rough estimation of β/α^2 given in Table I, the values of α_1 should be in the range between 0.8 and 0.4 $(eV)^{-1}$ showing a large discrepancy from the values given in Table III. This discrepancy would show that the Born approximation used by Barrie was not good.

§ 5. Transverse Galvanomagnetic and Thermomagnetic Effects

In our model, the negative value of β does not mean the "hole-conduction." The positive hole model gives the positive Hall coefficients, but our model gives the negative Hall coefficients showing the character of "electronic-conduction" irrespectively of the sign of β. Both the usual free electron and the positive hole models give the positive Ettingshausen and Ettingshausen-Nernst coefficients at high temperatures, but actually these coefficients of noble metals are negative. Our model can give an interpretation of the negative coefficients of noble metals.

The transverse galvanomagnetic and thermomagnetic effects have been calculated by Sondheimer[26] for the two band model composed of the usual free electron band and the inverted band of positive hole. Here we will calculate these effects for the general spherical band model. Since the spherical band model is not good approximation in the case of low temperatures, we consider only the case of high temperatures in which the time of relaxation τ exists.

We consider a metal strip with its surface in the xy-plane, carrying an electric current J_x or a thermal current w_x in the x-direction and subjected to a magnetic field $\boldsymbol{H}$ in the z-direction. The Boltzmann equation is

$$-\frac{e}{\hbar}\left(\boldsymbol{F}+\frac{1}{c}\boldsymbol{v}\times\boldsymbol{H}\right)\cdot\mathrm{grad}_k f+\boldsymbol{v}\cdot\mathrm{grad}_r f=-\frac{f-f_0}{\tau}, \tag{66}$$

where $\boldsymbol{F}$ is the electric field, $\boldsymbol{v}$ the velocity of electron and c the velocity of light. In (66) F is in electrostatic unit and H is in electromagnetic unit. If we put

$$f=f_0-\boldsymbol{k}\cdot\boldsymbol{c}(E)\frac{\partial f_0}{\partial E}, \tag{67}$$

(66) gives[27]

$$\frac{\hbar k}{\tau\, dE/dk}\boldsymbol{c}(E)-\frac{e}{\hbar c}\boldsymbol{H}\times\boldsymbol{c}(E)=-e\boldsymbol{F}-T\,\mathrm{grad}\left(\frac{\zeta}{T}\right)-\frac{E}{T}\,\mathrm{grad}\,T\,. \tag{68}$$

The x and y components of (68) are

$$\left.\begin{aligned}\frac{\hbar}{\tau}k\left(\frac{dE}{dc}\right)^{-1}c_1+\frac{eH}{\hbar c}c_2&=-eF_x-T\frac{\partial}{\partial x}\frac{\zeta}{T}-\frac{E}{T}\frac{\partial T}{\partial x}\\ -\frac{eH}{dk}c_1+\frac{\hbar}{\tau}k\left(\frac{dE}{dk}\right)^{-1}c_2&=-eF_y-T\frac{\partial}{\partial y}\frac{\zeta}{T}-\frac{E}{T}\frac{\partial T}{\partial y}\end{aligned}\right\} \tag{69}$$

where c_1 and c_2 are x and y components of $\boldsymbol{c}$.

The electric and thermal current densities are given by

$$\left.\begin{aligned}J_x&=\frac{e}{3\pi^2\hbar}\int k^3c_1\frac{\partial f_0}{\partial\eta}d\eta\,,\\ J_y&=\frac{e}{3\pi^2\hbar}\int k^3c_2\frac{\partial f_0}{\partial\eta}d\eta\,,\\ w_x&=-\frac{1}{3\pi^2\hbar}\int Ek^3c_1\frac{\partial f_0}{\partial\eta}d\eta\,,\\ w_y&=-\frac{1}{3\pi^2\hbar}\int Ek^3c_2\frac{\partial f_0}{\partial\eta}d\eta\,.\end{aligned}\right\} \tag{70}$$

Now we consider only the case of weak field ($H\to 0$). After a straightforward calculation we find

$$\left.\begin{aligned}J_x&=K_{11}e\left(eF_x+T\frac{\partial}{\partial x}\frac{\zeta}{T}\right)+K_{12}\frac{e}{T}\frac{\partial T}{\partial x}-K_{13}e\left(eF_y+T\frac{\partial}{\partial y}\frac{\zeta}{T}\right)-K_{14}\frac{e}{T}\frac{\partial T}{\partial y}\,,\\ J_y&=K_{13}e\left(eF_x+T\frac{\partial}{\partial x}\frac{\zeta}{T}\right)+K_{14}\frac{e}{T}\frac{\partial T}{\partial x}+K_{11}e\left(eF_y+T\frac{\partial}{\partial y}\frac{\zeta}{T}\right)+K_{12}\frac{e}{T}\frac{\partial T}{\partial y}\,,\\ w_x&=-K_{21}\left(eF_x+T\frac{\partial}{\partial x}\frac{\zeta}{T}\right)-K_{22}\frac{1}{T}\frac{\partial T}{\partial x}+K_{23}\left(eF_y+T\frac{\partial}{\partial y}\frac{\zeta}{T}\right)+K_{24}\frac{1}{T}\frac{\partial T}{\partial y}\,,\\ w_y&=-K_{23}\left(eF_x+T\frac{\partial}{\partial x}\frac{\zeta}{T}\right)-K_{24}\frac{1}{T}\frac{\partial T}{\partial x}-K_{21}\left(eF_y+T\frac{\partial}{\partial y}\frac{\zeta}{T}\right)-K_{22}\frac{1}{T}\frac{\partial T}{\partial y}\,,\end{aligned}\right\} \tag{71}$$

where

$$\left.\begin{aligned}K_{11}&=-\frac{1}{3\pi^2\hbar^2}\int k^2\frac{dE}{dk}\tau\frac{\partial f_0}{\partial\eta}d\eta\,,\\ K_{12}&=-\frac{1}{3\pi^2\hbar^2}\int Ek^2\frac{dE}{dk}\tau\frac{\partial f_0}{\partial\eta}d\eta=K_{21}\,,\\ K_{22}&=-\frac{1}{3\pi^2\hbar^2}\int E^2k^2\frac{dE}{dk}\tau\frac{\partial f_0}{\partial\eta}d\eta\,,\\ K_{13}&=-\frac{eH}{3\pi^2\hbar^4c}\int k\left(\frac{dE}{dk}\right)^2\tau^2\,dE\,,\\ K_{14}&=-\frac{eH}{3\pi^2\hbar^4c}\int Ek\left(\frac{dE}{dk}\right)^2\tau^2\,dE=K_{23}\,,\\ K_{24}&=-\frac{eH}{3\pi^2\hbar^4c}\int E^2k\left(\frac{dE}{dk}\right)^2\tau^2\,dE\,.\end{aligned}\right\} \tag{72}$$

From (72), it is seen that K_{mn}'s satisfy Onsager's reciprocal relations.

Putting grad $T=0$ and $J_y=0$ in (71), we find the Hall coefficient R as follows:

$$R=\frac{F_y}{HJ_x}=-\frac{K_{13}}{e^2HK_{11}^2}=-\frac{3\pi^2}{eck_0^3}=-\frac{1}{nec}\,. \tag{73}$$

Eq. (73) shows that the Hall coefficient is al-

ways negative in our model.

Putting $J_y=0$, $w_y=0$, $\partial T/\partial x=0$, we find the Ettingshausen coefficient A_E:

$$A_E=-\frac{\partial T/\partial y}{HJ_x}=\frac{T(K_{11}K_{14}-K_{12}K_{13})}{eHK_{11}(K_{11}K_{22}-K_{12}^2)}\,. \tag{74}$$

Putting (72) into (74), we hove

$$A_E=\frac{T}{nc}\left(-\frac{1}{\alpha k_0}+\frac{\beta}{\alpha^2}+\frac{1}{\tau}\frac{d\tau}{dE}\right). \tag{75}$$

Putting $J_x=J_y=\partial T/\partial y=0$ in (71), we find the isothermal Ettingshausen-Nernst coefficient B^i_{EN}:

$$B^i_{EN}=-\frac{F_y}{H\partial T/\partial x}=\frac{1}{HeT}\frac{K_{11}K_{14}-K_{12}K_{13}}{K_{11}^2}\,, \tag{76}$$

and putting (72) into (76), we have

$$B^i_{EN}=\frac{\pi^2\kappa^2T\alpha\tau}{3c\hbar^2k_0}\left(-\frac{1}{\alpha k_0}+\frac{\beta}{\alpha^2}+\frac{1}{\tau}\frac{d\tau}{dE}\right). \tag{77}$$

Putting $J_x=J_y=w_x=0$, we find the Righi-Leduc coefficient B_{RL}:

$$B_{RL}=\frac{\partial T/\partial y}{H\partial T/\partial x}$$

$$=\frac{K_{11}^2K_{24}+K_{12}^2K_{13}-2K_{11}K_{12}K_{14}}{HK_{11}(K_{12}^2-K_{11}K_{22})}\,, \tag{78}$$

and putting (72) into (78), we have

$$B_{RL}=-\frac{e\alpha\tau}{\hbar ck_0}\,. \tag{79}$$

The electrical and thermal conductivities are given by

$$\sigma=e^2K_{11}=\frac{e^2}{3\pi^2\hbar^2}k_0^2\alpha\tau\,, \tag{80}$$

$$\kappa_T=\frac{K_{11}K_{22}-K_{12}^2}{TK_{11}}\,, \tag{81}$$

$$=\frac{\kappa^2T}{9\hbar^2}k_0^2\alpha\tau\,. \tag{82}$$

From (74), (76) and (81), we have

$$A^i_{EN}\equiv\frac{B^i_{EN}}{\kappa_T}=\frac{A_E}{T}\,. \tag{83}$$

Using the second law of thermodynamics, Bridgman derived[28] (83), and Callen[29] derived (83) from Onsagers's reciprocal relations.

From (73), (78), (80) and (82) we have

$$R\sigma=B_{RL}\,, \tag{84}$$

and

$$\frac{RB^i_{EN}}{A_EB_{RL}}=\frac{\pi^2}{3}\left(\frac{\kappa}{e}\right)^2. \tag{95}$$

These relations were also derived by Bridgman by a phenomenological consideration[28], and by Sondheimer[26] for the free electron model. It is known that the relations (83), (84) and (85) generally hold for many metals including noble metals[28].

Now, from (52) and (75) we can eliminate both unknown parameters β and λ, and we have

$$\frac{1}{T}\left(ncA_E+\frac{3e}{\pi^2\kappa^2}S\right)=-\frac{3}{\alpha k_0}\,. \tag{86}$$

5.1. *Pure Metals*

Putting (47) into (75) and (77), we have

$$A_E=\frac{T}{nc}\left(\frac{1-\lambda}{\alpha k_0}+\frac{2\beta}{\alpha^2}\right), \tag{87}$$

$$B^i_{EN}=\frac{\pi^2\kappa^2T}{3c\hbar^2}\left(\frac{1-\lambda}{\alpha k_0}+\frac{2\beta}{\alpha^2}\right)\frac{\tau}{\alpha k_0^2}\,. \tag{88}$$

Therefore

$$A_E>0,\ B^i_{EN}>0 \quad \text{if} \quad \beta+\frac{\alpha}{2k_0}(1-\lambda)>0 \tag{89a}$$

and

$$A_E<0,\ B^i_{EN}<0 \quad \text{if} \quad \beta+\frac{\alpha}{2k_0}(1-\lambda)<0\,. \tag{89b}$$

Both free electron and positive hole models give negative values of A_E and B^i_{EN}. However, noble metals and many other metals have negative Ettinguishausen and Ettingshausen-Nernst coefficients. No model has yet been worked out for which A_E and B^i_{EN} are negative at high temperatures. Now from our simple model, A_E and B^i_{EN} are negative if the condition (89b) holds.

The condition (89b) is less stringent than the condition (56b), so that A_E and B^i_{EN} are negative for the metals which have positive thermoelectric powers. Noble metals are in this case. For alkali metals (except for Li), A_E and B^i_{EN} have not yet been measured. But from the values of S_0/T and αk_0 shown in Table II and Eq. (86), we see that Li and Cs may have negative values of A_E and B^i_{EN} at room temperatures. The measurement on Li[30] shows, however, the positive B^i_{EN} and make an unfortunate exception.

Now we will compare (86) with the experiments for pure noble metals. Our theory is applicable for the case of high temperatures ($T\gg\Theta$), but the available experimental data for A_E are only the measurements on noble metals in room timperature region ($T\simeq\Theta$). Therefore we are compelled to use the room

Table IV.

Metals	$cA_E/T\times10^{11}$ (erg^{-1} cm^3)	T (°K)	$n\times10^{-22}$ (cm^{-3})	ncA_E/T (eV^{-1})	$3eS_0/\pi^2\kappa^2T$ (eV^{-1})	T (°K)	$1/\alpha k_0$ Calculated from (86) (eV^{-1})	$1/\alpha k_0$ Calculated from (58) (eV^{-1})
Ag	0.57[a]	291	5.9[c]	0.54	0.25–0.33	500–1000	0.10–0.07	0.086
Cu	0.55[a]	291	8.5[c]	0.75	0.23	500–1000	0.17	0.10
	0.48[b]	298–358	〃	0.65	〃	〃	0.14	〃

a) reference 31)
b) reference 32)
c) taken to be equal to the number of atoms per unit volume

temperature data of A_E and the high temperature data of S_0, and then we have the results shown Table IV.

Considering that the data of A_E are those at room temperatures, we may conclude that the agreement of the theory with the experiments is fairly good. Owing to a curious exception that A_E/T of Au is not constant with temperatures[32], we have omitted Au from Table IV.

In Table V, we summarized the qualitative results on the sign of the thermoelectric powers and the coefficients of the transverse galvanomagnetic and thermomagnetic effects.

Table V.

		R	A_E	B_{EN}	B_{RL}	S
Free electron Model		−	+	+	−	−
Positive hole Model		+	+	+	+	+
Present Model	$\beta>-\alpha/2k_0$	−	+	+	−	−
	$-\alpha/2k_0>\beta>-2\alpha/k_0$	−	−	−	−	−
	$-2\alpha/k_0>\beta$	−	−	−	−	+
Observation	Cu, Ag, Au,	−	−	−	−	+
	Na, K	−				−
	Li	−		+		+

5.2. *Effect of Impurity*

Putting (50) with (47) and (51) into (75) and (87), we have the expressions of the Ettingshausen and Ettingshausen-Nernst coefficients for case of any impurity concentration. From these expressions, we easily obtain the initial increases as follows,

$$\left(\frac{\partial A_E}{\partial p}\right)_{p=0}=-\frac{\xi_i T}{nc\rho_0}\left(\frac{4-\lambda}{\alpha k_0}+\gamma_1\right), \tag{90}$$

$$\left(\frac{\partial B^i_{EN}}{\partial p}\right)_{p=0}=\xi_i\frac{\pi^2\kappa^2T}{3e^2cn\rho_0{}^2}\left(\frac{2\lambda-1}{\alpha k_0}-\frac{2\beta}{\alpha^2}-\gamma_1\right). \tag{91}$$

Using (59) and (55a), we can eliminate the parameters λ and β from (90) and (91), and thus we find

$$\frac{3e}{\pi^2\kappa^2}\left(\frac{\partial S}{\partial p}\right)_{p=0}+nc\left(\frac{\partial A_E}{\partial p}\right)_{p=0}=0\,, \tag{92}$$

$$\frac{3e}{\pi^2\kappa^2T}\left[-S_0+\frac{\rho_0}{\xi_i}\left\{\left(\frac{\partial S}{\partial p}\right)_{p=0}+ecn\rho_0\left(\frac{\partial B^i_{EN}}{\partial p}\right)_{p=0}\right\}\right]=\frac{3}{\alpha k_0}\,. \tag{93}$$

From (90), (91) and (87), we have also

$$\frac{A_E}{T}+\frac{\rho_0}{T\xi_i}\left[\frac{3e^2\rho_0}{\pi^2\kappa^2}\left(\frac{\partial B^i_{EN}}{\partial p}\right)_{p=0}-\left(\frac{\partial A_E}{\partial p}\right)_{p=0}\right]=0\,. \tag{94}$$

Since (92), (93) and (94) do not include the parameters β, λ and γ_1, these equations are suitable to test the agreement of the theory with experiments. In many cases $\partial S/\partial p$ is negative, so that we see from (92) that the Ettingshausen coefficients should increase by a small content of impurity atoms. It is unfortunate that the measurements on the effects of impurities on the Ettingshausen and Ettingshausen-Nernst coefficients of noble metals have never been worked out.

Acknowledgement

The author wishes to express his hearty thanks to Prof. T. Okada and Prof. T. Nakamura for their valuable discussions. This study was financed by the Scientific Research Fund of the Ministry of Education.

Appendix

Influence of Exchange and Correlation on Electron Transport in Metals*

Bohm and Pines have developed a new

* In the short note reported previously[33], Eqs. (4) and (7) were invalid, so that we correct the errors in this appendix.

method for treating exchange and correlation effects in an electron gas. By their collective description of electron interaction, one electron energy in a metal is given by[34]

$$E(\boldsymbol{k})=\frac{3.68}{r_s^2}\left(\frac{k}{k_0}\right)^2\frac{m}{m^*}-\frac{0.611}{r_s}\left[1-2\beta+\frac{\beta^2k_0^2-k_0^2+3k^2}{2kk_0}+\frac{k_0^2-k^2}{k_0k}\ln\left(\frac{k_0+k}{\beta k_0}\right)\right], \tag{A-1}$$

where E is in rydbergs, r_s is the average interelectronic distance in units of Bohr radius, and β is a measure of the screening of the Coulomb interaction ($\beta=0.353r_s^{1/2}$). In the course deriving (A-1), it was assumed that, in the Hartree approximation, the one electron energy is given by that of quasi-free electron:

$$E_0(\boldsymbol{k})=\frac{3.68}{r_s^2}\frac{m}{m^*}\left(\frac{k}{k_0}\right)^2. \tag{A-2}$$

Blatt[35] calculated the change produced in the conductivity and thermoelectric power of metals when one uses Bohm and Pines' $E-k$ curve (A-1) instead of the usual standard curve (A-2). Since there were errors in Blatt's paper, Barrie[10] has corrected these errors and has found that the conductivity changes markedly. But there are also errors in his paper. In this appendix, we correct these errors by using the results obtained in the text.

If we assume the validity of the use of Bohm and Pines' curve (A-1) in the transport equation (14), we have, from (29), (32), (36) and (37),

$$\frac{\sigma}{\sigma_0}=\frac{\kappa}{\kappa_0}=\left(\frac{X_1}{2A}\right)^2, \tag{A-3}$$

$$\frac{S}{S_0}=\begin{cases}\dfrac{2A(2X_1+X_2)}{3X_1^2} & \text{at } T\gg\Theta, \quad \text{(A-4)}\\[2ex] \dfrac{2A}{X_1} & \text{at } T\ll\Theta, \quad \text{(A-5)}\end{cases}$$

where σ, κ and S are electric- and thermal conductivities and thermoelectric power for the modified band (A-1) and σ_0, κ_0 and S_0 are those for free-electron band (A-2), and

$$A=\frac{3.68}{r_s^2}\frac{m}{m^*},$$

$$X_1\equiv\left(k\frac{dE}{dk}\right)_{E=\zeta}=2A+B[\tfrac{1}{2}\beta^2-2+2\ln(2/\beta)],$$

$$X_2\equiv\left(k^2\frac{d^2E}{dk^2}\right)_{E=\zeta}=2A+B[3-\beta^2-2\ln(2/\beta)],$$

$$B=\frac{0.611}{r_s}.$$

The numerical results are shown in Table A-I.

Table A-I.

	Li	Na	K	Rb	Cs
σ/σ_0	1.43	1.23	1.14	1.12	1.08
$S/S_0(T\gg\Theta)$	0.82	0.91	0.97	0.99	1.02
$S/S_0(T\ll\Theta)$	0.84	0.90	0.94	0.95	0.97

If the U-processes are taken into account, the values of S/S_0 shown in Table A-I will be slightly modified.

The values of σ/σ_0 are smaller than those obtained by Barrie. For thermoelectric powers, the influence of exchange and correlation is rather small compared to the effect of the departure of one electron Hartree energy level from that of quasi-free electrons.

References

1) P. G. Klemens: Proc. Roy. Soc. **A 67** (1954) 194.
2) L. Davis: Phys. Rev. **56** (1939) 93.
3) H. Jones: Proc. Phys. Soc. **A 68** (1955) 1191. Handbuch der Physik, Vol. **19**, P. 277 (1956).
4) P. G. Klemens: Phil. Mag. **45** (1954) 881.
5) D. K. C. MacDonald and S. K. Roy: Phil. Mag. **44** (1953) 1364.
6) I. I. Hanna and E. H. Sondheimer: Proc. Roy. Soc. **A 239** (1957) 247.
7) M. Kohler: Z. Phys. **124** (1948) 772, **125** (1949) 679.
E. H. Sondheimer: Proc. Roy. Soc. **A 203** (1950) 75.
8) J. Bardeen: Phys. Rev. **52** (1937) 688.
9) J. M. Ziman: Proc. Roy. Soc. **A 226** (1954) 436.
10) R. Barrie: Phys. Rev. **103** (1956) 1581.
11) N. F. Mott and H. Jones: The Theory of Metals and Alloys (1936).
12) R. Barrie: Proc. Phys. Soc. **B 69** (1956) 553.
13) A. Sommerfeld and H. Bethe: Handbuch der Physik, Vol. **24/2** (1934).
14) P. G. Klemens: Handbuch der Physik, Vol. **14**, P. 233 (1956).
15) See for instance, A. H. Wilson: The Theory of Metals, 2nd ed., Chapter 9, (1953).
16) See for instance, A. H. Wilson: ibid. Chapter 10.
17) D. L. C. MacDonald and W. B. Pearson: Proc. Roy. Soc. **A 219** (1953) 373, **A 221** (1954) 534.
18) See for instance, C. J. Gorter: Progress in Low Temperature Physics, Vol. **1**, Chapter 11 (1955).
19) F. A. Otter: J. Appl. Phys. **27** (1956) 197.
20) W. S. Corak et al: Phys. Rev. **98** (1955) 1699.

21) Calculated from Bidwell's data (from International Critical Tables, Vol. **6**) and the absolute thermoelectric power of Pt.
22) C. Kittel: Introduction to Solid State Physics, 2nd ed., P. 317 (1956).
23) D. H. Parkinson and J. E. Quarrington: Proc. Phys. Soc. **A 68** (1955) 762.
24) J. Callaway: Phys. Rev. **103** (1956) 1219.
25) C. A. Domenicali and F. A. Otter: Phys. Rev. **95** (1954) 1134.
26) E. H. Sondheimer: Proc. Roy. Soc. **A 193** (1948) 484.
27) See for instance, A. H. Wilson: op. cit. Chapter 8.
28) See for instance W. Meissner: Handbuch der Experimentalphysik, Vol. **11/2** (1935).
29) H. B. Callen: Phys. Rev. **73** (1948) 1349.
30) A. H. Smith's measurement (from W. Meissner, op. cit. Table 130).
31) F. Unwin's measurement (from W. Meissner: op. cit. Table 137).
32) E. H. Hall's measurement (from J. Meixner: Ann. d. Phys. (5) **35** (1939) 701, Table 2).
33) M. Tsuji: J. Phys. Soc. Japan **12** (1957) 828.
34) D. Pines: Phys. Rev. **92** (1953) 626.
35) F. J. Blatt: Phys. Rev. **99** (1955) 1735.

JOURNAL OF THE PHYSICAL SOCIETY OF JAPAN Vol. 13, No. 2, FEBRUARY, 1958

Thomas-Fermi Function for Impurity Atom Dissolved in a Matrix Metal

By Kwai UMEDA
Department of Physics, Okayama University, Okayama
and Shigehiro KOBAYASHI
Department of Physics, Kagawa University, Takamatsu

(Received October 26, 1957)

The scale transformation keeping invariant the TF equation for an impurity atom dissolved with infinite dilution in a matrix metal of very large size was established. It enabled us to reduce the double sequence of solutions of the TF equation specified by two parameters to a single sequence of master solutions specified by one parameter only. Starting from the asymptotic expansion of solution derived here anew the inward numerical integration of the TF equation was carried out. The screened Coulomb potential was compared with our numerical solutions to measure its degree of approximation.

§ 1. Introduction

According to Fujiwara's[4] notation, the electrostatic potential $V(r)$ around a Z_0+Z-valent impurity atom dissolved with infinite dilution in a Z_0-valent matrix metal of very large size can be expressed as

$$V(r)\equiv(e/r)\phi(x) \tag{1}$$

by means of the Thomas-Fermi (TF) function $\phi(x)$, i.e. the solution of the modified TF equation

$$\frac{d^2\phi}{dx^2}\equiv\phi''=\frac{\phi^{3/2}}{x^{1/2}}-A^{3/2}x \tag{2}$$

subject to the initial and boundary condition

$$\phi(x=0)=Z \tag{3}$$

and

$$\phi(x\to\infty)\to Ax \tag{4}$$

respectively, where x is the distance from the impurity atom as origin measured in the standard (unit atomic number) TF unit $\mu_0(=0.88534\,a_{\mathrm{H}})$

$$x=r/\mu_0 \tag{5}$$

and A is a constant depending on atomic valency Z_0 and atomic radius r_0 of solvent metal

$$A^{3/2}\equiv\left(\frac{3\pi}{4}\right)^3\left(\frac{Z_0}{2\pi}\right)\left(\frac{a_{\mathrm{H}}}{r_0}\right)^3. \tag{6}$$

Accordingly $V(r)$ has the normalization $V(\infty)=eA/\mu_0$.

Then, $\phi(x)$ is specified by two parameters Z and A as $\phi(x;Z,A)$. The special natures

of solute and solvent can be taken into account solely through parameters Z and A respectively. The solution of Eq. (2) was given first by Mott[1] in the first order approximation (linearization of Eq. (2)) of the screened Coulomb form which was refined by Friedel[2] in the so-called second order approximation and by Sugiyama *et al*[3] with use of variational method, and then by Fujiwara[4] and Alfred-March[5] using the direct numerical integration which was carried out outwards as usual on starting in accordance with Eq. (3) from the point ($x=0$, $\phi=Z$) by series expansion having the initial slope adjustable to satisfy Eq. (4), as shown schematically in Fig. 1 and accurately in Fujiwara's Fig. 1. This numerical solution is very sensitive to the value of the initial slope and besides it is fairly difficult to discriminate numerically the asymptotic convergence required by Eq. (4). In addition, in order to obtain one correct

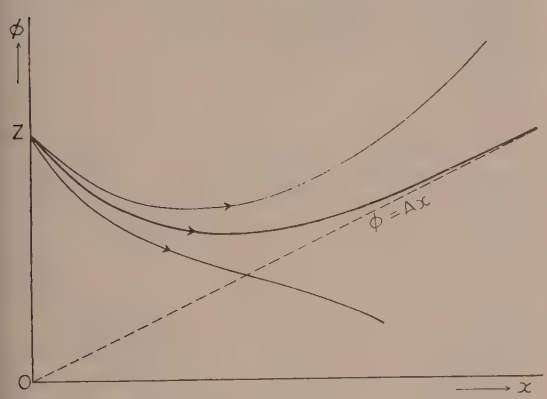

Fig. 1. Customary method: outward integration of the TF equation, Eq. (2).

solution we have to calculate a number of trial solutions in vain. This circumstance lets us try to solve Eq. (2) rather by the inward integration which was previously proved by us[6] to be efficient for the ordinary TF and TFD equation, as then all of calculated solutions can be significant ones.

§ 2. Derivation of Master Solutions

For definiteness we take as a master solvent the one for which A has a definite value C (e.g. in the present work $C=0.182044\approx A_{Ag}$, $C^{3/2}=0.0776723$ since we took $\lambda=(3/2)^{1/2}C^{1/4}=0.8$ sharp to make the computation of the asymptotic expansion, Eq. (14), easy). Denoting ϕ and x by Φ and X respectively we consider any master solution of the fundamental equation corresponding to Eq. (2)

$$\frac{d^2\Phi}{dX^2}\equiv\ddot{\Phi}=\frac{\Phi^{3/2}}{X^{1/2}}-C^{3/2}X \tag{7}$$

subject to the boundary condition

$$\Phi(X\to\infty)\to CX \tag{8}$$

only. Then $\Phi(X)$ will take on the other boundary $X=0$ its proper definite value, i.e. its initial value

$$\Phi(X=0)\equiv\Phi_0 \tag{9}$$

which represents the excess valency Z in this case and specifies the considered master solution.

To investigate the asymptotic behavior of $\Phi(X)$, we put conveniently $\Phi(X)$ for very large values of X in the form

$$\Phi(X)\equiv CX+Y(X) \tag{10}$$

$Y(X)$ vanishing asymptotically.

In the first order approximation, Eq. (7) is simplified to a linear homogeneous equation

$$\ddot{Y}=\lambda^2 Y \tag{11}$$

with

$$\lambda^2\equiv(3/2)C^{1/2} \tag{12}$$

or

$$C^{3/2}=(8/27)\lambda^6\,. \tag{12a}$$

The form of the solution of Eq. (11)

$$Y=ae^{-\lambda X} \tag{13}$$

suggests us that, in the higher order approximation, $Y(X)$ should be expressed by a power series of $e^{-\lambda X}$ and followingly the exact asymptotic solution should take the form

$$\Phi=CX+\sum_{k=1}^{\infty}a_k(X)e^{-k\lambda X} \tag{14}$$

$$=\frac{4}{9}\lambda^4 X\left[1+\sum_{k=1}^{\infty}\frac{9}{4}\frac{a_k(X)}{\lambda^4 X}e^{-k\lambda X}\right]. \tag{14a}$$

Inserting Eqs. (14a) and (12a) into Eq. (7) we obtain the recurrence formulas for the expansion coefficients $a_k(X)$ as follows.

i) In order of $e^{-\lambda X}$:

$$\ddot{a}_1-2\lambda\dot{a}_1=0\,, \tag{15}$$

$$\therefore\quad a_1=\text{const}\equiv a\,. \tag{16}$$

This reproduces obviously the solution in the first order approximation given above, Eq. (13), which results with $a=\Phi_0$ the Mott potential, Eq. (28).

ii) In order of $e^{-2\lambda X}$:

$$\ddot{a}_2-4\lambda\dot{a}_2+3\lambda^2 a_2\equiv\frac{9}{16}\frac{a^2}{\lambda^2 X}\,, \tag{17}$$

$$\therefore\ a_2=\frac{3}{16}\frac{a^2}{\lambda^4 X}\left[1-\frac{4}{3}\frac{1}{\lambda X}+\frac{26}{9}\frac{1}{(\lambda X)^2}-\frac{80}{9}\frac{1}{(\lambda X)^3}+\cdots\right]. \tag{18}$$

iii) In order of $e^{-3\lambda X}$:

$$\ddot{a}_3-6\lambda\dot{a}_3+8\lambda^2 a_3=\frac{9}{8}\frac{\dot{a}a^2}{\lambda^2 X}-\frac{27}{128}\frac{a^3}{\lambda^6 X^2}, \tag{19}$$

$$\therefore\ a_3=-\frac{9}{256}\frac{a^3}{\lambda^8 X^2}\left[0+\frac{1}{\lambda X}-\frac{53}{12}\frac{1}{(\lambda X)^2}+\frac{221}{12}\frac{1}{(\lambda X)^3}-\cdots\right]. \tag{20}$$

It is peculiar that a_3 is not of $O(1/(\lambda^8 X^2))$ but of $O(1/(\lambda^9 X^3))$.
iv) In oder of $e^{-4\lambda X}$:

$$\ddot{a}_4-8\lambda\dot{a}_4+15\lambda^3 a_4=\frac{9}{16}\frac{a_2^2+2aa_3}{\lambda^2 X}-\frac{81}{128}\frac{a^2a_2}{\lambda^6 X^2}+\frac{729}{4096}\frac{a^4}{\lambda^{10}X^3}, \tag{21}$$

$$\therefore\ a_4=\frac{27}{5120}\frac{a^4}{\lambda^{12}X^3}\left[1-\frac{23}{30}\frac{1}{\lambda X}+\cdots\right]. \tag{22}$$

v) In order of $e^{-5\lambda X}$:

$$a_5-10\lambda\dot{a}_5+24\lambda^2 a_5$$
$$=\frac{9}{8}\frac{aa_4+o_2a_3}{\lambda^2 X}-\frac{81}{128}\frac{aa_2^2+a^2a_2}{\lambda^6 X^2}+\frac{729}{1024}\frac{a^3a_2}{\lambda^{10}X^3}-\frac{6561}{32768}\frac{a^5}{\lambda^{14}X^4}, \tag{23}$$

$$\therefore\ a_5=-\frac{567}{163840}\frac{a^5}{\lambda^{16}X^4}\left[1-\cdots\right]. \tag{24}$$

Thus, we see that a alone is the only parameter specifying any master solution $\Phi(X)$ in such a way that a definite value of a allows to evaluate the values of $\Phi(X)$ for several very large values of X and followingly it determines the entire curve of $\Phi(X)$ which will meet finally the Φ-axis at a finite point Φ_0, Eq. (9), as shown in Fig. 2. The finite slope at this point $\dot{\Phi}_0$ makes possible to determine Φ_0 very accurately. In this way we have obtained for a sequence of values of a the corresponding sequence of master solutions $\Phi(X)$ and particularly the corresponding sequence of values of Φ_0 and $\dot{\Phi}_0$ as columned in Table I. The basic relation of Φ_0 versus a is illustrated in Fig. 3. The full table of values of $\Phi(X)$ over the whole range of X will be published in the Memoirs of the Faculty of Liberal Arts & Education, Kagawa University, Japan.

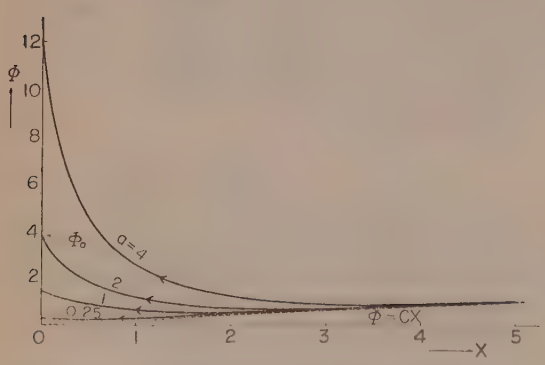

Fig. 2. Present method: inward integration of the master TF equation, Eq. (7).

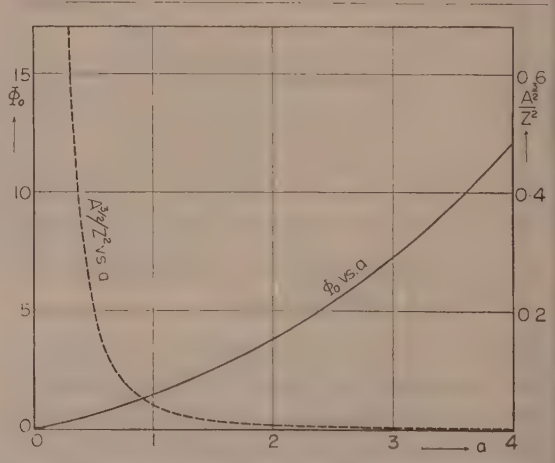

Fig. 3. Relations of Φ_0 and $A^{3/2}/Z^2$ versus a, cf. Eqs. (9), (27) and (16) respectively.

Table I. Values of Φ_0 and $\dot{\Phi}_0$ of the master solutions specified by a and values of $A^{3/2}/Z^2$ for the cases (Z, A) reducible to the master solutions.

a	Φ_0	$\dot{\Phi}_0$	$A^{3/2}/Z^2$
0.00	0	+ 0.18204	∞
0.25	0.28060	− 0.15976	0.98649
0.50	0.61546	− 0.72139	20505
0.75	1.0047	− 1.5028	076940
1.00	1.4466	− 2.5138	37115
1.25	1.9447	− 3.7792	20537
1.50	2.5001	− 5.3200	12427
1.75	3.1177	− 7.1703	$0^2$79910
2.00	3.8001	− 9.3600	53786
2.25	4.5487	−11.9159	37539
2.50	5.3695	−14.8829	26940
2.75	6.2702	−18.3157	19757
3.00	7.2497	−22.240	14778
3.25	8.3153	−26.713	11233
3.50	9.4714	−31.787	$0^3$86584
3.75	10.7256	−37.528	67519
4.00	12.0852	−44.010	53181

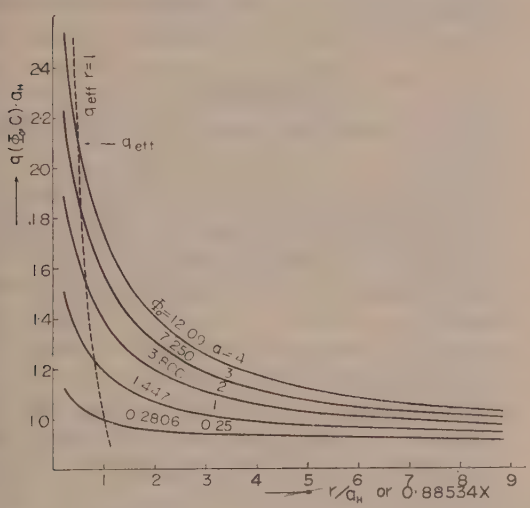

Fig. 4. Variation of the screening parameter $q_{(\Phi_0,C)}(X)$ of the screened Coulomb potential fitted to the master solutions by Eq. (29a). The full lines are the curves Eq. (29a) and the broken line is the definition curve $q_{\text{eff}}\cdot r=1$. The crossing points determine $q_{\text{eff}}(\Phi_0)$.

§ 3. Reduction of the TF Function for General Case to One of Master Solutions

Eqs. (2) to (4) are obviously invariant for the following scale transformation with a scale factor c

$$\left.\begin{aligned} \phi &\to (1/c)\phi\,, \\ x &\to c^{1/3}x\,, \\ A^{3/2} &\to (1/c)^2 A^{3/2}\,, \\ Z &\to (1/c)Z\,. \end{aligned}\right\} \tag{25}$$

Based on this, the master solution $\Phi(X)$ specified by a value of a or by the corresponding value of Φ_0 deduced from the Φ_0-a-relation (Table I and Fig. 3), i.e. the solution for the case $(Z=\Phi_0\,,\ A=C)$ can afford immediately the correct solution for the case (Z, A) satisfying Eqs. (2) to (4) by the following scale transformation with $c=\Phi_0/Z$

$$\left.\begin{aligned} (Z/\Phi_0)\Phi &= \phi\,, \\ (\Phi_0/Z)^{1/3}X &= x\,, \\ (Z/\Phi_0)^2 C^{3/2} &= A^{3/2}\,, \\ (Z/\Phi_0)\Phi_0 &= Z\,. \end{aligned}\right\} \tag{26}$$

Inversely, the correct solution $\phi(x; Z, A)$ for an arbitrary case (Z, A) can be derived in turn from the master solution $\Phi(X; \Phi_0\,, C)$ specified by the initial value

$$\Phi_0 = Z(C/A)^{3/4} = (Z^2/A^{3/2})^{1/2}C^{3/4} \tag{27}$$

or by the value of a associated to this value of Φ_0 due to the Φ_0-a-relation (Table I and Fig. 3). The needed master solution should be obtained by interpolation. The dependence of ϕ on x is given by the first two equations of Eq. (26), the scale factor Φ_0/Z being conveniently replaced by $(C/A)^{3/4}$.

It should be noted that all cases with identical value of $A^{3/2}/Z^2$, i.e. ratio of parameter of the TF equation to squared excess valency of impurity atom, can be reduced to the same master solution specified by the definite value of Φ_0 (or equivalently a) given by Eq. (27). Thus, a double sequence with two parameters Z and A can be simplified to a single sequence with one parameter Φ_0 (or equivalently a) only.

The values of $A^{3/2}/Z^2$ for general case (Z, A) (i.e. the value of $A^{3/2}$ of matrix metal for $Z=1$) reducible to each of master solutions obtained above are given in Table I. The dependence of $A^{3/2}/Z^2$ (or $A^{3/2}(Z=1)$) on a is illustrated in Fig. 3.

The practical need for existing metallic elements ($A^{3/2}=0.01\sim0.29$ and $Z=1\sim4$) can be sufficiently covered by such ranges of the values of Φ_0 and a as given in Table I and Fig. 3 ($\Phi_0=0\sim12$ and $a=0\sim4$).

§ 4. Comparison of the Screened Coulomb Potential with the Master Solution

As Alfred-March[5] (their Fig. 1) as well as Fujiwara[4] (his Fig. 2) pointed out, the screened Coulomb potential (Mott[1] potential) normalized to $V(\infty)=0$

$$V(r)=(Ze/r)e^{qr} \tag{28}$$

or correspondingly

$$\phi(x)=Ax+Ze^{-q\mu_0 x} \tag{28a}$$

cannot fit over whole range the exact solution. It is also clear from that $Y(X)$, Eqs. (10) and (14), cannot be represented by single exponential term. The degree of approximation of Eq. (28) would be measured by the dependence of the shielding parameter q on x defined by Eq. (28a), $\phi(x)$ being regarded as the exact solution obtained numerically. Then, inserting Eq. (26) into Eq. (28a) we can reduce the general case (Z, A) to the master case (Φ_0, C) as

$$q_{(Z,A)}(x)=q_{(\Phi_0,C)}(X)\cdot(A/C)^{1/4} \tag{29}$$

with

$$q_{(\Phi_0,C)}(X)=[\ln \Phi_0-\ln(\Phi-CX)]/\mu_0 X\,. \tag{29a}$$

Therefore it is sufficient if we investigate the dependence of $q_{(\Phi_0,C)}$ on X as given in Fig. 4. With Eq. (13), $q_{(\Phi_0,C)}$ converges asymptotically as

$$q_{(\Phi_0,C)}(X\to\infty)\approx\frac{1}{\mu_0}\left(\lambda+\frac{\ln(\Phi_0/a)}{X}\right)\to\frac{\lambda}{\mu_0} \tag{30}$$

which establishes that $q_{(\Phi_0,C)}$ increases monotonically with excess valency Φ_0 because Φ_0/a increases monotonically with Φ_0 as seen from Fig. 3. From Fig. 4 the constant shielding parameter seems to be valid only in the range distant enough from the impurity atom.

Alfred-March[5] used rather the effective shielding parameter q_{eff} which corresponds to the crossing point of the curve Eq. (29a) given above and the definition curve $q_{\text{eff}}\cdot r=1$. It is noticeable that

$$q_{\text{eff}}>q(\infty)(=\lambda/\mu_0) \tag{31}$$

and q_{eff} increases with excess valency Φ_0 in accordance with the q_{eff}-Z-curve for copper given in Alfred-March's Fig. 2. The values $q_{\text{eff}}(\Phi_0)$ determined from Fig. 4 were ascertained to lie just on their q_{eff}-Z-curve for copper, $q_{\text{eff}}(\Phi_0)$ and Φ_0 being multiplied with $(A_{\text{Cu}}/C)^{1/4}$ and $(A_{\text{Cu}}/C)^{3/4}$ respectively. Conversely, their q_{eff}-Z-curve for copper can be transformed into the one for matrix metal A, the ordinate $q_{\text{eff, Cu}}$ and the abscissa Z being multiplied in turn with $(A/A_{\text{Cu}})^{1/4}$ and $(A/A_{\text{Cu}})^{3/4}$ respectively.

Acknowledgements

The authors wish to express their sincere thanks to Professor T. Satō of Kobe University for his valuable mathematical discussion. The present work was supported by the Grant in Aid for Fundamental Researches administrated by the Japanese Ministry of Education given to the Research Group for the Study of Molecular Structure.

References

1) N. F. Mott: Proc. Camb. Phil. Soc. **32** (1936) 281.
2) J. Friedel: Adv. in Phys. **3** (1954) 446.
3) A. Sugiyama, T. Inoue and M. Inagaki: presented at the Osaka (1956) and Tokyo (1957) meetings of the Physical Society of Japan.
4) H. Fujiwara: J. Phys. Soc. Japan **10** (1955) 339, 727.
5) L. C. R. Alfred and N. H. March: Phil. Mag. **46** (1955) 759.
6) S. Kobayashi, T. Matsukuma, S. Nagai and K. Umeda: J. Phys. Soc. Japan **10** (1955) 759; K. Umeda: J. Fac. of Sci., Hokkaido Univ., Japan Ser. III **5** (1942) 171

JOURNAL OF THE PHYSICAL SOCIETY OF JAPAN Vol. 13, No. 2, FEBRUARY, 1958

Defects in Ionic Crystals
I. Improvement of the Method of Mott and Littleton and its Applications to Simple Defects

By Tatsumi KUROSAWA

The Institute for Solid State Physics, University of Tokyo

(Received October 30, 1957)

An improvement of the method of Mott and Littleton is proposed, and its applications to simple defects are treated. The formation energies of Schottky defects in LiF, NaCl, NaBr, KCl, KBr, RbBr and AgCl crystals, and that of a Frenkel defect in AgCl crystal are calculated. More complicated defects will be treated in forthcoming papers.

§ 1. Introduction

Hitherto, the calculations of the formation energy of defects in ionic crystals have been carried out by the method of Mott and Littleton[1]. Although this method is very ingenious, it is not such a formulation that considers the total energy of the lattice to be a function of the displacements and the electronic polarizations of ions. If such a formulation were developed, it might have two merits. (1) Since the total energy takes its minimum value when the displacements and the electronic polarizations of ions are in equilibrium, the calculated energy may be a good approximation even when the values of the displacements or the poralizations are not exact. This fact would prove of particular value in the case of complicated defects. (2) While the method of Mott and Littleton is applicable only when the lattice around defect is in equilibrium, such a limitation does not exist in the above mentioned formulation.

Such an attempt may have also practical importance, because knowledge about the interionic potentials and the dielectric properties of ionic crystals has been increased, and experimental data on the formation energy of defects have also accumulated, since the work of Mott and Littleton.

In this paper, we attempt to develop such a formulation, that is, to express the energy approximately as a function of displacements and electronic polarizations of the ions. Here we apply the method to evaluate the formation energy of simple defects. More complicated defects in equilibrium, and such cases as the lattice around a defect not being in equilibrium, will be treated in forthcoming papers.

§ 2. The Improvement of the Method of Mott and Littleton

We try to express the energy as a function of the displacements and the electronic polarizations of ions around a defect. The exact description of the energy for an arbitrary configuration of ions is prohibitively complicated, so that we are obliged to introduce an approximate expression. For this purpose, we divide the crystal into two regions, i.e., (I) the region near the defect, and (II) the outer region. We write the displacements and the polarizations of the ions in the region (I) symbolically as $X_1, X_2, \cdots, X_j, \cdots$, and those in the region (II) as $x_1, x_2, \cdots, x_\mu, \cdots$. We frequently write them X and x for simplicity. We take as the origins of X and x the state in which the ions form an undeformed lattice and the electronic polarizations are zero.

When the defect is absent, the energy change due to the deformation of the lattice and the ions is formally

$$E(X, x)=A(X)+\sum_{\mu} f_\mu(X)x_\mu+\frac{1}{2}\sum_{\mu,\nu} a_{\mu\nu}x_\mu x_\nu\,, \tag{2.1}$$

where we assume that x_μ's are all small and only the terms of the lowest order are retained. When the defect is present, the following terms must be added

$$\phi_0+\sum_{\mu}\phi_\mu x_\mu+\Phi(X)\,. \tag{2.2}$$

These terms represent the energy necessary to create a defect with the fixed configuration (X, x). For instance, this is the negative of

the interaction energy between an ion which is to be removed from the lattice to infinity and its surrounding ions. The first two terms come from the region (II), and the last term from (I). If the forces between ions are the two-body type, ϕ_μ is independent of X; we make this assumption. Now, the total energy is

$$W(X, x)=\frac{1}{2}\sum_{\mu,\nu} a_{\mu\nu}x_\mu x_\nu+\sum_\mu f_\mu(X)x_\mu+A(X)+\phi_0+\sum_\mu \phi_\mu x_\mu+\Phi(X)\,. \tag{2.3}$$

Since it is prohibitively difficult to compute the energy for an arbitrarily given value of X and x, we substitute for this expression the following approximation.

Let us consider the equilibrium state of the defect, which is given by the following Eqs.:

$$\left(\frac{\partial W}{\partial x_\mu}\right)_{X=X^0,\,x=x^0}=\sum_\nu a_{\mu\nu}x_\nu{}^0+\phi_\mu+f_\mu(X^0)=0 \quad \text{(for all } \mu)\,, \tag{2.4}$$

and

$$\left(\frac{\partial W}{\partial X_j}\right)_{X=X^0,\,x=x^0}=0 \quad \text{(for all } j)\,. \tag{2.5}$$

If we put x^0 into Eq. (2.3), in virtue of Eq. (2.4), we have

$$W(X, x^0)=\phi_0+\sum_\mu\left\{f_\mu(X)-\frac{1}{2}f_\mu(X^0)+\frac{1}{2}\phi_\mu\right\}x_\mu{}^0+A(X)+\Phi(X)\,. \tag{2.6}$$

If we take the region (I) sufficiently large, $x_\mu{}^0$'s may rapidly approach the values which are determined by the continuous model of Mott and Littleton. Practically we have to choose the region (I), such that the values determined by the continuous model are a comparatively good approximation of x^0 and the calculation of $f_\mu(X)$, $A(X)$ and $\Phi(X)$ of Eq. (2.6) for a given value of X is not too cumbersome. If we minimize $W(X, x^0)$ with respect to X, we obtain the energy of the defect in the equilibrium state, so far as $x_\mu{}^0$'s are exactly given.

On the other hand, when the defect is complex and the values of X^0 and x^0 are known only approximately, we are obliged to substitute these approximate values $\overline{X}^0=X^0+\delta X$ and $\overline{x}^0=x^0+\delta x$ for X, X^0 and x^0 in Eq. (2.6). This procedure is equivalent to substituting $\overline{X}^0$ and $\overline{x}^0$ in the following expression:

$$\overline{W}(X, x)=\phi_0+\frac{1}{2}\sum_\mu\{\phi_\mu+f_\mu(X)\}x_\mu+A(X)+\Phi(X)\,. \tag{2.7}$$

And the result of this substitution is:

$$\overline{W}(\overline{X}^0, x^0)=W(X^0, x^0)+\frac{1}{2}\sum_\mu\{f_\mu(X^0)+\phi_\mu\}\delta x_\mu-\frac{1}{2}\sum_{\mu,j}\frac{\partial f_\mu(X^0)}{\partial X_j}x_\mu{}^0\delta X_j+(\text{the second order terms of } \delta x \text{ and } \delta X)\,, \tag{2.8}$$

where we used Eq. (2.5). The linear terms of δx and δX can be transformed into

$$\frac{1}{2}\sum_\mu\{f_\mu(X^0)+\phi_\mu\}\left[\delta x_\mu-\sum_j\left\{\frac{\partial x_\mu(X)}{\partial X_j}\right\}_{X=X^0}\delta X_j\right]\,, \tag{2.9}$$

where $x_\mu(X)$ is given by

$$\sum_\nu a_{\mu\nu}x_\nu(X)+f_\mu(X)+\phi_\mu=0\,, \tag{2.10}$$

that is, the equilibrium value of x_μ for an X. Compared with the present technique, the method of Mott and Littleton is nearly equivalent to using the following expression instead of $\overline{W}(X, x)$:

$$\overline{W}_{ML}(X, x)=\phi_0+\Phi(0)+\frac{1}{2}\sum_\mu \phi_\mu x_\mu+\frac{1}{2}\{\Phi(X)-\Phi(0)\}\,. \tag{2.11}$$

And the result of the substitution, $\overline{X}^0$ for X and $\overline{x}^0$ for x, is

$$\overline{W}_{ML}(\overline{X}^0, \overline{x}^0)\simeq W(X^0, x^0)+\frac{1}{2}\sum_\mu \phi_\mu\delta x_\mu+\frac{1}{2}\sum_j\left(\frac{\partial\Phi}{\partial X_j}\right)_{X=X^0}\delta X_j+(\text{the second order terms of } \delta x \text{ and } \delta X)\,. \tag{2.12*}$$

The main error comes from the term $(\partial\Phi/\partial X)\delta X$, since both $\partial\Phi/\partial X$ and δX are large. On the other hand, we can expect that the coefficient of δX in the expression (2.9) may be much smaller than $\partial\Phi/\partial X$ comparing their physical meanings, especially when the region (I) is large. For this reason, we use $\overline{W}(X, x)$ for $\overline{W}_{ML}(X, x)$. In the case of the complicated defects for which the exact determination of X^0 is cumbersome, our method may be useful.

As the simplest example, we calculate the energy of a point charge e located on a lattice point (000) of a fictitious crystal; simple cubic lattice, κ (dielectric constant)$=4$ and the atoms being fixed at their equilibrium posi-

* Generally $\overline{W}_{ML}(X^0, x^0)\neq W(X^0, x^0)$ by the reason which is explained at the end of this chapter.

tions. This example was treated by Mott and Littleton in detail. We consider the six (100) ions as the region (I), and the others as (II). In this case $x_\mu{}^0$ means the dipole moment of the μth atom. According to Mott and Littleton, we take $x_\mu{}^0$ as $(ea^3/4\pi r^2)(1-1/\kappa)$, where r is the distance of the μth atom from the origin and a is the lattice constant. Then, $\sum_\mu \phi_\mu x_\mu{}^0$ is the potential at the origin created by these dipoles:

$$\frac{1}{2}\sum_\mu \phi_\mu x_\mu{}^0 = -\frac{1}{2}\sum_{r>(100)} \frac{a^4}{r^4} = -5{,}266\ , \quad (2.13)$$

where the unit of energy is $(e^2/4\pi a)(1-1/\kappa)$. $\Phi(0)$ and ϕ_0 are trivial and we neglect them. $\sum_\mu f_\mu(X)x_\mu{}^0$ is the interaction energy between the electric field at (100) created by the dipoles in the region (II) and the dipoles on the (100) atoms. The former is: $-(2.353e/4\pi a^2)\times(1-1/\kappa)$, and the latter is; $m=(ea/4\pi)\times(1-1/\kappa)X$. Thus we have:

$$\sum_\mu f_\mu(X)x_\mu{}^0 - \frac{1}{2}\sum_\mu f_\mu(X^0)x_\mu{}^0 = 0.843X - 0.421X^0\ . \quad (2.14)$$

Next, $A(X)$ is the sum of the polarization energy of the (100) atoms and the interaction energy between the dipoles on (100), that is, $6(m^2/2\alpha + 2.371m^2/2a^3)$, where α is the polarizability; or in the above unit it becomes:

$$A(X) = 1.500X^2 + 0.425X^2\ . \quad (2.15)$$

Finally, $\Phi(X)-\Phi(0)$ is the interaction energy between the extra point charge at (000) and the (100) dipoles

$$\Phi(X)-\Phi(0) = -6X\ . \quad (2.16)$$

Then, we have:

$$W(X, x^0) = 1.925X^2 - 5.157X - 5.266 - 0.421X^0\ . \quad (2.17)$$

If we determine X^0 from the condition

$$\left\{\frac{\partial W(X, x^0)}{\partial X}\right\}_{X=X^0} = 3.850X^0 - 5.157 = 0\ , \quad (2.18)$$

we obtain

$$X^0 = 1.340\ .$$

Substituting this value into Eq. (2.17), we obtain

$$W(X^0, x^0) = -9.29\ .$$

This procedure gives exactly the same value as that of the Mott-Littleton's first approximation.

Next, if we regard X^0 as unity, which corresponds to the Mott-Littleton's 0th approximation, and substitute this into $\overline{W}(X, x^0)$, we have

$$\overline{W}(1, x^0) = -8.92\ .$$

The 0th approximation of Mott and Littleton gives, however, $-8{,}27$, and the most exact value (the fourth approximation of their computation) is $-9{,}25$. In Fig. 1, we show

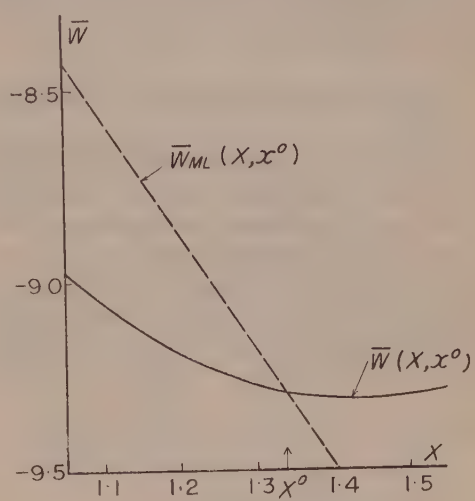

Fig. 1. $\overline{W}(X, x^0)$ and $\overline{W}_{ML}(X, x^0)$.

$\overline{W}(X, x^0)$ (in the solid line) and $\overline{W}_{ML}(X, x^0) = -3X - 5.266$ (in the broken line), for the values of X near X^0. Evidently our formulation gives much better values as compared with the energy form due to Mott and Littleton, when X^0 is not exact.

Moreover, if $A(X)$ has terms higher than X^2, or $f_\mu(X)$ and $\Phi(X)$ have those higher than X, and in fact this is the real case, the method of Mott and Littleton is not very accurate, that is, such a simple procedure in which we

Table I. Comparison of the present method and the method of Mott and Littleton using the same repulsive energy and polarizabilities.

	Mott-Littleton	From Eq. (2.6)
W_+	4,62 ev	4,54 ev
W_-	5,18	5,05
W_L	7,94	7,94
W_S	1,86	1,65

W_+; Work necessary to remove a positive ion.
W_-; Work necessary to remove a negative ion.
W_L; Lattice energy.
W_S; Formation energy of Schottky defect.

regard the deformation energy of the surrounding medium as one half of the potential energy at the center due to the surrounding polarization, is rather crude. For instance, we recalculated the energy of the Schottky defect in NaCl by Eq. (2.6) with the same repulsive energy and polarizabilities as Mott and Littleton had used. The results are given in Table I. The differences come from the above mentioned reason, but are rather small in this simple example.

§ 3. The Formation Energy of a Schottky Defect

The interionic potentials, the polarizabilities and the sohrt range effects of the electronic polarizations are given in the Appendix. We take the six (100) ions as the region (I), and write the displacements of these ions $a\xi$ and the electronic polarizations $ea\eta$. Each term of Eq. (2.6) for NaCl type crystal with lattice constant a is as follows

$$\begin{aligned} A(X)=&3\left(\frac{1}{2}+2\sqrt{2}+\frac{1}{2+2\xi}+\frac{2\sqrt{2}}{1+\xi}-\frac{2}{2+\xi}\right.\\ &\left.-\frac{8}{\sqrt{2+2\xi+\xi^2}}\right)\frac{e^2}{a}+6\eta f(\xi)\frac{e^2}{a}\\ &+\frac{7.113}{(1+\xi)^3}\eta^2\frac{e^2}{a}+3\eta^2\left(\frac{a^3}{\alpha}\right)\frac{e^2}{a}\\ &+6[u(a+a\xi)+u(a-a\xi)+4u(a\sqrt{1+\xi^2})-6u(a)]\\ &-21.5\xi^4\frac{e^2}{a}\pm 6ea\eta A_{\mp}e^{-a/\rho}(e^{(a/\rho)\xi}-e^{-(a/\rho)\xi}-4\xi)\,, \end{aligned} \tag{3.1}$$

and

$$\begin{aligned} f(\xi)=&4\left\{\frac{1+\xi}{(2+2\xi+\xi^2)^{3/2}}-\frac{1}{2\sqrt{2}\,(1+\xi)^2}\right\}\\ &+\left\{\frac{1}{(2+\xi)^2}-\frac{1}{(2+2\xi)^2}\right\}, \end{aligned} \tag{3.2}$$

where the first three terms in Eq. (3.1) represent the change in the coulomb interaction energy due to the displacements and the polarizations of the (100) ions, the fourth term is the deformation energy of the ions, α is the polarizability of the (100) ion. The fifth is the change in the short range potential, $u(r)$ being the short range potential between different ions and we have neglected those between ions of like sign. The sixth term comes from the crystalline field. The last term represents the short range effect of electronic polarizations, which is explained in the Appendix, where $+A_-$ stands for the case that the (100) ions are negative and vice versa.

The energy required to remove a (000) ion from the lattice to infinity with the fixed configuration $X=(\xi,\eta)$ and $x=0$, is given by

$$\begin{aligned} \phi_0+\Phi(X)=&\frac{\alpha_M e^2}{a}-\frac{6\xi}{1+\xi}\frac{e^2}{a}-\frac{6\eta}{(1+\xi)^2}\frac{e^2}{a}\\ &-6u(a+a\xi)\pm 6ea\eta A_{\mp}e^{-(a/\rho)\cdot(1+\xi)}\,, \end{aligned} \tag{3.3}$$

where the first three terms are the coulomb energy (and α_M is the Medelung constant).

Finally,

$$\begin{aligned} &\sum_{\mu}\left\{\frac{1}{2}\phi_\mu+f_\mu(X)-\frac{1}{2}f_\mu(X^0)\right\}x_\mu{}^0\\ &=-\frac{1}{2}(4.198M_{\mp}+6.335M_{\pm})\frac{e^2}{a}\\ &\quad+6(0.388M_{\mp}+1.965M_{\pm})\left(\xi+\eta-\frac{\xi_0}{2}-\frac{\eta_0}{2}\right)\frac{e^2}{a}\\ &\quad+6M_d a\left[\frac{u'(a)-u'(a-a\xi)}{4}\right.\\ &\quad\left.+\sqrt{2}\left\{u'(a)-\frac{1-\xi}{\sqrt{1+\xi^2}}u'(a\sqrt{1+\xi^2})\right\}\right]\\ &\quad-3M_d a\left[\frac{u'(a)-u'(a-a\xi_0)}{4}\right.\\ &\quad\left.+\sqrt{2}\left\{u'(a)-\frac{1-\xi_0}{\sqrt{1+\xi_0{}^2}}u'(a\sqrt{1+\xi_0{}^2})\right\}\right], \end{aligned} \tag{3.4}$$

where M_+, M_- and M_d have been introduced by Mott and Littleton, and are explained in the Appendix. When the (100) ions are negative, we take the upper part of the double suffix, and vice versa. The first term comes from the polarization in the region (II), and the last three terms are due to the interaction between the region (I) and (II). The notations ξ_0 and η_0 mean the equilibrium values of ξ and η respectively. We have neglected in Eq. (3.4) the terms which involve A_+ or A_-, because they are very small.

We sum up these three Eqs. (3.1), (3.3) and (3.4), differentiate with respect to ξ and η, and put the results equal to 0:

$$\frac{\partial W(\xi,\eta)}{\partial\xi}=\frac{\partial W(\xi,\eta)}{\partial\eta}=0\,. \tag{3.5}$$

These equations give ξ_0 and η_0, and this procedure is formally equivalent to that of Mott and Littleton. The values of ξ_0 and η_0 are given in Table II.

If we substitute these ξ_0 and η_0 into Eq. (2.6), we obtain the energy required to remove

an ion from the lattice to the infinity. The values are listed in Table III, and the formation energy of the Schottky defect in several

Table II.

	+ ion is removed		− ion is removed	
	ξ_0	η_0	ξ_0	η_0
LiF	0.075	0.035	0.091	0.003
NaCl	0.049	0.049	0.073	0.008
NaBr	0.043	0.060	0.072	0.007
KCl	0.049	0.036	0.062	0.023
KBr	0.042	0.046	0.061	0.020
RbBr	0.044	0.040	0.059	0.028
AgCl	0.036	0.052	0.050	0.058

Table III. Energy of Schottky defect (in ev).

	W_+	W_-	W_L	W_S (theory)	W_S (experiment)
LiF	6.67	6.76	11.09	2.34	2.7[3]
NaCl	5.03	5.11	7.95	2.20	2.02[4]
〃 (M.L.)	4.62	5.18	7.94	1.86	
NaBr	4.71	4.83	7.54	2.01	
KCl	4.77	4.68	7.20	2.25	2.4[5]
〃 (M.L.)	4.47	4.79	7.18	2.08	2.1[6]
KBr	4.53	4.49	6.88	2.14	
〃 (M.L.)	4.23	4.60	6.91	1.92	
RbBr	4.46	4.36	6.72	2.10	
AgCl	5.58	5.31	8.92	1.98	
〃 (A)	5.50	5.35	8.89	1.96	

crystals is also shown. For the purpose of comparison, we show the experimental values, the computed values due to Mott and Littleton (denoted by M.L.) and in our previous paper[2] (denoted by A). Generally, the present values are larger than those of Mott and Littleton, mainly because of the presence of A_+ and A_-. For the positive (negative) ion vacancy, $A_-(A_+)$ works to decrease (increase) ξ_0 and η_0 and to increase (decrease) $W_+(W_-)$, and the effect of A_- is generally larger than that of A_+. It may be expected that our values are somewhat better than those of M.L. and A, because of the more careful determination of interionic interactions and of the more exact formulation of the energy. The adoption of the ionic model, however, will limit the accuracy.

§4. The Formation Energy of a Frenkel Defect in AgCl

The formation energy of the Frenkel defect in AgCl crystal has been calculated in paper A. The main differences between the present calculation and the previous one are the taking account of A_+ and A_-, and the adoption of a new formulation for the energy. Moreover, because of the importance of the van der Waals potential Dr^{-6} between the Ag^+ ions, we calculate the energy for three values of D, that is

$$Da^{-6}=0,\ -0.100 \text{ and } -0.200\times10^{-12}\,\text{erg}\,.$$

On the other hand, according to Mayer's estimation,

$$Da^{-6}=-0.145\times10^{-12}\,\text{erg}\,.$$

As $\overline{W}(X)$ is only slightly dependent on X near X^0, we calculated the energy for three values of D with the same X^0, which is the equilibrium position of ions when Da^{-6} is $-0{,}100\times10^{-12}$ erg.

The results are in Table IV. The recalcu-

Table IV. Energy of Frenkel defect (in ev).

	I	II	III	A
W_+	5.58	5.58	5.58	5.50
W_I	−2.35	−2.72	−3.09	−3.66
W_F	3.23	2.86	2.49	1.83

I) $Da^{-6}=0$.
II) $Da^{-6}=-0{,}100\times10^{-12}$ erg.
III) $Da^{-6}=-0{,}200\times10^{-12}$ erg.
W_I; Work necessary to bring a positive ion into the interstitial site.
W_F; Formation energy of Frenkel defect.

lated energy is again larger than that of A. It is to be noted, that the Ag^+–Ag^+ potential has little effect on the properties of the perfect crystal, and then does not affect the determination of the short range potential treated in the Appendix, but has a large effect on the energy of a Frenkel defect.

The observed value of the formation energy of lattice defects in AgCl seems to be 1,0∼1,3 ev. In the case of the alkali halides the calculated formation energies of Schottky defects are reasonable, so that we may expect the same to hold true for AgCl. On the other hand, for the Frenkel defect, the calculated energy may have large error. That is, our interaction energies which are determined in the Appendix may not be reliable for such

small distances as we meet in the case of the Frenkel defect, and the Ag^+–Ag^+ potential can not be determined either empirically or theoretically with reliable precision. Moreover the energy difference between the 5s level of the interstitial Ag^+ ion and the 3p level of the nearest Cl^- ion is small and a sort of covalency may be expected. So that we may conclude that the predominant lattice defect in AgCl at low temperatures should be of the Frenkel type as concluded in A.

The author is greatly indebted to Professor J. Yamashita for his helpful discussions.

Appendix The Determination of the Interionic Potentials and others

For the determination of the interionic potentials, the polarizabilities of ions and the short range effects of the electronic polarizations, we use the data which have been alalysed in § 5 and § 6 of A. In this analysis, we have assumed the energy change of a polarized crystal as follows

$$\Delta E = a_+ p_+^2 + a_- p_-^2 + c p_x^2 - \frac{1}{2}\frac{4\pi}{3v}(p_+ + p_- + p_x)^2 + a_{+-} p_+ p_- + b_+ p_+ p_x + b_- p_- p_x \,, \quad \text{(per ion pair)} \tag{A.1}$$

where p_x is the polarization due to the displacement of ions, being equal to ex, and x is the relative displacement of ions. p_+ and p_- is the electronic polarization of a positive ion and a negative ion respectively and v is $2a^3$. The fourth term is the so-called Lorentz correction term, and the last three terms are due to the short range interaction between the polarizations.

From the experimental data, i.e., high frequency dielectric constant κ_0, static dielectric constant κ and infra-red absorption frequency ω_t, we have estimated the above coefficients. Using these results, we determine the values necessary for the calculations in § 3 and § 4 in the following manner.

a) Electronic polarizability

In paper A, we have suggested that it is reasonable to take $a_{+-} \simeq 0$, and a_+ and a_- are only dependent on the ion itself but independent on its partner. This is apparently equivalent to the additivity rule of the crystal polarizability, which had been suggested by Shockley and others[7]. The polarizability α of an ion is given by

$$\alpha_+ = \frac{1}{2a_+} \quad \text{and} \quad \alpha_- = \frac{1}{2a_-} \,, \tag{A.2}$$

and the values of α's are listed in Table V.

Table V. Polarizability (10^{-24} cm^3).

Ions	α	Ions	α
Li^+	0.05	Ag^+	2.14
Na^+	0.28	F^-	0.86
K^+	1.13	Cl^-	2.92
Rb^+	1.79	Br^-	4.12

b) Interionic potentials

The procedure used to determine these potentials is similar to that in § 7 of A. We neglect the short range interaction between ions of like sign. We assume the interaction form as

$$u(r) = Ae^{-r/\rho} \quad \text{for Alkali Halides} \,, \tag{A.3}$$

and

$$u(r) = Ae^{-r/\rho} + Cr^{-6} \quad \text{for AgCl} \,. \tag{A.4}$$

For the determination of A, ρ and C, we have four data; lattice energy W_L, lattice constant a, compressibility χ and c in Eq. (A.1). Assuming appropriate probable errors for these data, we determine A and ρ by the least square method. For AgCl, we have assumed three values of C, i.e., $Ca^{-6} = -0.14$, -0.18 and -0.27×10^{-12} erg, and determined A and ρ for each case. The sum of two terms is almost the same in three cases for $0.8a \leq r \leq 1.1a$, although each term differs case by case. Thus, as pointed out in paper A, the separation of the interionic potential into the repulsive energy and the van der Waals energy has no definite meaning, at least empirically. In the practical calculation, we used the last C. In Table VI, we listed A, ρ and C determined in such a way, and the data which are used (denoted by Exp.) and are calculated using the above-determined potential (denoted by Cal.) too. We can determine two parameters A and ρ from four data consistently, although the consistency is somewhat poor for AgCl. This fact seems to be an indirect confirmation of our assumptions.

c) The short range effects of the electronic polarization

Let us take a pair of ions, the interaction energy between them is $-e^2/r + u(r)$, when the polarization is absent. When the ions polarize, the interaction energy changes, and

Table VI. Interionic potential

	LiF	NaCl	NaBr	KCl	KBr	RbBr	AgCl	Unit
$Ae^{-a/\rho}$	0.376	0.267	0.247	0.215	0.204	0.169	0.365	10^{-12} erg
a/ρ	7.86	8.77	8.92	9.93	10.05	11.16	10.85	
Ca^{-6}							−0.273	10^{-12} erg
W_L (Exp.)	256.4*	182.8	173.3	164.4	156.2	153.3	205.7	Kcal/mole
W_L (Cal.)	255.7	183.3	173.8	166.0	158.6	154.8	205.5	〃
a (Exp.)	2.01	2.81	2.97	3.14	3.29	3.42	2.77	10^{-8} cm
a (Cal.)	1.99	2.83	2.99	3.17	3.32	3.44	2.75	〃
χ (Exp.)	1.54	4.20	5.08	5.63	6.70	7.94	2.26	10^{-12} cm³/erg
χ (Cal.)	1.48	4.25	5.18	5.52	6.41	7.42	2.58	〃
a^2e^2c (Exp.)	16.8	17.0	16.0	18.6	18.2	18.6	22.0	10^{-12} erg
a^2e^2c (Cal.)	17.3	15.9	15.2	16.9	16.5	17.3	26.6	〃
M_+	0.059	0.051	0.046	0.059	0.054	0.060	0.078	
M_-	0.083	0.080	0.086	0.066	0.072	0.067	0.068	
M_d	0.056	0.045	0.041	0.040	0.038	0.036	0.034	

* Estimated from the recent data on the affinity by Pritchard[8], 83,5±2 Kcal/mole.

the change consists of that of the coulomb energy and of the short range energy. The latter may be written generally in the following form:

$$p_+ \cos\vartheta_+ B_+(r) + p_- \cos\vartheta_- B_-(r) .$$

where $\vartheta_+(\vartheta_-)$ is the angle between $\vec{p}_+(\vec{p}_-)$ and the vector from the positive (negative) ion to the negative (positive) ion. Since $B_+(r)$ and $B_-(r)$ result from the overlap between ions, we may assume a form

$$B_+(r) = -A_+ e^{-r/\rho} \tag{A.5}$$

and

$$B_-(r) = -A_- e^{-r/\rho} , \tag{A.6}$$

and the same ρ as in $u(r)$. From these, we can derive

$$eb_+ = -A_+ e^{-a/\rho}\left(\frac{2}{\rho} - \frac{4}{a}\right)$$

and

$$eb_- = A_- e^{-a/\rho}\left(\frac{2}{\rho} - \frac{4}{a}\right) . \tag{A.7}$$

Moreover, we have suggested the following relations in A,

$$b_+ \simeq -0.3c \qquad b_- \simeq 0.9c . \tag{A.8}$$

We can determine A_+ and A_-, from Eqs. (A.7) and (A.8).

d) M_+, M_- and M_d

The polarization P and the electric field F are connected by a relation

$$P = \frac{1}{4\pi}(\kappa - 1)F . \tag{A.9}$$

The dipole moment per ion pair is

$$p = vP = \frac{1}{4\pi}(\kappa - 1)vF , \tag{A.10}$$

p consists of three parts: the electronic dipole moment of the negative ion p_-, that of the positive ion p_+ and the dipole moment due to the displacement p_x. According to paper A, they are given by

$$p_x = \frac{3}{4\pi}\frac{\kappa - \kappa_0}{\kappa_0 + 2}\frac{e}{e^*(0)}vF , \tag{A.11}$$

$$p_+ = \left\{\frac{v}{4\pi}(\kappa - 1)F - p_x\right\}\frac{\alpha_+}{\alpha_+ + \alpha_-} - \frac{b_+ - b_-}{2(a_+ + a_-)}p_x \tag{A.12}$$

and

$$p_- = \left\{\frac{v}{4\pi}(\kappa - 1)F - p_x\right\}\frac{\alpha_-}{\alpha_+ + \alpha_-} + \frac{b_+ - b_-}{2(a_+ + a_-)}p_x , \tag{A.13}$$

where

$$e^*(0)^2 = \frac{3v}{4\pi}\frac{3\mu\omega_t^2}{(\kappa_0 + 2)^2}(\kappa - \kappa_0) , \tag{A.14}$$

and μ is the reduced mass of ions.

Due to the definition of Mott and Littleton, M_+, M_- and M_d are given by

$$M_\pm = \frac{1}{2\pi}\left(1 - \frac{1}{\kappa}\right)\frac{p_\pm + \frac{p_x}{2}}{p_+ + p_- + p_x} \tag{A.15}$$

and

$$M_d = \frac{1}{4\pi}\left(1-\frac{1}{\kappa}\right)\frac{p_x}{p_+ + p_- + p_x}. \quad \text{(A.16)}$$

The values of M_+, M_- and M_d are shown in Table VI.

References

1) N. F. Mott and M. J. Littleton: Trans. Faraday Soc. **34** (1938) 485.
2) J. Yamashita and T. Kurosawa: J. Phys. Soc. Japan **10** (1955) 610.
3) I. Haven: Rec. Trav. Chim. **69** (1950) 1259.
4) H. W. Etzel and R. J. Maurer: J. Chem. Phys. **18** (1950) 1003.
5) H. Kelting and H. Witt: Z. Physik **126** (1949) 697.
6) C. Wagner and P. Hantelmann: J. Chem. Phys. **18** (1950) 72.
7) J. R. Tessman, A. H. Kahn and W. Shockley: Phys. Rev. **92** (1953) 890.
8) H. O. Pritchard: Chem. Rev. **52** (1953) 529.

JOURNAL OF THE PHYSICAL SOCIETY OF JAPAN Vol. 13, No. 2, FEBRUARY, 1958

On Solvent Effects in Dipole Moment Determinations*

By Kisaburo SHOGENJI**

Faculty of Engineering, Nagoya University, Nagoya

(Received November 6, 1957)

A new theory of the solvent effects is presented in this paper, in which the solute molecule is assumed to have a spheroidal form and have an electric dipole moment directed in the axis of rotation at its centre. The cavity field and the reaction field, etc. are calculated as the functions of the shape of the solute molecule and the dielectric constant of the solvent, and the molecular polarization is also calculated. Theoretical curve, expressing the molecular polarization *vs.* the dielectric constant of the solvent, obtained from this theory shows a fairly good agreement with the experimental results. The curve shows that the molecular polarization has a maximum value for a small dielectric constant of the solvent and its value decreases for larger dielectric constants.

§ 1. Introduction

In measuring the dipole moment of a molecule by using its solution, the solvent effects must be taken into consideration. There are many theories for the solvent effects. Higasi calculated an additive moment, which was due to the polarization of the medium surrounding the molecule: this polarization was induced by the dipolar field of the molecule. Ross and Sack,[2] on the other hand, calculated in detail the effects of the electric field acting on the molecule, which depended upon the shape of the molecule and the dielectric constant of the solvent. In these theories the shape of the molecule and the dielectric constant of the solvent determine the magnitude of the solvent effects.

Here we consider carefully the effects of the induced moment and of the electric fields acting on the molecule. As for the electric fields we calculate cavity field, reaction field, etc. for a spheroidal molecule as Onsager[3] did for a spherical molecule, and we adopt Higasi's calculation[1] for the induced moment. After the calculation of the interaction energy between the dipole and the fields, the molecular polarization is obtained. Thus the solvent effects are calculated as the functions of the shape of the dipolar molecule and of the dielectric constant of the solvent.

The assumptions, on the basis of which this calculation is made, are as follows: (i) The dissolved dipolar molecule is of spheroidal shape, whose semi-axes are a and b respectively, the former being the axis of revolution. (ii) The molecule has a point dipole moment at the centre of it, and the direction of the dipole is the same as the axis of revolu-

* This paper was published in Japanese: Busseiron Kenkyu No. 70 (1954), 1.

** Present address: Hitachi Central Research Laboratory, Kokubunji, Tokyo.

tion and the magnitude of the moment in vacuum is μ. (iii) The molecule can be considered as a continuous medium with the dielectric constant n^2, where n is the refractive index. (iv) The solvent can be thought as a continuous medium with the dielectric constant ε, and it surrounds the dissolved molecule tightly. (v) The solution is sufficiently dilute so that the mutual interaction between dissolved molecules can be considered as negligible. On the basis of the above assumptions the potentials inside and outside the molecule are calculated electrostatically by using the spherical functions in § 2. The approximate expressions for the fields derived from the above potentials are given in § 3. These expressions have convenient forms common to both prolate and oblate, while the exact formulae have different forms for two spheroids. The expressions contain, as a special case, the well-known expressions for the sphere obtained by Onsager[3]. Using the results obtained and Higasi's theory[1], we calculate the polarization of molecule in a given direction relative to the external field, then obtain the molecular polarization in § 4. This result is compared with the experiments in § 5. The experimental values used in the comparison are those of chlorobenzene and tert-butyl chloride.

§ 2. Calculation of Potentials

The electrostatic potentials, Ψ's, in space free from charges are expressed as the solutions of Laplace's equation, aside from constant factors, as follows:—

$$\Psi = LMN\,, \tag{2.1}$$

where

$$L=\begin{cases}(\pm\kappa)^{n-m}\mathrm{P}_n{}^m(\kappa\xi)\\ \kappa^{n+m+1}\mathrm{Q}_n{}^m(\kappa\xi)\end{cases},\qquad M=\begin{cases}\mathrm{P}_n{}^m(\eta)\\ \mathrm{Q}_n{}^m(\eta)\end{cases},$$

$$N=\begin{cases}\cos m\varphi\\ \sin m\varphi\end{cases}, \tag{2.2}$$

and

$$x=c\sqrt{\xi^2\mp 1}\sqrt{1-\eta^2}\cos\varphi\,,$$

$$y=c\sqrt{\xi^2\mp 1}\sqrt{1-\eta^2}\sin\varphi\,,\quad z=c\xi\eta\,, \tag{2.3}$$

$$c^2=\pm(a^2-b^2) \tag{2.4}$$

ξ, η and φ being spheroidal coordinates, x, y and z ordinary rectangular coordinates. For brevity's sake, notation κ is used, which we make to express unity for prolate and imaginary unit for oblate, namely,

$$\kappa=\begin{cases}1 & \text{for prolate}\\ i & \text{for oblate}\end{cases},$$

and the upper sign (+ or −) in the above equations refers to prolate and the lower one to oblate. These notation and convention are used hereafter.

Extensions of Onsager's theory[3] to spheroidal molecule have already been done by several authors, e. g. Fujishiro[4], Abbott and Bolton[5] and Buckingham[6]. Also a similar attempt is made in this section.

(a) *Potential due to dipole.* Let the distance between two points $r_1(\zeta_1, \eta_1, \varphi_1)$ and $r(\xi, \eta, \varphi)$ be d, the former being nearer than the latter to the origin of the coordinate. Then

$$1/d=1/c\Bigg[\sum_{n=0}^{\infty}(2n+1)(\pm 1)^n\kappa^{2n+1}\mathrm{P}_n(\kappa\xi_1)\mathrm{P}_n(\eta_1)\mathrm{Q}_n(\kappa\xi)\mathrm{P}_n(\eta)$$
$$+2\sum_{n=1}^{\infty}(2n+1)\sum_{m=1}^{n}(-1)^m(\pm 1)^{n-m}\kappa^{2m+1}\left\{\frac{(n-m)!}{(n+m)!}\right\}^2\mathrm{P}_n{}^m(\kappa\xi_1)\mathrm{P}_n{}^m(\eta_1)\mathrm{Q}_n{}^m(\kappa\xi)\mathrm{P}_n{}^m(\eta)\cos m(\varphi_1-\varphi)\,, \tag{2.5}$$

as given by Neumann and Heine[7].

When there is a dipole at point r_1, the magnitude of whose moment is μ and the direction of whose axis is z-direction, the potential at point r is, in general, given by $(\partial/\partial z_1)(1/d)$. Therefore assuming that there is a dipole μ at the origin r_1 pointing to z-direction, the potential Ψ_d due to the dipole is obtained by differentiating Eq. (2.5). Thus

$$\Psi_d=(\mu/c^2)\sum_{n=0}^{\infty}(\pm 1)^n\kappa^{2(n+1)}(2n+1)\dot{\mathrm{P}}_n(0)\mathrm{Q}_n(\kappa\xi)\mathrm{P}_n(\eta)\,, \tag{2.6}$$

$\dot{\mathrm{P}}_n(0)$ expressing the value of first derivative of P_n at 0. Differentiations used here are $(1/c)(\partial/\partial\eta_1)(1/d)$ at $\xi_1=1$ and $\eta=0$ for prolate and $(1/c)(\partial/\partial\xi_1)(1/d)$ at $\xi_1=0$ and $\eta_1=1$ for oblate. It is clear that Eq. (2.6) is a solution of Laplace's equation by referring to Eq. (2.2).

(b) *Potentials inside and outside spheroid.* (i) We assume that dissolved molecule is of spheroid and the ratio of its two semi-axes is $k=a/b$ and the dielectric cons-

tant inside the spheroid is n^2 and that of solvent outside is ε. If there exists an electric field E in z-direction, which is the direction of revolution of spheroid, the potential is $-zE$ at a large distance from the spheroid. Let the potentials outside and inside the spheroid be Ψ_{01} and Ψ_{i1}, respectively. Then we may put

$$\Psi_{01}=\mp\kappa cE_z\mathrm{P}_1(\kappa\xi)\pm B_{11}\mathrm{Q}_1(\kappa\xi)\mathrm{P}_1(\eta)\ , \quad (2.7)$$

$$\Psi_{i1}=\pm\kappa C_{11}\mathrm{P}_1(\kappa\xi)\mathrm{P}_1(\eta)\ . \quad (2.8)$$

Using

$$(\Psi_0)_{\xi=a/c}=(\Psi_i)_{\xi=a/c}\ , \quad (2.9)$$

and

$$-\varepsilon(\partial\Psi_0/\partial\xi)_{\xi=a/c}=-n^2(\partial\Psi_i/\partial\xi)_{\xi=a/c}\ , \quad (2.10)$$

as boundary conditions, we get

$$B_{11}=\frac{\kappa(\varepsilon-n^2)\mathrm{P}_1\dot{\mathrm{P}}_1cE_z}{\varepsilon\mathrm{P}_1\dot{\mathrm{Q}}_1-n^2\dot{\mathrm{P}}_1\mathrm{Q}_1}\ , \quad (2.11)$$

$$C_{11}=\frac{-\kappa(\mathrm{P}_1\dot{\mathrm{Q}}_1-\dot{\mathrm{P}}_1\mathrm{Q}_1)\varepsilon cE_z}{\varepsilon\mathrm{P}_1\dot{\mathrm{Q}}_1-n^2\dot{\mathrm{P}}_1\mathrm{Q}_1}\ , \quad (2.12)$$

where P_1, Q_1 and $\dot{\mathrm{P}}_1$ etc. represent the values of spherical functions and its first derivatives at a/c or ia/c.

(ii) When the electric field is directed in x-direction, being perpendicular to the axis of revolution, we get the potentials in a similar way as made in (i) as follows:—

$$\Psi_{02}=\mp\kappa cE_x\mathrm{P}_1^1(\kappa\xi)\pm\kappa B_{21}\mathrm{Q}_1^1(\kappa\xi)\mathrm{P}_1^1(\eta)\cos\varphi\ , \quad (2.13)$$

$$\Psi_{i2}=C_{21}\mathrm{P}_1^1(\kappa\xi)\mathrm{P}_1^1(\eta)\cos\varphi\ . \quad (2.14)$$

From the boundary conditions

$$B_{21}=\frac{\kappa(\varepsilon-n^2)\mathrm{P}_1^1\dot{\mathrm{P}}_1^1cE_x}{\varepsilon\mathrm{P}_1^1\dot{\mathrm{Q}}_1^1-n^2\dot{\mathrm{P}}_1^1\mathrm{Q}_1^1}\ , \quad (2.15)$$

$$C_{21}=\frac{-\kappa(\mathrm{P}_1^1\dot{\mathrm{Q}}_1^1-\dot{\mathrm{P}}_1^1\mathrm{Q}_1^1)c\varepsilon E_x}{\varepsilon\mathrm{P}_1^1\dot{\mathrm{Q}}_1^1-n^2\mathrm{P}_1^1\mathrm{Q}_1^1}\ , \quad (2.16)$$

(iii) When there exists a dipole at the centre of the spheroid pointing to z-direction, we may put

$$\Psi_{03}=\sum_{n=0}^{\infty}\kappa^{n+1}B_{3n}\mathrm{Q}_n(\kappa\xi)\mathrm{P}_n(\eta)\ , \quad (2.17)$$

$$\Psi_{i3}=\sum_{n=0}^{\infty}\{(\pm\kappa)^nC_{3n}\mathrm{P}_n(\kappa\xi)+\kappa^{n+1}D_{3n}\mathrm{Q}_n(\kappa\xi)\mathrm{P}_n(\eta)\}\ . \quad (2.18)$$

From Eq. (2.6) we can see

$$D_{3n}=\frac{(2n+1)\mu(\pm1)^n\kappa^{n+1}\dot{\mathrm{P}}_n(0)}{n^2c^2}\ ,$$

$$D_{30}=0\ ,\quad D_{31}=\frac{3\mu}{n^2c^2}\ ,\quad D_{32}=0\ , \quad (2.19)$$

$$D_{33}=-\frac{21\mu}{2n^2c^2}\ .$$

Using the boundary conditions mentioned above we get

$$B_{3n}=\frac{n^2(\mathrm{P}_n\dot{\mathrm{Q}}_n-\dot{\mathrm{P}}_n\mathrm{Q}_n)D_{3n}}{\varepsilon\mathrm{P}_n\dot{\mathrm{Q}}_n-n^2\dot{\mathrm{P}}_n\mathrm{Q}_n}\ , \quad (2.20)$$

$$C_{3n}=\frac{\pm\kappa(\varepsilon-n^2)\mathrm{Q}_n\dot{\mathrm{Q}}_nD_{3n}}{\varepsilon\mathrm{P}_n\dot{\mathrm{Q}}_n-n^2\dot{\mathrm{P}}_n\mathrm{Q}_n}\ . \quad (2.21)$$

§ 3. Approximate Formulae Expressing Fields

In this section we get approximate expressions for the results of the preceding section. These approximate expressions are simpler than the preceding results, and from them we may easily derive those of fields. Using these approximate formulae, we calculate cavity field, self field and reaction field, whose expressions include, as a special case, the well-known formulae for sphere[3].

(a) *Approximate expressions for results of the preceding section.* If we expand the spherical functions in the formulae of the preceding section in the series and keep the main terms only, neglecting others, we obtain approximate expressions for the potentials by using Eq. (2.4) and the ratio k of semi-axes as follows:—

$$\Psi_{01}=-zE_z-\frac{(\varepsilon-n^2)a^3E_z\cos\theta}{\{(3k^2-1)\varepsilon+n^2\}r^2}\ , \quad (3.1)$$

$$\Psi_{i1}=-\frac{3k^2E_zz}{(3k^2-1)\varepsilon+n^2}\ , \quad (3.2)$$

corresponding to Eqs. (2.7) and (2.8), and

$$\Psi_{02}=-xE_x-\frac{2(\varepsilon-n^2)a^3E_x\cos\theta'}{\{(3k^2+1)\varepsilon+(3k^2-1)n^2\}r^2}\ , \quad (3.3)$$

$$\Psi_{i2}=-\frac{6k^2\varepsilon E_xx}{(3k^2+1)\varepsilon+(3k^2-1)n^2}\ , \quad (3.4)$$

$$\Psi_{03}=\frac{3k^2\mu\cos\theta}{\{(3k^2-1)\varepsilon+n^2\}r^2}\ , \quad (3.5)$$

$$\Psi_{i3}=-\frac{(\varepsilon-n^2)(3k^2-1)\mu z}{\{(3k^2-1)\varepsilon+n^2\}n^2a^3}+\frac{\mu z}{n^2r^2}\ . \quad (3.6)$$

In the above equations r expresses the distance from the origin, θ the angle between z-axis and the line connecting the point under consideration to the origin, and θ' the angle

between x-axis and the line. These approximate equations have the same expressions for both prolate and oblate, privided that is k greater than $1/\sqrt{2}$. For the values of k smaller than $1/\sqrt{2}$, the approximate expressions, which are obtained by expanding the spherical functions in the series, are different from those for the values of k greater than $1/\sqrt{2}$, so that the above approximate expressions are not applicable.

(b) *Cavity field.* (i) When we put $n^2=1$ in Eq. (2.8) or (3.2), we get cavity field F_{zc} in z-direction since no self field and no reaction field act inside the spheroid, there being no dielectric. Its approximate form is as follows:—

$$F_{zc}\equiv\gamma_z E_z \simeq \frac{3k^2\varepsilon E_z}{(3k^2-1)\varepsilon+1}\,. \tag{3.7}$$

(ii) For x-direction we get similarly

$$F_{xc}\equiv\gamma_x E_x \simeq \frac{6k^2\varepsilon E_x}{(3k^2+1)\varepsilon+3k^2-1}\,. \tag{3.8}$$

(c) *Self field.* (i) When there is no dielectric outside the spheroid and no permanent dipole inside, and the external field is E, then the field inside the spheroid, which we denote E_{zi}', is obtained from Eq. (2.8) or (3.2) by putting $\varepsilon=1$. In this case the cavity field is obtained from the same equation by putting $\varepsilon=1$ and $n^2=1$, then this becomes in accordance with the external field. Thus self field F_{zs} is considered as the difference between the above two fields, because the reaction field does not act in this case. This field and its approximate form are as follows:—

$$F_{zc}=E_{zi}'-E_z=\frac{(n^2-1)\dot{\mathrm{P}}_1\mathrm{Q}_1E_z}{\mathrm{P}_1\dot{\mathrm{Q}}_1-n^2\dot{\mathrm{P}}_1\mathrm{Q}_1}$$

$$\simeq-\frac{(n^2-1)E_z}{3k^2-1+n^2}\,. \tag{3.9}$$

On the other hand the polarization P_z inside the spheroid is

$$P_z=\frac{(n^2-1)E_{zi}'}{4\pi}\,. \tag{3.10}$$

Therefore

$$F_{zs}=\frac{4\pi\dot{\mathrm{P}}_1\mathrm{Q}_1P_z}{\mathrm{P}_1\dot{\mathrm{Q}}_1-\dot{\mathrm{P}}_1\mathrm{Q}_1}\simeq-\frac{4\pi P_z}{3k^2}\,. \tag{3.11}$$

(ii) For x-direction we get similarly

$$F_{xs}=E_{xi}'-E_x=\frac{(n^2-1)\dot{\mathrm{P}}_1{}^1\mathrm{Q}_1{}^1E_x}{\mathrm{P}_1{}^1\dot{\mathrm{Q}}_1{}^1-n^2\dot{\mathrm{P}}_1{}^1\mathrm{Q}_1{}^1}$$

$$\simeq-\frac{(3k^2-1)(n^2-1)E_x}{3k^2+1+(3k^2-1)n^2}\,, \tag{3.12}$$

$$F_{xs}=\frac{4\pi\dot{\mathrm{P}}_1{}^1\mathrm{Q}_1{}^1P_x}{\mathrm{P}_1{}^1\dot{\mathrm{Q}}_1{}^1-\dot{\mathrm{P}}_1{}^1\mathrm{Q}_1{}^1}\simeq-\frac{4\pi(3k^2-1)P_x}{6k^2}\,. \tag{3.13}$$

(d) *Reaction field.* (i) When the molecule has a dipole, the reaction field acts on the molecule, which is due to the polarization of the surrounding dielectric induced by the original dipole.

At first the reaction field, when a molecule has a dipole due to homogeneous polarization P_z in z-direction, is calculated. As the field derived from Eq. (2.8) can be considered as consists of the cavity, self and reaction fields, the reaction field F_{zr} is obtained by subtracting the cavity and self fields from the field mentioned above. Thus we get

$$E_{zr}\equiv g_z m_z=E_{zi}-F_{zs}-F_{zc}$$

$$=-\frac{4\pi\mathrm{P}_1\mathrm{Q}_1\dot{\mathrm{P}}_1\dot{\mathrm{Q}}_1(\varepsilon-1)P_z}{(\mathrm{P}_1\dot{\mathrm{Q}}_1-\dot{\mathrm{P}}_1\mathrm{Q}_1)(\varepsilon\mathrm{P}_1\dot{\mathrm{Q}}_1-\dot{\mathrm{P}}_1\mathrm{Q}_1)} \tag{3.14}$$

using Eqs. (3.10) and (3.11), where m_z is the dipole moment. An approximate expression is

$$F_{zr}\simeq\frac{(3k^2-1)(\varepsilon-1)m_z}{\{(3k^2-1)\varepsilon+1\}a^3}\,, \tag{3.15}$$

where

$$m_z=VP_z=\frac{4\pi a^3P_z}{3k^2}\,, \tag{3.16}$$

V being the volume of the spheroid.

(ii) For x-direction we get

$$F_{xr}\equiv g_x m_x=E_{xi}-F_{xs}-F_{xc}$$

$$=-\frac{4\pi\mathrm{P}_1{}^1\mathrm{Q}_1{}^1\dot{\mathrm{P}}_1{}^1\dot{\mathrm{Q}}_1{}^1(\varepsilon-1)P_x}{(\mathrm{P}_1{}^1\mathrm{Q}_1{}^1-\mathrm{P}_1{}^1\mathrm{Q}_1{}^1)(\varepsilon\dot{\mathrm{P}}_1{}^1\dot{\mathrm{Q}}_1{}^1-\dot{\mathrm{P}}_1{}^1\mathrm{Q}_1{}^1)}$$

$$\simeq\frac{(3k^2+1)(3k^2-1)(\varepsilon-1)m_x}{2\{(3k^2+1)\varepsilon+3k^2-1\}a^3} \tag{3.17}$$

(iii) When a dipole μ exists at the centre of the spheroid and points to z-direction, the reaction field is obtained from the first term of Eq. (2.18) putting $n^2=1$. The approximate expression for the reaction field, which is obtained from Eq. (3.6) by putting $n^2=1$, is the same as Eq. (3.15), although the first term of the series expressed in Eq. (2.18) alone is not rigorously the same as Eq. (3.14).

§ 4. Molecular Polarization

The molecular polarization is calculated in this section. At first the polarizability of molecule is calculated, using the approximate expressions of the preceding section, and this is easily seen to be in accord with that of sphere in the case of $k=1$[3]. Next we cite the results of Higasi's theory briefly, as it is needed for the following calculation. Then the statistical mean of the component parallel to the external field of permanent and induced dipole moment is obtained. The value of this is easily, though not very simply, calculated numerically, and is to be compared with experimental values.

(a) *Polarizability.* The polarizability of molecule may be gotten from equation

$$m=\alpha F\,, \tag{4.1}$$

where m is the dipole moment induced by the field F acting on the molecule, and α the polarizability of the molecule, which is calculated in this section for the cases where F is directed in z- and x-directions respectively. When no permanent dipole exists, the field acting on the molecule is given by

$$F=\gamma E+gm\,, \tag{4.2}$$

E being the external field. With Eqs. (4.1) and (4.2) we obtain

$$m=\frac{\alpha\gamma E}{1-\alpha g}\,. \tag{4.3}$$

(i) For z-direction, using Eqs. (3.10), (3.16), (4.3) and the approximate expressions for γ_z and g_z, we get

$$\alpha_z=\frac{(n^2-1)a^3}{3k^2-1+n^2}\,. \tag{4.4}$$

(ii) For x-direction we obtain similarly

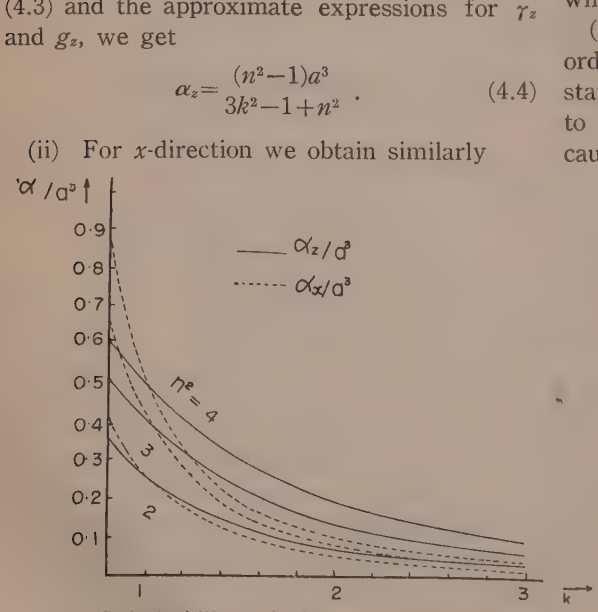

Fig. 1. Polorizability calculated by Eq. (4-4) and (4-5).

$$\alpha_x=\frac{2(n^2-1)a^3}{(3k^2+1)+(3k^2-1)n^2}\,. \tag{4.5}$$

Fig. 1 shows the polarizability as a function of k.

(b) *Higasi's theory*[1]. According to Higasi the reason that the apparent moment of molecule in the solvent differs from the moment in vacuum is as follows: When a dipolar molecule is put into solvent, the surrounding solvent gets polarization due to the field of the diople. If the molecule has a spherical form, this polarization has no effect on measuring the dipole moment. In other cases, this polarization between the molecule and the sphere circumscribing it affects the dipole moment determination as if the induced moment of this polarization were a part of the original dipole moment. Thus the apparent moment in the solvent depends not only on the original moment but also on the shape of the molecule and the dielectric constant of the solvent. The additive moment due to the solvent for the spheroidal molecule is

$$\mu_{ad}=\{(\varepsilon-1)/(\varepsilon+1)\}\mu\begin{cases}A\\A'\end{cases}, \tag{4.6}$$

$$A=-\frac{3}{k^2-1}\left\{1-\frac{k}{\sqrt{k^2-1}}\ln|k+\sqrt{k^2-1}|\right\}-1\,, \tag{4.7}$$

$$A'=\frac{3k'^2}{k'^2-1}\left\{1-\frac{1}{\sqrt{k'^2-1}}\sin^{-1}\frac{\sqrt{k'^2-1}}{k'}\right\}-1\,, \quad k'=1/k \tag{4.8}$$

where A is for prolate and A' for oblated.

(c) *Statistical mean of dipole moment.* In order to obtain the molecular polarization, the statistical mean of the dipole moment parallel to the external field should be calculated, because the dipoles point to various directions even under the external field.

The component of the dipole in z direction is given by

$$m_z=\mu+\alpha_z F_z\,. \tag{4.9}$$

Combining Eqs. (4.2) and (4.9) m_z may be solved as

$$m_z=\frac{\mu+\alpha_z\gamma_z E_z}{1-\alpha_z g_z}\,. \tag{4.10}$$

And also we get

$$m_x=\frac{\alpha_x\gamma_x E_x}{1-\alpha_x g_x}\,. \tag{4.11}$$

If the axis of revolution of the spheroid makes an angle θ with respect to the

external field E, then the components of the external field are $E_z=E\cos\theta$ and $E_x=E_x\sin\theta$ respectively. Substituting these and Eqs. (4.10) and (4.11) into Eq. (4.2) we obtain

$$F_z=\frac{\mu g_z+\gamma_z E\cos\theta}{1-\alpha_z g_z}, \tag{4.12}$$

$$F_x=\frac{\gamma_x E\sin\theta}{1-\alpha_x g_x}. \tag{4.13}$$

The torque acting on the molecule is given by the vector product of F and m. By integrating it with respect to the angle, the potential energy $w(\theta)$ may be obtained as a function of θ. It is, however, necessary that the torque to the additive moment calculated in § 4 (b) should be included in the total torque. It will not introduce any serious error if the field acting on it is assumed to be a Lorentz field. Then the torque is $\{(\varepsilon-1)/3\}A\mu E\sin\theta$. By integrating the total torque, the above term being included, we get

$$w(\theta)=\frac{1}{(1-\alpha_z g_z)(1-\alpha_x g_x)}\{(\alpha_x g_z-1)\gamma_x\mu E\cos\theta +(\alpha_x-\alpha_z)\gamma_z\gamma_x E^2\cos^2\theta\} +\frac{\varepsilon-1}{3}A\mu E\cos\theta. \tag{4.14}$$

When the angle between the axis of revolution and the external field is θ, the component of dipole moment parallel to the external field, including the additive moment calculated above, is given by

$$m_E(\theta)=\frac{\{1+(\varepsilon-1)A/(\varepsilon+2)\}\mu+\alpha_z\gamma_z E\cos\theta}{1-\alpha_z g_z}\cos\theta +\frac{\alpha_x\gamma_x E}{1-\alpha_x g_x}\sin^2\theta. \tag{4.15}$$

The statistical mean of it is obtained from

$$\overline{m}_E=\frac{\int_0^\pi m_E(\theta)\exp(-w/kT)\sin\theta\,d\theta}{\int_0^\pi \exp(-w/kT)\sin\theta\,d\theta}. \tag{4.16}$$

This calculation is rather complicated, but in ordinary conditions the terms of higher order with respect to E can be neglected. The procedures employed in the calculation of the numerator are as follows: after integration by parts, $\exp(-w/kT)$ contained in the resultant is expanded in a series and then the terms proportional to E are only picked up, the others being neglected, and they are rearranged. For the denominator the first term alone is also kept. Then

$$\overline{m}_E=\left[\frac{\{1+(\varepsilon-1)A/(\varepsilon+2)\}\mu^2}{3kT}\frac{(1-\alpha_x g_z)\gamma_x}{(1-\alpha_z g_z)(1-\alpha_x g_x)} +\frac{\varepsilon-1}{3}A+\frac{1}{3}\left(\frac{\alpha_z\gamma_z}{1-\alpha_z g_z}+\frac{2\alpha_x\gamma_x}{1-\alpha_x g_x}\right)\right]E. \tag{4.17}$$

Of course this becomes accord with the formula for the sphere[3], when α, γ and g are taken for sphere and A is put equal to zero. That the first term in Eq. (4.17) is more complicated than that for the sphere is mainly due to the fact that the magnitude and direction of dipole and the field vary in a complicated way as the functions of k and ε. The factors A in Eq. (4.17) is caused by the additive moment and the consequent torque. The molecular polarization P_m is given by

$$P_m=\frac{4\pi\overline{m}_E L}{(\varepsilon+2)E}, \tag{4.18}$$

where L is Avogadro's number.

§ 5. Comparison with Experiments

The experimental values for chlorobenzene and tert-butyl chloride are shown in Figs. 2 and 3, respectively. The values used in the

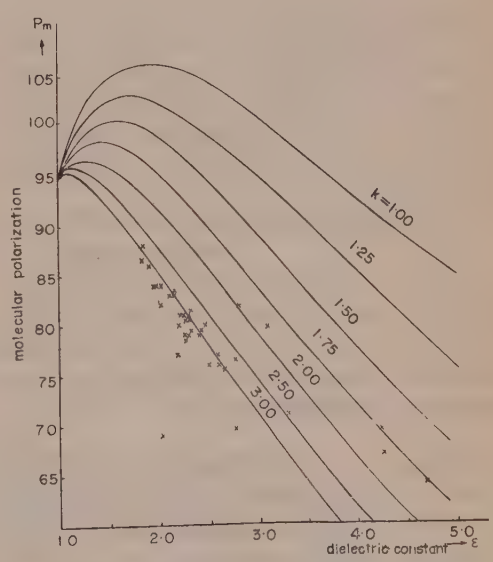

Fig. 2. Comparison between theoretical and experimental values P_m of molecular polarization of chlorobenzene.

calculations are as follows: $T=300°K$; $\mu=1.70$ for chlorobenzene and $\mu=2.13$ for tert-butyl chloride in Debye unit; $n^2=2.34$ for chlorobenzene and $n^2=1.91$ for tert-butyl chloride. The lengths a's of semi-axis of revolution used here are shown in Fig 4, which are

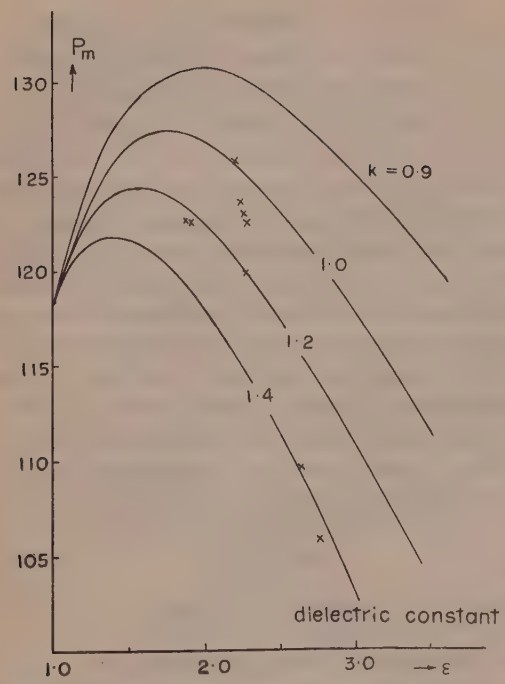

Fig. 3. Comparison between theoretical and experimental values P_m of molecular polarization of tert-butyl chloride.

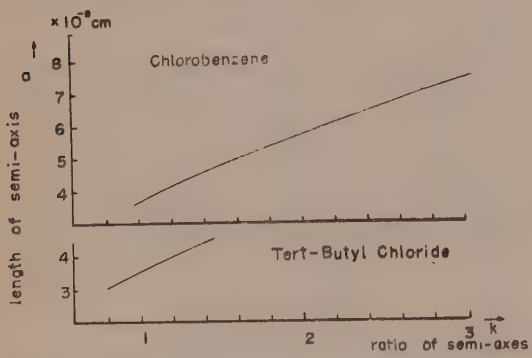

Fig. 4. The value of semi-axis used in calculation molecular polarizability.

determined so as to make the theoretical value of P_m calculated from Eq. (4.18) with $\varepsilon=1$ and μ mentioned above equal to the experimental value at $\varepsilon=1$.

The features of these theoretical curves are as follows: As the dielectric constant of solvent increases from unity, the molecular polarization generally increases at first and reaches its maximum and then decreases. The slope of this decreasing curve is steeper than that of Higasi's theory so that agreement with experiments becomes better. In general the smaller the ratio k becomes, the larger the maximum of the curve becomes and the larger the value of dielectric constant of solvent becomes, at which the curve reaches its maximum. Thus the apparent moment in the solvent can be larger than the true moment for small dielectric constant of solvent even for prolate. On the other hand for larger dielectric constant of solvent the apparent moment becomes smaller even for oblate. These features seem to represent the experimental characteristics.

It should be noted that Eq. (4.17) is only approximate formula. And the more k differs from unity, the worse the approximation becomes. That the calculation given here is made on the basis of the assumptions given at first should be noticed also. In spite of these approximation and simplifying assumptions, this calculation can show a fairly good agreement with experiments.

The writer should express his sincere thanks to Professor K. Higasi, Hokkaido University, for his kind guidance and encouragement, without which this work might have been left unfinished. He was also encouraged by interest shown to this work by Dr. J. W. Smith, University of London.

References

1) K. Higasi: Sci. Pap. Inst. Phys. Chem. Res., Tokyo **28** (1936) 284.
2) I. G. Ross and R. A. Sack: Proc. Phys. Soc. Soc. London **B 63** (1950) 893.
3) L. Onsager: J. Amer. Chem. Soc. **58** (1936) 1486.
4) R. Fujishiro: J. Chem. Soc. Japan **65** (1944) 352.
5) J. A. Abbott and H. C. Bolton: Trans. Faraday Soc. **48** (1952) 422.
6) A. D. Buckingham: *ibid.* **49** (1953) 881.
7) E. W. Hobson: The Theory of Spherical and Ellipsoidal Harmonics. Chap. X. (Cambridge, 1931).
8) K. B. McAlpine and C. P. Smyth: J. Chem. Physics **3** (1935) 55.
9) J. W. Smith and L. B. Witten: Trans. Faraday Soc. **47** (1951) 1404.

JOURNAL OF THE PHYSICAL SOCIETY OF JAPAN Vol. 13, No. 2, FEBRUARY, 1958

Study on the Ordered Alloy Ag_3Mg

By Kunio FUJIWARA†, Makoto HIRABAYASHI, Denjiro WATANABE and Shiro OGAWA

The Research Institute for Iron, Steel and Other Metals, Tohoku University, Sendai, Japan

(Received November 11, 1957)

One-dimensional anti-phase domain structure of the ordered alloy Ag_3Mg has been confirmed by X-ray diffraction study using a single crystal as well as polycrystals and by electron diffraction study with evaporated thin films. The measurements of specific heat and electrical resistivity have also been done, and these results have been qualitatively discussed in connection with the structure of this alloy.

§ 1. Introduction

The existence of the superlattice Ag_3Mg in the face-centred cubic α phase of silver-magnesium alloy system was first suggested by Clarebrough and Nicholas[1] and confirmed by Kachi's investigation[2] mainly from the electrochemical properties of this alloy. As to the atomic arrangement of this superstructure, however, nothing was known. In 1954, from the results of the X-ray diffraction study, Schubert, Kiefer, Wilkens and Haufler[3] concluded that the ordered alloy Ag_3Mg has a one-dimensional anti-phase domain structure like Cu_3Au in the partially ordered state. They came to this conclusion only by using powder specimens. It seemed, therefore, to be desirable that this result was examined with a single crystal. In the present work, the anti-phase domain structure of Ag_3Mg has clearly been confirmed by X-ray diffraction study using a single crystal as well as polycrystals and also by electron diffraction study with evaporated single-crystal-like films. Measurements of electrical resistivity and a series of calorimetries on the alloys in the α phase and the $\alpha+\beta$ two phase region (see Fig. 1) were also carried out, in order to elucidate the relation between these physical properties and the peculiarities of the structure. No quantitative conclusion, however, has been obtained in the present work.

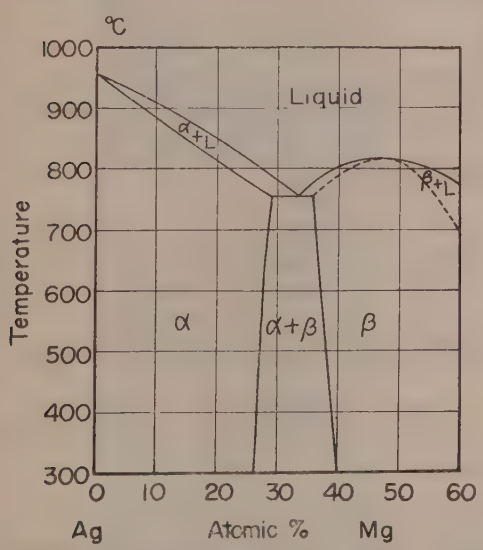

Fig. 1. Silver-rich side of the phase diagram of silver-magnesium system. (After Amer. Soc. Metals, *Metals Handbook* (1948)).

† Now at the Institute for Solid State Physics, Tokyo University, Tokyo.

§ 2. The Model of Superstructure of the Present Alloy.

As mentioned above, Schubert and his collaborators adopted the concept of a one-dimensional anti-phase domain structure in order to explain the result of their X-ray diffraction study with powder specimens.

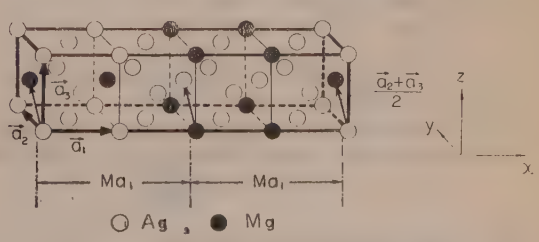

Fig. 2. Illustraction of a one-dimensional anti-phase domain structure ($M=2$).

Fig. 2 illustrates such a structure. The fundamental lattice of this structure is considered to be a face-centred tetragonal lattice

with the atomic arrangement similar to that in perfectly ordered Cu_3Au. An out-of-step vector in atomic arrangement, $(\vec{a}_2+\vec{a}_3)/2$, however, exists at every M cells along the x direction, where $\vec{a}_1$, $\vec{a}_2$ and $\vec{a}_3$ represent three fundamental vectors of face-centred tetragonal lattice, the tetragonal axis being $\vec{a}_1$. Nothing particular occurs in the atomic arrangements along the y and z axes, and so a unit cell of this structure must be taken as outlined by the thick lines in the figure. The intensity distribution in reciprocal space corresponding to such a structure is illustrated in Fig. 3-(a), where the splittings of the superlattice reflections having odd $k+l$ are shown. The indices of these split spots are $(h+1/2M, k, l)$ and $(h-1/2M, k, l)$ in terms of the fundamental face-centred tetragonal lattice. In the actual crystal, however, the tetragonal axis will distribute not only along x but also along y and z directions, and the superposed intensity distribution is illustrated in Fig. 3-(b).

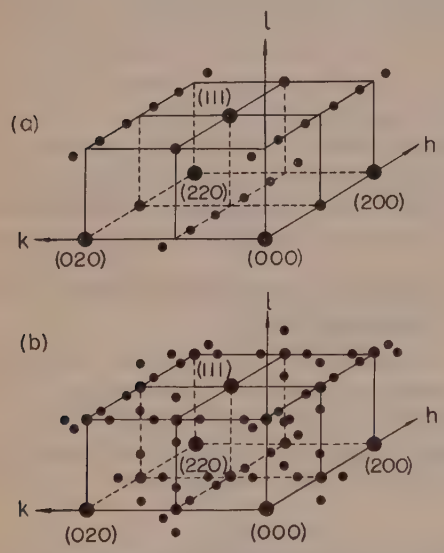

Fig. 3. Intensity distributions in reciprocal space
(a) corresponding to Fig. 2,
(b) corresponding to the superposition of three orientations, where tetragonality is neglected, since $c/a \sim 1$ in Ag_3Mg.

§ 3. X-ray Diffraction Study

a) Experimental Methods

A single crystal specimen was prepared by sawing out a relatively large grain from a specimen for calorimetry. The powder specimens whose compositions range from 9 to 33 per cent* were prepared by sucking up the melt into silica capillaries. It is disadvantageous for annealing that the vapour pressure of magnesium is considerably high. In all annealing process, therefore, specimens were enclosed in small glass tubes filled with argon. This procedure was effective to prevent the evaporation of magnesium to a large extent. After annealing the specimens were always etched in nitric acid in order to remove the surface layers from which some quantity of magnesium might have been lost by evaporation, and then their compositions were determined. The method of chemical analysis was inexpedient, as it required the consumption of considerably large amount of specimen in order to obtain high accuracy in composition determination, and so it was applied only to several specimens in the $\alpha+\beta$ two phase region. The compositions of the alloys in the α phase were determined by measuring the lattice constants in disordered state quenched from 500°C and comparing with the standard curve illustrated in Fig. 4.

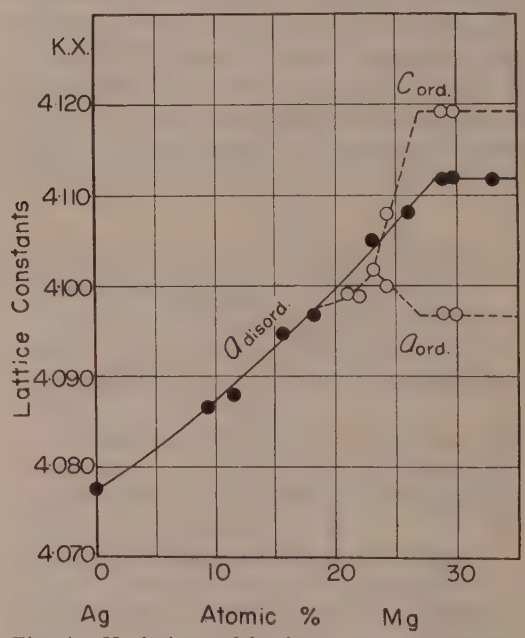

Fig. 4. Variations of lattice constants with composition.

The preparation of this standard curve was made by using the specimens for calorimetry, and the details will be described in § 5-(a).

A 7 cm oscillation camera and an 11.46 cm

* In the present paper, mere 'per cent' will be used in place of 'atomic per cent of magnesium'.

powder camera were used for the single crystal specimen and the powder specimens respectively. All photographs were taken with copper radiation on the Fuji industrial high speed films. The lattice parameters were determined from Debye-Scherrer photographs by means of the graphical-extrapolation method.

b) Experimental Results

The lattice variation caused by ordering were first noticed. The results obtained from powder photographs are summarized in Fig. 4. In this figure, the full curve depicts the disordered state quenched from 500°C into water, while the dotted curves depict the almost completely ordered state induced by slow cooling from 400°C to 250°C in 22 days. For the ordered specimens containing magnesium

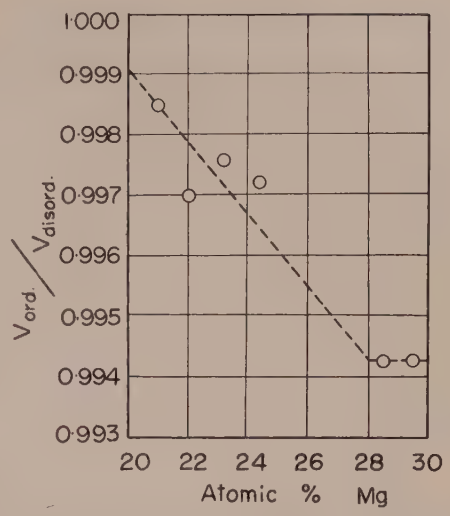

Fig. 5. Volume ratio of ordered to disordered state.

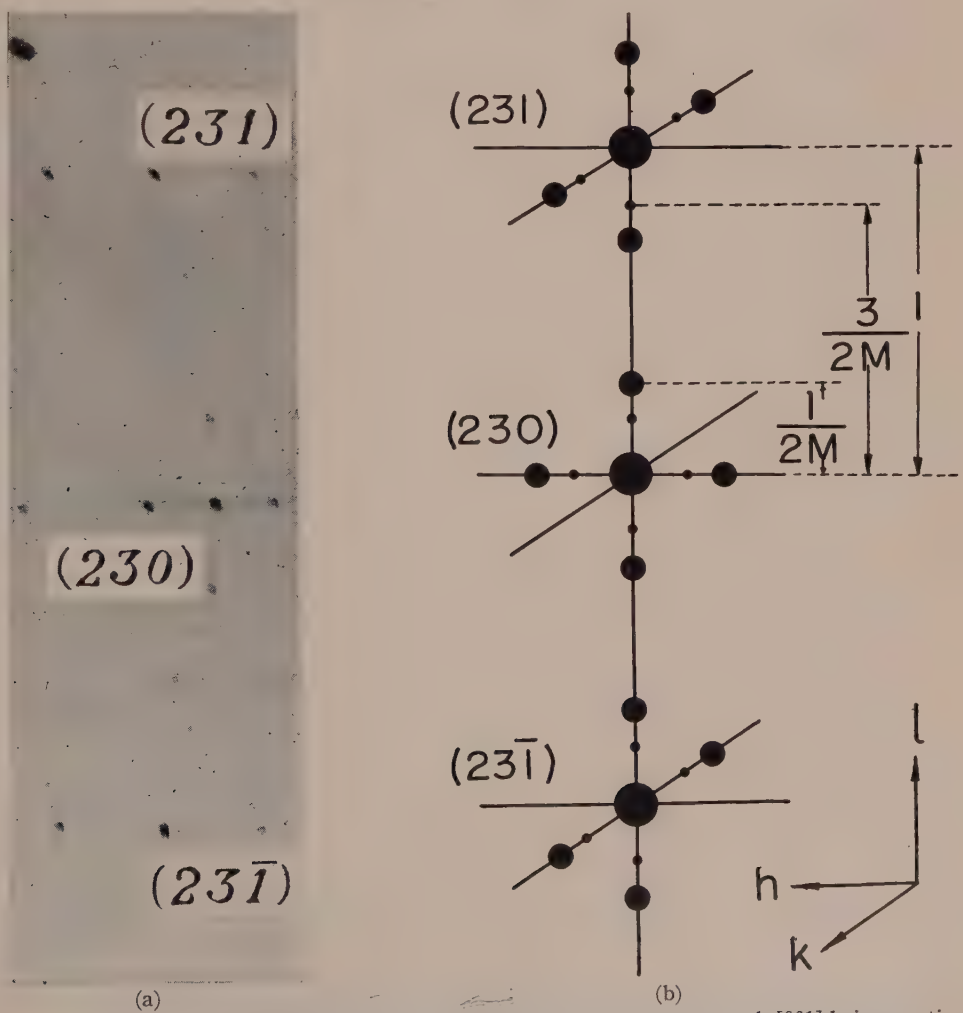

(a) (b)

Fig. 6. (a) A portion of oscillation photograph of 25 per cent single crystal, [001] being vertical.
(b) Intensity distribution in reciprocal space corresponding to (a).

less than about 23 per cent the lattice remains in the face-centred cubic form, although the lattice constant contracts a little. The transformation to the face-centred tetragonal form** accompanies ordering, however, in the alloys containing magnesium more than about 23 per cent. The tetragonality, c/a, increases monotonously with composition until the boundary between the α-phase and the $\alpha+\beta$ two phase region is reached, where it has the maximum value 1.006. The corresponding volume change is illustrated in Fig. 5 in terms of the volume ratio of ordered and disordered state.

The single crystal specimen containing 25 per cent magnesium was slowly cooled from 390°C to 250°C in 14 days. Fig. 6–(a) shows a portion of an oscillation photograph. Unfiltered copper radiation was used, [001] being vertical and oscillation angle being 15°. The cross-like splits of three superlattice reflections, (231), (230) and $(23\bar{1})$***, are clearly shown. The observed intensity distribution in reciprocal space corresponding to Fig. 6–(a) is illustrated in Fig. 6–(b), and accords well with Fig. 3–(b), the existence of a one-dimensional anti-phase domain structure being confirmed. Besides the primary split spots, $(h\pm 1/2M, k, l)$ and so on, the faint secondary splittings, e.g. $(h\pm 3/2M, k, l)$, are also observed in Fig. 6. The value of the period of out-of-steps, M, can be calculated from the separation of split spots, and is 1.77 in this specimen. In Fig. 7, the values of M observed mainly from powder patterns are plotted against composition.

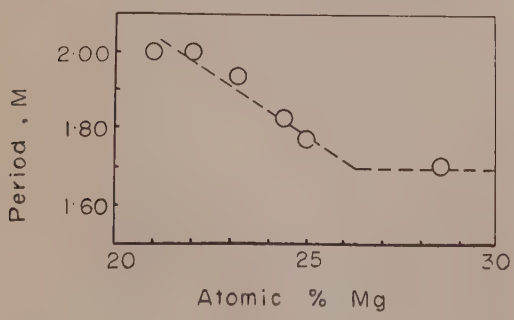

Fig. 7. Period of out-of-step, M, versus composition.

** It should be noticed, however, that the face-centred tetragonal cell can no longer be a unit cell in the ordered lattice.

*** Miller's indices of the superlattice reflection are used in terms of the fundamental face-centred tetragonal lattice, as described in § 2.

§ 4. Electron Diffraction Study

a) Experimental Method

The specimens were prepared in the following way. Single-crystal-like films of silver were first formed by evaporation *in vacuo* onto cleavage surfaces of rocksalt heated at 180~210°C, and then they were detached from the substrata in water and mounted on nickel supporters. Magnesium was evaporated *in vacuo* onto these silver films at room temperature, and then the films were quickly heated up to 300°C and slowly cooled in the apparatus for homogenization. High vapour pressure of magnesium, however, hindered the formation of the alloy films having expected composition. The amount of magnesium to be evaporated was, therefore, always increased by a few times as much as that corresponding to the desired composition. The thickness of the alloy films estimated from the evaporated quantities was 600–700Å.

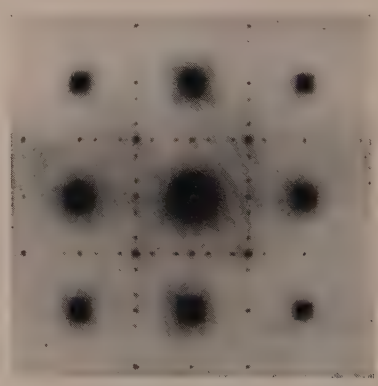

Fig. 8. (a) Electron diffration pattern from a film containing about 25 per cent Mg.

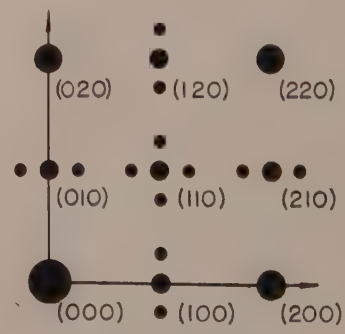

Fig. 8. (b) Intensity distribution in reciprocal space corresponding to (a). The difference in size between (a) and (b) should be noticed.

Since a precise determination of the lattice constants such as in the X-ray study was not expected in the electron diffraction study, the compositions of films were estimated by comparing the observed values of the period of out-of-step with the X-ray data as shown in Fig. 7, although such procedure is undesirable from the view point of structure analysis. Annealing of specimens was carried out in flow of argon, and this attempt brought fairly good results to avoid the evaporation and oxidation of magnesium during annealing.

A diffraction camera made by the Hitachi Co. was used, the applied voltage being about 50 KV. All diffraction photographs were taken at the normal incidence.

b) Experimental Results

Alloy films which were not completely homogenized before annealing exhibited unknown complex spot patterns as well as body-centred cubic rings due to the β phase, besides face-centred cubic spots with split superlattice reflections. As the annealings of specimens advanced, however, the extra spots and rings disappeared gradually. On the other hand, the superlattice reflections due to the α phase grew more intense. Fig. 8–(a) shows a diffraction photograph of a specimen annealed at 150°C for 18 hours, and Fig. 8–(b) shows the corresponding intensity distribution in reciprocal space in terms of the fundamental face-centred tetragonal lattice. Cross-like splittings of superlattice reflections can be clearly observed, and thus the one-dimensional anti-phase domain structure of Ag_3Mg is confirmed also by electron diffraction method. The composition of this film is estimated to be about 25 per cent from the observed value of M, 1.79. Further annealing of this specimen did not bring any essential change to the diffraction pattern, though the background intensity increased perhaps by contamination of the specimen.

§ 5. Calorimetric Study

a) Experimental Methods

An adiabatic calorimeter of the Nagasaki-Takagi type[4] was used to measure the specific heat. The specimens were made of ingots which had been homogenized by annealing at 750°C. Each of the specimens has three holes, one of which is for heating coil and the other two are for thermocouples, and its mass is about 30 gr on the average. In annealing processes the specimens were enclosed in glass tubes filled with argon, and all measurements were carried out under one atmospheric pressure of argon. The rate of heating of specimens was about 2°C per min. in the region of normal specific heat. The compositions of specimens in the α phase were calculated by using the measured values of their specific gravities and lattice constants in disordered state quenched from 500°C into water. The effects of vacancy, other lattice defects and grain boundaries were all neglected in this calculation. The results were plotted in Fig. 4 and used as the standard curve for the specimens for X-ray diffraction study, as already described. For the specimens in the $\alpha+\beta$ two phase region, the chemical analyses were employed.

b) Experimental Results

A series of calorimetric experiments was carried out on the alloys whose compositions

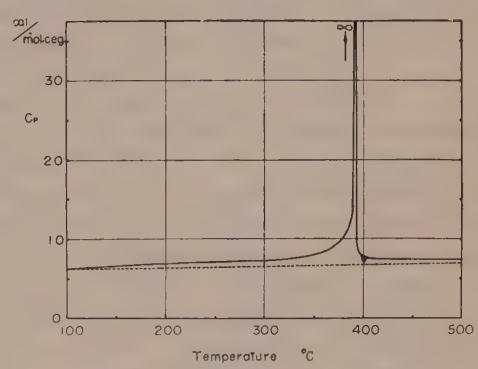

Fig. 9. Specific heat versus temperature curve of 25.4 per cent alloy. (I)

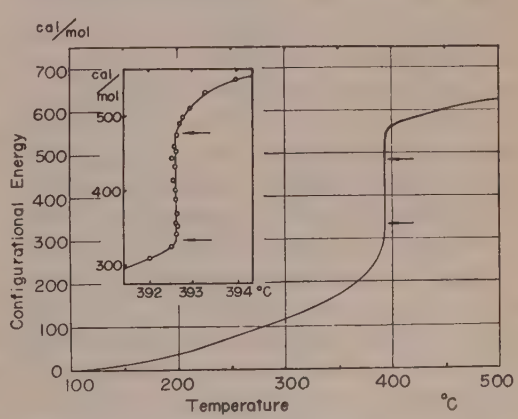

Fig. 10. Configurational energy versus temperature curve corresponding to Fig. 9.

range from 15.6 to 33.0 per cent. Figs. 9, 10 and 11 depict the results on the 25.4 per cent alloy as an example. The full curve in

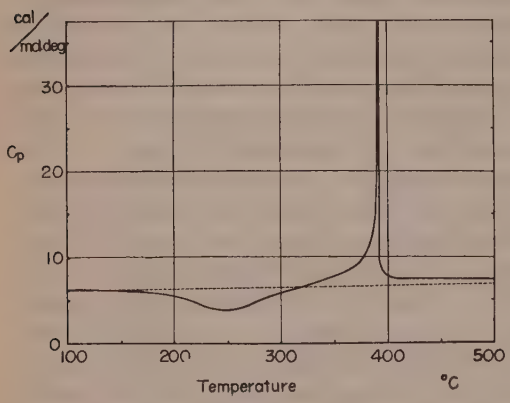

Fig. 11. Specific heat versus temperature curve of 25.4 per cent alloy. (II)

Fig. 9 illustrates the specific heat versus temperature curve. In this case the specimen was initially in a highly ordered state by slow cooling from 400°C to room temperature in 24 days. A typical λ-type transformation with anomalous residual specific heat above the critical temperature can be seen in this figure. The corresponding energy versus temperature curve is drawn in Fig. 10. Latent heat is observed at 393°C between two arrows in the figure, and it amounts to about 150 cal/mol. Fig. 11 depicts another specific heat versus temperature curve of the same specimen, the initial state in this case being a disordered state attained by quenching from 500°C into water. The decrease of specific heat due to the development of order begins at about 100°C, and the most highly ordered state of this alloy in the course of this measurement is realized at about 320°C, where the specific heat comes back onto the normal value indicated by the dotted line. The endothermic value in the disordering process was a little higher than the calorific value in the preceding, ordering process. This fact suggests that a perfectly disordered state of the specimen was not obtained by quenching. Latent heat at the critical temperature could not be observed in this measurement. The variations of the critical temperature and the configurational energy with composition are summarized in Figs. 12 and 13, respectively. Here, the data obtained from 15.6 and 18.1 per cent specimens have

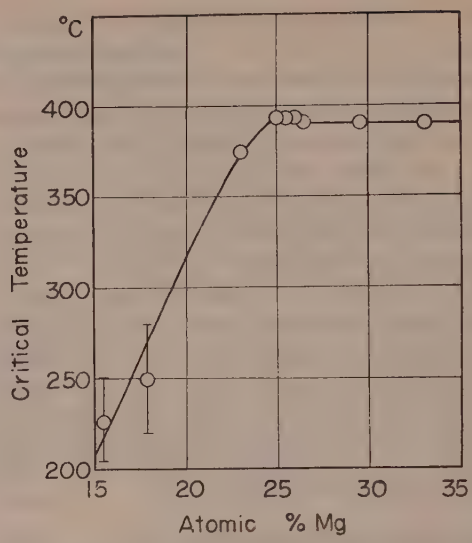

Fig. 12. Critical temperature versus composition.

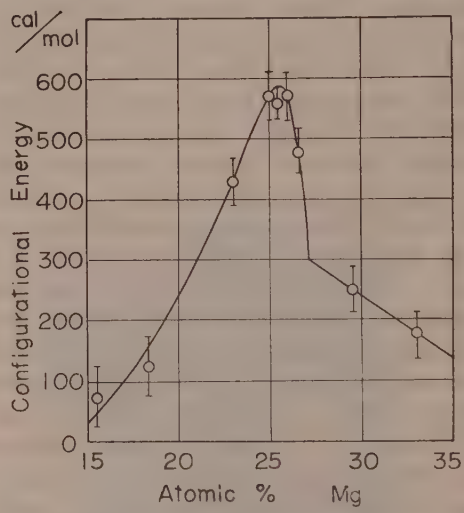

Fig. 13. Configurational energy just above T_c versus composition.

relatively low accuracy, as they showed only broad peaks in the specific heat measurements.

§ 6. Measurement of Electrical Resistivity

A wire of 24.8 per cent alloy was used as a specimen, whose dimensions were 8.5 cm in length and 0.8 mm in diameter. This specimen was initially quenched from 500°C into water, and then the variation of electrical resistivity with temperature was measured at the heating rate of about 100°C per hour under one atmospheric pressure of argon gas. Fig. 14 depicts the result. It should be noticed that the anomalous increase of re-

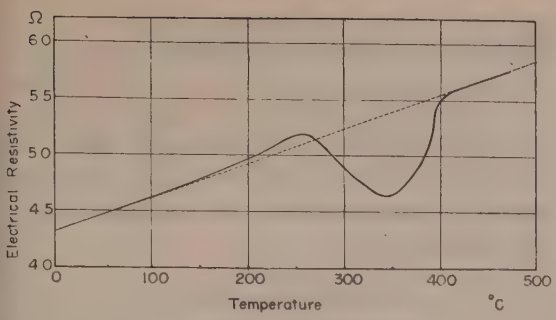

Fig. 14. Electrical resistivity versus temperature curve of 24.8 per cent alloy.

sistivity can be detected bewten 100°C and 260°C prior to the decrease in 260~400°C. This fact will be discussed in the next paragraph in comparison with the specific heat versus temperature curve.

§ 7. Discussions

a) Discussions on the Diffraction Experiments

Recently, Hill and Axon[5] measured the lattice spacings of the α solid solution of silver-magnesium alloy system. The present result on the lattice spacings of the disordered α phase, as shown in Fig. 4, agrees well with their results within the experimental error. On the other hand, the values reported by Letner and Sidhu[6], who failed to discover the superlattice Ag_3Mg, are considerably smaller than those of the present work, probably owing to the formation of order to a certain extent in their specimens. As to the lattice spacings in the ordered state, the results of Schubert *et al.* are in good qualitative agreement with those of the present work shown in Fig. 4. The slight difference in composition is, however, found between these two works, but the origin is not clear at the present stage.

The X-ray oscillation photograph of a single crystal specimen and the electron diffraction pattern of an evaporated thin film, as shown in Fig. 6 and Fig. 8 respectively, can well be explained by the one-dimensional anti-phase domain structure model. Thus, the result of Schubert *et al.* has been confirmed. The values of the period of out-of-step, M, decreases gradually from 2.0 to 1.7 as the concentration of magnesium increases (Fig. 7). Such a result is also in accord with that of Schubert *et al.* qualitatively. An attention should be paid, however, to the fact that the observed values of M are generally not integral in spite of the sharpness of split superlattice reflections. This fractional property of M has already been discussed by one of the present authors (K.F.)[7]. That is to say, the fractional value of M can be interpreted by considering a model in which a few, different periods of anti-phase domain are mixed uniformly but probably with some irregularity. For details reference may be made to the original paper.

Schubert *et al.* reported that several, faint, additional lines were found in their powder photographs of the alloy containing magnesium more than 26 per cent. In the present work, however, no additional pattern could be observed. In the electron diffraction patterns of CuAu II[8], Cu_3Pd[9] and Au_3Mn[10], which have also anti-phase domain structures, the strange satellites flanking normal spots have been observed. The appearance of such satellites may be expected in the case of Ag_3Mg, too. They were, however, not observed even in the highly ordered specimen which had been annealed at 150°C for 106 hours.

b) Discussions on the Calorimetries and the Measurement of Electrical Resistivity

The values of the critical temperature determined by calorimetries agree quite well with those of Clarebrough and Nicholas[1] and of Kachi[2] deduced with different experimental methods. The present work has, however, failed to reveal the quantitative relationship between configurational energy and period of out-of-steps owing to the complexity of the phenomena and the relatively low accuracies of experiments. The peak of configurational energy versus composition curve, as shown in Fig. 13, seems not to lie just in 25 per cent but to shift to a little higher concentration of magnesium. This slight shift is not thought to relate to the value of M which decreases monotonously as the concentration of magnesium increases. Such a phenomenon may be considered in connection with the degree of volume contraction in ordering process which increases with composition as shown in Fig. 5.

It is unfortunate for the results of the present calorimetries that all extant theories can tell nothing about the anti-phase domain structure. Nevertheless, some comparisons

between theories and experiments were made in Table I, where $E(Tc+)$, $\Phi(Tc+)$ and Q represent the configurational energy and

Table I. Comparison between theories and the data of calorimetry.

	Experiment (25.4% alloy)	Theories (A_3B-type)	
		Bragg-Williams	Peierls
Tc	666°K	—	—
$E(Tc+)$	560±25 cal/mol	—	—
$\Phi(Tc+)$	0.94±0.05 cal/deg. mol	—	—
Q	150±10 cal/mol	—	—
$RTc/E(Tc+)$	2.37±0.11	2.19	2.38
$\Phi(Tc+)/R$	0.47±0.03	0.562	0.46
Q/RTc	0.11±0.01	0.100	0.27

entropy just above the critical temperature and the latent heat, respectively. Fairly good coincidence exists between them, and thus no singularity due to the existence of anti-phase domains could be detected.

It is interesting to compare the specific heat versus temperature curve of 25.4 per cent alloy, as shown in Fig. 11, with the electrical resistivity versus temperature curve of 24.8 per cent alloy, as shown in Fig. 14. Both specimens were initially quenched from 500°C into water, and then they were heated up at the almost similar rates. Owing to the development of order, the decrease of specific heat appears at about 100°C, while the electrical resistivity begins, on the contrary, to increase anomalously at the similar temperature, and then turns to decrease at about 260°C. Such an anomalous increase of electrical resistivity in the initial process of ordering can be seen also in the data of Clarebrough and Nicholas[1], though they did not point it out. Similar phenomena have been observed in other superlattice alloys such as Cu_3Au[11] and Cu_3Pd[12], and they seem to relate to the anti-phase domain structure in the following way. The development of order in a domain may induce the decrease of electrical resistivity, while the formation of anti-phase domain boundaries may, on the other hand, induce the increase. If the latter effect is thought to overcome the former at the early stage of ordering, such a curious phenomenon may be expected.

Acknowledgements

The authors wish to express their sincere thanks to Dr. S. Kachi for the kind dispensation of his own specimens and for the useful discussions and also to Mr. S. Ikeda for his kind offices on the chemical analyses of several specimens.

The present investigation has partly been supported by the fund of the Ministry of Education in Aid of Scientific Researches.

References

1) L. M. Clarebrough and J. F. Nicholas: Aust. J. Sci. Res. **A3** (1950) 284.
2) S. Kachi: J. Japan Inst. Metals **19** (1955) 382. Sci. Rep. Res. Inst. Tohoku Univ. **A7** (1955) 351.
3) K. Schubert, B. Kiefer and M. Wilkens: Zeit. Naturfor. **9a** (1954) 987.
K. Schubert, B. Kiefer, M. Wilkens and R. Haufler: Z. Metallkde. **46** (1955) 692.
4) S. Nagasaki and Y. Takagi: J. Appl. Phys. Japan **17** (1948) 104.
5) R. B. Hill and H. J. Axon: J. Inst. Met. **85** (1956) 109.
6) H. R. Letner and S. S. Sidhu: J. Appl. Phys. **18** (1947) 833.
7) K. Fujiwara: J. Phys. Soc. Japan **12** (1957) 7.
8) S. Ogawa and D. Watanabe: J. Phys. Soc. Japan **9** (1954) 475.
9) D. Watanabe and S. Ogawa: J. Phys. Soc. Japan **11** (1956) 226.
10) S. Ogawa and D. Watanabe: read at the International Conference of Crystallography in 1957.
11) F. P. Burns and S. L. Quimby: Phys. Rev. **97** (1955) 1567.
12) F. E. Jaumot Jr. and A. Sawatzky: Acta Met. **4** (1956) 118.

JOURNAL OF THE PHYSICAL SOCIETY OF JAPAN Vol. 13, No. 2, FEBRUARY, 1958

The Paramagnetic Susceptibility of Some Nickel Salts

By Taiichiro HASEDA and Muneyuki DATE

The Research Institute for Iron, Steel and Other Metals, Tōhoku University, Sendai, Japan

(Received November 15 1957)

Paramagnetic susceptibilities of some nickel salts were measured in the temperature range between 1.40°K and 290°K. The flat behavior of the susceptibility *vs* temperature curve in the lowest temperature region was especially prominent in $NiCl_2 \cdot 6H_2O$. The paramagnetic susceptibility of a powdered specimen of the nickel salt was calculated with the low field approximation. The characteristic behavior of a nickel ion in various salts was explained as due to the Stark splitting of the lowest spin triplet. The measured values of susceptibility were analysed and consistent results were obtained. Especially in $NiCl_2 \cdot 6H_2O$, the crystalline field was expected to be much deformed from cubic symmetry and this is consistent with the fact that the paramagnetic resonance could not be detected at 9800 and 18000 Mc/sec in this salt.

§ 1. Introduction

The development of the microwave technique makes it facillitate to determine the energy splitting of the paramagnetic ions in crystalline field. Numerous investigations have been made on various salts. However, there are also a number of salts in which the paramagetic resonance is not detected. The reason for the failure to detect the resonance is attributed to too short spin-lattice relaxation times in some cases or to too large energy splittings in some cases. Thus, in these salts, an alternative procedure is necessary to determine the energy levels of the salts; the determination of the parameters in the energy splitting expression by comparing the calculated susceptibility with the experimental values in a wide temperature range, is yet a very useful method now.

Some measurements have been made on the susceptibility or on the magnetic anisotropy of hydrated nickel salts in the temperature range mostly from 14°K to 290°K,[1] and these results have been interpreted using Schlapp and Penney's theory[2] or more carefully in some cases.[3] As is well known, the orbital levels of divalent nickel ions in a cubic field split like those of trivalent chromium, leaving an orbital singlet lowest. So, a rather long spin-lattice relaxation time is expected. In fact, paramagnetic resonance has been detected in many nickel salts at room temperature. If the crystal structure is also known, a theoretical analysis can be made in detail. However, there are also some nickel salts of which the crystal structure are not known exactly in addition to the failure of paramagnetic resonance data. The analysis of susceptibility data in these cases give only ambiguous results. Notwithstanding these unfavourable conditions, it may still be worthwhile to get a qualitative information about energy levels in these cases. From this point of view, the expression of susceptibility of a nickel salt in powdered form especially at very tow temperatures is given in this paper. It is intended to account for the nature of the susceptibility of $NiCl_2 \cdot 6H_2O$ under the hypothesis of considerable distortion of the crystalline field from cubic symmetry.

§ 2. Experimental

Susceptibilities of powdered samples of $NiCl_2 \cdot 6H_2O$, $Ni(NH_4)_2(SO_4)_2 \cdot 6H_2O$, $NiK_2(SO_4)_2 \cdot 6H_2O$ and $NiSiF_6 \cdot 6H_2O$ were measured in the temperature range from 1.40°K to 290°K. The method used was a usual a.c. bridge method. The frequency used was 90 c/s. The effective measuring field was about two or three gauss.

The experimental results are given in Table I and Fig. 1. Susceptibility of $NiNH_4$ Tutton salt was measured by Jackson down to liquid hydrogen temperatures, and the Weiss constant was given to be about −4°K.[4] However, as can easily be seen from Table I, the Weiss constant is almost zero in two

Table I. Molar Susceptibility of Nickel Salts

T°K	$NiCl_2 \cdot 6H_2O$			$NiK_2(SO_4)_2 \cdot 6H_2O$			$Ni(NH_4)_2(SO_4) \cdot 6H_2O$			$NiSiF_6 \cdot 6H_2O$		
	χ_M	$1/\chi_M$	$\chi_M \cdot (T+7)$	χ_M	$1/\chi_M$	$\chi_M \cdot T$	χ_M	$1/\chi_M$	$\chi_M \cdot T$	χ_M	$1/\chi_M$	$\chi_M \cdot T$
290	$40.1\ 10^{-4}$	250	1.19	$41.6\ 10^{-4}$	240	1.21	$41.8\ 10^{-4}$	240	1.21	$42.2\ 10^{-4}$	237	1.22
78	142	70.5	1.18	160	62.5	1.25	155	64.7	1.21	160	62.1	1.26
20.4	413	24.2	0.84	590	16.0	1.20	592	16.9	1.21	610	16.4	1.24
18.1	445	22.5	0.80	660	15.2	1.20	—	—	—	—	—	—
14.6	511	19.6	0.75	820	12.2	1.20	822	12.2	1.20	835	12.0	1.22
4.20	670	14.9	0.28	2570	3.90	1.08	2600	3.85	1.09	2860	3.50	1.20
2.50	678	14.7	0.17	3950	2.53	0.99	4270	2.35	1.06	4880	2.07	1.21
1.54	678	14.7	0.10	5310	1.88	0.82	5920	1.69	1.01	8000	1.25	1.20

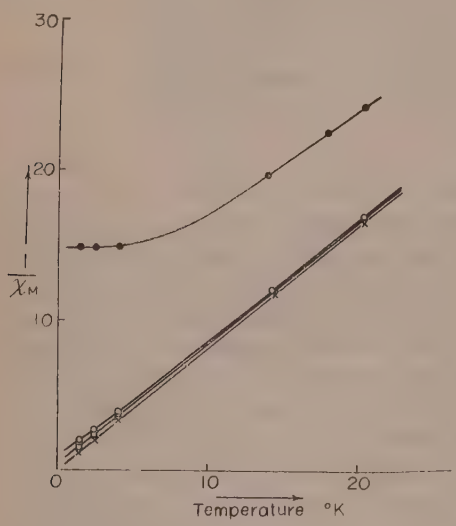

Fig. 1. Reciprocal of molar susceptibility of nickel salts.
● $NiCl_2 \cdot 6H_2O$
○ $NiK_2(SO_4)_2 \cdot 6H_2O$
□ $Ni(NH_4)_2(SO_4)_2 \cdot 6_2HO$
× $NiSiF_6 \cdot 6H_2O$

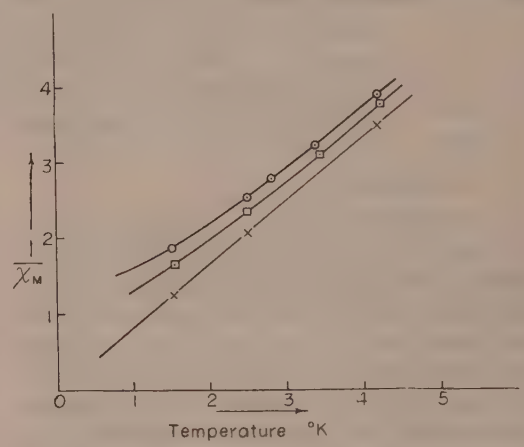

Fig. 2. Reciprocal of molar susceptibility of nikel salts at very low temperatures.
⊙ $NiK_2(SO_4)_2 \cdot 6H_2O$
▣ $Ni(NH_4)_2 \cdot 6H_2O$
× $NiSiF_6 \cdot 6H_2O$

Tutton salts and in fluosilicate. The reason for so large θ can not be found out theoretically even if the exchange interaction is taken into account.

A characteristic feature is distinct in $NiCl_2 \cdot 6H_2O$ at very low temperatures. χ_M is quite flat below about 5°K. Measurement on paramagnetic resonance was undertaken at 9800 and 18000 Mc/sec, but any resonance line was not observed. This will be accounted for naturally from the discussions described in the following section.

In Fig. 2, susceptibilities of the former three salts at liquid helium temperatures are shown. It is evident that the characteristics to be flat at the lowest temperature are common in two Tutton salts. Fluosilicate, as is well known, has a trigonal crystalline field and there remains spin degeneracy at the lowest temperature. Values obtained do not show any tendency to be flat at the lowest temperature. These facts are consistent, indeed, with the consideration mentioned below.

§ 3. Calculation of the Paramagnetic Susceptibilities

As is described in the preceeding section, the deviation of the susceptibilities of $NiCl_2 \cdot 6H_2O$ from the Curie law is remarkable at low temperatures. This deviation of Ni^{++} ion was investigated by Schlapp and Penney[2] who pointed out the importance of temperature independent part which is called high frequency term. This is important for the analysis of the susceptibilites at high tempe-

ratures because the susceptibility following the Curie law is small at high temperatures. However, Schlapp-Penney's calculation is not so important in the low temperature region and our experimental result cannot be explained by their theory. In this section, it is shown that this low temperature anomaly can be explained by the crystalline Stark separation of the lowest spin triplet. We used the spin Hamiltonian which is familiar in the analysis of the paramagnetic resonance. As Schlapp-Penney's term is not so important at low temperatures as described before, we will neglect it except the analysis of the experimental data at high temperatures observed in our experiments.

As is well known, the ground state of N^{++} ion is ^3F and the degeneracy of ^3F is removed by the cubic crystalline field. Under these conditions, the lowest state is spin triplet that is perfectly degenerate. In most crystals, however, the crystalline electric field have lower symmetries such as trigonal, tetragonal or rhombic. In general, this can be described by the following spin Hamiltonian:[5)6)]

$$H=DS_z^2+E(S_x^2-S_y^2)+g\beta \boldsymbol{HS}\,, \qquad (1)$$

where D and E are axial and rhombic crystalline field constant, respectively, and the last term represents the Zeeman energy. The solution of Eq. (1) can be represented as follows:

$$-W^3+2DW^2+(E^2-D^2+g^2\beta^2H^2)W -g^2\beta^2H^2\{D(l^2-m^2)-E(l^2-m^2)\}=0\,, \qquad (2)$$

where, l, m, n represent the direction cosine of the angle between magnetic field H and principal axis. Eq. (2) can easily be solved when H is parallel to the principal axes,

(a) $H//x$

$$\left.\begin{aligned} W_1&=\frac{D+E}{2}-\sqrt{\left(\frac{D+E}{2}\right)^2+g^2\beta^2H^2}\,,\\ W_2&=D-E\,,\\ W_3&=\frac{D+E}{2}+\sqrt{\left(\frac{D+E}{2}\right)^2+g^2\beta^2H^2}\,,\end{aligned}\right\} \qquad (3)$$

(b) $H//y$

$$\left.\begin{aligned} W_1&=D+E\,,\\ W_2&=\frac{D-E}{2}-\sqrt{\left(\frac{D-E}{2}\right)^2+g^2\beta^2H^2}\,,\\ W_3&=\frac{D-E}{2}+\sqrt{\left(\frac{D-E}{2}\right)^2+g^2\beta^2H^2}\,,\end{aligned}\right\} \qquad (4)$$

(c) $H//z$

$$\left.\begin{aligned} W_1&=D-\sqrt{E^2+g^2\beta^2H^2}\,,\\ W_2&=D+\sqrt{E^2+g^2\beta^2H^2}\,,\\ W_3&=0\,.\end{aligned}\right\} \qquad (5)$$

These results are illustrated in Fig. 3.

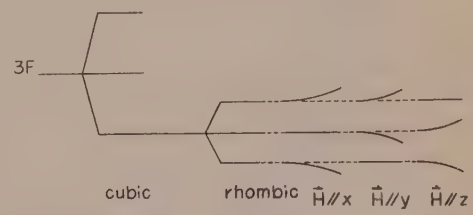

Fig. 3. Energy level splitting of Ni^{+2} ion (not to scale).

As is well known, the general formula of the magnetic susceptibility is

$$\chi=\frac{NkT}{H}\frac{\partial}{\partial H}\log Z\,, \qquad (6)$$

where Z is the partition function and N is the number of magnetic ions.

Forming the partition function from Eqs. (3), (4) and (5), and using the relation (6), we can get the principal susceptibilities as follows:

$$\chi_x=\frac{2Ng^2\beta^2}{\frac{D+E}{2}}\frac{\sinh\frac{D+E}{2kT}}{\exp\left(\frac{3E-D}{2kT}\right)+2\cosh\frac{D+E}{2kT}}\,, \qquad (7)$$

$$\chi_y=\frac{2Ng^2\beta^2}{\frac{D-E}{2}}\frac{\sinh\frac{D-E}{2kT}}{\exp-\left(\frac{3E+D}{2kT}\right)+2\cosh\frac{D+E}{2kT}}\,, \qquad (8)$$

$$\chi_z=\frac{2Ng^2\beta^2}{E}\frac{\sinh\frac{E}{kT}}{\exp\left(\frac{D}{kT}\right)+2\cosh\frac{E}{kT}}\,. \qquad (9)$$

To get the equation (7)~(9), the low field approximation is used. The results in the case of $NiNH_4$ Tutton salt are shown in Fig. 4.

The energy levels can also be obtained for the arbitrary directions with the low field approximation. The results are as follows:

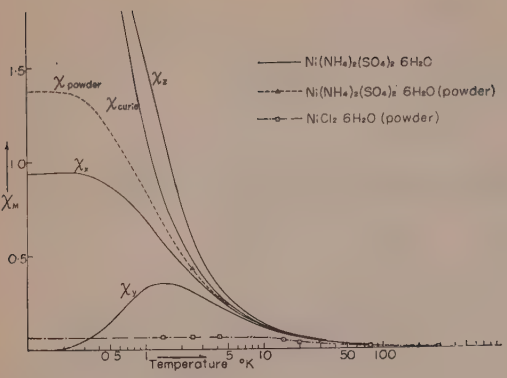

Fig. 4. Molar susceptibility of nickel salts. χ_{curie} shows the susceptibility of $D=E=0$, $g=2.25$.

$$\left.\begin{aligned} W_1 &= D-E-\frac{g^2\beta^2H^2}{2E} \\ &\quad +\frac{g^2\beta^2H^2}{2E(D-E)}\{D(l^2+m^2)-E(l^2-m^2)\}, \\ W_2 &= D+E+\frac{g^2\beta^2H^2}{2E} \\ &\quad -\frac{g^2\beta^2H^2}{2E(D+E)}\{D(l^2+m^2)-E(l^2-m^2)\}, \\ W_3 &= -\frac{g^2\beta^2H^2}{D^2-E^2}\{D(l^2+m^2)-E(l^2-m^2)\}, \end{aligned}\right\} \quad (10)$$

Then, using Eq. (6) and averaging for all directions, we get the susceptibility for powdered samples,

$$\chi_p=\frac{2Ng^2\beta^2}{3(D^2-E^2)}\,\frac{2D-\left\{\dfrac{3E^2-D^2}{E}\sinh\dfrac{E}{kT}+2D\cosh\dfrac{E}{kT}\right\}\exp\left(-\dfrac{D}{kT}\right)}{1+2\exp\left(\dfrac{-D}{kT}\right)\cosh\dfrac{E}{kT}}. \quad (11)$$

At $T=0$, Eq. (11) becomes

$$\chi_{p,\,T\to 0}=2Ng^2\beta^2\frac{-(D+3E)}{6E(D+E)}. \quad (12)$$

It must be noticed that the powder susceptibility becomes temperature independent at sufficiently low temperatures and the example is illustrated in Fig. 4 in the case of $Ni(NH_4)_2(SO_4)_2\cdot 6H_2O$ which has been investigated by means of paramagnetic resonance[3),5)] and D, E and g are well known ($D=-2.24$, $E=-0.39$, $g=2.25$). Though the deviation from Curie's law is small, the theoretical results show a satisfactory coincidence with experimental ones. Then let us consider the anomaly of $NiCl_2\cdot 6H_2O$. This can be explained if we assume D and E, about twenty times greater than that of $NiNH_4$ Tutton salts. This means the presence of a large deformed electric field on Ni^{++} ion in the crystal. The precise results may be obtained by paramagnetic resonance which could not be observed in the usual microwave region. Submillimeter wave may be necessary for this purpose. It must also be noticeed that, D and E are assumed to be large compared to the Zeeman energy and therefore our results are not used in the case of $NiSiF_6\cdot 6H_2O$ in which Ni^{++} ion is subjected to a crystalline field of trigonal symmetry and $E=0$.

It may also be interesting to investigate the effect of the exchange interaction, especially on $NiCl_2\cdot 6H_2O$, concerning the above mentioned behaviour.

References

1) L. C. Jackson: Phil. Trans. Roy. Soc. Lond. **224** (1924) 1.
B. C. Guha: Proc. Roy. Soc. A **206** (1951) 353.
2) R. Schlapp and W. G. Penney: Phys. Rev. **42** (1932) 666.
3) J. H. E. Griffiths and J. Owen: Proc. Phys. Soc. A **64** (1951) 583. Proc. Roy. Soc. A **213** (1952) 459.
R. P. Penrose and K. W. H. Stevens: Proc. Phys. Soc. A **63** (1950) 29.
4) J. Becquerel and J. van den Handel: Physica **6** (1939) 1034.
5) M. Date: Sci. Rep. RITU A **6** (1954) 390.
6) B. Bleaney and K. W. H. Stevens: Report on Progress in Physics (1953) 108.

JOURNAL OF THE PHYSICAL SOCIETY OF JAPAN Vol. 13, No. 2, FEBRUARY, 1958

X-ray Studies on the Structures of Solid Solutions $NaCl$-$CaCl_2$ III. Influence of Heat Treatments on the Diffuse Reflexions of X-rays due to {111} and {310} Plate-Zones

By Kazuo SUZUKI

Tokyo Institute of Technology, Oh-Okayama, Meguro, Tokyo

(Received October 30, 1957)

As reported in previous papers (J. Phys. Soc. Japan, **9** (1954) 702; *ibid.* **10** (1955) 794), single crystals of solid solutions $NaCl$-$CaCl_2$ contain two kinds of plate-zones extending parallel to {111} and {310} planes of the matrix. The present study concerns with the change of these plate-zones by heat treatments at various temperatures. Single crystals of solid solutions $NaCl$-$CaCl_2$ containing 10 mole per cent $CaCl_2$, which have been made uniform solid solutions by pre-heating at 400°C (being slightly above the solid-solubility limit of the phase diagram of $NaCl$-$CaCl_2$ system), were aged at room temperature or heated at higher temperatures. It is found that the {310} plate-zone is stable only at low temperatures, while the {111} plate-zone is more stable at higher temperatures. As the heating temperature is raised, the {111} plate-zone gradually tends from a coherent structure to an incoherent structure. Rotating-crystal X-ray photographs for the crystal heat-treated at 300°C (being slightly below the solid-solubility limit of the phase diagram) reveal that the final products of the precipitation have the crystal structure of $CaCl_2$, with an orientation favouring the structure model of the {111} plate-zones proposed in Part II.

§ 1. Introduction

In previous papers,[1),2),3)] it was reported that single crystals of the solid solutions of NaCl with a few mole per cent of $CaCl_2$ give the characteristic diffuse reflexions of X-rays corresponding to a rod-like distribution of the intensity around reciprocal-lattice points for the matrix. These diffuse reflexions were interpreted as being due to precipitation of small plate-like structures (called the *plate-zones*), parallel to {111} or {310} planes of the matrix lattice. In order to explain the fact that the rods in reciprocal space appear only at the normal reciprocal-lattice points of the matrix but not at any super-reciprocal-lattice points, it was assumed that each of the plate-zones was composed of smaller regions (called *platelets*), which possess a quasi-crystalline structure with super-lattice periods and are clustered together rather compactly with anti-phase relations among themselves (Part I).

In Part II of the paper, the structure of the platelets were proposed by anticipating that the arrangement of ions around a Ca^{++} ion in each platelet is somewhat similar to the crystal structure of $CaCl_2$, and a good agreement was obtained between calculated and observed intensities of the rods, especially for the $\langle 111 \rangle_r$ rods.

In the present paper, the influence of the heat treatments of samples on the diffuse scattering is reported in more detail than that briefly described in Part II. It was confirmed, in particular, that at higher temperatures the patterns due to the $\langle 111 \rangle_r$ rods change to spotty patterns due to the crystallites of $CaCl_2$ with orientations favouring the proposed structure model in Part II for the {111} platelets.

§ 2. Experimental

Single crystals of solid solutions of NaCl containing 10 per cent $CaCl_2$* are used for the specimen, because these can give intense diffuse reflexions. The procedure of heat treatment of the samples is as follows. The crystal suitably shaped by cutting and etching according to the processes described in Part I is put in a small vessel made of thin nickel plate (0.07 mm thick), and heated in an electric furnace kept at a desired temperature. After heating for about 1 hour, the vessel is quickly

* As to the implication of the percentage of $CaCl_2$, cf. Part I § 2 *a*).

cooled by placing it on a copper plate kept at room temperature (about 15°C). Because of small heat capacity of the vessel as well as of the specimen, it is conceived that the high temperature states can be quenched sufficiently well to the room temperature by the above procedure.

The specimens heat-treated as above were studied at the room temperature by the stationary-crystal or the rotating-crystal X-ray methods, using Ni-filtered Cu radiation. The distance from specimen to film were 4 cm.

§ 3. Influence of Heat Treatments on the $\langle 111 \rangle_r$ and $\langle 310 \rangle_r$ Rods

The present study on the influence of heat treatment was made by starting from the crystals which were pre-heated at 400°C for 1 hour followed by quenching to a room temperature. As seen in Fig. 1*a*, the diffraction photograph taken with this crystal shows almost no extra reflexions, indicating that Ca^{++} ions and vacancies are almost uniformly distributed at the atomic sites of NaCl crystal.** It is supposed that the heating at 400°C for the crystal used corresponds to the point "*A*" in the phase diagram, and it is brought to the point "*B*" by the quenching (Fig. 2).

The specimens thus treated were subjected to two kinds of treatments; i.e., i) the aging at room temperature, and ii) the heating at higher temperatures.

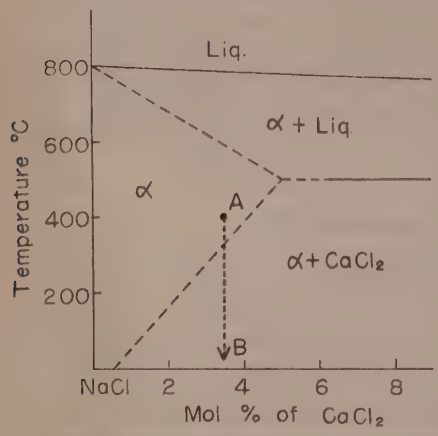

Fig. 2. Part of the phase diagram for NaCl-$CaCl_2$ system at lower $CaCl_2$ compositions.

** The patterns contain no diffuse reflexions except a faint diffuse reflexion located at $(\frac{1}{2}\frac{1}{2}\frac{1}{2})$. This reflexion suggests a new type of imperfection to exist in the matrix lattice at this stage (cf. Part I § 3 *a*)).

i) *Room-temperature aging*

Fig. 1*b* shows the diffraction photograph taken when the preheated specimen was kept for 3 days at room temperature. The photograph was taken with the [001] axis vertical and $\varphi=23°$. φ is the angle between the incident beam and the horizontal $[0\bar{1}0]$ axis. In this photograph the diffuse reflexions due to $\langle 310 \rangle_r$ rods can already be seen around the (200) point of the matrix. The diffuse reflexions due to $\langle 111 \rangle_r$ rods are, however, not yet appearing. Fig. 1*c* corresponds to the specimen kept for a month, in which we can see that the diffuse spots due to the $\langle 310 \rangle_r$ rods grew intense still further, and at the same time, those due to the $\langle 111 \rangle_r$ rods began to appear.

ii) *High-temperature treatments*

The influence of heat treatments was studied in the following way. A pre-heated crystal was heated at first at a temperature, say 50°C, and quenched to room temperature and then examined by X-rays. The same sample was next heated at a higher temperature, say 100°C, and quenched to room temperature and again examined by X-rays: and so on. The pre-heat treatment of the specimen was not applied at the stage between two successive heat treatments, because the crystal became imperfect when the specimen was subjected to many cycles of heat treatments across the solid-solubility limit of the phase diagram.

Figs. 3*a*~*f* show examples of the stationary-crystal photographs. The orientation of the crystal with respect to the incident X-ray beam is nearly the same as in the case of Fig. 1. By the heating at 50°C, there occurred no appreciable changes as compared with the case of Fig. 1*a*. When heated at 100°C (Fig. 3*b*), both the $\langle 111 \rangle_r$ and $\langle 310 \rangle_r$ rods began to appear. Diffuse spots due to the $\langle 310 \rangle_r$ rods were, however, considerably weaker than those due to the $\langle 111 \rangle_r$ rods. When heated at 150°C, diffuse spots due to the $\langle 111 \rangle_r$ rods became very strong, although the length of the rods became short; on the other hand, those due to the $\langle 310 \rangle_r$ rods were completely disappeared (Fig. 3*c*).

In the same photograph there appear many sharp and strong extra spots, and also streaks

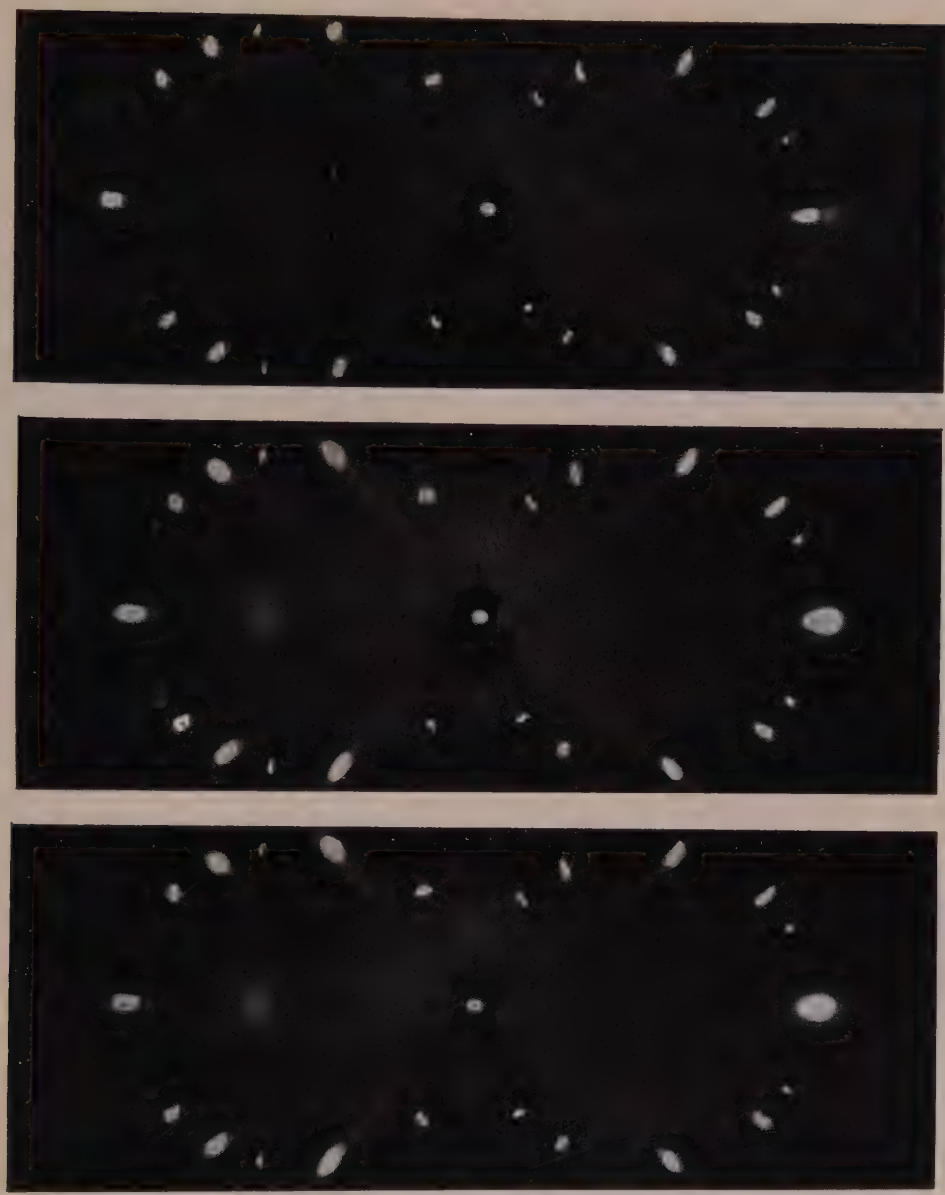

(a)

(b)

(c)

Fig. 1. Stationary-crystal X-ray photographs for the single crystal of NaCl-$CaCl_2$ solid solution containing 10 % $CaCl_2$ at several stages of aging at room temperature after being pre-heated at 400°C and quenched to a room temperature. [001] axis vertical, $\varphi=23°$. Filtered Cu radiation, 40 kV, 10 mA, 8 h. Flat films. (*a*) Immediately after the heat treatment; (*b*) 3 days after the heat treatment; (*c*) 4 weeks after the heat treatment.

which are either passing through or lying between the spots. Though it appears at first sight that some of the spots due to the $\langle 111 \rangle_r$ rods (indicated by arrows) are stronger than the rest of the spots due to the same rods, these are overlapped by weak extra reflexions. When the temperature of heat treatment is raised, the reflexions overlapping at the $\langle 111 \rangle_r$ rods increase their intensities and sharpness, and are gradually separating from the $\langle 111 \rangle_r$ rods. At the same time, the streaks change gradually to sharp spots as seen in Figs. 3*c*~*e*.

At 300°C (Fig. 3*f*), the reflexions due to the $\langle 111 \rangle_r$ rods and also all the streaks were perfectly changed to sharp spots. The arrangement of these spots is rather complex

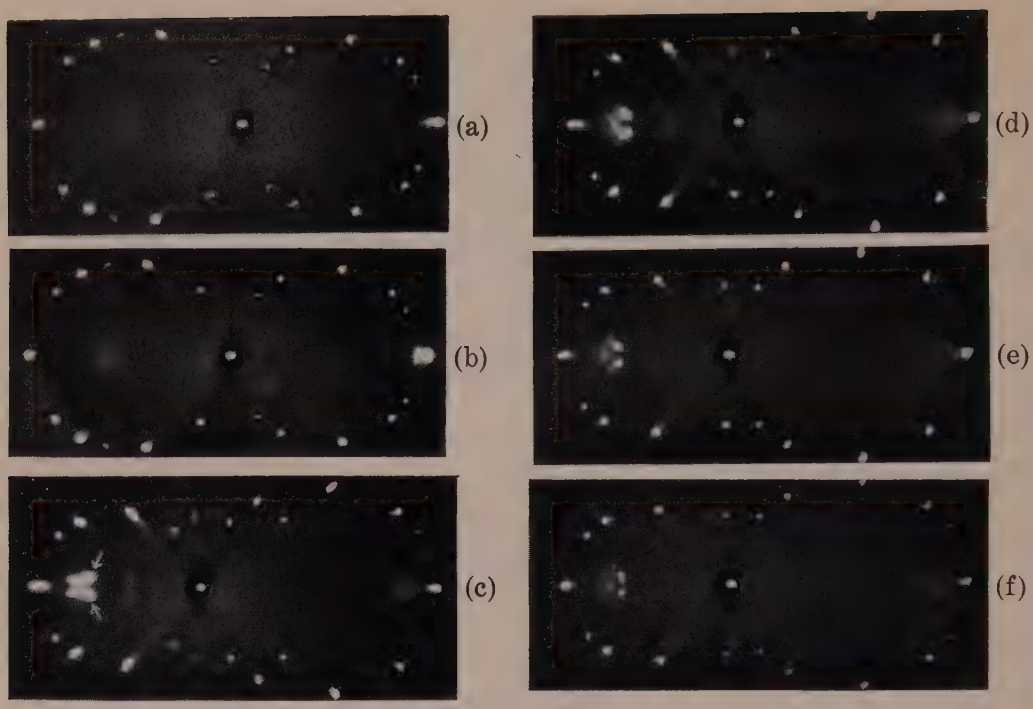

Fig. 3. Stationary-crystal X-ray photographs for the pre-heated single crystal of NaCl-$CaCl_2$ solid solution containing 10 % $CaCl_2$ at several stages of heat treatments. Photographs were taken at room temperature. [001] axis vertical, $\varphi=24°$. Filtered Cu radiation, 40 kV, 10 mA, 4 h. Flat films. (*a*) After 1 hour's heating at 50°C; (*b*) after 1 hour's heating at 100°C; (*c*) after 1 hour's heating at 150°C; (*d*) after 1 hour's heating at 200°C; (*e*) after 1 hour's heating at 250°C; (*f*) after 1 hour's heating at 300°C.

Fig. 4. Rotating-crystal X-ray photograph for the single crystal of NaCl-$CaCl_2$ solid solution containing 10 % $CaCl_2$ which has been quenched to room temperature after heating at 300°C for 1 hour. [001] axis rotation. Filtered Cu radiation, 35 kV, 13 mA, 6 h. Flat film.

but symmetric with respect to the Laue diffraction pattern due to the matrix lattice, indicating preferred orientations of a certain kind of precipitated particles in the matrix. By taking rotating-crystal X-ray photographs as described in the next section, these precipitates are found to be $CaCl_2$ crystallites.

§ 4. Crystal Structure of Precipitates and their Arrangement relative to the Matrix Lattice

a) Rotating-crystal X-ray photographs

Rotating-crystal photographs were taken for the specimen heat-treated at 300°C, which gave the Laue diffraction pattern of the type as shown in Fig. 3*f*. The crystal was rotated around either [001] or [101] axis of the crystal. On Fig. 4 corresponding to the [001] axis rotation there appear weak but sharp reflexions superposed on the strong reflexions due to the matrix lattice. The weak reflexions are grouping on several rings of different spacings. In the first column of Table I, the

Table I. Lattice spacings, *d*, of the precipitates and those of $CaCl_2$.

precipitates	$CaCl_2$	
d(Å)	*d*(Å)	(*hkl*)
4.46, 4.51, 4.51	4.49	(110)
3.42	3.46	(101), (011)
3.02, 3.02, 3.03	3.05	(111)
2.84, 2.85	2.85	(210), (120)
2.33, 2.32, 2.32, 2.34, 2.34, 2.35	2.33	(211), (121)
2.24, 2.24	2.24	(220)

spacings corresponding to the observed spots are given. The spacings of lattice planes of $CaCl_2$ crystals[4] are also tabulated for comparison. We see that the lattice spacings of the precipitates coincide with those of $CaCl_2$.

b) Orientation of $CaCl_2$ particles

In analysing the rotating-crystal photograps, it is convenient to use the cylindrical co-ordinates ξ, ζ and ω for representing the positions of the reciprocal-lattice points (Fig. 5). For the photograph shown in Fig. 4, the ζ-axis is taken parallel to the $[001]_r$ axis of the matrix, while the ξ-axis is lying in the $(001)_r$ plane. When the crystal is rotated around $[001]_r$, each reciprocal-lattice point moves on a circle with the radius ξ. The crossing points of these rings with the sphere of reflexion determine the conditions for the Bragg reflexions. In the case of the flat-film method, ξ and ζ are given by

$$\left.\begin{aligned} \xi &= \left\{1+\frac{D^2+x^2}{D^2+r^2}-\frac{2D}{\sqrt{D^2+r^2}}\right\}^{1/2}, \\ \zeta &= \frac{y}{\sqrt{D^2+r^2}}, \end{aligned}\right\} \quad (1)$$

where x and y are the co-ordinate values of each reflexion spot measured on the film, re-

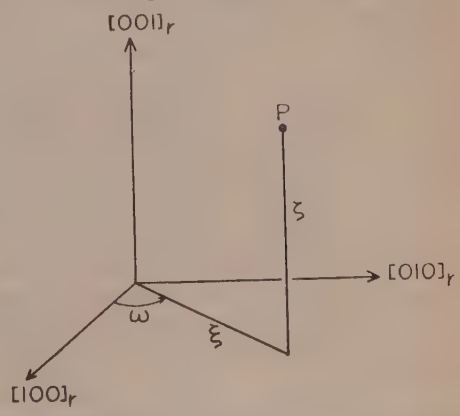

Fig. 5. Cylindrical co-ordinates for a reciprocal-lattice point *P*.

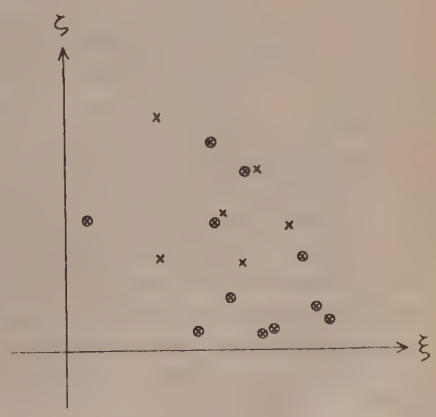

Fig. 6. (ξ, ζ)-diagram corresponding to weak reflexions in Fig. 4. Crosses which are enclosed by circles show the reflexions explained by Fig. 8; those not enclosed show the reflexions explained by Fig. 10.

spectively parallel and perpendicular to the equator line; D is the distance between the crystal and the film, and $r=(x^2+y^2)^{1/2}$.

Fig. 6 shows the (ξ, ζ)-diagram for the weak reflexions appearing in Fig. 4. After some trials, we could find that at least some of the reflexions in Fig. 6 are explained by assuming that the precipitated crystallites of $CaCl_2$ structure (C) take relative orientations with respect to the matrix (M) as follows:

$$\left.\begin{array}{l}(100)_C \text{ or } (010)_C // \{111\}_M\,, \\ [001]_C // \langle 110\rangle_M\,.\end{array}\right\} \qquad (2)$$

Fig. 7 shows the projection of reciprocal-lattice space for $CaCl_2$ crystal and that for the matrix related by the condition (2); the plane of projection is $(110)_{M,r}$* which is parallel to $(001)_{C,r}$. The $(hk0)$ points of $CaCl_2$ ($l=0$) lies on the plane of the projection, whereas the points with $l \neq 0$ are aligned on the line perpendicular to the plane of the projection

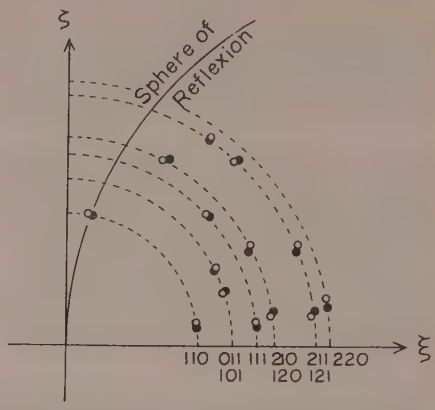

Fig. 8. (ξ, ζ)-diagram of the reflexion spots corresponding to the rotation of the reciprocal lattice of Fig. 7 around $[001]_{M,r}$.

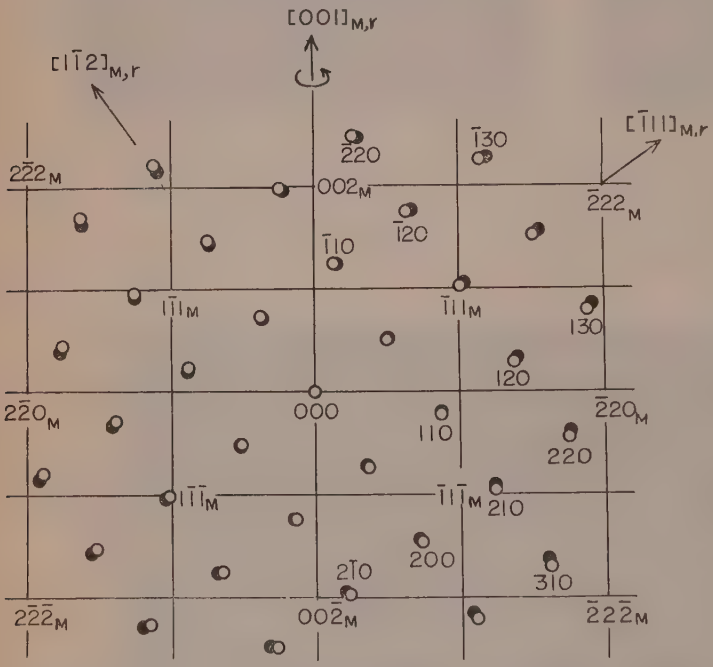

Fig. 7. Projection of reciprocal space for $CaCl_2$ crystal to the $(110)_{M,r}$ plane of the matrix which are related by the condition (2). Open circles correspond to reciprocal-lattice points of $CaCl_2$ which is oriented according to the relation $[010]_{C,r} // [\bar{1}11]_{M,r}$; filled circles correspond to those of $CaCl_2$ which is oriented according to the relation $[100]_{C,r} // [\bar{1}11]_{M,r}$. Indices are referred to open circles. Reciprocal space for the matrix is represented by solid lines; its reciprocal-lattice points are indicated by "M".

passing through the corresponding $(hk0)$ point. The open and filled circles correspond respectively to the two alternative cases of the first relation in (2). Because of the smallness of the difference of the length of a- and b-axis of the $CaCl_2$ structure ($a=6.24$ Å, $b=6.43$ Å), the two kinds of points are almost overlapping except for higher indices.

The (ξ, ζ)-diagram of the reflexion spots corresponding to the rotation of the reciprocal lattice of Fig. 7 around $[001]_{M,r}$ is shown in Fig. 8. The spots explained by Fig. 8 are enclosed by circles in Fig. 6. The spots remain unexplained can be interpreted as follows. Though we have considered so far only the case where $[001]_C$ is parallel to $[110]_M$, it is possible to occur the cases in which $[001]_C$ is parallel to $[101]_M$ or $[011]_M$. We can equally construct the (ξ, ζ)-diagram for the latter cases, although the process of construction is rather complex and some elementary geometrical considerations are needed because the axis of the rotation, $[001]_{M,r}$, is not contained in the $(101)_{M,r}$ or $(011)_{M,r}$ plane (Fig. 9). Fig. 10 shows the result of the construction.

* $(hkl)_{M,r}$ and $[hkl]_{M,r}$ denote the lattice planes and lattice rows in reciprocal space of the matrix respectively, and $(hkl)_{C,r}$ and $[hkl]_{C,r}$ denote those in reciprocal space of $CaCl_2$. Cf. Part I, p. 705.

We can see that all of the observed spots indicated in Fig. 6 are explained in this way.

As seen in Fig. 4, some of the reflexion spots due to the precipitates are broad and some are sharp. Moreover, some of the spots

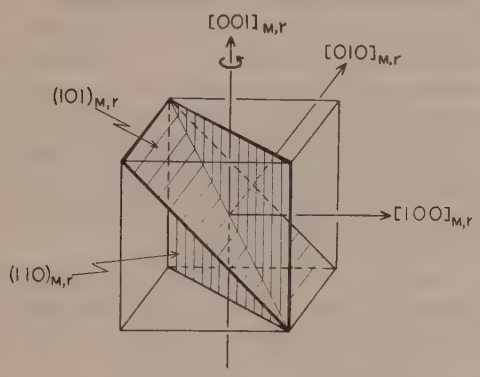

Fig. 9. Reciprocal space of the matrix showing two kinds of orientational relationship between the $[001]_{M,r}$ axis and the $\{110\}_{M,r}$ planes. $(011)_{M,r}$ plane is not shown since this is equivalent to $(101)_{M,r}$.

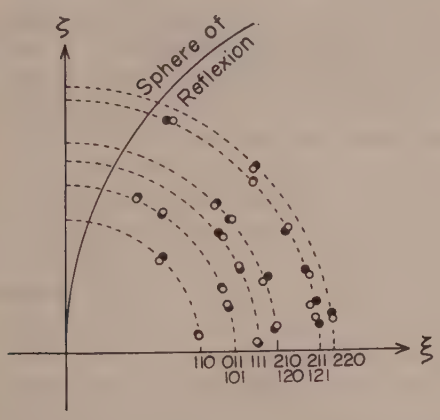

Fig. 10. (ξ, ζ)-diagram of the reflexion spots corresponding to the $[001]_{M,r}$ axis rotation of the reciprocal lattice of $CaCl_2$ being in the relation $(001)_{C,r}//(101)_{M,r}$ with respect to the matrix.

are long and some are short. These features are explained as follows. As seen in the Fig. 8 or 10, each reciprocal-lattice point is composed of two kinds of crystallites represented by open and filled circles, orienting according to the relation $(010)_C//\{111\}_M$ and $(100)_C//\{111\}_M$, respectively. Some of such paires of the reciprocal-lattice points are closer, and some are apart. Besides, some of the reciprocal-lattice points in Fig. 8 are situated at positions very close to those to those in Fig. 10. Superposing the both figures results in the various features of individual reflexion spot ovserved in Fig. 4.

§ 5. Discussion

As was stated in Part I of the paper, the diffraction patterns due to the single crystals of solid solutions $NaCl\text{-}CaCl_2$ which are characterized by the rod-like distributions of the intensity weight in reciprocal space have analogous features with those due to many age-hardenimg alloys such as Al-Cu, Al-Ag, etc. Moreover, many analogous features with the case of the alloys can be found also with respect to the change of pattern with the heat treatments as described in § 3. These analogous features are expected to take place because of similar thermodynamical conditions on the phase diagram of the solid solutions $NaCl\text{-}CaCl_2$ and of the age-hardening alloys.

Since the crystals were pre-heated at 400°C and then quenched to the room temperature, each crystal was initially in a state of unstable super-saturation at the room temperature. Thus the precipitations of the {111} and {310} plate-zones took place by the aging at this temperature. Rate of precipitation of both kinds of plate-zones are, however, different. When the crystal was kept for 3 days at room temperature, precipitations were composed of {310} plate-zones only, and the {111} plate-zones scarcely appeared after a month. This fact suggests that at room temperature the activation energy for the formation of the {310} plate-zones is lower than for the {111} plate-zones.

As seen in the series of photographs in Fig. 3, the rate of precipitation of the both types of the plate-zones is considerably promoted by heating the crystal at higher temperatures. When the crystal was heated at 150°C, however, the $\langle 310\rangle_r$ rods which had appeared by the heating at 100°C were perfectlydisappeared, while the $\langle 111\rangle_r$ rods became very strong. This fact suggests that the {310} plate-zone is stable only at relatively low temperatures, and the {111} plate-zone is more stable at higher temperatures, although as mentioned above the activation energy for the formation of the latter seems to be higher than that for the {310} plate-zone.

At 150°C, the extra spots also began to appear superposing on some of the $\langle 111\rangle_r$ rods, and these became gradually strong and sharp as the heating temperature was elevated (Figs. 3*b*~*d*). We can infer from this fact

that at 150°C the {111} plate-zone, which has been coherent with the matrix when it was formed by the heat treatment at lower temperatures, have considerably grown up, and are now tending to an incoherent structure. Though the degree of incoherency seems to be still quite small at this stage, it is conceived that the incoherency becomes larger as the heating temperature is elevated further, and finally, to the extent that the particles of $CaCl_2$ crystals are deposited in the matrix.

Summarizing the above observations it is concluded that the features of the change of the diffraction patterns at relatively low temperatures are characterized by the existence of unstable plate-like regions or the plate-zones. Such unstable regions are well known in the case of age-hardening alloys by the name of Guinier-Preston zones.

In the case of the age-hardening alloys, the coagulation of vacancies in the quench-annealed alloys is considered to be an important factor for the formation of the Guinier-Preston zones.[5] As was stated in Part I, when $CaCl_2$ is dissolved in NaCl at higher temperatures, a Na^+ ion at a lattice site of NaCl is replaced by a Ca^{++} ion, and at the same time, another Na^+ ion is removed from the crystal to satisfy the requirement of the neutrality of electric charge, leaving a positive ion vacancy. So that at least as many positive ion vacancies as the number of the Ca^{++} ions dissolved are frozen-in in the matrix lattice of the NaCl-$CaCl_2$ solid solutions. The fact that the plate-zones are formed at room temperature suggests that such vacancies can migrate in the interior of the matrix at this temperature, and they aggregate so as to form planar layers. Therefore, it is likely that in the case of NaCl-$CaCl_2$ solid solutions also the vacancies play an important role in the formation of the {111} and {310} plate-zones.

In conclusion, the author wishes to express his hearty thanks to Professor S. Miyake for his valuable discussions and helpful advices.

References

1) S. Miyake and K. Suzuki: Acta Cryst. **7** (1954) 514.
2) S. Miyake and K. Suzuki: J. Phys. Soc. Japan **9** (1954) 702.
3) K. Suzuki: J. Phys. Soc. Japan, **10** (1955) 794.
4) J. D. Hanawalt, H. W. Rinn and L. K. Frevel: Ind. Eng. Chem., Anal. Ed. **10** (1938) 457.
5) K. Hirano, Y. Takagi and H. Maniwa: J. Phys. Soc. Japan **10** (1955) 587.

JOURNAL OF THE PHYSICAL SOCIETY OF JAPAN Vol. 13, No. 2, FEBRUARY, 1958

Collective Electron Ferromagnetism, III. Relative Magnetization of Ferromagnetic Alloys*

By Hiroshi WATANABE

The Research Institute for Iron, Steel and Other Metals, Tohoku University, Sendai

(Received August 20, 1957)

Here is studied the relative magnetization (ζ_0) at absolute zero of temperature of ferromagnetic alloys composed of the first transition metals (except manganese). Based on Stoner's representation of the reduced inverse susceptibility *vs* reduced temperature curves, ζ_0 values are found from the measured values of saturation magnetization at absolute zero (σ_0), of the Curie temperature (θ) and of the mass susceptibilities above the Curie temperature (χ). With the estimated values of ζ_0, the number of carriers of ferromagnetism is plotted against the number of outer electrons. It is found from experiments on some body-centered cubic alloys of iron that ζ_0 is not much less than unity for these alloys, and hence it is concluded that for body-centered cubic alloys the lower half of the d band is not responsible for ferromagnetism. A similar analysis for face-centered cubic alloys shows that ζ_0 values of face-centered cubic cobalt-iron and nickel-iron alloys decrease gradually as the iron content increases, and the number of carriers of ferromagnetism becomes greater than 2 per atom near the composition of the body- and face-centered cubic boundary. Some other examinations are also made on the band theory of ferromagnetism in relation to the neutron diffraction experiments made by Shull and Wilkinson.

§ 1. Introduction

Collective electron theory of ferromagnetism has been successfully applied to some of the cobalt alloys[1] as well as to quite a number of nickel alloys.[2)3)] And it has also been emphasized that it is much more difficult to interpret the experimental data on iron alloys with the theory.[4)] There are many theories concerning the ferromagnetism of iron and its alloys with other elements, both on the side of the localized electron and on the side of the band picture, but none of them seems to have been accepted as being preferable to the others.

As for the band picture, there are two categories: one of them which has been suggested by Coles and Hume-Rothery[5)6)] assumes a fairly low value of ζ_0 of 0.76 for iron, assigning + spins for 4.65 d-electrons per atom and—spins for 2.45 d-electrons per atom (n_d, the total number of d-electrons, being assumed to be 7.1 per atom). The magnitude of the exchange energy of the electrons has been regarded as insufficient to align all the spins in one direction. And further, they attribute the departure of ζ_0 from unity to the broadening of d band, which would be expected to occur along the series nickel→cobalt→iron. The other, put forward by Pauling,[7)] assumes two types of d-functions, one responsible for ferromagnetism, the other for cohesive energy. With this picture the value of ζ_0 should be close to unity for iron provided that the electrons of the latter type are excluded from the carriers of ferromagnetism.

The primary purpose of this paper is to get experimental informations concerning ζ_0 from the measurements of paramagnetic susceptibilities above the Curie temperature, and of the saturation magnetization at absolute zero of temperature (σ_0) for body-centered cubic iron alloys, as well as for face-centered cubic alloys, and to interpret the magnetic properties of alloys composed of the first transition elements on a unified basis.

§ 2. Experimental Procedure and Results

As is well known, alloys rich in iron crystallize in body-centered cubic structure, but, in general, they are apt to be transformed into face-centered cubic structure at high tempera-

* This work has been supported in part by the Grant-in-Aid of Fundamental Scientific Research of Ministry of Education.

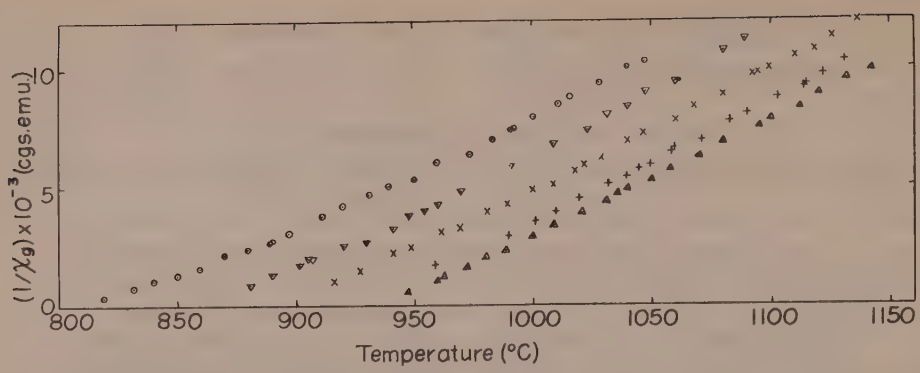

Fig. 1 *a*. Inverse mass susceptibility *vs* temperature curves of Fe–Co–V alloys, atmic percentages of Fe: Co: V being

⊙ 94.4 : 0 : 5.6 ▽ 87.1 : 7.3 : 5.6
× 84.3 : 10.2 : 5.5 + 78.9 : 15.4 : 5.7
△ 71.4 : 22.8 : 5.8

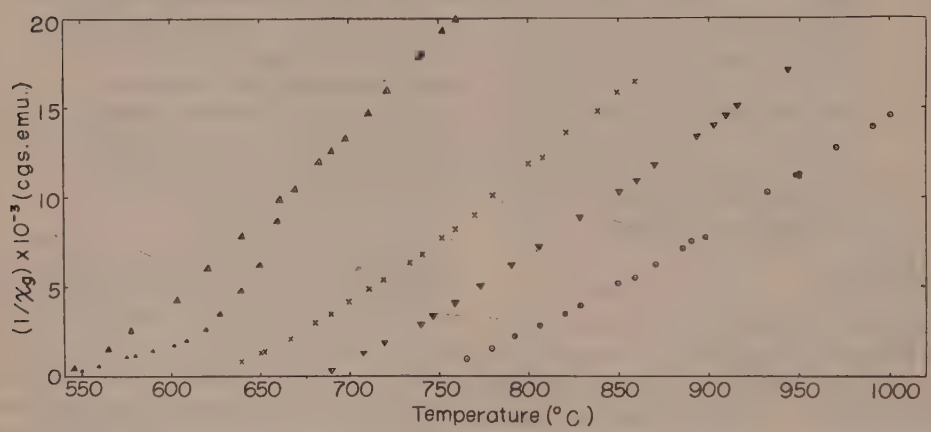

Fig. 1 *b*. Inverse mass susceptibility *vs* temperature curves of Fe–Cr–V alloys, atomic percentages of Fe:Cr:V being

⊙ 84.9 : 10.0 : 5.1 ▽ 79.4 : 14.9 : 5.7
× 74.2 : 20.5 : 5.3
△▲ } 65.5 : 29.4 : 5.2* △ Heating ▲ Cooling

* This was the only specimen, which showed thermal hysteresis.

tures, the susceptibility undergoing thereby an abrupt change. In order to avoid this tranformation we have added a few percent (approximately 5%) vanadium to all of the samples studied in order to suppress this transformation.

Experimental results are shown in Figs. 1 and 2. In Figs. 1*a* and *b*, inverse mass susceptibilities of iron-cobalt-vanadium and iron-chromium-vanadium alloys, respectivety, are plotted against temperature. The susceptibilities were measured with a pendulum magnetometer and an electromagnet. The samples were put in a small vessel, and were evacuated and sealed off. The measurements showed no thermal hysteresis for the samples studied here (cobalt content less than 20% for iron-cobalt-banadium alloys, and chromium content less than 30% for iron-chromium-vanadium alloys).

In Fig. 2*a* and *b*, the saturation magnetization at absolute zero and the ferromagnetic Curie temperature of both of the alloy systems, respectively, are plotted against composition. For comparison, data of vanadium-free alloys are taken from other author's measurements and are also shown in the figures by the dotted lines (the saturation magnetization of the iron-cobalt alloys are due to Weiss and Forrer,[8] that of the iron-chro-

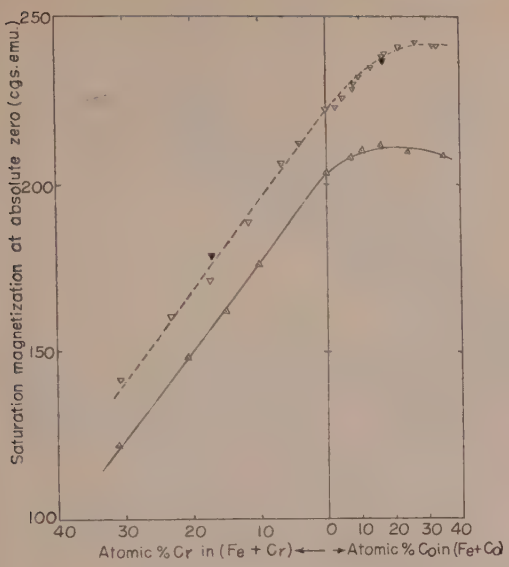

Fig. 2*a*. Saturation magnetization *vs* composition of Fe–Co–V and Fe–Cr–V alloys (△), together with that of V-free alloys (▽). Experimental points of Fe–Co alloys are due to Weiss and Forrer,[8] and those of Fe–Cr alloys due to Fallot.[9]

▼ Additional measurements on V-free alloys by the author.

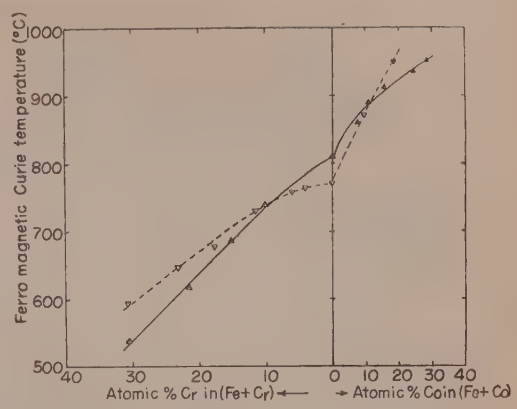

Fig. 2*b*. Ferromagnetic Curie temperature *vs* composition of Fe–Co–V and Fe–Cr–V alloys (△), together with that of V-free alloys (▽). Experimental points of Fe–Co alloy are due to Forrer,[10] and those of Fe-Cr alloys due to Fallot.[9]

mium alloys due to Fallot,[9] the Curie temperature of the iron-cobalt alloys due to Forrer,[10] and that of the iron-chromium alloys due to Fallot[9]). Saturation magnetizations were measured after Weiss and Forrer's method[8] at room temperature, and were extrapolated to absolute zero referring to the known temperature dependence of vanadium-free alloys

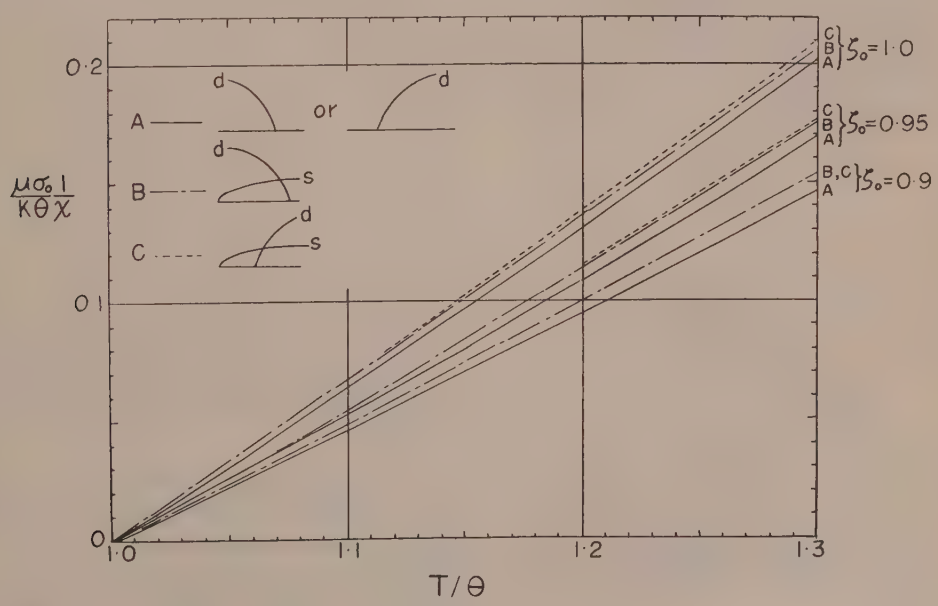

Fig. 3*a*. Theoretical reduced inverse susceptibility *vs* reduced temperature curves for some postulated electronic structures, in the temperature range $\theta < T < 1.30\theta$

A: Single parabolic d band.

B: Overlapping parabolic bands, d band being closed on the high energy side.

C: Overlapping parabolic bands, d band being closed on the low energy side.

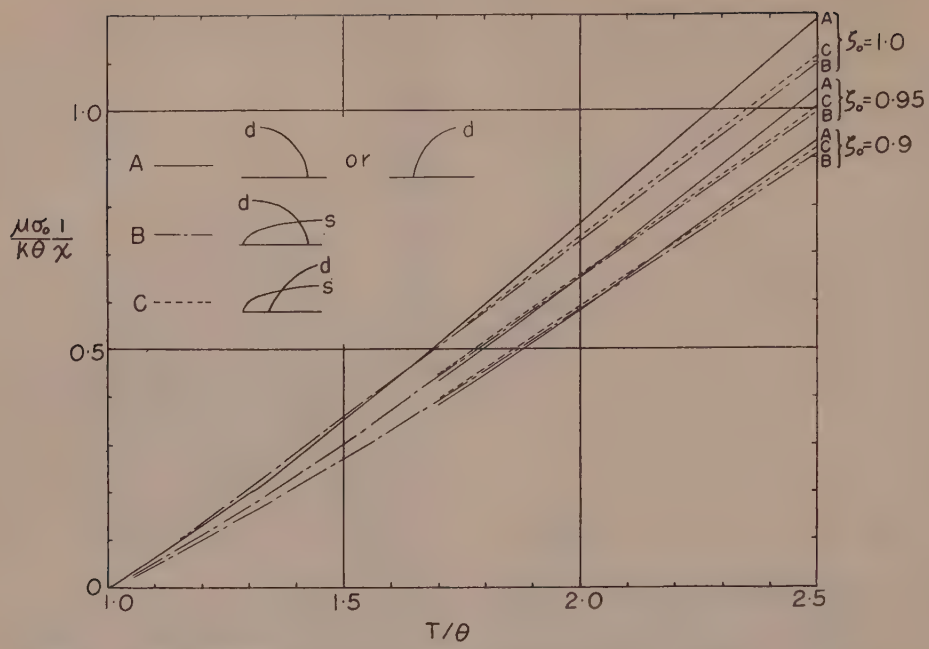

Fig. 3 *b*. The same as Fig. 3 *a*, but the temperature range is wider: $\theta < T < 2.5\theta$.

and iron-vanadium alloys.

In Fig. 3*a*, we have given a few computational results of reduced inverse susceptivility against reduced temperature. Curve A is the original Stoner curve[11], obtained by assuming a single parabolic band. Other curves will be explained in the next section. We have summarized our data in Figs. 4*a* and 4*b* in a similar representation. The comparison of points in these figures with curve A in Fig.

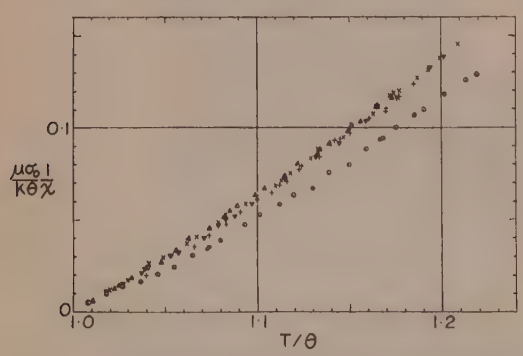

Fig. 4 *a*. Experimental reduced inverse susceptibility *vs* reduced temperature relation for Fe–Co–V alloys. Symbols of points are the same as those in Fig. 1 *a*.

3 readily gives an estimation of ζ_0 values of the measured alloys. Then we find that the values of ζ_0 of these alloys are within the range of values between 0.95 and 1.

We should have extended our measurements to the alloys containing chromium more than 30 percent if there had been no complications as to the phase diagram[12)13)], but it was given

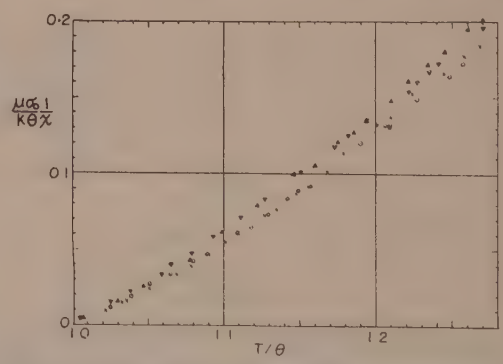

Fig. 4 *b*. Experimental reduced inverse susceptibility *vs* reduced temperature relation for Fe–Cr–V alloys. Symbols are the same as those in Fig. 1 *b*.

up for the present since a test measurment revealed that the added vanadium had little power to reduce these complications.

A similar comparison of the experimental data due to other authors of iron[14)15)], iron-chromium (3:1 at.)[15)] and iron-vanadium[16)] and iron-vanadium[16)] (3:1 at.) given in Fig. 4*c* can be made with Fig. 3*b*. Here also are the values of ζ_0 between 0.95 and 1.

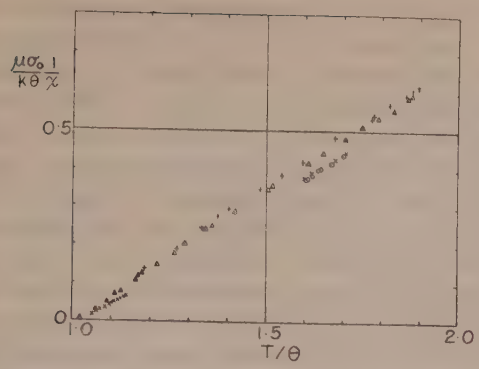

Fig. 4*c*. Experimental reduced inverse susceptibility *vs* reduced temperature relation, due to other authors, of
× bcc Fe, due to Sucksmith and Pearse,[14]
⊙ bcc Fe, due to Nakagawa,[15]
+ Fe–Cr (3:1 at) due to Nakagawa,[15]
△ Fe–V (3:1 at) due to Nakagawa.[15]

§ 3. Criticism of the Estimation of the Relative Magnetization

The procedure of the estimation of ζ_0 value from Stoner's curve is based on a single parabolic band model, while the band structure of actual alloys, of course, can by no means be described by such a simplified picture. So their remains a questions that the estimated value of ζ_0 would not be a good approximation to the actual alloys. Probably, we should take into account the band overlap effect, and also more general form of the relevant bands. The former effect can be treated analytically with a few assumptions which may be regarded as reasonable. Such a calculation has been made by Wohlfarth for nickel and nickel-copper alloys[2] and reavealed that the value of ζ_0 is changed only slightly from that derived from the single band model. We made a similar calculation in the case of iron, assuming the degree of overlapping of the *s* band to be roughly equal to that in the case of nickel, and taking the exchange transfer effect* of electrons from *d* to *s* band into account. The result of the calculation is shown by curve *B*** in Fig. 3*a*, and it is seen that ζ_0 value to be obtained by referring to curve *B* is not changed by over 2% from that to be obtained from curve *A*. Further, the result does not change materially if we take a model in which the carriers of ferromagnetism are not holes but electrons. Curve *C*** in Fig. 3*a* is the result of a calculation based on such a model, again with the assumption of overlapping *s* and *d* bands.

To summarize, the effect of band overlapping is not of primary significance for the evaluation of ζ_0 value.

It is more difficult to solve the problem of the band shape. It is almost impossible to manage the general case of band structure in an analytical form. Some calculations have been made for several cases other than that where the band form is parabolic or rectangular by Elcock *et al*[16], but their studies are restricted to paramagnetics, and it is not easy to see how the results would come out in the case of ferromagnetics. At least, however,

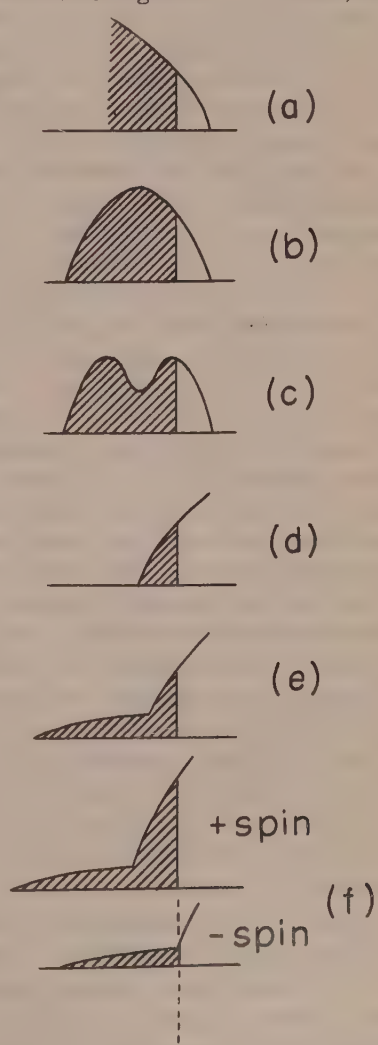

Fig. 5. (*a*)–(*e*): Some representative curves of band structure discussed qualitatively in **3**. (*f*): The detail of case (*e*). The shaded regions are occupied levels.

* Cf. Appendix I.
** Cf. Appendix II.

we may say that in our case the estimated values of ζ_0 would not be changed appreciably if the band form does not differ considerably from the standard one. For instance, if we take the band form to be rectangular, the result is $\zeta_0=1$ wherever ($0<\zeta_0<1$ being inhibited in this case), and the conclusion is substantially unchanged. A further qualitative discussion can be made with the help of our previous work on the condition of the occurrence of ferromagnetism[4]. Some representative cases were treated there: In the first case where the state density *vs* energy curve is a decreasing function of energy near the Fermi level (Fig. 5(*a*)), the minimum exchange energy required for ζ_0 to be unity should be an increasing function of the electron concentration. If in the actual case of ferromagnetic elements, ζ_0 takes the value 1 for nickel or cobalt, while it takes a value less than 1 for iron, the exchange energy should be definitely smaller for iron than for nickel or cobalt. This case corresponds to a slight generalization of the standard band form (the case of curve *A* in Fig. 3*a*), and we may expect a smaller slope of the reduced inverse susceptibility *vs* reduced temperature curve for iron than for nickel or cobalt, which is contradictory to the experiment. This conclusion may not be changed appreciably if the band is closed on the low energy side (Fig. 5(*b*)). The second case is that shown in Fig. 5 (*c*), in which the band has a low state density range in the middle. If the position of the Fermi level of iron were like what is given in the figure, and ζ_0 for iron were appreciably smaller than unity, then ferromagnetism would be observed for elements of lower electron concentrations, say for chromium or vanadium, as far as the band form and the exchange energy are regarded not to change appreciably with concentration. This does not seem likely to be true. The third case is one that represented in Fig. 5 (*d*), in which the state density curve is an increasing function of energy at the Fermi level (Fig. 1 of reference 4). In this case the slope of the state density curve is essential for the slope of the equi-exchange interaction curve as given in that figure; in order to explain the slope of the saturation magnetization *vs* electron concetration curve for iron-chromium alloys on the assumption of constant exchange interaction, the slope of the state density curve around the Fermi level of iron should be taken to be fairly steep that the state density in the region of non-ferromagnetic alloys is very small. This is what we have assumed in calculating curve *B* in the previous section. The remaining possibility that our estimation on ζ_0 would fail is one shown in Fig. 5 (*e*), where the band has a long tail in the low energy part. In this case, the relative movement of the + and − spin bands would be such as is indicated in Fig. 5 (*f*), unless the exchange integral takes an extremely high value in the region of low state density. Then ζ_0 would be less than unity while the reduced inverse susceptibility *vs* reduced temperature relation is not altered essentially from the case (*d*). The difference between cases (*d*) and (*e*), however, may be trivial as far as ferromagnetism is concerned, since we are not inquiring as to whether the electron spins in the low energy part of *d* band have positive or negative interaction. We shall call that part of the *d* band is not resposible for ferromagnetism.

§ 4. Discussion

Based on the experiments described in **2** and on the considerations sketched in **3**, we may make some inquiries on the band structure of body-centered cubic ferromagnetic alloys. We can also make similar inquiries if we utilize the experimental results of other authors of face-centered cubic or hexagonal alloys. Such a discussion will be given below. In Fig. 6 are summarized the necessary data of the saturation magnetization at absolute zero, and the number of carriers of ferromagnetism deduced from the estimated value of ζ_0.

(1) *Body-centered cubic alloys.*

As stated above, ζ_0 value is not much less than unity as far as the experimentally investigated alloys are concerned. We assume this is also true of other alloys. Then there are two cases which fit this fact according as the carriers of ferromagnetism are considered to be holes or electrons. The one is that the number of *d* electrons is equal to 10 minus the observed magnetic moment per atom (for iron, for instance, $n_d=10-2.2=7.8$, $n_s=8-7.8=0.2$); this possibility does not seem to be probable, since, for alloys with total number of outer electrons less than 7.9 per atom, we

would have negative values of n_s.

The other is that the maximum number of carriers of ferromagnetism of body-centered cubic alloy is roughly equal to 2.5 per atom, since this is the maximum observed value of saturation magnetization at absolute zero in Bohr magnetons forbody-centered cubic alloys. From this standpoint, the number of energy levels of the band responsible for ferromagnetism should be equal to $2.5\times2=5$, which leads to a separation of d band into two halves:

$$d=d_1+d_2\ ,$$

where d_1 and d_2 are sub-bands not responsible and responsible for ferromagnetism, respectively, each sub-band accommodating 5 electrons per atom.*

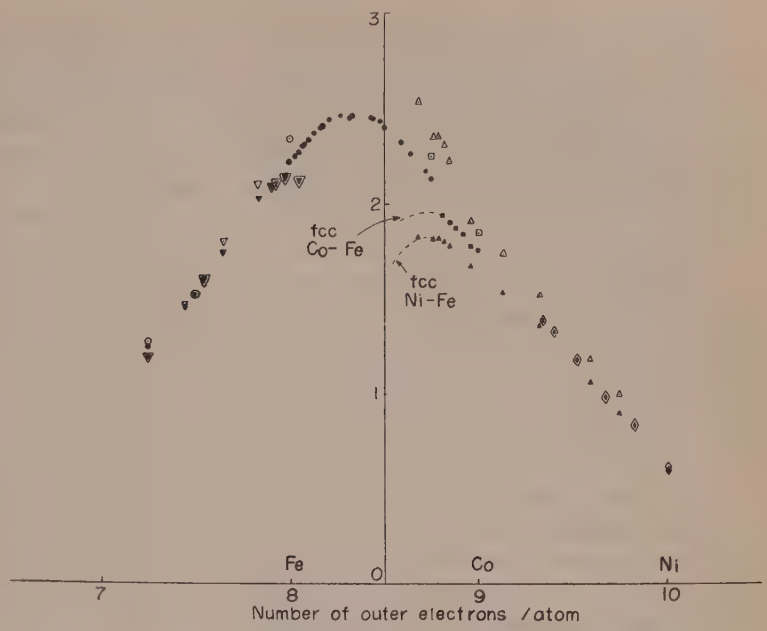

Fig. 6. Saturation magnetization (black points) in Bohr magnetons and number of carriers of ferromagnetism (open points) per atom of ferromagnetic alloys of elements of the first transition group against the number of outer electrons per atom.

▼ and ▽ Fe-Co-V and Fe-Cr-V.
● and ⊙ Fe-Cr, Fe-V, and bcc Fe-Co.
▣ and ▣ fcc Co-Fe.
▲ and △ fcc Ni-Fe.
◆ and ◇ fcc Ni-Co.

Now let us compare our result with the picture of Coles and Hume-Rothery referred to in the introduction. In view of our measurements and of the discussion given in the preceding section, the only case where ζ_0 becomes appreciably less than unity should be that indicated in the diagram (*e*) of Fig. 5; the small value of ζ_0, however, is not caused by the broadening of the band width with the decrease of electron concentration as they imagine, but is caused by the increasing significance of the low-state-density part of the d band.**

(2) *Face-centered cubic and hexagonal alloys.*

Nickel and its alloys with copper are the most fully investigated ones of this group. According to Wohlfarth's analysis[2] of the experimental data of them, ζ_0 value for nickel is just equal to unity, whereas it decreases with addition of copper at first slightly but more rapidly as the copper concentration becomes appreciable, falling to zero at about 60 at % copper. Although no detailed analysis has been given for nickel-zinc alloys, we may expect a similar situation for them.

Nickel-cobalt alloys have also been analysed by Wohlfarth[18] with the conclusion that ζ_0 is close to unity over the whole concentration range. According to a recent measurement of susceptibilities up to the melting point of cobalt made by Nakagawa[15], the value of ζ_0 is 0.95.

If we look at the range from cobalt to iron, the data of saturation magnetization due to Weiss and Forrer[8] and those of susceptibility due to Nakagawa[15] are available. Nakagawa measured the high temperature susceptibilities of cobalt-iron (3:1 at.) alloy. This alloy lies near the composition of the boundary between body- and face-centered cubic phases at room

* This conclusion is the same as that given by Bader *et al*[17], though the agreement is merely accidental.

** A part of Coles' earlier concept presented in the discussion of electronic structure of titanium alloys is rather closer to our picture.

Cf. J. Inst. Met. **80** (1951) 702.

temperature, and Weiss and Forrer's data for face-centered cubic alloys can easily be extrapolated to this composition, giving the moment of 2.0 Bohr magnetons per atom. Analysing these data, we find that $\zeta_0=0.89$ for this alloy. The number of carriers of ferromagnetism is then estimated to be approximately 2.3 per atom.

Other data giving informations concerning the face- acd body-centered cubic phase boundary are those of nickel-iron alloys. This system has been studied in great detail by Peschard,[19] and we can take out necessary data from his measurements.* The result of the analysis for this alloy system in the face-centered cubic range is that ζ_0 is still less than that in the system of face-centered cubic cobalt-iron alloys. At the phase boundary, which lies at the composition of 34.1 at % nickel, $\zeta_0=0.72$, and the estimated number of carriers of ferromagnetism is approximately equal to 2.5 per atom.**

The author believes that the mechanism proposed by Coles and Hume-Rothery for body-centered cubic iron alloys should be really called for to explain the fall of ζ_0 value with increase of iron content in face-centered cubic iron alloys.

(3) *Chromium or vanadium added to face-centered cubic alloys.*

The saturation magnetization of nickel-chromium and nickel-vanadium alloys deviate from the so-called Slater-Pauling curve[7]***. To explain this deviation, it has been proposed by Carr[21], in connection with the Zener theory of antiferromagnetic coupling between *d* eclectrons of adjacent atoms[22], that the moments of chromium or vanadium align antiparallel to those of solvent atoms. His proposition is, however, doubtful, since the neutron diffraction experiment of cobalt-chromium by Shull and Wilkinson[23] does not support such a spin configuration.

* Y. Nakagawa[20] has also reported the susceptibility data of this system up to 1600°C, which are in good agreement with Peschard's in the solid state.

** This value is apparently greater than the maximum number of carriers of ferromagnetism predicted by Bader *et al.*, *viz.* 2 per atom.

*** *Cf.*, for instance, R. M. Bozorth, *Ferromagnetism* (D. van Nostrand Company, Inc., New York 1951) *p.* 441.

A model much more consistent with the neutron diffraction data can be obtained by assuming that the outer electrons of chromium enter the unoccupied levels of nickel or cobalt, leaving no appreciable moment on chromium atoms. Such an idea has long been proposed by Hirone[24] and Wohlfarth[2] for nickel alloys, and by the author[1] for cobalt alloys. The neutron diffraction data give two possible configurations of spins, and no one can decide which is the correct one. In the case of cobalt-chromium, one gives small absolute values of chromium moment, while the other gives moment of 1.5–2 Bohr magnetons per atom which is parallel to the cobalt moments. Either configuration gives for cobalt atoms a decreasing moment with increasing chromium content. The above picture is compatible with the former configuration. We do not know, however, the precise number of electrons per chromium atom which enter into the *d* band of nickel, *viz.* the valency of chromium in this case. We have drawn the diagram in Fig. 7 on a somewhat arbitrary assumption

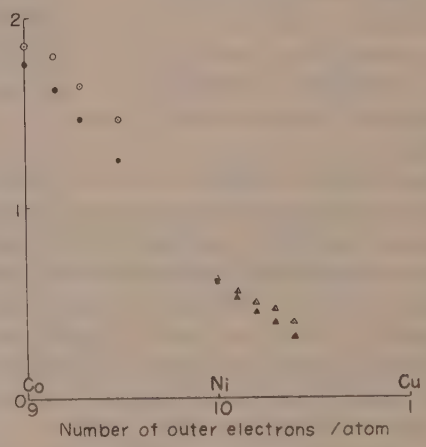

Fig. 7. Saturation magnetization (black points) in Bohr magnetons and number of carriers of ferromagnetism (open points) per atom of
● and ⊙ CO-Cr,
▲ and △ Ni-Cr,
against the number of outer electrons per atom. Here a Cr atom is assumed to throw all of its outer electrons to the *d* holes of Co or Ni.

that all of the 3*d* and 4*s* electrons of chromium enter into the *d* band of nickel or cobalt (Saturation magnetization data of cobalt alloys are due to Farcas,[25] and susceptibility data due to our previous work[1]). The points do not lie on a clearly defined straight line, but

the discrepancy may partly be due to the ambiguity mentioned above of the valency of chromium, and partly to the change of band structure with addition of chromium.

(4) *Number of s electrons, n_s.*

As can be expected from the general grounds, the s electrons of nickel have the tendency to be transferred to the d levels to fill them up. Naturally this tendency is counteracted by another effect which is common to transition elements *i.e.*, that some of the s levels lie lower than the d levels. The actual feature of electronic structure will be dependent on the relative magnitude of these competing factors. If we go from nickel to cobalt, and from cobalt to iron, it is expected that the former effect should be weakened, and hence, that overlapping of s and d bands should be strengthened. The increase of n_s along this series indicated in Fig. 8 (n_s being calculated from the estimated number of carriers of ferromagnetism) is in agreement with the expectation from the above consideration.

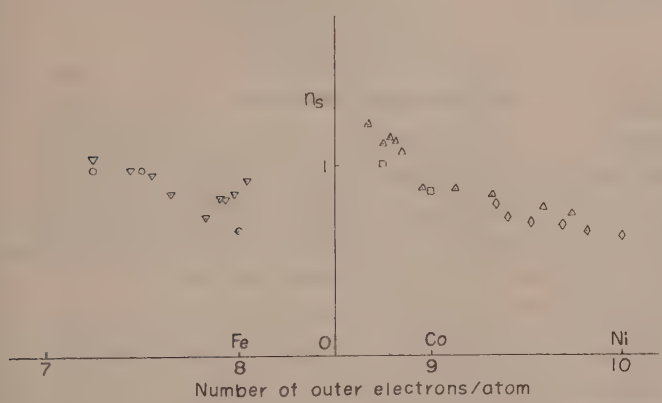

Fig. 8. n_s, the number of s electrons per atom against the number of outer electrons per atom. The symbols are the same as those in Fig. 6.

§ 5. Conclusion

By analysing the experimental results of susceptibility and saturation magnetization of ferromagnetic alloys, we have observed a definite distinction between the band structures of body- and face-centered cubic alloys. Among the current views on the electronic structure of such alloys, the Pauling picture is the best approach to the experimental results as far as body-centered cubic alloys are concerned. On the contrary, we encounter very low values of relative magnetization in some face-centered cubic alloys, which is caused by the effective smallness of the exchange integral or of the density of energy states.

Finally a brief discussion will be made of the collective electron theory in the light of the results of neutron diffraction experiment obtained by Shull and Wilkinson.[23] The collective electron theory, in its original form, does not distinguish between moments of different kind in an alloy, which is not consistent with the result offered by the neutron diffraction experiment that atoms of different kind have, in general, different moments. It may be noted, however, that the moments of constituent atoms are comprehensible by the theory.

A possible revision of the theory which takes account of the above situation may be made by considering the bands of constituent atoms separately,* an electron in one band is subjected not only to the molecular field due to the magnetization of the band to which it belongs but also to that due to the magnetization of the other band. In dilute alloys, the effect of the solute atom is determined primarily by the interaction between solvent and solute bands. In the case of face-centered cubic nickel-iron alloys, the interaction between nickel and iron bands may be estimated from the initial rate of increase of the Curie temperature with increasing iron content, while thedecrease of the Curie temperature at higher iron concentrations may be attributed to the broadening of the iron band and to a consequent decrease of ζ_0 in the same band. In the case of face-centered cobalt-iron alloys, the interaction between electrons in cobalt and iron bands is expected to be weaker than that between electrons in the cobalt band, as is indicated by the initial decrease of the Curie temperature with addition of iron to cobalt. The data for γ-iron itself are rather less conclusive; Wilkinson and Shull[27] studied coherent and incoherent magnetic scattering in iron at high temperatures and found magnetic diffuse scattering corresponding to ferro-

* A similar picture has been proposed by Coles[26] for the interpretation of the properties of copper rich nickel-copper alloys.

magnetic short range order in γ-iron, while Weiss have suggested that γ-iron is antiferromagnetic by extrapolating the neutron diffraction data on iron-manganese alloys[28] to γ-iron. The disagreement may be reconciled by considering that the lattice expansion due to heating changes the antiferrogmagnetic coupling into a ferromagnetic one, but further experimental studies will be necessary before the problem is settled.

Acknowledgements

The author wishes to express his hearty thanks to Dr. E. P. Wohlfarth who has kindly given him valuable advices concerning the exchange transfer effect, and also to Dr. C. G. Shull, who has notified him of some of the details of the neutron diffraction data on γ-iron and body-centered iron-cobalt. Thanks are also due to Mr. K. Ito for his assistance in the experiments.

APPENDIX I

The Exchange Transfer Effect

When there are two overlapping electronic bands, and the exchange integral in each of the bands is different in magnitude from each other, the electron distribution among these bands may be different in general from the case where no such difference exists. We shall call this effect the exchange transfer effect. We shall evaluate the magnitude of this effect in the simple case of overlapping d and s bands, both assumed to be parabolic, in which it is assumed that s electrons have no exchange integral with one another. An additional assumption will also be made, which is not really justifiable in the strict sense, that the total exchange energy of d electrons is proportional to the square of the net moment.* This case has been treated mathematically by Wohlfarth[2] and the result of the analysis has been applied to the interpretation of magnetic properties of nickel-copper alloys by the same author, without including this effect in his calculation.

It can easily be shown from the consideration of energy relation at absolute zero that the quantities related to the Fermi level of each band in Fig. 9 are connected by the following relationship:

$$\frac{1}{2}(\varepsilon_d^- + \varepsilon_d^-) = E - \varepsilon_s ,$$

with $$E = \varepsilon_{d_0} + \varepsilon_{s_0} ,$$

where ε_{d_0} and ε_{s_0} are ε values corresponding

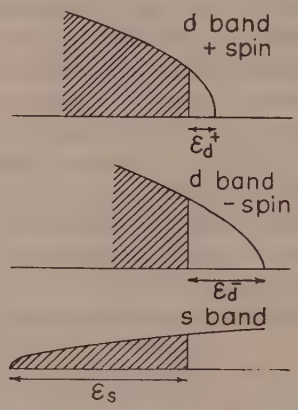

Fig. 9. Relative movement of d and s bands in an overlapping band model.

to the case with no exchange integral in the d band. With the same assumptions as Wohlfarth's of the value of $\gamma_0 = \varepsilon_{s_0}/\varepsilon_{d_0}$, and the interaction constant θ' satisfying the relation $k\theta'/\varepsilon_{d_0} = 2^{-\frac{1}{3}}$ for nickel, we may ask how his results would be modified.

The main feature of the modification is summarized in the following two points for the nickel-copper series of alloys. One is that the critical composition at which the d band is filled (and θ' falls to zero) is shifted to a slightly lower concentration of copper, *viz.* $C_{\text{crit}} = 0.6728$, from the value $C_{\text{crit}} = 0.6922$ given by Wohlfarth.** The other is that the number of s electrons at absolute zero is increased by the exchange transfer effect, since the additional kinetic energy will be more than offset by the gain in exchange energy due to the

* One may carry through the calculation with a better approximation by ommitting this assumption. It is doubtful, however, if the result so obtained would be really improved in describing actual state of affairs, since there are many other factors which should be taken into account to this approximation.

** The composition at which ferromagnetism vanishes has been considered to be approximately 60 at % copper, from the measurement of saturation magnetization due to Alder,[29] Marian, &c.[30] A recent report by Ahern and Sucksmith[31] suggests, however, a slightly steeper slope of the saturation magnetization *vs* composition curve. This might be due to the general trend of the relative movement of s and d bands. Since the above analysis neglects this effect, a more detailed discussion of C_{crit} would be superfluous.

increased number of d holes. This effect is the more significant the lower the copper concentration. In the analysis, we fix the number of d holes at absolute zero N_{d_0} at 0.6 per atom for nickel, so that, as the temperature is raised from absolute zero, the exchange transfer effect will decrease, and this will have an effect to reduce the value of N_d. If the temperature is raised further, the normal transfer effect as treated by Wohlfarth becomes predominant. Fig. 10 is a

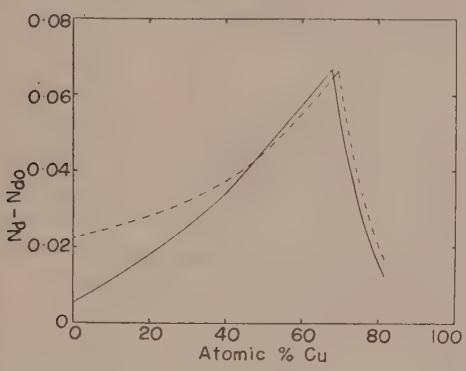

Fig. 10. Increase in the number of d holes as the temperature is raised from absolute zero to $T=\frac{(\varepsilon_{d0})_{Ni}}{2k}$, against copper concentration. Dotted line: Wohlfarth's calculation.[2] Solid line: Present calulation including the exchange transfer effect.

manifestation of such a modification plotting N_d–N_{d_0} against concentration of copper, where N_d is the value at the temperature $T=\frac{(\mathcal{E}_{d_0})_{Ni}}{2}$ (=773°K in our analysis). As can be seen from the figure, the modification as a whole is not serious in this case. The same can be said for the susceptibilities, and the qualitative aspects of Wohlfarth's results are not in error.

APPENDIX II

Specification of Models in Figs. 3a and 3b.

As for curve A of the single parabolic band model, the reader is referred to Stoner's original papers[11] and also to Wohlfarth's.[2] The calculation for curves B and C of overlapping band models was made for iron with the assumption that the ratio $\gamma_0=\mathcal{E}_{s_0}/\mathcal{E}_{d_0}$, which is a measure of the degree of overlapping of the two bands, is equal to 2. This value was chosen because this gives for case B approximately the same degree of overlapping as addopted for nickel by Wohlfarth. This can easily be seen from the relations:

$$N_d=\frac{4}{3}a_d\mathcal{E}_d^{\frac{3}{2}} \quad \text{and} \quad N_s=\frac{4}{3}a_s\mathcal{E}_s^{\frac{3}{2}}$$

The following formula may be obtained provided a_d and a_s are the same for nickel and for iron:

$$(\gamma_0)_{Fe}=(\gamma_0)_{Ni}\left(\frac{N_d}{N_s}\right)_{Ni}^{\frac{2}{3}}\Big/\left(\frac{N_d}{N_s}\right)_{Fe}^{\frac{2}{3}}.$$

If we put the values $(\gamma_0)_{Ni}=10$, $\left(\frac{N_d}{N_s}\right)_{Ni}=\frac{0.6}{0.6}=1$ and $\left(\frac{N_d}{N_s}\right)_{Fe}^{\frac{2}{3}}=\left(\frac{2.22}{0.22}\right)^{\frac{2}{3}}=4.67$, we obtain $(\gamma_0)_{Fe}=2.14$, which was substituted by the round number 2. For the analysis of case C, the same value of a_d/a_s as in B has been adopted, since we have no information of its accurate value. N_d and N_s for the calculation of the case of $\xi_0=1$ were chosen to be equal to 2.22 and 0.78, respectively, in accordance with the postulation suggested in the text of dividing the d band into two halves.

References

1) W. Hume-Rothery, H. M. Irving and R. J. P. Williams: Proc. Roy. Soc. **208 A** (1951) 431; H. Watanabe, Sci. Rep. RITU **6A** (1954) 343.
2) E. P. Wohlfarth: Proc. Roy. Soc. **195A** (1949) 434.
3) H. Watanabe: J. Phys. Soc. Japan **3** (1948) 317.
4) H. Watanabe: J. Phys. Soc. Japan **3** (1948) 12.
5) W. Hume-Rothery and B. R. Coles: Advances in Physics **3** (1954) 149.
6) B. R. Coles and W. R. Bitler: Phil. Mag. (8) **1** (1956) 477.
7) L. Pauling: Phys. Rev. **54** (1938) 899.
8) P. Weiss and R. Forrer: Ann. d. Physique (10) **12** (1929) 279.
9) M. Fallot: Ann. d. Physique (11) **6** (1936) 305.
10) R. Forrer: J. d. Physique (7) **1** (1930) 49.
11) E. C. Stoner: Proc. Roy. Soc. **165A** (1938) 372; Proc. Leeds Phil. Soc. **3** (1938) 457.
12) Y. Imai and K. Kumada: Sci. Rep. RITU **5A** (1953) 520; S. Takeda and N. Nagai, Mem. Fac. Eng. Nagoya Univ. **8** (1956) 1.
13) V. K. Bungardt and W. Spyra: Arch. f. Eisenhüt. **27** (1957) 777; W. Köster and A. v. Kienlin: ibid **27** (1957) 787; A. v. Kienlin and W. Köster, ibid **27** (1957) 793.
14) W. Sucksmith and R. R. Pearce: Proc. Roy. Soc. **167A** (1938) 189.
15) Y. Nakagawa: J. Phys. Soc. Japan **11** (1956) 855.
16) E. W. Elcock, P. Rhodes and A. Teviotdale: Proc. Roy. Soc. **221A** (1954) 53.
17) F. Bader, K. Ganzhorn and U. Dehlinger: ZS. f. Phys. **137** (1954) 190.

18) E. P. Wohlfarth: Phil. Mag. (7) **40** (1949) 1095.
19) M. Peschard: Rev. d. Mét. **22** (1925) 490, 581, 663.
20) Y. Nakagawa: J. Phys. Soc. Japan **12** (1957) 700.
21) W. J. Carr: Phys. Rev. **85** (1952) 590.
22) C. Zener: Phys. Rev. **81** (1951) 440.
23) C. G. Shull and M. K. Wilkinson: Phys. Rev. **97** (1955) 304.
24) T. Hirone: Sci. Rep. Tohoku Univ. **27** (1938) 101.
25) T. Farcas: Ann. d. Physique (11) **8** (1937) 146.
26) B. R. Coles: Proc. Phys. Soc. **65B** (1952) 221.
27) M. K. Wilkinson and C. G. Schull: Phys. Rev. **103** (1956) 516.
28) Unpublished data due to Corliss, Hastings and Weiss, cited by R. J. Weiss and K. J. Tauer in *Theory of Alloy Phases* (A. S. M. Cleveland, Ohio, 1956) p. 290.
29) M. Alder: Thesis, Zurich, 1916.
30) V. Marian: Ann. d. Physique **7** (1936) 459; M. A. Wheeler: Phys. Rev. **56** (1939) 1137: A. Krupkowski: Rev. d. Mét. **26** (1929) 131; 193.
31) S. A. Ahern and W. Sucksmith: Proc. Phys. Soc. **67B** (1956) 1050.

JOURNAL OF THE PHYSICAL SOCIETY OF JAPAN Vol. 13, No. 2, FEBRUARY, 1958

On the Effect of High Energy Radiation to Polymers

I. Cross-linking and Degradation

By Osamu SAITO

Faculty of Engineering, Chuo University, Tokyo

(Received October 28, 1957)

Integro-differential equations are obtained, which describe the variation of molecular weight distributions in a polymer substance caused by irradiation. The solutions of these equations give the gel point and the average molecular weights. In the case of cross-linking without cyclization, the results agree with those obtained by other authors. The problems involving cyclization and branching are also solved, showing that the gel formation is retarded by cyclization and that the weight average branching number diverges at the gel point, while the number average branching number does not. As for degradation, the molecular weight distributions for an arbitrary radiation dose are obtained, and it is shown that for any initial distribution the final molecular weight distribution becomes Poisson-like. The problem which deals with the case where cross-linking and degradation coexist is also discussed, and it is shown that for any initial distribution the gel formation occurs only when the ratio of the two probabilities concerning degradation and cross-linking is smaller than 4.

§ 1. Introduction

It is well known that when long chain polymers are irradiated by high energy radiation, new chemical bindings between molecules and also molecular scissions are produced. These effects are classified into cross-linking, degradation and end-linking. Cross-linking is the chemical binding by which two molecules are combined at their side bonds. Degradation results from the scission of molecular main chains. When the molecular ends newly produced by scission are active, they may combine with other molecules at the side bonds. This type of linking is called end-linking. On the other hand, when links are formed between monomers which belong to the same molecule, they are called cyclization. For larger radiation doses, the links become numerous resulting in the formation of gel part which is insoluble in any solvent. This part is composed of macromolecules and the instance when the gel part appears first is

called gel point. Theories of the cross-linking without cyclization were given by Flory[1-4], Stockmayer[5,6], and Charlesby[7-9]. Flory obtained the gel point and the average molecular weights for uniform initial distribution and Stockmayer obtained those for arbitrary initial distribution. These theories are concerned with the polymers before the gel point. On the contrary, Charlesby's theory deals with the polymers after the gel formation, giving the gel point and the sol fraction. Charlesby[10,11] also developed similar theories about degradation and end-linking, in which cyclization was likewise neglected.

The author develops a new theory concerning the variation of molecular weight distribution induced by cross-linking and obtains the gel point and the average molecular weights, which are the same as those already published by other authors. A similar equation is given in the appendix of Stockmayer's paper, in which he uses discrete degree of polymerization and obtains only the solution for the most probable distribution, not for an arbitrary initial distribution. The theory in this paper is concerned with the most general cases and gives solutions for arbitrary initial distributions. Moreover, this theory can be extended to cases including cyclization and branching, which have not yet been treated. When degradation occurs, the distribution of polymerization is given by a formula in a closed form. The case where cross-linking and degradation coexist is also discussed.

The variation of viscosity of irradiated polymers have been measured by many researchers. However, no sufficient use of these results has been made to understand the behaviours of irradiated polymers, because there has been no exact theory concerning the variation of viscosity of irradiated polymers. The theory given in this paper gives a direct method to obtain the viscosity average molecular weight, so that experimental results are compared with it and interesting results are obtained, which will be described in later papers.

It is known that many irradiated polymers suffer at the same time two or all of the effects of cross-linking, degradation and end-linking. However, the details are not well established. To accomplish this each effect must be separately and accurately studied, and a theory in which these three effects coexist must be established. These details will also be discussed in later papers.

§ 2. Cross-linking without Cyclization

Let us consider the case where an exposure to high energy radiation gives cross-linkings to long chain polymers, while no cyclization occurs. For the sake of simplicity, the following assumptions are made: (1) cross-linking takes place at random (all monomer units being equally likely to become cross-linked), (2) the number of cross-links is small compared with the number of monomer units available for cross-linking, (3) cyclization does not occur, (4) degree of polymerization can be treated as continuous (from zero to infinity).

Let a polymer be exposed to radiation with total dose R and the number of molecules having the degree of polymerization p be $n(p, R)$. When the radiation dose increases from R to $R+dR$, the number of molecules which have only one active centre and whose degree of polymerization is p is $pn(p, R)\dot{c}dR$. In this expression $\dot{c}$ represents the probability that a monomer, irradiated by unit radiation dose, has an active centre. Any molecule is assumed to have only one active centre, the number of those molecules which have two active centres at the same time being proportional to $(dR)^2$ and accordingly neglected. Those molecules which have active centres are cross-linked with other molecules, resulting in the increase of the degreee of polymerization. Therefore, $n(p, R)$ decreases by the amount given above. Furthermore, those molecules whose degree of polymerization is p and which have no active centre may be cross-linked with molecules with an active centre. The number of such molecules is given by

$$\frac{pn(p, R)}{\int_0^\infty pn(p, R)dp}\int_0^\infty pn(p, R)\dot{c}dRdp$$

$$=pn(p, R)\dot{c}dR\,.$$

This effect also contributes to the decrease of $n(p, R)$.

The number of those molecules, which are formed by cross-linking between two molecules, one having the degree of polymerization l and an active centre, and the other having the degree of polymerization $p-l$ and no

active centre, is

$$\frac{(p-l)n(p-l,\ R)}{\int_0^\infty pn(p,\ R)dp} ln(l,\ R)\dot{c}dR$$
$$=\frac{\dot{c}}{N} l(p-l)n(l,\ R)n(p-l,\ R)dR\,,$$

where N denotes the total number of monomers. This contributes to the increase of $n(p,\ R)$.

From the foregoing induction, we obtain the following relation

$$dn(p,\ R)=-2pn(p,\ R)\dot{c}dR$$
$$+\frac{\dot{c}}{N}\int_0^p l(p-l)n(l,\ R)n(p-l,\ R)dRdl\,.$$

Putting $\dot{c}R=t$ and $n(p,\ R)/N=m(p,\ t)$, it follows:

$$\frac{\partial m(p,\ t)}{\partial t}+2pm(p,\ t)$$
$$=\int_0^p l(p-l)m(l,\ t)m(p-l,\ t)dl\,. \qquad (1)$$

Multiplying this equation by p^k and integrating it with respect to p from zero to infinity, we obtain

$$\frac{df_k}{dt}+2f_{k+1}=\sum_{i=0}^{k} {}_kC_i f_{i+1}f_{k-i+1}\,, \qquad (2)$$

where

$$f_k=\int_0^\infty p^k m(p,\ t)dp$$

and k is integer. When $k=1$, if follows

$$\frac{df_1}{dt}=2f_2(f_1-1)\,.$$

f_1 represents the total number of monomers devided by N, and has a constant value unity. When $k=0$,

$$\frac{df_0}{dt}=f_1(f_1-2)=-1\,,$$

therefore

$$f_0=f_{0,0}-t\,,$$

where

$$f_{0,0}=\int_0^\infty m(p,\ 0)dp\,.$$

The number average molecular weight M_n is given by

$$M_n=M_{n,0}f_{0,0}/(f_{0,0}-t)\,, \qquad (3)$$

where $M_{n,0}$ is the number average molecular weight before irradiation. If we use the notation u for the number average degree of polymerization of polymers before irradiation, we obtain

$$M_n=M_{n,0}/(1-ut)\,. \qquad (4)$$

This does not depend on the initial form of the distribution except through u. When $k=2$, Eq. (2) gives

$$\frac{df_2}{dt}=2f_2{}^2\,.$$

The solution is

$$f_2=f_{2,0}/(1-2tf_{2,0})\,,$$

where

$$f_{2,0}=\int_0^\infty p^2 m(p,\ 0)dp\,.$$

The weight average molecular weight M_w is given by

$$M_w=M_{w,0}/(1-2tf_{2,0})\,, \qquad (5)$$

where $M_{w,0}$ denotes the initial weight average molecular weight.

If the initial distribution is Poisson-like, i.e. $m(p,\ 0)=(1/u^2)\exp(-p/u)$, it follows

$$f_2=2u/(1-4ut)\,.$$

And if the initial distribution is uniform, it becomes

$$f_2=u/(1-4ut)\,.$$

Therefore

$$M_w=\begin{cases} M_{w,0}/(1-4ut) & \text{for Poisson distr.,} \\ M_{w,0}/(1-2ut) & \text{for uniform distr.} \end{cases} \qquad (6)$$

These results are the same as those deduced by Flory, Stockmayer, and Charlesby, if we put $\gamma=2ut$, $\delta=4ut$.

We can obtain higher average molecular weight M_z, M_{z+1}, etc. from Eq. (2). However, the viscosity average molecular weight M_v is not deduced from the equation. For this purpose we must resort to other method to solve Eq. (1).

If we apply to Eq. (1) the Laplace transformation

$$f(s,\ t)=\int_0^\infty m(p,\ t)e^{-sp}dp\,,$$

we obtain

$$\frac{\partial f}{\partial t}=2\frac{\partial f}{\partial s}+\left(\frac{\partial f}{\partial s}\right)^2 \qquad (7)$$

The characteristic equation is easily integrated and the solution under $t=0$, $s=s_0$ and

$$f=g(s_0)=\int_0^\infty m(p,\ 0)\exp(-s_0p)dp$$

is given by

$$\left.\begin{aligned} f&=g(s_0)-\{g'(s_0)\}^2t\,, \\ s&=s_0-2\{1+g'(s_0)\}t\,. \end{aligned}\right\} \qquad (8)$$

When $s=0$, Eq. (8) gives

$$\frac{\partial f}{\partial s}=g'(s_0)=\frac{s_0}{2t}-1\,.$$

On the other hand, we obtain from the definition of f the following relation

$$\left(\frac{\partial f}{\partial t}\right)_{s=0}=-\int_0^\infty pm(p,\ t)dp=-f_1=-1\,.$$

Therefore, we know that s_0 must be zero at $s=0$. Other f_k's are given as follows:

$$f_k=(-1)^k\left(\frac{\partial^k f}{\partial s^k}\right)_{s=0},$$

and the average molecular weights are given from these f_k's.

When the initial distribution is Poisson-like, it follows

$$g(s_0)=1/u(1+us_0)\,.$$

For $s=0$, we obtain

$$f=1/u-t\,,$$
$$\partial f/\partial s=-1\,,$$
$$\partial^2 f/\partial s^2=2u/(1-4ut)\,,\quad \text{etc.}$$

These are the same as the preceding results for f_k.

For the uniform initial distribution, we must use $g(s_0)=(1/u)\exp(-s_0u)$, and then we can obtain the same results as f_k and the average molecular weights, described before, for the uniform distribution.

For the viscosity average molecular weight, we need the formula

$$\int_0^\infty p^{\alpha+1}m(p,\ t)dp\,,\quad \frac{1}{2}\leqq\alpha\leqq 1\,,$$

which can be calculated by integration if we know $m(p,\ t)$. $m(p,\ t)$ is given from f_k, as follows[9]:

$$\left.\begin{aligned} m(p,\ t)&=e^{-p/u}\sum_{i=0}^{\infty}c_iL_i\left(\frac{p}{u}\right),\\ c_i&=\sum_{k=0}^{i}\frac{(i!)^2(-1)^k}{k!(i-k)!}\,\frac{f_k}{u^{k+1}}\,,\end{aligned}\right\}\qquad(9)$$

where $L_i(x)$ is Laguerre's polynomial.

This method of calculating $m(p,\ t)$ is very complicated and f_k cannot be obtained easily for large k. More simple method may be desirable, which will be discussed in forth coming papers.

The argument of this section shows that the solution of Eq. (1) gives the same results as those obtained by other authors. In following sections we will extend the argument.

§ 3. Cross-linking with Cyclization

When long chain polymers are irradiated by high energy radiation, both inter- and intra-molecular cross-linkings occur. In this section both linkings will be considered.

The assumptions mentioned at the beginning of section 2 are accepted in this section except assumption (3), which is replaced by "(3) cyclization occurs". The probability that an active centre in a molecule composed of p monomers may cross-link with a monomer unit of other molecules is assumed to be, on the average, a function of p and N, say $\varphi(p,\ N)$.

When radiation dose increases from R to $R+dR$, the number of molecules whose degree of polymerization is p, each of which has an active centre, and which will cross-link with other molecules with no active centre is

$$\varphi(p,\ N)pn(p,\ t)dt\,.$$

And the number of molecules with no active centre whose degree of polymerization is p and which will cross-link with other molecules with an active centre is

$$\frac{pn(p,\ t)}{N}\int_0^\infty\varphi(l,\ N)ln(l,\ t)dldt\,,$$

Putting $n(p,\ t)/N=m(p,\ t)$, we obtain

$$\begin{aligned}&\frac{\partial m(p,\ t)}{\partial t}+pm(p,\ t)\int_0^\infty\varphi(l,\ N)lm(l,\ t)dl\\ &\quad+\varphi(p,\ N)pm(p,\ t)\\ &=\int_0^p\varphi(l,\ N)l(p-l)m(l,\ t)m(p-l,\ t)dl\,.\end{aligned}\qquad(10)$$

For the simplest case we may assume $\varphi(p,N)=1-p/N$. In this case the integral in the right hand side of Eq. (10) can be modified into a symmetric form as follows:

$$\begin{aligned}I&=\int_0^p\left(1-\frac{l}{N}\right)l(p-l)m(l,\ t)m(p-l,\ t)dl\\ &=\int_0^p\left(1-\frac{p-l}{N}\right)(p-l)lm(p-l,\ t)m(l,\ t)dl\\ \therefore\ I&=\left(1-\frac{p}{2N}\right)\int_0^p l(p-l)m(l,\ t)m(p-l,\ t)dl\,.\end{aligned}$$

Then Eq. (10) becomes for $p\leqq N$:

$$\begin{aligned}&\frac{\partial m(p,\ t)}{\partial t}+pm(p,t)\int_0^N\left(1-\frac{l}{N}\right)lm(l,\ t)dl\\ &\quad+\left(1-\frac{p}{N}\right)pm(p,\ t)\end{aligned}$$

$$=\left(1-\frac{p}{2N}\right)\int_0^p l(p-l)m(l,\ t)m(p-l,\ t)dl\,, \tag{11}$$

for $p>N$: $m(p,\ t)=0$.

Eq. (11) may be solved by PLK method[12]. Assume

$$\left.\begin{aligned} m(p,\ t)&=m_0(p,\ x)+\varepsilon m_1(p,\ x)+\cdots \\ t&=x+\varepsilon\varphi_1(x)+\cdots \end{aligned}\right\} \tag{12}$$

where $\varepsilon=1/N$, and the unknown functions m_0, m_1 and φ_1 are determined from the following relations. Substitute Eq. (12) into Eq. (11), multiply (11) by p^2, and integrate it with respect to p from zero to infinity, then we obtain the following equations by equating the coefficients of each powers of ε to zero:

$$\frac{df_2}{dx}=2f_2^2, \tag{13}$$

$$\frac{dg_2}{dx}=4f_2g_2+2f_2\left(f_2\frac{d\varphi_1}{dx}-f_3\right), \tag{14}$$

where

$$g_2=\int_0^\infty p^2m_1(p,\ x)dp\,.$$

From Eq. (13), we get

$$f_2=f_{2,0}/(1-2xf_{2,0})\,. \tag{15}$$

Assume that φ_1 satisfies the relation

$$f_2\frac{d\varphi_1}{dx}-f_3=0\,, \tag{16}$$

and that $\varphi_1=0$ at $x=0$, then g_2 always vanishes. From Eq. (2) we obtain

$$f_3=f_{3,0}/(1-2xf_{2,0})^3, \tag{17}$$

where

$$f_{3,0}=\int_0^\infty p^3m(p,\ 0)dp\,.$$

Inserting Eqs. (15) and (17) in Eq. (16) and solving it, we get

$$\varphi_1(x)=f_{3,0}x/f_{2,0}(1-2xf_{2,0})\,. \tag{18}$$

Finally,

$$\left.\begin{aligned} &\int_0^\infty p^2m(p,\ t)dp=f_{2,0}/(1-2xf_{2,0})\,, \\ &t=x+\varepsilon f_{3,0}x/f_{2,0}(1-2xf_{2,0})\,. \end{aligned}\right\} \tag{19}$$

The weight average molecular weight is then given by

$$M_w=M_{w,0}/(1-2xf_{2,0})\,.$$

In the preceding section where cyclization does not occur, we assume that the value of t at the gel point is given from the condition that f_2 diverges at the point. The value of f_2 being unable to exceed N, this condition for the gel point is not correct. However, if we calculate the value of t at the gel point by using the correct condition that f_2 has the value of the order of N at the gel point, we can easily obtain the result that the discrepancy between the true and the approximate value of t at the gel point is merely of the order of $1/N$, which is negligible. We can, therefore, obtain the correct result by assuming the approximate condition. On the contrary, in the case of cyclization we must assume the correct condition as follows.

If we consider that at the gel point the number of monomers contained in the largest molecule is kN, where $0<k<1$, then

$$\int_0^\infty p^2m(p,\ t)dp\doteqdot k^2N\,.$$

The value of t at the gel point is given by

$$t_g=\frac{1}{2}\left(\frac{1}{f_{2,0}}-\frac{1}{k^2N}\right)\left(1+k^2\frac{f_{3,0}}{f_{2,0}^2}\right).$$

Being $k^2N\gg 1$, t_g is expressed in good approximation by the following formula:

$$t_g=\frac{1}{2f_{2,0}^2}\left(1+k^2\frac{f_{3,0}}{f_{2,0}^2}\right). \tag{20}$$

This shows the fact that the gel formation is retarded by cyclization. k may depend on the method of measurement. For instance, the value of k determined from the measurement of melting point may be larger than that from the measurement of viscosity. The value of t_g for the both kinds of initial distributions are:

$$t_g=\begin{cases}\dfrac{1}{4u}\left(1+\dfrac{3}{2}k^2\right) & \text{for Poisson distr.,} \\[2ex] \dfrac{1}{2u}(1+k^2) & \text{for uniform distr.}\end{cases} \tag{21}$$

On the same way, we can obtain the number average molecular weight as follows:

$$\left.\begin{aligned} M_n&=M_{n,0}/(f_{0,0}-x), \\ t&=x-\varepsilon\log\sqrt{1-2xf_{2,0}}. \end{aligned}\right\} \tag{22}$$

The value of k in Eq. (21) may be small, so that the retardation of the gel formation due to cyclization may be negligible. We may estimate the value of k by the following experiment.

Let two polymers of the same species whose number average degrees of polymerization are u_1 and u_2 and both of which have the Poisson distribution, be solved in some sol-

vent. Then evaporate the solvent and make the polymers solid. The distribution of polymerization will be

$$m(p,\ 0)=\frac{c_1}{u_1^2}\exp\left(-\frac{p}{u_1}\right)+\frac{c_2}{u_2^2}\exp\left(-\frac{p}{u_2}\right),$$

where $c_1:c_2$, $(c_1+c_2=1)$, represents the weight concentration ratio. At the gel point t takes the following value:

$$t_g=\frac{1}{4(c_1u_1+c_2u_2)}\left\{1+\frac{3(c_1u_1^2+c_2u_2^2)}{2(c_1u_1+c_2u_2)^2}k^2\right\}. \quad (23)$$

If we plot $1/t_g$ to $c_1:c_2$, the curve is straight when k is negligible. In case where k cannot be neglected, it may be determined from the deviation from straight line.

§ 4. Branching of Cross-linked Molecules

In this section we consider the case where cross-linking without cyclization takes place. The number of end points of any molecule is always even. Let us call one half of the number of end points branching index. In the polymers irradiated by radiation dose R, the number of molecules which have the degree of polymerization p and the branching index q, both treated as continuous, is $n(p,\ q,\ R)$. Putting $n(p,\ q,\ R)/N=m(p,\ q,\ t)$, we obtain the following equation which represents the variation of distribution:

$$\frac{\partial m(p,\ q,\ t)}{\partial t}+2pm(p,\ q,\ t)$$
$$=\int_0^q ds\int_0^p l(p-1)m(l,s,t)m(p-l,q-s,t)dl. \quad (24)$$

Multiply this equation by p^iq^j and integrate it with respect to p and q from zero to infinity, then the following formula is obtained:

$$\frac{df_{ij}}{dt}+2f_{i+1j}$$
$$=\sum_{h=0}^{i}\sum_{k=0}^{j}{}_iC_h\,{}_jC_k f_{h+1\,k}f_{i-h+1\,j-k}\,, \quad (25)$$

where

$$f_{ij}=\int_0^\infty\int_0^\infty p^iq^jm(p,\ q,\ t)dpdq\,.$$

Making $i=0$, $j=1$, we get

$$\frac{df_{01}}{dt}=2f_{11}(f_{10}-1)=0\,.$$

By integration

$$f_{01}=1/u\,.$$

Accordingly, the number average branching index B_n becomes

$$B_n=f_{01}/f_{00}=1/(1-ut)\,. \quad (26)$$

On the other hand, inserting $i=1$, $j=1$ in Eq. (25) and integrating it, we obtain the following formula:

$$f_{11}=1/(1-2tf_{2,0})\,,$$

where $f_{2,0}$ is given in section 2. Therefore, the weight average branching index B_w is

$$B_w=f_{11}/f_{10}=1/(1-2tf_{2,0})\,. \quad (27)$$

Eqs. (26) and (27) indicate that the weight average branching index diverges at the gel point, while the number average branching index does not.

§ 5. Degradation

We consider in this section the case where linear polymers are degraded by irradiation and the molecular weight distribution is altered. Assumptions made are: (1) degradation takes place at random (all monomer units being equally likely to be ruptured), (2) all polymers are linear, (3) degree of polymerization can be treated as continuous (from zero to infinity).

We use the notation $\dot{r}$ to indicate the probability of the event that a monomer is ruptured by unit radiation dose. When radiation dose varies from R to $R+dR$, the number of molecules which have the degree of polymerization p and are newly ruptured is $pn(p,\ R)\dot{r}dR$ and the number of molecules which have the degree of polymerization p and are formed by the rupture of molecules which have degree of polymerization greater than p is

$$2\int_p^\infty n(l,\ R)\dot{r}dldR\,.$$

Therefore, the variation of distribution is represented as follows:

$$\frac{\partial n(p,\ \tau)}{d\tau}+pn(p,\ \tau)=2\int_p^\infty n(l,\ \tau)dl\,, \quad (28)$$

where $\tau=\dot{r}R$. The solution is

$$n(p,\tau)=\left\{n(p,\ 0)+2\tau\int_p^\infty n(p,\ 0)dp\right.$$
$$\left.+\tau^2\int_p^\infty dp\int_p^\infty n(p,\ 0)dp\right\}e^{-p\tau}\,, \quad (29)$$

where $n(p,\ 0)$ represents the initial distribution.

When τ is large enough, the first two terms in the brackets of Eq. (29) can be neglected. Then this formula becomes approximately

$$n(p,\ \tau)\propto\tau^2e^{-p\tau}\,.$$

This is the Poisson distribution. We know that whatever the initial distribution may be, the distribution of polymerization becomes Poisson-like for large radiation dose. This feature was discussed by Charlesby, but his discussion was only about the behaviour of f_2.

When the initial distribution is Poisson-like, i.e. $n(p, 0)=(N/u^2)\exp(-p/u)$, the solution (29) gives

$$n(p, \tau)=N\left(\frac{1}{u}+\tau\right)^2 e^{-(1/u+\tau)p}.$$

This shows that when the initial distribution is Poisson-like, the distribution conserves the same type. We obtain also the number and the weight average molecular weight as follows:

$$\left.\begin{aligned} M_n&=M_{n,0}/(1+u\tau)\,,\\ M_w&=M_{w,0}/(1+u\tau)\,.\end{aligned}\right\} \tag{30}$$

When the initial distribution is uniform, i.e. $n(p, 0)=(N/u)\delta(p-u)$, Eq. (29) gives

$$n(p, \tau)=\begin{cases}(N/u)\{\delta(p-u)+2\tau+(u-p)\tau^2\}e^{-p\tau}\,, & p\leqq u\,,\\ 0\,, & p>u\,,\end{cases}$$

where

$$\delta(x)=\begin{cases}0 & x<-\varepsilon/2\,,\\ 1/\varepsilon & -\varepsilon/2\leqq x\leqq\varepsilon/2\,,\\ 0 & \varepsilon/2<x\,.\end{cases}$$

And the average molecular weights are

$$\left.\begin{aligned} M_n&=M_{n,0}/(1+u\tau)\,,\\ M_w&=2M_{w,0}(e^{-u\tau}-1+u\tau)/(u\tau)^2\,.\end{aligned}\right\} \tag{31}$$

These results are the same as those obtained by Charlesby.

The viscosity average molecular weight for an arbitrary initial distribution has not yet been obtained, but we now easily find it out as follows:

$$M_v=\frac{w}{N}\left\{\int_0^\infty p^{\alpha+1}n(p, \tau)\,dp\right\}^{1/\alpha}, \tag{32}$$

where α is constant and w is the mass of a monomer. For the Poisson and the uniform initial distribution, it becomes respectively

$$M_v=\begin{cases}M_{v,0}/(1+u\tau),\\ M_{v,0}\left\{(\alpha+1)e^{-u\tau}-\dfrac{(\alpha+1)(\alpha-u\tau)}{u^{\alpha+1}}\right.\\ \qquad\left.\times\displaystyle\int_0^u p^\alpha e^{-p\tau}dp\right\}^{1/\alpha},\end{cases} \tag{33}$$

where $M_{v,0}$ means the initial value of the viscosity average molecular weight.

§ 6. Cross-linking with Degradation

In this section we consider the case where irradiated polymers are cross-linked and degraded, but cyclization may be neglected. Basic assumptions are the same as those in sections 2 and 5. In addition to these, we assume that cross-linking and degradation occur independently of each other. This assumption may be permissible when the densities of cross-linking and degradation are small.

Now we consider two molecules A and B whose degree of polymerization are p_A and p_B, and a third molecule with an active centre C. Generally speaking, the probability that an active centre cross-links with a molecule is proportional to the degree of polymerization. Now suppose that after the centre C cross-links with the molecule A or B, the molecule A is ruptured into two molecules A_1 and A_2 whose degrees of polymerization are p_{A1} and p_{A2}, respectively. Then the probabilities that C cross-links finally with A_1, A_2 and B are p_{A1}/N, p_{A2}/N and p_B/N respectively, where $N=p_{A1}+p_{A2}+p_B$. Next suppose that after A is ruptured into A_1 and A_2, C cross-links with A_1, A_2 or B. Then the probabilities that C cross-links ultimately with A_1, A_2 and B are similarly p_{A1}/N, p_{A2}/N and p_B/N respectively. Therefore, the statistical result is independent of the order of cross-linking and degradation. When they coexist, we may treat them as if degradation occurs first and then cross-linking follows.

Let us consider the case when a polymer substance the molecules of which are all linear and distributed initially as given by $n(p, 0)$ is irradiated, and cross-linking and degradation occur. First, the consideration of degradation will lead to a new distribution function $n(p, \tau)$ given by Eq. (29), and the consideration of cross-linking will then give the average molecular weights given by Eqs. (4) and (5).

For example, when the initial distribution is Poisson-like, the average molecular weights are given by

$$M_n=\frac{M_{n,0}}{1+u(\tau-t)}=\frac{M_{n,0}}{1+(\dot{r}-\dot{c})uR}, \tag{34}$$

and

$$M_w=\frac{M_{w,0}}{1+u(\tau-4t)}=\frac{M_{w,0}}{1+(\dot{r}-4\dot{c})uR}. \tag{35}$$

From the last formula, we know that the gel

formation occurs only when $\dot{r}/\dot{c}<4$. This condition of gel formation holds for any initial distribution (*cf* the appendix).

When the initial distribution is uniform, we obtain similarly the average molecular weights:

$$M_n=\frac{M_{n,0}}{1+u(\tau-t)}\,,$$
$$M_w=\frac{M_{w,0}}{u}\Big/\left\{\frac{u\tau^2}{2(e^{-u\tau}-1+u\tau)}-2t\right\}. \tag{36}$$

§ 7. Discussion

There may be considered three effects of high energy radiation to long chain polymers. They are cross-linking, degradation and end-linking. In this paper the effects of the first two are discussed. Among several possible methods to investigate these, the author uses the one in which integro-differential equations for the variation of molecular weight distributions are solved. First, in the case of cross-linking the same results as those obtained by Flory, Stockmayer, and Charlesby are given. This fact may be an indirect evidence that this integro-differential equation is valid. Further, by extending this equation to the case including cyclization, it is shown that the gel formation is retarded by the presence of cyclization, but this retardation may not be remarkable. However, the probability $\varphi(p,\ N)=1-p/N$ used in this case is the simplest one, so that it may be necessary to consider steric hindrance of molecules and to use some more practical formula for $\varphi(p,\ N)$. As for branching index, some experimental facts may be obtained by chemical measurement of the end groups, and compared to the theory. Although the effect of degradation has already been discussed by Charlesby, the distribution function $n(p,\ \tau)$ was not given in his theory. In this paper it is obtained in a closed form, from which many important quantities can be calculated. In the case where cross-linking and degradation coexist, it is assumed that correct statistical results are obtained by considering that degradation occurs first and then cross-linking follows. A mathematical proof of the validity of this assumption is considered. The treatment developed in this paper gives the result that whatever the initial distribution may be, the gel formation occurs only when $\dot{r}/\dot{c}$ is smaller than 4. This may show the fact that the gel formation depends only on $\dot{r}$ and $\dot{c}$, but not on the initial distribution.

It is in viscosity that the experimental effect of radiation to polymers appears for rather small radiation dose. Theoretical deduction of viscosity average molecular weight has not been done. It may, however, be possible to obtain it by the author's theory. The details will be described in part II, where the effect of end-linking will also be discussed.

Acknowledgments

The author wishes to express his sincere thanks to Dr. A. Amemiya for his advices about mathematical treatments, to Dr. A. Harasima for his suggestions about statistical aspects, to Dr. K. Shinohara for his informations about experimental features, and to Mr. M. Inokuti for his assistances in mathematical treatments. He also thanks Mr. T. Watanabe and others, the members of the Group for the Study of Irradiated Polymers in Tokyo, to whose discussions the author owes much.

Appendix

The result that, when cross-linking and degradation coexist, whatever initial distribution may be, the gel formation occurs only when $\dot{r}/\dot{c}$ is smaller than 4 is verified as follows:

The gel point is given by the equation

$$1-2tf_{2,0}=0\,, \tag{37}$$

where

$$\begin{aligned} f_{2,0}&=\int_0^\infty p^2m(p,\ \tau)dp\\ &=\int_0^\infty p^2m(p,\ 0)e^{-p\tau}dp+2\tau\int_0^\infty p^2e^{-p\tau}dp\\ &\quad\times\int_p^\infty m(l,\ 0)dl\\ &\quad+\tau^2\int_0^\infty p^2e^{-p\tau}dp\int_p^\infty dl\int_l^\infty m(h,\ 0)dh\,. \end{aligned}$$

By changing the order of integrations we obtain

$$f_{2,0}=\frac{2}{\tau}-\frac{2}{\tau^2}\int_0^\infty m(l,\ 0)(1-e^{-l\tau})dl\,.$$

Inserting this formula in Eq. (37) and considering $t=\dot{c}R$ and $\tau=\dot{r}R$, the value of τ at the gel point is given by the following equation

$$\frac{\dot{r}}{\dot{c}}-4+\frac{4}{\tau}\int_0^\infty m(l,\ 0)(1-e^{-l\tau})dl=0\,.$$

This leads to the condition $\dot{r}/\dot{c}<4$.

References

1) P. J. Flory: J. Am. Chem. Soc. **63** (1941) 3083.
2) P. J. Flory: J. Am. Chem. Soc. **63** (1941) 3091.
3) P. J. Flory: J. Am. Chem. Soc. **63** (1941) 3096.
4) P. J. Flory: J. Phys. Chem. **46** (1942) 132.
5) W. H. Stockmayer: J. Chem. Phys. **11** (1943) 45.
6) W. H. Stockmayer: J. Chem. Phys. **12** (1944) 125.
7) A. Charlesby: J. Poly. Sci. **11** (1953) 513
8) A. Charlesby: Proc. Roy. Soc. **A222** (1954) 60.
9) A. Charlesby: Proc. Roy. Soc. **A222** (1954) 542
10) A. Charlesby: Proc. Roy. Soc. **A224** (1954) 120.
11) A. Charlesby: Proc. Roy. Soc. **A231** (1955) 521.
12) Y. H. Kuo: J. Aeron. Sci. **23** (1956) 125.

JOURNAL OF THE PHYSICAL SOCIETY OF JAPAN Vol. 13, No. 2, FEBRUARY, 1958

Paramagnetic Resonance Absorption in Two Copper Salts at Wavelengths of 5.4 mm and 6.6 mm

By Kazuo ÔNO and Mieko OHTSUKA

Institute for Solid State Physics, University of Tokyo

(Received October 30, 1957)

Paramagnetic resonance absorption in single crystals of $CuSO_4\cdot 5H_2O$ and $K_2CuCl_4\cdot 2H_2O$ has been investigated at wavelengths of 5.4 mm and 6.6 mm. The shapes of absorption lines vary remarkably with orientation of the crystal in the magnetic field. This is interpreted in terms of exchange interaction between copper ions. The line shapes are compared with result calculated recently by Anderson. And then the exchange frequencies are estimated to be 1.0×10^{10} and 1.1×10^{10} for $CuSO_4\cdot 5H_2O$ and $K_2CuCl_4\cdot 2H_2O$ respectively.

§ 1. Introduction

Paramagnetic resonance absorption of $CuSO_4\cdot 5H_2O$ has been investigated in great detail at the range of centimeterwaves.[1] The crystals contain two dissimilar ions in a unit cell. If there is no exchange coupling between copper ions, two absorption lines would be observed corresponding to the two dissimilar ions. Experimentally, only one line has been observed at longer wavelengths. At the shorter wavelength, $\lambda=8.5$ mm, however, two lines were found under the appropriate condition. But the result is a very brief one. Similar circumstances have been observed in single crystals of $K_2CuCl_4\cdot 2H_2O$.[2]

In the present experiments the shapes of absorption lines in single crystals of $CuSO_4\cdot 5H_2O$ and $K_2CuCl_4\cdot 2H_2O$ were studied for various orientations of the crystal in the static magnetic field. All of these measurements were done at room temperature and wavelengths of 5.4 mm and 6.6 mm.

Recently, Anderson,[3] and Yokota and Koide[4] have quantitatively calculated the line shapes of resonance absorption in two inequivalent ions under strong exchange coupling. The comparison between the calculated and observed line shapes with orientation of the crystals is made in the present paper.

§ 2. Crystallographic Data

The X-ray analysis of the crystal structure of $CuSO_4\cdot 5H_2O$ given by Beevers and Lipson[5] shows that there are two inequivalent ions in a unit cell, with parameters (0 0 0) and ($\frac{1}{2}$ $\frac{1}{2}$ 0). Each ion is surrounded by a nearly octahedral arrangement consisting of four water molecules and two oxygen atoms; the angle between the planes of water molecules of the two ions is calculated to be about 82°. The

Cu^{++} ion may be acted by a crystalline electric field of tetragonal symmetry and its g-tensor must be also tetragonal. Since $CrSO_4 \cdot 5H_2O$, which may be isomorphous with $CuSO_4 \cdot 5H_2O$, has a very small value of fine structure parameter due to a rhombic symmetry compared with that due to an axial symmetry,[6] then the assumption mentioned above may be reasonable. That of $K_2CuCl_4 \cdot 2H_2O$ given by Chrobak[7] shows that two inequivalent ions are situated at (0 0 0) and ($\frac{1}{2}$ $\frac{1}{2}$ $\frac{1}{2}$) respectively. Each ion is surrounded by four chlorine atoms forming a rhomb in the a–a plane and by two water molecules located on the normal of this

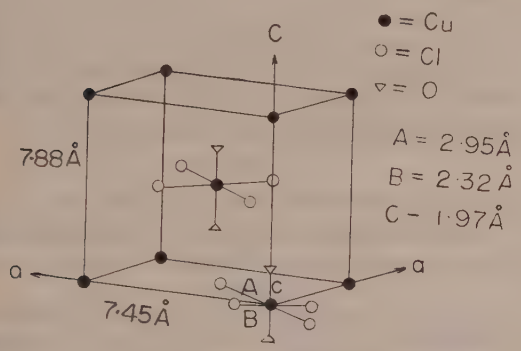

Fig. 1. Atomic arrangement of $K_2CuCl_4 \cdot 2H_2O$.

plane passing the ion as shown in Fig. 1.

Two rhombs in unit cell are rotated each other by 90° about the c-axis, the line of the two water molecules. Then the Cu^{++} ion may be affected by a crystalline field of rhombic symmetry.

§ 3. Apparatus and Experimental Results

The experimental method consisted in detecting the change in Q value caused by the absorption in the specimen and the detailed description of this apparatus has been given elsewhere.[8)2)]

a) $CuSO_4 \cdot 5H_2O$

The resonance absorption curves observed in $CuSO_4 \cdot 5H_2O$ at $\lambda=5.4$ mm with orientation for H in the plane containing the two tetragonal axes γ_1 and γ_2 are shown in Fig. 2.

Great variation of the line shape was found in the Figure. For H parallel to γ', the external bisector of γ_1 and γ_2, the width is very small ($\Delta H=100$ gauss) and seems to be independent of wavelength. The line width increases rapidly with θ, the angle between H and γ', until the two lines are resolved at

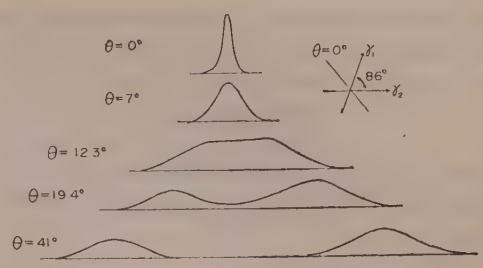

Fig. 2. Variation of line shape of $CuSO_4 5H_2O$ in the $\gamma_1-\gamma_2$ plane at $\lambda=5.4$ mm.

$\theta=15°$.

The two separated lines have a remarkable feature. That is; the intensity of the absorption observed at the higher magnetic field is always stronger than that at the lower one.

The line widths at $\theta=45°$ are 740 ± 50 gauss and 650 ± 50 gauss for the higher and lower magnetic field respectively with $\lambda=5.4$ mm.

The line width to be expected from magnetic dipolar interaction alone is about 450 gauss and is narrower than that observed. The effect of broadening the line is caused by the exchange interaction between inequivalent Cu^{++} ions. Thus the exchange energy may be determined reliably from the line width.

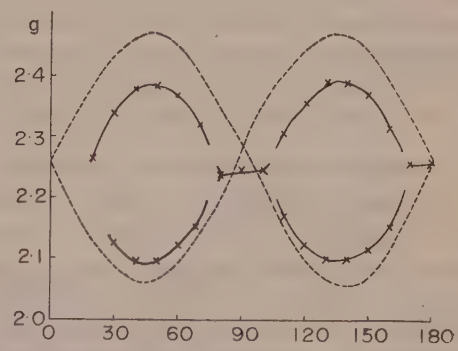

Fig. 3. Variation of g values of $CuSO_4 5H_2O$ in $\gamma_1-\gamma_2$ plane at $\lambda=6.6$ mm. Solid curves are obtained from the experimental results. Dashed curves are calculated with the assumption that there is no exchange interaction.

Fig. 3 shows the observed g-values in the γ_1–γ_2 plane at $\lambda=6.6$ mm. The determination of g-values was performed by comparing the magnetic field for absorption peak of the sample with that of α-diphenyl β-picryl hydrazyl ($g=2.00$ $\Delta H=$several gauss). The directions where the g-values are maximum coincide with those of the γ_1 and γ_2 axes. So the angle between γ_1 and γ_2 is observed to be

86°±2°. In the figure, dashed curves indicate the calculated g-values with the assumption that there is no exchange interaction and g-values are assumed to be $g_{//}=2.46$ and $g_{\perp}=2.06$.[1] It is noted that difference between observed and calculated g-values at the higher magnetic field is always smaller than that at the lower one.

b) $K_2CuCl_4 \cdot 2H_2O$

The resonance absorption curves at $\lambda=5.4$ mm in the a–a plane are shown in Fig. 4.

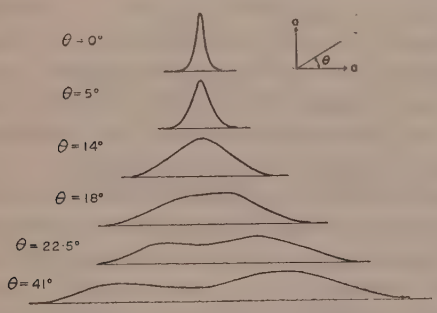

Fig. 4. Variation of line shape of $K_2CuCl_4 \cdot 2H_2O$ in the $a-a$ plane at $\lambda=5.4$ mm.

The features are qualitatively the same as those in $CuSO_4 \cdot 5H_2O$. The line widths are about 100 gauss with H parallel to a-axis and 1150 gauss and 920 gauss with H parallel to γ', the bisector of the two a-axes. The calculated dipolar width is about 380 gauss.

§ 4. Estimation of Exchange Frequency

The effect of exchange coupling in resonance absorption was first qualitatively discussed by Gorter and Van Vleck[9] and Kumagai et al.[10] Recently, Anderson and Weiss,[11] Anderson,[3] and Yokota and Koide[4] have quantitatively investigated this problem and Anderson has given some simple formulae for the widths and shapes of the absorptions.

According to Anderson, the intensity of the spectrum can be represented to be

$$I(\omega)=\frac{8\omega_e^3 x^2}{\omega^4+2\omega^2\omega_e^2(2-x^2)+\omega_e^4 x^4}$$
$$=\frac{8\omega_e\omega_0^2}{\omega^3+2\omega^2(2\omega_e^2-\omega_0^2)+\omega_0^4} \qquad (1)$$

where $\pm\omega_0$ are two possible frequency shifts, ω_e is an parameter specifying the rate at which jumping takes place back and forth between two frequencies, and x is ω_0/ω_e. Then we take

$$\omega_0=\frac{(g_{//}-g_{\perp})}{2\hbar}\beta H \sin 2\theta \sin\alpha$$

where θ is the angle between the direction of the external magnetic field H and γ', and α is the angle between two tetragonal axes.

We can calculate ω_e from the absorption curves in Fig. 1 and Fig. 3 and equation (1). For example ω_e is calculated as follows:

A) At certain angle where one resonance line is near being resolved into two lines, ω_e is

$$\omega_e=\omega_0/\sqrt{2} \qquad (2)$$

B) The actual maximum frequency shift observed is not ω_0 but $\delta\omega$, which is

$$(\delta\omega)^2=\omega_0^2-2\omega_e^2 \qquad (3)$$

C) Neglecting the line width due to the dipolar interaction, the widths of resolved line can be asymptotically represented to be

$$\Delta\omega=2\omega_e \qquad (4)$$

as ω_e/ω_0 goes to zero.

The estimated values of ω_e from A), B) and C) are summarized in Table I.

Table 1. The values of ω_e estimated from experimental results with $\lambda=5.4$ mm and $\lambda=6.6$ mm using Eqs. (2), (3) and (4).

	ω_e in 10^{10}		
	$CuSO_4 \cdot 5H_2O$		$K_2CuCl_4 \cdot 2H_2O$
	$\lambda=5.4$ mm	$\lambda=6.6$ mm	$\lambda=5.4$ mm
(A)	0.90	1.06	0.88
(B)	1.22	1.19	1.33
(C)	0.70	0.82	0.98

In the calculation, we assume the crystalline field to have a tetragonal symmetry. Then g-values are calculated from the results with the longer wavelengths[1)2)] to be $g_{\perp}=2.06$ and $g_{//}=2.46$ in $CuSO_4 \cdot 5H_2O$ and $g_{\perp}=2.06$ and $g_{//}=2.38$ in $K_2CuCl_4 \cdot 2H_2O$. This is reasonable in copper sulphate considering the crystalline field may have tetragonal symmetry.

The values of ω_e in Table I show no large divergences from each other. Comparing the resonance absorption curves measured at $\lambda=5.4$ mm and $\lambda=6.6$ mm with Eq. (1) we can ultimately estimate the exchange frequencies to be 1.0×10^{10} and 1.1×10^{10} for $CuSO_4 \cdot 5H_2O$ and $K_2CuCl_4 \cdot 2H_2O$ respectively.

For copper salts, an estimate of the exchange frequency can be made from the Curie-

Weiss law $\chi=c/(T+\Theta)$, with Θ obtained from the Weiss molecular field equation as

$$2k\Theta=Jz$$

where z is the number of nearest neighbours. The exchange integral J can be expressed[7] for a simple cubic lattic structure,[3]

$$\omega_e=2.12(J/\hbar)^2$$

From the results of the static susceptibility measurements, Θ is found to be $0.6°\pm0.05°$K in $CuSO_4\cdot5H_2O$ by Benzie and Cooke[1] and ω_e is calculated to be 3.8×10^{10}. Accordingly, these two estimates of the exchange frequency are fairly consistent.

The reasons for the minor differences may be attributed to the following considerations.

1) In the calculation, g is not treated as a tensor.
2) The dipolar interaction between copper ions is neglected.
3) The exchange interaction between similar and dissimilar ions may be different.
4) Crystal structure may not be a simple cubic lattice structure.
5) The crystalline electric field of tetragonal symmetry is assumed.
6) The exchange interaction may be a function of the temperature.

On the other hand, in the case of $K_2CuCl_4\cdot2H_2O$, the susceptibility does not obey the Curie-Weiss law exactly.[12] So the exchange frequency can not be estimated from the susceptibility measurements.

References

1) D. M. S. Bagguley and J. H. E. Griffiths: Proc. Roy. Soc. **A201** (1950) 366.
2) H. Abe, K. Ôno, I. Hayashi, J. Shimada and K. Iwanaga: J. Phys. Soc. Japan **9** (1954) 814. K. Ôno, H. Abe and J. Shimada: Phys. Rev. **92** (1953) 551.
3) P. W. Anderson: J. Phys. Soc. Japan **9** (1954) 316.
4) M. Yokota and S. Koide: Busseiron Kenkyu **76** (1954) 46.
5) C. A. Beevers and H. Lipson: Proc. Roy. Soc. **A146** (1934) 570.
6) K. Ôno, S. Koide, H. Sekiyama and H. Abe: Phys. Rev. **96** (1954) 38.
7) L. Chrobak: Z. Krist. **88** (1934) 35.
8) K. Ôno: Rikoken Hokoku 7 (1953) 209. K. Ôno: J. Phys. Soc. Japan **12** (1957) 1231.
9) C. J. Gorter and J. H. Van Vleck: Phys. Rev. **72** (1947) 1128.
10) H. Kumagai, K. Ôno, and I. Hayashi: Phys. Rev. **85** (1952) 925. H. Kumagai et al: J. Phys. Soc. Japan **9** (1954) 369.
11) P. W. Anderson and P. R. Weiss: Rev. Mod. Phys. **25** (1953) 269.
12) B. C. Guha: Proc. Roy. Soc. **A206** (1951) 353.

JOURNAL OF THE PHYSICAL SOCIETY OF JAPAN Vol. 13, No. 2, FEBRUARY, 1958

A Hydrodynamical Model for the Sedimentation

By Mitutosi KAWAGUTI

Institute of Science and Technology, University of Tokyo

(Received October 14, 1957)

The flow of a viscous fluid past a sphere in a frictionless circular pipe is investigated by using Faxén's procedure and the results are applied to the problem of sedimentation. Thus we obtained a formula for the sedimentation velocity V in the form: $V/V_0=1-1.6493(d_v/M^3)^{1/3}+0.7968(d_v/M^3)$, where V_0 is the terminal velocity of a particle, d_v the volume concentration and M a constant of order unity which depends on the distribution of sedimenting particles. Although our model is rather rough, it gives as good results as those given by other theories.

§ 1. Introduction

Recently H. Noda[3] measured the sedimentation velocity of tiny particles of polystyrene in a medium of salted water. On the other hand, J. Happel and N. Epstein[2] measured the pressure drop in a flow of water through

a circular pipe in which an assemblage of smooth spheres of equal diameter is mechanically suspended and immobilized.

It is also interesting to consider theoretically the relationship between the sedimentation velocity and the concentration of particles in a medium. On this problem, many theoretical investigations have been published (e.g. Burgers,[1] Uchida[5]), but so far as the author is aware, no satisfactory solution is known even in the Reynolds number range where Stokes' approximation is valid, owing to mathematical complexity.

Thus, in order to take into account the interaction between neighbouring particles, we consider the flow past a sphere in a fictitious frictionless circular pipe as a model flow for the sedimentation. The ratio of the radius of the pipe to that of a particle will be determined on a geometrical ground.

To deal with the model flow mentioned above, we shall use Faxén's procedure. It is to be noted that the same problem but with different boundary conditions on the surface of the circular pipe has recently been studied by Wakiya.[6] The interaction effects between the wall and the obstacle in the flow of a viscous fluid have also been studied by Wakiya[7] and Takaisi.[4]

In § 2 we shall study the flow of a viscous fluid past a sphere in a frictionless circular pipe, with a view to applying it to the problem of sedimentation in § 3.

§ 2. Viscous Flow past a Sphere in a Frictionless Circular Cylinder

2.1. We consider a sphere of radius a whose centre is on the axis of a circular pipe of radius $r_0 a$. The flow in the pipe is assumed to have uniform velocity U far upstream and downstream. Thus the flow will be axisymmetrical. We make the problem non-dimensional by choosing a, U, ρ as the units of length, velocity and density, respectively.

For an axisymmetrical flow, Stokes' approximate equations of motion and continuity can be written in non-dimensional forms as

$$\frac{\partial p}{\partial r}=\frac{2}{Re}\left(\nabla^2-\frac{1}{r^2}\right)v_r\,, \tag{2.1}$$

$$\frac{\partial p}{\partial z}=\frac{2}{Re}\,\nabla^2 v_z\,, \tag{2.2}$$

$$\frac{\partial}{\partial r}(rv_r)+\frac{\partial}{\partial z}(rv_z)=0\,, \tag{2.3}$$

with cylindrical polar coordinates (r, φ, z), where

$$\nabla^2=\frac{\partial^2}{\partial r^2}+\frac{1}{r}\frac{\partial}{\partial r}+\frac{\partial^2}{\partial z^2}\,, \tag{2.4}$$

and v_r, v_z are the r- and the z-components of velocity, p the pressure, and $Re=2aU/\nu$ is the Reynolds number, ν being the kinematic viscosity.

The equations (2.1)~(2.4) can be transformed in the spherical polar coordinates (R, θ, φ) as

$$D^4\psi=0\,, \tag{2.5}$$

where

$$D^2=\frac{\partial^2}{\partial R^2}-\frac{1}{R^2}\frac{\cos\theta}{\sin\theta}\frac{\partial}{\partial\theta}+\frac{1}{R^2}\frac{\partial^2}{\partial\theta^2}, \tag{2.6}$$

and ψ is Stokes' stream function from which the R- and θ-components of velocity v_R, v_θ are given as

$$v_R=\frac{1}{R^2\sin\theta}\frac{\partial\psi}{\partial\theta}\,,\qquad v_\theta=-\frac{1}{R\sin\theta}\frac{\partial\psi}{\partial R}\,. \tag{2.7}$$

The boundary conditions appropriate for our problem are

$$\left.\begin{array}{l} v_z\to 1\\ v_r\to 0\end{array}\right\}\ \text{as}\ \ z\to\pm\infty\,, \tag{2.8}$$

i.e. $\psi\to\frac{1}{2}r^2\sin^2\theta$ as $z\to\pm\infty$,

and

$$v_z=v_r=0 \quad \text{at}\quad R=1\,, \tag{2.9}$$

$$v_r=\partial v_z/\partial r=0 \quad \text{at}\quad r=r_0\,. \tag{2.10}$$

Putting

$$\boldsymbol{v}=\boldsymbol{u}_0+\boldsymbol{u}_1+\boldsymbol{u}_2+\cdots,\ \boldsymbol{v}_n=\sum_{i=0}^{n}\boldsymbol{u}_i\,, \tag{2.11}$$

where

$$u_{0z}=1,\quad u_{0r}=0\,, \tag{2.11'}$$

i.e. $\psi_0=\frac{1}{2}r^2\sin^2\theta$,

we shall obtain the velocity $\boldsymbol{v}$ iteratively.

2.2. It is well known that Stokes' solution for the uniform flow past a sphere:

$$\psi_1=\left(\frac{1}{2}R^2-\frac{3}{4}R+\frac{1}{8}\frac{1}{R}\right)\sin^2\theta\,, \tag{2.12}$$

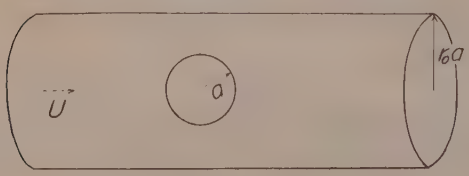

Fig. 1.

satisfies the boundary conditions (2.8) and (2.9) but not (2.10). The velocity components are given as follows:

$$v_{1z}=\left(1-\frac{3}{2}\frac{1}{R}+\frac{1}{2}\frac{1}{R^3}\right)+\frac{3}{4}\left(\frac{1}{R}-\frac{1}{R^3}\right)\sin^2\theta\,, \tag{2.13}$$

$$v_{1r}=-\frac{3}{4}\left(\frac{1}{R}-\frac{1}{R^3}\right)\sin\theta\cos\theta\,. \tag{2.14}$$

Thus we have for the perturbation quantities

$$u_{1z}=\left(-\frac{3}{2}\frac{1}{R}+\frac{1}{2}\frac{1}{R^3}\right)+\frac{3}{4}\left(\frac{1}{R}-\frac{1}{R^3}\right)\frac{r^2}{R^2}\,, \tag{2.15}$$

$$u_{1r}=-\frac{3}{4}\left(\frac{1}{R}-\frac{1}{R^3}\right)\frac{zr}{R^2}\,, \tag{2.16}$$

$$p_1=-\frac{4}{Re}\left(\frac{3}{4}\frac{1}{R}\right)\frac{z}{R^2}\,. \tag{2.17}$$

We shall modify the expressions (2.15)~(2.17) into forms which are convenient for the consideration of the boundary conditions (2.10). To this end, we note the formula (Ref. 8, p. 388)

$$\frac{1}{R}=\frac{2}{\pi}\int_0^\infty K_0(r\lambda)\cos z\lambda d\lambda\,. \tag{2.18}$$

Differentiating (2.18) with respect to r and z, we have

$$\frac{r}{R^3}=\frac{2}{\pi}\int_0^\infty K_1(r\lambda)\lambda\cos z\lambda d\lambda\,, \tag{2.19}$$

$$\frac{z}{R^3}=\frac{2}{\pi}\int_0^\infty K_0(r\lambda)\lambda\sin z\lambda d\lambda\,, \tag{2.20}$$

$$\frac{3rz}{R^5}=\frac{2}{\pi}\int_0^\infty K_1(r\lambda)\lambda^2\sin z\lambda d\lambda\,, \tag{2.21}$$

$$\frac{2}{R^3}-\frac{3r^2}{R^5}=-\frac{2}{\pi}\int_0^\infty K_0(r\lambda)\lambda^2\cos z\lambda d\lambda\,. \tag{2.22}$$

Introducing (2.19)~(2.22) in the expressions (2.15)~(2.17), we have

$$u_{1z}=\frac{2}{\pi}\int_0^\infty\left\{\frac{3}{4}r\lambda K_1(r\lambda)-\left(\frac{3}{2}+\frac{1}{4}\lambda^2\right)K_0(r\lambda)\right\}\cos z\lambda\, d\lambda\,, \tag{2.23}$$

$$u_{1r}=-\frac{2}{\pi}\int_0^\infty\left\{\frac{3}{4}r\lambda K_0(r\lambda)-\frac{1}{4}\lambda^2K_1(r\lambda)\right\}\sin z\lambda d\lambda\,, \tag{2.24}$$

$$p_1=-\frac{4}{Re}\frac{2}{\pi}\int_0^\infty\frac{3}{4}\lambda K_0(r\lambda)\sin z\lambda d\lambda\,. \tag{2.25}$$

2.3. It is easily shown that

$$u_{2z}=\frac{2}{\pi}\int_0^\infty[F(\lambda)r\lambda I_1(r\lambda)+\{2F(\lambda)+G(\lambda)\}I_0(r\lambda)]\cos z\lambda d\lambda\,, \tag{2.26}$$

$$u_{2r}=\frac{2}{\pi}\int_0^\infty[F(\lambda)r\lambda I_0(r\lambda)+G(\lambda)I_1(r\lambda)]\sin z\lambda d\lambda\,, \tag{2.27}$$

$$p_2=\frac{4}{Re}\frac{2}{\pi}\int_0^\infty F(\lambda)\lambda I_0(r\lambda)\sin z\lambda d\lambda \tag{2.28}$$

are a set of solutions of Eqs. (2.1)~(2.3), where $F(\lambda)$ and $G(\lambda)$ are arbitrary functions of z.

As a next step, we shall determine $\boldsymbol{u}_2$ so that $\boldsymbol{u}_1+\boldsymbol{u}_2$ will satisfy the boundary conditions (2.10):

$$\left.\begin{aligned} u_{1r}+u_{2r}&=0\,, &(2.29)\\ \frac{\partial}{\partial r}(u_{1z}+u_{2z})&=0 &(2.30)\end{aligned}\right\}\quad \text{at}\quad r=r_0$$

($\boldsymbol{u}_0$ satisfies the conditions (2.10)). Substituting (2.23), (2.24), (2.26) and (2.27) into (2.29) and (2.30), we have

$$\int_0^\infty[F(\lambda)r_0\lambda I_0(r_0\lambda)+G(\lambda)I_1(r_0\lambda)-\frac{3}{4}r_0\lambda K_0(r_0\lambda)+\frac{1}{4}\lambda^2K_1(r_0\lambda)]\sin z\lambda d\lambda=0\,, \tag{2.31}$$

$$\int_0^\infty\left[F(\lambda)r_0\lambda^2I_0(r_0\lambda)+\{3F(\lambda)+G(\lambda)\}\lambda I_1(r_0\lambda)-\frac{3}{4}r_0\lambda^2K_0(r_0\lambda)+\left(\frac{9}{4}+\frac{1}{4}\lambda^2\right)\lambda K_1(r_0\lambda)\right]\cos z\lambda d\lambda=0. \tag{2.32}$$

Since (2.31) and (2.32) must be satisfied for an arbitrary value of z, we have

$$r_0\lambda I_0(r_0\lambda)F(\lambda)+I_1(r_0\lambda)G(\lambda)=\frac{3}{4}r_0\lambda K_0(r_0\lambda)-\frac{1}{4}\lambda^2K_1(r_0\lambda)\,, \tag{2.33}$$

$$\{r_0\lambda^2 I_0(r_0\lambda)+3\lambda I_1(r_0\lambda)\}F(\lambda)+\lambda I_1(r_0\lambda)G(\lambda)=\frac{3}{4}r_0\lambda^2 K_0(r_0\lambda)-\left(\frac{9}{4}+\frac{1}{4}\lambda^2\right)\lambda K_1(r_0\lambda)\,. \tag{2.34}$$

Solving these equations for $F(\lambda)$ and $G(\lambda)$, we have

$$F(\lambda)=-\frac{3}{4}\frac{K_1(r_0\lambda)}{I_1(r_0\lambda)}\,, \tag{2.35}$$

$$G(\lambda)=\frac{3r_0\lambda I_0(r_0\lambda)K_1(r_0\lambda)}{4\{I_1(r_0\lambda)\}^2}+\frac{3r_0\lambda K_0(r_0\lambda)}{4I_1(r_0\lambda)}-\frac{\lambda^2 K_1(r_0\lambda)}{4I_1(r_0\lambda)}\,. \tag{2.36}$$

Although the solution thus obtained satisfies the boundary conditions (2.10), it cannot satisfy (2.9) exactly. Then we shall be content with the approximate condition that (2.9) may be satisfied by our solution on an average. Putting

$$v_z=1+c(u_{1z}+u_{2z})\,, \tag{2.37}$$

$$v_r=\quad c(u_{1r}+u_{2r})\,, \tag{2.38}$$

$$p=\quad c(p_1+p_2)\,,\ c\text{: const}, \tag{2.39}$$

we shall determine the constant c by the condition that the mean velocity over the surface of the sphere ($R=1$) vanishes:

$$\int_0^\pi v_z\sin\theta d\theta=0\,,\qquad \int_0^\pi v_r\sin\theta d\theta=0\,. \tag{2.40}$$

It is easily seen that

$$\left.\begin{aligned} v_z(\theta)&=v_z(\pi-\theta)\,,\\ v_r(\theta)&=-v_r(\pi-\theta)\end{aligned}\right\}\ \text{on}\quad R=1, \tag{2.41}$$

so that second equation in (2.40) is automatically satisfied, and the first one reduces to

$$\int_0^{\pi/2} v_z\sin\theta d\theta=0\,,\qquad \text{on } R=1\,. \tag{2.42}$$

We can easily show that

$$\int_0^{\pi/2} 1\times\sin\theta d\theta=1\,, \tag{2.43}$$

$$\int_0^{\pi/2} [u_{1z}]_{R=1}\sin\theta d\theta=-1\,, \tag{2.44}$$

$$\int_0^{\pi/2} [u_{2z}]_{R=1}\sin\theta d\theta=\frac{2}{\pi}\int_0^\infty F(\lambda)\frac{\lambda^2}{3}d\lambda+\frac{2}{\pi}\int_0^\infty\{2F(\lambda)+G(\lambda)\}d\lambda\,, \tag{2.45}$$

using the formula (Ref. 8, p. 376)

$$\int_0^x (x^2-t^2)^{\frac{1}{2}\nu}\cos t\, I_\nu(\sqrt{x^2-t^2})dt=\frac{\Gamma(\frac{1}{2})\,x^{2\nu+1}}{2^{\nu+1}\Gamma(\nu+\frac{3}{2})}\,, \tag{2.46}$$

for the calculation of (2.45). Substituting (2.43)~(2.45) into (2.42), we can determine the constant c as

$$c^{-1}=1-\frac{2}{\pi}\int_0^\pi\left[F(\lambda)\frac{\lambda^2}{3}+2F(\lambda)+G(\lambda)\right]d\lambda\,. \tag{2.47}$$

Using the explicit forms for $F(\lambda)$ and $G(\lambda)$ as given by (2.35) and (2.36) respectively, we have

$$\int_0^\infty F(\lambda)\frac{\lambda^2}{3}d\lambda=-\frac{1}{4}\frac{1}{r_0^3}\int_0^\infty \Lambda^2\frac{K_1(\Lambda)}{I_1(\Lambda)}d\Lambda\,, \tag{2.48}$$

$$\int_0^\infty[2F(\lambda)+G(\lambda)]\,d\lambda=-\frac{1}{4}\frac{1}{r_0^3}\int_0^\infty\Lambda^2\frac{K_1(\Lambda)}{I_1(\Lambda)}d\Lambda+\frac{3}{4}\frac{1}{r_0}\int_0^\infty\frac{1}{I_1(\Lambda)}\left\{\Lambda K_0(\Lambda)+\frac{\Lambda K_1(\Lambda)I_0(\Lambda)}{I_1(\Lambda)}-2K_1(\Lambda)\right\}d\Lambda\,. \tag{2.49}$$

These integrals can be evaluated numerically. Thus we have

$$\int_0^\infty F(\lambda)\frac{\lambda^2}{3}d\lambda=-0.62580\,r_0^{-3}\,, \tag{2.50}$$

$$\int_0^\infty[2F(\lambda)+G(\lambda)]\,d\lambda=2.59072\,r_0^{-1}-0.62580\,r_0^{-3}. \tag{2.51}$$

Substituting (2.50) and (2.51) into (2.47), we finally have

$$c^{-1}=1-1.64931\,r_0^{-1}+0.79680\,r_0^{-3}\,. \tag{2.52}$$

2.4. For determining the drag D, we first consider the pressures far upstream and downstream. Clearly we have $[p_1]_{z\to\pm\infty}=0$ and from (2.28) and (2.35) we have

$$[p_2]_{z\to\pm\infty}=-\frac{6}{Re\pi}\lim_{z\to\pm\infty}\int_0^\infty\frac{K_1(r_0\lambda)}{I_1(r_0\lambda)}\lambda I_0(r\lambda)\sin z\lambda d\lambda$$

$$=\mp\frac{6}{r_0^2}\frac{1}{Re}\,, \tag{2.53}$$

applying Dirichlet's integral theorem. Hence, in order to maintain the total flux through the pipe in the presence of a sphere at a value corresponding to the undisturbed uniform flow, a pressure difference Δp must be applied such that

$$\Delta p = \frac{1}{Re}\frac{12}{r_0^2}c\,, \tag{2.54}$$

between the upstream and downstream ends of the pipe.

Thus the drag coefficient can be given as:

$$C_D = \frac{D}{\frac{1}{2}\rho U^2 \pi a^2} = \frac{24c}{Re}$$
$$= \frac{24}{Re}\frac{1}{1-1.64931\,r_0^{-1}+0.79680\,r_0^{-3}}\,. \tag{2.55}$$

§ 3. Application to the Problem of Sedimentation

It is interesting to relate the solution thus obtained with the problem of sedimentation or the flow past many particles.

In the course of sedimentation, the distribution of the particles in the medium becomes random so that we may consider that the effects of particles far upstream and downstream of the particle under consideration will be cancelled on an average and we may assume that the flow is uniform there. But we cannot neglect the effects of the particles in the neighbourhood of the particle considered, because of the fact that the existence of these particles leads to the increase of effective mean velocity near the particle, and hence to the increase of the drag of the particle under consideration. These effects will be roughly taken into account by assuming the existence of a fictitious frictionless circular pipe around the particle under consideration. Then the solution obtained in the preceding section may be used as a model for the problem of the sedimentation.

We consider a system of equal spherical particles whose radius and density are a and ρ_p respectively in a medium of density ρ_s. Then the force acting on a particle due to the gravitational accelaraction g is given as

$$(\rho_p-\rho_s)\frac{4}{3}\pi a^3 g\,. \tag{3.1}$$

On the other hand, the drag of one sphere can be given from (2.55) as

$$D = 6\pi a U\mu(1-1.6493\,r_0^{-1}+0.7968\,r_0^{-3})^{-1}\,. \tag{3.2}$$

Thus the terminal velocity V can be determined, by equating the force (3.1) and the drag (3.2):

$$V = (1-1.6493\,r_0^{-1}+0.7968\,r_0^{-3})\,\frac{2}{9}(\rho_p-\rho_s)\frac{a^2 g}{\mu}\,. \tag{3.3}$$

The effective radius of smooth pipe can be determind in the following manner. Let the mass concentration of the particles (the ratio of the total mass of the particles to that of the medium and the particles) be d_m and the number of the particles in unit volume be n, then we have

$$n = \frac{d_m \rho_s}{\frac{4}{3}\pi a^3\{\rho_p-(\rho_p-\rho_s)d_m\}}\,. \tag{3.4}$$

If we assume the simple cubic and the body-centred lattice configuration of the particles, the relations between n and b are found to be

(a) $b = n^{-1/3}$, (simple cubic) (3.5a)

(b) $b = (n/2)^{-1/3}$, (body-centred) (3.5b)

respectively where b is the distance between neighbouring particles. Then we assume

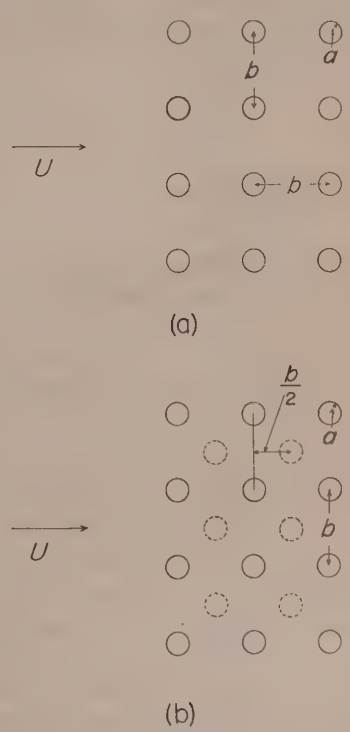

Fig. 2. Lattice configuration; a) simple cubic lattice, b) body-centred lattice.

that the effective radius of frictionless circular pipe $r_0 a$ is given by the relation:

$$2(r_0 a)^2 \pi = 2b^2 . \tag{3.6}$$

From (3.4)~(3.6), we have

$$r_0 = M \sqrt[3]{\frac{\rho_p - (\rho_p - \rho_s) d_m}{d_m \rho_s}} , \tag{3.7}$$

M being 0.9095 and 1.1458 for the cases (a) and (b) respectively.

In the formula (3.7), we can neglect the term $(\rho_p - \rho_s) d_m$ compared with ρ_p, considering that $(\rho_p - \rho_s)$ and d_m are both small in the problem of sedimentation. Then we have

$$r_0 = M \sqrt[3]{\frac{\rho_p}{d_m \rho_s}} = M (d_v)^{-1/3} , \tag{3.8}$$

where d_v is the volume concentration of the particles. Thus we have for the velocity of sedimentation

$$V = \left[1 - 1.6493 \sqrt[3]{\frac{d_v}{M^3}} + 0.7968 \frac{d_v}{M^3} \right] \frac{2}{9} (\rho_p - \rho_s) \frac{a^2 g}{\mu} . \tag{3.9}$$

When there is a single particle, its terminal velocity V_0 is given as

$$V_0 = \frac{2}{9} (\rho_p - \rho_s) \frac{a^2 g}{\mu} , \tag{3.10}$$

by making $r_0 \to \infty$ in (3.3). Thus we finally have

$$\frac{V}{V_0} = 1 - 1.6493 \sqrt[3]{\frac{d_v}{M^3}} + 0.7968 \frac{d_v}{M^3} , \tag{3.11}$$

where

$$\left. \begin{array}{ll} \text{(a)} & M = 0.9095 , \\ \text{(b)} & M = 1.1458 \end{array} \right\} \tag{3.12}$$

for the simple cubic and the body-centred lattice approximations respectively.

Comparison with the Experiments. In Fig. 3, the relation between the sedimentation velocity V/V_0 and the concentration d_v is plotted, and is compared with other theoretical and experimental results. Noda's experimental data[3] were obtained from the measurement of sedimentation velocities of the spherical particles of polystyrene (Dow polystyrene latex 580 G lot 2584), whose radius and density are $a = 134\ \mathrm{m}\mu$ and $\rho_p = 1.052$ respectively, in a salted water ($\rho_s = 1.0042$). On the other hand, Happel and Epstein[2] measured the pressure drop in a flow of water through a circular pipe of diameter 10 cm in which an assemblage of smooth cellulose acetate spheres of equal diameter (4.90 mm) is mechanically suspended and immobilized at simple cubic lattice points.

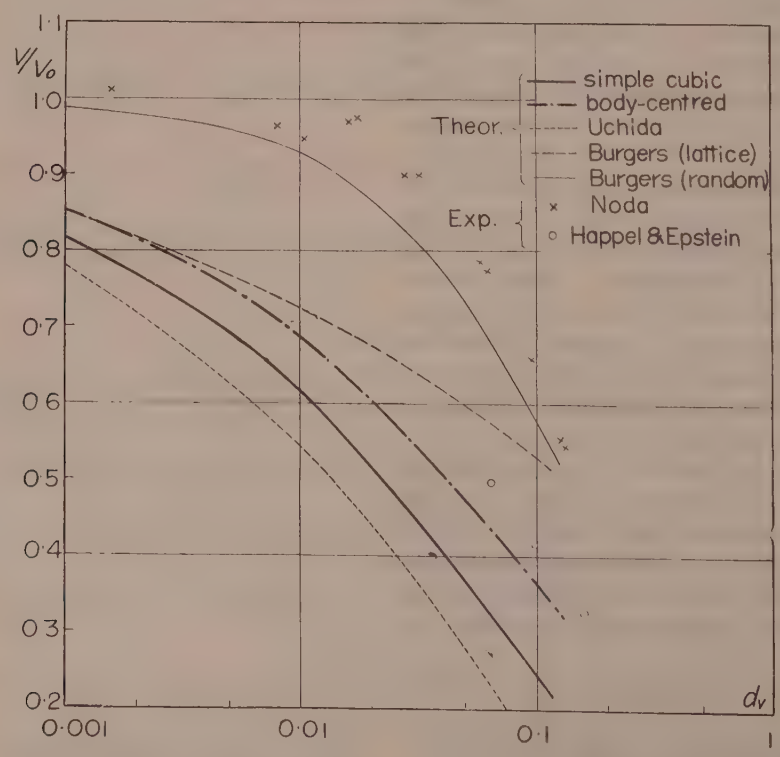

Fig. 3. Sedimentation velocity vs. volume concentration.

Although our model for the problem of sedimentation is rather rough, yet it gives as good results as those of other calculations[1),5)] based on the assumption that particles are situated at lattice points. It is also noteworthy that our data agree well with Happel and Epstein's experiments of the flow through pipe past spherical particles in lattice configurations. As for the origin of the discrepancy between our theory and the experiments of the sedimentation, it seems to the author that although in the theory all the distances between the neighbouring particles are assumed to be nearly equal, the distribution of the sedimenting particles will not be uniform but rather completely at random as to the distances between the neighbouring particles, and this fact may lead to the reduction of the drag of each particle and consequently to the increase of the sedimentation velocity.

§ 4. Summary

The flow of a viscous fluid past a sphere in a frictionless circular pipe is investigated by using Faxén's procedure and the results are applied to the problem of sedimentation. Although our model is rather rough, it gives as good results as those given by other theories.

Acknowledgements

In conclusion, I wish to express my hearty gratitude to Professors Isao Imai and Saburô Asaka for their discussion and kind inspection of the manuscript, to Professor Haruo Noda who kindly showed me unpublished data, and to Professor Shōichi Wakiya for his advice.

References

1) J. M. Burgers: Proc. Ned. Acad. Wet. **44** (1941) 1045, 1177; **45** (1942) 9, 126.
2) J. Happel and N. Epstein: Industrial and Engineering Chemistry **46** (1954) 1187.
3) H. Noda: Bulletin Chem. Soc. Japan **30** (1947) 495.
4) Y. Takaisi: J. Phys. Soc. Japan **10** (1955) 407, 685; **11** (1956) 1004, 1009, 1092; Mem. Ehime Univ. Sec. II **2** (1956) 89.
5) S. Uchida: Rep. Inst. Sci. Technol. Tokyo **3** (1949) 97.
6) S. Wakiya: J. Phys. Soc. Japan **8** (1953) 254; Res. Rep. Fac. Eng. Niigata Univ. **4** (1956) 157.
7) S. Wakiya: Res. Rep. Fac. Eng. Niigata Univ. **5** (1956) 1; **6** (1957) 155; J. Phys. Soc. Japan **12** (1957) 1130.
8) G. N. Watson: *A Treatise on the Theory of Bessel Functions* (Cambridge Univ. Press, 1922).

JOURNAL OF THE PHYSICAL SOCIETY OF JAPAN Vol. 13, No. 2, FEBRUARY, 1958

On a Theorem for Estimating Eigenvalues

By Hiroshi FUJITA and Tosio KATO

Department of Physics, Faculty of Science, University of Tokyo

(Received November 15, 1957)

Elementary proof is given for a theorem estimating eigenvalues of linear transformations with the form T^*T, which was used elsewhere in calculating the fundamental frequency of a square plate with free edges.

§ 1. Introduction

Some time ago one [3] of the authors of the present note proposed an approximation method for the eigenvalue problem of a self-adjoint transformation of the type T^*T in a Hilbert space. This method is based on the theorems stated in Section 3 and Section 4, which were proved with the aid of the Neumann-Murray theory [5, 7] concerning transformations T^*T, TT^* and a generalization of the Temple formula [2] [4, p. 103–105]. The purpose of the present note is to give elementary and direct proofs of these theorems. For simplicity we shall treat the

problem in the case of finite-dimensional vector spaces, though the application of these theorems lies mostly in systems with infinite degrees of freedom. The generalization of the results to the latter cases is straightforward and does not offer any essential difficulty.

Section 2 is devoted to a brief exposition of some known results regarding transformations T^*T and TT^*. In Section 3 and Section 4, we state and prove the theorems. Section 5 contains some remarks for the application of these theorems to continuous systems.

§ 2. Preliminary Remarks

Let $\mathfrak{H}$ and $\mathfrak{H}'$ be two (possibly identical) real Euclidean vector spaces with the inner products and the norms defined and denoted in the ordinary way. We consider a linear transformation T from $\mathfrak{H}$ into $\mathfrak{H}'$. T^*, the adjoint of T, is a linear transformation from $\mathfrak{H}'$ into $\mathfrak{H}$ and satisfies, by definition, the identity

$$(Tu, v)=(u, T^*v) \tag{1}$$

for any $u\in\mathfrak{H}$ and any $v\in\mathfrak{H}'$. T^*T and TT^* are symmetric transformations in $\mathfrak{H}$ and $\mathfrak{H}'$ respectively. The obvious relations

$$(T^*Tu, u)=\|Tu\|^2\geq 0\,, \quad (TT^*v, v)=\|T^*v\|^2\geq 0 \tag{2}$$

show that the symmetric transformations T^*T, TT^* and therefore their eigenvalues are non-negative. If we designate by $\mathfrak{N}$ the zero point set of T^*T, i.e., the set of u such that $T^*Tu=0$, (2) shows that $\mathfrak{N}$ is at the same time the zero point set of T:

$$Tu=0 \quad \text{for any} \quad u\in\mathfrak{N}\,. \tag{3}$$

Similarly, it holds that

$$T^*v=0 \quad \text{for any} \quad v\in\mathfrak{N}'\,, \tag{4}$$

where $\mathfrak{N}'$ is the zero point set of TT^*. 0 is an eigenvalue of T^*T (TT^*) if and only if $\dim\mathfrak{N}\neq 0$ ($\dim\mathfrak{N}'\neq 0$), i.e., $\mathfrak{N}\neq\{0\}$ ($\mathfrak{N}'\neq\{0\}$).

Let $\lambda_1^2, \lambda_2^2, \cdots, \lambda_\sigma^2$, ($\lambda_k>0$, $k=1, 2, \cdots, \sigma$), be the totality of the *positive* eigenvalues of T^*T and let

$$\mu_1^2\leq\mu_2^2\leq\cdots\leq\mu_n^2\leq\cdots\leq\mu_p^2\,,$$
$$(\mu_n>0,\ n=1, 2, \cdots, p)\,, \tag{5}$$

be the arrangement of $\{\lambda_k^2\}$ in the ascending order, where any degenerate eigenvalue is to appear repeatedly in comformity with its multiplicity. It should be remarked that $p=\dim\mathfrak{H}-\dim\mathfrak{N}$. We introduce a system $\{\varphi_n;\ n=1, 2, \cdots, p\}$ of eigenvectors of T^*T such that

$$T^*T\varphi_n=\mu_n^2\varphi_n\,,$$
$$(\varphi_n, \varphi_m)=\delta_{nm}\,, \quad (n, m=1, 2, \cdots, p)\,. \tag{6}$$

Evidently $\{\varphi_n\}$ is complete in $\mathfrak{H}\ominus\mathfrak{N}$. Furthermore, if we put

$$\psi_n=\frac{1}{\mu_n}T\varphi_n\,, \quad (n=1, 2, \cdots, p)\,, \tag{7}$$

then ψ_n is an eigenvector of TT^* with the eigenvalue μ_n^2 and the system $\{\psi_n\}$ is orthonormal, for the relations

$$\left.\begin{aligned} &TT^*\psi_n=\frac{1}{\mu_n}TT^*T\varphi_n=\mu_nT\varphi_n=\mu_n^2\psi_n\,,\\ &\mu_n\mu_m(\psi_n, \psi_m)=(T\varphi_n, T\varphi_m)\\ &=(T^*T\varphi_n, \varphi_m)=\mu_n^2(\varphi_n, \varphi_m)=\delta_{nm}\mu_n^2 \end{aligned}\right\} \tag{8}$$

are true for $n, m=1, 2, \cdots, p$. Moreover, $\{\psi_n\}$ is complete in $\mathfrak{H}'\ominus\mathfrak{N}'$. In fact, let v be an eigenvector of TT^* with a positive eigenvalue $\mu'^2(\mu'>0)$, i.e.,

$$TT^*v=\mu'^2v\,, \quad (\mu'>0,\ v\neq 0)\,. \tag{9}$$

Then, $\|T^*v\|^2=(TT^*v, v)=\mu'^2\|v\|^2\neq 0$ and

$$T^*T(T^*v)=T^*(TT^*v)=\mu'^2T^*v\,,$$

which means that T^*v is an eigenvector of T^*T with the positive eigenvalue μ'^2. Hence T^*v is to be expressible as

$$T^*v=\sum_{n=s}^{t}a_n\varphi_n\,, \tag{10}$$

where $\mu_s=\mu_{s+1}=\cdots=\mu_t=\mu'$. Thus, by means of (9) we obtain

$$v=\frac{1}{\mu'^2}TT^*v=\frac{1}{\mu'^2}\sum_{n=s}^{t}a_nT\varphi_n=\frac{1}{\mu'}\sum_{n=s}^{t}a_n\psi_n \tag{11}$$

showing the desired completeness of $\{\psi_n\}$.

Summarizing the results obtained above, we conclude:* The multiplicities being taken into account, the set of the positive eigenvalues of T^*T is identical with that of TT^*; we can choose a pair of orthonormal systems $\{\varphi_n\}$, $\{\psi_n\}$, $(n=1, 2, \cdots, p)$, such that $\{\varphi_n\}$ and $\{\psi_n\}$ are complete in $\mathfrak{H}\ominus\mathfrak{N}$ and $\mathfrak{H}'\ominus\mathfrak{N}'$ respectively (thus, $p=\dim\mathfrak{H}-\dim\mathfrak{N}=\dim\mathfrak{H}'-\dim\mathfrak{N}'$) and are connected with each other by the relations

$$T\varphi_n=\mu_n\psi_n\,, \quad T^*\psi_n=\mu_n\varphi_n\,, \quad (n=1, 2, \cdots, p)\,. \tag{12}$$

* These results correspond to Schmidt's theorem [8] concerning "pairs of adjoint eigenfunctions" of nonsymmetric integral equations. Also the Neumann-Murray theory can be regarded as a generalization of these results to general transformations in Hilbert spaces.

§ 3. Estimation of Eigenvalues

For any $u \in \mathfrak{H}$ and $v \in \mathfrak{H}'$ subjected to the conditions

$$\|u\|^2=1\,, \qquad \|v\|^2=1\,, \tag{13}$$

$$(Tu, v) \geq 0\,, \tag{14}$$

we define the following quantities

$$\eta=(Tu, v)=(u, T^*v)\,, \tag{15}$$

$$\mathcal{E}^2=\frac{1}{2}[\|Tu\|^2+\|T^*v\|^2]-\eta^2\,, \quad (\mathcal{E} \geq 0)\,. \tag{16}$$

The use of the notation $\mathcal{E}^2(\mathcal{E} \geq 0)$ is seen to be legitimate in virtue of the relation

$$2\mathcal{E}^2=\|Tu-\eta v\|^2+\|T^*v-\eta u\|^2\,, \tag{17}$$

which is an easy consequence of (15) and (16). Also (17) implies that $\mathcal{E}=0$ occurs if and only if both of the equalities

$$Tu=\eta v\,, \qquad T^*v=\eta u \tag{18}$$

are satisfied, i.e., if and only if u and v are respectively eigenvectors of T^*T and TT^* with the eigenvalue η^2.

Making use of φ_n, ψ_n $(n=1, 2, \cdots, p)$ introduced in Section 2, we can write

$$\left.\begin{aligned} u&=u_0+a_1\varphi_1+a_2\varphi_2+\cdots+a_p\varphi_p\,, \\ v&=v_0+b_1\psi_1+b_2\psi_2+\cdots+b_p\psi_p\,, \end{aligned}\right\} \tag{19}$$

where $u_0 \in \mathfrak{N}$, $v_0 \in \mathfrak{N}'$ are the projections of u, v on $\mathfrak{N}, \mathfrak{N}'$ respectively, and where

$$a_n=(u, \varphi_n)\,, \qquad b_n=(v, \psi_n)\,, \qquad (n=1, 2, \cdots, p)\,. \tag{20}$$

In view of (3), (4) and (12), we observe

$$\left.\begin{aligned} Tu&=\mu_1a_1\psi_1+\mu_2a_2\psi_2+\cdots+\mu_pa_p\psi_p\,, \\ T^*v&=\mu_1b_1\varphi_1+\mu_2b_2\varphi_2+\cdots+\mu_pb_p\varphi_p\,. \end{aligned}\right\} \tag{21}$$

If we put

$$\|u_0\|=a_0\,, \qquad \|v_0\|=b_0 \tag{22}$$

and introduce

$$\mu_0=0\,, \tag{23}$$

by convention, (13), (15) and (16) are reduced to the following forms:

$$\sum_{n=0}^{p} a_n^2=1\,, \qquad \sum_{n=0}^{p} b_n^2=1\,, \tag{24}$$

$$\eta=\sum_{n=1}^{p} \mu_n a_n b_n=\sum_{n=0}^{p} \mu_n a_n b_n\,, \tag{25}$$

$$2(\mathcal{E}^2+\eta^2)=\sum_{n=1}^{p} \mu_n^2(a_n^2+b_n^2)=\sum_{n=0}^{p} \mu_n^2(a_n^2+b_n^2)\,. \tag{26}$$

We now prove the following Lemma.

Lemma 1. Let η and $\mathcal{E}$ be as given above. Let ρ be a positive number and set

$$r=r(\rho)=\sqrt{\mathcal{E}^2+(\rho-\eta)^2}\,. \tag{27}$$

Then under the condition $\mathcal{E}>0$, each of the half-closed intervals $(\rho-r, \rho+r]$ and $[\rho-r, \rho+r)$ contains at least one of $\mu_0, \mu_1, \cdots, \mu_p$.

Proof. Multiplying both sides of

$$(\mu_n-\rho)^2-r^2=\mu_n^2-2\rho\mu_n+(\rho^2-r^2)$$

by $a_n^2+b_n^2$ and then summing up both sides with respect to n, we have

$$\begin{aligned} &\sum_{n=0}^{p} [(\mu_n-\rho)^2-r^2](a_n^2+b_n^2) \\ &=\sum_{n=0}^{p} \mu_n^2(a_n^2+b_n^2)-4\rho \sum_{n=0}^{p} \mu_n a_n b_n \\ &\quad +(\rho^2-r^2) \sum_{n=0}^{p} (a_n^2+b_n^2)-2\rho \sum_{n=0}^{p} \mu_n(a_n-b_n)^2 \\ &=2(\mathcal{E}^2+\eta^2)-4\rho\eta+2(\rho^2-r^2)-2\rho \sum_{n=0}^{p} \mu_n(a_n-b_n)^2 \\ &=2[\mathcal{E}^2+(\rho-\eta)^2-r^2]-2\rho \sum_{n=0}^{p} \mu_n(a_n-b_n)^2\,, \end{aligned}$$

by means of (24), (25) and (26). Thus, by virture of (27),

$$\sum_{n=0}^{p} [(\mu_n-\rho)^2-r^2](a_n^2+b_n^2) +2\rho \sum_{n=0}^{p} \mu_n(a_n-b_n)^2=0\,. \tag{28}$$

Suppose now that the interval $(\rho-r, \rho+r]$ does not contain any of $\mu_0(=0), \mu_1, \cdots, \mu_p$. (The other interval can be treated similarly.) Then each term in (28) is non-negative and therefore must vanish. Noting that $\mu_0=0$ and $\mu_n>0$ $(n \geq 1)$, we should conclude that

$$a_n=b_n \qquad \text{for} \quad n=1, 2, \cdots, p \tag{29}$$

and that

$$a_n=b_n=0 \qquad \text{if} \quad \mu_n \neq \rho-r\,. \tag{30}$$

If $\mu_n \neq \rho-r$ for every n, (30) evidently contradicts (24). On the other hand, if $\mu_s=\mu_{s+1}=\cdots=\mu_t=\rho-r$ $(0 \leq s \leq t \leq p)$ and the other $\mu_n \neq \rho-r$, (29) and (30) yield $\eta=\rho-r$ and

$$2(\mathcal{E}^2+\eta^2)=2(\rho-r)^2\,,$$

by means of (24), (25) and (26). In consequence we are led to $\mathcal{E}=0$, which again contradicts the assumption and complete the proof.

We are now ready to proceed to the following Theorem.

Theorem 1. Let T, T^* be as above. For $0 \leq \alpha < \beta$, let the open interval (α^2, β^2) contain at most one eigenvalue of T^*T. For a pair of $u \in \mathfrak{H}$, $v \in \mathfrak{H}'$ subjected to (13) and (14), let the inequality

$$(\eta-\alpha)(\beta-\eta)>\mathcal{E}^2 \tag{31}$$

be satisfied, where η and $\mathcal{E}$ are given by (15)

and (16).

Then there certainly exists a positive eigenvalue $\tilde{\lambda}^2$ of T^*T in the interval (α^2, β^2) such that

$$\xi \leq \tilde{\lambda} \leq \zeta , \tag{32}$$

where

$$\xi = \eta - \frac{\varepsilon^2}{\beta - \eta}, \qquad \zeta = \eta + \frac{\varepsilon^2}{\eta - \alpha}. \tag{33}$$

Proof. First we remark that (31) implies

$$\alpha < \xi \leq \eta \leq \zeta < \beta . \tag{34}$$

The two cases $\varepsilon > 0$ and $\varepsilon = 0$ are dealt with separately. In the case $\varepsilon > 0$, we determine a positive number ρ' in such a way that

$$\rho' - r(\rho') = \alpha .$$

Then Lemma 1 asserts that the interval $(\alpha, \rho' + r(\rho')]$ contains at least one μ_n $(n = 0, 1, \cdots, p)$. ρ' is determined by noting that $\rho' - \eta - r(\rho') = \alpha - \eta$ and $r(\rho')^2 - (\rho' - \eta)^2 = \varepsilon^2$. The result is

$$\rho' = \frac{1}{2}\left[\eta + \alpha + \frac{\varepsilon^2}{\eta - \alpha}\right],$$

$$r(\rho') = \frac{1}{2}\left[\eta - \alpha + \frac{\varepsilon^2}{\eta - \alpha}\right].$$

Hence

$$\rho' + r(\rho') = \eta + \frac{\varepsilon^2}{\eta - \alpha} = \zeta .$$

Evidently the interval $(\alpha, \zeta]$ excludes $\mu_0 = 0$ so that $(\alpha^2, \zeta^2]$ contains at least one positive eigenvalue λ'^2 of T^*T. On the other hand, if another positive number ρ'' is chosen in such a way that

$$\rho'' + r(\rho'') = \beta ,$$

we get similarly

$$\rho'' - r(\rho'') = \eta - \frac{\varepsilon^2}{\beta - \eta} = \xi$$

and see, according to Lemma 1, that the interval $[\xi, \beta)$ contains at least one μ_n $(n = 0, 1, \cdots, p)$. Since $[\xi, \beta)$ cannot contain $\mu_0 = 0$ by virtue of $0 < \xi$, there exists at least one positive eigenvalue λ''^2 of T^*T included in $[\xi^2, \beta^2)$.

It follows from these results, combined with the assumption that (α^2, β^2) contains at most one eigenvalue of T^*T that the above-mentioned λ' and λ'' are both unique and mutually identical. Thus the validity of the Theorem has been established for the case $\varepsilon > 0$.

If $\varepsilon = 0$, η^2 itself turns out to be an eigenvalue of T^*T as shown near the beginning of this Section. On the other hand, we have clearly, $\xi = \eta = \zeta$. Hence the Theorem is also true on account of (34).

§ 4. Estimation of Eigenvectors

Theorem 2. In Theorem 1, let $\tilde{\lambda}^2$ be non-degenerate and let $\tilde{u}$ be the eigenvector of T^*T with the eigenvalue $\tilde{\lambda}^2$ nomalized as

$$\|\tilde{u}\|^2 = 1 , \qquad (u, \tilde{u}) \geq 0 . \tag{35}$$

Then, $\tilde{v} = \text{const.}\ T\tilde{u}$ is an eigenvector of TT^* with the same eigenvalue $\tilde{\lambda}^2$. If $\tilde{v}$ is normalized as

$$\|\tilde{v}\|^2 = 1 , \qquad (v, \tilde{v}) \geq 0 , \tag{36}$$

we have

$$\frac{1}{2}[\|u - \tilde{u}\|^2 + \|v - \tilde{v}\|^2] \leq \frac{\varepsilon^2}{\delta^2}\left(1 - \frac{\varepsilon^2}{\delta^2}\right)^{-1/2}, \tag{37}$$

provided that $\varepsilon < \delta = \min(\eta - \alpha, \beta - \eta)$.

Proof. Let all notations be as before. The fact that $\tilde{v}$ is an eigenvector of TT^* with the eigenvalue $\tilde{\lambda}^2$ was already proved in Section 2. Also we may assume without loss of generality that

$$\tilde{\lambda} = \mu_r \neq \text{the other } \mu_n , \qquad \tilde{u} = \varphi_r , \qquad \tilde{v} = \psi_r$$

for some $r \geq 1$. Thus we have

$$(u, \tilde{u}) = (u, \varphi_r) = a_r \geq 0 , \quad (v, \tilde{v}) = (v, \psi_r) = b_r \geq 0 . \tag{38}$$

We further suppose that $\eta - \alpha \leq \beta - \eta$, i.e., $\delta = \eta - \alpha$, since the other case can be treated quite similarly. According to Theorem 1, μ_r and only μ_r is contained in the open interval (α, β') among all μ_n $(n = 0, 1, 2, \cdots, p)$ where $\beta' = \eta + \delta$, for

$$\zeta = \eta + \frac{\varepsilon^2}{\eta - \alpha} = \eta + \frac{\varepsilon^2}{\delta} < \eta + \delta = \beta' .$$

If we introduce the quadratic expression $f(x) = (x - \alpha)(x - \beta')$, it follows that $f(\mu_r) < 0$ and $f(\mu_n) \geq 0$ for $n \neq r$. Also $f(-\mu_n) \geq 0$ holds for $n = 0, 1, \cdots, p$ by virtue of $0 \leq \alpha$, $0 \leq \mu_n$. Hence we have

$$\sum_{n=0}^{p} f(\mu_n)(a_n + b_n)^2 + \sum_{n=0}^{p} f(-\mu_n)(a_n - b_n)^2 \geq f(\mu_r)(a_r + b_r)^2 . \tag{39}$$

By means of (24), (25) and (26), the left side of (39) is reduced to

$$2 \sum_{n=0}^{p} \mu_n^2 (a_n^2 + b_n^2)$$

$$+2\alpha\beta'\sum_{n=0}^{p}(a_n^2+b_n^2)-4(\alpha+\beta')\sum_{n=0}^{p}\mu_n a_n b_n$$
$$=4(\mathcal{E}^2+\eta^2)+4\alpha\beta'-4(\alpha+\beta')\eta$$
$$=4[\mathcal{E}^2+f(\eta)]$$
$$=4(\mathcal{E}^2-\delta^2)\,,$$

where at the last step use is made of $f(\eta)=-\delta^2$. On the other hand,

$$f(\mu_r)\geq\min f(x)=f(\mu)=-\delta^2\,.$$

In this way, we are led to

$$4(\mathcal{E}^2-\delta^2)\geq-\delta^2(a_r+b_r)^2\,,$$

namely,

$$\left(\frac{a_r+b_r}{2}\right)^2\geq 1-\frac{\mathcal{E}^2}{\delta^2}\,. \tag{40}$$

Since, by (35), (36) and (38)

$$\frac{1}{2}[\|u-\tilde{u}\|^2+\|v-\tilde{v}\|^2]=2\left(1-\frac{a_r+b_r}{2}\right), \tag{41}$$

we arrive at the desired inequality (37) with the aid of (40) and the elementary inequality $2(1-x)\leq(1-x^2)/x\,,\ (x>0)\,.$

Remark. In theorem 2, the assumption of non-degeneracy of $\tilde{\lambda}^2$ is essential. For example, if $\mu_r=\mu_{r+1}=\tilde{\lambda}$, it may occur that $\tilde{u}=\varphi_r$, $u=\varphi_{r+1}$, $\tilde{v}=\psi_r$, $v=\psi_{r+1}$. Then the left side of (37) is equal to 2, while the other side vanishes owing to $\mathcal{E}=0$.

§ 5. Concluding Remarks

Remark 1. Our results stated in Theorem 1 and Theorem 2 can be generalized to more general cases in which $\mathfrak{H}$, $\mathfrak{H}'$ are complex Hilbert spaces and T is a closed linear (in general unbounded) transformation from $\mathfrak{H}$ into $\mathfrak{H}'$ with its domain $\mathfrak{D}_T$ dense in $\mathfrak{H}$ [3]. Then T^* exists and turns out to be a closed linear transformation from $\mathfrak{H}'$ into $\mathfrak{H}$ with its domain $\mathfrak{D}_{T^*}$ dense in $\mathfrak{H}'$. In such cases, Theorem 1 and Theorem 2 retain their validity, if u, v are subjected to the additional conditions

$$u\in\mathfrak{D}_T\,,\qquad v\in\mathfrak{D}_{T^*}\,, \tag{42}$$

so that η, $\mathcal{E}^2$ given by (15), (16) are meaningful.

Remark 2. From the view point of practical application, our Theorems, in particular Theorem 1, can be regarded as an appromimation method of variational character. According to Theorem 1 we can calculate an approximate value, with error estimation, of the eigenvalue $\tilde{\lambda}^2$ in question as soon as we can construct suitable "admissible vectors" u, v and also are provided, in one way or another, with α^2 and β^2, i.e., a rough upper bound for the next lower eigenvalue and a rough lower bound for the next upper eigenvalue. Thus the scope of application of our Theorems is rather wide, for most eigenvalue problems differential systems in mathematical physics can be reduced to the form $T^*Tu=\lambda^2u$ by a suitable choice of $\mathfrak{H}$, $\mathfrak{H}'$. Though some of the conveniences of this method was illustrated by a simple example in [3], as typical examples of this application we refer the readers to papers by us and our collaborators on the vibration problem of an elastic plate with free edges. One [6] of them gives rather rough approximate values by using simple admissible vectors, while the other [1] adopts more complicated admissible vectors and gives much improved approximate values as the result. Also some detailed prescriptions of auxilliary procedures needed for good estimation and brief discussions of the relative advantages and disadvantages of this method in comparison with other methods can be found in [1].

References

1) T. Kato, H. Fujita, Y. Nakata and M. Newman: J. Research NBS **59** (1957) 169 to 186.
2) T. Kato: J. Phys. Soc. Japan **4** (1949) 334 to 339.
3) T. Kato: Math. Ann. **126** (1953) 253 to 262.
4) T. Kato: Technical Report No. 7, Dept. of Math., Univ. of Calif. (1955).
5) F. J. Murray: Trans. Amer. Math. Soc. **37** (1935) 301 to 338.
6) Y. Nakata and H. Fujita: J. Phys. Soc. Japan **10** (1955) 823 to 824.
7) J. von Neumann: Ann. of Math. **33** (1932) 301 to 338.
8) E. Schmidt: Math. Ann. **63** (1907) 433 to 476.

Short Notes

This section is intended to secure prompt publication of important discoveries in physics. The reports should not exceed 800 words in length. A figure of size 7 cm × 7 cm will be counted as 150 words.

J. PHYS. SOC. JAPAN **2** (1958) 220

Anomalous g-shifts of Excited States of Cr^{3+} in Ruby

By Ikuji TSUJIKAWA

Research Institute for Iron, Steel and Other Metals, Tohoku University, Sendai

and Satoru SUGANO

Department of Physics, Tokyo University, Tokyo

(Received December 5, 1957)

In the previous note, Tanabe and one of the present authors[1] tried to explain the Zeeman effect of the characteristic doublets R_1 and R_2 of ruby observed at 83°K by Lehmann[2] and found that the thoretical results contradicted with his odservations only in quantitative aspects.

Under these circumstances, we have repeated studies of the Zeeman effects[3] on the same absorption lines at 20°K and 4.2°K, using a concave grating of dispersion 2.5Å/mm (1st order) and a magnetic field $H_0=24000\,\phi$. As it was found in preliminary experiments that the spectral widths were broad at high Cr^{3+} concentration (a few per cent), we have used synthetic ruby of 4 mm thickness which contains 0.28 weight percent Cr_2O_3.

Our results show that the quantitatively strange points in Lehmann's results are removed and Zeeman levels of the ground states which are observed directly in the Zeeman patterns of R_1, R_2 when $H_0 \perp C_3$ (since $g_{0\perp} \sim 0$[1]) agree well with those observed by the paramagnetic resonance method.[4] However, the $g_{e//}$-shifts of the excited states of R_1 and R_2 are found to be anomalous; $g_{e//}(R_1) \approx 2+2\Delta$, $g_{e//}(R_2) \approx 2-2\Delta (\Delta \approx 0.2)$ and so $g_{e//}(R_1)+g_{e//}(R_2) \approx 4$.

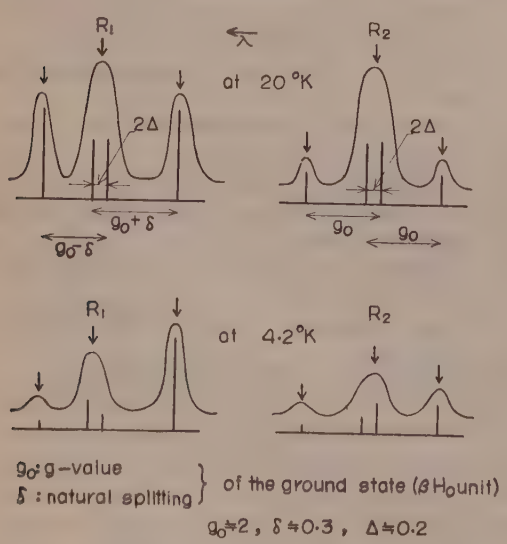

Fig. 1. The observed Zeeman patterns of R_1 and R_2 absorption when $E \perp C_3$ and $H_0 // C_3$.

One of our results which shows these anomalies is schematically described in Fig. 1. While the main three Zeeman components are completely resolved on our photographic plates, the central two lines closely located each other appear as a somewhat broad line. The superposition of these central lines is only found from its apparent shift relative to the side components when temperature is varied from 20°K to 4.2°K. This apparent shift is due to the decrease of the electron population of the upper Zeeman levels of the ground state at 4.2°K. The other strong evidence which confirms the anomalous behavior of $g_{e//}$-shifts is seen in the observed separations of the side components which are $\approx 2(2+\Delta)$ for both R_1 and R_2 when the electric vector E of the incident light is parallel to the optic axis C_3.

The observed remarkable relation $g_{e//}(R_1)+g_{e//}(R_2) \approx 4$ and the shift $\Delta g_{e//}(R_1) \approx 0.4$ can be explained by the dominant effect of the third order perturbation $L_Z \cdot V \cdot V \cdot \beta H_0$ (V is the trigonal field) which is linear in H_0 and involves no term of spin-orbit interaction H_{S0}. In these excited states of ruby none of the second order perturbations contributes to the g-shift and the contributions from the other types of the third order's which involve H_{S0} are all small because $H_{S0} < V$.[5]

The Zeeman effects on the other lines B_1 and B_2 located at $\sim 21000\,cm^{-1}$ have also been studied and the remarkably large splittings were found in one of them. The experimental details and other results will be published soon.

One of the authors S. S. should like to express his sincere thanks to Prof. E. Kanda and other members of Research Institute for I. S. O. M. for their hospitality.

References

1) Y. Tanabe and S. Sugano: J. Phys. Soc. Japan **12** (1957) 556.
2) H. Lehmann: Ann. d. Phys. (5) **19** (1934) 99.
3) Prof. G. H. Dieke of the Johns Hopkins University has kindly informed us that Zeeman experiment on ruby has also been completed in his laboratory but the results are not published yet.
4) A. A. Manenkov and A. M. Prokhorov: J. E. T. P. **28** (1955) 762.
M. M. Zaripov and Iu. Ia. Shamonin: J. E. T. P. **30** (1956) 291.
J. E. Geusic: Phys. Rev. **102** (1956) 1252.
5) S. Sugano and Y. Tanabe: to be published.

J. PHYS. SOC. JAPAN **2** (1958) 221

Theoretical Considerations on Radiation-Induced Reactions of Saturated Long-Chain Hydrocarbons

By Mitio INOKUTI and Tsutomu WATANABE

Department of Applied Physics, Faculty of Engineering, University of Tokyo, Tokyo

(Received November 2, 1957)

Proposed mechanisms of radiation-induced cross-linking of saturated long-chain hydrocarbons, based on the observed linear dose-dependence of both the amount of evolved hydrogen gas and the number of crosslinks, require the following process as an essential step.[1]

$$-CH_2-CH_2- + H \longrightarrow -CH_2-CH- + H_2 \qquad (1)$$

Using a semiempirical method of bond-eigenfunctions, the adiabatic potential of the ground doublet state of the reacting system was calculated by perturbation procedure, taking as bases the wave-function ψ_1 describing the hydrocarbon and the hydrogen atom infinitely separated from each other, and ψ_2 describing the hydrocarbon radical and the hydrogen molecule infinitely separated from each other. The Hamiltonian matrixelements were then reduced to linear combinations of two-body interactions, neglecting higher-order permutations and many-center integrals:

$$\mathscr{H}_{11}=E(C_0H)+E(H_0H)+U \qquad (2)$$

$$\mathscr{H}_{22}={}^1E(H_0H)+(3/4)\,{}^3E(C_0H_0) -(3/4)\,{}^1E(C_0H_0)+E(C_0H)+U \qquad (3)$$

$$\mathscr{H}_{12}=(1/2)\{{}^1E(H_0H)+{}^3E(C_0H)+U\} \qquad (4)$$

$$U=E(H_0'H)+2\sum_{\nu=1}^{\infty}E(C_\nu H) +2\sum_{i=1}^{\infty}\{E(H_iH)+E(H_i'H)\} \qquad (5)$$

${}^1E(XY)$ and ${}^3E(XY)$ are the adiabatic potentials for the lowest ${}^1\sum$ and ${}^3\sum$ state of the molecule XY, $E(XY)$ being their multiplicity-average. We remark, however, that ${}^1E(CH)$ or ${}^3E(CH)$ means the potential, not of the real CH molecule, but of a virtual one bonded by an electron in 1s hydrogen AO and one in the tetrahedrally hybridized carbon AO directed to the hydrogen. Suffixes and primes refer to the atoms in hydrocarbon as seen in Fig. 1. The non-orthogonality ($\psi_1\psi_2$) turns out 1/2 in our approximation. The perturbed energy is shown to be lowest when the hydrogen atom lies on the straight line along a CH-bond so that (2), (3), (4) and numerical work refer to this case. ${}^1E(HH)$ and ${}^3E(HH)$ were obtained by good approximate formulas by Hirschfelder and Linnett[3]. ${}^1E(CH)$ was approximated by a Morse function, parameters determined by spectroscopic and thermochemical data of lower hydrocarbons. An approximate formula for ${}^3E(CH)$ was established by a semiempirical Heitler-London type calculation.

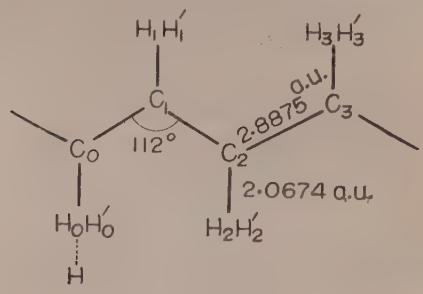

Fig. 1. (After Bunn[2]).

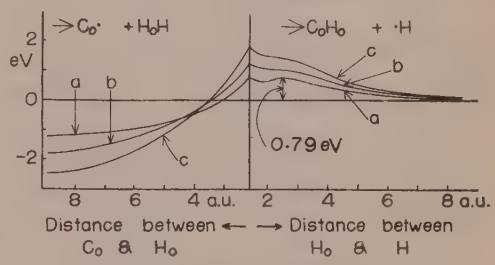

a) CH_4+H b) $-CH_2CH_3+H$,
c) $-CH_2CH_2-+H$

Fig. 2.

Our results are given in Fig. 2, with the cases $-CH_2-CH_3+H$ and CH_4+H, obtained by proper modifications in (5). The calculated activation energy for (1) seems rather high. But in solid hydrocarbon samples the reacting hydrogen atom is originally not at zero-potential, but at a finite potential; moreover there may be some attractive polarization forces and changes of hybridization in ψ_2, not taken into account here. These situations may reduce the activation energy appreciably in solid state. The reaction of hydrogen atom with a chain-end methyl group requires much lower activation enrgy than with a mid-chain. The calculated activation energy for CH_4+H, 0.79 ev, may be compared with the observed value, 0.40~0.56 ev,[4] Our treatment should be superior to Gorin at al's,[5] resulting in too low activation energy and a doubtful prediction of a stable complex CH_5, because of their adoption of a too short-range potential as ${}^3E(HH)$, which contributes to U remarkably.

We are grateful to Prof. A. Amemiya for helpful discussions throughout the work.

References

1) R. W. Pearson: J. Polym. Sci. **25** (1957) 189; R. Simha and L. A. Wall: J. Phys. Chem. **61** (1957) 425.
2) C. W. Bunn: Trans. Faraday Soc. **35** (1939) 483.
3) J. O. Hirschfelder and J. W. Linnett: J. Chem. Phys. **18** (1950) 130.
4) T. G. Majury and E. W. R. Steacie: Disc. Faraday Soc. **14** (1953) 45.
5) E. Gorin et al: J. Chem. Phys. **7** (1939) 633.

J. PHYS. SOC. JAPAN **2** (1958) 222~223

Liquid-Like Layers in the Adsorbed Film of H_2O on Glass

By Koji KAWASAKI, Kyoichi KANOU and Yoshiyasu SEKITA

Electrotechnical Laboratory, Nogatacho, Tokyo, Japan

(Received November 11, 1957)

The adsorption isotherm of water vapour and the d.c. surface conductivity were measured for some kinds of glass as given in Table I. The isotherms

Table I.

Material	No.	SiO_2	Al_2O_3	CaO	Na_2O
Glass-A	4	62.34	8.48	7.80	21.38
	6	59.75	11.82	7.97	20.46
Glass-B	3	75		7	18.91
	5	67		15	16.86

in ωt %

were obtained by the gravimetric method using powdered specimens; the d.c. conductivity was measured on glass plates by means of a galvanometer.[1] The samples had been cleaned with NaOH aqueous solution, chromic acid mixture and distilled water.

The surface conduction current i divided by i_0, the current for $\theta=0$, is plotted in Fig. 1 *versus*

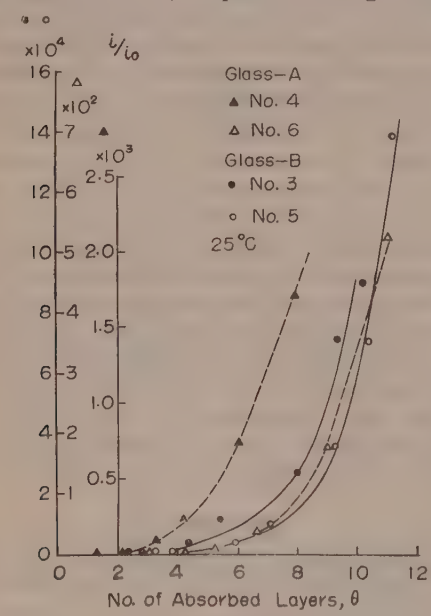

Fig. 1.

the number of the adsorbed layers θ as determined by the BET method. It can be seen that i/i_0 linearly increases with θ when θ exceeds some critical value which is characteristic to the specimen. This could be explained if one assumes that the lower, or the inner, adsorbed layers are immobile being under the influence of the strong attraction field of the glass surface, while the upper, or the outer, layers are mobile: the conduction current would increase materially only when the mobile or the liquid-like layers are present.

The above assumption is supported by the following consideration.

The calculations by Hill[2] and others show that, for the case of the liquid-like adsorbate, in which the effective molecular interaction is supposed to be exclusively of the van der Waals type the adsorption isotherm is represented by

$$lnx=ln(p/p_0)=-K/\theta^3\,, \qquad (1)$$

where θ is the number of layers at a pressure p, and p_0 is the saturation pressure. K is a certain constant which depends on various parameters characterizing the molecular interactions. Eq. (1) is a special case of the more general equation proposed by Halsey[3]:

$$ln(p/p_0)=-K/\theta^s\,. \qquad (2)$$

Now, the adsorption isotherms we obtained experimentally for Glass-B are plotted in Fig. 2. The

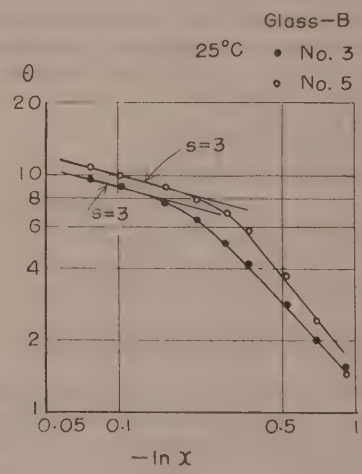

Fig. 2.

curves are, at high relative pressures, in good agreement with the theoretical isotherms with $s=3$ in Eq. (2), suggesting that the adsorbed layers are liquid-like. The values of s for representing the experimental isotherms at high relative pressures for Glass-A, Nos. 4 and 6, by Eq. (2) are 2.0 and 3.2 respectively.

In conclusion, we would like to point out that our adsorption isotherms are qualitatively in good agreement for $p/p_0 \leq 0.93$ with the one obtained by Garbatski and Folman[4] for a well defined glass plate. Investigations on the adsorption at very high relative pressures when capillary condensation may have pronounced influence are wanted.

References

1) K. Kawasaki: to be published in J. Appl. Phys. Japan.
2) T. L. Hill: J. Chem. Phys. **17** (1949) 590, 668.
3) G. D. Halsey, Jr.: J. Chem. Phys. **16** (1948) 931.
4) U. Garbatski & M. Folman: J. Phys. Chem. **60** (1956) 793.

J. PHYS. SOC. JAPAN **2** (1958) 223

Current Amplification by Electron Bombardment in the Semiconductor Barrier Layer

By Kenichi TAKEYA and Keiichi NAKAMURA

Technical Research Laboratory, Broadcasting Corporation of Japan, Tokyo

(Received December 4, 1957)

The experiment described in this paper is intended to find how much excess current will flow when a semiconductor barrier layer is bombarded by high energy electron beams. It is expected that the characteristic features of these excess current are closely related with those observed in a *p–n* function photo-diode, since the phenomena arise from the separation of free electron-hole pairs excited near the barrier field region. No one has hitherto tried experiment of this sort so extensively, except that W. Ehrenberg and his co-workers (1) carried out the measurement of electron voltaic effect of some selenium and cuprous oxide cells. For Se photo-cells, under best conditions, they obtained a max. current gain of about 500 when bombarding electron energy was in the vicinity of 50 KV. and for Cu_2O, about 150 at 90 KV.

Using similar Se photo-cell, and giving proper reverse bias voltage to the barrier layer, we obtained very large current gain under electron bombardment. In the experiments, the Se photocell was bombarded by electron beam perpendicular to its barrier layer. Furthermore, these experiments were performed for alloyed Ge– and grown and diffused, Si *p–n* junctions. In these cases, except for Si diffused junction, electron beam was directed so as to strike bare *p–n* junction region nearly parallel to its junction layer. For Si diffused junction, the arrangement was the same as that of Se photo-cell.

Excess currents were measured potentiometrically. The current gain δ was defined as the ratio of excess current i_2 to bombarding current i_1. The observed δ versus reverse bias voltage V_B characteristics were shown in the figures (1–4). The energy of bombarding electron is indicated on each curve. For Se photo-cell, no reasonable explanation for the observed properties has yet been found. Probably, expotential rise of δ as V_B increases will be the increase in collection efficiency of charge carriers released by electron bombardment. For Ge and Si *p–n* junctions, these characteristics are just those expected

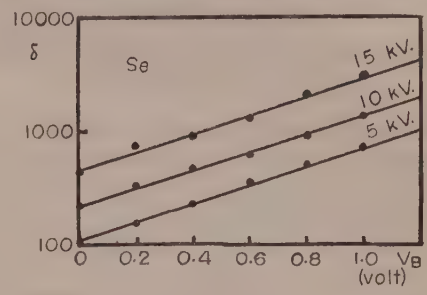

Fig. 1.

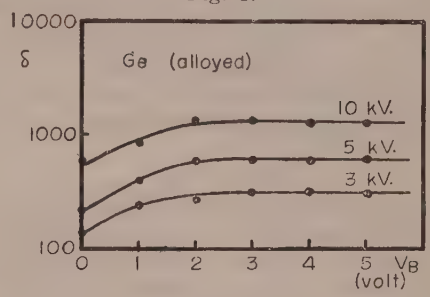

Fig. 2.

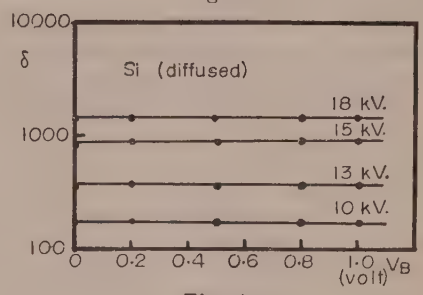

Fig. 4.

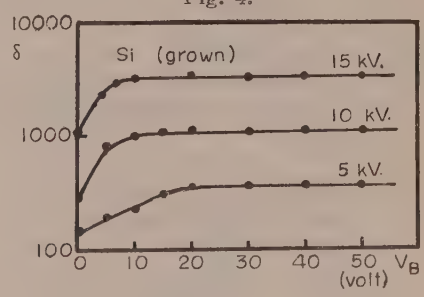

Fig. 3.

from the rectifying I–V characteristics and analogous to the photo-diode properties.

These results indicate, as Ehrenberg et al. suggested, a new method of measuring electron beams and of multiplication of electrons created in vaccum.

Reference

1) W. Ehrenberg, Chi-Shi Lang and R. West: Proc. Phys. Soc. **64** (1951) 424.

J. PHYS. SOC. JAPAN **2** (1958) 224

Fading of Coloration of Irradiated Glass*

By Sohei KONDO

National Institute of Genetics, Misima, Japan

(Received November 30, 1957)

Schulman, Klick and Rabin[1] found that changes in absorption coefficient of phosphate glass provide a simple method of measuring radiation doses up to 2×10^6 röntgen which 5% accuracy. If has also been found that ordinary slide glass[2] and window glass plates[3] are surprisingly homogeneous with respect to γ-ray induced absorption changes. For further improvement of the accuracy of glass dosimetry, correction for fading must be taken into account. The fading of coloration of gamma irradiated phosphate glass was studied by Rabin and Price[4]. They found the following fading formula.

$$\mu(t) \propto t^{-0.067}, \qquad (1)$$

where $\mu(t)$ is the change in absorption coefficient of glass measured at t hours after short exposures. A similar relation holds for fading of coloration of ordinary window glass irradiated by Co^{60} gamma rays as shown in Fig. 1.

It has been found that the following equation for fading gives a very good agreement with observed data over wide temperature ranges,

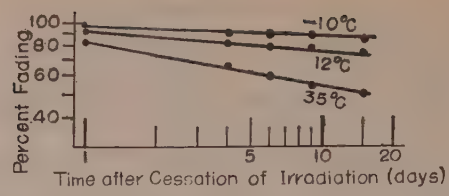

Fig. 1. Fading of irradiated window glass. These specimens were exposed to Co^{60} γ-rays for about one day at various dose rates.

$$\mu(t) \propto t^{-\lambda}, \qquad (2)$$

$$\lambda = e^{-A+BT}, \qquad (3)$$

where A and B are constants dependent only on glass and the used wavelength**, and T denotes the absolute temperature. A comparison of (3) with the experimental data is shown in Fig. 2 for ordinary window glass. Integration of (2) shows that the change in absorption coefficient $\mu(\tau, t)$ induced by τ hour irradiation fades with time t after cessation of the irradiation as follows (see also reference 4):

$$\mu(\tau, t)=\mu(\tau, t_0)\,\frac{(1+t/\tau)^{1-\lambda}-(t/\tau)^{1-\lambda}}{(1+t_0/\tau)^{1-\lambda}-(t_0/\tau)^{1-\lambda}} \qquad (4)$$

The relative fading $\mu(\tau, t)/\mu(\tau, 0)$ depends only on t/τ and λ. Then, it is convenient to express the fading in terms of t/τ. A comparison of (4) with observed values is given in Table I where numerical values of λ are taken from Fig. 2. It may be concluded that equations (2), (3) and (4) hold, in general, for fading of coloration of irradiated glasses. The detailed discussion will be presented elsewhere. This work was supported in part by a Grant-in-Aid for Radiation Research from the Ministry of Education.

Table I. Fading of relative absorption coefficient, $\mu(\tau, t)/\mu(\tau, 0)$, with time t for τ=16 hr at 22°C with dose rate about 3 Kr/h.

°C \ fading \ t (hr)		1	4 (+5)	8.5 (+10.5)	23 (+25)	46 (+48)	63 (+71)
16°C λ=0.1	calculated	0.973	0.926+	0.891+	0.838+	0.795+	0.766+
	observed	(**)	0.930+	0.909+	0.848+	0.785+	0.746+
36°C λ=0.18	calculated	0.947	0.880	0.826	0.729	0.666	0.608
	obsetved	(**)	0.854	0.798	0.706	0.659	0.582
58°C λ=0.35	calculated	0.875	0.750	0.657	0.519	0.428	0.376
	obsetved	(**)	0.732	0.625	0.532	0.442	0.391

** adjusted to equal the observed values.

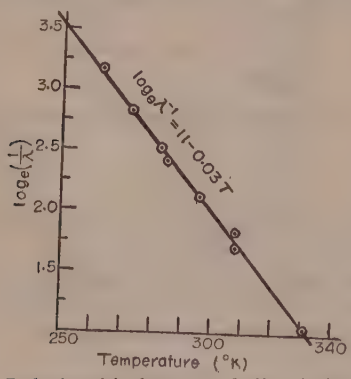

Fig. 2. Relationship between fading index λ given in (2) and temperature T.

* Contribution No. 225 from National Institute of genetics.

References

1) J. H. Schulman, C. C. Klick, and H. Rabin: Nucleonics **13** (1955) No. 2, 30.
2) R. G. Bauman: Nucleonics **14** (1956) No. 6, 90.
3) S. Kondo: Ann. Report. National Inst. Genetics (Japan) No. 7, (1957) 98. Busseiron Kenkyu **2** (1957) No. 1, 29.
4) H. Rabin and W. E. Price: Nucleonics **13** (1955) No. 3, 33.

** All measurements of μ were made at 4200 Å in the present paper.

J. Phys. Soc. Japan **2** (1958) 225

Surface Area Variation of Evaporated Barium Film by Oxidation

By Yutaka Tuzi and Hiroaki Okamoto

Matsuda Research Laboratory, Tokyo Shibaura Electric Co., Kawasaki

(Received November 6, 1957)

It seems that the surface area determination of an evaporated barium film[1] by the B. E. T. method has never been tried, probably because of its high activity and its small size. We tried it successfully using ethylene as the adsorbate.[2]

In the experimental procedures, special attentions were paid to the following points: (1) Prior to the experiment, the sample chamber was thoroughly evacuated (baked out at 360°C, 8 hr.). (2) No grease cocks were used in the high vacuum side of the liquid oxygen trap. The details of the experimental device have been published elsewhere.[3]

The barium film was evaporated uniformly on to the inner wall of a spherical glass bulb (ca. 50 cm^2) at room temperatures and $10^{-1}\sim10^{-3}$ μHg. The results of the repeated measurements of the surface area of a barium film are shown in Fig. 1. We can infer from this curve as well as from the hysteresis of the adsorption isotherms at the liquid oxygen temperature that the ethylene is chemisorbed on fresh barium surfaces even at -183°C[4]. Let us assume that the difference between the first and the third measurement is due to chemisorption, and adopt the steady value obtained after the third measurement as the real surface area S_r. S_r is again decreased if the film is annealed for 30 min. at 105°C or higer temperatures (Fig. 1); a similar decrease can be observed when the high temperature annealing is carried out immediately after the evaporation. It is supposed that, in these cases, a few monolayers of barium oxide are formed on the evaporated film.

Further variation of S_r was pursued allowing the film to absorb oxygen. In Fig. 2, the surface area S_r as well as the rate of absorption of oxygen (determined by the constant volume method) are plotted versus the amount of oxygen absorbed. The weights of the films examined and the temperatures at which the annealing or the measurement was carried out are also jotted in the figure.

The following points would be worth mentioning: (1) S_r is 4$\sim$10 times as large as the geometrical area of the film. (2) S_r decreases as Q, the amount of oxygen absorbed, increases, reaches a minimum value at Q=10$\sim$20 1 μHg (3$\sim$10 layers of BaO), and then increases almost linearly with Q. (3) The rate of increase of S_r depends on the thickness (i.e. weight) of the film.

Our experiment also gives a suggestion to the mechanism of the increase in the rate of absorption of oxygen at the beginning. This has been explained assuming that the oxidation starts exclusively at some specific points on the barium film.[5] Fig. 2 suggests, however, that the change of the rate of oxygen absorption has something to do with the variation in the physical nature (e.g. S_r) of the oxide film.

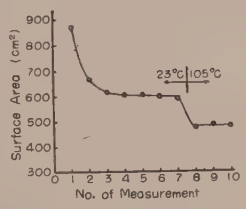

Fig. 1. Surface area vs. number of measurement. Weight of film =2.9 mg.

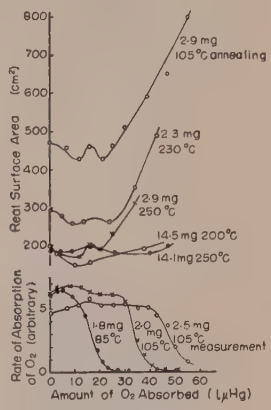

Fig. 2. Real surface area and rate of absorption of O_2 vs. amount of O_2 absorbed.

The authors are indebted to Dr. S. Asao for his kindness in reading the original manuscript, and Mr. H. Oda for his helpful aid.

References

1) Y. Mizushima, Z. Oda and O. Ochi: J. Phys. Soc. of Japan **12** (1957) 355.
2) L. A. Wooten and Y. R. C. Brown: J. Amer. Chem. Soc. **65** (1943) 113.
3) H. Okamoto and Y. Tuzi: Vacuum Techniques (Shinkû Gijutsu), **4** (1955) 79 (in Japanese).
4) B. M. W. Trapnell: Proc. Roy. Soc. **218 A** (1953) 566.
5) T. Arizumi and S. Kotani: J. Phys. Soc. of Japan **7** (1952) 300.
R. N. Bloomer: Brit. J. Appl. Phys. **8** (1957) 321.

J. Phys. Soc. Japan **2** (1958) 226

Crystal Growth of CdS by the Vacuum Sealed Method

By Hirosuke Yamashita and Sumiaki Ibuki

Engineering Laboratory, Mitsubishi Elec. Mfg. Co., Amagasaki-City, Japan

(Received November 1, 1957)

Last year we reported a method of growing CdS single crystals utilizing the condensation of sublimated vapor from polycrystalline powders heated in nitrogen gas flows.[1] As results of our trials, we could obtain fairly large single crystals and some interesting informations about the growth of single crystals,[2] neverthless it was too difficult to get thick crystals. We describe here about the CdS single crystals being recrystalized in a vacuum sealed vessel at high temperatures.

Putting chemically purified CdS powders into a quartz container, we seal it off at high vacuum after sufficiently outgassing the powders. The sealed vessel is kept at a temperature from 1,000°C to 1,200°C for several hours in an electric furnace having a proper temperature gradient, is thereafter slowly cooled at the rate of about 10°C/hr. Thus we can obtain several large single crystals having the sizes of about $10 \times 8 \times 5$ mm.

Some interesting samples grown at 1,2000°C are shown in Fig. 1 and 2. We can observe that crystals are used to grow along the direction parallel to the c-axis in the case of lower temperature, but at higher temperature they grow keeping a definite oblique angle and spirally around the c-axis.

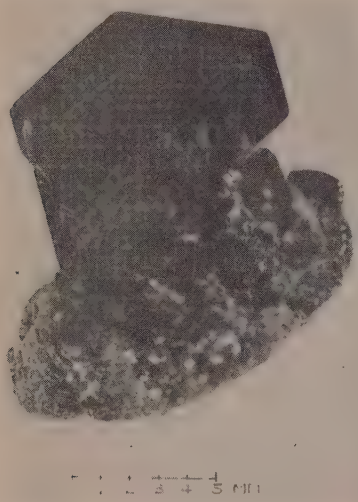

Fig. 1. Grown crystal.

Fig. 2. Grown crystal.

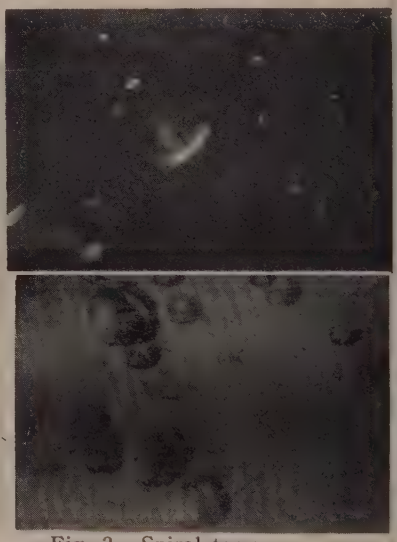

Fig. 3. Spiral terraces.

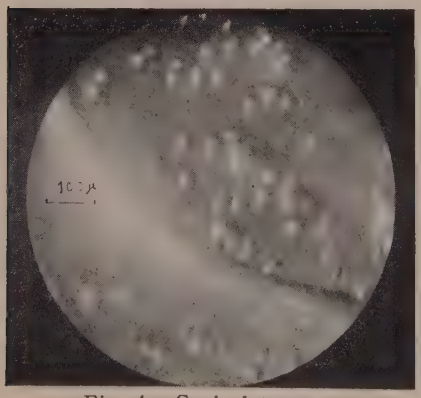

Fig. 4. Conical terraces.

On the surfaces of these crystals, furthermore, several types of terraces and pits are observed. Some features of the surfaces etched by HCl sol. are shown in Fig. 3 and 4. On (001) surfaces there are found pretty number of conical terraces, and some of them are spiral terraces as shown in Fig. 3. There are also observed some spiral pits having similar appearances as those on Ge and Si surfaces,[3] which indicate the presence of spiral dislocations. Several terraces of trigonal prisms are found on (110) surfaces, those of hexagonal half-piramids on (010) surfaces.

Orange crystals which are grown at lower temperature emit weak green fluorescence at the room temperature when irradiated by 3650 Å ultraviolet rays.

Details of the above-mentioned report will be published later.

References

1) S. Ibuki and K. Awazu: J. Phys. Japan **11** (1956) 1297.
2) S. Ibuki: to be published.
3) M. Kikuchi and S. Denda: J. Phys. Soc. Japan **12** (1957) 105.
Y. Matukura and T. Suzuki: J. Phys. Soc. Japan **12** (1957) 976.

J. PHYS. SOC. JAPAN **2** (1958) 227~228

Asymmetry of Proton Resonance Signals in Some Hydrates of Iron Group Salts

By Syukuro YANO and Sōji SASAKI

Department of Applied Physics, Kyoto University, Kyoto

Tunahiko SIDEI

Department of Nuclear Science, Kyoto University, Kyoto

(Received October 30, 1957)

We have observed many asymmetric proton resonance signals from hydrated salts of iron group elements in powdered form at room temperature. The typical line shapes are shown in Fig. 1. Table I shows the asymmetry of the resonance lines and their apparent shifts which mean the difference of magnetic field in gauss between maximum point of the absorption signal and the normal free water

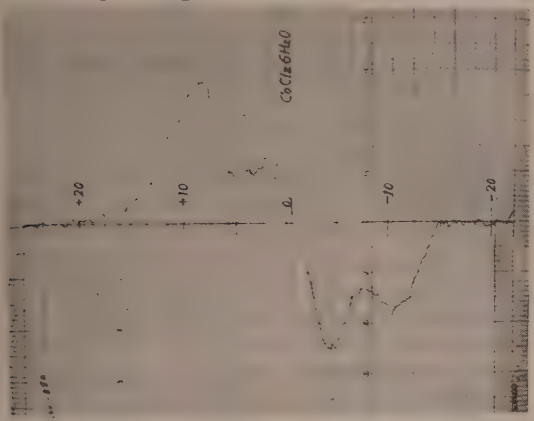

Fig. 1. A record of proton resonance derivative in powdered $CoCl_2 6H_2O$ at 20°C.

resonance field. This results show the parallelism between shift and asymmetry.

To confirm that these asymmetric lines come

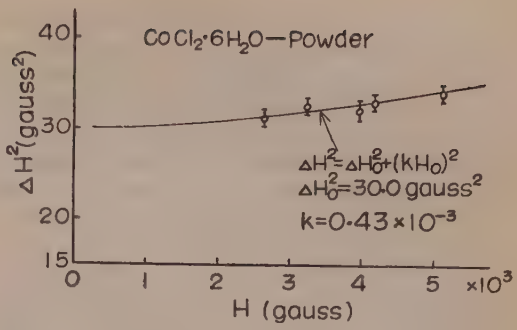

Fig. 2. Second moment of proton resonance in powdered $CoCl_2 6H_2O$ at room temperature in different external fields.

from paramagnetism of iron group ions, we measured the lines of $CoCl_2 6 H_2O$ in several different magnetic fields. The lines showed marked field dependence in their shapes and second moments. The variation of second moment with external magnetic fields are shown in Fig. 2. These values were calculated from the center of gravity of the integrated absorption curve which nearly fell on the point 1 gauss higher than the zero point of absorption derivative. The values of $(kH_0)^2$ in Fig. 2 are in agreement with $(\bar{\mu}/r^3)^2$ in order of magnitude, taking $r=2.5$ A and $\bar{\mu}=5\mu_p$ for about 4000 gauss and room temperature, where $\bar{\mu}$ represents the effective magnetic moment of cobalt ion and μ_p represents the magnetic moment of proton. Field independent part of the second moment of about 30 gauss² comes from nuclear dipole-dipole interaction.

The line shapes of $CoCl_2 \cdot 6H_2O$ can be decomposed into three displaced parts. The shifts of these component lines originating from electronic paramagnetism contribute to the second moment of the composed curve and this term corresponds to teh field dependent part of Fig. 2.

Theoretical line shapes for a pair of single nuclear

Table I.

Sample	Asymmetry*	Apparent shift (gauss) at about 4200 gauss	Second moment (gauss²) at about 4200 gauss
$CrF_3 3 H_2O$	(+)	≅+1.0	
$CrCl_3 6 H_2O$	(+)		
$FeCl_2 4 H_2O$	(−)		
$FeSO_4 7 H_2O$	(+)	≅−1.0	32
$CoCl_2 6 H_2O$	(+)	−0.8~−1.0	33.0±1.0 (+21°C) 37.4±1.0 (−20°C)
$CoBr_2 6 H_2O$	(+)	≅−2.5	
$CoSO_4 7 H_2O$	(+)	≅−1.0	
$NiCl_2 6 H_2O$	(−)	<0.5	30
$NiSO_4 6 H_2O$	(+)	+0.3	27
$CuF_2 2 H_2O$	(−)	<0.1	
$CuCl_2 2 H_2O$**	(−)	<0.5	21.5
$CuSO_4 5 H_2O$	(−)	−0.6~−1.3	
$ZnSO_4 7 H_2O$**	(−)	<0.1	26

* (+) indicates the line has asymmetry and (−) no asymmetry.
** For both paramagnetic $CuCl_2 2 H_2O$ and diamgnetic $ZnSO_4 7 H_2O$ as a reference sample, line shapes were those of two spin system.

spin and an electronic spin of a magnetic ion, are easily calculated assuming that the electronic spins are parallel or antiparallel to the external field. This result does not give a gaussian shape but an asymmetric and displaced line. When three spin system which is composed of a pair of nuclear spins and an electronic spin is treated,[1] the calculated lines have an asymmetry which is in nearly agreement with experimental curves.

Another origin of assymmetry may arise from the anisotropy of g-factor of the magnetic ion,[2] which may well be large for the cobalt salts. The order of magnitude is nearly equal to the anisotropy of the paramagnetic shift above stated.

It is interesting to note that some information about the states of paramagnetic ions and crystalline field will be obtained by proton resonance further, when these experiments are carried out at low temperature.

References

1) N. Bloembergen: Physica **16** (1950) 95.
2) W. C. Dickinson: Phys. Rev. **81** (1951) 717.

J. Phys. Soc. Japan **2** (1958) 228~229

Magnetostriction Constants of Nickel-Copper and Nickel-Cobalt Alloys

By Mikio Yamamoto and Takurô Nakamichi
The Research Institute for Iron, Steel and Other Metals, Tôhoku University, Sendai

(Received November 28, 1957)

We have determined, for the first time, the magnetostriction constants, λ_{100} and λ_{111}, of Ni–Cu and face-centered cubic Ni–Co alloys at room temperature, using single-crystal specimens and the strain gauge technique.[1] The specimens used are disks with (110) or (100) plate surfaces, cut out from single crystal ingots prepared from nickel and copper or cobalt, all of electrolytic origin, by the Bridgeman method in a vacuum Tammann furnace. Ni–Cu crystal disks containing 0, 7.0, 16.4, and 25.8 at.-% Cu are 15 mm in diameter and 1.5 mm in thickness, and Ni–Co crystal disks containing 10.5, 21.3, 32.8, 44.7, and 54.2 %Co are 10 mm in diameter and 1.0 mm in thickness. The out-put unbalanced voltage of a Wheatstone bridge formed by a strain gauge cemented along a certain crystallographic direction on the plate surface of the specimen together with other three similar gauges, which was proportional to the strain of the specimen, was detected directly by a galvanometer. The strain sensitivity was 0.53 $\times 10^{-6}$ per mm of the scale. The specimen was placed in magnetic field of some 4000 Oe, strong enough to saturate it, as produced from a rotable

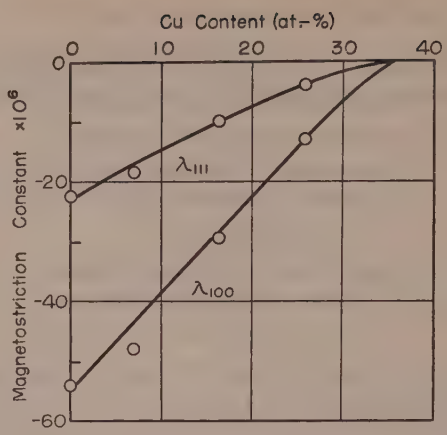

Fig. 1. Concentration dependence of the magnetostriction constants of Ni-Cu alloys.

electromagnet and its magnetostrictive strain along the fixed direction was measured as a function of the direction of the magnetic field.

The two principal magnetostriction constants, λ_{100} and λ_{111}, thus obtained are plotted against the alloy composition in Figs. 1 and 2 for Ni–Cu and Ni–Co alloys, respectively. Values of λ_{100} and λ_{111} for nickel are -54.1 and -22.4×10^{-6}, respectively, which are in good agreement with available data[2]. In Ni–Cu alloys, both constants are negative irrespective of the composition and their absolute values decrease monotonously with increasing copper content, vanishing at some 35 at.-%Cu, as may be expected from the magnetostriction vs. magnetic field curves for polycrystalline specimens.[3] The absolute values of saturation magnetostriction, $|\lambda_s|$, for isotropic polycrystals as calculated from our single crystal constants according to the formula $\bar{\lambda}_s=(1/5)(2\lambda_{100}+3\lambda_{111})$

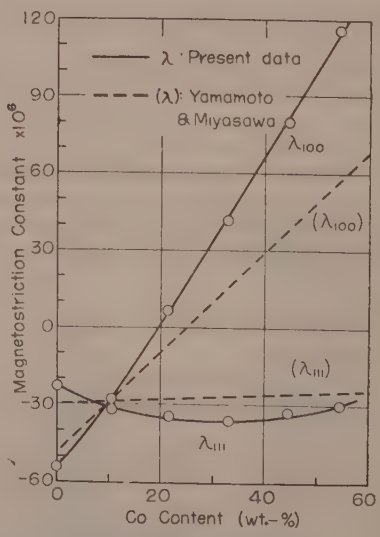

Fig. 2. Concentration dependence of the magnetoriction costants of Ni-Co alloys.

are somewhat higher than the measured data for polycrystalline specimens.[3,4] This discrepancy may be due mainly to the non-uniformity of domain distribution at unmagnetized state in polycrystalline specimens.

In face-centered cubic Ni–Co alloys, the concentration dependence is quite different for λ_{100} and λ_{111}; λ_{111} is negative irrespective of the composition, showing a flat minimum centered at about 30%Co, while λ_{100} increases almost linearly with increasing cobalt content and, passes through zero at about 20%Co, reaching to the large value of 116×10^{-6} at 55%Co. The present data agree qualitatively well, but quantitatively not so well, particularly for high-cobalt alloys, with the data obtained previously by one of the authors and Miyasawa[5] from the analysis of the magnetostriction vs. magnetic field curves of polycrystalline specimens (cf. Fig. 2). This discrepancy may due mainly to the lack of saturation of the magnetostriction vs. field curves measured by them. The values of saturation magnetostriction for isotropic polycrystals calculated in the same way as in the above-mentioned case of Ni–Cu alloys are in good agreement with the measured data by Went[4] who used magnetic field strong enough to saturate specimens.

References

1) J. E. Goldman: Phys. Rev. **72** (1947) 529.
2) R. M. Bozorth and R. W. Hamming: Phys. Rev. **89** (1953) 865. W. D. Corner and G. H. Hunt: Proc. Phys. Soc. **A 68** (1955) 133.
3) Y. Shirakawa and K. Numakura: Nippon Kinzoku Gakkaishi **18** (1954) 73 (in Japanese).
4) J. J. Went: Physica **17** (1951) 99.
5) M. Yamamoto and R. Miyasawa: Sci. Rep. RITU **A 5** (1953) 113.

Errata

Studies on the Radial Distribution Analysis in Diffraction Methods

II. Effect of Non-nuclear Scattering and Analysis of the Radial Distribution Curve

By Kinya KATADA

J. Phys. Soc. Japan **13** (1958) 51

Page	Column	Place		(should be read)
51	right	line 3 in the footnote***	$r(D)r$	$rD(r)$
52	left	denominator of Eq. (3)	$r_{ij}\sum_i Z_i^2\phi_i^2(s)$	$r_{ij}\sum_i Z_i^2\phi_i^2(s)$
52	right	Eq. (6)	$rd(r)^z_{(ij)}$	$rd^z_{(ij)}(r)$
52	right	Eq. (8)	$rd^\phi_{(ij)}(r)$	$rd^\phi_{(ij)}(r)$
53	left	Eq. (10)	$m_{(ij)}s$	$m_{(ij)}(s)$
53	left	Eq. (13)	$A_{CCl,2}=0.23$	$A_{CCl,2}=0.13$
53	right	lines 2 and 3 in the note for Fig. 2	$rd(r)$	$rd(r)$
56	right	line 4	$\Delta r_{ij}D^c(r_{ij})$	$\Delta r_{ij}D^c(r_{ij})$
56	right	line 6	$r=2.9_{ClCl}$Å	$r_{ClCl}=2.9$Å
56	right	column 4 in Table I	2.0	9.0

Eq. (15) should be in the place following right column, line 22 in the same page.

PROGRESS OF THEORETICAL PHYSICS

CONTENTS

Progress of Theoretical Physics Vol. 18, No. 6, December 1957

A New Approach to a Bound State ..... Tsutomu IMAMURA..559
Nuclear Magnetic Relaxation in Liquid Hydrogen ..... Tôru MORIYA..567
Description of Pauli Matter as a Continuous Assembly of Small Rotating Bodies
..... T. TAKABAYASI and J. P. VIGIER..573
Multiple Production of Particles and Hydrodynamical Aspect of Quantum
Theory of Fields ..... M. NAMIKI and C. ISO..591
On the Theory of the Unstable Particle, II ..... Kunio NAITO..614
Electrodisintegration of He^4 Nucleus ..... T. MUTO and T. SEBE..621
Photodisintegration of Deuteron near 11 Mev ..... Shih-Hui HSIEH..637
Electronic Energy Levels of Polyene Chains ..... S. HUZINAGA and T. HASINO..649

Letters to the Editor:
On the Ground State Spin of Ti^{47} and Mn^{55} ..... S. YANAGAWA..661
A Comment on Bardeen's Theory of Superconductivity .....
..... S. NAKAJIMA and T. KASUYA..662
Angular Correlation of Internal Bremsstrahlung and Successive Nuclear Gamma-Ray in the Radiative K-Capture .....
..... Y. KOH, O. MIYATAKE and Y. WATANABE..663
Spin and Size of Λ^0 Particle ..... K. NISHIMURA..665
The Utility of the "Individual Γ_5 Transformation" .....
..... K. FUJII and K. IWATA..666
Low Lying Levels of P^{32} and jj Coupling ..... S. P. PANDYA..668
Contents of Journ. of Phys. Soc. Japan Vol. 12, No. 10 670
Contents and Authors Index to Volume 10 ..... i~viii

Price $ 1.25 per copy
$ 15.00 per year (postage inclusive)
Annual dues for foreign members (individual subscribers)
$ 12.00 (postage inclusive)
" for foreign members of the Physical Society of Japan
$ 10.00 (postage inclusive)
Application for members, subscriptions and orders for back numbers should be sent, directly or through book-dealers, to

The Publication Office
in
Yukawa Hall, Kyoto University, Kyoto, Japan

JOURNAL OF THE PHYSICAL SOCIETY OF JAPAN Vol. 13, No. 3, MARCH, 1958

Elastic Scattering of 5.7 Mev Protons from Fe, Cr and Ti

By Michiya KONDO, Takashi YAMAZAKI, Atsutomo TOI*, Ryuzo NAKASIMA** and Shotaro YAMABE

Department of Physics, Osaka University, Osaka
**Department of Nuclear Engineering, Osaka University, Osaka*
***Research Institute for Atomic Energy, Osaka City University*

(Received October 2, 1957)

Using 5.7 Mev protons from the cyclotron, the angular distributions of protons elastically scattered from Fe, Cr and Ti were investigated by means of nuclear emulsion technique. The angular distributions of the elastically scattered protons by these nuclei were similar to that of Ni, that is, the differential cross sections in the ratio to those of the Rutherford scattering increase linearly at large angles. Some qualitative arguments are given about this characteristic feature of these nuclei, together with previously measured elements Ni[1)2)] and Zn[1)].

§ 1. Introduction

As was pointed out in Bromley and Wall's paper[1)] and our previous works[2),3)], the differential cross sections of the elastically scattered protons from even-Z nuclei in the medium weight region were expected to show the characteristic feature in comparison with odd-Z nuclei. According to the previous measurements[1),2)], the behaviours at large scattering angles were very different between even-Z and odd-Z nuclei; i.e., the differential cross sections in the ratio to the Rutherford cross sections for even-Z nuclei (Ni and Zn) increase linearly with the scattering angles, while they do not rise for odd-Z nuclei (Co and Cu). Bromley and Wall[1)] suggested, based on their experiments using 5.25 Mev protons, that the difference seemed to be depending on target spins, and we[2)] concluded, from the experiments of 5.7 Mev protons, that the behaviour was not sensitive to the incident energy for Ni and Cu.

Kliucharev, Bolotin and Lutsik[4)] have investigated the elastic scattering of 5.4 Mev protons by some elements in light and medium weight region, and have obtained the angular distributions in the ratio to the Rutherford cross sections having similar form for all cases of Zn, Cu and Ni, and these angular dependences are quite similar to our previous result for Cu. They pointed out the qualitative similarity in the form of the angular distributions from neighboring nuclei, but it is contrast with the above mentioned Bromley and Wall's suggestion and also with our expectation. Therefore, in order to obtain the further informations, it is required to accumulate the many experimental data for the elastic scattering of protons at various energies and from a number of nuclei in such medium weight region.

In the present work, we have extended these investigations to adjacent even-Z nuclei, Fe (Z=26), Cr (Z=24) and Ti (Z=22), by the use of 5.7 Mev proton beam from Osaka University cyclotron[5)] and the nuclear emulsion technique.

§ 2. Experimental

The experimental arrangement and procedure were same as our previous experiments[2)]. In the present investigation, the used nuclear emulsions were Ilford C2 and Fuji ET-6B, and their thicknesses were 100 μ and 70 μ, respectively.

The Ti target was a rolled foil of 1.2 mg/cm^2 thickness. The Cr foil of 3.7 mg/cm^2 thick was prepared by electroplating method. The thickness of Fe target was 3.8 mg/cm^2 and it was also a rolled foil. All these targets were self supporting and set at 45° with respect to the beam direction.

The beam current was collected by the Faraday cup connected to 0.025 μF polystylene condenser and was measured by electrometer.

§ 3. Results and Discussions

In order to check the experimental arrangement and the geometrical accuracy of the camera, the differential cross sections for Au

were measured and satisfactory results were obtained as was shown already in our preliminary report[3]. As the targets were rather thick in the both cases of Cr and Fe, the complete separation of the inelastically scattered proton groups from low lying levels of each isotopes were not expected, but the amounts of the target impurities were negligible. In Fig. 1, the typical range distribution of the scattered protons from Fe target is shown. The experimental errors causing from the various parts of the experimental arrangement and procedure were described already in previous paper[2].

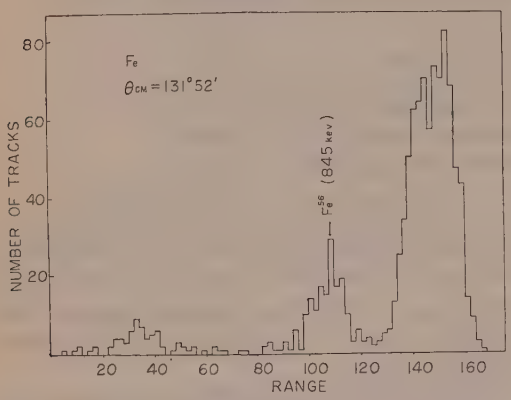

Fig. 1. The typical range distribution of the scattered protons from Fe. (1 div. = 1.2 μ)

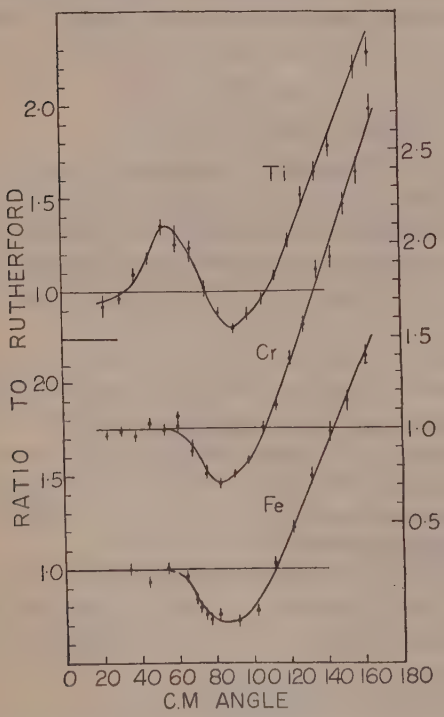

Fig. 2. Ratios of measured cross sections in the center of mass system to the Rutherford for Ti, Cr and Fe. Errors were only statistical ones.

The angular distributions in the ratio to the Rutherford cross sections are shown in Fig. 2. The overall tendencies of the angular dependences for these elements are similar to the case of Ni. Fig. 3 contains all these curves together, with the previous results of Ni[2]

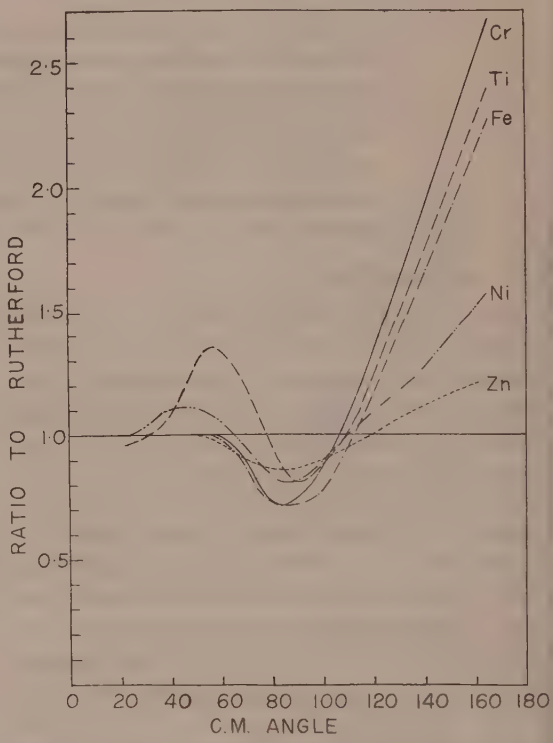

Fig. 3. A composite presentation of the experimental curves obtained in the scattering of 5.25 Mev (Zn)[1] or 5.7 Mev (Ti, Cr, Fe and Ni) protons from the even-Z nuclei.

and Zn[1] to compare the angular distributions from even-Z nuclei. From Figs. 2 and 3, one may point out that there are two characteristic features in all cases of elements; one is the appearence of a remarkable valley at 80° ~90° and the other is monotonous rise at large scattering angles. Comparing these five curves for even-Z nuclei in Fig. 3 with the results[1),2)] for odd-Z nuclei, the behaviour at large scattering angles seems to be characteristic property of even-Z nuclei in medium weight region for incident energy of few Mev, though with exceptions of Kliucharev, *et al.*'s 5.4 Mev results[4] for Ni and Zn.

The appearence of a valley at 80°~90° in

all cases may be interpreted in terms of cloudy crystal ball model, since according to this model, the pattern in the differential cross section is expected to be quite similar for neighbouring elements. For the behaviour at large scattering angles, the effect of the potential edge may be important, because the situation in backward direction is affected strongly by incident waves with the higher angular momentum which are determined mainly at the edge of potential well. Then, the different behaviour between even-Z and odd-Z nuclei at large angles may be explained by the use of the different shape of the potential edge for even-Z and for odd-Z nuclei.

For the Kliucharev, *et al.*'s 5.4 Mev data on Ni and Zn which differ from Bromley and Wall's (5.25 Mev) and our (5.7 Mev) results, we cannot give the reasonable interpretation but one may speculate that in this energy region the scattering may be affected by elastic contribution from the compound nucleus. We have an attempt to continue the investigation with various incident energies.

Acknowledgments

We are indepted to Mr. W. Watari for valuable discussions and also thank to Fuji Film Corporation for supplying the nuclear plates for us.

References

1) D. A. Bromley and N. S. Wall: Phys. Rev. **102** (1956) 1560.
2) M. Takeda, et al.: J. Phys. Soc. Japan **12** (1957) 561.
3) M. Takeda, et al.: J. Phys. Soc. Japan **12** (1957) 979.
4) A. P. Kliucharev, L. I. Bolotin and V. A. Lutsik: J. Exptl. Theoret. Phys. (U.S.S.R.) **30** (1956) 573.
5) S. Kikuchi, et. al.: Ann. Rep. Fac. Sci. Osaka Univ. **3** (1955) 1.

JOURNAL OF THE PHYSICAL SOCIETY OF JAPAN Vol. 13, No. 3, MARCH, 1958

Excited States of ^{40}Ca

Yasuo HIRAO, Eiji OKADA, Iwao MIURA and Tetsuo WAKATSUKI

Department of Physics and the Laboratory of Nuclear Studies
Faculty of Science, Osaka University, Osaka, Japan

(Received October 7, 1957)

By bombarding a natural calcium target with 5.7 MeV protons, gamma rays of energy 3.7 MeV and 3.9 MeV were observed with a NaI(Tl) three crystal pair spectrometer. The intensity of 3.7 MeV gamma ray is about 25% of 3.9 MeV gamma ray.

Angular distribution of these gamma rays was measured with a single crystal scintillation spectrometer. The result can be expressed as follows: $1+1.90\cos^2\theta-1.03\cos^4\theta$.

From comparison with theory it is highly probable that 3.90 MeV state has spin 2.

§ 1. Introduction

^{40}Ca is a nucleus with doubly magic nucleon number. In the shell model the first excited state of a doubly magic nucleus should lie relatively high. The removal of one nucleon from the closed configuration implies the breaking of a pair, and the pairing energy can be estimated to be 2 to 3 MeV at Z and $N=20$. An excited state brought about by the removal of two nucleons from the $d_{3/2}$ level into $f_{7/2}$ level should therefore lie not much higher than a single particle excitation state, because for two nucleons the pairing energy in the $f_{7/2}$ level can even overbalance the energy which is required for raising the second particle from the $d_{3/2}$ into the $f_{7/2}$ level. The configuration $(d3/2)^{-1}(f7/2)^1$ has odd parity and spin$\geq$2, while the configuration $(d3/2)^{-2}(f7/2)^2$ has even parity and most probably zero spin in its lowest state.

On the other hand the experimental result of the magnetic analysis of protons inelastically scattered by ^{40}Ca[1] showed that the level energies of the first, second and third excited states are 3.35, 3.73 and 3.90 MeV respectively. These energies are in general accord with the above considerations.

R. D. Bent, T. W. Bonner and J. H. McCrary[2] showed that the first level is followed by no gamma transition but nuclear pair emission. The spin and parity of this state is, therefore, 0+ and the configuration is inferred as $(d3/2)^{-2}(f7/2)^2$.

In our present experiment the higher excited states were investigated by the analysis of gamma rays in the inelastic scattering of protons by ^{40}Ca.

§ 2. Experimental Methods

Molecular ion beam of hydrogen accelerated by Osaka University 44 inch cyclotron was focused onto calcium target located at about 7 meters from the cyclotron by a wedge type focussing magnet through concrete shield wall of 1.5 meters in thickness. The energy of the proton was estimated to be 5.7±0.1 MeV from the measurements of range in air and in nuclear emulsion. The beam defining slit was made of a gold plate with a circular hole one centimeter in diameter. Proton current was about a few hundredths of a microampere.

A thin target of natural calcium of a few mg/cm² in thickness was prepared by evaporating the metal onto a thick gold backing.

We have used a NaI(Tl) three crystal pair spectrometer[3] to observe gamma ray spectrum. The energy resolution of this spectrometer was about 6% for 4.43 MeV gamma ray. For the measurement of the pulse height distribution a 20 channel pulse height analyzer was used.

We have also used a single crystal spectrometer with NaI(Tl) 1½ inches in diameter and 2 inches in length for the measurement of angular distribution.

To avoid the background gamma rays, the spectrometers were surrounded by lead blocks ten centimeters in thickness, and moreover the beam was lead onto the target through lead wall ten centimeters in thickness.

§ 3. Results

Fig. 1 shows the gamma ray spectrum observed with the three crystal spectrometer placed at right angles with the proton beam

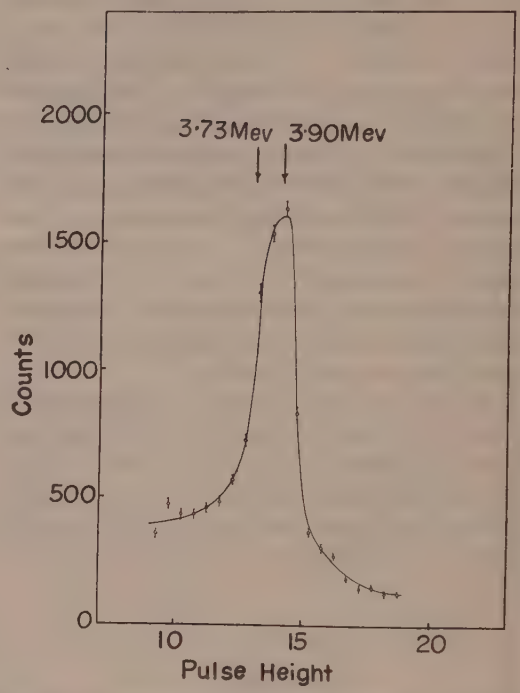

Fig. 1. Three crystal pair spectrum: calcium+proton at 5.7 MeV and 90° with respect to the proton beam.

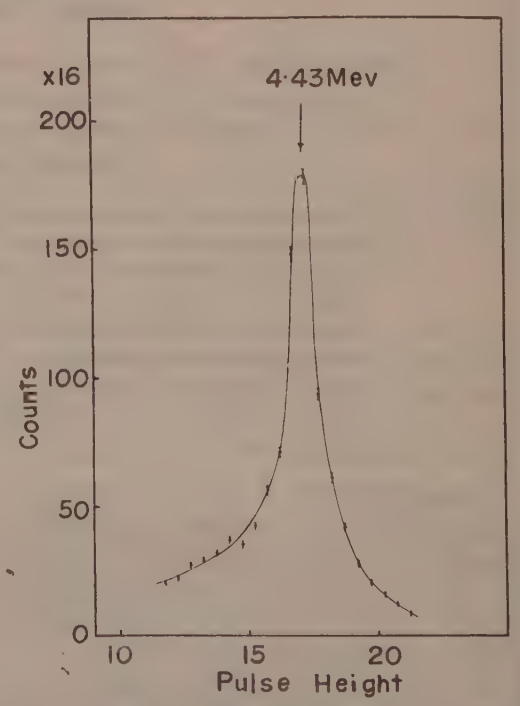

Fig. 2. Three crystal pair spectrum: polyethylene +proton at 5.7 MeV and 90° with respect to the proton beam.

when the thin calcium target was bombarded by 5.7 MeV protons.

Fig. 2 shows the spectrum of well known 4.43 MeV gamma ray in $^{12}C(p, p'\gamma)^{12}C$ reaction by the same spectrometer with a polyethylene target.

In these observations these two targets were bombarded alternately many times in order to ensure the determination of the gamma ray energies. The energy shift of the detector was less than 3% throughout the measurement.

By comparison of these two spectra, the peak is estimated to be at 3.90 MeV. Subtracting the spectrum of 3.90 MeV gamma ray whose shape is deduced from the 4.43 MeV gamma ray, we may get the residual gamma ray spectrum. It is inferred that this spectrum is due to 3.73 MeV gamma ray and the intensity is about 25% of the 3.90 MeV gamma ray. These results are consistent with the experiment by Braams on the inelastic scattering of protons by ^{40}Ca[1].

Fig. 3 shows angular distribution of the gamma rays whose energies are greater than 2.5 MeV. This angular distribution is due for the most part to the 3.90 MeV gamma ray but includes the influence of 3.73 MeV gamma ray.

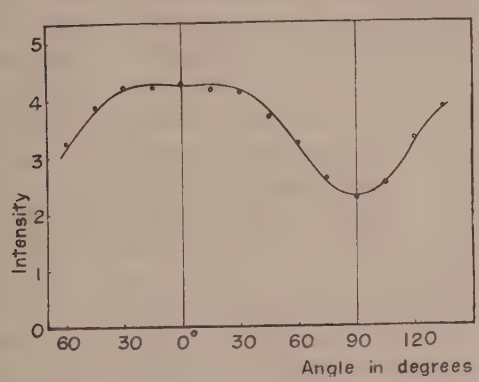

Fig. 3. Angular distribution of the gamma rays higher than 2.5 MeV. The curve shows $W(\theta)=1+1.90\cos^2\theta-1.03\cos^4\theta$.

§ 4. Discussions

The angular distribution in Fig. 3 has the form $W(\theta)=1+A\cos^2\theta+B\cos^4\theta$. The measured values of these coefficients in $W(\theta)$ are 1.90 and -1.03 ± 0.09 respectively.

Further analysis of the distribution consisted of an attempt to compare the measured values of the coefficients with those calculated for the inelastic scattering process.

By the aid of the formula for the angular distribution of a two stage particle reaction followed by gamma emission as given by A. A. Kraus, J. P. Schiffer, F. W. Prosser, and L. C. Biedenharn[4], one can calculate these coefficients for every case. The expansion coefficients of $P_\Delta(\cos\theta)$ for l, $l'\leq3$, $j\leq3$ and except for interference term are given in Table I, where l and l' are the incoming and outgoing proton angular momenta, J is the spin of the compound state, j is the spin of the gamma emitting state, and $P_\Delta(\cos\theta)$ is Legendre function. These coefficients were calculated by Dr. S. Takagi and Mr. S. Yamazaki in our University.

According to Kraus et al.[4], if the outgoing particle is not observed incoming l values and channel spins add coherently and incoherently respectively, while outgoing l values and channel spins add incoherently and coherently respectively. Moreover, since Δ is only even for sharp angular momentum j, there are no interference terms between states of opposite parity. In other words, the cross section can be broken into two parts, one part for even parity compound states and the other for odd parity states.

As a probable case for this energy of protons, we assumed a process due to the absorption of a d-wave proton followed by emission of a s-wave proton. If the gamma emitting state has spin 2+, only one channel spin is possible for either angular momentum for the compound state and therefore coherent interference does not exist.

The angular distribution is as follows:

$$\sigma(\theta)=1+\cos^2\theta \qquad \text{for} \quad J=3/2+$$

$$\sigma(\theta)=1+6\cos^2\theta-5\cos^4\theta \qquad \text{for} \quad J=5/2+$$

Compounding these two distributions in the ratio of 4:1, one can get as follows:

$$1+2\cos^2\theta-\cos^4\theta$$

in conformity with the experimental result.

As another case, we may consider a process due to the absorption of a p-wave proton followed by emission of a s-wave proton. If the gamma emitting state has spin 2−, the angular distribution is as follows:

$$\sigma(\theta)=1+\cos^2\theta \qquad \text{for} \quad J=3/2-$$

If the absorption of a f-wave proton is followed by emission of a s-wave proton and the gamma emitting state has spin 2−, the angular distribution is as follows:

Table I. The coefficients of $P_\Delta(\cos\theta)$ in the angular distribution of the gamma ray in the inelastic scattering of proton by even-even nucleus. l and l' are the angular momenta of incoming and outgoing proton respectively, s' is outgoing channel spin, J and j is the spin of compound and gamma emiting state respectively, and $P_\Delta(\cos\theta)$ is Legendre function.

$J=3/2$ ($l=1, 2$)					
j	s'	l' \ Δ	0	2	4
1	1/2	0	—	—	—
		1	1	0	0
		2	1	0	0
	3/2	0	1	−1/2	0
		1	1	−1/10	0
		2	1	3/10	0
		3	1	−1/10	0
2	3/2	0	1	1/2	0
		1	1	1/10	0
		2	1	−3/10	0
		3	1	1/10	0
	5/2	1	1	2/5	0
		2	1	−2/35	0
		3	1	−0.31	0
3	5/2	1	1	1/5	0
		2	1	−1/35	0
		3	1	−0.156	0
	7/2	2	1	5/28	0
		3	1	−0.059	0

$J=5/2$ ($l=2, 3$)					
j	s'	l' \ Δ	0	2	4
1	1/2	2	1	0	0
		3	1	0	0
	3/2	1	1	−2/5	0
		2	1	2/35	0
		3	1	0.31	0
2	3/2	1	1	2/5	0
		2	1	−2/35	0
		3	1	−0.31	0
	5/2	0	1	4/7	−4/7
		1	1	92/245	4/49
		2	1	2/35	2/7
		3	1	−0.236	−0.258
3	5/2	0	1	2/7	1/7
		1	1	46/245	−1/49
		2	1	1/35	−1/14
		3	1	−0.118	0.0646
	7/2	0	1	0	0
		1	1	25/98	9/98
		3	1	5/42	−1/14
		4	1	−0.0339	−0.0408

$$\sigma(\theta)=1+6\cos^2\theta-5\cos^4\theta \qquad \text{for} \quad I=5/2-$$

Same result can be obtained in this case as above described.

These calculated coefficients show good agreement with the measured values within 5%. The curve in Fig. 3 shows this calculated angular distribution. For other processes, we can not get good agreement even if we consider interference terms. From the estimation of barrier penetrability it is reasonable that the incoming and outgoing l value is assumed to be ≤ 3.

Then it is highly probable that the gamma emitting state, whose energy is 3.90 MeV, has spin 2.

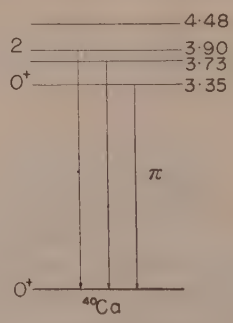

Fig. 4. The level diagram of ^{40}Ca.

§ 5. Acknowledgment

The authors wish to thank Prof. S. Kikuchi for his kind interest in this work, and Dr. S. Takagi and Mr. S. Yamazaki who calculated the coefficients of angular distributions and Mr. Y. Oda for his helpful discussion.

This work was supported by the Grant for Scientific Research of the Ministry of Education.

References

1) C. M. Braams: Phys. Rev. **101** (1956) 1764.
2) R. D. Bent, T. W. Bonner and J. H. McCrary: Phys. Rev. **98** (1955) 1325.

3) I. Miura, Y. Hirao, E. Okada and T. Wakatsuki: Genshikaku Kenkyu (in Japanese) Vol. 3, No. 1 (1957) 76.
J. Phys. Soc. Japan **12** (1957) 1178.
4) A. A. Kraus, J. P. Schiffer, F. W. Phosser and L. C. Biedenharn: Phys. Rev. **104** (1956) 1667.

JOURNAL OF THE PHYSICAL SOCIETY OF JAPAN Vol. 13, No. 3, MARCH, 1958

Angular Distribution of Protons Inelastically Scattered from Mg^{24}

By Shotaro YAMABE
Department of Physics, Osaka University, Osaka

(Received October 24, 1957)

The angular distributions of protons inelastically scattered from Mg^{24} ($Q=-1.368$ MeV) were measured from 22.5° to 165° in the laboratory system at incident proton energies of 5.1 and 5.4 MeV. The 44″ Osaka University cyclotron was used to provide a proton beam, and the scattered protons were detected by nuclear emlusion technique. Both distributions obtained show an asymmetry about the center of mass scattering angle $\theta=90°$ and a strong dependence with the energy of primary protons.

§ 1. Introduction

Up to the present time, the angular distributions of protons inelastically scattered from Mg^{24}, being left in the first excited level (1.368 MeV, 2, +), have been measured at various proton energies from 4.7 MeV to 18 MeV[1)-9)]. All these data indicate the asymmetry about the center of mass scattering angle $\theta=90°$ without any exception.

From the compound nucleus picture, it may be plausible that at such energies of the incident protons the compound states are in an intermediate region of the two extreme, that is, the region where the reaction proceeds through a single level of the compound nucleus —resonance region— or through the continuum region of the compound nucleus —statistical region—, in both cases the angular distributions are predicted to be symmetric about $\theta=90°$.[10)-12)] But the range of the excitation energy of compound state produced by protons of energies from 4.7 MeV to 18 MeV, is so large that it cannot be attributed only to this circumstance.

Fischer[5)] has interpreted his 10 MeV data by combining the statistical theory of the compound nucleus and the direct interaction proposed by Austern, Butler and McManus[13)]. Besides the direct interaction proposed by Austern, et al., Hayakawa and Yoshida[14)] have shown theoretically that the other possibility may be considered as the excitation of the rotational level of the nucleus.

Greenlees, et al.[6),7)] suggested an interference effect between the processes of compound nucleus formation and of direct interaction to explain the rapid change of the angular distributions with the incident proton energies in their experiments of 8∼10 MeV region.

In this paper the angular distributions of inelastically scattered protons from Mg^{24} are studied at proton energy 5.1 MeV and 5.4 MeV by means of nuclear emulsion technique.

§ 2. Experimental Arrangement and Procedure

The 44″ Osaka University Cyclotron[15)] was used to provide a beam of 5.7±0.1 MeV protons, and nuclear emulsion was used to detect the scattered protons. The experimental details concerning the scattering chamber, the collimator system, and the current integrator were same as mentioned in the previous paper[16),17)] of Osaka University plate group.

In Fig. 1 the schematic arrangement is shown. The foil changer box, contained ten sectors of aluminium foil, was inserted in front of the collimator system to reduce the primary proton energy by a step of about one hundred keV. Two plate cameras were constructed, the one (No. 1 camera) was for the study of angular distributions, the other (No.

2 camera) was for the study of excitation functions. The grancing angles of the plate were increased to 15° for both cameras in order to reduce the background track due to elastic portion which escaped from emulsion and had the same range in emulsion as inelastic group.

No. 1 camera had plate-holders at an interval of 7.5° from −7.5° to −75° and from 15° to 165° with respect to the incident beam direction in the laboratory system, and was set in the scattering chamber in the case of the measurement of angular distributions. Since the numbers of the elastically scattered protons at small angles were very large, the exposure of the plates at small angles was made about one-fifth of that of the plates at large angles by the shutter in front of the camera, and the normalization in angular distribution was done at 75° both from the ratios of the integrated current and of the intensities of elastically scattered protons.

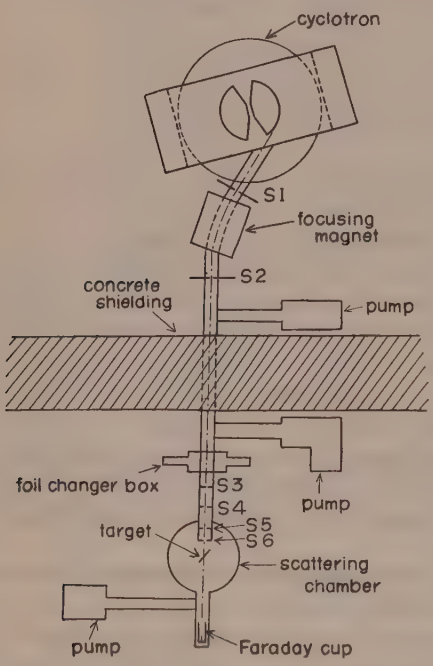

Fig. 1. The schematic illustration of experimental arrangement.

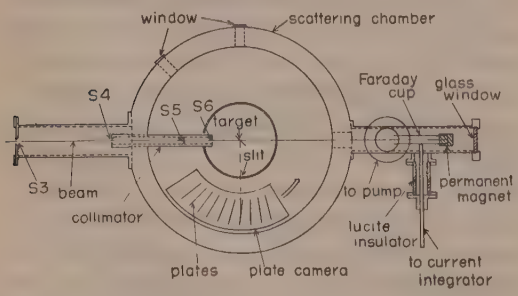

Fig. 2. The experimental arrangement for obtaining the excitation function.

No. 2 camera also had ten plate-holders at an interval of 7.5°. The experimental procedure obtaining the excitation function is shown in Fig. 2. The camera could be rotated in the horizontal plane around the axis of the scattering chamber. The plates were blinded by the aluminium blinder in front of the camera. This blinder had a slit at 90° with respect to beam direction, and the exposures of the plates were done one by one with the rotation of the camera. The proton energy could be changed by aluminium foil in front of the collimator system, thus the excitation functions could be obtained.

The target was a self-supporting Mg foil 1.2 mg/cm² thickness, and was prepared by vacuum evaporation onto a glass plate and was peeled off by a blade of a safty razor. Though the target was stored in vacuum, a small amounts of contaminations of hydrogen and oxygen could not be removed. The used emulsions were Ilford C–2 (200 μ, 100 μ) and Fuji ET–6B (70 μ) nuclear emulsions.

§ 3. Result and Discussions

In order to check the experimental procedure for No. 2 camera, preliminary run was made for the excitation function of the elastic scattering of protons from Au at 90° in the laboratory system. Incident energies of protons were changed from 5.7 MeV to 4.8 MeV by a step of 100 keV. The results are illu-

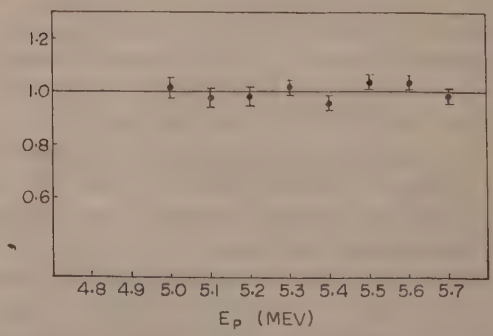

Fig. 3. The excitation function of the elastic scattering of protons from Au at 90° in the laboratory system. Ordinate indicates the product of the differential cross section and the square of incident energy in arbitary scale.

strated in Fig. 3. It is a plausible estimation that in these energy region the differential cross sections for Au are approximately equal to Rutherford cross sections, so the product of the differential cross section and the square of incident erergy of protons must be constant. The result obtained here is very satisfactory.

The excitation function obtained for Mg^{24} ($Q=-1.368$ MeV) is illustrated in Fig. 4 together with the previous results of Greenlees[8].

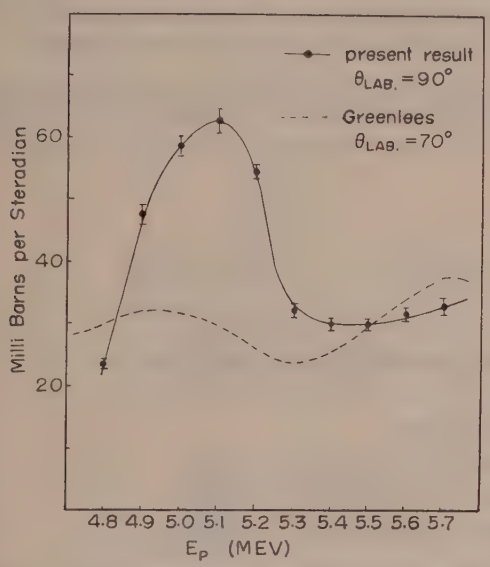

Fig. 4. The excitation function for Mg^{24}($Q=-1.368$ MeV) together with the previous results of Greenlees.

The uncertainty in the absolute cross section were estimated to be about 20% both for the excitation function and the angular distribution. There is a resonance feauture at the incident proton energy of 5.1 MeV, which agrees qualitatively with the previous result and the distributions were measured at 5.1 MeV and 5.4 MeV.

The typical range distribution is shown in Fig. 5 and the angular distributions obtained are shown in Fig. 6. These curves show apparent asymmetries about 90° and the shape changes with variation of incident proton energy. In the present case, the excitation energies of compound states of Al^{25} were considerably low, so it would be expected that so many levels were not excited. Then the asymmetry and the energy variation of the angular distribution might be explained by the interference of levels of different parties.

To obtain further information about the mechanism of the reaction the experiment for the angular distribution at other bombarding energies is now undertaking and then the detailed discussion will be given.

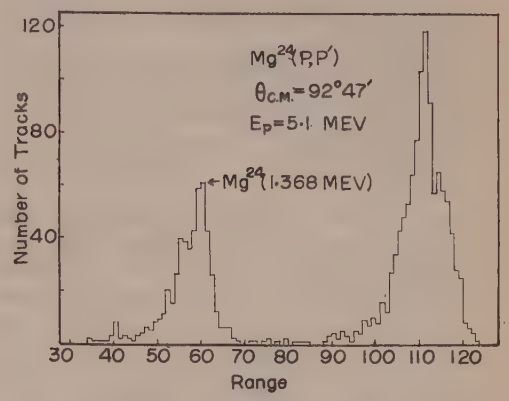

Fig. 5. The typical range distribution (1 div= 1.2 μ).

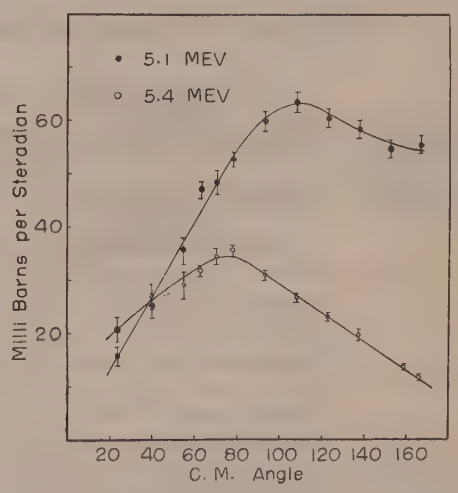

Fig. 6. Angular distribution of protons inelastically scattered from Mg^{24} measured at 5.1 MeV and 5.4 Mev.

Acknowledgements

The author wishes to express cordial thanks to Professor T. Wakatsuki for his kind advises, to Mr. M. Kondo and Mr. T. Yamazaki for their contributions throughout the course of this investigation, and to Fuji Film Corporation for the preparation of nuclear plates.

The author also gratefully acknowledges a financial support to the Nishina Memorial Fundation.

References

1) E. H. Rhoderick: Proc. Roy. Soc. **201** (1950) 348.
2) T. R. Wilkins: Phys. Rev. **60** (1941) 365.
3) Baker, Dodd and Simmons: Phys. Rev. **85** (1952) 1051.
4) H. E. Gove and H. F. Stoddart: Phys. Rev. **86** (1952) 572.
5) G. E. Fischer: Phys. Rev. **96** (1954) 704.
6) G. W. Greenlees and A. E. Souch: Proc. Phys. Soc. **A69** (1956) 686.
7) G. W. Greenlees et al.: Proc. Phys. Soc. **A70** (1957) 331.
8) H. E. Conzett: Phys. Rev. **105** (1957) 1324.
9) P. C. Gugelot and P. R. Phillips: Phys. Rev. **101** (1956) 1614.
10) J. M. Blatt and V. F. Weisskopf: Theoretical Nuclear Physics.
11) L. Wolfenstein: Phys. Rev. **82** (1951) 690.
12) W. Hauser and H. Feshbach: Phys. Rev. **87** (1952) 366.
13) Austern, Butler and McManus: Phys. Rev. **92** (1953) 350.
14) S. Hayakawa and S. Yoshida: Proc. Phys. Soc. **A68** (1955) 656.
Progr. Theoret. Phys. **14** (1955) 1.
15) S. Kikuchi, et al.: Ann. Rep. Fac. Sci. Osaka Univ. **3** (1955) 1.
16) M. Takeda, et al.: Jour. Phys. Soc. Japan **12** (1957) 561.
17) M. Kondo, et. al.: Jour. Phys. Soc. Japan in press.
18) G. W. Greenless: Proc. Phys. Soc. **A68** (1955) 97.

JOURNAL OF THE PHYSICAL SOCIETY OF JAPAN Vol. 13, No. 3, MARCH, 1958

Magnetic Moment of the First Excited State of $_{62}Sm^{152}$

By Kenzo SUGIMOTO

Department of Physics, Faculty of Science, Osaka University, Osaka

(Received November 28, 1957)

The first excited state (122-keV) of the even-even nucleus Sm^{152} was excited by the Coulomb excitation with 2-MeV protons. The angular distribution of the de-excitation radiation was investigated. The attenuation factor of the angular distribution $G_2 \sim 0.6$ was obtained using a samarium oxide target. The rotational change of the pattern in the angular distribution was examined under the condition of applying an external magnetic field vertical to the incident protons. The apparent g-factor for this state obtained was $g(Sm^{152}, 2^+) = +(0.36 \pm 0.16)$ n.m. A brief discussion about the effect of nuclear surroundings affecting the present determination was given.

§ 1. Introduction

A possibility of the determination of the magnetic moment in the nuclear excited state was pointed out by Brady and Deutsch[1], by investigating the influence of an external magnetic field on the angular correlation of successive nuclear radiations. This method was successfully applied to the determination of the magnetic moment of the first excited state of Cd^{111} by Zürich group[2]. Recently, this method was also applied to the $(p, p'\gamma)$ reaction and the magnetic moment of the second excited state of F^{19} was determined by several investigators[3].

The determination of the magnetic moment depends on the nuclear precession in the magnetic field during the life of the excited state, and if one investigates the rotational change of the pattern in the angular correlation of radiations, one may hope to determine the magnetic moment of the short lived excited state in the range of 10^{-9} sec. The so-called fast E2-transition from the first to the ground state in the rotational spectrum of the strongly deformed nucleus lies in this range of life, and one may hope to get a direct information

about the g-factor of the strongly deformed even-even nucleus. The first excited states of these nuclei can be excited by the Coulomb excitation, and the angular distribution of the de-excitation radiation can be predicted theoretically[4]. As the first example of the strongly deformed nucleus, Sm^{152} was investigated in the present work, because of its very marked position of neutron number 90 from which a distinct group of nuclei having the rotational spectrum arises.

§ 2. Instruments and Experimental Procedure

2 MeV protons accelerated by the static generator of Osaka University were used to initiate the Coulomb excitation.

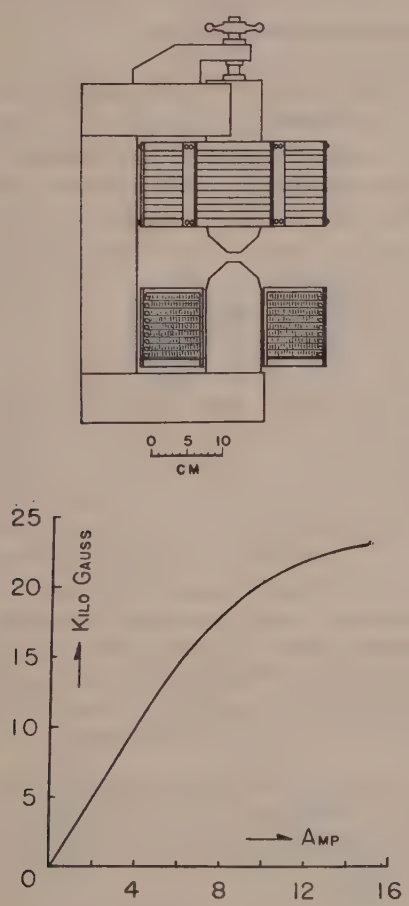

Fig. 1. Electro-magnet and its excitation curve. The pole pieces are made of cobalt-iron alloy. The pole face is 18 mm in diameter and the pole gap is 12.3 mm wide. The winding of the coil is 2400 turns, and the maximum dissipation is 1.6 kilo watts for producing the field of 23000 gauss.

An electro-magnet was specially designed for this work. The pole pieces of the magnet were made of cobalt-iron alloy. And the magnetic field up to 23000 gauss can be produced. The schematic drawing and the excitation curve of the magnet are shown in Fig. 1.

The target assembly is shown in Fig. 2. The target was prepared by depositing the natural samarium oxide* on a copper foil of 7-microns in thickness, and mounted in an aluminium container. The thickness of the target was thick for protons and thin for gamma-rays.

A magnetic shielding for the incident protons minimized the deflection of the beam by the stray magnetic field. In order to determine the deflection of the beam, a photograph was taken by exposing a photographic plate to the proton beam at the target. The photograph by the magnetic field of 23000-gauss is shown in Fig. 3. The deflection angle of the incident protons was measured as $10.4° \pm 0.5°$ for 23000-gauss.

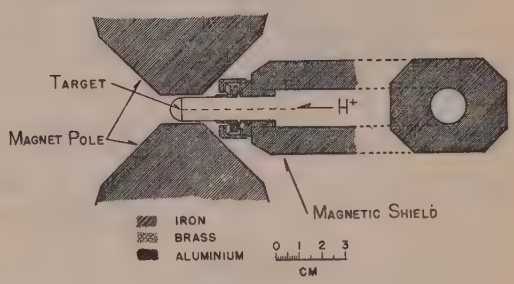

Fig. 2. Target apparatus and magnetic shield for incident protons.

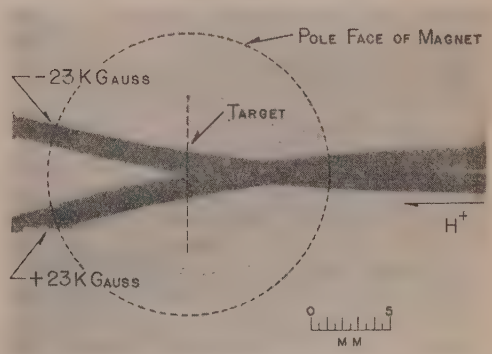

Fig. 3. Photograph of the beam path around the target.

* This sample was produced by Johnson, Matthey & Co., Limited (Hatton Garden, London), and the nominal purity was 99.95%.

The detector arrangement is shown in Fig. 4. Gamma-rays were detected with a NaI (Tl) scintillation spectrometer 1.5-in. in diameter and 1.5-in. in length. The effect of the magnetic field on the spectrometer was examined utilizing a gamma-ray source of Cs^{137},

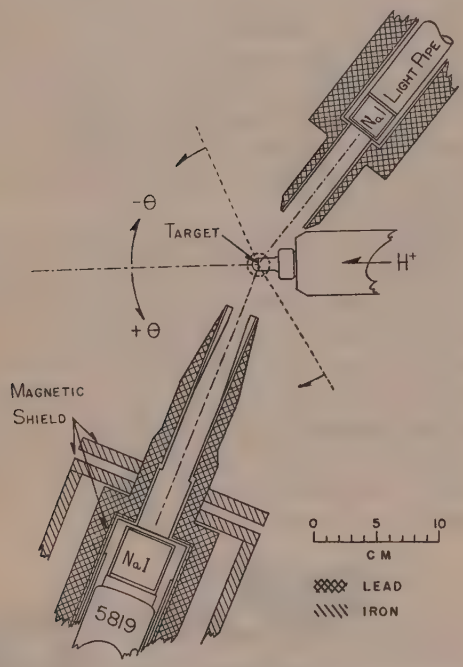

Fig. 4. Plan view of the detector arrangement.

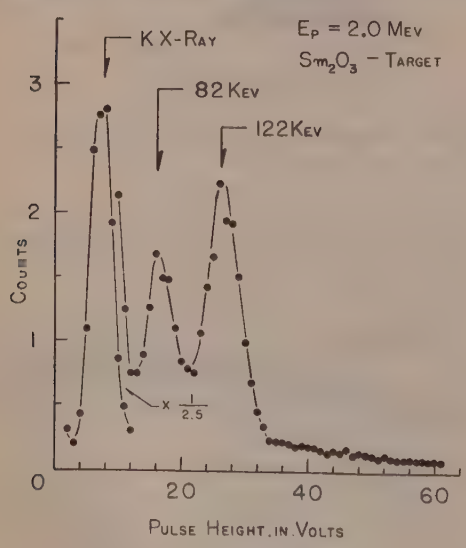

Fig. 5. Pulse height spectrum obtained by bombarding the samarium oxide target with 2 MeV protons. The 122 keV and 82 keV peaks were identified with the de-excitation radiation from the samarium isotopes of Sm^{152} and Sm^{154} respectively.

and the variation of the pulse height spectrum was reduced within 2% with the magnetic shielding of heavy iron plates on the photomultiplier. The geometrical centering of the arrangement was checked by measuring the intensity of gamma-rays from the source of Cs^{137} placed at the target, and the centering was corrected within 1%.

The pulse height spectrum of the scintillation spectrometer obtained by bombarding the samarium oxide target with 2-MeV protons is shown in Fig. 5. Radiation from a tantarum target was used to calibrate the energy scale. When the angular yield was measured, the net yield for the 122-keV radiation was determined from the count of the peak portion of the spectrum by subtracting the back ground which was estimated by extrapolating the just upper part of the spectrum.

§ 3. Experimental Results and Derivation of *g*-factor

The observed angular distributions of the 122-keV radiation at the magnetic field of ±22000-gauss are shown in Fig. 6.

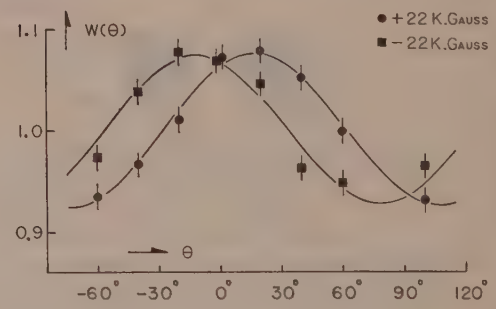

Fig. 6. The angular distribution of the 122 keV radiation at the magnetic field of ±22000 gauss. The solid curves are least-squares fits of the distribution to the form $W(\theta)=a+b\cdot\cos 2\theta+c\cdot\sin 2\theta$. The angular deflection of the pattern includes the deflection of the incident protons.

The theory of the Coulomb excitation predicts the angular distribution of the 122-keV radiation following the excitation by 2-MeV protons as follows,

$$W(\theta)=1+0.142\cdot\cos 2\theta+0.002\cdot\cos 4\theta\ .$$

When the analysis of the observed distribution was done, the term of $\cos 4\theta$ was neglected. And the experimental points were fitted by the method of least-squares. The apparent angular shift of the pattern thus obtained was

subtracted by the deflection angle of the incident protons, and the angular shift $\Delta\theta$ due to nuclear precession was obtained as $2\Delta\theta = 8.7° {}^{+3.6°}_{-3.8°}$.

The relation between the nuclear precession and the angular shift of the pattern in the angular distribution for the present case, by neglecting the influence of nuclear surroundings, can be given by[5]

$$2\Delta\theta = \mathrm{tg}^{-1}(2\omega\tau)\ , \quad \text{where} \quad \omega = g\cdot\mu_N\cdot H/\hbar\ ,$$

and where τ is the life time, ω is the Larmor frequency, g is the nuclear g-factor, and μ_N is the nuclear magneton. Using the value of the half life $T_{1/2} = (1.40\pm0.10)\cdot10^{-9}$ sec. obtained by Sunyar[6], the apparent g-factor was obtained to be

$$g(\mathrm{Sm}^{152}, 2^+) = +(0.36\pm0.16)\cdot\mu_N\ .$$

The present value is in good agreement in magnitude with the value obtained by Scharenberg and Goldring[7].

Though the effects of the nuclear surroundings affecting the present determination are complex, the effects can be estimated from the attenuation factor $\mathbf{G}_2$ of the coefficient in the angular distribution when the external magnetic field was not applied. $\mathbf{G}_2$ can be determined by comparing the observed distribution with the theoretical one. $\mathbf{G}_2 \sim 0.6$ was obtained by the present measurement in agreement with the result obtained by Simmons, et al.[8] using a samarium oxide target. Scharenberg and Goldring[7] have observed the distribution using a metallic samarium target and also a target in liquid form, and obtained $\mathbf{G}_2 = 0.65$ and $\mathbf{G}_2 = 0.95$ respectively.

The effects of the surroundings which cause the attenuation of the angular distribution, especially for the solid target, are considered as follows. Because of the recoil energy up to 50-keV, the recoil atom will find itself at a strange position of the lattice, so that the excited nucleus will be exposed to a strong electric field gradient. The effect due to the atomic hyperfine structure must also be considered, because of the special character of the atomic $4f$ electrons of the samarium atom. But this atomic moment is believed to fluctuate very rapidly ($\lesssim 10^{-12}$ sec.) relative to the nuclear precession ($\sim 10^{-9}$ sec.) above the room temperature. It is, therefore, reasonable to consider that the difference between the attenuation factor $\mathbf{G}_2$ for the solid targets and the liquid target is attributed to the difference in electric quadrupole interaction, so that the apparent g-factor may be increased at most by 40% from this cause.

Another cause which is due to the strong paramagnetism will strengthen the effective magnetic field at the nucleus, because the atom is partially polarized along the external magnetic field. This effect was estimated by considering the behavior of the atomic $4f$ electrons[9], and the effect on the determination of the g-factor was calculated to be 20% at 300°K and 10% at 700°K, so that the apparent g-factor must be decreased about 10% from this cause.

In spite of these uncertainties, the sign of the g-factor could be conclusive. It is interesting to remember that the uniform model predicts the g-factor $g \sim Z/A \sim 0.41$ irrespective of the deformability of the nucleus.

Acknowledgement

It is a pleasure to acknowledge the continued interest and encouragement of Professor S. Kikuchi and Professor T. Wakatsuki in this work. The author would like to thank Professor T. Nagamiya and Dr. J. Kanamori for their discussion and numerical estimations about the extra nuclear effects. He also wishes to thank Mr. A. Mizobuchi for his indispensable aid and Mr. H. Iwata for his technical assistance.

References

1) E. L. Brady and M. Deutsch: Phys. Rev. **78** (1950) 558.
2) H. Aeppli, H. Abers-Schönberg, H. Frauenfelder and P. Scherrer: Helv. Phys. Acta. **25** (1952) 339.
3) M. Lehman, A. Lévêque and M. Fiehrer: Comp. Rend. **241** (1955) 700.
P. B. Treacy: Nature **176** (1955) 923.
K. Sugimoto and A. Mizobuchi: Phys. Rev. **103** (1956) 739.
4) K. Alder, A. Bohr, T. Huus, B. Mottelson and A. Winther: Rev. Mod. Phys. **28** (1956) 432.
5) *e.g.* H. Frauenfelder: Beta- and Gamma-Ray Spectroscopy, Ed. K. Siegbahn (North Holland Publ.Co., Amsterdam, 1955) Ch. XIX, p. 531.
6) A. W. Sunyar: Phys. Rev. **98** (1955) 653.
7) R. P. Scharenberg and G. Goldring: Bull. Am. Phys. Soc. **2**, No. 1 (1957) 69: NRC 57-2-93 Sm^{152} 57 # 2.
8) B. E. Simmons, K. F. Famularo and G. D. Freier: Phys. Rev. **100** (1955) 1265 (A).
9) R. J. Elliot and K. W. H. Stevens: Proc. Roy. Soc. London A **219** (1953) 387.

JOURNAL OF THE PHYSICAL SOCIETY OF JAPAN Vol. 13, No. 3, MARCH, 1958

Optical Study on the Resultant Movement of Many Walls in Rochelle Salt

By Ryuji ABE

Department of Physics, Osaka University, Osaka

(Received September 24, 1957)

A new optical device to study the resultant movement of many walls in rochelle salt was constructed. It was found that the rotating angle of the optical plane is nearly in proportion to the spontaneous polarization. Some characteristics of the resultant wall motion were studied from the information of the rotating angle. From these experimental results we are inclined to conclude that the fatigue effect will be caused by either the displacement of dislocations or neutral vacancies.

§ 1. Introduction

Recently the domain structure and the wall motion in rochelle salt have been observed by several investigators[1)-3)] by means of polarizing microscope. These direct observations are very useful to investigate the mechanism of the individual motion of every wall. They are, however, not sufficient to study the essential mechanism of wall motions as a whole, because the observed motion of a wall is sensitively influenced by the local stresses in the vicinity of the wall. This influence of local stresses can be excluded in the measurement of the resultant movement of many walls, because the influence on every walls are averaged over. Therefore such a resultant measurement is also important to study the mechanism of the wall motion.

In the present experiment we have investigated various characteristics of the resultant movement of many walls by means of the high sensitive optical system. It was found that this optical method is very useful to study the characteristics of wall motion at very low frequencies. The measuring device is given in § 2 and some experimental data on the fatigue effect and the other phenomena are given in § 3.

§ 2. Experimental

Specimen. The crystal used in the present experiment was thin slab normal to *a*-axis, of which dimension is about $3\times2\times0.2\,\mathrm{cm}^3$. Silver electrodes were evaporated *in vacuo* on both sides of the slab. The thickness of the electrodes was limited within a few hundred Å so that a measurable intensity of light passes through the crystal.

Chamber that contains specimen. To keep the temperature and the humidity constant during an experiment the crystal was set in the closed chamber (Fig. 1). The temperature was controlled by circulating water which was kept at a constant temperature, while the humidity was controlled by changing the con-

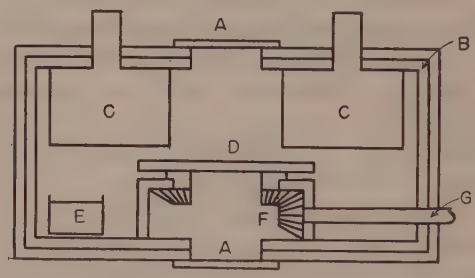

Fig. 1. Specimen chamber.

A: Glass plate B: Brass chamber
C: Water bath D: Specimen
E: Sulphuric acid F: Bevel-gear
G: Shaft

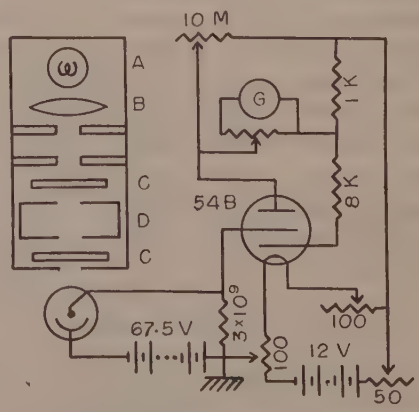

Fig. 2. Diagram of circuit

A: Light source B: Lens
C: Polarizer D: Specimen chamber

centration of sulphuric acid in the chamber. The crystal was placed on a disk which rotates around its center by operating the outer dial.

Circuit. The diagram of the circuit is shown in Fig. 2, where the polarized light falls in parpendicular onto an a-plate crystal and the light which has passed through the crystal is introduced into photo-electric tube. The induced photoelectric current is amplified by electrometer tube and the amplified current is detected by high sensitive galvanometer. The area of the crystal surface which was irradiated by the polarized light was about $1.5\times1.5\ \mathrm{cm}^2$.

§ 3. Experimental Result

Rotation of optical plane versus temperature. Rochelle salt crystal is orthorhombic in its paraelectric region and its optical axes exist in (010) plane[4]. If the polarized light is thrown in parpendicular to a-plane, it is divided into two extraordinary rays i.e. the one ray which oscillates in b-plane and the other ray which oscillates in c-plane. These two rays are recombined when they have passed through the crystal and a certain component of the recombined ray passes through the analyzer which is crossed to the polarizer. Then the intensity of the light which has passed through the crystal is given by

$$I=\gamma I_0 \sin^2 2\theta=\frac{1}{2}\gamma I_0(1-\cos 4\theta) \qquad (1)$$

where I_0 is the intensity of incident polarized light, θ is the angle between b-plane and the plane of the polarization of the incident light. γ is a certain constant which becomes $\sin(2\pi\Delta/\lambda_0)$ if the wave length of polarized light is a constant λ_0 and the crystal surfaces are prefectly flat, where Δ is the optical path difference between the two extraordinary rays. In the ferroelectric region the crystal becomes monoclinic and the optical plane differs from the b-plane*. Therefore the previous Eq. (1) must be modified to be

$$I^a=\frac{1}{2}\gamma I_0(1-\cos 4(\theta-\varphi_s)) \qquad (1)'$$

for the state (a) (Fig. 3), and

$$I^b=\frac{1}{2}\gamma I_0(1-\cos 4(\theta+\varphi_s)) \qquad (2)''$$

* Here the b-plane denotes b-plane in the paraelectric state.

for the state (b), where φ_s is the angle between the optical plane and the b-plane when the polarization of the crystal is saturated in one direction. If the state of the crystal changes from (b) to (a) by applying electric field, then the intensity of the light which has passed through the crystal changes by

$$I_a=\gamma I_0 \sin 4\theta \sin 4\varphi_s\ . \qquad (2)$$

$(\theta-\varphi_s)$ in Eq. (1)′ and $\sin 4\varphi_s$ in Eq. (2) are approximately equal to θ and $4\varphi_s$ respectively, because φ_s is smaller than 1° as proved later. Hence, from equations (1)′ and (2) φ_s is given by

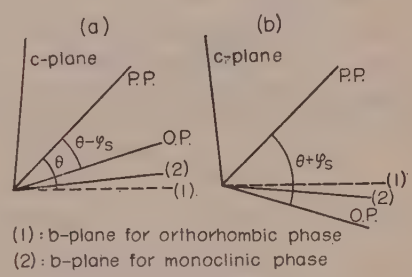

Fig. 3. Two polarizing states of rochelle salt.
P.P.: Plane of polarized light
O.P.: Optical plane
The broken line indicates b-plane in the paraelectric state.

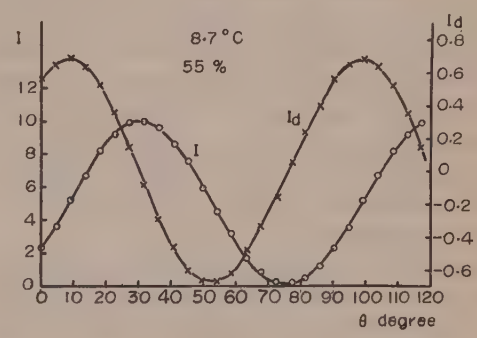

Fig. 4.

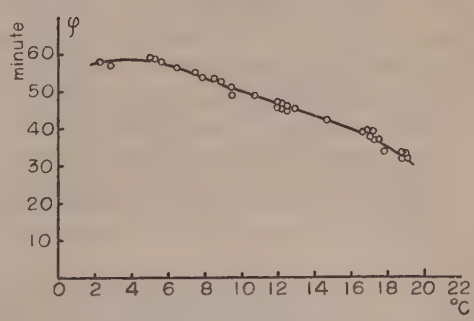

Fig. 5. Dependence of rotating angle on temperature.

$$\varphi_s = \frac{(I_d)_{\theta=\pi/8}}{4(I)_{\theta=\pi/4}} \quad . \qquad (3)$$

Therefore if the relative intensities of both $(I_d)_{\theta=\pi/8}$ and $(I)_{\theta=\pi/4}$ are measured, the absolute value of φ_s for every temperature* can be obtained. The dependences of φ_s on temperature and on spontaneous polarization are shown in Fig. 5 and Fig. 6 respectively, and some values of φ_s are given in Table I. These

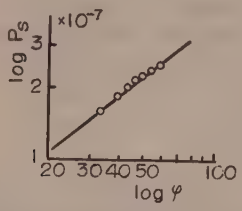

Fig. 6. Rotating angle versus spontaneous polarization.

Table I.

Temp. (°C)	2.2	5.2	8.5	11.9	14.6	17.8	19.2
φ_s (min)	58.0	58.9	53.6	45.8	43.0	37.4	32.5

figures clearly show that φ_s is proportional to P_s^{n}**. The value of n is determined to be 1.25 ± 0.2 from the experiment data.

It will be noted here that φ_s is nearly proportional to spontaneous polarization, because the value of n nearly equals unity. In the following experiment, accordingly, we use the resultant rotating angle φ as the measure of the resultant displacement of many walls. φ is given by $\varphi = V_+\varphi_s - V_-\varphi_s$, where V_+ and V_- are the volumes of positive and negative domain respectively.

Dependence of φ on electric field. Under a constant temperature and a constant humidity, φ increases with the increase of applied field, as shown in Fig. 8. It is clearly seen from this figure that in the ferroelectric region φ increases abruptly at a certain field. This "critical field" will correspond to the coercive field in the hysteresis loop obtained by Sawyer and Tower method. The "crytical field", however, is much lower than the coercive field given by Sawyer-and-Tower-hysteresis loop and the slope near the crytical field is fairly steeper than the slope in the hysteresis loop. The same conclusion has been obtained from different experimental measurement by a few investigators[5)-6)]. This conclusion indicates that the coercive field is dependent on the changing rate of field with time. An explanation for this dependence is given in our previous paper[8)].

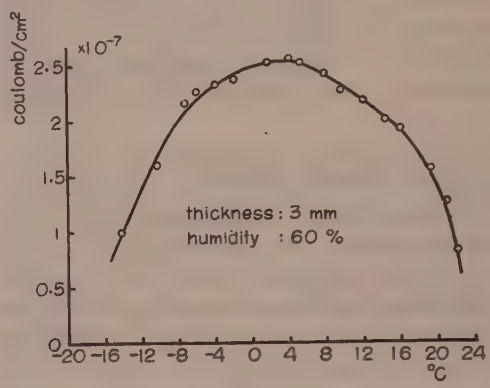

Fig. 7. Dependence of spontaneous polarization on temperature.

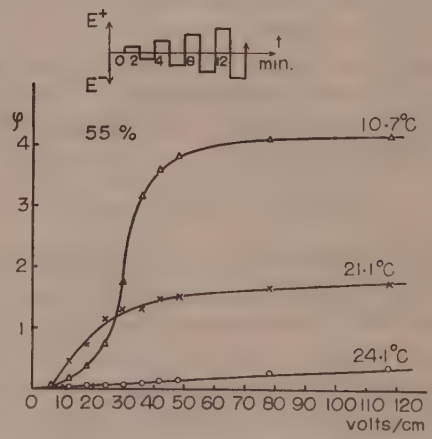

Fig. 8. Rotating angle versus applied field.

As shown in the following, φ changes with time remarkably, and shows a marked fatigue effect. Hence it was necessary to apply static fields to a crystal successively, as shown in the upper part of Fig. 8 in order to avoid the influence of the fatigue effect.

Change of φ with time. The angle φ reaches the equilibrium value soon after the application of field if the field is higher than the critical field mentioned above. However, it does not reach the equilibrium value within 20~30 sec after the application of field if the

* It is really ascertained that the simple relations (1) and (2) are satisfied for the persent crystal (Fig. 4).

** Temperature dependence of spontaneous polarization is a little affected by humidity. Here we use the data of spontaneous polarization obtained from the hysteresis loop at 60% humidity (Fig. 7).

field is lower than the critical field (Fig. 9). This phenomenon corresponds to the phenomenon found by Takahashi and Hara[5] by electrical means, although the present saturation frequency is about 3~4 times higher than their saturation frequency.

Fatigue effect. It is well known that rochelle salt comes to fatigue when a static field is applied to a crystal for a long time. About

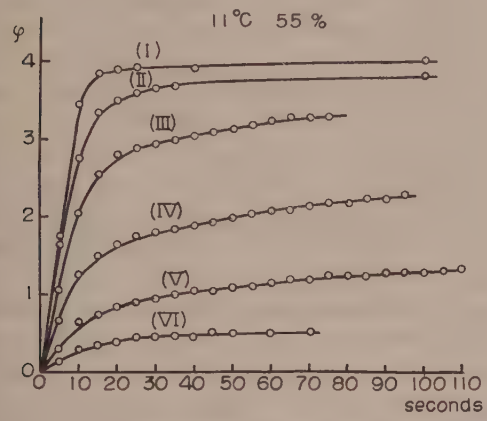

Fig. 9. The change of φ with time after the application of field.

(I)	50 volts/cm	(II)	45 volts/cm
(III)	40 volts/cm	(IV)	35 volts/cm
(V)	30 volts/cm	(VI)	25 volts/cm

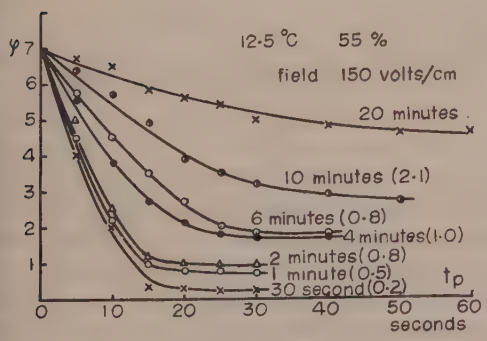

Fig. 10.

the origin of this effect, however, no satisfactory explanation has yet been proposed, because the experimental data on this effect are very complicated and fluctuated. Therefore for the study of this origin a more concentrated and detailed experiment must be done.

In the present experiment we have investigated various features of this effect by means of the present optical method. This method was very advantageous to study the displacement of walls at very low frequencies, because the measurement is not influenced by the existence of surface leak and ionic current. Fig. 10 gives an example of the recovery of φ with time after the removal of applied field which is high enough to saturate the polarization of crystal in one direction (150 volts/cm). The ordinate is φ in arbitrary scale and the abscissa is the time t_p that lapsed after the removal of field. The duration of field τ is given by the figures near the every curve and the quasi-equilibrium value* of φ is given by the figures in the parentheses. Though the result is not shown in this figure, the crystal almost recovers its original state after a sufficiently long time has lapsed. In Fig. 11 the change of the initial value of recovering velocity is shown as a function of the duration of field. The ordinate is the ini-

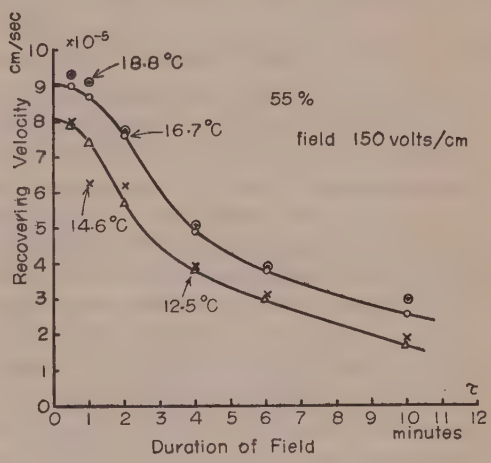

Fig. 11.

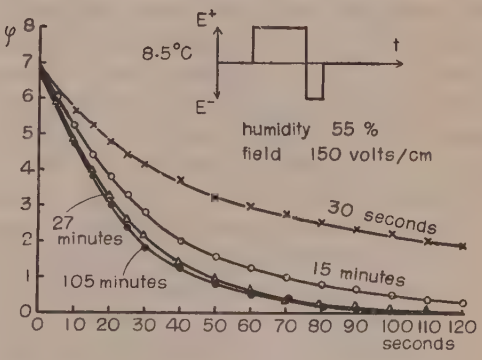

Fig. 12.

* The quasi-equilibrium value means the value of φ when the same period as the duration of applied field has lapsed after the removal of applied field.

tial value of recovering velocity which is determined by the gradient of φ-t_p curve at $t_p=0$, and the abscissa is the duration of applied field τ. In Fig. 12 the change of φ is shown when the reverse field is applied for 30 sec after the removal of the forward field. The ordinate is φ in arbitrary scale and the abscissa is the time that lapsed after the removal of the reverse field. The strength of field equals in both direction (150 volts/cm) and is high enough to saturate the polarization of the crystal. These experimental results are almost reproducible for the same crystal and the characteristic features of each curve are similar respectively for another crystal with the dimension, $3.5\times2.5\times0.5$ cm^3.

Now from these experimental results we can obtain some informations useful to discuss about the origin of the fatigue effect: (1) the crystal does not recover its original state for a few hours if the duration of field is longer than about 10 minutes, although it recovers the original state after the sufficiently long time. This fact suggests that a certain change of internal structure such as the dislocation or the movement of ions or vacancies is caused in the crystal. This suggestion is also supported by the result that the recovering velocity in the reverse direction increases with increase of duration of the forward field (Fig. 12). (2) the recovering velocity of wall becomes the order of 10^{-5} cm/sec, if we assume that the crystal is composed of equivalent lamellae of 180° domains with the breadth of $10^{-3}\sim10^{-4}$ cm (according to our observation) and the walls move only sideways (Fig. 11). This velocity is much lower than the velocity of wall at low fields observed by Mitui and Furuichi[1]. (3) the fatigue begins to appear abruptly when the duration of applied field is longer than about 30 sec (Fig. 11). This fact seems to mean that the velocity of the imperfections which cause the fatigue is the order of d/30 cm/sec, where d is the distance between the imperfection and the source of the recovering force. (4) the recovering velocity changes a little with the change of sign of the applied field. Therefore, it is likely that the source of the recovering force is related with the secondary structures of the crystal or the surface states of the electrodes. (5) the initial value of recovering velocity increases a little with the increase of temperature (Fig. 13). The recovering velocity, accordingly, seems to be independent of spontaneous polarization. Refering these experimental results a few discussions on the origin of the fatigue effect will be given in the following section.

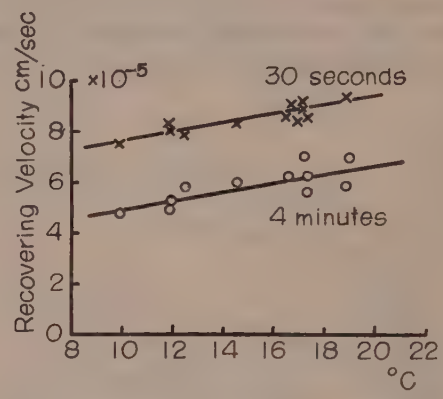

Fig. 13. Dependence of initial recovering velocity on temperature.

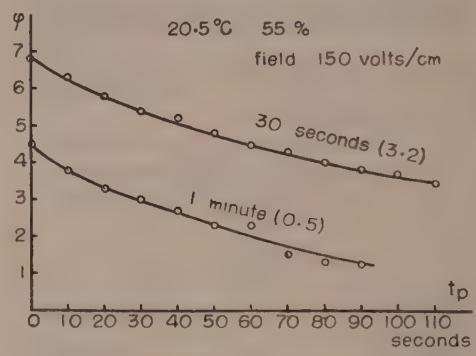

Fig. 14.

Effect of surface charge. In the foregoing experiments, to avoid the appearance of true charge both electrodes were shortcircuited when the applied field was removed. On the contrary, if both electrodes are left open when the applied field is removed, it will be expected that all domains little recover their original volumes for a short time, because the true charge induced in the electrodes prevent the movement of every domain. Actually at 10°C and at 55% humidity no change of φ was observed at least for 2 minutes after the removal of applied field which was high enough to saturate the polarization of crystal, although at the temperatures higher than about 20°C the fairly rapid change of φ was observed*

* The drastic increase of the recovering velocity may be due to the increase of the surface conductivity of the crystal.

(Fig. 14). This fact indicates that the rochelle salt crystal is a good insulator even at relatively high humidity.

§ 4. Discussions

1) The surface-charge layers due to ionic current will influence the recovery of crystal. This mechanism may be proposed as a possible explanation of the fatigue effect. This explanation seems to be adequate, because it reminds us the fact that surface space-charge layers exist in $BaTiO_3$ crystal[9),10)]. Rochelle salt, however, is a good insulator as proved by Takahasi and Hara[11)], and therfore the ionic current in the crystal is very small. For example if the resistance of the crystal is $10^{15}\Omega$ (refering to the Takahasi and Hara's data) and the applied field is 500 volts/cm, the charge caused by ionic current is smaller than about 1×10^{-11} coulomb/cm^2 for 10 minutes. This charge is much small than the charge caused by spontaneous polarization. Therefore the surface-charge layers in rochelle salt will little affect the recovering velocity of every domain. This fact seems to suggest that the fatigue of the crystal may be due to either the movement of dislocations or neutral vacancies, and independent of charge movement.

2) In the recent paper Kinase and Takahasi[12)] pointed out that the defects in electrodes may cause the nucleation of new domains because depolarizing charges appear at the defects. For the present specimen such defects may also be the important sources of new domains because the evaporated electrodes are very thin, and therefore many defects may be contained. As discussed in 1), however, the depolarizing charge on the crystal surface is little neutralized by true charge for a short time. Therefore to explain the observed fatigue effect i.e. the decrease of the recovering velocity, it is rather favorable to consider that the other origin of the recovering force exists in the crystal besides the surface defects. Screw dislocations[13)] or impurities in the crystal may be the important causes of the recovering force.

Finally the author wishes to express his appreciation to M. Y. Fuzishiro and Mr. K. Ichie for their helpful assistances. This work was suported by the Scientific Research Fund of the Ministry of Education.

References

1) T. Mitui and J. Furuichi: Phys. Rev. **90** (1953) 193.
2) M. Marutake: J. Phys. Soc. Japan **7** (1952) 25.
3) T. Nakamura: J. Phys. Soc. Japan **11** (1956) 624.
4) P. Groth: Chemische Kristallographie.
5) H. Takahasi and S. Hara: J. Phys. Soc. Japan **4** (1949) 257.
6) T. Nakamura: J. Phys. Soc. Japan **12** (1957) 477.
7) R. Abe: J. Phys. Soc. Japan **11** (1956) 104.
8) R. Abe: Busseiron-Kenkyu No. 94 (1956) 49; R. Abe: Busseiron-Kenkyu No. 102 (1956) 1, in Japanese.
9) W. Känzig: Phys. Rev. **98** (1955) 549.
10) A. G. Chynoweth: Phys. Rev. **102** (1956) 705.
11) H. Takahasi and S. Hara: J. Phys. Soc. Japan **4** (1949) 261.
12) W. Kinase and H. Takahasi: J. Phys. Soc. Japan (1957) 464.
13) T. Nakamura: Rep. Inst. Sci. and Tech., Univ. of Tokyo **7** (1953) 113.

JOURNAL OF THE PHYSICAL SOCIETY OF JAPAN Vol. 13, No. 3, MARCH, 1958

On the Screened Field around an Impurity Atom in Metal

By Hiroshi FUJIWARA

Department of Physics, Minami-Bunko
Hiroshima University, Minami-machi-3
Hiroshima City

(Received December 5, 1957)

By using a newly proposed model, in which the positive charges of bare nuclei of an impurity atom and the matrix atoms are put at the lattice points and all the electrons, valence electrons as well as core ones, are treated by Thomas-Fermi method, the deviation of the potential from the periodic one for the pure matrix metal due to the presence of an impurity atom has been calculated and compared with the screened Coulomb potential obtained in previous papers.

In the case of pure metals, a similar treatment was made by Slater and Krutter, so that our model may be regarded as an extension of theirs to the case of substitutional impurity.

Our obtained potential is nearly proportional to ΔZ, where $\Delta Z = Z_i - Z$, Z_i and Z being atomic numbers of the impurity and the matrix atom respectively and in this paper, we have treated the cases of $\Delta Z = \pm 2$ and ± 1.

§ 1. Introduction

As one of the applications of the Thomas-Fermi (to be referred to as T.F. hereafter) approximation, we have been investigating the screened potential around an impurity atom in the dilute solid solution which consists of two metals with different valencies.

Up to date, we have treated the case where a trace of di- or trivalent metal is disolveds as a substitutional impurity in a monovalent metal; for example, Zn or Ga in Cu.

Our previous studies[1], as well as most of the work done by other investigators[2], were based on the following model: i.e., only the valence electrons of atoms of matrix and impurity metals were treated in T.F. method; the charge $(\Delta Z)e$, where ΔZ is the excess of the valency of the impurity over that of the matrix, was concentrated at the position of the nucleus of the impurity atom and the remaining charges due to core electrons and the nuclei were smeared out so as to form a uniform positive charge distribution.

On this model, the problem was rather easy to treat and it reduces to the construction of a spherical symmetric solution of the T.F. equation.

This model has, however, several unsatisfactory features; (a) In the first place, because of the smearing out of the charge, the lattice structure of the matrix metal is completely lost in our model, so that, e.g., the crystal symmetry of the matrix metal cannot be taken into account. (b) Secondly, the impurity atom is characterized by a single parameter ΔZ, so that this model cannot distinguish between the different impurity atoms of the same valency, e.g., Zn and Cd or Ga and In. As to the matrix, it is characterized by the average density of valence electrons, which determines the Fermi energy. (c) In the case when ΔZ is negative, a negative point charge $(\Delta Z)e$ is to be put at the position of the nucleus of the impurity atom. In this connection, we encounter a further difficulty when we want to treat impurity atoms of transition metals. Let us consider, for example, the case of dilute solution of Co in Cu. According to our model negative charges of 28 electrons per atom (corresponding to $(1s)^2(2s)^2(2p)^6(3s)^2(3p)^6(3d)^1$ configuration) and the positive nuclear charge $29e$ (corresponding to Cu nuclei) are smeared out uniformly so as to yield a constant positive volume charge of $+e$ per atom as the background, and a negative point charge $-2e$ $(=(Z_{Co}-Z_{Cu})e)$ is put at the position of Co nucleus. Since positive holes of electrons are not allowed in T.F. method, our model requires that Co impurity atom must exist at least as singly ionized negative ion Co^-, which does not seem to be physically plausible. If we want to assume the Co atom, which is not

mally in $(3d)^7(4s)^2$ configuration, to contribute two $4s$ electrons to valence electrons which are to be included in our T.F. treatment, we have to locate $+e$ at the position of Co nucleus; in this formulation, however, we could not distinguish between Co and Zn cases.

From a somewhat different point of view, this difficulty may be considered as due to the ambiguity of assignning the number of valence electrons in transition metals.

In view of these unsatisfactory features of the simple model, we propose here a new model, in which the positive charges of bare nuclei are put at the lattice points and all the electrons, valence electrons as well as core ones, are treated by T.F. method. In the case of pure metals, the similar treatment was made by Slater and Krutter[3] some twenty years ago, so that our model may be regarded as an extension of theirs to the case of substitutional impurity.

Assuming the concentration of the impurity to be so small that the interaction between impurity atoms is negligible, we may treat the case in which at all lattice points are located the positive charges Ze except a single lattice point where a point charge Z_ie is located. Hereafter we denote the atomic number of matrix atom and that of impurity atom by Z and Z_i respectively. We expect that in the vicinity of the impurity atom, electron distribution will adjust itself so as to screen the excess charge $(Z_i \sim Z)e$, and as we go farther and farther from the impurity atom, electron distribution will tend more and more closely to the periodic one characteristic to the pure matrix metal. This electron distribution, as well as the corresponding potential distribution, will be determined by T.F. method.

This is nothing but the most straightforward and consistent way of applying T.F. method to our problem, and no ambiguity is left, for instance, about the choice of the number of electrons to be treated.

In this model, $|Z_i - Z|$ may be quite large; in fact, we could treat the case of vacancy simply by putting $Z_i = 0$. And the lattice structure can be fully taken into account.

Further our calculation may be of some interest from the mathematical point of view as an application of cellular method to crystals containing an impurity atom.

We do not believe, however, that our model is completely satisfactory. Since, T.F. method cannot account for the shell structure of electrons in atoms, the concept of "valency" is almost completely lost in our present model. The observed trend of the residual electric resistance, for instance, seems to show the significance of the concept of valency, at least as a guide to rough estimation.

In order to preserve the concept of closed shells, valency, etc. and at the same time, to take the lattice structure and other properties about individual element of the periodic table into account, it seems to us desirable to represent the distribution of core electrons by the use of Hartree and Hartree-Fock field, and to treat the electrons outside these cores by T.F. method. We are now proceeding this way and we hope to report the results in a near future.

§ 2. General Considerations about Our New Model

We consider the introduction of a single foreign impurity atom (hereafter abbreviates as i-atom) by substituting one of the solvent matrix atoms (hereafter abbreviates as m-atoms) which are arranged in a face-centered cubic crystal.

The lattice point thus substituted by an i-atom is denoted by $\boldsymbol{R}_0$, while those occupied by m-atoms are $\boldsymbol{R}_n$ $(n \neq 0)$.

In order to remove the deficits in the former model as stated in the introduction, all the electrons in the crystal are taken into consideration and we assume that the bare nuclei with positive charges $+Ze$ and $+Z_ie$ of m-atoms and an i-atom are located at $\boldsymbol{R}_n$ and $\boldsymbol{R}_0$ as point charges.

The fundamental problem in obtaining the crystal potential is to find the solution of the T.F. equation which is appropriate for this arrangement of positive point charges. Now let $u(\boldsymbol{r})$ be the electrostatic potential at the point $\boldsymbol{r}$ valid over the entire impure crystal in which every atom is supposed to be at rest at its lattice point. Then, $u(\boldsymbol{r})$ is given from the solution of usual T.F. equation:

$$\nabla^2 u(\boldsymbol{r}) = \alpha u^{3/2} \tag{1}$$

where

$$\alpha = \frac{32\pi^2 e}{3h^3} \cdot (2me)^{3/2} \tag{2}$$

under the following conditions in the vicinity of each lattice point, due to the presence of bare nuclei

$$u(\boldsymbol{r}):\quad (=u_0)=\frac{Z_i e}{|\boldsymbol{r}-\boldsymbol{R}_0|}+(\text{finite terms})\quad \text{near } \boldsymbol{R}_0 \tag{3a}$$

$$(=u_n)=\frac{Ze}{|\boldsymbol{r}-\boldsymbol{R}_n|}+(\text{finite terms})\quad \text{near } \boldsymbol{R}_n\quad (n\neq 0) \tag{3b}$$

In order to solve this problem, we use the "cellular method", i.e., we subdivide the crystal into polyhedra of equal size and form neglecting the distortion of the lattice due to the presence of an impurity atom. Each polyhedron, except one in which the bare nucleus of an i-atom is located at its center, has the bare nucleus of m-atom at its center.

We shall denote, hereafter, the polyhedron belonging to an i-atom or its neighboring m-atoms by P_0 or P_n and the solutions of (1) in P_0 and P_n by u_0 and u_n respectively.

Then, u_0 and u_n must be smoothly connected over the surface of each neighboring polyhedron, i.e., the continuity of the potentials and their derivatives must hold.

Rigorously speaking, the boundary conditions must be satisfied at all points on the surface of the polyhedron. In the case of the face-centered cubic lattice, the surface consists of twelve planar polygons, and the distance r of the surface points from the center falls in the range $(1/2\sqrt{2})a<r<(1/2)a$, a being the lattice constant. Since we introduce only a finite number of adjustable parameters in the actual calculation, we impose the boundary conditions only at the centers of polygons, which are midpoints between $\boldsymbol{R}_0$ and $\boldsymbol{R}_n$. We replace, however, in this calculation the distance $(1/2\sqrt{2})a$ by the radius $r_c=(3/16\pi)^{1/3}a$ of the atomic sphere whose volume is equal to the atomic polyhedron; since r_c is an average of the distances of the surface points from the center, we hope to be able thereby to take account, to some extent, of the fact that the distances of the surface points from the center are not constant.

Therefore, we replace the polyhedra P_0 and P_n, by the spheres of S_0 and S_n of equal volume, and, instead of at the midpoint between the centers of two polyhedra, apply the boundary conditions at the points where the line $\overline{R_0R_n}$ intersects with the atomic sphere, on the surface of the atomic sphere. Then our problem reduces to solving the T.F. equation within these spheres S_0 and S_n. This approximation seems to be particularly good for cubic metal which has very symmetrical atomic polyhedra.

While Slater and Krutter solved T.F. equation by using the cellular method for pure metals, our new model may be regarded as an extension of theirs to the case of impure metals.

Hitherto, for pure metals*, the potential in each atomic sphere has always been assumed as spherically symmetric. But, in our study of impure metals, we have to take account of the deviation of the potential in the atomic sphere from the spherical symmetry. Of course, the potential in the distance from the impurity must be the same as in the pure matrix metal, which we assume as spherical symmetric in each atomic sphere. On the other hand, in the atomic sphere S_0 for the impurity atom, the potential must have octahedral symmetry, and the deviation from the spherical symmetry appears only in the 4th degree spherical harmonics, so that we may safely neglect this deviation. In the atomic spheres S_n neighboring to S_0, however, the potential has much lower symmetry, and we take into account of the lower symmetry by writting:

$$u_n=U(r)+f_n(r,\theta,\varphi)\qquad n\neq 0 \tag{4}$$

where $U(r)$ is the potential for undisturbed matrix metal and the small term f_n depends not only on r but also on the direction θ, φ (r, θ, φ are the spherical polar co-ordinates with its origin at the center of S_n).

The potentials u_0 in S_0 and u_n in its neighboring spheres S_n obtained by integrating T.F. equation involve a certain number of parameters, which we shall determine by virtue of an appropriate set of boundary conditions.

* Even for the case of pure metals, when the symmetry of the crystal is low, the cellular polyhedron is not well approximated by a sphere, for example in diamond-type structure. Therefore, the angular terms in the potential within the polyhedron may be of some importance. From this side of the non-spherical properties of crystal potential, recently Bell et al.[4] investigated on lead sulphide, and March[5], using T.F. method, has made an attempt to estimate the size of the angular terms for silicon.

The details will be described in the following section.

§ 3. Equation in Each Atomic Sphere and the Boundary Conditions

(i) Let us first consider the solution u_0 of T.F. equation within the atomic sphere S_0 of the impurity atom. u_0, being spherical symmetric due to the consideration stated in § 2, satisfies:

$$\frac{1}{r}\frac{d^2(u_0 r)}{dr^2}=\alpha u_0^{3/2} \qquad (5)$$

Near the center, u_0 is given as follows:

$$u_0=Z_i e/r+c_1+\cdots \qquad (6)$$

If the screening of the excess charge $(Z_i \sim Z)e$ is complete in S_0 itself, the total charge contained within this sphere must be zero, i.e., the neutrality condition $(\partial u_0/\partial r)=0$ is to be satisfied at r_c, as is the case for the pure metal. But, in the actual case, the screening will be more or less incomplete and the distribution of the excess charge has its tail outside of S_0 to some extent, so that the neutrality condition does not hold. Therefore, we have to leave c_1 in (6) as an adjustable parameter, and determine its value in such a way that u_0 may be smoothly joined to u_n in the nearest neighbors.

(ii) As to the potential u_n within the spheres of m-atoms in the neighborhood of i-atom, we assume, in the first approximation, as follows:

(α) the deviation f_n does not vanish within the spheres of the nearest and 2nd neighbors.

(β) u_n does not deviate from spherical symmetry any longer within the spheres of further than 2nd neighbors and is equal to $U(r)$ of the pure matrix metal.

Both potentials u_n and U satisfy the T.F. equation:

$$\nabla^2 u_n=\alpha u_n^{3/2} \qquad (7)$$

$$\nabla^2 U=\alpha U^{3/2} \qquad (8)$$

$U(r)$, the potential for pure matrix metal, was already obtained by Slater and Krutter[6] from the solution of equation (8) subject to the boundary conditions:

$$U\to Ze/r \quad \text{as} \quad r\to 0 \qquad (9a)$$

$$(\partial U/\partial r)=0 \quad \text{at} \quad r=r_c \qquad (9b)$$

In order to show the geometrical relations about neighboring atoms to an impurity i-atom, we use such projection for face-centered cubic crystal as is shown in Fig. 1(a). In this projection, open circles denote those atoms located on the plane of the paper and the solid circles are on a plane at the $(\pm\frac{1}{2}a)$ height from the plane of the paper. In this figure, we assume i to be an impurity atom, then

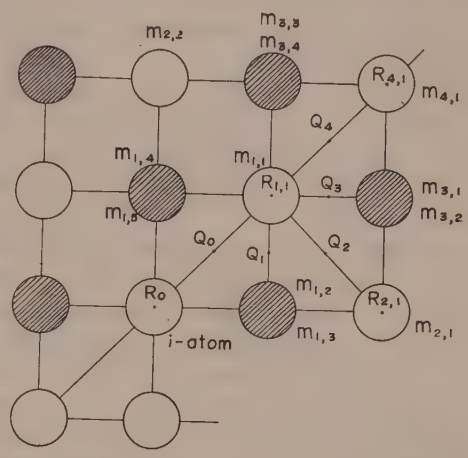

Fig. 1 (a) The projection to show the geometrical relations about neighboring atoms to an impurity i-atom in the face-centered cubic crystal.
Open circles ○ denote those atoms located on the plane of the paper and the solid circles ◍ are on a plane at the $(\pm\frac{1}{2}a)$ height from the plane of the paper.

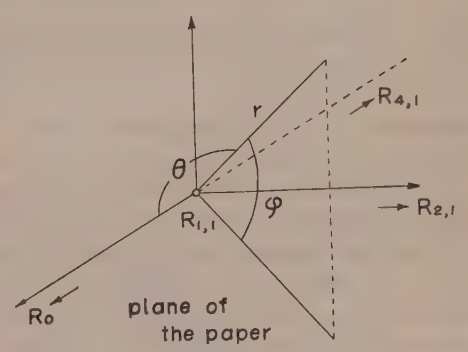

Fig. 1 (b)

the atoms $m_{1,j}$ (i.e., $m_{1,1}$, $m_{1,2}$, $m_{1,3}$, $m_{1,4}$, etc.) are the nearest neighbors to i-atom, $m_{2,k}$ (i.e., $m_{2,1}$, $m_{2,2}$, ete.) are the 2nd neighbors, and so on. Hereafter, the lower suffix n, expressing the matrix m-atom, is substituted by the double suffixes (k, j). First suffix k is the order of neighborhood and second one j is the number for m-atoms. And the atomic spheres corresponding to the atoms $m_{1,1}$, $m_{1,2}$,, $\cdots$ etc.

are denoted as $S_{1,1}$, $S_{1,2}$, $\cdots$ etc..

The potentials in the twelve atomic spheres corresponding to the nearest neighbors have the same form and are different only in the orientation in space. Therefore, we pay our attention to one representative m-atom $m_{1,1}$ among the twelve nearest neighbors $m_{1,j}$. Twelve nearest neighbors to this $m_{1,1}$ consist of one impurity atom, four $m_{1,j}$ atoms, two $m_{2,k}$ atoms, four $m_{3,h}$ atoms and one $m_{4,1}$, as is shown in Fig. 1(a).

The boundary conditions to be satisfied by our solutions are constructed between twelve pairs of atomic spheres, i.e., between the central sphere $S_{1,1}$ and each one of its twelve nearest neighbors.

According to the discussions in § 2, the boundary conditions concerning each of the above pairs can be imposed at one representative point Q_p, on the surface of the sphere $S_{1,1}$ and there are twelve these points. But, due to the symmetry properties of u_n in each sphere, there are only five independent points (five independent pairs) among these twelve pairs.

As is shown in Fig. 1(b), the polar coordinates r, θ, φ in $S_{1,1}$ are constructed in such a way that its origin is at $m_{1,1}$, i.e., the center of $S_{1,1}$, θ is taken from the line $\overrightarrow{R_{1,1}R_0}$ and φ is the angle from the plane of the paper.

Thus, our boundary conditions are formulated at five points $Q_0(r_c, \theta_0, \varphi_0)$, $Q_1(r_c, \theta_1, \varphi_1)$, $Q_2(r_c, \theta_2, \varphi_2)$, $Q_3(r_c, \theta_3, \varphi_3)$ and $Q_4(r_c, \theta_4, \varphi_4)$ corresponding to five independent pairs of spheres, i.e., $(S_{1,1}, S_0)$, $(S_{1,1}, S_{1,2})$, $(S_{1,1}, S_{2,1})$, $(S_{1,1}, S_{3,1})$ and $(S_{1,1}, S_{4,1})$ respectively.

These circumstances are also shown in Fig. 1(a). Since the line $\overline{R_{1,1}R_0}$ is two-fold symmetry axis, the term f_n, expressing the deviation from the spherical symmetry, can be expanded in spherical harmonics as follows:

$$\begin{aligned} f_n(r, \theta, \varphi) = a_0\chi_0(r) &+ a_1\chi_1(r)P_1(\cos\theta) \\ &+ a_2\chi_2(r)P_2(\cos\theta) + \cdots \\ &+ b_2\chi_2(r)P_2^2(\cos\theta)\cos 2\varphi \\ &+ b_3\chi_3(r)P_3^2(\cos\theta)\cos 2\varphi + \cdots \end{aligned} \tag{10}$$

In this expansion, the coefficients a_0, a_1, $\cdots$ and b_2, $\cdots$ are adjustable parameters which should be determined by the boundary conditions and it depends on the number of our boundary conditions that how many terms we can take into our consideration.

On these preparations, our boundary conditions can be formulated as follows:

(1) at Q_0: $\theta_0 = 0$

$$u_n(r_c, \theta_0, \varphi_0) = u_0(r_c) \tag{11}$$

$$(\partial u_n/\partial r)_{r_c} + (\partial u_0/\partial r)_{r_c} = 0 \tag{12}$$

(2) at Q_1: $\theta_1 = \dfrac{\pi}{3}$, $\varphi_1 = \dfrac{1}{2}\cos^{-1}\left(-\dfrac{1}{3}\right)$

As the potential within $S_{1,2}$ is the same one as in $S_{1,1}$, except the orientation, the continutiy condition for the potential itself is automatically satisfied. The condition for the derivatives is

$$(\partial u_n/\partial r) = 0 \tag{13}$$

(3) at Q_2: $\theta_2 = \dfrac{\pi}{2}$, $\varphi_2 = 0$

According to our assumptions, u_n in $S_{2,1}$ will deviate from $U(r)$ to some extent, and its form is not known in advance. In order to utilize the boundary condition at Q_2, we have to treat u_n in $S_{1,1}$ and in $S_{2,1}$ simultaneously and this would complicate the calculation considerably. Under these circumstances, it may be a reasonable approach to our problem to drop the boundary condition at Q_2 in the first approximation, and on finding u_n in $S_{1,1}$, to determine u_n in $S_{2,1}$ in the next stage. Further , the facts that there are only two points of Q_2 whereas there are four points of Q_1 and Q_3, and that 10 points of Q_0, Q_1, Q_3 and Q_4 are distributed rather uniformly over the surface of $S_{1,1}$ may be considered as suggesting that the neglect of the boundary condition at Q_2 is not so serious.

(4) at Q_3 and Q_4:

$$\theta_3 = \frac{2}{3}\pi, \quad \varphi_3 = \frac{1}{2}\cos^{-1}\left(-\frac{1}{3}\right); \quad \theta_4 = \pi$$

From the assumption (β) in this section, both potentials within $S_{3,1}$ and $S_{4,1}$ are taken as equal to U. Therefore, we can obtain the condition of the same form for these two cases, i.e.,

$$u_n(r_c, \theta_3, \varphi_3) = U(r_c) \tag{14}$$

$$(\partial u_n/\partial r)_{r_c} = 0 \tag{15}$$

$$u_n(r_c, \theta_4, \varphi_4) = U(r_c) \tag{16}$$

$$(\partial u_n/\partial r)_{r_c} = 0 \tag{17}$$

With these seven conditions from (11) to

(17), six adjustable parameters a_0, a_1, a_2, a_3, b_2 and b_3 in f_n can be determined, besides the remaining parameter c_1 in (6).

The equation which the term f_n should satisfy, is obtained as follows: We substitute the formula $u_n=U+f_n$ into (7) and, assuming f_n to be small in comparison with U, expand the equation in powers of f_n. Then we obtain the following differential equation:

$$\nabla^2 f_n=\frac{3}{2}\cdot\alpha\sqrt{U}\cdot f_n \tag{18}$$

by taking the equation (8) into account and neglecting the terms higher than the second order in f_n.

Then inserting the expression (10) as to f_n into (18), we find that the radial function $\chi_l(r)$ satisfies the following equation:

$$\frac{d^2\chi_l}{dr^2}+\frac{2}{r}\frac{d\chi_l}{dr}+\left(-\frac{l(l+1)}{r^2}-\frac{3}{2}\alpha\sqrt{U}\right)\chi_l=0 \tag{19}$$

If we put:

$$\chi_l(r)=r^{-1}R_l(r) \tag{20}$$

the equation (19) reduces to:

$$\frac{d^2R_l}{dr^2}=\left(\frac{l(l+1)}{r^2}+\frac{3}{2}\alpha\sqrt{U}\right)R_l \tag{21}$$

From (11), (12) and the condition (9b), the following relations between u_0 and u_n are obtained.

$$[a_0\chi_0+a_1\chi_1+a_2\chi_2+a_3\chi_3]_{r=r_c}=u_0(r_c,\ c_1)-U(r_c) \tag{22}$$

$$[a_0\chi_0'+a_1\chi_1'+a_2\chi_2'+a_3\chi_3']_{r=r_c}=-(\partial u_0/\partial r)_{r_c} \tag{23}$$

On the other hand, each of the five conditions (13) to (17) is written as a linear homogeneous relation for a_0, a_1, a_2, a_3, b_2 and b_3, so that by solving these simultaneous equations, we can express $a_1, \cdots$ and b_3 as definite multiples of a_0. Therefore, the ratio of left-hand sides of (22) and (23) is completely determined in terms of $\chi_l(r_c)$ and $\chi_l'(r_c)$. This ratio, which we denote by A_0, is to be equated to the ratio of their right-hand sides:

$$A_0=\frac{u_0(r_c,\ c_1)-U(r_c)}{-(\partial u_0/\partial r)_{r_c}} \tag{24}$$

And the parameter c_1 is determined by this implicit equation. With this value of c_1, the function u_0 is completely determined, and further the explicit value of a_0 can be determined from either (22) or (23).

§ 4. The Solutions of the Thomas-Fermi Equations

First, we have to find the solution $U(r)$ of T.F. equation for the pure metal. The method is essentially the same as that of the Slater and Krutter, and is briefly described as follows:

By the substitutions,

$$U(r)=\frac{Ze}{r}\cdot\phi \tag{25a}$$

$$r=\mu_m x \tag{25b}$$

(here, $\mu_n=0.8853a_h/Z^{1/3}$, a_h being Bohr radius), the Poisson equation is transformed into dimensionless form:

$$\frac{d^2\phi}{dx^2}=\frac{\phi^{3/2}}{\sqrt{x}} \tag{26}$$

with the boundary condition:

$$\phi=1 \quad \text{at} \quad x=0 \tag{27}$$

In the region where x is small, ϕ is expanded in powers of $x^{1/2}$ with an adjustable initial slope C:

$$\phi=1+Cx+\frac{4}{3}x^{3/2}+\frac{2}{5}Cx^{5/2}+\cdots \tag{28}$$

Then, the numerical integration is performed from the origin to large x for several different values of C. We determine the value of C corresponding to the correct solution in such a way that the boundary condition (9b) is satisfied, which is expressed in our notation as:

$$\phi'(x_c)=\frac{\phi(x_c)}{x_c} \tag{29}$$

at $x_c=r_c/\mu_m$.

Secondly, we construct the function $u_0(r_c,\ c_1)$ valid in S_0. By the substitution similar to (25a) and (25b), i.e.,

$$u_0=\frac{Z_l e}{r}\phi_0\,, \qquad r=\mu_l x$$

$$\mu_l=0.8853a_h/Z_l^{1/3} \tag{30}$$

we obtain the same equation:

$$\frac{d^2\phi_0}{dx^2}=\frac{\phi_0^{3/2}}{\sqrt{x}} \tag{31}$$

$$\phi_0=1+C_0x+\frac{4}{3}x^{3/2}+\cdots \tag{32}$$

we carry out the numerical integration for different values of C_0, for the interval x which corresponds to the interval $(0,\ r_c)$ of r. The

value of x which corresponds to r_c will be denoted by x_i, which is different for different choice of the i-atom.

The equation (21) is expressed in (x, ϕ) coordinates as follows:

$$\frac{d^2R_l(x)}{dx^2}=\left[\frac{l(l+1)}{x^2}+\frac{3}{2}\sqrt{\frac{\phi}{x}}\right]R_l(x) \qquad (33)$$

with the value of ϕ previously obtained above. $R_l(x)$ is obtained by performing the numerical integration of the differential equation (33) from the origin to large x starting with the initial condition $R_l(x)=x^{l+1}$. The amplitude of $R_l(x)$ may be taken arbitrary, because the product $a_lR_l(x)$ is independent of the change of normalization of $R_l(x)$.

§ 5. Calculations

In this paper, we take Cu as the matrix metal and Ga, Zn, Ni and Co as the impurity atoms. These impurities are chosen as examples for the cases of $\Delta Z=+2$, $+1$, -1 and -2 respectively. Hereafter, (ϕ_0, C_0) corresponding to the impurity atom Ga or Zn or Ni or Co and (ϕ, C) corresponding to the matrix pure metal Cu are denoted as (ϕ_{Ga}, C_{Ga}) or (ϕ_{Zn}, C_{Zn}) or $\cdots$ and (ϕ_{Cu}, C_{Cu}) respectively. The numerical integration of the dimensionless T.F. equation (26) and (31) are performed on the electronic computor "Fujic" of Fuji Photographic Film Co. Ltd.

The (x, ϕ) tables thus obtained may be useful for the investigations of metals or complex ions besides atoms or molecules, so the full tables, including those of ϕ which have not been used in this paper, will be published in separate paper.

From these tables, the initial slope C_{Cu} corresponding to the correct solution ϕ_{Cu} for the pure metal Cu is found to be -1.587855. And by using this ϕ_{Cu} for ϕ in (33), $R_l(x)$ is obtained by numerical integration with previously stated procedures. Further χ_l and χ_l' are calculated.

Thus, the adjustable parameters a_1, a_2, a_3, b_2 and b_3 are obtained as multiples of a_0 and a_0 itself is also calculated from (22) for each choice of the impurity.

These values for the coefficients are tabulated in Table I.

The value of A_0 calculated from $\chi_l(r_c)$ and $\chi_l'(r_c)$ is 0.48. The correct numerical values of C_0 as a quantity characterizing the solution

Table I.

(A) The values of the coefficients in f_n (expressed as the multiples of a_0).

a_1	$0.533a_0$	b_2	$-0.044a_0$
a_2	$0.048a_0$	b_3	$-0.003a_0$
a_3	$0.001a_0$		

(B) The values of a_0 for different choise of impurity.

Impurity atom	ΔZ	a_0*
Co	-2	$-0.000032e$
Ni	-1	$-0.000011e$
Zn	$+1$	$+0.000014e$
Ga	$+2$	$+0.000029e$

* The values of a_0 are the average of the two values corresponding to two values of C_0 which are tabulated in Table II.

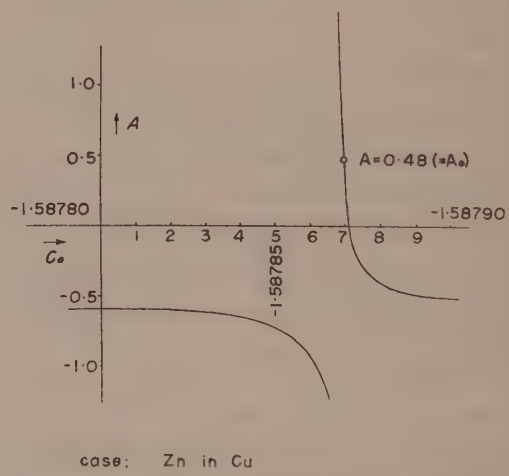

Fig. 2. The curve representing the relation between A and C_0.
The figure in the abscissa indicates the 5th place of decimals, i.e., for example, -1.58787 corresponds to figure 7.

ϕ_0 for each impurity i-atom is obtained from ϕ_0 with which the right-hand side value (to be denoted as A) of (24) is equal to A_0.

As to the numerical values of ϕ or ϕ_0 in the vicinity of x_c or x_i, there is about 1% difference between those two values of ϕ, which correspond to their C's having unit difference at their sixth place of decimals.

The curve representing the relation between A and C_0 are of the hyperbolic form and is shown in Fig. 2 for the case of Zn in Cu as an example.

Table II. The values of the initial slopes C_0 and $C_{0,p}$.

Impurity atom	ΔZ	C_0	$C_{0,p}$
Co	−2	between $\left\{\begin{matrix}-1.587821^{*}\\ 22\end{matrix}\right.$	between $\left\{\begin{matrix}-1.587827\\ 28\end{matrix}\right.$
Ni	−1	between $\left\{\begin{matrix}-1.587838\\ 39\end{matrix}\right.$	−1.587842
Zn	+1	between $\left\{\begin{matrix}-1.587869\\ 70\end{matrix}\right.$	−1.587867
Ga	+2	between $\left\{\begin{matrix}-1.587882\\ 83\end{matrix}\right.$	between $\left\{\begin{matrix}-1.587878\\ 79\end{matrix}\right.$

* The figure, for example as to the case of C_0 of Co,

$$\text{between}\left\{\begin{matrix}-1.587821\\ 22\end{matrix}\right.$$

shows the following affair;

$$-1.587821 > C_0 > -1.587822\,.$$

Similarlity is referred to other figures concerning other C_0 and $C_{0,p}$.

Certainly, the potential u_0 within S_0 for the i-atom which is introduced into the m-atom, should be different from that of pure i-metal (to be referred to u_0 (pure)). u_0 (pure) is obtained in the same way as for pure Cu. The values of C_0 corresponding to u_0 and that of u_0 (pure), denoted as $C_{0,p}$, are listed in Table II.

§ 6. The Screened Potential around an Impurity Atom

From our present model, the screened Coulomb potential is expressed as follows:

$$V(r) = -e(u_0 - U) - e^2\left[\frac{Z_i}{r}\phi_0\left(\frac{r}{\mu_i}\right) - \frac{Z}{r}\phi_{\mathrm{Cu}}\left(\frac{r}{\mu_m}\right)\right] \qquad (34)$$

where ϕ_0 for the four kinds of impurities (i.e., ϕ_{Ga}, ϕ_{Zn}, ϕ_{Ni} and ϕ_{Co}) and ϕ_{Cu} are obtained numerically.

Then it is found that the numerical values in the bracket of (34) are proportional to ΔZ and $V(r)$ can be expressed as:

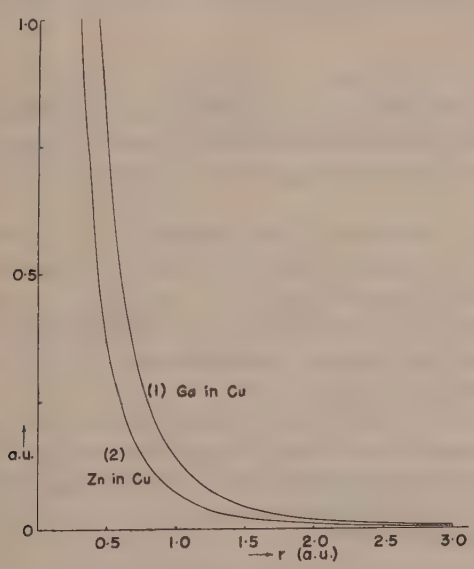

Fig. 3. The curves of the values in the bracket of (34),

i.e., $\dfrac{Z_i}{r}\phi_0\left(\dfrac{r}{\mu_0}\right) - \dfrac{Z}{r}\phi_{Cu}\left(\dfrac{r}{\mu_m}\right)$

Curve 1: impurity Ga ($\phi_0 \equiv \phi_{Ga}$).

Curve 2: impurity Zn ($\phi_0 \equiv \phi_{Zn}$).

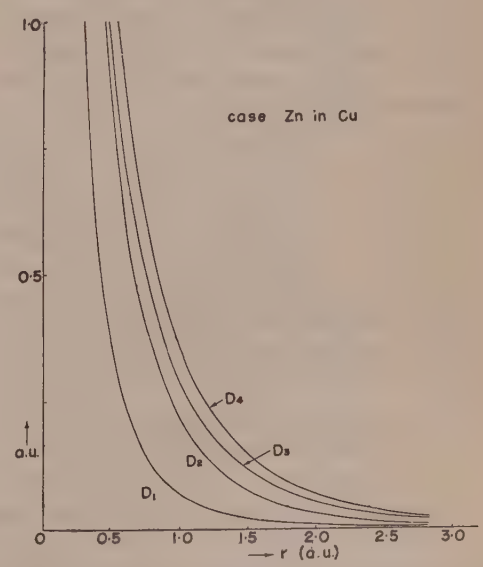

Fig. 4. The behavior of the potential due to the methods of treatment.

Curve D_1: present result.

Curves D_2, D_3 and D_4: results in the previous work and stated in the sentence.

$$V(r)=-\frac{e^2}{r}\cdot\Delta Z\cdot F(r) \tag{35}$$

within the limit of 1% error.

The curves for the cases of Ga in Cu and Zn in Cu are shown in Fig. 3.

To compare $V(r)$ in this paper with those obtained in the previous work, four curves are plotted in Fig. 4. The case of Zn in Cu is taken as an example.

In this figure, the curve D_1 corresponds to that of (34), D_2, D_3 are those obtained in our previous work (D_2: with exchange[7], D_3: without exchange[8]) and D_4 is the usual one obtained analytically from the linearized T.F. equation i.e., $V(r)=-(e^2/r)\cdot\Delta Z\cdot\exp(-qr)$[9].

As stated in the early part of § 3, the degree of the screening of excess charge $(\Delta Z)e$ will be incomplete within S_0 itself.

Table III. The values of ρ.

(A) The variations of ρ due to the method of treatments (the case is Zn in Cu, i.e., $\Delta Z=+1$).

Case	ρ
D_1 (present one)	$0.03e$
D_2 (previous ones)	$0.12e$
D_3 (previous ones)	$0.21e$
D_4 (previous ones)	$0.28e$

(B) The variations of ρ due to the choise of impurities according to the present model.

Impurity	ΔZ	ρ
Co	-2	$-0.06e$
Ni	-1	$-0.03e$
Zn	$+1$	$+0.03e$
Ga	$+2$	$+0.06e$

The remaining charge ρ which can not be screened completely within the sphere S_0 is calculated from the following formula:

$$\rho=\int\rho'(r)dV=-\frac{1}{4\pi}\int\frac{\partial(u_0-U)}{\partial r}dS$$
$$=-r_c^2\left(\frac{\partial(u_0-U)}{\partial r}\right)_{r_c}\cdot e \tag{36}$$

We take the case of Zn in Cu as an example and the calculated values of ρ for the four cases from D_1 to D_4 just stated above, are tabulated in Table III.

And in this Table, also those ρ's for the cases of $\Delta Z=\pm2$ and ±1 in this paper are listed respectively.

§ 7. Results and Discussions

The work reported in this paper, is done for the purpose of removing the deficits in the previous model that we could not take the lattice distortion of the matrix metal into account and so on, as stated in the introduction, and the following results are obtained.

(i) The convergency of the values of coefficients in f_n, is comparatively fast and the deviation from spherical symmetry is small even at Q_0, where f_n may be largest.

The magnitude of $f_n(r_c, \theta_0, \varphi_0)$ is estimated about 1% or less of $U(r_c)$. And since the corresponding value at Q_2 is very small, it is not serious that the boundary condition at Q_2 has been neglected.

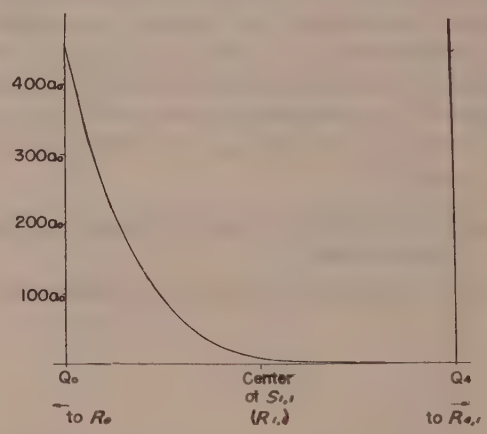

Fig. 5. The variations of f_n in the atomic sphere $S_{1,1}$ along the line $\overline{R_0R_{4,1}}$.

The behavior of the variation of f_n within $S_{1,1}$ is shown in Fig. 5 as the multiples of a_0. f_n is calculated along the line $\overline{R_0R_{4,1}}$. It is found from this figure that the deviation f_n from the spherical symmetric one U, almost vanishes at the center of $S_{1,1}$. This fact may be regarded as a justification of our assumption that the potential u_n within the sphere of higher than the 2nd neighbors to an impurity atom equals to $U(r)$ of pure metal.

(ii) As is indicated in Table II, the values of $C_{0,p}$ corresponding to the pure i-metal subject to the neutrality condition on its atomic sphere, are, to some extent, different from C_0 for i-atom when it is present as an impurity. $|C_0|$ is larger than $|C_{0,p}|$ for the case

of Ga or Zn and the opposite result is obtained for Ni or Co. This is conformity with the situation that Ga or Zn atom (i.e., $\Delta Z>0$) is positively ionized to some extent when it is introduced into Cu and Ni or Co atom ($\Delta Z<0$) exists as a negative ion in Cu.

(iii) The two curves in Fig. 3 for the cases of Ga ($\Delta Z=+2$) and Zn ($\Delta Z=+1$) in Cu, coincide almost exactly with those of Co ($\Delta Z=-2$) and Ni ($\Delta Z=-1$) with each other, except their signs and the perturbed potential $V(r)$ can be expressed in the form (35). This result shows that the change of the potential due to the introduction of an impurity atom is very nearly proportional to $\Delta Z=Z_i-Z$, at least for $-2\leqq\Delta Z\leqq+2$. In a certain sense, this result is what we may expect from the beginning, provided that the change of the potential is small compared with the potential itself and may be treated as a small perturbation to the potential of the pure metal. In fact, our potential $u(x, y, z)$ is determined by the equation (1) valid throughout the crystal under the boundary conditions (3a) and (3b) near the lattice points as stated in § 2.

On the other hand, the potential U of pure matrix metal satisfies the following condition.

$$\left.\begin{array}{ll}\nabla^2 U=\alpha U^{3/2} & \text{throughout the crystal}\\ U\sim Ze/|\boldsymbol{r}-\boldsymbol{R}|+\cdots & \text{near the lattice point } \boldsymbol{R}\end{array}\right\} \tag{37}$$

Now, if the change due to the impurity is small, we should be allowed to treat f defined by $u=U+f$ as a small quantity compared with U. Thus the differential equation satisfied by f is found to be

$$\nabla^2 f=\frac{3}{2}\cdot\alpha\sqrt{U}\cdot f \tag{38}$$

and the conditions at the lattice points are

$$f\sim\begin{cases}(\Delta Z)e/\boldsymbol{r}+\cdots & \text{at } \boldsymbol{r}\sim R_0\\ \text{finite} & \text{at all other } \boldsymbol{R}_n\end{cases} \tag{39}$$

Taking into account that the differential equation (38) is linear, we can see quite easily that if $f^{(1)}$ is the solution of (38) with the conditions (39) for $\Delta Z=1$, $f=(\Delta Z)f^{(1)}$ satisfies all the conditions for f in the general case. Hence the solution has the form:

$$f=(\Delta Z)\cdot f^{(1)} \tag{40}$$

where $f^{(1)}$ does not depend on ΔZ.

The above argument does not make use of the cellular method. If we use the cellular method, however, $u-U$ in each cell is proportional to ΔZ:

$$\left.\begin{array}{ll}u_0-U=(\Delta Z)\cdot F_1(r) & \text{in } S_0\\ u_n-U=(\Delta Z)\cdot F_2(r) & \text{in } S_n\end{array}\right\} \tag{41}$$

In our calculation, we employed the linearized equation (38) only in the atomic sphere of m-atom and we solved the equation numerically. The results shows, however, that we might make use of the linearized equation (38), even in the impurity cell itself.

(iv) As to the case of $\Delta Z>0$, the potential falls off more rapidly than those obtained in the previous work advancing from D_4 to D_1 as is shown in Fig. 4. It indicates that the screening radius becomes smaller and smaller in accordance with the case advancing from D_4 to D_1. They are also found from Table III concerning the remainning charge which is not screened off.

As was found from our previous investigations, these results seem to diminish the disagreement between the calculated and experimental values of residual electric resistance of binary alloys.

The perturbed potential $-(\Delta Z/r)e^2\cdot\exp(-qr)$ which was obtained by Mott from linearized T.F. equation, is also proportional to ΔZ, but, our present one (33) falls off more rapidly as is shown in Fig. 4. March et al.[10] have found that the potential obtained from numerical integration is represented by the asymptotic form $-(\Delta Z/r)e^2\cdot A\cdot\exp(-qr)$ at some distance from the origin for the case of $\Delta Z>0$. And Alfred and March[11] also obtained the values of A for the cases of negative ΔZ. Their results were that the obtained values of A were larger than those corresponding to positive ΔZ (same $|\Delta Z|$), show that the screening of the excess charge $(\Delta Z)e$ is weak for the negative ΔZ in comparison with that for the cases of positive ΔZ.

As stated before, our present calculations show that the obtained potential (35) for the cases of $\Delta Z=-2$ or -1 coincides almost exactly with that of $\Delta Z=+2$ or $+1$ respectively.

But, due to the experimental results of the residual electric resistances which are related directly to the dimensions of the potentials, of binary alloys, the resistances for the cases of $\Delta Z<0$ are comparatively larger than the corresponding values for $\Delta Z>0$.

Therefore, there remains some ambiguity in our results for the cases of $\Delta Z < 0$, and we hope to solve this point in our further investigations by using our improved model stated in the following sentence.

(v) As stated in the latter part of § 1, our present model is not completely satisfactory, since T.F. method cannot account for the shell structure of electrons in atoms.

We are now taking into account, in our model of this problem, the distribution of core electrons by the use of Hartree or Hartree-Fock fields and treating the electrons outside these cores by T.F. method. We are now proceeding this way and we hope to report the results in a near future.

§ 8. Acknowledgements

The author wishes to express his sincere thanks to Prof. Masao Kotani of University of Tokyo for his continued guidance and encouragements throughout this work and to Professors N. H. March, F. J. Blatt and K. Umeda, and Dr. S. Kobayashi for their kind interests and discussions. The author's appreciations are to Director S. Fujisawa and Dr. B. Okazaki of Fuji Photographic Film Co. Ltd. at Odawara for their kind permissions to use their electronic computor "Fujic" and especially to Mr. S. Tatsuoka who kindly operated the "Fujic" to make the tables of the solutions of T.F. equation. He further appreciates the valuable and kind assistance of Mrs. H. Komuro in the numerical work and the analysis of Fujic's data.

He is also indebted to the Ministry of Education and the members of Kotani Laboratory of University of Tokyo for their financial aids and his thanks are also due to Professors M. Suzuki and S. Matsumoto of Hiroshima University for their kind interests.

References

1) H. Fujiwara: a) J. Phys. Soc. Japan **10** (1955) 339.
b) ibid. **11** (1956) 376.
2) N. F. Mott: Proc. Camb. Phil. Soc. **32** (1936) 281.
N. F. Mott and H. Jones: 1936 Theory of Properties of Metals and Alloys, p. 293.
D. Lazarus: Phys. Rev. **93** (1954) 973.
J. Friedel: Advances in Physics **3** (1954) 446.
F. J. Blatt: Phys. Rev. **99** (1955) 600, 1708.
L. C. R. Alfred aud N. H. March: Phil. Mag. **46** (1955) 759; Phys. Rev. **103** (1956) 877.
N. H. March: Advances in Physics **6** (1957) 1.
3) J. C. Slater and H. M. Krutter: Phys. Rev. **47** (1935) 559.
4) D. G. Bell, D. M. Hum, L. Pincherle, D. W. Sciam and P. M. Woodward: Proc. Roy. Soc. **A217** (1953) 71.
E. G. Bell, R. Hensman, D. P. Jenkins and L. Pincherle: Proc. Phys. Soc. **A67** (1954) 562.
5) N. H. March: "Symposium on Band Structure" Proceedings of a Symposium held at R. R. E. Malvern on September, 1954.
6) J. C. Slater and H. M. Krutter: see 3).
7) see 1) b.
8) see 1) a.
9) N. F. Mott: loc. cit.
10) N. H. March: Phil. Mag., loc. cit.
H. Fujiwara: loc. cit.
11) L. C. R. Alfred and N. H. March: Phys. Rev., loc. cit.

JOURNAL OF THE PHYSICAL SOCIETY OF JAPAN Vol. 13, No. 3, MARCH, 1958

Calculation of the Energy Band Structure of the β-SiC Crystal by the Orthogonalized Plane Wave Method

By Syoiti KOBAYASI

Department of Physics, Faculty of Science, Hiroshima University Hiroshima, Japan

(Received December 7, 1957)

The energy band structure of the β- (zincblende-type) SiC crystal is worked by the orthogonalized plane wave (OPW) method. Since this crystal will be the typical one of the IV–IV compounds, the results of calculation for its electronic structure will be useful for systematic understanding of the transitions of the electron-behavior from the group-IV valence-crystals to the III–V compounds etc.. Our results show that the conduction band-minima occur at X-point or its immediate neighbor, while the valence band-maximum perhaps at Γ-point. Hence the indirect interband-transitions in the long wave limit will be expected to occur between these two states with the energy difference of 2.2 ev, and the direct interband-transitions at X-point will take place at a photon energy of 6.3 ev. Further the approximate charge-distribution in the crystal is worked by making use of the obtained Γ-valence eigenfunctions, which result seems to show that the electrons in its $\vec{k}=0$ levels of the β-SiC will be approximately a covalent-like distribution as far as Γ-eigenfunctions do concern. Finally, an idea is proposed to improve the slow-convergence of the OPW method for conduction bands of insulators. Its practical application is now in progress for the β-SiC.

§ 1. Introduction

Recently, many efforts have been made to calculate the detailed energy-band structures for the diamond-type group-IV valence-crystals (diamond, silicon, and germanium)[1,2,3]. Following these investigations, the speculation of rough features of the energy band structure in zincblende-type crystals has been attempted by Herman[4] on the basis of his own treatment of diamond and germanium[1], and recently the elaborate programs for InSb[5], ZnS[6] and others[6] have already been started by some workers.

There would be two appreciable differences, however, between the general nature of the energy band structure for Ge-group and InSb-group, for the following reasons. In the first place, the space group of the latter[7] is referred to as the point space group T_d^2, while that of the former, O_h^7, is not a point space group. Secondly, for binding property, the latter may be supposed to be of partly ionic and partly covalent character, while the former will naturally be pure homopolar.

Between these two groups, there seems to lie IV-IV compounds, in which the typical one will be the β- (zincblende-type) SiC crystal. The β-SiC has a similar symmetry property to that of InSb-group, while the former crystal seems to have close resemblance to the Ge-group rather than the InSb-group, for the reason that the constituent atoms belong to the group-IV and have the similar electron configuration.

Thus, a knowledge of the electronic structure of the IV-IV compounds will be useful for the systematic understanding of the transitions of the behavior of electrons from the monatomic crystals of diamond-type to the zincblende-type compounds.

In a preliminary investigation[8], we have already computed the rather rough picture of the band structure in the β-SiC by the tight-binding method. The main results were as follows. The minimum separation between the valence and the conduction bands occurred at $\vec{k}=0$, and was about 6 ev. The valence bands were divided into two branches with the minimum separation of 10 ev, at the Brillouin zone-edge along [1, 0, 0], and hence in the preceding paper we conjectured that this fact would be the characteristic difference between the valence band-shape of the zincblende-type compounds and that of diamond-

type monatomic crystals, the valence bands of the latter giving no separation[1,2,3].

Of course, the mentioned results of the tight-binding computation were not sufficient quantitatively, especially in the conduction bands which became very flat compared with the valence bands, probably because of the too much simplified assumptions in which no excited Bloch wave function was included and all energy-integrals were neglected except for those between the neighboring two kinds of atoms of the crystal.

Next we have attempted to go a step further by making use of the orthogonalized plane wave (OPW) method[9]. As well known, the OPW method has already been applied successfully to the several metals[10] and to the nonmetallic diamond-type valence crystals mentioned above[1,2]. This is the reason why the OPW method was adopted in our present computation.

According to the present results of the β-SiC given in Sec. 2, the conduction band-minima occur at X-point ($\vec{k}=(2\pi/a)$ [1, 0, 0]) or its immediate neighbor; a is the edge length of the cube which contains four unit cells, and the valence band-maximum perhaps at Γ-point ($\vec{k}=0$). Hence the indirect inter-band transitions in the long wave limit will be expected to appear near the band edge, its energy difference being 2.2 ev corresponding to the transition from the valence Γ_{15}-state to the conduction X_3- (or its neighboring-) state. Besides, the direct transitions connected with the energy difference of 6.3 ev may be anticipated to occur at the X-point. Regarding these aspects of the absorption spectra of the β-SiC, Herman[4,6] and Choyke and Patrick[11] have so far given some similar speculations.

Further, as shown in Sec. 3, we have estimated the charge distribution corresponding to $\vec{k}=0$ levels of the valence bands by making use of the four computed Γ-eigenfunctions of the valence bands. The results show that the electrons in the $\vec{k}=0$ levels of the β-SiC is approximately of covalent-like character.

It is well-known that in nature there are the two distinct crystalline-species of silicon carbide; i.e., the cubic one named as a β-type with which we now concern, and the hexagonal varieties, grouped as an α-type which is so called carborundum. Many experimental investigations of the actual SiC crystals have been made so far, regarding the electronic conductivity[12,13], the Hall effect[12], the injected light emission[14], the radiation damage[15], and the ultraviolet absorption of light near the band-edge[11,16]. But every specimen used for these experiments was the "α" one, probably because of the reason that rather large size of the α-type single crystal could be synthesized far more easily than that of the β-type one[17]. In view of the above situations, the experimental studies on the β-type specimen in place of the ordinary α ones, are highly required in order to compare with our results.

Finally, concerning one of the computational difficulties; i.e., of the slow-convergence problem in the OPW method when applied to non-metals, a revised procedure will be proposed in Sec. 4 which may be useful for computing the conduction bands of such valence crystals and insulators.

§ 2. Potential Construction and the Obtained Energy Band Structure

The primitive translation vectors in the reciprocal lattice (Fig. 1 (i)) are given by

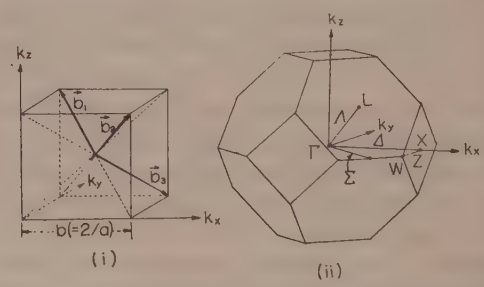

Fig. 1. Dimensions of the β (zincblende-type) SiC crystal. (i) The primitive translation in reciprocal lattice. $a=4.348$Å$=8.217a_H$ (a_H=Bohr radius). (ii) The first Brillouin zone.

$$\left.\begin{aligned}&\vec{b}_1=(1/a)[-1,\ 1,\ 1],\quad \vec{b}_2=(1/a)[1,\ -1,\ 1],\\ &\text{and}\qquad \vec{b}_3=(1/a)[1,\ 1,\ -1],\end{aligned}\right\}\qquad(1)$$

where a denotes the edge length of the cube which contains four unit cells, being $a=4.348$Å $=8.217a_H$[18] (a_H=Bohr radius). From (1) $\vec{K}$-vectors are defined as

$$\vec{K}_m=2\pi\sum_{i=1}^{3}m_i b_i\,. \qquad (2)$$

The first Brillouin zone can be taken as a truncated octahedron shown in Fig. 1 (ii) toge-

ther with the symmetry points and lines.

The crystal potential $U(\vec{r})$ can be expanded, by making use of (2), as follows:

$$U(\vec{r})=\sum_m U[\vec{K}_m]\exp(-i\vec{K}_m\cdot\vec{r})\,. \qquad (3)$$

The appropriateness of the assumed crystal potential can effect on the final result decisively. According to Howarth's results[19], even the relative order of the electronic levels at a symmetry point depends often upon the detailed behavior of the potential form. However, there seems to be no convincing criterion for setting up a suitable crystal potential except for the comparison of the final results with the experimental values, of which, at present, we have little knowledge for the β-SiC crystal as mentioned in Sec. 1, in spite of the abundant informations for the α-type ones.

In view of such unsettled situations, the crystal potential was constructed in the following conventional form

$$U(\vec{r})=\sum_\nu^{(Si)} V^{Si}(\vec{r}-\vec{R}_\nu)+\sum_\mu^{(C)} V^C(\vec{r}-\vec{R}_\mu), \qquad (4)$$

where $U(\vec{r})$ is determined through the assumption that a sort of cutting-off of the tail-part in each constituent atom-potential $V(\vec{r})$ is introduced in the following way. In (4) ν and μ refer to the lattice-sites in the entire crystal, and

$$\left.\begin{aligned} &V^{Si}(\vec{r})=(e^2/r)\cdot Z_p{}^{Si}(r)\\ \text{and}\quad &V^C(\vec{r})=(e^2/r)\cdot Z_p{}^C(r)\end{aligned}\right\} \qquad (5)$$

are the contribution to $U(\vec{r})$ from the individual atoms which have spherically symmetric charge distributions corresponding to the valence state ^5S of each constituent isolated-atom. In (5), $Z_p(r)$ includes the contributions from the nuclei, from the Coulomb interaction between the electrons on the same atoms, and from the exchange interaction which is represented by Slater's average exchange potentials due to the free electron approximation[20], where only the contribution to the exchange potential from the intra-atomic charge-overlap is included. The radial eigenfunctions of the valence electrons around C and Si atoms are taken over from the Hartree[21] and the Hartree-Fock[22] data, respectively.

Now the evaluation of numerical values of the expansion coefficients of (3); i.e.,

$$U[\vec{K}_m]=\Omega^{-1}\int_\Omega U(\vec{r})\exp(i\vec{K}_m\cdot\vec{r})d\tau_0 \qquad (6)$$

is required, where the integrations are to be taken over the unit cell with volume Ω. In the case of the β-SiC, (6) is given by

$$\begin{aligned} U[\vec{K}]=&(4\pi e^2/\Omega K)\\ &\times\Big\{\exp(i\vec{K}\cdot\vec{R}_\nu)\int_0^{r_{Si}} Z_p{}^{Si}(r)\sin(Kr)dr\\ &+\exp(i\vec{K}\cdot\vec{R}_\mu)\int_0^{r_C} Z_p{}^C(r)\sin(Kr)dr\Big\}, \end{aligned} \qquad (7)$$

and

$$\begin{aligned} U[0]=&(4\pi e^2/\Omega)\\ &\times\Big\{\int_0^{r_{Si}} Z_p{}^{Si}(r)rdr+\int_0^{r_C} Z_p{}^C(r)rdr\Big\}, \end{aligned} \qquad (8)$$

where r_{Si} and r_C are defined by the simultaneous equations:

$$(4\pi/3)r_{Si}{}^3+(4\pi/3)r_C{}^3=\Omega\,,$$
$$r_{Si}/r_C=\langle r_{Si}\rangle/\langle r_C\rangle\,.$$

Here

$$\langle r_{Si}\rangle=\frac{1}{4}\int_0^\infty r\{[P_{3s}{}^{Si}]^2+3[P_{3p}{}^{Si}]^2\}dr$$

and

$$\langle r_C\rangle=\frac{1}{4}\int_0^\infty r\{[P_{2s}{}^C]^2+3[P_{2p}{}^C]^2\}dr$$

are the average radii of both atoms, whose values are, by simple numerical integration, given by

$$\langle r_{Si}\rangle=2.06a_H \text{ and } \langle r_C\rangle=1.81a_H\,.$$

Then it follows,

$$r_{Si}=2.71a_H \text{ and } r_C=2.37a_H\,.$$

In (7) and (8), the integrations extend from 0 to r_{Si} around the Si-nucleus and 0 to r_C around the C-nucleus, respectively, according to our cut-off procedure mentioned before. The reason for such procedure is the following. In Slater's average free electron approximation of exchange potential adopted here[20], its contribution to the crystal potential is relatively appreciable in the tail-part of the assumed atomic orbitals of the valence electrons. On the other hand, as mentioned above, the assumed atomic orbitals adopted in our case are the solutions[21] of Hartree (not Hartree-Fock) equation in the valence state of the isolated carbon atom, and those[22] of Hartree-Fock equation of the isolated Si^{+3} ion (not of

Si-atom). Hence, concerning the tail-parts of both the atomic-functions, there are considerable unbalances, as anticipated in advance. For this reason, we used a sort of the cut-off procedure of the tail-parts of $P(r)$'s, in order to avoid the unfavorable part of the mentioned unbalances.

In this connection, Woodruff[2] has recently proposed a procedure regarding the construction of potential and the corresponding determination of ion-cores, and has obtained the Γ-solutions with very rapid convergence for silicon crystal. Further, Herman[6] has proposed to form the crystal potential by try-and-error method through comparing with the X-ray term values. At any rate, the mentioned difficulty in the construction of crystal potential remains unsettled yet, in spite of its decisive importance in the calculation of the energy band structure.

Thus the energy band structure of the β-SiC has been calculated. The wave functions associated with the irreducible representations of the wave-vector group of a given symmetry point in $\vec{k}$-space may be easily obtained in the same manner as in the case of symmetry-molecules[23] by making use of Parmenter's group-theoretical consideration[7].

Thus we have computed the energy values on the following several symmetry-points and lines; Γ, [0, 0, 0]; X, [1, 0, 0] (in the unit of $2\pi/a$, and so forth); W, [1, 0, 1/2]; L, [1/2, 1/2, 1/2]; a point along the Σ-axis, [1/2, 1/2, 0]; among which the energy values of the Σ-point have been less precise than those at the other points. The reason for this result is that Σ has rather low symmetry compared with the others, hence we are forced to include only small number of the OPW-terms for this point as far as the desk-calculator is

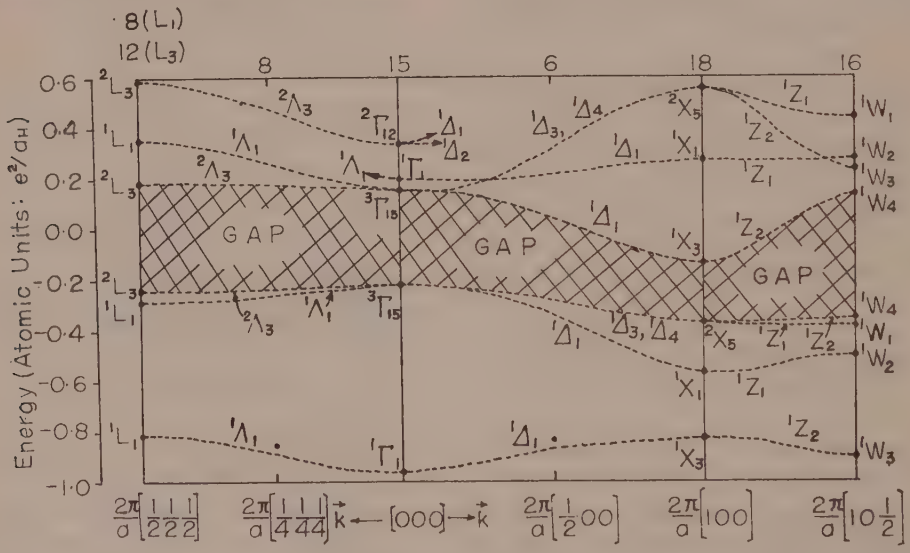

Fig. 2. Energy band structure of the β-SiC crystal obtained in the present OPW-calculation. The numbers at the upperside of the figure represent those of the OPW-terms involved.

at our disposal. (Further, the lowest valence-levels for the mid-points along the Δ- and Λ-axes; i.e., for [1/2, 0, 0] and [1/4, 1/4, 1/4], have been calculated. These values are also written in Fig. 2, though they seem to be not in good convergence owing to the same reason as in Σ.)

Hence, we could not fully investigate the convergence of the eigenvalues, especially for the lower-symmetry points and lines. The obtained energy contours are shown in Fig. 2, together with the convergence behaviors for X and Σ in Figs. 3 and 4, respectively. The numbers at the upperside of the Fig. 2 represent those of the OPW-terms involved. The spin-orbit coupling effect is neglected in view of the present degree of approximation. The terminology of BSW[24] is used to denote the group representation and the points and lines of symmetry.

As mentioned in Sec. 1, the present results seem to show that in the β-SiC the conduc-

tion band minima occur at the X-point or in its vicinity, and the valence band maximum perhaps at the zone-center (Γ-point), so that the indirect interband transitions in the long wave limit will be expected from the valence band-top (Γ_{15}) to the conduction band bottom (X_3) with a photon energy of 2.2 ev, while the direct transitions connected with the smallest energy 6.3 ev will occur from X_5 of the valence band to X_3 of the conduction band, within the accuracy of the present computation. These results seem approximately to agree with Herman's[4,6] and Choyke and Patrick's[11] speculations.

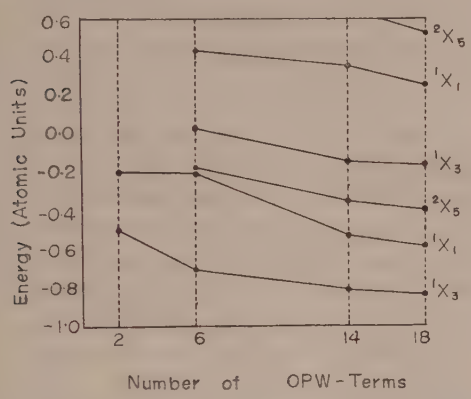

Fig. 3. Convergence-behaviors of the X-eigenvalues, showing comparatively good convergence.

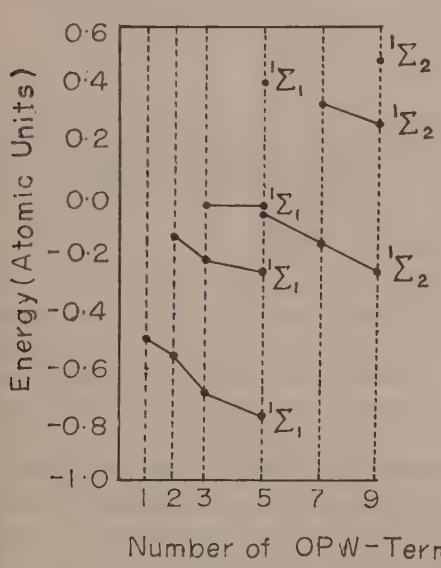

Fig. 4. Convergence-behaviors of the Σ-eigenvalues. (The example of insufficient convergence.)

§ 3. Additional Numerical Computation

Since the convergence of the eigenvalues for each symmetry point in $\vec{k}$-space may be supposed to be not sufficient enough as seen from Figs. 3 and 4, then we have further attempted to solve the secular equation for Γ involving 27 OPW-terms. The convergence-behaviors are shown in Fig. 5. (But, in Fig. 2, we have chosen the Γ-eigenvalues corresponding to 15 terms rather than to 27 terms, in order to keep balance in the whole contour of the energy bands.) The noticeable facts in Fig. 5 will be as follows. First, the convergence in the lowest valence band Γ_1 seems

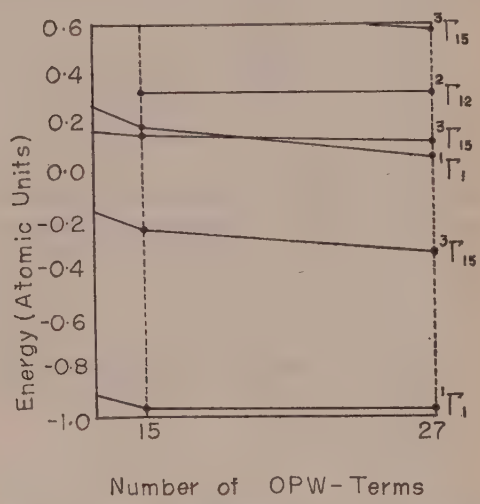

Fig. 5. Further examination of convergence-behaviors of Γ-eigenvalues when 27 OPW-terms are involved. The convergence in the lowest valence band (Γ_1) seems to be extremely sufficient. The two lowest conduction bands, Γ_{15} (triplet) and Γ_1 (singlet) are reversed with each other in this case.

to be extremely sufficient, and secondly, the two lowest conduction bands Γ_{15} (triplet) and Γ_1 (singlet) are reversed with each other and Γ_1 is turned down to be the lowest as shown in Fig. 5. In diamond[1] and silicon[2] the lowest conduction bands in Γ are both the triplet Γ_{15}, while in germanium[1] it is the singlet Γ_2' (it corresponds to Γ_1 of zincblende-type crystal[7]). Since the β-SiC is a compound of silicon and carbon, it would be natural to suppose that the lowest conduction bands in Γ would be triplet. But carrying through the computation beyond the present one will be prohibitibly laborious without automatic machines.

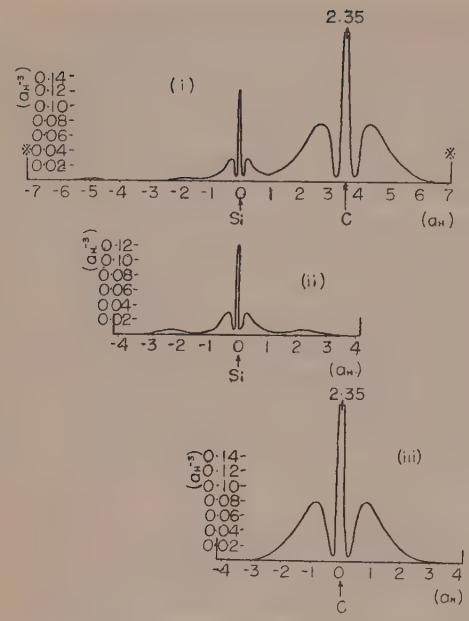

Fig. 6. Charge density according to the lowest valence-eigenfunction $\psi^{Val}(\Gamma_1)$ normalized in the unit cell. (i) The component along the line connecting Si- and C-sites ([1,1,1] direction). (ii) The component along [1,0,0] direction through Si-sites alone. (iii) The same as (ii) but through C-sites alone. In (ii) and (iii) of this figure the charge distributions along [0,1,0] or [0,0,1] directions are quite same as that for [1,0,0].

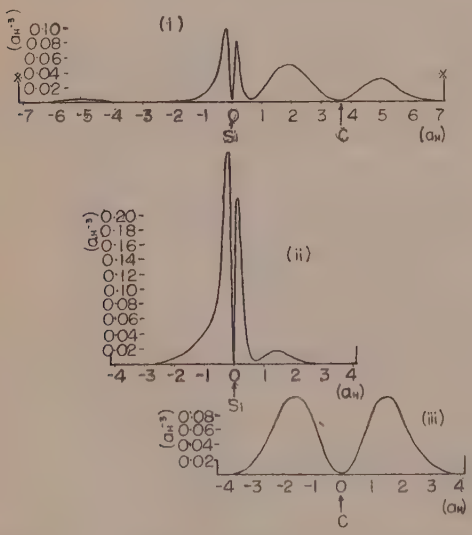

Fig. 7. The similar figure as in Fig. 6, for $|\psi_x^{Val}(\Gamma_{15})|^2$. (i), (ii), and (iii) of this figure correspond to (i), (ii), and (iii) of Fig. 6, respectively. The components along both [0,1,0] and [0,0,1] directions through Si- or C-site vanish. The situations are quite similar for $|\psi_y^{Val}(\Gamma_{15})|^2$ and $|\psi_z^{Val}(\Gamma_{15})|^2$.

Next, in order to obtain some knowledge of the behaviors of crystal electrons, for illustration, the charge density of Γ-electrons has been worked by making use of the obtained valence-electron wave functions. These wave functions are $\psi^{Val}(\Gamma_1)$, $\psi_x^{Val}(\Gamma_{15})$, $\psi_y^{Val}(\Gamma_{15})$, and $\psi_z^{Val}(\Gamma_{15})$, normalized in the unit cell. The behaviors of $|\psi^{Val}(\Gamma_1)|^2$ in the unit cell is drawn in Fig. 6 (i), (ii) and (iii). And $|\psi_x^{Val}(\Gamma_{15})|^2$ are shown in Fig. 7 (i), (ii) and (iii), along the similar directions as in Fig. 6. The apparent difference between $|\psi^{Val}(\Gamma_1)|^2$ and $|\psi_x^{Val}(\Gamma_{15})|^2$ is that the former is s-like, while the latter is p-like. The situations are quite similar for the cases of $|\psi_y^{Val}(\Gamma_{15})|^2$ and $|\psi_z^{Val}(\Gamma_{15})|^2$. Thus we have

$$|\psi_\Gamma^{Val}|^2=|\psi^{Val}(\Gamma_1)|^2+|\psi_x^{Val}(\Gamma_{15})|^2 +|\psi_y^{Val}(\Gamma_{15})|^2+|\psi_z^{Val}(\Gamma_{15})|^2, \qquad (9)$$

which represents the charge distribution of Γ electrons. The [1, 1, 1] component of (9) is drawn in Fig. 8, which seems to show that the charge density in the space region between the Si- and the C-site as well as in

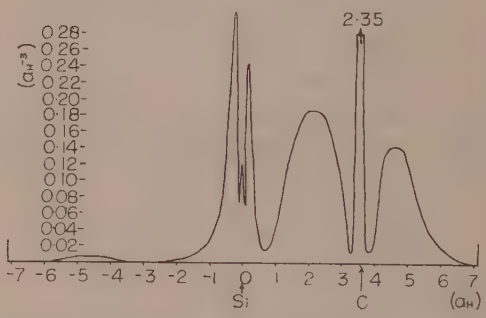

Fig. 8. The component along [1,1,1] direction of the charge density according to the total distribution belonging to $|\psi^{Val}(\Gamma_1)|^2+|\psi_x^{Val}(\Gamma_{15})|^2+|\psi_y^{Val}(\Gamma_{15})|^2+\psi_z^{Val}(\Gamma_{15})|^2$.

the vicinity of both the atoms will be considerably large compared with the other parts, representing the covalent-like distribution. However, if (9) or Fig. 8 is looked over from the standpoint of ionicity, the rather rough estimation shows that the charges corresponding to the Γ-valence electrons around the Si- and the C-position seem to be approximately $-3e$ and $-5e$, respectively, in spite of the present starting potential corresponding to $-4e$ and $-4e$, respectively. Then, in the ionic-viewpoint, β-SiC may be considered to be described approximately by $Si^{+x}C^{-x}$,

where $x \sim 1$. This result seems to agree with the semi-empirical values of electronegativity[25]: 1.8 and 2.5 for Si and C, respectively. But, after all, it will be rather right to imagine that the charge distribution in Fig. 8 is covalent-like, for the reason of the large charge-density in the mid-parts between the nearest Si and C.

At any rate, in order to obtain the binding mechanism of the β-SiC crystal, it is essentially required to work the total charge distribution of valence electrons which is given by $\sum_{\vec{k}} |\psi^{Val}(\vec{k}, \vec{r})|^2$, and which calculation is now in progress.

In the present paper, we omitted the minor details of the calculation. These will be described in the Journal of Science of Hiroshima University, Ser. A, later on.

§ 4. A Revising Method of the OPW Approximation for the Conduction Bands of Insulators

In this section we shall propose a new procedure for obtaining the better variation functions for conduction bands of insulators.

For simplicity, let us now consider a crystal whose unit cell contains only one atom. $u_s(\vec{r}-\vec{R}_n)$ are the ion-core atomic-orbitals which belong to the n-th atom and the corresponding Bloch sums are written as

$$\phi_s(\vec{k}, \vec{r}) = N^{-1/2} \sum_n \exp(i\vec{k}\cdot\vec{R}_n) u_s(\vec{r}-\vec{R}_n), \quad s=1, 2, \cdots, m, \tag{10}$$

where m is the number of the so called ion-cores, and N is the number of the unit cells in the crystal. Then the variation functions (OPW-terms) for the valence bands, which are orthogonalized to all the ion-cores (10), are

$$Y(\vec{k}, \vec{r}) = (N\Omega)^{-1/2} \exp(i\vec{k}\cdot\vec{r}) - N^{-1/2} \sum_s \sum_n \exp(i\vec{k}\cdot\vec{R}_n) \cdot A_s(\vec{k}) u_s(\vec{r}-\vec{R}_n), \tag{11}$$

of which the valence-band eigenfunctions are made up as

$$\psi^{Val}(\vec{k}, \vec{r}) = \sum_i \beta(\vec{k}+\vec{K}_i) Y(\vec{k}+\vec{K}_i, \vec{r}), \tag{12}$$

$\beta(k+K_i)$ being determined by group-theoretical consideration and by solving corresponding secular equations.

Then, the Wannier functions[26] of the valence bands will be constructed from the Bloch orbitals (12) as follows:

$$a^{Val}(\vec{k}, \vec{r}-\vec{R}_n) = N^{-1/2} \sum_{\vec{k}} \exp(-i\vec{k}\cdot\vec{R}_n) \psi^{Val}(\vec{k}, \vec{r}). \tag{13}$$

The Fourier transforms of (13); i.e., $\psi^{Val}(\vec{k}, \vec{r})$ are represented by

$$\psi^{Val}(\vec{k}', \vec{r}) = N^{-1/2} \sum_n \exp(i\vec{k}'\cdot\vec{R}_n) a^{Val}(\vec{k}', \vec{r}-\vec{R}_n). \tag{14}$$

Now we suppose that $\psi^{Val}(\vec{k}, \vec{r})$ have been obtained by applying the usual OPW method. $\psi^{Val}(\vec{k}, \vec{r})$, of course, are orthogonal to all the $\phi_s(\vec{k}, \vec{r})$ in (10). Hence, $a^{Val}(\vec{k}, \vec{r}-\vec{R}_n)$ for the valence bands play a similar role as those of the atomic orbitals in the lower ion-core bands. Then, the variation functions (OPW-terms) for the conduction bands can be constructed by includung the Wannier-functions of the valence bands in addition to the usual atomic orbitals belonging to the ion-core levels:

$$Y(\vec{k}, \vec{r}) = (N\Omega)^{-1/2} \exp(i\vec{k}\cdot\vec{r}) - N^{-1/2} \sum_s \sum_n \exp(i\vec{k}\cdot\vec{R}_n) A_s(\vec{k}) u_s(\vec{r}-\vec{R}_n) - N^{-1/2} \sum_t \sum_n \exp(i\vec{k}\cdot\vec{R}_n) A_t^{Val}(\vec{k}) \cdot a_t^{Val}(\vec{k}, \vec{r}-\vec{R}_n). \tag{15}$$

In the conventional OPW method, the valence bands and conduction bands of insulators have been solved at the same time, so that the convergence in the upper-lying conduction bands may be in general anticipated to be insufficient compared with that of the lower-lying valence bands, because the solutions for the higher energy levels can not be obtained until the secular determinants of rather high-order are solved. This fact is shown in Fig. 3 and 4. Then, we now propose that in the first step, the valence bands are calculated on the basis of (11) by the usual OPW method, secondly, the Wannier functions (13) of the valence bands are set up through the Fourier transform of the obtained $\psi^{Val}(\vec{k}, \vec{r})$, and in the final step, the conduction bands are computed on the basis of (15), instead of (11), by the usual OPW method. Then, this procedure would lead to more rapid conver-

gence for the conduction bands than usual.

After all, according to the present proposition, the labor for solving the higher-order secular-equation is replaced by that for getting the Wannier functions of the valence bands. For practical application, it is necessary that the labor for obtaining these Wannier functions must be rather simple and easy in the actual problem. Application of this method to the conduction bands of the β-SiC crystal is now in progress.

Acknowledgement

The author wishes to express his sincere gratitude to Professor T. Muto of Tokyo University for suggesting this work as well as for constant guidance. He is grateful to Professor H. Tazaki and Professor E. Hirahara of Hiroshima University for their constant interest and advice. Thanks are also due to Dr. J. Yamashita, Dr. F. Herman, Mr. E. Yamaka, Mr. M. Fukuchi, and Dr. A. Morita for their kind criticism and discussion.

References

1) F. Herman: Phys. Rev. **88** (1952) 1210; **93** (1954) 1214; Physica **20**(1954) 801; F. Herman and J. Callaway: Phys. Rev. **89** (1953) 518.
2) T. O. Woodruff: Phys. Rev. **98** (1955) 1741; **103** (1956) 1159.
3) G. E. Kimball: J. Chem. Phys. **3** (1935) 560; A. Morita: Sci. Rep. Tôhoku Univ. **33** (1949) 92; J. F. Mullaney: Phys. Rev. **66** (1944) 326; E. Yamaka and T. Sugita: Phys. Rev. **90** (1953) 992; Rep. ECL, NTT (Tokyo) **2** (1954) 24.
4) F. Herman: J. Electronics, Ser. 1, **1** (1955) 103.
5) T. Igo, E. Yamaka, and M. Yatani: Lecture on the 12th annual meeting of the Phys. Soc. Japan (October 18, 1957, at Tokyo).
6) F. Herman: Private communication.
7) R. H. Parmenter: Phys. Rev. **100** (1955) 573.
8) S. Kobayasi: J. Phys. Soc. Japan **11** (1956) 175.
9) C. Herring: Phys. Rev. **57** (1940) 1169; C. Herring and A. G. Hill: ibid. **58** (1940) 132.
10) C. Herring: Phys. Rev. **55** (1939) 598; R. H. Parmenter: ibid. **86** (1952) 552; J. Callaway: ibid. **97** (1955) 933; **99** (1955) 500; M. Fukuchi: Progr. Theor. Phys. (Kyoto) **16** (1956) 222; J. Callaway: Phys. Rev. **103** (1956) 1219.
11) W. J. Choyke and L. Patrick: Phys. Rev. **105** (1957) 1721.
12) G. Busch: Helv. Phys. Acta **19** (1946) 167; **19** (1946) 189: G. Busch and H. Labhart: ibid. **19** (1946) 463.
13) J. H. Racette: Phys. Rev. **107** (1957) 1542.
14) K. Lehovec, C. A. Accardo, and E. Jamgochian: Phys. Rev. **83** (1951) 603; **89** (1953) 20; R. W. Sillars: ibid. **85** (1952) 136.
15) W. Primak, L. H. Fuchs, and P. P. Day: Phys. Rev. **103** (1956) 1184.
16) O. Weigel: Nachr. Ges. Wiss. Göttingen (1915) p. 264.
17) H. N. Baumann, Jr.: J. Electrochemical Soc. **99** (1952) 109.
18) R. W. G. Wyckoff: *Crystal Structures Vol.* **1**, (1948), Chap. 3, Table-Page 29.
19) D. J. Howarth: Phys. Rev. **99** (1955) 469.
20) J. C. Slater: Phys. Rev. **81** (1951) 385; G. W. Pratt, Jr.: ibid. **88** (1952) 1217.
21) C. C. Torrance: Phys. Rev. **46** (1934) 388.
22) W. Hartree, D. R. Hartree, and M. F. Manning: Phys. Rev. **60** (1941) 857.
23) Eyring, Walter, and Kimball: *Quantum Chemistry* (1944), Chaps. 10 and 13.
24) L. P. Bouckaert, R. Smoluchowski, and E. Wigner: Phys. Rev. **50** (1936) 58.
25) L. Pauling: *Nature of the Chemical Bond* (1940), Chap. 2.
26) G. H. Wannier: Phys. Rev. **52** (1937) 191.

JOURNAL OF THE PHYSICAL SOCIETY OF JAPAN Vol. 13, No. 3, MARCH, 1958

The Crystallographic Aspect of the Mechanical Twinning in Ti and α-U

By Hiroshi KIHO

Department of Physics, Kyoyo-bu, University of Kyoto

(Received November 15, 1957)

A crystallographic study on the mechanical twinning in Ti and α-U is made by a method similar to that in a previous paper, allowing more kinds of atom movements, and the twin elements, K_1, K_2, η_1 and η_2, are determined. It is found that $\{11\bar{2}2\}$ and $\{11\bar{2}4\}$ twins in Ti are reciprocal to each other and that the elements of $\{11\bar{2}1\}$ twin are in agreement with Hall's result. It is also found that a general result that a plane having the smallest shear S is liable to twin in order nearly holds in Ti and α-U.

§ 1. Introduction

In a previous paper[1], the present author carried out, the crystallographic calculations on the atom movements of mechanical twinning, under several assumptions, and the twin elements, K_1, K_2, η_1 and η_2, have been determined. There η_1 was denoted by $[uvw]$ and η_2 by $[m_0n_0p_0]$. It has thus been shown that the observed twins have the smallest shear S among crystallographically possible twins.

Recently, the same problem was treated, independently of the present author, by M. A. Jaswon and D. B. Dove[2,10], who introduced the concept of homogeneous shear for a simple lattice and semi-homogeneous shear for a multiple lattice, and determined the atom movements. They used the inequality theorem in order to find a plane having the smaller twinning shear, thus obtaining the results similar to those of the present author. But, twins in Ti and Zr were not accounted for by them.

The assumptions used in the previous paper cited above are as follows:

I. There are only a few atom movements, $\boldsymbol{U}$, and these appear alternatively when the twin boundary moves;

II. The atom which comes in a twin lattice site is at the nearest matrix lattice site to it. This is justified by the fact that the twin dislocation is movable;

III. An atom movement $\boldsymbol{U}$ consists of the Burgers vector $\boldsymbol{b}$ of a twinning dislocation and a shuffle. Since the two parts divided by the path of the twinning dislocation shift each other by $\boldsymbol{b}$ on a average, the vector sum of the shuffles diminishes to zero.

Now, the ith lattice site is denoted by $\boldsymbol{R}_i=m\boldsymbol{a}_1+n\boldsymbol{a}_2+p\boldsymbol{a}_3$, where $\boldsymbol{a}_1$, $\boldsymbol{a}_2$ and $\boldsymbol{a}_3$ are primary lattice vectors. If atoms at the origin (000) as well as at $(m_0n_0p_0)$ undergo the same movement $\boldsymbol{U}$, so that the atom at $(m_0n_0p_0)$ comes to the twin origin $(0'0'0')$ and the atom at (000) comes to $(m_0'n_0'p_0')$ of the twin lattice, we may have

$$m_0=m_0', \quad n_0=n_0', \quad p_0=p_0', \tag{1}$$

where $(m_0n_0p_0)$ belongs to the same Bravais lattice as (000). By Eq. (6) in the previous paper, $[m_0n_0p_0]$ is equal to η_2.

The atom movements are conveniently investigated in the modified lattice in which the twin shear magnitude or $\boldsymbol{b}$ of the twin dislocation diminishes to zero. Using the above assumptions, it can be determined how apart $(m_0n_0p_0)$ is from (000). Twin planes are classified into three types as follows:

Type I: All atom movements are equal to $\boldsymbol{b}$ and shuffles are zero.

Type II: There are two atom movements, $\boldsymbol{U}_\perp$, in which shuffles are perpendicular to the twin plane, which are of the same magnitude but opposite to each other.

Type III: In addition to Type II, there are two more atom movements, $\boldsymbol{U}_\parallel$, in which shuffles are parallel to the twin plane, so that the number of the atom movements is four in all*.

* Type I corresponds to the homogeneous shear in Jaswon and Dove's treatment, while Types II and III correspond respectively to Y and X modes of the semi-homogeneous shear.

Based upon this method, mechanical twins of Ti and α-U are examined, and to this end it becomes necessary that more atom movements are to be allowed.

§ 2. General Treatment

In the previous paper, it was considered that when the distances between (hkl) planes parallel to a twin plane are all equal, each plane is quite equivalent as for the atom movement, and the atom movement is only of one kind (Type I). As will be shown below, the observed twin planes of Ti and Zr come under this case, but in applying the atom movement of Type I, the assumption II is not satisfied. Thus, also in the case where the distances between (hkl) planes are all equal in a multiple lattice, the twinning is allowed to have a few atom movements (i.e., Type II or III). Then, in the case in which $f=1/2$ is contained in Type II, while the case in which $f=0$ or $f=1/2$ is contained in Type III, fd being the minor fractional distance between (hkl) planes.

Types IV. In the above treatment, the number of atom movements is only four. But, twinning types having more movements are possible geometrically and one way to obtain them stepwise is as follows.

If, in Type II, there is $(m_f n_f p_f)$, nearer to $(0'0'0')$ than $(m_0 n_0 p_0)$, on the (hkl) plane apart from $(m_0 n_0 p_0)$ by fd, this Type II is converted to Type III by the assumption II. Again, similarly, when, in Type III, $(m_g n_g p_g)$ is on the (hkl) plane apart from $(m_0 n_0 p_0)$ by fd, it happens that

$$|\boldsymbol{T}_g+\boldsymbol{b}|<|\boldsymbol{U}_\perp|\,, \tag{2}$$

where $\boldsymbol{U}_\perp$ and $\boldsymbol{T}_g+\boldsymbol{b}$ are respectively the displacements from $(m_0 n_0 p_0)$ and $(m_g n_g p_g)$ to $(0'0'0')$, and $\boldsymbol{T}_g$ is the component of $\boldsymbol{R}_g$ parallel to the (hkl) plane. Then, an atom at $(m_g n_g p_g)$, instead of that at $(m_0 n_0 p_0)$, should come to $(0'0'0')$. Since $(m_g n_g p_g)$ does not belong to the same Bravais lattice as (000), $(m_g n_g p_g)$ does not take the same atom movement $\boldsymbol{U}$ as that of (000) and the new $(m_0 n_0 p_0)$ lies on the sixth double plane. Then, if $\boldsymbol{N}$ denotes a unit vector normal to the twin plane, we have, as shown in Fig. 1,

$$\left.\begin{aligned} \boldsymbol{U}_\perp &= \boldsymbol{b}\pm fd\boldsymbol{N}\,,\\ \boldsymbol{U}_\parallel &= \boldsymbol{b}\pm(\boldsymbol{T}_f+\boldsymbol{b})\,,\\ \boldsymbol{U}_\parallel' &= \boldsymbol{b}\pm(\boldsymbol{T}_g+2\boldsymbol{b})\,,\\ \boldsymbol{b} &= -\boldsymbol{T}_0/3\,. \end{aligned}\right\} \tag{3}^*$$

Here, when $(m_0 n_0 p_0)$ on the sixth double plane is not the nearest neighbour to $(0'0'0')$, the atom movement $\boldsymbol{U}$ of $(m_0 n_0 p_0)$ is not equal to $\boldsymbol{U}$ of (000) as in the above and Type IV is converted to another type, and so on. However, the twin origin $(0'0'0')$, to which an atom at $(m_0 n_0 p_0)$ comes, has the mirror-image relation with the matrix origin (000), so that it is not likely that $(m_0 n_0 p_0)$ is far distant from (000). Thus, only Type IV is taken up in addition to Types I, II and III.

When $(m_f n_f p_f)$ or $(m_g n_g p_g)$ does not lie on the plane apart from $(m_0 n_0 p_0)$ by fd, the atom movements are not of the above types, but are rather complex. However, these can be obtained similarly.

Reciprocal twin. The modified lattices of a twin and its reciprocal one are identical with each other and the atom movement of the latter is similar to the former, excepting the case where the assumption II does not hold for the reciprocal twin, because their shear directions are perpendicular to each other. A pair of $\{hkl\}$ planes of the same magnitude

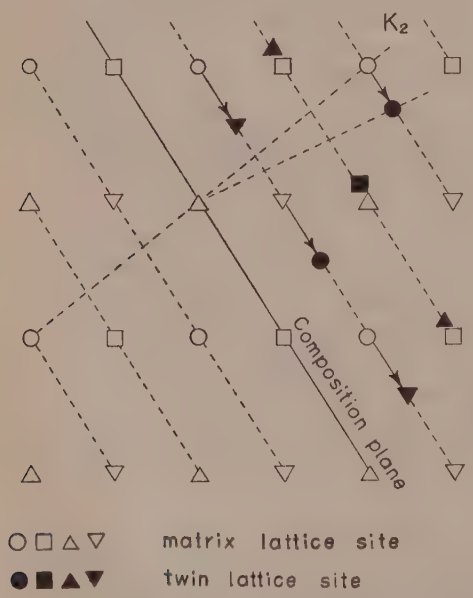

Fig. 1. The atom movement of Type IV. ($f=0$)

* $\boldsymbol{b}$ is reasonably the smallest one and does not always mean the Burgers vector of a real twin dislocation, because it is possible for dislocations of $\boldsymbol{b}$ to be combined, in consequence of alternative appearance of the different structures of the twin boundary.

as shown in Fig. 2 are reciprocal to each other, while the reciprocal of a single $\{hkl\}$ plane in it is the $\{hkl\}$ plane itself, or it cannot exist.

§ 3. Applications

Case of Ti and Zr

The mechanical twins in Ti (h.c.p.) were reported by C. J. McHargue and J. P. Hammond[3], J. D. Rosi et al.[4], and A. T. Churchman[5], while those in Zr (h.c.p.) were reported by E. J. Rapperport[6]. The observed twins are $\{10\bar{1}2\}$, $\{11\bar{2}1\}$, $\{11\bar{2}2\}$, $\{11\bar{2}3\}$ and $\{11\bar{2}4\}$. These, except for $\{10\bar{1}2\}$, are not contained in Table V in the previous paper*.

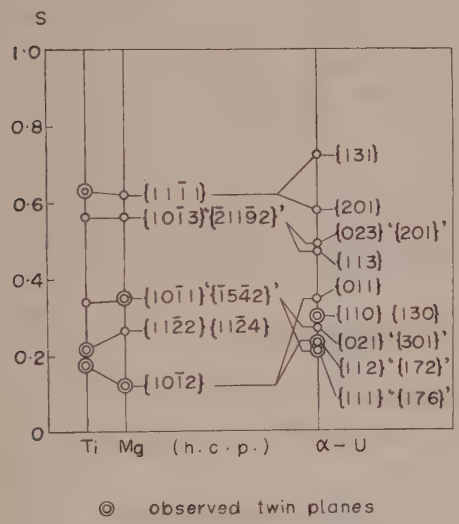

Fig. 2. Twinning shear.

Table I. Twin elements in Ti and Zr (r_0 being the distance between the nearest neighbours)

K_1	K_2	η_1	η_2	S	b/r_0	Type
$(10\bar{1}2)$	$(10\bar{1}\bar{2})$	$[\bar{1}011]$	$[10\bar{1}1]$	0.175	0.10	III
$(11\bar{2}1)$	(0001)	$[\bar{1}\bar{1}26]$	$[11\bar{2}0]$	0.630	0.31	II
$(11\bar{2}2)$	$(11\bar{2}\bar{4})$	$[11\bar{2}\bar{3}]$	$[22\bar{4}3]$	0.218	0.094	IV
$(11\bar{2}3)$†	...	...	...	...	...	
$(11\bar{2}4)$	$(11\bar{2}\bar{2})$	$[22\bar{4}\bar{3}]$	$[11\bar{2}3]$	0.218	0.069	IV

† When another complex type of the atom movement is considered, the elements of $\{11\bar{2}3\}$ twin, for which the assumption II holds, are $K_1=(11\bar{2}3)$, $K_2=(11\bar{2}2)$, $\eta_1=[11\bar{2}\bar{2}]$, $\eta_2=[11\bar{2}3]$ and $S=0.514$, and its reciprocal twin cannot exist.

* $K_1=(112)$, $K_2=(30\bar{2})$ in Table V in the previous paper must be abandoned, because $(m_0\, n_0\, p_0)$ does not belong to the same Bravais lattice as (000).

The twin elements as determined by the above method are given in Table I and the geometrically possible twins are shown in Fig. 2. The $\{11\bar{2}3\}$ twin rarely observed cannot twin and is exceptional in the present treatment. The $\{11\bar{2}2\}$ and $\{11\bar{2}4\}$ twins are reciprocal to each other, in contradiction to E. O. Hall's results that both of these twins are reciprocal to themselves respectively. It may be thought that the former is more liable to twin, since its shear magnitude S is smaller.

Next, the twin elements determine the stress in favour of twinning. Since the values of η_1 of $(11\bar{2}4)$ are $[22\bar{4}\bar{3}]$ and $[\bar{2}\bar{2}43]$ respectively, they have different orientation dependence: the $(11\bar{2}4)$ twin having $\eta_1=[22\bar{4}\bar{3}]$ is operative in the case where the axis of extension is nearly parallel to the basal plane, while the $(11\bar{2}4)$ twin having $\eta_1=[\bar{2}\bar{2}43]$ is operative in the case where the said axis is nearly perpendicular to the basal plane. Referring to the experimental result[4], which shows the $(11\bar{2}4)$ twin for extension of $(11\bar{2}0)$ pole, the former may be profitable for twin element, in spite of the absence of direct determination of twin element by measuring the tilt of twin surface. Elements of the $\{11\bar{2}1\}$ twin coincide for both treatments, and do not contradict to the observed orientation to twin[4]. Experimental data about the orientation dependence of the $\{11\bar{2}2\}$ twin are not only scanty but also scattered[3,4,5], so that they are not sufficient to discuss its reciprocity to $\{11\bar{2}4\}$.

Case of α-U.

As already pointed out by many authors, the crystal structure of α-U resembles to that of h.c.p., so that probable twin planes is α-U also resemble to those in h.c.p. However, the difference of the crystal structure reveals that, as shown in Fig. 2, the order of shear magnitude S of some planes does not agree with each other. The results for the twin elements of {130}, {112} and '{172}' agree with those of Cahn[8] and Hall[7], while the results for the twin elements of '{176}' agree with Lloyd and Chiswick's results[9]. Our results agree also with those obtained by Jaswon and Dove in their recent paper[10]. However, the {121} twin as reported by Cahn, which was not observed by Lloyd and Chiswick, is not conceivable in the present treatment.

It was pointed out in the previous paper that the observed twins have the smallest S in order. Such a result holds also in the cases of α-U and Ti, and, as shown in Fig. 2, the shear S of the observed twins is small enough. However, the twinning is not so simple that the present crystallographic analysis cannot be considered to be conclusive, and probably the dislocation theory of twin nucleation and the evaluation of the energy of the twin boundary should be necessary for the complete explanation of the twin phenomena.

In conclusion, the author expresses his cordial thanks to Professor Kenzo Tanaka, University of Kyoto, for his encouragement and discussions. The auther is also indebted to Mr. Saiyu Maruyama, Osaka Women's University, for his useful discussions.

References

1) H. Kiho: J. Phys. Soc. Japan **9** (1954) 739.
2) M. A. Jaswon and D. B. Dove: Acta Crystallographica **9** (1956) 621.
3) C. J. McHargue and J. P. Hammond: Acta Metallurgica **1** (1953) 702.
4) F. D. Rosi, C. A. Dube and B. H. Alexander: J. Metals **5** (1953) 257;
F. D. Rosi: Ibid. **6** (1954) 58;
F. D. Rosi, F. C. Perkins and L. L. Seigle: Ibid. **8** (1956) 115.
5) A. T. Churchman: Proc. Roy. Soc. **A226** (1954) 216.
6) E. J. Rapperport: Acta Metallurgica **3** (1955) 208.
7) E. O. Hall: *Twinning* (1954) p. 56.
8) R. W. Cahn: Acta Metallurgica **1** (1953) 49.
9) L. T. Lloyd and H. H. Chiswick: J. Metals **7** (1955) 1206.
10) M. A. Jaswon and D. B. Dove: Acta Crystallographica **10** (1957) 10.

JOURNAL OF THE PHYSICAL SOCIETY OF JAPAN Vol. 13, No. 3, MARCH, 1958

Ferroelectricity of $NaNH_4$-Tartrate

By Yutaka TAKAGI and Yasuharu MAKITA
Tokyo Institute of Technology, Oh-okayama, Tokyo

(Received December 6, 1957)

Below the transition point 109°K a crystal plate of $NaNH_4$-tartrate shows a domain structure under a polarizing microscope if viewed in the direction parallel to the b axis. The polarization in each domain lies parallel to $+b$ or $-b$ axis, and can be reversed by shearing stress. The spontaneous polarization is 0.21μ Coul/cm² at 92°K and it is probably constant below the transition temperature.

§ 1. Introduction

As known well $NaNH_4$-tartrate and its isomorph NaK-tartrate can form a continuous series of solution. The series were investigated first by Kurtschatow *et al.*[1] and afterward by Melmed *et al*[2]. Substitution of very small amount of $NaNH_4$-tartrate reduces the temperature range of ferroelectric activity in NaK-tartrate very rapidly. Substitution of about two per cent eliminates the spontaneous polarization entirely. The ferroelectric activity, however, reappears in the crystals containing more than about eighteen per cent of $NaNH_4$-tartrate. These mixed crystals show a single Curie point at low temperatures, the exact position of the transition depending upon the concentration. The Curie point-composition curve goes down linearly from about twenty per cent to about sixty per cent and then bends downward steeply at about eighty per cent. $NaNH_4$-tartrate thus seems to have no Curie point or, if any, one at extremely low temperature. In fact, Kurtschatow *et al.* reported that $NaNH_4$-tartrate did not reveal any dielectric anomaly from room temperature down to 83°K.

However, Jona and Pepinsky[3] have recently foundt hat $NaNH_4$-tartrate shows a small anomaly in the dielectric constants at 109°K, so small that there is no wonder why Kurt-

schatow *et al.* overlooked it. The anomaly was detected along its three crystallographic principal axes. The Curie-Weiss law does not hold in any of these axes. The dc biasing field of 10 Kv/cm super-imposed on an ac field of 10 v/cm does not change the value of dielectric constant. All these characters are very peculiar if compared with the well established properties of the NaK-tartrate and of the mixed ferroelectric crystals derived from them. Hoping to make clear the nature of the above mentioned transition in $NaNH_4$-tartrate, we have made a pyroelectric test of this crystal along its three principal axes and found that this crystal yields a pyroelectric charge along its crystallographic *b* axis. The details will be given in the following sections.

§ 2. Pyroelectric Study

Pyroelectric charge developed on the crystal surface during the temperature variation through the transition point has been measured by means of a Shimizu type electrometer[4]. The sensitivity of about 5×10^{-11} Coul/division can easily be attained by this device.

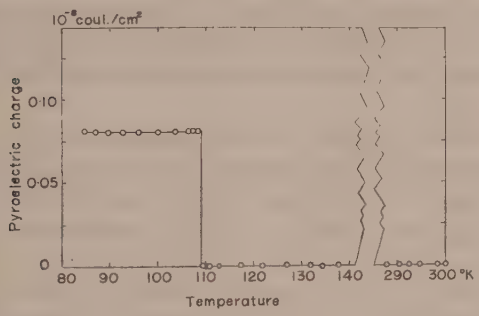

Fig. 1. Pyroelectric charge developed on the crystal surface cut perpendicularly to the *b* axis.

It has been observed that an electric charge occurs abruptly on the crystal surface cut perpendicularly to the *b* axis just when the crystal passes through the transition point. The charge remains constant below the transition point. One example is shown in Fig. 1. The amount of the charge turned out to be different from specimen to specimen, covering the range 2.5 to 15×10^{-10} Coul/cm². Moreover the charge developed on the same surface of the same specimen varied after various treatments. The effect of field cooling is clearly demonstrated in Fig. 2. Prior to each run of the measurements, the specimen was cooled from 118°K to 85°K under various dc field strength. At 85°K the electrodes were short-circuited for a few seconds and then immediately connected to the electrometer. Then the temperature was raised very slowly.

The figures beside each curve denote the dc field strength. Plus or minus sign means that the field was applied in the direction parallel or inverse to the sign of the charge observed in the virgin state. The figures in the circles denote the order of experiments.

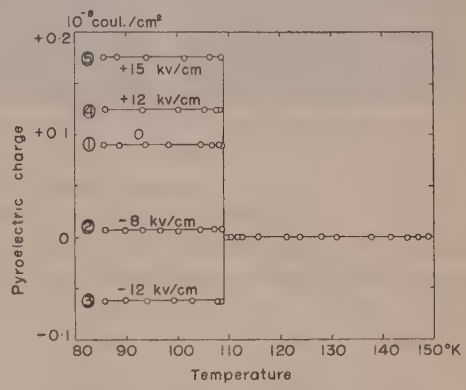

Fig. 2. Effect of field cooling on the pyroelectric charge. The number enclosed in the circle denotes the order of the experiment. The figures beside each curve denote the field strength under which the crystal was cooled from 118° to 85°K.

The diversity of the amount of charge suggests strongly that the crystal is made up of many tiny domains, each being polarized parallel to the $+b$ or the $-b$ direction. It is to be noted, moreover, that the crystal has a self bias; a slightly positive charge was observed in the second run even after a strong negative field had been applied throughout the cooling period. The specimens cut perpendicularly to the *a* or the *c* axis did not show any trace of pyroelectricity at their passage through the transition point.

§ 3. Observation of Domain Structure

Above the transition point $NaNH_4$-tartrate belongs to the orthorhombic symmetry class $P2_12_12$ and is therefore optically biaxial. The acute bisectrix is the *c* axis, the plane of the optic axes is (100) plane, and the crystal is optically negative. This fixes the position of the indicatrix with respect to the crystallographic axes:

$$a_{\text{ortho}}=Y,\ \ b_{\text{ortho}}=Z,\ \ c_{\text{ortho}}=X,$$

where X, Y and Z are the indicatrix axes. A b-plate therefore shows straight extinction, and the extinction positions correspond to the axes X and Y of the indicatrix.

If it is true that the crystal below the transition point polarizes spontaneously in the direction of the orthorhombic b axis, the symmetry must become monoclinic $P2_1$ owing to the spontaneous shear strain $z_x°$. This means that in a single domain crystal one of the monoclinic axes deviates from the original orthorhombic axis by an angle equal to $z_x°$. Of course this angle itself may be very small, but it is probable, as is so in the case of Rochelle salt, that the indicatrix axes rotates by an angle far larger than $z_x°$, for neither X nor Y is required to coincide with the monoclinic c or a axis. Only one condition necessary for this crystal symmetry is the coincidence of the b_{mono} axis with Z_{mono} (Fig. 3). If the angle between the c_{mono} axis and the X_{mono} axis happens to be sufficiently large, the domains will be observed through a polarizing microscope, if viewed in the direction parallel to the b axis (Fig. 3).

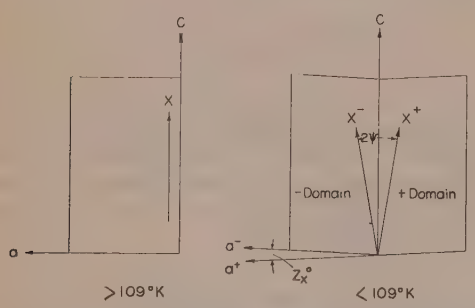

Fig. 3. The relation between the crystallographic axes and the optical indicatrix axes (schematic). Left, Orthorhombic phase; Right, Monoclinic phase.

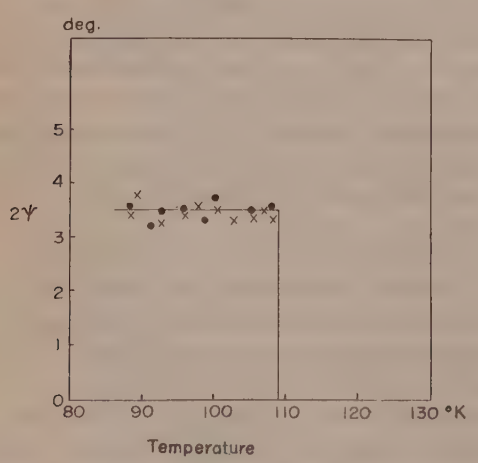

Fig. 4. The angle between the extinction positions of neighboring domains.

Fortunately this turned out to be the case. Parallel stripes with alternately bright and dark appearence were actually observed if the b plate was kept below the transition temperature. The stripes were long in the direction of the c axis, and the width of them was about a few hundred microns. The angle between the extinction positions of the neighboring domains is constant below the transition point (Fig. 4).

§ 4. Hysteresis Curve Induced by Shearing Stress

We tried many times in vain to get the electric displacement *vs.* electric field hysteresis loops characteristic of normal ferroelectric crystals, though all the evidences thus far obtained indicate unambiguously that there exists spontaneous polarization along the b axis below the transition point of $NaNH_4$-tartrate. The D–E relation was linear up to the maximum electric field of 20Kv/cm which we could apply without destroying the crystal.

There remains however another way of influencing the polarization, for the crystal is strongly piezoelectric. The shear stress Z_x can as well affect the electric polarization as the electric field can. We made a 45°-cut of the crystal of which one edge bisects the a and the c axes and thickness of the plate lies along the b axis. The slab was set between the cross nicols of a polarizing microscope, and a normal stress P was applied on one pair of narrow surfaces. The result of observation is shown in Fig. 5. As the stress is increased, the fractional area of bright stripes decreases, until the whole area becomes dark at the pressure of about 95 Kg/cm². As the stress is reduced, bright stripes reappear in most cases, but in a few cases the crystal remains dark even after the external stress is completely removed. The fractional decrease of bright stripes roughly estimated from two sets of photographs is shown in Fig. 6.

If these stripes really represent the $+b$ or the $-b$ domains, the cycle of the area frac-

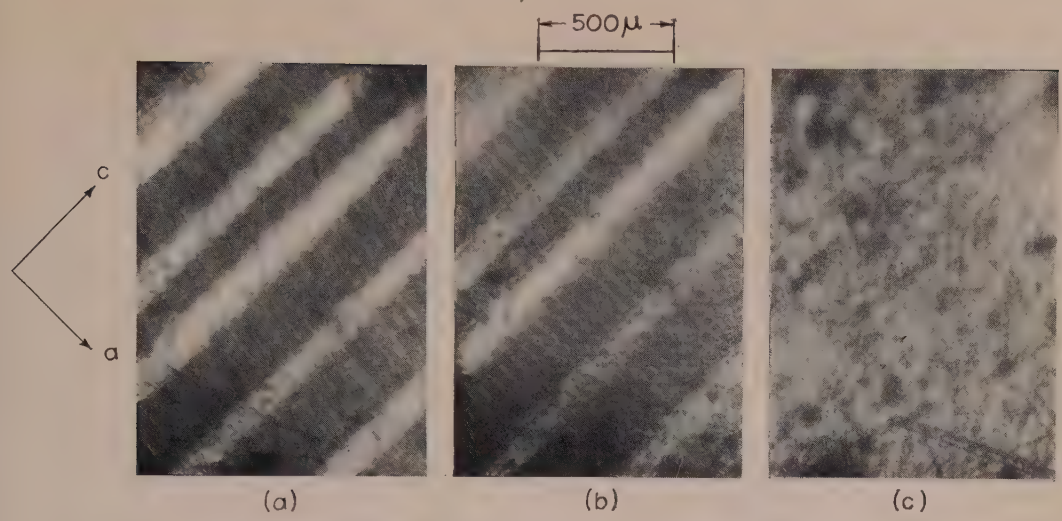

Fig. 5. Photographs showing the effect of shearing stress. (at 98.4°K).
a: Pressure=0, b: Pressure=62.5 Kg/cm², c: Pressure=98.7 Kg/cm².

tion such as shown in Fig. 6 should be accompanied by a cycle of the net polarization of the crystal slab. It turned out to be the case as shown in Fig. 7. The stress was increased and decreased step by step and the charge developed on the crystal surface was measured by the electrometer. Each pair of points connected by a short vertical line shows the value of charge immediately after the respective stress was applied and the value of charge when the electrometer deflection attained a steady value after a few minutes had elapsed under the constant stress. As known well in NaK-tartrate, we have here also the two components of electric polarization, one of which responds very slowly. It took 44 minutes to perform the stress cycle shown in the figure.

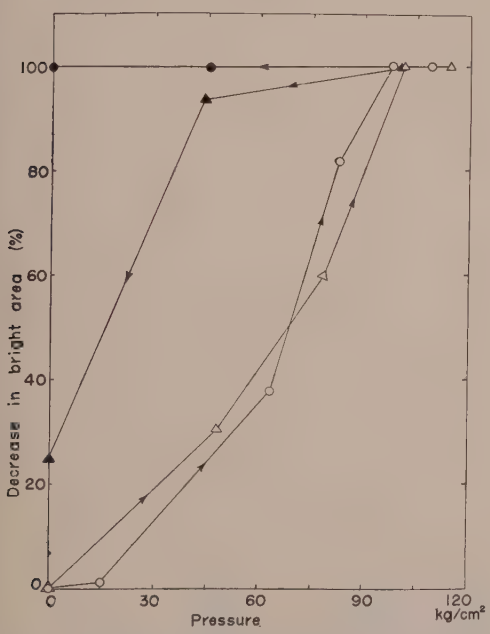

Fig. 6. Decrease in bright area *vs.* mechanical stress. Circles: at 98.4°K, Triangles: at 96.0°K, Hollow marks: for increasing stress. Solid marks: for decreasing stress.

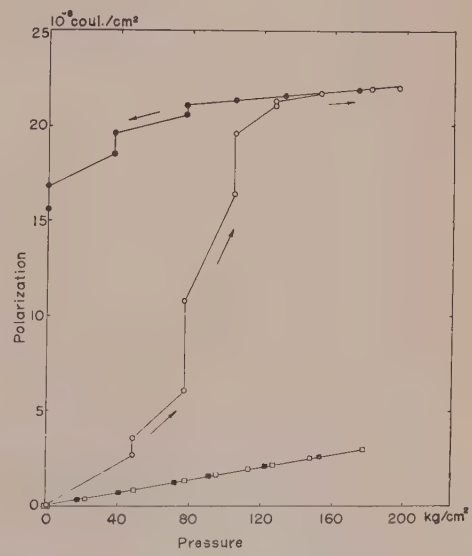

Fig. 7. Polarization *vs.* mechanical stress. Circles: at 92°K. Squares: at 126°K. Hollow marks: for increasing stress. Solid marks: for decreasing stress.

The same experiment was carried out at 126°K, above the transition point. The coincidence within the limit of accuracy of the measurements of the back and forth branches obtained in the stress cycle which took as long a time as 26 minutes assures that there is no appreciable leakage of electricity through the specimen and the measuring apparatus. The large hysteresis observed at 92°K is, therefore, a real effect due to the domain re-orientations. The spontaneous polarization estimated from this curve is 21×10^{-8} Coul/cm². The spontaneous polarization may perhaps be temperature independent as the pyroelectric charge remains constant below the transition point.

§ 5. Discussion and Conclusion

As is generally accepted, the mere existence of a spontaneous polarization is by itself insufficient to justify one in calling a certain crystal ferroelectric. Besides, we must have at least one way of reversing the direction of the spontaneous polarization. Of course the ferroelectricity is usually tested by applying the electric field, but in a wider sense of terminology the ferroelectricity may be tested by any means which can affect the electrical polarization. We feel, therefore, we are justified to call $NaNH_4$-tartrate a ferroelectric crystal with its spontaneous polarization along the b axis, in spite of its very peculiar behaviors as compared with other normal ferroelectrics. The most striking feature from the theoretical point of view is surely the failure of the Curie-Weiss law above the transition point (Fig. 8).

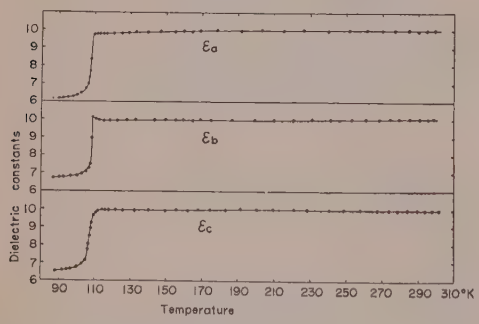

Fig. 8. Dielectric constants in the direction of three crystallographic axes.

When we took up the stress experiment we were led by the following reasoning. The shear stress is related with the electric field through the piezoelectric constant d_{25} and the dielectric susceptibility κ_2. But the maximum stress at which the crystal breaks mechanically does not necessarily coincide with the maximum field strength at which the crystal breaks down electrically. There is, at least in a fortunate case, a possibility to give a stronger influence by mechanical means than by electrical means without destroying the specimen. After the experiment performed along this line proved to be successful, we came to realize that our original idea was an over-simplification. In fact, if translated into the electric field necessary to induce the same polarization, the pressure of about 100 Kg/cm² on a 45°-cut slab should be equivalent to the electric field of about 14 Kv/cm, far less than the maximum amplitude which we applied of 20 Kv/cm. The situation must be analysed in more details.

We have for a piezoelectric crystal the equations,

$$Z_x = c_{55}z_x + f_{25}P_y$$
$$E = f_{25}z_x + \chi_2 P_y\ .$$

We need therefore a plane to represent a given state of the crystal since there are two independent variables. For the electric field experiment, we have the solutions

$$Z_x = 0, \quad z_x = -\frac{f_{25}}{c_{55}}P_y\ ,$$

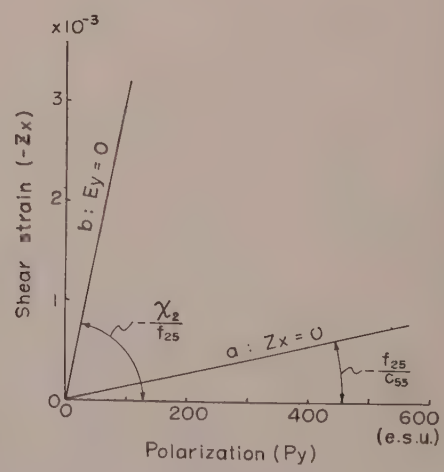

Fig. 9. The two different paths on which the crystal proceeds. a: the electric field experiment, b: the shearing stress experiment. The curves are obtained by using the Mason's values[7]: $d_{25}=-95.0\times10^{-8}$ e.s.u., $s_{55}=33\times10^{-12}$ c.g.s., $\varepsilon_y=8.9$.

and

$$E_y=\left(\chi_2-\frac{f_{25}}{c_{55}}\right)P_y\ ,$$

and similarly for the stress experiment, we have the solutions

$$E_y=0\ ,\quad z_x=-\frac{\chi_2}{f_{25}}P_y\ ,$$

and

$$Z_x=\left(f_{25}-\frac{c_{55}\chi_2}{f_{25}}\right)P_y\ .$$

As clearly shown by the second relations of the above two sets of solutions, the crystal proceeds on the different paths in the above two experiments (Fig. 9). That is, if we had translated into the electric field necessary to produce the same strain, instead of polarization, the same pressure of about 100 Kg/cm^2 should have been found equivalent to an electric field of about 500 Kv/cm. This situation may be the reason why we have observed different coercivities.

It is of some interest to note here that, below their transition points, $LiNH_4$-tartrate monohydrate[5] has its spontaneous polarization along the *b* axis while LiTl-tartrate monohydrate[6] has its spontaneous polarization along the *a* axis, though they are isomorphous above the transition temperature.

Finally we wish to thank Professor H. Takahasi for his invaluable advice and Mr. H. Maniwa for his helpfull discussions. This work was partly supported by the Scientific Research Fund of the Ministry of Education.

References

1) B. Kurtschatow and M. Eremejew: Z. Sowj. **1** (1932) 140.
2) A. Melmed, F. Jona and R. Pepinsky: Tech. Rept. No. 20 Contract AF **33** (616)-2133 (1954), Wright Air Development Center.
3) F. Jona and R. Pepinsky: Phys. Rev. **92** (1953) 1577.
4) T. Shimizu: Japanese Journ. Phys. I. **9-10** (1923) 107.
5) W. J. Merz: Phys. Rev. **82** (1951) 562.
6) B. T. Matthias and J. K. Hulm: Phys. Rev. **82** (1951) 108.
7) W. P. Mason: *Piezoelectric Crystals and Their Application to Ultrasonics*, D. Van Nostrand Co. Inc., New York, 1950.

JOURNAL OF THE PHYSICAL SOCIETY OF JAPAN Vol. 13, No. 2, MARCH, 1958

On the Temperature Diffuse Scattering of Electrons

I. Derivation of General Formulae

By Satio TAKAGI

Institute of Physics, College of General Education,
University of Tokyo
Komaba, Meguro-ku, Tokyo

(Received September 7, 1957)

The perturbation theory of the temperature diffuse scattering of electrons is presented taking account of the fact that each of the primary and secondary waves in the crystal consists of many plane waves. Formulae for the intensity of the diffuse scattering from a monatomic crystal forming a primitive lattice are obtained for each of the perturbation potentials due to Bloch and to Nordheim. When each of the primary and secondary waves does not excite any Bragg reflexions and can be given by a plane wave, the Nordheim potential gives the same result and the Bloch potential gives practically the same result as that of the current X-ray diffraction theory applied to electron diffraction. The result may be applied to explain the formation of the Kikuchi pattern by the temperature diffuse scattering and the anomalous intensity variation of the diffuse spot from some single crystals.

§ 1. Introduction

According to the dynamical theory of electron diffraction developed by Bethe,[1] the position of diffraction spots formed by reflexion from a perfectly smooth surface of a stationary crystal is determined completely by the surface lattice of the crystal. Miyake, Kohra and Takagi[2] have pointed out that circular arrays of sharp spots which appear in the reflexion patterns from cleavage faces of crystals (Fig. 1, a, b) arise from this dynamical effect, although previously several authors ascribed them to the two-dimensional diffraction from uppermost layer of the crystal on account of strong absorption of electrons.[3][4][5]

Besides these sharp spots there appear actually a number of diffuse spots at positions which are approximately in accordance with the conditions of ordinary three-dimensional diffraction. Co-existence of diffuse spots and arrays of sharp spots is observed on many kinds of crystals and is regarded as a general phenomnon not peculiar to a particular kind of crystal. As the the reflexion pattern from a smooth surface of a perfect crystal should be composed of only these arrays of spots

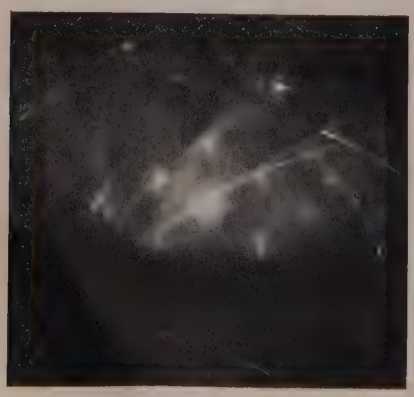

Fig. 1. (a)

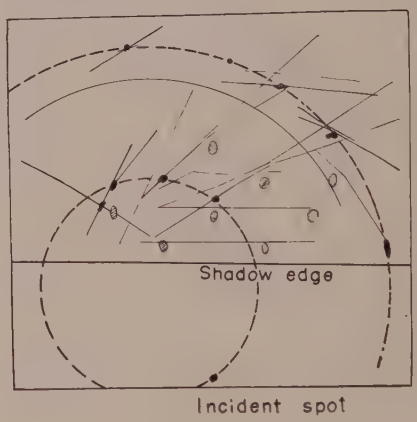

Fig. 1. (b).

Fig. 1. (a) Electron diffraction pattern from a cleavage face of zincblende. Incident beam, nearly parallel to [111]. (b) The sketch of the pattern. Broken circles indicate that the sharp spots lie on circles. Small hatched circles show the diffuse spots.

besides the patterns resulting from the secondary scattering such as Kikuchi patterns, the origin of the diffuse spots may be attributed to some kinds of lattice distortion. Miyake[6] has pointed out that they may be the temperature diffuse scattering.

The present paper treats the theory of the temperature diffuse scattering taking account of the dynamical effects. There are some experimental evidence that Kikuchi patterns, which are believed to be due to the inelastic collision of an electron with lattice electrons[7][8][9], may be partly attributable to the temperature scattering. According to the investigations of Watanabe[10] and Hashimoto, Yoda and Maeda,[11] the energy spectrum of Kikuchi patterns contained parts corresponding to electrons with energy loss of less than 1~2 ev. They have pointed out that these electrons cannot be considered as ones inelastically scattered.* The theory of the temperature diffuse scattering may also be necessary for the detailed explanation of Kikuchi patterns.

§ 2. Basic Formulation of the Theory

The quantum mechanical theory of the temperature diffuse scattering of X-rays was developed by Born and Sarginson[12] and Born[13]. The result is practically the same as that of the classical theories of Waller[14], Laval[15] and James.[16] In these theories each of the incident and thermally scattered waves is assumed to be a single plane wave. So far as this assumption holds, the result of the theory can also be applied to the case of electron diffraction with appropriate substitution of the atomic scattering factor. When dynamical effects are observed, however, many plane waves having wave vectors related by

$$\boldsymbol{k}_h = \boldsymbol{k}_o + \boldsymbol{b}_h \tag{1}$$

are excited with a definite phase relationship, where $\boldsymbol{k}_h$ and $\boldsymbol{k}_o$ are wave vectors and $\boldsymbol{b}_h$ is a reciprocal lattice vector. These coexisting waves should be taken into account.

A solution of the Schrödinger equation for an electron in a periodic potential is given by a Bloch function

$$\psi_k = \frac{1}{\sqrt{\Omega}} \sum_h c_{k,h} \exp(2\pi i \boldsymbol{k}_h \cdot \boldsymbol{r}) , \tag{2}$$

where Ω is the volume of the crystal and the summation is over all the reciprocal lattice points. For convenience, $c_{k,h}$ is normalized in the whole crystal, i.e.

$$\sum_h |c_{k,h}|^2 = 1 . \tag{3}$$

Putting (2) into the Schrödinger equation, we obtain an infinite set of linear homogeneous equations or the fundamental equations of the dynamical theory.[7][8][17] In practical calculations, only a finite number of component wave with appreciable amplitude are considered, so that the number of equations becomes finite. Possible values of $\boldsymbol{k}_0$ are obtained by solving the secular equation and are designated by $\boldsymbol{k}_0^{(i)}$. The wave field in the crystal is expressed by a linear combination of (2).

$$\psi_c = \frac{1}{\sqrt{\Omega}} \sum_i \alpha_i \sum_h c_{k,h} \exp(2\pi i \boldsymbol{k}_r^{(i)} \cdot \boldsymbol{r}) \tag{4}$$

which satisfies appropriate boundary conditions. Each of the vacuum waves outside the crystal has a wave vector with tangential component coinciding with that of one of the component waves in (4). These vacuum waves are the only waves observed so long as the atoms are at rest. However, when the crystal is set in thermal motions, the electron in the state (4) will make transitions to other states. The vacuum waves having the tangential component of the wave vectors corresponding to the end states constitute the temperature diffuse scattering.

§ 3. Interaction Between an Electron and Lattice Vibrations

In the ordinary perturbation theory of the interaction between an electron and lattice vibrations, the perturbation potential is assumed to be the difference between the potential energy of an electron in the vibrating crystal $V(\boldsymbol{r})$ and that in the stationary crystal $V_s(\boldsymbol{r})$[18]. However, a better approximation will be obtained by replacing $V_s(\boldsymbol{r})$ with the time average of $V(\boldsymbol{r})$, so that the perturbation potential $U(\boldsymbol{r})$ is put as

$$U(\boldsymbol{r}) = V(\boldsymbol{r}) - \langle V(\boldsymbol{r}) \rangle , \tag{5}$$

where $\langle\ \rangle$ means the time average.

There are several methods of getting $V(\boldsymbol{r})$. One, originally due to Bloch,[19] assumes

$$V(\boldsymbol{r}) = V_s(\boldsymbol{r} - \boldsymbol{u}(\boldsymbol{r})) , \tag{6}$$

* In this paper the term "inelastical scattering" means the scattering accompanied by a change in the electronic state of the scatterer.

where $\boldsymbol{u}(\boldsymbol{r})$ is a continuous function whose value at the position of an atom describes the displacement of the atom as the result of lattice vibration. Another, due to Nordheim,[20] replaces (6) with

$$V(\boldsymbol{r})=\sum_n v_n(\boldsymbol{r}-(\boldsymbol{r}_n+\boldsymbol{u}_n)) , \qquad (7)$$

where $v_n(\boldsymbol{r})$ signifies the contribution of the nth atom to the potential energy of an electron at distance $\boldsymbol{r}$ from the centre of the atom, and $\boldsymbol{r}_n$ and $\boldsymbol{u}_n$, the mean position and the displacement of the atom, respectively. As it is not easy to decide which of the approximations is more appropriate for the present purpose, we shall first adopt (6) which is simplar and treat (7) in the appendix.

$V_s(\boldsymbol{r})$ can be expanded in a three-dimensional Fourier series

$$V_s(\boldsymbol{r})=\sum_g V_g \exp(2\pi i\, \boldsymbol{b}_g\cdot \boldsymbol{r}) , \qquad (8)$$

where $\boldsymbol{b}_g$ is the reciprocal lattice vector. Substituting (8) into (6) and using the relation[12)21)]

$$\langle \exp(2\pi i\, \boldsymbol{b}_g\cdot \boldsymbol{u})\rangle = \exp(-2\pi^2\langle(\boldsymbol{b}_g\cdot \boldsymbol{u})^2\rangle) ,$$

we obtain

$$\langle V(\boldsymbol{r})\rangle=\sum_g V_g' \exp(2\pi i \boldsymbol{b}_g\cdot \boldsymbol{r}) , \qquad (9)$$

where

$$V_g' = V_g \exp(-M) , \qquad (10)$$

and M is the Debye temperature factor given by

$$M=2\pi^2\langle(\boldsymbol{b}_g\cdot \boldsymbol{u})^2\rangle = 2\pi^2|\boldsymbol{b}_g|^2\langle u_g{}^2\rangle , \qquad (11)$$

u_g being the component of $\boldsymbol{u}$ along $\boldsymbol{b}_g$. Thus we obtain as the first approximation

$$\begin{aligned} U(\boldsymbol{r}) &= \sum_g V_g' \exp(2\pi i \boldsymbol{b}_g\cdot \boldsymbol{r})[\exp(-2\pi i \boldsymbol{b}_g\cdot \boldsymbol{u}+2\pi^2\langle(\boldsymbol{b}_g\cdot \boldsymbol{u})^2\rangle)-1] \\ &= -2\pi i \sum_g (\boldsymbol{b}_g\cdot \boldsymbol{u}) V_g' \exp(2\pi i \boldsymbol{b}_g\cdot \boldsymbol{r})^* \qquad (12) \\ &= -(\boldsymbol{u}\cdot \mathrm{grad}\langle V(\boldsymbol{r})\rangle) .^* \qquad (12') \end{aligned}$$

§ 4. The Transition Probability

For the sake of simplicity, let us assume a monatomic crystal composed of N unit cells, each of which contains only one atom. The displacement of an atom $\boldsymbol{u}_n$ can be expressed by the normal coordinate as[18]

$$\boldsymbol{u}_n=\frac{1}{\sqrt{m_a N}}\sum_{q,t} \boldsymbol{e}_{q,t}\{a_{q,t}\exp(2\pi i\, \boldsymbol{q}\cdot \boldsymbol{r}_n)+a^*_{q,t}\exp(-2\pi i\, \boldsymbol{q}\cdot \boldsymbol{r}_n)\} , \qquad (13)$$

where m_a is the mass of the atom, $\boldsymbol{q}$, the wave vector of a lattice wave, $t(=1, 2, 3)$ distinguishes directions of polarizations, $\boldsymbol{e}_{q,t}$, a polarization vector for the mode $(\boldsymbol{q}, t)$ and $a_{q,t}$, the normal coordinate. The magnitude of $\boldsymbol{q}$ is restricted within the first Brillouin zone. Substituting (13) into (12), we get

$$U(\boldsymbol{r})=-\frac{2\pi i}{\sqrt{m_a N}}\sum_l V'_l \sum_{q,t}(\boldsymbol{b}_l)_{q,t}\{a_{q,t}\exp(2\pi i(\boldsymbol{b}_l+\boldsymbol{q})\cdot \boldsymbol{r})+a_{q,t}{}^*\exp(2\pi i(\boldsymbol{b}_l-\boldsymbol{q})\cdot \boldsymbol{r})\} , \qquad (14)$$

where $(\boldsymbol{b}_l)_{q,t}$ is the component of $\boldsymbol{b}_l$ along $\boldsymbol{e}_{q,t}$.

The Schrödinger equation for the unperturbed state of electrons is written as

$$\Delta\psi_{\boldsymbol{k}}+\frac{8\pi^2 m}{h^2}(E_{\boldsymbol{k}}-\langle V(\boldsymbol{r})\rangle)\psi_{\boldsymbol{k}}=0 , \qquad (15)$$

where $E_{\boldsymbol{k}}$, m and h have usual meanings and $\psi_{\boldsymbol{k}}$ is given by the Bloch function (2). We now calculate the transition probability from the state $(\psi_{\boldsymbol{k}}, N_{q,t})$ to the state $(\psi_{\boldsymbol{k}'}, N'_{q,t})$ where $\boldsymbol{k}'$ signifies the wave number vector of the electron in the final state, $N_{q,t}$ and $N'_{q,t}$, the quantum numbers of the vibrational mode in the initial and final states, respectively. If only the first power term in $\boldsymbol{u}(\boldsymbol{r})$ is retained, the transition probability has non-zero value only when the quantum number of one vibrational mode changes by 1 or -1, those of the other modes being constant. The matrix element of $U(\boldsymbol{r})$ is then written as

* Within the limit of the approximation (12), we can replace V_g' in (12) by V_g so that $\langle V(\boldsymbol{r})\rangle$ in (12′) by $V_s(\boldsymbol{r})$. We, however, adopt (12′) in order to compare the result with that of X-ray diffraction theory. The adoption of $\langle V(\boldsymbol{r})\rangle$ instead of $V_s(\boldsymbol{r})$ as the unperturbed potential in (5) is significant for the calculation of unperturbed wave functions.

$$(\boldsymbol{k}'.\ N'_{\boldsymbol{q}t}|U(\boldsymbol{r})|\boldsymbol{k},\ N_{\boldsymbol{q}t})$$

$$=\left\{\begin{array}{l} -\dfrac{2\pi i}{\sqrt{m_a N}}\sum_l V_l'(\boldsymbol{b}_l)_{\boldsymbol{q}t}\left\{\int\psi_{\boldsymbol{k}'}{}^*\psi_{\boldsymbol{k}}\exp(2\pi i\,(\boldsymbol{b}_l+\boldsymbol{q})\cdot\boldsymbol{r})\,d\boldsymbol{r}\right\}\sqrt{\dfrac{h}{8\pi^2\nu_t(\boldsymbol{q})}N_{\boldsymbol{q}t}}\ , \\ \qquad\qquad \text{when} \qquad N'_{\boldsymbol{q}t}=N_{\boldsymbol{q}t}-1 \\ -\dfrac{2\pi i}{\sqrt{m_a N}}\sum_l V_l'(\boldsymbol{b}_l)_{\boldsymbol{q}t}\left\{\int\psi_{\boldsymbol{k}'}{}^*\psi_{\boldsymbol{k}}\exp(2\pi i(\boldsymbol{b}_l-\boldsymbol{q})\cdot\boldsymbol{r})\,d\boldsymbol{r}\right\}\sqrt{\dfrac{h}{8\pi^2\nu_t(\boldsymbol{q})}(N_{\boldsymbol{q}t}+1)}\ , \\ \qquad\qquad \text{when} \qquad N'_{\boldsymbol{q}t}=N_{\boldsymbol{q}t}+1 \end{array}\right\} \tag{16}$$

where $\nu_t(\boldsymbol{q})$ is the frequency of the mode $(\boldsymbol{q},\ t)$. The integral in (16) which is over the whole crystal is given by

$$\int\psi_{\boldsymbol{k}'}^*\psi_{\boldsymbol{k}}\exp(2\pi i(\boldsymbol{b}_l\pm\boldsymbol{q})\cdot\boldsymbol{r}\,d\boldsymbol{r}=\frac{1}{\Omega}\sum_{h'}\sum_h c_{k'h'}{}^*c_{kh}\int\exp(2\pi i\,(-\boldsymbol{k}_0'+\boldsymbol{k}_0-\boldsymbol{b}_{h'}+\boldsymbol{b}_h+\boldsymbol{b}_l\pm\boldsymbol{q})\cdot\boldsymbol{r})\,d\boldsymbol{r}$$

$$=\sum_{h'}\sum_h c_{k'h'}^*c_{kh}\,\delta_{\boldsymbol{k}'_0,\,\boldsymbol{k}_0+\boldsymbol{b}_g\pm\boldsymbol{q}}\ ,$$

where $\boldsymbol{g}=-\boldsymbol{h}'+\boldsymbol{h}+\boldsymbol{l}$. When $\boldsymbol{k}_0'$ and $\boldsymbol{k}_0$ are given, the reciprocal lattice vector $\boldsymbol{b}_g$ which satisfies $\boldsymbol{k}_0'=\boldsymbol{k}_0+\boldsymbol{b}_g\pm\boldsymbol{q}$ is uniquely determined, as the magnitude of $\boldsymbol{q}$ is restricted in the first Brillouin zone. So, in the summation over $\boldsymbol{l}$ in eq. (16), only a term remains which satisfies $\boldsymbol{l}=\boldsymbol{g}+\boldsymbol{h}'-\boldsymbol{h}$, and (16) becomes

$$(\boldsymbol{k}',\ N'_{\boldsymbol{q}t}|U(\boldsymbol{r})|\boldsymbol{k},\ N_{\boldsymbol{q}t})$$

$$=\left\{\begin{array}{ll} -\dfrac{i}{\sqrt{m_a N}}\sqrt{\dfrac{h}{2\nu_t(\boldsymbol{q})}N_{\boldsymbol{q}t}}\ \sum_{h'}\sum_h c_{k'h'}{}^*c_{hk}\,(\boldsymbol{b}_{g+h'-h})_{\boldsymbol{q}t}\,V_{g+h'-h}\ , & \\ \qquad\qquad \text{when}\ \ N'_{\boldsymbol{q}t}=N_{\boldsymbol{q}t}-1\ \ \text{and}\ \ \boldsymbol{k}_0'=\boldsymbol{k}_0+\boldsymbol{b}_g+\boldsymbol{q} & \\ -\dfrac{i}{\sqrt{m_a N}}\sqrt{\dfrac{h}{2\nu_t(\boldsymbol{q})}(N_{\boldsymbol{q}t}+1)}\ \sum_{h'}\sum_h c_{k'h'}{}^*c_{hk}(\boldsymbol{b}_{g+h'-h})_{\boldsymbol{q}t}\,V'_{g+h'-h}\ , & \\ \qquad\qquad \text{when}\ \ N'_{\boldsymbol{q}t}=N_{\boldsymbol{q}t}+1\ \ \text{and}\ \ \boldsymbol{k}_0'=\boldsymbol{k}_0+\boldsymbol{b}_g-\boldsymbol{q} & \\ 0 \qquad\qquad \text{otherwise}\ . & \end{array}\right\} \tag{17}$$

The probability per unit time of the transition is then given by

$$\frac{1}{\hbar^2}|(\boldsymbol{k}',\ N'_{\boldsymbol{q}t}\mid U(\boldsymbol{r})\mid\boldsymbol{k},\ N_{\boldsymbol{q}t})|^2\frac{\partial}{\partial t}\left(\frac{\sin\xi t}{\xi}\right)^2, \tag{18}$$

where

$$\xi=\frac{1}{2\hbar}\{E_{\boldsymbol{k}'}-E_{\boldsymbol{k}}+(N'_{\boldsymbol{q}t}-N_{\boldsymbol{q}t})h\nu_t(\boldsymbol{q})\}\ ,$$

$E_{\boldsymbol{k}}$ being the energy of electron in the state $\boldsymbol{k}$. Integrating (18) over the end states, as in the ordinary procedure,[22] we get

$$\frac{\Omega}{\hbar^2}\,d\omega\,|(\boldsymbol{k}',\ N'_{\boldsymbol{q}t}|U(\boldsymbol{r})|\boldsymbol{k},\ N_{\boldsymbol{q}t})|^2\,\frac{\partial}{\partial t}\int_0^\infty\left(\frac{\sin\xi t}{\xi}\right)^2 k'^2dk'$$

$$=\frac{2\pi\Omega}{\hbar}\,d\omega|\,(\boldsymbol{k}',\ N'_{\boldsymbol{q}t}\,|U(\boldsymbol{r})|\boldsymbol{k},\ N_{\boldsymbol{q}t})|^2k'^2\Big/\frac{\partial E_{\boldsymbol{k}'}}{\partial k'}\ . \tag{19}$$

We can assume, for fast electrons,

$$E_{\boldsymbol{k}'}=\frac{h^2}{2m}k'^2\ .$$

The probability (19) then turns out to be

$$\frac{m\Omega k'\,d\omega}{2\pi\hbar^3}|(\boldsymbol{k}',\ N'_{\boldsymbol{q}t}|U(\boldsymbol{r})\mid\boldsymbol{k},\ N_{\boldsymbol{q}t})|^2\ .$$

Since $E_k \gg h\nu_t(\boldsymbol{q})$, the electrons scattered by the transitions

$$(\boldsymbol{k}, N_{\boldsymbol{q}t}) \longrightarrow (\boldsymbol{k}+\boldsymbol{b}_g+\boldsymbol{q},\ N_{\boldsymbol{q}t}-1)$$

and

$$(\boldsymbol{k}, N_{-\boldsymbol{q}t}) \longrightarrow (\boldsymbol{k}+\boldsymbol{b}_g-(-\boldsymbol{q}),\ N_{-\boldsymbol{q}t}+1)$$

which differ in energy by the amount $2h\nu_t(\boldsymbol{q})$ can not be practically distinguished. Summing up for these two transitions and also for t, and considering that $\nu_t(\boldsymbol{q})=\nu_t(-\boldsymbol{q})$ and $\langle N_{\boldsymbol{q}t}\rangle=\langle N_{-\boldsymbol{q}t}\rangle=\{\exp(h\nu_t(\boldsymbol{q})/kT)-1\}^{-1}$, we obtain the transition probability per unit time $P_{k',k}d\omega$ for which the wave vector of the scattered electron lies in the solid angle $d\omega$ in the direction of $\boldsymbol{k}'$ as

$$\begin{aligned} P_{k'k}d\omega &= \frac{m\Omega}{2\pi\hbar^3}k'\frac{1}{m_aN}\sum_t\frac{h}{2\nu_t(\boldsymbol{q})}\{2\langle N_{\boldsymbol{q}t}\rangle+1\}\,|\sum_{h'}\sum_h c_{k'h'}{}^*c_{kh}(\boldsymbol{b}_{g+h'-h})_{\boldsymbol{q}t}V'_{g+h'-h}|^2\,d\omega \\ &= \frac{m\Omega_0}{\hbar^2m_a}k'\sum_t|\sum_{h'}\sum_h c_{k'h'}{}^*c_{kh}(\boldsymbol{b}_{g+h'-h})_{\boldsymbol{q}t}V'_{g+h'-h}|^2\frac{1}{\nu_t(\boldsymbol{q})}\left\{\frac{1}{\exp(h\nu_t(\boldsymbol{q})/kT)-1}+\frac{1}{2}\right\}d\omega\,, \end{aligned} \tag{20}$$

where $\Omega_0\equiv\Omega/N$ is the volume of the unit cell.

§ 5. The Intensity Formulae for the Diffuse Scattering

Let us calculate the intensity of the diffuse scattering when the primary wave in the crystal is given by a single Bloch function (2). When the intensity of the incident electron is designated by J_0, its density ρ is given by[23)]

$$\rho = J_0/v = J_0m/hK_0\,,$$

where v is the velocity of the incident electron and K_0 is its wave number in vacuum. In the calculation of the preceding section, the wave function of the primary wave is normalized in the whole crystal so that the electron density is $1/\Omega$. The intensity $J_{s,h'}$ of the component plane wave of the secondary wave in vacuum having the wave vector $\boldsymbol{K}'_{h'}$ is consequently given by

$$J_{s,h'}=(P_{k'k}|c_{k'h'}|^2/R^2)\{(J_0m/hK_0)/(1/\Omega)\}\tau\frac{d\omega}{d\omega_0} \tag{21}$$

where R is the distance from the crystal to the point of measurement, τ is the transmissivity of electrons at the exist surface, and $d\omega/d\omega_0$ indicate the effect of refraction at the exit surface, where the solid angle $d\omega$ of the secondary ray in crystal changes into $d\omega_0$ in vacuum on passing the surface, as shown schematically in Fig. 2. Substituting (20) into (21) and remembering that $k'\approx K$, we obtain

$$\begin{aligned} J_{s,h'} &= \frac{J_0}{R^2}\frac{N}{m_a}|c_{k'h'}|^2\sum_t|\sum_{h'}\sum_h c_{k'h'}{}^*c_{kh}(\boldsymbol{b}_{g+h'-h})_{\boldsymbol{q}t}f_{e',g+h'-h}|^2 \\ &\quad\times\frac{h}{\nu_t(\boldsymbol{q})}\left\{\frac{1}{\exp(h\nu_t(\boldsymbol{q})/kT)-1}+\frac{1}{2}\right\}\tau\frac{d\omega}{d\omega_0}\,, \end{aligned} \tag{22}$$

where

$$f'_{e,h}=f_{e,h}\exp(-M)\,,\qquad f_{e,h}=-\frac{m\Omega_0}{2\pi\hbar^2}V_h\,. \tag{23}$$

If the electron distribution around each atom is the same as for free atoms, V_h is given by

$$V_h=-e^2(Z-f_{x,h})/\pi\Omega_0|\boldsymbol{b}_h|^2\,, \tag{24}$$

where Z is the atomic number, $f_{x,h}$, the atomic scattering factor for X-rays and e, the electronic charge. Putting (24) into (23), we get

$$f_{e,h}=\frac{2e^2m}{h^2|\boldsymbol{b}_h|^2}(Z-f_{x,h})\,, \tag{25}$$

which states that f_e is the atomic scattering factor for electrons.

If Nordheim's potential (7) is assumed instead of Bloch's (6), we obtain following intensity formula of the temperature diffuse scattering (see Appendix).

$$J_{s,h'}=\frac{J_0}{R^2}\frac{N}{m_a}\,|\,c_{k'h'}\,|^2\sum_t\,|\,\sum_{h'}\sum_h c_{k'h'}{}^*\,c_{kh}\,(\boldsymbol{b}_{g+h'-h}+\boldsymbol{q})_{qt}\,f'_e(\boldsymbol{b}_{g+h'-h}+\boldsymbol{q})\,|^2$$
$$\times\frac{h}{\nu_t(\boldsymbol{q})}\left\{\frac{1}{\exp(h\nu_t(\boldsymbol{q})/kT)-1}+\frac{1}{2}\right\}\tau\,\frac{d\omega}{d\omega_0}\,. \tag{26}$$

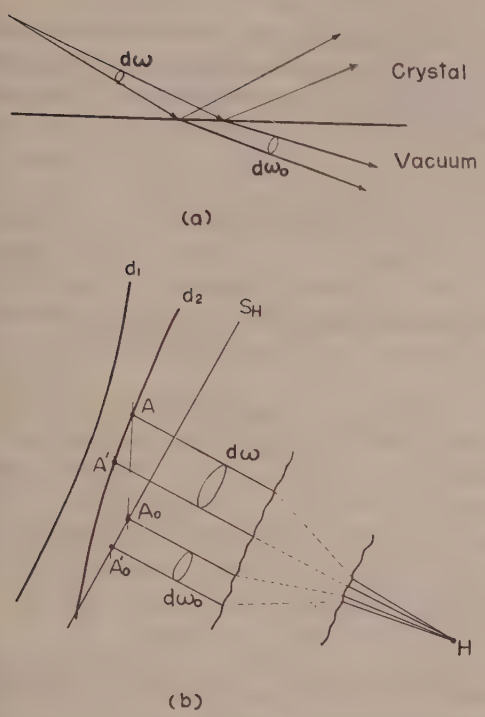

Fig. 2. (a) Showing the effect of reflexion and refraction at the exit surface. (b) Illustrating the relation between $d\omega$ and $d\omega_0$ in terms of the dispersion surface. H is the reciprocal lattice point, d_1 and d_2, two branches of the dispersion surface, S_H, a sphere of radius K_0 with H as centre. $\overrightarrow{AH}$ and $\overrightarrow{A'H}$ are the wave vectors of the crystal waves, $\overrightarrow{A_0H}$ and $\overrightarrow{A_0'H}$, those of the vacuum waves. $\overline{AA_0}$ and $\overline{A'A'_0}$ are perpendicular to the surface.

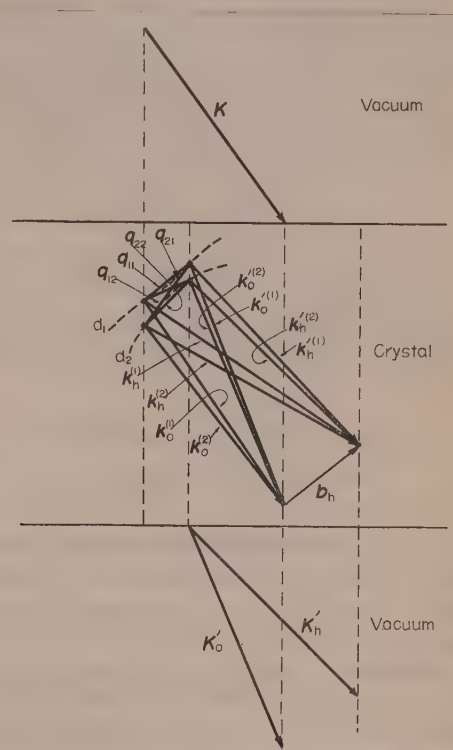

Fig. 3. Showing the relation between the wave vectors of crystal, vacuum and lattice waves. b_h is the reciprocal lattice vector. K's, k's and q's are the wave vectors of crystal, vacuum and lattice waves, respectively. Those with dash refer to the secondary or scattered waves, and without dash to primary or incident waves.

The difference between (22) and (26) is that the reciprocal lattice vector $\boldsymbol{b}_{g+h'-h}$ and the atomic scattering factor $f'_{e,g+h'-h}$ in (22) is replaced by $\boldsymbol{b}_{g+h'-h}+\boldsymbol{q}$ and $f_e'(\boldsymbol{b}_{g+h'-h}+\boldsymbol{q})$, respectively, in (26). The difference is unimportant when $|\boldsymbol{q}|$ is negligible compared with $|\boldsymbol{b}_{g+h'-h}|$.

In general, the primary wave in the crystal is given by the combination of Bloch functions (4) where $\boldsymbol{k}_0{}^{(i)}$ $(i=1, 2, \cdots)$ has the same tangential component as that of the incident wave, and many Bloch functions with the wave vectors having the equal tangential component can be connected to a single vacuum wave $\exp(2\pi i\boldsymbol{K}'_h\cdot\boldsymbol{r})$. So, in calculating the intensity of the vacuum wave, we should take account of many transitions $\psi_{\boldsymbol{k}}{}^{(i)}\to\psi_{\boldsymbol{k}'}{}^{(j)}$ $(i, j=1, 2, \cdots)$. As these transitions are related to different modes of vibrations which are mutually independent, the *intensity* of the vacuum wave is given by the sum of the *intensities* of the component wave resulting from each of the transitions,

$$J_{s,h'}=\sum_i\sum_j|\alpha_i|^2 J_{s,h'}{}^{ij}\,, \tag{27}$$

where i and j are the suffices for Bloch functions in the primary and secondary waves, α_i is the coefficient of the component Bloch functions in the primary wave (4), and $J_{s,h'}{}^{ij}$ is given by (22) with $\boldsymbol{q}$ replaced by $\boldsymbol{q}_{ij}$ which is given by

$$\boldsymbol{q}_{ij} = \boldsymbol{k}_0{}'^{(j)} - \boldsymbol{k}_0{}^{(i)} - \boldsymbol{b}_g \,. \tag{28}$$

The relation between the wave vectors of crystal, vacuum and lattice waves is shown in Fig. 3, where the case that each of the primary and secondary waves is given by the sum of two Bloch functions and that $\boldsymbol{b}_g=0$ is illustrated.

§ 6. Case of Plane Waves

When each of the primary and secondary waves in the crystal does not excite any Bragg reflexions, each wave is given by a single plane wave, i.e.

$$c_{k,h}=\delta_{h,0} \quad \text{and} \quad c_{k'h'}=\delta_{h',0} \,.$$

Let us further assume that the effect of reflexion and refaction at the exit surface can be neglected, i.e. $\tau d\omega/d\omega_0=1$. Then (26) becomes

$$J_{s,0}=\frac{J_0}{R^2}\frac{N}{m_a}\sum_t(\boldsymbol{b}_g+\boldsymbol{q})^2{}_{q,t}\, f'_e(\boldsymbol{b}_g+\boldsymbol{q})\frac{h}{\nu_t(\boldsymbol{q})}\left\{\frac{1}{\exp(h\nu_t(\boldsymbol{q})/kT)-1}+\frac{1}{2}\right\},$$

$$J_{s,h'}=0 \qquad (\boldsymbol{h}' \neq 0) \,. \tag{29}$$

This is exactly the same result as that of the current theory of the temperature diffuse scattering.[16] On the other hand, (22) gives

$$J_{s,0}=\frac{J_0}{R^2}\frac{N}{m_a}\sum_t(\boldsymbol{b}_g)^2{}_{qt}\, f'_{e,g}\,\frac{h}{\nu_k(\boldsymbol{q})}\left\{\frac{1}{\exp(h\nu_t(\boldsymbol{q})/kT)-1}+\frac{1}{2}\right\},$$

$$J_{s,h'}=0 \qquad (\boldsymbol{h}' \neq 0) \,. \tag{30}$$

which will be obtained by replacing $\boldsymbol{b}_g+\boldsymbol{q}$ and $f_e'(\boldsymbol{b}_g+\boldsymbol{q})$ in (29) by $\boldsymbol{b}_g$ and $f_e'{}_{,g}$, respectively. This difference is caused by the adoption of different perturbation potentials. In Nordheim's method, it is assumed that each atom vibrate with the electron clould rigidly fixed to the nucleus, as in the current theory.

§ 7. Discussions

In this paper we have treated the temperature diffuse scattering of electrons by the perturbation theory. The treatment is kinematical so far as the diffuse scattering is concerned, since we have neglected the double diffuse scattering. On the other hand, we have taken account of the Bragg reflexion by the dynamical theory. The influence of the Bragg reflexion on the temperature diffuse scattering may be important when the Bragg reflexion is much more intense than the diffuse scattering. Eq. (22) and (26) shows, however, that in general the intensity of the diffuse scattering is the same, at least in *order of magnitude* whether the primary or secondary waves in the crystal satisfies the Bragg condition or not. In the latter case which we have treated in the preseding section, the ratio of the intensity of the diffuse scattering to that of the Bragg reflexion is the same as for X-rays for which, as is well known, this ratio is very small.

The diffuse scattering obtained in the present study is only the first order diffuse scattering produced by the emission or the absorption of one quantum of a vibrational mode. This result is obtained by the adoption of the perturbation potential (12) in which we have neglected the higher power terms in $u(\boldsymbol{r})$. If we take account of higher terms, we shall have higher order diffuse scatterings which result from the transitions accompanied by simultaneous emission or / and absorption of more than one quantum of vibrational modes, even if we neglect the double diffuse scattering. Higher order diffuse scatterihg of X-rays has been studied by Laval.[15] According to his result it is important at large scattering angles and at high temperatures.[24] This may be also valid for electron diffraction.

It is worth noticing that there is a slight difference between the intensity formulae given by Nordheim's potential and by Bloch's potential. In the case of a single plane wave these formulae are given by (29) and (30). The iso-diffusion surfaces around a reciprocal

lattice point have centre of symmetry at the reciprocal lattice point for (30), but not for (29). Lack of centre of symmetry in the case of the X-ray diffuse scattering from sylvine has been demonstrated by Laval.[26] It is possible to decide which of the perturbation potentials (6) or (7) is more appropriate for the present purpose by careful measurement of the intensity, provided that the relatively high background caused by the inelastical scattering and by the scattering at lattice imperfections could be eliminated. However, this elimination especially the elimination of the scattering at lattice imperfections may be difficult in the present stage of development. In this connection it must be noted that in detailed comparison of the calculated and measured intensities, the effect of weak waves must be taken into account which we have neglected in deriving (29) and (30).

We have assumed in this paper that the crystal is monatomic and a unit cell contains only one atom. When the unit cell contains more than one atom, a similar treatment holds for scatterings near a reciprocal lattice point which constitute most part of the temperature scattering at low and moderate temperatures. Because for these scatterings for which long lattice waves are concerned the acoustical mode is significant, since the frequency of the acoustical mode is much smaller than that of the optical mode for long waves. The result in the preceding sections are valid for long acoustical waves, if we replace the mass of an atom by the mass of a unit cell, since for long waves atoms in a unit cell oscillate almost in phase.

Application of the present theory to some simple cases of practical importance will be given in the next paper.

The author wishes to express his thanks to Prof. S. Miyake for his valuable discussions. The work was partly supported by a resarch grant of the Minstry of Education.

Appendix

Intensity Formula Derived from Nordheims's Potential

If Nordheim's potential is assumed, the perturbation potential becomes

$$U(\boldsymbol{r})=-2\pi i\int\sum_n(\boldsymbol{b}\cdot\boldsymbol{u}_n)u'(\boldsymbol{b})\exp(2\pi i\boldsymbol{b}\cdot(\boldsymbol{r}-\boldsymbol{r}_n))\,d\boldsymbol{b}\,, \tag{31}$$

for monatomic crystals, where $\boldsymbol{b}$ is a vector in the reciprocal space and

$$u'(\boldsymbol{b})=u(\boldsymbol{b})\exp(-M)=u(\boldsymbol{b})\exp(-2\pi^2\langle(\boldsymbol{b}\cdot\boldsymbol{u}_n)^2\rangle)\,,$$

$u(\boldsymbol{b})$ being the Fourier tranform of $v(\boldsymbol{r})$ defined by

$$u(\boldsymbol{b})=\int v(\boldsymbol{r})\exp(-2\pi i\boldsymbol{b}\cdot\boldsymbol{r})\,d\boldsymbol{r}\,.$$

Substituting (13) into (31), we obtain an expression for $U(\boldsymbol{r})$ and the matrix element becomes

$$\begin{aligned}&(\boldsymbol{k}',N'_{qt}\mid U(\boldsymbol{r})\mid\boldsymbol{k},N_{qt})\\&=-\frac{2\pi i}{\sqrt{m_aN}}\int u'(\boldsymbol{b})(\boldsymbol{b})_{qt}\sum_n\exp(-2\pi i(\boldsymbol{b}-\boldsymbol{q})\cdot\boldsymbol{r}_n)\left\{\int\psi_{\boldsymbol{k}'}^*(\boldsymbol{r})\psi_{\boldsymbol{k}}(\boldsymbol{r})\exp(2\pi i\boldsymbol{b}\cdot\boldsymbol{r})d\boldsymbol{r}\right\}d\boldsymbol{b}\sqrt{\frac{h}{8\pi^2\nu_t(\boldsymbol{q})}N_{qt}}\,,\\&\qquad\text{when}\qquad N'_{qt}=N_{qt}-1\,.\end{aligned} \tag{32}$$

Replacing $-\boldsymbol{q}$ and N_{qt} by $\boldsymbol{q}$ and $N_{qt}+1$, respectively, we get the expression for $N'_{qt}=N_{qt}+1$. The summation over n has non-zero value N, only when $\boldsymbol{b}-\boldsymbol{q}=\boldsymbol{b}_g$, where $\boldsymbol{b}_g$ is a reciprocal lattice vector. The second integral in (32), over the whole crystal, becomes

$$\int\psi_{\boldsymbol{k}'}^*(\boldsymbol{r})\psi_{\boldsymbol{k}}(\boldsymbol{r})\exp(2\pi i\boldsymbol{b}\cdot\boldsymbol{r})\,d\boldsymbol{r}=\frac{1}{\Omega}\sum_{h'}\sum_h c_{\boldsymbol{k}'h'}^*c_{\boldsymbol{k}h}\,\delta(\boldsymbol{b}-(\boldsymbol{k}'_{h'}-\boldsymbol{k}_h))\,,$$

Thus the matrix element turns out to be

$$(\boldsymbol{k}', N'_{\boldsymbol{q}t} \mid U(\boldsymbol{r}) \mid \boldsymbol{k}, N_{\boldsymbol{q}t})$$

$$= \left\{ \begin{array}{l} -\dfrac{i}{\Omega_0\sqrt{m_a N}}\sqrt{\dfrac{h}{2\nu_t(\boldsymbol{q})}N_{\boldsymbol{q}t}}\sum_{h'}\sum_{h} c_{\boldsymbol{k}'\boldsymbol{h}'}{}^{*}c_{\boldsymbol{k}\boldsymbol{h}}(\boldsymbol{b}_{g+h'-h}+\boldsymbol{q})_{\boldsymbol{q}t}\,u'(\boldsymbol{b}_{g+h'-h}+\boldsymbol{q}), \\ \qquad \text{when} \quad N'_{\boldsymbol{q}t}=N_{\boldsymbol{q}t}-1 \quad \text{and} \quad \boldsymbol{k}'_0=\boldsymbol{k}_0+\boldsymbol{b}_g+\boldsymbol{q}, \\ -\dfrac{i}{\Omega_0\sqrt{m_a N}}\sqrt{\dfrac{h}{2\nu_t(\boldsymbol{q})}(N_{\boldsymbol{q}t}+1)}\sum_{h'}\sum_{h} c_{\boldsymbol{k}'\boldsymbol{h}'}{}^{*}c_{\boldsymbol{k}\boldsymbol{h}}(\boldsymbol{b}_{g+h'-h}+\boldsymbol{q})_{\boldsymbol{q}t}\,u'(\boldsymbol{b}_{g+h'-h}+\boldsymbol{q}), \\ \qquad \text{when} \quad N'_{\boldsymbol{q}t}=N_{\boldsymbol{q}t}+1 \quad \text{and} \quad \boldsymbol{k}'_0=\boldsymbol{k}_0+\boldsymbol{b}_g-\boldsymbol{q}. \end{array} \right\} \tag{33}$$

It is easily shown that

$$f_e(\boldsymbol{b}) = -\frac{2\pi m}{h^2}u(\boldsymbol{b})$$

is the atomic scattering factor for electrons. Putting $f_e' = f_e \exp(-M)$ and using (33) in the derivation of the intensity formula, we obtain (26).

References

1) H. Bethe, Ann. Physik, **87** (1928), 72.
2) S. Miyake, K. Kohra and M. Takagi, Acta Cryst. **7** (1954) 393.
3) F. Kirchner and H. Raether, Phys. Zeits. **33** (1932) 510.
4) H. Raether, Zeits. Phys. **78** (1932) 527.
5) S. Kikuchi and S. Nakagawa, Sci. Pap. Inst. Phys. Chem. Res. Tokyo, **21** (1933) 80, 256.
6) S. Miyake, Kagaku, **12** (1941) 54 (in Japanese).
7) M. von Laue, *Materiewellen und ihre Interferenzen*, Akademische Verlagsgesellschaft, Leipzig, 1948, Kap, V.
8) Z. G. Pinsker, *Electron Diffraction*, Butterworths Scientific Publications, London, 1953, Chap. 8.
9) Y. Kainuma, Acta Cryst. **8** (1955) 247.
10) H. Watanabe, J. Phys. Soc. Japan, **10** (1955) 908.
11) H. Hashimoto, E. Yoda and H. Maeda, J. Phys. Soc. Japan, **11** (1956) 464.
12) M. Born and K. Sarginson, Proc. Roy. Soc. **A 179** (1941) 69.
13) M. Born, Proc. Roy. Soc. **A 180** (1942) 397.
14) I. Waller, Zeits. Phys. **17** (1923) 398.
15) J. Laval, Bull. Soc. Franç. Minerall. **64** (1941) 1, J. Phys. Radium, **15** (1954) 545, 658.
16) R. W. James, *Optical Principles of the Diffraction of X-rays*, G. Bell & Sons, Ltd., London, 1954, Chap. V.
17) G. P. Thomson and W. Cochrane, *Theory and Practice of Electron Diffraction*, MacMillan, London, 1939, Chap. XIX.
18) See for example, A. Sommerfeld and H. Bethe, *Handbuch der Physik*, XXIV/2, J. Springer, Berlin, 1933, Kap. 3, Ziff. 34.
19) F. Bloch, Zeits. Phys. **52** (1928) 555.
20) L. Nordheim, Ann. Physik, **9** (1931) 607.
21) H. Ott, Ann. Physik, **23** (1935) 169.
22) See for example N. F. Mott and H. Jones, *Theory of the Properties of Metals and Alloys*, Oxford, Clarendon Press, 1936, p. 250.
23) D. E. Wooldridge, Phys. Rev. **56** (1939) 562.
24) See also G. N. Ramachandran and W. A. Wooster, Acta Cryst. **4** (1951) 335.
25) J. Laval, Bull. Soc. franç, Mineral. **62** (1939) 137.

JOURNAL OF THE PHYSICAL SOCIETY OF JAPAN Vol. 13, No. 3, MARCH, 1958

On the Temperature Diffuse Scattering of Electrons

II. Applications to Practical Problems

By Satio TAKAGI

Institute of Physics, College of General Education, University of Tokyo Komaba, Meguro-ku, Tokyo

(Received November 16, 1957)

The results of the perturbation theory of the temperature diffuse scattering of electrons developed in the preceding paper are applied to practical problems with the assumption of two plane waves.

It is shown that the intensity of the diffuse scattering does not become infinite at a reciprocal lattice point as it does in the current theory but remains finite, that the temperature diffuse scattering gives rise to Kikuchi patterns, and that the intensity of diffuse spots changes abruptly when the incident wave excites a Bragg reflexion. The anomalous intensity variation of the diffuse spots from the surface of some single crystals may be due to this effect. In the Bragg case the direction of the diffuse scattering can be obtained by the modified Ewald construction which replaces the Ewald sphere by the equi-energy surface in the reciprocal space.

The possibility of treating the Kikuchi pattern due to the inelastical collision of incident electrons with lattice electrons by the present method is also discussed.

1. Introduction

In part I of the present paper[1)]* we have developed a perturbation theory of the temperature diffuse scattering of electrons and have derived the intensity formulae taking into account the circumstance that each of the primary and secondary waves** may excite Bragg reflexions. The general formulae for the intensity of the first order temperature diffuse scattering from monatomic crystals are given by (27–I)* with $J^{ij}_{s;h'}$ given by (22–I) or by (26–I), respectively, according as the Bloch or the Nordheim perturbation potentials are assumed. The formulae will now be applied to some simple cases of practical importance. The simplest case is that each of the primary and secondary waves does not excite any Bragg reflexions and is given by a single plane wave, as has been treated in Section 6–I. In this case the same result as that of the current X-ray diffraction theory applied to electron diffraction was obtained by the Nordheim potential, and also by the Bloch potential with a sufficient approximation except for small scattering angles.

In the following we consider the case in which each of the primary and secondary waves is given by a combination of at most two plane waves, disregarding the simultaneous Bragg reflexions and the effect of weak waves.

2. Application to the Laue Case

Let us consider the case of transmission through a thin crystal bounded by two parallel planes and assume that each of the wave vectors of the waves contained in the primary and secondary waves makes a small angle with the surface normal. In this case the effect of reflexion and refraction at the entrance and exit surfaces can be neglected. The parameter W introduced by Bethe[2)] (Selektionsfehler) describing the deviation from the Bragg condition is then given by (see Appendix I)

* In the following, Part I is referred to as [I]. Equations, sections and figures in Part I are cited by adding I, such as (27–I), Section 6–I etc.

** In this paper the primary or the secondary wave means the wave expressed by a Bloch function (2–I) and not a single plane wave contained in this function. The primary wave gives rise to the secondary wave by the process of temperature scattering.

$$W=-\frac{(\boldsymbol{K}+\boldsymbol{b}_h/2)\cdot\boldsymbol{b}_h}{|v_h'|}\,,\ * \qquad (1)$$

where $\boldsymbol{b}_h$ is the reciprocal lattice vector and

$$v_h'=(2m/h^2)V_h'\,, \qquad (2)$$

V_h' being the Fourier coefficient of $\langle V(\boldsymbol{r})\rangle$ or the time mean of the potential energy of an electron in the crystal. $\boldsymbol{K}$ is the wave vector of the primary wave in the mean potential V_0. The magnitude of $\boldsymbol{K}$ is given by

$$K^2=K_0^2-v_0\,,** \qquad (3)$$

where v_0 is given by $v_0=(2m/h^2)V_0$, the tangential component being equal to that of the incident wave.

Subject to these assumptions, the ratio of the amplitude of the two component waves is given by

$$c_{\boldsymbol{k},\boldsymbol{h}}^{(i)}/c_{\boldsymbol{k},o}^{(i)}=W\pm\sqrt{W^2+1}\ **$$
$$(+\text{ for } i=1,\ -\text{ for } i=2.), \qquad (4)$$

where the superscript i $(=1, 2)$ indicates the branch of the dispersion surface on which the wave point lies. If we put

$$W=\cot\beta, \qquad 0\leq\beta\leq\pi\,, \qquad (5)$$

we have $W+\sqrt{W^2+1}=\cot(\beta/2)$, $W-\sqrt{W^2+1}=-\tan(\beta/2)$, and since c's are normalized by (3–I), we get

$$\left.\begin{aligned} c_{\boldsymbol{k},o}^{(1)}&=\sin(\beta/2)\,, & c_{\boldsymbol{k},\boldsymbol{h}}^{(1)}&=\cos(\beta/2)\,,\\ c_{\boldsymbol{k},o}^{(2)}&=\cos(\beta/2), & c_{\boldsymbol{k},\boldsymbol{h}}^{(2)}&=-\sin(\beta/2)\,. \end{aligned}\right\} \qquad (6)$$

α's in (4–I) then become

$$\alpha_1=\sin(\beta/2)\,,\quad \alpha_2=\cos(\beta/2)\,,$$

and the wave function of the primary wave is given by

$$\psi_{\boldsymbol{k}}=(1/\sqrt{\Omega})[\sin(\beta/2)\{\sin(\beta/2)\exp(2\pi i\boldsymbol{k}_0^{(1)}\cdot\boldsymbol{r})+\cos(\beta/2)\exp(2\pi i\boldsymbol{k}_h^{(1)}\cdot\boldsymbol{r})\}$$
$$+\cos(\beta/2)\{\cos(\beta/2)\exp(2\pi i\boldsymbol{k}_0^{(2)}\cdot\boldsymbol{r})-\sin(\beta/2)\exp(2\pi i\boldsymbol{k}_h^{(2)}\cdot\boldsymbol{r})\}]$$

which is to be connected to the incident wave of electron density $1/\Omega$. We now consider the transition to the state designated by W'. Putting $W'=\cot\beta'$ $(0\leq\beta'\leq\pi)$, we get similar expressions as (6) for the secondary waves and obtain from (27–I) and (22–I)

$$J_{\mathrm{s},\boldsymbol{h}}=\sin^2\frac{\beta}{2}(J_{\mathrm{s},\boldsymbol{h}}^{11}+J_{\mathrm{s},\boldsymbol{h}}^{12})+\cos^2\frac{\beta}{2}(J_{\mathrm{s},\boldsymbol{h}}^{21}+J_{\mathrm{s},\boldsymbol{h}}^{22})\,,$$

$$J_{\mathrm{s},\boldsymbol{h}}^{11}=\frac{J_0}{R^2}\frac{N}{m_a}\cos^2\frac{\beta'}{2}\sum_t\left\{\cos\left(\frac{\beta}{2}-\frac{\beta'}{2}\right)(\boldsymbol{b}_g)_{q,t}f'_{\mathrm{e},g}\right.$$
$$\left.+\sin\frac{\beta'}{2}\cos\frac{\beta}{2}(\boldsymbol{b}_{g-h})_{q,t}f'_{\mathrm{e},g-h}+\cos\frac{\beta'}{2}\sin\frac{\beta}{2}(\boldsymbol{b}_{g+h})_{q,t}f'_{\mathrm{e},g+h}\right\}^2\frac{Q_t(\boldsymbol{q}_{11})}{\nu_t^2(\boldsymbol{q}_{11})}\,,$$

$$J_{\mathrm{s},\boldsymbol{h}}^{12}=\frac{J_0}{R^2}\frac{N}{m_a}\sin^2\frac{\beta'}{2}\sum_t\left\{\sin\left(\frac{\beta}{2}-\frac{\beta'}{2}\right)(\boldsymbol{b}_g)_{q,t}f'_{\mathrm{e},g}\right.$$
$$\left.+\cos\frac{\beta'}{2}\cos\frac{\beta}{2}(\boldsymbol{b}_{g-h})_{q,t}f'_{\mathrm{e},g-h}-\sin\frac{\beta'}{2}\sin\frac{\beta}{2}(\boldsymbol{b}_{g+h})_{q,t}f'_{\mathrm{e},g+h}\right\}^2\frac{Q_t(\boldsymbol{q}_{12})}{\nu_t^2(\boldsymbol{q}_{12})}\,, \qquad (7)$$

$$J_{\mathrm{s},\boldsymbol{h}}^{21}=\frac{J_0}{R^2}\frac{N}{m_a}\cos^2\frac{\beta'}{2}\sum_t\left\{-\sin\left(\frac{\beta}{2}-\frac{\beta'}{2}\right)(\boldsymbol{b}_g)_{q,t}f'_{\mathrm{e},g}\right.$$
$$\left.-\sin\frac{\beta'}{2}\sin\frac{\beta}{2}(\boldsymbol{b}_{g-h})_{q,t}f'_{\mathrm{e},g-h}+\cos\frac{\beta'}{2}\cos\frac{\beta}{2}(\boldsymbol{b}_{g+h})_{q,t}f'_{\mathrm{e},g+h}\right\}^2\frac{Q_t(\boldsymbol{q}_{21})}{\nu_t^2(\boldsymbol{q}_{21})}\,,$$

$$J_{\mathrm{s},\boldsymbol{h}}^{22}=\frac{J_0}{R^2}\frac{N}{m_a}\sin^2\frac{\beta'}{2}\sum_t\left\{\cos\left(\frac{\beta}{2}-\frac{\beta'}{2}\right)(\boldsymbol{b}_g)_{q,t}f'_{\mathrm{e},g}\right.$$
$$\left.-\cos\frac{\beta'}{2}\sin\frac{\beta}{2}(\boldsymbol{b}_{g-h})_{q,t}f'_{\mathrm{e},g-h}-\sin\frac{\beta'}{2}\cos\frac{\beta}{2}(\boldsymbol{b}_{g+h})_{q,t}f'_{\mathrm{e},g+h}\right\}^2\frac{Q_t(\boldsymbol{q}_{22})}{\nu_t^2(\boldsymbol{q}_{22})}\,,$$

where

$$Q_t(\boldsymbol{q})=h\nu_t(\boldsymbol{q})\left\{\frac{1}{\exp(h\nu_t(\boldsymbol{q})/kT)-1}+\frac{1}{2}\right\}$$

* Bethe's first approximation is used throughout this paper. i.e. we put $V_{11}=V_{22}=0$, $V_{12}=v_h$ in Bethe's notations (Reference 2, p. 78).

** v_k is real and negative. See (24–I)

and $J_{s,h}$ is the intesity of the scattered wave in vacuum which is connected to the waves $\exp(2\pi i \boldsymbol{k}_h'^{(1)}\cdot\boldsymbol{r})$ and $\exp(2\pi i \boldsymbol{k}_h'^{(2)}\cdot\boldsymbol{r})$ in the crystal at the surface. $\boldsymbol{k}_h'^{(j)}$ is given by

$$\boldsymbol{k}_h'^{(j)}=\boldsymbol{k}_0'^{(j)}+\boldsymbol{b}_h$$
$$=\boldsymbol{k}_0^{(i)}+\boldsymbol{b}_{g+h}+\boldsymbol{q}_{ij} \quad (i, j=1, 2). \quad (8)$$

The relation between $\boldsymbol{q}$'s, $\boldsymbol{k}$'s and $\boldsymbol{k}'$'s, in the case that $\boldsymbol{b}_g=0$, is illustrated in Fig. 3–I.

3. Intensity of the Temperature Diffuse Scattering Extremely Near a Reciprocal Lattice Point

We assume now that the Ewald sphere passes near the reciprocal lattice point designated by H. The primary wave then satisfies closely the Bragg condition concerning H, and we can obtain the intensity of the diffuse scattering around H by putting $\boldsymbol{b}_g=0$ in (7). Particularly interesting is the case when

$$\beta=\pi/2(W=0) \text{ and } \beta'\to\pi/2(W'\to 0). \quad (9)$$

Then (7) gives the intensity of the diffuse scattering extremely near the Bragg spot when the incident wave exactly satisfies the Bragg condition. According to the current theory the intensity tends to infinity at the reciprocal lattice point[3], while the present theory gives a finite value as is shown below.

For the sake of simplicity, the reciprocal lattice vector $\boldsymbol{b}_h$ is assumed to be parallel to the surface. In this case, (9) means that

$$\boldsymbol{q}_{11},\ \boldsymbol{q}_{22}\to 0 \text{ and } \boldsymbol{q}_{12},\ -\boldsymbol{q}_{21}\to \boldsymbol{q}_0\,, \quad (10)$$

where $\boldsymbol{q}_0$ is the vector in the reciprocal space drawn from the vertex of a branch of the

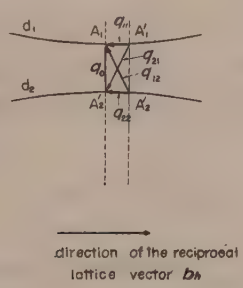

Fig. 1. Showing the relation between the wave vectors q_{ij} concerned in one transition. The reciprocal lattice vector $\boldsymbol{b}_h$ is parallel to the surface. A_1 and A_2 are the wave points of the primary waves and A_1' and A_2' are those of the secondary waves. Dotted lines are normal to the surface.

dispersion surface d_2 to that of d_1 (Fig. 1). Since the magnitude of $\boldsymbol{q}$'s are sufficiently small, we can put

$$Q_t(\boldsymbol{q}_{ij})=kT \quad (11)$$

and

$$\nu_t(\boldsymbol{q}_{ij})=c_t q_{ij}\,, \quad (12)$$

where $c_t(t=1, 2, 3)$ are the velocities of elastic waves in the crystal. Putting (9), (10), (11), (12) and $\boldsymbol{b}_g=0$ into (7), we obtain

$$J^{11}_{s,h}=\frac{1}{2}\frac{J_0}{R^2}\frac{N}{m_a}f'^2_{e,h}kT\cos^2\frac{\beta'}{2}\frac{1-\sin\beta'}{q_{11}^2}$$
$$\times\sum_t\frac{(\boldsymbol{b}_h)_{q,t}^2}{c_t^2} \quad \text{etc.} \quad (13)$$

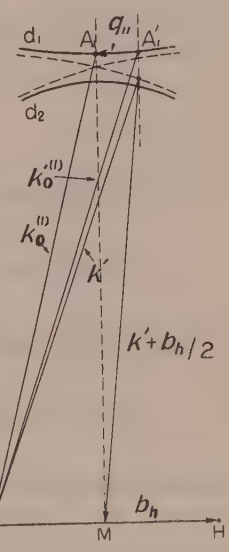

Fig. 2. Showing the relation between $\boldsymbol{k}_o$, $\boldsymbol{b}_h$ and $\boldsymbol{q}$ in the case that $\boldsymbol{b}_h$ is parallel to the surface. O and H are the origin and the point of the reciprocal lattice, respectively and M is the middle point of $\overline{OH}$.

When $\beta=\pi/2$ and $\boldsymbol{q}$'s are very small, $\boldsymbol{q}_{11}$ and $\boldsymbol{q}_{22}$ are nearly parallel to, and $\boldsymbol{q}_{12}$ and $\boldsymbol{q}_{21}$ are nearly perpendicular to $\boldsymbol{b}_h$. We see by Fig. 2 that

$$W'=-(\boldsymbol{K}'+\boldsymbol{b}_h/2)\cdot\boldsymbol{b}_h/|v_h'|=\pm|\boldsymbol{q}_{11}||\boldsymbol{b}_h|/|v_h'| \quad (14)$$

and we obtain

$$\frac{1-\sin\beta'}{q_{11}^2}=\frac{W'^2}{2q_{11}^2}=\frac{|\boldsymbol{b}_h|^2}{2|v_h'|^2}\,.$$

We now further assume that the crystal is elastically isotropic so that three vibrational modes associated with a wave vector are a longitudinal and two transverse waves. Then we get

$$J_{s,h}=\frac{1}{2}(J^{11}_{s,h}+J^{12}_{s,h}+J^{21}_{s,h}+J^{22}_{s,h})$$
$$=\frac{1}{2}\frac{J_0}{R^2}\frac{N}{m_a}|\boldsymbol{b}_h|^2 f'^2_{e,h}kT$$
$$\times\left\{\frac{1}{4}\frac{|\boldsymbol{b}_h|^2}{|v_h'|^2 c_l^2}+\frac{1}{q_0^2 c_{tr}^2}\right\}, \qquad (15)$$

where c_l and c_{tr} are the velocities of the longitudinal and transverse waves, respectively. The result of the dynamical theory gives $q_0=|v_h'|/K$ * and since $b_h/K=2\sin\theta$, where θ is the Bragg angle, is of the order of 1/100 in ordinary conditions, the first term in the curly bracket of (15) can be neglected. (15) then becomes

$$J_{s,h}=\frac{1}{2}\frac{J_0}{R^2}\frac{N}{m_a}f'^2_{e,h}|\boldsymbol{b}_h|^2 kT/c_{tr}^2|\boldsymbol{q}_0|^2 \qquad (16)$$

(16) means that the transition probability to the state on the same branch of the dispersion surface as that of the initial state is negligible compared with that to the different branch and that the intensity corresponding to the latter is equal to a half of the intensity, calculated by the current theory, at the vector distance $\boldsymbol{q}_0$ from the reciprocal lattice point H. This conclusion is also valid for the Nordheim potential (see Appendix II).

4. Kikuchi Patterns

We now consider the case when $\beta\to 0$: i.e. when the primary wave does not excite any Bragg reflexion and the secondary wave does excite a Bragg reflexion ($\boldsymbol{h}$). In this case (7) becomes

$$J_{s,h}=J^{21}_{s,h}+J^{22}_{s,h}$$
$$J^{21}_{s,h}=\frac{J_0}{R^2}\frac{N}{m_a}\sum_t\left\{\cos^2\frac{\beta'}{2}\sin^2\frac{\beta'}{2}(\boldsymbol{b}_g)^2_{\boldsymbol{q},t}f'^2_{e,g}+\cos^4\frac{\beta'}{2}(\boldsymbol{b}_{g+h})^2_{\boldsymbol{q},t}f'_{e,g+h}\right.$$
$$\left.+2\sin\frac{\beta'}{2}\cos^3\frac{\beta'}{2}(\boldsymbol{b}_g)_{\boldsymbol{q},t}(\boldsymbol{b}_{g+h})_{\boldsymbol{q},t}f'_{e,g}f'_{e,g+h}\right\}\frac{Q_t(\boldsymbol{q}_{21})}{\nu_t^2(\boldsymbol{q}_{21})}$$
$$J^{22}_{s,h}=\frac{J_0}{R^2}\frac{N}{m_a}\sum_t\left\{\cos^2\frac{\beta'}{2}\sin^2\frac{\beta'}{2}(\boldsymbol{b}_g)^2_{\boldsymbol{q},t}f'^2_{e,g}+\sin^4\frac{\beta'}{2}(\boldsymbol{b}_{g+h})^2_{\boldsymbol{q},t}f'^2_{e,g+h}\right.$$
$$\left.-2\sin^3\frac{\beta'}{2}\cos\frac{\beta'}{2}(\boldsymbol{b}_g)_{\boldsymbol{q},t}(\boldsymbol{b}_{g+h})_{\boldsymbol{q},t}f'_{e,g}f'_{e,g+h}\right\}\frac{Q_t(\boldsymbol{q}_{22})}{\nu_t^2(\boldsymbol{q}_{22})}.$$

Since q_0, the distance between the vertices of the dispersion surface, is very small ($\sim 10^{-4}$ A^{-1}, for $V_h=1$ volt and $\lambda=0.06$A), we can put $\boldsymbol{q}_{21}=\boldsymbol{q}_{22}=\boldsymbol{q}$, when $\boldsymbol{q}$'s are not too small. Then we get a more simple expression

$$J_{s,h}=\frac{J_0}{R^2}\frac{N}{m_a}\left\{\sum_t(\boldsymbol{b}_{g+h})^2_{\boldsymbol{q},t}f'^2_{e,g+h}\frac{Q_t(\boldsymbol{q})}{\nu_t^2(\boldsymbol{q})}+\frac{1}{2(W'^2+1)}\sum_t[(\boldsymbol{b}_g)^2_{\boldsymbol{q},t}f'^2_{e,g}-(\boldsymbol{b}_{g+h})^2_{\boldsymbol{q},t}f'^2_{e,g+h}]\frac{Q_t(\boldsymbol{q})}{\nu_t^2(\boldsymbol{q})}\right.$$
$$\left.+\frac{W'}{W'^2+1}\sum_t(\boldsymbol{b}_g)_{\boldsymbol{q},t}(\boldsymbol{b}_{g+h})_{\boldsymbol{q},t}f'_{e,g}f'_{e,g+h}\frac{Q_t(\boldsymbol{q})}{\nu_t^2(\boldsymbol{q})}\right\} \qquad (17)$$

by utilizing the relations $2\cos^2(\beta'/2)\sin^2(\beta'/2)=1/2(W'^2+1)$, $\cos^4(\beta'/2)+\sin^4(\beta'/2)=1-1/2(W'^2+1)$ and $2\sin(\beta'/2)\cos^3(\beta'/2)-2\sin^3(\beta'/2)\cos(\beta'/2)=W'/(W'^2+1)$. When (11) and (12) hold, (17) becomes

$$J_{s,h}=\frac{J_0}{R^2}\frac{N}{m_a}\frac{kT}{q^2}\left\{|\boldsymbol{b}_{g+h}|^2 f'^2_{e,g+h}\sum_t\frac{\cos^2\vartheta_{g+h,\boldsymbol{q}t}}{c_t^2}+\frac{1}{2(W'^2+1)}\left[|\boldsymbol{b}_g|^2 f'^2_{e,g}\sum_t\frac{\cos\vartheta_{g,\boldsymbol{q}t}}{c_t^2}\right.\right.$$
$$\left.\left.-|\boldsymbol{b}_{g+h}|^2 f'^2_{e,g+h}\sum_t\frac{\cos^2\vartheta_{g+h,\boldsymbol{q}t}}{c_t^2}\right]+\frac{W'}{W'^2+1}|\boldsymbol{b}_g||\boldsymbol{b}_{g+h}|f'_{e,g}f'_{e,g+h}\sum_t\frac{\cos\vartheta_{g,\boldsymbol{q}t}\cos\vartheta_{g+h,\boldsymbol{q}t}}{c_t^2}\right. \qquad (18)$$

where $\vartheta_{g,\boldsymbol{q}t}$ is the angle between $\boldsymbol{b}_g$ ant $\boldsymbol{e}_{\boldsymbol{q}t}$. $J_{s,h}$ in (17) and (18) signifies the intensity of the diffuse scattering in the direction $\boldsymbol{k}_h'$ which is given by (8)**. The relation between the wave vectors of the primary, the secondary and the lattice wave is shown in Fig. 3.

* See footnote * on p. 288.

** The difference of $\boldsymbol{k}_h'$'s designated by the superscript (i) is insignificant in the present case.

This result is analogous to that of Kainuma's theory[4] which treat the Kikuchi pattern as the result of the inelastical scattering*. The variation of the functions $1/2(W'^2+1)$ and $W'/(W'^2+1)$ in (17) or (18) with W' is shown in Fig. 4. The first term in the curly bracket of (17) or (18) correspond to the ordinary temperature diffuse scattering, the second term to the Kikuchi line and the third term to the Kikuchi band. The Kikuchi line is black or white according as the coefficient of $1/2(W'^2+1)$ is positive or negative, which is the intensity of the ordinary temperature diffuse scattering in the direction $\boldsymbol{k}_g'$ minus that in the direction $\boldsymbol{k}'_{g+h}$. The factor $|\boldsymbol{b}_g|^2 \cdot f'^2_{e,g}$ which is important in determining the intensity of the temperature diffuse scattering is shown in Fig. 5.

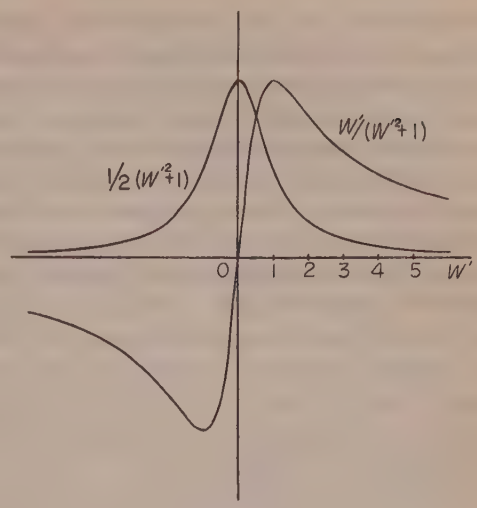

Fig. 4.

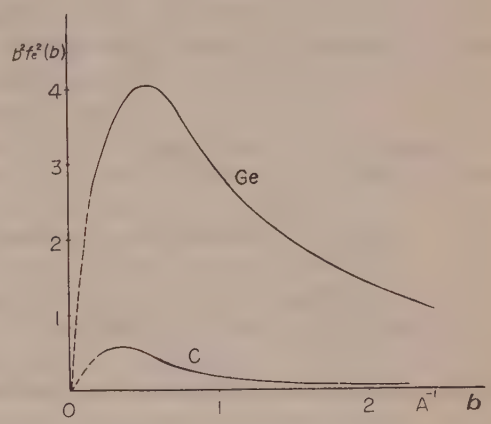

Fig. 5. $b=2\sin\theta/\lambda$.
$f_e(b)$: atomic scattering factor for electrons.

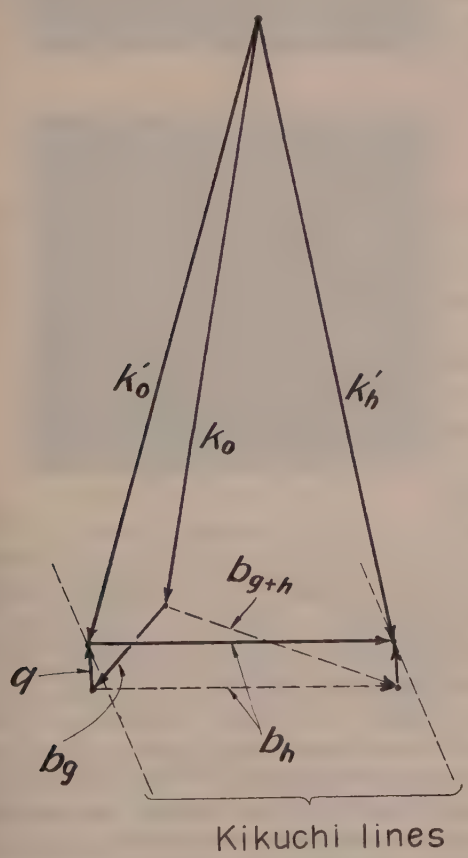

Fig. 3. Showing the relation between the wave vector of the primary wave $\boldsymbol{k}_o$, those of the secondary wave $\boldsymbol{k}_o'$ and $\boldsymbol{k}_h'$, that of lattice wave $\boldsymbol{q}$ and reciprocal lattice vectors. The direction of the Kikuchi line is also shown.

The intensity given by (17) or (18) will contribute to the intensity of the Kikuchi pattern actually observed. However, the intensity distribution is considerably different from the total intensity of the ordiary Kikuchi pattern. $J_{s,h}$ given by (18) is inversely proportional to q^2, so that it has a significant value only when q is small or only at points close to the reciprocal lattice point $(\boldsymbol{g}+\boldsymbol{h})$. The same is valid for $J_{s,h}$ given by (17). Thus the first order temperature scattering contributes to the intensity of the Kikuchi line only at points near a diffuse spot. The remaining part of the line is due to the other kind of scattering, mostly to the inelastical scattering. The intensity of some Kikuchi line is actually enhanced when they pass near a diffuse spot. The first order temperature scattering may actually contribute to the enhanced part. In

* See footnote * on p. 279 of [I].

this connection, it must be noted that Hashimoto and his collaborators[5] have studied the energy loss of diffracted electrons, from molybdenite, forming Kikuchi patterns and Kossel-Möllenstedt (K-M) patterns, by eliminating electrons with energy loss of more than a certain value, Δv, and observing the fading away of the patterns. On decreasing Δv, they observed that a part of Kikuchi lines far from the K-M pattern faded away, but a part near a K-M pattern remained even for $\Delta v=$ 2ev. This observation is consistent with the present result. This point may be further clarified by measuring the energy loss of electrons along a Kikuchi line.

Higher order temperature diffuse scattering which we have not treated in the present papers may also contribute to Kikuchi patterns. According to the approximate calculation for X-rays[6], the intensity of the second order scattering is inversely proportional to q instead of q^2 in the case of the first order scattering. Higher order temperature scatterings are less dependent on q. The intensity variation of the Kikuchi pattern with q may be slower for the higher order scattering than for the first order scattering.

5. Variation of the Intensity of Diffuse Spots with Change of the Direction of the Incident Wave

In this section, we shall treat the inverse case of the preceding section: i.e. the case when the primary wave excites a Bragg reflexion and the secondary wave does not, so that $\beta'\to 0$. The secondary wave is composed only of a plane wave with the wave vector $\boldsymbol{k}_0'=\boldsymbol{k}_0+\boldsymbol{b}_g+\boldsymbol{q}$ and the intensity of this wave $J_{s,o}$ is obtained by exchanging $\sin^2(\beta'/2)$ and $\cos^2(\beta'/2)$ in (7) and putting $\beta'=0$. The result is

$$\left.\begin{aligned}
J_{s,o}&=\sin^2\frac{\beta}{2}J^{12}_{s,o}+\cos^2\frac{\beta}{2}J^{22}_{s,o}\\
J^{12}_{s,o}&=\frac{J_0}{R^2}\frac{N}{m_a}\sum_t\left\{\sin\frac{\beta}{2}(\boldsymbol{b}_g)_{\boldsymbol{q},t}f'_{e,g}+\cos\frac{\beta}{2}(\boldsymbol{b}_{g-h})_{\boldsymbol{q},t}f'_{e,g-h}\right\}^2\frac{Q_t(\boldsymbol{q}_{12})}{\nu_t^2(\boldsymbol{q}_{12})}\\
J^{22}_{s,o}&=\frac{J_0}{R^2}\frac{N}{m_a}\sum_t\left\{\cos\frac{\beta}{2}(\boldsymbol{b}_g)_{\boldsymbol{q},t}f'_{e,g}-\sin\frac{\beta}{2}(\boldsymbol{b}_{g-h})_{\boldsymbol{q},t}f'_{e,g-h}\right\}^2\frac{Q_t(\boldsymbol{q}_{22})}{\nu_t^2(\boldsymbol{q}_{22})}
\end{aligned}\right\}\tag{19}$$

When $\boldsymbol{q}_{12}$ and $\boldsymbol{q}_{22}$ can be put equal as before, we get

$$\begin{aligned}
J_{s,o}=\frac{J_0}{R^2}\frac{N}{m_a}\Bigg\{&\sum_t(\boldsymbol{b}_g)^2_{\boldsymbol{q},t}f'_{e,g}\frac{Q_t(\boldsymbol{q})}{\nu_t^2(\boldsymbol{q})}+\frac{1}{2(W^2+1)}\sum_t\left[(\boldsymbol{b}_{g-h})^2_{\boldsymbol{q},t}f'_{e,g-h}-(\boldsymbol{b}_g)^2_{\boldsymbol{q},t}f'^2_{e,g}\right]\frac{Q_t(\boldsymbol{q})}{\nu_t^2(\boldsymbol{q})}\\
&-\frac{W}{W^2+1}\sum_t(\boldsymbol{b}_{g-h})_{\boldsymbol{q},t}(\boldsymbol{b}_g)_{\boldsymbol{q},t}f'_{e,g-h}f'_{e,g}\frac{Q_t(\boldsymbol{q})}{\nu_t^2(\boldsymbol{q})}\Bigg\}.
\end{aligned}\tag{20}$$

The results (19) and (20) predict that when the primary wave excites a Bragg reflexion the intensity of the diffuse spots generally varies abruptly. The variation with the W-value of the primary wave is similar to the intensity variation across a Kikuchi pattern discussed in the previous section. This effect is not yet observed in the transmission experiment. However, Miyake[7] has pointed out that the intensity of the diffuse spots from a cleavage face of zincblende is enhanced when the specular reflexion spot or the regular reflexion of the incident beam by the surface comes on a Kikuchi line which implies the occurance of a Bragg reflexion in the crystal, as has been pointed out by Miyake, Kohra and Takagi[8]. The enhanced diffuse spots are shown in Fig. 1–I. The effect is most remarkable when the reflected beam (Bragg reflexion) makes a small angle with the surface, the normal component of its wave vector being either positive (Laue case) or negative (Bragg case). This effect may be attributed to the same effect as predicted by (19) or (20), since the present argument in the case of normal incidence can also be applied with a slight modification at least to the Laue case with oblique incidence.

Particularly interesting is the case when the specular reflexion spot deviates slightly from the Kikuchi line. This case is shown in Fig. 6 a, b. The diffuse spots are more

intense in (a) than in (b), while the deviation of the specular reflexion spot from the Kikuchi line is equal in magnitude but opposite in direction. This may be explained by the third term in the curly bracket of (19) or (20). The problem of enhancement of the diffuse spot will be treated in more detail elesewhere.

(a)

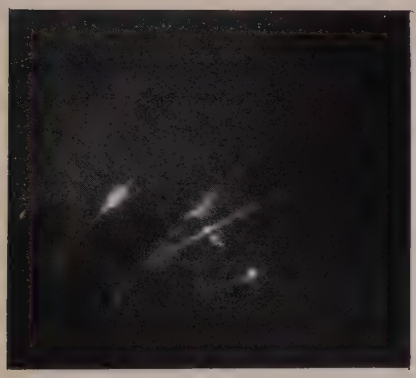

(b)

Fig. 6. Electron diffraction patterns from a cleavage face (110) of zincblende. The incident beam satisfies closely the Bragg condition concerning (260). The azimuth of the incident beam is slightly different in the two photographs. The specular reflexion spots are indicated by arrows. The incident spots are not shown.

6. Comments on the Bragg Case

In the Laue case, when the primary wave can be expressed by a combination of two plane waves, the wave field in the crystal which is connected to the incident wave is composed of two primary waves. In the Bragg case, however, only one primary wave out of the two is permitted in the crystal when the crystal is sufficiently thick, so that the incident electrons can not penetrate through the crystal. It is well known that in the range of selective reflexion, the crystal wave has a complex wave vector that it suffers absorption even if the crystal is non-absorbing in the ordinary sense. The absorption coefficient of one of the crystal waves is negative, i. e. the amplitude increases on penetrating into the crystal. The wave with negative absorption coefficient is not permitted in the crystal with sufficient thickness. Kohler[9] has pointed out that the same is valid for incidences outside the range of selective reflexion, if the true absorption is taken into account. In this case also, one of the primary wave has the negative absorption tion coefficient and it is not permitted even if the absorption is very weak, provided that μD is large, where μ is the absorption coefficient and D, the thickness of the crystal.

In the range of selective reflexion, the wave vector of the crystal wave is complex. These waves can not be treated by the present theory, because we have assumed that the wave field in the crystal can be expressed by a combination of plane waves with real wave vector. Outside this range, however, we can assume that the waves in the crystal have real wave vector (negligible absorption) but that there is only one primary wave permitted in the crystal. Then we can treat the problem in the Bragg case in the similar way as that given in the preceding sections. However, we shall not discuss the problem in detail but only comment some qualitative results.

(1) In deriving (17) and (18) for the intensity of the Kikuchi pattern, we have assumed that the primary wave in the crystal is a plane wave. (17) and (18) can therefore be applied to the Bragg case if the effect of reflexion and refraction at the entrance andexist surfaces is taken into acccount.

(2) The variation of the intensity of diffuse spots with change in the direction of the incident wave in the Laue case which is given by (19) or (20) is composed of two contributions from two primary waves. So, the variation in the Bragg case is different from that in the Laue case, though the variation itself will be observed in both cases.

(3) It is shown that in order to obtain the position of the diffuse spot, it is sufficient to consider only one transition from the state

represented by a wave point corresponding to a primary wave to the state represented by a wave point on the different branch of the dispresion surface from that of the initial state. The position of the diffuse spot is then obtained by the "modified Ewald construction" which replaces the Ewald sphere in the ordinary Ewald construction by an equi-energy surface which is the locus of the terminus of the wave vector of the crystal wave, drawn from a point, corresponding to the energy of the incident wave and which is congruent to and equally orientated as the dispersion surface. The detailed procedure is is given in Appendix III and illustrated in Fig. 7. The position of the diffuse spots obtained by this method is approximately equal to that obtained by the ordinary Ewald construction or by the kinematical theory,

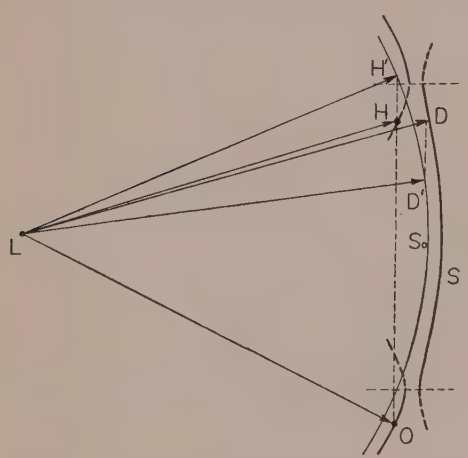

Fig. 7. The modified Ewald construction.

while the position of the sharp spots (given by LH′ in Fig. 7) is given by the dynamical theory and is such that they were produced by the two-dimensional diffraction from the surface lattice of the crystal, as has been pointed out by Bethe[2] and by Miyake, Kohra and Takagi[8].

7. Conclusions and Discussions

In this paper we have presented the results of the theory of the temperature diffuse scattering of electrons developed in [I] in some simple cases. The main results are the following.

(1) The intensity of the temperature diffuse scattering at a reciprocal lattice point is finite and is equal to a half of the intensity, given by the current theory, at a point which is the vector distance $\boldsymbol{q}_0$ apart from the reciprocal lattice point, where $\boldsymbol{q}_0$ is the smallest vector distance between two branches of the dispersion surface.

(2) Temperature diffuse scatterings give rise to Kikuchi patterns. The characteristic intensity variation across the Kikuchi line or band is the same as that given by Kainuma's theory. However, the intensity varies considerably along a Kicuchi line. Observed Kikuchi line becomes intense when it passes near a diffuse spot. The increased portion of the intensity may be due to the temperature scattering.

(3) When the incident beam excites a Bragg reflexion, the intensity of a diffuse spot changes abruptly. The variation of the intensity with change in the W-value of the incident wave is similar to the intensity varition across a Kikuchi pattern. This result may explain the anomalous intensity variation of the diffuse spots from the surface of some single crystals observed by Miyake[7].

(4) In the Bragg case, the position of diffuse spots are different from that of the sharp spots which appear on circular arrays. The positions can be determined by the "modified Ewald construction" which replaces the Ewald sphere by the equi-energy surface in the reciprocal space. The position of the diffuse spots in vaccum is approximately equal to that obtained by the ordinary Ewald construction.

We have obtained the Kikuchi pattern by the perturbation method without the rather complicated notion of "reciprocal waves" used in the theories of von Laue and of Kainuma. The Kikuchi pattern resulting from inelastical scattering* may also be treated by this method. The interaction of an incident electron and a lattice electron has been treated by several authors in the theories of the secondary electron emmission[10]. The theory of the Kikuchi pattern may be developed along similar lines.

The author wishes to express his thanks to Prof. S. Miyake for his valuable discussions. This work was partly supported by a research grant of the Ministry of Education.

* See footnote * on p. 279 of [1].

Appendix I. "Selektionsfehler" W in the Case of the Transmission though a Parallel-sided Crystal

In the notation of the present paper, W is given by[11]

$$W=-\frac{K\zeta}{|v_h'|\sqrt{\cos\vartheta_2/\cos\vartheta_1}}$$

Here v_h' and K is given by (2) and (3), respectively, ϑ_1 and ϑ_2 are the angle between the surface normal and $\boldsymbol{k}_o$ and $\boldsymbol{k}_h$, the wave vectors of the component waves of the primary wave, and ζ is the "Resonanzfehler" defined by $\zeta=\mathrm{LO}-\overline{\mathrm{LH}}$, where L is the Laue point, O and H are the origin and the point of the reciprocal lattice, respectively. As $\mathrm{LO}=K$ and $\mathrm{LH}=|K+\boldsymbol{b}_h|$, we have

$$\zeta=K-|\boldsymbol{K}+\boldsymbol{b}_h|=-(\boldsymbol{K}+\boldsymbol{b}_h/2)\cdot\boldsymbol{b}_h/K\,.$$

When ϑ_1 and ϑ_2 are small, $\cos\vartheta_2/\cos\vartheta_1\approx 1$, and we get Eq. (1).

Appendix II. Intensity of the Temperature Diffuse Scattering Extremely Near a Reciprocal lattice Point, in the Case of Nordheim's Potential

Putting $\boldsymbol{b}_g=0$, $\beta=\pi/2$ and $\beta'\to\pi/2$ in (27–I) and (26–I), we get, in the case of two plane waves,

$$J_{s,h}=\frac{1}{2}(J^{11}_{s,h}+J^{12}_{s,h}+J^{21}_{s,h}+J^{22}_{s,h})$$

$$J^{11}_{s,h}=J^{22}_{s,h}=\frac{1}{2}\frac{J_0}{R^2}\frac{N}{m_a}kT$$
$$\times\left\{f_e'(0)-\frac{1}{2}\frac{b_h^2}{|v_h'|}f_e'(\boldsymbol{b}_h)\right\}^2\Big/c_1^2$$

$$J^{12}_{s,h}=J^{21}_{s,h}=\frac{1}{2}\frac{J_0}{R^2}\frac{N}{m_a}\boldsymbol{b}_h^2f'^2_{e,h}kT/q_0^2c_{tr}^2$$

where we put

$$f_e'(\boldsymbol{b})=f_e'(\boldsymbol{b}_h)=f'_{e,h}\qquad(\boldsymbol{b}=\boldsymbol{b}_h\pm\boldsymbol{q}_0)\,,$$

since $|q_0|$ is small. This can also be written as

$$J_{s,h}=\frac{J_0}{R^2}\frac{N}{m_a}b_h^2f'^2_{e}{}_h kT$$
$$\times\left\{\frac{1}{2b_h^2}\left[\frac{f_e'(0)}{f_e'(\boldsymbol{b}_h)}-\frac{1}{2}\frac{b_h^2}{|v_h'|}\right]^2\Big/c_1^2\right.$$
$$\left.+\frac{1}{2q_0^2}\Big/c_r^2\right\}\,. \tag{21}$$

Values of $f_e(0)/f_e(\boldsymbol{b}_h)$ and $b_h^2/|v_h|$ for Ni are listed in Table I. $f_e(0)/f_e(\boldsymbol{b}_h)$ is at most of the same order of magnitude as, and in general much smaller than $b_h^2/|v_h|$. So the first term in the curly bracket of (21) is at most of the same order of magnitude as the first term in the curly bracket of (15) which can be neglected. Thus (16) is also valid in the present case.

Table I.

hkl	$f_e(0)/f_e(\boldsymbol{b}_h)$	$b_h^2/\|v_h\|$
111	4.02	2.73
222	9.7	20.4
333	17.2	85.5
444	26	259

Values of v_h are obtained from the values of V_h given by Bethe[2]. Values of $f_e(\boldsymbol{b}_h)$ are obtained by interpolation from those given by Mott and Massey[12].

Appendix III. The "Modified Ewald Construction"

The procedure of obtaining the position of the diffuse spot by the modified Ewald construction is shown in Fig. 7. In this figure S is the equi-energy surface corresponding to the energy of the incident wave, L is its centre and O is the origin of the reciprocal lattice. The tangential component of $\overrightarrow{\mathrm{LO}}$ is equal to that of the incident wave. $\overrightarrow{\mathrm{LO}}$ gives the wave vector of the primary wave in the crystal and if S passes near a reciprocal lattice point H, the primary wave contains also a plane wave with wave vector $\overrightarrow{\mathrm{LH}}$ which correspond to a sharp diffraction spot. The wave vector of the crystal wave corresponding to the centre of the diffuse spot is given by $\overrightarrow{\mathrm{LD}}$, where D is the point on S being nearest to H or more exactly the point of contact of S with an iso-diffusion surface around H. The directions of the corresponding vacuum waves are given by $\overrightarrow{\mathrm{LH}'}$ and $\overrightarrow{\mathrm{LD}'}$ as in the ordinary procedure, where H′ and D′ lie on S′, a sphere of radius K drawn around L, $\overline{\mathrm{HH}'}$ and $\overline{\mathrm{DD}'}$ being normal to the surface.

Though the position of the diffuse spot obtained by the present method is approximately equal to that obtained by the ordinary method as is mentioned in the text, the directions of the diffuse scattering in the crystal obtained by the two methods are somewhat different from each other.

References

1) S. Takagi, J. Phys. Soc. Japan, **13** (1958),
2) H. Bethe, Ann. Physik, **87** (1928), 55.
3) See for example: R. W. James, *Optical principles of the diffraction of X-rays*, G. Bell Sons, London, 1954, p. 210.
4) Y. Kainuma, Acta Cryst. **8** (1955), 247.
5) H. Hashimoto, E. Yoda and H. Maeda, J. Phys. Soc. Japan, **11** (1956), 464.
6) G. N. Ramachandran and W. A. Wooster, Acta Cryst. **4** (1951), 335.
7) S. Miyake, private communication.
8) S. Miyake, K. Kohra and M. Takagi, Acta Cryst. **7** (1954), 393.
9) M. Kohler, Ann. Phyisk, **18** (1933), 265.
10) See for example: D. E. Wooldridge, Phys. Rev. **56** (1939), 562.
11) G. P. Thomson and W. Cochrane, *Theory and Practice of Electron Diffraction*, McMillan, London, 1939, p. 292.
12) N. F. Mott and H. S. W. Massey, *Theory of atomic collisions*, Oxford, 1949. p. 190.

JOURNAL OF THE PHYSICAL SOCIETY OF JAPAN Vol. 13, No. 3, MARCH, 1958

Optical and Electrical Properties of Tin Oxide Films

By Kozo ISHIGURO, Taizo SASAKI, Toshihiro ARAI and Isamu IMAI

Department of Physics, College of General Education; Institute of Science and Technology, University of Tokyo

(Received June 29, 1957)

The electrical and optical properties of the transparent conducting tin oxide films were studied experimentally. The observed Hall effect and Seebeck effect show that the present specimens are n-type conductor whose carrier density is $10^{19}\sim10^{20}\,\mathrm{cm}^{-3}$. The optical measurements made it clear that the fundamental energy gap was about 4 ev and the plasma frequency of the conducting carriers lied in the near infrared region. By comparing the observed optical transmission and reflection with the theoretical values which can be calculated with the electrically measured constants, the effective mass of the carriers was determined to be about 1/5 of the free electron mass. It will be discussed in conclusion that, to satisfy the thermoelectric power relation with this small effective mass, we must assume that the Coulomb scattering of impurity ions is the predominant scattering mechanism in the transparent conducting tin oxide films.

§1. Introduction

Since the interesting properties of transparent conducting coating on glass surface were discovered, a large number of experimental works in this field have been reported[1]. But these have been confined almost exclusively to the refinement of the method of preparation and very few papers have refered to the analysis of their physical properties. The object of the present paper is to report on the experimental results carried out in our laboratory to make clear the optical and electrical properties of the typical transparent conducting coating, tin oxide film. In particular, the contribution of the free carriers, whose nature can be estimated from the electrical measurements, to the optical properties in the near infrared region will be discussed in some detail.

§2. Preparation of Samples

Among the various methods of preparation, the simplest one was adopted. Namely, one component solution of $SnCl_4 5H_2O$ crystal or $SnCl_4$ liquid in distilled water or in ethyl alcohol was sprayed by a small atomizer on the glass, fused silica or rock salt plates. The effect of mixing the impurities of III or V valency according to Verwey's principle of controlled valency[2] will not be discussed in

the present paper.

As shown in Fig. 1, the substrate was held downward in a main cylindrical electric furnace and the solution was sprayed onto it from the underlying atomizer. After passing through the preheating furnace, the atomized fog of $SnCl_4$ was poured upon the heated substrate. The adequate temperature of the main furnace was 500~600°C.

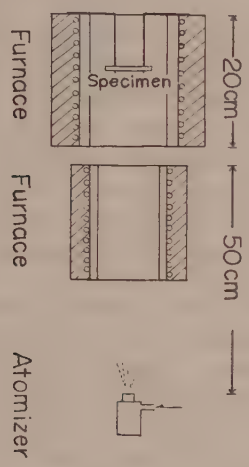

Fig. 1. Arrangement for preparing samples.

According to the electron diffraction observation, the main pattern coincides with that of SnO_2 and the rings are fairly sharp, indicating that the film is composed of crystallites not so small as to be interpreted as amporphous state.

§ 3. Electrical Properties

The experimental arrangement used for the conductivity measurement is shown schematically in Fig. 2. Knowing the film thickness, the conductivity of the sample can be calculated from the potential difference between the fixed points A and B, if a constant current is maintained in the sample from left to right in the figure. The potential difference was measured by the usual potentiometric method whose sensitivity was ca. 5 micro volts. To assure the ohmic contacts in the arrangement, careful pre-examinations had been repeated until the result was satisfactory. Table I summerizes the measured values for several different samples.

The Seebeck E.M.F. Θ was also measured by giving a temperature difference of several degrees between the point contacts A and B.

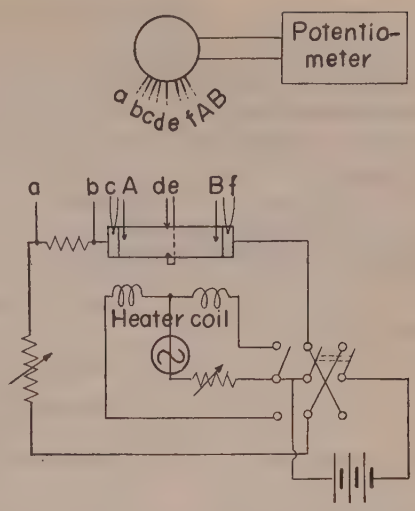

Fig. 2. Schematic diagram of circuit used for measurements of electric properties.

Since the Seebeck E.M.F. of tin oxide is much larger than that of copper which was used as point contact probes, the direction of thermoelectric power directly suggests the type of the free carriers in tin oxide. The conclusion is that our specimens are n-type carriers in accordance with Aichison[3] and Bauer[4].

The temperature dependence of Θ is given by the formula[5]

$$\left.\begin{aligned} \mathfrak{S} = -e\frac{d\Theta}{dT} &= \left(\frac{p}{6}+\frac{1}{2}\right)\pi^2 k \Big/ \xi \\ &\qquad \text{(in the degenerate case)} \\ &= \left(\frac{p}{2}+\frac{5}{2}-\xi\right)k \\ &\qquad \text{(in the non-degenerate case)} \end{aligned}\right\} \quad (1)$$

where

$\xi = \zeta / kT$,

ζ = Fermi energy,

p = scattering index defined from the proportionality of relaxation time τ to v^p.

p is an adjustable parameter chosen so as to give the best representation of τ. The limiting values of p are -1 and 3. The former corresponds to the scattering by the acoustical lattice vibrations and the latter to the Coulomb scattering by ionized atoms. In our specimens, the number of free electrons is such that they cannot be treated as a non-degenerate gas and it is necessary to consider them a transition case from classical to quantum statistics.

The correct Fermi energy and effective

Table I. Electrical constants of tin oxide films

Sample Number		15	16	18
Film thickness l (mμ)		110	42	82
Conductivity	σ (Ω cm)$^{-1}$ (room temp.)	430	63	155
	$d\sigma/dT$	~0	>0	>0
Hall coeff. H_R (cm^3/coul) (room temp)		0.075	0.145	0.11
Seebeck E.M.F. (μV/deg)	$\mathfrak{S}=\frac{d\Theta}{dT}$ (room temp.)	70	122	95
	$d\mathfrak{S}/dT$	0.18	~0.00	—
Photo conductivity	rise time (min)	2~3	1~3	1~3
	decay time (min)	~7	5~10	3~4
	$\Delta\sigma/\sigma$ (%)	0.3	—	1~2

Sample Number	15			18		
Carrier density n (cm^{-3}) (room temp.)	8.4×10^{19}			5.8×10^{19}		
Hall mobility μ_H (cm^2/volt. sec)(room temp.)	32			17		
Scattering index p	−1	0	3	−1	0	3
Fermi level $\zeta=(h^2/8m^*)(3n/\pi)^{2/3}$ (ev)	0.12	0.18	0.36	0.08	0.12	0.23
Effective mass m^*/m	0.59	0.39	0.20	0.71	0.47	0.24
Degenerate temp. T_{deg} (K°)	1400	2600	4100	900	1400	2700
Relaxation time τ (sec)	1.1×10^{-14}	7.1×10^{-15}	3.6×10^{-15}	6.7×10^{-15}	4.5×10^{-15}	2.2×10^{-15}
Mean free path $l=(2\zeta/m^*)^{1/2}\tau$	29 Å			13 Å		
Plasma frequency $\nu_P=(\sigma/\pi\tau)^{1/2}$ (sec^{-1})	1.07×10^{14}	1.32×10^{14}	1.84×10^{14}	0.82×10^{14}	1.00×10^{14}	1.42×10^{14}
Relaxation frequency $\nu_A=(1/2\pi\tau)$ (sec^{-1})	1.48×10^{13}	2.24×10^{13}	4.37×10^{13}	2.38×10^{13}	3.54×10^{13}	7.25×10^{13}
ν_B(sec^{-1})	1.559×10^{15}					
$\bar{\nu}_B$(sec^{-1})	2.802×10^{15}					
$(1/l)^3$ (cm^{-3})	4.1×10^{19}†			4.4×10^{20}		

† It may be interesting to notice that $n\approx(1/l)^3$ in the present case.

mass of carriers may be estimated from (1) by appropriate interpolations. However, as it is generally admitted that the effective mass m^* determined from the Seebeck effect gives too small value, we did not adopt the calculated value itself but assumed that the upper and lower limits of the effective mass were the free electron mass m and 1/10 of it respectively. The optical transmission and reflection calculated assuming these limiting values of the effective mass are compared with the measured values which are to be given in the next section.

The samples of relatively high electric conductivity change their conductivity neither by temperature variation nor by evacuation

But the low conductivity samples were rather unstable and the results obtained were similar to those of G. Bauer[4], who investigated the temperature dependence of conductivity, Seebeck E.M.F. and Hall coefficient of tin oxide films prepared by the oxidation of Sn films evaporated on fuzed quartz plates. Assuming that the temperature dependence of the low conductivity specimens is given by

$$\sigma = a \exp(-\varepsilon/kT),$$

the activation energy ε is estimated at 0.01~0.04 ev. By evacuation, however, the conductivity increases to about 10 times this value under the normal condition. It may be concluded, therefore, that the low conductivity samples are typical reduction type semiconductors, the excess Sn atoms supplying the conduction electrons.

A ceramic specimen with dimension $10\times2\times2$ mm showed the resistance of about 10^{11} ohms, which remained unchanged even after the bombardment with 2 Mev deuterons of ca. 10^{14} per cm² density generated by the cyclotron of Inst. of Science and Technology*. When the same specimen was evacuated, however, the resistance was found to decrease remarkably. This may be due to the escape of oxygen atoms from the surface layer.

The Hall constant R_H was obtained with some difficulties, since the effect was fairly small, especially for high conductivity samples whose constants were about $R_H = 0.075\,\mathrm{cm^3/coul}$. The measured constants indicates that the specimens are n-type in accordance with the Seebeck effect measurement. From the Hall constant of the typical sample No. 15, we estimate the carrier concentration N and Hall mobility μ_H as follows:

$$N = 8.4\times10^{19}\,\mathrm{cm^3}$$

$$\mu_H = 32\,\mathrm{cm^2/volt\cdot sec}\,.$$

§ 4. Optical Properties

The transmission and reflection in the wavelength region from 0.25 to 4.0 μ were measured by a small quartz spectro-photometer, and the transmission of the longer wavelength region was recorded by a Parkin Elmer spectro-photometer and a rock salt double monochrometer, Koken Type 301. As the substrates, fuzed quartz and rock salt plates were used. Fuzed quartz is superior than rock salt in the durability for the humidity and the mechanical impinging. Since it does not transparent for longer wavelength region than 4 μ, however, we must use rock salt plate for the mersurements in the region from 4 μ to 15 μ. Fig. 3 shows transmissivity

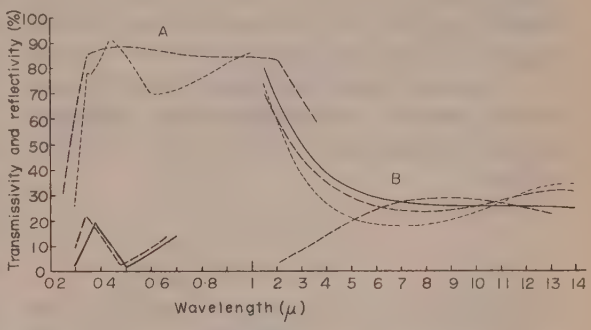

Fig. 3. Observed transmissivity and reflectivity of tin oxid films as a function of wavelength.
A: fuzed quartz substrate.
B: rock salt substrate.
—— , - - - , - - - - represent different specimens

versus wavelength curves. The substrate of sample A was a fuzed quartz plate and that of sample B was a rock salt plate. The specimens sprayed on rock salt plate generally show very low D.C. conductivity. Microscopic observation revealed that many cracks are present on these specimens, however, and the A.C. measurement proved that the conductivity remarkably increased already at 10 k.c. Therefore, these low D.C. conductivity is not the intrinsic nature of the film on rock salt substrate but is caused only by a macroscopic boundary effect of the cracks. Then the apparent low D.C. conductivity will not have any important influence on optical properties, if the scattering loss of the incident light by these cracks is corrected to give a smooth transmission curve connecting the values for the quartz and rock salt substrates.

A general survey of the curves shows that the specimens are almost perfectly transparent in visible region and the fundamental absorption begins at about 0.3 μ extending to shorter wave length. In the infrared region, the transmissivity decreases gradually whereas

* The bombardment was darried out by the courtesy of Prof. K. Ôno.

the reflectivity begins to increase*.

The absorption coefficients at the fundamental absorption edge are shown in Fig. 4. The correlation between the absorption coefficient and the D.C. conductivity was not detected.

The refractive index in the transparent region and the film thickness were obtained from the determination of the wavelengths corresponding to the interference maxima and minima and the reflectivities at these wavelengths. The film thickness was also checked by Tolansky's multiple beam interference method, and the refractive indices measurement was supplemented by Abelès' reflection method[7].

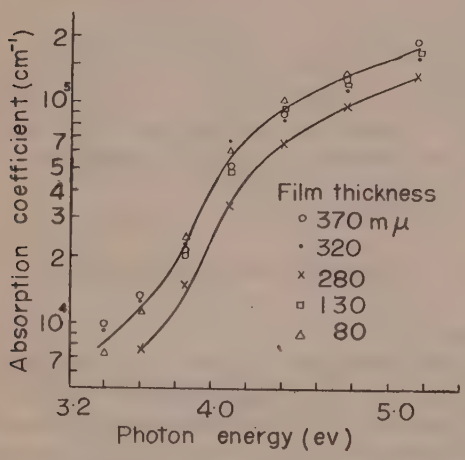

Fig. 4. Absorption coefficient at the fundamental absorption edge as a function of photon energy.

Some measurements were also made of the photo-conductivity. The photo current of about 1% of the dark current was observed when the specimen was exposed to light from a high pressure mercury lamp with a filter transmitting only ultra violet light. This observation confirms that the fundamental absorption edge corresponds to the energy gap between the valence band and the conduction band. But it should be noticed that the rise and decay time of photo-conductivity of the present specimens are several minutes or more. Since the correction of the thermoelectric effect induced by the temperature rise of the specimen by illumination of intense light has been considered, these slow time response cannot be explained by the thermal effect. It is not clear at present why such slow time response should occur in the specimens with so many dark free carriers which will immediately fill up the holes made by photo electrons.

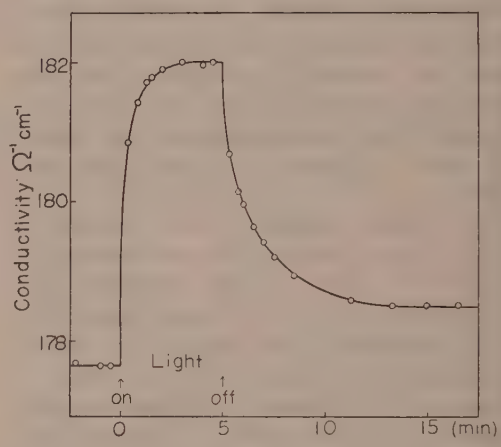

(a)

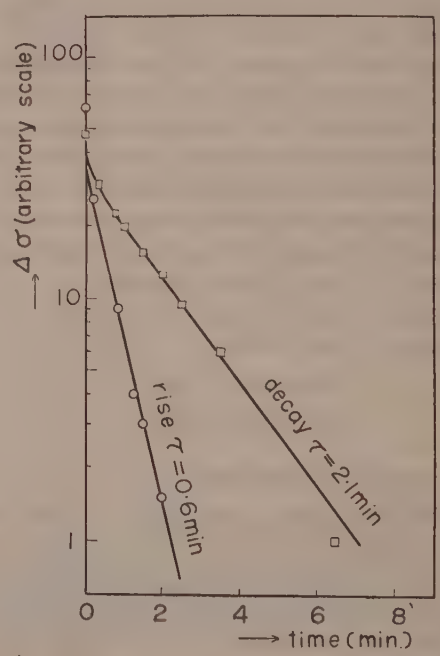

(b)

Fig. 5 (a), (b). Time dependency of photo-conduction.

* Aitchison reported that tin oxide was transparent from 0.2 to 14 microns[3]. But our observations do not support his results. He adopted reflection method and the sensitivity of the reflection method is high only when the absorption is very large and this may explain the cause of his neglect of absorption.

§ 5. Unified Discussions of Electrical and Optical Properties[9)]

E. Kanai[8)] proposed to adopt the well known optical theory of metals to explain the characteristics of tin oxide. He attributes the difference between the usual metals and tin oxide to the difference of the free carrier concentration. Though the plasma frequency of metals of high carrier concentration lies in the ultra violet region, that of tin oxide lies in the near infrared owing to the low carrier concentration. In his opinion, this is the cause of the optical transparency of tin oxide in spite of its metallic conduction. If this is the case, the measurements of optical properties may afford a supplemental method to determine effective mass and the scattering mechanism of free carriers even when the specimen is unstable for temperature change. This will be discussed below.

In germanium, the plasma frequency lies in the far infrared region owing to the low concentration of carriers, which makes its study very difficult. But in the case of semi metallic conductor such as tin oxide, we can investigate the optical anomalies expected at the plasma frequency without large experimental difficulty.

Let us suppose that the refractivity of tin oxide is caused by the combined effect of the intrinsic absorption continuum lying in the ultra violet region corresponding to the excitation of oxygen ions and the infrared absorption by the ohmic conduction of free carriers and, therefore, that it is not necessary to consider the absorption by lattice vibration.

The dispersion of refractive index, then, is given by the usual Drude-Krönig-Fujioka's formula

$$n^2-k^2=A_\nu-\frac{\nu_P^2}{\nu^2+\nu_A^2}$$

$$2nk=\frac{\nu_P^2\nu_A}{\nu^2+\nu_A^2}\frac{1}{\nu}+B_\nu\nu\ ,$$

where

$$n-ik=\text{complex refractive index}\ ,$$

$$\nu_P=\text{plasma frequency}$$

$$=(e^2N/m^*\pi)^{1/2}$$

$$=(\sigma/\pi\tau)^{1/2}\ ,$$

$$\nu_A=1/2\pi\tau\ ,$$

$$A_\nu=\bar{\nu}_B^2/(\nu_B^2-\nu^2)\ ,$$

$$B_\nu=\bar{\nu}_B\nu_C/(\nu_B^2-\nu^2)^2$$

and ν_B, $\bar{\nu}_B$, ν_C represent the mean effect of the fundamental electronic transitions in the ultra violet region.

For the longer wavelength region than the visible, one may put $B_\nu=0$, since the experiment shows that no absorption is present in the visible region. ν_B and $\bar{\nu}_B$ can be calculated from the observed refractive indices in the visible region, and ν_P and ν_A are determined from the electrical measurements. With these values, one can calculate the complex refractive index at any given frequency in the infrared region as shown in Table II.

If we assume that the film thickness is so large, say 10 μ, that the interference effect

Table II. Calculated refractive index and extinction coefficient as a function of wavelength

	$m^*=m$		$m^*=0.35m$		$m^*=0.1m$		experiment	
$\lambda(\mu)$	n	k	n	k	n	k	n	k
0.5	1.943	0.000	1.934	0.000	1.900	0.000	1.96	0.00
0.7	1.860	0.000	1.843	0.000	1.774	0.020	1.85	0.00
0.9	1.822	0.000	1.792	0.000	1.675	0.046		
1.0	1.811	0.000	1.774	0.000	1.633	0.062		
2·0	1.708	0.000	1.565	0.042	1.156	0.567		
3.0	1.604	0.022	1.227	0.177	1.187	1.414		
4.0	1.433	0.050	0.786	0.627	1.479	2.012		
5.0	1.186	0.114	0.696	1.311	1.792	2.448		
10.0	0.508	1.991	1.504	3.397	3.072	3.756		
15.0	0.905	3.435	2.471	4.652	3.997	4.599		
20.0	1.421	4.609	3.350	5.544	4.746	5.280		
50.0	4.881	8.986	6.965	8.647	7.840	8.188		

may be neglected, then one can write the reflectivity R and transmissivity T

$$R=\frac{(n_2-n)^2+k^2}{(n_2+n)^2+k^2},$$

$$T=\frac{16n_0n_2(n^2+k^2)}{\{(n+n_2)^2+k^2\}\{(n+n_0)^2+k^2\}}e^{-\alpha l},$$

where n_0 is the refractive index of the substrate and n_2 is that of the incident side medium. (Fig. 7)

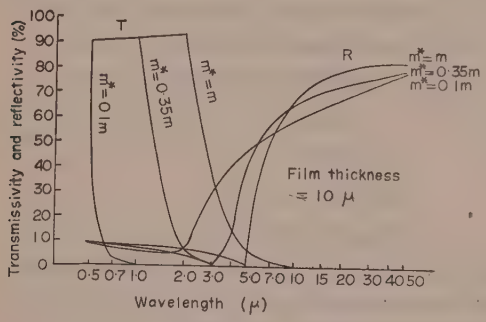

Fig. 6. Transmissivity and reflectivity calculated as a function of wavelength with the assumed effective mass; m*=0.1 m, 0.35 m and m. (film thickness=10 μ).

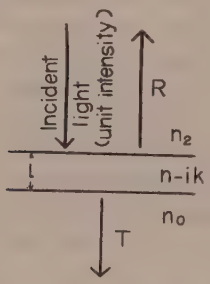

Fig. 7. Schematic explanation of transmissivity and reflectivity of film.

The calculated values are shown in Fig. 6. It is expected from them that the reflection increases remarkably for wavelengths longer than the wavelength corresponding to plasma frequency, and that the transmission decreases rapidly at the same wavelength region[13]. However, the actual specimens do not have such a large thickness and are only 0.1~0.3 μ thick. Then one cannot neglect the interference effect and must use the exact formula which involves the interference effect[10]:

$$R=e^{-\alpha l}\left\{\left(\frac{M_2}{N_2}\right)^2e^{\alpha l}+\left(\frac{M_0}{N_0}\right)^2e^{-\alpha l}-2\left(\frac{M_0M_2}{N_0N_2}\right)\cos(D+\Phi)\right\}|f|^2,$$

$$T=e^{-\alpha l}\frac{16n_0n_2(n^2+k^2)}{\{(n+n_2)^2+k^2\}\{(n+n_0)^2+k^2\}}|f|^2,$$

and

$$|f|^2=\frac{e^{\alpha l}}{\left\{e^{\alpha l}+\left(\frac{M_0M_2}{N_0N_2}\right)^2e^{-\alpha l}-2\left(\frac{M_0M_2}{N_0N_2}\right)\cos(D+\Psi)\right\}}$$

where

$$n_j-n_1=M_j\exp i\phi_j \qquad M_j^2=(n_j-n)^2+k^2$$
$$n_j+n_1=N_j\exp i\theta_j \qquad N_j^2=(n_j+n)^2+k^2$$
$$(j=0 \text{ or } 2)$$

$$(M_0M_2N_0N_2)\cos\Phi=(n^2+k^2)^2+n_0^2n_2^2-(n_0^2+n_2^2)(n^2+k)^2+4n_0n_2k^2$$
$$(M_0M_2N_0N_2)\sin\Phi=2k(n_0-n_2)(n^2+k^2+n_0n_2)$$
$$(M_0M_2N_0N_2)\cos\Psi=(n^2+k^2)^2+n_0^2n_2^2-(n_0^2+n_2^2)(n^2+k^2)-4n_0n_2k^2$$
$$(M_0M_2N_0N_2)\sin\Psi=2k(n_0+n_2)(n^2+k^2-n_0n_2).$$

In Fig. 8, the results of the calculations for the effective mass $m^*=0.1m$, $0.35m$ and m are

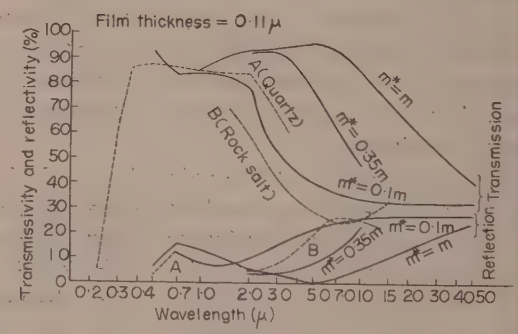

Fig. 8. Comparison of the observed transmissivity and reflectivity of tin oxide film with the calculated values with the assumed effective mass of free carriers: m*=0.1 m, 0.35 m and m. Full line=calculation, Dotted line=observation (film thickness=0.11 μ).

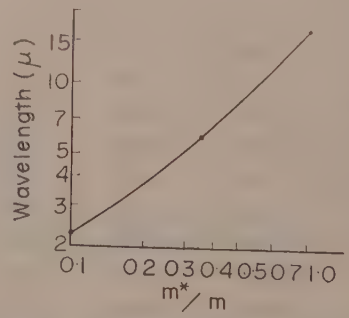

Fig. 9. Calculated wavelength corresponding to transmissivity 70% of tin oxide film of 0.11 μ thick as a function of m*/m.

compared with the experimental values (No. 15) where m is the free electron mass. To make the calculated one coincide with the experimental value, one may be inclined to adopt $m^* \approx 0.15m$. (Fig. 9) Then, if the equation (1) is valid for the present case, the scattering index p must be 3 in order to give such effective mass in the degenerate case (Table I). Then it may be concluded that, in the present specimens, the Coulomb scattering by ionized atoms is the rather predominant scattering mechanism.

§ 6. Discussions

The electrical and optical properties of tin oxide films mentioned above don't have the remarkable differences from the other oxides such as In_2O_3, CdO, ZnO etc., except the fact that the density of the free carriers are easily increased by the simple method and the films are strong and durable. Furthermore, it is reported by several authors[11] that the transparent electrodes are also made by In_2O_3 and CdO films prepared by sputtering method in an atmosphere of the adequate oxygen pressure and the mobilities of electrons are also in the range of $1 \sim 100\ cm^2/volt \cdot sec$. When these oxides are heated above 200°C, complex irreversible change due to adsorption, dissociation and diffusion of oxygen occurs and the interpretation of conductivity versus temperature curves must be cautions of these effects and the details of our experimental results of conductivity change with temperature of SnO and SnO_2 films will be reported later in another paper. Considering these circumstances, one of the interesting points of the study of SnO_2 films is to determine the source of the free carriers of such large density and our conclusion that the impurity scattering of free carriers is the predominant process in the conduction mechanism may be suggestive. But it must be noticed that the conclusion was derived by applying the well known usual theory of metals and only the scattering of lattice vibration of the acoustical mode was considered and the effect of optical vibration was neglected. But if the ionic character of the binding of SnO_2 crystal is large, such approximation may not be allowed.

Percentage ionic character P of SnO bonding is given by[12]

$$P = 16|x_{Sn} - x_0| + 3.5|x_{Sn} - x_0|^2$$
$$= 37.3\%$$

where $x_{Sn} \approx 1.8$ and $x_0 = 3.5$. This is fairly small comparing with the values of alkali halides. However, considering the fact that SnO_2 crystal is rutile type and Madelung constant is very large, the ionic character in bonding might be the considerable amount and the neglection of the interaction of the electron wave with the optical vibration of lattice may not be good approximation. On the other hand, however, the fact that the effective mass of our sample is small and same order with the homopolar crystals such as Ge and Si support the opposite stand point that the effect of optical mode is small. Because, with the increasing ionic character of the lattice, the free electron will be afforded the nature of polaron and the mass must be increased. The measurements of the absorption of infrared radiation in the residual ray region are desirable to make this problem clear. Finally, it will need some explanation that whereas the carrier density changed easily in order of 10^{19} by thermal treatment, the change by deuteron bombardment could not be detected. The number of the displaced atoms per unit volume from their regular sites by deuteron bomberdment are given approximately by $\rho(Z/M)\sigma N$, where ρ, Z and M are density, atomic number and mass number respectively and σ is the cross section of collision of the atom with deuteron and N is the number of irradiating deuterons per cm^2. In our experimental condition, if the carrier density change is proportional to the deficient number of oxygen atoms, it is anticipated that to obtain the possitive results the cross section of collision must be larger than 0.1 barns. Our negative result may suggest smaller cross section of collision between oxygen atom and deuteron.

§ 6. Summary

The electrical and optical properties of tin oxide films prepared by the spraying method were studied. The experiments carried out so far show that tin oxide is a conductor with n-type carriers and the optical properties in the near infrared region is influenced strongly by the properties of free carriers. In order to unify the optical and electrical measurement, the effective mass of the carriers must be taken as $1/5 \sim 1/7$ of the free

electron mass and the scattering index of the carriers p equal to 3. Compared with metals, tin oxide has some advantages in investigating the electric conduction mechanism and optical properties of free carriers, since the samples are transparent for wide frequency region and the specimens with the different carrier concentration can be prepared easily.

The authors wish to express their thanks to Mr. Kin'ichi Nakamura of N.H.K. for the presentation of the problem, to Mr. T. Kurachi and Prof. K. Kudo for their help in the infrared measurements, to Mr. M. Kuriyama and Prof. S. Takagi for the identification of the diffraction pattern and also to Prof. K. Takahashi for measurement of high resistance.

Furthermore, the authors wish to express their thanks to Dr. Hisao Miyazawa and Prof. Jiro Yamashita for their advices regarding several general properties of semiconductors.

References

1) H. A. McMaster: Chem. Abst. **41** (1948) 3925d, US Patent 2429420.
M. J. Zunick: Chem. Abst. **44** (1950) 11054e, US Patent 2516663.
J. M. Mochel: Chem. Abst. **45** (1951) 1318e, US Patent 2522531.
J. K. Davis: Chem. Abst. **46** (1952) 228a. US Patent 2564677.
J. M. Mochel: Chem. Abst. **46** (1952) 228b, US Patent 2564707, 2564987, 2564709, 2564710, 2564706, 2564708.
R. A. Gaiser and J. W. McAuley: Chem. Abst. **45** (1951) 10535i, US Patent 2567331.
W. O. Lytle and A. E. Junge: Chem. Abst. **46** (1952) 1373i, US Patent 2566346.
R. L. Gaiser: Chem. Abst. **46** (1952) 9234h, US Patent 2602032.
M. S. Tarnopol: Chem. Abst. **46** (1952) 11616i, US Patent 2606566.
R. F. Raymond and B. J. Dennison: Chem. Abst. **47** (1953) 7751g, US Patent 2617745.
W. O. Lytle and A. E. Junge: Chem. Abst. **48** (1954) 971c, US Patent 2651585.
T. K. Young and J. W. McAuley: Chem. Abst. **48** (1954) 6296e, US Patent 2667428.
R. Gomer: Rev. Sci. Inst. **24** (1953) 993.
2) E. J. W. Verwey: *Semiconducting materials* (Conference at Reading) 151 (1951).
F. A. Kroger and H. J. Vink: Physica XX (1954) 950,
3) R. E. Aitchison: Aust. J. App. Sci. **5** (1954) 10.
4) G. Bauer: Ann. d. Phys. **30** (1937) 433.
5) A. H. Wilson: The theory of metals 2nd ed. (1953) 232.
6) G. Kuwabara and K. Ishiguro: J. Phys. Soc. Japan **7** (1952) 72.
7) F. Abelés: J. Phys. et Rad. **11** (1950) 366.
8) E. Kanai: Report of Asahi Glass Co. V No. 1 (1955) 60 (in Japanese).
A. Fischer: Z. Naturforsch. **9a** (1954) 508.
9) H. Y. Fan and M. Becker: *Semiconducting materials* (Conference at Reading) 145 (1951).
E. Groschwitz and R. Wiesener: Z. Angew. Phys. **8** (1956) 391.
J. S. Benedict and W. Shockley: Phys. Rev. **89** (1953) 1152.
10) K. Ishiguro and G. Kuwabara: *Methods of optical measurement, Series of Modern Physics*, Iwanami Press (1955), (in Japanese).
11) L. Holland and G. Siddall: Vacuum III (1953).
A. Thelen and H. König: Naturwissenschaften **43** (1956) 297.
F. Lappe: Z. Phys. **137** (1954) 380.
12) C. A. Coulson: Valence (1952) 134.
Added references in proof.
13) W. G. Spitzer and H. Y. Fan: Phys. Rev. **106** (1957) 882.
W. G. Spitzer and H. Y. Fan: Phys. Rev. **108** (1957) 268.

JOURNAL OF THE PHYSICAL SOCIETY OF JAPAN Vol. 13, No. 3, MARCH, 1958

Statistical Aspect in Accelerating Creep and Creep Fracture of OFHC Copper

By Takeo YOKOBORI
Department of Mechanical Engineering, Tohoku University, Sendai
and Hideharu OHARA
Central Research Lab., Hitachi Ltd., Kokubunji, Tokyo

(Received December 5, 1957)

A large number of creep rupture tests on OFHC copper wire have been carried out at stress levels of 24.0~25.0 Kg/mm² and temperatures of 8~40°C. The F-test was made for the differences in variance between time for initiation of accelerating creep and time for rupture measured from the initiation of accelerating creep, and the regression analysis between these times was carried out. The scatter observed for these times appears to be an inherent characteristic of the material itself associated with a Markoff process—dynamic statistical process— as a rate process.

§ 1. Introduction

The scatter of the time for creep fracture under assumedly identical conditions is much larger than has generally been believed[1)-3)]. The recent studies indicate that the most of the scatter observed in creep life of metals appears to be an inherent characteristic of the material[1)-3)]. The statistical variations were interpreted as a Markoff process—dynamic statistical process—which are explained as a kind of rate process[1),2)]. In order to obtain more detailed knowledge on the problem, the creep fracture process was divided into the following two stages in the present study. These are Stage 1, from the instant of the application of the load till the initiation of accelerating creep, the period of which is denoted by t_1; and Stage 2, from the initiation of accelerating creep till fracture, the period of which is denoted by t_2. In the preliminary study on commercial copper by one (T. Yokobori) of the authors, there was no correlation between t_1 and t_2 at the 10% level of significance at the stress of 28.8 Kg/mm² and 28°C. In the present paper, the authors have attempted to verify the validity of independency of t_2 on t_1 at any stress level and temperature, and the validy of interpreting the Markoff process—dynamic statistical process—as a kind of rate process. While in the previous study[1),2)], commercial copper wire as cold-drawn was used, in the present study the specimens of OFHC copper as annealed were tested.

§ 2. Material and Treatment

The OFHC copper was obtained by vacuum melting. It is spectroscopically fine having the chemical analysis as shown in Table I,

Table I. Result of gas analysis.

Element	Content (%)
O_2	0.00033
H_2	0.00003
N_2	tr.

and was cold drawn to wire of 0.5 mm diameter from 10 mm diameter without intermediate annealing. The wire was cut into 130 specimens, the length between two chucks being kept at about 90 mm. The test specimens were annealed for 30 minutes at 300°C. The grains obtained are shown in Fig. 1.

§ 3. Procedures and Testing Equipment

The general arrangement of test equipment is shown in Fig. 2. The two similar equipments were used. The elongation of the test specimens was not magnified, but was recorded by a pen using a string. The ends of specimens were inserted into grooves of two chucks respectively, and tighted with small bolts. The temperature of atmosphere around the specimen did not vary throughout the test by more than ±0.5°C by regulating it at the room temperature. Applied stress and temperature are 24.0 Kg/mm², 24.5 Kg/mm², 25.0 Kg/mm² and 8°C, 20°C, 30°C, 40°C as shown

Table II. Summary of testd data*.

Specimen Number	Group Number**																	
	1 24.0 Kg/mm² 20°C		2 24.0 Kg/mm² 30°C		3 24.0 Kg/mm² 40°C		4 24.5 Kg/mm² 8°C		5 24.5 Kg/mm² 20°C		6 24.5 Kg/mm² 40°C		7 25.0 Kg/mm² 8°C		8 25.0 Kg/mm² 20°C		9 25.0 Kg/mm² 30°C	
1	105	37	85.5	6.5	5.5	2.5	160	19	9.5	1.5	0.63	0.37	72	35	5.2	3.8	5.7	4.3
	142	35.1	92	34.5	8	33.3	179	33.3	11	31.1	1	35.2	107	37.7	9	31.6	10	35.5
2	49.2	16.8	34.7	3.3	2.7	2.3	151	10	167	54	1.2	1.8	262	52	18.6	12.4	2	1
	66	29.2	38	30.5	5	34.1	161	29.0	221	33.3	3	35.1	314	37.7	31	32.1	3	36.1
3	282	60	20	3	27.3	26.7	162	30	61	34	1.3	0.7	32.8	25.2	12	5	6.7	1.3
	342	31.1	23	31.1	54	35.6	192	32.7	95	35.4	2	35.1	58	37.9	17	32.0	8	35.5
4	206	57	37.5	15.5	24.4	15.6	164	36	7.5	7.5	7.3	4.7	149	30	6.9	4.1	5.5	2.5
	263	32.0	53	30.7	40	29.9	200	37.2	15	35.1	12	25.2	179	42.2	11	30.7	8	33.9
5	63.6	22.4	14.5	8.5	4.7	1.3	190	36	8.7	9.3	1.9	5.1	40	21	14.9	4.1	2.3	1.7
	86	31.4	23	32.0	6	35.9	226	32.2	18	32.6	7	35.0	61	32.2	19	36.7	5	34.4
6	66	42	28.6	16.4	7.4	7.6	209	46	35.4	10.6	5.7	6.3	14.8	1.2	20.4	17.6	3.6	1.4
	108	31.8	45	35.0	15	28.2	255	33.0	46	29.0	12	35.5	16	31.1	38	29.5	5	32.9
7	28.4	30.6	47.4	58.6	6.9	7.1	246	61	64.5	24.5	6.9	1.1	20.0	18.8	23.4	11.6	2.3	1.7
	59	31.5	106	31.8	14	34.0	307	35.0	89	31.1	8	35.5	39	30.1	35	32.2	4	35.5
8	47	195	3.7	4.3	21.2	6.8	560	115	265	41	9.4	4.6	22	11	11.4	6.6	3.8	0.2
	242	35.5	8	31.1	28	43.4	675	36.8	306	29.5	14	32.5	33	31.7	18	35.5	4	35.5
9	236	28	44.3	9.7	4.5	7.5	706	24	22	0	0.8	0.2	10	5	52.1	38.9		
	264	35.0	54	37.7	12	34.4	730	35.6	22	22.4	1	34.6	15	31.1	91	33.5		
10	286	54	20	6	7.4	5.6	193	644	10.5	8.5	2.6	1.4	61.6	71.4	25.5	4.5		
	340	25.6	26	31.8	13	35.5	837	35.5	19	22.8	4	35.7	133	31.1	30	23.9		

11	240	44		8	1	1320	205	34.2	13.8	4.5	0.5	20.2	1.8	9.3	3.7		
	284	32.5		9	28.0	1525	34.5	48	33.0	5	40.5	22	36.6	13	34.5		
12	172	108		1.6	0.4	325	263	27.4	12.6	1.6	0.4	15.3	12.7	4.7	4.3		
	280	30.0		2	31.3	588	34.5	40	34.5	2	31.3	24	30.7	9	35.5		
13	132	28		2.4	6.6	425	187	2.9	1.1	1.6	0.4	37.4	11.6	3	3		
	160	23.3		9	36.1	612	37.2	4	23.0	2	37.8	49	35.1	6	35.5		
14	307	125		39.3	3.7	316	161	88.4	12.6	3.4	2.6	29.2	27.8	6.9	5.1		
	432	39.5		43	31.8	477	35.6	101	33.0	6	35.4	57	34.0	12	34.5		
15	372	108		3.4	2.6	280	80			3.8	2.2	19	7	23	16		
	480	36.6		6	32.1	360	37.7			6	34.3	26	28.4	39	33.5		
16	95	67		3.9	4.1	305	50			3.3	1.7	44.5	19.5	12.9	9.1		
	162	33.0		8	35.5	355	32.8			5	32.5	64	33.5	22	34.5		
17	157	50		1.1	0.9	42.6	34.4					18.7	5.3				
	207	30.7		2	30.0	77	31.1					24	27.5				
18				2.7	1.3	131	21					13.7	7.3				
				4	27.8	152	30.0					21	26.7				
19				3.2	5.8							18.9	5.1				
				9	32.7							2.4	41.0				
20				1.9	4.1												
				6	33.3												

* e.g. Group No. 2 85.5 6.5 = t_1=85.5 min. t_2=6.5 min.
Specimen No. 1 92 34.5 t_3=92 min. 34.5% Elongation

** Specimens of each group were chosen at random in respect of position in the original long wire.

Table II. Eight to twenty specimens were tested at each of stress levels and temperatures. The data of specimens which fractured near (at the distance less than 4 mm from) the chuck were excluded.

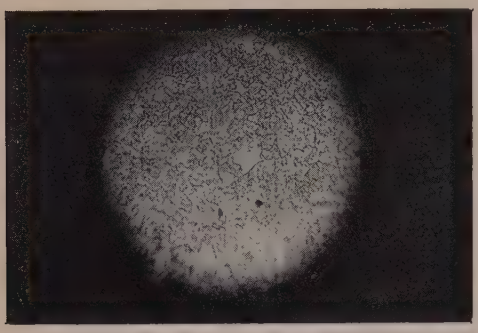

Fig. 1. Microstructure of OFHC copper. ×80.

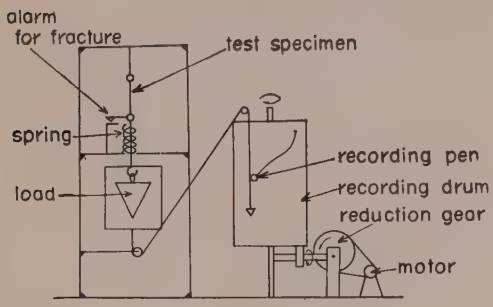

Fig. 2.

§ 4. Results

The type of fracture at the tested range of stress and temperature was necking type as shown in Fig. 3. The following notations are used in accordance with Fig. 4.

t_1=the time period for the initiation of accelerating creep measured from the instant of load application,

t_2=the time period for fracture measured from the instant of the initiation of accelerating creep, and

t_3=the time period for fracture measured from the instant at load application, that is, t_1+t_2.

t_1, t_2 and t_3 were determined from automatically recorded strain versus time curve (creep curves). t_3 was determined from automatically recorded strain versus time diagrams (creep curves). In the case of short value of t_3, the results were checked with stop-watch and the agreement was satisfactory. t_1 was determined from the same diagrams by trying to draw tangential straight lines to the curves and finding inflexion points. t_2 was obtained as t_3-t_1. t_1 determined in this manner seems rather slightly arbitrary because of always involved visual effect. The results, however, obtained by several trials in one curve show

Fig. 3. Fractured area of the specimen. ×245.

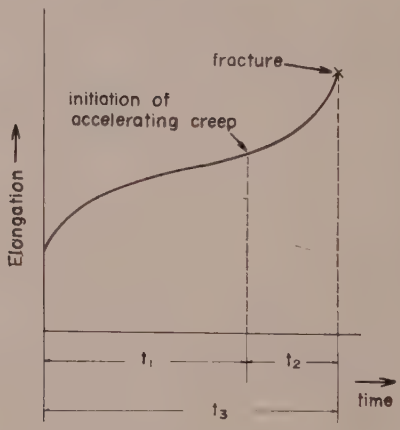

Fig. 4. Definition of t_1, t_2 and t_3.

that the scatter (error) of t_1 determined in this way was smaller than 15% of t_1 of the curve. Since the coefficient of variation of t_1 itself was almost 100%, the following treatment and conclusions in this articles may not be affected seriously by this method of determination of t_1, t_2 and t_3. The rawtest data are summarized in Table II.

§ 5. Statistical Analysis

The scatters of t_1 and t_2 were very remarkable and the frequency distributions appear to be roughly exponential type in all cases. Examples of the histograms are presented in Fig. 5. The F-test was applied to determine whether the differences in variance for t_1 and t_2 are significant at the 5% level of confidence. The logarithms of t_1 and t_2 were used, since exponential distribution is approximated with

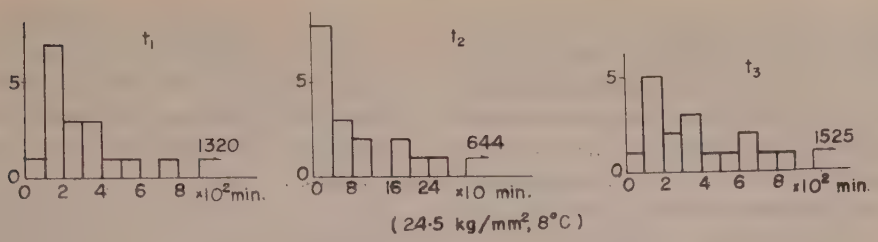

Fig. 5. Histogram of t_1, t_2 and t_3.

Table III. Summary of statistical analysis of test data.

Temperature °C	Stress Kg/mm²	Number of specimens tested	An unbiased value of despersion of log t_1	An unbiased value of despersion of log t_2	Result of F test at 5% level	Result of regression analysis of t_1 and t_2
8	24.5	18	0.108	0.245	Not Significant	Not Significant ($\alpha^*=50\%$)
	25.0	19	0.161	0.156	Not Significant	Not Significant ($\alpha=5\%$)
20	24.0	17	0.448	0.042	Significant	Not Significant ($\alpha=60\%$)
	24.5	14	0.342	0.055	Significant	Not Significant ($\alpha=10\%$)
	25.0	16	0.183	0.124	Not Significant	Not Significant ($\alpha=0.5\%$)
30	24.0	10	0.115	0.191	Not Significant	Not Significant ($\alpha=50\%$)
	25.0	8	0.068	0.019	Not Significant	Not Significant ($\alpha=80\%$)
40	24.0	20	0.198	0.169	Not Significant	Not Significant ($\alpha=2.5\%$)
	24.5	16	0.147	0.176	Not Significant	Not Significant ($\alpha=1\%$)

* α=The level of significance.

log normal distribution. In all cases except two, the differences in variance for t_1 and t_2 are not significant at the 5% level of confidence as shown in sixth column of Table III. Hence we may be justified to conclude that the scatter of t_1 and t_2 are of the same order of magnitude and very large.

Next, the regression analysis[4] was applied to determine whether the period t_2 of Stage 2 is dependent on the period t_1 of Stage 1. The results of the analysis are summarized in Table III. An examples of corresponding values of t_1 and t_2 are presented in Fig. 6. In five cases of nine tested the t-values were within the critical region corresponding to the level of significance larger than 10% as shown in Table III.

Consequently it can be concluded that there is no correlation between t_1 and t_2, and creep fracture process may be assumed as at least two successive events of Stage 1 and Stage 2.

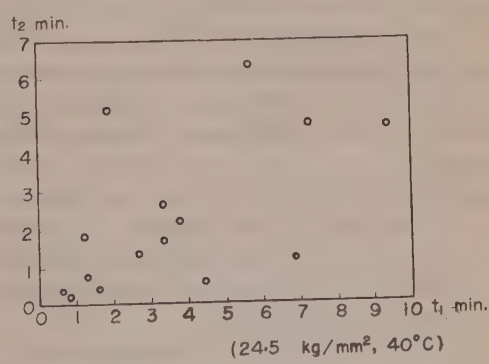

Fig. 6. Scatter diagram of t_1 and t_2.

§ 6. Physical Interpretation of Statistical Nature of Creep Fracture

The problems of the initiation of fracture

or yielding appears to have been interpreted as a Markoff process—dynamic statistical process[1),2),5),6),7),8)]. Let us take this approach in the present case and consider the physical nature of the statistical aspect. Let us denote the probability that the accelerating creep will initiate in the next interval of time dt, provided it has not initiated already, as

$$\mu_1(t)dt \qquad (1)$$

If $P_1(t)$ is the probability that the accelerating creep has not initiate at time t, the probability that it will initiate between times t and $t+dt$ is

$$P_1\mu_1 dt = -dP_1 \,. \qquad (2)$$

P_1 can be obtained using the frequency distribution curve $q_1(t)dt$ or approximately by the relation

$$P_1 = 1 - \frac{\nu}{n+1} \qquad (3)$$

Eq. (3) is the mean frequency of the νth of n observed observations. When t_1 is plotted as abscissae and the logarithm of P_1 as ordinates, then μ_1 is given by negative tangent of $\log P_1 - t_1$ plot. On integrating Eq. (2) we get

$$P_1(t) = \exp\left(-\int_0^t \mu_1(t)\right)dt \,. \qquad (4)$$

If μ_1 is independent of time, Eq. (4) reduces to

$$P_1(t) = \exp(-\mu_1 t) \,. \qquad (5)$$

In this case the frequency distribution curve is written as:

$$q_1 dt = \frac{-dP_1}{dt}dt = \mu_1 \exp(-\mu_1 t)dt \,. \qquad (6)$$

Next, let us take the same approach for Stage 2. The treatment is quite similar as for Stage 1 except the following notations instead of μ_1, q_1 and P_1 respectively and time is measured from the initiation of the accelerating creep.

$\mu_2(t)dt$ = the probability that the crack will occur in the next interval of time dt, provided it has not occured already, and

$P_2(t)$ = the probability that the crack has not occurd at time t.

The same formulae are obtained as Eq. (1), (2), (3), (4), (5) and (6) with μ_2, q_2 and P_2 instead of μ_1, q_1 and P_1 respectively. Logarithms of P_1 and P_2 were plotted against t_1 and t_2, respectively, for each applied stress and temperature. Examples of $\log P_1$ versus t_1, and $\log P_2$ versus t_2 plots are presented in Fig. 7. In all cases, $\log P - t$ plots may be approximated with straight lines except the initial portion corresponding to larger value of P. The averaged value $\bar{\mu}_1$ and $\bar{\mu}_2$ of μ_1 and μ_2 over the range of scatter of t_1 and t_2 were determined asuming the linearity of $\log P_1 - t_1$ and $\log P_2 - t_2$ plots respectively. The values of $\bar{\mu}_1$ and $\bar{\mu}_2$ obtained were plotted against reciprocal of absolute temperature T for each constant stresses as shown in Fig. 8. It appears that μ_1, $\bar{\mu}_2$ and T may be approximately related by:

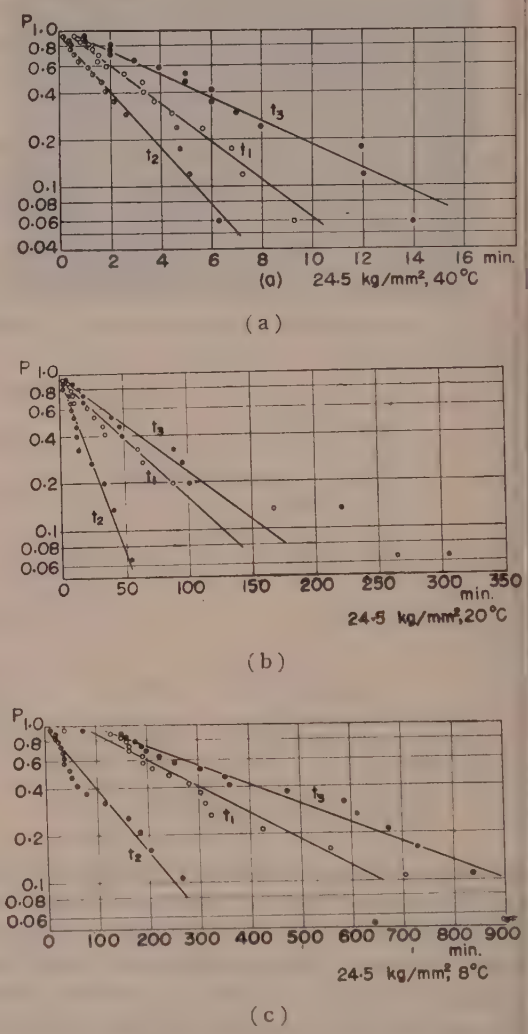

Fig. 7. The curve of $\log P - t$.
○, ◑ and ● denote t_1, t_2 and t_3, respectively.
P = the probability of non-fracture.

$$\bar{\mu}_1 = C_1 \exp(-U_1/RT) \qquad (7)$$

and

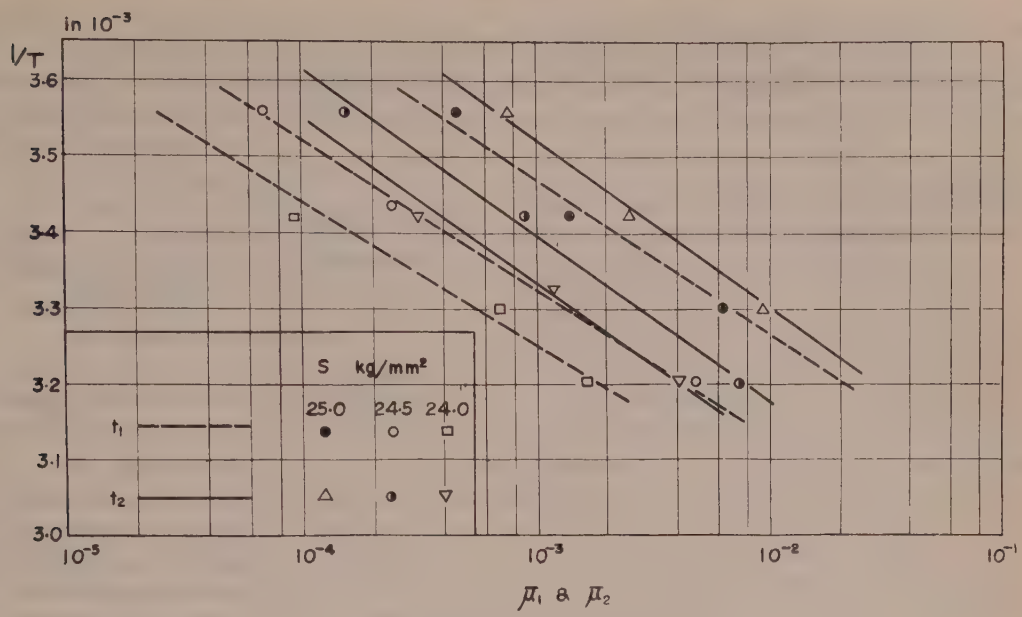

Fig. 8. The relation of $1/T$ to μ_1 and μ_2.
T=absolut temperature

$$\bar{\mu}_2 = C_2 \exp(-U_2/RT) \qquad (8)$$

where R is gas constant, C_1, C_2, U_1 and U_2 are constants. Eqs. (7) and (8) are of the same type as the rate in rate process, and U_1 and U_2 are regarded as activation energy. U_1 and U_2 can be determined from the tangent of the straight line in Fig. 8. In the range

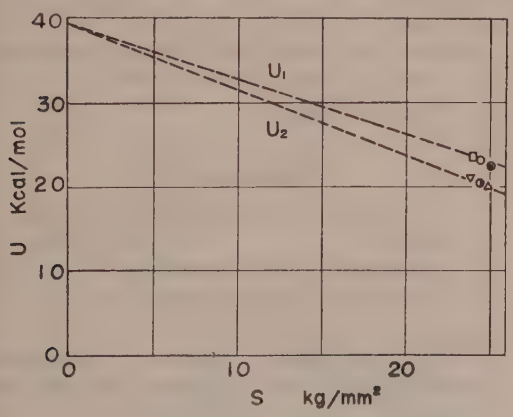

Fig. 9. The relation between activation energy U and stress level.

of 24.0 Kg/mm²~25.0 Kg/mm², U_1 and U_2 are 22.5~24.0 Kcal/mol. and 20~21 Kcal/mol. respectively. If U_1 and U_2 are plotted against stress as shown in Fig. 9, it appears that there is linearity between activation energy and stress. It is interesting that the straight lines can be extrapolated to pass through the value of 39.4 Kcal/mol., which is nearly equal to the activation energy of the creep of the same material obtained by one (Ohara) of the authors[9], or of the other pure copper[10].

The same approach was also applied assuming a whole process including Stage 1 and 2 as a Markoff process—dynamic statistical process. In this case, μ, q and P are used instead of μ_1 (or μ_2), q_1 (or q_2) and P_1 (or P_2). log P—t plot appears also to be linear as shown in Fig. 7. $\bar{\mu}$ determined by the same procedure has also approximately the same type as the rate in rate process as shown in Fig. 10. That is, we get:

$$\bar{\mu} = C \exp(-U/RT) \qquad (9)$$

where R, T, U and C have the same meaning as Eqs. (7) and (8). Hence it can be seen that a whole process may be at least formally well explained as a single rate process. This may be due to the fact that each of Stage 1 and 2 is a rate process and activation energies and stress dependence in both prosecess are almost equal respectively as seen from Fig. 9. If $\bar{\mu}$ is assumed to be approximately almost independent of time, then frequency distribution curve, qdt, of fracture time t_3 is given by the same type of equation as Eq. (6). On the other hand, Eq. (6) if approximated with log normal distribution function. In this sense, the scatter of creep fracture

time may assume log normal distribution. It can be seen from Eq. (9) that the scatter of time for fracture is smaller, the higher the temperature for constant stress and the higher the stress for constant temperature, since the variance D^2 of time for fracture is expressed by $1/\bar{\mu}^2$ in this case.

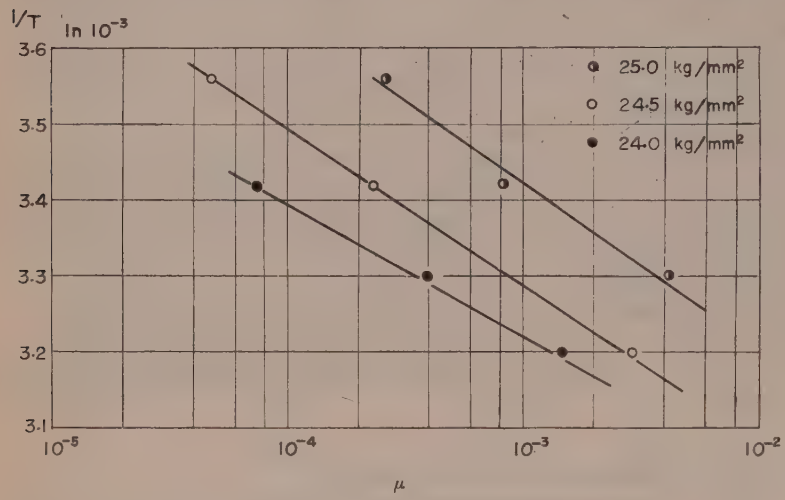

Fig. 10. The relation of $1/T$ to $\bar{\mu}$.

§ 7. Conclusion

Creep fracture tests on OFHC copper wire at 24.0 Kg/mm²~25.0 Kg/mm² and 8°C~40°C have been carried out and the results were statistically analysed. In the present case creep fracture process was divided into the following two stages: Stage 1, from the instant of load application to the initiation of accelerating creep, the period of which is denoted by t_1; and Stage 2, from the initiation of accelerating creep till fracture, the period of which is denoted by t_2. Then,

(1) Both of Stage 1 and 2 appear to be of statistical nature.

(2) Creep fracture process may be assumed as statistically at least two successive events of Stages 1 and 2, each of which is regarded as a Markoff process—dynamic statistical process.

(3) Creep fracture is not accurately described as a single process as usually treated.

(4) Each of Stage 1 and 2 is considered as a kind of rate process.

(5) The scattering of t_1 and t_2 can be interpreted as associated with a Markoff process—dynamic statistical process which is identified with a rate process.

(6) Since in the present case activation energies and the stress dependence in both rate processes are almost equal respectively, the whole process can approximately be expressed by a single rate process with the same activation energy.

(7) The following characteristic of scatter in creep life may be explained.

(i) The scatter of creep fracture time is of a log normal type of distribution, and

(ii) the scatter of creep life becomes smaller, the higher the temperature for constant stress and the higher the stress for constant temperature.

Acknowledgments

The present work was carried out by the financial aid of the Ministry of Education of Japan. The authors are greatly indebted to Dr. T. Kikuta, the Director of Central Research Laboratory, Hitachi Ltd., Prof. Y. Suezawa, Tokyo Institute of Technology, Prof. T. Akutagawa and Prof. R. R. Hasiguti, Department of Metallurgy, Univ. of Tokyo, for helpful advice and kindness. Appreciation is also due to Prof. M. Hirata for his useful advices and kindness.

References

1. T. Yokobori: J. Physical Society, Japan **6** (1951) 78.
2. T. Yokobori: Ibid. **7** (1952) 48.
3. C. W. Phillips and M. J. Sinnott: Trans. Amer. Soc. Metals **46** (1954) 63.
4. W. J. Dixon and F. J. Massey: "Introduction to Statistical Analysis," New York (McGraw-Hill Book Co., Inc.), (1950) 153.
5. T. Yokobori: Physical Rev. **88** (1952) 1423.
6. T. Yokobori: J. Appl. Physics. **25** (1954) 593.
7. T. Yokobori: J. Chemical Phys. **22** (1954) 951.
8. M. Hirata: Bulletin of Mathematical Statistics (in Japanese) **3** (1949) 57.
9. H. Ohara: J. Japan Inst. Metals **20** (1956) 105.
10. J. E. Dorn: "Creep aud Fracture of Metals at High Temperatures." London (N.P.L. and H.M.S.O.) (1956) 89.

Short Notes

This section is intended to secure prompt publication of important discoveries in physics. The reports should not exceed 800 words in length. A figure of size 7 cm × 7 cm will be counted as 150 words.

J. PHYS. SOC. JAPAN **13** (1958) 313

A Method for Measuring the Dynamic Viscosity & Dynamic Rigidity of Visco-elastic Liquids I.

Ali Abdel Kerim Ibrahim

Physics department, Faculty of Science, The University, Alexandria, Egypt

(Received November 19, 1957)

Consider a viscoelastic liquid of dynamic viscosity η_D in gm. cm.$^{-1}$ sec.$^{-1}$ dynamic rigidity N in dyne cm.$^{-2}$ is filling the annular gap between two coaxial cylinders. The outer cylinder (of inner radius b incm.) is oscillating through very small angles about 1° at various frequencies n in sec.$^{-1}$, the inner cylinder (of radius a in cm., length of immersion L in cm. and moment of inertia I in gm. cm.^{2}) is suspended by a delicate wire of torsion constant τ in gm. cm.^{2} sec.$^{-2}$.

If θ_0 is the angle of deflection of inner cylinder and ϕ_0 is that of the outer, then[1],

$$|\psi|^2=\frac{e^{6d/R}|\eta|^2}{e^{6d/R}|\eta|^2+4\gamma^2\omega^2d^2-4dN[\gamma(1+3d/R)+\rho d]} \tag{1}$$

where,

$$|\eta|^2=\left(\frac{N}{\omega}\right)^2+\eta_D{}^2$$

$$d=\frac{b-a}{2}$$

$$R=\frac{b+a}{2}$$

$$\omega=2\pi n$$

$$\gamma=\frac{I\omega^2-\tau}{K\omega^2}$$

$$K=2\pi La^3$$

and,

$$\psi=\theta_0/\phi_0\,.$$

After some rearrangement equation (1) becomes,

$$e^{6d/R}[\psi^{-2}-1]|\eta|^2=-4dN[\gamma(1+3d/R)+d\rho]+4\gamma^2\omega^2d^2 \tag{2}$$

Then, if ω is kept constant while the dimensions of the apparatus were varied then, ψ also varies and two equations are obtained. From these two equations the dynamic rigidity and dynamic viscosity can be determined.

A calculation of data on the rheometer as used for viscoelastic liquids follows. Using the symbols defined previously, the constants (Using Oldryed apparatus and results (2)) have the following values.

i) First case apparatus dimensions.

$R=2.1462$ cm. $\quad d=0.025$ cm.

$I=2677$ gm.cm.^{2}

$\gamma=1.294$ gm.cm.$^{-2}$ $\quad n=2.5$ sec.$^{-1}$

$\tau=2.79\times10^6$ gm.cm.^{2} sec.$^{-2}$ $\quad L=25.4$ cm.

With a mixture of poly (methyl methacrylate) and pyridine at 25°C (density 0.98 gm./ml.) in the rheometer, the value of ψ is 0.91.

Now equation (2) becomes,

$$1.902|\eta|^2=0.5853\,N+19.87 \tag{3}$$

ii) Second case of apparatus dimensions.

$R=2.1207$ cm. $\quad d=0.0505$ cm.

$I=2468$ gm.cm.^{2}

$\gamma=1.2445$ gm.cm.$^{-2}$ $\quad n=2.5$ sec.$^{-1}$

$\tau=2.79\times10^6$ gm.cm.^{2} sec.$^{-2}$ $\quad L=25.4$ cm.

With the same liquid in the rheometer the value of ψ is 0.39 and that equation (2) becomes,

$$6.411|\eta|^2=1.316\,N+94.17 \tag{4}$$

From equations (3) & (4), the value of N & η_D can be determined, the results are,

$$N=41.33 \text{ dyne cm.}^{-2}$$

$$\eta_D=4.03 \text{ Poise.}$$

Table (I) gives the values of the dynamic viscosity and dynamic rigidity of a mixture of poly (methyl methacrylate) and pyridine at various frequencies.

Table I.

n in sec.$^{-1}$	η_D in Poise	N in dyne cm.$^{-2}$
2.5	4.03	41.33
3	3.606	54.68
4	3.224	59.17
10	2.13	80.55

References

1) Ali Abdel Kerim Ibrahim: Ind. J. Phys. (In the press)

2) Oldroyed J. G. et al: Proc. Phys. Soc. London P. 44, 1951

J. PHYS. SOC. JAPAN **13** (1958) 314

Magneto-resistance Effect in Cadmium Sulphide

By Shōji TANAKA and Taizō MASUMI

Department of Applied Physics
University of Tokyo, Tokyo, Japan

(Received December 27, 1957)

At present, a little knowledges[1~5] have been given about the electronic energy band structures in cadmium sulphide single crystals, though the photoconductive properties have been largely investigated. Kroeger et al.[1,5] have measured the Hall effect in several impurity-doped conducting crystals and photoconducting crystals for the temperature range from 20°K to 700°K. The present work reported here is the measurement of magneto-resistance effect in impurity-doped cadmium sulphide single crystals at several temperatures.

The samples used for the experiment are the conducting flaky CdS single crystals doped with Ga or Cl or with excess-Cd that have hexagonal crystal structure being of Wurtzite lattice type. The c-axis of the crystal lies in the flaky surface and the surface is perpendicular to one of the three a-axes. The sizes of thin flake specimens are the order of 4 mm×2 mm×0.1 mm and the electrodes are indium-melted ones forming good ohmic contacts. Measurements have been made of relative changes of resistivity due to magnetic field $\boldsymbol{H}$, $(\rho-\rho_0)/\rho_0=(\Delta\rho)_H/\rho$, as a function of magnetic field strength H and the angle θ between the current $\boldsymbol{I}$ (or the direction of the fixed axis in some cases) and $\boldsymbol{H}$ at several temperatures. Some examples of the experimental results, the relation between $(\Delta\rho)_H/\rho$ and H for the $\boldsymbol{I}$-direction $[01\bar{1}0]$ (perpendicular to the a-axis said above and also to c-axis) and $\boldsymbol{H}$-direction $[2\bar{1}\bar{1}0]$ (parallel to the a-axis said above and perpendicular to c-axis) at 160°K and the angular dependence of $(\Delta\rho)_H/\rho H^2$ upon θ at the same temperature, are illustrated in Fig. 1 and 2 for a Ga-doped crystal, where θ is the angle between the $\boldsymbol{I}$-direction $[01\bar{1}0]$ and $\boldsymbol{H}$-direction on the curve (a) in Fig. 2, while, on the curve (b), it is the angle between the direction [0001] (parallel to c-axis) and $\boldsymbol{H}$-direction with the rotation axis $[01\bar{1}0]$.

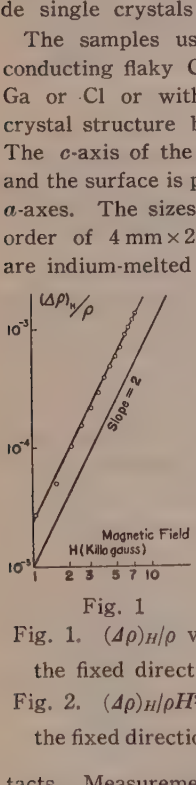

Fig. 1

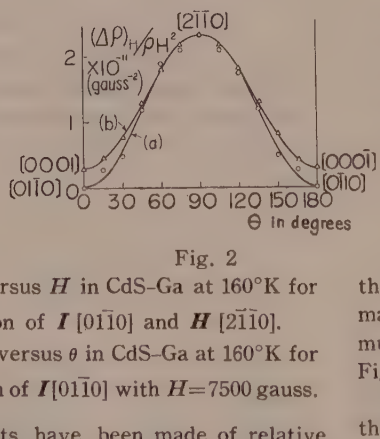

Fig. 2

Fig. 1. $(\Delta\rho)_H/\rho$ versus H in CdS–Ga at 160°K for the fixed direction of $\boldsymbol{I}$ $[01\bar{1}0]$ and $\boldsymbol{H}$ $[2\bar{1}\bar{1}0]$.

Fig. 2. $(\Delta\rho)_H/\rho H^2$ versus θ in CdS–Ga at 160°K for the fixed direction of $\boldsymbol{I}[01\bar{1}0]$ with $H=7500$ gauss.

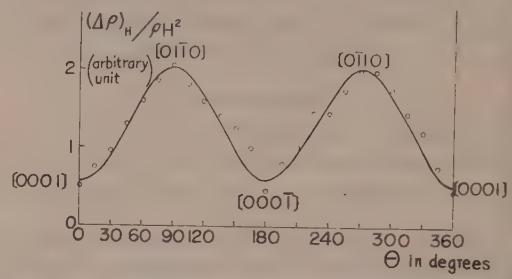

Fig. 3. $(\Delta\rho)_H/\rho H^2$ versus θ in CdS–Cd at 180°K for the fixed direction of $\boldsymbol{I}$ [0001] with $H=4900$ gauss.

Similar example for the $\boldsymbol{I}$-direction [0001] in a crystal with excess-Cd at 180°K is shown in Fig. 3, No appreciable differences between the results obtained for the CdS-Cd crystals and those for the CdS-Ga and CdS-Cl crystals have been observed. The absolute values of $(\Delta\rho)_H/\rho H^2$ in this case are much smaller than those for the $\boldsymbol{I}$-direction $[01\bar{1}0]$, and the angular dependence in Fig. 3 presents different appearences from that in Fig. 2 (a).

The general features of the $(\Delta\rho)_H/\rho$ versus H^2 relation shows good proportionality below 8×10^3 gauss in both cases. Temperature dependence of $(\Delta\rho)_H/\rho H^2$ for the fixed configuration and the results of Hall effect measurement[6] also support that the impurity scattering for electrons has not always a predominant effect in our observations. The angular dependences in Fig. 2 and 3 suggest the existence of anisotropic energy surfaces of conduction band in hexagonal cadmium sulphide although the correction of $(\Delta\rho)_H/\rho H^2$ for the transverse magneto-resistance effect in short samples[7] also must be considered in the case of the curve (b) in Fig. 2.

Further investigations are now in progress and they are likely to give some informations about the problem.

References

1) F. A. Kroeger, H. J. Vink and J. Volger: Physi- ca. **20** (1954) 1095.
2) E. Grillot, M. Grillot, P. Pesteil and A. Zmerli: Compt. Rend., **242** (1956) 1794.
3) G. Dresselhauss: Phys. Rev. **105** (1957) 135.
4) S. Tanaka and T. Masumi: to be published.
5) F. A. Kroeger, H. J. Vink and J. Volger: Philips Research Reports, **10** (1955) 39.
6) H. Miyazawa: Private communications.
7) E. W. J. Mitchell and P. T. Wedepohl: Proc. Phys. Soc. **B70** (1957) 527.

J. PHYS. SOC. JAPAN **13** (1958) 315~316

Absorption Lines in the Antiferromagnetic States of $MnCl_2 \cdot 4H_2O$ and $MnBr_2 \cdot 4H_2O$

By Ikuji TSUJIKAWA
The Research Institute for Iron, Steel and Other Metals
Tohoku University, Sendai

(Received January 13, 1958)

When paramagnetic salts become antiferromagnetic, we can expect polarization and energy shift of the absorption spectrum. We have chosen the monoclinic crystals of $MnCl_2 \cdot 4H_2O$ and $MnBr_2 \cdot 4H_2O$ as the Néel temperatures of these salts are easily attainable (1,6°K and 2,2°K respectively[1,2]). Furthermore the Mn^{2+} ions have line shape absorptions. We measured the violet doublet absorption between 20°K and 1,4°K with a grating spectrograph with 2.5Å per mm dispersion.

We ascertained that there is no phase change at T_N by observation with parallel light and crossed Nicols. In Table I, the relative intensities of V_1 and V_2 (designated from the longer wave length side) at different temperatures are shown. There are anisotropies in both salts, especially in bromide. In the case of L (incident light)$//a$, E (electric vector of L)$//c'(c' \perp a,b)$ and in the case of $L//b$, $E//c'$, we obtain similar polarization so that these absorptions are caused by electric dipole.

The measured oscillator strength is the order of 10^{-8}. Above and below T_N, we find remarkable changes of polarization. In the antiferromagnetic state V_2 becomes very weak relative to V_1. This should not occur, if the excited state consists of two orbital components originating from ^4E[3] and it is probable that these are the crystalline Stark components $\pm 3/2$, $\pm 1/2$ of ^4A. In Fig. 1, temperature dependence of the wave number of V_1 and V_2 is shown. Both lines shift to the shorter wave length when temperature lowers in the neighbourhood of T_N.

Table I. Relative intensities of V_1 and V_2.

Salt	$MnCl_2 \cdot 4H_2O$						$MnBr_2 \cdot 4H_2O$					
Temp.	20°K		4,2°K		1,4°K		20°K		4,2°K		1,6°K	
Line	V_1	V_2	V_1	V_2	V_1	V_2	V_1	V_2	V_1	V_2	V_1	V_2
$L//b$, $E//a$	4	5	4	6	4	2	40	40	40	40	25	15
$L//b$, $E//c'$	5	6	5	4	10	3	9	10	10	8	20	2
$L//a$, $E//b$	3	5	3	4	4	6	2	6	4	6	5	0
$L//a$, $E//c'$	5	6	5	4	10	3	8	9	8	6	20	2

Below T_N, both the ground and excited states should be in the molecular field which causes the splitting of spin components in each state. Firstly we assume that the $\pm 3/2$ component is lower in the excited state and the g-value is 2. From Henry's magnetization data, the measured molecular field at 1,4°K in chloride is 9,000ϕ and at 1,6°K in bromide is 16,500ϕ. These molecular fields cause splittings 0,84 cm^{-1}, 1,54 cm^{-1} respectively between two neighbour components M_s, $M_s \pm 1$. From these considerations, we can expect that V_1 and V_2 shift to shorter wave length by 0,84 cm^{-1} or 1,54 cm^{-1}. The measured shifts are in good accordance with such expectation. For the polarization, if we assume the b axis as the preferred axis and that transition moments do not vary above and below T_N and take into consideration the electron population for each spin component, the calculated intensities qualitatively explain the experimental results in bromide but quantitatively there are some discrepancies.

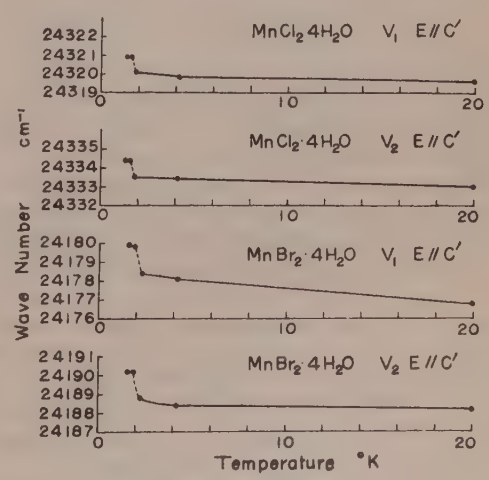

Fig. 1. Temperature dependence of wave number.

The conclusion that the preferred axis is the b

axis is in accordance with the antiferromagnetic resonance experiments[4]. However, in chloride, augmentation of intensity of V_2 at 1,4°K in the case of $L//a$, $E//b$ is anomalous and we cannot explain this fact.

References

1) S. A. Friedberg and J. D. Wasscher: Physica **19** (1953) 1072.
2) W. E. Henry: Phys. Rev. **94** (1954) 1146.
3) Y. Tanabe and S. Sugano: J. Phys. Soc. Japan **9** (1954) 766.
4) B. Bolger: Conférence de Physique des Basses Températures, Paris, September 1955.

J. PHYS. SOC. JAPAN **13** (1958) 316

Magnetic After-Effect Due to Quenched-in Vacancies in Nickel

By Yoji NAKAMURA
Faculty of Science, Kyoto University
and Jin-ichi TAKAMURA
Department of Metallurgy, Kyoto University

(Received December 10, 1957)

The purpose of this note is to describe the contribution of non-equilibrium point defects to the magnetic property of metals. For detecting the effect, the magnetization intensity measurements were made with astatic magnetometer in the magnetic field corresponding to the range of initial permeability. In order to introduce point defects into a metal, quenching from high temperatures was done, since it has some merit in creating in abundance only one kind of point defects, i.e. vacancies. If the magnetic property is influenced by quenched-in vacancies, it may be expected that the magnetization intensity in the quenched specimen would change its magnitude in the recovery process which tends to maintain thermodynamical equilibrium by eliminating excess vacancies.

The specimen used for the experiment was nickel, which is most stress-sensitive due to its large magnetostriction. Quenching was done by the method of allowing the nickel wire (99.98% of purity, 2 mm dia) to drop into the iced-brine bath of −10°C. Specimens were set in the earth magnetic field in such a way that the torque due to the quenched specimen was compensated by the torque of well annealed specimen. The change in the magnetization intensity of the quenched specimen was measured at room temperature.

Some of the results are shown in Fig. 1. The rate of the change is maximum initially, and then decreases with continued recovery. The change went to completion at room temperature in about ten days or more. With increasing the quenching temperature, the amount of the change increased, as expected from the concentration of frozen-in vacancies.

The observed change of magnetization intensity with time runs in parallel to that of volume during the corresponding period (Fig. 2). The volume change is attributable to the disappearance of excess vacancies and it was deduced from the contraction in length[1].

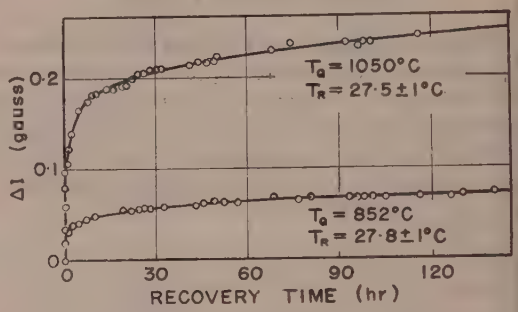

Fig. 1. Increase in magnetization intensity, ΔI, in Ni as a function of rocovery time, after quenching. T_Q is the quenching temperature, T_R the recovery temperature.

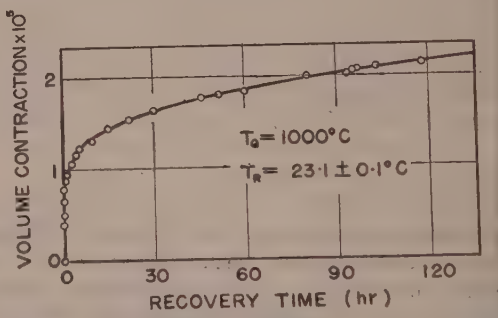

Fig. 2. Volume change as a function of recovery time in Ni, after quenching.

These effects could not be observed in well annealed specimens. Hence it may be safely said that the magnetic effect would be ascribed to the elimination of excess vacancies and not to the after-effect of thermal fluctuation[2]. In conclusion, the large increase of the magnetization intensity we observed may not be understood by the change in intrinsic magnetization due to the volume change obtained during the recovery, but it is to be interpreted in terms of domain boundary displacements.

The authors wish to express their hearty thanks to Professor H. Takaki for his interest in this work and to Dr. N. Kawai who kindly lent them the astatic magnetometer and gave valuable discussions.

References

1) J. Takamura: Metal Phys. Japan **2** (1956) 112. (in Japanese)
2) L. Neel: J. Phys. Radium **12** (1951) 339.

J. Phys. Soc. Japan **13** (1958) 317

Electrical Properties of Ag_2Se

By Shin-ya Miyatani
Department of Physics, Faculty of Science, Niigata University

(Received December 11, 1957)

Ag_2Se has similar electrical properties to those of Ag_2S or Ag_2Te about which we have already reported[1,2]. Using the same experimental method with that described there, the electronic conductivity, σ_e, ionic conductivity, σ_i, Hall constant, R, thermoelectric power, Θ, and Nernst coefficient, Q, can be measured as functions of the e.m.f., E, of the galvanic cell Ag|AgI|Ag_2Se|Pt or the deviation from the stoichiometric composition.

Now, Fig. 1 shows $\log \sigma_e$, $\log R\sigma_e$, $\Theta e/k$, and Q vs eE/kT in the αAg_2Se (stable above about 140°C). Since the values of eE represent the position of the Fermi level relative to that in an Ag-saturated composition, these plots can be compared with the theoretical curves; $\log F_r$, $\log (F_{2r-1/2}F_r^{-1})$, $(2+r)F_{r+1}(1+r)^{-1}F_r^{-1}-\eta$, and $ke^{-1}R\sigma_e((r+2)F_{r+1}(r+1)^{-1}F_r^{-1}-(2r+3/2)F_{2r+1/2}(2r+1/2)^{-1}F_{2r-1/2})$ vs η[3,4] respectively, where η is the reduced Fermi energy and related to eE/kT by $\eta=\eta_s(T)-eE/kT$ ($\eta_s(T)$ is η in Ag-saturated Ag_2Se.), $F_r=\int_0^\infty x^r(1+\exp(x-\eta))^{-1}dx$, and the mean free path of conduction electron, l, is assumed to be expressed as $l=l_0(\varepsilon/kT)^r$(ε is the kinetic energy of conduction electron). Adjusting the origins of the experimental and theoretical graphs, the fitness between them is tested. Fig. 1 shows that the theoretical curves for $r=0$ fit fairly well with experimental plots except Θ. Thus, assuming $r=0$, we obtain l_0 and the effective mass of conduction electron as 244Å and $0.174m$ at 170°C, 227Å and $0.174m$ at 220°C, and 202Å and $0.184m$ at 280°C respectively.

Further, the concentration of the excess Ag relative to a certain composition, N, is known from the quantity of electricity sent across the galvanic cell Ag|AgI|Ag_2Se|Pt. The R^{-1} vs eN plots show that they are related to each other by a simple equation; $R^{-1}=eN+\text{const}$. Adjusting the additive constant, we have $R^{-1}=eN_a$ where N_a can be regarded as the concentration of excess Ag over the stoichiometric composition. Since R^{-1} is equal to en (n: carrier concentration) in a highly degenerate case like the present one, we have $n=N_a$. The numbers added to the equi-Ag/Se ratio lines in Fig. 1 are such eN_a-values in $C\,\text{cm}^{-3}$. By the way, the contribution of hole is not too large even at the maximum of E where the evaporation of Se begins to take place.

On the other hand, the ionic conductivity, σ_i, is obtainable from the relaxation time, τ, of the ionic polarization effect with the use of the equation; $\sigma_i=L^2/(\pi^2\tau|dE/d(eN)|)$[2] where L is the total length of the specimen. The measurements of τ show that σ_i is independent of the composition since $\tau dE/d(eN)$ is independent of E. Thus we obtain σ_i as $3.6\Omega^{-1}\text{cm}^{-1}$ at 220°C and this value slightly increases with increasing temperature.

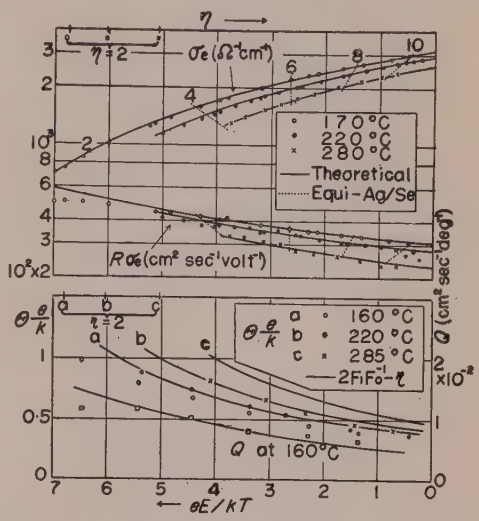

Fig. 1. $\log \sigma_e$, $\log R\sigma_e$, $\Theta e/k$, and Q vs eE/kT in α-Ag_2Se. The degeneracy is high as shown by the positions for $\eta=2$ on the upper abscissa.

Finally, in the β Ag_2Se (stable below about 130°C), $R\sigma_e$ decreases slightly with increasing E (it increases if $r=0$ and does not change if $r=1/2$.), where the accuracy of E is poor since the σ_i's in Ag_2Se and AgI are very small in this temperature range. Moreover the potential from the Nernst effect, V_N, is far smaller than that from the Righi-Leduc effect, V_R ($V_N/V_R\approx 1/2$ if $r=0$ and $V_N=0$ if $r=1/2$). These facts suggest that the scattering mechanism in the β phase is different from that in the α phase and r may be rather near to 1/2 than to 0. Assuming $r=1/2$, the mobility and effective mass of conduction electron are obtained as 810 $\text{cm}^2\,\text{sec}^{-1}\,\text{volt}^{-1}$ and $0.11m$ at 130°C respectively. By the way, such a change of r at the $\alpha-\beta$ transition takes place also in Ag_2Te and will be reported in near future.

References

1) S. Miyatani: J. Phys. Soc. Japan **9** (1955) 786.
2) S. Miyatani: J. Phys. Soc. Japan **13** (1958) No. 4.
3) F. Seitz: The modern Theory of Solids (1940).
4) R. W. Wright: Proc. Phys. Soc. **A64** (1951) 984.

J. PHYS. SOC. JAPAN **13** (1958) 318~319

The Effect of G-P (1) and G-P (2) Aggregates on the Plastic Deformation of an Age-Hardenable Al-Cu 4% Alloy

By Keisuke MATSUURA,
Hokkaido Gakugei Univ.
Sôichi IZUMI and Shigeyasu KODA
Hokkaido Univ.

(Received December 3, 1957)

The authors previously reported that the effect of G-P (2) or G-P (1) aggregates on the plastic deformation was different from that of the precipitates of θ' phase according to the experiment on Al-Cu 4% alloys aged at 160°, 200° and 240°C, respectively[1]. To clarify the effect of G-P (1) and G-P (2) more particularly the authors have examined the stress-strain curves and slip patterns of the specimens aged at 130°C. At this temperature of ageing, the age-hardening occurs in two stages separated by a flat plateau of constant hardness. The initial rise and flat plateau are attributed to the formation of G-P (1) aggregates and the second rise is mainly due to the formation of G-P (2)[2]. At the peak hardness, besides the G·P(2) aggregates, about 5–10% of the total possible θ' phase may be formed, however its contribution to the hardness seems to be negligible.

In the present experiment, polycrystalline wires of 1 mm. diameter for tensile testing, and strips of 1 mm. thickness for the observation of slip patterns were prepared. They were solution-treated for 30 min. at 530°C, air-quenched on a sheet of iron and then aged at 130°C for various periods. To eliminate the effect of the formation of G-P (1) during plastic deformation[3], the tensile testing was carried on in liquid nitrogen (Fig. 1), however the specimens for the observation of slip patterns were stretched at room temperature (Photo. 1, 2 and 3).

In Fig. 1, the following characteristics are recognized. Although the yield strength increases appreciably with ageing, the rate of strain-hardening changes only a little during the second rise

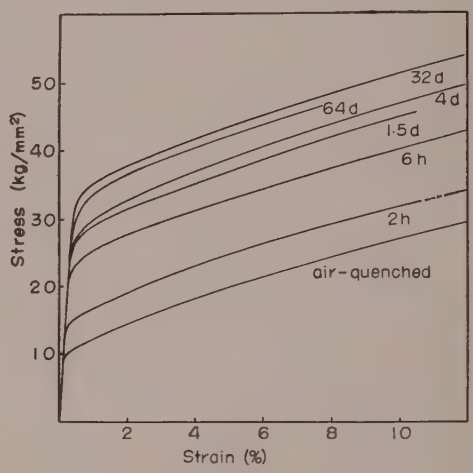

Fig. 1. Variation of stress-strain curves at −196°C with Ageing at 130°C.

of hardness. Corresponding to this fact, there is no distinct difference in the slip patterns among the air-quenched specimen, the one aged for 12 hrs. which is hardened with G-P (1), and the one aged for 9 days which is hardened with G-P (2). However, the slip lines in the specimen aged for 9 days seem to be a little longer and straighter than those of the air-quenched specimen.

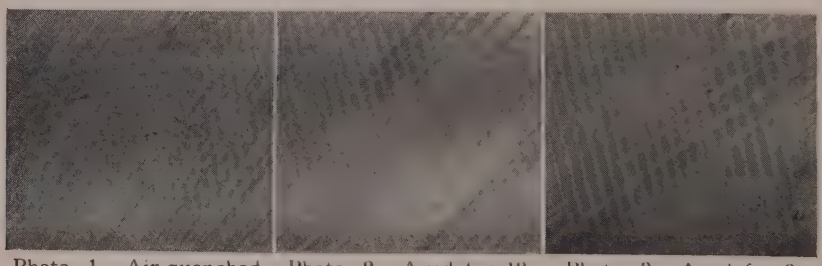

Photo. 1. Air-quenched (840×4/3) Photo. 2. Aged for 12 hours at 130°C (840×4/3) Photo. 3. Aged for 9 days at 130° (840×4/3)

Photo. 1, 2, 3. Sliplines on polycrystalline Al-Cu 4% alloys after several % extension.

These results suggest that the mechanism of plastic deformation of the specimens hardened with G-P (1) or G-P (2) is almost the same as that of the air-quenched one. Therefore, the avarage internal stress due to the formation of G-P zones, as proposed by Mott and Nabarro[4], is considered as an important cause of age-hardening, since the mode of plastic deformation is not necessarily affected by such hardening. This idea assumes that dislocations can pass through G-P (1) or G-P (2)

aggregates on the plastic deformation. From a calculation of Kelly and Fine[5], it seems that this assumption is reasonable.

References

1) K. Matsuura, R. Nagasaki and S. Koda: Nippon Kinzoku Gakkaishi, **10** (1957) 618.
2) J. M. Silcock, T. J. Heal and H. K. Hardy: J. Inst. Metals, **82** (1953–54) 239.
3) K. Matsuura, Y. Hamaguchi and S. Koda: J. Phys. Soc. Japan **12** (1957) 1424.
4) N. F. Mott and F. R. N. Nabarro: Report on Strength of Solids, (1948) 1.
5) A. Kelly and M. E. Fine: Acta Met., **5** (1957) 365.

J. Phys. Soc. Japan **13** (1958) 319

Some Observations on Germanium Bi-crystals

Makoto Kikuchi and Sigeru Iizima
Electrotechnical Laboratory, Tokyo, Japan

(Received January 11, 1958)

It has been tried to make germanium bi-crystals with two single crystal seeds. A pulled bi-crystal is show in Fig. 1. In this case, the seeds are [111] and [100], one of whose <110> edges are arranged to be nearly in parallel.

The crystal was sliced into wafers of 2 mm in thickness perpendicular to the axes. Fig. 2 and

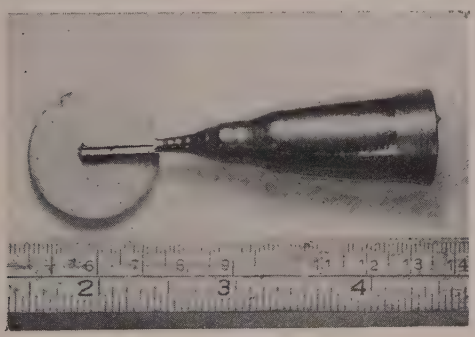

Fig. 1. A pulled bi-crystal.

3 show the slices after being etched with superoxol. The same slices are shown in Fig. 2 and 3 with different angles of illumination, since it is not possible to make all regions to be apparent by only one illuminating condition. The slices from the top towards the bottom of the crystal correspond to the slices of upper-left to lower-right in the figures.

In the crystal illustrated, unexpected third crystal originated at the joint of the [100] [111] grain boundary and the crystal periphery, as shown in Fig. 4. Though the direction of this third crystal is not yet defined, it is seen from the figures that this axis becomes predominant as the crystal is grown up and finally pushes out the [100] region.

It has been observed in other [100] [111] bicrystals, that the relative predominance of [100] and [111] in the growth of bi-crystals depends on the relative orientation of these two crystal axes.

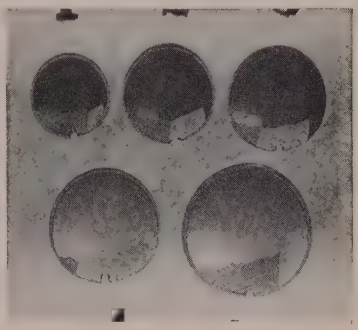

Fig. 2. Slices of bi-crystal.

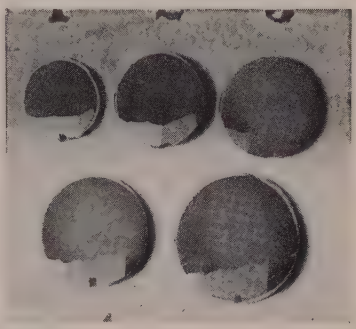

Fig. 3. Slices of bi-crystal.

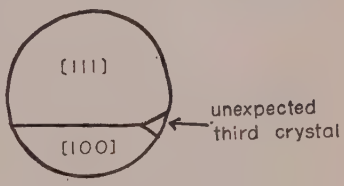

Fig. 4.

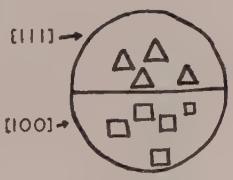

Fig. 5.

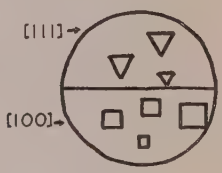

Fig. 6.

When [111] and [100] are contacting with <110> edge at the boundary, and the etched pattern is as shown in Fig. 5, [111] crystal becomes predominant over [100] as the crystal is grown. On the other hand, in the case of Fig. 6, ([111] axis is rotated 180°) [100] crystal becomes predominant over [111].

J. PHYS. SOC. JAPAN **13** (1958) 320

The Consecutive Observations on the Twin Intersections

By Hiroshi KIHO
Department of Physics, Kyoyo-bu, Kyoto University
and Saiyu MARUYAMA
Department of Physics, Osaka Women's University

(Received December 7, 1957)

Differing from the intersections of slip lines, it is not easy to distinguish between the crossing and the crossed twins, because the misfits of the twin bands are not the direct result of the shear of the crossing twins. The interpretations of the intersections in $\alpha-U$[1], in Zn[2], in $\beta-Sn$[3] and in Ti[4] have all been made on the pictures already intersected. In our previous work[3], to decide between the crossing and the crossed twins and to determine the modes of strain accomodation, we took up all the possible cases of intersection satisfying our criterion, and classified the pictures into these cases. Here, instead of the said method, we carried out the consecutive observations on the course of twin intersections in Bi, and observing directly the crossing and the crossed twins, confirmed our criterion on the modes of strain accomodation.

The specimens were prepared in the form of a thin strip ($1\times1.5\times15$ mm) by cleaving off from mother Bi single crystals. Their axes were in the direction of $[1\bar{1}0]$. The twin lamellae developed consecutively by pressing the specimen on the outer surfaces of metal rings with varying curvatures, or by pressing the centre of the specimen by a screw keeping the ends fixed.

When a twin band (110) crosses another, (101), which was formed prior to (110), it sometimes splits into two secondary twins, $(110)_t$ and $(011)_t$, in the crossed twin (101) (Plate 1). (Here subscript t means that the indices are referred to the crystal axes within the crossed twin.) The former $(110)_t$ is a mirror-image of the crossing twin (110), and the trace of $(110)_t$ coincides with that of the said crossing twin in the K_1 plane of the crossed. While the latter $(011)_t$ is the other secondary twin, and the trace of which does not coincide with that of the crossing twin (110) in the K_1 plane of the crossed. Each of them contributes to the strain accomodation. It is understandable by adding the effect of the surface to our previous criterion[3].

Several facts were disclosed in addition by the consecutive observations on the cleavage surfaces. The following ***A*** and ***B*** show, respectively, the crossing and the crossed twins.

(1) When the angle between the crystal surface and ***B*** is acute (Plate 2, "X" region), ***A*** is stopped by ***B*** and it grows with tapering. The accomodation kink appears above the intersection line of ***A*** and ***B***. This, together with the tapering of ***A***, accomodates the strain. On the other hand, when the angle between them is obtuse (Plate 2, "Y" region), ***A*** broadens without tapering, the accomodation kinking does not occur because of the lack of the intersection line of ***A*** and ***B*** in "Y", but the secondary twin $(110)_t$ and sometimes the secondary twin $(011)_t$ and basal slip $(111)_t$ appear in ***B*** to accomodate the residual strains (Plate 1).

Plate 1. ×200

Plate 2. ×220

←→ Specimen axis

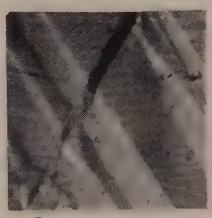

Plate 3. ×240

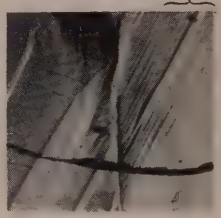

Plate 4. ×180

(2) The broadness of the twin bands has nothing to do with the determination of ***A*** and ***B***. In Plate 3, one might recognize the slender twin to be ***A***, but the consecutive observations show it to be ***B*** having the secondary twins in it.

(3) The apparent penetration of ***A*** into ***B*** by a short distance is due to the result of the boundary movement of ***B*** after ***A*** has been stopped (Plate 2). This mechanism often results in the misfit of ***B***.

(4) When the specimen is unbent in a reverse way, untwinning of ***A*** accompanies untwinning of the secondary twin, and untwinning of ***B*** does not accompany that of the secondary twin (Plate 4).

The authors express their cordial thanks to Prof. K. Tanaka, Kyoto University, for valuable advices and constant encouragement.

References

1) R. W. Cahn: Acta Met. **1** (1953) 49.
2) P. L. Pratt: *ibid.* **1** (1953) 692.
3) S. Maruyama and H. Kiho: J. Phys. Soc. Japan **11** (1956) 516.
4) F. D. Rosi: Acta Met. **5** (1957) 337.

J. Phys. Soc. Japan **13** (1958) 321

Microwave Spectrum of Hydrazine

By Takeshi Kojima
Department of Liberal Arts, Toyama University, Toyama
Hiromasa Hirakawa and Takeshi Oka
Department of Physics, Tokyo University, Tokyo

(Received January 16, 1958)

The microwave spectrum of hydrazine N_2H_4 was observed in the frequency range from 4.7 to 30 kMc/sec. About two hundred lines were found, all exhibiting quadratic Stark effects. Their frequencies f and intensities I were listed in Table I. The spectrum is complicated by the internal rotation of one NH_2 group with respect to the other and further by the inversion of each NH_2 group similar to that occurring in ammonia and methylamine. For some lines the hyperfine structures due to the electric quadrupole coupling of two N nuclei with the overall and internal rotation of the molecule were found.

Stark effects were observed for stronger lines and the numbers of resolved components n are shown in the last column of Table I. Fairly large number of lines were found to show no splitting in spite of the Stark shift of about 10 Mc/sec at the electric field of 2000 volt/cm.

Table I. Microwave spectrum of hydrazine. (in Mc/sec)

f	I	n
4764.0	WW	
4879.4	WW	
5386.0	WW	
5562.53	W	
5568.98	W	
5992	WW	
6144	WW	
6498.3	WW	
6575.71	MW	
6588.6	WW	
6759.91	W	
7444.9	WW	
7977.76	MW	1?
8134.63	WW	
8147.09	M	1
8270.73	WW	
8273.57	WW	
8478.7	WW	
8824.0	WW	
9227.5	WW	
9543.51	W	
9555.23	S	1
9689.62, 9689.72, 9689.80	MS	1
9697.59	WW	
11351.2, 11351.39, 11351.56	M	
11363.00	WW	
11388.0	WW	
11390.0	WW	
11406.2	WW	
11413.67	WW	
12424.12	WW	
12772.8	WW	
12946.29, 12946.61, 12946.99	M	≧3
13151.3	WW	
13191.71, 13192.5, 13193.29, 13194.13	MW	
13279.22, 13279.62, 13280.02	M	≧5
13291.33	WW	
13422.6	WW	
13542.53	WW	
13557.30	WW	
13632.40	WW	
13988.41	WW	
14065.4	WW	
14441.59	W	
14475.4	WW	
14556.31	MW	≧4
14570.8	WW	
14687.29	MW	1
14700.4	WW	
14900.5	WW	
15062.1	WW	
15067.9	WW	
15091.2	WW	
15099.30, 15099.86, 15100.72, 15101.32, 15102.67, 15103.40, 15104.37	MW	
15892.15	W	
15921.66	WW	
16045.67	WW	
16286.4	WW	
16313.92	WW	
16376.94	W	
16598.20	WW	
16767.90	W	
17071.6, 17073.10, 17074.41	WW	
17077.2, 17078.17, 17078.73, 17079.32, 17079.94, 17080.5	W	
17092.35, 17093.19	W	
17103.84, 17104.58, 17105.42	M	2
17125.84	W	
17326.69	W	
17332.72	MW	
17797.71	WW	
17865.95	W	
18086.02	W	1?
18118.9	WW	
18663.70	MW	
18687.31	MW	1?
18691.44	MW	
18781.43	W	1?
18824.0	WW	
18830.96, 18831.28	MS	≧5
18842.22	W	
18940.14	WW	
19088.39	WW	
19118.8	W	
19125.6, 19126.2, 19126.93, 19127.65, 19128.26, 19128.86, 19129.54, 19129.88	M	≧5
19341.02, 19341.23, 19341.5	M	1?
19352.35, 19352.65, 19353.0	W	
19488.29	W	
19505.92	W	
19559.0, 19561.4	W	
19672.93	WW	
19804.8, 19806.06	WW	
19874.46, 19875.04	W	
19945.6	WW	
20073.28, 20073.78	M	
20414.9	W	
20797.01	MW	
20950.65	MW	
21107.10, 21110.25	M	
21127.0	W	
21153.63	M	
21165.43	W	
21221.74	MS	1
21233.40	MW	
21236.46	W	
21239.52	W	
21527.14	W	
21661.71	W	
22235.35	M	
22413.3	W	
22516.50	W	
22766.98	MS	1
22779.30	W	
22839.43, 22839.91	MW	
22902.87	MS	1
23119.2	W	
23130.70, 23131.19	M	1
23230.27	MW	
23771.02	W	
24120.0	W	
24285.79, 24286.23	MW	
24377.18	W	
24824.59	M	
24923.34	M	1
24935.41	W	
25078.38	M	
25201.35	MW	
25213.53	M	
26162.06	W	
26346.36	W	
26605.60	WW	
26872.2	WW	
26874.2	WW	
26883.58	MW	
26895.45	S	1
26934.06, 26937.28	M	1
26945.52	S	1
26950.5	W	
26992.83, 26995.23	S	1
27027.4	W	
27088.7	W	
28002.87	W	
28025.6	W	
28207.9	WW	
28218.66	W	
28222.08	W	
28830.5	W	
28844.4	W	
28855.40, 28855.75	W	
28933.1	W	
29010.24, 29011.74, 29012.73	M	
29199.6	W	
29240.5	W	
29251.64, 29252.01	M	1
29491.6	W	1

PROGRESS OF THEORETICAL PHYSICS

CONTENTS

Progress of Theoretical Physics Vol. 19, No. 1, January 1958

Many-Body Pseudopotential for Hard-Sphere Interaction .....Ryuzo ABE..1
Two-Pion-Exchange Nuclear Potential ...M. KONUMA, H. MIYAZAWA and S. OTSUKI.. 17
Multipole Mixing in Odd Mass Spheroidal Nuclei .....
.....R. NAKASIMA, S. YAMASAKI and Y. YOSHIZAWA.. 31
Dispersion Relation for the Photoproduction of K-Mesons .....Susumu OKUBO.. 43
On the Form Factor of Liquid He^4 at Absolute Zero, I .....Ryuzo ABE.. 57
On the Propagation of the Hydromagnetic Waves in Compressible Ionized Fluid
..... Tosiya TANIUTI.. 69
Note on the Collision Matrix for the Nuclear Reactions, I .....
.....M. KAWAI and M. NAGASAKI.. 77
The Dispersion Relations for the Scattering of Photons from Proton .....
.....T. AKIBA and I. SATO.. 93
On the Decay Interactions of Strange Particles. .....Yoshihiko MIYACHI..112

Letters to the Editor:
Molecular Orbital Treatment of $1s\sigma 2p\sigma^3 \sum_u$ State of H_2.....S. HUZINAGA..125
Contents of Journ. of Phys. Soc. of Japan, Vol. 12, Nos. 11, 12.....127
Rules for Contribution and Proofreading .....i~iv

Price $ 1.25 per copy
$ 15.00 per year (postage inclusive)
Annual dues for foreign members (individual subscribers)
$ 12.00 (postage inclusive)
" for foreign members of the Physical Society of Japan
$ 10.00 (postage inclusive)
Application for members, subscriptions and orders for back numbers should be sent, directly or through book-dealers, to

The Publication Office
in
Yukawa Hall, Kyoto University, Kyoto, Japan

JOURNAL OF THE PHYSICAL SOCIETY OF JAPAN Vol. 13, No. 4, APRIL, 1958

On the Low Lying Levels of Mn^{55}

By Sadaaki YANAGAWA

Department of Applied Physics, Faculty of Engineering, University of Tokyo, Tokyo

(Received December 24, 1957)

In this calculation of the low lying energy levels of Mn^{55}, the same treatment as in our previous note[1] is extended from the standpoint of the configurational mixings. One assumes that the potential between nucleons is $V(r_{12})[1+a(\sigma_1\cdot\sigma_2)]$: $V(r)=V_0e^{-r^2/r_0^2}$, and the wave functions are the harmonic oscillator type due to Talmi[2]. λ is the ratio of the potential range r_0 to $1/\sqrt{\nu}$ which determines the extension of the wave function. The values of a and λ are determined from the experimental data of the energy splittings of the $J=0$, 2 and 4 levels for Fe^{56}. And for these values of parameters, the competition of the low lying levels $J=7/2$, 5/2 and 3/2 for Mn^{55} is discussed.

§ 1. Introduction

In a previous note[1], we have discussed about the difference of the ground state spin of Mn^{55} and Ti^{47}. In this case, the important feature is the fact that the ratio of the energy splitting of the 1st to the 2nd excited state measured from the ground state for Fe^{56} and Ti^{48} are abnormally small. We have assumed that the ground configuration for protons of Fe^{56} and for neutrons of Ti^{48} are $(f_{7/2})^2$ and the states of neutrons of Fe^{56} and of protons of Ti^{48} are frozen to the $\{(j)^2: 0\}$ states. The configurations for protons of Mn^{55} and for neutrons of Ti^{47} are taken as $(f_{7/2})^3$. Other kinds of nucleon group can be handled similarly. As is shown in the reference (1) the $J=5/2$ state is the lowest one. But the fact that the $J=3/2$ state lies at the position just above 7/2 level, is not in good agreement with the experiments. Some improvement is necessary.

It is questionable whether the freezing one kind of nucleon group in even-even nuclei to the seniority zero state is good or not. However, we have here tried to improve the results quantitatively from the standpoint of the configurational mixings, and examined to see how far this treatment is near the truth.

The method of the configurational mixing for Fe^{56} is completely analogous to the one used in the calculation for Ca^{42} by Komoda and the author[3]. We assume as in the reference (3) $V(r_{12})[1+a(\sigma_1\cdot\sigma_2)]$ for the two body nuclear potential, where $V(r)$ is Gaussian potential ($=V_0\times e^{-r^2/r^2_0}$, r_0 the potential range parameter). We used as before the harmonic oscillator wave function for the nucleon state function, the radial part of which is defined by

$$R_{nl}(r)=N_{nl}e^{-(\nu/2)r^2}r^{l+1}L^{l+1/2}_{n+l+1/2}(\nu r^2)\ .$$

N_{nl} is a normalization factor and L is an associated Laguerre polynominal. $\nu=\omega m/\hbar$ where m and ω are the constants contained in the Hamiltonian of the harmonic oscillator

$$\mathscr{H}=\frac{1}{2m}(p^2+m^2\omega^2r^2)\ .$$

The explicit expression for $L^{l+1/2}_{n+l+1/2}$ is given in Talmi's paper[2]. The excitation energies of a single nucleon from $f_{7/2}$ to $f_{5/2}$ and $p_{3/2}$ are taken from the experimental values of the 1st and 2nd excited states of Co^{57}. They are 1.4 and 1.5 Mev. respectively.

§ 2. Calculation for Fe^{56}

For Fe^{56} the proton configurations are assumed to be the mixings of $(f_{7/2})^2$, $(f_{7/2}f_{5/2})$ and $(f_{7/2}p_{3/2})$ configurations. Especially for $J=0$ state, $(f_{5/2})^2$ and $(p_{3/2})^2$ configurations are taken into account. And the part of neutrons are disregarded as in the previous note.

For several fixed values of parameters a and λ $(=r_0\sqrt{\nu})$, the secular equations are solved for $J=0$, 2 and 4 energy states for Fe^{56}, of which dimensions are all 3.

The ratio of the experimental energy value of $J=2$ state to that of $J=4$ for Fe^{56} is about 2.46. We can determine the values of a and λ so as to make the theoretically calculated ratio coincide with the experimental one 2.46. For these special parameters a and λ, the pairing energy E_p is determined from the experimental energy value of $J=2$ state; 0.845

Mev. for Fe^{56}. The results out of our calculations which seem suitable are tabulated in Table I.

Table I.

a	λ	E_p
0.1	0.66	3.4
0.2	0.45	3.0

(E_p is the pairing energy in Mev.)

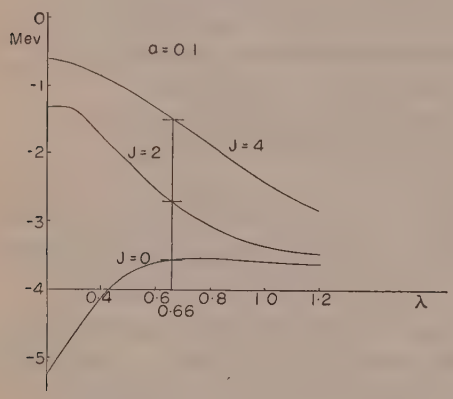

Fig. 1.

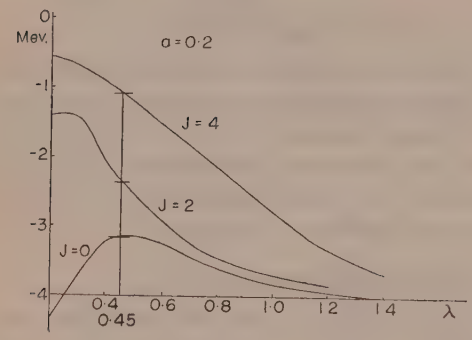

Fig. 2.

For $a=0.1$ and 0.2, the energy diagrams are plotted against λ in the figures. If a becomes large (for example $a=0.3$), λ and E_p decrease ($\lambda\sim0.3$, $E_p\sim1.5$), and conversely as a becomes smaller than 0.1 (for example $a=0$: Wigner force only), λ and E_p increase rapidly ($\lambda\sim1.5$, $E_p\sim9$).

§ 3. The Calculation for Mn^{55}

For Mn^{55} the proton configurations are assumed to be the mixings of $(f_{7/2})^3$, $(f_{7/2})^2f_{5/2}$ and $(f_{7/2})^2p_{3/2}$, and the group of neutrons are frozen. The state functions are $\{(f_{7/2})^3:J\}$, $\{(f_{7/2})^2(J'), f_{5/2}:J\}$ and $\{(f_{7/2})^2(J'), p_{3/2}:J\}$, $J'=0, 2, 4$ and 6. Then the dimensions of secular equations for energy matrices are 6 for $J=7/2$ and 5/2 and 5 for 3/2. For the above parameter values, we have solved the equations by the usual perturbation method and obtained the lowest root of the secular equations. The results are tabulated in Table II.

Table II.

a	$E(7/2)$	$E(3/2)$
0.1	0.23	1.27
0.2	0.33	1.25

(measured from the ground state $J=5/2$ in Mev.)

§ 4. Discussions

As shown in the Table II the state $J=5/2$ is the lowest. The fact that the $J=3/2$ state lies at the position of about 1 Mev. above the ground state 5/2, is the remarkable result, considering that among the present experimental data, there is no level up to about 1 Mev. from the ground except the 7/2 level. The nucleus radius parameter R_0 is determined roughly from the equation $1/\sqrt{\nu}=2.21R_0$ by demanding that the root mean square radius of the nucleus Fe^{56} should agree with the usual formula $R=R_0A^{1/3}$. In this way we obtain $R_0=1.41\times10^{-13}$cm. for $\lambda=0.45$ and $R_0=0.96\times10^{-13}$ cm. for $\lambda=0.66$, if the parameter of potential range r_0 is taken as 1.4×10^{-13}cm. For the nucleus Ti^{47} too, we can treat completely in the same manner as for Mn^{55}.

Our fundamental assumption that the neutron's group is "frozen" to the lowest seniority state, might not be tenable in the theory of the shell model. Nevertheless, our calculation shows that the method of the configurational mixings gives fairly correct results. It would be of interest to see how far the results are improved by taking the higher seniority states into account.

References

1) S. Yanagawa: Prog. Theor. Phys. **18** (1957) 661.
2) I. Talmi: Helv. Phys. Acta **25** (1952) 185.
3) T. Komoda and S. Yanagawa: to be published elsewhere.

JOURNAL OF THE PHYSICAL SOCIETY OF JAPAN Vol. 13, No. 4, APRIL, 1958

Alpha Particles from the Interaction of 14.8-Mev Neutrons with Medium Weight Nuclei

By Isao KUMABE

Department of Physics, Faculty of Science, University of Kyoto

(Received December 25, 1957)

The angular and energy distributions of alpha particles resulting from $V^{51}(n, \alpha)Si^{48}$ and $S^{32}(n, \alpha)Si^{29}$ reactions induced by 14.8-Mev neutrons were measured with Ilford C2 nuclear plates. It was found that the angular distributions for the entire energy regions in the center-of-mass system are concave upward and approximately 90° symmetrical, and the energy distributions show that the alpha particles with energies below the Coulomb barrier are more emitted than expected. Also the curve on a semilog plot of the relative level density calculated from the energy distributions of the alpha particles fits a straight line which would correspond to Maxwellian distributions with the temperatures of about 0.9 Mev for Sc and about 1.5 Mev for Si.

The total cross sections of V and S are 126 mb±15% and 109 mb± 15% respectively. Experimental data on (n, α) reaction so far obtained by us are summarized and discussed in detail.

§ 1. Introduction

The angular and energy distributions of the alpha particles emitted, when various nuclei are irradiated by fast neutrons, yield information concerning the basic mechanism of such interactions.

The activation cross sections were measured for many elements bombarded with 14.5-Mev neutrons by Paul and Clarke.[1] They have shown that the (n, p) and (n, α) reaction cross sections for large mass number are too larger than those predicted by the evaporation theory, but the $(n, 2n)$ reaction cross sections are approximately in agreement with the theory. They suggested the existence of the non-compound process in the cases of (n, p) and (n, α) reactions. Experimental data of the angular and energy distributions on (n, α) reactions for various nuclei may give more reliable information on these problems.

Several experiments[2-6] have been performed to measure the density of energy levels on excitation energy. In those experiments, measurements were made of the energy distributions of neutrons and protons from reaction and inelastic scattering on various nuclei. The presence of non-compound-nucleus processes throws serious doubt on the interpretation of the results of those experiments and prompts a search for new experiments which might provide less ambiguous information about the energy level density. On the other hand, experimental data (n, α) reactions may give more reliable information on the energy level density, since it seems improbable that alpha particles will be emitted by direct interaction.

Brady[7] has measured the angular and energy distributions of the alpha particles resulting from the (p, α) reactions for several elements at 18 Mev. However, the detailed data have not been reported.

Except for light nuclei, angular and energy distribution of the (n, α) reaction have been measured so far only for zirconium,[8] for which the angular distribution above 120° has not been measured and the energy distribution has not been reported in detail.

In previous papers[9][10], we have reported the angular and energy distributions of the alpha particles resulting from $Al^{27}(n, \alpha)Na^{24}$, $Co^{59}(n, \alpha)Mn^{56}$ and $Mn^{55}(n, \alpha)V^{52}$ reactions induced by 14.8-Mev neutrons. It has been found that the angular distributions for the entire energy region of particles are concave upward and approximately 90° symmetrical, and the energy distributions show that the alpha particles with energies below the Coulomb barrier are more emitted than has been expected by the evaporation theory.

In this paper the measurement extended to the target nuclei of vanadium and sulphur are reported. Since the target nuclei of the so far measured (n, α) reactions were Al^{27},

Co^{59} and Mn^{55} and resultant residual nuclei were limited to odd-odd, sulphur was chosen for the target element in spite of 95.06% abundance of S^{32}.

§ 2. Experimental Procedure

The experimental arrangement is shown schematically in Fig. 1. Neutrons were provided by the d-T reaction, employing magnetically analyzed molecular deuterium of 220 Kev from a Cockcroft-Walton machine. The tritium target consisted of 0.5 curies absorbed in a 0.2 mg/cm² zirconium foil and was bombarded with a steady beam of about 100 μA. Neutron production was $\sim 5\times 10^8$ neutrons/sec. Neutron flux was monitored by a modified Mc Kibben[11] BF_3 proportional counter which had been calibrated by an argon-filled proportional counter counting the accompanying alpha particles from the $T(d, n)\alpha$ reaction. The argon-filled counter was placed at 90° direction with respect to the beam.

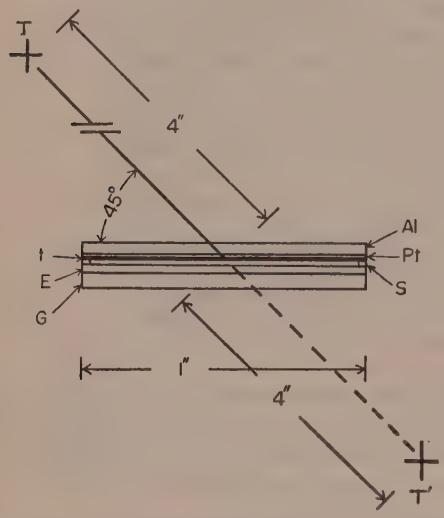

Fig. 1. Experimental arrangement. Al: aluminum backing holder (thickness 1 mm). Pt: platinum backing (thickness 60 mg/cm²). t: target. S: celluloid spacer (thickness 0.1 mm). E: Emulsion. G: Glass. T or T′: tritium target. When the tritium target is placed in the position T, the emulsion detects alpha particles emitted in the forward direction, and when the tritium target is placed in the position T′, the emulsion detects alpha particles emitted in the backward direction.

The targets of vanadium and sulphur were vacuum evaporated onto halves of platinum foil of thickness 60 mg/cm² which were used to reduce the background. Target thicknesses used were 2.54 mg/cm² for V and 2.43 mg/cm² for S respectively. 1.5″×1″ Ilford C2 plates (thickness 200 μ) were used.

An incident angle of 45° for the neutrons was chosen. Advantages of incident angle 45° are as follows.

1. If neutron incidence is normal or parallel to the plane, on account of large absorption loss of particles emitted parallel to the plane, the errors arising from the correction of absorption loss increase near $\theta=90°$ or 0° and 180°, and then the uncertainty of the angular distribution increases. However, if an incident angle of 45° is chosen, the particles which are emitted parallel to the plane and suffer a large absorption loss distribute between $\theta=45°$ and 135° and then the errors arising from the correction are averaged and decrease.

2. There is a possibility that a part of tracks emitted in the direction normal to the plane may be missed in scanning, but in the case of the incident angle of 45° for the neutrons, these contribute to only a small part of the angular distribution near $\theta=45°$ or 135°.

3. The errors arising from the estimation of the shrinkage factor in the case of an incident angle of 45° is averaged over all angles and become smaller than in the case of parallel or normal incidence to the plane. The disadvantage of incident angle of 45° is that the complicated calculation is needed for the angular distribution.

In order to discriminate alpha particles from protons in the emulsion, the plates were processed by the temperature method[12] using low pH (6.6) amidol developer[13], and for the hot stage, we chose the values of 15 minutes and 18°C for the suitable time and temperature respectively after several trials. And the soaking of the emulsions in a glycerine solution to prevent their shrinkage after development significantly improved the accuracy in the measurement of the alpha tracks.

The processed emulsions were secanned using "Tiyoda" microscope and "Nippon Kogaku" microscope at magnification of 1350. Acceptance critera required for tracks is to begin at the emulsion surface. The shrinkage factor (2.3) was obtained by measuring the horizontal and vertical components of the

lengths of Polonium alpha tracks. Data were obtained by two different observers, working in different areas of the plates. The data were analyzed separately and combined only after it was established that the two sets displayed the same general features. The background tracks were measured in the half without the target material of the emulsion. The range-energy relation in C2 plate used was obtained from the range-energy curve of Rotblat[14] corrected with *Po-α*.

§ 3. Results

The anglar distributions in the center-of-mass system of the alpha particles from the interaction of 14.8-Mev neutrons with vanadium and sulphur for the entire energy region are shown in Fig. 2. The uncorrected

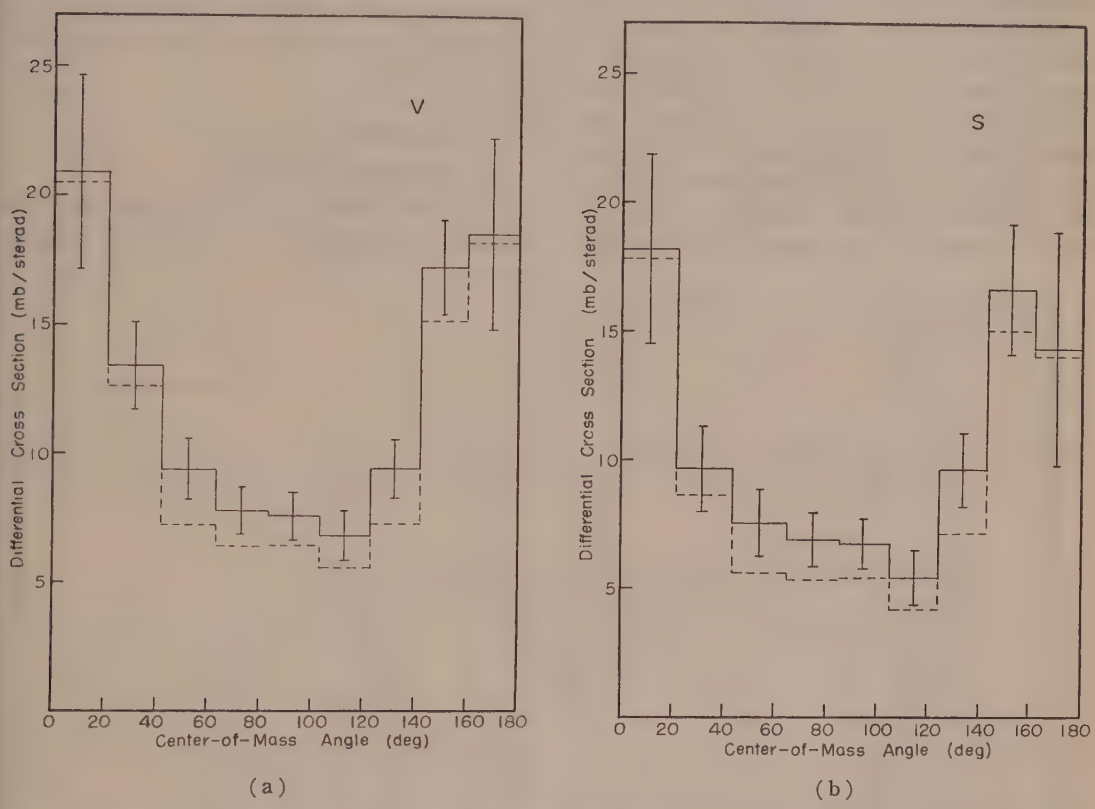

Fig. 2. Angular distributions of alpha particles from the V^{51} (n, α) Sc^{48} and S^{32} (n, α) Si^{29} reactions. The dashed lines show the observed angular distributions, while the solid lines show the corrected angular distributions.

angular distribution is divided into two energy regions, namely, a high-energy region (>6 Mev) and a low-energy region (<6 Mev), and it was found that the angular distributions for these two regions are nearly similar to each other. Therefore we assumed that the angular distributions for various energy regions are all the same. Thus the correction for the energy loss of alpha particles in the target material was carried out for the uncorrected energy distribution in Fig. 3, using the angular distribution. Then, making use of this corrected energy distribution, the correction for the absorption loss of alpha particles stopped in the target material was carried out for the uncorrected angular distribution. The final results obtained by the successive corrections are shown by the solid line in Fig. 2 and by the solid curve in Fig. 3. The procedures of the correction are presented in Appendix. The errors in Figs. 2 and 3 are the statistical errors derived from the track counts of the target and background data.

It is assumed that the relation between the measured alpha particle energy distributions

and the level densities of the residual nucleus is given by the following formula[15]:

$$n(\mathcal{E})d\mathcal{E}=\text{const. } \mathcal{E}\sigma_c(\mathcal{E})\omega(\mathcal{E}_r)d\mathcal{E},$$

where $n(\mathcal{E})d\mathcal{E}$ = number of alpha particles emitted with energy between $\mathcal{E}$ and $\mathcal{E}+d\mathcal{E}$, $\sigma_c(\mathcal{E})$[16] is the cross section, including the effects of barrier penetration for a nuclear radius of $1.5\times10^{-13}A^{1/3}$ cm, for the formation of the compound nucleus in the same state of excitation by the reverse reaction, in which particles of energy $\mathcal{E}$ strike the excited residual nucleus, and $\omega(\mathcal{E}_r)$ is the density of energy level of the rediual nucleus at excitation $\mathcal{E}_r=\mathcal{E}_{max}-\mathcal{E}$. $\mathcal{E}_{max}$ is the maximum energy which the emitted particle may have. Fig. 4 shows the results presented by plotting the measured energy spectra divided by $\mathcal{E}\sigma_c(\mathcal{E})$. Except for low energy side, the data fit a straight line which would correspond to a Maxwellian distribution with the temperatures of about 0.9 Mev for Sc and about 1.5 Mev for Si. The temperatures at the low energy side (7 Mev for Sc and 7 Mev for Si) are not included in the present discussion because of the contribution of the second alpha particles from $(n, n\alpha)$ events.

The total cross sections of V and S are 126 and 109 mb respectively. Combined systematic and statistical uncertainties are estimated to be roughly 15% in the total cross sections.

§ 4. Discussions

(1) *Angular distributions*

As in the cases of Al, Co and Mn, the angular distributions for the entire energy

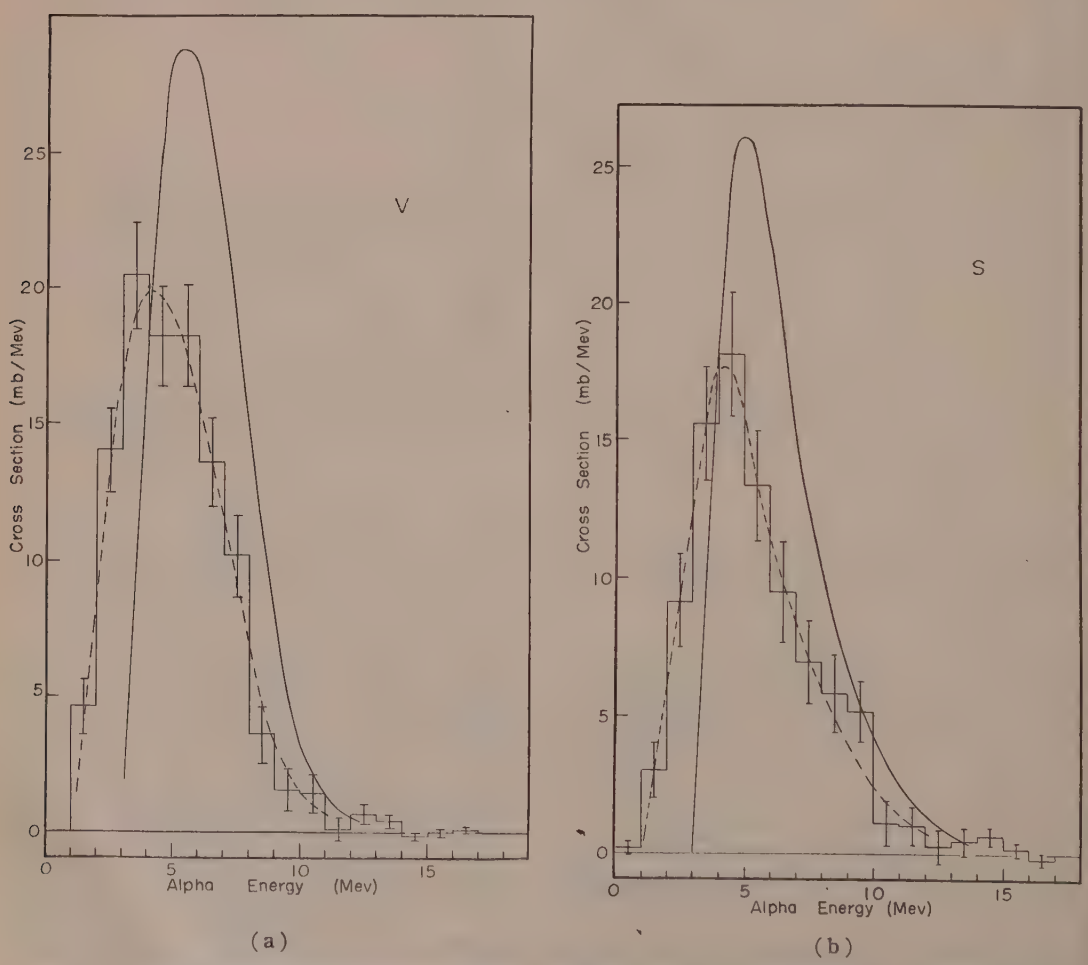

Fig. 3. Energy distributions of alpha particles from the $V^{51}(n, \alpha)Sc^{48}$ and $S^{32}(n, \alpha)Si^{29}$ reactions. The histograms and dashed curves show the observed energy distributions, while the solid curves show the corrected energy distributions.

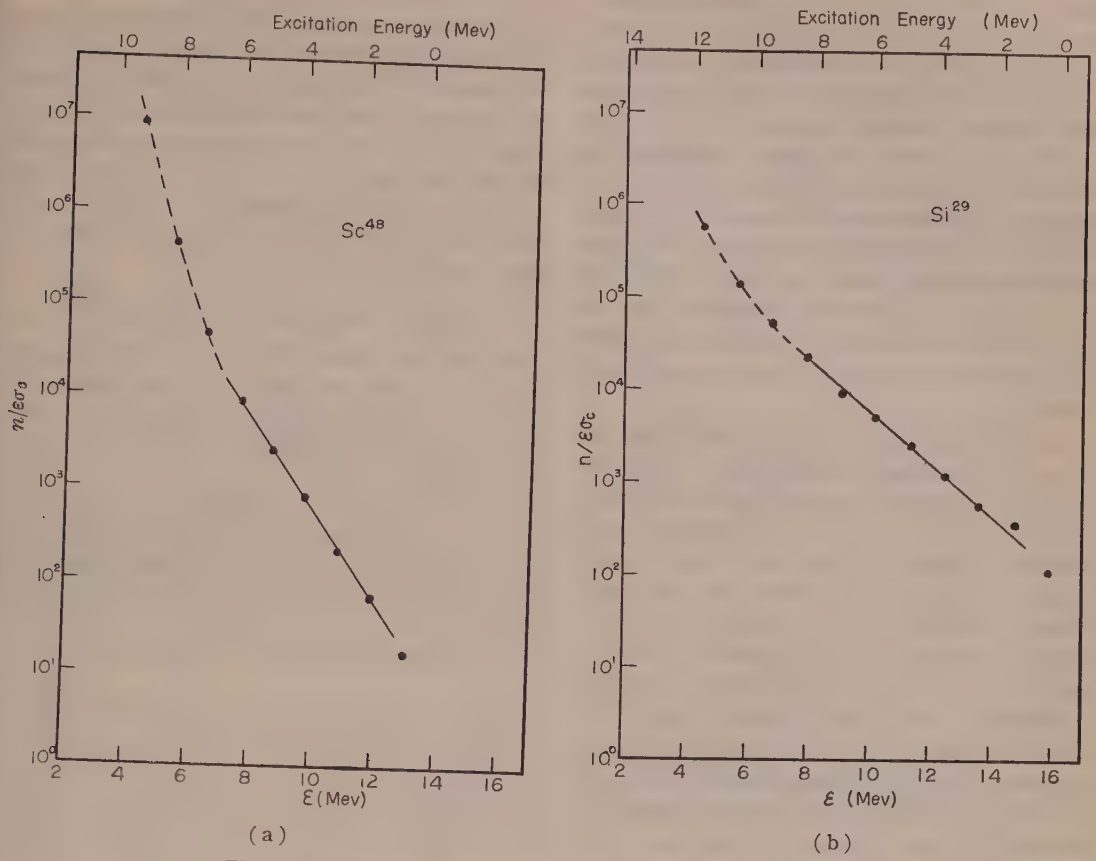

Fig. 4. The relative level densities $\omega = n/\varepsilon\sigma_c$ of Sc^{48} and Si^{29}.

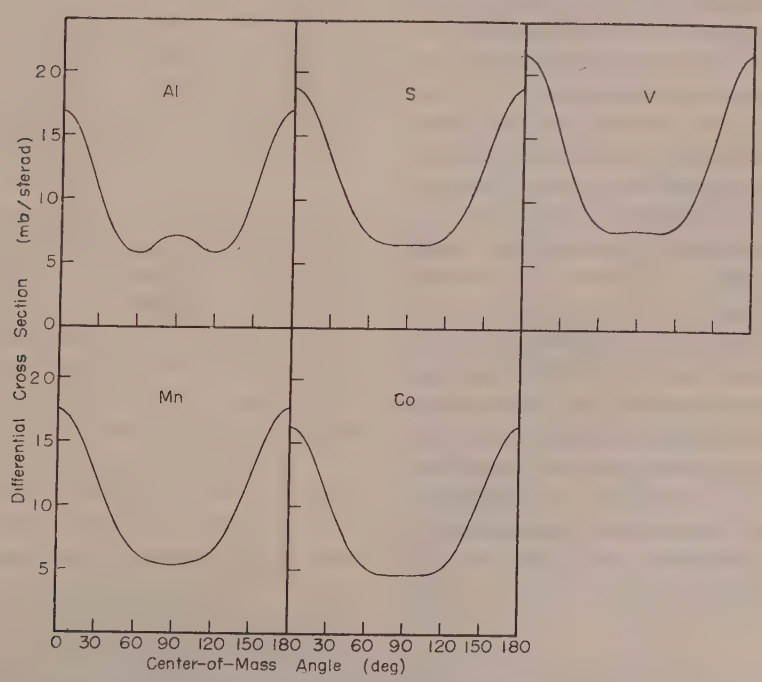

Fig. 5. Summary of the (n, α) angular distributious. These were obtained by a least-squares fit to $A_0 + A_2P_2(\cos\theta) + A_4P_4(\cos\theta)$ weighted according to statistics

region in the cases V and S are also approximately 90° symmetrical and concave upward.

The (n, α) angular distributions measured by us are summarized in Fig. 5. These were obtained by least-squares fit to $A_0+A_2P_2(\cos\theta)+A_4P_4(\cos\theta)$ weighted according to statistics. As shown in Fig. 5, all the angular distributions are concave upward and show the simillar shape to each other. Thus it may be concluded that the angular distributions of the alpha particles from the interaction of 14.8-Mev neutrons with light medium weight nuclei show the above-mentioned shape.

Rosen and Stewart[17] have measured the energy and angular distributions of neutrons from 14-Mev neutron interactions with heavy elements, while Ahn and Roberts[18] have measured with Zr. Allan[6] has measured the angular distribution of protons from the interaction of 14-Mev neutrons with Cu^{63}. Their results indicated that the angular distributions of the high energy particles are strongly peaked in the forward direction and those of the low energy particles are isotropic. A marked contrast between those results and the results of the (n, α) reaction should be remembered.

Our results are expected to contain the alpha particle group from the $(n, n\alpha)$ reaction. Since the inelastically scattered neutrons from the $(n, n\alpha)$ reaction are of low energy, the angular distribution of these neutrons seems to be isotropic as the above data and consequently the angular distribution of the corresponding alpha particles seems to be also isotropic. Therefore it is considered that most of the observed deviation from isotropy are due to the contribution from the (n, α) reaction.

The appoximate 90° symmetry of the angular distribution of the alpha particles indicates the fact that most of the reactions probably occur through the formation of the compound nucleus although the fairly large deviation from isotropy cannot be explained by the statistical theory of nuclear reactions[19]. The observed deviation from isotropy may be explained by introducing a kind of selection rule for the emission of the alpha particles such as the isotopic spin selection rule[20] or by furthur development of an intermediate coupling model such as proposed by Lane, Thomas and Wigner[21].

The (p, α) reactions of several elements at 18 Mev were observed by Brady[7]. He showed that the particles "evaporating" with low energy show almost isotropic angular distributions and the angular distribution of emitted fast particles is always in the forward direction. The disagreement of Brady's and ours might be due to different incident nucleons and energies.

(2) *Energy spectrum and level density*

As in the cases of Al, Co and Mn, the energy distributions show, in the cases of V and S too, that the alpha particles with energies below the Coulomb barrier are more emitted than expected.

The relative level densities measured by us are summarized in Fig. 6, and the nuclear temperatures in Table I. In the cases of Co (n, α) and Mn (n, α), values averaged over

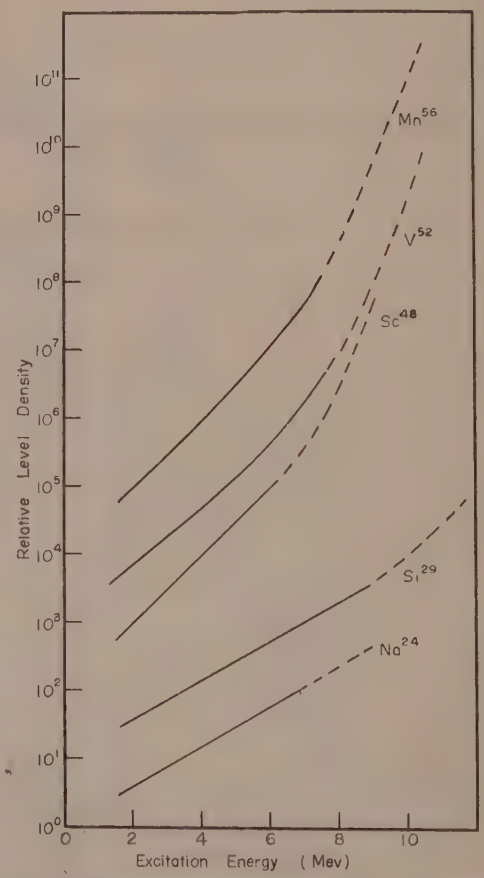

Fig. 6. Summary of the relative level densities. The dashed curves show the regions which are expected to contain the second alpha particles from $(n, n\alpha)$ events.

energy interval between 2 and 7.5 Mev of the excitation energy are listed. Gugelot[4] obtained the nuclear temperature 2.7 Mev for Al (p, p) and 2.6 Mev for Fe (p, p), respectively. It is remarkable that the temperatures obtained by us are always lower than Gugelot's values.

Table I. Summary of the nuclear temperatures in Mev.

Nucleus	Na^{24}	Si^{29}	Sc^{48}	V^{52}	Mn^{56}
Temperature	1.45	1.5	0.9	0.85	0.7

The shape of the energy level distribution determined from the 40-Mev (α, p) experiment[3] was compatible with the Fermi gas model density formula $\omega(\mathcal{E}_r)=\text{const}\exp\sqrt{a\mathcal{E}_r}$. On the other hand, the parameter a was found to have the same value for Cu, Ag, and Au. According to the Fermi gas model a should increase linearly with the atomic number.

The results of our experiment, when analyzed in terms of the statistical theory, are not compatible with the Fermi gas model for the nucleus. The experimentally measured level density increases much less rapidly at low excitation energies than the Fermi gas level density. On the other hand, in contrast to the (α, p) result, the rate of increase of level density with the excitation energy measured in our experiment increases with mass number as can be seen in Fig. 6. This is a general prediction of most nuclear model.

Ribe[22] has observed the energy spectrum of disintegration particles produced by 14-Mev neutrons in argon-gas counter fillings which has two peaks. It is considered that a low energy peak is due to (n, p) reaction and a high energy peak is due to (n, α) reaction. The position of the high energy peak is about 5 Mev which is in fairly good agreement with our data in the cases of V and S.

Brady[23] has observed the energy distribution of the alpha particles resulting from the Ni (p, α) Co reaction. The curve on a semi-log plot of the relative level density calculated from this energy distribution fits a straight line which would correspond to Maxwellian distribution with a temperature of about 0.6 Mev. This temperature is in fairly good agreement with our value of Mn calculated from the Co (n, α) Mn reaction.

Allan[6] has measured the energy distribution of protons from the interaction of 14-Mev neutrons with several medium weight nuclei and suggested that the large low energy proton excess might come from the (n, np) reaction because of the reason that the emission of a second neutron is energetically impossible over most of the range of target nucleus excitation and proton emission (n, np) is in competition only with γ-emission. In our cases, however, as shown in Table II

Table II. Binding energies in Mev. These binding energies were derived from the table of Martin.[24]

Target nucleus	neutron	proton	α particles
Al^{27}	13.73	5.96	8.05
S^{32}	14.88	9.13	7.02
V^{51}	10.73	7.68	7.35
Mn^{55}	10.96	7.18	6.64
Co^{59}	11.14	6.65	6.06

alpha particle emission $(n, n\alpha)$ is in competition with proton emission (n, np) because of the small difference between the alpha particle and proton binding energy, and the large low energy alpha particle excess cannot be explained by the $(n, n\alpha)$ reaction only.

The evaporation of charged particles is favoured by depression of the Coulomb barrier due to the expansion of highly excited nuclei, but this effect is negligible at the temperature concerned here. Further, by introducing a choice of large nuclear radii, we may interprete the larger yield of low energy alpha particles well, but nuclear radii larger than $r_0=1.5\times10^{-13}$cm is in disagreement with other experiments. In view of above considerations, it may be probable that the actual boundary of the nuclear potential is not a square well with sharp boundary but rather has a diffuse nuclear surface because the diffuseness of nuclear surface makes the penetration of the potential barrier easier. Recently, Kikuchi[25] has reported in this connexion that the energy distribution of the alpha particles of the Al^{27} (n, α) Na^{24} reaction, which gives somewhat lower temperature than those of others, can be explained with the temperature of 2 Mev by introducing a diffuse potential.

Considerable modification of the theory of Coulomb barrier penetrabilities or of the level density function of the residual nuclei, would be required to explain our (n, p) results.

(3) *Cross sections*

The total cross sections obtained by other authors and by us are shown in Table III.

Table III. Comparison of cross sections (mb)

Target	Present experiment		Activation methods $(n, \alpha\gamma)$			Theoretical $(n, \alpha\gamma)$
	$(n, \alpha\gamma)+(n, \alpha n)+(n, n\alpha)$	$(n, \alpha\gamma)$	Paul and Clarke	Hughes*	Yasumi	
Al	92±15	82.0±17	78.9±16	110±20	120±14.4	273
S	109±16	38.2±7.6				
V	126±19	43.2±8.6	28.6±12	30±10		4.6
Mn	96±14	39.4±8.0	52.5±7.9	30±12		4.5
Co	84±13	25.0±5.0	39.1±7.8	52± 8		3.7

* These data are summarized by Hughes and Harvey. Theoretical cross sections were derived from the calculation by Paul and Clarke[1].

Column I gives the cross section of $(n, \alpha\gamma)+(n, \alpha n)+(n, n\alpha)$ reactions, while column II gives the cross sections of $(n, \alpha\gamma)$ reactions only which are compared directly with those obtained by other authors[1)26)] with the activation method. When the emission of the first alpha particles leaves the residual nucleus in states with an excitation energy below neutron binding energy, only γ-ray emission can occur. Therefore when the energy distribution of the alpha particles is cut off at $(14.8+Q-B_n)\times(A-3)/(A+1)$ Mev, it is possible to attribute the high energy part of the energy distribution to the $(n, \alpha\gamma)$ process, where Q is the Q value of (n, α) reaction, B_n the neutron binding energy and A the mass number of target nucleus. Q and B_n were derived from the papers of Martin[24)], Segre[27)] and Endt *et al*[28)]. Our $(n, \alpha\gamma)$ cross sections are in fairly good agreement with those obtained by other authors[1)26)]. Except in the cases of Al and S, the experimental cross sections are higher by a factor of about 10 than those expected from the evaporation theory.

The approximately 90° symmetrical angular distributions and the low energy alpha particle excess might suggest that the large experimental (n, α) cross sections are not due to the non-compound processes but rather to the large penetrabilities which are explained by introducing a diffuse potential.

Table IV. The relation between $\sigma(\theta)\sin\theta d\theta$ and $\sigma(\varphi)\sin\varphi d\varphi$. $\int_{\varphi}^{\varphi+10^\circ}\sigma(\varphi)\sin\varphi d\varphi$ is the value of the sum of each column.

θ \ φ	0°	10°	20°	30°	40°	50°	60°	70°	80°	90°	100°	110°	120°	130°	140°	$\int_{\theta}^{\theta+10^\circ}\sigma(\theta)\sin\theta d\theta$
0°				0.18a	0.62a	0.20a										a
10°			0.09b	0.27b	0.22b	0.32b	0.11b									b
20°		0.05c	0.17c	0.14c	0.14c	0.16c	0.25c	0.08c								c
30°	0.30d	0.12d	0.10d	0.10d	0.10d	0.11d	0.14d	0.23d	0.06d							d
40°	0.07e	0.08e	0.08e	0.08e	0.09e	0.09e	0.10e	0.13e	0.19e	0.06e						e
50°	0.02f	0.11f	0.08f	0.08f	0.08f	0.08f	0.09f	0.10f	0.12f	0.19f	0.06f					f
60°		0.03g	0.12g	0.09g	0.08g	0.08g	0.08g	0.08g	0.09g	0.11g	0.18g	0.05g				g
70°			0.03h	0.14h	0.09h	0.08h	0.08h	0.08h	0.08h	0.09h	0.11h	0.17h	0.08h			h
80°				0.04 i	0.15 i	0.09 i	0.09 i	0.08 i	0.08 i	0.08 i	0.09 i	0.10 i	0.17 i	0.04 i		i
90°																

Acknowledgements

The author wishes to express his sincere thanks to Profs. K. Kimura and S. Yasumi for their valuable suggestions and continual encouragments throughout the work. His thanks are also due to Prof. M. Kobayasi and his colleagues for valuable theoretical discussions, and to Mr. H. Ogata, Mr. Y. Tsuneoka, Mr. S. Ōki, Mrs. E. Takekoshi and Miss N. Shiomi for their cooperative efforts. This work has been supported by the Scientific Research Expenditure of the Ministry of Education.

Appendix

(1) *The relation between* $\sigma(\theta)\sin\theta d\theta$ *and* $\sigma(\varphi)\sin\varphi d\varphi$

Assume that the target is placed on the emulsion as indicated in Fig. 1. Let θ be the angle between the lines of flight of the incoming neutron and of the alpha particle, and φ the angle between the inward drawn normal to the plate and the alpha particle direction. When an incident angle of 45° is chosen for the neutrons, $\sigma(\varphi)\sin\varphi d\varphi$ must be calculated from $\sigma(\theta)\sin\theta d\theta$, since the energy loss and absorption loss are functions of φ, where $\sigma(\theta)$ is a differential cross section per unit solid angle in the laboratory system, and $\sigma(\varphi)\sin\varphi d\varphi$ is the cross section of alpha particles emitted in the direction between φ and $\varphi+d\varphi$.

The relation between $\sigma(\theta)\sin\theta d\theta$ and $\sigma(\varphi)\sin\varphi d\varphi$ is shown in Table IV obtained by graphical calculation. Using Table IV we can calculate $\sigma(\varphi)\sin\varphi d\varphi$ from $\sigma(\theta)\sin\theta d\theta$.

(2) *The correction of energy loss for energy distribution*

The alpha particles resulting from the (n, α) reaction are produced uniformly in the target, since the absorption of the neutron in the target is negligibly small. If $R(E_0)$ represents the range in the material of the target of an alpha particle of energy E_0, a particle emitted in the direction φ at the upper surface loses the energy $E_0-f[R(E_0)-T\sec\varphi]$ before emerging from the target, where $f(R)$ is the inverse function of $R(E_0)$ and T is the target thickness. If we assume that the energy loss per unit length between E_0 and $f[R(E_0)-T\sec\varphi]$ is constant, the emerging particles distribute uniformly between E_0 and $f[R(E_0)-T\sec\varphi]$. When the number of particles emitted in the direction between φ and $\varphi+d\varphi$ with an energy between E_0 and E_0+dE_0 in the target is $N(E_0, \varphi)\,dE_0d\varphi$, the number of particles emerging from the target with an energy between E and $E+dE$ is given by

$$\frac{N(E_0, \varphi)dE_0d\varphi}{E_0-f[R(E_0)-T\sec\varphi]}F(E, E_0, \varphi)\,, \qquad (1)$$

where the function $F(E, E_0, \varphi)$ is defined by

$$\begin{aligned} F(E, E_0, \varphi)&=1 \\ \text{for}\quad & E_0>E>f[R(E_0)-T\sec\varphi] \\ &=0 \\ \text{for}\quad & E>E_0,\ E<f[R(E_0)-T\sec\varphi]\,. \end{aligned}$$

If the number of particle emitted with an energy between E_0 and E_0+dE_0 in the target is $n(E_0)dE_0$, $N(E_0, \varphi)dE_0d\varphi$ can be written as

$$N(E_0, \varphi)dE_0d\varphi=n(E_0)\frac{2\pi\sigma(\varphi)\sin\varphi d\varphi dE_0}{\sigma_{\text{total}}}\,, \qquad (2)$$

using the assumption that the angular distribution for various energy regions are all the same.

Then we get, from (1) and (2), the energy distribution $N(E)dE$ for the particles emerging from the target in the form:

$$N(E)dE=\int_0^{E_0\,\max}\int_0^{\pi/2}\frac{n(E_0)F(E, E_0, \varphi)\,2\pi\sigma(\varphi)\sin\varphi d\varphi}{\{E_0-f[R(E_0)-T\sec\varphi]\}\sigma_{\text{total}}}dE_0dE$$

If, for convenience of calculation, we divide the energy and angle into 1 Mev and 10° intervals, respectively, we have

$$N(E)dE\fallingdotseq\sum_{E_0=1,2.\cdots}\int_{E_0}^{E_0+1}n(E_0)\,dE_0\left[\sum_{\varphi=5^\circ,15^\circ,\cdots,85^\circ}\frac{F(E, E_0,\varphi)\,2\pi\int_{\varphi-5^\circ}^{\varphi+5^\circ}\sigma(\varphi)\sin\varphi d\varphi}{\{E_0-f[R(E_0)-T\sec\varphi]\}\sigma_{\text{total}}}\right]dE\,. \qquad (3)$$

Using this equation, we can calculate the corrected energy distribution $n(E_0)dE_0$ from the observed energy distribution $N(E)dE$.

(3) *Correction of absorption loss for angular distribution*

For a particle leaving the target with energy E and at angle φ, the following relation holds

$$(T-T')\sec\varphi=R(E_0)-R(E)\ ,$$

where T' is the depth and E_0 the energy of a particle at the point of generation. Assuming that we omit the particle of $E<1$ Mev from scanning, the absorption rate A' is expressed by

$$A'=\frac{T'}{T}=\frac{T\sec\varphi-\{R(E_0)-R(1)\}}{T\sec\varphi}F'(E,E_0,\varphi)\ ,$$

where the function $F'(E, E_0, \varphi)$ is defied by

$$\begin{aligned} F'(E,E_0,\varphi)&=1 \quad \text{for} \quad T\sec\varphi>R(E_0)-R(1)\ ,\\ &=0 \quad \text{for} \quad T\sec\varphi<R(E_0)-R(1)\ . \end{aligned}$$

Therefore, when the particles generated with the energy distribution $n(E)dE$ and angular distribution $\sigma(\varphi)$ emerge from the target, the absorption rate A is expressed by

$$A=\int_0^{\pi/2}\int_0^{E_{0\,\max}}\frac{n(E_0)dE_0}{n_{\text{total}}}\left(1-\frac{R(E_0)-R(1)}{T\sec\varphi}\right)\frac{2\pi\sigma(\varphi)\sin\varphi d\varphi}{\sigma_{\text{total}}}F'(E,E_0,\varphi)\ .$$

If, for convenience of calculation, we divide the energy and angle into 1 Mev and 10° intervals, respectively, we get

$$A\fallingdotseq\sum_{\varphi=5^\circ,15^\circ,\ldots,85^\circ}\ \sum_{E_0=1,2,\ldots}\int_0^{E_0+1}\frac{n(E_0)dE_0}{n_{\text{total}}}\left(1-\frac{R(E_0)-R(1)}{T\sec\varphi}\right)\frac{2\pi\int_{\varphi-5^\circ}^{\varphi+5^\circ}\sigma(\varphi)\sin\varphi d\varphi}{\sigma_{\text{total}}}F'(E,E_0,\varphi)\ .$$

References

1) E. B. Paul and R. L. Clarke: Can. J. Phys. **31** (1953) 267.
2) E. R. Graves and L. Rosen: Phys. Rev. **89** (1953) 343.
B. G. Whitmore and G. E. Dennis: Phys. Rev. **84** (1951) 296.
D. M. Thomson: Proc. Phys. Soc. (London) A**69** (1956) 447.
P. C. Gugelot: Phys. Rev. **81** (1951) 51.
R. Britten: Phys. Rev. **88** (1952) 283.
3) R. M. Eisberg, G. Igo and H. E. Wegner: Phys. Rev. **100** (1955) 1309.
4) P. C. Gugelot: Phys. Rev. **93** (1954) 425.
5) "Statistical Aspects of the Nucleus" Brookhaven National Laboratory Report BNL-331, p. 91 (1955) (unpublished).
6) D. L. Allan: Proc. Phys. Soc. (London) A**70** (1957) 195.
7) These data were introduced by P. C. Gugelot in Physica **22** (1956) 1019.
8) F. L. Ribe and W. Davis: Phys. Rev. **99** (1955) 331.
9) I. Kumabe, E. Takekoshi, H. Ogata, Y. Tsuneoka and S. Ōki: Phys. Rev. **106** (1957) 155.
10) I. Kumabe, E. Takekoshi, H. Ogata, Y. Tsuneoka and S. Ōki: J. Phys. Soc. Japan **13** (1958) 129.
11) A. O. Hanson and J. L. Mc Kibben: Phys. Rev. **72** (1947) 673.
12) A. D. Dainton, A. R. Gattiker and W. O. Lock: Phil. Mag. **42** (1951) 396.
13) B. Stiller, M. M. Shapiro and F. W. O'Dell: Rev. Sci. Inst. **25** (1954) 340.
14) J. Rotblat: Nature **167** (1951) 550.
15) V. F. Weisskopf: Phys. Rev. **52** (1937) 295.
16) J. M. Blatt and V. F. Weisskopf: *Theoretical Nuclear Physics* (John Wiley and Sons, Inc., New York, 1952), p. 353.
17) L. Rosen and L. Stewart: Phys. Rev. **107** (1957) 824.
18) S. A. Ahn and J. H. Roberts: Phys. Rev. **108** (1957) 110.
19) W. Hauser and H. Feshbach: Phys. Rev. **87** (1952) 366.
20) B. Cassen and E. U. Condon: Phys. Rev. **50** (1936) 846.
21) A. M. Lane, R. C. Thomas and E. P. Wigner: Phys. Rev. **98** (1955) 694.
22) F. L. Ribe: Phys. Rev. **103** (1956) 741.
23) Reference 5, p. 92.
24) C. N. Martin: *Tables Numériques de Physique Nucleaire* (Gauthier-Villars, Paris, 1954).
25) K. Kikuchi: Prog. Theor. Phys. **17** (1957) 643.
26) S. Yasumi: J. Phys. Soc. Japan **12** (1957) 443.
D. J. Hughes and J. A. Harvey: *Neutron Cross Sections* (Mc Graw-Hill Book Company, Inc., New York, 1955).
27) E. Segre: *Experimental Nuclear Physics*, Vol. I (John Wiley and Sons, Inc., New York 1953), p. 720.
28) P. M. Endt and J. C. Kluyver: Rev. Mod. Phys. **26** (1954) 95.

JOURNAL OF THE PHYSICAL SOCIETY OF JAPAN Vol. 13, No. 4, APRIL, 1958

Some Studies on the Ternary System (Ba-Pb-Ca)TiO_3*

By Takuro IKEDA

Kobayasi Institute of Physical Research, Kokubunji, Tokyo

(Received December 19, 1957)

The phase relation and the dielectric and mechanical properties of ceramic samples on the ternary system (Ba–Pb–Ca)TiO_3 are studied. The ferroelectricity of the solid solution (Ba–Pb)TiO_3 decreases with increasing Ca concentration and disappears at about 50 mole percent of $CaTiO_3$; and then the structure changes to cubic, pseudocubic and orthorhombic. A certain insoluble region exists in the vicinity along (Ba–Ca)TiO_3 side. The dielectric and piezoelectric constants of $BaTiO_3$ decrease with increasing concentration of $PbTiO_3$ and $CaTiO_3$. The dielectric and mechanical Q's vary in parallel with composition.

§ 1. Introduction

It is well-known that dielectric and mechanical properties of $BaTiO_3$ are varied by the addition of $PbTiO_3$ or $CaTiO_3$. Especially, ceramics of solid solutions of these materials are used for electromechanical transducers and show better properties than pure $BaTiO_3$ ceramics.

Structural studies on the binary system (Ba–Pb)TiO_3 have been performed by G. Shirane[1] and other authors. With concentration of $PbTiO_3$, Curie point becomes higher, and the tetragonality increases.

The system (Ba–Ca)TiO_3 was investigated by R. C. DeVries and R. Roy[2], and M. McQuarrie and F. W. Behnke[3]. The Curie point decreases gradually with increasing concentration of Ca, and there is a wide insoluble range of concentration.

E. Sawaguchi *et al*[4] reported phase relations of (Pb–Ca)TiO_3 system and indicated that the tetragonality of $PbTiO_3$ decreases with increasing mole percent of $CaTiO_3$ and disappears at about $(Pb_{0.6}–Ca_{0.4})TiO_3$. The phase of solid solution containing more than 40 mole percent of $CaTiO_3$ is prescribed as pseudocubic.

Properties of $CaTiO_3$ were investigated by L. W. Coughanour, R. S. Roth and others[5], and M. McQuarrie[6] and H. F. Kay *et al*[7]. Kay's previous paper (which is quoted in McQuarrie's report[6]) reported that $CaTiO_3$ has a pseudomonoclinic structure at room temperature and transitions occur at 600° and 1000°C. Roth *et al* performed complete X-ray study and indicates that $CaTiO_3$ has an orthorhombic structure at room temperature; lattice parameters are $a=5.381$ A, $b=7.645$ A, $c=5.443$ A and pseudomonoclinic angle is $\beta'=90°40'$. Recently, Kay[7] determined the atomic position in $CaTiO_3$ and it was shown to be antiferroelectric. McQuarrie studied the phase relation of system (Ca–Sr)TiO_3. He concluded that the orthorhombic structure of $CaTiO_3$ changes into tetragonal at 1100°C and cubic at 1200°C. Gränicher[8] studied also the system (Ca–Sr)TiO_3, and showed the existence of some other phases. But, as for the phase transition of $CaTiO_3$, there are some ambiguities. In the present paper, so far as $CaTiO_3$ is concerned, the phase transition temperatures reported by McQuarrie and the structural investigation by Roth *et al* are quoted.

As materials for electromechanical transducers, mechanical and piezoelectric properties of this system have been investigated by some authors. W. P. Mason[9] showed that the addition of $PbTiO_3$ to $BaTiO_3$ increases coercive field and decreases the temperature dependence of various properties. D. A. Berlincourt and F. Kulcsar[10] examined the effect of addition of $PbTiO_3$ or $CaTiO_3$. Mason[11][12] reported subsequently the better quality of the solid solution (Ba–Pb–Ca)TiO_3. Their experiments, however, have been restricted to the vicinity of $BaTiO_3$.

The present studies were begun chiefly for two purposes: of examining the phase relation from the ferroelectric range to the antiferroelectric $CaTiO_3$, and of obtaining the systematic information on the electromechanical properties of the system.

Recently, M. McQuarrie[13] reported the

* The summary of the present report was read at the Meeting of the Physical Society of Japan, on 11th, April, 1957.

structural study on the same system. He measured dielectric properties, showed the complete phase diagram, and emphasized the evaporating loss of PbO.

The present author has independently studied this system and obtains similar diagram. Furthermore, the mechanical and piezoelectric properties of ceramics of the system are measured and systematic results are obtained.

§ 2. Experimental Procedure

(a) *Preparation of Samples*

The c.p. grade of $BaCO_3$, $CaCO_3$, PbO and TiO_2 are mixed with various mole concentration and calcined at 1200°~1050°C. They were crushed and pressed in the disc shape with diameter of 30 mm and thickness of 2~4 mm, and then sintered at 1420°~1250°C. Porosities of the samples are mostly 10~20%.

In the sintering process of those with larger Pb concentrations, the evaporation loss of PbO are not ignorable. Then, some lumps of PbO are laid in the crusible and the sintering is done in the atmosphere of PbO at lower temperature (less than 1300°). None the less, some part near surface of piled up discs of the same composition appear to be a little deficit of Pb, and so inner parts are used for samples. The compositions of samples after sintering are not examined.

In Fig. 1, the compositions (before sintering) of the tested samples are indicated by points.

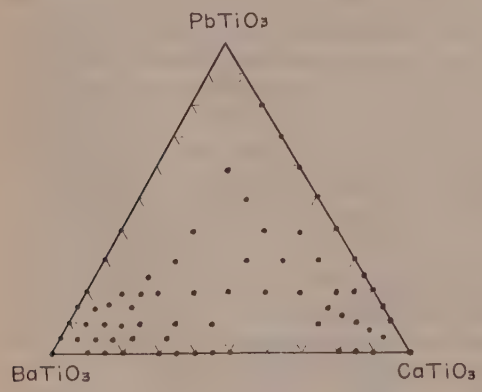

Fig. 1. Tested samples of the system (Ba-Pb-Ca)TiO_3.

(b) *Temperature Dependence of Dielectric Constant.*

On the small square plates are glazed silver electrodes. They are immersed in the silicone oil bath and temperature is varied. The dielectric measurement is done at 550 Kc/s by the resonance-substitution-method with a precise variable air-condenser. The temperature corresponding to a peak of dielectric constant is taken as Curie point.

(c) *Dielectric and Electromechanical Measurement of Prepolarized Sample.*

The ceramic discs with silver electrodes (diameter of ca. 26 mm) are prepolarized by field cooling precess with d.c. fields of 5~15 KV/cm, and aged at 60°~80°C for one or two days. The resonant frequencies of most of them in radial mode vibration are about 120 Kc/s.

Their dielectric quantities are measured at 50 Kc/s by the Radio Frequency Impedance Bridge of Yokogawa Electric Works at room temperature. A measured impedance is the capacity C^F and resistance R_e in series (Fig. 2 (a)). From them, free dielectric constant $\varepsilon_3{}^F$ and dielectric Q value Q_e are computed by the following formulae:

$$C^F=\frac{\varepsilon_3{}^F(\pi a^2)}{4\pi d} \quad \text{and} \quad \omega C^F R_e=\frac{1}{Q_e}, \qquad (2.1)$$

where a=radius and d=thickness.

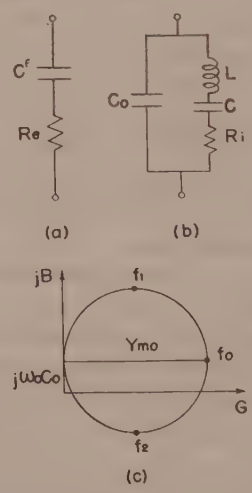

Fig. 2. Equivalent circuit and admittance diagram.

The piezoelectric and elastic properties are measured by the resonance curve method and admittance loop method in the radial mode vibration. By denoting the frequencies corresponding to maximum and minimum admittance as f_m and f_n, the electromechanical radial coupling coefficient k_r is calculated by

$$k_r{}^2=K\frac{f_n-f_m}{f_m}, \qquad K=\frac{R_1{}^2-(1-\sigma^2)}{1+\sigma} \qquad (2.2)$$

where the factor $R_1=2.03$ and $K=2.51$ for a value of Poisson's ratio $\sigma=0.27$* (cf. Mason's book[9]). k_r^2 is

$$k_r^2=\frac{2}{1-\sigma}\cdot\frac{4\pi d_{31}^2}{s_{11}^E\varepsilon_3^{\sigma}}, \qquad (2.3)$$

where d_{31}=transverse piezoelectric constant, s_{11}^E=elastic compliance coefficient for constant electric field. The resonant frequency of the radial vibration is

$$f_0=\frac{R_1}{2\pi a}\sqrt{\frac{1}{\rho s_{11}^E}\frac{1}{1-\sigma^2}}, \qquad (2.4)$$

where ρ=density. In ordinary case, $f_m\approx f_0$. From the measured values of f_m, f_n and C^F, the piezoelectric constant d_{31} is obtained.

The mechanical Q factor Q_m of the vibrator is measured from the admittance circle: that is, by denoting the quadrantal frequencies as f_1 and f_2 (in Fig. 2 (c)), the value of Q_m is given by

$$Q_m=f_0/(f_2-f_1). \qquad (2.5)$$

In the case of the vibrator with small electromechanical coupling or low Q factor, the resonance curve method is unsuitable for obtaining the value of k_r^2. Then, from the admittance diagram,

$$C/C_0=1/Q_m\cdot Y_{m0}/(\omega_0 C_0), \qquad (2.6)$$

where C_0=clamped capacity, C=capacity in the piezoelectric branch, Y_{m0}=diameter of admittance circle=reciprocal of internal friction resistance R_l and $\omega_0=2\pi f_0$ (Fig. 2 (b) and (c)). Using this value of C/C_0 instead of $(f_n-f_m)/f_m$ in eq. (2.2), more certain value of k_r^2 can be obtained.

(d) *Elastic Measurement of Non-piezoelectric Ceramic Sample.*

As described later, the samples in the region near $CaTiO_3$ show no anomalies in the curve of dielectric properties vs. temperature. Then, the elastic measurements of them are adopted here for ascertaining phase changes. They have not piezoelectricity, and so the temperature variation of elastic modulus and dissipation are measured by the composite-bar method. That is, the resonant frequencies and the minimum to maximum admittance ratio of the composite bar, which consists of the X-cut and Y-long quartz rod and the specimen being cemented endwise, are observed with varying temperature. The anomalies of these quantities vs. temperature curve are considered to correspond to the phase transformations. (cf. an earlier report on the elastic properties of lead zirconate and other solid solutions[14]).

(e) *X-ray Measurement*

Debye photographs are taken by the Weissenberg camera with a goniometer, using Cu-Kα radiation. Its diameter is 57.3 mm. The lattice parameters and superstructure lines are examined.

§ 3. Experimental Results

(a) *Ferroelectric Phase*

In Fig. 3, the temperature variations of the dielectric constants of $(Ba_{0.7-x}-Pb_{0.3}-Ca_x)TiO_3$ and $(Ba_{0.8-x}-Pb_{0.2}-Ca_x)TiO_3$ are shown. The temperature of maximum dielectric constant is considered as Curie point T_c. The distribution of Curie points is indicated in Fig. 4. Under these temperatures, the samples are to be of the same phase as that of $BaTiO_3$, namely ferroelectric and of tetragonal structure. X-ray pattern of $(Pb_{0.6}-Ca_{0.4})TiO_3$, as

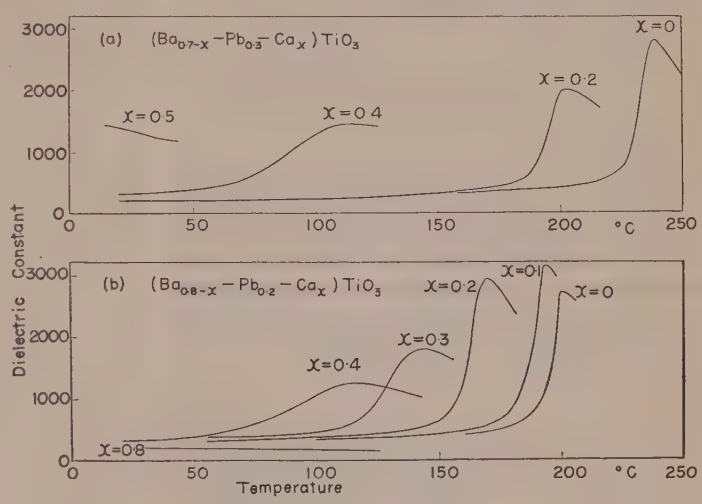

Fig. 3. Temperature variation of dielectric constant.
(a) $(Ba_{0.7-x}-Pb_{0.3}-Ca_x)TiO_3$
(b) $(Ba_{0.8-x}-Pb_{0.2}-Ca_x)TiO_3$

* The factors R_1 and K are different corresponding to various values of σ. Namely, $R_1=2.03$, 2.07 and $K=2.51$, 2.55 for $\sigma=0.27$, 0.33, respectively. But these differences are not important in the present paper.

an example, is analyzed and proved to be tetragonal as in $BaTiO_3$.

(b) *Insoluble Region*

Ordinarily, Curie point of the solid solution shifts smoothly with composition. When the composition enters the insoluble region, Curie point jumps or becomes unchanged. The insoluble limit in Fig. 4 is thus determined. The limited boundary near $CaTiO_3$ is drawn according to the X-ray measurement; for example, the pattern of $(Ba_{0.125}$–$Pb_{0.125}$–$Ca_{0.75})TiO_3$ is analyzed as that of mixed crystal.

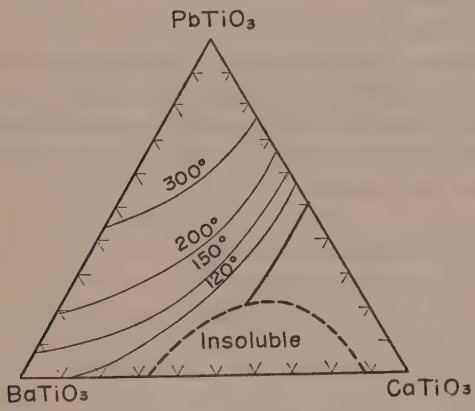

Fig. 4. Curie point in the ferroelectric phase

(c) *Phase of the Sample in the Vicinity of $CaTiO_3$.*

In the case of the sample with concentration of $CaTiO_3$ more than 50 mole percent (the right side of the solid line in Fig. 4), the dielectric constant goes on decreasing and tan δ increasing. With rising temperature no anomalies are found. The neighbouring region to tetragonal phase is of cubic structure, but $CaTiO_3$ is known to be orthorhombic. According to the previous paper of McQuarrie[6], orthorhombic $CaTiO_3$ transforms to tetragonal and then to cubic. A tetragonal region, therefore, may exist between the cubic and orthorhombic phases in the diagram. Debye photographs of several samples in this region are analyzed. Those in the nearest vicinity of $CaTiO_3$ can be indexed by assuming same structures as that of $CaTiO_3$ reported by Roth *et al* and are orthorhombic. That of $(Pb_{0.4}$–$Ca_{0.6})TiO_3$ may be considered to be cubic. It cannot be comfirmed if the structures of intermediate compositions are tetragonal or not. Nevertheless, the Debye patterns show a little deviation from cubic. So they are indicated as pseudo-cubic rather than tetragonal.

The phase boundaries cannot be definitely determined by X-ray measurements, and, therefore, the elastic properties are examined *versus* temperature by the composite bar method. When the phase transition occurs, any anomalies may appear at the transition temperature. For example, the resonant frequency and the minimum to maximum current ratio (a measure for internal friction) vs. temperature of the composite bar (of $(Pb_{0.25}$–$Ca_{0.75})TiO_3$) are shown in Fig. 5 (a). The measurements are done to about 400°C. In Fig. 5 (b), the temperatures thus obtained are plotted by circles. The transition temperatures, 1100° and 1200°C, of $CaTiO_3$ are those in the previous report of McQuarrie[6]. The dots in Fig. 5 (b) are the temperatures corresponding to peaks of dielectric constant curve, or the

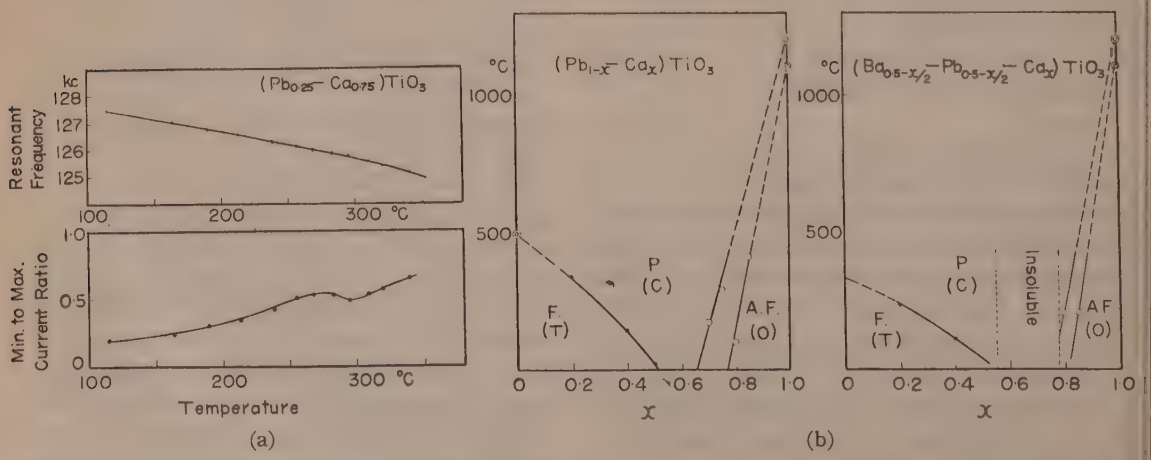

Fig. 5. (a) Elastic measurement by the compositebar method. (b) Determination of phase boundaries.

Curie points, under which the phase is ferroelectric and tetragonal. That of $PbTiO_3$ is 490°C by Shirane[1]. Combining these points, the phase boundaries are located. These results thus determined are not inconsistent with X-ray measurements.

(d) *Phase Diagram*

From above results, the phase diagram of the whole system is obtained in Fig. 6. This result resembles, but is a little different from McQuarrie's recent report.

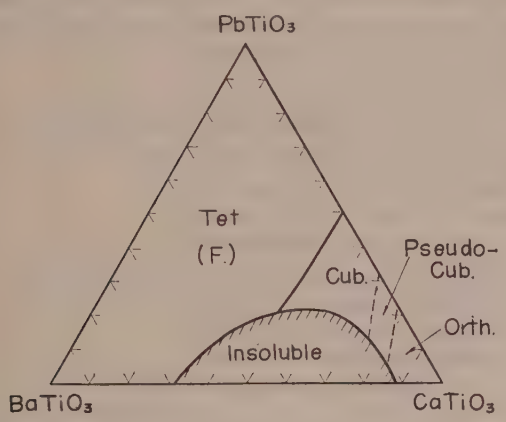

Fig. 6. Phase diagram of the system (Ba-Pb-Ca)TiO_3.

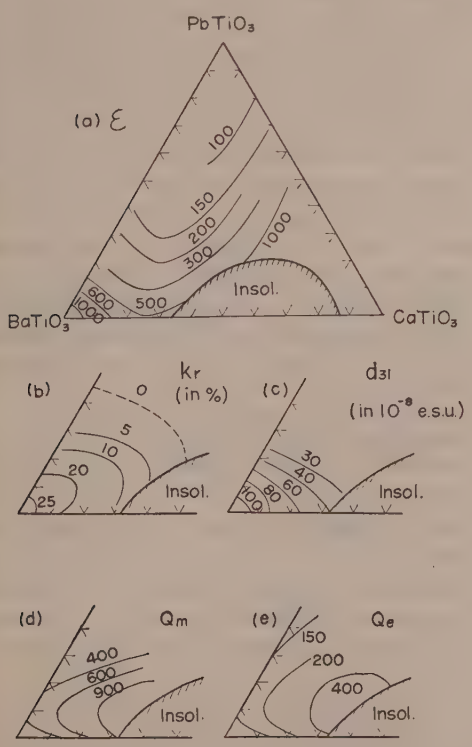

Fig. 7. Dielectric, piezoelectric and mechanical properties.

(e) *Dielectric, Piezoelectric and Mechanical Properties.*

In Fig. 7, the maps of dielectric constant (ε in (a)), electromechanical coupling coefficient (k_r in (b)) and transverse piezoelectric constant (d_{31} in (c)) of the ceramic sample at room temperature are shown. The indicated values of the dielectric constants are those of ε_3^F for the prepolarized ceramics and ε_0 for the unpolarized one. The electromechanical coupling of ceramics decreases with concentrations of $PbTiO_3$ and $CaTiO_3$.

The mechanical and dielectric Q values (Q_m and Q_e) are shown in Fig. 7 (d) (e). Certain regularities are found in them.

§ 4. Discussions

(a) *Phase Diagram*

It is well-known that the solid solutions of $BaTiO_3$ with $PbTiO_3$ have higher Curie points and with $CaTiO_3$ lower ones, and it has been discussed from standpoints of ionic radius and polarizability. In the system (Ba–Pb–Ca)TiO_3, it may be comprehensible to some extent that Curie points becomes lower from the binary (Ba–Pb)TiO_3 side towards $CaTiO_3$. The ferroelectric to paraelectric phase boundary lies near the composition of about 50 mole percent $CaTiO_3$. But, the present boundary lies a little nearer to $CaTiO_3$ than those of Sawaguchi[4] and McQuarrie[13]. This is presumably due to lower purity of $CaCO_3$ used here. As for other, phase boundaries in the vicinity of $CaTiO_3$ there may be any suspicion. The pseudocubic phase in the present diagram corresponds to tetragonal of McQuarrie[13], but tetragonality cannot be confirmed by the Debye patterns. Furthermore, the location of these boundaries are a little different from his report.

The insoluble region is narrower than McQuarrie's. His earlier paper[6] on the system (Ba–Ca–Sr)TiO_3 reported smaller insoluble range along Ba–Ca binary than his recent report and the result is rather close to the present one. The samples in his recent data are sintered at 1250°C on account of avoiding evaporation loss of PbO, and it is lower than that in this study. The discrepany between the present and his insoluble limit may be caused by the difference of sintering temperature or of the purity of chemicals used.

(b) *Dielectric and Electromechanical Properties*

With concentrations of $PbTiO_3$ and $CaTiO_3$, the Curie points rise or only a little decrease, and on the other hand, the second transition temperatures fall rapidly. Then, the properties at room temperature tend to keep away from any influence of the transition. Although the properties of single crystals of the solid solution have never been studied, the diminution of dielectric constant and piezoelectric constant may be supposed to be caused by these effects; particularly, by the lowering of the second transition temperature. Furthermore, the addition of $PbTiO_3$ increases the coercive field, and makes the prepolarizing operation more difficult, and so the piezoelectric constant of the ceramics tends to decrease. The increasing of dielectric constants near the ferro- to paraelectric boundary is due to approach of the Curie point.

Mason has measured the mechanical and dielectric Q factors of this system, particularly, in relation to the aging phenomena. In the present result, the systematic variation of the Q values with composition is observed. According to the author's previous study[15], the internal friction of $BaTiO_3$ ceramics is mainly the dissipation in the single domain crystal. It may be the case also in the present study. In the samples with higher Q_m, however, the dissipation due to ceramic form will become no longer ignorable. It is not yet revealed if the dissipation in the single crystal has a mechanical origin or a dielectric one. As the piezolectric properties of the single crystals of the solid solutions are not known, further detailed discussions are impossible. Nevertheless, the solid solution with larger dielectric Q has higher mechanical Q in this system.

When the piezoelectric ceramics are used as ultrasonic transducers, the higher mechanical Q and Curie point are necessary for avoiding the influence of heat generation by the internal loss[16] and the larger piezoelectric constant is required for low impedance at resonance. These requirements, however, are often incompatible. Which must be taken up depends on the intention.

§ 5. Conclusion

The following results are derived from the present studies:

(1) The phase diagram of the ternary system (Ba–Pb–Ca)TiO_3 is indicated. The ferroelectric and tetragonal phase changes to the orthorhombic structure of $CaTiO_3$ through cubic and pseudocubic phases.

(2) Some systematic results on the dielectric, piezoelectric and mechanical properties of this system are obtained.

In conclusion, the author wishes to express his sincere thanks to Dr. O. Nomoto, Mr. M. Marutake and Mr. A. Takeda for their useful discussions. He is also grateful to Dr. H. Hagihara and Mr. H. Yamashita for X-ray measurement by the Weissenberg camera and to Mr. Y. Kanda for his help to some part of this experiment.

The present studies were supported by the Scientific Expenditure of the Ministry of Education.

References

1) G. Shirane and K. Suzuki: J. Phys. Soc. Japan **6** (1951) 274–8.
2) R. C. DeVries and R. Roy: J. Am. Cer. Soc. **38** (1955) 142–6.
3) M. McQuarrie and F. W. Behnke: *ibid.* **37** (1954) 539–43.
4) E. Sawaguchi and T. Mitsuma: J. Phys. Soc. Japan **11** (1956) 1298 (S. N.).
5) L. W. Coughanour, R. S. Roth, S. Marzullo and F. E. Sennett: J. Res. NBS **54** (1955) 149–62.
6) M. McQuarrie: J. Am. Cer. Soc. **38** (1955) 444–9.
7) H. F. Kay and P. C. Bailey: Acta Cryst. **10** (1957) 219–26; Kay's previous report in 1951 was read in ref. 6).
8) H. Gränicher and O. Jakits: Nuovo Cimento **11** Suppl. (1954) 480–520.
9) W. P. Mason: *Piezoelectric Crystals and Their Application to Ultrasonics* (1946).
10) D. A. Berlincourt and F. Kulcsar: J. Acoust. Soc. Amer. **24** (1952) 709–13.
11) W. P. Mason: Acustica **4** (1954) 200–2; J. Acoust. Soc. Amer. **27** (1955) 73–85.
12) W. P. Mason and R. F. Wick, Proc. IRE **42** (1954) 1606–20.
13) M. McQuarrie: J. Am. Cer. Soc. **40** (1957) 35–41.
14) M. Marutake and T. Ikeda, J. Phys. Soc. Japan **10** (1955) 424–8.
15) T. Ikeda: J. Phys. Soc. Japan (in contribution).
16) T. Ikeda and K. Negishi: Bull. Kobayasi Inst. **7** (1957) 112–5.

JOURNAL OF THE PHYSICAL SOCIETY OF JAPAN Vol. 13, No. 4, APRIL, 1958

Electrical Properties of Ag_2Te

By Shin-ya MIYATANI

Department of Physics, Faculty of Science, Niigata University

(Received September 2, 1957)

The electronic conductivity, σ_e, Hall constant, R, and thermoelectric power, Θ, in α Ag_2Te are measured as the Ag/Te ratio is varied by the use of the galvanic cell Ag|AgI|Ag_2Te|Pt, where the e.m.f. of the cell, E, represents the position of the Fermi level relative to Ag-saturated Ag_2Te. According as Ag is removed across the cell, starting from the Ag-saturated composition, σ_e decreases at first, and then increases. Θ changes its sign at the minimum of σ_e, although R is always n-type, duing to the large mobility ratio ($\sim$100). The energy gap is, therefore, as narrow as several kT. When Ag is removed further, σ_e decreases again, keeping E constant. This is a mixed state of Ag_2Te and a new phase mentioned below. After a minimum of σ_e is attained, σ_e and E increase again, suggesting a new phase, $Ag_{\sim 1.93}Te$. The energy gap of this phase is fairly larger than that in Ag_2Te phase and the mobilities of electron and hole are far smaller than those in Ag_2Te. When Ag is removed still further, σ_e and E become to be independent of the composition, indicating the precipitation of Te or Te rich compound. Those experimental data are compared with the Lorentz-Sommerfeld theory, proving a good accordance between them. On the other hand, ionic conductivity is estimated from the ionic polarization effect.

§ 1. Introduction

Ag_2Te is one of the Ag_2S group in which electrons and Ag ions are mobile. The author has been engaged in the researches of "ion-mobile semiconductors" and the present paper is concerned to one of such series of experiments. Now, recently, Appel[1),2)] has carried out the detailed investigation of the electrical and optical properties of this substance. Regarding the electrical properties, our data are similar to his one in many respects, although our interpretation is considerably different from his one. In particular, the galvanic cell Ag|AgI|Ag_2Te|Pt has been used in our present research and it has made the interpretation very easy. The reason is as follows: With the use of the cell, Ag content in Ag_2Te can be varied easily and moreover the e.m.f. of the cell represents the position of the Fermi level relative to that in the Ag-saturated Ag_2Te. In this respect, the ion-mobile semiconductors are very convenient to research only if a proper ionic conductor for the cell exists, like AgI in our present case.

§ 2. Theoretical

To begin with, let us summarize the theoretical formulae which will be used in the later sections.

(*a*) The galvanic cell Ag|AgI|Ag_2Te|Pt[3,4)]

AgI is a purely ionic conductor and hence the amount of Ag supplied to or removed from the Ag_2Te across AgI is equal to the amount of electricity sent across the cell divided by e, Q/e. Moreover, Ag_2Te is an average crystal[5)] and hence the chemical potential of Ag ion in Ag_2Te is independent of the composition (Ag/Te ratio), resulting in the conclusion that the e.m.f. of the cell, E represents the position of the Fermi level in the Ag_2Te relative to that in the Ag-saturated Ag_2Te.

(*b*) Formulae for σ_e, R, and Θ

The concentration of carrier, n (or p), the electronic conductivity, σ_e, Hall coefficient, R, and the thermoelectric power, Θ, are given by[6,7,8)]

$$n=4\pi(2m^*kT)^{3/2}h^{-3}F_{1/2}\equiv\frac{2}{\sqrt{\pi}}N_nF_{1/2}\,, \quad (1)$$

$$\sigma_e=16\pi m^*e^2kTl_0(3h^3)^{-1}(r+1)F_r\,, \quad (2)$$

$$R=\frac{1}{ne}\frac{3}{2}\frac{2r+(1/2)}{(r+1)^2}\frac{F_{1/2}F_{2r-(1/2)}}{F_r^2}\,, \quad (3)$$

$$\Theta=\frac{k}{e}\left(\frac{2+r}{1+r}\frac{F_{r+1}}{F_r}-\eta\right), \quad (4)$$

$$F_r\equiv\int_0^\infty\frac{x}{1+\exp(x-\eta)}dx\,, \quad (5)$$

where η is the reduced Fermi energy (Fermi energy/kT), the mean free path, l, is assumed to be expressed as $l=l_0(\mathcal{E}/kT)^r$ ($\mathcal{E}$ is the kinetic energy of a carrier), m^* is the effective mass of the carrier, and e, k, h, and T are usual notations. By the way, r will be assumed as 1/2 in the present paper.

When there are both electrons and holes, σ_e, R, and Θ are expressed as

$$\sigma_e=\sigma_n+\sigma_p\ , \tag{6}$$

$$R=\left(\frac{\sigma_n}{\sigma_e}\right)^2 R_n+\left(\frac{\sigma_p}{\sigma_e}\right)^2 R_p\ , \tag{7}$$

$$\Theta=\left(\frac{\sigma_n}{\sigma_e}\right)\Theta_n+\left(\frac{\sigma_p}{\sigma_e}\right)\Theta_p\ , \tag{8}$$

where the suffices n and p represent the electron and hole components of the quantities concerned respectively.

(*c*) Ionic conduction

The ionic conductivity, σ_i, can be obtained by the "polarization method" which we have already reported.[4,9,10] We shall review it in brief for the later reference.

When a direct current of a constant intensity is sent to a specimen through the platinum electrodes (see Figs. 1 and 7), mobile Ag ions move toward the cathode, and accumulate there. If the applied voltage is not so large as the condition of deposit is fulfilled, that is, if the chemical potential of Ag atom at the cathode is smaller than that in an Ag-saturated specimen, ionic current decreases with time and at last vanishes, leaving electronic current only. Such a state will be called a stationary state (*Polarization process*). When the current is switched off after such a stationary state is attained, a residual potential is left and decays according as the polarization decays (*Decay process*).

For such processes, the electronic and ionic components of the current density, I_e and I_i can be given respectively by

$$I_e=\sigma_e\frac{d}{dx}\left(\frac{\zeta_e}{e}-\Phi\right), \tag{9}$$

$$I_i=-\sigma_i\frac{d\Phi}{dx}\ , \tag{10}$$

where ζ_e is the Fermi energy of electron and Φ is the electrostatic potential. Eq. (10) has not the diffusion term of ions since Ag_2Te is an average crystal like Ag_2S. For the stationary state, putting $I_i=0$, we have

$$I=I_e=\sigma_e\frac{d}{dx}\left(\frac{\zeta_e}{e}\right). \tag{11}$$

When σ_e is a known function of ζ_e, Eq. (11) can be integrated as

$$\int_{\zeta_0}^{\zeta}\sigma_e d\zeta_e=Iex\ , \tag{12}$$

which gives the stationary potential distribution $V_s(x)=(\zeta(x)-\zeta_0)/e$, where ζ_0 is σ_e at one end of the specimen. In particular, if ζ_e can be expressed as $A\times F_r(\eta)$, then Eq. (12) is expressed as

$$\int_{\eta_0}^{\eta}F_r(\eta)d\eta=\frac{Iex}{AkT}\ . \tag{13}$$

Next, at the instant of switching off, we have the relations as

$$\frac{V_r}{V_s}=\frac{\sigma_i}{\sigma_i+\sigma_e}\ ,\qquad \frac{V_c}{V_s}=\frac{\sigma_e}{\sigma_i+\sigma_e}\ , \tag{14}$$

where V_s, V_r and V_c are the potential difference between two probes in the stationary state, that at the instant of switching off, and the potential difference between two AgI cells arranged near the two electrodes at the instant of switching off, respectively (see Fig. 4 in the reference (4)). Thus, σ_i can be obtained from V_r/V_s if it is not too small (*Residual method*). Further, the relaxation time of the polarization and decay processes is deduced from the following consideration: The equation of continuity for mobile ions is given by

$$e\frac{\partial N}{\partial t}=-\frac{\partial I_i}{\partial x}\ , \tag{15}$$

where N is the concentration of the excess mobile ions. When the applied voltage is sufficiently small (In our present work, ~10 mV has been used usually), Eq. (15) can be reduced with the use of Eqs. (9), and (10) to

$$\frac{\partial N}{\partial t}=\frac{\sigma_i\sigma_e}{e(\sigma_i+\sigma_e)}\frac{\partial^2(\zeta_e/e)}{\partial x^2}\ . \tag{16}$$

If ζ_e is a known function of N, Eq. (16) can be expressed as

$$\frac{\partial N}{\partial t}=\frac{\sigma_i\sigma_e}{\sigma_i+\sigma_e}\frac{\partial^2 N}{\partial x^2}s\ , \tag{17}$$

where s is defined as $\partial/(\zeta_e/e)/\partial(eN)$ and so a known function of ζ_e or N. Then Eq. (17) can be integrated with the boundary condition that there is neither supply nor removal of ions at the electrodes. Thus, the relaxation time, τ, is obtained as

$$\frac{1}{\tau}=\left(\frac{\pi}{L}\right)^2 s\frac{\sigma_i\sigma_e}{\sigma_i+\sigma_e}\approx\left(\frac{\pi}{L}\right)^2 S\sigma_i \text{ if } \sigma_i \ll \sigma_e\,, \quad (18)$$

where L is the length of the specimen. From the measurement of τ, therefore, we can obtain σ_i if s is known (*τ-method*). When σ_i/σ_e is so small that the residual method is not available, the τ method can be used, where τ is the relaxation time of the potential difference between two AgI cells AgI (probes) as shown in Fig. 7.

§ 3. Experimental

(*a*) Arrangements

The samples are prepared as follows: Ag (reduced from $AgNO_3$) and Te(Merck) are put in a hard glass tube in a proper proportion. Then the tube is evacuated, sealed and then heated up to 600°C. Duing to the large ionic mobility in Ag_2Te, the reaction takes place rapidly and so the compound can be prepared easily. The sample obtained in such a way is cut and ground to a proper size. The method of measurements of σ_e, R, and Θ is as usual (Fig. 1). Those electrical

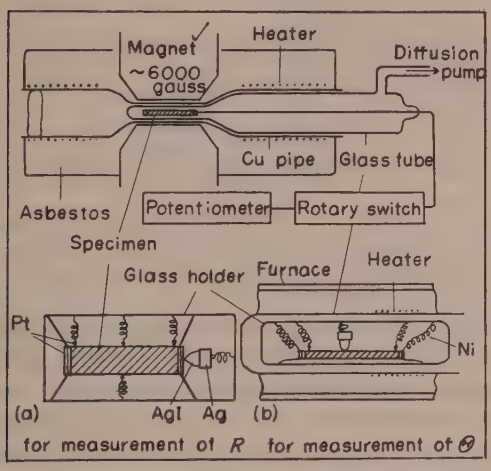

Fig. 1. Schematic diagram of the experimenta method for measurements of σ_e, R, and Θ.

quantities are measured as functions of the e.m.f. of the cell, E, or the composition, N, and the temperature, T.

(*b*) Results

(1) *General comments.* Ag_2Te has two phases; α phase (stable above about 150°C) and β phase (stable below). In the α phase, the ionic conductivity is fairly large and hence the galvanic cell Ag|AgI|Ag_2Te|Pt is very effective. We shall, therefore, begin with the description of the electrical properties in the α Ag_2Te. Fig. 2 shows the change of

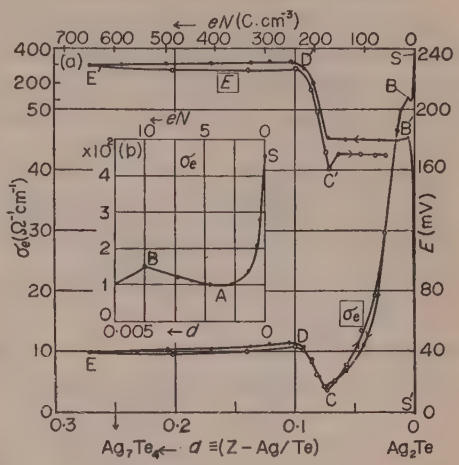

Fig. 2. (a) The change of σ_e and E vs. $d\equiv 2-\mathrm{Ag/Te}$ ratio by removing and supplying Ag at 225°C. (b) σ_e vs. d in the range of small d in a different scale. The value of eN (upper abscissa) is related to d by $d=eN/2400$, where N is the concentration of deficit Ag, and the density of Ag_2Te is assumed as 8.5 g/cm³.

σ_e and E when Ag is removed from and then supplied to an Ag_2Te specimen across the cell. The figure shows that, starting from the Ag-saturated composition designated by S in the figure, σ_e decreases and E increases rapidly at first according as Ag is removed, and then σ_e increases after passing a minimum (A) and attains a maximum (B). From this point, σ_e decreases remarkably and reaches the second minimum (C), while E is kept constant. At further removal of Ag, both E and σ_e increase again and σ_e reaches the second maximum (D). At still further removal of Ag, E and σ_e do not show any remarkable changes. Let us divide the whole range into four regions; from S to B, B to C, C to D, and D to E. For convenience, they will be called α_1, mixture α_2, and precipitation regions respectively. In the following sections, the electrical properties in each region will be described in proper order.

(2) *α_1 region.* Fig. 3 shows log σ_e and log R vs. E. The Hall constant is always n-type while the thermoelectric power, Θ, changes its sign near the minimum point of σ_e. From the figure, the following conclusion will be easily deduced; the energy gap is as narrow as several kT and the mobility ratio μ_n/μ_p is

very large. The detailed analysis will be tried in § 4.

(3) *Mixture region.* As mentioned in (1), σ_e begins to decrease when Ag is removed further. In this region, the uniformity of the specimen is not held, as illustrated by Fig. 4, which represents the potential distribution along a specimen in the mixture region when a constant current is sent. That is, when Ag is removed at an end of a specimen, σ_e decreases at this end and such a small σ_e region extends according as Ag is removed, until the whole specimen becomes small σ_e. This ununiformity does not disappear by a heat treatment of a fairly long period and so the state in this range of composition is regarded as a mixture of α_1 and a different phase from α_1, that is, α_2. The constancy of E also supports this view-point. (see also Fig. 5)

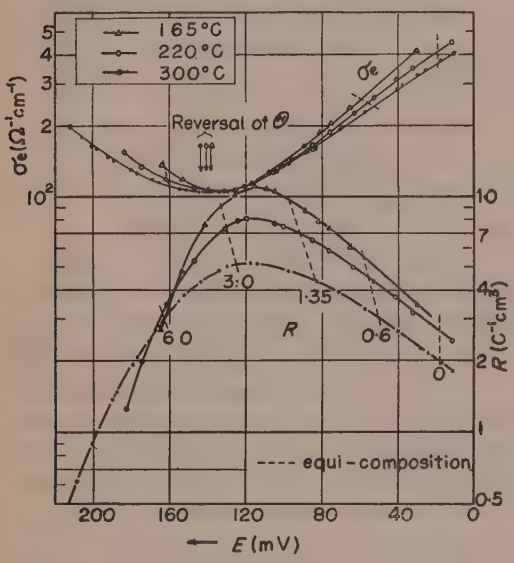

Fig. 3. $\log \sigma_e$ and $\log R$ vs. E at three temperatures. The broken lines represent the equi-compositions with the values of eN(C cm^{-3}) relative to a certain composition near Ag-saturated.

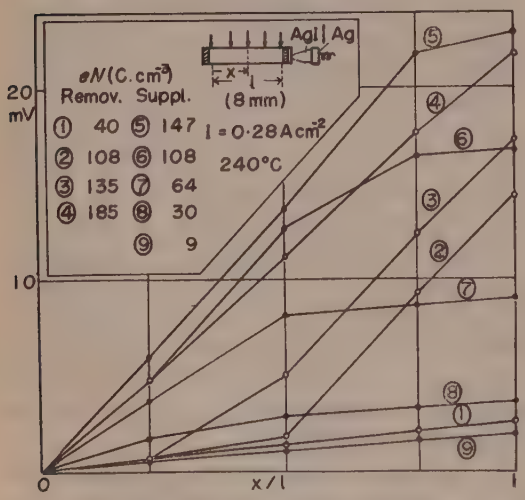

Fig. 4. Potential distribution along the specimen whose Ag content is varied by the Ag|AgI arranged at the right end. Each curve is regarded as composed of two straight lines of different inclinations, indicating σ_e changes suddenly at a certain point.

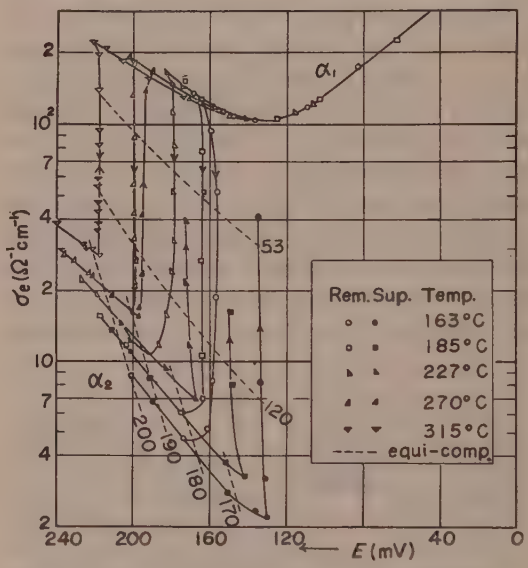

Fig. 5. $\log \sigma_e$ vs. E at various temperatures. The broken lines represent the equi-compositions with the eN values attached on them.

(4) *α_2 region.* After the whole specimen becomes to be of small σ_e, σ_e increases again together with E at further removal of Ag. Fig. 5 shows $\log \sigma_e$ vs. E at various temperatures. In the α_2 phase, R is comparatively small but still n-type, while Θ is p-type. Therefore, the mobility ratio will be very large and the energy gap is comparatively small just as in the α_1 phase.

(5) *Precipitation region.* When Ag is removed still further σ_e and E become to be independent of the composition. This independence may be due to the precipitation of Te or Te rich compound, where the precipitation may be formed not to disturb the conduction of electrons. By the way, there is no indication of Ag_7Te_4 as shown in Fig. 2.

(6) *Ionic conductivity in the α phase.* There

are two methods to obtain the ionic conductivity, σ_i; One is the residual method and the other is the τ method as mentioned in § 2 (*c*). The former is not available without correction in the α_1 phase since σ_i/σ_e is so small that the residual potential is masked by the potential due to the Peltier effect, while the latter is not available with ease since s in Eq. (18) can not be easily determined. Fig. 6 shows $\log \tau$ and $\log (1/s)$ vs. E

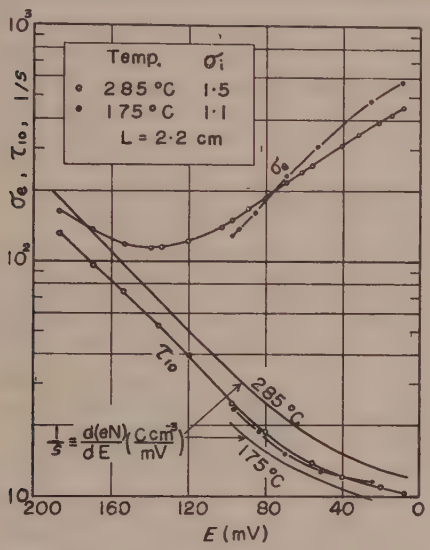

Fig. 6. $\log \sigma_e$, τ_{10} and $1/s$ vs. E. $\tau_{10}=2.3\tau$. The $1/s$ and τ_{10} curves are parallel to each other, indicating a constant ionic conductivity.

in the α_1 region, where τ is the relaxation time of the potential difference between two cells. They are parallel to each other, indicating that σ_i is independent of E and accordingly the composition. Further, Fig. 7 shows the stationary potential distribution along the specimen. The feature of curves is just as expected.

On the other hand, Fig. 8 shows $\log \sigma_e$ and σ_i vs. the composition in the mixture and α_2 regions, where σ_i is obtained by the residual method. As mentioned above, s is not so definitely determined in these ranges as in the α_1 range, since σ_e does not attain its equilibrium value instantly after Ag is removed or supplied, and so the residual method is preferable although the τ method gives a similar value of σ_i to that from the residual method. For instance, $L=0.7$ cm, $E=145$ mV, $\sigma_e=3\,\Omega^{-1}\,cm^{-1}$, $\tau=13$ sec, $s=4.4$ mV $C^{-1}\,cm^3$, resulting in $\sigma_i=0.9\,\Omega^{-1}\,cm^{-1}$ at 165°C with the use of Eq. (18). Thus, as far as the ionic conduction is concerned, there is no remarkable difference between the α_1 and α_2 phase.

(7) *$\alpha-\beta$ transition.* Fig. 9 shows E and $\log \sigma_e$ vs. temperature including the transition point, [where σ_i of AgI below about 140°C and σ_i of β Ag_2Te are very small and hence the measurement of E is not too reliable.

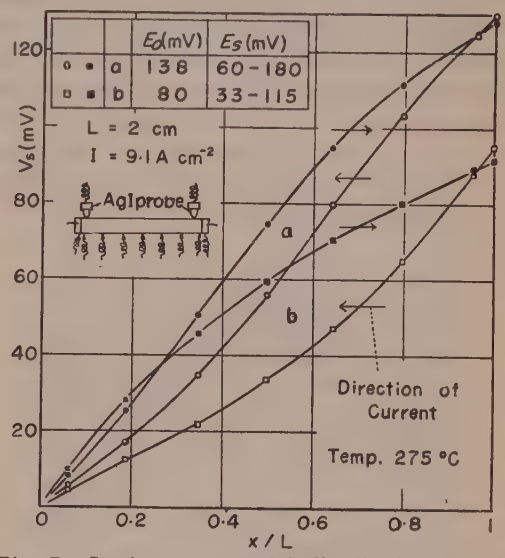

Fig. 7. Stationary potential distribution. E_0 is E in the initial state and E_s is E of two cells in the stationary state. The inclination of curves is proportional to $1/\sigma_e$. It is most steep at the anode in the case of (b), while it is at the middle in the case of (a) as expected from the respective values of E.

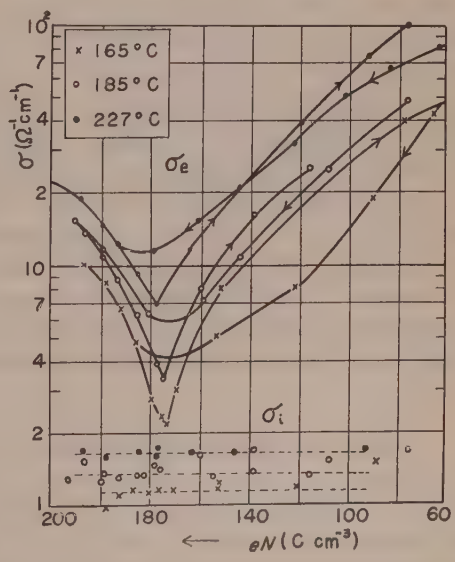

Fig. 8. $\log \sigma_e$ and σ_i vs. eN, where σ_i is obtained by the residual method.

Now, σ_e decreases at the transition $\beta \rightarrow \alpha_1$. This decrease is not due to the change of mobility but to the decrease of the concentration of electrons owing to the sudden increase of the energy gap at the transition, as seen later. In the case of the α_2 phase, the transition temperature for $\alpha_2 \rightarrow \beta$ is lowered remarkably with increasing deficiency of Ag while that for $\beta \rightarrow \alpha_2$ is not too much changed. Moreover, the change of σ_e at the transition $\alpha_2 \rightarrow \beta$ is very slow. This may be due to the precipitation of Te at the transition. On the other hand, at the $\beta \rightarrow \alpha_2$ transition, it is necessary to heat the specimen to somewhat higher temperature in order for the precipitated Te to re-enter the matrix.

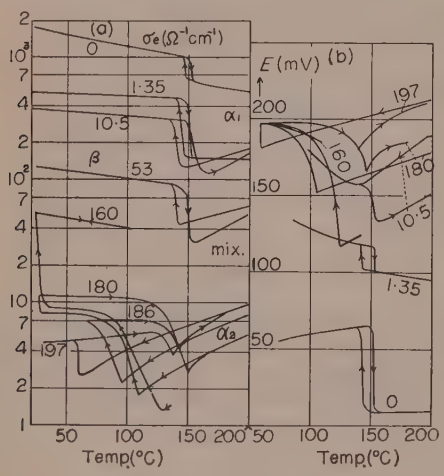

Fig. 9. (a) $\log \sigma_e$ vs. temperature, and (b) E vs. temperature corresponding to (a). The numbers attached on them are the values of eN (C cm^{-3}).

(8) *β phase.* As shown in Fig. 9, σ_e decreases with increasing deficiency of Ag and there is no indication of another phase at least in the range of composition under consideration. Further, when eN is larger than about 10 C cm^{-3}, E is almost independent of eN, suggesting the mixed state like that in the α phase. Thus the decrease of σ_e may be attributed mainly to the decrease of the mobilities of electron and hole in the mixed state.

§ 4. Analysis of Data and Discussion

(a) α_1 phase

Fig. 10 shows $\log \sigma_e$, $\log R\sigma_e^2$ vs. eE/kT at 300°C and Fig. 11 shows σ_e and eE/kT vs. eN (relative) at 300°C and 220°C. These figures can be analyzed graphically as follows: First let us separate σ_n from σ_e. Now, the hole component, σ_p, will be negligible in a small E region. $R\sigma_e^2$ is more suitable for such neglection since $R\sigma_e^2 = \sigma_n\mu_n - \sigma_p\mu_p$ and μ_n/μ_p will be large. Therefore, $\log R\sigma_e^2$ vs. eE/kT plot is at first compared with the theoretical graph, $\log F_{\frac{1}{2}}$ vs. η, assuming $r=1/2$ in Eqs. (2) and (3). From such a comparison (overlapping two graphs to each other), the position of $\eta=0$ is obtained. As seen in Fig. 10, the experimental plot of $R\sigma_e^2$ shows a remarkable

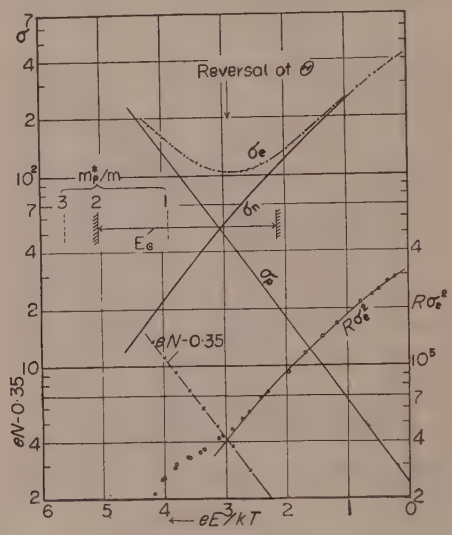

Fig. 10. $\log \sigma_e$ and $\log R\sigma_e^2$ vs. eE/kT in the α_1 Ag_2Te. The σ_n and σ_p are obtained graphically as described in text.

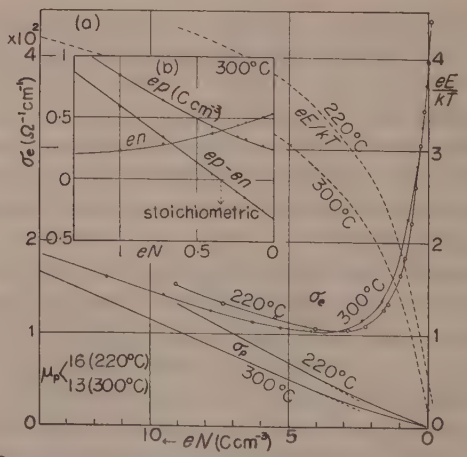

Fig. 11. (a) σ_e and eE/kT vs. eN (relative) at 220° and 300°C. The σ_p obtained from Fig. 10 is also plotted against eN. From the inclination of the σ_p curve, the mobility of holes is estimated as shown in the figure. (b) en and ep vs. eN in the composition range in which en and ep are comparable order of magnitude.

deviation from the theoretical curve in a large E range. This deviation is opposite to what would be expected from the contribution of holes, and it is negligible at 165°C and increases with increasing temperature. The cause of such a deviation is not certain (a change of μ_n or of the energy gap with increasing Ag ion vacancies?) and we shall neglect it in the present paper.

Using the zero point of η determined as mentioned above, the $\log \sigma_n$ vs. eE/kT curve can be drawn so that it coincide with the experimental $\log \sigma_e$ vs. eE/kT plot in the range of small E. Further, subtracting σ_n from σ_e we have the hole component of σ_e, σ_p, which can be expressed as

$$\log \frac{\sigma_p}{e\mu_p N_p} = \frac{\zeta_p}{kT} = \frac{eE}{kT} + \text{const.} \qquad (19)$$

Thus both σ_n and σ_p are obtained. The mobility and effective mass of conduction electron can be obtained with the use of the position of η, R and σ_n as listed in the table at the end of this section.

Next, although the mobility of hole, μ_p, can not be obtained from R, it can be estimated as follows: As shown in Fig. 11, σ_p obtained by the procedure mentioned above is proportional to eN except in the small E region, indicating that the number of holes changes by just the amount of Ag ions removed or supplied. That is, the number of hole, p, is far larger than that of electron, n, and accordingly the change of n is negligible. This view is supported by the fact that eN can be expressed as $\log(eN) = eE/kT + \text{const.}$ only if a small additive constant for eN is adjusted as also shown in Fig. 10. Thus, the mobility of hole, μ_p, can be obtained from the inclination of the σ_p vs. eN curve. On the other hand, n and p become comparable in the small E region, and then we have

$$ep - en = eN_a\,, \qquad (20)$$

where N_a is the absolute concentration of the deficit Ag. Fig. 11 (b) shows that this is in fact the case.

Now the distribution of holes in the valence band is classical and hence the position of the top of the valence band can not be determined as in the case of the conduction band. In order to determine it, the thermoelectric power is available. Fig. 12 shows an example

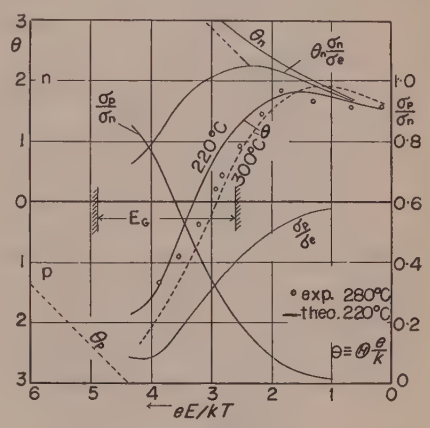

Fig. 12. The graphical deduction of theoretical curve of thermoelectric power, where the energy gap is determined so that the theoretical reversal point of Θ coincides with the experimental one. The potential probes are Nichrome wires whose Θ against Cu is about $-3.3\mu V/°C$ ($\theta = 0.04$).

of graphical construction of the theoretical Θ given by Eqs. (4) and (8). The energy gap, E_G, can be determined so that the theoretical reversal point of Θ coincides with the experimental one. Then we have the effective mass of hole. The several quantities obtained so far are listed in the following table.

Temp (°C)	μ_n ($cm^2v^{-1}sec^{-1}$)	m_n^*/m	μ_p ($cm^2v^{-1}sec^{-1}$)	m_p^*/m	E_G (mV)
165	1440	0.054	18	1.0	55
220	1100	0.059	16	1.4	95
300	750	0.069	13	2.0	140

Here, we don't intend to insist that these values are accurate, but we can say with confidence that the energy gap is as small as several kT and the mobility ratio is very large.

(**b**) α_2 phase

Fig. 13 shows an example of analysis at 165°C. As shown in the figure, when Ag is removed from the specimen in the mixture region, σ_e decreases, R (n-type) increases to

some extent, and Θ (p-type) increases until the whole specimen becomes the α_2 phase. At supplying Ag, they changes in the opposite direction although there is a hysteresis effect, particularly at a comparatively low temperature (see also Fig. 5) duing to the large relaxation time of such a phase change.

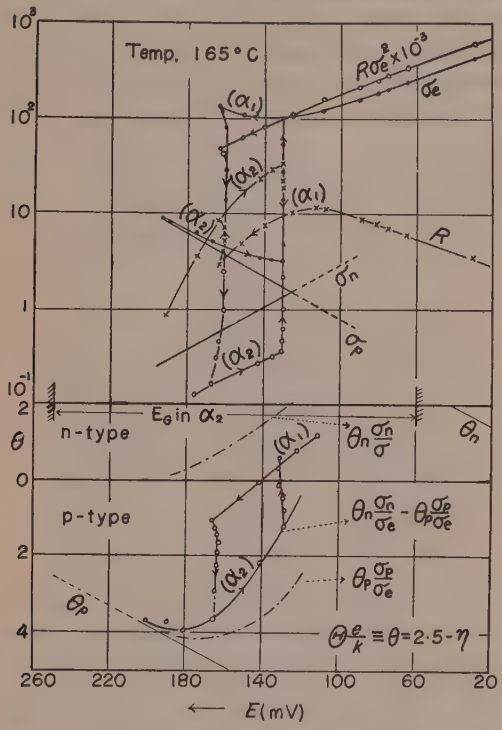

Fig. 13. $\log\sigma_e$, $\log R$, $\log R\sigma_e^2$, and $\Theta\, e/k\equiv\theta$ vs. E at 165°C.

Now, in the α_2 phase, σ_n and σ_p can be determined by trial and error so that both is expressed as classical as shown in the figure. Since $R\sigma_e^2$ is considered to be equal to $\sigma_n\mu_n$ as in the α_1 phase, we have the mobility of electron as 300 $cm^2\,v^{-1}\,sec^{-1}$. The mobility of hole can be also estimated from σ_p vs. eN curve just as in the α_2 phase as follows: Fig. 14 shows σ_e vs. eN plot. Since p seems to be far larger than n, we may consider that p is equal to the concentration of ionized Ag ion vacancies. If it is assumed that every removed Ag ion forms Ag ion vacancy, then the majority of Ag ion vacancies should be neutral, that is, the Ag ion vacancies should have acceptor levels, the majority of which are occupied by holes. This view can not, however, account for the behavior as shown in Fig. 14. We suggest, therefore, an alternative models as follows: In the α_2 phase, a complex compound $Ag_{2-x}Te$ may be formed, where x is about 0.071 at 165°C, and 0.067 at 240°C, for example, $Ag_{27}Te_{14}\sim Ag_{31}Te_{16}$, and the deviation from such a complex composition supplies ionized vacancies, the number of which is equal to the hole. Further, according as the temperature is raised, the crystal changes its form so that the number of Ag ion vacancies increases, resulting in the increase of the number of holes and accordingly the increase of σ_e. This model may not be conclusive but it accounts for the data at least phenomenologically.

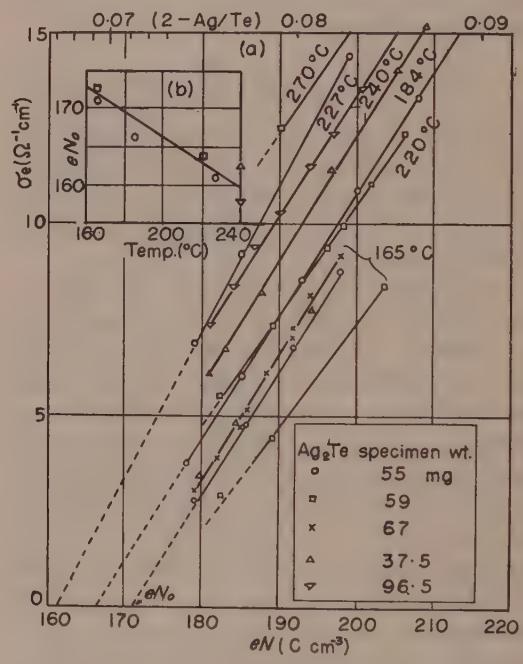

Fig. 14. (a) σ_e vs. eN in the α_2 phase. They are straight lines of the almost same inclination. (b) eN_0 vs. temperature, where eN_0 is the eN value corresponding to $\sigma_e=0$.

Thus, the mobility of hole is estimated as $0.3\sim0.4$ $cm^2\,v^{-1}\,sec^{-1}$, which is almost independent of the temperature. With those values of σ_n, σ_p, μ_n, and μ_p, theoretical Θ vs. E curve can be drawn so that it fits to the experimental plot as shown in Fig. 13. From such a comparison, the effective mass of electron and holes and the energy gap can be estimated as $m_n^*=0.024m$, $m_p^*=6m$, and $E_G=190$ mV. At higher temperature, the accuracy of analysis becomes poor because of the smallness of σ_n/σ_p (e.g. at 240°C, $\mu_n=125$, $m_n^*=0.036m$, $\mu_p=0.33$, $m_p^*=7m$, assuming the

energy gap is equal to that at 165°C i.e. 190 mV).

(**c**) β phase

As mentioned above, σ_i's of AgI and β Ag_2Te are very small and so the Ag content can not be varied at a fixed temperature in the β phase, and moreover, the accuracy of the measurement of E is not too well. Therefore, the reliability of analysis is not so large as in the α phase.

Now, β Ag_2Te can be divided into the pure state and the mixed state as described in § 3 (8). Fig. 15 shows $\log \sigma_e$, $\log R\sigma_e^2$, and Θ vs. eE/kT in the pure region. The mobility and effective mass of conduction electron are obtainable by the procedure mentioned in (**a**) as shown in the figure. Fig. 16 shows E vs. eN in the β Ag_2Te, and a similar plot in the α phase (188°C) is also shown for the reference. The origin of the abscissa is fixed from an analysis in the α phase. Now, σ_p can be obtained by subtracting σ_n from σ_e, although the accuracy is not very well because of the smallness of σ_p. Then μ_p is estimated as 11 $cm^2\,v^{-1}sec^{-1}$ from σ_p vs. eN plot as shown in Fig. 16. Thus ep and en are obtained, and accordingly the value of E corresponding to the stoichiometric composition is obtained as 86 mV at 125°C. This value is in accordance with that obtained from Fig. 16. supporting our analysis in the β phase. The energy gap obtained from Θ is very narrow as shown in the figure.

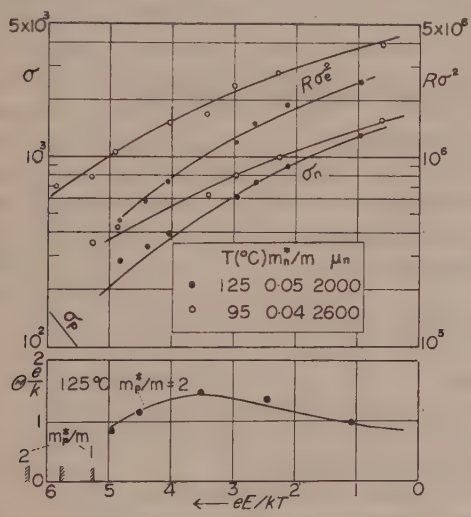

Fig. 15. (a) $\log \sigma_e$, and $R\ \sigma_e^2$ vs. eE/kT at 125°C and 95°C. (b) $\Theta\, e/k$ vs. eE/kT at 125°C. The energy gap is very narrow (might be negative).

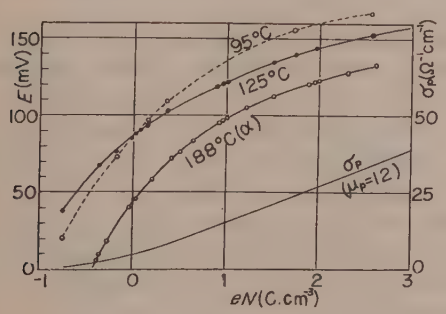

Fig. 16. E vs. eN (absolute) in β Ag_2Te. The stoichiometric position is determined in the α phase (183°C). Besides, σ_p obtained from Fig. 15 is also plotted against eN.

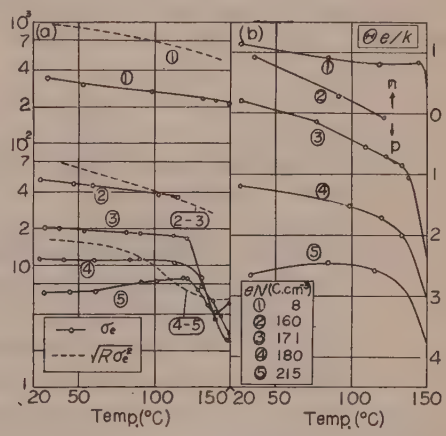

Fig. 17. (a) $\log \sigma_e$ and $\log (R\ \sigma_e^2)^{1/2}$ vs. temperature, and (b) $\Theta\ e/k$ vs. temperature corresponding to (a), where (2–3) and (4–5) represent that their σ_e are in the middle between No. 2 and 3, and No. 4 and 5, respectively.

In the mixed region, the precipitation of Te (?) takes place very slowly and the uniformity of the specimen is not too well, and so we shall only discuss it qualitatively. Fig. 17 shows $\log \sigma_e$, $\log (R\sigma_e^2)^{1/2}$ and Θ vs. temperature when the temperature is raised from the room temperature. From the figure, it is seen that σ_n and σ_p decrease but σ_p/σ_n increases with increasing deficiency of Ag. The decrease of σ_n and σ_p seems to be due mainly to the decrease of the mobility. More detailed discussion will be left to the future.

(**d**) Remarks

In the present analysis, the energy dependence of the mean free path of conduction electron has been assumed as $l=l_0(\mathcal{E}/kT)^{1/2}$. This assumption may be, however, not necessarily allowed. In fact, other dependence, l=constant, can account for our data with

almost same extent of fitness, resulting in somewhat different values of effective mass and the energy gap, although the essential features so far mentioned are not changed. More detailed experiments and consideration will be necessary in order to determine which dependence is right. In collaboration with Mr. Yokota, the author wishes to discuss this subject in the future.

The author wishes to express his sincere thanks to the members of our Department of Physics, especially to Mr. Yokota, Mr. Suzuki, and Mr. Haga for their kind advices and discussions. The present work was supported by the research grant of the Ministry of Education.

References

1) J. Appel and G. Lautz: Physica **20** (1954) 1110.
2) J. Appel: ZS. Naturforschung **10**a (1955) 530.
3) C. Wagner: J. Chem. Phys. **21** (1953) 1819.
4) S. Miyatani: J. Phys. Soc. Japan **10** (1955) 786.
5) P. Rahlfs: Z. physik. Chem. B **31** (1935) 157.
6) F. Seitz: The modern Theory of Solids (1940).
7) R. W. Wright: Proc. Phys. Soc. A **64** (1951) 984.
8) W. Schockley: Electrons and Holes in Semiconductors (1950).
9) I. Yokota: J. Phys. Soc. Japan **8** (1953) 595.
10) M. H. Hebb.: J. Chem. Phys. **20** (1952) 185.

JOURNAL OF THE PHYSICAL SOCIETY OF JAPAN Vol. 13, No. 4, APRIL, 1958

On the Backward Leakage Current in the Alloyed Germanium p-n Junction

By Makoto KIKUCHI

Electrotechnical Laboratory, Tokyo, Japan

(Received December 12, 1957)

It has been observed that the "creep" phenomenon often found in the backward direction of the alloyed germanium p-n junction occurred in the so-called "leakage current component". It has also been found that in some of the alloyed junction transistor samples, the characteristics of the collector junction was influenced by the creep in the emitter junction. The experimental procedures and results are described.

Although we have no complete theory to explain these experimental observations at present, some essential remarks are given from theoretical consideration. In the last section, an experimental result which might be an evidence for the correlation between the creep phenomenon and the surface field effect is given.

§ 1. Introduction

It is often observed that the electrical characteristic of $p-n$ junctions, either alloyed or grown, does not obey the Shockley's formula[1]. One of the most serious discrepancies is the non-saturable backward current, which is often encountered in the physical experiments and technical procedures.

In general, the backward current of the $p-n$ junction consists of three components, i.e., the saturation current, the leakage current, and the breakdown current. In these components, the saturation and the breakdown components can be treated theoretically at present, while the leakage current component has been kept rather untouched from the theoretical point of view. Some works on the leakage current[2] have been published, which considered its dependence on the humidity and its correlation with the channel conduction, but the theoretical current-voltage characteristic has not yet been derived satisfactorily.

Another characteristic behavior found in the "real" junction is the "creep" phenomenon[3]. The creep is defined as the variation

of the current under a fixed applied voltage. In the transistor and diode technology, this undesirable phenomenon is to be avoided by rinsing the specimens in the distilled water and baking them in vacuum or dry atmosphere. These treatments are expected to take off any ions from the surface. Hence, it may be thought that the ions on the surface are playing important role in the creep. Nevertheless, simple theory based on the model of the ions on the surface can explain straightforward neither the i–v characteristic of the leakage current nor the creep phenomenon. We have been performing transistor lifetest for about three years, and it has come out very difficult to explain the electrical characteristics, such as collector cutoff current, collector impedance, current amplification factor, etc., of the deteriorated transistors from simple channel theory.

Recently, Plummer[4] has reported that the creep of the backward current occurred in the saturation current component. He adopted such an experimental procedure that the current-voltage characteristic can be taken for the same surface condition. Moreover, he observed the growth of channel during the drift and its rapid disappearance after the cessation of the applied voltage.

We have really observed the creep of the saturation current component but do not belive that is only the case. In the course of analysis of the transistor lifetest results, we found two types of creep as shown in Fig. 1, one is the increase of saturation current under the applied voltage (Fig. 1 (a)), and the other is the increase of leakage current (Fig. 1 (b)). These experimental results were obtained by an $X-Y$ recorder varying the bias voltage more slowly than the time constant of the recorder but fast enough to prevent the creep during the voltage variation. The creep was observed keeping the junction under the bias voltage for three minutes, as shown in Fig. 1. When we observed these two types of creep, i.e., the creep in the saturation and the leakage current component, we tried to attribute the former to the formation of the channel conduction and the latter to simple surface ohmic leakage. To check these models, photocurrent was observed at the same time as the creep was going on. Fig. 2 shows the experimental results, where (a) and (b) correspond to the saturation and the leakage component creep, respectively. As are shown in the figure, the photocurrent (which was observed by a weak chopped light) varies in parallel with the current for the case of leakage creep. This might be thought to be

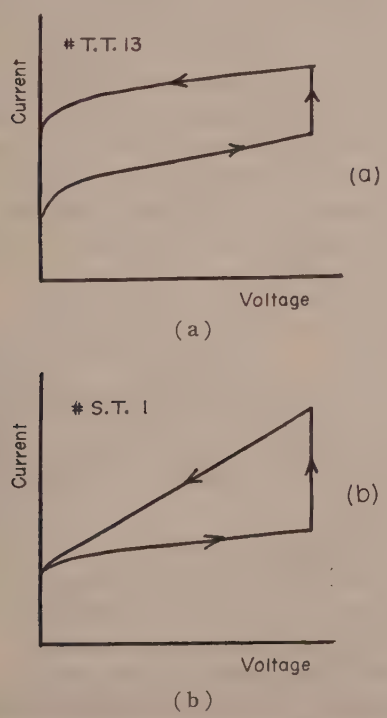

Fig. 1. Examples of the two typical creeps.

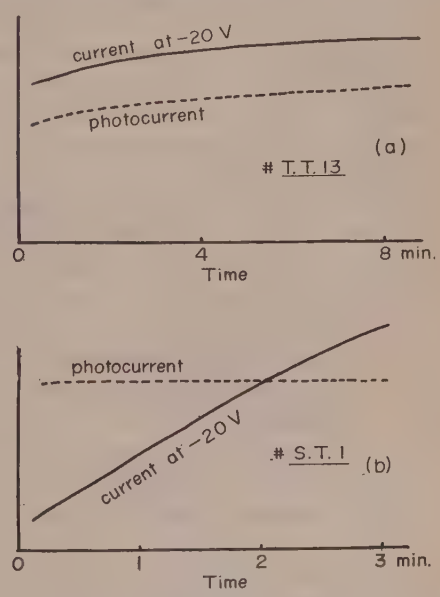

Fig. 2. Results of the simultaneous measurement of the photocurrent and the creeping current. (a) the saturation creep, and (b) the leakage creep.

an evidence for the above mentioned models, but it soon turned out to be very difficult to explain all of the characteristics of the deteriorated transistors on the basis of such a simple model[5].

In this paper, experiments especially on the drift of the leakage current component, and on the correlation between the surface conditions and the leakage current are described. Typical present theories are surveyed in trying to explain these experimental results. In the last section, a possibility that the drift phenomenon has correlation with the surface field effect is suggested with the help of the experimental results of time variation of the current.

§ 2. Creep Phenomena

(2.1) *Experimental apparatus*

As mentioned above, the creep phenomena can be observed with an $X-Y$ recorder. Strictly speaking, however, the time constant of the recorder can not be neglected. A simple measuring circuit has been devised to avoid the effect of measuring operation on the creep effect. The circuit is shown in Fig. 3. The key switches in the figure which are encircled by dotted lines are being set under a purely mechanical pendulum. Setting the pendulum free, it opens these switches in the order of No. 1, 2 and 3 with desired time lags of the order of milliseconds. At first, these three switches are closed and the junction is forced to creep under the applied valtage of V_1. When the switch No. 1 is opened, the creep stops, and the junction is subjected to no bias. At the next instant, the switch No. 2 is opened, therefore is the switch S closed, and hence the current flows through the junction by virtue of the battery voltage V_2. This current continues to flow until the switch No. 3 is opened at the next moment. In this way, the current voltage characteristics of the junction for the junction conditions just at the moment of the cessation of the voltage V_1. (At least within some milliseconds after that moment.)

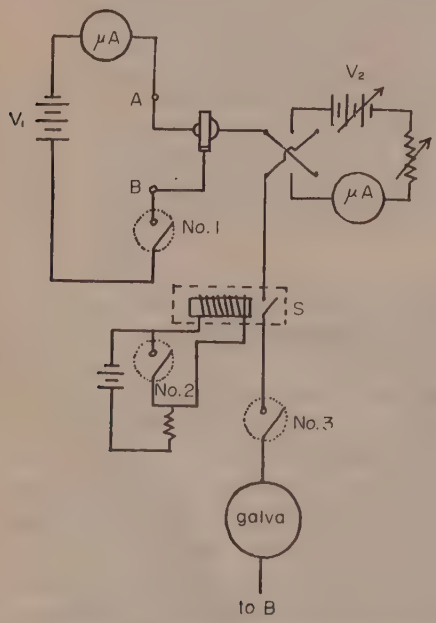

Fig. 3. Circuit for measuring the instantaneous characteristics.

The current was measured using the galvanometer ballistically, and with the aid of calibrated data. The result of calibration of the relation between the current and the deflection of ballistic galvanometer is shown in Fig. 4. The linearlity is fairly good as shown. The arrangement shown in Fig. 3 is for the case of measurement of the effect of the emitter creep on the collector characteristic of junction transistor about which mentioned in the next section.

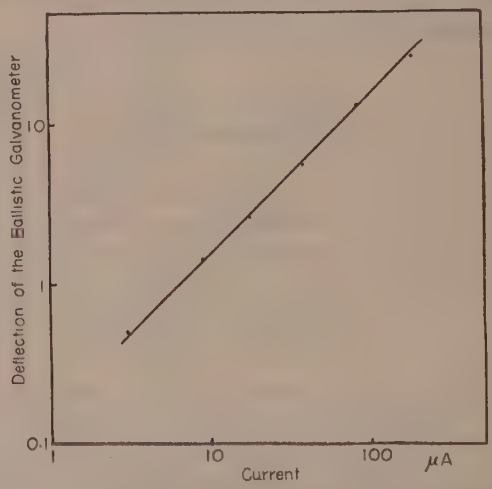

Fig. 4. The result of the calibration of the ballistic galvanometer. (ballistic use of usual galvanometer

(2.2) *Experimental results*

A typical example of the negative creep is shown in Fig. 5. The sample #A-1 is a deteriorated alloy junction transistor. Therefore, the initial current at the reverse voltage of 16 volts is above 100 microamperes. As the negative creep goes on, however, it de-

creases to about 30 microamperes in 70 seconds. In general, the decay of the current can not be expressed by a simple exponential function, as in the case of the same kinds of phenomena[8]. If the result of Fig. 5 is replotted in a semi-log scale, it is usually noticed that the apparent decay time constant increases as the time goes on.

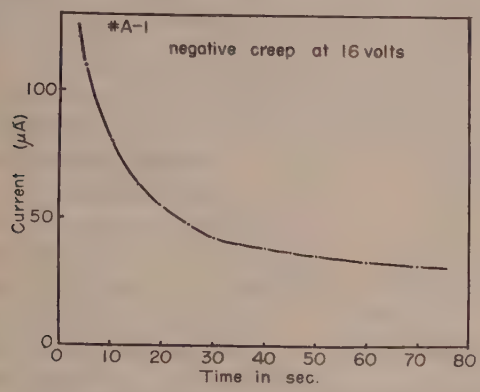

Fig. 5. Negative creep observed in a deteriorated alloy junction transistor.

The fact that the negative creep occurs in the leakage current component will be seen in Fig. 6. The variation of the current voltage characteristic by the creep as shown in the figure is quite typical in the creep phenomena observed in this experimental work. As is seen in the figure, the saturation current component is not altered, while the leakage current component is remarkably reduced by the creep. The characteristic curves in the figure do not contain cumulative creep effect by virtue of the circuit in Fig. 3. It is noticed that the ratio of the leakage current before and after the creep is nearly

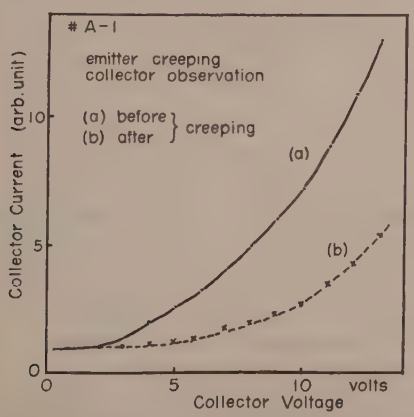

Fig. 6. Variation of the current voltage characteristic of a junction by the creep effect.

independent of the bias voltage. The leakage currents (total current minus saturation current) are plotted in semi-log scale in Fig. 7. Though, apparently, the currents are nearly exponential for the bias voltage, it is not exactly the case for the wider range of voltage. It is noticed, however, that the two lines are nearly parallel, which means that the ratio of the currents does not depend on the voltage.

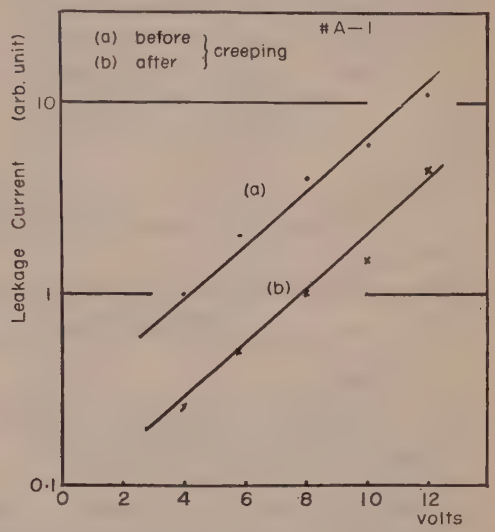

Fig. 7. Semi-log plot of the leakage currents before and after the creep.

The effect of the emitter creep on the collector characteristic has been observed by the circuit arrangement as shown in Fig. 3. A typical result is shown in Fig. 8. At the time 0 in the figure, reverse voltage of 35 volts is applied to the emitter of the alloy junction transistor # A-5, which is one of the detriorated transistors after about 10000 hours' lifetest, and the collector current is observed for 30 seconds. At that moment, the emitter is opened, and then the recovery of the collector characteristic is observed for 60 seconds. As is shown, the collector characteristic is remarkably changed by the emitter creeping. Fig. 6 shows the change in the current voltage characteristic of the collector corresponding to this kind of measurement. It is observed that very similar change in the current voltage characteristic of the collector junction as shown in Fig. 6 is caused both by the emitter creep and the creep of the collector itself. The interaction of the collector and emitter creep on each other has been observed

not in all of the samples investigated. The probability of finding this effect was about 30 percent.

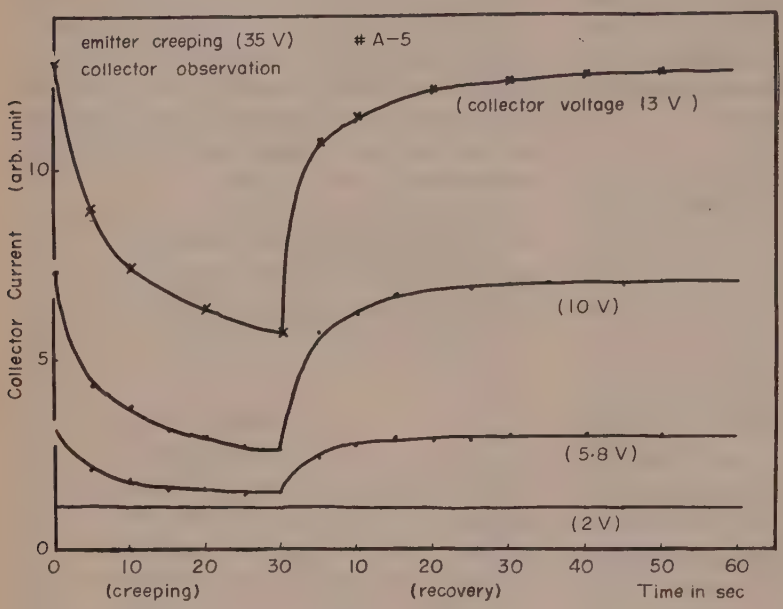

Fig. 8. Negative creep observed in the collector junction of an alloy transistor forced by the emitter creep.

In general, it may be concluded that the time constant of the creep is considerably less than that of its recovery. This has been already pointed out by some of the workers[7] and also by the author[8]. For instance, owing to our previous (unpublished) work, the time constants in the two types of creep mentioned in the introduction, (Fig. 1), were found to be as shown in Table I.

Table I. Time constants of the creep and its recovery.

	time constants of the	
	creeping	recovery
saturation current creep	294 min.	10.4 min.
leakage current creep	9.5 min.	6.5 sec.

In both cases, the time constants of the recovery is smaller than that of creeping. It will not be so worthwhile to compare the absolute values of the time constants found in the different experiments, since they are believed to be sensitively dependent on the surface conditions.

It must also be noticed here, that these experimental results of the creep phenomena can not be attributed to the thermal effect in the junction. This may easily be verified from the fact that the saturation current is not altered. In fact, temperature rise in the junction was sometimes observed when the creep was forced by relatively high reverse voltages. This effect, however, was small and turned out to be negligible.

§ 3. Effect of Glow Discharge on Germanium Surfaces

On the course of the work to investigate the effect of ambient atmosphere on the transistor characteristics, it has been found out that the collector characteristic was remarkably changed by the discharge in the Geisler tube connected between the rotary pump and the glass bell jar. The effect occurred only when the vacuum was rather low and therefore the glow discharge could be observed extending to the bell jar from Geisler tube. The change in the collector characteristic was the remarkable increase of the *leakage current*. Experiments on the effect of glow discharge in low vacuum on the junction characteristic and on the surface recombination velocity was performed.

(3.1) *The effect on diode characteristics*

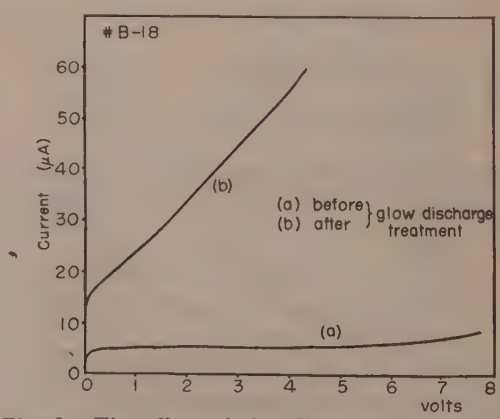

Fig. 9. The effect of glow diacharge on the backward characteristc of a junction.

The junction diode specimens were mounted in a bell jar and kept at the earth potential, and the jar was evacuated by a rotary pump. The diode characteristic was measured by an $X-Y$ recorder, the results are illustrated in Fig. 9.

The curves (a) and (b) correspond to before and after the discharge, respectively. As is shown, the leakage current component is increased about one or two orders of magnitude, while the saturation current component is increased only about three times or so.

The increase in the saturation current could easily be understood on the basis of the increased surface recombination velocity by the glow discharge. It seemed, however, to be difficult to explain the change in the leakage current by the change in the recombination velocity. Therefore, another model which took into account the local surface breakdown was imagined.

This model was checked by the following experiment using the local photocurrent technique[9]. As is shown in the right-hand side of Fig. 10, a small light spot is moved along on the periphery of the alloyed In dot of the junction. The local photoresponse is measured and plotted in Fig. 10. From the previous experimental results[9], it has been established that if a small breakdown region is formed on the periphery, a sharp peak comes out at that point in the photoresponse curve. The curve (a) is the photoresponse before the discharge, and (b) and (c) are after the discharge. As is seen from the figure, no peak appears after the discharge, while the response is reduced at every point. These results compel us to believe that the local breakdown model is not the case and to go back to the surface recombination velocity model again.

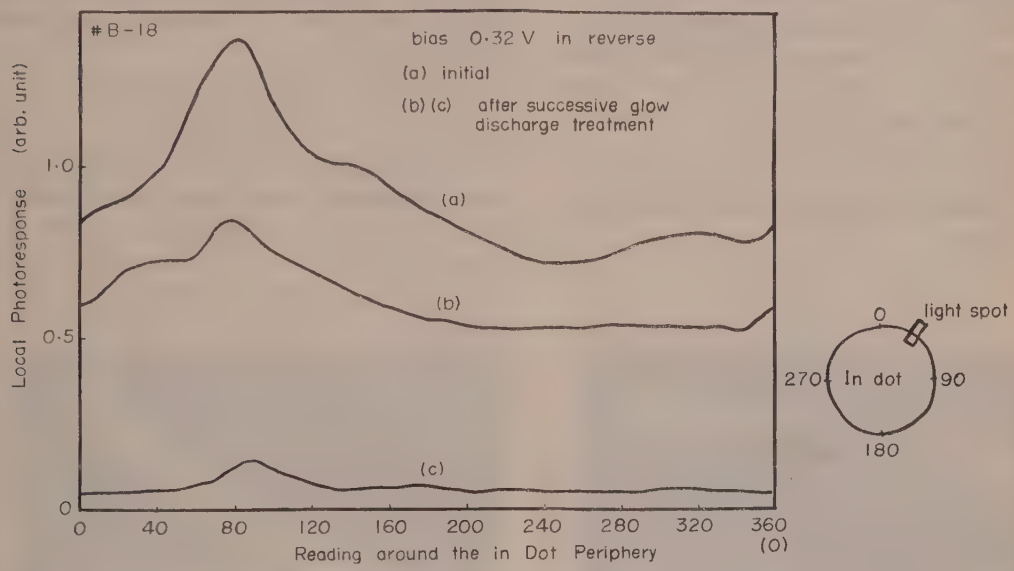

Fig. 10. Result of the local photocurrent measurements to check the occurrance of surface breakdown.

(3.2) *The effect on surface recombination velocity*

To confirm the effect of glow discharge on the surface recombination velocity, the local photoresponse along on the germanium rod was examined. For constant geometry, the photoresponse is a unique function of the surface recombination velocity, provided that

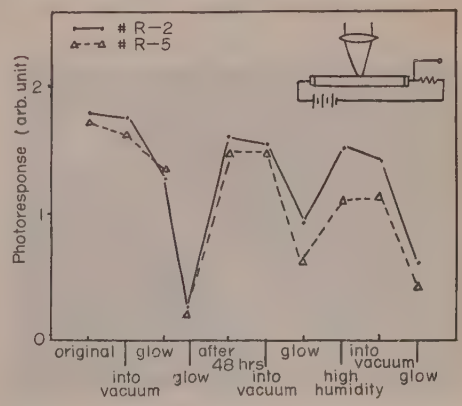

Fig. 11. The effect of glow discharge on the surface recombination velocity measured on the rod of germanium single crystal.

the temperature is kept constant. The experimental results are shown in Fig. 11. Germanium rod of $0.2\times3\times20$ mm in dimension is etched and the photoresponse is measured. The photoresponse shows no change after five minutes exposure to vacuum of 10^{-2}–10^{-3} mmHg. When the surface is subjected to the discharge in the vacuum, however, the photoresponse is reduced drastically as shown in the figure. The response recovered its initial value after 48 hours' exposure to the room air. In the next run, recovery occurred by high humidity. From these results, it will be concluded that the discharge affects the surface in enhancing the surface recombination velocity. Therefore, a question remains that how the large increase in the leakage current be explained from the increase of surface recombination velocity.

§ 4. Effect of Alcohol on Germanium Surfaces

It has often been experienced in the course of experiments on germanium diodes and germanium surfaces that the characteristics of the diodes and surfaces are considerably affected when they are subjected to alcohol.

Since it is difficult to treat the effect of alcohol quantitatively, only the experimental results are mentioned here and qualitative considerations are postponed to the following section.

(4.1) *The effect on diode characteristics*

The effect of alcohol on the current voltage characteristic has been observed on an oscilloscope as shown in Fig. 12. In the pictures of Fig. 12, units of the current and voltage are as follows,

current....50 microamp. per div.

voltage.... 5 volts per div..

When the diode is wetted by alcohol, the initial characteristic as shown in (a) is changed to that shown in (b). Because of the long

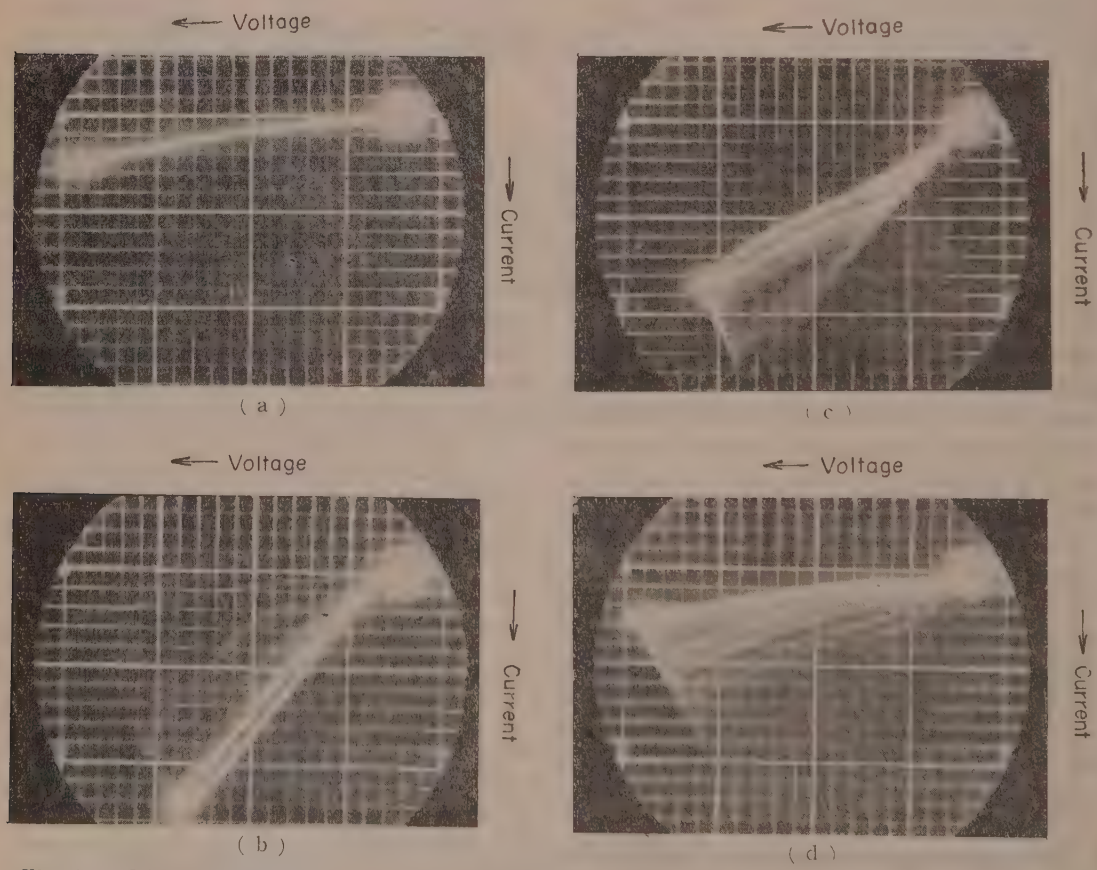

Fig. 12. Effect of alcohol on the current voltage characteristic of a junction. current; 50 microamp. per div., voltage; 5 volts per div.

persistance of the cathode ray tube, the characteristic corresponding to the intermediate state (or transient) can be seen in the figure. As the alcohol vaporizes in the room air, the characteristic recovers gradually as shown in the figures (c) and (d).

It must be noticed that when the surface of the diode is wet, considerable creep (hysteresis) appears as seen from (b) and (c). This hysteresis disappears when the surface is dried again. Another point which must be noticed is the fact that the alcohol induces *leakage current* remarkably. By rough estimation, the characteristic of (b), which corresponds to the most wetted state, may be understood as the result of shunting the diode by ohmic resistance of the liquid alcohol. The intermediate state characteristics, however, can not be understood by such a simple model, since they are not of ohmic character and have rather complicated shapes as shown in (c) and (d). For instance, when the alcohol begins to evaporate, the corresponding change in the characteristic occurs for higher voltages, while the current for lower voltages are kept almost unchanged, as shown in (c). The drift of the characteristic curve is illustrated schematically in Fig. 13. These instantaneous current voltage characteristic curves can not be fitted by any existing theories.

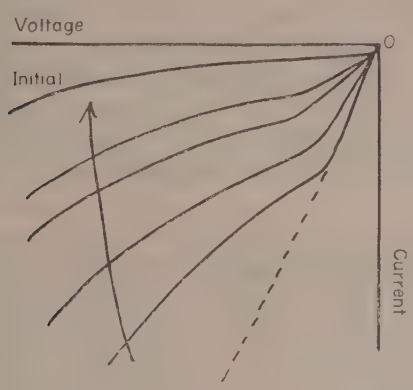

Fig. 13. Schematic representation of the recovery of the characteristic curve.

(4.2) *The effect on surface recombination velocity*

The effect of alcohol on the surface recombination velocity has ever been observed in many kinds of minority carrier lifetime measurements. For instance, in the Morton-Haynes method, the output signal is increased by wetting the surface by alcohol. This signal recovers its initial value as the alcohol evaporates. In the Haynes-Shockley method, similar increase in the collector signal by alcohol is observed. When a germanium slab of 0.2 mm in thickness is used in this kind of measurement, as shown in Fig. 14, the signal on the oscilloscope is changed from (a) to (b) when the surface is wetted by alcohol.

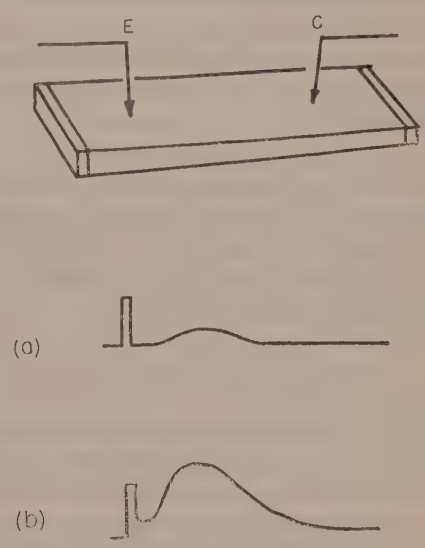

Fig. 14. Effect of alcohol on the lifetime measurement. (Haynes-Shockley method)

These experimental observations seem to show that the surface recombination velocity is reduced by alcohol. There is, of course, another possibility that the alcohol enhances the collectivity (or intrinsic alpha) of the point contact, but it has not been tried to ensure or rule out this possibility. At any rate, the reduction of the surface recombination velocity by alcohol was confirmed by the experiment using germanium rod in the same manner as mentioned referring to Fig. 11.

It is an open question that in spite of the opposite effect on the surface recombination velocity, glow discharge and alcohol show the the similar influence on the leakage current component of the junction diode.

§ 5. Discussion

Summarizing above mentioned experimental results, problems may be picked out as follows;

(1) What is the nature of the creep phenomena ?

(2) Through what kind of mechanism do the creep of emitter and collector of a transistor correlate ?

(3) Have we any junction rectification theories which involve the leakage current component that may creep under the influence of applied voltage ?

Since it is quite difficult to answer these questions and explain all of the experimental results mentioned above, it is intended here to make a critical survey on some existing theories in the following at first, and then a discussion on the correlation between the creep and the field effect is given.

(5.1) *The leakage current*

Eriksen[10] has presented a theory of junction characteristics taking channel conduction into account. According to his theory, leakage current which flows in the channel may be expressed in the form;

$$I=\sqrt{2j_0}C\left(\int_0^V g(V')dV'\right)^{1/2}, \qquad (1)$$

where j_0 is the saturation current across the surface $p-n$ junction, C the length along the periphery of the junction on the surface, g the surface conductivity. He assumed that j_0 is constant and independent of the position along on the channel. It has been observed that the surface conductivity g is roughly inversely proportional to the applied voltage across the surface junction (V' in this case)[11]. Therefore, it is not so crude to substitute this voltage dependence into Eq. (1), which results in the following equation;

$$I=\sqrt{2j_0}Ca\log\frac{V+V_0}{V_0}, \qquad (2)$$

where V_0 is a constant introduced to avoid the divergence of the integration, and a is the proportionality constant.

As is seen from the equation, the leakage current calculated in this way does not represent the characteristic of the actual diodes. The leakage current observed in the actual diodes shows steady growing up, or strictly speaking, has positive second derivative with respect to the voltage, while Eq. (2) gives only negative second derivative. It can also be shown that this discrepancy has occurred not because of the assumed special voltage dependence of g.

Eriksen has already pointed out that the geometry must be taken into account when this theory is applied to the alloyed junctions, since above equation is the result for the grown junction. It has been found by rough estimation, however, that even if the geometry is considered, the above mentioned discrepancy would not disappear, as long as the *usual* voltage dependence of g is assumed.

Cutler has calculated independently the leakage current in Si fused junction on the similar channel model[12]. In this case, g was assumed to be independent of the voltage difference across the surface junction, while the theoretical junction current was used for the surface junction instead of the simple saturation current j_0 in the Eriksen's formula. The result is expressed as follows;

$$I=\sqrt{2gC^2j_0\frac{kT}{q}\left(e^{qV/kT}-\frac{qV}{kT}-1\right)}^{1/2}, \qquad (3)$$

where the notations are rearranged for the convenience of the comparison with Eq. (1). In this calculation, geometry was considered only for the grown junctions.

As is seen from Eq. (3), the leakage current derived in this way has negative second derivative, as was the case of Eriksen's result.

A remark which has been given independently by these authors, is the invalidity of assuming j_0 to be independent of the position along on the channel. We believe this is one of the most important factors that must be considered hereafter, since it involves the correlation between the leakage current and the surface recombination velocity. One difficulty occurs in this model when the experimental results of the creep phenomenon are considered. Since the result show the independentness of the change in the leakage current on the bias voltage, as mentioned referring to Fig. 7, the factor which is changed by the creep phenomenon must be involved in the quantites that can be put *out of the integral* in Eq. (1). If this is the case, the insertion of j_0 into the integral is utterly meaningless.

It must be noticed here that there is another blindspot in the consideration of these channel models. It is usually believed that g is almost inversely proportional to the voltage difference across the surface junction, so the assumption made by Cutler that g is a constant with respect to the voltage seems to be crude. If, however, the voltage dependence of the surface conductivity g is assumed to

be unknown, it is possible, in principle, to deduce the dependence from the experimental results. By rough estimation, it promptly turns out that the voltage dependence of g so determined is quite unusual and no longer is a monotonic decreasing function of the voltage[13].

In considering the creep phenomenon on this point of view, one must also estimate the validity of the assumption used so far that the surface potential φ_s is constant with respect to the voltage difference.

In the above discussion, the possibility of the ionic conduction as proposed by Law[14] has not been considered. It has been ruled out since the electrical characteristic was observed under relatively low humidity, and also since no ohmic character was measured in the experiments.

(5.2) *Creep phenomena and the surface field effects.*

Attention is focused on the creep phenomenon again in this section. If, in general, the current is expressed;

$$I=F(V,\alpha)\,, \qquad (4)$$

the effect of the creep appears in the factor α. The time dependence of the creep and its recovery is understood as that of α. The nature of the quantity α is still in question at present, but it may be believed that the phenomenon is not the thermal one and is essentially connected with the *surface properties*. This is evident since the creep appears in the deteriorated transistors and diodes which exhibited no creep before the deterioration.

One of the most striking feature of the creep phenomenon is the *large time constant*. The time constants associated with the creep are of the order of seconds or minutes, which are several orders of magnitude larger than the ordinary electronic reactions in the semiconductors.

It is noticed here, however, that such long time effects are rather familiar to the investigators of the semiconductor surface phenomena. In the surface field effect, relaxation with the time constants of the order of minutes are commonly experienced which results from the slow transportation of electrons across the surface oxide layer. The time constants are dependent upon the thickness of the oxide layer[15]. In both of the above two phenomena, creep and filed effect, slow effect is observed under the application of the electric field on the surface. Hence, there may be some correlations between them. In the field effect, it is believed that the fast reaction occurs at first and then follows the slow reaction. The former completes within the time comparable to the minority carrier lifetime while the latter takes seconds or minutes depending on the surface conditions. Therefore, the response of the field effect is generally observed as reported by Many et al[16].

Hence, it is quite natural to expect to find out the similar fast process at the beginning of the creep, if it is really correlated to the field effect. According to the field effect mechanism, this fast process must be of opposite direction with respect to the following slow creep.

Experimental evidence has been obtained by single sweep method as shown in Fig. 15, and 16. The photographs show the variation of the current under a constant voltage as a function of time from the application. As is seen from the figures, the expected fast process could be observed. For instance, fast positive creep occurs in 1 millisec. after the application of the voltage, after which slow negative creep follows as shown in Fig. 15. In another junction shown in Fig. 16, fast negative creep is followed by a slow positive creep. Denoting the time constants of the fast and slow creep by τ_1 and τ_2, respectively, the results are summarized in the Table II. The signs in the table are referred to the direction of the creep.

Table II. Time constants of the fast and slow creep.

	τ_1	τ_2
# 5	−240 microsec.	+ 1.2 sec.
#15	+550 microsec.	−165 millisec.
# 4	− 22 microsec.	+430 millisec.
#11	−100 microsec.	+130 millisec.

It was not possible to observe the fast creep in all of the samples tested. Two reasons are imagined, i.e., too small time constants to be detected by the apparatus used, or the lack of the effect itself.

One may notice at once seeing the results of Table II that τ_1 is somewhat larger than the time constants of the fast process in the field effect experiment, since the time constant of the fast process in the field effect is believed to be of the order of the carrier lifetime. However, we have some informations concerning on this result.

Fig. 17 and 18 show the results of the measurement of the field effect mobility as a function of frequency. As are shown in the figures, field effect mobility is sensitively affected by the surface conditions. In some cases, inflection appears in the curve. Montgomery[17] has already pointed out that this inflection point corresponds to the minority carrier lifetime. In our experimental results, however, the time constants obtained from the inflection point were sometimes considerably larger than that expected from the lifetime. The similar results are published by Iwata et al[18] on the surface experiments of Si. The time constant of the fast decay was ranging from several hundred microseconds

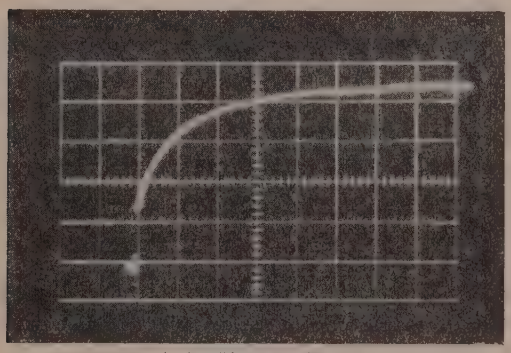

(a) 500 μ sec/5 div

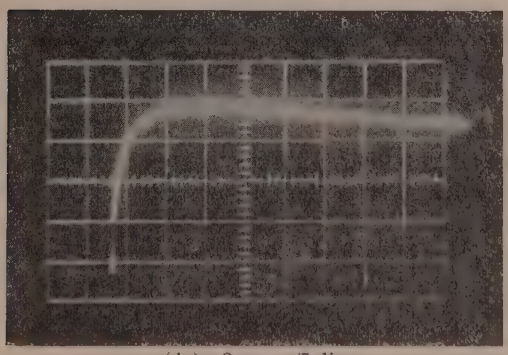

(b) 2 m sec/5 div

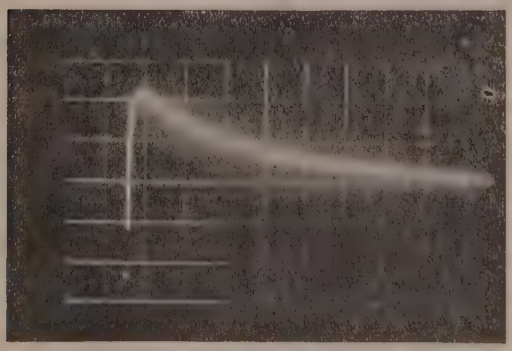

(c) 20 m sec/5 div

Fig. 15. Result of the single sweep experiment. The unit of the time scales are: (a) 500 microsec./5 div, (b) 2 milli-sec./5 div, (c) 20 milli-sec/5 div. (sample # 15)

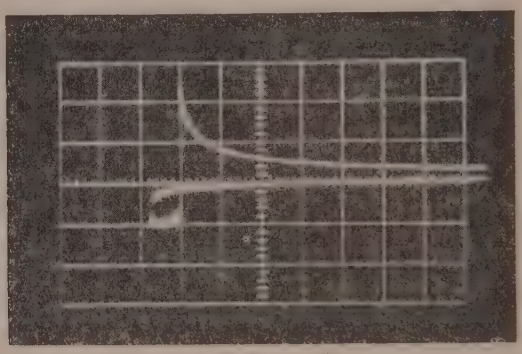

(a) 200 μ sec/div

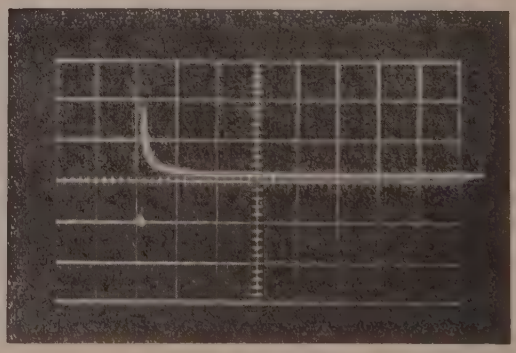

(b) 500 μ sec/div

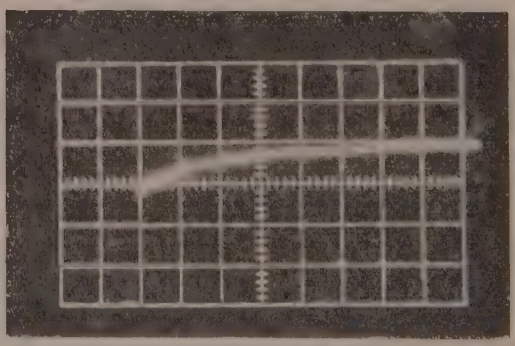

(c) 500 μ sec/5 div

Fig. 16. Result of the single sweep experiment. The unit of the time scales are; (a) 200 microsec./5 div, (b) 500 microsec./5 div, (c) 500 millisec./5 div. (sample # 13)

to some milliseconds[19]. Hence, it seems that there remains some questions on the belief that the time constant of the fast process in the field effect should be correlated with the carrier recombination.

It must be noticed that the discovery of the fast process in the creep phenomenon may give a strong evidence for the correlation between the surface field effect and the creep.

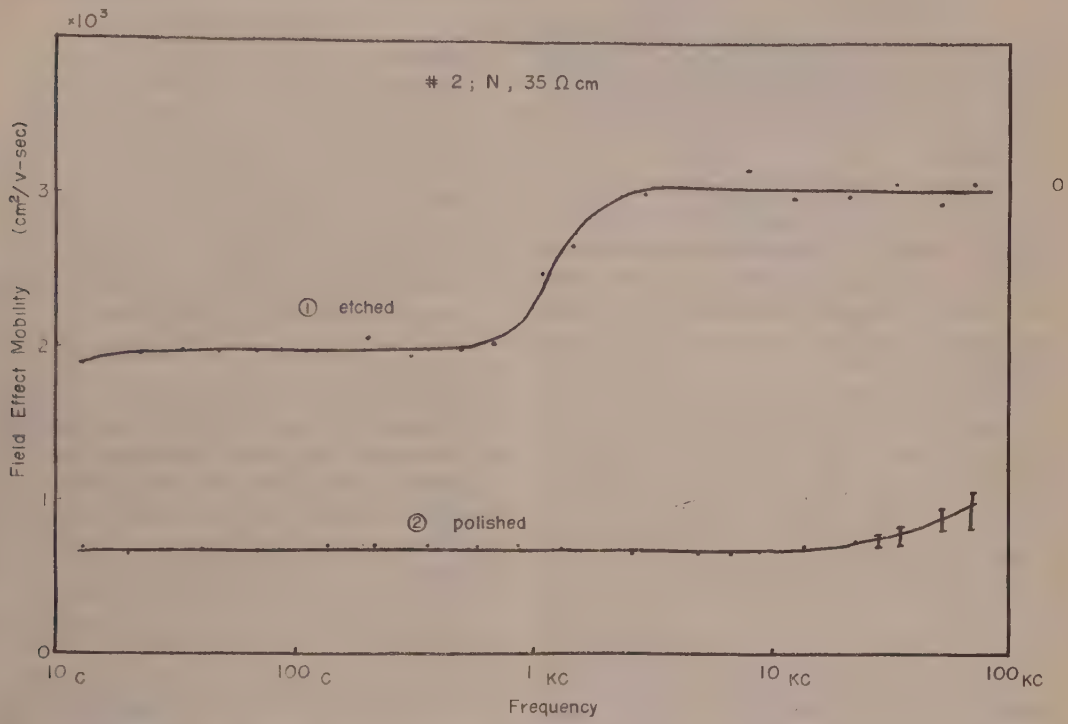

Fig. 17. Field effect mobility as a function of the frequency. 1, etched, 2, polished surface, respectively.

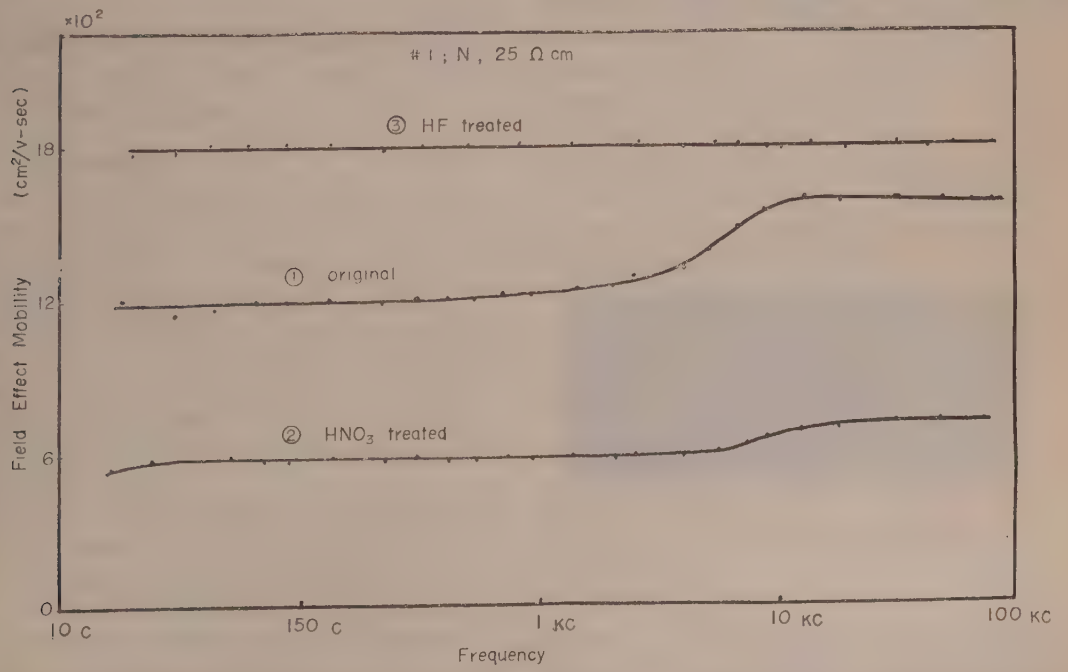

Fig. 18. Field effect mobility as a function of the frequency. 1, original, 2, HNO_3 treated, respectively.

§ 6. Conclusion

Experimental results on the backward characteristic and the creep phenomenon of the junction diodes have been given with the related surface and diode phenomena. The difficulties encountered in explaining the results on the basis of the present theories have been surveyed. It is noticed that no existing theories are successful in the explanation without introducing some additional models or concepts.

It has been pointed out that there is a possibility that the creep is caused by the same mechanism which is underlying the surface field effect. Though it is still a *possibility*, the experimental evidence presented by the single sweep observation seems to support the model strongly.

As a final comment, it should be noticed that there are at least two kinds of creep phenomenon, i.e., the creep in the relatively low humidity ambient and in high humidity, respectively. The former may be treated on the basis of electronic process, while it will not be adequate to treat the latter on the same basis. The same will be true for the case of the surface effects of semiconductors. Thus, the discussion of the surface properties whether they are of electronic or ionic without specifying the surface conditions may sometimes further introduce more confusions than clarify the situation.

Acknowledgement

The author wishes to express his thanks to Mr. Tarui for the assistance for the circuit arrangement, and to Mr. Denda for the preparation of thin germanium samples.

References

1) Shockley: B. S. T. J. **33** (1949) 435.
2) Christensen: P. I. R. E. **42** (1954) 1371.
McWhorter: P. I. R. E. **42** (1954) 1376.
Law: P. I. R. E. **42** (1954) 1367.
3) It is sometimes called "drift" or "gradual shift," but the term "creep" has been commonly used in Japan.
4) Plummer: Proc. Phys. Soc. **69** (1956) 539.
5) Kikuchi et al: Research Rep. of Electrotechnical Lab. No. 555. (in Japanese)
6) Morrison: Phys. Rev. **102** (1956) 1297.
7) Ref. 4).
8) Ref. 5).
9) Kikuchi: J. Phys. Soc. Japan **12** (1957) 133.
10) Eriksen et al: J. A. P. **28** (1957) 133.
11) Kingston: Phys. Rev. **93** (1954) 346.
12) Cutler et al: P. I. R. E. **45** (1957) 39.
13) Fig. 4, Fig. 5, in ref. 10).
14) Law: J. A. P. **26** (1955) 1265.
15) Lasser et al: Phys. Rev. **105** (1956) 491.
Kikuchi: Journ. Phys. Soc. Japan **12** (1957) 756.
16) Many et al: Phys. Rev. **101** (1956) 1433.
Harnick et al: Phys. Rev. **101** (1956) 1434.
17) Montgomery: Phys. Rev. **106** (1957) 441.
18) Iwata et al: J. A. P. Japan **26** (1957) 577. (in Japanese)
19) See also Burgess: Brit: J. A. P. **8** (1957) 62.

JOURNAL OF THE PHYSICAL SOCIETY OF JAPAN Vol. 13, No. 4, APRIL, 1958

Effect of External Stress on the Domain Structure of WO_3

By Sigetosi TANISAKI

Faculty of Literature and Science, Yamaguchi University

(Received December 23, 1957)

WO_3 is monoclinic at room temperature and has a domain structure with walls of (110) and (100) twin planes. The (110) wall is displaced sideways by a pressure externally applied along the b axis, resulting in the change of the axis b to the shorter axis a. The (100) domains change to a single domain by stress X_z. The single domain crystal obtained in this way is used to determine the optic elasticity axes of WO_3. Two peculiar types of domain structure appear by a pressure along the c axis, which can be understood as resulting from the change of the axis c to the axis a by the stress. This sensitivity of domain structure to the stress seems to be due to the monoclinic and pseudosymmetric structure of this crystal.

§ 1. Introduction

Tungsten trioxide, WO_3, was first reported to be a ferroelectric by Nagasawa[1] and Matthias[2] and then there have been many reports in relation to the ferroelectricity or antiferroelectricity. According to Ueda and Kobayashi[3] WO_3 is monoclinic and has an antiferroelectric atomic arrangement at room temperature and the unit cell dimensions are $a=7.274$Å, $b=7.501$Å, $c=3.824$Å, $\beta=90°56'$. It has a domain structure with walls of (110) and (100) twin planes which is sensitive to external stress. Hirakawa[4] and, Ueda and Ichinokawa[5], reported on the effect of stress on (110) domains. In the present paper, the effect of external stress on both (110) and (100) domains and two peculiar types of domain structure which appear by stress will be reported.

§ 2. Experiments

The crystals used in this experiments are thin plate crystals with well-developed c surfaces produced by sublimation of purified tungstic acid in the same way as was reported in the previous paper[6]. The purer is tungstic acid, the fewer and the greater are the domains of the crystals obtained, and such crystals are convenient to observe the effect of external stress on the domain structure.

a) (110) *domain*

When a c surface of plate crystal is observed by the metallurgical microscope, (110) and (100) domain walls can be seen clearly because the crystal is monoclinic and therefore the c surface is not flat but zigzag on account of its domain structure. Five straight lines which make an angle of 45° to the crystal edges in Photo. 1 (a) are (110) domain walls, and the many fine parallel lines which are parallel or perpendicular to the crystal edges are (100) walls and so the direction of the b axis of the crystal can be known easily from these (100) walls. When a pressure is applied along the a or b axis of such crystal, (110) walls are displaced sideways and the domains whose b axis is perpendicular to the pressure widen and the domains whoes b axis is parallel to the pressure narrow. On being applied a sufficiently strong pressure all (110) walls are displaced and disappear in a thin crystal. But in a thicker crystal it is not easy to move (110) walls and sometimes the crystal is destroyed by severe stress before wall displacements are observed. Photo. 1 (b) shows the effect of the pressure shown by arrows on (110) walls. Among the five (110) walls of Photo. 1 (a), two pairs of walls disappear and there is one short wall left near the right lower corner of the crystal.

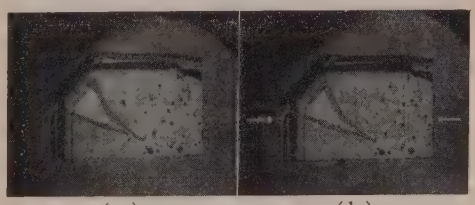

(a) (b)

Photo. 1. Effect of the pressure shown by arrows on (110) walls.

b) (100) *domain*

In order to observe (100) domains, it is better to observe a b surface of the crystal by

a polarizing microscope. Because one of the three optic elasticity axes of WO_3 is coincident with the crystallographic *b* axis and the other two in the *b* plane are different from *a* and *c* axes by a small angle in the monoclinic phase. Therefore extinction positions are different in each adjacent domains, and so a beautiful domain pattern is observed between crossed nicols as shown in Photo. 2 (a). The dark and bright parts of the domain pattern can be interchanged by a rotation of the crystal. When shearing stress X_z is applied to this crystal, it can be changed into a single domain crystal as shown in Photo. 2 (b). The orientation of the two optic elasticity axes in the *b* plane can be determined by observing the extinction positions of such single domain crystal in consideration of the sense of the applied shearing stress. Fig. 1 shows the positions of optic elasticity axes with respect to the crystallographic axes. A gipsum plate was used in order to distinguish the X′ axis from the Z′ axis.

These changes of (110) and (100) domain structure by the external stress do not recover even if the stress is removed.

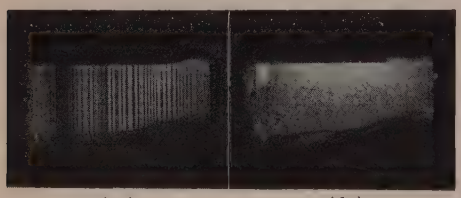

(a) (b)

Photo. 2. Effect of the stress X_z on (100) walls.

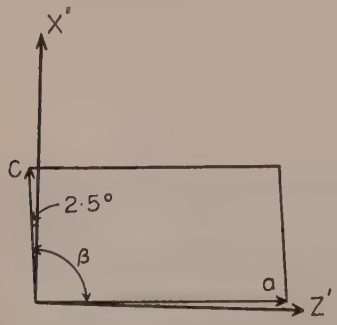

Fig. 1. Optic elasticity axes of WO_3.

c) two peculiar types of domain structure

When a *b* surface is observed, a new type of domain structure produced by a pressure applied along the *c* axis is found. If the pressure is increased slowly, wedge-shaped domains making about 45° to the *c* axis are nucleated at the crystal edges and extend across the crystal (Photo. 3). When the stress is removed, only small wedges in the initial stage of formation disappear at once, but the other large new domains do not show any change of appearance. These new domains extend through the thickness of the crystal. When such crystal is observed by the polarizing microscope using only a polarizer, the new domains and the original part of the crystal show the dichroism, and the difference of the absorption of two parts of the crystal is maximum

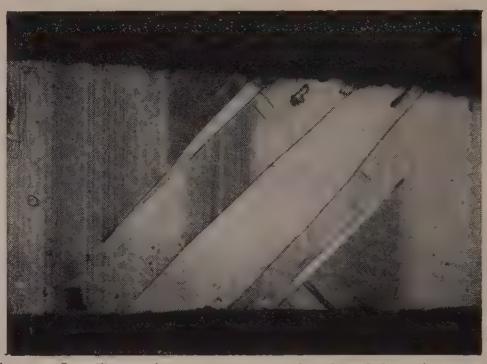

Photo. 3. Domain structure obtained by the pressure along the *c*-axis.

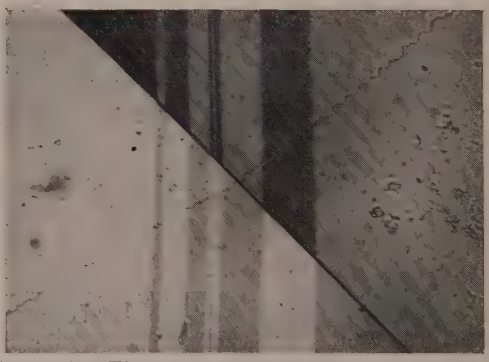

Photo. 4. First type of the domain structure obtained by the pressure along the *c*-axis.

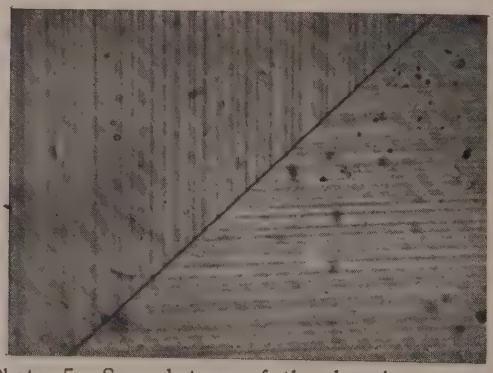

Photo. 5. Second type of the domain structure obtained by the pressure along the *c*-axis.

in the position in which the c axis of the original crystal is parallel to the direction of polarization and the contrast is reversed at the perpendicular position to this. From this fact it seems that in the new domains the orientation of the a and c axes is interchanged with respect to that of the original part of the crystal. This is ascertained by taking X-ray rotation photographs of a crystal, which mostly consists of new domains, and is obtained by widely applying a pressure to the c surface.

Inside this new domain many fine laminar domains are observed between crossed nicols, which extend nearly perpendicularly or parallel to the c surface of the crystal. Their domain walls seem to be (001) and (100) twin planes respectively judging from the reversal of the a and c axes. Such indices of planes in the new domains are expressed for convenience with a prime like (100)′ and indices without prime are used only for the original part of the crystal in the following. These (001)′ domains are related to the original (100) domains at the boundary as shown in Photo. 4 and 5. These photographs show the two standard types of domain structure near the boundary. In Photo. 4 the right upper side of the boundary is the original part of the crystal and the left lower side of it is the new domain part, and in Photo. 5 the left upper side is the original part and the right lower side is the new domain part. In the first type the upper dark (100) domains link to the lower bright (001)′ domains and the bright (100) domains to the dark (001)′ domains and an angle between the (100) and (001)′ walls measured on the photograph is about 177°. In contrast to this, in the second type the dark (100) domains link to the dark (100)′ domains and the bright (100) domains to the bright (100)′ domains and an angle between the (100) and (100)′ walls is about 87°.

Those two peculiar types of domain structure can be explained as follows by taking into consideration the reversal of the a and c axes on either side of the boundary. The orientation of the crystallographic axes of each domain in the first type can be determined, as shown in Fig. 2, from the domain pattern observed between crossed nicols and the orientation of the optic elasticity axes relative to the crystallographic axes shown in Fig. 1. Then the boundaries of the original and new domains seem to be (201) or (201)′, and $(20\bar{1})$ or $(20\bar{1})'$, which are their twin planes, and the angle between (100) and (001)′ in each case is calculated to be 177°10′ and 177°4′ respectively from the crystallographic data by Ueda and Kobayashi[3]. There is a difference of angle 6′ between them but the calculated value and the measured one coincide very well. In order to maintain the condition of continuity at the domain boundary so that the crystal does not show any crack or overlapping, there must be in the crystal a strain caused by this difference of angle 6′. Sometimes very fine (100)′ domains which seem to be due to this strain can be observed inside the (001)′ domains.

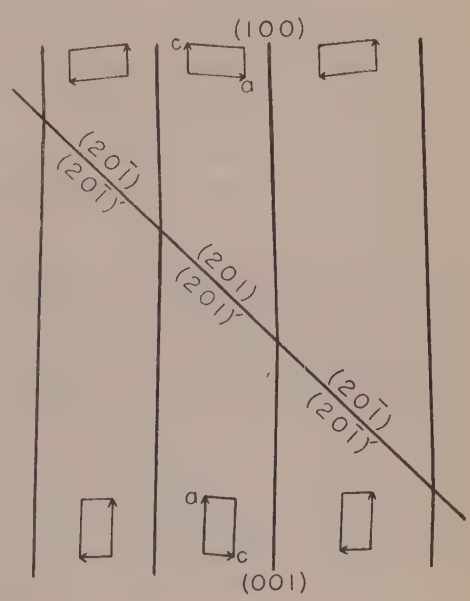

Fig. 2. Crystal axes of each domain in the first type.

In the same way as in the first type, the orientation of the crystallographic axes of each domain in the second type can be determined as shown in Fig. 3. There is no boundary plane of low indices in which the condition of continuity is completely fulfilled. Among several probable combinations of boundary planes, for example (201) $(20\bar{1})'$, (101) $(40\bar{1})'$, (403) $(30\bar{1})'$, (302) $(80\bar{3})'$, and (805) $(50\bar{2})'$ etc., a combination of (302) and $(80\bar{3})'$ shows the best fitness and so the orientation of the boundary plane seems to be very close

to (302) and $(80\bar{3})'$, or $(80\bar{3})$ and $(302)'$. When it is assumed to be (302) and $(80\bar{3})'$ themselves, calculated values of angles between (302) and (100) and between $(80\bar{3})'$ and $(100)'$ are 51°10′ and 35°49′ respectively, and the sum of them is 86°59′ which coincides very well with the measured value 87°.

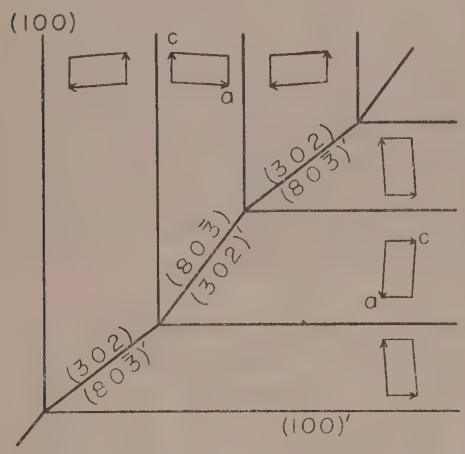

Fig. 3. Crystal axes of each domain in the second type.

Thus the characteristics of the two types of domain structure can be almost explained, but the condition of continuity at the boundary is not fulfilled completely in both cases. In fact, the real domain structure is not always one or the other of the above two standard types, but is a complex structure in which the two types are mixed together and sometimes a few domains disapper at the boundary in such a way that the strain caused in the crystal becomes as small as possible.

§ 3. Discussions and Conclusions

The fundamental unit of the structure of this material is a WO_6 octahedron formed by a tungsten atom and octahedrally coordinating six oxygen atoms, and these octahedra are coupled together by sharing corners to form a three dimensional crystal lattice. WO_3 is not cubic but monoclinic at room temperature and there are four somewhat distorted WO_6 octahedra per unit cell. Therefore the a and b axis lengths are each approximately twice the c axis length and the relation, $a<b<2c$, is noticed between the three axis lengths. In the above experiments, the (110) wall is displaced sideways by a pressure along the b axis with the change of the axis b to the shorter axis a, and the (100) domains change to a single domain by stress X_z, and two peculiar types of domain structure appear by the pressure along the c axis with the change of the axis c to the axis a. Judging from the monoclinic and pseudosymmetric structure above described, all these changes of the domain structure are not astonishing and needs only a small displacement of each atom. Thus the sensitivity of domain structure to the external stress seems to be due to the monoclinic and pseudosymmetric crystal structure of this material.

In conclusion the author wishes to express his hearty thanks to Prof. K. Tanaka of Kyoto University for his continual guidance and encouragement, and to Dr. T. Nakamura of Tokyo University for his valuable suggestions. This work was supported partly by the Scientific Research Expenditure of the Ministry of Education.

References

1) S. Nagasawa: Denki Kagaku **16** (1948) 13, 57.
2) B. T. Matthias: Phys. Rev. **76** (1949) 430.
3) R. Ueda and J. Kobayashi: Phys. Rev. **91** (1953) 1565.
J. Kobayashi: Mem. Sch. Sci. & Eng. Waseda Univ. **18** (1954) 92.
4) K. Hirakawa: Busseiron Kenkyu **26** (1950) 42.
5) R. Ueda and T. Ichinokawa: J. Phys. Soc. Japan **6** (1951) 122.
6) S. Tanisaki: J. Phys. Soc. Japan **11** (1956) 620.

JOURNAL OF THE PHYSICAL SOCIETY OF JAPAN Vol. 13, No. 4, APRIL, 1958

Ferroelectric and Optical Properties of Na(K-NH_4)-tartrate Mixed Crystals

By Yasuharu MAKITA and Yutaka TAKAGI

Tokyo Institute of Technology, Oh-okayama, Tokyo

(Received January 10, 1958)

The phase diagram of the mixed crystals composed of NaK-tartrate and its isomorph $NaNH_4$-tartrate has been investigated over the whole range of the concentration. The properties of each phase have been studied by dielectric and pyroelectric measurements and by optical observations. In 90.5 per cent $NaNH_4$-tartrate crystal three kinds of polymorphic modification have been found, that is, successively, a ferroelectric phase with spontaneous polarization along the crystallographic b axis, another ferroelectric phase with spontaneous polarization along the crystallographic a axis and a paraelectric phase. The phase of compositions near the pure $NaNH_4$-tartrate has been confirmed to be ferroelectric with spontaneous polarization along the b axis.

§ 1. Introduction

It has recently been found that $NaNH_4$-tartrate is ferroelectric below the transition point of $-164°C$ with a spontaneous polarization in the direction parallel to the b axis[1]. The crystal shows many peculiar properties: 1) Its dielectric constant along each crystallographic axis does not follow the Curie-Weiss law above the transition point, and the pyroelectric charge developed on the crystal surface at the transition point remains constant for further cooling. 2) The domain structure is not affected by an ac electric field of 20 Kv/cm, while it can easily be affected by a shearing stress Z_x. These properties form striking contrasts if compared with those of NaK-tartrate (Rochelle salt) or other normal ferroelectrics.

As well known, the non-polar phase of $NaNH_4$-tartrate ($NaNH_4C_4H_4O_6 \cdot 4H_2O$) is isomorphous with the non-polar phase of NaK-tartrate ($NaKC_4H_4O_6 \cdot 4H_2O$), and they can form a continuous series of solid solution over the whole range of concentration. These mixed crystals were first investigated by Kurtschatow *et al.*[2] and have recently been re-examined by Melmed *et al.*[3] Substitution of very small amount of $NaNH_4$-tartrate reduces the temperature range of ferroelectric activity in NaK-tartrate very rapidly. Substitution of about two per cent eliminates the spontaneous polarization entirely. The ferroelectric activity, however, reappears in the crystals containing more than about eighteen percent of $NaNH_4$-tartrate. These crystals show a single Curie point at low temperatures, exact position of the transition depending upon the concentration. The Curie point-composition curve goes down linearly from about 20 per cent to about 60 per cent. It seemed to be difficult to foretell how it can be connected with the transition point of $-164°C$ of $NaNH_4$-tartrate. Moreover, it must be emphasized that the spontaneous polarization of $NaNH_4$-tartrate lies in the direction parallel to the b axis while the spontaneous polarization of NaK-tartrate and those of all the mixed crystals which have been so far investigated lie in the direction parallel to the a axis. So it can not be expected that the Curie point-composition curve given by the previous investigators should be connected smoothly with the transition point of $NaNH_4$-tartrate.

However, Melmed *et al.* have found that the crystal containing 98.1 per cent of $NaNH_4$-tartrate shows a small anomaly in the dielectric constant at $-155°C$, the behavior of which being quite similar to that observed in the pure $NaNH_4$-tartrate. It seems, therefore, that this transition point of $-155°C$ of the 98.1 per cent crystal should be connected with the transition point of $-164°C$ of the pure $NaNH_4$-tartrate.

Our primary concern in the present paper is to study in more detail the dielectric, pyroelectric and optical properties of the mixed crystals of the compositions near the pure $NaNH_4$-tartrate. Our second purpose is to re-

examine and to complete the phase diagram over the whole range of this system.

§ 2. Preparation of the Crystal Plates

The crystals were grown by cooling method in a 2-litre beaker filled with saturated aqueous solution. It usually required two weeks to decrease the temperature from 28°C to 26°C; the regulation was achieved by a thermoregulator.

The composition of the crystal depends upon the composition of the solution, as shown in Fig. 1. The data have been obtained by chemical analysis through the measurement of the weight of potassium contained in the crystal; the accuracy of the analysis is within 0.5 per cent. The results are in fairly good agreement with those obtained by Melmed *et al.*, though slightly different from those obtained by Kurtschatow *et al.* The latter investigators did not give the temperature of crystallization used in their experiment.

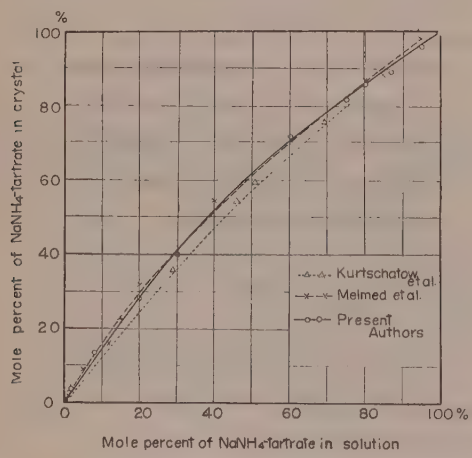

Fig. 1. The relation between the compositions of the crystals and the solutions.

The pure $NaNH_4$-tartrate and the mixed crystals around it show a pronounced tendency to dehydrate, while the pure NaK-tartrate and the mixed crystals around it sometimes show a tendency to deliquesce. In the course of our studies, therefore, the crystals have always been preserved in five desiccators, each being kept at a suitable humidity according to the composition of the mixed crystals, except the short time when the crystals were set in the measuring apparatus. The specimens used were cut out of mother crystals by means of a wet thread saw and then ground on a linen cloth with the abrasive of fine powder of chrome oxide suspended in liquid paraffin. In the cutting and grinding processes, special attention was paid to the orientation of the crystal plates with reference to the crystallographic axes.

§ 3. Dielectric Properties

1. *Dielectric Constants*

As the electrodes, silver-foils have been attached by absolute alcohol on the surfaces of the specimens of the area 0.7 to 6 cm² and the thickness 0.7 to 1.5 mm. The dielectric constants have been measured over the temperature range from about 30°C down to −190°C by a usual bridge method with an ac field of 1 KC/sec and the field intensity of 5 to 10 v/cm.

According to the dielectric properties, it is convenient to divide the mixed crystals into four groups, as was done so by Kurtschatow *et al.* and Melmed *et al.*

The first group covers the range 0 to 2.5 per cent. This group is characterized by the typical NaK-tartrate behavior, all crystals except the 2.5 per cent one having two transition points. In the pure NaK-tartrate, as known well, there are two high peaks in the dielectric constant along the *a* axis, ε_a, at the two transition points of −18°C and 24°C, respectively. In the crystal containing only 2.5 percent $NaNH_4$-tartrate, the upper and the lower transition points merge with each other at −5.5°C. It is observed that the effect of the addition is much more pronounced for the upper transition point than for the lower one. The results are shown in Fig. 2.

The second group covers the range 2.5 to 18 per cent. This group is characterized by

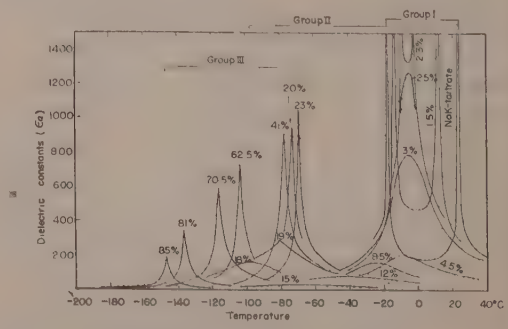

Fig. 2. Dielectric constants along the *a* axis in the crystals belonging to the groups I, II and III.

a low and broad peak in the dielectric constant, ε_a. The peak is lowest for about 15 per cent $NaNH_4$-tartrate (Fig. 2).

The third group covers the range 18 to 85 per cent. This group exhibits a pronounced single peak in the dielectric constant, ε_a, of which the peak value decreases as the concentration of $NaNH_4$-tartrate increases (Fig. 2).

On the whole, our results of the dielectric constant along the *a* axis of the crystals containing less than 85 per cent of $NaNH_4$-tartrate are in fairly good agreement with those obtained by Melmed *et al.* In these groups, the dielectric constants along the *b* and *c* axes (ε_b and ε_c) have also been carefully examined. They show no anomalies at the transition points mentioned above, as shown in Fig. 3a.

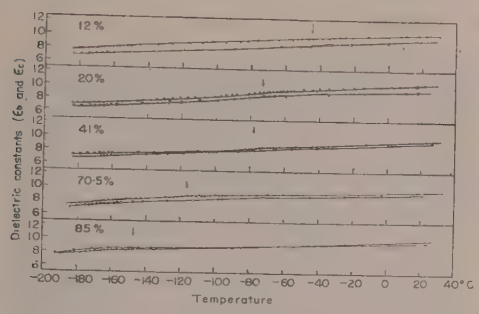

(a)

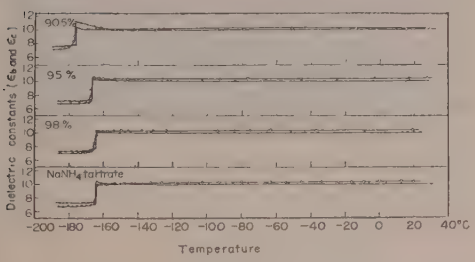

(b)

Fig. 3. Dielectric constants along the *b* and *c* axes.
Solid circles: ε_b, Open circles: ε_c.
(a): The groups II and III.
The arrows show the temperature where the peak of the dielectric constant along the *a* axis appears.
(b): The group IV.

The fourth group covers the range 92.5 to 100 per cent. This group is characterized by a small anomaly in all three dielectric constants ε_a, ε_b and ε_c with a discontinuity at the lower temperature side of the transition point (Figs. 3b and 4). A small peak is observed in ε_a in the crystals containing about 92.5 per cent $NaNH_4$-tartrate, but it tends to disappear as the composition approaches 100 percent, as shown in Fig. 4. The locus of these transition points proves to be a phase boundary.

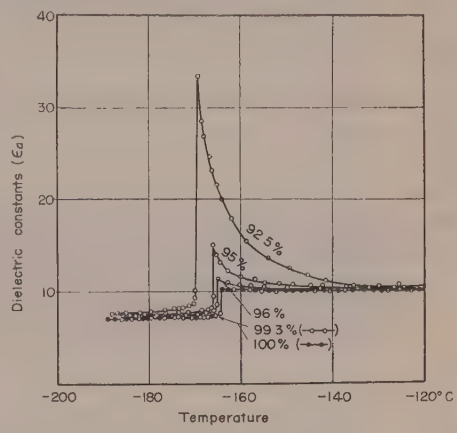

Fig. 4. Dielectric constants along the *a* axis of the crystals belonging to the group IV.

The 90.5 per cent crystal, lying between the groups III and IV, reveals two phase transitions at −163°C and −176°C. It has been confirmed that the upper transition is the same as those observed in crystals of the group III, because it is accompanied with a fairly large peak of only one dielectric constant ε_a, while the lower transition is the same as those observed in the crystals of the group IV, because it is accompanied with a small anomaly of all three dielectric constants ε_a, ε_b and ε_c (Fig. 5).

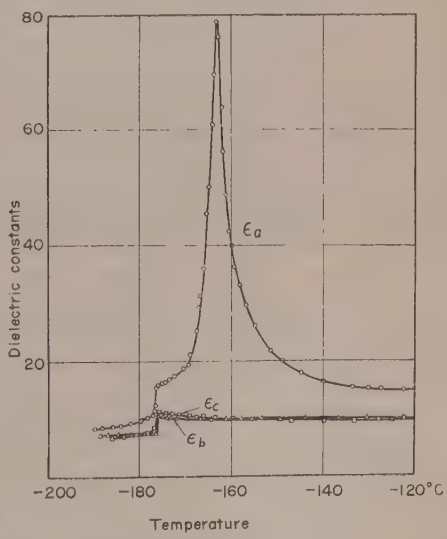

Fig. 5. Dielectric constants along the three crystallographic axes of the 90.5 per cent crystal.

2. *Dielectric Hysteresis Loops*

Under a high ac field of 50 cycles/sec applied parallel to the *a* axis, the dielectric hysteresis loop has been observed on a cathode ray oscilloscope. The crystals belonging to the group I reveal ferroelectric hysteresis loops at temperatures between their two transition points (Fig. 6).

On the other hand the 12 per cent crystal, which belongs to the group II, does not display a ferroelectric hysteresis loop for an applied field of 25 Kv/cm. Contrary to our expectation, we observed hysteresis curves much resembling those of ferroelectrics in the crystals just outside the phase boundaries of the groups I and III.

The crystals belonging to the group III reveal ferroelectric hysteresis loops below the transition points. The coercive field increases not only with decreasing temperature but also with increasing concentration of $NaNH_4$-tartrate.

The crystals belonging to the group IV reveal only straight lines instead of the hysteresis loops all over the temperature range from 30°C to −190°C under an applied field as strong as 25 Kv/cm.

It has been found that the 90.5 per cent crystal reveals ferroelectric hysteresis loops only at temperatures between the upper and the lower transition points, although an ac field strength of 20 Kv/cm was not enough to bring about the saturation, as shown in Fig. 7.

The hysteresis curve has also been sought under a high ac field parallel to the *b* or the *c* axis. But it turned out that all the crystals, including those belonging to the group IV, display only straight lines instead of the hystersis loops all over the temperature range from 30°C to −190°C under an applied field of 25 Kv/cm.

In the course of the study of hysteresis penomena, some double hysteresis loops have been observed. The 20 percent crystal is very notable with its peculiar properties. With this crystal, it is possible to observe a double hysteresis loop at temperatures ranging from about −76°C (the transition point) down to about −150°C and under a relatively weak field (Fig. 8a). This anomalous hysteresis phenomenon is very similar to those recently observed by Yurin[4)]* in NaK-tartrate crystal which had been intensely irradiated by γ-ray for several hours. However, there exists a striking difference: in our case the double hysteresis loop changes into an ordinary ferroelectric hysteresis loop as the applied field is increased, while in the Yurin's experiment the double hysteresis loops are observed to persist even under the field high enough to cause the saturation. Moreover, the life time of the double hysteresis loop is usually very short after a high field had been applied to our specimen and it becomes much shorter if the temperature of the crystal is changed several times up and down across the transition point under a high ac or dc field. After such a treatment the double loop often disappears, giving rise to the normal loop, and both the maximum electric polarization and the slope of the hysteresis loop become much larger than those observed before the treatment (Fig. 8 (b), (c)). It is very interesting to notice that the coercive field observed after treatment is often smaller than the threshold field (Fig. 8d). The recovery to the initial state with its double hysteresis loop requires several weeks or more, and it appears that the longer we keep the specimen at a temperature below the transition point, the more stable becomes the double hysteresis loop.

The double or the double-like hysteresis loops are also observed in other crystals at compositions adjacent to the phase boundaries between the group II and its neighboring groups on both sides under the same experimental conditions as above. Some examples are shown in Fig. 9.

§ 4. Pyroelectric Properties

In order to make clear the peculiar properties described in the preceding sections, the pyroelectric tests have been carried out by means of Simizu-type electrometer[5)]. The sensitivity of about 5×10^{-11}Coul/division can be attained by this device. A cooling rate of 1°C/min was adopted.

As will be expected, all the crystals cut perpendicularly to the *a* axis (*X*-cut specimen) belonging to the group I, except the 2.5 per

* The writers are grateful to Dr. T. Nakamura and Dr. T. Sakudo for the information about the Russian references.

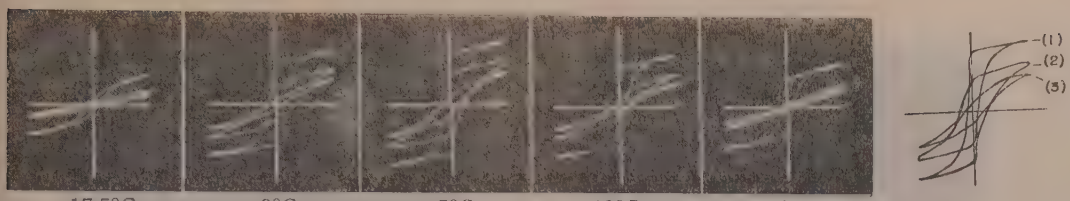

−17.5°C −9°C −5°C 13°C 18°C

Fig. 6. Dielectric hysteresis loops in the crystals belonging to the group I. The horizontal line denotes the maximum field (E_{scale}).

(1): The pure NaK-tartrate, E_{sc}=6 Kv/cm.
(2): 1.5 per cent, E_{sc}=4.5 Kv/cm.
(3): 2.5 per cent, E_{sc}=6 Kv/cm.

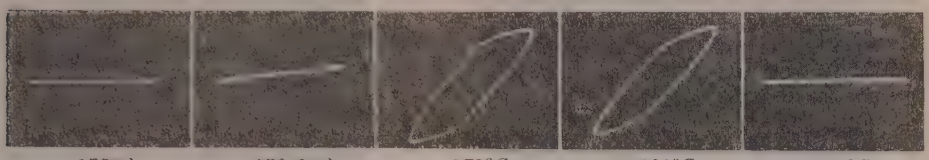

−177°C −176.5°C −172°C −168°C −155°C

Fig. 7. A series of the dielectric hysteresis loops in the 90.5 per cent *X*-cut specimen under the applied field parallel to the *a* axis. E_{sc}=20 Kv/cm.

Fig. 8. The double hysteresis loops observed in the 20 per cent crystal and the effects of various treatments. The vertical line denotes the polarization scale (P_{sc}) and the horizontal line denotes the maximum field (E_{scale}).

(a): Before the treatments. $P_{sc}=3.84\times10^{-8}$ Coul/cm², E_{sc}=758 v/cm. The threshold field E_t=405 v/cm.

(b): After the temperature cycling through the transition point 2 times under a high *ac* field.
E_{sc}=300 v/cm, $P_{sc}=1.53\times10^{-8}$ Coul/cm².

loop (1): the moment field was applied to the specimen.

loop (2): after 4 seconds.

(c): After the temperature cycling through the transition point 3 times under a high *ac* field. The short linear line at the center of the figure was obtained with an *ac* field less than the threshold field. $P_{sc}=1.79\times10^{-8}$ Coul/cm², E_c=354 v/cm.

(d): Under a high *ac* field. $P_{sc}=6.38\times10^{-8}$ Coul/cm², E_{sc}=2.3 Kv/cm².

cent one, show a pronounced pyroelectricity at temperatures between the upper and the lower transition points.

The *X*-cut specimen of 12 percent crystal, which belongs to the group II, did not show any trace of pyroelectricity at its passage through the dielectric peak point.

The *X*-cut specimens belonging to the group III show a pronounced pyroelectricity below the transition point. The results for some representative crystals are shown in Fig. 10.

The crystals cut perpendicularly to the *b* or the *c* axis (*Y*- or *Z*-cut specimens), belonging to the groups I, II and III did not show any trance of pyroelectricity at their passage through the transition points or the dielectric peak points.

The pyroelectric tests of the *X*-, the *Y*- and the *Z*-cut specimens belonging to the group IV have been carried out. The *Y*-cut specimens show a sudden occurrence of pyroelectricity just at the transition point and the charge amount proves to be temperature independent, as shown in Fig. 11. The *X*- or the *Z*-cut specimen did not show any trace of pyroelectricity at its passage through the transition point.

As expected, the 90.5 per cent *X*-cut specimen, lying between the groups III and IV, displays a pyroelectricity characteristic of the normal ferroelectrics at temperatures only between the upper and the lower transition points. Moreover, the *Y*-cut specimen of this

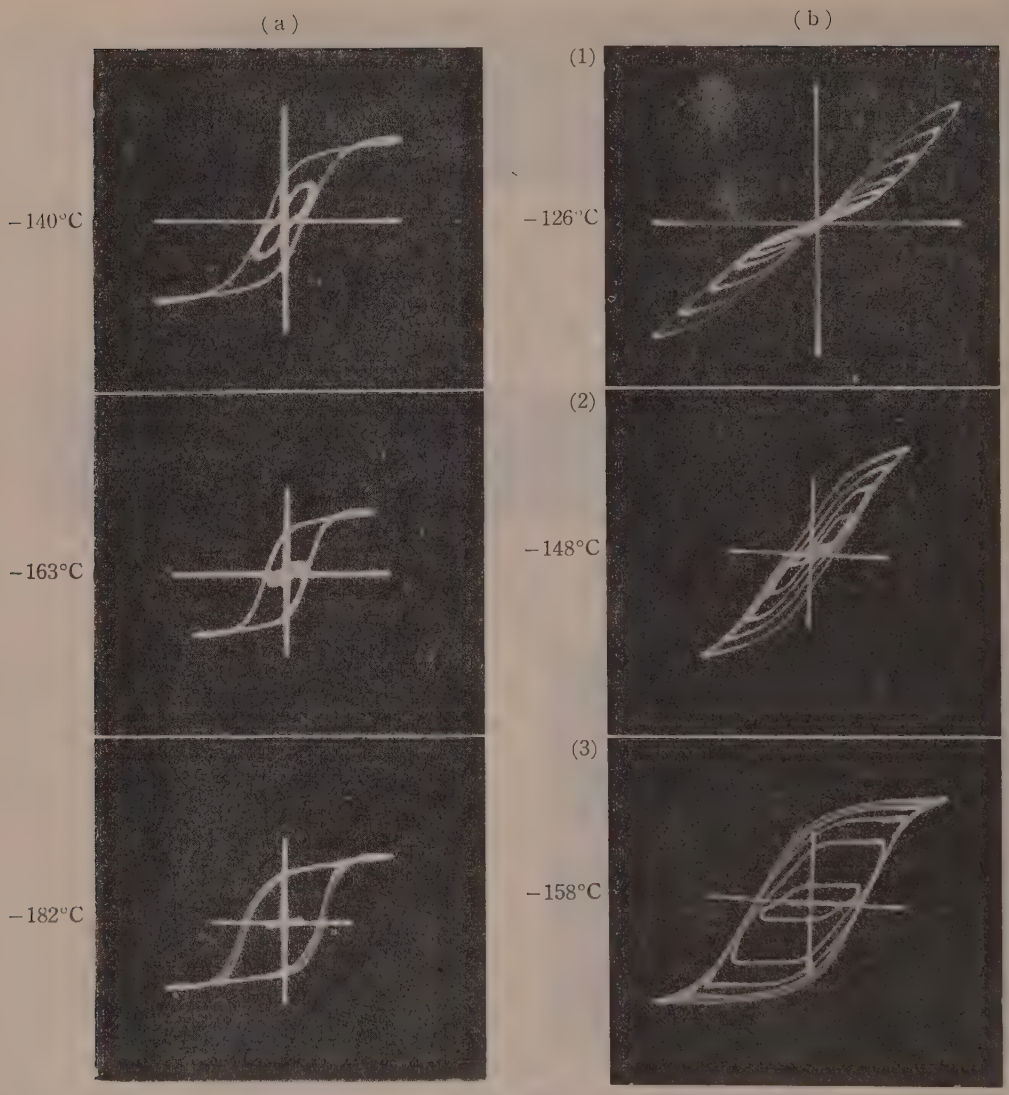

Fig. 9. Dielectric hysteresis loops under various field strength.
(a): The 23 per cent crystal. $P_{sc}=30.7\times10^{-8}$ Coul/cm², $E_{sc}=6$ Kv/cm.
(b): The 19 per cent crystal.
loop (1): under relatively weak fields. $P_{sc}=5.4\times10^{-8}$ Coul/cm², $E_{sc}=2.4$ Kv/cm.
loops (2) and (3): $P_{sc}=23.4\times10^{-8}$ Coul/cm², $E_{sc}=4$ Kv/cm.

crystal reveals the same type of pyroelectricity as those observed in the crystals belonging to the group IV only below the lower transition point, as clearly demonstrated in Fig. 11.

The Z-cut specimen of this crystal did not show a trace of pyroelectricity. The results mean undoubtedly that this crystal begins to polarize spontaneously in the direction parallel to the a axis at the upper transition point, and spontaneous polarization increases until the temperature reaches the lower transition point, at which its direction rotates suddenly by 90° towards the direction parallel to the

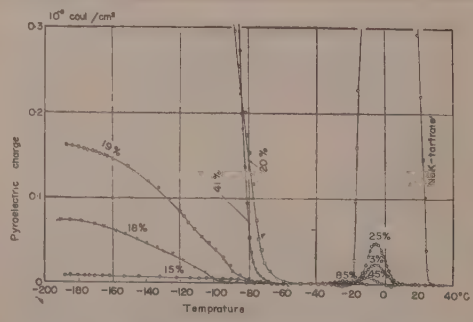

Fig. 10. Behaviors of pyroelectric charge in the X-cut specimens of the crystals belonging to the groups I, II and III.

b axis and thereafter its magnitude seems to remain constant.

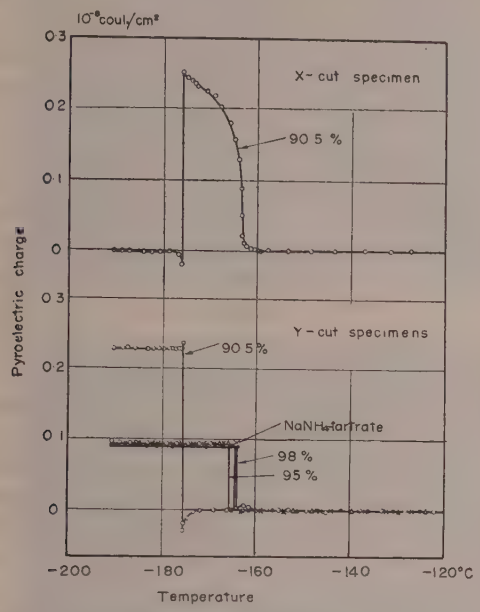

Fig. 11. Behaviors of pyroelectric charge in the 90.5 per cent crystal and those of the group IV.

It is to be noted that: 1) The *X*-cut specimens of the 20 per cent crystal yield a considerable amount of pyroelectric charge of the order comparable to those measured in the pure NaK-tartrate, though the values of pyroelectricity vary according to various pre-treatments. The effect of a field cooling treatment is clearly shown in Fig. 12. 2) It seems very likely that the pyroelectric charge detected in the *X*-cut specimens of the 3 per cent crystal arises from a certain kind of inhomogeneous monoclinicity: although the monoclinicity should disappear just at the composition of 2.5 per cent, if the crystal happened to be perfect. 3) Even at temperatures in the paraelectric region but not far from the transition point, all mixed crystals reveal a small amount of pyroelectricity, though it is almost negligible in unstressed crystals if compared with normal pyroelectricity caused by the spontaneous polarization. The pyroelectricity may be ascribed to crystal imperfections: to the internal strain and/or perhaps to the space charge stored somewhere in the interior of the crystals. 4) The *Y*-cut specimens of the crystals of the group IV as well as in the pure $NaNH_4$-tartrate are affected by means of field cooling, though the effect is very small if compared with that due to stress cooling (Z_x).

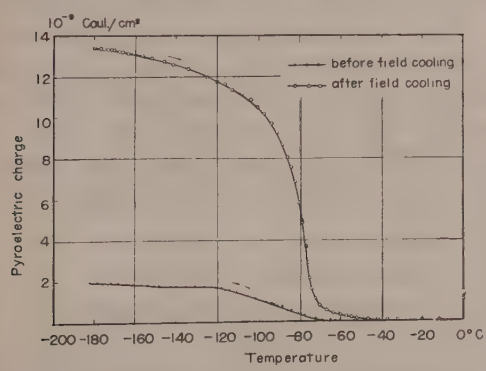

Fig. 12. Effect of the field cooling on the pyroelectricity in the 20 per cent crystal (*X*-cut specimen).

§ 5. Electric Polarization Induced by Shearing Stresses in the Crystals of Group IV

In the preceding paper, we reported that the shear stress Z_x can easily affect the electric polarization in the pure $NaNH_4$-tartrate crystal. We made, therefore, several 45° cut slabs of the crystals of which one edge bisects the *a* and *c* axis and the thickness of the plates lies along the *b* axis (45° *Y*-cut specimens), and applied a normal stress on one pair of narrow surfaces of each slab. The specimens below the transition point reveal a pronounced hysteresis curve in the shear stress *vs.* the electric polarization relation ($Z_x - P_y$ curve), while above the transition point they show only a linear relation.

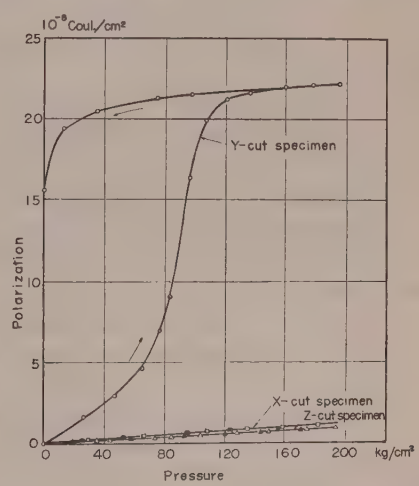

Fig. 13. Hysteresis curve induced by shearing stress in the 98 per cent crystal, at −183°C.

On the other hand, the 45° X-cut specimens and the 45° Z-cut specimens displays only linear relations in the shear stress *vs.* the electric polarization curves, the Y_z-P_x curves and the X_y-P_z curves respectively. The results in the 98 per cent crystal are shown, as an example, in Fig. 13.

The spontaneous polarization estimated from those cycles turns out to be 0.21μ Coul/cm^2, being independent of the concentration within the accuracy of the experiment.

It has also been confirmed that the 45° X-cut specimens belonging to the groups I and III, display pronounced hysteresis curves in the relation, the shear stress *vs.* the electric polarization (Y_z-P_x curves), at temperatures in their ferroelectric range; while the 45° Y-cut and the 45° Z-cut specimens show only linear relation in the Z_x-P_y curves and the X_y-P_z curves.

§ 6. Optical Properties

1. *Domain Structure*

At temperatures between the upper and the lower transition points, the crystals belonging to the group I become monoclinic owing to the spontaneous shear strain y_z^0, since the crystals polarize spontaneously along orthorhombic a axis. There is a possibility for us to observe domain structures through a polarizing microscope, because the angle between the monoclinic a axis and one of the indicatrix axes of the monoclinic phase is far larger than the spontaneous shear strain y_z^0 [6]. The direction of observation must be parallel to the a axis. The same situration is also expected with regards the crystals belonging to the group III.

The crystals belonging to the group IV becomes monoclinic owing to the spontaneous shear strain z_x^0, since the spontaneous polarization lies as proved in the preceding sections along the orthorhombic b axis. These crystals must, therefore, be observed in the direction parallel to the b axis.

The crystals belonging to the group II have no spontaneous polarization both above and below the temperature at which there is a broad peak in the dielectric constant *vs.* temperature curve. If it is true, the crystals must remain orthorhombic below the peak temperature, the domain should not be observed anywhere.

Fortunately all these expectations turned out to be true. The X-cut specimens belonging to the group I reveal the domain structure consisting of many fine stripes which are parallel to the c axis, only if the specimens are kept at temperatures between the upper and the lower transition points. The X-cut specimens belonging to the group II do not show a domain pattern even at temperatures below the broad peak point. The X-cut specimens belonging to the group III also reveal the domain structure which is quite similar to those observed in the group I, if the specimens are cooled below the transition point.

On the other hand, the Y-cut specimens belonging to the group IV display a domain structure consisting of many stripes which are parallel to the c axis at temperatures below the transition point, while the X-cut and the Z-cut specimens have never shown a domain pattern.

The behavior of the X-cut specimens of the 90.5 per cent crystal, which lies between the groups III and IV, is very interesting. It displays a domain structure consisting of a lot of stripes which are parallel to the c axis, if the specimens are kept at temperatures between the upper and the lower transition points, whereas the pattern suddenly disappears at the moment the crystal is cooled through the lower transition point. On the other hand, the Y-cut specimens at temperatures between the upper and the lower transition points do not show a domain pattern, but they display a domain structure, when they are cooled below the lower transition point. This comfirms that a sudden change of the spontaneous shear strain from y_z^0 to z_x^0 occurs at the lower transition point. The effect of the shear stress Z_x upon the domain boundaries in the Y-cut specimens of this crystal is not very different from those observed in the Y-cut specimens of the crystals belonging to the group IV, as shown in Fig. 14.

2. *Optically Biaxial Properties*

Both the pure $NaNH_4$-tartrate and the pure NaK-tartrate are optically biaxial. Lavinir[7], using sodium light, has determined the principal refractive indices. The values at 20°C are as follows:

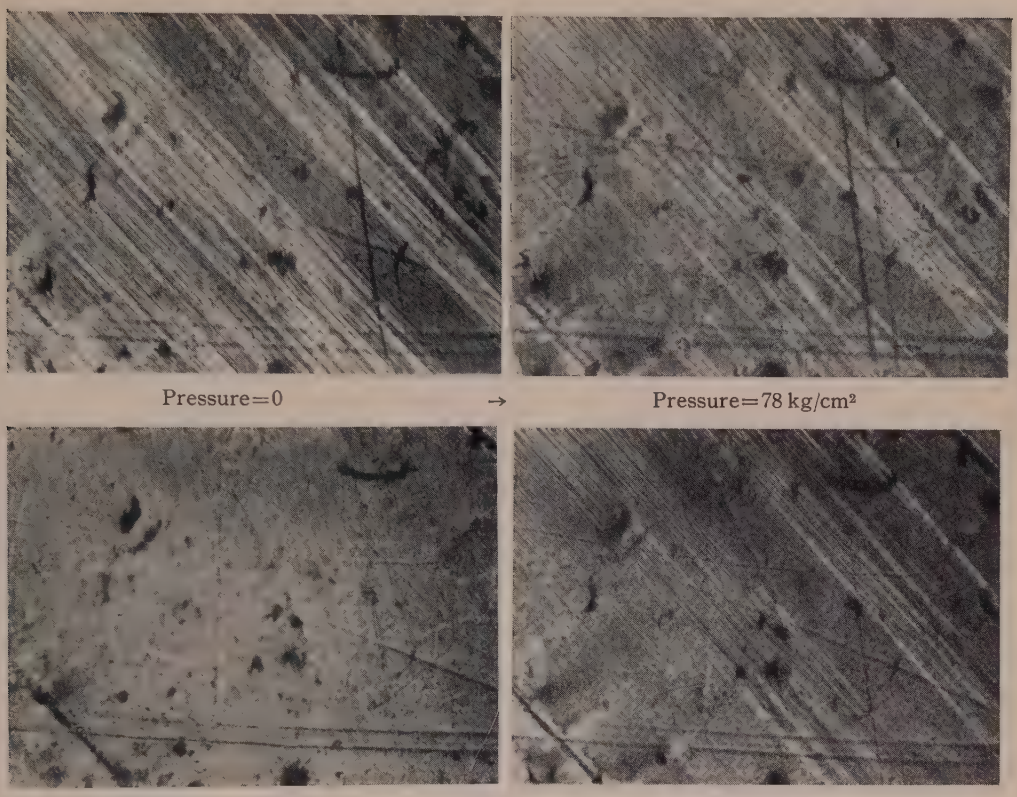

Fig. 14. Response of the domain structure to the shearing stress Z_x in the 90.5 per cent Y-cut specimen, at $-186°C$.

$\alpha=1.4900$, $\beta=1.4920$, $\gamma=1.4954$, for NaK-tartrate,
$\alpha=1.4953$, $\beta=1.4985$, $\gamma=1.4996$, for $NaNH_4$-tartrate.

On using these values, we obtain for the optical angle (2Ω):

$\Omega=37°20'$ for NaK-tartrate,
$\Omega=59°40'$ for $NaNH_4$-tartrate.

Hence NaK-tartrate is optically positive. As known well, the optical plane is (010), and the acute bisectrix is the a axis. We get therefore the following identification:

$n_a=\gamma$, $n_b=\beta$, $n_c=\alpha$, for NaK-tartrate,

where n_a, n_b and n_c denote the refractive indices for the light of which the electric vector lies along the crystallographic a, b and c axes, respectively. On the other hand, $NaNH_4$-tartrate is optically negative. We have confirmed that the optical plane is (100) and the acute bisectrix is the c axis. We get therefore

$n_a=\beta$, $n_b=\gamma$, $n_c=\alpha$, for $NaNH_4$-tartrate.

We have examined the crystals at room temperature in convergent polarized light. In NaK-tartrate the optical axes lie in fact in (010) plane. The optical axes approach gradually the crystallographic c axis on increasing the concentration of $NaNH_4$-tartrate. It seems that the two optical axes coincide with the c axis at the concentration of about 65 per cent, though we could not obtain a uniaxial figure, since the crystal of requisite composition was missing. On further increasing the concentration of $NaNH_4$-tartrate the optical axes get away from the crystallographic c axis. If the refractive indices change linearly with the composition, the optically uniaxial crystal must be located at somewhere

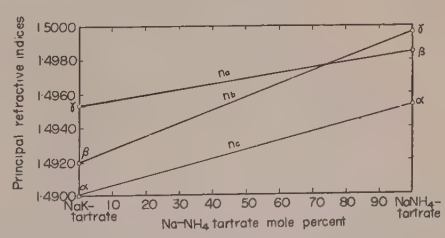

Fig. 15. Refractive indices *vs.* composition curves.

about 74 percent as shown in Fig. 15. The reason of the discrepancy between our observation and the expectation derived from Fig. 15 is not clear yet.

§ 7. Conclusion and Discussion

The phase diagram summarizing the result of the present investigation is shown in Fig. 16, where the phase boundaries obtained by Kurtschatow *et al.* and Melmed *et al.* are also included for the convenience of comparison.

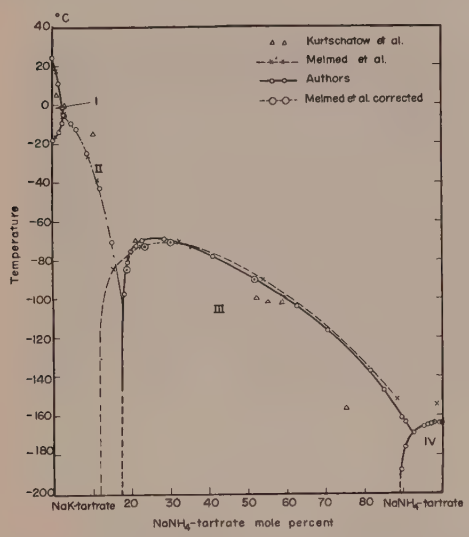

Fig. 16. The phase diagram of Na(K-NH_4)-tartrate mixed crystals. The chain line shows the temperature where the broad dielectric peak appears.

The phase boundary of the region I is in good agreement with those determined by previous investigators. On the other hand, the phase boundary on the left hand side of the region III appears to be slightly different from that determined by Melmed *et al.* The discrepancy is, however, mainly due to the fact that they used directly the chemically analized values themselves, in place of the values which should be obtained if they used their own curve which is shown in Fig. 1. In fact, if we were allowed to correct their value by means of their curve, it turns out that their phase boundary shifts to agree quite well with ours as shown by dotted lines in the figure.

In the phase diagram, the phase I is ferroelectric and the crystals in this temperature range are monoclinic, while the phase II is paraelectric and the crystals in this temperature range are orthorhombic. The phase III is ferroelectric and the crystals are monoclinic with the same type of spontaneous shear strain y_x^0 as those in the phase I. On the other hand, the phase IV is another ferroelectric phase with spontaneous polarization parallel to the *b* axis and crystals in the temperature range are monoclinic owing to the spontaneous shear strain z_x^0.

The properties of the crystals belonging to the group IV are very peculiar as compared with other groups. The Curie-Weiss law does not hold above the transition point. The transition seems to be of the first order. The spontaneous polarization is independent of temperatures below the transition point.

It is of some interest to notice that direction of spontaneous polarization in NaK-tartrate as well as $NaNH_4$-tartrate is parallel to the direction of the maximum refractive index, although the correspondence is actually not so perfect as to give the uniaxial crystal just at the boundary between the groups III and IV. The correspondence should become better at low temperatures, if the optically uniaxial composition would go towards the right as the temperature is decreased. But the indices *vs.* temperature formulae given by Lavinir predicts that the contrary is the case. We have observed that it really goes towards NaK-tartrate side from the room temperature values with decreasing temperature.

The authors wish to express their hearty thanks to Professor H. Takahasi of Tokyo University, Dr. M. Marutake of Kobayashi Institute, Dr. G. Shirane of Westinghause Research Laboratories, Dr. E. Sawaguchi of Electrotechnical Laboratory, Dr. T. Mitsui of Pensylvania State University, and Dr. H. Maniwa of Tokyo Institute of Technology, for their very illuminating discussions. The chemical analysis of all the specimens has been carried out by Dr. T. Katsura under the direction of Professor I. Iwasaki of Tokyo Institute of Technology. The authors greatly appreciate the kindness of both of them. The authors are also indebted to Mr. S. Takayanagi for his cooperation in this study in its early stage. The expenditure of this study has been defrayed from the Science Research Grant of the Ministry of Education.

References

1) Y. Takagi and Y. Makita: J. Phys. Soc. Japan **13** (1958) 272
2) B. Kurtschatow and B. Eremejew: Z. Sowj. **1** (1932) 140
3) A. Melmed, F. Jona and R. Pepinsky: Tech. Rept. No. 20 Centract AF 33 (616)-2133, Wright Air Development Center, (1954)
4) V. A. Yurin: Izbestia Akad. Nauk. SSSR Ser. Fiziki, **21** No. 3 (1957) 329
5) T. Shimizu: Japanese Journ. Phys. **I.** 9-10 (1923) 107
6) T. Mitsui and J. Furuichi: Phys. Rev. **90** (1953) 193
7) A. Lavinir: Bull. Soc. Fr. Min. **17** (1894) 153

JOURNAL OF THE PHYSICAL SOCIETY OF JAPAN Vol. 13, No. 4, APRIL, 1958

The Change of Carrier Concentration in the Simple Semiconductors with Static Magnetic Field

By Yasutada UEMURA and Masaharu INOUE

Department of Physics, University of Tokyo

(Received January 11, 1958)

The change of carrier-concentration with static magnetic field is discussed by using the simple model of the semiconductors. The attention is mainly focused on whether the concentration of free carriers increases or decreases with the field. The situations are classified into three cases [A], [B] and [C] according to the degree of concentration of the centers.

[A] The concentration of the trapping centers is dilute and a center can trap only one carrier. In this case the carrier concentration n is a monotonously decreasing function of the field H, namely $dn/dH^2 \geq 0$,

[B] The impurity levels lose the locality and form a band so called "impurity band," however, the width of which is still smaller than kT. In this case we obtain

$$(dn/dH^2)_{\text{weak } H} > 0 \qquad \text{when } (m/m^*) < \sqrt{3\delta}$$
$$(dn/dH^2)_{\text{weak } H} < 0 \qquad \text{when } (m/m^*) > \sqrt{3\delta}$$

where m^* is the effective mass of carriers and δ means the degree of compensation, namely $\delta = (N_d - N_c)/Nd$.

[C] The width of impurity band is larger than kT and the Fermi-level ζ_0 at $H=0$ lies in this band. In this case we obtain

$$(dn/dH)_{\text{weak } H} > 0 \qquad \text{when } (m/m^*) < \sqrt{3(1-s)}$$

where

$$s = kT\left[\frac{\partial}{\partial E}\log D(E)\right]_{E=\zeta_0}.$$

$D(E)$ means the state density of the impurity band.

It seems that there is no possibility to explain the so-called "magneto-conductive" phenomena observed in p-InSb from this stand-point.

§ 1. Introduction

The aim of this paper is to investigate the change of carrier-concentraction in the simple semiconductors with the static magnetic field. Our attention is mainly focused on whether the concentration increases or decreaces with the field. This problem has been considered by several authors[(1)(2)(3)] to explain the increase of the carrier-concentration due to the magnetic field, so called magneto-conductive phenomena, observed in the p-type InSb. The characteristics of their standpoints and

Table I

	Mackintosh[1]	Stevens[2]	Appel[3]	This paper
The effects taken into account	spin paramagnetism of trapped electrons	spin paramagnetism of current carriers and trapped electrons	orbital dismagnetism of current carriers. spin paramagnetism of trapped electrons	orbital dia and spin paramagnetism of current carriers. spin paramagnetism of trapped electrons
The distribution function for trapped electrons	$\frac{1/2}{1+\exp\frac{E_{\pm}-\zeta}{kT}}$	$\frac{1/2}{1+\exp\frac{E_{\pm}-\zeta}{kT}}$	$\frac{1/2}{1+\exp\frac{E_{\pm}-\zeta}{kT}}$	The situations are classified into three cases according to the concentration of trapping centers
The statistics for current carriers	Fermi	Fermi	Maxwell Boltzmann	Maxwell Boltzmann
applied to	InSb-p	general	InSb-p	general
whether magnetoconductive phenomena in InSb-p can be explained or not	Yes		No	perhaps No

their results are summarized in the Table I, comparing with those of this paper shown in the last column of the table.

In the former researches there remained some questions about the choice of the distribution function for the trapped state of carriers. As shown in the Table I, they used the distribution function $f_{\pm}=\frac{1}{2}[\exp(E_{\pm}-\zeta/kT)+1]^{-1}$, which would lead us to the conclusion that the distribution function of Trapped carriers without the magnetic field might be $f=f_{+}+f_{-}=[\exp(E-\zeta/kT)+1]^{-1}$. This conclusion is not correct and it is supposed that it should be $f=[\frac{1}{2}\exp(E-\zeta/kT)+1]^{-1}$ when a trapping center can trap only one electron and it should be $f=2[\exp(E-\zeta/kT)+1]^{-1}$ when a trapping center can trap two electrons. In order to discuss the change of carrier concentration, it is important that the correct types of distribution function are used for the different concentrations of the trapping centers. In this paper we classify the situations into three typical cases and for each of them we took the correct types of the distribution function of the trapped carriers. The effect of the compensation of carriers which was neglected in the former papers is also considered in this paper.

For the simplicity we assume that the distribution of the free carriers is classical, and then discuss the effects of the orbital diamagnetism and spin paramagnetism on the change of the carrier-concentration with the static magnetic field.

§ 2. A Simple Model

Here we take a simple model of a semiconduction which has one conduction band, a single donor level, and some acceptors. The levels of acceptors are assumed that they are sufficiently far apart from the level of donors in the energy scale. We further assume that the energy surface of the free carriers is spherical and the effective mass of them is m^*. (Fig. 1A).

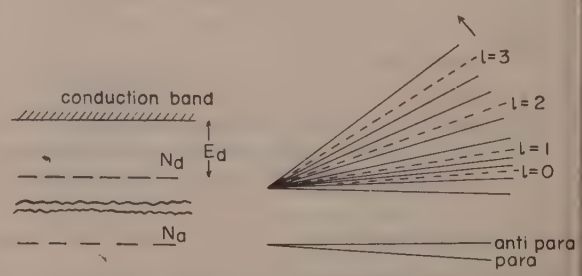

Fig. 1. (a, b)

If the magnetic field H is applied in the z direction the motion of the free carriers in x-y plane is orbitally quantized. Their states

are described by the discrete quantum number l and the momentum p_z in the z direction. The energy of a free carrier $E_\pm$ consists of three terms, i.e. the kinetic energy in the z direction, the quantized energy of the circular motion in the x-y plane which is represented by the energy of a simple harmonic oscillator, and the Zeeman-energy due to the spin of the carrier.

$$E_\pm = \frac{p_z^2}{2m^*} + 2\mu^* H(l+\tfrac{1}{2}) \mp \mu H$$

$$\mu = \frac{e\hbar}{2m^*} \qquad \mu^* = \frac{e\hbar}{2m^* c}$$

$$l = 0, 1, 2, \cdots$$

In the Fig. 1 (B), the field dependence of $E_\pm$ is shown when $p_z = 0$.

For the trapped state, only the effect of the spin paramagnetism is taken into account, and the effect of the orbital diamagnetism is negelected in this paper. It is noticed that the orbital diamagnetism of trapped carriers should be included when the m^* is small and the field H is large.

By assuming the classical distribution of the free carriers, their concentration $n_\pm$ is expressed as follows:

$$n_\pm = \frac{4\pi}{h^3} \frac{\hbar e H}{c} \sum_{l=0}^{\infty} \int_{-\infty}^{+\infty} dp_z \exp\left(\frac{\zeta + E_\pm}{kT}\right)$$

where $(\pm)$ refers to+or−spin respectively, and ζ means the Fermi-energy.

For the convenience, let us introduce the following nondimensional parameters such as ε, η, θ and θ^* which are defined by:

$$\varepsilon \equiv \frac{E_d}{kT} \qquad \eta = \frac{\zeta}{kT} \qquad \theta \equiv \frac{\mu H}{kT}$$

$$\theta^* = \frac{\mu^* H}{kT}$$

As to the concentrations we introduce the following quantities:

$$N_0^* \equiv 2\left(\frac{2\pi m^* kT}{h^2}\right)^{3/2} \qquad A \equiv \frac{N_0^* e^\varepsilon}{2N_d}$$

$$\delta \equiv \frac{N_d - N_a}{N_d}$$

where N_d and N_a are the concentrations of the donors and acceptors. The non-dimensional parameter δ represents the degree of the compensation and is assumed to be $1 \geqq \delta > 0$. In the usual cases, A is sufficiently smaller than 1 especially at the low temperature.

By using these notations, the concentration of free carriers n can be written as follows:

$$n = n_+ + n_-$$

$$n_\pm = \tfrac{1}{2} N_0^* e^\eta \frac{\theta}{\sinh\theta^*} e^{\pm\theta} \qquad (1)$$

Fermi-energy η in the above equation should be determined by the neutrality condition which is

$$n_+ + n_- + N_+ + N_- = N_d - N_a \qquad (2)$$

$N_\pm$ is the concentrations of trapped electrons. The suffix $(\pm)$ corresponds to their $(\pm)$ spin. In the following three sections, we get three different expressions of $n(H)$ from the equation (2) by using the best fitted forms of $N_\pm$ in each cases.

§ 3. Case A. The Concentration of the Donor is Dilute and a Donor-center can Trap Only One Carrier

In this case $N_\pm$ is not given by the Fermi-distribution in a perfect sense of the one body approximation but is given by the following modified form:[4][5]

$$N_\pm = \frac{N_d}{1 + e^{\varepsilon \mp \theta - \eta} + e^{\mp 2\theta}} \qquad (3)$$

By using the equations (1), (2), (3), n can be obtained as follows:

$$\frac{n}{N_d} = \frac{1}{2}\left[-(a+1-\delta) + \sqrt{(a+1-\delta)^2 + 4\delta a}\right]$$

$$a \equiv A\theta^*/\sinh\theta^* \qquad (4)$$

The equation (4) can be written approximately in the simple expressions when $a \ll 1$.

$$\frac{n}{N_d} \doteqdot \begin{cases} \sqrt{a} & (\delta = 1) \\ \dfrac{\delta}{1-\delta} a & (a \ll (1-\delta)^2) \end{cases}$$

Some remarks should be made in the equation (4), that is to say, n does not include θ. This means that the effect of the spin paramagnetisms does not appear explicitly. As it is easily proved that dn/dH^2 is always negative in the case A, so n is a monotonously decreasing function of H.

§ 4. Case B. The Donor Levels Lose the Locality and from a Band so Called "Impurity Band", However, the Width of which is Still Smaller than kT.

In this case the Fermi-destribution function can be applied to the trapped electrons and $N_\pm$ is given by:

$$N_{\pm}=\frac{N_d}{1+e^{\varepsilon\mp\theta-\eta}} \tag{5}$$

By introducing the quantities z, β_1 and β_2 which are defined by

$$Z\equiv n/N_dA$$

$$\beta_{\frac{1}{2}}\equiv\frac{\theta^*}{\sinh\theta^*}(1+e^{\mp 2\theta}) \tag{6}$$

and substituting (1) and (5) into (2), the following equation is obtained:

$$A+\frac{1}{Z+\beta_1}+\frac{1}{Z+\beta_2}=\frac{\delta}{Z} \tag{7}$$

If we get the solution z of this equation, we can see how the concentration of carriers n depends on the magnetic fild H through β_1 and β_2. But the exact root z is complicated and is not convenient to understand the dependence of n on the parameters A, β_1, β_2 and δ. In stead of (5). Appel used $N_{\pm}=\frac{1}{2}N_d/1+e^{\varepsilon\mp\theta-\eta}$ and solved the equation (7) in the cuse $\delta=1$.

In order to obtain the physical insight of the situation we consider to solve the equation (7) approximately. As to the parameter A, we mentioned in § 2 that A is sufficiently smaller than 1 ($A\ll 1$), so that as the first approximation we neglect the first term of the left side of equation (7). The root $\bar{z}$ of this approximate equation can be easily obtained as follows:

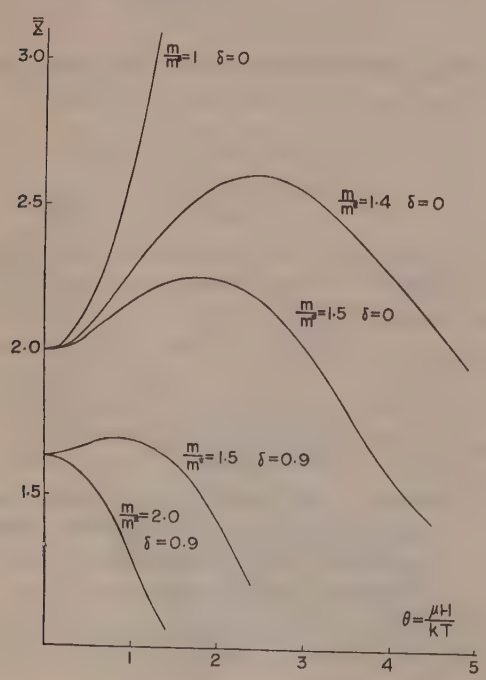

Fig. 2.

$$\bar{z}=\frac{1}{2(2-\delta)}[(\beta_1+\beta_2)(\delta-1)$$
$$+\sqrt{(\beta_1+\beta_2)^2(\delta-1)^2+4(2-\delta)\delta\beta_1\beta_2}] \tag{8}$$

The change of $\bar{z}$ with θ is shown in the Fig. 2.

The behavior of $\bar{z}$ in the range of the weak magnetic field can be seen by expanding the formula (8) as the power series of θ.

$$\bar{z}\doteqdot\frac{2\delta}{2-\delta}[1+\tfrac{1}{2}\theta^2(\delta-\tfrac{1}{3}r^2)+\cdots\cdot]$$
$$r\equiv m/m^* \tag{9}$$

The expression (9) means that

$$\left(\frac{dn}{dH^2}\right)_{\text{weak }H}>0 \quad \text{if } \frac{m}{m^*}<\sqrt{3\delta}$$

$$\left(\frac{dn}{dH^2}\right)_{\text{weak }H}<0 \quad \text{if } \frac{m}{m^*}>\sqrt{3\delta}$$

We can see that the effect of the orbital diamagnetism exceeds the effect of the spin paramagnetism when the effective mass m^* of free carriers is small, ($m^*<m/\sqrt{3\delta}$) and the concentration n decreases with the magnetic field. In other words we can expect the increase of n with the magnetic field only when the effective mass of free carriers is not too small ($m^*>m/\sqrt{3\delta}$) and the effect of the spin paramagnetism is predominant.

§ 5. Case C. The Concentration of the Donors is sufficiently Dense and the Width of Their "Impurity Band" is Larger than kT. The Fermi-level ζ_0 at $H=0$ lies in this Band.

This case was not discussed in the former papers, but is supposed to be realized in the most semiconductors at the low temperature.

The total density N of electrons in the impurity band at $H=0$ is as follows:

$$N=2\int_{-\infty}^{+\infty}\frac{D(E)dE}{1+e^{\varepsilon-\eta_0}}$$

where η_0 means the Fermi-level at $H=0$ and $D(E)$ is the state density of impurity band.

The Fermi-level $\eta(H)$ can be determined approximately by the equation:

$$F(\eta+\theta;\ T)+F(\eta-\theta;\ T)\doteqdot 2F(\eta_0;\ T) \tag{10}$$

The function $F(x;\ T)$ is defined by the following integral:

$$F(x;\ T)=\int_{-\infty}^{+\infty}\frac{\rho(\varepsilon kT)}{1+e^{\varepsilon-x}}d\varepsilon \tag{11}$$

where

$$\rho=\rho(E)=\frac{\Delta E}{N_d}D(E)$$

in which ΔE means the width of impurity band. The quantity ρ is non-dimensional and corresponds to the state density of the impurity band.

To see the behavior of η in the small range of θ, the expansion is made in (10) and if we put

$$\eta=\eta_0+\gamma$$

Then γ is given by:

$$\gamma=-\frac{F''}{2F'}\theta^2$$

where F' and F'' mean dF/dx and d^2F/d^2x respectively.

By introducing the parameter s which is defined by:

$$s=\left(\frac{F''}{F'}\right)_{\eta=\eta_0}=\left[\frac{d}{d\eta}\log F'\right]_{\eta=\eta_0} \tag{12}$$

the γ is written as follows:

$$\gamma=-\tfrac{1}{2}s\theta^2 \tag{13}$$

By using the equation (13) and (1) we get:

$$n=n_{H=0}\frac{\theta^*}{\sinh\theta^*}\cosh\theta e^{\gamma}$$
$$\doteqdot n_{H=0}\left[1+\frac{1}{2}\theta^2\left(1-s-\frac{r^2}{3}\right)+\cdots\right] \tag{14}$$

In (14) we can see that $(dn/dH^2)_{\text{weak } H}$ is positive if $(m/m^*)<\sqrt{3(1-s)}$.

When kT is sufficiently small and the carriers in the impurity can be considered as the Fermi-gas, the equation (13) becomes

$$s\doteqdot kT\left[\frac{\partial}{\partial E}\rho(E)/\rho(E)\right]_{E=\zeta_0} \tag{15}$$

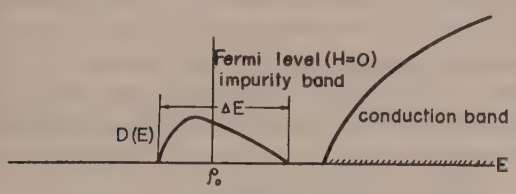

Fig. 3.

In order to be $(dn/dH^2)_{\text{weak } H}>0$ in the case of the small effective mass m^* of the free carriers, s should be negative such as the case shown in the Fig. 3.

§ 6. Discussions

Above results suggest us that it is hard to be $(dn/dH^2)_{\text{weak } H}>0$ for the large m/m^* because of the effect of the orbital diamagnetism. In the cases A and B we cannot reduce the origin of so-called "magneto-conductive" phenomena in the p-InSb to the change of carrier concentration due to magnetic field. However, if the situation is such as the case C the conclusion is not definite. It will be needed to know n and $N=N_++N_-$ by the phenomenological treatment of the impurity band and to consider whether the phenomena can be explained by the results of equation (14) or not where we take into account the large difference of mobilities of carriers between in the impurity band and in the conduction band. But the last possibility to explain the "magneto-conductive". phenomena seems to be rare when we see that n itself is very small at the sufficiently tow temperature. Then we may write the answer "perhaps no" in the last column of the Table I.

§ 7. Acknowledgement

The authors express their cordial thanks to the valuable discussions given by Prof. R. Kubo and the members of his research group. This research was partialy supported by the research grant of the Ministry of Education.

References

1) I. M. Mackintosh: Proc. Phys. Soc. A**69** (1956) 403.
2) K. W. Stevens: Proc. Phys. Soc. A**69** (1956) 406.
3) J. Appel: Z. Naturforsch. **11**a (1956) 689.
4) P. T. Landsberg: Proc. Phys. Soc. A**65** (1952) 604.
5) M. Tsuji: Memories, Fac. Sci. Kyushu Univ. B**1** (1954) 106.

JOURNAL OF THE PHYSICAL SOCIETY OF JAPAN Vol. 13, No. 4, APRIL, 1958

The Change of Carrier Concentration in the Graphite with Static Magnetic Field

By Yasutada UEMURA and Masaharu INOUE

Department of Physics, University of Tokyo

(Received January 11, 1958)

The change of carrier concentration with static magnetic field in a single crystal of graphite is considered and the Hall coefficient R is discussed from this point of view.

The Wallace's model of the two dimensional zone and its orbital quantization proposed by McClure are the starting point of the analysis. By comparing with the Kinchin's experiment we propose that the acceptor levels exist at 11×10^{-3} eV. above the bottom of the conduction band and their concentration is 1.7×10^{18}/c.c.. As to the Wallace's resonance integral γ_0 we estimate its value as 1.43 eV. semiempirically. The ratio of the mobilities of two carriers $b=\mu_p/\mu_n=0.87$ gives the best fit of R at the low temperature under the strong magnetic field. By using these resonable values of the parameters the Hall coefficient R is plotted as the function of temperature and magnetic field. The agreement with experimental data may be good except the low field region. The origins of discrepancy are discussed.

§ 1. Introduction

In the previous paper[1] it has been considered how the concentration of carriers changes with the static magnetic field in a simple extrinsic semiconductor. In this paper we treat the carrier concentration in the graphite as an example of intrinsic case and would like to propose that the interesting change of the Hall coefficient with magnetic field observed by Kinchin[2] in a single crystal of graphite may be interpreted from this point of view.

The model of the graphite crystal assumed in this paper is the simple one in which we take the two dimensional zone treated by Wallace[3] as the band structure of the host crystal which has a single acceptor level in the conduction band. We further assume that the mobility μ_n of conduction electrons is slightly larger than that of holes μ_p and their ratio μ_p/μ_n is denoted by b.

In the § 2 we review briefly the interesting nature of the Hall effect in the single crystal of graphite observed by Kinchin and point out some possible ways to interpret it. In this paper we pick up the one of them in which the change of carrier concentration due to the magnetic field is mainly considered. In the § 3, the orbital quantization of the Wallace's two dimensional zone is discussed and the interband effect pointed by McClure[4] is especially mentioned. In the § 4, the distribution of carriers is determined in the usual way and the concentration of electrons and holes is calculated as the functions of the temperature and the magnetic field. In the § 5, the parameters appeared in our model such as γ_0, one of the reasonance integrals defined by Wallace, b, E_a, the energy separation between the acceptor level and the bottom of canduction band, and the acceptor density N_a, are determined semiempirically by comparing the result of calculation in the § 4 with the observed data by Kinchin. Further we examine the behavior of the Hall coefficient R in the whole range of the temperature and the field by using the estimated values of the parameters. The agreement with experiment seems to be good except in the low field region. In the last section (§ 6) the origins of the discrepancy are discussed and the relation between the galvano-magnetic phenomena and the other such as the de-Haas van Alphen effect and the diamagnetic susceptibility is pointed out briefly.

§ 2. The Hall Effect of Graphite

In 1953 Kinchin[2] observed the Hall effect of the single crystal of the natural graphite in which he applied the magnetic field H along the c-axis of the crystal. As shown in the Fig. 1, his result exhibits the very inter-

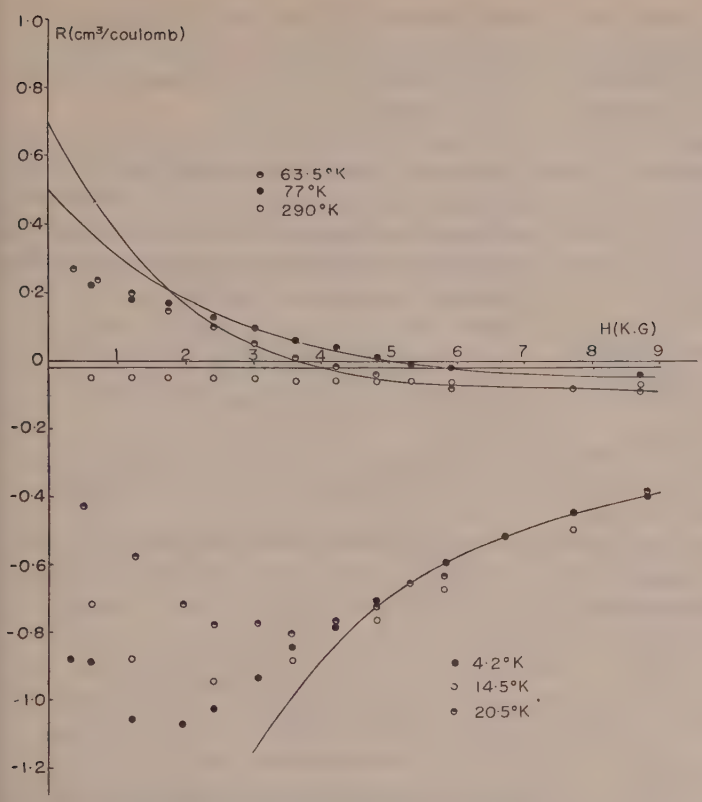

Fig. 1. The Hall coefficient of Graphie. The solid lines are calculated values and experimental data are taken from Kinchin.

esting nature especially in the field dependence of the Hall coefficient R and the satisfactory explanation of his data has not been given by any one else.

The Fig. 1 shows that in the limit of low magnetic field ($H \to 0$) the sign of R is negative in the low temperature range. As the temperature rises, it changes to positive, but in the sufficiently high temperature it becomes negative again. In order to interpret this behavior Kinchin proposed that the crystal contains the acceptors and the level of which lies in the conduction band. He assumed that the mobility μ_n of the electrons is larger than that of holes μ_p so that the Hall coefficient R is negative in the low temperature range. As the temperature rises the acceptors begin to trap the electrons and the concentration of free electrons becomes smaller than that of holes to change the sign of R. However if the temperature reaches sufficiently high the effect of trapped electron should be neglected compared with the large concentration of free carriers and then the sign of R is determined again by the difference of the mobilities between electrons and holes. Kinchin suggested in his paper that E_a is 6×10^{-3} eV., N_a is 10^{18}/c.c. and the value of $b=\mu_p/\mu_n$ falls between 0.8 and 1.

What is the origin of the field dependence of R? Several origins may be considered to give the possible explanations of this interesting nature. We mention the three of them.

(i) In the recent experiment of the cyclotron resonance[5),6)] of the graphite it is shown that there are four kinds of current carriers such as the majority electrons and holes and the minority electrons and holes. It may be possible to interpret the field dependence of R by the usual treatment of the theory of conduction if we take into account the four components of the current carriers. The existence of carriers which have the very light mass seems to be preferable.

(ii) The radious of the circular motion of free carriers under the strong magnetic field is comparable to the mean free path of them in the low temperature range, so that we may expect some anomalous effects in the scattering processes, such as that the relaxation time depends on the magnetic field. The origin of the interesting field dependence of R may be attributed to the anomalous effects mentioned above.

(iii) The diamagnetic susceptibility of the graphite is comparatively large so that it is possible that the change of carrier concentration due to the magnetic field may play an important role in the field dependence of R.

At the present situation there are no detailed discussions about these possibilities. In this paper the last case is picked up so that we assume that the Hall coefficient R is given in the following expression

$$R=\frac{3\pi}{8|e|}\frac{1}{p}\frac{b^2-(n/p)}{[b+(n/p)]^2} \qquad (1)$$

which is obtained by the usual theory of conduction in the semiconductor containing free

electrons and free holes as the current carriers, where n and p mean respectively the concentration of them. The field dependence of R is given by (1) in which n and p depend on the magnetic field as the result of the orbital quantization. Exactly speaking the factor $3\pi/8$ in (1) should be 1 if the carriers are degenerate, however, the factor is not important in the following discussions so that we always use (1) approximately.

§ 3. The Two Dimensional Wallace's Model and its Orbital Quantization due to the Magnetic Field

The investigation of the band structure of the graphite has been made by many authors[3),7),8),9),10)] in both theoretical and experimental aspects. In this paper we take rather simple one in which we assume the two dimensional model (single hexagonal layer) after Wallace[3)]. According to his results, the Hamiltonian $\mathscr{H}$ is given by:

$$\mathscr{H}=\begin{pmatrix} H_{11} & H_{12} \\ H_{21} & H_{22} \end{pmatrix} \tag{2}$$

where

$$H_{11}=H_{22}$$
$$=E_0-2\gamma_0'(\cos\kappa_y a+2\cos\frac{\sqrt{3}\,\kappa_x a}{2}\cos\frac{\kappa_y a}{2}$$
$$H_{12}=H_{21}^*$$
$$=-\gamma_0(e^{-i(1/\sqrt{3})\kappa_x a}+2\cos\tfrac{1}{2}\kappa_y a\, e^{i(1/2\sqrt{3})\kappa_x a})\,.$$

The parameters γ_0 and γ_0' are the resonance integrals and $a=2.46$Å is a distance between the nearest identical atoms in the hexagonal layer. By using above $\mathscr{H}$ it is shown that there are two bands, the one is called the conduction band and the other is called the valence band, which touch each other at the corners of the first Brillouin zone. The attention may be focussed on the structure near the corner points and the approximate expression of (2) near this point is given as follows

$$\mathscr{H}=\begin{pmatrix} -\frac{3}{4}\gamma_0'a^2[\kappa_x^2+\kappa_y^2] & \hbar v i e^{(\pi/3)i}[\kappa_x+i\kappa_y] \\ -\hbar v i e^{-(\pi/3)i}[\kappa_x-i\kappa_y] & -\frac{3}{4}\gamma_0'a^2[\kappa_x^2+\kappa_y^2] \end{pmatrix} \tag{3}$$

where $\hbar v\equiv(\sqrt{3}/2)\gamma_0 a$ and the energy is measured from the origin of $E_0+3\gamma_0'$ and κ_x, κ_y are measured from the corner of the first Brillouin zone.

Let be the magnetic field H applied in the z direction. In this case κ_x and κ_y in (3) are not commutable each other and by considering the method of Kohn and Luttinger[7)] they are regarded as the operators which satisfy the following commutation relation

$$[\kappa_x,\kappa_y]=\frac{1}{i}\frac{eH}{\hbar c}\,. \tag{4}$$

By introducing the operators κ_+ and κ_- defined by

$$\kappa_+\equiv\frac{1}{\sqrt{2}}[\kappa_x+i\kappa_y]\,,\quad \kappa_-\equiv\frac{1}{\sqrt{2}}[\kappa_x-i\kappa_y]$$

the following wellknown relations are obtained

$$\begin{aligned} &[\kappa_-,\kappa_+]=\frac{eH}{\hbar c}\equiv s \\ &\kappa_- u_n=(ns)^{1/2}u_{n-1} \\ &\kappa_+ u_n=[(n+1)s]^{1/2}u_{n+1} \\ &\kappa_+\kappa_- u_n=nsu_n \\ &\kappa_-\kappa_+ u_n=(n+1)su_n \end{aligned} \tag{5}$$

where u_n means the eigenfunction of a simple harmonic oscillator and n indicates its quantum number.

The $\mathscr{H}$ in (3) is written by κ_+ and κ_- as follows:

$$\mathscr{H}=\begin{pmatrix} -\frac{3}{4}\gamma_0'a^2[\kappa_+\kappa_-+\kappa_-\kappa_+] & \sqrt{2}\,\hbar v i e^{(\pi/3)i}\kappa_+ \\ -\sqrt{2}\,\hbar v i e^{-(\pi/3)i}\kappa_- & -\frac{3}{4}\gamma_0'a^2[\kappa_+\kappa_-+\kappa_-\kappa_+] \end{pmatrix}.$$

The Schrodinger equation is

$$\mathscr{H}\Psi=\varepsilon\Psi \tag{6}$$

in which we use the above expression of $\mathscr{H}$.

The solution of (6) is easily obtained if we put Ψ as follows

$$\Psi=\begin{pmatrix} c_1u_n \\ c_2u_{n-1} \end{pmatrix} \qquad \text{for} \quad n\geq 1$$

$$\Psi=\begin{pmatrix} c_1'u_0 \\ 0 \end{pmatrix} \qquad \text{for} \quad n=0$$

where c_1, c_2 and c_1' should be determined by the following equations

$$\begin{pmatrix} -\frac{3}{4}\gamma_0'a^2[2n+1]s & \sqrt{2}\,\hbar v i e^{(\pi/3)i}[ns]^{1/2} \\ -\sqrt{2}\,\hbar v i e^{-(\pi/3)i}(ns)^{1/2} & -\frac{3}{4}\gamma_0'a^2[2n-1]s \end{pmatrix}\begin{pmatrix} c_1 \\ c_2 \end{pmatrix}=\varepsilon\begin{pmatrix} c_1 \\ c_2 \end{pmatrix} \qquad \text{for} \quad n\geq 1 \tag{7}$$

$$\begin{pmatrix} -\frac{3}{4}\gamma_0'a^2 s & 0 \\ 0 & 0 \end{pmatrix}\begin{pmatrix} c_1' \\ 0 \end{pmatrix}=\varepsilon\begin{pmatrix} c_1' \\ 0 \end{pmatrix} \qquad \text{for} \quad n=0\,. \tag{8}$$

The eigen value $\mathcal{E}$ of the equations (7) and (8) is solved as follows.

$$\left.\begin{aligned} \mathcal{E}_n &= -\tfrac{3}{4}\gamma_0' a^2 s \cdot 2n \pm \sqrt{(\tfrac{3}{4}\gamma_0' a^2)^2 s^2 + 2\hbar^2 v^2 n s} && \text{for } n \geq 1 \\ \mathcal{E}_0 &= -\tfrac{3}{4}\gamma_0' a^2 s && \text{for } n = 0 . \end{aligned}\right\} \tag{9}$$

In the following discussions of the Hall effect the role of γ_0' is not important, so that we take into account the resonance integral only between the nearest neighbors and neglect γ_0' as the approximation.

Then the energy levels (9) are reduced to the following simple expression.

$$\left.\begin{aligned} \mathcal{E}_l &= \pm\nu\sqrt{sl} \qquad (l=0, 1, 2, \cdots) \\ \nu &\equiv \sqrt{2}\,\hbar v = \sqrt{3/2}\,\gamma_0 a . \end{aligned}\right\} \tag{9'}$$

The state density w of each levels is given by (10)

$$w = qs = 8(2\pi)^{-3}(2\pi/c_L)(2\pi s) \tag{10}$$

where $c_L = 6.74$Å is the distance between the identical layers. The energy spectra of (9′) and the state density (10) were at first obtained by McClure[4] and were used to discuss the diamagnetic susceptibility of the graphite. McClure attributed the origin of the comparatively large value of the susceptibility to the anomalous energy spectra of (9′) in which the 0-point energy disappears owing to a kind of the interband effect. By comparing with the observed data McClure estimated the value of γ_0 as 2.6 eV semiempilically. We would like to show in the following discussions that in the field dependence of the Hall coefficient R this effect may also play an important role.

The orbital quantization due to the magnetic field is discussed for the case of a more complicated model in the same way, however its details will be discussed in the forthcoming paper. (See the additional note.)

§ 4. The Concentration of Carriers

By using the results of (9′) and (10) the concentration of the free electrons n and the free holes p are given as follows

$$\left.\begin{aligned} n &= \frac{q(kT)^2}{\nu^2}\sum_{l=0}^{\infty}\frac{\alpha}{1+e^{\sqrt{\alpha l}-\eta}} \\ &= \frac{q(kT)^2}{\nu^2}F(\alpha;\,-\eta) \\ p &= \frac{q(kT)^2}{\nu^2}\sum_{l=0}^{\infty}\frac{\alpha}{1+e^{\sqrt{\alpha l}+\eta}} \\ &= \frac{q(kT)^2}{\nu^2}F(\alpha;\,+\eta) \end{aligned}\right\} \tag{11}$$

where α is the nondimensional parameter defined by

$$\left.\begin{aligned} \alpha &\equiv \frac{\nu^2 s}{(kT)^2} = \left(\frac{2\mu H}{kT}\right)\frac{3}{2}\left(\frac{\gamma_0}{kT}\right)\left(\frac{\gamma_0}{\hbar^2/ma^2}\right) \\ \mu &\equiv \frac{e\hbar}{2mc} \end{aligned}\right\} \tag{12}$$

and η is the Fermi energy divided by kT.

The concentration n of electrons which are trapped in the acceptor level is given by

$$n_a = \frac{2N_a}{1+e^{\varepsilon_a-\eta}} ; \qquad \varepsilon_a = \frac{E_a}{kT} . \tag{13}$$

Because of the large effect of the orbital diamagnetism we neglect the effect of the spin paramagnetism for the simplicity. The Fermi level is determined by the following neutrality condition.

$$F(\alpha;\,\eta) = F(\alpha;\,-\eta) + \frac{2\nu^2 N_a}{q(kT)^2}\,\frac{1}{1+e^{\varepsilon_a-\eta}} . \tag{14}$$

If the approximation is allowed that the distributions of both carriers can be treated as classical (non-degenerate), $F(\alpha, \pm\eta)$ is written as follows:

$$F(\alpha, \pm\eta) = e^{\mp\eta}\sum_{l=0}^{\infty}\alpha e^{-\sqrt{\alpha l}} \equiv e^{\mp\eta}G(\alpha) . \tag{15}$$

The function $G(\alpha)$ is calculated by the following approximate formula

$$\left.\begin{aligned} G(\alpha) &\fallingdotseq \alpha + 2[1+\sqrt{\alpha}+\tfrac{1}{4}\alpha]e^{-\alpha} \\ G(0) &= 2 . \end{aligned}\right\} \tag{16}$$

The function (16) is shown in the Fig. 2

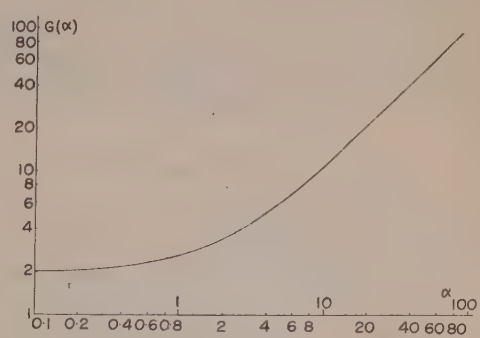

Fig. 2.

and the validity of the approximation is examined in the Appendix. It is supposed to be good to use the classical distribution function for n_a however there remains some ques-

tion to assume that the distribution of free carriers is also classical. As to the n and p it is rather better in the case of n than in the case of p to use the classical distribution. Taking into account this point we use (17) in the analysis of the data at the low temperature under the strong magnetic field where $\alpha \gg 1$.

$$\left.\begin{aligned} F(\alpha, \pm\eta) &\doteqdot \frac{\alpha}{1+e^{\pm\eta}} \\ G(\alpha) &\doteqdot \alpha \qquad \alpha \gg 1 . \end{aligned}\right\} \tag{17}$$

§ 5. The Empirical Determination of the Parameters

In this section, the evaluation of E_a, N_a, $b=\mu_p/\mu_n$ and γ_0 is made and it is discussed in the § 6 whether these values are plausible or not. Further the temperature and the magnetic field dependence of the Hall coefficient R is investigated in detail. The values of these parameters are determined mainly by the observed condition where R vanishes. ($R=0$) The condition $R=0$ implies that in the formula (1) the numerator must vanish and by using the relations (11) and (13) the following condition is obtained.

$$b^2=\frac{n}{p} \doteqdot \left[1+\frac{K(T)}{G(\alpha)}\right]^{-1} \tag{18}$$

$$K(T) \equiv \frac{2\nu^2 N_a}{q(kT)^2} e^{-\varepsilon_a} \tag{19}$$

where non-degenerate approximation for the trapped state is used. The equation (18) can be written as follows

$$\frac{2\nu^2 N_a}{q(kT)^2} e^{-\varepsilon_a} = G(\alpha)\frac{1-b^2}{b^2} . \tag{20}$$

[A] *The value of E_a*: If the temperatures T_1 and T_2 at which R vanishes are known in the limiting case of the weak magnetic field ($H \to 0$), the following relation is deduced from (20)

$$\left(\frac{T_2}{T_1}\right)^2 e^{-(\varepsilon_{a_1}-\varepsilon_{a_2})}=1$$

so that E_a is estimated by

$$E_a=2k\left(\frac{T_1 T_2}{T_1-T_2}\right)\ln\left(\frac{T_1}{T_2}\right) \equiv kT_a . \tag{21}$$

By comparing with the Kinchin's data shown in the Fig. 1, it is found that $T_1=29°$K and $T_2=192°$K and by substituting these values in (21) we get $E_a=11\times10^{-3}$ eV. $T_a=129°$K.

[B] *The determination of γ_0*: If the magnetic field H' at which R vanishes is known at the fixed temperature T', we get the following relation from (20)

$$\begin{aligned} G(\alpha') &= 2\left(\frac{T_1}{T'}\right)^2 e^{-(\varepsilon_{a_1}-\varepsilon_{a'})} \\ &= 2\left(\frac{T_1}{T'}\right)^2 e^{-(T_a/T_1-T_a/T')} . \end{aligned} \tag{22}$$

The value α' is then estimated by using the graph $G(\alpha)$ of Fig. 2. By the definition (12) of α, γ_0 is known as follows.

$$\gamma_0=\left(\frac{\hbar^2}{ma^2}\right)\sqrt{\frac{\alpha'(kT')}{\hbar^2/ma^2}} \cdot \sqrt{\frac{(kT')}{3(\mu H')}} . \tag{23}$$

The Kinchin's data show $T_1=29°$K, $T'=77°$K, $H'=5$ K gauss and by using these values and $T_a=129°$K obtained in [A], $G(\alpha)$ is found as 4.54 and the corresponding value of α' is 3.82. The resonance integral γ_0 is then estimated as $\gamma_0=1.43$ eV by (23). We also tried to estimate the value of γ_0 by using the data at $T'=63.5°$K and got the same value of it.

[C] *The relation between N_a and b*: In the case where $H \to 0$ so that $\alpha \to 0$, the value $G(\alpha)$ tends to 2 and in this consideration we deduce (24) from (20).

$$\frac{2(1-b^2)}{b^2}=\frac{3\pi}{4} c_L a^2 N_a \left(\frac{\gamma_0}{kT_1}\right)^2 e^{-T_a/T_1} . \tag{24}$$

This equation is rearranged as follows:

$$N_a=\frac{8}{3\pi}\frac{(1-b^2)}{b^2}\frac{1}{c_L a^2}\left(\frac{kT_1}{\gamma_0}\right)^2 e^{T_a/T_1} . \tag{25}$$

If we know the value of b we can estimate N_a from (25) by substituting the obtained values of γ_0, T_1, and T_a. As being shown in the following discussions [D], we get $b=0.87$ as an appropriate value so that N_a is estimated 1.7×10^{18}/c.c..

[D] *The Hall coefficient at the low temperature under the strong magnetic field*: In this case α is sufficiently larger than 1 ($\alpha \gg 1$) and the Fermi level η is supposed to be nearly zero. By using the equation (1), (11), (17), and (23) we have R in this condition as follows.

$$\begin{aligned} R &= \frac{3\pi}{8e}\frac{1}{p}\frac{b-1}{b+1} \\ &= \left(\frac{b-1}{b+1}\right)\left(\frac{c_L a^2}{e}\right)\left(\frac{9\pi^2}{32}\right)\frac{1}{\alpha'}\left(\frac{\gamma_0}{kT'}\right)^2\left(\frac{H'}{H}\right) . \end{aligned} \tag{26}$$

It is noticed that in the limit of low temperature and strong magnetic field ($\alpha \gg 1, \eta=0$), the Hall coefficient R is inversely proportional

to the field strength H and does not depend on the temperature. This characteristic feature is also found in the Kinchin's experimental data. If the observed value $R=-0.5$ cm³/coulomb at $H=7$ K. gauss is fitted to the expression (26), the value of b is estimated as $b=0.87$. As being shown in Fig. 1 the behaviour of R calculated by (26) seems to agree well with the observed data in the range of the low temperature and the strong magnetic field.

[E] *The Hall coefficient R calculated by using the parameters determined above*: By using the above obtained values of the parameters E_a, N_a, γ_0 and b, the dependence of the R on the temperature and the magnetic field is plotted in the Fig. 1. We can not well reproduce the observed tendency in the weak field range by our calculation. The discrepancy is especially remarkable at the low temperature where observed R exhibits the minimum at certain magnetic field. However in the other range the calculated curves of R reproduce well the nature of observed data qualitatively or even semi-quantitavely.

§ 6. Discussions

At first we discuss that the values of the parameters determined in § 5 are plausible or not.

As to N_a, E_a, and b, Kinchin suggested $N_a=2\times10^{18}$/c.c., $E_a=6\times10^{-3}$ eV, and $1>b\geq 0.8$. Our results are $N_a=1.7\times10^{18}$/c.c., $E_a=11\times10^{-3}$ eV, and $b=0.87$. There is a difference in the value of E_a which seems to be the result of using the two dimensional model in our consideration.

It is an important point for understanding the magnetic field dependence of R whether the value of γ_0 is plausible or not. The theoretical calculations of the γ_0 suggested that it should be nearly between 0.9 and 3 eV. As it is already mentioned in the § 3, McClure proposed $\gamma_0=2.6$ eV by using the observed data of the diamagnetic susceptibility. Our result $\gamma_0=1.43$ eV determined by using the Kinchin's data of the Hall effect seems to be plausible. The value determined in this paper may be somewhat smaller one because of our somewhat larger value of E_a. It is supposed that we can not ignore the effect discussed in this paper if the value of γ_0 is larger than this value.

The calculated curve of R seems to have a good agreement with the observed data except in the range of the low temperature and the low magnetic field. The characteristic behavior of R in the low temperature under the strong magnetic field reffered in [D] of § 5 suggests that our considerations show the part of the essential features of the phenomena. The physical meaning of the expression (26) is that the almost part of the carriers occupies the level $l=0$ in the spectra (9′) because of the conditions of $\alpha\gg1$, $\eta=0$. The inverse proportionality of R to H has its origin in the proportionality of the state density w to H. Here we see that the absence of the 0-point energy in (9′) plays an important role in our considerations as in the discussions on the diamagnetism presented by McClure[4].

The discrepancy between the theory and the experiment is found rather in the low field region especially at the low temperature and the origins of which seem to be in the simple assumption of the two dimensional band structure. In our model the n and p tend to zero as the temperature tends to the absolute zero. However if the actual band exhibits the slight overlap of the energy surface then n and p do not tend to zero as the temperature tends to zero. The observations on the de Hass van Alphen effect[12], the oscillatory behaviour of the galvano-magnetic effects[13], and the cyclotron resonance[5),6] suggest that there exists the slight overlap in the energy surface so that in order to interpret the behavior of R at the low temperature it is necessary to take into account these fine structures of the energy band. The discussions of the effect of the magnetic field on the complicated band remain as the problem in the forthcoming paper.

§ 7. Acknowledgement

The authors express their cordial thanks to Prof. R. Kubo and the members of his research group for the valuable discussions. This work was partially supported by the research grant of the Ministry of Education.

Additional Note

Recently, after this paper had been prepared we read the paper entitled "Band Structure of Graphite and de Haas-van Alphen

Effect" by J. W. McClure[14]. According to his paper the six kinds of parameters γ_0, γ_1, γ_2, γ_3, γ_4 and Δ are proposed to characterize the fine structure of the energy band. The γ_3 plays a role to give the bands of minority carriers and the γ_2 is the origin of the band overlap. By using his Hamiltonian and neglecting the effect of γ_3 and γ_4, we try to find the quantized energy levels due to the magnetic field in the same way as § 2.

The quantized energy levels $\mathcal{E}_n$ are obtained as solutions of the following equations

$$\begin{aligned}&(E_1-\mathcal{E}_0)(E_2-\mathcal{E}_n)(E_3-\mathcal{E}_n)^2\\&\quad-(\hbar v)^2(2n+1)S(E_1-\mathcal{E}_n)(E_3-\mathcal{E}_n)\\&\quad-(\hbar v)^2(2n+1)S(E_2-\mathcal{E}_n)(E_3-\mathcal{E}_n)\\&\quad+4(\hbar v)^4n(n+1)S^2=0 \qquad (\text{for } n\geqq 1)\\&(E_1-\mathcal{E}_0)(E_2-\mathcal{E}_0)(E_3-\mathcal{E}_0)-(E_1-\mathcal{E}_0)(\hbar v)^2S\\&\quad-(E_2-\mathcal{E}_0)(\hbar v)^2S=0 \qquad (\text{for } n=0)\\&\mathcal{E}_{-1}=E_3=\frac{1}{2}\gamma_2P^2 \qquad (\text{for } n=-1)\end{aligned}$$

where E_1, E_2, E_3 and Γ represent

$$E_1=\gamma_1\Gamma+\Delta$$
$$E_2=-\gamma_1\Gamma+\Delta$$
$$E_3=\frac{1}{2}\gamma_2\Gamma^2$$
$$\Gamma=2\cos\frac{k_zc_2}{2}$$

In the case of the semiclassical limit ($n\gg 1$), we get

$$\mathcal{E}_n=\frac{1}{2}(E_1+E_3)\pm\sqrt{\frac{1}{4}(E_1-E_3)^2+2(\hbar v)^2nS}$$
$$\mathcal{E}_n=\frac{1}{4}(E_2+E_3)\pm\sqrt{\frac{1}{4}(E_2-E_3)^2+2(\hbar v)^2nS}$$

The lowest level which corresponds to $l=0$ in (9′) is found to be

$$\mathcal{E}_{-1}=\frac{1}{2}\gamma_2l'^2\ ;$$

If the effect of band overlap is neglected ($\gamma_2\to 0$) the level $\mathcal{E}=0$ appears also in the three dimensional case. In the condition of the low temperature $T\to 0$ there remains the finite concentration of carriers owing to the parameter γ_2 which indicates the effect of band overlap.

Is it necessary to assume the existence of the acceptors in order to explain the temperature dependence of R at $H\to 0$, even if the effect of γ_3 is considered? It is a difficult problem and no satisfactory answer seems to be proposed at present time.

Appendix

The derivation of $G(\alpha)$ in (16)

$$G(\alpha)\doteqdot\alpha+2[1+\sqrt{\alpha}+\tfrac{1}{4}\alpha]e^{-\sqrt{\alpha}}\ .$$

In the Euler's formula

$$\sum_{j=m}^{n}f(j)=\int_m^n f(x)\,dx+\tfrac{1}{2}[f(m)+f(n)]$$
$$+\sum_{k>1}(-)^k\frac{B_k}{(2k)!}[f^{(2k-1)}(m)-f^{(2k-1)}(n)]$$

we put $f(j)=\alpha e^{-\sqrt{\alpha j}}$, then we get

$$G(\alpha)\doteqdot\alpha+\int_1^\infty\alpha e^{-\sqrt{\alpha x}}\,dx+\tfrac{1}{2}[f(1)+f(\infty)]$$
$$=\alpha+2[1+\sqrt{\alpha}+\tfrac{1}{4}\alpha]e^{-\sqrt{\alpha}}\ .$$

The error of this approximation is given by

$$|R_1|<\frac{B_1}{2}[f'(1)-f'(\infty)]<\frac{B_1}{2}\frac{\alpha\sqrt{\alpha}}{2}e^{-\sqrt{\alpha}}$$
$$\therefore\quad |R_1|<\frac{1}{24}\alpha\sqrt{\alpha}\,e^{-\sqrt{\alpha}}<\frac{27}{24e^3}=0.0564\ .$$

On the other hand $G(\alpha)\geqq 2$ so that the approximate formula (16) is supposed to be good.

References

1) Y. Uemura, M. Inoue: J. Phys. Soc. Japan **13** (1958) 377.
2) G. H. Kinchin: Proc. Roy. Soc. **A 217** (1953) 9.
3) P. R. Wallace: Phys. Rev. **71** (1947) 633.
4) J. W. McClure: Phys. Rev. **104** (1956) 666.
5) Galt. Yager. Dail: Phys. Rev. **103** (1956) 1586.
6) B. Lax, H. J. Zeiger: Phys. Rev. **105** (1957) 1466.
7) W. M. Lomer: Proc. Roy. Soc. **A 227** (1955) 330.
8) D. F. Johnston: Proc. Roy. Soc. **A 227** (1955) 349.
9) S. Mrozowski: J. Chem. Phys. **21** (1953) 492.
10) M. Yamazaki: J. Chem. Phys. **26** (1957) 930.
11) J. M. Luttinger, W. Kohn: Phys. Rev. **97** (1955) 869.
J M. Luttinger: Phys. Rev. **102** (1956) 1030.
12) D. Shoenberg: Phil. Trans. Roy. Soc. (London) **245** (1952) 1.
13) T. G. Berlincourt and M. C. Steele: Phys. Rev. **98** (1955) 956.
14) J. McClure: Phys. Rev. **108** (1957) 612.

JOURNAL OF THE PHYSICAL SOCIETY OF JAPAN Vol. 13, No. 4, APRIL, 1958

Effect of the Basic Strength of Attached Groups on Light Absorption Spectra III: Dissociations in the Excited States of Naphthalene Derivatives

By Reikichi ITOH

Kobayashi Institute of Physical Research, Kokubunzi, Tokyo

(Received January 8, 1958)

The dissociations in the excited states of the derivatives of naphthalene, i.e., α- and β-naphthylamine, and α- and β-naphthol are discussed by the molecular orbital treatment using semi-empirical L.C.A.O. method. The difference of the proton dissociation constant between the excited and the ground state, pK_1-pK_2, is expressed by a certain parameter connecting the coulomb integral with the basic strength of attached groups. The value of the parameter is derived by the light absorption spectra of the similar molecules. The calculated values of the differences, pK_1-pK_2, are 5.0 and 5.5 in the case of β-naphthylamine and α-naphthol in good agreement with the experimental values of 6.0 and 6.0 respectively. The similar calculations for the case of β-naphthol give considerably smaller value of which discussion is given briefly as well as the experiment.

§ 1. Introduction

The dissociation in the excited state of a molecule has been discussed by several authors[1] from the experimental point of view in the cases of naphthalene- and oxypyrene-derivatives. It was pointed out that pH dependence of the light absorption spectra of those molecules shows different behavior from that of the fluorescent spectra, and that the changing point of the absorption spectra is higher about 6 units in pH scale than that of the florescent spectra. Förster[1] has made the experiments on the derivatives of naphthalene and oxypyrene, and Weeler[1] has calculated the dissociation constants in the excited states of naphthol and its sulfonate derivative on the ground of chemical kinetics. The present author[1] gave a method of estimating the dissociation constant in the excited state from the experimental data on the light absorption. However, no theoretical explanation of these experiments on the ground of molecular orbital treatment has appeared till now. Weeler's treatment which leads to a quantitative result in the case of naphthol and its sulfonate derivative is not based upon the electronic theory of the molecules. The present work gives the explanation of the nature of dissociation in the excited states of naphthol and naphthlamine from the electronic point of view by using the semi-empirical L. C. A. O. method.

§ 2. pH-dependences of Absorption and Fluorescent Spectra

At first, we summarize experimental results of Föster and Weeler.

a) β-naphthol

The proton dissociation constant pK_a of the molecule in the ground state at 20°C is 9.6. Both of the absorption and fluorescent spectra of the dissociated form (ion) shift towards longer wavelength than those of undissocated molecule. The change of the absorption spectrum takes place at pH=8, i. e. the shift from 3250 A to 3470A, and that of the fluorescence at pH=2 corresponds to the shift from ultraviolet (3500 A) to blue (4200 A). Since the fluorescence arises from the electronic excited state of the molecule, the aspect of the dissociation in the excited state should change at pH=2, while that of the ground state changes at pH=8.

b) α-naphthol

In this case the behavior of both of absorption and fluorescent spectra through the change of pH is similar to those of β-naphthol, except that the ultraviolet fluorescent spectra is lacking in water solution and the complete quenching process occurs in strong acidic solution with pH <2. The reaction for the proton dissociation in the excited and ground state will be given by

$$AOH+H_2O=AO^-+H_3O^+.$$

c) β-naphthylamine

The absorption spectrum changes at pH=4 from 2750 A to 2800 A or 3400 A, while that of the fluorescence at pH=−2 (Hammett's scale) from ultraviolet (3400 A) to blueviolet (4100 A) and at pH=12 from blueviolet to green (5000 A), the former corresponding to the change from cationic to neutral form and the latter from neutral to anionic form of the molecule respectively. These reactions are expressed by the equations;

$$ANH_3^+ + H_2O = ANH_2 + H_3O^+,$$
$$ANH_2 + OH^- = ANH^- + H_2O$$

respectively, where A denotes the naphthalene. It is expected that these reactions occur in the excited state (fluorescence change) as well as in the ground state (absorption change). The change of the absorption spectra in the second equation is observed in the very strong alkaline solution of pH∼20, which will be realized in the special solution as liquid ammonia solution and is not observed in the ordinary alkaline solutions.

d) α-naphthylamine

The behavior of the absorption spectra is similar to that of β-naphthylamine, while that of fluorescent spectrum is completely quenched and the intensity of the fluorescence is too weak to be observed.

The changes of absorption and fluorescent spectra of those four derivatives against pH scale are summarized in Fig. 1 schematically.

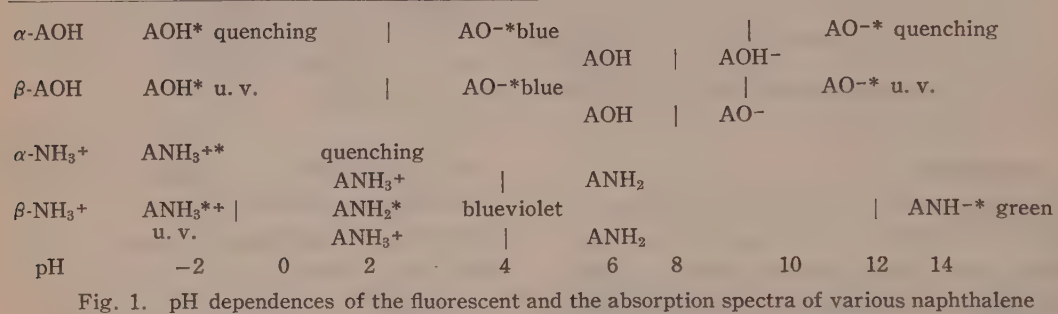

Fig. 1. pH dependences of the fluorescent and the absorption spectra of various naphthalene derivatives are shown, where A is the naphthalene and the molecule in the excited state is denoted by a star.

§ 3. Ground and Excited Electronic States

Substances considered in this paper are composed of a parent molecule A (naphthalene and a substituent BH (hydroxyl or amino group). The latter has two non-bonding electrons constaining π-component or lone pair electrons. It is naturally expected that the non-bonding electrons in the substituent could migrate to the parent molecule in consequence of the interaction between A and BH. Since the mode of interaction between A and BH is different for the different electronic state of A, the rate of the migration in the ground state is assumed to be different from that of the excited state of the molecule A. Here, we denote the rate of the migration of the former state by λ_g and that in the latter by λ_e, respectively. Both of them can be calculated by assuming the interaction between the occupied π-electron level of the non-bonding electrons of BH, χ, and the lowest level of the vacant orbital of A in the ground state, ω_2, or between χ and that of the vacant orbital in the first excited state, ω_1, as the perturbation. The absorption spectrum of A is given by the difference of ω_2 and ω_1. As the relation $\chi<\omega_1<\omega_2<0$ is expected, the interaction between χ and ω_1 is stronger than that between χ and ω_2. It is likely that the mixing rate, λ_1, of π- orbital of BH, ϕ_s (χ level), with that of A, ψ_1 (ω_1 level), is larger than λ_2, the mixing rate of ϕ_s with ψ_2 (ω_2 level). The above considerations lead to the following relations,

$$\lambda_g = 2\lambda_2, \qquad \lambda_e = \lambda_1 + \lambda_2, \qquad (1)$$

which show that λ_e is larger than λ_g. Now, densities of the π-electrons in BH under the influence of the ground and the excited state of A which are denoted by q_g and q_e respectivery, are given by

$$q_g = q_0 - 2\lambda_2^2, \quad q_e = q_0 - (\lambda_1^2 + \lambda_2^2). \qquad (2)$$

It is concluded also from equation (2) that q_g is larger than q_e and this leads us to the following considerations;

a) By the so called inductive effect of the

σ-electrons in BH bond on the π-electrons of B atom, the degree of localization of σ-electron in BH bond is conversely affected by the change of π-density of B atom*;

b) Then it is natural to assume that the larger π-density on the B atom leads to the smaller density of σ-electrons of the atom, the effect of which drives the σ-electrons to the more locarization in the BH bond and consequently brings about the stronger BH bond;

c) Since the bond strength of BH directly relates to the proton affinity for protonic dissociation, $BH=B^-+H^+$, a stronger BH bond is more basic, or less acidic, than a weaker BH bond. By the same reason it is also concluded that the excited state is more acidic than the ground state. This conclusion is consistent with the observation.

The similar correlation is found for the cases of various aromatic compounds with OH or NH_2 group through the solvent effect on their absorption spectra[2]. For example, we consider the effect of hydrogen bond formation on the near ultraviolet absorption spectra of benzene derivatives such as aniline and phenol. In these molecules it is well known that their absorption spectra shift to longer wave length (so called red shift) when the solvent is changed from non-polar to polar one, e. g., from carbontetrachloride to dioxane. When these molecules form the hydrogen bonds, the bond length of BH (OH or NH_2) group becomes larger by 0.02~0.03 A due to the attraction on the proton by the proton accepter of the polar solvent[3]. By this effect, the σ-electrons in BH bond tend to localize more strongly on the B atom than without it, and this causes the migration of non-bonding electron on B atom to the parent molecule much more strongly and results in the red shift of the absorption spectra.

In the case of the absorption spectra, the delocarization of σ-electrons in BH bond affect the electron migration, while in the case of the proton dissociation treated in this paper, the electron migration to the parent molecule in the excited state arising from light absorption brings about the delocalization of σ-electron in the bond conversely. Thus the origin of the effect is the correlation between σ- and π-electrons through the induction effect in both cases. In this paper, the magnitude in the difference of the proton dissociation constant in the ground and the excited states of the derivatives are estimated from the difference of the degree of the electron migration in the ground and the excited state of the parent molecule.

* The so called red shift[2] in the absorption spectra through the hydrogen bond formation is caused by the inductive effect of σ-electrons in the bond of the attached group on the π-electrons of the same group as discussed in later place. The effect conventionaly goes from σ- to π-electrons, but the one in the present phenomena goes from π- to σ-electrons in the attached group due to the induction effect between σ- and π-electron and the word, conversely, means the latter situation.

§ 4. Relation between the Basic Strength of Attached Group and Its Coulomb Integral

In the previous papers, I and II[4], the author has pointed out that there exists a linear relation between the basic strength, pK_b, of the attached group and the value of the coulomb integral, α, for the cases of triphenylmethane dyes and aniline derivatives. Thereby it was given by

$$\alpha_i-\alpha_j=k(pK_{b_j}-pK_{b_i}), \qquad (3)$$

where the constant k was taken to be about 0.4 eV so that equation (3) was consistent with the spectroscopic data of these molecules. In this paper it is also assumed that there exists a similar relation

$$\alpha_2-\alpha_1=k(pK_{a_1}-pK_{a_2}), \qquad (4)$$

where the suffixes 1 and 2 refer to the ground and the excited state of the molecule respectively and pK_a the proton dissociation constant (i. e. acidic strength) of the whole molecule, instead of the attached group itself. The change of pK_a of the former, however, will be proportional to that of the latter, because the dissociation of the molecule takes place at the attached group. The main difference between equations (3) and (4) is that (3) is concerned with the relation before the perturbation to the molecule A by BH is introduced, while (4) is the relation after the introduction of the perturbation. In other words, the quantities in (3) are for the attached group only, while those in (4) are for the molecule as a whole, though the both equations are expressed by the same parameters, the

coulomb integral and the basic strength pK.

The attached groups hitherto considered are amino groups only. When another sort of groups such as OH is attached to the parent molecule, the value of the parameter k should be changed because of the different electronic configuration between N (sp^4, V_3) in NH_2 and O (s^2p^4, V_2) in OH. Therefore it is necessary to use different parameters k_n and k_0 for these two cases separately. Now it is convenient to determine the values of the parameters from the experimental data of the red shift in the absorption spectra. Since the bond length of OH bond is nearly equal to that of NH bond (1.07 A and 1.08 A respectively), it is expected that nearly equal degree of the delocalization of σ-electron for the two bond is caused through the effect of the hydrogen bond formation with the solvent which makes the bond length longer by about 0.02~0.03 A which localizes more σ-electrons on B atom. This localization effect of σ-electrons reveals the red shifts, the ammount of which are 300 cm^{-1} (phenol) and 610 cm^{-1} (aniline)[5]. It is possible to consider that the localization of σ-electron induces π-electron migration in the same manner for naphthol to naphthylamine as for phenol to aniline. Owing to the different configuration of electrons in O and N, the rate of the migration of π-electrons accompanied by the same amount of localization is different in both cases.

The above considerations are summarized as

$$\Delta\tilde{\nu}_{OH}/\Delta\tilde{\nu}_{NH}=\Delta\mathcal{E}_{OH}/\Delta\mathcal{E}_{NH} \quad (5)$$

$$=\Delta\alpha_{OH}/\Delta\alpha_{NH} \quad (6)$$

$$=k_0\Delta pK/k_n\Delta pK \quad (7)$$

$$=k_0/k_n \quad (8)$$

where $\Delta\tilde{\nu}$ is the red shift due to the hydrogen bond formation, and $\Delta\mathcal{E}$ is the corresponding energy of stabilization which is in the first approximation given by[6]

$$\Delta\mathcal{E}_i=\Sigma c_i^2\Delta\alpha_i$$

$\Delta\alpha$ is the change of the value of the coulomb integral due to the hydrogen bond formation and c_i is the A. O. coefficient of attached group in M. O. of the iso-electronic homocyclic molecule under consideratain. The suffixes, OH and NH, refer to phenol and aniline respectively, and ΔpK is assumed to be nearly equal in both cases because the degree of localization of σ-electron is almost same in both cases. As in the previous papers k_n is determined to be about 0.4 eV, while k_0 is to be 0.2 eV according to equation (8). As in the paper I, the coulomb integral of B atom (N or O) is expressed semi-empirically by[7]

$$\alpha_r=I_r-1/2\cdot q_r(E_r-I_r), \quad (9)$$

where q_r is the π-electron density, I_r is the ionization potential and E_r is the electron affinity of the atom respectively. However, it will be better to use the first and the second ionization potential of B atom instead of the electron affinity and the first ionization potential respectively, because of the neglect of the contribution from proton in M. O.'s of the parent molecule. When q_r takes different value for the excited state from that for the ground state, the difference of the coulomb integrals, α_1 and α_2, is expressed by

$$\alpha_2-\alpha_1=1/2\ (q_e-q_g)\ (I_1-I_2) \quad (10)$$

$$=1/2\ (\lambda_1^2-\lambda_2^2)\ (I_1-I_2)$$

according to equation (2), and combining this equation to (4), it is obtained that

$$k(pK_{a_1}-pK_{a_2})=1/2\ (\lambda_1^2-\lambda_2^2)\ (I_1-I_2), \quad (12)$$

where k is to be 0.4 eV or 0.2 eV according to that attached group is NH_2 or OH. It is now neccessary to evaluate the rates of migration, λ_1 and λ_2, in order to calculate the dissociation constant in the excited state.

§ 5. Results and Discussions

As the same process of the calculation of λ_1 and λ_2 as in the previous paper II is adopted for evaluating the rate of migration, λ_1 and λ_2, the details of the calculation are not reproduced except to give the neccessary data for calculation. The wave function, $\Phi(\nu)$, and the potential, $H(\nu)$, for the migrating electron are given as

$$\Phi(\nu)=\Sigma a_i\psi_i+b\phi_s, \quad H(\nu)=H_p+H_s$$

where the summation is taken over the vacant orbitals of the parent molecule, and H_p and and H_s denote the potential for the migrating electron in the parent molecule and the substituent respectively. As the result of the perturbation calculation minimizing the energy for the total molecule, the expression

$$\lambda_i=a_i/b=(\rho_i-T_i\chi)/(\chi-\omega_i) \quad (13)$$

is obtained. ρ_i and T_i are the resonance and the overlap integral between ψ_i and ϕ_s and are given by

$$\rho_i = c_k/2\ (\gamma + s(\chi + \omega_i)), \quad T_i = c_k S,$$

where $S=(\phi_k \mid \phi_s)$, $\gamma=(\phi_k \mid H \mid \phi_s)$ and c_k is the A. O. coefficient of M. O. for the atom in the parent molecule to which the substituent attaches. In the case of naphthalene, ψ_i's are given by[8]

$$\psi_1 = 0.4085(\phi_1 - \phi_4 + \phi_5 - \phi_8) + 0.2883(\phi_2 - \phi_3 + \phi_6 - \phi_7),$$

$$\psi_2 = 0.4142(\phi_1 - \phi_4 + \phi_5 - \phi_8) - 0.2801(\phi_2 - \phi_3 + \phi_6 - \phi_7).$$

Now the relation $\gamma/\gamma_0 = s/s_0$[9]$=1.2$ (for NH_2) or 1.4 (for OH) is assumed, where γ_0 and s_0 are the resonance and overlap integral of A. O.'s for the M. O.'s in benzene respectively, and the values $\gamma_0=-5.0$ eV and $S_0=0.25$ are taken throughout the calculation. The values for energy levels, ω_i and χ, have been given as

$$\omega_1 = -8.10\ \text{eV}^{10)},\ \omega_2 = -2.67\ \text{eV},\ \chi = -9.8\ \text{eV}$$

(for NH_3) or -10.8 eV (for OH) respectively[11], where the difference, $\omega_2-\omega_1$, corrpesponds to the absorption at 2200 A[12] in naphthalene molecule. The values for the ionization potentials I_2 and I_1 are taken from Mulliken's work[13].

I_1: $N(sp^4,\ V_3)$, $N^+(sp^3,\ V_4)$, -12.24 eV

I_2: $N^+(sp^3,\ V_4)$, $N^{++}(sp^2,\ V_5)$?

and

I_1: $O(s^2p^4,\ V_2)$, $O^+(s^2p^3,\ V_3)$ -13.73 eV

I : $O(s^2p^4,\ V_2)$, $O^{++}(s^2p^2,\ V_4)$ -36.68 eV,

where $I=I_1+I_2$. However, in the case of NH_2, $I_2-I_1=-14.98$ eV was derived from the data for the free atomic state instead of for the valence state, since the available data is lacking, and in the case of OH, $I_2-I_1=-9.22$ V was estimated from the Mulliken's data in the valence state. The result of the calculation is listed in Table I.

Table I. Results of the Calculation

attached group	λ_1	λ_2	$\Delta\lambda^2$	$\Delta\alpha$	$\Delta pK_{calc.}$	$\Delta pK_{obs.}$
α-NH_3^+	0.75	0.11	0.55	4.1 eV	10.0	—
β-NH_3^+	0.53	0.08	0.27	2.0	5.0	6.0
α-OH	0.50	0.10	0.24	1.1	5.5	6.0
β-OH	0.35	0.12	0.12	0.6	3.0	6.0

As seen from Table I, the differences of pK are in good agreement with observation for the β-naphthylamine and α-naphthol, while it is too smaller than the one for the β-naphthol, though the calculated value is not certain due to the estimation of the ionization data I_2-I_1. Since the fluorescence of α-naphthylamine is completely quenched, the calculated value of pK can not be compared with the observed one, and only the relative change from β-derivatives is brought here.

In this connection we note that such considerations will be usefull also for discussing the difference of the chemical chracter between α- and β-derivatives as follows. As easily shown by the simple L. C. A. O. theory, the densities of π-electrons for α- and β-derivatives in the stable ground state are[14]

$$q_\alpha = 1.45, \quad q_\beta = 1.53$$

respectively. According to the consideration on the inductive effect given in § 3, the strength of the BH bond should be stronger in β-than α-derivatives, since the localization of σ-electrons in BH bond is presumably less in the latter by the induction effect between σ- and π-electrons. This is to be the case of naphthol and naphthylamine, where the observation shows that α-naphthol ($pK_a=9.2$)[15] is more acidic than β-naphthol ($pK_a=9.6$)[15] and α-naphthylamine ($pK_b=10.1$)[16] is less basic (more acidic) than β-naphthylamine ($pK_b=9.9$)[16]. These facts are the other strong support for us to the assumption in the correlation between σ- and π-electron in the attached group. When these molecules are brought in the excited state by the absorption of light, π-electron density of attached group is reduced much more in the α-derivatives than in the β-derivatives, the difference of which is about 0.1~0.3, and this means that in the excited state as well as in the ground state, α-derivatives should be more acidic than β-derivatives and α-derivatives are more liable to set its proton free towards the solvent than to stabilize itself after the emission of fluorescence. Thus α-derivatives would be likely to be rendered to the quenching process by the formation of hydrogen bond in strong acidic solution, or for the anionic forms in alkaline solution the effect of hydration may play the same role. These are possibly the reasons why the ultraviolet fluorescence of α-naphthol and α-naphthylamine are lacking in the solutions.

Our conclusion that the excited molecule is more acidic than in the ground state as the result of the difference in the migration of

non-bonding electrons of the attached group between the ground and the excited state, have been derived on the ground of a reasonable electronic structure of the molecules.

The author thanks Prof. I. Oshida for his helpful discussions. This work was supported by the Scientific Research Fund granted by the Ministry of Education.

References

1) Th. Förster: Z. Electrochem. **54** (1950) 42, 531, A. Weeler: ibid. **56** (1952) 662, M. Koizumi and N. Mataga: Nature **175** (1955) 731, R. Itoh: J. Phys. Soc. Japan **12** (1957) 829.
2) S. Nagakura and H. Baba: J. A. C. S. **74** (1952) 5693, H. Tsubomura: J. Chem. Soc. Japan **73** (1952) 841, 920, H. Baba: Monograph Series of the Research Institute of Applied Electricity, Hokkaido University, **No. 4** (1954) 61, R. Miyasaka (R. Itoh): Busseiron Kenkyu **No. 62** (1953) 94 (in Japanese), S. Nagakura and M. Gouterman: J. Chem. Phys. **26** (1957) 881.
3) M. Davies: J. Chem. Phys. **15** (1947) 739
4) R. Itoh: J. Phys. Soc. Japan **12** (1957) 644 and **12** (1957) 809, (hereafter refered as I and II, respectively)
5) See reference 2) R. Itoh
6) See the previous paper I
7) See the previous paper II
8) C. M. Moser: J. Chim. Phys. **52** (1955) 24.
9) L. E. Orgel, T. L. Cottrell, W. Dick and L. E. Sutton: Trans. Farad. Soc. **47** (1951) 113.
10) W. C. Price: Chem. Rev. **41** (1947) 257.
11) F. A. Matsen: J. A. C. S. **72** (1950) 5243.
12) C. Daglish: J. A. C. S. **72** (1950) 4861.
13) R. S. Mulliken: J. Chem. Phys. **2** (1934) 782.
14) H. C. Longuet-Higgins: J. Chem. Phys. **18** (1950) 275
15) See reference 1) Förster.
16) Handbook of Chemistry (*Kagaku Binran*) Chem. Soc. Japan (1954) Maruzen, Tokyo (in Japanese).

JOURNAL OF THE PHYSICAL SOCIETY OF JAPAN Vol. 13, No. 4, APRIL, 1958

On the Absorption Spectra of Complex Ions

IV. The Effect of the Spin-orbit Interaction and the Field of Lower Symmetry on *d* electrons in Cubic Field

By Yukito TANABE

Department of Applied Physics, Faculty of Engineering, University of Tokyo

and Hiroshi KAMIMURA

Department of Physics, Faculty of Science, University of Tokyo

(Received January 11, 1958)

It is shown that the matrix elements of the crystalline field of lower symmetry than cubic and of the spin-orbit interaction for d-electrons in octahedral complex ions can be easily evaluated by the method of tensor operators, and the tables necessary to evaluate these elements by this method are given. It is also pointed out that the effective Hamiltonian which plays the same role as the spin Hamiltonian for the non-degenerate states can be constructed for the degenerate orbital states and will be useful for the analysis of line spectra of these complexes.

§ 1. Introduction

Since 1951, many investigations have been carried out on the absorption spectra of the transition-metal complex ions and we have now fairly complete knowledge of the electronic excited states which correspond to the spin-allowed absorption bands of these ions. Further progress will be made by studying the spin-forbidden bands, the line spectra (especially the Zeeman effect of these), the optical anisotropy observed in the complexes of lower symmetry, etc. Some of these pro-

blems were already treated in part by several authors. It seems to us, however, many problems remain unsolved. In order to clarify these points, it is first necessary and will be important to consider the effects of the crystalline field of lower symmetry than cubic and of the spin-orbit interaction which were neglected in the previous paper.[1)]

We will therefore present here the matrix elements of these operators in the form suitable to any application. To this end, the method of tensor operators is most useful and we will develop the algebra of tensor operators in § 2 and show that the matrix elements in question can be evaluated by simple multiplication of several factors which will be given here. Before applying the matrix elements evaluated in this way to practical problems, we will discuss a general treatment by the effective Hamiltonian in § 3 that will be useful in the analysis of line spectra of complex ions, in which we are interested and for which this calculation was first carried out. Practical application of the results will be given in a later paper.

§ 2. Method of Tensor Operators

As in (I), we want to evaluate the matrix elements of the spin-orbit interaction and of the field of low symmetry in $S\Gamma$ scheme. Namely, the basic functions are $\Psi(f_{2g}^{n}(S_1\Gamma_1)e_g^{n'}(S_2\Gamma_2)S\Gamma M_S\gamma)$. (We write f_{2g}, e_g in place of $d\varepsilon$, $d\gamma$ in order to indicate that they need not necessarily be constructed from the d functions.) Since the evaluation is most conveniently carried out by using the method of tensor operators, we study first the properties of tensor operators.

i) Tensor operators

We define as irreducible tensor operators of type Γ each operator $\mathbf{X}(\Gamma)$, whose (Γ) (=dimension of the irreducible representation Γ) components $X_\gamma(\Gamma)$ transform in the same way as the basis of the irreducible representation $\varphi(\Gamma\gamma)$ under the operations of the octahedral group. For example, the so-called "Kubic Harmonics" are the components of such tensor operators. The non-cubic perturbation V can thus be written as the sum of irreducible tensors $V_\gamma(\Gamma)$ as follows:

$$\begin{aligned} V = {} & V(A_{2g}) + \Sigma_\gamma c_\gamma V_\gamma(E_g) + \Sigma_\gamma c_{1\gamma} V_\gamma(F_{1g}) \\ & + \Sigma_\gamma c_{2\gamma} V_\gamma(F_{2g}) + V(A_{1u}) + V(A_{2u}) \\ & + \Sigma_\gamma c_\gamma' V_\gamma(E_u) + \Sigma_\gamma c_{1\gamma}' V_\gamma(F_{1u}) \\ & + \Sigma_\gamma c_{2\gamma}' V_\gamma(F_{2u}) , \end{aligned} \tag{2.1}$$

where $V_\gamma(\Gamma)$ may be expanded in terms of Kubic Harmonics, namely

$$\begin{aligned} & V(A_{2g}) = f_6(A_{2g}|r)\Sigma x^4(y^2-z^2)+\cdots, \\ & \begin{cases} V_u(E_g) = f_2(E_g|r)(3z^2-y^2)+\cdots, \\ V_v(E_g) = f_2(E_g|r)\sqrt{3}(x^2-y^2)+\cdots, \end{cases} \\ & V_\gamma(F_{1g}) = f_4(F_{1g}|r)xy\sqrt{3}(x^2-y^2)+\cdots, \text{ (cycl.)} \\ & V_\zeta(F_{2g}) = f_2(F_{2g}|r)xy+\cdots, \text{ (cycl.)} \end{aligned} \tag{2.2*}$$

and

$$\begin{aligned} & V(A_{1u}) = f_9(A_{1u}|r)xyz\Sigma x^4(y^2-z^2)+\cdots, \\ & V(A_{2u}) = f_3(A_{2u}|r)xyz+\cdots, \\ & V_u(E_u) = f_5(E_u|r)xyz\sqrt{3}(x^2-y^2)+\cdots, \\ & V_v(E_u) = f_5(E_u|r)xyz(-3z^2+r^2)+\cdots, \\ & V_\gamma(F_{1u}) = f_1(F_{1u}|r)z+\cdots, \text{ (cycl.)} \\ & V_\zeta(F_{2u}) = f_3(F_{2u}|r)z\sqrt{3}(x^2-y^2)+\cdots, \text{ (cycl.)} \end{aligned}$$

where (cycl.) shows that the other components α, β (or ξ, η) of $V(F_1)$ (or $V(F_2)$)** can be derived from the component γ (or ζ) by cyclic change of x, y, z.

One may observe that $V_u(E)$ and $V_\gamma(F_1)$ have (axial+) tetragonal symmetry, and $V(A_2)$, $V_v(E)$ and $V_\zeta(F_2)$ rhomibc, while, $V(A_2)$, $(1/\sqrt{3})\Sigma_\gamma V_\gamma(F_1)$ and $(1/\sqrt{3})\Sigma_\gamma V_\gamma(F_2)$ are of trigonal symmetry with respect to the threefold symmetry axis of the octahedron.

One also observes that these non-cubic perturbations (the fields of low symmetry or coupling with the nuclear motion) are not only hermitian but also real, namely the matrix elements of these operators are real if we

* Note that (2.2) also could be used as the definition of the basic functions $\varphi(\Gamma\gamma)$ of the irreducible representation Γ. One may observe that this choice of bases is different from that made in (I). In (3.7) of (I), we chose the bases of F_{1u} and F_{2g} in the following way: $\alpha\propto -x$, $\beta\propto y$, $\gamma\propto -z$; $\xi\propto -yz$ $\eta\propto zx$, $\zeta\propto -xy$. That is not a convenient choice of phases, so we make here the usual choice of phases $\alpha\propto x$, $\beta\propto y$, $\gamma\propto z$; $\xi\propto yz$, $\eta\propto zx$, $\zeta\propto xy$ as in (2.2). However, the matrix elements, tables and formulae given in (I) need not be changed at all even if this choice of phases were adopted, excluding, of course, (3.7), so that the matrix elements evaluated in this paper can be used together with the energy matrices of the coulomb interaction given in (I) without any modification.

** We will suppress the suffices g, u when there is no fear of confusion or when the statement aplies both to g and u.

refer to the real basic functions. We denote such operators as $V_\gamma(\Gamma)$. In practice, however, pure imaginary operators also appear, for example, the angular momentum operator $\boldsymbol{l}$, which is of the type F_{1g}. These will be denoted as $T_\gamma(\Gamma)$. They always appear in the form combined with the spin operator $\boldsymbol{s}$ as in the spin-orbit interaction or with an external magnetic field $\boldsymbol{H}$ as in the Zeeman term, in the Hamiltonian.

The problem to evaluate the matrix elements of the non-cubic perturbations is thus reduced to the evaluation of the matrix elements of $V_{\bar\gamma}(\bar\Gamma)$: $(\alpha\Gamma\gamma|V_{\bar\gamma}(\bar\Gamma)|\alpha'\Gamma'\gamma')$. This matrix element can, however, be factorized into two factors, one of which depends on γ, γ' and $\bar\gamma$, while the other does not, as is easily shown.

$$(\alpha\Gamma\gamma|V_{\bar\gamma}(\bar\Gamma)|\alpha\Gamma'\gamma') = (\alpha\Gamma\|\mathbf{V}(\bar\Gamma)\|\alpha'\Gamma')(\Gamma)^{-1/2}(\Gamma\gamma|\Gamma'\gamma',\bar\Gamma\bar\gamma)\,, \quad (2.3)$$

where $(\Gamma\gamma|\Gamma'\gamma',\bar\Gamma\bar\gamma)$ is the Wigner (or Clebsch-Gordan) coefficient given in (I). This may be compared with the formula for the general tensor operators $T_q^{(k)}$

$$(\alpha jm|T_q^{(k)}|\alpha'j'm') = (\alpha j\|\mathbf{T}^{(k)}\|\alpha'j')(2j+1)^{-1/2}(jm|j'm'kq) \quad (2.4)$$

given by Racah[2]. Thus we only need to evaluate the double barred matrices $(\alpha\Gamma\|\mathbf{V}(\bar\Gamma)\|\alpha'\Gamma')$. Since our Wigner coefficients have the following property,

$$(\Gamma)^{-1/2}(\Gamma\gamma|\Gamma'\gamma'\bar\Gamma\bar\gamma) = \varepsilon(\Gamma\bar\Gamma\Gamma')(\Gamma')^{-1/2}(\Gamma'\gamma'|\Gamma\gamma\bar\Gamma\bar\gamma)\,, \quad (2.5)$$

where

$$\varepsilon(\Gamma A_1\Gamma') = \varepsilon(\Gamma F_2\Gamma') = 1\,, \qquad \varepsilon(\Gamma A_2\Gamma') = \varepsilon(\Gamma F_1\Gamma') = -1 \quad (2.6)$$

and $\varepsilon(\Gamma E\Gamma') = 1$

except for $\varepsilon(F_1EF_2) = \varepsilon(F_2EF_1) = -1$,

it follows for real operators

$$(\alpha\Gamma\|\mathbf{V}(\bar\Gamma)\|\alpha'\Gamma') = \varepsilon(\Gamma\bar\Gamma\Gamma')(\alpha'\Gamma'\|\mathbf{V}(\bar\Gamma)\|\alpha\Gamma), \quad (2.7)$$

so that particularly

$$(\alpha\Gamma\|\mathbf{V}(\bar\Gamma)\|\alpha\Gamma) = 0 \text{ for } \bar\Gamma = A_2\,, F_1\,. \quad (2.8)$$

(2.3) is valid also for operators $\mathbf{T}$. For these operators the double barred matrices are pure imaginary and

$$(\alpha\Gamma\|\mathbf{T}(\bar\Gamma)\|\alpha'\Gamma') = -\varepsilon(\Gamma\bar\Gamma\Gamma')(\alpha'\Gamma'\|\mathbf{T}(\bar\Gamma)\|\alpha\Gamma)\,, \quad (2.9)$$

so that particularly

$$(\alpha\Gamma\|\mathbf{T}(\bar\Gamma)\|\alpha\Gamma) = 0 \text{ for } \bar\Gamma = A_1, E, F_2\,. \quad (2.10)$$

The matrix elements of the spin-orbit interaction operator is of the form

$$V_{so} = \sum_{\sigma\bar\gamma} a_{\sigma\bar\gamma} \sum_{i=1}^{N} s_{i\sigma}t_{i\bar\gamma} = \sum_{\sigma\bar\gamma} a_{\sigma\bar\gamma}V_{\sigma\bar\gamma}(1F_1)\,, \quad (2.11)$$

where $\mathbf{t}$ (usually written as $\zeta\boldsymbol{l}$) is the operator of the type F_{1g}, and the suffices σ and $\bar\gamma$ run over x, y, z and α, β, γ respectively. For the isotropic spin-orbit interaction

$$a_{x\alpha} = a_{y\beta} = a_{z\gamma} = 1$$

$$a_{\sigma\bar\gamma} = 0 \qquad \text{for other pair of } \sigma \text{ and } \bar\gamma.$$

Since our scheme is $S\Gamma M_s\gamma$, it is more convenient to evaluate the matrix elements of following operators $V_{q\bar\gamma}(1F_1)$ instead of $V_{\sigma\bar\gamma}(1F_1)$:

$$V_{+1\bar\gamma}(1F_1) = -\frac{1}{\sqrt{2}}(V_{x\bar\gamma} + iV_{y\bar\gamma}) = \sum_i s_{i+1}t_{i\bar\gamma}\,,$$

$$V_{0\bar\gamma}(1F_1) = V_{z\bar\gamma} = \sum_i s_{i0}t_{i\bar\gamma}\,,$$

$$V_{-1\bar\gamma}(1F_1) = \frac{1}{\sqrt{2}}(V_{x\bar\gamma} - iV_{y\bar\gamma}) = \sum_i s_{i-1}t_{i\bar\gamma}\,. \quad (2.12)$$

Then we can show for such double tensors

$$(\alpha S\Gamma M_s\gamma|V_{q\bar\gamma}(1F_1)|\alpha'S'\Gamma'M_s'\gamma') = (\alpha S\Gamma\|\mathbf{V}(1F_1)\|\alpha'S'\Gamma')((2S+1)(\Gamma))^{-1/2} \times (SM_s|S'M_s'1q)(\Gamma\gamma|\Gamma'\gamma'F_1\bar\gamma)\,, \quad (2.13)$$

where the Wigner coefficients $(SM_s|S'M_s'1q)$ are, for instance, given in TAS[3]. The double barred matrices are imaginary and

$$(\alpha S\Gamma\|\mathbf{V}(1F_1)\|\alpha'S'\Gamma') = (-1)^{S-S'}(\alpha'S'\Gamma'\|\mathbf{V}(1F_1)\|\alpha S\Gamma)\,. \quad (2.14)$$

It is to be noted that the double barred matrices of an irreducible tensor operator defined above are independent of the choice of basic functions, if the components of the tensor operator are properly defined corresponding to the new choice of bases. When new bases $\varphi(\Gamma M)$ are derived from the old bases $\varphi(\Gamma\gamma)$ in the following way

$$\varphi(\Gamma M) = \sum \varphi(\Gamma\gamma)(\Gamma\gamma|\Gamma M)\,, \quad (2.15)$$

the invariancy of double barred matrix is assured if we define $\bar M$ component of the tensor operator $\mathbf{X}(\bar\Gamma)$ by the relation

$$X_{\bar M}(\bar\Gamma) = \sum_{\bar\gamma} X_{\bar\gamma}(\bar\Gamma)(\bar\Gamma\bar\gamma|\bar\Gamma\bar M) \quad (2.16)$$

and the Wigner coefficient in the new scheme by

$(\Gamma M|\Gamma'M'\bar\Gamma\bar M)$

$$= \sum_{\gamma\gamma'\bar{\gamma}} (\Gamma M|\Gamma\gamma)(\Gamma\gamma|\Gamma''\gamma', \overline{\Gamma}\bar{\gamma})(\Gamma''\gamma'|\Gamma''M')$$
$$\times(\overline{\Gamma}\bar{\gamma}|\overline{\Gamma}\overline{M}) , \tag{2.17}$$

since

$$(\Gamma M|X_{\overline{M}}(\overline{\Gamma})|\Gamma'M')$$
$$= \sum_{\gamma\gamma'\bar{\gamma}} (\Gamma M|\Gamma\gamma)(\Gamma\gamma|X_{\bar{\gamma}}(\overline{\Gamma})|\Gamma''\gamma')$$
$$\times(\overline{\Gamma}\bar{\gamma}|\overline{\Gamma}\overline{M})(\Gamma''\gamma'|\Gamma''M')$$
$$=(\Gamma\|\mathbf{X}(\overline{\Gamma})\|\Gamma'')(\Gamma)^{-1/2} \sum_{\gamma\gamma'\bar{\gamma}} (\Gamma M|\Gamma\gamma)$$
$$\times(\Gamma\gamma|\Gamma'\gamma'\overline{\Gamma}\overline{M})(\Gamma''\gamma'|\Gamma''M')(\overline{\Gamma}\bar{\gamma}|\overline{\Gamma}\overline{M})$$
$$=(\Gamma\|\mathbf{X}(\overline{\Gamma})\|\Gamma'')(\Gamma)^{-1/2}(\Gamma M|\Gamma''M'\overline{\Gamma}\overline{M}) . \tag{2.18}$$

ii) The evaluation of the matrix elements for a given configuration

We now proceed to the evaluation of the double barred matrix elements of spin-independent operators $\mathbf{X}(\overline{\Gamma})$ ($\mathbf{X}=\mathbf{V}$ or $\mathbf{T}$)

$$X_{\bar{\gamma}}(\overline{\Gamma}) = \sum_i x_{i\bar{\gamma}}(\overline{\Gamma}) = \sum_{i=1}^{n} x_{i\bar{\gamma}}(\overline{\Gamma}) + \sum_{i=n+1}^{n+n'} x_{i\bar{\gamma}}(\overline{\Gamma})$$
$$= X_{\bar{\gamma}}(\overline{\Gamma})_n + X_{\bar{\gamma}}(\overline{\Gamma})_{n'} . \tag{2.19}$$

The elements which are diagonal with respect to the number of electrons in the f_2 and e shells can be written as the sum of two terms, thus

$$(f_2{}^n(S_1\Gamma_1)e^{n'}(S_2\Gamma_2)S\Gamma\|\mathbf{X}(\overline{\Gamma})\|f_2{}^n(S_3\Gamma_3)e^{n'}(S_4\Gamma_4)S\Gamma')$$
$$=(f_2{}^n(S_1\Gamma_1)e^{n'}(S_2\Gamma_2)S\Gamma\|\mathbf{X}(\overline{\Gamma})_n\|f_2{}^n(S_3\Gamma_3)e^{n'}(S_2\Gamma_2)S\Gamma')\delta(S_2S_4)\delta(\Gamma_2\Gamma_4)$$
$$+(f_2{}^n(S_1\Gamma_1)e^{n'}(S_2\Gamma_2)S\Gamma\|\mathbf{X}(\overline{\Gamma})_{n'}\|f_2{}^n(S_1\Gamma_1)e^{n'}(S_4\Gamma_4)S\Gamma')\delta(S_1S_3)\delta(\Gamma_1\Gamma_3) , \tag{2.20}$$

where $\mathbf{X}(\overline{\Gamma})_n$ and $\mathbf{X}(\overline{\Gamma})_{n'}$ operate on the f_2 and e shell electrons respectively. These matrices can now be evaluated be means of the following general formulae the proof of which will be given in Appendix:

$$(\alpha\Gamma_a\beta\Gamma_b\Gamma\|\mathbf{X}(\overline{\Gamma})_a\|\alpha'\Gamma_a'\beta\Gamma_b\Gamma')=(\alpha\Gamma_a\|\mathbf{X}(\overline{\Gamma})\|\alpha'\Gamma_a')(\Gamma_a\Gamma_b\Gamma[\overline{\Gamma}]\Gamma_a'\Gamma_b\Gamma') \tag{2.21}$$

and

$$(\alpha\Gamma_a\beta\Gamma_b\Gamma\|\mathbf{X}(\overline{\Gamma})_b\|\alpha\Gamma_a\beta'\Gamma_b'\Gamma')=(\beta\Gamma_b\|\mathbf{X}(\overline{\Gamma})\|\beta'\Gamma_b')(\Gamma_a\Gamma_b\Gamma[\overline{\Gamma}]\Gamma_a\Gamma_b'\Gamma') , \tag{2.22}$$

where $\mathbf{X}(\overline{\Gamma})_a(\mathbf{X}(\overline{\Gamma})_b)$ acts only on the first (second) state in the resultant coupled state, and

$$(\Gamma_a\Gamma_b\Gamma[\overline{\Gamma}_a]\Gamma_a'\Gamma_b\Gamma')=[(\Gamma)/(\Gamma_a)]^{1/2}(\Gamma_a'\overline{\Gamma}_a(\Gamma_a)\Gamma_b\Gamma|\Gamma_a'\Gamma_b(\Gamma')\overline{\Gamma}_a\Gamma) . \tag{2.23}$$

Similarly,

$$(\Gamma_a\Gamma_b\Gamma[\overline{\Gamma}_b]\Gamma_a\Gamma_b'\Gamma')=[(\Gamma)/(\Gamma_b)]^{1/2}(\Gamma_a, \Gamma_b'\overline{\Gamma}_b(\Gamma_b)\Gamma|\Gamma_a\Gamma_b'(\Gamma')\overline{\Gamma}_b\Gamma) . \tag{2.24}$$

(2.23) and (2.24) are thus easily calculated from the transformation matrices between different coupling schemes which were used in the calculation of the matrices of the coulomb interaction. It is to be noted that $(\Gamma_a\Gamma_b\Gamma[\overline{\Gamma}_a]\Gamma_a'\Gamma_b\Gamma')$ vanishes unless all the representation $\Gamma_a\times\Gamma_b\times\Gamma$, $\Gamma_a'\times\Gamma_b\times\Gamma'$, $\Gamma_a\times\Gamma_a'\times\overline{\Gamma}_a$ and $\Gamma\times\Gamma'\times\overline{\Gamma}_a$ contain the identity representation A_1, while $(\Gamma_a\Gamma_b\Gamma[\overline{\Gamma}_b]\Gamma_a\Gamma_b'\Gamma')$ vanishes unless $\Gamma_a\times\Gamma_b\times\Gamma$, $\Gamma_a\times\Gamma_b'\times\Gamma'$, $\Gamma_b\times\Gamma_b'\times\overline{\Gamma}_b$ and $\Gamma\times\Gamma'\times\overline{\Gamma}_b$ all contain A_1.

From (2.20), (2.21) and (2.22),

$$(f_2{}^n(S_1\Gamma_1)e^{n'}(S_2\Gamma_2)S\Gamma\|\mathbf{X}(\overline{\Gamma})\|f_2{}^n(S_3\Gamma_3)e^{n'}(S_4\Gamma_4)S\Gamma')$$
$$=(f_2{}^nS_1\Gamma_1\|\mathbf{X}(\overline{\Gamma})\|f_2{}^nS_1\Gamma_3)\delta(S_1S_3)\delta(S_2S_4)\delta(\Gamma_2\Gamma_4)(\Gamma_1\Gamma_2\Gamma[\overline{\Gamma}]\Gamma_3\Gamma_2\Gamma')$$
$$+(e^{n'}S_2\Gamma_2\|\mathbf{X}(\overline{\Gamma})\|e^{n'}S_2\Gamma_4)\delta(S_2S_4)\delta(S_1S_3)\delta(\Gamma_1\Gamma_3)(\Gamma_1\Gamma_2\Gamma[\overline{\Gamma}]\Gamma_1\Gamma_4\Gamma') . \tag{2.25}$$

Similar formula for the spin-orbit interaction is obtained:

$$(f_2{}^n(S_1\Gamma_1)e^{n'}(S_2\Gamma_2)S\Gamma\|\mathbf{V}(1F_1)\|f_2{}^n(S_3\Gamma_3)e^{n'}(S_4\Gamma_4)S'\Gamma')$$
$$=(f_2{}^nS_1\Gamma_1\|\mathbf{V}(1F_1)\|f_2{}^nS_3\Gamma_3)\delta(S_2S_4)\delta(\Gamma_2\Gamma_4)(S_1S_2S[1]S_3S_2S')(\Gamma_1\Gamma_2\Gamma[F_1]\Gamma_3\Gamma_2\Gamma') , \tag{2.26}$$

since

$$(e^{n'}S_2\Gamma_2\|\mathbf{V}(1F_1)\|e^{n'}S_4\Gamma_4)=0\ .$$

The definition of $(S_1S_2S[1]S_3S_2S')$ is similar to (2.23), namely

$$(S_1S_2S[1]S_3S_2S')=[(2S+1)/(2S_1+1)]^{1/2}(S_3S_2(S')1S|S_31(S_1)S_2S)\ ,$$

or

$$=\sqrt{(2S+1)(2S'+1)}\,W(S'1S_2S_1;\ SS_3) \tag{2.27}$$

in terms of Racah's W-function.

The matrix elements of $\mathbf{X}(\overline{\Gamma})$ and $\mathbf{V}(1F_1)$ considered in this section are thus simply evaluated by multiplying several factor, e.g., $(f_2{}^nS_1\Gamma_1\|\mathbf{X}(\overline{\Gamma})\|f_2{}^nS_1\Gamma_3)$, $(\Gamma_1\Gamma_2\Gamma[\overline{\Gamma}]\Gamma_3\Gamma_2\Gamma')$ etc, once these are calculated and tabulated.

The matrices $(f_2{}^nS_1\Gamma_1\|\mathbf{X}(\overline{\Gamma})\|f_2{}^nS_1\Gamma_3)$ can be evaluated in terms of the double barred matrices for one electron by means of the following formula which is essentially (23) of RIII[4].

$$\begin{aligned}&(f_2{}^nS_1\Gamma_1\|\mathbf{X}(\overline{\Gamma})\|f_2{}^nS_1\Gamma_3)\\&=n(f_2\|\mathbf{x}(\overline{\Gamma})\|f_2)((\Gamma_1)/(f_2))^{-1/2}\sum_{S_1'\Gamma_1'}(f_2{}^nS_1\Gamma_1\{|f_2{}^{n-1}(S_1'\Gamma_1')f_2)(f_2{}^{n-1}(S_1'\Gamma_1')f_2|\}f_2{}^nS_1\Gamma_3)\\&\times(\Gamma_1'F_2(\Gamma_3)\overline{\Gamma}\Gamma_1|\Gamma_1'F_2\overline{\Gamma}(F_2)\Gamma_1)\ .\end{aligned} \tag{2.28}$$

Similar formula can also be written down for $(e^{n'}S_2\Gamma_2\|\mathbf{X}(\overline{\Gamma})\|e^{n'}S_2\Gamma_4)$.

For the spin-orbit interaction, we have

$$\begin{aligned}&(f_2{}^nS_1\Gamma_1\|\mathbf{V}(1F_1)\|f_2{}^nS_3\Gamma_3)\\&=n(\tfrac{1}{2}f_2\|\mathbf{st}\|\tfrac{1}{2}f_2)[(2S_1+1)(\Gamma_1)/2(f_2)]^{1/2}\sum_{S_1'\Gamma_1'}(f_2{}^nS_1\Gamma_1\{|f_2{}^{n-1}(S_1'\Gamma_1')f_2)(f_2{}^{n-1}(S_1'\Gamma_1')f_2|\}f_2{}^nS_3\Gamma_3)\\&\times(S_1'\tfrac{1}{2}(S_3)1S_1|S_1'\tfrac{1}{2}1(\tfrac{1}{2})S_1)(\Gamma_1'F_2(\Gamma_3)F_1\Gamma_1|\Gamma_1'F_2F_1(F_2)\Gamma_1)\ .\end{aligned} \tag{2.29}$$

$(f_2{}^nS\Gamma\|\mathbf{X}(\Gamma)\|f_2{}^nS\Gamma')$, $(e^{n'}S\Gamma\|\mathbf{X}(\Gamma)\|e^{n'}S\Gamma')$ and $(f_2{}^nS\Gamma\|\mathbf{V}(1F_1)\|f_2{}^nS'\Gamma')$ evaluated by these formulae are given in Table I. It is to be notde that, for half filled shells ($n=3$ and/or $n'=2$), not only the diagonal elements of $\mathbf{V}$-operators vanish but also certain off-diagonal elements vanish. This fact is peculiar to the half filled shells and will perhaps be the cause of sharp absorption lines in the spectra of $Cr^{3+}(f_2{}^3)$ $Mn^{2+}(f_2{}^3e^2)$ and $Ni^{2+}(f_2{}^6e^2)$ complexes, since this means that the states of half filled shells are not perturbed by the nuclear motion to the first order.

In Tables II and III all the necessary matrix elements of $(\Gamma_a\Gamma_b\Gamma[\overline{\Gamma}_a]\Gamma_a'\Gamma_b\Gamma')$, $(\Gamma_a\Gamma_b\Gamma[\overline{\Gamma}_b]\Gamma_a\Gamma_b'\Gamma')$ and $(S_aS_bS[1]S_a'S_bS')$ are given.

Since we do not know at present which matrix elements are needed for future analyses, we shall rather content ourselves with the preparation of these tables than proceed to the tabulation of all the matrix elements of (2.25) and (2.26)

Before leaving this section, definitions of the double barred matrices for one electron should be given. According to (2.8) and (2.10), only the followings do not vanish among the diagonal double barred matrix elements of $\mathbf{V}$ and $\mathbf{T}$ operators:

$$\begin{aligned}&(f_2\|\mathbf{v}(E)\|f_2)=\sqrt{3}\,(f_2\zeta|\mathbf{v}_u(E_g)|f_2\zeta)\ ,\\&(f_2\|\mathbf{v}(F_2)\|f_2)=\sqrt{6}\,(f_2\xi|\mathbf{v}_\xi(F_{2g})|f_2\eta)\ ,\\&(f_2\|\mathbf{t}(F_1)\|f_2)=\sqrt{6}\,(f_2\xi|\mathbf{t}_\gamma(F_{1g})|f_2\eta)=\sqrt{6}\,ik\ ,\\&(e\|\mathbf{v}(E)\|e)=-2(eu|\mathbf{v}_u(E_g)|eu)\ ,\\&(e\|\mathbf{t}(A_2)\|e)=\sqrt{2}\,(eu|\mathbf{t}(A_{2g})|ev)\ .\end{aligned} \tag{2.30}$$

Table Ia. $(f_2{}^nS\Gamma\|\mathbf{X}(\overline{\Gamma})\|f_2{}^nS'\Gamma')$

$\mathbf{X}(\overline{\Gamma})=\mathbf{V}(E)$

$n=1,\ 5\quad (f_2\|\mathbf{v}(E)\|f_2)=-(f_2{}^5{}^2F_2\|\mathbf{V}(E)\|f_2{}^5{}^2F_2)$

$n=2,\ 4\quad (f_2{}^2S\Gamma\|\mathbf{V}(E)\|f_2{}^2S\Gamma')$

$\qquad =\pm(f_2{}^4S\Gamma\|\mathbf{V}(E)\|f_2{}^4S\Gamma')$

$S\Gamma$ \ $S'\Gamma'$	$^1A_1$	$^3F_1$	^1E	$^1F_2$
$^1A_1$			$2/\sqrt{3}$	
$^3F_1$		∓1		
^1E	$2/\sqrt{3}$		$\mp2/\sqrt{3}$	
$^1F_2$				∓1

$\times(f_2\|\mathbf{v}(E)\|f_2)$

Take upper sign for $n=2$, and lower sign for $n=4$. The elements without double sign are same both for $n=2$ and 4.

$n=3\quad (f_2{}^3S\Gamma\|\mathbf{V}(E)\|f_2{}^3S'\Gamma')$

$S\Gamma$ \ $S'\Gamma'$	$^4A_2$	^2E	$^2F_1$	$^2F_2$
$^4A_2$				
^2E				
$^2F_1$				$\sqrt{3}$
$^2F_2$			$-\sqrt{3}$	

$\times(f_2\|\mathbf{v}(E)\|f_2)$

$\mathbf{X}(\overline{\Gamma})=\mathbf{V}(F_2)$

$n=1,\ 5\quad (f_2\|\mathbf{v}(F_2)\|f_2)=-(f_2{}^5{}^2F_2\|\mathbf{V}(F_2)\|f_2{}^5{}^2F_2)$

$n=2,\ 4\quad (f_2{}^2S\Gamma\|\mathbf{V}(F_2)\|f_2{}^2S\Gamma')$

$\qquad =\pm(f_2{}^4S\Gamma\|\mathbf{V}(F_2)\|f_2{}^4S\Gamma')$

$S\Gamma$ \ $S'\Gamma'$	$^1A_1$	$^3F_1$	^1E	$^1F_2$
$^1A_1$				$2/\sqrt{3}$
$^3F_1$		∓1		
^1E			$\mp\sqrt{2}/\sqrt{3}$	
$^1F_2$	$2/\sqrt{3}$		$\mp\sqrt{2}/\sqrt{3}$	±1

$\times(f_2\|\mathbf{v}(F_2)\|f_2)$

$n=3\quad (f_2{}^3S\Gamma\|\mathbf{V}(F_2)\|f_2{}^3S'\Gamma')$

$S\Gamma$ \ $S'\Gamma'$	$^4A_2$	^2E	$^2F_1$	$^2F_2$
$^4A_2$				
^2E				$\sqrt{2}$
$^2F_1$				-1
$^2F_2$		$\sqrt{2}$	-1	

$\times(f_2\|\mathbf{v}(F_2)\|f_2)$

$\mathbf{X}(\overline{\Gamma})=\mathbf{T}(F_1)$

$n=1,\ 5\quad (f_2\|\mathbf{t}(F_1)\|f_2)=(f_2{}^5{}^2F_2\|\mathbf{T}(F_1)\|f_2{}^5{}^2F_2)$

$n=2,\ 4\quad (f_2{}^2S\Gamma\|\mathbf{T}(F_1)\|f_2{}^2S'\Gamma')$

$\qquad =(f_2{}^4S\Gamma\|\mathbf{T}(F_1)\|f_2{}^4S'\Gamma')$

$S\Gamma$ \ $S'\Gamma'$	$^1A_1$	$^3F_1$	^1E	$^1F_2$
$^1A_1$				
$^3F_1$		-1		
^1E				$\sqrt{2}$
$^1F_2$			$\sqrt{2}$	-1

$\times(f_2\|\mathbf{t}(F_1)\|f_2)$

$n=3\quad (f_2{}^3S\Gamma\|\mathbf{T}(F_1)\|f_2{}^3S'\Gamma')$

$S\Gamma$ \ $S'\Gamma'$	$^4A_2$	^2E	$^2F_1$	$^2F_2$
$^4A_2$				
^2E			$\sqrt{2}$	
$^2F_1$		$\sqrt{2}$	1	
$^2F_2$				1

$\times(f_2\|\mathbf{t}(F_1)\|f_2)$

Table Ia′. $(f_2{}^nS\Gamma\|\mathbf{V}(1F_1)\|f_2{}^nS'\Gamma')$

$n=1,\ 5\quad (\frac{1}{2}f_2\|\mathbf{st}\|\frac{1}{2}f_2)=-(f_2{}^5{}^2F_2\|\mathbf{V}(1F_1)\|f_2{}^5{}^2F_2)$

$n=2,\ 4\quad (f_2{}^2S\Gamma\|\mathbf{V}(1F_1)\|f_2{}^2S'\Gamma')$

$\qquad =\pm(f_2{}^4S\Gamma\|\mathbf{V}(1F_1)\|f_2{}^4S'\Gamma')$

$S\Gamma$ \ $S'\Gamma'$	$^1A_1$	$^3F_1$	^1E	$^1F_2$
$^1A_1$		$-\sqrt{2}/\sqrt{3}$		
$^3F_1$	$\sqrt{2}/\sqrt{3}$	∓1	$\mp1/\sqrt{3}$	$\mp1/\sqrt{2}$
^1E		$\pm1/\sqrt{3}$		
$^1F_2$		$\pm1/\sqrt{2}$		

$\times(\frac{1}{2}f_2\|\mathbf{st}\|\frac{1}{2}f_2)$

$n=3\quad (f_2{}^3S\Gamma\|\mathbf{V}(1F_1)\|f_2{}^3S'\Gamma')$

$S\Gamma$ \ $S'\Gamma'$	$^4A_2$	$^2E_1$	$^2F_1$	$^2F_2$
$^4A_2$				$2/\sqrt{3}$
^2E				$-\sqrt{2}/\sqrt{3}$
$^2F_1$				-1
$^2F_2$	$-2/\sqrt{3}$	$-\sqrt{2}/\sqrt{3}$	-1	

$\times(\frac{1}{2}f_2\|\mathbf{st}\|\frac{1}{2}f_2)$

Table Ib. $(e^n S\Gamma \| \mathbf{X}(\Gamma) \| e^n S'\Gamma')$

$\mathbf{X}(\overline{\Gamma})=\mathbf{V}(E)$

$n=1,\ 3 \quad (e\|\mathbf{v}(E)\|e)=-(e^{3\,2}E\|\mathbf{V}(E)\|e^{3\,2}E)$

$n=2 \quad (e^2 S\Gamma\|\mathbf{V}(E)\|e^2 S'\Gamma')$

$S\Gamma$ \ $S'\Gamma'$	$^1A_1$	$^3A_2$	^1E
$^1A_1$			$\sqrt{2}$
$^3A_2$			
^1E	$\sqrt{2}$		

$\mathbf{X}(\overline{\Gamma})=\mathbf{T}(A_2)$

$n=1,\ 3 \quad (e\|\mathbf{t}(A_2)\|e)=(e^{3\,2}E\|\mathbf{T}(A_2)\|e^{3\,2}E)$

$n=2 \quad (e^2 S\Gamma\|\mathbf{T}(A_2)\|e^2 S'\Gamma')$

$S\Gamma$ \ $S'\Gamma'$	$^1A_1$	$^3A_2$	^1E
$^1A_1$			
$^3A_2$			
^1E			-2

Table IIa. $(\Gamma_a\Gamma_b\Gamma[\overline{\Gamma}_a]\Gamma_a'\Gamma_b\Gamma')$

$\overline{\Gamma}_a=E \quad (\Gamma_a A_1\Gamma_a[E]\Gamma_a' A_1\Gamma_a')=1\,,$
$(\Gamma_a A_2\Gamma_a{}^*[E]\Gamma_a' A_2\Gamma_a'^*)-1\,,$
except for $(EA_2E[E]EA_2E)=-1,$
where $\Gamma^*=A_2\times\Gamma\,.$
$(\Gamma_a E\Gamma[E|\Gamma' E\Gamma_a')$

Γ_a	Γ \ Γ_a'	A_1	A_2	E		
	Γ'	E	E	A_1	A_2	E
A_1	E			$1/\sqrt{2}$	$-1/\sqrt{2}$	1
A_2	E			$-1/\sqrt{2}$	$1/\sqrt{2}$	1
E	A_1	$1/\sqrt{2}$	$-1/\sqrt{2}$			$1/\sqrt{2}$
	A_2	$-1/\sqrt{2}$	$1/\sqrt{2}$			$1/\sqrt{2}$
	E	1	1	$1/\sqrt{2}$	$1/\sqrt{2}$	

Γ_a	Γ \ Γ_a'	F_1	F_2	F_2	
	Γ'	F_1	F_2	F_1	F_2
F_1	F_1	1			1
	F_2		1	1	
F_2	F_1		1	1	
	F_2	1			1

$\overline{\Gamma}_a=F_2 \quad (\Gamma_a A_1\Gamma_a[F_2]\Gamma_a' A_1\Gamma_a')=1$
$(\Gamma_a A_2\Gamma_a{}^*|F_2|\Gamma_a' A_2\Gamma'^*{}_a)=1$
$(\Gamma_a E\Gamma|F_2|\Gamma_a' E\Gamma')=(\Gamma_a' E\Gamma'|F_2|\Gamma_a E\Gamma)$

Γ_a	Γ \ Γ_a'	F_1	F_2	F_2	
	Γ'	F_1	F_2	F_1	F_2
A_1	E			1	1
A_2	E	1	1		
E	A_1		$-1/\sqrt{2}$		$1/\sqrt{2}$
	A_2	$1/\sqrt{2}$		$-1/\sqrt{2}$	
	E	$1/\sqrt{2}$	$-1/\sqrt{2}$	$1/\sqrt{2}$	$-1/\sqrt{2}$

Γ_a	Γ \ Γ_a'	F_1	F_2	F_2	
	Γ'	F_1	F_2	F_1	F_2
F_1	F_1	$-1/2$	$\sqrt{3}/2$	$-\sqrt{3}/2$	$-1/2$
	F_2	$\sqrt{3}/2$	$-1/2$	$-1/2$	$-\sqrt{3}/2$
F_2	F_1	$-\sqrt{3}/2$	$-1/2$	$-1/2$	$\sqrt{3}/2$
	F_2	$-1/2$	$-\sqrt{3}/2$	$\sqrt{3}/2$	$-1/2$

$\overline{\Gamma}_a=F_1 \quad (\Gamma_a A_1\Gamma_a[F_1]\Gamma_a' A_1\Gamma_a')=1$
$(\Gamma_a A_2\Gamma_a{}^*|F_1|\Gamma_a' A_2\Gamma_a'^*)-1$
except for $(F_1A_2F_2[F_1]F_1A_2F_2)=-1$
$(F_2A_2F_1[F_1|F_2A_2F_1)=-1$
$(\Gamma_a E\Gamma[F_1|\Gamma_a' E\Gamma')=(\Gamma_a' E\Gamma'[F_1]\Gamma_a E\Gamma)$

Γ_a	Γ \ Γ_a'	F_1	F_2	F_2	
	Γ'	F_1	F_2	F_1	F_2
A_1	E	1	1		
A_2	E			1	1
E	A_1	$1/\sqrt{2}$		$-1/\sqrt{2}$	
	A_2		$-1/\sqrt{2}$		$1/\sqrt{2}$
	E	$-1/\sqrt{2}$	$1/\sqrt{2}$	$-1/\sqrt{2}$	$1/\sqrt{2}$

Γ_a	Γ \ Γ_a'	F_1	F_2	F_2	
	Γ'	F_1	F_2	F_1	F_2
F_1	F_1	$-1/2$	$-\sqrt{3}/2$	$\sqrt{3}/2$	$-1/2$
	F_2	$-\sqrt{3}/2$	$1/2$	$-1/2$	$-\sqrt{3}/2$
F_2	F_1	$\sqrt{3}/2$	$-1/2$	$1/2$	$\sqrt{3}/2$
	F_2	$-1/2$	$-\sqrt{3}/2$	$\sqrt{3}/2$	$-1/2$

Table IIb. $(\Gamma_a\Gamma_b\Gamma[\overline{\Gamma}_b]\Gamma_a\Gamma_b'\Gamma')$

$\overline{\Gamma}_b = E$ $\quad (A_1\Gamma_b\Gamma_b[E]A_1\Gamma_b'\Gamma_b')=1$
$(A_2\Gamma_b\Gamma_b^*[E]A_2\Gamma_b'\Gamma_b'^*)=1$
except for $(A_2EE[E]A_2EE)=-1$
$(E\Gamma_b\Gamma[E]E\Gamma_b'\Gamma)$

	Γ_b' Γ	A_1 E	A_2 E	E A_1	A_2	E
Γ_b Γ						
A_1 E				$1/\sqrt{2}$	$1/\sqrt{2}$	1
A_2 E				$-1/\sqrt{2}$	$-1/\sqrt{2}$	1
E A_1		$1/\sqrt{2}$	$-1/\sqrt{2}$			$1/\sqrt{2}$
A_2		$1/\sqrt{2}$	$-1/\sqrt{2}$			$-1/\sqrt{2}$
E		1	1	$1/\sqrt{2}$	$-1/\sqrt{2}$	

$(F_1\Gamma_b\Gamma[E]F_1\Gamma_b'\Gamma')$

	Γ_b' Γ'	A_1 F_1	A_2 F_2	E F_1	F_2
Γ_b Γ					
A_1 F_1				$\sqrt{3}/\sqrt{2}$	$-\sqrt{3}/\sqrt{2}$
A_2 F_2				$-\sqrt{3}/\sqrt{2}$	$\sqrt{3}/\sqrt{2}$
E F_1		$\sqrt{3}/\sqrt{2}$	$\sqrt{3}/\sqrt{2}$	$-\sqrt{3}/2$	$-\sqrt{3}/2$
F_2		$\sqrt{3}/\sqrt{2}$	$\sqrt{3}/\sqrt{2}$	$\sqrt{3}/2$	$\sqrt{3}/2$

$(F_2\Gamma_b\Gamma[E]F_2\Gamma_b'\Gamma)$

	Γ_b' Γ'	A_1 F_2	A_2 F_1	E F_1	F_2
Γ_b Γ					
A_1 F_2				$-\sqrt{3}/\sqrt{2}$	$\sqrt{3}/\sqrt{2}$
A_2 F_1				$\sqrt{3}/\sqrt{2}$	$-\sqrt{3}/\sqrt{2}$
E F_1		$\sqrt{3}/\sqrt{2}$	$\sqrt{3}/\sqrt{2}$	$\sqrt{3}/2$	$\sqrt{3}/2$
F_2		$\sqrt{3}/\sqrt{2}$	$\sqrt{3}/\sqrt{2}$	$-\sqrt{3}/2$	$-\sqrt{3}/2$

$\overline{\Gamma}_b = A_2$ $\quad (A_1\Gamma_b\Gamma_b[A_2]A_1\Gamma_b^*\Gamma_b^*)=1$
$(A_2\Gamma_b\Gamma_b^*[A_2]A_2\Gamma_b^*\Gamma_b)=1$
$(E\Gamma_b\Gamma[A_2|E\Gamma_b'\Gamma')$

	Γ_b' Γ'	A_1 E	A_2 E
Γ_b Γ			
A_1 E			$\sqrt{2}$
A_2 E		$\sqrt{2}$	

	Γ_b' Γ'	E A_1	A_2	E
Γ_b Γ				
E A_1			$-1/\sqrt{2}$	
A_2		$-1/\sqrt{2}$		
E				-1

$(F_1\Gamma_b\Gamma[A_2]F_1\Gamma_b'\Gamma')$

	Γ_b' Γ'	A_1 F_1	A_2 F_2
Γ_b Γ			
A_1 F_1			$\sqrt{3}$
A_2 F_2		$\sqrt{3}$	

	Γ_b' Γ'	E F_1	F_2
Γ_b Γ			
E F_1			$\sqrt{3}/\sqrt{2}$
F_2		$\sqrt{3}/\sqrt{2}$	

$(F_2\Gamma_b\Gamma[A_2]F_2\Gamma_b'\Gamma')$

	Γ_b' Γ'	A_1 F_2	A_2 F_1
Γ_b Γ			
A_1 F_2			$\sqrt{3}$
A_2 F_1		$\sqrt{3}$	

	Γ_b' Γ'	E F_1	F_2
Γ_b Γ			
E F_1			$\sqrt{3}/\sqrt{2}$
F_2		$\sqrt{3}/\sqrt{2}$	

Table III. $(S_aS_bS[1]S_a'S_bS')$

$(S_a0S_a[1]S_a'0S_a')=1$

$(S_a1S[1]S_a'1S')$

S_a	S_a' / S	0 / 1	1 / 0	1	2
0	1		$1/\sqrt{3}$	1	$\sqrt{5}/\sqrt{3}$
1	0	$1/\sqrt{3}$		$-1/\sqrt{3}$	
	1	-1	$1/\sqrt{3}$	$1/2$	$-\sqrt{5}/2\sqrt{3}$
	2	$\sqrt{5}/\sqrt{3}$		$\sqrt{5}/2\sqrt{3}$	$\sqrt{5}/2$

S_a	S	S_a' / S': 1/2 / 1/2	3/2	3/2 / 1/2	3/2	5/2
1/2	1/2	$-1/3$	$-2\sqrt{2}/3$	$2/3$	$\sqrt{5}/3$	
	3/2	$2\sqrt{2}/3$	$\sqrt{10}/3$	$1/3\sqrt{2}$	$2/3$	$\sqrt{3}/\sqrt{2}$
3/2	1/2	$-2/3$	$1/3\sqrt{2}$	$\sqrt{5}/3\sqrt{2}$	$-\sqrt{2}/3$	
	3/2	$\sqrt{5}/3$	$-2/3$	$\sqrt{2}/3$	$11/15$	$\sqrt{6}/5$
	5/2		$\sqrt{3}/\sqrt{2}$		$\sqrt{6}/5$	$3\sqrt{7}/5\sqrt{2}$

$(S_a\tfrac{1}{2}S[1]S_a'\tfrac{1}{2}S')$

S_a	S	S_a' / S': 0 / 1/2	1 / 1/2	3/2
0	1/2		$\sqrt{2}/\sqrt{3}$	$2/\sqrt{3}$
1	1/2	$-\sqrt{2}/\sqrt{3}$	$2/3$	$-\sqrt{2}/3$
	3/2	$2/\sqrt{3}$	$\sqrt{2}/3$	$\sqrt{10}/3$

S_a	S	S' / S: 1/2 / 0	1	3/2 / 1	2
1/2	1/2		$-1/\sqrt{2}$	$1/\sqrt{2}$	
	1	$1/\sqrt{2}$	1	$1/2$	$\sqrt{5}/2$
2/3	1	$1/\sqrt{2}$	$-1/2$	$\sqrt{5}/2\sqrt{2}$	$-1/2\sqrt{2}$
	2		$\sqrt{5}/2$	$1/2\sqrt{2}$	$3/2\sqrt{2}$

The off-diagonal elements are as follows

$$
\begin{aligned}
&(f_2\|\mathbf{v}(F_2)\|e)=(e\|\mathbf{v}(F_2)\|f_2)=\sqrt{3}\,(f_2\zeta|\mathbf{v}_\zeta(F_{2g})|eu)\,,\\
&(f_2\|\mathbf{v}(F_1)\|e)=-(e\|\mathbf{v}(F_1)\|f_2)=-3(f_2\zeta|\mathbf{v}_\gamma(F_{1g})|ev)\,,\\
&(f_2\|\mathbf{t}(F_1)\|e)=(e\|\mathbf{t}(F_1)\|f_2)=-3(f_2\zeta|\mathbf{t}_\gamma(F_{1g})|ev)=-2\sqrt{3}\,ik'\,,\\
&(f_2\|\mathbf{t}(F_2)\|e)=-(e\|\mathbf{t}(F_2)\|f_2)=\sqrt{3}\,(f_2\zeta|\mathbf{t}_\zeta(F_{2g})|eu)\,.
\end{aligned}
\tag{2.31}
$$

For the spin-orbit interaction operator;

$$
\begin{aligned}
&(\tfrac{1}{2}f_2\|\mathbf{st}\|\tfrac{1}{2}f_2)=6(\tfrac{1}{2}f_2+\tfrac{1}{2}\xi|\mathbf{s}_0\mathbf{t}_\gamma|\tfrac{1}{2}f_2+\tfrac{1}{2}\eta)=3i\zeta\,,\\
&(\tfrac{1}{2}f_2\|\mathbf{st}\|\tfrac{1}{2}e)=(\tfrac{1}{2}e\|\mathbf{st}\|\tfrac{1}{2}f_2)=-3\sqrt{2}\,(\tfrac{1}{2}f_2+\tfrac{1}{2}\zeta|\mathbf{s}_0\mathbf{t}_\gamma|\tfrac{1}{2}e+\tfrac{1}{2}v)=-3\sqrt{2}\,i\zeta'\,.
\end{aligned}
\tag{2.32}
$$

If f_2 and e are constructed from the d-functions and $\mathbf{t}(F_1)=\boldsymbol{l}$, $\mathbf{t}=\zeta\boldsymbol{l}$, then $k=k'=1$ and $\zeta'=\zeta$ will be the spin-orbit coupling parameter for a d electron.

iii) The evaluation of the off-diagonal elements

Since the operators we are interested in are of one electron type and (2.7), (2.9) and (2.14) are still valid, we have only to calculate the double barred matrix elements of the following type in this section:

$$
(f_2{}^n(S_1\Gamma_1)e^{n'}(S_2\Gamma_2)S\Gamma\|\mathbf{X}(\overline{\Gamma})\|f_2{}^{n-1}(S_3\Gamma_3)e^{n'+1}(S_4\Gamma_4)S\Gamma')
\tag{2.33}
$$

which can be calculated by using the formula (28) of RIII as follows:

$$
=\sum_{\underset{\sim}{S}\,\underset{\sim}{\Gamma}}\sqrt{n}\,(f_2{}^nS_1\Gamma_1\{|f_2{}^{n-1}(S_3\Gamma_3)f_2)(e,\ e^{n'}(S_2\Gamma_2)|\}e^{n'+1}S_4\Gamma_4)\sqrt{n'+1}
$$

$$\times(S_3\Gamma_3 f_{2n}(S_1\Gamma_1)S_2\Gamma_2 S\Gamma\|\mathbf{x}_n(\overline{\Gamma})\|S_3\Gamma_3 e_n(\underset{\sim}{S\Gamma})S_2\Gamma_2 S\Gamma'')$$
$$\times(S_3\Gamma_3 \tfrac{1}{2}e(\underset{\sim}{S\Gamma})S_2\Gamma_2 S\Gamma''|S_3\Gamma_3 \tfrac{1}{2}eS_2\Gamma_2(S_1\Gamma_4)S\Gamma'') \,. \tag{2.34}$$

Now, applying (2.21) and (2.22), we obtain

$$=\sqrt{n(2S_1+1)(\Gamma_1)}\,(f_2{}^nS_1\Gamma_1\{|f_2{}^{n-1}(S_3\Gamma_3)(ee^{n'}(S_2\Gamma_2)|\}e^{n'+1}S_4\Gamma_4)\sqrt{(n'+1)(2S_4+1)(\Gamma_4)}$$
$$\times(f_2\|\mathbf{x}(\overline{\Gamma})\|e)[S_1S_2S|S_3S_4S]\,[\Gamma_1\Gamma_2\Gamma[\overline{\Gamma}]\Gamma_3\Gamma_4\Gamma''] \,, \tag{2.35}$$

where

$$[S_1S_2S|S_3S_4S]=[(2S_1+1)(2S_4+1)]^{-1/2}(S_3\tfrac{1}{2}(S_1)S_2S|S_3\tfrac{1}{2}S_2(S_4)S)=W(S_3\tfrac{1}{2}SS_2;\ S_1S_4) \tag{2.36}$$

and

$$[\Gamma_1\Gamma_2\Gamma[\overline{\Gamma}]\Gamma_3\Gamma_4\Gamma'']$$
$$=[(\Gamma)/(f_2)(\Gamma_1)(\Gamma_4)]^{1/2}(\Gamma_3,\ E\overline{\Gamma}(F_2)(\Gamma_1)\Gamma_2\Gamma|\Gamma_3,\ E\Gamma_2(\Gamma_4)(\Gamma')\overline{\Gamma}\Gamma')$$
$$=[(\Gamma)/(f_2)(\Gamma_1)(\Gamma_4)]^{1/2}\sum_{\underset{\sim}{\Gamma}}(\Gamma_3E(\underset{\sim}{\Gamma})\overline{\Gamma}\Gamma_1|\Gamma_3,\ E\Gamma(F_2)\overline{\Gamma}_1)(\underset{\sim}{\Gamma}\Gamma_2(\Gamma'')\Gamma\Gamma'|\underset{\sim}{\Gamma}\overline{\Gamma}(\Gamma_1)\Gamma_2\Gamma')$$
$$\times(\Gamma_3E(\underset{\sim}{\Gamma})\Gamma_2\Gamma'|\Gamma_3,\ E\Gamma_2(\Gamma_4)\Gamma'')$$
$$=[(\Gamma_1)(\Gamma_4)]^{-1/2}\sum_{\underset{\sim}{\Gamma}}(\Gamma_3F_2\Gamma_1[\overline{\Gamma}]\Gamma_3E\underset{\sim}{\Gamma})(\Gamma_1\Gamma_2\Gamma[\overline{\Gamma}]\underset{\sim}{\Gamma}\Gamma_2\Gamma')(\Gamma_3E(\underset{\sim}{\Gamma})\Gamma'|\Gamma_3,\ E\Gamma_2(\Gamma_4)\Gamma'') \,. \tag{2.37}$$

For the spin-orbit interaction, we have similarly

$$(f_2{}^n(S_1\Gamma_1)e^{n'}(S_2\Gamma_2)S\Gamma\|\mathbf{V}(1F_1)\|f_2{}^{n-1}(S_3\Gamma_3)e^{n'+1}(S_4\Gamma_4)S'\Gamma'')$$
$$=\sqrt{n(2S_1+1)(\Gamma_1)}\,(f_2{}^nS_1\Gamma_1\{|f_2{}^{n-1}(S_3\Gamma_3)f_2)(ee^{n'}(S_2\Gamma_2|\}e^{n'+1}S_4\Gamma_4)\sqrt{(n'+1)(2S_4+1)(\Gamma_4)}$$
$$\times(\tfrac{1}{2}f_2\|\mathbf{st}\|\tfrac{1}{2}e)[S_1S_2S[1]S_3S_4S'][\Gamma_1\Gamma_2\Gamma[F_1]\Gamma_3\Gamma_4\Gamma''] \,, \tag{2.38}$$

where

$$[S_1S_2S[1]S_3S_4S']$$
$$=(2S+1)(2S'+1)\sum_{\underset{\sim}{S}}(2\underset{\sim}{S}+1)W(S_3\tfrac{1}{2}S_11;\ \underset{\sim}{S}\tfrac{1}{2})W(S'1S_2S_1;\ S\underset{\sim}{S})W(S_3\tfrac{1}{2}S'S_2;\ SS_4) \,, \tag{2.39}$$

The off-diagonal elements are thus easily evaluated by the multiplication of several factors which appear on the right hand sides of (2.35) and (2.38). The coefficients of fractional parentage are already given in (I), so that only $(e,\ e^n(S'\Gamma')|\}e^{n+1}S\Gamma)$ which are obtained from $(e^n(S'\Gamma')e|\}e^{n+1}S\Gamma)$ by (3.3) of (I) are given here (Table IV). The matrices $[\Gamma_a\Gamma_b\Gamma[\overline{\Gamma}]\Gamma_c\Gamma_a\Gamma'']$, $[S_aS_bS[1]S_cS_aS']$ and $[S_aS_bS|S_cS_aS]$ are given in Table V, VI, and VIII, respectively.

We have thus essentially finished the evaluation of all the matrix elements of tensor operators among the states Ψ $(f_2{}^n(S_1\Gamma_1)e^{n'}(S_2\Gamma_2)S\Gamma\cdot M_s\gamma)$ that will be needed in practical problems. The value of the necessary matrix elements are readily obtained simply by multiplying appropriate factors given in Table I–VII according to the formulae (2.25), (2.26), (2.35) and (2.38).*

Table IV. $(e,\ e^n(S'\Gamma')|\}e^{n+1}S\Gamma)$

$(ee^n(S'\Gamma')|\}e^{n+1}S\Gamma)=1$ for $n=0,1,3$

for $n=2$ $(ee^2(S'\Gamma')|\}e^3{}^2E)$

$S'\Gamma'$	^2E
$^1A_1$	$1/\sqrt{6}$
$^3A_2$	$-1/\sqrt{2}$
^1E	$-1/\sqrt{3}$

$(f_2{}^{n-1}(S'\Gamma')f_2|\}f_2{}^nS\Gamma)=1$ $n=1,2,6$

Values for $n=3,4,5$ are given in Table II of (I).

§ 3. The Effective Hamiltonian for the Orbitally Degenerate States

The method of the spin-Hamiltonian for the non-degenerate orbital multiplets[6] has been

* It must be, however, noted that the formulae (2.25), (2.26), (2.35) and (2.38) are not to be used when $N=n+n'\geq 6$. The matrix elements of operators in this case should be evaluated by the following formula;

$$(f_2{}^n(S_1\Gamma_1)e^{n'}(S_2\Gamma_2)S\Gamma\|\mathbf{X}\,|f_2{}^{n''}(S_3\Gamma_3)e^{n'''}(S_4\Gamma_4)S'\Gamma'')$$
$$=\pm(f_2{}^{6-n}(S_1\Gamma_1)e^{4-n'}(S_2\Gamma_2)S\Gamma\|\mathbf{X}\|f_2{}^{6-n''}(S_3\Gamma_3$$
$$\times e^{4-n'''}(S_4\Gamma_4)S'\Gamma') \,,$$

where $-$ sign is used for $\mathbf{X}=\mathbf{V}(\overline{\Gamma})$ or $\mathbf{V}(1F_1)$, while $+$ sign should be taken for $\mathbf{X}=\mathbf{T}(\overline{\Gamma})$.

Table Va. $[\Gamma_a\Gamma_b\Gamma[F_1]\Gamma_c\Gamma_d\Gamma']$

$[\Gamma_a A_1\Gamma_c[F_1]\Gamma_c E\Gamma'] = -[\Gamma_c E\Gamma'[F_1]\Gamma_a A_1\Gamma_c]$

Γ_c	Γ'	A_1	A_2	E	A_2	E	F_1	F_2	F_1	F_2
Γ_a	Γ	E	E	A_1			F_1		F_1	
A_1	A_1								$1/\sqrt{6}$	
A_2	A_2							$1/\sqrt{6}$		
E	E							$1/\sqrt{6}$	$1/\sqrt{6}$	
F_1	F_1		$1/\sqrt{6}$	$-1/2\sqrt{3}$		$-1/2\sqrt{3}$	$-1/2\sqrt{2}$	$-1/2\sqrt{6}$	$-1/2\sqrt{6}$	$1/2\sqrt{2}$
F_2	F_1	$1/\sqrt{6}$			$-1/2\sqrt{3}$	$1/2\sqrt{3}$	$1/2\sqrt{2}$	$1/2\sqrt{6}$	$-1/2\sqrt{6}$	$1/2\sqrt{2}$

$[\Gamma_c A_2\Gamma_a{}^*[F_1]\Gamma_c E\Gamma'] = +[\Gamma_c E\Gamma'[F_1]\Gamma_a A_2\Gamma_a{}^*]$

Γ_c	Γ'	A_1	A_2	E	A_2	E	F_1	F_2	F_1	F_2
Γ	Γ	E	E	A_1			F_1		F_1	
A_1	A_2									$1/\sqrt{6}$
A_2	A_1						$1/\sqrt{6}$			
E	E						$1/\sqrt{6}$			$1/\sqrt{6}$
F_1	F_2		$1/\sqrt{6}$		$1/2\sqrt{3}$	$1/2\sqrt{3}$	$-1/2\sqrt{6}$	$1/2\sqrt{2}$	$1/2\sqrt{2}$	$1/2\sqrt{6}$
F_2	F_1	$1/\sqrt{6}$		$1/2\sqrt{3}$		$-1/2\sqrt{3}$	$-1/2\sqrt{6}$	$1/2\sqrt{2}$	$-1/2\sqrt{2}$	$-1/2\sqrt{6}$

$[\Gamma_a E\Gamma'[F_1]\Gamma_c E\Gamma']$

Γ_c	Γ'	A_1	A_2	E	A_2	E	F_1	F_2	F_1	F_2
Γ_a	Γ	E	E	A_1			F_1		F_1	
A_1	E								$1/2\sqrt{3}$	$-1/2\sqrt{3}$
A_2	E						$-1/2\sqrt{3}$	$1/2\sqrt{3}$		
E	A_1						$1/2\sqrt{6}$		$1/2\sqrt{6}$	
	A_2							$1/2\sqrt{6}$		$1/2\sqrt{6}$
	E						$1/2\sqrt{6}$	$1/2\sqrt{6}$	$-1/2\sqrt{6}$	$-1/2\sqrt{6}$
F_1	F_1		$1/2\sqrt{3}$	$-1/2\sqrt{6}$		$-1/2\sqrt{6}$		$1/2\sqrt{3}$	$1/2\sqrt{3}$	
	F_2		$-1/2\sqrt{3}$		$-1/2\sqrt{6}$	$-1/2\sqrt{6}$	$-1/2\sqrt{3}$			$1/2\sqrt{3}$
F_2	F_1	$-1/2\sqrt{3}$		$-1/2\sqrt{6}$		$1/2\sqrt{6}$	$-1/2\sqrt{3}$			$-1/2\sqrt{3}$
	F_2	$1/2\sqrt{3}$			$-1/2\sqrt{6}$	$1/2\sqrt{6}$		$-1/2\sqrt{3}$	$1/2\sqrt{3}$	

Table Vb. $[\Gamma_a\Gamma_b\Gamma[F_2]\Gamma_c\Gamma_d\Gamma']$

$[\Gamma_a A_1\Gamma_c[F_2]\Gamma_c E\Gamma'] = +[\Gamma_c E\Gamma'[F_2]\Gamma_a A_1\Gamma_c]$

Γ_c	Γ'	A_1	A_2	E	A_2	E	F_1	F_2	F_1	F_2
Γ_a	Γ	E	E	A_1			F_1		F_1	
A_1	A_1									$1/\sqrt{6}$
A_2	A_2						$1/\sqrt{6}$			
E	E						$1/\sqrt{6}$			$1/\sqrt{6}$
F_1	F_1		$1/\sqrt{6}$		$1/2\sqrt{3}$	$1/2\sqrt{3}$	$-1/2\sqrt{6}$	$-1/2\sqrt{2}$	$1/2\sqrt{2}$	$-1/2\sqrt{6}$
F_2	F_2	$1/\sqrt{6}$		$1/2\sqrt{3}$		$-1/2\sqrt{3}$	$-1/2\sqrt{6}$	$1/2\sqrt{2}$	$-1/2\sqrt{2}$	$-1/2\sqrt{6}$

$$[\Gamma_a A_2 \Gamma^* [F_2] \Gamma_c E \Gamma'] = -[\Gamma_c E \Gamma' [F_2] \Gamma_a A_2 \Gamma_a^*]$$

Γ_a	Γ	Γ_c / Γ'	A_1 / E	A_2 / E	E / A_1	A_2	E	F_1 / F_1	F_2	F_2 / F_1	F_2
A_1	A_2									$1/\sqrt{6}$	
A_2	A_1								$1/\sqrt{6}$		
E	E								$1/\sqrt{6}$	$1/\sqrt{6}$	
F_1	F_2			$1/\sqrt{6}$	$-1/2\sqrt{3}$		$-1/2\sqrt{3}$	$-1/2\sqrt{2}$	$-1/2\sqrt{6}$	$-1/2\sqrt{6}$	$1/2\sqrt{2}$
F_2	F_1		$1/\sqrt{6}$			$-1/2\sqrt{3}$	$1/2\sqrt{3}$	$1/2\sqrt{2}$	$-1/2\sqrt{6}$	$-1/2\sqrt{6}$	$-1/2\sqrt{2}$

$$[\Gamma_a E \Gamma [F_2] \Gamma_c E \Gamma']$$

Γ_a	Γ	Γ_c / Γ'	A_1 / E	A_2 / E	E / A_1	A_2	E	F_1 / F_1	F_2	F_2 / F_1	F_2
A_1	E									$1/2\sqrt{3}$	$-1/2\sqrt{3}$
A_2	E							$-1/2\sqrt{3}$	$1/2\sqrt{3}$		
E	A_1								$-1/2\sqrt{6}$		$-1/2\sqrt{6}$
	A_2							$-1/2\sqrt{6}$		$-1/2\sqrt{6}$	
	E							$-1/2\sqrt{6}$	$-1/2\sqrt{6}$	$1/2\sqrt{6}$	$1/2\sqrt{6}$
F_1	F_1			$-1/2\sqrt{3}$		$-1/2\sqrt{6}$	$-1/2\sqrt{6}$	$-1/2\sqrt{3}$			$-1/2\sqrt{3}$
	F_2			$1/2\sqrt{3}$	$-1/2\sqrt{6}$		$-1/2\sqrt{6}$		$1/2\sqrt{3}$	$1/2\sqrt{3}$	
F_2	F_1		$1/2\sqrt{3}$			$-1/2\sqrt{6}$	$1/2\sqrt{6}$		$1/2\sqrt{3}$	$1/2\sqrt{3}$	
	F_2		$-1/2\sqrt{3}$		$-1/2\sqrt{6}$		$1/2\sqrt{6}$	$-1/2\sqrt{3}$			$-1/2\sqrt{3}$

Table VI. $[S_a S_b S[1] S_c S_a S']$

$$[S_a S_b S[1] S_c \tfrac{1}{2} S'] = (-)^{S_a+S_b+S+S_c+1/2+S'} [S_c \tfrac{1}{2} S'[1] S_a S_b S]$$

S_a	S_b	S	S_c / S': 1/2, 0	1	3/2, 1	2
0	0	0		$1/2$		
1		1	$-1/2\sqrt{3}$	$1/\sqrt{6}$	$-1/2\sqrt{6}$	$\sqrt{5}/2\sqrt{6}$
0	1	1	$1/2\sqrt{3}$	$1/\sqrt{6}$		
1		0		$-1/6\sqrt{3}$	$1/3\sqrt{3}$	
		1	$1/3\sqrt{2}$		$1/4$	$\sqrt{5}/12$
		2		$\sqrt{5}/3\sqrt{3}$	$\sqrt{5}/12\sqrt{3}$	$\sqrt{5}/4\sqrt{3}$

$$[S_a S_b S[1] S_c \tfrac{1}{2} S'] = (-)^{S_a+S_b+S+S_c+1/2+S'} [S_c \tfrac{1}{2} S'[1] S\ S_b S]$$

S_a	S_b	S	S_c / S': 0, 1/2	1, 1/2	3/2
1/2	0	1/2	$1/2$	$-1/6$	$\sqrt{2}/3$
3/2		3/2		$-1/3$	$\sqrt{5}/6$
1/2	1	1/2	$-1/6$	$5/18$	$\sqrt{2}/9$
		3/2	$\sqrt{2}/3$	$\sqrt{2}/9$	$\sqrt{10}/9$
3/2	1	1/2		$1/9$	$-1/9\sqrt{2}$
		3/2		$\sqrt{5}/9$	$1/18$
		5/2			$1/\sqrt{6}$

very useful in the semi-quantitative (in the sense that empirical parameters are introduced) analysis of paramagnetic resonance spectra[6]. Even when the ground multiplets were orbitally degenerate, the spin-Hamiltonian could be constructed and used for the final ground state (Kramers' doublet) in which we were interested in the case of paramagnetic resonance.[7]. In the case of optical spectra, however, we are rather interested in the whole levels split from a multiplet $^{2S+1}\Gamma$ due to the action of the field with low symmetry and of the spin-orbit

Table VII. $[S_a S_b S | S_c S_d S]$

$S=0$ $[S_a S_a 0 | S_c S_c 0] = [S_c S_c 0 | S_a S_a 0]$

S_a	S_b	S_c / S_d 1/2 1/2
0	0	$1/\sqrt{2}$
1	1	$1/\sqrt{6}$

$S=1$ $[S\ S_b 1 | S_c \tfrac{1}{2} 1]$
$= -(-)^{S_a+S_b+S_c+1/2}[S_c \tfrac{1}{2} 1 | S_a S_b 1]$

S_a	S_b	S_c 1/2	3/2
1	0	$1/\sqrt{6}$	$1/\sqrt{6}$
0	1	$-1/\sqrt{6}$	0
1	1	1/3	$-1/6$

$S=2$ $[1\,1\,2 | \tfrac{3}{2}\tfrac{1}{2} 2] = -[\tfrac{3}{2}\tfrac{1}{2} 2 | 1\,1\,2] = -1/2\sqrt{3}$

$S=1/2$ $[S_a S_b \tfrac{1}{2} | S_c \tfrac{1}{2}\tfrac{1}{2}] = (-)^{S_a+S_b+S_c+1/2}[S_c \tfrac{1}{2}\tfrac{1}{2} | S_a S_b \tfrac{1}{2}]$

S_a	S_b	S_c 0	1
1/2	0	1/2	1/2
1/2	1	1/2	$-1/6$
3/2	1		1/3

$S=3/2$ $[S_a S_b \tfrac{3}{2} | 1 \tfrac{1}{2}\tfrac{3}{2}] = (-)^{S_a+S_b+3/2}[1 \tfrac{1}{2}\tfrac{3}{2} | S_a S_b \tfrac{3}{2}]$

S_a	S_b	S_c 1
3/2	0	$1/2\sqrt{2}$
1/2	1	$-1/3$
3/2	1	$\sqrt{5}/6\sqrt{2}$

Table VIII. $(\Gamma_1 m_1 \Gamma_2 m_2 | \Gamma m)$
$= (\Gamma m | \Gamma_1 m_1 \Gamma_2 m_2)^*$

$A_2 \times E$

		Γ / m	E u_+	u_-
m_1	m_2		$-i$	
	u_+			
e_2	u_-			i

$A_2 \times F_1$

		Γ / m	F_2 x_+	x_-	x_0
m_1	m_2				
	a_+		1		
e_2	a_-			1	
	a_0				1

$A_2 \times F_2$

		Γ / m	F_1 a_+	a_-	a_0
m_1	m_2				
	x_+		-1		
e_2	x_-			-1	
	x_0				-1

$E \times E$

		Γ / m	A_1 e_1	A_2 e_2	E u_+	u_-
m_1	m_2					-1
u_+	u_+					
	u_-		$-1/\sqrt{2}$	$-i/\sqrt{2}$		
u_-	u_+		$-1/\sqrt{2}$	$i/\sqrt{2}$		
	u_-				1	

$E \times F_1$

		Γ / m	F_1 a_+	a_-	a_0	F_2 x_+	x_-	x_0
m_1	m_2							
	a_+			$1/\sqrt{2}$			$i/\sqrt{2}$	
u_+	a_-				$-1/\sqrt{2}$			$-i/\sqrt{2}$
	a_0		$1/\sqrt{2}$			$i/\sqrt{2}$		
	a_+				$-1/\sqrt{2}$			$i/\sqrt{2}$
u_-	a_-		$-1/\sqrt{2}$			$i/\sqrt{2}$		
	a_0			$1/\sqrt{2}$			$-i/\sqrt{2}$	

$E \times F_2$

		Γ / m	F_1 a_+	a_-	a_0	F_2 x_+	x_-	x_0
m_1	m_2							
	x_+			$-i/\sqrt{2}$			$1/\sqrt{2}$	
u_+	x_-				$i/\sqrt{2}$			$-1/\sqrt{2}$
	x_0		$-i/\sqrt{2}$			$1/\sqrt{2}$		
	x_+				$-i/\sqrt{2}$			$-1/\sqrt{2}$
u_-	x_-		$-i/\sqrt{2}$			$-1/\sqrt{2}$		
	x_0			$i/\sqrt{2}$			$1/\sqrt{2}$	

$F_1 \times F_1$

	Γ	A_1	E		F_1			F_2		
	m	e_1	u_+	u_-	a_+	a_-	a_0	x_+	x_-	x_0
m_1	m_2									
	a_+			$-1/\sqrt{3}$					$-\sqrt{2}/\sqrt{3}$	
a_+	a_-	$1/\sqrt{3}$					$i/\sqrt{2}$			$-1/\sqrt{6}$
	a_0		$-1/\sqrt{3}$		$i/\sqrt{2}$			$1/\sqrt{6}$		
	a_+	$1/\sqrt{3}$					$-i/\sqrt{2}$			$-1/\sqrt{6}$
a_-	a_-		$1/\sqrt{3}$					$\sqrt{2}/\sqrt{3}$		
	a_0			$-1/\sqrt{3}$		$-i/\sqrt{2}$			$1/\sqrt{6}$	
	a_+		$-1/\sqrt{3}$		$-i/\sqrt{2}$			$1/\sqrt{6}$		
a_0	a_-			$-1/\sqrt{3}$		$i/\sqrt{2}$			$1/\sqrt{6}$	
	a_0	$-1/\sqrt{3}$								$-\sqrt{2}/\sqrt{3}$

$F_1 \times F_2$

	Γ	A_2	E		F_1			F_2		
	m	e_2	u_+	u_-	a_+	a_-	a_0	x_+	x_-	x_0
m_1	m_2									
	x_+			$-i/\sqrt{3}$		$\sqrt{2}/\sqrt{3}$				
a_+	x_-	$1/\sqrt{3}$					$1/\sqrt{6}$			$i/\sqrt{2}$
	x_0		$i/\sqrt{3}$		$-1/\sqrt{6}$			$i/\sqrt{2}$		
	x_+	$1/\sqrt{3}$					$1/\sqrt{6}$			$-i/\sqrt{2}$
a_-	x_-		$-i/\sqrt{3}$		$-\sqrt{2}/\sqrt{3}$					
	x_0			$-i/\sqrt{3}$		$-1/\sqrt{6}$			$-i/\sqrt{2}$	
	x_+		$i/\sqrt{3}$		$-1/\sqrt{6}$			$-i/\sqrt{2}$		
a_0	x_-			$-i/\sqrt{3}$		$-1/\sqrt{6}$			$i/\sqrt{2}$	
	x_0	$-1/\sqrt{3}$					$\sqrt{2}/\sqrt{3}$			

$F_2 \times F_2$

	Γ	A_1	E		F_1			F_2		
	m	e_1	u_+	u_-	a_+	a_-	a_0	x_+	x_-	x_0
m_1	m_2									
	x_+			$1/\sqrt{3}$					$\sqrt{2}/\sqrt{3}$	
x_+	x_-	$-1/\sqrt{3}$					$-i/\sqrt{2}$			$1/\sqrt{6}$
	x_0		$1/\sqrt{3}$		$-i/\sqrt{2}$			$-1/\sqrt{6}$		
	x_+	$-1/\sqrt{3}$					$i/\sqrt{2}$			$1/\sqrt{6}$
x_-	x_-		$-1/\sqrt{3}$					$-\sqrt{2}/\sqrt{3}$		
	x_0			$1/\sqrt{3}$		$i/\sqrt{2}$			$-1/\sqrt{6}$	
	x_+		$1/\sqrt{3}$		$i/\sqrt{2}$			$-1/\sqrt{6}$		
x_0	x_-			$1/\sqrt{3}$		$-i/\sqrt{2}$			$-1/\sqrt{6}$	
	x_0	$1/\sqrt{3}$								$\sqrt{2}/\sqrt{3}$

interaction than in one of them. Therefore it is of some value to point out we can also construct the effective Hamiltonian for the orbitally degenerate multiplet $^{2S+1}\Gamma$, the correct zeroth-order wave function for the split levels and thus the behavior of these levels in the magnetic field (Zeeman effect) if it could be observed, besides the optical anisotropy. Of course, for the multiplets which are perturbed to the first order by the field of low symmetry or the spin-orbit interaction, we can discuss these properties without much labor, using the first order perturbation theory. However, for certain multiplets, especially those of half

filled shells, the first order perturbation generally vanishes, and the treatment by the effective Hamiltonian will be useful for these states.

Since we already know the form of the effective Hamiltonian for the orbitally non-degenerate multiplets ${}^{2S+1}A_1$ or ${}^{2S+1}A_2$, i.e., the usual spin-Hamiltonian, we will consider here only the multiplets ${}^{2S+1}\Gamma(\Gamma=E, F_1, F_2)$ and study how to construct the effective Hamiltonian for these. First we note that the matrix of the effective Hamiltonian for ${}^{2S+1}\Gamma$: $(\alpha^{2S+1}\Gamma M_S\gamma|\mathfrak{H}_{\text{eff.}}|\alpha^{2S+1}\Gamma M_S'\gamma')$ is $(2S+1)\times(\Gamma)$ dimensional and this matrix can be represented as linear combination of matrices of $(2S+1)$ irreducible spin operators: 1, $\boldsymbol{S}^{(1)}=(S_x, S_y, S_z)$, $\boldsymbol{S}^{(2)}=(3S_z^2-S(S+1), \sqrt{3}(S_x^2-S_y^2), \frac{1}{\sqrt{2}}(S_yS_z+S_zS_y), \frac{1}{\sqrt{2}}(S_zS_x+S_xS_z), \frac{1}{\sqrt{2}}(S_xS_y+S_yS_x)$, $\boldsymbol{S}^{(3)}=\cdots$ up to tensors of the degree $2S$, of (Γ) irreducible orbital operators of type $\Gamma_i(\Gamma\times\Gamma=\sum\Gamma_i)$: 1, $\boldsymbol{T}(A_2)$, $\boldsymbol{V}(E)$, $\boldsymbol{T}(F_1)(=\boldsymbol{L})$, $\boldsymbol{V}(F_2)$ whose double barred matrices are

$$\begin{aligned}
&(\alpha E\|\boldsymbol{T}(A_2)\|\alpha E)=\sqrt{2}\,i\,, && (\alpha E\|\boldsymbol{V}(E)\|\alpha E)=\sqrt{2}\,,\\
&(\alpha F_1\|\boldsymbol{T}(F_1)\|\alpha F_1)=-\sqrt{6}\,i\,, && (\alpha F_1\|\boldsymbol{V}(E)\|\alpha F_1)=\sqrt{6}\,,\\
& && (\alpha F_1\|\boldsymbol{V}(F_2)\|\alpha F_1)=3\sqrt{2}\,.\\
&(\alpha F_2\|\boldsymbol{T}(F_1)\|\alpha F_2)=\sqrt{6}\,i\,, && (\alpha F_2\|\boldsymbol{V}(E)\|\alpha F_2)=\sqrt{6}\,,\\
& && (\alpha F_2\|\boldsymbol{V}(F_2)\|\alpha F_2)=3\sqrt{2}\,,
\end{aligned} \tag{3.1}$$

and of the products of spin and orbital operators such as $S_\sigma T(A_2)$, $S_\sigma T_\gamma(F_1)$ etc. Next we note that spin-tensors of odd degree combine only with T-type orbital operators and those of even degree only with V-type orbital operators in the effective Hamiltonian. We further note that only the former types of operators, spin-tensors of odd degree and T-type orbital operators, combine with the external magnetic field. These considerations enable us to write down at once the general form of the effective Hamiltonian for ${}^{2S+1}E$: (assuming for simplicity $S\leqq 1$,)

$$\mathfrak{H}_{\text{eff.}}=\mathfrak{H}_S+\boldsymbol{E}\cdot\boldsymbol{V}(E)+\boldsymbol{S}^{(2)}\cdot\boldsymbol{E}^{(2)}\cdot\boldsymbol{V}(E)+\boldsymbol{S}\cdot\lambda\boldsymbol{T}(A_2)+\beta\boldsymbol{H}\cdot\boldsymbol{g}\cdot\boldsymbol{S}+\beta\boldsymbol{H}\cdot\boldsymbol{g}_0\cdot\boldsymbol{T}(A_2)+\beta\boldsymbol{H}\cdot\boldsymbol{g}_{(E)}\cdot\boldsymbol{V}(E)\cdot\boldsymbol{S} \tag{3.2}$$

and for ${}^{2S+1}F_1$ and ${}^{2S+1}F_2$: (again assuming $S\leqq 1$)

$$\begin{aligned}\mathfrak{H}_{\text{eff.}}=\mathfrak{H}_S&+\boldsymbol{E}\cdot\boldsymbol{V}(E)+\boldsymbol{S}^{(2)}\cdot\boldsymbol{E}^{(2)}\boldsymbol{V}(E)+\boldsymbol{F}\cdot\boldsymbol{V}(F_2)+\boldsymbol{S}^{(2)}\cdot\boldsymbol{F}^{(2)}\cdot\boldsymbol{V}(F_2)+\boldsymbol{S}\cdot\lambda\cdot\boldsymbol{T}(F_1)\\
&+\beta\boldsymbol{H}\cdot\boldsymbol{g}\cdot\boldsymbol{S}+\beta\boldsymbol{H}\cdot\boldsymbol{g}_0\cdot\boldsymbol{T}(F_1)+\beta\boldsymbol{H}\cdot\boldsymbol{g}_{(E)}\cdot\boldsymbol{V}(E)\cdot\boldsymbol{S}+\beta\boldsymbol{H}\cdot\boldsymbol{g}_{(F_2)}\cdot\boldsymbol{V}(F_2)\cdot\boldsymbol{S}\,,\end{aligned} \tag{3.3}$$

where $\mathfrak{H}_S$ is the usual spin Hamiltonian constructed with the spin tensors of even degree up to $2S$, and $\boldsymbol{E}$, $\boldsymbol{F}$, λ, $\boldsymbol{g}$, $\boldsymbol{g}_0$ are parameters to be determined empirically. As in the case of the spin-Hamiltonian $\mathfrak{H}_S$ the coefficients of operators in (3.2) and (3.3) should be chosen so as to produce the invariant forms appropriate to the symmetry of the problem. It is also to be noted that the terms which contain spin-tensors of degree k: $\boldsymbol{S}^{(k)}$ appear when $k\leqq 2S$ and, except for the Zeeman term, they usually come from k-th (or higher) order perturbation with respect to the spin-orbit interaction as long as we neglect the spin-spin interaction.

As a simple example of the treatment by the effective Hamiltonian, we will discuss the splitting and the Zeeman effect of ${}^2E$, ${}^2F_1$ and ${}^2F_2$ levels under the action of trigonal crystalline field and of the external magnetic field along the trigonal axis of the octahedron. The formal considerations given below will be found useful for the analysis of the line spectra of ruby to be reported later[8].

For this purpose, it is convenient to use the following bases which are quantized in the direction of the symmetry axis, namely for $E(u, v)$,

$$u_+=-(u+iv)/\sqrt{2}\,,\qquad u_-=(u-iv)/\sqrt{2}\,, \tag{3.4}$$

for $F_1(\alpha, \beta, \gamma)$,

$$a_+=-(\omega\alpha+\bar{\omega}\beta+\gamma)/\sqrt{3}\,,\quad a_-=(\bar{\omega}\alpha+\omega\beta+\gamma)/\sqrt{3}\,,\quad a_0=(\alpha+\beta+\gamma)/\sqrt{3}\,, \tag{3.5}$$

and for $F_2(\xi, \eta, \zeta)$,

$$x_+=-(\omega\xi+\bar{\omega}\eta+\zeta)/\sqrt{3}\,, \qquad x_-=(\bar{\omega}\xi+\omega\eta+\zeta)/\sqrt{3}\,, \qquad x_0=(\xi+\eta+\zeta)/\sqrt{3}\,,$$

where $\omega=e^{2\pi i/3}$ and $\bar{\omega}=\omega^2$.

The Wigner coefficients in this scheme are given in Table VIII.

The effective Hamiltonian for ^2E is very simple, if we drop the last term in (3.2) for simplicity

$$\mathfrak{H}_{\text{eff.}}=\lambda S_z T(A_2)+g_{//}\beta H S_z+g_{0//}\beta H T(A_2)\,, \tag{3.6}$$

where z-axis is taken along the direction of the trigonal axis. Note that trigonal invariant does not appear from $V(E)$. The eigenfunctions and the corresponding eigenvalues are at once written down:

$$W_{1\pm}'=\frac{\lambda}{2}\pm\left(\frac{g_{//}}{2}+g_{0//}\right)\beta H \qquad \begin{cases}\Psi(^2E\tfrac{1}{2}u_+)\\ \Psi(^2E-\tfrac{1}{2}u_-)\end{cases} \tag{3.7}$$

and

$$W_{2\pm}'=-\frac{\lambda}{2}\pm\left(\frac{g_{//}}{2}-g_{0//}\right)\beta H \qquad \begin{cases}\Psi(^2E\tfrac{1}{2}u_-)\\ \Psi(^2E-\tfrac{1}{2}u_+)\end{cases} \tag{3.8}$$

Since the main contribution to the first term in (3.6) comes from the second order perturbation $V_{S0}\cdot V_{\text{trig.}}$, we may say that ^2E is split by the interplay between the spin-orbit interaction and the trigonal field. The split components show the linear Zeeman effect and the corresponding g-values are $g_{//}+2g_{0//}$ and $g_{//}-2g_{0//}$. Since $\boldsymbol{L}$ is quenched in E state, thus $g_{//}\sim 2$ and $g_{0//}\sim 0$, so we can predict that the sum of the g-values of the split components will be almost equal to 4. This will be really seen in the Zeeman effect of the characteristic doublet R_1, R_2 of ruby, $Cr^{3+}:Al_2O_3$[9].

Both for $^2F_1$ and $^2F_2$, the effective Hamiltonian is of the same form. Dropping again the last two terms in (3.3) for simplicity,

$$\mathfrak{H}_{\text{eff.}}=FV_0(F_2)+\lambda(S_xT_x+S_yT_y)+\lambda_0S_zT_z+g_{//}\beta HS_z+g_{0//}\beta HT_z\,. \tag{3.9}$$

Moreover, the matrix elements of V are entirely same for both F_1 and F_2, and those of T for F_1 can be obtained from those for F_2 merely changing the sign (Table VIII). Therefore, we will consider here only the case of $^2F_2$. (For $^2F_1$, change λ, $\lambda_0\to-\lambda$, $-\lambda_0$ and $g_0\to-g_0$ in the following.)

The matrix of the above Hamiltonian for $^2F_2$ is

$$\begin{array}{c|cccccc|}
 & x_+ & x_+ & x_0 & x_0 & x_- & x_- \\
 & \tfrac{1}{2} & -\tfrac{1}{2} & \tfrac{1}{2} & -\tfrac{1}{2} & \tfrac{1}{2} & -\tfrac{1}{2} \\
\hline
x_+\ \tfrac{1}{2} & -F-\frac{\lambda_0}{2}+\beta H\left(\frac{g_{//}}{2}-g_{0//}\right) & & & & & \\
x_+\ -\tfrac{1}{2} & & -F+\frac{\lambda_0}{2}-\beta H\left(\frac{g_{//}}{2}+g_{0//}\right) & -\lambda/\sqrt{2} & & & \\
x_0\ \tfrac{1}{2} & & -\lambda/\sqrt{2} & 2F+\beta H\frac{g_{//}}{2} & & & \\
x_0\ -\tfrac{1}{2} & & & & 2F-\beta H\frac{g_{//}}{2} & -\lambda/\sqrt{2} & \\
x_-\ \tfrac{1}{2} & & & & -\lambda/\sqrt{2} & -F+\frac{\lambda_0}{2}+\frac{\beta}{2}H\left(\frac{g_{//}}{2}+g_{0//}\right) & \\
x_-\ -\tfrac{1}{2} & & & & & & -F-\frac{\lambda_0}{2}-\beta H\left(\frac{g_{//}}{2}-g_{0//}\right)
\end{array} \tag{3.10}$$

The eigenvalues and the corresponding eigenfunctions are:

$$W_{0\pm}=-F-\frac{\lambda_0}{2}\pm\beta H\left(\frac{g_{//}}{2}-g_{0//}\right),\quad \begin{cases}\Psi(^2F_{2\frac{1}{2}}x_+)\\ \Psi(^2F_{2-\frac{1}{2}}x_-)\end{cases} \tag{3.11}$$

and neglecting the second order Zeeman effect,

$$W_{1\pm}=-F+\frac{\lambda_0}{2}-\frac{\lambda}{\sqrt{2}}\tan\alpha\pm\beta H\left[-\frac{g_{//}}{2}\cos 2\alpha-g_{0//}\cos^2\alpha\right],$$

$$\begin{cases}\Psi(^2F_{2\frac{1}{2}}x_0)\sin\alpha+\Psi(^2F_{2-\frac{1}{2}}x_+)\cos\alpha\\ \Psi(^2F_{2-\frac{1}{2}}x_0)\sin\alpha+\Psi(^2F_{2\frac{1}{2}}x_-)\cos\alpha\end{cases} \tag{3.12}$$

$$W_{2\pm}=-F+\frac{\lambda_0}{2}+\frac{\lambda}{\sqrt{2}}\cot\alpha\pm\beta H\left[\frac{g_{//}}{2}\cos 2\alpha-g_{0//}\sin^2\alpha\right],$$

$$\begin{cases}\Psi(^2F_{2\frac{1}{2}}x_0)\cos\alpha-\Psi(^2F_{2-\frac{1}{2}}x_+)\sin\alpha\\ \Psi(^2F_{2-\frac{1}{2}}x_0)\cos\alpha-\Psi(^2F_{2\frac{1}{2}}x_-)\sin\alpha\end{cases} \tag{3.13}$$

where

$$\tan 2\alpha=+\sqrt{2}\,\lambda\Big/\left(3F-\frac{\lambda_0}{2}\right),\quad 0\leqq 2\alpha<\pi\,. \tag{3.14}$$

These results may be used for the analysis of the spectra, e.g., the optical anisotropy, intensity distribution in the Zeeman pattern, assuming suitable parameters F, λ, λ_0, g, g_0 chosen so as to fit the observed natural splitting and the Zeeman splitting. Theoretical problem is thus reduced to the explanation of these empirically determined values, just as in the case of the usual spin-Hamiltonian.

Acknowledgement

The authors wish to express their sincere thanks to Professor M. Kotani for his interest and encouragement. They are also indebted to Professor Chr. Klixbüll Jφrgensen of Technical University of Denmark for his valuable suggestion and correspondence, and to Mr. S. Sugano for his helpful discussions. They further appreciate the secretary assistance of Mrs. Y. Yuminami.

Appendix

The proof of (2.21) goes as follows: by definition, we have

$$(\alpha\Gamma_a\beta\Gamma_b\Gamma\gamma|\mathbf{X}_{\bar\gamma}(\bar\Gamma)_a|\alpha'\Gamma_a'\beta\Gamma_b\Gamma''\gamma')=(\alpha\Gamma_a\beta\Gamma_b\Gamma\|\mathbf{X}(\bar\Gamma)_a\|\alpha'\Gamma_a'\beta\Gamma_b'\Gamma'')(\Gamma)^{-1/2}(\Gamma\gamma|\Gamma''\gamma'\bar\Gamma\bar\gamma)\,, \tag{A.1}$$

while

$$=\sum_{\gamma_a,\gamma_a',\gamma_b}(\Gamma\gamma|\Gamma_a\gamma_a\Gamma_b\gamma_b)(\alpha\Gamma_a\gamma_a|\mathbf{X}_{\bar\gamma}(\bar\Gamma)_a|\alpha'\Gamma_a'\gamma_a')(\Gamma_a'\gamma_a'\Gamma_b\gamma_b|\Gamma'\gamma')$$

$$=(\alpha\Gamma_a\|\mathbf{X}(\bar\Gamma)\|\alpha'\Gamma_a')(\Gamma_a)^{-1/2}\sum_{\gamma_a,\gamma_a',\gamma_b}(\Gamma\gamma|\Gamma_a\gamma_a\Gamma_b\gamma_b)(\Gamma_a\gamma_a|\Gamma_a'\gamma_a'\bar\Gamma\bar\gamma)(\Gamma_a'\gamma_a'\Gamma_b\gamma_b|\Gamma'\gamma')\,. \tag{A.2}$$

Using the definition of the transformation matrix

$$(\Gamma_a'\bar\Gamma(\Gamma_a)\Gamma_b\Gamma|\Gamma_a'\Gamma_b(\Gamma')\bar\Gamma\Gamma)\delta(\Gamma\Gamma'')\delta(\gamma\gamma'')$$

$$=\sum_{\gamma_a,\gamma_a',\gamma_b,\bar\gamma}(\Gamma\gamma|\Gamma_a\gamma_a\Gamma_b\gamma_b)(\Gamma_a\gamma_a|\Gamma_a'\gamma_a'\bar\Gamma\bar\gamma)(\Gamma_a'\gamma_a'\Gamma_b\gamma_b|\Gamma'\gamma')(\Gamma'\gamma'\bar\Gamma\bar\gamma|\Gamma''\gamma'')\,, \tag{A.3}$$

the summation in (A.2) can be transformed inthe following way:

$$=(\alpha\Gamma_a\|\mathbf{X}(\bar\Gamma)\|\alpha'\Gamma_a')(\Gamma_a)^{-1/2}(\Gamma_a'\bar\Gamma(\Gamma_a)\Gamma_b\Gamma|\Gamma_a'\Gamma_b(\Gamma')\bar\Gamma\Gamma)(\Gamma\gamma|\Gamma'\gamma'\bar\Gamma\bar\gamma)\,. \tag{A.3}$$

Thus (2.21) has been proved. (2.22) may be proved in the same way.

Note added in proof. Equation (2.3), which is the basic formula for the present calculation, has been used without proof. Recently, G. F. Koster has given the proof including more general cases. Phys. Rev. **109** (1958) 227.

References

1) Y. Tanabe and S. Sugano: J. Phys. Soc. Japan **9** (1954) 753, to which we refer as I.
2) G. Racah: Phys. Rev. **62** (1942) 438, cited as RII.
3) E. U. Condon and G. H. Shortley: Theory of Atomic Spectra (Cambridge, 1953), which we denote by TAS.
4) G. Racah: Phys. Rev. **63** (1943) 367, cited as RIII.
5) M. H. L. Pryce: Proc. Phys. Soc. **A63** (1950) 25.
6) B. Bleaney and K. W. H. Stevens: Rep. Prog. Phys. **16** (1953) 108.
K. D. Bowers and J. Owen: Rep. Prog. Phys. **18** (1955) 304.
7) A. Abragam and J. H. L. Pryce: Proc. Roy. Soc. **A205** (1951) 135.
8) S. Sugano and Y. Tanabe: to be published in this Journal.
9) I. Tsujikawa and S. Sugano: J. Phys. Soc. Japan **13** (1958) 220.

Journal of the Physical Society of Japan Vol. 13, No. 4, April, 1958

A new Probe Method for Measuring Ionized Gases

By Takayoshi Okuda and Kenzo Yamamoto

Faculty of Engineering, Nagoya University, Nagoya

(Received December 18, 1957)

A new probe method is proposed. This method is based upon the idea that the end of a cylindrical probe affects the surface area of the sheath. The first stage of this method is to measure the sheath radius by using a variable-length structure. The procedure is to extrapolate the probe current to $l=0$ along the straight line of the plot of current vs. length of probe and to measure the slope of the straight line and thus to derive the radius of the sheath. Experimental results of ion sheath for Ar are fairly well consistent with the theoretical radius expected from simple theories, except for low plasma density. The discrepancy between the theory and the experiment is caused by the disturbance.

By taking into account a correction factors, namely, depletion in ion collection due to elastic scattering, plasma density can be exactly estimated by measuring the radius of ion sheath without having any knowledge of the adequate space charge equation. Thus, the reliability of the probe method is increased.

§ 1. Introduction

In Langmuir's probe theory,[1] the conditions to be satisfied are (i) no collisions between charged particles and gas atoms; (ii) both energy distribution and density of charged particle at the plasma-sheath boundary being the same as in undisturbed plasma, in other words, behavior of plasma near probe unchanged by insertion of probe into plasma.

The first is obviously not fulfilled for plasma of such high pressure that thickness of the sheath is greater than the mean free path of the charged particle. From this point of view, expressions in which velocity of ion is defined by use of the term "mobility" have been suggested and developed by some investigators.[2-7]

The second is concerned with investigations on the boundary between plasma and sheath. This is one of the most interesting problems of the probe theory today. It arises primarily from a need to overcome the contradiction that application of the ordinary probe theory results in an ion temperature which is larger than or is of the order of electron temperature. Body solved the boundary problem on the

criterion that ion sheath can not be formed stably unless it fulfills a certain condition, and he obtained an expression for ion current independent of ion temperature.[8] Other aspects of the problem were suggested by F. Wenzel[9] and D. Bohm,[10] who gave ion collection formulae independent of ion temperature by analyzing the density distribution of the charged particle under the assumption that density distribution is governed by orbital motion around the probe through the effect of probe potential.

In addition to the situation of the plasma-sheath boundary in the probe measurement, a complicated condition develops at high pressure. This is a depletion of collected charged particle due to elastic scattering, which was emphazed by B. Davydov and L. Zimadovskaya,[11] D. Bohm,[10] Y. M. Kagan,[12] G. J. Schulz and S. C. Brown.[5]

In practical use, besides such a depletion, there is a disturbing effect, i.e. formation of a disturbed region near the probe because of penetration of probe voltage into the plasma. This phenomena was touched upon in previous papers,[13] so we will not go into it further here.

We consider it essential to determine sheath radius for probe measurement exactly, i.e. to verify the conduction equation in sheath and to find both behavior of plasma-sheath boundary and disturbance due to penetration of probe voltage into plasma. Of course, sheath radius is an important quantity to estimate plasma density.

Nevertheless, a method for determining the radius of ion sheath exactly has not yet been developed. The cathetometer method usually provides only crude estimation because the sheath is thin and the boundary between it and the plasma is not clearly observed; consequently, it is difficult to determine the exact boundary between the plasma and the sheath of a probe having the usual negative potential. Also this method is not applicable for electron sheath which is not visible. Turning to the ion sheath, a high negative voltage must be used to make it visible. At high negative voltage, there are secondary processes, such as ejection of secondary electrons by positive ion or metastable atom which complicate the situation and finally lead to a breakdown of the ion sheath. From the fact that the critical voltage for such secondary processes is lowered with rising pressure, at high pressure especially there is no experimental method for determining radius of the ion sheath free from such secondary processes.

We propose here a new method using a cylindrical probe of variable-length. The end of the probe as well as the side of cylinder collect currents of ions or electrons from the plasma. The current flowing into the end is a function of the sheath radius and can not be neglected so far as a finite dimension of the sheath is concerned, even when the probe is thin.

After verifying the priciple of our method by preliminary experiment in this paper, we apply the results of our measurement to a criterion for the most suitable space charge equation as well as to the correction necessary to eliminate the disturbing effect from the measurement of the plasma density. In this way we can increase the reliability of the measured plasma density.

§ 2. Preliminary Experiment

We first consider the end effect quantitatively. Whatever the shape of the end sheath of the cylindrical probe may be, the additional collection through the end sheath can be written in the term of equivalent extention Δl of the probe length l. Thus, total collection is given by

$$i=i_0(l+\Delta l)\,, \qquad (1)$$

where i_0 is the ion current per cm of length of the side of cylinder of the probe, and Δl must be a function of both the probe radius r_p and the sheath radius a. The latter radius can be found by experiment as follows. Under the conditions that secondary processes do not occur and that the sheath radius is large

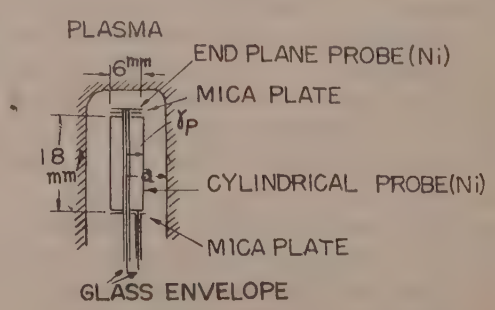

Fig. 1. Probe structure for examining end effect.

enough in low pressure so that we can determine it by visual observation, the ion current flowing through the end sheath is measured as a function of the radius of the sheath covering the side of cylinder. We prepare a device (see Fig. 1) in which there is an end plane probe separated from the main cylindrical probe. The same negative potential as applied to the main probe is, through a different probe voltage source, applied to the end plane probe. The radius of sheath a is then measured by means of the cathetometer and the ion current flowing into the end probe is simultaneously measured. The thickness of the end sheath is nealy equal to that of the main probe, although slightly curved in shape, as shown in Fig. 1.

As an example, in Table I we tabulate the experimental data for Hg vapour at room temperature and for the discharge current of 50 mA. We assume the three shapes for the end sheath as indicated in Fig. 2 where (a) represents a cylindrical and (b) and (c) represent semi-spherical shapes. In such assumed forms, Δl in each case can be

Table I. Preliminary test for end effect in cylindrical probe. Mercury vapour plasma at room temperature, discharge current 50 mA. i_{end} denotes ion current flowing into end plane probe.

Probe Voltage (V)	i_{end} (μA)	a (mm)	i_0 (μA/mm)			
			from main probe	(a) $i_{end}/1.5a-r_p$	(b) $i_{end}/a-r_p$	(c) i_{end}/a
200	42	7.0	5.6	5.7	10.5	6.0
300	50	7.4	6.1	6.1	11.4	6.7
400	56	8.0	6.3	6.2	11.2	7.0
500	62	8.5	6.4	6.4	11.3	7.3
600	68	9.1	6.6	6.4	11.1	7.5
800	82	10.0	6.9	6.8	11.7	8.2

(a), (b) and (c) represent that Eq. (2), (3) and (4) are used, respectively.

$$\Delta l = 1.5a - r_p\,, \tag{2}$$

$$\Delta l = a - r_p\,, \tag{3}$$

$$\Delta l = a\,. \tag{4}$$

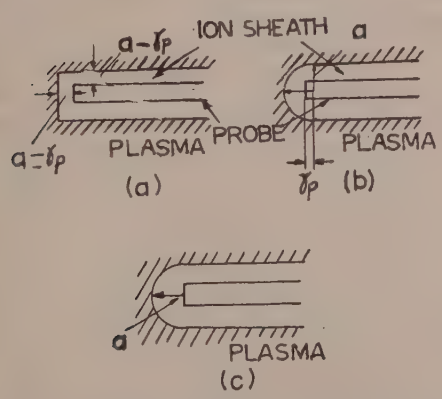

Fig. 2. Assumed shapes of ion sheath at end. (a) a cylindrical end, (b) and (c), hemi-spherical end.

The equivalent ion current per unit length $i_{end}/\Delta l$ for the three forms is computed from the experimental results given in Table I where i_{end} is the ion current flowing into the end probe. Values of $i_{end}/\Delta l$ with various negative voltages in the case of (a) fairly agree with i_0 which is deduced from the current flowing into the main probe. Thus the validity of the form (a) is confirmed.

Thus equation (1) for determining sheath radius can be rewritten as

$$i = i_0(l + 1.5a - r_p)\,. \tag{5}$$

A more convenient way for evaluating the radius of the sheath is to estimate the ion current i_{00} at $l=0$ by extending line i vs. l having a slope of $i_0 = di/dl$ (see Fig. 4). Then, instead of equation (5), we can write

$$i_{00} = i_0(1.5a - r_p)\,. \tag{6}$$

This is valid not only for an ion sheath, but also for an electron sheath, of course.

§ 3. Experiment and Results

Here, we use two probes of different diameters with lengths that can be varied by using an external magnet, as shown in Fig. 3. A large spherical vessel is used to eliminate

the asymmetric disturbance usually arising in the ordinary cylindrical tube, which is long with a small cross-section. Here the asymmetric disturbance is a phenomenon in which plasma densities and potentials are different on the cathode and anode sieds of the probe. Special precaution must be taken to completely eliminate any excess collection of ions coming through the small gap between probe and glass envelope.

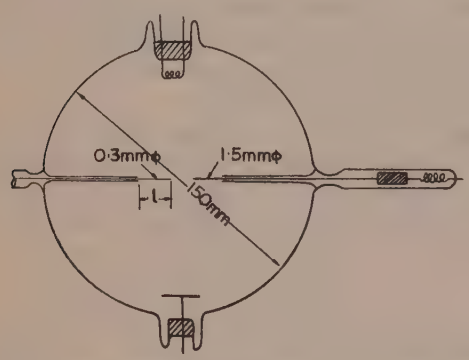

Fig. 3. Variable-length probes for measuring radius of ion sheath.

Examples of plots of ion current vs. probe length are given in Fig. 4. Except for the range of small l the plot is a straight line. Deviation from the straight line for small l seems to be due to the disturbance caused by the very thin glass envelope.

To verify validity of this method, we compare the sheath radius calculated by equation (6) with that measured by visual observation, at a particular condition. The sheath radius is made visible when the probe is set at a very high negative potential and in such a low pressure that no secondary processes occur on the probe surface. Table II gives results for Ar in pressure of 4.10^{-3} mm Hg, indicating that there is good agreement between calculated and measured radius when form (a) is assumed, while if form (b) or (c) is assumed there is no agreement between them.

Sheath radii a for Ar measured in this method are tabulated in Table III. The pressure of gas is from 10^{-3} mm Hg to 5 mm Hg, and discharge current from 0 to 200 mA.

We now compare the measured sheath radius with the theoretical radius derived from various space charge equations. According to Y. Watanabe and H. Kobayashi,[4] following three different equations are applicable.

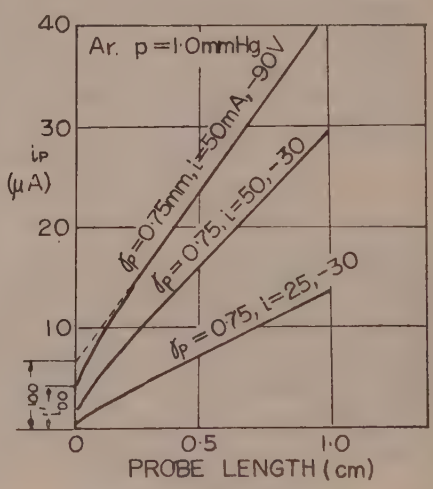

Fig. 4. Plots of ion current vs. probe length at various negative potentials.

Table II. Comparison of radius of ion sheath measured by variable-length probe method with that by visual observation, in the case of Ar of pressure of 4.10^{-3} mm Hg.

Discharge current (mA)	Probe voltage (V)	i_0 (μA/cm)	i_{00} (μA)	probe radius r_p (cm)	sheath radius a (cm)			
					Variable-length probe method			Visual observation
					(a)	(b)	(c)	
50	200	51	18	0.015	0.25	0.38	0.35	0.26
〃	400	82	34	〃	0.29	0.44	0.41	0.32
〃	200	61	26	0.075	0.33	0.50	0.43	0.37
〃	400	88	65	〃	0.54	0.81	0.74	0.57
200	200	144	34	0.015	0.17	0.26	0.24	0.18
〃	400	200	75	〃	0.26	0.39	0.33	0.27
〃	200	200	70	0.075	0.28	0.42	0.35	0.35
〃	400	250	140	〃	0.42	0.63	0.64	0.43

(a), (b) and (c) represent that Eq. (2), (3) and (4) are used, respectivety.

(a) Langmuir's law

$$3.43\cdot10^{-7}M^{-1/2}V^{3/2}(r_p\beta^2)^{-1}=i\,. \qquad (7)$$

(b) μ-law

$$5.56\cdot10^{-13}p^{-1/2}\mu_0V^{3/2}(\phi_c r_p)^{-3/2}=i\,. \qquad (8)$$

(c) b-law

$$5.55\cdot10^{-13}p^{-1}b_0V^2(\psi_c r_p)^{-2}=i\,. \qquad (9)$$

Notations used are as follows:

i: collecting ion current per cm (A/cm)
V: negative voltage (volts)
a: radius of ion sheath (cm)
r_p: radius of probe (cm)
M: atomic weight, e.g., for O_2, $M=16$
j_p: random ion current density (A/cm²)
v: velocity of ion (cm/sec)
β^2, ϕ_c and ψ_c: geometrical factors corresponding to Langmuir's law, μ- and b-laws, respectively, being functions of a/r_p
p: pressure (mm Hg)
μ_0: mobility coefficient of ion at 1 mm Hg (cm$^{3/2}$. mm Hg$^{1/2}$/V$^{1/2}$. sec) by which the velocity of ion is defined as $v=\mu_0(E/p)^{1/2}$, where E is field strength, e.g., for Ar and Ne, μ_0's are 0.8×10^4, and 1.6×10^4, respectively
b_0: mobility of ion at 1 mm Hg (cm². mm Hg/V. sec) by which velocity of ion is defined as $v=b_0$ (E/p), i.e., for Ar and Ne, b_0's are $1.24.10^3$ and $3.34.10^3$, respectatively.[14]

In Table III, theoretical values of ion sheath radius evaluated from Langmuir's, μ- and b-laws are denoted as a_2, a_3 and a_4, respectively. From the experimental results, we may come to the following conclusions:

A) At pressures lower than 10^{-2} mm Hg, measured a_1 approximates evaluated a_2 based upon Langmuir's law;
B) At moderate pressures of the order of $10^{-1}\sim1$ mm Hg, measured a_1 approximates evaluated a_3 based upon μ-law.
C) At pressures higher than several mm Hg, measured a_1 approximates evaluated a_4 based upon b-law;
D) In each case, measured a_1 agrees with or is less than evaluated a;
E) In each case, the discrepancy between measured a_1 and evaluated radius increases with decreasing discharge current or with plasma density.

From the above measurements, we have increased our knowledge of negative probe, e.g., we can now understand qualitatively the conditions under which each space charge equation is applicable.

Now the question arises as to where the discrepancy between the sheath radius measured by are variable-length probe method and the evaluated radius based upon the corresponding simple space charge equation comes from.

Table III. Measured and evaluated sheath radii, sheath voltage, R, α, β and evaluated plasma density for Ar.

Pressure (mm Hg)	Discharge current (mA)	Probe radius (cm)	Negative Voltage (V)	i_0 (μA/cm)	i_{00} (μA)	a_1 (cm)	a_2 (cm)	a_3 (cm)	a_4 (cm)	V′ (V)	R	α	β	n (10^{10}/cm³)
0.026	5	0.015	30	5.0	0.4	0.063	0.27	0.35	0.65	4.5	0.95	1.24	0.44	0.51
〃	〃	〃	90	8.2	1.5	0.13	0.75	0.62	1.25	14.0	〃	1.15	〃	0.51
〃	50	〃	〃	43.0	4.0	0.072	0.26	0.28	0.66	23.0	〃	1.22	0.67	37.5
〃	200	0.075	30	72.0	11.5	0.16	0.18	0.22	0.42	24.0	0.82	1.49	0.39	2.6
〃	〃	〃	90	93.0	26.0	0.24	0.32	0.36	0.76	60.0	〃	1.55	〃	2.4
0.15	5	0.015	30	2.5	0.4	0.12	0.47	0.32	0.42	6.6	0.55	1.82	0.57	0.1
〃	〃	0.075	〃	3.2	0.6	0.18	0.67	0.50	0.62	3.8	0.26	2.61	0.50	0.08
1.00	〃	〃	60	5.4	1.3	0.21	1.20	0.43	0.47	14.8	0.041	13.5	0.47	0.08
〃	50	〃	〃	31.0	4.8	0.15	0.44	0.23	0.27	22.0	〃	9.55	0.67	0.53
2.00	200	0.015	90	28.0	3.7	0.094	0.35	0.13	0.16	55.0	0.063	9.90	0.78	0.58
5.00	5	〃	60	2.4	0.48	0.14	1.05	0.23	0.20	35.2	0.025	27.8	0.35	0.014
	100	〃	〃	21.5	2.8	0.097	0.27	0.093	0.099	55.0	〃	23.5	0.55	0.33

We first consider how the simple space charge equation must be modified when various other processes are to be considered. If the ion at the sheath-plasma boundary posses an initial velocity, the sheath radius would be large (Malter and Webster),[15] which is a fact contrary to measurements. Also, an addition to the diffusion term in the equation of current flow leads to a large sheath radius, an effect contrary to the measurement.

Ion sheath radius is usually evaluated from space charge equation by using the value of ion current, which is measured to be small because of elastic scattering sideways and backwards. Consequently the sheath radius is estimated to be large. Such loss through elastic scattering might be considered the source of the discrepancy. In general, elastic scattering is increased with increasing gas pressure. However elastic scattering is not a possible source because of the experimental fact that the discrepancy does not depend upon the pressure. Moreover, the range in which the plot i vs. l is not linear is too large to be explained by elastic scattering.[12]

Another probable source may come from an estimation of the true sheath voltage. If the negative voltage penetrate into plasma to some degree, it can be expected that sheath voltage is lower than applied voltage deduced from the probe characteristic.

Assuming the penetration, we can expect the sheath voltage V' from the measured sheath radius and the corresponding space charge equation, to be as given in Table III. For example, with a pressure of 2.6×10^{-2} mm Hg and a discharge current of 200 mA, using a probe having a diameter of 1.5 mm in the tube, as shown in Fig. 3, expected sheath voltages of 24, 35 and 60 volts can be obtained for an applied negative voltage of 30, 60 and 90 volts, respectively. Also, the experiment indicates that the difference between the sheath voltage and the applied voltage increases as the discharge current or the plasma density decreases. Such a penetration is characterized by formation of a penetrating sheath outside the ion sheath. Disturbance due to penetration will be described in another paper.

§ 4. Determination of Plasma Density

To determine plasma density, it is essential that elastic scattering effect must be taken into account.

The elastic scattering occuring near a probe leads to depletion of the collection of ions or electrons, which has been discussed by Brown and Schultz,[5] Bohm[10] and Kagan.[12] This effect has a tendency to become pronounced with increasing gas pressure.

Analogous to Bohm's theory for spherical probe stood on an idea that collection is determined by the diffusion flow at the point which is one mean free path distant from the probe, we get the expression of the collection on a cylindrical probe in terms of the probe radius r_p, the mean free path λ, and probe length l as follows;

$$R_1=j/j_0=\lambda/\{\lambda+r_p\log l/(r_p+\lambda)\}\,, \qquad (10)$$

where j and j_0 are electron current densities flowing into the probe, with and without the depletion, respectively.

Thus, such a depletion depends upon the mean free path of the charged particle as well as on both the radius and length of probe, but is independent of plasma density. Kagan[12] found that this depletion becomes effective in the vicinity of the probe within several times the radius of the probe. Equation (10) applies also for ion or electron sheath.

Eq. (10) is derived by assuming that no sheath is formed around the probe. So far as ion collection in negative probe is concerned, it is necessary to consider the effect of the existence of an ion sheath on the depletion.

According to our analysis which is analogous to Kagan's theory of spherical probe, the density distribution as a function of distance r from a cylindrical probe is expressed by

$$n_v=(F_v/2\pi r_p v)\{(r_p/r)\cos\theta_r + (2r_p/\lambda)\log(r/r_p)+\pi/2\}\,, \qquad (11)$$

where F_v is total flow to the probe, v velocity of charged particle and $\theta_r=\sin^{-1}r_p/r$.

Setting $r=r_p$, we find the density at probe surface as follows:

$$n_v(r_p)=F_v/4r_p v\,. \qquad (12)$$

Since scattering does not occur in the ion sheath, as we shall discuss in detail in another paper, the existence of an ion sheath increases collection of ion determined by the density outside the sheath. Consequently, ion collection with ion sheath is greater than that without ion sheath; the condition of the latter can

not be found in the usual probe method.

Considering the effect of ion sheath having radius a, the resultant expression of the depletion factor can be given by

$$R' = R\alpha\,, \tag{13}$$

and

$$\alpha = n_v(a)/n_v(r_p)$$
$$= (2/\pi)\{(r_p/a)\cos\theta_{ri} + (2r_p/\lambda)\log(a/r_p) + \pi/2\}\,, \tag{14}$$

where $\theta_{ri} = \sin^{-1} r_p/a$.

Finally, the correct plasma density can be found by the following equation:

$$n = \frac{i}{2\pi ae}\frac{1}{R'}\left(\frac{2\pi M'}{kT_p}\right)^{1/2} \tag{15}$$

where e is elementary charge, K Boltzmann constant, M' mass of ion and T_p ion temperture.

The plasma densities obtained by Eq. (15) are given in Table III. It is found that numerical values of plasma density obtained at different negative voltages agree fairly well with eath other. Without above correction, there is a poor agreement.

Finally, we may add following description concerning to the disturbance. The disturbance accompanying with negative probe is characterized by formation of penetrating sheath and "transition region" which appears outside the penetrating sheath. The transition region is formed as a result of loss of charged particles near the probe. Owing to such disturbance, the plasma density near the probe is decreased. In fact, the extent of the disturbance observed as a range in which the plot of probe current vs. probe length is not linear, increases with decreasing plasma density. Also, the ratio β of the measured ion current at $l=0$ to the ion current extrapolated to $l=0$ along the straight line, increases with increasing plasma density, as shown in Fig. 5 in which measured β as well as the electron current flowing into the probe holding at the space potential as a measure of plasma density are plotted against pressure.

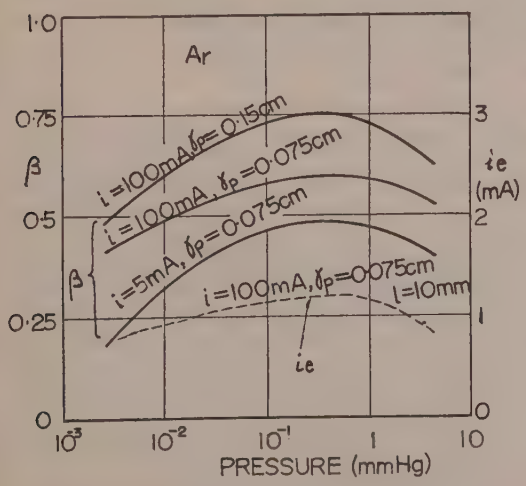

Fig. 5. Ratio β and elctron current at plasma potential as a function of pressure.

Those non-linearity can not be caused by the scattering effect because the scattering effect is located so close to the glass envelope that its range is usually covered by the ion sheath around the probe. Therefore it is seen that the formation of transition region results in the non-linearity and consequently the transition region expands with decreasing plasma density.

§ 5. Conclusion

We propose a new method for determining sheath radius and plasma density. This method has the merit that it is not necessary in principle to use the space charge equation and that error due to disturbance can be eliminated. Also it offers information of the most adequate space charge equation and clarifies how disturbance in negative probe leads to error in the measurement.

It especially emphasizes that the disturbance must not be ignored even in low pressure plasma where the elastic scattering effect can be neglected, and that tne boundary problem should be interpreted basing upon the disturbance.

References

1) I. Langmuir and H. Mott-Smith: G. E. Rev. **27** (1924), 449, 538, 616, 762, 810, Phys. Rev. **28** (1926) 729.
2) W. H. McCurdy: Phys. Rev. **27** (1926) 157.
3) J. D. Cobine: Gaseous Conductors, McGraw-Hill, New York, 1948.
4) Y. Watanabe and H. Kobayashi: Technol. Rep. Tohoku Univ., **18** (1954) 235.
5) G. J. Schultz and S. C. Brown: Phys. Rev. **98** (1956) 1642.
6) D. Kamke and H. J. Rose: Zeit. f. Physik **145** (1956) 843.
7) F. Borgnis: Ann. der Physik **31** (1938) 497, 745.
8) R. L. F. Boyd: Proc. Roy. Soc. **201A** (1950) 329.

9) F. Wenzel: Zeit. f. ang. Physik **2** (1950) 59.
10) D. Bohm: in "A. Guthrie and R. K. Wakering: The Characteristics of Electrical Discharges in Magnetic Fields", McGraw-Hill, New York, first edition pp. 41 and 77.
11) B. Davydov and L. Zimanovskaya: Zhr. Tekh. Fiz. **6** (1936) 1244.
12) Yu. M. Kagan: Zhr. Tekh. Fiz. **24** (1954) 889.
13) T. Okuda and K. Yamamoto: J. Phys. Soc. Japan **11** (1956) 177, K. Yamamoto and T. Okuda: J. Phys. Soc. Japan **11** (1956) 57.
14) J. A. Hornbeck: Phys. Rev. **84** (1951) 615.
15) L. Malter and W. H. Webster: R. C. A. Rev. **12** (1951) 191.

JOURNAL OF THE PHYSICAL SOCIETY OF JAPAN Vol. 13, No. 4, APRIL, 1958

Oscillation of the Wake behind a Flat Plate parallel to the Flow

By Sadatoshi TANEDA
Kobe University of Mercantile Marine

(Received December 27, 1957)

Oscillation of the pure laminar wake behind a flat plate placed in a uniform stream at zero incidence angle was investigated experimentally at Reynolds numbers between 10^2 and 10^5. (The Reynolds number R is Ul/ν, where U is the model speed, l is the plate length and ν is the kinematic viscosity.)

For a sufficiently small R the corresponding wake was perfectly laminar and vortex filament was seen nowhere. But when R of about 700 was reached, the wake began to oscillate sinusoidally some distance downstream. As R was increased further the oscillation became more and more conspicuous and discrete vortex filaments appeared in the loop of the sinusoidal wave. Frequency N was measured by the hot-wire technique and it was found that the Strouhal number Nl/U is nearly proportional to 1/2 power of R. On the other hand, wave length λ was determined from the photographs taken by aluminium dust method, and the relation between l/λ and R was obtained. Spacing ratio and velocity of the vortex filaments were also estimated.

These experimental results were compared with those of the wakes behind various bluff bodies, and some knowledges about the origin of oscillation of the wake were obtained. The value of wake Strouhal number was nearly constant for all shapes of body, while the wave velocity changed remarkably with the shape of the body.

§ 1. Introduction

It has long been recognized that the wake behind a bluff cylindrical body oscillates and arranges itself in a regular vortex street in the intermediate Reynolds number range. Though an appropriate explanation of the geometry of the vortex street was provided by the well known theory of von Karman[1], the reason why the wake should oscillate or why a vortex street must appear, has not yet been made clear.

In the case of a bluff body, the flow separates from the surface of the body and twin vortices are formed immediately behind the body at the beginning of motion. Then they become more and more elongated in the flow direction, take up an asymmetrical position and move away from the body. In this way a regular vortex street is set up. These experimental results seem to indicate that the oscillation of a wake is due to the instability of twin vortices.

On the other hand, it should be noticed that the wake behind a bluff body is a separated

wake, and is composed of two parts, the twin vortices and the laminar wake. Therefore the laminar wake can also be considered as the origin of oscillation, and it is still a matter of speculation which of the twin vortices or the laminar wake is to be looked upon as the true origin of oscillation. In order to make clear this point, the investigation about a pure laminar wake is needed. However, literatures in which the pure laminar wakes were dealt with seem to be scanty. The pure laminar wake can be produced by a flat plate placed parallel to the flow, since separation does not occur and twin vortices do not appear in the flow. Though several authors (Fage and Johansen[2]; Tyler[3]; Blenk, Fuchs and Liebers[4]) have investigated the wake behind an inclined flat plate in the past, little work has been done for the case of zero incidence angle. A careful measurement about the pure laminar wake behind a flat plate parallel to the flow was first made by Hollingdale[5]. He has obtained several valuable results about the stability and the configuration of the pure laminar wake, but his observation was made only for R lower than about 2×10^3 and the results seem to be inadequate to draw any general conclusion as to the variation of the frequency, wave length and wave velocity with the Reynolds number.

In the present report, further observations on the pure laminar wake behind a flat plate parallel to the flow, at various Reynolds numbers from about 10^2 to 10^5, are described, together with some remarks on the experimental method and possibe significance of the results.

§ 2. Apparatus and Experimental Method

All the experiments were made with a research water tank of 300 cm in length, 20 cm in width and 20 cm in depth. A small carriage, to which a model was fixed upright, was towed, by a steel wire uniformly along rails mounted over the water tank, using a 100 watt a. c. motor. The velocity of the carriage could be varied smoothly from 1 to 20 cm/s by controlling a friction gear fitted to the motor. General arrangement of the apparatus is shown in Fig. 1.

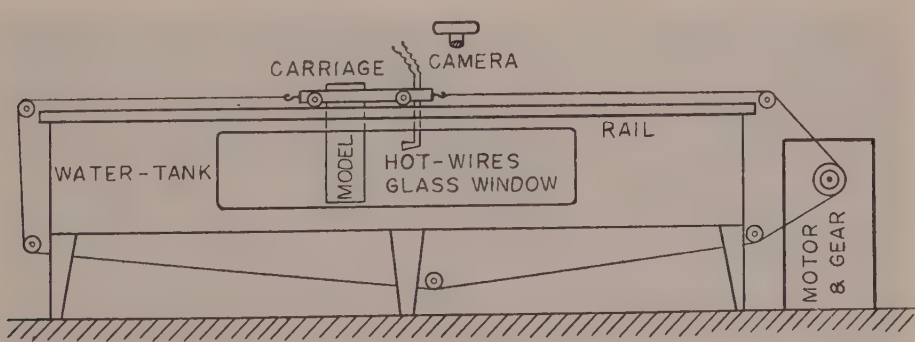

Fig. 1. Schematic diagram of the apparatus.

Thin flat plates of five different sizes, all of which were tapered carefully and smooth to sharp edges, were used as models. Sizes of the models are given in Table I. All ratios of the thickness to length of the plates used were less than 125^{-1}, and no influence of the thickness was detected in the wake measurement.

Wave length and spacing ratio of the vortex street were determined, by examining photographs taken by aluminium dust method[6]. The central horizontal plane of the tank was illuminated from a side by a sheet of intense

Table I.

l (mm)	t (mm)	l/t	L (mm)	L/l
400	1.0	400	190	0.48
223	1.0	223	190	0.85
140	1.0	140	190	1.36
101	0.50	202	190	1.88
37	0.24	154	140	3.78
20	0.16	125	120	6.00

l: Length of the plate.
t: Thickness of the plate.
L: Span of the plate.

light from incandescent lamps behind a narrow slit, and photographs showing the movement of aluminium dust suspended in the water were taken from above with a camera fixed to the water tank.

The frequency was measured with a hot-wire speed meter. Hot-wire technique has usually been applied only to air stream because its use in water is met with a great difficulty due to electrolysis, air bubbles in, or a large conductivity of water etc. We used the technique, however, in the water and succeeded in measuring the frequency after a considerable amount of study. In order to eliminate the influence of electrolysis, a. c. was used to heat the hot wire. Two Pt-wires, each 30 μ in diameter and about 5 mm in length, were used, one in the wake, and the other outside the wake. They were heated by 250 cycle a. c. from an audio frequency oscillator, and the change of electric resistance of the hot wires, caused by a fluctuating flow, was amplified and recorded on the photographic paper of an electromagnetic oscillograph. The velocity of the carriage and the time mark were also recorded on the same paper. Fig. 2 shows the block diagram of the electronic set-up used in the frequency determination.

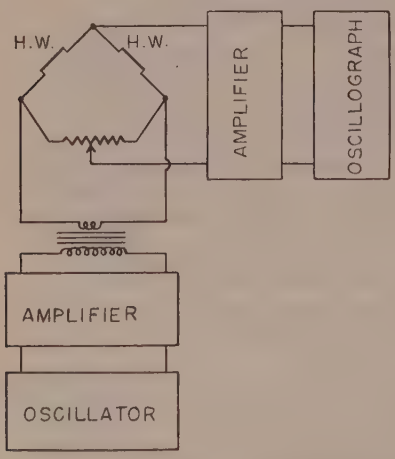

Fig. 2. Block diagram of the electronic set-up used in the frequency determination.

The velocity of the wave form was determined from the photographs of one part of the field taken successively by measuring the distance the wave had travelled in the known time interval between two consecutive exposures.

§ 3. Flow pattern of the Wake

Many photographs were taken, of the flow pattern behind a flat plate moving in the water at various Reynolds numbers between 10^2 and 10^5. Some of them are shown in Fig. 3.

The change of the flow pattern which occurs in the wake when R is increased stepwise is as follows. For R lower than about 700, the wake is perfectly laminar. When R of about 700 is reached, however, a very faint oscillation appears some distance downstream of the flat plate, as was clarified already in the previous paper[7]. This value of 700 is in approximate accordance with the value of 600 observed by Hollingdale. For R from about 700 to 1000 the oscillation is not regular. Frequently the oscillation persists for a few wave lengths, then dies out, and the wake becomes sensibly laminar again. For R higher than about 10^3, however, the oscillation does not show any tendency to die away, and the wake shows a regular sinusoidal form. The whole sinusoidal wave form is observed to move slowly in the direction of motion of the body. When R is slightly higher than 10^3, the sinusoidal wave form extends far downstream but discrete vortex filament does not appear in the whole wake. On increasing R further, the oscillation becomes more and more noticeable, and discrete vortices appear in the hollows of the sinusoidal wave form. They arrange themselves for some distance in a configuration corresponding to that of a Karman vortex street. The vortices do not arrange themselves on two parallel rows with a definite spacing ratio (the ratio of lateral spacing between the rows to the distance between two consecutive vortices in the same row), but the wake tends to widen out downstream, and the spacing ratio changes. At the beginning of the wake the spacing ratio is about 0.3, while far downstream it is about 0.6. These values are much larger than the theoretical value 0.28 obtained by von Karman.

For higher R the regular vortex street is soon deformed and destroyed into pieces. But it was frequently observed that these scattered vortices were soon united and arranged themselves again to a new regular vortex street, the dimension of which was much larger than that of the primary one.

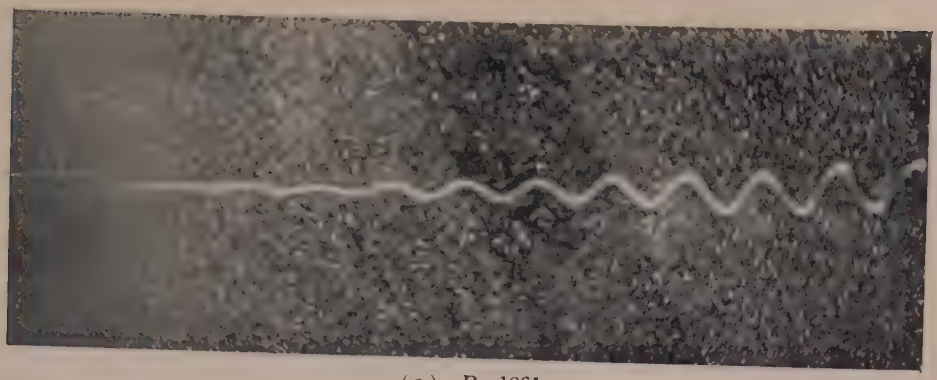

(a) $R=1861$

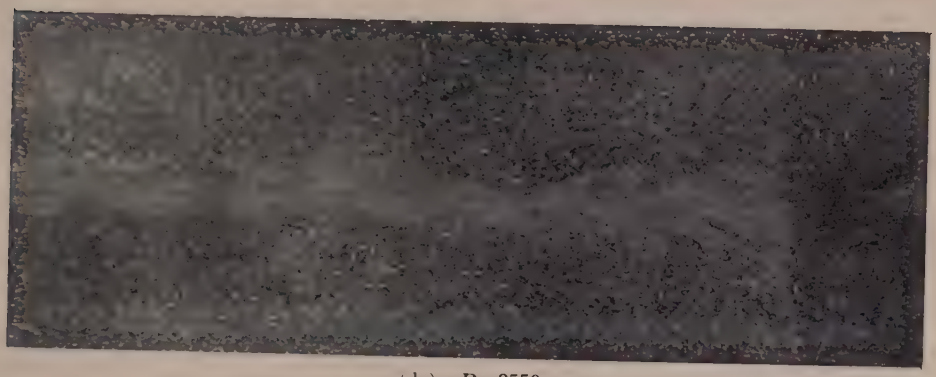

(b) $R=3550$

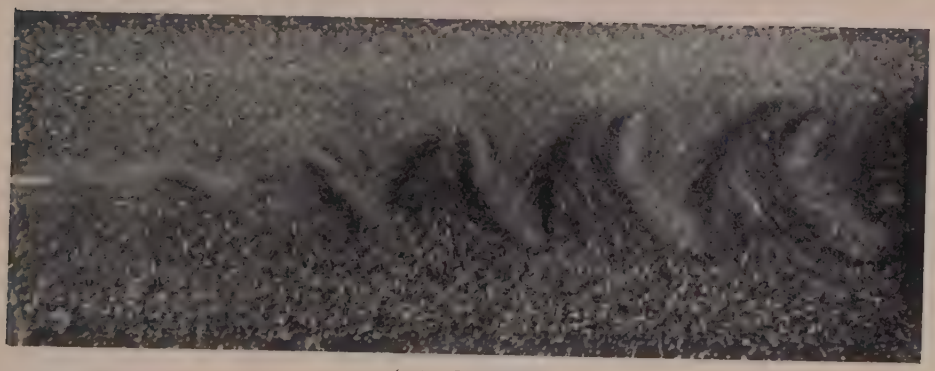

(c) $R=15800$

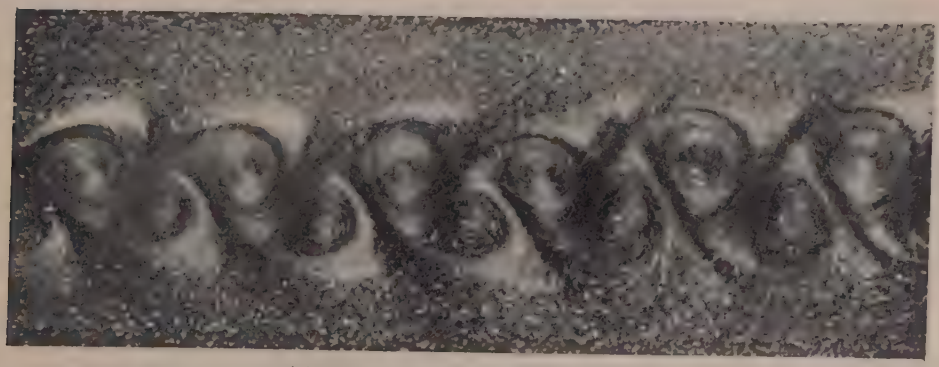

(d) $R=15800$; continued from (c)

Fig. 3. Photographs showing flow pattern in the oscillating wake behind flat plate moving in the water.

§ 4. Measurement of the Frequency

The frequency of the oscillating wake was measured with a hot wire speed meter. When R is lower than about 700, the wake is sensibly laminar and no oscillating signal can be detected. Then it follows a range of R in which the frequency is very irregular. In the range from about 700 to 1000 of R, the commencement of the oscillation seems to depend largely on a very small residual motion of the water. Consequently it is very difficult to determine the frequency. At R higher than about 10^3, however, a regular frequency is observed. Of course even for R higher than 10^3, any signal of oscillation can be detected in the immediate rear of the plate, since the flow is always laminar there. Therefore a hot wire should be placed always at some distance behind a plate. The frequency increases with the model speed, while for a fixed model speed frequency is constant throughout the whole field of the wake. The best signal was obtained when the hot wire was located about 1 to 2 plate length behind the plate and about 5 mm off the centre of the wake. As the direction of the flow cannot be detected with a single hot wire, the frequency of the fluctuation in the middle of the vortex street is always double that outside. The double frequency component decreased rapidly with distance from the centre of the wake, and disappeared almost completely at about 5 mm from the wake centre. The typical oscillographs are shown in Fig. 4.

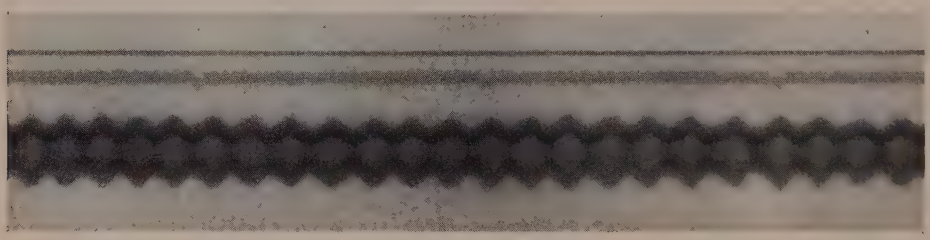

(a) $R=5760$

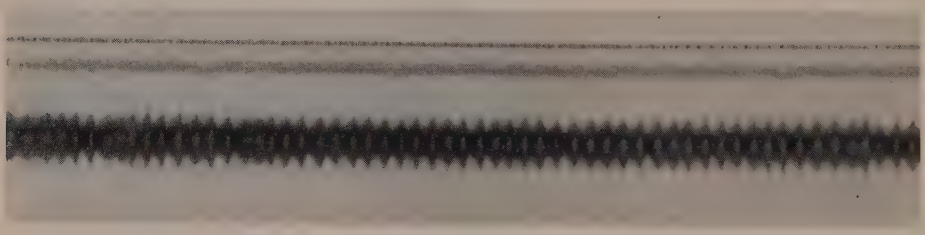

(b) $R=15800$

Fig. 4. Velocity fluctuation records.

The results are expressed in terms of the dimensionless Strouhal number $S=Nl/U$, where N is the frequency, l is the plate length and U is the model speed. The Strouhal number S is considered to depend on R as well as external disturbances. The present measurements of $S(R)$ are given in Fig. 5.

From this figure it will be seen that there exists a functional relation

$$\frac{Nl}{U}=\text{const.}\left(\frac{Ul}{\nu}\right)^{1/2} \qquad (1)$$

Hence

$$N=\text{const.}(\nu l)^{-1/2}U^{3/2} \qquad (2)$$

Namely, the frequency N is nearly proportional to 3/2 power of the flow speed. It should be noticed that this relation is in accordance with that observed in the case of a laminar half jet (Sato[8]).

As is seen from Fig. 5, the scatter of observed values is fairly large for the whole range of R. It seems that this is not due to the inaccuracy of experiment, but to the essential properties of the pure laminar wake.

§ 5. Measurements of the Wave Length and the Wave Velocity

The wave length and the wave velocity were determined from the photographs of the flow pattern. When R is lower than about

10^3, it was rather difficult to measure the wave length owing to the irregularity of the wave form, so all measurements were made only for R higher than 10^3. Even for R higher than 10^3 the measurement was very difficult, because the amplitude of the wave was very small immediately behind the flat plate. The wave length varied in different places, i.e. the wave length showed a tendency to increase downstream. For these reasons measurements were all made at the place where a distinct sinusoidal wave form appeared first in the wake. The curve of l/λ against R is given in Fig. 6. As is seen from the figure the functional relation

$$\frac{l}{\lambda}=\text{const.}\left(\frac{Ul}{\nu}\right)^{1/2} \tag{3}$$

can be established. A large scattering of the observed values is similar to that in the case of the frequency measurements.

The wave velocity was determined from the successive photographs of the vortex street. If we know the time between the two successive exposures, then the wave velocity V can be calculated by measuring the distance the

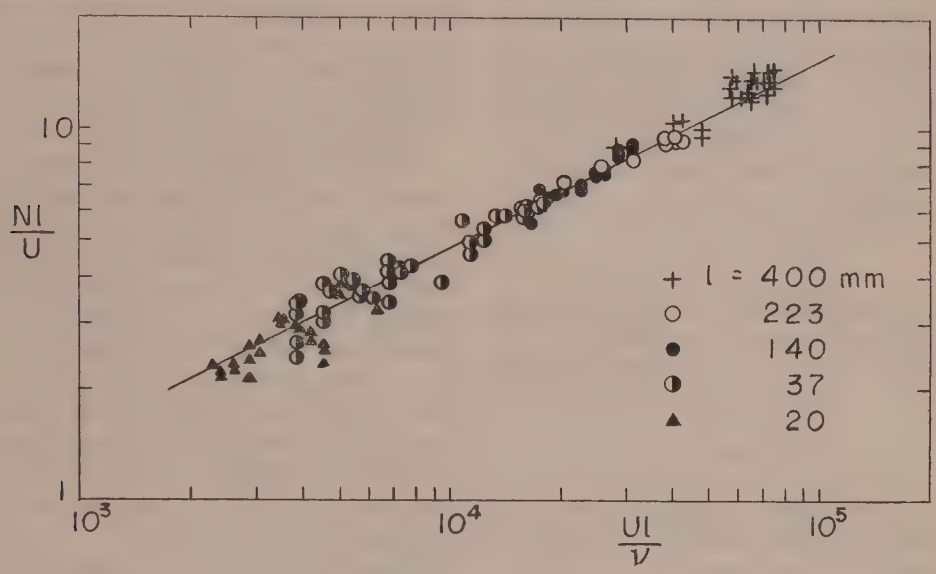

Fig. 5. Plot of $\log S$ against $\log R$.

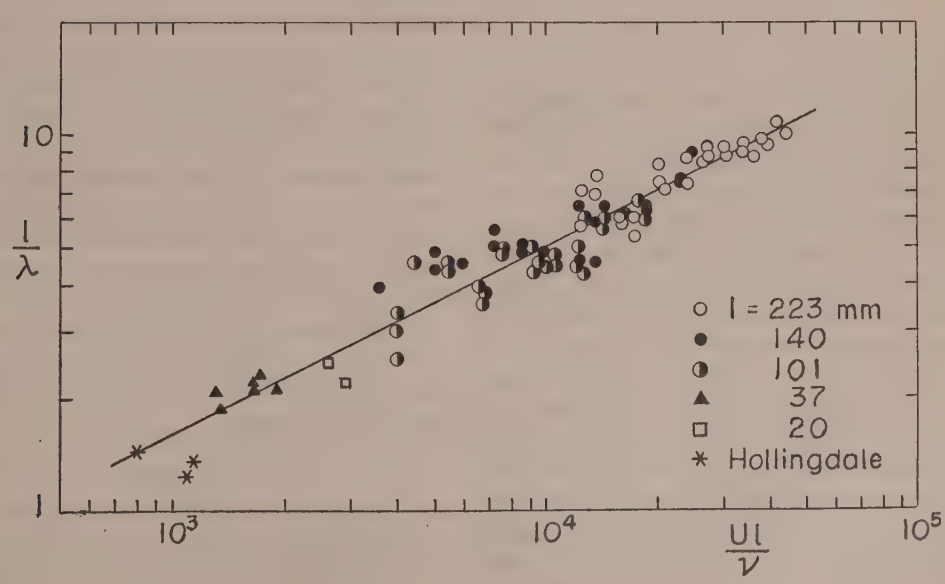

Fig. 6. Plot of $\log l/\lambda$ against $\log R$.

wave had travelled during that time interval. From many observations it was found that the value of V/U is nearly 0.08 and does not vary greatly with the Reynolds number. It should be noted that this value of 0.08 is much less than that for the bluff body. In the case of a circular cylinder the value of V/U is about 0.14 (Karman and Rubach[9]; Richards[10]). The value of V/U shows a weak tendency to decrease downstream.

§ 6. Discussion

In the case of a flat plate, N is, as is shown in § 4, nearly proportional to $U^{3/2}$, while in the case of a bluff body, N is proportional to U^1 (Karman and Rubach[9]; Fage and Johansen[2]; Tyler[3]; Blenk, Fuchs and Liebers[4];). Thus there is a conspicuous difference between the two cases of a flat plate and a bluff body. But if we use the wake width δ, instead of the plate length l in equation (1), we get

$$\frac{N\delta}{U}=\text{const.} \qquad (4)$$

for a flat plate, because δ is proportional to $R^{-1/2}$ from the boundary layer theory.

On the other hand in the case of a bluff body

$$\frac{Nd}{U}=\text{const.} \qquad (5)$$

where d is the breadth of the bluff body across the stream. Since the wake width δ is nearly proportional to d, we have

$$\frac{N\delta}{U}=\text{const.} \qquad (6)$$

Thus the wake Strouhal number $N\delta/U$ remains practically constant in both wakes, those behind a flat plate and behind a bluff body. Moreover if δ is the wake width at the position where the difference between the velocities at the centre and the outside of the wake is equal to U, the value of the constant is found to be nearly universal for bodies in any shape.

The reasoning mentioned above leads us to the conclusion that there is no essential difference between the two wakes, the pure laminar wake and the separated wake. The frequency seems to be the function of only U and δ, and is independent whether twin vortices are present or not. Though the viscosity is effective in producing a wake, it has little relation to the frequency.

On the other hand it should be noticed that the scattering in the observed frequency for the flat plate is much larger than that for the bluff body. In the case of the bluff body scattering is very small when Reynolds number is comparatively low (Roshko[11]; Kovasznay[12]). These facts give us an important suggestion as to the origin of oscillation of the wake and the behaviour of the twin vortices.

As was described above the value of $N\delta/U$ is nearly independent of the shape of the body producing the wake, while the wave velocity V/U changes conspicuously with the shape of the body (§ 5). That is, V is a function of not only U and δ, but also the shape of the body. It seems that the shape of a body has an influence upon the velocity distribution in a wake and consequently the wave velocity changes according to the shape. But the wave velocity is not affected greatly by the viscosity.

As for the spacing ratio of the vortex street behind a bluff body, there has been many investigations made and it is believed that the initial value of the spacing ratio near the body is about 0.3, and it increases up to about 0.5 downstream. This is in agreement with the results obtained for the flat plate (§ 3). That is, as for the spacing ratio there is no signifficant difference between both cases of the pure laminar wake and the separated wake. The observed spacing ratio is always larger than the value 0.28 of von Karman obtained theoretically.

Though the wake Strouhal number $N\delta/U$ is nearly constant and is independent of the Reynolds number for bodies in any shape and form, the wake Reynolds number at which oscillation first appears in the wake, changes with the shape of the body. In the case of a flat plate parallel to the flow, the critical wake Reynolds number is about 200, while in the case of a circular cylinder it is about 100. There seems to be a general relation that the smaller the bluffness of a body, the higher is the critical Reynolds number.

In conclusion, the author wishes to express his thanks to Professor Hikoji Yamada for constant advice and encouragement in the course of this work.

References

1) Th. von Karman: Gött. Nachr. [Math. Phys. Kl] (1912) 547.
2) A. Fage and F. C. Johansen: Proc. Roy. Soc. A, **116** (1927) 170.

3) E. Tyler: Phil. Mag. (7) **11** (1931) 849.
4) H. Blenk, D. Fuchs and F. Liebers: Lufo. **12** (1935) 38.
5) S. H. Hollingdale: Phil. Mag. (7) **29** (1939) 209.
6) S. Taneda: Rep. Res. Inst. App. Mech. **1** (1952) 131.
7) S. Taneda: J. Phys. Soc. Japan **11** (1956) 302.
8) H. Sato: J. Phys. Soc. Japan **11** (1956) 702.
9) Th. von Karman and H. Rubach: Phys. Zeits. **13** (1912) 49.
10) G. J. Richards: Phil. Trans. A, **233** (1934) 279.
11) A. Roshko: N. A. C. A. Tech. Note **2913** (1953) 1.
12) L. S. G. Kovasznay: Proc. Roy. Soc. A, **198** (1949) 174.

Short Notes

This section is intended to secure prompt publication of important discoveries in physics. The reports should not exceed 800 words in length. A figure of size 7 cm × 7 cm will be counted as 150 words.

J. Phys. Soc. Japan **13** (1958) 426

Transport Phenomena in Monovalent Metals

By Mikio Tsuji

General Education Department, Kyushu University, Fukuoka

(Received January 16, 1958)

Taking into account the departure of the distribution function for phonons from its thermal equilibrium value, Hanna and Sondheimer[1] have calculated the electrical and thermal conductivities and the absolute thermoelectric powers of monovalent metals based on the quasi-free electron model. Their expressions have been obtained by interpolation from the solutions at high temperatures and those at low temperatures, and the latter have been obtained by the assumption that the change of the distribution function for electrons due to the impurity scattering is larger than that due to the lattice scattering. Therefore it is not obvious whether their results are applicable for the case of intermediate temperature range and for the pure metals at low temperatures.

We have obtained the formulae which are approximately correct at all temperatures and for any concentration of impurities including the case of pure metals. The Boltzmann equations for the electrons and phonons are written in the form:

$$\frac{1}{\hbar K}\frac{dE}{dK}E^{n-1}\frac{\partial f_0}{\partial E}=\mathscr{L}_1(c^{(n)})+\sum_j\mathscr{L}_{2,j}(b_j^{(n)}), \quad (1)$$

$$(n-1)\frac{\hbar u_0^2}{kT}\frac{\partial N_0}{\partial z}=\mathscr{L}_{3,j}(c^{(n)})+\mathscr{L}_{4,j}(b_j^{(n)}), \quad (2)$$

where $\mathscr{L}$'s are the collision operators and $c^{(n)}$ and $b_j^{(n)}$ are the functions related to the distribution for electrons and phonons. (See reference (1) and (4).) If we put

$$c^{(n)}=c_0^{(n)}+c_1^{(n)}\eta, \quad (3)$$

and insert (3) into (2), $b_j^{(n)}$ are obtained as linear functions of $c_0^{(n)}$ and $c_1^{(n)}$. Putting these $b_j^{(n)}$ into (1), we have an integral equation of the type

$$\mathscr{L}_1(c^{(n)})=\frac{1}{\hbar K}\frac{dE}{dK}E^{n-1}\frac{\partial f_0}{\partial E}+c_0^{(n)}A_0(E)+c_1^{(n)}A_1(E)+B^{(n)}(E). \quad (4)$$

Using the well known symmetricity of the integral operator $\mathscr{L}_1$, we can solve (4) by a modification of Kohler's variational method[2]. We have assumed the general spherical energy band model for electrons and the Debye model for phonons. The results are as follows:

$$\frac{1}{\sigma}=\rho=\rho_e-\rho_g \quad (5)$$

$$\rho_g=\frac{3\pi^2\hbar}{e^2}q_0^2\left(\frac{T}{\Theta}\right)^5\sum_j\Lambda_j^{-1}P_{j,6}, \quad (6)$$

$$\kappa=\kappa_e+\kappa_g, \quad (7)$$

$$\kappa_g=\frac{(kT)^2}{3\pi^2\hbar}\left(\frac{T}{\Theta}\right)^2K_0^4q_0^{-2}\alpha^2\sum_j\Lambda_jP_{j,4}, \quad (8)$$

$$S=S_e(1+\delta)+S_g, \quad (9)$$

$$S_g=-\frac{k}{e}\left(\frac{T}{\Theta}\right)^3\sum_j P_{j,5} \quad (10)$$

where $\alpha=(dE/dK)_\zeta$, q_0 is the maximum wave number of phonons and other simbols have the same meanings as those used by Hanna and Sondheimer. For the quasi-free electron model, the expressions for σ and κ coincide completely with those obtained by Hanna and Sondheimer, and thus the interpolation formulae of Hanna and Sondheimer have been justified. For the absolute thermoelectric power S, Eq. (9) differs from the expression of Hanna and Sondheimer in the point that the latter have not the term δS_e. δ is a complicated function of temperature, and at low temperatures and for ideally pure metals, if we assume the phonons are scattered only by electrons, the value of δ reaches to 1/2. However, in many cases, δ is small compared to unity, and so the results of Hanna and Sondheimer are justified practically except for certain special cases.

We have also shown that a general variational principle of Ziman[3] and Dorn[4] gives the same results if we put

$$c^{(n)}=c_0^{(n)}+c_1^{(n)}\eta, \quad (11)$$

$$b_j^{(n)}=\frac{b_{j,0}^{(n)}}{z+\Gamma_j}+\frac{z}{z+\Gamma_j}b_{j,1}^{(n)}, \quad (12)$$

where Γ_j has the same meaning as reference (1). The author believes, however, that his new method above described is more convenient in the point that the best forms of the trial functions of $b_j^{(n)}$ are automatically and uniquely determined if the trial function of $c^{(n)}$ is given. The details will soon appear in Memoirs of the Faculty of Science, Kyushu University, Series B Vol. 2, No. 4.

References

1) I. I. Hanna and E. H. Sondheimer: Proc. Roy. Soc. **A 239** (1957) 247.
2) M. Kohler: Zs. f. Physik **124** (1948) 772; **125** (1949) 679.
3) J. M. Ziman: Canad. J. Phys. **34** (1956) 1256.
4) D. Dorn: Zs. f. Naturf. **12a** (1957) 739.

J. PHYS. SOC. JAPAN **13** (1958) 427–428

Observation of a Beryllium Hyperfragment

By Shigeo MATSUMOTO

Institute of Polytechnics, Osaka City University, Osaka

(Received January 10, 1958)

A beryllium hyperfragment has been found in 600 microns thick Ilford G5 emulsions which were flown at 70,000 feet during four hours from Bristol. The fragment was emitted from a nuclear disintegration of the type $20+1_p$. After traveling 6×10^{-12} seconds, it came to rest and gave rise to a four prong star. The track of the fragment exhibited the "thin-down", and it was not accompanied by delta rays near the secondary star. The residual ranges of the fragment and its decay products are given in Table I. The masses of particles 1 and 2 were found to be $(1.0\pm0.24)M_p$ and $(3\pm1.1)M_p$** respectively by making use of the constant sagitta method, where M_p represents the protonic mass. The former agrees well with the result obtained by the range-ionization method. If particle 2 is an alpha particle, the detectable number of delta rays longer than 2 microns along the track are expected to be four. Since even such a delta ray could not be observed, the particle seems to be singly charged. The identifications of 3 and 4 could not be established, but they appear to be singly changed. The emitted angles of decay products indicate that one or more neutrons should be emitted.

Table I. Characteristics of the hyperfragment and its decay products.

Track	Residual range	Identity	Energy*(Mev)
Fragment	137 μ	${}_\Lambda Be^8({}_\Lambda Be^9)$	53
1	6.5±0.21 mm	p	41.5±0.8
2	218±7 μ	t(or d)	8.9 (or 7.7)
3	34±1.7 μ	p, d, t	1.8, 2.3, 2.6
4	29±1.6 μ	p, d, t	1.6, 2.0, 2.3

When we assume various identities of 2, 3, and 4, a number of hypothetical disintegration schemes are made. Assuming that only one neutron, indicated as 5, has carried away the residual momentum from charged particles, the binding energy of a Λ^0 particle in the hyperfragment—B_Λ—can be calculated for the disintegration schemes. Most of the disintegration schemes except for the three shown in Table II can be excluded, because B_Λ are too large or too small. The mass measurement of particle 2 indicates that it was perhaps a triton, so scheme (b) is less probable than (a). Scheme (c) is also less probable, because the B_Λ is a little smaller as compared with the values reported by other authors.[4)5)] Scheme (a) seems to be the most probable, because the identities of each particle fit to observation and the binding energy—$B_\Lambda=7.2\pm2.0$ Mev—agrees fairly well with the values otained by other authors[5)6)]. Tati and Tati[7)] and Kwon et al.[8)] have indicated that B_Λ increases gradually with increasing mass number of hyperfragment. Their theoretical prediction is compatible with the B_Λ in (a). In conclusion, we would like to take note of the following. When a beryllium hyperfragment decays, a helium or heavier recoil nucleus is usually involved in the decay products. It acquires interest from the fact that such a nucleus has not been observed in the present example.

Table II. Probable disintegration schemes of the beryllium hyperfragment.

	Decay products					
Fragment	1	2	3	4	5	B_Λ(Mev)
(a) ${}_\Lambda Be^8$	p	t	d	p	n	7.2±2.0
(b) ${}_\Lambda Be^9$	p	d	t	d	n	5.8±2.0
(c) ${}_\Lambda Be^9$	p	t	d	d	n	2.2±2.0

The auther wishes to express his cordial thanks to Prof. Y. Watase for his interest and encouragement, and to Prof. Y. Yamaguchi for some criticisms. Thanks are also due to Mr. S. Kaneko for his constant guidance, and to Mr. O. Kusumoto for his valuable advice.

* The range-energy relation of Fay et al.[1)] was used for shorter tracks, and that of Barkas et al.[2)] for longer one. We have employed the value of stopping power which was measured by Imaeda and Kazuno[3)] for the same emulsions as those used here.

** If particle 2 is doubly charged, the value is changed to $(2.3\pm0.9)M_p$.

References

1) H. Fay, K. Gottstein, and K. Hain: Suppl. Nuovo Cim. **11** (1954) 234.
2) W. H. Barkas, P. H. Barrett, P. Cüer, H. H. Heckman, F. M. Smith, and H. K. Ticho: Phys. Rev. **102** (1956) 583. W. H. Barkas: University of California Radiation Laboratory Report UCRL-3384 (unpublished).
3) K. Imaeda and M. Kazuno: J. Phys. Soc. Janan **11** (1956) 85.
4) W. F. Fry, J. Schneps, and S. Swami: Phys. Rev. **101** (1956) 1526.
5) W. Slater, E. Silverstein, R. Levi-Setti, and V. L. Telegdi: Bull. Amer. Phys. Soc. Ser. II, **1** (1956) 319.
6) W. F. Fry, J. Schneps, and M. S. Swami: Phys. Rev. **99** (1955) 1561. M. Blau: Phys. Rev. **102** (1956) 495. K. Gottstein, B. Roederer, J. Roederer, N. Varshneya, and P. Waloshek: Z.

Naturforschg. **11a** (1956) 152.
7) T. Tati and H. Tati: Nuovo Cim. **3** (1956) 1136.
8) Y. Poc Kwon, J. Ôba, and T. Gotô: Nuovo Cim. **6** (1957) 832.

J. PHYS. SOC. JAPAN **13** (1958) 428–429

Asymptotic Expansions of Weber's Functions

By Ryozo YAMADA
Faculty of Science and Engineering
Meijo University, Nagoya, Japan

(Received January 20, 1958)

In our previous paper[3], we obtained the asymptotic expansions of the solutions of modified Weber's equation $y''+(\gamma+x^2/4)y=0$, whose validity was limited to the range $\pi/4>\arg x>-\pi/4$. This paper deals with the expansions of the solutions of Weber's equation $y''+(\gamma-x^2/4)y=0$, valid for $\pi/4>\arg x>-\pi/4$. By these two sets of asymptotic expansions, we can evaluate $D_n(x)$, $D_{-n-1}(ix)$ for arbitrary order and argument in the whole complex domain, together with Whittaker's expression of these functions in Kummer's function and the asymptotic expansions of Whittaker[2),3)]. The integral representation of the functions are[2)]

$$D_n(x)=-\frac{\Gamma(n+1)}{2\pi i}e^{-1/4\cdot x^2}\int_{\infty}^{0}e^{-xt-1/2\cdot t^2}(-t)^{-n-1}dt$$

$$=\frac{\Gamma(n+1)}{2\pi i}x^{-n}e^{in\pi}\int_{\infty}^{\infty+2\pi i}e^{-x^2f(w)}dw\,,$$

$$D_{-n-1}(ix)=\frac{e^{-1/2(n-1)i\pi}}{\sqrt{2\pi}}x^{-n}e^{in\pi}\int_{\infty}^{\infty+\pi i}e^{-x^2f(w)}dw$$

where $f(w)=1/4+\exp w+\frac{1}{2}\exp 2w-(w/4)\sinh^2 w_0$, $t=x\exp w$, and

$$-n=(x^2/4)\sinh^2 w\equiv(x^2/4)\sinh^2(\alpha+i\beta).$$

The stationary points of this integrand are

$$w_1=\log\sinh^2\tfrac{1}{2}w_0\,,\quad w_2=\log\sinh^2\tfrac{1}{2}(w_0+i\pi)\,.$$

If we write

$$\phi_1=\mathrm{Im}\,\{f(w)-f(w_1)\}\,,\quad \phi_2=\mathrm{Im}\,\{f(w)-f(w_2)\}\,,$$

the contours of integration that pass through w_1 and w_2 are determined by $\phi_1(w)=0$, $\phi_2(w)=0$. These contours have different shapes by the signs of $\phi_1(w_2)$, $\phi_1(w_2-2\pi i)$, i.e.,

$$\begin{matrix}\phi_1(w_2)\\ \phi_1(w_2-2\pi i)\end{matrix}=\sinh\alpha\sin\beta$$
$$-\frac{\sinh 2\alpha\sin 2\beta}{4}\log\frac{\cosh\alpha+\cos\beta}{\cosh\alpha-\cos\beta}$$
$$+\frac{\cosh 2\alpha\cos 2\beta-1}{2}\left(\tan^{-1}\frac{\sin\beta}{\sinh\alpha}\mp\frac{\pi}{2}\right).$$

We divide the domain of values of complex w_0 into six subdomains named 1, 2, 3, 1′, 2′, 3′ as shown in Fig. 1. By the method of the steepest

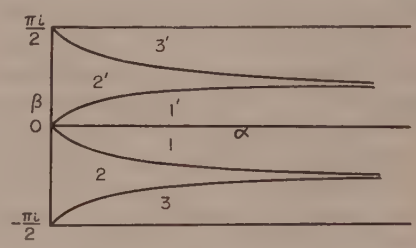

Fig. 1. w_0-plane. $\phi_1(w_2)$ is negative in 1, 1′ and 2′ and is positive in 2, 3 and 3′. $\phi_1(w_2-2\pi i)$ negative in 3, 2′ and 3′ and is positive in 1, 2 and 1′.

descents[1)], the integral $\int\exp(-x^2f(x))dw$ along the contours that pass through w_1, $w_1+2\pi i$ and w_2 which are denoted as (w_1), $(w_1+2\pi i)$ and (w_2) are

$$(w_1)=-\sqrt{\frac{2\pi}{x\cosh w_0}}\exp\left[-\frac{x}{4}\left\{\cosh w_0+\tfrac{1}{2}\sinh^2 w_0-\sinh^2 w_0\log\sinh^2\tfrac{1}{2}w_0\right.\right.$$
$$\left.\left.+\frac{2}{x^2}\log(x\sinh^2\tfrac{1}{2}w_0)\right\}\right]\left(1+\frac{1}{24x^2}\frac{8\cosh^2 w_0-11\cosh w_0-5}{\sinh^2\tfrac{1}{2}w_0\cosh^3 w_0}-\cdots\right),$$

$$(w_1+2\pi i)=-\sqrt{\frac{2\pi}{x\cosh w_0}}\exp\left[-\frac{x^2}{4}\left\{\cosh w_0+\tfrac{1}{2}\sinh^2 w_0-\sinh^2 w_0(\log\sinh^2\tfrac{1}{2}w_0+2\pi i)\right.\right.$$
$$\left.\left.+\frac{2}{x^2}\log(x\sinh^2\tfrac{1}{2}w_0)\right\}\right]\left(1+\frac{1}{24x^2}\frac{8\cosh^2 w_0-11\cosh w_0-5}{\sinh^2\tfrac{1}{2}w_0\cosh^3 w_0}-\cdots\right),$$

$$(w_2)=\sqrt{\frac{2\pi}{x\cosh w_0}}\exp\left[\frac{x^2}{4}\left\{\cosh w_0-\tfrac{1}{2}\sinh^2 w_0+\sinh^2 w_0(\log\cosh^2\tfrac{1}{2}w_0-i\pi)\right.\right.$$
$$\left.\left.-\frac{2}{x^2}\log(x\cosh^2\tfrac{1}{2}w_0)\right\}\right]\left(1+\frac{1}{24x^2}\frac{8\cosh^2 w_0+11\cosh w_0-5}{\cosh^2\tfrac{1}{2}w_0\cosh^3 w_0}-\cdots\right).$$

Considering the integral representations and the end points of contours, we can construct the tables of $D_n(x)$, $D_{-n-1}(ix)$ in terms of (w_1), $(w_1+2\pi i)$ and (w_2) when w_0 lies in the subdomain 1, 2, 3, 1′, 2′, 3′.

	1	2	3	1′	2′	3′
$\frac{2\pi i e^{-in\pi}x^n}{\Gamma(n+1)} D_n(x)$	(w_1) $-(w_1+2\pi i)$	$-(w_1+2\pi i)$	(w_2) $-(w_1+2\pi i)$	(w_2) $-(w_1+2\pi i)$	(w_1)	$(w_1)-(w_2)$
$\sqrt{2\pi}\, e^{-1/2(n-1)\pi i} x^n D_{-n-1}(ix)$	$(w_1)+(w_2)$	(w_2)	(w_2)	$(w_1)+(w_2)$	$(w_1)+(w_2)$	(w_1)

Asymptotic expansions in the transitional region are also obtained by a similar method;

$$D_n(x) \approx \frac{\Gamma(n+1)\, e^{i(n+1/6)\pi}}{x^{(n+2/3)}(12)^{1/6}} \exp\left[\frac{x^2}{4}(\tfrac{1}{2}+\log 2-i\pi)+\varepsilon(\log 2-i\pi)\right]\left(\frac{v}{2}\right)^{1/3} H_{1/3}^{(1)}(ve^{-i\pi}) ,$$

$$D_{-n-1}(ix) \approx \frac{\sqrt{2\pi}\, e^{i(1/2\cdot n+1/6)\pi}}{x^{(n+2/3)}(12)^{1/6}} \exp\left[\frac{x^2}{4}(\tfrac{1}{2}+\log 2-i\pi)+\varepsilon(\log 2-i\pi)\right]\left(\frac{v}{2}\right)^{1/3} H_{1/3}^{(1)}(v) ,$$

where $\varepsilon=n-x^2/4$, and $v=4\varepsilon^{3/2}/3x$. These asymptotic expansions are valid for $|\arg x|<\pi/4$. $D_n(-x)$, $D_{-n-1}(-ix)$ can be obtained by the circuit relations[2].

References

1) G. N. Watson: Theory of Bessel Functions, Cambridge, 1922, 262–268.
2) Whittaker and Watson: Modern Analysis, 4th ed., Cambridge, 347.
3) R. Yamada: J. Phys. Soc. Japan **10** (1955) 71.

Errata

Thomas-Fermi Function for Impurity Atom Dissolved in a Matrix Metal

By Kwai UMEDA and Shigehiro KOBAYASHI

J. Phys. Soc. Japan **13** (1958) 148

Page	Column	Line		(should be read)
149	left	bottom	X	X
	right	bottom	$\equiv$	$=$
150		3	a^2	a_2
		6	oder	order
		7	λ^3	λ^2
		10	$a_5-\cdots$	$\ddot{a}_5-\cdots$
		11	$aa_4+o_2a_3$	$aa_4+a_2a_3$
		11	$aa_2{}^2+a^2a_2$	$aa_2{}^2+a^2a_3$
152	left	7	e^{qr}	e^{-qr}

PROGRESS OF THEORETICAL PHYSICS

CONTENTS

Progress of Theoretical Physics Vol. 19, No. 2, February 1958

An Attempt at Reformulating Pion-Nucleon Interection, I—*Introduction of K-Space*—..... O. HARA, Y. FUJII and Y. OHNUKI..129
Invariants in $K_{\mu 3}$ and K_{e3} Decays .....R. GATTO..146
Effect of Electron Exchange on the Dispersion Relation of Plasma Oscillations ..... H. KANAZAWA and S. TANI..153
General Theory of Infrared Divergence .....N. NAKANISHI..159
Theory of Direct Interaction in Nucleon Inelastic Scattering .....S. YOSHIDA..169
Multiple Meson Production in Antinucleon-Nucleon Annihilation ....N. YAJIMA and K. KOBAYAKAWA..192
Remarks on Spin-Wave Theory for the Ferromagnetic Exchange Problem .... I. MANNARI..201
Letters to the Editor:
The Exciton-Lattice Interaction and the Line Shape of the Exciton Absorption Band .....Y. TOYOZAWA..214
On Puppi's Determination of the Pion-Nucleon Coupling Constant .. ..K. MATUMOTO, S. OTSUKI, H. SHIMODAIRA and E. YAMADA..216
On the Applicability of the Pion-theoretical Nuclear Potential .... S. OTSUKI, R. TAMAGAKI and W. WATARI..217
High Energy Gamma-Rays from the Crab Nebula.....S. HAYAKAWA..219
Contents of Journ. of Phys. Soc. of Japan, Vol. 13, No. 1 220

Price $ 1.25 per copy
$ 15.00 per year (postage inclusive)
Annual dues for foreign members (individual subscribers)
$ 12.00 (postage inclusive)
" for foreign members of the Physical Society of Japan
$ 10.00 (postage inclusive)

Application for members, subscriptions and orders for back numbers should be sent, directly or through book-dealers, to

The Publication Office
in
Yukawa Hall, Kyoto University, Kyoto, Japan

JOURNAL OF THE PHYSICAL SOCIETY OF JAPAN Vol. 13, No. 5, MAY, 1958

Excitation Curve for the Reaction $P^{31}(n, p)$ Si^{31}

By Susumu MORITA

Department of Physics, Faculty of Science, Kyushu University, Fukuoka, Japan

(Received February 6, 1958)

The excitation curve for the reaction $P^{31}(n, p)Si^{31}$ was measured in the energy range of neutron from 3.0 MeV to 5.2 MeV by activation method. A large resonance peak of 160 mb was found at the neutron energy of 4.9 MeV.

§ 1. Introduction

Paul and Clarke[1] found that the cross sections for (n, p) reactions with 14 MeV neutrons were considerably larger than the theoretical values predicted by the assumption of compound nucleus formation. Then, it has been attempted by several authors to measure the excitation function, and energy spectrum and angular distribution of the emitted protons in these reactions[2),3)]. We obtained also the preliminary result for the excitation function of the reaction $P^{31}(n, p)Si^{31}$ for neutron energies of 3.0 MeV to 5.2 MeV by the activation method. The reaction $P^{31}(n, p)Si^{31}$ has the threshold energy of 0.9 MeV and the resultant Si^{31} decays by emitting a beta ray with the maximum energy of 1.5 MeV and has a half life of 159 min.[4]. Accordingly, this reaction has proved to be a valuable "threshold detector" for the measurement of continuous neutron spectrum, particularly, the fast neutron flux in a nuclear reactor[5].

The cross section of this reaction has been measured for neutron energies up to 3.6 MeV with good energy resolution[6], and the behavior of the cross section is primarily determined by the Coulomb barrier penetrability for the emitted proton in the energy region near the threshold[7]. As the neutron energy gets higher, the existence of resonance structure has been shown. We tried in the present work to extend the cross section measurement to somewhat higher energy.

§ 2. Experimental Procedures and Results

The reaction $D(d, n)He^3$ was used as the neutron source. The change of energy of incident deuteron, as well as the variation of neutron energy with angle of emission, were used in order to get the neutrons of various energies. The deuteron beam, accelerated by the Van de Graaff generator at Kyushu University, entered the target chamber of 4 cm in length through a nickel foil. The bombardments with deuterons of 1.93 MeV and 2.28 MeV were made with a nickel foil of 1.59 mg/cm² thick and deuterium gas of 43.5 cm Hg and those with deuterons of 1.70 MeV and 2.13 MeV were undertaken with a nickel foil of 1.09 mg/cm² thick and deuterium gas of 10.21 cm Hg. The energy loss and spread of deuteron beam in the nickel foil and deuterium gas was estimated by the data given by Allison and Warshow[8] and Segre[9].

The samples of red phospher were arranged in the directions of 0, 20, 40, 60 and 80 degrees relative to the deuteron beam and the distances between the center of target chamber and the centers of the surface of samples were 138 mm.

Each sample was made by pressing the red phospher into a circular vessel of 35 mm diameter. The thickness of red phospher was enough to get the saturation of self absorption for the beta-ray of Si^{31}, and the densities of induced activity were measured.

After the bombardment of about four hours by deuteron beam of a few microamperes, the activity induced in these samples by the neutrons were followed with a G.M. counter of thin mica window. The samples were placed closely against the window of the counter to give 2π counting geometry. For example, the decay curves for five samples obtained with deuteron of 2.28 MeV are shown in Fig. 1. In this figure, the straight lines A, B, C, D and E, with the half life of 159 min.[4], correspond to the activity of samples placed at 0, 20, 40, 60 and 80 degrees, respectively. As these lines are well fitted with our experimental data, all the coudting rates of each sample were followed back to the

initial activity assuming the above value of half life, and the weighted mean of these values was obtained for each sample. The counting rate of initial activity divided by the neutron intensity incident on the sample was taken as the measure of the relative cross section of this reaction at the corresponding

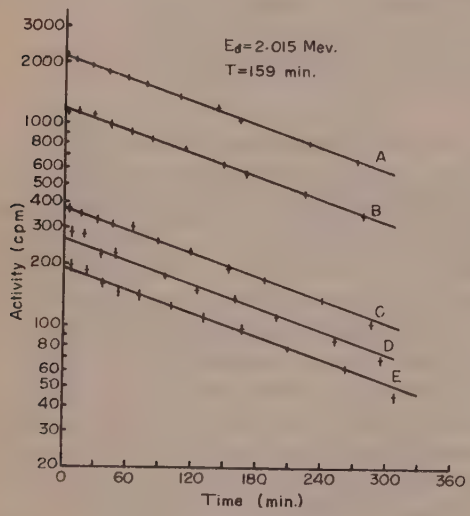

Fig. 1. Decay curves of activity of Si^{31} induced by *d-d* neutrons, obtained with deuteron beam of 2.28 MeV. The lines A, B, C, D and E, with half life of 159 min., correspond to the activity of samples placed at 0, 20, 40, 60 and 80 degrees, respectively.

neutron energy. As the geometrical extent of target chamber and those of samples were rather large in our arrangement, the intensity of neutron impinging on each sample and its uncertainty were estimated by the following procedures. The target chamber of 4 cm in length was divided into four sections of 1 cm in length and each section was approximated by a point neutron source sitiuated at their center. The neutron intensities incident on samples from these point sources were estimated, considering the deuteron energies at these points, angle of emission of neutron and the solid angles for each sample subtended by these point sources. The values of cross section for the *d-d* reaction as a function of deuteron energy and angle of emission of neutron was referred to the summary given by Fowler and Brolley[10].

The uncertainties in neutron intensity are considerably large for the samples placed at the directions of 20 and 40 degrees, owing to the rapid change of the angular distribution of *d-d* neutrons in these directions. Also, the energy spread of neutrons becomes larger with the increase of angle of emission and their spreads for the samples placed at 80 degrees were estimated to be 3.26±0.17 MeV, 3.25±0.23 MeV, 3.13±0.22 MeV and 3.10±0.20 MeV, corresponding to the four values of bombarding energy of deuterons. As these values are well overlapped, the average of the cross section was obtained for the average value of these neutron energies. This average value is normalized to the absolute value of the cross section obtained by Ricamo[11]. The values of cross section for a certain energy of neutron, obtained with different deuteron energies but overlapped energy region of neutron, were also averaged. The result thus obtained is shown in Fig. 2. The values of

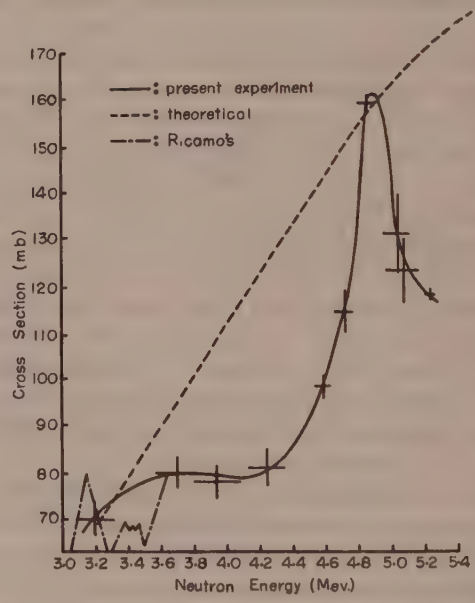

Fig. 2. Excitation curve of the reaction P^{31} (*n*, *p*) Si^{31}. Present result was normalized to the absolute cross section obtained by Ricamo at the neutron energy of 3.2 MeV.

the absolute cross section, shown in the ordinate, has an uncertainty of about 15 per cent, owing to the difference in the energy resolution between Ricamo's experiment and ours.

As can be seen in Fig. 2, a remarkable resonance of about 160 mb was found at neutron energy of 4.9 MeV. A small resonance at neutron energy of 3.7 MeV is probable but not certain. The dotted curve in Fig. 2, shows the theoretical excitation curve calculated by assuming the compound nucleus for-

mation with the value of $R=(1.4\times A^{1/3})\times 10^{-13}$ cm for nuclear radius and the value of 0.9 MeV for the threshold energy of this reaction. The general behavior of the theoretical curve, in the region below the barrier height of 5.4 MeV, is determined by the penetrability of emitted proton against the Coulomb barrier. This theoretical curve is well fitted with the experimental points in the energy range below 3.0 MeV, but seems somewhat too large in the range above 3.0 MeV, as was suggested by Grimeland[7]. But the value of 3.3 MeV, suggested by Grimeland for the barrier height of Si^{31}, will be too small. On the other hand, the theoretical curve was obtained with the assumption that the available energy of this reaction is small compared with the threshold energy and this assumption is not valid in our energy range. Accordingly, the excitation curve in these energy range will not be conclusive to estimate the barrier height. The excitation curve in the range above the barrier height, where the theoretical curve becomes nearly flat and the direct interaction will become important, will be desirable.

The author wishes to express his cordial thanks to Prof. I. Nonaka and all staff of the nuclear laboratory of Kyushu University. This work has been supported by the Scientific Research Expenditure of the Ministry of Education.

Note added in proof; After this paper was received by the Physical Society of Japan, measurements of the excitation curve of the reaction $P^{31}(n, p)Si^{31}$ in the more extended range of neutron energies than our's were reported by J. A. Grundl et al in Phys. Rev. 109 (1958(425. Their results are consistent with the present one in general behavior, although the resonance peak in their result is not so remarkable as in our result. This may be due to the diffrence in the energy resolution of neutron.

References

1) E. B. Paul and R. L. Clarke: Canad. J. Phys. **31** (1953) 267.
2) G. Brown, G. C. Muirhead and W. T. Morton: Phil. Mag. **2** (1957) 785.
3) V. V. Verbinski, T. Hurlimann, W. E. Stephens and E. T. Winhold: Phys. Rev. **108** (1957) 779.
4) E. Lüscher, R. Ricamo, P. Scherrer and W. Zünti: Helv. Phys. Acta. **23** (1950) 561.
5) D. J. Hughes: Pile Neutron Research.
6) R. Ricamo: Nuovo Cimento. **8** (1951) 383.
7) B. Grimeland: Nuovo Cimento. **11** (1955) 1336.
8) S. K. Allison and S. D. Warshow: Rev. Mod. Phys. **25** (1953, 779.
9) E. Segre: Experimental Nuclear Physics. Vol. 1. Part 2.
10) J. L. Fowler and J. E. Brolley Jr.: Rev. Mod. Phys. **28** (1956) 103.

JOURNAL OF THE PHYSICAL SOCIETY OF JAPAN Vol. 13, No. 5, MAY, 1958

Electronic Structure of Bismuth Type Crystals

By Shoichi MASE

Department of General Education, University of Nagoya

(Received December 17, 1957)

A study is made of calculating the electronic energy bands in bismuth type crystals by making use of the Bloch method (with the inclusion of spin-orbit interaction) for the purpose of clarifing the relation between the low temperature diamagnetic susceptibility and the energy bands. The peculiar feature of the de Haas-van Alphen effect in bismuth type crystals (the small effective mass tensor) is explained by our calculated energy bands but the ordinary main term of the Landau-Peierls susceptibility expected from the energy bands is considerably small compared with the experimental value. Then, unlike Jones theory, the most part of the extraordinary large constant susceptibility seems to be attributed to the non-diagonal term which is usually neglected.

§ 1. Introduction

As is well known, the electronic and magnetic properties of bismuth type crystals, particularly bismuth, are extremely anomalous and they have been studied by many workers. On the consideration of the magnetic property and others, Jones[1] deduced that the energy surfaces of electrons are extremely oblong spheroids, the longest axis of which is parallel to the trigonal axis, and that of holes is ob late spheroid, the shortest axis of which is in trigonal axis. On the analysis of the de Haas-van Alphen effect of bismuth, Blackman[2] and Shoenberg[3] deduced that, besides Jones' ellipsoids, there are another three ellipsoids with 120° symmetry about the trigonal axis.

According to Shoenberg's study, the contribution to the susceptibility by the de Haas-van Alphen electrons in bismuth is less than 10% of the experimental value, the detail of which is shown in Table I. One object in the present paper is to study whether the observed anisotropic small effective mass tensor in the de Haas-van Alphen effect is reasonably explained from the view point of the energy bands. The other object is to investigate whether or not the susceptibility of about 90% of the experimental value minus the ion core part is contributed by other ellipsoids which do not show periodic phenomena as appreciable.

Table I. The specific susceptibility of bismuth at low temperatures (after Shoenberg[3]).

	$\chi_{\parallel}\times 10^6$	$\chi_{\perp}\times 10^6$
Contribution from the de Haas electrons	−0.0072	−0.184
Experimental value	−1.22	−1.84

Morita[4] investigated the electronic structure of bismuth crystal with use of the tight binding approximation and tried to explain Jones' and Shoenberg's results. We extend his theory with the inclusion of the spin-orbit interaction in an approximate manner.

§ 2. The Symmetry Properties of Energy Bands

Bismuth type crystal has the space group symmetry D_{3d}^5-R3m but the crystal structure is very similar to that of simple cubic lattice. The crystal is composed of sublattices A and B. We take here the binary and trigonal axis as x- and z-axis respectively, then the

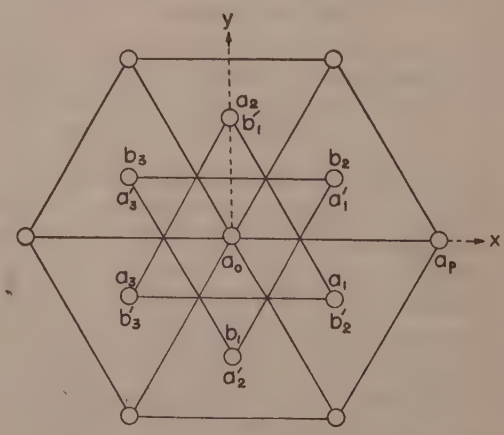

Fig. 1. The lattice structure of bismuth type crystal.

atom configuration projected to the perpendicular plane to z-axis becomes as shown in Fig. 1. The positions of atoms in the figure are

$$a_0=(0,0,0)u\ ,$$

$$a_1=\left(\frac{\sqrt{2}}{2}\ ,\ -\frac{\sqrt{6}}{6}\ ,\ \frac{2\sqrt{3}}{3}(1+3\omega)\right)u\ ,$$

$$a_2=\left(0,\ \sqrt{\frac{2}{3}}\ ,\ \frac{2\sqrt{3}}{3}(1+3\omega)\right)u\ ,$$

$$a_3=\left(-\frac{\sqrt{2}}{2}\ ,\ -\frac{\sqrt{6}}{6}\ ,\ \frac{2\sqrt{3}}{3}(1+3\omega)\right)u\ ,$$

$$a_p=(2,0,0)u\ ,$$

$$b_1=\left(0,\ -\sqrt{\frac{2}{3}},\ \frac{\sqrt{3}}{3}(1+3\omega+3\varepsilon)\right)u\ ,$$

$$b_2=\left(\frac{\sqrt{2}}{2}\ ,\ \frac{\sqrt{6}}{6}\ ,\ \frac{\sqrt{3}}{3}(1+3\omega+3\varepsilon)\right)u\ ,$$

$$b_3=\left(-\frac{\sqrt{2}}{2}\ ,\ \frac{\sqrt{6}}{6}\ ,\ \frac{\sqrt{3}}{3}(1+3\omega+3\varepsilon)\right)u\ ,$$

$$b_1'=\left(0,\ \sqrt{\frac{2}{3}}\ ,\ -\frac{\sqrt{3}}{3}(1+3\omega-3\varepsilon)\right)u\ .$$

In the case of bismuth ω, ε and u take the following values*,

$$\omega=0.0173\ ,$$
$$\varepsilon=0.0548\ ,$$
$$u=3.24\text{Å}\ .$$

u is approximately the nearest neighbour distance. The primitive translation vectors of the lattice are $\overrightarrow{a_0a_1}$, $\overrightarrow{a_0a_2}$ and $\overrightarrow{a_0a_3}$, hence the first Brillouin zone is such as indicated in Fig. 2.

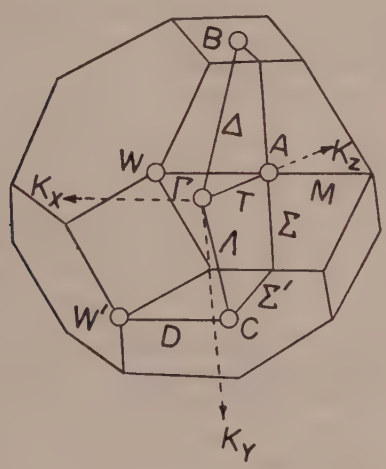

Fig. 2. First Brillouin zone.

The effect of the crystal symmetry on the energy bands can be derived by well known Bouckaert, Smoluchowski and Wigner's method[5] or Elliot's method[6] in double group. The typical elements of symmetry operations which make the lattice invariant are as follows:

(i) E is the unit element,

(ii) C_3^+ and C_3^- are $\pm 120°$ rotation around the trigonal axis,

(iii) S_1, S_2 and S_3 are the reflections in the planes through a_0a_2, a_0a_3, a_0a_1 and z-axis respectively,

(iv) J is the inversion at the origin followed by the non-primitive translation $\tau\equiv\overrightarrow{a_0b_2}$,

(v) JC_3^+ and JC_3^-,

(vi) JS_1, JS_2 and JS_3.

By the operations (i), (ii) and (iii), the atoms A-site are transformed into A-site and by the operations (iv), (v) and (vi), the atom of A-site into B-site. The characters of irreducible representations of the double groups of wave number $\boldsymbol{k}$ are given in Table II. The plus and minus signs attached on some characters in (a) and (c) mean that the upper sign corresponds to the representation without dash sign and the lower sign corresponds to the other. Additional degeneracies due to time reversal symmetry are also shown in Table II. In Table III is shown the compatibility relations.

If we neglect ω and ε, Bragg reflections from hexagonal faces in Fig. 2 disappear and symmetry lines T and Λ extend to the point which is equivalent to Γ. In the real crystal, however, the energy band should split at the faces through the middle points A and C along T and Λ, and nearly full and nearly empty bands should be separated by small energy gap. Then we should expect electrons or holes with very small effective mass at A or C. From the crystal symmetry alone, A is the point with zero slope along T, Σ and M. C is the point with zero slope along Λ, Σ' and D. B is also the point with zero slope along three directions similar as the

* These values was cited from reference 4.

Table II. Character tables for representations of double groups of $\boldsymbol{k}$.

(a) Γ, A

	E	$\bar{E}$	$2C_3$	$2\bar{C}_3$	$3S$	$3\bar{S}$	J	$\bar{J}$	$2JC_3$	$2J\bar{C}_3$	$3JS$	$3J\bar{S}$
Γ_1, Γ_1'	1	1	1	1	1	1	±1	±1	±1	±1	±1	±1
Γ_2, Γ_2'	1	1	1	1	-1	-1	±1	±1	±1	±1	∓1	∓1
${}^2\Gamma_3$, ${}^2\Gamma_3'$	2	2	-1	-1	0	0	±2	±2	∓1	∓1	0	0
Γ_4, Γ_4'	1	-1	-1	1	i	$-i$	±1	∓1	∓1	±1	$\pm i$	$\mp i$
Γ_5, Γ_5'	1	-1	-1	1	$-i$	i	±1	∓1	∓1	±1	$\mp i$	$\pm i$
${}^2\Gamma_6$, ${}^2\Gamma_6'$	2	-2	1	-1	0	0	±2	∓2	±1	∓1	0	0

D_i	Γ_1	Γ_2	${}^2\Gamma_3$	Γ_1'	Γ_2'	${}^2\Gamma_3'$
$D_i\times D_{1/2}$	${}^2\Gamma_6$	${}^2\Gamma_6$	$\Gamma_4+\Gamma_5+{}^2\Gamma_6$	${}^2\Gamma_6'$	${}^2\Gamma_6'$	$\Gamma_4'+\Gamma_5'+{}^2\Gamma_6'$

Γ_4, Γ_5 and Γ_4', Γ_5' are degenerated by time reversal.

(b) T

	E	$\bar{E}$	$2C_3$	$2\bar{C}_3$	$3S$	$3\bar{S}$
T_1	1	1	1	1	1	1
T_2	1	1	1	1	-1	-1
${}^2T_3$	2	2	-1	-1	0	0
T_4	1	-1	-1	1	i	$-i$
T_5	1	-1	-1	1	$-i$	i
${}^2T_6$	2	-2	1	-1	0	0

D_i	T_1	T_2	${}^2T_3$
$D_i\times D_{1/2}$	${}^2T_6$	${}^2T_6$	$T_4+T_5+{}^2T_6$

T_4 and T_5 are degenerated by time reversal.

(c) B, C

	E	$\bar{E}$	S_1	$\bar{S}_1$	J	$\bar{J}$	JS_1	$J\bar{S}_1$
B_1, B_1'	1	1	1	1	±1	±1	±1	±1
B_2, B_2'	1	1	-1	-1	±1	±1	∓1	∓1
B_3, B_3'	1	-1	i	$-i$	±1	∓1	$\pm i$	$\mp i$
B_4, B_4'	1	-1	$-i$	i	±1	∓1	$\mp i$	$\pm i$

D_i	B_1	B_2	B_1'	B_2'
$D_i\times D_{1/2}$	B_3+B_4	B_3+B_4	$B_3'+B_4'$	$B_3'+B_4'$

B_3, B_4 and B_3', B_4' are degenerated by time reversal.

(d) $\Lambda, \Delta, \Sigma, \Sigma'$

	E	$\bar{E}$	S_1	$\bar{S}_1$
Λ_1	1	1	1	1
Λ_2	1	1	-1	-1
Λ_3	1	-1	i	$-i$
Λ_4	1	-1	$-i$	i

D_i	Λ_1	Λ_2
$D_i\times D_{1/2}$	$\Lambda_3+\Lambda_4$	$\Lambda_3+\Lambda_4$

Λ_3 and Λ_4 are degenerated by time reversal.

(e) M, D ($\xi=\sqrt{2}\pi uk_x$)

	E	$\bar{E}$	JS_1	$J\bar{S}_1$
M_1	1	1	$e^{-i\xi}$	$e^{-i\xi}$
M_2	1	1	$-e^{-i\xi}$	$-e^{-i\xi}$
M_3	1	-1	$ie^{-i\xi}$	$-ie^{-i\xi}$
M_4	1	-1	$-ie^{-i\xi}$	$ie^{-i\xi}$

D_i	M_1	M_2
$D_i\times D_{1/2}$	M_3+M_4	M_3+M_4

M_3 and M_4 are degenerated by time reversal.

Table III. Compativility relations.

Γ_1	Γ_2	${}^2\Gamma_3$	Γ_1'	Γ_2'	${}^2\Gamma_3'$	$\Gamma_4+\Gamma_5$	${}^2\Gamma_6$	$\Gamma_4'+\Gamma_5'$	${}^2\Gamma_6'$
T_1	T_2	${}^2T_3$	T_1	T_2	${}^2T_3$	T_4+T_5	${}^2T_6$	T_4+T_5	${}^2T_6$
Λ_1	Λ_2	$\Lambda_1+\Lambda_2$	Λ_1	Λ_2	$\Lambda_1+\Lambda_2$	$\Lambda_3+\Lambda_4$	$\Lambda_3+\Lambda_4$	$\Lambda_3+\Lambda_4$	$\Lambda_3+\Lambda_4$
A_1	A_2	${}^2A_3$	A_1'	A_2'	${}^2A_3'$	A_4+A_5	${}^2A_6$	$A_4'+A_5'$	${}^2A_6'$
Σ_1	Σ_2	$\Sigma_1+\Sigma_2$	Σ_1	Σ_2	$\Sigma_1+\Sigma_2$	$\Sigma_3+\Sigma_4$	$\Sigma_3+\Sigma_4$	$\Sigma_3+\Sigma_4$	$\Sigma_3+\Sigma_4$
M_1	M_2	M_1+M_2	M_2	M_1	M_1+M_2	M_3+M_4	M_3+M_4	M_3+M_4	M_3+M_4

C_1	C_2	C_1'	C_2'	C_3+C_4	$C_3'+C_4'$
Λ_1	Λ_2	Λ_1	Λ_2	$\Lambda_3+\Lambda_4$	$\Lambda_3+\Lambda_4$
D_1	D_2	D_2	D_1	D_3+D_4	D_3+D_4

point C. T is the line with zero slope (T_4, T_5) or finite slope ($^2T_6$) in directions perpendicular to the T. Λ and Δ are points of zero slope in two directions perpendicular to the Λ and Δ axis. M is the line of zero slope in two directions perpendicular to the line. W is not special symmetry point on M and then generally a point of finite slope along M. These considerations are useful to study some detail of the band structure in the following sections.

§ 3. Calculation of Energy Bands

Bismuth, antimony and arsenic atoms have five valency electrons and the upper most p states are halfly occupied by the electrons. In crystals, the atomic levels become broad and overlap. Since, however, the cohesive energy of bismuth metal is comparatively small, we may expect from Wiger's theory[7] of cohesion that the overlapping of p-and d-bands is presumably not so large. Then we neglect here the d state. As seen from Fig. 1, each half of six neighbouring atoms is slightly different in the atomic distances and this is taken into account to obtain the matrix elements. Here we take the two centre approximation and further for the two centre integrals take the following approximation:

$$(pp\sigma)_{R+\Delta R}, (pp\pi)_{R+\Delta R}, (ss\sigma)_{R+\Delta R}, (sp\sigma)_{R+\Delta R} = (pp\sigma)_R, (pp\pi)_R, (ss\sigma)_R, (sp\sigma)_R\left(1-r_i\frac{\Delta R}{R}\right), \tag{3.1}$$

where $r_i=r_1, r_2, r_3, r_4$ for the first···and the fourth respectively. Neglecting the higher power than second of ε, ω to unity, matrix elements in the case without spin are given in Appendix A.

Now we consider the spin-orbit interaction. For arsenic, antimony and bismuth atoms, the spin-orbit coupling parameter λ for p^3 electron configuration are the order of 0.2 ev, 0.4 ev and 1.3 ev[8] respectively. If the values of these are not considerably reduced in metals, we should take account of the spin-orbit interaction Hamiltonian H_{SO} in zeroth order approximation, not as small perturbation, because λ is the same order of magnitude as the nearest neighbour energy integrals for the electro static potential. H_{SO}, however, may be very small in the middle of lattice points where wave functions particularly well overlap. Then even the nearest neighbour integral for H_{SO} is certainly small compared with the energy integral in the same atom, which is the order of λ, and the former should be also small compared with the nearest neighbour integrals for the electro static potential. Then it may be not so bad to neglect the migration of atomic wave functions into neighbouring atoms and approximate H_{SO} as spherically symmetrical about each nucleus. In such a approximation the matrix element for H_{SO} is independent of $\boldsymbol{k}$. Because of the periodic potential term, however, the magnitude may be somewhat different from that is appeared in the theory of atomic spectra.

Noting that spin functions transform by the spinor representation, Bloch functions which belong to the irreducible representations are obtained by group theoretical method[9]. The results are listed in Appendix B. α and β show two spin functions. The bar on the subscript means that the wave functions are constructed from atomic functions located at B-site. We can set up secular equations for each representation as shown in Appendix C.

Now we determine the values of parameters to obtain energy curves. Many knowledge are obtained from soft X-ray emission band but unfortunately no experiment is made for this type of lattice. Then we determine the parameters in rough manner. With use of approximately determined two centre integrals with reference to the existing calculations of energy bands for germanium and others and estimated value of $E_{xx}(0)-E_{ss}(0)$, we found that the overlapping of s and p bands is small. Therefore we neglect the s state in numerical calculation. We evaluate the energy eigenvalue with use of ε and ω for bismuth and several values of λ and with the assumption of the following values for the other parameters,

$$\begin{aligned}(pp\sigma)&=1.1\text{ ev},\\ (pp\pi)&=-0.35\text{ ev},\\ r_1&=3,\quad r_2=6.\end{aligned} \tag{3.2}$$

The energy *versus* $\boldsymbol{k}$ curves are shown in Fig. 3. This figure was drawn by performing numerical calculation for only a few points on the secular equations in Appendix C. In the case of $\lambda>0.7$ ev, the energy of A_4' becomes higher than that of $^2\Gamma_6'^{\alpha}$ and the band structure becomes similar as that of good conductor. Then we deduce that λ is fairly small compared with that of atom in bismuth.

Along the line Δ, the energy extremum does not occurs in the case of $\lambda=0$. With the inclusion of spin-orbit interaction, qualitative feature of energy curve will be unchanged.

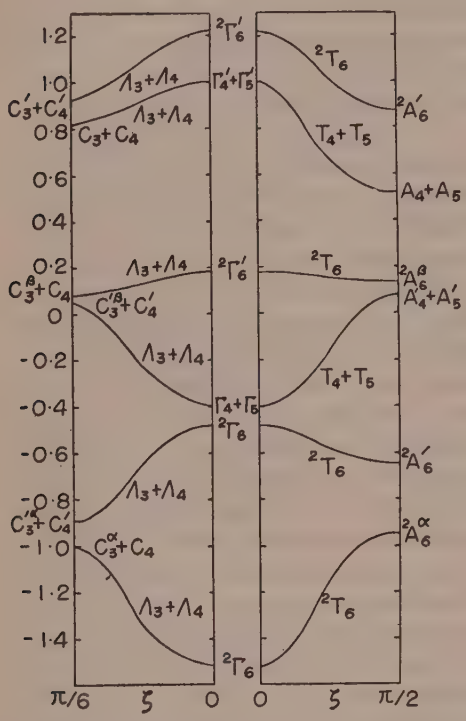

Fig. 3. Energy *versus* $\boldsymbol{k}$ curve. The origin of the energy is arbitrary. (Units ev.).

Although the lattice constants are almost the same in bismuth, antimony and arsenic, the values of parameters in (3.2) will be generally different in three cases and the energy curves in three cases will be unable to obtain only by changing the value of λ. We can say, however, that the pocket of holes does not occur at A in antimony and arsenic, since the energies for A_4' and $^2\Gamma_6'$ are considerably reduced and raised respectively by diminishing the value of λ and on the other hand the values of C_3, C_3' and $^2A_6$ are more insensitive on the value of λ, as far as λ is not so small. Apart from the kind of charge carriers, however, we should expect the points A and C for possible points where electrons or holes are located.

§ 4. The Shape of the Energy Surfaces of Electrons and Holes

We proceed to investigate finer detailes of the band structure and discuss the comparison with experiments of susceptibility. Total susceptibility consists of the diamagnetic and paramagnetic susceptibility of conduction electrons and the contribution from ion core. The latter part is -0.14×10^{-6}/gr in bismuth[10] and this value is about 10% of total value. On the other hand the spin paramagnetic susceptibility of conduction electrons is very small compared with Landau susceptibility in bismuth. Then we may consider that about 90% of the experimental value of χ in bismuth is orbital diamagnetism (or sums of orbital diamagnetism and paramagnetism) of conduction electrons. In antimony and arsenic the percentage of the orbital part to total susceptibility becomes much smaller.

To calculate the energy surfaces in the neighbourhood of A and C, we expand the matrix elements as power series of $\boldsymbol{k}-\boldsymbol{k}_A$ or $\boldsymbol{k}-\boldsymbol{k}_C$ and solve the secular equations with keeping up to the second order of wave number. Further we retain only the leading term in expansion of $\mathcal{E}$ and ω.

First we consider the energy surface at C. The energy surface connected with C_3 is given by

$$E_C(\boldsymbol{k})=E(C_3)+\frac{h^2}{2m}(\alpha_{11}(C_3)k_x^2+\alpha_{22}(C_3)k_y^2+\alpha_{33}(C_3)k_z^2+2\alpha_{23}(C_3)k_yk_z)\,. \quad (4.1)$$

The energy surface connected with C_3' is quite similar as that of C_3. The expression of $\alpha_{ij}(C_3)$ is shown in Appendix D. The other two ellipsoids are obtained from (4.1) by $\pm120°$ rotation about the trigonal axis. We subsequently correspond these ellipsoids to the de Haas-van Alphen ellipsoids. The magnitude of all $\alpha_{ij}(C_3)$ or $|\alpha_{ij}(C_3')|$ are generally the same order. We note, however, the numerators of α_{22}, α_{33} and α_{23} are composed of the sum of terms with plus and minus signs of comparable order but α_{11} is composed of only terms with same sign.

Secondly we study the structure of the energy surface at A. In the neighbourhood of this point, the energy connected with the representation A_4' is given by

$$E_A(\boldsymbol{k})=E(A_4')+\frac{h^2}{2m}(\alpha_{11}(A_4')k_x^2+\alpha_{11}(A_4')k_y^2+\alpha_{33}(A_4')k_z^2)\,. \quad (4.2)$$

The energy surface connected with $^2A_6$ is quite similar as that of A_4'. The expression of $\alpha_{ij}(A)$ is shown in Appendix D. The

magnitude of $|\alpha_{33}(A)|$ is generally not so large, because $(pp\sigma)+2(pp\pi)$ in numerator is small positive quantity and the denominator is not so small. On the other hand the magnitude of $|\alpha_{11}(A)|$ is generally large if the energy gap between ${}^2A_6{}^\beta$ and A_4' is small.

Along the line M and D, the energy gap between occupied and unoccupied bands may be as small as at the points A and C. Since W and W' are not the points with zero slope, we must study in detail whether or not energy extremum occurs somewhere along the line. This is very tedious and here we do not pursue this problem. But we wish to point out that the energy surfaces at the points along these lines have not the same symmetry properties as those of the de Haas-van Alphen ellipsoids Shoenberg have found.

Now we compare theoretical values of α_{ij} with the experimental values evaluated from the de Haas-van Alphen effect. Table IV (a) is the experimental values for bismuth, antimony and arsenic and IV (b) is theoretical values of $\alpha_{ij}(C_3)$ and $\alpha_{ij}(A_4')$ with use of the values of parameters in (3.2) and the value $\lambda=0.6$ ev. The characteristic feature of the experimental results are that all α_{ij} is fairly larger than unity except α_{22} in bismuth and any principal axis of ellipsoids is not in the direction of the trigonal axis but inclines by some degree ($\alpha_{23}\neq 0$). Then we can correspond the energy surface at C with the de Haas-van Alphen ellipsoids. The discrepancy between theoretical and experimental values of α_{22}, α_{33} and α_{23} can be attributed to improper cancelation in numerator of (D.2) but the discrepancy of α_{11} can not be interpreted in such manner. To explain the extremely large value of α_{11} in bismuth, we must suppose that the energy gap between C_3 and C_3' should be the order of one half or one third of the present calculation, in which the energy gap is 0.025 ev. On the other hand, if we assume that the energy gap in antimony is the order of 0.1~0.2 ev, then we can understand that the experimental values of all α_{ij} are the order of ten in antimony. The single energy surface pocket at A_4' is extremely oblong ellipsoid. In order to explain that the de Haas-van Alphen effect by the holes is not perceptible in bismuth, we must consider that the energy gap between ${}^2A_6$ and A_4' is larger than two times of 0.05 ev in present calculation and then $|\alpha_{11}(A_4')|$ is <70. On the other hand two types of period are observed in arsenic[11]. We correspond one type of period

Table IV. Effective mass tensor coefficients. (a) experimental values, (b) theoretical values.

(a)

	α_{11}	α_{22}	α_{33}	α_{23}
Bi	417	0.8	40	4.0
Sb	20	5.3	10	6.7
As	5.2	13	7.9	9.8
	32	32	4.3	0

(b)

	α_{11}	α_{22}	α_{33}	α_{23}
C_3	136	−3.0	112	−4.6
A_4'	−148	−148	−1.3	0

(the longer period part) with the energy surface at ${}^2A_6{}^\beta$ in accordance with the shape of the energy surface derived from experiments.

According to Abeles and Meiboom's experiment of galvanomagnetic effect of bismuth[12], the number of conduction electrons per atom is the order of 1.6×10^{-5} at 80°K. This is almost equal as the value 1.5×10^{-5} per atom evaluated from the de Haas-van Alphen effect. This fact shows that the de Haas-van Alphen electrons themselves are majority carriers. Thus we suppose that electrons and holes are located at the points C and A respectively. The present theory predicts that the electrons at C are depleted by alloying antimony in bismuth by the effect from large change of λ. This depletion should cause remarkable change in electronic phenomena as conductivity.

Since the contribution to the susceptibility $\chi_\perp$ from holes at A is very small compared with that of de Haas-van Alphen ellipsoids, the contribution to the ordinary main term of Landau-Peierls diamagnetism from all electrons and holes in bismuth is clearly smaller than two times of the contribution from the

de Haas-van Alphen electrons, i.e. 20% of experimental value of $\chi_\perp$. We can obtain similar conclusion of $\chi_\parallel$. Then we obtain at most 30% of the experimental value from ionic and Landau susceptibilities.

§ 5. Conclusion

To summarize, it is most plausible that three ellipsoids of electrons (or holes) at C are responsible for the de Haas-van Alphen effect. The shape of the energy surface we found here is in accord with Shoenberg's model. Extreme anisotropy of α_{ij} in bismuth can be understood as accidental approach of two energy bands at C, the energy gap of which is estimated to the order of 0.01 ev, and proper cancelation in numerator of α_{22}, α_{33} and α_{23}. The energy surface pocket of holes (or electrons) which is expected to occur at A is extremely oblong single ellipsoid and we expect longest period of the de Haas-van Alphen oscillation in the magnetic field parallel to the trigonal axis. Such oscillation is observed only in arsenic. If we supposed that $\alpha_{11}(A_4')=-50\sim70$ in bismuth and then $E(A_6^\beta)-E(A_4)\sim0.1$ ev, the longest period by the holes is the same order with $\chi_\parallel$ component of Shoenberg's ellipsoids and these are both too short compared with $\chi_\perp$ component of Shoenberg's ellipsoids. The calculated value of $\alpha_{11}(A_4')$ is fairly accord with but $|\alpha_{33}(A_4')|$ is considerably small compared with the value derived from galvanomagnetic effect or cyclotron resonance[13] of bismuth. This inevitable discrepancy may be due to crude approximation in the present paper.

In the present paper one remarkable point to be noted is that total contribution to the ordinary Landau-Peierls susceptibility from possible ellipsoids of electrons and holes in bismuth may be less than 20% of the experimental value. Such a unexpected result in Landau-Peierls theory was also met in the theory of diamagnetic susceptibility of graphite[14]. We suppose that the small energy gap at C in bismuth should be related to the particular importance of the non-diagonal term which was pointed out by Adams[15].

Appendix A. Matrix Elements in the Case without Spin

We take into account of only six nearest neighbours.

$$H_{ss}=E_{ss}(0)\,,$$

$$H_{xx}=H_{yy}=H_{zz}=E_{xx}(0)\,,$$

$$H_{\bar{s}s}\exp i\mu=2c\{(X+Y+Z)+ir_3\varepsilon(P+Q+R)\}\,,$$

$$H_{\bar{x}x}\exp i\mu=\{(a+b)-2\omega(a-b)\}(X+Y)+2bZ+2ir_2\varepsilon bR+i\varepsilon\{(r_1+2)a+(r_2-2)b\}(P+Q)\,,$$

$$H_{\bar{y}y}\exp i\mu=\frac{1}{3}\{(a+5b)-2\omega(a-b)\}(X+Y)+\frac{2}{3}\{(2a+b)-4\omega(a-b)\}Z$$
$$+\frac{1}{3}i\varepsilon\{(r_1+2)a+(5r_2-2)b\}(P+Q)+\frac{2}{3}i\varepsilon\{2(r_1+2)a+(r_2-4)b\}R\,,$$

$$H_{\bar{z}z}\exp i\mu=\frac{2}{3}\{(a+2b)+4\omega(a-b)\}(X+Y+Z)-\frac{2}{3}i\varepsilon\{(4-r_1)a-2(r_2+2)b\}(P+Q+R)\,,$$

$$H_{\bar{x}y}\exp i\mu=\frac{\sqrt{3}}{3}(1-2\omega)(a-b)(X-Y)+\frac{\sqrt{3}}{3}i\varepsilon\{(2+r_1)a-(r_2+2)b\}(P-Q)\,,$$

$$H_{\bar{x}x}\exp i\mu=\frac{\sqrt{6}}{3}(1+\omega)(a-b)(X-Y)-\frac{\sqrt{6}}{3}i\varepsilon\{(1-r_1)a+(r_2-1)b\}(P-Q)\,,$$

$$H_{\bar{z}y}\exp i\mu=\frac{\sqrt{2}}{3}(1+\omega)(a-b)(X+Y)-\frac{2\sqrt{2}}{3}(1+\omega)(a-b)Z-\frac{\sqrt{2}}{3}i\varepsilon\{(1-r_1)a+(r_2-1)b\}(P+Q)$$
$$+\frac{2\sqrt{2}}{3}i\varepsilon\{(1-r_1)a+(r_2-1)b\}R\,,$$

$$H_{\bar{s}x}\exp i\mu=-\sqrt{2}\,i(1-\omega)d\cdot(P-Q)-\sqrt{2}\,\varepsilon(r_4+1)d\cdot(X-Y)\,,$$

$$H_{\bar{s}y}\exp i\mu=-\frac{\sqrt{6}}{3}i(1-\omega)d\cdot(P+Q)+\frac{2\sqrt{6}}{3}i(1-\omega)d\cdot R-\frac{\sqrt{6}}{3}\varepsilon(r_4+1)d\cdot(X+Y)$$
$$+\frac{2\sqrt{6}}{3}\varepsilon\cdot(r_4+1)d\cdot Z\,,$$

$$H_{\bar{s}s}\exp i\mu=-\frac{2\sqrt{3}}{3}i(1+2\omega)d\cdot(P+Q+R)+\frac{2\sqrt{3}}{3}\varepsilon(2-r_4)d\cdot(X+Y+Z)\,,$$

where

$$X=\cos(\xi+\eta+\zeta)\,,\qquad Y=\cos(-\xi+\eta+\zeta)\,,\qquad Z=\cos(-2\eta+\zeta)\,,$$

$$P=\sin(\xi+\eta+\zeta)\,,\qquad Q=\sin(-\xi+\eta+\zeta)\,,\qquad R=\sin(-2\eta+\zeta)\,,$$

$$\xi=\sqrt{2}\,\pi uk_x\,,\qquad \eta=\frac{\sqrt{6}}{3}\pi uk_y\,,\qquad \zeta=\frac{2\sqrt{3}}{3}(1+3\omega)\pi uk_z\,,\qquad \mu=2\sqrt{3}\,\varepsilon\pi uk_z\,,$$

$$a=(pp\sigma)\,,\qquad b=(pp\pi)\,,\qquad c=(ss\sigma)\,,\qquad d=(sp\sigma)\,.$$

Appendix B. Basis Functions for Irreducible Representations of Double Groups of k

We use abbraviate notation s, x, y, z and $s, \bar{x}, y, z$ for Bloch functions constructed from atomic functions ϕ_s, ϕ_{p_x}, ϕ_{p_y}, ϕ_{p_z} located at sublattice A and ϕ_s, ϕ_{p_x}, $\phi_{\bar{p}_y}$, $\phi_{\bar{p}_z}$ located at sublattice B respectively. The sign of plus and minus in the expression means that the wave functions in the first and second line take the upper and lower sign respectively. $\nu=\varepsilon\pi/2(1+3\omega)$.

(i) Γ, A: $p=1$ for Γ, $p=-i\exp(-3\nu i)$ for A.

$$\left.\begin{matrix}\psi(\Gamma_4)\\ \psi(\Gamma_4')\end{matrix}\right\}=\frac{\sqrt{8}}{8}\,[(x+iy)\alpha-(x-iy)\beta\mp p\{(\bar{x}+i\bar{y})\alpha-(\bar{x}-i\bar{y})\beta\}]\,,$$

$$\left.\begin{matrix}\psi(\Gamma_5)\\ \psi(\Gamma_5')\end{matrix}\right\}=\frac{\sqrt{8}}{8}\,[(x+iy)\alpha+(x-iy)\beta\mp p\{(\bar{x}+i\bar{y})\alpha+(\bar{x}-i\bar{y})\beta\}]\,,$$

$$\left.\begin{matrix}\psi_1(^2\Gamma_6)\\ \psi_1(^2\Gamma_6')\end{matrix}\right\}=\frac{\sqrt{2}}{2}(s\alpha\pm p\bar{s}\alpha)\,,\qquad \left.\begin{matrix}\psi_1'(^2\Gamma_6)\\ \psi_1'(^2\Gamma_6')\end{matrix}\right\}=\frac{\sqrt{2}}{2}(s\beta\pm p\bar{s}\beta)\,,$$

$$\left.\begin{matrix}\psi_2(^2\Gamma_6)\\ \psi_2(^2\Gamma_6')\end{matrix}\right\}=\frac{\sqrt{4}}{4}\{(x+iy)\beta\mp p(\bar{x}+i\bar{y})\beta\},\qquad \left.\begin{matrix}\psi_2'(^2\Gamma_6)\\ \psi_2'(^2\Gamma_6')\end{matrix}\right\}=\frac{\sqrt{4}}{4}\{(x-iy)\alpha\mp p(\bar{x}-i\bar{y})\alpha\},$$

$$\left.\begin{matrix}\psi_3(^2\Gamma_6)\\ \psi_3(^2\Gamma_6')\end{matrix}\right\}=\frac{\sqrt{2}}{2}(z\alpha\mp pz\alpha)\,,\qquad \left.\begin{matrix}\psi_3'(^2\Gamma_6)\\ \psi_3'(^2\Gamma_6')\end{matrix}\right\}=\frac{\sqrt{2}}{2}(z\beta\mp p\bar{z}\beta)\,.$$

(ii) T

$$\left.\begin{matrix}\psi_1(T_4)\\ \psi_1(T_5)\end{matrix}\right\}=\frac{\sqrt{4}}{4}\{(x+iy)\alpha\mp(x-iy)\beta\}\,,$$

$$\left.\begin{matrix}\psi_2(T_4)\\ \psi_2(T_5)\end{matrix}\right\}=\frac{\sqrt{4}}{4}\{(\bar{x}+i\bar{y})\alpha\mp(\bar{x}-i\bar{y})\beta\}\,,$$

$$\psi_1(^2T_6)=s\alpha\,,\qquad \psi_1'(^2T_6)=s\beta\,,$$

$$\psi_2(^2T_6)=\frac{\sqrt{2}}{2}(x+iy)\beta\,,\qquad \psi_2'(^2T_6)=\frac{\sqrt{2}}{2}(x-iy)\alpha\,,$$

$$\psi_3(^2T_6)=z\alpha\,,\qquad \psi_3'(^2T_6)=z\beta\,,$$

$$\psi_4(^2T_6)=\bar{s}\alpha\,,\qquad \psi_4'(^2T_6)=\bar{s}\beta\,,$$

$$\psi_5(^2T_6)=\frac{\sqrt{2}}{2}(\bar{x}+i\bar{y})\beta\,,\qquad \psi_5'(^2T_6)=\frac{\sqrt{2}}{2}(\bar{x}-iy)\alpha\,,$$

$$\psi_6(^2T_6)=\bar{z}\alpha\,,\qquad \psi_6'(^2T_6)=\bar{z}\beta\,.$$

(iii) B, C: $p=\exp(-2\nu i)$ for B, $p=-i\exp(-\nu i)$ for C

$$\left.\begin{matrix}\psi_1(C_3)\\ \psi_1(C_3')\end{matrix}\right\}=\frac{\sqrt{4}}{4}\{s\alpha+s\beta\pm p(\bar{s}\alpha+\bar{s}\beta)\}\,,\qquad \left.\begin{matrix}\psi_1(C_4)\\ \psi_1(C_4')\end{matrix}\right\}=\frac{\sqrt{4}}{4}\{s\alpha-s\beta\pm p(\bar{s}\alpha-\bar{s}\beta)\}\,,$$

$$\left.\begin{matrix}\psi_2(C_3)\\ \psi_2(C_3')\end{matrix}\right\}=\frac{\sqrt{4}}{4}\{x\alpha-x\beta\mp p(x\alpha-\bar{x}\beta)\}\,,\qquad \left.\begin{matrix}\psi_2(C_4)\\ \psi_2(C_4')\end{matrix}\right\}=\frac{\sqrt{4}}{4}\{x\alpha+x\beta\mp p(x\alpha+\bar{x}\beta)\}\,,$$

$$\left.\begin{matrix}\psi_3(C_3)\\ \psi_3(C_3')\end{matrix}\right\}=\frac{\sqrt{4}}{4}\{y\alpha+y\beta\mp p(\bar{y}\alpha+\bar{y}\beta)\}\,,\qquad \left.\begin{matrix}\psi_3(C_4)\\ \psi_3(C_4')\end{matrix}\right\}=\frac{\sqrt{4}}{4}\{y\alpha-y\beta\mp p(\bar{y}\alpha-\bar{y}\beta)\}\,,$$

$$\left.\begin{matrix}\psi_4(C_3)\\ \psi_4(C_3')\end{matrix}\right\}=\frac{\sqrt{4}}{4}\{z\alpha+z\beta\mp p(\bar{z}\alpha+\bar{z}\beta)\}\,,\qquad \left.\begin{matrix}\psi_4(C_4)\\ \psi_4(C_4')\end{matrix}\right\}=\frac{\sqrt{4}}{4}\{z\alpha-z\beta\mp p(\bar{z}\alpha-\bar{z}\beta)\}\,.$$

(iv) $\Lambda, \Delta, \Sigma, \Sigma'$

$$\left.\begin{matrix}\psi_1(\Lambda_3)\\ \psi_1(\Lambda_4)\end{matrix}\right\}=\frac{\sqrt{2}}{2}(s\alpha\pm s\beta)\,,$$

$$\left.\begin{matrix}\psi_2(\Lambda_3)\\ \psi_2(\Lambda_4)\end{matrix}\right\}=\frac{\sqrt{2}}{2}(\bar{s}\alpha\pm\bar{s}\beta)\,,$$

$$\left.\begin{matrix}\psi_3(\Lambda_3)\\ \psi_3(\Lambda_4)\end{matrix}\right\}=\frac{\sqrt{2}}{2}(y\alpha\pm y\beta)\,,$$

$$\left.\begin{matrix}\psi_4(\Lambda_3)\\ \psi_4(\Lambda_4)\end{matrix}\right\}=\frac{\sqrt{2}}{2}(\bar{y}\alpha\pm\bar{y}\beta)\,,$$

$$\left.\begin{matrix}\psi_5(\Lambda_3)\\ \psi_5(\Lambda_4)\end{matrix}\right\}=\frac{\sqrt{2}}{2}(z\alpha\pm z\beta)\,,$$

$$\left.\begin{matrix}\psi_6(\Lambda_3)\\ \psi_6(\Lambda_4)\end{matrix}\right\}=\frac{\sqrt{2}}{2}(\bar{z}\alpha\pm\bar{z}\beta)\,,$$

$$\left.\begin{matrix}\psi_7(\Lambda_3)\\ \psi_7(\Lambda_4)\end{matrix}\right\}=\frac{\sqrt{2}}{2}(x\alpha\mp x\beta)\,,$$

$$\left.\begin{matrix}\psi_8(\Lambda_3)\\ \psi_8(\Lambda_4)\end{matrix}\right\}=\frac{\sqrt{2}}{2}(\bar{x}\alpha\mp\bar{x}\beta)\,.$$

(v) D, M: $p=\exp(-\nu i)$ for D, $p=\exp(-3\nu i)$ for M

$$\left.\begin{matrix}\psi_1(D_3)\\ \psi_1(D_4)\end{matrix}\right\}=\frac{\sqrt{2}}{2}(s\alpha\mp ips\beta)\,,$$

$$\left.\begin{matrix}\psi_2(D_3)\\ \psi_2(D_4)\end{matrix}\right\}=\frac{\sqrt{2}}{2}(x\alpha\mp ip\bar{x}\beta)\,,$$

$$\left.\begin{matrix}\psi_3(D_3)\\ \psi_3(D_4)\end{matrix}\right\}=\frac{\sqrt{2}}{2}(y\alpha\pm ip\bar{y}\beta)\,,$$

$$\left.\begin{matrix}\psi_4(D_3)\\ \psi_4(D_4)\end{matrix}\right\}=\frac{\sqrt{2}}{2}(z\alpha\pm ip\bar{z}\beta)\,,$$

$$\left.\begin{matrix}\psi_5(D_3)\\ \psi_5(D_4)\end{matrix}\right\}=\frac{\sqrt{2}}{2}(s\beta\mp ips\alpha)\,,$$

$$\left.\begin{matrix}\psi_6(D_3)\\ \psi_6(D_4)\end{matrix}\right\}=\frac{\sqrt{2}}{2}(x\beta\mp ip\bar{x}\alpha)\,,$$

$$\left.\begin{matrix}\psi_7(D_3)\\ \psi_7(D_4)\end{matrix}\right\}=\frac{\sqrt{2}}{2}(y\beta\pm ip\bar{y}\alpha)\,,$$

$$\left.\begin{matrix}\psi_8(D_3)\\ \psi_8(D_4)\end{matrix}\right\}=\frac{\sqrt{2}}{2}(z\beta\pm ip\bar{z}\alpha)\,.$$

Appendix C. Secular Equations

We give secular equations for some representations. The s state is neglected.

(i) $T(0,0,\zeta)$: $\zeta=0\sim\pi/2$.

The secular equations are

$$\begin{vmatrix} E_{xx}(0)+\dfrac{\lambda}{2}-E(T_4+T_5) & H_{x\bar{x}} \\ H_{\bar{x}x} & E_{xx}(0)+\dfrac{\lambda}{2}-E(T_4+T_5)\end{vmatrix}=0\,,$$

$$\begin{vmatrix} E_{xx}(0)-\dfrac{\lambda}{2}-E(^2T_6) & -\dfrac{\sqrt{2}}{2}\lambda & H_{x\bar{x}} & 0 \\ & E_{xx}(0)-E(^2T_6) & 0 & H_{z\bar{z}} \\ \text{compl. conj.} & & E_{xx}(0)-\dfrac{\lambda}{2}-E(^2T_6) & -\dfrac{\sqrt{2}}{2}\lambda \\ & & & E_{xx}(0)-E(^2T_6)\end{vmatrix}=0\,.$$

These equations split into two parts respectively at Γ and A, as known from Table III.

(ii) $\Lambda(0,2\zeta,\zeta)$: $\zeta=0\sim\pi/6$,

$\Delta(0,-\zeta,\zeta)$: $\zeta=0\sim\pi/3$,

$\Sigma\left(0,\eta,\dfrac{\pi}{2}\right)$: $\eta=0\sim\dfrac{\pi}{4}\left\{1+\dfrac{\omega(2+3\omega)}{(1+3\omega)^2}\right\}$.

The secular equation is

$$\begin{vmatrix} E_{xx}(0)-E & H_{y\bar{y}} & -\frac{i}{2}\lambda & H_{y\bar{z}} & \frac{i}{2}\lambda & 0 \\ & E_{xx}(0)-E & H_{\bar{y}z} & -\frac{i}{2}\lambda & 0 & \frac{i}{2}\lambda \\ & & E_{xx}(0)-E & H_{z\bar{z}} & \frac{\lambda}{2} & 0 \\ \text{compl. conj.} & & & E_{xx}(0)-E & 0 & \frac{\lambda}{2} \\ & & & & E_{xx}(0)-E & H_{x\bar{x}} \\ & & & & & E_{xx}(0)-E \end{vmatrix} = 0 .$$

This equation splits into two parts at B and C, as known from Table III.

(iii) $M\left(\xi, 0, \frac{\pi}{2}\right)$: $\xi = 0 \sim \frac{\pi}{2}\left\{1+\frac{\omega(2+3\omega)}{(1+3\omega)^2}\right\}$,

$D\left(\xi, \frac{\pi}{3}, \frac{\pi}{6}\right)$.

The secular equation is

$$\begin{vmatrix} E_{xx}(0)-E & iH_{\bar{x}y}e^{i\mu} & iH_{\bar{z}x}e^{i\mu}+\frac{\lambda}{2} & iH_{\bar{x}x}e^{i\mu} & -\frac{i}{2}\lambda & 0 \\ & E_{xx}(0)-E & 0 & -\frac{i}{2}\lambda & -iH_{\bar{y}y}e^{i\mu} & -iH_{\bar{y}z}e^{i\mu}-\frac{i}{2}\lambda \\ & & E_{xx}(0)-E & 0 & -iH_{\bar{z}y}e^{i\mu}+\frac{i}{2}\lambda & -iH_{\bar{z}z}e^{i\mu} \\ & & & E_{xx}(0)-E & iH_{\bar{x}y}e^{i\mu} & iH_{\bar{z}x}e^{i\mu}-\frac{1}{2}\lambda \\ \text{compl. conj.} & & & & E_{xx}(0)-E & 0 \\ & & & & & E_{xx}(0)-E \end{vmatrix} = 0 .$$

Appendix D. Effective Mass Tensor Coefficients

(i) $\alpha_{ij}(C_3^\beta)$

$$\begin{aligned}\alpha_{11}(C_3^\beta) = &-\frac{16m\pi^2u^2(a-b)^2}{3h^2\Delta E_{\alpha\beta}\Delta E_{\gamma\beta}\Delta E_{\alpha'\beta}\Delta E_{\beta'\beta}\Delta E_{\gamma'\beta}}\Big[\Big(\Delta E_{5\beta}\Delta E_{6\beta}-\gamma^2-\frac{\lambda^2}{4}\Big)\Big\{\Big(\Delta E_{1\beta}\Delta E_{3\beta}-\frac{\lambda^2}{4}\Big) \\ &+2\Big(\Delta E_{1\beta}\Delta E_{2\beta}-\frac{\lambda^2}{4}\Big)+2\sqrt{2}\,\gamma\Delta E_{1\beta}\Big\}+\Big(\Delta E_{2\beta}\Delta E_{3\beta}-\gamma^2-\frac{\lambda^2}{4}\Big)\Big\{\Big(\Delta E_{4\beta}\Delta E_{6\beta}-\frac{\lambda^2}{4}\Big) \\ &+2\Big(\Delta E_{4\beta}\Delta E_{5\beta}-\frac{\lambda^2}{4}\Big)-2\sqrt{2}\,\gamma\Delta E_{4\beta}\Big\}-\frac{\lambda^2}{4}\Big\{4\Delta E_{2\beta}\Delta E_{5\beta}+2\Delta E_{3\beta}\Delta E_{6\beta} \\ &+2\sqrt{2}\,\gamma(\Delta E_{5\beta}\Delta E_{6\beta}-\Delta E_{2\beta}\Delta E_{3\beta})+\lambda(2\Delta E_{2\beta}+\Delta E_{3\beta}+2\Delta E_{5\beta}+\Delta E_{6\beta})-6\Big(\gamma^2-\frac{\lambda^2}{4}\Big)\Big\}\Big], \end{aligned} \tag{D.1}$$

$$\begin{aligned}\alpha_{ij}(C_3^\beta) = &-\frac{16m\pi^2u^2a^2}{3h^2\Delta E_{\alpha\beta}\Delta E_{\gamma\beta}\Delta E_{\alpha'\beta}\Delta E_{\beta'\beta}\Delta E_{\gamma'\beta}}\Big[a_{ij}\Big(\Delta E_{2\beta}\Delta E_{3\beta}-\gamma^2-\frac{\lambda^2}{4}\Big)\Big(\Delta E_{5\beta}\Delta E_{6\beta}-\gamma^2-\frac{\lambda^2}{4}\Big) \\ &+\frac{1}{9}b_{ij}\Big(\Delta E_{1\beta}\Delta E_{3\beta}-\frac{\lambda^2}{4}\Big)\Big(\Delta E_{4\beta}\Delta E_{6\beta}-\frac{\lambda^2}{4}\Big)+\frac{2}{9}(1-s)^2c_{ij}\Big\{\Big(\Delta E_{1\beta}\Delta E_{3\beta}-\frac{\lambda^2}{4}\Big) \\ &\times\Big(\Delta E_{4\beta}\Delta E_{5\beta}-\frac{\lambda^2}{4}\Big)+\Big(\Delta E_{1\beta}\Delta E_{2\beta}-\frac{\lambda^2}{4}\Big)\Big(\Delta E_{4\beta}\Delta E_{6\beta}-\frac{\lambda^2}{4}\Big)-2\gamma^2\Delta E_{1\beta}\Delta E_{4\beta} \end{aligned}$$

$$-\frac{\lambda^2}{2}\left(\Delta E_{1\beta}+\frac{\lambda}{2}\right)\left(\Delta E_{4\beta}+\frac{\lambda}{2}\right)\Big\}+\frac{2}{9}(1+2s)^2 d_{ij}\left(\Delta E_{1\beta}\Delta E_{2\beta}-\frac{\lambda^2}{4}\right)\left(\Delta E_{4\beta}\Delta E_{5\beta}-\frac{\lambda^2}{4}\right)$$

$$+\frac{1}{6}e_{ij}\lambda^2\left\{\left(\Delta E_{3\beta}+\frac{\lambda}{2}\right)\left(\Delta E_{6\beta}+\frac{\lambda}{2}\right)-\gamma^2\right\}+\frac{\sqrt{2}}{6}(1-s)\lambda^2\gamma f_{ij}(\Delta E_{2\beta}+\Delta E_{3\beta}-\Delta E_{5\beta}-\Delta E_{6\beta})$$

$$+\frac{1}{6}(1+2s)\lambda^2 g_{ij}\left\{\left(\Delta E_{2\beta}+\frac{\lambda}{2}\right)\left(\Delta E_{5\beta}+\frac{\lambda}{2}\right)-\gamma^2\right\}+\frac{2\sqrt{2}}{9}(1-s)\gamma l_{ij}\Big\{\Delta E_{4\beta}\left(\Delta E_{1\beta}\Delta E_{3\beta}-\frac{\lambda^2}{4}\right)$$

$$-\Delta E_{1\beta}\left(\Delta E_{4\beta}\Delta E_{6\beta}-\frac{\lambda^2}{4}\right)\Big\}+\frac{1}{9}(1+2s)\lambda^2 m_{ij}\left\{\frac{\lambda^2}{2}\left(\Delta E_{1\beta}+\frac{\lambda}{2}\right)\left(\Delta E_{4\beta}+\frac{\lambda}{2}\right)-2\gamma^2\Delta E_{1\beta}\Delta E_{4\beta}\right\}$$

$$+\frac{2\sqrt{2}}{9}(1-s)(1+2s)\gamma n_{ij}\left\{\Delta E_{4\beta}\left(\Delta E_{1\beta}\Delta E_{2\beta}-\frac{\lambda^2}{4}\right)-\Delta E_{1\beta}\left(\Delta E_{4\beta}\Delta E_{5\beta}-\frac{\lambda^2}{4}\right)\right\}\Big], \tag{D.2}$$

where

$$\Delta E_{\alpha\beta}=E(C_3^{\alpha})-E(C_3^{\beta}),$$

$$\Delta E_{\alpha'\beta}=E(C_3'^{\alpha})-E(C_3^{\beta}), \quad \text{etc.},$$

$$\left.\begin{matrix}\Delta E_{1\beta}\\ \Delta E_{4\beta}\end{matrix}\right\}=E_{xx}(0)\pm 2\varepsilon\{(2+r_1)a-2b\}-E(C_3^{\beta}),$$

$$\left.\begin{matrix}\Delta E_{2\beta}\\ \Delta E_{5\beta}\end{matrix}\right\}=E_{xx}(0)\pm\frac{2}{3}\varepsilon\{-(2+r_1)a+2(1+2r_2)b\}-E(C_3^{\beta}),$$

$$\left.\begin{matrix}\Delta E_{3\beta}\\ \Delta E_{6\beta}\end{matrix}\right\}=E_{xx}(0)\mp\frac{2}{3}\varepsilon\{(4-r_1)a-2(2+r_2)b\}-E(C_3^{\beta}),$$

$$\gamma=-\frac{4\sqrt{2}}{3}\varepsilon\{(r_1-1)a-(r_2-1)b\}, \qquad s=b/a,$$

and

$$a_{22}=(1+3s)^2, \quad b_{22}=(5+7s)^2, \quad c_{22}=1, \quad d_{22}=8,$$

$$a_{33}=2, \quad b_{33}=2(1-4s)^2, \quad c_{33}=8, \quad d_{33}=1,$$

$$a_{23}=\sqrt{2}(1+3s), \quad b_{23}=-\sqrt{2}(5+7s)(1-4s), \quad c_{23}=-2\sqrt{2}, \quad d_{23}=2\sqrt{2},$$

$$e_{22}=(1+3s)(5+7s), \quad f_{22}=1+3s, \quad g_{22}=4(1+3s), \quad l_{22}=(5+7s),$$

$$e_{33}=-2(1-4s), \quad f_{33}=-4, \quad g_{33}=2, \quad l_{33}=4(1-4s),$$

$$e_{23}=2\sqrt{2}(1+2s+3s^2), \quad f_{23}=-\frac{\sqrt{2}}{2}(1+6s), \quad g_{23}=\frac{\sqrt{2}}{2}(5+3s), \quad l_{23}=-\frac{\sqrt{2}}{2}(11+10s),$$

$$m_{22}=4(5+7s), \quad n_{22}=4,$$

$$m_{33}=-2(1-4s), \quad n_{33}=-4,$$

$$m_{23}=\frac{\sqrt{2}}{2}(1+23s), \quad n_{23}=-\frac{7\sqrt{2}}{2}.$$

(ii) A

$$\alpha_{11}(A_4')=\frac{16m\pi^2u^2(a-b)^2}{h^2(E(^2A_6)^{\alpha}-E(A_4'))(E(^2A_6)^{\beta}-E(A_4'))}\left[\lambda-\frac{8}{3}\{(2r_1+1)a+(4r_2-1)b\}\varepsilon\right],$$

$$\alpha_{33}(A_4')=-\frac{32m\pi^2u^2(a+2b)^2}{3h^2(E(A_4)-E(A_4'))},$$

$$\alpha_{11}(^2A_6)^{\beta}=-\frac{32m\pi^2u^2(a-b)^2}{3h^2}\left[\frac{4(2r_1+1)\varepsilon a+4(4r_2-1)\varepsilon b-\frac{3}{2}\lambda}{(E(^2A_6)^{\alpha}-E(^2A_6)^{\beta})(E(A_4')-E(^2A_6)^{\beta})}\right.$$

$$\left.+\frac{\Delta E_{1\beta}\Delta E_{3\beta}+\Delta E_{2\beta}\Delta E_{4\beta}-\lambda^2}{\Delta E_{\alpha\beta}\Delta E_{\alpha'\beta}\Delta E_{\beta'\beta}}\right],$$

$$\alpha_{33}(^2A_6)^\beta = -\frac{32m\pi^2u^2(a+2b)^2}{3h^2\Delta E_{\alpha\beta}\Delta E_{\alpha'\beta}\Delta E_{\beta'\beta}}[\Delta E_{1\beta}\Delta E_{2\beta}+\Delta E_{3\beta}\Delta E_{4\beta}+\lambda^2]\,,$$

where

$$\Delta E_{\alpha\beta}=E(^2A_6{}^\alpha)-E(^2A_6{}^\beta)\,,$$

$$\Delta E_{\alpha'\beta}=E(^2A_6{}')^\alpha-E(^2A_6{}^\beta)\,,$$

$$\Delta E_{\beta'\beta}=E(^2A_6{}')^\beta-E(^2A_6{}^\beta)\,,$$

$$\left.\begin{matrix}\Delta E_{1\beta}\\ \Delta E_{2\beta}\end{matrix}\right\}=E_{xx}(0)\pm 2\{(r_1+2)a+2(r_2-1)b\}\mathcal{E}-\frac{\lambda}{2}-E(^2A_6{}^\beta)\,,$$

$$\left.\begin{matrix}\Delta E_{3\beta}\\ \Delta E_{4\beta}\end{matrix}\right\}=E_{xx}(0)\pm 2\{(4-r_1)a-(4+2r_2)b\}\mathcal{E}-E(^2A_6{}^\beta)\,.$$

References

1) H. Jones: Proc. Roy. Soc. **A 147** (1934) 396.
2) M. Blackman: Proc. Roy. Soc. **A 166** (1938) 1.
3) D. Shoenberg: Proc. Roy. Soc. **A 170** (1939) 341.
4) A. Morita: Science Repts. Tohoku Univ. **33** (1949) 144.
5) Bouckaert, Smoluchowsky and Wigner: Phys. Rev. **50** (1936) 58.
6) R. J. Elliot: Phys. Rev. **96** (1954) 280.
7) E. Wigner: Proc. 1953 Intern. Conf. Theor. Phys., Tokyo (1954) 649.
8) Condon and Shortly: *The Theory of Atomic Spectra* (1935).
9) Eyring, Walter and Kimball: *Quantum Chemistry* (1944).
W. M. Lomer: Proc. Roy. Soc. **A 227** (1955) 330.
10) Mott and Jones: *The Theory of the Properties of Metals and Alloys* (1936).
11) Ted G. Berlincourt: Phys. Rev. **99** (1955) 1716.
12) B. Abeles and S. Meiboom: Phys. Rev. **101** (1956) 544.
T. Okada: Annual Meeting of the Phys. Soc. of Japan (1956).
13) Lax, Button, Zeiger and Roth: Phys. Rev. **102** (1956) 715.
14) J. E. Hove: Phys. Rev. **100** (1955) 645.
S. Mase: Busseiron Kenkyu **98** (1956) 101 (in Japanese).
15) E. N. Adams: Phys. Rev. **89** (1953) 633.

JOURNAL OF THE PHYSICAL SOCIETY OF JAPAN Vol. 13, No. 5, MAY, 1955

Effects of Impurities on Nuclear Quadrupole Resonance in *p*-Dichlorobenzene

By Shoji KOJIMA, Shizuko OGAWA, Midori MINEMATSU and Makoto TANAKA

Department of Physics, Tokyo University of Education, Otsuka, Tokyo

(Received December 27, 1957)

The resonance of Cl^{35} in α phase *p*-dichlorobenzene containing various impurities was studied. The used impurities were *p*-BrϕCl, *p*-$Br_2\phi$, *p*-$I_2\phi$, *p*-OHϕCl, *p*-$CH_3\phi$Cl, *p*-$NH_2\phi$Cl, *p*-$NO_2\phi$Cl, *p*-$NO_2\phi CH_3$ and *p*-$(CH_3)_2\phi$. The characteristic number which represents the number of resonant nuclei which is affected by an impurity molecule was measured. This characteristic number depends on the volume difference of the resonant and impurity molecules and independent on the difference in dipole moment. The results of the theoretical discussions supported the experiment.

The height, width, shape and the integrated intensity of the resonance line were also measured. The integrated intensity was almost constant in the range of small concentration of impurity and then decreased.

1. Introduction

Duchsene and Monfils[1] and Dean[2] found in their experiments on *p*-dichlorobenzene that presence of impurities in the sample leads to a broadening of the quadrupole resonance line. Segel and Lutz[3] gave a brief report on the decrease in the line height as a result of presence of impurities. Recently Monfils and Grosjean[4] studied the decrease of the line height in detail. They indicated that the effectiveness of an impurity molecule in reducing the line height depends on both the difference in volume and the difference in electric dipole moment of the resonant and impurity molecules. Michel and Spence[5], however, found in their experiment on monochlorobenzene no evidence for the dependence on dipole moment. In the present work the effects of impurities have been studied with a larger number of impurities than those used by Monfils and Grosjean.

It was mentioned by Segel and Lutz that the integrated intensity of the line was independent on the impurity concentration[3]. Michel and Spence, however, mentioned that the main effect of impurities on the resonance was to reduce its intensity without appreciable broadening[5]. The height, the width and the integrated intensity of the line have been carefully measured in the present experiments.

2. Experimental Procedures

The resonance of Cl^{35} in α phase *p*-dichlorobenzene containing the various impurities was studied. The frenquency of the resonance was about 34.23 Mc.

The spectrometer used was a signal feed back oscillator which was described by Wang[6]. The working level of oscillation was about 5.8 volt in all the experiments. The height of resonance line was observed with a video amplifier and an oscilloscope. In order to measure the width and the shape of the resonance line a set of a narrow band amplifier and recorder was used. In this case, adopting frequency modulation of small amplitude, the derivative curve of the resonance line was recorded. The width was determined from the recording as the difference of the frequen-

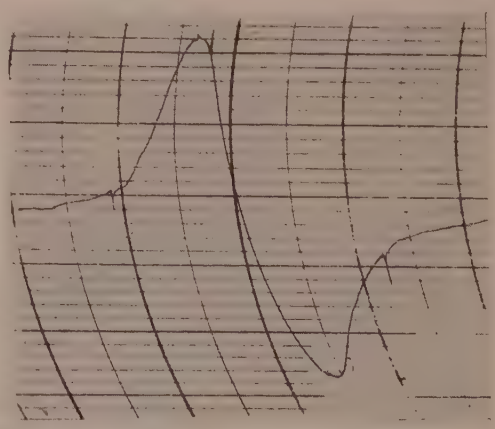

Fig. 1. Recording of the nuclear quadrupole resonance of Cl^{35} in p-$Cl_2\phi$ with impurities of p-BrϕCl 0.1%. Kicks are frequency markers.

cies corresponding to the extreme points of the derivative curve. An example of recordings is reproduced in Fig. 1.

The samples were produced by melting the mixture of pure *p*-dichlorobenzene and impurities of known molar percent with the aid of a hot water bath. The produced samples in the hot water bath were let cool naturally and its temperature reached to room temperature during 24 hours.

3. The height of the Resonance Line

The studied samples were those containing the impurities of *p*-BrϕCl, *p*-$Br_2\phi$, *p*-$I_2\phi$, *p*-OHϕCl, *p*-$CH_3\phi$Cl, *p*-$NH_2\phi$Cl, *p*-$NO_2\phi$Cl, *p*-$NO_2\phi CH_3$ and *p*-$(CH_3)_2\phi$. The height of the resonance line decreased when the concentration of impurity was increased. Monfils and Grosjean deduced from a simple assumption a theoretical equation expressing the relation between the intensity and the concentration of impurity. If we apply their equation for the height of resonance, A, we obtain

$$A = A_0 \exp(-NC) \qquad (1)$$

where C is the molar concentration of impurity and N is a characteristic number. This characteristic number represents the number of resonant nuclei per impurity molecule whose resonances have been so shifted that they can no longer contribute to the central portion of the line.

The observed height was plotted logarithmically against the concentration of impurity. The plots are reproduced in Figs. 2, 3 and 4, where the plotted height is normalized as the height on the pure sample is unity. For small impurity concentrations the experimental data fit to the straight lines which

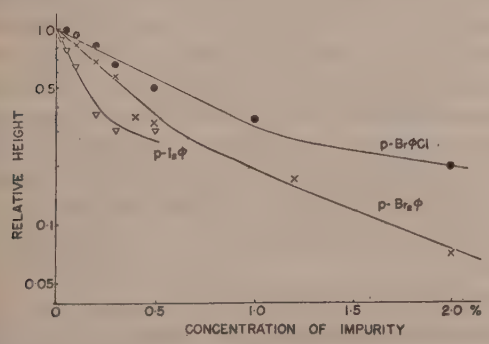

Fig. 2. The height of the resonance line *vs.* impurities of p-BrϕCl, p-$Br_2\phi$ and p-$I_2\phi$.

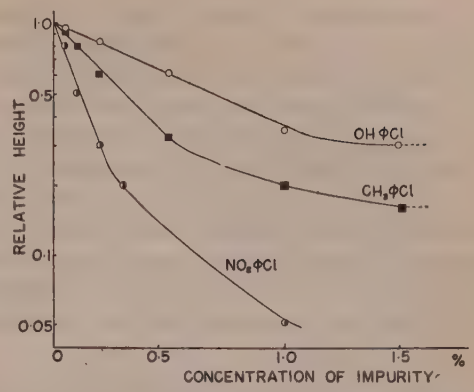

Fig. 3. The height of the resonance line *vs.* impurity concentration for the impurities of p-OHϕCl, p-$CH_3\phi$Cl and p-$NO_2\phi$Cl.

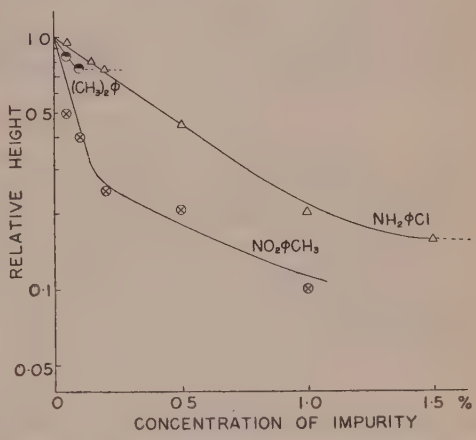

Fig. 4. The height of the resonance line *vs.* impurity concentration for the impurities of p-$(CH_3)_2\phi$, p-$NH_2\phi$Cl and p-$NO_2\phi CH_3$.

Table I.

Impurity	N	N'	N (M. G)
p-BrϕCl	105	100	87
p-$Br_2\phi$	190	200	164
p-BrϕI			330
p-$I_2\phi$	510		
p-OHϕCl	100	60	135
p-$NH_2\phi$Cl	160		435
p-$NH_3\phi$Cl	230		204
p-$(CH_3)_2\phi$	380		
p-$NO_2\phi$Cl	600	500	
p-$NO_2\phi CH_3$	830		

* Monfils and Grosjean[4]

are expressed by Eq. (1). From the slope of the straight line, the characteristic number N was determined. The values obtained are

listed in the second column of Table I. Those reported by Monfils and Grosjean are also listed in the fourth column of the table. It indicates close agreement between their results and the present results except for the case of impurity of p-$NH_2\phi Cl$. This sample, however, showed in the experiment an appreciable change with time. The present data were measured after one day from solidification. Measurements after a few weeks showed further decrease in height for the sample of impurity concentration of about 0.05, 0.1 and 0.2 percent and no appreciable change for the pure sample and those of large impurity concentrations. So that these measurements give a greater characteristic number than the mentioned above. We have used the data of the measurement on the fresh sample which was considered to be free from chemical change.

Figs. 2, 3 and 4 indicate that the plots deviate from the straight lines for large concentration. In these range of concentration it seems that the volumes influenced by an impurity molecule are overlapping. The critical concentration C_c, above which the overlapping begins, is estimated from the equation of

$$C_c \simeq 1/N\,. \qquad (2)$$

The critical concentrations obtained from the knick points of the curves and those calculated from Eq. (2) are listed in Table II.

Table II.

Impurity	C_c (percent)	$1/N\times 100$
p-$Br\phi Cl$	1.0~1.3	0.95
p-$Br_2\phi$	0.6~0.7	0.55
p-$I_2\phi$	0.2	0.20
p-$OH\phi Cl$	1.2	1.00
p-$CH_3\phi Cl$	0.6	0.43
p-$(CH_3)_2\phi$	>0.1	0.27
p-$NH_2\phi Cl$	1.0~1.3	0.63
p-$NO_2\phi CH_3$	0.2	0.17
p-$NO_2\phi Cl$	0.3	0.12

The agreement between them is satisfactory. This means that the linear relation in the logarithmic plot of the height holds until the height decreases to $1/e$ of the initial value, where e is the base of natural logarithm.

For the samples mixed with p-$OH\phi Cl$, p-$CH_3\phi Cl$, p-$(CH_3)_2\phi$ and p-$NH_2\phi Cl$ the decrease of height stopped at the concentration of 1.5, 1.5, 0.1 and 1.5 percent respectively, which are shown by dotted lines in Figs. 3 and 4. They presumably arise from nonmixing of the impurity above those concentration. These data are omitted from the plots.

4. The Line Width

The line width, Γ, was measured for the samples containing impurities of p-$OH\phi Cl$, p-$Br\phi Cl$, p-$Br_2\phi$ and p-$NO_2\phi Cl$. On the contrary to the case of Michel and Spence the broadening of the line was always observed. The relative broadening denfined by $(\Gamma-\Gamma_0)/\Gamma$, where Γ_0 is the width for the pure sample, was plotted against the impurity concentration C, as shown in Fig. 5. It indicates that the

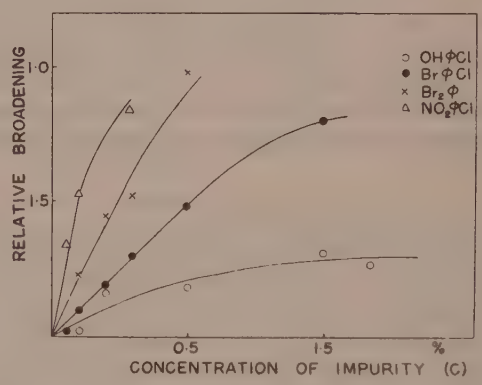

Fig. 5. The broadening of the resonance line *vs.* impurity concentration for the impurities of p-$Br\phi Cl$, p-$Br_2\phi$, p-$OH\phi Cl$ and p-$NO_2\phi Cl$.

relative broadening is proportional to the concentration in the range of small concentration. This linear relation can be expressed

$$(\Gamma-\Gamma_0)/\Gamma_0 = N'C \qquad (3)$$

where N' is again the characteristic number. The N', however, is defined slightly differently from N. It means the number of resonant nuclei whose resonance has been shifted to produce observable broadening. The characteristic number N' was determined from the initial slope of the curve. The obtained results are listed in the third column of Table I. The characteristic numbers obtained from both methods, N and N', are in close agreement.

When the concentration increased the plots of broadening deviate from the straight lines. The effective value of characteristic number, which is determined from the tangent of the

curve, decreased as the impurity concentration increased. The origion of decrease of N' is the same as the previous case.

5. The Integrated Intensity

The shape of the resonance line was determined by graphical integration of the recording. The obtained patterns of the resonance lines for the various concentration of impurities of p-BrϕCl are reproduced in Fig. 6, where the

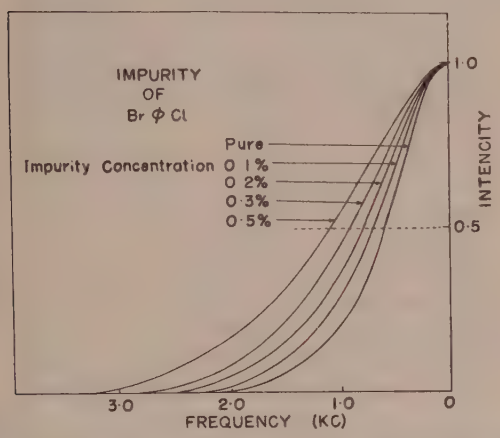

Fig. 6. The shape of resonance line (the left half is shown) for various concentration of p-BrϕCl impurity.

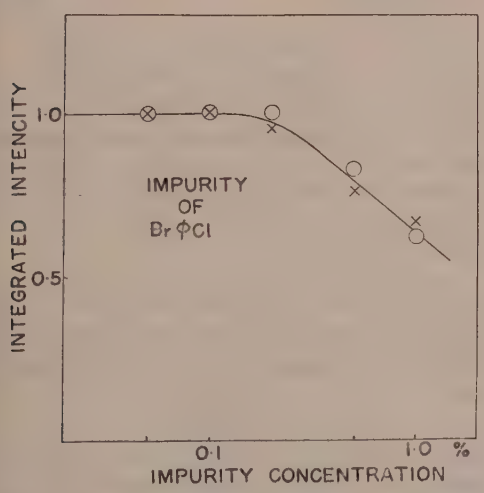

Fig. 7. The integrated intensity *vs.* impurity concentration for the impurity of p-BrϕCl. ○ obtained from the area of the resonance line. × obtained from the product of the height and the width.

all patterns are normalized as the intensity maximum is unity. It indicates that the patterns are similar to Gaussian curve. The integrated intensity, I, was obtained as the area of pattern. The plots of the integrated intensity against the impurity concentration is reproduced in Fig. 7.

If the shape of the line is expressed by $A\exp(-2\nu^2/\Gamma^2)$, the area is obtained by $(\pi/2)^{1/2}A\Gamma$. The product $A\Gamma$ is also plotted in the Fig. 7. Both plots fit excellently.

The curve shown in Fig. 7 indicates that the integrated intensity is constant below the impurity concentration of 0.2 percent. For such small concentration Eqs. (1) and (3) give

$$A\Gamma = A_0\Gamma_0\{1+(N-N')C\}\,. \qquad (4)$$

The previous result that N' is equal to N leads to the constancy of the integrated intensity.

When the impurity concentration was increased above 0.2 percent, the integrated intensity decreased gradually. This is presumably arisen from that the tails of the resonance curve sink below the noise level.

6. Interpretation of Characteristic Number

Monfils and Grosjean connected the characteristic number N with difference in volume and difference in electric dipole moment. For the impurities of monoatomic substituents the difference in volume of the resonant and impurity molecules is calculated as the difference of the van der Waals volumes of corresponding atoms. For the impurities of radical substituents the volume is not so clearly defined as the previous case. The shape of the radical is determined by giving the spheres of van der Waals radii for each atoms, whose center is located at the known bond distance and the known bond angle. At first the volume of such shape of the radical is calculated (V_a). At room temperature, however, the radicals may rotate around its axis. The volume taking into account rotation around one axis is then calculated (V_b). Another definition of the volume is given by the circumscribed sphere of the above mentioned static shape of the radical (V_c). The differences in volumes of resonant and impurity molecules calculated on these three definitions are listed in Table III with the notation of ΔV_a, ΔV_b and ΔV_c, respectively.

The relation between the characteristic number N and the volume difference is shown in Fig. 8 for the impurities of monoatomic substituents and in Fig. 9 for the impurities of the radical substituents. In Fig. 9 the

Table III.

Impurity	N	ΔV_a (10^{-24} cm^3)	ΔV_b (10^{-24} cm^3)	ΔV_c (10^{-24} cm^3)	ΔV_{exp} (10^{-24} cm^3)
p-OHϕCl	100	−8.89	4.75	− 0.9	6.8
p-NH$_2\phi$Cl	190	−4.23	5.87	11.7	13.0
p-CH$_3\phi$Cl	220	0.31	7.00	14.4	15.0
p-(CH$_3$)$_2\phi$	380	0.62	14.00	28.8	26.8
p-NO$_2\phi$Cl	600	1.02	23.03	41.0	40.7
p-NO$_2\phi$CH$_3$	830	1.33	30.0	55.4	56.2

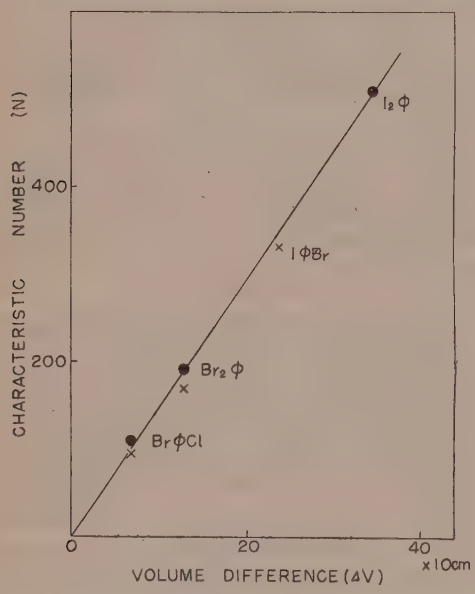

Fig. 8. The characteristic number *vs.* the volume difference for the impurities of momoatomic substituents. × is the value measured by Monfils and Grosjean.

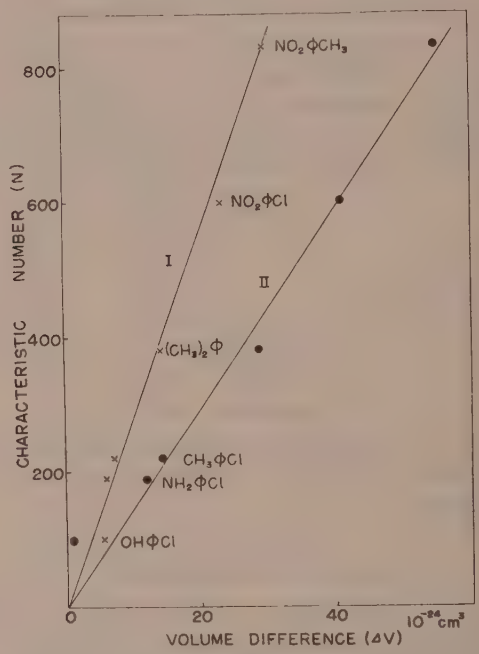

Fig. 9. The characteristic number *vs.* the volume difference for the impurities of radical substituents. × based on the volume difference defined as ΔV_b, ○ based on the volume difference defined as ΔV_c.

crosses denote the plot of N against ΔV_b and the full circles denote the plot of N against ΔV_c. Figs. 8 and 9 indicate that the characteristic number is proportional to the volume difference. The straight line in Fig. 8 is expressed by an equation:

$$N = k\Delta V\,, \qquad (5)$$

where k is 14.5×10^{24} cm^{-3}. This relation accords with the result of Monfils and Grosjean not only qualitatively, but also quantitatively.

If the definition of volume V_c is used, the straight line II in Fig. 9 is obtained. This straight line is just expressed by Eq. (5). On the other hand, if the definition V_b is used, the obtained straight line, which is shown by the line I in Fig. 9, has a larger slope than that expressed by the equation. Then the difference between them may attribute to the effect of the dipole moment of molecule. The difference between the observed characteristic number and the number calculated from the volume difference by using the Eq. (5), *ie*, $N-k\Delta V_b$, was plotted against the difference in dipole moment of the resonant and impurity molecules*. The plot is reproduced in Fig. 10. It shows no correlation between the characteristic number and the difference in dipole moment. In view of the present result the definition of the volume V_c seems to be adequate. And if this definition is used the

* The values of dipole moment used are almost the same as those used by Monfils and Grosjean. But for the p-OHϕCl 2.27 Debye is used instead of 1.62 Debye.[7]

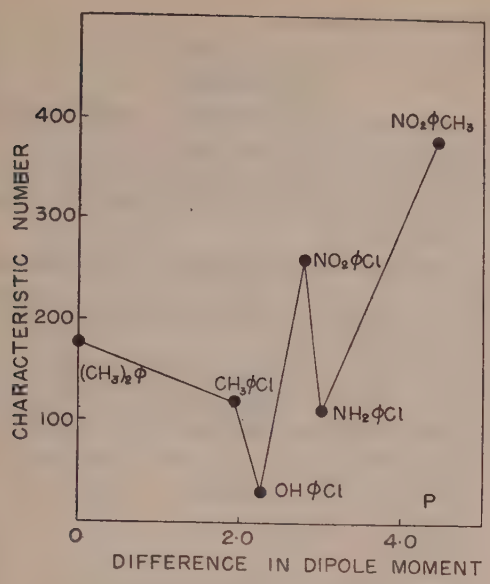

Fig. 10. The characteristic number *vs.* the difference in dipole moment. The plotted characteristic number is subtracted the number corresponding to the volume difference.

dependency of characteristic number on the volume difference is expressed by the same equation as the case of the monoatomic impurities.

7. Theoretical Estimations

a) Effect of the dipole moment

When a molecule possess a dipole moment P, the field gradient produced by it at a distance r is expressed by

$$q_{zz}=\frac{\partial}{\partial z}\frac{3(\boldsymbol{Pr})z-rP_z}{r^5}=\alpha\frac{P}{r^4}, \qquad (6)$$

where numerical factor α is 2~3 in usual cases. Since the shift of resonance frequency due to the effect of dipole field, $\Delta\nu$, is equal to $eQq_{zz}/2h$, then we obtain

$$\Delta\nu\approx 6\times 10^{19}Pr^{-4} \quad (c/s) \qquad (7)$$

Putting $P=1$ Debye and $\Delta\nu=400$ c/s, which is the half of width of the resonance line on pure sample, we obtain $r=6.4\times 10^{-8}$ cm. The resonant nuclei in the sphere of this radius do not contribute to the central portion of the resonance line. Since the density of molecule is about $5.28\times 10^{-21}/\mathrm{cm}^3$, this sphere contains only six molecules. This number is very small with respect to the observed characteristic number N. If the dipole moment of a part of the molecule in place of the dipole moment of whole molecule were accounted, the situation would not be altered. Therefore, the difference in dipole moment of the resonant and impurity molecules is not responsible for the characteristic number.

b) Effect of volume

An impurity molecule whose volume is different from that of surrounding molecules produces strain on the surrounding medium. For simplicity we assume that the impurity molecule is spherical and the radial displacement alone is produced. Then the nonvanishing strain tensors in polar coordinate are given by

$$e_{rr}=\frac{\partial u}{\partial r} \qquad e_{\theta\theta}=e_{\varphi\varphi}=u/r, \qquad (8)$$

where u is the radial displacement. Generally u is expressed by the form $ar+br^{-2}$. In the present case, however, a vanishes as the case of point imperfection. If the volume change ΔV is introduced on the surface of the spherical molecule whose radius is r_0, then $(u)_{r_0}=\Delta V/4\pi r_0^2$. From this condition b is determined. So that,

$$u=\Delta V/4\pi r^2 \qquad (9)$$

Since the dilatation $e_{rr}+e_{\theta\theta}+e_{\varphi\varphi}$ vanishes by Eqs. (8) and (9), the stress tensors are expressed by

$$\left.\begin{aligned} S_{rr}&=2\mu e_{rr}=-\frac{4}{3}\mu\frac{\Delta V}{V}\\ S_{\theta\theta}&=2\mu e_{\theta\theta}=\frac{2}{3}\mu\frac{\Delta V}{V}\\ S_{\varphi\varphi}&=2\mu e_{\varphi\varphi}=\frac{2}{3}\mu\frac{\Delta V}{V}\end{aligned}\right\} \qquad (10)$$

where μ is Lamé constant or the rigidity and $V=(4\pi/3)r^3$. These equations give the stresses on the surface of the sphere of volume V.

The relation between the frequency shift and the stress was measured by Kushida, Benedeck and Bloembergen on p-dichlorobenzene.[8] Their result is $\frac{\partial\nu}{\partial p}=28$ c/s/kg/cm² at 24.8°C. This figure was obtained by applying simple hydrostaic pressure p. In the present case, however, radial commpression and tangential tensions are applied. Therefore the shift may be different from the homogeneous deformation. Since such data are not available, we use tentatively above figure. The rigidity μ is estimated to be 2.7×10^4 kg/cm² from the volume compressibility used by Kushida *et al.* and Poisson ratio to be 0.3 as

usual substances have. Then the frequency shift of the resonant molecules which located on the surface of the sphere of volume V is

$$\Delta\nu = 28 \times \frac{4}{3}\mu\frac{\Delta V}{V} \qquad (11)$$

For the impurity of p-dibromobenzene, ΔV is equal to $13\times10^{-24}\,\mathrm{cm}^3$. Then the Eq. (11) gives V of $3.3\times10^{-20}\,\mathrm{cm}^3$ in order to yield the shift of 400 c/s. The volume contains about 174 molecules. This figure fits to the observed characteristic number. The estimations above mentioned supports the experimental evidence that the effect of impurity is interpreted with the volume effect alone.

The present work was partially supported by the Scientific Research Expenditure of the Ministry of Education.

References

1) J. Duchesne and A. Monfils: Comptes Rendus Acad. Sci. (Paris) **238** (1954) 1801.
2) C. Dean: J. Chem. Phys. **23** (1955) 1734 (L).
3) S. L. Segel and B. C. Litz: Phys. Rev. **98** (1955) 1183 (A).
4) A. Monfils and D. Grosjean: Physica **22** (1956) 541.
5) R. E. Michel and R. D. Spence: J. Chem. Phys. **27** (1957) 957 (L).
6) T. C. Wang: Phys. Rev. **99** (1955) 566.
7) C. P. Smyth: *Dielectric Behaviour and Structure*, McGraw-Hill New York; (1955).
8) T. Kushida, G. B. Benedek and N. Bloembergen: Phys. Rev. **104** (1956) 1364.

JOURNAL OF THE PHYSICAL SOCIETY OF JAPAN Vol. 13, No. 5, MAY, 1958

Origin of the Magnetic Anisotropy Energy of Antiferromagnetic Cr_2O_3

By Masashi TACHIKI and Takeo NAGAMIYA
Department of Physics, Osaka University, Osaka, Japan

(Received January 27, 1958)

The magnetic anisotropy constant Cr_2O_3 arising from the dipolar interactions among the chromic ions was calculated to be $-0.059\,\mathrm{cm}^{-1}$ per ion at absolute zero, and the magnetic anisotropy constant due to the crystalline field combined with the spin-orbit coupling was estimated from the fine-structure coupling constant of ruby and compared with that deduced from the antiferromagnetic resonance experiment by Dayhoff. The value from ruby is too large. The temperature dependence of the anisotorpy constant and that of the antiferromagnetic resonance frequency at zero field are discussed.

§ 1. Introduction

Since Honda and Soné[1] first made measurements of the powder susceptibility of chromium sesquioxide, Cr_2O_3, there appeared a number of experimental studies of the magnetic properties of this substance.[2-5] The neutron diffraction study by Brockhouse[2] has indicated that an antiferromagnetic arrangement of the spins of the chromic ions occurs below 308°K (Fig. 1). The spins align along the unique crystallographic axis according to the single crystal measurements of the magnetic susceptibility by McGuire *et al*,[3] and recently this has been supported also by a neutron diffraction study.[4] Information about the magnetic anisotropy energy can most conveniently be obtained from measurements of the antiferromagnetic resonance absorption, and Dayhoff,[5] carrying out such an experiment, determined the anisotropy energy as a function of temperature in the neighbourhood of the Néel point, 308°K.

The origin of the magnetic anisotropy energy in chromium sesquioxide may consist of three parts: the magnetic dipolar interactions among the chromic ions, the fine-structure coupling of the individual chromic ion, i.e., the spin-orbit interaction combined with the interaction between the orbital angular momentum and the crystalline electric field,

and the anisotropic exchange interactions. The purpose of this paper is to calculate the first of these three and to give some considerations on the other two.

§ 2. Anisotropy Energy arising from the Magnetic Dipolar Interactions among the Ions

Chromium sesquioxide has a corundum structure of rhombohedral symmetry. Chromic ions lie on the [111] body diagonal of the rhombohedral unit cell, and the magnetic structure deduced from neutron diffraction measurements is as shown in Fig. 1. Since

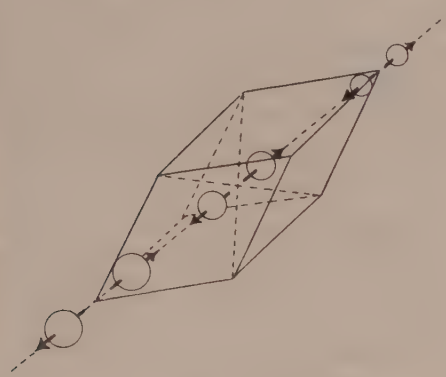

Fig. 1. The rhombohedral unit cell of Cr_2O_3 after Brockhouse; only Cr ions with spins are indicated.

the crystal has a three-fold symmetry about the [111] axis, the anisotropy energy arising from the dipolar interactions has uniaxial symmetry about the same axis. We calculated this anisotropy energy using the Fourier method developed Nagamiya *et al.*[6]. Assuming an isotropic g-factor and using Eqs. (4.1), (4.3) and (4.5) of their paper, the following expression is obtained for this anisotropy energy:

$$E=\Big[g^2\mu_B{}^2S^2\frac{4\pi}{V}\sum_{hkl}\{1+(-1)^{h+k+l}\}^2 \times\{\sin 2\pi(h+k+l)u\}^2\{3\cos^2\theta_{hkl}-1\} \times\sigma^2{}_{hkl}\Big]\cos^2\theta\ , \qquad (1)$$

where θ is the angle between the spin axis and the [111] axis, V the volume of the rhombohedral unit cell, θ_{hkl} the polar angle of the reciprocal lattice vector (hkl), σ_{hkl} means the form factor of the spherical charge distribution placed at each position of the chromic ion (given by Eq. (6.4) of the paper quoted above) and u is the parameter indicating position of the chromic ions. As we could not find the observed value of u, we assumed $u=0.105$, referring to those for α–Al_2O_3 and α–Fe_2O_3 ($u=0.105$ for both). With the use of $g=1.97$ obtained from the paramagnetic resonance experiment,[8] the following numerical result is obtained:

$$E=-0.059\cos^2\theta\ \mathrm{cm}^{-1}\ \text{per ion at absolute zero.} \qquad (2)$$

It is interesting to compare this negative small value of the coefficient of $\cos^2\theta$ with corresponding value, $1.15\,\mathrm{cm}^{-1}$, of α–Fe_2O_3.[9] The crystalline structure is the same for these two compounds but the spin superstructure is different. The trivalent metallic ions, which are located at the interstices of the approximately hexagonal close-packed lattice of the oxygen ions, form slightly uneven honey-comb nets. In α–Fe_2O_3, spins on each honey-comb net plane point in the same direction, and alternate nets of opposite spins are piled up, so that a strong dipolar anisotropy energy favouring the magnetization direction in the plane of the nets is expected. On the other hand, each of the honey-comb nets in Cr_2O_3 consists of plus and minus spins, arranged in an antiferromagnetic way as shown in Fig. 2. The negative sign in Eq. (2) indicates a stronger coupling between

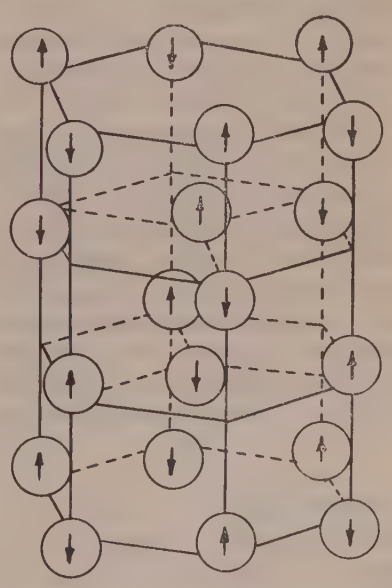

Fig. 2. Nearly hexagonal net planes of Cr ions in Cr_2O_3.

neighbours in the same honey-comb net plane of Cr_2O_3 and it favours the spin direction along the body diagonal, [111]. This is consistent with the experimental results mentioned in section 1.

§ 3. Other Anisotropy Energies

Geusic[10], and Zaripov and Shamonin[11] observed by paramagnetic resonance measurements in ruby (Al_2O_3 contaminated with Cr_2O_3) that the fine-structure coupling constant D of Cr^{3+} is $-0.19\ \mathrm{cm}^{-1}$, the negative sign having been known from the optical Zeeman effect[12]. We might expect approximately the same fine-structure coupling constant for the Cr^{3+} ions in Cr_2O_3. The corresponding anisotropy energy is $-0.29\cos^2\theta\ \mathrm{cm}^{-1}$ per ion at absolute zero ($DS(S-1/2)=-0.29\ \mathrm{cm}^{-1}$, S being 3/2) which is about five times as large as that arising from the dipolar interactions. However, we shall see in the next section that such a large anistropy energy is incompatible with the results of the experiment of antiferromagnetic resonance absorption, which gives a value about one third of it.

The anisotropy constant arising from the anisotropic exchange interaction may have a magnitude of $K_{f-s}\cdot\Delta E_{ex}/\Delta E_{cry}$ if one denotes by K_{f-s} the fine-structure anisotropy constant ($-0.29\ \mathrm{cm}^{-1}$ in case the above argument were valid), by ΔE_{ex} the change of energy when the spin of a chromic ion changes its component in the direction of the Weiss molecular field by one, and by ΔE_{cry} the separation between the ground and excited orbital levels in the crystalline field. ΔE_{ex} is $3kT_N/(S+1)$ in the approximation of molecular field ($T_N=308°\mathrm{K}$, $S=3/2$) and ΔE_{cry} is known to be of the order of $20000\ \mathrm{cm}^{-1}$ [12] from the optical absorption spectrum of ruby, so that $K_{f-s}\cdot\Delta E_{ex}/\Delta E_{cry}\sim10^{-2}\cdot K_{f-s}$, which is negligibly small compared with K_{f-s}. A closer analysis will show that this underestimates the anisotropy constant arising from the anisotropic exchange interaction by a factor of about 4, but it is still negligible compared with K_{f-s}.

§ 4. Discussion

Antiferromagnetic resonance studies by Dayhoff[6] show that the temperature dependence of the anisotropy energy, represented by $-K\cos^2\theta$ in the temperature range of 18° below the Néel point, is given through

$$K=8300\,(T_N-T)^{0.87\pm0.03}\ \mathrm{erg/cm^3}\,. \tag{3}$$

In order to compare this with the theoretical anisotropy constant based on the arguments in section 2 and 3, we first derive the theoretical temperature dependence of the dipolar and fine-structure anisotropy constants. Taking the approximation of the molecular field, they are expressed as

$$K_{dip}=-NC\langle S_\zeta\rangle^2/S^2,\quad C=-0.059\ \mathrm{cm}^{-1}, \tag{4}$$

$$K_{f-s}=-ND\{3\langle S_\zeta^2\rangle-S(S+1)\}/2\,, \tag{5}$$

where S_ζ is the component of the spin angular momentum operator of each ion in the direction of the internal field and N the number of ions in one cubic centimeter. For (5), the spin Hamiltonian DS_z^2 has been assumed for each ion, z being the direction of [111]. The molecular field approximation gives the following expression:[13]

$$\langle S_\zeta\rangle^2=S^2\mathrm{B}_s^2(z)\,, \tag{6}$$

$$\frac{1}{2}\left\{3\langle S_\zeta^2\rangle-S(S+1)\right\}=S(S+1)-\frac{3}{2}S\,\mathrm{B}_s(z)\coth\frac{z}{2S}\,, \tag{7}$$

$$z=g\mu_\mathrm{B}SH/kT\,, \tag{8}$$

where B_s is the Brillouin function and H the magnitude of the internal field. Further, there is a relation between z and T:

$$\frac{T}{T_N}=\frac{3S}{(S+1)}\cdot\frac{\mathrm{B}_s(z)}{z}\,. \tag{9}$$

Expanding (6), (7) and (9) in powers of z in the vicinity of the Néel temperature, we obtain

$$\langle S_\zeta^2\rangle=\frac{(S+1)^2}{9}z^2\,,$$

$$\frac{1}{2}\left\{3\langle S_\zeta^2\rangle-S(S+1)\right\}=\frac{1}{15}\frac{(S+1)}{S}\left(S-\frac{1}{2}\right)\left(S+\frac{3}{2}\right)z^2\,,$$

$$z^2=\frac{30\,S^2}{(S+1)^2+S^2}\frac{T_N-T}{T_N}\,. \tag{10}$$

Inserting (10) into (4) and (5), and putting $S=3/2$, we get

$$K_{dip}=3.84\times10^3\,(T_N-T)\ \mathrm{erg/cm^3}, \tag{11}$$

$$K_{f-s}=-2.65\times ND(T-T_N)/T_N\,. \tag{12}$$

Both are proportional to (T_N-T) and so that they cannot give the temperature dependence of (3). The deviation from 1 of the power of (T_N-T) in expression (3) may probably

arise from changes in the lattice parameters in the neighbourhood of the Néel temperature. Greenwald[14] observed by X-ray diffraction method that the c-axis (in hexagonal setting) elongates and the a-axis contracts as the crystal is cooled through the antiferromagnetic transition region. These changes would make the trigonal part of the crystalline field acting on Cr^{3+} decrease and hence would lower the value of D. If so, one would expect a milder dependence on temperature of the anisotropy constant. Also, the exchange coupling constants would be affected by these changes; if they are diminishing with lowering temperature, one would also expect a milder dependence.

If we replace (3) simply by 8300 (T_N-T) and combine it with (11), we obtain $K_{I-S}=4.46\times10^3\,(T_N-T)$ erg/cm^3. The corresponding value of D is $-0.063\,\mathrm{cm}^{-1}$ per ion, which is about one third of that deduced from experiments on ruby. Considering a possible difference in the crystalline field in Cr_2O_3 and in ruby, this factor of 1/3 may not be improbable. The corresponding critical magnetic field (H_c, the field at which the spin axis turns from the easy axis to the direction perpeudicular to it when the field is applied along the easy axis) at absolute zero is calculated to be 136 kilo gauss. Dayhoff extrapolated expression (3) to absolute zero and obtained 110 kilo gauss. With dipolar interactions only it would turn out to be 85 kilo gauss.

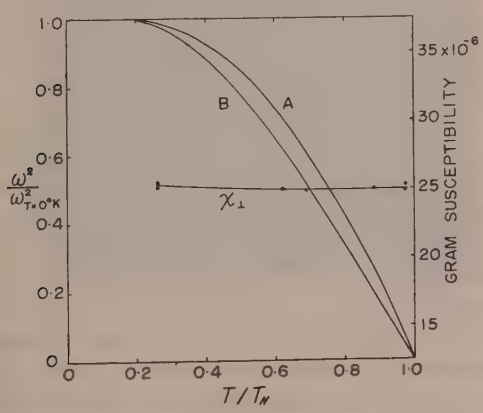

Fig. 3. The temperature dependence of the zero field antiferromagnetic resonance frequency $\omega/2\pi$ calculated (A) for dipolar interactions only and (B) for fine-structure coupling only. Experimental perpendicular susceptibility after McGuire *et al.*, which was used in the calculation, is also plotted.

Fig. 3 shows the dependence on temperature of $2K/\chi_\perp$, which is the square of antiferromagnetic resonance frequency ω/γ in the absence of external magnetic field, for the case (A) where the anisotropy energy arises solely from the dipolar interaction and for the case (B) where it arises solely from the fine-structure coupling, using experimental values of $\chi_\perp$ given by McGuire *et al.*[3]. The latter is also plotted in the same figure. To get an accurate estimate of the anisotropy constant due to the fine-structure coupling, extention of the measurements of antiferromagnetic resonance to lower temperature will be valuable.

References

1) K. Honda and T. Soné: Science Repts. Tohoku Imp. Univ. **3** (1914) 223.
2) B. N. Brockhouse: J. Chem. Phys. **21** (1953) 961.
3) T. R. McGuire, E. J. Scott and F. H. Grannis: Phys. Rev. **102** (1956) 1000.
4) R. Nathans, T. Riste, G. Shirane and C. G. Shull: Bull. A. P. S. II Vol. 2 No. 1 FA6 (1957).
5) E. S. Dayhoff: Phys. Rev. **107** (1957) 84.
6) J. Kanamori, T. Moriya, K. Motizuki and T. Nagamiya: J. Phys. Soc. Japan **10** (1955) 93.
7) R. W.G. Wyckoff: The structure of Crystals (Interscience Publishers, Inc., New York, 1948) Chapter V.
8) L. R. Maxwell and T. R. McGuire: Rev. Mod. Phys. **25** (1953) 279.
9) A. Hirota, H. Suzuki, A. Tsubaki and T. Nagamiya: Presented at the Meeting of Phys. Soc. Japan, April, 1957.
10) J. E. Geusic, Phys. Rev. **102** (1956) 1252.
11) M. M. Zaripov and Iu. Ia. Shamonin: Soviet Phys. (JETP) **3** (1956) 171.
12) G. Kuwahara, S. Sugano and Y. Tanabe: Presented at the Meeting of Phys. Soc. Japan, April, 1957.
S. Sugano and Y. Tanabe: Presented at the Meeting of Phys. Soc. Japan, October, 1957.
See also Y. Tanabe and S. Sugano: J. Phys. Soc. Japan **12** (1957) 556 and H. Lehmann: Ann. d. Phys. [5] **19** (1934) 99.
13) K. Yosida: Prog. Theor. Pnys. **6** (1951) 691.
14) S. W. Greenwald: Nature **177**, (1956) 286.

JOURNAL OF THE PHYSICAL SOCIETY OF JAPAN Vol. 13, No. 5, MAY, 1958

Anisotropy of Hot Electrons in n-type Germanium

By Wataru SASAKI, Motoichi SHIBUYA and Kanji MIZUGUCHI

Electrotechnical Laboratory, Nagatacho, Tokyo

(Received February 8, 1958)

Electromotive force perpendicular to the current flowing in n-type germanium samples is observed. The deviation angle of electric field vector from current vector is a function of current orientation, temperature, and field strength, and in some cases exceeds 20°. This effect can be attributed to the anisotropy in electric conduction due to the ellipsoidal energy surfaces.

§ 1. Introduction

Electric conduction in cubic crystals is isotropic so long as Ohm's law is applicable. However, under high electric field, where Ohm's law fails, cubic crystals do not always conduct isotropically. If anisotropy occurs in conduction, and the current direction does not lie on any of the symmetry axes of the crystal, electric field vector deviates from current vector. This deviation produces electric field transverse to the current and could be detected by transverse electrodes attached to the crystal in the same way as the Hall effect.

This effect was considered theoretically by one of us, M. S., for semiconductors with spheroidal energy surfaces[1]. Preliminary experiment carried out by us[2] showed that this effect occurs in n- and p-type germanium, and that the deviation observed in n-type germanium agrees qualitatively with Shibuya's calculation.

In this paper details of the experiment on n-type germanium are described and the experiment is compared with the above-mentioned theory, and mechanisms are suggested to explain the quantitative disagreement between the theory and experiment.

§ 2. Experimental

n-type germanium samples with room-temperature resistivity of 6~15 ohm-cm were chosen from crystals prepared by M. Kikuchi of our Laboratory. Slices of about 3 mm thick were cut along (110) plane of the crystal lattice, and filaments with large current electrodes and transverse potential electrodes, as shown in Fig. 1, were prepared by a magnetostriction cutter. Filaments lying along various direction between ⟨001⟩ and ⟨110⟩ were prepared. The angle θ defining the filament direction is chosen as shown in Fig. 1.

Filaments were etched with CP 4 to minimize spurious effects caused by hole injection from surface imperfections under high electric field.

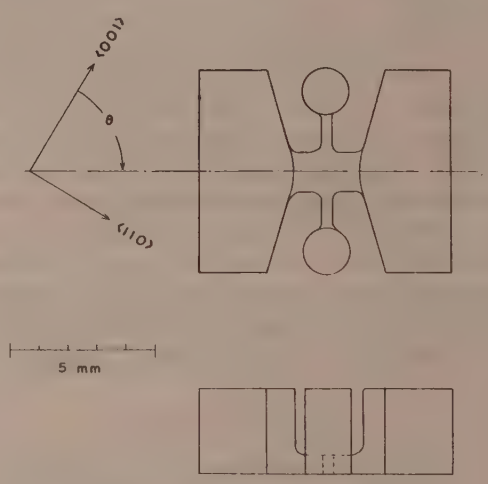

Fig. 1. Shape of specimen.

In order to avoid temperature rise in filaments under high electric field, measurements were carried with pulsed current. The apparatus arrangement is shown in Fig. 2. The voltage applied on the filament was measured through terminals A, the current through terminals B, and the transverse voltage through terminals C. These voltages were measured by measuring the pulse height on the cathode-ray tube of a synchroscope. Fig. 3 shows the wave form of these pulses on the synchroscope. For minimizing the temperature rise the duration time of the pulse must be chosen as small as possible, while too short pulse makes the estimation of the pulse height uncertain due to transient phenomena caused by the floating capacities of the pulse transformer. In many cases pulses of 0.3~0.5

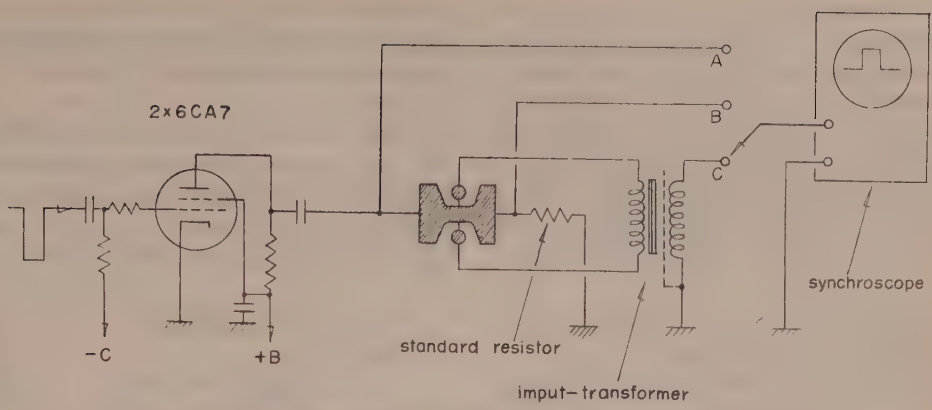

Fig. 2. The apparatus arrangement for pulse measurement.

Longitudinal voltage, pulse height:800 v

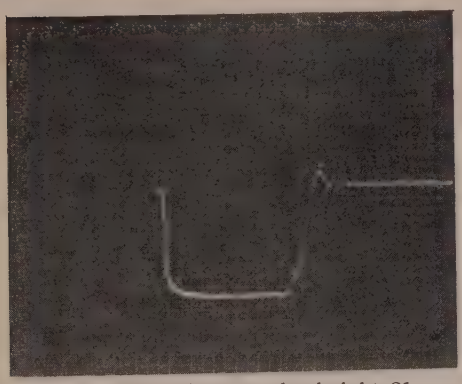

Transverse voltage, pulse height:21 v

Fig. 3. Wave form of voltage pulses.

microsecond duration and repetition rate of 50 pulses per second were used.

The pulse transformer was loaded with 1 kΩ resistor in order to obtain the best wave form. This impedance is rather low and the electric field in the filament is disturbed by insertion of this transformer when transverse electric field is produced. Thus, though the transverse voltage measured at terminals C is proportional to the transverse field without the transformer, the absolute amount of the field should require a method of calibration. This was done as follows. When magnetic field is applied the electric field vector deviates from the current vector by an angle $\mathcal{E}$, the Hall angle, in the plane perpendicular to the magnetic field. Hall angle is given by

$$\mathcal{E}=\mu_R B$$

where μ_R is the Hall mobility, a function of temperature and the purity of the specimen, and B is the magnetic induction. When the transverse electrodes of our specimen are used as Hall electrodes and magnetic field is applied, the *Hall field* caused by magnetic field is disturbed by the insertion of the imput transformer in the same way as the *anisotropy field* caused by the high electric field, and the measured transverse voltage at terminals C caused by magnetic induction B corresponds to the deviation of electric field vector from current vector by an angle $\mathcal{E}$, given by the above equation, when there is no such disturbance as is caused by insertion of pulse transformer. Thus the angle of deviation of electric field vector from current vector is estimated from the pulse voltage measured at terminals C. This estimation becomes underestimation when electric field is so high that the resistivity of the filament becomes higher than the low field resistivity; however, the effect is smaller than 10 per cent at the highest field.

The measurement was carried at temperatures of 290°K, 200°K and 90°K

§ 3. Results of Experiment

Fig. 4 shows the field dependence of the current density and the transverse voltage, observed at terminals C, of an n-type germa-

nium filament whose direction deviates by 30° from ⟨001⟩ axis, at 90°K. Three regions are seen in the current-density curve as has been pointed out by Ryder and Shockley[3)-6)]. In the first region Ohm's law is valid, in the second Ohm's law fails and the current is nearly proportional to the square root of electric field, and in the third current is almost constant.

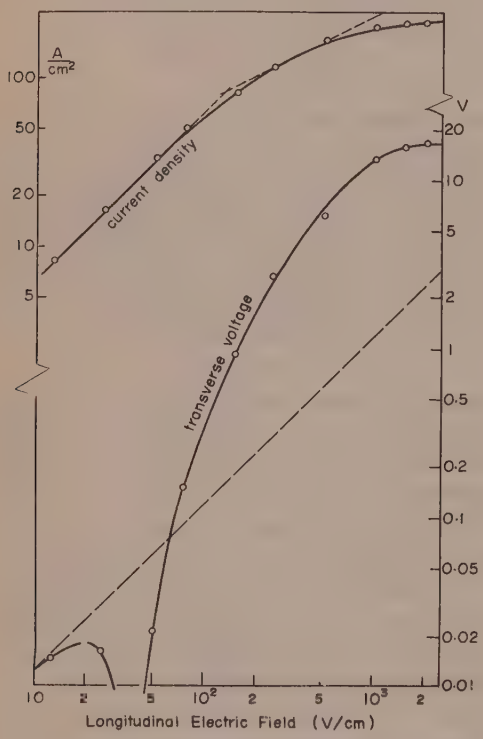

Fig. 4. Electric field dependence of current density and transverse voltage for an n-type germanium filament with $\theta=30°$. Broken line corresponds to spurious voltage due to probe asymmetry.

Spurious transverse voltage proportional to longitudinal electric field, caused by asymmetry in transverse probes, appears in the first region. Another component of transverse voltage, which differs from that in the first region in regard to its dependence on longitudinal field, appears in the second region. This component grows rapidly and attains its maximum value before the third region begins.

In order to estimate the transverse field due to anisotropy of hot electrons, the spurious component due to probe asymmetry, which is proportional to longitudinal field and is easily estimated from the low field data, is subtracted from the observed voltage. Thus the tangent of the angle ε between current and electric field vectors due to anisotropy of hot electrons is calculated and is shown in Figs. 5 and 6.

In Fig. 5 tan ε is plotted against longitudinal electric field for filament whose direction deviates 30° from ⟨001⟩ axis measured at three temperatures are shown. It is seen that the lower the temperature the lower is the field

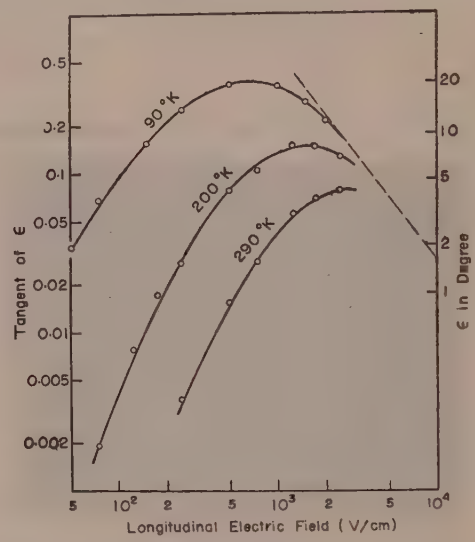

Fig. 5. Electric field dependence of tan ε for an n-type germanium specimen with $\theta=30°$.

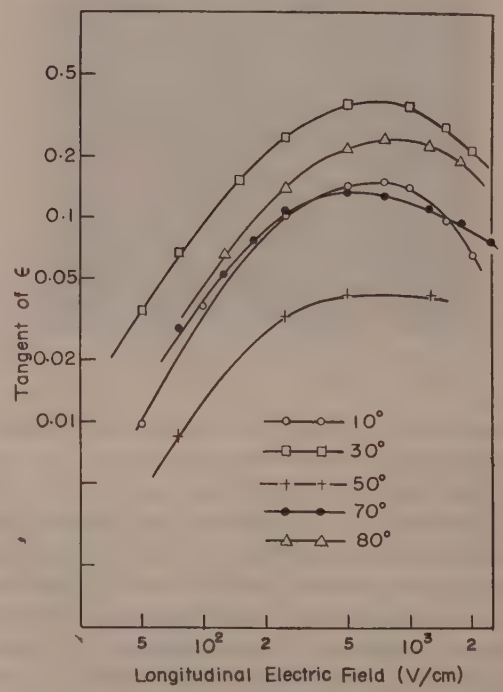

Fig. 6. Electric field dependence of tan ε for specimens with various values of θ.

where the angle becomes observable, the lower the field E_d where the angle attains the maximum value, and the larger the maximum angle. It seems that these three curves tend asymptotically to a single curve for the field higher than E_d.

In Fig. 6 $\tan \varepsilon$ curves for various filaments with different direction of crystal axis measured at 90°K are shown. The direction of deviation of the electric field vector from the current vector is such that the electric field lies nearer to ⟨111⟩ axis in (110) plane than the current vector in every case. Fig. 7 shows the angle ε at longitudinal field of 750 v/cm as a function of θ. The sign of ε was taken positive for specimens with θ smaller than 50°.

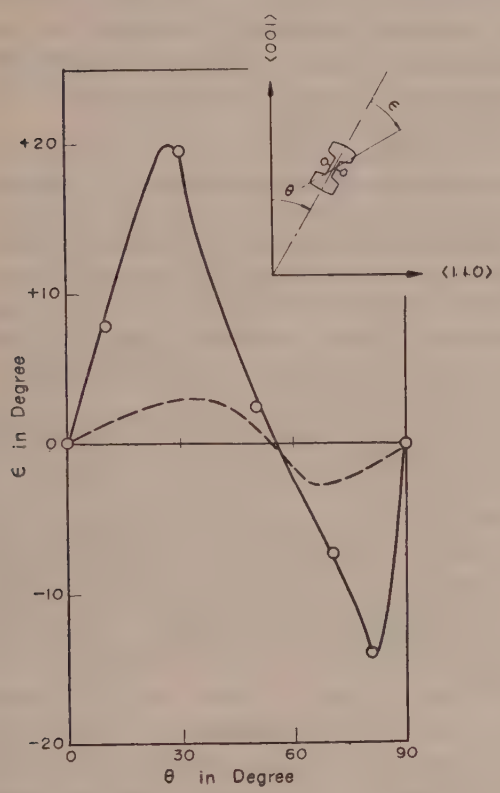

Fig. 7. Dpendence of ε on θ.

The shapes of the curves in Fig. 6 are very similar to one another, and the curves do not seem to tend asymptotically to a single curve in the highest field, in contrast to the curves in Fig. 5.

§ 4. Discussions

The anisotropy of hot electrons in cubic semiconductors with spheroidal energy surfaces was calculated by Shibuya[1]. He considers the different contributions to the current shared by the electron groups from different energy valleys in k-space, caused by different temperature rise and hence the difference in mobility of the electrons in these groups at high electric fields. His calculation hence results in anisotropy angle which is constant over the electric field where current is proportional to the square root of electric field and is also independent of temperature. The angle of anisotropy thus obtained is shown in Fig. 6 by broken line, which is in good qualitative agreement with experiment.

This effect may be understood with a sim-

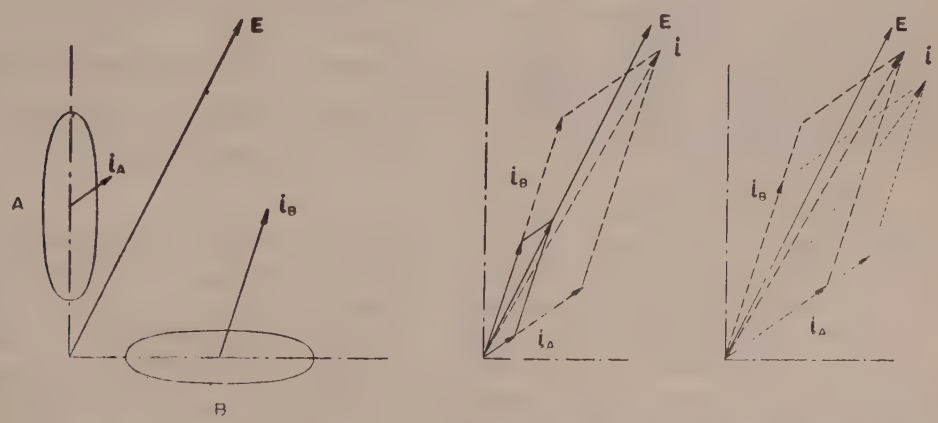

Current directions in low field (full lines) and in high field (broken lines).

Current directions in high field without (broken lines) and with (dotted lines) intervalley electron transfer.

Fig. 8. Simplified spheroidal energy surface model for explaining high field anisotropy.

plified model in Fig. 8. Only two spheroids A and B are considered. An electric field E is applied in the direction nearer to the rotation axis of spheroid A. Electric current produced by electrons with prolate-spheroidal energy surfaces lies farther from the axis of rotation, and such current components as shown in Fig. 8 are produced. These components make an electric current vector parallel to electric field when Ohm's law holds. The magnitude of effective mass of an electron with prolate energy surfaces is a function of the direction of the electric field relative to the axis of rotation of the spheroid, and is the larger the smaller the angle between electric field and the rotation axis. When the electric field becomes larger, the temperature of electrons in valley B, with smaller effective mass, becomes higher than that of A, and this difference of electron temperatures makes the current shared by A group larger than that by B group at higher electric field. These situations are shown in Fig. 8. In n-type germanium eight spheroids lying on $\langle 111 \rangle$ axes make the situation more complicated.

The disagreement in quantitative respects including the field and temperature dependence of $\mathcal{E}$ seems to suggest other mechanisms involved in this problem.

In Shibuya's calculation it is assumed that the number of electrons in a valley does not change from that at thermal equilibrium in spite of the difference between the temperatures of the electrons in different energy valleys. There must be a natural tendency, however, that the electrons in a valley at higher temperature are scattered to a valley at lower temperature, and the electron number in high temperature valleys become smaller than that in low temperature valleys. This tendency will make the current carried by electrons in high temperature valley less and that in low temperature valleys more than the case calculated by Shibuya, thus the angle of deviation will become larger. This situation in a simplified model is also shown in Fig. 8. If it is taken into account that the frequency of intervalley scattering is dependent on the lattice and electron temperatures the field and temperature dependence of the angle of deviation will be realized.

The existence of maximum in $\mathcal{E}$ *versus* field curve suggests that the difference in number of electrons in different valleys becomes smaller in field higher than E_a probably due to occurence of very frequent intervalley transitions of electrons, which depends little on the thermally excited intervalley phonons as may be supposed from the asymptotic character of the curves in Fig. 5.

Quantitative calculation for explaining the phenomenon described above is being carried.

We wish to represent our thanks to M. Kikuchi for preparation of germanium single crystals, to Z. Ishii for X-ray determination of crystal axes of the specimen, and to G. M. Hatoyama for interests and discussions to this work.

References

1) M. Shibuya: Phys. Rev. **99** (1955) 1189.
2) W. Sasaki and M. Shibuya: J. Phys. Soc. Japan **11** (1956) 1202.
3) E. J. Ryder and W. Shockley: Phys. Rev. **81** (1951) 139.
4) W. Shockley: Bell System Tech. J., **30** (1951). 990.
5) E. J. Ryder: Phys. Rev. **90** (1953) 766.

JOURNAL OF THE PHYSICAL SOCIETY OF JAPAN Vol. 13, No. 5, MAY, 1958

Magnification Calibration of Electron Microscopes by Crystal Lattice Spacings

By Ryozi UYEDA,
Physical Institute, Nagoya University, Nagoya, Japan
Tatsunosuke MASUDA, Hiroshi TOCHIGI,
Akashi, Ltd., Naka 8th Bldg., Marunouchi, Tokyo, Japan
Kazuo ITO and Haruo YOTSUMOTO
Japan Electron Optics Lab. Co. Ltd., Kamirenjaku, Mitaka, Tokyo, Japan

(Received January 30, 1958)

By an electron microscope Brindley, Comer, Uyeda and Zussman (Acta Cryst. **11** (1958), 99) found fringes corresponding to superlattice of about 90 Å spacing in antigorite. We tried to use the fringes for magnification calibration of electron microscopes. In this paper the trial and new observations in the course of the trial are shortly described.

§ 1. Introduction

The magnification of electron microscopes is usually calibrated by replicas of optical gratings. Since, however, the smallest spacing of optical gratings is about one micron, calibration at magnification over 10,000 times is very difficult. Although for this purpose other methods are known[1], they are not so convenient as using grating replicas. Therefore, gratings of smaller spacings are required. It is well known that Menter[2] observed direct images of crystal lattice of phthalocyanines. Since, however, the spacing of phthalocyanine is about 12 Å, it is too small for the magnification calibration. Recently, Brindley, Comer, Uyeda and Zussman[3] reported direct images of superlattice spacing of about 90 Å in an antigorite*, a lamellar variety of surpentine. We tried to use this spacing for the magnification calibration. In this note, we report on our trial and give some interesting observations made in the course of the experiment.

§ 2. Magnification Calibration

We determined the superlattice spacing by the superposed specimen method of electron diffraction as follows: Thallium chloride (TlCl) was deposited on an antigorite specimen by vacuum evaportion and then electron diffraction patterns and electron micrographs of the superposed specimen were taken (Fig. 1). In the diffraction pattern (Fig. 1a) Debye-rings of TlCl are appearing superposed on the diffraction pattern of an antigorite single crystal. Taking the spacing of TlCl (a=3.834 kx) as the standard[4], we determined the superlattice spacing to be 89.7 Å*. In the micrograph (Fig. 1b) fringes corresponding to the superlattice spacing are appearing and we used them for the magnification calibration. The fringes usually appeared undistorted and we found that they are adequate for our purpose. Since, however, the specimen of antigorite with the superlattice structure is rare, we must look for another appropriate specimen. We believe that the use of moiré patterns[5] is worthy of consideration.

§ 3. New Observations

In Figs. 2–7 some of the most interesting micrographs are reproduced. Fringes generally appeared with better contrast by under focussing. In Fig. 2 fringes are sharper than those in other pictures and a weak line is appearing between two strong ones. Fig. 3 gives an example of fringes with spacings one-half those in other figures. Broad and curved bands are observed where two crystal sheets are overlapping. They may be moiré pattern on overlapping sheets[5]. In Fig. 4 a micrograph of a distorted crystal is reproduced. Dark bands are appearing along or between which we can observe stepped structures of the fringes. We thought at first that the dark bands are of the same origin as those

* Specimen from Manchuria, called *Yu Yen Stone* (U.S. National Museum, No. 94356).

* The x-ray value of the same specimen is not available.

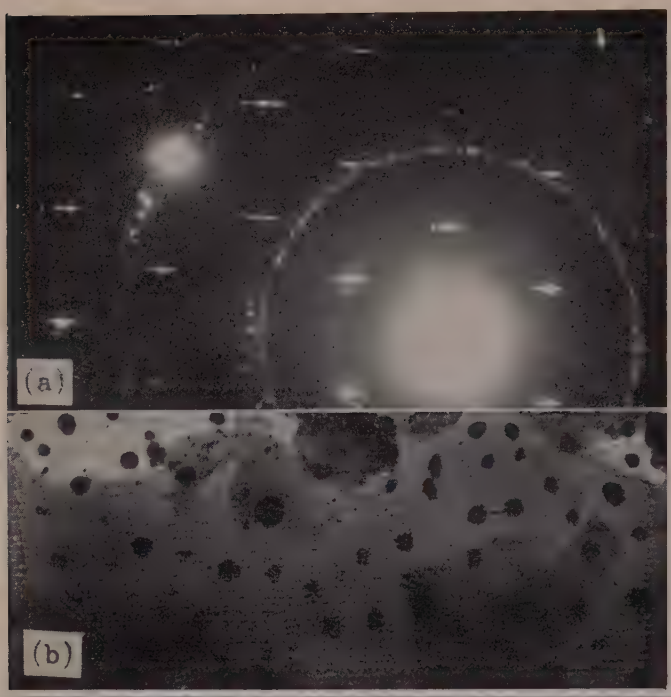

Fig. 1. Superposed specimen Antigorite-TlCl
(a) Diffraction pattern
(b) Electron micrograph
Black spots in (b) are TlCl crystal grains.

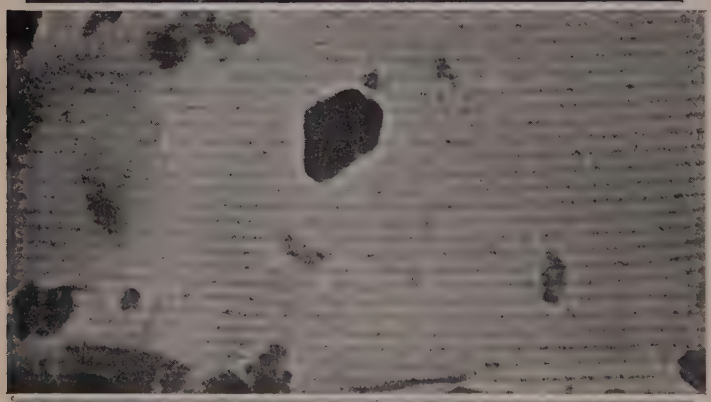

Fig. 2. Sharp fringes ×240,000

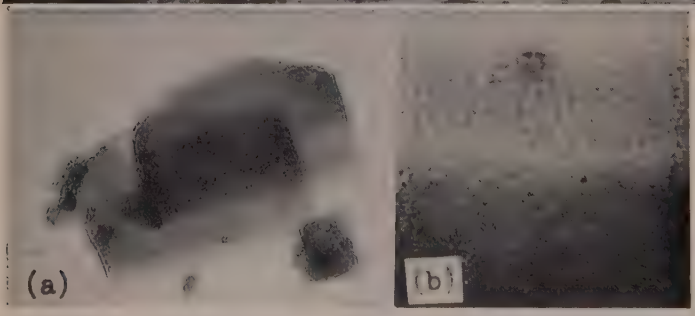

Fig. 3. Fringes of one-half spacing
(a) ×60,000
(b) A part of (a) enlarged ×220,000

of Fig. 3 and called them broadly "screw dislocations". Hashimoto[6] and Cowley[7], however, have advanced different interpretations. We recognized that the dark bands have moved during observation (Fig. 5). In some parts of Fig. 4, superlattice fringes split into two and the split distance sometimes amounted to one-half the superlattice spacing (Fig. 6). It is also worth noting that a few edge dislocations were observed (Fig. 7). We must, however, be deliberate in *deciding whether or not apparent imperfections represent those actually in the crystal.*

§ 4. Acknowledgement

The authors' hearty thanks are due to Dr.

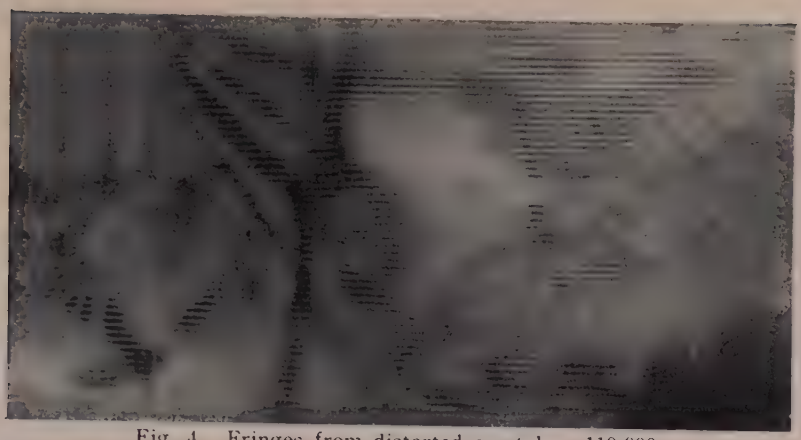

Fig. 4. Fringes from distorted crystal ×110,000

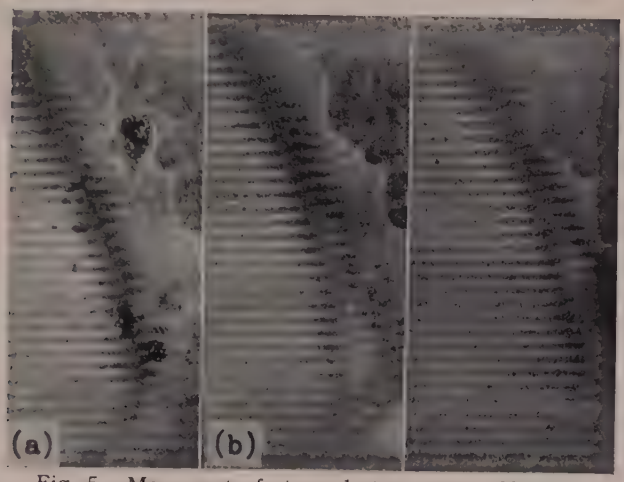

Fig. 5. Movement of stepped structure ×200,000

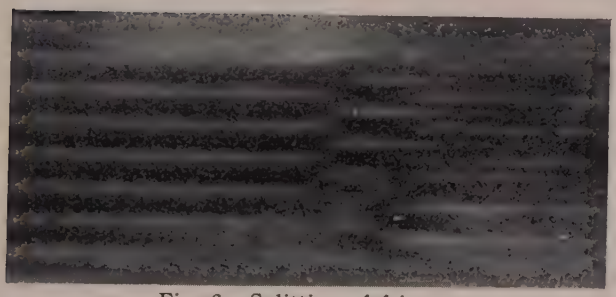

Fig. 6. Splitting of fringes ×470,000

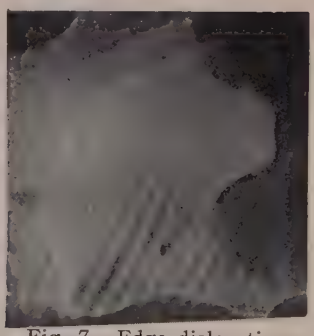

Fig. 7. Edge dislocation ×240,000

G. W. Brindley and Dr. J. Zussman for furnishing antigorite specimen and to Drs. H. Hashimoto and J. M. Cowley for valuable discussions.

References

1) C. H. Hall: Introduction to Electron Microscopy, Chap. 11 (McGraw Hill, 1953).
2) J. W. Menter: Proc. Roy. Soc. **A236** (1956), 119.
3) G. W. Brindley, J. J. Comer, R. Uyeda and J. Zussman: Acta Cryst., **11** (1958), 99.
4) F. W. C. Boswell: Proc. Phys. Soc. London, **A64** (1951), 465.
5) T. Mitsuishi, H. Nagasaki and R. Uyeda: Proc. Japan Academy, **27** (1951), 86.
D. W. Pashley, J. W. Menter and G. A. Bassett: Nature **179** (1957), 752.
6) H. Hashimoto: Private communication.
7) J. M. Cowley: Private communication.

JOURNAL OF THE PHYSICAL SOCIETY OF JAPAN Vol. 13, No. 5, MAY, 1958

An Application of the Thomas-Fermi Method to Complex Ions

Hiroshi KAMIMURA,
Department of Physics, Faculty of Science, University of Tokyo

Shoichiro KOIDE*,
College of General Education, University of Tokyo

Satoru SUGANO,
Department of Physics, Faculty of Science, University of Tokyo

and

Yukito TANABE
Department of Applied Physics, Faculty of Engineering, University of Tokyo

(Received February 6, 1958)

Although the covalency character has been found even in the normal complexes by the analyses of the paramagnetic resonance spectra and optical absorption experiments recently performed, any reliable model for the electronic structures of complex ions has not yet been established. To clarify this problem, the electron distribution in a complex ion $[Co(NH_3)_6]^{3+}$ is determined by means of the Thomas-Fermi method. To avoid the difficulty of multi-centre problem, the smoothing approximation is adopted. The Thomas-Fermi equation is reexamined from the standpoint of the variation principle, in order to investigate the validity of this approximation. In this paper, by the use of a trial function of spherical symmetry, the charge distributions for the total, valence- and core-electrons are calculated. Among these charge distributions, the charge distribution for valence-electrons seems most reliable and to approximate well the real situation in the complex ion. All faults brought by the smoothing approximation are discussed. In Appendix, the treatment of a trial function including an angle-dependent term is discussed.

§ 1. Introduction

As is well known, the binding between constituents of a complex ion is fairly strong so that we can treat it as a structural unit just like a single "molecule". A typical one of such ions is the so-called octahedral complex XY_6, in which the central metallic ion X is surrounded by a (nearly) regular octahedron composed of six "ligands" Y's. The electronic structure or the bond property of such a complex has been a long-pending problem for many physicists and chemists.

Since in complex salts the behaviour of electrons responsible for the magnetic properties is different from that of free metallic ions, a good deal of information on the electronic structure of these complexes has been obtained from their magnetic properties, i.e. magnetic susceptibilities and paramagnetic resonance spectra. For instance, magnetic susceptibility of the ferricyanide ion $[Fe(CN)_6]^{3-}$ is much smaller than that of the ferric ion in the simple salts. Pauling[1] has explained this peculiar property by his famous model in which covalent bondings are assmued between σ orbitals of ligands and the d^2sp^3 hybridized orbitals of the Fe^{3-} ion, while Van Vleck has pointed out that the same result can be predicted assuming that extremely strong cubic electric field due to six CN ions acts on the Fe^{3+} ion. These models correspond to the two limiting cases of the charge distribution between the central atom and ligands: i.e. $[Fe^{3-}(CN)_6]$ and $[Fe^{3+}(CN)^-{}_6]$.

Van Vleck[2] has also shown that these two can be derived as special cases of the charge distribution if one uses the molecular orbital method. In the molecular orbital picture, the

* Present adress: H. H. Wills Physics Laboratory, University of Bristol, Royal Fort, Bristol 8, England.

orbitals of the incomplete shell electrons may spread all over the complex ion.

The recent detailed analyses of the paramagnetic resonance and optical absorption experiments have shown that there exists the above-mentioned effect (conventionally called "covalency") even in the normal complexes which had been considered to be described by the ionic or crystalline field model.[3)4)] From these standpoints, it seems appropriate to treat the electronic structure of complexes by the molecular orbital method. In fact, several attempts in the LCAO MO approximation have been made in order to analyze the experimental data. In most of these analyses, however, the basic approximation is the ionic model and the quantitative results are restricted at most to the semi-empirical determination of the degree of covalency. After all, at present we have no reliable model which can be a starting point of our further investigations.

In view of these circumstances, it is highly desirable to obtain accurate MO wave functions, e.g. LCAO SCF wave functions. But this requires first of all some knowledge of the charge distribution in these complex ions. For such a complex ion as treated here $[Co(NH_3)_6]^{3+}$, the ionic model $[Co^{3+}(NH_3)_6]$ will not be adequate as well as Pauling's covalent model $[Co^{3-}(NH_3)^+{}_6]$. The real situation may be between these two. In fact, recently Pauling[5)] proposes "the neutrality principle" that the central atom should be regarded as neutral on an average. In MO treatments, one may start either with the $[Co^{3+}(NH_3)_6]$ or $[Co^{3-}(NH_3)^+{}_6]$ model if LCAO SCF calculations were carried out to the final stage, varying not only the coefficients of linear combination of atomic orbitals but also the orbital exponent of the central atomic orbital. The labour of finding the correct wave function is, however, greatly dependent on the Hartree field assumed at the beginning of the calculations, and it is thus necessary to have a reliable model for the charge distribution in advance.

We shall, therefore, adopt the Thomas-Fermi method to infer the charge distribution between the central atom and ligands. The main difficulty in applying this method to a polyatomic system arises from the lack of spherical symmetry. Fortunately, the geometrical shape of an octahedral complex is of good symmetry, and March has shown that in such molecules the smoothing or spherical approximation gives fairly good results, especially for the distribution of valence electrons. In the present paper, therefore, we shall try as the first step to find the radial charge distribution of valence electrons under this approximation.

Before presenting the results, the Thomas-Fermi equation will be reexamined from the standpoint of the variational principle, in order to investigate the validity of this approximation (§ 2). § 3 is devoted to the elucidation of the method. Numerical results obtained for $[Co(NH_3)_6]^{3+}$ using the smoothing approximation will be shown and discussed in § 4.

§ 2. The Thomas-Fermi Equation and the Variational Principle

The purpose of the present investigation is to obtain the charge distribution $e\rho(\boldsymbol{r})$ and the potential $V(\boldsymbol{r})$ in the octahedral molecular ion $[Co(NH_3)_6]^{3+}$ by means of the Thomas-Fermi (T.F.) method. It is, however, quite difficult to solve the TF equation directly in this case, for lack of spherical symmetry. In order to avoid this difficulty, March et al.[6)] have considered the similar problem using the so-called smoothing approximation in which the potential due to nuclei is averaged over angles. It is not easy, however, to estimate the contribution from the angle-dependent terms of the TF potential neglected in this approximation.

We will, therefore, try to reduce the TF equation to an equivalent variational problem and to solve the latter. While usual derivation of the TF equation by the variational method is based on the principle of energy minimum,[7)] we will show here that the TF equation can also be derived from the principle of "complementary energy" minimum.[8)]

Let us consider a molecular system consisting of several nuclei (charge $Z_l e$ and position $\boldsymbol{R}_l$) and of N electrons. Using the conventional notations, the total energy of such a system in the statistical treatment is given by the expression:

$$E\left(\frac{1}{4\pi}\nabla V_e,\ e\rho,\ T\right)$$

$$=\int d\tau\left\{\frac{1}{8\pi}(\nabla V_e)^2+\frac{1}{4\pi}\nabla V_e\cdot\nabla V_N\right\}$$
$$+\int_T d\tau\kappa\rho^{5/3} \qquad (1)$$

where

$$\kappa=(3h^2/10\,m)(3/8\pi)^{2/3}\,,$$

V_e and V_N are electrostatic potentials due to the electrons and nuclei respectively and T is the region occupied by electrons. The first term on the right hand side of Eq. (1) represents the energy of repulsion between electrons, the second the interaction energy between electrons and nuclei, and the last term expresses the kinetic energy of N electrons.

As is readily seen, the well-known relation between the charge density $e\rho$ and the potential $V(=V_e+V_N)$

$$4\pi e\rho=\mu(V-V_0)^{3/2},\quad \mu=4\pi e(3e/5\kappa)^{3/2} \qquad (2)$$

can be derived by minimizing the above expression (1) under the following subsidiary conditions

$$\nabla\cdot\frac{1}{4\pi}\nabla V_e=\begin{cases}e\rho & \text{in } T\\ 0 & \text{otherwise}\end{cases} \qquad (3)$$

and

$$\int_T e\rho\, d\tau=Ne\,, \qquad (4)$$

where $-eV_0$ is the maximum energy of an electron in the complex ion. Applying the Friedrichs' or involutory transformation to (1), (3) and (4), one can prove that our problem is equivalent to the procedure of minimizing the complementary energy $-I$ expressed by the following function

$$-I(U,\,T')=\int d\tau\frac{1}{8\pi}(\nabla U-\nabla V_N)^2$$
$$+\int_{T'} d\tau\frac{1}{4\pi}\frac{2}{5}\mu U^{5/2}-NeU(\infty). \qquad (5)$$

Here T' is the region where $U>0$, and $U(\infty)$ stands for the value of U at infinity. No subsidiary condition is imposed on this function $U(\boldsymbol{r})$. Applying the variational principle to the function U, one can obtain the TF equation

$$\Delta U=\begin{cases}\mu U^{3/2}-4\pi\sum_i Z_i e\delta(\boldsymbol{r}-\boldsymbol{R}_i) & \text{in } T'\\ 0 & \text{otherwise}\end{cases} \qquad (6)$$

and the conditions

$$U(\boldsymbol{r})\sim U(\infty)+(\sum Z_i-N)e/r,\ \text{as } r\to\infty$$

and

$$\frac{1}{4\pi}\int_{T'} d\tau\mu U^{3/2}=Ne\,.$$

Comparing (6) with (2) (3) (4), one can see that for the correct U and V,

$$U=V-V_0\,,\quad U(\infty)=-V_0\,.$$

Equivalence between these two procedures to minimize (1) and (5) can be confirmed by proving the following inequalities

$$I(U,\,T')\leq E_0<E\left(\frac{1}{4\pi}\nabla V_e,\,T\right), \qquad (7)$$

where E_0 denotes the minimum value of the expression (1), i.e. the correct TF energy. The equalities in (7) hold only when the correct solutions of V_e and of U are substituted. We will therefore restrict our discussion to the verification of the inequalities (7).

If we express the function E in terms of $(1/4\pi)\nabla V_e$, then

$$E-I=\int d\tau\left\{\frac{1}{8\pi}(\nabla V_e)^2+\frac{1}{4\pi}\nabla V_e\cdot\nabla V_N\right.$$
$$+\int_T d\tau\frac{3}{5}\left(\frac{4\pi}{\mu}\right)^{2/3}\left(\nabla\cdot\frac{1}{4\pi}\nabla V_e\right)^{5/3}$$
$$+\int d\tau\frac{1}{8\pi}(\nabla U-\nabla V_N)^2$$
$$+\int_{T'} d\tau\frac{1}{4\pi}\frac{2}{5}\mu U^{5/2}-NeU(\infty). \qquad (8)$$

The sum of the first- and the third term on the right hand side can be transcribed as

$$\int d\tau\left\{\frac{1}{8\pi}(\nabla V_e)^2+\frac{1}{4\pi}\nabla V_e\cdot\nabla V_N\right\}$$
$$+\int d\tau\frac{1}{8\pi}(\nabla U-\nabla V_N)^2$$
$$=\int d\tau\frac{1}{8\pi}(\nabla U-\nabla V_e-\nabla V_N)^2$$
$$-\frac{1}{4\pi}\int_T d\tau\, U\Delta V_e+NeU(\infty)\,. \qquad (9)$$

Substituting this into (8), we get

$$E-I=\int d\tau\frac{1}{8\pi}(\nabla U-\nabla V_e-\nabla V_N)^2$$
$$+\frac{\mu}{4\pi}\left[\int_{T'} d\tau\frac{2}{5}U^{5/2}+\int_T d\tau\frac{3}{5}\left(\frac{\Delta V_e}{\mu}\right)^{5/3}\right.$$
$$-\int_T d\tau\, U\frac{\Delta V_e}{\mu}\,. \qquad (10)$$

Evidently the first term cannot be negative and vanishes only when $\nabla U=\nabla(V_e+V_N)$. The second term can be written as

$$\int_{T\times T'} d\tau\left[\frac{2}{5}U^{5/2}+\frac{3}{5}\left(\frac{\Delta V_e}{\mu}\right)^{5/3}-U\frac{\Delta V_e}{\mu}\right]$$
$$+\int_{T'-T\times T'} d\tau\frac{2}{5}U^{5/2}$$
$$+\int_{T-T\times T'} d\tau\frac{3}{5}\left(\frac{\Delta V_e}{\mu}\right)^{5/3}-\int_{T-T\times T'} d\tau U\frac{\Delta V_e}{\mu}, \tag{11}$$

where $T\times T'$ expresses the common region of T and T'. If we utilize the well-known inequality for $x, y>0$

$$\frac{1}{p}x^p+\frac{1}{q}y^q-xy\geq 0, \quad \frac{1}{p}+\frac{1}{q}=1,$$

where the equality holds only when $x^p=y^q$, then we can readily see that the first term on the right hand side of (11) is non-negative and becomes zero only when

$$\Delta V_e=\mu U^{3/2}. \tag{12}$$

Then second- and the third term are obviously non-negative. The last term also cannot be negative, since $-U\Delta V_e/\mu$ is positive in the region $T-T\times T'$. All these terms become zero when $T=T'$. Thus we ultimately get

$$E\left(\frac{1}{4\pi}\Delta V_e,\ T\right)\geq I(U,\ T'). \tag{13}$$

If we substitute the correct solution in V_e and U alternately, we obtain the inequalities of (7).

Let us denote the correct solution by V_e^0 and U^0, then (10) becomes

$$E\left(\frac{1}{4\pi}\nabla V_e,\ T\right)-I(U,\ T')$$
$$=E\left(\frac{1}{4\pi}\nabla V_e,\ T\right)-I(U^0,\ T^0)$$
$$+E\left(\frac{1}{4\pi}\nabla V_e^0,\ T^0\right)-I(U,\ T')$$
$$>\int d\tau\frac{1}{8\pi}(\nabla U-\nabla V_e^0-\nabla V_N)^2$$
$$+\int d\tau\frac{1}{8\pi}(\nabla U^0-\nabla V_e-\nabla V_N)^2. \tag{14}$$

One can thus estimate the mean square errors of the approximate ∇V_e or ∇U by calculating the left hand side of this expression.

§ 3. Application of the Method to a Complex Ion

Now we will apply the above-mentioned variational principle to an octahedral complex ion $[Co(NH_3)_6]^{3+}$. The reasons why we choose this ion as the object of our study are that it is a diamagnetic cation with the ligands of well-known character and that its high symmetry and the small distance between the metal ion and the ligands are considered to be favourable for the smoothing approximation adopted below.

As the first step, we try to minimize the expression (5) taking a spherical variation function:

$$U=U_0(r), \tag{15}$$

where r is the distance measured from the Co nucleus*. From the physical point of view, this is equivalent to the procedure to smooth out the positive charges of the nitrogen and hydrogen nulei over the spherical surfaces of radii R_1 and R_2 respectively, where R_1 is the distance Co-N and R_2 that of Co-H (smoothing approximation).** Starting from (1), (3) and (4), March has made similar justification of the smoothing approximation.[9]

Substituting (15) into (5) and taking the variation with respect to the radial function $U_0(r)$, one obtains the Euler equation

$$\frac{1}{r^2}\frac{d}{dr}\left(r^2\frac{d}{dr}U_0(r)\right)$$
$$=\begin{cases}\mu\{U_0(r)\}^{3/2} & r<R_b\\ 0 & r>R_b,\end{cases} \tag{16}$$

together with the boundary conditions

(a) $U_0^{(1)}(r)\to Ze/r$ as $r\to 0$,

(b) $U_0^{(1)}(R_1)=U_0^{(2)}(R_1)$,

* It is unfortunate, however, that the inequality (14) cannot be used directly to judge the accuracy of U_0 obtatined in this way. When this U_0 is substituted for U in the expression (5), $I(U,\ T)$ becomes infinite, because U_0 does not show correct (singular) behavior near the position of the ligand nuclei. The infinity of $I(U,\ T)$, however, does not imply infinite error in V_e or the electronic charge distribution. In fact, the appearance of infinity may be avoided by adopting $U_0-V_{N0}+V_N$ as U instead of U_0, where V_{N0} is the spherical part of V_N, but then the evaluation of the integral

$$\frac{1}{4\pi}\cdot\frac{2}{5}\int_{T'}\mu U^{5/2}d\tau$$

will be rather difficult. At present we confine ourselves to such qualitative discussions as given below.

** R_1 is taken as 1.99 Å which is approximately equal to the sum of covalent radii of Co and N, while R_2 is taken as 2.55 Å assuming that the molecular constants of the ligand NH_3 are equal to those of a free NH_3 molecule.

$$(c)\quad U_0^{(2)}(R_2)=U_0^{(3)}(R_2)\,,$$

$$(d)\quad -\left(\frac{dU_0^{(1)}}{dr}\right)_{R_1}+\left(\frac{dU_0^{(2)}}{dr}\right)_{R_1}=-\frac{N_1e}{R_1^2}\,, \qquad (17)$$

$$(e)\quad -\left(\frac{dU_0^{(2)}}{dr}\right)_{R_2}+\left(\frac{dU_0^{(3)}}{dr}\right)_{R_2}=-\frac{N_2e}{R_2^2}\,,$$

$$(f)\quad U_0^{(3)}(R_b)=0\,,$$

$$(g)\quad \frac{1}{4\pi}\int_{T'} d\tau\mu U^{3/2}=Ne\,,$$

where Ze is the charge of Co nucleus, N_1e and N_2e are the nuclear charges of nitrogen and hydrogen respectively. R_b represents the finite radius of the positive complex ion, exactly as in the case of atomic ions, and $U_0^{(1)}$, $U_0^{(2)}$ and $U_0^{(3)}$ represent U_0 for $r\leq R_1$, $R_1\leq r\leq R_2$ and $R_2\leq r$ respectively. If we set

$$U_0=\frac{Ze}{r}\phi_0\,,\quad r=bx\,, \qquad (18)$$

where

$$b=(3/32\pi^2)^{2/3}(h^2/2me^2Z^{1/3})\,,$$

then (16) is transformed into its usual dimensionless form

$$\frac{d^2\phi_0}{dx^2}=\sqrt{\frac{\phi_0^3}{x}} \qquad (19)$$

and the boundary conditions (17) become correspondingly,

$$(a)\quad \phi_0^{(1)}(0)=1\,,$$

$$(b)\quad \phi_0^{(1)}(X_1)=\phi_0^{(2)}(X_1)\,,$$

$$(c)\quad \phi_0^{(2)}(X_2)=\phi_0^{(3)}(X_2)\,,$$

$$(d)\quad \left(\frac{d\phi_0^{(1)}}{dx}\right)_{X_1}-\left(\frac{d\phi_0^{(2)}}{dx}\right)_{X_1}=\frac{N_1}{X_1Z}\,, \qquad (20)$$

$$(e)\quad \left(\frac{d\phi_0^{(2)}}{dx}\right)_{X_2}-\left(\frac{d\phi_0^{(3)}}{dx}\right)_{X_2}=\frac{N_2}{X_2Z}\,,$$

$$(f)\quad \phi_0^{(3)}(X_b)=0\,,$$

$$(g)\quad \frac{z}{Z}=-X_b\left(\frac{d\phi_0^{(3)}}{dx}\right)_{X_b}\,,$$

where z is number of excess positive charge 3 of this ion, $\phi_0^{(1)}$, $\phi_0^{(2)}$ and $\phi_0^{(3)}$ correspond to $U_0^{(1)}$, $U_0^{(2)}$ and $U_0^{(3)}$, and X_1, X_2 and X_b are R_1, R_2 and R_b in dimensionless unit. As is well-known, the condition $(20g)$ is easily derived from $(17g)$, using the equation (16) and the other conditions $(a)\sim(f)$.

According to March, the smoothing approximation seems to give fairly good results in certain cases. However, in order to take the actual arrangement of nuclei in complex ions into account, it will, of course, be more adequate to assume a trial function including the angle-dependent terms, in addition to the term of spherical symmetry. For instance, if the cubic term of potential is added as the second step, the form of a trial function becomes

$$U(\boldsymbol{r})=U_0(r)+C(\theta,\ \varphi)U_4(r)\,, \qquad (21)$$

where

$$C(\theta,\ \varphi)=\sqrt{7/12}\{Y_4^0+\sqrt{5/14}(Y_4^4+Y_4^{-4})\}\,. \qquad (22)$$

Substituting (21) into (5) and then taking variation for U_0 and U_4, a set of differential equations for U_0 and U_4 are obtained together with their boundary conditions. The purpose of this paper is, however, to discuss the results of the smoothing approximation, which could also be used as initial solution to these equations. We shall, therefore, content ourselves only with the derivation of these equations (which will be given in Appendix), and now proceed to the discussion of the present results.

§ 4. Results and Discussion

We solved numerically the equation (19) under the boundary condition (20). Numerical integration was performed using the electronic digital computor FUJIC in the region $r\leq R_1$. Then, on account of the functional limitation of the computor, the solution had to be extended to the outer region $r\geq R_1$ by means of the desk machine as usual. In the course of integration it was found that the TF potential for the inner region $\phi_0^{(1)}$ was rather insensitive to the boundary condition $(20g)$, while $\phi_0^{(2)}$ and $\phi_0^{(3)}$ depended on it.

The numerical values of the TF potential $\phi_0(r)$ thus obtained are given in Table I, and the curve of corresponding $U_0(r)$ *vs* r is given in Fig. 1. It may be noticed that the potential curve reveals a minimum in the region $r\leq R_1$ as if an attractive force for electrons from the sphere passing through the ligands (ligands' sphere) does exist in spite of the fact that in the spherical approximation the nuclear charges of the ligands are smeared out so that the potential due to these charges becomes constant inside the sphere. This is due to the formation of sphere of neutral charge in the region $r<R_1$, the radius of which is just given by the position of potential minimum $R_n=1.33$Å ($X_n=8.5$). Outside this sphere, electrons at r are repelled towards ligands by the excess negative charges lying between r and R_n. Thus this is the cause

Table I. The numerical values of the T. F. potential $\phi_0(x)$.

x	$\phi_0(x)$	x	$\phi_0(x)$
0.04	0.9470	5.44	0.0815
0.08	0.9022	5.76	0.0775
0.12	0.8623	6.08	0.0745
0.16	0.8262	6.40	0.0723
0.20	0.7931	6.72	0.0710
0.24	0.7626	7.04	0.0703
0.28	0.7342	7.36	0.0704
0.32	0.7077	7.68	0.0712
0.36	0.6830	8.00	0.0727
0.40	0.6597	8.32	0.0749
0.44	0.6378	8.64	0.0778
0.48	0.6171	8.96	0.0815
0.52	0.5975	9.28	0.0860
0.56	0.5790	9.60	0.0914
0.60	0.5614	9.92	0.0976
0.64	0.5447	10.24	0.1049
		10.56	0.1132
0.72	0.5136	10.88	0.1227
0.80	0.4853	11.20	0.1336
0.88	0.4594	11.52	0.1460
0.96	0.4356	11.84	0.1600
1.04	0.4138	12.16	0.1760
1.12	0.3935	12.48	0.1942
1.20	0.3748		
1.28	0.3575	12.75	0.2113
1.36	0.3413	13.11	0.1933
1.44	0.3263	13.47	0.1783
1.52	0.3122	13.83	0.1659
1.60	0.2990	14.19	0.1560
1.68	0.2867	14.55	0.1481
1.76	0.2751	14.91	0.1422
1.84	0.2643	15.27	0.1381
1.92	0.2540	15.63	0.1357
2.00	0.2444	15.99	0.1350
2.08	0.2353	16.35	0.1359
2.16	0.2267		
2.24	0.2186	16.75	0.1225
2.32	0.2109	17.15	0.1107
2.40	0.2036	17.55	0.1003
2.48	0.1967	17.95	0.0911
2.56	0.1902	18.35	0.0830
2.64	0.1840	18.75	0.0757
2.72	0.1781	19.15	0.0693
2.80	0.1725	19.55	0.0635
2.88	0.1671	19.95	0.0582
2.96	0.1621	20.35	0.0535
3.04	0.1572	20.75	0.0492
		21.15	0.0454
3.20	0.1483	21.55	0.0418
3.36	0.1401	21.95	0.0385
3.52	0.1327	22.35	0.0355
3.68	0.1259	22.75	0.0328
3.84	0.1197	23.15	0.0302
4.00	0.1141		
4.16	0.1089	23.95	0.0255
4.32	0.1042	24.75	0.0214
4.48	0.0996	25.55	0.0177
4.64	0.0961	26.35	0.0143
4.80	0.0925	27.15	0.0111
4.96	0.0893	27.95	0.0081
5.12	0.0864	28.75	0.0051
		29.55	0.0022

of the apparent attraction from the ligands' sphere. It will be interesting to compare R_n with Pauling's covalent radius $R_c=1.22$Å.

The calculated radial charge densities of total, valence- and core-electrons are given in Fig. 2, Fig. 3 and Fig. 4 respectively.

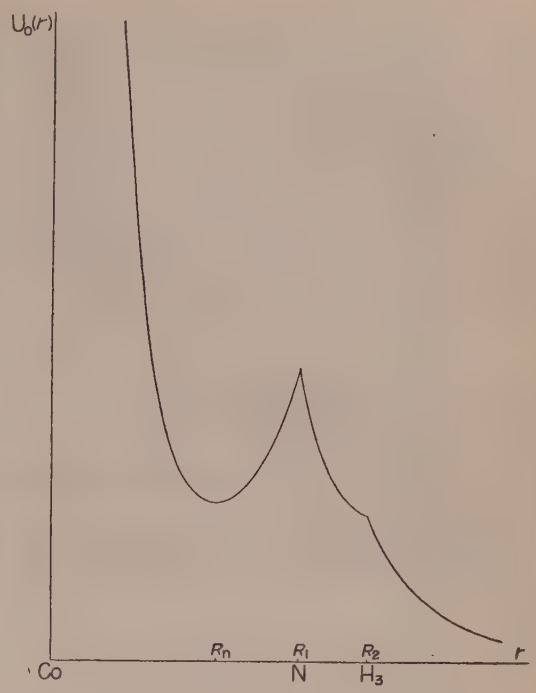

Fig. 1. The curve of the potential $U_0(r)$

The density of valence-electrons is determined by subtracting K-shell, L-shell, $3s$- and $3p$-electrons of Co and K-shell electrons of six N's as core-electrons from the density of total electrons. This can be done, after Coulson and March,[10] by seeking the energy E_l below which 30 core-electrons lie;

$$2\int_{-\infty}^{E_l} N(E)dE=30\,, \tag{23}$$

where the level density $N(E)$ is given by the formula

$$N(E)=\frac{16\pi^2(2m^3)^{1/2}}{h^3}\int_{E+eV>0}(E+eV)^{1/2}r^2\,dr\,. \tag{24}$$

After the value of E_l is obtained (in our present case $E_l=-0.99$ a.u.), the radial charge distribution of valence-electrons $D_{val}(r)$ can be calculated by the formula

$$D_{val}(r)=\frac{4r^2}{3\pi}\left[\{2(E_0+V)\}^{3/2}-\{2(E_l+V)\}^{3/2}\right], \tag{25}$$

where $E_0=-eV_0$ is the maximum energy and is found to be -0.34 a.u.

The discrimination between valence- and core-electrons adopted here is made from the difference of their orbital energies. Hartree's orbital energies of electrons in a free Co^{2+}

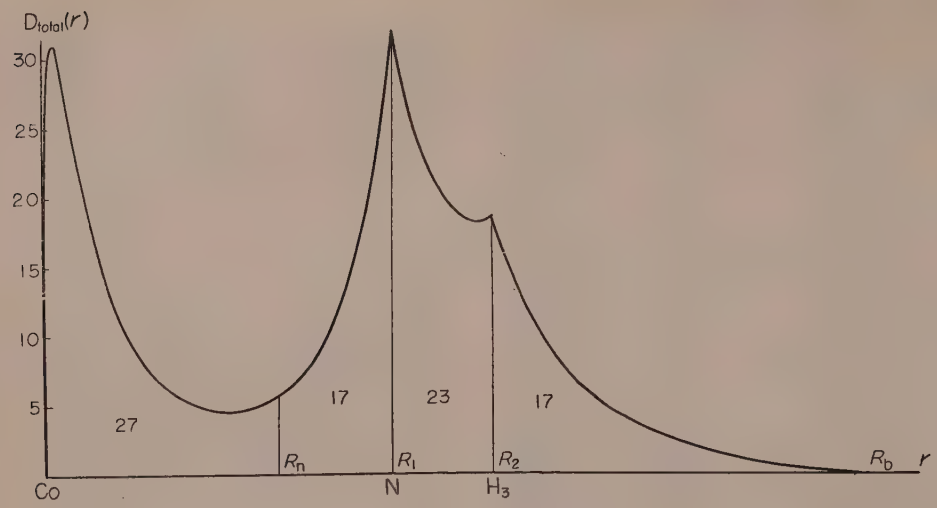

Fig. 2. The calculated radial charge density of total electrons. The approximate numbers of total electrons distributed in each region $o \leq r < R_n$, $R_n \leq r < R_1$, $R_1 \leq r < R_2$ and $R_2 \leq r$ are also given.

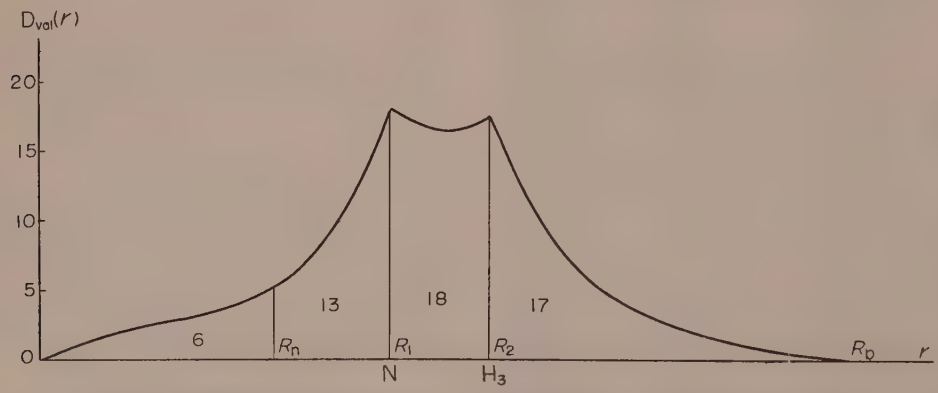

Fig. 3. The calculated radial charge density of valence-electrons. The approximate numbers of valence-electrons distributed in each region $o \leq r < R_n$, $R_n \leq r < R_1$, $R_1 \leq r < R_2$ and $R_2 \leq r$ are also given.

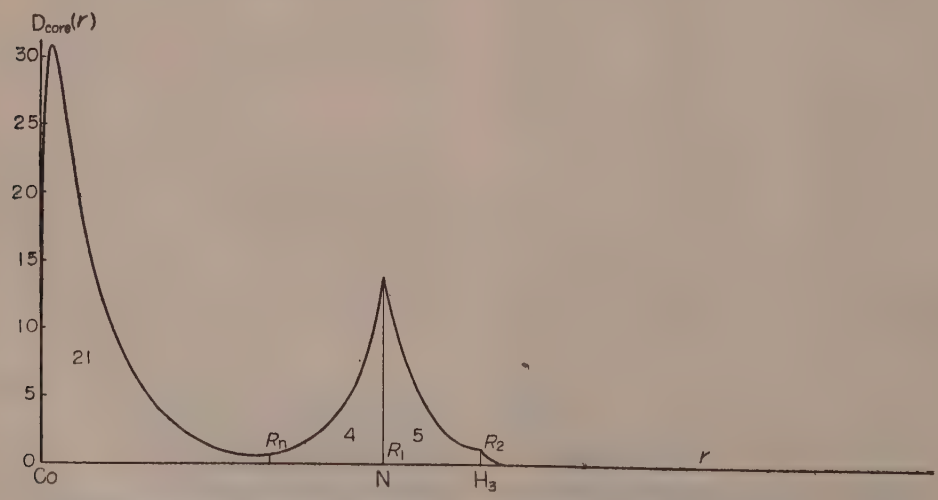

Fig. 4. The calculated radial charge density of core-electrons. The approximate numbers of core-electrons distributed in each region $o \leq r < R_n$, $R_n \leq r < R_1$, and $R_1 \leq r < R_2$ are also given.

ion[11] and the ionization energies of $2s$- and $2p$-electrons in an NH_3 molecule[12] are given in Table II for reference. Even if the orbital energy of $3p$-electrons is somewhat lifted when Co becomes neutral, it will be still lower than $2s$ orbital energy of an NH_3 molecule.

Table II. Hartree's orbital energies of Co^{2+} and ionization potentials of an NH_3 molecule.

Co^{2+}		NH_3	
$1s$	7711.2 ev	$2s$	27 ev
$2s$	916.6		
$2p$	810.6	$2p_\pi$	16
$3s$	119.7	(bonding)	
$3p$	85.0	$2p_\sigma$	11
$3d$	28.8	(non-bonding)	

Before we discuss the calculated charge distribution, an attention must be paid to such fault of the spherical approximation that core-electrons of the ligands drastically move into the region ($0 \leq r \leq R_n$) when this approximation is adopted, as March has pointed out in his treatment of CCl_4 molecule. In fact this fault also appears in our case; when the distribution of 22 electrons is examined excluding 8 $3s$-, $3p$-electrons out of 30 core-electrons, we find only two or three electrons in the region of the ligands. This should be 12 for correct charge distribution, so that 10 electrons out of 12 have been missed from the region of the ligands.

In spite of the above fact, the resultant number of our core-electrons (30 electrons) distributed in the region ($R_n \leq r \leq R_2$), which is 9 as Fig. 4 shows, seems rather near 12 which can be expected in the real situation. This will be interpreted as follows: As the result of the movement of some core-electrons of the ligands into the central region, most of the $3s$- and $3p$-core-electrons of Co are overflowed outwards so that the missing core-electrons of the ligands are almost made up for by these overflowed. This overflowing will be due to the repulsive force of the negatively charged sphere in the central region and to the exclusion principle operating there. In Fig. 4 we can also partly see these circumstances in the fact that the core-electrons in the ligands' region are too scattered to be the K-shell electrons of N's.

On the other hand, the distribution of valence-electrons obtained in this way should be nearer to the truth than that of total electrons, since core-electrons play a role in shielding the nuclear charges of ligands as well as in allowing the exclusion principle to be operated so that the wrong tendency of the spherical approximation, i.e., the movement of electrons towards the central region, is suppressed for valence-electrons. This fact was also pointed out by Banyard and March[13].

Further considerations show, however, that for valence-electrons there is another possibility that their distribution obtained becomes too diffuse rather than contracted. As already mentioned, the spherical approximation makes the distribution of electrons, especially that of deeply lying core-electrons, too compact in the central region and as the result of this the central nuclear charges are over-screened by these electrons, so that we can expect rather diffuse distribution of the valence-electrons which are mainly populated in the relatively shallow parts of the potential energy. The previously explained phenomenon of "overflowing" may be considered as the similar effect, though in this case it is the $3s$- and $3p$-core-electrons which spread out, but not the valence-electrons. Further, the more enhanced tail of curve 2 than that of curve 1 in Fig. 4 of Banyard and March's paper might be interpreted to show such effect clearly.

Keeping all these possible deviations in the calculated distribution from the real one in our mind, we now return to the discussion of our result for the density of valence-electrons (Fig. 3). It shows that in the region $R_1 \leq r$ 35 electrons are distributed. This should be compared with 36 electrons which is expected when a pair of electrons is used in each N-H bond of an NH_3 molecule. Although our result shows that in the region $r \leq R_n$, 6 valence-electrons are distributed and that in the region $R_1 \geq r \geq R_n$ 12 valence-electrons are distributed, it will be premature to conclude from this that Co is trebly ionized and 12 electrons form lone pair electrons of 6 NH_3 molecules in $[Co(NH_3)_6]^{3+}$ complex ion. This is because, apart from the problems of the accuracy in our result and from the meaning of R_n, the orbital of $3d$-electron is so spread that we can not determine the

ionicity of Co by the number of the valence electrons distributed in such limited region as $r \leq R_n$.

Considering from the fact that 35 electrons are found in the region $r > R_1$ we may expect there is little possibility for valence-electrons to be too diffuse in the present case. This is reasonable, since, compared with CCl_4 molecule treated by March et al, our object is of higher symmetry and has smaller value of $(N_1+N_2)/Z$, which seems to give certain measure for the validity of the smoothing approximation.

Thus being encouraged to believe that our results for valence-electrons approximate well the real situation despite the crude approximation adopted here, we hope our results, especially the distribution of valence-electrons and the potential for them, will serve as a good starting point for the future.

Acknowledgements

The authors would like to express their sincere thanks to Professor Masao Kotani for his much instructive advices and continual encouragement during the course of this work. They further wish to express their gratitudes to Mr. S. Tatsuoka of the Fuji Film Co. for his kindness to operate "Fujic" to provide the table of the T.F. solution. They are also indebted to the Ministry of Education and to the members of Kotani laboratory for their financial aids. Finally, they would like to thank Mrs. H. Komuro and Miss. S. Kosugi for their valuable assistance in the numerical work.

Appendix

We shall consider here the case in which the trial function (21) is assumed. As it is more convenient to work in terms of the usual T.F. dimensionless quantities, we express (21) in the following form

$$U=\frac{Ze}{r}\phi_0(r)+C(\theta,\ \varphi)\frac{Ze}{r}\phi_4(r) \qquad \text{(A1)}$$

and set $r=bx$. Then, substituting (A1) into (5) and minimizing $-I$ with respect to ϕ_0 and ϕ_4, we obtain the following simultaneous differential equations for ϕ_0 and ϕ_4 in the region T'

$$\begin{cases} \dfrac{d^2\phi_0}{dx^2}=\dfrac{1}{\sqrt{x}}\displaystyle\int\frac{1}{4\pi}(\phi_0+C(\theta,\ \varphi)\phi_4)^{3/2}d\Omega & \text{(A2)} \\ \dfrac{d^2\phi_4}{dx^2}-\dfrac{20}{x^2}\phi_4 \\ \qquad =\dfrac{1}{\sqrt{x}}\displaystyle\int C(\theta,\ \varphi)(\phi_0+C(\theta,\ \varphi)\phi_4)^{3/2}d\Omega, & \text{(A3)} \end{cases}$$

and for ϕ_0 and ϕ_4 outside the region T'

$$\begin{cases} \dfrac{d^2\phi_0}{dx^2}=0 & \text{(A4)} \\ \dfrac{d^2\phi_0}{dx^2}-\dfrac{20}{x^2}\phi_4=0\,, & \text{(A5)} \end{cases}$$

where $d\Omega$ is the solid angle, togeter with the boundary conditions

$$(a)\quad \begin{cases} \phi_0^{(1)}(0)=1 \\ \phi_4\sim x^5 \qquad \text{for small } x \end{cases}$$

$$(b)\quad \begin{cases} \phi_0^{(1)}(X_1)=\phi_0^{(2)}(X_1) \\ \phi_4^{(1)}(X_1)=\phi_4^{(2)}(X_1) \end{cases}$$

$$(c)\quad \begin{cases} \phi_0^{(2)}(X_2)=\phi_0^{(3)}(X_2) \\ \phi_4^{(2)}(X_2)=\phi_4^{(3)}(X_2) \end{cases}$$

$$(d)\quad \begin{cases} \left(\dfrac{d\phi_0^{(1)}}{dx}\right)_{X_1}-\left(\dfrac{d\phi_0^{(2)}}{dx}\right)_{X_1}=\dfrac{N_1}{X_1Z} \\ \left(\dfrac{d\phi_4^{(1)}}{dx}\right)_{X_1}-\left(\dfrac{d\phi_4^{(2)}}{dx}\right)_{X_1} \\ \qquad =\sqrt{21\pi}\,\dfrac{N_1}{X_1Z} \end{cases} \qquad \text{(A6)}$$

$$(e)\quad \begin{cases} \left(\dfrac{d\phi_0^{(2)}}{dx}\right)_{X_2}-\left(\dfrac{d\phi_0^{(3)}}{dx}\right)_{X_2}=\dfrac{N_2}{X_2Z} \\ \left(\dfrac{d\phi_4^{(2)}}{dx}\right)_{X_2}-\left(\dfrac{d\phi_4^{(3)}}{dx}\right)_{X_2} \\ \qquad =\sqrt{21\pi}\,\dfrac{N_2}{X_2Z}\,\mathrm{P}_4(\cos\alpha) \end{cases}$$

$$(f)\quad \phi_0(X_b)+C(\theta,\ \varphi)\phi_4(X_b)=0$$

$$(g)\quad \int d\Omega X_b(\theta,\varphi)\left(\frac{d}{dx}(\phi_0^{(3)}+C(\theta,\varphi)\phi_4^{(3)})\right)_{X_b(\theta,\varphi)} -20\int d\Omega C(\theta,\varphi)\int_{X_2}^{X_b(\theta,\varphi)}\frac{1}{x}\phi_4^{(3)}(x)\,dx =-4\pi\frac{Z}{Z}$$

where α is $\angle$H—Co—N.

As is seen in (f), in this case the finite radius of the positive complex ion R_b depends on angular variables θ, φ. The condition (g) is easily derived from the condition

$$\frac{1}{4\pi}\int_{T'}\Delta V d\tau=Ne$$

using the equations (A2), (A3) and the other boundary conditions $(a)\sim(f)$.

Though equations (A2) and (A3) were not solved numerically in this paper, we will remark the numerical procedure here. As a first approximation we assume for ϕ_0 the solution calculated in the present paper. Then, with this ϕ_0 we solve (A3) to obtain ϕ_4. With these ϕ_0 and ϕ_4, we can obtain X_b as a function of θ, φ from the condition (f) and then examine whether they satisfy the condition (g) or not. If they do not satisfy (g), we then solve (A2) with ϕ_4 obtained now. Thus such a procedure is repeated until the condition (g) becomes to be satisfied.

References

1) L. Pauling: J. Am. Chem. Soc. **53** (1931) 1367.
2) J. H. Van Vleck: J. Chem. Phys. **3** (1935) 817.
3) J. Owen: Proc. Roy. Soc. A **227** (1955) 183.
4) Y. Tanabe and S. Sugano: J. Phys. Soc. Japan **9** (1954) 766.
5) L. Pauling: *Report of International Conference, Echangé isotropiques et structure moléculaire* (1948).
6) N. H. March: Proc. Camb. Phil. Soc. **48** (1952) 665.
7) P. Gombas: *Die Statistische Theorie des Atoms*, Wien, 1949.
8) Y. Tanabe: J. Phys. Soc. Japan **12** (1957) 974.
9) R. A. Ballinger and N. H. March: Proc. Camb. Phil. Soc. **51** (1955) 517.
10) C. A. Coulson and N. H. March: Proc. Camb. Phil. Soc. **52** (1958) 114.
11) M. Ariyama, K. Kayama and M. Sugimoto: J. Phys. Soc. Japan **12** (1957) 285.
12) R. S. Mulliken: J. Chem. Phys. **3** (1935) 506.
13) K. E. Banyard and N. H. March: Proc. Camb. Phil. Soc. **52** (1956) 280.

JOURNAL OF THE PHYSICAL SOCIETY OF JAPAN Vol. 13, No. 5, MAY, 1958

Macroscopic Foundation of Plasma Dynamics

By Taro KIHARA

Department of Physics, Faculty of Science, University of Tokyo

(Received February 6, 1958)

A fluid which comprises several species of charged and neutral particles is treated macroscopically. Basic equations, energy and momentum theorems, and law of similarity are discussed. The condition under which current equation reduces to the usual form is considered; and one-dimensional transverse waves are treated as an example. Quasi-stationary phenomena are examined as a particular case; and it is pointed out that one of the usual basic equations of hydromagnetics, the Ohm's law $\boldsymbol{J}=\sigma(\boldsymbol{E}+\boldsymbol{v}\times\boldsymbol{B})$, should be replaced by $\mathrm{rot}(\boldsymbol{E}+\boldsymbol{v}\times\boldsymbol{B}-\sigma^{-1}\boldsymbol{J})=0$, $\boldsymbol{v}$ being the velocity of the mean mass flow. An axially symmetric solution is obtained and applied to a self-pinched column, whose stability is explained in an elementary manner.

§ 1. Introduction

Both for cosmic problems and for thermonuclear fusion, study of ionized fluid, plasma, is needed. Theoretically, the plasma can be and must be investigated from two points of view, i.e. macroscopic and microscopic. The present article is a treatment from the former point of view.

The macroscopic or phenomenological theory of plasma has not well been developed in comparison with the theory of electromagnetic field or classical fluid dynamics. The electromagnetic field is treated on the basis of the Maxwell equations; fluid flow is treated on the basis of the Euler equation and the equation of continuity. These basic equations are "exact" and there is no alternative or arbitrariness. As regards plasma, on the other hand, choice of basic equations is not fixed. Spitzer[1] treated fully ionized gases composed of only electrons and one type of positive ion. He neglected all the quadratic terms in fluid

velocity and current density. His equation of the plasma flow is, therefore, not the usual Euler equation but a linear approximation. Alfvén[2] and Cowling[3] treated quasi-stationary neutral plasma. They simply assumed Ohm's law in a magnetic field, which does not hold in general. Their system of equations, therefore, cannot be regarded as a basis of the plasma dynamics, although it is effective for discussing cosmic problems.

The aim of the present article is to consolidate, in an elementary way, the foundation for the plasma dynamics and hydromagnetics.

The electromagnetic field in a plasma is determined by four vectors, electric field $\boldsymbol{E}$, magnetic flux density $\boldsymbol{B}$, electric displacement $\boldsymbol{D}$, and magnetic field $\boldsymbol{H}$, which satisfy the Maxwell equations

$$\operatorname{rot}\boldsymbol{E}+\frac{\partial\boldsymbol{B}}{\partial t}=0\,, \tag{1.1}$$

$$\operatorname{div}\boldsymbol{B}=0\,, \tag{1.2}$$

$$\operatorname{rot}\boldsymbol{H}-\frac{\partial\boldsymbol{D}}{\partial t}=\boldsymbol{J}\,, \tag{1.3}$$

$$\operatorname{div}\boldsymbol{D}=\rho^* \tag{1.4}$$

where $\boldsymbol{J}$ and ρ^* are current and charge densities. From (1.3) and (1.4) we have the equation of continuity for the flow of electric charge

$$\operatorname{div}\boldsymbol{J}+\frac{\partial\rho^*}{\partial t}=0\,. \tag{1.5}$$

Between $\boldsymbol{E}$ and $\boldsymbol{D}$ on one hand, and $\boldsymbol{B}$ and $\boldsymbol{H}$ on the other we assume the usual linear relations

$$\boldsymbol{D}=\varepsilon\boldsymbol{E} \quad\text{and}\quad \boldsymbol{B}=\mu\boldsymbol{H} \tag{1.6}$$

with two constants ε and μ. In this article the MKS rational system of units is used throughout.

§ 2. Basic Equations

We consider a plasma which comprises several species of charged and neutral particles (electrons, ions, atoms) in which neither ionization nor recombination occurs. Let us denote by m_j, n_j and $\boldsymbol{v}_j$ the particle mass, the number density and the mean velocity of the jth species, respectively. Then the equation of continuity for the jth species is simply

$$\operatorname{div}(m_jn_j\boldsymbol{v}_j)+\frac{\partial m_jn_j}{\partial t}=0\,. \tag{2.1}$$

For each species we assume the Euler equation of motion

$$\frac{\partial}{\partial t}(m_jn_j\boldsymbol{v}_j)=e_jn_j(\boldsymbol{E}+\boldsymbol{v}_j\times\boldsymbol{B})-m_jn_j\operatorname{grad}\phi+\boldsymbol{R}_j-\operatorname{Div}(\mathbf{P}_j+m_jn_j\boldsymbol{v}_j\boldsymbol{v}_j) \tag{2.2}$$

($\operatorname{Div}_x\mathbf{P}\equiv\partial P_{xx}/\partial x+\partial P_{yx}/\partial y+\partial P_{zx}/\partial z$, etc.) Here e_j and $\mathbf{P}_j$ are, respectively, the particle electric charge and the partial-pressure tensor of jth species; $\boldsymbol{R}_j$ is the resistance acting on the jth species per unit volume; and ϕ is the gravitational potential. As regards $\boldsymbol{R}_j$ we consider only friction with other species, hence

$$\Sigma\boldsymbol{R}_j=0 \qquad (\Sigma\equiv\Sigma_j)\,. \tag{2.3}$$

Electric charge and current densities are given by

$$\rho^*=\Sigma e_jn_j \quad\text{and}\quad \boldsymbol{J}=\Sigma e_jn_j\boldsymbol{v}_j\,. \tag{2.4}$$

Let us introduce the mass density ρ and the mass-flow velocity $\boldsymbol{v}$ by the relation

$$\rho=\Sigma m_jn_j \quad\text{and}\quad \rho\boldsymbol{v}=\Sigma m_jn_j\boldsymbol{v}_j\,. \tag{2.5}$$

Then, adding all equations (2.1) together, we have

$$\operatorname{div}(\rho\boldsymbol{v})+\frac{\partial\rho}{\partial t}=0\,, \tag{2.6}$$

which is the equation of continuity of the mass-flow.

From (2.2) we obtain similarly

$$\frac{\partial}{\partial t}(\rho\boldsymbol{v})=\rho^*\boldsymbol{E}+\boldsymbol{J}\times\boldsymbol{B}-\rho\operatorname{grad}\phi-\operatorname{Div}(\mathbf{P}+\rho\boldsymbol{v}\boldsymbol{v})\,, \tag{2.7}$$

which is the equation of motion for the plasma as a whole. Here $\mathbf{P}$ is the total-pressure tensor which has connection with the partial pressure tensors as

$$\mathbf{P}+\rho\boldsymbol{v}\boldsymbol{v}=\Sigma(\mathbf{P}_j+m_jn_j\boldsymbol{v}_j\boldsymbol{v}_j)\,. \tag{2.8}$$

For gaseous plasma pressure tensors are given by

$$\mathbf{P}_j=m_jn_j\langle(\boldsymbol{c}_j-\boldsymbol{v}_j)(\boldsymbol{c}_j-\boldsymbol{v}_j)\rangle$$

and

$$\mathbf{P}=\Sigma m_jn_j\langle(\boldsymbol{c}_j-\boldsymbol{v})(\boldsymbol{c}_j-\boldsymbol{v})\rangle\,,$$

where $\boldsymbol{c}_j$ is particle velocity and $\langle\ \rangle$ means the average according to the velocity distribution (hence $\boldsymbol{v}_j=\langle\boldsymbol{c}_j\rangle$). Equation (2.8) can be derived by use of these relations, both sides being equal to $\Sigma m_jn_j\langle\boldsymbol{c}_j\boldsymbol{c}_j\rangle$. The equations (2.6) and (2.7) can be expressed in alternative forms

$$\left(\frac{\partial}{\partial t}+\boldsymbol{v}\cdot\operatorname{grad}\right)\rho+\rho\operatorname{div}\boldsymbol{v}=0\,, \tag{2.6a}$$

$$\rho\left(\frac{\partial}{\partial t}+\boldsymbol{v}\cdot\text{grad}\right)\boldsymbol{v}$$
$$=\rho^*\boldsymbol{E}+\boldsymbol{J}\times\boldsymbol{B}-\rho\,\text{grad}\,\phi-\text{Div}\,\mathbf{P}\,, \quad (2.7a)$$

in which $\partial/\partial t+\boldsymbol{v}\cdot\text{grad}$ is the so-called substantial derivative.

Multiplying (2.2) by e_j/m_j and taking summation over the subscript j we obtain a differential equation for the current density:

$$\frac{\partial \boldsymbol{J}}{\partial t}=\Sigma\frac{e_j^2n_j}{m_j}(\boldsymbol{E}+\boldsymbol{v}_j\times\boldsymbol{B})-\rho^*\,\text{grad}\,\phi+\Sigma\frac{e_j}{m_j}\boldsymbol{R}_j$$
$$-\text{Div}\,\Sigma\frac{e_j}{m_j}(\mathbf{P}_j+m_jn_j\boldsymbol{v}_j\boldsymbol{v}_j)\,. \quad (2.9)$$

This equation will be reduced to a simpler form in § 4.

§ 3. Energy and Momentum Theorems, Law of Similarity

From (2.2) we have

$$\Sigma\boldsymbol{v}_j\cdot\frac{\partial}{\partial t}(m_jn_j\boldsymbol{v}_j)=\boldsymbol{J}\cdot\boldsymbol{E}-\rho\boldsymbol{v}\cdot\text{grad}\,\phi+\Sigma\boldsymbol{v}_j\cdot\boldsymbol{R}_j$$
$$-\Sigma\boldsymbol{v}_j\cdot\text{Div}\,(\mathbf{P}_j+m_jn_j\boldsymbol{v}_j\boldsymbol{v}_j)\,,$$

which can be transformed into

$$\frac{\partial}{\partial t}\left(\Sigma\frac{1}{2}m_jn_jv_j^2+\phi\rho\right)=\boldsymbol{J}\cdot\boldsymbol{E}+\Sigma\boldsymbol{v}_j\cdot\boldsymbol{R}_j$$
$$-\Sigma\boldsymbol{v}_j\cdot\text{Div}\,\mathbf{P}_j-\text{div}\left(\Sigma\frac{1}{2}m_jn_jv_j^2\boldsymbol{v}_j+\phi\rho\boldsymbol{v}\right),$$

the left-hand side being the time rate of increase of the kinetic and potential energies per unit volume. From this equation and the energy theorem for electromagnetic field,

$$\frac{\partial}{\partial t}\left(\frac{1}{2}\boldsymbol{E}\cdot\boldsymbol{D}+\frac{1}{2}\boldsymbol{H}\cdot\boldsymbol{B}\right)=-\boldsymbol{J}\cdot\boldsymbol{E}-\text{div}\,(\boldsymbol{E}\times\boldsymbol{H})\,,$$

we obtain the energy theorem for the system composed of plasma and electromagnetic field:

$$\frac{\partial}{\partial t}\left(\Sigma\frac{1}{2}m_jn_jv_j^2+\phi\rho+\frac{1}{2}\boldsymbol{E}\cdot\boldsymbol{D}+\frac{1}{2}\boldsymbol{H}\cdot\boldsymbol{B}\right)$$
$$=\Sigma\boldsymbol{v}_j\cdot\boldsymbol{R}_j-\Sigma\boldsymbol{v}_j\cdot\text{Div}\,\mathbf{P}_j$$
$$-\text{div}\left(\Sigma\frac{1}{2}m_jn_jv_j^2\boldsymbol{v}_j+\phi\rho\boldsymbol{v}+\boldsymbol{E}\times\boldsymbol{H})\right). \quad (3.1)$$

First and second terms on the right-hand side are work done by the friction and by the partial pressure, respectively. It is to be noted that an equation for the heat flow must be considered if necessary.

The momentum theorem for the electromagnetic field is given by

$$\frac{\partial}{\partial t}(\varepsilon\mu\boldsymbol{E}\times\boldsymbol{H})=-(\rho^*\boldsymbol{E}+\boldsymbol{J}\times\boldsymbol{B})+\text{Div}\,\mathbf{T}\,,$$

where $\mathbf{T}$ is Maxwell's stress tensor. From this equation and the equation of motion (2.7) we obtain the momentum theorem for the system composed of plasma and electromagnetic field:

$$\frac{\partial}{\partial t}(\rho\boldsymbol{v}+\varepsilon\mu\boldsymbol{E}\times\boldsymbol{H})$$
$$=-\rho\,\text{grad}\,\phi-\text{Div}\,(\mathbf{P}+\rho\boldsymbol{v}\boldsymbol{v}-\mathbf{T})\,. \quad (3.2)$$

All the equations given in the foregoing are invariant with respect to the transformation

$$(\boldsymbol{r},t)\to s^{-1}(\boldsymbol{r},t)\,,$$
$$\varepsilon,\ \mu,\ \phi,\ m_j,\ e_j,\ \boldsymbol{v}_j \text{ unaltered},$$
$$(\boldsymbol{E},\boldsymbol{B},\boldsymbol{D},\boldsymbol{H})\to s(\boldsymbol{E},\boldsymbol{B},\boldsymbol{D},\boldsymbol{H})\,,$$
$$(\boldsymbol{J},\rho^*,\rho,n_j,\mathbf{P}_j,\mathbf{T})\to s^2(\boldsymbol{J},\rho^*,\rho,n_j,\mathbf{P}_j,\mathbf{T})\,,$$
$$\boldsymbol{R}_j\to s^3\boldsymbol{R}_j\,,$$

s being any positive number. This is a form of the similarity law.

§ 4. Two-Component and Quasi-Two-Component Systems

Among our basic equations (2.6), (2.7) and (2.9), the equation of electric current is most complicated. This equation, however, can be reduced to a simpler form in some cases by virtue of the fact that the mass of an electron is much smaller than those of other constituent particles.

We first consider the case where the plasma is a fully ionized gas composed of only electrons and one type of positive ion. Let the particle mass, particle charge and number density of electrons be m, $-e$ and n, respectively, and assume $en\gg|\rho^*|$. The mean velocities of positive ions and electrons are approximately equal to $\boldsymbol{v}$ and $\boldsymbol{v}-(en)^{-1}\boldsymbol{J}$ respectively. In the equation (2.9), $\Sigma e_j^2n_j/m_j$ can be replaced by e^2n/m, and $\Sigma e_j^2n_j\boldsymbol{v}_j/m_j$ by $e(en\boldsymbol{v}-\boldsymbol{J})/m$. The gravitation can usually be neglected. Let us assume that the friction $\boldsymbol{R}$ is proportional to the relative velocity between electron-fluid and ion-fluid; namely $\Sigma e_j\boldsymbol{R}_j/m_j$ is assumed to be proportional to the current density $\boldsymbol{J}$. Finally, $\Sigma(e_j/m_j)(\mathbf{P}_j+m_jn_j\boldsymbol{v}_j\boldsymbol{v}_j)$ has the meaning $\Sigma e_jn_j\langle\boldsymbol{c}_j\boldsymbol{c}_j\rangle$ in molecular terms. When the particle velocity $\boldsymbol{c}$ of electrons is much larger than the mean velocities and the velocity distribution of electrons is nearly isotropic, this quantity is reduced to a scalar $-eP_e/m$, P_e being the partial pressure of electrons. Thus in the two-component system under the above-mentioned

conditions we obtain the usual approximation

$$\frac{m}{e}\frac{\partial \boldsymbol{J}}{\partial t}=en\left(\boldsymbol{E}+\boldsymbol{v}\times\boldsymbol{B}-\frac{1}{\sigma}\boldsymbol{J}\right)-\boldsymbol{J}\times\boldsymbol{B}+\text{grad}\,P_e \tag{4.1}$$

to the equation of current. Here σ indicates the electric conductivity.

The approximation (4.1) holds not only for the two-component system but also for more general systems under the condition that all species of heavier constituents (ions and neutral atoms) have nearly equal mean velocities, which are therefore close to $\boldsymbol{v}$. This type of plasma may be called quasi-two-component. This condition is satisfied when the magnetic field is not very strong. Let us make an investigation for a slightly ionized gas.

We consider a slightly ionized gas at rest, which is uniform, steady and neutral as a whole. The gas is supposed to contain, besides neutral atoms, electrons and one type of monovalent positive ion. Let their number densities be both n, which is much smaller than the number density of neutral atoms. Then equations (2.2) for electrons and ions are

$$K_e(\boldsymbol{E}+\boldsymbol{v}_e\times\boldsymbol{B})-\boldsymbol{v}_e=0\ ,$$
$$K_i(\boldsymbol{E}+\boldsymbol{v}_i\times\boldsymbol{B})-\boldsymbol{v}_i=0\ ,$$

respectively. Here $\boldsymbol{v}_e$ aud $\boldsymbol{v}_i$ are mean velocities of electrons and ions, $K_e\equiv-|K_e|$ and K_i are mobilities of electrons and ions, respectively. From these equations we obtain

$$\boldsymbol{v}_e=(1+K_e^2B^2)^{-1}[K_e\boldsymbol{E}+K_e^2(\boldsymbol{E}\times\boldsymbol{B})+K_e^3(\boldsymbol{E}\cdot\boldsymbol{B})\boldsymbol{B}]$$

and

$$|\boldsymbol{v}_e|^2=K_e^2[E^2+K_e^2(\boldsymbol{E}\cdot\boldsymbol{B})^2]/(1+K_e^2B^2)$$

with similar expressions for the ion. Since $|K_e|\sim10^3K_i$ and

$$\frac{|\boldsymbol{v}_i|}{|\boldsymbol{v}_e|}\lesssim\frac{K_i}{|K_e|}(1+K_e^2B^2)^{1/2}$$

our condition is satisfied when $|K_eB|\ll10^3$.

Eqs. (2.6), (2.7), (4.1), and the Maxwell equations compose a system of basic equations for the usual plasma dynamics. The similarity law is that these equations are invariant with respect to the transformation

$$(\boldsymbol{r},\,t)\to s^{-1}(\boldsymbol{r},\,t)\ ,$$
$$\varepsilon,\ \mu,\ \phi,\ m/e,\ \boldsymbol{v}\ \text{unaltered},$$
$$(\boldsymbol{E},\,\boldsymbol{B},\,\boldsymbol{D},\,\boldsymbol{H},\,\sigma)\to s(\boldsymbol{E},\,\boldsymbol{B},\,\boldsymbol{D},\,\boldsymbol{H},\,\sigma)\ ,$$
$$(\boldsymbol{J},\,\rho^*,\,en,\,\rho,\,\mathbf{P},\,P_e)\to s^2(\boldsymbol{J},\,\rho^*,\,en,\,\rho,\,\mathbf{P},\,P_e)$$

with any positive number s.

§ 5. Transverse Plane Wave

As an example transverse plane wave will be treated in brief. Let us confine ourselves to the case of a neutral gravitation-free plasma in which the partial pressure of electrons is constant ($\rho^*=0$, grad $\phi=0$, grad $P_e=0$). Taking the z-axis in the direction of propagation we denote the x, y, z components of the vectors by

$$\boldsymbol{B}=(b_x(z,\,t),\ b_y(z,\,t),\ B_0)\ ,$$
$$\boldsymbol{J}=(J_x(z,\,t),\ J_y(z,\,t),\ 0)\ ,$$
$$\boldsymbol{v}=(v_x(z,\,t),\ v_y(z,\,t),\ 0)\ ,$$
$$\boldsymbol{E}=(E_x(z,\,t),\ E_y(z,\,t),\ 0)\ .$$

Here $\boldsymbol{B}_0\equiv(0,\,0,\,B_0)$ is a constant magnetic flux; and all other components are assumed to be so small that any product of them is negligible.

Using such notations as

$$b_x+ib_y=\tilde{b}\ ,\quad J_x+iJ_y=\tilde{J}\ ,\qquad \text{etc.},\ (i^2=-1)\ ,$$

we have from (1.1)

$$i\frac{\partial\tilde{E}}{\partial z}+\frac{\partial\tilde{b}}{\partial t}=0$$

and from (1.3)

$$i\frac{\partial\tilde{b}}{\partial z}-\varepsilon\mu\frac{\partial\tilde{E}}{\partial t}=\mu\tilde{J}\ .$$

Eliminating $\tilde{b}$ we obtain

$$\frac{\partial^2\tilde{E}}{\partial z^2}-\varepsilon\mu\frac{\partial^2\tilde{E}}{\partial t^2}=\mu\frac{\partial\tilde{J}}{\partial t}\ . \tag{5.1}$$

From the equation of motion (2.7), which reduces to

$$\rho\frac{\partial\boldsymbol{v}}{\partial t}=\boldsymbol{J}\times\boldsymbol{B}_0-\text{Div}\,\mathbf{P}$$

in the present case, we have

$$\rho\frac{\partial\tilde{v}}{\partial t}=-iB_0\tilde{J}+\eta\frac{\partial^2\tilde{v}}{\partial z^2}\ , \tag{5.2}$$

where use has been made of the relation

$$P_{zx}=-\eta\frac{\partial v_y}{\partial z}\ ,\quad P_{zy}=-\eta\frac{\partial v_y}{\partial z}$$

η being the coefficient of viscosity effective for the present phenomenon. Finally, from the current equation, which reduces to

$$\frac{m}{e}\frac{\partial\boldsymbol{J}}{\partial t}=en(\boldsymbol{E}+\boldsymbol{v}\times\boldsymbol{B}_0-\sigma^{-1}\boldsymbol{J})-\boldsymbol{J}\times\boldsymbol{B}_0\ ,$$

we have

$$\frac{m}{e}\frac{\partial\tilde{J}}{\partial t}=en(\tilde{E}-iB_0\tilde{v}-\sigma^{-1}\tilde{J})+iB_0\tilde{J}\ . \tag{5.3}$$

In order to get a dispersion relation we investigate the case in which (z, t)-dependence is such as $\exp(-i\omega t+ikz)$, thus

$$\tilde{E}=E_0 \exp(-i\omega t+ikz)\,, \qquad \text{etc.}$$

Then we have from (5.1)

$$(-k^2+\omega^2\mathcal{E}\mu)E_0=-i\omega\mu J_0\,,$$

from (5.2)

$$(\omega\rho+ik^2\eta)v_0=B_0J_0\,,$$

and from (5.3)

$$\left(\omega\frac{m}{e}+B_0+i\frac{en}{\sigma}\right)J_0=ienE_0+enB_0v_0\,.$$

Eliminating E_0, J_0, and v_0 we finally obtain the dispersion relation

$$\left(\omega\frac{m}{e}+B_0+i\frac{en}{\sigma}-\frac{enB_0^2}{\omega\rho+ik^2\eta}\right)(\omega^2\mathcal{E}\mu-k^2)=en\mu\omega. \tag{5.4}$$

In the particular case where damping due to the resistivity σ^{-1} and the viscosity η can be ignored, the equation becomes

$$\left(\omega\frac{m}{e}+B_0-\frac{en}{\omega\rho}B_0^2\right)(\omega^2\mathcal{E}\mu-k^2)=en\mu\omega\,. \tag{5.5}$$

Fig. 1, which shows this relation, clearly explains the well-known fact that the wave motion can exist in two separate regions of ω indicating the electric wave and the hydromagnetic wave.

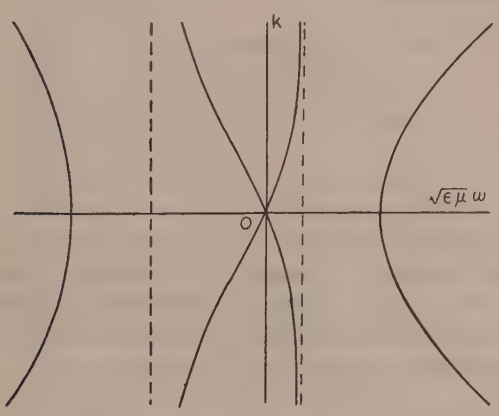

Fig. 1.

§ 6. Quasi-Stationary and Quasi-Static Phenomena in a Neutral Plasma

Let us consider the case where a neutral plasma satisfies the following three conditions: the displacement current in (1.3) is negligible, i.e.

$$\boldsymbol{J}=\text{rot}\,\boldsymbol{H}\,, \tag{6.1}$$

the electron inertia term in (4.1) is negligible; and grad n is parallel to grad P_e. Under these conditions we have from (4.1)

$$\text{rot}\,[\boldsymbol{E}+\boldsymbol{v}\times\boldsymbol{B}-(en)^{-1}\boldsymbol{J}\times\boldsymbol{B}-\sigma^{-1}\boldsymbol{J}]=0\,. \tag{6.2}$$

Substituting this relation into (1.1), we obtain

$$\frac{\partial\boldsymbol{B}}{\partial t}=\text{rot}\,(\boldsymbol{v}\times\boldsymbol{B})-\text{rot}\left(\frac{\boldsymbol{J}}{en}\times\boldsymbol{B}\right)-\text{rot}\frac{\boldsymbol{J}}{\sigma}$$

from which follows, by virtue of (6.1),

$$\frac{\partial\boldsymbol{B}}{\partial t}=\text{rot}\,(\boldsymbol{v}\times\boldsymbol{B})-\text{rot}\left(\frac{\boldsymbol{J}}{en}\times\boldsymbol{B}\right)-\frac{1}{\mu}\,\text{rot}\left(\frac{1}{\sigma}\,\text{rot}\,\boldsymbol{B}\right) \tag{6.3}$$

In many cases of importance the second term on the right-hand side vanishes or can be ignored. In quasi-static case, for example, where $\partial(\rho\boldsymbol{v})/\partial t$, $\boldsymbol{vv}$, rot $(n^{-1}\,\text{Div}\,\mathbf{P})$, and rot $(n^{-1}\rho\,\text{grad}\,\phi)$ are all small, we have an approximation to (2.7),

$$\text{rot}\,(n^{-1}\boldsymbol{J}\times\boldsymbol{B})=0\,. \tag{6.4}$$

Another example will be seen in the next section. When (6.4) holds true, Eqs. (6.2) and (6.3) reduce to

$$\text{rot}\,(\boldsymbol{E}+\boldsymbol{v}\times\boldsymbol{B}-\sigma^{-1}\boldsymbol{J})=0\,, \tag{6.5}$$

and

$$\frac{\partial\boldsymbol{B}}{\partial t}=\text{rot}\,(\boldsymbol{v}\times\boldsymbol{B})+\frac{1}{\mu\sigma}\nabla^2\boldsymbol{B} \tag{6.6}$$

($\nabla^2\equiv$grad div$-$rot rot), where the conductivity σ has been supposed to be uniform.

Eq. (6.6) is the so-called induction equation in hydromagnetics. In usual hydromagnetics Ohm's law in a magnetic field, $\boldsymbol{J}=\sigma(\boldsymbol{E}+\boldsymbol{v}\times\boldsymbol{B})$ is assumed as one of the basic equations, from which the induction equation is derived. The present assumption is not the Ohm's law itself but instead Eq. (6.5). The simple Ohm's law does not hold true in general and most results in hydromagnetics can be obtained by use of (6.5) instead of the simple ohm's law.

Within a perfectly conducting plasma Eq. (6.6) is reduced to

$$\frac{\partial\boldsymbol{B}}{\partial t}=\text{rot}\,(\boldsymbol{v}\times\boldsymbol{B})\,,$$

which, as pointed out by Alfvén[2], shows that the lines of magnetic flux are "frozen in" the material.

§ 7. An Axially Symmetric Solution

We consider quasi-stationary neutral plasma with axial symmetry assuming that no gravitational force is acting. By use of cylindrical

coordinates r, φ, z with respect to the axis, all the quantities are supposed to be independent of φ and z and furthermore of the form

$$(B_r, B_\varphi, B_z)=(0, B_\varphi(r, t), B_z(r, t)) ,$$
$$(J_r, J_\varphi, J_z)=(0, J_\varphi(r, t), J_z(r, t)) , \qquad (7.1)$$
$$(v_r, v_\varphi, v_z)=(v_r(r, t), v_\varphi(r, t), v_z(r, t)) .$$

The equation of continuity for the electric current, (1.5), is satisfied identically since $\rho^*=0$. The equation of continuity for the mass-flow, (2.6), becomes

$$\frac{1}{r}\frac{\partial}{\partial r}(r\rho v_r)+\frac{\partial\rho}{\partial t}=0 . \qquad (7.2)$$

Denoting unit vectors in the direction of (r, φ, z) by $(\boldsymbol{u}_r, \boldsymbol{u}_\varphi, \boldsymbol{u}_z)$ we have in general

$$\mathrm{Div}\,\mathbf{P}=\frac{1}{r}\frac{\partial}{\partial r}(r\boldsymbol{u}_r\cdot\mathbf{P})$$
$$+\frac{1}{r}\frac{\partial}{\partial\varphi}(\boldsymbol{u}_\varphi\cdot\mathbf{P})+\frac{\partial}{\partial z}(\boldsymbol{u}_z\cdot\mathbf{P}) .$$

Since

$$\boldsymbol{u}_r\cdot\mathbf{P}=P_{rr}\boldsymbol{u}_r+P_{r\varphi}\boldsymbol{u}_\varphi+P_{rz}\boldsymbol{u}_z , \qquad \text{etc.}$$

and

$$\partial\boldsymbol{u}_\varphi/\partial\varphi=-\boldsymbol{u}_r , \quad \partial\boldsymbol{u}_r/\partial\varphi=\boldsymbol{u}_\varphi ,$$

and furthermore since all components of $\mathbf{P}$ in the present coordinate system are independent of φ and z, we obtain

$$\mathrm{Div}\,\mathbf{P}=\boldsymbol{u}_r\left[\frac{1}{r}\frac{\partial}{\partial r}(rP_{rr})-\frac{1}{r}P_{\varphi\varphi}\right]$$
$$+\boldsymbol{u}_\varphi\left[\frac{1}{r}\frac{\partial}{\partial r}(rP_{r\varphi})+\frac{1}{r}P_{\varphi r}\right]$$
$$+\boldsymbol{u}_z\frac{1}{r}\frac{\partial}{\partial r}(rP_{rz})$$

or

$$\mathrm{Div}\,\mathbf{P}=\boldsymbol{u}_r\left[\frac{\partial}{\partial r}P_{rr}+\frac{1}{r}(P_{rr}-P_{\varphi\varphi})\right]$$
$$+\boldsymbol{u}_\varphi\frac{1}{r^2}\frac{\partial}{\partial r}(r^2P_{r\varphi})$$
$$+\boldsymbol{u}_z\frac{1}{r}\frac{\partial}{\partial r}(rP_{rz}) ,$$

where the symmetry relation $P_{r\varphi}=P_{\varphi r}$ has been used. Similarly,

$$\mathrm{Div}\,(\rho\boldsymbol{vv})=\boldsymbol{u}_r\left[\frac{1}{r}\frac{\partial}{\partial r}(r\rho v_r^2)-\frac{\rho}{r}v_\varphi^2\right]$$
$$+\boldsymbol{u}_\varphi\left[\frac{1}{r}\frac{\partial}{\partial r}(r\rho v_r v_\varphi)+\frac{\rho}{r}v_r v_\varphi\right]$$
$$+\boldsymbol{u}_z\frac{1}{r}\frac{\partial}{\partial r}(r\rho v_r v_z) .$$

By use of these expressions the equation of motion (2.7),

$$\frac{\partial}{\partial t}(\rho\boldsymbol{v})-\boldsymbol{J}\times\boldsymbol{B}+\mathrm{Div}\,(\mathbf{P}+\rho\boldsymbol{vv})=0$$

can be evaluated. The r-component is

$$\rho\left(\frac{\partial}{\partial t}+v_r\frac{\partial}{\partial r}\right)v_r-\frac{\rho}{r}v_\varphi^2+\frac{\partial}{\partial r}\left(\frac{B^2}{2\mu}+P_{rr}\right)$$
$$+\frac{B_\varphi^2}{\mu r}+\frac{1}{r}(P_{rr}-P_{\varphi\varphi})=0 , \qquad (7.3)$$

where the relation $\mu\boldsymbol{J}=\mathrm{rot}\,\boldsymbol{B}$ has been used and $B^2=B_\varphi^2+B_z^2$. The φ- and z-components are

$$\rho\left(\frac{\partial}{\partial t}+v_r\frac{\partial}{\partial r}\right)v_\varphi+\frac{\rho}{r}v_r v_\varphi+\frac{1}{r^2}\frac{\partial}{\partial r}(r^2P_{r\varphi})=0 \qquad (7.4)$$

and

$$\rho\left(\frac{\partial}{\partial t}+v_r\frac{\partial}{\partial r}\right)v_z+\frac{1}{r}\frac{\partial}{\partial r}((rP_{rz})=0 \qquad (7.5)$$

respectively.

In these equations $\partial/\partial t+v_r\cdot\partial/\partial r$ is the substantial derivative, $\rho v_\varphi^2/r$ is the centrifugal force, $-\rho v_r v_\varphi/r$ is (a part of) the Coriolis force. Eq. (7.3) simply explains the well-known fact that magnetic flux has a hydrostatic pressure of the amount $B^2/2\mu$ plus a longitudinal tension B^2/μ. It can be shown that Eqs. (7.3) and (7.5) agree with the Navier-Stokes equation if a constant isotropic viscosity η is introduced by

$$P_{rr}=P+\frac{2}{3}\eta\,\mathrm{div}\,\boldsymbol{v}-2\eta\frac{\partial v_r}{\partial r} ,$$
$$P_{\varphi\varphi}=P+\frac{2}{3}\eta\,\mathrm{div}\,\boldsymbol{v}-2\eta\frac{v_r}{r} ,$$
$$P_{r\varphi}=-\eta r\frac{\partial}{\partial r}\left(\frac{v_\varphi}{r}\right), \quad P_{rz}=-\eta\frac{\partial v_z}{\partial r} .$$

In reality, however, the plasma viscosity is not necessarily isotropic in a magnetic field.

Eq. (6.4) is identically satisfied in the present case and (6.5) holds. Hence we have the induction equation (6.6) which becomes

$$\frac{\partial B_\varphi}{\partial t}=-\frac{\partial}{\partial r}(v_rB_\varphi)+\frac{\partial}{\partial r}\left(\frac{1}{\mu\sigma}\frac{1}{r}\frac{\partial}{\partial r}(rB_\varphi)\right) , \qquad (7.6)$$

$$\frac{\partial B_z}{\partial t}=-\frac{1}{r}\frac{\partial}{\partial r}(rv_rB_z)+\frac{1}{r}\frac{\partial}{\partial r}\left(\frac{r}{\mu\sigma}\frac{\partial B_z}{\partial r}\right) . \qquad (7.7)$$

Within a perfectly conducting plasma we obtain, from these equations and the equation of continuity (7.2),

$$\left(\frac{\partial}{\partial t}+v_r\frac{\partial}{\partial r}\right)\frac{B_\varphi}{r\rho}=0 \tag{7.8}$$

and

$$\left(\frac{\partial}{\partial t}+v_r\frac{\partial}{\partial r}\right)\frac{B_z}{\rho}=0\,. \tag{7.9}$$

Thus B_z and B_φ/r are proportional to the mass density at a substantial point of the fluid flowing with the velocity $\boldsymbol{v}$. The ratio B_φ/rB_z is invariant at any substantial point:

$$\left(\frac{\partial}{\partial t}+v_r\frac{\partial}{\partial r}\right)\frac{B_\varphi}{rB_z}=0\,. \tag{7.10}$$

As an important example let us consider a fully ionized plasma column with both longitudinal and circular currents. We assume that no current is flowing outside the plasma and that magnetic field in region distant from the column in weak. When the longitudinal current is increased the plasma column is compressed or "pinched" by the newly increased magnetic flux circling the current. As the pinch advances the longitudinal flux B_z within the plasma becomes dominant in comparison with the circular flux B_φ, because B_φ/rB_z is invariant at any substantial point. When the increase of current occurs rapidly, newly added current flows near the surface and the distribution of the flux may become such as shown in Fig. 2. As a result a self-

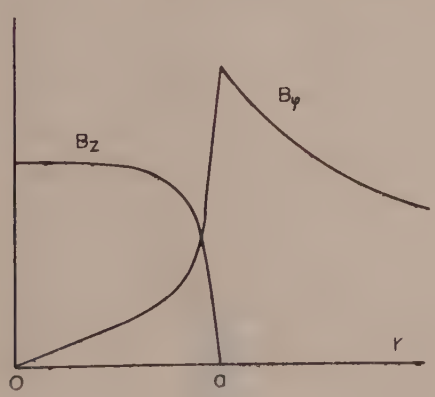

Fig. 2.

pinched plasma can be represented by an idealized model with sheet current

$$\sigma=\begin{cases}\infty & \text{for } 0\leq r<a\\ 0 & \text{for } r<a\,,\end{cases}$$

$$(B_r,\,B_\varphi,\,B_z)=\begin{cases}0,\,0,\,P_0) & \text{for } 0\leq r<a\\ 0,\,P_1a/r,\,0) & \text{for } r>a\,,\end{cases} \tag{7.11}$$

where $a(t)$ is the radius of the column, B_0 and B_1 are functions of t only. We also assume the density to be uniform in the plasma.

Let us confine ourselves to the case where $v_\varphi=v_z=0$ and the inertia term in (7.3), $\rho(\partial/\partial t+v_r\cdot\partial/\partial r)v_r$, can be neglected. Then the distribution of particle velocities in the plasma may be isotropic within a plane perpendicular to the z-axis:

$$P_{rr}=P_{\varphi\varphi}(\neq P_{zz}\text{ in general}) \tag{7.12}$$

(compare Watson[4]). Hence P_{rr} is uniform for $r<a$. Since sum of material and magnetic pressures must be equal on both sides of the column boundary in equilibrium, we obtain

$$P_{rr}+(2\mu)^{-1}B_0^2=(2\mu)^{-1}B_1^2 \tag{7.13}$$

assuming $P=0$ outside the column. The total flux Φ frozen in the column is πa^2B_0 which is constant; the total longitudinal current I is given by $\mu I=2\pi aB_1$. Inserting these into (7.13) we have

$$P_{rr}+\frac{1}{2\mu}\left(\frac{\Phi}{\pi a^2}\right)^2=\frac{\mu}{2}\left(\frac{I}{2\pi a}\right)^2. \tag{7.14}$$

When P_{rr} is proportional to ρ^γ or $a^{-2\gamma}$ with $\gamma<2$, the magnetic-pressure term on the left-hand side becomes predominant as the pinch progresses; and hence the radius of a highly pinched column is inversely proportional to the total longitudinal current. The ratio P_{rr}/ρ which is proportional to $\rho^{\gamma-1}$ or $a^{-2(\gamma-1)}$, is a measure of the plasma temperature. The temperature of a highly pinched column is therefore proportional to $I^{2(\gamma-1)}$. For $\gamma=2$, it is easy to see that both the density and the temperature are proportional to I^2.

§ 8. Stability of a Self-pinched Plasma

A column of very large current is compressed or "pinched" by the magnetic flux circling the current. But this pinched column is unstable: any small constriction and any small kink will grow[5)-7)]. A known idea to stabilize (to some extent at least) the pinched column is to create not only a pinching magnetic field around the plasma but also a strong longitudinal magnetic field within the plasma column. Although Shrafranov[8)] has discussed the problem mathematically, an elementary explanation will be helpful. We consider a column of perfectly conducting neutral plasma which has radius a in equilibrium. The pressure outside the column is assumed to be zero. The sheet current model (7.11) with the condi-

tion (7.13) in equilibrium will be treated.

If the column suffers quasi-statically a gently-sloping small constriction and the radius becomes $a(1-\delta)$ at one part, then $\boldsymbol{B}$ will become at this part

$$(0,\ 0,\ B_0(1-\delta)^{-2}) \quad \text{for} \quad 0 \leqq r < a(1-\delta)\ ,$$
$$(0,\ B_1 a/r,\ 0) \quad \text{for} \quad r > a(1-\delta)\ .$$

The sum of material and magnetic pressures in the column is $P_{rr}+B_0^2(1-\delta)^{-4}/2\mu$ or $P_{rr}+B_0^2(1+4\delta)/2\mu$ for small δ; the magnetic pressure just outside the boundary is $B_1^2(1-\delta)^{-2}/2\mu$ or $B_1^2(1+2\delta)/2\mu$ for small δ. Hence the condition for stability against gently-sloping constrictions is $2B_0^2 > B_1^2$.

For sharply-sloping constrictions the magnetic flux in the plasma is denser near the boundary surface than near the axis; hence the stability condition is less severe. In conclusion, therefore, the column (7.11) is stable against constrictions if $2B_0^2 > B_1^2 (> B_0^2)$ and unstable otherwise. The result agrees with that of Shrafranov's analytical treatment.

Although sufficiently strong longitudinal magnetic flux stabilizes a plasma column against constrictions, it does not stabilize the column against gently-curving kink, as shown by Shrafranov. The situation can be explained in an elementary way. When the column suffers a gently-curving kink with radius of curvature R, then the force due to the longitudinal flux is $\pi a^2 B_0^2/\mu R$ per unit length, which acts in the direction of stabilization. It will be shown that this quantity is smaller than the destabilizing force due to the pinching magnetic flux when a/R is sufficiently small.

Supposing that a kinked column of radius a forms a circle of radius $R(\gg a)$, we choose a quantity δ such as $a \ll \delta R \ll R$. Then the force acting on the part δR of the circle is directed outward, and it can be calculated by use of Biot-Savart's law. Let the total longitudinal current be I, then the force is equal to (compare Fig. 3a)

$$\frac{\mu I^2}{4\pi}\int_0^\delta\int_{\delta-\xi}^{2\pi-\xi} \frac{\sin(\theta/2)}{[2R\sin(\theta/2)]^2} R^2 d\theta d\xi$$
$$= \frac{\mu I^2}{4\pi}\int_0^\delta\int_{\delta-\xi}^{2\pi-\xi} \frac{d\theta}{4\sin(\theta/2)} d\xi$$
$$= -\frac{\mu I^2}{4\pi}\int_0^\delta \ln\tan\frac{\xi}{4} d\xi$$
$$\fallingdotseq -\frac{\mu I^2}{4\pi}\int_0^\delta \ln\frac{\xi}{4} d\xi$$
$$= \frac{\mu I^2}{4\pi}\,\delta\left(\ln\frac{4}{\delta}+1\right).$$

Since $\mu I = 2\pi a B_1$ the destabilizing force is

$$\pi a^2 B_1^2 \mu^{-1}\delta[\ln(4/\delta)+1]\ ,$$

which is greater than the stabilizing force acting on this part $\pi a^2 B_0^2 \mu^{-1}\delta$, which is directed inward. Hence the present plasma is unstable against gently-curving kinks.

This kink instability of a plasma column with longitudinal electric current and magnetic flux can not be avoided by an external magnetic flux parallel to the axis. When the column kinks gently in such a way as shown in Fgi. 3b, point A moves toward this side and

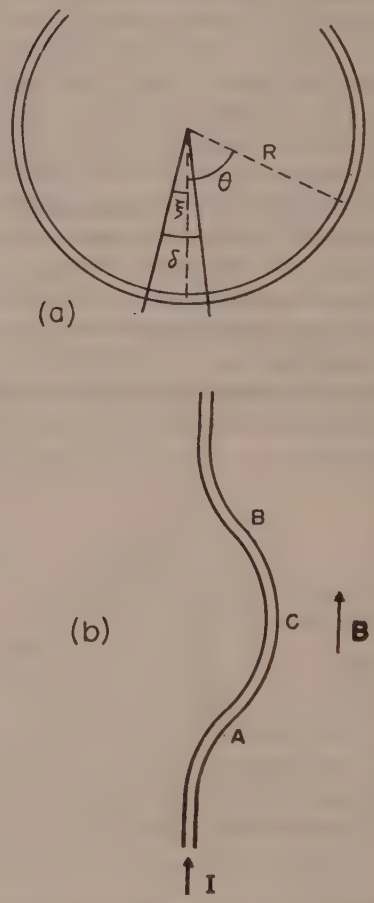

Fig. 3.

B that side. Hence the column becomes helix-like, and, at a point C, the Lorentz force acts toward outside. For a helix with long spatial period, this outward force predominates, resulting in an instability of the plasma column. (For a helix with constant A and $\tan\theta$,

$$x = A\cos\tau\ ,\quad y = A\sin\tau\ ,\quad z = A\tau\tan\theta\ ,$$

the curvature is given by $\cos^2\theta/A$; and the sine of the angle between z-axis and a tangent to the helix is $\cos\theta$. If a column of plasma kinks into this helix under the condition $a/A \ll 1 \ll \tan\theta$, then the stabilizing force due to the magnetic tension, which is proportional to $\cos^2\theta/A$, is less effective than the unstabilizing Lorentz force which is proportional to $\cos\theta$.)

When the plasma is constricted in a tube with a conducting wall and the radius of the tube is sufficiently small compared with that of the plasma column, then the column is expected to be stable against any mode of deformation. The condition of stability was recently calculated by Tayler[9] and independently by the present author. For the sheet-current model (7.11) in a tube of radius b and for the displacement which is proportional to $\exp(ikz+im\varphi)$ with $k>0$ and an integer m as regards z and φ dependencies, the column is stable if and only if B_0^2/B_1^2 is greater than the value given by

$$\frac{B_0^2}{B_1^2}=\frac{I_m'(ka)}{kaI_m(ka)}[1+m^2F(ka,kb)]\,, \tag{8.1}$$

$$F=-\frac{K_m(ka)I_m'(kb)-I_m(ka)K_m'(kb)}{ka[K_m'(ka)I_m'(kb)-I_m'(ka)K_m'(kb)]}\,.$$

Here $I_m(x)$ and $K_m(x)$ are the modified Bessel functions and $I_m'(x)\equiv dI_m/dx$, etc. Curves are shown in Fig. 4. (Modes of deformation with $m\geqq 2$ are more stable.) Since B_0^2/B_1^2 must be smaller than 1, the column is unstable (against kink for which $m=1$) when $b>5a$. For $b=4a$ the necessary and sufficient condition for stability is $B_0^2/B_1^2>0.82$; for $b=3a$ it is $B_0^2/B_1^2>0.60$.

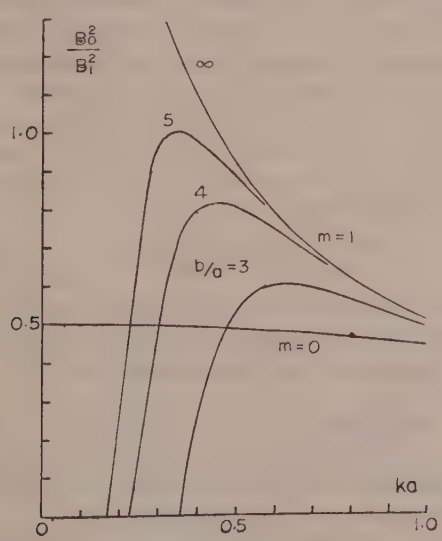

Fig- 4.

Without making results greatly complicated, we can generalize the model (7.11) to

$$(B_r, B_\varphi, B_z)=\begin{cases}(0,\ B_0\alpha r,\ B_0) & \text{for } 0\leqq r<a\\ (0,\ B_1a/r,\ B_2) & \text{for } a<r<b\,.\end{cases} \tag{8.2}$$

Here B_0, B_1 and B_2 are constants and αa is assumed to be so small that its square may be neglected (compare Fig. 2 for $B_2=0$). Then the pressure in the plasma is uniform as in the foregoing and the equilibrium condition is

$$P_{rr}+(2\mu)^{-1}B_0^2=(2\mu)^{-1}(B_1^2+B_2^2)\,. \tag{8.3}$$

A relation giving the critical value of B_0^2/B_1^2 for stability is the following:

$$\frac{B_0^2}{B_1^2}\left(1+\frac{2m\alpha}{k}\right)=\frac{1}{(ka)^2}\left[\frac{kaI_m'(ka)}{I_m(ka)}+\frac{2m\alpha}{k}\right]\times\left[1+\left(m+ka\frac{B_2}{B_1}\right)^2F(ka,kb)\right], \tag{8.4}$$

which is a generalization of (8.1).

The author wishes to thank Prof. I. Imai, Prof. G. Miyamoto, and Mr. Y. Midzuno for useful discussions.

References

1) L. Spitzer: *Physics of Fully Ionized Gases* (Interscience Publishers, 1956).
2) H. Alfvén: *Cosmical electrodynamics* (Oxford 1950).
3) T. G. Cowling: *Magnetohydrodynamics* (Interscience Publishers, 1957). See also S. I. Surovatskij: Uspehi Fiz. Nauk **62** (1957) 247.
4) K. M. Watson: Phys. Rev. **102** (1956) 12, Eq. (44).
5) R. F. Post: Revs. Modern Phys. **28** (1956) 338; Scientific American (December, 1957).
6) M. D. Kruskal and M. Schwarzschild: Proc. Roy. Soc. (London) **A223** (1954) 348.
7) R. J. Tayler: Proc. Phys. Soc. **B70** (1957) 31.
8) V. D. Shrafranov: Atomnaya Energia **1** (1956) 38 or J. Nuclear Energy II **5** (1957) 86.
9) R. J. Tayler: Proc. Phys. Soc. **B70** (1957) 1049.

JOURNAL OF THE PHYSICAL SOCIETY OF JAPAN Vol. 13, No. 5, MAY, 1958

Externally Pinched Plasma

By Tihiro OHKAWA and Taro KIHARA

Department of Physics, Faculty of Science, University of Tokyo

(Received February 6, 1958)

A new process of pinching a plasma column is treated theoretically. A column of plasma with no longitudinal current can be pinched by an external magnetic field parallel to the column; and the plasma thus pinched will not show any instability. The process depends on the effective value of γ, the ratio of specific heats. For $\gamma=2$ in particular, the temperature of a perfectly conducting plasma with no heat loss will rise in proportion to the external magnetic field.

The self-pinched plasma column with longitudinal current has been well investigated both theoretically and experimentally as a possible method of achieving thermonuclear reaction. A known method of making the plasma stable is to create a longitudinal magnetic flux within the plasma, and surround the column with a tube with a conducting wall. The condition for the stability is that the radius of the tube must be smaller than five times the radius of the plasma column in an ideal case.[1)2)] Because of this severe condition, another method is needed.

A preferable approach is to use a plasma column with no longitudinal current and pinch the column with external magnetic field parallel to the column.

The field may be produced by a solenoid energized by a discharge of a condenser bank or an impulse generator. Closed current will be induced in the plasma and the plasma will be compressed radially by the Lorentz force $\boldsymbol{J}\times\boldsymbol{B}$. The system has a larger inductance than the usual self-pinched plasma and hence requires a larger stored energy in the power supply.

In the following, this type of pinch effect is discussed. We consider a neutral plasma in which both the displacement current and the inertia term of the electron mass motion can be neglected (quasi-stationary neutral plasma).[2)]

The equation of continuity and the equation of motion for the plasma flow are

$$\mathrm{div}\,(\rho\boldsymbol{v})+\partial\rho/\partial t=0\,, \qquad (1)$$

and

$$\rho[\partial\boldsymbol{v}/\partial t+(\boldsymbol{v}\cdot\mathrm{grad})\boldsymbol{v}]=\boldsymbol{J}\times\boldsymbol{B}-\mathrm{Div}\,\mathbf{P}\,, \qquad (2)$$

respectively [Eqs. (2.6) and (2.7a) of reference 2]. Here ρ is the density of the fluid; $\boldsymbol{v}$ is the flow velocity; $\boldsymbol{J}\times\boldsymbol{B}$ is the Lorentz force density on the neutral plasma; $-\mathrm{Div}\,\mathbf{P}$ is the mechanical force density. In addition to these comes the equation

$$\frac{\partial\boldsymbol{B}}{\partial t}=\mathrm{rot}\,(\boldsymbol{v}\times\boldsymbol{B})+\frac{1}{\mu\sigma}\nabla^2\boldsymbol{B}-\mathrm{rot}\,[(\mathrm{en})^{-1}\boldsymbol{J}\times\boldsymbol{B}] \qquad (3)$$

($\nabla^2\equiv\mathrm{grad\ div}-\mathrm{rot\ rot}$) [Eq. (6.3) of reference 2]. Here $-e$ is the electron charge, n the number density of electrons, and σ the electrical conductivity assumed to be uniform.

By use of a cylindrical coordinate system (r,φ,z) we investigate the case in which all the quantities are independent of φ and z, $\boldsymbol{B}$ has only the z-component $B(r,t)$, and $\boldsymbol{v}$ has only the r-component $v(r,t)$. Then the current density $\boldsymbol{J}$ has only the φ-component $J(r,t)$. As the domain of the independent variables we choose $0\leqq r<R$ and $t>0$. In this case the last term of (3) vanishes and we have

$$\frac{\partial B}{\partial t}=-\frac{1}{r}\frac{\partial}{\partial r}(rvB)+\frac{1}{\mu\sigma}\frac{1}{r}\frac{\partial}{\partial r}\left(r\frac{\partial B}{\partial r}\right). \qquad (3a)$$

Eq. (1) becomes

$$\frac{1}{r}\frac{\partial}{\partial r}(rv\rho)+\frac{\partial\rho}{\partial t}=0\,. \qquad (1a)$$

If the isotropy of the pressure tensor in (r,φ)-plane, is assumed, $P_{rr}=P_{\varphi\varphi}$, and the r-component of Eq. (2) becomes,

$$\rho\left(\frac{\partial v}{\partial t}+v\frac{\partial v}{\partial r}\right)+\frac{\partial}{\partial r}\left(P_{rr}+\frac{B^2}{2\mu}\right)=0\,, \qquad (2a)$$

$B^2/2\mu$ being the so-called magnetic pressure. [Compare Eq. (7.3) of reference 2].

As an idealized model let us consider a perfectly conducting fully ionized cylindrical plasma of radius $a(<R)$, a being a function of the time t, which is "pinched" by the external magnetic pressure. We namely assume the conductivity to be

$$\sigma=\begin{cases}\infty & \text{for} \quad 0\leqq r<a\\ 0 & \text{for} \quad a<r<R;\end{cases}$$

the magnetic flux density B and the pressure P are assumed to be continuous

$$B=\begin{cases}B(r,t)\\ B(a,t)\end{cases} \quad P_{rr}=\begin{cases}P_{rr}(r,t) & \text{for } 0\leqq r<a\\ P_{rr}(a,t)\equiv 0 & \text{for } a<r<R\,.\end{cases}$$

Inside the plasma we then have, from (3a) and (1a),

$$\left(\frac{\partial}{\partial t}+v\frac{\partial}{\partial r}\right)B+\frac{B}{r}\frac{\partial}{\partial r}(rv)=0\,, \tag{3b}$$

$$\left(\frac{\partial}{\partial t}+v\frac{\partial}{\partial r}\right)\rho+\frac{\rho}{r}\frac{\partial}{\partial r}(rv)=0\,, \tag{1b}$$

from which we obtain

$$\left(\frac{\partial}{\partial t}+v\frac{\partial}{\partial r}\right)\frac{B}{\rho}=0\,, \tag{4}$$

[Eq. (7.9) of reference 2]. The magnetic flux density is proportional to the fluid density at any substantial point of the fluid flowing with the radial velocity v. Eq. (2a) is reduced, at such high pressures as the inertia term may be neglected, to

$$P_{rr}(r,t)+(2\mu)^{-1}B(r,t)^2=(2\mu)^{-1}B(a,t)^2\,. \tag{5}$$

Now we will suppose the adiabatic condition to be satisfied. When the pressure is isotropic, it is proportional to ρ^γ (hence to B^γ) at any substantial point of the fluid, γ being the ratio of the specific heats, 5/3. The plasma temperature is determined by P/ρ; it is proportional to $\rho^{\gamma-1}$ (hence to $B^{\gamma-1}$) at any substantial point. A relation between B at a substantial point and the external $B(a,t)$ can be found from (5). In the part of the domain where the magnetic pressure is much smaller than the fluid pressure the flux density B at a substantial point is proportional to $B(a,t)^{2/\gamma}$, and hence the temperature to $B(a,t)^{2-2/\gamma}$. Under very high magnetic pressures, on the other hand, the B at a substantial point is close to the external $B(a,t)$, and hence the plasma temperature is proportional to $B(a,t)^{\gamma-1}$.

Our assumption of perfect conductivity may be close to the reality when the plasma is pinched suddenly. For a sudden radial compression, however, the pressure is not isotropic; P_{rr} and $P_{\varphi\varphi}$ are larger than P_{zz}. In this case P_{rr} is nearly proportional to ρ^γ with γ somewhat larger than 5/3.

For $\gamma=2$ in particular there exists a simple solution of our equations. If we namely assume the "similar compression"

$$v=\frac{r}{a}\frac{da}{dt}\,, \tag{6}$$

we obtain from (3b) and (1b)

$$\left(\frac{\partial}{\partial t}+v\frac{\partial}{\partial r}\right)(a^2B)=0\,, \tag{7}$$

and

$$\left(\frac{\partial}{\partial t}+v\frac{\partial}{\partial r}\right)(a^2\rho)=0\,, \tag{8}$$

which indicate that both a^2B and $a^2\rho$ at a substantial point are constant. In particular, $a^2B(a,t)$ is independent of the time (see Fig. 1). Taking Eq. (5) into account we know that

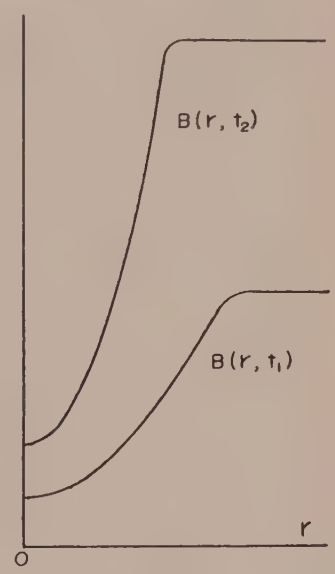

Fig. 1.

P_{rr} at a substantial point is proportional to a^{-4} or ρ^2. Hence the assumption (6) corresponds to $\gamma=2$. In this case *the temperature at any substantial point rises simply in proportion to the external magnetic field.* It is to be noted that the general solution of (7) is

$$a^2B=f(r/a)\,,$$

f being any differential function, and then

$$P_{rr}=\frac{1}{2\mu}B(a,t)^2\left[1-\frac{f(r/a)^2}{f(1)^2}\right].$$

The authors wish to thank Prof. G. Miyamoto and Dr. G. Iwata for useful discussions.

References

1) R. J. Tayler: Proc. Phys. Soc. **B 70** (1957) 1049.
2) T. Kihara: J. Phys. Soc. Japan **13** (1958) 473.

JOURNAL OF THE PHYSICAL SOCIETY OF JAPAN Vol. 13, No. 5, MAY, 1958

The Arc Spectrum of Iodine and the Quadrupole Moment of I^{127}

By Kiyoshi MURAKAWA

Institute of Science and Technology, University of Tokyo, Komaba-machi, Meguro-ku, Tokyo

(Received January 20, 1958)

The analysis of the arc spectrum of iodine has been continued, and the identification of the term sequence $(^3P_2)nf$ has been fairly well completed, and some other levels newly detected. From the hyperfine structure of $(^3P_2)7p\,^4D_{7/2}$ the quadrupole moment without shielding correction was found to be $Q'(I^{127})=-0.63$ barn, whereas the value that was deduced from $(^3P)6s\,^4P_{5/2}$ previously was $Q'(I^{127})=-0.71$ barn. The mean of these two values is $Q'(I^{127})=-0.67\pm0.04$ barn. This is in agreement with the value $Q'(I^{127})=-0.66$ barn that is deduced from the hfs of the ground term $5p^5\ ^2P_{3/2}$ whose measurement is given in the literature. Assuming the shielding correction $\Delta=-0.07$, the true quadrupole moment $Q(I^{127})=-0.62$ barn has been obtained.

§ 1. Introduction

About twenty years ago the author analysed the spark spectrum of iodine (I II) and published a preliminary description of I I[1] (referred to as Part I in the following: all the previous literatures are quoted there). Suwa and the author (to be referred to as Part II) improved the light source and extended the analysis of I I[2].

Schmidt[3] (to be referred to as S) analysed the hyperfine structure (hfs) of I I for the first time and calculated the quadrupole moment (Q) of I^{127}, while the author calculated $Q(I^{127})$ from the hfs of I II[4]. Eshbash and Fisher[5] (to be referred to as EF) studied the far infra-red spectrum of I I; their result will be quoted later.

The purpose of the present paper is to extend the analysis of I I published in Parts I and II, to review critically the wave functions used in Part II in order to calculate Q, and to obtain Q from the hfs of $(^3P_2)7p\,^4D_{7/2}$ whose wave function can be regarded as simple.

§ 2. Experimental Procedure

The light source used was an electrodeless discharge tube described in Part II, the technique of the high frequency being similar to that of Lacroute[6]. The red part of the spectrum was photographed with a plane grating equipped with a large concave mirror. The dispersion was 8A/mm in the first order and 4A/mm in the second. This grating gives strong intensity only in the red and green region. In order to obtain wave length standard a small amount of neon was sometimes mixed with iodine. In the region shorter than λ4600 the spectrum was photographed with a two-prism spectrograph having a camera-lens with one-meter focal length.

The infra-red plates that are available (since 1945) in this country are sensitive only to the region λ7900–6700 and the sensitivity falls off rapidly from λ8100 towards longer wave length, although that of the pre-war plates reached λ10000. In the region λ7544–5000 in which the neon lines are abundant the wave length was measured directly against neon standards. In the region longer than λ7544 in which neon lines are scarce, data that were obtained with plates taken with the same plane grating equipped with a lens of shorter focal length were utilized.

In order to resolve the hfs a Fabry-Pérot etalon was used, which was crossed with the prism spectrograph. In the infra-red region lines are crowded in a space of low dispersion, so the hfs had to be measured using thin spacers, except in a very few strong and isolated lines.

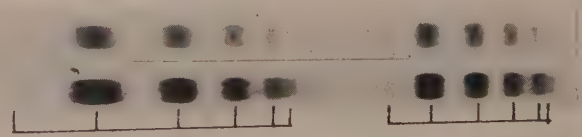

Fig. 1. Enlargement of the interference pattern of I I λ4862, taken with a 8mm etalon. Two copies of a same plate are shown. One was printed with medium strength; the other was printed somewhat strongly.

An example of the interference pattern of the spectaum of iodine is shown in Fig. 1.

§ 3. Analysis of the Arc Spectrum of Iodine

In order to test whether the wave function of $(^3P)7p\,^4D_{7/2}$ is perturbed or not the level $(^1D)6p^2F_{7/2}$ must be detected. For this purpose the hfs of the levels $(^1D)6p^2F_{7/2}$ and $(^3P)5d^4D_{5/2}$ were approximately calculated assuming that they are not perturbed, and then the hfs of the transition $(^3P)5d^4D_{5/2}-(^1D)6p^2F_{7/2}$ was constructed. Then a line having the desired hfs was searched, and it was at once found that only $\lambda 7700$ satisfies this condition (see Fig. 2). The hfs of the lines having $(^3P)5d^4D_{5/2}$ as the final level was studied and it was found that the hfs splittings of $(^3P)5d^4D_{5/2}$ are identical with those of the level with $J=5/2$ contained in $\lambda 7700$ within the accuracy of 0.02 cm^{-1}. It was therefore concluded that $\lambda 7700$ corresponds to the above-mentioned transition. In a similar way other lines were classified. In Figs. 3–7 hfs of some lines which served as key to the classification are shown. Most of them are situated either close to strong lines or close to each other, so the hfs given in Figs. 2–7 serve merely to prove the classification, and do not claim any great accuracy.

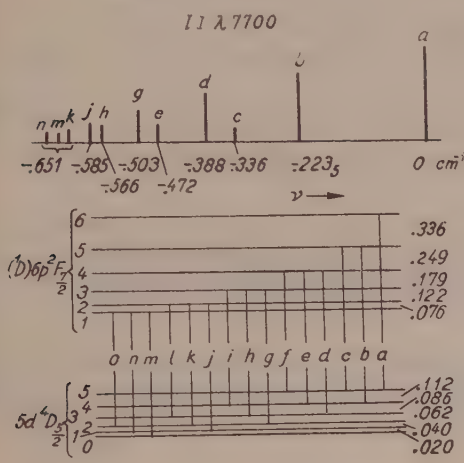

Fig. 2. Hfs of the line $\lambda 7700$.

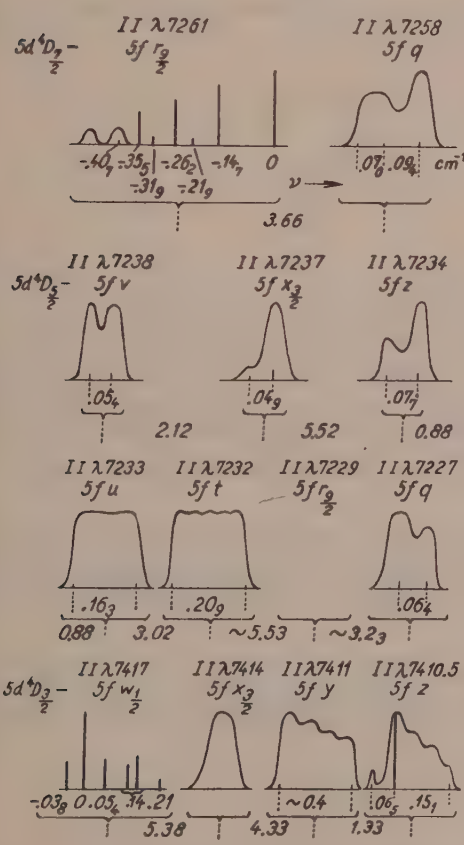

Fig. 3. Hfs of the lines of the transitions $5d\,^4D_{7/2,\ 5/2,\ 3/2}-5f$.

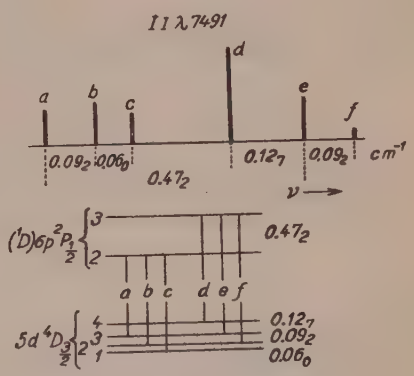

Fig. 4. Hfs of the line $\lambda 7491$.

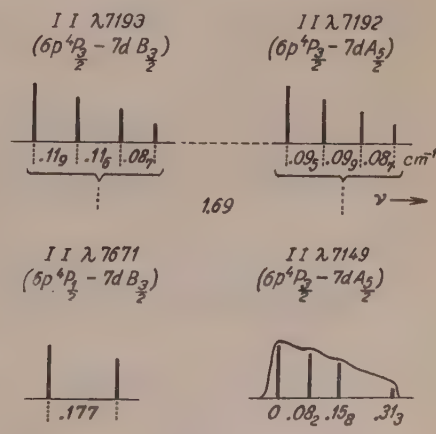

Fig. 5. Hfs of the lines $\lambda\lambda 7193$, 7192, 7671 and 7149.

Table I Spectrum of I I in the region λ14460–4690

Int.	λ(air)	ν(vac)	Term combination		Int.	λ(air)	ν(vac)	Term combination	
(80)	14460.19	6913.64	$6p\ ^4P_{3/2}$—$7s\ ^4P_{5/2}$	EF**	1	7414.62	13483.16	$6s\ ^2P_{3/2}$—$7p\ ^4P_{1/2}$	
(170)	14287.22	6997.35	$6p\ ^4D_{7/2}$—$7s\ ^4P_{5/2}$	EF*	5	7413.63	13484.96	$5d\ ^4D_{3/2}$—$5f\ x_{3/2}$	
(40)	13958.37	7162.21	$5d\ ^4F_{5/2}$—$4f\ X_{7/2}$	EF	2	7411.25	13489.29	$5d\ ^4D_{3/2}$—$5f\ y$	
(520)	11236.45	8897.18	$6s\ ^4P_{3/2}$—$6p\ ^4P_{3/2}$	EF**	2.5	7410.52	13490.62	$5d\ ^4D_{3/2}$—$5f\ z$	
(2190)	10466.60	9551.59	$6s\ ^4P_{5/2}$—$6p\ ^4P_{5/2}$ (?)	FE	6	7402.12	13505.93		
(680)	10238.91	9763.99	$6s\ ^4P_{3/2}$—$6p\ ^4P_{1/2}$	EF	1	7305.50	13684.55	$5d\ ^4D_{3/2}$—$(^1D)6p\ ^2D_{3/2}$	
1.5 (2480)	9731.80	10272.78	$6s\ ^4P_{5/2}$—$6p\ ^4D_{7/2}$	EF*	1	7260.61	13770.18	$5d\ ^4D_{7/2}$—$5f\ r_{9/2}$	
1 (1280)	9653.14	10356.49	$6s\ ^4P_{5/2}$—$6p\ ^4P_{3/2}$	EF**	2	7258.14	13773.85	$5d\ ^4D_{7/2}$—$5f\ q$	
(140)	9427.02	10604.90	$6s\ ^4P_{1/2}$—$6p\ ^4D_{1/2}$	EF**	1	7243.66	13801.37	$6s\ ^2P_{3/2}$—$7p\ ^4D_{3/2}$	
4 (240)	9335.13	10709.29	$6s\ ^2P_{3/2}$—$6p\ ^2D_{5/2}$	EF	1	7237.94	13812.28	$5d\ ^4D_{5/2}$—$5f\ v$	
10 (580)	9113.91	10969.23	$6s\ ^4P_{3/2}$—$6p\ ^4D_{3/2}$	EF	5	7236.83	13814.40	$5d\ ^4D_{5/2}$—$5f\ x_{3/2}$	
0.5 (30)	9098.95	10987.27	$6s\ ^2P_{3/2}$—$6p\ ^2D_{3/2}$	EF**	1	7233.94	13819.92	$5d\ ^4D_{5/2}$—$5f\ z$	
8 (1840)	9058.35	11036.52	$(^1D)6s\ ^2D_{5/2}$—$5f\ x_{3/2}$	EF	1	7233.48	13820.80	$5d\ ^4D_{5/2}$—$5f\ u$	
4 (100)	9022.49	11080.38	$6s\ ^4P_{1/2}$—$6p\ ^4S_{3/2}$	EF	3	7231.90	13823.82	$5d\ ^4D_{5/2}$—$5f\ t$	
4	8898.40	11234.89	$6s\ ^2P_{3/2}$—$6p\ ^2P_{3/2}$		0.5	7229.01	13829.35	$5d\ ^4D_{5/2}$—$5f\ r_{9/2}$	
5	8857.45	11286.83	$\begin{cases} 5d\ ^4D_{5/2}—4f\ X_{7/2} \\ 6s\ ^2D_{3/2}—5f\ w_{1/2} \end{cases}$		2	7227.32	13832.58	$5d\ ^4D_{5/2}$—$5f\ q$	
					4	7192.59	13899.38	$6p\ ^4P_{3/2}$—$7d\ B_{3/2}$	
5	8853.36	11292.05	$(^1D)6s\ ^2D_{3/2}$—$5f\ x_{3/2}$		4	7191.71	13901.07	$6p\ ^4P_{3/2}$—$7d\ A_{5/2}$	
5	8393.45	11910.78	$6s\ ^4P_{1/2}$—$6p\ ^2D_{3/2}$		5	7148.66	13984.78	$6p\ ^4D_{7/2}$—$7d\ A_{5/2}$	
15 (90)	8043.78	12428.55	$6s\ ^4P_{5/2}$—$6p\ ^4D_{3/2}$	EF	2	7063.68	14153.03	$6s\ ^4P_{1/2}$—$7p\ ^4P_{3/2}$	
0.5	8042.1	12431.1	$6s\ ^2P_{1/2}$—$7p\ ^4D_{3/2}$		1	6993.6	14294.8	$6s\ ^4P_{1/2}$—$7p\ ^4D_{5/2}$	
6	8003.67	12490.84	$6s\ ^4P_{1/2}$—$6p\ ^2P_{1/2}$		2	6939.36	14406.58	$6s\ ^4P_{1/2}$—$7p\ ^4P_{1/2}$	
1	7972.85	12539.12	$5d\ ^4D_{1/2}$—$5f\ w_{1/2}$		2	6789.32	14724.96	$6s\ ^4P_{1/2}$—$7p\ ^4D_{3/2}$	
4	7969.53	12544.35	$5d\ ^4D_{1/2}$—$5f\ x_{3/2}$		5	6732.08	14850.16	$5d\ ^4D_{3/2}$—$6f\ q$	
10	7700.24	12983.04	$5d\ ^4D_{5/2}$—$(^1D)6p\ ^2F_{7/2}$		3	6726.97	14861.44	$5d\ ^4D_{3/2}$—$6f\ v$	
8	7670.98	13032.56	$6p\ ^4P_{1/2}$—$7d\ B_{3/2}$		2	6698.51	14924.58	$6p\ ^4P_{3/2}$—$(^1D)5d\ ^2D_{5/2}$	
6	7556.73	13229.60	$6s\ ^2P_{3/2}$—$7p\ ^4P_{3/2}$		5	6661.14	15008.31	$6p\ ^4D_{7/2}$—$(^1D)5d\ ^2D_{5/2}$	
6	7554.31	13233.84			7	6619.62	15102.44		***
3	7490.62	13346.36	$5d\ ^4D_{3/2}$—$(^1D)6p\ ^2P_{1/2}$		6	6585.27	15181.22	$5d\ ^4D_{5/2}$—$6f\ r$	
7	7469.08	13384.85			8	6583.71	15184.82	$5d\ ^4D_{5/2}$—$6f\ t$	
2	7416.59	13479.58	$5d\ ^4D_{3/2}$—$5f\ w_{1/2}$		4	6582.84	15186.82	$5d\ ^4D_{5/2}$—$6f\ u$	

Int.	λ(air)	ν(vac)	Term combination	
3	6580.46	15192.32	$5d\ ^4D_{5/2}-6f\ w$	
1	6577.51	15199.13	$5d\ ^4D_{5/2}-6f\ x$	
10	6566.44	15224.75	$6s\ ^2P_{1/2}-(^1D)6p\ ^2P_{3/2}$	
5	6488.15	15408.46	$6s\ ^4P_{3/2}-6p\ ^4D_{1/2}$	
1	6433.40	15539.59	$6s\ ^2P_{3/2}-4f\ W_{5/2}$	
3	6378.72	15672.80	$5d\ ^4D_{3/2}-7f\ q$	
1	6376.38	15678.56	$5d\ ^4D_{3/2}-7f\ t$	
9	6371.68	15690.12	$6p\ ^4P_{3/2}-7d\ C_{5/2}$	
10	6359.10	15721.16	$6s\ ^4P_{3/2}-6p\ ^2S_{1/2}$	
3	6355.71	15729.54	$6p\ ^4P_{5/2}-(^1D)5d\ ^2D_{5/2}$	
10	6339.44	15769.91		
5	6337.86	15773.84	$6p\ ^4D_{7/2}-7d\ C_{5/2}$	
5	6330.35	15792.56	$6p\ ^4P_{3/2}-(^1D)5d\ ^2F_{5/2}$	
4	6296.97	15876.27	$6p\ ^4D_{7/2}-(^1D)5d\ ^2F_{5/2}$	
10	6293.91	15883.99	$6s\ ^4P_{3/2}-6p\ ^4S_{3/2}$	
3	6246.03	16005.75	$5d\ ^4D_{5/2}-7f\ r$	
1.5	6245.24	16007.77	$5d\ ^4D_{5/2}-7f\ t$	
1	6244.49	16009.69	$5d\ ^4D_{5/2}-7f\ u$	
4	6244·36	16010.03	$5d\ ^4D_{5/2}-7f\ v$	
1.5	6243.90	16011.21	$5d\ ^4D_{5/2}-7f\ w$	
1.5	6243.05	16013.39	$5d\ ^4D_{5/2}-7f\ x$	
1.5	6242.57	16014.62	$5d\ ^4D_{5/2}-7f\ y$	
6	6191.89	16145.70		****
15	6082.409	16436.31	$6s\ ^4P_{3/2}-6p\ ^2D_{5/2}$	
3	6056.04	16507.88	$5d\ ^4D_{5/2}-8f\ q$	
2	6055.14	16510.34	$6s\ ^4P_{1/2}-4f\ V_{3/2}$	
2	6054.09	16513.20	$5d\ ^4D_{5/2}-8f\ r$	
2.5	6053.65	16514.40	$5d\ ^4D_{5/2}-8f\ t$	

Int.	λ(air)	ν(avc)	Term combination	
2.5	6053.47	16514.89	$5d\ ^4D_{5/2}-8f\ u$	
10	6024.04	16595.57	$6s\ ^2P_{3/2}-(^1D)6p\ ^2P_{3/2}$	
0.5	6005.93	16645.61	$6s\ ^2P_{1/2}-5f\ w_{1/2}$	
1	6004.99	16648.21	$6s\ ^2P_{1/2}-5f\ x_{3/2}$	
0	6002.70	16654.57	$6s\ ^2P_{1/2}-5f\ y$	
2	5984.25	16705.91	$6p\ ^4P_{3/2}-9s\ ^4P_{5/2}$	
1	5954.42	16789.61	$6p\ ^4D_{7/2}-9s\ ^4P_{5/2}$	
8	5893.98	16961.77	$6s\ ^4P_{3/2}-6p\ ^2P_{3/2}$	
0	5882.22	16995.68	$6s\ ^2P_{3/2}-8p\ ^4P_{3/2}$ (?)	
3	5780.63	17294.37	$6s\ ^4P_{3/2}-6p\ ^2P_{1/2}$	
10	5764.32	17343.30	$6s\ ^4P_{5/2}-6p\ ^4S_{3/2}$	
9	5586.67	17894.79	$6s\ ^4P_{5/2}-6p\ ^2D_{5/2}$	
1	5546.36	18024.8	$6s\ ^2P_{3/2}-5f\ y$	P
2	5500.92	18173.7	$6s\ ^4P_{3/2}-6p\ ^2D_{3/2}$	P
8	5427.04	18421.14	$6s\ ^4P_{5/2}-6p\ ^2P_{3/2}$	
0	5297.33	18872.2	$6s\ ^4P_{3/2}-7p\ ^4P_{5/2}$	P
1	5273.75	18956.6	$6s\ ^4P_{3/2}-7p\ ^4P_{3/2}$	P
10	5234.58	19098.43	$6s\ ^4P_{3/2}-7p\ ^4D_{5/2}$	
7	5204.14	19210.14	$6s\ ^4P_{3/2}-7p\ ^4P_{1/2}$	
15	5119.28	19528.57	$6s\ ^4P_{3/2}-7p\ ^4D_{3/2}$	
10	4916.98	20332.03	$6s\ ^4P_{5/2}-7p\ ^4P_{5/2}$	
8	4896.76	20415.98	$6s\ ^4P_{5/2}-7p\ ^4P_{3/2}$	
1	4863.03	20557.6	$6s\ ^4P_{5/2}-7p\ ^4D_{5/2}$	P
20	4862.31	20560.63	$6s\ ^4P_{5/2}-7p\ ^4D_{7/2}$	
10	4763.35	20987.78	$6s\ ^4P_{5/2}-7p\ ^4D_{3/2}$	
0.5	4712.51	21214.2		P
6	4700.94	21266.41	$6s\ ^4P_{3/2}-4f\ W_{5/2}$	
6	4690.60	21313.29	$6s\ ^4P_{3/2}-4f\ V_{3/2}$	

EF: wave length according to Eshbach and Fisher; the intensity given by EF is shown in parentheses.
* classification according to EF.
** classification of EF somewhat modified.
*** hfs narrow.
**** hfs similar to λ7402.
P: wave length measured with prisms only.

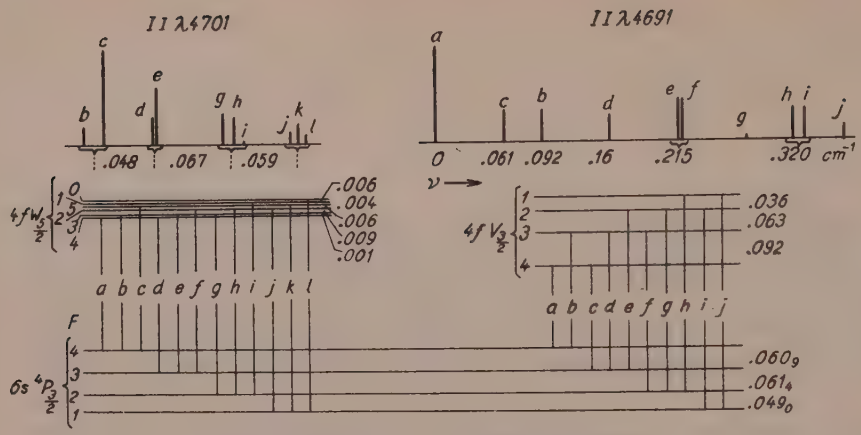

Fig. 6. Hfs of the lines λλ4701 and 4691.

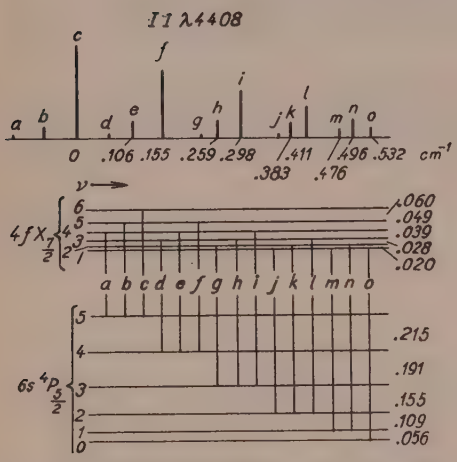

Fig. 7. Hfs of the line λ4408. The upper level has two levels in the neighborhood, so it should be perturbed. The accuracy of the measurement was not sufficient for detecting this perturbation, however.

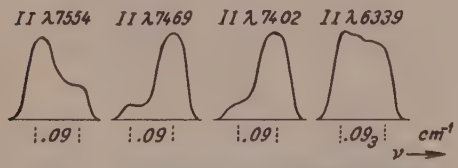

Fig. 8. Hfs of four unclassified lines.

All the classified lines of I I in the region λ14460–4690 are listed in Table I. Unclassified lines with intensity larger than 5 are also listed, with the indication of their hfs either in footnote or in Fig. 8. It will be seen that the hfs of these unclassified lines are of poor value for the classification, but it may be concluded that none of them contains any level with $J=1/2$. All the lines of I I in the region shorter than λ4500 with intensity larger than 2 were contained in Table I of Part II, so they will not be repeated here. Some supplement is given in Table II in which all the unclassified lines in this region with intensity larger than 0.5 (they are only four in number) are also listed.

All the terms of I I that have been hitherto detected are given in Table III. The first column lists the labels of terms adopted in the present work (and also in Parts II and I). They were named so that analogy with the spectrum of F I is good, although none of the terms of I I is of LS-coupling. In case where the label of Part II is changed, the old one is given in square brackets. The second column lists the values of levels measured from the ground level of I II, while in the third column distances from the ground level of I I ($5p^{62}P_{3/2}$) are given.

Table II. Supplement to the list of the Spectrum of I I in the violet region (λ4500—3600)

Int.	λ(air)	ν(vac)	Term combination
3	4409.20	22673.5	$6s\ ^4P_{5/2}$—$4f\ R$
10	4408.04	22679.5	$6s\ ^4P_{5/2}$—$4f\ X_{7/2}$
1	4406.54	22687.2	$6s\ ^4P_{5/2}$—$4f\ Q$
0	4389.96	22772.9	$6s\ ^4P_{5/2}$—$4f\ V_{3/2}$
1	4384.03	22803.7	
4	4203.75	23781.6	$6s\ ^4P_{5/2}$—$(^1D)6p\ ^2P_{3/2}$
2	4159.73	24033.3	$6s\ ^4P_{3/2}$—$(^1D)6p\ ^2D_{5/2}$
1	4069.49	24566.2	
1	4059.23	24628.3	
0.5	3846.42	25990.9	
0.5	3827.33	26120.5	

Most of the J-values of the levels $(^3P_2)\ 5f$ could not be determined by the hfs data alone except in $5fw_{1/2}$ and $5f\ r_{9/2}$ where the hfs

Table III. Term-value of I I

$5p\ ^2P_{3/2}$	84260.8	0
$5p\ ^2P_{1/2}$	76658.1	7602.7
$(^3P_2)6s\ ^4P_{5/2}$	29630.8	54630.0
$(^3P_2)6s\ ^4P_{3/2}$	28171.5	56089.3
$(^3P_0)6s\ ^4P_{1/2}$	23367.9	60892.9
$(^3P_1)6s\ ^2P_{3/2}$	22444.5	61816.3
$(^3P_1)6s\ ^2P_{1/2}$	21073.6	63187.2
$(^1D)6s\ ^2D_{5/2}$	15460.7	68800.1
$(^1D)6s\ ^2D_{3/2}$	15716.2	68544.6
$(^3P_2)5d\ ^4D_{7/2}$	18179.5	66081.3
$(^3P_2)5d\ ^4D_{5/2}$	18238.6	66022.2
$(^3P_2)5d\ ^4D_{3/2}$	17909.2	66351.6
$(^3P_2)5d\ ^4D_{1/2}$	16968.5	67292.3
$(^3P_2)5d\ ^4F_{5/2}$	14113.5	70147.3
$(^1D)5d\ ^2F_{5/2}$	3481.7	80779.1
$(^1D)5d\ ^2D_{5/2}$	4349.7	79911.1
$(^3P_2)7s\ ^4P_{5/2}$	12360.7	71900.1
$(^3P_2)7s\ ^4P_{3/2}$	11961.5	72299.3
$(^3P_2)9s\ ^4P_{5/2}$	2568.4	81692.4
$7d\ B_{3/2}$	5374.9	78885.9
$7d\ A_{5/2}$	5373.2	78887.6
$7d\ C_{5/2}$	3584.2	80676.6
$(^3P_2)6p\ ^4D_{7/2}$	19358.0*	64902.8
$(^3P_2)6p\ ^4D_{5/2}$	—	
$(^3P_2)6p\ ^4D_{3/2}$	17202.2	67058.6
$(^3P_2)6p\ ^4P_{5/2}$	20079.2(?)	64181.6(?)
$(^3P_2)6p\ ^4P_{3/2}$	19274.3**	64986.5
$(^3P_2)6p\ ^4P_{1/2}$	18407.5	65853.3
$(^3P_{1,0})6p\ ^4D_{1/2}$	12763.0	71497.8
$(^3P_{1,0})6p\ ^4S_{3/2}$	12287.5	71973.3
$(^3P_{1,0})6p\ ^2D_{5/2}$	11735.2	72525.6
$(^3P_{1,0})6p\ ^2D_{3/2}$	11457.2	72803.6
$(^3P_{1,0})6p\ ^2P_{3/2}$	11209.6	73051.2
$(^3P_{1,0})6p\ ^2P_{1/2}$	10877.1	73383.7
$(^3P_{1,0})6p\ ^2S_{1/2}$	12450.3	71810.5
$(^1D)6p\ ^2F_{7/2}$	5255.6	79005.2
$(^1D)6p\ ^2F_{5/2}$	4138.2	80122.6
$(^1D)6p\ ^2D_{3/2}$	4224.2[Y]	80036.6
$(^1D)6p\ ^2P_{3/2}$	5848.9	78411.9
$(^1D)6p\ ^2P_{1/2}$	4562.9	79697.9
$(^3P_2)7p\ ^4D_{7/2}$	9070.2	75190.6
$(^3P_2)7p\ ^4D_{5/2}$	9073.1	75187.7
$(^3P_2)7p\ ^4D_{5/2}$	8642.9	75617.9
$(^3P_2)7p\ ^4P_{5/2}$	9299.0	74961.8
$(^3P_2)7p\ ^4P_{3/2}$	9214.9	75045.9
$(^3P_2)7p\ ^4P_{1/2}$	8961.5	75299.3
$(^3P_2)8p\ ^4D_{7/2}$	5420.4	78840.4
$(^3P_2)8p\ ^4D_{5/2}$	5410.0	78850.8
$(^3P_2)8p\ ^4D_{3/2}$	5039.9	79220.9
$(^3P_2)8p\ ^4P_{5/2}$	5531.8	78729.0
$(^3P_2)8p\ ^4P_{3/2}$	5448.8	78812.0
$(^3P_2)9p\ ^4D_{7/2}$	3603.2	80657.6
$(^3P_2)9p\ ^4D_{5/2}$	3801.4	80459.4
$(^3P_2)9p\ ^4D_{3/2}$	3466.4	80794.4
$(^3P_2)4f\ R_{(5/2)}$	6957.3	77303.5
$(^3P_2)4f\ X_{7/2}$	6951.3	77309.5
$(^3P_2)4f\ Q$	6943.6	77317.2
$(^3P_2)4f\ W_{5/2}$	6905.1	77355.7
$(^3P_2)4f\ V_{3/2}$	6858.2	77402.6
$(^3P_2)5f\ w_{1/2}$	4429.6	79831.2
$(^3P_2)5f\ v_{(9/2)}$	4426.3	79834.5
$(^3P_2)5f\ x_{3/2}$	4424.2	79836.6
$(^3P_2)5f\ y_{(5/2)}$	4419.9	79840.9
$(^3P_2)5f\ z_{(7/2)}$	4418.6	79842.2
$(^3P_2)5f\ u_{(5/2)}$	4417.8	79843.0
$(^3p_2)5f\ t_{(3/2)}$	4414.8	79846.0
$(^3P_2)5f\ r_{(3/2)}$	4409.3	79851.5
$(^2P_2)5f\ q_{(7/2)}$	4406.0	79854.8
$(^3P_2)6f\ q$	3059.0	81201.8
$(^3P_2)6f\ r$	3057.4	81203.4
$(^3P_2)6f\ t$	3053.8	81207.0
$(^3P_2)6f\ u$	3051.8	81209.0
$(^3P_2)6f\ v$	3047.8	81213.0
$(^3P_2)6f\ w$	3046.3	81214.5
$(^3P_2)6f\ x$	3039.5	81221.3
$(^3P_2)7f\ q$	2236.4	82024.4
$(^3P_2)7f\ r$	2232.9	82027.9
$(^3P_2)7f\ t$	2230.8	82030.0
$(^3P_2)7f\ u$	2228.9	82031.9
$(^3P_2)7f\ v$	2228.6	82032.2
$(^3P_2)7f\ w$	2227.4	82033.4
$(^3P_2)7f\ x$	2225.2	82035.6
$(^3P_2)7f\ y$	2224.0	82036.8
$(^3P_2)8f\ q$	1730.7	82530.1
$(^3P_2)8f\ r$	1725.4	82535.4
$(^3P_2)8f\ t$	1724.2	82536.6
$(^3P_2)8f\ u$	1723.7	82537.1

* according to EF.

** according to EF. EF call this level $6p\ ^4P_{5/2}$, but the J-value 5/2 is not consistent with the hfs of λ7193 and λ7192 (see Fig. 5).

data allow us to determine J uniquely and in $5f\ x_{3/2}$ where the combination relations seem to justify the J-determination. It was tried to determine the J-values by comparison with the theory of Condon and Shortley[7], but, since some indications of existence of small perturbations were apparent, this was abandoned. The J-values that seem to fit the hfs data qualitatively but are not altogether unique are given in parentheses.

§ 4. Quadrupole Moment of I^{127}

In order to confirm the hfs of $6s^4P_{5/2}$, hfs of further lines were measured. Since the hfs of the level $6s^4P_{3/2}$ was accurately determined in Part II, λ6294 and λ5894 having the same final level were measured (see Fig. 9) and the hfs of the initial levels determined. Then the hfs of the lines ending on $6s^4P_{5/2}$ and starting with the same levels were measured (see Fig. 10), and the hfs of $6s^4P_{5/2}$ given

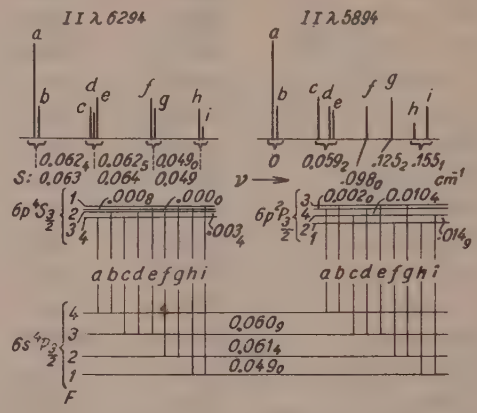

Fig. 9. Hfs of the lines $\lambda\lambda$6294 and 5894.

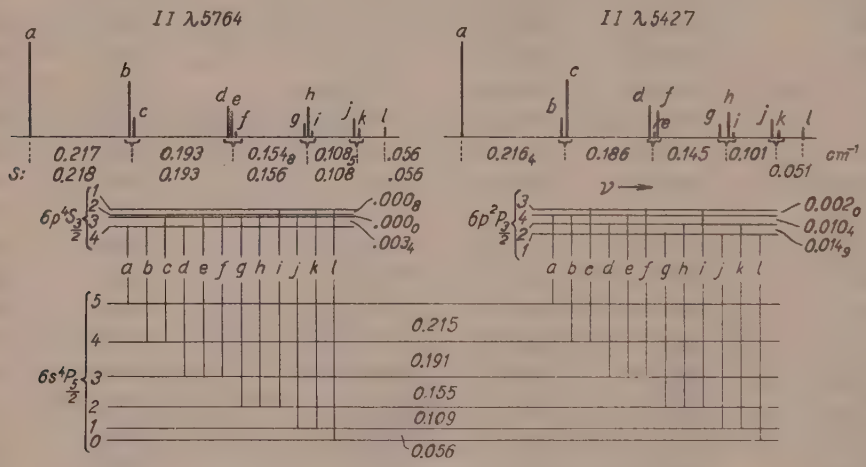

Fig. 10. Hfs of the lines $\lambda\lambda$5764 and 5427.

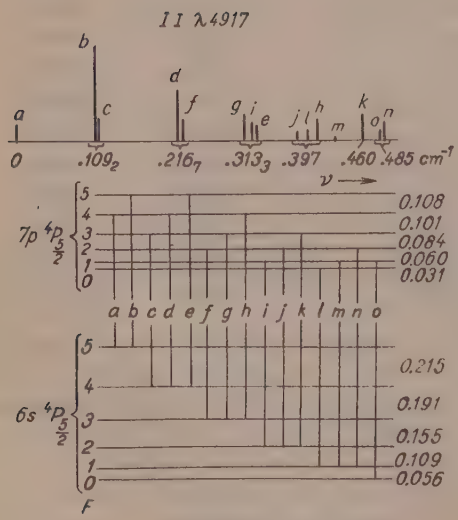

Fig. 11. Hfs of the line λ4917.

in Part II or by Schmidt was confirmed. Also the complicated hfs of λ4917 can be interpreted using the same hfs of $6s^4P_{5/2}$ (see Fig. 11).

The hfs of λ4862 and λ4129 are given in Fig. 12. Both of them are qualitatively identical. The initial level of λ4862 namely $(^3P_2)7p\ ^4D_{7/2}$ is close to $(^3P_2)7p\ ^4D_{5/2}$, which is characteristic of jj-coupling. The hfs of the latter level is obtained from λ5235 (see Fig. 13) in which the components are so close together that the accuracy of measurement is not great. The amount of perturbation in $7p^4D_{7/2}$ can be calculated, using the theory of Casimir[8]. The hfs levels of $7p\ ^4D_{7/2}$ $F=5$, 4, 3, 2 and 1 are pushed upwards by the amount 0.003, 0.004, 0.003, 0.002 and 0.001 cm^{-1} respectively

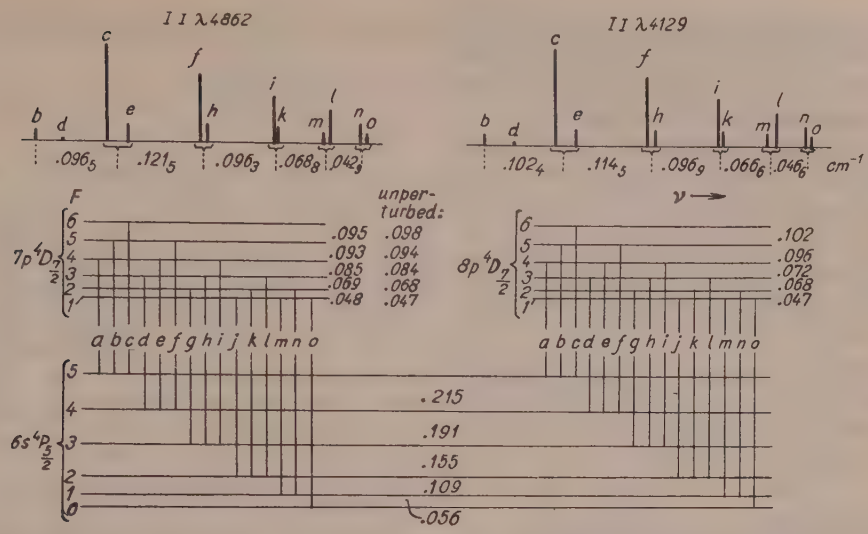

Fig. 12. Hfs of the lines λλ4862 and 4129. The accuracy of measurement of λ4129 is somewhat inferior to that of λ4862, so that no attempt was made to calculate Q from the hfs of the level $8p\,^4D_{7/2}$. *Correction*: The splitting of $8p\ ^4D_{7/2}$, $F=4-3$ should read .084 instead of .072.

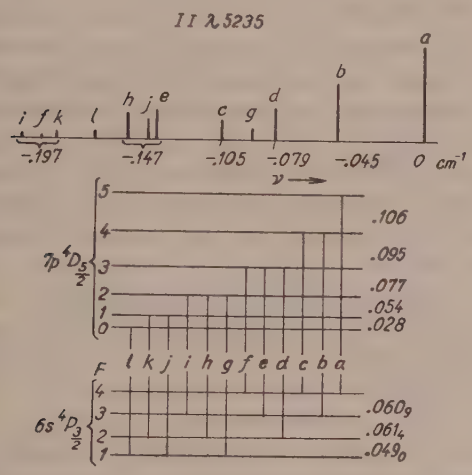

Fig. 13. Hfs of the line λ5235. The components h, j and e were recognized to form a broad band, but they were not resolved.

owing to the perturbation by $7p\ ^4D_{5/2}$. The unperturbed hfs of $(^3P_2)7p\ ^4D_{7/2}$ is given by $A=0.01909$ and $B=-0.057\times10^{-3}\text{cm}^{-1}$.

The level $(^3P_2)7p\ ^4D_{7/2}$ is so highly excited that we can assume the wave function to be a product of $^3P_2$ and $7p_{3/2}$. Using the values $\zeta_{5p}=5760\ \text{cm}^{-1}$ given by Robinson and Shortley[9], Schmidt calculated the wave function:

$$\psi(^3P_2{}^2)=c_1[p_{3/2}^{3/2}p_{1/2}^{1/2}]_2{}^2+c_2[p_{3/2}^{3/2}p_{3/2}^{1/2}]_2{}^2,$$

$$c_1=0.300,\qquad c_2=0.955\,.$$

We get therefore $(\omega=3\cos^2\theta-1)$

$$(^4D_{7/2}|\omega/r^3|^4D_{7/2})=\frac{2}{5}(c_1{}^2R_1{}'-2\sqrt{2}\,c_1c_2S_1)\langle r_{5p}^{-3}\rangle-\frac{2}{5}R_1{}'\langle r_{7p}^{-3}\rangle.$$

ζ_{7p} is so small compared with ζ_{5p} that the second term can be neglected. Thus, putting $R_1{}'=1.11$ and $S_1=1.19$ in this expression, we get

$$(^4D_{7/2}|\omega|^4D_{7/2})=-0.3458.$$

Putting this and $\zeta_{5p}=5760\ \text{cm}^{-1}$, $H_1=1.06$, $Z_{5p}^*=53-4=49$, $I=5/2$, and $J=7/2$ in the usual formula (see Part II), we obtain

$$Q'=-0.63\ \text{barn}\qquad\text{from } (^3P_2)7p\,^4D_{7/2}$$

where Q' means that the shielding correction has not been included.

In Part II, the energy matrix for $5p^46s$ was solved and $\zeta(5p)=5284$, $F_2=1454$, $G_1=681\ \text{cm}^{-1}$ were obtained. The solutions are listed in Table IV. According to the calculation 6s

Table IV. Calculated and observed term values of the $5p^4$ 6s-configuration

	Calculated	Observed	Δ
$(^3P)6s\ ^4P_{5/2}$	54631	54630	+ 1
$(^3P)6s\ ^4P_{3/2}$	56087	56089	− 2
$(^3P)6s\ ^4P_{1/2}$	60870	60893	− 23
$(^3P)6s\ ^2P_{3/2}$	61412	61816	−404
$(^3P)6s\ ^2P_{1/2}$	62879	63187	−308
$(^1D)6s\ ^2D_{5/2}$	68805	68800	+ 5
$(^1D)6s\ ^2D_{3/2}$	68958	68545	+413

$^3D_{3/2}$ should lie higher than $6s\ ^2D_{5/2}$. This situation does not change even if we alter the parameter values in reasonable range. This is not in agreement with the observation, so we have to assume that $6s\ ^2D_{3/2}$ and $6s\ ^2D_{5/2}$ are perturbed by higher lying $5p^4\ 5d$ levels containing large percent of LS-coupling $5d\ ^2D_{3/2}$ and $5d\ ^2D_{5/2}$ wave functions respectively. The fact that $6s\ ^2D_{3/2}$ lies deeper than $6s\ ^2D_{5/2}$ shows that $6s\ ^2D_{3/2}$ is perturbed more strongly than $6s\ ^2D_{5/2}$. From this it can be assumed that $6s\ ^2P_{3/2}$ is also somewhat perturbed and $6s\ ^4P_{3/2}$ slightly perturbed. This explains why somewhat discrepant values of Q' were obtained in *P*art II:

$Q'=-0.71$ barn from $6s\ ^4P_{5/2}$,
$Q'=-0.75$ barn from $6s\ ^4P_{3/2}$,
$Q'=-0.51$ barn from $6s\ ^2P_{3/2}$.

We shall therefore adopt $Q'=-0.71$ barn as the best value from $5p^4\ 6s$. When this is combined with the above-mentioned Q' obtained from $7p\ ^4D_{7/2}$, we get

$$Q'=-0.67\pm0.04 \text{ barn.}$$

Some time ago Jaccarino et al.[10] measured the hfs of $5p^5\ ^2P_{3/2}$ by the atomic beam resonance method and obtained $A=0.0275755$ cm^{-1}, $B=0.47765\times10^{-3}$ cm^{-1}, $C=0.00454\times10^{-6}$ cm^{-1}. From this B, the present author deduced[11]

$Q'=-0.66_4$ barn from $5p^5\ ^2P_{3/2}$.

The above-mentioned spectroscopic value of Q' is in agreement with this.

In order to obtain the true quadrupole moment $Q=(1+\Delta)Q'$, we have to get Δ. The value of Δ was calculated by Sternheimer[12] only for $3p^5$ of Cl I, so we shall extrapolate Δ for I I, as shown by the dotted curve in Fig. 14. and consider $\Delta=-0.07$ the best value available at present. Under this assumption, we get

$$Q(\mathrm{I}^{127})=-0.62 \text{ barn.}$$

Naturally the values of Δ for $5p^5$, $5p^4\ 6s$ and $5p^4\ 7p$ would be different in a strict sense. It is possible that the above-mentioned slight differences between $Q'(5p^5\ ^2P_{3/2})$, $Q'(5p^4\ 6s\ ^4P_{5/2})$ and $Q'(5p^4\ 7p)$ are real and are partly explained by the differences of Δ's. But at present we have no means of confirming or disproving such an assumption.

Measurement of all of the plates was finished in December, 1956. Since then much effort has been made toward calculating the shielding correction for iodine theoretically, but

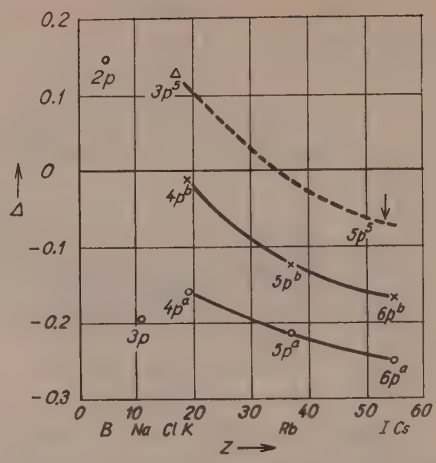

Fig. 14. The shielding corrections (Δ) for various states plotted *versus* the charge number Z. All of the values were calculated by Sternheimer. Two kinds of wave functions (a and b) for alkali atoms were used by him. The graph shows that the result of calculation is sensitive to the wave functions chosen. The value for iodine was obtained by extrapolation (dotted curve) from chlorine.

this has been found to be a hard task for the author and has therefore been abandoned. The extrapolation from chlorine is not altogether free from objection, so the value of $Q(\mathrm{I}^{127})$ presented here would perhaps require a small correction in the end, but it is not likely that this would be materially altered.

§ 5. Correction to Part I and Part II

Everywhere read $4f$ and $5f$ in place of $5f$ and $6f$ respectively.

References

1) K. Murakawa: Z. Physik **109** (1938) 162.
2) K. Murakawa and S. Suwa: Z. Physik **137** (1954) 575.
3) T. Schmidt: Z. Physik **112** (1939) 199.
4) K. Murakawa: Z. Physik **114** (1939) 651.
5) F. E. Eshbach and R. A. Fisher: J. Opt. Soc. Amer. **44** (1954) 868.
6) P. Lacroute: Ann. Physique **3** (1935) 5.
7) E. U. Condon and G. H. Shortley: *The Theory of Atomic Spectra*, Cambridge University Press, London (1935).
8) H. Casimir: Verhandel. Teylers Tweede Genootschap, Haarlem **11** (1936).
9) H. A. Robinson and G. H. Shortley, Phys. Rev. **52** (1937) 713.
10) V. Jaccarino, J. G. King, R. A. Satten, and H. H. Stroke: Phys. Rev. **94** (1954) 1798.
11) K. Murakawa: Phys. Rev. **100** (1955) 1369.
12) R. M. Sternheimer: Phys. Rev. **95** (1954) 736; **105** (1957) 158.

JOURNAL OF THE PHYSICAL SOCIETY OF JAPAN Vol. 13, No. 5, MAY, 1958

Viscous Flow at Low Reynolds Numbers past an Infinite Row of Equal Circular Cylinders

By Tosio MIYAGI

Junior College of Engineering, University of Osaka Prefecture

(Received January 31, 1958)

Steady viscous flow at low Reynolds numbers passing through an infinite row of parallel circular cylinders of the same radius is investigated on the basis of the Stokes equations of motion. Tamada and Fujikawa's expansion formula for the drag coefficient has been extended up to the 14th power of the diameter-distance ratio of the row. An alternative simple formula is presented for the case where the said ratio approaches unity so that the above-mentioned expansion formula becomes divergent. Numerical discussion is made on the drag coefficient *versus* the diameter-distance ratio of the row.

§ 1. Introduction

In a recent paper[1], Tamada and Fujikawa have treated, according to Oseen's approximation, the steady viscous flow at low Reynolds numbers passing through an infinite row of equal circular cylinders. They have thus found among others that at sufficiently low Reynolds numbers the drag D experienced by any one of the cylinders is of Stokes's type, namely it becomes directly proportional to the product of the viscosity coefficient μ and the undisturbed flow speed U. This result seems to suggest that an appropriate solution may also be found when the problem is considered on the basis of the Stokes equations of motion. (In this connexion one may remember the well-known so-called Stokes's paradox that there exists no solution of the Stokes equations for the case of flow past a single cylinder.) It is the object of the present paper to report such an analysis. As will be seen later, the computation required is far simpler than in Tamada and Fujikawa's case. The expansion formula for $D/\mu U$ as a power series in the diameter-distance ratio of the row has been extended up to the 14th power. (Tamada and Fujikawa's result includes only the 10th power.) Also an alternative simple formula has been deduced for the case where the diameter-distance ratio approaches unity so that the above-mentioned expansion formula becomes useless. Numerical discussion is made on the drag coefficient *versus* the diameter-distance ratio of the row, especially for the values of the ratio close to unity.

§ 2. Stokes Equations of Motion and their Solution

Let us consider the steady two-dimensional flow of a viscous fluid passing through an infinite row of equal circular cylinders of radius a, spaced regularly at a distance $2h$ between the centres and lying in a plane perpendicular to the uniform stream of velocity U. We take the rectangular coordinates (x, y) in the plane of fluid motion in such a way that the origin coincides with the centre of any cylinder of the row and the x-axis is along the direction of the uniform stream.

Let u and v be the x- and y-components of the fluid velocity at any point in the field of flow, μ the viscosity coefficient, and p the pressure. Then the Stokes equations of motion and the equation of continuity are given by

$$\left.\begin{aligned} \partial p/\partial x=\mu\Delta u\ , \qquad \partial p/\partial y=\mu\Delta v\ , \\ \partial u/\partial x+\partial v/\partial y=0\ , \end{aligned}\right\} \qquad (1)$$

where Δ stands for $\partial^2/\partial x^2+\partial^2/\partial y^2$.

Elimination of p yields

$$\Delta\omega=0, \quad \text{or} \quad \partial^2\omega/\partial z\partial\bar{z}=0\ , \qquad (2)$$

where ω is the vorticity defined as

$$\omega=\partial v/\partial x-\partial u/\partial y=2i\partial w/\partial\bar{z}\ ,$$

and

$$z=x+iy\ , \qquad \bar{z}=x-iy\ , \qquad w=u-iv\ . \qquad (3)$$

Since ω should be real, the general solution of (2) is given in the form:

$$\omega=\Omega(z)+\overline{\Omega}(\bar{z})\ , \qquad (4)$$

where $\Omega(z)$ is an arbitrary analytic function of z and $\overline{\Omega}(\bar{z})$ is its conjugate complex function. Further, ω must be one-valued through-

out the field of flow and should vanish at infinity. Therefore, taking, in addition, the periodicity of the field into account, we may put the function $\Omega(z)$ in the form:

$$\Omega(z)=\frac{\pi U}{ih}\sum_{n=0}^{\infty}a_{2n}\frac{d^{2n}}{d\zeta^{2n}}\coth\zeta\,,\qquad \zeta=\frac{\pi z}{2h}\,. \tag{5}$$

Here arbitrary constants a_{2n}'s turn out to be real owing to the symmetry of the field under consideration.

Inserting (4) and (5) into (3), and integrating with respect to $\bar{z}$, we obtain

$$\frac{w}{U}=a_0[\log(2\sinh\overline{\zeta})-\overline{\zeta}\coth\zeta]$$
$$+\sum_{n=1}^{\infty}a_{2n}\left[\frac{d^{2n-1}}{d\zeta^{2n-1}}\coth\overline{\zeta}-\overline{\zeta}\frac{d^{2n}}{d\zeta^{2n}}\coth\zeta\right]+f(\zeta)\,.$$

The boundary condition at infinity (i.e., $w\to U$ when $|\zeta|\to\infty$) together with the periodicity of the w-field restricts the form of the arbitrary function $f(\zeta)$ and we obtain

$$\frac{w}{U}=a_0[\log(2\sinh\overline{\zeta})+\log(2\sinh\zeta)-(\zeta+\overline{\zeta})\coth\zeta]$$
$$+\sum_{n=1}^{\infty}a_{2n}\left[\frac{d^{2n-1}}{d\zeta^{2n-1}}\coth\overline{\zeta}-(\zeta+\overline{\zeta})\frac{d^{2n}}{d\zeta^{2n}}\coth\zeta\right]$$
$$+\sum_{n=1}^{\infty}b_{2n}\frac{d^{2n-1}}{d\zeta^{2n-1}}\coth\zeta\,. \tag{6}$$

§ 3. Boundary Condition on the Cylinders

We next proceed to the fulfilment of the boundary condition on the surface of each cylinder. In virtue of the periodicity of (6), it is obviously sufficient to apply the condition on any one of the cylinders. Thus,

$$w/U=-1\,,\quad \text{at}\quad |z|=a\quad\text{or}\quad \overline{\zeta}=t^2/\zeta\,,\quad t=\pi a/2h\,. \tag{7}$$

Substituting $\overline{\zeta}=t^2\zeta^{-1}$ into (6), expanding the right-hand side into Laurent series in ζ and equating the resulting expression to -1, we get an infinite set of algebraic equations for determining the constants a_{2n}'s and b_{2n}'s.

Thus, after tedious but straightforward calculation we arrive at the following result:

$$a_0[1-2\log(2t)+k_1t^2]-\sum_{n=1}^{\infty}(2n-1)!\,k_na_{2n}+\sum_{n=1}^{\infty}(2n+1)!\,k_{n+1}t^2a_{2n}-\sum_{n=1}^{\infty}(2n-1)!\,k_nb_{2n}=1\,, \tag{8}$$

$$a_0\left[\frac{2s-1}{2s}k_s+k_{s+1}t^2\right]+(2s-1)!\,t^{-4s}a_{2s}+\sum_{n=1}^{\infty}\frac{(2n+2s-1)!}{(2s-1)!}k_{n+s}a_{2n}$$
$$+\sum_{n=1}^{\infty}\frac{(2n+2s+1)!}{(2s+1)!}k_{n+s+1}t^2a_{2n}-\sum_{n=1}^{\infty}\frac{(2n+2s-1)!}{(2s)!}k_{n+s}b_{2n}=0\,, \tag{9}$$

$$a_0\left[\frac{k_s}{2s}t^{4s}\right]+\sum_{n=1}^{\infty}\frac{(2n+2s-1)!}{(2s)!}k_{n+s}t^{4s}a_{2n}-(2s)!\,a_{2s}-(2s-2)!\,t^2a_{2s-2}-(2s-1)!\,b_{2s}=0\,, \tag{10}$$

where

$$k_s=(-1)^{s-1}2^{2s}B_s/(2s)!\qquad (s=1,2,3,\cdots)\,, \tag{11}$$

and B_s's are Bernoulli numbers.

Further, we can eliminate b_{2n}'s from these equations and we obtain

$$a_0\left[1-2\log(2t)+2k_1t^2-\sum_{n=1}^{\infty}\frac{k_n^2}{2n}t^{4n}\right]+\sum_{n=1}^{\infty}a_{2n}\left[(2n-1)(2n-1)!\,k_n+2(n+1)(2n)!\,k_{n+1}t^2\right.$$
$$\left.-\sum_{s=1}^{\infty}\frac{(2n+2s-1)!}{(2s)!}k_sk_{n+s}t^{4s}\right]=1\,, \tag{12}$$

$$a_0\left[\frac{2s-1}{2s}k_s+2(s+1)k_{s+1}t^2-\sum_{n=1}^{\infty}\frac{(2n+2s-1)!}{(2s)!\,(2n)!}k_nk_{n+s}t^{4n}\right]+(2s-1)!\,t^{-4s}a_{2s}$$
$$+\sum_{n=1}^{\infty}a_{2n}\left[\frac{(2n+2s)!}{(2s)!}k_{n+s}+\frac{(2n+2s+2)!}{(2n+1)(2s+1)!}k_{n+s+1}t^2-\sum_{j=1}^{\infty}\frac{(2j+2s-1)!\,(2j+2n-1)!}{(2s)!\,(2j-1)!\,(2j)!}k_{j+s}k_{n+j}t^{4j}\right]=0\,,$$
$$(s\geqq 1)\,. \tag{13}$$

Close examination of these equations shows that a_{2n} is $O(t^{4n})$ and first n equations determine the expansion of a_0 up to the $(4n-2)$th power of t. In the following lines we content ourselves with taking only four equations. These can be solved successively and we obtain

$$\frac{1}{a_0}=1-2\log(2t)+\frac{2}{3}t^2-\frac{1}{9}t^4+\frac{8}{135}t^6-\frac{53}{1350}t^8+\frac{1112}{42525}t^{10}-\frac{241643}{13395375}t^{12}+\frac{18776}{1488375}t^{14}-\cdots,$$

$$\frac{a_2}{a_0}=-\frac{t^4}{6}\left[1-\frac{8}{15}t^2+\frac{1}{3}t^4-\frac{1072}{4725}t^6+\frac{2153}{14175}t^8-\frac{5816}{55125}t^{10}+\cdots\right],$$

$$\frac{a_4}{a_0}=\frac{t^8}{360}\left[1-\frac{16}{21}t^2+\frac{20}{27}t^4-\frac{544}{945}t^6+\cdots\right],$$

$$\frac{a_6}{a_0}=-\frac{t^{12}}{68040}\left[1-\frac{24}{25}t^2+\cdots\right]. \tag{14}$$

Further we find from (10)

$$\frac{b_2}{a_0}=-t^2\left[1-\frac{1}{2}t^2+\frac{8}{45}t^4-\frac{11}{90}t^6+\frac{1156}{14175}t^8-\frac{4651}{85050}t^{10}+\frac{18832}{496125}t^{12}-\cdots\right],$$

$$\frac{b_4}{a_0}=\frac{t^6}{18}\left[1-\frac{3}{4}t^2+\frac{17}{35}t^4-\frac{599}{1575}t^6+\frac{17}{63}t^8-\cdots\right],$$

$$\frac{b_6}{a_0}=-\frac{t^{10}}{1800}\left[1-\frac{25}{27}t^2+\frac{844}{945}t^4-\cdots\right],$$

$$\frac{b_8}{a_0}=\frac{t^{14}}{476280}\left[1-\cdots\right]. \tag{15}$$

§ 4. Drag Formula and Numerical Discussion

By summing up the stress acting on a cylinder one can verify a general formula

$$D+iL=\oint(ip+\mu\omega)dz\,, \tag{16}$$

where D and L are the x- and y-components of the force experienced by the cylinder and the integration is carried along the surface of the cylinder. Moreover, it can be seen without difficulty that to Stokes approximation

$$ip+\mu\omega=2\mu\Omega(z)\,. \tag{17}$$

Therefore, inserting this together with (5) into (16), we obtain a very simple result:

$$D+iL=8\pi\mu Ua_0\,,$$

or

$$D/\mu U=8\pi a_0\,,\qquad L=0\,. \tag{18}$$

Inserting the expression for a_0 in (14), it will readily be seen that our expansion formula for the drag is in perfect agreement with Tamada and Fujikawa's formula up to the 10th power of t.

In Table I are shown the values of $D/\mu U$ against a/h as calculated by the formula (18). Also, the values of $(D/\mu U)^{-1}$ are plotted against a/h in Fig. 1. It will be seen that the value of $D/\mu U$ increases rapidly as the ratio a/h approaches unity. At the same time, the convergency of the series for a_0 in (14)

Table I. Values of $D/\mu U$ against a/h.

a/h	$D/\mu U$
0.01	3.17
0.04	4.88
0.1	7.54
0.2	12.60
0.4	31.74
0.5	52.82
0.55	70.15
0.6	98.60
$2/\pi\fallingdotseq 0.64$	119.69
0.7	170.64

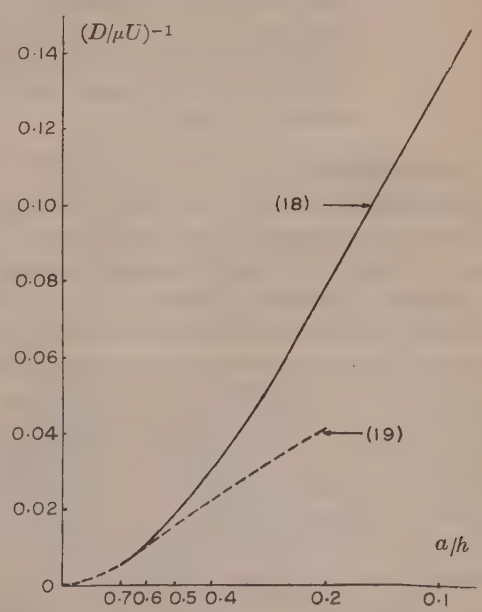

Fig. 1.

becomes worse so that our expansion formula seems to be hardly applicable beyond the value 0.7 of a/h. However, as will be seen from Fig. 1, a formula of the form

$$D/\mu U = \text{const.}\,\{1-(a/h)\}^{-2} \tag{19}$$

seems to hold in this range of difficulty. In fact, this form is verified for the case of flow past a flat screen[2]. Analytical deduction of the exact value of the constant in (19) seems to be hopeless for the present problem. However, approximate evaluation of it can be achieved by numerical matching with the results in Table I. Thus, using the values of $D/\mu U$ for $a/h=0.6$, $2/\pi$, 0.7, we find that

$$\text{const.}=15.8\,. \tag{20}$$

With this value, the formula (19) gives, for example, the values 176, 395, 1580 of $D/\mu U$ when a/h is 0.7, 0.8 and 0.9 respectively.

The writer wishes to express his cordial thanks to Professor S. Tomotika for his interest and encouragement. The writer's thanks are also due to Professor K. Tamada for his suggestion of the present problem and to Professor H. Fujikawa for his valuable discussions.

References

1) K. Tamada and H. Fujikawa: Quart. J. Mech. Appl. Math. **10** (1957) 423.
2) H. Hasimoto: to be published.

JOURNAL OF THE PHYSICAL SOCIETY OF JAPAN Vol. 13, No. 5, MAY, 1958

The Wall-effect upon the Forces experienced by an Elliptic Cylinder in a Viscous Liquid.

By Yorisaburo TAKAISI

Department of Physics, Faculty of Education, Ehime University, Matuyama

(Received January 31, 1958)

The steady slow motion of an elliptic cylinder with an arbitrary angle of attack in a viscous liquid bounded either by a plane wall or by two parallel plane walls is discussed on the basis of Oseen's linearized equations of motion. The analytical expressions for the lift and drag coefficients are obtained to a first approximation, and numerical calculations are carried out for the thickness ratio $t=0$, 0.1, 0.5 and 1. It is found that the wall-effect upon the lift is in either case much greater than that on the drag.

§ 1. Introduction

Since Harrison's study[1] in 1924, the steady flow of an unbounded viscous liquid past an elliptic cylinder at small Reynolds numbers was studied by several authors on the basis of Oseen's linearized equations of motion, and approximate expansion formulae for the forces experienced by the cylinder were obtained. As far as the present writer is aware, however, there have been few works concerning the wall-effect upon the forces experienced by an elliptic cylinder moving in a viscous liquid.

Recently, the present writer has made investigations[2][3] on the wall-effect upon the forces experienced by a circular cylinder moving in a viscous liquid bounded either by a plane wall or by parallel plane walls on the basis of Oseen's linearized equations of motion, by developing a similar analysis to that of Faxén[4] in his treatment of the wall-effect upon the forces experienced by a sphere moving in a viscous liquid.

In this paper, we study similar problems relating to an elliptic cylinder moving with low speeds at an arbitrary angle of attack in a viscous liquid.

§ 2. Fundamental Equation and its Solutions

Let us assume that a cylindrical obstacle is placed in a uniform flow of velocity U streaming parallel to the x-axis. Then Oseen's linearized equations of motion for the two-

dimensional steady motion of a viscous liquid can be written in the form

$$\psi=\psi_1+\psi_2\ , \tag{2.1}$$

$$\Delta\psi_1=0\ , \tag{2.2}$$

$$(\Delta-k^2)(e^{-kx}\psi_2)=0\ , \tag{2.3}$$

where ψ is the stream function for the perturbation and is connected with the components of the perturbation velocity as:

$$u=\partial\psi/\partial y\ ,\quad v=-\partial\psi/\partial x\ , \tag{2.4}$$

and $k=U/2\nu$, ν is the kinematic viscosity of the liquid and Δ stands for $\partial^2/\partial x^2+\partial^2/\partial y^2$.

According to L. N. G. Filon[5], the appropriate solutions of (2.2) and (2.3) which satisfy the boundary conditions at infinity are given respectively by

$$\psi_1=A_0\ln r+B_0\theta+\sum_{n=1}^{\infty}r^{-n}(A_n\cos n\theta+B_n\sin n\theta)\ , \tag{2.5}$$

$$\psi_2=a_0e^{kx}K_0(kr)+b_0\int_0^{\theta}kr\{K_1(kr)+K_0(kr)\cos\theta\}e^{kr\cos\theta}d\theta+e^{kx}\sum_{n=1}^{\infty}K_n(kr)(a_n\cos n\theta+b_n\sin n\theta)\ , \tag{2.6}$$

where $x=r\cos\theta$, $y=r\sin\theta$, and

$$b_0=-B_0\ . \tag{2.7}$$

$K_n(x)$ is the modified Bessel function of the second kind. The condition (2.7) ensures that the stream function $\Psi=Uy+\psi$ is one-valued and continuous throughout the whole field of flow.

If we confine ourselves to the first order approximation, it suffices to take only the first two terms in (2.5) and (2.6) respectively. Then, as shown in our previous paper[2], the conjugate complex velocity $w=u-iv$ $(i=\sqrt{-1})$ can be expressed in integral forms as

$$w=\frac{1}{2}k\int_{-\infty}^{\infty}\left(\frac{y}{|y|}+\frac{\beta}{|\beta|}\right)(A_0-iB_0)e^{k(i\beta x-|\beta||y|)}d\beta-\frac{1}{2}k\int_{-\infty}^{\infty}\left\{\left(\frac{y}{|y|}+\frac{\beta}{\lambda}\right)a_0+i\left(\frac{y}{|y|}+\frac{\lambda}{\beta}\right)b_0\right\}\times e^{k(i\beta x-\lambda|y|)}d\beta\ , \tag{2.3}$$

where $\lambda=\sqrt{\beta^2+2i\beta}$

We introduce elliptic coordinates ξ, η, related with x, y by the equation

$$x+iy=ce^{-i\vartheta}\cosh(\xi+i\eta)\ . \tag{2.9}$$

Then the surface of the elliptic cylinder is given by $\xi=\xi_0$, and the angle between the uniform flow and the major-axis of the ellipse is ϑ.

If we take

$$\sigma=\exp(-\xi_0)\ ,\quad c=2\sigma\ , \tag{2.10}$$

the half-length of the major-and minor-axes are given respectively by

$$a=c\cosh\xi_0=1+\sigma^2\ ,\quad b=c\sinh\xi_0=1-\sigma^2\ . \tag{2.11}$$

We insert (2.9) into (2.8) and expand the integrands with respect to $e^{i\eta}$, retaining only constant terms as well as terms involving $e^{-i\eta}$. Then, after some calculations, we obtain

$$(w/k)_{\xi=\xi_0}=1/2\cdot ia_0(2S-1-\sigma^2e^{2i\vartheta})+1/2\cdot b_0(2S+1+\sigma^2e^{2i\vartheta})+e^{-i\eta}k^{-1}\{i(A_0-a_0)e^{i\vartheta}+(B_0+b_0)e^{i\vartheta}\}+O(ka)\ , \tag{2.12}$$

with

$$S=-\ln(1/2\cdot k)-\gamma\ , \tag{2.13}$$

where $\gamma=0.57721\cdots$ is Euler's constant.

§ 3. Elliptic Cylinder in a Semi-infinite Viscous Liquid

Suppose that an elliptic cylinder is moving, with constant slow velocity U, from right to left in a semi-infinite viscous liquid otherwise at rest parallel to its bounding plane wall (Fig. 1). Referring to rectangular coordinates

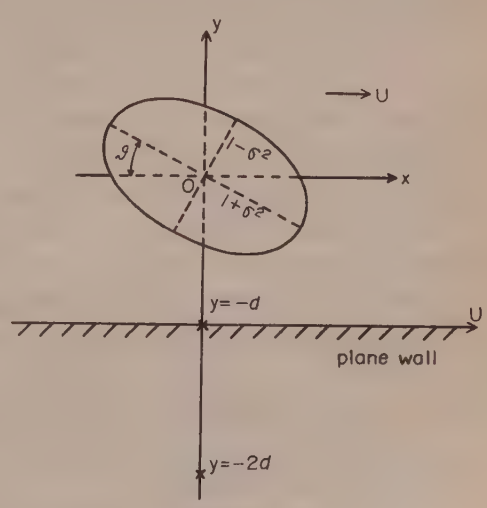

Fig. 1.

with its origin at the centre of the cylinder, the fluid at infinity flows, with constant velocity U, past the cylinder at rest in the positive direction of the x-axis. In this case the bounding plane wall should also move, with the same velocity U, from left to right in its own plane, so as to satisfy the boundary conditions.

As in our previous paper[2], in order to satisfy the boundary conditions on the bounding plane wall, we now superpose an image flow which is defined as

$$w^*=u^*-iv^*$$
$$=-\frac{1}{2}k^2\int_{-\infty}^{\infty}(\beta+|\beta|)f_1^{(1)}(\beta)e^{k\{i\beta x-|\beta|(y+2d)\}}d\beta$$
$$-\frac{1}{2}k^2\int_{-\infty}^{\infty}(\lambda+\beta)f_2^{(1)}(\beta)e^{k\{i\beta x-\lambda(y+2d)\}}d\beta\ , \tag{3.1}$$

where $f_1^{(1)}(\beta)$ and $f_2^{(1)}(\beta)$ are determined by the boundary condition on the bounding plane wall $(w+w^*)_{y=-d}=0$, and are expressed in terms of the unknown constants A_0, B_0, a_0 and b_0 as:

$$\left.\begin{aligned} f_1^{(1)}(\beta)&=\frac{1}{2k}\left\{-i\frac{(\lambda+|\beta|)^2}{\beta|\beta|}A_0+\frac{(\lambda+|\beta|)^2}{\beta^2}B_0\right\}+\frac{1}{k}\left\{i\frac{\lambda+|\beta|}{\beta}a_0+\frac{\lambda(\lambda+|\beta|)}{\beta^2}b_0\right\}e^{-l(\lambda-|\beta|)}\ ,\\ f_2^{(1)}(\beta)&=\frac{1}{k}\left\{i\frac{\lambda+|\beta|}{\beta}A_0-\frac{\lambda+|\beta|}{|\beta|}B_0\right\}e^{l(\lambda-|\beta|)}+\frac{1}{2k}\left\{-i\frac{(\lambda+|\beta|)^2}{\lambda\beta}a_0-\frac{(\lambda+|\beta|)^2}{\beta^2}b_0\right\}\ ,\end{aligned}\right\} \tag{3.2}$$

where $l=kd$.

If we insert (2.9) and (3.2) into (3.1) and expand the integrands with respect to $e^{i\eta}$, retaining only constant terms as well as terms involving $e^{-i\eta}$, we obtain, after some lengthy calculations,

$$\begin{aligned}(w^*/k)_{\xi=\xi_0}=&A_0(G_1+iG_2)+B_0(G_6+iG_7)+a_0(G_{11}+iG_{12})+b_0(G_{16}+iG_{17})\\ &+ke^{-i\eta}[A_0\{iG_3e^{i\vartheta}+\sigma^2(G_4+iG_5)e^{-i\vartheta}\}+B_0\{iG_8e^{i\vartheta}+\sigma^2(G_9+iG_{10})e^{-i\vartheta}\}\\ &+a_0\{iG_{13}e^{i\vartheta}+\sigma^2(G_{14}+iG_{15})e^{-i\vartheta}\}+b_0\{iG_{18}e^{i\vartheta}+\sigma^2(G_{19}+iG_{20})e^{-i\vartheta}\}]\ ,\end{aligned} \tag{3.3}$$

where, for the sake of simplicity, we have put

$$\left.\begin{aligned}
G_1&=1/2\cdot l^{-1}+1/4\cdot\pi\{J_0(2l)+J_2(2l)\}\cos 2l+1/4\cdot\pi\{Y_0(2l)+Y_2(2l)\}\sin 2l-g_2(l)\ ,\\
G_2&=-1/4\cdot l^{-2}+1/4\cdot\pi\{J_0(2l)+J_2(2l)\}\sin 2l-1/4\cdot\pi\{Y_0(2l)+Y_2(2l)\}\cos 2l-1/2\cdot h_1(l)+h_2(l)\ ,\\
G_3&=-1/2\cdot l^{-2}-1/2\cdot h_1(l)+h_2(l)\ ,\\
G_4&=1/4\cdot l^{-3}+1/2\cdot l^{-1}+1/8\cdot\pi\{2J_0(2l)+Y_1(2l)+2J_2(2l)+Y_3(2l)\}\cos 2l\\
&\quad+1/8\cdot\pi\{2Y_0(2l)-J_1(2l)+2Y_2(2l)-J_3(2l)\}\sin 2l-1/4\cdot g_1(l)-5/4\cdot g_2(l)+g_3(l)\ ,\\
G_5&=1/8\cdot\pi\{2J_0(2l)+Y_1(2l)+2J_2(2l)+Y_3(2l)\}\sin 2l\\
&\quad-1/8\cdot\pi\{2Y_0(2l)-J_1(2l)+2Y_2(2l)-J_3(2l)\}\cos 2l+3/4\cdot h_2(l)-h_3(l)\ ,\\
G_6&=1/4\cdot l^{-2}+1/4\cdot\pi\{Y_0(2l)+Y_2(2l)\}\cos 2l-1/4\cdot\pi\{J_0(2l)+J_2(2l)\}\sin 2l+1/2\cdot h_1(l)+h_2(l)\ ,\\
G_7&=-1/2\cdot l^{-1}+1/4\cdot\pi\{J_0(2l)+J_2(2l)\}\cos 2l+1/4\cdot\pi\{Y_0(2l)+Y_2(2l)\}\sin 2l-g_1(l)+g_2(l)\ ,\\
G_8&=-g_1(l)+g_2(l)\ ,\\
G_9&=1/8\cdot\pi\{2Y_0(2l)-J_1(2l)+2Y_2(2l)-J_2(2l)\}\cos 2l\\
&\quad-1/8\cdot\pi\{2J_0(2l)+Y_1(2l)+2J_2(2l)+Y_3(2l)\}\sin 2l+1/2\cdot h_1(l)+3/4\cdot h_2(l)-h_3(l)\ ,\\
G_{10}&=1/4\cdot l^{-3}+1/8\cdot\pi\{2J_0(2l)+Y_1(2l)+2J_2(2l)+Y_3(2l)\}\cos 2l\\
&\quad+1/8\cdot\pi\{2Y_0(2l)-J_1(2l)+2Y_2(2l)-J_3(2l)\}\sin 2l-1/4\cdot g_1(l)+5/4\cdot g_2(l)-g_3(l)\ ,\\
G_{11}&=-1/3\cdot l+1/4\pi\{I_0(2l)+I_2(2l)-\mathbf{L}_0(2l)-\mathbf{L}_2(2l)\}-g_1(l)+g_2(l)\ ,\\
G_{12}&=-1/4\cdot l^{-2}-1-1/2\cdot K_0(2l)+1/2\cdot K_2(2l)+1/2\cdot\pi\{I_1(2l)-\mathbf{L}_1(2l)\}-1/2\,h_1(l)+h_2(l)\ ,\\
G_{13}&=1/4\cdot l^{-2}-1-1/2\cdot K_0(2l)+1/2\cdot K_2(2l)+1/2\cdot\pi\{I_1(2l)-\mathbf{L}_1(2l)\}\ ,\\
G_{14}&=1/4\cdot l^{-3}-1/3\cdot l+1/4\cdot K_1(2l)-1/4\cdot K_3(2l)+1/4\cdot\pi\{I_0(2l)+I_2(2l)-\mathbf{L}_0(2l)-\mathbf{L}_2(2l)\}\\
&\quad-5/4\cdot g_1(l)+9/4\cdot g_2(l)-g_3(l)\ ,\\
G_{15}&=-1/3+1/15\cdot l^2-1/2\cdot K_0(2l)+1/2\cdot K_2(2l)+1/8\cdot\pi\{I_1(2l)-I_3(2l)-\mathbf{L}_1(2l)+\mathbf{L}_3(2l)\}\\
&\quad-1/2\cdot h_1(l)+7/4\cdot h_2(l)-h_3(l)\ ,\\
G_{16}&=-1/4\cdot l^{-2}+1-1/2\cdot K_0(2l)+1/2\cdot K_2(2l)-1/2\cdot\pi\{I_1(2l)-\mathbf{L}_1(2l)\}-1/2\cdot h_1(l)-h_2(l)\ ,\\
G_{17}&=-l^{-1}+1/3\cdot l-1/4\cdot\pi\{I_0(2l)+I_2(2l)-\mathbf{L}_0(2l)-\mathbf{L}_2(2l)\}+g_2(l)\ ,\\
G_{18}&=1/3\cdot l-1/4\cdot\pi\{I_0(2l)+I_2(2l)-\mathbf{L}_0(2l)-\mathbf{L}_2(2l)\}\ ,\\
G_{19}&=1/4\cdot l^{-2}+2/3+1/15\cdot l^2-1/8\cdot\pi\{3I_1(2l)+I_3(2l)-3\mathbf{L}_1(2l)-\mathbf{L}_3(2l)\}\\
&\quad-1/2\cdot h_1(l)-3/4\cdot h_2(l)+h_3(l)\ ,\\
G_{20}&=-1/4\cdot l^{-3}-1/2\cdot l^{-1}-1/4\cdot K_1(2l)+1/4\cdot K_3(2l)+1/4\cdot g_1(l)+5/4\cdot g_2(l)-g_3(l)\ ,
\end{aligned}\right\} \tag{3.4}$$

where $J_n(x)$ is the Bessel function of the first kind, $Y_n(x)$ is Neumann's Bessel function of the second kind, $I_n(x)$ is the modified Bessel function of the first kind and $\mathbf{L}_n(x)$ is Struve's function[6] of imaginary argument defined as:

$$\mathbf{L}_n(x)=\sum_{m=0}^{\infty}\frac{(1/2\cdot x)^{n+2m+1}}{\Gamma(m+3/2)\Gamma(n+m+3/2)}\,. \tag{3.5}$$

also, the functions $g_n(x)=\int_0^\infty (u^2+1)^{-n}e^{-xu}du$ and $h_n(x)=\int_0^\infty u(u^2+1)^{-n}e^{-xu}du$ $(n=1, 2, 3)$ are given by

$$\left.\begin{aligned}
g_1(x)&=\mathrm{Ci}(x)\sin x-\mathrm{Si}(x)\cos x+1/2\cdot\pi\cos x\,,\\
g_2(x)&=1/2\{\mathrm{Ci}(x)\sin x-\mathrm{Si}(x)\cos x+1/2\cdot\pi\cos x\}\\
&\quad-1/2\cdot x\{\mathrm{Ci}(x)\cos x+\mathrm{Si}(x)\sin x-1/2\cdot\pi\sin x\}\,,\\
g_3(x)&=1/8\cdot x+3/8\{\mathrm{Ci}(x)\sin x-\mathrm{Si}(x)\cos x+1/2\cdot\pi\cos x\}\\
&\quad-3/8\cdot x\{\mathrm{Ci}(x)\cos x+\mathrm{Si}(x)\sin x-1/2\cdot\pi\sin x\}\\
&\quad-1/8\cdot x^2\{\mathrm{Ci}(x)\sin x-\mathrm{Si}(x)\cos x+1/2\cdot\pi\cos x\}\,,
\end{aligned}\right\} \tag{3.6}$$

$$\left.\begin{aligned}
h_1(x)&=-\mathrm{Ci}(x)\cos x-\mathrm{Si}(x)\sin x+1/2\cdot\pi\sin x\,,\\
h_2(x)&=1/2-1/2\cdot x\{\mathrm{Ci}(x)\sin x-\mathrm{Si}(x)\cos x+1/2\cdot\pi\cos x\}\,,\\
h_3(x)&=1/4-1/8\cdot x\{\mathrm{Ci}(x)\sin x-\mathrm{Si}(x)\cos x+1/2\cdot\pi\cos x\}\\
&\quad+1/8\cdot x^2\{\mathrm{Ci}(x)\cos x+\mathrm{Si}(x)\sin x-1/2\cdot\pi\sin x\}\,,
\end{aligned}\right\} \tag{3.7}$$

with

$$\mathrm{Si}(x)=\int_0^x\frac{\sin u}{u}du\,,\qquad \mathrm{Ci}(x)=-\int_x^\infty\frac{\cos u}{u}du\,. \tag{3.8}$$

Since the boundary conditions at infinity as well as on the bounding plane wall are already satisfied by w and w^* as given respectively by (2.8) and (3.1), we have only to consider the boundary condition at the surface of the elliptic cylinder. It is

$$(w+w^*)_{\xi=\xi_0}=-U\,. \tag{3.9}$$

Inserting (2.12) and (3.3) into (3.9), we have, on neglecting terms of $O(ka)$,

$$a_0=A_0\,, \tag{3.10}$$

$$b_0=-B_0\,, \tag{3.11}$$

$$A_0=\frac{U}{k}\,\frac{F_1(kd)-1/2\cdot\sigma^2\sin 2\vartheta}{\{1/2(1+\sigma^2\cos 2\vartheta)-F_3(kd)\}^2-\{F_1(kd)\}^2-\{-S+F_2(kd)\}^2+1/4\cdot\sigma^4\sin^2 2\vartheta}\,, \tag{3.12}$$

$$B_0=\frac{U}{k}\,\frac{1/2(1+\sigma^2\cos 2\vartheta)-F_3(kd)+\{-S+F_2(kd)\}}{\{1/2\cdot(1+\sigma^2\cos 2\vartheta)-F_3(kd)\}^2-\{F_1(kd)\}^2-\{-S+F_2(kd)\}^2+1/4\cdot\sigma^4\sin^2 2\vartheta}\,, \tag{3.13}$$

where, for the sake of convenience, we have used the same notations as in our previous paper[2], namely:

$$\left.\begin{aligned}
F_1(l)&=G_1+G_{11}=G_7-G_{17}\\
&=1/2\cdot l^{-1}-1/3\cdot l+1/4\cdot\pi\{J_0(2l)+J_2(2l)\}\cos 2l+1/4\cdot\pi\{Y_0(2l)+Y_2(2l)\}\sin 2l\\
&\quad+1/4\cdot\pi\{I_0(2l)+I_2(2l)-\mathbf{L}_0(2l)-\mathbf{L}_2(2l)\}-g_1(l)\,,\\
F_2(l)&=1/2\cdot(-G_2+G_6-G_{12}-G_{16})\\
&=1/2\cdot l^{-2}+1/2\cdot K_0(2l)-1/2\cdot K_2(2l)-1/4\cdot\pi\{J_0(2l)+J_2(2l)\}\sin 2l\\
&\quad+1/4\cdot\pi\{Y_0(2l)+Y_2(2l)\}\cos 2l+h_1(l)\,,\\
F_3(l)&=1/2\cdot(G_2+G_6+G_{12}-G_{16})=-1+1/2\cdot\pi\{I_1(2l)-\mathbf{L}_1(2l)\}+2h_2(l)\,.
\end{aligned}\right\} \tag{3.14}$$

The relation (3.11) has been obtained again independently of (2.7).

As in the case of a circular cylinder in a viscous liquid bounded either by a plane wall or by parallel plane walls, the lift L and the drag D experienced by the elliptic cylinder under discussion per unit length can be expressed as:

$$L=2\pi\rho UA_0\,, \tag{3.15}$$

$$D=2\pi\rho UB_0\,, \tag{3.16}$$

where ρ is the density of the liquid concerned.

Hence, if use is made of (3.12) and (3.13), we obtain for the lift and drag coefficients $C_L^{(1)}$ and $C_D^{(1)}$

$$\begin{aligned} C_L^{(1)}&=L/(1/2\cdot\rho U^2\cdot 2a)\\ &=\frac{8\pi}{R}\,\frac{F_1(kd)-1/2\cdot\sigma^2\sin 2\vartheta}{\{1/2\cdot(1+\sigma^2\cos 2\vartheta)-F_3(kd)\}^2-\{F_1(kd)\}^2-\{-S+F_2(kd)\}^2+1/4\cdot\sigma^4\sin^2 2\vartheta} \end{aligned} \tag{3.17}$$

$$\begin{aligned} C_D^{(1)}&=D/(1/2\cdot\rho U^2\cdot 2a)\\ &=\frac{8\pi}{R}\,\frac{1/2\cdot(1+\sigma^2\cos 2\vartheta)-F_3(kd)+\{-S+F_2(kd)\}}{\{1/2\cdot(1+\sigma^2\cos 2\vartheta)-F_3(kd)\}^2-\{F_1(kd)\}^2-\{-S+F_2(kd)\}^2+1/4\cdot\sigma^4\sin^2 2\vartheta}\,, \end{aligned} \tag{3.18}$$

where $R=4ka$.

For a circular cylinder, we have only to put $\sigma=0$ in (3.17) and (3.18), thus

$$\left.\begin{aligned} C_L^{(1)}&=\frac{8\pi}{R}\,\frac{F_1(kd)}{\{1/2-F_3(kd)\}^2-\{F_1(kd)\}^2-\{-S+F_2(kd)\}^2}\,,\\ C_D^{(1)}&=\frac{8\pi}{R}\,\frac{1/2-F_3(kd)+\{-S+F_2(kd)\}}{\{1/2-F_3(kd)\}^2-\{F_1(kd)\}^2-\{-S+F_2(kd)\}^2}\,, \end{aligned}\right\} \tag{3.19}$$

which are in perfect agreement with the formulae obtained recently by the present writer.

When the bounding plane wall recedes far away to infinity from the centre of the cylinder, the value of kd tends to infinity and our case is reduced to the case of an elliptic cylinder in an unbounded stream of viscous liquid. The value of ka is, however, kept to be small.

Making use of the well-known asymptotic expressions for the Bessel functions $J_n(x)$, $Y_n(x)$ and $K_n(x)$, and also for $\mathrm{Si}(x)$ and $\mathrm{Ci}(x)$, together with

$$I_n(x)-\mathbf{L}_n(x)=\frac{1}{\pi}\sum_{m=0}^{p-1}(-1)^m\,\frac{\Gamma(m+1/2)}{\Gamma(n+1/2-m)(1/2\cdot x)^{2m-n+1}}+\mathrm{O}(x^{n-2p-1})\,, \tag{3.20}$$

we easily find that

$$\lim_{kd\to\infty} F_n(kd)\longrightarrow 0\quad (n=1,2,3)$$

Thus, we have ultimately

$$C_{L\infty}=\lim_{kd\to\infty} C_L^{(1)}\longrightarrow\frac{16\pi}{R}\,\frac{\sigma^2\sin 2\vartheta}{4S^2-(1+2\sigma^2\cos 2\vartheta+\sigma^4)}\,, \tag{3.21}$$

$$C_{D\infty}=\lim_{kd\to\infty} C_D^{(1)}\longrightarrow\frac{16\pi}{R}\,\frac{2S-(1+\sigma^2\cos 2\vartheta)}{4S^2-(1+2\sigma^2\cos 2\vartheta+\sigma^4)}\,. \tag{3.22}$$

As should be expected, (3.21) and (3.22) are in perfect agreement with the first approximation obtained previously by H. Hasimoto[7], I. Imai[8] and others for the case of an elliptic cylinder in an unbounded viscous liquid.

On the other hand, in case when the value of kd becomes small subject to the restriction $d>a$ so that all terms higher than $(kd)^2$ can be neglected, we can make use of the well-known expansion formulae for the various functions used in $F_n(kd)$'s. Thus, we get ultimately approximate formulae for $C_L^{(1)}$ and $C_D^{(1)}$, which are valid for sufficiently small ka and kd, in the forms:

$$C_L^{(1)}=\frac{16\pi}{R}\frac{\sigma^2\sin 2\vartheta+kd}{4\omega_1^2-(1+2\sigma^2\cos 2\vartheta+\sigma^4)}, \tag{3.23a}$$

$$\approx\frac{16\pi}{R}\frac{\sigma^2\sin 2\vartheta}{4\omega_1^2-(1+2\sigma^2\cos 2\vartheta+\sigma^4)}, \tag{3.23b}$$

$$C_D^{(1)}=\frac{16\pi}{R}\frac{2\omega_1-(1+\sigma^2\cos 2\vartheta)}{4\omega_1^2-(1+2\sigma^2\cos 2\vartheta+\sigma^4)}, \tag{3.24}$$

where

$$\omega_1=\ln(2d)-1/2\,. \tag{3.25}$$

§ 4. Elliptic Cylinder in a Viscous Liquid bounded by Two Parallel Plane Walls

In the special case when an elliptic cylinder is moving midway between two bounding plane walls, we superpose flows due to images, which are defined as:

$$w^*=-\frac{1}{2}k^2\int_{-\infty}^{\infty}(|\beta|+\beta)f_1^{(2)}(\beta)e^{k(i\beta x-|\beta|y)}d\beta$$
$$-\frac{1}{2}k^2\int_{-\infty}^{\infty}(\lambda+\beta)f_2^{(2)}(\beta)e^{k(i\beta x-\lambda y)}d\beta\,, \tag{4.1}$$

$$w^{**}=\frac{1}{2}k^2\int_{-\infty}^{\infty}(|\beta|-\beta)f_3^{(2)}(\beta)e^{k(i\beta x+|\beta|y)}d\beta$$
$$+\frac{1}{2}k^2\int_{-\infty}^{\infty}(\lambda-\beta)f_4^{(2)}(\beta)e^{k(i\beta x+\lambda y)}d\beta\,, \tag{4.2}$$

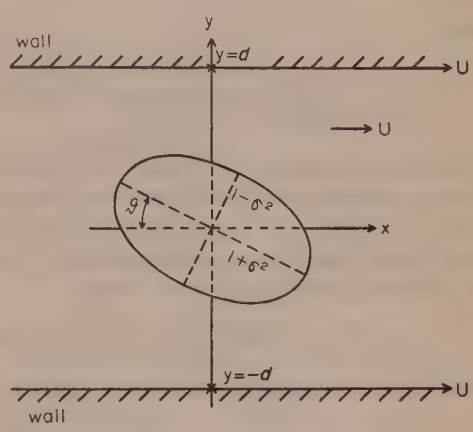

Fig. 2.

where $f_n^{(2)}(\beta)$'s are unknown functions to be determined by the boundary conditions on the bounding plane walls.

Remembering the relations (3.10) and (3.11), it is natural to put $a_0=A_0$ and $b_0=-B_0$. Thus, we have

$$\left.\begin{aligned}
\begin{matrix}f_1^{(2)}\\ f_3^{(2)}\end{matrix}(\beta)&=[(\lambda+|\beta|)e^{i(\lambda-|\beta|)}-(\lambda-|\beta|)e^{-i(\lambda+|\beta|)}-2|\beta|]A_0/k|\beta|M_1(\beta)\\
&\quad\pm[(\lambda+|\beta|)e^{i(\lambda-|\beta|)}+(\lambda-|\beta|)e^{-i(\lambda+|\beta|)}-2\lambda]B_0/ik\beta M_2(\beta)\,,\\
\begin{matrix}f_2^{(2)}\\ f_4^{(2)}\end{matrix}(\beta)&=[(\lambda+|\beta|)e^{-i(\lambda-|\beta|)}+(\lambda-|\beta|)e^{-(\lambda+|\beta|)}-2\lambda]A_0/k\lambda M_1(\beta)\\
&\quad\pm[(\lambda+|\beta|)e^{-i(\lambda-|\beta|)}-(\lambda-|\beta|)e^{-i(\lambda+|\beta|)}-2|\beta|]B_0/ik\beta M_2(\beta)\,,
\end{aligned}\right\} \tag{4.3}$$

where we have put for brevity

$$\begin{matrix}M_1\\ M_2\end{matrix}(\beta)=(\lambda+|\beta|)\{e^{i(\lambda-|\beta|)}-e^{-i(\lambda-|\beta|)}\}$$
$$\pm(\lambda-|\beta|)\{e^{i(\lambda+|\beta|)}-e^{-i(\lambda+|\beta|)}\}\,. \tag{4.4a}$$

We insert (2.9), (4.3) and (4.4a) into (4.1) and (4.2) and expand the integrands with respect to $e^{i\eta}$, retaining only constant terms as well as terms involving $e^{-i\eta}$. Then we obtain

$$(w^*/k+w^{**}/k)_{\xi\sim\xi_0}$$
$$=-A_0\left\{\int_0^{\infty}[(\lambda+\beta)e^{i(\lambda+\beta)}-(\lambda-\beta)e^{-i(\lambda+\beta)}-2\beta]d\beta/M_1'(\beta)\right.$$
$$\left.+\int_0^{\infty}\beta[(\lambda+\beta)e^{-i(\lambda-\beta)}+(\lambda-\beta)e^{-i(\lambda+\beta)}-2\lambda]d\beta/\lambda M_1'(\beta)-\text{C.C.}\right\}$$

$$+iB_0\left\{\int_0^\infty[((\lambda+\beta)e^{l(\lambda-\beta)}+(\lambda-\beta)e^{-l(\lambda+\beta)}-2\lambda]d\beta/M_2'(\beta)\right.$$

$$\left.+\int_0^\infty\lambda[(\lambda+\beta)e^{-l(\lambda-\beta)}-(\lambda-\beta)e^{-l(\lambda+\beta)}-2\beta]d\beta/\beta M_2'(\beta)-\text{C.C.}\right\}$$

$$+i\,e^{-i\eta}\left[k\,e^{i\vartheta}A_0\left\{\int_0^\infty(\lambda^2-\beta^2)[(\lambda+\beta)e^{-l(\lambda-\beta)}+(\lambda-\beta)e^{-l(\lambda+\beta)}-2\lambda]d\beta/2\lambda M_1'(\beta)+\text{C.C.}\right\}\right.$$

$$-k\sigma^2e^{-i\vartheta}A_0\left\{\int_0^\infty\beta[(\lambda+\beta)e^{l(\lambda-\beta)}-(\lambda-\beta)e^{-l(\lambda+\beta)}-2\beta]/M_1'(\beta)\right.$$

$$\left.+\int_0^\infty(\lambda^2+\beta^2)[(\lambda+\beta)e^{-l(\lambda-\beta)}+(\lambda-\beta)e^{-l(\lambda+\beta)}-2\lambda]d\beta/2\lambda M_1'(\beta)+\text{C.C.}\right\}$$

$$+ik\sigma^2e^{-i\vartheta}B_0\left\{\int_0^\infty\beta[(\lambda+\beta)e^{l(\lambda-\beta)}+(\lambda-\beta)e^{-l(\lambda+\beta)}-2\lambda]d\beta/M_2'(\beta)\right.$$

$$\left.\left.+\int_0^\infty\lambda[(\lambda+\beta)e^{-l(\lambda-\beta)}-(\lambda-\beta)e^{-l(\lambda+\beta)}-2\beta]d\beta/M_2'(\beta)+\text{C.C.}\right\}\right], \tag{4.5}$$

where

$$\begin{matrix}M_1'\\M_2'\end{matrix}(\beta)=(\lambda+\beta)\{e^{l(\lambda-\beta)}-e^{-l(\lambda-\beta)}\}\pm(\lambda-\beta)\{e^{l(\lambda+\beta)}-e^{-l(\lambda+\beta)}\}\,. \tag{4.4b}$$

In (4.5) the notation C.C. stands for "the conjugate complex of the foregoing integrals".

Since it seems very difficult to evaluate exactly the integrals in (4.5), we confine ourselves to the evaluation of the integrals for sufficiently small values of kd such that all terms higher than $(kd)^{1/2}$ can be neglected. After straightforward calculations similar to those in our previous paper[3], we have finally

$$(w^*/k+w^{**}/k)_{\xi=\xi_0}=iA_0\{\ln(1/2\cdot kd)+0.4569\}-B_0\{\ln(1/2\cdot kd)-0.8384\}\,. \tag{4.6}$$

Making use of the relations $a_0=A_0$ and $b_0=-B_0$ we have from (2.12)

$$\begin{aligned}(w/k)_{\xi=\xi_0}=&1/2\cdot A_0\sigma^2\sin 2\vartheta-1/2\cdot B_0\{2S+(1+\sigma^2\cos 2\vartheta)\}\\&+i[1/2\cdot A_0\{2S-(1+\sigma^2\cos 2\vartheta)\}-1/2\cdot B_0\sigma^2\sin 2\vartheta]\,.\end{aligned} \tag{4.7}$$

The boundary condition at the surface of the elliptic cylinder is

$$(w+w^*+w^{**})_{\xi=\xi_0}=-U\,. \tag{4.8}$$

Inserting (4.6) and (4.7) into (4.8), we obtain

$$\left.\begin{aligned}A_0&=\frac{U}{k}\frac{2\sigma^2\sin 2\vartheta}{4\omega_2^2-(0.0872-0.5906\sigma^2\cos 2\vartheta+\sigma^4)}\,,\\B_0&=\frac{U}{k}\frac{2\{2\omega_2-(-0.2953+\sigma^2\cos 2\vartheta)\}}{4\omega_2^2-(0.0872-0.5906\sigma^2\cos 2\vartheta+\sigma^4)}\,,\end{aligned}\right\} \tag{4.9}$$

where

$$\omega_2=\ln d-\gamma-0.1908\,. \tag{4.10}$$

The lift L and the drag D experienced by the elliptic cylinder can also be calculated by (3.15) and (3.16) respectively. Thus we have for the lift and drag coefficients $C_L^{(2)}$ and $C_D^{(2)}$

$$C_L^{(2)}=L/(1/2\cdot\rho U^2\cdot 2a)=\frac{16\pi}{R}\frac{\sigma^2\sin 2\vartheta}{4\omega_2^2-(0.0872-0.5906\,\sigma^2\cos 2\vartheta+\sigma^4)}\,, \tag{4.11}$$

$$C_D^{(2)}=D/(1/2\cdot\rho U^2\cdot 2a)=\frac{16\pi}{R}\frac{2\omega_2-(-0.2953+\sigma^2\cos 2\vartheta)}{4\omega_2^2-(0.0872-0.5906\sigma^2\cos 2\vartheta+\sigma^4)}\,. \tag{4.12}$$

We may put $\sigma=0$ for a circular cylinder, and then (4.11) and (4.12) reduce simply to

$$\left.\begin{aligned} C_L^{(2)}&=0 \\ C_D^{(2)}&=\frac{8\pi}{R}\frac{1}{\ln d-0.9156} \end{aligned}\right\} \qquad (4.13)$$

which are in perfect agreement with the formulae obtained previously by the present writer for a circular cylinder.

§ 5. Numerical Discussions

Numerical calculations were made for the cases $t=0$ (flat plate), 0.1, 0.5 and 1 (circular cylinder), where $t=b/a$ is the thickness ratio of the cylinder.

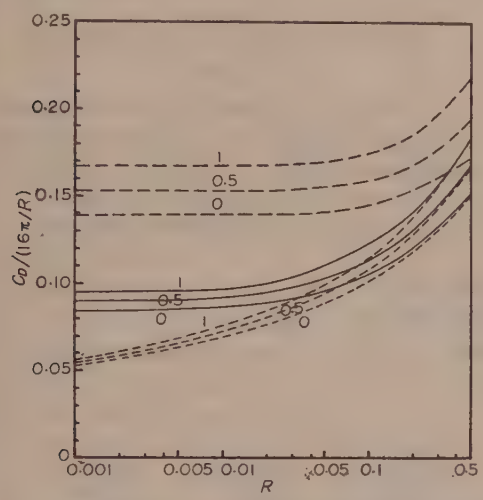

Fig. 3. Values of $C_D^{(1)}/(16\pi/R)$ plotted against Reynolds number R. Values of thickness ratio are indicated on the curves.
— — —, $d/a=10$, } calculated by (3.18);
———, $d/a=100$, }
- - - - -, $d/a\to\infty$, calculated by (3.22).

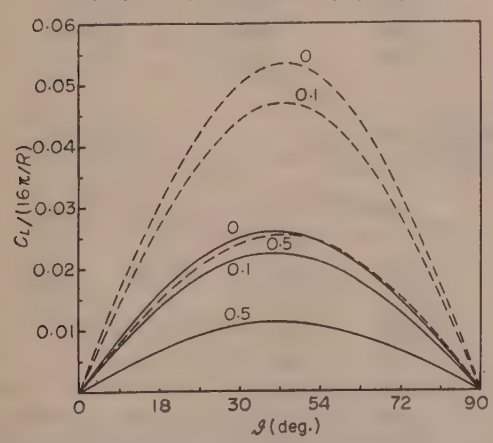

Fig. 4. Values of $C_L/(16\pi/R)$ at very low speeds ($R\approx 0$) plotted against angle of attack ϑ, for $d/a=10$. Values of thickness ratio are indicated on the curves.
———, single wall, calculated by (3.23b);
— — —, double walls, calculated by (4.11).

The values of $C_D^{(1)}/(16\pi/R)$ have been calculated by using the formulae (3.18) and (3.22) for various values ranging from 0.002 to 0.4 of the Reynolds number R. They are plotted in Fig. 3.

Table I and Fig. 4 give the values of $C_L/(16\pi/R)$ for sufficiently small Reynolds numbers R and $R^*(=Ud/\nu)$, calculated by using the formulae (3.23b) and (4.11), for various values of ϑ ranging from 0 to 90 deg., where the value of the ratio $d/a=10$.

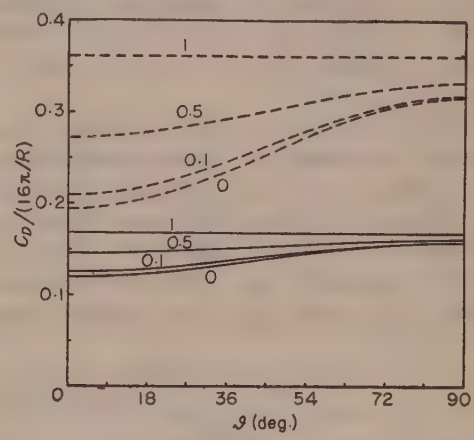

Fig. 5. Values of $C_D/(16\pi/R)$ at very low speeds ($R\approx 0$) plotted against angle of attack ϑ, for $d/a=10$. Values of thickness ratio are indicated on the curves.
———, single wall, calculated by (3.24);
— — —, double walls, calculated by (4.12).

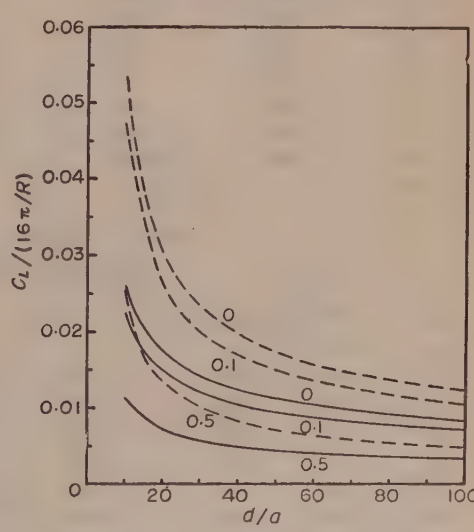

Fig. 6. Values of $C_L/(16\pi/R)$ at very low speeds ($R\approx 0$) plotted against d/a, for $\vartheta=45$ deg. Values of thickness ratio are indicated on the curves.
———, single wall, calculated by (3.23b);
— — —, double walls, calculated by (4.11).

Table II and Fig. 5 give the values of $C_D/(16\pi/R)$ for sufficiently small Reynolds numbers R and R^*, calculated by using the formulae (3.24) and (4.12), for various values of ϑ ranging from 0 to 90 deg., where the value of the ratio $d/a=10$.

It is worth noticing that the values of $C_L/(16\pi/R)$ and $C_D/(16\pi/R)$ for sufficiently small Reynolds numbers R and R^* are indpendent of them.

Table III and Fig. 6 give the values of $C_L/(16\pi/R)$, calculated by using the formulae (3.23b) and (4.11), for various values of the ratio d/a ranging from 10 to 100, where $\vartheta=45$ deg.

Table IV and Fig. 7 give the values of $C_D/(16\pi/R)$, calculated by using the formulae (3.24) and (4.12), for various values of the ratio d/a ranging from 10 to 100, where $\vartheta=45$ deg.

Table V and Fig. 8 give the values of $C_L/C_{L\infty}$, calculated by using the formulae (3.23b), (4.11) and (3.21), for various values

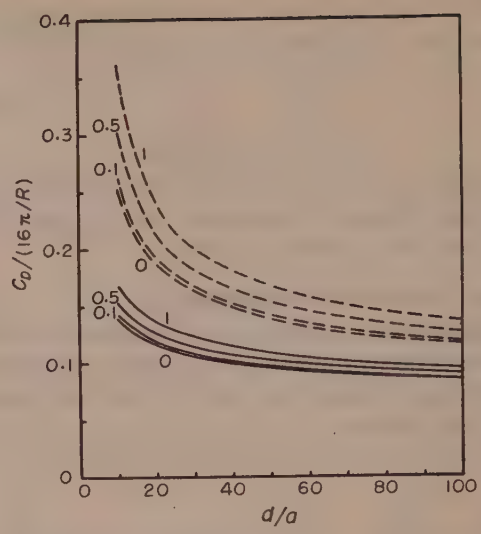

Fig. 7. Values of $C_D/(16\pi/R)$ at very low speeds ($R\approx 0$) plotted against d/a, for $\vartheta=45$ deg. Values of thickness ratio are indicated on the curves. ———, single wall, calculated by (3.24); — — —, double walls, calculated by (4.12).

Table I. Values of $C_L/(16\pi/R)$ for $d/a=10$
[I, Single wall; II, double walls.]

ϑ	$t=0$ flat plate		$t=0.1$		$t=0.5$	
(deg.)	I	II	I	II	I	II
0	0	0	0	0	0	0
9	0.0084	0.0160	0.0072	0.0141	0.0035	0.0078
18	.0159	.0306	.0136	.0270	.0067	.0148
27	.0216	.0423	.0186	.0374	.0091	.0204
36	.0250	.0502	.0216	.0443	.0107	.0241
45	.0259	.0533	.0224	.0469	.0112	.0255
54	.0242	.0512	.0210	.0450	.0105	.0243
63	.0203	.0439	.0176	.0386	.0089	.0207
72	.0146	.0321	.0127	.0282	.0064	.0152
81	.0076	.0170	.0066	.0149	.0034	.0080
90	0	0	0	0	0	0

Table II. Values of $C_D/(16\pi/R)$ for $d/a=10$
[I, single wall; II, double walls.]

ϑ	$t=0$ flat plate		$t=0.1$		$t=0.5$		$t=1$ circular cylinder	
(deg.)	I	II	I	II	I	II	I	II
0	0.1194	0.1938	0.1249	0.2089	0.1449	0.2715	0.1669	0.3605
9	.1204	.1966	.1258	.2114	.1453	.2730	〃	〃
18	.1233	.2049	.1282	.2185	.1465	.2771	〃	〃
27	.1277	.2178	.1320	.2303	.1482	.2836	〃	〃
36	.1332	.2344	.1367	.2450	.1504	.2919	〃	〃
45	.1390	.2532	.1417	.2616	.1528	.3011	〃	〃
54	.1447	.2723	.1466	.2785	.1552	.3104	〃	〃
63	.1497	.2899	.1509	.2940	.1573	.3189	〃	〃
72	.1535	.3040	.1542	.3064	.1590	.3258	〃	〃
81	.1560	.3132	.1563	.3145	.1601	.3300	〃	〃
90	.1568	.3164	.1570	.3173	.1604	.3316	〃	〃

Table III. Values of $C_L/(16\pi/R)$ for $\vartheta=45$ deg.
[I, single wall; II, double walls.]

d/a	$t=0$ flat plate		$t=0.1$		$t=0.5$	
	I	II	I	II	I	II
10	0.0259	0.0533	0.0224	0.0469	0.0112	0.0255
20	.0172	.0303	.0147	.0262	.0071	.0133
40	.0122	.0196	.0104	.0168	.0049	.0081
60	.0103	.0157	.0087	.0135	.0040	.0064
100	.0084	.0123	.0071	.0105	.0033	.0049

Table IV. Values of $C_D/(16\pi/R)$ for $\vartheta=45$ deg.
[I, single wall; II, double walls.]

d/a	$t=0$ flat plate		$t=0.1$		$t=0.5$		$t=1$ circular cylinder	
	I	II	I	II	I	II	I	II
10	0.1390	0.2532	0.1417	0.2616	0.1528	0.3011	0.1669	0.3605
20	.1161	.1857	.1180	.1907	.1260	.2121	.1355	.2404
40	.0997	.1471	.1013	.1504	.1073	.1638	.1141	.1083
60	.0922	.1312	.0935	.1338	.0987	.1445	.1044	.1573
100	.0842	.1155	.0853	.1176	.0896	.1259	.0094	.1355

ranging from 0.001 to 0.1 of the Reynolds number R, where $\vartheta=45$ deg. and the value of the ratio $d/a=10$.

Table VI and Fig. 9 give the values of $C_D/C_{D\infty}$, calculated by using the formulae (3.24), (4.12) and (3.22), for various values ranging from 0.001 to 0.1 of the Reynolds number R, where $\vartheta=45$ deg. and the value of the ratio $d/a=10$.

As can seen from Tables V and VI, the wall-effect upon the lift is in either case much greater than that on the drag.

In conclusion, the writer wishes to express his cordial thanks to Professor S. Tomotika for his continual guidance and also for his kind inspection of the manuscript. The

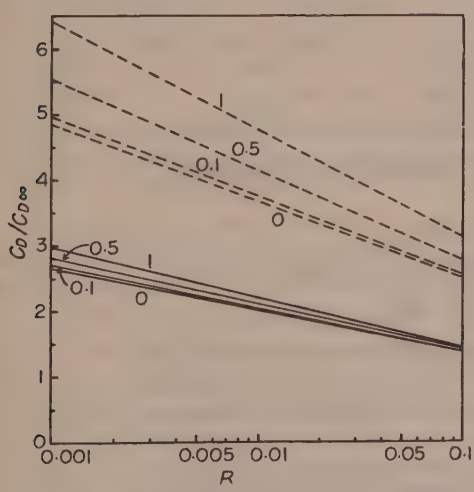

Fig. 9. Ratio $C_D/C_{D\infty}$ at very low speeds ($R\approx 0$) plotted against Reynolds number R, for $\vartheta=45$ deg. and $d/a=0$. Values of thickness ratio are indicated on the curves.
———, single wall, calculated by (3.24) and (3.22);
— — —, double walls, calculated by (4.12) and (3.22).

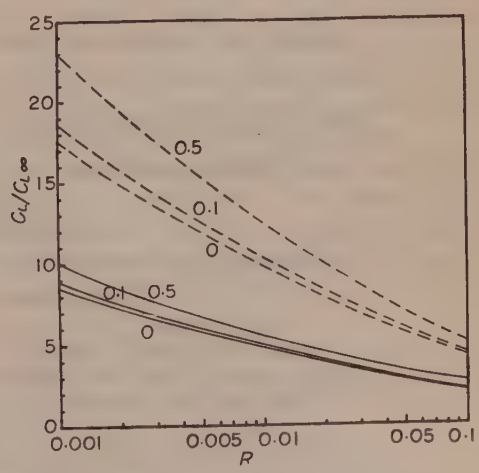

Fig. 8. Ratio $C_L/C_{L\infty}$ at very low speeds ($R\approx 0$) plotted against Reynolds number R, for $\vartheta=45$ deg. and $d/a=10$. Values of thickness ratio are indicated on the curves.
———, single wall, calculated by (3.23b) and (3.21);
— — —, double walls, calculated by (4.11) and (3.21).

Table V. Values of $C_L/C_{L\infty}$ for $\vartheta=45$ deg. and $d/a=10$
[I, single wall; II, double walls.]

R	$t=0$ flat plate		$t=0.1$		$t=0.5$	
	I	II	I	II	I	II
0.001	8.521	17.56	8.820	18.52	10.09	23.03
0.005	5.757	11.86	5.935	12.46	6.688	15.27
0.01	4.732	9.751	4.867	10.22	5.439	12.39
0.05	2.736	5.637	2.792	5.862	3.029	6.916
0.1	2.041	4.206	2.073	4.353	2.205	5.035

Table VI. Values of $C_D/C_{D\infty}$ for $\vartheta=45$ deg. and $d/a=10$
[I, single wall; II, double walls.]

R	$t=0$ flat plate		$t=0.1$		$t=0.5$		$t=1$ circular cylinder	
	I	II	I	II	I	II	I	II
0.001	2.662	4.849	2.689	4.964	2.810	5.537	2.974	6.424
0.005	2.212	4.030	2.231	4.120	2.317	4.567	2.437	5.264
0.01	2.019	3.677	2.034	3.756	2.016	4.149	2.206	4.674
0.05	1.567	2.855	1.575	2.909	1.613	3.179	1.669	3.605
0.1	1.372	2.500	1.377	2.542	1.401	2.760	1.438	3.105

writer's thanks are also due to the Ministry of Education for a grant-in-aid for fundamental scientific research.

References

1) W. J. Harrion: Trans. Cambr. Phil. Soc. **23** (1924) 71.
2) Y. Takaisi: J. Phys. Soc. Japan **10** (1955) 407.
3) Y. Takaisi: J. Phys. Soc. Japan **10** (1955) 685.
4) H. Faxén: Diss. Uppsala (1921).
5) L. N. G. Filon: Proc. Roy. Soc. A **113** (1926) 7.
6) G. N. Watson: *Theory of Bessel Functions.* (2nd ed. Cambridge Univ. Press (1948)) 329.
7) H. Hasimoto: J. Phys. Soc. Japan **8** (1953) 653.
8) I. Imai: Proc. Roy. Soc. A **224** (1954) 141.

JOURNAL OF THE PHYSICAL SOCIETY OF JAPAN Vol. 13, No. 5, MAY, 1958

The Forces Experienced by Two Elliptic Cylinders in a Uniform Flow at Small Reynolds Numbers

By Shinji KUWABARA

Department of Physics, Faculty of Science, University of Tokyo

(Received February 4, 1958)

Using Imai's general method of solving two-dimensional Oseen's equations, the drag and lift coefficients for one of two parallel elliptic cylinders in a uniform flow at small Reynolds numbers are calculated. When the thickness ratios of both elliptic cylinders are taken to be unity, the general expressions for these coefficients reduce to those for the case of two circular cylinders which have been obtained in the author's previous paper. The expressions for the case of two flat plates are also included as a special case.

§ 1. Introduction and Summary

In a previous paper[1], the author studied the forces experienced by two circular cylinders in a uniform flow at small Reynolds numbers. H. Fujikawa also studied the same problem[2),3)] and further obtained the expressions for the drag and lift in power series in $1/d$ up to $O(1/d^4)$, where d is the distance

between the two circular cylinders[4]. His expressions are considered to be valid even when the two cylinders are close to each other. In the present paper, studies on the flow past two elliptic cylinders at small Reynolds numbers will be carried out by Oseen's approximation.

As in the previous paper, we make use of Imai's general method of solving two-dimensional Oseen's equations[5]. On the basis of his method, Imai himself investigated the uniform flow past an elliptic cylinder at an arbitrary angle of incidence and obtained the expressions for the velocity distribution near the elliptic cylinder as well as for the drag and lift up to a third approximation. In § 2 we give the outline of Imai's method, and in § 3 we apply it to the case of two elliptic cylinders in a modified form.

The effects of the elliptic cross-sections and the angles of incidence of both elliptic cylinders make the expressions for the drag and lift much more complicated than in the case of two circular cylinders. These effects are characterized by the following parameters: σ_1, σ_2, β_1 and β_2, where $1+\sigma_1^2$, $1-\sigma_1^2$ and β_1 are respectively the semi-major axis, the semi-minor axis and the angle of incidence of the first elliptic cylinder and $a(1+\sigma_2^2)$, $a(1-\sigma_2^2)$ and β_2 are those of the second elliptic cylinder. The parameters which characterize the flow past two elliptic cylinders are σ_1, σ_2, β_1, β_2, a, d, α and R. a, d, α and R appeared already in the previous investigation, but R, the Reynolds number, is here based on the major axis of the first elliptic cylinder, so that $R=2U(1+\sigma_1^2)/\nu$ instead of $R=2U/\nu$.

In particular, if we put σ_1 and σ_2 equal to unity, then we have the formulae for the two flat plates, while if we make σ_1 and σ_2 vanish, the formulae reduce to those for the two circular cylinders which were obtained in the previous paper.

Numerical calculations were carried out in the following cases: (i) $a=1$; $h=10$; $t_1=t_2=0, 0.1, 0.5$; $\alpha=90°$; $\beta_1=-\beta_2=0°\sim 90°$; $R=0.04\sim 1.0$; (ii) $a=1$; $h=10$; $t_1=t_2=0, 0.1, 0.5$; $\alpha=0°, 180°$; $\beta_1=0°, 90°$; $\beta_2=0°, 90°$; $R=0.04\sim 1.0$, where $t_1=(1-\sigma_1^2)/(1+\sigma_1^2)$, $t_2=(1-\sigma_2^2)/(1+\sigma_2^2)$ are the thickness ratios of the two cylinders respectively and $h=d/(1+\sigma_1^2)$.

§ 2. Imai's Method of Solving Oseen's Equations

In the previous paper[1], we have given the general expression for the complex velocity to the Oseen approximation. But it is inconvenient for the application to the elliptic cylinder. Therefore, we need the expression for the complex velocity which can be applied to arbitrary profiles. We derive this, following Imai's deduction[5].

We introduce the complex variables

$$z=x+iy=re^{i\theta}\,, \qquad \bar{z}=x-iy=re^{-i\theta}\,, \tag{2.1}$$

and

$$W=u-iv\,, \tag{2.2}$$

where (x, y) are the Cartesian coordinates, (u, v) the velocity components and (r, θ) the polar coordinates. In the previous paper, we obtained the complex velocity to Oseen's approximation as

$$W=\frac{i}{2k}e^{kx}\left\{A_1K_0(kr)+\sum_{n=1}^{\infty}(A_{n+1}e^{ni\theta}-\overline{A}_ne^{-ni\theta})K_n(kr)\right\}+\frac{df}{dz}\,, \tag{2.3}$$

and

$$f(z)=Uz+\frac{m+i\Gamma}{2\pi}\ln z+O\left(\frac{1}{z}\right), \tag{2.4}$$

which satisfies the boundary conditions at infinity. Here $2k=U/\nu$ (U is the velocity of the uniform flow in the direction of the x-axis and ν the kinematic viscosity), A_n's are complex coefficients, m and Γ are real constants and K_n is the modified Bessel function of the second kind.

If we consider only the state near the cylinder, the argument kr of the Bessel function is expected to be $O(R)$, R being the Reynolds number which is assumed small. Hence, we can expand Bessel functions in the power series of kr, then we have

$$W=\frac{df}{dz}-\frac{i}{2k}e^{kx}\left[\frac{8}{k^3}g''(z)+\frac{4}{k^2}\bar{g}'(\bar{z})+\frac{2}{k}\bar{z}g'(z)+z\bar{g}(\bar{z})-\frac{k^3}{32}\overline{A}_1z\bar{z}^2\left(\ln\bar{z}-2S-\frac{3}{2}\right)-\frac{k}{4}A_2z(\ln z-2S-1)\right], \tag{2.5}$$

where

$$S=\ln(2/k)-\gamma\,, \tag{2.6}$$

$$g(z)=\frac{1}{32}k^3A_1\{z^2\ln z-\frac{1}{2}z^2-(2S+1)z^2\}$$

$$+\frac{1}{8}k^2\bar{A}_1 z(\ln z-1)-\frac{1}{4}k\bar{A}_2\ln z$$
$$+\frac{1}{4}k\sum_{n=3}^{\infty}(n-3)!\,\bar{A}_n\left(\frac{1}{2}kz\right)^{2-n}. \tag{2.7}$$

If we assume the following forms, in view of the form of W,

$$\bar{A}_1=k(a_0+ka_1+k^2a_2+\cdots)\,, \tag{2.8a}$$
$$\bar{A}_2=k^2(b_0+kb_1+k^2b_2+\cdots)\,, \tag{2.8b}$$
$$g(z)=k^3\{g_0(z)+kg_1(z)+k^2g_2(z)+\cdots\}\,, \tag{2.8c}$$
$$f(z)=k^{-1}\{f_0(z)+kf_1(z)+k^2f_2(z)+\cdots\}\,, \tag{2.8d}$$

we have from (2.7) and (2.8)

$$g_0''(z)=\frac{1}{8}\frac{a_0}{z}+\frac{1}{4}\frac{b_0}{z^2}+\cdots\,, \tag{2.9a}$$
$$g_m''(z)=\frac{1}{16}\bar{a}_{m-1}(\ln z-2S)+\frac{1}{8}\frac{a_m}{z}+\frac{1}{4}\frac{b_m}{z^2}+\cdots$$
$$(m=1,2,\cdots) \tag{2.9b}$$

The condition $W=0$ at the surface of the cylinder, or the modified condition:

$$e^{-kz}W=0 \tag{2.10}$$

is sufficient to determine the analytic functions $f(z)$ and $g(z)$. Equating to zero the coefficients of each power of k of the left-hand side of (2.10), we have a series of equations:

$$f_0'(z)=4ig_0''(z)\,, \tag{2.11a}$$
$$f_1'(z)=\tfrac{1}{2}(z+\bar{z})f_0'(z)+4ig_1''(z)+2i\bar{g}_0'(\bar{z})\,, \tag{2.11b}$$
$$f_2'(z)=\tfrac{1}{2}(z+\bar{z})f_1'(z)-\tfrac{1}{8}(z+\bar{z})^2f_0'(z)$$
$$+i\{4g_2''(z)+2\bar{g}_1'(\bar{z})+\bar{z}g_0'(z)\}\,, \tag{2.11c}$$

on the profile. Then, we rearrange (2.5) and obtain the complex velocity near the cylinder as

$$W=e^{kz}\sum_{n=0}^{\infty}k^n\{F_{n+1}(z)-G_n(z,\bar{z})\}\,, \tag{2.12}$$

where

$$F_n(z)=f_n'(z)-4ig_n''(z) \tag{2.13}$$

and

$$G_0(z,\bar{z})=\tfrac{1}{2}(z+\bar{z})f_0'(z)+2i\bar{g}_0'(\bar{z})\,, \tag{2.14}$$
$$G_1(z,\bar{z})=\tfrac{1}{2}(z+\bar{z})f_1'(z)-\tfrac{1}{8}(z+\bar{z})^2f_0'(z)$$
$$+i\{2\bar{g}_1'(\bar{z})+\bar{z}g_0'(z)\}\,, \tag{2.15}$$

and so on. The terms of $O(k^{-1})$ in (2.12) have been omitted on account of the boundary condition (2.11a) which holds throughout the field of flow.

The boundary conditions on the profile are

$$F_{n+1}(z)=G_n(z,\bar{z})\,. \tag{2.16}$$

To a first approximation, we have

$$F_1(z)=G_0(z,\bar{z})\,, \tag{2.17}$$

with

$$F_1(z)=f_1'(z)-4ig_1''(z)\,, \tag{2.18}$$
$$G_0(z,\bar{z})=\tfrac{1}{2}(z+\bar{z})f_0'(z)+2i\bar{g}_0'(\bar{z})\,. \tag{2.19}$$

We assume that the region outside the profile can be mapped onto the region outside a unit circle in the Z-plane by the transformation function

$$z=\omega(Z)\,. \tag{2.20}$$

Then (2.17) becomes

$$F_1[\omega(\zeta)]=G_0[\omega(\zeta),\overline{\omega(\zeta)}]\quad\text{for }\zeta=e^{i\theta}\,. \tag{2.21}$$

Substituting from (2.4), (2.9) and (2.20) into (2.18), we have

$$F_1[\omega(\zeta)]=U-\tfrac{1}{4}i\bar{a}_0\{\ln\omega(\zeta)-2S\}+P(Z^{-1})\,, \tag{2.22}$$

where $P(Z)=\sum_{n=1}^{\infty}C_nZ^n$. (2.21) and (2.22) lead to an integro-differential equation for the function $g_0'(z)$ of the form:

$$\oint_C\frac{G_0[\omega(\zeta),\overline{\omega(\zeta)}]+\frac{1}{4}i\bar{a}_0\ln\omega(\zeta)}{\zeta-Z}d\zeta$$
$$=2\pi i(U+\tfrac{1}{2}i\bar{a}_0S)\,, \tag{2.23}$$

where C is the unit circle. Thus, the first approximation has been completed. The successive approximations can be carried out in the same way.

§ 3. Application of Imai's Method to the Case of Two Elliptic Cylinders

In the general cases of two elliptic cylinders submerged in a uniform flow at small Reynolds numbers, we assume the following form for the complex velocity

$$W(z_1,z_2)=W_1(z_1)+W_2(z_2)+U\,, \tag{3.1}$$

with

$$W_1(z_1)=e^{kx_1}\sum_{n=1}^{\infty}k^n\{F_{n+1}^{(1)}(z_1)-G_n^{(1)}(z_1,\bar{z}_1)\}\,, \tag{3.2}$$
$$W_2(z_2)=\frac{i}{2k}e^{kx_2}\left\{A_1^{(2)}K_0(kr_2)+\sum_{n=1}^{\infty}(A_{n+1}^{(2)}e^{ni\theta_2}\right.$$
$$\left.-\bar{A}_n^{(2)}e^{-ni\theta_2})K_n(kr_2)\right\}+\frac{df^{(2)}}{dz_2}\,, \tag{3.3}$$

near the first elliptic cylinder E_1 and with

$$W_1(z_1)=\frac{i}{2k}e^{kx_1}\left\{A_1^{(1)}K_0(kr_1)+\sum_{n=1}^{\infty}(A_{n+1}^{(1)}e^{ni\theta_1}\right.$$
$$\left.-\bar{A}_n^{(1)}e^{-ni\theta_1})K_n(kr_1)\right\}+\frac{df^{(1)}}{dz_1}\,, \tag{3.4}$$
$$W_2(z_2)=e^{kx_2}\sum_{n=1}^{\infty}k^n\{F_{n+1}^{(2)}(z_2)-G_n^{(2)}(z_2,\bar{z}_2)\}\,, \tag{3.5}$$

near the second elliptic cylinder E_2 alternatively. Here $F_{n+1}^{(1)}(z_1)$, $F_{n+1}^{(2)}(z_2)$, $G_n^{(1)}(z_1,\bar{z}_1)$,

$G_n^{(2)}(z_2, \bar{z}_2)$, $f^{(1)}(z_1)$, $f^{(2)}(z_2)$ and so on have forms similar to those obtained in § 2 except that they are devoid of the terms corresponding to the uniform flow. Also z_1 and z_2 are the vectors drawn from the centres of the elliptic cylinders E_1 and E_2 to the point in

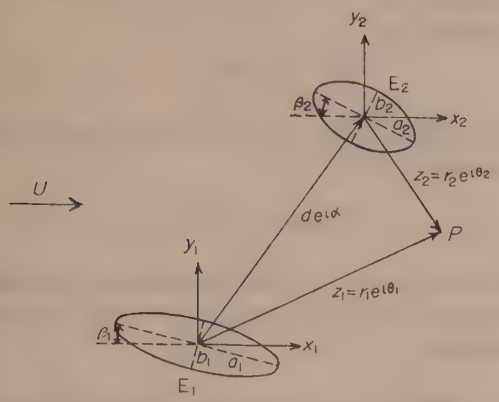

Fig. 1. The general configuration of two elliptic cylinders.

question and $de^{i\alpha}$ is the vector connecting the centres of E_1 and E_2 (*cf.* Fig. 1.).

By the transformation function

$$z_1=C_1\left(Z_1+\frac{\sigma_1^2}{Z_1}\right), \qquad (0\leq\sigma_1\leq 1,\ C_1=c^{-i\beta_1}) \tag{3.6}$$

the unit circle $Z_1=e^{i\theta}$ in the Z_1-plane is mapped onto the first ellipse which is inclined at an angle β_1 with respect to the x_1-axis and whose semi-major and semi-minor axes are respectively

$$a_1=1+\sigma_1^2\,, \qquad b_1=1-\sigma_1^2\,. \tag{3.7}$$

The expressions corresponding to (3.6) and (3.7) for the second ellipse E_2 are

$$z_2=C_2\left(Z_2+\frac{\sigma_2^2}{Z_2}\right), \quad (0\leq\sigma_2\leq 1,\ C_2=ae^{-i\beta_2})\,, \tag{3.8}$$

$$a_2=a(1+\sigma_2^2)\,, \qquad b_2=a(1-\sigma_2^2)\,. \tag{3.9}$$

In this paper we shall confine ourselves to the first approximation. Thus we take only the terms of $O(k^0)$ in the complex velocity. Then, (3.2) and (3.5) reduce to

$$W_p(z_p)=F_1^{(p)}(z_p)-G_0^{(p)}(z_p, \bar{z}_p) \qquad \text{near } E_p. \tag{3.10}$$

Here as well as in what follows, $p=1$ and 2 correspond to the first and the second ellipse respectively. From (2.4), (2.9), (2.11a), (3.6) and (3.8), we have

$$f_1^{(p)\prime}(z_p)=P(Z_p^{-1})\,, \tag{3.11}$$

$$g_1^{(p)\prime\prime}(z_p)=\frac{1}{16}\bar{a}_0^{(p)}(\ln C_pZ_p-2S)+P(Z_p^{-1})\,, \tag{3.12}$$

$$\bar{g}_0^{(p)\prime}(\bar{z}_p)=\frac{1}{8}\bar{a}_0^{(p)}\ln\bar{C}_p\bar{Z}_p+P(\bar{Z}_p^{-1})\,, \tag{3.13}$$

$$f_0^{(p)\prime}(z_p)=4ig_0^{(p)\prime\prime}(z_p)$$
$$=\frac{1}{2}ia_0^{(p)}C_p^{-1}Z_p^{-1}\{1+P(Z_p^{-1})\}\,. \tag{3.14}$$

Hence, by (2.13) and (2.14) we have

$$F_1^{(p)}(z_p)=-\tfrac{1}{4}i\bar{a}_0^{(p)}(\ln C_pZ_p-2S)+P(Z_p^{-1})\,, \tag{3.15}$$

$$G_0^{(p)}(z_p, \bar{z}_p)=\tfrac{1}{4}ia_0^{(p)}(1+\sigma_p^2\bar{D}_p^2)-\tfrac{1}{4}i\bar{a}_0^{(p)}\ln C_pZ_p$$
$$+2i\{\bar{g}_0^{(p)\prime}(\bar{z}_p)-\tfrac{1}{8}\bar{a}_0^{(p)}\ln\bar{C}_p\bar{Z}_p\}+P(Z_p^{-1})\,, \tag{3.16}$$

where $D_p=e^{-i\beta_p}(=C_1$ or C_2/a according as $p=1$ or 2). By use of (3.15) and (3.16), we can rewrite (3.10) explicitly as

$$W_p(z_p)=-\tfrac{1}{4}ia_0^{(p)}(1+\sigma_p^2\bar{D}_p^2)+\tfrac{1}{2}i\bar{a}_0^{(p)}S_p$$
$$+2i\{\bar{g}_0^{(p)\prime}(\bar{z}_p)-\tfrac{1}{8}\bar{a}_0^{(p)}\ln\bar{C}_p\bar{Z}_p\}+P(Z_p^{-1}) \qquad \text{near } E_p, \tag{3.17}$$

where

$$S_1=\ln(2/k)-\gamma\,, \qquad S_2=\ln(2/ka)-\gamma\,. \tag{3.18}$$

We now assume that $kd\geqq O(1)$ so that $K_n(kd)=O(1)$*. Taking the terms of $O(k^0)$ in (3.3) and (3.4), we obtain

$$W_q(z_q)=\frac{i}{2k}e^{kd\cos(\alpha+p\pi)}(A_1^{(q)}K_0$$
$$-\bar{A}_1^{(q)}e^{-i(\alpha+p\pi)}K_1)+\frac{1}{k}\frac{df_0^{(q)}}{dz_q}+P(Z_p) \text{ near } E_p,$$

where $q\neq p$, that is, $q=3-p$ and we have put $K_n(kd)=K_n$ for brevity. By use of (2.8) and (3.14), which hold throughout the field of flow, we rewrite the above expressions as follows.

$$W_q(z_q)=\frac{i}{2}(K_1e^{kd\cos(\alpha+p\pi)}-1/kd)e^{-i(\alpha+p\pi)}a_0^{(q)}$$
$$+\frac{i}{2}K_0e^{kd\cos(\alpha+p\pi)}\bar{a}_0^{(q)}+P(Z_p)\,. \tag{3.19}$$

The boundary conditions are

$$W(z_1, z_2)=W_1(z_1)+W_2(z_2)+U=0\,, \tag{3.20}$$

on the surfaces of E_1 and E_2. Substituting from (3.17) and (3.19) into (3.20), we obtain

$$g_0^{(p)\prime}(z_p)-\tfrac{1}{8}a_0^{(p)}\ln C_pZ_p+P(Z_p^{-1})$$
$$=\tfrac{1}{8}\{4iU+2a_0^{(p)}S_p-\bar{a}_0^{(p)}(1+\sigma_p^2D_p^2)$$
$$+2K_0e^{kd\cos(\alpha+p\pi)}a_0^{(q)}$$

* If $kd\to\infty$, then $K_n(kd)\to 0$. The following argument is also valid for such a case.

$$+2(K_1e^{kd\cos(\alpha+p\pi)}-1/kd)e^{i\alpha}\bar{a}_0^{(q)}\}+P(Z_p) \tag{3.21}$$

on the profile $Z_p=e^{i\theta}$. From (2.9), we find that the left-hand side of (3.21) is $P(Z^{-1})$, while the right-hand side is $P(Z)$. Hence both sides must be separately equal to zero. Thus we have

$$g_0^{(p)\prime}(z_p)=\tfrac{1}{8}a_0^{(p)}\ln C_pZ_p\ , \tag{3.22}$$

$$\begin{aligned}4iU=&-2a_0^{(p)}S_p+\bar{a}_0^{(p)}(1+\sigma_p^2D_p^2)\\&-2K_0e^{kd\cos(\alpha+p\pi)}a_0^{(q)}\\&-2(K_1e^{kd\cos(\alpha+p\pi)}-1/kd)e^{i\alpha}\bar{a}_0^{(q)}\ .\end{aligned} \tag{3.23}$$

From (3.23) and its complex conjugate, we can determine $a_0^{(1)}$ and $a_0^{(2)}$.

Substituting (3.22) into (2.11a) and using (3.6), we obtain

$$f_0^{(1)\prime}=4i\frac{dg_0^{(1)\prime}(z_1)}{dZ_1}\Big/\frac{dz_1}{dZ_1}=\frac{ia_0^{(1)}}{2C_1}\frac{Z_1}{Z_1^2-\sigma_1^2}+P(Z_1^{-2})\ . \tag{3.24}$$

Now the drag coefficient $C_D^{(p)}$ and the lift coefficient $C_L^{(p)}$ for the elliptic cylinder E_p are respectively defined as

$$C_D^{(p)}=\frac{X_p}{\frac{1}{2}\rho U^2 2a_p}\ ,\qquad C_L^{(p)}=\frac{Y_p}{\frac{1}{2}\rho U^2 2a_p}\ , \tag{3.25}$$

where X_p and Y_p are the drag and lift of the elliptic cylinder E_p $(p=1, 2)$.

It is known[5] that the drag X and the lift Y of a cylinder are given by

$$X=\rho Um\ ,\qquad Y=\rho U\Gamma\ , \tag{3.26}$$

where $(m+i\Gamma)/2\pi$ is the coefficient of $1/z$ in the asymptotic expansion of df/dz, as given by (2.4). Hence it may be supposed that we can put

$$X_p=\rho Um_p\ ,\qquad Y_p=\rho U\Gamma_p\ , \tag{3.27}$$

where $(m_p+i\Gamma_p)/2\pi$ is the coefficient of $1/z_p$ in the asymptotic expansion of $df^{(p)}/dz_p$.

It is obviously sufficient to consider the lift and drag coefficients of the first cylinder E_1 only. Now, we have from (2.8d)

$$\frac{df^{(1)}}{dz_1}=\frac{1}{k}\{f_0^{(1)\prime}+kf_1^{(1)\prime}+\cdots\}\ .$$

Hence, we obtain from (3.24), in the first approximation,

$$\frac{m_1+i\Gamma_1}{2\pi}=\frac{ia_0^{(1)}}{2k}\ . \tag{3.28}$$

Substituting from (3.27) and (3.28) into (3.25), we have

$$C_D^{(1)}+iC_L^{(1)}=\frac{4\pi ia_0^{(1)}}{UR}\ , \tag{3.29}$$

where $R=4(1+\sigma_1^2)k$ is the Reynolds number based on the major axis of the first elliptic cylinder.

§ 4. The Case of the Symmetrical Configurations with the Central Line Perpendicular to the Uniform Flow

In this section, we apply the method given in the last section to the flow past two equal elliptic cylinders placed symmetrically with the central line perpendicular to the oncoming uniform flow, that is, $a=1$, $\sigma_1=\sigma_2=\sigma$, $\beta_1=-\beta_2=\beta$ and $\alpha=\pi/2$ so that $S_1=S_2=S$, $C_1=\bar{C}_2=C=e^{-i\beta}$ (*cf.* Fig. 2 (a)). In this case, in view of symmetry, we find

$$W_1(z)=\bar{W}_2(z)\ ,$$

so that

$$a_0^{(1)}=-\bar{a}_0^{(2)}\ , \tag{4.1}$$

and consequently (3.23) can be written as

$$\begin{aligned}4iU=&-2\{S-i(K_1-1/kd)\}a_0^{(1)}\\&+(1+\sigma_1^2C_1^2+2K_0)\bar{a}_0^{(1)}\ .\end{aligned} \tag{4.2}$$

From (4.2) and its complex conjugate, we have

$$a_0^{(1)}=-2iU\times\frac{(S-\frac{1}{2}-\frac{1}{2}\sigma^2\cos 2\beta-K_0)+i(K_1-4/Rh+\frac{1}{2}\sigma^2\sin 2\beta)}{(S+\frac{1}{2}+\frac{1}{2}\sigma^2\cos 2\beta+K_0)(S-\frac{1}{2}-\frac{1}{2}\sigma^2\cos 2\beta-K_0)+(K_1-4/Rh+\frac{1}{2}\sigma^2\sin 2\beta)(K_1-4/Rh-\frac{1}{2}\sigma^2\sin 2\beta)}\ , \tag{4.3}$$

where $h=d/(1+\sigma^2)$ is the ratio of the distance between the two cylinders to the semi-major axis of the elliptic cylinder.

Substituting from (4.3) into (3.29) and taking the real and imaginary parts, we obtain

$$C_D^{(1)}=\frac{8\pi}{R}\times\frac{S-\frac{1}{2}-\frac{1}{2}\sigma^2\cos 2\beta-K_0}{(S+\frac{1}{2}+\frac{1}{2}\sigma^2\cos 2\beta+K_0)(S-\frac{1}{2}-\frac{1}{2}\sigma^2\cos 2\beta-K_0)+(K_1-4/Rh+\frac{1}{2}\sigma^2\sin 2\beta)(K_1-4/Rh-\frac{1}{2}\sigma^2\sin 2\beta)}\ , \tag{4.4}$$

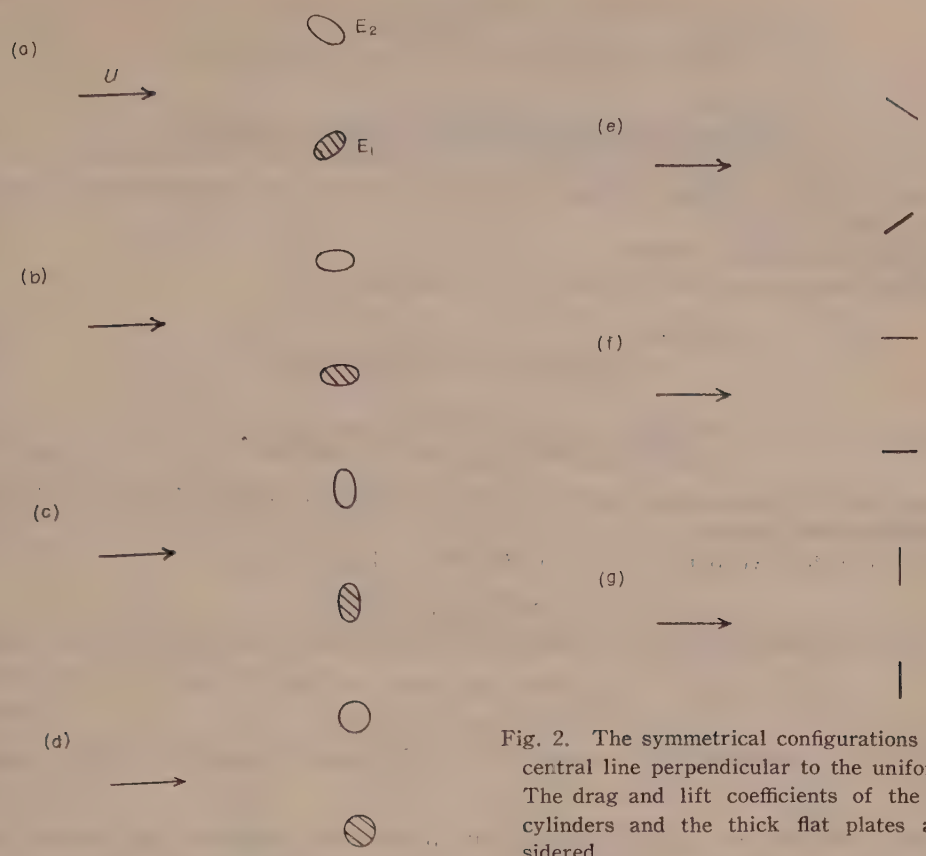

Fig. 2. (a)–(d)

Fig. 2. The symmetrical configurations with the central line perpendicular to the uniform flow. The drag and lift coefficients of the hatched cylinders and the thick flat plates are considered.

$$C_L^{(1)}=\frac{8\pi}{R}$$

$$\times\frac{K_1-4/Rh\frac{1}{2}+\sigma^2\sin 2\beta}{(S+\frac{1}{2}+\frac{1}{2}\sigma^2\cos 2\beta+K_0)(S-\frac{1}{2}-\frac{1}{2}\sigma^2\cos 2\beta-K_0)+(K_1-4/Rh+\frac{1}{2}\sigma^2\sin 2\beta)(K_1-4/Rh-\frac{1}{2}\sigma^2\sin 2\beta)}, \tag{4.5}$$

where
$$R=2(1+\sigma^2)U/\nu\,, \tag{4.6}$$

$$S=\ln[8(1+\sigma^2)/R]-\gamma\,, \tag{4.7}$$

$$K_0=K_0(Rh/4)\,,\qquad K_1=K_1(Rh/4)\,, \tag{4.8}$$

and
$$h=d/(1+\sigma^2)\,. \tag{4.9}$$

Next, we consider some special cases of interest.

(A) Case when the elliptic two cylinders are both parallel or perpendicular to the flow direction. Putting $\beta=0$ in (4.4) and (4.5), we have

$$C_D^{(1)}=\frac{8\pi}{R}\frac{S-\frac{1}{2}-\frac{1}{2}\sigma^2-K_0}{(S+\frac{1}{2}+\frac{1}{2}\sigma^2+K_0)(S-\frac{1}{2}-\frac{1}{2}\sigma^2-K_0)+(K_1-4/Rh)^2}\,, \tag{4.10}$$

$$C_L^{(1)}=\frac{8\pi}{R}\frac{K_1-4/Rh}{(S+\frac{1}{2}+\frac{1}{2}\sigma^2+K_0)(S-\frac{1}{2}-\frac{1}{2}\sigma^2-K_0)+(K_1-4/Rh)^2}\,, \tag{4.11}$$

for the first of the two elliptic cylinders both with their major axes parallel to the flow direction (*cf.* Fig. 2 (b)). Also, putting $\beta=\pi/2$, we have

$$C_D^{(1)}=\frac{8\pi}{R}\frac{S-\frac{1}{2}+\frac{1}{2}\sigma^2-K_0}{(S+\frac{1}{2}-\frac{1}{2}\sigma^2+K_0)(S-\frac{1}{2}+\frac{1}{2}\sigma^2-K_0)+(K_1-4/Rh)^2}, \tag{4.12}$$

$$C_L^{(1)}=\frac{8\pi}{R}\frac{K_1-4/Rh}{(S+\frac{1}{2}-\frac{1}{2}\sigma^2+K_0)(S-\frac{1}{2}+\frac{1}{2}\sigma^2-K_0)+(K_1-4/Rh)^2}, \tag{4.13}$$

for the first of the two elliptic cylinders with their major axes perpendicular to the flow direction (*cf.* Fig. 2 (c)).

(B) Case of two circular cylinders.

In this case, we put $\sigma=0$ in (4.4) and (4.5). Thus we have

$$C_D^{(1)}=\frac{8\pi}{R}\frac{S-\frac{1}{2}-K_0}{(S+\frac{1}{2}+K_0)(S-\frac{1}{2}-K_0)+(K_1-4/Rd)^2}, \tag{4.14}$$

$$C_L^{(1)}=\frac{8\pi}{R}\frac{K_1-4/Rd}{(S+\frac{1}{2}+K_0)(S-\frac{1}{2}-K_0)+(K_1-4/Rd)^2}; \tag{4.15}$$

They agree with the expressions (3.41) and (3.42) given in the previous paper[1] (*cf.* Fig. 2(d)).

(C) Case of two flat plates.

For two flat plates, we put $\sigma=1$ in (4.4) and (4.5). Thus, we have

$$C_D^{(1)}=\frac{8\pi}{R}\frac{S-\frac{1}{2}-\frac{1}{2}\cos 2\beta-K_0}{(S+\frac{1}{2}+\frac{1}{2}\cos 2\beta+K_0)(S-\frac{1}{2}-\frac{1}{2}\cos 2\beta-K_0)+(K_1-4/Rh+\frac{1}{2}\sin 2\beta)(K_1-4/Rh-\frac{1}{2}\sin 2\beta)}, \tag{4.16}$$

$$C_L^{(1)}=\frac{8\pi}{R}\frac{K_1-4/Rh+\frac{1}{2}\sin 2\beta}{(S+\frac{1}{2}+\frac{1}{2}\cos 2\beta+K_0)(S-\frac{1}{2}-\frac{1}{2}\cos 2\beta-K_0)+(K_1-4/Rh+\frac{1}{2}\sin 2\beta)(K_1-4/Rh-\frac{1}{2}\sin 2\beta)}, \tag{4.17}$$

for the first of the two flat plates symmetrically placed with respect to the uniform flow at arbitrary angles of incidence (*cf.* Fig. 2 (e)). In particular, putting $\beta=0$, we have

$$C_D^{(1)}=\frac{8\pi}{R}\frac{S-1-K_0}{(S+1+K_0)(S-1-K_0)+(K_1-4/Rh)^2}, \tag{4.18}$$

$$C_L^{(1)}=\frac{8\pi}{R}\frac{K_1-4/Rh}{(S+1+K_0)(S-1-K_0)+(K_1-4/Rh)^2}, \tag{4.19}$$

for the first of the two flat plates both parallel to the uniform flow (*cf.* Fig. 2 (f)). Also, putting $\beta=\pi/2$, we have

$$C_D^{(1)}=\frac{8\pi}{R}\frac{S-K_0}{(S+K_0)(S-K_0)+(K_1-4/Rh)^2}, \tag{4.20}$$

$$C_L^{(1)}=\frac{8\pi}{R}\frac{K_1-4/Rh}{(S+K_0)(S-K_0)+(K_1-4/Rh)^2}, \tag{4.21}$$

for the first of the two flat plates perpendicular to the uniform flow (*cf.* Fig. 2 (g)).

§ 5. The Case of Symmetrical Configurations with the Central Line Parallel to the Uniform Flow

In the case when the two elliptic cylinders are placed symmetrically with the central line parallel to the uniform flow (*cf.* Fig. 3), that is, $\beta_1=0$ or $\pi/2$, $\beta_2=0$ or $\pi/2$ and $\alpha=0$ or π, we find in view of symmetry that the lifts of both cylinders vanish, so that we can suppose that $a_0^{(1)}$ and $a_0^{(2)}$ are purely imaginary. Thus

$$a_0^{(1)}=-\bar{a}_0^{(1)}, \qquad a_0^{(2)}=-\bar{a}_0^{(2)}. \tag{5.1}$$

We can solve (3.23) for $a_0^{(1)}$, and then substituting it into (3.29), we obtain

$$C_D^{(1)}=\frac{8\pi}{R}$$

$$\times\frac{S_2+\frac{1}{2}+\frac{1}{2}\sigma_2^2\cos 2\beta_2-(K_0-K_1\cos\alpha)e^{-Rh\cos\alpha/4}-4\cos\alpha/Rh}{(S_1+\frac{1}{2}+\frac{1}{2}\sigma_1^2\cos 2\beta_1)(S_2+\frac{1}{2}+\sigma_2^2\cos 2\beta_2)-\{(K_0+K_1)e^{Rh/4}-4/Rh\}\{(K_0-K_1)e^{-Rh/4}+4/Rh\}}\,, \tag{5.2}$$

where

$$R=2(1+\sigma_1^2)U/\nu\,, \tag{5.3}$$

$$S_1=\ln[8(1+\sigma_1^2)/R]-\gamma\,,\qquad S_2=\ln[8(1+\sigma_1^2)/Ra]-\gamma\,, \tag{5.4}$$

$$K_0=K_0(Rh/4)\,,\qquad K_1=K_1(Rh/4)\,. \tag{5.5}$$

They include many configurations according to the parameters α, β_1, β_2, σ_1 and σ_2, as sketched in Fig. 3. Next, we consider some special cases of interest.

(A) Case of two equal elliptic cylinders.

In this case, $a=1$. Hence we put $S_1=S_2=S$ and $\sigma_1=\sigma_2=\sigma$ in (5.2). Then, we have

(i) $\beta_1=\beta_2=0$; $\alpha=0$ or π (*cf.* Fig. 3 (a) and (b)):

$$C_D^{(1)}=\frac{8\pi}{R}\frac{S+\frac{1}{2}(1+\sigma^2)-(K_0\mp K_1)e^{\mp Rh/4}\mp 4/Rh}{\{S+\frac{1}{2}(1+\sigma^2)\}^2-\{(K_0+K_1)e^{Rh/4}-4/Rh\}\{(K_0-K_1)e^{-Rh/4}+4/Rh\}}\,, \tag{5.6}$$

where as well as in what follows the upper and lower signs correspond to $\alpha=0$ and $\alpha=\pi$ respectively.

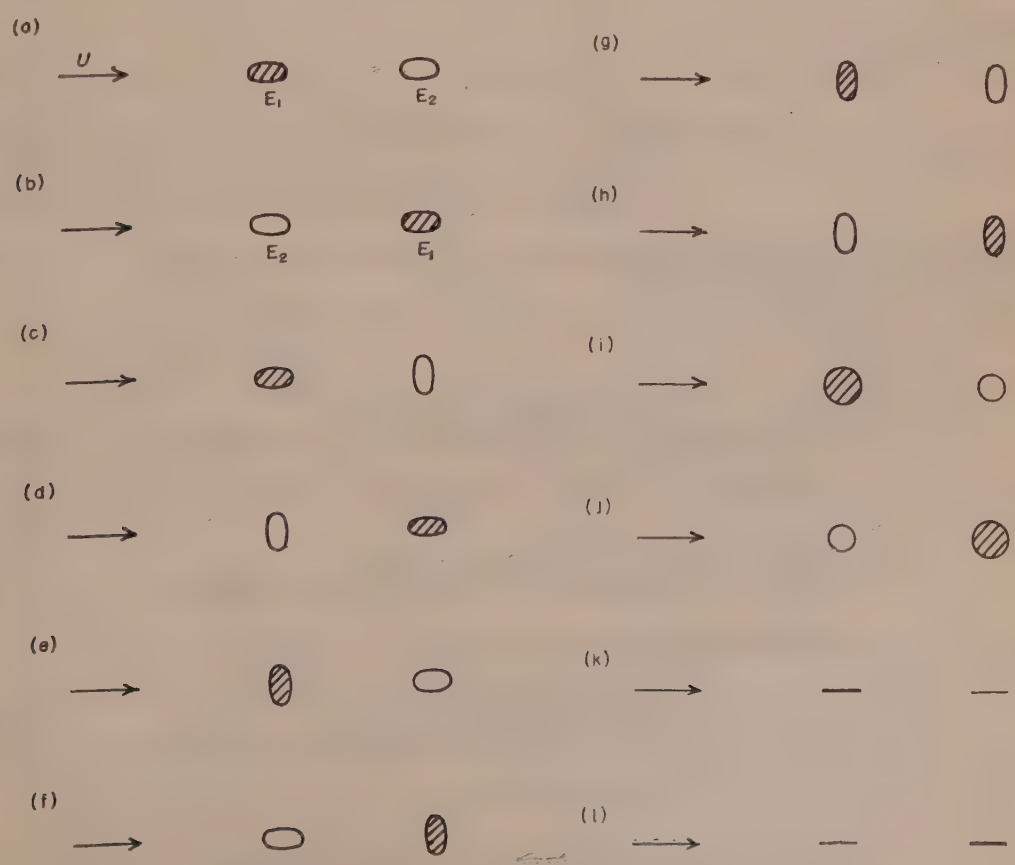

Fig. 3. (a)-(f) Fig. 3. (g)-(l).

(ii) $\beta_1=0$, $\beta_2=\pi/2$; $\alpha=0$ or π (*cf.* Fig. 3 (c) and (d)):

$$C_D^{(1)}=\frac{8\pi}{R}\frac{S+\frac{1}{2}(1-\sigma^2)-(K_0\mp K_1)^{\mp Rh/4}\mp 4/Rh}{\{S+\frac{1}{2}(1+\sigma^2)\}\{S+\frac{1}{2}(1-\sigma^2)\}^2-\{(K_0+K_1)e^{Rh/4}-4/Rh\}\{(K_0-K_1)e^{-Rh/4}+4/Rh\}}, \tag{5.7}$$

(iii) $\beta_1=\pi/2$, $\beta_2=0$; $\alpha=0$ or π (*cf.* Fig. 3 (e) and (f)):

$$C_D^{(1)}=\frac{8\pi}{R}\frac{S+\frac{1}{2}(1+\sigma^2)-(K_0\mp K_1)e^{\mp Rh/4}\mp 4/Rh}{\{S+\frac{1}{2}(1+\sigma^2)\}\{S+\frac{1}{2}(1-\sigma^2)\}-\{(K_0+K_1)e^{Rh/4}-4/Rh\}\{(K_0-K_1)e^{-Rh/4}+4/Rh\}}. \tag{5.8}$$

(iv) $\beta_1=\beta_2=\pi/2$; $\alpha=0$ or π (*cf.* Fig. 3 (g) and (h)):

$$C_D^{(1)}=\frac{8\pi}{R}\frac{S+\frac{1}{2}(1-\sigma^2)-(K_0\mp K_1)e^{\mp Rh/4}\mp 4/Rh}{\{S+\frac{1}{2}(1-\sigma^2)\}^2-\{(K_0+K_1)e^{Rh/4}-4/Rh\}\{(K_0-K_1)e^{-Rh/4}+4/Rh\}}, \tag{5.9}$$

where

$$R=2(1+\sigma^2)U/\nu\,, \tag{5.10}$$

$$S=\ln[8(1+\sigma^2)/R]-\gamma\,. \tag{5.11}$$

(B) Case of two circular cylinders (*cf.* Fig. 3 (i) and (j)).

In this case, we put $\sigma_1=\sigma_2=0$ and then (5.2) becomes

$$C_D^{(1)}=\frac{8\pi}{R}\frac{S_2+\frac{1}{2}-(K_0\mp K_1)e^{\mp Rd/4}\mp 4/Rd}{(S_1+\frac{1}{2})(S_2+\frac{1}{2})-\{(K_0+K_1)e^{Rd/4}-4/Rd\}\{(K_0-K_1)e^{-Rd/4}-4/Rd\}}, \tag{5.12}$$

where

$$R=2U/\nu\,, \tag{5.13}$$

$$S_1=\ln(8/R)-\gamma\,,\qquad S_2=\ln(8/Ra)-\gamma\,, \tag{5.14}$$

$$K_0=K_0(Rd/4)\,,\qquad K_1=K_1(Rd/4)\,. \tag{5.15}$$

The formula (5.12) agrees with (3.43) and (3.44) given in the previous paper[1].

(C) Case of two equal flat plates.

In this case, we put $S_1=S_2=S$, $\sigma_1=\sigma_2=1$ and $a=1$. Then, we have

(i) $\beta_1=\beta_2=0$; $\alpha=0$ or π (*cf.* Fig. 3 (k) and (l)):

$$C_D^{(1)}=\frac{8\pi}{R}\frac{S+1-(K_0\mp K_1)e^{\mp Rh/4}\mp 4/Rh}{(S+1)^2-\{(K_0+K_1)e^{Rh/4}-4/Rh\}\{(K_0-K_1)e^{-Rh/4}+4/Rh\}}, \tag{5.16}$$

(ii) $\beta_1=0$; $\beta_2=\pi/2$; $\alpha=0$ or π (*cf.* Fig. 3 (m) and (n)):

$$C_D^{(1)}=\frac{8\pi}{R}\frac{S-(K_0\mp K_1)e^{\mp Rh/4}\mp 4/Rh}{S(S+1)-\{(K_0+K_1)e^{Rh/4}-4/Rh\}\{(K_0-K_1)e^{-Rh/4}+4/Rh\}}, \tag{5.17}$$

(iii) $\beta_1=\pi/2$; $\beta_2=0$; $\alpha=0$ or π (*cf.* Fig. 3 (o) and (p)):

$$C_D^{(1)}=\frac{8\pi}{R}\frac{S+1-(K_0\mp K_1)e^{\mp Rh/4}\mp 4/Rh}{S(S+1)-\{(K_0+K_1)e^{Rh/4}-4/Rh\}\{(K_0-K_1)e^{-Rh/4}+4/Rh\}}, \tag{5.18}$$

(iv) $\beta_1=\beta_2=0$; $\alpha=0$ or π (*cf.* Fig. 3 (q) and (r)):

$$C_D^{(1)}=\frac{8\pi}{R}\frac{S-(K_0\mp K_1)e^{\mp Rh/4}\mp 4/Rh}{S^2-\{(K_0+K_1)e^{Rh/4}-4/Rh\}\{(K_0-K_1)e^{-Rh/4}+4/Rh\}}, \tag{5.19}$$

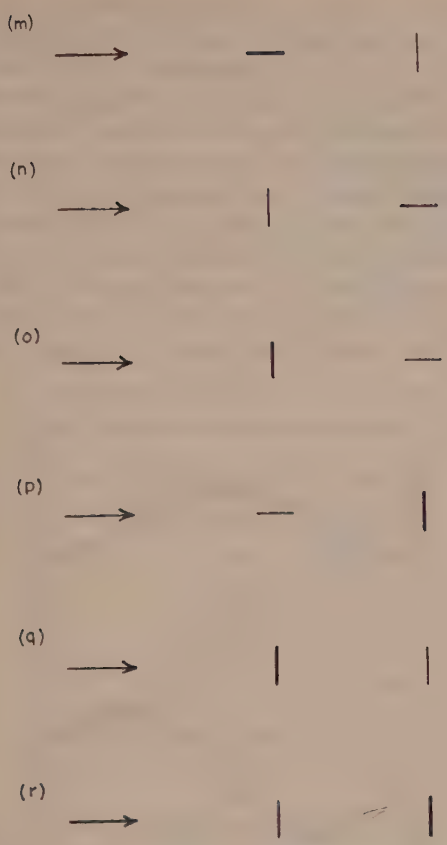

Fig. 3. The symmetrical configurations with the central line parallel to the uniform flow. The drag coefficients of the hatched cylinders and the thick flat plates are considered.

where

$$R=4U/\nu\ , \tag{5.20}$$

$$S=\ln(16/R)-\gamma\ , \tag{5.21}$$

$$K_0=K_0(Rh/4)=K_0(Rd/8)\ ,$$

$$K_1=K_1(Rh/4)=K_1(Rd/8)\ . \tag{5.22}$$

§ 6. The General Case

The general case can be dealt with in quite a similar manner to § 4 and § 5. Thus, we have

$$C_D{}^{(1)}=\frac{8\pi}{R}\frac{\Delta_X{}^{(1)}}{J}\ , \tag{6.1}$$

$$C_L{}^{(1)}=\frac{8\pi}{R}\frac{\Delta_Y{}^{(1)}}{J}\ , \tag{6.2}$$

with

$$\begin{aligned}J=&(o_1o_2-n_1{}^2)(o_3o_4-n_2{}^2)+(p_1p_2-q_1{}^2)(p_3p_4-q_2{}^2)\\&-(o_1p_2+q_1n_1)(o_3p_3-q_2n_2)\\&-(o_2p_1+q_1n_1)(o_4p_4-q_2n_2)\\&+(o_1q_1+p_1n_1)(o_4q_2-p_3n_2)\\&+(o_2q_1+p_2n_1)(o_3q_2-p_4n_2)\ ,\end{aligned} \tag{6.3}$$

$$\begin{aligned}\Delta_X{}^{(1)}=&o_2(o_3o_4-n_2{}^2)+p_2(p_3p_4-q_2{}^2)\\&-p_2(o_3p_3-q_2n_2)-o_2(o_4p_4-q_2n_2)\\&+(q_1+n_1)(o_4q_2-p_3n_2)\ ,\end{aligned} \tag{6.4}$$

$$\begin{aligned}\Delta_Y{}^{(1)}=&n_1(o_3o_4-n_2{}^2)-q_1(p_3p_4-q_2{}^2)\\&+q_1(o_3p_3-q_2n_2)-n_1(o_4p_4-q_2n_2)\\&+(o_1-p_1)(o_4q_2-p_3n_2)\ ,\end{aligned} \tag{6.5}$$

where

$$o_1,\ o_2=S_1\pm\tfrac{1}{2}(1+\sigma_1{}^2\cos 2\beta_1)\ , \tag{6.6}$$

$$o_3,\ o_4=S_2\pm\tfrac{1}{2}(1+\sigma_2{}^2\cos 2\beta_2)\ , \tag{6.7}$$

$$p_1,\ p_2=K_0e^{Rh\cos\alpha/4}\pm(K_1e^{Rh\cos\alpha/4}-4/Rh)\cos\alpha\ , \tag{6.8}$$

$$p_3,\ p_4=K_0e^{-Rh\cos\alpha/4}\pm(K_1e^{-Rh\cos\alpha/4}-4/Rh)\cos\alpha\ , \tag{6.9}$$

$$q_1,\ q_2=(K_1e^{\pm Rh\cos\alpha/4}-4/Rh)\sin\alpha\ , \tag{6.10}$$

$$n_p=\tfrac{1}{2}\sigma_p{}^2\sin 2\beta_p\ ,\qquad (p=1,\ 2) \tag{6.11}$$

and

$$R=2(1+\sigma_1{}^2)U/\nu\ , \tag{6.12}$$

$$S_1=\ln[8(1+\sigma_1{}^2)/R]-\gamma\ ,$$

$$S_2=\ln[8(1+\sigma_1{}^2)/Ra]-\gamma\ , \tag{6.13}$$

$$K_0=K_0(Rh/4)\ ,\qquad K_1=K_1(Rh/4)\ . \tag{6.14}$$

If we put $\sigma_1=\sigma_2=0$, then $n_1=n_2=0$ and (6.1)–(6.11) agree with (3.25)–(3.39) in the previous paper for two circular cylinders in the general configurations.

Making use of the asymptotic form of $K_n(kd)$, we have the limiting forms of (6.1) and (6.2) for $kd\to\infty$ as

$$C_D{}^{(1)}=\frac{8\pi}{R}\frac{S_1-\frac{1}{2}(1+\sigma_1{}^2\cos 2\beta_1)}{S_1{}^2-\frac{1}{4}(1+\sigma_1{}^4+2\sigma_1{}^2\cos 2\beta_1)}\ , \tag{6.15}$$

$$C_L{}^{(1)}=\frac{8\pi}{R}\frac{\frac{1}{2}\sigma_1{}^2\sin 2\beta_1}{S_1{}^2-\frac{1}{4}(1+\sigma_1{}^4+2\sigma_1{}^2\cos 2\beta_1)}\ , \tag{6.16}$$

which coincide with the first approximate expressions for the case of a single elliptic cylinder obtained by Imai[5], Tomotika and Yosinobu[6] and Hasimoto[7].

It can be proved that the general expressions (6.1)–(6.11) reduce to the previous results in § 4 and § 5 by taking $\alpha=\pi/2,\ 0,\ \pi$.

§ 7. Numerical Discussions

The parameters to characterize the flow past the two elliptic cylinders are σ_1, σ_2, β_1, β_2, a, h, α and R. The effects of a, h and α may be expected to be qualitatively similar to those for the case of two circular cylinders. Therefore we shall here confine ourselves to the investigation of the effects of the new parameters σ_1, σ_2, β_1 and β_2. Further, we fix

$h=d/(1+\sigma_1^2)=10$ and consider only the cases of symmetrical configurations of two equal cylinders.

Numerical calculations have been carried out for the cases:

(i) $a=1$; $h=10$; $t_1=t_2=0, 0.1, 0.5$; $\alpha=90°$; $\beta_1=-\beta_2=0°-90°$; $R=0.04-1.0$ by using (4.4) and (4.5) and their simplified forms (4.10)–(4.21),

(ii) $a=1$; $h=10$; $t_1=t_2=0, 0.1, 0.5$; $\alpha=0°, 180°$; $\beta_1=0°, 90°$; $\beta_2=0°, 90°$; $R=0.04-1.0$ by using (5.6)–(5.25). They are shown in Figs. 4 and 5 and tabulated in Tables I and II.

In the case (i) with the perpendicular central line, the curves of the drag coefficients $C_D^{(1)}$ vs. $\beta=\beta_1=-\beta_2$ is symmetrical about $\beta=\pi/2$, so that the reversal of the flow direction does not change the values of the drag, in the first approximation. In the case (ii) with the parallel central line, comparison of the four configurations: I. $\alpha=0°$, $\beta_2=0°$ (Fig. 3 (a)), II. $\alpha=180°$, $\beta_2=0°$ (Fig. 3 (b)), III. $\alpha=0°$, $\beta_2=90°$ (Fig. 3 (c)) and IV. $\alpha=180°$, $\beta_2=90°$ (Fig. 3 (d)) shows that, irrespectively of β_1 (=0° or 90°), the drag is the largest for case I and

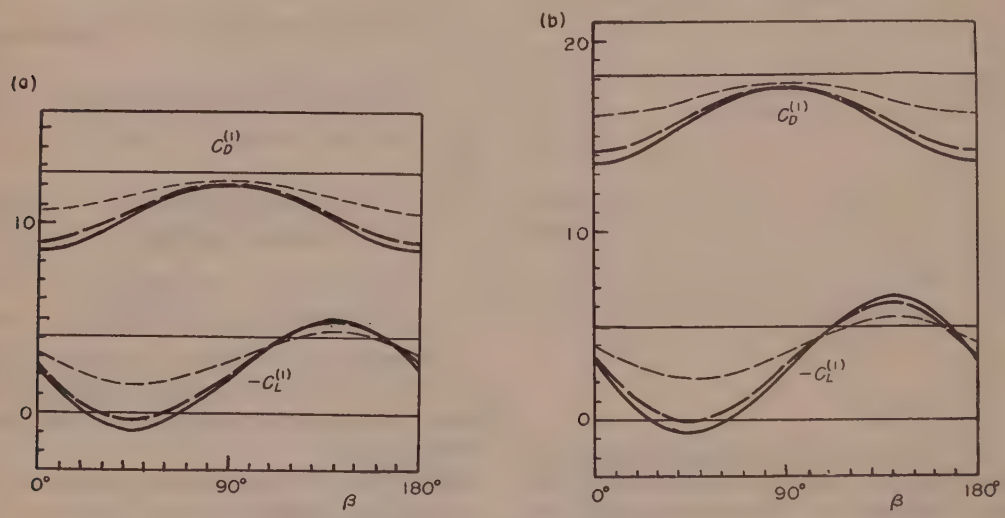

Fig. 4. $C_D^{(1)}$ and $C_L^{(1)}$ vs. $\beta=\beta_1=-\beta_2$ in the symmetrical configurations with the central line perpendicular to the uniform flow when $a=1$ and $h=10$. (a) $R=0.4$; (b) $R=0.8$.

——————— equal circular cylinders,
— — — — — equal elliptic cylinders with the thickness ratio $t=0.5$,
—— —— —— equal elliptic cylinders with the thickness ratio $t=0.1$,
——————— equal flat plates.

Table I. Calculated values of $C_D^{(1)}$ and $C_L^{(1)}$ for various values of β and R of the symmetrical configurations with the central line perpendicular to the uniform flow when $a=1$ and $h=10$.

(a) Two flat plates

$C_D^{(1)}$

R \ β	0°	18°	36°	54°	72°	90°
0.04	70.980	72.099	74.728	77.481	79.390	80.056
0.08	41.892	42.680	44.547	46.527	47.914	48.401
0.2	21.696	22.242	23.554	24.973	25.985	26.343
0.4	13.581	14.033	15.126	16.323	17.186	17.494
0.6	10.416	10.836	11.853	12.965	13.767	14.053
0.8	8.650	9.059	10.042	11.106	11.866	12.136
1.0	7.499	7.907	8.877	9.910	10.636	10.891

$C_L^{(1)}$

R \ β	0°	18°	36°	54°	72°	90°	108°	126°	144°	162°
0.04	−5.221	5.114	10.552	9.661	4.056	−3.917	−12.081	−18.234	−19.916	−15.234
0.08	−4.768	1.445	4.842	4.461	1.165	−3.653	−8.638	−12.409	−13.468	−10.710
0.2	−3.964	−0.559	1.396	1.300	−0.463	−3.142	−5.948	−8.069	−8.667	−7.176
0.4	−3.198	−0.819	0.575	0.539	−0.690	−2.588	−4.583	−6.081	−6.490	−5.437
0.6	−2.717	−0.651	0.556	0.521	−0.548	−2.195	−3.924	−5.223	−5.577	−4.662
0.8	−2.388	−0.429	0.702	0.654	−0.356	−1.896	−3.513	−4.737	−5.086	−4.232
1.0	−2.158	−0.207	0.897	0.828	−0.168	−1.665	−3.236	−4.444	−4.813	−3.991

(b) Two elliptic cylinders with the thickness ratio $t=0.1$

$C_D^{(1)}$

R \ β	0°	18°	36°	54°	72°	90°
0.04	72.505	73.408	75.564	77.878	79.517	80.096
0.08	42.958	43.599	45.139	46.808	48.002	48.426
0.2	22.416	22.866	23.959	25.165	26.039	26.352
0.4	14.150	14.526	15.448	16.473	17.224	17.494
0.6	10.921	11.274	12.137	13.097	13.798	14.050
0.8	9.117	9.462	10.301	11.225	11.894	12.133
1.0	7.939	8.285	9.116	10.017	10.661	10.890

$C_L^{(1)}$

R \ β	0°	18°	36°	54°	72°	90°	108°	126°	144°	162°
0.04	−5.345	3.359	8.102	7.512	2.754	−4.180	−11.291	−16.552	−17.853	−13.771
0.08	−4.900	0.351	3.316	3.091	0.292	−3.899	−8.246	−11.482	−12.318	−9.917
0.2	−4.105	−1.206	0.505	0.475	−1.026	−3.360	−5.813	−7.645	−8.132	−6.834
0.4	−3.341	−1.298	−0.071	−0.067	−1.119	−2.781	−4.533	−5.836	−6.176	−5.257
0.6	−2.857	−1.071	−0.001	−0.001	−0.922	−2.372	−3.900	−5.038	−5.335	−4.533
0.8	−2.525	−0.822	0.188	0.177	−0.698	−2.063	−3.501	−4.581	−4.876	−4.123
1.0	−2.294	−0.588	0.407	0.379	−0.489	−1.824	−3.232	−4.305	−4.620	−3.890

(c) Two elliptic cylinders with the thickness ratio $t=0.5$

$C_D^{(1)}$

R \ β	0°	18°	36°	54°	72°	90°
0.04	77.439	77.794	78.682	79.710	80.488	80.774
0.08	46.463	46.721	47.368	48.120	48.692	48.903
0.2	24.856	25.045	25.523	26.082	26.510	26.668
0.4	16.145	16.310	16.730	17.222	17.600	17.740
0.6	12.740	12.900	13.305	13.778	14.141	14.275
0.8	10.837	10.997	11.399	11.866	12.222	12.353
1.0	9.596	9.758	10.129	10.630	10.983	11.112

$C_L^{(1)}$

R \ β	0°	18°	36°	54°	72°	90°	108°	126°	144°	162°
0.04	−5.910	−1.926	0.479	0.461	−1.750	−5.251	−8.865	−11.384	−11.808	−9.755
0.08	−5.489	−3.055	−1.543	−1.491	−2.793	−4.914	−7.134	−8.706	−9.009	−7.802
0.2	−4.723	−3.343	−2.456	−2.382	−3.086	−4.278	−5.548	−6.462	−6.662	−6.009
0.4	−3.971	−2.966	−2.312	−2.247	−2.751	−3.618	−4.547	−5.219	−5.371	−4.903
0.6	−3.492	−2.538	−2.000	−1.941	−2.393	−3.169	−4.002	−4.607	−4.747	−4.329
0.8	−3.167	−2.280	−1.705	−1.649	−2.089	−2.841	−3.650	−4.242	−4.387	−3.984
1.0	−2.950	−2.037	−1.443	−1.393	−1.839	−2.599	−3.419	−4.028	−4.174	−3.787

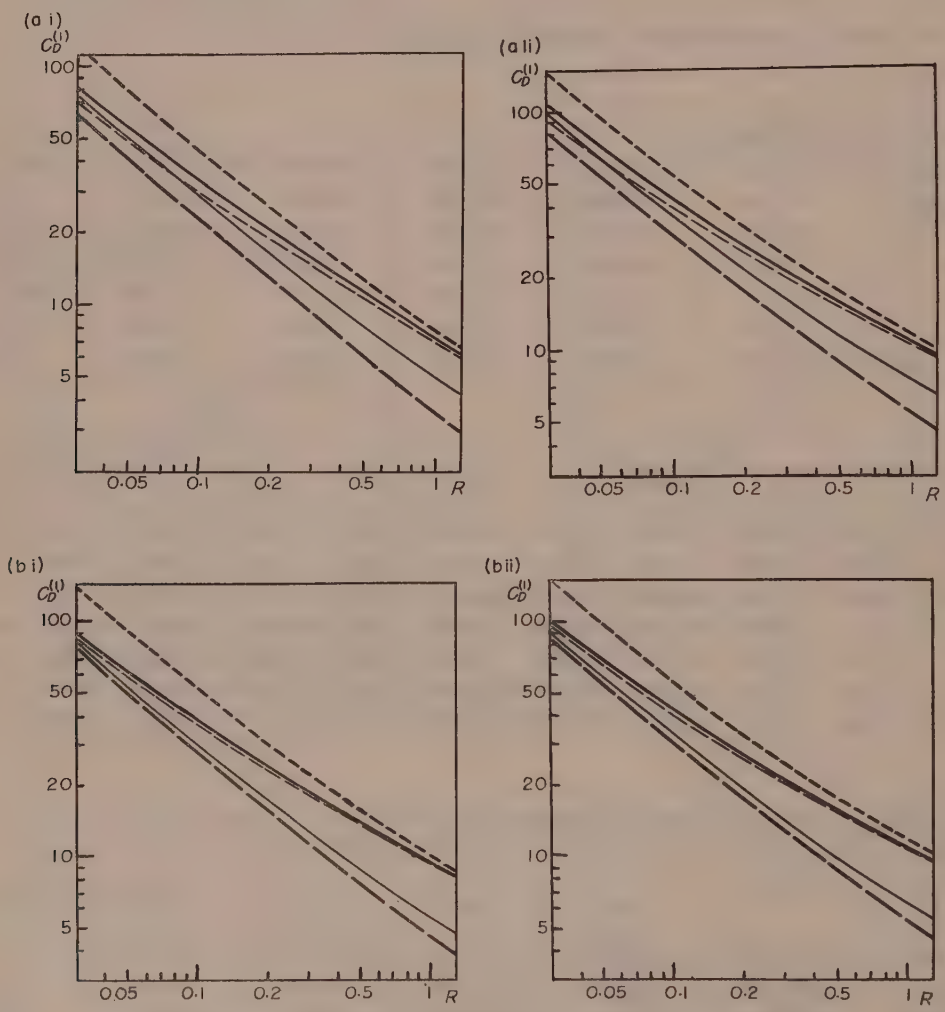

Fig. 5. $C_D^{(1)}$ vs. R, in the symmetrical configurations with the central line parallel to the uniform flow when $a=1$ and $h=10$. (a) equal flat plates; (b) equal elliptic cylinders with the thickness ratio $t=0.5$, (i) $\beta_1=0°$; (ii) $\beta_2=90°$.

——— $\alpha=0°$, $\beta_2=0°$,
——— $\alpha=180°$, $\beta_2=0°$,
— — — — $\alpha=0°$, $\beta_2=90°$,
—— —— —— $\alpha=180°$, $\beta_2=90°$,
- - - - - - - - - a single flat plate in (a) and a single elliptic cylinder in (b)

Table II. Calculated values of $C_D^{(1)}$ for various values of R in the symmetrical configurations with the central line parallel to the uniform flow when $a=1$ and $h=10$.

(a) Two flat plates

	$\beta_1=0°$				$\beta_1=90°$			
R \ α	0°	180°	0°	180°	0°	180°	0°	180°
R \ β_2	0°	0°	90°	90°	0°	0°	90°	90°
0.04	66.927	60.681	58.278	50.290	85.583	77.596	76.209	65.764
0.08	39.813	34.216	35.383	28.143	51.493	44.254	46.685	37.134
0.2	20.854	16.366	19.130	13.183	27.636	21.689	25.766	17.756
0.4	13.100	9.608	12.294	7.513	17.939	13.157	17.064	10.428
0.6	10.045	7.143	9.528	5.435	14.168	10.075	13.607	7.762
0.8	8.343	5.834	7.961	4.322	12.103	8.464	11.687	6.345
1.0	7.240	5.011	6.932	3.611	10.792	7.470	10.458	5.447

(b) Two elliptic cylinders with the thickness ratio $t=0.1$

	$\beta_1=0°$				$\beta_1=90°$			
R \ α	0°	180°	0°	180°	0°	180°	0°	180°
R \ β_2	0°	0°	90°	90°	0°	0°	90°	90°
0.08	68.426	61.636	60.899	52.534	84.292	75.928	76.259	65.785
0.04	40.892	34.787	37.028	29.437	50.849	43.258	46.723	37.145
0.2	21.594	16.665	20.083	13.827	27.404	21.149	25.794	17.760
0.4	13.675	9.803	12.965	7.912	17.844	12.792	17.088	10.429
0.6	10.547	7.302	10.089	5.745	14.116	9.773	13.629	7.762
0.8	8.802	5.975	8.461	4.584	12.071	8.194	11.709	6.344
1.0	7.670	5.141	7.395	3.843	10.771	7.219	10.479	5.446

(c) Two elliptic cylinders with the thickness ratio $t=0.5$

	$\beta_1=0°$				$\beta_1=90°$			
R \ α	0°	180°	0°	180°	0°	180°	0°	180°
R \ β_2	0°	0°	90°	90°	0°	0°	90°	90°
0.04	73.446	64.477	69.656	59.775	80.916	71.034	77.030	66.103
0.08	44.591	36.437	42.632	33.613	49.322	40.303	47.316	37.306
0.2	24.219	17.473	23.442	15.913	27.032	19.503	26.241	17.812
0.4	15.778	10.299	15.405	9.209	17.844	11.647	17.465	10.440
0.6	12.425	7.690	12.190	6.757	14.229	8.806	13.981	7.756
0.8	10.555	6.307	10.369	5.444	12.237	7.313	12.050	6.327
1.0	9.348	5.437	9.194	4.605	10.972	6.382	10.819	5.418

the smallest for case IV, and that the drag for case III is larger than for case II above a certain value of R.

Acknowledgement

The author wishes to express his sincere thanks to Professor Isao Imai and Professor Saburô Asaka for their continual guidance and encouragement throughout this study. He is also indebted to Dr. Mitutosi Kawaguti, Dr. Hidenori Hasimoto and Mr. Hideo Takami for their invaluable advice and discussions.

References

1) S. Kuwabara: J. Phys. Soc. Japan **12** (1957) 291.
2) H. Fujikawa: J. Phys. Soc. Japan **11** (1956) 558.
3) H. Fujikawa: J. Phys. Soc. Japan **11** (1956) 690.
4) H. Fujikawa: J. Phys. Soc. Japan **12** (1957) 423.
5) I. Imai: Proc. Roy. Soc. **A 224** (1954) 141.
6) S. Tomotika and H. Yosinobu: Mem. Coll. Sci. Univ. Kyoto **27** (1954).
7) H. Hashimoto: J. Phys. Soc. Japan **8** (1953) 653.

JOURNAL OF THE PHYSICAL SOCIETY OF JAPAN Vol. 13, No. 5, MAY, 1958

Experimental Studies on the Initiation of Electric Arcs

By Tasaburô YAMAGUTI

Physical Institute, College of Arts and Sciences, Chiba University

(Received January 8, 1958)

Concerning the initiation of stable arcs under atmospheric pressure it is pointed out that the customary theories have some difficulties in their explanations. Considering that the boiling point of the electrode and the work function of the cathode may take part in the initiation, arcs between electrodes with remarkably different boiling points are experimentally investigated. The results are qualitatively explained by two stability conditions: (a) an arc spot of one of the electrodes at least must be in boiling state, and (b) the ionization potential of the evaporated metal vapour must be larger than double the work function of the cathode material.

§ 1. Introduction

In preliminary experimental studies on the initiation of stable arcs between electrodes connected to an *ac* power source by excitation of high frequency oscillations, it is observed that the arcs kindle in both possitive and negative half cycles of the power source between a carbon rod and an iron plate, whereas between an iron rod and an iron plate arc starts predominantly in the half cycles of positive rod. Interpretations of these experiments with the customary theories for arc formation, however, meet with some difficulties. In these experiments it is also observed that the arc spot on the plate reaches the temperature of boiling point when the plate is faced to a carbon rod electrode, whereas the spot facing an iron rod may be below the boiling point.

The effect of boiling of the arc spot on the initiation of arc was studied by Nottingham[1] and Suits.[2] The former shows that the arc potential increases gradually with the boiling point of the electrode material, while the latter shows that no such regular relation can be obtained from more accurate data. As any certain relation between the boiling point and the arc formation is not yet known, it will be worth-while to experimentally investigate the conditions of the initiation with electrodes of different materials, which have boiling points distributed in a wide range of temperature.

In the present experiment, the initiation and stability of the arc are studied by connecting the electrodes to an alternating source (50 c/s) and superposing high frequency oscillations in every other half cycle of the *ac*. The stability of the arc is examined by measurement of the arc current or by observation of its oscillogram, which numbers of the igniting half cycles are responsible to. Thus, it can be said that the present experiment offers a convenient method of observation which is equivalent to a large number of experiments on *dc* arc initiation.

§ 2. Experimental Methods

Electrical connection of the experimental apparatus is shown in Fig. 1, which is similar to that of the previous paper[3] in the point

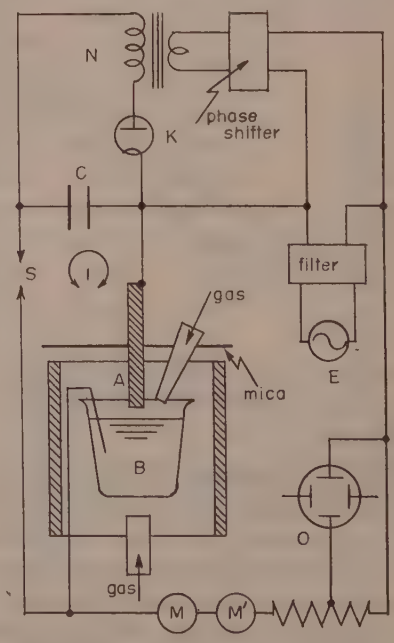

Fig. 1. Schematic diagram of the experimental apparatus.

that the low voltage arc is initiated between electrodes separated by a small gap by means of the superposition of high frequency oscillations. By the action of a kenotron K, arcs can first ignite only in every other half cycle in which the rod electrode A has one and the same polarity, and its sign can be interchanged by exchange of connections of the primary terminals of the neon transformer N of 6000 volts. When the kenotron is in short circuit, the oscillations are superposed in every half cycle. The high frequency oscillations are started in circuit (1), where C is 2000 pF and the spark gap S is 1 mm.

To determine certainty of the initiation and stability of the arc, it is investigated whether the arc can kindle or not between electrodes in the following cases: when the high frequency oscillation is superposed in both half cycles of the *ac*, when the oscillation is superposed only in the half cycles when the rod is positive, and when the rod negative. It is also observed whether the arc still continues to kindle when the superposition is ceased.

The initiation and stability of the arc can be seen from the readings of an *ac* ammeter M and of a *dc* ammeter M' or from wave forms of the arc current observed on an oscillograph O. In cases when the self-rectifying action of the arc is remarkable, M' indicates about 5.5 A and M 11 A. Whereas, in arcs kindled on carbon electrodes M' indicates nearly zero A and M about 17 A.

Materials of the rod electrode are iron (4 mm in diameter), tungsten (3 mm) and carbon (5 mm), and those of the plate electrode iron, zinc, cadmium and tungsten. To diminish oxidation of the electrodes, arcs are kindled always in methane gas flames. When the plate electrode materials have low melting points (Cd and Zn) they are pre-heated by methane gas flame in crucibles of 25 cc capacity as shown in the figure to nearly 600°C with an expectation that the temperature will be raised to the boiling point by the arc, and their melted surfaces are used as plate electrodes.

§ 3. Experimental Results

Experimental results on the initiation of arc are shown in Table I. The first vertical column represents chemical symbols of the plate materials and the first horizontal row those of the rod electrodes. Symbols + and − of the second row represent the half cycles, during which the rod polarity is positive or negative respectively. Symbol s in the third row denotes the superposition of high frequency oscillations during the corresponding half cycles, and symbols c of the same row represent that the superposition is ceased after the arc has started steadily and the electrodes have attained high temperature by the heating action of the arc. Circles ○ given in coordinate points mean that the arc initiates with certainty between the given two electrodes, and black circles ● with less certainty in the half cycles of superposed oscillations. With regard to every other half cycle with no superposed oscillations ◎ is given for easy starting of arc, triangle △ for an uncertain initiation, and cross × for no initiation. When the arc still kindles on even after the stop of the superposed oscillation (columns with symbol c), they are marked too with double circles, and no initiation with crosses. In the following some details how the arcs kindle between rods and plates are given for some electrode materials.

(a) *Iron rod electrode*

As will be seen from Table I, arcs surely start by the superposition in the half cycles of positive rod. However, for the negative rod, after the plate temperature reached the melting points arcs do not start in cases of iron and zinc plates even when the oscillation is applied. Only for cadmium plate steady arcs are initiated and kindle even after the cease of the superposition.

Deformations of the electrodes caused by the arc, which are most typical in the case of iron electrodes, give suggestions for the working mechanism of the electric discharge machining:[4] the melted material of the anode is stretched toward the cathode and forms a needle-like shape. Contrary to this, softened and melted part of the cathode forms a rather flat convex surface as if it is pressed by fast flow of positive ions, and especially for a rod-shaped cathode its top becomes flat having area more than two times the cross section of the rod. In open air, however, both electrodes are covered by thick layers of oxides and are deformed less remarkably.

(b) *Tungsten rod electrode*

By application of the high frequency oscil-

Table I. Stability of arcs formed between materials, which have boiling and melting points distributed in a wide range.

Rod / Plate	Fe						W						C					
	−	+	−	+	−	+	−	+	−	+	−	+	−	+	−	+	−	+
		S	S		C	C		S	S		C	C		S	S		C	C
Fe	×	○	●	×	×	×	×	○	●	×	×	×	◎	○	○	◎	◎	◎
Zn	×	○	●	×	×	×	◎	○	●	×	◎	◎	◎	○	○	◎	◎	◎
Cd	△	○	○	◎	◎	◎	◎	○	○	◎	◎	◎	◎	○	○	◎	◎	◎
W							◎	○	○	△	◎	◎						

lations the arc starts when the rod is positive, whereas in negative half cycles the initiation is uncertain for iron and zinc plates. On the contrary, once the alternating current arc starts between the rod and a zinc or cadmium plate by high frequency excitation, the arc continues to kindle even after the high frequency oscillations are stopped. In case of a tungsten rod and a tungsten plate, the arc started by the excitation shows such an oscillogram of arc current as shown in Fig. 2a:

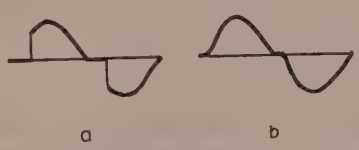

Fig. 2. Schematic diagram of arc current oscillogram, a: a-type arc formed on boiling electrode, b: b-type arc due to thermal emission.

the current begins to flow at certain potential of the *ac* source. However, after the electrodes glew in brilliant white the oscillogram changes from type *a* to type *b* of the figure. The arc current is larger than the former and the phase angle of current start is remarkably decreased in the latter. Thus it will be natural to consider that the arc of type *b* is due to thermal emission of electrons and that of type *a* as due to field emission. Once an arc of type *b* starts between the electrodes, the arc continues in each half cycle even though the excitation is ceased, although it fades away in a short time by heat loss at the arc spots due to thermal conduction through the electrodes.

(c) *Carbon rod electrode*

Between a carbon rod and all metal plates examined arcs are formed always by the excitation irrespective of the rod polarity, and moreover the arcs start even with no excitation after the electrode became white heated. When the carbon rod is heated in brilliant white, oscillogram of arc current is the *b* type in half cycle of negative carbon rod.

§ 4. Explanation of the Experimental Results

According to the usual theories arcs are classified to a thermionic emission type and a field emission type. Some arcs in the present experiment are also to be attributed to thermionic emission type when the electrodes are not in boiling state and hence can not supply considerable amount of vapours as in the case of tungsten-tungsten arc. However, stability of arcs kindled on electrodes evaporating violently can hardly be explained by a simple field or spray discharge theory as will be shown in the following. In this work, therefore, a criterion that *the ionization potential of vapour of an electrode material must be larger than double the work function of a cathode* is introduced to explain the stability of arc. Its physical meaning is that each positive ion draws out two electrons from the cathode taking one for neutralization of itself and another for maintainance of the arc. Since the above criterion concerns with vapour ions evaporated from an electrode the arc stability depends on the boiling temperature of electrodes, more stable for electrodes of lower boiling point. It must be noted here, however, that the temperature of an electrode depends on the property of the opposite electrode. Namely, it is probable that there are cases in which an arc spot on an electrode may reach its boiling point or not according to the mode of partition for two electrodes of the input power supplied to the discharge gap. In other words, the temperature of the

spot on a plate seems to depend on materials of rod electrode. For instance, when the arcs are formed between a carbon rod and an iron plate, flames accompanied by thick smoke grow from the spot on the melt, showing the temperature of the plate reaching the boiling point of iron. Whereas when an iron or a tungsten rod is faced to an iron plate, smoky flames are not observed and the spot on the plate is considered as being in temperatures below the boiling point. Further, when cadmium is used as the plate smoky flame rises strongly from the spot showing rapid evaporation of the metal for all kinds of the rod used: iron, tungten and carbon. These phenomena show that the temperature of the cadmium plates reaches the boiling point which is remarkably below the melting points of the rod materials used.

The melting and boiling points of electrode materials are given in Table II for reference. As will be seen from Table I and the descriptions of the last section the arcs burn more steadily in regular order of increasing melting points of the rod electrodes and of decreasing boiling points of the plate electrodes as far as the present experiment is concerned.

Table II. The melting and boiling points of electrode materials.

Material	Cd	Zn	Fe	W	C	(Fe_3O_4)	(Fe_2O_3)	(ZnO)
Melting point (°C)	320.9	419.5	1530	3380	3600	1538	1560	1975
Boiling point (°C)	764	907	3200	5900	4000		(1200)	

Now, for one or two seconds after the initiation of the arc between iron electrodes, the arc current is alternating one, but gradually reveals rectifying property with rise of temperature of the electrodes and becomes nearly perfect direct current within a few seconds. The initial arc current of alternating property can be explained by a mechanism of spray discharge or field emission. In order to explain by the same idea the fact that there are no initiation of arc between an iron positive plate and an iron negative rod, it will have to be assumed that the positive charges, which cause the spray of electrons, can not accumulate on the white heated cathode owing to evaporation of the insulating surface layer. This assumption seems very plausible for iron electrodes, but can not interpret the arcs of alternating property, which are formed between an iron rod and a cadmium plate or between a carbon rod and an iron plate. For, in these cases, too, presence of the thin layer is hardly conceivable on white glowing iron electrodes. Thus usual theories can not explain these arc phenomena without contradiction.

As already stated, in half cycles in which the iron or zinc plates are in positive potential the arcs initiate more stably when the plate are faced to rod electrodes of higher melting points. To interpret these phenomena it will be sufficient only to assume thermal emission of electrons from carbon or tungsten rod. This assumption, however, fails in explaining other arc phenomena: a negative tungsten rod keeps arc stably, after interruption of the superposition, in the cases of a zinc or cadmium positive plate, but does not for a positive iron plate. As there are such several arc phenomena that can not be explained by the usual theories, conditions for stability of arcs are necessary to be investigated taking these experimental results into consideration.

Before proceeding to the interpretation of the arc initiation, it must be noted that arcs formed on negative carbon rod is due to the thermal electron emission and that the arc which kindles on a tungsten cathode after the electrode is heated white by arc current is also the thermal type. Such arcs of thermal type are distinguished from others by the large value of the arc current and also by the current osillogram of *b*-type of Fig. 2.

Now, the conditions necessary to explain the experimental facts can be reduced to two. The first is that one of the electrodes at least is in boiling state to supply thick metal vapour in which the arc can start. The second is that the ionization potential E of the evaporating electrode materials must be larger than two times the work function ϕ of the cathode, enabling every positive ion to draw out two electrons from the cathode, one electron to neutralize itself and another to maintain the arc. This second condition proves of great use as stability criterion.

The values of E and ϕ of electrode materials are given in Table III as well as in Fig. 3, where E's are shown with circles and ranges of 2ϕ values[5] obtained experimentally by various investigators with segments. In oder to show varidity of the present criterion, the 2ϕ values of liquid state, which may be considered to be smaller than those of solid state, must be used for the interpretation of the experimental results. Since the values of liquid are not yet known, it is required in the first place what ranges of 2ϕ values may satisfy the stability condition, where to E being given the values in Table III. If the ranges of the values thus determined are included in those of solid state or less than them, then it can be said that the 2ϕ values of liquid state are in these ranges determined if they have both the upper and the lower limits, or merely that the 2ϕ values are less than the upper limits determined if any lower limits are not obtained. The second condition of the stability of the arc can be written as

$$E\,(\text{vapour}) > 2\phi\,(\text{cathode})\ ,$$

and hence the extinction condition as $E < 2\phi$.

Table III. Maximum and minimum values observed for 2ϕ and E in volts.

Material	C	Cd	Fe	Zn	W
2ϕ max. (V)	9.62	8.20	9.54	8.61	9.38
2ϕ min. (V)	8.00	7.36	7.82	6.16	8.50
E (V)	11.2	8.96	7.83	9.35	8.1

Since the above condition concerns with cathode, each electrode material is discussed as a cathode. The arcs formed on the same material used as an anode are discussed in connection with other cathode materials coupled with this anode.

a) *Cadmium cathode*

In this case dense cadmium vapour exists in the gap, hence the stability criterion is written as

$$E(\text{Cd}) > 2\phi(\text{Cd})\ ,$$

which is satisfied by the measured E and 2ϕ as shown in Fig. 3. This explains the result that cadmium arc is stable for any anode material.

b) *Iron cathode*

Arcs do not initiate between iron electrodes unless high frequency oscillations are superposed. Thus either the electrode temperature must be below the boiling point or the condition $E(\text{Fe}) < 2\phi(\text{Fe})$ must hold, which is actually satisfied as is shown in Fig. 3. Whether the temperature reaches the boiling point or not can not be said immediately, but depends on the anode material.

As the arc between Fe and Cd is stable and cadium evaporates densely $2\phi(\text{Fe})$ must be less than $E(\text{Cd}) = 8.96$ volts. This condition is satisfied by the observed values except larger ones of ϕ. Iron-zinc arcs are unstable. The origin may be ascribed to temperature of zinc being below the boiling point or to that zinc is covered by a layer of compounds of higher boiling point. If the zinc temperature were above the boiling point, then the extinction condition would have to hold: $2\phi(\text{Fe}) > E(\text{Zn}) = 9.35$ volts, which is satisfied only by larger 2ϕ given in Fig. 3. Moreover

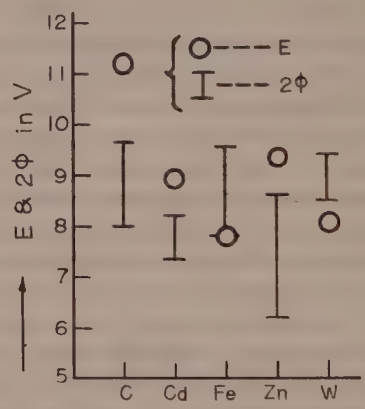

Fig. 3. Ionization potential E and two times the work function 2ϕ of the electrode materials.

this limitation of $2\phi(\text{Fe})$ contradicts with that for the iron-cadmium arc, that is, $2\phi(\text{Fe})$ must be smaller than 8.96 volts. It is considered, therefore, that the surface of zinc electrode is below the boiling point due to contamination by its compounds. The extinction of the arc between iron and tungsten can be explained by $2\phi(\text{Fe}) > E(\text{Fe})$ and by the temperature of iron below the boiling point. Stable initiation of arc between iron cathode and carbon anode can be explained by the large value of $E(\text{C})$ considering that carbon can evaporate easily. The iron plate is boilling, but $E(\text{Fe})$ can not explain the stability.

Thus it can be said that arcing between an iron cathode and other materials is explained by taking 2ϕ of iron to be less than 8.96 volts,

although some questions about iron-zinc arcs remain for future investigation.

c) *Zinc cathode*

Between a zinc cathode and an iron anode arcs do not initiate without the superposition of oscillations. As stated above it will be natural to consider that zinc surface is below the boiling point due to oxide layer. To explain stable arcs between a zinc cathode and tungsten anode zinc must be considered as being above the boiling point considering that tungten has much higher melting point. Accordingly zinc vapour must be predominant and the relation $2\phi(\mathrm{Zn})<E(\mathrm{Zn})=9.35$ volts well explain the stability. Carbon-zinc arcs are stable. Since both of $E(\mathrm{C})$ and $E(\mathrm{Zn})$ are larger than $2\phi(\mathrm{Zn})$, stability should be very well.

d) *Tungsten cathode*

Between iron and tungsten electrodes no arcs are initiated unless the high frequency oscillations are superposed. Hence if iron is in boiling state there must be the relation $2\phi(\mathrm{W})>E(\mathrm{Fe})$, and this is actually satisfied by the measured values. Stable arcs are formed between zinc and tungsten electrodes by the superposition though uncertain initiations are observed when tungsten is the cathode. Considering zinc being above and tungsten below their own boiling points, the condition $2\phi(\mathrm{W})<E(\mathrm{Zn})=9.35$ volts must hold; and this condition is satisfied by main part of $2\phi(\mathrm{W})$ except the largest value 9.38 volts. Cadmium-tungsten arcs are stably formed even after interruption of the superposition. The stability condition is $E(\mathrm{Cd})>2\phi(\mathrm{W})$, which is satisfied only with small values of $2\phi(\mathrm{W})$ according to Fig. 3. In case both electrodes are tungsten, the arc starts by the superposition. After the electrodes glew white by arc current the arc initiates without oscillations, but fades away in a short time as temperature of electrodes is lowered by heat conduction. Fig. 3 shows that $E(\mathrm{W})<2\phi(\mathrm{W})$, that is, the tungsten vapour can not account for the arcing. The arc must be accounted for by the thermal emission of electrons from the tungsten cathode. Eventually the experiments on the tungsten cathode arc show that 2ϕ value of tungsten must be less than $E(\mathrm{Cd})=8.96$ and larger than $E(\mathrm{Fe})=7.83$ volts.

e) *Carbon cathode*

Between a carbon cathode and any metal examined arcs kindle stably even after the excitation is ceased. The initiation of the arc, when the carbon electrode is cathode, can be explained by thermal emission of electrons from white heated carbon and also by the stability conditions $E(\mathrm{C})>2\phi(\mathrm{C})$, $E(\mathrm{Cd})>2\phi(\mathrm{C})$ and $E(\mathrm{Zn})>2\phi(\mathrm{C})$, which are satisfied by the known values of E and ϕ. For iron anode, however, it can be explained by the thermal emission. Since the arc formed on a carbon cathode can be interpreted by thermal emission, much can not be said about the work function of carbon.

§ 5. Discussion

As stated above the initiation of the arc can be explained by the proposed stability criterion. The high frequency current between the electrodes may be due to the field emission of electrons as usually considered. Since the instantaneous value of this high frequency current must be considerably large estimating from the duration ($\sim 1\mu s$) of its first impulse, the condenser capacity (2000 pF) and the secondary voltage of the neon-transformer (6 kV), and since the area of the discharge spots on the electrodes are very small, the spot of either one of the electrodes at least will soon reach its boiling point and will supply considerable amount of neutral particles. These particles are ionized between the electrodes, beat the cathode and are to release electrons therefrom. If the above mentioned stability condition is fulfilled, the arc current will build up with the temperature rise of electrodes, and when either cathode or anode begins heavy evaporation by boiling the arc will continue to kindle even after the superposition is ceased.

According to the general conception of arc discharges ratio of number of electrons liberated from the cathode by the impinging positive ions to those drawn out by the field of positive space charges is considered to be small. However, the present experiments show that the electrons of the former origin play an important part in the initiation of the arc.

The values of the work function used in the present interpretation are those obtained for solid state. Although the work function is known as being nearly independent of temperature,[6] the values for liquid state are more desirable for the present purpose, about

which anything is not yet known. However, if the present criterion is valid it may be said that 2ϕ values of the materials in the melted state lie within the limits obtained by the present experiment. While it is likely to happen that the surfaces of melted metals are covered by thin layers of oxides, which must also affect the work function. In this respect experimental investigations on the stability of vacuum arcs are desirable. At present, accordingly, it will not be adequate to discuss in more detail about the effect of the work function on the arc initiation.

In conclusion the author's thanks are due to Prof. K. Honda of Tokyo University for his kind advices.

References

1) W. B. Nottingham: Phys. Rev. **28** (1926) 764.
2) C. G. Suits: Phys. Rev. **46** (1934) 252.
3) T. Yamaguti: J. Phys. Soc. Japan. **12** (1957) 204.
4) Reference 3, p. 207.
5) H. B. Michaelson: J. App. Phys. **21** (1954) 536.
6) S. Seely: Phys. Rev. **59** (1941) 75.

JOURNAL OF THE PHYSICAL SOCIETY OF JAPAN Vol. 13, No. 5, MAY, 1958

The Thermoluminescence of Glasses

By Takeo KIKUCHI

Institute of Polytechnics, Osaka City University

(Received January 30, 1958)

The thermoluminescence of soda-silicate glass and fused quartz, as well as ctystalline quartz, were observed below room temperature. The glow curves of glasses have broad bands without any structure. The luminescence shows the slow decay continuing for more than ten minutes at any fixed temperature between 100°K and 350°K. The dependence of these curves on the irradiation temperature and on the X-ray dose, and the effect of the heat treatments were studied. The decay curves, which do not obey the simple monomolecular or bimolecular law, are analysed by the model that the trapping levels are distributed continuously and uniformly beneath the conduction band. The discussions on the relation between the trapping centers and the random network structure of the glasses are presented.

§ 1. Introduction

In the work of the thermoluminescence for fused quartz, R. Yokota has observed that the glow curve of fused quartz has the broad band, and suggested that this represents the characteristic features of the glassy states.[1] The author has found soda-silicate glass shows the glow curve with two broad bands, one at the temperature above the room temperature, and the other at the temperature below it.[2] And he has pointed out that these two groups of the bands indicate the existence of two groups of the electron trapping levels, deep and shallow, in glass, corresponding to the model for the electronic structure of the amorphous substances proposed by H. Förhlich with regards to the theory of the dielectric breakdown.[3] In the present paper we shall describe the experiments on the thermal glow and the decay of the luminescence for soda-silicate glass, fused quartz and crystalline quartz irradiated previously with X-ray at low temperatures. And from these results we shall discuss the electron trapping levels in the glassy states.

§ 2. Experimental Procedure

The specimens were soda-silicate glass, fused quartz and crystalline quartz, which were kindly offered by R. Yokota. The molecular formula of soda-silicate glass is $0.6Na_2O \cdot 2SiO_2$. Each specimen has the surface of about 1 cm² and the thickness of about 0.5 mm, which was attached on the

copper block of the cryostat at the distance of 20 mm from the window of the X-ray tube. At a constant temperature, the specimen was irradiated with X-ray (W-target) of a constant intensity (40 kv, 16 ma, unless especially denoted).

The measurements of the luminescence intensity were performed by the use of the photomultiplier 931A, dc amplifier and a recorder. During the X-ray irradiation, the intensity of the luminescence emitted by the specimen reached the saturation value in a few minutes. As soon as the irradiation was ceased, the intensity dropped quickly by a considerable amount and then decayed more or less slowly. After the observation of the decay for about 10 or 20 minutes, the temperature of the specimen was raised with a constant speed, the glow curve being recorded.

§ 3. Results

(1) *Glasses and Crystal*

The glow curves of each specimen are shown in Fig. 1. At a lower temperature, the

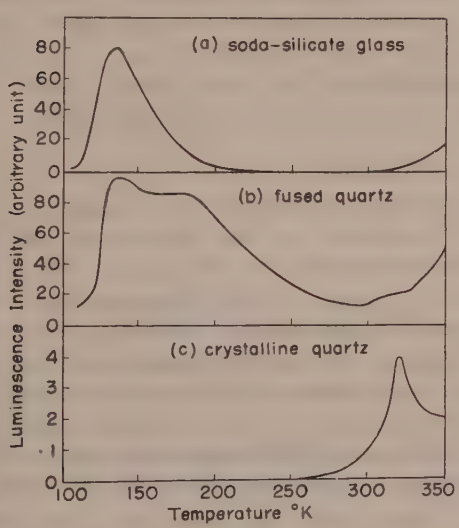

Fig. 1. Glow curves of glasses and crystal. (a) and (b); irradiated with X-ray for 32 minutes. (c); irradiated with X-ray for 11 hours.

broad bands are found in the glow curves for soda-silicate glass and fused quartz, while such a band is not found for the crystal. This seems to indicate that the shallow electron traps associated with the broad band at low temperature are characteristic to the glassy states.

(2) *Temperature Dependence*

The glow curves of glasses irradiated at various temperatures are shown in Fig. 2. We see each curve has a nearly similar slope at the side of higher temperature, and the peak shifts to the lower temperature indefinitely, as the irradiation temperature is lowered. This shows that a band of the glow curve is not due to one type of trapping center, but due to many trapping centers whose levels are distributed over the wide range.

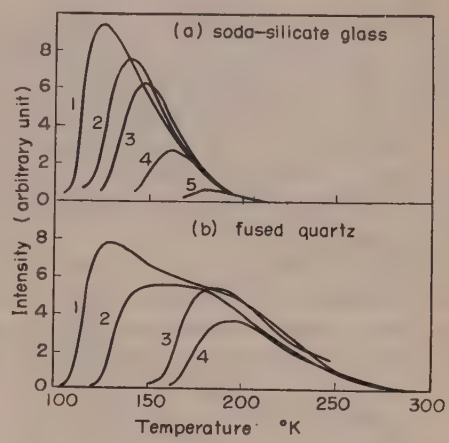

Fig. 2. Glow curves of glasses irradiated (a); for 2 minutes, at 1; 102°K, 2; 114°K, 3; 123°K, 4; 142°K, 5; 166°K, (b); for 10 minutes at 1; 102°K, 2; 118°K, 3; 149°K, 4; 160°K.

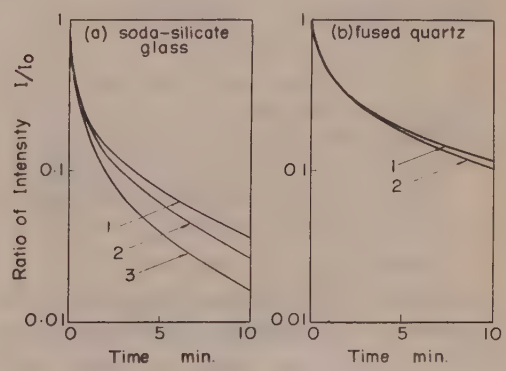

Fig. 3. Decay curves of glasses irradiated (a); for 2 minutes, at 1; 102°K, 2; 123°K, 3; 166°K, (b); for 10 minutes, at 1; 102°K, 2; 290°K.

Fig. 3 shows the time decay of the luminescence of soda-silicate glass and fused quartz at various temperatures. The ordinate indicates the ratio of the luminescence intensity I to the intensity I_0 immediately after the cease of the irradiation. The lumine-

scence intensity decays rapidly at first and then decays more slowly. These decay curves do not obey the simple mono- or bimolecular law. The temperature dependence of the decay time is not found for fused quartz and is very small even for soda-silicate glass compared with the conventional model in which only one or a few trapping levels are assumed. As discussed later, these facts are well understood by considering many trapping levels which are assumed to be in the glasses.

(3) *Dependence on the X-ray Dose*

To examine the dependence of the decay on the X-ray intensity, the X-ray current is changed from 3 ma to 20 ma at 40 kv. The decay curves are similar to those shown in Fig. 3 independent of the X-ray intensity in this range. This fact indicates that the present phenomena are not due to the bimolecular processes.

On the other hand, if the duration of the X-ray irradiation is changed, the X-ray current being fixed, the decay time changes. This is shown in Fig. 4. The more the

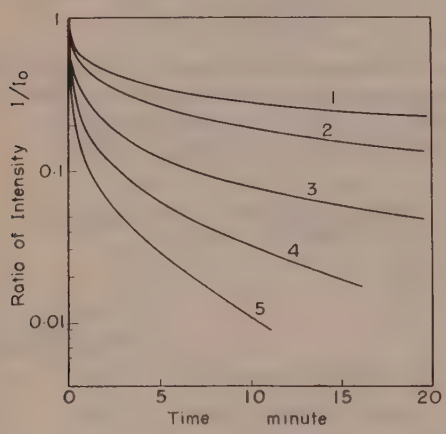

Fig. 4. Decay curves of soda-silicate glass irradiated for 1; 128 minutes, 2; 32 minutes, 3; 8 minutes, 4; 2 minutes, 5; 0.5 minutes at 102°K.

duration of the X-ray irradiation, the slower is the decay. This suggests that during the irradiation the redistribution of the trapped electrons are allowed to tend to the equilibrium distribution which favors the deeper traps. The shape of the glow curve is independent of the duration of the irradiation, though the luminescence intensity rises as the duration increases.

(4) *The Effect of Heat Treatment*

In Fig. 5 the decay curves of the luminescence intensities for the specimens of soda-silicate glasses are shown. These specimens are prepared by different heat treatments;

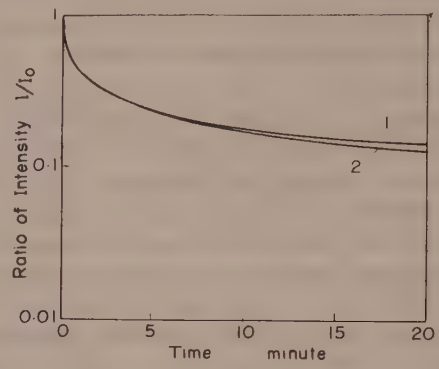

Fig. 5. Decay curves of soda-silicate glass irradiated for 32 minutes at 102°K. 1; annealed at 550°C for 15 hours, 2; quenched after heated at 800°C for 10 minutes.

that is, one is annealed at 550°C for about 15 hours, and the other quenched after heated at 800°C for about 10 minutes. The quenched specimen shows the slightly rapid decay compared with the annealed one. As for the experiments of the glow curves, these two specimens show nearly the same shape.

§ 4. Discussion

Now we shall consider the processes which will contribute to the phenomena of the thermoluminescence of the glasses described in the last section, and the distribution and structure of the electron trapping centers of the glasses. As already suggested in 3. (2) from the dependence of the glow curves on the temperature of the X-ray irradiation, many trapping levels are presumed to be distributed continuously beneath the conduction band. And the fact that the decay curve does not depend on the X-ray intensity, as described in 3. (3), shows that the decay is mainly determined by the rate at which electrons are released thermally from many trapping levels. Hence the processes in which we are interested are to be that the electrons ionized to the conduction band, are trapped in the trapping centers whose energy levels are distributed continuously beneath the conduction band, and after the irradiation is ceased, these electrons are released ther-

mally and then rapidly recombine.

Now the features of the luminescence decay may be interpreted as follows. If the depth of a trapping level from the bottom of the conduction band is $\mathcal{E}$ and the density of the trapping level occupied by the electrons in the range from $\mathcal{E}$ to $\mathcal{E}+d\mathcal{E}$ immediately after the cease of X-ray irradiation is $Z(\mathcal{E})d\mathcal{E}$, the intensity of the luminescence $I(t)$ at a time t after the irradiation is ceased may be expressed as

$$I(t)=\int_0^\infty Cb\exp(-bt\,e^{-\varepsilon/kT})\,Z(\mathcal{E})d\mathcal{E}\,, \qquad (1)$$

where b is the frequency factor, k the Boltzmann's constant, T the absolute temperature and C a constant. Although $Z(\mathcal{E})$ could be obtained directly by analysing the decay curves, we shall rather assume the form of $Z(\mathcal{E})$ at first and calculate $I(t)$ according to Eq. (1), which is to be compared with experimental curves. We assume, for simplicity, that the trapped electrons are distributed uniformly from the levels E_d to E_s, as shown in Fig. 6. That is,

$$\begin{aligned} &0<\mathcal{E}<E_s\,, && Z(\mathcal{E})=0 \\ &E_s\leq\mathcal{E}\leq E_d\,, && Z(\mathcal{E})=A \\ &E_d<\mathcal{E}\,, && Z(\mathcal{E})=0\,. \end{aligned} \qquad (2)$$

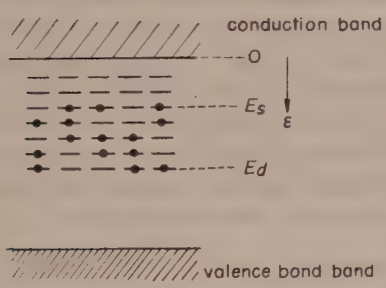

Fig. 6. Distribution of trapped electrons. E_s is the most shallow occupied level. E_d is the deepest occupied level. It is assumed that electrons uniformly and continuously occupy the levels from E_s to E_d.

In this equation, E_s and E_d are the most shallow and the deepest trapping levels occupied by the electrons respectively, at $t=0$. Substituting Eq. (2) in Eq. (1), we obtain

$$I(t)=\int_{E_s}^{E_d} A\cdot Cb\,e^{-\varepsilon/kT}\exp(-bt\,e^{-\varepsilon/kT})d\mathcal{E} \qquad (3)$$

$$=I_0\cdot\frac{\exp(-bx_dt)\{1-\exp[-b(x_s-x_d)t]\}}{b(x_s-x_d)t}\,, \qquad (4)$$

where

$$x_s=\exp(-E_s/kT),\quad x_d=\exp(-E_d/kT) \qquad (5)$$

and I_0 is the luminescence intensity at $t=0$. Since $x_s\gg x_d$ in general, Eq. (4) may be written approximately as follows,

$$I(t)\simeq I_0\cdot\frac{1-\exp(-bx_st)}{bx_st}\,. \qquad (6)$$

In this equation, we should notice that the factors determining the decay time are E_s and T, if b is assumed to be fixed. The curves of Eq. (6) are shown in Fig. 7 in the broken lines. In this figure, the solid curves are the same as the observed ones shown in Fig. 3. Although the agreements of both curves are not sufficiently well, the following estimations may be possible. Assuming b to be 10^{10} sec^{-1}, from Fig. 7 we can estimate for soda-silicate glass the approximate values of E_s to be 0.21 ev and 0.33 ev at the temperature of 102°K and 165°K respectively. For fused quartz, the value of E_s changes considerably with temperature, i.e. E_s are 0.22 ev and 0.66 ev at 102°K and 300°K respectively.

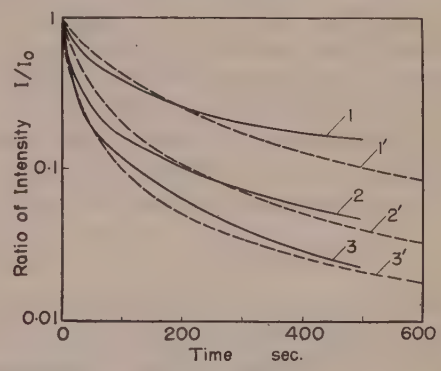

Fig. 7. Decay curves of glasses.
Experimental, 1; fused quartz irradiated at 102°K for 10 minutes, 2; soda-silicate glass irradiated at 102°K for 2 minutes, 3; irradiated at 166°K for 2 minutes.
Calculated, 1'; $bx_s=0.02$, 2'; $bx_s=0.05$, 3'; $bx_s=0.1$.

The results described in 3. (3) that the decay time of luminescence is independent of X-ray intensity show that the value of E_s does not change with the intensity of the X-ray. On the other hand, the decay time is considerably dependent upon the duration of the X-ray irradiation. In fact, for soda-silicate glass at 102°K the values of E_s are estimated to be 0.22 ev in the case of the irradiation of 128 minutes and to be 0.20 ev in the case of the irradiation of 0.5 minutes. We shall make some speculation with respect

to these points. If we assume that the number of trapping centers is far more than the number of electrons available and that the probability for the electron to be captured by the trap is independent of the depth of the trap, the electrons ionized by X-ray may be captured uniformly by each trapping level. Therefore, the dose rate of X-ray does not affect the distribution of the trapped electrons. Since, during the irradiation, the electrons trapped in the upper trapping levels will be released thermally more rapidly than those in the lower levels, the distribution of the trapped electrons will tend to be dense in the lower levels with the increase of the duration of the irradiation. A part of electrons released thermally may recombine rapidly and the other part of those may be captured again by the lower trapping levels. This retrapping processes may greatly promote such a redistribution of trapped electrons. Due to these trapping processes, the level E_s, which divides the trapping levels into empty and uniformly occupied, may be expected to be lowered with the increase of the duration of the X-ray irradiation.

As is well known, the depth of the occupied trapping level $\mathcal{E}$ is obtained from the glow curve according to the approximate equation,

$$\mathcal{E} \simeq kT_G \ln\left(\frac{bT_G}{\beta}\right), \tag{7}$$

where T_G is the temperature corresponding to the maximum of the glow curve and β is the speed of the temperature rise. Assuming b to be 10^{10} sec^{-1} as before, we may obtain from Fig. 1 the values of $\mathcal{E}$ to be ranged from 0.22 ev to 0.40 ev for soda-silicate glass and from 0.22 ev to 0.54 ev for fused quartz, in the case that each specimen is irradiated at 102°K. We find the least ones of these values approximately agree with the values of E_s estimated from the decay curves.

Next we shall discuss briefly the model of the shallow trapping centers of electrons, the detail of which were previously manifested by the author.[4] According to the theory of random network structure of glasses, we may expect the existence of the volume fluctuation or the local volume dilations and compressions in glasses which is to be associated with the randomness of the Si-O-Si bond angle. The effective potential $V(r)$ for an electron may be assumed to be proportional to the volume dilation $\Delta(r)$ and may be expressed as

$$V(r)=E_1\Delta(r)\,, \tag{8}$$

where E_1 is a proportional constant. In this equation $\Delta(r)$ may be determined by the randomness of the glass structure, or its thermal history of the specimen which defines the fictive temperature τ.[5] We shall assume that the volume dilations are confined within the spheres of a certain radius. These dilated spheres may form trapping centers for conduction electrons. Using Eq. (8) we can obtain the energy level $\mathcal{E}$ of the traps as the function of E_1, τ and a the radius of the dilated sphere. $\mathcal{E}$ may be found to increase with τ and E_1 and to decrease with a. The values of the trapping level $\mathcal{E}$ estimated from our experiments are obtained from the appropriate values of them; that is, for τ from 1000°K to 1500°K which are considered to be the fictive temperature of our specimens, and for a around 10 Å and for E_1 around 20 ev which seem to be reasonable values in the model adopted here.

Interpreting the experimental results of the heat treatments seems to be difficult. The quenched specimen has a higher fictive temperature, probably near 1000°K, than the annealed one, whose fictive temperature is considered to be about 823°K. The experimental results described in 3. (4) show that this difference of the fictive temperature of the specimens has less effects than expected from the model above mentioned.

§ 5. Summary

We have observed the thermoluminescence of glasses and examined its dependence on the temperature and the X-ray dose. From the glow curves the electrons ionized by X-ray are found to be trapped in the levels from nearly 0.2 ev to 0.5 ev. The decay curves exhibits slow decays continuing for more than ten minutes, and the decay times are considerably affected by the duration of the X-ray irradiation. These phenomena are well understood by the terms of the electron trapping levels which are uniformly and continuously distributed beneath the conduction band. The distribution of the trapped electrons or the highest level occupied by the electrons E_s is determined by the temperature and the duration of X-ray irradiation.

The model of the trapping center was proposed which is based on the glass structure, essentially affected by the fictive temperature of the specimen. The values of the trapping levels obtained from this model fit approximately with the observed ones. In order to interpret the effect of the heat treatments of the specimens, the more profound considerations are desirable.

§ 6. Acknowledgement

The author wishes to thank Dr. R. Yokota for his offering the valuable specimens, and he also wishes to thank Professor H. Kawamura for his guidance throughout the course of this work.

References

1) R. Yokota: Phys. Rev. **91** (1953) 1013.
2) T. Kikuchi: J. Phys. Soc. Japan **10** (1955) 826.
3) H. Fröhlich: Proc. Roy. Soc. **188** (1947) 521.
4) T. Kikuchi: Busseiron Kenkyu **100** (1956) 1.
5) A. Q. Tool: J. Amer. Ceram. Soc. **29** (1946) 240.
E. Kanai and T. Satoh: J. Phys. Soc. Japan **9** (1954) 417.

Short Notes

This section is intended to secure prompt publication of important discoveries in physics. The reports should not exceed 800 words in length. A figure of size 7 cm × 7 cm will be counted as 150 words.

J. PHYS. SOC. JAPAN **13** (1958) 532–533

Orientation Dependence of the Uniaxial Ferromagnetic Anisotropy Induced by Magnetic Annealing in 20% Co-Ni Single Crystals

By Keizô AOYAGI, Satoshi TANIGUCHI and Mikio YAMAMOTO

The Research Institute for Iron, Steel and Other Metals, Tôhoku University, Sendai

(Received January 13, 1958)

Previously, We[1] and, independently, Néel[2] developed a theory of uniaxial ferromagnetic anisotropy induced by magnetic annealing in cubic solid solutions by assuming that the energy of atom pairs depends both on their kinds and on the orientation of the magnetization vector, and obtained results which agree qualitatively well with the experimental results available at that time. In order to check the theory more precisely, we have measured the induced uniaxial anisotropy as dependent on the alloy composition, annealing temperature, annealing time, orientation of magnetic field applied during annealing, etc. for polycrystalline and monocrystalline Ni-Co alloys. We shall present here the results concerning the orientation dependence of the uniaxial anisotropy induced in 20%Co-Ni single crystals.

The specimen used was a $(1\bar{1}0)$ circular disk of 15.26 mm in diameter and 0.61 mm in thickness. The anisotropy measurement was made by using a torque magnetometer, which was designed to allow the repetition of heat treatment and torque measurement without removing the specimen, so that the torque curve associated with the induced uniaxial anisotropy can be obtained as a difference between curves of the states annealed with and without magnetic field. After finishing the measurement of the curve for the annealing without magnetic field, the specimen was annealed at 650°C (above the Curie temperature) for 30 minutes, cooled down to 450°C at the rate of about 30°C/min., held at that temperature for 15 minutes and consecutively for 5 hours in the presence of magnetic field of about 1500 Oe directed along a desired crystallographic direction, and then rapidly cooled to the room temperature. In this way, the uniaxial anisotropy constant, K_u, and its easy direction, θ_0, were determined as functions of the direction of the magnetic field applied during annealing, θ_T.

In Figs. 1 (a) and (b), $K_u/K_{u[111]}$ and $\Delta\theta=\theta_0-\theta_T$ are plotted against θ_T, in comparison with the theoretical formula for the induced uniaxial anisotropy, E_u:

$$E_u=-K(k_1\sum_i \alpha_i^2\beta_i^2+k_2\sum_{i>j}\alpha_i\alpha_j\beta_i\beta_j)\,,$$

where K, k_1 and k_2 are the constants and α_i's and β_i's are the direction cosines of the magnetization vector and magnetic field applied during annealing, respectively. The figures clearly show that the experimental results agree completely with the theoretical formula by taking the value of k_2/k_1 as 3, while the theoretical value of k_2/k_1 under the nearest neighbour assumption is 4.

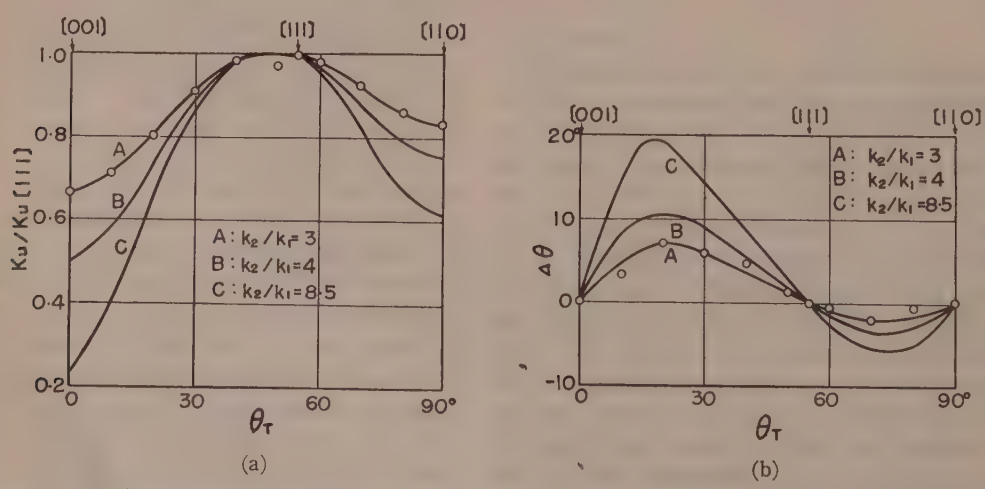

Fig. 1. Uniaxial ferromagnetic anisotropy constant relative to that in the [111] direction, $K_u/K_{u[111]}$, and the deviation of its direction of easy magnetization from that of magnetic field applied during annealing, $\Delta\theta$, as dependent on the direction of annealing field, θ_T.

Chikazumi[3] recently made a similar measurement with a Ni_3Fe single crystal and found that his result was fitted to the theoretical formula by taking a rather large value, about 8.5, of k_2/k_1. It does not seem, however, that the large discrepancy between theory and experiment with Ni_3Fe single crystal is originated from the geometrical coordination of lattice points in face-centered cubic crystal as proposed by Chikazumi[3], since 20% Co-Ni single crystal has also the face-centered cubic lattice. We are now pursuing the discrepancies between theory and experiment for Ni-Co and Ni_3Fe crystals.

References

1) S. Taniguchi and M. Yamamoto: Sci. Rep. Res. Inst. Tôhoku Univ., **A** 6 (1954), 330.
S. Taniguchi: *ibid.* **A** 7 (1955), 269.
2) L. Néel: J. Phys. Rad. **15** (1954), 225.
3) S. Chikazumi: J. Phys. Soc. Japan **11** (1956), 551.

J. Phys. Soc. Japan **13** (1958) 533

Pits on Germanium Surface Formed by Molten Indium

By Sei-ichi Denda
Electrotechnical Laboratory, Tokyo, Japan

(Received March 1, 1958)

It is well known that small pits are formed on germanium surface when a strong acid etching solution is used. Recently we have been observed the same kind of pits which appeares on germanium when it is immersed into molten indium.

The small piece of slice of n-type germanium single crystal with (111) surface is polished with emery paper, and is soldered by the pellet of indium with diluted $ZnCl_2+HCl$ as a flux, and then immersed into a large volume of molten indium with some agitation at 350°C. In 2 minutes it is suddenly picked out of indium, and the indium remaining on the surface is removed by Hg.

Fig. 1 and Fig. 2 show the photographs of the treated germanium surface on which pits pattern appears. This is not obtained on the whole wetted region but on the small portion of that region. The density of these pits is nearly the same as that of the etch pits on the spacimen which is cut out of a same single crystal. Fig. 2 also shows different kind of type of very small pits whose density is one order of magnitude greater than that of the big one. However, its properties are not known yet.

If the temperature of molten indium is 200°C, Fig. 3 which shows triangles, characteristic structure of (111) plane, is obtained.

Pits in Fig. 1 and Fig. 2 resemble the etch pits

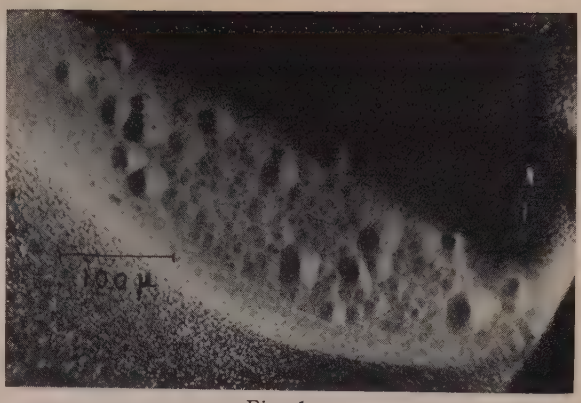

Fig. 1.

Fig. 2.

Fig. 3.

formed by CP-4 which is a strong etching solution, and the situation in Fig. 3 is seen on the surface treated by superoxol which is a weak etchant. Thus there is a close analogy between chemical etching and metallic dissolution of germanium.

It has been visualized that the edge dislocation affects the flatness and uniformity of the alloyed p-n junction which is important in the transistor fabrication[1].

Reference

1) Goldstein: RCA Rev. **18** (1957) 213.

J. PHYS. SOC. JAPAN **13** (1958) 534

Stepped Structure in Moiré Fringe

By Hatsujiro HASHIMOTO

Kyoto Technical University, Matsugasaki, Sakyoku, Kyoto, Japan

(Received February 28, 1958)

The moiré fringes of crystal lattice were observed[1] in the electron microscopic images of two crystalline films superposed. Such fringes appear only on the extinction contour bands due to Bragg reflections. The dislocation in moiré fringe was shown[2] to reveal the dislocation in crystal lattice. The present author observed stepped structures in moiré fringes of CuS and ZnS films as shown in Figs. 1, 3 and 4.

Fig. 1 is a moiré fringe formed on a single contour band of Bragg reflection in which stepped structures of steps of 1/2 and 1 spacing can be seen. Such structure may be interpreted by light optical analogue as follows. Fig. 2 (a) is a grating containing a disorder in spacing near its center whose amount is half the spacing in total and its range covers 5 lines. Fig. 2 (b) is a perfect grating. Fig. 2 (c) is a moiré pattern obtained by superposing (a) and (b) with small twist angle in which a structure of the steps of 1/2 spacing is formed. Fig. 2 (d) is also a moiré pattern obtained by similar method, which shows a stepped structure of 1 spacing. Fig. 3, which is a fringe on a single contour band, indicates two crossed fringes. Each of which may be interpreted as the combination of two edge dislocations of the same sign as is shown in Fig. 3 (c).

Fig. 1. (a) is moiré fringe of CuS with a guide (b) (× 300,000).

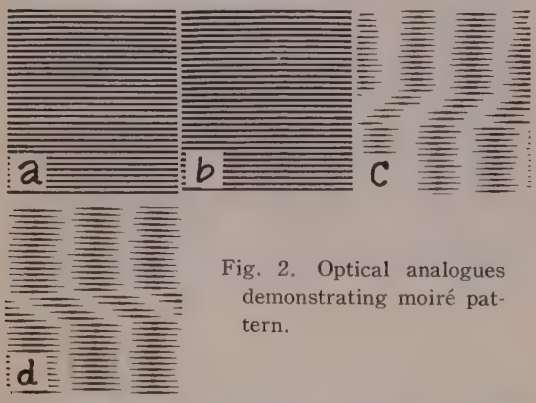

Fig. 2. Optical analogues demonstrating moiré pattern.

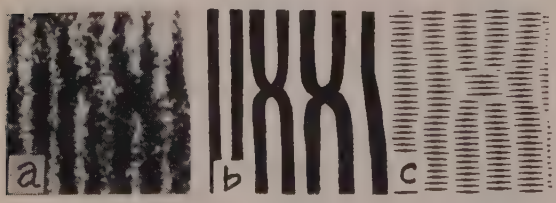

Fig. 3. (a) is moiré fringe of CuS film with a guide (b) (× 400,000). (c) Optical demonstration of cross-steped structure.

Fig. 4 is a moiré fringe on two extinction bands

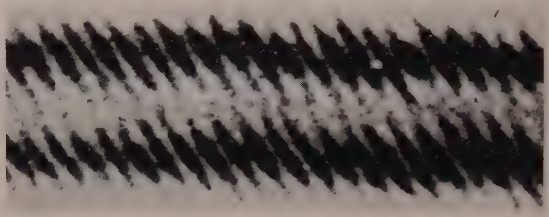

Fig. 4. Moiré fringe on two extinction bands (× 300,000)

due to principal maxima of $(h\ k\ 0)$ and $(\bar{h}\ \bar{k}\ 0)$ reflections. Between two parts of the fringe, we can detect similar stepped structure described above. Such structure was observed on almost every coupled extinction bands but the amount of shift of steps was different in each case. In moiré fringes on the two extinction bands which seem to be due to a principal and its subsidiary maxima or the first and the second Bragg reflections, we also observed stepped structures. These structures may not be interpreted as the disorder of original lattice because the structures moved with the movement of extinction bands and therefore the structures are expected to have no relation with disorder in original lattice. These structures seem to be due to the dynamical interaction of electron with crystal.

The author expresses his sincere thanks to Prof. K. Tanaka of Kyoto University and Prof. R. Uyeda of Nagoya University for their kind discussions.

References

1) T. Mitsuishi, H. Nagasaki and R. Uyeda; Proc. Japan, Acad. **27** (1951) 86. Y. Seki; J. Phys. Soc. Japan **8** (1953) 149, W. C. T. Dowell, J. L. Farrant and A. L. G. Rees; Proc. Regional Conf. Electron Microscopy, Tokyo (1957) 320.

2) H. Hashimoto and R Uyeda; Acta Cryst, **10** (1957) 143.
D. W. Pashley, J. W. Menter and G. A. Bassett; Nature **179** (1957) 752.

J. PHYS. SOC. JAPAN **13** (1958) 535

On the Superstructure of the Alloy Au_3Mn

By Denjiro WATANABE

The Research Institute for Iron, Steel and Other Metals, Tohoku University, Sendai

(Received February, 23, 1958)

It was found by Raub *et al.*[1] that the alloy Au_3Mn has an ordered structure with tetragonal symmetry below 625°C., but its atomic arrangement has not yet been determined. On the other hand, it was elucidated by Meyer[2] that the ordered alloy is metamagnetic like Au_2Mn, having the Néel point of antiferromagnetism at about 145°K. A full explanation of the above magnetic property, however, has not been given due to lack of information on the crystal structure. The present author was able to determine the complex ordered structure of Au_3Mn by electron diffraction.

Fig. 1 shows a diffraction pattern of a thin alloy film containing about 25 atomic % Mn, which was slowly cooled from 450°C. after annealing at 450~500°C. for 2 hrs. The pattern resembles that of the ordered alloy Cu_3Pd[3] in the splitting of superlattice reflections. In order to explain this splitting, a model of a two-dimensional anti-phase domain structure was proposed, as shown in Fig. 2. In this model, it can be seen that the fundamental lattice is a face-centred orthorhombic one with an atomic arrangement similar to Cu_3Au but that the stepshifts, $\pm\frac{1}{2}(\vec{a}_2\pm\vec{a}_3)$ and $\pm\frac{1}{2}(\vec{a}_3\pm\vec{a}_1)$, occur at every cell and at every two cells of the fundamental lattice along the x and y directions respectively. The lattice constants of the fundamental lattice are: $a_1=4.08$, $a_2=4.05$, $a_3=4.03$Å. It is noticeable that both types of shifts belong to the first kind[3] and, therefore, the present two-dimensional anti-phase domain structure is different from that found in Cu_3Pd[3].

The intensity distribution in reciprocal space corresponding to the model in Fig. 2 can well explain the details of the pattern in Fig. 1, except the following two points.

(1) Strictly speaking, the positions of the split superlattice reflections do not coincide with those expected from the above model. This disagreement is attributable to the fact that the extensions of the domain along the x and y directions are not a_1 and $2a_2$, as considered in Fig. 2, but are $1.2a_1$ and $2.2a_2$, respectively. This fractional property of domain size means a mixture of different sizes of domains in the actual lattice[4]. Thus, it should be noticed that the model in Fig. 2 corresponds to an idealized lattice of the ordered Au_3Mn, and for the actual, fractional domain size an enormous unit cell will have to be taken as an exact unit cell. The lattice spacings obtained from an X-ray Debye photograph of 26.5 atomic % Mn alloy by Raub *et al.*[1] are almost explained by the present model with the domain size, $1.0a_1$ and $2.2a_2$.

(2) In Fig. 1 satellites are observed arround the intense normal spots, while their intensities cannot be derived from the present model. The circumstance is the same as in CuAu(II)[5] and Cu_3Pd[4].

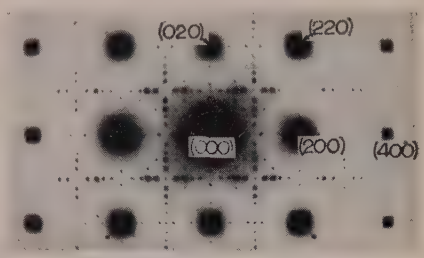

Fig. 1. Electron diffraction pattern of the ordered Au_3Mn film; normal incidence. Indices assigned to normal reflections are referred to the disordered cubic lattice.

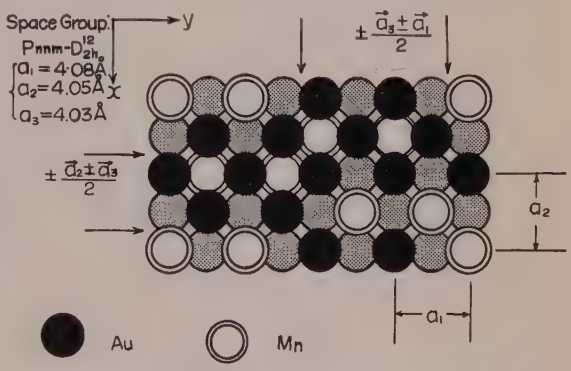

Fig. 2. The Au_3Mn superstructure, viewed along $[001]_{cub.}$ Stepshifts occur at places indicated by arrows.

It is sure that the satellites arise from the lattice modulation, such as a periodic change of the lattice spacing or of the scattering factor, with the same period as that of anti-phase domains, but the explanation of the origin of such a modulation has not yet been given. The author measured the intensities of diffraction spots photometrically and tried Fourier analysis for the potential distribution, in order to obtain more information about the nature of the lattice modulation, and he succeeded in getting a clue to the solution.

A full report will be published elsewhere.

The author wishes to express his sincere thanks to Prof. S. Ogawa for his kind guidance.

References

1) E. Raub, U. Zwicker and H. Baur: Z. Metallk. **44** (1953) 312.
2) A. J. P. Meyer: Compt. Rend. **244** (1957) 2028.
3) D. Watanabe and S. Ogawa: J. Phys. Soc. Japan **11** (1956) 226.
4) K. Fujiwara: J. Phys. Soc. Japan **12** (1957) 7.
5) S. Ogawa and D. Watanabe: J. Phys. Soc. Japan **9** (1954) 475.

J. PHYS. SOC. JAPAN **13** (1958) 536–537

Ultrasonic Velocity and Adiabatic Compressibility of Mixture of Sulfuric Acid and Water

By Yoshio ISHIDA

Faculty of Education, Shimane University, Matsue

(Received February 7, 1958)

The ultrasonic velocity in aqueous solution of the sulfuric acid was measured at the frequency of 5 Mc/sec and at two temperatures 30°C and 15°C, by use of the rotary grating method[1,2,3] which is a variation of the Debye-Sears light diffraction method[4].

After finishing it, the author was informed about the publication by Porosorow[5] and very glad to have an opportunity to make comparison as shown in Table I.

Table I.

The author's value at 30°C		
Conc. % (weight)	Velocity (m/sec)	Density (g/cm³)
0	1509	0.996
10.1	1512	1.062
18.6	1526	1.123
26.0	1546	1.180
32.2	1563	1.230
37.2	1567	1.271
45.0	1577	1.340
57.7	1567	1.466
68.7	1553	1.587
77.1	1536	1.684
82.4	1515	1.743
86.8	1480	1.783
91.5	1416	1.811
96.2	1327	1.826
99.3	1253	1.823

Porosorow's value at 29°C		
Conc. % (weight)	Velocity (m/sec)	Density (g/cm³)
0	1508	0.996
8.2	1510	1.050
14.1	1521	1.091
24.5	1549	1.165
30.0	1574	1.210
36.1	1579	1.262
39.0	1582	1.28
45.2	1587	1.35
51.0	1583	1.41
60.0	1580	1.49
66.0	1564	1.56
76.0	1548	1.66
91.0	1452	1.801

In Fig. 1, the concentration is expressed in the mole fraction of the sulfuric acid and the adiabatic compressibility is computed by the formula $1/\rho V^2$. The velocity-curves have maxima, while the compressibility-curves minima. The position of maximum of the velocity-curve shifts to the higher-concentration side as the temperature decreases. The position of minimum of the compressibility-curve does not shift appreciably, but the

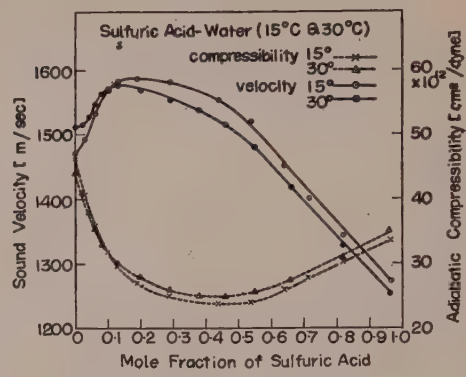

Fig. 1. Ultrasonic velocity and adiabatic compressibility *versus* concentration.

value of minimum decreases with the temperature.

The feature that velocity-curve has maximum is common to all of the mixtures of methyl alcohol-water[7], ethyl alcohol-water[6], acetone-water[6], pyridine-water[7], formic acid-water[3], acetic acid-water[9,7], nitric acid-water[5], carbon tetrachloride-liquid paraffin[10] and others. We ascertained that the volume contraction always took place when these mixtures were prepared. Since the sulfuric acid-water mixture shows both of the volume contraction and the above-mentioned ultrasonic feature, it belongs to the group of these mixtures. Thus, there is a relation between the volume contraction and the existence of minimum in the compressibility curve.

Supported by a scholarship of the Ministry of Education in 1957, the present research was performed at the Department of Physics, Faculty of Science, Kyoto University. The author wishes to thank Professor I. Takahashi for his continual encouragement and valuable discussions. His thanks are also due to Professor M. Ishibashi of the same University for his kind guidance in the technique of acidimetry.

References

1) I. Takahashi, Y. Ishida and M. Ota: Memoirs Coll. Sci. Univ. Kyoto A **27** (1953) 41.
2) I. Takahashi and Y. Ishida: J. Appl. Phys. Japan **25** (1956) 248, (in Japanese).
3) Y. Ishida: Sci. Report Shimane Univ. **7** (1957), 30.
4) P. Debye and F.W. Sears: Proc. Nat. Acad. Sci. **18** (1932) 409.
5) P. Porosorow: Zh. Fiz. Kim. **14** (1940) 391 (See B. B. Kudrjawzew: Anwendung von Ultraschallverfahren bei Physikalisch-Chemischen Untersuchungen, Deutscher Verlag der Wissenschaften, Berlin (1955), translated from the Russian Edition (1952)).
6) I. G. Mikhailov: C. R. (Doklady) URSS **26** (1940) 147.
7) ———: C.R. (Doklady) URSS **31** (1941) 324.

8) ———: C. R. (Doklady) URSS **31** (1941) 550. (Concerning the last three, see O. Nomoto: Chôonpa, Kawade-Shobo, Tokyo (1948)).
9) A. W. Smith and L. M. Ewing: J. Chem. Phys. **7** (1939) 632.
10) P. J. Ernst: J. Acous. Soc. America **19** (1947) 372.

J. PHYS. SOC. JAPAN **13** (1958) 537

Excitation of π Electrons in Benzene by Fast Electron According to FE Model

By Mitio INOKUTI

Department of Applied Physics, Faculty of Engineering, University of Tokyo, Tokyo

(Received February 17, 1958)

It has been empirically known that an aromatic hydrocarbon undergoes strikingly little chemical change under high energy radiations as compared with other organic compounds.[1] The radiation-insensitivity of aromatic hydrocarbons seems to have not received clear-cut explanation, though some proposed to attribute it to easy transfers of excitations.[2] However, it is also desirous to examine primary excitation processes due to radiations, and so we tried an estimation of cross sections for excitation of π electrons in benzene by impact of a fast electron.

We adopt a simple FE model to describe the molecule, whose skeleton is represented by a circular ring of radius a. ($a=2.767$ atomic unit, adjusted by observed 1st excitation energy.) Then an EF orbital is

$$u_m(\chi)=(2\pi)^{-1/2}e^{im\chi}, \quad m=0, \pm 1, \pm 2, \cdots. \quad (1)$$

where χ is the electronic angular coordinate. Born approximation gives the differential cross section I for excitation $i \to f$ as*

$$I=4(k'/k)K^{-4}|(f|T|i)|^2,$$

$$T=\sum_{s=1}^{6} \exp(i\boldsymbol{K}\cdot\boldsymbol{r}_s), \quad (2)$$

where $\boldsymbol{r}_s$ ($s=1, 2, \cdots, 6$) are electronic positions, $\boldsymbol{k}$ and $\boldsymbol{k}$ momentum of the colliding electron before and after scattering respectively and $\boldsymbol{K}=\boldsymbol{k}'-\boldsymbol{k}$. If $\boldsymbol{k}$ is perpendicular to the molecular plane,** we can integrate (2) to get the total cross sections $Q_m^{(0)}$ and $Q_m^{(4)}$ for the formation of the excited states where a π electron is excited into the levels $\pm m$ from the levels ± 1 or the level 0, respectively, as

$$Q_m^{(0)}=2q(1, m)+2q(-1, m),$$

$$Q_m^{(4)}=2q(0, m), \qquad m=2, 3, 4, \cdots, \quad (3)$$

where

$$q(n, m)=(8\pi a^2/k^2)\int_v^w J_{n-m}^2(z)z^{-3}dz,$$

$$v, w=ka\mp\sqrt{(ka)^2-m^2+n^2}. \quad (4)$$

The integral in (4) can be evaluated analytically for $|m-n|>1$, while it must be computed numerically for $|m-n|=1$.

Table

incident energy (ev)	$Q_2^{(0)}$	$Q_2^{(4)}$	$\sum_{m\geq 3}(Q_m^{(0)}+Q_m^{(4)})$
	(π atomic unit)		
100	11.457	0.684	1.562
200	6.451	0.345	0.781
300	4.582	0.230	0.561
400	3.586	0.173	0.391
700	2.216	0.099	0.223
1000	1.625	0.069	0.156
1500	1.140	0.046	0.104

Numerical results, given in Table, show that π electrons are very apt to be excited to the lowest excited level; it is physically expected on account of the mobile character of π electrons. For comparison we remark that the cross section for excitation of σ electrons, roughly estimated by means of the additivity-hypothesis[3] that the cross section of a molecule is nearly the sum of those of the constituent atoms, amounts only about 10% of $Q_2^{(0)}$. As we disregarded exchange collisions, the excited levels concerned are singlets and so they may be deactivated by fluorescence or collisional deactivation in a short period, so that they may contribute little to initiation of secondary processes leading to over-all radiation effects. On the basis of the above argument we can interpret the radiation-insensitivity of benzene in terms of the large cross section for excitation of π electrons at least qualitatively.

With the present result we can point out that primary excitation processes sometimes become dependent on molecular structure and significant in radiation chemistry, contrary to current ideas. Excitation to lower triplet states deserves examination also, but it is difficult as exchange collisions generally become important at low energies where Born approximation is inapplicable.

The author is grateful to Prof. A. Amemiya for his discussions and encouragements throughout the work.

References

1) M. Tolbert and R. M. Lemmon, U. S. Atomic Energy Commission Unclassified Document UCRL-2704 (1954).
2) M. Burton et al, Disc. Faraday Soc. **12** (1952) 88; J. Phys. Chem. **56** (1952) 560.
3) J. W. Otvos and D. P. Stevenson, J. Am. Chem. Soc. **78** (1955) 546.

* The Hartree atomic unit is used in all the expressions.

** Cases with other incident directions, offering mathematical complexities, have not been treated exactly, but seem never to yield features essentially different from the simple case closely examined.

J. PHYS. SOC. JAPAN **13** (1958) 538

Contact Behavior of Metals to CdSe, CdTe, ZnSe and ZnTe

By Hirosi TUBOTA and Hiromichi SUZUKI
General Education Department, Kyusyu University

(Received February 25, 1958)

Behavior of the contact between metals and II-VI intermetallic compounds such as CdSe, CdTe, ZnSe and ZnTe were studied. These compounds were prepared as polycrystalline materials by a dry method in our laboratory. CdSe was n-type and had the hexagonal structure, while the others were p-type and had the cubic structure. Cu, Ag, Au, Zn, Cd, In and Pb were used as contact metals.

The ingots of these compounds were cut and polished up into a parallelepiped and cleaned. Then, a film of the metal mentionded above was evaporated onto two opposite surfaces with the largest area as the electrodes. The dc current-voltage characteristics were obtained by a usual method at room temperature in the dark. From these characteristic curves, we observed the linearity and obtained the threshold voltage (V_0) for zero current. This voltage is defined as the extrapolation of the linear part of the characteristic curve to zero current, and this magnitude may be used as a measure of deviation from the ohmic behavior. The results are shown in the following table, and also the typical curves of current-voltage characteristics in In-CdSe and Au-CdSe are shown in Fig. 1.

In the case of CdSe, measurements were made with many samples. Particularly, in In-CdSe, about one dozen of samples were tried and it was found that V_0 were very close to zero for all of the samples and the linearity were very good up to several volts. It is of interest that the result is in agreement with the fact observed in In-CdS and Ga-CdS by Smith.[1]

Observed values of the threshold voltage (V_0)

Group number in the periodic table		I			II		III	IV
Electrode metal		Cu	Ag	Au	Zn	Cd	In	Pb
Work function[3] (in eV)		4.47	4.28	4.58	3.74	3.92	3.9	4.02
V_0 (in volt)	CdSe (n)	0.05	0.1	0.1	0.05	0.05	0.00	0.05
	CdTe (p)	0.2	0.2	0.1	0.2	0.4	0.3	0.5
	ZnSe (p)	—	—	0.2	0.4	—	—	—
	ZnTe (p)	0.05	—	—	—	—	—	—

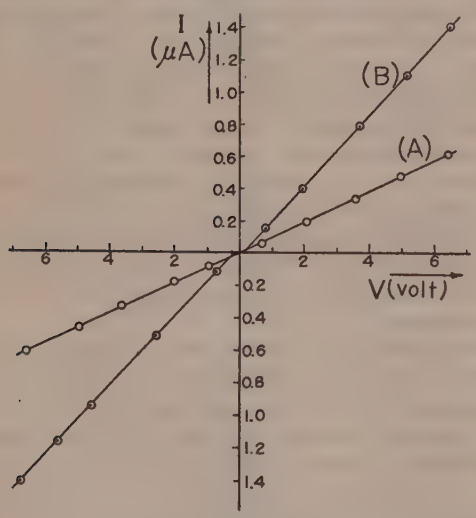

Fig. 1. Dc current-voltage charactertistic curves. (A) for In-CdSe contact, (B) for Au-CdSe contact.

In the cases of CdTe, ZnSe and ZnTe, measurements were made with several samples and no metals were found to present the good ohmic behavior. Furthermore, in ZnSe and ZnTe, almost all metals used showed such poor linearity that the threshold voltages could not be determined.

If the barrier height in metal-semiconductor contact is determined only by the work function difference between metal and semiconductor, it should be expected that, as the work function of metal becomes larger, so does the deviation from the ohmic behavior, and hence the threshold voltage increases in n-type materials. This expectation seems to be satisfied qualitatively in CdSe as shown in the table. On the other hand, as the reverse is the case in p-type, the results obtained in the case of CdTe seem qualitatively explicable on the same way.

In order to explain the ohmic behavior by the model of the conductive layer formed by diffusion of metal into semiconductor, we must have more sufficient knowledge of the diffusion of the present materials. However, at least, in the case of In-CdSe contact showing a good ohmic behavior, it seems that there may be a strongly n-type conductive layer formed in CdSe next to the electrodes, as proposed by F. A. Kröger[2] for In-CdS and Ga-CdS contacts.

The authors wish to express their sincere thanks to Prof. A. Okazaki for his continual advice and encouragement.

References

1) R. W. Smith: Phys. Rev. **97** (1955) 1525.
2) F. A. Kröger, G. Diemer and H. A. Klasens: Phys. Rev. **103** (1956) 279.
3) H. B. Michaelson: J. Appl. Phys. **21** (1950) 536.

Errata

On the Temperature Diffuse Scattering of Electrons I. Derivation of General Formulae

By Saito TAKAGI

J. Phys. Soc. Japan **13** (1958) 278.

P. 279, eq. (4), $2\pi i \boldsymbol{k}_r^{(i)} \cdot \boldsymbol{r}$ should be read $2\pi i \boldsymbol{k}_h^{(i)} \cdot \boldsymbol{r}$.
P. 281, 2nd line of eq. (17), $V_{g+h'-h}$ should be read $V'_{g+h'-h}$.
P. 281, 2nd and 4th line of eq. (17), c_{hk} should be read c_{kh}.
P. 282, 10th line from the bottom, $k' \approx K$ should be read $k' \approx K_0$.

On the Temperature Diffuse Scattering of Electrons II. Applications of Practical Problems

By Satio TAKAGI

J. Phys. Soc. Japan **13** (1958) 287.

P. 290, 2nd line of the equation following eq. (16), (eq. for $J^{21}_{s,h}$) $f'_{e,g+h}$ should be read $f'^2_{e,g+h}$.
P. 290, 1st line of eq. (18), $\sum_t \frac{\cos\theta_{g\,qt}}{c_t^2}$ should be read $\sum_t \frac{\cos^2\theta_{g\,qt}}{c_t^2}$.
P. 291, left column, line 2, treat should be read treats.
P. 295, 3rd line of eq. (21), $\frac{1}{2q_0^2}\ c^{\ 2}$ should be read $\frac{1}{2q_0^2}\Big/c_{tr}^2$.
P. 295, right column, 10th line from the bottom, S′ should be read S_0.
P. 296, Reference (1), the number of page, 278, should be added.

On the Absorption Spectra of Complex Ions IV

By Y. TANABE and H. KAMIMURA

J. Phys. Soc. Japan 13 (1958) 394

Page		Wrong	Correct
402	Table III	$\left(\frac{3}{2}1\frac{3}{2}[1]\frac{3}{2}1\frac{5}{2}\right)=\sqrt{6}/5$	$=-\sqrt{6}/5$
403	Eq. (2.35)	$(f_2^n S_1\Gamma_1\{\|f_2^{n-1}(S_3\Gamma_3)$	$(f_2^n S_1\Gamma_1\{\|f_2^{n-1}(S_3\Gamma_3)f_2)$
407	6th line from the bottom	....degenerate multiplet ${}^{2S+1}\Gamma$, ...	degenerate multiplets ${}^{2S+1}\Gamma$, which enables us to predict the splitting of the multiplet, ...
408	Eq. (3.1)	$(\alpha E\|\|\boldsymbol{T}(A_2)\|\|\alpha E)=\sqrt{2}\,i$	$=-\sqrt{2}\,i$
		$(\alpha F_1\|\|\boldsymbol{T}(F_1)\|\|\alpha F_1)=-\sqrt{6}\,i$	$=+\sqrt{6}\,i$

PROGRESS OF THEORETICAL PHYSICS

CONTENTS

Progress of Theoretical Physics Vol. 19, No. 3 March 1958

Quantum Electrodynamics with the Indefinite Metric—*Non-Lorentz-Invariance of the Gupta Formalism*—.....S. SUNAKAWA..221
Dispersion Relations for K Meson-Nucleon Scattering.....K. IGI..238
On the Longitudinal and Transverse Polarization of Positrons in μ^+-Meson Decay.....S. HORI, H. SEGAWA and A. WAKASA..249
Theory of Cohesive Energy of LiH Crystal—*The Method of Semi-Localized Crystalline Orbital (SLCO), I*—.....A. MORITA and K. TAKAHASHI..257
Antinucleon-Nucleon Interactions.....Z. KOBA and G. TAKEDA..269
Formulas in the Fermi Theory of Beta-Decay, I—*Beta-Spectrum*—.....Z. MATUMOTO and M. YAMADA..285
On the Static Approximation of the γ_5 Meson Theory.....A. KANAZAWA..330
Letters to the Editor:
On the Recombination Processes by the Auger Effect.....M. NAGAE..339
On the Auger Effect in the Deep Traps in Si.....M. NAGAE..341
Mass Levels and Relative Parities of Baryons.....H. KATSUMORI..342
Effect of Electron-Electron Scattering on Hall Mobility of Electrons in n Semiconductors.....M. S. SODHA and P. C. EASTMAN..344
Density of the Normal Component for Solutions of He^3 and He^4.....S. K. TRIKHA..346
The Non-Indication of the "Anomalous" Scattering of Mu-Mesons.....S. FUKUI, T. KITAMURA and Y. WATASE..348
Ground State Energy of Bose System with Lennard-Jones Potential.....R. ABE..350
Contents of Journ. of Phys. Soc. of Japan, Vol. 13, No. 2 352

Price $ 1.25 per copy
$ 15.00 per year (postage inclusive)
Annual dues for foreign members (individual subscribers)
$ 12.00 (postage inclusive)
" for foreign members of the Physical Society of Japan
$ 10.00 (postage inclusive)

Application for members, subscriptions and orders for back numbers should be sent, directly or through book-dealers, to

The Publication Office
in
Yukawa Hall, Kyoto University, Kyoto, Japan

JOURNAL OF THE PHYSICAL SOCIETY OF JAPAN Vol. 13, No. 6, JUNE, 1958

Gamma Rays from the Proton Bombardment of Silicon

By Eiji OKADA, Iwao MIURA, Tetsuo WAKATSUKI and Yasuo HIRAO

Department of Physics and the Laboratory of Nuclear Studies, Faculty of Science, Osaka University, Osaka

(Received February 10, 1958)

Gamma ray spectrum from silicon bombarded by 5.7 MeV protons has been studied by a scintillation spectrometer. The following gamma rays due to inelastic scattering of protons were observed. 1.78 MeV (^{28}Si 1st—ground), 1.28 MeV (^{29}Si 1st—ground), 2.03 MeV (^{29}Si 2nd—ground), 2.43 MeV (^{29}Si 3rd—ground), 2.24 MeV (^{30}Si 1st—ground). Excitation curves for the 1.78 MeV gamma rays have been measured in the proton energy range from 2.2 to 5.7 MeV. Resonances were found at 2.9, 3.5, 4.4, 5.0 and 5.4 MeV. At 5.4 MeV, the angular distribution of the 1.78 MeV gamma rays was measured. By comparison with theory, the corresponding compound level of ^{29}P at 7.9 MeV was assigned $d_{5/2}$. The cross section for this process is 250 mb.

§ I. Introduction

The yield of gamma rays from silicon bombarded with protons has been studied by a number of workers. In the low energy region of proton energies below 2 MeV, the spectrum of gamma ray energies and the yields were measured for the reactions ^{29}Si$(p, \gamma)^{30}$P[1] and ^{30}Si$(p, \gamma)^{31}$P[2]. Many resonances have been found for each reaction. As the proton energy becomes higher, gamma rays following inelastic scattering of protons become predominant. Cohn, Bair, Kington and Willard[3], observing 1.78 MeV gamma rays from the first excited state of ^{28}Si due to proton inelastic scattering, found 13 resonances in the range of proton energies from 2.6 to 4.9 MeV.

Bromley, Gove, Paul, Litherland and Almqvist[4] studied the gamma radiation associated with the ^{29}Si$(p, p'\gamma)^{29}$Si inelastic scattering reaction in the proton energy range from 2.5 to 3.0 MeV.

The present paper describes measurements of the energy spectrum, yield and angular distribution of gamma rays following inelastic scattering of protons by natural silicon target at proton energies extending up to 5.7 MeV.

§ 2. Experimental Methods

Molecular ion beam of hydrogen accelerated by 44 inch cyclotron has been used to study the gamma rays following inelastic scattering of protons by silicon. The outer beam of protons passed through a focussing magnet, concrete shield wall 1.5 meter thick and aluminium absorbers of different thicknesses before reaching a target. The distance from the cyclotron to the target is about 7 meters. The upper limit of the proton energy was 5.7 MeV and the energy was degraded at 0.1 MeV intervals down to 2.2 MeV by the aluminium absorbers placed about 1 meter in front of the target. The intense gamma rays from aluminium by Al$(p, p'\gamma)$ reaction were shielded by a lead block with a beam hole 1 cm in diameter placed just behind the absorber in a vacuum vessel. But a considerable fraction of gamma rays from aluminium absorbers was observed in a forward direction and a correction was necessary in angular distribution measurement.

The corrections amount to about 100% for 0°, 4% for 135° and 1 ~ 2% for all the other angles. The energy of those back ground gamma rays was found to be 1.74 MeV corresponding to the transition from the fourth to the second excited state of ^{27}Al.[5]

The beam was defined by a defining slit made of gold plate 4 mm wide and 10 mm high.

The proton current incident on the target was measured by a current integrater consisting of a highly insulated condenser and a string electrometer. A monitor scintillation counter was also used.

The gamma rays were measured with a sodium iodide crystal spectrometer consisting of a crystal 3 in. in diameter and in length, viewed by a Dumont 6364 photomultiplier,

The pulses were fed from the amplifier to a 20 channel pulse height analyzer. The crystal and the lead shield for the crystal were mounted on a turntable which enabled them to be set at angles between $-60°$ to $+135°$ with respect to the proton beam. The distance from the target to the surface of the crystal was 30 cm. No collimation for the

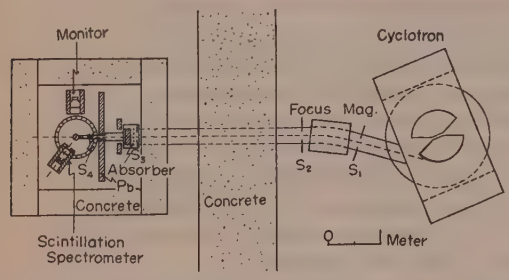

Fig. 1. Schematic diagram of experimental equipment.

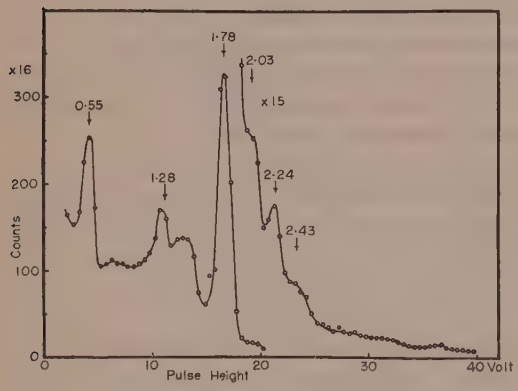

Fig. 2. Gamma ray spectrum from Si bombarded by 5.7 MeV protons observed at 90° with respect to the proton beam.

gamma ray was used for the measurement of the yield and the spectrum, but a lead slit of 3.5 cm in diameter and 7 cm thick was placed in front of the crystal for the measurement of angular distribution to improve the geometrical condition.

The geometry of the system is shown schematically in Fig. 1.

§ 3. Results and Discussions

Fig. 2 shows the gamma ray spectrum observed at right angles to the beam at proton energy of 5.7 MeV. The arrows indicate the positions of the peaks and the energies of the gamma rays expected from the known excited levels of ^{28}Si (abundance 92.2%), ^{29}Si (4.7%) and ^{30}Si (3.1%)[5] by inelastic scattering.

As is evident from the Fig. 2, the energy of the most intense gamma ray is 1.78 MeV (^{28}Si 1st—ground) corresponding to the deexcitation from the first excited state to the ground state in ^{28}Si. The 2.67 MeV (^{28}Si 2nd—1st) and 3.13 MeV (^{28}Si 3rd—1st) were too weak to be observed. Gamma rays of 1.28, 2.03 and 2.43 MeV were identified as the deexcitation from the first, second and third excited state to the ground state of ^{29}Si. Gamma ray of 2.24 MeV energy corresponding to the transition from the first excited state to the ground state of ^{30}Si has also been observed. The 550 keV gamma ray was ascribed to be due to the gold backing.

Next, the yield of the 1.78 MeV radiation from the reaction ^{28}Si$(p, p'\gamma)^{28}$Si, as a function of the proton bombarding energy was measured at right angles to the beam. The result is shown in Fig. 3. The resonant yields were

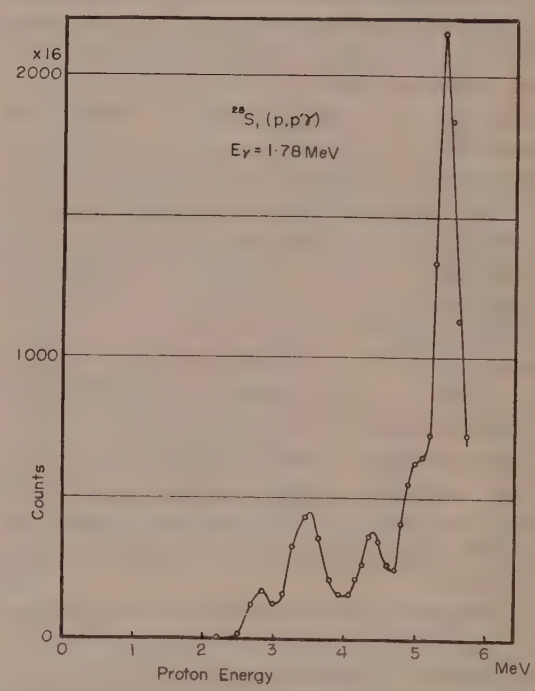

Fig. 3. Yield of the 1.78 MeV radiation from the ^{28}Si$(p, p'\gamma)$ reaction as a function of the bombarding proton energy.

observed at proton energies of 2.9, 3.5, 4.4, 5.0 and 5.4 MeV. As the proton energy was changed by the absorber, the spread of the proton energy is considerably large and the levels spaced closely are not resolved. Thus our value 2.9 MeV can be supposed to include

2.64 and 3.11 MeV resonances, 3.5 MeV includes 3.35, 3.58 and 3.71 MeV resonances, 4.4 MeV includes 4.25 and 4.44 MeV resonances, and 5.0 MeV includes 4.70, 4.82 and 4.86 MeV resonances as reported by Cohn et al.[3]

Newly found resonace level at 5.4 MeV has very strong intensity and the corresponding level of ^{29}P is 7.9 MeV. To determine the spin of this level, the angular distribution of 1.78 MeV gamma ray was measured at proton energy of 5.4 MeV. The results of this measurement are shown in Fig. 4 and the solid line in this figure represents a curve calculated theoretically as is discussed later.

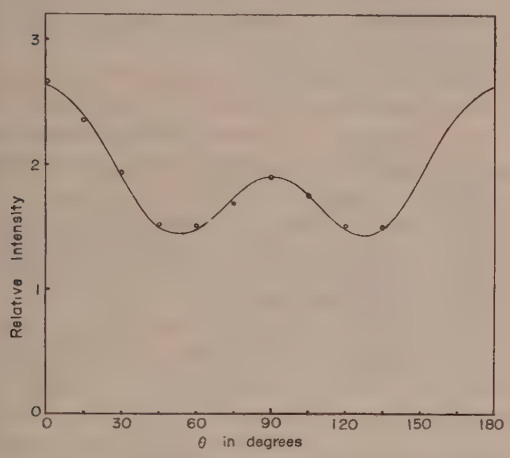

Fig. 4. Angular distribution of the 1.78 MeV radiation relative to the direction of the incident protons at proton energy of 5.4 MeV. The solid curve was calculated assuming 5/2+compound state and $1=1'=2$.

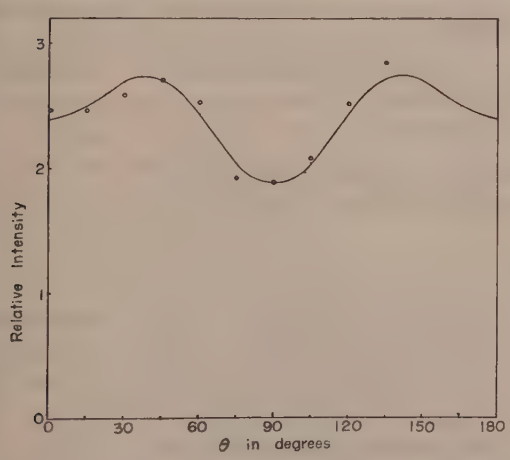

Fig. 5. Angular distribution of the 1.78 MeV radiation at proton energy of 5.7 MeV. The solid curve is a least square fit to the experimental points using even Legendre polynomials up to P_4.

The measurement was also made at proton energy of 5.7 MeV and the results are shown in Fig. 5. The solid line in this figure represents a least squares fit to the data, using even Legendre polynomials up to P_4, and is given by

$$W(\theta)=\alpha\{1+0.239P_2(\cos\theta)-0.225P_4(\cos\theta)\}$$

As the spins of the ground and the first excited state at 1.78 MeV of ^{28}Si are known to be 0^+ and 2^+ respectively, the angular distribution of the gamma ray corresponding to the transition from the first excited state to the ground state can be calculated if appropriate spin is assumed for the compound level of ^{29}P. The general expression was given by Kraus, Schiffer, Rrosser and Biedenharn[6] and the numerical coefficient of the Legendre polynomials for the present case can be obtained from Table I in our previous work[7] for $1, 1' \leqq 3$ and except for interference term. (1 and 1′ are incoming and outgoing angular momentum for protons respectively.) For the resonance level of ^{29}P at 7.9MeV ($E_p=5.4$MeV), the assigment of $5/2^+$ to the level and $1=1'=2$ gives satisfactory agreement with the experiment. In this case the theory gives[8]

$$\begin{aligned}\sigma(\theta)=&a_{3/2}12(12-\cos^2\theta)\\&+a_{5/2}(151-138\cos^2\theta+175\cos^4\theta)\\&+a_{3/2\cdot5/2}24(1-18\cos^2\theta+25\cos^4\theta)\end{aligned}$$

where the first term is that due to 3/2 channel spin, the second is due to 5/2 channel spin and the final term is due to interference effects. The solid curve in Fig. 4 represents the theoretical curve with the values $a_{5/2}=1/2\cdot a_{3/2}$ and $a_{3/2\cdot5/2}=1/2\cdot a_{3/2}$. The relative values of $a_{5/2}$ or $a_{3/2\cdot5/2}$ to $a_{3/2}$ other than this choice also explain the experimental curve to some extent. But the value of the spin J other than $5/2^+$ can not give the angular distribution observed by the experiment. The values $J=5/2^+$ $1=1'=2$ are consistent with the observation on the angular distribution of the inelastically scattered protons from the 1.78 MeV level of ^{28}Si at proton energy of 5.4 MeV carried out by Yamabe, Kondo and Yamazaki[9] in our laboratory.

It is therefore concluded that ^{29}P has $d_{5/2}$ level at 7.9 MeV. But it is not certain that the level is single or not.

The angular distribution of the 1.78 MeV gamma ray at proton energy of 5.7 MeV is

shown in the Fig. 5. General character of the curve seems to be expressed by the theoretical curve assuming compound level $d_{5/2}$ and $1=2$, $1'=0$.

The absolute cross section for the excitation of 1.78 MeV gamma ray at 5.4 MeV proton energy has been measured by comparison of the intensity with that of 1.17 and 1.34 MeV gamma rays from a standard ^{60}Co source* placed at the position of the target. The result is 24 mb/ster. at 90°. From the curve shown in Fig. 4, the total cross section can be calculated as 250 mb.

§ 4. Acknowledgements

The authors wish to thank Prof. S. Takagi, Prof. S. Yamabe, Mr. M. Kondo and Mr. T. Yamazaki for their discussions.

This work was supported by the Grant for Scientific Research of the Ministry of Education.

References

1) P. M. Endt, J. C. Kluyver and C. Van der Leun: Phys. Rev. **95** (1954) 580.
S. Milani, J. N. Cooper and J. C. Harris: Phys. Rev. **99** (1955) 645.
C. Broude, L. L. Green, J. J. Singh and J. C. Wilimott: Phys. Rev. **101** (1956) 1052.
L. W. Seagondollar, J. A. Woods, H. G. de Sonza and W. A. Glass: Bull. Am. Phys. Soc. **2** (1957) 304.
N. K. Green, R. F. Wiseman and E. A. Milne: Bull. Am. Phys. Soc. **2** (1957) 377.
2) E. B. Paul, G. A. Bartholomew, H. E. Gove and A. E. Litherland: Bull. Am. Phys. Soc. **1** (1956) 39.
3) H. O. Cohn, J. K. Bair, J. D. Kington and H. B. Willard: Phys. Rev. **99** (1955) 644.
4) D. A. Bromley, H. E. Gove, E. B. Paul, A. E. Litherland and E. Almqvist: Can. Journ. Phys. **35** (1957) 1042.
5) P. M. Endt and J. C. Kluyver: Rev. Mod. Phys. **26** (1954) 95.
6) A. K. Kraus, J. P. Shiffer, P. W. Prosser and L. C. Biedenharn: Phys. Rev. **104** (1957) 1667.
7) Y. Hirao, E. Okada, I. Miura and T. Wakatsuki: Journ. Phys. Soc. Japan **13** (1958) 233.
8) J. P. Shiffer, M. S. Moore, and C. M. Class: Phys. Rev. **104** (1956) 1661.
9) S. Yamabe, M. Kondo and T. Yamazaki: To be published.

* Prepared at Oak Ridge National Laboratory.

JOURNAL OF THE PHYSICAL SOCIETY OF JAPAN Vol. 13, No. 6, JUNE, 1958

Magnetic Spectrometer having Inclined Plane Pole-Faces for Low-energy Electrons

By Susumu KATO

Laboratory for Applied Physics, Faculty of Engineering, Osaka University, Higashinoda, Osaka, Japan

(Received January 29, 1958)

A magnetic spectrometer with inclined plane pole-faces has been constructed for the velocity analysis of low-energy electrons. The magnetic field strength H at a point P satisfies

$$H=H_1/r\ ,$$

where H_1 is a constant and r is the distance from the line of intersection of the two pole-planes to P. The momentum dispersion of our spectrometer is about 3 times larger and the solid angle of the collection is more than 10 times wider than those of a conventional semi-circular spectrometer of similar dimensions. The equation which determines the momentum dispersion was obtained and the conditions for focusing were discussed.

§ 1. Introduction

An electron, ejected from one point into a uniform magnetic field in a direction perpendicular to the lines of magnetic force, describes a circle whose radius depends on the velocity of the electron and on the strength

of the magnetic field. Thus various momenta may be selected by changing either the radius of the selected paths or the value of the magnetic field. This is the principle of the conventional semi-circular spectrometers. The resolving power of a semi-circular spectrometer is mainly defined by three terms, i.e. the momentum dispersion, broadening of the image of the emitting source focused on the collecting slit and the collecting slit width.

Various attempts have been done for increasing the resolving power.[1] One of the method which has been used is to give a small amounts of departure from uniformity in the magnetic field, for example—by altering the profile of the pole-faces of the magnet. In order to get good reproducibility and ease of construction, the simplest possible profile is evidently desirable.

It is thus of interest to utilize the non-uniform magnetic field between two inclined plane pole-faces. The field is the same as that due to a current flowing along the line of intersection of the two planes, and the lines of force are a family of circular arcs. This kind of field was first discussed by Richardson[2] mathematically, and has further been studied in the case of a sector field by several investigators.[1]

We have constructed a magnetic spectrometer which has an inclined plane pole-faces magnet. In our spectrometer the whole paths of electrons from the source to the collecting point exist in the magnetic field as in usual semi-circular focusing systems but somewhat different from the paths suggested by Richardson. The spectrometer has the high dispersion and resolving power together with a fairly large solid angle of collection, and the lack of uniformity of the edge of magnetic field does not affect the paths of electrons.

§ 2. The Orbits of Electrons

Let r, z, and ϕ be cylindrical coordinates representing radial, longitudinal and azimuthal displacements with respect to the axis $r=0$ defined by the line of intersection of the two planes which contain the faces of the magnetic pole-pieces. The equipotential planes $\phi=$constant all intersect along this axis, on which lie the centers of the circular lines of force. The field H satisfies

$$H=H_1/r\,, \tag{1}$$

where H_1 is the intensity at $r=1$.

The three-dimensional equations of the orbits from a point source lying in the mid-plane $\phi=0$ at $r=r_s$ were given by Richardson. However the integrands which were used in his equations are not convenient for numerical calculations to design a spectrometer. Fortunately in a spectrometer the image will be formed by the orbits which lie in or near the mid-plane $\phi=0$. In this case, the equations of the family of coplaner orbits are given also by Richardson,

$$r=r_s\cdot\exp\{K(\cos\psi-\cos\psi_s)\}\,, \tag{2}$$

$$z=-K\cdot r_s\cdot\exp(-K\cos\psi_s)\times\int\cos\psi\cdot\exp(K\cos\psi)d\psi\,, \tag{3}$$

where, ψ is the angle between the velocity vector V at a point P on the orbit and a vector through P parallel to the axis $r=0$, pointing in the direction of increasing z and $\psi=\psi_s$ at the source S. K is related to the momentum $m_t\cdot v$ by

$$K=\frac{m_t\cdot v}{H_1\cdot e_0}\,. \tag{4}$$

Now we consider the nature of the orbits.

A. *Estimation of orbits.*

On designing the spectrometer it is convenient to know the approximate forms of the orbits before the rigorous calculations. From the above equations of the orbits, the radius of curvature ρ at a point P on the paths is

$$\rho=Kr\,. \tag{5}$$

Then, if we know the position of a source S and ψ_s, we can show a orbit lying in the mid-plane as a series of loops in which the radius of curvature is equal to Kr. r takes a value between $A\exp K$ and $A\exp(-K)$ periodically, with maxima at $\psi=2n\pi$ and minima at $(2n+1)\pi$, where n is an integer and

$$A=r_s\cdot\exp(-K\cos\psi_s)\,.$$

The z-displacement in a complete loop increases rapidly with K. Orbits with the same value of K have the same shapes but different sizes, because both r and z are proportional to $\exp(-K\cos\psi_s)$, which varies with the angle of emission ψ_s.

For the actual calculation of eq. (3) it will be convenient to use the values of $\int_0^\psi\cos\psi\cdot$

$\exp(K\cos\psi)d\psi$ given by Richardson. A part of his work is shown in Table I.

Table I. Values of $\int_0^{\psi}\cos\psi\cdot\exp(K\cos\psi)d\psi$ for $K=1$.
(quoted from a part of Richardson's table[2])

$\psi°$	I	$\psi°$	I
10	0.46965	100	2.23040
20	0.91157	110	2.19582
30	1.30243	120	2.14771
40	1.62648	130	2.09147
50	1.87685	140	2.03071
60	2.05483	150	1.96774
70	2.16785	160	1.90386
80	2.22688	170	1.83976
90	2.24395	180	1.77550

B. Conditions for focusing.

In spectrometers it is necessary that the rays emitted from a point source with small angular divergence $\Delta\xi_s$ should be converged to a point. However the general conditions for focusing of the rays in the field H of Eq. (1) have not been studied yet. Then we have derived the general condition from Eqs. (2) and (3) as followings,

$$\frac{\partial r}{\partial\psi_s}=rK\sin\psi_s\,, \qquad (6)$$

$$\frac{\partial z}{\partial\psi_s}=K(z\sin\psi_s+r_s\cos\psi_s)\,. \qquad (7)$$

Eq. (6) becomes zero when

$$\psi_s=n\pi\,, \qquad (n=0,1,2,\cdots)\,, \qquad (8)$$

and for Eq. (7) the condition which makes it zero is

$$\cos\psi_s=\pm\sqrt{\frac{z^2}{z^2+r_s^2}}=\pm\sqrt{\frac{w^2}{w^2+1}}\,, \qquad (9)$$

where $z=w\cdot r_s$.

Unfortunately we have no ψ_s's satisfying the conditions (8) and (9) simultaneously except when the emitting source lies on the line of intersection of the two magnetic pole-planes so we can not design such spectrometer. Then we must choose the value of (r, z) which indicates the position of the collecting slit so as to minimize the broadning of the emitted rays estimated from both Eqs. (3) and (9).

The relations between ψ_s and w are shown by the dotted lines in Fig. 1 and the corresponding values of z calculated from Eq. (3) by full lines. The intersections satisfy both Eqs. (3) and (9). But for perfect focusing Eq. (8) should also be considered, then the points A_1 and A_2 in Fig. 1 are the most suitable ones for spectrometers of this kind.

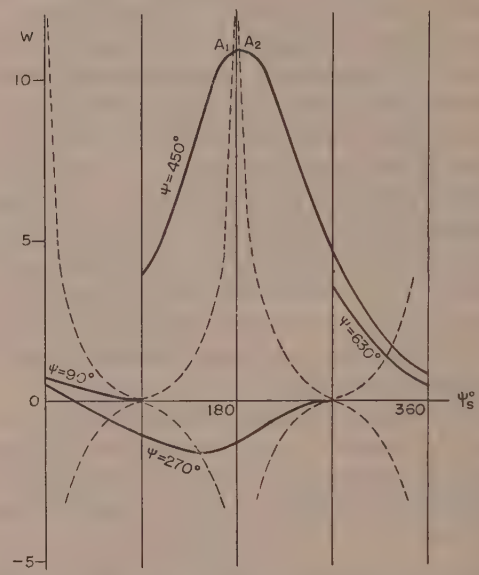

Fig. 1. Focusing of the orbits lying in the mid-plane for $K=1$. The relations between emitting angle ψ_s and $w=z/r_s$ derived from Eq. (9) are shown with the dotted lines. The corresponding values of z calculated from Eq. (3) are shown by full lines. ψ represent the positions of the collecting slit. The intersecting points satisfy both Eqs. (3) and (9). Among these points A_1 and A_2 are most suitable for the spectrometers.

C. Momentum dispersion and resolving power

In the conventional semi-circular spectrometer the distance from the source to the image z_i is,

$$z_i=2\rho=\frac{2p}{H\cdot e_0}\,,$$

where p is the momentum of an electron. Thus

$$p\frac{dz_i}{dp}=\frac{2p}{H\cdot e_0}=z_i\,.$$

The dispersion is proportional to the length of the spectrometer. With inclined poles Richardson calculated the dispersion of z-direction for only a case when K is near to or greater than unity and ψ_s is near to π. However to obtain the best dispersion available in this type of magnetic field we must calculate for both r and z-directions in the

general case. We have derived following Eqs. of momentum dispersion.

From Eq. (2)

$$p\frac{dr}{dp}=K\frac{dr}{dK}=Kr(\cos\psi-\cos\psi_s)\ . \qquad (10)$$

The maximum value of Eq. (10) is $2r$ when $K=1$, which represents two times the dispersion of a semi-circular spectrometer of the same length. The dispersion of z-direction is given from Eq. (3)

$$p\frac{dz}{dp}=K\frac{dz}{dK}=z\left\{1-K\cos\psi_s+\frac{K(\partial I/\partial K)}{I}\right\}\ , \qquad (11)$$

where

$$I=\int_{\psi_s}^{\psi}\cos\psi\cdot\exp(K\cos\psi)d\psi\ , \qquad (12)$$

thus

$$\frac{\partial I}{\partial K}=\int_{\psi_s}^{\psi}\cos^2\psi\cdot\exp(K\cos\psi)d\psi\ . \qquad (13)^*$$

Values of $\partial I/\partial K$ are given in Table II. for $K=1$. The momentum dispersion for z-direction derived from Eq. (11) is shown in

Table II. Values of $\frac{\partial I}{\partial K}=\int_0^{\psi}\cos^2\psi\cdot\exp(K\cos\psi)d\psi$ for $K=1$.

$\psi°$	$\partial I/\partial K$	$\psi°$	$\partial I/\partial K$
10	0.467	100	1.862
20	0.894	110	1.871
30	1.248	120	1.891
40	1.513	130	1.924
50	1.691	140	1.967
60	1.794	150	2.018
70	1.842	160	2.076
80	1.858	170	2.138
90	1.860	180	2.202

Fig. 2. The maximum value occurs near at $\psi=450°$, $\psi_s=180°$ and fortunately this is in the neighbourhood of points A_1 and A_2 indicated in Fig. 1. The dispersion in this point is larger than semi-circular spectrometer by more than 3 times. Orbits in the mid-plane of our spectrometer and the arrangement of the electrodes are shown in Fig. 3. The axis of the collecting slit i.e. the perpendicular line of the baffles of our spectrometer is sat normal to the z-axis but the direction of the perpendicular line of the spectrometer which was suggested by Richardson is arranged normal to the r-axis. From the point of view of adjustment our slit system is more con-

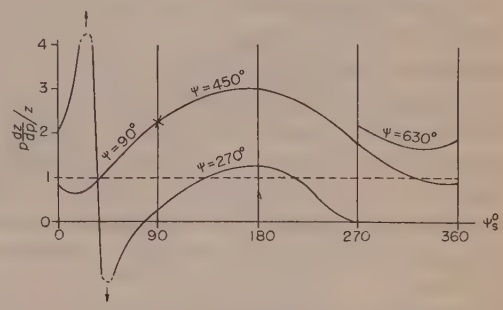

Fig. 2. Momentum dispersions. The values were calculated from Eq. (11) and shown in full lines. The dotted line corresponds to the momentum dispersion for conventional semi-circular spectrometers.

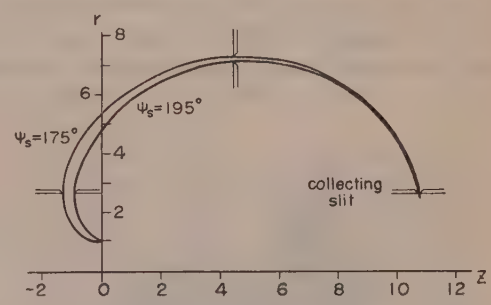

Fig. 3. Orbits in the mid-plane between inclined plane pole-faces in our spectrometer. The positions of the centers of the two baffles and the collecting slit are adjusted for the values $\psi=270°$, $360°$ and $450°$ of the orbit with $K=1$, $\psi_s=185°$ which was represented as pt. A_2 in Fig. 1 and 2.

venient than the Richardson's one. In his paper he described that his spectrometer has 4.24 times the dispersion of a semi-circular spectrometer of the same length but when we calculated his case with both his equation and our Eq. (11) we have not obtained 4.24 but 3.24.

D. Solid angle of collection.

Richardson has found that the inclined pole spectrograph which was suggested by him has a solid angle of collection about 16.5 times that of a parallel pole spectrograph with a slit of equal width using the same

* Differentiation with respect to K was done under the assumption that the both limits of the integral were constants. When the width of the beam of the emitted rays is not so wide the error caused by this assumption is negligibly small.

source-image distance. In our spectrometer the angle has been calculated according to Richardson's method and the results was better 10 times or more compared to the semi-circular spectrometer of the same length.

§ 3. Construction of a Spectrometer

We have constructed a spectrometer with inclined pole-faces magnet. The orbits of electrons in the mid-plane of the spectrometer are shown in Fig. 3. The source to slit distance is 11.10 cm. The momentum dispersion is $3.0\,z$ which is about 3 times the dispersion of a semi-circular spectrometer of the same length and the displacement of z-direction was 1.65 mm/volt for 100 volts electrons.

A vacuum box has been constructed by soldering brass plates of 1 cm in thickness. The collecting slit has been assembled so that its position and width can be adjusted from the outside of the box, two O-rings being used for this purpose. The box was evacuated by a high speed oil diffusion pump and pressures of about 1×10^{-5} mm H_g could be obtained.

Fig. 4. Magnetic spectrometer having inclined plane pole-faces. The main purpose of the construction of this apparatus is to analyse the velocity distributions of the photoelectrons which were ejected by soft X-rays or ultra-violet rays. The spectrometer (right) and the soft X-ray tube (left) are shown.

The magnet has been constructed with two 20 cm squar silicon steel. The narrowest gap near the intersecting line of the plates was 4 mm and for low energy electrons, i.e. weak magnetic field strength, the approach to saturation of the magnetic induction is not conceivable. The intersecting angle between two pole plates was 90°.

The spectrometer is shown in Fig. 4. The main purpose of the construction of this apparatus is to analyse the velocity distributions of the photoelectrons which are ejected by soft X-rays or ultra-violet rays so the velocity of the electrons is up to about 100 v.

§ 4. Discussion

The inclined plane pole-faces magnetic spectrometer described above has following advantages. The momentum dispersion is about 3 times larger and the solid angle of the collection is more than 10 times wider than those of a conventional semi-circular spectrometer of similar dimension. For example when the source to image distance is 11.10 cm the displacement of the image is 0.555 mm/volt for 100 volts electrons in the case of semi-circular spectrometer, and in our spectrometer the value becomes 1.65 mm/volt with an appropriate solid angle of collection.

One of the disadvantages of this type of spectrometers is that the space near the source and the collecting slit is not so large. But in our spectrometer the space for the slit is somewhat improved from the one suggested by Richardson. Richardson designed a spectrometer of different type in which the inclined planes were bevelled so as to become parallel at their closest parts. But the construction and the adjustment of the apparatus are seemed to be more complicated.

In our spectrometer the gap at the intersecting line of the two pole-faces is very narrow and the flux density at the part is somewhat stronger than in the semi-circular spectrometer for the analysis of electrons of the same momentum. This is not so inconvenient for the spectroscopy of low-energy electrons.

Acknowledgements

The author wishes to acknowledge Professor G. Shinoda for his encouragement and helpful discussion during the course of this work. He is grateful also to Assistant Professor T. Suzuki for his kind advice throughout this calculation.

References

1) K. Siegbahn: Beta-and Gamma-ray Spectroscopy (North-Holland Publishing Company, Amsterdam 1955).
2) H. O. W. Richardson: Proc. Phys. Soc. **59** (1947) 791.

JOURNAL OF THE PHYSICAL SOCIETY OF JAPAN Vol. 13, No. 6, JUNE, 1958

On the Magnetic Annealing Effect in 2% Cobalt-Copper Alloy
I. Induced Ferromagnetic Anisotropy

By Tadayasu MITUI

Department of Physics, Faculty of Science, University of Hokkaido, Sapporo, Japan

(Received September 26, 1957)

The behavior of ferromagnetic precipitates in copper-cobalt alloy containing ca. 2 wt. % cobalt heat-treated with magnetic field was studied with the object of making clear a physical origin of the induced uniaxial anisotropy observed. The magnitude of magnetic anisotropy induced by magnetic annealing was measured as functions of the aging temperature, aging time, and intensity of magnetic field. It has been found that almost all of the experimental results can be explained by the fine-particle behavior of ferromagnetic precipitates. It is shown that the origin of magnetic annealing can be explained neither by the magneto-elastic anisotropy of directional deformation nor by the magnetocrystalline anisotropy, but by the shape anisotropy of precipitated particles, which is distributed preferentially along the direction of magnetic field applied during annealing. It is also shown that the magnetic annealing affects remarkably the initial precipitation process rather than the over-growth stage of precipitation.

§ 1. Introduction

Since it has been found that the presence of magnetic field during heat treatment induces a uniaxial magnetic anisotropy in various ferromagnetic alloys and ferrites such as, permalloys, perminvars, Alnico V, and cobalt ferrite, the effectiveness of magnetic heat-treatment has been studied by many investigators for many years and a number of explanations have been proposed.

As for magnetically hard materials, this phenomenon was first found with Alnico II by Oliver and Shedden[1] who observed an increase in residual induction by cooling in the presence of magnetic field. This effect was also found in some other permanent magnetic alloys such as MK Alloy, Alnico V, and Alcomax. Especially, Alnico V has been studied by several investigators for the purpose of clarifying a physical origin of the induced uniaxial anisotropy; Heidenreich and Nesbitt[2,3] and Kronenberg[4] succeeded in the direct observation of various interesting phenomena in precipitation by means of the electron microscope and clarified the mechanism of magnetic annealing in this case. They found that Alnico V was divided into plates of precipitates and that the nuclei grew parallel to the direction of magnetic field applied during heat treatment, which suppressed completely the nucleation of precipitates perpendicular to its direction. These experimental works confirmed substantially the physical origin of uniaxial anisotropy, in this case, namely the so-called "shape-effect", which has been referred to for the interpretations of the magnetic behavior of precipitation-type alloys[5,6,7]. The significant feature of this effect is that the precipitate grows in the form of prolate ellipsoid elongated in the direction of magnetic field applied during heat treatment.

On the other hand, Néel[8], Chikazumi and Oomura[9], and Taniguchi and Yamamoto[10] proposed independently a new mechanism based on the idea of "directional order", in terms of which they could explain almost all features of the magnetic annealing effect in high-permeability alloys, such as permalloys and perminvars. This mechanism was also proposed by Néel for the magnetic annealing of Alnico-type alloys, but his interpretation may be only a possible one and has not yet been confirmed experimentally. Although the shape effect is found by the microscopic observation in Alnico V, the mechanisms of directional order and surface anisotropy proposed by Néel may also be possible interpretations of magnetic behavior of precipitation-type alloys. Then, the limit of compatibility

of these mechanisms to precipitation-type alloys should be established.

In precipitation-type alloys which respond to magnetic annealing, magnetic field may affect the precipitation process in some way. However, the origin of the anisotropy of Alnico V is incompletely uderstood, because the precipitation reaction has not yet been definitely studied and also the composition, magnetic saturation, Curie points, and crystal structures of the phases involved have not yet been established. So, we suppose that, in order to find out contributions of various mechanisms on the origin of the uniaxial anisotropy induced by magnetic annealing in precipitation alloys, it is necessary to used alloys metallographically simpler than Alnico V, which is practically important but rather complex.

For the above-mentioned purpose, we have used copper-cobalt alloy containing ca. 2 wt. % of cobalt, with which we previously discovered[11] the magnetic annealing effect. We shall report the measurements of the uniaxial magnetic anisotropy induced during various magnetic heat-treatments in this alloy and discuss the machanism of the effect on the precipitation process.

§ 2. Preparations of the Specimens and the Apparatus

Tammann and Oelsen[12] determined by measuring the specific magnetization the solubility of cobalt in copper and Hashimoto[13] determined in more detail the phase diagram of Cu–Co alloys, which is shown in Fig. 1. As seen from the figure, cobalt is soluble

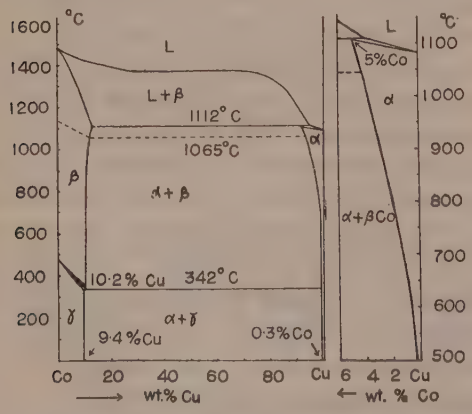

Fig. 1. Phase diagram of Copper-Cobalt alloy system.

only to the extent of 5% at 1100°C, 3% at 940°C, and 0.3% at 400°C. The Curie temperature of precipitate of cobalt-rich phase (β-phase) is higher than temperatures of solid solubility if cobalt is contained less than about 4%.

With Cu–Co alloys containing less than 5% Co, it is possible to precipitate by aging the ferromagnetic phase containing approximately 10% copper in the non-ferromagnetic matrix, and the content of 2% cobalt is suitable to avoid a very small trace of ferromagnetism due to imperfect quenching from the high-temperature region of solid solution, because nucleation of the precipitates proceeds extremely rapidly at the temperatures studied, perhaps due to the extremely rapid precipitation at grain boundaries or other imperfections.

Alloy specimens containing about 2% Co were made from electrolytic copper of 99.9% purity and cobalt of 99.8% purity. Weighed metals were melted in a hydrogen atmosphere in a Tammann furnace. After casting in an iron mold, the ingot was forged to avoid segregation and internal cavity and then homogenized at about 1000°C for more than 20 hours.

Specimens were cut out from the ingot and were lathe-machined into disks, 13.3 mm in diameter and 5.2 mm in thickness. Then, to eliminate the internal strain due to forging and machining and to disperse grains finely and randomly, they were in a vacuum heated from room temperature to 700°C at the rate of ca. 50°C an hour, kept at 700°C for 5 hours and cooled slowly to room temperature. Chemical analysis of the specimens gave the following values: 97.7% Cu, 2.2% Co, and less than 0.1% other metals.

The specimens used for the study of magnetic annealing were aged at various temperathres for an appropriate time in an externally applied magnetic field, after the solution treatment of ca. 2 hours at ca. 1000°C, in vacuum electric furnace.

The magnetic anisotropy was measured by means of the torque magnetometer as described previously[11]. The disk-shaped specimens are placed in a strong and uniform magnetic field of ca. 10,000 Oe, and the torques necessary to fix the disk on arbitary directions are measured. The magnetic field is supplied by

a Weiss-type electromagnet. The specimen holder of the torque magnetometer is supported by a jewel bearing on the lower end of a helical spring made of phosphor-bronze, so that the horizontal displacement of the specimen due to slightly irregular field of the electromagnet can be avoided.

§ 3. Details of the Experimental Procedure

The specimens were solution-heat-treated in a vacuum at ca. 1000°C, rapidly quenched in water, and then aged at 750°C for ca. 20 hours without a magnetic field. For all specimens prepared by the above-mentioned procedure, the parasitic torque due to the irregular distribution of intergrains was preliminarily examined by the torque magnetometer, of which the results are shown in Fig. 2. We have selected the specimens showing a negligibly small specific torque (curve C) of ca. 10^2 dyne/cm^2, and omitted the specimens having remarkable irregular torque values (curves A and B).

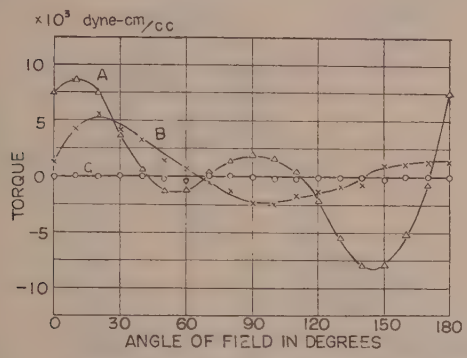

Fig. 2. Torque curves of the 2% Co–Cu alloy specimens aged without magnetic field.

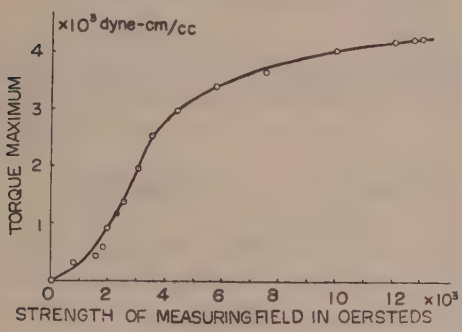

Fig. 3. Dependence of the torque maximum upon the intensity of magnetic field in 2% Co–Cu alloy.

The precipitation treatments were conducted in a vacuum electric funace at various temperatures and all the specimens were quenched into water at suitable intervals of the aging. Measurements of torque were carried out at room temperature. The intensity of magnetic field applied in the measurements was about 10,000 Oe, although this intensity is not yet enough to induce the saturated intensity of the torque maximum, as seen from Fig. 3 showing the dependence of the torque maximum upon the intensity of magnetic field.

§ 4. Experimental Results

(1) *Precipitation process affected by magnetic field.*

In order to test a possibility that the magnetic field present during aging is able to influence on the initial stage of precipitation rather than on the over-growth stage, we varied the time of magnetic annealing. For the specimens quenched and then aged at 750°C for 4.0 hours with the magnetic field of 1000 Oe, we obtained the value of 4×10^3 ergs/cc for the constant, K_u of the induced anisotropy, which was found to be expressed experimentally as

$$E=-K_u\cos^2\Theta\,, \qquad (1)$$

where Θ is the angle between the direction of magnetic field applied during annealing and that of the measuring field, as seen from the torque curve shown in Fig. 4. This indicates that magnetic field applied during aging produces an uniaxial magnetic anisotropy with an easy direction along the field. On the other hand, the value of K_u found for

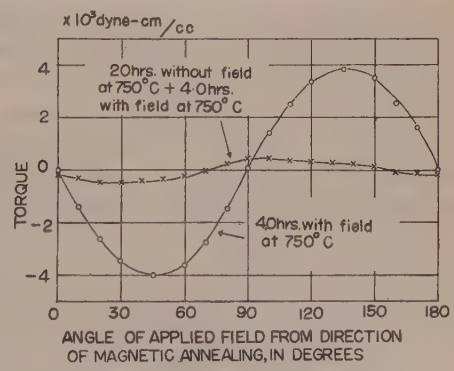

Fig. 4. Torques brought about by magnetic annealing at 750°C in 2% Co–Cu alloy.

the specimens quenched and then aged for 20 hours without magnetic field and consecutively for 4 hours with the field of 1000 Oe is only ca. 4×10^2 ergs/cc, as seen from the torque curve shown in Fig. 4, being the same order of magnitude as that at the final stage of 750°C-isothermal treatment with field of 1000 Oe observed in the previous work[11]. It may thus be concluded that the influence of magnetic field during precipitation process is only effective for the nucleation and initial precipitation process.

(2) *Change of the induced magnetic anisotropy with the time of magnetic annealing at various temperatures.*

Values of the anisotropy energy induced during aging with the field of 3000 Oe at 750°C, 720°C, 650°C and 550°C are plotted against the aging time in Fig. 5, which indicates the marked increase of the induced anisotropy energy at the early stage and its large decrease at the over-aging stage. Such a change of the induced anisotropy with the time of magnetic annealing has a trend similar to the changes of the hardness and coercive force of the alloy, as will be shown later.

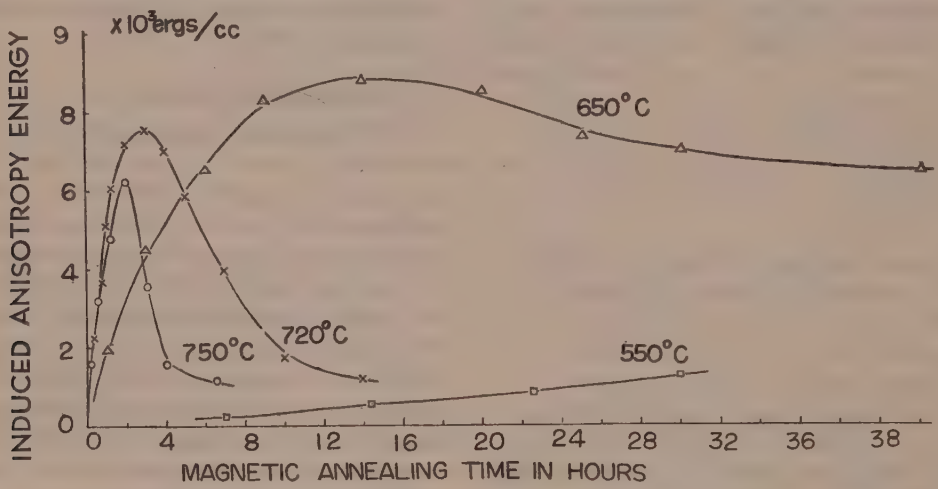

Fig. 5. Anisotropy energy as dependent on the time of annealing with an applied field of 3000 Oe in 2% Co–Cu alloy.

We may expect from Fig. 5 that the change of the anisotropy constant with aging time at the initial stage of aging is a relaxation process. In fact, the logarithm of the relaxation time, τ, is plotted against the reciprocal of the absolute temperature, T, in Fig. 6, from which we obtain, as the temperature dependence of the relaxation time,

$$\tau=\tau_0 \exp(E/kT)\,. \qquad (2)$$

The value of the activation energy E, is ca. 36 Kcal/mol, being lower than the value of the activation energy for the diffusion of Co-atom in the Cu-matrix determined with single crystals of Cu–Co which is 55.14 Kcal/mol[14]. This is reasonable if one takes into account the fact that diffusive processes in the precipitation process may, in general, be much

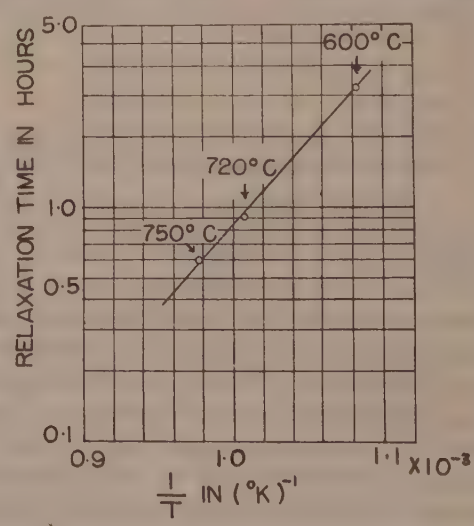

Fig. 6. Relaxation time of the effect of magnetic annealing in a 2% Co–Cu alloy specimen. The activation energy is 36 K cal/mol.

more rapid at grain boundaries and other imperfections than in the interior of the matrix.

(3) *Change of the induced magnetic anisotropy with the strength of magnetic field applied during aging.*

The anisotropy constant as a function of the time of magnetic annealing at 750°C is shown in Fig. 7, which shows that the anisotropy constant approaches to the maximum value after ca. 2 ~ 3 hours at 750°C, independently of the strength of magnetic field applied during magnetic annealing. The maximum value of the induced anisotropy constant is plotted against the strength of magnetic field applied during magnetic annealing in Fig. 8, which indicates that the maximum value of the anisotropy constant approaches to saturation with increasing field, as was also observed in our previous work[11]. On the other hand, in order to test the effect of removing the field during magnetic annealing, the specimen was aged at 750°C for one hour under the field of 5000 Oe and then without field for suitable time intervals. Fig. 9 shows that the anisotropy constant decreases exponentially after the field has been removed.

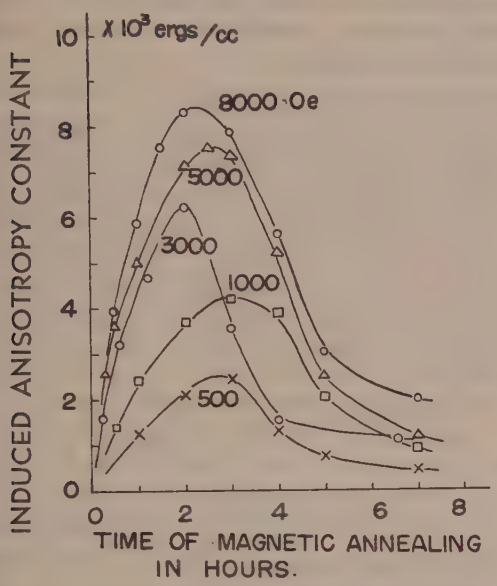

Fig. 7. Anisotropy as dependent on the time of magnetic annealing at 750°C in 2% Co–Cu alloy, as determined from the torqus curves measured in magnetic field of ca. 10,000 Oe at room tomperature.

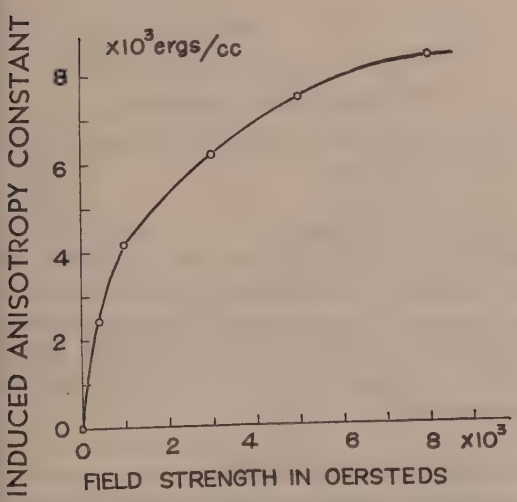

Fig. 8. Effect of the strength ot magnetic field applied during annealing at 750°C on the magnetic anisotropy constant in 2% Co–Cu alloy as determined from the torque curves measured in field of ca. 10,000 Oe at room temperature.

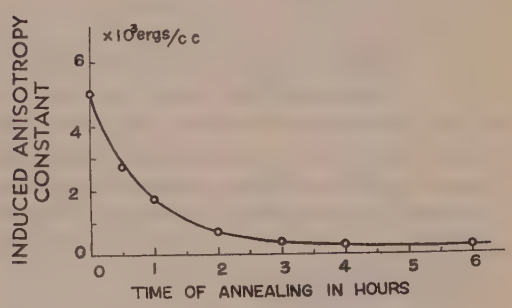

Fig. 9. Magnetic Anisotropy constant of 2% Co–Cu alloy dependent on the time of annealing at 750°C after the field has been removed.

(4) *Effect of double magnetic annealing.*

To observe the change of magnetic behavior as the relaxation properties caused by different magnetic annealing, the effect of double magnetic annealing was studied.

After the specimen was annealed at 750°C for 4 hours with field of 2000 Oe (initial magnetic annealing) and its torque was measured. It was annealed again at the same temperature for 4 hours with the same field applied newly in the direction orthogonal to the previous one (second magnetic annealing). Although the initial magnetic annealing induced the anisotropy of pure two-fold rotational symmetry containing no four-fold term, the second magnetic annealing induced the anisotropy of four-fold symmetry, as shown in Fig. 10.

Such magnetic annealing was also extended over-aging stage. Curve A of Fig. 11 shows the torque measured after the specimen had been held at 750°C for 4 hours with the field of 2000 Oe, while the torque measured after

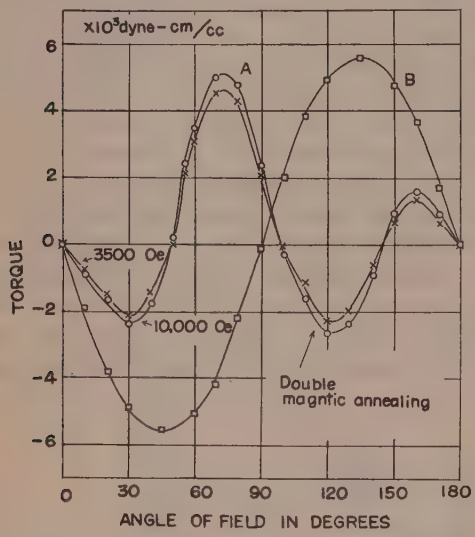

Fig. 10. Torque curves of 2% Co–Cu alloy, obtained after the double magnetic annealing. Curve A shows the effect of the initial magnetic annealing and curves B show the effect of changing the direction of magnetic annealing by 90° degrees from the direction of the former magnetic annealing.

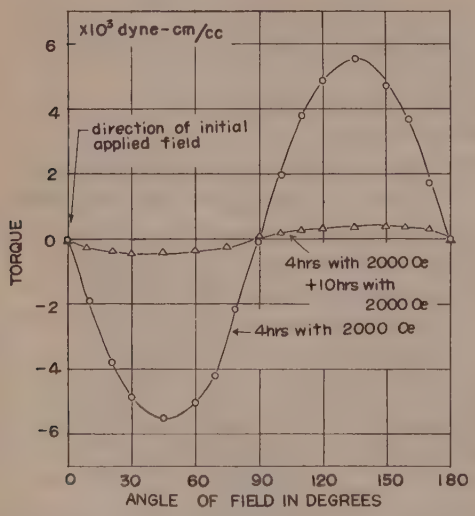

Fig. 11. Torque curves of 2% Co–Cu alloy obtained after the double magnetic annealing extended over the overaging stage.

the same specimen had been held again at the same temperature for 10 hours with the field applied only in the direction changed by 90 degrees is shown in curve B. This torque curve obtained after the double magnetic annealing made over the over-aged stage has the two-fold symmetry and has the easy direction of anisotropy along the direction in which the field is applied initially. Thus, the curves obtained after the double magnetic annealing made during the precipitation process show pronounced differences for the initial stage of precipitation from for the over-growth stage.

(5) *Effect of cold working*

The anisotropy constant obtained with the specimen which was cold-worked by press in the solid-solution state and aged at 750°C for 4 hours isothermally with magnetic field of 1000 Oe is about 10^4 ergs/cc, being greater than the value of 4×10^3 ergs/cc obtained after the same treatment with the uncold-worked specimen, as shown in Fig. 12. This increase

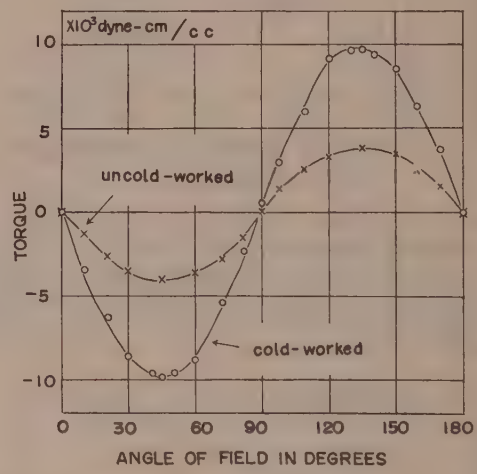

Fig. 12. Effect of cold-work on the torque curve of 2% Co–Cu alloy.

of the uniaxial anisotropy may naturally be interpreted by the fact that the precipitation rate is rapidly increased by cold-working and the number of precipitates in the cold-worked specimen responsible for the uniaxial anisotropy is greater than those in the uncold-worked one.

§ 5. Discussion of Results

(1) *Precipitation process and magnetic behavior of precipitate particles.*

There have been many experimental and theoretical works on the magnetic behaviors of precipitated particles depending on their

size and shape. Theories on the most interesting aspect of the behavior of fine particles, have been developed by Kittel[15], Néel[16], Stoner and Wohlfarth[17], and Jacobs and Bean[18]. Detailed expositions of this field may be found in the survey by Kittel and Galt[19].

During the isothermal aging of Cu–Co solid solution, the following changes might take place; first, Co atoms migrate and aggregate to form small Co-rich regions, and secondly the face-centered cubic Co-rich phase, which is coherent to the matrix, precipitates and consequently each precipitated particle become ferromagnetic. In this stage, however, precipitates are so small that the directions of magnetization fluctuate thermally, and the bulk specimen does not show any ferromagnetic behavior. The phenomenon of this kind in Cu–Co alloy was recently studied by Becker[20] and Weil and Gruner[21] independently, and was termed "super-paramagnetism" by Bean[22]. Moreover, with increasing aging time the precipitated particles becomes too large for thermal fluctuation and become the stable single-domain permanent-magnets. For this stage it seems likely that the nucleation comes to an end and the total volume of precipitation become constant, since changes of the electric resistance and of the saturation magnetization have not been observed in this stage, as seen from Fig. 13.

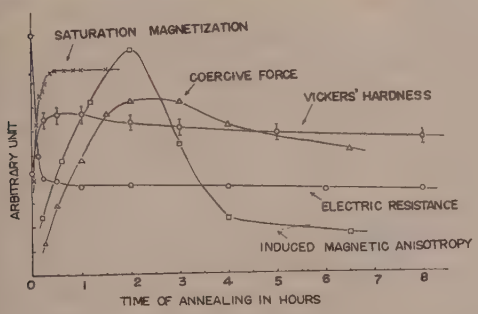

Fig. 13. Precipitation kinetics and magnetic annealing of 2% Co–Cu alloy at 750°C.

When the aging is continued further, the so-called coagulation takes place, i.e., the volume of each precipitate increases and the number of precipitates decreases. The increase of the particle size results in the division of single magnetic domain into two or more domains, which is energitically favorable. Such multi-domain gives rise to the low coercivity due to the displacements of domain walls in the precipitates. Such characteristics of Cu–Co alloy were found by Bate, Schofield and Sucksmith[23]. More recently, Becker[24] also showed that there were magnetically three types of precipitated particles in the precipitation process of Cu–Co alloy containing 2% Co. According to his classification, precipitated particles of the type I are those in a stage of nucleation which show a super-paramagnetic behavior. Precipitated particle having the stable single-domain size in a further aging are belonged to the type II, and the type III involves particles precipitated in the multi-domain size stage in which precipitates continue to grow and the coercivity decreases. On this basis Becker showed that it was possible to explain the change in coercive force with aging time at 800°C. Figure 13 demonstrates the similar results obtained by us. Many kinds of measurements on the 750°C isothermal aging give the experimental confirmation of the suggestion that the induced anisotropy as well as the high coercive force arises from fine particle behavior, because the maximum of the anisotropy corresponds to that of the coercive force. Moreover, the result of the magnetic saturation measurement shows that the nucleation stage of precipitation is completed before the rise of the anisotropy to its maximum, since the magnetic saturation corresponds the total amount of ferromagnetic precipitated particles. Accordingly, it seems likely that changes of the induced anisotropy during magnetic annealing are related to a change in particle size in the growth stage of precipitated particles having a constant total amount. Taking into account of single domain precipitates, all of the present experiments may be explained consistently.

(2) *Origin of the ferromagnetic anisotropy of precipitated particles.*

The above-mentioned relations between the coercive force and aging process suggests that the coercive force of the alloy may be due to the particle anisotropy: hence, an examination of high coercive force of the alloy may simultaneously clarify the origin of the uniaxial anisotropy. On the experimental side, the work of Bate, Schofield and Sucksmith[23] has shown that the high coercive force in Cu–Co alloy arises from fine-particle

behavior of precipitated particles. Accordingly, the discussion in the following paragraph is concerned with the comparison of the observed with the theoretical values of the coercive force.

Generally the high coercive force of finely dispersed particles arises from the crystal anisotropy, the magnetoelastic anisotropy or the shape anisotropy. Now we estimate the coercive forces of the Cu-Co alloy due to these three causes separately. First, the coercive force due to the magnetoelastic origin is expressed by $H_c=3\lambda T/I_s$, as given by Stoner and Wohlfarth[17]. Taking 10^{-5} for λ, the coefficient of magnetostriction, 10^{10} dynes/cm^2 for T, a reasonable upper limit of the internal stress, and 1300 for I_s, the saturation magnetization, gives ca. 230 Oe for H_c. Accordingly, the magnetoelastic anisotropy does not play the major role, as the maximum coercive force of ca. 1500 Oe was observed by Bate *et al.*[23] Next, the coercive force due to the crystal anisotropy is $H_c=0.64\,K/I_s$ for cubic crystallites oriented at random. Taking 5×10^5 ergs/cc for K, the crystal anisotropy constant, gives only about 250 Oe. Finally, the coercive force due to the shape anisotropy of randomly oriented particles should be $H_c=0.48(N_t-N_0)I_s$, where N_0 and N_t are the demagnetizing factors of the spheroid along the major and minor axes, respectively, according to the calculation by Stoner and Wohlfarth (1948)[17]. The upper limit on the coercive force of highly elongated particle is $(0.48)\times2\pi I_s=3700$ Oe. On the other hand, particles with a N_t-N_0 of 0.7 which is estimated from the photographs, the coercive force of ca. 1400 Oe is predicted. Thus, the observed coercive force can be reasonably explained by the shape anisotropy.

(**3**) *Possible origin of the uniaxial ferromagnetic anisotropy.*

In the Cu-Co alloy, it seems that the induced uniaxial ferromagnetic anisotropy results only from the shape anisotropy of the precipitated particles and the degree to which they are orientated to the direction of applied field during magnetic annealing, since the matrix is non-ferromagnetic and only the precipitated phase is ferromagnetic. In fact, the curve C of Fig. 2 shows no torque for aging without field, because precipitated particles in the polycrystalline specimen are distributed at random in the orientation, whatever an effective anisotropy of precipitates and interactions between precipitates themselves are. However, if the specimen has anisotropic orientations of crystal grains, it shows an irregular torque curve for aging without field, as seen from curves A and B of Eig. 2. As already stated, we are inclined to explain the uniaxial ferromagnetic anisotropy by the shape of precipitated particles. We must, however, examine possibilities of other origins of the anisotropy: magnetoelastic, magnetocrystalline and of the so called "directional order" together with the shape anisotropy.

The anisotropy energy due to the magnetostrictive strain fixed in the direction of applied field is given by

$$K_u=(3/2)\lambda^2E\,, \qquad (3)$$

where λ is the coefficient of magnetostriction, and E is Young's modulus. This mechanism gives only the energy of 3×10^2 ergs/cc if λ is 10^{-5} and E is 2×10^{12} dynes/cm^2. This is much less than ca. 10^5 ergs/cm^3 of precipitate and thus it seems unlikely that strain anisotropy plays the major role. As to the crystalline anisotropy, X-ray study has confirmed that the particles precipitated during the aging process show the face-centered cubic structure, as will be shown in Part II, and naturally it makes few contribution to the uniaxial anisotropy.

In order to test the possibility that the anisotropy of the precipitated particles is primarily the shape anisotropy, we has investigated the shape of precipitates directly by electron and light microscopes, as will be shown in Part II.

Thus, as a matter of fact, it seems clear that the particle shape accounts for the uniaxial ferromagnetic anisotropy in Cu-Co alloy. According to the theory of Néel *et al.*, the uniaxial anisotropy constant, K_u, is expressed by

$$K_u=(1/2)N(\Delta I_s)^2V(1-V)\,, \qquad (4)$$

where N is the demagnetizing factor of the precipitate particles, ΔI_s the difference in saturation magnetization between the precipitated phase and the matrix phase, and V the fractional volume of the orientated precipitates. If we take $\Delta I_s=1300$ which is the saturation magnetization of the precipitates, $V=$

0.01 which is estimated from the photographs, the averaged value $N=0.7$ which is estimated from the photographs, we obtain the induced anisotropy energy of about 5×10^4 ergs/cc which is approximately in agreement with the observed maximum value of $10^4\sim8\times10^3$ ergs/cc. There are reasons that the observed values are less than predicted, by the same reason in the before-mentioned case of the coercive force of fine particles. In addition, the value of the shape anisotropy constant is in general connected to the amount of the orientated precipitates and unrelated to the total amount of ferromagnetic phase present. Accordingly, $V=0.01$ is perphaps over-estimated, since the volume fraction of the total amount of the phase precipitated completely at the aging temperatures studied is about $0.01\sim0.02$ in view of the phase diagram. Consequently, it may be inferred that the induced anisotropy is caused by the precipitates having the anisotropic distribution along the field applied during aging.

The next step in understanding the compatibility of the mechanisms is to discuss the possibilities of the directional order and the surface anisotropy. Ae we have seen from the experimental results (§ 4, (1), (2) and (4)), it seems unlikely that the directional order plays the major role, since the change of the anisotropy is influenced sensitively by the size of the precipitates and the precipitation process. Especially, the mechanism of directional order cannot interpret the experimental fact regarding the anisotroyy of the fourfold symmetry induced by double magnetic annealing, because the dipole-dipole interaction, which depends on the kind of atom pairs and the direction of spontaneous magnetization relative to the axis of the atom pair, yields only the directional equilibrium of solute atom pairs in the precipitated phase. Furthermore, the saturation magnetization reaches a constant value very early before the aging time corresponding to the maximum of the induced anisotropy, as illustrated in Fig. 13. This means that the total volume and the compositions of the precipitates reach to nearly a constant value very early during the initial stage of precipitation. Consequently, it seems that the induced anisotropy does not depend on the concentration of the atom pairs, so that the directional order may not play the major role. The qualitative disagreements between the observed result and the predicted result from directional order are provided by the effective response to magnetic annealing on the initial precipitation and by the phenomenon of disappearence of induced anisotropy during the over-aging.

On the other hand, although the surface anisotropy of precipitated particle seems attractive, we have few available data supporting it, since the mechanism of surface anisotropy relates sensitively to the size, shape and atomic concentration of precipitated particles and it is difficult to separate the effective part due to this mechanism from the other mechanism.

There are some points of interest in our experimental facts on the effect of magnetic annealing. First, the anisotropy energy rises to the maximum and then falls with increasing time of magnetic annealing at various temperatures, as shown in Fig. 5. Such curious phenomena were found first by the author *et al*[11] and also recently by Becker[24] for shorter annealing times at 800°C. In the precipitation process at the various temperatures studied, the maxima of the anisotropy shift to longer aging time with decreasing temperature. This shows that a suitable growth time corresponding to the critical size for precipitated particles of single domain shifts to longer aging time as the aging-temperature is lowered. The critical time corresponding to the single domain formation was known from some properties, such as the coercive force which was considered to be a very sensitive indicator of the average size of precipitated particles. The aging time corresponding to the maximum of the anisotropy coincides approximately with the time of maximum of the coercive forces as shown in Fig. 13. Accordingly, it seems likely that the behavior is due to the formation of single domain and the decreasing anisotropy for the longer time is due to the behavior of multi-domains in larger precipitated particles, just as mentioned above in § **5**, (**1**). Presumably such behavior due to over-aging would also be observed in other alloys of the precipitation type and would be remarked as a characteristic phenomenon of magnetic annealing.

Secondly, Fig. 7 shows that the dependency

of the induced anisotropy on the strength of the applied field is remarkable. Tendency of the saturation of the induced anisotropy suggests that the field applied during aging causes the alignment of precipitated particles to line up in the direction of the field. In general, if the field applied during aging is high enough and the direction of magnetization in precipitated particles orientates to the direction of external field, the induced anisotropy frozen in by the magnetic annealing will be approached to their saturation values and will be independent of field applied during aging. When the direction of the magnetic field coincides no longer with directions of magnetizations of precipitated particles, the consideration for the phenomenon is much more complicated. Pressumably the behavior would be decided by interaction between the force of magnetic field acting on the precipitated particle and the crystal force due to the favored coherency of the matrix, just as in the case of Alnico V.

Thirdly, the anisotropy of four-fold symmetry is produced by the double magnetic annealing during initial stage of precipitation, as illustrated in Fig. 10. Such an unusual phenomenon is not fully understood. If the precipitated particles are aligned to favor in the two directions of fields which have been applied in the double magnetic annealing, the torque curve having four-fold symmetry may correspond to the torque curves obtained in the experiment of Nesbitt *et al.*[25] However, the maximum torque obtained in Fig. 10 increases with increasing strength of the measured field which is not yet enough to produce magnetic saturation of the precipitates, contrary to the experiments of Nesbitt *et al.* in which the anisotropy diminishes with increasing field strength and is due to the shape anisotropy of the precipitated particle. This behavior of polycrystal can not be due to the shape anisotropy of the precipitates alone and perhaps the consideration of the origin of the other anisotropy and mutual interaction of precipitates are necessary to explain it.

In addition to these, there is the fact that magnetic field is able to influence the nucleation or initial precipitation rather than overgrowth stage of precipitates. Recently, Nesbitt and A. G. Williams[26] showed that magnetic field affects the nucleation process only in Alnico V. They also indicated that the mechanism of Kittel *et al.* was the more important one. Thus, it seems likely that such behavior of the Cu–Co alloy as well as Alnico V is the characteristic of magnetic annealing in the precipitation-type alloys.

From the arguments mentioned above, it may be seen that the shape anisotropy and directional orientation of precipitated particles are the most resonable origin of the magnetic annealing effect of the Cu–Co alloy.

§ 6. Summary

A number of phenomena of magnetic annealing have been observed during the various precipitation process of 2% Co–Cu alloy. We have examined the possibility of magnetic behavior arising from the particle anisotropy and clarified that the uniaxial anisotropy properties of this alloy are explained by the shape effect proposed by Nèel and Kittel *et al.*, as offered to be correct for alnico V. Moreover, it has been observed that magnetic field applied during aging is able to influence the nucleation stage or initial precipitation stage rather than over-growth stage of precipitation, as shown by Nesbitt *et* al. with Alnico V.

The author wishes to express his sincere thanks to Prof. S. Miyahara for his kind guidance. The contributions of the members of our research group are gratefully acknowledged.

A part of this work was financed by the Scientific Research Fund of the Ministry of Education.

References

1) D. A. Oliver and J. W. Shedden: Nature **142** (1938) 209.
2) R. D. Heidenreich and E. A. Nesbitt: J. Appl. Phys. **23** (1952) 352.
3) E. A. Nisbitt and R. D. Heidenreich: J. Appl. Phys. **23** (1952) 366.
4) K. J. Kronenberg: Z. Metallkunde **45** (1954) 440.
5) L. Néel: Compt. rend. **225** (1947) 109.
6) C. Kittel, E. A. Nesbitt, and W. Shockley: Phys. Rev. **77** (1950) 839.
7) A. Shubina and Y. S. Shur: J. Tech. Phys. (U.S.S.R.) **19** (1949) 88.
8) L. Néel: Compt. rend. **237** (1953) 1468; J. Phys. radium (8) **15** (1954) 225.

9) S. Chikazumi and T. Oomura: J. Phys. Soc. Japan **10** (1955) 842.
10) S. Taniguchi and M. Yamamoto: Sci. Rep. Res. Inst. Tôhoku Univ. **A6** (1954) 330.
S. Taniguchi: Sci. Rep. Res. Inst. Tôhoku Univ. **A7** (1955) 269.
11) S. Miyahara and T. Mitui: J. Fac. Sci. Hokkaido Univ. **4** (1953) 275.
T. Mitui and S. Miyahara: J. Phys. Soc. Japan **10** (1955) 1023.
12) G. Tammann and W. Oelsen: Z. anorg. Chem. **186** (1930) 257.
13) U. Hashimoto: Nippon Kinzoku Gakkai-Si **1** (1937) 19.
14) T. Hirone, M. Sakamoto, and N. Kunitomi: Read November, 1956 at the Meeting of the Phys. Soc. of Japan (not yet published).
15) C. Kittel: Phys. Rev. **70** (1946) 965.
16) L. Néel: Compt. rend. **224** (1947) 1550.
17) E. C. Stoner and E. P. Wohlfarth: Nature **160** (1947) 650; Phil. Trans. Roy. Soc. **A240** (1948) 599.
18) S. Jacobs and C. P. Bean: Phys. Rev. **100** (1955) 1060.
19) C. Kittel and J. K. Galt: Solid State Physics **Vol. 3** (1957) 437.
20) J. J. Becker: Journal of Metals **9** (1957) 59.
21) L. Weil and L. Gruner: Compt. rend. **243** (1956) 1629.
22) C. P. Bean: J. Appl. Phys. **26** (1955) 1381.
23) G. Bate, D. Schofield and W. Sucksmith: Phil. Mag. **46** (1955) 621.
24) J. J. Becker: Private communication and to be published.
25) E. A. Nesbitt, H. J. Williams and R. H. Bozorth: J. Appl. Phys. **25** (1954) 1014.
26) E. A. Nesbitt and A. J. Williams: Proceedings, Conference on Magnetism and Magnetic Materials, Boston (1956) Oct.

JOURNAL OF THE PHYSICAL SOCIETY OF JAPAN Vol. 13, No. 6, JUNE, 1958

Electrical and Optical Properties of Ges

By Tadaichi YABUMOTO

Institute of Electrical Engineering, Shizuoka University, Hamamatsu, Japan

(Received December 12, 1957)

High purity germanium monosulfide was prepared and its semiconducting properties were measured. Samples are obtained by the reaction of germanium and sulfur in vacuum at high temperature and reducing in ammonium gas to remove germanium disulfide. Dark resistivities of evaporated layers and polycrystalline blocks of GeS prepared by the above method are $10^{10}\Omega$ cm or more.

1. The thermal activation energy for dark current is 0.74 ~ 1.0 ev and about 0.25~0.5 ev at higher and lower temperature regions, respectively.
2. The absorption edge is found at about 700 mμ from the optical measurements.
3. At room temperature the maximum spectral sensitivity of photoconductivity is observed at the wavelength of about 700 mμ in vacuum and of about 800 mμ in room air.
4. The sign of the observed thermoelectric power is that of p type at high temperature, and its magnitude is about 1 mv/deg.

§ 1. Introduction

Semiconducting properties of sulfides of the elements in the first and second groups of periodic table have been reported in many literatures, but those of the elements in the elements in the fourth group have hardly been investigated up to the present.

GeS was selected as such an example, and its main features of electrical and optical properties were measured with high purity samples.

§ 2. Preparation and Purification of Samples

GeS samples used in the experiments were obtained by the reaction of germanium and sulfur powders of about stoichiometric ratio

in an evacuated quartz tube at high temperature.

Germanium powder was prepared by grinding high purity single crystals, and sulfur powder was purified by recrystallization in CS_2 three times or more and then by vacuum distillation.

These germanium and sulfur powders were put into a quartz tube which was kept free from impurities by a previous heat treatment in high vacuum, and then the tube was sealed off after evacuation.

Reaction of germanium and sulfur was done by heating the quartz tube in an electric furnace at about 800°C and then at 1050°C for about six hours each. Since there are some GeS_2 and sulfur as impurities in the samples prepared by this method, they were again treated in ammonium gas. These samples were heated at 800°C for an hour in quartz tube through which pure ammonium gas was slowly passed at the rate of about 2~3 c.c./sec.

GeS was sublimated and crystallized on the wall of the quartz tube at lower temperature in the stream of ammonia gas. In this treatment the purity of these samples was increased, and a very small amount of impurities such as Fe, Al, Cu, was found spectroscopically and high resistivity was observed.

GeS has a lattice structure like stressed rocksalt and the lattice constants are a=4.29Å b=10.42Å and c=3.64Å. By means of x-ray analysis it was confirmed that these samples were certainly germanium monosulfides.

§ 3. Experimental Procedure and Results

Measurements described below were made on sandwich type evaporated layers and on polycrystalline blocks of GeS samples prepared by the above mentioned method. Electric current was measured by Du-Bridge Brown's circuit whose current sensitivity is the order of 10^{-14} amperes.

(a) Dark conductivity

GeS is not stable at high temperatures in air, so the measurements were made in high vacuum tubes. Sandwich type samples were composed of an evaporated GeS layer placed between electrodes of sputtered platinum and evaporated aluminium layers as shown in Fig. 1.

The polycrystalline block type samples have two platinum sputtered layers on opposite surfaces as electrodes. These tubes were heated in an oil bath, and the temperature was measured by copper-constantan thermocouple.

Temperature dependence of dark current was measured for both type samples between room temperature and 200°C.

Figs. 2 and 3 show the data on evaporated layers and on a polycrystalline block respectively.

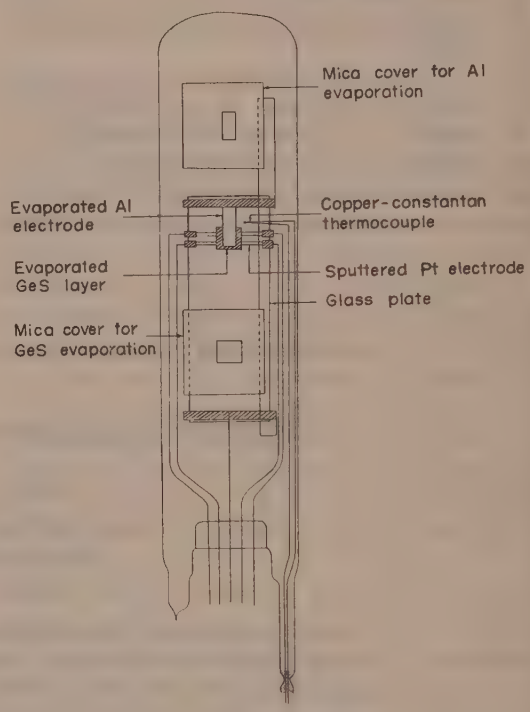

Fig. 1. Experimental tube to measure the conductivity of sandwich type GeS layer.

From these figures the thermal activation energy for dark conductivity is calculated to be 0.74~1.0 ev and in the case of evaporated of about layers there is lower activation energy portion 0.25~0.5 ev at lower temperature region.

From the results the specific resistance is also calculated to be 10^9~10^{14} Ωcm for the evaporated layer and 10^{10} Ωcm or more for the polycrystalline blocks at room temperature.

(b) Optical absorption

Optical absorption was measured with evaporated layers at room temperature. Samples were prepared by evaporation on quartz plates. The thickness of the layers is 0.2~1 μ which is determined by optical interference and colorimetric measurement.

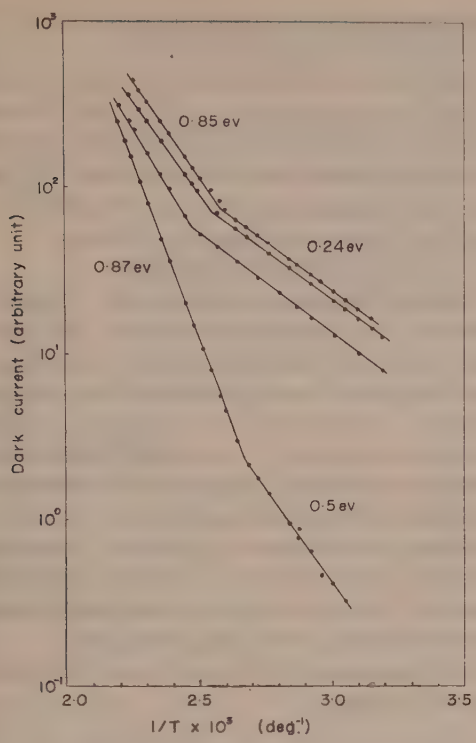

Fig. 2. Temperature dependence of dark current in sandwich type samples.

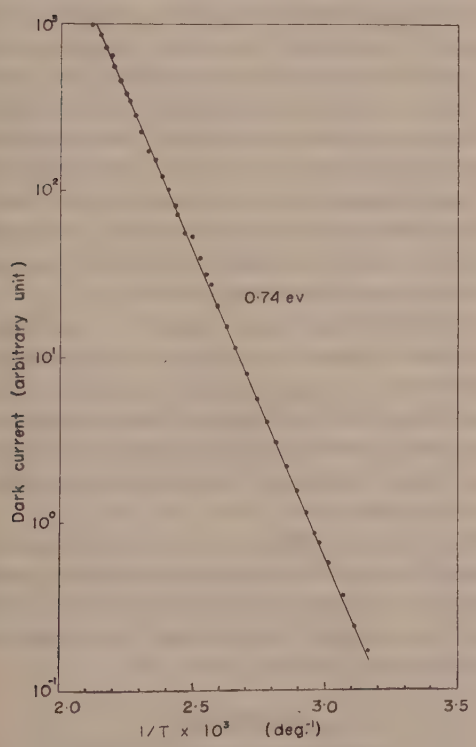

Fig. 3. Temperature dependence of dark current in polycrystalline block type sample.

A tungsten filament was used for the light source, and the radiation was made to monocromatic light by a Beckmann type monochromator or a minimum dispersion type spectrometer. After passing through the layer, the monocromatic light was detected by an antimony- cesium photo-tube or a photo-multiplier. A curve of absorption coefficient calculated from the absorption experiments is shown against the wavelength in Fig. 4. From

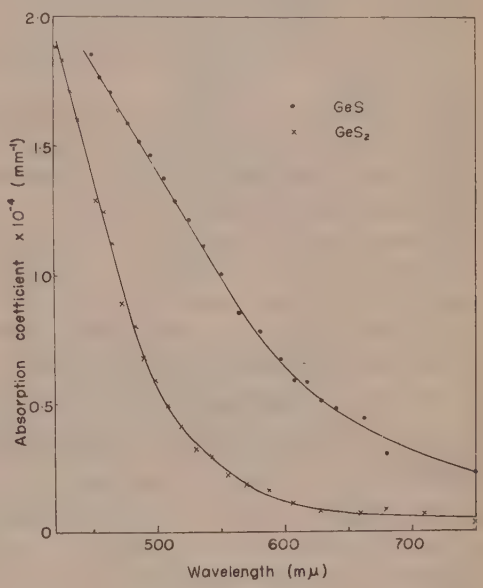

Fig. 4. Optical absorption of GeS and GeS_2.

this figure it is seen that the absorption edge of fundamental absorption band lies at about 700 mμ (1.8 ev). In Fig. 4 the similar result obtained with GeS_2 is also plotted. Its absorption edge lies at about 540 mμ (2.3 ev).

(c) Photoconductivity

Experimental results on spectral sensitivity of photo-current at room temperature are shown in Fig. 5. Sandwich type samples are composed of thin evaporated GeS layer placed between transmitting electrode and evaporated alminium electrode. Nesa coating was used as the transmitting electrode on the quartz glass. Polycrystalline block sample has two evaporated gold layers as electrodes.

Light source and monocromator are similar to those used in the absorption experiment, and the detection of light intensity was made by thermopile.

As seen from this figure there is a maximum of sensitivity at about 700 mμ in wavelength for both type samples. On the polycrystalline

block the maximum shifts to about 800 mμ in room air. As the curves (1), (2), (3) of this figure show the order of measurement, it is

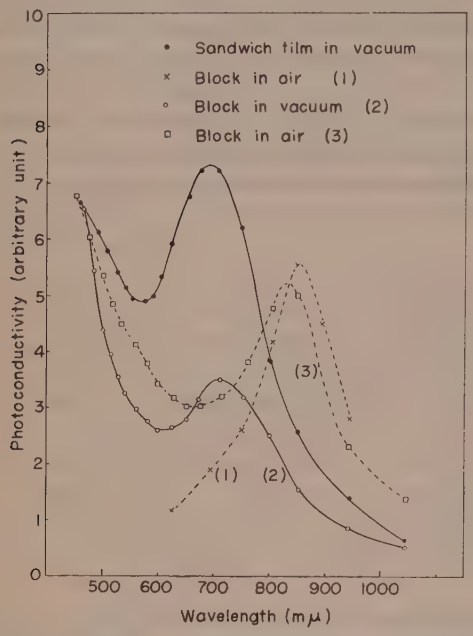

Fig. 5. Spectral photocurrent for equal energy illumination.

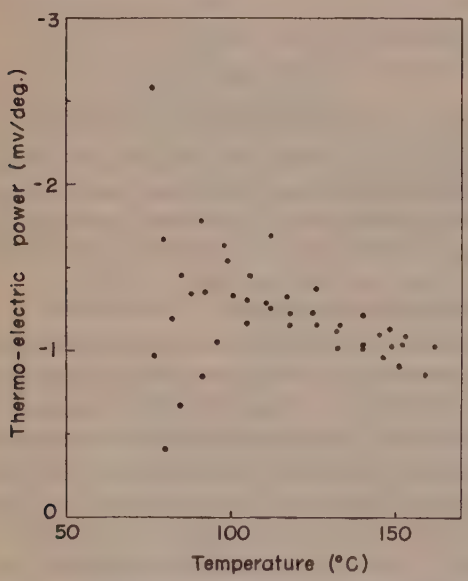

Fig. 6. Temperature dependence of thermolectric power.

seen that the shift of its maximum is reversible.

It will be interesting to study this phenomena further. It is also seen from this figure that the sensitivity rapidly increases below the wavelength of about 550 mμ.

This wavelength is almost the same as that of the absorption edge in GeS_2, but it seems that the increase is not related to GeS_2, because no photocurrent was observed in GeS_2 with the irradiation of 100 watt tungsten lamp and high pressure mercury arc lamp.

(d) Thermoelectromotive force

Thermoelectromotive force was measured between the temperature of 70° and 160°C with a potentiometer, and the temperature was measured by copper-constantan thermocouples. In Fig. 6 the results are plotted against temperature. For temperatures below 100°C the accuracy of data is low because of the high resistance of samples.

Although it seems that the conduction process is intrinsic above 100°C as seen from Figs. 2 and 3, the sign of the electromotive force observed is that of p type ones.

The magnitude of thermo electric power is about 1 mv/deg.

§ 4. Conclusions and Acknowledgements

In this paper some electrical and optical properties of GeS are described. High purity GeS samples were obtained by heating in the stream of ammonia gas after being prepared by heat treatment of germanium and sulfur in quartz tube. The energy gap of GeS is calculated as 1.5~2.0 ev from thermal activation energy, about 1.8 ev from the maximum of photoconductivity and these values are in good agreement with each other. Dark resistivity of GeS as high as 10^{10} Ωcm or more is obtained at room temperature.

In evaporated layers there is a conduction of lower activation energy which seems to come from some impurity centre. It is interesting that the sign of thermoelectromotive force is that of holes at higher temperature region where intrinsic conduction seems to take place.

The auther wishes to express his sincere thanks to Mr. Sakio Suzuki, Mr. Shoji Yamada and Dr. Shinichiro Narita for their contributions in making the samples and taking the experimental data of this work.

Reference

1) W. H. Zachariasen: Phys. Rev. **40** (1932) 917.

JOURNAL OF THE PHYSICAL SOCIETY OF JAPAN Vol. 13, No. 6, JUNE, 1958

Electronic Structure and Diamagnetism of Graphite

By Shoichi MASE

Department of General Education, University of Nagoya

(Received December 17, 1957)

We studied the electronic energy bands of graphite by the Bloch method and then calculated the diamagnetic susceptibility. The calculated value of the main term in Peierls' constant susceptibility (parallel component to c-axis) is about 0.3 times the experimental value, and the theoretical value of periods (on the basis of Onsager's theory) of two types with regard to the de Haas-van Alphen effect is about 2.5 times the experimental value. The cause of such discrepancy is discussed.

§ 1. Introduction

As is well known, in a strong diamagnetic substance like graphite or bismuth or antimony, conduction electrons, i.e. so-called de Haas-van Alphen electrons, cause a non-periodic part of susceptibility which is fairly small compared with the experimental value.[1] Blackman[2] suggested that the periodic part and most of the non-periodic part of the susceptibility of bismuth are caused by electrons found in separate places in the Brillouin zone. However, it is difficult to explain why the electrons giving rise to a large non-periodic part of susceptibility do not so appreciably to the periodic part. Hence on the basis of Blackman's suggestion, we have to expect an extreme anisotropy in energy bands.

According to Wallace,[3] Coulson[4] and others, the electrons and holes in graphite occupy the corner states of the Brillouin zone of hexagonal prism and there is no energy gap between the lower and the upper bands. Then, since the characteristic quantities of the electrons and holes are estimated as nearly equal, there is no reason to assume two types of energy pockets, as Blackman did, and we must consider that the electrons causing the periodic and non-periodic susceptibilities are electrons of the same type.

In this paper we study the relation between the diamagnetic susceptibility and the energy bands. For the purpose of determining the values of the parameters required in later sections, in § 2 we consider how the energy integrals in the Bloch method are affected by the inclusion of the overlapping of wave functions. In § 3 the exact secular equation for the π-electron in three dimensional lattice is set up and the energy distribution is investigated in detail on the basis of this equation. In § 4 the constant diamagnetic susceptibility is calculated by using the parameters which were determined in § 2 and § 3. In § 4 it is shown that, in the magnetic field parallel to the c-axis, the c-axis component of the ordinary main term of the Landau-Peierls' diamagnetism is only about 30 % of the experimental value and that the perpendicular component is also much smaller than the susceptibility of diamond. Hence we conclude that the observed value of the perpendicular component consists mostly of atomic susceptibility. In § 5 the de Haas-van Alphen effect is analysed. It is shown there that correct value of periods can not be obtained within the limits of either π-electron or the one band model.

§ 2. π-bands of Two Dimensional Lattice. Effect of the Overlapping of Wave Functions

In the Bloch method, the overlapping of wave functions is usually neglected to simplify the calculation. Wallace[3] worked along this line. Coulson and Tayler,[4] however, took into account the overlapping of wave functions between nearest neighbours and calculated the state density, and obtained a result differing remarkably from Wallace's. From Table I, however, we suppose that the overlapping of higher orders gives rise to an effect of the same order as the overlapping of lower order when proceeding to a higher approximation, since the distance to a higher neighbour is not very much longer than that to the nearest neighbour; that is to say, it is possible that the effect of the overlapping was wrongly estimated in the first step of

the approximation. We shall therefore take into account the effect of the overlapping of wave functions more fully.

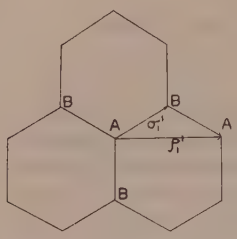

Fig. 1. Crystal structure of two dimensional lattice.

Table I. Classes of neighbouring atoms; a is the atomic distance to nearest neighbour. (Cf. Fig. 1.)

Type	Distance R/a	Number in a class	$(a/R)^4$
σ_1	1	3	1
ρ_1	$\sqrt{3}$	6	1/9
σ_2	2	3	1/16
σ_3	$\sqrt{7}$	6	1/49
ρ_2	3	6	1/81
ρ_3	$2\sqrt{3}$	6	1/144

We show in Fig. 1 the crystal lattice of two dimensional graphite composed of two sublattices, A and B, as marked there. Defining ϕ as the atomic $2p_z$ function, and φ as Löwdin's orthogonalized atomic function, we have

$$\left.\begin{aligned} \varphi(\boldsymbol{r}-\boldsymbol{r}_j)&=\sum_i \phi_i(1+\boldsymbol{S})_{ij}^{-1/2}\,, \\ S_{ij}&=\int \phi_i^*\phi_j d\tau\,. \end{aligned}\right\} \tag{2.1}$$

Using the orthogonalized function φ instead of the usual non-orthogonalized function ϕ for the Bloch sums ψ_A and ψ_B corresponding to types A and B respectively of atoms in a unit cell, energy eigenvalues are given by

$$E=H_{AA}\pm|H_{BA}|\,, \tag{2.2}$$

where the matrix elements are

$$H_{AA}=E(0)+\sum_\mu E(\rho_\mu)a_\mu{}^\rho(\boldsymbol{k})\,, \tag{2.3a}$$

$$H_{BA}=\sum_\nu E(\sigma_\nu)a_\nu{}^\sigma(\boldsymbol{k})\,, \tag{2.3b}$$

and where

$$a_\mu{}^\rho(\boldsymbol{k})=\sum_j \exp(-2\pi i\boldsymbol{k}\cdot\boldsymbol{\rho}_\mu{}^j)\,,$$

$$a_\nu{}^\sigma(\boldsymbol{k})=\sum_j \exp(-2\pi i\boldsymbol{k}\cdot\boldsymbol{\sigma}_\nu{}^j)\,.$$

We make use of symbols $\boldsymbol{\rho}$ and $\boldsymbol{\sigma}$ to denote the distance vectors from the referred atom to atoms of the same type and of different type; the suffix μ and ν denote the μ- and ν-th neighbours in each species, and j is to distinguish an atom from those in the same neighbouring order; $E(0)$, $E(\rho_\mu)$ and $E(\sigma_\nu)$ are integrals

$$E(0)=\int \varphi^*(\boldsymbol{r})H\varphi(\boldsymbol{r})d\tau\,, \tag{2.4a}$$

$$E(\rho_\mu)=\int \varphi^*(\boldsymbol{r}-\boldsymbol{\rho}_\mu)H\varphi(\boldsymbol{r})d\tau\,, \tag{2.4b}$$

$$E(\sigma_\nu)=\int \varphi^*(\boldsymbol{r}-\boldsymbol{\sigma}_\nu)H\varphi(\boldsymbol{r})d\tau\,. \tag{2.4c}$$

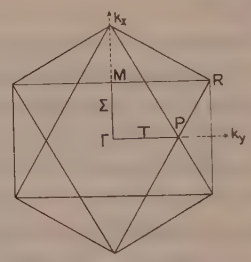

Fig. 2. The Brillouin zones for two dimensional lattice.

Now, to calculate the electric and magnetic properties, we study the electronic states in the neighbourhood of point P shown in Fig. 2. We use an expansion in a power series of wave vectors, $\boldsymbol{k}'=\boldsymbol{k}-\boldsymbol{k}_P(|\boldsymbol{k}'|\ll|\boldsymbol{k}|)$

$$a_\nu{}^\sigma(\boldsymbol{k})=\sum_j \exp(-2\pi i\boldsymbol{k}_P\cdot\boldsymbol{\sigma}_\nu{}^j)$$
$$\times\left\{1-2\pi i\boldsymbol{k}'\cdot\boldsymbol{\sigma}_\nu{}^j-\frac{1}{2}(2\pi\boldsymbol{k}'\cdot\boldsymbol{\sigma}_\nu{}^j)^2+\cdots\right\}.$$

Since for any number of ν we can show that $a_\nu{}^\sigma(P)=0$, H_{BA} identically vanishes at P. Further, we have

$$a_\mu{}^\rho(\boldsymbol{k})=\sum_j \cos 2\pi\boldsymbol{k}_P\cdot\boldsymbol{\rho}_\mu{}^j$$
$$-\frac{1}{2}\sum_j(2\pi\boldsymbol{k}'\cdot\boldsymbol{\rho}_\mu{}^j)^2\cos 2\pi\boldsymbol{k}_P\cdot\boldsymbol{\rho}_\mu{}^j+\cdots\,.$$

Because the first term H_{AA} of (2.2) is quadratic in $\boldsymbol{k}'$ and the second term H_{BA} giving rise to splitting into two bands is linear in $\boldsymbol{k}'$, the two bands have no overlapping in the neighbourhood of P. The energy value $E_P(\boldsymbol{k})$ in the neighbourhood of P is then given by

$$\begin{aligned} &E_P(\boldsymbol{k}) \\ &=E(0)-3(E(\rho_1)-2E(\rho_2)+E(\rho_3)+\cdots) \\ &\quad\pm 3\pi a(-E(\sigma_1)+2E(\sigma_2)+E(\sigma_3)+\cdots)|\boldsymbol{k}-\boldsymbol{k}_P|\,. \end{aligned} \tag{2.5}$$

This formula shows that the shapes of the

two bands are symmetric as regards P. This fact is due to the crystal symmetry. The widths of the lower and the upper bands, $\Delta E_L = E(P) - E(\Gamma)$ and $\Delta E_U = E(R) - E(P)$, where $E(\Gamma)$ and $E(R)$ are respectively the energy at points Γ and R, are given by

$$\Delta E_L = -\sum_\nu a_\nu^\sigma(\Gamma) E(\sigma_\nu) + \sum_\mu (a_\mu^\rho(P) - a_\mu^\rho(\Gamma)) E(\rho_\mu) , \quad (2.6a)$$

$$\Delta E_U = -\sum_\nu a_\nu^\sigma(\Gamma) E(\sigma_\nu) - \sum_\mu (a_\mu^\rho(P) - a_\mu^\rho(\Gamma)) E(\rho_\mu) . \quad (2.6b)$$

By writing integrals (2.4) in terms of the non-orthogonalized functions, we can investigate the effect of the overlapping of wave functions on the width of the energy band. Defining $S(n)$, $\overline{E}(0)$ and $\overline{E}(n)$ as

$$S(n) = \int \phi^*(\boldsymbol{r} - \boldsymbol{r}_n) \phi(\boldsymbol{r}) d\tau , \quad (2.7a)$$

$$\overline{E}(0) = \int \phi^*(\boldsymbol{r})(V - U) \phi(\boldsymbol{r}) d\tau , \quad (2.7b)$$

$$\overline{E}(n) = \int \phi^*(\boldsymbol{r} - \boldsymbol{r}_n)(V - U) \phi(\boldsymbol{r}) d\tau , \quad (2.7c)$$

where V is the crystal potential and U the potential of an isolated atom, we can rewrite $E(\sigma_1)$ etc. in terms of (2.7). Thus we obtain

$$\begin{aligned} E(\sigma_1) = {} & (1 + 5S^2(\sigma_1) + 31S^4(\sigma_1) + 213S^6(\sigma_1))\beta(\sigma_1) \\ & - 2(S(\sigma_1)\beta(\rho_1) + S(\rho_1)\beta(\sigma_1)) \\ & + 2S(\sigma_1)(2S(\sigma_2)\beta(\sigma_1) + S(\sigma_1)\beta(\sigma_2)) + \cdots , \end{aligned} \quad (2.8a)$$

$$\begin{aligned} E(\rho_1) = {} & -S(\sigma_1)(1 + 8S^2(\sigma_1) + 60S^4(\sigma_1))\beta(\sigma_1) \\ & + (\beta(\rho_1) + 10S(\sigma_1)S(\rho_1)\beta(\sigma_1) \\ & - 2S(\rho_1)\beta(\rho_1) + 5S^2(\sigma_1)\beta(\rho_1)) \\ & - (S(\sigma_2)\beta(\sigma_1) + S(\sigma_1)\beta(\sigma_2)) \\ & - (S(\sigma_3)\beta(\sigma_1) + S(\sigma_1)\beta(\sigma_3)) + \cdots , \end{aligned} \quad (2.8b)$$

where

$$\beta(\sigma_\nu) = \overline{E}(\sigma_\nu) - S(\sigma_\nu)\overline{E}(0) ,$$

$$\beta(\rho_\mu) = \overline{E}(\rho_\mu) - S(\rho_\mu)\overline{E}(0) .$$

The width of lower band is

$$\begin{aligned} \Delta E_L = {} & (1 + \sum_\nu a_\nu^\sigma(\Gamma) S(\sigma_\nu) + \sum_\mu a_\mu^\rho(\Gamma) S(\rho_\mu))^{-1} (1 + \sum_\mu a_\mu^\rho(P) S(\rho_\mu))^{-1} \{ -\sum_\nu a_\nu^\sigma(\Gamma) \beta(\sigma_\nu) \\ & + \sum_\mu (a_\mu^\rho(P) - a_\mu^\rho(\Gamma)) \beta(\rho_\mu) + (\sum_{\mu,\mu'} a_\mu^\rho(P) \beta(\rho_\mu) a_{\mu'}^\rho(\Gamma) S(\rho_{\mu'}) - \sum_{\mu,\mu'} a_\mu^\rho(\Gamma) \beta(\rho_\mu) a_{\mu'}^\rho(P) S(\rho_{\mu'})) \\ & + (\sum_{\mu,\nu} a_\mu^\rho(P) \beta(\rho_\mu) a_\nu^\sigma(\Gamma) S(\sigma_\nu) - \sum_{\mu,\nu} a_\mu^\rho(P) S(\rho_\mu) a_\nu^\sigma(\Gamma) \beta(\sigma_\nu)) \} . \end{aligned} \quad (2.6)'$$

To find the order of magnitude, we assume that the resonance integral is proportional to the overlapping integral $S(n)$, and that $S(n)$ is inversely proportional to the fourth power of distance. Then we have

$$\beta(R) = \frac{S(R)}{S(\sigma_1)} \beta(\sigma_1) = \left(\frac{a}{R}\right)^4 \beta(\sigma_1) ,$$

and

$$\Delta E_L = -\frac{\beta(\sigma_1)}{S(\sigma_1)} \times \frac{(1 + \sum_\nu a_\nu^\sigma(\Gamma) S(\sigma_\nu) + \sum_\mu a_\mu^\rho(\Gamma) S(\rho_\mu)) - (1 + \sum_\mu a_\mu^\rho(P) S(\rho_\mu))}{(1 + \sum_\nu a_\nu^\sigma(\Gamma) S(\sigma_\nu) + \sum_\mu a_\mu^\rho(\Gamma) S(\rho_\mu))(1 + \sum_\mu a_\mu^\rho(P) S(\rho_\mu))} \quad (2.6)''$$

Adopting the values 1/4 and -3.0 ev. for $S(\sigma_1)$ and $\beta(\sigma_1)$ respectively, as proposed by Coulson and Tayler, we study how the magnitude of the calculated band width is affected, taking into account the contribution of higher neighbours; results are given in Table II. Naturally in the approximation of nearest neighbours, (2.6)′ agrees with the result of Coulson and Tayler. Potential $V - U$ is large half way between any two atoms, and then the overlapping of wave functions in this neighbourhood contributes largely to $E(0)$ and $\overline{E}(\sigma_1)$. Therefore we may suppose that $E(0)$ and $\overline{E}(\sigma_1)$ are of the same order. Hence we have a value -4.0 ev. for $E(\sigma_1)$. Neglecting the overlapping of wave functions and taking into account the contribution of the nearest neighbours alone, we have 12 ev. as the width of the lower band. Although the contribution of $S(\sigma_1)$ considerably reduces the width of the lower band, the effect is cancelled fairly well by the contributions of $S(\rho_1)$ and $\overline{E}(\rho_1)$. Thus the final value converges into some

value between the value of zeroth approximation (12 ev.) given in the second column in Table II, and that of nearest neighbour approximation (5.1 ev.). While $E(\sigma_1)$ is found to be nearly equal to the value of the lowest approximation in which the overlapping is not included, $E(\rho_1)$ is much more affected than $E(\sigma_1)$ and the sign is the opposite of the sign expected from the two-centre approximation. The absolute value of $E(\rho_1)$, however, is fairly small as compared with $E(\sigma_1)$. Hence, when overlapping is neglected, the theoretical result is wrong even when the resonance integrals of higher neighbours are taken into account. However, when only the nearest neighbours are taken into account, no good result can be obtained even should the overlapping be calculated exactly, since many other terms of comparable order are neglected. As to these points, Wohlfarth[6] got similar results by calculating the effect of overlapping for a simple one-dimensional lattice.

Table II. The overlapping effect on energy integrals in units of ev. The first row shows the distance to the farthest neighbouring atom whoes contribution is taken into account.

	$\sigma_1(S(\sigma_1)=0)$	σ_1	ρ_1	σ_2	$R=\infty$
ΔE_L	12.0	5.1	6.8	7.0	7.6

	$E(\sigma_1)$	$E(\rho_1)$
$S=0$	-4.0	-0.4
$S\neq 0$	~ -4.2	~ 1.3

§ 3. π-bands of Three Dimensional Lattice

In three dimensional lattice, the binding only between the succesive layers (the layer distance c=3.35 Å) is extremely weak (the binding energy is about 4 kcal/mole)[7] and so the feature of stacking can be easily changed by something such as mechanical treatments.[8] Therefore it is possible that the observed electric and magnetic properties are not those of a uniformly stacked lattice but are those of a mixture of various stackings.

There are three types of stacking, viz, aa type, ab type and abc type. The difference between the electronic structures of these three types is ordinarily not so remarkable, but it does have an important effect on the electronic properties at low temperatures. For example, in abc type the total number of electronic states per atom in the lowest B.Z. is 0.998. This type of lattice, therefore, would be expected to behave like a metal. Compared with the number of conduction electrons in graphite ($\sim 10^{-5}$ per atom at 0°K) as estimated from experiments on Hall effect and others, the number 0.002 in the abc type of lattice is considerably large. There are experimental reports that some crystals contain abc type of lattice to about 15 %.[9] Depending on whether this abc type is contained in large blocks or in small pieces in the background of the ab type, the effect on diamagnetic property differs very much, i.e. the effect is far smaller in the latter case. According to Brennan,[7] the cohesive energy for ab type is lower than that for aa type by about 0.36 kcal/mole. Although the cohesive energy has not been compared for abc and ab types, it is probable that abc type is energetically more stable than aa type. However, it is not probable that abc type is contained in the form of a large block in crystals. In the present paper we consider only regular lattice of ab type.

Taking orthogonal atomic wave functions φ for the four atoms A, B, A′ and B′ respectively in a unit cell, and taking into account that the circumstances around the A and B sites are the same as those around the B′ and A′ sites, we construct four Bloch sums from these functions which then give the following matrix elements:

$$H_{AA}=E_{zz}(0)+\sum_{\mu}E_{zz}(\rho_\mu,0)\cdot a_\mu{}^\rho(\boldsymbol{k})+2\sum_{n}E_{zz}(0,2nc)\cdot\cos 4\pi nck_z$$
$$+2\sum_{n,\mu}E_{zz}(\rho_\mu,2nc)\cdot a_\mu{}^\rho(\boldsymbol{k})\cdot\cos 4\pi nck_z\,, \tag{3.1a}$$
$$H_{BB}=E_{\bar{z}\bar{z}}(0)+\sum_{\mu}E_{\bar{z}\bar{z}}(\rho_\mu,0)\cdot a_\mu{}^\rho(\boldsymbol{k})+2\sum_{n}E_{\bar{z}\bar{z}}(0,2nc)\cdot\cos 4\pi nck_z$$
$$+2\sum_{n,\mu}E_{\bar{z}\bar{z}}(\rho_\mu,2nc)\cdot a_\mu{}^\rho(\boldsymbol{k})\cdot\cos 4\pi nck_z\,, \tag{3.1b}$$
$$H_{BA}=\sum_{\nu}E_{\bar{z}z}(\sigma_\nu,0)\cdot a_\nu{}^\sigma(\boldsymbol{k})+2\sum_{n,\nu}E_{\bar{z}z}(\sigma_\nu,2nc)\cdot a_\nu{}^\sigma(\boldsymbol{k})\cdot\cos 4\pi nck_z\,, \tag{3.1c}$$

$$H_{B'A}=2\sum_{n}E_{zz}(0,(2n-1)c)\cdot\cos 2\pi(2n-1)ck_z$$
$$+2\sum_{n,\mu}E_{zz}(\rho_\mu,(2n-1)c)\cdot a_\mu{}^\rho(\boldsymbol{k})\cdot\cos 2\pi(2n-1)ck_z\,, \tag{3.1d}$$
$$H_{A'A}=2\sum_{n,\nu}E_{\bar{z}\bar{z}}(\sigma_\nu,(2n-1)c)\cdot a_\nu{}^\sigma(\boldsymbol{k})^*\cdot\cos 2\pi(2n-1)ck_z\,, \tag{3.1e}$$
$$H_{A'B}=2\sum_{n,\nu}E_{\bar{z}\bar{z}}(\sigma_\nu,(2n-1)c)\cdot a_\nu{}^\sigma(\boldsymbol{k})\cdot\cos 2\pi(2n-1)ck_z\,, \tag{3.1f}$$

where n denotes the number of layers and other indices have the same meaning as in the preceding section. It is noted that $\boldsymbol{k}$ is a two-dimensional wave vector. The secular equation is written

$$\begin{vmatrix} H_{AA}-E & H_{BA}^* & H_{B'A} & H_{A'A}^* \\ H_{BA} & H_{BB}-E & H_{A'A}^* & H_{A'B}^* \\ H_{B'A} & H_{A'A} & H_{AA}-E & H_{BA} \\ H_{A'A} & H_{A'B} & H_{BA}^* & H_{BB}-E \end{vmatrix}=0. \tag{3.2}$$

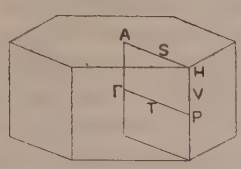

Fig. 3. The Brillouin zones which contain one electron per atom.

Since it can be seen from an approximate solution of this equation that the position of the highest energy in the lower zone and that of the lowest energy in the upper zone are on line $\overline{\mathrm{PH}}$ in Fig. 3, we shall investigate the neighbourhood of this line only. Because $a_\nu{}^\sigma(P)=0$, as was seen in § 2, $H_{A'A}$ and $H_{A'B}$ are negligibly small compared with $H_{B'A}$ and are of the order of about 1/10 of H_{BA}. Hence these terms are neglected here. In this approximation, the solution of the secular equation is in form the same as obtained by Carter and Krumhansle,[10] i.e.

$$E=H_{BB}-\frac{1}{2}(H_{BB}-H_{AA}+H_{B'A})$$
$$\pm\left\{|H_{BA}|^2+\frac{1}{4}(H_{BA}-H_{AA}+H_{B'A})^2\right\}^{1/2}. \tag{3.3}$$

The two bands touch at point Q, where $H_{BB}-H_{AA}+H_{B'A}=0$, and on lines $\overline{\mathrm{QH}}$ and $\overline{\mathrm{PQ}}$ we have exactly $E=H_{BB}(\boldsymbol{k}_P,k_z)$. The value of $|k_z|$ at Q, where the two bands contact is somewhat larger than 1/4 c. As seen from (3.1), the leading term among the terms depending on k_z in $H_{BB}(\boldsymbol{k}_P,k_z)$ is $2E_{\bar{z}\bar{z}}(0,2c)\cos 4\pi ck_z$. Then if $E_{\bar{z}\bar{z}}(0,2c)>0$, as expected from the two-centre approximation, $H_{BB}(\boldsymbol{k}_P,k_z)$ has its maximum value at $k_z=0$, $k_z=\pm 1/2\,c$ and minimum value at $k_z=\pm 1/4\,c$. The difference is $4E_{\bar{z}\bar{z}}(0,2c)$. Hence the lower and upper bands overlap by $4E_{\bar{z}\bar{z}}(0,2c)$.[11] We measure the energy in the lower band from its top, that in the upper band from its bottom, and write them as $\mathcal{E}_h$ and $\mathcal{E}_e$ respectively. Further we neglect in the matrix elements terms other than the leading terms. Then we can rewrite (3.3)

$$\mathcal{E}_h=9\pi^2a^2\gamma_0'k^2+4\gamma_1'(\cos^2 2\pi ck_z-1)-\frac{\delta}{2}-\gamma_1\cos 2\pi ck_z$$
$$-\left\{9\pi^2a^2\gamma_0{}^2k^2+\frac{1}{4}(\delta+2\gamma_1\cos 2\pi ck_z)^2\right\}^{1/2}, \tag{3.4a}$$
$$\mathcal{E}_e=9\pi^2a^2\gamma_0'k^2+4\gamma_1'\cos^2 2\pi ck_z-\frac{\delta}{2}-\gamma_1\cos 2\pi ck_z$$
$$+\left\{9\pi^2a^2\gamma_0{}^2k^2+\frac{1}{4}(\delta+2\gamma_1\cos 2\pi ck_z)^2\right\}^{1/2}, \tag{3.4b}$$

where

$$\gamma_0=E_{\bar{z}\bar{z}}(\sigma_1,0)\,,\qquad \gamma_0'=\frac{1}{2}(E_{\bar{z}\bar{z}}(\rho_1,0)+E_{zz}(\rho_1,0))\,,\qquad \gamma_1=E_{zz}(0,c)\,,$$
$$\gamma_1'=E_{\bar{z}\bar{z}}(0,2c)\,,\qquad \delta=E_{\bar{z}\bar{z}}(0)-3E_{\bar{z}\bar{z}}(\rho_1,0)-E_{zz}(0)+3E_{zz}(\rho_1,0)\,.$$

The area of cross-section perpendicular to k_z-axis of the reduced energy surface is denoted

by $A(k_z)$. Then, $A(k_z)$ for the upper band and the lower band is given respectively by

$$A_h(k_z)=\frac{1}{9\pi a^2\gamma_0^2}\{\mathcal{E}_h^{\max}+4\gamma_1'(1-\cos^2 2\pi ck_z)\}\{\mathcal{E}_h^{\max}+4\gamma_1'(1-\cos^2 2\pi ck_z)+\delta+2\gamma_1\cos 2\pi ck_z\}\,, \tag{3.5a}$$

$$A_e(k_z)=\frac{1}{9\pi a^2\gamma_0^2}(\mathcal{E}_e^{\max}-4\gamma_1'\cos^2 2\pi ck_z)\{\mathcal{E}_e^{\max}-4\gamma_1'\cos^2 2\pi ck_z+\delta+2\gamma_1\cos 2\pi ck_z\}\,. \tag{3.5b}$$

In the region $k_z\geq 0$, $A_h(k_z)$ takes the maximum value at $k_z=1/2\,\mathrm{c}$

$$A_h^{\max}(1/2\,\mathrm{c})=-\frac{2\mathcal{E}_h^{\max}\gamma_1}{9\pi a^2\gamma_0^2}\left(1-\frac{\mathcal{E}_h^{\max}}{2\gamma_1}-\frac{\delta}{2\gamma_1}\right). \tag{3.6}$$

The value of k_z for which $A_h(k_z)=0$, is obtained from the formula,

$$\cos 2\pi ck_z=-(1-|\mathcal{E}_h^{\max}|/4\gamma_1')^{1/2}\,.$$

Thus, $k_z\sim 3/8\,\mathrm{c}$, by $|\mathcal{E}_h^{\max}|\sim 2\gamma_1'$. On the other hand, the values of k_z for which $A_e(k_z)=0$, are determined from formulas

$$\cos 2\pi ck_z\approx-\frac{\mathcal{E}_e^{\max}+\delta}{2\gamma_1}\,,$$

$$\cos 2\pi ck_z=\left(\frac{\mathcal{E}_e^{\max}}{4\gamma_1'}\right)^{1/2}.$$

Consequently, by assuming that $\mathcal{E}_e^{\max}+\delta\sim 0.2\gamma_1$, we obtain $k_z=1/4\,\mathrm{c}+\Delta k_z$ ($\Delta k_z\sim 0.016/\mathrm{c}$), and $k_z\sim 1/8\,\mathrm{c}$. Accordingly, the number of energy pockets of electrons is twice that of holes. Now, we must calculate the number of states to evaluate the chemical potentials ζ_{0e}, ζ_{0h} of electrons and holes. Denoting the number of occupied states of electrons and holes per unit volume by n_{0e}, n_{0h}, we determine ζ_{0e} ζ_{0h} from the following

$$\left.\begin{aligned}&\zeta_{0e}+\zeta_{0h}=4E_{zz}^{-}(0,2c)\,,\\&n_{0e}=n_{0h}\,.\end{aligned}\right\} \tag{3.7}$$

We should have used the formula (3.4) to calculate the value of n_0, but the calculation is cumbersome on account of the presence of the term containing γ_1'. Therefore, for the present, we investigate the qualitative features by means of an approximate calculation. If we approximate the constant energy surfaces of the electrons and holes by ellipsoids, we have the relation

$$A_h^{\max}K_{zh}=A_e^{\max}K_{ze}\,, \tag{3.8}$$

where K_{zh} is the length of k_z from point H to the point at which $A_h(k_z)=0$ and where K_{ze} is the diffenence between two values of k_z so that $A_e(k_z)=0$. Since $A_e^{\max}$ becomes considerably smaller than $A_h^{\max}$ because of the appearance of γ_1', we have $K_{ze}>K_{zh}$. Thus the points where $A_h(k_z)=0$, $A_e(k_z)=0$, are given by $k_z\gtrsim 3/8\,\mathrm{c}$, $k_z\lesssim 1/8\,\mathrm{c}$ respectively, we have the relation $\zeta_{0e}\gtrsim\zeta_{0h}$. Next, we make a rough estimation of the orders of ζ_{0e} and ζ_{0h}, which as seen from (3.7), are of the order of $2E_{zz}^{-}(0,2c)$. Assuming that the resonance integral is inversely proportional to the fourth power of the distance, as in § 2, we obtain $E_{zz}^{-}(0,2c)\sim 1/16\cdot E_{zz}(0,c)$. Taking the value 0.09 ev. for $E_{zz}(0,c)$ as was given by Coulson, we obtain the value 0.011 ev. for ζ_0, i.e. 128°K in terms of degeneracy temperature. This temperature is in good agreement with the result obtained from the analysis of the de Haas-van Alphen effect.

Based on the above qualitative discussion, we assume the values for the energy integrals as shown in Table III, where T_{0e} and T_{0h} are the degeneracy temperatures obtained from two periods of the de Haas-van Alphen effect. The values of $E_{zz}^{-}(\sigma_1,0)$ and $E_{zz}(\rho_1,0)$ are determined on the basis of the calculation in § 2 so that the calculated width of π-band is in agreement with the estimated value from the experiment. Carter and Krumhansl gave the value $\gtrsim 0.01$ ev. for δ but we take here a somewhat larger value. With use of Table III, the maximum value of $A_e(k_z)$ is found at $k_z\sim 0.18/\mathrm{c}$ and is given by

$$A_{0e}^{\max}\left(\frac{0.18}{c}\right)=0.351\times\frac{2\zeta_{0e}\gamma_1}{9\pi a^2\gamma_0^2}\,. \tag{3.9}$$

Thus we obtain the result $A_{0e}^{\max}/A_{0h}^{\max}=0.54$. In Fig. 4, we show schematically the electron distribution in the Brillouin zone at 0°K. The shape of the constant energy surface looks

like an ellipsoid but $A(k_z)$ varies as a function of k_z more gently than in an ellipsoid. In a certain sense, this energy surface has the intermediate character of ellipsoid and cylinder.

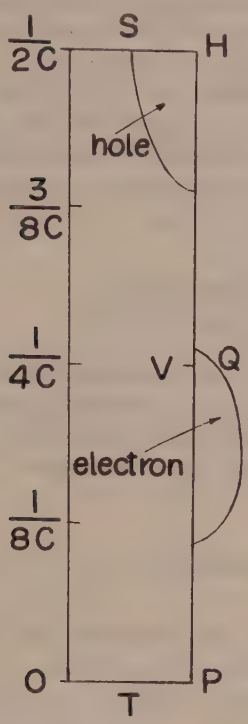

Fig. 4. Schematic representation of the distribution of electrons and holes at 0°K.

Table III. Estimated values of energy integrals in units of ev.

ζ_{0e}	0.015 ($T_{0e}=169°K$)	$E_{zz}(0, c)$	0.20
ζ_{0h}	0.010 ($T_{0h}=116°K$)	$E_{zz}(0, 2c)$	0.0063
$E_{zz}(\sigma_1, 0)$	−3.20	δ	0.02
$E_{zz}(\rho_1, 0)$	0.33		

It is seen in (3.5), that in our approximation, the integrals between the second nearest neighbours do not contribute to $A(k_z)$. Hove[12] calculated the density of state using a formula neglecting γ_1' and δ in (3.4) and obtained the result that the density of the upper band becomes higher than that of the lower band owing to the contribution of the term containing γ_0'. It is noted, however, that the value of parameter γ_0' should take the sign opposite to that expected from the two-centre approximation. Thus, we may say that the effect of γ_0' term is the reverse of that concluded by Hove. Furthermore, the ratio $\pi\gamma_0'\gamma_1/2\gamma_0^2$ of the first term of the correction arising from γ_0' term to the main term is estimated as 0.01 by using Table III. As this could be 0.05 at most, we may neglect the effect of γ_0' term. This is our ground for the expression (3.5).

Now we study whether the characteristic features of the constant energy surface of electrons and holes, as shown in Fig. 4, remain the same after neglecting the γ_1' term. If this term is neglected, both degeneracy temperatures reduce to 0°K and there is no way to explain various properties at low temperatures. Therefore, we assume here finite degeneracy temperatures, although we neglect γ_1' and γ_0' terms in (3.4). In such an approximation, two separate parts for the distribution of electrons in which energies are the lowest at $k_z=\pm 1/4\,c$, contact each other and the shape of the energy surface becomes similar to a cylinder, and the numbers of pockets of electrons and holes become equal. The numbers n_{0e} and n_{0h} are given by

$$\left.\begin{aligned} n_{0e}&=\frac{8\gamma_1\zeta_{0e}}{9\pi^2a^2c\gamma_0^2}\left\{1+\frac{\pi}{4}\frac{\delta}{\gamma_1}+\frac{1}{8}\left(\frac{\delta}{\gamma_1}\right)^2+\frac{\pi}{4}\left(\frac{\zeta_{0e}}{\gamma_1}\right)+\frac{1}{8}\left(\frac{\zeta_{0e}}{\gamma_1}\right)^2+\frac{1}{4}\frac{\zeta_{0e}\delta}{\gamma_1^2}+\cdots\right\},\\ n_{0h}&=\frac{8\gamma_1\zeta_{0h}}{9\pi^2a^2c\gamma_0^2}\left\{1-\frac{\pi}{4}\frac{\delta}{\gamma_1}+\frac{1}{8}\left(\frac{\delta}{\gamma_1}\right)^2+\frac{\pi}{4}\left(\frac{\zeta_{0h}}{\gamma_1}\right)+\frac{1}{8}\left(\frac{\zeta_{0h}}{\gamma_1}\right)^2-\frac{1}{4}\frac{\zeta_{0h}\delta}{\gamma_1^2}+\cdots\right\}.\end{aligned}\right\}\tag{3.10}$$

By using Table III, these become $n_{0e}=4.4\times10^{18}$/cc, $n_{0h}=2.5\times10^{18}$/cc. Kinchin[13] estimated the number of conduction electrons from his measurements of Hall coefficient. His results are $n_e\approx n_h=1.2\times10^{18}$/cc at 4°K and 6.2×10^{18}/cc at room temperature. Since at low temperatures the Hall coefficient depends on the magnetic field anomalously, we can not apply any simple theory to calculate the number of conduction electrons but for the present we will suppose that n_0 is of the order of $1\sim4\times10^{18}$/cc at 0°K. Hence we may say that the above theoretical values are of the right order of magnitude. Since, however, the number of electrons and holes should be equal, we calculate the degeneracy temperatures by taking $n_{0e}=n_{0h}$. The result becomes $T_{0e}<T_{0h}$, which is contrary to that in Table

III. It is essential that we take into account the γ_1' term in order to clarify the difference in the behaviour of electrons and holes.

§ 4. Anisotropy of Constant Diamagnetic Susceptibility

As is well known, the diamagnetic susceptibility of graphite is very large and shows an extremely large anisotropy. Wallace concluded in his paper that the anisotropy in both magnetism and conductivity have the same order of magnitude. In this section, we make clear how the anisotropy is related to the structure of the energy band.

According to Peierls,[14] the diamagnetic susceptibility per gram originating from quasi bound electrons is composed of three terms $\chi^{(1)}$, $\chi^{(2)}$ and $\chi^{(3)}$ where $\chi^{(2)}$ is the atomic like susceptibility and $\chi^{(3)}$ is the term which has its analogue in neither the susceptibility of atom nor in that of free electron. Here $\chi^{(1)}$, which is normally an important term, is given by

$$\chi_z{}^{(1)}=\frac{(e/2h\bar{c})^2}{12\pi^2\rho}\iint_{(S)}\left\{\frac{\partial^2\mathcal{E}}{\partial k_x{}^2}\frac{\partial^2\mathcal{E}}{\partial k_y{}^2}-\left(\frac{\partial^2\mathcal{E}}{\partial k_x\partial k_y}\right)^2\right\}\frac{2dS}{|\mathrm{grad}\,\mathcal{E}|}\frac{\partial f_0}{\partial\mathcal{E}}d\mathcal{E}\,, \tag{4.1}$$

where ρ is the density and $\bar{c}$ the light velosity. Since, as was mentioned in § 3, the right order of magnitude of the effective number of electrons can be obtained even in the approximation neglecting γ_1' term in (3.4), we take the same approximation as used in the calculation of n_0. In this approximation, we can also obtain the right order of magnitude of the susceptibility. Then we get

$$\mathcal{E}=-\frac{\delta}{2}-\gamma_1\cos 2\pi ck_z\pm\left\{\gamma_0{}^2x+\frac{1}{4}(\delta+2\gamma_1\cos 2\pi ck_z)^2\right\}^{1/2}, \tag{4.2}$$

where $x=9\pi^2a^2(k_x{}^2+k_y{}^2)$. We denote the susceptibility in the magnetic field parallel and perpendicular to the c-axis by $\chi_{\parallel}$ and $\chi_{\perp}$ respectively.

(1) $\chi_{\parallel}{}^{(1)}$

The bracket in the integrand of (4.1) becomes

$$\frac{\partial^2\mathcal{E}}{\partial k_x{}^2}\frac{\partial^2\mathcal{E}}{\partial k_y{}^2}-\left(\frac{\partial^2\mathcal{E}}{\partial k_x\partial k_y}\right)^2=4\mathcal{E}^2(9\pi^2a^2\gamma_0{}^2)^2\cdot\frac{(\gamma_0{}^2x-\mathcal{E}^2)^2}{(\gamma_0{}^2x+\mathcal{E}^2)^4}. \tag{4.3}$$

Substituting this into (4.1) and using the suffix e to mean the upper band, we obtain

$$\begin{aligned}\chi_{\parallel e}^{(1)}(\mathcal{E})&=\frac{4(e/2h\bar{c})^2(9\pi^2a^2\gamma_0{}^2)^2 4\mathcal{E}^2}{12\pi^2\rho\cdot 18\pi^2a^2c\mathcal{E}}\int_0^{(\varepsilon^2+\varepsilon(\delta+2\gamma_1))/\gamma_0{}^2}\frac{(\gamma_0{}^2x-\mathcal{E}^2)^2dx}{(\gamma_0{}^2x+\mathcal{E}^2)^3\{\gamma_1{}^2\mathcal{E}^2-(\gamma_0{}^2x-\mathcal{E}^2-\mathcal{E}\delta)^2/4\}^{1/2}}\\&=\frac{6a^2\gamma_0{}^2(e/2h\bar{c})^2}{c\gamma_1\rho}\left[\left\{\left(1+\frac{\eta^2}{8}\right)\log 4-2-\frac{\eta^2}{2}\right\}-\left(1+\frac{\eta^2}{8}\right)\log\xi-\frac{3}{2}\left(\frac{5}{2}-\log 4\right)\eta\xi\right.\\&\quad\left.-\frac{3}{2}\eta\xi\log\xi-3\left(\frac{85}{48}-\log 4\right)\xi^2-3\xi^2\log\xi+\cdots\right],\end{aligned} \tag{4.4}$$

where $\xi=\mathcal{E}/\gamma_1$, $\eta=\delta/\gamma_1$. Integrating over $\mathcal{E}$, the limits are 0 and γ_1, but we can replace the upper limit γ_1 by the infinity without giving rise to a serious error if $kT\ll\gamma_1$. Then we get

$$\begin{aligned}\chi_{\parallel e}^{(1)}=\frac{6a^2\gamma_0{}^2(e/2h\bar{c})^2}{c\gamma_1\rho}&\left[\left\{\left(1+\frac{\eta^2}{8}\right)\log 4-2-\frac{\eta^2}{2}\right\}J_1-\left(1+\frac{\eta^2}{8}\right)J_2-\frac{3}{2}\left(\frac{5}{2}-\log 4\right)\eta J_3\right.\\&\left.-\frac{3}{2}\eta J_4-3\left(\frac{85}{48}-\log 4\right)J_5-3J_6\right],\end{aligned} \tag{4.5}$$

where

$$J_1=-\frac{1}{\exp(-\zeta_e/kT)+1},$$

$$J_2=-\frac{\log \zeta_e/\gamma_1}{\exp(-\zeta_e/kT)+1}-C\left(1-\frac{1}{\exp(-\zeta_e/kT)+1}\right)+\sum_r(-1)^{r+1}\exp(-r\zeta_e/kT)$$
$$\times\{\mathrm{Ei}(r\zeta_e/kT)-\log(r\zeta_e/kT)\}+\sum_r(-1)^{r+1}\exp(r\zeta_e/kT)\,\mathrm{Ei}(-r\zeta_e/kT)\,,$$

$$J_3=-\frac{\zeta_e}{\gamma_1}-\frac{kT}{\gamma_1}\log(1+\exp(-\zeta_e/kT))\,,$$

$$J_4=-\log\left(\frac{\zeta_e}{\gamma_1}\right)\left\{\frac{\zeta_e}{\gamma_1}+\frac{kT}{\gamma_1}\log(1+\exp(-\zeta_e/kT))\right\}-\frac{kT}{\gamma_1}\log(1+\exp(-\zeta_e/kT))$$
$$+\frac{kT}{\gamma_1}\sum_r(-1)^{r+1}\frac{1}{r}\exp(r\zeta_e/kT)\,\mathrm{Ei}(-r\zeta_e/kT)-\left(\frac{kT}{\gamma_1}\right)\sum_r\frac{(-1)^{r+1}}{r}\exp(-r\zeta_e/kT)$$
$$\times\{\mathrm{Ei}(r\zeta_e/kT)-\log(r\zeta_e/kT)\}+C\left(\frac{kT}{\gamma_1}\right)\log(1+\exp(-\zeta_e/kT))\,,$$

$$J_5=-\left(\frac{\zeta_e}{\gamma_1}\right)^2-\frac{\pi^2}{3}\left(\frac{kT}{\gamma_1}\right)^2+2\left(\frac{kT}{\gamma_1}\right)^2\sum_r\frac{(-1)^{r+1}}{r^2}\exp(-r\zeta_e/kT)\,,$$

$$J_6=-\log\left(\frac{\zeta_e}{\gamma_1}\right)\left\{\left(\frac{\zeta_e}{\gamma_1}\right)^2+\frac{\pi^2}{3}\left(\frac{kT}{\gamma^1}\right)^2-2\left(\frac{kT}{\gamma_1}\right)^2\sum_r\frac{(-1)^{r+1}}{r^2}\exp(-r\zeta_e/kT)\right\}$$
$$-\left[\frac{\pi^2}{2}\left(\frac{kT}{\gamma_1}\right)^2-3\left(\frac{kT}{\gamma_1}\right)^2\sum_r\frac{(-1)^{r+1}}{r^2}\exp(-r\zeta_e/kT)-2\left(\frac{kT}{\gamma_1}\right)^2\sum_r\frac{(-1)^{r+1}}{r^2}\exp(r\zeta_e/kT)\right.$$
$$\times\mathrm{Ei}(-r\zeta_e/kT)-2\left(\frac{kT}{\gamma_1}\right)^2\sum_r\frac{(-1)^{r+1}}{r^2}\exp(-r\zeta_e/kT)\{\mathrm{Ei}(r\zeta_e/kT)-\log(r\zeta_e/kT)\}$$
$$\left.+2C\left(\frac{kT}{\gamma_1}\right)^2\sum_r\frac{(-1)^{r+1}}{r^2}\exp(-r\zeta_e/kT)\right].$$

Here C is Euler's constant and Ei is exponential integral. By replacing ζ_e and η by ζ_h and $-\eta$, we get a similar expression for the positive holes. From the condition $n_e=n_h$, ζ_e and ζ_h are determined. While formula (4.5) is rather complicated, nevertheless in the regions $\zeta_e/k\gg T$, we can obtain

$$\chi_{\parallel e}^{(1)}=-\frac{6a^2\gamma_0^2(e/2h\bar{c})^2}{c\gamma_1\rho}\left[\left\{1+\frac{3}{2}\eta\frac{\zeta_{0e}}{\gamma_1}+\frac{\eta^2}{8}+3\left(\frac{\zeta_{0e}}{\gamma_1}\right)^2\right\}\log\frac{1}{\zeta_{0e}/\gamma_1}\right.$$
$$\left.-2\left\{1+\frac{\eta^2}{4}-\left(1+\frac{\eta^2}{8}\right)\log 2\right\}-3\left(\frac{5}{4}-\log 2\right)\eta\frac{\zeta_{0e}}{\gamma_1}-6\left(\frac{85}{96}-\log 2\right)\left(\frac{\zeta_{0e}}{\gamma_1}\right)^2\right]. \tag{4.6}$$

A similar expression is obtained for holes.

(2) $\chi_\perp^{(1)}$

Since the Landau-Peierls' term is very small compared with the atomic susceptibility, as will be seen later, for convenience we calculate by assuming $\eta=0$. Substituting the expression

$$\frac{\partial^2\mathcal{E}}{\partial k_z^2}\frac{\partial^2\mathcal{E}}{\partial k_y^2}-\left(\frac{\partial^2\mathcal{E}}{\partial k_z\partial k_y}\right)^2=8\pi^2c^2(9\pi^2a^2\gamma_0^2)\mathcal{E}^4\left\{\frac{(\gamma_0^2x-\mathcal{E}^2)}{(\gamma_0^2x+\mathcal{E}^2)^3}+\frac{4\gamma_1^2\gamma_0^2x}{(\gamma_0^2x+\mathcal{E}^2)^4}\right\} \tag{4.7}$$

into (4.1), we have

$$\chi_\perp^{(1)}(\mathcal{E})=\frac{8c\gamma_1(e/2h\bar{c})^2}{3\rho}\left\{1-\frac{3}{4}\xi^2\log\frac{4}{\xi}+\frac{11}{8}\xi^2+\cdots\right\}. \tag{4.8}$$

By integrating (4.8), we obtain

$$\chi_\perp^{(1)}=\frac{16c\gamma_1(e/2h\bar{c})^2}{3\rho}\left\{J_1(\zeta)+\left(\frac{11}{8}-\frac{3}{2}\log 2\right)J_5(\zeta)+\frac{3}{4}J_6(\zeta)\right\}, \tag{4.9}$$

where $J_1(\zeta)$, $J_5(\zeta)$ and $J_6(\zeta)$ have already been defined. In the temperature range $T\ll\zeta/k$, (4.9) becomes

$$\chi_{\perp}^{(1)}=-\frac{16c\gamma_1(e/2h\bar{c})^2}{3\rho}\left\{1-\frac{3}{4}\left(\frac{\zeta_0}{\gamma_1}\right)^2\log\frac{4}{\zeta_0/\gamma_1}+\frac{11}{8}\left(\frac{\zeta_0}{\gamma_1}\right)^2+\cdots\right\}. \tag{4.10}$$

(3) Comparison with experiments

Adopting the values of parameters γ_0 and others as given in Table III, we get $\chi_{\parallel e}^{(1)}=-3.9\times10^{-6}$, $\chi_{\parallel h}^{(1)}=-4.6\times10^{-6}$ and then $\chi_{\parallel}^{(1)}=-8.5\times10^{-6}$. According to Krishnan and Ganguli's experiment,[15] $\chi_{\parallel}$ is -30×10^{-6}, independent of temperatures below about 90°K. The contribution from the corner electrons, as just calculated, at most is 30% of this experimental value. If we take the larger value for γ_0 and the smaller value for γ_1 so that the calculated value approaches the experimental, we get too small a value for n_0 and too large a value for the width of the π-band, values which contradict the experimental values. Thus this disagreement can not be removed by taking appropriate values for parameters. We then think that either the basic equation (4.2) is wrong or $\chi_{\parallel}^{(3)}$ can not be neglected. Within the limits of π-electron, (4.2) is an approximate but adequate formula. Jonston[11] calculated the effect of the mixing of σ- and π-orbitals on the Fermi surface and got new results on the overlapping of energy bands, results which differ from ours in the energy distribution of the upper band. Since, by estimating the effect of the mixing based on his evaluation, it seems that the new effect would not be so serious as to affect the qualitative aspect of our result, we must look for another cause of the discrepancy in $\chi_{\parallel}$, i.e. we must look in other terms which are not taken into account in usual Peierls' formula.

Now it is noteworthy that (4.5) and $\chi_{\parallel h}^{(1)}$ are in fair accord with the experimental fact that the diamagnetic susceptibility decreases with the adding of impurities;[16] but, first, the above statement is meaningless because $\chi_{\parallel}^{(1)}$ is too small, and, second, it is useless to study the temperature dependence[17] on the basis of (4.5) or on its approximate formula unless we calculate $\chi_{\parallel}^{(3)}$.

On the other hand, $\chi_{\perp}^{(1)}$ is $\sim-3.7\times10^{-8}$ for $T\ll\zeta/k$. Therefore $\chi_{\perp}^{(2)}$ and $\chi_{\perp}^{(3)}$ can not be neglected when calculating $\chi_{\perp}$. The susceptibility of carbon per gram is -0.5×10^{-6} and consequently it is expected that $\chi_{\perp}$ for graphite will be of the same order of magnitude, which actually agrees well with the experiment. Then it is expected that $\chi_{\perp}$ is almost constant in the whole temperature region.

§ 5. de Haas-van Alphen Effect and Summary

The calculation in the previous section, based upon Peierls' theory can not be used in the low temperature region. For the free electron model, exact expressions of susceptibility have been given by several authors. The periodic part of the susceptibility is

$$\chi\propto\sum_r\frac{(-1)^r\sin(\pi r\zeta/\beta^*H-\pi/4)}{r^{1/2}\sinh(\pi^2rkT/\beta^*H)}.$$

If we make use of the cylindrical energy surface which is a simple approximate form of (3.4), we get essentially the same period and temperature dependence of the amplitude as in the expression for the susceptibility obtained by using the ellipsoidal model, although it gives rise to a difference in the phase as well as in the field dependency of the amplitude. The shape of the energy sorface is known from the determination of the values of ζ and β. Onsager[18] gave a more general form for the period, which is given by a quantity instead of $2\beta/\zeta$, and which can be given by

$$\frac{2\beta}{\zeta}\rightarrow\frac{e}{hcA^{\max}}. \tag{5.1}$$

Then the ratio of the period of electrons and holes can be given by

$$\frac{2\beta_h/\zeta_h}{2\beta_e/\zeta_e}\rightarrow\frac{A_e^{\max}}{A_h^{\max}}=0.54. \tag{5.2}$$

Onsager's theory is essentially the one-band model.

According to Shoenberg,[1] two independent periods are observed in graphite. The result of his analysis based upon the assumption of ellipsoidal energy surfaces is given in Table IV. For comparison, the result of our calculation is listed in Table V. We must conclude that the first component $T_0=169$°K in Table IV comes from the electrons and that the second component $T_0'\sim116$°K comes from the holes. As we can see by comparing Tables IV and V, the theoretical and experimental

values of various parameters are in fair accord but not perfectly so. Particularly, there is a considerable difference between the values given in the second column of Table IV and of Table V. If we took the value of $A^{\max}$ 2~3 times that in Table V, we should be able to eliminate this difference. As is known from (3.6), (3.9), and (3.10), however, this would result in too large a value for n_0 which is approximately proportional to $A^{\max}$, and therefore in too small a value for $\chi_{\parallel}^{(1)}$. This discrepancy is significant because the calculation of $A^{\max}$ is based upon an adequate energy formula.

Table IV. Experimental values of parameters derived under the assumption of ellipsoidal energy surface (after Shoenberg).

$T_0=169°K$	$2\beta/\zeta=2.20\times10^{-5}$	$\frac{2\beta'/\zeta'}{2\beta/\zeta}=0.75$	$n=3.88\times10^{18}$/cc	$\chi_{\parallel}^{(1)}=-3.4\times10^{-6}$	$m_{\perp}/m=0.036$
$T_0'\sim116°K$	$2\beta'/\zeta'=1.65\times10^{-5}$		$n'=1.6\sim7.98\times10^{18}$/cc	$\chi_{\parallel}^{(1)}=-0.4\sim-2.6\times10^{-6}$	$m_{\perp}'/m\sim0.07$

Table V. Theoretical values of periods, etc.

Formula	(5.1)	(5.2)	(3.10)	(4.6)
T_{0e}	$2\beta_e/\zeta_e=6.7\times10^{-5}$	$\frac{2\beta_h/\zeta_h}{2\beta_e/\zeta_e}=0.54$	$n_e\sim4.4\times10^{18}$/cc	$\chi_{\parallel e}^{(1)}\sim-3.9\times10^{-6}$
T_{0h}	$2\beta_h/\zeta_h=3.6\times10^{-5}$		$n_h\sim2.5\times10^{18}$/cc	$\chi_{\parallel h}^{(1)}\sim-4.6\times10^{-6}$

From the above consideration, we confirmed that the agreement between theory and experiment can be obtained in neither non-periodic nor periodic parts of susceptibility without the inclusion of a non-diagonal term.

Adams[19] showed that in some cases the non-diagonal term is of comparable order of magnitude to the usual Peierls' term and that it becomes larger accordingly as the energy gap becomes smaller. As was seen in § 3, the energy gap between the lower and upper bands, which are nearly full and nearly empty respectively, is very small in the neighbourhood of Q at which these two bands are in contact. Since the non-diagonal term may be more sensitively dependent on the feature of the band structure, 2s and higher states having a slight effect on the energy band structure found here should be taken into account in the calculation of the non-diagonal term which is a very complicated problem.

The writer acknowledges his debt to Professor K. Ariyama for his valuable guidance and expresses his appreciation to Professor H. Nakano for his helpful discussions.

References

1) D. Shoenberg: Phil. Trans. **A 245** (1952) 1.
2) M. Blackman: Proc. Roy. Soc. **A 166** (1938) 1.
3) P. R. Wallace: Phys. Rev. **71** (1947) 622.
4) C. A. Coulson: Nature **159** (1947) 265, and also C. A. Coulson and R. Tayler: Proc. Phys. Soc. **A 65** (1952) 815.
5) P. O. Löwdin: J. Chem. Phys. **18** (1950) 365.
6) E. P. Wohlfarth: Proc. Phys. Soc. **A 66** (1953) 889.
7) R. O. Brennan: J. Chem. Phys. **20** (1952) 40.
8) G. E. Bacon: Acta. Cryst. **5** (1952) 392.
9) J. Hoerni: Nature **164** (1949) 1046.
10) J. L. Carter and J. A. Krumhansl: J. Chem. Phys. **21** (1953) 2238.
11) J. C. Slonzewski and P. R. Weiss (Phys. Rev. **99** (1955) 636), D. F. Jonston (Proc. Roy. Soc. **A 227** (1955) 349, **A 237** (1956) 48), and others obtain similar overlapping of energy bans.
12) J. E. Hove: Phys. Rev. **97** (1955) 1717.
13) G. H. Kinchin: Proc. Roy. Soc. **A 217** (1953) 9.
14) R. Peierls: Z. Phys. **80** (1933) 763.
15) W. Ganguli and K. S. Krishnan: Proc. Roy. Soc. **A 117** (1941) 168.
16) R. Smoluchowski: Rev. Mod. Phys. **25** (1953) 178.
17) K. Ariyama and S. Mase: Prog. Theor. Phys. **12** (1954) 246. J. E. Hove: Phys. Rev. **100** (1955) 645.
18) L. Onsager: Phil. Mag. **43** (1952) 1006.
19) E. N. Adams: Phys. Rev. **89** (1953) 633.

JOURNAL OF THE PHYSICAL SOCIETY OF JAPAN Vol. 13, No. 6, JUNE, 1958

Electron Spin Resonance of Z_1-centers in Potassium Chloride

By Hazimu KAWAMURA and Keiko ISHIWATARI

Department of Physics, Osaka City University, Osaka

(Received January 18, 1958)

The paramagnetic resonance due to a Z_1-center electrons in potassium chloride is investigated. Since Z_1-centers are always accompanied by F-centers, the contribution from F-centers ought to be substracted from the resultant curve in order to get the absorption curve due to Z_1-center alone, which is found to be Gaussian with the half width of 79 oersteds and g value of 1.999. The result is annalyzed according to the model that an electron is trapped by a divalent cation substituted for a cation of the bulk crystal.

§ 1. Introduction

Pick[1] has found a prominent absorption band which is called Z_1-band on the longer wave length side of the F-band in additively colored specimens of KCl and NaCl to which divalent ions have been introduced. His work has been followed by several authors[2)3)4)], and it is now accepted that the model for the Z_1-center is one electron trapped by a divalent cation substituted for a cation of the bulk crystal as shown in Fig. 1, which first proposed by Seitz[5].

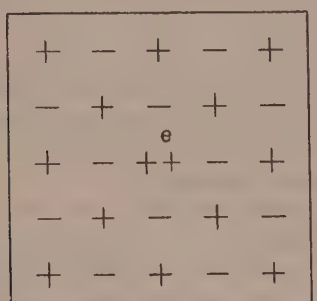

Fig. 1. The model for Z_1-center consisting of an electron bound to a divalent ion substituted for cation.

Since the divalent ion such as calcium, strontium or barium has no nuclear magnetic moment, only the spins of the neighboring nuclei have strong magnetic coupling with the trapped electron. Hence the situations are quite similar to those of the F-center, except that the nearest neighbors are anion nuclei instead of cation ones. The broadening of the electron spin resonance of Z_1-center will, therefore, be mainly due to hyperfine coupling with the nuclear moments of the nearest anions, and will give some information about the electronic structure of the center just as in the case of F-center.

§ 2. Experimental Procedure

Single crystals of potassium chloride were grown from the melt which contained about 10^{-3} mole fraction of calcium chloride or strontium chloride. Although we did not measure the actual concentration of the divalent ions in the crystal, it would at most be 1/10 of the initial concentration in the melt. The crystals were then additivly colored by heating them at 580°C for five hours in the sodium vapor. The specimens for spin resonance measurements with the dimension of $2\times6\times9\,\mathrm{mm}^3$ were cut from the colored crystals. In this stage the specimens contain many complex centers beside F- and Z_1-centers. So by heating them at 400°C for 20 seconds and quenching on a copper block kept at room temperature, we got crystals purely with F-centers. Finally, the F-centers were converted into Z_1-centers, by irradiating with a sodium lamp whose spectrum lies in the F-band.

The details of the equipment for electron spin resonance were described in the last paper[6]. The microwave of 9500 Mc/sec generated by 2K25 reflex klystron was fed to a rectangular cavity through a coaxial cable. The transmitted power was detected by 1N23 crystal. The magnetic field was modulated at 455 Kc/sec through a small coil wound directly around the specimen. The detected power was resonant amplified and lock-in detected. Although the spin density was as small as $5\times10^{16}\,\mathrm{cm}^{-3}$, the S/N ratio at the peak was larger than 10 as shown in Fig. 2 by virtue of the high frequency modulation,

and, therefore, we can speak of the curve shape in detail by repeating the run.

After the spin resonance experiment was over, the same specimen was further cleaved to the thickness of about 0.5 mm and the optical absorption was measured at −150°C.

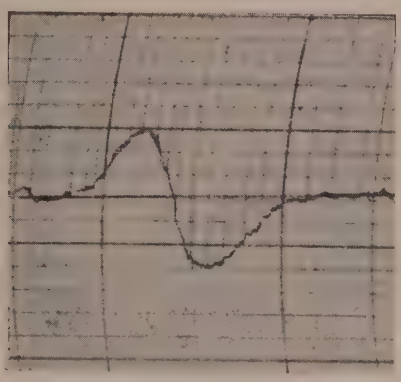

Fig. 2. An example of the record for spin resonance absorption curve of specimen No. 1 which contains both Z_1-centers and F-centers.

§ 3. Experimental Results

The measurments were done with two specimens; one was doped with calcium chloride and the other with strontium chloride. First we shall describe the optical measurements which reveal the characteristic features of the specimens. Fig. 3a shows the plots of the optical density of a quenched crystal as the function of wave numbers in ev measured at −150°C. It has a simple F-band at 2.30 ev with the half width of 0.25 ev followed by a trace of band on the shorter wave length

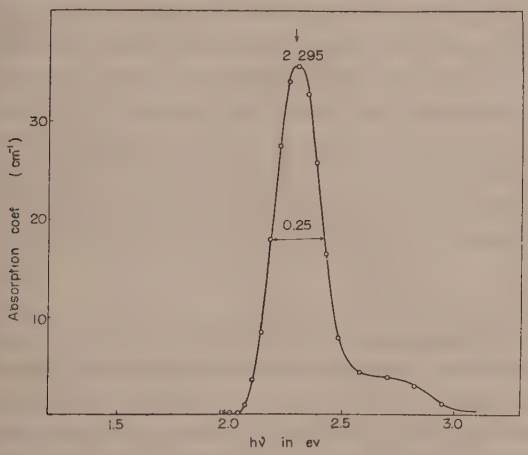

Fig. 3a. Optical absorption band of KCl doped with Sr, additively colored, and quenched. Only F-band appears.

side. When the specimens were irradiated with sodium lamp from the distance of 10 cm for 20 minutes, the Z_1-band grows up at the expense of the F-band as shown in Fig. 3b and Fig. 3c. The shape and position of the Z_1-band alone can be determined uniquely by subtracting the contribution from the F-band as shown in these figures. The peak position and the half width are almost equal for Ca

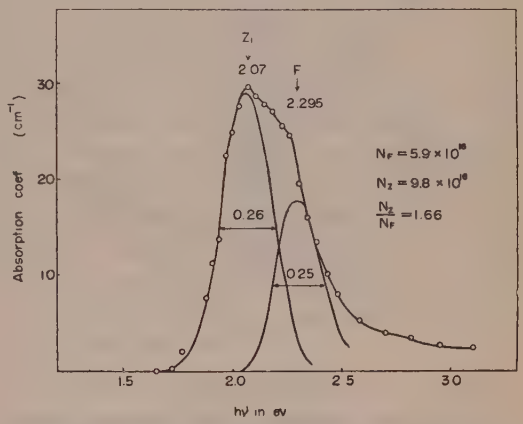

Fig. 3b. Optical absorption of KCl doped with Ca, additively colored, quenched and irradiated with F-light. The absorption curve is decomposed into F-band and Z_1-band.

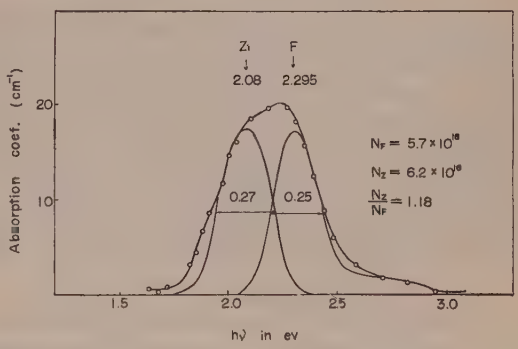

Fig. 3c. Optical absorption of KCl doped with Sr, additively colored, quenched and irradiated with F-light. The absorption curve is decomposed into F-band and Z_1-band.

Z_1-center and Sr Z_1-center within the experimental errors as shown in Table I. The densities N_{Z_1} of Z_1-centers in both cases were calculated employing the value 0.84 for the oscillator strength of Z_1-center, which was obtained by Camagni *et al.*[4]. These are also shown in the Table with the densities N_F of remaining F-centers in each specimen.

Fig. 4a and Fig. 4b are the plots of the

Table I.

No.	doped with	peak position of Z_1-band (ev)	half width of Z_1-band (ev)	N_{Z_1} density of Z_1-centers (cm^{-3})	N_F density of F-centers (cm^{-3})
1	Ca	2.07 ± 0.01	0.26 ± 0.01	9.8×10^{16}	5.9×10^{16}
2	Sr	2.08 ± 0.02	0.27 ± 0.02	6.2×10^{16}	5.7×10^{16}

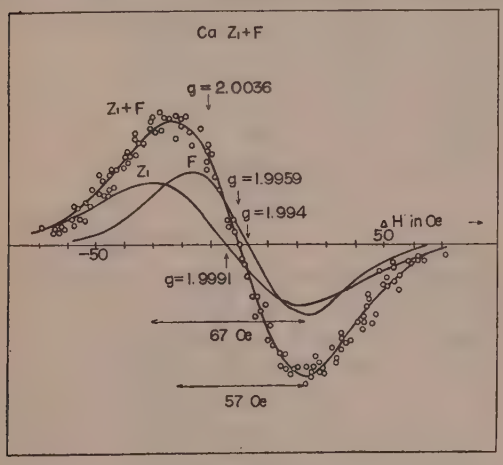

Fig. 4a. The derivative of spin resonance absorption for the specimen No. 1 which contains Ca Z_1-centers and F-centers with the ratio of 1.7. The contributions from Z_1-centers and F-centers are also shown.

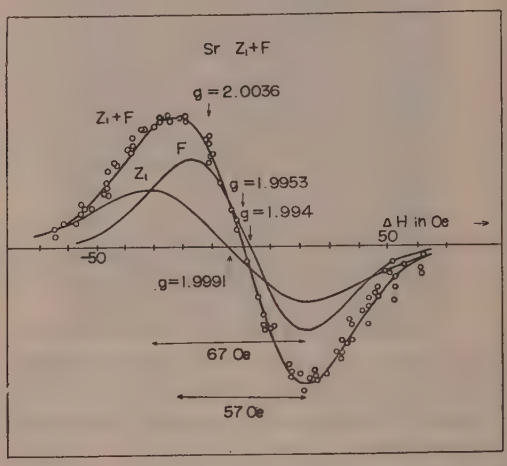

Fig. 4b. The derivative of spin resonance absorption for the specimen No. 2 which contains Sr Z_1-centers and F-centers with the ratio of 1.2. The contributions from Z_1-centers and F-centers are shown.

derivatives of the spin resonance absorption curves reproduced from the records, where in 4a the result for the specimen No. 1 with Ca Z_1-center and in 4b No. 2 with Sr Z_1-center are shown. The peak to peak separations and g values* at the absorption peak for these specimens are clearly different from those for F-center alone as indicated in Table II, the

Table II.

specimen	peak to peak (oersteds)	g	N_{Z_1}/N_F (optical)
No. 1 (Ca)	57 ± 3	1.9959 ± 0.0005	1.7
No. 2 (Sr)	57 ± 3	1.9953 ± 0.0005	1.2
F-center alone	49.5	1.994	

latter being reproduced from our last paper[6]. Since we know the ratio of the density of Z_1-centers to that of F-centers in addition to the shape and the position of the absorption curve of F-center, we can, as indicated in Fig. 4, obtain uniquely the absorption curve due to Z_1-center alone by subtracting the definite contribution due to F-center, so that the ratio of $(\Delta H)^2\times D$ for the component curves** is equal to the ratio N_{Z_1}/N_F which is determined optically, where D is the peak value of the each component curve and ΔH the peak to peak separation. The resulting curves for both cases are Gaussian with half width of 79 ± 8 oersteds and situated at $g=1.9991\pm0.005$. We could not recognize any difference beyond experimental error between Z_1-centers doped with calcium and strontium.

§ 4. Discussion

Now we shall discuss the electronic structure of the Z_1-center according to the model shown in Fig. 1. There is no paramagnetic electron except the Z_1-center electron, since all ions may have the closed shell configulations.

* g value was determined being refered to the sharp line of diphenyl trinitrophenyl hydrazyl, a small speck of which was attached on the modulaing coil.

** Of course, we assume the shape of both component curves is Gaussian.

Further, we can safely neglect the magnetic effect of the nuclei of the divalent ions at the centers, since Ca^{40} whose abundance is 96.92% has no nuclear magnetic moment and the isotope of strontium with nonzero moment is only Sr^{87} whose abundance is 6.96%. Hence we shall be able to assume that the broadening of the spin resonance absorption is mainly due to the hyperfine coupling between the Z_1-electron and the nuclear spins of the surrounding chlorine ions. The effect of the potassium ions at the position of the next nearest neighbors may be neglected as shown later.

The Hamiltonian for the hyperfine interaction between the nucleus with magnetic moment operator μ_n and the electron with spin magnetic moment μ_s and wave function $\psi(\boldsymbol{r})$ is given by

$$\mathscr{H}=(8\pi/3)|\psi(\boldsymbol{R})|^2\mu_n\mu_s\ , \qquad (1)$$

where $\boldsymbol{R}$ is the position of the nucleus, Thus the nucleus produces an additional magnetic field

$$\Delta H_m=-(8\pi/3)(\mu/I)m|\psi(\boldsymbol{R})|^2\ , \qquad (2)$$

where μ and I are the values of the magnetic moment and the spin of the nucleus and m is the eigenvalue of the z-component of the nuclear spin. Since each of the six nearest neighbors gives the contribution given by (2), the mean square deviation of the magnetic field is given by

$$\langle\Delta H^2\rangle=\langle\sum_i(8\pi/3)^2(\mu_i/I_i)^2|\psi(\boldsymbol{R}_i)|^4\langle m_i^2\rangle\rangle\ , \qquad (3)$$

where $\langle m_i^2\rangle=\langle I_{iz}^2\rangle=(1/3)I_i(I_i+1)$. Since all μ_i's and I_i's are equal and further $\psi(\boldsymbol{R}_i)$'s are equal to each other for a spherically or cubically symmetric wave function, we have

$$\langle\Delta H^2\rangle=(128/9)\pi^2[(I+1)/I][\mu|\psi(\boldsymbol{R})|^2]^2\ . \qquad (4)$$

As indicated by Kip *et al.*[7], the shape of the line resulting from the distribution of four possible values of m to the six nearest nuclei is nearly Gaussian. Hence, the half width of the resonance line is given by 2.35 times of $\langle\Delta H^2\rangle)^{1/2}$, which is to be compared with 79 oersteds obtained by the experiment. Taking I to be 3/2 and μ to be 0.790 in nuclear magnetons, which is the root of weighted mean square value for natural chlorines, we find

$$|\psi(\mathrm{Cl})|^2=0.55\times10^{24}\ \mathrm{cm}^{-3}\ . \qquad (5)$$

Now for the purpose of order estimation we shall take the effective mass approximation and assume that the wave function of the Z_1-center is given by

$$\psi(\boldsymbol{r})=F(\boldsymbol{r})\psi_0(\boldsymbol{r})\ , \qquad (6)$$

where $\psi_0(\boldsymbol{r})$ is the Bloch function for the conduction electron at the bottom of the band, and $F(\boldsymbol{r})$ is a solution of the effective mass equation for the periodic field perturbed by the substituted divalent ions. For $\psi_0(\boldsymbol{r})$ we shall employ the solution obtained by one of us making use of cellular method for KCl[8]. Unfortunately the solution is not orthogonal to the inner core s-state. However, a fairly good $\psi_0(r)$ may be obtained by orthogonalizing this solution to 1s, 2s and 3s electrons of a free chlorine ion by making use of the Schimdt method. Further, $\psi_0(r)$ employed in (6) must be normalized so that integration of $|\psi_0(r)|^2$ over unit cell is equal to the volume of unit cell. Thus we find;

$$|\psi_0(\mathrm{Cl})|^2=320\ . \qquad (7)$$

Just likewise the value of $|\psi_0(r)|^2$ at the position of potassium is found to be

$$|\psi_0(K)|^2=470\ . \qquad (8)$$

As for the effective mass equation we shall take electron mass as effective mass and $1/\kappa^*r$ as the perturbing potential, where κ^* is the effective dielectric constant. Even this crude assumption would indeed be rather sensible for the calcium Z_1-center, since calcium ion has the same configuration with potassium ion; but it may considerably distort the true aspect for the strontium Z_1-center. We shall, however, go ahead with this, being encouraged by the experimental fact the behaviors of optical absorptions and spin resonances are the same for the calcium and strontium Z_1-centers. The solution of this effective mass equation is given by

$$F(\boldsymbol{r})=(1/\pi\alpha^3)^{1/2}\exp(-r/\alpha) \qquad (9)$$
$$\alpha=\kappa^*a_0\ ,$$

where a_0 is the Bohr radius. Since Z_1-electron is fairly concentrated about the center and hence the displacement of ion may be very small, we may take the optical dielectric constant as κ^* for rough estimation. Inserting $\kappa^*=2.2$ and $r=3.14$Å, we get

$$|F(\mathrm{Cl})|^2=0.92\times10^{21}\ \mathrm{cm}^{-3}\ . \qquad (10)$$

Thus finally we obtain

$$|\psi(\mathrm{Cl})|^2=|F(\mathrm{Cl})|\cdot|\psi_0(\mathrm{Cl})|^2=0.30\times10^{24}\,\mathrm{cm}^{-3}\,, \tag{11}$$

which is to be compared with the experimental value of $0.55\times10^{24}\,\mathrm{cm}^{-3}$. The value of $|F(\boldsymbol{r})|^2$ at the next nearest neighbors becomes $9.3\times10^{19}\,\mathrm{cm}^{-3}$. Hence combining with (8) we get $|\psi(\mathrm{K})|^2=0.044\times10^{24}\,\mathrm{cm}^{-3}$. This contribute 0.71 (oersted)^2 to $\langle\Delta H^2\rangle$, which can be neglected compared with the contribution from the nearest chlorines, since the latter is found to be 340 (oersted)^2 from (4) and (11). Further the energy of the optical absorption due to the transition $1s$—$2p$ is given by $13.6\times(1/\kappa^*)^2[1-(1/2)^2]=2.1$ ev. However, it may not so reasonable to compare this value with the experimental value of the absorption peak position, since the validity of the effective mass approximation is quite suspicious because the electron density is distributed only over a small number of ions.

So far we have dealt with the Z_1-center upon the model due to Seitz as shown in Fig. 1. However, Pick[1] had proposed a different model. He considered that an electron is bound by a divalent ion accompanied by a psoitive ion vacancy. If this is the case, the bound electron may be found preferentially near the two chlorine ions which are at the opposite side of the positive ion vacancy. In this case the resonance line may be triangular in shape. Althrough this triangle may be rounded off due to the distribution of the electron cloud to the other ions, our result that the resonance line is Gaussian may favor the model due to Seitz.

While the donor level of silicon crystal varies from 0.049 ev to 0.039 ev as the doping element is changed from As to Sb, the choice of divalent ion, calcium or strontium, does make difference less than few percent in the position of Z_1-band. This is rather surprising, since the Z_1-electron is far more concentrated and hence its energy is expected to be much more affected by the core potential of central ion compared with the donor electron in Si.

This work was partly supported by the Grant for Scientific Research from the Ministry of Education.

References

1) H. Pick: Ann. Physik **35** (1939) 73.
Z. S. Physik **114** (1939) 127.
2) G. Heiland and H. Kelting: Z. S. Physik **126** (1949) 689.
3) H. Kelting and H. Witt: Z. S. Physik **126** (1949) 697.
4) P. Camagni G, Chiarotti, F. G. Fumi and L. Guilotto: Phil. Mag. **45** (1954) 225.
5) F. Seitz: Phys. Rev. **83** (1951) 134.
6) H. Kawamura and K. Ishiwatari: Jour. Phys. Soc. Japan. **13** (1958) 33.
7) A. F. Kip, C. Kittel, R. A. Levy and A. M. Portis: Phys. Rev. **91** (1953) 1066.
8) H. Kawamura: Physics and Chemistry of Solid, (to be published.)

JOURNAL OF THE PHYSICAL SOCIETY OF JAPAN Vol. 13, No. 6, JUNE, 1958

Magnetic Anisotropy Measurements of NiO Single Crystal*

By Hisamoto KONDOH, Enji UCHIDA,
Department of Physics, University of Osaka Prefecture
Yoshihide NAKAZUMI
Tochigi Chemical Industrial Co., Ltd., Osaka
and Takeo NAGAMIYA
Department of Physics, Osaka University

(Received February 5, 1958)

The magnetic anisotropy of NiO single crystal grown by the Verneuil method was measured using a torque balance. An X-ray study showed that the crystal, despite its outward appearance of a single crystal, is composed of small rhombohedral domains twinned through {100} planes. By applying a pressure along one of the [111] axes of the crystal during annealing from above the Néel temperature, the twin structure was partly removed. Torque measurements in a homogeneous magnetic field and their analysis showed that in pressure-annealed crystals domains with trigonal axis pointing along the direction of the pressure dominate but antiferromagnetic domains in each crystallite are distributed at random. The spin axis was found to be in the plane parpendicular to the trigonal axis within $\pm 16°$.

§ 1. Introduction

From powder measurements of the magnetic susceptibility by Trombe[1], Foëx and Blanchetais[2] and Bizette[3], the monoxide of nickel is known to be antiferromagnetic with a Néel point in the region of 523°K to 600°K. The neutron diffraction study of NiO first made by Shull et al[4] showed that it has a so-called Néel type magnetic superstructure, with alternating (111) sheets of plus spins and minus spins. The direction of the spins was found to be one of the cubic principal axis, but Kaplan[5] inferred, by calculating the dipolar interaction energy, that (111) would be the easy plane of magnetization. Keffer and O'Sullivan[6] showed that there are certain infinite number of orientational configurations of spins on the four sublattices with equal minimum dipolar energy, if the crystal were strictly cubic, but he suggested that the actually observed[7),8] small rhombohedral distortion would make (111) the easy plane of magnetization. Kanamori[9] considered the small rhombohedral contraction to be due to the balance between a decrease in exchange energy and an increase in elastic energy. Roth's new[10] measurements of the neutron diffraction line intensities appear to support that the (111) plane is the easy plane. Singer[11] measured the magnetic susceptibility of a single crystal grown by the Verneuil method and cooled through the Néel point applying a pressure along one of the [111] directions. He found that the spin direction can not be along one of the cubic principal axes and that it probably is in the (111) plane. The present writers independently carried out similar experiments measuring torque, instead of magnetic susceptibility, and have come to the same conclusion. Later the susceptibility measurements were also made, but since the results do not go beyond those of Singer, they will not be reported here.

Crystals grown by Verneuil method (flame fusion method) are apparently single crystals but they have twin structures consisting of small rhombohedral crystallographic domains, as the crystals become rhombohedral below the Néel point. More domains can be made aligned along a chosen [111] direction by growing the crystal from a seed which is suitably oriented, or by cooling the crystal with application of a pressure along a chosen [111] direction, or even by giving a mechanical shock or a supersonic to the crystal. After developing the technique of growing good crystals and applying these methods of aligning domains, we could get crystals with domains

* This paper has been read at the annual meeting of the Phys. Soc. of Japan, Nov. 24th 1956 at Osaka University.

aligned at maximum by 76 percent (assuming the sublattice magnetizations to lie in the (111) plane). In Singer's experiment, he could obtain an alignment of 50 percent. It can be shown that no accurate determination of the direction of the sublattice magnetizations can be made before a completely aligned crystal is obtained, but some interesting experimental results and their interpretation will be reported in the present paper.

§ 2. Experimental

Single crystals of NiO were grown[12] by the Verneuil (flame fusion) method. They have bullet-like shapes as shown in Fig. 1 and can be cleaved along {100} to rectangular parallelpipeds. The Laue back reflection X-ray patterns and the oscillation photograph of reflections from a (422) plane showed[13] that their structure is of NaCl type slightly deformed rhombohedrally and that, despite their outward appearance as single crystals, they are composed of fine crystallographic domains with a repeated twin structure, the twin planes being {100}. Crystals prepared in three different ways, which we shall designate as A, B and C, were used in the present measurements. Crystals of kind A were grown with no seeds, crystals of kind B with seeds which were so placed that their [001] axis points vertically, i.e. along the direction in which the specimens grew, and crystals of kind C with seeds whose [111] axis pointed vertically. In Fig. 1 their crystallographic orientations can be recognized by the shapes of their tops and by the inclinations of the cleavage planes at their bottoms. These different kinds of crystals show different anisotropic properties, as we shall see later.

From X-ray studies made by Rooksby[8] and Shimomura and Nishiyama[7] we know that NiO crystals have cubic symmetry above their Néel temperature but suffer a slight rhombohedral contraction below this temperature. This deformation should be responsible for the twinning observed at room temperature. By applying a pressure along one of the [111] directions while cooling slowly from above the Néel temperature, we may expect a partial removal of this twinning. We prepared samples of a shape shown in Fig. 2(b), a column of regular hexagon whose basal planes are (111) and lateral planes $\{11\bar{2}\}$. This shape is convenient for the purpose of giving a homogeneous stress and for the purpose of getting clear marks of crystal orientations. The misorientations of the surfaces were confirmed to be within 3° by observing X-ray pictures for perpendicular incidence. In the early stage of our experiment, only a set of parallel (111) planes were ground from a cleavage cube of

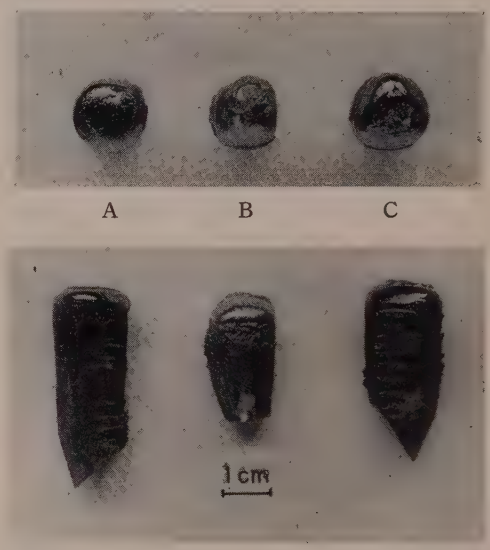

Fig. 1. The vertical and horizontal views of NiO crystals grown by the Verneuil method. Crystals of kind A have circular tops, those of kind B rectangular tops, and those of kind C triangular tops. Cleavage planes at the bottom are (100) planes.

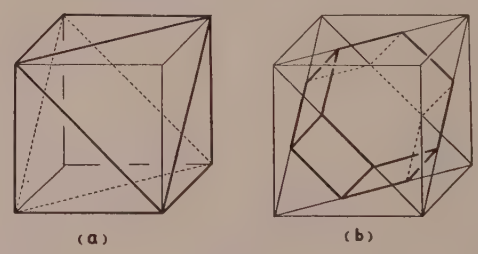

Fig. 2. Made out shapes of the samples. The cubes represent mother crystals.

edges of about 1 cm length, so that the samples had a shape shown in Fig. 2(a). This shape was less satisfactory in removing twin structures. Fig. 3 schematically represents our device of stress-annealing; weight up to 45 kg was applied on the crystal.

Magnetic torque measurements were made by using a torsion balance. The apparatus and the method are almost the same with those developed by Stout and Griffel[14] in their

magnetic anisotropy measurements of $NiSO_4$-$6H_2O$. The torsion fiber is a ribbon wire of phosphor bronze, 1 mm wide and 0.03 mm thick. For the suspension ribbon of a length of 15 cm, the torsion constant was 3.35 dyn cm radian^{-1}. No significant change of this value with temperature and time has been observed during the measurements. In order to mount the sample with a desired orientation, the leg

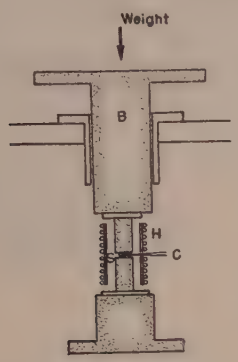

Fig. 3. The schematical representation of stress-annealing device. B: brass cylinder, S: sample, H: heating coil, C: thermocouple.

of the suspension was made of a silica rod of 7.1 mm in diameter whose bottom surface was ground flat with a suitable inclination to the axis of rotation, and the sample was glued to it with collodion cement. The angular position of the freely hung crystal, relative to the pole pieces of the magnet, was checked by observations with a telescope and read at the torsion head. The magnitude of the torque which the sample underwent in the homogeneous horizontal magnetic field was measured by reading the rotation of the torsion head which is necessary to bring the sample back to its normal position in zero field.

The results for this torque, T, could be summarized within experimental errors by a formula

$$T = C\cos 2(\theta + \varepsilon) \qquad (1)$$

where C is the amplitude, θ the angle between a fixed horizontal axis of the crystal and the field direction, and ε a phase constant. If the centering of the suspension and sample is not done correctly, the field exerts an additional torque on the suspension itself, which varies approximately as $\cos\theta$. Care was taken to eliminate this effect up to about 8000 oe, which was the usual field intensity in the present measurements.

§ 3. Results

Singer[11] reports that unstressed crystal shows an almost isotropic susceptibility. Our annealed but unstressed crystals of kind A

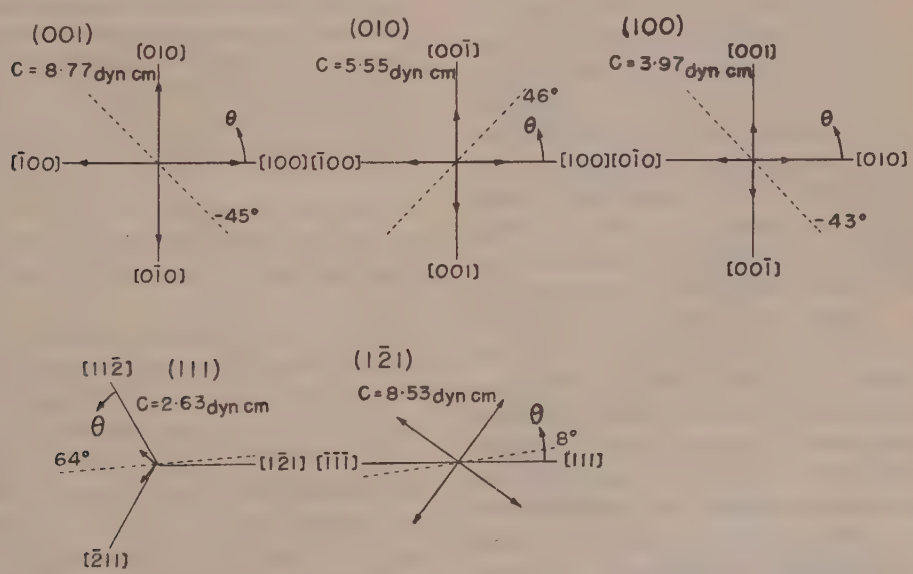

Fig. 4. Magnetic torque data obtained with an unstressed crystal of kind A. Arrows indicate crystallographic direction in which the torque attains its maximum and minimum values, the lengths of the arrows representing their relative values. Broken lines are positions of vanishing torque.

showed anisotropy without exception; an example of torque measurements for them is shown in Fig. 4, in which the attached indices of planes represent the planes of rotation in the respective series of experiments, θ measures the angle of the magnetic field relative to the crystal, arrows indicate the position of maximum (positive) and minimum (negative) torques, and a broken line the *stable* position of zero torque; there is another unstable position of zero torque which is prependicular to that indicated by this broken line. These positions and torque amplitude varied from sample to sample. Crystals of kind B showed even stronger anisotropy without stress-annealing and the results of their torque measurements when the samples were made into the shape shown by Fig. 2(b)* were similar to those represented by Fig. 6, which corresponds to a stress-annealed crystal of kind A (the same sample with that which gave Fig. 4 without stress). Crystals of kind C, if unstressed, showed no anisotropy.

Stress annealing from 800°K produces a unique anisotropic character of the crystal but a subsequent re-annealing at 1000°K without applying a force recovers the original anisotropy.

The amplitude of torque, C, for the sample corresponding to Fig. 4 and 6 is plotted in Fig. 5 as a function of the force applied during the process of annealing. The shape of the sample was somewhat like that shown in Fig. 2(a) but the [111] corners were not so much cut off as this; the edge length of the cube from which the sample was cut out was 0.74 cm, the triangular cut-out surfaces had edges of a length of 0.75 cm and the thickness was 0.44 cm. In obtaining these plots the crystal was restored to its original state each time before annealing under a stress. The amplitude clearly increases with increasing weight but shows a saturation beyond approximately 30 kg (120 kg/cm²), except for the amplitude of torque for the plane (111) which merely fluctuates. Excessive weight of >70 kg rather diminished the torque amplitude. The unique characteristic of the stress-annealed crystals of kind A and particularly of kind B can be summarized as follows:

1) The directions of maximum, minimum, and zero torques are definite crystallographic directions, as shown in Fig. 6.

2) The ratio of the amplitudes for different planes of rotation is constant, independent of the magnitude of the applied stress.

3) In the (111) plane, i.e. the plane perpendicular to the stress axis, the crystal is almost isotropic, yielding no torque.

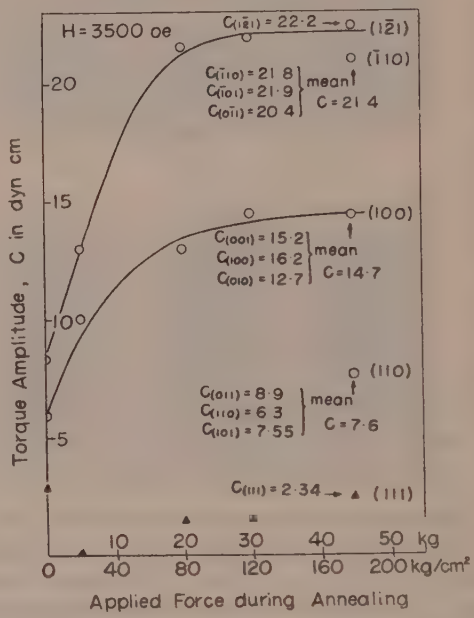

Fig. 5. Plots of the torque amplitude against the magnitude of the applied pressure during annealing. Each point at saturation for the rotation plane of (100) represents the mean of the three values obtained for (100), (010) and (001). These three values are equal to one another when there is no torque in the (111) plane.

4) If (1$\bar{2}$1) is the plane of rotation, the torque vanishes when the (111) surfaces of the sample become perpendicular to the magnetic field.

Crystals of kind B made into the shape of Fig. 2(b) posses these characteristics even before receiving stress annealing, possibly due to the effect of grinding out (see § 5).

The amplitudes corresponding to Fig. 6 and their ratio are listed in Table I, together with the phase angles, ε. We shall theoretically interpret these ratio and phase angles in the next paragraph, and the results obtained are also included in this Table.

Fig. 7 shows the temperature dependence of the torque amplitude for the plane (1$\bar{2}$1).

* The mechanical shocks in the process of working out seem to endow or enhance the anisotropy.

The Néel temperature estimated from this curve is 523°K.

§ 4. Interpretation of the Results

Our samples consist of twinned crystallographic domains of four kinds with rombohedral axis along four possible body diagonals. Furthermore, it is conceivable that each of these domains is subdivided into three kinds of antiferromagnetic domains with three different directions of sublattice magnetizations since each crystallographic domain has a trigonal

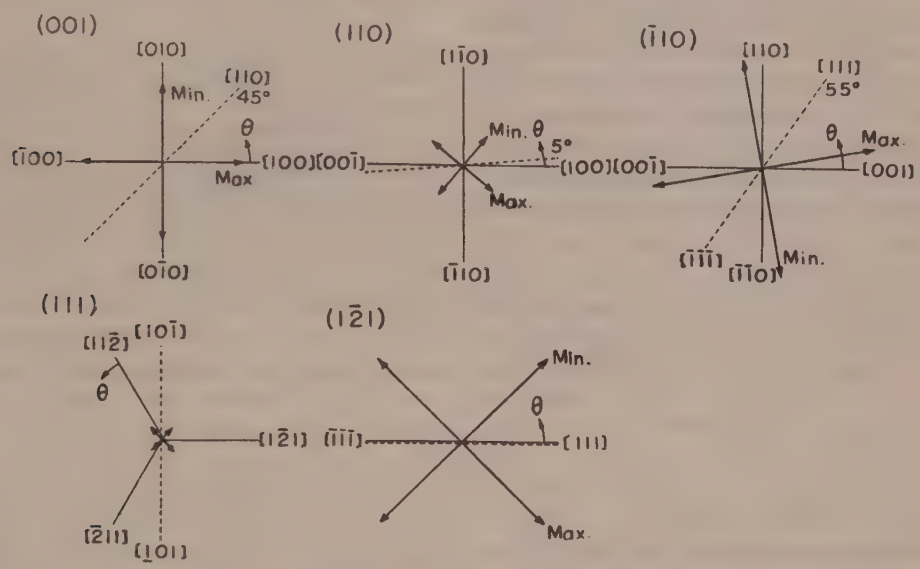

Fig. 6. Magnetic torque data obtained with a stress-annealed crystal of kind A.

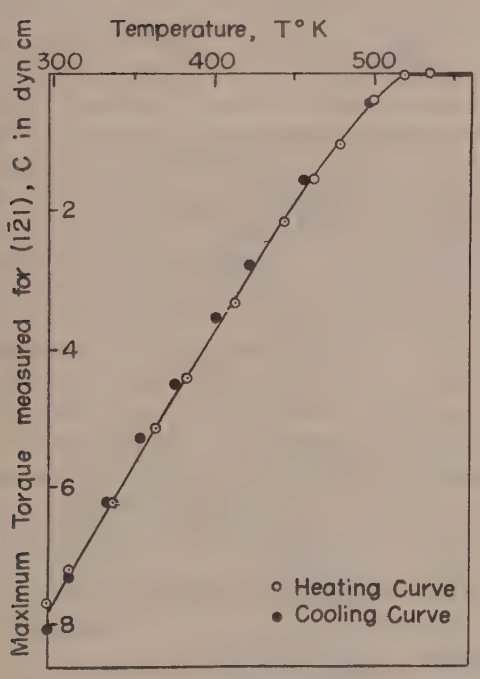

Fig. 7. The temperature dependence of the maximum torque measured for (1$\bar{2}$1) as the plane of rotation. The maximum occurs at an angle of −45° from [111].

axis. In all, there may exist domains of 12 kinds. In order to derive theoretical formula for the torque, we may first write out the formula of the (Gibbs) free energy per unit volume of each subdomains. Let the direction cosines of the spin axis be (α, β, γ) and the direction cosines of the applied magnetic field (a, b, c), both referring to the cubic principal axes. Then, for sufficiently weak field intensity, H (for which the torque is proportional to H^2 and the susceptibility independent of H) the free energy per unit volume can be written

$$F = -\tfrac{1}{2}\chi_{//}H_{//}^2 - \tfrac{1}{2}\chi_{\perp}H_{\perp}^2$$
$$= \tfrac{1}{2}(\chi_{\perp}-\chi_{//})(\alpha a+\beta b+\gamma c)^2H^2 - \tfrac{1}{2}\chi_{\perp}H^2 \,. \quad (2)$$

One may multiply this by the corresponding volume of the same kind of domains and sum over 12 kinds of domains to obtain the total free energy. The torque needed to bring the crystal back to its original position, i.e. the position in zero field, is calculated by

$$T = -\partial F_{total}/\partial\theta \,, \quad (3)$$

if the angle θ is measured from a fixed axis of the crystal to the direction of the magnetic

field. Equation (1) follows immediately from (2) and (3), since F_{total} is a quadratic function of a, b, c; C and ε depend on the abundance ratio of different kinds of domains.

We shall specialize our problem by confining ourselves to our stress-annealed crystals which show no anisotropy within the (111) plane. For these crystals it is plausible to assume that out of four kinds of crystallographic domains one with the trigonal axis along [111] is more abundant than the remaining three (with trigonal axes along $[1\bar{1}\bar{1}]$, $[\bar{1}1\bar{1}]$ and $[\bar{1}\bar{1}1]$, respectively) and that the three antiferromagnetic subdomains (with spin axes possibly along $[\bar{2}11]$, $[1\bar{2}1]$, $[11\bar{2}]$ or along $[1\bar{1}0]$, $[\bar{1}01]$, $[01\bar{1}]$ in the case of the dominant kind of crystallographic domains, for instance) are equally abundant in each kind of crystallographic domains. Then we can take out the excess volume occupied by the dominant kind over each of those occupied by the others and consider the rest of the volume of the sample to be magnetically isotropic. The total free energy effective for the torque in this case is given by

$$F_{total}=\tfrac{1}{3}\sum_{(\alpha\beta\gamma)}\tfrac{1}{2}(\chi_{\perp}-\chi_{//})(\alpha a+\beta b+\gamma c)^2H^2pV\,, \tag{4}$$

where the summation is taken over cyclic permutations of α, β, γ, p is the fraction of the excess volume, and V the total volume. (If the susceptibilities refer to a unit mass, the volume is replaced by the total mass.) The above formula can be put into another form:

$$F_{total}=\tfrac{1}{3}(\chi_{\perp}-\chi_{//})VH^2p(\beta\gamma+\gamma\alpha+\alpha\beta)\times(bc+ca+ab)\,, \tag{5}$$

leaving out the isotropic part. The torque

Table I.

Plane of rotation	{100}	{110}	$\{\bar{1}10\}$	(111)	$(1\bar{2}1)$
Average torque amplitude, C, in dyn cm	14.7	7.6	21.4	2.3	22.2
$C/C_{\{100\}}$ (exp.)	1	0.52	1.46	<0.15	1.51
Phase constant, ε, in degree (exp.)	0	40	−10		45
k (cal.)	−1/3	−1/6	−1/2	0	−1/2
$k/k_{\{100\}}=C/C_{\{100\}}$ (cal.)	1	0.5	1.5	0	1.5
ε (cal.)	0	45	−9.8		45

Table II. Data used for the evalution of pS.

Kind of the crystal	B
Ultrasonic oscillations applied normal to (111)	27 kc/sec, 30 min.
Static pressure applied simultaneously on (111)	35 kg/cm²
Plane on which H lies	$(1\bar{2}1)$
Constant, k, for $(1\bar{2}1)$	$k=-1/2$
Mass of the crystal, m	$m=0.368$ g
Magnetic field, H	$H^2=45.1\times10^6$ (oe)²
Néel point, T_c (Fig. 7)	$T_c=523$°K
Temp. of the measurement, T	$T=303$°K
$\chi_{//}/\chi_{\perp}$ at 303°K*	$\chi_{//}/\chi_{\perp}=0.50$
$\chi_{\perp}$**	$\chi_{\perp}=12.2\times10^{-6}$ emu
Difference susceptibility at 303°K	$\chi_{\perp}-\chi_{//}=6.1\times10^{-6}$ emu
Maximum deflection observed	327 deg.
Torsion constant of the suspension, b	$b=3.35$ dyn cm rad.$^{-1}$
Torque amplitude, C	$C=19.1$ dyn cm
Calculated value of pS	$pS=-0.377$

* The value of $\chi_{//}/\chi_{\perp}$ at 303°K was calculated from the formula derived by Van Vleck[16].

** After Foëx and Blanchetais or Singer.

can be calculated by differentiating the last factor, $bc+ca+ab$, with respect to the angle of rotation. It has a form

$$T=C\cos 2(\theta+\varepsilon)\ , \qquad (1)$$

where

$$C=kVH^2(\chi_\perp-\chi_{//})pS\ , \qquad (6)$$

$$S=\beta\gamma+\gamma\alpha+\alpha\beta\ ,$$

k and ε being certain constants which depend on the kind of the plane of rotation.

It is noted that the torque amplitude, C, is proportional to pS so that the value of S alone cannot be known from our experiment. However, that the spin axis is along [001] or its equivalents is excluded, since in this case S vanishes. The analysis of our experimental results with the use of the above formulas shows that S is negative and most probably $-1/2$ which corresponds to spin axis being in the (111) plane· Measurement of the anisotropy of the susceptibility should in principle also be unable to yield the values of p and S separately, since the formula of it can be derived from the same free energy (5).

Comparison of our formulas (1) and (6) with the results described in the preceding paragraph is very satisfactory, as one sees in Table I. The relative magnitudes of the torque amplitudes and the values of the phase constant, ε, measured for different planes of rotation agree within experimental errors with those calculated theoretically. For these values of ε the theoretical k values are negative (see Table 1), which implies that S is negative, since C is positive. The absolute measurements of the torque yield a value of pS for each sample, and the highest value of $p|S|$ obtained was 0.38, which corresponds to $p=76\%$ if S is assumed to be $-1/2$. We can conclude at least that the spin axis lies within $\pm 16°$ from the (111) plane, since $p<1$ and so $|S|>0.38$ ($[(1+2S)/3]^{1/2}$ is the sine of the angle between the spin axis and the (111) plane). An example of evaluating pS is shown in Table II.

§ 5. Further Experimental Facts and Discussion

We have seen at the end of the preceding paragraph that the torque measurements yield the product pS. The maximum attainable absolute value of this quantity should be 1/2, whereas the highest value actually attained was 0.38. Attempts were made to elevate the absolute value of pS, by varing the condition of stress-annealing and growing the crystals from seeds. Crystals of kind B were most suitable for this purpose. In the meanwhile, it happened when a crystal was dropped carelessly on the floor that a considerable reduction in torque amplitude took place. Also, when the (111) surfaces of a crystal were polished by sand paper, a marked increase in torque amplitude was observed. These indicate that mechanical shocks at room temperature alter the twin structure of the crystal. Therefore we applied ultrasonic oscillations of 27 kc/sec in the direction normal to the (111) surfaces applying simultaneously a pressure on these surfaces and could even more efficiently increase the torque amplitude for samples annealed without stress. With stress-annealing only the value of $p|S|$ could not exceed approximately 0.25 in most cases but with supersonic it could be elevated to 0.38 in the best case.

Effect of a magnetic field on the alignment of domains was not much studied. Application of a high magnetic field should turn the magnetizations in the easy plane so as to bring them perpendicular to the field, overcoming a small anisotropy energy (of sixfold symmetry) in that plane and the resistaces of magnetic domain boundaries. One may except a departure from the proportionality between the torque and H^2 and a hysteresis effect, i.e. a change in the magnetic anisotropy of the sample after the application of the field. There were a few examples in which a sort of these effects was observed above 10000 oe but they were not fully investigated. We hope to study them further. Antiferromagnetic resonance experiments in the region of far infra-red will give informations of the magnetic anisotropy in NiO, and this will be our next program.

It is the authors' pleasure to acknowledge the warm encouragement given by Professor Y. Mashiyama of the University of Osaka Prefecture. They also appreciate the assistance of Messrs. M. Kojima and S. Saito in the X-ray study and N. Fukuoka in the magnetic measurements. Thanks are due to the member of Azuma Precision Metal Pattern Works in Osaka for their kind help in preparing a precision pressing apparatus. A part of the present investigation was supported by the

Scientific Research Expenditure of the Education Ministry.

References

1) F. Trombe: J. Phys. Radium **12** (1951) 170.
2) M. Foëx and C. H. Blanchetais: Compt. Rend. **222** (1949) 1579.
3) H. Bizette: J. Phys. Radium **12** (1951) 161.
4) Shull, Strauser and Wollen: Phys. Rev. **83** (1951) 331.
5) J. I. Kaplan: J. Chem. Phys. **22** (1954) 1709.
6) F. Keffer and W. O'sullivan: Phys. Rev. **108** (1957) 637.
7) Y. Shimomura and Z. Nishiyama: Mem. Inst. Sci. and Indust. Resea. Osaka Univ. **6** (1948) 30.
8) H. P. Rooksby: Acta Cryst. **1** (1948) 226; Nature **152** (1943) 304.
9) J. Kanamori: Progr. Theor. Phys. **17** (1957) 177.
10) W. L. Roth: Annual Meeting American Crystallographic Association, June, 1956.
11) J. R. Singer: Phys. Rev. **104** (1956) 929.
12) Y. Nakazumi: J. Chem. Soc. Japan, Ind. Chem. Sec. **59** (1956) 1304.
13) X-ray study on the present crystal by Y. Shimomura, M. Kojima and S. Saito (University of Osaka Prefecture).
14) J. W. Stout and M. Griffel: J. Chem. Phys. **18** (1950) 1449.
15) J. H. Van Vleck: J. Chem. Phys. **9** (1941) 85.

JOURNAL OF THE PHYSICAL SOCIETY OF JAPAN Vol. 13, No. 6, JUNE, 1958

Fine Structures of X-ray K Absorption Spectra of Nickel in Oxides of Nickel

Kenjirō TSUTSUMI

Department of Physics, Faculty of Science, Osaka University

(Received December 5, 1957)

The fine structures of X-ray K absorption spectra of nickel in metallic nickel, NiO, Ni_2O_3 and $NiO_2 \cdot nH_2O$ were photographed by a bent crystal spectrograph. The fine structures of absorption spectra of metallic nickel and NiO agree well with those published by previous authors, but those of Ni_2O_3 do not coincide with those reported by Hayasi and Cauchois. Also Cauchois' data of Ni_2O_3 do not coincide with Hayasi's data. This seems to be due to doubtful chemical structures of Ni_2O_3 and it is supposed that the three specimens used by the three authors might have different chemical structures. The first absorption maxima A are much more pronounced with increasing oxygen proportion and the general features of α, β, C and γ of the absorption spectra of oxides are similar respectively. However, the second small absorption maxima B are less pronounced with increasing oxygen proportion. These facts are expected from Coster and Kiestra's and Cauchois' considerations. It may be considered from the comparison of the present curves of absorption spectra only that nickel sesquioxide is a mixture of NiO and $NiO_2 \cdot nH_2O$.

§ 1. Introduction

An investigation into the fine structures of the X-ray absorption spectra of metallic oxides may be interest to obtain some information about solid state problems. Coster and Kiestra[1] investigated the various oxides of Mn, Fe and Zn and concluded that the fine structure at a shorter distance from the main edge depended not so much on the crystal structure but it seemed to be chiefly determined by the field in a closer neighborhood of the atom in question. Cauchois,[2,3,4] in her experiments on the fine structures of the absorption spectra of some oxide of copper and nickel, investigated the white line (R.B.) which occurred immediately on the high frequency side of K absorption edge. As it has been reported that there exists a series of

nickel oxides with various proportions of oxygen, the author investigated the fine structures of X-ray absorption spectra of nickel in metallic nickel (Ni), nickel monoxide (NiO), nickel sesquioxide (Ni_2O_3) and nickel dioxide hydrate ($NiO_2 \cdot nH_2O$).

§ 2. Experiments

The nickel foil was prepared by electrolysis. Its thickness was about 8μ. The oxides were supplied by Hutaba Chemical Industry. NiO, Ni_2O_3 and $NiO_2 \cdot nH_2O$ respectively were 96.21, 99.58 and 97.57% in purity, and were grey green, grey black and green.

The X-ray diffraction patterns of all the samples were photographed. They are reproduced in Photo. 1. The diffraction pattern of $NiO_2 \cdot nH_2O$ shows only amorphous halos, and that of Ni_2O_3 is not a superposition of those of NiO and $NiO_2 \cdot nH_2O$. The diameter

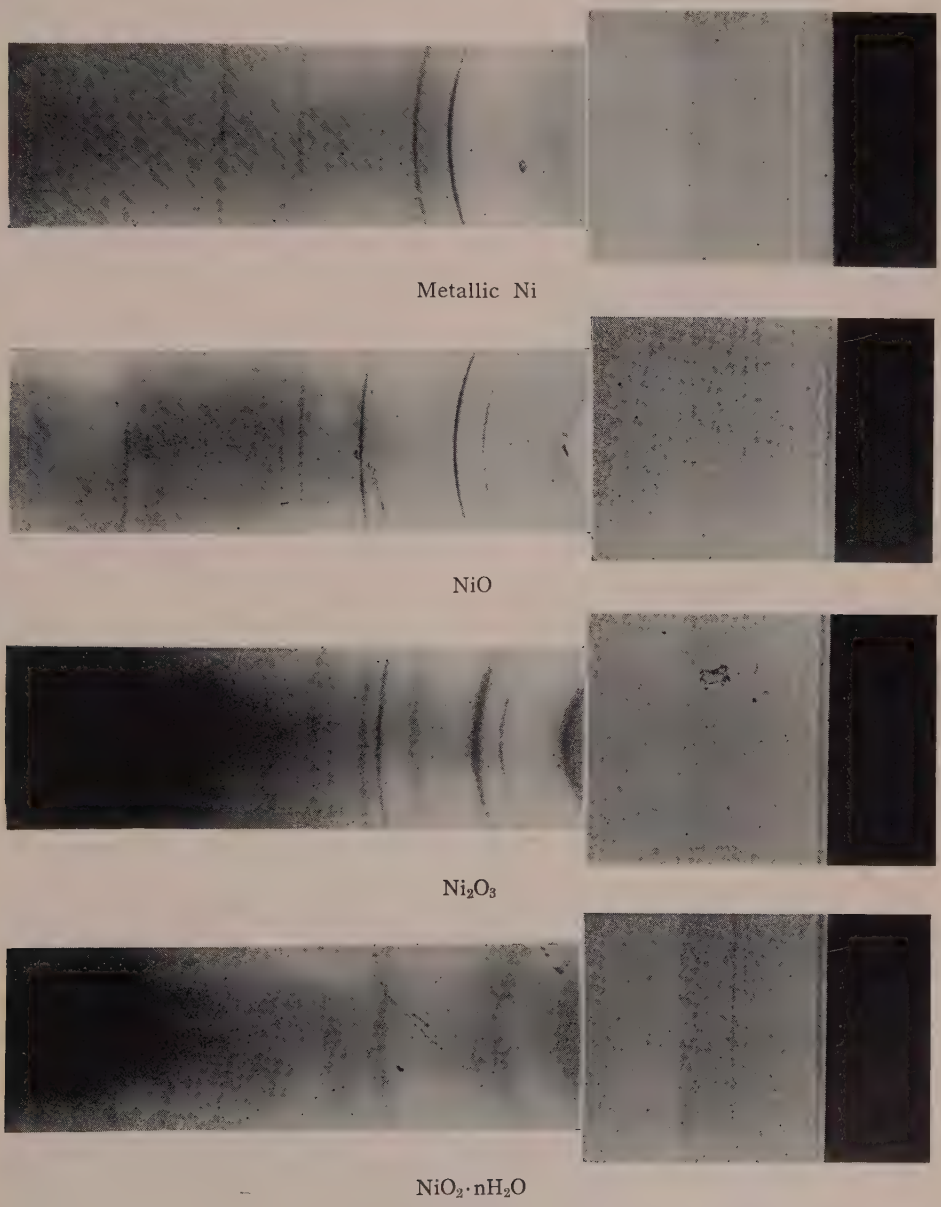

Photo. 1. X-ray diffraction patterns of metallic nickel and its oxides on about 1/1 of original size.

Photo. 2. Ni *K* absorption spectra of metallic nickel and its oxides on about 3.7/1 of original size.

of the powder camera was 7.03 cm. The X-ray tube with a copper target was loaded with 20 kV and 20 mA. The time of exposure was about 1.5 hours.

The fine structures of X-ray K absorption spectra of nickel in Ni, NiO, Ni_2O_3 and $NiO_2 \cdot nH_2O$ were taken with a bent crystal spectrograph of transmission type having a focusing circle of diameter of 20 cm. The second order reflection from (1 0 0) plane of a quartz crystal was used, and the dispersion in the region of Ni K absorption edge was about 18.9 *x.u.* per mm on the photographic plate. The gas ion X-ray tube with a molybdenum target was used to avoid W $L\alpha$ emission lines and was loaded with 14 kV (peak) and 8 mA. The time of exposure was varied 15 to 20 hours. In the case of oxides the ab-

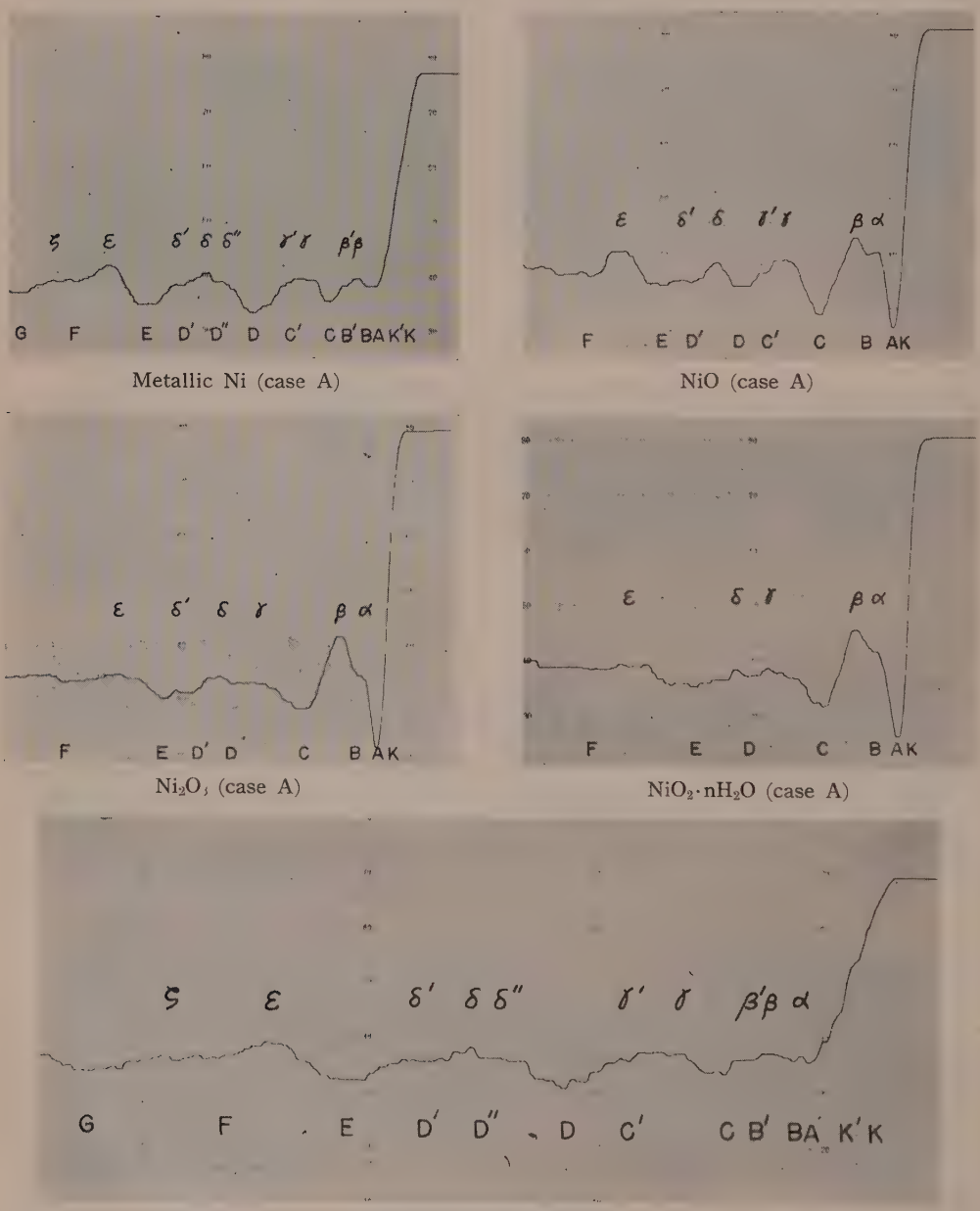

Photo. 3. The microphotometric trace of Ni K absorption spectra of metallic Nickel and its oxides on about 1/3.25 of original size.

sorbers were made by mixing a small amount of grease with the finely pulverized specimen and spreading the mixture on a thin paper up to the required amount 7 mg/cm² to 20 mg/cm². The microphotometric traces with the dispersion of about 2.5 *x.u.* per cm were taken (case A), and in the case of nickel another trace with the dispersion of about 1.25 *x.u.* per cm was taken to see the ditails of the fine structures near the absorption edge (case B). The spectrograms and corresponding microphotometer traces are reproduced in Photo. 2 and Photo. 3. The measurements of wavelengths were carried out referring to the Ni $K\alpha_1$, Cu $K\alpha_1$, Mo $K\alpha_1$ and Cu $K\beta_1$ photographed on the same plate. Table I shows the wavelength values of the fine structures of K absorption spectra of nickel in Ni, NiO, Ni_2O_3 and $NiO_2 \cdot nH_2O$ respectively, and Table II shows their energy separations from the Ni K absorption edges of these substances.

Table I. Wavelength values of fine structures of Ni K absorption spectra of metallic nickel and its oxides. (in *x.u.*)

	Ni	NiO	Ni_2O_3	$NiO_2 \cdot nH_2O$
K	1484.9_9	1483.2_2	1483.0_9	1483.1_0
K'	1483.3_8			
A	1481.3_8	1481.6_8	1481.6_0	1481.7_8
α	$1480._8$	$1479._9$	$1479._7$	$1479._6$
B	$1480._4$	$1478._6$	$1479._3$	$1478._7$
β	$1479._1$	$1477._5$	$1477._5$	$1477._3$
B'	$1478._4$			
β'	$1477._8$			
C	$1476._6$	$1473._4$	$1473._0$	$1473._2$
γ	$1474._5$	$1469._5$	$1468._5$	$1467._6$
C'	$1472._0$	$1467._6$		
γ'	$1471._1$	$1466._7$		
D	$1468._1$	$1464._8$	$1466._1$	$1465._3$
δ''	$1464._8$			
D''	$1463._5$			
δ	$1462._7$	$1461._6$	$1464._7$	$1463._9$
D'	$1461._3$	$1459._3$	$1461._8$	
δ'	$1460._0$	$1456._8$	$1459._9$	
E	$1456._5$	$1454._8$	$1458._4$	$1459._0$
ε	$1452._3$	$1451._0$	$1453._7$	$1452._0$
F	$1448._3$	$1446._4$	$1447._9$	$1447._7$
ζ	$1445._9$			
G	$1441._9$			
η	$1436._6$			

Table II. Energy separations of fine structures from Ni K main edges of metallic nickel and its oxides. (in eV.)

	Ni	NiO	Ni_2O_3	$NiO_2 \cdot nH_2O$
K	0	0	0	0
K'	8.9_1			
A	20.1_4	8.6_4	8.3_6	7.4_1
α	$23._5$	$18._7$	$19._0$	$19._7$
B	$25._8$	$26._0$	$21._3$	$24._8$
β	$33._1$	$32._2$	$31._4$	$32._7$
B'	$37._1$			
β'	$40._5$			
C	$47._2$	$55._5$	$57._0$	$55._9$
γ	$59._1$	$77._7$	$82._6$	$87._9$
C'	$73._4$	$88._6$		
γ'	$78._5$	$93._7$		
D	$95._6$	104	$96._4$	101
δ''	114			
D''	122			
δ	126	123	105	109
D'	135	136	122	
δ'	142	151	133	
E	162	162	141	137
ε	187	184	169	179
F	210	212	203	204
ξ	224			
G	248			
η	280			

§ 3. Discussions

The wavelength values of the fine structures of Ni K absorption spectra of metallic nickel and NiO agree well with those already published by Cauchois[2] (Ni and NiO) and Hayasi[5,6] (Ni) within the limit of experimental errors, but those of Ni_2O_3 do not coincide with those obtained by Hayasi[6] and Cauchois[2]. Also the values of Ni_2O_3 given by Cauchois do not agree with those obtained by Hayasi. This seems to be due to some doubtful chemical structures of Ni_2O_3. Several reports[7] hitherto made on the chemical structures of nickel sesquioxide indicate that Ni_2O_3 may be a mixture of NiO and amorphous NiO_2, that even the ordinary anhydrous substance may contain some water molecules, and that anhydrous Ni_2O_3 may not

exist. It is considered that the specimens used for the above three experiments might have different chemical structures owing to the different procedure of their preparation.

The first absorption maxima A are more pronounced with increasing oxygen proportion. Absorption maximum A corresponds to the transition of the K electron to the $4p$-level. According to Coster and Kiestra[1] the atomic wave-functions are much more maintained as more oxygen is added and the metal ions are located apart from each other. This implies that the width of the p-band becomes smaller and then the fine structure is more pronounced.

The general features of the small absorption minima α, large minima β, maxima C and minima γ of absorption spectra of these oxides are similar respectively. Coster and Kiestra[1,8] considered that in these regions the fine structures were determined by immediate surroundings of the atom in question. This consideration is well supported by the present experimental results. However, the second small absorption maxima B are less pronounced with increasing oxygen proportion. This seems to be due to the coordinations of oxygen atoms which become more complex with increasing oxygen proportion.

It is believed that the fine structure, in the high energy region from the main edge, is determined by the type of the crystal lattice. Nickel crystallises in the face centered cubic lattice and NiO also crystallises in nearly the face centered cubic lattice. However, recently it is reported that the NiO crystallises in the rhombohedral lattice[9] at the room temperature. Moreover, because of the large difference of structure factors of nickel and NiO, the comparison of the fine structures of these two substances was not made.

Finally it may be considered only from the comparison of the present curves of absorption spectra of NiO, Ni_2O_3 and $NiO_2 \cdot nH_2O$ that nickel sesquioxide is a mixture of NiO and $NiO_2 \cdot nH_2O$. In conclusion the author well supports Coster and Kiestra's[1,8] and Cauchois'[4] considerations.

The author express my sincere thank to Professor M. Sawada for his encouragement to this work.

References

1) D. Coster and S. Kiestra: Physica **14** (1948) 175.
2) Y. Cauchois and I. Manesco: J. de Chimie Physique **47** (1950) 892.
3) Y. Cauchois: J. de Chimie Physique **46** (1949) 307.
4) Y. Cauchois and N. F. Mott: Phil. Mag. **40** (1949) 1260.
5) T. Hayasi: Sci. Report Tohoku Imp. Univ. **25** (1937) 1.
6) T. Hayasi: Sci. Report Tohoku Imp. Univ. **25** (1937) 606.
7) J. W. Mellor: A Comprehensive Treatiese on Inorganic and Theoritical Chemistry, XV. Longmans Green and Co. 1936, London.
8) S. Kiestra: Conference on the Application on X-ray Spectroscopy to Solid State Problems, Oct., 1950, Madison.
9) H. P. Rooksby: Acta. Cryst. **1** (1948) 226.

JOURNAL OF THE PHYSICAL SOCIETY OF JAPAN Vol. 13, No. 6, JUNE, 1958

Fine Structures of the X-ray Absorption by the Single Crystal of Germanium

Kenjiro TSUTSUMI* and Masayoshi OBASHI**

*Department of Physics, Faculty of Science, Osaka University
**North College, Osaka University

(Received February 23, 1958)

The fine structures of X-ray absorption by single crystals of germanium were investigated. These crystals were used as an analysing crystal of a spectrometer and at the same time as an absorber. The intensities of general radiation reflected from (1 0 0), (1 1 0) and (1 1 1) planes were investigated. The fine structures of intensities reflected from these planes were in agreement with those of absorption spectrum reported by Doran and Stephenson obtained by the transmission method using a single crystal as an absorber. However, they reported that they observed a weak fine structure near the absorption edge which was not observed by us. The observed fine structure of the absorption can be interpreted in terms of Kronig's theory, while the absence of the fine structure near the absorption edge is due to the anomalous scattering of germaninum on the one hand and to the thickness effect reported by Parratt, Hempstead and Jossem on the other.

§ 1. Introduction

A convenient technique to measure the fine structure of the absorption spectrum using a single crystal has been proposed by Stephenson[1] and Krogstad, Nelson and Stephenson[2] who used a single crystal as an analysing crystal and at the same time as an absorber. They claimed that the results obtained by this technique were in agreement with those obtained by the transmission method in the cases of KBr[1], KCl and NaCl[2]. However, Nelson[3] could not obtain by this technique any fine structure of absorption with germanium which was reported by Hulbei and Cauchois[4].

As good single crystals of germanium were available, we investigated the fine structures of the absorption of germanium by this technique and compared these with those given in the literature[3].

§ 2. Experiments

By using the North American Philips Diffraction Unit and Wide Range Spectrometer, modified to a tube spectrometer described by Coster and De Lang[5], we recorded automatically the fine structures of absorption by single crystals of germanium. The details of our modified method have been published in our previous papers[6]. The maximum divergency of the slit system is about 0.0004 radians. As the analysing crystals we used germanium single crystals of N type which contained arsenic as impurity and the faces parallel to (1 0 0), (1 1 0) and (1 1 1) were used. The number of etch pits by CP-4 was about $10^4/cm^2$.

The reflections of the fourth order from (1 0 0) plane, the second order from (1 1 0) plane and the first order from (1 1 1) plane were used. The perfectness of the crystals was examined by recording Mo $K\alpha_{1,2}$ emission lines reflected from these planes. They are reproduced in Photo. 1. The same emission lines reflected from a good calcite crystal were also recorded for comparison. They are reproduced in Photo. 2. The widths of the half maxima of the lines by germanium are slightly wider than those given by calcite, but the crystals of germanium can safely be used as analysing crystals.

The general radiation was analysed by these crystals of germanium in the region of Ge K absorption edge. They are reproduced in Photo. 3. The X-ray tube with a molybdenum target was loaded with 15–20 mA at 20 kV. The scanning speed of the Geiger-Müller tube was 1/8° per minute and the time constant of the rate-meter was 8 seconds. The intensities on the long and the short wavelength sides of Ge K absorption edge were not recorded on one and the same chart, be-

cause the number of counts was too few to detect the fine structure of the reflected intensity on the short wavelength side when the intensities of both sides were so recorded as to avoid the dead time correction of the counter.

Table I shows the wavelength values (in A) of the fine structures of reflected intensities and Table II shows their energy separations (in eV) from the Ge K absorption edge. The last columns of the both tables show the wavelength values and the energy separations measured by Doran and Stephenson[3], who investigated the fine structure of the absorption spectrum using a single crystal absorber of germanium by the transmission method.

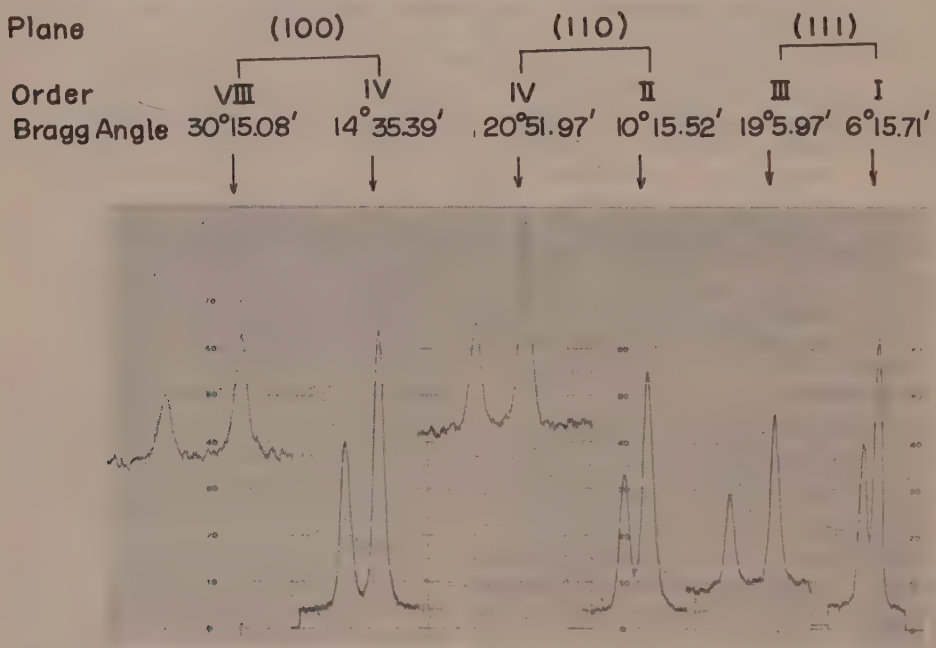

Photo. 1. Mo K_{α_1,α_2} emission lines reflected from various planes of germanium crystals.

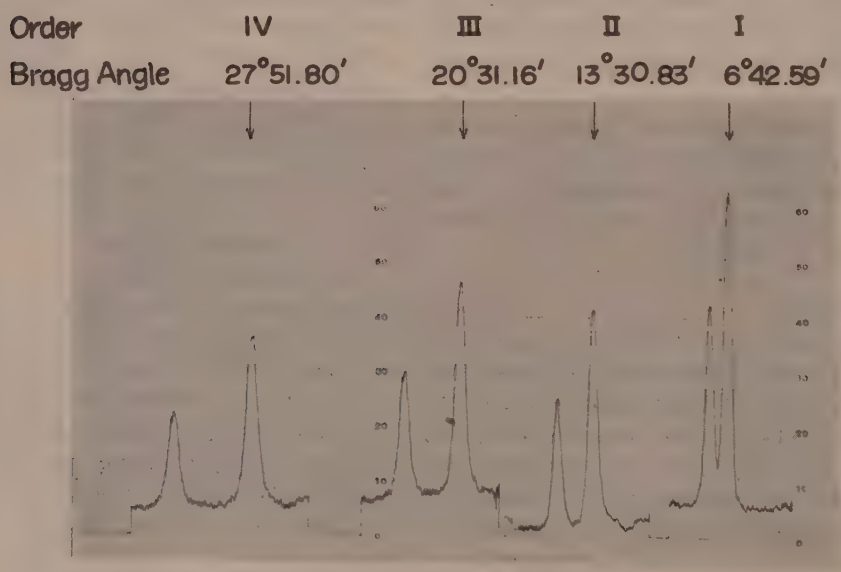

Photo. 2. Mo K_{α_1,α_2} emission lines reflected from a good calcite.

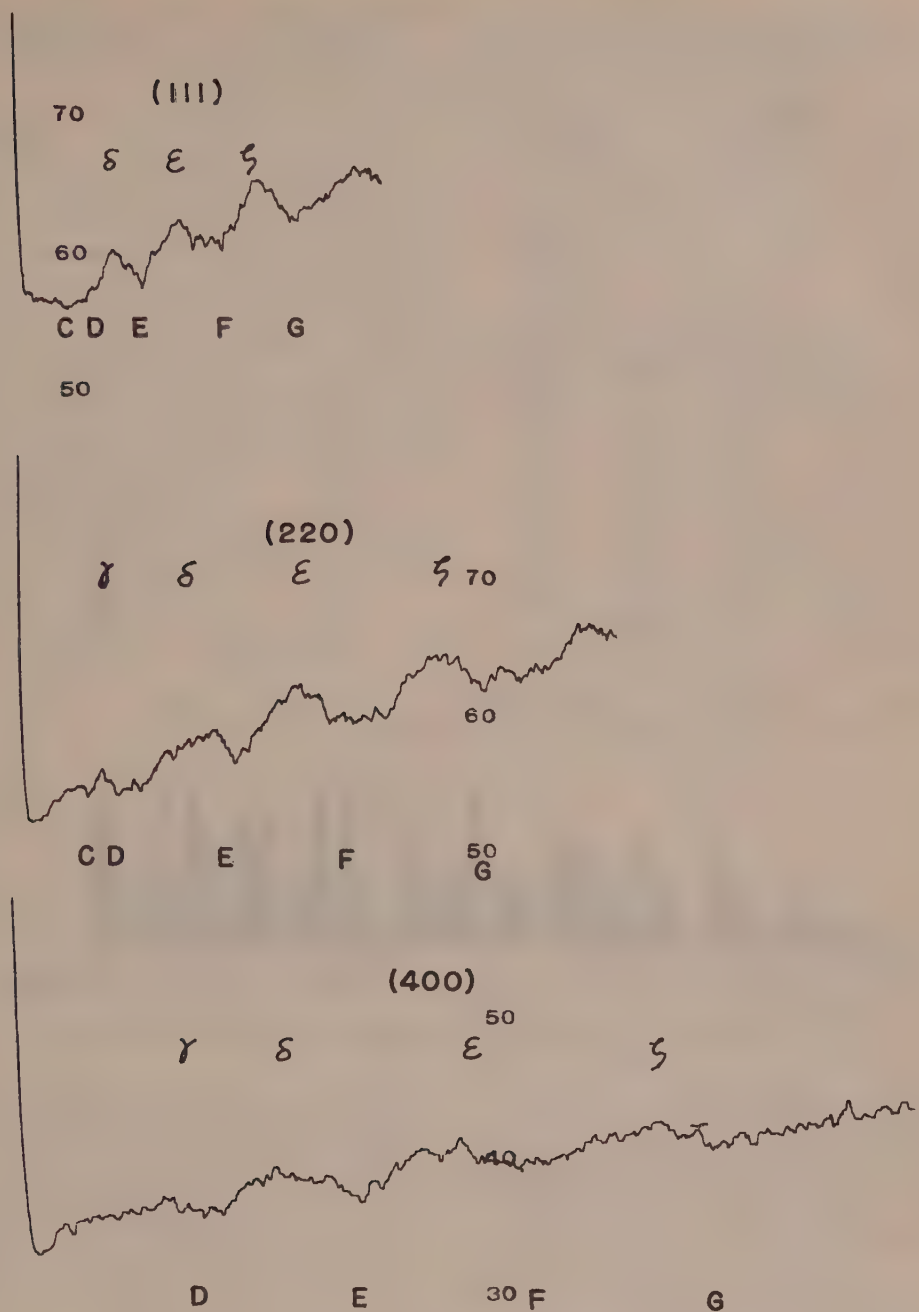

Photo. 3. Fine structures of reflected intensities from various planes of germanium single crystals.

§ 3. Discussions

By comparing Table I and II it will be seen that the fine structures of intensities reflected from the various planes of germanium single crystals and those given by Doran and Stephenson agree well with each other, except near the absorption edge. The weak fine structure within 50 eV from the absorption edge which was observed by Doran and Stephenson is not observed in our reflected intensity curves. In this region our results coincide with those of Nelson.

These facts are considered to be due to the following:

Table I. Wavelength values of fine structures of absorption of germanium single crystals. (in A)

	Present work			Doran and Stephenson
	(400)	(220)	(111)	
K				1.117_0
A				1.116_0
α				1.115_2
B				1.114_1
β				1.113_4
C		1.111_1	1.110_3	1.111_6
γ	1.110_5	1.110_0		1.110_5
D	1.108_8	1.108_9	1.108_7	1.109_7
δ	1.105_4	1.105_4	1.105_1	1.105_2
E	1.102_1	1.102_1	1.102_2	1.102_0
ε	1.097_7	1.097_7	1.097_6	1.098_1
F	1.095_6	1.095_3	1.094_2	1.094_6
ζ	1.090_0	1.089_7	1.090_1	1.090_0
G	1.087_5	1.087_0	1.087_2	

Table II. Energy separations of fine structures of absorption of germanium single crystals from the K absorption edge of germanium. (in eV.)

	Present work			Doran and Stephenson
	(400)	(220)	(111)	
K	0	0	0	0
A				6.7
α				15.7
B				25.2
β				31.7
C		59	67	48
γ	65	70		61
D	81	81	83	79
δ	116	116	120	114
E	150	150	149	147
ε	195	195	196	186
F	217	220	231	223
ζ	275	278	274	271
G	301	306	304	

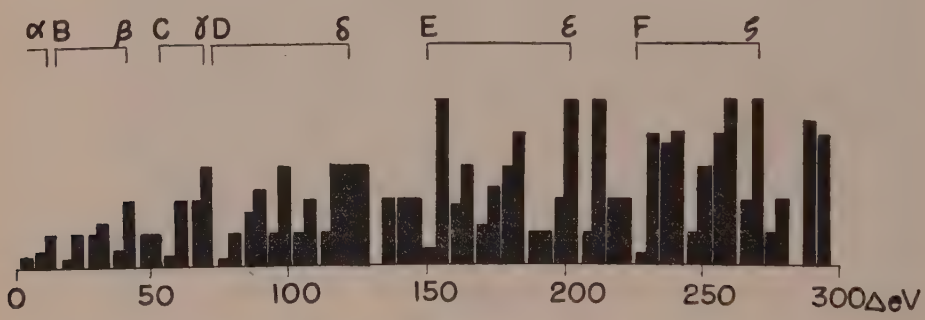

Fig. 1. Magnitudes of absorption discontinuities of germanium *vs* energies.

1. If we assume that the fine structure of the reflected intensity is caused by absorption by the analysing crystal itself, the fluctuations (discontinuities) in the absorption coefficient will occur at the enery values[7]

$$W=\frac{h^2}{8md^2}(h^2+k^2+l^2)\,, \qquad (1)$$

as measured from the mean potential of the crystal since it belongs to the cubic system, where d is the lattice constant, m the electron mass and $(h,\ k,\ l)$ are Miller-indices. The magnitudes of discontinuities are proportional to

$$I_{hkl}=H_{hkl}(V_{hkl})^2, \qquad (2)$$

where H_{hkl} is the abundance factor of the (hkl) planes and V_{hkl} is the Fourier coefficient of the potential in the crystal. According to Kronig's simplified method[7], however, I_{hkl} is considered to be proportional only to H_{hkl}. We plotted this quantity, I_{hkl}, against energy value given by (1) for the case of germanium (Fig. 1). One can distinguish groups $A-\alpha$, $B-\beta$, $C-\gamma$, $D-\delta$, $E-\varepsilon$ and $F-\zeta$. Their

Table III. Separations of gravity centers of absorption discontinuities of germanium. (in eV.)

Group	Theoretical	Present experiments	Doran and Stephenson
α	13		15.7
$B-\beta$	29		29
$C-\gamma$	62	65	55
$D-\delta$	98	98–102	97
$E-\varepsilon$	177	173	167
$F-\zeta$	248	246–253	247

centers of gravity agree with those of the observed structures as seen in Table III. In our case reflected X-rays are partially polarized, so that when these polarized X-rays are absorbed by a single crystal all photoelectrons are not uniformly ejected in all directions, and therefore some planes do not contribute to the discontinuities. This effect is more influential near the absorption edge than in the high energy region, because in Fig. 1 the abundance factor and the number of overlapping planes with different Miller-indices are small in this region. Thus the fluctuations in the absorption coefficient are less pronounced in this region than those when unpolarized X-rays are absorbed by a polycrystalline absorber.

2. The total energy I diffracted from a face of a single crystal, according to kinematical theory, is given by

$$\frac{I}{I_0}=\frac{1}{2\mu}\left(\frac{N\lambda_i^3e^4}{Zm^2c^4\sin 2\theta}\cdot\frac{1+\cos^2 2\theta}{2}\right)|F|^2$$
$$\equiv\frac{Q'}{2\mu}|F|^2\,, \qquad (3)$$

where I_0, μ, N, Z, λ_i, θ, F and e are the power of the incident radiation, atomic absorption coefficient, number of unit cells per unit volume, number of atoms per unit cell, wavelength of the incident radiation, Bragg angle, structure factor and the charge of an electron, respectively. In the case of germanium the structure factor becomes

$$F=f(1+e^{(\pi i/2)(h+k+l)})(1+e^{\pi i(h+k)}+e^{\pi i(h+l)}$$
$$+e^{\pi i(k+l)})\equiv f\cdot p\,, \qquad (4)$$

f being the atomic scattering factor of germanium. We must consider the anomalous scattering in the present case because the frequency ω_i of the incient radiation is near the frequency ω_k of the absorption edge of the scattering atom. In this case f is written as

$$f=f_0+f'+if''\,,$$

where f_0 is the atomic scattering factor for frequencies high in comparison with the atomic absorption frequency ω_k and for a particular reflection it is independent of the incident wavelength itself, and f' and f'' are the real and imaginary parts of f which depend on the frequency. Then equation (3) can be written

$$I=\frac{I_0Q'p^2}{2\mu(\omega_i)}\{(f_0+f')^2+f''^2\}\,, \qquad (5)$$

in which I_0, f_0 and p are independent of frequency and Q' varies monotonically with frequency. From the classical theory[8] of dipole-oscillator f' and f'' are expressed as

$$f'=\frac{mc}{2\pi^2e^2}\int_{\omega_k}^{\infty}\frac{\omega^2\mu(\omega)}{\omega_i^2-\omega^2}d\omega\,, \qquad (6)$$

$$f''=\frac{mc}{4\pi e^2}\omega_i\mu(\omega_i)\equiv g'\mu(\omega_i),\quad \omega_i>\omega_k, \qquad (7)$$

$$f''=0\,,\qquad \omega_i<\omega_k\,.$$

When $\mu(\omega)$ varies monotonically with frequency the general features of f' and f'', as functions of frequency, are shown in Fig. 2.

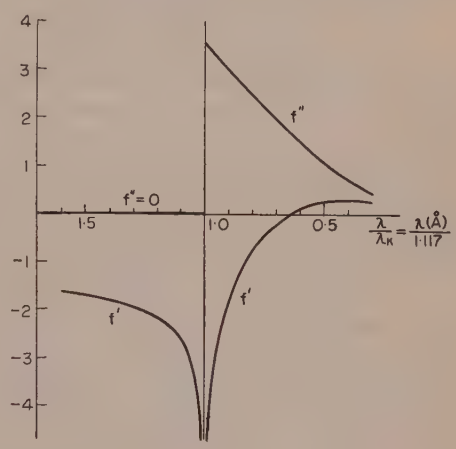

Fig. 2. General features of f' and f'' against frequency.

It is estimated* from equation (6) that the maximum magnitude of fluctuation $\Delta f'$ depending on the small fluctuation $\Delta\mu$ in μ is nearly equal to that of $g'\Delta\mu$ when $\Delta\mu$ varies sinusoidally. The fluctuation $\Delta f''$ depending on $\Delta\mu$ is $g'\Delta\mu$ from equation (7). Table IV shows the values of f_0, f' and f'' when the damping constant of oscillators is taken to be 10^{-4}.

From equation (5) the fluctuation in I depending on $\Delta\mu$ is

---

* From equation (6) it can be shown that only the following integral contributes to the fluctuation in f'.

$$\frac{mc}{2\pi^2e^2}\cdot\frac{\omega_i}{2}\int_{\omega_k}^{\infty}\frac{\Delta\mu}{\omega-\omega_i}d\omega=\Delta f'(\omega_i)\,,$$

where $\Delta\mu$ is a fluctuating part in μ. If we assume that $\Delta\mu$ is $a\cdot\sin m\omega$, then the maximum magnitude of $\Delta f'(\omega_i)$ can be given approximately as

$$\frac{mc}{2\pi^2e^2}\cdot\frac{\omega_i}{2}\cdot 4\cdot\frac{a\pi}{2}=2ag.$$

Table IV. Values of f_0, f' and f''.

λ/λ_K	λ (A)	f_0 (400)	f_0 (220)	f_0 (111)	f'	f''
1	1.117_0				−9.77	3.74
0.995	1.114_4				−7.17	3.70
0.99	1.105_8	18.4	21.7	26.2	−4.57	3.66
0.985	1.100_2				−4.06	3.63
0.98	1.094_7				−3.72	3.59
0.975	1.089_1				−3.44	3.55

$$\Delta I=\frac{I_0Q'p^2}{2\mu^2}[-\{(f_0+f')^2-f''^2\}\Delta\mu +2(f_0+f')\mu\Delta f']. \quad (8)$$

The maximum magnitude of $\mu\Delta f'$ is nearly equal to that of $g'\mu\Delta\mu\equiv f''\Delta\mu$, and the fluctuation $\Delta f'$ shows quite a different variation with ω_i from that of the fluctuation $\Delta\mu$. As can be seen in Fig. 2 and Table IV, $(f_0+f')^2-f''^2$ and $2(f_0+f')\cdot f''$ near the absorption edge are much smaller than their respective values in the high frequency region. Thus the fluctuations in the reflected intensity are less pronounced near the absorption edge than in the high energy region. Besides, $\Delta\mu$ cannot affect I near the absorption edge as $(f_0+f')^2$ is comparable to f''^2. It is supposed that the maximum magnitude of the small fluctuation $\Delta f'$ is actually smaller than that of $g'\Delta\mu$ because in our experimental results the fluctuations in the reflected intensity in the high energy region from the absorption edge are similar to those of the absorption spectrum by the transmission method and therefore are not affected by $\Delta f'$. Therefore the influence of $\Delta f'$ on the reflected intensity is considered to be very small in the whole frequency region. When the magnitudes of f' and f'' become small with increasing frequency, $\Delta\mu$ much affect the reflected intensity and then the fluctuations in the reflected intensity become more pronounced.

3. The effect similar to the thickness effect in the absorption spectrum which was investigated by Parratt, Hempstead and Jossem[9] by the transmission method is considered to occur in our case, particularly in the case of low dispersion of the spectrometer. In their investigation they concluded that the fine structure of the absorption spectrum near the absorption edge became less pronounced with increasing absorber thickness on account of the tail of the spectral window (the tail of the focal spot of the X-ray tube in our case) and the enormous asymmetric shape of the absorption edge. Therefore, in our case also, the fluctuations in the reflected intensity are less pronounced near the absorption edge than in the high energy region.

We express our sincere thanks to Professor M. Sawada for his encouragement in this work.

References

1) S. T. Stephenson: Phys. Rev. **44** (1933) 349.
2) R. Krogstad, W. Nelson and S. T. Stephenson: Phys. Rev. **92** (1953) 1394.
3) D. G. Doran and S. T. Stephenson: Phys. Rev. **105** (1957) 1156.
4) M. Hulbei and Y. Cauchois: C. R. Acad. Sci. Paris **211** (1940) 316.
5) D. Coster and H. De Lang: Physica **13** (1947) 379.
6) K. Tsutsumi, A. Hayase and M. Sawada: J. Phys. Soc. Japan **12** (1957) 793, Norelco Reporter 1958 to be published.
7) R. de L. Kronig: Zs. f. Phys. **70** (1931) 317, **75** (1932) 191.
8) R. W. James: The Optical Principles of the Diffraction of X-rays: G. Bell and Sons, Ltd., 1950.
9) L. G. Parratt, C. F. Hempstead, and E. L. Jossem: Phys. Rev. **105** (1957) 1228.

JOURNAL OF THE PHYSICAL SOCIETY OF JAPAN Vol. 13, No. 6, JUNE, 1958

Nuclear Magnetic Resonance Experiment on Metal Cadmium. II

Yoshika MASUDA

Department of Physics, Kobe University

(Received December 12, 1957)

The spin-lattice relaxation time, T_1 and the spin-spin relaxation time, T_2, of the resonance line in metal cadmium were measured by use of a nuclear magnetic resonance technique. The contribution of p-character in the conduction electron to the relaxation was estimated. The line width was measured at a temperature between the room temperature and 250°C. It was shown that the exchange broadening between unlike spins underwent a motional narrowing. The inverse line width or spin-spin relaxation time, T_2, was interpreted in terms of the lattice diffusion theory. These analyses yielded for the coefficient of self-diffusion D the value 0.05 cm²/sec exp (−17.6 kcal/mol-RT).

§ 1. Introduction

Nuclear magnetic resonance measurements in metal cadmium have already yielded significant results for the interpretation of its metallic properties[1]. The line shape, linewidth, and Knight shift of the resonance line have given much informations concerning the properties of the conduction electrons.

The nuclear relaxation in metals is usually determined by the interaction of nuclear spins and conduction electron spins. When one takes into account only the Fermi-interaction, the relation between the spin-lattice relaxation time and the Knight shift is well known as the "Korringa relation"[2]. From the fact that the isotropic shift in metal cadmium is 0.43 per cent, we determined the s-content ξ of the wave function to be about 20 per cent. The resonance line is asymmetric indicating an anisotropy of the Knight shift. From the analysis of these line profiles we estimated the asymmetry in p-character of the conduction electron. The anisotropic shift, $(\Delta H_{//} - \Delta H_{\perp})/H_0$, is 0.039 per cent, where $\Delta H_{//}$ and $\Delta H_{\perp}$ are the shifts parallel and perpendicular to the c-axis, respectively. The symmetric line broadening, $\delta_{\text{max. sl.}}=1.5$ gauss, was originated from the indirect exchange coupling between neighboring nuclei which involves conduction electrons[1]. The deviation of the measured relaxation time T_1 from the Korringa time may be due to the contribution of p-electron to the relaxation.

Owing to the local magnetic field at a resonating nucleus produced by its neighbors, nuclear magnetic resonance line in solids usually has a width of several gauss. It is well known that sufficiently rapid motion of the nuclei can reduce the effective local field, so that the onset of such motion can be observed as a reduction in line width. In metals, where the possibility of any rotational motion is excluded, the motion is presumably connected with a diffusion process. A general theory on the T_1's and T_2's which result from interactions of the nuclei with fluctuating local magnetic fields has been given by Bloembergen, Purcell, and Pound[3] and Kubo and Tomita[4]. The BPP theory deals with nuclear dipolar-dipolar interactions and the effects of diffusional motion of the nuclei. Line width transition in solid alkali metals[5),6] and in aluminum[7] have been reported and interpreted to be due to self-diffusion. But we must concern with the effect of nuclear motion on the exchange interaction as the line width are related in this case, to the exchange interaction between unlike spins[8)9].

We shall discuss the motional narrowing in this case. From the analysis of this narrowing, the self-diffusion coefficient will be estimated.

§ 2. Experiment

The experimental procedures and equipments employed for the measurement were described previously[1]. The samples were consisted of foil rolled to a thickness of about 15 μ. Layers of foil were separated by mica. To avoid oxidation, the metal sample was sealed at

reduced pressure into a thin-walled glass tube. The specimen was annealed at 300°C for two hours to eliminate the effects of grain boundary diffusion.

The specimen with its coil was mounted inside a Dewer vessel, into which the heated air was blown by an air compressor through a small electric furnace. A chromel-alumel thermocouple was attached to the sample vial. The temperature inhomogeneity in the vessel was found not to exceed 1°C. The experiment was performed on the Cd^{113} (abundance ratio 12.34 per cent) at the field of 3900 gauss with a permanent magnet using a resonance frequency of 3.71 Mc/sec. For the measurement of the relaxation time we employed the ordinary saturation method.

§ 3. Results and Discussion

a) *The Spin-Lattice Relaxation Time.*

For the evaluation of T_1 from saturation factor $(\gamma H_1)^2 T_1 T_2$, we employed the T_2 as determined from the symmetric line broadening δ and not from the overall width which is of the inhomogeneous type. It results in T_1 of 0.5×10^{-3} sec. for Cd^{113} which is one half of the Korringa time of 1.1×10^{-3} sec. estimated from the measured shift. We shall consider this deviation.

The Hamiltonian for the nuclear spin-electron spin interaction is given by

$$\mathscr{H}=\frac{8\pi}{3}g\beta g_N\beta_N \mathbf{I}_i\cdot\mathbf{S}\delta(\mathbf{r}_i)$$
$$+g\beta g_N\beta_N \mathbf{I}_i\cdot\{\mathbf{S}r_i^{-3}-3r_i^{-5}(\mathbf{S}\cdot\mathbf{r}_i)\mathbf{r}_i\}\,, \quad (1)$$

where $\mathbf{r}_i$ is the radius vector of the electron with the nucleus at the origin and β is the Bohr magneton. The electron in the solid may be adequately described by one-electron wave function of Bloch type,

$$\left.\begin{aligned}\Psi_k&=e^{i\mathbf{k}\cdot\mathbf{r}}u_k(\mathbf{r})\,,\\ V^{-1}\int\Psi_k^*\Psi_k d\tau&=1\,,\end{aligned}\right\} \quad (2)$$

where V is the volume of the metal under consideration. $u_k(\mathbf{r})$ has the periodicity of the lattice, and within the atomic polyhedron, it is assumed to be a mixture of s- and p-functions. Bardeen[10], Silverman and Kohn[11], and Kohn[12] have shown that the periodic function $u_k(\mathbf{r})$ in the Bloch wave function (2) can be expanded in a fairly rapidly converging power series in $\mathbf{k}$. This is an expansion in spherical harmonics containing the angle Θ_1 between $\mathbf{r}_i$ and $\mathbf{k}$,

$$u_k(\mathbf{r})=c_0u^0(r)+ikc_1u^1(r)P_1(\cos\Theta_1)\,, \quad (3)$$

where $u^0(r)$ is the normalized s-solution of the Schrödinger equation, the $u^1(r)$ is the radial part of the p-solution. The c_1 and $u^1(r)$ are independent of k. The coefficient c_1 may be determined by the boundary conditions of the wave function on the Wigner-Seitz sphere. The c_1 was evaluated accurately in case of lithium and sodium[11)12)]. In cadmium, however, it was estimated from the shift in reference 1, since we have no accurately calculated value.

The first term of the Hamiltonian (1) represents the hyperfine interaction and the second term the dipolar interaction between two dipoles. It is well known that the diagonal elements of the hyperfine interaction produce an isotropic Knight shift, whereas the off-diagonal elements contribute to the relaxation time T_1. The expression of relaxation time first presented by Korringa[2] is as follows:

$$\left(\frac{1}{T_1}\right)_s=\frac{4\pi kT}{\hbar}\Omega^2N(E_0)^2\left(\frac{(\Delta E)_s}{2I+1}\right)^2\xi^2\,, \quad (4)$$

where Ω is the atomic volume, $N(E_0)$ the number of states, for a unit volume of the metal, per unit energy interval, $(\Delta E)_s$ the h.f.s. splitting of the atom with one s-electron outside closed shells, and ξ the s-content of the conduction electron.

Actually the part of the electronic wave function with non s-character (p-, d-, etc.) will also contribute to the relaxation time, but not to the shift in the absence of the asymmetry in p-character of electron at the top of the conduction band. We shall consider the relaxation time originated from the p-part of the electronic wave function.

Consider the dipolar part of the Hamiltonian (1). Since the nuclear- and electron-spins are quantized with respect to the external field $\mathbf{H}$, the dipolar interaction between nuclear spin $\mathbf{I}_i$ and electron spin $\mathbf{S}$ can be expanded in spherical harmonics containing the polar angle θ and Φ in the $\mathbf{r}_i$ space, where the polar axis is in the direction of $\mathbf{H}$,

$$\mathscr{H}_{dip}=g\beta g_N\beta_N r_i^{-3}\Big[\Big(-2I_zS_z+\frac{1}{2}I_+S_-+\frac{1}{2}I_-S_+\Big)P_2(\cos\theta)$$

$$-\frac{1}{2}(I_+S_z+I_zS_+)P_2^1(\cos\theta)e^{-i\phi}-\frac{1}{2}(I_-S_z+I_zS_-)P_2^1(\cos\theta)e^{+i\phi}$$
$$-\frac{1}{4}I_+S_+P_2^2(\cos\theta)e^{-2i\phi}-\frac{1}{4}I_-S_-P_2^2(\cos\theta)e^{+2i\phi}\Big]. \tag{5}$$

I_z and S_z are the components of spin parallel to the magnetic field $\mathbf{H}$; I_+, I_-, S_+, and S_- are the usual spin raising and lowering operators. The state of a nucleus of spin I is characterized by the quantum number m and $s=\pm\frac{1}{2}$ is the spin quantum number of the electron.

The energy exchange between a nucleus and a conduction electron is due to their magnetic interaction and is determined by the matrix elements $(\Psi_k;\ m, s\rightarrow\Psi_{k'}, m', s')$ of the Hamiltonian (5). They are

$$\left(m, s\left|-2I_zS_z+\frac{1}{2}I_+S_-+\frac{1}{2}I_-S_+\right|m', s'\right)\Delta kk'c_1c_1'\int P_1(\cos\Theta_1)P_1(\cos\Theta_2)P_2(\cos\theta)d\omega$$
$$-\frac{1}{2}(m, s|I_+S_z+I_zS_+|m', s')\Delta kk'c_1c_1'\int P_1(\cos\Theta_1)P_1(\cos\Theta_2)P_2^1(\cos\theta)e^{-i\phi}d\omega$$
$$-\frac{1}{2}(m, s|I_-S_z+I_zS_-|m', s')\Delta kk'c_1c_1'\int P_1(\cos\Theta_1)P_1(\cos\Theta_2)P_2^1(\cos\theta)e^{+i\phi}d\omega$$
$$-\frac{1}{4}(m, s|I_+S_+|m', s')\Delta kk'c_1c_1'\int P_1(\cos\Theta_1)P_1(\cos\Theta_2)P_2^2(\cos\theta)e^{-2i\phi}d\omega$$
$$\frac{1}{4}(m, s|I_-S_-|m', s')\Delta kk'c_1c_1'\int P_1(\cos\Theta_1)P_1(\cos\Theta_2)P_2^2(\cos\theta)e^{+2i\phi}d\omega\,, \tag{6}$$

where

$$\Delta=g\beta g_N\beta_N\int_0^{r_s}u^{1*}(r_i)u^1(r_i)r_i^{-1}dr_i \tag{7}$$

and Θ_2 is the angle between $\mathbf{r}_i$ and $\mathbf{k}'$. The integration over r_i is extended only over the Winger-Seitz sphere with radius $r_s=\left[\frac{3}{4\pi}\frac{\Omega}{2}\right]^{1/3}$. Carrying out the integral over the solid angle $d\omega$, the matrix elements take the forms

$$\left(m, s\left|-2I_zS_z+\frac{1}{2}I_+S_-+\frac{1}{2}I_-S_+\right|m', s'\right)\Delta kk'c_1c_1'\frac{4}{15}\pi\{3P_1(\cos\theta_1)P_1(\cos\theta_2)-P_1(\cos\chi)\}$$
$$-(m, s|I_+S_z+I_zS_+|m', s')\Delta kk'c_1c_1'\frac{2}{5}\pi\{P_1(\cos\theta_2)P_1^1(\cos\theta_1)e^{-i\varphi_1}+P_1(\cos\theta_1)P_1^1(\cos\theta_2)e^{-i\varphi_2}\}$$
$$-(m, s|I_-S_z+I_zS_-|m', s')\Delta kk'c_1c_1'\frac{2}{5}\pi\{P_1(\cos\theta_2)P_1^1(\cos\theta_1)e^{+i\varphi_1}+P_1(\cos\theta_1)P_1^1(\cos\theta_2)e^{+i\varphi_2}\}$$
$$-(m, s|I_+S_+|m', s')\Delta kk'c_1c_1'\frac{2}{5}\pi P_1^1(\cos\theta_1)P_1^1(\cos\theta_2)e^{-i(\varphi_1+\varphi_2)}$$
$$-(m, s|I_-S_-|m', s')\Delta kk'c_1c_1'\frac{2}{5}\pi P_1^1(\cos\theta_1)P_1^1(\cos\theta_2)e^{+i(\varphi_1+\varphi_2)}\,, \tag{8}$$

where k_1, θ_1, φ_1 are the polar coordinates in the $\mathbf{k}$ space and k_2, θ_2, φ_2 in the $\mathbf{k}'$ space, the polar axis being in the direction of $\mathbf{H}$. χ is the angle between $\mathbf{k}$ and $\mathbf{k}'$. Picking up the non-secular parts of Eq. (8), which are responsible for the relaxation time, we obtain

$$(\mathscr{H}_{kk'})_{rel}=(I_+S_-+I_-S_+)W_B(kk')+(I_+S_z)W_C(kk')+(I_-S_z)W_D(kk')$$
$$+(I_+S_+)W_E(kk')+(I_-S_-)W_F(kk') \tag{9}$$

with

$$\left.\begin{aligned}
W_B(kk') &= \Delta kk'\, c_1c_1'\frac{2}{15}\pi\{3P_1(\cos\theta_1)P_1(\cos\theta_2)-P_1(\cos\chi)\}\,,\\
W_C(kk') &= \Delta kk'\, c_1c_1'\frac{2}{15}\pi\{P_1(\cos\theta_2)P_1^1(\cos\theta_1)e^{-i\varphi_1}+P_1(\cos\theta_1)P_1^1(\cos\theta_2)e^{-i\varphi_2}\}\,,\\
W_D(kk') &= \Delta kk'\, c_1c_1'\frac{2}{15}\pi\{P_1(\cos\theta_2)P_1^1(\cos\theta_1)e^{+i\varphi_1}+P_1(\cos\theta_1)P_1^1(\cos\theta_2)e^{+i\varphi_2}\}\,,\\
W_E(kk') &= \Delta kk'\, c_1c_1'\frac{2}{5}\pi P_1^1(\cos\theta_1)P_1^1(\cos\theta_2)e^{-i(\varphi_1+\varphi_2)}\,,\\
\text{and}\quad W_F(kk') &= \Delta kk'\, c_1c_1'\frac{2}{5}\pi P_1^1(\cos\theta_1)P_1^1(\cos\theta_2)e^{+i(\varphi_1+\varphi_2)}\,.
\end{aligned}\right\}\tag{10}$$

The change of $N(m)$, the number of nuclear spins in the state m, due to the interaction with the conduction electrons is calculated with time dependent perturbation theory, using the Fermi-statistics for the electrons[2]. Then we obtain

$$\begin{aligned}
\frac{\partial N(m)}{\partial t} &= U_B\{N(m+1)C_m-N(m)(C_m\exp\gamma+C_{m-1})+N(m-1)C_{m-1}\exp\gamma\}\\
&\quad+(U_C+U_C')\{N(m+1)C_m-N(m)(C_m+C_{m-1})+N(m-1)C_{m-1}\}\\
&\quad+U_E\{N(m+1)C_m\exp\gamma-N(m)(C_m+C_{m-1}\exp\gamma)+N(m-1)C_{m-1}\}
\end{aligned}\tag{11}$$

with

$$\left.\begin{aligned}
U_B &= \frac{2\pi}{\hbar}\frac{\Omega^2}{(2\pi)^6}\int d\mathbf{k}\int d\mathbf{k}'\,|W_B(kk')|^2\delta(E_{k'}^{-}-E_k^{+}-g_N\beta H)\\
&\quad\times\{1+\exp(-\alpha)\}^{-1}\{1+\exp(\alpha+\gamma)\}^{-1}\,,\\
U_C &= \frac{2\pi}{\hbar}\frac{\Omega^2}{(2\pi)^6}\frac{1}{4}\int d\mathbf{k}\int d\mathbf{k}'\,|W_C(kk')|^2\delta(E_{k'}^{+}-E_k^{+}-g_N\beta H)\\
&\quad\times\{1+\exp(-\alpha)\}^{-1}\{1+\exp\alpha\}^{-1}\,,\\
U_C' &= \frac{2\pi}{\hbar}\frac{\Omega^2}{(2\pi)^6}\frac{1}{4}\int d\mathbf{k}\int d\mathbf{k}'\,|W_C(kk')|^2\delta(E_{k'}^{-}-E_k^{-}-g_N\beta H)\\
&\quad\times\{1+\exp(-(\alpha+\gamma))\}^{-1}\{1+\exp(\alpha+\gamma)\}^{-1}\,,\\
\text{and}\quad U_E &= \frac{2\pi}{\hbar}\frac{\Omega^2}{(2\pi)^6}\int d\mathbf{k}\int d\mathbf{k}'\,|W_E(kk')|^2\delta(E_{k'}^{+}-E_k^{-}-g_N\beta H)\\
&\quad\times\{1+\exp(-\alpha)\}^{-1}\{1+\exp(\alpha+\gamma)\}^{-1}\,,
\end{aligned}\right\}\tag{12}$$

where $\alpha=(E_k^{+}-E_0)/kT$, $\gamma=g_N\beta_N H/kT$, $|(I_-)_{mm'}|^2=C_m\delta(m,m'+1)$, $|(I_+)_{mm'}|^2=C_{m-1}\delta(m,m'-1)$, and $S_\pm=\delta(s,s'\pm1)$. The spin-lattice relaxation time is given by $1/T_1=U_B+2U_C+U_E$. This gives,

$$\left(\frac{1}{T_1}\right)_p=\frac{304}{135}\frac{\pi^3kT}{\hbar}\Omega^2N(E_0)^2\Delta^2k_m^4c_1^4\,,\tag{13}$$

where k_m is the value of the wave number at the Fermi level E_0. The quantity Δ calculated from Eq. (7) is related to the atomic p-type hyperfine splitting $(\Delta E)_p$:

$$\Delta=\frac{(\Delta E)_p}{2I+1}(1-\xi).$$

We estimated the relaxation time by p-electrons, by Eq. (13), using the value of c_1 determined from the shift obtained in reference 1, as

$$(1/T_1)_p=0.43\times10^3\ \mathrm{sec}^{-1}.$$

On the other hand, employing the values obtained in reference 1, we estimated the relaxation time by Eq. (4),

$$(1/T_1)_s=1.1\times10^3\ \mathrm{sec}^{-1}.$$

Defining the resultant relaxation time as, $(1/T_1)=(1/T_1)_s+(1/T_1)_p$, we get

$$T_1=0.65\times10^{-3}\ \mathrm{sec}.$$

Comparing this value with the experimental one of 0.5×10^{-3} sec. we see a good agreement which may partly be accidental. We may, however, conclude that at least a part of the deviation from Korringa time is due to the contribution of p-electron to the relaxation.

As an example other than cadmium, we apply Eq. (13) to lithium and sodium employing the value of s-content calculated by Jones and

Schiff[13], Kohn[14], and Kjeldaas and Kohn[15]. Jones and Schiff estimated the s-content in lithium to be 25 per cent and that in sodium 65 per cent. In the case of sodium, calculations show that the Fermi energy, E_0 is almost exactly the value given by free electron approximation. In the case of lithium, however, where the conduction electrons behave very differently from free electrons, the value of E_0 is not so certain. Schiff[16] found $E_0=2.69$ eV but free electron approximation gives $E_0=4.72$ eV. The interaction of the p-part would reduce the relaxation time calculated from the Korringa relation by about 2 per cent in lithium. But there is a negligible contribution to the relaxation in sodium. Although the hyperfine interaction of p-orbits is usually much smaller than that of s-orbit, being only 6 per cent of that in the s-state in the case of lithium, it becomes dominant in the case of a heavier element.

This effect of p-electrons on the relaxation must be further examined in heavier elements.

b) *The Spin-Spin Relaxation Time*

The experimental data are the values of T_2, the inverse line width or spin-spin relaxation time, measured at a temperature between a room temperature and 250°C. Figure 1 shows the variation of the overall width with temperature. As the observed anisotropy in line profile is proportional to the magnetic field as stated in reference 1, the line becomes nearly symmetric with the anisotropic shift $\Delta H_{//}-\Delta H_{\perp}=1.52$ gauss which is comparable to $\delta_{\text{max. sl.}}=1.5$ gauss, at the low field employed in the present experiments. Accordingly, δ has a considerable contribution to the line broadening in this case. δ was proved to originate from the indirect exchange coupling between neighboring nuclei which involves conduction electrons. As an anisotropic Knight shift is produced by the nuclear spin-electron spin dipolar coupling when the charge distribution of electron deviates from spherical symmetry about the nucleus, we can consider that the asymmetry of p-electron will be unchanged by the atomic self-diffusion process. We consider that only the symmetric line broadening δ can undergo a motional narrowing, keeping the value of $(\Delta H_{//}-\Delta H_{\perp})/H_0$ constant. The variation of the overall width with temperature was converted to the variation of the symmetric line broadening δ. It is shown in Figure 1 by notation δ.

The diffusion may also have an effect on T_1, the spin-lattice relaxation time. Because of a poor signal-to-noise ratio we could not measure the temperature dependence of the spin-lattice relaxation time. But it has presumably a negligible contribution to the line width. If the asymmetry in p-character of

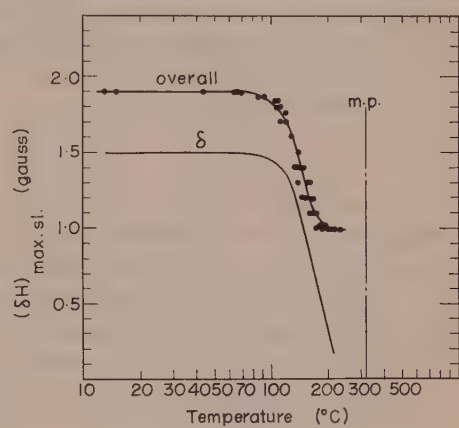

Fig. 1. Line width data.

conduction electrons is unchanged by the diffusion process, the asymmetry of line profile must become more striking as the diffusion progresses. But, unfortunately, we could not observe the variation with temperature of line profile and Knight shift.

δ is seen to decrease as the temperature is increased over about 80°C, and it narrows out at about 200°C. The ambiguity of measurements is rather large in high temperature region, since the resonance line becomes much less intense and reliable measurements become increasingly difficult. Though it was desirable to make measurements in rather high temperature region where the melting phenomenon heralds the breakdown of the forces which holds the lattice rigid, we could not detect the resonance line in such region.

We shall be interested in the effect of nuclear motion on the exchange interaction as the line width are related to exchange interaction between unlike spins. A pure rotation, leaving the internuclear distance between the two nuclei unchanged, has no effect because the exchange interaction has no angular dependence. Unlike the dipolar interaction, it does not average out on rotation. An analysis

of this motional narrowing of exchange broadening will be given next.

Ramsey and Purcell[8], and Ruderman and Kittel[9] have shown that the nuclear spin-electron spin interaction will in second-order perturbation theory give rise to an exchange type of coupling between nuclear spins in molecules or in metals.

The Hamiltonian for the nuclear spin-electron spin interaction is given by Eq. (1), and the electronic wave function by Eq. (2). Ruderman and Kittel[9] found the exchange interaction in a metal to be of the form

$$\mathscr{H}^{exch}=\sum_{i>j}\sum_{j} A_{ij}\mathbf{I}_i\cdot\mathbf{I}_j\ , \qquad (14)$$

where

$$A_{ij}=-2^{-5}(|\Delta_{ij}|^2)_{Av}m'\pi^{-3}\hbar^2R_{ij}^{-4}$$
$$\times[\sin(2k_mR_{ij})-2k_mR_{ij}\cos(2k_mR_{ij})]\ . \qquad (15)$$

A pair of nuclear spins is introduced at positions $\mathbf{R}_i$ and $\mathbf{R}_j$ in the lattice, and one writes $\mathbf{R}_{ij}=\mathbf{R}_i-\mathbf{R}_j$, and m' is the effective mass. The average over k and k' is introduced,

$$(|\Delta_{ij}|^2)_{Av}=\langle\Delta_i(kk')\Delta_j(kk')\rangle_{eff}\ , \qquad (16)$$

where

$$\Delta_i(kk')=(8\pi/3)g\beta g_N\beta_N u_k(\mathbf{R}_i)u_{k'}^*(\mathbf{R}_i)\ . \qquad (17)$$

If we assume that the spin $\mathbf{I}_i$ only interacts with a spin $\mathbf{I}_j$ in the nearest neighbor sites, the exchange interaction is modified as follows

$$\mathscr{H}^{exch}=\sum_{i>j}\sum_{j} A\,\mathbf{I}_i\cdot\mathbf{I}_j\,\delta(|\mathbf{R}_{ij}(t)|-a)\ . \qquad (18)$$

It is necessary to sum over all spins $\mathbf{I}_j$, because of the self-diffusion. $\delta(|\mathbf{R}_{ij}(t)|-a)$ is unity when $\mathbf{I}_i$ and $\mathbf{I}_j$ are in the nearest neighbor sites, otherwise zero, where a is the nearest neighbor distance. But the summation over j may be restricted to the nearest neighbor because of the nearest neighbor interaction only. Hamiltonian, Eq. (18), can be written as[17]

$$\mathscr{H}_i^{exch}=\sum_{j=1}^{n} A\mathbf{I}_i\cdot\mathbf{I}_j e^{i\phi_j(t)}=\sum_{j=1}^{n} A(t)\mathbf{I}_i\cdot\mathbf{I}_j\ , \qquad (19)$$

where $\phi_j(t)$ is the phase which varies in a random manner with the exchange of unlike spin in the nearest neighbor sites and n is the number of nearest neighbor sites. The correlation function of $A(t)$ is

$$\langle A(t)A^*(t+\tau)\rangle=A^2e^{-\tau/\tau_e}\ , \qquad (20)$$

where τ_e is the correlation time for an indirect exchange coupling. Using this correlation function, we can calculate the transition probabilities by Solomon's procedure[18] and these results will give the spin-spin relaxation time T_2. If we consider only spins of value $\frac{1}{2}$, we obtain

$$\frac{1}{T_2}=\frac{A^2nf}{4\hbar^2}\left[\tau_e+\frac{\tau_e}{1+(\omega_{I_i}-\omega_{I_j})^2\tau_e^2}\right], \qquad (21)$$

where f is the abundance ratio of unlike spins. In the extremely narrow case, the spin-spin relaxation time is given by

$$\left(\frac{1}{T_2}\right)_{ex}=\left(\frac{A}{\hbar}\right)^2\frac{\tau_e}{2}nf\ . \qquad (22)$$

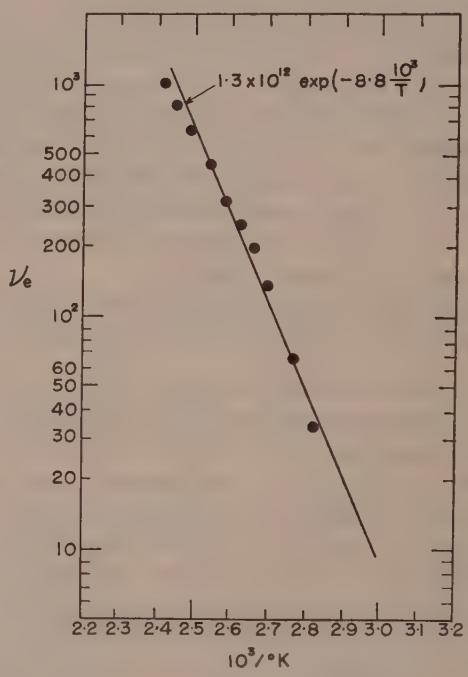

Fig. 2. Plot of ν_e against reciprocal temperature, obtained from analysis of line width data.

Turning to the line width data, we can calculate the frequency of exchange motion ν_e at a given temperature. The equation $\nu_e=\nu_{e0}\exp(-E_D/RT)$ is then employed to find the activation energy E_D for self-diffusion. As Eq. (22) is valid only in the case of the extremely narrow condition $(\omega_{I_i}-\omega_{I_j})^2\tau_e^2\ll 1$, it cannot be applied to the early stage of narrowing under consideration. Fig. 2 shows the frequency of exchange ν_e as a function of $1/T$, obtained from the analysis of the line width data[19]. The data are fitted by an exponential formula, corresponding to a ν_{e0} value of $1.3\times10^{12}\,\mathrm{sec}^{-1}$, and $E_D=17.6$ kcal/mole. The observed atomic diffusion coefficients are usually expressed in terms of two constants, D_0 and E_D, as follows:

$$D=D_0 \exp(-E_D/RT) . \quad (23)$$

The theoretical diffusion coefficient for translational diffusion has a form

$$D=\frac{a^2}{12\tau_D} . \quad (24)$$

Here a is the lattice constant and τ_D is the mean time-of-stay in one nearest neighbor position between jumps. As the mean time-of-stay τ_D has the heat of activation, we obtain

$$\tau_{D_0}=\tau_D \exp(-E_D/RT) . \quad (25)$$

The constant τ_{D_0} is found by a crude approximation to be given by

$$\tau_{D_0}^{-1}=\frac{n(2\pi\nu_{e0})}{f} . \quad (26)$$

Upon comparing above equations, we obtain for D_0 the following theoretical equation

$$D_0=\frac{n\pi a^2 \nu_{e0}}{6f} . \quad (27)$$

This equation gives the result as follows:

$$D_0 \sim 0.05 \text{ cm}^2/\text{sec} .$$

The experiment of self-diffusion by the radioactive tracer method gave the bulk and grain boundary diffusion coefficient[20]. The bulk diffusion constants as measured in single crystals are given by

$$D_{v//}=0.05 \text{ cm}^2/\text{sec} \exp(-18.2 \text{ kcal/mol}-RT)$$

and

$$D_{v\perp}=0.10 \text{ cm}^2/\text{sec} \exp(-19.1 \text{ kcal/mol}-RT) ,$$

where $D_{v//}$ and $D_{v\perp}$ refer to diffusion parallel and perpendicular to the hexagonal axis respectively. These values are not much different from our value of D_0. The thermodynamical relation of Nachtrieb et al.[21] gives

$$E_D=16.5\, L_m ,$$

where L_m is the latent heat of melting. Introducing the observed value of latent heat for cadmium, $L_m=13.2$ cal/gr., it predicts E_D to be 10.5 kcal/mole. Employing the Van Liempt relation[22]

$$E_D=32\times(\text{melting temperature}) ,$$

it predicts 19 kcal/mole. These values of activation energy are consistent with the value obtained in our experiment 17.6 kcal/mole. Also, inserting the observed value of $E_D=17.6$ kcal/mole into the Dashman-Langmuir's relation[23],

$$D_0=E_D d^2/Nh ,$$

where d is the atomic distance and N is the Avogadro's number, D_0 is estimated to be 0.17 cm²/sec.

Because of a poor sensitivity of the experiment and a crude approximation made in analysis there may be an appreciable error in our diffusion constant. We can not say so much about the quantitative result. Finally, it may be noted that we can not hope to detect the variation of diffusion with direction by nuclear resonance study, even if the single crystal is employed.

Acknowledgements

The author wishes to thank Professor T. Kanda for his continued help and encouragement throughout the progress of this work. Particular thanks are due to Professor T. Nagamiya and Professor J. Itoh for many helpful discussions and advice. This work has been supported in part by the Scientific Research Expenditure of the Ministry of Education.

References

1) Y. Masuda: J. Phys. Soc. Japan **12** (1957) 523.
2) J. Korringa: Physica **16** (1950) 601.
3) Bloembergen, Purcell, and Pound: Phys. Rev. **73** (1948) 679.
4) R. Kubo and K. Tomita: J. Phys. Soc. Japan **9** (1954) 888.
5) H. S. Gutowsky: Phys. Rev. **83** (1951) 1073.
6) D. F. Holcomb and R. E. Norberg: Phys. Rev. **98** (1955) 1074.
7) E. F. W. Seymour: Proc. Phys. Soc. **A66** (1953) 85.
8) N. F. Ramsey and E. M. Purcell: Phys. Rev. **85** (1952) 143.
N. F. Ramsey: Phys. Rev. **91** (1953) 303.
9) M. A. Ruderman and C. Kittel: Phys. Rev. **96** (1954) 99.
10) J. Bardeen: J. Chem. Phys. **6** (1938) 367.
11) R. A. Silverman and W. Kohn: Phys. Rev. **80** (1950) 912.
12) W. Kohn: Phys. Rev. **87** (1952) 472.
13) H. Jones and B. Schiff: Proc. Phys. Soc. **A67** (1954) 217.
14) W. Kohn: Phys. Rev. **96** (1954), 590.
15) T. Kjeldaas and W. Kohn: Phys. Rev. **101** (1956) 66.
16) B. Schiff: Proc. Phys. Soc. **A67** (1954) 2.
17) I. Solomon and N. Bloembergen: J. Chem. Phys. **25** (1956) 261.
18) I. Solomon: Phys. Rev. **99** (1955) 559.
19) H. S. Gutowsky and G. E. Pake: J. Chem. Phys. **18** (1950) 162.

20) Wajda, Shirn, and Huntington: Acta Metallurgica **3** (1955) 39.
21) Nachtrieb, Weil, Catalano, and Lawson: J. Chem. Phys. **20** (1952) 1189.
22) Van Liempt: Z. Phys. **96** (1935) 534.
23) S. Dashman and I. Langmuir: Phys. Rev. **20** (1922) 113.

JOURNAL OF THE PHYSICAL SOCIETY OF JAPAN Vol. 13, No. 6, JUNE, 1958

Effects of Ionizing Radiations on Polyethylene

By Kenichi SHINOHARA,
Scientific Research Institute, Tokyo
Ayao AMEMIYA and Akibumi DANNO*
Faculty of Engineering, University of Tokyo, Tokyo

(Received January 28, 1958)

Polyethylene films were irradiated in the air by deuterons accelerated by a cyclotron and by gamma rays from cobalt-60 source. Gel fraction, swelling ratio, weight changes and infrared absorption spectra of irradiated specimens were measured. It was found that the specimen irradiated by deuterons was cross-linked and became insoluble in xylene. The effects of deuteron irradiation seem almost the same as those of other ionizing radiations such as pile or gamma rays. Infrared absorption spectra reveals some difference in that the ratio of E_{co}/E_{cc} is 0.65 in the deuteron irradiation and is smaller than the value of 14.0 resulting from gamma ray irradiation, where E_{co} is the optical density of carbonyl groups and E_{cc} that of unsaturation. Some considerations are given on the possible explanation of this difference.

§ 1. Introduction

Many studies have been made on the irradiation of polyethylene by ionizing radiations. Charlesby and his coworkers[1)-4)] have investigated the rod-shaped polyetylene irradiated in a pile and observed the liberation of gas, the changes in weight, density, solubility and in melting point. Infrared absorption spectra have also been investigated by Dole and his coworkers[5)], Ballentine et al[6)] and Miller, Lowton and Balwit[7)] for polyethylene films irradiated in a pile, or irradiated by the gamma rays from cobalt-60 or by high energy electrons. Their results suggest that the production of unsaturated bonds in polyethylene is important among other radiation effects.

In the present paper, some results will be presented on the radiation effects on polyethylene which are dependent on the character of ionizing radiations, especially on the infrared absorption spectra of polyethylene films irradiated by deuterons and gamma rays from cobalt-60.

§ 2. Experimental Procedure

Deuteron beam produced by the cyclotron at the Scientific Research Institute was applied for polyethylene with the dimension shown below. Deuterons were extracted from the cyclotron at the exit port covered with aluminum foil approximately 28 μ in thickness. The energy of the beam was 3.8 MeV after acceleration, and about 2 MeV after passing through the aluminum window. The beam bombarded a sample after travelling through 1.5 cm in the air, with the energy of about 1.4 MeV.

The irradiation of the sample was carried out using an aluminum rotating-drum as shown in Fig. 1. The rotating-drum was 50 mm in diameter and 50 mm in height. The film to be irradiated was mounted on the surface of this drum. The drum was rotated while mov-

* Present adress; Japan Atomic Energy Research Institute, Tokyo.

ing up and down in order to irradiate the sample uniformely. The revolution rate of the drum was variable in the range from 20 to 100 rpm, so that the absorbed dose can be adjusted from 4.2×10^7 to 22.5×10^7 rads per one exposure during one course of up and down. Dose applied to the sample during one

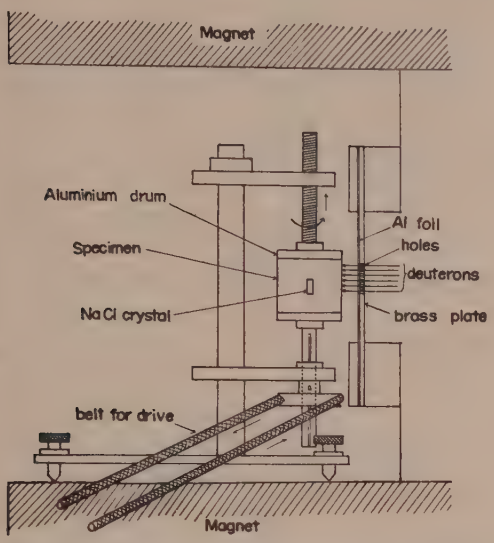

Fig. 1. Schematic diagram of irradiation experiment.

course was defined as one exposure, for instance, when the rate of revolution was 60 rpm and the deuteron current was 10 μA, one exposure was equivalent to 7.0×10^7 rads. Total amount of the dose applied to the sample was, also measured independently by the activity of ^{24}Na produced in NaCl crystal which had been attached on the surface of the sample.

In the second experiment, the films of polyethylene were irradiated by gamma rays from cobalt-60 source of about 120 curies. The dose rate in the center of the source cylinder was 7.5×10^4 r/hr as measured by the ferrous sulphate dosimetry.

The semples of polyethylene were the films commercially obtained with the thickness of 0.03 mm. The size of the specimen was 150 mm in length and 38 mm in width. The average molecular weight was determined as 5.15×10^4 by the measurement of viscosity.

§ 3. Experimental Results

(i) *Formation of cross-links and the change of weight*

Irradiation of polyethylene by deuterons caused a similar change in its character as by the pile radiation or gamma rays. The polymer cross-linked and formed an insoluble gel in organic solvents such as xylene or benzene. The analysis of the swelling experiments revealed that the number of cross-links increased linearly with absorbed dose.

Changes of weight caused by irradiation also showed a similar behaviour to the results obtained by Charlesby[1]. The weight at first increased, reaching a maximum at the absorbed dose of 4.2×10^8 rads and then decreased. Fractional increase of the weight at the maximum, however, only about 2% and was smaller than the value of 8% obtained by Charlesby for the pile irradiation. The

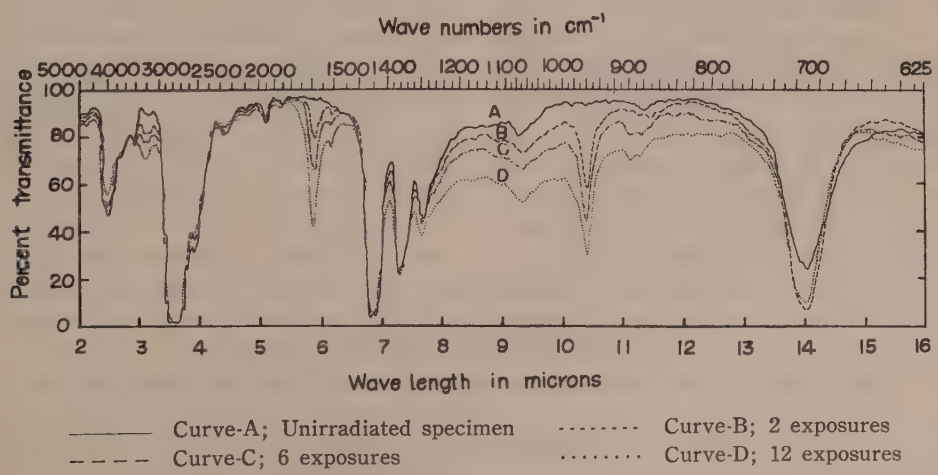

Fig. 2. Infrared absorption spectra of irradiated polyethylene.

thickness of the samples were of the same order of magnitude in both cases.

(ii) *Infrared absorption spectra*

Infrared absorption spectra of irradiated films of polyethylene were measured by the Baird Model B Double Beam Infrared Spectrophotometer. The films were held in place in the cell with a holder and compared against air.

Fig. 2 shows the infrared absorption spectra of polyethylene irradiated in the air by deuterons. Curve A is that for an unirradiated sample and curves B, C and D are those for the samples irradiated by deuterons. The number of exposures given to those specimens were 2, 6 and 12, and the absorbed dose given by the specimens were estimated as about 1.4×10^8, 4.2×10^8 and 8.4×10^8 rads, respectively. In these curves the characteristic band at 964 cm^{-1} arises from the absorption by the unsaturation of the type of PHC=CHR trans, the band at 1720 cm^{-1} by the carbonyl groups and the band 3450 cm^{-1} by the hydroxyl groups. The absorption at these characteristic bands increases with the absorbed dose showing that the unsaturations, carbonyl groups and hydroxyl groups had been produced in the irradiated samples. This is in accord with the results obtained in the experiments of pile irradiation carried out by Dole, Keeling and Rose[6], and also, of gamma ray irradiation by Ballentine et al[6].

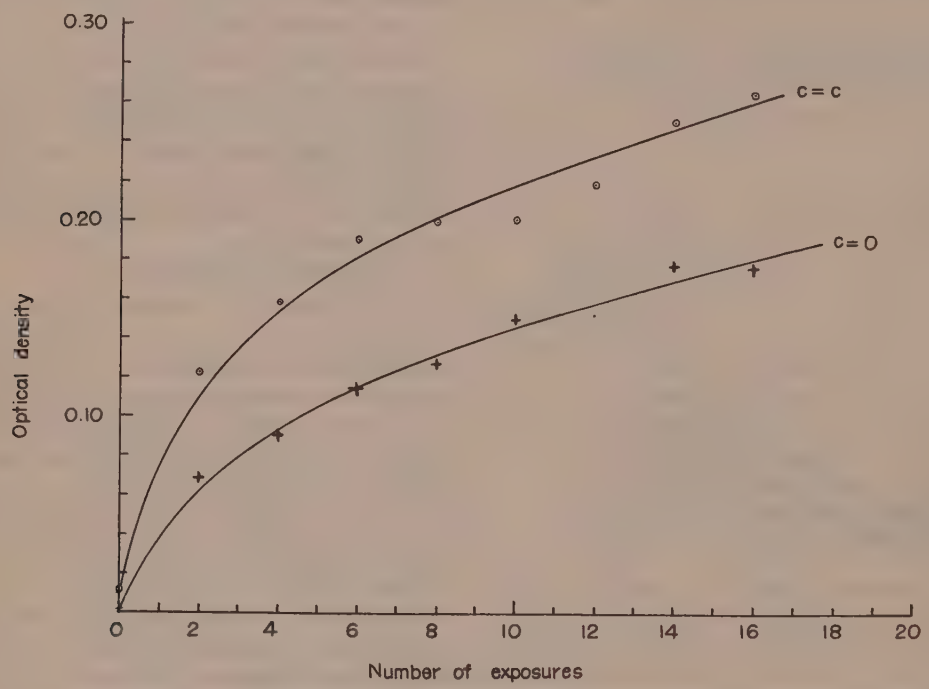

Fig. 3. Optical densities at 1720 cm^{-1}(C=0) and at 964 cm^{-1}(C=C).

The optical density at 1720 cm^{-1} increased with the number of exposures but the increase is not linear as shown in Fig. 3*. The optical density at 964 cm^{-1} also increased with the number of exposures. Moreover, the ratio of optical density of carbonyl groups, E_{co}, to that of unsaturation, E_{cc}, at a given absorbed dose was found to be approximately constant and its mean value was 0.65, as seen in Table I. If it is assumed that the molar extinction coefficients of carbonyl group and unsaturation are 188 and 85.4 mol/l/cm^8), respectively, the ratio of the yield of carbonyl groups to that of unsaturations turns to be 1:3. From this result, the yield of unsaturations is three times larger than that of carbonyl groups in the polyethylene irradiated by deuterons.

Results of gamma ray irradiation is given in Fig. 4. The dose rate used was 7.5 r/hr. The change in optical density at unsaturation

* In the calculation of optical density, a base line was selected as to connect the both tails of the absorption peak by a straight line.

Table I. The ratio of optical density of carbonyl groups and that of unsaturations.

I. Deuteron irradiation

Number of exposures	$E_{C=O}$	$E_{C=C}$	$E_{C=O}/E_{C=C}$
0	0.0	0.009	0.0
2	0.070	0.122	0.57
4	0.091	0.158	0.58
6	0.114	0.191	0.60
8	0.127	0.199	0.64
10	0.151	0.201	0.75
12	0.150	0.219	0.74
14	0.177	0.250	0.71
16	0.175	0.275	0.64

II. Gamma rays irradiation (does rate 7.0×10^4 rad/hr.)

Dose 10^6 rad	$E_{C=O}$	$E_{C=C}$	$E_{C=O}/E_{C=C}$
15.3	0.221	0.029	7.8
40.4	0.536	0.039	13.7
60.8	0.675	0.035	19.2
81.1	1.029	0.067	15.2

produced by gamma ray irradiation is smaller than that of deuteron irradiation. The change at carbonyl groups, on the other hand, produced by the former is larger than the by the latter. Hence, the ratio of E_{CO}/E_{CC} in the gamma ray irradiation is much larger as seen in Table I.

This result may be compared with the result obtained by Ballentine, Dienes, Manowitz, Ander and Mesrobian[6], that the value of E_{CO}/E_{CC} was 0.65 when irradiated by electrons of 2 MeV and was 4.5 by gamma rays from cobalt-60 with dose rate of 2.5×10^{-5} r/hr.

§ 4. Discussion

It is seen above that there is some difference in E_{CO}/E_{CC} between deuteron and gamma ray irradiation, gamma ray giving a larger value of E_{CO}/E_{CC} and also of E_{CO}. Since the oxidation of polyethylene was not observed in the irradiation in vacuum[9], the presence of oxygen in polyethylene resulting from the diffusion from the surrounding atomsphere must be related to the oxidation process, i.e. the formation of carbonyl groups[10]. The concentration of oxygen in polyethylene in air at one atomsphere is calculated to be about 2.2×10^{-4} mol/cc, when the permeability constant of oxygen in the sample is taken as 40×10^{-10} cc/cm²/sec/cm in Hg at 20°C[11]. On the other hand, the consumption of oxygen during the irradiation of deuterons can be estimated as 2×10^{-6} mol/cc per 2.3×10^7 rads from the number of carbonyl groups formed. The amount of consumption of oxygen is, therefore, only a small fraction of oxygen in polyethylene, in both deuteron and gamma ray irradiation. This shows that the process of diffusion is not important in giving the

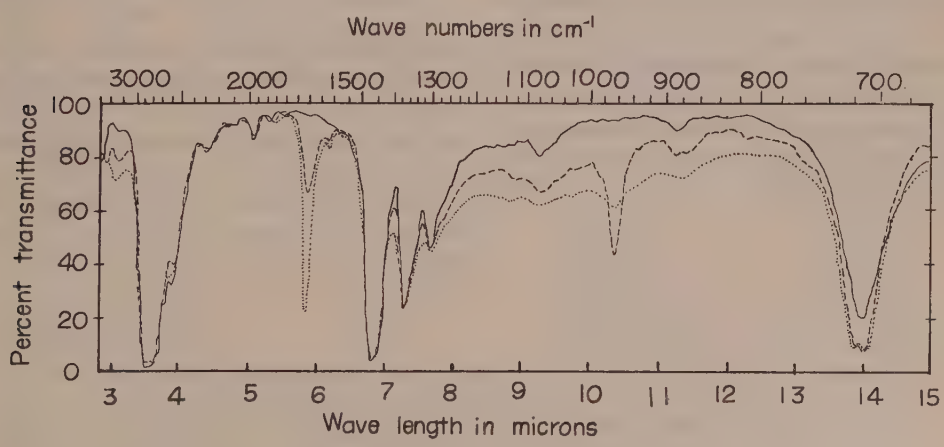

Fig. 4. Infrared absorption spectra of polyethylene irradiated by deuterons and gamma rays.

——— unirradiated sample
– – – – irradiated by deuterons
····· irradiated by gamma rays

difference in the effect between the deuteron and gamma ray irradiation.

The difference of E_{co}/E_{cc} between deuterons and gamma ray irradiation may be explained in the following way be considering the character of radiations. The chemical changes produced in polyethylene by ionizing radiations may be interpreted in general, by postulating primary processes and secondary processes[12)-14)]. One of the primary processes is the rupture of side-bonds giving rise to the formation of polymer radicals and liberation of free hydrogen atoms. The secondary processes will include the recombination of these radicals and free hydrogen atoms and other entities. Also, the dihydrogenation process will cause the formation of unsaturations as follows,

$$\begin{array}{c} H \\ -C-\dot{C}- \\ H\ H \end{array} + H \longrightarrow \begin{array}{c} -C=C- \\ H\ H \end{array} + H_2 \qquad (1)$$

In the samples irradiated by deuterons, the specific ionization along the track is very high compared with that due to the secondary electrons from gamma rays from cobalt-60. The density of polymer radicals and free hydrogen atoms will also be very high, and their mutual recombination will occur so frequently, that the formation of unsaturation will be very prominent. In the case of irradiation by gamma rays, the specific ionization is low, and radicals and hydrogen atoms will be distributed some distance apart from each other. Therefore, their chance of mutual recombination will be much less than in the case of deuteron irradiation. The chance of reaction of polymer radicals with oxygen atoms, on the other hand, will be about the same resulting in the relative increase of the formation of carbonyl groups.

The experiment of Ballantine et al, also give a similar tendency for E_{co}/E_{cc}, i.e. a lower value for electron beams which, most probably, will have a much larger density of ionization than gamma rays, though the numerical values do not coincides with ours. In this case, if the radicals formed in the samples have life time not very short compared with the time required for the irradiation, the average density of radicals will be rather high, giving rise to smaller value for E_{co}/E_{cc}.

References

1) A. Charlesby: Proc. Roy. Soc. **A215** (1952) 187.
2) A. Charlesby and N. H. Hancock: Proc. Roy. Soc. **A217** (1953) 122.
3) A. Charlesby and M. Ross: Proc. Roy. Soc. **A218** (1953) 245.
4) A. Charlesby: Proc. Roy. Soc. **A222** (1954) 60.
5) M. Dole, C. D. Keeling and D. G. Rose: J. Ame. Chem. Soc. **76** (1954) 4304.
6) D. S. Ballentine, G. J. Dienes, B. Manowitz, A. Ander and R. B. Mesrobian: J. Polymer Sci. **13** (1954) 410.
7) A. A. Miller, E. J. Lawton and L. S. Balwit: J. Phys. Chem. **60** (1956) 599.
8) L. H. Cross, R. B. Richards and H. A. Willis: Disc. Faraday Soc. **9** (1950) 235.
9) Б. П. Карпов: Сессия Акаамии Науксссp по Мирному Использованию Атомной Знергии: Июая (1955) 4.
10) A. Chapiro: J. Chim. Phys. **52** (1955) 246.
11) W. Heilman, V. Tammela, J. A. Meyer, V. Stannett and M. Szwarc: Ind. Engin. Chem. **48** (1956) 821.
12) K. H. Sun: Mordern Plastic **32** (1954) 141.
13) H. Okamoto and A. Ishihara: J. Polymer Sci. **20** (1956) 115.
14) R. W. Pearson: J. Polymer Sci. **25** (1957) 189.

JOURNAL OF THE PHYSICAL SOCIETY OF JAPAN Vol. 13, No. 6, JUNE, 1958

Effects of ionizing radiations on polyvinyl alcohol
I. Breakdown of main-chain and formation of carbonyl groups

Akibumi DANNO*

Faculty of Engineering, University of Tokyo, Tokyo.

(Received February 1, 1958)

Polyvinyl alcohol in the form of film and powder were irradiated in the air by gamma rays from cobalt-60 source, and by deuterons accelerated by a cyclotron. Weight changes, viscosity, solubility and infrared absorption spectra of irradiated samples were measured as a function of absorbed dose. The reduction of the molecular weight of the irradiated specimens was observed suggesting that the effect was one of degradation. Infrared absorption spectra showed the formation of the carbonyl groups in the irradiated specimen.

§ 1. Introdnction

It has been shown that the chemical changes produced by ionizing radiations on long-chain polymers bring about either cross-linking or degradation depending on the chemical structure of the material and on the mode of irradiation[1,2,3]. For example, cross-linking has been observed for polyethylene[4], natural rubber[5] and polystyrene[6], while degradation for polymethyl methacrylate[7] and polytetrafluoroethylene[8].

The physical properties of the irradiated polyvinyl alcohol have not been reported in detail. The only article referring to it is the general review of Charlesby[1]. In this articl, polyvinyl alcohol was classified in the group of polymer which crosslinks.

In the present experiment polyvinyl alcohol was irradiated in the air by deuterons accelerated by the cyclotron at the Scientific Research Institute, and also by gamma rays from cobalt-60. After irradiation the sample turned brittle and became easily soluble in water. The molecular weight of the irradiated specimen decreased with the absorbed dose.

§ 2. Experimental

Deuteron irradiation was carried out on the films of polyvinyl alcohol. The film to be irradiated was mounted on the surface of an aluminum rotating-drum as reported in the previous paper[9]. The drum was rotated while moving up and down in order to radiate the sample uniformely. The rate of revolution of the drum was variable in the range from 20 to 100 rpm, so that the absorbed dose can be adjusted from 4.2×10^7 to 22.5×10^7 rads per one exposure during one course of up and down.

Gamma rays from cobalt-60 of about 120 curies were used to irradiate, both, films and powder of polyvinyl alcohol. The dose rate in the center of the source cylinder was 7.5×10^4 r/hr as measured by ferrous sulphate dosimetry.

Films used for the experiment were of the thickness of 0.02 mm and 0.04 mm. The thinner one was used for the measurement of infrared absorption spectra, and the thicker one for the measurement of the weight change and solubility. Viscosities and solubilities were also measured for powdered samples irradiated by gamma rays. The degree of polymerization of the samples were as follows,

polyvinyl alcohol	degree of polymerization
film-A	780
film-B	1670
film-C	2680
powder-A	760
powder-B	1660
powder-C	2680

§ 3. Experimental results

(i) *Changes in weight in polyvinyl alcohol films*

Changes of weight in the fims of polyvinyl alcohol irradiated in the air, by deuterons were measured as a function of the number

* Present adress; Japan Atomic Energy Research Institute, Tokyo.

of exposures. The behaviour of this change was different from that of polyethylene. In the latter case the sample increases its weight at first, to reach a maximum value, and then decreases gradually. The weight of irradiated polyvinyl alcohol decreased exponentially with the number of exposures as shown in Fig. 1.

Microchemical analysis was carried out for the irradiated films. The percentages of carbon and hydrogen in weight were calculated by the carbon dioxide and water formed on combution. According to the results of analysis, the weight fraction of carbon in the

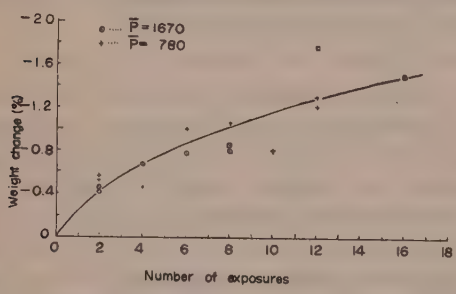

Fig. 1. Weight changes of polyvinyl alcohol films irradiated by deuterons.

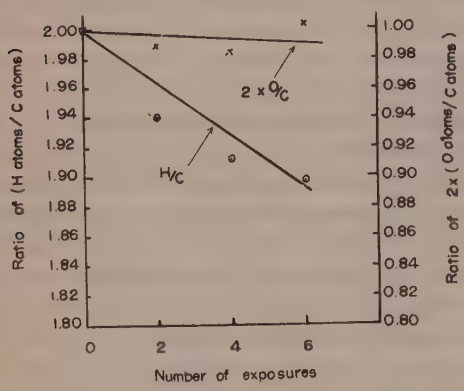

Fig. 2. The results of the Micro-chemical analysis of polyvinyl alcohol films irradiated by deuterons.

unirradiated specimen was slightly smaller than that of the theoretical value calculated from the chemical formula. This may be due to the water adsorbed in the sample, since the polyvinyl alcohol is very hygroscopic. This adsorbed water turned out to be 3.7% in weight. As shown in Fig. 2, the ratio of the number of hydrogen atoms to that of carbon atoms, H/C, decreased with the absorbed dose, but the ratio of the number of oxygen atoms to that of carbon atoms, O/C, remained almost constant. From these results, it was assumed that the gases evolved by the irradiation in the air was mostly hydrogen.

Direct analysis of the gas evolved by the irradiation was also carried out as follows. Powdered sample of polyvinyl alcohol was sealed in an evacuated glass tube and irradiated to about 10^7 rads by gamma rays from cobalt-60. The gases evolved by the irradiation were analyzed by a mass-spectrometer. Table I shows the result of the analysis. Small amount of carbon-monoxide and -dioxide were also liberated.

Table 1. Results of mass-spectrographic analysis of gases liberated by the irradiation of polyvinyl alcohol in vaccum.

molecules	H_2	CO	O_2	CO_2
volume %	91.0	6.2	0.8	1.5

(ii) *Viscosity measurement*

Powdered sample of polyvinyl alcohol irradiated by gamma rays in the air, was found to be more easily soluble in water compared with unirradiated specimen. The molecular weight of these samples were obtained by viscosity measurement using the the formula (1)[10],

$$[\eta]=8.87\times10^{-4}P^{0.62} \qquad (1)$$

where $[\eta]$ is the intrinsic viscosity and P the

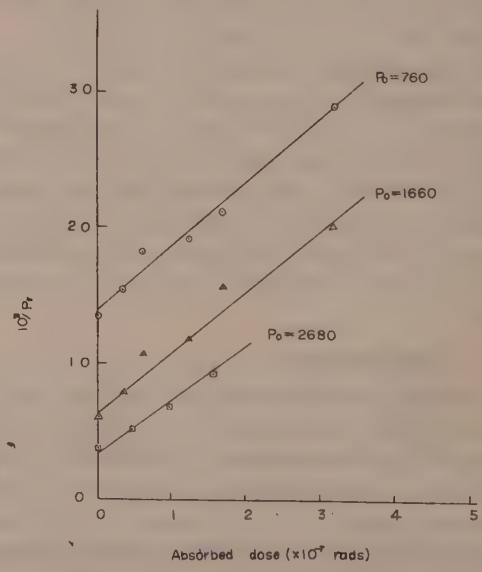

Fig. 3. The relation between the degree of polymerization, P_r, and the absorbed dose, R.

degree of polymerization. Viscosity average molecular weight, M_v is calculated as wP, where w is the mass of monomer unit (CH_2–CHOH). For the Poisson distribution of molecular weight, number average molecular weight, M_n can be derived from the viscosity average molecular weight[7],

$$M_n = M_v/((\beta+1)\Gamma(\beta+1))^{1/\beta}, \quad \beta=0.62 \quad (2)$$

where β is the power of Staudinger's law unsed in equation (1), and is equal to 0.62.

Linear relation is obtained between $1/P$ and the absorbed dose, R, as shown in Fig. 3. In this figure, results of the measurements for different initial degree of polymerization were listed. This linear relationship between $1/P$ and R can be expressed by

$$1/P_r - 1/P_0 = \alpha R \quad (3)$$

where P_0 and P_r are the degree of polymerization of initial and the irradiated specimen, respectively. As all three curves in Fig. 3 are nearly parallel, we may be taken a single value for α, i.e.

$$\alpha = 4.5 \times 10^{-11}/\text{rad} \quad (4)$$

(iii) *Change of the infrared absorption spectra*

Infrared absorption spectra of irradiated films of polyvinyl alcohol were measured by the Perkin-Elmer Model 21 infrared spectrophotometer. Results are shown in Fig. 4. Curve-A in this figure is the absorption spectra of the unirradiated sample, curve-B that of the sample irradiated by cobalt-60 gamma rays, the absorbed dose being 6.0×10^7 rads and curve-C that of the sample irradiated by deutron, the absorbed dose being about 14×10^7 rads. In both irradiated specimens the prominent absorption is observed at 1710–1720 cm^{-1}, which was scarcely detectable in the initial specimen.

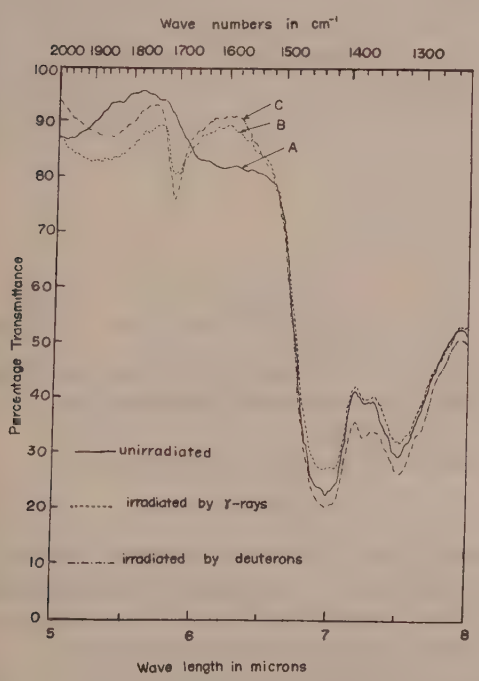

Fig. 4. Infrared absorption spectra of polyvinyl alcohol irradiated by deuterons and cobalt-60 gamma rays.

It is known that[11] a carbonyl group situated in saturated open chain ketones always exhibit a strong band near 1725–1705 cm^{-1}, while normal unconjugated alkyl aldehyde shows their carbonyl band at slightly higher frequency than the corresponding ketones in the range of 1740–1720 cm^{-1}. On the other hand, non-basic aliphatic acids shows the absorption band in the range between 1725–1715 cm^{-1}, when examined in the solid or liquid state. Therefore, the absorption spectra observed at 1720–1710 cm^{-1} shows the formation of ketonic and acidic type carbonyl.

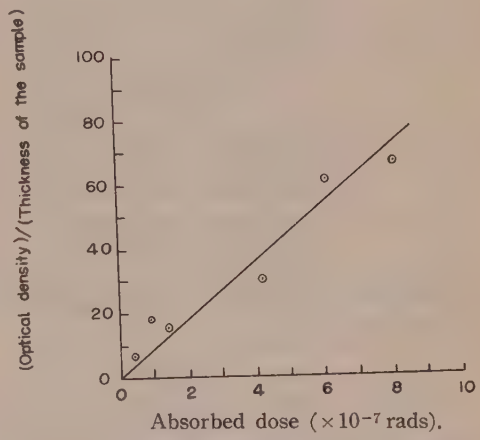

Fig. 5. Change of optical density at 1720–1710 cm^{-1} divided with the thickness of the sample.

The number of carbonyl groups in the sample produced by the radiation may be estimated from the optical density. As shown in Fig. 5, the relation between the optical density of carbonyl groups and the absorbed dose is approximately linear in the specimens irradiated by cobalt-60 gamma rays.* The

* In the calculation of optical density, a base line was selected as to connect the both tails of the absorption peak by a straight line,

carbonyl concentration in the sample was obtained from the value of optical density by dividing it by the molar extinction coefficient. The value of the latter was given as 188 mol /l/cm by Cross, Richard and Willis[12,13]. Fig. 5 gives the increase of the optical density with absorbed dose can be used to get the rate of formation of carbonyl group in a given monomer unit. The result obtained is 2.6×10^{-10}/rad.

§ 4. Discussions

It is seen above when polyvinyl alcohol is irradiated by ionizing radiations in the air, breakdown of main-chain and formation of carbonyl groups take place. One possible mechanism for such a breakdown of main-chain and formation of acidic carbonyl groups by the irradiation in the air is

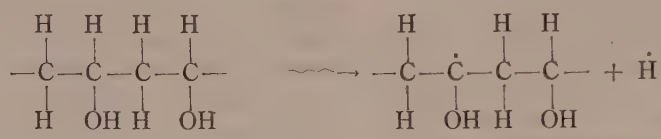

(5)

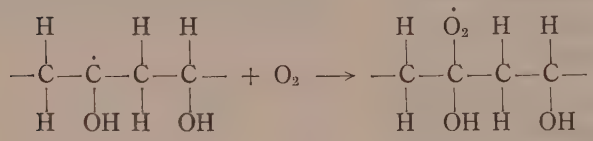

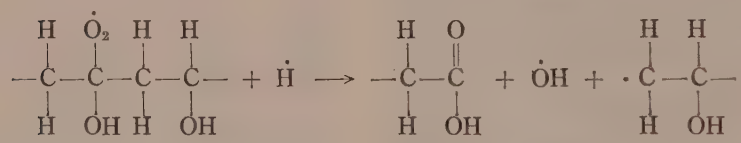

(6)

The formation of ketonic carbonyl groups and the liberation of hydrogen molecules may be explained as

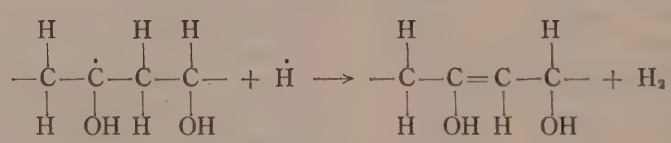

(7)

If the distribution of molecular weight of the unirradiated specimen could by expressed by an exponential low, and if the breakdown of the main-chain bond occurs at random along the chain and is proportional to absorbed dose, R, then the probability of a given bond between monomers being broken by the radiation, μ, is obtained by the slope of the molecular weight *vs* dose curve (Fig. 3). The relation between the viscosity average molecular weight of irradiated specimen, M_r, and the number average molecular weight M_n, obtained by the theoretical calculation[7], may be written for polyvinyl alcohol as $M_r=1.8\,M_n$. Thus

$$1/M_r-1/M_0=\mu R/1.8\,w \qquad (8)$$

where M_0 is the viscosity average molecular weight of unirradiated specimen and w the mass of monomer unit.

This relation can also be written as

$$1/P_r-1/P_0=\mu R/1.8 \qquad (9)$$

where p_r and P_0 are the average degree of polymerization of irradiated and unirradiated specimen, respectively, which can be determined by the viscosity measurement.

It was already stated above that the result of experiment can be expressed as

$$1/P_r-1/P_0=4.5\times10^{-11}\,R \qquad (4')$$

Comparing (4′) with the theoretical formula (9), the value of μ may be determined as $\mu = 8.1 \times 10^{-11}$/rad. Therefore, the absorption of the dose of 10^8 rads will results in the breakdown of 0.8% of the bonds in the main-chain skeleton. There are 1.36×10^{22} monomer units in one gram of polyvinyl alcohol, so that 11.0×10^{11} main-chain bonds between these monomers will be fractured by one rad. By definition, one rad of absorbed dose liberats 6.2×10^{13} eV per gram of the substance irradiated. Therefore, the energy expenditure per main-chain fracture is 56 eV.

As was seen above, the probability of formation of carbonyl groups in a given monomer unit was estimated as 2.6×10^{-10}/rad from the infrared analysis. Thus 10^8 rads results in the formation of carbonyl groups of 2.6% of total monomer units. Comparing this value with the probability of breakdown of main-chain, it is seen that the probability of formation of carbonyl groups is three times larger, and the energy expenditure per carbonyl formation is 18 eV.

§ 5. Acknowledgement

The auther wishes to express his sincere thanks to Dr. K. Shinohara of the Scientific Research Institute, Dr. A. Amemiya of Faculty of Engineering, University of Tokyo and Dr. A. Harashima of Tokyo Institute of Technology for their constant encouragement and also to Dr. M. Tomonari of the Kurashiki Rayon Company for kindly preparating the samples of polyvinyl alcohol. He also wishes thank the Tokyo Polymer Irradiation Group for their helps in the experiment.

References

1) A. Charlesby: Nucleonics, 12, June (1954) 18.
2) K. H. Sun: Mordern Plastics, Sep. (1954) 141.
3) A. A. Miller, E. J. Lawton and J. B. Balwit: J. Polymer Sci. **14** (1954) 503.
4) A. Charlesby: Proc. Roy. Soc. A, **215** (1952) 187.
A. Charlesby and N. H. Hancock: Proc. Roy. Soc. A, **217** (1953) 122.
A. Charlesby and M. Ross: Proc. Roy. Soc. A, **218** (1953) 245.
5) A. Charlesby: Atomics, 5, Jan. (1954) 12.
6) A. Charlesby: J. Polymer Sci. **11** (1953) 513.
7) P. Alexander and A. Charlesby: Proc. Roy. Soc. A, **223** (1954) 392.
8) J. W. Ryan: Mordern Plastics Oct. (1954) 152.
9) K. Shinohara, A. Amemiya and A. Danno: to J. Phys. Soc. Japan **13** (1958).
10) H. Staudinger and H. Warth: J. Prakt. Chem. **155** (1940) 261.
I. Sakurada and T. Chiba: Kogyo Kagaku **49** (1944) 137.
11) L. J. Bellamy: The Infrared Spectra of Complex Molecules (1954).
12) J. T. Clarke and E. R. Blot: J. Polymer Sci. **1** (1946) 419.
13) L. H. Cross, R. B. Richards and H. A. Willis: Discs. Faraday Soc. **9** (1950) 235.

Effects of Ionizing Radiation on Polyvinyl Alcohol
II. Changes of Physical Properties of the Irradiated Specimen Caused by Heat Treatment

By Akibumi DANNO*

Faculty of Engineering, University of Tokyo, Tokyo,

(Received February 1, 1958)

The physical Properties of polyvinyl alcohol irradiated by deuterons or gamma rays were found to change remarkably by heat treatment. Irradiation causes the decrease of the molecular weight and the increase of the carbonyl groups. When these specimens are heated above 120°C, however, the solubility diminishes considerably and even gel formation occurs for highly irradiated ones. Infrared absorption spectra revealed that the number of carbonyl groups formed by the irradiation decreased greatly as a result of heat treatment. Some discussion are given on the process of gel formation.

§ 1. Introduction

It is usually believed that physical properties of polymers irradiated by ionizing radiatiohs remain unchanged after irradiation[1].

In polyvinyl alcohol, it was found, in the previous paper[2], that considerable number of carbonyl groups are formed by the irradiation. Since carbonyl groups are rather active, the sample were subjected to heat treatment and the resulting changes of properties, which, it is thought, might arise from the action of carbonyl groups, were investigated. Two effects of heat treatment have been observed; gel formation and the disappearance of carbonyl groups.

§ 2. Experiment

Films of polyvinyl alcohol were irradiated by deuterons accelerated by a cyclotron[3]. Polyvinyl alcohol in the form of films and powder were also irradiated by gamma rays from cobalt-60 as reported in the previous paper[2].

Films of thickness of 0.02 mm and 0.04 mm were used. The thinner one was used for the measurement of solubility. Solubility and gel fraction were also measured for the powdered sample irradiated by gamma rays.

Heat treatment was carried out by keeping irradiated samples at a certain temperature above 120°C for more than ten minutes in a thermostat. The samples were kept in air during the heat treatment.

* Present adress; Japan Atomic Energy Research Institute, Tokyo.

§ 3. Experimental Result

(i) *Changes of weight in heat treatment*

Weight changes of polyvinyl alcohol due to irradiation by deuterons or gamma rays and also by subsequent heat treatment were measured. As reported in the previous paper[2], weight of irradiated specimens decreased with increasing radiation dose. A further change of weight in these specimens were observed after heating for one hour at 150°C. The relation between the decrease of weight and the absorbed dose is given in Fig. 1.

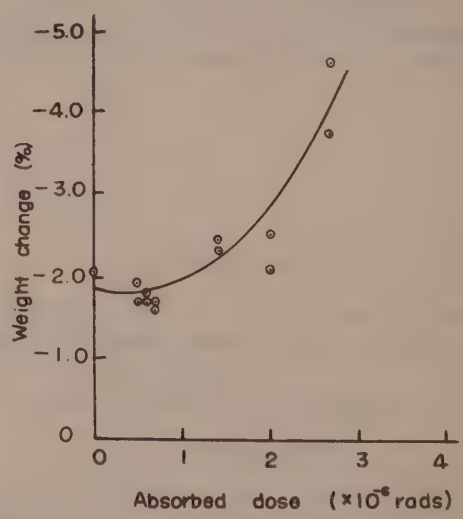

Fig. 1. Weight change of irradiated polyvinyl alcohol after heated at 150°C for one hour.

A set of micro-chemical analysis of heat treated specimens was carried out. The results are shown in Fig. 2. The ratio of num-

ber of hydrogen atoms to that of carbon atoms, H/C, decreases from 1.97 in the unirradiated specimen to 1.86 for highly irradiated specimen. On the other hand, the ratio of number of oxygen atoms to that of carbon atoms, O/C, decreases from 0.50 in the unirradiated specimen to 0.48 for highly irrdiated specimen.

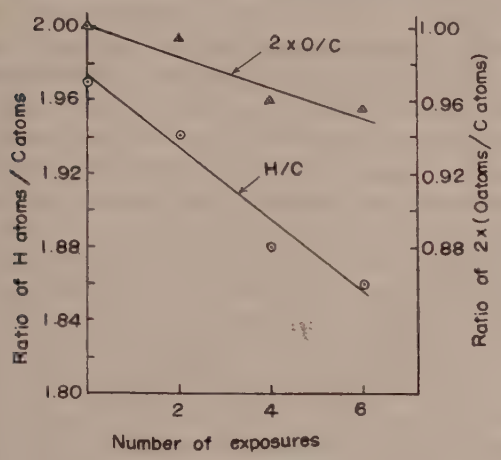

Fig. 2. Micro-chemical analysis of heat treated polyvinyl alcohol (0.02 mm in thickness).

Since the slope of the curve of H/C is greater than that of $2\times$O/C, the liberation of hydrogen in the process of irradiation and heat treatment is more predominate than that expected from the liberation of H_2O. Since the liberation of H_2O is known to occur for unirradiated polyvinyl alcohol by heat treatment, the change of weight of the irradiated specimen by the heat treatment may be attributed to the liberation of H_2 and H_2O.

(ii) *Gel formation of irradiated specimen caused by heat treatment*

When the powder of polyvinyl alcohol irradiated by gamma rays was heated to a temperature above 120°C for over ten minutes after irradiation, considerable fraction of the powder became insoluble in boilling water. Films of polyvinyl alcohol which were irradiated by deuterons and were heated above 120°C, also, became insoluble in hot water above 150°C in an autoclave, and swelled to an extent depending on the amount of absorbed dose.

Gel fractions of the powdered polyvinyl alcohol after heat treatment were measured. The results are given in Fig. 3. In this figure, the ordinate in the gel fraction and abscissas gives r/i, where $i=1/P_i$ and $i+r=1/P_r$. P_i and P_r are the average degree of polymerization of initial and irradiated specimens measured by viscosity. r/i gives, therefore, the ratio of the number of molecules fractured to that of molecules which existed before irradiation. When the value of r/i was smaller

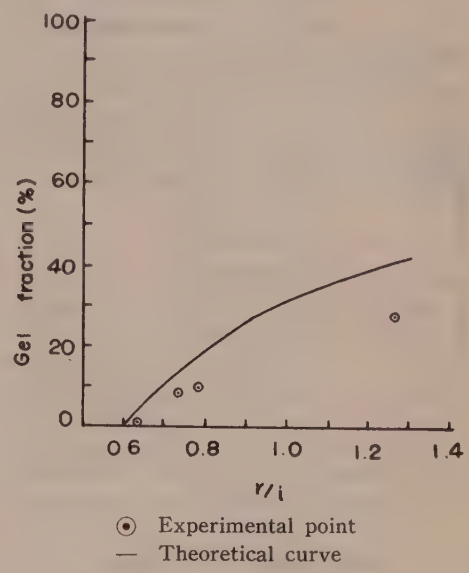

Fig. 3. Gel fraction of irradiated polyvinyl alcohol powder after heat treatment.

than 0.6, the heat treated specimen was also completely soluble, and gel formation first occured when r/i became about 0.6. This indicates that at $r/i=0.6$ the linkage between molecules which are caused by heat treatment became so abandant that they finally form an infinite network.

(iii) *The change of infrared absorption spectra due to heat treatment*

Infrared absorption spectra of films of polyvinyl alcohol irrodiated by deuterons and subjected to heat treatment were measured. Results are shown in Fig. 4 and Fig. 5. Fig. 4 is that of unirradiated specimen which is heated at 150°C for one hour. Fig. 5 is that of a film subjected to the same treatment after irradiation of 6.5×10^7 rads.

In the unirradiated specimen, no significant change on the infrared absorption spectra was observed before and after heat treatment. In the irradiated specimen, however, the absorption at 1720–1710 cm^{-1} due to carbonyl groups is considerably diminshed after the heat treatment. These specimen did not di-

solve as was stated above in boiling water.

It may be not unreasonable to conclude from these facts that carbonyl groups produced by the radiation disappear during the heat treatment, and this disappearance has some conection to the formation of intermolecular linkages which are formed.

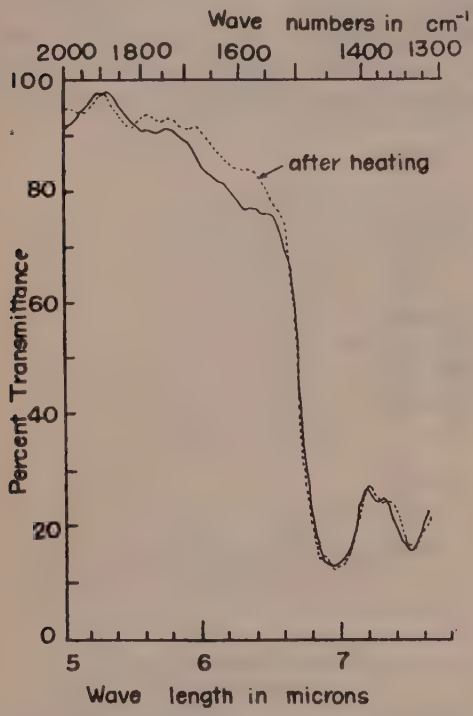

Fig. 4. The change of infrared absorption spectra of unirradiated specimen by the heat treatment.

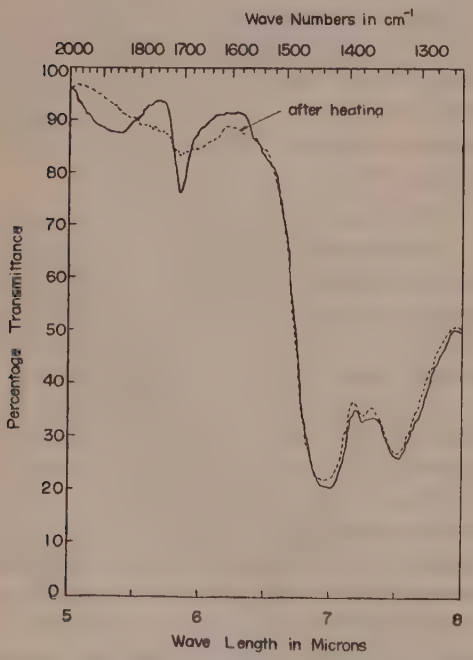

Fig. 5. The change of infrared absorption spectra of irradiated specimen by the heat treatment.

§ 4. Discussion

It is known that some intermolecular linkages are produced by heat treatment[4], in ordinary polyvinyl alcohol which is not irradiated but contains carbonyl groups. The irradiation of polyvinyl alcohol in air causes the main-chain bond fracture and the decrease in molecular weignt as shown by our experiment. Large number of carbonyl groups, however, are formed in this process and the heat treatment, carried out after the irradiation, produces so many intermolecular linkages that even an infinite net-work is formed when the absorbed dose is high.

Following tentative explanation may be given to the process of forming an intermolecular linkage, i.e. the reaction of the carbonyl group reacts with a neighbouring molecule to form a ketale linkage;

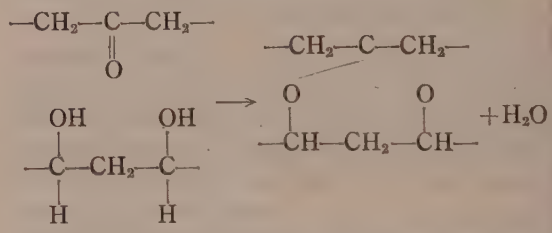

In order to make some calculation on the condition of gel formation by main-chain bond fracture of polyvinyl alcohol, it is assumed that the molecular weight distribution of the unirradiated specimen follows an exponential law, and the breakdown of the main-chain bond occurs at random along the chain. The number of molecules existing in the initial and irradiated specimen are given by the following formula,

$$n(P_i)=N_0/P_i=N_0 i$$
$$n(P_i)=N_0/P_r=N_0(i+r)$$

Where N_0 is the total number of monomer units in the specimen. The difference r $(=1/P_r-1/P_i)$ represents the probability of a fracture of the bond between two adjacent monomer units due to radiation. A calculation giving gel point was published by Charlesby[5] for the case, when the active groups are produced at the ends of fractured mole-

cules. In this calculation, it was assumed that only a certain proportion σ of the end-groups become active. In the case of polyvinyl alcohol, active groups seem to be formed in the intramolecular site and not at the ends as shown in the previous paper. However, a similar calculation can be carried out. In this case, if the number of these active groups are σ times the number of fractured molecules, the gel point is given as the point where the ratio r/i becomes

$$r/i=1/(4\sigma-1)$$

The sol fraction can be given by

$$S=\left\{\frac{1-i/r}{2}-S\right\}^2$$

In this treatment, it is assumed that active groups are never produced at fractured end, but are always produced in the middle part of molecules only, and the end groups of the fractured molecules do not make linkages. Notwithstanding this difference, the same results was obtained for the gel point as that given by Charlesby[6].

Experimentally, gel point obtained was at $r/i=0.6$, so that the efficiency of formation of active groups, σ, is about 2/3. Therefore, at least 4/3 carbonyl groups are produced per one fractured molecule.

§ 5. Acknowledgement

The auther wishes to express his sincere thanks to Dr. K. Shinohara of the Scientific Research Institute, Dr. A. Amemiya of Faculty of Engineering, University of Tokyo and Dr. A. Harashima of Tokyo Institute of Technology for their constant encouragement.

References

1) A. Charlesby: Nucleonics, **12**, June (1954) 18.
2) A. Danno: J. Phys. Soc. Japan **13** (1958).
3) K. Shinohara, A. Amemiya and A. Danno: J. Phys. Soc. Japan **13** (1958).
4) J. T. Clarke and E. R. Blout: J. Polymer Sci. **1** (1946) 419.
5) A. Charlesby: Proc. Roy. Soc. **A231** (1955) 521.
6) A. Charlesby: Proc. Roy. Soc. **A222** (1954) 542.

JOURNAL OF THE PHYSICAL SOCIETY OF JAPAN Vol. 13, No. 6, JUNE, 1958

Nuclear Quadrupole Resonances in Arsenic and Antimony Trihalides and Sulphur Molecular Addition Compounds

By Shizuko OGAWA

Department of Physics, Faculty of Science, Ochanomizu University, Tokyo

(Received Eebruary 8, 1958)

Nuclear quadruploe resonances of I, Br, Cl, As and Sb isotopes in solids $AsCl_3$, $SbCl_3$, $SbBr_3$, AsI_3, SbI_3, $AsI_3 \cdot 3S_8$, $SbI_3 \cdot 3S_8$, SnI_4, $SnI_4 \cdot 2S_8$ and $SnI_4 \cdot 4S_8$ have been measured systematically. The newly obtained coupling constants eQq and asymmetry parameters η of the I^{127} resonances at 77°K are as follows: $eQq=1383.03$, 1402.68 Mc: $\eta=0.002$, 0.039 in $SnI_4 \cdot 2S_8$, $eQq=1364.3$, 1368.3, 1405.0 Mc and $\eta=0.00$, 0.00, 0.03 in $SnI_4 \cdot 4S_8$. In $SnI_4 \cdot 4S_8$ an additional line was observed at 219.04 Mc corresponding to the first resonance. The second resonance of SbI_3 was at 254.637 Mc with $eQq=895.83$ Mc and $\eta=0.565$. Resonance frequencies of As^{75} in AsI_3 and $AsI_3 \cdot 3S_8$ at 77°K were 29.338 and 49.501 Mc, respectively. The first resonance of Sb^{121} in SbI_3 was 25.406 Mc at 77°K and the corresponding resonance in $SbI_3 \cdot 3S_8$ was 37.461 Mc at 297°K. $SbBr_3$ showed two crystal forms which gave Sb^{121} coupling constants of 319.920 and 316.02 Mc and asymmetry parameters of 0.082 and 0.182 at 304°K, respectively. On the Br resonances of $SbBr_3$ three resonance lines instead of two hitherto reported were observed in both crystal forms.

Coupling constants of trihalides were compared with their chemical bond properties. The constants of AsI_3 and SbI_3 are different from those of other compounds, while their sulphur moleculor addition compounds are in rather good agreement.

AsI_3 showed positive temperature dependency for arsenic isotope as for the case of iodine isotope.

§ 1. Introduction

The nuclear quadrupole resonances of I^{127} in AsI_3 were first observed by Kojima, Tsukada, Ogawa, Shimauchi and Abe[1]. On the I^{127} resonance in SbI_3 only the lower frequency line was reported by Schawlow[2] and Barnes and Bray[3], while on the resonances in the sulphur molecular addition compounds, $AsI_3 \cdot 3S_8$ and $SbI_3 \cdot 3S_8$, the lower and higher frequency lines were measured at 77°K by Robinson, Dehmelt and Gordy[4]. They also mentioned the resonance of I^{127} in $SnI_4 \cdot 4S_8$. The resonance frequency, however, was not reported.

Two resonance lines of each Br isotope in $SbBr_3$ which come from the nonequivalent positions of atoms were reported by Robinson, Dehmelt and Gordy[4] at 77°K, while ealier Schawlow[2] observed only one resonance line in Br^{81} at room temperature. On $AsBr_3$ three resonance lines of each Br isotope were observed by Kojima *et al.*[1]. Three lines were also observed on Cl^{35} resonance in $AsCl_3$ by Livingston[5]. The Cl isotope in $SbCl_3$ exhibited two resonance lines[6),7)], one of which had double the intensity of the other. Since the crystal structure of $SbBr_3$ seems to be similar to $AsBr_3$, $AsCl_3$ and $SbCl_3$, three resonance lines of Br isotope corresponding three nonequivalent Positions of atoms in a molecule should be expected.

The resonance of As^{75} in $AsBr_3$ was measured by Kojima *et al.*[1] and the resonances in $AsCl_3$, $AsBr_3$, AsI_3 were measured by Barnes and Bray[8]. Among these resonance frequencies the frequency of AsI_3 is unreasonably high as expected from the nature of the chemical bond.

The resonances of Sb isotopes in $SbCl_3$ were studied by Dehmelt[6], Wang[7] and Ogawa[9], and Wang also measured the resonance in $SbBr_3$ at room temperature. The Sb resonance in SbI_3, however, had not been reported.

The present measurements have been made on the isotopes, of As, Sb, Cl, Br, and I in trihalides and sulphur molecular addition triiodides in the temperature range between 77°K and room temperature. A systematic

relation between the nuclear quadrupole coupling and the nature of chemical bond was obtained. SnI_4 and its sulphur molecular addition compounds were also investigated.

§ 2. Experimental Procedure

The frequencies to be observed cover a very wide frequency range from about 20 Mc to 450 Mc. Four superregenerative oscillators were used for the detection. A tuned type transmission line which was described by Kojima *et al.*[10] was used above 100 Mc frequency range. In the frequency region below 100 Mc, *LC* tuned push pull feed back oscillators were used, which were described in detail in the previous paper[9]. The frequency range from 20 Mc to 70 Mc was covered with one oscillator by using coils of various dimensions. Reactions in the oscillator coils produced by resonating nuclei were amplified by three stage audio amplifier and displayed on an oscilloscope.

While the nuclei whose spin number is 3/2 have only one resonance line, the nuclei having spin of 5/2 have two resonances, i.e., the first resonance ν_1 $(3/2 \leftrightarrow 1/2)$ and the second resonance ν_2 $(5/3 \leftrightarrow 3/2)$. When the both resonances are measured, the asymmetry parameter of the field gradient tensor, η, can be determined. For the determination the two resonances must be measured at the same temperature of the sample. Otherwise the error in η calculated from ν_1 and ν_2 will be large because of the difference in temperature at the sample. This precaution is essential when the asymmetry parameter has small value. In those cases a similar measuring procedure as previouly described[9] was used. For a sample which has a large asymmetry parameter the above mentioned difference of temperature did not lead to a significant error in the calculation of the asymmetry parameter.

The frequency between 10 Mc and 200 Mc was measured by the aid of an oscillator of the frequency range from 10 Mc to 15 Mc which was calibrated by standard frequency of JJY. For measurements above 200 Mc, a single generator of the frequency range from 30 to 300 Mc was used as a marker, and this marker frequency was measured with the frequency meter.

§ 3. Resonances of Cl and Br Isotopes

The nuclei Br^{79}, Br^{81} and Cl^{35} have a spin of 3/2. Nuclear quadrupole resonances of these nuclei exhibit only one resonance line, whose frequency is expressed as follows:

$$\nu = \frac{1}{2} eQq_{zz}\left(1 + \frac{1}{3}\eta^2\right)^{1/2}, \qquad (1)$$

where Q is nuclear quadrupole moment of nucleus. The asymmetry parameter, η, is defined by $|q_{xx} - q_{yy}/q_{zz}|$ where q_{zz} is field gradient tensor component along the principal axis. Although asymmetry parameter is not obtained, nuclear quadrupole coupling constant eQq can be obtained by doubling the observed frequency unless the asymmetry parameter is large.

The resonance frequencies of Cl^{35} in $AsCl_3$ and $SbCl_3$ were measured. The results are listed in Table I. $AsCl_3$ is liquid at room temperature and freezes about $-16°C$. Below this temperature three resonance lines were always observed. The obtained values are consistent with Livingston's results at 77°K. Since the As resonance in $AsCl_3$ showed only one resonance line as described below, the three Cl resonance lines must belong to the same molecule. Cl^{35} in $SbCl_3$ shows two resonance lines, one of which has a large intensity of about twice of the other. This arises from the fact that there are two nonequivalent sites of the chlorine atoms of the molecule in crystal lattice.

Table I. Cl^{35} resonances in $AsCl_3$ and $SbCl_3$.

Compound	Temp. (°K)	Resonance frequency ν (Mc/sec)		
		I	II	III
$AsCl_3$	249	24.424±0.001	24.485±0.001	24.754±0.002
	212	24.581±0.002	24.652±0.002	24.941±0.002
	77	24.951±0.002	25.052±0.002	25.391±0.002
$SbCl_3$	302	19.187±0.003	20.383±0.001	

Table II. Br resonances in $SbBr_3$.

Crystal	Isotope	Temp. (°K)	Resonance frequency ν (Mc/sec) I	II	III
I	Br^{79}	297	161.677±0.003	161.887±0.004	167.885±0.002
		246	162.355±0.002	162.689±0.003	168.958±0.001
		77	164.492±0.003	164.768±0.002	171.576±0.002
	Br^{81}	298	135.047±0.001	135.253±0.001	140.277±0.002
		246	135.620±0.001	135.921±0.003	141.150±0.001
		77	137.403±0.010	137.630±0.005	143.324±0.001
II	Br^{81}	299	132.071±0.002	139.621±0.002	140.640±0.002
		245	132.507±0.005	140.275±0.005	141.261±0.005
		77	133.499±0.005	141.923±0.003	142.622±0.002

The measured resonance frequencies of Br^{79} and Br^{81} in $SbBr_3$ as listed in Table II. $SbBr_3$ (Crystal form I) was obtained by slow heating of mixture of bromine dissolved in carbon disulphide and antimony powder. After distillation of the solution the crystal of $SbBr_3$ was deposited. Results in Table II show three lines. The measured resonance frequencies agree partially with the results of Schawlow indicating 135.56 Mc in Br^{81} at 24°C and with those of Robinson *et al.* indicating 137.428 Mc and 144.490 Mc at 77°K, the latter is higher about 1 Mc than the highest line in the present experiment. The existence of three resonance lines, however, differs from their results. The samples which were obtained in commercial (Crystal from II) exhibited different three resonance lines. The observation of the resonance frequencies in the temperature from 77°K to room temperature indicated that these two forms of crystals did not interchange from one another by varying the temperature. Some informations about these crystal forms might be obtained with a Zeeman analysis.

Temperature variations of the resonance frequencies for these crystals are shown in Fig. 1 together with the values of other observers. The ratio of the coupling constants of Br^{79} to that of Br^{81} is equal to the ratio Q^{79}/Q^{81} and has an average value of 1.19713± 0.00008 at the temperature used.

§ 4. Resonances of I^{127} Isotope

The isotope I^{127} has a spin of 5/2 and the resonance frequencies of it expressed by the following equations;

$$\left.\begin{aligned}\nu_1&=\frac{3}{20}eQq_{zz}\left(1+\frac{59}{54}\eta^2-\frac{11093}{17496}\eta^4\right),\\ \nu_2&=\frac{3}{10}eQq_{zz}\left(1-\frac{11}{54}\eta^2+\frac{2837}{17496}\eta^4\right).\end{aligned}\right\}\quad(3)$$

If these two frequencies can be observed, the asymmetry parameter, η, is determined. The equations are approximate solutions of the

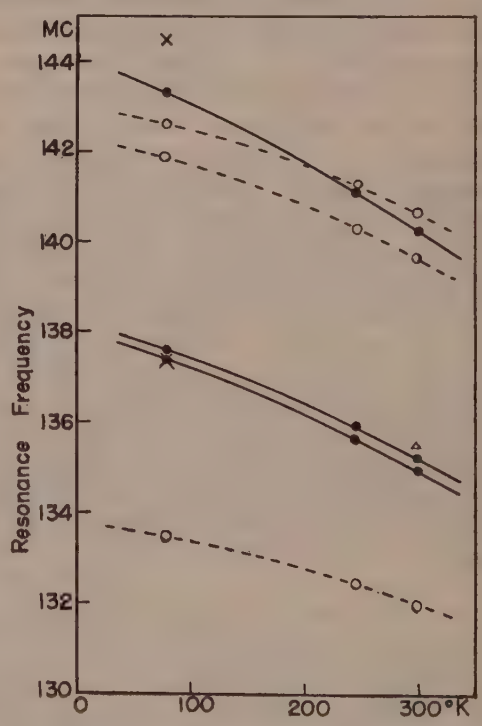

Fig. 1. Temperature dependency of the resonance frequencies of Br^{81} in $SbBr_3$. Solid line shows crystal form I and dotted line shows crystal form II. It also shows the measured values by Robinson, Dehmelt and Gordy. (×), and by Schawlow (△).

secular equations[11]. The higher terms of η^2 are required when η is larger than about fifteen percents.

S_8 compounds were made by distillation or crystalization from a carbon disulphite solution containing iodide and sulphur. $AsI_3 \cdot 3S_8$ is a very stable compound and forms a large orange crystal. Resonance is also observed in the compound made by mixing melted iodide and sulphur.

The resonance of I^{127} in AsI_3, the first resonance of SbI_3 and the resonances in the corresponding sulphur molecular addition compounds, $AsI_3 \cdot 3S_8$ and $SbI_3 \cdot 3S_8$, at 77°K were reported by several investigators. In the present experiment these resonance frequencies were also measured from 77°K to room temperature to compare the tri-iodides with the corresponding sulphur molecular addition compounds. The resonance frequencies of I^{127} in iodides are listed in Table III.

The second resonance of I^{127} in SbI_3 was first looked for by Schawlow unsuccessfully. He interpreted this result by supposing that the frequencies ν_1 and ν_2 coincided so that only one resonance would be observed. The present survey at 77°K from about 350 Mc to the lower frequencies, however, revealed the existence of the resonance at the unexpectedly low frequency of about 260 Mc. It yielded an asymmetry parameter of 0.565. The iodine resonance of SbI_3 could not be observed at room temperature. At about −30°C a broad weak line appeared, and then the intensity increased and the line width seemed to become narrower as the temperature was decreased. At 77°K the signal to noise ratio of ν_1 was as large as twenty. The signal to noise ratio of ν_2 at 77°K was about four, so that it was difficult to observe this resonance at the higher temperature. The deep red crystal at room temperature changed to a yel-

Table III. I^{127} resonances.

Compound	Temp. (°K)	ν_1 (Mc/sec)	ν_2 (Mc/sec)	eQq (Mc/sec)	η
AsI_3	312	206.553±0.003	401.985±0.010	1345.75	0.1467
	245	206.485±0.005	400.707±0.010	1342.08	0.1544
	77	207.023±0.005	395.979±0.010	1330.23	0.1891
$AsI_3 \cdot 3S_8$	302	224.462±0.003	448.920±0.009	1496.40	0.000
	245	405.408±0.003	450.817±0.008	1502.72	0.003
	77	227.543±0.006	455.059±0.008	1516.86	0.007
SbI_3	218	181.825±0.006	——		
	77	174.356±0.001	254.637±0.050	895.83	0.565
$SbI_3 \cdot 3S_8$	297	183.125±0.002	366.023±0.050	1220.33	0.02
	77	184.151±0.010	367.023±0.050	1226.25	0.03
SnI_4	301	203.470±0.005	406.902±0.005	1356.36	0.008
		204.490±0.005	408.988±0.005	1363.28	0.000
$SnI_4 \cdot 2S_8$	301	204.019±0.005	408.008±0.010	1360.04	0.002
		206.784±0.005	413.153±0.010	1377.40	0.028
	77	207.458±0.005	414.907±0.010	1383.03	0.002
		210.746±0.005	420.675±0.010	1402.68	0.039
$SnI_4 \cdot 4S_8$	301	201.961±0.02	403.897±0.040	1346.3	0.00
		202.036±0.020	404.081±0.040	1346.9	0.00
		206.853±0.020	413.238±0.040	1377.7	0.03
		213.148±0.020	——		
	77	204.64 ±0.03	409.35 ±0.10	1364.3	0.0
		205.25 ±0.03	410.50 ±0.10	1368.3	0.0
		210.99 ±0.03	421.40±0.10	1405.0	0.03
		219.04 ±0.03	——		

low one at low temperature. This seems to indicate some gradual phase change or rotation of the molecule.

SnI_4 is one of the substances which produces sulphur molecular addition compounds. As a comparison, the resonance of the pure single crystal of SnI_4 was measured, although it had already been measured by Dehmelt[13] and others[4),14)]. The results are also included in Table III. On account of the large asymmetry parameter of SbI_3 the equations containing the terms up to η^8 were used for the determination of eQq.

§ 5. Resonances in As and Sb Isotopes

The measured resonance frequencies of As^{75} in arsenic compounds are shown in Table IV.

Table IV. As^{75} resonances in arsenic compounds.

Compound	Temp. (°K)	Resonance Frequency ν (Mc/sec)
$AsCl_3$	243	76.207±0.004
	213	76.873±0.002
	77	78.866±0.004
AsI_3	373	33.057±0.002*
	302	32.198±0.003
	213	31.079±0.003
	77	29.338±0.005
$AsI_3 \cdot 3S_8$	303	47.545±0.003
	217	48.398±0.005
	72	49.501±0.005

* high temperature phase.

The resonance in $AsCl_3$ was observed at all range of temperature up to the melting point, −16°C. Although it was observed at 77°K by Barnes and Bray[8)], the resonance at higher temperature has not been observed. The resonance frequency at 77°K obtained in the present experiment is lower about 80 kc than the value reported by them. The signal to noise ratio was rather good so that the measured value at 77°K will be more reliable than their value. Resonance of As^{75} in AsI_3 was observed about 32 Mc at room temperature but in powdered sample the signal to noise ratio was very poor. In the single crystal, of about 3 cm^3, the signal to noise ratio was only about four and the line width was about 20 kc. Resonance of As^{75} in AsI_3 was also reported by Barnes and Bray[8)], however, their value of 116 Mc seems very high. The resonance frequency may be roughly estimated by using the equation of $(1/2)\cdot 3\cos\theta(1+2\beta)eQq_{atom}$, where 2β is 0.5 being electronegativity difference between As and I and θ is the angle of I–As–I which is known to be about 87° from the asymmetry parameter of the iodine resonance[1)] or crystal structure[16)]. The estimated resonance frequency is about 48 Mc. The present result is reasonable from this estimation. The As^{75} resonance of $AsI_3 \cdot 3S_8$ was 47.5 Mc at room temperature having more good signal to noise ratio.

As^{75} whose spin number is 3/2 has one resonance, therefore η is not determined. But since $AsCl_3$ exhibits three Cl resonance lines corresponding to three nonequivalent Cl atoms in a same molecule and the latter two samples show only one I resonance line, it is supposed that the asymmetry parameter of $AsCl_3$ is finite and those of AsI_3 and $AsI_3 \cdot 3S_8$ are zero.

The measured resonance frequencies of Sb in antimony compounds are shown in Table V. Abundances of two isotopes Sb^{121} and Sb^{123} are about 57 and 43 percent respectively. For the resonance frequencies of Sb^{121} having a spin of 5/2, the equetions (2) are applicable and for Sb^{123} having a spin of 7/2 the resonance frequencies are expressed by following equations:

$$\left.\begin{aligned} \nu_1 &= \frac{1}{14}eQq_{zz}\left(1+\frac{109}{30}\eta^2-\frac{196093}{27000}\eta^4\right), \\ \nu_2 &= \frac{2}{14}eQq_{zz}\left(1-\frac{17}{30}\eta^2+\frac{50207}{27000}\eta^4\right), \\ \nu_3 &= \frac{3}{14}eQq_{zz}\left(1-\frac{1}{10}\eta^2-\frac{487}{27000}\eta^4\right). \end{aligned}\right\} \quad (3)$$

The Sb resonance in $SbBr_3$ occurs at two different frequencies corresponding to bromine resonances in two crystal forms. The reported frequencies of Sb in $SbBr_3$ by Wang[7)] corresponds to crystal form I. In crystal form II the Sb atom has a large asymmetry parameter of about 18 percent. These samples gave so large electric loss on the oscillator coil that the resonance frequency of Sb^{123} could not be measured accurately. In the case of SbI_3 the line was very broad and the side bands of the line which shifted by the quenching frequency are overlapped each other. Only the first resonance of Sb^{121} was observed. The Sb atom has a axially symmetric field gradient with respect to the three I atoms similar to AsI_3, so the second resonance could

Table V. Sb resonance.

Compound	Isotope	Temp. (°K)	ν_1 (Mc/sec)	ν_2 (Mc/sec)	ν_3 (Mc/sec)	eQq (Mc/sec)	η
$SbBr_3$ I	Sb^{121}	304	48.439±0.005	95.836±0.005		319.920	0.083
	Sb^{123}		29.821±0.005	58.016±0.005	87.279±0.010	407.35	0.082
	Sb^{121}	77	50.273±0.003	99.215±0.010		343.95	0.100
	Sb^{123}		31.186±0.004	60.107±0.003		422.987	0.095
$SbBr_3$ II	Sb^{121}	304	49.061±0.004	94.160±0.010		316.02	0.181
	Sb^{123}		31.990±0.005	56.544±0.005	85.989±0.010	402.689	0.182
SbI_3	Sb^{121}	77	25.406±0.010	—		169.37	0*
$SbI_3 \cdot 3S_8$	Sb^{121}	297	37.461±0.06	—		249.74	0*
		250	37.77 ±0.06	—		251.8	0*

* The value are assumed from the crystal structures.

be expected to be twice the first resonance. However, the resonance could not be found in the frequency range between 45 Mc to 52 Mc. It is probably due to a small signal to noise ratio.

$SbI_3 \cdot 3S_8$ which was studied at room temperature, exhibited some spurious lines with intensities comparable to the true resonance line. Therefore, it was necessary to verify this resonance line by smearing it out with a magnetic field. The spurious resonances were more abundant in the frequencies below 30 Mc. They probably originate from electric vibrations in the crystal domains[16]. A few spurious lines were also observed in $AsI_3 \cdot 3S_8$.

§ 6. Discussion on Sulphur Molecular Addition Compounds

Several iodides have been known to have sulphus molecular addition compounds which are composed of its original compounds and definite multiples of the sulphur molecule[17]. Robinson, Dehmelt and Gordy[4] considered the quadrupole coupling constants of AsI_3 and SbI_3 to be approximately equal to those of $3S_8$ compounds by the reason that the observed resonance frequency of $SnI_4 \cdot 4S_8$ was near that of SnI_4.

As shown in Fig. 3, AsI_3 has a structure of macromolecular sheets and not molecular structure. On the other hands $AsI_3 \cdot 3S_8$, investigated by Hertel, has a single molecular structure, where the molecule AsI_3 is surrounded with six sulphur ring molecules as shown in Fig. 4[17]. The effect of the sulphur molecules is to decrease the intermolecular bonds between the molecules of AsI_3. In fact, the observed coupling constant of the I^{127} resonance increased by about twenty megacycles indicating stronger covalent structure. For SbI_3 the same interpretation is true. Small intermolecular bonding results in a large amount of covalent structure. The observed

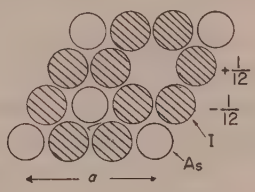

Fig. 2. Crystal structure of AsI_3. a=7.187 A. It shows a sheet in a unit cell which is normal to c axis of crystal.

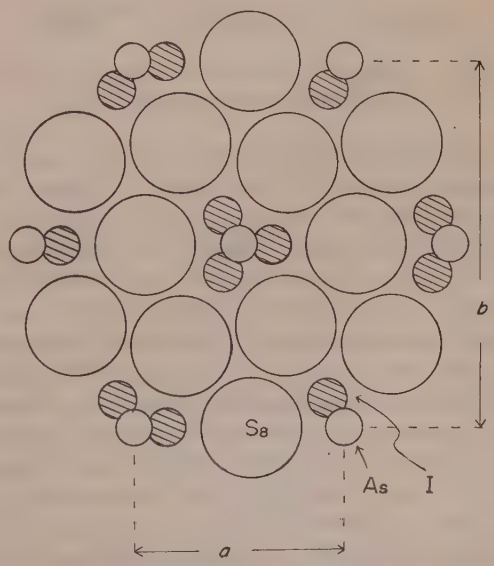

Fig. 3. Crystal structure of $AsI_3 \cdot 3S_8$. a=14.2 A. Bond angle I–As–I is 101.7°[18]

asymmetry parameters are large in AsI_3 and SbI_3, but their S_8 compounds have very small values. Indeed an accurate relative measurements of the first and the second resonances of $AsI_3 \cdot 3S_8$ at room temperature yielded zero asymmetry parameter. The measurement at 77°K gave a small asymmetry parameter which came partially from unavoidable temperature difference between two samples in the separate detectors. The resonance in I^{127} in $SbI_3 \cdot 3S_8$ has less signal to noise ratio. However, it seems that asymmetry parameter is finite.

Sulphur molecular addition compounds of SnI_4 showed resonances which has less signal to noise ratio and broader width than those of pure SnI_4. Robinson *et al.* indicated the structure of $4S_8$ but Hertel showed $2S_8$. Indeed the amount of sulphur played a complex role in the present experiment. Fig. 4 shows

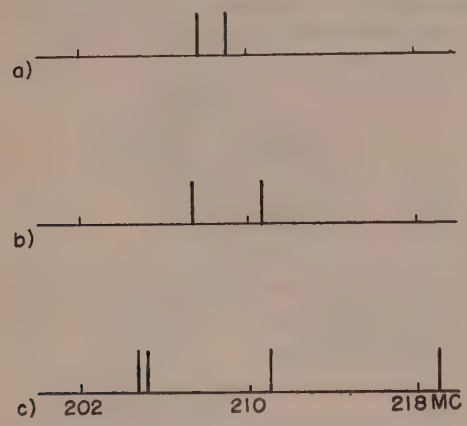

Fig. 4. Splitting of the I^{127} resonance lines in SnI_4 (a), $SnI_4 \cdot 2S_8$ (b) and $SnI_4 \cdot 4S_8$ (c).

the resonance frequencies of SnI_4 as the amount of sulphur is increased. $2S_8$ and $4S_8$ might give the different type of crystals. When the mixing of sulphur was insufficient the resonance lines of two types were often observed. When SnI_4 was mixed with more than $4S_8$ the intensity of resonance line decreased abruptly. The samples of SnI_4 used to make those compounds were single crystals and powder which was not applied to special purification. Powder material easily gave $SnI_4 \cdot 2S_8$ and $SnI_4 \cdot 4S_8$. Pure single crystals, however, yielded $SnI_4 \cdot 2S_8$ but not $SnI_4 \cdot 4S_8$. Crystal structures of sulphur molecular addition compounds of SnI_4 have not been reported.

The resonance frequencies of $SnI_4 \cdot 2S_8$ and $SnI_4 \cdot 4S_8$ were plotted against the temperature. The results are reproduced (in Fig. 5). Two lines of $SnI_4 \cdot 2S_8$ have the same intensities. This fact indicates that these lines are due to two pairs of iodine atoms in one molecule. The splitting of multiplet in $SnI_4 \cdot 4S_8$ was about 20 Mc. It shows that the intermolecular bonding is larger than SnI_4 and the asymmetry of molecule is disturbed.

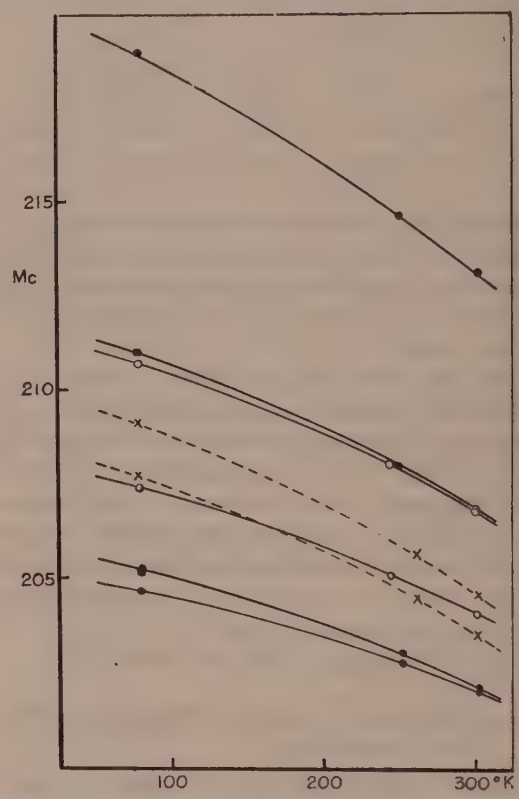

Fig. 5. Temperature dependcy of first resonance of I^{127} in SnI_4 (dotted line), $SnI_4 \cdot 2S_8$ (○) and $SnI_4 \cdot 4S_8$(●). Points at 257°K in SnI_4 was measured by A. Schimauchi and S. Hagiwara.

The line widths in $AsI_3 \cdot 3S_8$ and $SbI_3 \cdot 3S_8$ were narrower than those of AsI_3 and SbI_3. It seems that the intermolecular interaction between AsI_3 molecules is reduced by the presence of sulphur molecules. On the other hand, addition of sulphur molecule in SnI_4 reduced the intensity of resonance by a factor of a few tenths and broadened the widths of resonance line. The effect of S_8 molecule is opposite in both cases.

§ 7. The Quadrupole Coupling and the Electronegativity

The coupling constant is related with the

number of unbalanced p electrons U_p and with the coupling constant for a pure p electron which is twice that of free atom.

$$eQq_{\text{obs.}}=|U_p\cdot eQq_{\text{pure } p}| \ . \qquad (4)$$

U_p is a quantity depending upon electronic structure of the molecule.

The molecules of interest here are type MX_3, i.e., arsenic and antimony trihalides and sulphur molecular addition compounds of triiodides. When double bond character and d hybridization are not considered for simplicity, the atom M has s–p hybridized orbitals which form three covalent bonds and an unshared pair. On account of electronegativity difference between M and X atoms, M is positively charged in these cases. U_{pM} is expressed by Gordy as follows[19];

$$U_{pM}=-3\alpha_M\{1-3\beta+4\beta(1+c)\} \ , \qquad (5)$$

where α_M represents percent s character of the bonding orbitals, β is ionic character of each bond, and c is a correction for the change in screening caused by the charge. In this expression the s character is depends on the bond angle, of X–M–X, θ, in the following relation

$$\alpha=\cos\theta/(1-\cos\theta) \ , \qquad (6)$$

This angle is approximately same in these molecules[20)21)]. For the atom X, a single bond is formed to complete its octet. The principal axis of the field gradient tensor is along the bond direction. U_{pX} is as follows;

$$U_{pX}=(1-\alpha_X)(1-\beta) \ . \qquad (7)$$

where α_X represent percent s character of X atoms.

The atomic coupling constants for iodine, bromine and chlorine atoms are now known accurately by the results of the atomic beam experiments[22)–24)]. The values of 2292, 769 and 109.6 Mc were used for I^{127}, Br^{79} and Cl^{35}. For arsenic and antimony atoms the atomic couplings were calculated with the values of 426 and 734 Mc respectively which are estimated from the values of electric field gradient q obtained from optical hyperfine structure[23)] and the values of nuclear quadrupole moment Q[26)].

Table VI shows the values of U_p and the differences of the electronegativities of the bonded atoms[27)]. Molecular coupling constants investigated here and by other references are shown together in this table. $1-|U_p|$ is the deviation of the coupling from that of pure covalent p bond and gives a measure of the ionic character. Figs. 6 and 7 show the plots

Table VI.

Compound	Isotope	$eQq_{\text{obs.}}$ (Mc/sec)	$\lvert U_p\rvert$	$\lvert x_M-x_X\rvert$
$AsCl^{35}$	Cl^{35}	50.4[a]	0.460	1.0
	As^{75}	157.73	0.371	1.0
$AsBr_3$[c]	Br^{79}	414.1[a]	0.538	0.8
	As^{75}	122.63	0.288	0.8
AsI_3	I^{127}	1330.23	0.580	0.5
	As^{75}	58.63	0.138	0.5
$AsI_3 3S_8$	I^{127}	1516.86	0.662	0.5
	As^{175}	99.00	0.233	0.5
$SbCl_3$	Cl^{35}	40.4[a]	0.368	1.2
	Sb^{121}	383.67[d]	0.523	1.2
$SbBr_3$	Br^{79}	334.0[a,b]	0.434	1.0
	Sb^{121}	318.0[b]	0.451	1.0
SbI_3	I^{127}	895.83	0.390	0.7
	Sb^{121}	169.73	0.231	0.7
$SbI_3\cdot SS_8$	I^{127}	1226.25	0.535	0.7
	Sb^{121}	251.8	0.343	0.7

[a] averaged over multiple lines.
[b] averaged for two crystal forms.
[c] from Kojima et al.
[d] from Dehmelt.

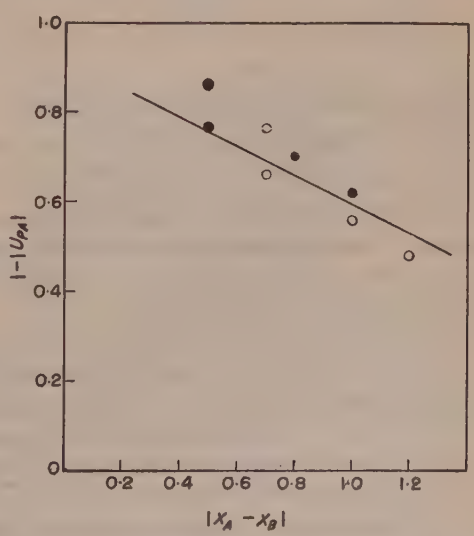

Fig. 6. The values of $1-|U_{pM}|$ versus electronegativity difference $|x_M-x_X|$ in M atoms. ● is As compound and ○ is Sb compound.

of $1-|U_p|$ against the electronegativity difference. Except for AsI_3 and SbI_3 these plots are represented by the following equations.

$$|U_{pM}|=0.08+0.37|x_M-x_X| \ , \qquad (8a)$$

$$|U_{pX}|=0.86-0.38|x_M-x_X| \ . \qquad (8b)$$

The relation (8b) is considered as expressing qualitatively the dependency expected from Eq. (7), since the s character, α_X, is about 14 percent and the ionic character of each bond, β, is nealy a half of the electronegativity difference between bonded atoms. The relation (8a), however, results very small value of s character for M atom adopting the same value of ionic character β for X atom. The smallness of s character contradicts with the result calculated from the bond angle X–M–X. The assumption of s–p hybridized configuration alone is insufficient to interprete the experimental result, therefore d hybridization or double bond character should be considered together with s–p hybridization.

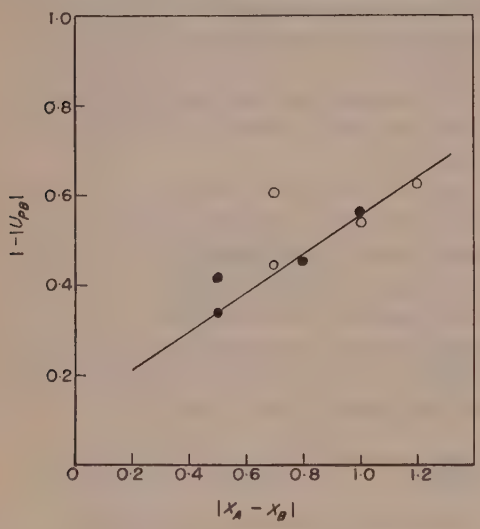

Fig. 7. The values of $1-|U_{pX}|$ versus electronegativity difference $|x_M-x_X|$ in X atoms. ● is As compound and ○ is Sb compound.

The coupling constants for both M and X atoms in AsI_3 and SbI_3 are obviously apart from the linear relation (8). This fact indicates that the crystal structures of these molecules are quite different from those of others and these molecules deform appreciably in the crystalline state. In fact, AsI_3 and SbI_3 do not form molecular crystals. On the other hand, sulphur molecular addition compounds of AsI_3 and SbI_3 satisfy the linear relation. In the compounds the molecules of AsI_3 and SbI_3 are remained without large change.

§ 8. Temperature Dependency

Generally, the frequency of nuclear quadrupole resonance line decreases with increasing temperature. This character was interpreted by Bayer[28] with the concept of the effective field gradient which is averaged field gradient for the thermal vibrations whose frequencies are large compared to the quadrupole resonance frequency. The effective field gradient and consequently observed frequency decreased when temperature increased. The observed resonance frequencies of Cl^{35} in $AsCl_3$ are plotted in Fig. 8, which also includes the low temperature values obtained by Livingston. Since the vibrational effect is diminished at low temperature frequency change of resonance line becomes very small at low temperature.

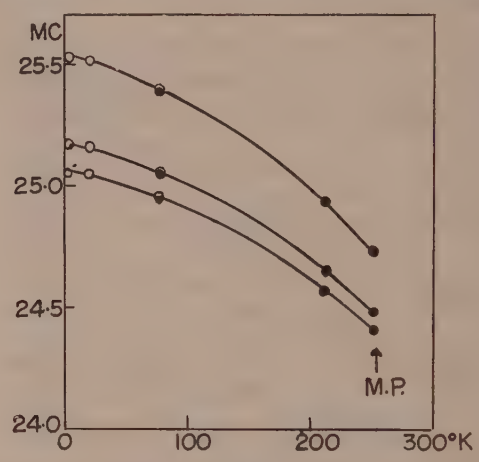

Fig. 8. Temperature dependency of the Cl^{35} resonance frequency in $AsCl_3$. Open circles show Livingston's measurement.

In Table VII the calculated values of logarithmic temperature coefficient $1/\nu\cdot\partial\nu/\partial T$ at 77°K is shown. From these figures it is concluced that the temperature dependency of M atom in MX_3 type molecule is about two or three times larger than X atoms.

In the case of AsI_3 the observed frequency changes of both the nuclei As and I were positive, that is, decreasing temperature decreases the resonance frequency. Fig. 9 shows the temperature changes of As resonance frequencies in AsI_3 and $AsI_3\cdot 3S_8$. Positive temperature coefficient could not be interpreted

with Bayer's theory. Kushida, Benedeck and Bloembergen[29] studied the pressure effect for quadrupole resonances. The variable quantity of nuclear quadrupole frequency with temperature is expressed

Table VII. Logarithmic temperature coefficients $1/\nu \cdot \partial\nu/\partial T$ (10^4/°K).

	$AsCl_3$	$AsBr_3$	AsI_3	$AsI_3 \cdot 3S_8$
As	−1.8	−1.7[b]	4.4	−1.2
Halogen	−0.9	−1.0[b]	0.56	−0.59
	$SbCl_3$	$SbBr_3$	SbI_3	$SbI_3 \cdot 3S_8$
Sb	−0.9[a]	−1.6∼2.0	—	−1.7
Halogen	−0.4 ∼−1.3[c]	−0.5[c]	−0.73	−0.35

[a] from Bray and Barnes.
[b] from Kojima et al.
[c] from Wang

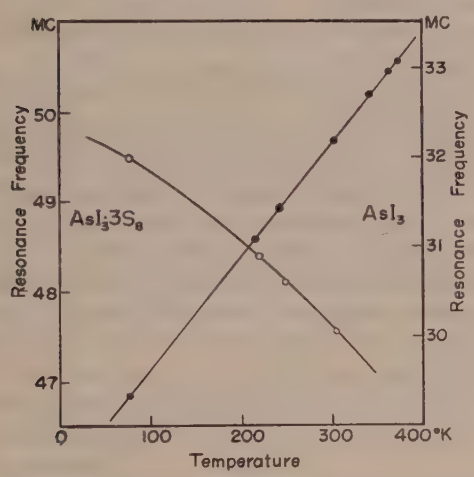

Fig. 9. Temperature dependency of the As^{75} resonance frequency in AsI_3 (●) and $AsI_3 \cdot 3S_8$ (○).

$$\frac{1}{\nu}\left(\frac{\partial\nu}{\partial T}\right)_p = \frac{V}{\nu}\left\{\frac{\partial\nu}{\partial q_0}\frac{dq_0}{dV} + \frac{\partial\nu}{\partial\eta_0}\frac{d\eta_0}{dV} + \sum_i \frac{\partial\nu}{\partial\xi_i^0}\left(\frac{\partial\xi_i^0}{\partial V}\right)_T\right\}\frac{1}{V}\left(\frac{\partial V}{\partial T}\right)_p + \frac{1}{\nu}\sum_i \frac{\partial\nu}{\partial\xi_i^0}\left(\frac{\partial\xi_i^0}{\partial T}\right)_V . \quad (9)$$

The first term represents the volume dependency of quadrupole resonance frequency and the second term is the Bayer's term. ξ_i^0 is the amplitude of the normal modes of the vibration. In the case of AsI_3, η in I^{127} resonance increased with decreasing temperature. This term gives a decrease of coupling when temperature is decreased. However, in As^{75} resonance η would be very small, probably zero, for the links of six iodine atoms. Therefore the second term in the bracket has a small effect. The first term in bracket indicates a volume effect. The volume of AsI_3 decreases with decreasing temperature. This may produce a decrease of the p character of the field gradient and an increase of the hybridization of the intramolecular bond by increase bonding to surrounding molecules. Probably, the hybridization in AsI_3 has some d character and produces large ionic character which is expected from Figs. 6 and 7. Thus, in the case of AsI_3 the first term in bracket which shows volume effect is predominant and over-compensates the effects of the other terms in above equation.

The As resonance in AsI_3 indicates a phase change at about 92°C which is shown in Fig. 10. It corresponds to that the iodine resonance in AsI_3 split into three multiplets above 90°C[1]. Smallness of deviation of the resonance frequency at this phase change indicates that the crystal structure is not affected so much.

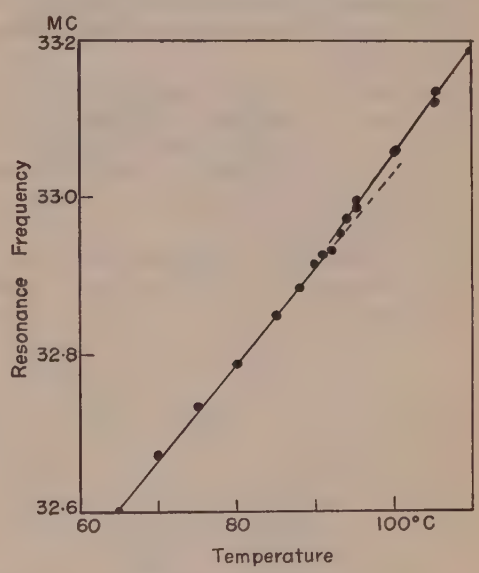

Fig. 10. Temperature dependency of As^{75} resonance frequency in AsI_3 at above room temperature. Phase transition was observed at about 90°C.

Acknowledgements

The author wishes to express her thanks to Professor Shoji Kojima of Tokyo University of Education for his guidance and encouragement, and also for permission to perform this

experiment in his laboratory. She thanks to the members of his laboratory for helps on experiment, and to Dr. Y. Abe for the supply of single crystal of AsI_3. This work was supported by the Scientific Research Expenditure of the Ministry of Education.

References

1) S. Kojima, K. Tsukada, S. Ogawa, A. Shimauchi and Y. Abe: J. Phys. Soc. Japan **9** (1954) 805.
2) A. L. Schawlow: J. Chem. Phys. **22** (1954) 1211.
3) R. G. Barnes and P. J. Bray: J. Chem. Phys. **23** (1955) 1177.
4) H. Robinson, H. G. Dehmelt and W. Gordy: J. Chem. Phys. **22** (1954) 511.
5) R. Livingston: Science **118** (1953) 61.
6) H. G. Dehmelt and H. Krüger: Z. Physik **130** (1951) 3851.
7) T. C. Wang: Phys. Rev. **99** (1955) 566.
8) R. G. Barnes and P. J. Bray: Chem. Phys. **23** (1955) 407.
9) S. Ogawa: J. Phys. Soc. Japan **12** (1957) 1105.
10) S. Kojima, K. Tsukada, A. Shimauchi and Y. Hinaga: J. Phys. Soc. Japan **9** (1954) 795.
11) R. Bersohn: J. Chem. Phys. **20** (1952) 1505.
12) I. Tatsuzaki and Y. Yokozawa: J. Phys. Soc. Japan **12** (1957) 802.
13) H. G. Dehmelt: Z Physik **130** (1951) 356.
14) R. Livingston and H. Zeldes: Phys. Rev. **90** (1953) 609.
15) R. W. G. Wyckoff: "*Crystal Structure*," Interscience Publishers, Inc. New York, (1951).
16) S. Kojima, K. Tsukada, S. Ogawa and A. Shimauchi: Phys. Rev. **92** (1953) 1571, S. Kojima, K. Tsukada, S. Ogawa, A. Shimauchi and N. Matsumiya: J. Phys. Soc. Japan **10** (1955) 165. S. Ogawa: Sci. Report of Ochanomizu University **5** (1955) 228.
17) E. Hertel: Z Phys. Chem. **15** (1932) 51.
18) Y. Abe: to be published.
19) W. Gordy, Smith and Trambarulo "*Microwave Spectroscopy*", John Wiley and Sons, Inc. New York (1953) p. 280.
20) A. H. Gregg, G. C. Hampson, G. I. Jekins, P. L. F. Jones and L. F. Sutton: Trans. Feraday Soc. **33** (1937) 852.
21) K. Shimomura: J. Phys. Soc. Japan **12** (1957) 1386.
22) V. Jaccarino, J. G. King, L. F. Satton and J. Stroke: Phys. Rev. **94** (1954) 1798.
23) J. G. King and V. Jaccarino: Phys. Rev. **94** (1954) 1610.
24) V. Jaccarino and J. G. King: Phys. Rev. **83** (1951) 471.
25) R. G. Barnes and W. V. Smith: Phys. Rev. **93** (1954) 95.
26) N. F. Ramsey: "*nuclear Moments*", John Wiley and Sons, Inc. New York (1953).
27) L. Pauling: "*Nature of Chemical Bonds*", Cornell Uhiv. Press New York 1940.
28) H. Bayer: Z. Physik **130** (1951) 227.
29) T. Kushida, G. B. Benedeck and N. Bloembergen: Phys. Rev. **104** (1956) 1364.

JOURNAL OF THE PHYSICAL SOCIETY OF JAPAN Vol. 13, No. 6, JUNE, 1958

A Torsion Magnetometer for Determining Free Radicals in Some Organic Solutions

By Hideo TAKAKI, Naoto KAWAI, Chie MIYAKE and Tadasuke MORITA

Faculty of Science, Kyoto University

(Received February, 14, 1958)

A torsion pendulum magnetometer whose sensitivity is 1×10^{-10} c.g.s.e.m.u./division was made with fused silica. By using this, a process in which the free radicals appear and disappear was traced magnetically from time to time during the reduction of duroquinone with glucose, and the result showing a fair agreement with Michaelis' was obtained. Secondly, we examined similar reactions by changing reducing agents, their concentrations and the temperature. Finally, the mean life time of free radicals was calculated from the observation. Then it was found to be shown as an exponentially decreasing function with temperature, and to be about 20 minutes at room temperature.

§ 1. Introduction

For several decades free radicals have been one of the leading subjects of investigation in the field of organic chemistry. A series of experiments have been made and a number of hypotheses have been set up severally on the nature, behavior and kinetics of what is called the radical reaction. On the other hand, the free radicals, having been found in most of all the living matters, have accentuated the attention of many biologists, biochemists and biophysicists. For instance, Bauer[1] has found in the living cells a plenty of free radicals which disappear with the death of the cells, suggesting that life depends on an excited state of protein molecules in the protoplasm.

Of all the characteristics the said radicals possess, the most remarkable property is their magnetism. Since they always contain odd or unpaired electrons, they reveal themselves to be paramagnetics in a magnetic field. Consequently, the free radicals are the subjects to be investigated preferably by the magnetic measurement. By any other method the way of detection itself is extremely difficult. It is indeed Bauer and Michaelis who first introduced the magnetic method into this investigation. Michaelis[2] studied in detail the reducing or oxidizing process of dyestuff in 1938.

In recent years much has been studied on them by the resonance absorption experiments. B. Commoner, J. Townsend and G.E. Pake[3] have proved that the concentration of free radicals abundant in living cells, such as leaves, roots, rabbit tissue, carrots, frog egg, etc. is in the range from about 2 too $200(\times10^{-8})$

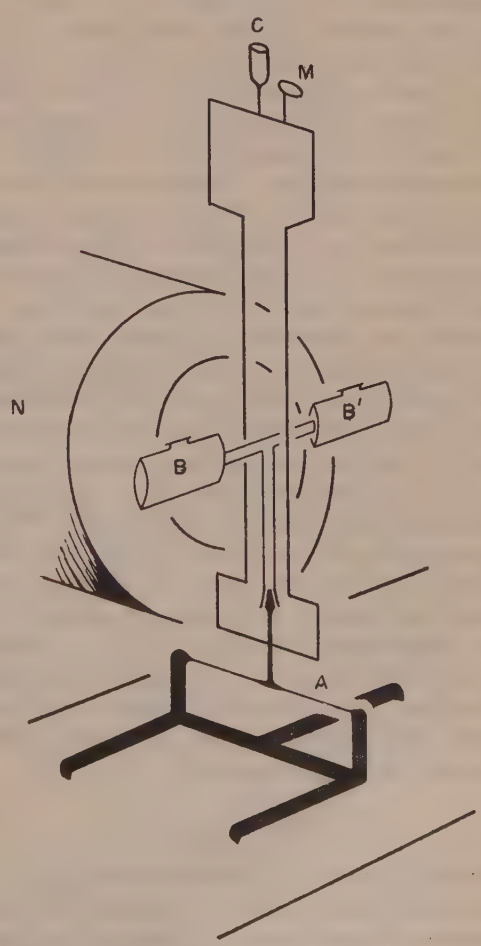

Fig. 1. Apparatus.

moles per gram; while H. M. McConell,[4] R. Bersohn,[5] J. E. Wertz,[6] etc., we learn, are going to further determine the hyperfine structure of semiquinone group.

Thus, the investigators' interest has so largely been focused upon the problems involving the radical reactions that it seems to be of fundamental importance to set up a sensitive apparatus capable of measuring the magnetic susceptibility of organic substances from time to time during the reaction, and then to infer how the free radical arises, reacts and disappears in the course of the radical reaction. The following is the descriptions of the magnetometer newly designed by us, together with some of the results.

§ 2. Apparatus

A sensitive torsion magnetometer was made with fused silica in the following way. As shown in Fig. 1, pendulum system of the magnetometer (C, M, B and B') is fixed to a tripod through a thin quartz fiber (A) in such a way that the center of gravity of the whole pendulum system may be higher than the fulcrum. The solution to be measured is placed into a reaction vessel (B) and a suitable solution into a compensating vessel (B'). By placing the above-mentioned vessel symmetrically on either side of the truncated pole pieces of the electromagnet (N), the basic diamagnetism of both the two kinds of solution can completely be offset and only susceptibility change related with the reaction can be taken out. The amounts of the change can be measured directly from the deflection angle of the pendulum with the aid of a lamp-scale and a reflecting mirror (M). As already mentioned, the center of gravity (G) of the pendulum system is located higher than the torsion wire, so the restoring couple vector due to the torsion wire, is much reduced by the couple vector of the gravity, which, acting at the center of gravity of pendulum system downward, will rotate the system in the opposite direction to that of the former. The situation may be expressed by

$$\frac{\theta}{f}=\frac{r}{\tau-mgl}$$

where θ, represents the deflection angle; f, horizontal component of paramagnetic attraction between the magneticfield and the solution; τ, torsion constant of the torsion wire; l and r, the distance from the foot of pendulum to G and to center of cylindrical vessel respectively; m, the total of the pendulum system; and g, the force of gravity.

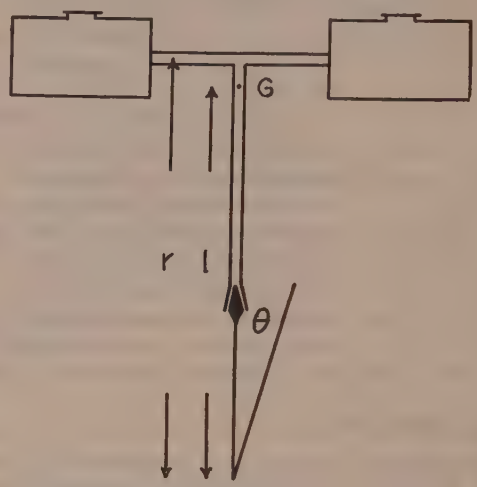

Fig. 2. Scheme of magnetometer.

Sensitivity of our apparatus can be raised, when by adding suitable mass to the top of the pendulum (C) we elevate its center of gravity, because τ-mgl can be decreased. Hence a very sensitive magnetometer is to be attained, so far as τ-mgl is kept positive. The highest sensitivity ever reached by this adjustment was 1×10^{-10} c.g.s.e.m.u. volume susceptibility per division. It is one of the characteristics of the equipment that the samples, however large the charge may be, can be measured without changing the sensitivity.

The calibration of our magnetometer is carried out in the following way; first, a small counter weight, say, 1 mg is mounted upon the dish attached to the B, the resultant deflection is determined, and then the scale constant per unit force (dyne/div) is calculated. The attraction between total paramagnetics in the reaction vessel and the magnetic field is further expressed by

$$f=A\chi\int H\frac{\partial H}{\partial x}dx$$

where A is the cross sectional area of the vessel, and χ the paramagnetic volume susceptibility of the solution which varies with time.

§ 3. Determination of free radicals

One of the results we obtained by using

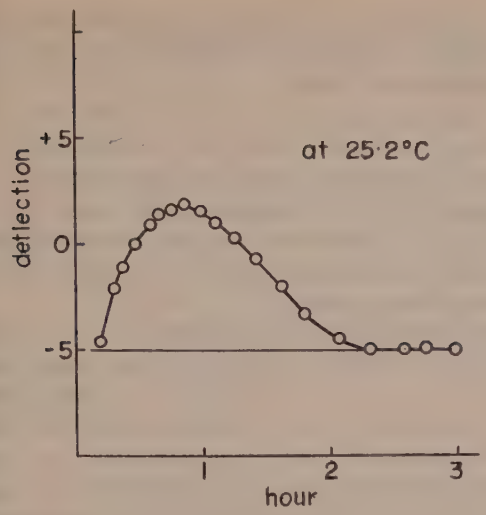

Fig. 3. Solution of 0.020 g. of duroquinone; 1 cc. of 1.0-N sodium hydroxide and 1 cc. of pyridine, mixed with water up to 5 cc., and 20 mg of glucose added.

this apparatus is given in Fig. 3. In the present experiment, we took up the reaction system containing H_2O, NaOH, pyridine, duroquinone and glucose, in which process there arises the free radical in question, as

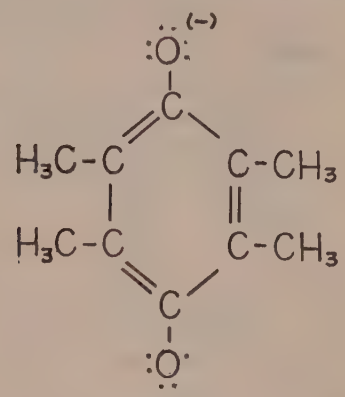

Fig. 4. Durosemiquinone radical.

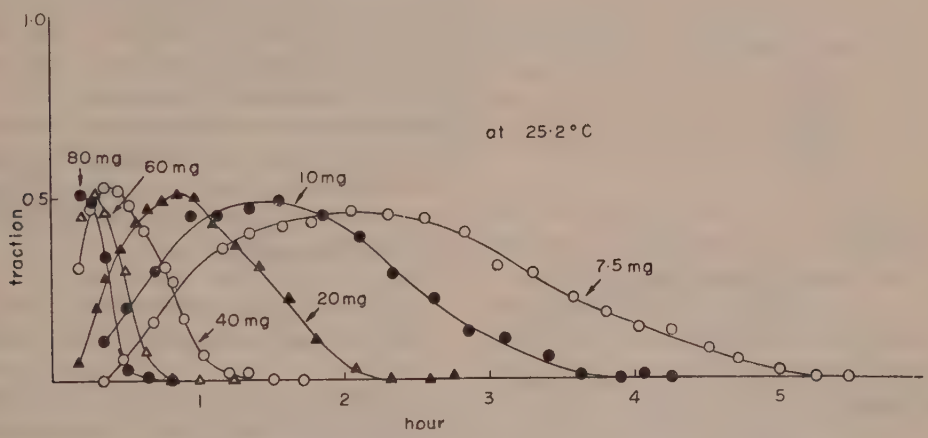

Fig. 5. Monosaccarides concentration dependency of reaction.

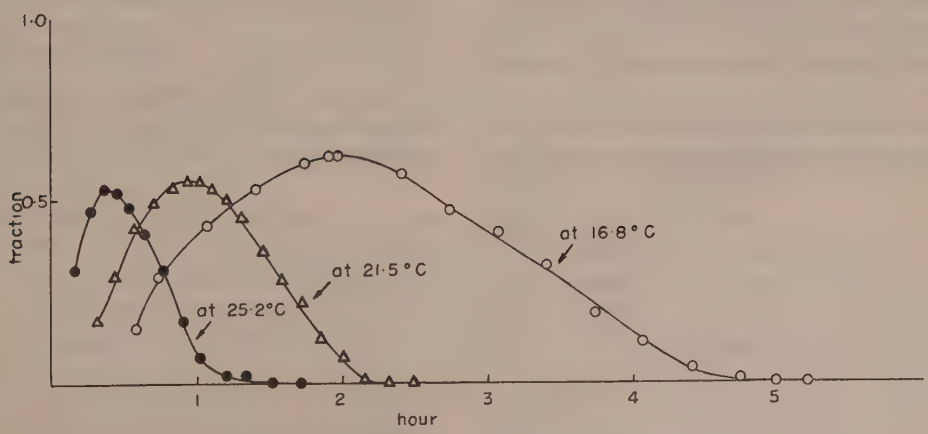

Fig. 6. Temperature dependency of reaction.

an intermediate product of semiquinone, having paramagnetism as shown in Fig. 4. The positive shift of magnetometer in the Fig. 3, therefore, corresponds to the free radical accumulation.

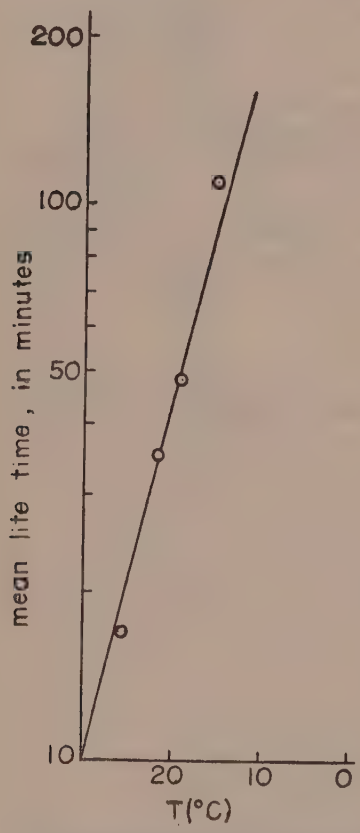

Fig. 7. Temperature dependency of mean lifetime of free radical.

We further examined the process of reactions by various monosaccarides, such as glucose, fructose, mannose, etc.. The results can be summarized in the following items in descending order:

That, if the temperature under which the reaction proceeds is kept constant, the velocity is the fastest in fructose, the slowest in mannose and the intermediate in glucose, respectively.

That, in every monosaccaride, both the rate of production of free radicals and that of their decay are strictly in proportion to the concentration of monosaccaride, (see Fig. 5), while Fig. 6 shows the temperature dependency of the reaction, citing, as a representative case, that of glucose.

Order of magnitude estimation of the mean life time of free radicals: The mean life time of semiquinone radicals was determined by integrating the concentration curve (represented in fractions) with respect to time, and them by dividing it by the total number of molecules. Thus, the obtained temperature dependency of the life time in the case of fructose is shown in a semilogalithmic diagram Fig. 7. The life time of radicals depends upon the temperature, the concentration of monosaccaride and the kind of monosaccaride. It is worth while to note here that the life time is remarkably prolonged as temperature falls. Extrapolate the line at the boiling temperature of liquid oxygen, then the life time will amount up to about 10^{17} years.

We wish to express our thanks to Professor R. Goto for his encouragement and assistance in preparing duroquinone.

References

1) E. Bauer and A. Raskin: Nature **138** (1936) 801.
2) L. Michaelis, M. P. Schubert, R. K. Reber, J. A. Kuck and S. Granik: J. Am. Chem. Soc. **60** (1938) 1678.
3) B. Commoner, J. Townsend and G. E. Pake: Nature **174** (1954) 689.
4) H. M. McConell: J. Chem. Phys. **24** (1956) 632.
5) R. Bersohn: J. Chem. Phys. **24** (1956) 1066.
6) J. E. Wertz and J. L. Vivo: J. Chem. Phys. **23** (1955) 2441.

JOURNAL OF THE PHYSICAL SOCIETY OF JAPAN Vol. 13, No. 6, JUNE, 1958

On the Flow of a Viscous Fluid past a thin Screen at Small Reynolds Numbers

By Hidenori HASIMOTO

Department of Aeronautical Engineering, Faculty of Engineering, Kyoto University

(Received February 12, 1958)

The slow steady flow of a viscous incompressible fluid past a thin screen with holes or slits is investigated on the basis of the Stokes equations of motion. It is found that the flow conductance σ of the holes or slits (i.e. the ratio of the total flow Q to the pressure drop P) is given by

$$\sigma=\frac{Q}{P}=\frac{M}{8\rho\mu},$$

where ρ is the density of the fluid, μ the viscosity, and M the virtual mass of disks or strips which are congruent with the holes or slits, moving broadside-on in a perfect fluid. The drag D acting on a part of the wall δW of the screen is also given by

$$D=Pq_p,$$

where q_p is the total flow of the perfect fluid through δW in this movement with unit velocity.

As examples, the cases of a single elliptic hole, a single slit, two parallel equal slits, and a series of parallel equal and equidistant slits are considered. Especially, in the last case, the total drag for an intervening strip is shown to be $4\pi\mu U/\log|\cos(\varepsilon\pi/2)|$ where U is the velocity of the viscous fluid at infinity, and ε the relative aperture of the screen $(0<\varepsilon<1)$.

§ 1. Introduction

The flow of a fluid through an orifice or orifices in a screen is very important from the practical view-points, and many classical works are known, especially for the case of the perfect fluid.

When the area of the orifice and the rate of flow through it are small, the effect of viscosity is so great that we must in general appeal to the Navier-Stokes equations for the theoretical study.

However, the Stokes approximation seems to be adequate and useful in many cases, if we take into account the small Reynolds numbers of the flow field in the neighbourhood of an orifice.

In this paper the flow of a viscous incompressible fluid through an orifice or orifices in an infinitely thin screen is investigated from a general view-point, on the basis of the Stokes equations of motion.

It is found that the flow conductance of the orifice and the drag on a part of the wall are proportional respectively to the virtual mass and the rate of flow induced by the movement of the disks or strips congruent with the orifices in a perfect fluid.

About ten years ago Roscoe[1] studied the three dimensional flow past a plane obstacle and related its drag to its electrostatic capacity. Our studies owe greatly to his idea and may be regarded as the complement to his study in this respect. He confined his study to the case of three dimensions, perhaps being afraid of the failure of the Stokes equations in the case of the two-dimensional flow. The existence of the solution is ascertained, however, in the case of the flow past a screen, having pressure difference between its two sides. The presence of this pressure difference seems to be an essential feature of our problem.

As examples, the cases of a single elliptic hole, a single slit, two parallel and equal slits, and a series of parallel equal and equidistant slits are discussed. The first example is considered by Roscoe without noticing our relation (3.9). He also estimated the conductance of a slit (which is two-dimensional) making a limiting process, which is shown in

our second example to be erroneous unfortunately.

Recently, many studies have been made on the flow of a viscous fluid past an obstacle in the presence of other obstacles, e.g. walls or the same kind of obstacles, on the basis of the Oseen or the Stokes equations of motion. Most of these investigations must appeal to an expansion method assuming the ratio d/l to be small, where d is the representative length of obstacles (such as the diameter of a circular cylinder), and l is the distance between them. Our second and third examples, being the exact solutions of the Stokes equations, may be useful to fill up the deficiency of them, especially in the case of small aperture $d \gg l$. Tamada and Fujikawa[2] investigated in detail the flow past a lattice of circular cylinders on the basis of the Oseen equations. Kuwabara[3] also discussed the flow past a lattice of parallel flat plates. Their formulae for the drag on a cylinder agree with the result of the fourth example qualitatively in the limit of small Reynolds numbers and small d/l.

§ 2. Fundamental Equations

We take the x-axis perpendicularly to the plane of the screen, denoting unit vector parallel to the x-axis by $\boldsymbol{i}$. The pressure p of the fluid at $x=\pm\infty$ is taken to be $p=\mp P/2$ without loss of generality. Let us consider the motion of the fluid induced by this pressure difference P.

The Stokes equations for the steady slow motion of an incompressible viscous fluid are written as

$$\mu \Delta \boldsymbol{V} = \operatorname{grad} p, \tag{2.1}$$

$$\operatorname{div} \boldsymbol{V} = 0\,, \tag{2.2}$$

where Δ stands for

$$\partial^2/\partial x^2 + \partial^2/\partial y^2 + \partial^2/\partial z^2,$$
$$\boldsymbol{V} = (u,\ v,\ w)$$

is the velocity vector, and μ is the coefficient of viscosity.

Our problem is to solve (2.1) and (2.2) under the boundary conditions

i) $p \to \mp P/2$ as $x \to \pm\infty$, (2.3)

ii) $\boldsymbol{V}=0$ on the wall of the screen W at $x=0$, (2.4)

iii) p and $\boldsymbol{V}$ are regular, one-valued and finite (or zero) throughout the field of flow including infinity. (2.5)

We have only to consider the positive half space $x>0$, because the symmetry of (2.1)–(2.5) allows a solution in which u is even and v, w, p are odd with respect to x:

$$\begin{aligned} u(x,\ y,\ z) &= u(-x,\ y,\ z)\,, \\ v(x,\ y,\ z) &= -v(-x,\ y,\ z)\,, \\ w(x,\ y,\ z) &= -w(-x,\ y,\ z)\,, \\ p(x,\ y,\ z) &= -p(-x,\ y,\ z)\,. \end{aligned} \tag{2.6}$$

On account of continuity of $\boldsymbol{V}$ and p we can conclude from (2.6) that

$$v,\ w,\ p=0 \quad \text{on the holes H at } x=0. \tag{2.7}$$

The boundary value problem of this type in the positive half-space is quite similar to the stamp problem in the elasticity, and has the following solution

$$\boldsymbol{V} = \boldsymbol{i}\Phi - x \operatorname{grad} \Phi, \tag{2.8}$$

$$p = -2\mu \frac{\partial \Phi}{\partial x}\,, \tag{2.9}$$

which satisfy (2.1)–(2.5) and (2.7) provided that Φ is a harmonic function:

$$\Delta \Phi = 0 \tag{2.10}$$

and satisfy the following boundary conditions

$$\Phi = 0 \quad \text{on the wall W} \tag{2.11}$$

$$\partial\Phi/\partial x = 0 \quad \text{on the holes H,} \tag{2.12}$$

$$\operatorname{grad} \Phi \to \frac{P}{4\mu}\boldsymbol{i} \quad \text{as } x \to \infty, \tag{2.13}$$

grad Φ being one-valued and regular throughout the field of flow including infinity. H must not contain the element whose area is ∞^2. This exceptional case corresponds to the flow past a disk etc., which should be excluded from our problem. (2.8)–(2.10) are essentially the same formulae already used by Roscoe in the study of the flow past a plane obstacle.

The quantity of practical interest is the flow conductance of the holes:

$$\sigma = Q/P\,, \tag{2.14}$$

where

$$Q = \int_{\mathrm{H}} u\, dS \tag{2.15}$$

is the total flow through the holes H. By making use of (2.8) Q is represented in terms of Φ as follows:

$$Q = \int_{\mathrm{H}} \Phi\, dS\,. \tag{2.16}$$

The drag on a part of the wall δW is also expressed in terms of Φ as

$$D=-2\int_{\delta W} p\, dS=4\mu\int_{\delta W}\frac{\partial\Phi}{\partial x}dS\,, \qquad (2.17)$$

where use is made of (2.6) and (2.9).

§ 3. Flow of a Perfect Fluid past Complementary Disks or Strips

Let us consider the velocity potential Φ_p for the flow of a perfect fluid with uniform velocity U_p at $x=\pm\infty$, past disks or strips H which are congruent with the holes under consideration. It is well known that Φ_p satisfies the following equations and boundary conditions

$$\Delta\Phi_p=0\,, \qquad (3.1)$$

$$u_p=\partial\Phi_p/\partial x=0 \quad \text{on H}, \qquad (3.2)$$

$$\text{grad}\,\Phi_p\to iU_p \quad \text{as } x\to\infty, \qquad (3.3)$$

and grad Φ_p is regular and one-valued throughout the flow field including infinity.

It will be seen that (3.1)–(3.3) are perfectly equivalent to (2.10)–(2.13) provided that U_p and Φ_p satisfy

$$U_p=P/4\mu, \qquad (3.4)$$

and

$$\Phi_p=0 \quad \text{on W}. \qquad (3.5)$$

The condition (3.5) may be easily satisfied by taking a suitable additive constant in Φ_p if there is no circulation for each element of H. Thus if we know the velocity potential of a perfect fluid past H which is the complement of W, our problem is solved.

We next proceed to find a formula which expresses the flow conductance of holes for a viscous fluid in terms of a quantity which is familar in the case of a perfect fluid. For this purpose we consider the motion of H with velocity iU_p broadside-on in a perfect fluid. The velocity potential induced by this motion is evidently given by

$$\Phi_p-U_px \qquad (3.6)$$

using Φ_p determined by (3.1)–(3.3). The virtual mass M of H is defined

$$MU_p^2=2T$$

$$=\rho\int[\text{grad}\,(\Phi_p-U_px)]^2dV \qquad (3.7)$$

and is independent of U_p, where T is the induced kinetic energy of the fluid, ρ is the density, and dV the volume element of the flow field external to H.

Making use of Green's theorem and taking into account the relations (3.1)–(3.5) and the symmetry of the flow field, we have

$$MU_p^2=-2\rho\int_H(\Phi_p-U_px)\frac{\partial}{\partial x}(\Phi_p-U_px)dS$$

$$=2\rho U_p\int_H\Phi_p\, dS\,, \qquad (3.8)$$

assuming that the surface integral over a sphere of infinite radius tends to zero. This assumption is allowed unless the total area of H is infinite as in the case of an infinite series of slits. In such a case (3.7) becomes infinite and (3.8) loses its meaning. However it is convenient to define a partial virtual mass of a hole of area δH, taking δH instead of H as the domain of integration in (3.8).

Introducing (3.4) and (3.8) into (2.14) and (2.16) we obtain for Q and σ

$$Q=\frac{MU_p}{2\rho}=\frac{MP}{8\rho\mu}\,, \quad \sigma=\frac{M}{8\rho\mu}\,. \qquad (3.9)$$

When M denotes the partial virtual mass, Q gives of course the total flow through δH.

In addition, making use of (2.17) and (3.4), the drag D on a part of the wall δW is given by

$$D=4\mu\int_{\delta W}u_p\, dS=\frac{P}{U_p}\int_{\delta W}u_p\, dS=Pq_p\,, \qquad (3.10)$$

where q_p is the total flow of the perfect fluid through δW with uniform volocity $\boldsymbol{i}$ at infinity.

Equations (3.9) and (3.10) are the required results, and complement Roscoe's formula which relates the viscous drag D_d of a disk with its electrostatic capacity C by

$$D_d=8\pi\mu CU\,, \qquad (3.11)$$

where U is the normal velocity of the disk.

§ 4. Examples

1) A single elliptic hole.

The virtual mass of an elliptic disk H is known to be

$$M=\frac{4\pi}{3}\rho b^2c^2\Big/\int_0^{\pi/2}\sqrt{b^2\sin^2\theta+c^2\cos^2\theta}\,d\theta$$

$$=\frac{16\rho S^2}{3\pi s}\,, \qquad (4.1)$$

$$S=\pi bc, \quad s=4\int_0^{\pi/2}\sqrt{b^2\sin^2\theta+c^2\cos^2\theta}\,d\theta\,,$$

where b and c are the semi-axes, S is the area and s the periphery of H. Introducing (4.1) into (3.9) the conductance of the elliptic hole H is given by

$$\sigma=\frac{2S^2}{3\pi\mu s}, \tag{4.2}$$

which is the formula obtained by Roscoe without noticing the relation to M.

For the sake of reference the velocity distribution on the hole is found to be

$$V=\frac{SP}{\pi\mu s}\sqrt{1-\frac{y^2}{b^2}-\frac{z^2}{c^2}}\,\boldsymbol{i}. \tag{4.3}$$

(2) A single slit of width $2h$.

For a strip or a flat plate of width $2h$, M is known to be

$$M=\pi\rho h^2. \tag{4.4}$$

This gives for the conductance of a slit of width $2h$:

$$\sigma_{2h}=\frac{\pi}{8\mu}h^2\fallingdotseq 0.3927\frac{h^2}{\mu}. \tag{4.5}$$

Roscoe estimated this value to be $4h^2/(3\pi\mu)\fallingdotseq 0.4244\ h^2/\mu$ assuming (4.2) to be valid for a rectangle of width $2h$ and making its length L infinitely large. This interesting discrepancy seems to be due to the edge effect of the elliptic hole which becomes important as its thickness becomes small.

Now, according to classical results, the velocity potential of a perfect fluid past a strip $x=0$, $|y|\leqq h$ is given by

$$\begin{aligned}\Phi_p&=U_p\,\mathrm{Re}\,f(\zeta),\\ f(\zeta)&=\sqrt{\zeta^2+h^2},\\ \zeta&=x+iy.\end{aligned} \tag{4.6}$$

Introducing this into (2.8) and (2.9) we obtain for the velocity and pressure distribution on H and W

$$\boldsymbol{V}=i\boldsymbol{\Phi}=\begin{cases}\dfrac{Ph}{4\mu}\sqrt{1-\dfrac{y^2}{h^2}}\,\boldsymbol{i}, & |y|\leqq h,\\ 0, & |y|\geqq h.\end{cases} \tag{4.7}$$

$$p=\begin{cases}0, & |y|\leqq h,\\ \mp\dfrac{P}{2}\Big/\sqrt{1-\dfrac{h^2}{y^2}}, & |y|\geqq h,\ x=\pm 0,\end{cases} \tag{4.8}$$

$$\frac{dp}{dx}=-2\mu\frac{\partial^2\Phi}{\partial x^2}=2\mu\frac{\partial^2\Phi}{\partial y^2}=2\mu\frac{\partial^2|V|}{\partial y^2}$$
$$=\begin{cases}-\dfrac{P}{2h}\Big/\sqrt{\left(1-\dfrac{y^2}{h^2}\right)^3}, & |y|\leqq h,\\ 0, & |y|\geqq h.\end{cases} \tag{4.9}$$

$u-y$ curve is an ellipse in contrast with a parabola in the case of the Poiseuille flow.

The behaviour of the flow at a great distance r from the slit is also given by

$$\boldsymbol{V}\sim\mp\frac{Ph^2}{8\mu}x^2\cdot\mathrm{grad}\left(\frac{1}{r^2}\right),\quad \text{as } x\to\pm\infty \tag{4.10}$$

and

$$p\sim\mp\frac{P}{2}\left[1-\frac{h^2(x^2-y^2)}{2r^4}+O\left(\frac{1}{r^4}\right)\right], \tag{4.11}$$

making use of

$$\begin{aligned}\Phi&\sim\pm\frac{P}{4\mu}\mathrm{Re}\left(\zeta+\frac{h^2}{2\zeta}+\cdots\right)\\ &=\pm\frac{Px}{4\mu}\left[1+\frac{h^2}{2r^2}+\cdots\right].\end{aligned} \tag{4.12}$$

3) Two parallel slits of equal breadth

Let us consider two parallel slits $h>y>a$ and $-h<y<-a$ whose width l and distance d are $l=h-a$ and $d=2a$ respectively. In this case Φ is given by

$$\begin{aligned}\Phi&=\mathrm{Re}\,f(\zeta),\\ f(\zeta)&=U_p\int_0^\zeta\frac{\zeta^2+m^2}{\sqrt{(\zeta^2+a^2)(\zeta^2+h^2)}}d\zeta,\end{aligned} \tag{4.13}$$

which satisfies (2.11)–(2.13) provided that

$$\frac{\Gamma}{2}=U_p\int_a^h\frac{m^2-y^2}{\sqrt{(y^2-a^2)(h^2-y^2)}}dy=0 \tag{4.14}$$

or

$$m^2=h^2E(\sqrt{1-k^2})/K(\sqrt{1-k^2}),\ k=a/h, \tag{4.15}$$

where K and E are the complete elliptic integrals of the first and the second kind respectively. $f(\zeta)$ is the complex velocity potential of a two-dimensional perfect fluid past two flat plates ($x=0$, $a<|y|<h$) with uniform velocity iU_p. (4.14) is nothing but the condition of zero circulation around each plate, and is seen to assure (2.11), if we take into account that the integrand of (4.13) is real for $\zeta=iy$ in the intervals $|y|<a$ or $|y|>h$, and its contribution to (4.13) is purely imaginary.

Putting $\zeta=iy$ in (4.13) and substituting in (2.16) the total flow Q past a hole is given by

$$\begin{aligned}Q&=\int_a^h\Phi\,dy=y\Phi\Big|_a^h-U_p\int_a^h\frac{y(m^2-y^2)}{\sqrt{(y^2-a^2)(h^2-y^2)}}dy\\ &=\frac{\pi P}{8\mu}\left[\frac{a^2+h^2}{2}-m^2\right]\\ &=\frac{\pi h^2P}{8\mu}\left[\frac{1}{2}(1+k^2)-\frac{E(\sqrt{1-k^2})}{K(\sqrt{1-k^2})}\right],\end{aligned} \tag{4.16}$$

making use of $\Phi(0,h)=\Phi(0,a)=0$ and introducing (3.4).

The drag D acting on a plate $|y|<a$ is given by

$$\frac{D}{P}=\frac{2}{U_p}\int_0^a\frac{\partial\Phi}{\partial x}dy=2\int_0^a\frac{m^2-y^2}{\sqrt{(a^2-y^2)(h^2-y^2)}}dy$$

$$=2\left[\frac{m^2-h^2}{h}K(k)+hE(k)\right]=\frac{\pi h}{K'}\,, \qquad (4.17)$$

where we have used the relations (3.10) and (4.13) together with the Legendre relation

$$E'K-KK'+EK'=\frac{\pi}{2}\,, \qquad (4.18)$$

where

$$E'=E(k'),\ K'=K(k'),\ k'=\sqrt{1-k^2}=\sqrt{1-(a^2/h^2)}. \qquad (4.19)$$

Fig. 1 and Fig. 2 show the values of $8\mu\sigma/(\pi h^2)=\sigma/\sigma_{2h}$ and $D/(2hP)$, where σ_{2h} is the

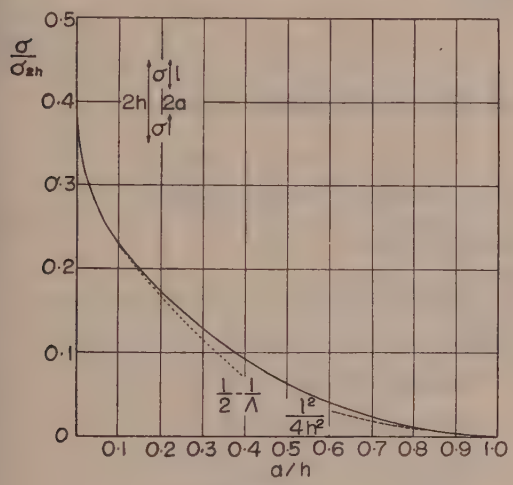

Fig. 1.

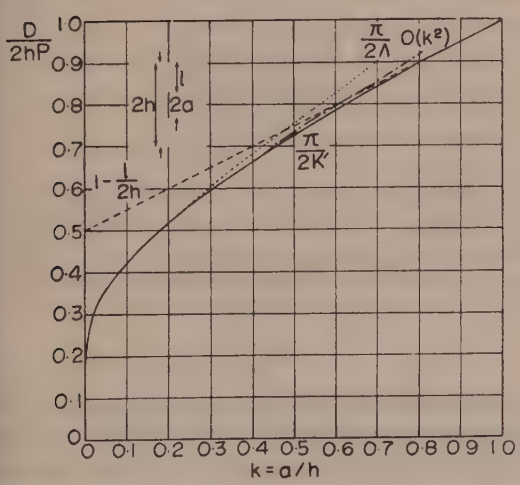

Fig. 2.

conductance of a single slit of width $2h$ given by (4.5). Making k $(=a/h)$ or k' $(=\sqrt{1-(a^2/h^2)}\sim\sqrt{(2l)/h})$ tend to zero we obtain

$$\frac{\sigma}{\sigma_{2h}}=\frac{1}{2}\left[1-\frac{2}{\Lambda}+\frac{k^2}{2\Lambda}\left(2-\frac{1}{\Lambda}\right)+O(k^4)\right] \qquad (4.20)$$

$$=\frac{1}{16}k'^4+O(k'^6)\sim\frac{l^2}{4h^2}\,, \qquad (4.21)$$

$$\Lambda=\log\left(\frac{4}{k}\right)=\log\left(\frac{4h}{a}\right)=\log\left(\frac{8h}{d}\right),$$

$$\frac{D}{2hP}=\frac{\pi}{2[\Lambda+(\Lambda-1)k^2/4+O(k^4)]} \qquad (4.22)$$

$$=\frac{1}{1+k'^2/4+O(k'^4)}\sim 1-\frac{l}{2h}\,. \qquad (4.23)$$

According to (4.20) the blocking effect of a small intervening strip (width $d=2a$) in a slit (width $2h$) is great on account of the presence of the logarithmic term. On the other hand if we keep the width of two slits $(l=h-a)$ constant and decrease the distance $2a$ between them σ increases from σ_l at $a=\infty$ to $\sigma_{2h}/2=2\sigma_l$ at $a=0$, on account of the interference between two slits.

(4.22) shows that the drag for a small obstacle in a slit experiences the force of the magnitude $\pi hP/\log(8h/d)$, and (4.23) shows that the deviation of D from $2hP$ is given by lP, being a half of $2lP$ which may be inferred from naive consideration.

4) A series of parallel equal and equidistant slits.

We now consider the case where

$$\Phi=A\,\mathrm{Re}\,F(\zeta) \qquad (A=\text{real}) \qquad (4.24)$$

with

$$F(\zeta)=\cosh^{-1}\left(\frac{1}{C}\cosh\frac{\pi\zeta}{h}\right),\quad C=\cos\frac{\pi l}{2h}\,. \qquad (4.25)$$

This Φ is an even periodic function of ζ with a period ih, since $\cosh^{-1}(-|\tau|)=\cosh^{-1}|\tau|+i\pi$, and we take F to be real and positive at $\zeta=0$.

On the imaginary axis $\zeta=iy$, $\cosh(\pi\zeta/h)$ equals $\cos(\pi y/h)$, and F becomes purely imaginary at the interval W except H:

$$\text{W:}\quad \frac{l}{2}+nh<y<-\frac{l}{2}+(n+1)h\,,$$

$$\text{H:}\quad -\frac{l}{2}+nh<y<\frac{l}{2}+nh\,,$$

$$n=0,\ \pm1,\ \pm2,\cdots. \qquad (4.26)$$

On the other hand

$$\frac{\partial F}{\partial x}=F'(\zeta)=\frac{\pi}{h}\frac{\sinh(\pi\zeta/h)}{\sqrt{\cosh^2(\pi\zeta/h)-C^2}} \qquad (4.27)$$

is purely imaginary at H and real at W.

If we make x infinitely large we find

$$F=\frac{\pi}{h}\zeta-\log C+O(e^{-(2\pi/h)x}) \text{ as } x\to\infty, \quad (4.28)$$

since

$$\cosh^{-1}\xi=\log(\xi+\sqrt{\xi^2-1})=\log(2\xi)+O\left(\frac{1}{\xi^2}\right). \quad (4.29)$$

These show that (4.24) and (4.25) in conjunction with (2.8) and (2.9) give the viscous flow through a series of parallel equal (width l), and equidistant (period h, distance $d=h-l$) slits, if we take

$$A=\frac{h}{4\pi\mu}P \quad (4.30)$$

according to (2.11)–(2.13).

Introducing (4.24) and (4.28) into (2.8) we obtain

$$V\to iU,\ U=-A\log C \quad \text{as } x\to\pm\infty. \quad (4.31)$$

This implies the existence of the uniform flow iU at ∞ which may be expected by considering that the total flow is infinite in the present case.

Taking into account the continuity and periodicity of the flow, we obtain

$$Q=Uh=\frac{Ph^2}{4\pi\mu}\left|\log\cos\frac{\pi l}{2h}\right| \quad (4.32)$$

for the total flow past one slit, or

$$\sigma=\frac{Q}{P}=\frac{h^2}{4\pi\mu}\left|\log\cos\frac{\pi\varepsilon}{2}\right|,\quad \varepsilon=\frac{l}{h} \quad (4.33)$$

for the conductance of a slit, where ε is the relative aperture of the screen.

The force D acting on a strip, e.g.

$$\frac{l}{2}<y<-\frac{l}{2}+h,$$

is given by

$$D=Ph=\frac{4\pi\mu U}{\left|\log\cos\frac{\pi\varepsilon}{2}\right|}, \quad (4.34)$$

by use of the momentum and periodicity consideration together with (4.30) and (4.31).

Of course (4.32) and (4.34) can be obtained from (2.16) and (2.17) directly, but these integrals are reducible to the integrals at $x=\infty$ if we make use of contour integrals along a rectangle

$$-\frac{i}{2}h\to\frac{i}{2}h\to\frac{i}{2}h+\infty\to-\frac{i}{2}h+\infty,$$

and note that Φ and $\partial\Phi/\partial x$ are periodic harmonic functions, satisfying (2.11)–(2.12).

Fig. 3 shows the values of $D/(\mu U)=h^2/(\mu\sigma)$

$$=4\pi\Big/\left|\log\cos\frac{\pi}{2}\varepsilon\right|.$$

Making ε or $\varepsilon'=1-\varepsilon$ tend to zero we obtain

$$\frac{h^2}{\mu\sigma}=\frac{D}{\mu U}=\frac{32}{\pi\varepsilon^2}-\frac{4\pi}{3}+O(\varepsilon^2) \quad (4.35)$$

$$=\frac{4\pi}{\left|\log\sin\frac{\pi}{2}\varepsilon'\right|}$$

$$=\frac{4\pi}{\log\frac{1}{\tau}+\sum_{n=1}^{\infty}\frac{2^{2n-1}B_n}{n(2n)!}\tau^{2n}}\sim\frac{4\pi}{\log\frac{1}{\tau}+\frac{\tau^2}{6}}, \quad (4.36)$$

where

$$\varepsilon'=1-\varepsilon=\frac{h-l}{h}=\frac{d}{h},\quad \tau=\frac{\pi\varepsilon'}{2}=\frac{\pi d}{2h}, \quad (4.37)$$

and B_n is the Bernoulli number:

$$B_1=\frac{1}{6},\ B_2=\frac{1}{30},\ B_3=\frac{1}{42},$$
$$B_4=\frac{1}{30},\ B_5=\frac{5}{66},\cdots. \quad (4.38)$$

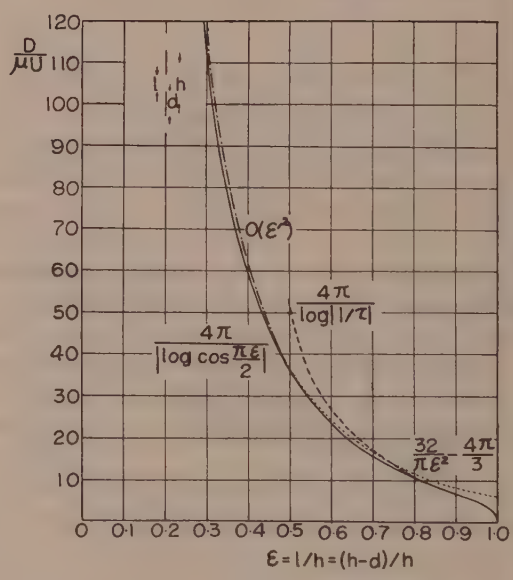

Fig. 3.

According to (4.35) the drag on a strip is inversely proportional to the square of the relative aperture ε, and $\sigma\sim\pi l^2/32\mu\sim\sigma_l$ (see (4.5)), provided ε is small. It is remarkable that the expansion formulae afford very good approximations even in the intermediate values of ε, if we take only the first two terms (see Fig. 3).

Recently Tamada and Fujikawa investigat-

ed[2] the flow past a lattice of circular cylinders (diameter d) on the basis of the Oseen equations and obtained a formula for the drag on a cylinder in the limit of small Reynolds numbers and d/h. Their values are qualitatively similar to that obtained from (4.36) and are a little larger for the same values of d/h. Kuwabara's result for a lattice of flat plates which are parallel to the main flow is also similar to (4.36) and give smaller values for the same values of d/h. These are in accordance with our intuition.

In conclusion the author expresses his hearty gratitude to Professor Ko Tamada, Professor Isao Imai and Professor Susumu Tomotika for their continual suggestion and encouragement throughout this work. The author's thanks are also due to the Ministry of Education for a grant in aid for fundamental research.

References

1) R. Roscoe: Phil. Mag. **40** (1949) 338.
2) K. Tamada and H. Fujikawa: Quart J. Mech. and Appl. Math. **10** (1957) 423.
3) S. Kuwabara: to be published.
4) H. Lamb: Hydrodynamics, Cambridge Univ. Press, 6th edition, 1932.

JOURNAL OF THE PHYSICAL SOCIETY OF JAPAN Vol. 13, No. 6, JUNE, 1958

Asymptotic Behaviour of the Response Function of an Optical System with the Primary Spherical Aberration

By Hirosi ITÔ

Department of Applied Physics, Faculty of Engineering, Osaka University

(Received April 1, 1958)

An asymptotic calculation of the response function of an optical system which has the primary spherical aberration is carried out in the presense of a defect of focus. The evaluation of the integral for the response function is calculated by the aid of the approximate formulae for Fresnel's integral when the coefficient of the spherical aberration is sufficiently large compared with the wave length of light. The response function denotes an interesting behaviour for various focal shifts even for a fixed value of the coefficient of the spherical aberration. When the shift is small, it has a strong decreasing character, and for larger values of it, the function becomes larger and begins to denote an oscillating property at last. The spatial frequency s extends from zero to 2 and the result is not valid in the neighbourhoods of the end points because of the simplification of the calculation which is used. The result is compared with an experiment.

§ 1. Introduction

Recently, many authors introduced "*information theory*" into the discussion of the characteristics of the optical systems, and some of the concepts which have prevailed up to now in this field are being reconsidered from this new standpoint. One of the most interesting new ideas which have been brought forth by this theory is that, we can assume an optical system as a kind of linear filter which has the frequency response. The frequency response function derived from this assumption is now considered as the most powerful concept which would play an essential role in the performance test for optical systems, Duffieux[1], Hopkins[2] and Linfoot[3] have introduced a reasonable definition for it. The complex amplitude in the image of a point source situated on the optical axis of an optical system can be given by the Fourier

transform of the pupil function. If we consider the frequency spectrum of the intensity in the diffraction image of the point source, it can be represented by the correlation function and is given by the formula (1) in § 2. This function has just the same form as that of the time correlation function in the theory of time series although the spatial frequency stands as time. Numerous investigations[4)5)6)] have been done about the measurement of this function for various optical systems, but there are very few about the analytical calculations. Hopkins[2)] calculated the effect of defocussing, and De[7)] did that of the function for an astigmatic optical system with defect of focus. However, any direct analysis is supposed to be difficult when the system includes every kind of aberration and even the numerical calculation seems awfully hard when the coefficients of the aberrations become large. On the other hand, it seems us that, there is a benefitable condition in case of the usual photographic lenses to try approximate calculations by it. The aberration function appears as the phase of the pupil function and includes Seidel's aberration coefficients. Although these constants are sufficiently small, the optical wave length is still smaller compared with them. We must notice that, these coefficients are considered to become smaller effectively as the aperture is reduced down smaller, and such discussion will fail for extreme cases. Taking advantage of this fact, we could expect to get some asymptotic expression for the response function. Although this thought is valid in principle, it is still difficult in general case. Fortunately, since the aberration function for the presence of the primary spherical aberration and the defect of focus is not complicated, such treatment is possible. Its calculation appears in § 3 and § 4, and the higher order approximation which gives some correction for it is in § 5. The detailed calculation of the most important integral which plays an essential role is given in Appendix. The calculated values and observed values are compared for a single lens which is assumed to have only the primary spherical aberration.

§ 2. General Formulae

The definition of the response function is given as the following when an incoherently lit or self-luminous object is imaged through an optical system in question. Of course, we assume that the image is isoplanatic.

$$\varphi(s)=\frac{1}{\pi}\iint f\left(x+\frac{s}{2},y\right)f^*\left(x-\frac{s}{2},y\right)dxdy\,, \tag{1}$$

where

$$\left.\begin{aligned} f(x,y)&=\exp\left[ikW(x,y)\right]. & (x^2+y^2\leq 1)\\ &=0\,. & (x^2+y^2>1)\end{aligned}\right\} \tag{2}$$

$W(x,y)$ is the aberration function of the optical system and $k=2\pi/\lambda$. λ is the optical wave length. When the system has the primary spherical aberration in the presence of a defect of focus, the pupil function $f(x,y)$ is given by

$$\exp\left[ik\left\{A(x^2+y^2)+\frac{1}{4}W_1(x^2+y^2)^2\right\}\right]. \tag{3}$$

A represents the marginal optical distance between a reference sphere centered on the chosen focal plane and the section of the emergent wave front in the sagittal meridian. W_1 is the coefficient of the primary spherical aberration when the exit pupil is considered as a circle of which radius is 1. Using (3), the integrand of (1) is written as

$$\exp\left[i(px+qxy^2+qx^3)\right]. \tag{4}$$

p and q are both the functions of the spatial frequency s, and are defined by

$$\left.\begin{aligned} q&=kW_1s\\ p&=\frac{kW_1s}{4}\left(s^2-\frac{1}{n}\right),\end{aligned}\right\} \tag{5}$$

where we put

$$A=-\frac{W_1}{8n}\,. \tag{6}$$

By proper choice of the parameter n, we can realize any focal setting for a given W_1. n takes negative values as well as positive ones. From (5), p changes its sign from negative to positive at $s_0=(1/\sqrt{n})$.

The region of integration for (1) is given by the shadowed region in Fig. 1 on the exit pupil plane. Then the response function is

$$\varphi(s)=\text{real part of }\frac{4}{\pi}\int_0^{1-s/2}\exp\left[i(qx^3+px)\right]dx \times\int_0^{\sqrt{1-(x+s/2)^2}}\exp\left[iqxy^2\right]dy \tag{7}$$

where the limits of integration are written explicitly.

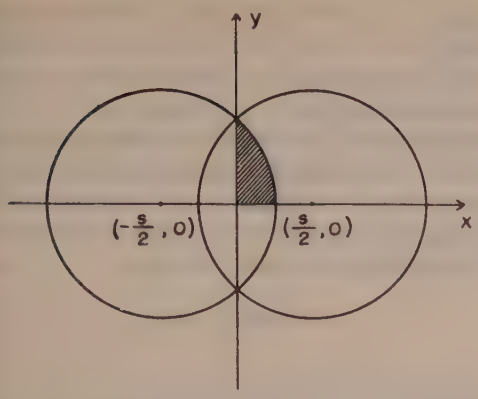

Fig. 1. Domain of integration of (7).

§ 3. Fresnel's Integral

Instead of (7), it is more convenient to treat the integral

$$\Phi(s)=\int_0^{1-(s/2)} \exp\left[i(qx^3+px)\right]dx \times \int_0^{\sqrt{1-(x+s/2)^2}} \exp\left[iqxy^2\right]dy\,. \qquad (8)$$

Putting the integral related to y as

$$f(x)=\int_0^{\sqrt{1-(x+s/2)^2}} \exp\left[iqxy^2\right]dy\,,$$

and replacing $\sqrt{qxy}$ by a new variable σ, we get

$$f(x)=\frac{1}{\sqrt{qx}}\int_0^{\sqrt{qx\{1-(x+s/2)^2\}}} \exp\left[i\sigma^2\right]d\sigma\,. \qquad (9)$$

$\sqrt{qx}f(x)$ is exactly Fresnel's integral[8] of which property is well-known. However, as the result is not represented by a simple function, we must be satisfied with its approximation. When we put

$$qx\left\{1-\left(x+\frac{s}{2}\right)^2\right\}=u\,, \qquad (10)$$

Fresnel's integral is represented by

$$\sqrt{qx}f(x)=\left\{\begin{array}{ll}\dfrac{\sqrt{\pi}}{2}e^{\pi/4\cdot i} & (u\gg 0)\\ u^{1/2}e^{iu} & (u\sim 0)\end{array}\right\} \qquad (11)$$

as the first approximation. These two functions are connected with each other at $\pi/4$ continuously but not smoothly. The true function oscillates around this value and the error caused by this smoothing process will be estimated later. The values of x corresponding to $u=(\pi/4)$ can be obtained by solving the equation

$$qx\left\{1-\left(x+\frac{s}{2}\right)^2\right\}=\frac{\pi}{4}\,. \qquad (12)$$

Since p and q are very large for almost all values of s, there is a conventional method to get these values. In Fig. 2, the maximum values of u are sketched as the function of s when $kW_1=400$. This function is

$$M=kW_1s\left\{-\frac{s}{3}+\frac{s^3}{108}+\left(\frac{2}{9}+\frac{s^2}{54}\right)\sqrt{3+\frac{1}{4}s^2}\right\} \qquad (13)$$

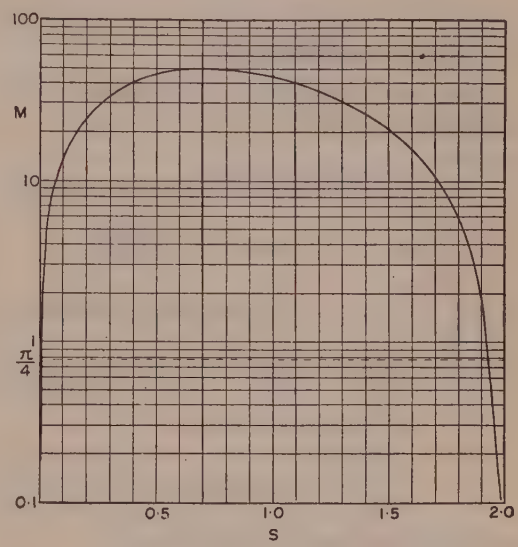

Fig. 2. Maximum value of $qx\{1-(x+s/2)^2\}$ as the function of spatial frequency.

Except the neighbourhoods of $s=0$ and $s=2$, M is sufficiently larger than $\pi/4$. This function u is zero at the both ends $x=0$ and $1-(s/2)$, and has only one maximum between these points. From this fact, we may assume that there are two values of x which satisfy $u=(\pi/4)$, and the one is very near the point $x=0$ while the other is in the neighbourhood of $x=1-(s/2)$. These values are given approximately by

$$x_1\sim\frac{\pi}{4q\left(1-\frac{s^2}{4}\right)} \qquad x_2\sim 1-\frac{s}{2}-\frac{\pi}{8q\left(1-\frac{s}{2}\right)}\,. \qquad (14)$$

These become infinite at $s=0$ or $s=2$, so that the result which comes from this simplification can not be applied near these points. The number of lines per millimeter on the object plane to be resolved by some optical system is too numerous for the region of s which exceeds 1, when the aberration is large. Probably, the usual lenses have no response effectively for such high values. Therefore, it will be sufficient for us not to consider the neighbourhood of $s=2$, although the divergence

near zero is undesirable and limits the application of the result. Within this reasoning, we are going to use the following representation for $f(x)$, that is

$$f(x)=\left\{\begin{array}{l} f_1(x)=\dfrac{\sqrt{\pi}}{2}e^{\pi/4\cdot i}\ (x_1<x<x_2)\ . \\ f_2(x)=e^{iu}\left(\dfrac{u}{qx}\right)^{1/2}\left(\begin{array}{l}0\leq x\leq x_1\\ x_2\leq x\leq 1-(s/2)\end{array}\right). \end{array}\right\} \tag{15}$$

§ 4. First Approximation

Using the relation (15), the integral with respect to x is given by

$$\int_0^{1-(s/2)} f_1(x)\exp[i(qx^3+px)]dx$$
$$+\int_0^{x_1}(f_2(x)-f_1(x))\exp[i(qx^3+px)]dx$$
$$+\int_{x_2}^{1-(s/2)}(f_2(x)-f_1(x))\exp[i(qx^3+px)]dx \tag{16}$$

The first term in (16) is also written as

$$\int_0^\infty f_1(x)\exp[i(qx^3+px)]dx$$
$$-\int_{1-(s/2)}^\infty f_1(x)\exp[i(qx^3+px)]dx\ . \tag{17}$$

The second term of this becomes

$$-\frac{\sqrt{\pi}}{2i}\frac{\exp\left[i\left\{q\left(1-\frac{s}{2}\right)^3+p\left(1-\frac{s}{2}\right)\right\}\right]}{\sqrt{q\left(1-\frac{s}{2}\right)}\left\{3q\left(1-\frac{s}{2}\right)^2+p\right\}}$$
$$+O(q^{-5/2}) \tag{18}$$

by partial integration. Note that this process also makes the result not to be applied in the neighbourhood of $s=2$. According to the definition (7), one of the necessary terms which comes from (18) is

$$I_1=-\frac{2\sin\left\{q\left(1-\frac{s}{2}\right)^3+p\left(1-\frac{s}{2}\right)+\frac{\pi}{4}\right\}}{\sqrt{\pi\left(1-\frac{s}{2}\right)q}\left\{3q\left(1-\frac{s}{2}\right)^2+p\right\}}\ . \tag{19}$$

The error is the order of $q^{-5/2}$ which is not serious unless s is very small. The first term in (17) is

$$\frac{\sqrt{\pi}}{2}\frac{e^{\pi/4\cdot i}}{\sqrt{q}}\int_0^\infty\frac{\exp[i(qx^3+px)]}{\sqrt{x}}dx\ . \tag{20}$$

By putting $qx^3=t^3$, this becomes

$$\frac{\sqrt{\pi}}{2}\frac{e^{\pi/4\cdot i}}{q^{2/3}}\int_0^\infty\frac{\exp[i(t^3+\alpha t)]}{\sqrt{t}}dt\ , \tag{21}$$

where α is defined by $(p/q^{1/3})$ which changes its sign at $s_0=(1/\sqrt{n})$. Apart from the coefficient, the property of this integral is closely similar to that of Airy's integral and its evaluation can be also done in the same manner as that. Its detailed calculation is shown in Appendix. The result is not unique and is divided into several cases. By the definition of p and q, α is given by

$$\alpha=\frac{(kW_1s)^{2/3}\left(s^2-\frac{1}{n}\right)}{4}\ . \tag{22}$$

For a value of s smaller than $(1/\sqrt{n})$, α takes a negative value and becomes positive for an s larger than this value. This change of sign is very important, since the asymptotic behaviour of (21) for positive α is quite different from that for negative α. For a negative value of α, and for its large absolute value (21) becomes

$$I_2=\frac{2}{\sqrt{|p|q}}\left\{\sin 2\left(\frac{|\alpha|}{3}\right)^{3/2}-\frac{5}{18}\frac{\cos 2\left(\frac{|\alpha|}{3}\right)^{3/2}}{2\left(\frac{|\alpha|}{3}\right)^{3/2}}\right.$$
$$\left.-\frac{205}{648}\frac{\sin 2\left(\frac{|\alpha|}{3}\right)^{3/2}}{\left(2\left(\frac{|\alpha|}{3}\right)^{3/2}\right)^2}+\cdots\cdots\right\}. \tag{23}$$

If α is positive and large, its asymptotic expansion is

$$I_2'=\frac{2}{kW_1s^2}\exp\left[-\frac{kW_1s^4}{12\sqrt{3}}\right]$$
$$\cdot\left\{1-\frac{5}{18}\frac{1}{2\left(\frac{\alpha}{3}\right)^{3/2}}+\frac{205}{608}\frac{1}{\left(2\left(\frac{\alpha}{3}\right)^{3/2}\right)^2}-\cdots\right\}. \tag{24}$$

I_2' decreases exponentially as s becomes larger while the decreasing property of I_2 is not so strong. It denotes an oscillating property. When α is small, the integral (21) is represented by the following infinite series.

$$I_2''=\frac{2}{3\sqrt{\pi}\,q^{2/3}}\sum_{m=0}^\infty\frac{(\pm|\alpha|)^m}{m!}\Gamma\left(\frac{m}{3}+\frac{1}{6}\right)$$
$$\times\cos 2\pi\left(\frac{m}{3}+\frac{1}{6}\right). \tag{25}$$

This result is most important since α is not so large in almost all the region of s which we are interested in. It gives the largest contribution to the response function because it is the order of $q^{-2/3}$. I_1 is of the order of

$q^{-3/2}$ and any one of the other terms of which derivation will be shown later is the order of q^{-1} or $q^{-3/2}$.

Now we are in the stage to calculate the remaining integrals which may be considered as the correction terms as well as I_1. In the following, we take two integrals among them as the examples and show their evaluations. One of the integrals which appear in (16) is

$$\int_0^{x_1} f_2(x)\exp[i(qx^2+px)]dx$$
$$=\int_0^{x_1}\sqrt{1-\left(x+\frac{s}{2}\right)^2}\exp\left[i\left\{p+q\left(1-\frac{s}{4}\right)\right\}\times x-iqsx^2\right]dx\,. \tag{26}$$

The factor qsx^2 is quite small even at the upper limit of integration, so that we assume that

$$\exp\left[i\left\{p+q\left(1-\frac{s_2}{4}\right)\right\}x-iqsx^2\right]$$
$$\sim\exp\left[i\left\{p+q\left(1-\frac{s^2}{4}\right)\right\}x\right].$$

Expanding the square root term around $x=0$, and integrating by x, we get

$$I_3=4\sqrt{1-\frac{s^2}{4}}\,\frac{\sin\dfrac{\pi}{4-s^2}}{q}+O(q^{-2})\,. \tag{27}$$

Another integral which is in (16) is

$$\int_{x_2}^{1-(s/2)}\sqrt{1-\left(x+\frac{s}{2}\right)^2}\exp\left[i\left\{p+q\left(1-\frac{s^2}{4}\right)\right\}x-iqsx^2\right]dx\,. \tag{28}$$

We put $x=1-s/2-\xi$ and take the following approximations

$$\sqrt{1-\left(x+\frac{s^2}{2}\right)^2}\sim\sqrt{2\xi}$$
$$\exp\left[i\left\{p+q\left(1-\frac{s^2}{4}\right)\right\}x-iqsx^2\right]\sim\exp\left[-iqs\left(1-\frac{s}{2}\right)^2+i\left\{p+q\left(1-\frac{s^2}{4}\right)\right\}\left(1-\frac{s}{2}\right)\right.$$
$$\left.+2iqs\left(1-\frac{s}{2}\right)\xi-i\left\{p+q\left(1-\frac{s^2}{4}\right)\right\}\xi\right].$$

Inserting these results into (28), we get

$$C\int_0^{\pi/8q(1-s/2)}\sqrt{\xi}\exp\left[\left\langle 2qsi\left(1-\frac{s}{2}\right)-i\left\{p+q\left(1-\frac{s^2}{4}\right)\right\}\right\rangle\xi\right]d\xi$$

where

$$C=\sqrt{2}\exp\left[i\left\langle -qs\left(1-\frac{s}{2}\right)^2+\left\{p+q\left(1-\frac{s^2}{2}\right)\right\}\left(1-\frac{s}{2}\right)\right\rangle\right].$$

This is evaluated as the following by partial integration.

$$\sqrt{\frac{\pi}{8q\left(1-\dfrac{s}{2}\right)}}\,\frac{\exp\left[i\pi\left\{p+q\left(2s-1-\dfrac{3}{4}s^2\right)\right\}\Big/8q\left(1-\dfrac{s}{2}\right)\right]}{i\left\{q\left(2s-1-\dfrac{3}{4}s^2\right)+p\right\}}$$
$$-\frac{1}{2i\left\{q\left(2s-1-\dfrac{3}{4}s^2\right)+p\right\}^{3/2}}\int_0^{-\pi/4\cdot(s-1)^2/(2-s)}\frac{e^{it}}{\sqrt{t}}dt\,. \tag{29}$$

The integral which appears here is also Fresnel's integral. The upper limit of this integral is not so small even if we limit the domain of s up to 1. Therefore, the first approximation which has been used before is not sufficient. Taking into account the second order approxition, this becomes

$$I_4=\frac{1}{6\sqrt{2}\pi}\left(\frac{\pi}{q\left(1-\frac{s}{2}\right)}\right)^{3/2}\cos\frac{\pi}{4}\frac{(s-1)^2}{2-s}+O(q^{-2})\ . \tag{30}$$

Just the same kind of approximation is applied to the remaining two integrals in (16). The results are

$$I_5=-\frac{2\cos\left\{\frac{\pi}{4-s^2}\right\}}{q\sqrt{1-\frac{s^2}{4}}}+O(q^{-3})\ ,$$

$$I_6=\frac{4\sin\left\{\frac{\pi}{16q}\frac{p+3q\left(1-\frac{s}{2}\right)^2}{1-\frac{s}{2}}\right\}\cos\left\{q\left(1-\frac{s}{2}\right)^3+p\left(1-\frac{s}{2}\right)-\frac{\pi}{16q}\frac{p+3q\left(1-\frac{s}{2}\right)^2}{1-\frac{s}{2}}+\frac{\pi}{4}\right\}}{\sqrt{q\left(1-\frac{s}{2}\right)\pi}\left\{p+3q\left(1-\frac{s}{2}\right)^2\right\}}$$

$$+O(q^{-5/2})\ .$$

Now the value of the response function is given by the sum of these six terms.

$$I=I_1+I_2+I_3+I_4+I_5+I_6+O(q^{-2})\ . \tag{31}$$

Although we use the symbol I_2, I_2'' must be employed for small values of s, and I_2' or I_2 is applied for larger values of s. In Fig. 3, five examples are given for different values of W_1 and n by using (31). Three I_2's should be used carefully, and I_2'' has been used actually for almost all region of s for all of them.

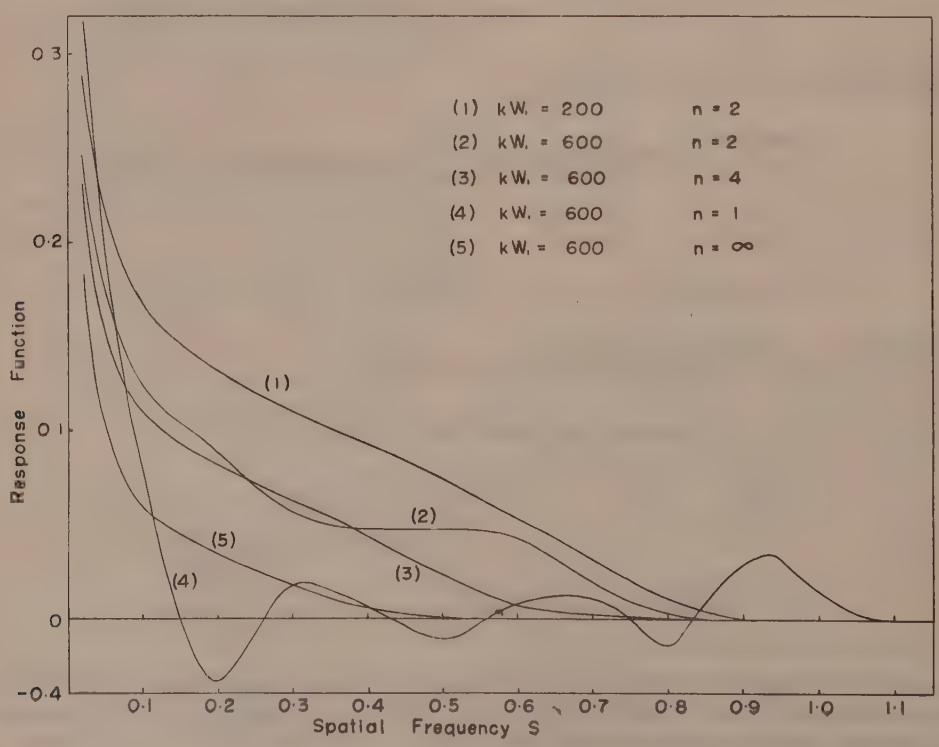

Fig. 3.

§ 5. Second Order Approximation

The calculation of the response function which was expounded in the foregoing sections is quite consistent so far as we take (15) as the first approximation of Fresnel's integral. As pointed out, I_2'' is the principal part and the largest correction terms are of the order of q^{-1}. If the second order contribution of Fresnel's integral is the same order, we must add this to the result. If we take into account the second term, Fresnel's integral is represented by

$$\int_0^z \frac{e^{it}}{\sqrt{t}} = \begin{cases} \sqrt{\frac{\pi}{2}}(1+i) - i\frac{e^{iz}}{\sqrt{z}}\,. & (z \gg 0) \quad (32) \\ 2z^{1/2}e^{iz} - \frac{4}{3}iz^{3/2}e^{iz}\,. & (z \sim 0) \quad (33) \end{cases}$$

When we use this expression, the curve is not continuous at x_1 or x_2 if we use the original values. However, the discrepancies are not serious, so that these simple values will be still used. The integral which arises from the second term of (32) is

$$-\frac{i}{2}\frac{1}{q}\int_{x_1}^{x_2} \frac{\exp\left[i\left\{p+q\left(1-\frac{s^2}{4}\right)\right\}x - iqsx^2\right]}{x\sqrt{1-\left(x+\frac{s}{2}\right)^2}}dx\,,$$

where the following approximation is used.

$$\frac{1}{\sqrt{1-\left(x+\frac{s}{2}\right)^2}} \sim \frac{1}{\sqrt{1-\frac{s^2}{4}}}\left(1+\frac{x}{2\left(1-\frac{s^2}{4}\right)}x\right).$$

Then we get

$$-\frac{i}{2}\frac{1}{q\sqrt{1-\frac{s^2}{4}}}\left(\int_{x_1}^{x_2}\frac{\exp\left[i\left\{p+q\left(1-\frac{s^2}{4}\right)\right\}x-iqsx^2\right]}{x}dx\right.$$

$$\left.+\frac{s}{2\left(1-\frac{s^2}{4}\right)}\int_{x_1}^{x_2}\exp\left[i\left\{p+q\left(1-\frac{s^2}{4}\right)\right\}x-iqsx^2\right]dx\right),$$

where only the first integral is necessary because the second one is of the order of q^{-2}. The first one can be rewritten as follows:

$$\int_0^\infty g(x)\,dx - \int_0^{x_1} g(x)\,dx - \int_{x_2}^\infty g(x)dx\,, \tag{34}$$

where

$$g(x) = \exp\left[i\left\{p+q\left(1-\frac{s^2}{4}\right)\right\}x - iqsx^2\right]\Big/x\,.$$

The result which comes from the second integral of (34) is

$$I_7 = -\frac{1-\frac{1}{4n}}{2q\left(1-\frac{s^2}{4}\right)^{3/2}}\left\{1-\frac{1}{18}\left(\frac{\pi}{4}\right)^2\left(\frac{1-\frac{1}{4n}}{1-\frac{s^2}{4}}\right)^2\right\}+O(q^{-2})\,. \tag{35}$$

The real part of the integral

$$-\frac{i}{2}\frac{1}{q\sqrt{1-\frac{s^2}{4}}}\int_{x_2}^{\infty}\frac{\exp\left[i\left\{p+q\left(1-\frac{s^2}{4}\right)\right\}x-iqsx^2\right]}{x}dx\,.$$

can be easily shown to be of the order of q^{-2}. The integral which comes from the first term in (34) is

$$\frac{2}{q\pi\sqrt{1-\frac{s^2}{4}}}\int_0^{\infty}\frac{\sin\left(\left\{p+q\left(1+\frac{s^2}{4}\right)\right\}x-qsx^2\right)}{x}dx\,.$$

Putting $qsx^2=\xi^2$, it becomes

$$\frac{2}{q\pi\sqrt{1-\frac{s^2}{4}}}\int_0^{\infty}\frac{\sin\left\{\sqrt{kW_1}\left(1-\frac{1}{4n}\right)\xi-\xi^2\right\}}{\xi}d\xi\,.$$

This integral is also evaluated by the method of the steepest descent, and its result is

$$I_8=\frac{1}{q\sqrt{1-\frac{s^2}{4}}}\left[1-\frac{\frac{4}{\sqrt{\pi}}}{\sqrt{kW_1}\left(1-\frac{1}{4n}\right)}\sin\left\{\frac{kW_1}{4}\left(1-\frac{1}{4n}\right)^2-\frac{\pi}{4}\right\}\right]+O(q^{-5/2})\,.$$

Therefore, the correction which comes from (32) is

$$I_8+I_7\,.$$

Now we consider the integrals which come from the second term of (33). The calculation is done in the same line as before, and one of the results is

$$I_9=-\frac{2}{3}\frac{\sqrt{1-\frac{s^2}{4}}}{kW_1s\left(1-\frac{1}{4n}\right)}\cos\frac{\pi}{4}\frac{1-\frac{1}{4n}}{1-\frac{s^2}{4}}\,.$$

The integral

$$-i\left(\frac{4}{\pi}\right)\frac{2}{3}q\int_{x_2}^{1-s/2}x\left\{1-\left(x+\frac{s}{2}\right)^2\right\}^{3/2}\exp\left[i\left\{p+q\left(1-\frac{s^2}{4}\right)\right\}x-iqsx^2\right]dx$$

is of the order of $q^{-3/2}$, and is

$$\frac{2}{3}\frac{\sqrt{\frac{\pi}{4}}}{q^{3/2}\left\{2s\left(1-\frac{s}{2}\right)-\left(1-\frac{1}{4n}\right)\right\}}\cos\left\{q\left(1-\frac{s}{2}\right)^2\left(s-\frac{1-\frac{1}{4n}}{1-\frac{s}{2}}\right)-\frac{\pi}{4}\left(s-\frac{1-\frac{1}{4n}}{2-s}\right)\right\}+O(q^{-5/2})$$

Any one of the terms which are of the order of $q^{-3/2}$ is very small in fact, so that we take

$$I_7+I_8+I_9$$

as the correction which comes from (32) and (33).

§ 6. Discussion and Comparison with the Experiment

The error introduced by the calculation up to now will be necessary to be explained. The absolute value of the error increases as

the spatial frequency decreases. At $s=0$, it becomes infinite and also so at $s=2$. However, if kW_1 is very large, it does not become serious even for sufficiently small values of s. For example, the orders of the error at $s=0.001$ and $s=0.1$ are 10^{-2} and 10^{-4} respectively when $kW_1=600$.

From the examples which are given in Fig. 3, several interesting features will be revealed. When kW_1 becomes larger, the response becomes smaller as we easily imagine. However, for a fixed value of W_1, the response changes remarkably for different choice of focal shift. The curves (2) (3) (4) and (5) have the same value of kW_1, but different n's. $n=\infty$ means no focal shift. When n becomes smaller, magnitude of defocussing becomes larger. Of course, we are now considering only the case where n is positive. This means that, the curve of the spherical aberration and the image plane are in the same direction from the gaussian plane. Otherwise, response becomes considerably smaller than the ones given here. The behaviour of the curve is similar to the case where $n=\infty$. Among these curves, (2) has the highest response almost everywhere. Probably, it corresponds to the best focus.

The behaviour of the curve (4) is very interesting. It has an oscillating property and has several peaks. The last one is larger than the preceding ones. This phenomena has been recognized by numerical calculations[6] when the aberration is large.

In order to know the behaviour of the response function for the increase of the parameter n, we consider the first term of (23), and take the phase factor. The argument of the function

$$\frac{2}{\sqrt{pq}}\sin\frac{kW_1 s}{4\cdot 3^{3/2}}\left(\frac{1}{n}-s^2\right)^{3/2} \tag{36}$$

takes its maximum value

$$\mu=\frac{kW_1}{64n^2}$$

at $s_0'=(1/2\sqrt{n})$. (36) becomes zero at $s=0$ and $s=2$. However near these points, this expression is not valid because of the small values of α, so that we do not take these end points. If we assume $\mu<\pi$, there is no node. If $\pi<\mu<2\pi$, the function (36) takes zeros two times, and the corresponding response functions crosses s-axis twice. By the rule stated above, the number of nodes of the curve (4) must be four while the true number is six. The calculated value of μ is 9.375 and is nearly equal to 3π. If μ is a little larger than 3π, two more nodes will appear. By this fact, this example is somewhat critical and not said to be a good one. Nevertheless, this method of estimation is very convenient to know the rough behaviour of the response function. About the other cases, μ's are all smaller than π, and this means no node for every curve as we can see from Fig. 3.

Recently, my friend, Dr. T. Suzuki designed

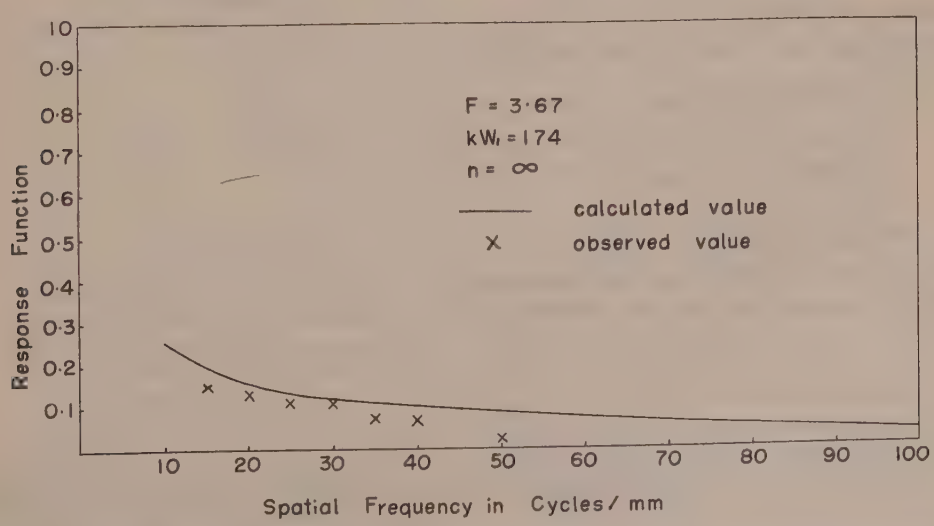

Fig. 4. Comparison of the calculated values and observed values of the response function for a single lens. F number is 3.67, $kW_1=174$ and $n=\infty$.

and constructed a device which measured the response of optical systems. An experiment is done for a single lens which has only the primary spherical aberration. The experimental values are shown in Fig. 4 and compared with theoretical values. The correction which is given in § 5 is now considered. The coincidence of them can be said good although the calculated values are always larger than the observed ones. We are not in the stage to analyze the errors of this experiment or to estimate the magnitude of them at present. However, since this experiment is difficult, one of them might come from some incompleteness of the instrument*. The discrepancy between them increases as s increases. However, the loss of high frequency components is always inevitable in such kind of experiments. From the comparison with the experiment, the result obtained here seems to be still good even for small values of s. By our experience, the result is not reliable when W_1 is comparable with λ. For smaller values of W_1 or s, the numerical calculation[10] is recommended by using a good table of Fresnel's integral.

I should like to express my gratitudes to Mr. R. Kōno and S. Lee and Dr. T. Suzuki. Kōno and Lee helped me in deriving the curves appeared here. Dr. Suzuki presented me valuable advices and data.

Appendix

Evaluation of the Integral (21)

α changes its sign at $s_0=(1|\sqrt{n})$, so that we must consider the following two integrals

$$\int_0^\infty \frac{\exp[i(t^3+|\alpha|t)]}{\sqrt{t}}dt\,, \qquad (1)$$

$$\int_0^\infty \frac{\exp[i(t^3-/\alpha|t)]}{\sqrt{t}}dt\,. \qquad (2)$$

1. α is sufficiently large.

Instead of the real value t, we consider a complex variable z and take the function

$$\zeta(z)=i(z^3\pm|\alpha|z)\,, \qquad (3)$$

and the following contour integral is considered. In case when positive α is taken, the path of integration on complex plane is taken in Fig. 5. The one corresponding to negative sign is in Fig. 6.

$$\frac{1}{2\pi i}\int_\Gamma \frac{e^\zeta}{\sqrt{z}}dz\,. \qquad (4)$$

The saddle points are obtained by solving the algebraic equation

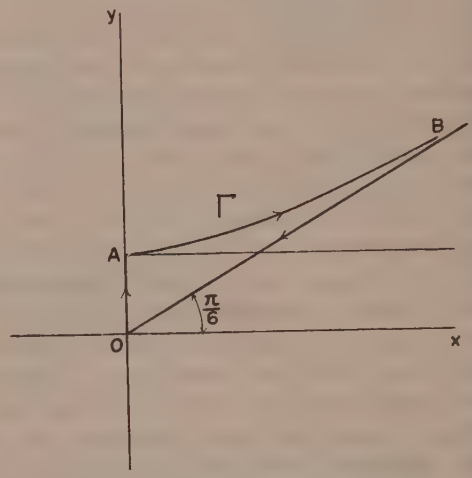

Fig. 5. The contour Γ for the integral (4) when α is positive.

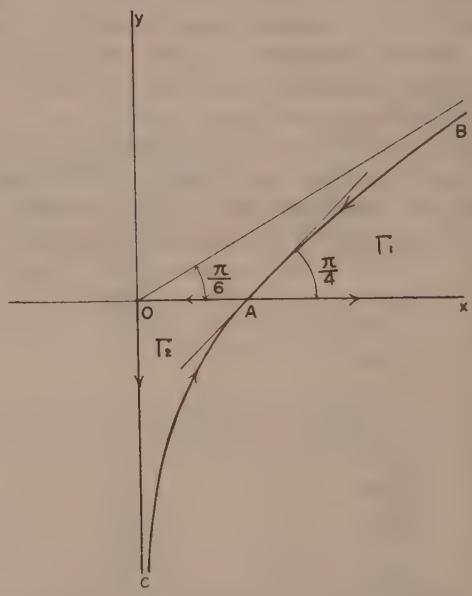

Fig. 6. The contour Γ for the integral (5) when α is negative.

$$\zeta'(z_0)=3z_0^2+\alpha=0\,, \qquad (4)$$

where

$$z_0=\begin{cases} \pm i\sqrt{\dfrac{|\alpha|}{3}} & (\alpha \text{ is positive}=\text{case I}) \\ \pm\sqrt{\dfrac{|\alpha|}{3}} & (\alpha \text{ is negative}=\text{case II}) \end{cases}$$

* T. Suzuki is now planning to make a device which has better respose.

The path of the integration which passes through the saddle point A is given by

$$x^2-3y^2+|\alpha|=0\,, \qquad \text{(case I)}$$

$$x^3-3xy^2-|\alpha|x+2\left(\frac{|\alpha|}{3}\right)^{3/2}=0\,. \qquad \text{(case II)}$$

The tangent line at A is parallel to x axis in case I and makes the angle $\pi/4$ with x axis case II. The integrals along y axis are pure imaginary in both cases, so that we need only the paths which pass through A's. Expanding $\zeta(z)$ in the neighbourhood of $z=z_0$, we get

$$\zeta(z)=\zeta(z_0)+\frac{\zeta''(z_0)}{2!}(z-z_0)^2\,\frac{\zeta'''(z_0)}{3!}(z-z_0)^3\,.$$

where $\zeta'(z_0)=0$ since z_0 is a saddle point. After expanding $1/\sqrt{z}$ near the point $z=z_0$, we put $z-z_0=\rho$ in case I and $z-z_0=\rho e^{\pi/4\cdot i}$ in case II. Then we integrate with respect to ρ from $-\infty$ to $+\infty$ because any one of the integrands has a sharp maximum at A if α is large. Then we get the results (23) and (25).

2. α is small.

In this case, integration is done along the path OB for both cases. Putting $z=\rho e^{\pi/6\cdot i}$, it becomes

$$\int \frac{\exp\left[i(z^3\pm|\alpha|z)\right]}{\sqrt{\rho}}\,dz$$

$$=e^{\pi/6\cdot i}\int_0^\infty \frac{\exp\left[i(-\rho^3\pm e^{2/3\cdot\pi i}|\alpha|\rho)\right]}{\sqrt{\rho}}d\rho$$

$$=e^{\pi/6\cdot i}\sum_{m=0}^{\infty} e^{2/3\cdot m\pi i}\frac{(\pm|\alpha|)^m}{m!}\int_0^\infty \rho^{m-1/2}\exp(-\rho^3)d\rho.$$

Putting $\rho^3=\tau$, we can easily evaluate the integral and get the result.

References

1) P. M. Duffieux: *L'integrale de Fourier et ses applications a l'optique*, Rennes (1946).
2) H. H. Hopkins: Proc. Roy. Soc. **A 231** (1955) 91.
3) E. H. Linfoot: Jour. Opt. Soc. Am. **45** (1955) 808.
4) J. W. Coltman: Jour. Opt. Soc. Am. **44** (1954) 468.
5) P. Lindberg: Optica Acta **1** (1954) 80.
6) Y. Ukita and J. Tsujiuchi: Jour. Mech. Lab. **10** (1956) 155. (in Japanese)
7) M. De: Proc. Roy. Soc. **A 233** (1955).
8) G. N. Watson: *A Treatise on the Theory of Bessel functions*. Cambridge Univ. Press (1922) 91.
9) G. N. Watson: The book cited in (8). p. 188.
10) H. Itô, R. Kōno and S. J. Lee: Journ. Appl. Phys. Japan **26** (1957) 539. (in Japanese)

JOURNAL OF THE PHYSICAL SOCIETY OF JAPAN Vol. 13, No. 6, JUNE, 1958

Adsorption of Water Vapour on Glass and Other Materials in Vacuum

By Hiroaki OKAMOTO and Yutaka TUZI

Matsuda Research Laboratory, Tokyo Shibaura Electric Co., Kawasaki

(Received February 28, 1958)

The adsorption of water vapour on lead borosilicate glass, soda lime glass, copper, nickel and alumina ceramic in high vacuum was studied by the time lag method of molecular flow originated by Barrer. The amount of adsorption at 273°~403°K and 2×10^{-5} mmHg was found to be less than 1 % of a monolayer. It is suggested that the adsorption of water vapour in this pressure region will not be a simple physical adsorption.

§ 1. Introduction

One of the main components of the residual gases in vacuum apparatus is water vapour.[1),2)] It is often supposed that many kinds of phenomena observed in vacuum systems are complicated due to this residual water vapour. Although the adsorption of water vapour has been extensively studied,[3),4),5)] there are only a few data which will contribute to the high vacuum technique. Experimental difficulties

associated with the measurement of pressure have restricted most investigations to the high pressure region. The most sensitive pressure gauge in high vacuum technique, the ion gauge, cannot be used because of its incandescent tungsten filament.[1),6),7)] Other instruments for pressure measurement are all insensitive for the study of adsorption in very low pressure region.

In the present paper, a preliminary study for the estimation of the rate of adsorption of water vapour on glass, copper, nickel and alumina ceramic by using the time lag method of molecular flow is described.

§ 2. Principle of the Time Lag Method

The principle of this method is similar to that of Barrer,[8)] and is illustrated in Fig. 1.

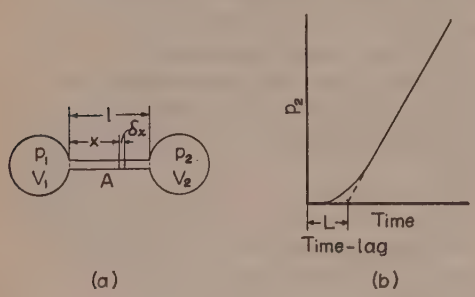

Fig. 1. Principle of time lag method.

The sample is packed into a tube A connecting two vessels V_1 and V_2. The whole apparatus is maintained at a constant temperature. At the beginning of each experiment, the apparatus is evacuated to a fine vacuum. When the pressure p_1 in V_1 is increased by introducing a gas, the pressure p_2 in V_2 also rises by diffusion of the gas through A, but the latter pressure rise takes place with a time lag behind the former. The amount of time lag depends on the adsorption of gas in A.

In the first part of this section, 2.1, we will consider the diffusion process and the time lag assuming no adsorption in A. In part 2.2, the influence of adsorption will be discussed. In part 2.3 we will finally discuss the estimation of adsorption by the time lag method.

2.1. *The Diffusion Process and the Time Lag when No Adsorption Takes Place in A*[9)]: Assuming that the flow is molecular, the transient isothermal flow along the axis of A will be expressed by the equation of diffusion

$$\frac{\partial c}{\partial t}=D\frac{\partial^2 c}{\partial x^2}, \qquad (0<x<l) \qquad (1)$$

where c represents the concentration in A, D the diffusion constant and l the length of A. If c_1, c_2 are the concentrations in V_1 and V_2 respectively and if $c=0$ at $t=0$, the approximate value of c_2 at time $t=t$ will be obtained as

$$c_2=\frac{\pi r^2}{V_2}\int_0^t D\left(-\frac{\partial c}{\partial x}\right)_{x=l} dt, \qquad (2)$$

where r represents the radius of A and V_2 represents the volume of V_2. If $c_1 \gg c_2$ is always valid, the approximate value of the concentration gradient at $x=l$ can be obtained by solving Eq. (1) with the boundary conditions $c=c_1$ at $x=0$ and $c=0$ at $x=l$, and the initial condition $c=0$ at $t=0$ $(0<x<l)$.

The calculated variation of c_2 versus t is illustrated by the curve in Fig. 1. (b), which asymptotically approaches a straight line. If we elongate the asymptotic straight line to cut the time axis, we obtain the intercept $\boldsymbol{L}$ which is defined as the "time lag". For the system shown in Fig. 1. (a), it can be proved that

$$\boldsymbol{L}=\frac{l^2}{6D}. \qquad (3)$$

2.2. *The Diffusion Process and the Time Lag when Adsorption Takes Place in A*: The adsorption is expected to modify the rate of diffusion in the following way. If the adsorbed film is immobile as would be approximately correct at a very low pressure,

$$v\frac{\partial c_g}{\partial t}=vD\frac{\partial^2 c_g}{\partial x^2}-a\frac{\partial c_a}{\partial t}, \qquad (4)$$

where c_g and c_a represent the concentration of the gas phase and the adsorbed film respectively, and v and a represent the total volume of the pores and the surface area of the adsorbent per unit length of A respectively. If one assumes that the adsorption equilibrium is reached very rapidly,

$$\frac{\partial c_a}{\partial t}=\frac{\partial f(c_g)}{\partial t} \qquad (5)$$

and $\boldsymbol{L}$ can be evaluated from Eq. (4) and (5) for two limiting cases.

In the first case we assume that the amount of adsorption is proportional to the pressure. For this case Barrer[8)] and Clausing[10)] solved the problem in the following way. Namely, in this case,

$$k_s c_g = c_a \tag{6}$$

where k_s is a constant, and therefore Eq. (5) becomes

$$\frac{\partial c_a}{\partial t} = k_s \frac{\partial c_g}{\partial t} . \tag{7}$$

From Eq. (4) and (7),

$$\frac{\partial c_g}{\partial t} = \frac{D}{\left(1+k_s \frac{a}{v}\right)} \cdot \frac{\partial^2 c_g}{\partial x^2} . \tag{8}$$

Thus the time lag L becomes

$$L = \frac{l^2\left(1+k_s \frac{a}{v}\right)}{6D} . \tag{9}$$

Eq. (9) shows that L is independent of c_1.

In the second case, it is assumed that the adsorption of the gas takes place completely in a region before the gas begins to diffuse into the next region.[11] For this case, with an additional assumption that the diffusion constant of the adsorbing gas in A is fairly large compared to the migration velocity of the adsorbate, Clausing obtained a simplified solution in the following way.[10] Let the pressure at δx (Fig. 1 (a)) at an arbitrary moment be zero, and let N represent the number of adsorption sites per unit surface area of the adsorbent, and K the conductance

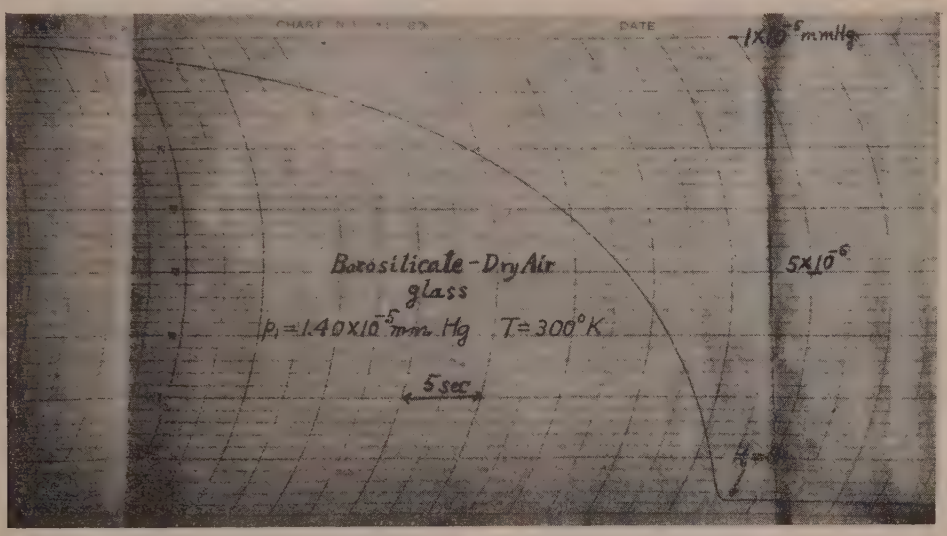

(a) Dry air

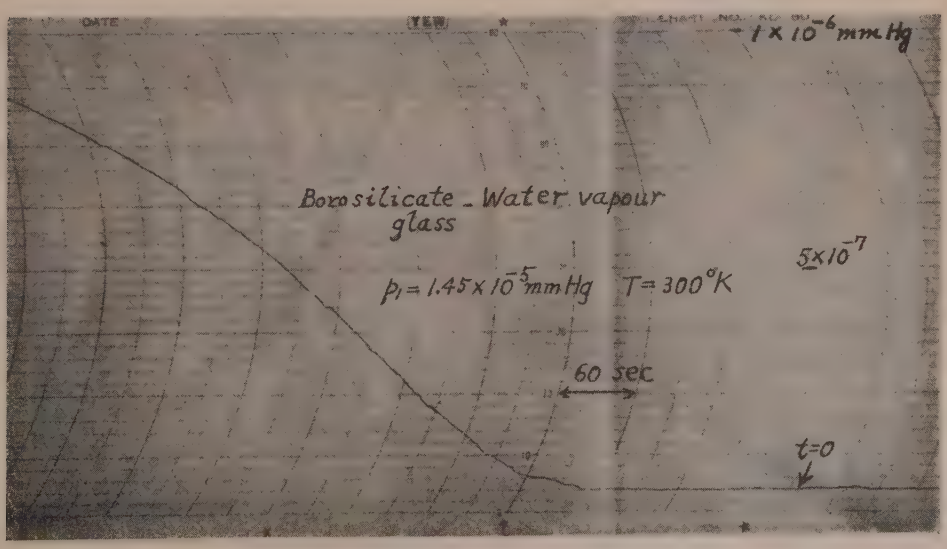

(b) Water vapour

Fig. 2. Time lag and build up of p_2, in typical experiment.

per unit length of A. If all molecules which flow into δx during the time interval δt are adsorbed on the adsorption sites existing in δx, the following equation will hold:

$$\frac{Kc_1}{x}\delta t = Na\delta x\,. \tag{10}$$

Gas molecules will flow into the region next to δx only after the completion of adsorption on all sites in δx. Thus it will take a time $\boldsymbol{L}$ for molecules to occupy all sites in A before they begin to diffuse into V_2. $\boldsymbol{L}$ can be obtained by integrating Eq. (10):

$$\boldsymbol{L} = \int_0^t dt = \int_0^t \frac{Nax}{Kc_1}dx\,, \tag{11}$$

or

$$\boldsymbol{L} = \frac{1}{2}\frac{Nal^2}{Kc_1} = \frac{1}{2}\frac{N\times(\text{molar volume})\times 760\times T\times a\times l^2}{(\text{Avogadro's number})\times 273\times K\times p_1} \tag{12}$$

where T represents the temperature of experiment in °K and p_1 is expressed in mm Hg. Eq. (12) shows that $\boldsymbol{L}$ is inversely proportional to p_1.

2.3. *The Estimation of Adsorption by the Time Lag Method*: The time lag $\boldsymbol{L}'$ which an adsorbable gas (e.g. H_2O) of molecular weight M would show if it were non adsorbing can be estimated by the following relation, if we know the time lag $\boldsymbol{L}_0$ of a non adsorbing gas (e.g. air) of molecular weight M_0:

$$\boldsymbol{L}' = \boldsymbol{L}_0\sqrt{\frac{M}{M_0}}\,. \tag{13}$$

This is because

$$D \propto \sqrt{M}\,. \tag{24}$$

The difference $\boldsymbol{L}-\boldsymbol{L}'$ will give an estimate of the amount of adsorption. As shown in Fig. 2 (a), (b), there actually is a very remarkable difference between the time lag of dry air and that of water vapour.

§ 3. Experimental

Samples used in this study are lead borosilicate glass (Nonex type), soda lime glass, OFHC copper, vacuum melted nickel and alumina ceramic (92~93 % Al_2O_3). Glass samples were crushed into 10~20 mesh particles, washed in tap water, distilled water, ethyl alcohol and ethyl ether successively. Metal samples were hacked into pieces of about 1×1 mm size, washed in water, ethyl alcohol and ethyl ether successively, and reduced in hydrogen. They were again reduced in dry hydrogen after the insertion into the apparatus. Alumnina ceramic was crushed into 10~20 mesh particles, boiled in sulphuric acid for 1 hr., washed in water, and fired in a gas furnace at a temperature of 1100°C for 30 min*). The real surface area of each sample was determined by the BET method using ethylene as the adsorbate[12),13)]

*) More detailed discussions of these treatments were reported in Ref. (7) and (13).

Table I. Condition of the Experiments.

Sample	Lead borosilicate glass	Soda lime glass			Copper	Nickel	Alumina ceramic
Shape	10~20 mesh particles	10~20 mesh particles			1×1 mm pieces	1×1 mm pieces	10~20 mesh particles
Weight (g)	38.5	—	23.3	25.3	93.0	56.1	33.0
Specific surface area ($cm^2\ g^{-1}$)	67	33			6.0	40	57.5
Length of A (cm)	12.8	4.3	7.3	8.1	8.2	8.8	8.1
Radius of A (cm)	0.85	0.81	0.85	0.81	0.84	0.83	—
Conductance for dry air, K/l at 300°K ($cm^3\ sec^{-1}$)	14.3	60	36	29	70.7	63.2	66.7
Conductance for H_2O, K/l at 300°K ($cm^3\ sec^{-1}$)	18.1	76	45.5	36.5	89.8	80.2	84.6

(Table I). The water vapour was supplied from distilled water which had been thoroughly degassed and stored in the experimental apparatus.

The whole apparatus was constructed with Nonex type lead borosilicate glass, special taps without grease were used in high vacuum side. Details of this apparatus has been described elsewhere.[7]

Prior to each experiment, the whole apparatus was baked out at 380°C in high vacuum and evacuated to a pressure of less than 1×10^{-8} mm Hg. The ion gauge with which p_2 was measured had been throughly processed by electron bombardment.

The pressure p_1 was kept at a constant value between 10^{-4} and 10^{-6} mm Hg by allowing the water vapour flow through a small leak into V_1 and evacuating it through a duct of appropriate conductance. p_1 was estimated by an oil manometer which was located in the high pressure side of the small leak. Throughout the time lag measurements, p_2 was maintained 10^{-7} mmHg to 10^{-8} mmHg so as to the relation $p_1 \gg p_2$ held at all times.

The water vapour which flowed into V_2 was examined by low temperature distillation. Hardly any decomposition products or impurities could be detected.

§ 4. Results and Discussions

The time lag versus pressure relation for each sample was obtained at a series of temperatures. The results for lead borosilicate glass, soda lime glass and nickel are shown as examples in Figs. 3, 4 and 5 respectively.

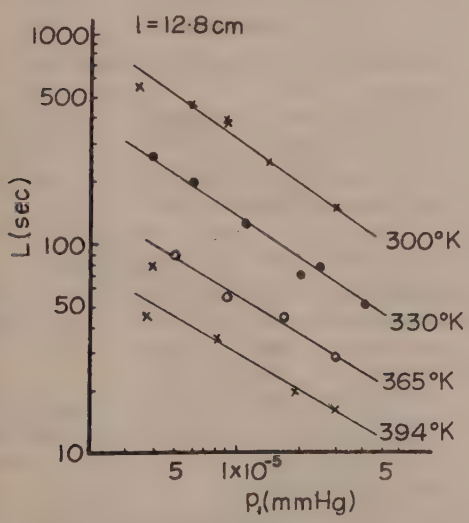

Fig. 3. Time lag of water vapour for lead borosilicate glass.

The variation of time lag as a function of the tube length l was investigated for soda lime glass at 330°K and $p_1=2.1\times10^{-5}$ mm Hg, and is given in Fig. 6.

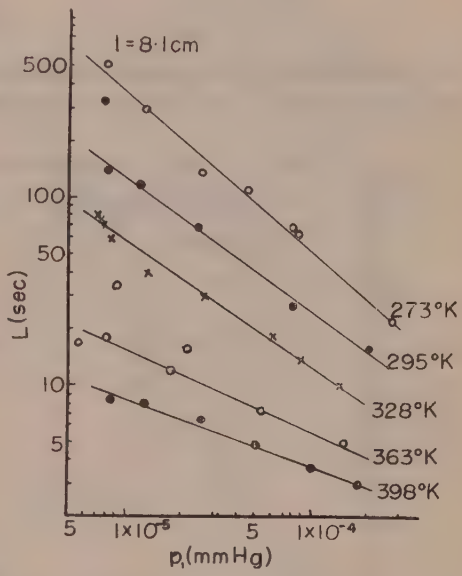

Fig. 4. Time lag of water vapour for soda lime glass.

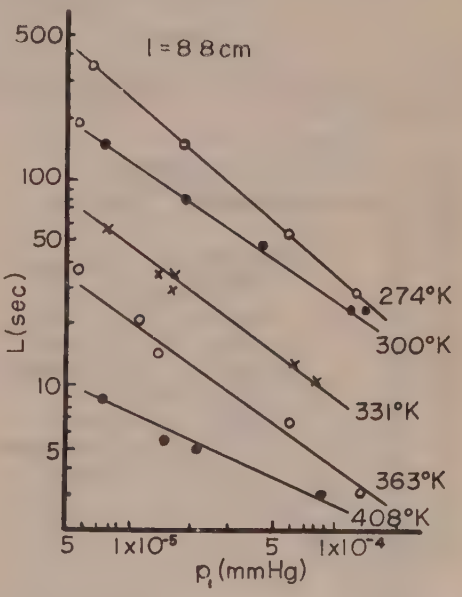

Fig. 5. Time lag of water vapour for nickel.

The amount of adsorption at $p_1=2\times10^{-5}$ mm Hg was evaluated assuming Eq. (12). For this calculation, it is necessary to estimate K, the conductance of A. This can be carried

out in the following way: As is seen in Fig. 2, p_2 reaches a saturation value p_{2f} as time goes on because of the pumping action of the ion gauge with which p_2 is measured. In this saturation state, the following relation is known to hold:

$$\frac{K}{l}=\frac{p_{2f}S}{p_1-p_{2f}} \tag{15}$$

In this equation, S is the rate of absorption of gas by ion gauge, which can be determined

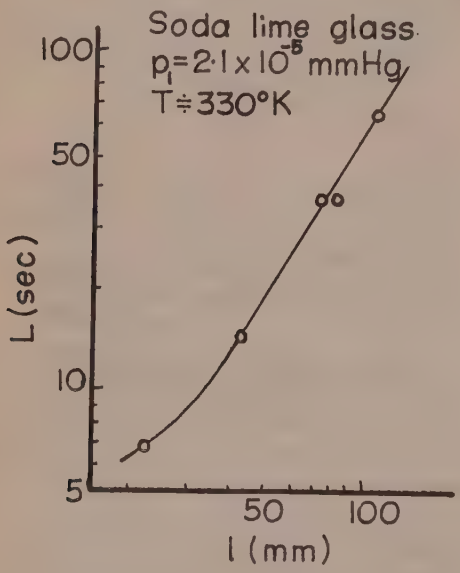

Fig. 6. Time lag of water vapour as a function of length of A.

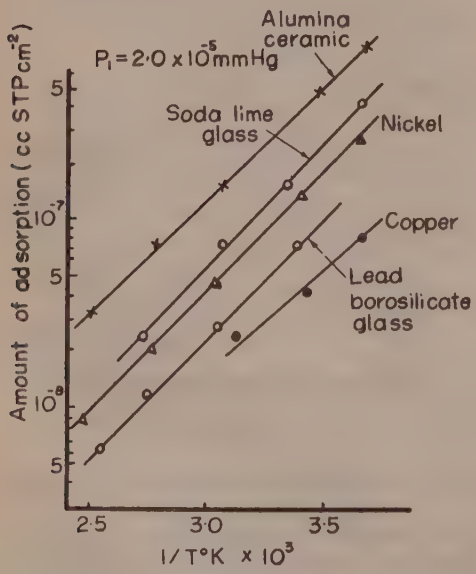

Fig. 7. Amount of adsorbed water vapour vs. temperature.

by the rate of pressure decrease in a known volume, and is approximately constant in this pressure region.[14] The values of K estimated in this way are given in Table I. The calculated amounts of adsorption for all samples investigated are illustrated in Fig. 7.

The following points can be concluded for all specimens studied: (1) The time lag $\boldsymbol{L}$ of water vapour is very much greater than the value estimated assuming no adsorption. (2) $\boldsymbol{L}$ is proportional to log p_1 and l^2 (at least for soda lime glass). (3) The temperature coefficient of $\boldsymbol{L}$ is negative. (4) The $\boldsymbol{L}\sim p_1$ relations are explained by neither of the assumptions in 2.2. (5) Therefore, the adsorption in this pressure region will not be a simple physical adsorption. (6) The amount of adsorption at 273°~403°K and $p_1=2\times10^{-5}$ mmHg is less than 1% of a monolayer (3.45×10^{-5} cc STP).[15]

Barrer *et al.* elongated the $\boldsymbol{L}\sim p_1$ curve (plotted to the ordinary scale) to cut the time lag axis and assumed this intercept to be the true time lag. They explained the pressure dependence of the time lag assuming that the molecules adsorbed on the completed first monolayer are mobile. In our cases, however, the above assumption is inadequate because the amount of adsorption is less than 1% of a monolayer.

The authors are indepted to Prof. K. Kinosita for his kindness in reading the manuscript, to Prof. G. Tominaga and Prof. Y. Uemura for their kind discussions.

References

1) J. Blears: J. Sci. Instrum., Supp. No. 1. p. 36 (1951).
2) K. Hisatake and K. Matsuda: J. Phys. Soc. Japan **8** (1953) 416.
3) R. I. Razouk and A. S. Salem: J. Phys. Colloid. Chem. **52** (1943) 1028.
4) K. Kinosita: J. Appl. Phys. Japan (Ôyô Butsuri), **24** (1955) 215 in Japanese.
5) S. Dushman: Scientific Foundation of Vacuum Technique, p. 506 (New York: John Wiley and Sons Inc., 1949)
6) S. Dushman: *Ibid.*, p. 673.
7) H. Okamoto and Y. Tuzi: J. Appl. Phys. Japan (Ôyô Butsuri), **25** (1956) 20 in Japanese.
8) R. M. Barrer and D. M. Grove: Trans. Farad. Soc. **47** (1951) 826.
9) R. M. Barrer: Diffussion in and through Solid, p. 18 (Cambridge Univ. Press, 1951).
10) P. Clausing: Ann. der Phys. **7** (1930) 136.

11) R. M. Barrer: Brit. J. Appl. Phys., Supp. No. 3, p. 41 (1954).
12) L. A. Wooten and J. R. C. Brown: J. Am. Chem. Soc., **65** 113 (1943).
13) H. Okamoto and Y. Tuzi: Vacuum Techniques (Shinkû Gijutsu), **7** (**6**) (1956) 218 in Japanese.
14) D. Alpert: J. Appl. Phys., **24** (1953) 860.
15) S. Dushman: *loc. cit.* p. 459.

Errata

Structural Investigation by Means of Nuclear Quadrupole Resonance II (Tin Tetrabromide)

By Kenji SHIMOMURA
Minami Branch, Hiroshima University, Hiroshima

J. Phys. Soc. Japan **12** (1957) 657

Page	Colum	Place		(should be read)
658	left	Fig. 1	$0 \neq H$, $0 = H$	$H=0$, $H \neq 0$
661	left	line 8	+ should be replaced by −	+ should be replaced by − and $\cos\frac{\alpha}{2}$ by $\sin\frac{\alpha}{2}$
667	right	Refer. 8)	C. Cean	C. Dean

Errata

The Thermoelectric, Galvanomagnetic and Thermomagnetic Effects of Monovalent Metals

By Mikio TSUJI

J. Phys. Soc. Japan **13** (1958) 133

Page	Column	Place		(should be read)
134	left	line 7 from bottom	,	(to be eliminated)
	right	line 11	**Surphace**	**Surface**
138		Eq. (32)	$(T/\Theta)^3$	T^2/Θ^3
139	right	line 4 from bottom	Zieman's	Ziman's
140	left	Fig. 1	q	q_0
	right	line 6	$u=u_0$	$u_0=\bar{u}_0$
141	right	line 11	these	thus
	right	line 13	Otters	Otter
144		Eq. (72)	dE	$\frac{\partial f_0}{\partial \eta}\alpha\eta$
145	left	Eq. (79)	$\hbar$	$\hbar^2$
	left	line 7 from bottom	(78)	(79)
	left	line 4 from bottom	(95)	(85)
	right	Eq. (88)	$\tau/\alpha k_0^2$	$\alpha\tau/k_0$

Short Notes

This section is intended to secure prompt publication of important discoveries in physics. The reports should not exceed 800 words in length. A figure of size 7 cm × 7 cm will be counted as 150 words.

J. PHYS. SOC. JAPAN **13** (1958) 656

Specific Heats of Copper Ferrite

By Tohru INOUE and Shuhichi IIDA

Department of Physics, Faculty of Science, University of Tokyo

(Received April 4, 1958)

The tetragonal distortion of the spinel structure such as $CuFe_2O_4$, $CuCr_2O_4$, $NiCr_2O_4$, Mn_3O_4, $ZnMn_2O_4$, etc, has recently discussed. Among these, $CuFe_2O_4$ is the only one that is ferromagnetic at room temperature. The tetragonal distortion of $CuFe_2O_4$ was explained by Goodenough[1] by using the idea of semicovalent bonding and recently by Dunitz et al.[2] by using the concept of Jahn-Teller effect. Bertaut[3] has found that $CuFe_2O_4$ becomes cubic after quenched from high temperature and concluded that the transition temperature from cubic to tetragonal is about 760°C. But this conclusion due to Bertaut is supposed to be incorrect because recently Miyahara and Ohnishi[4] showed this transition to occur about 400°c by means of X-ray high temperature camera and qualitative heat analysis. This transition temperature is below the magnetic Curie temperature. In this respect it should be noticed that Takei et al.[5] has early pointed out the existence of the anomaly at about 390°C from an abrupt change of the magnetization at constant magnetic field and Forrer et al.[6] has also pointed out the existence of the anomaly at about 360°C.

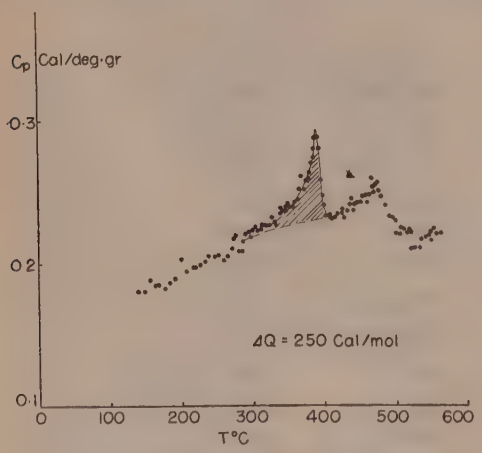

Fig. 1. Specific heats of copper ferrite

In this connection we have measured the specific heats for $CuFe_2O_4$. The result is shown in Fig. 1. It shows clearly the presence of a λ-point at 390°C corresponding to transition from cubic to tetragonal. The peak at about 470°C is that associated with the magnetic transition of this material.

The apparatus used is the improved one of the Takagi Nagasaki's adiabatic calorimeter[7]. The main heater which is situated outside of the copper container consists of the heating elements on the upper and lower surface of the cylinder as well as on the side, and inside of the main heater there is another outer heater for the fine adjustment.

The specimen was prepared as follows; the electrolytic iron and copper was dissolved in nitric acid, dried by infrared ray lamp, calcinated at 1000°C in air for 6 hours, and pressed into the shape of pot with lid. Then it was heated again at 1000°C for about 10 hours and annealed at about 900°C for several hours. The purpose of the last annealing is to transform all the cuprous ions into the cupric ions. The specimen was about 70 grams in weight. The measurements were performed at the pressure of about 0.04 mmHg and at the heating rate of 1.5 degrees per minute.

Inferring from the result of the measurement as high as 750°C, it is certain that there is no anomaly at 760°C. After rapid cooling in vacuum from 750°C, the anomaly at 390°C was disappeared. But it recovered again by an annealing in air at 900°C for several hours. The reason of this anomalous phenomenon might be due to the production of cuprous ions in the matrix and further study is now going on.

References

1) J. B. Goodenough and A. L. Loeb: Phys. Rev. **98** (1955) 391
2) J. D. Dunitz and L. E. Orgel: J. Phys. Chem. Solid. **3** (1957) 20
3) E. F. Bertaut: Compt. Rend. **230** (1950) 213 and J. Phys Rad. **12** (1951) 252
4) S. Miyahara and H. Ohnishi: J. Phys Soc. Japan **12** (1956) 1296 and unpublished work presented before the meeting of the Phys. Soc. of Japan, April 1957
5) T. Takei, T. Yasuda and S. Ishihara: Denkigakkai Shi in Japan **59** (1939) 568
6) R. Forrer, R. Baffie und P. Fourinier: J. de Phys. **6** (1945) 71
7) S. Iida: J. Phys. Soc. Japan **7** (1952) 373

J. PHYS. SOC. JAPAN **13** (1958) 656

The Q-value for the $N^{14}(n, \alpha)B^{11}$ Reaction

Tadayoshi DOKE, Shoji SUZUKI and Iwao OGAWA

Department of Physics, St. Paul's University, Tokyo

(Received April 4, 1958)

A gridded ionization chamber, with a cylindrical

effective volume 18.5 cm. in dia. and 8 cm. in height, filled with a mixture of 1-atm. nitrogen and 3~4-atm. argon gas was irradiated by *D-D* neutrons from a Cockcroft-Walton accelerator, and the Q-value for the $N^{14}(n, \alpha)C^{11}$ reaction was determined from the pulse-height distribution obtained either with a single channel pulse-height analyzer or with a gray wedge analyzer. The mean deviation of positions of peaks in the measured spectra was about 20 kev.

D-D neutrons were produced by bombarding a thick heavy ice-target with 150 kev deutrons, and those neutrons which were emitted at nearly a right angle to the D^+-beam were used to irradiate the chamber, since the neutron energy for this direction is least dependent upon deutron energies,[1] the energy in our case being $E_n=2.40$ MeV. The distance from the ice-target to the chamber was so chosen that the energy-spread of incident neutrons due to the angular width would not exceed ± 0.05 MeV.

An example of pulse-height spectra thus obtained is shown in Fig. 1. Several peaks are clearly seen, and have been interpreted as noted in the figure.

The relationship between pulse-height and particle energy was calibrated with five natural alpha-sources having well-known particle energies[2] (U^{238}, U^{234}, Po, ThC and ThC′). The extrapolated pulse-height vs energy straight line crossed the energy axis at less than about 100 kev, in good accordance with Cranshaw and Harvey's results[3] for pure argon.

The average Q-value obtained from the (n, α) peak and E_n was $Q=-0.12\pm 0.06$ Mev. On the other hand, Q became somewhat larger in the absolute value, when the neutrons in the 20°-direction to the D^+-beam were used ($Q=-0.17$ Mev). This value is, however, less reliable because of the uncertainty in the estimation of neutron energies.

Also, the peak II in Fig. 1 was used tentatively to check the results above. This peak can be assumed to correspond to the well-known (n, α) resonance reaction at $E_n=1.800\pm 0.015$ Mev[4] caused by the stray neutrons having a continuous energy-spectrum in this energy region. Such an interpretation affords $Q=-0.18\pm 0.05$ Mev, in agreement with the former result within the limits of probable error.

All these results give considerably smaller Q's as compared with other authors'.[5),6)] However, ours are in fair agreement with the current mass-Q-value ($Q_m=-0.15\pm 0.01$ Mev[7,8)]).

The reason that other authors—with the exception of Bollmann and Zünti—obtained too large values ($-0.2\sim -0.5$ Mev) is perhaps that they did not take into proper account the appreciable inconstancy, with respect to the particle species and energies, of the energy loss of the particle per ion pair for the undiluted N_2-gas they used, as was pointed out by Bollmann et al.[5] To reduce this effect, Bollmann et al. used argon-diluted nitrogen,

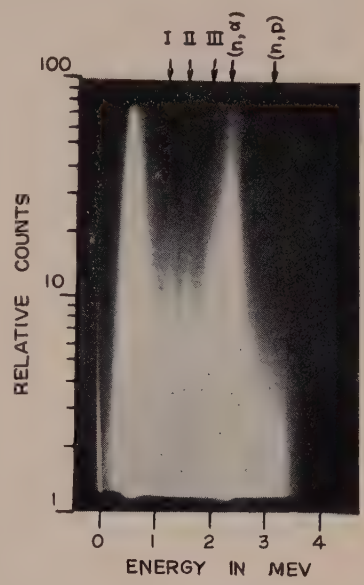

Fig. 1. Typical Gray-Wedge Pulse-Height Spectrum. Peaks noted as I, II and III are due to the (n, α) and (n, p) resonance reactionsinduced by stray neutrons with certain corresponding energies.

but their figures (-0.28 ± 0.08 Mev) still exceed the current Q_m. This is probably due to the possible (systematic) error in their estimation of E_n's, which might well become appreciable for the angle of neutron emission far different from a right angle.

References

1) J. L. Fowler and J. E. Brolley: Rev. Mod. Phys. **28** (1956) 103.
2) G. H. Briggs: Rev. Mod. Phys. **26** (1954) 1.
3) T. E. Cranshaw and J. A. Harvey: Can. Journ. Res. **A26** (1948) 243.
4) C. H. Johnson and H. H. Barschall: Phys. Rev. **80** (1950) 818.
5) W. Bollmann and W. Zünti: Helv. Peys. Acta **24** (1951) 517.
6) D. M. Van Patter and W. Whaling: Rev. Mod. Phys. **26** (1954) 402.
7) F. Ajzenberg and T. Lauritsen: Rev. Mod. Phys. **27** (1955) 77.
8) A. H. Wapstra: Physica **21** (1955) 367.

J. PHYS. SOC. JAPAN. **13** (1958) 658

A Richter Type Magnetic Loss in Yttrium-Iron Garnet

By Hisashi SEKIZAWA, Shūichi IIDA
Department of Physics, Faculty of Science, Tokyo University, Tokyo, Japan
and Tomonao MIYADAI
The Electrical Communication Laboratory, Nippon Telegraph and Telephone Public Corporation

(Received April 4, 1958)

A magnetic loss of Richter type has been found in ferrites containing ferrous ions[1], and it is attributed to the electron diffusion, i.e. the exchange of electrons between Fe^{2+} and Fe^{3+} ions. A similar phenomenon was observed for yttrium-iron garnet $3Y_2O_3 \cdot 5Fe_2O_3$.

The specimen was prepared from 99.9% yttrium and high purity iron oxide. The constituent oxides were mixed and pressed into toroidal form about 3 cm in outer diameter. Then, it was fired at 1430°C for 6 hours in air and cooled in the furnace. X-ray diffraction pattern of the powder specimen which was prepared together with the toroidal specimen showed only the lines belonging to garnet phase with $a=12.37$ A. Complex permeability of the specimen at fixed frequencies (2, 1, 0.5 and 0.25 Mc/s) was measured by means of an impedance bridge varying the temperature from ca. 120°C to −180°C. The results are shown in Fig. 1. There is a distinct peak of $\tan\delta$ for each frequency which shifts to higher temperatures for higher frequencies. The logarithms of the frequency at which the maximum of $\tan\delta$ takes place were plotted against the reciprocal of the temperature and found to lie on a straight line as shown in Fig. 2. The activation energy E obtained from the slope of the line is about 0.50 eV.

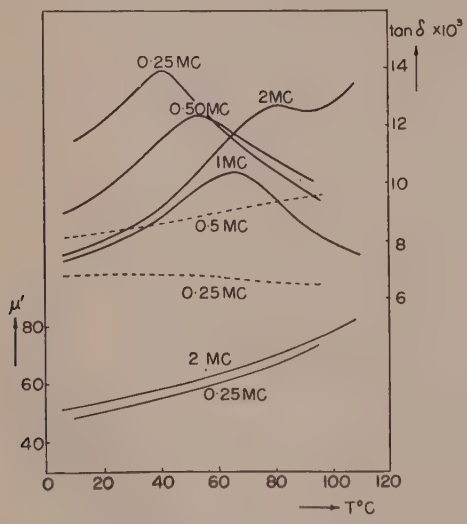

Fig. 1. $\tan\delta$ and μ' of yttrium-iron garnet.
—— $\tan\delta$; after fired at 1430°C and cooled in furnace.
--- $\tan\delta$, after heating up to 350°C.
—— μ; (Appreciable change was not observed by the heating up to 350°C.)

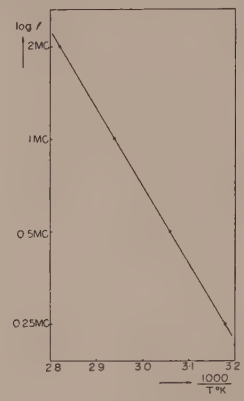

Fig. 2. Plots of $\log f$ vs. $1/T$ of the maximum of $\tan\delta$ for yttrium-iron garnet.

No anomalous behaviour was found in the lower temperature range down to liquid oxygen temperature. (Another specimen with lower purity had similar peaks below liquid oxygen temperature for the same set of frequencies). The measurements were performed again after the specimen was heated in air up to about 380°C, fairly above the Curie temperature (287°C). The peaks of $\tan\delta$ vanished by this heat-treatment as shown also in Fig. 1.

Yttrium-iron garnet contains no divalent metallic ions in stoichiometric composition[2]. But it has been found that the electrical resistivity of this garnet shows marked dependence on the firing temperature[3], and it can be accounted for only by assuming the existence of ferrous ions in it. This fact points to the conclusion that the garnet can oxydize or deoxydize without accompanying any phase change but with an appearance of certain imperfections (interstitial atoms etc.), as it is the case for most of the oxides. Thus it is also possible in the garnet that ferrous and ferric ions coexist in the same crystal sites and the electron diffusion among these ions may couple with the direction of the magnetic moment, as it is in the case of ferrites. Although the value of the activation energy obtained is higher than the one observed usually in ferrites, it is too small to be accounted for by the ionic diffusion. The disappearance of loss peak upon oxydation supports the mechanism mentioned above.

References

1) H. P. J. Wijn and H. van der Heide: Rev. Mod. Phys. **25** (1953) 98.
2) W. P. Wolf and G. P. Rodrigue: J. Appl. Phys. **29** (1958) 105.
3) L. G. Van Uitert; J. Appl. Phys. **28** (1957) 1513.

J. PHYS. SOC. JAPAN **13** (1958) 659

On the Measurement of Isotope Abundance of Lithium with Mass Spectrometer

By Itiro OMURA and Nozomu MORITO

Hitachi Central Research Laboratory
Kokubunji, Tokyo

(Received April 1, 1958)

An absolute measurement of the isotope abundance ratio of lithium has been carried out with a mass spectrometer. The instrument used is the Hitachi Mass Spectrometer, RMU-5, with a single filament surface ionization source. Samples used are lithium chloride N_1 on the market (Koso Chem. Co., Inc.), and purified lithium chloride B_5 which was provided through the courtesy of Prof. Titani of Tokyo Metropolitan University. A droplet (about 0.2 cc) of aqueous solution (0.5 mg/1) is placed on the filament and dried.

The values of the ion abundance ratio ($^7Li^+/^6Li^+$) obtained were 12.48 ± 0.05 for the sample N_1 and 13.69 ± 0.05 for B_5. The values which have been reported as the natural abundance ratio of lithium isotopes are scattered in a pretty wide range approximately from 11 to 13. The results for the sample N_1 lies in this range and without any correction according to the so-called isotope effect, it is equal to the value which has been believed to be the most reliable. The isotope constitution of the sample B_5 might have been changed during the purification[1].

The change of the ion current and the ion abundance ratio after a sudden changed of the filament temperature was observed. Other processes were tried successively after the current as the abundance ratio had become constant. In the first process the filament temperature was suddenly increased from 1025°C to 1075°C. In the second it was decreased from 1075°C to 1025°C for 30 seconds and again returned to 1075°C, while in the last process it was increased to 1175°C for 30 seconds and then reduced to 1075°C. After each of these processes, transient variation appeared not only in the curent but in the abundance ratio, as is shown in Figs. 1 and 2.

The abundance ratio of potassium isotopes was measured for reference. The ratio $^{39}K^+/^{41}K^+$ obtained was 13.96 ± 0.05. In this case, as well as in the case of lithium, the isotopic correction seemed to be unnecessary. Similar phenomena as shown in Figs. 1 and 2 were again observed.

The unexpected phenomena have a serious influence on the analysis, but their origin is not clear. The mechanism of surface ionization seems to be much complicated. Although there are several plausible reports published on the measurement of the abundance ratio of lithium isotopes as well as on the necessity of the isotopic correction[2-5] further investigation is desired.

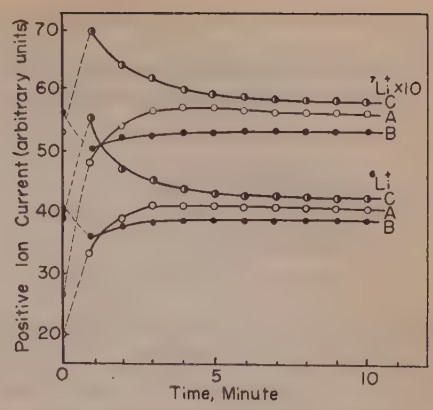

Fig. 1. Transient variation of ion current after a rapid change of filament temperature
Sample: LiCl (B_5)
Curve A: 1025°C→1075°C
Curve B: 1075°C→1025°C (30 sec)→1075°C
Curve C: 1075°C→1175°C (30 sec)→1075°C

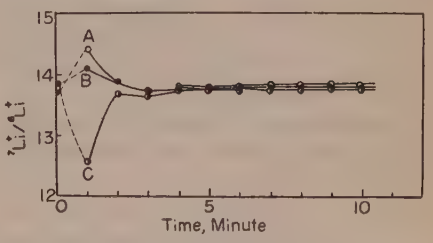

Fig. 2. Transient variation of ion abundance ratio after a rapid change of filament temperature
Simple: LiCl (B_5)
Curve A: 1025°C→1075°C
Curve B: 1075°C→1025°C (30 sec)→1075°C
Curve C: 1075°C→1175°C (30 sec)→1075°C

The authors wish to thank Dr. B. Tadano and all members of the Section of Mass Spectrometry of this laboratory for their helpful discussions and encouragement during this work.

References

1) G. Wagner und A. Pelz: Monatshefte für Chemie **86** (1955) 414.
2) A. K. Brewer: J. Chem. Phys. **4** (1936) 350.
3) K. Ordzhonikidze and V. Shiuttse: Soviet Physics JETP **2** (1956) 396.
4) J. R. White and A. E. Cameron: Phys. Rev. **74** (1948) 991.
5) H. Hintenberger: Naturwiss. **34** (1947) 52.

J. PHYS. SOC. JAPAN **13** (1958) 660

Higher order Transitions in Double Nuclear Resonance Experiments in Solids

By N. Bloembergen

Harvard University, Cambridge, Massachusetts, U. S. A.

(Received March 19, 1958)

Saito has in a recent paper[1] discussed the narrowing of one nuclear (A) resonance, while the other nuclear (B) resonance is driven hard by a large radiofrequency field near the resonance frequency $\omega_B{}^0$. The experiments were conducted in TlF and TlBr. Saito mentions two observations, which remained unexplained:

(1) The A resonance becomes asymmetric, when the driving frequency ω_B is slightly off the resonance value $\omega_B{}^0$.

(2) The A resonance "collapsed" at first for intermediate values of driving field at the resonance frequency $\omega_B{}^0$, before the narrowed line appears for larger driving fields.

It is the purpose of this note to call attention to some higher order nuclear spin transitions. Their existence has recently been demonstrated in double resonance experiments in cesiumhalides[2], and they may also account for the observations of Saito.

Consider for simplicity two nuclear species $I_A=I_B=\frac{1}{2}$, in a coordinate system rotating with the angular velocity ω_B. In this system of reference the B spins are quantized with respect to the effective field $H_B{}^{\mathrm{eff}}=xH_B{}^{\mathrm{rf}}(\omega_B)+z(\omega_B{}^0-\omega_B)/\gamma_B$. The A spins are still effectively quantized in the z-direction. The magnetization of the B-spins in the ρ-direction, i.e. parallel to $H_B{}^{\mathrm{eff}}$, which makes an angle Θ with the z-axis, can be obtained from Redfield's theory[3]. This author also showed that the part of the interaction between a pair of A and B spins to be retained is

$$\mathscr{H}^{\rho}_{AB}=C_{AB}I_{z,A}[I_z^{\rho}, B\cos\Theta+\tfrac{1}{2})(I^{\rho}_{+,B}+I^{\rho}_{-,B})\sin\Theta] \tag{1}$$

$$C_{AB}=a_{AB}+(\gamma_A\gamma_B h^2\tau_{AB}^{-3}+b_{AB})\ (1-3\cos^2\vartheta_{AB}). \tag{2}$$

Consider a radiofrequency field at the frequency $\omega_A=\omega_A{}^0+\gamma_B\,|\,H_B{}^{\mathrm{eff}}\,|=\omega_A{}^0+\gamma_B H_B{}^{\mathrm{rf}}\operatorname{cosec}\Theta$. Energetically this field can induce transitions in which an A-spin is flipped from the positive to the negative z-axis ($\Delta m_A=+1$), and simultaneously a B-spin is reversed with respect to the effective field ($\Delta m_{\rho,B}=+1$). The matrix element for this double transition is by second order perturbation theory

$$\frac{(\frac{1}{2},\frac{1}{2}\,|\,\gamma_A hH_A{}^{\mathrm{rf}}I_A{}^{+}\,|\,-\frac{1}{2},\frac{1}{2})(-\frac{1}{2},\frac{1}{2}\,|\,\frac{1}{2}C_{AB}I_{z,A}I^{\rho}_{+,B}\sin\Theta\,|\,-\frac{1}{2},-\frac{1}{2})}{\gamma_B h_B H_B{}^{\mathrm{rf}}\operatorname{cosec}\Theta} \tag{3}$$

Since C_{AB} and $\gamma_B h_B H_B{}^{\mathrm{rf}}$ are of the same order of magnitude, this second order transition has an intensity comparable to the first order transition, in which only A spin is flipped ($\Delta m_B=0$). Third and higher order transitions may also contribute appreciably[2]. Clearly the inverse process has a matrix element of the same magnitude. The processes $\Delta m_A=-\Delta m_{\rho,B}=\pm1$ also exist with a resonance frequency $\omega_A{}^0-\gamma_B H_B{}^{\mathrm{rf}}\operatorname{cosec}\Theta$. The relative intensities of the three transitions are given by the following table:

Resonant Frequency	*Relative Intensity*
$\omega_A{}^0+\gamma_B H_B{}^{\mathrm{rf}}\operatorname{cosec}\Theta$	$\{Z/(n_B{}^{+}+n_B{}^{-})\}(n_A{}^{+}n^{+}_{B\rho}-n_A{}^{-}n^{-}_{B\rho})(C_{AB}\sin^2\Theta/\gamma_B hH_B{}^{\mathrm{rf}})^2$
$\omega_A{}^0$	$n_A{}^{+}-n_A{}^{-}$
$\omega_A{}^0-\gamma_B H_B{}^{\mathrm{rf}}\operatorname{cosec}\Theta$	$\{Z/(n_B{}^{+}+n_B{}^{-})\}(n_A{}^{+}n^{-}_{B\rho}-n_A{}^{-}n^{+}_{B\rho})(C_{AB}\sin^2\Theta/\gamma_B hH_B{}^{\mathrm{rf}})^2$

Z is the number of nearest B neighbors to an A spin. $n^{+}_{B\rho}-n^{-}_{B\rho}$ can be determined from Redfield's theory. It is zero exactly at resonance ($\Theta=\pi/2$), and has opposite sign on either side of $\omega_B{}^0$. $n_A{}^{+}-n_A{}^{-}$ has the normal Boltzmann value for sufficiently weak fields $H_A(\omega_A)$.

It follows immediately that the absorption around $\omega_A{}^0$ is asymmetric, and that the asymmetry should be reversed, it $\omega_B-\omega_B{}^0$ changes sign.

The "collapse" can be explained as a severe broadening of the line by second and higher order transitions, when $\gamma_B hH_B{}^{\mathrm{eff}}\leq C_{AB}$. From Fig. 2 and Table I of reference 1 it can be seen that the collapse indeed occurs in this range. For $\gamma_B hH_B{}^{\mathrm{eff}}>C_{AB}$ the higher transitions move away from the A resonance and become much weaker in intensity. The narrowing then becomes observable.

References

1) Y. Saito: J. Phys. Soc. Japan **13** (1958) 72.
2) N. Bloembergen and P. P. Sorokin: Phys. Rev. to be published.
3) A. G. Redfield: Phys. Rev. **98** (1955) 1787.

J. PHYS. SOC. JAPAN **13** (1958) 661

Polarization Reversal in Triglycine Sulphate Crystal

By Kiyasu ZEN'ITI, Kazuo HUSIMI and Keisuke KATAOKA

Electrical Communication Laboratory, Nippon Telegraph and Telephone Public Corporation, Tokyo

(Received March 3, 1958)

Conventional methods for the study of switching processes in ferroelectrics use the switching current as the measure for switching of polarization. Such an observation cannot determine the absolute polarization of the crystal. We have applied the ultrasonic method[1] to study the switching process of triglycine sulphate crystal and compared the results with those obtained by the conventional pulse method.

The crystals have been grown by S. Waku of this Laboratory by volatilization process. The sample used is 0.5 mm in thickness and 4 mm² in area of electrode which was prepared by vacum evaporation of gold. The spontaneous polarization is 3.3μ c/cm², which is considerably larger than the value 2.2μ c/cm² already reported. The crystal is markedly piezoelectric in polarized state[2], which makes it very favourable for the ultrasonic method.

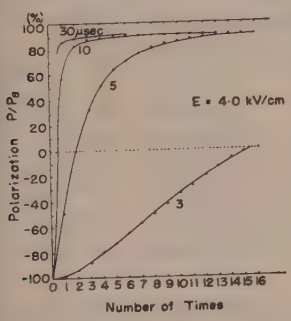

Fig. 1. Polarization Reversal under Successive Pulse Application.

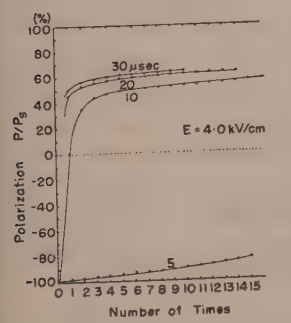

Fig. 3. Polarization Reversal under Successive Pulse Application. (Uncontrolled growth sample)

After setting the crystal to negative saturation by application of a field of 1.5 kV/cm for several seconds, the crystal is switched to the positive polarization step by step by successive application of voltage pulses from a pulse generator of low output impedance. The pulse widths are chosen from 10 μsec to 1 msec with logarithmically linear steps and the field strengths are from 1 kV/cm to 5.5 kV/cm with 0.5 kV/cm steps. The polarization vs. time curves are shown in Fig. 1 for the case of pulse height of 4 kV/cm.

As shown in Fig. 1 the switching velocity becomes very small near the saturation, therefore the value of switching times would depend much on its definition. We shall here define the switching time t_α by the equation

$$\int_0^{t_\alpha} i \cdot dt = (1+\alpha) P_s$$

where i is the switching current and α is the degree of polarization on reversal measured from the depolarized point. In Fig. 2 are shown three switching times $t_{0.0}$, $t_{0.4}$ and $t_{0.8}$ as the function of the switching field.

In conventional pulse method, the switching current has a sharp peak followed by a long and gradually decreasing tail. Strictly speaking, the switching time cannot be defined unambiguously in such a case, but for convenience we determine observed switching times t_{0b} from the end of the tail, and these are also shown in Fig. 2.

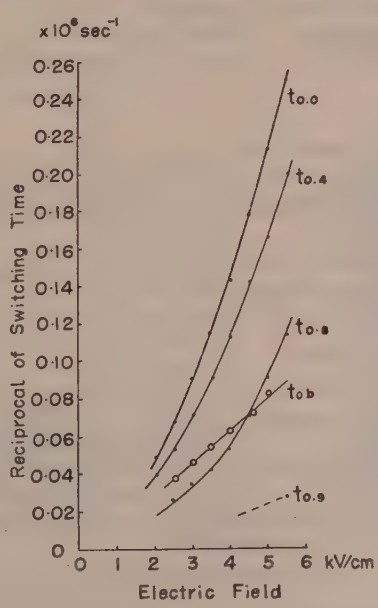

Fig. 2. Comparison of Switching Times among Various Definition.

The switching characteristics are influenced seriously by the crystalization conditions. The switching processes of another sample prepared in uncontrolled condition is shown in Fig. 3. Not only is the switching time larger for this sample, but there appears an apparent saturation near 50% of the true saturation polarization. This apparent saturation occurs even in a good crystal when an unsuitable electroed material such as conductive point is used, or the sample is measused in damp environment. The apparent saturation in an un controlled sample may be due to the wide distribution of the polarizing rates of different parts of the crystal. In a good crystal, it is probably caused by a layer of low polarizing rate which is formed under the surface by the surface condition such as electrode material or moisture.

References

1) Husimi, Kataoka: ECL Res. Rep. **801** (55–409) Oct. 1955.
2) Husimi, Kataoka: To be published.

Preliminary Announcement of Meetings of the Physical Society of Japan

1. Annual Meeting

The Annual Meeting for 1958 of the Physical Society of Japan will be held at the University of Kyoto, Kyoto, during October 15~20, 1958. There will be the following sections:

Theory of elementary particles. Nuclear reaction and nuclear structure (theoretical and experimental). Cosmic rays. Radiation physics. Ionic crystals. Optical properties of matter. Lattice imperfections. Plastic properties of matter. Metals. Magnetism. Dielectrics. Semi-conductors. Atoms and molecules. Low temperature physics. Statistical mechanics. Biophysics. High polymer physics. Electric discharge and plasma physics. Applied mathematics and mechanics. X-rays and electron diffraction. Optics. Apparatus and techniques. Acoustics.

There will be several sessions for invited papers and general lectures besides the sessions for contributed papers.

2. Symposium on Lattice Imperfections

A Symposium on Lattice Imperfection will be held in conjunction with the Annual Meeting. English will be adopted as the formal language of this symposium. Professors Maurer and Brown of Illinois University are being invited to give lectures.

PROGRESS OF THEORETICAL PHYSICS

CONTENTS

Progress of Theoretical Physics Vol. 19, No. 4 April 1958

π-N Interactions in Gev Region.....Y. KAKUDO, T. GOTO and R. NAKASHIMA..353
Parity-Nonconservation and the Spins of the Strange Particles.....K. ITABASHI..359
Separable Dynamical Systems of Staeckel in Flat Space.....G. IWATA..369
Perfect Imaging Dynamical Systems.....G. IWATA..375
Elastic Scattering of Deuterons by Heavy Nuclei.....Y. NISHIDA..389
Low Levels of Some Nuclei in the $d_{3/2}$—$f_{7/2}$ Shell.....S. P. Pandya..404
On the Form Factor of Liquid He^4 at Absolute Zero, II.....R. ABE..407
Nuclear Binding Energies and Low-Lying Energy Levels in the $2s_{1/2}$ and $1d_{3/2}$ Shells..... A. ARIMA..421
Letters to the Editor:
Quantization of Spin Wave Field.....I. MANNARI..451
Note on Energy Levels of Polyatomic Molecules.....S. D. MAJUMDAR..452
Natures of Nuclear Force Indicated by the Photodisintegration of the Deuteron, III.....S. H. Hsieh..453
An Attempt of a Nonliner Field Theory.....H. KITA..454
Contents of Journ. of Phys. Soc. of Japan, Vol. 13, No. 3.....457
Announcement on Supplement of Prog. Theor. Phys.....458

Price $ 1.25 per copy
$ 15.00 per year (postage inclusive)
Annual dues for foreign members (individual subscribers)
$ 12.00 (postage inclusive)
" for foreign members of the Physical Society of Japan
$ 10.00 (postage inclusive)

Application for members, subscriptions and orders for back numbers should be sent, directly or through book-dealers, to

The Publication Office
in
Yukawa Hall, Kyoto University, Kyoto, Japan

JOURNAL OF THE PHYSICAL SOCIETY OF JAPAN Vol. 13, No. 7, JULY, 1958

Isotope Shift in the Spectrum of W I*

By John A. VREELAND

Westinghouse Electric Corporation, Atomic Power Department, Pittsburgh, Pennsylvania, U.S.A.

and

Kiyoshi MURAKAWA

Institute of Science and Technology, University of Tokyo, Komaba-machi, Meguro-ku, Tokyo

(Received March 13, 1958)

By use of samples enriched in W^{183} and W^{180} respectively and of natural tungsten the isotope shift in the spectrum of W I was measured, and the ratio of the shift of the neighboring even isotopes was determined. The result is

$$\Delta\nu(186-184):\Delta\nu(184-182):\Delta\nu(182-180)=83\pm2:100:66\pm5\,.$$

Discrepant result of other observers is considered to be due to the neglect of the disturbing effect of the W^{183}-components.

§ 1. Introduction

Using separated tungsten isotopes whose compositions are shown in Table I, Vreeland and Murakawa[1] (referred to as Part I) measured the isotope shift of the even isotope in the hyperfine structure (hfs) of the spectrum of W I and calculated the nuclear magnetic moment of W^{183}. The isotope shift can be easily studied in the line $\lambda4269$, owing to the large magnitude of the shift, but unfortunately this line was masked by the strong aluminum hydride band. Somewhat later, using natural tungsten, Murakawa[2] (referred to as Part II) studied the hfs of $\lambda4269$ and of some other lines, and determined the ratio of the shift of the neighboring even isotopes: $\Delta\nu(186-184:\Delta\nu(184-182)=1:1.206\pm0.010=83\pm1:100$. Two years ago, using natural tungsten again, Murakawa[3] (referred to as Part III) detected a component due to W^{180} in the hfs of $\lambda4269$ and gave the ratio of the even isotope shifts: $\Delta\nu(186-184):\Delta\nu(184-182):\Delta\nu(182-180)=1:1.206\pm0.010:0.88\pm0.07=83\pm1:100:73\pm7$. Subsequently Barr and Jenkins[4] (referred to as

Table I. Isotopic constitution (percent) of the samples of tungsten.

Sample label	Isotope				
	180	182	183	184	186
183	0.098	4.19	86.21	7.14	2.36
180	4.95	50.75	15.28	17.89	11.14
Natural	0.14	26.4	14.4	30.6	28.4

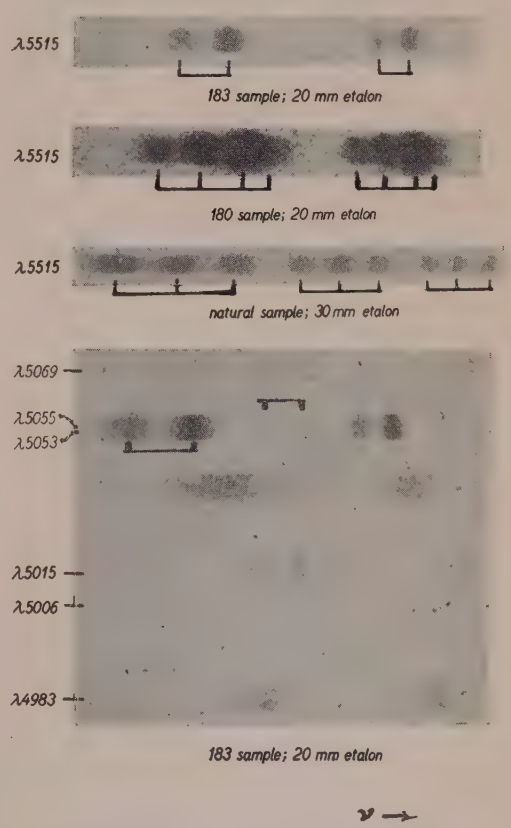

Fig. 1. Enlargement of the interference patterns of the spectrum of W I.

* The work with separated isotopes was performed in the University of Wisconsin in 1950–1951 and was supported by the U. S. Office of Naval Research.

B and J), using a sample enriched in W^{180}, measured the same ratio and obtained $\Delta\nu(186-184):\Delta\nu(184-182):\Delta\nu(182-180)=88:100:68$.

The ratio $\Delta\nu(184-182):\Delta\nu(182-180)$ given in Part III is in agreement with B and J within the experimental error of Part III, but the ratio $\Delta\nu(186-184):\Delta\nu(184-182)$ given in Part II (and also in Part III) differs from that of B and J beyond the limit of error of Part II.

The above-mentioned ratio was obtained in Parts II and III mainly by studying the hfs of $\lambda 4269$, whereas the conclusion of B and J is based on the hfs of $\lambda 5015$ and $\lambda 4983$[6]. In order to study the hfs of $\lambda 5015$ and $\lambda 4983$, samples enriched in W^{183} and W^{180} respectively (in addition to natural tungsten) must be used. The plates that were taken previously using separated isotopes have now been re-measured, confirming Parts II and III, and a result which is more accurate than Part III has been obtained.

§ 2. Experimental Procedure

As a light source a liquid-air cooled or water cooled aluminum hollow-cathode discharge tube was used, whose construction was described by Arroe and Mack[6]. Neon was used as carrier gas. The hfs was resolved by a silvered Fabry-Perot etalon. Some of the interference patterns are reproduced in Fig. 1.

§ 3. Result of Measurement

In each sample (see Table I) the isotope W^{183} is present and disturbs the determination of the positions of the components of W^{184} and W^{182}. On the other hand the sample W 183 contains the isotopes W^{184} and W^{182} (in addition to W^{183}, W^{186} and W^{180}) and the determination of the positions of the components of W^{183} ($I=1/2$) is disturbed by the components of W^{184} and W^{182}.

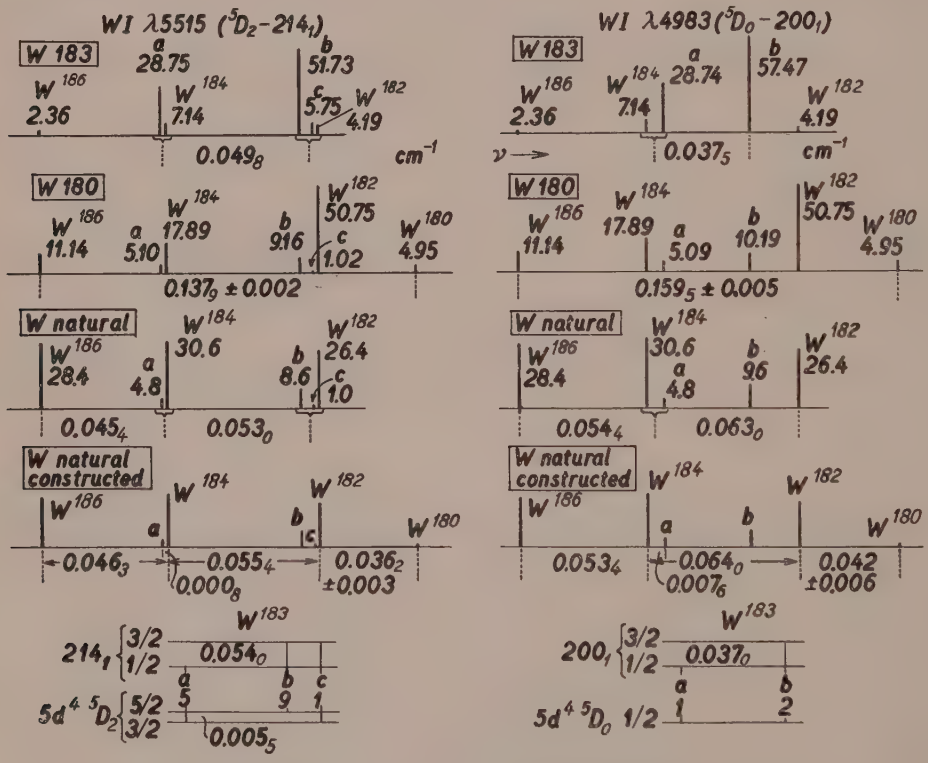

Fig. 2. Hfs of WI $\lambda\lambda$ 5515, and 4983.

We have therefore measured the patterns of both natural tungsten and W 183 and adjusted the positions of the components due to W^{184} and W^{182}, so that both sets of analysis may be consistent with each other (see Figs. 2 and 3)[7]. It was assumed that the center of gravity of the W^{183}-components lies just midway between the W^{184}-and W^{182}-components (Part II).

In Figs. 2 and 3 the hfs of the term $5d^4\ {}^5D$ was calculated assuming that the configuration $5d^4$ is of LS-coupling: Sogo and Jeffries'[8] $\mu(W^{183})=0.115\pm0.001$ nm was used; Racah's value[9] $\zeta(5d)=2089$ and the effective charge[10] $Z^*(5d)=74-20=54$ were assumed. This calculation would be sufficient for a one-digit discussion of the hfs of $5d^4\ {}^5D$. In the case of λ4404.5 (Fig. 3), the interval factor of the level $5d^4\ {}^3P_2{}^a$ is required. Since another level with $J=2$ lies near, an assumption of pure LS-coupling would certainly be a poor approximation for ${}^3P_2{}^a$, so that we have left the hfs of ${}^3P_2{}^a$ undetermined. In adjusting the positions of the components of W^{184} and W^{182} for λ4404.5 the component a was neglected.

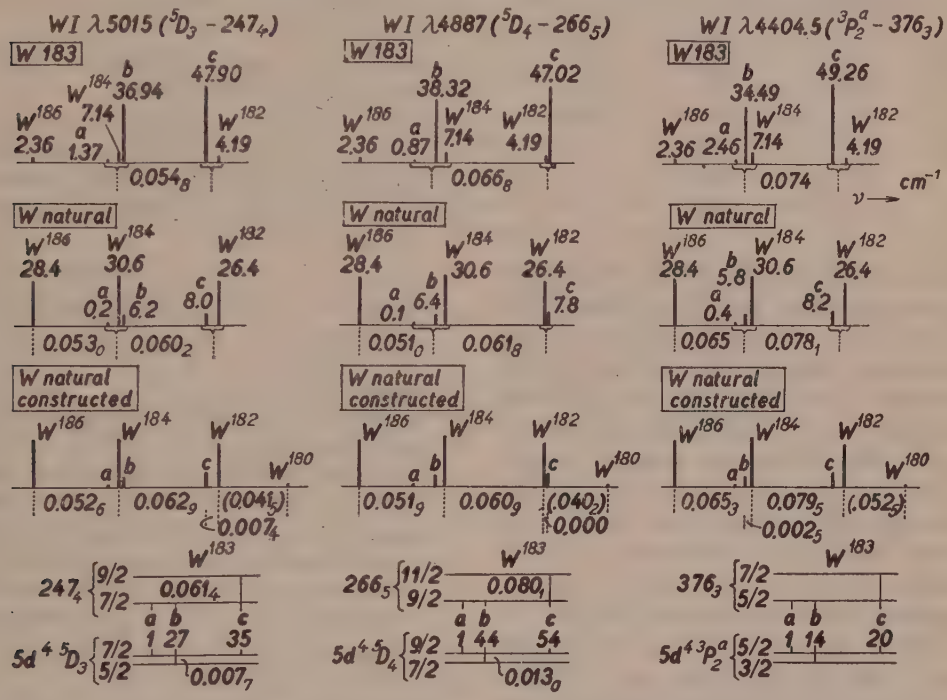

Fig. 3. Hfs of W I $\lambda\lambda$ 5015, 4887, and 4404.5. A number in parentheses was calculated.

Since this has only a small intensity, it would have a small influence on the determination of these components.

The position of the component W^{180} was measured by a comparator and a microphotometer. It was found that only the distance $W^{186}-W^{180}$ can be measured accurately. From this the calculated distance $W^{186}-W^{182}$ was subtracted and the distance $W^{182}-W^{180}$ was obtained. The best accuracy was attained for λ5515 (Figs. 1 and 2). In the case of λ4983 the accuracy is somewhat less. The component W^{180} of λ5015 appears over-exposed on all the plates that were taken using the sample W 180, so this was abandoned.

In our first publication (Part I) the process of obtaining the positions of W^{182} and W^{184} was somewhat different from that adopted in the present measurement, but we consider

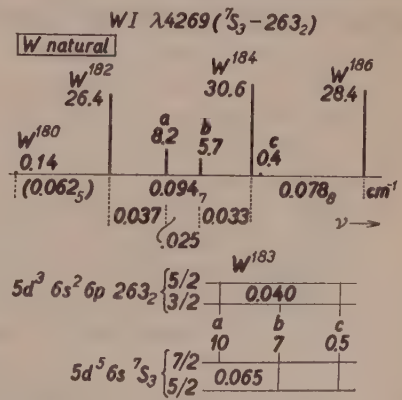

Fig. 4. Hfs of W I λ 4269. A number in parentheses was calculated.

the distance $\Delta\nu(182-180)$ obtained in the present work to be more accurate than Part I.

The ratio of the distances of the neigh-

boring isotopes that was determined from Figs. 2–4 (the hfs of $\lambda 4269$ is shown in Fig. 4 for the sake of completeness) is summarized in Table II, and the weighted mean is

$$\Delta\nu(186-184):\Delta\nu(184-182):\Delta\nu(182-180)$$
$$=83\pm2:100:66\pm5\ .$$

Table II. Isotope shift in W I.

Line	$\Delta\nu(186-184)$	:	$\Delta\nu(184-182)$	:	$\Delta\nu(182-180)$
$\lambda 5515$	84	:	100	:	66
$\lambda 5015$	83	:	100		
$\lambda 4983$	83	:	100	:	66
$\lambda 4887$	85	:	100		
$\lambda 4404$	82	:	100		
$\lambda 4269$	83	:	100		

The value of $\Delta\nu(186-184):\Delta\nu(184-182)$ given here is in agreement with Part II (and Part III), but not with the result of B and J. The value of $\Delta\nu(184-182):\Delta\nu(182-180)$ given here is in agreement with Part III and with B and J. B and J do not mention the use of separated isotope W 183. Since the isotope shift is small (of the order of $0.05\,\mathrm{cm}^{-1}$) in the case of $\lambda 5015$ and $\lambda 4983$ which were studied by B and J, the effect of the presence of W^{183} in the sample would certainly be not negligible. We therefore hope that by introducing correction due to the components of W^{183} to the data of B and J, the ratio $\Delta\nu(186-184):\Delta\nu(184-182):\Delta\nu(182-180)$ deduced from their data would come closer to our value.

Full details concerning the hfs of W^{183} (magnetic effect) will be published elsewhere.

References

1) J. A. Vreeland and K. Murakawa: Phys. Rev. **83** (1951) 229.

2) K. Murakawa: J. Phys. Soc. Japan **8** (1953) 215. All the literatures published before 1953 are quoted.
Correction: In Table I the hfs of $\lambda 5500.$ ($19_5'-380_4$) should read: 182: $-0.055\,\mathrm{cm}^{-1}$, 184: $0\,\mathrm{cm}^{-1}$, 186: $+0.046\,\mathrm{cm}^{-1}$.

3) K. Murakawa: J. Phys. Soc. Japan **11** (1956) 778.

4) W. L. Barr and F. A. Jenkins: Bull. Am. Phys. Soc. [2] **1** (1956) 389.

5) F. A. Jenkins: Private communication. The kindness of Prof. Jenkins of giving us the detailed information is greatly appreciated.

6) O. H. Arroe and J. E. Mack: J. Opt. Soc. Am. **40** (1950) 386.

7) The level notation and classification of W were taken from O. Laporte and J. E. Mack [Phys. Rev. **63** (1943) 246].

8) P. B. Sogo and C. D. Jeffries: Phys. Rev. **98** (1955) 265.
In Part I the present authors calculated $\mu(W^{183})$ from the interval factor of $5d^5\,6s\ {}^7S_3$. At that time the finite nuclear volume correction was not included. Somewhat later this correction was taken into account, at the same time improving the value of $(dn^*/dn)/n^{*3}$, and $\mu(W^{183})=+0.10\pm0.02\,\mathrm{nm}$ was obtained. This value was quoted by K. Murakawa and T. Kamei [Rep. Inst. Sci. Technology, Univ. Tokyo **7** (1953) 219].

9) G. Racah: quoted by R. E. Trees, W. F. Cahill and P. Rabinowitz [J. Research Natl. Bur. Standards **55** (1955) 335].

10) K. Murakawa: Phys. Rev. **98** (1955) 1285.

JOURNAL OF THE PHYSICAL SOCIETY OF JAPAN Vol. 13, No. 7, JULY, 1958

On the Electrical Properties of Polycrystalline Boron

By Ryosei UNO

Scientific Research Institute, Komagome-Kamifujimae, Bunkyo-ku, Tokyo, Japan

(Received January 23, 1958)

Several specimens of polycrystalline boron, which have various electrical conductivities at room temperature, ranging from 8 (ohm cm)$^{-1}$ to 5×10^{-3} or less, were obtained by reduction of distilled boron tribromide. The spectroscopic analysis and the observation by the Debye-Scherrer X-ray pattern were carried out. Some evidence was obtained showing that the conductivity at room temperature may not increase with the amount of impurities but it depends rather on the difference in the crystal structure. Assuming a simple model, carrier concentration and mobility were estimated from the data of conductivity and thermoelectric power. The result was that the carrier concentration may be nearly constant over the range from 100 to 1000°K and that the mobility may vary exponentially with the reciprocal of absolute temperature.

§ 1. Introduction

Electrical properties of bulk boron and boron films have been investigated by several workers, and an extensive survey of the experimental results together with some optical properties was given by Moss.[1] Weintraub[2] found the specific conductivity of bulk boron, produced by reduction of boron tribromide by hydrogen using high voltage electric arc, to be $5.9\times10^{-7}\Omega^{-1}\,\mathrm{cm}^{-1}$ at 23°C, increasing to about $1\,\Omega^{-1}\,\mathrm{cm}^{-1}$ at 1000°C and the thermal activation energy to be about 1.25 eV. According to Laubengayer *et al*,[3] however, the increase of electrical conductivity of a single crystal of boron prepared by them was less than one hundred fold between 20 and 600°C corresponding to an activation energy of less than 0.35 eV. Moreover, a measurement carried out by Henninger[4] on the bulk boron prepared by Weintraub[2] suggested that the specimen might have layers of low conductivity and the true conductivity of boron might be very low and have a small dependence on temperature. Recently, Lagrenaudie[5] measured various properties of boron on three groups of samples, *viz.*, those obtained by dissociation of boron tribromide, those obtained by cracking of boron hydride on glass plate, and those obtained by fusion of amorphous boron. Samples produced by the dissociation seem to be very pure and consisted of considereably large crystallin grains. Samples produced by the fusion were impure and those by cracking on glass were pure but amorphous. All the samples were *p*-type semiconductors, having an intrinsic activation energy of about 1.2~1.3 eV according to the measurements on electrical conductivity, optical transmission and photoconductivity. Several impurity levels, having activation energies of 0.06, 0.30, 0.40, 0.50, 0.60 and 0.84 eV, were also obtained from the gradient of curves of conductivity versus the reciprocal of absolute temperature. It was also reported that the Debye-Scherrer X-ray pattern of the sample produced by dissociation contains new lines other than those observed by Laubengayer. The rectification of boron was hardly observed, and the mobility of carrier was reported to be small because Hall effect could not be observed, and a value of 3 cm^2/volt-sec was estimated from an observation of the current variation due to induced charge. It may be concluded from his experiments that the energy difference between the valence band of boron and the first excited band is about 1.2~1.3 eV. Anomary of the reflection of light was not observed at the absorption edge and the observed difference of absorption, between samples produced by dissociation and those by fusion, could not be interpreted by the difference in the amount of impurities. Johnston *et al*[6] measured the temperature dependency of specific heat of boron and obtained a rather high value of 1219°K as the Debye characteristic temperature, between 60 and 150°K, which may be consistent with the small mobility.

* Now at Faculty of Literature and Science, Nihon University, Kamikitazawa, Setagaya-Ku, Tokyo.

In our experiments, several specimens of boron of different impurity contents were produced by the reduction of boron tribromide using more or less different procedures. Measurements made on these samples showed that the electrical conductivity did not depend much on the amount of impurities but might depend rather on the crystal structure of the samples. Measurements of the temperature dependence of electrical conductivity, thermoelectric power and Hall constant at temperatures between 100 and 1000°K, were also carried out in order to obtain some information about carrier concentration, mobility, effective mass and energy band structure. However, our measurements of Hall voltage using both direct current and alternating current carried out over a temperature range from 150 to 600°K were unsuccessful on account of very small Hall voltage. An analysis, therefore, was carried out using the data of thermoelectric power and electrical conductivity. The result obtained using a simple model was that the carrier concentration may be nearly constant over the range from 100 to 1000°K and that the mobility vary exponentially with the reciprocal of absolute temperature.

§ 2. Preparation of Samples

The preparation of samples was described in detail in the previous paper.[7] Following the method used by Laubengayer *et al*,[3] powder of boron was made from boron oxide by the reduction with magnesium, which was then changed over to boron tribromide. After the distillation, boron tribromide was thermally decomposed or reduced by hydrogen and the samples of pure boron were obtained. Five processes differing slightly from one another were used in this final procedure and samples having different properties were obtained.

In the first process, the boron was thermally decomposed in vacuum and pure boron was deposited on the filament of tantalum or tungsten. Bromine liberated was taken off by allowing it to combine with mercury. By this process, only sample No. 1 was obtained. In the second process, mixture of hydrogen and a small amount of boron tribromide vapour was allowed to flow through the reduction chamber in which the filament was held at a high temperature. Bromide was reduced at the filament and boron was deposited on it. No mercury was used except on glass taps, and blocks of boron large enough for our purposes were obtained. The reduction was carried out at a temperature of about 1300~1400°C, which was measured by an optical pyrometer looking through the glass wall of the reduction chamber. As the wall was blurred, the value of the temperature measured might have been lower than the actual temperature and could serve only as an indication. (from No. 2 to 10) By spectroscopic analysis of a sample produced by this process, some traces of mercury and beryllium was found. In the third process, silicone grease was used for glass joints and taps of the chamber to avoid mercury. The reduction was carried out at 1200~1300°C. (No. 11 to 17) The sample made by this procedure con-

Table I. The results of spectroscopic analysis.

Process	Sample: for electrical measurement	Sample: for spectroscopic analysis	Impurities: C	Na	Mg	Al	Si	Ca	Ni	W	Pb	Total	Reduction
First	No. 1											unknown	
Second	4	a								30		30	1400~1500°C
	5	b			0.2		2					2.2	
Third	14												
	15	c	3				9					12	1200~1300°C
	16	d	6	0.4	0.2	1.5	15	1	0.6			27.7	
Fourth	18	e				1	4	1				6	approx. 1100°C
	20	f					6				6	12	
Fifth	21	g			0.4		2					2.4	1150~1200°C

tained some silicon according to spectroscopic analysis. (Table I) In the fourth process, ordinary grease for high vacuum was used in place of silicone grease, attempting to reduce silicon. The reduction temperature was about 1100°C. (No. 18 and 20) The sample made in this process was not so pure as those in the third, in spite of reducing the amount of silicon. (see Table I) The boron tribromide used in this process was the same bromide as that used in the third process which had been kept in a container of hard glass for about half a year after the third process was carried out. It seems probable that bromine liberated from tribromide had attacked glass walls and produced various bromide during this period. In view of this, the reduction of bromide was carried out in the fifth process, as soon as possible after the distillation. The process used was that of the fourth. The reduction temperature was 1150~1200°C. (No. 21) The sample obtained in this way was the purest as shown in the table. There was an optimum reduction temperature for getting a large block of boron. If the temperature was too high, local heating was apt to occur in the filament and it was broken before a block of boron had grown up sufficiently. If the temperature was too low the rate of reduction was too low for a block of sufficient size to be grown in a few days.

All the samples used for the measurement were obtained when tantalum ribbon was used as the filament. After removing the tantalum ribbon and grinding with carborundum and water, specimens up to (5~10) ×(1.0~1.5)× (0.3~0.6) mm³ were prepared for the measurement.

The spectroscopic analysis were carried out on the material which were taken from the same blocks as those used in preparing samples for the electrical measurements. As the quantitative spectroscopic analysis was difficult, only relative amount of impurities are determined, assuming it to be proportional to the density of spectral line divided by its arc intensity value. As copper electrode was used, the content of copper could not be determined. The results are shown in Table I along with the reduction temperature. A sample produced in the third process was compared with commercial boron which contained 1.5 % carbon and 1 % other impurities, by a spectroscopic analysis using carbon electrode.* It is concluded that the impurity content of this sample may be about the same as the commercial boron. Samples obtained in the second and fifth process seem to be purest, about 99.5 %, and those in the third are most impure.

§ 3. Debye-Scherrer X-ray Patterns

Debye-Scherrer X-ray patterns obtained for various samples are shown in Fig. 1 together with that obtained by Laubengayer *et al*[3] on a tetragonal single crystal of boron (not ideal).

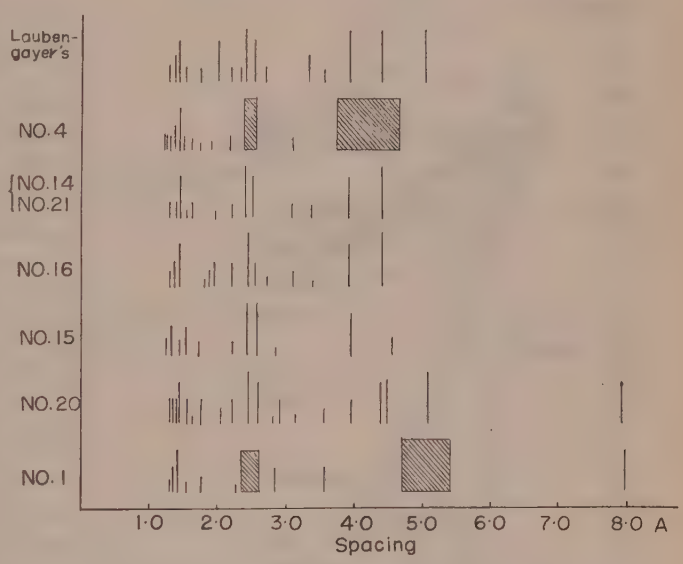

Fig. 1. Debye-Scherrer X-ray patterns, with that observed by Laubengayer *et al*, for reference.

They show that the crystal structure of our specimens except No. 20 is similar to that of the single crystal. The ideal structure of tetragonal single crystal of boron was reported by Hoard[8] to have a axis of 8.73±0.02 Å and c axis of 5.03±0.02 Å. Its unit cell contains four deformed isocahedra and four large holes, two of which are occupied by special atoms having only four first neighbours, interspread among the very compact isocahedral groups.

* For this spectroscopic analysis, we are indebted to Dr. Matsuo of Matsuda Research Laboratory, Tokyo-Shibaura Electric Co. Ltd.

The patterns shown in Fig. 1 indicate that No. 14 and No. 21 have the same structure although they may contain different amount of impurities, and that No. 14, 15 and 16 have different structures in spite of having nearly the same amount of impurities and that No. 21 shows a reflection from a plane of large spacing and its pattern resembles that of No. 1.

The pattern like that observed by Lagrenaudie[5] on a boron sample produced from boron tribromide was not observed.

§ 4. Electrical Conductivity

The electrical properties of the samples prepared in the first and second processes were reported previously.[7] In the previous report, the results on two kinds of boron, the one showing low conductivity (No. 1) and the other showing high conductivity (No. 3, 4 and 5) at room temperature, were presented. In the present paper, the resuls on the samples showing intermediate conductivity were included as well as the main results previously reported.

Electrical conductivity was measured by direct current in the temperature range between 120 and 1000°K. To assure good electrical contacts with the electrodes and probes, usual technique of sputtering of gold or platinium was used. The specimen was held in vacuum of about 10^{-3} mmHg during the measurements. It was varified on some of the typical samples that Ohm's law is satisfied in the range between 0.1 and 1.6 V/cm at room temperature and at about 700°K.

The results are shown in Fig. 2. Conductivities of all the samples increase exponentially with reciprocal of absolute temperature, showing that they have the usual characteristics of semiconductor. Absolute value of each curve may contain some error, because the shapes of some samples are irregular. If the conductivity in the range of straight line in Fig. 2, is expressed by the relation

$$\sigma=\sigma_0 \exp\left(-\frac{E}{2kT}\right) \qquad (1)$$

where E, k, T and σ_0 are the activation energy, Boltzmann's constant, absolute temperature and some constant respectively. The value of E's shown in the figure may be obtained for the points indicated on the curves. These values are not inconsistent with those obtained by Lagrenaudie[5] and others.[1]

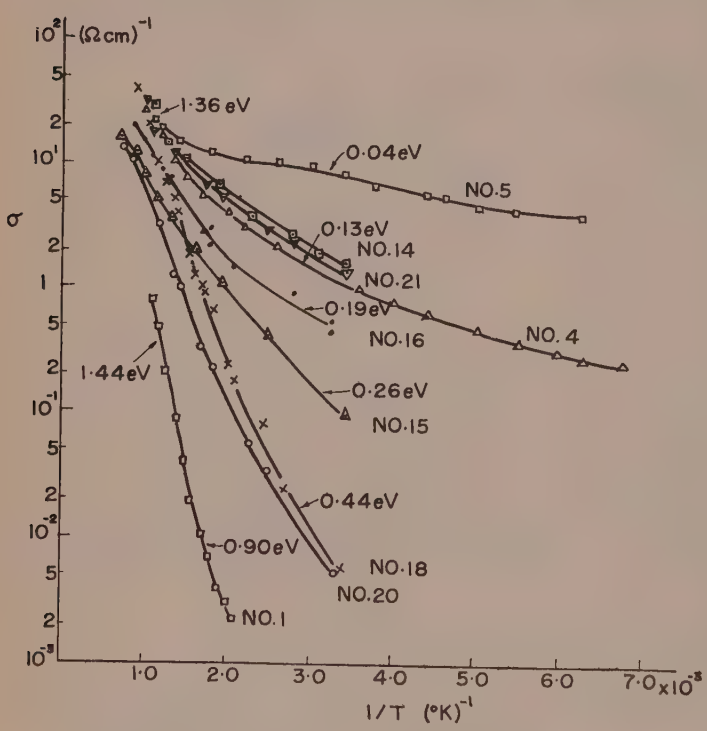

Fig. 2. Electrical conductivity.

All the samples seem to have intrinsic conductivity of about 10 Ω^{-1} cm^{-1} at 1000°K but their conductivity differ at lower temperatures from sample to sample, showing a structure sensitive characteristics. According to the usual interpretation of the behaviour of semiconducting characteristics, the higher conductivity should correspond to a lower amount of impurities. However, this does not seem necessarily to be the case for our boron samples. For example, No. 21 and No. 14 have almost the same conductivity, although the former seems to contain much smaller amount of impurities. On the other hand, No. 14, 15 and 16 which may contain about the same amount of impurities, show considerably different behaviours in conductivity. It seems, therefore, necessary to look for some other causes than

the impurity content of the samples to explain the difference in conductivity at lower temperatures. In this respect, it may be worth noting that the samples showing the same Debye-Scherrer pattern, No. 14 and 21, have almost the same conductivity and those showing different patterns, No. 14, 15 and 16, have different conductivities. It is also probable that there are some correlation between the temperature of reduction and the conductivity, that the samples reduced at lower temperature in the process of preparation generally show lower conductivity. Those facts suggest that the conductivity of boron depends, unlike usual semiconductors, more on the structure of the crystal than on the impurity content.

§ 5. Thermoelectric Power

Thermoelectric power Q was measured in the temperature range between 150 and about 1000°K. In the measurement above room temperature, the sample was placed between two electrodes of copper each of which had an auxiliary heater to produce temperature difference across the sample. Temperatures at both ends of the sample were measured with an alumel-chromel thermocouples of 0.25 mm in diameter, which were welded to each electrode. The entire system was held in a quartz tube which was evacuated and heated electrically. The observation below room temperature was conventionally carried out with an apparatus, only one electrode of which had an auxiliary heater. The apparatus was covered with a glass tube and immersed in liquid air. The temperature was measured by copper-constantan thermocouple. The thermoelectric power was obtained from the gradient of the thermoelectromotive force versus temperature difference across the sample, because the thermoelectromotive force did not vanish when the temperature difference measured was zero, although the relation between the electromotive force and the difference was almost linear. This arose probably from the small difference in temperature between the point on the sample where the electrode was applied and the point at which the temperature was measured.

All the samples measured were p-type and the results are shown in Fig. 3. In Fig. 4 the thermoelectric power is plotted against the logarithum of the absolute temperature, showing that there is approximately a linear relation expressed by

$$Q = Q_0 + \alpha \log T \qquad (2)$$

where Q_0 and α are constants. It seems that the sample showing lower conductivity at room temperature has larger value of α.

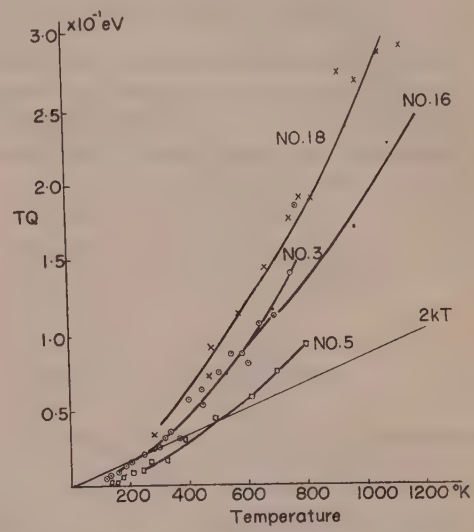

Fig. 3. Product of the thermoelectric power and the absolute temperature.

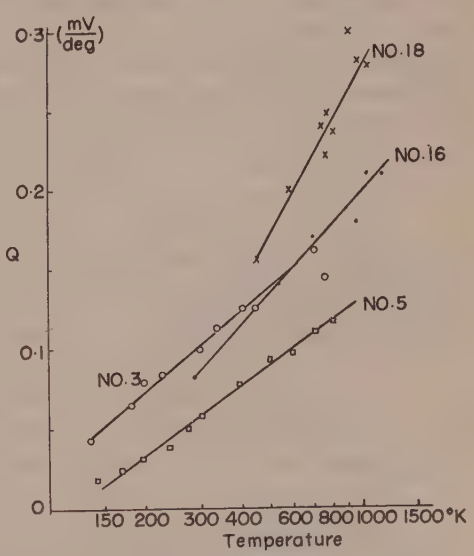

Fig. 4. The thermoelectric power against the logarithum of the absolute temperature.

§ 6. Carrier Concentration and Mobility

Carrier concentration and mobility of the boron samples were analysed from the data of conductivity and thermoelectric power.

As the samples are all p-type, all the carriers were assumed to be holes in a single band. According to the expression used by Johnson and Lark-Horovitz,[9] the product of thermoelectric power and the absolute temperature is given by,

$$eTQ=L_2/L_1-\zeta \qquad (3)$$

where $L_j=\int_0^\infty \varepsilon^j l\frac{\partial f}{\partial \varepsilon}d\varepsilon$, ζ is the Fermi energy, f the Fermi distribution function, ε the energy of holes, l the mean free path of holes, taking $\varepsilon=0$ at the top of valence band. If we assume the mean free path is independent of energy (lattice scattering),

$$L_2/L_1=\frac{2\int_0^\infty \varepsilon f(\varepsilon,\zeta)d\varepsilon}{\int_0^\infty f(\varepsilon,\zeta)d\varepsilon}$$

$$=2kT\frac{F_1(\eta)}{F_0(\eta)} \qquad (4)$$

where $F_j(\eta)=\int_0^\infty \frac{x^j dx}{e^{x-\eta}+1}$ and $\eta=\zeta/kT$. $F_1(\eta)/F_0(\eta)$ can be calculated by the expressions given by Stoner[10] when $\eta<0$ or $\eta>5$. For the region $0<\eta<5$ numerical calculation was carried out.* As L_2/L_1 was calculated as a function of ζ and T, the Fermi energy ζ was obtained as a function of temperature, substituting the experimental values of thermoelectric power in Eq. (3).

The concentration of holes was then calculated from

$$n_p(T)=2\int_0^\infty D(\varepsilon)f(\varepsilon,\zeta(T))d\varepsilon$$

where $D(\varepsilon)$ is the level density. If it is assumed that the ε-space has spherical symmetry, $D(\varepsilon)$ will be given by,

$$D(\varepsilon)=\frac{1}{4\pi}\left(\frac{2m^*}{\hbar^2}\right)^{3/2}\varepsilon^{1/2}$$

where m^* is the effective mass. Thus we get

$$n_p(T)=2\int_0^\infty \frac{1}{4\pi}\left(\frac{2m^*}{\hbar^2}\right)^{3/2}\varepsilon^{1/2}f(\varepsilon,\zeta)d\varepsilon$$

$$=\frac{1}{3\pi}\left(\frac{2m_0}{\hbar^2}\right)^{3/2}\left(\frac{m^*}{m_0}\right)^{3/2}(kT)^{3/2}F_{1/2}(\eta) \qquad (5)$$

where m_0 is the mass of electron. $F_{1/2}(\eta)$ can be calculated in the same way as $F_1(\eta)/F_0(\eta)$. If we assume that m^* is equal to m_0, the value of $n_p(T)$ can be obtained from Eq. (5), using the known value of $\zeta(T)$ given above. Finally, the mobility of holes $\mu_p(T)$ was obtained from $\mu_p(T)=\sigma(T)/en_p(T)$ using the experimental value of conductivity $\sigma(T)$.

The mobility may be obtained from Seitz's theory[11] of the mobility in homopolar crystal which gives

$$\mu_p=6\frac{e}{m^*}\frac{c^2\hbar^4}{C^2kT}\frac{M_0}{m^{*2}}n_0\sqrt{\frac{\pi m^*}{8kT}}$$

where M_0 is atomic weight, c the sound velocity, n_0 the density of unit cell and the constant C can be approximated by

$$C(eV)=1.7\times10^{-2}\Theta$$

where Θ is the Debye characteristic temperature. In evaluating this expression, the value of 1220°K, obtained from the observation on specific heat, was used for the Debye temperature. The sound velocity was interpolated as 1.4×10^6 cm/sec from a measurement of the threshold energy of various metals for sputtering.[12] The density of unit cell was obtained assuming that the crystal structure of our specimens agree with those reported by Hoard *et al.*[8] The result of the calculation gives $2.9\,(m_0/m^*)^{3/2}$ cm²/volt-sec as the value of the mobility at 300°K. To equate the value of mobility just obtained to the value obtained from the analysis of experiment,

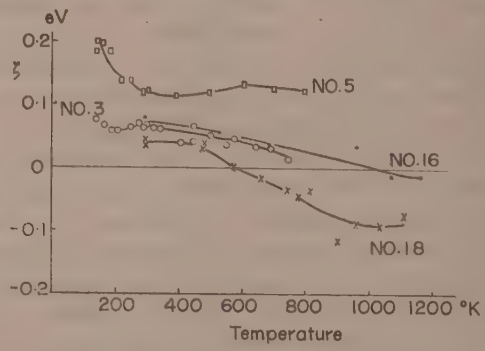

Fig. 5. The Fermi energy.

m^* must be taken equal to 150 m_0 for the sample No. 16 at room temperature. Such a large effective mass may be unreasonable, and it was thought preferable to assume m^* equal to m_0 in the later analysis.

The results of the analysis are shown in three figures. Fig. 5 gives the temperature dependency of Fermi energy, Fig. 6 the carrier concentration and Fig. 7 the mobility. Below 500°K the Fermi energies of the specimens

* The result of our calculation is in good agreement with those of H. Weiss, Z. Naturforschg. 11a (1956) 13.

are all positive, that is, they lie in the valence band at low temperature. The carrier concentration remain nearly constant from about 100 to 1000°K. The mobility varies exponentially with $1/T$. This dependence on $1/T$ is not so usual as a semiconductor.

The assumption made in the analysis may be too simple to interprete the properties of boron. From the temperature dependency of conductivity (Fig. 2), several acceptor levels may be assumed to exist, but, if such levels

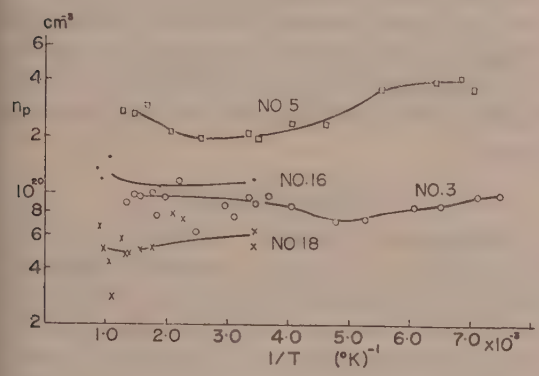

Fig. 6. Carrier concentration.

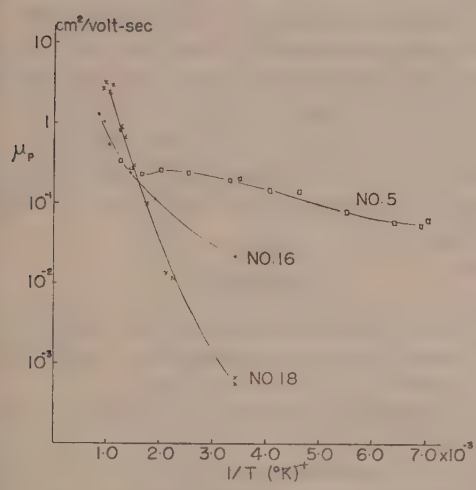

Fig. 7. Mobility.

are present, TQ (Fig. 3) must be constant in some range of temperature. It was not the case, however, the energy of the acceptor level could not, therefore, be obtained from the thermoelectric power. The very simple model was chosen only for simplicity. The results of analysis, of course, depend on the assumption we have made, but the dependence of mobility on the temperature obtained, resembles those of NiO reported by F. J. Morin.[13]

§ 7. Discussion

It was suggested above that the conductivity of boron may depend more on the structure of crystals than on the impurity contents. The first evidence which indicated this is the fact that sample No. 1 and No. 20, which have smaller conductivities (Fig. 2) compared to other samples have a line in the Debye-Scherrer photograph (Fig. 1) showing the existence of an extremely large spacing. The existence of this large spacing seems to show that the structure of these samples is monoclinic[14] whose axis are reported to be $a=10.0$ Å $b=17.8$ Å, $c=8.8$ Å and $\beta\approx 90°$. Most of the other samples which lack the evidence of this large spacing is expected to belong to the tetragonal structure as already reported above.

In the case of tetragonal crystals, the ideal structure has four large holes in a unit cell, two of which are always occupied. It has also been reported[15] that the Fourier projection of electron density on (001) plane gave a definite evidence for the presence of occasional "extra" boron atoms in these vacant holes. It seems most probable that these holes can be filled with extra boron atoms to a varying degree for different specimens. If this is the case, it may result in the difference of various properties such as electrical conductivity, density, and the difference of the intensities of Debye-Scherrer rings. All the atomic position of ideal structure are given by Hoard[8] in terms of $D_{2d}^{8}-P\bar{4}n2$. Two of 50 atoms occupy the position 2(b) and 48 atoms the position 8(i). As the position 2(a) has the same symmetry properties as 2(b), it seems probable that the extra atoms may occupy the position 2(a) partially. An attempt was made to calculated the intensity of Debye-Scherrer patterns by assuming various degree of occupation, but consistent results could not be obtained yet.

The densities of samples were measured by floating method and the results are shown in Table II, along with the conductivity at room temperature. If the extra atoms occupy the position 2(a) partially, the value of the density should fall between 2.31 and 2.40. The observed densities of the samples No. 14, 15 and 16, however, exceed the upper limit of 2.40. As those samples are prepared by

the third process which gave the highest impurity content, this shows that the contribution of impurities must not be neglected in evaluting density, and therefore, it is not possible, in this case too, to set the relation between the degree of occupation and the density by straightfoward calculation. As the position 2(a) and 2(b) have four nearest neighbours, it seems that some silicon atoms which were observed as impurities, may occupy these positions in place of boron atoms as they prefer to have four nearest neighbours. Nevertheless, there is some indication among No. 14, 15 and 16, that the sample having higher density shows higher conductivity.

Table II. The densities and the conductivities at room temperature.

Process	Sample	Density gr/cm^3	Conductivity at room temperature ohm^{-1} cm^{-1}
Third	No. 14	2.510	1.5
	15	2.436	9.4×10^{-2}
	16	2.444	5.3×10^{-1}
Fourth	20	2.362	5.0×10^{-3}
Fifth	21	2.362	1.3

As the samples we have used were all polycrystalline, the grain boundary may give some influence on the observed conductivity. As preliminary measurement[7] of high frequency effective resistance in the range from 100 to 5×10^6 cycles at and above room temperature showed that the decrease of resistance at higher frequency was observed on the sample No. 1 but not on No. 5. Lagrenaudie[16] also observes a dispersion of resistance at low temperature. More detailed experiment are in progress.

Morita[17] observed the optical properties of boron film produced by the evaporation of our sample, in visible and near infrared. He observed that the absorption edge lie at about 1 μ, corresponding to the activation energy of 1.2 eV. Lagrenaudie also observed the edge at about 1 μ, on the optical transmission and photoconductivity experiment. This optical properties may be inconsistent with the constancy of carrier concentration over wide temperature range except when the concentration is very large.

Recently a report of Shaw, Hudson and Danielson[18] appeared on the electrical properties of the single crystal of boron. Their result on the electrical conductivity is in good agreement with ours which is obtained from the experiment on the polycrhstalline specimens. This result suggests that the grain boundary of our specimens may not play a major role on the behavour of conductivity. It is also reported that the mobility of electrons and holes is 0.7 and 0.9 cm^2/volt sec respectively and that the effective mass calculated exceeds ten times that of the free electron and the mean free path is between one and one hundred minimum interatomic distance. Qualitatively, the results may not be inconsistent with our results which suggest a small mobility and a large effective mass.

Acknowledgement

The author is greately indebted to Mr. T. Irie of the Fuji Electrical Manufacturing Co. Ltd., who co-operated with him in this work. He is also indebted to Dr. K. Shinohara of our Laboratory, Prof. T. Muto and Assist. Prof. J. Yamashita of the University of Tokyo and Prof. I. Nitta of the Osaka University for valuable discussions and suggestions in connection with this work, and to Dr. K. Toishi and Mr. T. Yoshino for the spectroscopic analysis and to Prof. S. Yoshida of the Gakushuin University for X-ray analysis.

This work was supported by the Scientific Research Expenditure of the Ministry of Education.

References

1) T. S. Moss: Photoconductivity in the Elements, Butterworths Scie. Pub. London 1952 p. 78
2) E. Weintraub: J. Ind. Eng. Chem. **5** (1913) 106.
3) A. W. Laubengayer, D. T. Hurd, A. E. Newark and J. L. Hoard: J. Am. Chem. Soc. **65** (1953) 1924.
4) F. P. Henninger: Ann. Phys. Lpz. **28** (1937) 245.
5) J. Lagrenaudie: J. de Phys. et Rad **13** (1952) 354; ibid. 14 (1953) 14; ibid. **16** (1955) 731; and J. Chim. Phys. **50** (1953) 629.
6) H. L. Johnston, H. N. Hersh and E. C. Kerr: J. Am. Chem. Soc. **73** (1951) 1112.
7) R. Uno, T. Irie, S. Yoshida and K. Shinohara: J. of Scie. Res. Inst. **47** (1953) 216, and 223.
8) J. L. Hoard, S. Geller and R. E. Hughes: J. Am. Chem. Soc. **73** (1951) 1892.

9) V. A. Johnson and K. Lark-Horovitz: Phys. Rev. **92** (1953) 226.
10) E. C. Stoner: Phil. Mag. **21** (1956) 145.
11) F. Seitz: Phys. Rev. **73** (1938) 549.
12) G. K. Wehner; Phys. Rev. **93** (1954) 633.
13) F. J. Morin: Phys. Rev. **93** (1954) 1199.
14) J. L. Hoard: Nuclear Sci. Abst. 1954 488 (NYO-3945).
15) J. L. Hoard: Nuclear Sci. Abst. 1953 4615 (NYO-3944).
16) J. Lagrenaudie: J. de Phys et Rad. **16** (1955) 731.
17) N. Morita: J. Scie. Res. Inst **48** (1954) 8.
18) W. C. Shaw, D. E. Hudson, and G. C. Danielson: Nuclear Scie Abst. 1955 2788 (ISC-380); Phys. Rev. **107** (1957) 419.

JOURNAL OF THE PHYSICAL SOCIETY OF JAPAN Vol. 13, No. 7, JULY, 1958

Change of Oxygen Concentration with Temperature of the Nickel and Cobalt Oxide Solid Solutions

By Tamio SAKATA
Research Laboratory, Ohkura Electric Company, Tokyo
and Kimiko SAKATA
Institute of Science and Technology, University of Tokyo

(Received February 28, 1958)

The oxide solid solution MeO ($=n$ MiO$+m$ CoO) having a rock salt type structure is obtained; its lattice parameter varies with cation composition according to Vegard's law. The deviation from stoichiometry in MeO thus produced was found to be less than $10^{-2}\%$ (in excess of oxygen). Taking this well defined divalent oxide, MeO as a reference, change of oxygen concentration was studied as functions of both temperature and cation composition, with special reference to the correlation between the nature of the defects in oxides introduced by reaction with oxygen in air and the various physical and chemical properties which they exhibit. It turned out that the whole reaction process is divided into five distinct stages when the temperature is raised from room to higher temperatures. At the first and the second stages, surface and subsurface reactions predominate. The third stage is characterized by incorporation of gaseous oxygen into the lattice. The first step of incorporation takes place without change of crystal structure, resulting in formation of the oxide phase characterized by (1) having smaller unit cell dimension, (2) having random distribution of trivalent as well as divalent cations among the lattice sites and (3) having low activation energy for current carriers ($\sim$0.02 eV). The second step is the spinel formation, resulted from the more ordered re-arrangement of these cations. As the result, the activation energy increases to $\sim$0.1 eV. The fourth stage corresponds to transitional region in which the decomposition of the spinel into the rock salt type divalent oxide MeO occurs. The hysteresis is here appreciable in the reaction: oxide with spinel type structure $\rightleftarrows$ MeO. The reaction products at the fifth stage correspond to oxides with equilibrium *intrinsic defects* determined by the temperature and oxygen partial pressure of the atmosphere. Products of each reaction stage, without exception, proved to be p-type semiconductors.

§ 1. Introduction

The extensive studies of the semiconductive properties of oxides of iron group transition metals by C. Wagner and others[1),2)] led to the conclusions that in the nearly stoichiometric divalent oxide MeO, the lattice always carries cation defects due to the excess of oxygen and localized positive holes produced

as the result of the increasing valency, the configuration of which may well be more specifically described as:

$$(Me^{2+}_{1-3\delta},\ Me^{3+}_{2\delta},\ Hole_{\delta})O^{2-},$$

and that the positive hole conduction is accompanied by the exchange of the valence state of one cation with that of the neighbouring ones: $Me^{2+}+Me^{3+}\rightarrow Me^{3+}+Me^{2+}$. This concept has been clearly demonstrated in nickel oxide by the method of controlled valency[3], and in magnetite, Fe_3O_4, by the application of principle of dilution[3]. Moreover, a model has been proposed to explain the conduction in NiO and α-Fe_2O_3, taking the above concept into account[4),5)].

On the other hand, there still remain some difficulties in the experimental approach to the unified interpretation in case of the oxides of transition metals because of its intrinsic tendency of changing its valence quite easily. Thus, the semiconductive properties of the oxide are changed radically by the heat treatment as the result of the formation of oxide phases with varied oxygen composition (so called berthollide). In this connection, the systematic studies how the change of oxygen composition takes place with temperature in an oxide are required for the through understanding of the semiconductive properties of the oxide. We may well abreviate hereafter this reaction as oxide/oxygen reaction, because it is brought about by the reaction of the oxide with oxygen in the surrounding atmosphere.

We have studied this problem in cases of NiO, CoO and the oxide solid solution (4NiO+8CoO), the results proving to be quite instructive, because the physical and chemical behaviours of the same type of oxides with different cations against the same reaction were successfully compared here[6]. The present experiment was proposed, focusing an attention on the correlation between the lattice defects of the oxides and various physical and chemical properties in order to extend the results of the foregoing studies of oxide/oxygen reaction throughout the whole range of the mixing ratio of NiO and CoO. Specifically, we will take, in the following, a divalent oxide phase MeO as a reference, and will discuss the stoichiometric deviation of the products of MeO/oxygen reaction from it. Informations about such deviations may be supplied from conductivity measurements, upon the basis of above mentioned conduction mechanisum. In the present experiment, measurements of thermo electromotive force are also carried out in order to supplement the conductivity data.

§ 2. Preparation of Specimens

We have already established the procedure in obtaining the homogeneous oxide solid solution of nickel and cobalt, MeO ($=n$ NiO+m CoO), from their carbonates[6]. By the same method, series of the oxide solid solution are prepared with varying cation composition:

n	12	11	10	9	8	6	4	3	2	1	0
m	0	1	2	3	4	6	8	9	10	11	12
k*	0	8.34	16.7	25	33.2	50	66.8	75	83.3	91.7	100

* CoO percentage in divalent oxide, MeO.

The specimens are prepared from fine powder of these oxides, by mixing the material with lavender oil to a creamy consistency, spreading it in a film on a smooth mica plate, allowing the film to dry, cutting it into a desired size, pre-sintering it at 1000°C and finally being subjected to a heat treatment at 500°C during several hours. After the last treatment, a flake can be easily removed from the mica plate. The flake thus obtained is mounted upon free ends of four platinum wires of the stem shown in Fig. 1–a, using the above mentioned creamy mixture as a cement. Then, the flake attached to the stem, is subjected to heat treatment again after being allowed to dry, being sintered at 1200°C in air during 1 hour and finally being quenched rapidly. Throughout these procedures, the flake of specimen is well sintered—well annealed platinum wires (0.5 mm in diameter) never prevent the shrinking of the flake to take place—, at the same time, the platinum

wires are completely buried in the specimen, assuring its intimate contacts with oxide flake. The flake is made small in size and weight, so as to satisfy the necessary condition for the present experiment that an equiliblium of the oxide/oxygen reaction is readily established at a temperature within an appreciably short time and also that the state in question is easily frozen in by rapid quenching.

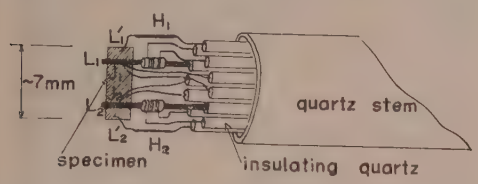

Fig. 1a. Specimen mounting and stem.

L_1, L_2 platinum wires (0.5 mm in diameter) serve as leads for measurements of resistivity and thermo electromotive force.

L_1', L_2' platinum wires (0.3 mm in diameter) serve as auxiliary leads for measurements.

H_1, H_2 small platinum heaters for temperature gradient along specimen.

J_1, J_2 Pt-PtRh couples for measurements of specimen temperature and temperature difference.

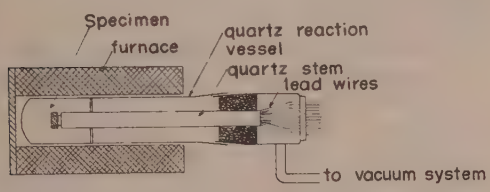

Fig. 1b. Setup of specimen and whole apparatus for investigation of oxide/oxygen reaction.

The setup of the specimen as well as the whole apparatus is given in Figs. 1a and 1b. The Pt-PtRh thermo-couples J_1 and J_2 are welded directly to the lead wires L_1 and L_2 respectively, so that the junctions are completely buried in the specimen. The small platinum heaters H_1 and H_2 produce a temperature gradient along the specimen for the measurement of thermo electromotive force. The auxiliary leads L_1' and L_2' are applied to the specimen in order to measure its resistivity by a potentiometer. All the contacts, however, were so intimate that the simple bridge method is applicable without any appreciable error.

The measurement of resistivity is carried out continuously throughout the treatments, which serves to indicate how the reaction is proceeding and what kind of product is obtained. Both measurements of the resistivity and thermo electromotive force can be carried out up to 1200°C under various surrounding atmospheres. The present report, however, concerns with the part of experiments carried out mainly in air, so in the following, if not specified, all experiments should be considered to be carried out in air.

§ 3. Oxide for Reference

We regard $MeO = n\,NiO + m\,CoO$, the divalent oxide, as stoichiometric oxide in the present system of the oxide solid solution and deal with the deviation from stoichiometry brought about through MeO/oxygen reaction. Nevertheless, the only one we can prepare is not such an ideal stoichiometric oxide but one with excess of oxygen deviating from stoichiometry, i.e., $Me_{1-\delta}O$ or more strictly $(Me^{2+}_{1-3\delta}Me^{3+}_{2\delta}Hole_{\delta})O^{2-}$.[7] We must, therefore, specify the nature of the reference state of an oxide more definitely.

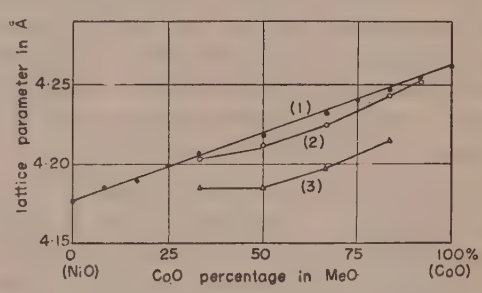

Fig. 2. Lattice parameter of oxides with rock salt type structure derived from the divalent oxide solid solution MeO ($=n\,NiO+m\,CoO$). abscissa: $m/(n+m)\times 100$.

(1) reference oxide satisfies Vegard's law.

(2) products at the third stage reaction have a shrinked unit cell.

(3) *over* shrinked oxide, coexisting with spinel type oxide.

As will be described in § 4, the specimen quenched after a heat treatment at 1200°C during 1 hour is identified with $Me_{1-\delta}O$, having a rock salt type structure irrespective of the previous history. δ cannot be determined analytically, but can be estimated to be less than 10^{-4} by comparing its resistivity with that of NiO with known amount of Li, i.e., $(Ni^{2+}_{1-2\delta}Ni^{3+}_{\delta}Li^{+}_{\delta})O^{2-}$. The cation composition in the oxide solid solution is accurate within 1 per cent. $Me_{1-\delta}O$ has a characteristic lattice parameter $a_{Me_{1-\delta}O}$ to each composition of com-

ponent oxides and is little affected by δ value so long as it remains within the order of magnitude mentioned above. It varies, however, with composition of component oxides satisfying Vegard's law:

$$a_{Me_{1-\delta}O}=\frac{n}{n+m}a_{NiO}+\frac{m}{n+m}a_{CoO}\,,$$

where $a_{NiO}=4.176$ Å and $a_{CoO}=4.262$ Å, as shown in Fig. 2. As the present experiment deals mainly with "large" variation in oxygen concentration and, furthermore, only the information about the direction in which oxide/oxygen reaction proceeds is important, the specification of the divalent oxides for reference just described will be quite sufficient.

§ 4. Procedure and Results of the Experiment

$Me_{1-\delta}O$/oxygen reaction is studied as a function of the temperature, observing the change in resistivity R and thermo electromotive force Θ. Three different ways of heat treatment are carried out for each of 11 different oxide solid solutions mentioned in § 2. We shall illustrate the procedures and results obtained in three typical cases of the oxide solid solution 4NiO+8NiO, CoO and NiO.

1) *Oxide solid solution* 4NiO+8CoO.

Heating process The temperature is raised gradually from room temperature to 1200°C, the formation temperature of $Me_{1-\delta}O$. The reference oxide has a high resistivity more than at least 10^8 ohm cm at the room temrerature, so that measurements cannot be made possible up to a certain temperature indicated as T_1 in Fig. 3. When the temperature is raised beyond T_1, the resistivity is at first, still high, but measurable, and is order of 10^6 ohm cm, then it decreases gradually. Thus a stationary $\log R-1/T$ relation is not obtainable in this region of temperature. It depends, not only upon the way how the measurement is made, but also upon the previous history.

An essential difference appears in the temperature region above T_2 in Fig. 3. If we observe the resistivity by fixing the temperature at any point above T_2, it decreases with time, and finally reaches a certain definite value within an accessible time. This fact indicates that a certain equilibrium exsist in the reaction $Me_{1-\delta}O$/oxygen above T_2. Thus, in reality, an definitely stationary $\log R-1/T$ (and $\Theta-1/T$) relation is obtainable, and it proves to be characteristic to the oxide solid solution. $\log R-1/T$ and $\Theta-1/T$ relations thus obtained are shown in Figs. 4 and 5, respectively.

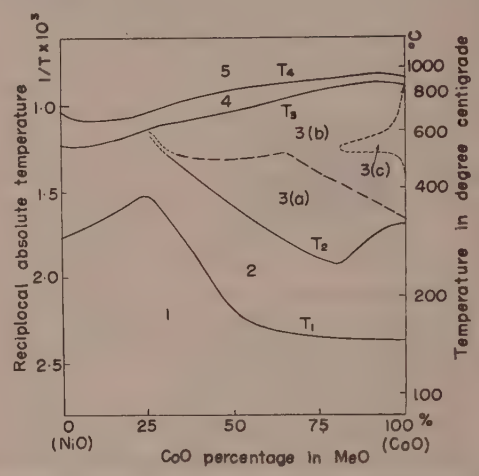

Fig. 3. Oxide/oxygen reaction in the oxide solid solution nNiO+mCoO proceeds with temperature. It can be divided into five temperature regions.
abscissa: $m/(n+m)\times 100$.
1: divalent oxide is metastable.
2: reaction proceeds at surface and subsurface of the oxide.
3: oxygen is incorporated into lattice.
(a) shrinked rock salt type oxide.
(b) spinel type oxide coexists with over shrinked rock salt type oxide.
(c) pure spinel oxide.
4: transition region for 3→5.
5: divalent oxide $Me_{1-\delta}O$ is stable, in which δ decreases with increasing temperature.

Sudden increases of resistivity and thermo electromotive force take place within a narrow temperature region from T_3 to T_4, thereafter they decrease with increasing temperarature. At this stage, the specimen returns back to its original divalent oxide phase, $Me_{1-\delta}O$.

The stationary $\log R-1/T$ and $\Theta-1/T$ relations shown in Figs. 4 and 5, respectively, are divided into two regions, namely, high temperature region and low temperature one, the discontinuity existing between T_3 and T_4.

Cooling process The temperature is lowered gradually from 1200°C, the formation temperature of the reference oxide, to room temperature. The stationary $\log R-1/T$ and $\Theta-1/T$

relations, in this process, are shown also in Figs. 4 and 5, respectively.

Comparing two stationary $\log R-1/T$ (and $\Theta-1/T$) relations of the heating and cooling processes, it is seen that the reaction is entirely reversible with respect to heating and cooling processes as far as the high temperature region is concerned. The sudden changes of resistivity and of thermo electromotive force are seen in both processes, but there is some difference in temperatures at which they occur.

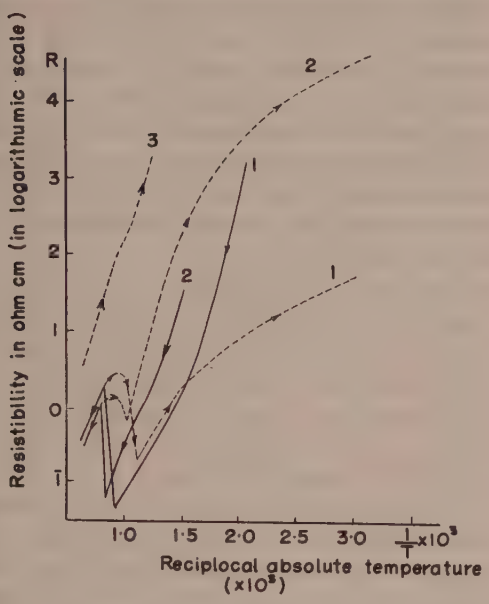

Fig. 4. Resistivity vs. temperature obtained in heating (solid line) and cooling (dotted line) process.
Reference oxides are:
1 oxide solid solution 4NiO+8CoO
2 CoO
3 NiO

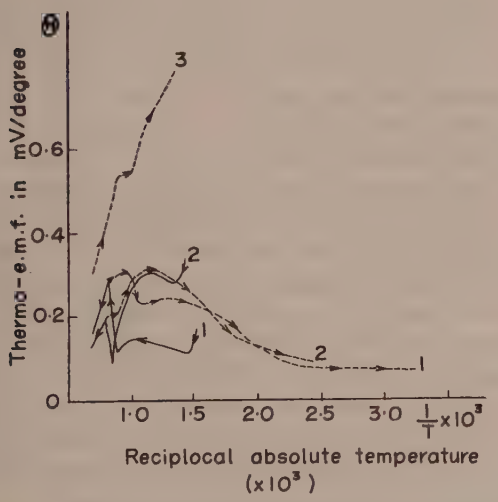

Fig. 5. Thermo e.m.f. vs. temperature obtained in heating (solid line) and cooling (dotted line) process.
Reference oxides are:
1 oxide solid solution 4NiO+8CoO
2 CoO
3 NiO

Quenching The equiliblium products at various temperatures are quenched from corresponding temperatures, defects being frozen in. Thus, the change in crystal structure with progress of the reaction is inferred from the results of the X-ray analysis of the quenched specimens. Results show that products corresponding to the higher temperature region of the stationary $\log R-1/T$ or $\Theta-1/T$ relations are identified with $Me_{1-\delta}O$, the reference state of the oxide itself, and, on the other hand, those obtained at the lower temperature region are, in the order of increasing temperature, as follows: (1) rock salt

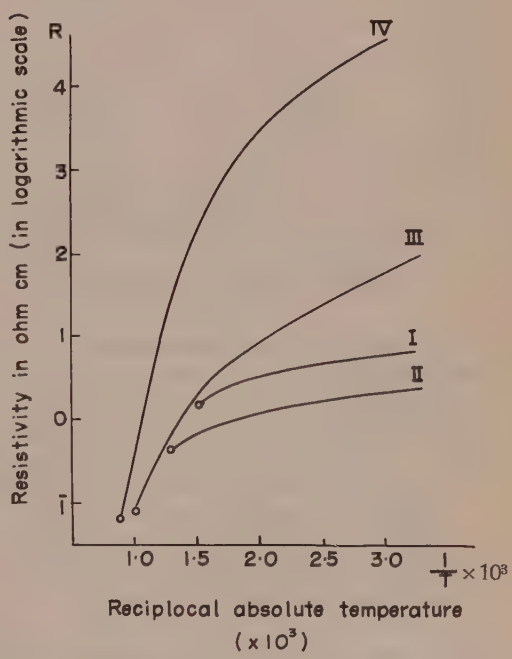

Fig. 6. The characteristic relations of resistivity vs. temperature for the 3rd. stage reaction products.
I, II: for $Me_{1-\delta}O$, shrinked rock salt type oxide.
III: for mixed oxide, in which one with spinel type predominates over one with shrinked rock salt type structure (reference oxide is solid solution 4NiO+8CoO).
IV: for the cobalt spinel oxide Co_3O_4 (reference oxide is CoO).

type oxide $Me_{1-\delta}O$, (2) rather amorphous oxide, (3) rock salt type oxide with shrinked unit cell compared with (1), (4) mixture of spinel type and shrinked rock salt type structure. The relative amount of oxygen increases from (1) to (4). The discontinuities in resistivity and thermo electromotive force are considered to result from the reaction: $(4) \rightleftarrows Me_{1-\delta}O$.

The $\log R-1/T$ and $\Theta-1/T$ relations for oxides (3) and (4) are measured in the temperature range between room and their formation temperatures. It is found out that these relations are independent of the direction of the temperature variation, indicating that these products are practically stable below their formation temperature. Some of the typical results are shown in Figs. 6 and 7 respectively.

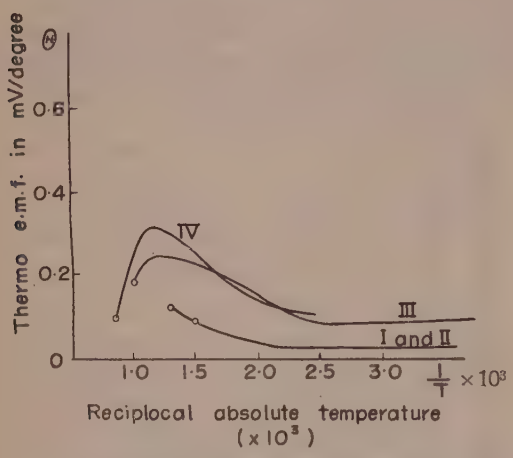

Fig. 7. The characteristic thermo e.m.f. *vs.* temperature relations for the 3rd. stage reaction products.

I, II: for $Me_{1-\delta}O$, shrinked rock salt type oxide.

III: for mixed oxide, in which one with spinel type predominates over one with shrinked rock salt type structure (reference oxide is oxide solid solution $4NiO+8CoO$).

IV: for the cobalt spinel oxide Co_3O_4 (reference oxide is CoO).

The curve III, the $\log R-1/T$ and $\Theta-1/T$ relations for the oxide (4) described above, coincides with one of the low temperature region of the stationary $\log R-1/T$ and $\Theta-1/T$ relations obtained in cooling process, respectively, so that we may conclude that even if the cooling was carried out very slowly, the reaction never proceeds reversibly at the temperature just below T_3 in Fig. 3. The product obtained in the slow cooling process is the mixed oxide (4).

2) *Pure cobalt oxide.*

The general behaviours are much the same with those described in the case of oxide solid solution $NiO+2CoO$. Only difference is the existence of a pure oxide with spinel type structure Co_3O_4. The $\log R-1/T$ and $\Theta-1/T$ curves for Co_3O_4 is shown in Figs. 6 and 7 respectively. The stationary $\log R-1/T$ and $\Theta-1/T$ relations for CoO/oxygen reaction obtained in the heating and the cooling process are shown in Figs. 4 and 5, respectively.

3) *Pure nickel oxide.*

In Ni-rich oxide solid solution, T_2 practically coincides with T_3 in Fig. 3. The reaction in narrow temperature region (T_3 to T_4) seems to correspond to the reaction: amorphous oxide $\rightleftarrows$ reference oxide, $Ni_{1-\delta}O$.

§5. Oxide/Oxygen Reaction

It follows from the foregoing experimental results that the progress of the $Me_{1-\delta}O$/oxygen reaction with increasing temperature can be divided into five distinct stages. Their temperature regions are shown in Fig. 3.

The first stage The divalent oxide shows no measurable change. We can tell nothing about this stage except that the resistivity is more than 10^8 ohm cm. Very likely, oxygen is adsorbed on the oxide surface.

The second stage No change in the crystal structure and the lattice parameter is detectable. The resistivity, however, decreases markedly to the order of 10^3 ohm cm. The reaction does not attain any definite equilibrium within finite period of time. The surface geometry and the initial δ value in the divalent oxide affects largely the reaction in this stage, so that no stationary resistivity and thermo electromotive force can be obtained, in the heating process. The reaction, moreover, seems to be fairly reversible. It is likely that the incorporation of oxygen in the reaction is taking place mainly at the oxide surface. The conductivity may principally due to the migration of charges through grain boundaries.

The third stage The interior of the oxide begins to take part in the reaction. An equilibrium state at a temperature, say T_a, is frozen in below this temperature. Therefore, $\log R-1/T$ and $\Theta-1/T$ relations which may considered to be characteristic of the reaction

product at T_a, are obtained in temperature region below its formation temperature, i.e. T_a. Some of such characteristic curves, are shown in Figs. 6 and 7 respectively. We may express the reaction product at this stage as $Me_{1-\varepsilon}O$, in order to distinguish it from a reference oxide, where ε measures a "large" deviation compared with δ. ε almost tends to the value corresponding to the composition in the oxide with spinel type structure. The crystal structure is still of rock salt type, but the lattice parameter decreases markedly with the progress of the reaction. The parallel relation between decrease of lattice parameter and increase in conductivity is much the same as is found in NiO substituted by known amount of Li atom, i.e., $(Ni^{2+}_{1-2\delta}Ni^{3+}_{\delta}Li^{+}_{\delta})O^{2-}$, where it is believed that the addition of Li^+ into the lattice results the formation of Ni^{3+} at normal cation site. The unit cell contracts owing to the difference in ionic radius between Ni^{2+} and Ni^{3+}, while the resistivity decreases in proportion to the amount of Li^+ incorporated into the lattice, or Ni^{3+} induced. In $Me_{1-\varepsilon}O$ the excess oxygen introduces cation vacancies and simultaneously cation sites trapping positive hole in the neibourhood of these vacancies, the structure being

$$(Me^{2+}_{1-3\varepsilon}Me^{3+}_{2\varepsilon}Hole_{\varepsilon})O^{2-}\ .$$

Therefore, number of trivalent cations is comparable with that of divalent cations. With increasing number of trivalent cations, the interaction between defects becomes more appreciable and at last the rearrangement of cations will take place, resulting in the oxide with spinel type structure:

rock salt type oxide with shrinked unit cell $\rightarrow$oxide with spinel type structure.

The transformation seems, in some respects, to be cooperative. The oxide with *over* shrinked rock salt type structure, however, can still coexist with spinel structure except in case of Co-rich oxide solid solution. The lattice parameter of the oxide with shrinked rock salt type structure is shown in Fig. 2 for the comparison with that of reference oxide. The rather smooth change of the stationary $\log R-1/T$ and $\Theta-1/T$ relations which are obtainable in the heating process, may be responsible for the existence of mixed oxide phase (oxide with spinel type and one with over shrinked rock salt type, the former becoming predominant with increasing temperature).

On the other hand, between the characteristic $\log R-1/T$ and $\Theta-1/T$ relations for the oxide with shrinked rock salt type and those for the mixed oxide in which one with spinal type structuture is predominant, there appears marked differences. Curves in Figs. 6 and 7 show the $\log R-1/T$ and $\Theta-1/T$ relations for such products obtained in the case of oxide solid solution 4NiO+8CoO and for Co_3O_4, the pure spinel type oxide, from which we can derive following results:

products	composition in solid solution from which products were derived	resistivity* (ohm cm)	ionization energy (eV)	thermo e.m.f.* (mV/°C)
oxide with shrinked rock salt type structure: $Me_{1-\varepsilon}O$	(4NiO+8CoO)	$3\cdot10^0$ $8\cdot10^0$	0.02 0.02	0.03 0.03
mixed oxide in which one with spinel type is predominant over one with rock salt type structure: spinel+$Me_{1-\varepsilon}O$	(4NiO+8CoO)	$7\cdot10^2$	0.1	0.09
pure spinel type oxide: Co_3O_4	CoO	$8\cdot10^4$	0.1	0.1

* at room temperature.

The $\log R-1/T$ relations in Fig. 6 for two products with shrinked rock salt type structure show the parallel displacement, indicating the difference in defect concentration in both cases, and at the same time the existence of definite low ionization energy of the current carrier ($\sim$0.02 eV). These results are consistent with that obtained from $\Theta-1/T$ relations in Fig. 7. On the other hand, the spinel rich oxide has a much more enhanced activa-

tion energy (~0.1 eV) and much higher resistivity. Comparing the $\log R-1/T$ and $\Theta-1/T$ relations for the spinel rich oxide derived from solid solution 4NiO+8CoO with those for the pure spinel type cobalt oxide, Co_3O_4, it is seen that the activation energy is rather insensitive to the cation composition. This fact suggests a somewhat regular local arrangement of cations in the spinel structure: octahedral sites may be preferentially occupied by cobalt ions and the conduction takes place through them as is believed to be the case in the magnetic spinel, Fe_3O_4.

This stage may be sub-divided into three temperature regions a, b and c as shown in Fig. 3, each of which corresponding mainly to following products:

3 (a) shrinked rock salt type oxide $Me_{1-\varepsilon}O$,
3 (b) mixed oxide of $Me_{1-\varepsilon}O$ with the spinel type oxide, the latter becoming predominant with increasing temperature,
3 (c) the pure spinel oxide.

The fourth stage There is a critical temperature for the oxides with *over* shrinked rock salt type and spinel type structure to be stable. Both of them, sustaining comparable number of trivalent and divalent cations, decompose into the divalent oxide with normal rock salt type structure, $Me_{1-\delta}O$, which is essentially the reference oxide itself. Surprisingly, when the decomposition takes place under low oxygen partial pressure, which is still high compared with dissociation pressure of cooresponding MeO, the oxide is readily reduced to a metal or a metallic alloy. As stated already in § 4, the discontinuity of the stationary $\log R-1/T$ and $\Theta-1/T$ relations which are obtainable in the course of heating and cooling processes, appears as the result of this decomposition.

The fifth stage The reaction at this stage proceeds with increasing temperature towards the desorption of oxygen. $Me_{1-\delta}O$ approaches the nearer to the ideal stoichiometry the more higher the temperature is raised. δ remains always positive and is a definite function of temperature, oxygen partial pressure and cation composition. This stage may be regarded as the *intrinsic defective* state referring to the above condition.

§ 6. Conclusion

In higher temperature region than T_3 (cf. Fig. 3), NiO and CoO form an homogeneous divalent oxide solid solution with rock salt type structure over whole range of component oxide composition. It has an inherent tendency to be a non-stoichiometric oxide with excess oxygen and may be expressed as $Me_{1-\delta}O$, in which δ never exceeds at least 10^{-4} and decreases with increasing temperature.

Provided the experimental conditions are suitably chosen, $Me_{1-\delta}O$/oxygen reaction equilibrium can be attained in the bulk of the oxide within an accessible time in temperature region between T_2 and T_3.

In the range of component oxide composition from 75% NiO to 100% NiO, general behaviour of $Me_{1-\delta}O$/oxygen reaction is found to be NiO-*like*, that is, the rock salt type structure of $Me_{1-\delta}O$ remains stable in temperature region lower than T_3.

On the other hand, CoO-*like* character may be taken to be a tendency to transform into the homogeneous oxide phase with spinel type structure Co_3O_4 through CoO/oxygen reaction taking place in temperature region lower than T_3.

In the range of component oxide composition from 25% CoO to 100% CoO, behaviours of the oxide solid solution are such that CoO-*like* character is modified continuously by incorporation of NiO, or *vice versa*. The spinel formation is suppressed to some degree by incorporation of NiO, while the affinity with gaseous oxygen is promoted by incorporation of CoO. Thus the third oxide phase, $Me_{1-\varepsilon}O$ appears, where $\varepsilon \gg \delta$.

The crystal form of $Me_{1-\varepsilon}O$ is mainly affected by NiO-*like* character. On the other hand, oxygen content in it is already comparable with that corresponding to the spinel type oxide. Thus, in this phase, number of trivalent cation is comparable with that of divalent and these cations are randomly distributed among crystallographically equivalent cation sites in the rock salt type oxide. It is pointed out that the unit cell dimension, here, is appreciably smaller than in the divalent oxide, $Me_{1-\delta}O$. The spinel formation from this phase may be considered as the result of ordered rearrangement of these cations.

In the present oxide system, the temperature region in which the third stage reaction proceeds, i.e., the temperature region from

T_2 to T_3 is rather narrow, so that the oxide phase $Me_{1-\delta}O$ never developes to bring about the oxide Me_2O_3, in which all cations are in trivalent state. Throughout all of three oxide phase mentioned above, number of trivalent cation is always less than number of divalent cation, and *p*-type semiconduction is predominant. On the other hand, in cases of iron or manganese oxides, a temperature corresponding to T_3 might be much higher. Thus the oxides such as Fe_2O_3 or Mn_2O_3 are really stable. It is interesting to note that in such oxides *n*-type conduction is sometimes produced[4),6)]. This difference which appears in $Me_{1-\delta}O$ phase is due to difference in the relative stability of divalent cations of transition elements in $Me_{1-\delta}O$ phase.

In case of transition elements, it must be noted that the reaction product depends largely upon the valence state of transition element in the reactant. Thus, for example, such oxides as Ni_2O_3 or Co_2O_3 never appear in the present experiment, although they are sometimes cited in chemical literatures.

Acknowledgement

We should like to express our sincere thanks to Prof. Y. Kakiuchi of Institute for Solid State Physics, University of Tokyo, for his continual guidance.

References

1) H. H. von. Baumbach and C. Wagner: Z. Physik. Chem., (B) **24** (1934) 59.
2) C. Wagner and E. Koch: Z. physik. Chem., (B) **32** (1936) 449.
3) E. J. W. Verwey, P. W. Haaijman, F. C. Romeijn and G. W. van. Oosterhout: Philips Research Reports, **5** (1950) 173.
4) F. J. Morin: Phys. Rev., **93** (1954) 1195.
5) F. J. Morin: Phys. Rev., **93** (1954) 1199.
6) T. Sakata, K. Sakata and K. Kigoshi: J. Phys. Soc. Japan., **10** (1955) 179.
7) A. L. G. Rees: Chemistry of the Defect Solid State, 1954.

JOURNAL OF THE PHYSICAL SOCIETY OF JAPAN Vol 13, No. 7, JULY, 1958

Paramagnetic Effect in Superconductors. Part I. Quasi-Paramagnetism and Resistance of Indium at the Superconducting Transition

Yoshio SHIBUYA

The Research Institute for Iron, Steel and Other Metals, Tohoku University, Sendai

(Received January 8, 1958)

As a continuation of the previous investigation on the paramagnetic effect in tin we have investigated the same effect in indium. The minimum of current I_0 necessary for the occurrence of the paramagnetic effect has been represented by the same functions of the temperature T and the maximum of external magnetic field H_0, beyond which we cannot observe the quasi-paramagnetism at that temperature, as in the case of tin i.e. $I_0=\xi\gamma d(T_c-T)$ and $H_0=\xi(T_c-T)-I_g/\gamma d$. Here I_g, ξ and T_c are characteristic constants of the superconductor and have values 0.6 amp., 94.4 oersted/deg. and 3.422°K respectively for the case of indium: γ is 0.27 amp./mm. oe. The maximum of external magnetic field H_0 and the specimen diameter d are measured in oersted and in mm. respectively. These formulas are understood in a good approximation as those for the intersection of the plane $I=I_g+\gamma dH$ with the transition surface in the $(I-H-T)$ space. In parallel with the measurement of the magnetic flux, plotted as a function of the current at constant temperature and external magnetic field, a measurement of the resistance of the same specimen has been performed. The results obtained are in good accordance with an expression derived in a modified form from the theory proposed by H. Meissner.

§ 1. Introduction

A superconductor through which an electric current flows in the presence of an external magnetic field shows a remarkable quasi-paramagnetism preceding the change to perfect diamagnetism, which is well-known now as the so-called paramagnetic effect in superconductors.[1] In the previous papers[2] we reported the experimental results of the paramagnetic effect in tin. In these reports we confirmed that the paramagnetic effect was not an apparent but an intrinsic one observed, irrespective of the measuring procedure, and claimed that the minimum of current required for the occurrence of the paramagnetic effect should be determined in the $(I-H-T)$ space, instead of merely on the $(I-H)$ plane as formerely proposed, where I, H and T were the current supplied, the external magnetic field and the temperature respectively.

H. Meissner formulated a theory of the paramagnetic effect[3] at about the same time of the publication of the paper I, basing upon the idea[4] that in the intermediate state the specimen current following a helical pat so as to connect the oblong superconductin grains oriented along the resultant field H (the vector sum of external field H and cur rent field H_I) produced a longitudinal flu greater than that due to the external field According to H. Meissner, the maximum o quasi-paramagnetism, e.g. at constant exter nal magnetic field and temperature, occur when the resultant field H_t is equal to th critical field H_c at that temperature. Ou previous result (the paper II) did not, how ever, agree with this prediction. Afterward H. Meissner gave a detailed analysis on ou experimental result (the paper II) and claim ed that our result substantiated rather tha invalidated his theory.[5]

In order to confirm this point we perform ed measurements on the paramagnetic effec in solid circular indium cylinders. Furthe the resistance measurement was though quite important for the understanding of th nature of the paramagnetic effect. Never theless it seemed that the simultaneou measurement of the resistance and the mag

netic flux was hitherto very scanty except those of W. Meissner and R. Doll[6] and of A. Sellmaier[7]. No quantitative analysis of the experimental result was, however, given in these investigations. Basing upon H. Meissner's theory, we have derived an expression for the resistance as a function of current at constant magnetic field and temperature. In order to compare this result with the experiment we performed the resistance measurement in parallel with the magnetic flux measurement.

In course of the present investigation it came to our notice that J. C. Thompson who obtained the same expression as ours for the resistance as a function of current at constant field and temperature, obtained, moreover, an analytical expression for the apparent permeability as a function of current at constant field and temperature.[8] Our result of magnetic measurement was compared with the expression for the apparent permeability derived by J. C. Thompson.

Special care was taken in the determination of the temperature within the specimen throughout the present investigation.

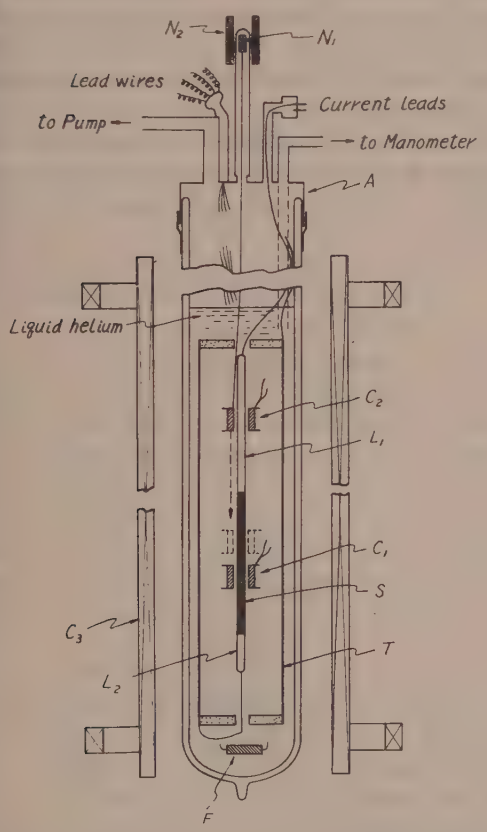

Fig. 1. Schematic diagram of the experimental apparatus. The outer Dewar vessel for containing liquid nitrogen and two pairs of large Helmholtz coils of square-type for nullifying the earth magnetic field are not shown.

§ 2. Experimental Details

The experimental apparatus used in this investigation is for the most part the same as used previously[2] except two pairs of large Helmholtz coils of square-type located perpendicularly to each other in place of the Helmholtz coils previously used and a thin walled, slotted copper tube used as the return current lead in place of the cylindrical copper mesh. The experimental apparatus is shown schematically in Fig. 1. A circular indium cylinder S and circular copper cylinders L_1 and L_2 of about the same diameter as that of S, soldered together with Wood's metal at the upper and the lower end of S, are placed in a uniform, external, longitudinal, magnetic field, and an externally supplied electric current flows down or up through them.

The magnetization of the specimens was measured with the use of a ballistic-type galvanometer which had a period of 13 sec. We employed mainly the so-to-speak dynamic method* of holding T constant throughout, taking H as a parameter and I as a variable which was changed in small steps: at each step the galvanometer deflection was measured when H was reversed. A search coil C_1 was fixed around the center of the specimen, and a compensating coil C_2 connected in opposition to C_1 was fixed in a uniform magnetic field, around a copper lead at a position sufficiently far from the specimen. The difference in the magnetic flux through two coils C_1 and C_2 induced a current in the ballistic-type galvanometer circuit, when the external magnetic field H was reversed. Two coils C_1 and C_2 have nearly the same structure. We confirmed also the intrinsic nature of the paramagnetic effect in indium

* We are indebted to H. Meissner who recommended us this dynamic procedure in place of the dynamic one, previously adopted, of holding T constant throughout, taking I as a parameter, and reversing H which was taken as a variable and changed in small steps. The latter procedure might yield some inaccuracy in the measurement in small magnetic field.

by the static method of measurement reported previously.

The thin-walled, slotted copper tube T surrounding the specimen concentrically is used as the return current lead in order to nullify the magnetic field around the specimen due to the return current. The P.V.F. wire-wound solenoid system C_3 is the same as used previously. The earth magnetic field was cancelled with two pairs of large Helmholtz coils of square-type located perpendicularly to each other (one horizontally, the other vertically) which were not shown in Fig. 1 for spatial reasons. A small heater F is placed in the bottom of the helium column. The manostat previously reported[2] was used to fix the helium vapour pressure to within 0.2 mm H_g. The helium vapour pressure was measured with a mercury manometer. The temperature within the specimen was determined together by vapour pressure thermometry using the 1948 Mond Laboratory Tables and by taking the liquid helium column head into consideration. The determination of the liquid helium column head was performed as follows. Observing the liquid helium levels at the beginning and at the end of the measurement at a given temperature, we determined the mean liquid helium level during the measurement at that tem perature and defined the mean liquid heliu column head by the distance of the mea liquid helium level from the specimen-centr The lowering of the liquid level during on run of measurements at a given temperatur was, generally speaking, considerable an sometimes amounted to about 10 cm, whe the level was high i.e. it lay near the liqui helium Dewar cap A in Fig. 1, but it becam 3~4 cm when the level lay far below the ca A. The helium vapour pressure above th liquid helium and the liquid helium colum head thus determined served to determin the true temperature within the specimen.

The indium specimens were prepared fro Johnson-Matthey spectroscopically pure indiu (>99.99% I_n). They were cast in vacuo i glass tubes and then drawn to the require diameter. After cutting the specimen t about 80 mm long, the specimen was seale in a evacuated glass tube and annealed a 100°C for several hours. Although the melt ing point of indium was relatively low (abou 156°C) and the room temperature annealin would be sufficient for indium, the annealin process above mentioned was performed b way of precaution. The specimen No. 1 wa 2.38 mm in diameter and about 80 mm i

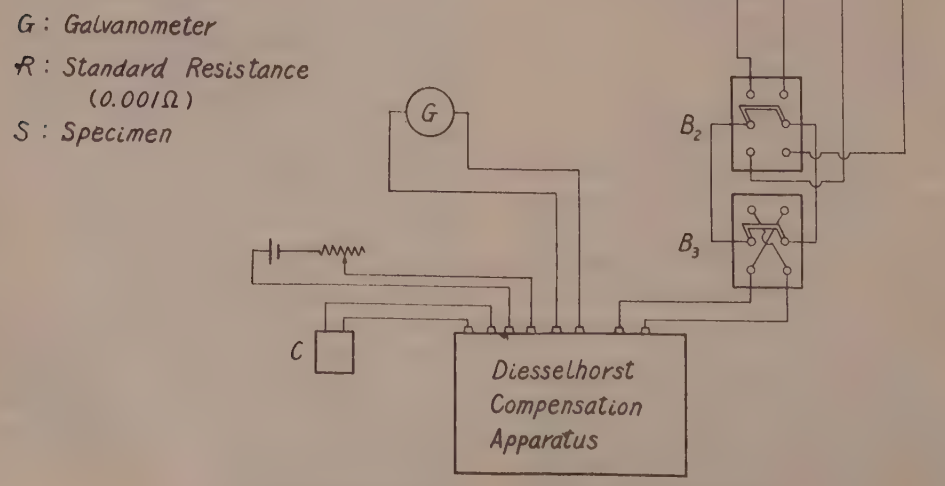

Fig. 2. Potentiometer circuit for measuring resistance.

length, and No. 2 was 1.63 mm in diameter and about 75 mm in length. Both specimens showed the same critical temperature 3.422 °K.

The resistance measurement was performed only with the specimen No. 2 by the use of a Diesselhorst compensation apparatus which ensured to measure such a small potential difference as 10^{-8} V. The galvanometer used for the resistance measurement had a voltage sensitivity of 3×10^{-8}V. Two BS# 38 enamelled wires soldered with Wood's metal to the specimen No. 2 near its both ends were used as the potential probes. The potentiometer circuit for measuring the resistance is shown in Fig. 2.

The parallel measurement of the magnetic flux and the resistance was carried out in such a way as follows. After measuring the potential drop between two potential probes for a certain value of I at constant values of H and T, we observed the ballistic deflection of the galvanometer caused by the reversal of H. Then I was somewhat increased while H and T were kept constant, and the same procedure was repeated. This procedure started with $I=0$ and ended with such a large current as 15 amp. The current I was increased by about 1 amp. except near the current I^* where the maximum of quasi-paramagnetism occurred. The current increase was made in smaller steps near I^*.

The method employed for finding the critical field H_c consisted in raising the field steadily and watching for signs from the search coil that flux was entering the specimen as the superconducting phase collapsed. This method was sometimes supplemented by the method of determining H_c from the magnetization curve of the specimen obtained by reversing H. We observed supercooling of some degree in both specimens.

§ 3. Experimental Results

1. The determination, in the $(I-H-T)$ space, of the minimum of current I_0 required for the occurrence of the paramagnetic effect.

In the magnetic flux measurement for this purpose we employed the dynamic method described above. Typical examples of results obtained with the specimens Nos. 1 and 2 are shown in Figs. 3 and 4 respectively. a/b shown in the inset of Fig. 3 or Fig. 4 gives the apparent permeability μ, which is a function of I only, provided H and T are constant. μ^* which designated the maximum of μ for

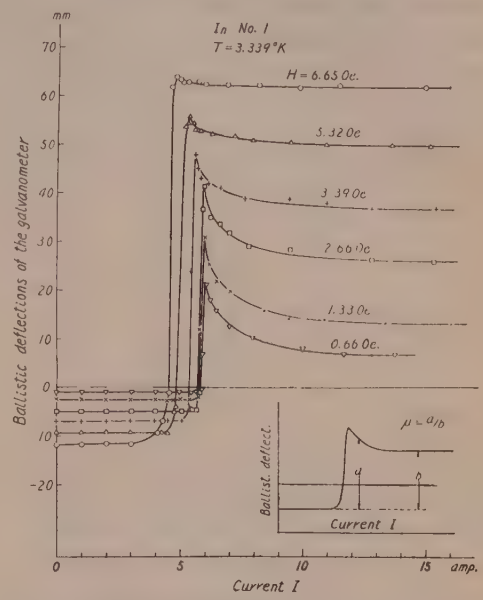

Fig. 3. Ballistic deflections of the galvanometer for No. 1 specimen as a function of current I for the specified values of magnetic field H, when H was reversed. a/b shown in the inset defines the apparent permeability μ.

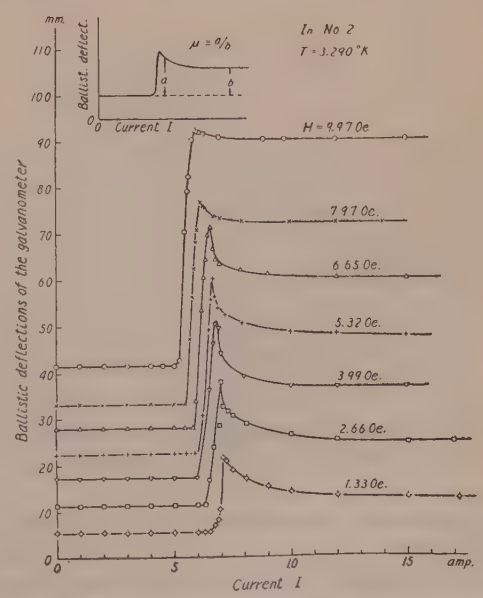

Fig. 4. Ballistic deflections of the galvanometer for No. 2 specimen as a function of current I for specified values of magnetic field H, when H was reversed. a/b shown in the inset gives the apparent permeability μ.

fixed values of H and T and plotted against I^* where μ^* occurred, and the extrapolation to the abscissa where $\mu^*=1$ defined the minimum of current I_0 at that temperature. I_0 changed with temperature and there was a one-to-one correspondence between I_0 and T. Figs. 5 and 6 show these extrapolations at

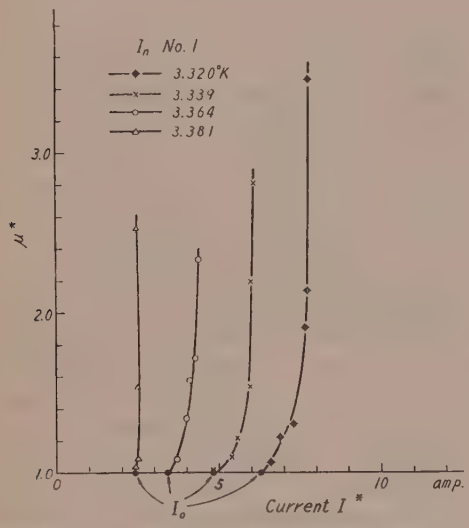

Fig. 5. μ^* for No. 1 specimen as a function of current I^* at the specified temperatures.

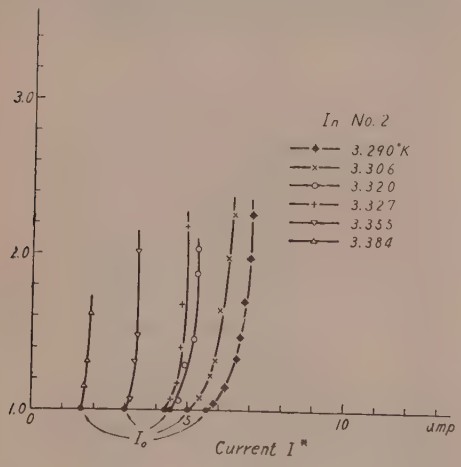

Fig. 6. μ^* for No. 2 specimen as a function of current I^* at the specified temperatures.

the specified temperatures for the specimens Nos. 1 and 2 respectively. From Figs. 5 and 6 we obtained the I_0-T relations for two specimens. In a similar way we plotted μ^* against H and obtained H_0, the maximum of magnetic field over which we could not observe the quasi-paramagnetism at a given temperature, by the extrapolation of μ^* to

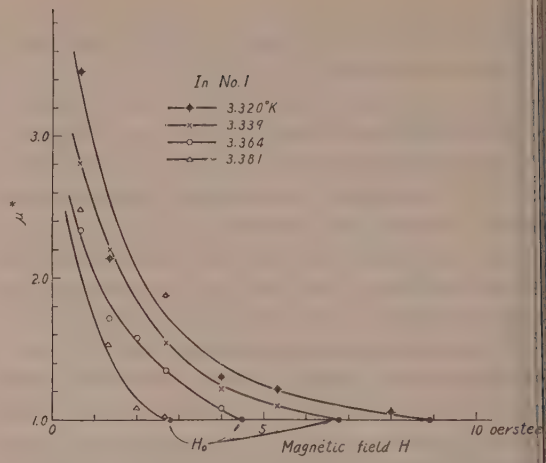

Fig. 7. μ^* for No. 1 specimen as a function of external magnetic field H at the specified temperatures.

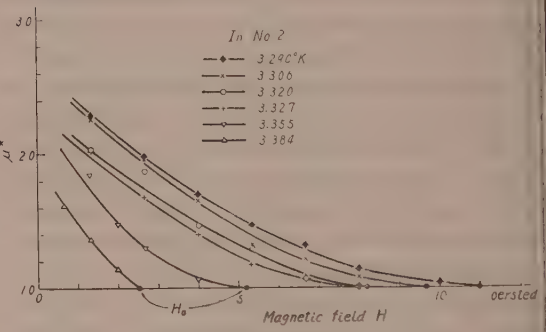

Fig. 8. μ^* for No. 2 specimen as a function of external magnetic field H at the specified temperatures.

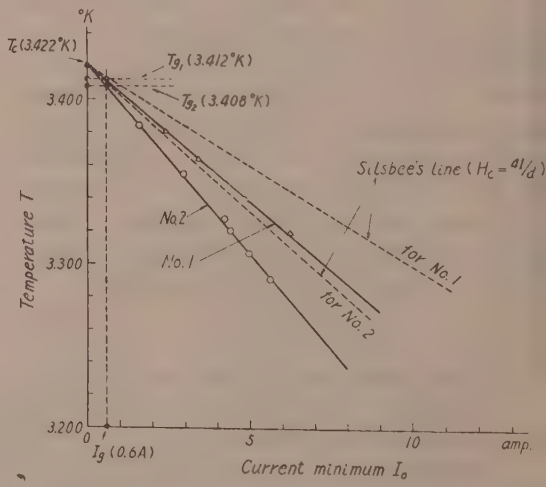

Fig. 9. I_0-T relations for the specimens Nos. 1 and 2.

the abscissa (Figs. 7 and 8). There was also a one-to-one correspondence between H_0 and T. Thus we obtained the H_0-T relations.

Further we obtained the I_0-H_0 relations for two specimens from Figs. 5, 6, 7 and 8. The I_0-T, the H_0-T and the I_0-H_0 relations thus obtained for two specimens are shown as straight lines at least in the measured region in Figs. 9, 10 and 11 respectively.

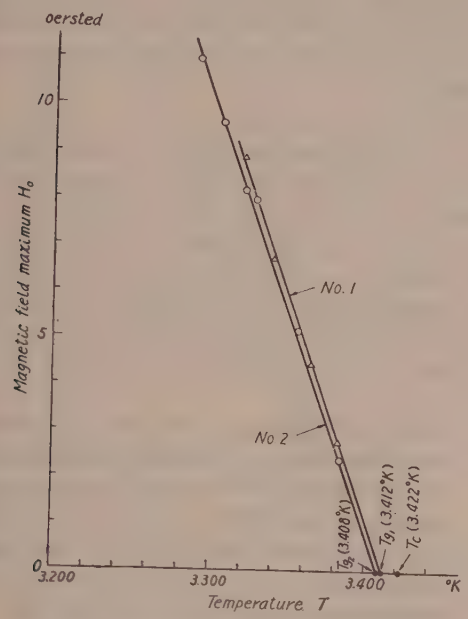

Fig. 10. H_0-T relations for two specimens.

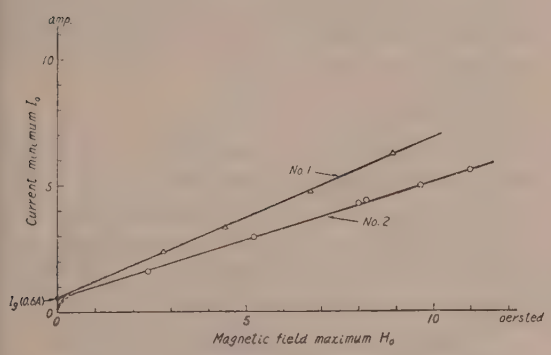

Fig. 11. I_0-H_0 relations for two specimens.

Just as in the case of tin, it was ascertained that the formula for the minimum of current required for the appearance of the paramagnetic effect was represented graphically by a straight line (the critical line) in the $(I-H-T)$ space, the orthogonal projections on the $(I-T)$, the $(H-T)$ and the $(I-H)$ plane of which are the straight lines shown in Figs. 9, 10 and 11 respectively.

The $(I-T)$ projections having inclinations, proportional to the specimen diameter d, to the T-axis point to the transition temperature T_c. The $(H-T)$ projections are approximately parallel to each other and T_c-T_g is inversely proportional to d, where T_g is the intersection of the projection with the T-axis (Fig. 12). The $(I-H)$ projections have inclinations, proportional to d, to the H-axis but intersect with the I-axis at a definite value of current I_g, irrespective of the specimen-diameter. Thus the critical lines terminate at the point (I_g, T_g) on the $(I-T)$ plane.

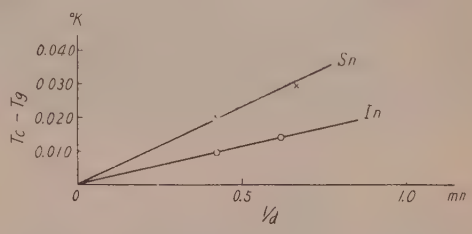

Fig. 12. Proportionality of T_c-T_g to the reciprocal of specimen diameter, $1/d$. The straight line for tin was drawn by using data obtained previously (the paper II).

In a similar way to the case of tin we obtained as the formulas for the $(I-T)$, the $(H-T)$ and the $(I-H)$ projection which satisfied those relations described above the following three equations (1), (2) and (3) respectively.

$$I_0=\xi\gamma d(T_c-T), \tag{1}$$

$$H_0=\xi(T_c-T)-I_g/\gamma d, \tag{2}$$

$$I_0=I_g+\gamma dH_0\,. \tag{3}$$

Here ξ, T_c and I_g are the characteristic constants of the superconductor. The value of γ which was believed formerly to be also a characteristic constant of the superconductor was found to scatter widely according to the recent measurement.[9] This may be mainly due to the fact that μ^* in Figs. 7 or 8 is a slowly varying function of H. It cannot be decided at the present stage of investigation whether γ is a characteristic constant of the superconductor, a constant originated merely from the circular nature of the specimen cross-section or a quantity depending upon the condition of the specimen surface. The numerical values of ξ, T_c, I_g and γ for two specimens are tabulated in Table I. Averaging the values for two specimens, we decided that $\xi=94.4$ oersteds/deg., $T_c=3.422$°K, $I_g=0.6$ amp. and $\gamma=0.27$ amp./mm. oerst. for indium. Of three equations (1), (2) and (3)

Table I. Numerical values of constants which appear in the formulas for the minimum of current I_0 for indium cylinders.

$$I_0=\xi\gamma d(T_c-T),$$
$$H_0=\xi(T_c-T)-I_g/\gamma d,$$
$$I_0=I_g+\gamma dH_0.$$

	In. No. 1 (2.38 mm ϕ / 80 mm l)	In. No. 2 (1.63 mm ϕ / 75 mm l)	Mean value
I_g (amp.)	0.6	0.6	0.6
ξ (oerst./deg.)	95.5	93.2	94.4
γ (amp./mm. oerst.)	0.26	0.28	0.27
T_c (°K)	3.422	3.422	3.422
[T_g (°K)]	3.412	3.408	

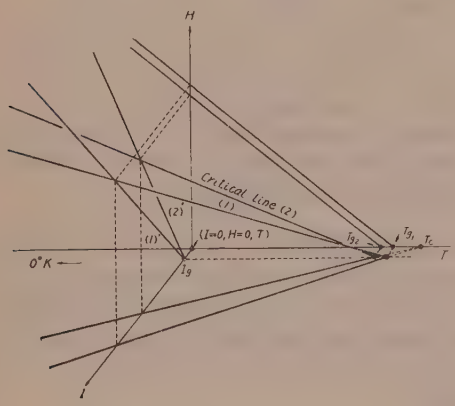

Fig. 13. Critical lines (lines of current minimum) for two specimens in the $(I-H-T)$ space. The $(I-H)$ projections (1)′ and (2)′ of the critical lines are represented well by Eq. (3) in the text which is analogous to the equation obtained by Meissner *et al* i.e. $I_0=I_g+\gamma dH$.

only arbitrary two equations are independent and the critical line in the $(I-H-T)$ space is represented by the simultaneous equations of the two. Fig. 13 shows schematically the critical lines for two specimens in the $(I-H-T)$ space. The quasi-paramagnetism can be observed only in the region of larger I and smaller H at each temperature than those given by the critical line. Eq. (3) coincides formally with formula $I_0=I_g+\gamma dH$, obtained by Meissner *et al.* T_g which does not appear explicitly in the above equations is given by $T_c-I_g/\xi\gamma d$.

It should be emphasized that such a somewhat systematic structure in the apparent permeability-curve as reported in the previous report (Fig. 16 in the paper II.) could not be observed throughout this investigation. The existence of such a structure in the μ-curve as found previously seems now to us to be apparent. Furthermore we could not obtain in this investigation such closed contours as found in the previous report (Fig. 17 in the paper II.). These results formerly obtained might be spurious and be attributed to the experimental procedure formerly adopted.

Although the extension of the I_0-T relation to the absolute zero of temperature would not be permissible, it seems, in a similar way to the case of tin, from this extension that there is a lower limit of specimen diameter, d_0 for the appearance of the paramagnetic effect. This limit can be deduced from the equation $I_g=\xi\gamma d_0T_c$. For the case of indium, d_0 becomes 6.9×10^{-3} mm.

2. The verification of the theory which predicts that the apparent permeability-maximum μ^* at a given temperature occurs at the point where the resultant magnetic field $H_t[=(H^2+H_I^2)^{1/2}]$ equals the critical field H_c at that temperature.

As the previous report II suffered critism in regard to this problem[5], we tried to confirm the prediction in this investigation. In Fig. 14 the resultant field

$$H_t[=(H^2+H_I{}^{*2})^{1/2}=(H^2+(4I^*/d)^2)^{1/2}]$$

at the surface of the specimen No. 2 for several temperatures, obtained at the point where μ^* occurred were compared with the critical field H_c. As can be seen in Fig. 14, most of measured points lie below the threshold curve $H_c=136(T_c-T)$ i.e.

$$H_t=[H^2+(4I^*/d)^2]^{1/2}<H_c(T).$$

Denoting provisionally H_t for the maximum of quasi-paramagnetism at a fixed temperature by $H_c{}^*(I^*,T)$ (the effective critical field),

$$H_c{}^*(I^*,T)<H_c(T).$$

However, we found the general trend that $H_c{}^*$ at a fixed temperature approached H_c with the decrease of current I^*, and $H_c{}^*$ at the point (I_0, H_0) lay nearly on the H_c-curve. This situation can be seen more cleary in Fig. 15, where the orthogonal projections, on the $(I-H)$ plane, of the intersections (the Silsbee's lines), for several temperatures, of

the planes T=const. with the transition surface $[H^2+(4I/d)^2]^{1/2}=H_c(T)$ are shown together with the μ^*-lines for the corresponding temperatures. It can be said that H_c^* at the point (I_0, H_0) coincides nearly with H_c in accordance with the theory proposed by H. Meissner. This point will be touched again in the following.

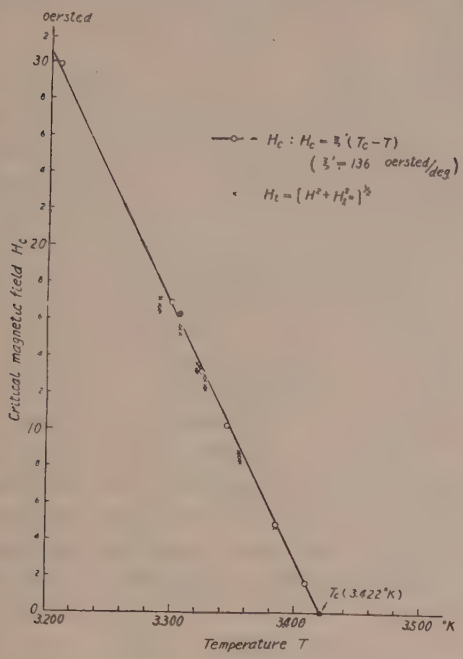

Fig. 14. Comparison of the resultant magnetic field H_t at the specimen surface (the vector sum of external field H and current field H_I^*) with the critical magnetic field H_c.

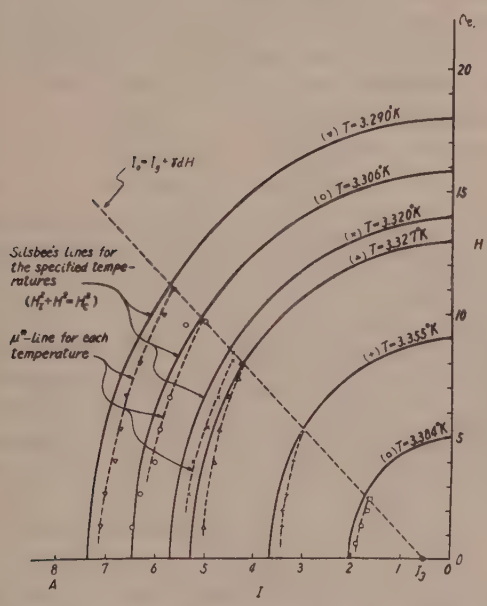

Fig. 15. Orthogonal projections, on the $(I-H)$ plane, of the intersections (the Silsbee's lines), for the specified temperatures, of the planes T=const. with the transition surface $[H^2+(4I/d)^2]^{1/2}=H_c(T)$, and the μ^*-lines for the corresponding temperatures.

3. Comparison of the resistance measurement at the superconducting transition with the theoretical prediction.

The ratio of electric resistance at 4.2°K of the specimen No. 2 to that at 290°K was 1.7 $\times 10^{-4}$. The result of resistance measurement for H=2.66 Oe. at 3.301°K are shown in Fig. 16 (lower figure) where the resistance

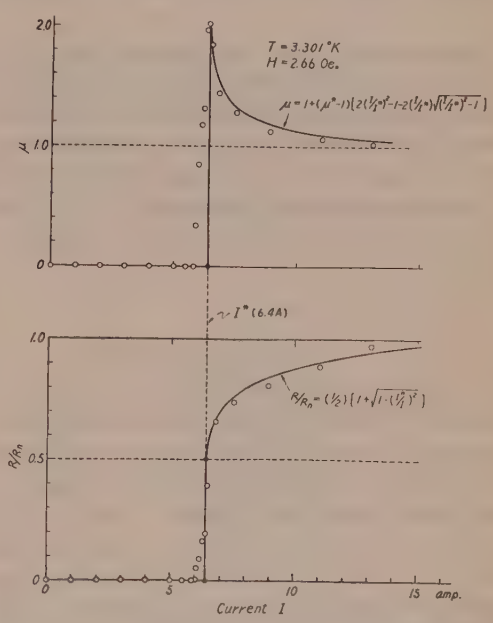

Fig. 16. Relative resistance R/R_n (lower figure) and μ (upper figure) as a function of current I for constant temperature and magnetic field.

is plotted as the relative resistance R/R_n against the current I. R_n, the resistance of the specimen in the normal state at that temperature which was measured in an external magnetic field strong enough to destroy superconductivity, was 2.1×10^{-7} ohms in this case. The solid curve represents the relative resistance as a function of the current at constant magnetic field and temperature, which was derived from a calculation based upon H. Meissner's theory (Appendix):

$$R/R_n=1/2[1+\sqrt{1-(I^*/I)^2}]\,,$$

where I^* represents the current where the

maximum of quasi-paramagnetism occurs. This expression is quite the same as that obtained by F. London[10] for the case of zero magnetic field. In accordance with the result that the perfect diamagnetism did not change abruptly to the maximum of quasi-paramagnetism at I^* but changed in the certain range of current to the maximum of quasi-paramagnetism at I^*, the relative resistance did not appear abruptly at I^* where according to the theory we should expect it to be 1/2, but left the abscissa at about the same current where the perfect diamagnetism began to be destroyed (see the upper figure in Fig. 16). It can be seen, however, that the agreement between theory and experiment is fairly good.

As described in the introduction J. C. Thompson who obtained the same expression as ours for the electric resistance as a function of current and found also a fair agreement between theory and experiment, obtained furthermore an expression for μ at constant values of H and T as a function of I i.e.

$$\mu=1+(\mu^*-I)[2(I/I^*)^2 -1-2(I/I^*)\sqrt{(I/I^*)^2-1}],$$

and found that the experiment showed a good agreement with the theory in this case also[8]. Our result of magnetic measurement performed in parallel with the resistance measurement above described is shown also in Fig. 16 (upper figure) in which μ was plotted against I. The solid curve represents the expression obtained by J. C. Thompson. The experiment agrees also fairly with the theory.

§ 4. Discussion and Conclusion

Although the same formulas for the minimum of current required for the appearance of the paramagnetic effect as obtained in the previous reports which dealt with tin specimens have been obtained in the present investigation with indium specimens, it has become adequate to consider from the present investigation that some of conclusions in the previous report (the paper II) was apparent. We have not been able to draw out from the present investigation some of the previous conclusions (i) that the closed contour lines for μ could be obtained on the $(I-H)$ planes at relatively higher temperatures near T_g, and (ii) that a somewhat systematic structure in the μ-curve as a function of H could be obtained also at relatively higher temperatures near T_g.

As once thought of by us[2], suggested also by J. T. Thompson* and pointed out by H. Meissner[5], the critical line (I_0-line) determined in the $(I-H-T)$ space can be understood as the intersection of the plane $I=I_g+\gamma dH$ with the transition surface $H_c^2=H^2+(4I/d)^2$. We obtain the following equations for the intersection.

$$I_0=\frac{I_g+\gamma\sqrt{(1+16\gamma^2)d^2H_c^2-16I_g^2}}{(1+16\gamma^2)},$$

$$H_0=\frac{-16\gamma(I_g/d)+\sqrt{(1+16\gamma^2)H_c^2-16(I_g/d)^2}}{(1+16\gamma^2)}.$$

Although these equations are not such linear equations as Eqs. (1) and (2) but quadratic ones, they can be approximated by the following linear equations respectively, provided $H_c \gg 4I_g/d$.

$$I_0=\frac{\xi'\gamma d(T_c-T)}{(1+16\gamma^2)^{1/2}}+\frac{I_g}{(1+16\gamma^2)},$$

$$H_0=\frac{\xi'(T_c-T)}{(1+16\gamma^2)^{1/2}}-\frac{16\gamma I_g}{(1+16\gamma^2)d},$$

since $H_c=\xi'(T_c-T)$. ξ should be understood as $\xi'/(1+16\gamma^2)^{1/2}$, which is 95.5 oerst./deg. for $\xi'=136$ oerst./deg. and $\gamma\sim 0.25$ amp./mm. oe. as compared with $\xi=94.4$ oerst./deg. (see Table I). Then we have

$$I_0=\xi\gamma d(T_c-T)+I_g/2, \qquad (4)$$

$$H_0=\xi(T_c-T)-I_g/\gamma d\times 0.5. \qquad (5)$$

Eq. (4) differs from Eq. (1) by the second constant term, which is only 0.3 amp. in the present case. Eq. (5) differs from Eq. (2) by a factor 1/2 in the second term. When allowance has been made for the difficulty of the quantitative measurement inherent in such a investigation as on the paramagnetic effect, it should be approved that the agreements between Eq. (1) and (4) and between Eq. (2) and (5) are good.

The result that the perfect diamagnetism and the zero resistance at constant values of H and T began to be destroyed at about the same current slightly smaller than I^* cannot be explained with the theory. This unexplained result may be due to other causes e.g. the end effect of the specimen.

* Private communication.

The result that the paramagnetic effect vanishes abruptly at I_g seems quite curious. What comes across the mind in this regard is that the line $I_0=I_g+\gamma dH_0$, though obtained as a straight line in the measured range, may not be a straight line near T_c but the one, shown in trial with a dotted line in Fig. 10, so curved as to lead the paramagnetic effect to appear at T_c and to be observed continuously from T_c down to lower temperatures. Such a speculation, however, would diminish in some measure the mystery of I_g. At the present stage of investigation we have no theoretical reason why the I_0-H_0 line should thus become curved. Alternatively the mysterious constant I_g may be connected with the boundary effect between normal and superconducting regions.[11] If this is the case, the fact that the paramagnetic effect vanishes abruptly at I_g may be not so curious as it seems. It may be, however, meaningless to continue such a speculation further without establishing a concrete theory.

As seen in Fig. 16, the specimen shows a small resistance of $R=1/2\ R_n$ at that current where μ^* occurs. If the heating due to the current causes the temperature of the specimen to be slightly higher than that of the liquid bath, we shall understand in some degree the discrepancy between H_c and H_c^*. If this is the case, the theory of the paramagnetic effect proposed by H. Meissner will be a fairly satisfactory one, except its drawback that it cannot explain the mysterious constant I_g. Although we cannot give an exact estimate of the heating of the specimen due to the current, it seems, however, unlikely that such small resistance of the specimen as 1×10^{-7} ohms, through which the current of 5~10 amp. flows, causes a noticeable change in the temperature of the specimen. At any rate an essentially new concept seems necessary for the explanation of the mysterious constant I_g.

Acknowledgement

The author would like to express his hearty thanks to Professor T. Fukuroi for his helpful suggestions and encouragements and to Mr. T. Aizawa for his sincere assistance. Thanks are also due to Professor H. Meissner, the Jones Hopskins University for kind suggestions and valuable discussions and to Dr. J. C. Thompson, the University of Texas for his helpful discussions. The present work was supported partly by the Grand in Aid for Fundamental Scientific Research from the Ministry of Education.

Appendix

As described in the text, the maximum of apparent permeability occurs for given external magnetic field H and temperature T at I^* where the resultant magnetic field H_t at the surface of the specimen is less than the critical field H_c:

$$H_t=[H^2+(I^*/\pi d)^2]^{1/2}$$
$$=H_c^*(I^*,\ T)<H_c(T)\ ,$$

where we used the rationalized mks-unit system in order to reconcile the unit system with that which was adopted by H. Meissner. As the current is increased above I^*, the apparent permeability does not drop at once from its maximum value to the normal state value but decreases slowly toward it.

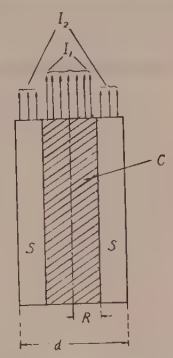

Fig. A1. Cylindrical specimen in the stage $I>I^*$ for constant temperature and magnetic field, where I^* is the current at which the paramagnetic maximum occurs. C is the intermediate core of radius R through which the current I_1 flows and S is the normal conducting sheath through which the current I_2 flows.

It seems reasonable to assume, following F. London and H. Meissner, that the specimen in this stage consists of an intermediate core C of radius R, through which the current I_1 flows, surrounded by a normal conducting sheath S through which the current I_2 flows (see Fig. A1). The radius of the intermediate core R is determined by the condition that the resultant field at R is equal to H_c^*:

$$I^*/\pi d = I_1/2\pi R\,. \qquad (1)$$

Regarding our H_c^* as H_c in H. Meissner's theory, from his theory [Equation (17)][3] we have

$$R = I^*/\pi d\sigma_n E\,, \qquad (2)$$

where E is the electric field and σ_n is the normal state conductivity.

Combining (1) and (2), we get

$$I_1 = 2I^*/\pi d^2\sigma_n E\,.$$

The current I_2, which passes through the normal conducting sheath, S, is given by

$$I_2 = \int_R^{d/2} 2\sigma_n E\pi r dr$$
$$= \sigma_n E\pi(d/2)^2 - I^{*2}/\pi d^2\sigma_n E\,.$$

The sum of the current I_1 and I_2 must be equal to the total current I. Then

$$I = I_1 + I_2 = \sigma_n E\pi(d/2)^2 + I^{*2}/\pi d^2\sigma_n E$$
$$= E/\Omega_n + \Omega_n I^{*2}/4E\,,$$

where

$$\Omega_n = [\pi(d/2)^2\sigma_n]^{-1}$$

is the normal resistance per unit length R_n/l, R_n and l being the normal resistance and the length of the specimen respectively.

Solving the above equation with respect to E, we get

$$E = 1/2\cdot I\Omega_n[1+\sqrt{1-(I^*/I)^2}]$$

or

$$\Omega = (\Omega_n/2)[1+\sqrt{1-(I^*/I)^2}]\,,$$

where

$$\Omega = E/I\,.$$

Then we have for the resistance $R = \Omega l$

$$R = (R_n/2)[1+\sqrt{1-(I^*/I)^2}]\,.$$

References

1) A historical bibliography is found in the reference (2).
2) Y. Shibuya and S. Tanuma: Phys. Rev. **98** (1955) 939: Sci. Rep. Res. Inst. Tohoku Univ. **A7** (1955) 549 referred to in the text as I and II.
3) H. Meissner: Phys. Rev. **97** (1955) 1672; **101** (1956) 31.
4) Meissner, Schmeissner and Meissner: Z. Physik **130** (1951) 529.
5) H. Meissner: Phys. Rev. **103** (1956) 39.
C. J. Gorter also gave a suggestive remark on this disagreement [Physica **23** (1957) 45].
6) W. Meissner and R. Doll: Z. Physik **140** (1955) 340.
7) A. Sellmaier: Z. Physik **141** (1955) 550.
8) J. C. Thompson: Journ. Phys. Chem. Solid **1** (1956) 61.
L. Rinderer who investigated only the resistance of cylindrical superconductors in the magnetic field obtained independently also the same expression for the resistance as a function of current as J. C. Thompson and we did [Helvetica Physica Acta **29** (1956) 339].
9) J. C. Thompson: Phys. Rev. **102** (1956) 1004.
10) F. London: Superfluids (New York, John Wiley and Sons), Vol. I, p. 120 (1950).
11) J. Bardeen: Theory of Superconductivity p. 340 [Handbuch der Physik Vol. **15** (1956)].

JOURNAL OF THE PHYSICAL SOCIETY OF JAPAN Vol. 13, No. 7, JULY, 1958

Paramagnetic Effect in Superconductors. Part II. Quasi-Paramagnetism in Non-Circular Cylindrical Tin Specimens

By Yoshio SHIBUYA

The Research Institute for Iron, Steel and Other Metals, Tohoku University, Sendai

(Received January 8, 1958)

Using circular cylindrical samples, we have shown in previous reports, that the minimum of current I_0 required for the appearance of the paramagnetic effect is composed of two terms I_g and γdH_0 and that I_g is independent of the sample size. In this paper, using the several kinds of non-circular cylindrical samples (rectangular, semi-circular, triangular, hollow circular, and three other forms which may show no paramagnetic effect), we have studied the same effect.

In the former four samples, the value of I_g has proved to be the same as in the case of circular cylinders. In the latter three samples (sandwich-type, cylinder and hollow cylinder with a longitudinal wedge-shaped slot) no paramagnetic effect has been found.

§ 1. Introduction

The formula $I_0=I_g+\gamma dH$[1] hitherto proposed for the minimum current requirement for the appearance of the paramagnetic effect in circular cylindrical superconductors has been shown, in the previous report,[2),3)] to be one for the orthogonal projection on the $(I-H)$ plane, of the critical line in the $(I-H-T)$ space, where I, H and T represent the current, the external magnetic field and the temperature respectively. The characteristic quantity d, the diameter of the specimen, which specifies the cross-section of the specimen appears only in the second term of the above formula. As I_g, the so-called mysterious constant in the paramagnetic effect, is independent of d in circular cylindrical samples, we are inclined to suppose that it should be the same in cylindrical superconductors of non-circular cross-section, if the paramagnetic effect should be observed in them. It may be some aids to the clarification of the origin of the mysterious constant I_g to ascertain whether non-circular cylinders, if the paramagnetic effect occurs in them, give the same I_g as the circular cylinders. This is the reason why we undertook an experiment with non-circular cylindrical superconductors. We observed the paramagnetic effect in a rectangular, a semi-circular, and a regular, triangular cylindrical tin specimen.

The critical line representing the minimum of current in the $(I-H-T)$ space was determined after the same procedure as in the case of circular cylinders. It is represented by the simultaneous equations:

$$I_0=\xi\beta(T_c-T)\,,$$
$$H_0=\xi(T_c-T)-I_g/\beta\,.$$

From these two equations the $I-H$ relation i.e. $I_0=I_g+\beta H_0$ could be derived as in the former case. Although β was different from specimen to specimen according to the shape of their cross-sections, I_g proved to be the same, irrespective of the shape of cross-section i.e. I_g was 1.2 amp. for tin.

Although it seems not adequate to deal here with the experiment with a hollow circular cylinder, a description of additional measurements performed with it is given. The result was in agreement with that reported already by W. Meissner *et al.*[4)]

Furthermore we performed an experiment with non-circular tin cylinders having reentrant cross-sections without observing the paramagnetic effect in them. We retraced also the experiment of W. Meissner and R. Doll[6)] with a tin specimen of sandwich-type consisted of two semi-circular cylinders which were insulated from each other by a mica foil and in accordance with their result we observed no paramagnetic effect in it.

§ 2. Experimental Details

As the experimental apparatus and procedure are almost the same as appeared in the previous reports[3),7)] here we do not repeat them. Most of the magnetic measurements were performed by the dynamic method and some by the static method.

All the tin specimens except the rectangular cylindrical one were prepared from Johnson-Matthey spectroscopically pure tin. The rectangular cylindrical tin specimen was prepared from Kahlbaum pure tin. The specimen was machined to the size of 5 mm in breadth, 1 mm in thickness and 80 mm in length. A tin rod of 6 mm in diameter was cut longitudinally right in two with a cutter of 0.5 mm in thickness, one of which was used as the semi-circular cylindrical specimen whose length was 80 mm. Therefore, strictly speaking, the specimen was not semi-circular. The tin specimen of sandwich-type was constructed from a pair of semi-circular cylinders thus prepared and an insulating mica foil. The regular triangular cylindrical tin specimen was prepared by machinning a tin rod to the size of 5 mm in an edge of the regular triangle and 70 mm in length. The hollow cylindrical specimen was machined so as to have the outer diameter of 5 mm, the inner diameter of 2 mm, and the length of 70 mm.

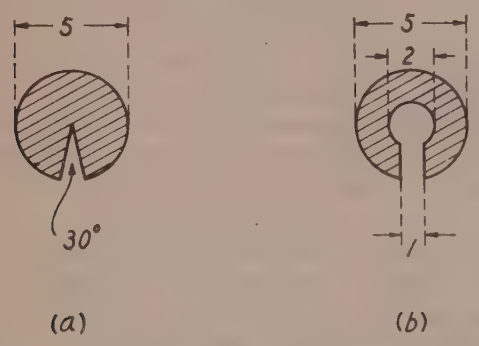

Fig. 1. Cross-sections of tin cylinders showing no paramagnetic effect. The length is in the unit of mm.

In three kinds of non-circular tin cylinders we could not observe the paramagnetic effect. One was prepared in such a way that a circular cylinder of 5 mm in diameter and 70 mm in length was cut away to the cylinder axis longitudinally with a cutter having the angle of 30° [see Fig. 1 (a)]. The other was prepared from a hollow cylinder of 5 mm in outer diameter, 2 mm in inner diameter and 70 mm in length by cutting it longitudinally and perpendicularly to its surface with a cutter of 1 mm thick at one side of the wall. Its cross-section is shown in Fig. 1 (b). The third was the specimen of sandwich-type afore-mentioned.

The annealing procedures of all the specimens were quite the same i.e. the specimens were sealed in evacuated glass tubes seperately and were annealed at 190°C for two hours.

All these specimens were soldered with Wood's metal at their upper ends to copper cylinders of the same cross-section and length as theirs respectively.

§ 3. Experimental Results

1. Non-circular cylinder showing the paramagnetic effect.

(*a*) *Rectangular cylinder.*

A typical result obtained by the dynamic method is shown in Fig. 2, in which the ballistic deflection of the galvanometer was plotted as a function of current I for a given field H at 3.691°K. According to the similar procedure to that adopted in the previous report the apparent permeability μ was defined. μ^* which corresponded to the maximum of quasi-paramagnetism for constant values of

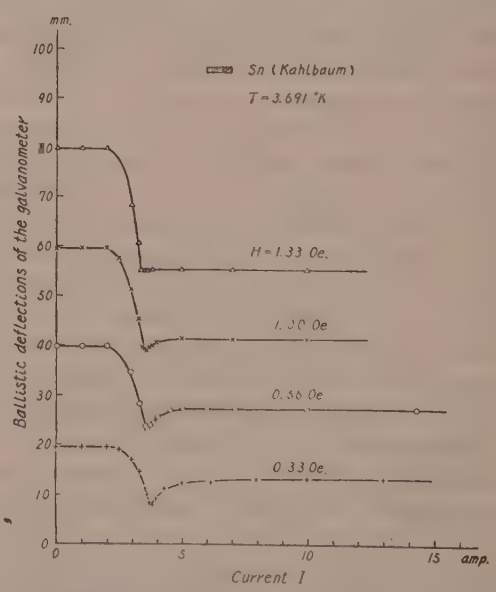

Fig. 2. Ballistic deflections of the galvanometer for the rectangular tin cylinder as a function of current I for the specified values of magnetic field H, when H was reversed.

magnetic field and temperature was plotted as a function of the current I^*, where μ^* occurred, in Fig. 3 (a). It can be seen that in this case also there exists the minimum of current I_0 for the occurrence of the paramagnetic effect. In the same way the maximum of external magnetic field H_0 at that temperature was determined (Fig. 3 (b)). I_0 and H_0 thus determined at several temperatures gave the I_0-T, the H_0-T, and the I_0-H_0 relation shown in Fig. 4 (a), (b) and (c) respectively. These three relations are

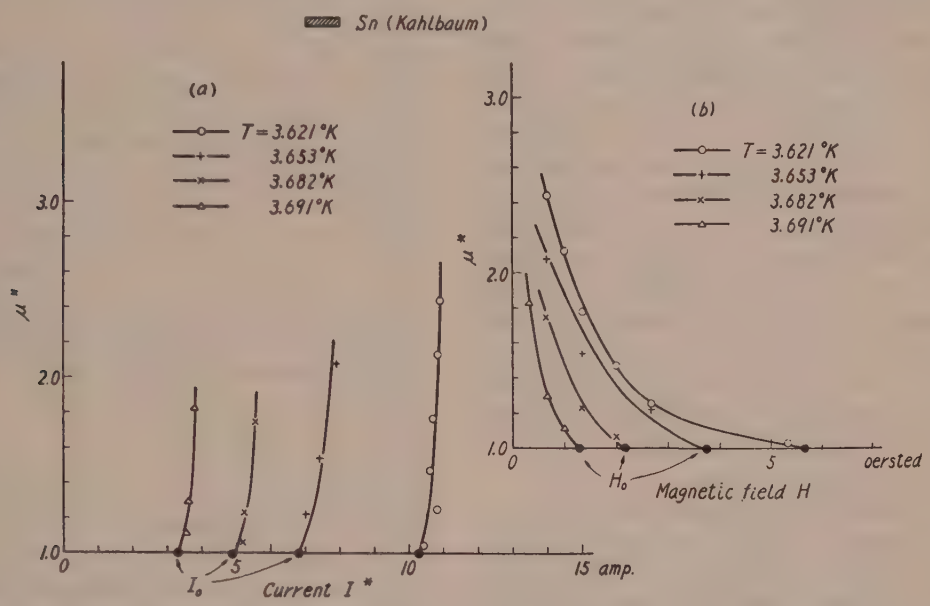

Fig. 3. (a) μ^* for the rectangular tin cylinder as a function of current I^* at the specified temperatures. (b) μ^* for the same as a function of external magnetic field H at the specified temperatures.

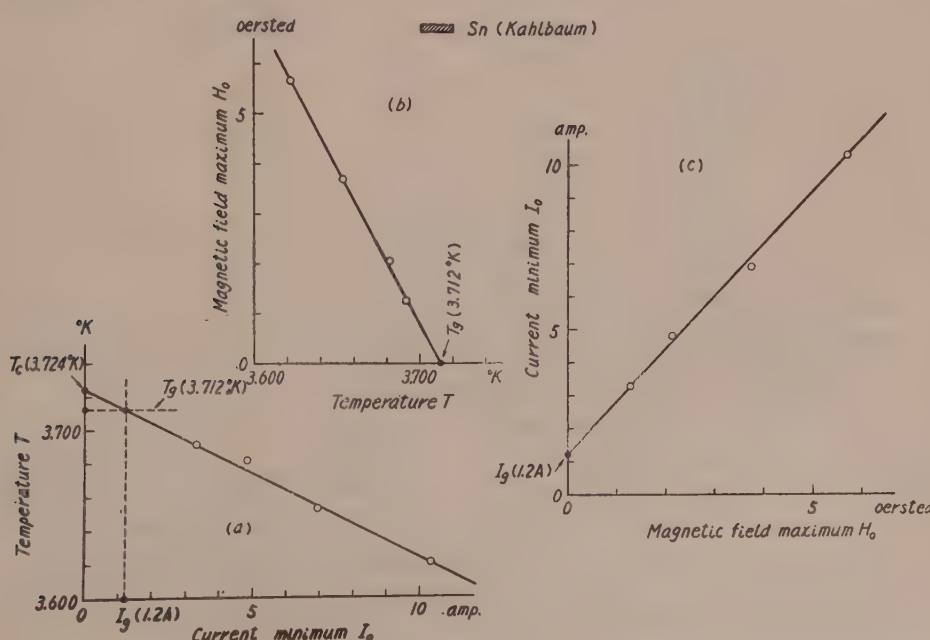

Fig. 4. (a) I_0-T relation, (b) H_0-T relation, and (c) I_0-H_0 relation for the rectangular tin cylinder.

represented by three equations as follows:

$$I_0=\xi\beta(T_c-T)\,, \qquad (1)$$

$$H_0=\xi(T_c-T)-I_g/\beta\,, \qquad (2)$$

$$I_0=I_g+\beta H_0\,, \qquad (3)$$

The critical line (the line for the minimum of current I_0) is represented in the $(I-H-T)$ space by the simultaneous equations of arbitrary two equations of the above three. These equations are quite similar to those obtained in the case of circular cylinders except γd replaced by β. The mysterious constant I_g exists also in the present case and its numerical value is quite the same as in circular cylinders, i.e. $I_g=1.2$ amp. Other constants are $T_c=3.724°$K, $\xi=62.0$ oerst./deg. and $\beta=1.61$ amp./oerst. Similarly to the case of circular cylinders the critical line terminates at the point $(I_g\,,\ T_g)$ on the $(I-T)$ plane, where T_g, which does not appear explicitly in above equations, is equal to $T_c-I_g/\xi\beta$ and its value is 3.712°K in this case.

(*b*) *Semi-circular cylinder.*

One example of the ballistic deflections of the galvanometer plotted against I is shown in Fig. 5 which was obtained for specified values of H at 3.672°K. It seems, at first sight, curious that whereas the ballistic deflections caused by reversing H in the superconducting state should be proportional to H, the figure does not show such a proportionality. This is due to the procedure that we changed

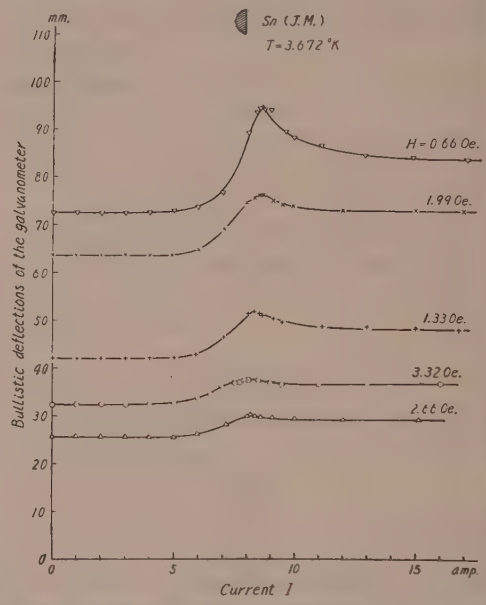

Fig. 5. Ballistic deflections of the galvanometer for the semi-circular tin cylinder as a function of current I for the specified values of magnetic field H, when H was reversed.

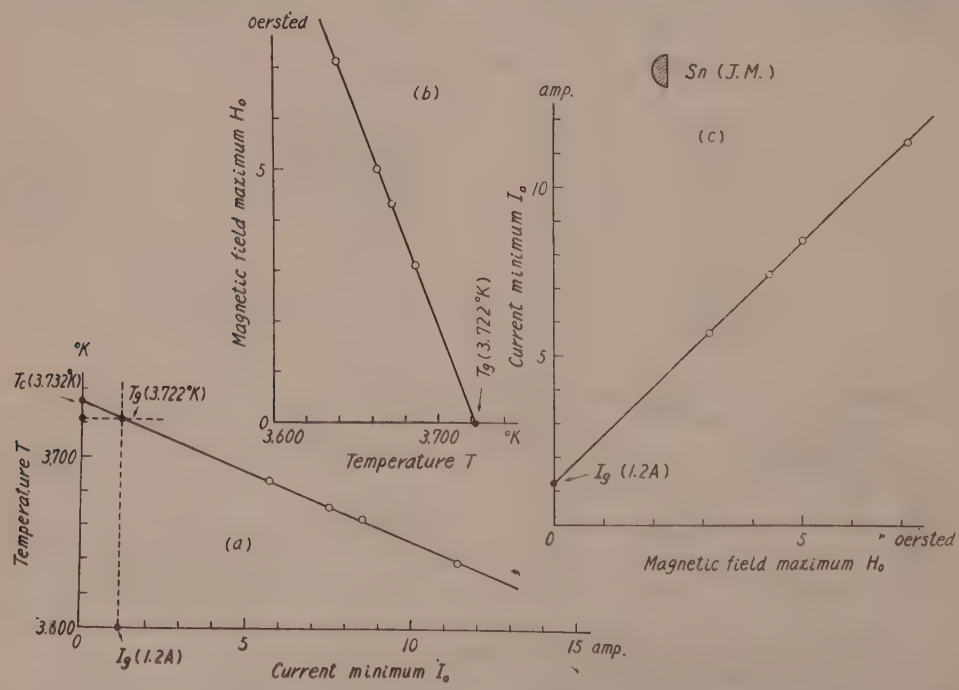

Fig. 6. (a) I_0-T relation, (b) H_0-T relation and (c) I_0-H_0 relation for the semi-circular tin cylinder.

the shunt-resistance of the galvanometer with the magnetic field in order to plot the ballistic deflections for the magnetic field from 0.66 Oe. to 3.32 Oe. in a limited space. This procedure does not, however, affect the determination of the apparent permeability μ. Determining I_0 and H_0 for several temperatures, we obtained the I_0-T, the H_0-T, and the I_0-H_0 relation shown in Fig. 6 (a), (b) and (c) respectively. These relations are represented also by above three equations. In this case also the mysterious constant I_g exists and its value is again 1.2 amp. Other constants appearing in the equations are $T_c=3.732°K$, $\xi=85.5$ oerst./deg. and $\beta=1.44$ amp./oerst. T_g is 3.722°K.

(c) *Regular triangular tin cylinder.*

The ballistic deflection curves obtained at 3.694°K by the dynamic method are shown in Fig. 7. The circumstances are quite similar to those in former two cases. The $(I-H)$, the $(H-T)$ and the $(I-H)$ projection of the critical line in the $(I-H-T)$ space are shown in Fig. 8 (a), (b) and (c) respectively. These projections are also represented well by the above three equations (1), (2) and (3). We obtained $I_g=1.2$ amp. in this case also. The values of T_c, ξ and β are 3.734°K, 81.9 oerst./deg. and 1.08 amp./oerst. respectively. T_g is 3.720°K.

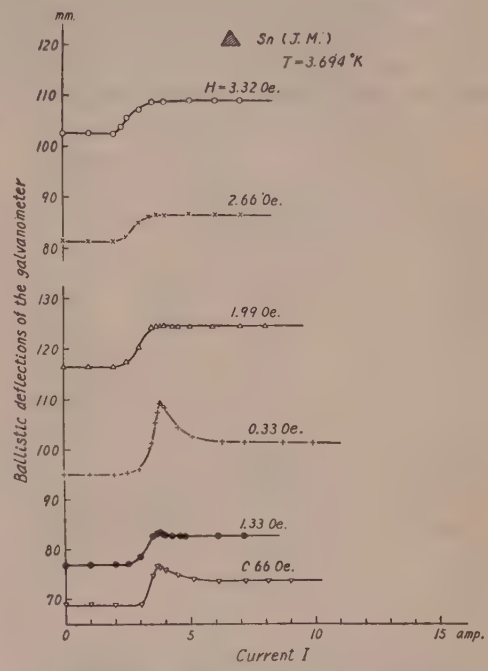

Fig. 7. Ballistic deflections of the galvanometer for the regular triangular tin cylinder as a function of current I for the specified values of magnetic field H, when H was reversed.

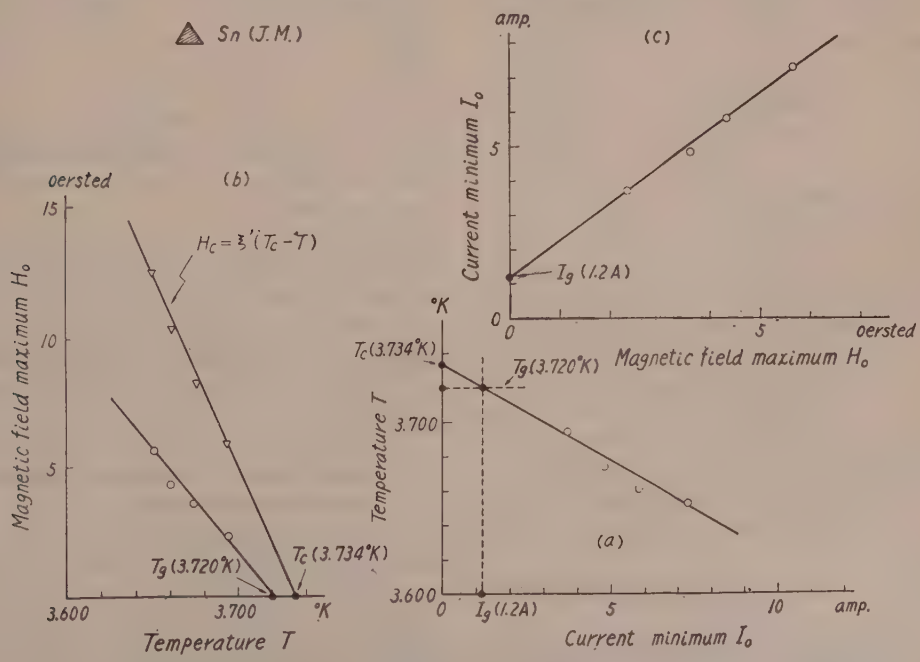

Fig. 8. (a) I_0-T relation, (b) H_0-T relation and (c) I_0-H_0 relation for the regular triangular tin cylinder. The critical field H_c is represented by $H_c=\xi'(T_c-T)$, where $\xi'=150.5$ oerst/deg. and $T_c=3.734°K$.

2. Hollow circular cylinder.

We observed the quasi-paramagnetism in this specimen both with a search coil surrounding the specimen and with a search coil placed into the hole. One of the results obtained by the dynamic method at 3.662°K is shown in Fig. 9. It can be seen that the flux increase occurred not only in the boc of the specimen but also in the hole.

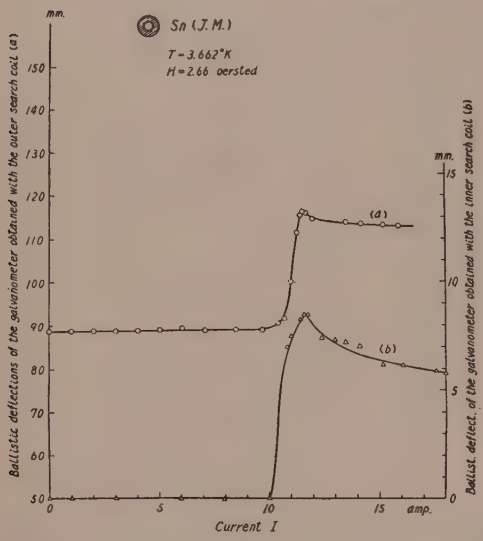

Fig. 9. (a) Ballistic deflections of the galvanometer for the hollow tin cylinder obtained with the outer search coil as a function of current I for H=2.66 oersteds and T=3.662°K, when H was reversed. (b) The same obtained with the inner search coil.

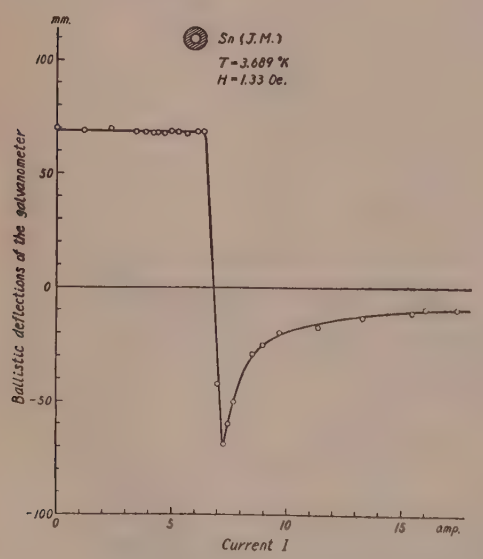

Fig. 10. Ballistic deflections of the galvanometer for the hollow tin cylinder as a function of current I for H=1.33 oersteds and T=3.689°K obtained by the static method.

The result obtained by the static metho is shown in Fig. 10 which ensures that th paramagnetic effect is not a transient, a parent phenomenon accompanying the chang in time of any one of I, H or T. The critic line for the minimum of current required fo the appearance of the paramagnetic effe was determined from the results obtaine with the outer search coil by the dynami method. It is represented in the (I—H—T space by the same equations as in circula tin or indium cylinders, which need not b repeated here. We did not ascertain the cu rent minimum requirement with the inne search coil placed in the hole. We observe a hysteresis in the magnetization curve wit I=0 in this specimen which was a character istic of hollow cylinders. The hysteresis i shown in Fig. 11 obtained by the stati

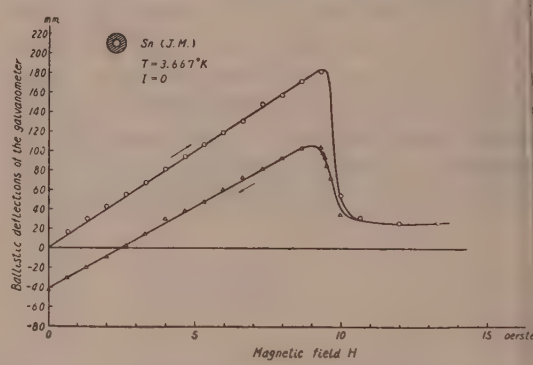

Fig. 11. Hysteresis in the magnetization curve for the hollow tin cylinder obtained by the static method.

method at 3.667°K. The magnetic field wa increased from 0 to 13.30 oerst. by smal steps, and vice versa; at each step a moving search coil connected to the galvanomete was dropped and the ballistic deflection wa measured.

3. Non-circular cylinders showing n paramagnetic effect.

(*a*) *Cylinder having a longitudinal, wedge shaped slot* (Fig. 1 (a)).

It may be justified both from Fig. 12 ob tained by the dynamic method and from Fig 13 by the static method to conclude that th quasi-paramagnetism cannot be observed i this specimen. This specimen showed

hysteresis in the magnetization curve with $I=0$, as shown in Fig. 14 which was obtained by the static method, in spite of the fact that the specimen was a singly-connected body.

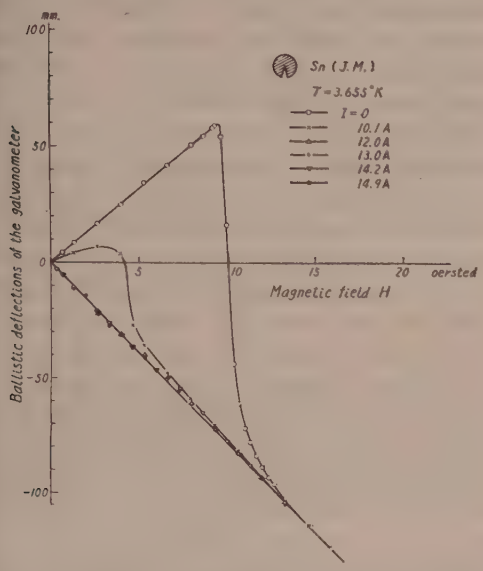

Fig. 12. Ballistic deflections of the galvanometer for the tin cylinder having a wedge-shaped longitudinal slot as a function of magnetic field H for the specified values of current I at 3.655°K, when H was reversed.

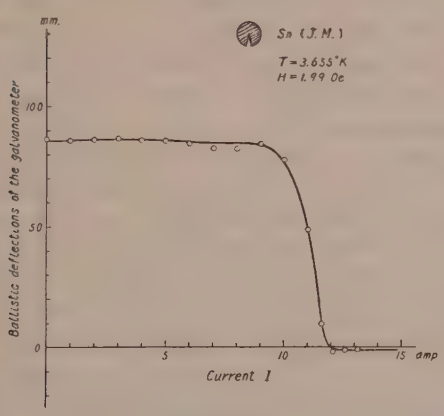

Fig. 13. Ballistic deflections of the galvanometer for the tin cylinder having a wedge-shaped longitudinal slot as a function of current I for H=1.99 Oe. and T=3.655°K obtained by the static method.

In Fig. 14 the ballistic deflections were plotted as a function of the magnetic field which varied from zero to 18.61 oerst. by small steps without returning back, and vice versa.

(*b*) *Hollow cylinder having a longitudinal slot at one side of its thickness* (see its cross-section in Fig. 1 (b)).

The ballistic deflection *vs.* current curve at 3.676°K for a fixed value of H which was reversed is shown in Fig. 15. We could not observe the quasi-paramagnetism in this specimen.

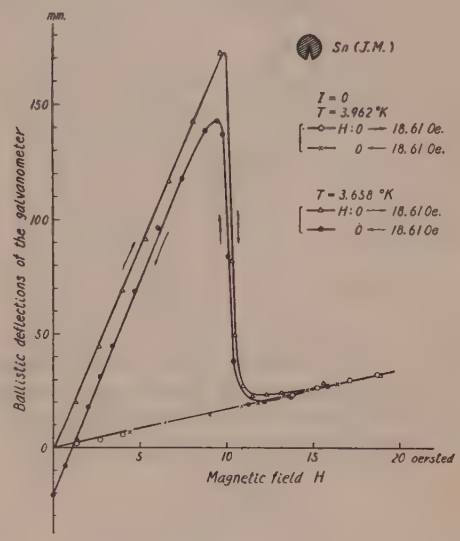

Fig. 14. Hysteresis in the magnetization curve for the tin cylinder having a wedge-shaped longitudinal slot obtained by the static method.

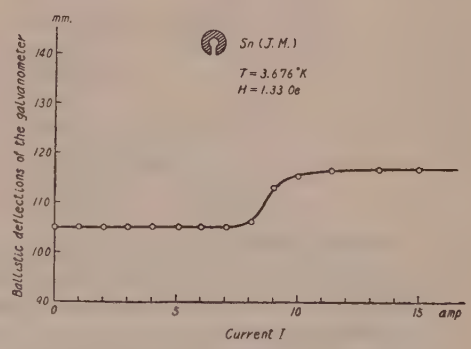

Fig. 15. Ballistic deflections for the hollow tin cylinder having a longitudinal slot as a function of current I for H=1.33 Oe. and T=3.676°K, when H was reversed.

(*c*) *Sandwich-type cylinder.*

The results of dynamic measurement and of static measurement are shown in Figs. 16 and 17 respectively. In this case also we found no paramagnetic effect.

§ 4. Conclusions

The results obtained with non-circular tin cylinders showing the paramagnetic effect as seen in § **3.1.** are tabulated in Table I. As the experimental results cannot be compared with

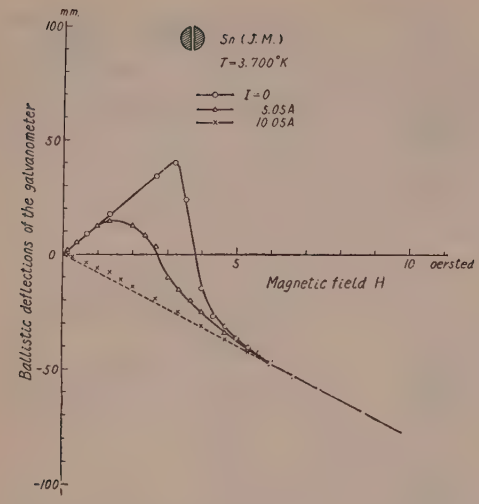

Fig. 16. Ballistic deflections for the tin cylinder of sandwich-type as a function of magnetic field H for the specified values of current I at 3.700°K, when H was reversed.

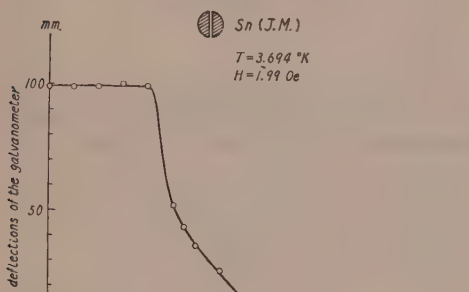

Fig. 17. Ballistic deflections for the tin cylinder of sandwich-type as a function of current I for H=1.99 Oe. and T=3.694°K obtained by the static method.

Table I. Numerical values of constants which appear in the formulas for the minimum of current I_0 for non-circular tin cylinders showing the paramagnetic effect.

$$I_0=\xi\beta(T_c-T)\ ,$$
$$H_0=\xi(T_c-T)-I_g/\beta\ ,$$
$$I_0=I_g+\beta H_0\ .$$

	Sn (Kahlbaum)	Sn (J. M.)	Sn (J. M.)
I_g (amp.)	1.2	1.2	1.2
ξ (oerst./deg.)	62.0	85.5	81.9
β (amp./oerst.)	1.61	1.44	1.08
T_c (°K)	3.724	3.732	3.734
[T_g (°K)]	3.712	3.722	3.720

the theory in contradiction to the case of circular cylinders, because the analytical expression for the magnetic field distribution around such specimens cannot be easily obtained, the critical field H_c was determined only for the triangular cylinder, which was represented by $H_c=\xi'(T_c-T)$ where $\xi'=150$ oerst./deg. and $T_c=3.734$°K.

The shapes of specimen cross-section dealt with in this paper were not, of course, geometrically accurate ones, because their edges were more or less rounded off. The fact that the paramagnetic effect can be observed in such specimens can be explained qualitatively with the idea[4] on which the theory of H. Meissner[5] bases. In such specimens also the resultant magnetic field of the external field and the field produced by the specimen current shows a helical path, irregular as it is, and the current flowing so as to connect the oblong superconducting grains which remain in the intermediate state along the resultant field produces a longitudinal flux greater than that due to the external field.

On the other hand in such specimens showing no paramagnetic effect as dealt with in **§ 3.3.** the paramagnetic effect may not be observed owing to the possibility that the helical path for the current cannot be completed.

β corresponds to γd in the formula obtained for circular cylinders where γ having the dimension amp./mm. oerst. is more or less constant i.e. nearly 0.25 in both cases of tin and indium and d is the specimen diameter in mm. β seems to depend on the cross-section of the specimen. It is not, however, clear from the present investigation in what way β depends on the cross-section of the specimen. Similar arguments can be said in regard to ξ. The difference of T_c between the rectangular and the semi-circular or the triangular cylinder should be ascribed to the difference of their sources.

The mysterious constant I_g which appeared in the formulas for the minimum of current I_0 in the $(I-H-T)$ space for circular cylinders was 1.2 amp. for tin. The fact that I_g exists also in non-circular cylinders and its value is also 1.2 amp., irrespective of the cross-section of the specimen, may throw a light on the explanation for I_g.

The discrepancies between our experiment reported in the previous paper[3] which dealt

with circular tin cylinders and the theory of H. Meissner[5] could not be removed completely by our recent results on circular indium cylinders[7]. However, the facts that our recent results showed a qualitative agreement with the theory and that the paramagnetic effect observed in some specimens of non-circular cylinders can be explained qualitatively with the idea due to W. Meissner *et al*[4] seem to substantiate to some extent the theory of H. Meissner on the paramagnetic effect[5]. Nevertheless the explanation for the origin of the mysterious constant I_g seems to be sought in a new direction.

Acknowledgement

The author would like to express his hearty thanks to Professor T. Fukuroi for his helpful suggestions and encouragements, to Mr. S. Tanuma for his discussions and to Mr. T. Aizawa for his sincere assistance. The author is also indebted to Professor H. Meissner, the Johns Hopkins University for his simulating correspondence. The present work was supported partly by the Grant in Aid for Fundamental Scientific Research from the Ministry of Education.

References

1) Meissner, Schmeissner and Meissner: Z. Physik **130** (1951) 529.
2) Y. Shibuya and S. Tanuma: Phys. Rev. **98** (1955) 938.
3) Y. Shibuya and S. Tanuma: Sci. Rep. RITU **A 7** (1955) 549.
4) Meissner, Schmeissner and Meissner: Z. Physik **132** (1952) 529.
5) H. Meissner: Phys. Rev. **97** (1955) 1672; **101** (1956) 31.
6) W. Meissner and R. Doll: Z. Physik **140** (1955) 340.
7) The preceding paper in this series.

JOURNAL OF THE PHYSICAL SOCIETY OF JAPAN Vol. 13, No. 7, JULY, 1958

The Effect of Tension on the Magnetostriction of Iron Single Crystals

BY Hideo TAKAKI and Jun-ichi HAYASHI

Faculty of Science, Kyoto University

(Received January 27, 1958)

Under various tensions the magnetostriction of iron single crystals was measured at room temperature by means of strain gauge technique. Two magnetostriction constants λ_{100} and λ_{111} were found to be independent of tension. Formerly one of the authors observed a tension-dependent magnetostriction constant by using a mechano-optical lever, which was found to be due to the overlooking of the fact that the long rod specimen is not uniformly magnetized over the whole length on account of its demagnetizing field. It was found that the magnetostriction of the rod specimen must be measured only in its uniformly magnetized portion. The mean values of magnetostriction constants were:

$$\lambda_{100}=19.2\times10^{-6}\,,\quad \lambda_{111}=-22.6\times10^{-6}\,.$$

§ 1. Introduction

In the previous work, one of the authors[1] observed the effect of tension below the elastic limit on the magnetization and the magnetostriction of the long rod single crystals of iron. In this case we observed that a sharp corner of the descending hysteresis curves of magnetization, which was called 'remanence', shifted by the application of tension to a little higher magnetic field side, the amount of the shift being dependent both on tension and on the crystal orientation of the rod axis of the specimen. The remanent magnetization, however, was insensitive to the application of tension, thus satisfying Kaya's law[2]. In other words, the distribution of magnetic domains

at the remanence point is determined uniquely by the crystal orientation of the rod axis. Therefore, taking the remanence and the saturation magnetization as two standard states, the magnetostriction constants were calculated from the descending hysteresis curves of magnetostriction of some single crystals which were observed by means of mechano-optical lever. It was concluded from this experiment that the λ_{100} decreases with increasing tension and falls to about half the value under the tension of 1.0 kg/mm², while the λ_{111} remained unchanged.

Recently one of the authors and Tsuji[3] observed the magnetostriction of the long rod single crystals of 3.2 percent silicon steel by using strain gauge technique, and compared the result with previous one obtained by the mechano-optical method. These two methods often gave a remarkable different result, which was thought to be due to the fact that the specimen is not to be uniformly magnetized over the whole length on account of the demagnetizing field, especially in lower magnetic field. The magnetization of the rod specimen has the maximum value at its centre and decreases gradually to the end of the specimen. Accordingly the magnetostriction can not be uniform over the whole length of the specimen, either. Since the magnetization measured by the ballistic method corresponds to that in the central portion of the specimen, the magnetostriction should also be observed in the same portion of the specimen. This requirement was not satisfied by the previous mechano-optical method of observing the change of a length over the greater part of the rod specimen, but it could easily be attained by the strain gauge technique.

Since an applied tension is below the elastic limit and the anisotropy energy is large in case of iron, tension may not affect the rotation of magnetic domains in low as well as high field. The magnetization of all magnetic domains, therefore, are oriented along any of the easy directions of magnetization below the remanence point, but their distribution may be affected considerably by tension as well as by magnetic field. But since the distribution may be affected considerably by tension as well as by magnetic field. But since the distribution of magnetic domains at the remanence point is to be uniquely determined it should be, and actually is, independent of external tension. So we can take the remanence point as one of the standard states for the calculation of the magnetostriction constants even in the case of measurement under the application of tension. According to the above consideration we have made the measurement by using strain gauge and calculated magnetostriction constants and their dependence on tension.

§ 2. Experiment

The specimens used were four single crystals of the cylindrical rod of about 2 mm in diameter and 20–30 cm in length, prepared by the strain anneal method from vacuum melted electrolytic iron. Three in them were the

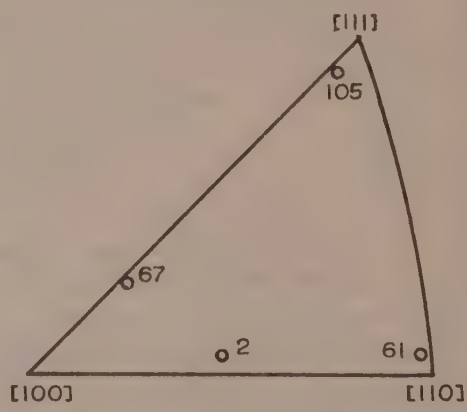

Fig. 1. Stereographic projection of the orientation of the specimens.

Table I.

Specimen number	Direction cosines			Length mm	Diameter mm	Demagnetizing factor	Remanent magnetization	Nearest orientation
	l	m	n					
61	0.036	0.697	0.717	236.8	1.990	0.00321	1155	[110]
105	0.522	0.542	0.659	230.4	1.955	0.00331	995	[111]
2	0.045	0.374	0.926	264.0	1.986	0.00265	1270	[210]
67	0.178	0.190	0.965	302.0	2.001	0.00212	1271	[411]

same as used in the previous measurement by the mechano-optical lever. The crystallographic directions and dimensions of these specimens are shown in Table I and Fig. 1. The strain gauge used was that of type K-12-1 manufactured by Kyowa Musen Kenkyusho Co.. Its gauge factor is 2.00±0.03 and its effective length is 23 mm. Two equal strain gauges, an active gauge and a dummy gauge were used, the former being fixed at the mid-position of the specimen by Duco cement, and the latter on a brass tube in order to avoid the temperature fluctuation. By using two additional gauges in two branches, a bridge circuit was constructed as shown in Fig. 2. After clamping the both

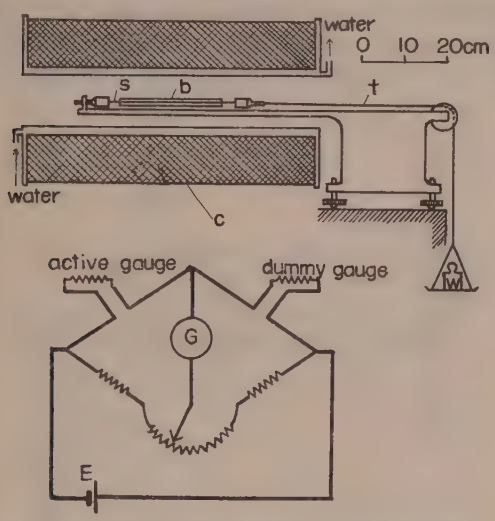

Fig. 2. Experimental apparatus and scheme of electric circuits.
s; specimen to be measured, *b*; brass tube bearing the dummy gauge, *c*; magnetizing coil, *t*; cotton cord, *w*; weight for loading tension.

ends of the specimen by the chucks for loading, the specimen was placed in the brass tube which was attached by the dummy gauge, then the whole system was inserted into the magnetizing coil which was kept at constant temperature by circulating water. The apparatus is also shown in Fig. 2. All measurements were carried out at room temperature. The change of length was read by the deflection of a mirror of galvanometer. The strain sensitivity was estimated to be 4×10^{-7} per 1 mm deflection of the scale at a distance of 2 m. We could attained more higher sensitivity, but the above value was found to correspond to a good dumping of the galvanometer. After demagnetizing the specimen in alternating field and then loading a tension on it, the hysteresis curves of magnetostriction were measured. The yield strength of the specimen was estimated from the stress-strain curves reported by Paxton and Churchman[4] for the single crystals of Armco iron which were prepared and treated in almost all the same way as ours. According to their result, the yield strength of the iron single crystals is about 3 kg/mm² (as tensile stress) nearly independent of the crystal orientation, and no upper yield point appears. As the purity of our specimens is believed to be higher

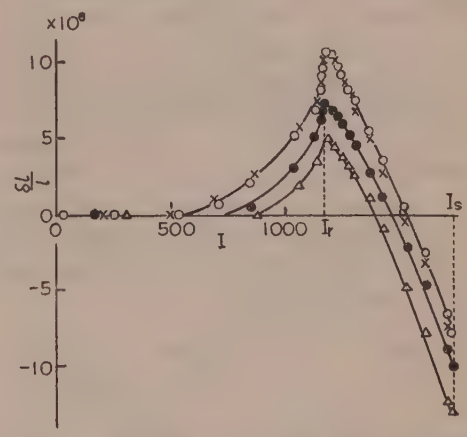

Fig. 3. Descending hysteresis curves of magnetostriction of specimen No. 61, near [110], under various tensions.
○——○ under no tension
●——● 0.35 kg/mm² tension
×——× 0.16 kg/mm² tension
△——△ 0.64 kg/mm² tension

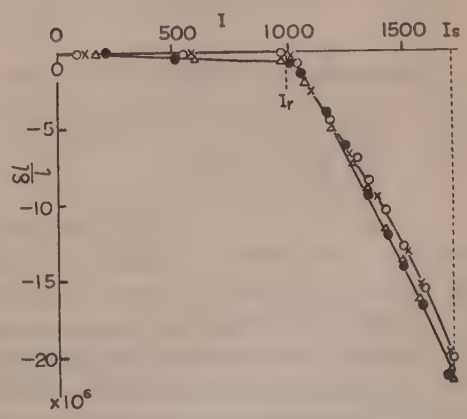

Fig. 4. Descending hysteresis curves of magnetostriction of specimen No. 105, near [111], under various tensions. The signs of measured points are the same as in Fig. 3.

than that of Armco iron, the yield point may be lower. Consequently, we limitted the tension within 0.6 kg/mm², in which range the material may be regarded as nearly elastic during the experiment. According to the Becker's consideration[5], the internal stress should be induced by magnetostriction and given by $\lambda_{100}E$ (E is the Young's modulas),

Fig. 5. Descending hysteresis curves of magnetostriction of specimen No. 2, near [210], under various tensions. The signs of measured points are the same as in Fig. 3.

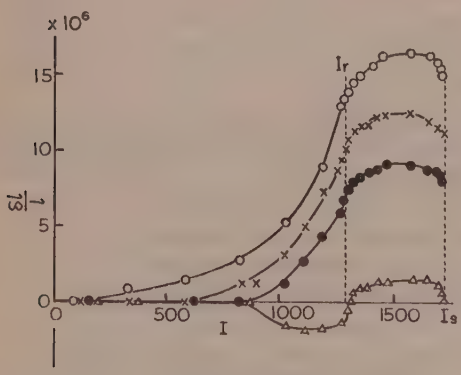

Fig. 6. Descending hysteresis curves of magnetostriction of specimen No. 67, near [411], under various tensions. The signs of measured points are the same as in Fig. 3.

which is evaluated for iron to be about 0.5 kg/mm². This value is comparable to the higher values of applied tension. Magnetostriction under 0.8 kg/mm² was also observed, but in this case the specimen showed a little tendency to creep and no satisfactory result for calculating the magnetostriction constants was obtained. Descending hysteresis curves of magnetostriction under various tensions are shown in Fig. 3 to Fig. 6.

§ 3. Discussion and Calculation of Magnetostriction Constants

Magnetization curves of each specimen has a sharp corner at remanence point, where the magnetization remained unchanged under various tensions. Magnetization curves of three specimens out of the four were shown in the previous paper[1], and the last one No. 67 is similar to them in its behaviour. Comparing the present result with the former one, we found that the behaviour of magnetostriction curves is somewhat different from each other. As already mentioned by Takaki and Tsuji[3], below the remanence point magnetostriction curves obtained by the two methods are considerably different from each other for the specimen except one with [111] orientation, an example of which is shown in Fig. 7. The above discrepancy between the

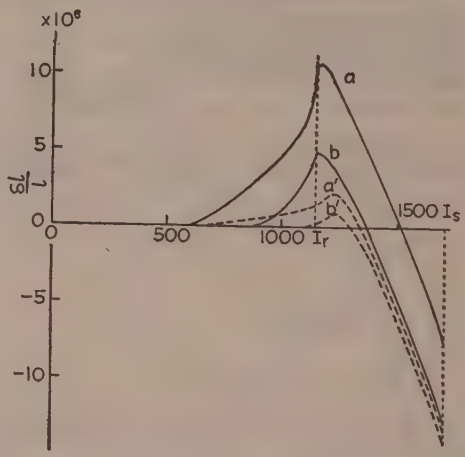

Fig. 7. Comparison of the descending hysteresis curves of magnetostriction obtained by two measuring methods, specimen No. 61, [110].
——— obtained with strain gauge.
- - - - - obtained with optical lever.
a, a' under no tension.
b, b' under 0.64 kg/mm².

two magnetostriction curves may be explained by the fact that the magnetostriction is not uniform over the whole length of the specimen but its value is variable below the remanence. For the specimen of nearly [111] direction, however, the two methods gave nearly the same descending hysteresis curves of magnetostriction, and below the remanence this specimen has the uniform and constant magnetostriction though it has not been uniformly magnetized (Fig. 6). This is because

that the magnetic domains are oriented along any of the easy directions of magnetization, which are directed symmetrically around the rod axis, and the magnetostriction has the same value in any portion of the specimen. From Fig. 3 to Fig. 6, magnetostriction varies considerably with tension below the remanence point, but does not depend on tension between saturation and remanence as shown in Table II and Fig. 8. This result is quite different from

Table II. Dfference of Magnetostriction between Saturation and Remanence under Various Tensions.

Specimen number	$-\left(\frac{\delta l}{l}\right)_{\text{sat-rem}} \times 10^6$ under tension			
	0 kg/mm²	0.15 kg/mm²	0.35 kg/mm²	0.64 kg/mm²
61	17.7	18.2	17.2	18.0
105	21.6	19.9	20.6	21.3
2	5.2	4.7_5	4.5_5	5.2
67	−1.3	−1.0	−1.2	−1.1

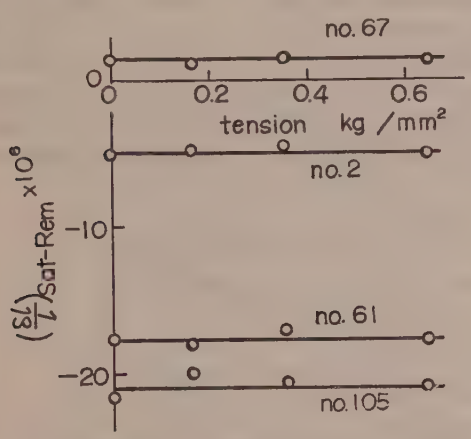

Fig. 8. Difference of magnetostriction between saturation and remanence of four specimens.

the previous result[1], which must be considered to be incorrect. The specimen with the orientation near [100] was also measured but gave no satisfactory result which was probably caused by the fact that this single crystal specimen has a curved form at initially prepared state and stretched by tension. But this specimen has only small effect on determining magnetostriction constants because the coefficients of λ_{100} and λ_{111} have small values in this orientation as shown in equation (1). Anyhow, it may be safely concluded that the magnetostriction constants do not vary with tension. This is further confirmed by the calculation of the magnetostriction constants for various tensions. The method of calculation is the same as in the previous report, that is, the difference of length between the state of saturation magnetization and remanence is expressed by the following relation,

$$\left(\frac{\delta l}{l}\right)_{\text{sat-rem}} = \lambda_{100}\left\{\frac{3}{2}\left(1-\frac{l^3+m^3+m^3}{l+m+n}\right) -3(l^2m^2+m^2n^2+n^2l^2)\right\} -3\lambda_{111}(l^2m^2+m^2n^2+n^2l^2)\,, \qquad (1)$$

where l, m and n are the direction cosines of the measured orientation referred to the cubic crystal axes. Using the equation (1) two magnetostriction constants λ_{100} and λ_{111} were calculated by the least square method. λ_{111} is also determined by the other method. Namely magnetostriction for [110] specimen can be expressed at near to its saturation by the following formula,

$$\left(\frac{\delta l}{l}\right)=\frac{3}{4}\lambda_{100}+\frac{3}{4}\lambda_{111}\left(2\frac{I^2}{I_s^2}-1\right) \quad \text{(above remanence)}, \qquad (2)$$

that is, the gradient of $(\delta l/l)$ versus I^2/I_s^2 curve gives the value of λ_{111}. Our specimen No. 61 deviates about 2° from [110] direction, but this deviation has only negligible effect on the calculated λ_{111}. The calculated magnetostriction constants are shown in Table III and

Table III. Magnetostriction Constants of Iron Single Crystals under Various Tensions.

Tension kg/mm²	$\lambda_{100}\times10^6$	$\lambda_{111}\times10^6$	$\lambda_{111}\times10^6$ calculated from [110] specimen.
0	19.3±1.0	−22.9±0.8	−22.9
0.16	19.7±1.3	−21.7±1.1	−22.7
0.35	19.4±0.6	−21.8±0.6	−21.4
0.64	18.4±1.1	−23.0±1.0	−24.3
Mean	19.2	−22.6	

Fig. 9 in comparison with the previous result. Their rather large probable error may come from the lack of the number of the specimens, but the two constants were independent of tension. The mean values of the magnetostriction constants over various tensions are: $\lambda_{100}=19.2\times10^{-6}$ and $\lambda_{111}=-22.6\times10^{-6}$. Although the values of λ_{111} obtained by the two measuring

methods are both independent of tension, yet the one obtained with strain gauge is larger than the one with mechano-optical lever. This difference may have the other origin. When we compare the mechano-optical method with the strain gauge method for the same portion of the same specimen, we get always greater value with the latter. Strain gauge being calibrated by a known strain, so we must suppose that the mechano-optical method contains some error probably caused by the multiplying factor of the mechano-optical lever. Therefore we believe that the present result obtained by using strain gauge is more reliable.

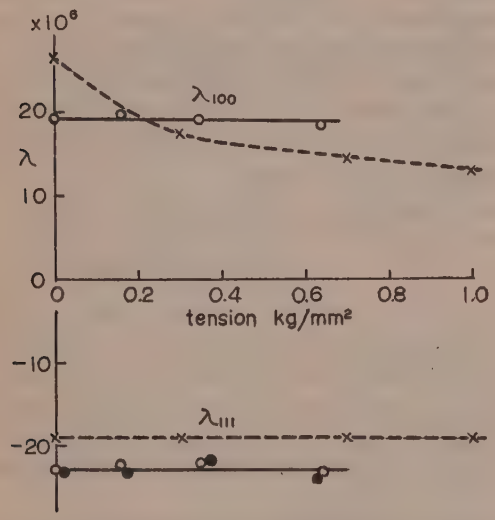

Fig. 9. Magnetostriction constants of iron versus tension.

○——○ Our results with strain gauge.
●——● Our results calculated from curves of specimen No. 61.
×----× Takaki's former results with mechano-optical lever.

In the above discussion we have assumed that the state of saturation and remanence are the two standards states*, but the process from saturation to remanence may somewhat vary with tension. From the exprimental results, the specimens [110] and [111] remain nearly unchanged under any tension, but the specimens having the orientation deviated from the principal axes take somewhat different values under varying tension. In the state of saturation and remanence the distribution of magnetic domains is uniquely determined, but this is not necessary the case on the way between the two states.

The main factors to determine the domain distribution are the magnetic anisotropy energy and the energy by external field. The energy by external tension is smaller than the above two energies, but when external tension is applied, it may affect the behaviour of magnetostriction in the process from saturation to remanence. For the specimen with the orientation of the principal axes, the distribution of magnetic domains is uniquely determined in the whole process between saturation and remanence. Generally speaking, magnetostriction below the remanence point decreases with increasing tension. In this case the magnetic anisotropy energy and the energy by external field become smaller and the energies from internal stress, surface free poles and other origins become comparable to the energy by external tension. Thus the condition of setting and fixing strain gauge become an important factor, so that the discussion about the domain distribution is insignificant below the remanence point. For example,

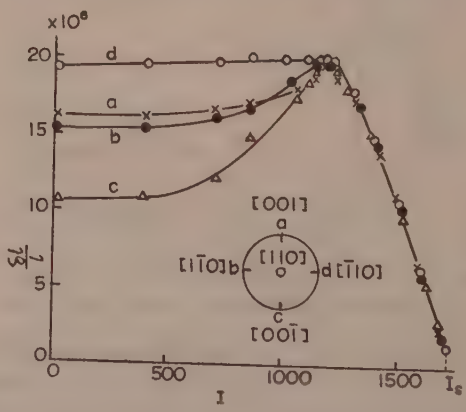

Fig. 10. Descending hysteresis curves of magnetostriction observed on the various lateral surfaces of specimen No. 61, near [110].

the magnetostriction of the specimen No. 61 of [110] direction was observed with strain gauge fixed on the various lateral surfaces of the cylindrical specimen in the central portion (Fig. 10). Two strain gauges on symmetrical position give the different results, which mean that the condition determining the domain distribution is very delicate and complex. Lee[6]

* The demagnetized state is often taken as the standard state, but it is incorrect because the distribution of magnetic domains is not uniquely determined in such a state.

discussed the effect of the surface closure domains in relation with the specimen size, but, for our specimen size this effect is concealed in the experimental error.

We wish to thank Mr. Y. Nakamura and Mr. T. Tsuji for their valuable assistance throughout the work. The expenses of this research were partly defrayed by the Scientific Research Expenditure of the Ministry of Education.

References

1) H. Takaki: Proc. Physico-Math. Soc. Japan **24** (1942) 875.
2) S. Kaya: ZS. f. Phys. **84** (1933) 705.
3) H. Takaki and T. Tsuji: J. Phys. Soc. Japan **11** (1956) 1153.
4) H. W. Paxton and A. T. Churchman: Acta Met. **1** (1953) 473.
5) Becker-Döring: Ferromagnetismus (1939) 132.
6) E. W. Lee: Proc. Phys. Soc. **68 B** (1955) 65.

JOURNAL OF THE PHYSICAL SOCIETY OF JAPAN Vol. 13, No. 7, JULY, 1958

Electronmicroscopic Observation of Coloured and Bleached Alkali-Halide Crystals

By Tadatosi HIBI and Kazuo ISHIKAWA

Research Institute for Scientific Measurements, Tōhoku University, Sendai, Japan

(Received June 18, 1957)

Alkali-halide crystals coloured with X-ray irradiation were observed electronmicroscopically using replica techniques. Crystals bleached by keeping them in air and by thermal treatment were also observed. Growth of crystallites was seen not only on the irradiated front face, but also on the side face and on the newly cleaved section. An interesting growth of crystallites was observed all over the front face with the progress in colouration. It was also seen on the side face that the growth of crystallites similar to that on the front face occured in accordance with the degree of colouration. At the inner part of coloured crystal, growth of crystallites was observed only along the steps or in the neighbouring part. By the process quite reverse to the crystal growth in colouration, crystallites grown during colouration disappeared in the process of bleaching. Results obtained were discussed.

§ 1. Introduction

With application of replica techniques, we found that small crystallites appeared on the surface of AgBr crystal in photographic emulsion after optical colouration while observing the print-out effect. This process was considered to be due to atomic or ionic diffusion to the surface from the inner part[1]. It was also found that the crystal MgO changed its shape with colouration due to the heating to high temperature[2]. From these phenomena crystal growth on the surface of alkali-halide crystal coloured with X-ray irradiation was expected. To confirm this, the present experiment was performed. While this experiment was in progress, several studies[3,4] were published on the surface change of the alkali-halide crystals by X-ray irradiation, in connection with the decrease in the density of alkali-halide crystals by colouration. These results will be discussed in comparison with our experimental results.

§ 2. Specimen and Experimental Method

In this experiment, transparent natural crystals of NaCl and KBr were used. The small crystals of $5\times3\times3$ mm cleaved in air from a single block of the crystal were used as coloured specimens on one hand and standard specimens on the other, respectively. Speci-

mens were always used without any pre-treatment such as water-polishing or annealing. The front-, the side- and the cleavage-face after colouration by X-rays were examined and compared with the standard un-irradiated specimens. Each face to be examined is shown schematically in Fig. 1, where the incident beam of X-rays hits normally the front-face. Specimens were all irradiated at room temperature in dark with X-rays of 40 KV, 5 mA from Fe target. The distance between the specimen and the target was about 4 cm. Aluminum foil of 0.02 mm thick was used as a window of X-ray tube. Chromium oblique replicas reinforced by carbon were used for the electronmicroscopic observation. In making oblique replicas, evaporation angle, measured from the crystal surface, was about $\tan^{-1}(1/3)$ for both the front and the side faces and about $\tan^{-1}(1/6)$ for the cleavage face. It took about 1 hour for replication. Coloured crystals were exposed to room light only during this time interval. Much care was paid to the shadowing for the determination of the orientations of crystallites grown on the surface, as shown in Fig. 2. We could also distinguish, the parts locating closed to detached from the front face, from the direction of the shadows.

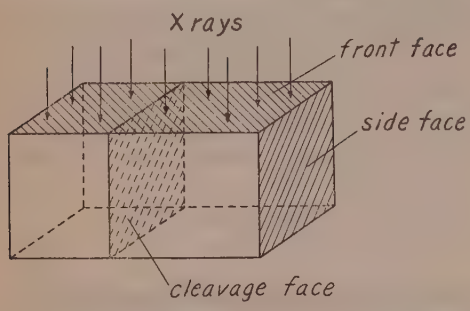

Fig. 1. Faces which was examined with the electronmicroscope.

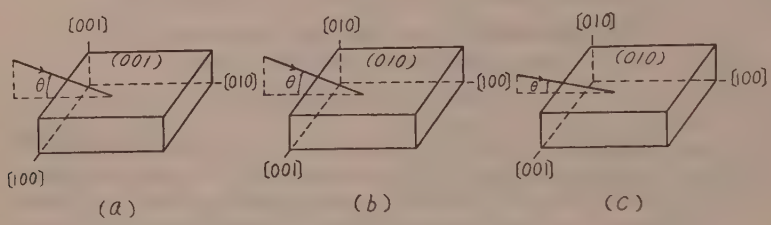

Fig. 2. Direction of evaporation in making oblique replicas. Arrows show the direction of evaporation. (a) front face: $\theta \simeq \tan^{-1}(1/3)$, (b) side face: $\theta \simeq \tan^{-1}(1/3)$, (c) cleavage face: $\theta \simeq \tan^{-1}(1/6)$.

§ 3. Experimental Results

First, two NaCl crystals, one of which was kept in the desiccator and another in air for 14 days, were compared. We could hardly find any difference between them, and so it can be said that humidity in air has no pronounced effect*.

Under a comparatively uniform condition of irradiation, the change of the front face of NaCl crystals with duration of X-ray irradiation was next observed. Fig. 3 (a) shows the electron micrograph of the surface of NaCl crystal without any X-ray irradiation, while (b), (c), (d), (e) and (f) show the electron images of the front face of crystals irradiated by X-rays for 10, 15, 30 minutes and 1 and 3.5 hours, respectively. The surface of the standard un-irradiated crystal is almost smooth and even in the special case it has only low steps as seen in (a). After the X-ray irradiation for a short time, fine crystallites having circular contour shown in (b) appear first here and there. It is known from (b) that crystallites are easy to appear along the steps. By further irradiation, crystallites grow to leaf-like pattern (c), and then the distinct parallelepipedal crystallites appear (d). Judging from the direction of shadows, the [100] direction of the crystallites is predominantly parallel to the cube edge of the base crystal and parallel to the diagonal of the base crystal. By still further irradiation, however, large circular crystal patterns appear. (e) shows a small portion of such a circular pattern. Crystallites still grow and distribute

* This experiment was made during the season of low humidity, but in the season of high humidity we should pay attention to the effect of humidity[5].

all over the front face. After irradiation for a sufficiently long period, very large crystallites are formed and the substrate becomes completely smooth (f). It should be noted that a very peculiar behaviour of the crystal growth appears with the increase of X-ray colouration and the surface change from (e) to (f) is very similar to the behaviour of ag-

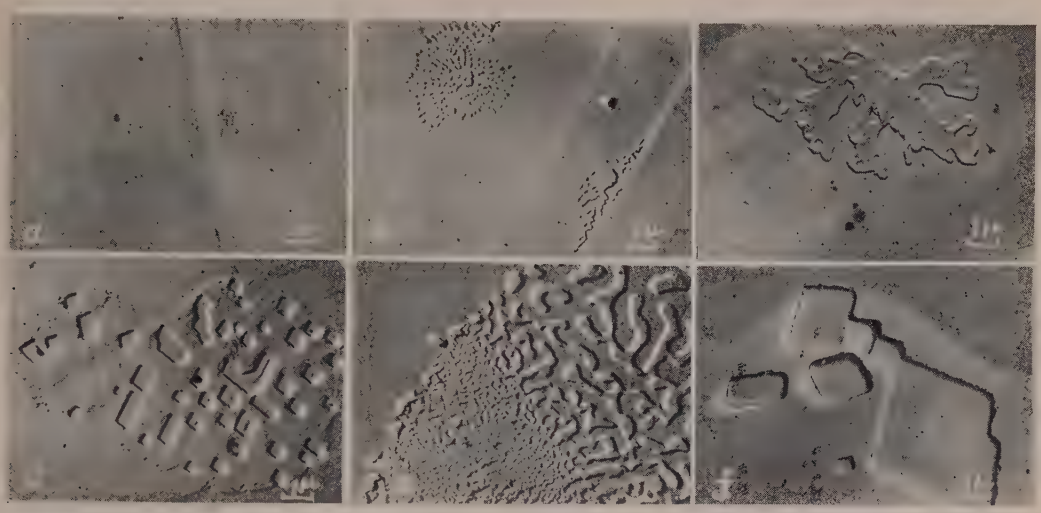

Fig. 3. The change of the front face of NaCl crystals by X-ray irradiation: (a) 0, (b) 10, (c) 15, (d) 30 minutes, (e) 1, (f) 3.5 hours.

Fig. 4. Electron images of the side face of NaCl crystal coloured by X-ray irradiation for 4 hours: (a) the place nearest to the front face (b), (c) the distant places farther from the front face.

Fig. 5. Electron images of the cleavage face of NaCl crystal coloured by X-ray irradiation for 4 hours: (a) the place nearest to the front face, (b), (c) the places farther alway from the front face.

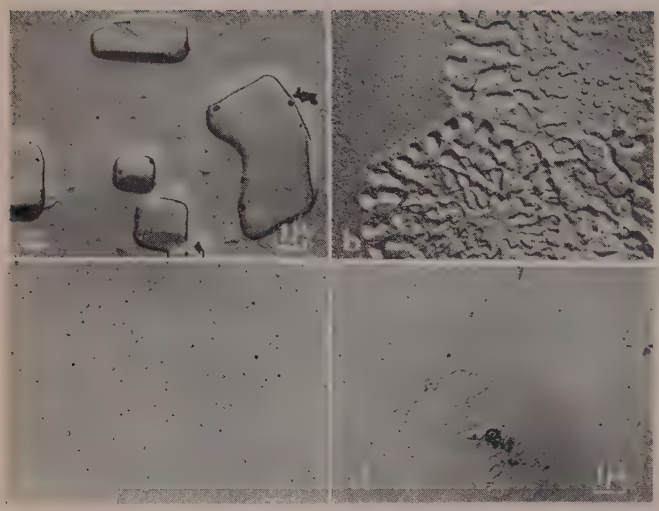

Fig. 6. The change of the front face of NaCl crystals by natural bleaching: (a) immediately after (b) 13 days after, and (c), (d) 33 days after the colouration by X-ray irradiation for 3 hours.

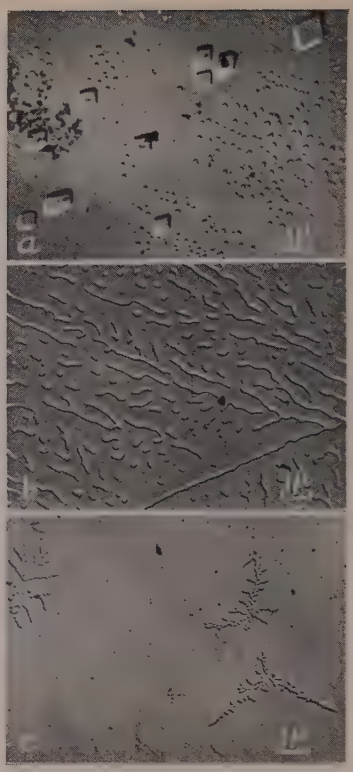

Fig. 7. Electron images of the side face of NaCl crystal bleached for 33 days after the colouration by X-rays for 3 hours: (a) the place nearest to the front face, (b), (c) the distant places farther from the front face.

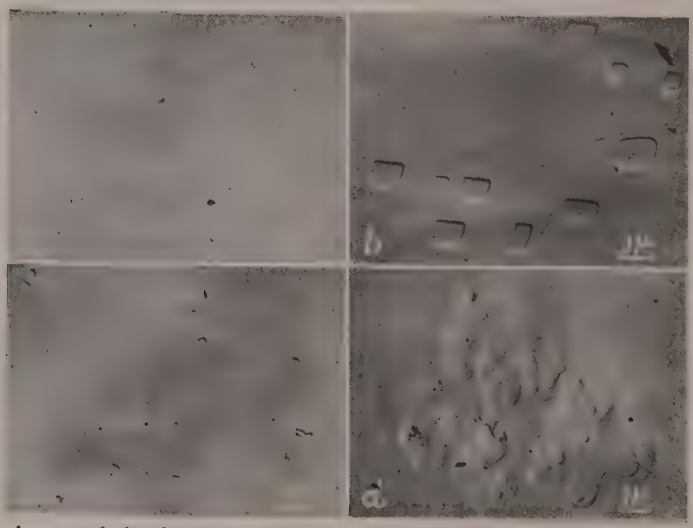

Fig. 8. The change of the front face of NaCl crystals by thermal bleaching: (a) the surface of uncoloured standard specimen after thermal treatment: (b) the front face immediately after colouration by X-ray irradiation for 3.5 hours, (c), (d) the front faces immediately after thermal bleaching.

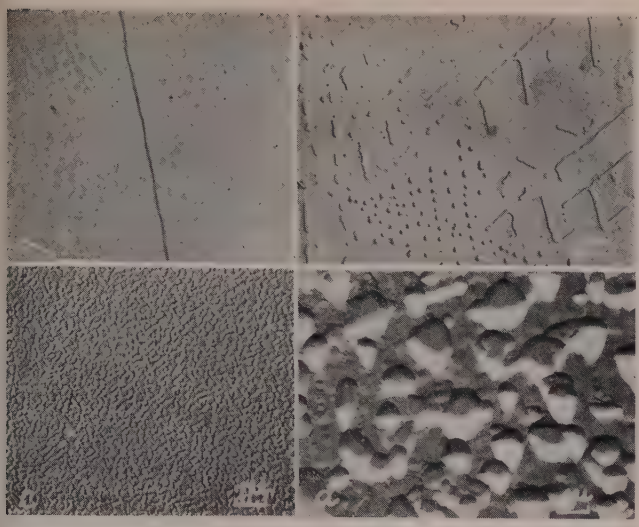

Fig. 9. The change of the front face of KBr crystals by X-ray irradiation: (a) 0, (b) 20 minutes, (c) 3, (d) 4 hours.

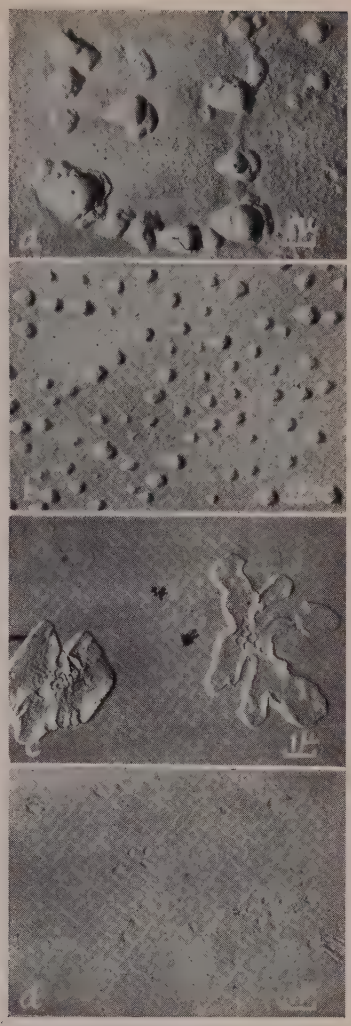

Fig. 10. Electron images of the side face of KBr crystal coloured by X-ray irradiation for 3.5 hours: (a) the place nearest to the front face, (b), (c), (d) the distant places in this order from the front face.

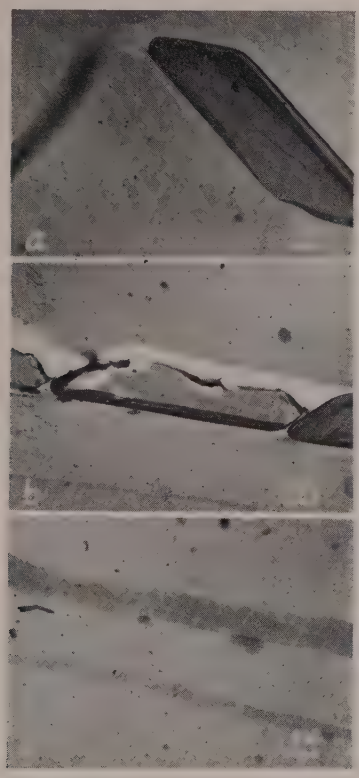

Fig. 11. Electron images of the cleavage face of KBr crystal coloured by X-ray irradiation for 3.5 hours: (a) the place nearest to the front face, (b), (c) the distant places farther away from the front face.

gregation of deposited thin film.

Fig. 4 shows the electron micrographs of the side face of NaCl crystal coloured by X-ray irradiation for 4 hours: (a) shows the image of the place nearest to the front face while (b) and (c) show those of the distant places from the front face. In (a) large crystallites are seen, while crystallites are small in (b) and a few steps only appear on the smooth plane in the deeper place (c). Therefore, it is found that the behaviour of crystal growth on the side face also changes with colouration degree. In the case of (a), it should be noted that the [100] direction of the

crystallites is approximately parallel to the edge of the base crystal.

For the observation of inner parts of coloured NaCl crystals, the section newly cleaved parallel to the side face of the crystal coloured by X-ray irradiation for 4 hours was examined. Fig. 5 shows the result obtained: (a) shows the image of the place nearest to the front face irradiated by X-rays, and (b) and (c) show those of the places farther away from the front face respectively. In (a), large crystallites are seen only along the steps or in the neighbouring place. While small crystallites are observed along steps in (b) and only a few steps are seen on the smooth plane in (c). It is noted that in (a) and (b) steps bend remarkably, while in (c) almost straight steps are only observed.

The bleaching behaviour was next examined by keeping the coloured crystals in the air for a long time. In Fig. 6, (a), (b) and (c) show this effect on the front faces of crystals which were photographed immediately after, 13 days and 33 days after the colouration by X-ray irradiation for 3 hours, respectively. (b) shows a part of a large circular crystal pattern and this is very similar to the pattern in Fig. 3 (e) which was observed in the process of crystal growth by X-ray irradiation. In this figure, (d) shows the image which was taken from the crystal bleached for 33 days after the colouration, and the crystallites in (d) are very similar to those in Fig. 3 (c). It is seen from these that the crystallites on the front face of NaCl crystal disappear on bleaching. Moreover, it might be conceivable from (b) and (d) that crystallites grown during colouration disappear during bleaching by the process quite reverse to crystal growth in colouration.

Fig. 7 shows the side face of NaCl crystal, which was bleached for 33 days after the colouration. (a) shows the image of the place nearest to the front face, while (b) and (c) show those of the distant places farther from the front face. It is interesting to note that the crystallites on the side face does not disappear completely after 33 days, notwithstanding almost complete disappearance of the crystallites on the front face. The crystallites in (c) are very similar to those in Fig. 3 (c).

It was found from the observation of the part of section near the front face of NaCl crystals bleached for 33 days after the colouration that crystallites still remained but steps became lower or nearly disappeared.

Fig. 8 shows the results obtained by thermal bleaching. After heating for 10 minutes at 300°C, specimens were slowly cooled to room temperature in 1 hour. (a) shows the image after the thermal treatment in the case of uncoloured standard specimen. Any change is hardly observed by thermal treatment. (b) shows the image of the front face immediately after the colouration by X-ray irradiation for 3.5 hours, while (c) and (d) show those of the front face immediately after the thermal bleaching. In (b) a pronounced crystal growth is seen, while in (c) crystallites are very small. Therefore, it is concluded that the front face becomes smooth also by the thermal bleaching. Stratified laminar crystallites as shown in (d), the lamellae of which are supposed to be formed in the earliest stage of crystal growth during colouration, were rarely observed on the front face of thermally bleached NaCl crystal.

KBr crystals were next observed electron-microscopically. Fig. 9 (a) shows the electron micrograph of the surface of KBr crystal without any X-ray irradiation. A step and the smooth plane are only seen. In this figure (b), (c) and (d) show the electron images of the front face of crystals coloured by X-ray irradiation for 20 minutes and 3 and 4 hours respectively. Rod-like and point-like patterns appear on the front face by X-ray irradiation for a short time. (b) shows the image of the place on the front face where the both kinds of crystal pattern appeared at the same time. After X-ray irradiation for 3 hours, a pattern very similar to deposited thin film was obtained all over the front face as shown in (c). By further irradiation, crystallites grow into larger ones and the substrate becomes smooth as in (d). Surface change from (c) to (d) is very similar to the behaviour of aggregation of deposited thin film as well as in the case of NaCl crystals. Fig. 10 shows the images of the side face of KBr crystal coloured by X-rays for 3.5 hours: (a) shows the pattern nearest to the front face, while (b), (c) and (d) show the patterns in the distant places in this order from the front face. In (a) and (b) many crystallites are seen and the substrate is not smooth, while in (c) and (d) leaf-like patterns such as in Fig. 3 (c) and small crystallites

are only observed on the almost smooth surface. This phenomenon is similar to the case of NaCl crystals. Fig. 11 shows the electron images of the cleavage face of KBr crystal coloured by X-ray irradiation for 3.5 hours. In this figure, (a) shows the image of the place nearest to the front face, and (b) and (c) show those in the distant places from the front face respectively. In this case, observation was made along the same one step. In (a), a large crystallite is seen only along the step and most parts of the section are smooth. The size of crystallites along the step becomes smaller with the distance from the front face as seen in (b). At a farther distance only a few steps appear on the smooth surface as in (c). It is to be noted that in (a) the step bends remarkably, while in (b) and (c) it is almost straight. These results are consistent with those of NaCl crystals.

The effect of thermal bleaching was also examined in the case of KBr crystals. It was observed that crystallites grown during colouration did not disappear completely by heating for 10 minutes at 300°C, although their complete disappearance may be expected by further treatment.

§ 4. Discussion of Results Obtained

It is clear from the present results that in the case of colouration of alkali-halide crystals by X-ray irradiation, crystal growth appears on the front face. The maximum height of crystallites was about 2500–3500Å. Recently Leider[4] found by electron diffraction that crystallites larger than several hundred Å appeared on the front face of NaCl crystal with X-ray irradiation. On the other hand, Smith, Leivo and Smoluchowski[3] found by multiple-beam interferometry that steps having the height of about 180–1400 Å only appeared on the front face of KCl crystal of X-ray irradiation. Leider's result agrees with our experiment. It has been found in electronmicroscopic observation of KCl crystal coloured in the vapour of potassium that the straight or wound steps appeared first, and then crystallites appeared on the surface with further colouration[6]. Therefore, it may be due to the sufficiently pure and well annealed KCl crystals that steps only were observed in the examination with multiple-beam interferometry in the case of Smith and others. Sakaguchi and Suita[7] also obtained the value of about 3000–4000 Å as the increase in thickness of alkali-halide crystals at the saturated colouration due to X-ray irradiation, from the measurement by electric micrometer. This value agrees with the maximum height of crystallites obtained in our experiment. Expansion of alkali-halide crystals due to X-ray irradiation of weak intensities was also observed by Lin[8]. The value of maximum relative linear expansion of 10^{-6} obtained by him does not conflict with our result. It is, therefore, considered as atomic or ionic diffusion to front face from inner part of crystal that crystallites grow on the front face by X-rays. It may be reasonably understood from this mechanism that time lag occurs on the expansion of alkali-halide crystals due to X-ray irradiation of weak intensities[8].

Crystal growth on the front face was observed as very peculiar behaviours in the course of colouration degree. In the case of appearance of the distinct parallelepipedal crystallites, the [100] direction of the crystallites is, in general, parallel to the cube edge of the base crystal and parallel to the diagonal of the base crystal, though Leider[4] did not confirm accurately this fact. This phenomenon is considered to be physically reasonable. In earlier stage of colouration, crystallites are easy to appear along the steps as shown in Fig. 3 (b). This phenomenon shows that ions or atoms are easy to diffuse to the surface from the inner part of crystal through steps or micro steps. In a later stage, however, a surface change is very similar to the behaviour of aggregation of deposited thin film in both cases of NaCl and KBr, and also pronounced steps could not be observed in both cases though there may be micro steps which is unresolvable in our experiment. In this stage, therefore, surface migration seems to be an important factor in the crystal growth on the surface. It should be also noted that patterns such as Fig. 3 (e) and Fig. 9 (c) perhaps show the colloidal state.

On the front face, crystal growth will appear not only along the steps, but also on the smooth area. On one hand, from the observations on cleaved faces, it appears that crystal growth mainly happens along the steps. To explain this it may be considered that ions aggregate to the mechanical imperfections—

cracks or slips (perhaps dislocations)— leaving vacancies behind. This mechanism seems to be very similar to that of the internal latent image formation[9] in the photographic emulsion. It was also, found that at the parts farther inside from the front face, crystal growth becomes less marked with difficulty of penetration of X-rays, and steps more straight. The winding of steps is considered to be connected with crystal growth, because the winding of steps is most pronounced at the part nearest to the front face.

Decrease in the density of alkali-halide crystals by X-ray irradiation, discussed by several investigators[7,8,10], may be explained from our experimental results which suggest that crystallites apear not only on the surface, but also vacancies are created inside the crystal, though Smith and others[3] attached great importance only to the internal mechanism. The surface structure appeared in earlier stage of X-ray irradiation may be explained on the standpoint of dislocation as a result of the climb of dislocation which occurs when the exciting radiation causes the dislocations to yield vacancies. This will explain some of the structure originated in the depth of the crystal where the radiation penetrates[11]. However, crystal growth in later stage of X-ray irradiation cannot be discussed here as climb of dislocations, because it is not yet clear whether surface migration connects with climb motion of dislocation or not.

It is very interesting that crystallites grown during colouration disappear in the course of bleaching, by the process quite reverse to crystal growth in colouration. If the coloured state is considered to be the excited one and the bleached state the normal one, it may be physically reasonable that in the bleaching process ionic diffusion occurs to the inner part of crystal to fill up the vacancies created by X-ray irradiation.

The delay of disappearance of crystallites on the side face grown by X-ray irradiation, as compared with that on the front face, may be due to the difference of degree of crystal growth. It has not yet been made clear from the observation whether crystallites appeared at the surface and the inner part of alkali-halide crystal are alkali crystal or alkali-halide one. However, both kinds of crystallites seem to appear perhaps at different stages of colouration.

Finally the relation between crystal growth and colouration is to be discussed. Positive or negative ions removed from the lattice points produce the crystallites and colouration of crystal occurs from many vacancies which are left in the crystal behind. It is reasonably understood that colouration is most pronounced at the part nearest to the front face and it becomes less marked at the part father inside from the front face. This mechanism does not conflict with the considerations hitherto accepted. From the results in our experiment, it seems that there is not only the interaction between colour centers and dislocations as reported by Amelinckx[12] but crystal growth is closely connected with them excepting surface migration stage. So, electronmicroscopic observation of crystal growth or steps will be very important in learning the behaviours of ions in alkali-halide crystals, though hardly any such observation has hitherto been made. However, some obscurities may remain on the above-mentioned phenomena and interpretations. To make these clear, several studies are being carried out under simpler conditions.

In conclusion, we wish to express our thanks to Prof. Y. Uchida, Kyōto University, Prof. M. Ueta and Dr. T. Suzuki, Tōhoku University for their kind interest. The authors would like to express their thanks to Prof. F. Seitz and Prof. J. S. Koehler, University of Illinois for their kind comments on this work.

References

1) T. Hibi: (to be published).
2) T. Hibi and K. Yada: (to be published).
3) W. J. Smith, W. J. Leivo and R. Smoluchowski: Phys. Rev. **101** (1956) 37.
4) H. R. Leider: Phys. Rev. **101** (1956) 56.
5) T. Hibi and K. Yada: (to be published).
6) T. Hibi and T. Tomiki: (to be published).
7) K. Sakaguchi and T. Suita: Tech. Repts. Osaka Univ. **2** (1952) 177.
8) L. Lin: Phys. Rev. **102** (1956) 968.
9) J. M. Hedges and J. W. Mitchell: Phil. Mag. **44** (1953) 357; J. Phot. Sci. **1** (1953) 110.
10) I. Estermann, W. J. Leivo and O. Stern: Phys. Rev. **75** (1949) 627.
11) S. Amelinckx, W. Bontinck, W. Dekeyser and F. Seitz: Phil. Mag. **2** (1957) 355.
12) S. Amelinckx: Phil. Mag. **1** (1956) 269.

JOURNAL OF THE PHYSICAL SOCIETY OF JAPAN Vol. 13, No. 7 JULY, 1958

A Note on Thermodynamics of the Harmonic Oscillator with Radiation Damping

By Nobuhiko SAITÔ

Department of Applied Physics, Waseda University, Tokyo

and Jun-ichi HORI

Department of Physics, Hokkaido University, Sapporo

(Received March 15, 1958)

Previously one of the authors showed that the system with positive real impedance can be described within the framework of irreversible thermodynamics. In this paper we first remark that the impedance of the system which is describable by irreversible thermodynamics should necessarily be positive real. This conclusion is immediately drawn from the theorem of network synthesis that a system with non-positive-real impedance cannot be constructed from elementary RLC circuit. That a system is constructed from RLC circuit is the necessary and sufficient condition for the system to be described by irreversible thermodynamics. Then we examine some statistical properties of the harmonic oscillator with radiation damping, a typical example of the system with non-positive real impedance, which will help us to apprehend the above conclusion somewhat more intuitively. The main point is that in the presence of radiation damping, we cannot set up the Fokker-Planck equation for the fluctuation without having recourse to an approximation. The result of this approximation is however at variance with the requirement of the rigorous irreversible-thermodynamical description.

§ 1. Introduction

In a recent paper[1], which in the following will be refered to as I, one of the authors showed that the system whose impedance is of the form

$$Z(i\omega)=z^{-1}/(i\omega)+z^0+(i\omega)z^1+\sum_{j=1}^{n+1} c_j/(i\omega-p_j) \quad (1.1)$$

(the so-called positive real impedance in the network theory) can be described within the frame work of irreversible thermodynamics. The problem whether the physical system whose impedance are not positive real can or cannot be described by irreversible thermodynamics, was however remained open. In I it was shown that the irreversible change (including fluctuation) of the system whose impedance is positive real can be described by a system of (say r) Langevin equations of the second order, if we introduce r–1 appropriatea inner variables, in addition to the variable x under consideration. In other words, such a system eventually reduces to a many-dimensional irreversibe-thermodynamical system as treated in § 2 of I. The problem mentioned above amounts to inquiring whether the system with non-positive-real impedance can or cannot be reduced to such a many-dimentional system. It is not self-evident that we can exculde the possibility of such a reduction, inasmuch as we have not examined the possibility of, e.g., taking the derivatives of the variable under consideration as inner variables, which seems to be natural in the case of the system with non-positive-real impedance, as will be seen below. The answer to this question is readily given by combining the well known theorem in the network theory that a network with non-positive-real impedance cannot be constructed from elementary RLC circuits (which means that such a system cannot be described macroscopically by a set of differential equations of the second order tractable by irreversible thermodynamics), together with the argument of Saitô[2], extending his formulation of the ordinary irreversible thermodynamics to a system described by a set of differential equations of the second order. This extension is easily carried out starting from his original treatment by making use of the technique of Ostrogradsky, as was pointed out by Saitô and Namiki[4],

In effect consider a set of differential equations of the second order

$$\sum_j (m_{ij}\ddot{x}_j + r_{ij}\dot{x}_j + s_{ij}x_j) = 0, \tag{1.2}$$

where the coefficients m_{ij}, r_{ij} and s_{ij} respectively form positive definite matrices. The fluctuating force $p_i(t)$ to be introduced into the right-hand sides of these equations have the statistical properties

$$\langle p_i(t)\rangle = 0,$$
$$\mathscr{P}_{ij}(i\omega) = (2/\pi)kTr_{ij}, \tag{1.3}$$

according to the fluctuation-disspation theorem, where $\mathscr{P}_{ij}(i\omega)$ is the spectral density, and hence

$$\langle p_i(t)p_j(t+\tau)\rangle = 2kTr_{ij}\delta(\tau). \tag{1.4}$$

These properties and further assumption that the distribution function of the fluctating forces is normal are necessary and sufficient for the system to be described irreversible-thermodynamically. A system with non-positive-real impedance cannot be described, as was mentioned above, by a set of differential equations of the form (1.2), and consequently it cannot be described in the framework of irreversible thermodynamics.

This is all that we want to conclude. We should like, however, to present a more detailed discussions on the harmonic oscillator with radiation damping, a typical system with non-positive-real impedance, in order to elucidate the nature of such a system.

We first examine in § 2 the many-dimensional irreversible-thermodynamical system treated in § 2 of I, in more detail, showing that the rank of the matrix of the quadratic from of dissipation function should be equal to that of the matrix whose elements are the coefficients of the diffusion terms of the Fokker planck equation describing this system. This means that the variables which contribute independently to the macroscopic entropy production or energy dissipation should necessarily contribute also to the diffusion terms of the Fokker-Planck equation. This is a natural consequence since the fundamental idea of irreversible thermodynamics is that each mechanism of energy dissipation is accompanied with a microscopic fluctuation, which should appear as a diffusion in the space in which the process under consideration becomes Markovian.

In § 3 we take up the harmonic oscillator with radiation damping, and show that we cannot obtain its Fokker Planck equation without having recourse to an approximation and if this approximation is admitted, the resulting Fokker-Planck equation has only one diffusion term, despite the fact that there are two mechanisms of, and hence two variables which contribute to, the energy dissipation. According to the above-mentioned characteristic property of the irreversible-thermodynamical system, this will mean that the harmonic oscillator with radiation damping cannot be reduced to a many-dimensional irreversible-thermodynamical system.

§ 2. A Characteristic Property of Irreversible-Thermodynamical System.

Let us consider a many-dimensional irreversible-thermodynamic system which is described by (I, 2.36), and assume that the matrix $\{L_{ij}\}$ is singular, i.e., its rank R is smaller than r. Since $\{L_{ij}\}$ is symmetric, it can be diagonalized by an orthogonal transformation*

$$C_k{}^i x^k = y^i, \tag{2.1}$$

as

$$G_i{}^k L_{kl} G_j{}^l = D_i \delta_{ij}, \tag{2.2}$$

where $r-R$ D_i's are zero. We can let $D_i=0$, $i=R+1,\ldots,r$, whithout loss of generality. By this transformation, (I, 2.16) and the entropy production become

$$Ts'_{ij}y^j + \sum_{j=1}^{R} D_j\dot{y}^j + Tm'_{ij}\ddot{y}^j = p_i'(t), \tag{2.3}$$

and

$$\Delta\dot{S} = \sum^{R}(1/T)D_j(\dot{x}^j)^2, \tag{2.4}$$

respectively, where $s'_{ij} = G_i{}^k s_{kl} G_j{}^l$ and $m'_{ij} = G_i{}^k m_{kl} G_j{}^l$. (2.3) and (2.4) indicate that there are only R variables which contribute to the energy dissipation.

If we derive the Fokker-Planck equation corresponding to (2.3), we see that the rank of the matrix whose elements are the coefficients of its diffusion terms is equal to R, provided that the matrices $\{s'_{ij}\}$ and $\{m'_{ij}\}$ are non-singular (this assumption bring about no loss of generality)[3]. The Fokker-Planck equation is none other than the diffussion equation for a Markov process in a $2r$-dimensional phase space V with the coordinates

* We use here the summation convention for the sum from 1 to r.

$\{y_i', \dot{y}_i'\}$, $i=1, 2, \ldots, r$. Now the above result shows that in the present case the process is completely causal and exhibits no fluctuation in a certain $2r-R$-dimensional subspace of V. Viewed from the angle of fluctuation, therefore, this is nothing but an R-dimensional process. Let us express this fact by saying that the process is stochastically only R-dimensional. In other words, there are only R independent mechanisms of diffusion; that is, those variables which independently contribute to the energy dissipation all contribute to the diffusion, whilst the variables other than these make no contribution.

As was already mentioned in the introductory section, this is a natural result in accordance with the fundamental idea of irreversible thermodynamics.

§ 3. Fokker-Planck Equation for the Harmonic Oscillator with Radiation Damping.

Saitô and Namiki[4] gave a general method of obtaining the Fokker-Planck equation corresponding to a given Langevin equation by throwing the theory of Brownian motion into the formalism of the quantum mechanics. In this section we try to derive after their method the Fokker-Planck equation for the harmonic oscillator with radiation damping.

The stochastic property of the fluctuating force to be introduced into the Langevin equation can easily be derived from the fluctuation-dissipation theorem. There seems to be no doubt about the validity of this theorem since it yields a correct results for the energy distribution of the radiation field which is in equilibrium with the oscillator[5]. As is well known, such an oscillator is described macroscocpically by the differential equation of the third order

$$\alpha\dddot{x}+m\ddot{x}+r\dot{x}+sx=0, \tag{3.1}$$

at least approximately, where $\alpha=-(2/3)e^2c^{-3}$ (e: the electric charge of the oscillator; c: the velocity of light) and $s=m\omega_0^2$ (ω_0: natural frequency of the oscillator). The impedance of the system is

$$Z(i\omega)=s/(i\omega)+r+m(i\omega)+\alpha(i\omega)^2, \tag{3.2}$$

and the fluctuation of the system is described by the Langevin equation

$$\alpha\dddot{x}+m\ddot{x}+r\dot{x}+sx=p(t), \tag{3.3}$$

which is obatined from (3.1) by adding the term of the fluctuating force $p(t)$. The spectral density of $p(t)$ is given by

$$\mathscr{P}(i\omega)=(2/\pi)kT\,\mathrm{Re}\,Z(i\omega)=(2/\pi)kT(r-\alpha\omega^2),$$

according to the fluctuation-dissipation theorem. This indicates that the term $\alpha\dddot{x}$ in (3.3) which represents the radiation damping and the term $r\dot{x}$ which corresponds to the ordinary viscous damping contribute independently to the energy dissipation, that is, that there are two independent variables which contribute to the energy dissipation. It is, therefore, reasonable to take x and $\ddot{x}$ as such variables.

The correlation function of $p(t)$ is given by

$$\langle p(t)p(t+\tau)\rangle=2T[r\delta(\tau)+\alpha\delta''(\tau)], \tag{3.5}$$

as can easily been from (3.4). It is to be noted that this contains a very singular term $\delta''(\tau)$. As was mentioned in § 1, a system with radiation damping has a non-positive-real impedance and hence cannot be describable by irreversible thermodynamics. This fact manifests itself in the right-hand side of (3.5) which contains a term proportional to $\delta''(t)$. However in order to cast the formalism into the framework of the irreversible thermodynamics, it is necessary to assume that the fluctuating force to be introduced into the right-hand side of (3.1) has a correlation function expressed by a δ-function. Thus we put

$$\langle p(t)p(t+\tau)\rangle=\gamma\delta(\tau), \tag{3.6}$$

instead of (3.5), where γ is a constant which is determined below. Physically speaking the functions δ and δ'' are only the idealized abstraction and should really be regarded as the functions such as, for example, those shown in Fig. 1 and Fig. 2, respectively with small correlation times τ_0 and τ'. The correlation time τ' is somewhat larger than τ_0. The irreversible thermodynamics is valid only when we neglect the behavior of the system within τ_0, looking only upon the coarse-grained phenomenon. The assumption (3.6) does not mean that the term $\delta''(t)$ can be neglected but it is an approximation to the whole right-hand side of (3.5) inculding the term $\delta''(t)$. The physical meaning of this approximation will be made clear in what follows.

In this connection it is noted that the values at different times of a stochastic variable with correlation function represented simply by a δ-function are completely independent, while

those of δ''-type correlation function are not independent at contiguous times as is seen in Fig. 2.

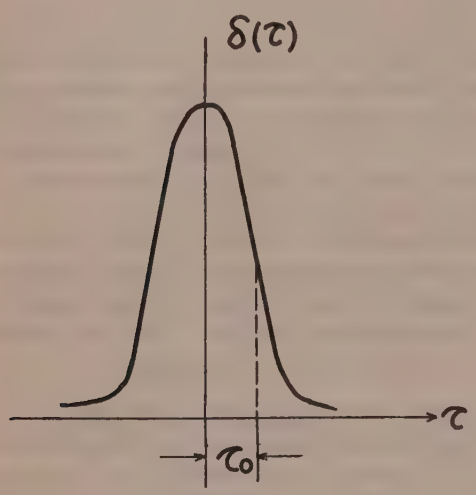

Fig. 1.

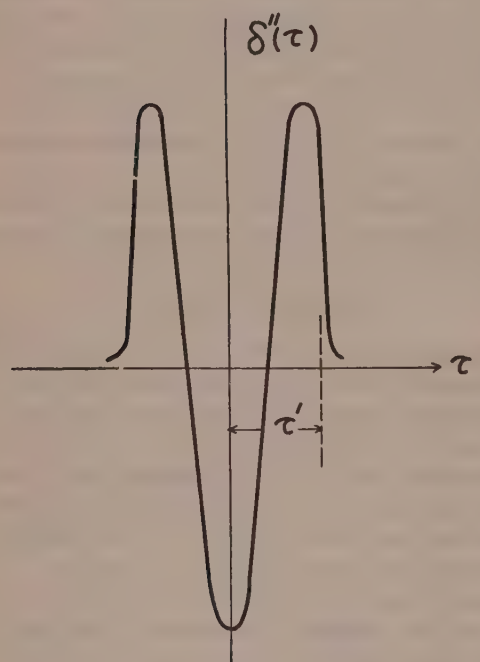

Fig. 2.

As the Lagrangian we should take $\mathscr{L}=(1/2)\{\alpha\dddot{x}+m\ddot{x}+r\dot{x}+sx\}^2$. Putting $\dot{x}=u$ and $\ddot{x}=w$ and regarding x, u and w as independent variables, we therefore obtain as the modified Lagrangian[4)]

$$\mathscr{L}'=(1/2)(\alpha\dot{w}+mw+ru+sx)^2 +p_1(\dot{x}-u)+p_2(\dot{u}-w). \tag{3.7}$$

The momenta and the coresponding differential operators are

$$\pi=\frac{\partial\mathscr{L}'}{\partial\dot{w}}=\alpha(\alpha\dot{w}+mw+ru+sx),$$
$$p_1=\frac{\partial\mathscr{L}'}{\partial\dot{x}}=p_1,\ p_2=\frac{\partial\mathscr{L}'}{\partial\mu}=p_2, \tag{3.8}$$

and

$$p_1\to-\gamma\partial/\partial x,\quad p_2\to-\gamma\partial/\partial u,\quad \pi\to-\gamma\partial/\partial w, \tag{3.9}$$

respectively, where the coefficient γ is to be determined below. The Hamiltonian then is

$$\mathscr{H}=\dot{w}\pi+\dot{x}p_1+\dot{u}p_2-\mathscr{L}' =up_1+wp_2+(\pi/2\alpha)(\pi/\alpha-2mw-2ru-2sx). \tag{3.10}$$

Thus the Fokker-Planck equation for the distribution function $W(x, u, w, t)$ is given immediately by

$$\gamma\partial W/\partial t=\mathscr{H}W=-\gamma u(\partial W/\partial x)-\gamma w(\partial W/\partial u) +(\gamma/2\alpha)(\partial/\partial w)[(\gamma/\alpha)(\partial W/\partial w) +2(mw+ru+sx)W] \tag{3.11}$$

It is not always necessary to solve this equation in order to obtain various average quantities. We have for example the equilibrium value of $\langle u^2\rangle$, by letting $t\to\infty$

$$(m/2)\langle u^2\rangle_\infty=\gamma/4(r-s\alpha/m).$$

Since this must be equal to $(1/2)kT$, γ is determined to be

$$\gamma=2kTr(1-s\alpha/mr). \tag{3.12}$$

The Fokker-Planck equation obtained above contains only *one* diffusion term: In the present case there are *two* variables contributing to energy dissipation, whereas the process looks stochastically like only one-dimensional, contrary to the requirement of rigorous thermodynamical description mentioned in § 2. In the coarse observation, which smoothes out the behavior within τ', the radiation damping does not accompany its own fluctuation, but only modify indirectly the magnitude of the fluctuation accompanying the ordinary viscous damping, according to Eq. (3.12).

It is a difficult problem to handle consistently the term $\delta''(\tau)$. We shall not however worry about it since it is evident from the argument given in § 1 that even if we could take into account the effect of this term rigorously, we cannot at any rate obtain the Fokker-Planck equation which has a full significance from the point of view of the irreversible thermodynamics. We think that

the peculiar property of the radiation damping mentioned above suggests the reason why the radiation damping cannot be treated by irreversible thermodynamics.

However in order to incorporate, consistently, the formalism of radiation damping into the framework of the irreversible thermodynamics, we put the first term of the differential equation of radiation damping (3.1) $\alpha\dddot{x}$ equal to $-\omega_0^2\alpha\dot{x}$, where ω_0 is the natural frequency given by $\omega_0^2=s/m$, as is usually done in simple calculation[7] assuming that the frequency of the motion is hardly affected by the radiation damping. Then the process can effectively be described by a differential equation of the second order with the coefficient of the damping term $r-s\alpha/m$. In this approximation, therefore, our system can be treated in the framework of irreversible thermodynamics. The approximation $\alpha\dddot{x}\approx-\omega_0^2\alpha\dot{x}$ will however be valid only for a narrow neighborhood of the particular frequency ω_0, and indeed the spectral density of the system in this approximation $(2/\pi)kT(r-s\alpha/m)$ is nothing but the equation (3.4) at the frequency $\omega=\omega_0$.

It is however interesting to note that the coefficient of the diffusion term $r-s\alpha/m$ just coincides with value of γ obtained above ((3.12)), and it should also be noted that the δ-function approximation (3.6) with $\gamma=2kT(r-s\alpha/m)$ given by (3.6) for the correlation function of the fluctuating force is strictly valid for the approximation $\alpha\dddot{x}\approx-\omega_0^2\alpha\dot{x}$. Our treatment in deriving Eq. (3–11) is, we surmise, a little better approximation than that of $\alpha\dddot{x}\approx-\omega_0^2\alpha\dot{x}$

§ 4. Conclusions

We have shown above that the impedance of irreversible-thermodynamical system should necessarily be positive real. That the fluctuation of any system with positive real impedance can be described by a system of Langevin equations of the second order means that we can regard the system described by a Langevin equation of the second order as the *fundamental* irreversible thermodynamical system, and every irreversible-thermodynamical system can be represented by a suitable combination of these fundamental systems. This conclusion corresponds to the well known fact in the network theory that every passive network can be constructed of elementary RLC circuits (which corresponds to our fundamental system). Our conclusion represents a generalization of the result of the network theory in the sense that the fluctuation has now been taken into account. It may be said that any system which can be represented macroscopically by a model of passive network can be described by the irreversible thermodynamics.

We can also say from the above result that the irreversible thermodynamics is valid only for the irreversible phenomenon which is described as an ordinary viscous damping proportional to the "*velocity*" $\dot{x}$. This corroborates the point of view of Cox[6] concerning the nature of irreversible thermodynamics.

This work is supported in part by a Grant in Aid from the Ministry of Education.

References

1) J. Hori: J. Phys. Soc. Japan **11** (1956) 1220.
2) N. Saitô: J. Phys. Soc. Japan **12** (1957) 1321.
3) M. C. Wang and G. Uhlenbeck: Rev. of Modern Phys. **17** (1945) 323.
4) N. Saitô and M. Namiki: Prog. Theor. Phys. **16** (1956) 71.
5) H. B. Callen and T. A. Welton: Phys. Rev. **83** (1951) 34.
6) R. T. Cox: Rev. of Modern Phys. **22** (1950) 238.
7) W. Heitler: *Quantum Theory of Radiation* (1954) p. 32.

JOURNAL OF THE PHYSICAL SOCIETY OF JAPAN Vol. 13, No. 7, JULY, 1958

Gel Formation of Aqueous Solution of Polyvinyl Alcohol Irradiated by Gamma Rays from Cobalt-60

Akibumi DANNO*

Faculty of Engineering, University of Tokyo, Tokyo

(Received March 6, 1958)

Experiments were carried out on the irradiation of aqueous solution of polyvinyl alcohol by gamma rays. For sufficient dose of radiation, the polymer molecules in the solution interlinked with each other and formed an insoluble gel. The change in degree of polymerization of the polymer with the absorbed dose, and the minimum dose R_g, required to produce a gel, were measured as a function of concentration of polyvinyl alcohol. In dilute solutions below the critical concentration, gel formation did not occur even for prolonged irradiation. Some considerations are given on the phenomena.

§ 1. Introduction

A number of works have been done on the radiation effects of water[1] and aqueous solutions of low molecular organic substances[2], but only a few reports have appeared on high polymer solutions. Examples are radiation-induced-polymerization of aqueous solution of acrylonitrile[3] and the gel formation of aqueous solution of polyvinyl pyrrolidone[4]. In both of these reports, it was suggested that the radicals formed in water play an important role in the polymerization of acrylonitrile or the gel formation of polyvinyl pyrrolidone. Such a phenomenon is frequently observed for the radiation-induced-decomposition of aqueous solution of low molecular weight substances[5]. Charlesby, in his work on the gel formation of polyvinyl pyrrolidone solution, reported that the minimum dose, R_g, required to produce gel varies as the concentration of the solute is changed. The value of R_g was minimum at a certain concentration and increased as the concentration is increased or decreased and below a certain concentration gel formation did not occur even for a prolonged irradiation.

No detailed study on the radiation effect of polyvinyl alcohol has appeared hitherto. In particular, the only article concerning its water solution is that of Charlesby in which it is simply stated that polyvinyl alcohol behaves in the same manner as polyvinyl pyrrolidone**. Polyvinyl alcohol is a polymer which belongs to the so-called degradation type polymer[7], but it is shown in the present experiment that it can be interlinked when irradiated in water.

§ 2. Experiments

The polyvinyl alcohol in the form of powder was used in this experiment. It was carefully fractionated to get uniform distribution of molecular weight and washed with methanol to eliminate residual sodium acetate. The amount of residual sodium acetate was estimated to be less than 0.06—0.08% in weight. Three samples differing in molecular weight were used. The degrees of polymerization, i.e. the degree of polymerization derived from the molecular weight divided by the monomer weight, of the samples were 1050, 1740 and 2680, respectively. They were dissolved in distiled water and solutions of concentration 1/16, 1/8, 1/4,, ···, 4, 6, 8 and 12 gr/100 cc were prepared. The solution was filled in a test tube of 170 mm in length and 12 mm in diameter, leaving the air of about 5 mm above the surface of solution, closed with a cork and sealed with paraffin wax.

* Present address; Japan Atomic Energy Research Institute, Tokyo.

** In the course of the preparation of the present manuscript, following paper on the irradiation of aqueous solution of polyvinyl alcohol has appeared. In this letter, Berkowitch, Charlesby and Desreeux studied the behaviour in the concentration range below 3% and they observed the formation of microgel[6].

Irradiation was carried out with a cylindrical cobalt-60 of approximately 120 curies. The source cylinder was constructed with 20 rods of cobalt-60 and each rod was of 170mm in length and 3 mm in diameter. These rods were arranged at equidistance on a circle of 64 mm in diameter to form a cylinder. To extend, along the axis, the uniform part of the field at both ends, two pairs of 20 rods of cobalt-60 of 20 mm in length and 3 mm in diameter were arranged at both ends.

The dose rate at the center of the cylinder, measured with the ferrous-ferric dosimeter, was 7.5×10^4 r/hr. The distribution of the field intensity in the cylinder and also outside of it was determined relatively to that of the center by the use of glass dosimeter.

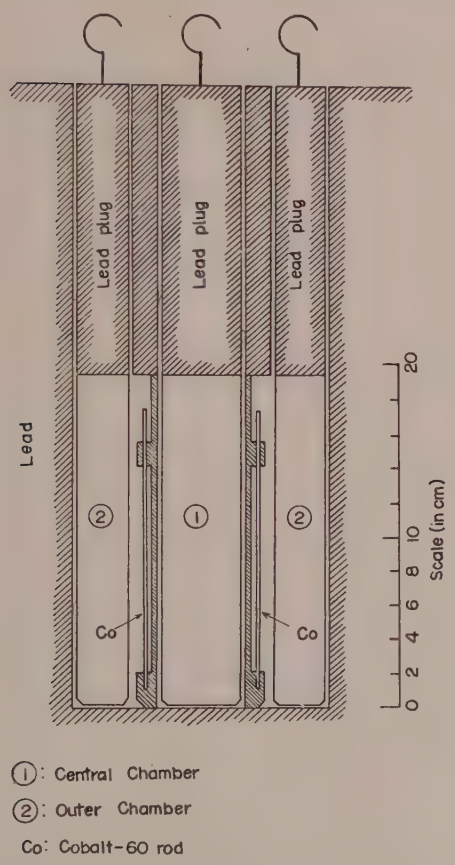

Fig. 1. Schematic diagram of Co-60 Source.

Fig. 1 shows the schematic diagram of the cobalt-60 source. Irradiation was carried out in the central chamber and also in the outer chamber, which is divided into six subchambers. The central irradiation chamber is 200 mm in height and 52 mm in diameter.

§ 3. Results of the Experiment

Aqueous solution of polyvinyl alcohol of various concentration, described above, was irradiated at about 5°C by gamma rays from cobalt-60. Fig. 2 shows, as an example, the degree of polymerization, P_r, of the polymer in the irradiated solution as obtained from the viscosity measurements. The initial degree of polymerization of this polymer was 1740.

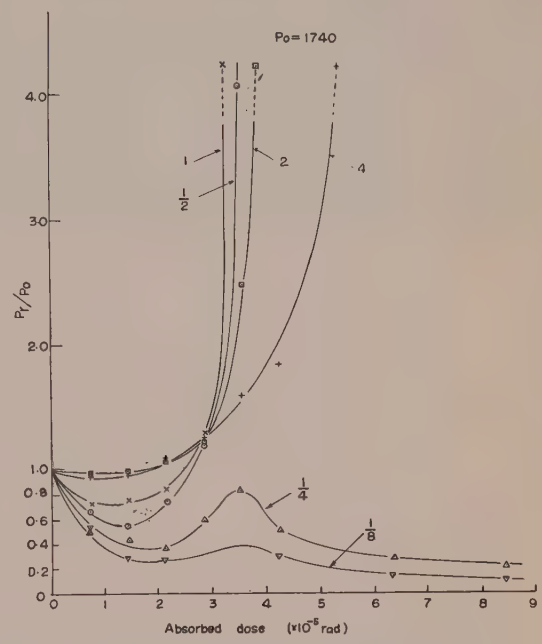

Fig. 2. Change of degree of polymerization, P_r of polyvinyl alcohol in aqueous solution.

Figures attached to each curve give the number of grams of the polymer dissolved in 100 cc of water.

For any concentration, P_r decreases at first as the absorbed dose increases but increases, in general, after passing a minimum value. For a further increase of the dose, P_r passes a maximum and decreases again, when the concentration is below a certain critical value. Above the critical concentration, P_r continues to rise rapidly showing that gelation occured. The critical concentration varies as the initial degree of polymerization of the polymer changes. For the sample of initial degree of polymerization 1740, the critical concentration was approximately 0.36 gr/100 cc.

In the solution above the critical concentration, insoluble gel is formed. Fig. 3 shows

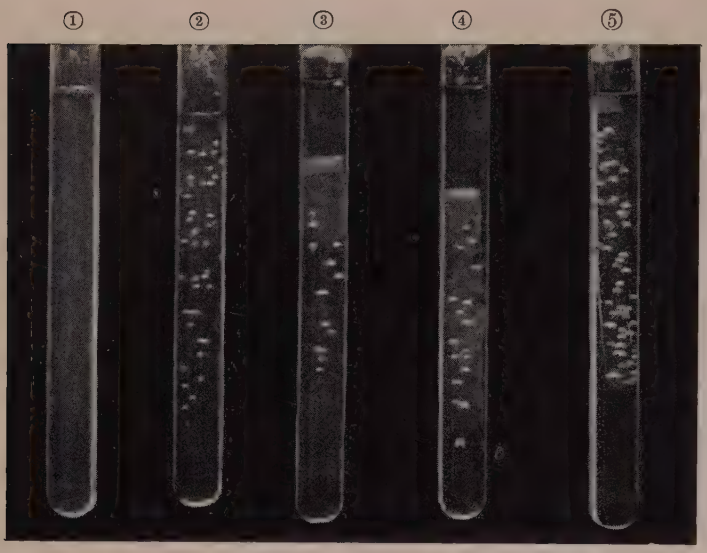

① unirradiated sample
② irradiated with 1.6×10^6 rads
③ 〃 3.3×10^6 rads
④ 〃 4.9×10^6 rads
⑤ 〃 13.3×10^6 rads

Fig. 3. Photograph of various phases of gel formation.
$P_0=1740$
concentration 4 g/100 cc
dose rate 7.5×10^4 r/hr

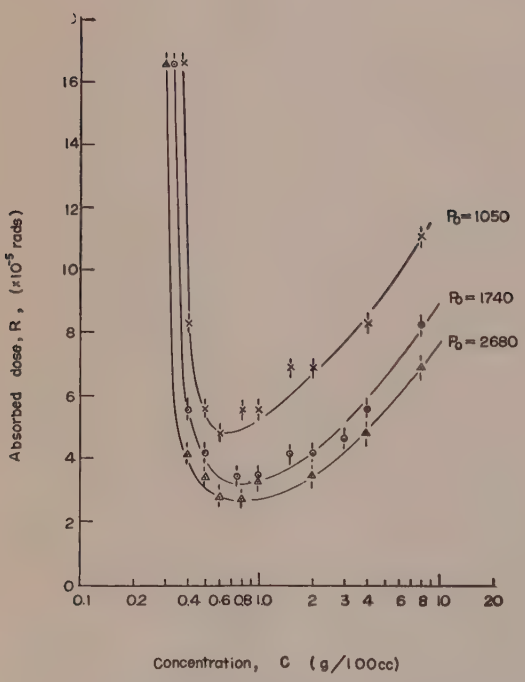

Fig. 4. Dependence of degree of polymerization of polymer on Min. Dose for Gel Formation, R_g.

various phases of gel formation. The solution as a whole turns to gel at first and the gel formed is similar to the fragile gelatine solution. On receiving further radiation the gel shrinks, giving off some water. The water given off increases with increasing dose. It dose not contain dissolved polyvinyl alcohol.

The gel of polyvinyl alcohol solution formed on receiving sufficient irradiation exhibits rubber like elasticity and often contains a number of bubbles. This rubber like substance is not dissolved even when boiled in hot water of 150°C in an autoclave for one hour. It also retains its original shape through boiling in 0.1 N HCl solution or in 0.1 N NaOH solution at 100°C for three hours. When the gel is dried up, it shrinkes remarkably to become a hard pale yellow substance but swells back to the original form when immersed in water.

Minimum dose R_g required for gel formation depends both on the degree of polymerization and the concentration of the polymer. Fig. 4 shows the relation between the minimum dose R_g and the concentration, C, defined as grams per 100 cc. As the degree of polymerization increases, the critical concentration increases, and at the same time the minimum point of the curve shifts to higher concentration. The curve, without much changing its shape moved upward, thus increasing the minimum dose R_g at the same concentration with decrease of the degree of polymerization.

§ 5. Discussion

It is known that degradation process rather than cross-linking occurs predominantly in polyvinyl alcohol irradiated by ionizing radiation. When it is irradiated in the coexistence of water, however, the cross-linking type of reaction occurs and gel is formed as is stated above. Importance of the role of water in gel formation of polyvinyl alcohol is also seen from an experiment on the irradiation

of films of polyvinyl alcohol swelled in water. In this experiment the yield of gel portion increased with the increase of the extent of swelling[8]. Present experiment indicates that the amount of water needed to make gel per one monomer of polyvinyl alcohol is rather large but, at the same time, too much water prevents gel formation as is seen from the existent of the critical concentration.

It would be natural to suppose that the energy absorbed by water from the radiation is transferred to molecules to cause some chemical reactions. If we write the total number of monomer units and the molecules of polyvinyl alcohol in the solution of 100 cc as N and M, respectively, the mass of monomer unit as w, and the degree of polymerization of the polyvinyl alcohol as P, then the concentration of the solution, C, and the number of molecules, M, is

$$C=wN, \quad M=N/P \tag{1}$$

It may be assumed, as a first approximation, that gel formation occurs at an absorbed dose of R_g which is needed to link each polymer molecules in one gram of the solution once on the average. For dilute solution, R_g may be taken as proportional to the total number of molecules, M. If the energy to make one cross-linking is represented by σ, then

$$R_g=K\sigma M \tag{2}$$

where K is a constant which varies with the life time of the active species of dissociated water, the interaction between these species and polymer molecules, the life time of polymer radicals produced by the reaction of active species with the polymer molecules, and the recombination probability of these species and the polymer radicals. In other words, K is a function of temperature and the distribution of molecules in the solution.

From equation (1) and (2) we get

$$R_g=K\sigma C/wP \tag{3}$$

The minimum dose R_g is, thus, expected to be proportional to C and inversely proportional to P. Fig. 5 shows the relation, obtained experimentally, between the product $R_g \times P$ and the concentration C. Above the critical concentration, a linear relation exists between $R_g \times P$ and C. Results obtained for three different degrees of polymerization i.e. 1050, 1740 and 2680, all lie on the same straight line, which is expressed by

$$R_g \times P=5.1\times 10^8+1.37\times 10^8\, C$$
$$=1.37(3.7+C)\times 10^8 \tag{4}$$

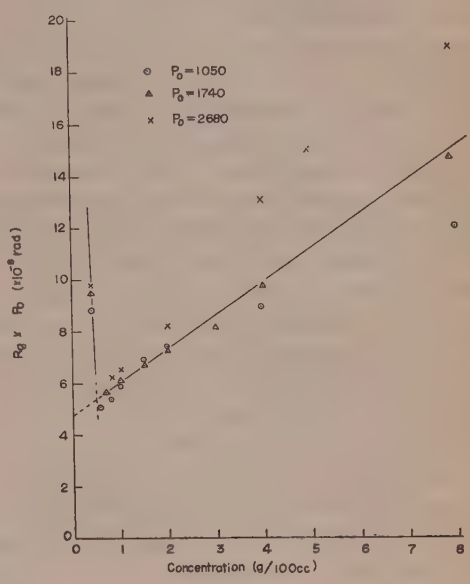

Fig. 5. Relation between $R_g \times P_0$ and concentration.

The line does not pass through the origin, but intersects with the ordinate. This fact may be interpreted as showing that some pre-irradiation is necessary to bring the solution to the state where equation (3) can be applied. The empirical formula (4) may be written in the form

$$R_g-R_0=K\sigma C/wP \tag{5}$$

The slope of the experimental curve, $1.37\times 10^8/P$ rad, is the dose absorbed by the solution which causes the interlinkage of all the molecules contained in one gram of the solution. Since the mass of the monomer (CH_2CHOH) is 7.36×10^{-23} gr, and the concentration C represents the grams of solute in 100 cc of water, the number of molecules in the unit mass of the solution is 1.36×10^{20} (C/P). By definition, one rad of absorbed dose liberates 6.2×10^{13} eV per gram of the substance irradiated. Therefore, the energy per one linkage absorbed from the solution may be estimated as 62 eV.

In the dilute solution below the critical concentration, the distance between polymer molecules in the solution becomes so large that the chance of linking which will be

caused by the collision of polymer radicals decreases to such an extent that the macro-gel will not be formed.

The critical concentration may correspond to the distribution of molecules at which neighboring molecules just interact. In this respect, following consideration may be of some interest. If all the molecules of polyvinyl alcohol are assumed to have the same degree of polymerization, P, and to have segmental configuration, then the square mean end to end distance of the polymer molecule is given by $l(P/n)^{1/2}$, where l is the length of the segment and n the number of monomer units in one segment. Since the mass of the monomer is 7.36×10^{-23} gr, and the critical concentration C_r represents the grams of solute in 100 cc of water, the number of molecules in the unit mass of the solution is $1.36\times(C_r/P)\times10^{20}$.

If we divide the solution into cubes of equal volume and allow one molecule to exist in each cube then the length of the side of cube, a, is given by

$$a=(7.36\times10^{-21}\cdot P/C_r)^{1/3}, \qquad (6)$$

For the case of $P=1740$, C_r is 0.36 gr/100 cc and we have

$$\left.\begin{aligned} l(P/n)^{1/2}&=43l(n)^{-1/2}\\ a&=3.3\times10^{-6}\text{ cm}\end{aligned}\right\} \qquad (7)$$

The length of the segment l can be taken to be equal to $1.54\times10^{-8}\times2n$ cm, where 1.54×10^{-8} cm is the length of the $C-C$ bond and n is a number usually smaller than 10. Therefore,

$$\begin{aligned} l(P/n)^{1/2}&=43\times1.54\times10^{-8}\times2n^{1/2}\\ &=1.32\times10^{-6}n^{1/2} \qquad (8)\end{aligned}$$

If, at the critical concentration, the length of the cube a is supposed to be equal to the square mean end to end distance of the polymers, i.e. $l(P/n)^{1/2}=a$, the value of n should be taken equal to 6 which is a reasonable value.

In the dilute solution below the critical concentration, the relation between the dose and the degree of polymerization is represented by curves with a minimum and a maximum as shown in Fig. 2. These results may be interpreted by considering that both degradation and cross-linking are taking place[9]. A theoretical treatment of this phenomena will be published by Saito elsewhere.

Above the critical concentration, a detailed discussion was given by Charlesby[4]. Gel formation was explained by him by postulating indirect action and the effect of end-linking. His argument was carried out on the aqueous solution of polyvinyl pyrrolidone, but it may also be applied to polyvinyl alcohol, as it does not rest upon any special chemical character of the polymers. Of course, the mere existence of the critical concentration and of the minimum of the minimum dose required for gel formation at a certain concentration can be explained by a simple probability calculation assuming that the energy absorbed by water is used for the gel formation if the effects of both cross-linking and degradation or even only of cross-linking is assumed to take place[4]. Extensive treatment of the mechanism is not, however, possible from the knowledge obtained from our experiment alone, and will not be concerned here.

§ 5. Conclusion

Polyvinyl alcohol which belongs to the so-called degradation type polymer can be cross-linked when irradiated in the presence of water. The mechanism underlying its process, however, can not be made clear without a more detailed physical experiments such as on the temperature effect* and also the chemical experiments are carried out. Especially, the interaction of H^+, OH^-, H, OH, H_2O_2, HO_2 etc. which are the products of irradiation of water, with the molecules of polyvinyl alcohol would be an important and an interesting problem which deserves detailed investigation.

§ 6. Acknowledgment

The author wishes to express his sincere thanks to Dr. K. Shinohara of the Scientific Research Institute, Dr. A. Amemiya of the Faculty of Engineering, University of Tokyo and Dr. A. Harashima of Tokyo Institute of Technology for their constant encouragement and also to Dr. M. Tomonari of the Kurashiki Rayon Company for kindly preparing the samples of polyvinyl alcohol. He also wishes to thank the Tokyo Polymer Irradiation Group for their helps in the experiment.

* Minimum dose required for the gel formation changes considerably when the temperature is changed.

References

1) A. O. Allen: The Science and Engineering of Nuclear Power **II** (1949) 207; Discs. Faraday Soc. **12** (1952) 72.
C. J. Hochanadel: Int. Conf. Peac. Atom. En. (Geneve) P/739 June (1955).
T. Rigg, C. Stein and J. Weiss: Proc. Roy. Soc. A, **211** (1952) 375; J. Am. Chem. Soc. **77** (1955) 4526.
2) A. Chapiro, C. Cousin, Y. Landler and M. Magat: Discs. Faraday Soc. **12** (1952) 98.
N. Bach: Int. Conf. Peac. Atom. En. (Geneve) P/683 June (1955).
3) E. Collinson and F. S. Dainton: Discs. Faraday Soc. **12** (1952) 234.
4) A. Charlesby and P. Alexander: J. Chim. Phys. **52** (1955) 699.
P. Alexander and A. Charlesby: J. Polymer Sci. **23** (1957) 355.
P. Alexander and A. Charlesby: Radiobiology Symposium (1954) 49.
5) E. Collinson and A. J. Swallow: Chem. Rev. **56** (1956) 471.
6) J. Berkowich, A. Charlesby and V. Desreux: J. Polymer Sci. **25** (1957) 490.
7) A. Danno: J. Phys. Soc. Japan. **13** (1958)
8) private communication from Dr. A. Amemiya.
9) A. Charlesby: Proc. Roy. Soc. A, **231** (1955) 521.

JOURNAL OF THE PHYSICAL SOCIETY OF JAPAN Vol. 13, No. 7, JULY, 1958

The Paramagnetic Resonance Absorption of Some Free Radicals in Sulfuric Acid Solution

By Yasaburo YOKOZAWA

Research Institute of Applied Electricity, Hokkaido University, Sapporo

(Received November 12, 1957)

The paramagnetic resonance absorptions in sulfuric acid solutions of some organic compounds, bianthrone, perylene and thio-compounds were observed at 9 kMc/sec under the range of room temperature to the liquid air temperature. One of these samples and the free radical of D.P.P.H. were attached to the different parts of the resonance cavity and their absorptions were separated through the difference of the static magnetic field in each position. The absorption intensities of the sample and the free radical were compared with each other and the number of unpaired electrons was calculated. In bianthrone the number was independent on temperature, while in perylene and thio-compounds it decreased with decreasing temperature. The activation energies of perylene and thio-compounds calculated from their temperature dependencies were respectively 1.7 kcal mol^{-1} and 5.8 kcal mol^{-1}. On the activation energies and the absorption intensities, some considerations were made.

§ 1. Introduction

There have been many papers on paramagnetic resonance absorptions of powders or liquid solutions of organic free radicals. The detection of the paramagnetic resonance absorption was attempted on such aromatic compounds as anthanthrone, benzanthrone, pyranthrone, perylene, violanthrone and violanthrene. However the absorptions were not detected except those of powder of violanthrone and violanthrene[1] and the sulfuric acid solutions of perylene[2], violanthrone and violanthrene. Of these substances we interested in perylene which had resonance absorption only in sulfuric acid solution. The paramagnetic resonance absorptions of bianthrone[3] and thio-compounds[4] in sulfuric acid were already reported. So the work was attempted to measure the temperature dependencies of absorption intensities of these substances.

The homogeneity of magnetic field of the electromagnet available in this work was too poor to resolve the hyperfine structures of paramagnetic absorption of free radicals. Only

the absorption area was thus studied at several temperatures. The inhomogeneity of magnetic field smoothened the hyperfine structures of absorption line and the sensitivity of the apparatus was reduced. However the smoothened resonance curve facilitated the measurement of absorption area.

Few papers have reported the temperature dependency of absorption area but it seems to be important in order to understand the nature of absorption of free radicals.

§ 2. Experimental Procedure

Measurements were made at a frequency of about 9 kMc/sec in the range of room temperature to the liquid nitrogen temperature. The method of magnetic modulation was used and to eliminate the crystal detection noise, two ways were employed. The first way was a superheterodyne detection system similar to the one by Schneider and England[5]. The reflected power from the resonance cavity was balanced using a magic tee to a level at which a superheterodyne receiver could be used. A slide screw tuner in the arm opposite to the cavity arm of the magic tee was adjusted to select the absorption signal in the detection arm correctly. In this way an absorption curve was observed by a C.R.O. and the absorption intensity was easily measured. When the cavity was cooled, beside the retuning of the cavity, the adjustment of the slide screw tuner was necessary not to include the dispersion signal. As it was very troublesome, the transmission cavity was employed as the second way. In this way only the retuning of the cavity was necessary in the cooling process, but as the level of transmitted power was not low the superheterodyne detection was not available. As usual, to a small absorption, the derivatives of absorption curves were recorded using a narrow band amplifier followed by a lock-in amplifier. The modulation frequency was 240 c/s and the time constant of recording system was about 3 sec and the time necessary to sweep a full curve had order of 3 to 5 minutes.

As sulfuric acid is dispersive in a microwave range and the Q of the cavity is greatly reduced, only a small amount of sample was available. A simple consideration shows that in the transmission cavity the optimum amount of sample is obtained when the Q loaded with the sample is 8/9 of the loaded Q without the sample[6]. The amount of sulfuric acid solution used in this work was selected not to decrease the Q remarkably and the amount of sample soluble into this solvent had the order of a few mg. The solution was closed in a polyethylene envelope and attached to the bottom of the cavity.

The 2.1 cm gap of the available electromagnet necessitated some device for the resonance cavity used at a low temperature as shown in Fig. 1. Both an input and an

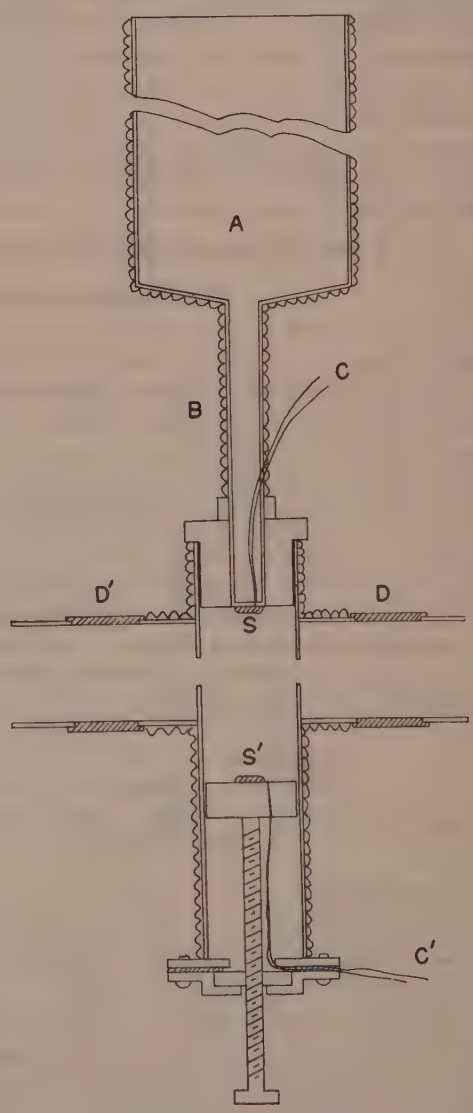

Fig. 1. The resonance cavity used in low temperatures, where A represents a liquid air vessel, B, an insulater coat of asbestos, C, C', copper constantan thermocouples, D, D', thermal insulating wave-guides and S, S' samples.

output waveguide feed were thermally insulated by bakelite waveguides, inside walls of which were plated by aluminium foils. Cooling was performed by the use of liquid nitrogen in the vessel attached to the cavity. Two samples were attached to the bottom and the ceiling of the cavity respectively and their temperatures were measured by two different copper constantan thermocouples. Though cooling was inherently inefficient, a constant temperature was obtained for a sufficiently long time to measure resonance absorptions.

The resonance absorption of α-diphenyl-β-picryl-hydrazyl (designated as D.P.P.H.) placed separately in the portion where the sample occupied had several peaks. From the spacings of these peaks, the inhomogeneity of the magnetic field was estimated about 3 oersteds at a field strength of 3000 oersteds. Though the shape of the absorption curve is thus deformed, the area of absorption is not influenced by the inhomogeneity, because each unit volume of sample contributes the equal area to the absorption intensity. By the inhomogeneity the hyperfine structure was not resolved and the sensitivity of apparatus was reduced, but the line shapes were simplified and the measurement of absorption area became facilitated by the lack of hyperfine structure.

§ 3. The Measurement of Susceptibility by Paramagnetic Resonance Absorptions

If the line width of paramagnetic resonance absorption is narrow, the next relation is easily obtained form Kramers' equation

$$\chi(0)=a\frac{A}{g}\,, \qquad (1)$$

where $\chi(0)$ is static magnetic susceptibility, g, g-factor, A, the area of magnetic resonance absorption and a, a proportional constant. Thus the static susceptibility is calculated from an absorption intensity. This method is superior to other methods when paramagnetic components are hidden in the diamagnetic part of molecules.

To obtain the absolute value of magnetic susceptibility, the areas of absorptions of both a sample to be tested and a standard sample with known susceptibility attached to the same cavity were compared. As a standard sample, D.P.P.H. or other free radical such as Wurster's blue was used and it was attached to the bottom (ceiling) of the cavity with the sample to the ceiling (bottom). The setting of the cavity was adjusted so as to separate the absorptions of two substances through the difference of magnetic fields at their positions in order to compare their intensities. To ascertain the correctness of this procedure, two samples with equal amount of free radical of Wurster's blue, were attached to the

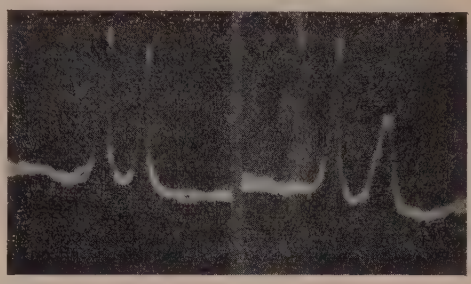

Fig. 2. Paramagnetic resonance absorptions of two samples with equal amount of Wurster's blue which are separated through the difference of the static magnetic fields in each position. In the right figure, one absorption line is broadened due to the inhomogeneity of static magnetic field, the absorption area remaining unchanged.

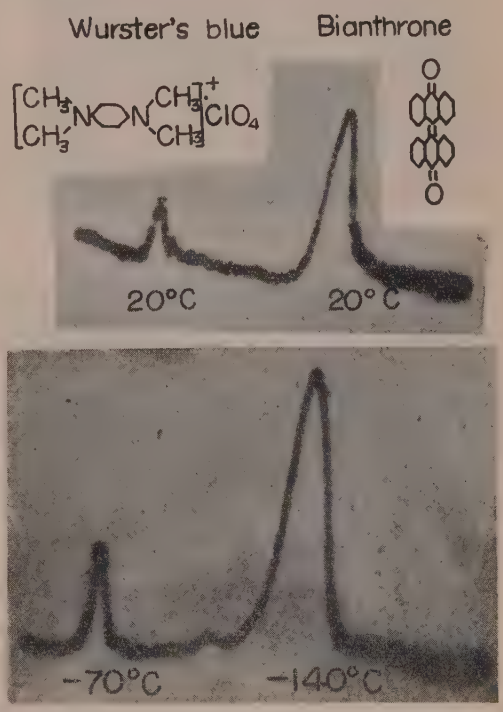

Fig. 3. Paramagnetic resonance absorptions of Wurster's blue and bianthrone in sulfuric acid at different temperatures.

cavity as described above and their absorption intensities were compared. Fig. 2 shows the results in different settings of the cavity. Both absorptions have equal areas in spite of the deformation of absorption curve. Moreover, it was ascertained that the same mole number of D.P.P.H. and Wurster's blue had same absorption area and correctness of this procedure was thus established.

§ 4. Results and Discussion

(a) Bianthrone

Photographs of the absorption of the sulfuric acid solution of bianthrone observed on a C.R.O. detected by a superheterodyne system are shown in Fig. 3. In this case, Wurster's blue was used as a standard free radical.

As magnetic susceptibility χ is expressed as follows;

$$\chi=\frac{g^2\beta^2NS(S+1)}{3kT}, \qquad (2)$$

where N is the number of paramagnetic centers and other notations have their usual meanings, the ratio of the resonance absorption intensity of samples to that of Wurster's blue at the same temperature, $\chi/\chi_{\text{w.b.}}$ is proportional to the numbers of unpaired electrons of sample, when the temperature of Wurster's blue is above 190°K[7] in which this free radical obeys the Curie's law. Though the temperatures of the samples and the free radical were different, the absorption intensity of the free radical at the sample temperature was calculated.

The ratio $\chi/\chi_{\text{w.b.}}$ was independent on temperature and the number of unpaired electrons did not change.

Heated bianthrone shows also the paramagnetic resonance absorption[8]. The products of heated material and the solution in sulfuric acid have probably the similar structures.

(b) Perylene

The absorptions of perylene detected by a derivative curve at different temperatures are shown in Fig. 4. D.P.P.H. was used as a standard free radical obeying Curie's law down to a very law temperature[9]. The ratio of susceptibility of the sample to that of D.P.P.H. $\chi/\chi_{\text{D.P.P.H.}}$ decreased with decreas-

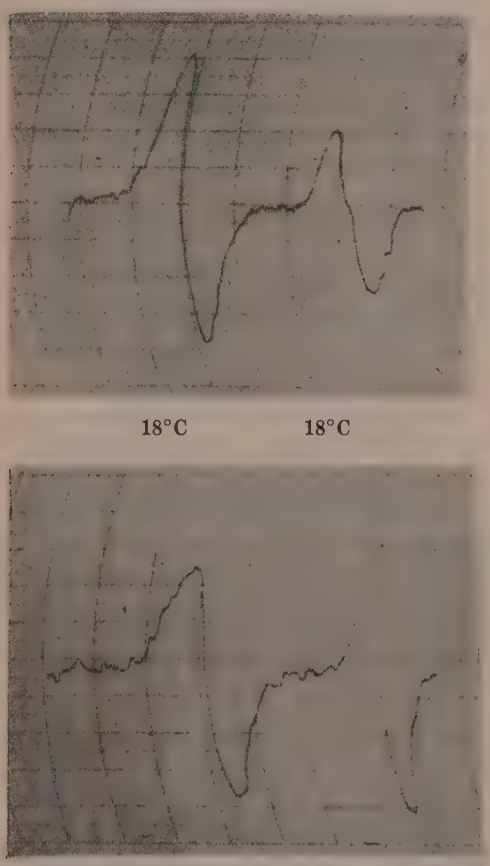

Fig. 4. Paramagnetic resonance absorptions of D.P.P.H. and perylene in sulfuric acid at a room temperature and in the low temperatures.

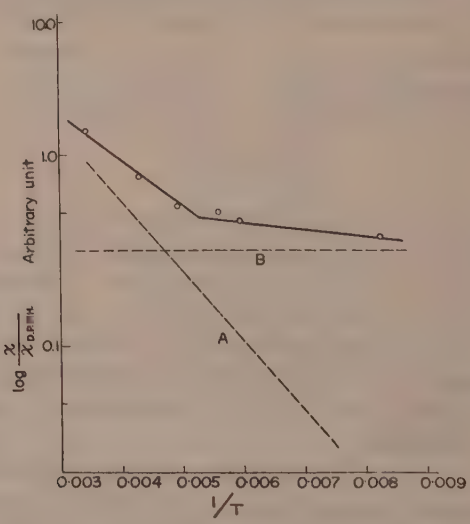

Fig. 5. The relation between the ratio of susceptibility of perylene in sulfuric acid to that of D.P.P.H. and temperatures. As for straight lines A and B, see the paper.

ing temperature and the relation between the logarism of the ratio and the inverse of absolute temperature is shown in Fig. 5. Nearly straight line with a bend at 180°K was obtained. This absorption may be considered to consist of two parts, A and B. The part A that is dependent on temperature may be assumed to be caused by an excited state and from the slope of the straight line A the activation energy ΔE is obtained as

$$\Delta E = 1.70 \text{ kcal mol}^{-1} . \qquad (3)$$

As an excited state which has a resonance absorption, a triplet state may be considered. Under the assumption that ΔE is equal to the energy difference between the ground singlet and excited triplet states, the populations of these two states N_1 and N_2 can be connected with each other by the following equation;

$$N_2/N_1 = 3 \exp(-\Delta E/kT) . \qquad (4)$$

From this relation N_2 is calculated using Eq. (3) and using Eq. (2), the magnetic susceptibily of the sulfuric acid solution of perylene is obtained. The results are shown in Table I. The susceptibility of the part B was neglected, for it had the order of 10% of the whole value at room temperature and was not important in the next rough estimation. Magnetic susceptibily is also measured by the absorption intensity. The total error consisted mainly 15% in measuring of line widths and a certain degree in measuring the amount of samples. The calculated and observed values are fairly in agreement.

Table I. Ratios of molar magnetic susceptibility of sample to that of D.P.P.H. at a room temperature

Samples	Structure formula	ΔE (kcal/mol)	$\chi/\chi_{D.P.P.H.}$ (observed)	$\chi/\chi_{D.P.P.H.}$ (calculated)
Perylene		1.7	0.32±0.06	0.40
Thiophenol	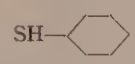	5.8	—	2×10^{-4}
Diphenylsulfide	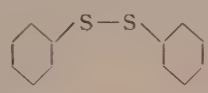	〃	0.06±0.01	〃
Thianthrene	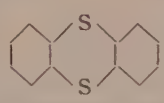	〃	0.05±0.01	〃

As the cause of the existence of contribution of the triplet state to magnetic susceptibility, next reasons may be considered:

(a) In sulfuric acid, the structure of perylene is deformed so that the energy of the triplet state lowers,

(b) Positive ions of perylene are formed in sulfuric acid so that an appreciable population of the triplet state at room temperature is yielded.

According to the private communication from Dr. Niira, there are two fourfold degenerate states in perylene when it is considered as a system of π electrons. The energy levels are shown in Fig. 6 together with those of naphthalene, where W is energy, α, a Coulomb integral and β, a resonance integral between neighbouring carbon atoms[10]. From this result, it is clear that the energy

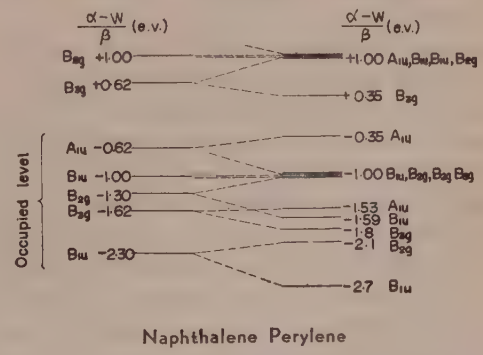

Fig. 6. The energy levels of π electrons in naphthalene and perylene. W: energy, α: Coulomb integral, β: resonance integral

necessary to excite the ground state to the triplet state is large and the condition of (a) is very unlike even in the sulfuric acid solution as was already stated by Weissman *et al*[11]. In order that (b) is correct, four positively charged ions, in which π electrons fill up to the lower fourfold degenerate level, must be considered. As the degeneracies of this level are removed by the interraction of next neighbour of carbon atoms, an excited triplet state exists near the ground singlet state. However, there are some questions about the appearance of four charged ions. Four charged ions may be not always necessary for the population of the triplet state at room temperature. The energy levels of positive ion may be different from Fig. 6 especially in sulfuric acid, and the possibility of existence of triplet state of divalent ion near the ground state may be admitted. Divalent positive ion of perylene in sulfuric acid may be the cause of resonance absorption.

There is no other evidence of triplet state near the ground state. As the optical transition from a triplet to a singlet state is forbidden, the triplet state is detected only as a weak phosphorescence, which will be hidden in the strong vibrational spectra of molecules and perhaps it will hardly be observed.

Weissmann *et al.*[11][12] reported the paramagnetic resonance absorptions of anthracene, tetracene and perylene in sulfuric acid solution and stated that singly charged positive ions were responsible for a part of resonance absorption. In the present work, the resonance absorption of anthracene in sulfuric acid solution was also detected but it was so small that its temperature dependency could not be measured.

Recently MacLean *et al.*[13] stated that the paramagnetism in sulfuric acid was due to oxidation products of the aromatics. As reported previously[2], the precipitates obtained by throwing the sulfuric acid solution into ice water showed a resonance absorption. It was very weak in the precipitate obtained from fresh sulfuric acid solution and became stronger in that obtained from old solution. This fact shows the existence of some chemical reaction in the sulfuric acid.

It seems that there is no decisive reason to determine which opinion is correct. On the nature of perylene in sulfuric acid, further experiments are desired.

(c) Thio-compounds

In the case of the sulfuric acid solution of thiophenol, two absorptions were obtained as stated by Wertz and Vivo[4] but the hyperfine structures of each line were not resolved due to the inhomogeneity of magnetic field. The sulfuric acid solution of diphenylsulfide and thianthrene was observed to have only one absorption line on the contrary to the results by Wertz and Vivo[4]. The appearance of two lines may depend on the condition of solving the sample into sulfuric acid. Even in the case of thiophenol, there was frequently the case that only one absorption line appeared. The results of the temperature dependency of thiophenol were previously reported[14].

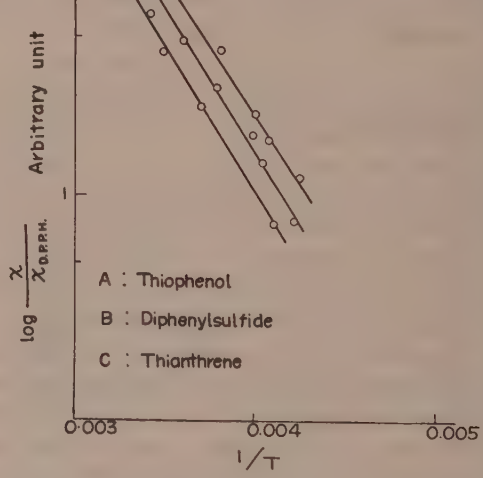

Fig. 7. The relation between the ratio of susceptibility of thio-compounds in sulfuric acid to that of D.P.P.H. and temperatures.

Fig. 7 shows the results obtained in diphenylsulfide and thianthrene with the results of one absorption line of thiophenol. The activation energies of thio-compounds were common and it was equal to

$$\Delta E = 5.80 \text{ kcal mole}^{-1}. \qquad (5)$$

The comparison of observed and calculated values of susceptibility is given in Table I. As thiophenol is liquid at room temperature, its amount was not measured and the comparison was not made. Contrary to the case

of perylene, even the orders of both values are not in agreement*.

This compounds may be in the dissociation equilibrium with free radicals in sulfuric acid solution. The temperature dependency of absorption intensity may be caused by the change of a dissociation constant. Their common value of activation energy shows the fact that the absorptions are caused by the same origin in these substances.

In conclusion some discussion must be done about the line widths. The unchange of line width is partly caused by the inhomogeneity of magnetic field. In the case of perylene, the line width was fairly narrow and showed the existence of exchange narrowing, whereas the diluted perylene in sulfuric acid solution was reported to have the hyperfine structures[11)12)] and fairly wide overall line width. Consequently, broadening of the resonance absorption in the process of decrease of temperature will be expected on account of the decrease of exchange narrowing with the decrease of unpaired electrons. In the case of thio-compounds the line width may be caused by the superposition of hyperfine structures, so the change of line width will not be observed.

The author wishes to express his sincere thanks to Dr. K. Niira, Tokyo Institute of Technology, for his helpful discussion. He is also grateful to Messrs. I. Miyashita and I. Tatsuzaki for their assistance throughout the work. This work was supported in part by a Grant in Aid from the Ministry of Education.

References

1) Y. Yokozawa and I. Tatsuzaki: J. Chem. Phys. **22** (1954) 2087.
H. Akamatu, S. Mrozowski and D. Wobschall: Carbon Conference in Buffalo (1957).
2) Y. Yokozawa and I. Miyashita: J. Chem. Phys. **25** (1956) 796.
3) J. M. Hirshon, D. M. Gardner and G. K. Fraenkel: J. Am. Chem. Soc. **75** (1953) 4115.
4) J. E. Wertz and J. L. Vivo: J. Chem. Phys. **23** (1955) 2193.
5) E. E. Schneider and T. S. England: Physica **17** (1951) 221.
6) M. W. P. Strandberg, M. Tinkham, I. H. Solt, Jr., and C. F. Davis, Jr.: Rev. Sci. Inst. **27** (1956) 596.
7) T. L. Chu, G. E. Pake, J. Townsend and S. I. Weissman: J. Phys. Chem. **57** (1953) 905.
8) W. G. Nielsen and G. K. Fraenkel: J. Chem. Phys. **21** (1953) 1619.
9) L. S. Singer and C. Kikuchi: J. Chem. Phys. **23** (1955) 1738.
H. J. Gerritsen, S. Okkes, H. M. Gijsman and J. van den Handel: Physica **20** (1954) 13.
10) K. Niira: Private communication.
B. Pullman and A. Pullman: *Les théorie électroniques de la chimie organique*, Masson et Cie (1952).
11) S. I. Weissman, E. de Boer and J. J. Conradi: J. Chem. Phys. **26** (1957) 963.
12) E. de Boer: thesis, Univesity of Amsterdam (1957).
13) C. MacLean and J. H. van der Waals: J. Chem. Phys. **27** (1957) 827.
14) Y. Yokozawa and I. Miyashita: J. Phys. Soc. Japan **12** (1957) 107.

* The statement in our previous paper[14)] should be corrected that the resonance absorption of thiophenol was due to a triplet states.

JOURNAL OF THE PHYSICAL SOCIETY OF JAPAN Vol. 13, No. 7, JULY, 1958

Moving Striations in Arc Discharge

By Hirosi YOSHIMOTO, Mituo SATO and Yasuhiro NAKAO
Department of Physics, Faculty of Science, Okayama University

(Received February 7, 1957)

In the same manner as in glow discharge, the moving striations are observed in arc discharge. From the patterns of light oscillation, a light intensity wave travelling towards the cathode is obtained. The phenomenon of the moving striations is one manifestation of the light intensity wave which occurs due to an interaction between the following two waves, a space charge wave travelling towards the cathode and an electron density wave. The former changes the electron emission of the cathode, and this produces the latter. The stationary striations observed in the positive column also seem to be one aspect of the light intensity wave.

§ 1. Introduction

In arc discharge as well as in glow discharge, oscillations are usually observed in tube voltage, current and light intensity. Hitherto many experimental data[1)~4)] have been reported concerning the striations in positive column of rare gas and mercury vapour discharge. These informations, however, are insufficient to give a theoretical explanation for striations. In particular, no relationship has been discovered between moving and stationary striations. In 1951, Donahue and Dieke[5)] reported the oscillatory phenomena in direct current glow discharge comprehensively.

One of the present writers has previously reported the oscillatory phenomena of arc in hot-cathode discharge tube like fluorescent lamp[6),7)]. In his reports the mechanisms of electrical oscillations have been discussed, but the moving striations accompanied by these oscillations have not been mentioned. The oscillations were not the so-called "Plasma Oscillation," and the frequencies were below 2000 cycle/sec. The circumstances of these oscillations mentioned in his reports may be summarized as follows.

The electrical oscillations are due to the periodical variation of the anode fall accompanied with sudden ionizations and are very much influenced by thermoionic emissivity of cathode, Hg vapour pressure, arc current, etc.. These oscillations can be easily controlled by ion-supply into the anode fall.

From these results we can say that, if there should happen periodical ionizations in front of the anode, the change of the space charge at the anode fall inevitably propagate towards cathode. In this view point we may expect that some sorts of moving striation appear in the positive column and the space charge wave modulates the thermoionic emission or the discharge current. We have already reported the phenomenon of moving striation several times[8)~10)]. In this paper we report collectively the experimental results of moving striation obtained hitherto. The discharge tube used is the same as ordinary fluorescent lamp, except that it has no fluorescent film on the inner surface of the tube wall. The cathode is self-heated by the discharge current itself, so that its thermoionic emissivity will change with current. This point is the special feature of this arc discharge which differs from the case of glow discharge.

§ 2. Experimental Apparatus and Technique

The experimental technique is almost the same as that of Donahue and Dieke. The experimental arrangement is shown in Fig. 1.

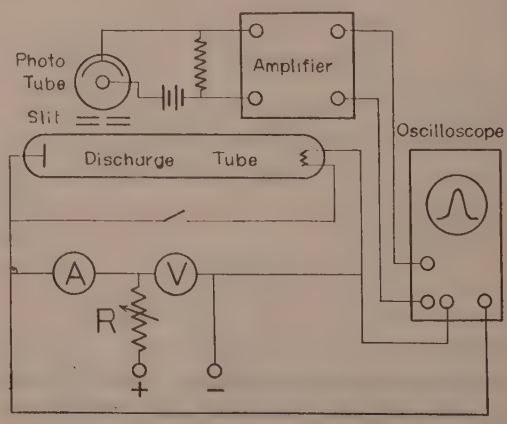

Fig. 1.

Discharge tube mounted horizontally has the same cathode as that of 20 watt fluorescent lamp and is filled with 4 mm Ar gas and Hg vapour. The arc discharge is maintained by a regulated rectifier power-supply in series with a variable resistance R. Photo-tube is movable horizontally almost in contact with the discharge tube. Light is admitted to the photo-tube through narrow slits. The electric circuit of photo-tube is shielded from the induction of electrical oscillations. Output currents from the photo-tube circuit flow through a resistance at the input terminals of an oscillograph, and the driven sweep of the oscillograph is triggered by the voltage oscillations. The light output about a selected point in the arc discharge is given by the pattern on the cathode ray tube screen as a function of time. Thus the moving striations can be easily observed by plotting the phase of the light intensity depending on the observation point of the arc discharge. The discharge voltage can be studied as a function of time, external resistance and ambient temperature merely by bringing leads directly from the electrodes to the oscillograph. The cathode filament can be externally heated by making current to flow through it by a suitable d.c. source, if it is needed to change the thermoionic emissivity of cathode.

§ 3. Modes of Moving Striations

Oscillations in the tube voltage, the current and the light intensity were observed for the current over the range 0.02–0.4 amp. Oscillations are unstable at a certain range of the current which is shifted to the smaller or larger value according to the increase or decrease of ambient temperature, as shown later. When the discharge is stable, regular oscillations are always observed and the positive column appears quite homogeneous or shows the appearance of stationary striations. The light intensity oscillations have always the same frequencies as that of the voltage oscillations. This shows that these two oscillations are different manifestations of the same phenomenon, as Donahue and Dieke have already pointed out. The light at any point of observation has two components, an a.c. one and a d.c. one. For the simplicity of the measurement, we observed the a.c. component.

Fig. 2 shows an example of the light intensity oscillations at different points in the tube. In this figure the zero of time is the moment at which the current takes its minimum value. The phase of the maxima of the light intensity oscillations retards and the amplitude of oscillation changes with the increasing distance

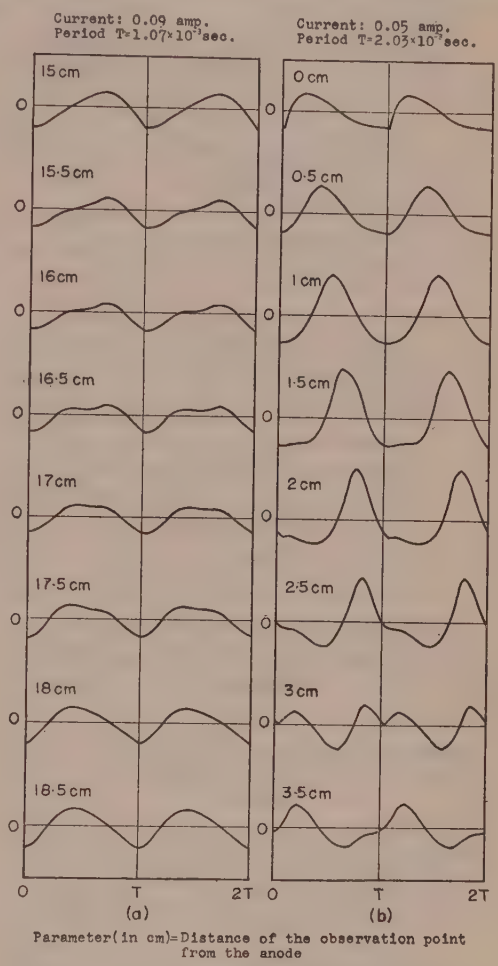

Fig. 2.

from the anode. This indicates that the maxima of light intensity oscillation travel from the anode towards the cathode. We shall call each of the maxima of the light intensity observed in the oscillation pattern a "striation" hereafter. Its movement over the whole length of the tube is shown in Fig. 3, where the abscissa is the distance of the observation point from the anode and the ordinate the time when a striation passes this point. This figure shows that there exist three different modes according to the current ranges. Mode (a): For the current 0.1–0.4 amp the moving

striation is observed only in the range 0–2 cm in front of the anode, but nowhere in the positive column. Mode (b): For the current 0.08–0.1 amp the moving striation is observed also in the cathode-side region of the positive column as well as in front of the anode. Mode (c): For the current below 0.08 amp

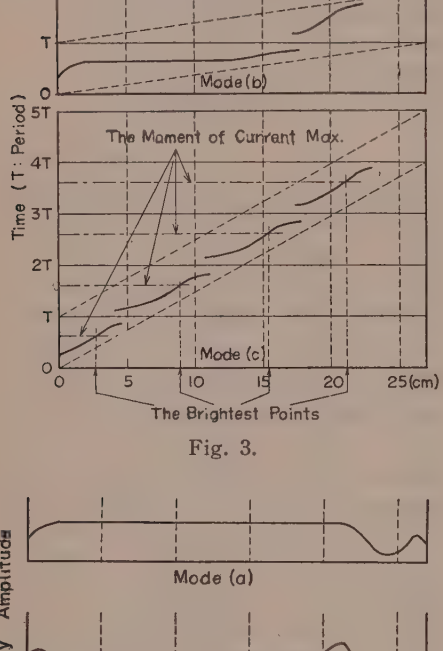

Fig. 3.

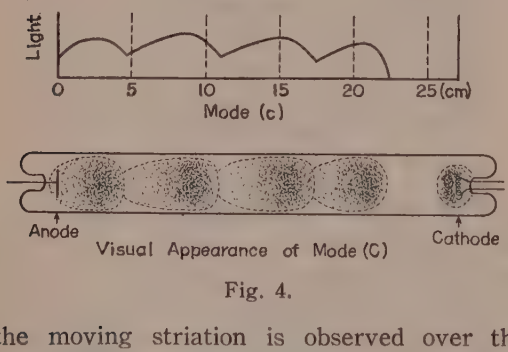

Fig. 4.

the moving striation is observed over the whole positive column. In this case the plot of striation is represented by curve segments discontinuous just at the moments of the current minimum, each segment, therefore, being always within one period. This discontinuity is, however, no characteristic property of the moving striation for the current below 0.08 amp, because for this current range we can get rather continuous curve by changing the experimental conditions, i.e. external resistance, ambient temperature, etc..

Next, the variation of the amplitude of the light oscillation versus the distance from the anode is shown in Fig. 4, where the modes (a), (b) and (c) correspond to the modes (a), (b) and (c) in Fig. 3 respectively. The curves in (a), (b) and (c) embody the visual appearances of discharge, as it is the case for mode (c). Generally, in the region where the moving striations are observed, the points at which the amplitude of light oscillation takes its maximum or minimum value correspond nearly to the brightest or darkest points in the tube respectively. From Figs. 3 and 4 it is obvious that the phase of the striation at the brightest points coincides just with that of the current maximum. These facts show that in this case the stationary striations may be understood to be one manifestation of moving striations.

Now we mention some essential features of light oscillation. When we keep our eyes on the phase of minimum of the light oscillation in Fig. 2, we notice that there are two types of patterns of oscillation as follows. The one has a character that, though the maximum of oscillation retards, the minimum doesn't and its phase coincides always with that of the current minimum as shown in Fig. 2 (a). The moving striations of modes (a) and (b) in Fig. 3 belong to this type. The other has a character that both the maximum and the minimum retard as shown in Fig. 2 (b). The moving striations of mode (c) in Fig. 3 belong to this type. On the other hand, we can notice that the patterns of oscillation have one or two maxima within one period of current oscillation according to the observation point. When the curve of the movement of striation is discontinuous as for mode (c) in Fig. 3, the patterns of oscillation have always two maxima at the neighorurhood of the discontinuity of the curve. If the movement of striation is represented by a continuous curve throughout the positive column, the patterns of oscillation will have only one maximum within one period at every point of observation.

We can get the instantaneous distribution of the variations of the light intensity throughout the positive column by measuring the

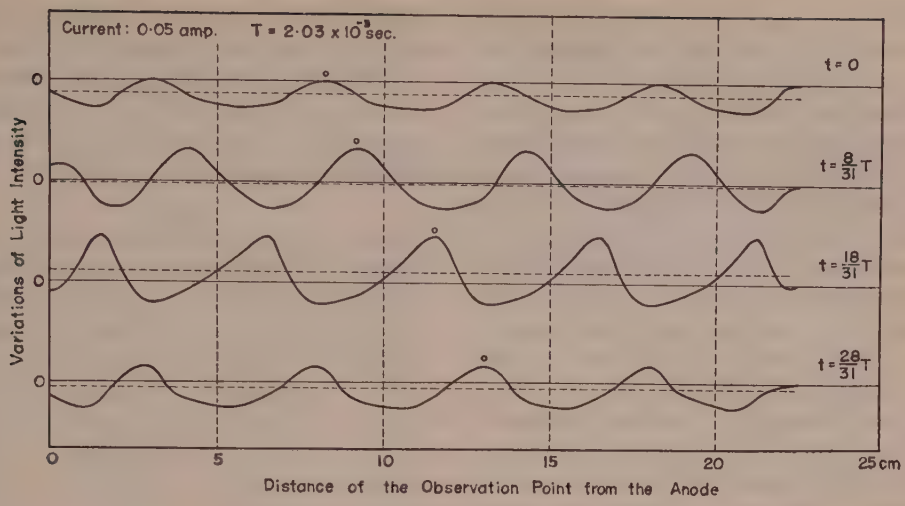

Fig. 5.

instantaneous deviations from the zero-level of light oscillation at different points of the tube. Fig. 5 shows a number of example of this distribution curve which were measured at different moments within one period of the oscillation. From these examples it is obvious that in the positive column there exists a travelling wave with a constant wave length towards the cathode. Both the amplitude and the shape of this wave are repeated periodicaly throughout the positive column. This means that in the positive column there is no singularity to be regarded as the cause of the stationary striations. This travelling wave, however, changes its amplitude, shape and velocity as it moves along the tube. Fig. 6 shows the changes of amplitude, zero-level and current with time. The zero-level of this wave (broken line in Fig. 5) oscillates periodically up and down with time in such a way that at the maximum or minimum current the displacement of the zero-level is maximum in the positive or negative side respectively and moreover the shape of this curve is similar to the current wave form (compare (b) with (c) in Fig. 6).

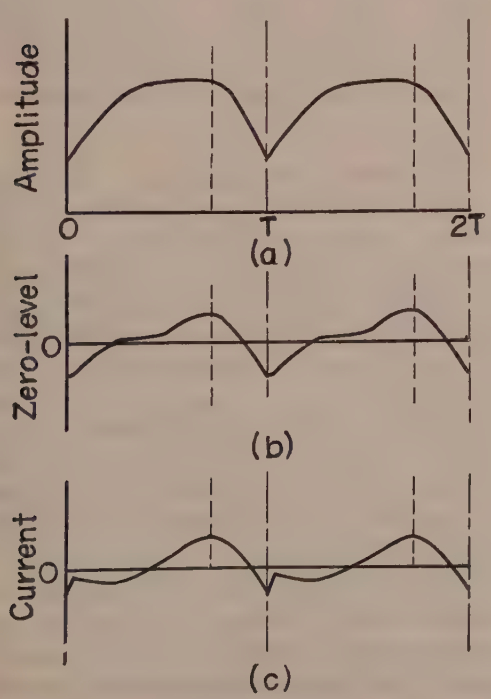

Fig. 6.

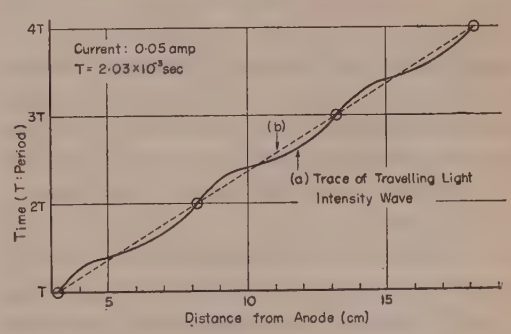

Fig. 7.

From the curves in Fig. 5, we can trace the movement of the travelling wave as shown by curve (a) in Fig. 7. This curve is continuous and quite different from that of the moving striation (see Fig. 3 (c)). It is noticeable that the points marked with (∘) at which this curve crosses with the horizontal lines

corresponding to the moments of the current minimum in Fig. 7 lie on the straight line (b). Since the gradient of the curve in Fig. 7 represents the velocity, the curve (a) shows that the velocity of this travelling wave changes oscillatorily about the constant value obtained from the straight line (b). This constant value is just equal to the product of the wave length and the frequency of oscillation. From the view point of the wave modulation, it is obvious that there exists a travelling wave with constant velocity and this wave must be modulated by a sort of wave in our present case. We can, therefore, say that the travelling light intensity wave shown in Fig. 5 appears due to an interaction of two waves. In order to make clear these circumstances, we must answer, moreover, to the next question, what is the wave modulating the travelling wave with constant velocity. About this problem we shall mention in detail later.

We can thus summarize these experimental results as follows. The time dependent part of the light intensity is composed of two components. One component is represented by a wave which depends on time only and whose wave form is similar to that of current (see Fig. 6 (b)), and the other by a travelling wave which moves towards the cathode changing its amplitude and velocity periodically (see Fig. 5). We may expect that these two components should appear naturally as a result of interaction of two waves as already mentioned. On the other hand, the time independent part of the light intensity depends on the observation point. The distribution of this part coinsides just with the visual appearance of the positive column and must be also given by the interaction of two waves.

§ 4. Velocity of Moving Striation

The velocity of the moving striation is apparently different from that of the travelling light intensity wave and varies as the striation moves along the tube. For the sake of convenience, we now consider the velocity calculated from the straight line (b) in Fig. 7 instead of that of the moving striation for the current over the range 0.02–0.08 amp. Table I shows these velocities for different value of current. The velocities for the current larger than 0,08 amp, however, are rough mean values of the moving striations observed only in front of the anode, because for these values of current the straight lines mentioned in the former case can't be obtained. We see that the velocity of the travelling wave or the moving striation increases with current.

Table I

Current (amp)	Voltage (volt)	Frequency (cycle/sec	Velocity (m/sec)
0.03	42.0	431	29.00
0.05	42.0	493	33.06
0.07	42.0	562	38.00
0.08	42.0	592	40.00
0.09	42.0	930	/
0.10	41.0	979	46.99
0.15	40.0	1125	49.09
0.20	40.0	1190	52.66
0.25	40.0	1149	57.95
0.30	39.0	1284	64.26
0.35	38.0	1338	82.95

Amb. Temp.: 23°C. Series Resistance: 54.8Ω. Gap between Electrodes: 27 cm.

Table II

Current (amp)	Velocity (m/sec)			
	13°C.	20°C.	25°C.	30°C.
0.025	36.95	32.12	32.30	26.96
0.040	42.95	34.30	34.06	27.77

Series Resistance: 150Ω. Gap between Electrodes: 48 cm.

This velocity is very sensitively influenced by the external conditions, i.e. ambient temperature, external resistance, etc.. Table II shows some examples of the dependence of the velocity on ambient temperature. We see that the increase of ambient temperature causes to decrease the velocity of the travelling wave.

The drift velocity of positive ion is equal to the product of its mobility and the field intensity. From the equation given by Compton and Langmuir, we obtain in our experimental conditions

mobility of Hg ion = 24.6 m/sec/volt/cm.

Since in our discharge tube the potential gradient in the positive column is about 1 volt/cm, the drift velocity of Hg ion is about 24 m/sec. From that the velocity of the ob-

served travelling wave is comparable with this drift velocity, it follows that the travelling wave might be a propagating density wave of positive ions.

§ 5. Characteristics of Frequency and Current Oscillation

It has been already mentioned that the light oscillations are always accompanied by current oscillations. The curve I in Fig. 8 shows the dependence of the frequency on the arc current. The frequency increases with the current in this case. It is noteworthy that the frequency changes suddenly at the current 0.1 amp. Corresponding to this, the visual appearance of discharge changes remarkably in such a way that for the current below the discontinuous point it is of the form such as stationary striations and for the current above the point it is of the form such as uniform positive column.

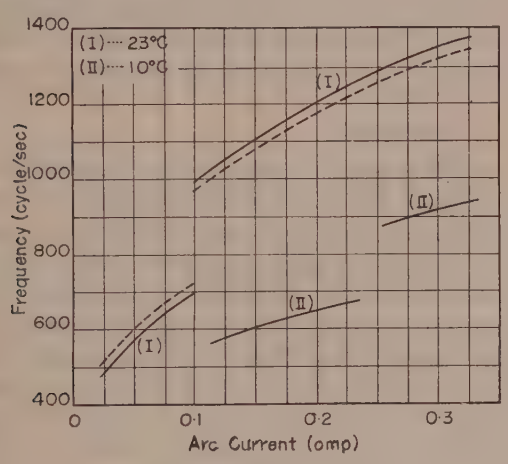

Fig. 8.

Next, expecting the enhancement of the electron emission, we have heated the cathode filament by d.c. 0.15 amp. Then the arc voltage apparently dropped a few volts. As shown by the broken curve in Fig. 8, for the current below the discontinuous point the frequency increases, while for the current above this point it decreases. The frequency change is about 30 cycle/sec. The ambient temperature which determines the Hg vapour density in the tube has great influence on the frequency as well as on the character of discharge. The decrease of the ambient temperature shifts the discontinuous point towards the larger current region and diminishes the frequency remarkably.

The wave form of the current is shown in Fig. 9. There is the portion of the sudden increase of current. This sudden increment and the amplitude of current increase with effective current. The ratio of the time when the current becomes maximum after the moment of its minimum to the period of the current oscillation decreases with the increasing current as shown in Fig. 10.

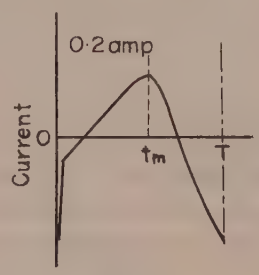

Fig. 9.

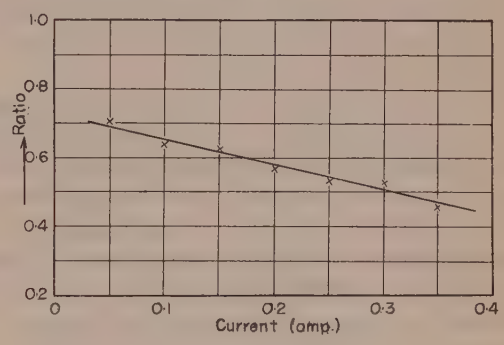

Fig. 10.

§ 6. Mechanism of Light Intensity Wave

We have already mentioned that, whenever the moving striations are observed in the discharge, there exists a light intensity wave in the positive column. In this section we consider the mechanism which produces this light intensity wave.

The oscillatory phenomena of discharge are considered to be necessary for the occurrence of the moving striations. In this sense, the causes of the current (or voltage) oscillation must be those of the light intensity wave. About the causes one of the writers has previously reported a theory[7]. Thus, we can say as follows, if his theory may be adopted here.

(1) In front of the anode there occur sudden ionizations periodically, and then a great deal of positive ions which are too much to

sustain the arc are created at each ionization. These positive ions will be immediately neutralized by the electrons coming from the cathode side and there appears a true plasma, so far as the supply of the electrons is just sufficient to neutralize the positive ions. On the contrary to this, if the supply of electrons is insufficient for neutralization, the positive ions remaining to be neutralized will move towards the cothode as a positive space charge. This may be considered as the origin of the space charge wave travelling towards the cathode.

Whether the supply of electrons is sufficient or not will presumably depend on the thermoionic emissivity of the cathode. Thus we can say these circumstances as follows.

(2) If at the instant of every ionization the cathode is able to emit immediately electrons necessary to neutralize completely the positive ions created at the anode, the space charge wave will not occur. In this case the neutralization must be performed instantaneously at the moment of ionization.

(3) If the cathode is unable to emit sufficient electrons for the neutralization, the space charge wave will appear and the moving striations also will be observed. Here, we must pay attention to the manners of neutralization. If it takes much time for the complete neutralization, during this period a space charge wave will appear and damp away gradually with time.

(4) The space charge wave accompanies necessarily an electric field intensity wave.

(5) Since the light intensity is proportional to the drift velocity of electron determined by the electric field, the electric field intensity wave should accompany a light intensity wave.

(6) The positive space charge wave arrives at the cathode and modulates the electron emission. According to this modulation, the electron density throughout the tube will change nearly instantaneously.

(7) By this change of the electron density the amplitude of the light intensity wave will be modulated, because the light intensity is proportional to the electron density.

From these fundamental processes, we can deduce further that the light intensity wave occurs as such a manifestation of the interaction between the electric field intensity wave and the electron density wave, as it is embodied by

$$L \propto \overline{Q}vn = \overline{Q}kEn \ ,$$

where L is the light intensity, $\overline{Q}$ the mean excitation cross-section for electron, v the drift velocity of electron, n the electron density, k the mobility of electron and E the electric field intensity. If the electron temperature does not vary so appreciably, it may be justified that $\overline{Q}$ is constant. Therefore, in this approximation, we can say that the light intensity wave can be given by the product of the electric field intensity wave and the electron density wave. The former is a travelling wave which moves towards the cathode and its amplitude will depend on the quantity of the positive ions in front of the anode remaining to be neutralized, and the latter is a wave which is expressed by a periodic function of time only and whose wave form is presumably similar to that of current. These two waves, of course, must have the same frequency as that of current.

§ 7. Conclusion

In the same manner as the case of glow discharge, the moving striations have been observed in arc discharge which was burned in a tube like fluorescent lamp with a self-heated oxide-coated cathode. This means that the cause and the characteristic properties of this phenomenon should be essentially the same in both discharges. From the patterns of light oscillations at various points of the positive column we have visualized a light intensity wave which travels towards the cathode changing its amplitude and velocity. The velocity of such a wave is apparently different from that of the moving striation. From the natures of this light intensity wave it has been deduced that there exist an electric field intensity wave travelling towards the cathode and an electron density wave which modulates the preceding wave periodically. Thus the light intensity wave occurs due to the interaction between these two waves. Not only the moving striations but also the visual appearance like stationary striations are apparent manifestations of this interaction. From the analysis of the moving striations we can get the informations of the movement of space charge in plasma.

In our experiment we could not detect a negative space charge wave which moves from the cathode towards the anode. But we believe that such a negative space charge wave corresponds presumably to the electron density wave mentioned above and, as the velocity of this wave is very fast, it is difficult to catch this wave accurately.

Concerning about the characteristic properties of moving striations deduced from our assumption that the light intensity wave is given by the product of the electric field intensity wave and the electron density wave, we shall discuss in detail in the following paper.

Acknowledgement

The writers wish to express their sincere thanks to Professor K. Honda of Tokyo University for his kind encouragement and helpful discussions. The writer's thanks are also due Professor K. Umeda of Okayama University for his kind advices and useful discussions. This research has been supported partly by Grant in Aid for Fundamental Scientific Research from the Japanese Ministry of Education.

References

1) F. W. Aston and T. Kikuchi: Proc. Roy Soc. **98** (1921) 50.
2) T. Kikuchi: Proc. Roy. Soc. **99** (1921) 257.
3) T. Takamine, T. Suga and A. Yanagihara: Sc. Pap. I. P. C. R. **20** (1933) 63.
4) W. Pupp: Phys. Z. S. **36** (1935) 61.
5) T. Donahue and G. H. Dieke: Phys. Rev. **81** (1951) 248.
6) H. Yoshimoto: J. Phys. Soc. Japan **8** (1953) 59.
7) H. Yoshimoto: J. Phys. Soc. Japan **8** (1953) 69.
8) H. Yoshimoto and M. Sato: Res. Notes, Dep't of Phys., Fac. of Sci., Okayama Univ. **10** (1954) 1. (in Japanese)
9) H. Yoshimoto and M. Sato: ditto. **10** (1954) 5. (in Japanese)
10) H. Yoshimoto and M. Sato: ditto. **10** (1954) 9. (in Japanese)

JOURNAL OF THE PHYSICAL SOCIETY OF JAPAN Vol. 13, No. 7, JULY, 1958

Moving Striations due to Space Charge Waves

By Hirosi YOSHIMOTO, Mituo SATO and Yasuhiro NAKAO

Department of Physics, Faculty of Science, Okayama University

(Received February 7, 1957)

In the positive columm there exists a light intensity wave travelling towards the cathode. This wave is assumed to be proportional to the product of the electron density wave and the electric field wave. The equation for such a light intensity wave is considered. All the characteristic properties of the moving striations deduced from the analysis of the equation are presented here and are in favor to those of the observed moving striations. From the phenomena of the moving striations, the informations of the space charge waves in plasma can be obtained.

§ 1. Introduction

As shown in the preceding paper[1], the phenomenon of moving striations is one manifestation of a travelling light intensity wave considered to occur due to the interaction between the electron density wave and the electric field wave in the positive column. We assume the light intensity wave to be proportional to the product of the electron density wave and the electric field wave.

In this paper we deduce the characteristic properties of moving striations from this assumption. For the sake of simplicity, the analysis is carried out for the essentially one-dimentional case in which there is no average charge density in the positive column and

the electric field wave travels towards the cathode keeping its amplitude and velocity constant.

§ 2. Light Intensity Waves in Uniform Plasma

The electron density wave is assumed to be a wave given by

$$n(t)=n_0\{1+\sum_k \eta_k \sin(k\omega t+\varepsilon_k)\}. \quad (1)$$

The electric longitudinal field wave is assumed to be the wave travelling in the $+x$ direction with a constant propagation velocity v_0 given by

$$E=(x,\ t)=E_0\{1+\sum_k \zeta_k \sin(k\omega\tau+\delta_k)\}, \quad (2)$$

where

$$\tau\equiv t-\frac{x}{v_0}. \quad (3)$$

Here, ω is the angular frequency of the electric oscillation, ε_k and δ_k are the phase constants of the kth harmonics of the two waves, η_k and ζ_k are fractions of the amplitudes of the kth harmonics, n_0 is the mean electron density, and E_0 is the mean electric field. According to our assumption mentioned above the fundamental formular of light intensity wave is given by

$$L=nE=L_0\{1+\sum \eta_k \sin(k\omega t+\varepsilon_k)\}\cdot\{1+\sum \zeta_k \sin(k\omega\tau+\delta_k)\}, \quad (4)$$

where

$$L_0=n_0E_0.$$

From (4) we can see first that this wave travels towards the cathode with periodically varying amplitude and with the same propagation velocity as that of the electric field wave.

§ 3. Analysis of Light Intensity Wave

The right side of Eq. (4) can be divided into three terms as follows.

$$L=\overline{L}(x)+L_0A(t)+L_0B(x,\ t), \quad (5)$$

where

$$\overline{L}(x)=L_0\left\{1+\frac{1}{2}\sum \eta_k\zeta_k\cos\left(k\omega\frac{x}{v_0}-\delta_k+\varepsilon_k\right)\right\}, \quad (6)$$

$$A(t)=\sum \eta_k \sin(k\omega t+\varepsilon_k), \quad (7)$$

$$B(x,\ t)=\sum \zeta_k \sin(k\omega\tau+\delta_k)-\frac{1}{2}\sum \eta_k\zeta_k\cos(k\omega t+k\omega\tau+\delta_k+\varepsilon_k)+\sum_{(k\neq l)}\sum \eta_k\zeta_l \sin(k\omega t+\varepsilon_k)\sin(l\omega\tau+\delta_l). \quad (8)$$

Here it must be noted that the third term in the right side of (8) doesn't contain the products of the same order harmonics.

Since the time averages of functions (7) and (8) vanish, the time average of L is just equal to $\overline{L}(x)$. This means that the visual appearance of the positive column should be not uniform and similar to that of stationary striations. The schematic characters of the three terms (6) to (8) match to those of the three components obtained in our experiment. For the sake of simplicity, we take only the fundamental harmonics $k=1$ into account, as

$$n(t)=n_0\{1+\eta \sin(\omega t+\varepsilon)\}, \quad (1)'$$

$$E(x,\ t)=E_0\left\{1+\zeta \sin\left(\omega t+\frac{\omega}{v_0}x+\delta\right)\right\}, \quad (2)'$$

and

$$\overline{L}(x)=L_0\left\{1+\frac{1}{2}\eta\zeta\cos\left(\frac{\omega}{v_0}x-\delta+\varepsilon\right)\right\}, \quad (9)$$

$$A(t)=\eta \sin(\omega t+\varepsilon), \quad (10)$$

$$B(x,\ t)=\zeta \sin(\omega\tau+\delta)-\frac{1}{2}\eta\zeta\cos\left(2\omega t-\frac{\omega}{v_0}x+\delta+\varepsilon\right), \quad (11)$$

omitting suffix 1.

§ 4. Travelling Part of Light Intensity Wave

Eq. (11) can be rewritten as

$$B(x,\ t)=\beta \sin\psi, \quad (12)$$

where

$$\beta\equiv\zeta\left\{1+\frac{1}{4}\eta^2+\eta \sin(\omega t+\varepsilon)\right\}^{1/2}, \quad (13)$$

$$\psi\equiv\omega\left(t-\frac{x}{v_0}\right)+\delta-\frac{1}{2}\eta\cos(\omega t+\varepsilon)+\frac{1}{8}\eta^2\sin 2(\omega t+\varepsilon)-\cdots. \quad (14)$$

We see that the function $B(x,\ t)$ represents a travelling wave which moves towards the cathode changing its amplitude as well as velocity. The amplitude β is a function of t only, and its maximum or minimum occur in phase with those of electron density n. Its maximum and minimum values are $(1+1/2\cdot\eta)\zeta$ and $(1-1/2\cdot\eta)\zeta$ respectively. So that the value of η can be determined from the ratio of the maximum value to the minimum

value measured experimentally. As

$$\omega t = 2n\pi + \frac{1}{2}\pi - \varepsilon$$

at the maximum of the amplitude β, this gives

$$\boldsymbol{B}(x, t) = \zeta\left(1 + \frac{1}{2}\eta\right)\cos\left(\frac{\omega}{v_0}x - \delta + \varepsilon\right). \quad (15)$$

By comparing (15) with (9), it will be known that the two waves $\overline{L}(x)$ and $B(x, t)$ are in phase at this time. This means that at the brightest or darkest points of the stationary striations the amplitude of the wave $B(x, t)$ is maximum or minimum. In our experiment, we have obtained also these relations.

Differentiating (14) with respect to t, we obtain the phase velocity v of the travelling wave $B(x, t)$ as follows.

$$v = v_0\left\{1 + \frac{1}{2}\eta\sin(\omega t + \varepsilon) + \frac{1}{4}\eta^2\cos 2(\omega t + \varepsilon) - \cdots\right\} \quad (16)$$

$$= v_0\left\{1 + \frac{1}{2}\eta\sin(\omega t + \varepsilon)\right\}, \quad (16\text{–a})$$

being neglected the second and the higher power of η.

By comparing (16–a) with (1)′, we see that the phase velocity v changes periodically in phase with the electron density $n(t)$ as shown in Fig. 1(a). At the instant when $n(t)$ is maximum or minimum the velocity v is also maximum or minimum. These features can be observed in our experiment. If the value of η is negligibly small, the velocity of the travelling wave $B(x, t)$ is nearly constant

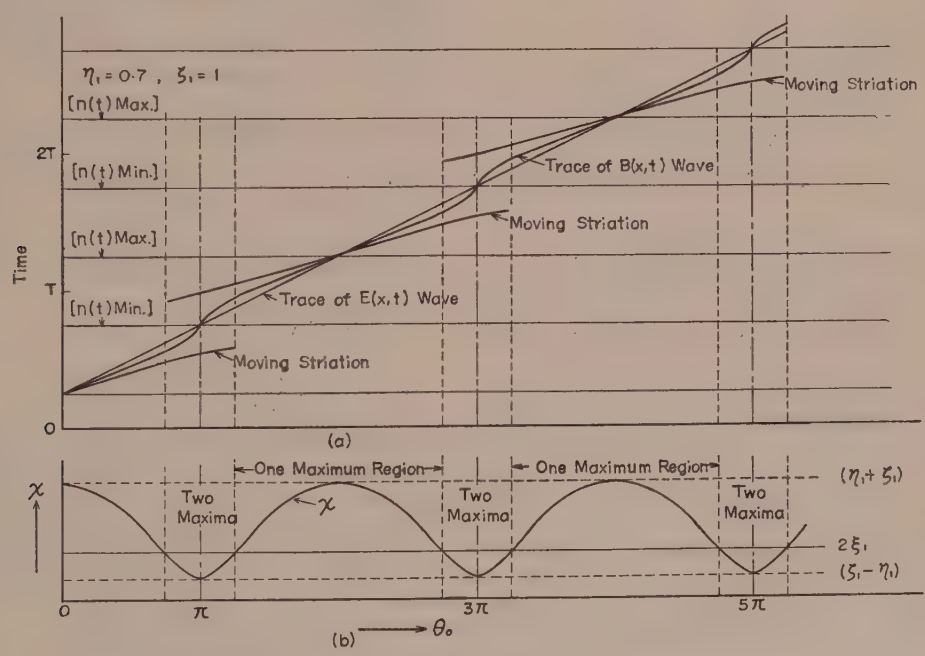

Fig. 1.

and equal to the velocity v_0 of the electric field wave.

In the preceding paper we have mentioned that the zero-level of the travelling wave oscillates periodically up and down. This point can also be explained clearly by (10) and (12). These two equations correspond just to the two components into which the a.c. part of the light intensity wave was divided. When the amplitude β of the travelling wave $B(x, t)$ is maximum or minimum, $A(t)$ is equal to η or $-\eta$. The former case means that the zero-level of the travelling wave is maximum at the positive side of the stationary zero-level, and the latter case means that it is minimum at the negative side.

§ 5. Time-dependent Part of Light Intensity Wave and Moving Striations

We will consider the moving striations. (10) and (11) can be rewritten as

$$\begin{aligned}\boldsymbol{A}(t)+\boldsymbol{B}(x,\ t)&=\{\eta\sin(\omega t+\varepsilon)+\zeta\sin(\omega\tau+\delta)\}\\&\quad-\frac{1}{2}\eta\zeta\cos(\omega t+\omega\tau+\delta+\varepsilon)\\&=\chi\sin(\omega t+\varepsilon-\varphi)\\&\quad+\xi\cos\left(2\omega t-\frac{\omega}{v_0}x+\delta+\varepsilon-\pi\right),\end{aligned}\tag{17}$$

where

$$\chi=\left\{\eta^2-\zeta^2+2\eta\zeta\cos\left(\frac{\omega}{v_0}x+\varepsilon-\delta\right)\right\}^{1/2},\tag{17-a}$$

$$\xi=\frac{1}{2}\eta\zeta\,.\tag{17-b}$$

The first term in the right side of (17) contains φ as a phase angle. This φ is a function of x and its expression changes with the relative magnitude of η and ζ as follows.

In the case, $\eta>\zeta$, φ is a periodic function of x, as

$$\begin{aligned}\varphi&=\frac{\zeta}{\eta}\sin\left(\frac{\omega}{v_0}x+\varepsilon-\delta\right)\\&\quad-\frac{1}{2}\left(\frac{\zeta}{\eta}\right)^2\sin 2\left(\frac{\omega}{v_0}x+\varepsilon-\delta\right)-\cdots.\end{aligned}\tag{18}$$

In the case, $\eta<\zeta$, φ is an increasing function of x, as

$$\begin{aligned}\varphi&=\left(\frac{\omega}{v_0}x+\varepsilon-\delta\right)-\frac{\eta}{\zeta}\sin\left(\frac{\omega}{v_0}x+\varepsilon-\delta\right)\\&\quad+\frac{1}{2}\left(\frac{\eta}{\zeta}\right)^2\sin 2\left(\frac{\omega}{v_0}x+\varepsilon-\delta\right)-\cdots.\end{aligned}\tag{19}$$

Let

$$\left.\begin{aligned}&\frac{\omega}{v_0}x+\varepsilon-\delta\equiv\theta_0,\qquad\theta_0-2\varphi\equiv\theta,\\&\theta_0-\varphi+\frac{\pi}{2}-\varepsilon\equiv\omega t_0,\ t-t_0\equiv t',\\&\boldsymbol{A}(t)+\boldsymbol{B}(x,\ t)\equiv\Gamma\cos\Phi.\end{aligned}\right\}\tag{20}$$

We then obtain from (17)

$$\Gamma\cos\Phi=\chi\cos(\omega t'+\theta)+\xi\cos(2\omega t'+\theta)\,.\tag{21}$$

In order to make clear the characteristic properties of the moving striations, it is important to know the time when $\Gamma\cos\Phi$ takes its maximum value. Now, differentiating (21) with respect to t, we can obtain

$$\begin{aligned}&\frac{d}{dt}(\Gamma\cos\Phi)\\&=\omega\left\{\chi\cos\left(\omega t'+\theta+\frac{\pi}{2}\right)\right.\\&\quad\left.+2\xi\cos\left(2\omega t'+\theta+\frac{\pi}{2}\right)\right\}=\omega\Gamma'\cos\Phi',\end{aligned}\tag{22}$$

where

$$\Gamma'\equiv(\chi^2+4\xi^2+4\xi\cos\omega t')^{1/2},\tag{22-a}$$

for the case $\chi>2\xi$,

$$\begin{aligned}\Phi'&=\omega t'+\theta+\frac{\pi}{2}+2\frac{\xi}{\chi}\sin\omega t'\\&\quad+2\left(\frac{\xi}{\chi}\right)^2\sin\omega t'+\cdots,\end{aligned}\tag{22-b}$$

and for the case $\chi<2\xi$,

$$\begin{aligned}\Phi'&=2\omega t'+\theta+\frac{\pi}{2}-\frac{1}{2}\frac{\chi}{\xi}\sin\omega t'\\&\quad+\frac{1}{8}\left(\frac{\chi}{\xi}\right)^2\sin\omega t'-\cdots.\end{aligned}\tag{22-c}$$

The valve of Γ' is always positive is so far as $\chi\neq 2\xi$. So the maximum or minimum value of $\Gamma\cos\Phi$ will be obtained from the condition: $\cos\Phi'=0$. And it will be immediately known that $\Gamma\cos\Phi$ takes its maximum value, if

$$\Phi'=2n\pi+\frac{\pi}{2}\,.\tag{23}$$

This equation yields for the case $\chi>2\xi$,

$$\omega t=2n\pi+\left(\frac{\pi}{2}-\varepsilon\right)+\varphi-2\frac{\xi}{\chi}\sin\omega(t-t_0)+\cdots,\tag{24}$$

and for the case $\chi<2\xi$,

$$\begin{aligned}\omega t&=n\pi+\left(\frac{\pi}{2}-\varepsilon\right)\\&\quad+\frac{\theta_0}{2}+\frac{\chi}{4\xi}\sin\omega(t-t_0)+\cdots.\end{aligned}\tag{25}$$

The coefficients of the sine terms in Eqs. (24) and (25) are smaller than unity. So neglecting the sine terms, we can say that the maxima of light intensity oscillation appear at interval of one or a half period respectively, that is, for the case $\chi>2\xi$, only one maximum will be observed within one period of the current oscillation while, for the case $\chi<2\xi$, two maxima will be observed.

§ 6. Relation between χ and ξ

From Eq. (17-a) we see that

$$\text{max. value of }\chi=\eta+\zeta>\eta\zeta=2\xi$$

as $\eta<1$ and $\zeta<1$, and

$$\text{min. value of }\chi=|\eta-\zeta|.$$

Here

$$\eta-\zeta\gtreqless\eta\zeta(=2\xi)\qquad(1>\eta>\zeta)$$

and

$$\zeta-\eta\gtreqless\eta\zeta(=2\xi).\qquad(1>\zeta>\eta)$$

For the case $|\eta-\zeta|=2\xi$,

$$\eta=\frac{\zeta}{1-\zeta}, \qquad (\eta>\zeta) \tag{26}$$

thus $1>\eta>0$ and $0.5>\zeta>0$, and

$$\eta=\frac{\zeta}{1+\zeta}, \qquad (\eta<\zeta) \tag{27}$$

thus $0.5>\eta>0$ and $1>\eta>0$. If

$$\eta>\frac{\zeta}{1-\zeta} \qquad (\eta>\zeta)$$

or

$$\eta<\frac{\zeta}{1+\zeta} \qquad (\eta<\zeta),$$

we obtain

$$\eta-\zeta>\eta\zeta \qquad (\eta>\zeta)$$

or

$$\zeta-\eta>\eta\zeta \qquad (\eta<\zeta)$$

respectively. Fig. 2 shows these circumstances graphically. If the point $(\eta\zeta)$ is in the domain A or D, $\chi>2\xi$ throughout the positive column. While, if the point $(\eta\zeta)$ is in

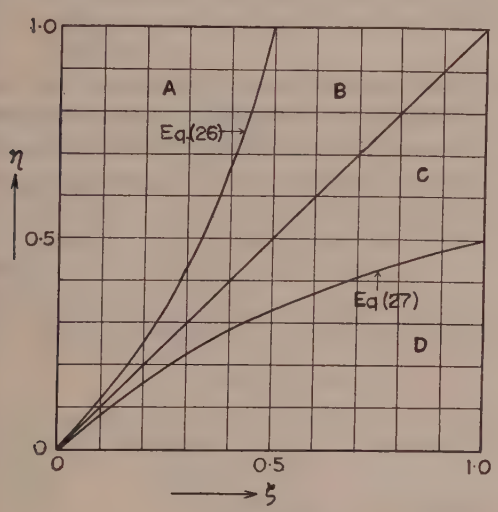

Fig. 2.

the domain B or C, in the positive column there are two sorts of regions, that is, the regions in which $\chi>2\xi$, and the regions in which $\chi<2\xi$. Fig. 1(b) shows this example. From this figure we see that these two sorts of regions situate alternately in the positive column. This is the reason why two different types of the light oscillation pattern (the one has only one maximum within one period and the other has two maxima) are observed in the positive column, and at the same time this is also the reason why the curve of the movement of striation is discontinuous. If χ is always larger than 2ξ throughout the positive column, only the type of the oscillation pattern having one maximum will be observed, and the curve of the movement of striation will be continuous.

§ 7. Movement of Striations

From (24) and (25) we can know the movement of striation. This movement will show quite different features according to whether η is larger or smaller than ζ. This is due to the facts that, as already mentioned, φ is a periodic or monotonic function of x according to the relative magnitude of η and ζ.

1. The case: $\eta>\zeta$. Neglecting the terms of the second and the higher power of ζ/η in (18) for the sake of simplicity, we obtain

$$\varphi=\frac{\zeta}{\eta}\sin\left(\frac{\omega}{v_0}x+\varepsilon-\delta\right)=\frac{\zeta}{\eta}\sin\theta_0\,. \tag{28}$$

If $\chi>2\xi$ throughout the positive column, inserting (28) into (24) we obtain

$$\omega t=2n\pi+\left(\frac{\pi}{2}-\varepsilon\right)+\frac{\zeta}{\eta}\sin\theta_0 - 2\frac{\xi}{\chi}\sin\omega(t-t_0)+\cdots. \tag{29}$$

If $\chi\gg 2\xi$, this yields approximately

$$\omega t=2n\pi+\left(\frac{\pi}{2}-\varepsilon\right)+\frac{\zeta}{\eta}\sin\theta_0\,. \tag{29-a}$$

Thus the maxima of the light intensity oscillation appear nearly at the same time throughout the positive column, and those phase differences will be shown as a periodic function of x. In such a case, therefore, the so-called "moving striation" will not appear, and the striation seems to move periodically back and forth according to the increase of x.

If there exist the regions of $\chi<2\xi$ in the positive column, the curve of the movement of the striation is discontinuous as shown in Fig. 3. In these regions the striations move towards the cathode with a velocity nearly equal to $2v_0$. Thus in such a case the moving striation will appear.

2. The case: $\eta<\zeta$. From (19) we obtain approximately

$$\varphi=\theta_0-\frac{\eta}{\zeta}\sin\theta_0\,. \tag{30}$$

If $\chi>2\xi$ throughout the positive column, the curve of the movement of the striation is continuous.

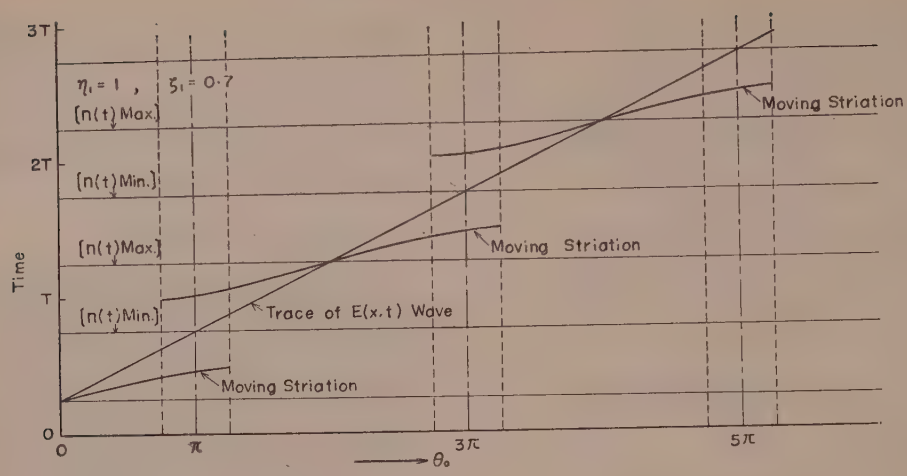

Fig. 3.

Inserting (30) into (24) we obtain

$$\omega t = 2n\pi + \left(\frac{\pi}{2} - \varepsilon\right) + \theta_0 - \frac{\eta}{\zeta}\sin\theta_0 - 2\frac{\xi}{\chi}\sin\omega(t-t_0) + \cdots. \quad (31)$$

If $\chi \gg 2\xi$, this yields approximately

$$\omega t = 2n\pi + \left(\frac{\pi}{2} - \varepsilon\right) + \theta_0 - \frac{\eta}{\zeta}\sin\theta_0 . \quad (31\text{–a})$$

As θ_0 is a monotonic function of x, this equation shows that t increases with x. Therefore, the striation moves towards the cathode and its velocity is more or less v_0. If $\eta \ll \zeta$, the velocity is just equal to v_0, and according to the increase of the value of η, it will become to change periodically. And, when the value of η becomes larger than $\zeta/(1+\zeta)$, in the positive column there appear the regions in which $\chi < 2\xi$, and the curve of the movement of the striation will become discontinuous. In such regions the velocity of the moving striation is nearly equal to $2v_0$. Thus, in this case ($\eta < \zeta$) the moving striations are always observed.

The coefficients η and ζ correspond to the modulation factors of the two waves (the electron density wave and the electric field intensity wave) respectively. Therefore, we can say that the features of the moving striations are greately influenced by the relative magnitude of the modulation factors of these two waves as follows. When the modulation factor of the electron density wave is far greater than that of the field intensity wave, the moving striations will not be observed. And, when the modulation factor of the former wave is smaller than that of the latter wave, the moving striations will be always observed. Moreover, when the magnitudes of the modulation factors of the two waves are comparable, the moving striations will be observed and the movement of the striation will be shown by curve segments.

§ 8. Relation between the Phases of the Minima of the Light Oscillations and those of the Electron Density Wave

In contrast to (23), the phases of the minima of the light oscillations are

$$\Phi' = 2n\pi + \frac{\pi}{2} + \pi . \quad (32)$$

This equation yields for the case $\chi > 2\xi$,

$$\omega t = \pi + 2n\pi + \left(\frac{\pi}{2} - \varepsilon\right) + \varphi - 2\frac{\xi}{\chi}\sin\omega(t-t_0) + \cdots, \quad (33)$$

and for the case $\chi < 2\xi$,

$$\omega t = \pi + n\pi - \varepsilon + \frac{\theta_0}{2} + \frac{\chi}{4\xi}\sin\omega(t-t_0) - \cdots, \quad (34)$$

corresponding to (24) and (25) respectively. While the phases of the minima of the electron density wave are given by

$$\omega t = \pi + 2n\pi + \left(\frac{\pi}{2} - \varepsilon\right). \quad (35)$$

Comparing (35) with (33) it will be known that, if $\eta > \zeta$, the minima of the light oscillations coincide nearly with that of the elec-

tron density wave and they seem only to oscillate periodically back and forth at definite points in the oscillation patterns. Alternatively, if $\eta < \zeta$, the minima of the light oscillations move towards the cathode with increasing x. These relations hold for the case $\chi > 2\xi$.

Next, we shall consider the case $\chi < 2\xi$. In this case, as already mentioned, the schematic characters of (34) are hardly affected by the relative magnitude of η and ζ, because (34) does not contain the term φ. The regions where $\chi < 2\xi$ situate always at the vicinity of the points at which the value of θ_0 is $(2n+1)\pi$ (refer to Fig. 1(b)). Thus the term $\theta_0/2$ in (34) has its value nearly equal to $(n+1/2)\pi$. This means that, though the light oscillation patterns in such regions have two minima within one period of the oscillation, one of these two minima always coincides nearly with the minima of the electron density wave.

§ 9. Electron Density Wave and Current Oscillation

As already mentioned, the modulation factor of the electron density wave η and then that of the electric field intensity wave ζ can be determined, if we measure the ratio of the maximum value to the minimum value of β given in (13). On the other hand, the modulation factor of the current oscillation is obtained from the oscillographic pattern of the current. Table I shows these moluation

Table I

Current (amp.)	E-Wave ζ	n-Wave η	Current Wave η'
0.020	0.96	0.092	0.098
0.025	0.86	0.087	0.092
0.030	0.80	0.090	0.088
0.040	0.70	0.069	0.073

Temp.: 30°C. Series Resistance: 150Ω. Gap between Electrodes: 48 cm.

factors obtained in our experiment. From this table we see that the modulation factor of the electron density wave is always nearly equal to that of the current wave. Here it should be noted that the modulation factor shows only the magnitude of the fundamental wave. If we consider our experiment from the viewpoint of the relationship between the phases of minima of the light oscillation and the electron density wave, the current wave seems to correspond to the electron density wave. Therefore, we may take the current wave instead of the electron density wave. However, as already mentioned in the preceding paper, the wave form of the current does not coincide with that of the electron density, though these wave forms are similar to each other. Fig. 4 shows this example.

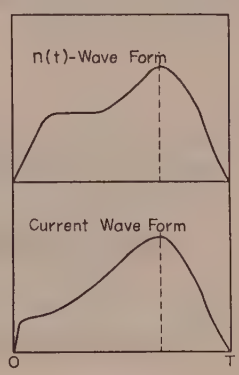

Fig. 4.

From this figure we see that the discrepancies between these two waves are remarkable at the earlier part of the period and negligibly small at the later part. From the harmonic analysis of these waves, the electron density wave seems to be obtained by neglecting the third and the higher harmonics of the current wave. At all events, the two wave forms are not identical, but the more the current changes slowly, the more the two wave forms will be similar to each other. In the discharge space the total energy consumed in unit time is equal to the product of current and field intensity. On the other hand, in our theory the energy radiated as light is proportional to the product of electron density and field intensity. Therefore, the wave form of the electron density allows to estimate the manner of contribution of the current to the light emission.

§ 10. Conclusion

The light intensity wave has been assumed to be represented by the product of the electric field intensity wave and the electron density wave. This basic assumption explains all the experimental results and establishes the characteristic properties of the moving

striations as well as the stationary striations. We believe that in the positive column there exists a space charge wave travelling towards the cathode. This seems to play an essential role for the phenomena of moving striations irrespectively of whether the discharge may be arc or glow.

Acknowledgement

The writers wish to express their sincere thanks to Professor K. Honda of Tokyo University for his kind encouragement and helpfull discussions. The writer's thanks are also due Professor K. Umeda of Okayama University for his kind advices and useful discussions. This research has been supported partly by Grant in Aid for Fundamental Scientific Research from the Japanese Ministry of Education.

References

1) H. Yosimoto, M. Sato and Y. Nakao: J. Phys. Soc. Japan **13** (1958) 734.

JOURNAL OF THE PHYSICAL SOCIETY OF JAPAN Vol. 13, No. 7 JULY, 1958

Flow Formation with Suction or Injection

By R. S. NANDA

Department of Mathematics, Indian Institute of Technology, Khargpur, India

(Received March 15, 1958)

The problem of boundary layer control with suction or injection is discussed for the cases, (1) flow formation between two planes at a finite distance apart, (2) flow formation in the annular space between two concentric circular cylinders.

Exact solutions of the full Navier-Stokes equations are obtained in both the cases. Results obtained by Hashimoto for an infinite flat plate are deduced as a special case.

§ 1. Introduction

With the aim of reducing the drag suffered by a body and increasing the maximum lift several methods have been devised for the purpose of artificially preventing separation and delaying transition to turbulence. The method of suction has been found particularly useful. Many authors have studied steady boundary layer problems with a normal velocity imposed on the body. In view of its immense utility, especially in the field of aeronautical engineering, it is worthwhile considering unsteady boundary layer problems with suction.

Hasimoto[1] has recently considered the unsteady motion of an infinite flat plate with suction or injection. He has obtained exact solutions of the Navier-Stokes equations for the cases when suction velocity is constant and when it varies as $t^{-1/2}$.

In the present paper we consider, (1) formation of couette motion and (2) flow formation in the annular space between two concentric circular cylinders, when one of the parallel boundaries is kept fixed and the other is started to move with a velocity $U(t)$ and simultaneously a normal velocity $V(t)$ is imposed on the moving boundary. The case (1) is shown to agree with Hasimoto's results for h, the distance between the two plates, tending to infinity.

§ 2. Formation of Couette Motion

Let us consider the unsteady motion of an incompressible viscous fluid between two parallel flat plates. Let h be the distance between the plates. We take a system of axes fixed in space; x-axis coinciding with one of the plates and y-axis normal to it. Let the plate $y=0$ be started at $t=0$ along x-axis with a velocity $U(t)$ and let the plate $y=h$

be kept fixed. Since the plates are infinite in length, all the physical quantities are independent of x. The Navier-Stokes equations and the equation of continuity reduce to

$$\frac{\partial u}{\partial t}+v\frac{\partial u}{\partial y}=\nu\frac{\partial^2 u}{\partial y^2}\,, \tag{1.1}$$

$$\frac{\partial v}{\partial t}+v\frac{\partial v}{\partial y}=\nu\frac{\partial^2 v}{\partial y^2}-\frac{1}{\rho}\frac{\partial p}{\partial y}\,, \tag{1.2}$$

$$\frac{\partial v}{\partial y}=0 \tag{1.3}$$

The boundary conditions to be satisfied are

$$0\leqslant y\leqslant h \qquad u=v=0 \qquad t\leqslant 0\,,$$

$$\left.\begin{array}{ll}\text{At} & y=0 \quad u=U(t);\ v=V(t);\\ \text{At} & y=h \quad u=0\end{array}\right\}\ t>0\,. \tag{1.4}$$

Equations (1.3) and (1.4) give

$$v=V(t)\,. \tag{1.5}$$

Equations (1.2) and (1.5) then give

$$p=p_0-\rho y\frac{dv}{dt}$$

where p_0 is the value of p at $y=0$ and ρ is the density of the fluid.

Equations (1.1) and (1.5) give

$$\frac{\partial u}{\partial t}+V\frac{\partial u}{\partial y}=\nu\frac{\partial^2 u}{\partial y^2}\,. \tag{1.6}$$

We shall now solve this equation in the cases $V=V_0=$constant and $V\propto t^{-1/2}$.

The case $V=V_0$

In this case let us first find a solution in the form

$$u=U(t)F(y)\,.$$

Substituting in (1.6) we get

$$\frac{U'}{U}=\nu\frac{F''}{F}-\frac{VF'}{F}\,. \tag{1.7}$$

Let

$$\frac{U'}{U}=A \qquad \text{i.e.} \quad U=U_0\exp(At)\,.$$

Then (1.7) reduces to

$$F''-2BF'-K_1F=0\,, \tag{1.8}$$

where $\frac{V}{\nu}=2B$; $\frac{A}{\nu}=K_1$. Boundary conditions to be satisfied are $F(0)=1$; $F(h)=0$. Solution of (1.8) satisfying the boundary conditions is

$$F(y)=\alpha\exp[y(B+\sqrt{B^2+K_1})]+B\exp[y(B-\sqrt{B^2+K_1})]\,, \tag{1.9}$$

where

$$\alpha=\frac{-\exp[-h\sqrt{B^2+K_1}]}{\exp[h\sqrt{B^2+K_1}]-\exp[-h\sqrt{B^2+K_1}]}\,,$$

$$\beta=\frac{\exp[h\sqrt{B^2+K_1}]}{\exp[h\sqrt{B^2+K_1}]-\exp[-h\sqrt{B^2+K_1}]}\,.$$

In order to obtain a general solution for the plate velocity as a general function of time we apply Laplace Transforms.

Let

$$u^*(y,p)=\int_0^\infty \exp(-pt)u\,dt$$

Equation (1.6) reduces to

$$\frac{d^2u^*}{dy^2}-2K\frac{du^*}{dy}-\frac{p}{\nu}u^*=0\,, \tag{1.10}$$

where

$$K=\frac{V_0}{2\nu}\,.$$

The boundary conditions to be satisfied are

$$\left.\begin{array}{l}u^*(0,p)=U^*(p)\,,\\ u^*(h,p)=0\,.\end{array}\right\} \tag{1.11}$$

Thus the solution of (1.10) satisfying (1.11) can be written as

$$u^*=U^*\exp(Ky)\left[\frac{\exp[(y-h)\sqrt{K^2+p/\nu}]-\exp[-(y-h)\sqrt{K^2+p/\nu}]}{\exp[-h\sqrt{K^2+p/\nu}]-\exp[h\sqrt{K^2+p/\nu}]}\right] \tag{1.12}$$

We are now to get the inverse of (1.12). The expression within brackets on the right hand side of Eq. (1.12) can be expanded in an infinite series and hence, we get

$$L^{-1}\left[\frac{\exp[(y-h)\sqrt{K^2+p/\nu}]-\exp[-(y-h)\sqrt{K^2+p/\nu}]}{\exp[-h\sqrt{K^2+p/\nu}]-\exp[h\sqrt{K^2+p/\nu}]}\right]$$

$$=\frac{\exp(-K^2\nu t)}{2\sqrt{\pi\nu t^3}}\left[\sum_{n=0}^{\infty}(2nh+y)\exp\left[-\frac{(2nh+y)^2}{4\nu t}\right]-\sum_{n=0}^{\infty}[(2n+1)h-y]\exp\left[-\frac{\{(2n+1)h-y\}^2}{4\nu t}\right]\right]$$

Finally making use of convolution theorem we get

$$u=\frac{\exp(Ky)}{2\sqrt{\pi\nu}}\int_0^t \frac{U(t-\tau)\exp(-K^2\nu\tau)}{\tau^{3/2}}\left[\sum_{n=0}^{\infty}(2nh+y)\exp\left[-\frac{(2nh+y)^2}{4\nu\tau}\right]\right.$$
$$\left.-\sum_{n=0}^{\infty}[2n+1)h-y]\exp\left[-\frac{\{(2n+1)h-y\}^2}{4\nu\tau}\right]\right]d\tau \tag{1.14}$$

As $h\to\infty$

$$u\to\frac{\exp(Ky)}{2\sqrt{\pi\nu}}\int_0^t y\exp\left(-K^2\nu\tau-\frac{y^2}{4\nu\tau}\right)\frac{U(t-\tau)}{\tau^{3/2}}d\tau\,,$$

which agrees with the result given by Hasimoto. Flow formation without suction can also be obtained from (1.14) by putting $K=0$ and $U=U_0$.

This gives

$$u=U_0[\sum_{n=0}^{\infty}\operatorname{erfc}(2n\eta_1+\eta)-\sum_{n=0}^{\infty}\operatorname{erfc}((2n+1)\eta_1-\eta)]\,,$$

a result agreeing with Schlichting,[2] where $\eta=y/2\sqrt{\nu t}$; $\eta_1=h/2\sqrt{\nu t}$.

The frictional drag D per unit area of the plate is given by

$$D=\frac{u}{2\sqrt{\pi\nu}}\int_0^t \frac{U(t-\tau)\exp(-k^2\nu\tau)}{\tau^{3/2}}\left[\sum_{n=0}^{\infty}\exp\left(\frac{-n^2h^2}{\nu\tau}\right)\left[\frac{2n^2h^2}{\nu\tau}-2nhk-1\right]\right.$$
$$\left.-\sum_{n=0}^{\infty}\exp\left[\frac{(2n+1)^2h^2}{-4\nu\tau}\right]\left[\frac{(2n+1)^2h^2}{2\nu\tau}+kh(2n+1)-1\right]\right]d\tau\,. \tag{1.15}$$

The case $V\propto t^{-1/2}$

As in Ref. (1) we take

$$u=U(t)G(\eta)\,,$$

where

$$\eta=\frac{y}{2\sqrt{\nu t}}\,.$$

Equation (1.6) then takes the form

$$\nu G''=4\nu t\frac{U'}{U}G-2\eta\nu G'+2V\sqrt{\nu t}\,G'\,. \tag{1.16}$$

In order that this may be reducible to an ordinary differential equation, we take

$$4\nu t\frac{U'}{U}=A\,,\qquad 2V\sqrt{\nu t}=B\,.$$

In particular, taking

$$A=2\nu\alpha\,,\qquad B=2\sqrt{\nu}\,V_0\,,$$

we have

$$U=U_0t^{\alpha/2};\qquad V=\frac{V_0}{\sqrt{t}}\,.$$

Equation (1.16) then becomes

$$G''+2(\eta-\eta_0)G'-2\alpha G=0\,, \tag{1.17}$$

where

$$\eta_0=\frac{V_0}{\sqrt{\nu}}\,.$$

Putting

$$G=\exp(-\xi^2)Z$$

where

$$\xi=\eta-\eta_0\,,$$

this gives

$$\frac{d^2Z}{d\xi^2}-2\xi\frac{dZ}{d\xi}-2(1+\alpha)Z=0\,. \tag{1.18}$$

Solution of (1.18) is $Z=\frac{d^\alpha\omega}{d\xi^\alpha}$ where ω satisfies the differential equation

$$\frac{d^2\omega}{d\xi^2}-2\xi\frac{d\omega}{d\xi}-2\omega=0\,. \tag{1.19}$$

Hence, the solution of (1.17) becomes

$$G=\exp[-(\eta-\eta_0)^2\frac{d^\alpha}{d\eta^\alpha}[K_1\exp[(\eta-\eta_0)^2]$$
$$\times\int\exp[-(\eta-\eta_0)^2]d\eta+K_2\exp[(\eta-\eta_0)^2]] \tag{1.20}$$

where K_1 and K_2 are constants to be evaluated from the boundary conditions

$$G(0)=1;\qquad G(\eta_1)=0\,, \tag{1.21}$$

where

$$\eta_1=\frac{h}{2\sqrt{\nu t}}\,.$$

For the Rayleigh's[3] case of impulsive start $U=U_0$ the expression (1.20) satisfying (1.21) becomes

$$G(\eta)=\frac{\operatorname{erf}(\eta_1-\eta_0)-\operatorname{erf}(\eta-\eta_0)}{\operatorname{erf}(\eta_0)+\operatorname{erf}(\eta_1-\eta_0)}\,.$$

In order to get the case of a flat plate we

again make $h\to\infty$ and get

$$G(\eta)=\frac{\operatorname{erfc}(\eta-\eta_0)}{\operatorname{erfc}(-\eta_0)}$$

which is the same as Hasimoto's result.

If the plate $y=0$ is started with a uniform acceleration (i.e. $\alpha=2$) we get

$$G=\exp\left[-(\eta-\eta_0)^2\frac{d^2}{d\eta^2}\left[K_1\exp\{(\eta-\eta_0)^2\}\int\exp\{-(\eta-\eta_0)^2\}d\eta+K_2\exp\{(\eta-\eta_0)^2\}\right]\right] \tag{1.22}$$

where K_1 and K_2 are given by

$$K_1=\frac{[1+2(\eta_1-\eta_0)^2]}{2N}, \qquad K_2=\frac{-[1+2(\eta_1-\eta_0)^2x_1+(\eta_1-\eta_0)\exp[-(\eta_1-\eta_0)^2]]}{2N}$$

$$N=[(1+2\eta_0^2)[1+2(\eta_1-\eta_0)^2][x_0-x_1]-\eta_0\exp(-\eta_0^2)[1+2(\eta_1-\eta_0)^2]$$
$$-[1+2\eta_0^2][\eta_1-\eta_0]\exp[-(\eta_1-\eta_0)^2]]$$

and

$$x_0=\left[\int\exp[-(\eta-\eta_0)^2]d\eta\right]_{\eta=\eta_0}; \qquad x_1=\left[\int\exp[-(\eta-\eta_0)^2]d\eta\right]_{\eta=\eta_1}$$

§ 3. Flow through Concentric Circular Cylinders

We shall now consider the unsteady motion of an incompressible fluid confined between two concentric circular cylinders of radii a and b ($b>a$). We introduce cylindrical coordinates x, y, θ, x-axis coinciding with the common axis of the cylinders. Let the cylinder $y=a$ be started at $t=0$ with a velocity $U(t)$ along x-axis and the cylinder $y=b$ be kept fixed. A normal velocity $V(t)$ imposed on the moving cylinder represents suction. Let u, v, w be the components of the velocity in the directions of x, y and θ increasing respectively. Evidently $w=0$. All the physical quantities are independent of x and θ. The equations of motion and the equation of continuity reduce to

$$\frac{\partial u}{\partial t}+v\frac{\partial u}{\partial y}=\nu\left[\frac{\partial^2 u}{\partial y^2}+\frac{1}{y}\frac{\partial u}{\partial y}\right] \tag{2.1}$$

$$\frac{\partial v}{\partial t}+v\frac{\partial v}{\partial y}=-\frac{1}{\rho}\frac{\partial p}{\partial y}+\nu\left[\frac{\partial^2 v}{\partial y^2}+\frac{1}{y}\frac{\partial v}{\partial y}-\frac{v}{y^2}\right] \tag{2.2}$$

$$\frac{\partial v}{\partial y}+\frac{v}{y}=0 \tag{2.3}$$

and the boundary conditions are

$$\begin{array}{llll} a\leqslant y\leqslant b & u=v=0 & t\leqslant 0 & \\ \text{At} \quad y=a & u=U(t); & v=V(t) & \\ \text{At} \quad y=b & u=0; & & \end{array}\Bigg\}\, t>0\,. \tag{2.4}$$

Equations (2.3) and (2.4) give

$$v=\frac{aV}{y} \tag{2.5}$$

Equations (2.2) and (2.5) then give

$$\frac{p-p_0}{\rho}=\frac{V^2}{2}\left(1-\frac{a^2}{y^2}\right)+a\frac{dV}{dt}\log\frac{a}{y},$$

where p_0 is the value of p at $y=a$ and ρ is the density of the fluid.

Equations (2.1) and (2.5) give

$$\frac{\partial u}{\partial t}+\frac{aV}{y}\frac{\partial u}{\partial y}=\nu\left[\frac{\partial^2 u}{\partial y^2}+\frac{1}{y}\frac{\partial u}{\partial y}\right]. \tag{2.6}$$

We shall now slove this equation in the case when $V=V_0=$constant. This equation can be easily solved by the method of separation of variables.

We write

$$u=U(t)G(y)\,.$$

Equation (2.6) then becomes

$$\frac{U'}{\nu U}=\frac{G''}{G}+\frac{1-R}{y}\frac{G'}{G}, \tag{2.7}$$

where

$$R=aV/\nu$$

Taking

$$U'/U=A \qquad \text{i.e.} \quad U=U_0\exp(At)\,,$$

equation (2.7) reduces to

$$G''+\frac{1-R}{y}G'-\frac{A}{\nu}G=0\,. \tag{2.8}$$

The boundary conditions to be satisfied are

$$G(a)=1\,, \qquad G(b)=0\,. \tag{2.9}$$

The solution of (2.8) satisfying (2.9) is

$$G=y^{R/2}[\alpha I_{R/2}(\sqrt{A/\nu}y)+\beta K_{R/2}(\sqrt{A/\nu}y)]\,, \tag{2.10}$$

where

$$\alpha=\frac{\alpha^{-R/2}K_{R/2}(\sqrt{A/\nu}b)}{I_{R/2}(\sqrt{A/\nu}a)K_{R/2}(\sqrt{A/\nu}b)-I_{R/2}(\sqrt{A/\nu}b)K_{R/2}(\sqrt{A/\nu}a)}\,,$$

$$\beta=\frac{-a^{-R/2}I(\sqrt{A/\nu}b)}{I_{R/2}(\sqrt{A/\nu}a)K_{R/2}(\sqrt{A/\nu}b)-I_{R/2}(\sqrt{A/\nu}b)K_{R/2}(\sqrt{A/\nu}a)}\,.$$

$I_{R/2}$ and $K_{R/2}$ are modified Bessel functions of order $R/2$.

To obtain the general solution when $U=U(t)$ we make use of Laplace transforms. Let us write

$$u^*(y,p)=\int_0^\infty \exp(-pt)u(y,t)dt\,.$$

Equation (2.6) then becomes

$$\frac{d^2u^*}{dy^2}+\frac{1-R}{y}\frac{du^*}{dy}-\frac{p}{\nu}u^*=0$$

the solution of which is easily found to be

$$u^*=y^{R/2}[BI_{R/2}(\sqrt{p/\nu}y)+CK_{R/2}(\sqrt{p/\nu}y)]\,,$$

and since $u^*(a,p)=U^*(p)$ and $u^*(b,p)=0$ we have

$$U^*(p)=a^{R/2}[BI_{R/2}(\sqrt{p/\nu}a)+CK_{R/2}(\sqrt{p/\nu}a)]\,,$$

and

$$0=BI_{R/2}(\sqrt{p/\nu}b)+CK_{R/2}(\sqrt{p/\nu}b)\,.$$

Solving we have finally

$$u^*=\frac{U^*(p)y^{R/2}}{a^{R/2}}\left[\frac{K_{R/2}(\sqrt{p/\nu}b)I_{R/2}(\sqrt{p/\nu}y)-K_{R/2}(\sqrt{p/\nu}y)I_{R/2}(\sqrt{p/\nu}b)}{I_{R/2}(\sqrt{p/\nu}a)K_{R/2}(\sqrt{p/\nu}b)-I_{R/2}(\sqrt{p/\nu}b)K_{R/2}(\sqrt{p/\nu}a)}\right]. \tag{2.11}$$

Now by the inversion theorem

$$L^{-1}\left[\frac{K_{R/2}(\sqrt{p/\nu}b)I_{R/2}(\sqrt{p/\nu}y)-K_{R/2}(\sqrt{p/\nu}y)I_{R/2}(\sqrt{p/\nu}b)}{I_{R/2}(\sqrt{p/\nu}a)K_{R/2}(\sqrt{p/\nu}b)-I_{R/2}(\sqrt{p/\nu}b)K_{R/2}(\sqrt{p/\nu}a)}\right]$$
$$=\frac{1}{2\pi i}\int_{c-i\infty}^{c+i\infty}\left[\frac{K_{R/2}(\sqrt{p/\nu}b)I_{R/2}(\sqrt{p/\nu}y)-K_{R/2}(\sqrt{p/\nu}y)I_{R/2}(\sqrt{p/\nu}b)}{I_{R/2}(\sqrt{p/\nu}a)K_{R/2}(\sqrt{p/\nu}b)-I_{R/2}(\sqrt{p/\nu}b)K_{R/2}(\sqrt{p/\nu}a)}\right]e^{pt}dp\,. \qquad c>0$$

We write $p=-\nu a^2$. Then

$$I_{R/2}(\sqrt{p/\nu}a)K_{R/2}(\sqrt{p/\nu}b)-I_{R/2}(\sqrt{p/\nu}b)K_{R/2}(\sqrt{p/\nu}a)$$
$$=-\frac{\pi}{2}[J_{R/2}(a\alpha)Y_{R/2}(b\alpha)-J_{R/2}(b\alpha)Y_{R/2}(a\alpha)]$$

Let the zeros of $J_{R/2}(a\alpha)Y_{R/2}(b\alpha)-J_{R/2}(b\alpha)Y_{R/2}(a\alpha)$ be $\alpha_1,\ \alpha_2,\ \cdots$.
Then the poles of the integrand are given by $-\nu\alpha_1^2,\ -\nu\alpha_2^2,\ \cdots$.
Let R_n denote the residue at $-\nu\alpha_n^2$

Then

$$R_n=\frac{-\pi\nu\alpha_n^2J_{R/2}(b\alpha_n)J_{R/2}(a\alpha_n)}{J^2_{R/2}(a\alpha_n)-J^2_{R/2}(b\alpha_n)}[J_{R/2}(y\alpha_n)Y_{R/2}(b\alpha_n)-J_{R/2}(b\alpha_n)Y_{R/2}(y\alpha_n)]e^{-\nu\alpha_n^2t}$$

Making use of the convolution theorem we get

$$u=$$
$$-\frac{\pi\nu}{a^{R/2}}\int_0^t y^{R/2}U(t-\tau)\sum_{n=1}^{\infty}\alpha_n^2 e^{-\nu\alpha_n^2\tau}\left[\frac{[J_{R/2}(y\alpha_n)Y_{R/2}(b\alpha_n)-J_{R/2}(b\alpha_n)Y_{R/2}(y\alpha_n)]}{J^2_{R/2}(a\alpha_n)-J^2_{R/2}(b\alpha_n)}\right]J_{R/2}(b\alpha_n)J_{R/2}(a\alpha_n)\,d\tau\,.$$

In conclusion, I wish to express my sincere thanks to Dr. Y. D. Wadhwa for suggesting the problem and to Prof. B. R. Seth for his valuable guidance throughout the work.

References

1) H. Hashimoto: J. Phys. Soc. Japan **12** (1957) 68.
2) H. Schlichting: Boundary Layer Theory, Pergamon Press (1955).
3) Lord Rayleigh: Phil. Mag. (6) **21** (1911) 697.

Short Notes

This section is intended to secure prompt publication of important discoveries in physics. The reports should not exceed 800 words in length. A figure of size 7cm×7 cm will be counted as 150 words.

J. PHYS. SOC. JAPAN **13** (1958) 754~755

The Magnetic Field at the Nucleus of Sm^{+++} induced by Paramagnetism of 4*f*-electrons

By Junjiro KANAMORI and Kenzo SUGIMOTO

Department of Physics, Osaka University, Osaka

(Received, April 22, 1958)

Recently, one of the present authors (K.S.) reported[1] the gyromagnetic ratio of the first excited state (122 kev.) of nuclide Sm^{152}, which was determined by investigating the influence of an external magnetic field on the angular distribution of de-excitation radiation following Coulomb excitation. As briefly discussed in the previous paper[1], the electronic magnetic moment of Sm^{+++} (of which the ground state is $^6H_{5/2}$) induces a magnetic field at the nucleus, which gives rise to some complicacy in the final interpretation of the experimental results. The purpose of this note is to give more detailed discussion on the calculation of the induced field.

In the present case, we assume that the nucleus interacts with a thermal average of the electronic magnetic moment. (The validity of this assumption was discussed in the previous paper[1]*.) Thus we take the thermal average of the interaction between the nucleus and the 4*f*-electrons over the electronic states. The Hamiltonian of the nucleus in external field is given by

$$\begin{aligned}\mathscr{H} &= \mathscr{H}_0+\mathscr{H}_1+\mathscr{H}_2 \\ &= \mathscr{H}_0-\mu_n \boldsymbol{H}_{ex}\cdot\boldsymbol{I}-\mu_n \boldsymbol{H}_{in}\cdot\boldsymbol{I}, \qquad (1)\end{aligned}$$

where $\mathscr{H}_0$ is the electronic energy which determines the thermal distribution among the electronic states; $\boldsymbol{H}_{ex}$ the external field; $\mathscr{H}_2$ the hyperfine coupling between the nucleus and the electrons. The effective Hamiltonian of $\mathscr{H}_2$ in the Russel-Saunders scheme is given by[2]

$$\begin{aligned}\mathscr{H}_2 = -\mu_n \boldsymbol{H}_{in}\cdot\boldsymbol{I} = 2\mu_n\mu_B\langle 1/r^3\rangle[(\boldsymbol{L}\cdot\boldsymbol{I}) \\ +\xi L(L+1)(\boldsymbol{S}\cdot\boldsymbol{I})-(3\xi/2)\{(\boldsymbol{L}\cdot\boldsymbol{S})(\boldsymbol{L}\cdot\boldsymbol{I}) \\ +(\boldsymbol{L}\cdot\boldsymbol{I})(\boldsymbol{L}\cdot\boldsymbol{S})\}], \qquad (2)\end{aligned}$$

$$\xi=(2l+1-4S)/S(2l-1)(2l+3)(2L-1) \quad (l=3),$$

where $\boldsymbol{L}$ is the total electronic orbital angular momentum; $\boldsymbol{S}$ the total electronic spin; $\langle 1/r^3\rangle$ the average of the inverse cubic power of the distance between the nucleus and the 4*f*-electrons. Using J, M quantization scheme of the electronic states, where $\boldsymbol{J}$ is the total electronic angular momentum, and neglecting the effect of the crystalline field which is not important at room temperature, the thermal average of $\boldsymbol{H}_{in}$ is calculated to be

$$\begin{aligned}\langle H^z_{in}\rangle = -\mu_B H_{ex}\cdot \sum_{J,M} \exp(-W_{OJ}/kT)\cdot \\ \times[(H^z_{inJJM}g_J M)/kT+\sum_{J'\neq J}(S^z_{JJ'M}H^z_{inJ'JM} \\ +H^z_{inJJ'M}S^z_{J'JM})/\Delta W_{J'J}] \\ \div \sum_{J,M}\exp(-W_{OJ}/kT), \qquad (3)\end{aligned}$$

where W_{OJ} is the energy of each J level; g_J its g-factor; $\Delta W_{J'J}=W_{OJ'}-W_{OJ}$; the z-axis is chosen as the direction of the external field.

In the case of Sm^{+++}, as van Vleck discussed in detail in the problem of its susceptibility[3], we cannot confine ourselves to the lowest J level in the summation in (3), because at room temperature both the population of the upper levels with large g-factors and the mixing of different J states caused by the external field make important contributions to $\langle H^z_{in}\rangle$. These effects destroy the proportionality of the susceptibility and the quantity $\langle H^z_{in}\rangle$ to inverse temperature, which would follow, if the upper levels were not considered. The explicit form of $\langle H^z_{in}\rangle$ for Sm^{+++} is given by

$$\begin{aligned}\langle H^z_{in}\rangle/H_{ex} = (0.6227/T)\cdot\langle 1/r^3\rangle\cdot 10^{-24} \\ \times[7.746+37.10e^{-7y}+76.4e^{-16y} \\ +132e^{-27y}+\cdots \\ -2.378(1-e^{-7y})/y \\ -3.02(e^{-7y}-e^{-16y})/y \\ -2.92(e^{-16y}-e^{-27y})/y-\cdots] \\ \div[3+4e^{-7y}+5e^{-16y}+\cdots], \qquad (4)\end{aligned}$$

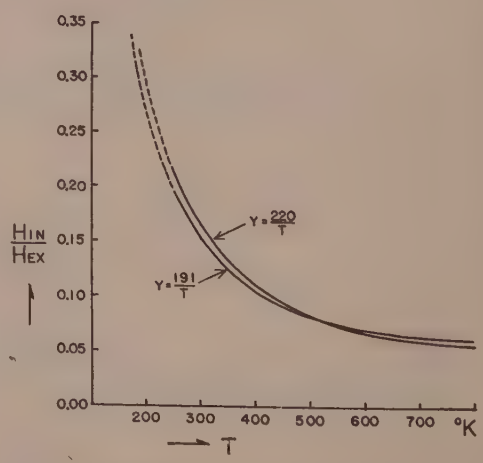

Fig. 1. Temperature variation calculated for the induced magnetic field "H_{in}" at the nucleus of Sm^{+++}.

* This assumption is also supported by recent work of Goldring and Scharenberg. We thank Dr. R. P. Scharenberg for sending us the preprint of their work.

where y is $|\lambda|/2kT$ and λ is the coefficient of the spin-orbit coupling. In the numerical calculation, we insert $\langle 1/r^3\rangle = 51(\pm 13)$ Å^{-3} after Elliot and Stevens[4] and either values, $220k$ and $191k$ for $|\lambda|/2$ after van Vleck[3]. The result is shown in Fig. 1.

In the case of other rare earth ions except Eu^{+++} and Pm^{+++} we can simplify (3) as follows:

$$\langle H^z_{in}\rangle = 2\mu_B^2 \langle 1/r^3\rangle \cdot C g_J J(J+1)/kT\,,$$
$$C = [(2-g_J) + \xi L(L+1)(g_J-1) - (3\xi/2)\{J(J+1) - L(L+1) - S(S+1)\}]\,,$$
$$g_J = 1 + [J(J+1) - L(L+1) + S(S+1)]/2J(J+1)\,. \qquad (5)$$

For instance, the induced field at the nucleus of Nd^{+++} is obtained as

$$\langle H^z_{in}\rangle = (392/T)\cdot H_{ex}\,, \qquad (6)$$

where we used $\langle 1/r^3\rangle = 40(\pm 10)$ Å^{-3} after Elliot and Stevens.[4]

We thank Prof. T. Nagamiya for kind discussions.

References

1) K. Sugimoto, J. Phys. Soc. Japan **13** (1958) 240.
2) A. Abragam and M. H. L. Pryce, Proc. Roy. Soc. **A205** (1951) 135.
3) J. H. van Vleck, "The theory of electric and magnetic susceptibilities" Clarendon Press Oxford (1932), P. 245.
4) R. J. Elliot and K. W. H. Stevens, Proc. Roy. Soc. **A219** (1953) 387.

J. Phys. Soc. Japan **13** (1958) 755~756

Plasma Oscillation in the Electrically Conductive Tin Oxide Film

By Kozo Ishiguro, Taizo Sasaki, Toshihiro Arai and Isamu Imai

Department of Physics, College of General Education, University of Tokyo

(Received April 16, 1958)

In the previous paper[1], the optical and electrical properties of the free electrons in the electrically conductive tin oxide films were reported. According to the conclusion of the paper that the effective mass m^* of the electrons in the conduction band should be 0.15~0.20 times of the free electron mass m, the complex refractive index of the specimen No. 15 was recalculated with the constants given under the column of $m^*=0.2m$ of Table I of that paper.

The formulae used to calculate n and k are;

$$n^2 - k^2 = A_\nu - \frac{\nu_p^2}{\nu^2+\nu_A^2}$$

$$2nk = \frac{\nu_p^2}{\nu^2+\nu_A^2}\cdot\frac{\nu_A}{\nu}$$

where

$$A_\nu = \frac{7.851}{2.430-(\nu/10^{15})^2}$$

$$\nu_p = \left(\frac{Ne^2}{\pi m^*}\right)^{1/2} = \text{plasma frequency} = 1.84\times 10^{14}\ \text{sec}^{-1}$$

$$\nu_A = \frac{1}{2\pi\tau} = \text{relaxation frequency} = 4.37\times 10^{13}\ \text{sec}^{-1}$$

and the results are given in column 4 and 5 of Table I of the present paper.

Table I.

ν (sec.$^{-1}$)	$h\nu$ (eV)	λ (μ)	n	k	$\frac{2nk}{(n^2+k^2)^2}$
6.00×10^{14}	2.48	0.50	1.92	0.00	0.00
4.00	1.65	0.75	1.80	0.00	0.00
3.00	1.24	1.00	1.73	0.00	0.00
2.00	0.83	1.50	1.58	0.06	0.03
1.50	0.62	2.00	1.38	0.15	0.11
1.20	0.50	2.50	1.14	0.33	0.38
1.10	0.46	2.72	1.02	0.47	0.60
1.00	0.41	3.00	0.92	0.67	0.73
0.95	0.39	3.2	0.89	0.80	0.69
0.90	0.37	3.3	0.87	0.95	0.60
0.85	0.35	3.5	0.87	1.10	0.49
0.80	0.33	3.8	0.88	1.27	0.39
0.60	0.25	5.0	1.10	2.03	0.16
0.30	0.12	10.0	2.33	3.77	0.05
0.20	0.08	15.0	3.36	4.77	0.03
0.10	0.04	30.0	5.53	6.65	0.01

It was shown recently by H. Fröhlich and H. Pelzer[2], and also by J. Hubbard[3] that the probability of the energy loss of a fast charged particle suffering a long range collision with free electrons in a solid was proportional to $2nk/(n^2+k^2)^2$. The numerical values of this quantity are also tabulated in the column 6 of Table I of the present paper and the curve plotted against the photon energy is shown in Fig. 1. The curve has a very sharp maximum at $h\nu_{max}=0.41$ eV, indicating that the energy loss of the electron beam penetrating the specimen would be observed in steps of $h\nu_{max}$. It should be noticed that as it was pointed out by Nozière and Pines[4], the real plasma frequency ν_{max} does not coincide with the so-called plasma frequency ν_p but is shifted to $\nu_p/1.84$ or $\nu_p/(A_\nu)^{1/2}$, in which A_ν represents the contribution of the valence and core electrons to the dielectric constant of the present specimen. It is also shown that as the half value width of the absorption band of the electron energy spectrum is given by $nkh\nu_{max}$, we can evaluate the lifetime τ of the plasma wave[5] in

the present specimen as $\tau=\hbar/nkh\nu_{max}\approx 2.6\times 10^{-15}$ sec.

Such an aspect of the plasma oscillation is already pointed out by Fröhlich and Pelzer[2] for Ag, but on the other materials, especially for semiconductors, no example has been as yet reported.

Since tin oxide film does not show any remarkable optical absorption due to lattice vibration between 0.32~200 μ except the two bands at $\lambda=33\,\mu$ and 39 μ (Fig. 1)* and the intrinsic absorption edge due to the transition between the valence and conduction band lies at $\lambda=0.32\,\mu$, it is free from any disturbances interacting with the plasma oscillation at $\lambda\approx 3\,\mu$, and the density of the free electrons in tin oxide is easily controlled by heat treatments. Therefore, the conductive tin oxide film presents an interesting example to study the plasma oscillation in a relatively simplified condition except that the impurity scattering of electrons is rather the predominant mechanism over the scattering caused by the lattice vibration to determine the electrical properties[1].

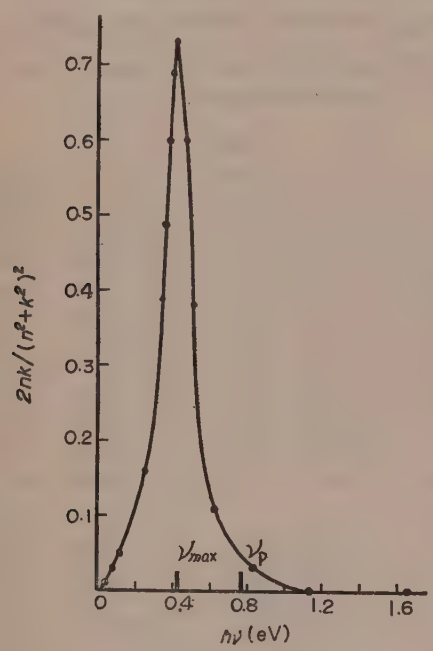

Fig. 1.

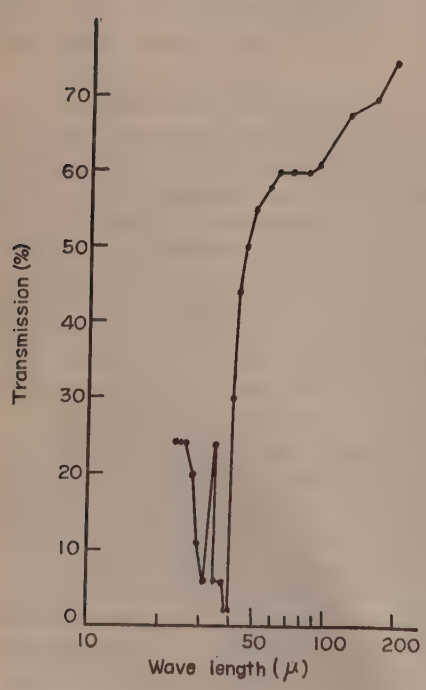

Fig. 2.

The authors should like to express their thanks to Prof. H. Kanazawa of our institute for his theoretical help and the introduction to the references.

References

1) K. Ishiguro, T. Sasaki, T. Arai and I. Imai: J. Phys. Soc. Japan **13** (1958) 296–304.
2) H. Fröhlich and H. Pelzer: Proc. Phys. Soc. **A 68** (1955) 525.
3) J. Hubbard: Proc. Phys. Soc. **A 68** (1955) 976.
4) P. Nozière and D. Pines: Phys. Rev. **109** (1958) 1062.
5) P. Wolf: Phys. Rev. **92** (1953) 18.
H. Kanazawa: Prog. Theor. Phys. **13** (1955) 227.

* The transmission spectrum over the wide wavelength range by the powdered specimen method was obtained by the courtesy of Prof. H. Yoshinaga.

J. Phys. Soc. Japan **13** (1958) 756~757

Magnetic Annealing of Fe_3Al Single Crystal

By Kenzō Suzuki
Department of Physics and Chemistry, Gakushuin University, Mejiro, Takyo, Japan

(Received May 29, 1958)

Recently, the magnetic annealing effect of cubic solid solution has been studied in detail by Chikazumi[1] on the single crystal of Ni_3Fe and by Yamamoto, Taniguchi and Aoyagi on the single crystal of Ni-Co alloy.[2] Their results were in rather good agreement with the theory, which was developed by Néel[3] and independently by Taniguchi-Yamamoto.[4] For the purpose of observing the same effect on the body-centred cubic crystal, which was expected to be insensitive to the annealing in $\langle 100 \rangle$ magnetic field, the author investigated this effect on Fe_3Al crystal.

The specimen used was Fe_3Al (110) disk (10.61 mm in diameter and 0.32 mm in thickness). First the specimen was heated up to 650°C and annealed for 30 minutes, and then it was cooled down at a controlled rate to room temperature in a magnetic field. After cooling the torque was measured. Then this torque data was analized by means of Fourier analysis and the anisotropy energy measured was separated into field-induced anisotropy E_u and usual crystal anisotropy E_k. Fig. 1 shows the obtained E_u and E_k *vs* θ_t curves for the cooling rate 3°C/min, where θ_t is the direction of annealing field. The $\Delta\theta$ is also plotted against θ_t in Fig. 2,

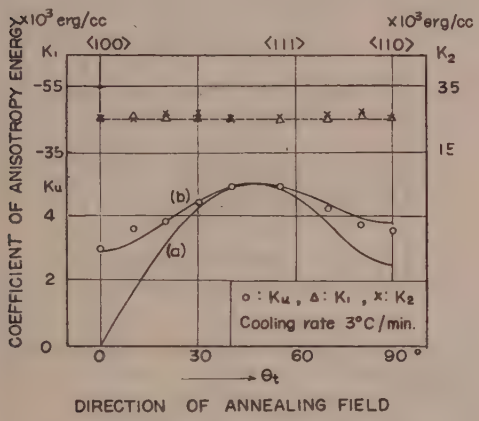

Fig. 1. E_u and E_k vs θ_t curve.
(a): Theoretical curve with $A_1=0$, $A_2=9.8\times10^3$ erg/cc.
(b): Experimental curve with $A_1=2.9\times10^3$ erg/cc, $A_2=9.8\times10^3$ erg/cc.

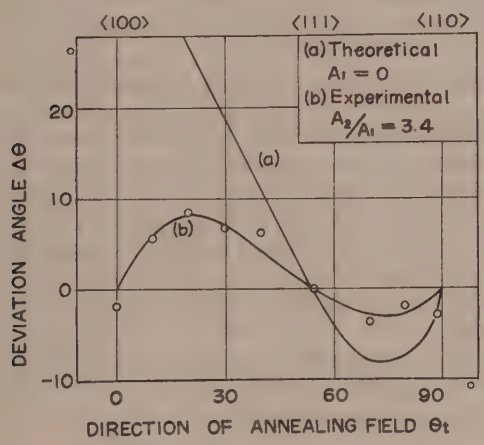

Fig. 2. $\Delta\theta$ vs θ_t curve.

where $\Delta\theta$ is the deviation angle between the annealing field direction θ_t and the minimum point θ_0 of E_u, i.e. $\Delta\theta=\theta_t-\theta_0$.

The anisotropy induced by magnetic annealing are generally represented by the formula.

$$E_u=-A_1\sum_i \alpha_i^2\beta_i^2-A_2\sum_{i>j}\alpha_i\alpha_j\beta_i\beta_j\,, \qquad (1)$$

where α_i and β_i are the direction cosines of intrinsic magnetization and magnetic field of annealing respectively, and A_1 and A_2 are the factors specified by the crystal structure. According to Néel and Taniguchi-Yamamoto's theory, A_1 should be zero for b.c.c. crystal, so E_u must vanish for the ⟨100⟩ magnetic annealing. The theoretical curves are also shown in Fig. 1 and Fig. 2. It was found, however, by the present experiment that the ⟨100⟩ magnetic annealing does give rise to a finite value of E_u, as seen in Fig. 1. The experimental curves in Fig. 1 and Fig. 2 was well fitted by Eq. (1) by assuming $A_1=2.9\times10^3$ erg/cc and $A_2=9.8\times10^3$ erg/cc. The finite value of A_1 can be interpreted by assuming the contribution of the 2nd nearest neighbor interaction. Since 2nd nearest neighbor atoms form a simple cubic lattice, the anisotropy due to 2nd nearest neighbors should be represented only by A_1 term. Therefore the A_1 term in experimental E_u is to be understood as the result of the anisotropic distribution of 2nd nearest neighbors.

By using experimental A_1 and A_2 values, we can obtain the ratio of the coefficient of dipole-dipole interaction between the 1st nearest neighbors l_1 to that between 2nd ones l_2,

$$l_1:l_2=\frac{3}{4}\sqrt{\frac{A_2}{A_1}}=1.35\,, \qquad (2)$$

the value of which would be rather reasonable. It should be pointed out that the contribution from 2nd nearest neighbors was also verified by the experiment of magnetic anisotropy induced by cold rolling on Fe_3Al single crystals.[5]

The author sincerely thanks to Prof. S. Chikazumi for his kind advice and important suggestions in the course of this investigation.

References

1) S. Chikazumi: J. Phys. Soc. Japan **11** (1956) 551.
2) M. Yamamoto, S. Taniguchi and K. Aoyagi: J. Phys. Soc. Japan **13** (1958) 532.
3) L. Néel: Compt. Rend. **237** (1953) 1613; J. Phys. et Rad. **15** (1954) 225.
4) S. Taniguchi and M. Yamamoto: Sci. Rep. Res. Inst. Tohoku Univ. **A6** (1954) 330, S. Taniguchi: Sci. Rep. Res. Inst. Tohoku Univ. **A7** (1955) 269.
5) S. Chikazumi, K. Suzuki and H. Iwata: unpublished.

J. PHYS. SOC. JAPAN **13** (1958) 758

Magnetic Properties of Nickel and Cobalt Ferrite-Chromite Series

By Syohei MIYAHARA and Tachiro TSUSHIMA

Department of Physics, Faculty of Science, Hokkaido University, Sapporo, Japan

(Received May 26, 1958)

Though Néel's theory on ferrimagnetism explains successfully the ferrimagnetism of various ferrites,[1] it does not succeed to explain sufficiently the magnetic character of chromites; especially the spontaneous magnetizations of chromites at absolute zero temperature were not explained as the difference of the moments of two sublattices. Thus, the problem of chromites are thought to be rather complicated. In this note an experimental study on magnetic properties of nickel and cobalt ferrite-chromite series is reported, that might make certain contribution to the problem of the ferrimagnetism of chromite.

Chemical formula of the samples is given by Ni (or Co) $Fe_{2-t}Cr_tO_4$, where t varies from 0 to 2. $NiFe_2O_4$ was made from the mixed solution of $NiCl_2$ and $FeCl_3$, and $NiCr_2O_4$ was also prepared from the solution of $NiCl_2$ and $CrCl_3$. Other samples of nickel series were made by mixing $NiFe_2O_4$ and $NiCr_2O_4$ in stoichiometric ratios.

The specimens of cobalt series were made from powders of extra-pure CoO, Fe_2O_3 and Cr_2O_3. All samples were heated at 1100°C for about ten hours in air, then quenched to room temperature and were identified by the X-ray diffraction patterns.

Magnetizations at various temperatures from liquid nitrogen to about 900°K were measured by Gouy's method. The maximum field strength used is about 8000 oersted, which is strong enough to saturate the specimens.

Saturation magnetization *vs* temperature curve shows normal form and decreases the magnitude as chromium content increases. Magnetizations at 0°K are obtained by extrapolating the curve from nitrogen temperature. Their changes with chromium content t are shown in Fig. 1.

The variation of lattice parameters with chromium content t is shown in Fig. 2, from which we can find that nickel ferrite-chromite has inverse spinel structure as long as $t<1.0$, and it changes gradually to normal as t further increases. On the other hand cobalt ferrite-chromite changes its structure from inverse to normal as t increases to 0.4 and remain normal for greater t.

If we assume that the chromium ion always occupies the octahedral site and nickel ion preferentially occupies the octahedral site[2], we can evaluate the difference of magnetic moments of the octahedral and tetrahedral sites of nickel ferrite-chromite. When $t<1$, it is expressed by $(2-2t)\beta$, which agrees well with the observed value; when $1<t<2$, it is expressed by $(4-4t)\beta$, which clearly differs from the observed value.

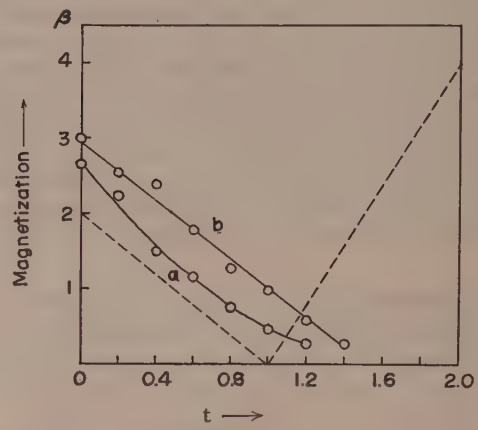

Fig. 1. Magnetization at 0°K in β.
a) Nickel series
—— observed
--- calculated
b) Cobalt series, observed

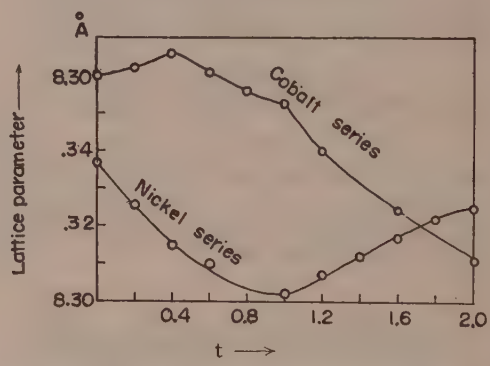

Fig. 2. Variation of lattice parameter with t.

Though we do not have enough information about cation distribution of cobalt ferrite-chromite to evaluate the magnetic moment, it is plausible to assume it to be a few Bohr-magnetons per atom. The magetizations of the samples extrapolated to 0°K are, however, much less than the above value in the cobalt chromite side. This discrepancy should not be due to especially small magnetic moments of the ions, because it is confirmed[3] by the Curie constant that the ions have ordinary magnetic moments due to spins.

References

1) L. Néel, Ann. Phys., **3** (1948) 137.
2) D. S. McClure, J. Phys. Chem. Solids, **3** (1957) 311.
J. D. Dunitz and I. E. Orgel, J. Phys. Chem. Solids, **3** (1957) 318.
3) McGuire et al., Ceramic Age, **60** (1952) 22.

J. PHYS. SOC. JAPAN **13** (1958) 759

On Magneto-Acoustic Resonance in Metals

By Nobuo MIKOSHIBA

Electrotechnical Laboratory, Tokyo, Japan

(Received April 21, 1958)

Recently Pippard[1),2)] has proposed a concept of magneto-acoustic resonance[3)] for transverse acoustic waves to interprete the experiments of Bömmel,[4)] who showed that the absorption coefficient in metals was markedly affected by the presence of a magnetic field. The object of this note is to point out the limitation of Pippard's concept and to propose other possible magneto-acoustic resonance for the absorption of longitudinal acoustic waves at low temperatures.

In general, the type of the interaction of acoustic waves with conduction electrons is different for three frequency ranges,[5)] i.e.

1) the low frequency range: $\omega\tau \ll 1$, $kl<1$,
2) the intermediate frequency range: $\omega\tau<1$, $kl>1$ and
3) the high frequency range: $\omega\tau>1$, $kl \gg 1$

where ω and k are the angular frequency and the wave vector of acoustic waves; τ and l are the relaxation time and the mean free path of conduction electrons, respectively. From the relations $\omega=sk$ (s: sound velocity) and $l=\tau v_0$ (v_0: Fermi velocity), we get

$$\omega\tau=\left(\frac{s}{v_0}\right)kl \qquad (1)$$

(s/v_0 is for example 1/350 for Cu), which gives classification of three frequency ranges.

In the low frequency range we must treat acoustic waves *classically* as waves of a potential for conduction electrons. But in the high frequency range, we can treat them as a *coherent acoustic phonon beam* and then the type of the interaction become very similar to the electron-thermal phonon interaction.[6),7),8)] Two approaches may be possible in the intermediate range; one is the approach from the low frequency range[5)] and the other from the high frequency range.[6)]

Pippard's concept of magneto-acoustic resonance is based on the approach from the low frequency range. His resonance conditions are as follows (see Fig. 1):

A) The mean free path of conduction electrons must be larger than the dimensions of the circular orbits,

$$l>2\pi r \quad \text{or} \quad \omega_c\tau>2\pi \qquad (2)$$

with the use of $r=v_0/\omega_c(\omega_c=eH/m^*c)$

B) The diameter of the circular orbits must be equall to

$$\frac{\lambda}{2}(2n+1)=\frac{\pi}{k}(2n+1), \qquad n=0,1,2,\cdots \qquad (3)$$

where λ is the wave length.

C) Transverse waves can produce a transverse electric field, only when thermal phonons scatter conduction electrons to follow the ionic vibrations.[5)] This scattering process is negligiblly small in the high frequency range; however, some amounts of it may remain in the intermediate frequency range. Then

$$\omega\tau<1 \qquad (4)$$

is required.

Above three conditions are reduced to

$$\omega=\pi\left(n+\frac{1}{2}\right)\left(\frac{s}{v_0}\right)\omega_c,\ \omega\tau<1, \text{ and } \omega_c\tau>2\pi \qquad (5)$$

In such high frequency range as Pippard's concept breaks down, longitudinal waves rather strongly interact with conduction electrons in a transverse magnetic field (see Fig. 2). The electronic motion in the plane perpendicular to the magnetic field is quantized, if $\omega_c\tau>2\pi$. When the energy of acoustic phonon $\hbar\omega$ is equal to the energy gap $n\hbar\omega_c$ ($n=1, 2, \cdots$) between quantized oscillator states, a new magneto-acoustic resonance absorption may occur. This resonance conditions can be written as

$$\omega=n\omega_c,\ \omega\tau>1 \quad \text{and} \quad \omega_c\tau>2\pi. \qquad (6)$$

If $l\sim10^{-2}$ cm at low temperatures, $\omega>10^{11}$ sec^{-1} is required for Cu. But for semi-metals the attainable frequency, 10^9 sec^{-1}, may be sufficient to observe the resonance.

We are indebted to Dr. M. Shibuya and Dr. W. Sasaki for their valuable discussions.

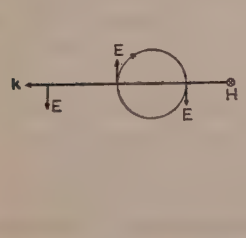

Fig. 1.

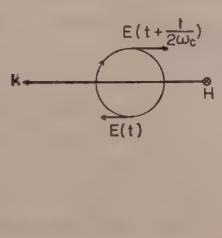

Fig. 2.

References

1) A. B. Pippard: Phil. Mag. **2** (1957) 1147.
2) R. W. Morse, H. V. Bohm and J. D. Gavenda [Phys. Rev. **109** (1958) 1394] has published their observation of magneto-acoustic resonance in the intermediate frequency range. But their interpretations contradict to Pippard's conditions.
3) W. P. Mason and H. E. Bömmel: J. Acoust. Soc. America **28** (1955) 930.
4) H. E. Bömmel: Phys. Rev. **100** (1955) 758.
5) A. B. Pippard: Phil. Mag. **46** (1955) 1104.
6) C. Kittel: Acta Metallurgica **3** (1955) 295.
7) B. V. Paranjape: Proc. Phys. Soc. **A66** (1953) 572.
8) Van Den Beukel: Appl. Sci. Research **B5** (1956) 459.

J. PHYS. SOC. JAPAN **13** (1958) 760~761

Space Charge Phenomena in Nitrobenzene under High Electric Field

By Pyong-un CHONG, Chiyoe YAMANAKA and Tokuo SUITA

Department of Electrical Engineering, College of Engineeriny, Osaka University

(Received April 15, 1958)

To study the dielectric breakdown in liquids, it is very important to investigate the prebreakdown phenomena which include essential mechanisms of destruction. We have studied the field distribution in nitrobenzene at room temperature using the Kerr electro-optical effect under conditions of D.C. and single rectangular pulse voltages.

We used a conventional setup[2] for optical measurement. The first slit, placed before the liquid cell, was 0.30 mm which was as wide as the gap length of the electrodes. The second slit, placed behind the cell, was 0.03 mm wide. It was made movable in the direction of the applied electric field by a micrometer, which enables to detect the transmitted light through one of ten sections between the electrodes.

The intensity of a light beam J under the electric field E, is given by

$$J=\tfrac{1}{2}J_0 \sin^2(\pi B l E^2)\,.$$

Where J_0 is the intensity of a incident light beam, B is Kerr constant (4.1×10^{-5} in esu for light of wavelength 5460 A at 20°C) and l is the length of the electrodes in the direction of the light beam (~0.30 mm). The intensity of the transmitted light beam was measured by a multiplier phototube 931 A. So we can calculate the electric field distribution between the electrodes.

In carrying out the experiments we took care of the following points.

a) We made the light beam parallel, uniform and not to be scattered by the electrodes very carefully. These were checked by measuring the light intensity of the ten sections between the electrodes with two Nicols made parallel without electric field.

b) We changed the polarity of electrode and carried out the same procedure. In both cases we got almost the same results.

c) In calculating the electric field strength from the intensity of the transmitted light beam, we tried to estimate it in a several ways, and made it sure that the results were consistent with each other.

In Fig. 1 we show the electric field distribution between the electrodes in $C_6H_5NO_2$. The increase of the field strength near the cathode was obviously seen. For example, under the application of 8 KV, the field strength at the cathode section was more than 115% as high as the mean field strength. Almost the same results were obtained in D.C. voltages and single pulse voltages whose durations ranged from 25 μ sec to 100 μ sec. In the case of single pulse voltages the observed light pulse always indicated a time delay to reach a steady value as

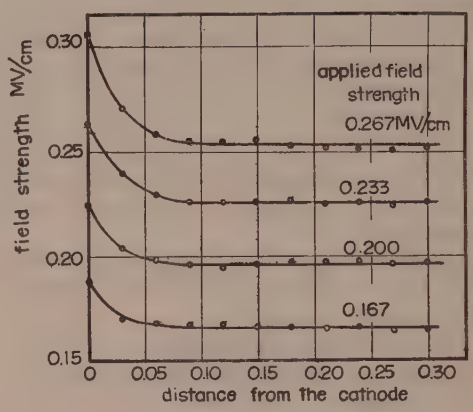

Fig. 1. Field distribution under applying pulse voltages.

Pulse voltage form (25 μs)

Light pulse form under 6 kV.

Light pulse form under 7 kV.

Light pulse form under 9 kV.

(a)

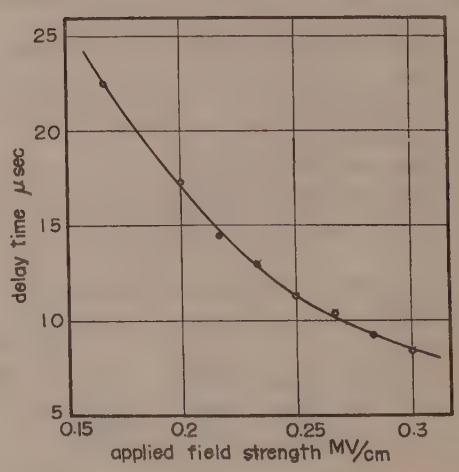

(b)

Fig. 2. Delay time of the light pulse under applying 25μ sec pulse voltages.

shown in Fig. 2. The delay time became shorter as the higher pulse voltages were applied. These phenomena seem to be caused by the movement of the positive ions. If we estimate the mobility of the positive ion, from this model, it is the order of 10^{-3} cm²/sec.volt.. This value seems to be a little larger than those reported before[3),4)].

As there are many factors to cause the overestimation, it may be the upper limits of the positive ion mobility in $C_6H_5NO_2$.

We are now measuring the field distortion in nonpolar liquid containing dipolar solute molecules in connection with the experiments mentioned above.

References

1) P. Chong, C. Yamanaka and T. Suita: Read at the Annual Meeting of the Phys. Soc. Japan, 1957.
2) A. M. Zarem, F. R. Marshall and F. L. Poole: A.I.E.E. 1. **68** (1949) 282.
3) D. W. Goodwin and K. A. Macfadyen: Proc. Phys. Soc. **B 66** (1953) 85.
4) C. Yamanaka, P. Chong and T. Suita: Tech. Rep. Osaka Univ. **6** (1956) 1.

J. Phys. Soc. Japan **13** (1958) 761~762

Electric Breakdown and Conduction in $BaTiO_3$ Single Crystals

By Yoshio Inuishi and Shigeyuki Uematsu
Faculty of Engineering, Osaka University

(Received April 9, 1958)

The nature of electric breakdown and conduction in single crystals of $BaTiO_3$ has been investigated[1)]. $BaTiO_3$ single crystals were grown by Remeika's method and diffused edge silver electrodes were attached to them by evaporation technique. The temperature dependence of D.C. breakdown strength along C axis is shown in Fig. 1 with the scattering of data. The mean breakdown strength of 0.3~0.5 MV/cm is rather insensitive to the temperature in comparison with large temperature dependence of low field conductance, although some drop in breakdown strength is seen above room temperature. It is interesting that no marked change in breakdown strength is seen at Curie temperature where the transition from ferro- to para-electric phase occurs.

The reported low value of breakdown strength[2),3)] in $BaTiO_3$ ceramic (0.02~0.05 MV/cm) seems to suffer from secondary factors. The low field conductance σ obtained from final conduction current at 500 V application is shown in Fig. 2 as a function of reverse temperature $1/T$ (°K).

Assuming the relation

$$\sigma=\sigma_0 \exp(-W/kT)\,.$$

We got 0.75 e.v. for activation energy W above 120°C Curie temperature.

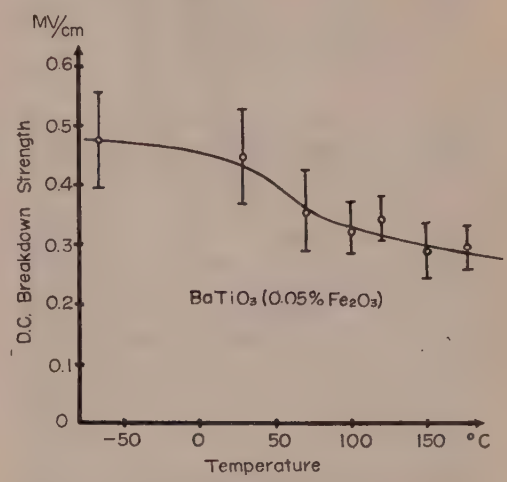

Fig. 1.

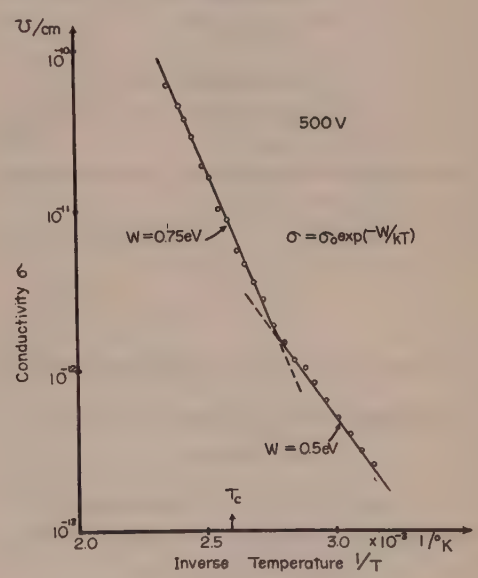

Fig. 2.

A possible mechanism may be the migration of K^+ ions introduced by KF. Fig. 3 shows the relation between final conduction current and applied field. At low field, Ohm's law is applicable. At higher field, however, current increases abruptly due to prebreakdown phenomena. From the temperature insensitivity of the breakdown strength, these prebreakdown current seems to be mainly electronic.

The measurements of photoconductivity and Hall effect are now in progress which, we expect, will

bring us much more information on electronic process in $BaTiO_3$ single crystals. We wish to express our cordial gratitude to Mr. Kisaka of Matsushita Electric Co. for providing $BaTiO_3$ single crystals.

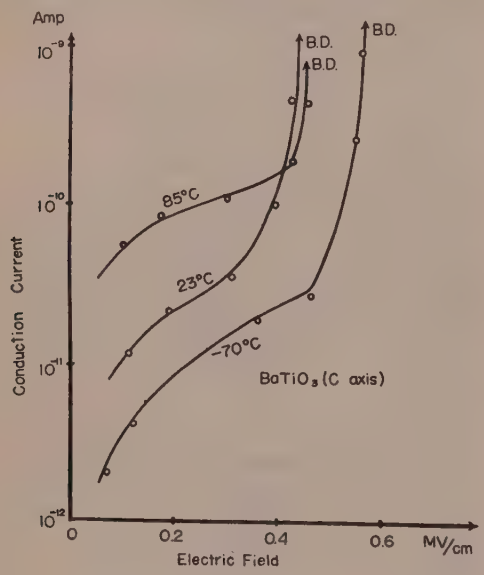

Fig. 3.

References

1) S. Uematsu and Y. Inuishi: Bull. Japan Phys. Soc. (Oct. 1957) 20M–13.
2) R. Fujimoto and K. Okazaki: Bull. Japan Phys. Soc. (April 1957) 11A 18.
3) P. H. Fang and W. S. Brower: Bull. American Phys. Soc. II **3** (Jan. 1958) 44.

J. Phys. Soc. Japan **13** (1958) 762~763

Diffusion of Iron in Single Crystals of Copper

By Yuzo Tomono and Akira Ikushima
Department of Physics, University of Tokyo

(Received April 4, 1958)

Transition elements, when they are dissolved dilutely in noble metals, exhibit anomalous behaviours in electrical and magnetic phenomena, and recently this problem has been investigated extensively. The experimental study on the diffusion of transition elements in noble metals also seems to offer one of the important informations about the problem mentioned above. And as the first step, the diffusion experiment of Fe^{55} in single crystals of pure copper was performed, and the following is the report of the result.

The specimens were prepared from 99.99% copper. Single crystals were grown in H_2 atmosphere by Tammann and Bridgeman method. Crystals thus grown were cut and etched with dilute HNO_3 into the form of short cylinders of 13 m diameter and 10~20 mm length. Then, they were annealed to remove any residual strain at about 950°C for about 10 hours in H_2 atmosphere. A subsequent etching with dilute HNO_3-alcohol solution showed that the specimens were still single crystals. The

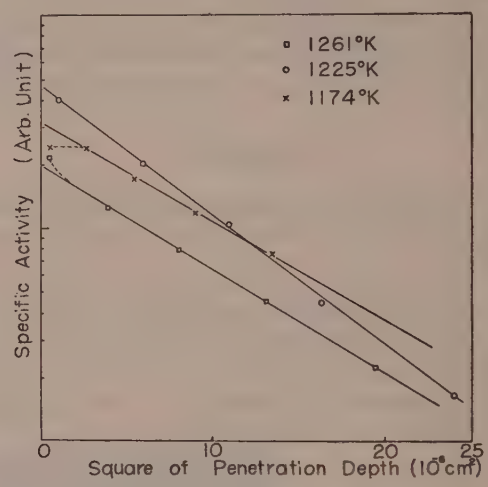

Fig. 1. Typical penetration plots.

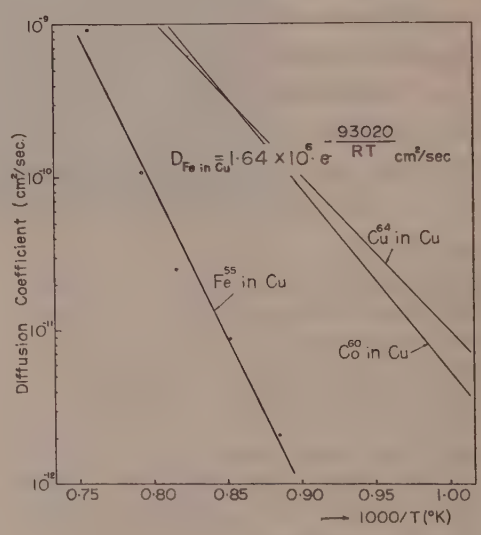

Fig. 2. Plot of $\log D$ *vs* $1/T$.

specimens were then plated electrolytically on their ends with the radioactive isotope Fe^{55} obtained from the Oak Ridge National Laboratory. The plating was made from a slightly basic $FeCl_3$ bath. During plating, the sides of the specimens were protected with vinyl tape. The thickness of the plated layer was estimated from the radioactivity to be about 5~10 A.

Diffusion heat treatments were made in Argon

atmosphere of 200 mm Hg at 5 different temperatures. The temperature at the specimen was measured with a calibrated Pt-13% RePt thermocouple. An electronic recorder was used during the heat treatments to watch any temperature fluctuations.

After the heat treatment, the specimen was mounted on a precision lathe, and the material from each cut by lathe was collected in a glass dish. In order to avoid the positional error of the collected matter and also avoid the error due to the absorption of the radiation from Fe^{55} tracer, the collected matter on the dish was dissolved with dilute HNO_3 and then dried by using an infrared ray lamp. The Geiger counter with the mica window of 1.18 mg/cm² thickness was used under the shield with the lead blocks.

Diffusion coefficients of Fe^{55} in Cu.

Temperature (°K)	Diffusion time (sec.)	Diffusion coefficient
1320±2	5.40×10^{3}	9.26×10^{-10}
1261±2	2.16×10^{4}	1.07×10^{-10}
1225±2	6.88×10^{4}	2.42×10^{-11}
1174±2	2.59×10^{5}	8.84×10^{-12}
1130±2	3.25×10^{5}	2.10×10^{-12}

The results thus obtained are shown in the table and the figures. The diffusion coefficient of Fe^{55} in Cu is expressed as $D=D_0 \exp(-Q/RT)$ cm²/sec. with

$$\log_{10}D_0=6.21\pm0.87 \quad (D_0 \text{ in cm}^2/\text{sec.})$$
$$Q=93020\pm4820 \quad \text{cal/mole.}$$

The errors are the probable errors. The activation energy and the entropy factor for the Fe^{55} in Cu are fairly larger than that of Co^{60} in Cu[1] and Cu^{64} in Cu[2]. This tendency seems to be consistent with that of the residual resistivities due to solute transition elements in Cu[3]. This result, however, disagrees with the data reported by Mackliet[4], and this discrepancy will be examined by the present authors. The diffusion experiment of Mn^{54} in Cu is now in progress.

The authors wish to thank Drs. Kunitomi and Sakamoto for many valuable advices. This work was partly supported by the Scientific Research Expenditure from the Ministry of Education.

References

1) N. Kunitomi and S. Sakamoto: private communication, to be published.
2) A. Kuper, H. Letaw, J. L. Slifkin, E. Sonder, and C. T. Tomizuka: Phys. Rev. **96** (1954) 1224, Phys. Rev. **98** (1955) 1870.
3) see, for example, J. O. Linde: Ann. der Phys. **10** (1931) 52, **15** (1932) 219.
4) C. A. Mackliet: Phys. Rev. **109** (1958) 1964.

J. Phys. Soc. Japan **13** (1958) 763~764

Beta and Gamma Ray Spectroscopy of Co^{60}

By Kazumasa Kamada,* Tomoyuki Teranishi** and Yasukazu Yoshizawa

Department of Physics, Faculty of Science Osaka University, Osaka

(Received May 27, 1958)

Beta ray and internal conversion electrons of 1.17 and 1.33 Mev gamma rays were measured by the two-directional focusing beta-ray spectrometer ($\rho=$ 40 cm).[1] The observed values of the maximum energy of beta ray, E_β, K-shell and total conversion coefficients, α_K and α, and $K/L+M$ rations are tabulated in Table I with values reported previously. Kurie plot of beta ray is shown in Fig. 1, where the deviation in the low energy part is due to the counter window thickness. The K-shell conversion coefficients are determined from the intensity ratio of the K electrons to the beta ray. K and L+M lines are not completely separated, as shown in Fig. 2, but one could obtain these ratios assuming that the shape of $L+M$ line was same as that of K line. In Table I are shown the extrapolated values of Rose's recent theoretical $E2$ conversion coefficients[2] with the finite nuclear size effect for K- and L-shells and without this for M-shell.

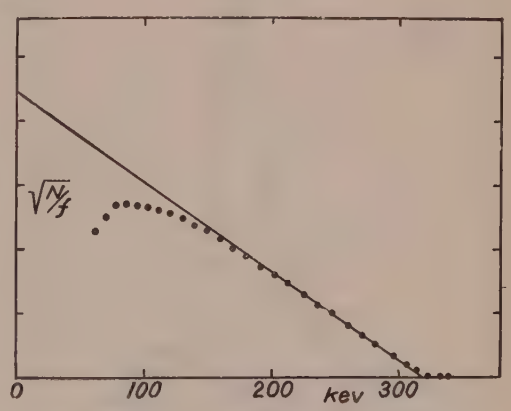

Fig. 1. Kurie plot of beta ray.

It is interesting that the experimental values of α_K of both gamma rays are in agreement with the theoretical values within experimental error, but $K/L+M$ are not. Gamma transitions among the 4^+, 2^+ and 0^+ states of Ni^{60} have been pointed out to be pure electric quadrupole by angular correlation experiments and others. It has been shown by another experiment[3] that $K/L+M$ of $E2$ gamma transitions from the excited states of Cr^{52} have the

* Now at Mitubishi Rayon Co.
** Now at Mitubishi Electric Manufacturing Co.

Table I. The maximum energy of beta ray, K-shell and total conversion coefficients, and $K/L+M$ rations of 1.17 and 1.33 MeV gamma rays.

		Present	Preceding	Theoretical
E_β	(keV)	319±3	316±3[4] 314[5] 306±5[6] 318±4[7] 309±3[8]	
$\alpha_K \times 10^4$	1.17γ 1.33γ	1.50±0.06 1.16±0.06		1.48 1.12
$\alpha \times 10^4$	1.17γ 1.33γ	1.65±0.07 1.29±0.07	1.7[6] 1.73[7] 1.2[6] 1.29[7]	1.67 1.27
$K/L+M$	1.17γ 1.33γ	9.1±0.5 9.1±0.5	~10[9] ~10[9]	7.6 7.6

same tendency. For 661 keV gamma ray of $Ba^{137\,m}$ the experimental value[1] $K/L/M$ was 5.661/1/0.27, whereas the theoretical one[2] for $M4$ transition is 5.66/1/0.42. Therefore, the discrepancies of $K/L+M$ may be due to those between experimental and theoretical M-shell conversion coefficients, in which the finite nuclear size effect is expected to be small.

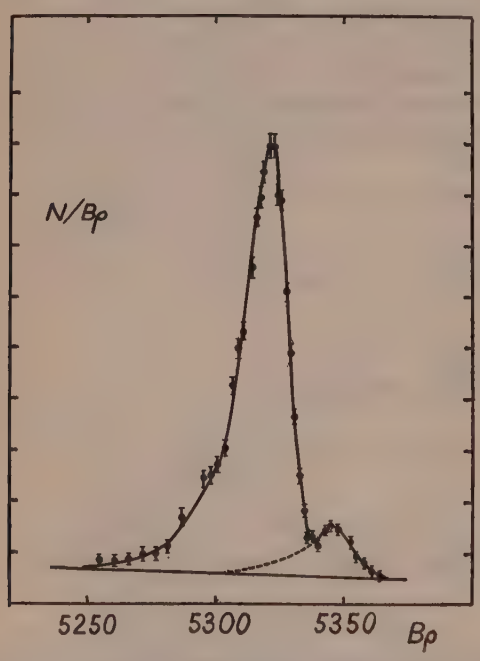

Fig. 2. Momentum distribution of internal conversion electrons of 1.17 MeV gamma transition.

References

1) Y. Yoshizaka: Nuc. Phys. **5** (1958) 122.
2) M. E. Rose: private communication.
3) Katoh, Nazawa, Yoshizawa and Koh: to be published.
4) Y. Yoshizaka: J. Phys. Soc. Japan **8** (1953) 435.
5) G. L. Keister and F. H. Schmidt: Phys. Rev. **93** (1954) 140,
6) C. Y. Fan: Phys. Rev. **87** (1952) 252.
7) Waggoner, Moon and Roberts: Phys. Rev. **78** (1950) 295; **80** (1950) 420.
8) Bolla, Terrani and Zappa: Nuo. Cim. **12** (1954) 875.
9) Lindström, Hedgran and Alburger: Phys. Rev. **89** (1953) 1303.
10) Note added in proof—Dr. M. E. Rose have kindly communicated that the discrepancy in the Co^{60} gamma rays is due to the neglect of screening in M-shell coefficients and these can be decreased by a factor 0.6. Using this factor the theoretical ratio becomes in agreement within experimental error with the experimental ones.

J. PHYS. SOC. JAPAN **13** (1958) 764~765

A Note on Direct Observation of Dislocations by Electron Microscopy

By Hatsujiro HASHIMOTO and Toshio NAIKI
Kyoto Technical University, Sakyoku, Kyoto, Japan

(Received February 28, 1958)

It is widely known that Menter[1] observed dislocations in phthalocyanine crystals by electron microscopy. Since one can understand his result by intuition, it has come to be generally believed that the electron microscopy can give the proof for the existence of dislocations. It must be noted, however, a dislocation appearing in an electron micrograph does not always represent a dislocation existing in the crystal lattice. The present authors demonstrated this by an analogy in light optics.

In our demonstration, a plane grating of 66 μ spacing was irradiated by an almost parallel light beam of wave-length 4,900 Å. This corresponds to the electron optical system where a thin sheet of phthalocyanine crystal (spacing 12 Å) is irradi-

ated by 80 K.V. electrons (wavelength 0.04 Å). We covered one-half of the grating with a slightly wrinkled sheet of transparent paper, leaving the other half uncovered. We took some photographs of the grating at out-of-focus as well as in exact focus (Fig. 1). In exact focus (Fig. 1a), striations of the grating appear straight over the area of both covered and uncovered parts. At out-of-focus (Figs. 1b and c), however, the covered part is remarkably distorted while the uncovered part remains unchanged. In Fig. 1b, edge dislocations are appearing (indicated by arrows) and in Fig. 1c,

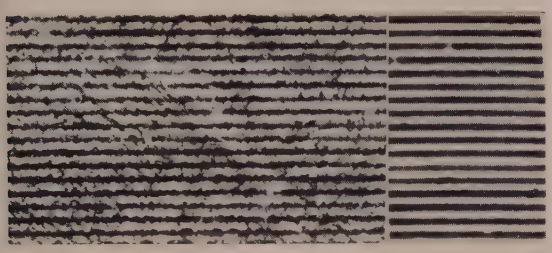

(a) $\Delta a = 0.0$ mm

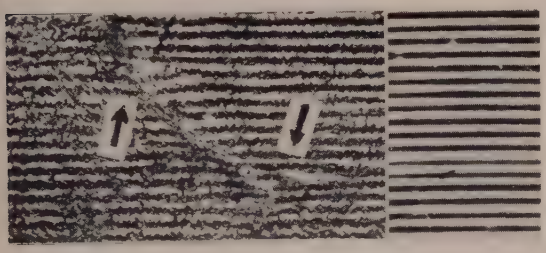

(b) $\Delta a = 1.0$ mm

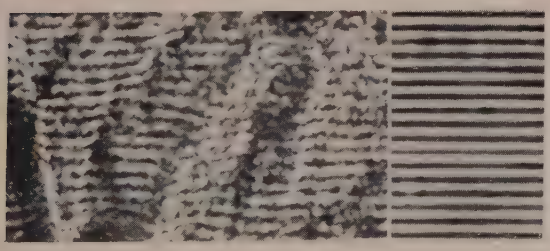

(c) $\Delta a = 9.4$ mm

Fig. 1. Light optical demonstration. Images of a plane grating covered with wrinkled paper (left) and uncovered (right). Δa indicates defocus, *i.e.* distance between the object and the object plane.

the distortions of the lattice look like dislocations with screw components. Similar phenomena are also observed when small segments of filaments are laid on the grating or when the grating is painted with transparent enamel, leaving brush traces. In any case, irregularities larger than the spacing produce distortions of the lattice in defocused images, often including ghost dislocations.

In electron microscopy, films supporting specimens often have defects and specimens are almost always covered with an uneven layer of contamination due to electron irradiation. Electron micrographs are usually taken at defocus of the order of 0.1 μ which corresponds to that in our demonstration. For example, defocus of $\Delta a = 9.4$ mm (Fig. 1c) corresponds to that of $\Delta a = 0.34\ \mu$ in the electron optical system. Thus it is highly probable that ghost dislocations appear in electron micrographs. According to our experiment, a ghost dislocation is usually accompanied by a diffuse region around or near it.

We feel that Menter's Figs. 6, 7 and 10 show true dislocations. However, we cannot entirely eliminate the possibility of ghost because diffuse regions similar to those observed in our demonstration are appearing in his micrographs. We examined many micrographs of dislocations taken in Japan[2] and found that some may possibly be ghosts. We think that a series of through-focus micrographs are needed to distinguish true dislocations from ghosts. The facts given in this paper are also applicable to dislocations in moiré fringes of crystal lattices[3),4)] and images of superlattices[5),6)].

The authors express their sincere thanks to Professor Kenzo Tanaka, Professor Ryozi Uyeda and Professor Keinosuke Kobayashi for their kind discussions.

References

1) J. W. Menter: Proc. Roy. Soc. **A 236** (1956) 119.
2) H. Watanabe and T. Komoda: Private communication.
K. Ito and H. Yotsumoto: Private communication.
R. Uyeda and Y. Kamiya: Private Communication.
S. Sakata: Private communication.
3) H. Hashimoto and R. Uyeda: Acta Cryst. **10** (1957) 143.
4) D. W. Pashley, J. W. Menter and G. A. Bassett: Nature **179** (1957) 752.
5) G. W. Brindley, J. J. Comer, R. Uyeda and J. Zussman: Acta Cryst. **11** (1958) 99.
R. Uyeda, T. Masuda, H. Tochigi, K. Ito and H. Yotsumoto: J. Phys. Soc. Japan **13** (1958) 461.
6) S. Ogawa, D. Watanabe, H. Watanabe and T. Komoda: Acta Cryst. In press.

J. Phys. Soc. Japan **13** (1958) 766

On the Auger Ejection of Electrons from Nickel by Inert Gas Ions

By Yoshiyuki Takeishi

Tokyo Shibaura Electric Co., 72, Horikawa-chō, Kawasaki, Japan

(Received April 30, 1958)

We have approximately calculated distribution in kinetic energy and total yield, γ, of the secondary electrons ejected from nickel surface by inert gas ions (except Kr^+ ion) of lower energy. The methods of calculations were essentially similar to the used one in our previous study[1] on clusty BaO-coated cathode, based upon the Hagstrum's one[2] for tungten. In this report, we will use the same notations as defined in the previous paper.[1]

The type of electron ejection in the present case is assumed the Auger neutralization for each inert gas ion, provided that the work function, φ, and the width of conduction band, ε_F, for nickel are 4.84 ev[3] and 4.70 ev[4], respectively.

Then, neglecting the atomic energy level shifts near metal and the effects of the movement of incident ion, the distribution in energy, $N_i(\varepsilon_K)$, of electrons excited in the process of Auger neutralization is expressed as follows:

$$N_i(\varepsilon_K)=c_1\rho(\varepsilon_K)\iint_0^{\varepsilon_F} n_c(\varepsilon_1)n_c(\varepsilon_2) \times\delta(\varepsilon_K-\varepsilon_1-\varepsilon_2+\varepsilon_0-E_i)d\varepsilon_1 d\varepsilon_2 \qquad (1)$$

which corresponds to Eq. (23)′ in the previous paper.[1] Here ε_0 is $\varepsilon_F+\varphi$, the energy difference between the zero vacuum level and the ground state in the conduction band, and E_i is the ionization energy of inert gas atom.

Assuming that $n_c(\varepsilon)$, the initial state density in the conduction band, is proportional to $\varepsilon^{1/2}$, and $\rho(\varepsilon_K)$, the density of final state, is given, as usual, by $c\varepsilon_K{}^{1/2}$, where c is a constant, $N_i(\varepsilon_K)$ can be calculated as follows:

$$\begin{aligned} N_i(\varepsilon_K)&=c_2\cdot\pi/2\cdot\varepsilon_K{}^{1/2}\cdot(\varepsilon_K+\varepsilon_0-E_i)^2\,, \\ &\qquad E_i-\varepsilon_0<\varepsilon_K<E_i-\varepsilon_0+\varepsilon_F \\ &=c_2\cdot\varepsilon_K{}^{1/2}[4\{\varepsilon_K-1/2(\varepsilon_K+\varepsilon_0-E_i)\}\cdot \\ &\quad\times\{\varepsilon_F(\varepsilon_K+\varepsilon_0-E_i)-\varepsilon_F{}^2\}^{1/2} \\ &\quad+(\varepsilon_K+\varepsilon_0-E_i)^2\sin^{-1}\{(\varepsilon_F-1/2(\varepsilon_K+\varepsilon_0-E_i))/ \\ &\quad(1/2(\varepsilon_K+\varepsilon_0-E_i))\}]\,, \\ &\qquad E_i-\varepsilon_0+\varepsilon_F<\varepsilon_K<E_i-\varepsilon_0+2\varepsilon_F\,. \end{aligned} \qquad (2)$$

In this calculation, the Auger transform was effectively used. Here, c_2 is the normalization factor and 1.197×10^{-3} for He^+, Ne^+, Ar^+ ions and 1.265×10^{-3} for Xe^+ ion.

For the above-calculated $N_i(\varepsilon_K)$ and the escape probability, $P_e(\varepsilon_K)$, the energy distribution, $N_0(\varepsilon_K)$, of electrons which escape from nickel surface, is obtained by

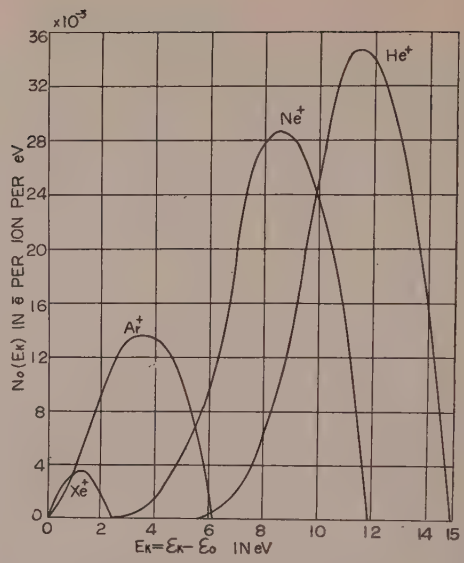

Fig. 1. Distribution in kinetic energy, $N_0(E_k)$, of secondary electrons.

$$N_0(\varepsilon_K)=N_i(\varepsilon_K)P_e(\varepsilon_K)\,. \qquad (3)$$

Assuming that the angular distribution of excited electron velocities is isotropic, $P_e(\varepsilon_K)$ is expressed by

$$P_e(\varepsilon_K)=\tfrac{1}{2}[1-(\varepsilon_0/\varepsilon_K)^{1/2}]\,, \qquad \varepsilon_K>\varepsilon_0\,. \qquad (4)$$

Upon this assumption, $N_0(\varepsilon_K)$ is calculated for each inert gas ion (except Kr^+ ion), as shown in Fig. 1, where the abscissa is scaled in $E_K=\varepsilon_K-\varepsilon_0$, that is, the kinetic energy of secondary electrons.

Finally, total electron yield, γ, per an incident ion, is easily obtained, by integrating $N_0(E_K)$ over E_K. γ values of 0.159, 0.128, 0.0506, and 0.0057 are obtained for He^+, Ne^+, Ar^+, and Xe^+ ions, respectively.

In spite of the over-simplified calculations, the obtained values of γ can fairly explain the cathodic phenomena with nickel cathode in normal glow discharges in inert gases, which will be partially reported in the following paper.[5] However, the calculated $N_0(E_K)$ and γ should be justified by their direct measurements. Accordingly, we will leave the discussions after the direct measurements are done in future.

In conclusion, the author wishes to express his sincere thanks to Mr. K. Nomura and Mr. R. Satō for their encourgements throughout this work.

References

1) Y. Takeishi: Jour. Phys. Soc. Japan, **11** (1956) 676.
2) H. D. Hagstrum: Phys. Rev. **96** (1954) 336.
3) H. B. Michaelson: Jour. Appl. Phys. **21** (1950) 536.
4) R. H. Kingston: Phys. Rev. **84** (1951) 944.
5) Y. Takeishi: following paper [Jour. Phys. Soc. Japan **13** (1958) 767].

J. PHYS. SOC. JAPAN **13** (1958) 767~768

A Note on the Normal Cathode Fall in the Glow Discharges in Inert Gases

By Yoshiyuki TAKEISHI

Tokyo Shibaura Electric Co., 72, Horikawa-chō, Kawasaki, Japan

(Received April 30, 1958)

1. The normal cathode fall, V_{cn} (obs.), has been measured for nickel cathode in glow discharges in He, Ne, Ar, and Xe gases, respectively (see Table I). Both cathode and anode were pure nickel and were same form of a dish, the diameter of which was 10 mm. The other experimental conditions and procedures were similar to that in our previous work.[1] After sufficient stabilization of the cathode, the *d. c.* tube drop,[1] V_{cn} (obs.), between anode and cathode was measured as the normal cathode fall.

2. We have attempted to obtain the theoretical normal cathode fall, V_{cn} (cal.), for nickel, inserting the values of γ calculated in the preceding paper,[2] into the following equation:

$$\left.\begin{aligned} V_{cn}(\text{cal.}) &= 3.0(B/A)\ln(1+1/\gamma)^{1)}, \\ \text{for He,} \quad &= 1.42(a_3/a_1)\ln(1+1/\gamma)^{3)}, \end{aligned}\right\} \qquad (1)$$

for Ne, Ar, Kr, and Xe.

The latter expression has been introduced by Dote[3]. It is resulted from modification in α/p expression; $\alpha/p = a_1\{1-\exp[(-E/p-a_2)/a_3]\}$[4], $E/p \geq a_2$, where a_1, a_2, and a_3 are numerical constants which are cited in Table II. The results of calculations using Eq. (1), are shown in Table I.

Table I. Normal Cathode Falls (in volt).

Cathode		He	Ne	Ar	Kr	Xe
nickel	p in mmHg	20.6	17.7	16.5	—	15.1
	V_{cn} (obs.)	145.0	143.0	142.5	—	196.5
	V_{cn} (cal.)	149.2	146.5	142.0	—	205.0
	γ (cal.)[2]	0.159	0.128	0.0506	—	0.0057
clusty barium oxide	p	15.1	15.0	14.9	—	6.6
	V_{cn} (obs.)[1]	80.5	73.5	56.0	—	46.5
	V_{cn} (cal.)	84.4	76.5	53.0	47.7	45.6
	γ (cal.)[1]	0.481	0.480	0.476	0.474	0.471
tungsten	p	20.0	36.0	10.0	—	6.6
	V_{cn} (obs.)[1]	121.0	114.5	117.0	—	250 ?
	V_{cn} (cal.)	116.4	118.1	114.4	128.3	173.3
	γ (obs.)[5]	0.290	0.213	0.095	0.050	0.013
molybdenum	p	42	40	10	5.8	5.4
	V_{cn} (obs.)[6]	109.5	107.0	103.6	120.0	134.4
	V_{cn} (cal.)	113.7	108.0	103.7	115.9	152.6
	γ (obs.)[5]	0.300	0.254	0.122	0.069	0.022

3. By Eq. (1), V_{cn} (cal.) has been computed again for tungsten cathode, using the corrected values of γ for 10 ev inert gas ions, reported by Hagstrum,[5] and also computed again for clusty BaO-coated cathode[1] (see Table I).

4. We have also tried to compute V_{cn} (cal.) for molybdenum cathode, using the values of γ for 10 ev ions measured by Hagstrum[5], and to compare V_{cn}(cal.) with V_{cn}(obs.), reported already by Jurriaanse et al[6] (see Table I).

5. It is seen in Table I that V_{cn}(cal.) are in good agreement with V_{cn}(obs.) for four cathodes. However there are some disadvantages: (i) For nickel and clusty BaO-coated cathodes, the values of γ obtained by our over-simplified calculations were used. (ii) For tungsten and molybdenum, secondary electrons can be ejected by metastable Ne atoms[7], which may be present in close proximity to cathode in glow discharges, nevertheless this effect is not included in Eq. (1). (iii) Both our calculations and Hagstrum's measurements were done for the "clean" surface adsorbed no molecules.

Table II. Numerical constants in α/p expression and Eq. (1).[4]

	a_1	a_2	a_3
Ne	4.18	9.4	200
Ar	13.93	24.5	455
Kr	17.17	26.5	510
Xe	27.84	41.8	780

Here we will only point out next two points for those problems: (i) It is easily deduced from Eq. (1), that $\Delta V_{cn}(\text{cal.})/\Delta\gamma = -1.42(a_3/a_1)\cdot 1/\gamma(1+\gamma)$, which indicates that the variation of 10% in γ gives the variation of at most several volt to V_{cn}(cal.). (ii) It is supposed in our mind that in glow discharges, the ions impacting cathode sputter probably the

adsorbed molecules, and a considerably "clean" surface may be realized.

In conclusion, the author is grateful to Mr. K. Nomura and Mr. R. Satō for their encouragements during this work.

References

1) Y. Takeishi: Jour. Phys. Soc. Japan **11** (1956) 676.
2) Y. Takeishi: preceding paper, ibid. **13** (1958) 766.
3) T. Dote: The print of Research Group of Cold Cathode Discharge Tubes, No. 97 (in Japanese), April, 1956.
4) T. Dote: Transactions of the 1956 joint convention of the three Electrical Institutes of Japan, the print No. 48 (in Japanese).
5) H. D. Hagstrum: Phys. Rev. **104** (1956) 672, 317.
6) T. Jurriaanse et al: Philips Res. Rep. **1** (1945) 225.
7) H. D. Hagstrum: Phys. Rev. **96** (1954) 336.

J. Phys. Soc. Japan **13** (1958) 768~769

Electron Spin Resonance of Eu^{++} in Natural CaF_2

By On Matumura, Kazumi Hōrai and Zen'emon Miduno

Department of Physics, Faculty of Science, Kyusyu University

(Received April 7, 1958)

The electron spin resonance of natural CaF_2 crystals (Fluorite from Weardale, England) containing a small amount of Eu^{++} has been analysed at 3 cm wavelength at room temperature. The typical spectrum is shown in Fig. 1.

Divalent europium has seven f electrons and a ground state of $^8S_{7/2}$. In the absence of external magnetic field, this state is split by a cubic crystal field into two twofold levels and one fourfold level. The overall separation is $8\boldsymbol{a}$, where $\boldsymbol{a}$ is the crystalline cubic field splitting parameter[1]. The theoretical treatments were carried out by Kittel and Luttinger[2], and De Boer and Van Lieshout[3]. Using their results, when the external magnetic field is perpendicular to |001| axis, the resonance fields are obtained for $\beta H \gg \boldsymbol{a}$ as,

$$M=1/2 \leftrightarrow -1/2:$$
$$H=H_0-\left(\frac{35}{32}-\frac{1155}{16}\phi+\frac{10875}{32}\phi^2\right)\left(\frac{a}{g\beta}\right)^2\frac{1}{H_0}$$

$$M=\pm 3/2 \leftrightarrow \pm 1/2: \quad H=H_0\mp 3(1-5\phi)\left(\frac{a}{g\beta}\right)+\left(\frac{5}{8}+\frac{195}{4}\phi-\frac{2115}{8}\phi^2\right)\left(\frac{a}{g\beta}\right)^2\frac{1}{H_0}$$

$$M=\pm 5/2 \leftrightarrow \pm 3/2: \quad H=H_0\mp\frac{5}{2}(1-5\phi)\left(\frac{a}{g\beta}\right)+\left(\frac{115}{3}\phi-\frac{2275}{12}\phi^2\right)\left(\frac{a}{g\beta}\right)^2\frac{1}{H_0}$$

$$M=\pm 7/2 \leftrightarrow \pm 5/2: \quad H=H_0\pm 5(1-5\phi)\left(\frac{a}{g\beta}\right)+\left(\frac{5}{8}-\frac{285}{4}\phi+\frac{1725}{8}\phi^2\right)\left(\frac{a}{g\beta}\right)^2\frac{1}{H_0}$$

The parameter $\phi=\cos^2\theta\sin^2\theta$ where θ is the angle between the magnetic field and |100| axis.

With $g=1.993$ and $\boldsymbol{a}=0.0186\ \mathrm{cm}^{-1}$, the calculated angular variation of the spectrum and the observed values for $H\perp|001|$ are shown in Fig. 2. The agreements seem to be almost satisfactory. The theoretical intensities of the fine structure components $M=7/2$; $M=-3/2$; $M=-5/2$; $M=1/2$; $M=5/2$; $M=3/2$; $M=-7/2$ are 7:15:12:16:12:15:7, and the observed intensity ratios are (measured from high to low fields) approximately 7:20:14:30:15:

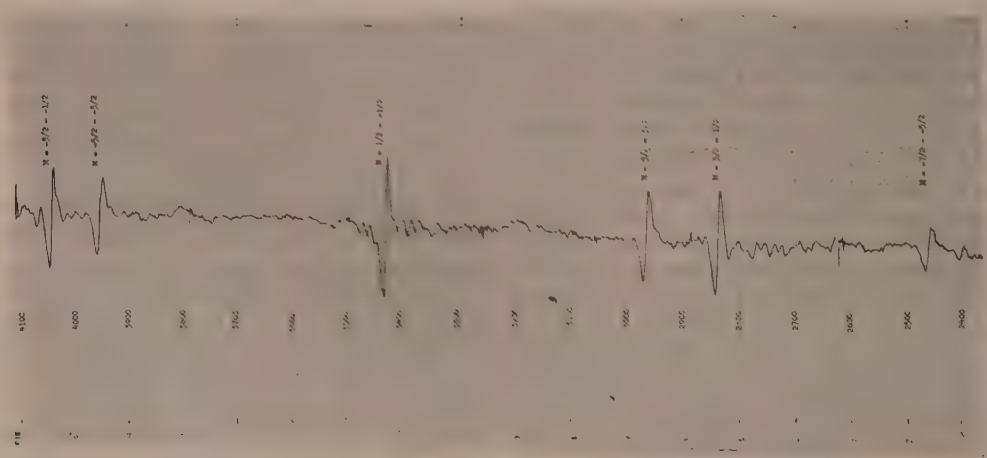

Fig. 1.

18:7. The anomalous large intensity of the central line may be due to other impurities or imperfections in the crystals. In addition, some rather weak complicated lines are also observed. The full report will be given in the near future.

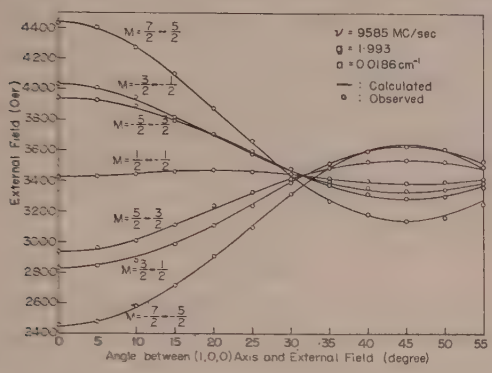

Fig. 2. Angular variation of the fine structure lines.

This research is partially supported by the Grant for Promotion of Science from the Ministry of Education.

References

1) W. Low: Phys. Rev. **105** (1957) 792.
2) C. Kittel and J. M. Luttinger: Phys. Rev. **73** (1948) 162.
3) J. De Boer and R. Van Lieshout: Physica **15** (1949) 570.

J. Phys. Soc. Japan **13** (1958) 769~770

Measurement of the Thermal Conductivity in Semiconductors

By Riro Nii

Electrical Communication Laboratory, Musashinoshi, Tokyo

(Received April 19, 1958)

We measured the thermal conductivity of Bi_2Te_3 and PbTe by Ångström method. The apparatus for our measurement is shown schematicaly in Fig. 1. The sample was soldered on the bar of copper which was wounded by the heater I. The thermocouples T_1 and T_2 of Cu constantan were soldered at the positions shown in the figure. When the on off current of period 4 sec was added to the heater I, the sineous temperature wave passed through the sample and diminished to zero amplitude before reaching to the other end of the sample. Then the thermoelectric motive force of the T_1 and T_2 were given by the next forms.

$$V_1 = A\cos\omega t + C_1$$

$$V_2 = B\cos(\omega t - \beta) + C_2$$

And there exist the following relation between A, B and β.

$$\varkappa = \frac{\omega l^2}{2\ln^2\frac{A}{B}} = \frac{\omega l^2}{2\beta^2} = \frac{K}{c\rho}$$

where K: thermal conductivity
c: specific heat
ρ: density
$\varkappa$: temperature conductivity

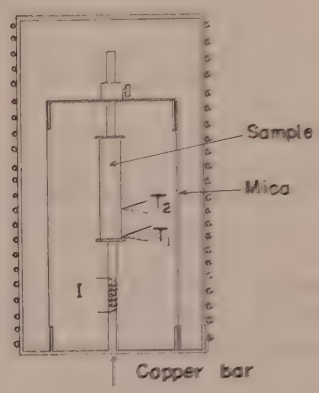

Fig. 1. The apparatus for the measurement.

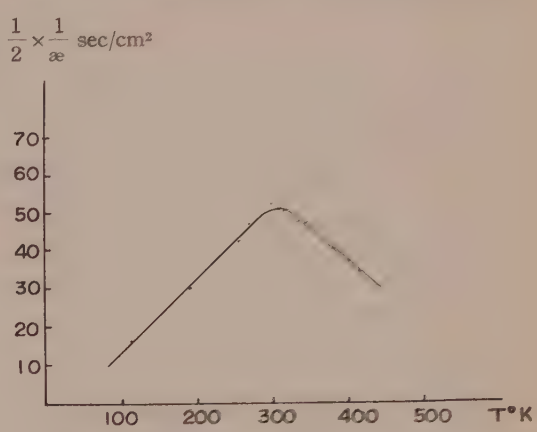

Fig. 2. Temperature conductivity of Bi_2Te_3.

Hence the measurement of the ratio A/B and phase difference β gave independently the temperature conductivity. The agreement of the values of calculated from A/B and β was fairly good, but the accuracy of measurement was better for the case of the ratio A/B. The point in the figures 2 and 3 are the values calculated for the measurment of A/B.

At first we show in Fig. 2 the temperature dependence of $1/\varkappa$ of Bi_2Te_3. As is shown there, the curve bends at the temperature where the Hall coefficient of the same sample begins to decrease, and this behaviour corresponds to the results given by Goldsmid[1] and Satterthwaite *et al.*[2]

Next we show in Fig. 3 the temperature dependence of K of PbTe. The values of thermal conductivity K, were calculated from the measured values of æ and the values of c and ρ. For the

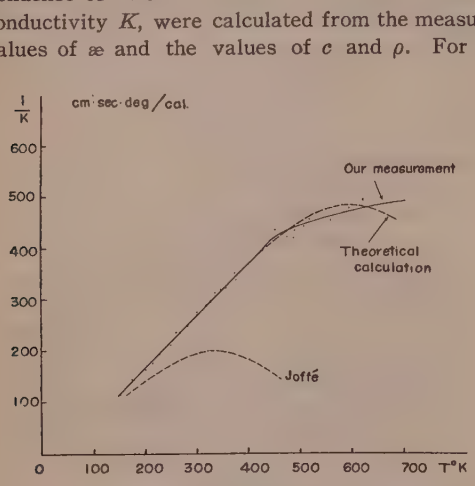

Fig. 3. The thermal conductivity of PbTe.

values of specific heat c of PbTe, we used the values given by Parkinson *et al*[3] below room temperature, and we assumed 12 cal./mol above room temperature. The dotted curve in Fig. 3 is the results given by Joffé.[4] He suggested from his results the heat conduction by excitons in PbTe, but our sample did not show the abnormal bend of thermal conductivity by excitons. The $1/K$ curve of our samples deviates from a straight line at higher temperature where the samples become intrinsic. Price[5] considered the energy transport by a bipolar diffusion due to a recombination of electrons and holes for Boltzmann statistics and gave a formula for the additional heat conductivity. The agreement between our results and the values of K calculated from the Price's formula is rather well.

References

1) Goldsmid: Proc. Phys. Soc. B. **69** (1956) 203.
2) Satterthwaite *et al*: Phys. Rev. **108** (1957) 1164.
3) Parkinson *et al*: Proc. Phys. Soc. **A67** (1954) 569.
4) Joffe: Canadian Journal of Physics **34** (1956) 1342.
5) Price: Phil. Mag. **46** (1955) 1252.

JOURNAL OF THE PHYSICAL SOCIETY OF JAPAN Vol. 13, No. 8, AUGUST, 1958

Elastic and Inelastic Scattering of Protons from Neon

By Michiya KONDO and Takashi YAMAZAKI

Department of Physics, Faculty of Science, Osaka University, Osaka

(Received April 7, 1958)

The angular distributions of protons elastically scattered from Ne and inelastically scattered from Ne^{20} ($Q=-1.63$ MeV) were measured from 30° to 165° in the laboratory system at bombarding energies of 4.7, 4.9, 5.1, 5.3 and 5.5 MeV. Photographic plates were employed for the detection of scattered particles. The distributions for the elastic scattering of protons varied markedly with the primary energies, while the five distributions for the inelastic scattering had roughly similar shapes.

§ 1. Introduction

The angular distributions of inelastically scattered protons have been studied about several light elements and the asymmetric distributions about the centre-of-mass scattering angle $\theta=90°$ were obtained except a few cases. To explain these angular distributions, the theories based on the mechanisms of compound nucleus formation,[1),2),3)] direct nucleon-nucleon interaction,[4),5),6)] and surface interaction,[7)8)] were considered. There are, however, many complexities on applying these theories. Even though only the compound nucleus mechanism is assumed among them, for instance, there exist some types of distributions. If the reaction proceeds through a single compound level, the angular distribution is expected to be symmetric about $\theta=90°$ and then the distribution is characterized by the spin and the parity of the compound level.[3)] If the interferences with other overlapping levels are important, the distribution becomes asymmetric about $\theta=90°$ and will change remarkably with the incident energy. If a large number of overlapping levels are involved in the compound nucleus and interference terms can be neglected statistically, the distribution becomes symmetric about $\theta=90°$.[1),2)] Moreover, if the contributions of the direct interaction were superposed upon the mechanism of the compopund nucleus formation, the distribution becomes more complex and it will be difficult to separate the contributions of each mechanism.

The angular distributions of protons elastically scattered and inelastically scattered from Ne^{20}, exciting it to 1.63 MeV, were measured at the proton energy of 9.5 MeV[9)] and the symmetric distribution about 90° was obtained for the inelastic group. The distribution peaked in the forward direction were reported for the inelastic group at the proton energy of 4.2 MeV.[10)] McManus[11)] has analyzed the 9.5 MeV data in terms of the direct interaction theory,[4)] because the large anisotropy is quite unlikely from the statistical consideration. Butler also fitted his theory[5)] on this data. A good agreement was obtained with these theories, but it could not be concluded that this reaction arises from a direct interaction.

In the present experiments the angular distributions of elastically and inelastically scattered protons from Ne^{20} were obtained in the energy region from 4.5 to 5.4 MeV. The excitation energy of the compound nucleus Na^{21} for 5 MeV protons is about 8 MeV and it is expected that the compound levels are rather widely spaced. In this case the statistical theory,[1),2)] of course, can not be applied but it must be needed to take account of the effects due to individual levels. And adding to this situation there might exist the contribution of the mechanisms other than compound process in this energy regions. However, a small number of inelastic scattering data[10),12),13)] has been reported at relatively low bombarding energies and these data were taken only at a fixed incident energy.[10),12)] Therefore it is interesting to investigate the angular distributions at various incident energies.

§ 2. Experimental Arrangement and Procedure

The 5.7 MeV proton beam extracted from the Osaka 44-inch cyclotron was focused into the scattering chamber. The photographic emulsion technique was employed to study

the scattering of protons by neon. The arrangement of the scattering chamber, the beam collimating system and the beam integrating system was same as described in the previous papers.[13),14)] As a gas target was used in this experiment, the detecting systems were slightly modified from that previously described.[13)]

The gas target system consisted of target cell, gas reservoir, mercury manometer and evacuating lead. The target cell was a brass cylinder of 7.5 cm in diameter, and the wall of the cylinder had a slot of 2.5 cm in width covered with aluminum foil of 9 micron thick allowing both the incident beam and the scattered particles to pass through. The axis of the cylinder was set at the center of the scattering chamber perpendicularly to the beam direction. The target system was filled with neon gas to the pressure of 15.0 cm Hg. The pressure was measured by the manometer and was constant within 1 per cent throughout the experiment. The energy loss of incident protons to reach the center of the gas target was about 200 keV.

The plate cameras used for the measurements of angular distributions and excitation function were same as the ones used for the foil-target experiments.[13)] In the measurements of angular distributions with gas-target, an annular slit-system was set at the interior of the plate camera. This had slits at 7.5° intervals corresponding to each plate, and the slits have baffles to prevent the scattered protons entering into the plate through the other neighboring slits and to decrease the slit-edge scattering. The slits, 1.5 mm in width, were cut by a milling machine and the accuracy of the widths was within 1 per cent. This arrangement was shown in Fig. 1.

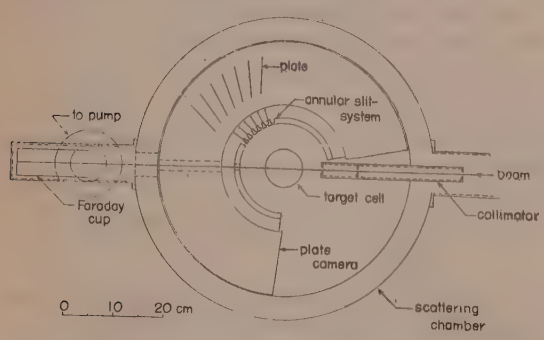

Fig. 1. The schematic diagram of scattering chamber and plate camera.

The position and the thickness of the target were defined by the width of the slit, the position of the slit, the scanned distance of of the plate, and the position of the centre of the plate. These relations were illustrated in Fig. 2.

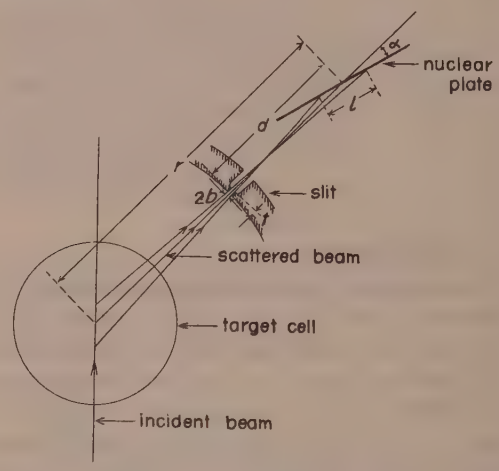

Fig. 2. Details of the detecting system. $2b$: 0.150 cm, r: 19.05 cm, d: 10.0 cm, t: 0.15 cm, α: 15.0°, l: 2.5 cm.

The differential cross section $d\sigma/d\Omega$ at the laboratory scattering angle θ_0 is given by

$$d\sigma/d\Omega = N_s \sin\theta_0 / N_i n G \qquad (1)$$

where

$$G = 2b\, A \sin\alpha / rd \qquad (2)$$

and N_s is the number of scattered particles obtained by scanning an area of A cm² on the plate. N_i is the number of incident particles and n the number of target atoms per cm³. $2b$ is the width of slit, α the glancing angle of plate, r the distance between the centre of the target and the centre of the plate, and d the distance between the slit and the centre of the plate.

The errors of relative cross sections from the glancing angle α were estimated to be less than 0.5 per cent and the errors from r and d were negligible. N_i and n were common to each scattering angle. The thickness of a edge of a slit was 1.5 mm, and the effect of this thickness to the relative cross section was negligible and was less than 1 per cent to the absolute value. Thus the whole systematic errors were estimated to be about one per cent in the relative cross section, combined the errors of the width of a slit. The absolute cross section, however,

might be accurate within ten per cent. The angular resolution was determined mainly by the scanned region of the plate and was about $\pm 1°$. The angular setting of the camera was accurate within 1/2°.

The effective target thickness at the scattering angle θ_0, T mg/cm², is expressed to be

$$T = 2br\rho/d \sin\theta_0 \qquad (3)$$

where ρ is the density of the neon gas in milligramme per cubic centimeter. In the present experiments the target thickness was about 0.050 mg/cm² at the scattering angle $\theta_0 = 90°$ and about 0.195 mg/cm² at $\theta_0 = 165°$.

The plate camera for obtaining the excitation function was same as described before,[13] but in this experiment it also had a similar slit system as the one used for measuring the angular distribution. The other experimental arrangements and procedures were same as previously reported.[13] The incident energies could be reduced with 100 keV intervals by changing a thickness of absorber.

The emulsion used were Ilford C-2 of 200μ and 100 μ and Fuji BT-6B of 150 μ in thickness.

§ 3. Results

Absolute cross sections could be obtained by observing the quantities involved in the formulae (1) and (2). As a check on the accuracy of the detecting system, the proton-proton scattering cross sections were measured at several scattering angles by using a propane gas as a target and an agreement with the interpolation of the available data was obtained within the accuracy of 5 per cent.

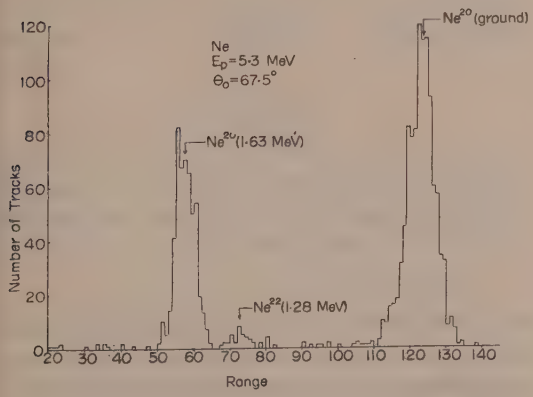

Fig. 3. The typical range distribution for the scattered protons from Ne, observed at the laboratory angle of 67.5°. 1 div.: 1.2 micron.

The range distributions for the scattered protons by neon at $\theta_0 = 62.5°$ are shown in Fig. 3. Since a natural neon gas was used for a target, a small amount of elastic group from Ne^{22} (9.7%) was contained within elastic group from Ne^{20} (90.0%). Inelastic groups were resolved corresponding to the 1st excited state of Ne^{20} ($Q = -1.63$ MeV) and the 1st excited state of Ne^{22} ($Q = -1.28$ MeV). Data were taken about the elastic group and the inelastic group from Ne^{20}, and about one thousand tracks were counted for each point.

Excitation curves for the Ne (p, p) Ne and Ne^{20} (p, p') Ne^{20} ($Q = -1.63$ MeV) were measured at a laboratory angle of 90° for the bombarding energies from 4.6 to 5.5 MeV. The bombarding energies were determined by considering both the thickness of absorbers and the range of tracks in emulsions. The energy spread of the incident protons were estimated to be less than 100 keV. The results are shown in Fig. 4.

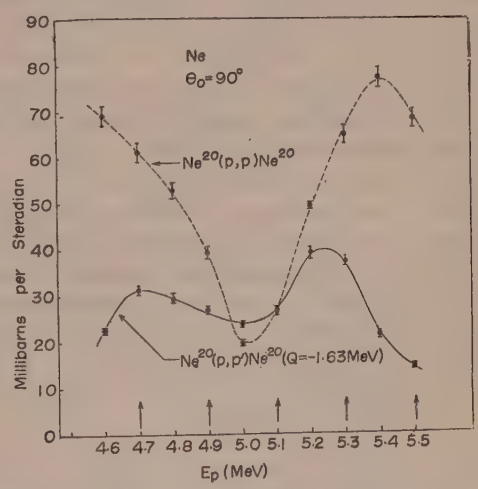

Fig. 4. The excitation functions for the reactions Ne(p, p)Ne and $Ne^{20}(p, p')Ne^{20}$($Q = -1.63$ Mev) at the laboratory angle of 90°.

Angular distributions were measured at the five bombarding energies indicated in Fig. 4 by arrows. The distributions of the elastic groups are shown in Fig. 5 and the distributions of the inelastic groups from Ne^{20} ($Q = -1.63$ MeV) are shown in Figs. 6 and 7. The cross sections of excitation curves and that of the angular distributions were consistent within expected experimental errors. The

angular distributions for inelastic scattering were fitted by the least square method with a series of the Legendre polynomials up to $P_4(\cos\theta)$. The coefficiects of P_3 and P_4 have,

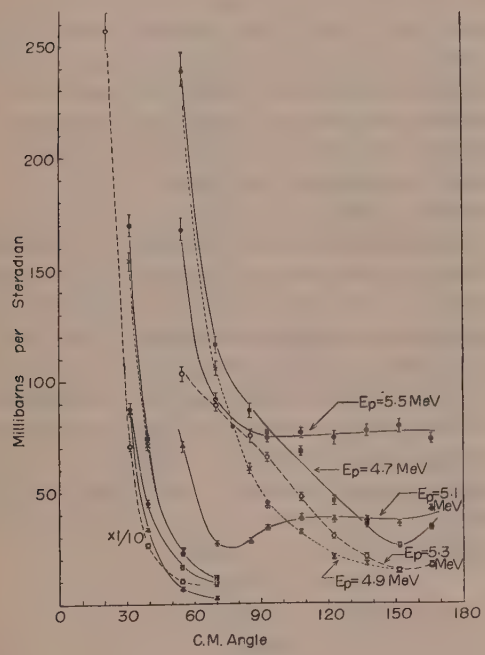

Fig. 5. The angular distributions of protons elastically scattered from Ne measured at E_p =4.7, 4.9, 5.1, 5.3, and 5.5 Mev.

Table I. The coefficients of the Legendre polynomials obtained by expanding the angular distributions of inelastically scattered protons from Ne^{20} and the integrated cross sections as a function of incident proton energies.
E_p: bombarding energy of protons,
A_L: the coefficient of $P_L(\cos\theta)$,
σ_T: integrated cross section

E_p	A_0	A_1	A_2	A_3	A_4	σ_T(mb)
4.7	30.8	2.7	−17.3	−4.2	−1.6	387
4.9	20.6	4.1	−15.4	−0.6	1.9	259
5.1	22.8	5.5	−13.1	0.5	2.3	287
5.3	30.8	4.4	−23.1	−7.2	0.6	387
5.5	11.4	1.1	− 5.6	−0.8	0.4	143

however, large uncertainties, if we take into account the statistical errors. These coefficients and integrated cross sections are listed in Table I. The curves in Figs. 6 and 7 are calculated from the coefficients given in Table I.

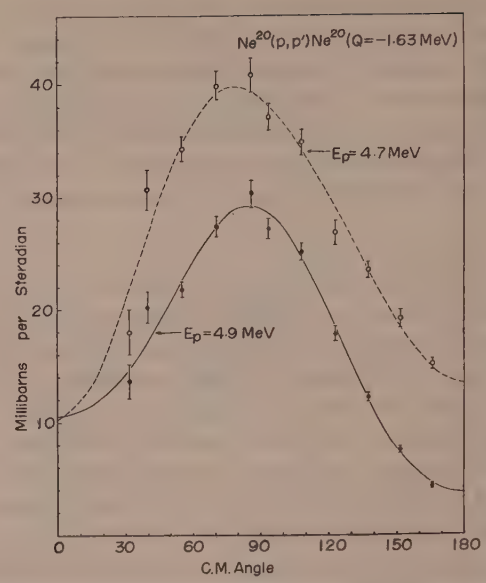

Fig. 6. The angular distributions of protons inelastically scattered from $Ne^{20}(Q=-1.63$ Mev) at E_p=4.7 and 4.9 Mev.

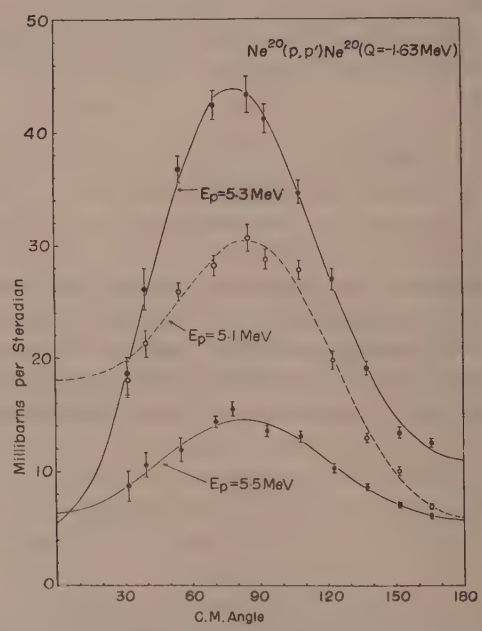

Fig. 7. The angular distributions of protons inelastically scattered from $Ne^{20}(Q=-1.63$ Mev) at E_p=5.1, 5.3, and 5.5 Mev.

§4. Discussions

As shown in Fig. 4, the excitation curves of both the elastic and the inelastic scattering indicate the resonance character. The total cross sections for inelastic scattering (Table I) vary with the primary energy and have large values at 4.7 and 5.3 MeV. Since

the energy resolution of the primary beam was not so good, we can not conclude that these peaks are due to a single resonance. But it is expected that these peaks are caused by few resonances or a certain strong resonance among the weak ones. The same situations were observed in the similar experiments on Si and Mg.[15] The angular distributions of the elastic scattering illustrated in Fig. 5 show the strong interference between the coulomb and the nuclear scattering and vary remarkably with the primary energy. These may be explained by assuming the occurence of resonance scatterings.

The angular distributions of inelastically scattered protons at five energies have similar shapes, although the integrated cross sections vary markedly with the incident energy. The coefficients of the odd terms of the Legendre polynomals are generally small as compared with that of even terms and therefore the distributions are nearly symmetric about 90°. The coefficients A_0 and A_2 are large in every case, but the coefficients A_4 are generally small and can be neglected by considering the experimental errors. The coefficients A_3 may also be neglected except the case of 4.7 and 5.3 MeV.

It is interesting that these distributions have similar shape to that obtained by Freemantle *et al.*[9] at 9.5 MeV, in spite of the different situations, that is in the present case few levels may be involved in the compound state while more levels may be involved in the case of 9.5 MeV. McManus[11] analyzed 9.5 MeV data in terms of direct interaction theory. The theories of direct interaction type[4),7)] predict an angular dependence of inelastic differential cross section as follows

$$d\sigma/d\Omega \propto \sum_L K_L j_L(qR)^2 \qquad (4)$$

where $q=|\boldsymbol{k}_i-\boldsymbol{k}_0|$ is the momentum change between incident and outgoing proton, R is the nuclear radius, j_L is the spherical Bessel function of order L, and L is restricted to

$$|\boldsymbol{J}_i+\boldsymbol{J}_f+\boldsymbol{1}|_{\max} \geqq L \geqq |\boldsymbol{J}_i+\boldsymbol{J}_f+\boldsymbol{1}|_{\min}$$

We cannot fit the present data with this theoretical distribution using the same parameter as McManus', because the present incident energy differs from that of Freemantle *et al.*[9] and a momentum change q at the same scattering angle differs from that of 9.5 MeV. Even if the other direct interaction theories are applied in this case, the rapid variation of the cross sections with the bombarding energy may not be explained. Moreover, it is difficult to assume the strong interference between compound nucleus and direct interaction mechanisms suggested by Greenless *et al.*[16] in the case of Mg^{24}. On the other hand, we can easily explain these features by assuming that only the compound nucleus mechanism contributes to this reaction, but we cannot exclude the existence of the direct interaction mechanisms.

If we assume only the compound nucleus formation, we can discuss the natures of the compound levels. As was mentioned above, it is expected that a single or few levels may contribute to the reaction, then the interference with the other neighbouring levels will appear in the angular distribution. However, the fact that the odd terms of the Legendre polynomials (Table I) are small shows the interferences between the levels of different parities to be small. When it is assumed that only a single incoming orbital angular momentum l, spin and parity of the compound level J_π, outgoing orbital angular momentum l', outgoing channel spin s' contribute to the angular distribution, we can determine the shape of the distribution using the Blatt and Biedenharn's formula.[3] Spins and parities of Ne^{20} for the ground and the 1st excited states are already known as 0+ and 2+ respectively. From the fact that the coefficients A_4 are very small as compared with the coefficients A_2 and from the values of A_2/A_0, the following cases will be probable

l	J_π	l'	s'	A_2/A_0
2	3/2+	2	5/2	−0·71
1	3/2−	1	3/2	−0.80
(1	3/2−	3	5/2	−0.20)
3	5/2−	1	5/2	−0.91

and observed A_2/A_0 are as follows

E_p	A_2/A_0
4.7 MeV	−0.56
4.9 MeV	−0.75
5.1 MeV	−0.58
5.3 MeV	−0.75
5.5 MeV	−0.50

We have neglected in the above calculations the even terms which are caused by the other types of proton waves or by the inter-

ferences between these proton waves. Actually the coefficients of these terms may be involved in the observed A_0 and A_2, but these can not be eliminated from the observed values. Therefore there are some ambiguities when the observed A_2/A_0 are compared with the theoretical ones. We also cannot know about the existence of the interference terms between the levels of same parities, while we see the interference terms between the levels of different parities being small. Consequently there may exist the levels of same parities in the energy region investigated here, i.e. the peaks at 4.7 and 5.3 MeV are due to the single level or the superposition of the above indicated levels of same parities. These conditions are different from that of the similar experiments on Mg^{24} $(0+ \rightarrow 2+)$, where a large odd terms have been observed.[13),15)]

Acknowledgement

The authors wish to thank Professor T. Wakatsuki for his kind advises, Dr. S. Yamabe for his great helps and guidances, Miss. M. Kitatani for her helps in scanning the plates, and Fuji Photo Film Corporation for the preparation of nuclear plates. The authors are also grateful to the Nishina Memorial Foundation for its financial support.

References

1) L. Wolfenstein: Phys. Rev. **82** (1951) 690.
2) W. Hauser and H. Feshbach: Phys. Rev. **87** (1952) 366.
3) J. M. Blatt and L. C. Bidednharn: Rev. Mod. Phys. **24** (1952) 157.
4) N. Austern, S. T. Butler and H. McManus: Phys. Rev. **92** (1953) 350.
5) S. T. Butler: Phys. Rev. **106** (1957) 272.
6) T. R. Lamarsh and H. Feshbach: Phys. Rev. **104** (1956) 1633.
7) S. Hayakawa and S. Yoshida: Proc. Phys. Soc. **A68** (1955) 656. Prog. Theor. Phys. **14** (1955) 1.
8) S. Yoshida: Proc. Phys. Soc. **A69** (1956) 668.
9) R. G. Freemantle, D. J. Prowse, A. Hossain and J. Rotblat: Phys. Rev. **96** (1954) 1270.
10) H. Heitler, A. N. May and C. F. Powell: Proc. Roy. Soc. **A190** (1947) 180.
11) McManus: Report of the Brookhaven Conference on the Satistical Aspects of Nucleus (1955).
12) E. H. Rhoderick: Proc. Roy. Soc. **201** (1950) 348.
13) S. Yamabe: Jour. Phys. Soc. Japan **13** (1958) 237.
14) M. Takeda *et al.*: Jour. Phys. Soc. Japan **12** (1957) 561.
15) S. Yamabe, M. Kondo, T. Yamazaki and A. Toi: To be published in Jour. Phys. Soc. Japan.
16) G. W. Greenlees, B. C. Haywood, L. G. Kuo and M. Petravić: Proc. Phys. Soc. **A70** (1957) 331.

JOUNAL OF THE PHYSICAL SOCIETY OF JAPAN Vol. 13, No. 8, AUGUST 1958

Angular Distribution of Protons Inelastically Scattered from Si^{28} and Mg^{24}

By Shotaro YAMABE, Michiya KONDO, Takashi YAMAZAKI and Atsutomo TOI*

Department of Physics, Faculty of Science, Osaka University, Osaka
**Department of Nuclear Engineering, Faculty of Engineering, Osaka University, Osaka*

(Received April 7, 1958)

The angular distributions and the excitation curves of protons inelastically scattered from Si^{28} ($Q=-1.78$ MeV) and Mg^{24} ($Q=-1.37$ MeV) have been measured in the energy range $E_p=4.8$ to 5.7 MeV. A broad resonance was observed in each excitation functions. The angular distributions in Mg^{24} show an asymmetry about the centre-of-mass scattering angle $\theta=90°$ and a strong dependence with the energy of incident protons, while in Si^{23} the angular distributions are rather symmetric than in Mg^{24}.

§ 1. Introduction

The angular distribution of the protons inelastically scattered from Si^{28}, being left in the 1.78 MeV level, was measured by Conzett at proton energy of 12 MeV.[1] He interpreted his result with the combination of a distribution symmetric about 90° and a distribution expected from a theory of the direct interaction.[2),3)] Similar experiments on the 1.37 MeV level of Mg^{24} were performed by many investigators at proton energies from 4.7 MeV to 18 MeV.[1),4)-12)] These results are all asymmetric about the centre-of-mass scattering angle $\theta=90°$. In the 10 MeV region[8),9),11)] the angular distributions change markedly with the incident proton energies. To explain this circumstance, Greenless *et al.*[11)] suggested an interference effect between the process of compound nucleus formation and direct interaction. Yoshida[13)] gave the treatment which regards the inelastic scattering of nucleons by a nucleus at medium energy as the surface interaction, and applied this theory to proton scattering by Mg^{24} at 10 MeV.[9)] He showed that the strong angular dependence of the inelastic scattering was due to the surface interaction while the main contribution came from the compound nucleus.

In the region of the incident proton energies up to 5.7 MeV, the excitation curve of the 1.78 MeV gamma rays following the inelastic scattering of protons from Si^{28} were studied[14),15)]. For the incident protons near 5 MeV, the excitation curves of the protons inelastically scattered from Mg^{24}, exciting to 1.37 MeV, were measured.[12),16)] They show the resonance features. In this relatively low incident energy region the excitation energies of the compound nucleus are considerably low for Mg^{24} and Si^{28}, so it would be expected that so many levels were not excited. The main feature will be explained by considering the overlapping of a few levels, if the compound nucleus formation is the predominant process in this energy region. But the possibility of direct interaction might be considered adding to the compound process.

In this paper the angular distributions for Si^{28} ($Q=-1.78$ MeV) were studied at 5.3, 5.4 and 5.5 MeV. The angular distributions for Mg^{24} ($Q=-1.37$ MeV) at 4.8 and 5.7 MeV were also measured as the extension of the previous investigation performed at 5.1 and 5.4 MeV[12)] by one of the present authors.

§ 2. Experimental Arrangement and Procedure

The 44-inch Osaka University Cyclotron was used to provide a beam of 5.7 MeV protons. The experimental arrangement and procedure were same as the previous experiments.[12),17)] The detectors were the Ilford *C-2* nuclear emulsions, 200 microns and 100 microns thick, and the Fuji *ET-6B* nuclear emulsions, 70 microns thick.

For the study of silicon a foil of fused silica, 0.9 mg/cm² thick, was used. The magnesium target of 1.2 mg/cm² thick was prepared by vacuum evaporation onto a glass plate and was peeled off by a blade of a

safety razor. These targets were self-supporting and were set at 45° with respect to the beam direction. The beam current was collected by the Faraday cup connected to 0.025μF polystyrene condenser and was measured by electrometer.

§ 3. Results

The range distribution of the scattered protons from silicon dioxide is shown in Fig. 1. Because of the large amount of oxygen in the target, the elastic scattering for silicon could not be resolved at small angles. The proton group of the first excited state at 1.78 MeV for Si^{28} (92.27%) was resolved from other inelastic proton groups for Si^{29} (4.68%) and Si^{30} (3.05%) except the proton group of 2.03 MeV state for Si^{29}. The contribution of this group for Si^{29} to the group of 1.78 MeV state for Si^{28} is considered to be almost negligible from the range distribution. A small amount of contamination of hydrogen was found in this target.

In the case of magnesium the proton group of the first excited state at 1.37 MeV for Mg^{24} (78.60%) is resolved from the other inelastic proton groups for Mg^{25} (10.11%) and Mg^{26} (11.29%), and the elastic proton groups. A small amount of contaminations of oxygen and hydrogen was found in the magnesium target. As the elastic proton groups for magnesium and oxygen could not be resolved at small scattering angles, the angular distributions of the elastic scattering of protons from magnesium could not be obtained. The uncertainty in the absolute cross section was estimated to be about 20% both for the excitation functions and the angular distributions, and it was caused mainly from the non-uniformity of the target thickness.

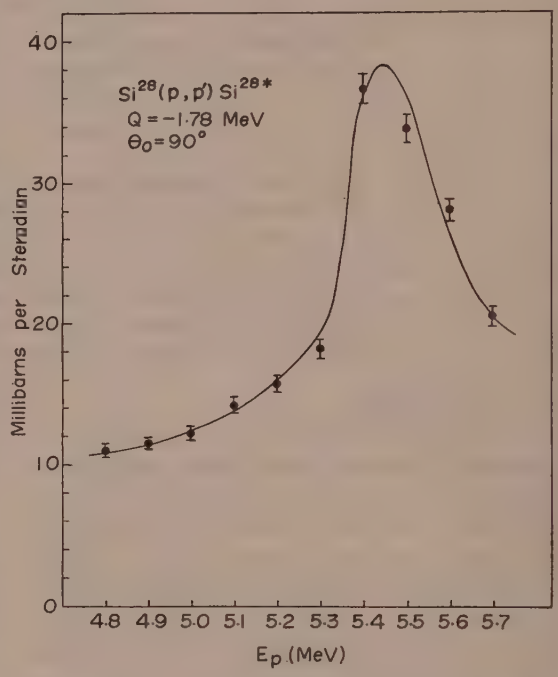

Fig. 2. The excitation function for $Si^{28}(Q=-1.78\,\text{MeV})$ at the laboratory angle of 90°. The errors are only the statistical ones.

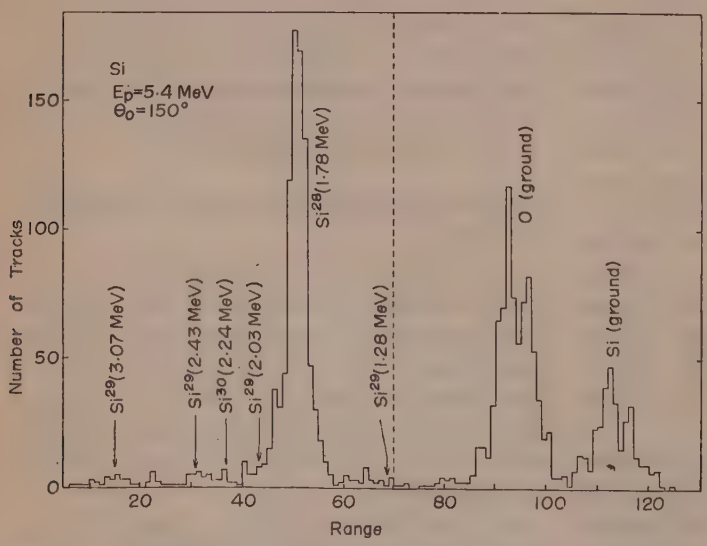

Fig. 1. The range distribution of protons scattered from SiO_2, observed at the laboratory angle of 150° (1 div=1.27 μ). The scanning area for the inelastic groups is 18 times of that for the elastic groups.

The excitation function obtained for Si^{28} ($Q=-1.78$ MeV) at the laboratory scattering angle $\theta_0=90°$ is shown in Fig. 2. There is a resonance feature at the incident proton energy of 5.4 MeV. This agrees with the result obtained by Okada and others[14] by studying the gamma-rays following the inelastic scattering of protons from Si^{28}. The angular distributions of protons were measured at incident energy of 5.3, 5.4 and 5.5 MeV. They are shown in Fig. 3.

The shape of the angular distributions does not change strongly near the peak of the resonance. At the forward angles the background increased mainly due to the elastic protons which had escaped from the emulsion surfaces. Moreover the proton groups due to the other levels of silicon, the amount of which was uncertain, were superposed on it. Therefore the estimation of the background at the forward angles has some ambiguity.

The excitation function[12] previously obtained for Mg^{24} ($Q=-1.37$ MeV) is illustrated in Fig. 4. There seems a resonance feature at the incident proton energy of 5.1 MeV. The angular distributions of the inlastically scattered protons were obtained at incident energies of 4.8 and 5.7 MeV. These results

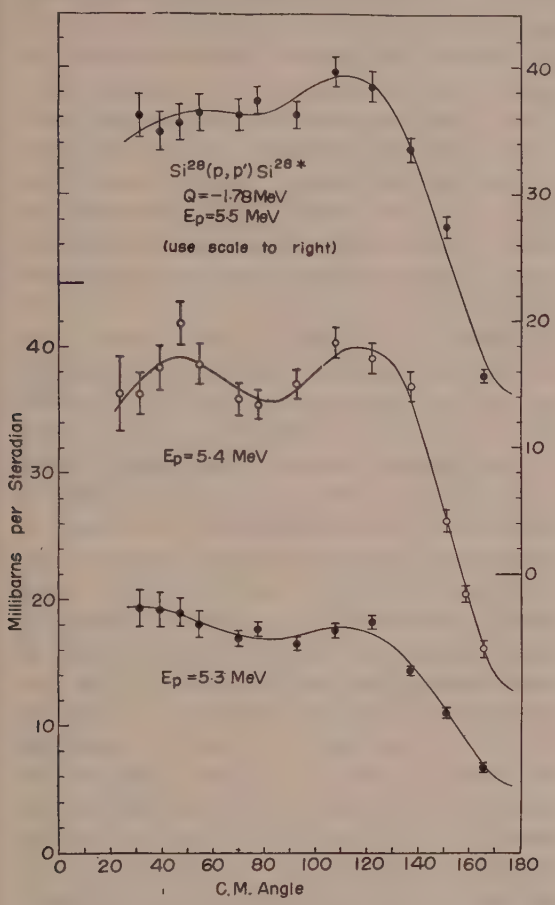

Fig. 3. The angular distributions of protons inelastically scattered from Si^{28} measured at E_p =5.3, 5.4 and 5.5 MeV. The errors are only the statistical ones.

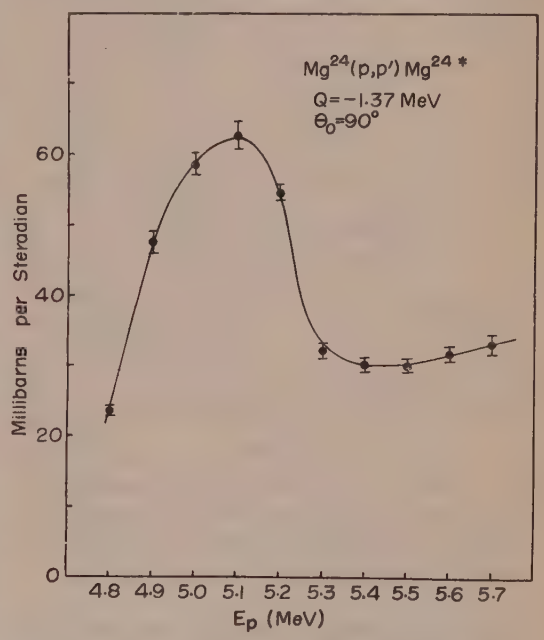

Fig. 4. The excitation function for Mg^{24}($Q=-1.37$ MeV) at the laboratory angle of 90°. The errors are only the statistical ones.

Table. 1. The coefficients of the Legendre polynomials obtained by expanding the angular distributions of protons inelastically scattered from Si^{28} and Mg^{24} and the integrated cross sections as a function of incident proton energies.

E_p: bombarding energies of protons, A_L: the coefficients of P_L (cos θ), σ_T: integrated cross sections.

	E_p	A_0	A_1	A_2	A_3	A_4	σ_T(mb)
Si^{28}	5.3	16.8	3.4	−2.2	3.5	−2.4	211
	5.4	36.3	3.1	−6.1	6.3	−8.3	456
	5.5	35.3	2.6	−7.5	6·0	−5.2	443
Mg^{24}	4.8	30.8	− 1.0	8.4	4.5	−1.2	387
	5.1	49.9	−22.4	−19.1	−1.9	0.1	627
	5.4	26.4	5.5	−11.8	−3.1	−0.5	332
	5.7	28.3	−12.9	−13.3	−0.1	−2.1	355

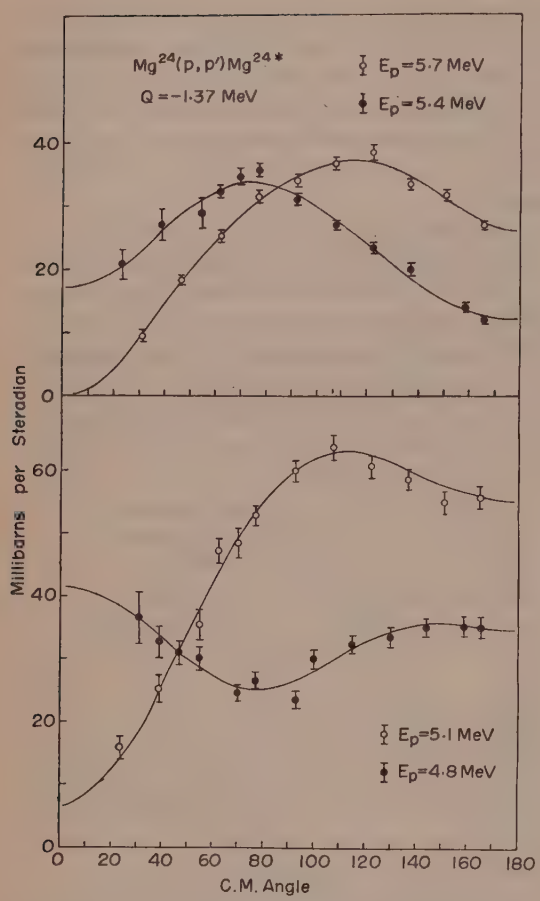

Fig. 5. The angular distributions of protons inelastically scattered from Mg^{24} measured at E_p =4.8, 5.1, 5.4 and 5.7 MeV. The errors are only the statiscal ones.

are shown in Fig. 5 together with the previously obtained results[12] at 5.1 and 5.4 MeV. These curves show apparent asymmetries about 90° and the shape changes with variation of incident proton energy.

All angular distributions were expanded into a series of Legendre polynomials by means of the least square method. These coefficients and the integrated cross sections are listed in Table I. The curves in Figs. 3 and 5 are calculated from the coefficients given in Table I.

§ 4. Discussions

A. Silicon

The excitation curve of Si^{28} obtained in this experiment shows a resonance feature, and the resonance at 5.4 MeV is very strong. This is also seen in the gamma-rays following the inelastic scattering of protons.[14] This indicates the existence of the contribution from the compound process, and it is expected that a single or a few levels may be excited. The shape of the angular distribution varies gradually near the peak of the resonance, that is, the tendensies between the expansion coefficients are similar at 5.3, 5.4 and 5.5 MeV. Then, assuming that only the compound nucleus formation contributes to the reaction and a single level contributes mainly to this process, the spin and the parity of the compound state will be assigned by the application of the formula of Blatt and Biedenharn[18] to the angular distribution.

The angular distribution of silicon at the resonance of 5.4 MeV protons could be fitted by the Legendre polynomials up to P_4 (cos θ). If the spin of the compound level is 1/2 or 3/2, the term P_4 (cos θ) should vanish. If it is 7/2, the coefficient of P_2 (cos θ) should be positive. It is improbable that the spin of this state is larger than 7/2, because the penetrability of protons for such a state of large spin is small. In the case of $5/2^+$, assuming that a process due to the emission of d-wave proton is predominant, and mixing the contributions of outgoing channel spin 3/2 and 5/2 to the reaction in a suitable ratio, the coefficients of P_2 (cos θ) and P_4 (cos θ) are shown to be negative. In the case of $5/2^-$, the sign of the coefficients of even terms in Legendre expansion can be explained by assuming the contribution from outgoing channel spin 5/2 to be predominant. Therefore, this angular distribution may be explained by assuming the spin 5/2 for the compound state P^{29} corresponding to the resonance at 5.4 MeV, but the parity of this state cannot be determined from this angular distribution because of the complexity of the channel spins and the interferences of different proton waves. Okada and others[14] measured the angular distribution of the gamma rays following the inelastic scattering of protons from Si^{28} at incident energy of 5.4 MeV, and assigned $5/2^+$ for this level. This is not inconsistent with our result.

B. Magnesium

The excitation curve of Mg^{24} also has a resonance feature, and the shape of the angular distribution shows a strong dependence

on the energy of incident protons. These variations of the cross section and the angular distribution can be explained by the compound process, and it seems that the reaction does not proceed through a single level of the compound nucleus because of the presence of large odd term P_1 (cos θ).

The angular distribution at 4.7 MeV measured by Rhoderick[5] shows a peak in the forward direction. Our distribution at 4.8 MeV has a slight rise in the forward direction and a minimum at about 80°. As the incident energy increases, a resonance feature appears in the excitation curve. But the angular distribution at 5.1 MeV shows an apparent asymmetry about $\theta=90°$. The angular distribution at 5.7 MeV is quite similar to that at 5.1 MeV. However, between these energies the coefficient of P_1 (cos θ) in the expansion of the angular distribution changes its sign, and the distribution falls in the backward direction.

The angular distribution at 5.1 MeV can be fitted by the Legendre polynomials up to P_2 (cos θ). Since the coefficients of P_3 and P_4 are regarded as zero and the coefficient of P_2 is negative, it would be expected to be 3/2 for the spin of the compound state contributed mainly to the reaction. But the process through the outgoing channel spin 5/2 from the compound state $5/2^-$ is also probable. As the angular distribution has the strong interference term between the levels of different parities and the process is rather complex, it is difficult to determine uniquely the nature of the compound nucleus from this distribution by using the formula[18] which has many adjustable parameters. Miura and others[19] also measured the angular distribution of gamma rays following the inelastic scattering of protons from Mg^{24} at 5.1 MeV.

Acknowledgement

The authors wish to thank to Fuji Photo Film Corporation for the preparation of nuclear plates, to Miss M. Kitatani for her help in scanning the nuclear plates, and to Mr. R. Nakashima for his discussion.

The authors also gratefully acknowledge a financial support to the Nishina Memorial Fundation.

References

1) H. E. Conzett: Phys. Rev. **105** (1957) 1324.
2) N. Austern, S. T. Butler and H. McManus: Phys. Rev. **92** (1953) 350.
3) S. Hayakawa and S. Yoshida: Proc. Phys. Soc. **A68** (1955) 656. Progr. Theoret. Phys. **14** (1955) 1.
4) T. R. Wilkins: Phys. Rev. **60** (1941) 365.
5) E. H. Rhoderick: Proc. Roy. Soc. **201** (1950) 348.
6) Baker, Dodd, and Simons: Phys. Rev. **85** (1952) 1051.
7) H. E. Gove and H. F. Stoddart: Phys. Rev. **86** (1952) 572.
8) G. E. Fisher: Phys. Rev. **96** (1954) 704.
9) G. W. Greenlees and A. E. Souch: Proc. Phys. Soc. **A69** (1956) 686.
10) P. C. Gugelot and P. R. Phillips: Phys. Rev. **101** (1956) 1614.
11) G. W. Greenlees, B. C. Haywood, L. G. Kuo and M. Petravić: Proc. Phys. Soc. **A70** (1957) 331.
12) S. Yamabe: Jour. Phys. Soc. Japan **13** (1958) 237.
13) S. Yoshida: Proc. Phys. Soc. **A69** (1956) 668.
14) E. Okada, I. Miura, T. Wakatsuki and Y. Hirao: Jour. Phys. Soc. Japan **13** (1958) 541.
15) H. O. Cohn, J. K. Bair, J. D. Kington and H. B. Willard: Phys. Rev. **99** (1955) 644 (A).
16) G. W. Greenlees: Proc. Phys. Soc. **A68** (1955) 97.
17) M. Takeda, et al.: Jour. Phys. Soc. Japan **12** (1957) 561.
18) J. M. Blatt and L. C. Biedenharn: Revs. Mod. Phys. **24** (1952) 258.
19) I. Miura, T. Wakatsuki, Y. Hirao and E. Okada: to be published.

JOURNAL OF THE PHYSICAL SOCIETY OF JAPAN Vol. 13, No. 8, AUGUST, 1958

An Experimental Study of Extensive Air Showers

By Saburo MIYAKE, Kensaku HINOTANI, Tatsunosuke KANEKO and Itsuo KATSUMATA

Institute of Polytechnics, Osaka City University, Osaka

(Received April 8, 1958)

An observation of extensive air showers has been performed at Mt. Norikura (2840 m above sea level and 25°N geomagnetic latitude) by the aid of two multiplate cloud chambers, sparsely distributed 90 GM counters and two sets of counter hodoscope pile. In this experiment, the structure of the air shower in the neighbourhood of shower axis was mainly investigated.

For each observed air shower, the shower size, N, and the location of the shower axis were estimated. The air showers were divided into three groups characterized by the core structure which depends upon the shower size. The first group is of the small size shower (less than 1.5×10^5) which has comparatively poor core which fluctuates by the behaviour of a few high energy particles. The second group is of the middle size shower ($1.5\times10^5-5.5\times10^5$) in which the decaying nuclear component and the electron component are in state of equilibrium, and the electron component lateraly distributes as proportional to $1/r$ in particle density and $1/r^2$ in energy flow near shower cores. The third group is of the large size shower (larger than 5.5×10^5) which contains many high energy nucleons and they are thought to be yet in the state of active nuclear cascade.

Integral size spectrum was obtained as $6.1\times10^{-9}(N/10^5)^{-1.5}\,\mathrm{cm}^{-2}\,\mathrm{sec}^{-1}\,\mathrm{sr}^{-1}$ for the showers with a total number of particles 1.5×10^5–5.5×10^5 and for large size showers the exponent of the spectrum increases with shower size reaching about -1.9 at $N=10^6$.

§ 1. Introduction

The showers studied here are known as extensive air showers, usually abbreviated as EAS. It is now evident that EAS are produced by ultra energetic primary particles whose energies are of the order of magnitude of 10^{14} to 10^{18} ev. The phenomena are understood as extremely energetic nucleonic cascade of which the electron cascade is an outgrowth. Some natures of EAS at various altitude have been investigated by many authors[1]; i.e. Density distribution, size-frequency distribution, angular distribution, attenuation length and so on. The EAS were so far detected and studied mainly by means of the electron component, but the chief concern may be now about the experimental information pertained to the high energy mesons and nucleons that are only a minute portion of all the particles. To gain the information about ultra energetic nuclear interactions, the other trials to observe the direct information, as in the case of nuclear emulsion, can not be expected due to the small frequency of the event. Some authors[2] have reported their theoretical calculations to explain the structure of EAS using the appropriate theory of multiple meson production assuming the interaction cross section and inelastisity at the collision of high energy nucleon and air nuclei. But little information is available as yet on the exact nature of the core of EAS which act essential part in the development of the EAS. One cannot be satisfied by experiments of the first approximation and by qualitative agreement between a theory and limited amount of experimental data near the shower axis. Though the detecting efficiency of the shower cores is low, it may be important to derive the experimental information concerning a small region in the EAS very near the central axis. A practical upper limit of the primary energies of events that can be studied in such detail is about 10^{16} ev because of the limited frequency with which shower axes hit very close to a particular detecting equipment.

The purpose of the present study is to observe the structure of the cores of EAS.

Total number of particles, the angle of incidence, the position of the axis, etc. are given for each EAS so that the view about the structure of the core depending upon these characters can be obtained. The present experiment has been done by the counter hodoscope and multiplate cloud chambers at 2840 m above sea level and 25°N geomagnetic latitude.

§ 2. Experimental Method and Apparatus

A schematic diagram of the layout of various pieces of the apparatus in a horizontal plane is shown in Fig. 1, and a more detailed discription of the individual part is given below. Firstly, it was necessary to have a "core selector" (abbreviated CS below) so that the distances from the other detecting apparatus to the cores of the EAS should not be large. Three air shower trays arranged on three apices of an equilateral triangle with a side of 4 m (abbreviated AS–1, AS–2 and AS–3 below) are used to catch EAS and to produce the master pulse by the coincidence with CS. A cross sectional diagram of the CS is shown in Fig. 2. The type of CS in this experiment is similar to Cocconi's one[3]. A five-fold coincidence of any two counters among four counters inside the shield and the three AS trays which consist of each 5 counters was interpreted as indicating a shower core which strikes nearby. The counters used in CS and AS trays were each of area 120 cm², and the shield was 10 cm Pb on the top, 10 cm Pb on the sides and at the ends, and 5 cm Pb underneath the counters. Since most of the showers are nearly vertical, the effective shield was 10 cm Pb.

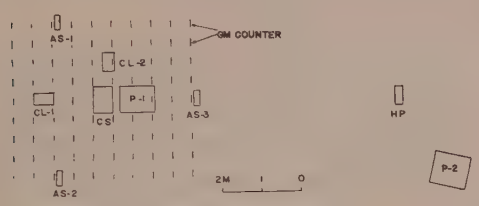

Fig. 1. Arrangement of apparatus. AS–1, 2, and 3; unshielded counter tray composed of five counters of area 120 cm² each. CS; core selector. P–1 and P–2; penetrating particle detector. CL–1 and CL–2; multiplate cloud chamber which contains five sheets of 1 cm lead plate. HP; hydrogen filled high pressure cloud chamber. 90 counters of area 50 cm² each are arranged in square lattice for determination of shower size and shower axis.

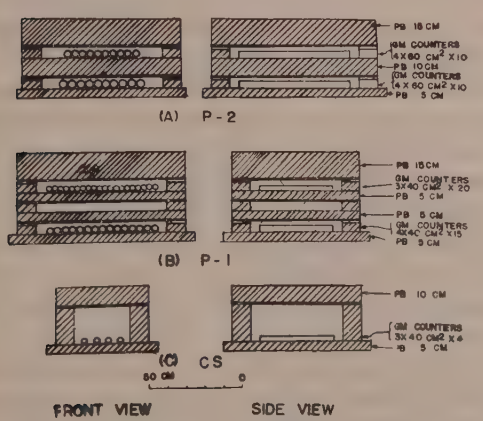

Fig. 2. Cross-sectional diagram of P–1, P–2 and CS.

A position (r, θ) of EAS core and a total number, N, of ionizing particles in EAS were determined by using 90 GM counters on a square lattice. Density gradients of charged particles along to the orthogonal axes (x and y axis) can be obtained from the data of the counter hodoscope and the position of EAS axis is deduced by the use of experimental result of the lateral distribution[4]. From the position of the core and the mean density of charged particles at CS, the total electron number of EAS is estimated. Each counter was connected to each neon bulb which shows the discharge of the counter, and they were driven by the triggering when the master pulse took place.

The apparatus labeled CL–1 and CL–2 in Fig. 1 were multiplate cloud chambers located near CS (1 m and 1.5 m apart from CS along to x and y axis respectively). The chambers were photographed from the perpendicular directions each other. The zenith angles of EAS, the nature of the penetrating particles (mainly that of N component), and the energies of electrons and photons in EAS are known from these cloud chambers. The sensitive area of each chamber is 0.119 m² and 0.116 m² with 10% error respectively. CL–1 contains five sheets of 1 cm Pb plate and CL–2 contains four sheets of 0.5 cm Pb plate and three sheets of 1 cm Pb plate.

Another associated pieces of apparatus were two penetrating particle detectors labeled P–1 and P–2 which show the particle density penetrating two layers of lead (15 cm and 25 cm Pb). Front view and side view of their

sections are shown in Fig. 2. Each counter was connected to hodoscope and the record of the hodoscope was triggered by the master pulse. These detectors were placed at two different distances from CS, so that the density of penetrating particles could be observed as a function of the air shower size and the distance from shower core.

§ 3. Determination of the Position of Core and the Shower Size

Using the lattice counters, the particle density, ρ, is given by the following equation;

$$\rho=\frac{1}{S}\ln\frac{n}{n-m}\,, \qquad (1)$$

were S is a sensitive area of the counter, n is a total number of the counters in the area and m is a number of discharged counters. And for the density on the limited region in the area (when the number of the counters used is smaller than 10) the following equation was used

$$\bar{\rho}(n,m)=\frac{1}{S}\,\frac{{}_nC_m\sum(-1)^i\{{}_mC_i/(n-m+i)\}}{1/(n-m)}\,. \qquad (2)$$

Assuming that the lateral distribution function does not depend on the size and Zenith angle of the EAS, the electron density, $\rho(r)$, at a distance r from the shower core can be expressed by the following equation;

$$\rho(r)=N\varphi(r)\,, \qquad (3)$$

where N is a total number of particles and $\varphi(r)$ is a lateral distribution function. The density, ρ, and the density gradients $d\rho/dx$ and $d\rho/dy$, are obtained from the data of lattice counters. So, position of the core axis, x and y, should be obtained mathematically for given function, $\varphi(r)$.

Practically, φ has, however, very complex form and so the experimental distribution function, $1/r$, was used in this experiment because the observed function is $r^{-0.95\pm0.05}$ in the region of distance, which covers the present experiment, of about 2 to 15 m from the shower core[4]. Then Eq. (3) is modified into following expression;

$$\rho(r)=A/r=N\varphi(r)\,, \qquad (4)$$

where A is a constant which have relation, $kA=N$ and k is determined as 616 by numerical integration of experimental lateral distribution curve[4]. From Eq. (4) r and θ can be easily obtained as follows;

$$r=\frac{\rho(x)}{\sqrt{(\partial\rho/\partial x)^2+(\partial\rho/\partial y)^2}}\,,\quad \theta=\tan^{-1}\frac{\partial\rho/\partial y}{\partial\rho/\partial x}\,, \qquad (5)$$

where $\rho(r)$ is a particle density at CS. The size (total number of the shower particles) N, is given by a value of $k\cdot r\cdot\rho(r)$.

On a occasion that a core falls within 2 m from CS, (in the region of lattice counters) x and y coordinates of the core are obtained from maximum points in histograms of the electron density along to the both axes, and the $\rho(r)$ is given by a mean value of densities at the center of each coordinate.

In the event that a shower core hits near CS or boundary of the lattice counter arrangement, the size N is determined as $\rho(r)\times(1/2$ or $2/3)\times L$ respectively where L is a half length of the side of the arrangement.

The obtained distance, r, contains the error of about 50 cm in the region of the lattice counter and about 30% errors on the outer domain of the area.

The above analysis is not applied to so large showers that the most of the lattice counters were discharged. These events will be caused by the density larger than about 1000 particles per m² over the lattice counter region.

§ 4. Examination of the Lateral Distribution

The assumption, in the preceeding section, that the average lateral distribution of the particles is proportional to $1/r$, is examined by the data of multiplate cloud chamber. In order to estimate a fluctuation of local density of the particles, the top space of the multiplate cloud chamber in which the tracks of 20~30 particles were observed was divided equally and the number of tracks in each space was counted. The histogram in Fig. 3 shows the frequency distribution of track number observed at the left half of the top space of CL-2. In the figure, a normalized binominal distribution in the case which total number is ten, fit well the histogram. This figure shows that the tracks at the top space randomly distributed in the unit of about two tracks. The distribution of the particles observed in cloud chamber should be corrected for the transition effect by the roof of the chamber (0.55 cm Fe). Under the chamber roof, a particle should multiply into about 1.44 using the Bethe's multiplication factor

$M_f=1+2(1-7.2/Z)t/X_0$ as cited by Williams[5]. In the factor, Z is the atomic number and t/X_0 is the thickness in radiation length of the wall materials traversed. From the multiplication factor, the distribution of the particles in the atomosphere is roughly considered to be random distribution in the unit of about 1.5 particles in average.

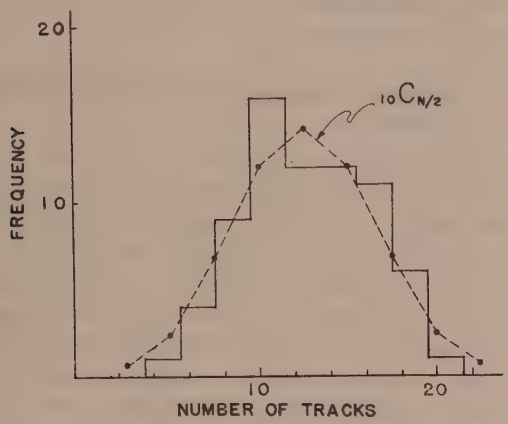

Fig. 3. The histogram shows the frequency distribution of track number observed at the left half of the top space of CL-2. The dotted line shows a normalized binomial distribution in the case of total number 10. This figure shows that the tracks at top space randomly distribute in the unit of about two tracks.

The particle density in the top space of the cloud chamber was compared with the expected density which is estimated from the size and the location of the shower axis obtained with the lattice counter's data using the lateral distribution function of $1/r$.

§ 5. The Lateral Distribution of Energy Flow

(1) *A character of the core detector*

Coincidences of counters shielded by thick lead plate may be caused in general either by a high energy electron or photon striking the lead, or by a local shower generated by a meson or nucleon contained in EAS. The coincidences by a penetrating shower are expected very few, because the density of meson and nucleon component in EAS at mountain altitude is only an order of one-hundredth of electron photon component which has only 10 to 100 particles in the area of CS. Five-fold coincidences used in the present experiment represent EAS which contains many high energy electrons and photons that can not be scattered far from the core of the EAS. Under the lead absorber more than 20 cm thickness, the coincidences represent preferably penetrating component. These explanation are clearly shown by the absorption curve of EAS by lead[6].

Under the thick absorber (about 10 radiation length or more) the shower particles decreases exponentially according to $k_0 \exp(-0.24\,t)$ and k_0 is approximately proportional to initial energy of the primary particle[7]. The absorption curve of EAS has also such relation from 0 to about 20 cm lead, but, in the casee of EAS, k_0 is thought to be correspond to sum of the energies of shower particles. In other words, the coincidence of CS indicates EAS containing a energy flow more than a certain value on CS. In the present experiment, the critical value of the energy flow for coincidence is estimated at about 50 Gev/m² from the lead layer of 10 cm and particle density of about 40/m² under the lead absorber.

(2) *The lateral distribution of energy flow*

As shown in the preceding section, the detection of EAS by CS depends mainly upon the integrated energy flow of the electron photon component. Fig. 4 shows the relation of observed frequencies of EAS axes versus distances between EAS axes and CS. It shows that the frequency of EAS axes detected in area of $2\pi r\,dr$ between r and $r+dr$ is proportional to the area up to about 2.5 m and at further distance the frequency decreases according to $r^{-2}dr$. We can deduce the lateral

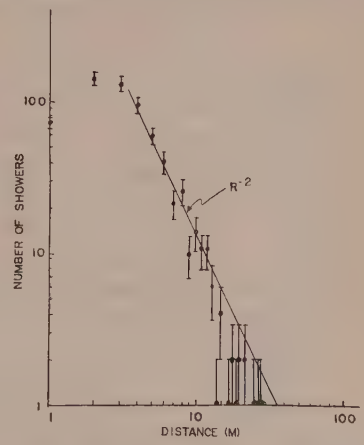

Fig. 4. The observed number of showers for all sizes as a function of the distance, R, of their axis from the CS.

distribution of the energy flow of the showers, if it was a smooth function of r without consideration of the fluctuation of the energetic particles and it's amplitude was proportional to the primary energy of the shower. Because, the observed frequency is estimated as follows;

$$F(r)dr=2\pi r\,dr\,k\int_{E_0}^{\infty} E^{-(\gamma+1)}dE=2\pi\,dr\,rk'\,E_0^{-\gamma} \quad (=Kr^{-2}dr)\,, \quad (6)$$

where E_0 is a critical energy of EAS which trigges CS at distance r from the core. Therefore, the funntion should be proportional to $r^{-3/\gamma}$. Using known exponent γ of the primary energy spectrum of 1.5 in the energy region, the function is proportional to r^{-2}.

The distributions are also shown in Fig. 5 dividing into four groups: i.e. less than $1.5\cdot10^5$, $1.5\cdot10^5$—$5.7\cdot10^5$, $5.7\cdot10^5$—$1.5\cdot10^6$ and more than $1.5\cdot10^6$ respectively. From these figures, we can also deduce the lateral variation of energy flows of the EAS near shower cores (0–15 m) as follows. The effective detecting area for EAS of size N was determined from the distance r_m which gives a maximum frequency for each curve. Since they were the limits of the detection area for EAS of the minimum energy in each group, it is concluded from the observed value that r_m for each group has following relation in the limited energy region,

$$\pi r_m^2=aN_m\,, \quad (7)$$

where a is a constant.

The detailed discussion comparing the electron photon component and nucleon or meson

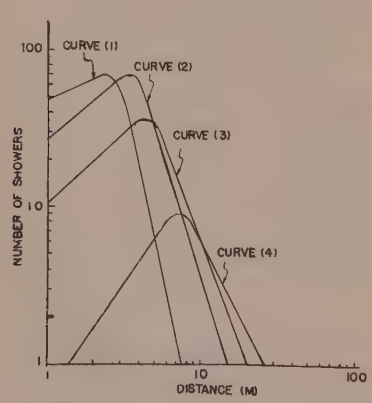

Fig. 5. The observed number of showers for each size group as a function of the distance, r, of their axis from the CS.

component for triggering CS over a wide range of primary energies are complicated. But it is reasonable to consider that the present detector was triggered by a certain value of energy flow and the energy flow is distributed proportional to r^{-2} at least for EAS of the size of $1.5\cdot10^5$ to 10^6 particles. The distribution is also expected from electromagnetic cascade theory too, when the shower age is nearly equal to 1.

§ 6. Energy Spectrum of Electron Photon Component

The energy of a cascade shower was estimated by means of multiplate cloud chamber. Practical ones are the track length and electron number at the cascade maximum, both of which depend on the shower energy approximately linearly. Although track length is undoubtedly prefered from the view point of the fluctuation, but in order to obtain this quantity experimentally one must have the whole shower development available for observation. There are some difficulties in such a case that the energy of initial electron or photon is so high that the cascade development does not finish in the chamber, and so in this case estimated total number of electrons and the number at cascade maximum are used with some correction.

The track length p is given by a product of total number of track segments n_{total} and radiation length of a lead plate measured along the direction of the shower axis and then the energy is given by

$$E_0=cp\,, \quad (8)$$

where c is a constant and has been estimated from conventional cascade theory[7)8)] and cloud chamber experiments[9)]. In the present case, the value of the constant c was taken as 25 Mev from a thickness of a lead plate of 10 mm.

The number of electrons in the cascade maximum $n_{\max}$ is a quantity which represents the maximum observable number of fast electrons in the foward half hemisphere. The factor which should be multiplied on $n_{\max}$ was determined experimentally. Since a ratio of n_{total} to $n_{\max}$ was about 4.0 around 1 Gev and it increased very slowly with energy, the factor was estimated at 100 Mev. The error of the estimation of energy seems to be about

30% on the average for energies of 300 Mev to 10 Gev.

The integral energy spectra of electron photon component, for each group of size and various distances from shower axis, were

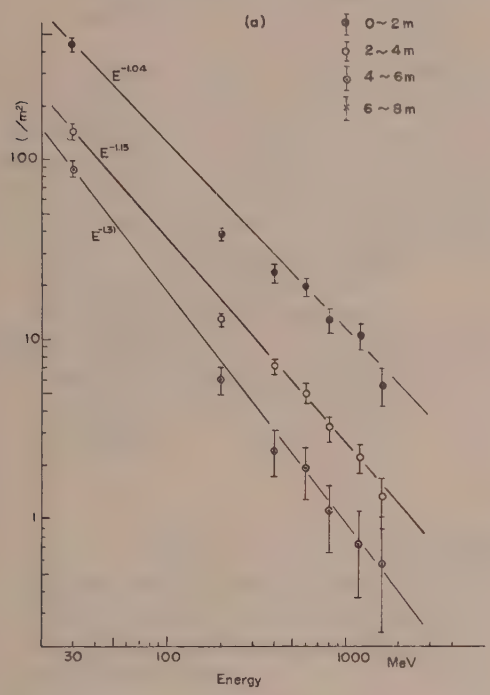

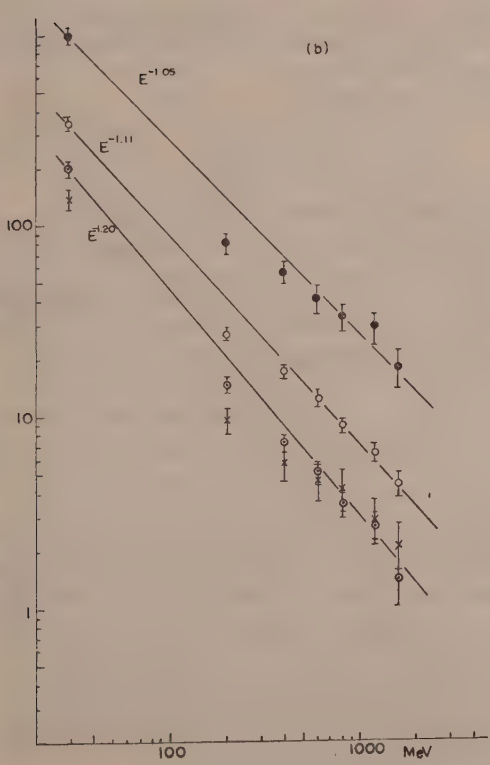

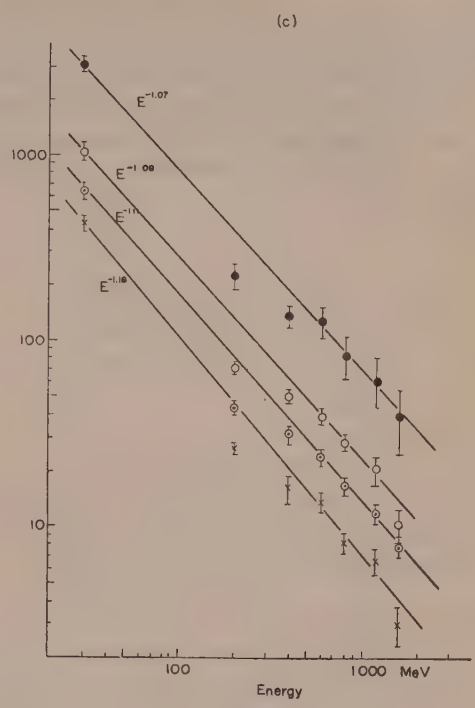

Fig. 6. The integral energy spectra of electron-photon component for group of size at various distance from shower axis.
a) 1.5×10^5
b) $1.5\times10^5-5.5\times10^5$
c) $5.5\times10^5-1.5\times10^6$

shown in Fig. 6. In these figures, we can see that the exponent of the spectra varies from 1.0 to 1.3 according to the distances (2 m to 8 m) from the shower axis.

In these figures, the points at 30 Mev are estimated from the number of the charged particles in the top space of the cloud chamber comparing with the integral energy spectrum, for energies smaller than critical energy in air, obtained by Richards and Nordheim[10], and the data at other energies contains both components of photons and electrons since shower primaries can not be distinguished whether they were photons or electrons.

The lateral distribution of the energy flow described in § 5 is also interpreted from the observations of the lateral distribution of the particles and of the energy spectra at the distances as follows;

1) In § 4, the lateral distribution of shower particles was estimated as r^{-1} on the average, but, as shown in Fig. 7, the distributions of various energy cut for group of each size have a tendency to be flatten in larger size

groups. It depends upon the detection efficiency of CS mentioned already. If we assume expediently that CS and the cloud chamber (particle detector) were placed at the same position, a frequency with which shower axes of size N hit the area between r and $r+dr$ is given by;

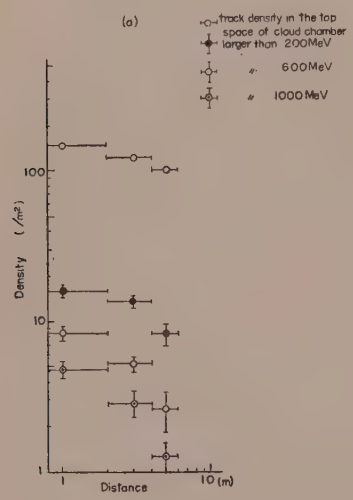

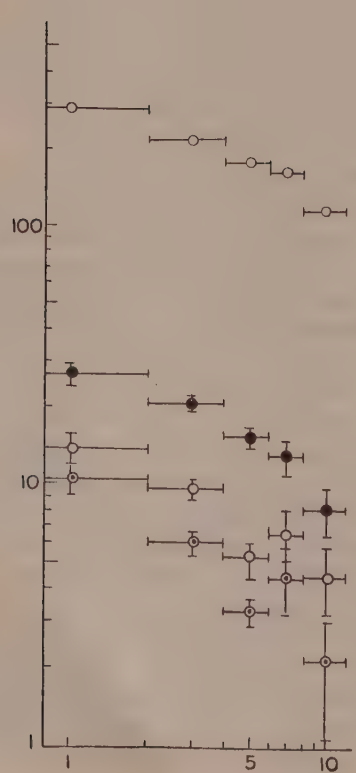

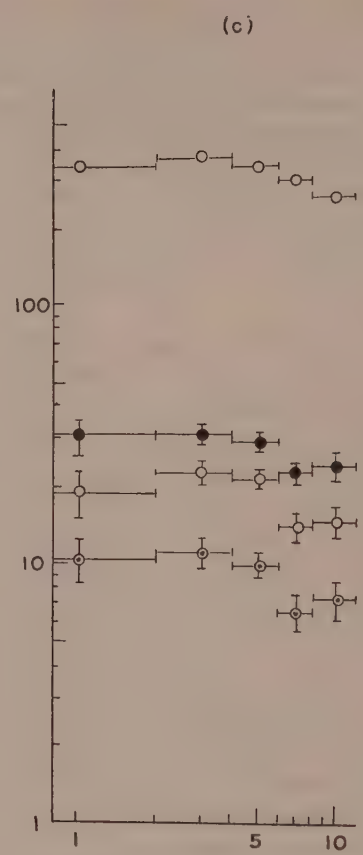

Fig. 7. The observed lateral distribution of the electron component of various energy cut for each group of size.
a) 1.5×10^5
b) $1.5\times10^5-5.5\times10^5$
c) $5.5\times10^5-1.5\times10^6$

$$\left.\begin{array}{ll} f(N,r)drdN=2\pi rdrF(N)dN & r^2<kN \\ f(N,r)drdN=0 & r^2>kN \end{array}\right\}, \quad (9)$$

where $F(N)$ is a differential size spectrum which is expressed as const$\cdot N^{-\gamma-1}$. Then observed density $\rho_{ob}(r)$ at distance, r, is;

$$\rho_{ob}(r)=\frac{\varphi(r)\int_{N_1}^{N_2}Nf(N,r)dN}{\int_{N_1}^{N_2}f(N,r)dN} \quad (10)$$

where $\varphi(r)$ is a distribution function ($\rho(r)=N\varphi(r)$) and N_1 and N_2 are lower and higher limit respectively in the range now concerned. In the region smaller than critical value r_1 ($r_1^2=kN_1$) in which detection efficiency is 100%, observed density distribution is correctly proportional to $\varphi(r)$ as shown by the integration of Eq. (10);

$$\rho_{ob}(r)=\varphi(r)\frac{\gamma}{\gamma-1}\cdot\frac{N_1^{1-\gamma}-N_2^{1-\gamma}}{N_1^{-\gamma}-N_2^{-\gamma}}=\text{const}\cdot\varphi(r)\,. \tag{11}$$

In the region that the distance, r, is larger than r_1, the integration is as follows;

$$\rho_{ob}(r)=N_2\left\{\varphi(r)\frac{\gamma}{\gamma-1}\frac{(r/r_2)^{2-2\gamma}-1}{(r/r_2)^{-2\gamma}-1}\right\}, \tag{12}$$

where $r_2^2=kN_2$. And the observed density distribution is somewhat differ from the true distribution. The observed value of group III for large r is increased by the reason shown in Eq. (12). Eq. (11) and the curves of group I and II, in the region larger than about 3 m, show that the real particle density distribution is proportional to r^{-1}.

2) If the differential energy spectrum was expressed as $f(r)E^{-s(r)-1}$, the observed energy flow distribution can be calculated as follows;

$$\int_{E_1}^{E_2} f(r)E^{-s-1}EdE=f(r)\frac{1}{1-s}(E_2^{-s+1}-E_1^{-s+1})$$
$$=\frac{k_1}{r^2}\,, \tag{13}$$

where E_1 and E_2 are energies determined from the integral energy spectrum in Fig. 6 as above assumption can be applied.

The observed density distribution is also similarly calculated;

$$\int_{E_1}^{E_2} f(r)E^{-s-1}dE=f(r)\frac{1}{-s}(E_2^{-s}-E_1^{-s})=\frac{k_2}{r}\,. \tag{14}$$

From Eq. (13) and (14), the mean energy is obtained as;

$$\frac{1}{E(r)}=\frac{s-1}{s}\cdot\frac{E_1^{-s}-E_2^{-s}}{E_1^{-s+1}-E_2^{-s+1}}=r\frac{k_2}{k_1}\,. \tag{15}$$

Under the practical conditions $s>1$ and $E_1\gg E_1$, Eq. (15) is simplified into following equation;

$$s=\frac{1}{1-E_1r(k_2/k_1)}\doteqdot 1+E_1r\frac{k_2}{k_1}\,. \tag{16}$$

Substituting the present data as following

$$E_1=30\,\text{Mev}\,,\quad k_2=1000\,,\quad k_1=10^6\,,$$

then s varies for the variation of r from 0 to 10 m about 0.3, and this shows good agreement with the present data of energy spectra in various distances from the core.

§ 7. Number Spectrum of EAS

The total number of the ionized particles of the observed EAS was estimated by the method described in § 3. From the observed integral number distribution shown in Fig. 8, the number spectrum can be obtained as follows, assuming that the differential number spectrum is given by a power law;

$$F(N)dN=SN^{-\gamma-1}dN\,, \tag{17}$$

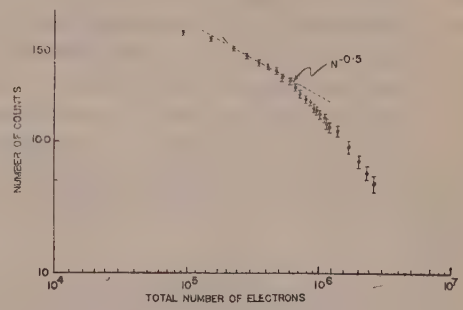

Fig. 8. The observed integral number spectrum. The dotted line shows $N^{-0.5}$. The number spectrum should be corrected for detecting area.

where γ and S may be taken as constants over a limited range of N. The observed frequency of the showers with the size larger than N_0 is given by the integration of the product of Eq. (17) and detecting area (Eq. (7));

$$\int_{N_0}^{\infty} SN^{-\gamma-1}dNaN=S_0aN_0\,. \tag{18}$$

From the experimental results described in § 5 (2), S_0 is obtained at $0.12\,\text{sec}^{-1}\,\text{cm}^{-2}$.

The integral number spectrum is therefore,

$$3.8\cdot10^{-9}(N/10^5)^{-1.5}\,\text{cm}^{-2}\,\text{sec}^{-1}\,,$$

within the range $1.5\cdot10^5<N<5.5\cdot10^5$. From the zenith angle distribution the effective solid angle of detection is 0.63 and so the integral number spectrum per steradian is

$$6.1\cdot10^{-9}(N/10^5)^{-1.5}\,\text{cm}^2\,\text{sec}^{-1}\,\text{sr}^{-1}\,,$$

and for higher energy region the exponent increases with the size reaching about -1.9 at 10^6.

The errors for above results can not be estimated correctly, but they seem to be about factor two and about a half for their upper and lower errors respectively.

§ 8. Meson and Nucleon Component

1) *Composition of nucleonic component*

Although several measurements of the ratio of neutral to charged N-particles has been reported[11], their variation with the shower size has not yet been investigated. So in this experiment, a very preliminary study of the

ratio was made by means of the multiplate cloud chamber.

For this purpose, 56 penetrating showers observed in the cloud chamber pictures were picked up, and the shower primary was investigated. Then, those events were omitted where the nature of the shower primary appeared doutfull because of possible obliteration of its track by the electron showers. Thus, only 49 events were classified. Among them, 17 cases had neutral primaries. Accordingly, a ratio neutral to charged primary was obtained at 0.53 ± 0.20 on the average of all showers.

To clarify the variation of the ratio with the shower size, the penetrating showers were classified with shower size, and the ratio was estimated at 0.72 ± 0.40 for shower size $N<6\cdot10^5$ and 0.40 ± 0.24 for $N>6\cdot10^5$. The ratio 0.72 is in agreement with earlier determinations[11].

From the results, we can deduce a conclusion that a contribution of charged π-mesons among the EAS becomes predominantly with increasing shower size, even though the statistical precision is not enough.

2) *Energy spectrum of nucleonic component*

The energy of the penetrating shower observed in the cloud chamber is estimated from the energy of the electron shower associated with the penetrating showers ($\pi^0-2\gamma$). Thus, the mean energy per secondary particle was estimated at 2.0 Gev. The energy per secondary particle was somewhat large for smaller multiplicity group than larger one, but the difference was not so much.

The energy spectrum is shown in Fig. 9 and a point plotted at 1 Gev was obtained from star frequency (the star means a nuclear interaction without more than one penetrating secondary particle, and the energy distributes around 1–2 Gev). The exponent of the integral energy spectrum was about -1.2.

Average energy of the observed penetrating showers belonged to the group of $N<6\cdot10^5$ is 6.2 Gev and that for $N>6\cdot10^5$ is 10.1 Gev.

3) *Abundance and abundance ratio*

By means of the hodoscope pictures of P–1 and P–2 detectors, a classification of the penetrating particles into "interacting" and "non interacting" particles is possible. In general, the former correspond to nucleon and

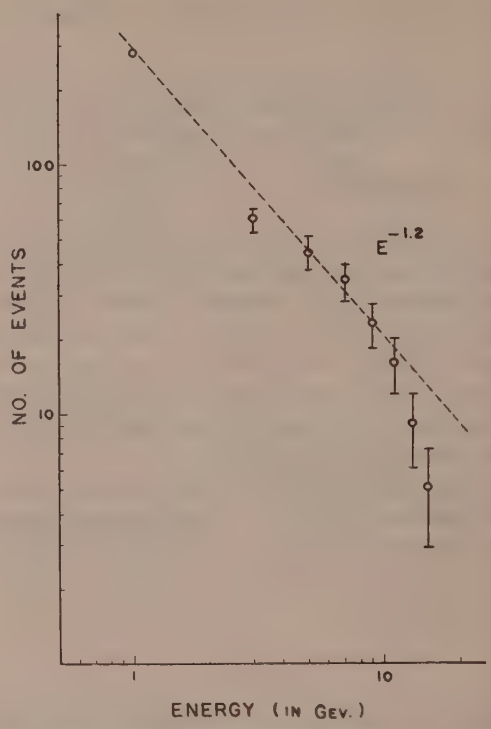

Fig. 9. The energy spectrum of nucleonic component which are obtained from the penetrating shower observed in the cloud chamber. A point plotted at 1 Gev was obtained from star frequency. Dotted line shows $E^{-1.2}$.

π meson component and the bulk of the latter correspond to μ-mesons. It should be considered that the latter category includes also all the charged nucleons and π-mesons which failed to interact, and that a corresponding number of unobserved neutrons has to be added to the total.

In the analysis of the hodoscope pictures, the event were classified as "non interacting" particles if one or two counters was discharged in two trays, and in such a way that a particle could reasonably be reconstructed comparing with the data from the cloud chamber. If more than two counters in first tray and more than three counters in second tray were discharged, and the projected zenigh angles estimated from the pictures were nearly equal to ones from the cloud chamber, the events were classified as interacting particles which interact at the top layer of 15 cm Pb. If one counter in first tray and more than three counters in second tray were discharged, the events were also classified as interaction at second layer of 10 cm Pb.

Table 1. Composition of EAS near the shower axis at 2840 m elevation.

Group	I	II	III
Shower size	$1.3\cdot10^4-1.8\cdot10^5$	$1.8\cdot10^5-6.0\cdot10^5$	$6.0\cdot10^5-1.5\cdot10^6$
pp./el. (%)	1.55 ± 0.26	1.15 ± 0.11	0.92 ± 0.08
μ/el. (%)	0.85 ± 0.19	0.67 ± 0.09	0.60 ± 0.06
N/el. (%)	0.70 ± 0.17	0.48 ± 0.07	0.33 ± 0.05
N/pp. (%)	45.0 ± 17.6	41.9 ± 10.0	35.4 ± 7.9

A summary of the results of the analysis of the penetrating events observed by hodoscope is given in Table I. The results are qualitatively in agreement with Kasnitz *et al*[11] data.

4) *Lateral distribution of penetrating particles*

The lateral distribution of N-component was obtained separately from μ-mesons as shown in Fig. 10. The distribution of N-component should be corrected for saturation effect of the lattice counters and detection efficiency of CS. The correction is so complicate that the lateral distribution can not be corrected exactly. However, it may be natural to think that the obtained lateral distribution has a tendency to flatten the real distribution. As a result, it seems that the distribution is $1/r$ or somewhat more steep function of r.

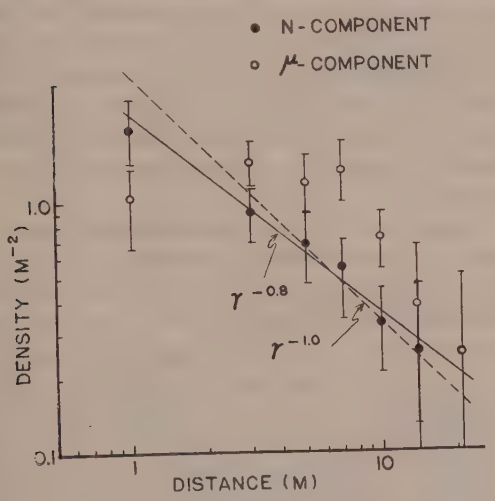

Fig. 10. The lateral distribution of nucleonic component and μ-mesons.

§ 9. Discussion

In this experiment, the lateral distribution of energy flow has been obtained as r^{-2} for showers with size $1.5\cdot10^5-5.5\cdot10^5$. The result shows that the lateral distribution of electrons is almost equal to one expected from the electromagnetic cascade theory for shower age 1, and so the angular distribution of the energy flow of secondaries in high energy interactions is thought to be considerably sharp. Therefore, in the high energy nuclear interactions which will develop into EAS, the greater part of the high energy secondaries will be contained in core region of about 2–3 m. The structure of observed small size shower (less than $1.5\cdot10^5$) is also similar to large showers, but one must noticed for inefficiency of detection caused by CS selection. The detection efficiency may be favour for young showers and small size showers seem to contain the showers of various ages and they have comparatively poor core (less than about 50 Gev/m²) in average.

The number spectrum and an analysis of nucleon component show that the EAS of large size is in the active state of development. So, in such a state, a greater part of shower energy is still reserved in core region. The observed number spectrum is somewhat different from one obtained by scintillation detector placed at large span. Namely, in a part of large size ($>6\cdot10^5$), the former spectrum is steeper than the latter. One of the reasons may be understood as that high energy nucleons are predominant (density of charged particles in core region is not so high expected by pure electromagnetic cascade theory) and the energy spectrum of high energy neutral π-mesons is steep. Although the population of the nucleons to shower electrons decreases as shower size becomes large, the observed mean energies of the nucleons rapidly increase. Nevertheless the maximum of the high energetic electron component which is favour to be detect by CS is higher altitude than maximum of total electron component about several radiation length. Then expected size is somewhat different by

the character of the detecting mechanisms and age of each shower.

If the average primary energy of EAS having a given number of charged particles at a particular depth in the atmosphere could be calculated, the number spectrum would lead directly to the energy spectrum of the cosmic ray primaries. But since the EAS do not develop and propagate like purely electronic cascade showers, and since the detailed features of the nuclear cascade are thought to be still largely unknown, one can not calculate with considerable reliability their relation theoretically.

Nevertheless, even if the calculation has been performed, the fluctuation problem in the very early stages of the shower's development and contribution of the heavy primary should be considered in the case when primary energy spectrum is derived. The fluctuation problem has been discussed by W. L. Kraushaar[12] and he concluded that one tends to overestimate primary particle intensities by a factor of 1.4 if fluctuations are neglected. One of the author of this paper has analysed absorption length and the following result[13] was obtained.

In lower atmosphere (lower than mountain altitude), under probably permissible approximation, the following relation was obtained;

$$\lambda_{ob}=L(1+r)\ , \tag{19}$$

where λ_{ob} is a observed attenuation length of EAS and L is a interaction mean free path of the primary particles of EAS. And r means a ratio of the primary particles, which have higher energies than the estimated energies corresponding to the observed shower sizes, to the other observed showers. Therefore, the true energy spectrum can be obtained by multiplying the factor $r/(1+r)$. This shows that the observed size spectrum contains lower energy events than the estimated energies. Provided that λ_{ob} is 90 g/cm^2 [14] and L is 80 g/cm^2 for the EAS with size $3\cdot10^6-3\cdot10^7$, the correction factor is about 0.1. So, if above interpretaion is correct, the intensity of primary particles with energy $10^{16}-10^{17}$ ev would be overestimated at about ten times.

The result of above correction shows a spectrum similar to obtained here but conclusions must be reserved because the estimation of sizes by the method used in the present experiment is not so accurate especially in high energy region.

Preliminary discussions for high energy events are as follows;

1) Two cases of very high energy nuclear interactions were observed by the cloud chamber when shower axis was very near the chamber. And some cases shows in the chamber photographs that there is a high density region of electron component compareing to other region of same core, and the area of the region was thought to be about 1 m diameter. These discontinuities also depend upon probably very high energetic nucleons in the core although their amount may be very small. Occasionally these are thought to be survivals of the primaries and it seems to be possible to estimate the inelastisity in high energy nuclear interactions, but in this case as mentioned already, it must be care that there are young EAS which has been started at considerably deep atmosphere.

2) High energy electron component has been studied concerning to nucleon component, and crude conclusion is that a separated young cascade shower, which is distinguished by accompanied photons and electrons from old cascade showers in chamber photographs, were mainly due to γ rays produced by the decay of π^0-mesons which were produced by nuclear interactions in air. It seems to be possible to estimate the intensity of high energy nucleons from these cascade showers. Detailed discussion will be appeared in next paper.

Finally, as a next step of experiment of EAS we are proceeding a plan that is to observe size dependency of observed absorption length and to investigate the behavior of N-component near shower core over determination of the shower age of each EAS. For this purpose we are now constructing very huge multiplate cloud chamber ($200\times127\times80$ cm^3) which contains twenty-one sheets of lead plate of 1 cm thickness.

Acknowledgement

The authors wish to express their thanks to Professor Y. Watase for his continual encouragements. This study has been supported in part be a Grant in Aid for Fundamental Scientific Research from the Ministry

of Education and from Cosmic Ray Laboratory of Tokyo University.

References

1) For example, see the references of K. Greisen "*Progress in Cosmic Ray Physics III*" edited by J. G. Wilson (North-Holland Publishing Company 1956.)
2) See the references of A. Ueda and N. Ogita Pro. Theor. Phys. **18** (1957) 269.
3) G. Cocconi, V. Cocconi Tongiorgi, and K. Greisen: Phys. Rev. **76** (1949) 1020.
4) G. B. Khristiansen: "*Oxford Conference Report*" p. 11 (1956).
N. A. Dobrotin, G. T. Zacepin, S. I. Nikolskji and G. B. Khristiansen: Nuovo Cimento Suppl. **3** (1956) 635.
5) R. W. Williams: Phys. Rev. **74** (1948) 1689.
6) N. A. Dobrotin et al.: UFN **49** (1953) 185.
7) R. R. Wilson: Phys. Rev. **86** (1952) 261.
8) B. Rossi and K. Greisen: Rev. Mod. Phys. **13** (1941) 240.
9) P. A. Bender: Nuovo Cimento **2** (1955) 980.
Y. B. Kim: Phys. Rev. **102** (1956) 882.
K. Hinotani, K. Suga and Y. Tanaka: Jour. Phys. Soc. Japan **9** (1954) 883.
10) J. A. Richards and L. W. Nordheim: Phys. Rev. **74** (1948) 1106.
11) K. Greisen and W. D. Walker: Phys. Rev. **90** (1953) 915.
H. L. Kasnitz and K. Sitte: Phys. Rev. **94** (1954) 977.
12) W. L. Kraushaar: *Fluctuations in shower Development* presented in Varenna Conference (1957).
13) S. Miyake: to be published.
14) G. Clark, J. Earl, W. Kraushaar, H. Linsley, B. Rossi and F. Scherb: Nature, **180** (1957) 353 and 406.

Journal of the Physical Society of Japan Vol. 13, No. 8, August, 1958

Recombination Centers in Germanium

By Jun'ichi Okada

Matsuda Research Laboratory, Tokyo Shibaura Electric Co., Kawasaki-city, Japan

(Received April 30, 1958)

The dependence of carrier lifetime in pure germanium upon injection level has been studied using a photoconductivity decay method. The data are analyzed in terms of the recombination theory for transient conditions including the case of high injection level. The results show that at least two recombination levels exist in pure germanium: one is active in n-type and the other in p-type. The recombination level in n-type germanium is at 0.28 eV from the conduction band and the cross section for capture of holes A_p is about 4.7 times larger than that for capture of electrons A_n. On the other hand, the recombination level in p-type germanium is at 0.25 eV from the valence band or 0.31 eV from the conduction band and A_n/A_p is about 9.8.

§ 1. Introduction

Recent experiments on carrier lifetime in germanium have shown that several lattice imperfections act as recombination centers for electrons and holes. Among these imperfections, copper and nickel have been most extensively studied[1)–5)]. For both impurities, the energy level was found to be close to the middle of the energy gap and the capture cross sections for electrons and holes were obtained. Similar properties have been found for "deep level" impurities, such as gold, iron, cobalt and manganese[6)]. It has also been shown that dislocations play a prominent role for recombination processes[5),7)–9)]. Furthermore, the centers produced by thermal quenching[10)] or by bombardment with high energy particles[11)] have been observed to act as recombination centers.

On the other hand, a number of studies have been made of recombination processes in pure germanium[1),5),12)–15)]. Most of them are the measurements of the temperature dependence of carrier lifetime which yield

only the positions of recombination levels in pure germanium. However, since the other properties of these centers have scarcely been studied, it is difficult to identify these levels to the known levels or imperfections.

In order to extend the information concerning the properties of recombination centers in pure germanium, we have studied the dependence of carrier lifetime on the injection level and equilibrium carrier concentrations. Similar experimental work has been made of silicon by Bittmann and Bemski[16].

According to the theory given below, the carrier lifetime at very low injection levels depends strongly on the electron or hole population of the recombination centers and the carrier densities. On the other hand, at very high injection levels, the lifetime approaches the limiting value which can be determined only from the capture cross sections and the concentrations of recombination centers. Thus, analyzing our data, we can obtain the information concerning the energy levels and capture cross sections of the recombination centers in pure germanium.

§ 2. Theory

Assuming that only one set of recombination centers is active, the recombination process can be characterized by the effective capture cross sections for an electron and hole, A_n and A_p, the concentration of centers N_r, the energy level of centers E_r and the equilibrium electron and hole densities n_0 and p_0.

In our experiments the time-decay of excess carriers injected by a pulse of light was measured. Thus it is interesting to solve the recombination equations of excess carries Δn and Δp under transient conditions. According to the analysis given in the Appendix B, the effective time of decay τ at any time t is given by

$$\tau=\frac{\tau_0+\tau_\infty\Delta\varphi}{1+\Delta\varphi}\,, \tag{1}$$

where τ is defined by

$$\frac{1}{\tau}=-\left(\frac{1}{\Delta\varphi}\right)\frac{d\Delta\varphi}{dt}\,, \tag{2}$$

and

$$\Delta\varphi=\frac{\Delta n}{n_0+p_0}=\frac{\Delta p}{n_0+p_0}\,. \tag{3}$$

In this expression, τ_0 and τ_∞ are the limiting values of lifetime at very low and high injection levels respectively, and are given by

$$\tau_0=\tau_{p0}\frac{n_0+n_1}{n_0+p_0}+\tau_{n0}\frac{p_0+p_1}{n_0+p_0}\,, \tag{4}$$

and

$$\tau_\infty=\tau_{p0}+\tau_{n0}\,, \tag{5}$$

where

$$\left.\begin{aligned}\tau_{n0}&=\frac{1}{v_nA_nN_r}\,,\\ \tau_{p0}&=\frac{1}{v_pA_pN_r}\,,\end{aligned}\right\} \tag{6}$$

and

$$\left.\begin{aligned}n_1&=N_C\exp\left[-(E_C-E_r)/kT\right]\,,\\ p_1&=N_V\exp\left[-(E_r-E_V)/kT\right]\,.\end{aligned}\right\} \tag{7}$$

Here N_C and N_V are the effective densities of states for conduction band and valence band respectively, E_C is the bottom energy of conduction band, E_V is the top energy of valence band, and v_n and v_p are the thermal velocities of electrons and holes respectively. These expressions are equivalent to the Shockley-Read expressions for steady-state lifetime[17] (see Appendix A) and provide means for determining the values of τ_0 and τ_∞.

From Eqs. (4) and (5), the ratio τ_0/τ_∞ is given by

$$\frac{\tau_0}{\tau_\infty}=\frac{1}{1+(\tau_{n0}/\tau_{p0})}\frac{n_0+n_1}{n_0+p_0}+\frac{1}{1+(\tau_{p0}/\tau_{n0})}\frac{p_0+p_1}{n_0+p_0}\,. \tag{8}$$

In an n-type material, where $n_0\gg p_0$, we have

$$\frac{\tau_0}{\tau_\infty}=\frac{1}{1+r_n}+\frac{1}{1+r_n}(n_1+r_np_1)\left(\frac{1}{n_0}\right)\,, \tag{8a}$$

with a similar relation,

$$\frac{\tau_0}{\tau_\infty}=\frac{1}{1+r_p}+\frac{1}{1+r_p}(p_1+r_pn_1)\left(\frac{1}{p_0}\right)\,, \tag{8b}$$

for a p-type material, where $p_0\gg n_0$. Here

$$\left.\begin{aligned}r_n&=\frac{\tau_{n0}}{\tau_{p0}}=\frac{A_p}{A_n}\,,\\ r_p&=\frac{\tau_{p0}}{\tau_{n0}}=\frac{A_n}{A_p}\,,\end{aligned}\right\} \tag{9}$$

with approximation $v_n=v_p$. Thus, the ratio of cross sections r_n (or r_p) and n_1 (or p_1) can be determined from the measurements of the dependence of τ_0/τ_∞ on electrical resistivity using Eq. (8).

§ 3. Experimental Method

The specimens used in this study were in the form of rods, about $0.3\times0.3\times1.3\,\mathrm{cm}^3$, which were cut from single crystals of n-type

Sb-doped germanium and p-type Ga- or In-doped germanium. The rods were carefully etched with CP-4 solution and ohmic contacts were soldered on the two ends.

Carrier lifetimes were measured by observing the time-decay of photoconductivity. The schematic diagram of apparatus is shown in Fig. 1. One surface of rods was illuminated

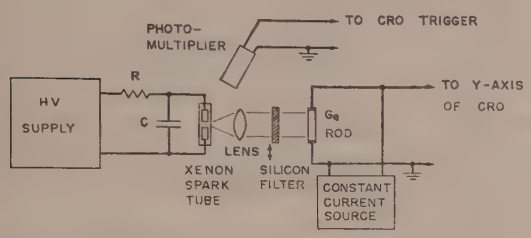

Fig. 1. Schematic diagram of measuring circuit and equipment.

by a short pulse of light approximately 2 μsec duration from a high pressure xenon spark tube which creates excess hole-electron pairs in the specimens. The resulting change $\Delta V(t)$ in the voltage across the rods, was displayed on the oscilloscope. In our experiments, a Tektronix type 545 oscilloscope was used in conjunction with a Tektronix type 53/54D plug-in unit.

The signal displayed on an oscilloscope is given by

$$\Delta V(t)=i\Delta R(t)$$

where $\Delta R(t)$ is the change in resistance of the specimen. As shown in Appendix C the time constant τ^* determined from $(1/\tau^*)=-(1/\Delta V)(d\Delta V/dt)$ is not equivalent to the carrier lifetime defined by Eq. (2). When the constant current is passed through the specimens, relation between τ and τ^* is given by

$$\tau=\left(1-\frac{\Delta V}{V_0}\right)\tau^*, \qquad (11)$$

where V_0 is the voltage across the specimens in equilibrium state.

From an oscilloscope trace apparent lifetime τ^* was obtained at any time t and converted into τ by Eq. (11). Varing the intensity of pulsed light the effective carrier lifetime τ was measured as a function of $\Delta\varphi$ calculated from ΔV.

Measurements were made at a temperature of 290°K. The values of fundamental parameters, such as mobilities and concentration products, were taken from the data of Morin and Maita[18] except the density-of-state masses for electron and hole, for which the value $m_n=m_p=0.75m_0$[19] was used.

§ 4. Experimental Results

According to Eq. (1) a plot of $\tau(1+\Delta\varphi)$ *versus* $\Delta\varphi$ should yield a straight line with intercept τ_0 at $\Delta\varphi=0$ and of slope τ_∞. An example is shown in Fig. 2 for specimen which is n-type with $n_0=1.06\times10^{14}/\text{cm}^3$.

Values of τ_0 and τ_∞ obtained for a number of different specimens are summarized in Table I.

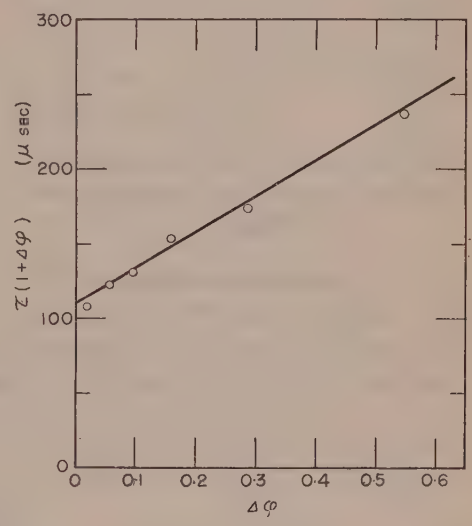

Fig. 2. Lifetime *versus* injected carrier density in n-type germanium $(1-n)$.

Table I. Summary of data on carrier lifetimes in pure germanium. τ_{n0} and τ_{p0} were calculated from τ_∞ and cross section ratio. (τ_{p0}) was obtained from the temperature dependence of carrier lifetime in n-type germanium.

Sample	Carrier density $\text{cm}^{-3}\times10^{-14}$	τ_0 μ sec	τ_∞ μ sec	τ_{n0} μ sec	τ_{p0} μ sec	(τ_{p0}) μ sec
1–n	1.06	110	240	198	42	43
2–n	0.882	176	350	289	61	58
3–n	5.03	66	305	251	54	—
4–n	1.60	186	490	404	86	—
1–p	1.66	128	280	26	254	—
2–p	3.14	313	1120	104	1016	—
3–p	5.64	70	340	32	308	—

Fig. 3 shows the plot of τ_0/τ_∞ *versus* the reciprocal of the electron density for n-type specimens. According to Eq. (8a), this plot should be a straight line. Using this linear

relationship, values of r_n and n_1 (or p_1) were obtained from the intercept and slope of the line. In this analysis, the equation for determining n_1 has quadratic form. Thus, we have two values of n_1 or E_r (calculated from n_1 by Eqs. (7)). One corresponds to $E_r > E_i$

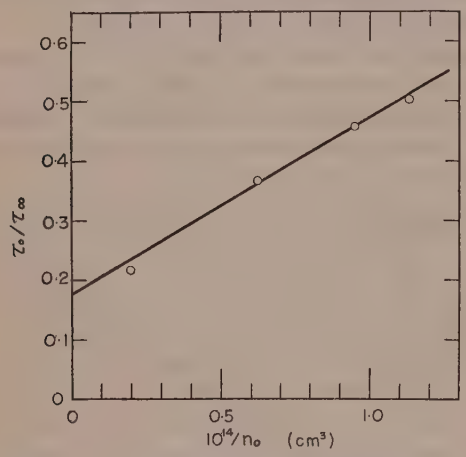

Fig. 3. τ_0/τ_∞ *versus* reciprocal of the equilibrium electron desity in n-type germanium.

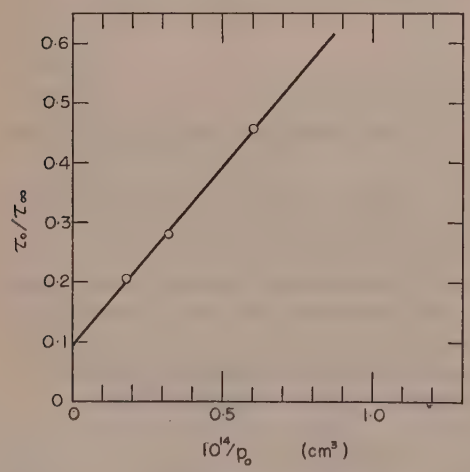

Fig. 4. τ_0/τ_∞ *versus* reciprocal of the equilibrium hole density in p-type germanium.

Table II. Results of analysis.

Type	Ratio of cross section $A_n:A_p$	Upper half of gap E_C-E_r eV	Lower half of gap E_r-E_V eV
n	1:4.7	0.28	0.32
p	9.8:1	0.31	0.25

(upper half of energy gap), and the other to $E_r < E_i$ (lower half of energy gap), where

$$E_i = \tfrac{1}{2}(E_C - E_V) + \tfrac{1}{2}kT \ln (N_V/N_C) .$$

A similar plot for p-type specimens is shown in Fig. 4.

Results of our analysis are presented in Table II.

§ 5. Discussion

The experimental results presented above show that two recombination levels are operative in pure germanium: one in n-type germanium and the other in p-type germanium. However, it is difficult to distinguish between two possibilities as to the location of the recombination level in the lower or upper half of the energy gap from our experiments as any other information concerning the energy level is unknown.

Fortunately, for n-type germanium, we have the data on the temperature dependence of carrier lifetime as described in the preceding paper[5]. They are shown in Fig. 5. In this

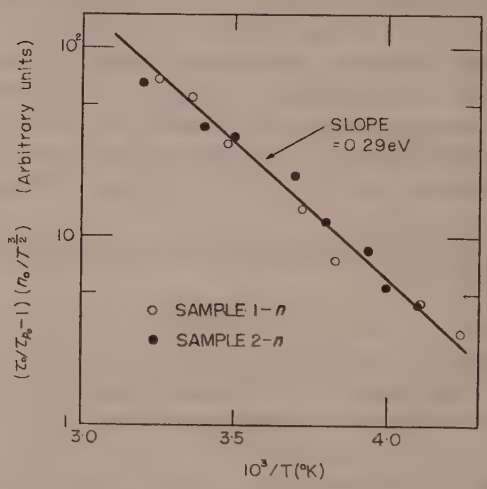

Fig. 5. $(\tau_0/\tau_{p0}-1)(n_0/T^{3/2})$ *versus* $1/T$.

case, the data are plotted as $(\tau_0/\tau_\infty - 1)(n_0/T^{3/2})$ *versus* inverse absolute temperature to facilitate comparison with theory. The slope corresponds to about 0.29 eV. This value is to be compared with the values shown in Table II. Thus, within the experimental error, it can be concluded that the recombination level in n-type germanium is at 0.28 eV from the conduction band. In addition, it is possible to obtain τ_{p0} from the measurements of carrier lifetime of n-type germanium at low temperature[5]. These values of τ_{p0} are also shown in Table I and are in good agreement with the values determined from τ_∞ and r_n.

It is interesting that the cross section ratio

of n-type germanium is opposite to that of p-type germanium. For n-type germanium the cross section for capture of holes is about 4.7 times larger than that for the capture of electrons. This result is to be expected if the recombination centers are acceptors so that the filled centers are negatively charged. Burton *et al.* have shown that copper and nickel act as the recombination centers of this sort[1]. On the contrary, for p-type germanium, the capture cross section for electrons is about 9.8 times that for holes. This suggests that donorlike recombination centers are operative in p-type germanium. Similar results have been obtained for the recombination centers in both p- and n-type silicon by Bittmann and Bemski[16].

From the values of recombination levels found in our experiments, $(E_C-E_r)^4:(E_r-E_V)^4$ is 1:5 for 0.28 eV level in n-type germanium and 10:1 for 0.25 eV level in p-type germanium using $E_C-E_V=0.70$ eV. These values are in good agreement with the values of r_n and r_p determined experimentally. Since any theoretical evidence is missing, this agreement may be fortuitous. However, if we accept this result, it is suggested that capture cross sections depend on the level of recombination centers with the relationship such as

$$A_n:A_p=(E_C-E_r)^4:(E_r-E_V)^4 .$$

It is interesting to identify the recombination levels found by our experiments to the known imperfections. A number of chemical impurities which possess more than one deep-lying level are known to act as recombination centers[20]. If a single impurity is operative in both n- and p-type germanium, Ni ($E_C-E_{r1}=0.30$ eV, $E_{r2}-E_V=0.22$ eV) and Co ($E_C-E_{r1}=0.30$ eV, $E_{r2}-E_V=0.25$ eV) are responsible for the observed recombination levels. If two sorts of impurities are active, Cu ($E_C-E_{r1}=0.26$ eV), Fe ($E_C-E_{r1}=0.27$ eV), Ni and Co are responsible for n-type, and Ni and Co for p-type. However, since the data of the capture cross sections are missing, it is difficult to discuss further.

Moreover, while the analysis described above is based on the assumption that a single recombination level is active in a given conductivity type, a few specimens show that multiple recombination levels model is valid[5]. An example of this is shown in Fig. 6. In this case, simple linear relation is not obtained. This deviation may be associated with multiple recombination levels, so no analysis has been made (see Appendix A).

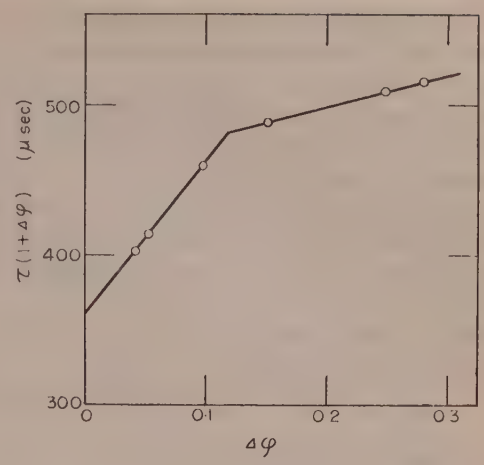

Fig. 6. Lifetime *versus* injected carrier density in n-type germanium ($6-n$).

Acknowledgements

The author would like to express his indebtedness to his co-workers at the Tokyo Shibaura Electric Co. for their aid in this work. In particular, he would like to thank Mr. Y. Ochiai for carring out much of the labor of sample preparation and measurements.

Appendix A: Carrier Lifetime for Steady-State Conditions

In this appendix, we shall consider the carrier lifetime in a nondegenerate semiconductor where the recombination occurs through multiple-levels. We have previously dealt with the case of low disturbances in carrier densities where only first-order terms need be considered[5]. It is the purpose of this appendix to extend the simple theory to the case of large disturbances in carrier densities.

For large values of injected carrier densities, Eq. (8) in the preceding paper must be rewritten in the form

$$\left.\begin{aligned}\Delta R_{nj}&=\gamma_{nj}\{N_{j0}^{+}\Delta n-(n_0+n_j+\Delta n)\Delta N_j^{-}\}\,,\\ \Delta R_{pj}&=\gamma_{pj}\{N_{j0}^{-}\Delta p-(p_0+p_j+\Delta p)\Delta N_j^{+}\}\,,\end{aligned}\right\}\tag{A1}$$

where R_{nj} and R_{pj} are the net rates of capture of free electrons and holes respectively by j-level, γ_{nj} and γ_{pj} are the rates of capturing an electron and hole by a single j-

trap, N_j^- and N_j^+ are the concentrations of filled and unfilled recombination centers, N_j is the concentration of recombination centers, and Δn and Δp are the changes of carrier densities n and p of electrons and holes respectively. Here subscript 0 refers to the thermal equilibrium condition, and n_j and p_j are the densities of free electrons and holes, respectively, when the Fermi level equals to the effective energy, E_j, of j-level.

For the steady-state case ($\Delta R_{nj}=\Delta R_{pj}$), using the condition of electrical neutrality

$$\Delta n=\Delta p+\sum_j \Delta N_j^+=\Delta p-\sum_j \Delta N_j^- , \qquad \text{(A2)}$$

it is easy to show that the lifetimes of electrons and holes defined by

$$\tau_n=\frac{\Delta n}{\sum_j \Delta R_{nj}} ,$$

and

$$\tau_p=\frac{\Delta p}{\sum_j \Delta R_{pj}} ,$$

are of the form

$$\left.\begin{aligned} \tau_n&=\frac{1+H_n}{\{(n_0+\Delta n)(1+H_p)+p_0(1+H_n)\}H} ,\\ \tau_p&=\frac{1+H_p}{\{n_0(1+H_p)+(p_0+\Delta p)(1+H_n)\}H} ,\end{aligned}\right\} \qquad \text{(A3)}$$

and the ratio of excess electrons and holes is given by

$$\frac{\Delta n}{\Delta p}=\frac{1+H_p}{1+H_n} , \qquad \text{(A4)}$$

where

$$H_n=\sum_j \frac{\gamma_{pj}N_{j0}^-}{B_j} ,$$

$$H_p=\sum_j \frac{\gamma_{nj}N_{j0}^+}{B_j} ,$$

$$H=\sum_j \frac{\gamma_{nj}\gamma_{pj}N_j}{B_j} ,$$

and

$$B_j=\gamma_{nj}(n_0+n_j+\Delta n)+\gamma_{pj}(p_0+p_j+\Delta p) .$$

If all N_j's are small compared to any one of the quantities n_0, p_0, n_j, p_j,

$$H_n \text{ and } H_p \ll 1$$

or

$$\Delta n=\Delta p ,$$

In this case, we have single lifetime τ given by

$$\frac{1}{\tau}=\frac{1}{\tau_n}=\frac{1}{\tau_p}=\sum_j \frac{1+\Delta\varphi}{\tau_{j0}+\tau_{j\infty}\Delta\varphi} , \qquad \text{(A5)}$$

where

$$\tau_{j0}=\frac{\tau_{pj}(n_0+n_j)+\tau_{nj}(p_0+p_j)}{n_0+p_0} ,$$

$$\tau_{j\infty}=\tau_{pj}+\tau_{nj} ,$$

$$\Delta\varphi=\frac{\Delta n}{n_0+p_0} ,$$

and

$$\tau_{nj}=\frac{1}{\gamma_{nj}N_j} , \qquad \tau_{pj}=\frac{1}{\gamma_{pj}N_j} .$$

This equation is the simple extension of the Shockley-Read equation for the dependence of lifetime upon carrier density[17].

Appendix B: Carrier Lifetime for Transient Conditions

For simplicity, we shall assume that a single recombination level is active. Then Eqs. (A1) and (A2) give

$$\left.\begin{aligned} -\frac{d\Delta n}{dt}&=\gamma_n(N_0^++n_0+n_1+\Delta n)\Delta n-\gamma_n(n_0+n_1+\Delta n)\Delta p ,\\ -\frac{d\Delta p}{dt}&=\gamma_p(N_0^-+p_0+p_1+\Delta p)\Delta p-\gamma_p(p_0+p_1+\Delta p)\Delta n .\end{aligned}\right\} \qquad \text{(B1)}$$

For the transient case, it is impossible to solve these equations exactly. We are interested in finding simple, approximate formula which may be used in analyzing experimental data.

We first define the effective time constants of decay at any time t to be

$$\left.\begin{aligned} \frac{1}{\tau_n}&=-\left(\frac{1}{\Delta n}\right)\frac{d\Delta n}{dt} ,\\ \frac{1}{\tau_p}&=-\left(\frac{1}{\Delta p}\right)\frac{d\Delta p}{dt} ,\end{aligned}\right\} \qquad \text{(B2)}$$

As a further simplification, we shall assume that N_r is small so that we may neglect the

change in carrier densities produced by changing concentrations in the recombination centers. In this case, $\tau=\tau_n=\tau_p$ and $\Delta n=\Delta p$. From Eq. (B1), we find that τ is given by

$$\frac{1}{\tau}=\gamma_n\gamma_p\frac{N_0^+N_0^-+N_0^-(n_0+n_1+\Delta n)+N_0^+(p_0+p_1+\Delta p)}{\gamma_n(N_0^++n_0+n_1+\Delta n)+\gamma_p(N_0^-+p_0+p_1+\Delta p)}, \tag{B3}$$

for

$$\{\gamma_n(N_0^++n_0+n_1+\Delta n)+\gamma_p(N_0^-+p_0+p_1+\Delta p)\}^2$$
$$\gg 4\gamma_n\gamma_p\{N_0^+N_0^-+N_0^-(n_0+n_1+\Delta n)+N_0^+(p_0+p_1+\Delta p)\}.$$

Neglecting N_0^+ and N_0^-, and putting $\Delta n=\Delta p$, we get

$$\tau=\frac{\tau_{p0}(n_0+n_1+\Delta n)+\tau_{n0}(p_0+p_1+\Delta n)}{n_0+p_0+\Delta n},$$

or

$$\tau=\frac{\tau_0+\tau_\infty\Delta\varphi}{1+\Delta\varphi}. \tag{B4}$$

Appendix C: Apparent Lifetime

The signal measured by the photoconductivity decay method is given by

$$\Delta V(t)=i\Delta R(t) \tag{C1}$$

where $\Delta R(t)$ is the change in resistance of the specimen. This change in resistance corresponds to the change in conductivity

$$\Delta\sigma=e(\Delta n\cdot\mu_n+\Delta p\cdot\mu_p). \tag{C2}$$

Experimentally, the apparent lifetime, τ^*, at any time t is given by

$$\frac{1}{\tau^*}=-\left(\frac{1}{\Delta V}\right)\frac{d\Delta V}{dt}, \tag{C3}$$

and in general differs from the effective lifetime τ defined by Eq. (B2). For convenience we define some dimensionless parameters as follows:

$$v=\Delta V/V_0,\quad r=\Delta R/R_0,\quad s=\Delta\sigma/\sigma_0, \tag{C4}$$

where subscript 0 refers to the equilibrium state. Then, from Eq. (C3)

$$\frac{1}{\tau^*}=-\left(\frac{1}{v}\right)\frac{dv}{dt}, \tag{C5}$$

and from Eqs. (B2) and (C2)

$$\frac{1}{\tau}=-\left(\frac{1}{s}\right)\frac{ds}{dt}, \tag{C6}$$

assuming that $\Delta n=\Delta p$.

When the specimen is driven by a constant current source,

$$v=r. \tag{C7}$$

Using the relation

$$r=s/(1+s), \tag{C8}$$

we get from Eqs. (C5), (C6) and (C7)

$$\frac{1}{\tau^*}=-\left(\frac{1}{v}\right)\frac{dv}{dt}$$
$$=-\left(\frac{1}{r}\right)\frac{dr}{dt}=\frac{1}{1+s}\frac{1}{\tau}. \tag{C9}$$

Thus, from (C7), (C8) and (C9), the relation between τ^* and τ is given by

$$\tau=(1-v)\tau^*. \tag{C10}$$

References

1) J. A. Burton, G. W. Hull, F. J. Morin and J. C. Severiens: J. Phys. Chem. **57** (1953) 853.
2) R. M. Baum and J. F. Battey: Phys. Rev. **98** (1955) 923.
3) J. F. Battey and R. M. Baum: Phys. Rev. **100** (1955) 1634.
4) R. G. Shulman and B. J. Wyluda: Phys. Rev. **102** (1956) 1455.
5) J. Okada: J. Phys. Soc. Japan **12** (1957) 1338.
6) See W. W. Tyler and H. H. Woodbury: Phys. Rev. **102** (1956) 647; H. H. Woodbury and W. W. Tyler: Phys. Rev. **105** (1957) 84 and references cited therein.
7) A. D. Kurtz, S. A. Kulin and B. L. Averbach: Phys. Rev. **101** (1956) 1285.
8) J. P. McKelvey: Phys. Rev. **106** (1957) 910.
9) G. K. Wertheim and G. L. Pearson: Phys. Rev. **107** (1957) 694.
10) See for example: R. A. Logan and M. S. Schwartz: Phys. Rev. **96** (1954) 46.
11) See for example: J. J. Loferski and P. Rappaport: Phys. Rev. **98** (1955) 1861.
12) H. Y. Fan, D. Navon and H. A. Gebbie: Physica **20** (1954) 855.

13) P. Ransom and F. W. G. Rose: Proc. Phys. Soc. (London) B **67** (1954) 646.
14) E. M. Pell: J. Appl. Phys. **26** (1955) 658.
15) M. S. Ridout: Report of the Rugby Meeting on Semiconductors (Phys. Soc. London) (1956) 33.
16) C. A. Bittmann and G. Bemski: J. Appl. Phys. **28** (1957) 1423.
17) W. Shockley and W. T. Read, Jr.: Phys. Rev. **87** (1952) 835.
18) F. J. Morin and J. P. Maita: Phys. Rev. **94** (1954) 1525.
19) T. H. Geballe and G. W. Hull: Phys. Rev. **94** (1954) 1134.
20) See for example: W. Kohn: Solid State Physics (Academic Press Inc., New York) **5** (1957) 320 Fig. 16.

JOURNAL OF THE PHYSICAL SOCIETY OF JAPAN Vol. 13, No. 8, AUGUST, 1958

One to One Correspondence between Etch Pits and Dislocations in KCl Crystals

By Masayoshi SAKAMOTO and Shunsuke KOBAYASHI

Department of Physics, Tokyo College of Science, Shinjuku-ku, Tokyo

(Received May 10, 1958)

Etch pits of KCl crystals obtained with dehydrated glacial acetic acid were observed. KCl is so soft, comparing with LiF, that dislocations are generated on it by slight mechanical shocks. Therefore, surfaces of KCl crystal are apt to be contaminated in the sense of the dislocation theory. It is supposed its depth usually reaches 100 μ or more and also most of these generated dislocations are surface half loops and isolated loops. One to one correspondence between etch pits and dislocations is discussed.

§ 1. Introduction

There have been some excellent reports on the etching of alkali halide crystals[1]. Recently, the authors could find a successive etching method for KCl crystals. From the observed results of these etching patterns, it is believed there should be one to one correspondence between etch pits and dislocations.

As KCl crystals are remarkably soft*, they should be treated very carefully during the preparation of specimens by cleavage and before and after the etching operation. Specimens increase pits density on their surface tremendously when they receive any slight mechanical shock from outside due to the operator's carelessness.

The same things also happen at the instant of cleavage when the cleavage front stops or when its speed drops below a certain value.

It is believed that most of these etch pits generated on the surface have resulted from dislocations consisting of surface half loops and isolated loops close to the surface which were already reported by J. J. Gilman and W. G. Johnston regarding LiF crystals[2].

§ 2. Etching Method

KCl ingots produced from melt* were cleaved successively into small specimens of $5\times5\times10\,\mathrm{mm}^3$. Glacial acetic acid fully dehydrated was used for etching and aceton for rinse after the etching**. The wet specimens just after rinse were dried by placing them upon a special kind of blotting paper. The last treatment seems to be most important throughout the whole process.

The duration of each etching was ranging from a few parts of a second to about 100 seconds. Specimens were remarkably dissolved at the initial instant by 10 cc etchant in a small bottle, but the dissolution tended to

* Values of c_{11} were reported: 0.40×10^{12} dyne/cm^2 in KCl, 1.18×10^{12} dyne/cm^2 in LiF.

* We used KCl ingots produced at Horiba Manufacturing Co. in Japan.

* Recently, we found a better etching reagent which is acetic acid saturated with Zn ions. Among several metal ions, Zn ion was the best.

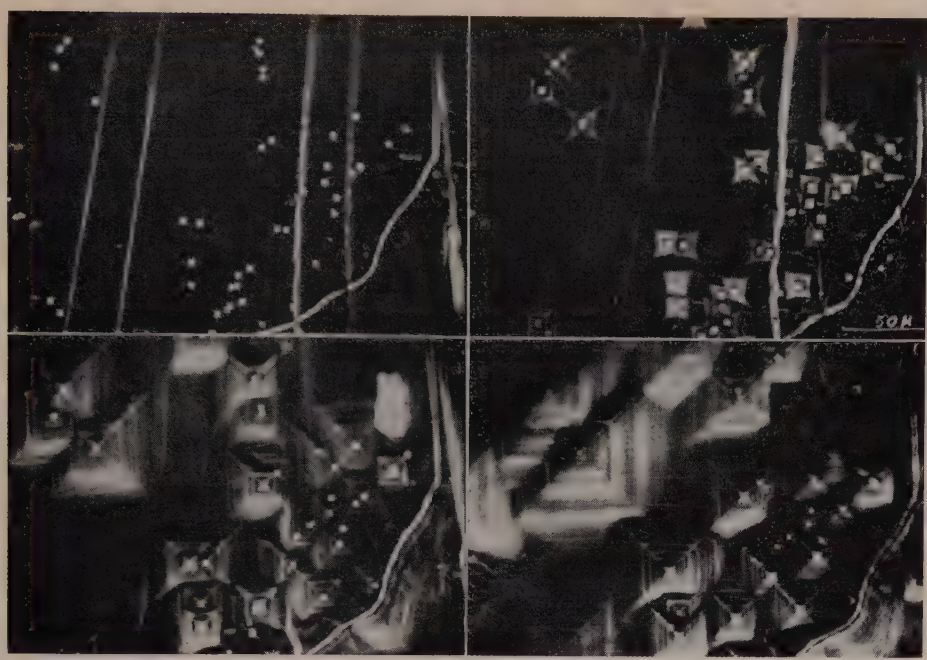

Fig. 1. An example of successive etching.
(a) First etching. (<1 sec.) (b) Second etching. (5 sec.)
(c) Third etching. (20 sec.) (d) Fourth etching. (30 sec.)

Fig. 2. An example of double etching. (1 sec.)

show a saturation in about 10 seconds.

Fig. 1 shows a typical example of successive etching. An etch pit appears in a pyramidal shape having a square base. The side edges of the base are parallel to [100] type directions. When the intensities with which the etch pits are produced are thought to be equal, all the pyramids are of the same size [Fig. 2], but the shape and size of etch pits are not generally so simple. Fig. 2 is a picture of the second etching in double etching. After the fast first etching, the specimen was lightly pressed with a finger on a spot of its surface, and then it was etched again for a short time. In this picture, there were two kinds of etch pits with large basal square of the same size: one shaped like a prefect pyramid, the other flat-topped. Both of them had appeared as small pyramids of the same size when they were first etched. It is presumed that the causes which had produced the large perfect pyramids had continued to exist from the first etching till the second one, and that the causes which had produced the flat-topped pyramids vanished during this process. On the other hand, there is another kind of etch pits, also shaped like pyramids but smaller in size. Those small pyramids, shown in this picture, may be thought as new etch pits which have come out during the second etching. So these pits must have been

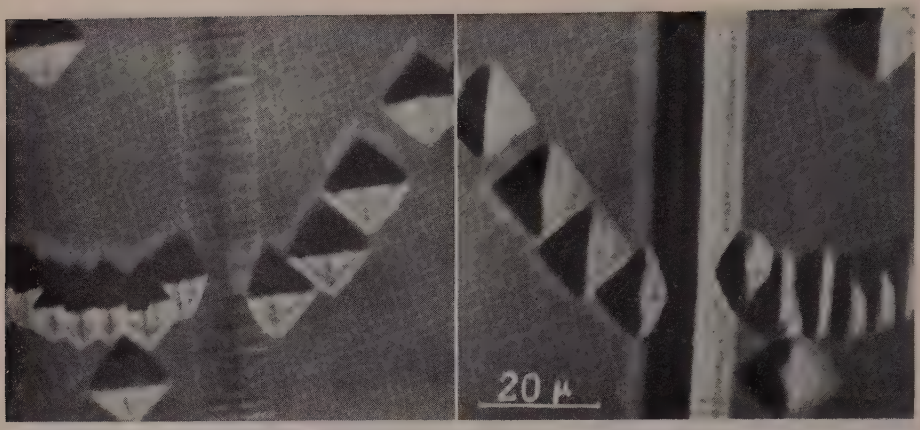

(a) (b)

Fig. 3. Symmetric pattern of matching cleaved pieces.

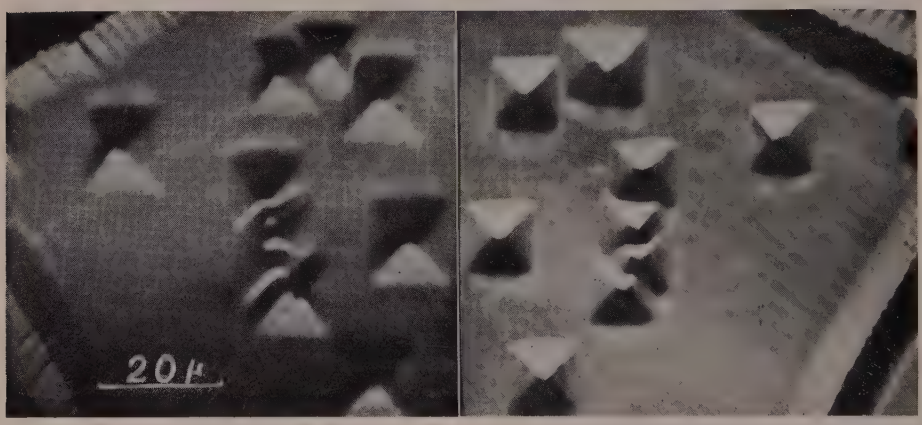

(a) (b)

Fig. 4. Asymmetric Pattern of matching cleaved pieces.

generated by the stresses given with a finger.

§ 3. Observed Results

(a) Symmetrical Pattern of Cleaved Pieces

When KCl crystals are carefully dealt with through the processes of cleavage and etching, perfectly symmetrical pattern of etching like Fig. 3 can be got at any time. If the specimens are treated without caution, it may be very difficult to obtain symmetrical pattern of matching cleaved pieces [Fig. 4]. Though these two pictures were those of matching cleaved pieces, there are some asymmatrie pits near the boundary in these pictures.

(b) Effects of Slight Mechanical Shocks

In Fig. 5 two pictures are compared: one taken before, and the other after, the cleaved surface of the specimen was dropped from the height of 1 cm on to the flat plate of an optical microscope in parallel with it. Pits density, which had been about $10^4/cm^2$ before the fall, increased to more than $10^6/cm^2$ after that. Especially, it is considered that numerous small surface loops must have been generated.

Fig. 6 shows a side picture of one of the spots where the specimen was stressed by a metal pincet with a minimum pressure barely enough to hold it. Picture (a) shows the specimen before holding, and (b) after that. In picture (a) pits density is about $10^3 \sim 10^4/cm^2$, but in (b) the generation of pits is remarkable and reaches deep. The white part on the left side of (b) means an off-focal region which resulted from this dilation. There also happened some breakdowns of the surface. Pits density near the surface is more than $10^8/cm^2$,

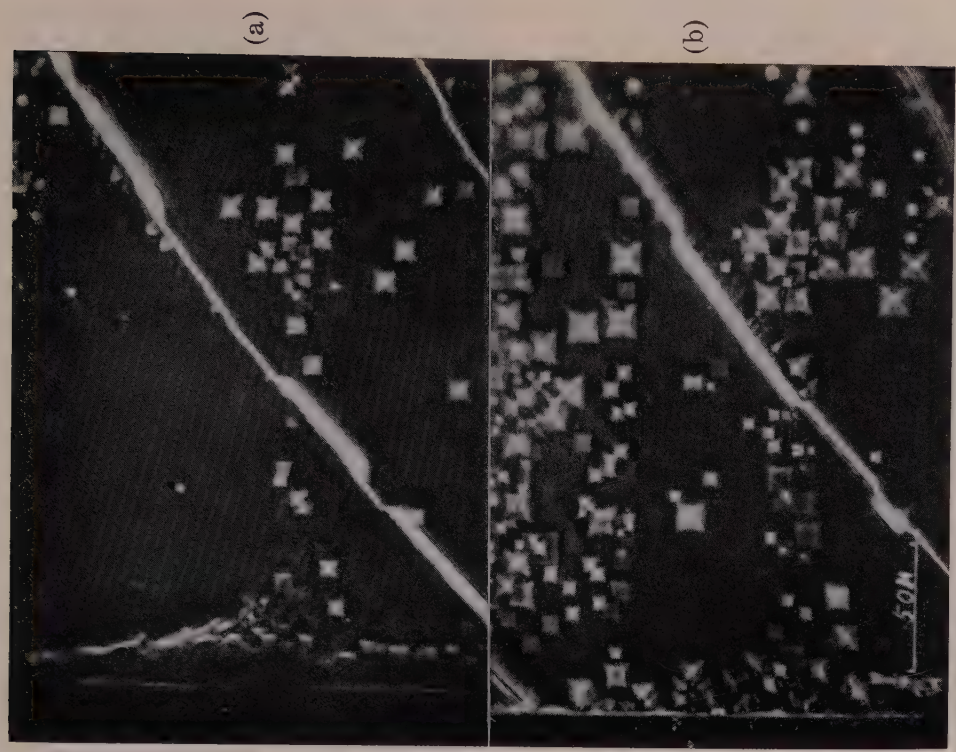

Fig. 5. Effect of a fall.
(a) Before the fall. (b) After the fall.

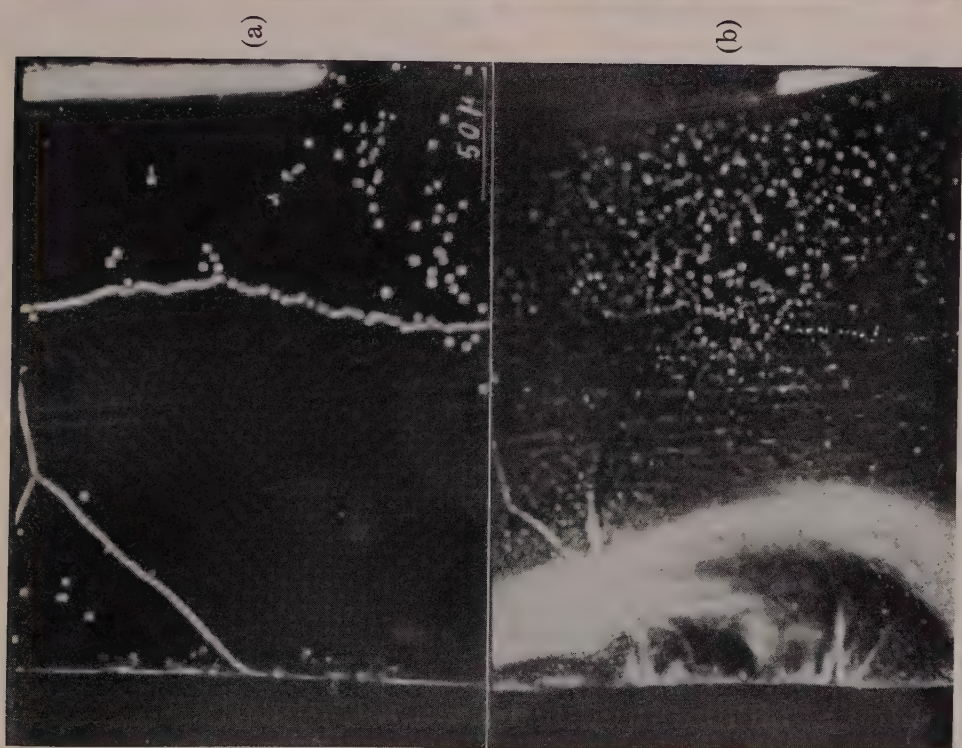

Fig. 6. Effect of a holding with a pincet.
(a) Before the holding. (b) After the holding.

which exceeds the resolving power of the microscope, and may reach $10^6/cm^2$ at the depth of about 250 μ.

Fig. 7 shows the effect of rubbing. The cleaved surface of the specimen was placed on a piece of silk cloth with its face downwards and then pulled in one direction for 3 cm as slightly as possible. Picture (a) shows

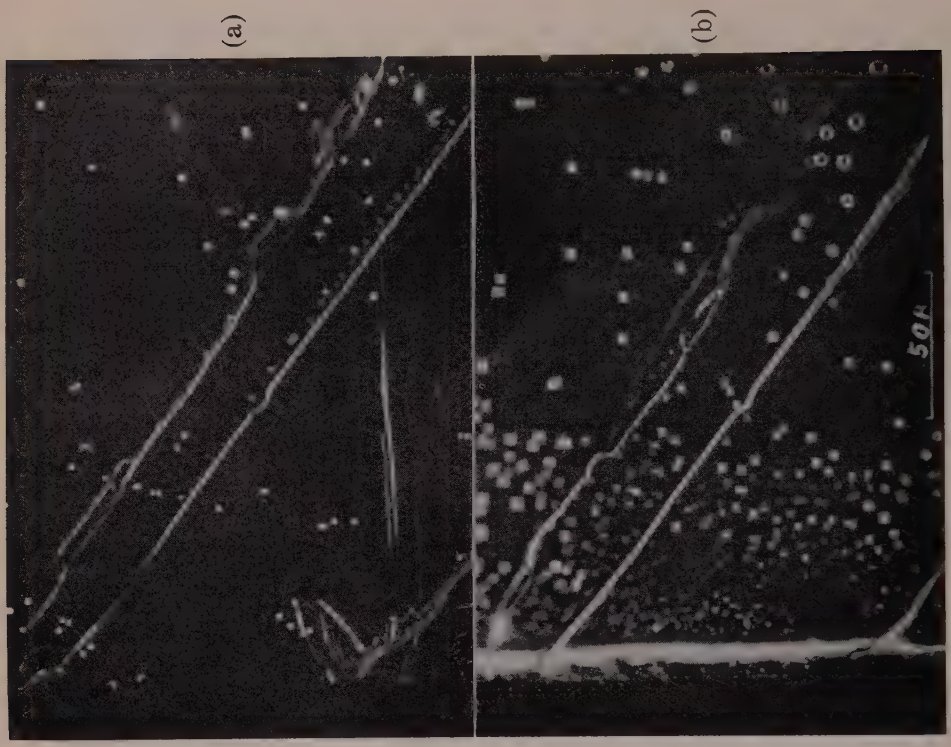

Fig. 7. Effect of a rubbing.
(a) Before the rubbing. (b) After the rubbing.

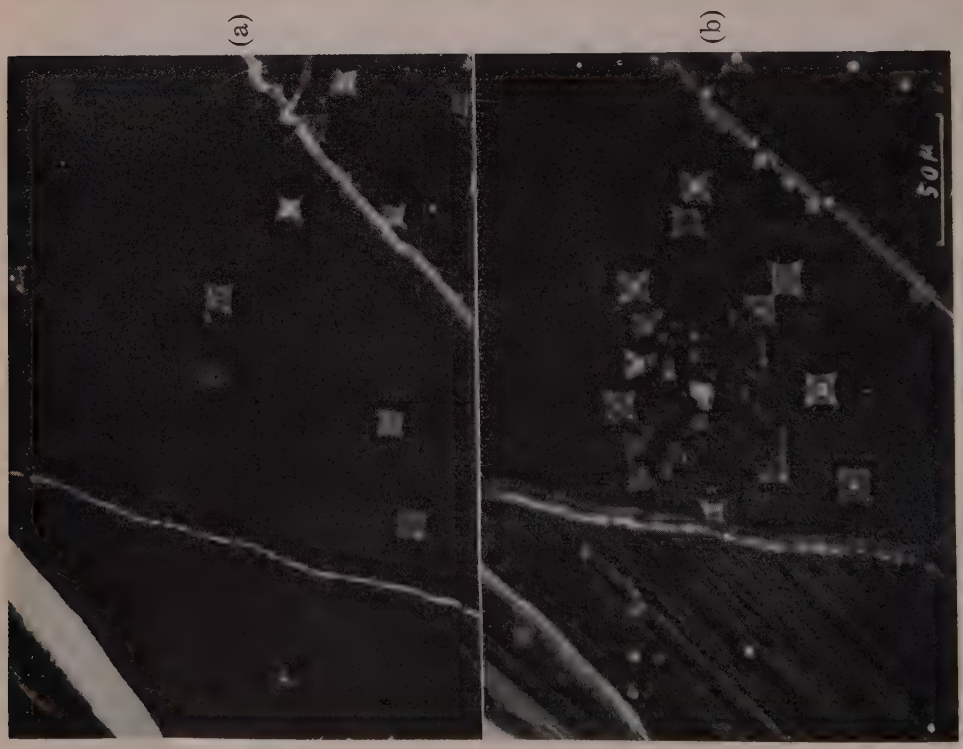

Fig. 9. Effect of an impact with a carborundum piece.
(a) Before the impact. (b) After the impact.

the specimen before the rubbing and (b) after that. Pits density of (a) is $10^3 \sim 10^4/cm^2$, but in (b) more than $10^8/cm^2$ close to the furface and about $10^6/cm^2$ in the interior. Effects have reached the depth of 100 μ. It must be noticed that a row of small pits along a cleavage step in (a) has vanished in (b). It is presumed that these pits resulted from shal-

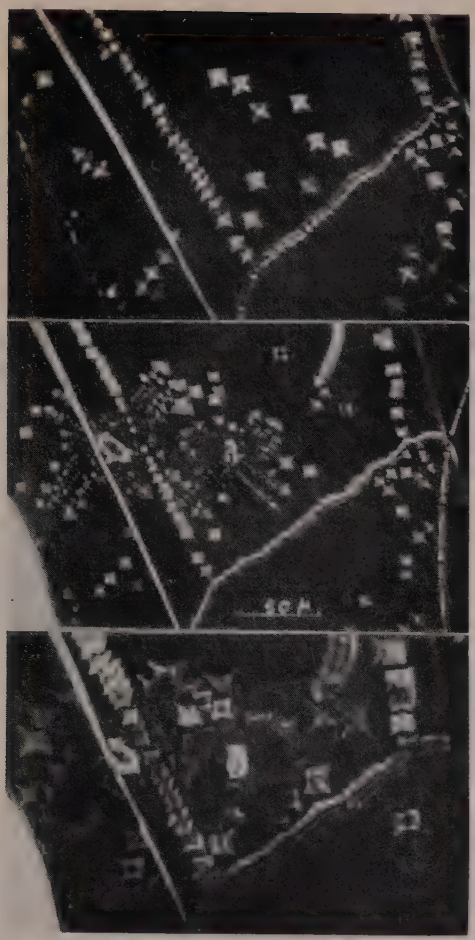

Fig. 8. Effect of an impact with a small Ni-rod.
(a) Before the impact.
(b) After the impact. Etching of 1 sec.
(c) Second etching after the impact (3 sec.).

low surface half loops.

Fig. 8 shows a picture of the successive etching when small Ni-rod, 4mm in length and 0.2 mm in diameter, was dropped upon a cleaved surface from the height of 1 cm. Picture (a) was taken before the fall, (b) and (c) after that. Letter X-like pattern in (b) resulted from the impact of Ni top on the cry stal surface. It is presumed that this pattern was consisted of rows of edge-type dislocations. In fact picture (c) seems to indicate that these generated pits consisted of dislocation loops.

Fig. 9 shows the pattern when carborundum particle, having mean size 400 μ [equal to about 65 mesh], was dropped upon the surface of the specimen from the height of 1 cm. The effect of this closely resembles the case of Fig. 8. Gilman and Johnston recognized this pattern with LiF up to 100 mesh carborundum but did not at 240 or more mesh. In the case of KCl, this was done up to 300 mesh [mean size 80 μ] carborundum but not at 600 [mean size 40 μ] or more mesh.

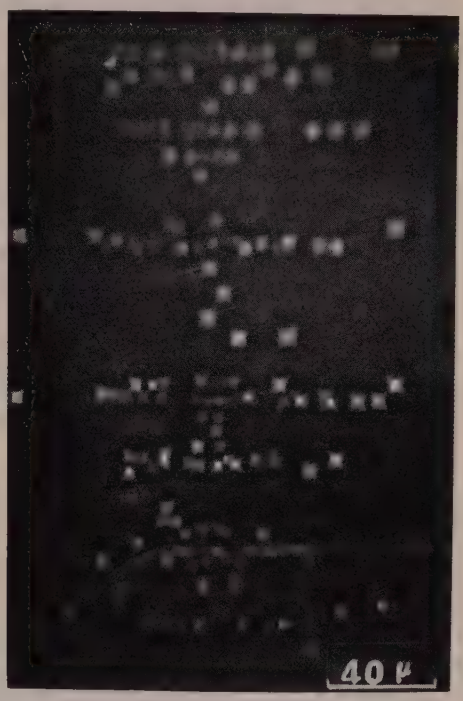

Fig. 10. Etching pattern of the place where the cleavage front seemed to stop.

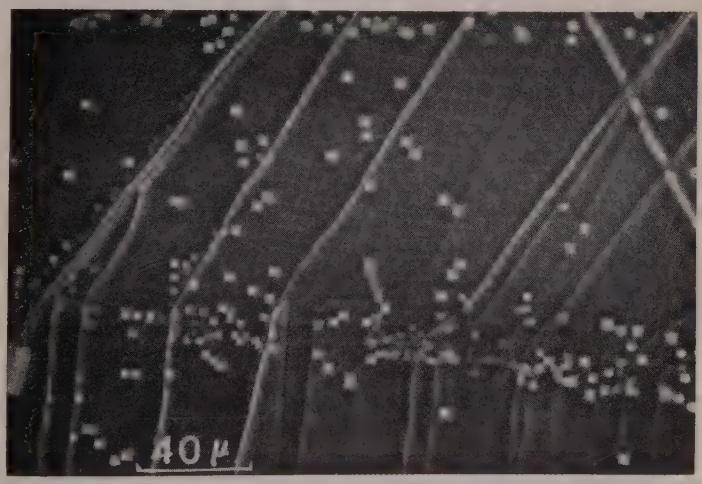

Fig. 11. Etching pattern of a cleavage surface.

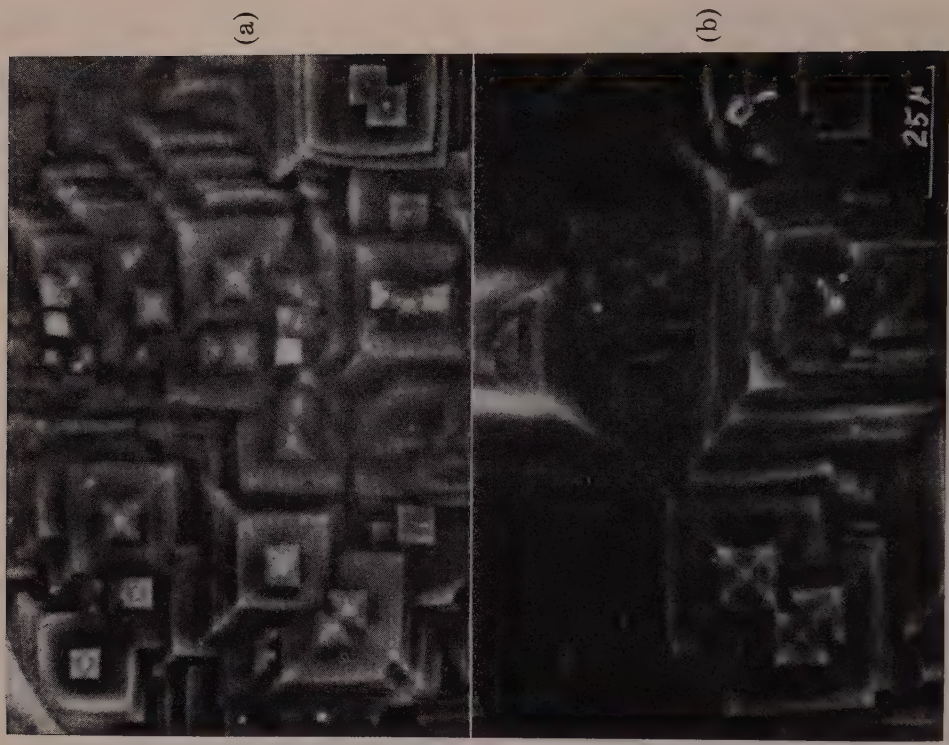

Fig. 12. A deep etching-pattern.
(a) Etching of 80 sec. (b) Etching of 100 sec.

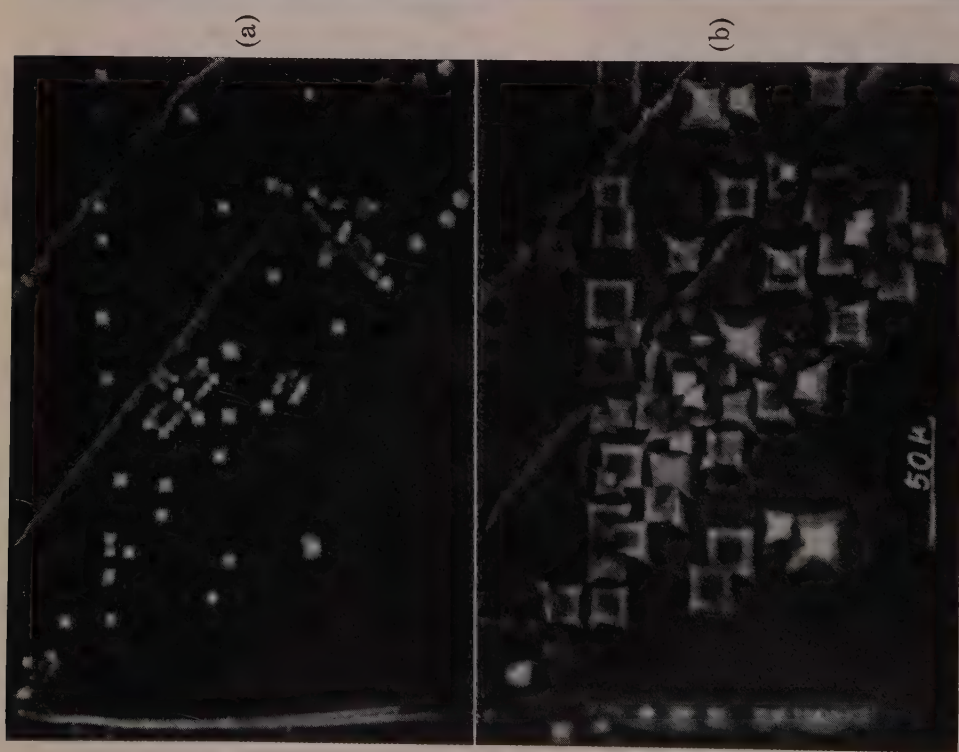

Fig. 13. An example of a cleaved surface impacted with small carborundum pieces.
(a) First etching. (1 sec.) (b) Second etching (2 sec.)

(c) Effects of Cleavage Itself

While an advancing cleavage front is accompanied by a stress field, numerous etch pits are generated especially in the regions where a cleavage front advances slowly and once stops. Characteristics of these pits are those, as shown in Fig. 10, that these are lining up parallel to [100] direction and may be

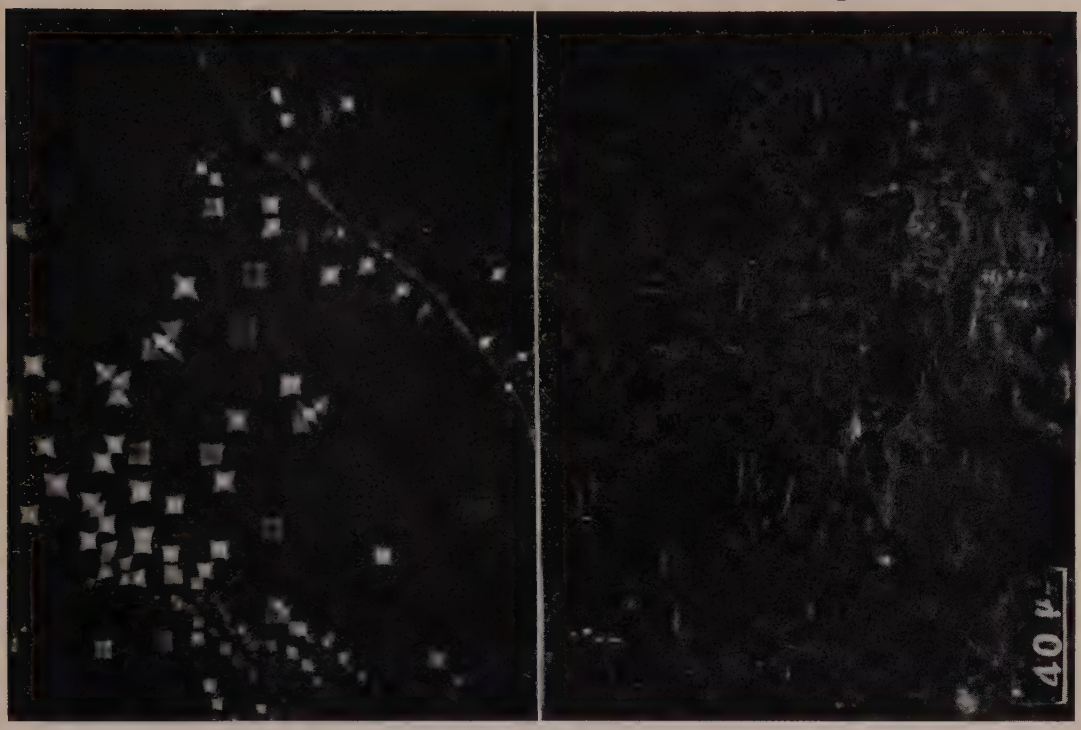

Fig. 15. Effect of human breathing.
(a) Before the breathing. (b) After the breathing.

Fig. 16. Effect of water vapor.

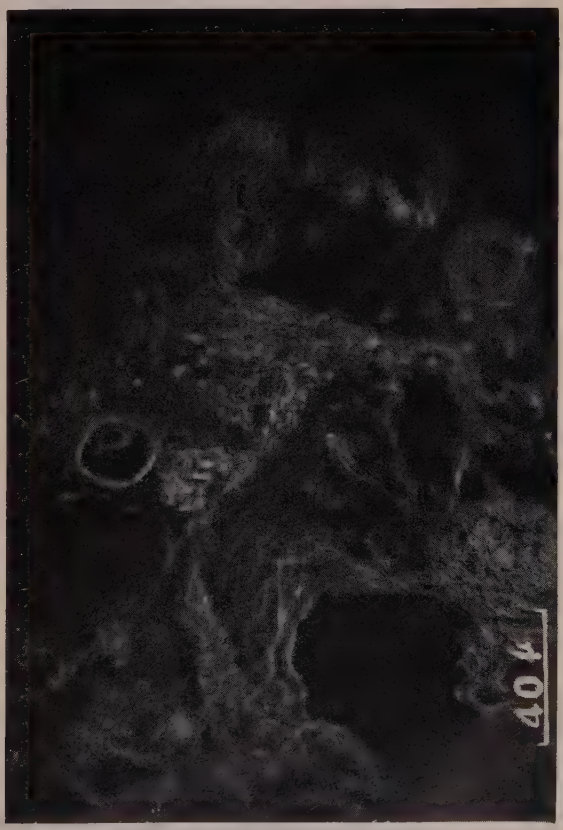

Fig. 17. Effect of water.

thought to result from groups of screw-type dislocation loops. However, when an acting stress field is not uniform, this pattern may be in more complicated situation, including some paired etch pits presumed as groups of edge-type dislocation loops [Fig. 11]. When the velocity of a cleavage front advancing through crystal is more than a certain value, the generation of new pits will never happen.

(d) Existence of Surface Half Loop and Isolated Loop

Fig. 12 and Fig. 13 show that most of newly generated etch pits on the crystal surface were probably surface dislocation half loops and isolated dislocation loops close to the surface. In Fig. 12, when the etching exceeded a certain depth by successive etching, several pairs of etch pits vanished in the same field of this picture.

Fig. 13 shows the same thing. In a fast first etching of cleaved KCl surface especially, it is noticed there are many paired etch pits. It may be known that this situation is essentially the same in Fig. 1, 8, 9, 11 and 12. Therefore, we may the scheme of Fig. 14 in order to understand any asymmetrical

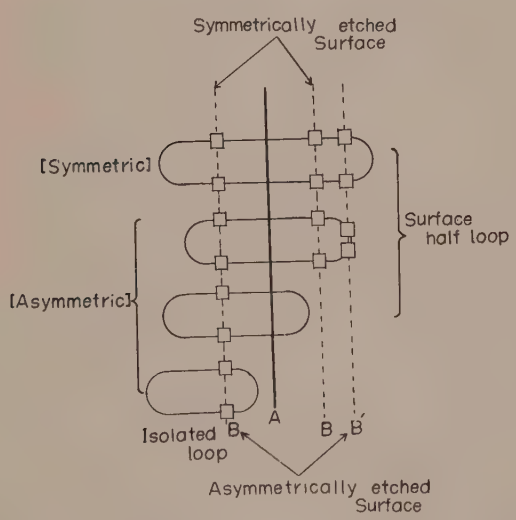

Fig. 14. Interpretation of aymmetric pattern of matching cleaved pieces.
A: Cleavage surface
B–B: Symmetrically etched surface
B–B′: Asymmetrically etched surface
Small squres show etchpits

pattern of matching cleaved surfaces like Fig. 4. Also, completely symmetrical pattern may be obtained with fully cautious treatment [Fig. 3].

(e) Effects of Breathing

KCl is so hygroscopic that the specimen should be protected against operator's breathing and other moistures. Fig. 15 (b) shows the case that the specimen accepted human breathing lightly on its surface and (a) the case not accepted. Fig. 16 shows the effect of water vapor. Fig. 17 shows the case that the specimen was once wetted and then dried out. These pictures are thought to be essentially the same.

§ 4. Discussions

It can not be thought that etch pits result from isolated impurities. Pits density of as grown crystals was usually about $10^4/cm^2$, but the impurities contained in used crystals were 0.00001 gr Ba, 0.00001 gr Ca and 0.00003 gr Fe per 100 gr KCl and therefore the number of expected defects due to these impurities will be about $10^9/cm^2$ or more.

It may not be insisted that etch pits must be present only when dislocations are accompanied by impurities as the situation of metals. Because edge-type patterns in Fig. 8 and 9 and screw-type patterns in Fig. 10 and 11 can be shown any time in the same specimen by the different stimulations respectively. This result was just the same even in the home-made crystals which were more impure.

§ 5. Conclusions

(a) Any etch pits can be persued spatially by the successive etching [Fig. 1].

(b) When KCl crystals are treated carefully, a complete symmetrical etch pattern of matching cleaved pieces can always be taken [Fig. 3].

(c) When any paired etch pits vanish at the almost same time in the successive etching, it may be interpreted that these pits consisted of any dislocation loops [Fig. 12, 13].

(d) Especially, the surface of KCl crystal is apt to generate many surface half loops or isolated loops close to the surface by any slight mechanical shocks. This may be the reason why a symmetrical pattern of matching cleaved pieces could not be taken so easily [Fig. 4, 14].

(e) The observed results of etch pits did not give any inconsistent facts with the dis-

location properties.

According to the reasons mentioned above, it is believed that there exists one to one correspondence between etch pits and dislocations in KCl crystals.

Acknowledgement

The authors wish to express their thanks to Dr. J. J. Gilman and Dr. W. G. Johnston at G. E. Research Laboratory for their valuable suggestions and discussions and also to Prof. Y. Uemura at Tokyo University who gave them many chances of discussion about this subject.

References

1) "Dislocations and Mechanical Properties of Crystals" edited by Fisher and others: John Wiley and Sons, Inc. (1957).
2) J. J. Gilman and W. G. Johnston: J. A. P. **27** (1956) 1018.

JOURNAL OF THE PHYSICAL SOCIETY OF JAPAN Vol. 13, No. 8, AUGUST, 1958

The Internal Friction of Barium Titanate Ceramics*

By Takuro IKEDA

Kobayasi Institute of Physical Research, Kokubunji, Tokyo

(Received April, 10, 1957, Revised May 5, 1958)

The internal friction of $BaTiO_3$ ceramics has been studied under various conditions. It depends on temperature, biasing field and vibration amplitude, but is nearly independent of frequency and porosity. It is concluded that its main part is not caused by the ceramic and domain structures but is the property of the single domain crystal, which is of intrinsically dielectric origin, acting through piezoelectric coupling.

§ 1. Introduction

Barium titanate ceramics are much used as transducers for generation of ultrasonic waves. Considerable heat, however, is generated in the transducer at a high power level, and thus limits the maximum radiated power. The origin of this effect has been investigated by some authors. Baerwald and Berlincourt[1] attributed it to the dielectric hysteresis, but its main cause was interpreted as the internal friction of $BaTiO_3$ ceramics by Hueter *et al*[2),3)] and the present author[4]. The temperature rise of the transducer becomes remarkable near its resonance, while the unpolarized one shows no anomalous rise. An example of these measurements is shown in Fig. 1(a)[4]; the solid and dotted lines are the temperature rise of polarized and unpolarized ceramics in an oil vessel, respectively. This dissipation of mechanical energy near the resonance must be represented by an internal resistance R_{int} in the equivalent circuit in Fig. 1(b). (R_{el}: dielectric resistance, R_{rad}: acoustic radiation resistance).

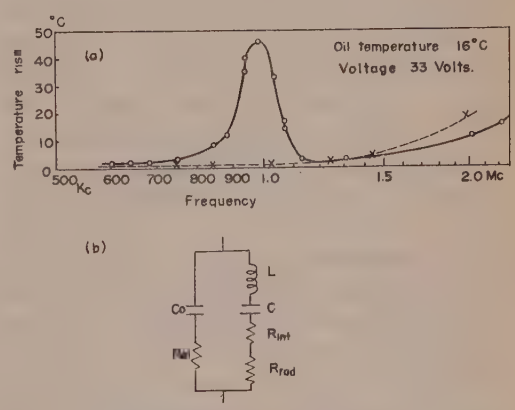

Fig. 1. (a) Temperature rise of $BaTiO_3$-ceramic-transducer.
(b) Its equivalent circuit.

Few papers refer to the internal friction of the $BaTiO_3$ ceramics. Mason[5] has reported that the dissipation of mechanical energy becomes smaller by aging. Hueter and Neuhaus[6] investigated the dependence of the ul-

* The summary of § 3 and 5 was read at the meeting of the Physical Society of Japan on 19th, July, 1956, and that of § 4 and 6 on 1st, Nov., 1956.

trasonic attenuation on temperature and biasing field by a pulse method, and attributed the anomalies in the biasing effect to the dislocations at the 90° domain boundaries on the basis of Mason's argument. However, this mechanism seems to be insufficient to explain the greater part of the attenuation.

The present paper attempts to study the subject in more detail; and at first to answer the question, whether the dissipation of vibrational energy in ceramic $BaTiO_3$ vibrator occurs mainly in the interior of grain crystallites, or it is caused by the ceramic structure. Dependence of the internal friction upon various parameters—temperature, frequency and porosity—will be examined, and as a result, it will be shown that the energy dissipation during mechanical vibration mainly occurs within each grain (§ 5). In order to find the origin of the internal friction in the grain crystallite, its dependence on biasing field and vibrational amplitude will be measured and, taking account of the following reasons, both internal friction and dielectric loss of the ceramics are examined in parallel.

A complication arises on account of the piezoelectric property of single crystal and prepolarized ceramics of $BaTiO_3$, since in the piezoelectric crystal we have no longer an unambiguous relation between stress and strain. Instead, we have several alternative sets of relations among the quantities—electric field, polarization, stress and strain, and different elastic coefficients corresponding to different electrical condition, which are in general complex. In such condition, the internal friction will also depend on the electrical condition of the crystal. For instance, the elastic loss factor, the "internal friction", of an unplated bar of piezoelectric crystal will be the $\tan\delta$ of s^D, the elastic compliance coefficient for constant electric displacement, while the loss factor of a plated and short-circuitted bar will be the $\tan\delta$ of s^E, the compliance coefficient for constant electric field. Similarly, $\tan\delta$ of the dielectric parameter, the "dielectric loss", depends upon mechanical condition of the crystal; namely, the loss of free crystal is the $\tan\delta$ of ε^F, the "free dielectric constant", and the loss of a clamped crystal is the $\tan\delta$ of ε^C, the "clamped dielectric constant".

This situation gives rise to various possibilities in the interpretation of internal friction of piezoelectric crystals, since energy dissipation of intrinsically dielectric origin can contribute to the internal friction under certain conditions. Namely, Mason[7] has shown for a plated 45°X-cut bar of Rochelle salt crystal that most of the dissipation of vibrational energy can be explained as the dielectric loss of the clamped crystal. Price[8] also confirmed Mason's view from the measurement of the attenuation of ultrasonic pulse in various directions.

Since the electromechanical coupling is very strong in the single domain crystal of $BaTiO_3$, we expect an effect similar to that in Rochelle salt, and it is the purpose of this paper to find that the same consideration applies to the interpretation of internal friction of pre-polarized ceramic $BaTiO_3$.

The internal friction and dielectric loss of the $BaTiO_3$ ceramics are found to be mostly caused by the dissipations within the grain crystallite, and the major contribution of the dissipation in the grain may be the average in some sense, involving mechanical and dielectric losses of single domain crystal. Observation of the internal friction and dielectric loss of the ceramics, taking account of the order of electromechanical coupling in the single crystal, leads to the conclusion that the main part of internal friction of ceramic $BaTiO_3$ is the dissipation of the dielectric origin.

Many reports have been published regarding the dielectric loss of the $BaTiO_3$ ceramics. The dielectric losses in the biased state of the $BaTiO_3$ ceramics were already investigated by Baerwald *et al*[1], but they appear to have confused the dielectric loss at low amplitude with that at high voltage accompanying the domain reversals. Accordingly, the biae dependence of the dielectric loss will be reexamined.

§ 2. Preparation of Samples and Experimental Procedure

(a) *Preparation of Samples*

Commercial $BaCO_3$ and TiO_2 have been mixed in 1 to 1 mole ratio, calcined at 1200°C, crushed and pressed, and sintered at 1400°~1450°C. Most of the samples have specific gravity 5.5~5.6, and the Curie points at about 116°C. Samples of various porosities have been prepared by sintering at various tem-

peratures. The specimens are in the shape of discs and bars. Silver eletrodes have been glazed on the proper faces.

(*b*) *Experimental Procedure*

The internal friction Q_m^{-1} have been measured by the resonance-curve-method, composite-bar method and bridge (admittance-loop) method.

In the resonance curve method, the frequency of driving voltage of constant amplitude applied on the specimen (prepolarized ceramics), is varied and one observes the electric current passing through maximum and minimum. Denoting the maximum and minimum currents by I_m and I_n, and the frequencies corresponding to them by f_m and f_n, respectively, the internal friction Q_m^{-1} is obtained by the following formula:

$$Q_m^{-1}=\frac{2(f_n-f_m)}{f_m}\sqrt{\frac{I_n}{I_m}}\,. \qquad (2.1)$$

This relation, however, holds true only in the case of small dissipation, and also requires a good sinusoidal wave-form of oscillator voltage. (Wave form distortion strongly affects the value of I_n.)

The composite-bar method consists in observing the resonance curve of a composite bar consisting of X-cut and Y-long quartz rod and the specimen cemented endwise[9]. The internal friction is calculated by

$$Q_m^{-1}=\left(1+\frac{m_q}{m_s}\right)\frac{2(f_n-f_m)}{f_0}\frac{(I_mI_n)^{1/2}}{I_m+I_n}\,, \qquad (2.2)$$

where m_q=mass of the quartz rod, m_s=mass of the specimen, f_0=resonant frequency of the composite bar, and other symbols have the same meaning as above.

Q_m^{-1} was also measured by the bridge method using a radio frequency impedance bridge (made by Yokogawa Electric Works). Admittance-loop was traced and the internal friction was computed by

$$Q_m^{-1}=(f_2-f_1)/f_0\,, \qquad (2.3)$$

where f_0 is the resonant frequency, and f_1 and f_2 are quadrantal frequencies (f_2-f_1 is the half-width).

Actually, the values obtained by the resonance curve method were often found to be larger by 20~40% than those from (2.3) on account of the distortion of wave form. Therefore, the bridge method was mainly adopted, and the resonance curve method was used in a few cases, where corrections were made to make the value consistent with the bridge method values.

§ 3. Experimental. A. Dependence of Internal Friction of Ceramic $BaTiO_3$ upon Various Parameters

(*a*) *Temperature Dependence*

The temperature variation of the internal friction of the $BaTiO_3$ ceramics was examined by the composite bar method. The specimen was *ca.* $3\times3\times24$ mm³ in size. Measurement was dode at the frequency of about 90 Kc/s and at temperatures between 20° and 140°C. Experiments were made with unpolarized and remanent-polarized (and short-circuited) state of the specimen. The effect of the polarization is hardly found, as shown in Fig. 2. The

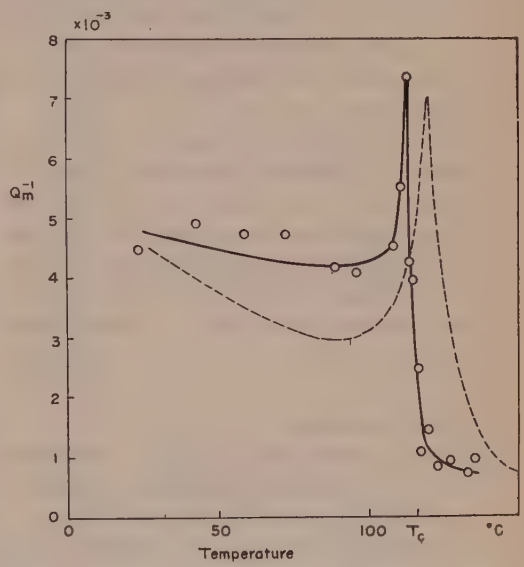

Fig. 2. Temperature variation of the internal friction.

values above T_C are not reliable and may be lower than shown, because of the error of small f_n-f_m in Eq. (2.2), the distortion of oscillator wave form, and the incomplete cementing, etc.

Even in this curve, however, the internal friction above the Curie point T_C is several times smaller than that below T_C. The dotted curve shows the result for $(Ba_{0.96}\text{–}Pb_{0.04})TiO_3$ by Hueter and Neuhaus[6], showing a similar behaviour.

(*b*) *Frequency Dependence*

Several prepolarized discs of $BaTiO_3$ cera-

mics with diameters of 18~58 mm were investigated in their radial and thickness modes of vibration. The internal frictions of these discs were measured with the impedance bridge at room temperature. The results are shown in Fig. 3. The dispersion of the measured values

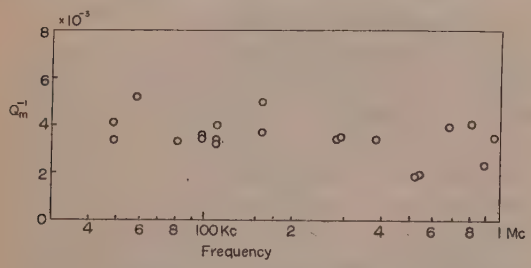

Fig. 3. Frequency dependence of the internal friction.

are likely to be due to the differences of aging and the errors in plotting the admittance loops, etc. In the thickness vibration, it is difficult to measure Q_m^{-1} because of the coupling with higher radial modes.

The internal friction is seen to be nearly independent of frequency between 50 and several hundred Kc/s. Hueter *et al*[6], on the other hand, report nearly constant attenuation per wave length of ultrasonic pulses for frequencies between 1~50 Mc/s. So it may be said that the internal friction is independent of frequency over a very wide frequency range.

(*c*) *Bias Dependence*

Polarized ceramic disc 2 mm in thickness and 26 mm in diameter was used. After it was aged at 82°C for 45 hours, the variation of the internal friction was examined with varying positive bias by the resonance curve method. Fig. 4 shows the measuring circuit.

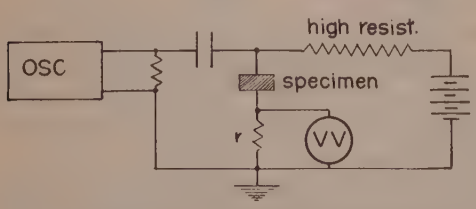

Fig. 4. Measurement of bias dependence.

The experiment was performed at 80°C. The Q^{-1} values obtained by this method and corrected as mentioned in § 2 are shown in Fig. 5. The biasing field was increased step by step, and the measurement was made in 6 to 10 minutes at each step. The internal friction

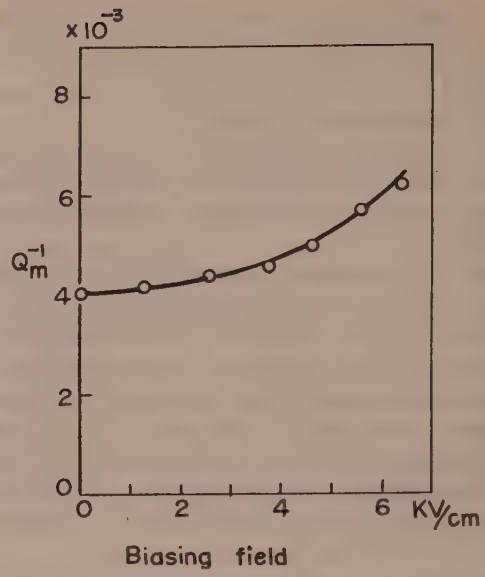

Fig. 5. Bias dependence of the internal friction.

of ceramics is found to increase by about 40% at the bias of 6 KV/cm.

(*d*) *Amplitude Dependence*

In Fig. 6(a), V_v gives the voltage applied on the specimen. V_i gives the potential difference across a small resistance r, and is proportional to the electric current through the vibrator. At each constant voltage, the frequency of the oscillator is adjusted to f_m, the frequency corresponding to the maximum current, and the corresponding values of V_v and V_i were observed. The equivalent circuit is shown in Fig.6(b). It is now assumed that ω_0, L, C and C_0 are independent of vibration amplitude and $1/\omega_0 C_0$ is larger than R_i. R_i is the internal resistance which is amplitude-dependent. When the amplitude of vibration

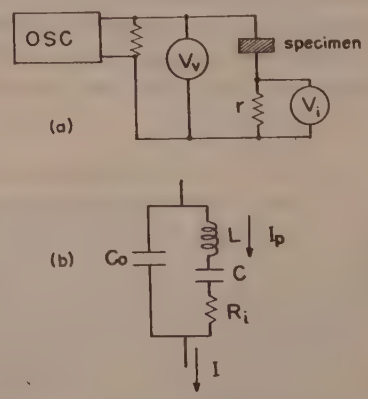

Fig. 6. (a) Measurement of amplitude dependenc.
(b) Equivalent circuit of the vibrator.

is small, R_i must be equal to the value obtained by the bridge method, $(R_i)_0$. Then

$$(Q_m^{-1})_0=\omega_0 C(R_i)_0 \quad \text{and} \quad Q_m^{-1}=\omega_0 C R_i \ . \tag{3.1}$$

Hence

$$Q_m^{-1}/(Q_m^{-1})_0=R_i/(R_i)_0 \approx (I_m/V_v)_0/(I_m/V_v) = (V_i/V_v)_0/(V_i/V_v) \ . \tag{3.2}$$

When the mode of vibration is radial, the strain amplitude (effective value) at the centre is

$$S_0=KI_p \ , \tag{3.3}$$

where I_p is the " piezoelectric current " through the LCR branch and K is the constant of specimen given by

$$K=\frac{4}{\omega_0 a^2}\frac{d_{31}}{\varepsilon_3^F}\frac{1}{k_r^2}\frac{x_1}{J_1(x_1)} \ , \tag{3.4}$$

(a=radius of the disc, ε_3^F=free dielectric constant, d_{31}=piezoelectric constant, k_r=electromechanical coupling coefficient for radial vibration, x_1=root of the Eq. $xJ_0(x)=(1-\sigma)J_1(x)$ where J_0 and J_1 are Bessel functions and σ is Poisson's ratio). At the frequency f_m, we have $I_m \approx (I_p)_{f_0}=V_v/R_i$; therefore, from (3.3),

$$S_0 \approx KV_v/R_i \ . \tag{3.5}$$

When V_i and V_v are measured with varying V_v, Q_m^{-1} and S_0 are determined at each amplitude by (3.2) and (3.5) by using the values of $(Q_m^{-1})_0$ and $(R_i)_0$.

Using the same specimen as employed in (c), the following values are chosen at 80°C;

$$\left.\begin{aligned} &K \approx 5.2\times10^{-4}\ (\text{amp.}^{-1}) \ , \\ &(R_i)_0 \approx 40\Omega \ , \\ &1/\omega_0 C_0 \approx 450\Omega \ . \end{aligned}\right\} \tag{3.6}$$

In the neighbourhood of 80°C, f_0 varies little with various V_v. From the measurement of V_i with varying V_v, Fig. 7 is obtained, using Eqs. (3.2), (3.5) and (3.6). The abscissa is shown in the strain amplitude S_0 (the effective amplitude) estimated approximately by (3.5). The internal friction is seen to increase rapidly at a certain strain amplitude.

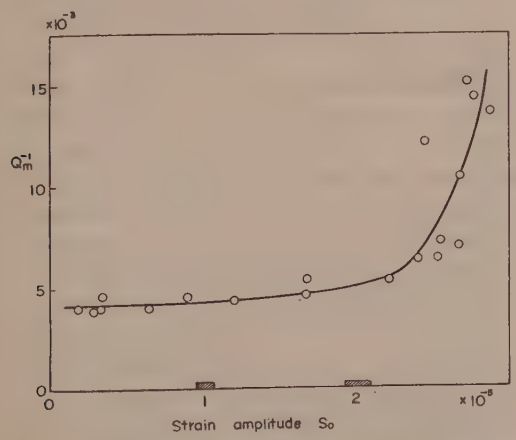

Fig. 7. Amplitude dependence of the internal friction.

(*e*) *Porosity Dependence*

Several specimens with disc shape were prepared at various sintering temperatures. Their apparent densities are 5.0~5.6 corresponding to different porosities, while the true density of the substance is 6.0. The internal friction was measured in radial vibrations by the resonance-curve method. The internal friction of a few specimens with lower densities could not be determined by that method, and so were measured by the compositebar method. Fig. 8 shows Q_m^{-1} and the radial coupling coefficient k_r, where the abscissa is shown in density instead of porosity. While k_r is considerably porosity-dependent, Q_m^{-1} is seen to be only slightly dependent on porosity in the range of this experiment.

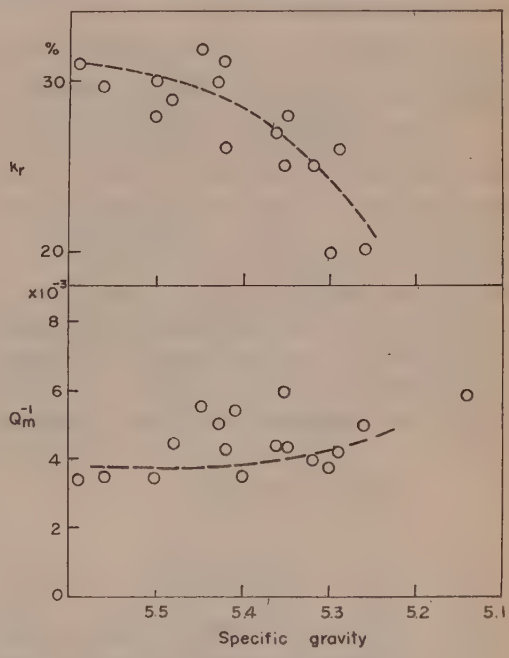

Fig. 8. Porosity dependence of the radial coupling coefficient and the internal friction.

§ 4. Experimental. B. Parallel Examination of the Internal Friction and Dielectric Loss

(*a*) *Bias Dependence and Aging Effect*

The specimen was the same disc as the one

used in § 3 (c). The dielectric tan δ, or Q_e^{-1}, was measured at 50 Kc/s with the impedance bridge under a biasing field. The result at 80°C is shown in Fig. 9. The measurement

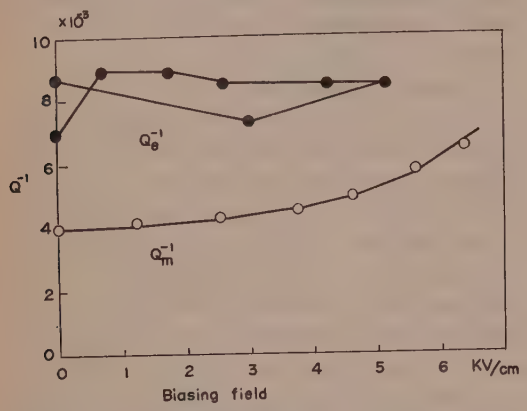

Fig. 9. Bias dependence of the internal friction and dielectric loss.

was done step by step, and the plotted values obtained are those after about 5 minutes at each step. The curve of the internal friction Q_m^{-1} is taken from Fig. 5. The internal friction increases with the biasing field (by 40% larger at the d.c. field of 6 KV/cm), but the dielectric loss is nearly independent of the bias.

The aged sample was now biased and aged for several hours, and next, after the removal of the bias, it was aged again. This cycle was repeated several times and the internal friction and dielectric loss were measured during these cycles. An example of the measurements is shown in Fig. 10. Internal friction in the aged condition also is seen to be larger in the biased state than in the unbiased state.

(*b*) *Temperature Variation*

The specimen was in the form of a bar made of prepolarized ceramics, about 0.8 mm thick, 2.6 mm wide and 18 mm long. The dielectric loss was measured by the impedance bridge, and the internal friction was obtained by the resonance-curve method in the longthwise longitudinal vibration. Fig. 11 shows the results. The dotted curve at the higher temperature shows the dielectric loss of the unpolarized ceramics. These measurements show that the internal friction and dielectric loss vary in parallel.

§ 5. Considerations.—The Internal Friction of the "Ceramic" $BaTiO_3$

On the ground of these knowledges on the dependence of the internal friction, this and next sections will deal with the problems on the mechanism of the dissipation in the $BaTiO_3$ ceramics.

The measured internal friction $\psi^*(\psi^*=Q_m^{-1})$ can be considered to consist of two parts: the internal friction in the grain crystallite ψ_{GC}, and that due to the ceramic structure ψ_{Cer}. Namely,

$$\psi^*=\psi_{GC}+\psi_{Cer} \tag{5.1}$$

The second part will be caused mostly in

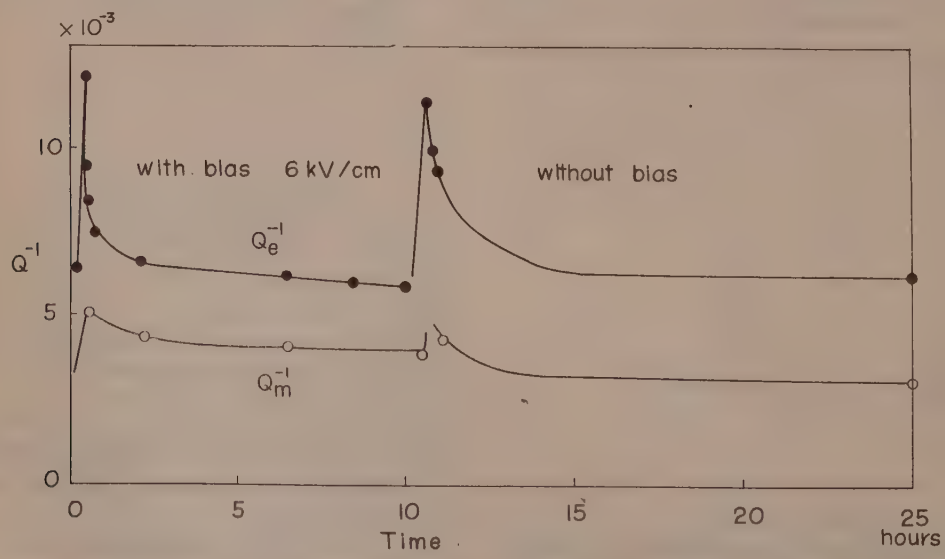

Fig. 10. Aging effects of the internal friction and dielectric loss with and without the bias.

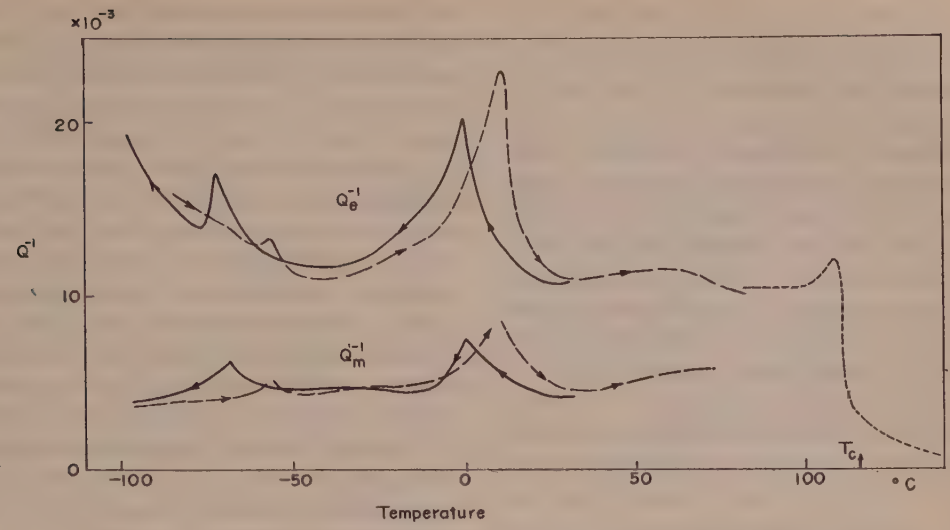

Fig. 11. Temperature variation of the internal friction and dielectric loss.

the grain boundary (ψ_{GB}). Its magnitude cannot be estimated directly, but it will be reasonable to assume that it dose not change appreciably above and below Curie point; then, ψ_{Cer} must be of the order of the internal friction above T_C, and is shown to be several times smaller than the value of ψ^* at room temperature. This means that most part of the internal friction of $BaTiO_3$ ceramics in the ferroelectric range is caused by the dissipation in the grain crystallite, ψ_{GC}. The dissipation due to the "ceramic" structure ψ_{Cer} will not be important in $BaTiO_3$ ceramics.

Porosity dependence measurement, which was performed in order to find the contribution of ψ_{Cer}, gave the internal friction which is nearly independent of porosity in the range examined. The result suggests again that the role of ψ_{Cer} must be small.

The first term of (5.1)—the internal friction ψ_{GC} in the grain crystallite—consists of the dissipation at domain boundaries, ψ_{DB}, and the contribution from that of the single domain crystal, ψ_{SD}. ψ_{DB} is not evaluable but it can be assumed to be small in the aged condition. (Its order of magnitude may be smaller than ψ_{GB}, because the walls are thinner than grain boundaries.) ψ_{SD} will be the average of the mechanical dissipations in all domains with various orientations. Since the internal frictions of the unpolarized and prepolarized ceramics are nearly equal, the averaging taking account of the domain distributions may hardly affect ψ_{SD}.

Further considerations of ψ_{DB} and ψ_{SD} will be given in the following section.

§ 6. Discussions.—In Relation to the Dielectric Loss in the Single Crystal

(*a*) *Piezoelectric Relation in the Dissipative Crystal*

In the piezoelectric crystals, the relation between stress and strain is complicated because of the piezoelectric coupling between electric and mechanical quantities. Denoting the electric field, polarization, stress and strain by E, P, T and S, we have alternative sets of relations, such as

$$\left.\begin{aligned} T&=c^P S-aP \\ E&=\chi^C P-aS \end{aligned}\right\}, \tag{6.1}$$

or

$$\left.\begin{aligned} T&=c^E S-eE \\ P&=\kappa^C E+eS \end{aligned}\right\}, \tag{6.2}$$

corresponding to different choices of independent variables. One set is derivable from another, and there seems to be no general argument in favour of any one of these sets.

In the ferroelectric substances, the dielectric loss may occur on account of the lag of reorientation of dipoles, and this suggests that polarization P is the proper independent variable to represent electrical state. Strain S is chosen for the mechanical variable, since it seems to be the less ambiguous measure for the internal elastic state. Then, Eq. (6.1) becomes fundamental relation between E, P, T and S, where the elastic constant and clamped

inverse susceptibility are complex, so that

$$c^P = c' + jc'' \quad \text{and} \quad \chi^C = \chi' + j\chi'' . \tag{6.3}$$

The piezoelectric coefficient a may also be complex and must be examined experimentally. However, the phase of a of the single domain crystal cannot be determined, using the present samples, which are of ceramic form. In the case of Rochelle salt, the piezoelectric coefficient f_{14}, which corresponds to a, has been shown to be unaffected by phase transition and considered as real by Mason[7]. Although $BaTiO_3$ differs from Rochelle salt in several important points, it may not be too unreasonable to assume here that a is real. Tan δ's of c^P and χ^C will be denoted by ψ and φ;

$$\psi = c''/c' \quad \text{and} \quad \phi = \chi''/\chi' . \tag{6.4}$$

(*b*) *Internal Friction and Dielectric Loss*

Tan δ of the elastic constant c^E for constant field and that of the free dielectric inverse susceptibility χ^F of the single domain crystal will be given by

$$\left.\begin{aligned} \psi(c^E) &= 1/(1-k^2)\cdot(\psi + k^2\varphi) \\ \varphi(\chi^F) &= 1/(1-k^2)\cdot(\varphi + k^2\psi) \end{aligned}\right\} , \tag{6.5}$$

where k is the appropriate electromechanical coupling coefficient and the second terms represent the piezoelectric coupling effect.

Although the elastic and dielectric constants of the ceramics may not be the simple averages of c^E and χ^F but depend on all the quantities, c^E, c^D, χ^F and χ^C of the single crystal, they may still be considered as the averages in some sense. Similar averaging may be considered for the phase of these quantities. Accordingly, denoting the internal friction and dielectric loss of ceramics by ψ^* and φ^* ($\psi^* = Q_m^{-1}$ and $\varphi^* = Q_e^{-1}$), they will be expressed as

$$\left.\begin{aligned} \psi^* &= A(\psi + f\varphi) + \psi' \\ \varphi^* &= A'(\varphi + f'\psi) + \varphi' \end{aligned}\right\} . \tag{6.6}$$

Experiments have shown that ψ^* as well as φ^* is almost the same for the unpolarized and the remanent-polarized states. The first term in the expression for ψ^* corresponds to ψ_{SD} in § 5. ψ' represents the dissipation except that within each domain; i.e. the dissipation in the grain boundary, in the domain boundary, etc. φ' is similarly the dielectrict loss due to the ceramic and domain structures.

In the prepolarized ceramics, the dissipation terms due to the macroscopic electromechanical coupling must be added to both formulae ($B\varphi'$ and $B'\psi'$ respectively). But, as the existence of the remanent polarization does not affect ψ^* and φ^*, these terms will not be considered here. (B and B' are of the order of k^{*2}, where k^* is the macro electromechanical coupling coefficient. As k^* is about 30%, these dissipations are at most 0.1×10^{-3} or less.)

The constants A, A', f and f' are certain averaged values and must depend on the distribution of domain orientations. But the absence of the differencs between the internal frictions of the unpolarized and prepolarized ceramics suggests that these constants are little influenced by the domain distributions.

The value of ψ' is supposed to be at most of the order of the value above T_C. Then it may be taken as

$$\psi' \lesssim (0.5 \sim 0.6)\times10^{-3} . \tag{6.7}$$

φ' may also be expected to be smaller than the dielectric loss above T_C, of which the dielectric tan δ of $\chi(=\chi^C=\chi^F)$ constitutes a main part; and then

$$\varphi' \ll 0.6\times10^{-3} . \tag{6.8}$$

At room temperature, the measured values of ψ^* and φ^* in sufficiently aged $BaTiO_3$ ceramics are

$$\left.\begin{aligned} \psi^* &\approx (3.1 \sim 3.8)\times10^{-3} , \\ \varphi^* &\approx (6 \sim 7)\times10^{-3} . \end{aligned}\right\} \tag{6.9}$$

When the relations

$$A = A' \quad \text{and} \quad f = f' \tag{6.10}$$

are assumed, and the values

$$f \approx 0.45 \sim 0.5 \tag{6.11}$$

are chosen, then

$$\left.\begin{aligned} &\psi \text{ is almost negligible} \\ &\varphi = (3 \sim 3.5)\times10^{-3} . \end{aligned}\right\} \tag{6.12}$$

Accordingly, most part of the internal friction ψ^* of the ceramics can be interpreted by the dielectric tan δ of χ^C in the clamped crystal, assuming a to be real.

(In the above discussions, the piezoelectric coefficient a has been assumed to be real. When a is complex and its tan δ is denoted by $\alpha/2$, another term $k^2/(1-k^2)\cdot\alpha$ must be added to both formulae in (6.5). Correspondingly, the term $Ag\alpha$ should be added to the first equation in Eq. (6.6) for ceramics and $A'g'\alpha$ to the second. But, if it is allowable to assume that $f = f' = g = g' \approx 0.45 \sim 0.5$, the magnitudes of ψ and α will be very small.)

This conclusion will be examined in the light of existing data on $BaTiO_3$. The interrelation among dielectric, piezoelectric and elastic properties of $BaTiO_3$ crystal has been investigated theoretically by Devonshire[10]. He ascribed the anomaly of $BaTiO_3$ to the dielectric one, and assumed that the elastic compliances s^P's for constant polarization did not vary at the transition. (It was shown that s^P varied at the transition by the amount corresponding to the change of the crystal lattice[9]. Its variation, however, is only of the order of 30%.) Accordingly, ψ, which is $\tan\delta$ of s^P, may be considered to be unchanged at the transition. Then, ψ may be smaller than 0.5×10^{-3}. As regards the electromechanical coupling coefficient, Mason *et al*[11] reported the value $k_{33}=67.5\%$ for the single crystal. From the reports of Devonshire and Mason, the values of the piezoelectric coupling for the single crystals that $k_{33}\sim65\%$, $k_{15}\sim80\%$ and $k_{31}\sim15\%$ will be used. As the constant f in Eqs. (6.6) is of the order of k^2, it may be permissible to assume that f is nearly equal to 0.5. The author has tentatively extended Marutake's calculation[12] on the physical constants of $BaTiO_3$ ceramics to the case of complex coefficients, and has also obtained $A=A'\sim1.9$ and $f=f'\sim0.48$. Above conclusions may, therefore, be permissible.

The frequency independence of the internal friction can be understood from the frequency-independence of dielectric loss already reported.

Biasing field causes the increase of the internal friction, while the dielectric loss is nearly independent of the bias, and so the increase of the internal friction cannot be interpreted by a change of φ. This may be mainly due to the increase of ψ_{DB}, which is presumably caused by the internal strains at the domain boundaries accompanying the 90° domain rotations (e.g. dislocations).

The amplitude dependence of the internal friction cannot be interpreted as that of φ, and it may be caused by the amplitude effect of the dissipation in the domain boundary or grain boundary. Further study will be desirable to elucidate these points.

The mechanism of the dielectric loss in the clamped crystal ($\tan\delta$ of χ^C) is not yet clear. Direct measurement of the phase of a on single domain crystals is also very desirable.

§ 7. Conclusions

From the preceding experiments and discussions, the following results are obtained:

(1) The internal friction of $BaTiO_3$ ceramics is dependent on vibration amplitude and biasing field, but independent of frequency and porosity in the range investigated.

(2) The main part of the internal friction of $BaTiO_3$ ceramics is the average of the dissipation of mechanical energy in the single domain crystals, and the dissipation due to the "ceramic" and domain structures is small.

(3) The dissipation in the single domain crystal cannot be considered to be the intrinsic mechanical loss, but considered to be caused by the dielectric $\tan\delta$ of χ^C of the clamped crystal, which acts through the piezoelectric coupling, assuming that the phase lag of the piezoelectric coefficient a is small.

In order to confirm the above conclusions, it is desirable that measurements are done on the internal friction, dielectric loss and the electromechanical coupling coefficients of the single crystal.

The author is very grateful for useful advice and discussions of Prof. H. Takahasi of the Tokyo University, and Dr. O. Nomoto and Mr. M. Marutake of the Kobayasi Institute. He also wishes to thank Mr. T. Nobuzawa and Mr. Y. Kanda of the Waseda University for their help to these experiments.

This study was supported partly by the Scientific Expenditure of the Ministry of Education.

References

1) H. G. Baerwald and D. A. Berlincourt: J. Acoust. Soc. Amer. **25** (1953) 703–710.
2) J. Kolb and T. F. Hueter: J. Acoust. Soc. Amer. **26** (1954) 139 (A).
3) T. F. Hueter, D. P. Neuhaus and J. Kolb: J. Acoust. Soc. Amer. **26** (1954) 696–703.
4) T. Ikeda: J. Acoust. Soc. Japan **11** (1955) 87–95 (in Japanese). Its main part was read at the meeting of the Acoustical Society of Japan on 14th, May, 1954.
5) W. P. Mason: Acustica **4** (1954) 200–2; J. Acoust. Soc. Amer. **27** (1955) 73–85.
6) T. F. Hueter and D. P. Neuhaus: J. Acoust. Soc. Amer. **27** (1955) 292–6.
7) W. P. Mason: Phys. Rev. **58** (1940) 744–56.
8) W. J. Price: Phys. Rev. **75** (1949) 946–52.
9) M. Marutake and T. Ikeda: J. Phys. Soc. Japan **10** (1955) 424–8.

10) A. F. Devonshire: Phil. Mag. **42** (1951) 1065–79.
11) W. L. Bond, W. P. Mason and H. J. McSkimin: Phys. Rev. **82** (1951) 442–3.
12) M. Marutake: J. Phys. Soc. Japan **11** (1956) 807–14.

JOURNAL OF THE PHYSICAL SOCIETY OF JAPAN Vol. 12, No. 8, AUGUST, 1958

The Thermoelectric, Galvanomagnetic and Thermomagnetic Effects of Monovalent Metals II
The Thermoelectric Powder for Anisotropic Media

By Mikio TSUJI

General Education Department, Kyushu University, Fukuoka

(Received April 23, 1958)

In the part I of this article, it has been shown that the thermoelectric power of monovalent metals at high temperatures is interpreted, at least semi-quantitatively, based on the spherical energy band model. However, it has also been shown that the model gives no possibility of the positive sign of the thermoelectric power of pure metals at low temperatures. Therefore, in this part II, the thermoelectric power at low temperatures is calculated for an arbitrarily anisotropic energy band. The results show that there is a possibility to give positive thermoelectric powder for pure metals at low temperatures if the shape of the energy surface is appropriate. The relation with the spherical band model used in I is discussed also.

§ 1. Introduction

In the previous paper[1] (to be referred to as I), we have investigated the thermoelectric effect and the transverse galvano- and thermomagnetic effects of monovalent metals using the model of the general spherical energy band, and have given an interpretation of the positive thermoelectric powers and the negative Ettingshausen and Ettingshausen-Nernst coefficients of noble metals at high temperatures. For the thermoelectric power of pure metals at low temperatures, however, the model of spherical band has given no possibility of the positive sign which are observed actually for noble metals[2]. As stated in I, for the change of the distribution function $f(\boldsymbol{k})$ of the conduction electrons due to the lattice scattering at high temperatures, each of the transitions to or from nearly all states $(\boldsymbol{k}')$ on the Fermi surface gives respective contribution to $(\partial f(\boldsymbol{k})/\partial t)_{\mathrm{coll}}$, and so the anisotropy is averaged out in a certain extent. The situation is quite similar in the scattering due to the impurity atoms or lattice defects. In these cases, the spherical band model is good, at least semiquantitatively, for the purpose of calculating the conductivities or thermoelectric power. (To calculate the magnetoresistance effect, it is necessary to take into account the anisotropy of the band structure even in these cases[3].) On the other hand, for the lattice scattering at low temperatures, only the electronic states $(\boldsymbol{k}')$ near the state $\boldsymbol{k}$ contribute to $(\partial f(\boldsymbol{k})/\partial t)_{\mathrm{coll}}$, and therefore $(\partial f(\boldsymbol{k})/\partial t)_{\mathrm{coll}}$ depends strongly on the local behaviour of the energy band near the state $\boldsymbol{k}$. Hence, in this case, the anisotropy of the band structure becomes important and the spherical band model becomes useless.

Therefore, in this paper, the electrical and thermal conductivities and the thermoelectric power of monovalent metals at low temperatures are calculated for an arbitrarily anisotropic energy band, and especially it is discussed qualitatively what kind of the band structure gives possibility of the positive thermoelectric power of pure noble metals at low temperatures. Since the effects of non-equilibrium distribution of the lattice waves give negative

contribution to the thermoelectric powers, the effects may be neglected for our purpose to investigate the possibility of the positive sign of the thermoelectric power.

Now, it is generally not easy to solve the Boltzman equation for the anisotropic energy band. Using the fact that the wave vectors of all the conduction electrons lie inside the Debye sphere of phonons for non-polar semiconductors, Radcliffe[4] has obtained the time of relaxation for arbitrarily anisotropic band structure. But his method can not be used in the case of monovalent metals.

Jones[5] has discussed qualitatively the thermoelectric power of noble metals based on the anisotropy of the band structure, but since his theory assumes the existence of the universal relaxation time, the theory can not be applied to the lattice scattering at low temperatures. However, the fact that the wave numbers of phonons which scatter the electrons are small compared to those of electrons on the Fermi surface makes the calculation tractable if we use the variational principle of Kohler[6] to obtain approximate solutions. Sondheimer's unpublished results of the calculation by such a method have been quoted by Wilson in his text-book[7]. But the calculations have had an important error. This is easily seen from the fact that the electrical conductivity σ given by (10.63.1) of Wilson's text becomes negative for a special case that the band structure is sherical and $(d^2E/dk^2)_{E=\zeta}$ is negative.

In § 2 a transport equation for a pure metal of anisotropic energy band at low temperatures is derived, and the solution of this equation is given in § 3, by using the variational principle. We discuss the results in § 4 and show:

(1) that the qualitative behavior of the temperature depence of the electrical and thermal conductivities is not modified essentially by the introduction of the anisotropy in the band structure,

(2) that the ratio of the electrical conductivity to the thermal conductivity at low temperatures is modified by the anisotropy, and

(3) that the thermoelectric power of pure metals at low temperatures is remarkably modified by the anisotropy, and if the feature of the band structure are appropriate, the thermoelectric power may become positive.

In § 5, the effects of the impurity scatterings are calculated and the relation between the calculation in this paper and the spherical band approximation used in I is discussed. Thus the meanings of the parameters α and β appeared in I become clearer.

§ 2. The Transport Equation

If the electric field $\boldsymbol{F}$ and the temperature gradient ∇T are in x direction, Boltzmann's equation can be written in the form,

$$\frac{1}{\hbar}\frac{\partial E}{\partial k_x}\frac{\partial f_0}{\partial E}\left(eF+T\frac{\partial}{\partial x}\frac{\zeta}{T}+\frac{E}{T}\frac{\partial T}{\partial x}\right)+\left(\frac{\partial f}{\partial t}\right)_{\text{coll}}=0\,, \tag{1}$$

where $f(\boldsymbol{k})$ is the distribution function of electrons, f_0 the Fermi distribution $(=1/(e^{\eta}+1)$, $\eta=(E-\zeta)/\kappa T)$, $-e$ the electronic charge, ζ the Fermi energy and the other simbols have their usual meanings. The collision term $(\partial f/\partial t)_{\text{coll}}$ is given by[8]

$$\begin{aligned}\left(\frac{\partial f}{\partial t}\right)_{\text{coll}}=\frac{C^2\Delta}{16\pi^3 M\kappa T}\int\frac{q^2}{\nu_q}N_q[&f_0(\boldsymbol{k})\{1-f_0(\boldsymbol{k}+\boldsymbol{q})\}\delta(E_{\boldsymbol{k}}-E_{\boldsymbol{k}+\boldsymbol{q}}+h\nu_{\boldsymbol{q}})\\&+f_0(\boldsymbol{k}+\boldsymbol{q})\{1-f_0(\boldsymbol{k})\}\delta(E_{\boldsymbol{k}}-E_{\boldsymbol{k}+\boldsymbol{q}}-h\nu_q)]\{\Phi(\boldsymbol{k}+\boldsymbol{q})-\Phi(\boldsymbol{k})\}d\boldsymbol{q}\,,\end{aligned} \tag{2}$$

where C is the interaction constant between electrons and lattice waves used by Wilson, Δ the volume of the unit cell, M the mass of lattice ion, $\boldsymbol{q}$ the wave number vector of phonon, ν_q the frequency of phonon, N_q the number of phonons of wave number $\boldsymbol{q}$, and Φ is given by

$$f=f_0-\Phi\frac{\partial f_0}{\partial E} \tag{3}$$

In (2), we have assumed that C does not depend on $\boldsymbol{k}$. Strictly speaking, C may depend on $\boldsymbol{k}$ and $\boldsymbol{q}$, but at low temperatures we may assume that C depends only on $\boldsymbol{k}$. However,

the effect of the anisotropy is derived principally from the geometry of the energy surface, and so we may neglect the dependency of C on $\boldsymbol{k}$ for the purpose of qualitative discussion.

Now, we put the solution of (2) in the form

$$\Phi = c(\eta)\frac{\partial E}{\partial k_z}\,. \tag{4}$$

The exact solution of (2) can not be written in such a simple from as (4) if the energy band is not spherical, but the physical quantities such as the electrical and thermal conductivities and the thermoelectric power calculated by the variational method take the stationary values when the trial function of Φ coincides with the exact solutions and so the physical quantities may be insensitive to the form of the trial function at least semiquantitatively. If we put (4) into (2), we can integrate with respect to the orientation of $\boldsymbol{q}$ and reduce the triple integral to a single integral as follows. We represent the vector $\boldsymbol{q}$ in the polar coordinates $(q, \vartheta, \tilde{\omega})$, in which the polar axis z' is taken in the direction of the outward normal vector $\boldsymbol{n}$ to the constant energy surface through the point $\boldsymbol{k}$ in the $\boldsymbol{k}$-space, (directed to the higher energy side), and the azimuthal angle $\tilde{\omega}$ is measured from the axis x' which are in the plane determined by z' and x axes. (See Fig. 1.) The radius of curvature ρ of the intersected curve between the energy surface and the plane determined by $\boldsymbol{n}$ and $\boldsymbol{q}$ vectors is given by

$$\frac{1}{\rho} = \frac{1}{\rho_1}\sin^2(\tilde{\omega}-\psi) + \frac{1}{\rho_2}\cos^2(\tilde{\omega}-\psi)\,, \tag{5}$$

where ρ_1 and ρ_2 are the two principal radii of curvature and ψ is the angle between x' axis and the dirction which gives the principal curvature $1/\rho_1$. The signs of ρ, ρ_1 and ρ_2 are taken to be positive if the centers of curvature C, C_1 and C_2 lie inside the energy surface and negative in the opposite case. Considering that $q \ll k \sim |\rho|$, we assume that the center of curvature of the intersected curve between the constant energy surface through the point $\boldsymbol{k}+\boldsymbol{q}$ and the plane determined by $\boldsymbol{n}$ and $\boldsymbol{q}$ vectors coincides with the center of curvature C. (See Fig. 2.) Then the radius of curvature ρ' is expanded in the form

$$\rho' = \rho + \left(q\cos\vartheta + \frac{q^2}{2\rho}\right) - \frac{1}{2\rho}\left(q\cos\vartheta + \frac{q^2}{2\rho}\right)^2 + \cdots\,, \tag{6}$$

in which it is noted that $q\cos\vartheta$ and q^2/ρ is the small quantities of the same order of magnitude from the energy conservation. The energy $E_{\boldsymbol{k}+\boldsymbol{q}}$ is expanded as

$$E_{\boldsymbol{k}+\boldsymbol{q}} = E_{\boldsymbol{k}} + \frac{\partial E}{\partial n}(\rho'-\rho) + \frac{1}{2}\frac{\partial^2 E}{\partial n^2}(\rho'-\rho)^2 + \cdots\,, \tag{7}$$

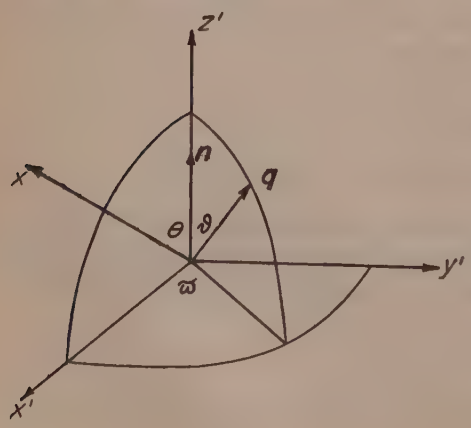

Fig. 1.

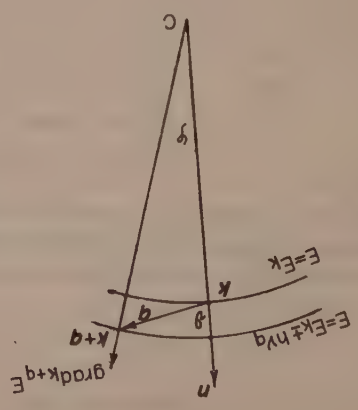

Fig. 2.

where $\partial E/\partial n$ $(=|\mathrm{grad}_k E|)$ and $\partial^2 E/\partial n^2$ are the derivatives of the energy E_k in the direction of $\boldsymbol{n}$. From (6) and (7) we have

$$E_{k+q}-E_k=\frac{\partial E}{\partial n}\left(q\cos\vartheta+\frac{q^2}{2\rho}\right)+\frac{1}{2}\left(\frac{\partial^2 E}{\partial n^2}-\frac{1}{\rho}\frac{\partial E}{\partial n}\right)\left(q\cos\vartheta+\frac{q^2}{2\rho}\right)^2. \tag{8}$$

Using (8), we can rewrite the δ-function in (2) in the form,

$$\begin{aligned}&\delta(E_{k+q}-E_k\pm h\nu_q)\\&=\frac{1}{q(\partial E/\partial n)}\left\{1\mp\frac{\partial^2 E/\partial n^2-(1/\rho)(\partial E/\partial n)}{(\partial E/\partial n)^2}h\nu_q\right\}\delta\left(\cos\vartheta+\frac{q}{2\rho}\mp\frac{h\nu_q}{q(\partial E/\partial n)}\right),\end{aligned} \tag{9}$$

in which we have used a theorem on the δ-function in which the argument is a quadratic from of a relevant variable. (See Eq. (11) in I.) In the term $\Phi(\boldsymbol{k}+\boldsymbol{q})-\Phi(\boldsymbol{k})$ in (2), if we use the form (4), there appear the terms of $\partial E/\partial k_x$ which are given by

$$\left(\frac{\partial E}{\partial k_x}\right)_k=\frac{\partial E}{\partial n}\cos\theta, \tag{10}$$

and

$$\left(\frac{\partial E}{\partial k_x}\right)_{k+q}=|\mathrm{grad}_{k+q}E|(\cos\varphi\cos\theta\pm\sin\varphi\cos\tilde{\omega}\sin\theta), \tag{11}$$

where φ is the angle shown in Fig. 2. The negative sign in (11) is taken in the case when the center of curvature C lies outside the energy surface. Now the contribution of the second term in the bracket of (11) vanishes when the Eq. (2) is integrated with respect to $\tilde{\omega}$, and so we neglect the second term hereafter. From the assumption that the two curves shown in Fig. 2 have a common center of curvature, we have

$$|\mathrm{grad}_{k+q}E|=\frac{\partial E}{\partial n}+\frac{\partial^2 E}{\partial n^2}(\rho'-\rho), \tag{12}$$

and from Fig. 2 and the energy conservation we have

$$\cos\varphi=1-\frac{q^2}{2\rho^2}\left(1\mp\frac{h\nu_q}{q(\partial E/\partial n)}\right). \tag{13}$$

Therefore, the first term of (11) becomes

$$\left(\frac{\partial E}{\partial k_x}\right)_{k+q}=\frac{\partial E}{\partial n}\cos\theta\left[1\pm\frac{\partial^2 E/\partial n^2}{(\partial E/\partial n)^2}h\nu_q-\frac{q^2}{2\rho^2}\left\{1\pm\left(\frac{\partial^2 E/\partial n^2}{(\partial E/\partial n)^2}-\frac{1}{\rho(\partial E/\partial n)}\right)h\nu_q\right\}\right]. \tag{14}$$

Putting (9), (10) and (14) into (2) and integrating with respect to $\tilde{\omega}$ and ϑ, we have

$$\begin{aligned}\left(\frac{\partial f}{\partial t}\right)_{\mathrm{coll}}=&-\frac{1}{\hbar\Lambda}\left(\frac{T}{\Theta}\right)^3\frac{\partial E/\partial k_x}{\partial E/\partial n}\frac{\partial f_0}{\partial E}\int_{-\Theta/T}^{\Theta/T}\left[\left\{1+\frac{\overline{(1/\rho)}}{\partial E/\partial n}\kappa Tz-\left(\frac{1}{\rho^2}\right)q_0^2\left(\frac{T}{\Theta}\right)^2z^2\right\}c(\eta+z)\right.\\&\left.-\left\{1-\frac{\partial^2 E/\partial n^2-\overline{(1/\rho)}\cdot\partial E/\partial n}{(\partial E/\partial n)^2}\kappa Tz\right\}c(\eta)\right]\frac{e^{\eta}+1}{e^{\eta+z}+1}\frac{z^2dz}{|1-e^{-z}|}\equiv-\frac{1}{\hbar}\frac{\partial E}{\partial k_x}\mathscr{L}(c),\end{aligned} \tag{15}$$

where $\Lambda^{-1}\equiv C^2\Delta hq_0^3/(8\pi^2Mu_0)$, $z\equiv h\nu_q/\kappa T$, Θ the Debye temperature, q_0 the maximum wave number of phonons, u_0 the sound velocity, and $\overline{(1/\rho)}$ and $\overline{(1/\rho^2)}$ are the average of $(1/\rho)$ and $(1/\rho^2)$ with respect to $\tilde{\omega}$. If we put

$$c(\eta)=\left(eF+T\frac{\partial}{\partial x}\frac{\zeta}{T}\right)c^{(1)}(\eta)+\frac{1}{T}\frac{\partial T}{\partial x}c^{(2)}(\eta),$$

the Boltzmann equation separates into two integral equations

$$E^{n-1}\frac{\partial f_0}{\partial E}=\mathscr{L}(c^{(n)}), \qquad n=1,\ 2. \tag{16}$$

Now, if the Fermi surface does not touch to the zone boundary, the effect of Umklapp processes may become negligibly small at low temperatures. But if the Fermi surfaces touches the boundary, we must not neglect, even at low temperatures, the Umklapp processes which are associated with the phonons of small wave numbers and transfer the states of the electrons near the zone boundary to the states near the same zone boundary in the adjacent zone (or the states near opposite boundary in the reduced zone scheme). We note here that in our calculation the Umklapp processes of this type are perfectly taken into account automatically.

§ 3. Solution of the Boltzman Equation

The variation principle used first by Kohler[6] states that the solution Φ of the Boltzmann equation is such as to make the integral

$$-\int \Phi\left(\frac{\partial f}{\partial t}\right)_{\text{coll}} dk \tag{17}$$

a maximum, subject to a certain subsidiary condition. In the present approximation, by putting (4) and (15) into (17), the integral (17) is replaced by

$$(c^{(n)},\ c^{(n)})=\kappa T\iint\frac{(\partial E/\partial k_x)^2}{\partial E/\partial n}c^{(n)}\mathscr{L}(c^{(n)})dSd\eta\,, \tag{18}$$

which is made a maximum, subject to the subsidiary condition

$$\kappa T\iint\frac{(\partial E/\partial k_x)^2}{\partial E/\partial n}c^{(n)}\mathscr{L}(c^{(n)})dSd\eta=\iint E^{n-1}\frac{(\partial E/\partial k_x)^2}{\partial E/\partial n}\frac{\partial f_0}{\partial \eta}c^{(n)}dSd\eta\,, \tag{19}$$

where dS is the surface element on the constant energy surface. Now if we put the trial function $c^{(n)}(\eta)$ in the form

$$c^{(n)}(\eta)=c_0{}^{(n)}+c_1{}^{(n)}\eta\,, \tag{20}$$

after the usual manipulation of the variational method, (See § 2 in I) we obtain the electrical conductivity σ, the thermal conductivity κ_T and the thermoelectric power S as follows;

$$\sigma=\frac{e^2}{4\pi^3\hbar}\frac{(\alpha_0{}^{(1)})^2}{d_{00}}\,, \tag{21}$$

$$\kappa_T=\frac{1}{4\pi^3\hbar T}\frac{(\alpha_0{}^{(1)}\alpha_1{}^{(2)}-\alpha_1{}^{(1)}\alpha_0{}^{(2)})^2}{(\alpha_0{}^{(1)})^2 d_{11}}\,, \tag{22}$$

$$S=-\frac{\kappa}{e}\frac{\alpha_1{}^{(1)}\alpha_2{}^{(1)}\,d_{00}-\alpha_0{}^{(1)}\alpha_2{}^{(1)}\,d_{01}+\alpha_0{}^{(1)}\alpha_1{}^{(1)}\,d_{11}}{(\alpha_0{}^{(1)})^2\,d_{11}}\,, \tag{23}$$

where

$$\alpha_r{}^{(n)}=\iint E^{n-1}\frac{(\partial E/\partial k_x)^2}{\partial E/\partial n}\frac{\partial f_0}{\partial \eta}\eta^r dSd\eta\,, \tag{24}$$

and

$$d_{rs}=\kappa T\iint\frac{(\partial E/\partial k_x)^2}{\partial E/\partial n}\eta^r\mathscr{L}(\eta^s)dS\,d\eta\,. \tag{25}$$

The calculations of $\alpha_r^{(n)}$ and d_{rs} are given in the appendix. Putting (24) and (25) into (21), (22) and (23), we have the final results:

$$\frac{1}{\sigma}=\frac{2\pi^2 h}{e^2\Lambda}\left(\frac{T}{\Theta}\right)^5 q_0^2\frac{f_3}{f_1^2}J_5\left(\frac{\Theta}{T}\right), \tag{26}$$

$$\frac{1}{\kappa_T}=\frac{18hT^2}{\Lambda\pi^2\kappa^2\Theta^3}\left\{1+q_0^2\left(\frac{T}{\Theta}\right)^2\frac{f_3}{f_2}\frac{\pi^2}{3}\right\}\frac{f_2}{f_1^2}J_5\left(\frac{\Theta}{T}\right), \tag{27}$$

$$S=-\frac{\pi^2\kappa^2 T}{3e}\frac{(f_2(df_1/dE)-f_1f_4)+(\pi^2/3)q_0^2(T/\Theta)^2\{2f_3(df_1/dE)-f_1(df_3/dE)\}}{f_1f_2\{1+(\pi^2/3)q_0^2(T/\Theta)^2\cdot f_3/f_2\}}, \tag{28}$$

where

$$J_n\left(\frac{\Theta}{T}\right)=\int_0^{\Theta/T}\frac{z^n dz}{(e^z-1)(1-e^{-z})},$$

and

$$\left.\begin{aligned} f_1&=\int\frac{(\partial E/\partial k_x)^2}{\partial E/\partial n}dS, & f_2&=\int\frac{(\partial E/\partial k_x)^2}{(\partial E/\partial n)^2}dS,\\ f_3&=\int\frac{(\partial E/\partial k_x)^2}{(\partial E/\partial n)^2}\left(\overline{\frac{1}{\rho^2}}\right)dS, & f_4&=\int\frac{(\partial E/\partial k_x)^2\,\partial^2E/\partial n^2}{(\partial E/\partial n)^4}dS,\end{aligned}\right\} \tag{29}$$

in which the integrations are taken on the constant energy surface in the first Brillouin zone. In Eqs. (26), (27) and (28), f_n ($n=1, 2, \cdots, 4$) and df_n/dE denote their values on the Fermi surface.

For the crystals which have cubic symmetry, (29) can be rewritten in simpler forms

$$\left.f_1=\frac{1}{3}\int\frac{\partial E}{\partial n}dS,\quad f_2=\frac{1}{3}\int dS,\quad f_3=\frac{1}{3}\int\left(\overline{\frac{1}{\rho^2}}\right)dS,\quad f_4=\frac{1}{3}\int\frac{\partial^2E/\partial n^2}{(\partial E/\partial n)^2}dS.\right\} \tag{30}$$

§ 4. Discussion

If the energy band is spherical, (30) becomes

$$\left.f_1=\frac{4\pi}{3}k^2\frac{dE}{dk},\quad f_2=\frac{4\pi}{3}k^2,\quad f_3=\frac{4\pi}{3},\quad f_4=\frac{4\pi}{3}k^2\frac{d^2E/dk^2}{(dE/dk)^2},\right\} \tag{31}$$

and so (26), (27) and (28) become

$$\frac{1}{\sigma}=\frac{3\pi hq_0^2}{2e^2\Lambda k_0^4\alpha^2}\left(\frac{T}{\Theta}\right)^5 J_5\left(\frac{\Theta}{T}\right), \tag{32}$$

$$\frac{1}{\kappa_T}=\frac{27hT^2}{2\pi^3\kappa^2k_0^2\alpha^2\Theta^3}\left\{1+\frac{\pi^2}{3}\frac{q_0^2}{k_0^2}\left(\frac{T}{\Theta}\right)^2\right\}J_5\left(\frac{\Theta}{T}\right), \tag{33}$$

$$S=-\frac{\pi^2\kappa^2T}{3e}\frac{2/\alpha k_0+\pi^2/3\,(4/\alpha k_0+2\beta/\alpha_2)(q_0^2/k_0^2)(T/\Theta)^2}{1+(\pi^2/3)(q_0^2/k_0^2)(T/\Theta)^2}, \tag{34}$$

(where $\alpha\equiv(dE/dk)_{E=\zeta}$ and $\beta\equiv(d^2E/dk^2)_{E=\zeta}$)

These results agree with Eqs. (29), (32) and (35) given in I. (Wilson's Eqs. (10.63.1) and (10.63.2) for σ and κ_T reduce to the right forms in the free electron model, but not in the general spherical band model.)

Now our results have been derived under the assumption that the temperature is much lower than the Debye characteristic temperature. But our results give the correct expression in the case of the spherical energy band and the model of the spherical energy band is ap-

proximately good at high temperatures at least semiquantitatively. Therefore, Eqs. (26), (27) and (28) may be regarded as an interpolation formulae which are valid at all temperatures at least semi-quantitatively. (There is a weak point, however, that these equations do not involve the effect of the Umklapp processes of usual type which are important at high temperatures and considered in I.)

From (26) and (27), it is seen that the temperature dependences of the electrical and thermal conductivities of the anisotropic media are not altered from those of isotropic media. This provides a justification of the usual approximation of spherical band model or the free electron model in the derivation of the temperature dependence of the electrical and thermal conductivities. The ratio of the electrical to thermal conductivities at low temperatures is given by

$$\frac{\sigma T^3}{\kappa_T}=\frac{9e^2}{\pi^4\kappa^2}\frac{\Theta^2}{q_0^2}\frac{f_2}{f_3}. \tag{35}$$

For the case of the spherical energy surface, the ratio f_2/f_3 becomes $(3\pi^2 n)^{2/3}$ where n is the number density of electrons. Klemens[10] has shown that the experimental values of $\sigma T^3/\kappa_T$ for monovalent metals are generally smaller than the theoretical values calculated by the assumption of the spherical energy band, and especially for noble metals, the experimental values are several times smaller than the theoretical values, and thus he has concluded that the Fermi surface of noble metals touches the zone boundary. These facts may be interpreted from our results as follows.

From (30), the ratio f_2/f_3 is given by

$$\frac{f_2}{f_3}=\int dS\Big/\int\left(\frac{1}{\rho^2}\right)dS$$

Now, in the region near the zone boundary, the Fermi surface may bulge outwards to the boundary, and the mean curvature should become larger than the curvature of the sphere of equal volume. Therefore, the value of the ratio f_2/f_3 would become smaller than the value expected for the spherical energy surface. Especially, if the Fermi surface touches the zone boundary, the absolute values of the principal curvatures $1/\rho_1$ and $1/\rho_2$ (one of which is negative) at the region near the zone boundary become very large, and so the value of the ratio f_2/f_3 would become very smaller than the value for the case of the spherical energy band.

The thermoelctric power of pure metals at low temperatures is given by

$$S=-\frac{\pi^2\kappa^2 T}{3e}\,\frac{f_2(df_1/dE)-f_1f_4}{f_1f_2}, \tag{37}$$

and, since f_1 and f_2 are positive, the sign of S is determined by the sign of $f_2(df_1/dE)-f_1f_4$. To calculate df_1/dE, we use the approximation of concentricity shown in Fig. 2, and, in (30), we expand $\partial E/\partial n$ and the surface element dS at the Fermi surface. Then $f_1(E)$ becomes

$$f_1(E)=\frac{1}{3}\int_{E=\zeta}\left[\frac{\partial E}{\partial n}+\left\{\frac{\partial^2 E}{\partial n^2}\left(\frac{\partial E}{\partial n}\right)^{-1}+2\left(\frac{1}{\rho}\right)\right\}(E-\zeta)\right]dS_0,$$

where dS_0 is the surface element on the Fermi surface. Therefore, we have

$$\left(\frac{df_1}{dE}\right)_{E=\zeta}=\frac{1}{3}\int_{E=\zeta}\left\{\frac{\partial^2 E}{\partial n^2}\left(\frac{\partial E}{\partial n}\right)^{-1}+2\left(\frac{1}{\rho}\right)\right\}dS_0, \tag{38}$$

and

$$9\left(f_2\frac{df_1}{dE}-f_1f_4\right)=\int dS\int\frac{\partial^2 E/\partial n^2}{\partial E/\partial n}dS+2\int dS\int\left(\frac{1}{\rho}\right)dS-\int\frac{\partial E}{\partial n}dS\int\frac{\partial^2 E/\partial n^2}{(\partial E/\partial n)^2}dS. \tag{39}$$

For the spherical energy band, (29) reduces to

$$2\int dS\int\frac{1}{k_0}dS=2(4\pi)^2k_0^3$$

and thus the thermoelectric power becomes negative as shown in I. Therefore, it must be the anisotropy of the band structure that gives the positive thermoelectric power for the pure noble metals at low temperatures.

For the anisotropic energy band, since the first and the third terms of the right side of (39) are of the same order of magnitude and of opposite signs, if the second term has large negative value, the thermoelectric power would become negative. (For the positive hole model, ρ (=constant) is negative and (39) becomes negative agreeing with the usual results.) Since, at present, the detailed behavior of the band structure is unknown, we can not calculate the right hand side of (39) with necessary accuracy. However, there might be a possibility of positive thermoelectric power if on the certain regions on the Fermi surface the mean curvature $(\overline{1/\rho})$ has very large negative value. As Klemens has shown, if the Fermi surface of noble metals touches to the zone boundary, the Fermi surface near the zone boundary must have a saddle type shape ($1/(\rho_1\rho_2)$ is negative), and the absolute value of the negative principal curvature would be larger than the positive principal curvature, and so $(\overline{1/\rho})$ would become negative.

However, since our results are only approximate solutions which may be good when the anisotropy is not so remarkable, further investigations must be required to obtain a decisive conclusion.

§ 5. Relation with the Spherical Band Approximation

Our method described in § 3 may be applicable approximately to the lattice scattering at high temperatures and the impurity scattering, if the anisotropy is not so remarkable. Therefore, by comparison of the results in these case with the results obtained in I based on the spherical band approximation, we can clarify the meanings of the parameters α and β appeared in I, where α and β have been defined based on the averaged spherical energy band which, however, have not clearly defined.

For the impurity scattering, the time of relaxation τ exists and it may be regarded approximately to be dependent of the energy of the $\boldsymbol{k}$ state only[3]. Therefore, the change of the distribution function due to the impurity scatterings can be written in the form,

$$\left(\frac{\partial f}{\partial t}\right)_i=-\frac{f-f_0}{\tau}=\frac{1}{\tau}\frac{\partial E}{\partial k_x}\frac{\partial f_0}{\partial E}c(\eta)\,. \tag{40}$$

This term gives to the electrical and thermal resistivities additional residual parts

$$\frac{1}{\sigma_i}=\rho_i=\frac{4\pi^3\hbar^2}{e^2f_1\tau}\,. \tag{41}$$

and

$$\frac{1}{\kappa_i}=\frac{12\pi\hbar^2}{\kappa^2f_1T\tau}\,, \tag{42}$$

respectively. Eqs. (41) and (42) coincide with more general expressions[11]

$$\sigma=\frac{e^2}{12\pi^3}\int\frac{\tau v^2dS}{|\mathrm{grad}_k E|}\,, \tag{43}$$

$$\kappa_T=\frac{\kappa^2T}{36\pi}\int\frac{\tau v^2dS}{|\mathrm{grad}_k E|}\,, \tag{44}$$

if we assume that τ depends only on the energy of electrons. If we use the spherical band

approximation, (41) and (42) agree with (28) and (31) in I. If we writte (28) and (31) in I in the form

$$\frac{1}{\sigma_i}=\frac{3\pi^2\hbar^2}{e^2k_0^2\alpha\tau}, \tag{45}$$

and

$$\frac{1}{\kappa_i}=\frac{9\hbar^2}{\kappa^2Tk_0^2\alpha\tau}, \tag{46}$$

and compare (45) and (46) with (41) and (42), we see that the parameter α appeared in I corresponds to

$$\alpha=\left\langle\frac{\partial E}{\partial n}\right\rangle, \tag{47}$$

where $\langle\ \rangle$ denotes the average on the Fermi surface.

For the thermoelectric power of impure metals, we easily obtain

$$S=-\frac{\pi^2\kappa^2T}{3e}\left[\rho_i\left(\frac{1}{f_1}\frac{df_1}{dE}+\frac{1}{\tau}\frac{d\tau}{dE}\right)+\rho_0\left\{\left(2\frac{1}{f_1}\frac{df_1}{dE}-\frac{1}{f_3}\frac{df_3}{dE}\right)+\left(\frac{\Theta}{T}\right)^2\frac{3}{\pi^2q_0^2}\left(\frac{f_2(df_1/dE)-f_1f_4}{f_1f_3}\right)\right\}\right]$$
$$\Big/\left[\rho_i+\rho_0\left\{1+\frac{3}{\pi^2q_0^2}\left(\frac{\Theta}{T}\right)^2\frac{f_2}{f_3}\right\}\right], \tag{48}$$

In (48), if we use the spherical band approximation to the term due to the impurity scatterings and the term which survive at high temperatures, we have

$$S=-\frac{\pi^2\kappa^2T}{3e}\left[\rho_i\left(\frac{2}{\alpha k_0}+\frac{\beta}{\alpha^2}+\frac{1}{\tau}\frac{d\tau}{dE}\right)+\rho_0\left\{\left(\frac{2\beta}{\alpha^2}+\frac{4}{\alpha k_0}\right)+\frac{3}{\pi^2q_0^2}\left(\frac{\Theta}{T}\right)^2\left(\frac{f_2(df_1/dE)-f_1f_4}{f_1f_3}\right)\right\}\right]$$
$$\Big/\left[\rho_i+\rho_0\left\{1+\frac{3}{\pi^2q_0^2}\left(\frac{\Theta}{T}\right)^2\frac{f_2}{f_3}\right\}\right], \tag{49}$$

and, therefore, we see that the parameter β appeared in I corresponds to

$$\beta\simeq\left\langle\frac{\partial E}{\partial n}\right\rangle\left\langle\frac{\partial^2E/\partial n^2}{\partial E/\partial n}\right\rangle. \tag{50}$$

From (47) and (50), the meanings of α and β have become clearer than those given in I. The exact expression of the parameter β in the case of complicated Fermi surface will not be written in such a simple form as (50). However, if we regard β as a phenomenological parameter which has the order of magnitude of the right hand side of (50), the calculations given in I would not lose general validity in the case of rather complicated band structure.

Appendix

Calculation of $\alpha_r^{(n)}$ and d_{rs}

The calculation of $\alpha_r^{(n)}$ is straightforward, and the results are as follows;

$$\alpha_0^{(1)}=-f_1,\qquad \alpha_0^{(2)}=-\zeta f_1,\qquad \alpha_1^{(1)}=-\frac{\pi^2}{3}\kappa T\frac{df_1}{dE},$$
$$\alpha_1^{(2)}=-\frac{\pi^2}{3}\kappa T\left(\zeta\frac{df_1}{dE}+f_1\right),\qquad \alpha_2^{(1)}=-\frac{\pi^2}{3}f_1. \tag{A-1}$$

The calculation of d_{00} and d_{11} is also straightforward, and we have

$$d_{00}=A^{-1}\left(\frac{T}{\Theta}\right)^5q_0^2f_3J_5\left(\frac{\Theta}{T}\right), \tag{A-2}$$

$$d_{11}=\Lambda^{-1}\left(\frac{T}{\Theta}\right)^3 f_2\left\{1+\frac{\pi^2}{3}q_0^2\left(\frac{T}{\Theta}\right)^2\frac{f_3}{f_2}\right\}J_5\left(\frac{\Theta}{T}\right). \tag{A-3}$$

We have neglected in d_{11} a term which has J_7, since this term gives numerically only a small contribution to d_{11} and is beyond our approximation.

d_{10} is given by

$$\begin{aligned} d_{10}=&-\Lambda^{-1}\left(\frac{T}{\Theta}\right)^3\int_{-\infty}^{\infty}d\eta\int_{-\Theta/T}^{\Theta/T}dz\int_{\eta=\text{const}}dS\frac{(\partial E/\partial k_x)^2}{(\partial E/\partial n)^2}\\ &\cdot\left\{\frac{\partial^2 E/\partial n^2}{(\partial E/\partial n)^2}\kappa Tz-\left(\overline{\frac{1}{\rho^2}}\right)\frac{q_0^2}{2}\left(\frac{T}{\Theta}\right)^2 z^2\right\}\frac{\eta}{(e^\eta+1)(e^{-\eta}+e^z)}\frac{z^2}{|1-e^{-z}|}\\ =&\Lambda^{-1}\left(\frac{T}{\Theta}\right)^3\kappa T f_4 J_5\left(\frac{\Theta}{T}\right)+\Lambda^{-1}\left(\frac{T}{\Theta}\right)^5\frac{q_0^2}{2}\iint\frac{f_3(E)\eta}{(e^\eta+1)(e^{-\eta}+e^z)}\frac{z^4}{|1-e^{-z}|}dzd\eta\\ =&\Lambda^{-1}\left(\frac{T}{\Theta}\right)^3\kappa T f_4 J_5\left(\frac{\Theta}{T}\right)+\Lambda^{-1}\left(\frac{T}{\Theta}\right)^5\frac{\pi^2}{3}\kappa T q_0^2\frac{df_3}{dE}J_5\left(\frac{\Theta}{T}\right). \end{aligned} \tag{A-4}$$

Here we have neglected also the term of J_7 arising from the integration which includes $f_3(E)$.

d_{01} is given by

$$\begin{aligned} d_{01}=&d_{10}+\Lambda^{-1}\left(\frac{T}{\Theta}\right)^3\iiint\left[\int\frac{(\partial E/\partial k_x)^2}{(\partial E/\partial n)^2}\left\{1+\left(\overline{\frac{1}{\rho}}\right)\left(\frac{\partial E}{\partial n}\right)^{-1}\kappa Tz\right\}dS\right]\frac{-z}{(e^\eta+1)(e^{-\eta}+e^z)}\frac{z^2dzd\eta}{|1-e^{-z}|}\\ &-\Lambda^{-1}\left(\frac{T}{\Theta}\right)^5\frac{q_0^2}{2}\iiint\left[\int\frac{(\partial E/\partial k_x)^2}{(\partial E/\partial n)^2}\left(\overline{\frac{1}{\rho^2}}\right)dS\right]\frac{-z^3}{(e^\eta+1)(e^{-\eta}+e^z)}\frac{z^2dzd\eta}{|1-e^{-z}|}. \end{aligned} \tag{A-5}$$

The second term of the right side of (A-5) vanishes, if we expand dS as

$$dS=dS_0\left\{1+2\left(\overline{\frac{1}{\rho}}\right)\left(\frac{\partial E}{\partial n}\right)^{-1}\kappa T\eta\right\},$$

and the third term gives a small term including J_7 which is neglected in our approximation. Thus we have

$$d_{01}=d_{10}, \tag{A-6}$$

from which Onsager's reciprocal relation can be derived easily.

References

1) M. Tsuji: J. Phys. Soc. Japan, **13** (1958) 133.
2) D. K. C. MacDonald and W. B. Pearson: Proc. Roy. Soc. **A219** (1953) 373. G. T. Pullan: Proc. Roy. Soc. **A217** (1953) 280.
3) R. Olson and S. Rodriguez: Phys. Rev. **108** (1957) 1212.
4) J. M. Radcliffe: Proc. Phys. Soc. **A68** (1955) 675.
5) H. Jones: Proc. Phys. Soc. **A68** (1955) 1191, Handbuch der Physik, Vol. 19, P. 277 (1956).
6) M. Kohler: Z. Phys. **124** (1948) 772, **125** (1949) 679.
7) A. H. Wilson: The Theory of Metals, 2nd ed. P. 323 (1953).
8) See for instance, A. H. Wilson: ibid, P. 260.
9) R. E. B. Makinson: Proc. Phys. Soc. **A67** (1954) 290.
10) P. G. Klemens: Australian J. Phys. **7** (1954) 70.
11) A. H. Wilson: loc. cit. Chapter 8.

JOURNAL OF THE PHYSICAL SOCIETY OF JAPAN Vol. 13, No. 8, AUGUST, 1958

An Order-Disorder Transformation Phenomenon in the $FeTiO_3$–Fe_2O_3 Solid Solution Series

By Yoshikazu ISHIKAWA*

Institute for Solid State Physics, University of Tokyo, Tokyo

(Received May 8, 1958)

The effects of heat treatments on the magnetic properties of the synthesized solid solution xFeTiO$_3$–$(1-x)$Fe$_2$O$_3$ of ilmenite and hematite were examined in detail for compositions x around 0.5. It was confirmed that a transformation from an ordered state (ferrimagnetic one) into a disordered state (antiferromagnetic one) takes place cooperatively at a distinct transition point. This transformation temperature is lowered with decrease in the ilmenite content from 1100°C for $x=0.65$ to 600°C for $x=0.45$. The completely disordered specimens could not be obtained for the composition $x \geqq 0.6$ by the quench method while the completely ordered state could not be attained in the specimens with $x \leqq 0.5$ because of decrease of the transformation temperature for these specimens and a reduction of the rate of ion diffusion at such low temperatures. The results obtained were discussed by using the Bragg-Williams approximation. It was noted briefly that the reverse thermo-remanent magnetism found in this system is closely related to the order-disorder transformation phenomenon which exists in this system.

§ 1. Introduction

The order-disorder transformation phenomenon which was first observed in a Cu–Au alloy[1] has been found in many substitutional binary alloys and investigations of this phenomenon have been carried out both experimentally and theoretically by many investigators. The results obtained have been reviewed in literatures[2].

On the other hand, such a transformation phenomenon has been observed very rarely in ionic compounds. This may be due to the situation that in the ionic compounds a change in the arrangement of cations usually increases the electrostatic energy greatly.

There are many magnetic oxides whose magnetic properties are greatly affected by the heat treatment. For example, in magnesium ferrite, $MgFe_2O_4$, which has a nearly inverse spinel structure and has the saturation moment of 1.1 μ_B when prepared by cooling slowly, the intensity of magnetization increases when it is quenched from high temperatures. This phenomenon is interpreted as a result of an increase in the magnesium content on the tetrahedral sites in the quenched specimen. Pauthenet and Bochirol have reported[3] that the value of x varies with temperature according to a Boltzmann distribution law given by Néel[4]:

$$x(1+x)/(1-x)^2=\exp(-E/T)\,,$$

where E is an energy involved in an interchange of a Mg ion on an octahedral site and a Fe ion on a tetrahedral site and is 1200°K for $MgFe_2O_4$. We can see by this equation that the change in the distribution of cations in this specimen does not take place cooperatively because for a cooperative phenomenon E must depend on x.

On the other hand, a change in the distribution of Li ions on the octahedral sites in $LiFe_5O_8$[5] or a change in the arrangement of holes in FeS_x[6] has been reported to take place cooperatively, but detailed investigations of such cooperative phenomena have not yet been made.

We have reported in previous paper that the magnetic properties of the solid solution of $FeTiO_3$ and Fe_2O_3: xFeTiO$_3$–$(1-x)$Fe$_2$O$_3$ are greatly affected by the heat treatment. For example, the specimen with x around 0.5 which is feebly ferromagnetic when it is quenched from 1200°C can be changed to strongly ferrimagnetic by an appropriate heat treatment[7]. Such a change in the magnetic properties by the heat treatment makes the magnetic properties of this series very complicated. It is, therefore, necessary to examine

* Present address; Department of Applied Physics, Faculty of Engineering, Tokyo University, Tokyo.

more carefully how these properties are affected by various heat treatments.

In the course of these experiments, we have found the change in the magnetic properties takes place cooperatively having a distinct transition point for the specimens with x around 0.5. As we have expected in the previous papers[7),8)] that the ferrimagnetism and feeble ferromagnetism in this series are correlated with the crystal symmetries $R\bar{3}$ and $R\bar{3}C$ respectively, this phenomenon may be explained as a kind of order-disorder transformation phenomenon where Ti and Fe ions are distributed at random in the feebly ferromagnetic specimen, while are arranged in order in the ferrimagnetic one. Hence it may be worthwhile to examine whether such a transformation phenomenon in the ionic compound can be explained by the theories which have been successfully applied to the order-disorder transformation phenomena observed in many alloys.

§ 2. Experimental Procedure

In order to investigate the order-disorder transformation phenomenon in the solid solution series, it must be necessary, first of all, to recognize what physical quantity is most affected by the heat treatment. We have reported in the previous paper that the electrical conductivity and Seebeck voltage have little correlation with the change of crystal symmetry[9)]. On the other hand, as the order-disorder transformation temperature lies far above the Curie temperature of the specimen and the magnetic susceptibility at such a high temperature was found to be little affected by the heat treatment[8)], the change in the ordering can not be observed directly at the temperature where such a change really occurs even by the magnetic method. Hence we detected the degree of order at a desired temperature of the specimen by measuring the intensity of magnetization at room temperature of the specimen quenched from that temperature where it had been left in thermal equilibrium.

The experiments were carried out by using six specimens having the composition x around 0.5, which had been prepared in advance by the method described in the previous paper[8)]*. Each specimen was sealed into a quartz capsule which was carefully evacuated to an approximated oxygen pressure so as not to reduce or oxidize the specimen or not to precipitate the spinel phase during the heat treatment. Then, the specimen was placed in a furnace and after having been annealed at a constant temperature until its equilibrium state it was quenched into water. It was confirmed that it required more than twenty four hours to attain the equilibrium state at low temperatures (400~500°C), only one hour at high temperatures (>700°C). The variation of the intensity of magnetization of the quenched specimen with temperature was measured in a field strength of 8500 Oe in order to find the Curie temperature of the specimen. This procedure can be carried out without disturbing the arrangement of cations because the Curie temperatures of all specimens used in this experiment are below 300°C and a rearrangement of cations can hardly take place at such low temperatures. By repeating the same procedure for the specimen quenched from each temperature on both heating and cooling processes we obtained the variation of the intensity of magnetization at room temperature with the quenching temperature for each specimen. The quenching temperature was limited below 1250°C, above which the oxygen ions might flow into the quartz capsule through its wall.

§ 3. Experimental Results

The results obtained by the above procedure were shown in Figs. 1–6. (a) of these figures show the variation of the magnetization at room temperature with the quenching temperature and (b) the thermomagnetic curves of the specimen when it was quenched from the temperature attached to each curve. In Fig. 1, a case for $x=0.51$ is given, where we found the magnetization at room temperature decreases with the quenching temperature and disappears sharply at 790°C. As we shall show in the latter section the magnetization at room temperature is approximately proportional to the long range order parameter S introduced by Bragg and Williams, hence we can consider this curve indicates the variation of the long range order with temperature. From this figure we can understand that the change in the magnetization or the crystal

* This paper will be referred to as I hereafter in this paper.

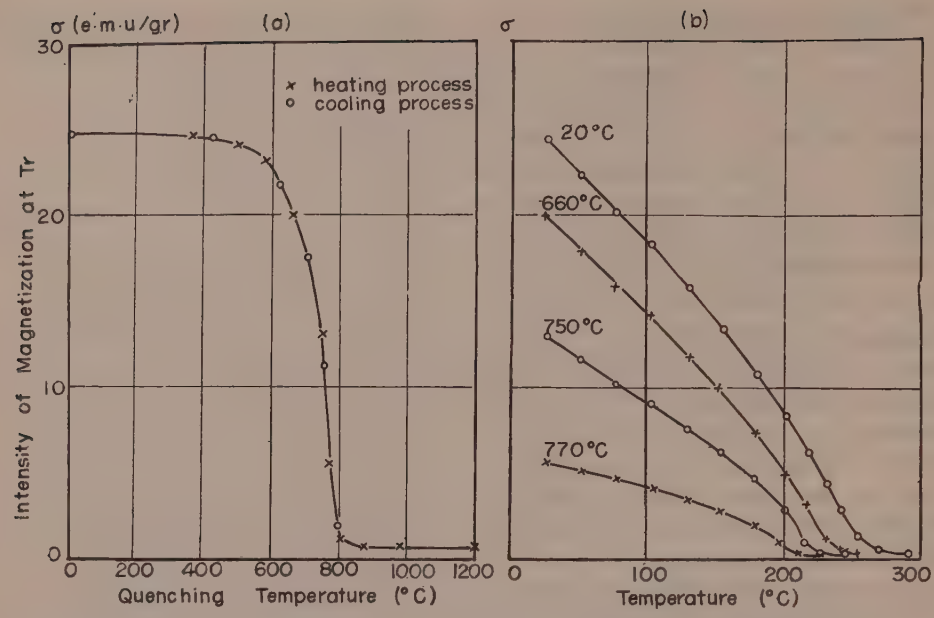

Fig. 1 (a). The variation of magnetization at room temperature of a specimen with $x=0.51$ *vs.* quenching temperature. (b). The thermomagnetic curves of the specimen quenched from temperatures attached to each curve. The magnetization is measured in a field strengh of 8500 Oe.

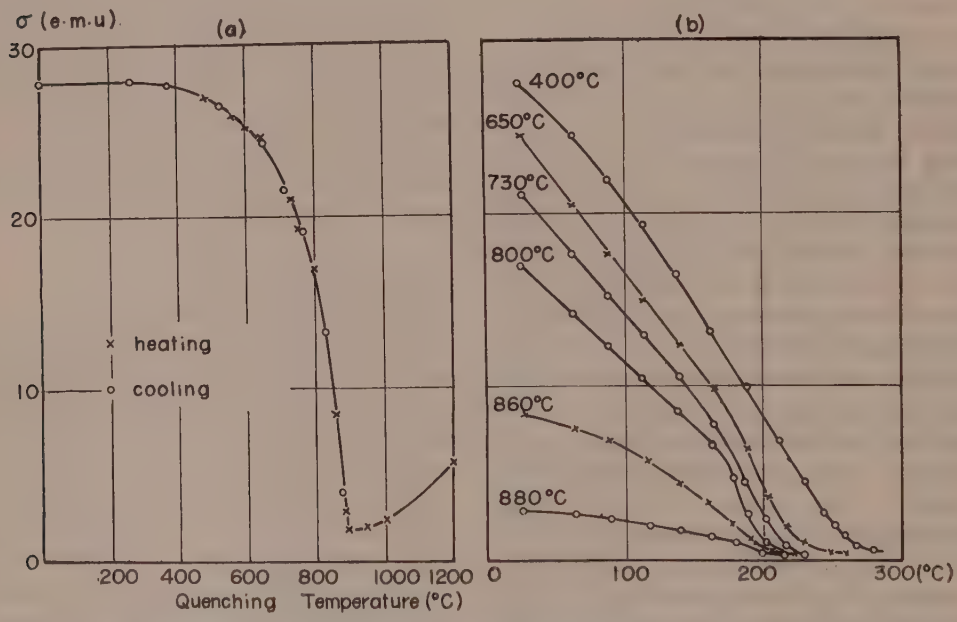

Fig. 2 (a). The variation of magnetization at room temperature of a specimen with $x=0.56$ *vs.* quenching temperature. (b). The thermomagnetic curves of the specimen quenched from temperature attached to each curve.

symmetry takes place cooperatively at a definite transition temperature. Furthermore we found the magnetizations measured on both heating and cooling processes accord well and no temperature hysteresis was observed at the critical temperature. It may, therefore, be concluded that this transition is of the second order. We found from Fig. 1(b) that when the specimen was quenched from higher temperatures and hence the magneti-

zation at room temperature was decreased, the Curie temperature was shifted to the low temperature side. Such a tendency has already been reported in I, where we showed only two extreme values in the perfectly ordered and the perfectly disordered states.

In Fig. 2(a) the variation of the magnetization at room temperature of the specimen for $x=0.56$ with the quenching temperature was shown. The magnetizations measured on both heating and cooling processes were also found to accord with one another. This curve is

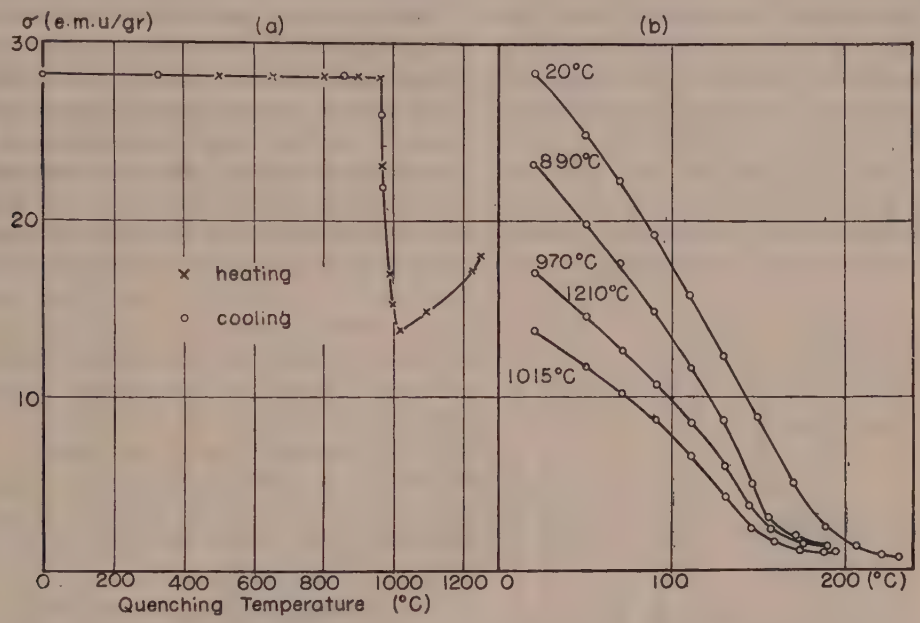

Fig. 3 (a). The variation of magnetization at room temperature of a specimen with $x=0.61$ *vs.* quenching temperature. (b). The thermomagnetic curves of the specimen quenched from temperature attached to each curve.

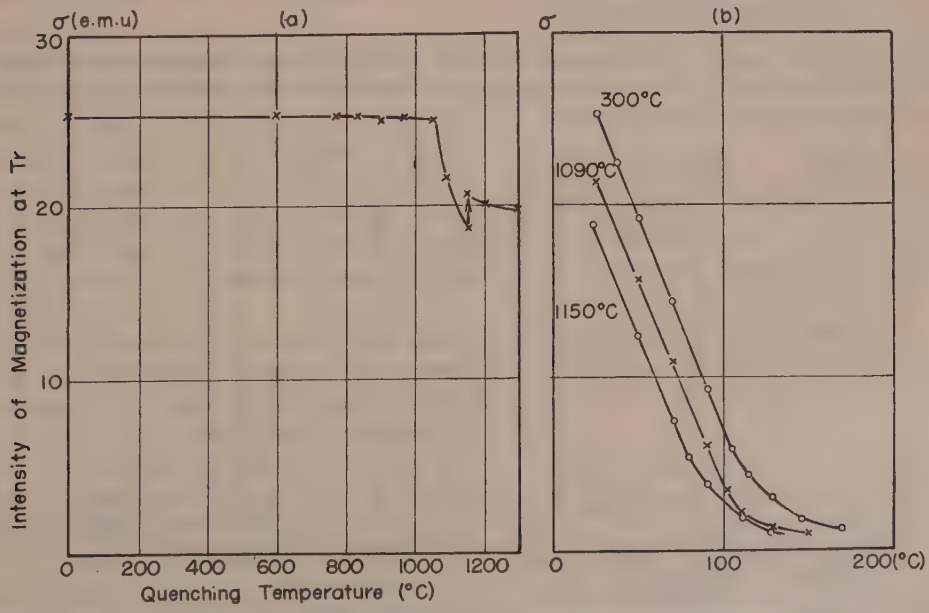

Fig. 4 (a). The variation of magnetization at room temperature of a specimen with $x=0.68$ *vs.* quenching temperature. (b). The thermomagnetic curves of the specimen quenched from temperature attached to each curve.

very similar to the one found in Fig. 1(a), but the transition temperature is raised up to 890°C in this case. Futhermore it must be noticed in the figure that when the specimen was quenched from a temperature higher than the critical temperature the magnetization at room temperature was rather increased. This strange phenomenon was observed in all specimens with x greater than 0.56. From Fig. 2(b) we fined the variation of the Curie temperature with the quenching temperature is similar to the case for $x=0.51$. In Fig. 3(a) a case for $x=0.61$ is shown. We find from the figure the situation is very different from the two former cases. In this case the decrease of magnetization began rather sharply at 960°C attaining to a minimum value at 1000°C. When the quenching temperature was higher than 1000°C the magnetization at room temperature was increased and the feebly ferromagnetic specimen or perfectly disordered one could not be obtained for this composition. In Fig. 4(a) a case for $x=0.68$ is snown, where we find the decrease in the magnetization at room temperature began to take place at the quenching temperature 1050°C, but the decrease is very small. It must be noticed, as we showed in the figure by an upward arrow, that when the specimen was quenched from 1150°C and the magnetization of the quenched specimen was measured soon after the quenching it took the value

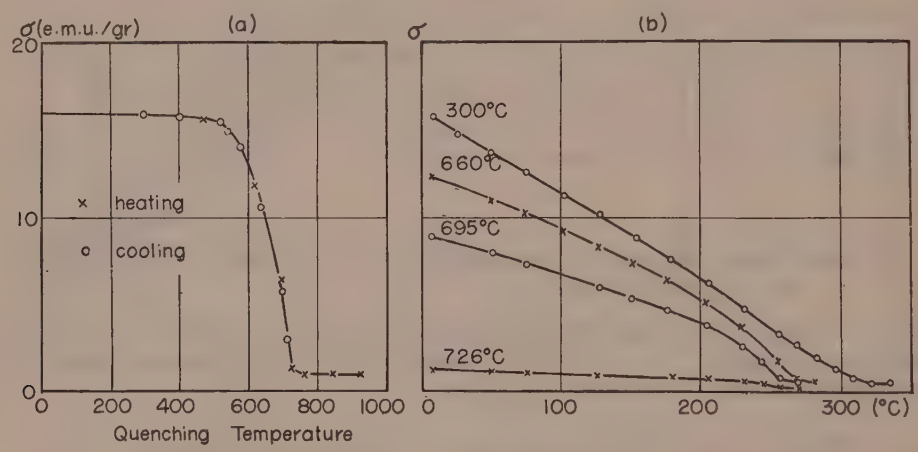

Fig. 5 (a). The variation of magnetization at room temperature of a specimen with $x=0.48$ *vs.* quenching temperature. (b). The thermomagnetic curves of the specimens quenched from temperatures attached to each curve.

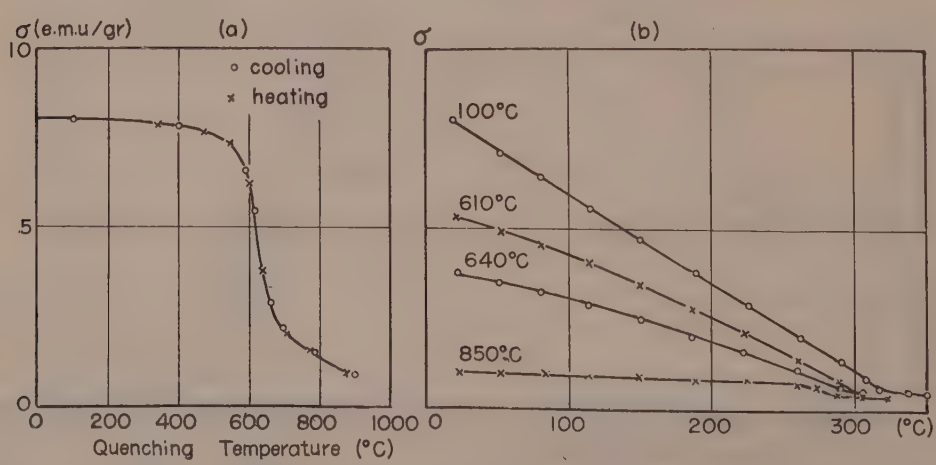

Fig. 6 (a). The variation of magnetization at room temperature of a specimen with $x=0.465$ *vs.* quenching temperature. (b). The thermomagnetic curves of the specimens quenched from temperatures attached to each curve.

18.6 e.m.u./gr at room temperature, but it was found to be increased up to 20.5 e.m.u./gr after keeping it at room temperature for a day, which means a recovery process can take place even at room temperature for this specimen. The decrease of the Curie temperature with the decrease in the magnetization at room temperature was also observed in both cases of $x=0.61$ and 0.68 as Figs. 3(b) and 4(b) show. It must be noticed in Fig. 3(b) that the thermomagnetic curves of the specimens quenched from 1210C° and 970°C accord well with one another, which suggests that the phenomenon of the reincreasement of the magnetization at room temperature above the critical temperature is not due to a different ordering mechanism but is due to a recovery of the ordering during a short period of the quenching which may be longer when the quenching temperature is higher. It is also expected that when the quenching temperature is higher the crystal imperfection is increased in the specimen, which may promote the rate of ordering in the recovery process as has been reported in the case of Cu_3Au alloy[10),11)]. The situation that the short range order might not be destroyed completely at about 1200°C in the specimen of the higher ilmenite content may also contribute to this phenomenon. It was thus found that the disordered state can not be established in the specimens for $x \geqq 0.6$.

On the other hand, in cases of $x=0.48$ and $x=0.465$, we can also find the critical temperature as are shown in Figs. 5(a) and 6(a), but the maximum values of the magnetization at room temperature are considerably smaller compared with those of the specimens with $x \geqq 0.5$, indicating the perfect ordering can not be established in these specimens at any cost. This situation may be explained by a fact that the transition temperatures were lowered to 700~600°C in these specimens. As the rate of diffusion of cations is greatly reduced when the annealing temperature is lowered below 500°C, the establishment of the ordered state becomes very difficult in these specimens. By carefully comparing Fig. 1(a) with Fig. 2(a), we may expect even in the specimen with $x=0.51$ the perfect ordering is not established. We have thus understood the situation that when the content of Fe_2O_3 exceeds 50 mol percent the saturation value of magnetization of the annealed specimen decreases sharply as has been reported in I. In every cases the magnetizations measured on both heating and cooling processes accord well each other and so the transition is expected to be that of the second order.

Through these results we have confirmed

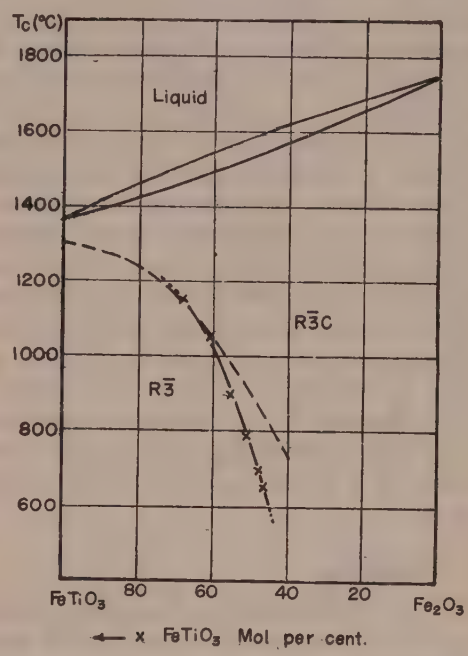

Fig. 7. The phase diagram of the $FeTiO_3$–Fe_2O_3 system. Cross marks indicate transition points determined experimentally, while a broken line is calculated by using the Bragg-Williams approximation.

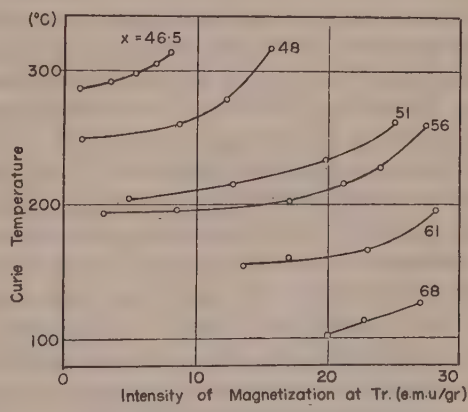

Fig. 8. The variation of the Curie temperature with the magnetization at room temperature or with the long range order parameter. Numerals attached to each curve indicate the $FeTiO_3$ mol. per cent.

that though the magnetization of all specimens used in this experiment is affected by the heat treatment, the transition from the perfectly ordered state to the perfectly disordered state is observed only in the specimen with $x=0.56$.

The critical temperatures of these specimens thus obtained are plotted in Fig. 7 against the composition. The liquidus-solidus lines drawn in the figure were estimated from the melting points of $FeTiO_3$ and Fe_2O_3. We can estimate from the figure that the critical temperature of the specimen with $x=0.4$ is about 550°C, hence the increase in the magnetization by annealing can not be expected in the specimen with x less than 0.4. In Fig. 8 we showed the variation of the Curie temperature with the magnetization at room temperature or with the degree of long rang order. As this figure shows all curves have the same characteristics that the rate of decrease in the Curie temperature is large for a slight decrease in the degree of order from the perfectly ordered state but its rate is decreased for a further decrease in the degree of order.

§ 4. Discussion

We have investigated in the above section the effect of the heat treatment on the magnetic properties and expected that the transformation from the ferrimagnetic state to the antiferromagnetic state corresponds to the transformation of the arrangement of cations from the ordered state to the disordered state. In order to confirm this expectation a neutron diffraction analysis was conducted by G. Shirane *et al* in both quenched and annealed specimens of $x=0.5$ and found that diffraction lines indexed by (100) and (111) were intensified greatly in the annealed specimen[12]. This fact indicates that the ordering of Ti and Fe ions was established by the annealing process, while patterns in the quenched specimen can be interpreted by assuming the disordering of Fe and Ti ions. We have, thus, confirmed that the phenomenon which we observed in the solid solution is a kind of order-disorder transformation, hence in this section we shall try to discuss this phenomenon by using the Bragg-Williams approximation.

In order to simplify the problem we neglect the difference between Fe^{+2} and Fe^{+3} ions. Such a simplification may be permissible because the interchange of the positions of Fe^{+2} and Fe^{+3} ions can take place merely through the electron transfer and therefore the required energy for an interchange of Fe^{+2} and Fe^{+3} ions is negligible compared with that of Ti and Fe ions. Hence the order-disorder transformation phenomenon in the solid solution $xFeTiO_3\cdot(1-x)Fe_2O_3$ is reduced to that in a binary alloy of $Fe_{2-x}Ti_x$. Since, as we have showed in I, the cation sites can be divided into four sublattices A_1, A_2, B_1 and B_2 in the rhombohedral structure, two types of superstructures among these four sublattices are possible in the Fe–Ti system. One is at FeTi and the other at Fe_3Ti. The former corresponds to pure ilmenite and the latter to the solid solution of $0.5\,FeTiO_3\cdot 0.5\,Fe_2O_3$. Though the former is really observed in pure ilmenite[13], the latter is not expected to exist because the critical temperature does not show any anomalous change for x around 0.5 in Fig. 7. Accordingly, we can neglect the difference between A_1 and A_2 or B_1 and B_2 in this system as we did in I. Then, the problem is reduced to a case where two kinds of cations Fe and Ti are distributed among two sublattices A and B. Let the total number of cations in one mol be, N. If f_{Fe} denotes the fraction of Fe ions, $f_{Ti}=1-f_{Fe}$ denotes that of Ti ions. As the fraction of A sites r_A does not generally agree with f_{Fe} in this system we put $f_{Fe}=r_A+\delta$, where $\delta \gtrless 0$ in our case. Accordingly f_{Ti} is given by $f_{Ti}=1-r_A-\delta$. Next we shall describe the fraction of A sites occupied by Fe ions by P_A which takes the value 1 in the perfectly ordered state and $r_A+\delta$ in the disordered state. We shall define the long range order parameter S as

$$S=\frac{P_A-r_A-\delta}{1-r_A} \qquad (1)$$

in this paper which takes the maximum value

$$S_m=1-\frac{\delta}{1-r_A} \qquad (2)$$

in the perfectly ordered state and is zero in the disordered state. The numbers of Fe ions on A sites [Fe/A] and on B sites [Fe/B] are expressed by using the above quantities as

$$[Fe/A]=P_A r_A N\,,$$
$$[Fe/B]=(r_A+\delta)N-[Fe/A]=(r_A+\delta-P_A r_A)N\,. \qquad (3)$$

If we assume the magnetic moments of one kind of sublattice are aligned in the same direction, coupling antiferromagnetically with those of another kind of sublattice, the resultant magnetization per mol J_s at 0°K is given by

$$J_s = J_{Fe}[Fe/A] - J_{Fe}[Fe/B] = J_{Fe}N(2P_A r_A - r_A - \delta)$$
$$= J_{Fe}N[2(1-r_A)r_A S + (2r_A - 1)(r_A + \delta)] , \quad (4)$$

where J_{Fe} is the magnetic moment of a Fe ion. In case of $Fe_{2-x}Ti_x$ Eq. (4) is reduced to

$$J_s = J_{Fe}S , \quad (5)$$

since $N=2N_a$, $r_A=\frac{1}{2}$ and $\delta=\frac{1}{2}(1-x)$, where N_a is the Avogadro number. This equation means that the resultant magnetization at 0°K is proportional to the long range order parameter S. In the actual case, the measurement is carried out at room temperature and the magnetization on the A sublattice is expected not to be saturated. The ordinates in Figs. 1–6(a), therefore, are not necessarily proportional to S in a strict meaning, but we can approximately say that these curves express the change in the degree of order with the temperature. In the perfectly ordered state, J_s is given as

$$J_s = J_{Fe}[1-(1-x)] = xJ_{Fe} = 4x . \quad (6)$$

The long range order parameter S can be calculated by the Bragg-Williams method and is found to be

$$S = 1 - 2\frac{\{(e^y + \delta^2(e^y-1)^2\}^{1/2} - 1}{e^y - 1} \quad (7)$$

in which $y = V/RT$ and the ordering energy V is assume to be

$$V = V_0 S \quad (8)$$

following the Bragg-Williams assumption[14]. The transition temperature T_c obtained from Eqs. (7) and (8) is

$$T_c = (V_0/4K)(1-4\delta^2) = (V_0/4K)x(2-x) . \quad (9)$$

In Fig. 9 we showed by the solid line the behavior of $S(T)$ obtained from Eqs. (7) and (8) by a graphical method in case of $x=0.56$ for which composition the most typical order-disorder transformation phenomenon could be observed. The broken line in the figure indicated the experimental results for $x=0.56$. Considering the roughness of the theory and the simplification made in the calculation, the agreement is rather well and the theoretical curve would approach to the experimental values if the short range order were taken into account. The variation of critical temperature with the composition x was also calculated from Eq. (9) by assuming $(V_0/4K)=1300$°K and the result was drawn by the broken line in Fig. 7. We found from the

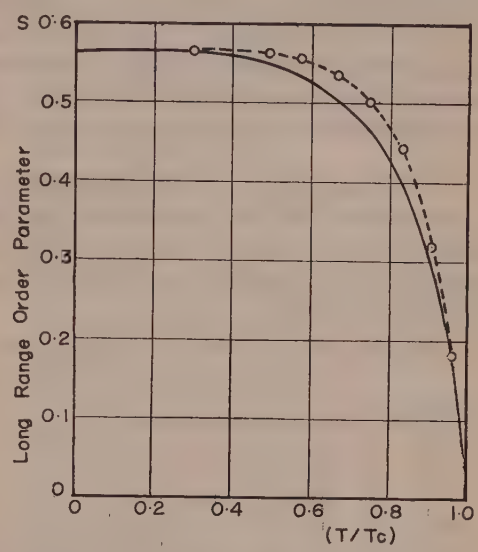

Fig. 9. The dependence of the long range order parameter $S(T)$ calculated in a case of $x=0.56$ upon temperature. Hollow marks indicate the the experimental results.

figure our theory explains well a tendency of the decrease of critical temperature with the composition. The deviation of the theoretical curve from the experimental result may be due to an effect of the short range order. We have thus found the order-disorder transformation phenomenon observed in the $FeTiO_3$–Fe_2O_3 solid solution series could be fairly well explained by the Bragg-Williams approximation.

On the other hand, the decrease in the Curie temperature with the decrease in the degree of order must be attributed to the situation that the number of pairs between Fe^{+2} and Fe^{+3} ions decreases and that between Fe^{+2} and Fe^{+2} ions increase with the decrease in the degree of order as we discussed in detail in I. It is, therefore, very difficult to obtain the dependence of the Curie temperature on the long range order parameter S because for this purpose we must distinguish Fe^{+2} from Fe^{+3} which difference has been neglected in our theory.

§ 5. The Reverse Thermo-Remanent Magnetism

The queer phenomenon of the reverse thermo-remanent magnetism* or shortly reverse TRM, was first discovered for certain ferromagnetic oxide minerals containing the ilmenite-hematite solid solution by T. Nagata S. Uyeda and S. Akimoto[15]. Uyeda has conducted a series of detailed studies on the mechanism of this phenomenon[16),17]. Main results of his study will be summarized as follows:

(1) The phenomenon of reverse TRM, being found not only in natural but also in synthesized solid solution series $x\mathrm{FeTiO_3}$–$(1-x)\mathrm{Fe_2O_3}$, is an intrinsic property of the solid solution series.

(2) Among the solid solution members, only those with $0.7 > x \geqq 0.45$ show the reverse TRM whereas those with different x values show only normally directed TRM as is shown in Fig. 10: the reverse TRM is a peculiar property of the specimens which show the order-disorder transformation dealt with in the present paper.

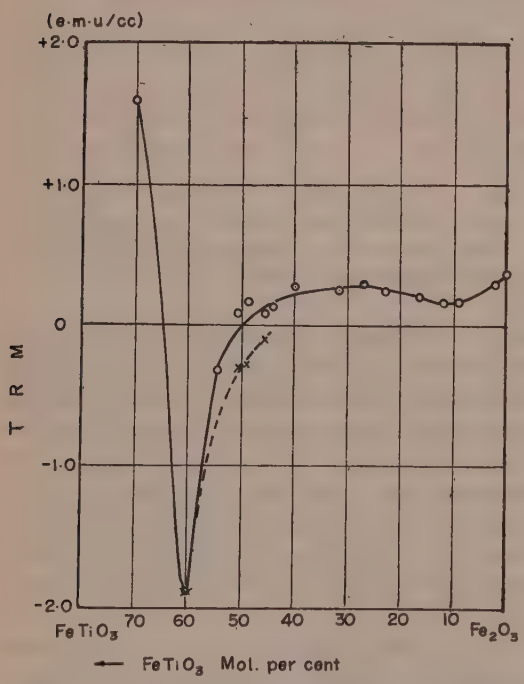

Fig. 10. The intensity of thermo-remanent magnetization at room temperature *vs.* composition: T R M plotted are the total T R M produced by field cooling in $H=2.0$ Oe.
○ Specimens quenched from 1200°C.
× Onnealed specimens.
(after Uyeda[17])

(3) As for the specimens showing the order-disorder transition, the TRM is normally directed in the disordered state and the reverse TRM develops with the increase of the degree of order. The reverse TRM seems to be preserved in the specimen which have seemingly been attained to the completely ordered state by prolonged heat treatment.

(4) When the composition and the degree of order of a specimen is properly chosen, the reverse TRM occurs even when the magnetic field applied during cooling is as intense as 2×10^4 Oe. Consequently, the origin of the phenomenon is considered to be related with a superexchange interaction and not with macroscopic magneto-static one, such as demagnetizing field.

Uyeda's study has further indicated the existence of weakly ferromagnetic second phase in the specimen having the reverse TRM and the Curie point of the second phase should be higher by 30~50°C than that of the bulk. Based upon these results, he considered the origin of the phenomenon as follows[17]. In the specimens with $0.70 > x \geqq 0.45$ of $x\mathrm{FeTiO_3}$–$(1-x)\mathrm{Fe_2O_3}$, a parasitically ferromagnetic disordered phase (A-phase) coexists with a ferrimagnetic ordered phase (B-phase), where $T_{cA} > T_{cB}$, the boundaries between them being in a good registry. The spins in the two phase are coupled in a way that their spontaneous magnetizations (J_s) are directed antiparallelly by some unknown mechanism related to the superexchange force over their boundaries. If such is the case, when the specimen undergoes a field cooling from above T_{cA}, the spins of the parasitically ferromagnetic phase are aligned in the direction of the field first, and then the spins of the ferrimagnetic phase are directed reversely. In order to explain the fact that the reverse TRM property is preserved even after the ordering has apparently completed, Uyeda pointed out that it would be necessary to assume some mechanism of "fossilization" of the disordered phase in the ordered matrix. However, ac-

* The reverse TRM is a phenomenon that the residual magnetization which a ferromagnetic specimen acquires when it is cooled through the Curie point in a magnetic field is oppositely directed to that of the applied field.

cording to our study reported in this paper, the Curie point was found to rise considerably with the increase of the degree of order. Therefore, it seems unlikely that the second phase (A-phase) is the residual part left disordered during the process of formation of the order. We should rather like to assume that the second phase (A-phase) may be something related with the surface structure of the ordered domain which develops in the disordered matrix. One expectation is that the A phase may be a ferrimagnetic thin layer on the surface of the ordered domain, whose composition and Curie point are slightly different from those within the domain. The existence of such a thin layer has ordinally been expected in the development of the ordered domain[18]. By such an assumption for A-phase, we can interpret more reasonablly the experimental fact that the reverse TRM is preserved even in the completely ordered specimen, because such a surface structure of the domain can be left undisappeared on the boundary of the domain even after these domains come to contact closely with each other.

As a concluding remark of this section we sould like to note that the detailed investigation of the reverse TRM will give us some light on the minute structure of the ordered domain in the process of the formation of order in these oxide specimens. A further study of the detailed mechanism of the reverse TRM is now under progress in cooperation with S. Uyeda.

Acknowledgement

The author wishes to express his hearty thanks to Prof. Shozo Sawada for his kind encouragement and guidance throughout this experiment. His thanks are also due to Dr. Akimoto for his X-ray alaysis and Dr G. Shirane for his neutron analysis. The section of the reverse TRM is entirely indebted to Dr. S. Uyeda.

References

1) G. Tammann: Zeit. f. Anogr. Allgen. Chem **107** (1919) 1.
2) T. Muto and Y. Takagi: Solid State Physics vol I, (1955) p. 193.
C. Nix and W. Schockley: Rev. Mod. Phys. **10** (1938) 1.
3) R. Pauthenet and L. Bochirol: J. Phys. Radium. **12** (1951) 249.
4) L. Néel: Compt. Rend. **230** (1950) 190.
5) F. K. Lotgering: Philips Res. Rep. **11** (1956) 190.
6) P. B. Braun: Nature **170** (1952) 1123.
7) Y. Ishikawa and S. Akimoto: Journ. Phys. Soc. Japan **12** (1957) 834.
8) Y. Ishikawa and S. Akimoto: Journ. Phys. Soc. Japan **12** (1957) 1083.
9) Y. Ishikawa: Journ. Phys. Soc. Japan **13** (1958) 37.
10) J. A. Brinkman, C. E. Dixon and C. J. Meechan: Act. Metall. **2** (1954) 38.
11) R. A. Dugdale and A. Green: Phil. Mag. (7) **45** (1954) 163.
12) G. Shirane, S. J. Pickart, Nathan and Y. Ishikawa: to be published.
13) F. W. Barth and E. Posnjak: Zeit fur Krist. **88** (1934) 265.
14) W. L. Bragg and Williams: Proc. Roy. Soc. Lond. **145A** (1934) 699.
W. L. Bragg and Williams: Proc. Roy. Soc. Lond. **151A** (1935) 540.
15) T. Nagata, S. Uyeda and S. Akimoto: Journ. Geomag. Geoelec. **4** (1952) 22.
T. Nagata, S. Uyeda and S. Akimoto: Journ. Geomag. Geoelec. **5** (1953) 168.
16) S. Uyeda: Journ. Geomag. Geoelec. **7** (1955) 9; **8** (1956) 39.
17) S. Uyeda: Journ. Geomag. Geoelec. **9** (1957) 61.
S. Uyeda: Japanese Journ. Geophys. **1** (1957).
18) C. Sykes and F. W. Jones: Proc. Roy. Soc. Lond. **157A** (1936) 213.

JOURNAL OF THE PHYSICAL SOCIETY OF JAPAN VOL. 13 No. 8 AUGUST 1958

Diffusion of Cadmium into Single Crystals of Copper*

Tokutaro HIRONE, Nobuhiko KUNITOMI,** Masanobu SAKAMOTO** and Hideo YAMAKI***

The Research Institute for Iron, Steel and Other Metals, Tohoku University, Sendai

(Received May 9, 1958)

The diffusivity of cadmium into single crystals of copper has been measured in the temperature range from 725°C to 950°C using radioactive isotope Cd^{115} as a tracer. The results indicate that $D_0=0.935\,cm^2/sec$ and $H=45{,}700$ cal/mol. These values are compared with the corresponding values for the diffusion of zinc into copper in order to investigate the effect of the difference in atomic radii.

§ 1 Introduction

In order to study the effect of excess valency on the activation energy of solute diffusion, the diffusion coefficients of several kinds of atoms into monovalent noble metals have been investigated experimentally and theoretically.[1),2),3),4)5)6)] However, the effect of the atomic size in the diffusion process has not yet been investigated sufficiently. Although this effect has been considered to contribute to the activation energy of the diffusion,[7),8)] the experimental evidences have revealed less effect than expected.[9),10)]

Since cadmium and zinc have different ionic radii and the same valence the comparison of the diffusivities of both atoms will give an information on the effect of atomic size. The purpose of the present paper is to measure the activation energy of cadmium diffusion into copper single crystals and to compare it with that of zinc which has been obtained by Hino, Tomizuka and Wert.[11)]

§ 2 Experiment

Single crystals of copper (99.98% pure) were grown by the Bridgeman technique. The specimens were formed from these crystals into drum shaped piecess. In order to obtain the specimen possibly free from the mosaic structure, the diffusion surface of the crystals was carefully cut with a jeweler's saw, ground with fine emery, whetted with a stone and etched carefully with dilute HNO_3 solution. The estimated thickness of the plated layers ranged below 200Å.

The specimens were then placed in pairs with active surfaces together, in quartz tube filled with argon gas of about a half atmosp heric pressure at room temperature. In some specimens which were annealed near melting point, a thin mica plate was used as the separater between two active surfaces in order to avoid the cohesion of both crystals. The temperature control was kept within ±2°C for every diffusion anneal.

After the diffusion anneal, the side surface layer of the specimen was removed by the Boley watchmaker's lathe to eliminate the effect of surface diffusion. The sections, 0.003 cm to 0.010 cm thick, were then removed by using this precision lathe, and the activity of each section was determined with a thin mica end-window Geiger-Müller counter tube in a standard scaling unit. Each cut was weighed to check their thickness and compared with the value obtained from the reading of the gauge. For the counting, two methods were actually used; the first was to measure the sample in a circular dish of the same geometry and the second was to measure by solving the sample in dilute HNO_3 solution in circular metaaclyle vessel. In our case, the accuracy of the counting was almost unchanged for two cases except less counting efficiency for the latter.

§ 3 Results

Diffusion runs were made at temperature in the range from 950°C to 725°C for periods ranging from 3 hours to slightly more than 4 days. As is shown in Fig. 1, a linear curve

* This work is supported partly by the Grant-in-Aid for the Sientific Research from the Ministry of Education.

** Now at Japan Atomic Energy Reserch Institute, Tokai-mura, Ibaragi.

*** Now at Hitachi Research Institute, Hitachi Co,. Hitachi, Ibaragi.

was obtained for every sample, when the logarithm of the concentration of radioactive cadmium was plotted against the square of the penetration distance indicating a little effect of imperfections in the crystals. The linear lines in this figure fitted for the measured points were obtained by the aid of the least square method, which allows the diffusion coefficient to be determined directly.

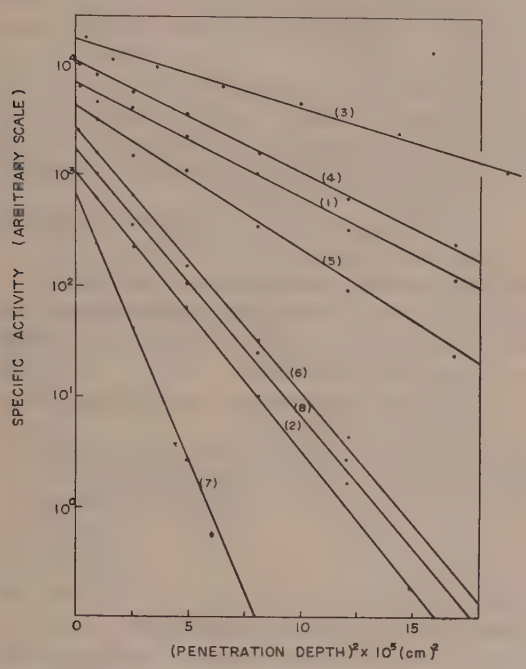

Fig. 1. Penetration curves for diffusion of cadmium into single crystals of copper.

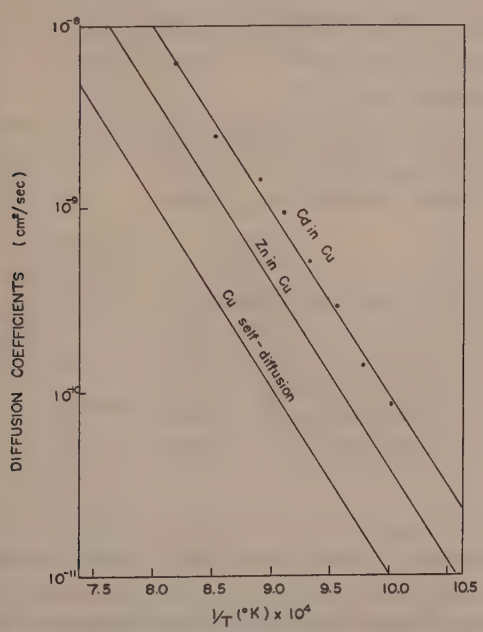

Fig. 2. Diffusion coefficients plotted as log D versus $1/T$.

The Table I summarizes the results of individual samples and Fig. 2 gaves the logarithm of diffusion coefficient as a function of the reciprocal absolute temperature. It was found that the measured values were expressed by the Arrhenius equation $D=D_0 exp(-H/RT)$. And the frequency factor D_0 and the activation enthalpy H were calculated by means of the least square method.

Table I. Diffusion Data of Cadmium into Copper

Curve	Temperature (deg. C)	Time (sec)	Diffusion Coeff. (cm²/sec)
1	950	9.87×10^3	8.74×10^{-11}
2	900	9.90×10^3	1.46×10^{-10}
3	850	7.56×10^4	2.88×10^{-10}
4	825	6.50×10^4	5.19×10^{-10}
5	800	8.64×10^4	9.51×10^{-10}
6	775	8.84×10^4	1.43×10^{-9}
7	750	8.64×10^4	2.45×10^{-9}
8	725	2.89×10^5	6.12×10^{-9}

The values thus calculated are

$$D^\circ=0.935\pm0.271\ \mathrm{cm^2/sec},$$

$$H=45{,}700\pm900\ \mathrm{cal/mol}.$$

§ 4 Discussion

Since the primary purpose of this work is to investigate the effect of atomic size of the solute atom, it is interesting to compare the obtained results with those for zinc into copper and with the theoretical value. The diffusion of zinc into single crystals of copper has been measured by Hino and others[11] and their results are represented by

$$D_0=0.34\ \mathrm{cm^2/sec},$$

and

$$H=45{,}600\ \mathrm{cal/mol}.$$

It should be noticed by comparing their results with ours that the activation enthalpy H is nearly the same for both cases, while the frequency factor is a little larger in our case.

From a theoretical consideration some difference of the activation enthalpy is expected due to the difference of ionic radii of zinc and cadmium. Firstly, it should have an influence upon the coulomb contribution to the formation vacancy. According to Blatt,[12] the redistribution of screened electrons near the impure

atom with positive excess valency should cause the larger formation energy of vacancy at the neighboring site of a larger impure atom, since the apparent excess valency becomes smaller than that of smaller impure atom. The more accurate theory of Fujiwara,[13] in which the exchange interaction of the core electrons has been taken into account, also indicates the less screening effect of cadmium atom than zinc in copper. This effect should cause the larger formation enthalpy of vacancy for cadmium than for zinc. Secondly, the migration enthalpy of the impure atom also increases in the case of cadmium diffusion because it has larger ionic radius Therefore, the theoretical consideration should result the larger activation enthalpy of cadmium diffusion than that of zinc diffusion in any case. Thus the theoretical expectation contradicts with the experimental results of the present authors and Sawatzky.

However, these conclusions are very tentative and more work should be carried out for the measurement of the diffusion of solute atoms which have different atomic size and the same atomic valence.

References

2) E. Sonder, L. Slifkin and C. T. Tomizuka: Phys. Rev. **93** (1954) 970.
2) C. T. Tomizuka and L. Slifkin: Phys. Rev. **96** (1954) 610.
3) M. Sakamoto: J. Phys. Soc. Japan.
4) D. Lazarus: Phys. Rev. **93** (1954) 973.
5) F. J. Blatt: Phys. Rev. **99** (1955) 600.
6) L. C. R. Alfred and N. H. March: Phys. Rev. **103** (1956) 877.
7) H. B. Huntington and F. Seitz: Phys. Rev. **61** (1942) 315.
8) F. G. Fumi: Phil. Mag. **46** (1955) 1007.
9) J. Sawatzky: Phys. Rev. **100** (1955) 1627.
10) F. E. Jaumot, Jr. and A. Sawatzky: J. Appl. Phys. **27** (1956) 1186.
11) J. Hino, C. T. Tomizuka and C. Wert: Acta. Meta. **5** (1957) 41.
12) F. J. Blatt: Phys. Rev. **108** (1957) 1204.
13) H. Fujiwara: private communication.

JOURNAL OF THE PHYSICAL SOCIETY OF JAPAN Vol. 13, No. 8, AUGUST, 1958

Diffusion of Cobalt into Iron-Cobalt Alloy**

Tokutaro HIRONE, Nobuhiko KUNITOMI* and Masanobu SAKAMOTO*

The Research Institute for Iron, Steel and Other Metals, Tohoku University, Sendai

(Received May 9, 1958)

The diffusivities of Co^{60} into 50–50 atomic percent iron-cobalt alloy were measured by means of the lathe sectioning method for the temperature range including f.c.c. to b.c.c. phase transformation. The experimental values were expressed by

$$D=1.1\times10^{-4}\exp(-41800/RT) \quad \text{cm}^2/\text{sec} \quad \text{for f.c.c. structure,}$$

$$D=2.6\times10^{-6}\exp(-27400/RT) \quad \text{cm}^2/\text{sec} \quad \text{for b.c.c. structure.}$$

The activation energies for diffusion in the b.c.c. and f.c.c. lattices were compared with the theoretical values calculated by the approximation of the closed shell repulsion with the Born-Mayer potential. And it is concluded that the vacancy mechanism is responsible for the diffusion in the body centered cubic metal in the same manner as in the face centered cubic metal.

§ 1. Introduction

The diffusion coefficient in solid solution alloy is affected not only by the physical character of each constituent atom but also by the lattice structure of the alloy. Among these, the effect of the physical character of each atom, such as the atomic size or the atomic valence, has been investigated by

* Now at Japan Atomic Energy Research Institute, Tokai-mura, Ibaragi.

** This research was supported in part by Grant in Aid for Scientific Research by the Ministry of Education.

many researchers.[1),2),3)] Few studies, however, have been carried out on the effect of lattice structure.[4)]

It has been considered in the crystal lattices of usual metals and alloys that the vacancy plays an important role for atomic diffusion.[5)] Especially in metals with the face centered cubic lattice, such as in the case of monovalent noble metals, it has been definitely shown from the observation of Kirkendall effect[6)] and the theoretical consideration[7)] based on the accurate results obtained by the tracer method that the vacancy migration is most predominant.

In the body centred cubic lattice, on the other hand, the both interstitial and vacancy mechanisms are considered to be approvable, although the ring diffusion process proposed by Zener[8)] and Le Claire[9)] is disproved by the recent observation of Kirkendall effect.[10)]

The purpose of this paper is to determine the mechanism of diffusion in the body centered cubic lattice by measuring the change of activation energy during b.c.c. to f.c.c. phase transformation, and by comparing the results observed with the corresponding values expected theoretically. Based on this idea, the specimen material should have a lattice transformation from the body centered cubic lattice to the face centered cubic lattice at an appropriate temperature. Fortunately, the iron-cobalt 50–50 atomic percent alloy has a phase transformation of the required type f.c.c. to b.c.c., at about 980°C and forms an ordered structure of the Cs-Cl type below 760°C, and satisfied the condition mentioned above.

§ 2. Experimental Method

Purity 99 percent iron and purity 98 percent cobalt were cast into cylinders of 15 mm diameter by the vacuum melting method. After forging, they were cut and machined into the drum-shaped specimens, 10 mm in diameter and about 20 mm in length. One face of each specimen was polished mechanically and electroplated Co^{60} for about 10 Å thickness. The plated specimens were sealed off in quartz tubes in which argon gas was filled, and placed in a furnance for diffusion anneals. The temperature was held constant within limits of ±2°C over the time of diffusion anneals which ranged from several hours to three months, depending on the temperature, covering the range 840°C–1250°C.

The measurement was performed by means of the lathe sectioning method which was concluded to be most accurate to determine the diffusion coefficient by using the radioactive isotope.[11)] After the diffusion annealing, the sectioning, was done on the Boley's precision lathe. In order to eliminate the effect of surface diffusion, a thickness of approximately $6(Dt)^{1/2}$ was removed from the side before sectioning where D is the expected diffusion coefficient and t the time of anneal. In sectioning, the thickness of each cut varied from 1/100 mm to 5/100 mm, and the depth of penetration of each cut was measured by a dial gauge and corrected by means of the weighing of all cuts. The material from each cut was placed under the Geiger-Müller counter tube upon the same geometrical conditions to determine the amount of radioactive cobalt.

In the case of volume diffusion the specific activity c which depends linearly on the Co^{60} concentration of each cut falls off exponentially with the square of the penetration depth x. That is

$$\ln c = -x^2/4Dt + \text{const.} \qquad (1)$$

where D is the diffusion coefficient and t is the time of diffusion anneal.

§ 3. Experimental Results

The diffusion measurements were performed at the different ten temperatures over the range 840°C–1250°C. Results plotted in Fig. 1 show that the specific activity of each cut decreases exponentially with the square of penetration depth. This fact indicates that there is no observable effect of the grain boundary or surface diffusion. According to Eq. (1), the diffusion coefficients corresponding to the temperatures of anneal were calculated from the penetration curves with the aid of the least square method. In Fig. 2, the logarithms of the diffusion coefficients thus calculated are plotted against the reciprocal of the absolute temperature.

The diffusion coefficients for five temperatures over the range of 1000°C–1250°C where the specimen has the face centered cubic lattice and those for three tempratures over the range 840°C–925°C were it has the body

centered cubic lattice exhibit to satisfy the Arrhenius equation, respectively. The value at 950°C is anomalous since its diffusion was carried out near the transition temperature. By means of the least square calculations, the temperature dependence of the diffusion coefficient in both structures is given by

$$D=1.1\times10^{-4}\exp(-41800/RT) \quad \text{cm}^2/\text{sec in f.c.c.}$$

$$D=2.6\times10^{-6}\exp(-27400/RT) \quad \text{cm}^2/\text{sec in b.c.c.}$$

where R is the gas constant and T is the absolute temperature. The probable errors of the activation energy and frequency factor are determined by the statistical analysis to be ±4 %, ±70 % in the face centered cubic lattice and ±3 %, ±40 % in the body centered cubic lattice, respectively.

Comparing both equations with each other, we find that the activation energy for diffusion in the body centered cubic lattice is by about 14.4 kcal/mol smaller than that in the face centered cubic lattice.

In recent years, Gerstricken and Dekhtyar reported very large values of the diffusion coefficients which was determined by the absorption method for the temperatures corresponding to the face centered cubic region of the same alloy.[12] This difference of diffusion coefficients is supposed to be due to the inevitable experimental inaccuracy of the absorption method.

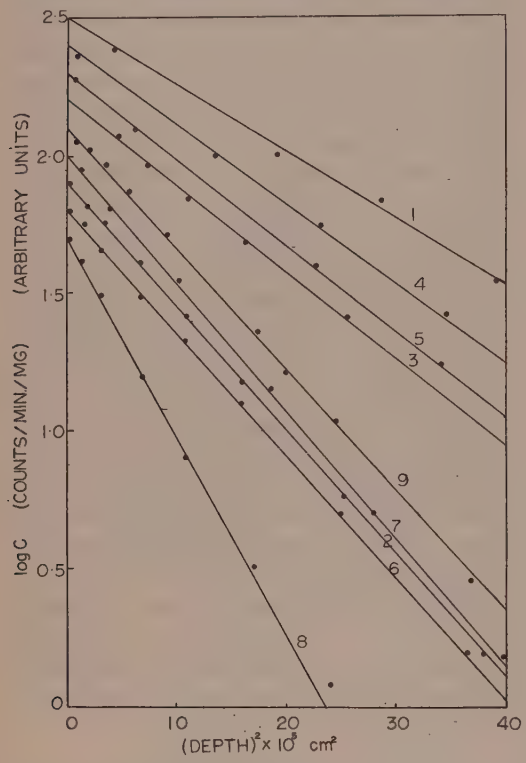

Fig. 1. Penetration curves for the diffusion of cobalt into iron-cobalt alloy.

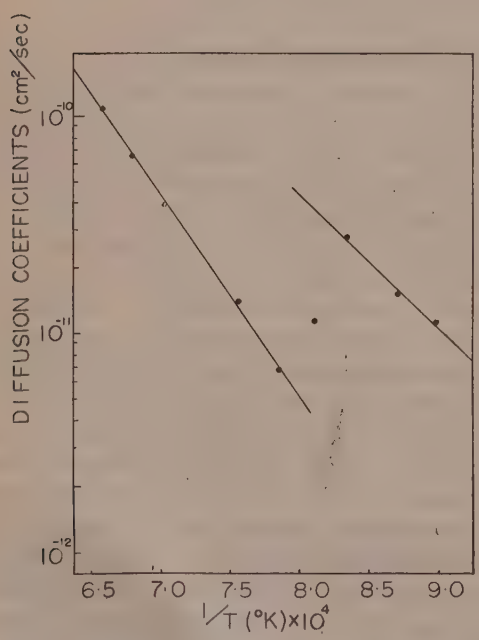

Fig. 2. Diffusion coefficients plotted as $\log D$ versus $1/T$.

§ 4. Discussion

It has been concluded from the observation of Kirkendall effect in the face centred cubic and body centered cubic metals that the diffusion mechanism in both lattices is attributed to the movement of lattice imperfections. There are, however, two fundamental mechanisms of atomic diffusion with lattice imperfections, namely diffusion by means of interstitial atom and of vacancy. The purpose of the following calculation is to determine the prefered mechanism in the body centered cubic structure. The activation energy for diffusion is mainly influenced by the cohesive character of metals which is consisted of two main factors, namely the coulomb and exchange interaction. Since the coulomb interaction is not appreciably affected by the change of the interatomic distance and it is more difficult to estimate theoretically, in this case the computation of activation energy has been restricted within the repulsion of closed shells.

The constants in this potential have been generally determined by the elastic moduli, but those for the iron-cobalt alloy have not yet been measured exactly. Therefore we emplyed the values derived by Huntington for copper[13] and corrected them by replacing the interatomic distances in the iron-cobalt alloy for each structure. The differences of atomic number among iron, cobalt and copper is very small and those have the atomic radii of the same order of magnitude. Hence it may not introduce any great error even if the constants for copper are used instead of those for iron and cobalt in Born-Mayer's potential. The expressions of potentials for this calculation are

$$E_r = 0.038 \exp 13.6(r_0 - r/r_0) \quad \text{e.v.} \quad \text{in f.c.c.}$$

$$E_r = 0.038 \exp 10.8(r_0 - r/r_0) \quad \text{e.v.} \quad \text{in b.c.c.}$$

In the following paragraphs, the results of calculation for the differences of the free energies between the normal and saddle point configurations for the two processes will be given by using the above formulas as the repulsive force. And these configurations for the two diffusion mechanisms and the two lattice structures are shown in Fig. 3.

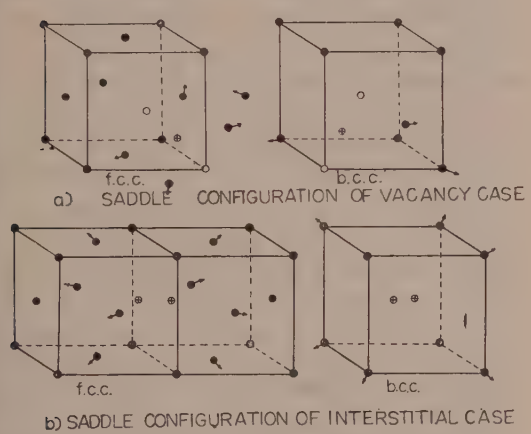

Fig. 3. Configurations involved in the vacancy and interstitial mechanism of diffusion. ● denotes an atom at an ordinary lattice site. ○ denotes vacancy. ⊕ denotes atom at a saddle point of migration.

1) Vacancy case

In Fig. 3a, the saddle configurations of vacancy mechanism for the face centered cubic and body centered cubic lattices are shown. In these configurations two atoms are taken off from adjointed positions in the metallic lattice leaving two vacancies after them. And then one atom is placed on the saddle point which is the middle point between the two vacancies. In the case of the face centered cubic lattice, one of the atoms which are taken off from the interior, is put on the surface with a net decrease of 17 repulsive bonds and the other atom is placed at the saddle point which has the four nearest neighbour atoms. These four atoms are mutually adjacent and displaced to the both vacancies in order to make the repulsive energy minimum. Similarly in the case of body centered cubic lattice 11 ordinary repulsions decrease and 4 new bonds take places between the diffusing atom and its nearest neighbours which are displaced so as to minimize the repulsive energy.

2) Interstitial case

Fig. 3b shows the saddle point configurations of the interstitial mechanisms for the face centered cubic and body centered cubic lattices respectively. In both cases, one atom is taken from the surface and another atom from ordinary lattice point which leaves a vacancy in the interior. These two atoms are placed on the saddle points which are on either side of the vacancy. In the face centered cubic

Table I. Diffusion of cobalt into iron- cobalt alloy.

Number of curve	Temperature (deg C)	Time (sec)	Diffusion coeff. D (cm^2/sec)
1	1250	4.18×10^5	1.14×10^{-11}
2	1200	5.02×10^5	6.63×10^{-11}
3	1150	8.75×10^5	3.93×10^{-11}
4	1050	2.47×10^6	1.46×10^{-12}
5	1000	2.88×10^6	7.02×10^{-12}
6	960	3.52×10^6	1.12×10^{-12}
7	925	9.50×10^5	2.77×10^{-12}
8	875	1.59×10^6	1.50×10^{-12}
9	840	7.52×10^6	1.13×10^{-12}

Table II. Calculated and experimental values of activation energy.

	f.c.c.	b.c.c.
Vacancy	0.53 e.v.	0.31 e.v.
Interstitial	5.9	3.2
Experiment	1.74	1.15

lattice, therefore, the calculation is performed under the conditions that on the surface 6 ordinary bonds are broken and on saddle points 8 atoms are displaced. For the body centered cubic lattice, in the same way, the processes contain 4 ordinary bonds broken and 8 atoms displaced at the saddle configuration. Results of the calculations of the activation energies due to these mechanisms mentioned here are shown in the table II with the experimental results.

The calculated values indicate that the activation energy in the body centered cubic lattice is much smaller than that in the face centered cubic lattice and this behavior is in qualitative agreement with that observed. Since the above computation does not include the electronic contribution for the activation energy, the calculated values are expected to show smaller values than those in which the electronic contribution is taken into account. In fact the calculated values are greater than those observed, therefore it is to be concluded that the interstitial mechanism of diffusion is unreasonable for both lattices.

One of the remarkable results of the present experiment is the very small frequency factor compared with that observed in the usual self-diffusion experiment. For example, the frequency factor D_0 for copper self-diffusion is 0.47 cm²/sec, while the present D_0 is 1.1×10^{-4} cm²/sec in the face centered cubic lattice and 2.6×10^{-6} cm²/sec in the body centered cubic lattice.

As well known, D_0 is expressed by

$$D_0=\nu a^2\gamma \exp(\Delta S/R) \quad \text{cm}^2/\text{sec}.$$

Where ν is the lattice vibrational freqency, a is the lattice parameter, γ is a geometrical parameter determined by the lattice structure and ΔS is the entropy of activation. According to the theoretical and experimental works published previously, the value of D_0 is small in the grain-boundary diffusion, because the restricted diffusion path decreases the entropy of activation. And also for the case of iron-cobalt alloy it seems to be probably that the diffusion path of cobalt are restricted by the kind of neighbouring atoms in the disordered distribution of iron and cobalt atoms.

The iron-cobalt alloy with the composition of 50–50 atomic percent shows the ordered structure below 750°C. Experiments to measure the activation energy and frequency factor of diffusion in the ordered structure will be obviously interesting in the consideration of ordering and diffusion mechanisms. But, since it must be performed in relatively low temperature range, there will be a number of experimental difficulties, e.g., the effect of grain-boundary diffusion and the extremely long period of diffusions anneal which is necessary because of the decreasing of the diffusion coefficients.

References

1) D. Lazarus: Phys. Rev. **93** (1954) 973.
2) C. T. Tomizuka and L. Slifkin: Phys. Rev. **96** (1954) 610.
3) L. C. R. Alfred and N. H. March: Phys. Rev. **103** (1956) 877.
4) L. Slifkin and C. T. Tomizuka: Phys. Rev. **97** (1955) 836.
5) Progress in Metal Physics. No. 5 p. 265 A. LeClaire: Diffusion in Metals.
6) A. S. Nowick: Phys. Rev. **88** (1952) 925.
7) B. Huntington and F. Seitz: Phys. Rev. **61** (1942) 315.
8) C. Zener: Acta. Cryst. **3** (1950) 346.
9) A. Le Clair: Acta. Meta. **1** (1953) 438.
10) P. G. Shewmon and J. H. Bechtold: Acta. Meta. **3** (1955) 452.
11) R. C. Smith, F. E. Jaumot, Jr. and L. A. Arne: Phys. Rev. **94** (1954) 1402.
12) S. D. Gertstricken and I. Y. Dekhtyar: A/CONF. 8/p/712.
13) H. B. Huntington: Phys. Rev. **91** (1953) 1092.

JOURNAL OF THE PHYSICAL SOCIETY OF JAPAN Vol. 13, No. 8, AUGUST, 1958

Diffusion of Cobalt into Single Crystals of Copper**

By Masanobu SAKAMOTO*

Research Institute for Iron, Steel and Other Metals, Tohoku University, Sendai

(Received May 9, 1958)

The measurements of diffusion coefficient of cobalt into copper have been carried out in the temperature range from 950°C to 700°C using Co^{60} as tracer. The result indicates that the diffusion coefficient is given by the equation $D=5.7\exp(-55200/RT)$ cm²/sec and, therefore, that the activation energy is appreciably larger than that of copper self-diffusion. From this experiment it has been definitely shown that, for the negative value of excess valency Z, the effect of screening on the solute diffusion in metals plays an effective role in the same manner as the effect observed for the positive value of Z.

§ 1. Introduction

The diffusion experiments of cadmium, indium, tin and antimony into single crystals of silver[1),2)] have indicated that the activation energy for diffusion decreases with increasing excess valency Z, which is the difference of valence electrons between solute and soluent atoms. This fact has been successfuly interpreted by Lazarus' theory[3)] which is based upon Thomas-Fermi approximation on the screening potential around impurity atoms. After that, Alfred and March[4)] have developed an improved theory in which they used corrected forms of screening potential. For positive values of Z, these theories have been proved to be fairly reasonable because the calculated values are in agreement with the experimental results, mentioned above.

On the other hand, for negative values of Z, experiments to examine the theory have not yet been performed. According to these theories, it will or may be expected that the activation energy has to be larger for the impurity atom diffusion with the negative value of Z than that of self-diffusion, in contrast with the prediction that the diffusion is accerelated by the local stress[5)]. The present report aims to be compared with the result for self-diffusion in copper and to confirm theoretical values of activation energy.

§ 2. Experimental Results

Cylindrical single crystals of copper were prepared by Bridgeman method, cut and machined to form drum-shaped specimens. The specimens were electro-plated with the layer of cobalt-60 of about 20Å thicknes from $CoCl_2$ solution, sealed off in quartz tube with argon gas, and annealed in the furnace in which temperature was held constant to within ±2°C, for periods of several hours to 20 days. Specimens which were annealed were sectioned on a precession lathe and analyzed by counting technique in the preceeding paper[6)].

Six diffusion runs were performed over the temperature range from 950°C to 700°C. The

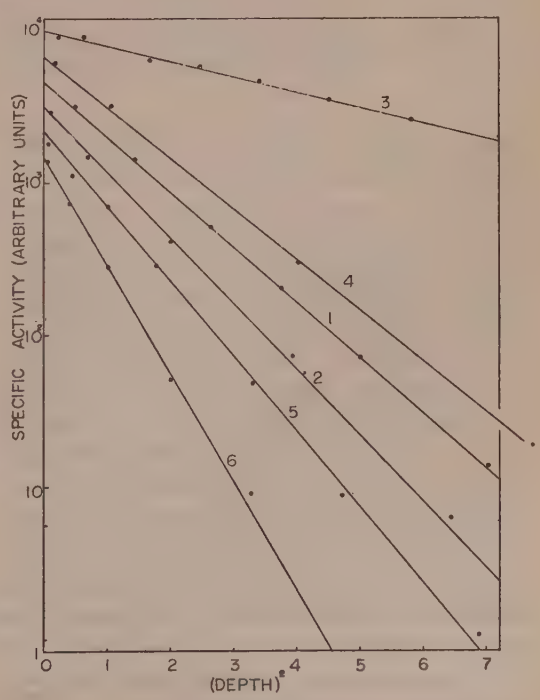

Fig. 1.

* Now at Japan Atomic Energy Research Institute, Tokaimura, Ibaragi.

** This work is supported partly by the Grant in Aid for the Scientific Research from the Ministry of Education.

penetration curves for all specimens are shown in Fig. 1 which indicate a strict proportionality between the logarithm of the specific activity and the square of the penetration depth. The logarithms of the diffusion coefficients, calculated from these data, are plotted against the reciprocal of the absolute temperature in Fig. 2 and a summary of the

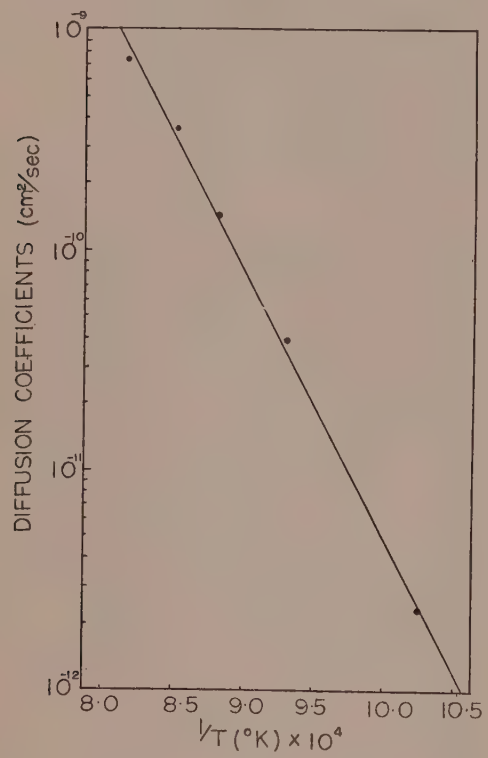

Fig. 2. Diffusion coefficients plotted as $\log D$ versus $1/T$.

Table I. Diffusion of cobalt into copper.

Curve	Unit of (depth)² (cm)²	Temperature (deg C)	Time (sec)	Diffusion coeff. D (cm²/sec.)
1	4.55×10^{-5}	950	7.20×10^{4}	7.05×10^{-10}
2	2.27×10^{-5}	900	4.14×10^{4}	3.42×10^{-10}
3	2.27×10^{-5}	860	4.32×10^{5}	1.42×10^{-10}
4	1.71×10^{-5}	800	2.43×10^{5}	3.88×10^{-11}
5	1.71×10^{-5}	750	6.62×10^{5}	9.27×10^{-12}
6	1.71×10^{-5}	700	1.90×10^{6}	2.31×10^{-12}

data are shown in Table I. The straight line obtained by a least-square method is given by the equation

$$D=5.7\exp(-55200/RT)\ \mathrm{cm^2/sec.}$$

Statistically estimated errors are ±2% for activation energy and ±6% for frequency factor.

§ 3. Discussion

It is interesting to compare the activation energies calculated by Lazarus, Alfred and March substituting the value $Z=-2$ for cobalt in copper, with the result mentioned above and the experimental data of self-diffusion for copper according to Kuper, *et al.*[7] These values for activation energy are shown in Table II.

Table II.

	Co in Cu (exp.)	Cu self. (exp.)	Lazarus (theo.)	Alfred, March (theo.)
Activation energy (kcal/mol)	55.2	47.1	53.9	59.8

According to a classical consideration, the local strain around an impurity atom reduces the difficulty of the atomic jump from one equilibrium position to the other in the crystal lattice. Therefore, the activation energy of the difiusion should decrease by the introduction of impure atom. And, in addition, the main contribution of closed shell repulsion also reduces the activation energy because the ionic radius of cobalt is smaller than that of copper. However, in contrary, the result of this report exhibits a increase of activation energy for the diffusion of cobalt into copper. Thus as a sole propable mechanism, one must take into account the effects of screening of the solute atoms on the Fermi electrons of solvent lattice.

In conclusion, one of the most interesting aspects of the present results is that the activation energy obtained here is about 8 kcal/mol larger than that of self-diffusion for copper. This provides the strong support for the expectation of theories, though it is hard to say that the calculated values are in numerical agreement with the observed one.

Finally, if the activation energies are measured for other impurities with the different values of negative Z in the same solvent, it might seem possible to justify the theory for the effect of screening on solute diffusion in higher accuracy.

The author wishes to express his sincere thank to Prof. T. Hirone for his kind inten-

tions and encouragement throughout the course of the present study and publishing. His heartiful thank is also due to Dr. N. Kunitomi for his valuable advices and his kind inspection of the manuscript.

References

1) E. Sonder, L. Slifkin and C. T. Tomizuka: Phys. Rev. **93** (1954) 970.
2) C. T. Tomizuka and L. Slifkin: Phys. Rev. **96** (1954) 610.
3) D. Lazarus: Phys. Rev. **93** (1954) 973.
4) L. C. R. Alfred and N. H. March: Phys. Rev. **103** (1956) 877.
5) A. S. Nowick: J. Appl. Phys. **22** (1951) 1182.
6) T. Hirone, N. Kunitomi, M. Sakamoto and H. Yamaki: J. Phys. Soc. Japan. **13** (1958) 827.
7) H. Kuper, H. Letaw, L. Slifkin, E. Sonder and C. T. Tomizuka: Phys. Rev. **96** (1954) 1224.

JOURNAL OF THE PHYSICAL SOCIETY OF JAPAN Vol. 13, No. 8, AUGUST, 1958

The Theory of the Fine Structure of the X-ray Absorption Spectrum

By Toshio SHIRAIWA, Tsutomu ISHIMURA and Masao SAWADA
Faculty of Science, Osaka University

(Received April 21, 1958)

In the interpretation of the fine structure of the X-ray absorption spectrum in solids, the life time of the state of the electron ejected by absorption of a photon is considered. The life time is mainly determined by the inelastic collision cross section between the ejected electron and the atoms in the crystal. With the assumption that the inelastic cross section has a magnitude of the order of one square Angstrom, Kronig's method for the molecule is applied to the solid in order to obtain the variation of the transition probability. The wave function of the final state of the transition is obtained as the sum of the plane wave, whose amplitude decreases with increasing distance from the absorbing atom, and the waves scattered by the neighboring atoms. The calculated results for the K-absorption spectra of copper, nickel and iron agree well with experiments.

§ 1. Introduction

An acceptable theory of the fine structure of the X-ray absorption spectrum was first proposed by Kronig.[1] According to his theory the origin of the fine structure is ascribed to the zone structure of the energy levels of the electrons in the crystal which is a result of the effect of the periodic field in the crystal. The X-rays are absorbed by the electrons which make transitions from the X-ray K levels to empty levels lying above the Fermi surface. These empty levels are grouped into zones and there exist forbidden and allowed bands. Because the absorption coefficient is proportional to the procuct of the transition probability and the state density, a fine structure occurs. In his theory the variation of the transition probability was neglected and the fine structure was explained mainly by the variation of the electronic state density. His computation of the latter, in which an electron in a lattice was treated as nearly free and the field of the lattice as a perturbing potential, is very precise. But his calculation predicts much more fine structure than experiment reveals. So he suitably grouped anomalies in the density of states curve and, by such grouping, explained the position of absorption maxima and minima of the fine structure.

On the other hand, for the fine structure of a gas molecule he computed[2] the fluctuation of the absorption coefficient caused by the variation of the transition probability and, in order to calculate the state function of the final state of the transition, he adopted the following method. An ejected electron, which is treated as a plane wave, is scattered

by the partner atoms in the molecule and the final state is assumed as the sum of the plane wave and the scattered waves. This method has been applied by several other authors.[2]

Hayashi[3] assumed that the wave of an ejected electron is reflected by atomic net planes and gives rise to a quasi-stationary standing wave around the atom which has ejected the electron, when the wavelength is such that the corresponding Bragg angle is equal to $\pi/2$. Since this standing wave has a large amplitude around the center atom, a strong absorption occurs. Among possible standing waves he took waves of p-type symmetry to consider the transition from the K level and calculated the positions of the absorption maxima, with considerable agreement with the results of experiments for Cu, Ni and Li. In his theory the net planes which cause the standing wave were chosen on the assumption that the reflecting power of the net planes is determined by the number of neighboring atoms and an atom must exist on the normal which is drawn from the center atom to the net plane. The neighboring atoms, then, play a major part in reflection. He suggested that the existence of this quasi-stationary state was due to the additional potential field caused by the missing K electron.

The following approximation has been proposed by Kostarev[4] to obtain the wave function of the ejected electron. The potential field of the neighboring atoms surrounding the absorbing atom is averaged to be spherically symmetrical. The ratio of the absorption coefficient of a solid to that of an isolated atom is given by the ratio of the transition probabilities which itself is given by the ratio of the squares of the amplitudes of the wave functions in the two cases. And in this calculation it is assumed that the both wave functions coincide at points distant from the absorbing atom.

The knowledge which has so far been obtained from experiments on the absorption spectrum of crystals is mainly as follows: The fine structure depends on the crystalline structure and for crystal lattices of the same structure the energy separation measured from the main edge is inversely proportional to the square of the lattice constant. These facts are explained qualitatively by Kronig's theory. Experimental results also show that the fine structure depends on the kind of element and the positions of the neighboring atoms in the region of comparatively high energy.[5] Hayashi's theory and Kostarev's theory conveniently explain this fact.

Kronig's theory is based on the calculation of the stationary state in the crystal and is easily acceptable theoretically. But as regards the comparison with experimental results, he has only proposed a graphical representation and this does not coincide with the experiments quantitatively.* This is indicated in (f) of Figs. 2, 3, and 4 which show the positions of the anomalies of the absorption coefficient by vertical lines according to Kronig's method. The height of each line corresponds to the multiplicity of the equivalent lattice planes which cause the discontinuous zone of the energy.

If we try to interpret the experimental results quantitatively, we must consider the following points. In the Kronig computation only the variation of the state density is considered, whereas one should also include the variation of the transition probability. Secondly, it is necessary to calculate in a more precise way than Kronig did the wave functions of the eigenstates, because in his theory only the degeneracy of the two states is considered near the discontinuous plane in wave number space, whereas near the cross line or point of these planes higher degeneracy occurs. These cross lines or points increase rapidly in number in the higher energy region so that the form of the zone must be changed considerably. If we could take account of these features and of the spreading of the spectral bands[7] caused by the life time of the state of the ejected electron and that of the K-excited state,[8),9] a fairly perfect interpretation of the fine structure would be given.

It will be shown in the present paper that if one considers the life time of the ejected electron, which can be done through a simplified calculation, one can more readily interpret the fine structure quantitatively. In the process of the transition by absorption of the photon energy, the electron ejected from an inner K-level to a nearly free space makes

* A modified graphical representation has been proposed by Kurylenko.[6]

a wave packet around the absorbing atom, corresponding to the uncertainty of the energy, and this wave packet spreads with the lapse of time. The wave function is the solution of the time dependent Schrödinger equation for the initial condition that the function is that of the K state, and the potential field which determines this wave function is the field within the wave packet. Then, in obtaining the transition probability, it may be possible to use wave functions which satisfy the time independent Schrödinger, equation with a potential field that extends over the inside of the wave packet but not outside of it, instead of using the eigenfunctions in the whole crystal. The amplitude of the wave function of the ejected electron decreases with time, and if the life time is sufficiently small the transition problem in the crystal could be limited to a small space around the absorbing atom.

The life time is determined by the incoherent cross section of the collision of the ejected electron due to the thermal motion of atoms and by the cross section of the inelastic collision with atoms. At room temperature it will be determined mainly by the inelastic collision except in the case of ionic crystals. The cross section of the inelastic collision will have a value larger than one square Angstrom and, for this value, the ejected electron almost decreases on passing through a few atomic layers. Therefore we can calculate the transition probability according to the principle mentioned above.

To calculate the wave function of the ejected electron, the authors adopted the method which had been used by Kronig and Petersen[2] for a gas molecule, modified by introducing the decrease of the amplitude caused by scattering. The calculation was applied to the case of copper, nickel and iron with the approximation that the potential field of each atom is of a well type.

§ 2. Calculations

The wave function of the ejected electron: As has been mentioned in § 1, we must obtain the wave function of the ejected electron, whose amplitude decreases with increasing distance from the absorbing atom. As the rough approximation, we may use the eigen-function obtained in the potential field of the neighboring atoms in the finite domain which we determine suitably by the life time. But when this problem is treated as the scattering problem, it will be possible to obtain a more proper solution.

The wave function of the ejected electron can be expressed by the sum of the wave for an isolated atom and the waves scattered by the neighboring atoms. In the first approximation, we have only to consider the primary scattered waves, but when we consider the multiply scattered waves the approximation will become better.

In the case of the isolated atom the ejected electron is expressed by a series of spherical waves and, at points distant from the absorbing atom where the field of the absorbing atom can be neglected, it can be replaced by a series of plane waves, $\exp(i\boldsymbol{kr})$, where $\boldsymbol{k}/2\pi$ is the wave number vector. The effect of the neighboring atoms is to decrease the amplitude of the ejected electron in the scattering process. The ratio of the intensity of the scattered wave to that of the incident wave in a collision is $\sigma_t=\sigma_{\mathrm{el}}+\sigma_{\mathrm{inel}}$, where σ_{el} and σ_{inel} are the cross section of the elastic and the inelastic collision respectively. We assume that the amplitude of the ejected electron decreases as $\exp(-\mu/2r)$, where μ is $(\sigma_{\mathrm{el}}+\sigma_{\mathrm{inel}})\,\rho$, ρ being the number of atoms per unit volume and r the distance from the absorbing atom. Now let the incident wave at the s-th atom at distant r_s from the absorbing atom, ψ_i, be equal to

$$\exp\left(-\frac{\mu}{2}r_s\right)\exp(i\boldsymbol{kr}). \qquad (1)$$

When σ_{inel} is zero or small and the decrease of the amplitude is due only to the elastic scattering, the total probability of existence of the electron does not change with collisions and therefore we must consider multiple scattering. In this case, the result gives the eigen-function in the whole crystal and Kronig's method for solids is more suitable than the present method. When σ_{inel} is large, the scattered waves from the distant atoms and the multiply scattered waves decrease and the present method is suitable.

The elastic and inelastic cross sections for slow electrons in crystals has not been measured, but it has been suggested by Farnsworth that slow electrons can only

Table I. Values of the cross sections of several elements for the collision of an electron: Experimental values are quoted from the reference 13). Theoretical values are calculated by numerical integration of the scattered amplitudes, which are obtained from the atomic structure factors for X-rays, with respect to the scattering angles. In the calculation of the inelastic cross section, Morse's method is used. The structure factors which are calculated from the Thomas-Fermi distributions are referred to the same reference.

Energy of the electron in eV.	Experimental values: Total cross section in A².				Elastic cross section in A².	Ionization cross section in A².		Calculated values for Cu: Elastic cross section in A².	Inelastic cross section in A².
	Zn	Hg	K	A	Hg	Hg	A		
25	25	15	120	13	4	3	1.5	200	384
50	20	17	80	9	3	5	3	114	206
100	18	13	34	6.5	2	5	3.2	61.6	110
200	12	9	20	4	2	4.8	3	32.9	57.9

penetrate a few atomic laryers.[10] The values calculated by the present authors using the form factor and Morse's[11] and Bethe's[12] methods seem to be too large, in comparison with the experimental data on gases. Measurements have been made for several elements, including rare gases, alkali metals, Zn and Hg.[13] These data are listed in Table I. We cannot use these values for the atoms in the crystal, but it is perhaps not too wrong to assume that the cross section for inelastic collision for a slow electron is larger than one square Angstrom. In the present paper the authors choose a few values of μ arbitrarily, and calculate the variation of the transition probability in each case. As will be shown in the result of the calculation, the small difference in the values does not affect the result.

The wave function ψ of the ejected electron is represented by

$$\psi=\psi_i+\sum_s \psi_s+\sum_{s,t} \psi_{s,t}+\sum_{s,t,u} \psi_{s,t,u}+\cdots, \qquad (2)$$

where ψ_i is the incident wave and ψ_s is the wave scattered by the s-th atom for the incident wave ψ_i and $\psi_{s,t}$ is the wave scattered by the t-th atom for the ψ_s, that is, the secondary scattered wave, and so on. Each wave is as follows:

1) *Incident wave*; ψ_i.

This is represented by

$$\exp\left(-\frac{\mu}{2}r+i\boldsymbol{kr}\right)$$

and near the nucleus of the absorbing atom situated at point A in Fig. 1, we put

$$\exp(i\boldsymbol{kr}). \qquad (3)$$

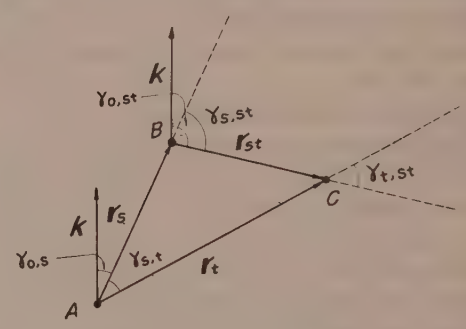

Fig. 1. Showing the relation between positions of the absorbing atom and the scattering atoms and the several vectors and angle used in the calculation. The absorbing atom is situated at A and the scattering atoms are situated at B and C. $\boldsymbol{k}/2\pi$ is the wave number vector of the incident wave.

2) *The primary scattered wave*; ψ_s.

The incident wave to the s-th atom is given by Eq. (1), and its scattered wave is represented by

$$\frac{f(\theta_s)}{r_b}\exp(ikr_b)\exp\left\{i\boldsymbol{kr}_s-\frac{\mu}{2}(r_s+r_b)\right\}, \qquad (4)$$

where θ_s is the scattering angle and r_b the distance from the s-th atom situated at B. In order to obtain the transition probability from a 1s state, it is enough to calculate the wave function in the spase where the wave function of the 1s state exists, concentrated in the vicinity of the nucleus. Then the spherical wave Eq. (4) is replaced by the plane wave,

$$q_s\exp(i\boldsymbol{k}_{s0}\boldsymbol{r}),$$

$$q_s=\frac{f(\pi-\gamma_{0,s})}{r_s}\exp\{(ikr_s+i\boldsymbol{kr}_s)-\mu r_s\}, \qquad (5)$$

where $\gamma_{0,s}$ is the angle between $\boldsymbol{r}_s$ and $\boldsymbol{k}$, and $\boldsymbol{k}_{s0}/2\pi$ is the wave number vector in the direction from B to A.

3) *The secondary scattered wave*; $\psi_{s,t}$.

The wave scattered by the s-th atom is a spherical wave, but we approximate the incident wave to the t-th atom by the plane wave,

$$\frac{f(\gamma_{0,st})}{r_{st}} \exp\left\{(ikr_{st}+ik\boldsymbol{r}_s)-\frac{\mu}{2}(r_s+r_{st})\right\} \cdot \exp(i\boldsymbol{k}_{st}\boldsymbol{r}_c)\,, \tag{6}$$

where $\gamma_{0,st}$ is the angle between $\boldsymbol{r}_{st}$ and $\boldsymbol{k}$, $\boldsymbol{r}_{st}$ the vector drawn from B to C, $\boldsymbol{r}_c$ the position vector from C, and $\boldsymbol{k}_{st}/2\pi$ is the wave number vector in the direction from B to C. The above approximation is not so good as the approximation of Eq. (4), but the secondary scattered wave is weak compared with the primary scattered wave, so that the above approximation should be permissible. The wave scattered by the t-th atom for the incident wave (6) becomes, near the point A,

$$q_{s,t} \exp(i\boldsymbol{k}_{t0}\boldsymbol{r})\,, \tag{7}$$

where

$$q_{s,t}=\frac{f(\gamma_{0,st})}{r_{st}}\frac{f(\pi-\gamma_{t,st})}{r_t} \cdot \exp\left\{(ikr_{st}+ikr_t+ik\boldsymbol{r}_s) -\frac{\mu}{2}(r_s+r_{st}+r_t)\right\}.$$

In the above formulae $\boldsymbol{k}_{t0}/2\pi$ is the wave number vector in the direction from the t-th atom to the absorbing atom, and $\gamma_{t,st}$ is the angle between $\boldsymbol{r}_t$ and $\boldsymbol{r}_{st}$.

4) *The third scattered wave*; $\psi_{s,t,u}$.

In the same way, the third scattered wave $\psi_{s,t,u}$ is obtained and the formula in the vicinity of A is as follows.

$$q_{s,t,u} \exp(i\boldsymbol{k}_{u0}\boldsymbol{r})\,, \tag{8}$$

$$q_{s,t,u}=\frac{f(\gamma_{0,st})}{r_{st}}\frac{f(\gamma_{st,tu})}{r_{tu}}\frac{f(\pi-\gamma_{u,tu})}{r_u} \cdot \exp\left\{(ikr_{st}+ikr_{tu}+ikr_u+ik\boldsymbol{r}_s) -\frac{\mu}{2}(r_s+r_{st}+r_{tu}+r_u)\right\},$$

where $\boldsymbol{r}_{tu}$ is the vector drawn from the t-th atom to the u-th atom. $\gamma_{st,tu}$ is the angle between $\boldsymbol{r}_{st}$ and $\boldsymbol{r}_{tu}$, $\gamma_{u,tu}$ is the angle between $\boldsymbol{r}_u$ and $\boldsymbol{r}_{tu}$, and $\boldsymbol{k}_{u0}/2\pi$ is the wave number vector from the u-th atom to the absorbing atom.

The scattered waves of higher orders are obtained in the same way, but, as these terms are not taken into the actual calculation, they are not given here.

The total wave function of the ejected electron is given from Eqs. (2), (3), (5), (6), (7) and (8) by

$$\psi=\exp(i\boldsymbol{k}\boldsymbol{r})+\sum_s Q_s \exp(i\boldsymbol{k}_{s0}\boldsymbol{r})\,, \tag{9}$$

where

$$Q_s=q_s+\sum_t q_{t,s}+\sum_{u,t} q_{u,t,s}+\cdots.$$

The transition probability from 1s state:

The transition probability from the 1s state to the state of which wave function is represented by Eq. (9) has been obtained by Kronig.[2] The transition probability is proportional to the quantity,

$$\sum_{x,y,z}\left|\int\psi_0^* x\psi d\tau\right|^2=\{1-\sum_s(Q_s^*+Q_s)\cos\gamma_{0,s} -\sum_{s\,s'}Q_s^*Q_{s'}\cos\gamma_{s,s'}\}\left|\int\psi_0^* z\exp(ikz)d\tau\right|^2 \tag{10}$$

where ψ_0 is the wave function of the 1s state, $\gamma_{s,s'}$ is the angle between $\boldsymbol{r}_s$ and $\boldsymbol{r}_{s'}$, and

$$\left|\int\psi_0^* z\exp(ikz)d\tau\right|^2$$

corresponds to the transition probability in the case of the isolated atom. Then, by calculating the term of the braces in Eq. (10), it is possible to obtain the variation of the transition probability relative to that of the isolated atom. The simplicity of Eq. (10) is due to the symmetry of ψ_0, and when the initial state is L, that is for an L absorption spectrum, the transition probability will have a more complicated formula.

When the incident ray is unpolarized and the absorber is an assembly of fine crystals, the transition probability represented by Eq. (10) is averaged over all directions of the vector $\boldsymbol{k}$. So the term which gives the difference of the transition probability from that of the isolated atom becomes

$$\frac{1}{4\pi}\int\{-\sum_s(Q_s^*+Q_s)\cos\gamma_{0,s} -\sum_{s,s'}Q_s^*Q_{s'}\cos\gamma_{s,s'}\}d\Omega$$

$$=\frac{1}{4\pi}\int\{-\sum_s(q_s^*+q_s)\cos\gamma_{0,s}$$

$$-\sum_{s,s'} q_s^* q_{s'} \cos\gamma_{s,s'} - \sum_{s,t} (q_{t,s}^* + q_{t,s}) \cos\gamma_{0,s}$$
$$-\sum_{s,t,u} (q_{u,t,s}^* + q_{u,t,s}) \cos\gamma_{0,s} + \cdots\} d\Omega, \quad (11)$$

where $d\Omega$ is the solid angle regarding to the $\boldsymbol{k}$ vector.

We proceed with the evaluation of Eq. (11). In the calculation it is assumed that the potential of each atom is a well type potential hole of radius a and with a depth V_0, and in order to obtain the scattered amplitude, $f(\theta)$, Born's approximation is used, that is,

$$f(\theta) = -\frac{2m}{\hbar^2} \int_0^\infty \frac{\sin(2kr\sin\theta/2)}{2kr\sin\theta/2} V(r) r^2 dr$$
$$= -\frac{2m}{\hbar^2} V_0 a^3 \left(\frac{\cos K}{K^2} - \frac{\sin K}{K^3} \right), \quad (12)$$

where

$$K = 2ka \sin\theta/2 .$$

In Eq. (11) we carry out the integration before the summation. The integrated formula of each term of Eq. (11) becomes as follows.

1) *Integration of the first term*: From (4)

$$\int q_s \cos\gamma_{0,s} d\Omega$$
$$= \frac{2\pi}{r_s} \exp(-\mu r_s + ikr_s) \int_{-1}^{1} \exp(ikr_s x) x F(x) dx , \quad (13)$$

where

$$x = \cos\gamma_{0,s} , \quad F(x) = f(\pi - \gamma_{0,s}) .$$

In Eq. (13) ka is small compared with kr_s, and kr_s has a comparative large value; for example, when the energy of the electron is 20 eV. and r_s is the distance to the nearest neighbor in Cu, the value of kr_s is 5.9 and k becomes larger as the energy of the electron increases. In the present paper the authors do not consider the fine structure in the vicinity of the main absorption edge, so the integration of Eq. (13) is expanded into a series whose n-th term includes the n-th power of $1/kr_s$ by partial integration:

$$\int_{-1}^{1} \exp(ikr_s x) x F(x) dx = \frac{1}{ikr_s} \exp(ikr_s) x F(x) \Big|_{-1}^{1}$$
$$- \frac{1}{(ikr_s)^2} \exp(ikr_s x) \frac{\partial}{\partial x} \{x F(x)\} \Big|_{-1}^{1} + \frac{1}{(ikr_s)^3} \exp(ikr_s x) \frac{\partial^2}{\partial x^2} \{x F(x)\} \Big|_{-1}^{1} \cdots , \quad (14)$$

and

$$\int q_s \cos\gamma_{0,s} d\Omega = 2\pi \left(-\frac{2m}{\hbar^2} V_0 a^3 \right) \exp(-\mu r_s)$$
$$\times \left[\frac{1}{ikr_s^2} \left[\exp(2ikr_s) \left\{ \frac{\cos 2ka}{(2ka)^2} - \frac{\sin 2ka}{(2ka)^3} \right\} - \frac{1}{3} \right] \right.$$
$$\left. + \frac{1}{k^2 r_s^3} \left[\exp(2ikr_s) \left\{ \frac{1}{4} \frac{\cos 2ka}{(2ka)^2} - \frac{1}{4} \left(\frac{1}{2ka} + \frac{1}{(2ka)^3} \right) \sin 2ka \right\} + \left(\frac{1}{3} + \frac{1}{15} k^2 a^2 \right) \right] + \cdots \right] . \quad (15)$$

Then the integrated formula of the first term, taking only the first term in (15), becomes

$$\frac{1}{4\pi} \int (q_s^* + q_s) \cos\gamma_{0,s} d\Omega \simeq \left(-\frac{2m}{\hbar^2} V_0 a^3 \right) \frac{\exp(-\mu r_s)}{kr_s^2} \sin 2kr_s \cdot M(K_0), \quad (16)$$

where

$$M(K_0) = \frac{\cos K_0}{K_0^2} - \frac{\sin K_0}{K_0^3} , \qquad K_0 = 2ka .$$

2) *Integration of the second term*:

$$q_s^* q_{s'} = \frac{1}{r_s r_{s'}} f^*(\pi - \gamma_{0,s}) f(\pi - \gamma_{0,s'}) \exp\{ik(r_{s'} - r_s) + i\boldsymbol{k}(\boldsymbol{r}_{s'} - \boldsymbol{r}_s) - \mu(r_s + r_{s'})\} .$$

The term which must be integrated with respect to $d\Omega$ appears below, and, in the same

manner as in 1) directly above, the authors use the partial integration method and take the first term alone.

$$\int f^*(\pi-\gamma_{0,s})f(\pi-\gamma_{0,s'})\exp\{ik(r_{s'}-r_s)\}d\Omega$$

$$=\int_0^\pi \exp(ikr_{ss'}\cos\gamma_{0,ss'})\sin\gamma_{0,ss'}\,d\gamma_{0,ss'}\int_0^{2\pi} f^*(\pi-\gamma_{0,s})f(\pi-\gamma_{0,s'})d\varphi$$

$$=-\frac{1}{ikr_{ss'}}\exp(ikr_{ss'}\cos\gamma_{0,ss'})\int_0^{2\pi} f^*(\pi-\gamma_{0,s})f(\pi-\gamma_{0,s'})d\varphi\Big|_{\gamma_{0,ss'}=0}^{\pi}$$

$$+\frac{1}{ikr_{ss'}}\int_0^\pi \exp(ikr_{ss'}\cos\gamma_{0,ss'})\,d\gamma_{0,ss'}\int_0^{2\pi}\frac{\partial}{\partial\gamma_{0,ss'}}\{f^*(\pi-\gamma_{0,s})f(\pi-\gamma_{0,s'})\}\,d\varphi$$

$$\simeq\left(-\frac{2m}{\hbar^2}V_0\,a^3\right)^2\frac{2\pi}{ikr_{ss'}}[\exp(ikr_{ss'})M\{K_+(\gamma_{s,ss'})\}-\exp(-ikr_{ss'})M\{K_-(\gamma_{s,ss'})\}]\,.$$

Where M is the same function as in Eq. (16),

where
$$K_+(\gamma_{s,ss'})=ka\sqrt{2(1+\cos\gamma_{s,ss'})}\,,$$
$$K_-(\gamma_{s,ss'})=ka\sqrt{2(1-\cos\gamma_{s,ss'})}\,,$$

and

$$\frac{1}{4\pi}\sum_{\substack{s,s'\\ s\neq s'}}\int q_s{}^*q_{s'}\cos\gamma_{s,s'}\,d\Omega=\frac{1}{8\pi}\sum_{\substack{s,s'\\ s\neq s'}}\int(q_s{}^*q_{s'}+q_sq_{s'}{}^*)\cos\gamma_{s,s'}\,d\Omega$$

$$=\frac{1}{2}\left(-\frac{2m}{\hbar^2}V_0a^3\right)^2\sum_{\substack{s,s'\\ s\neq s'}}\frac{\exp\{-\mu(r_s+r_{s'})\}}{kr_sr_{ss'}r_{s'}}\cos\gamma_{s,s'}[\sin k(-r_s+r_{ss'}+r_{s'})M\{K_+(\gamma_{s,ss'})\}$$

$$\times M\{K_+(\gamma_{s',ss'})\}-\sin k(-r_s-r_{ss'}+r_{s'})M\{K_-(\gamma_{s,ss'})\}M\{K_-(\gamma_{s',ss'})\}]\,. \tag{17}$$

When $\boldsymbol{r}_s=\boldsymbol{r}_{s'}$

$$\frac{1}{4\pi}\sum_s\int q_s{}^*q_s\cos\gamma_{s,s}\,d\Omega=\frac{1}{4\pi}\sum_s\frac{\exp(-\mu r_s)}{r_s{}^2}\int|f(\theta)|^2\,d\Omega\,.$$

The above term changes slowly with k, so that it is excluded from the calculation.

3) *Integration of the third term*:

In the same way we obtain the integrated formula of the third term.

$$\frac{1}{4\pi}\int(q_{t,s}{}^*+q_{t,s})\cos\gamma_{0,s}\,d\Omega=\left(-\frac{2m}{\hbar^2}V_0a^3\right)^2\frac{\exp\{-\mu/2\cdot(r_t+r_{ts}+r_s)\}}{kr_tr_{ts}r_s}\cos\gamma_{s,t}$$

$$\times[\sin k(r_t+r_{ts}+r_s)M\{K_-(\gamma_{t,ts})\}+\sin k(-r_t+r_{ts}+r_s)M\{K_+(\gamma_{t,ts})\}]M\{K_+(\gamma_{s,ts})\}\,. \tag{18}$$

4) *Integration of the fourth term*:

The fourth and other terms can be calculated in the same way; for example, the fourth term becomes

$$\frac{1}{4\pi}\int(q_{u,t,s}{}^*+q_{u,t,s})\cos\gamma_{0,s}\,d\Omega=\left(-\frac{2m}{\hbar^2}V_0\,a^3\right)^3\frac{\exp\{-\mu/2\cdot(r_u+r_{ut}+r_{ts}+r_s)\}}{kr_ur_{ut}r_{ts}r_s}\cos\gamma_{s,u}$$

$$\times[\sin k(r_u+r_{ut}+r_{ts}+r_s)M\{K_-(\gamma_{u,tu})\}+\sin k(-r_u+r_{ut}+r_{ts}+r_s)M\{K_+(\gamma_{u,tu})\}]$$

$$\times M\{K_-(\gamma_{ut,ts})\}M\{K_+(\gamma_{s,ts})\}\,. \tag{19}$$

§ 3. Application to Actual Crystals

The calculation was applied to copper, nickel and iron. The values of total cross section shown in Table II were chosen. The ejected electron decreases to $1/e$ as it moves as long as the cross section of the elastic collision is not large compared with that of the inelastic collision. From Eq. (16) the difference between the absorption coefficient* for solid and that for an isolated atom is proportional to the following term, if one assumes that

$$\left|\int \psi_0 z \exp(ikz)\, d\tau\right|^2$$

is constant:

$$-\sum_s \left(-\frac{2m}{\hbar^2} V_0 a^3\right) \frac{N_s}{r_s^2} \cdot \exp(-\mu r_s) \sin 2kr_s \left\{\frac{\cos 2ka}{(2ka)^2} - \frac{\sin 2ka}{(2ka)^3}\right\}, \quad (20)$$

where N_s is the number of atoms which are at equal distances from the absorbing atom and the summation extends all over the different r_s. The value of a is small compared with r_s, so that the term in braces in Eq. (20) is a modulating factor for $\sin 2kr_s$. The value of the summation is determined mainly by the terms of small r_s, even if the value of μ is small.

This follows from the consideration of several factors:

(1) For large r_s the terms $\sin 2kr_s$ have short periods with respect to k; (2) the amplitude N_s/r_s^2 decreases with increasing r_s; (3) the intervals between successive shells of neighboring atoms become smaller with increasing r_s.

* The absorption coefficient is given by the product of the transition probability and the state density, and in deriving Eq. (20), it is assumed that the state density is proportional to k as in the case of the isolated atom. Of course the state density will fluctuate in the solid, but the magnitude of the fluctuation is small compared with the fluctuation of the absorption coefficient.

Table II. The values of the total cross sections used in the calculation.

Element	Cu			Ni			Fe		
μ, in the lattice constant unit.	0.5	1	2	0.5	1	2	0.5	1	2
μ, in A^{-1}	0.069	0.138	0.277	0.071	0.142	0.284	0.087	0.174	0.349
σ_t, in A^{-2}	1.63	3.27	6.53	1.55	3.11	6.21	2.06	4.11	8.22

a distance 1/2, 1 or 2 times the lattice constant, respectively.

In Eq. (11), the first term is the largest and the second and the third term follow it, and we have only to consider the first term, Then the small difference in the value of μ and the domain of the summation do not affect the total summed value. Table III shows the values of N_s/r_s^2 for f.c.c. and b.c.c. crystals.

Table III. Distances from the absorbing atom to the neighboring shells and values of N_s/r_s^2 where N_s is the number of the atoms in each shell, in f.c.c. and b.c.c. crystals. r_s is expressed in unit of lattice constant.

	f.c.c.		b.c.c.	
No.	r_s	N_s/r_s^2	r_s	N_s/r_s^2
1	0.707	24.00	0.866	10.67
2	1.000	6.00	1.000	6.00
3	1.225	16.00	1.414	6.00
4	1.414	6.00	1.656	8.73
5	1.580	9.60	1.732	2.67
6	1.732	2.67	2.000	1.50
7	1.870	13.71	2.176	5.05
8	2.000	1.50	2.236	4.80
9	2.120	8.00	2.445	4.00
10	2.240	4.80	2.595	4.74
11	2.345	4.36	2.825	1.50
12	2.450	4.00	2.955	5.48
13	2.550	11.08	3.000	3.33
14			3.162	2.40
15			3.315	2.18

Figures 2, 3 and 4 show the calculated value of Eq. (20) for copper, nickel and iron for each value of μ. Curve (b) is the value summed up to the 7th shell in the f.c.c. lattice and up to the 8th shell in the b.c.c. lattice, when μ is zero. The curves (f) in the figures show the positions of the anomalies of the absorption coefficients according to Kronig's method. The height of each verti-

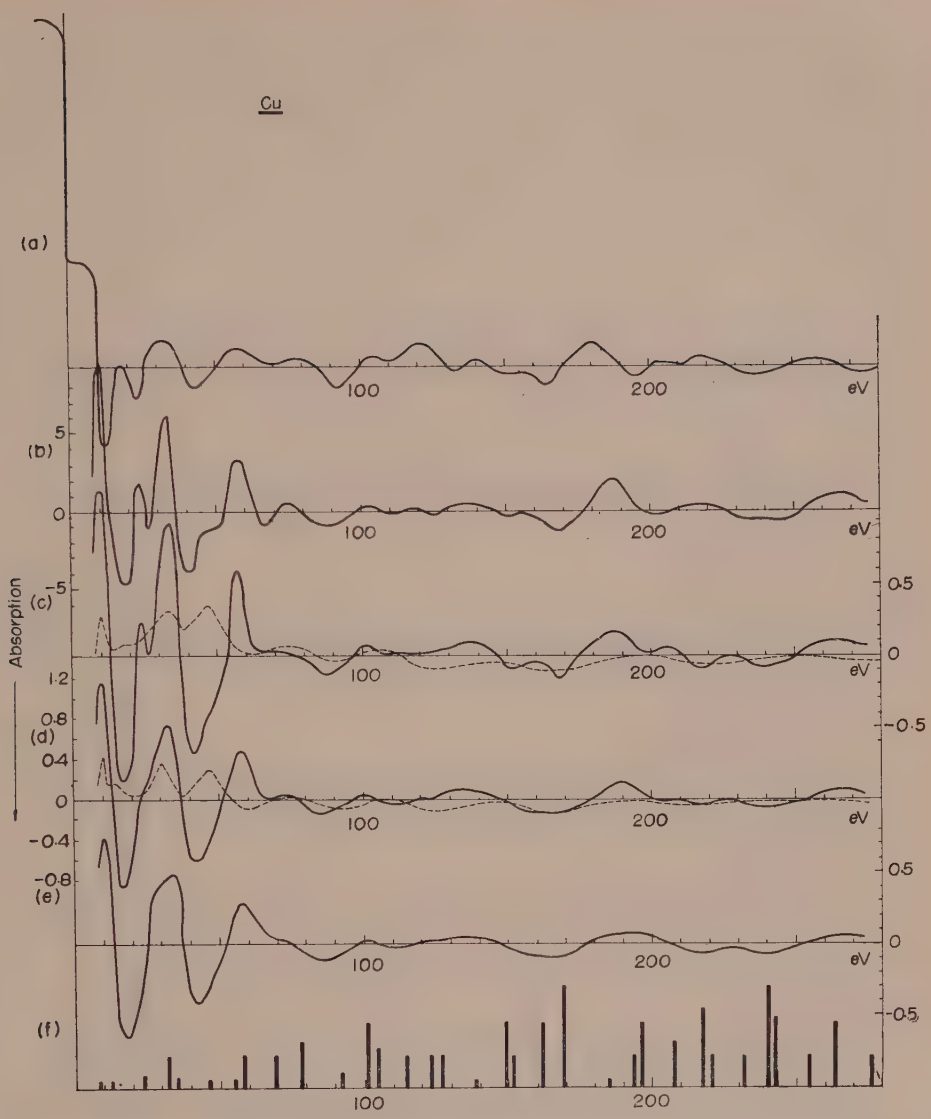

Fig. 2. The fine structure of the X-ray absorption spectrum of Cu at K absorption edge. Solid lines.

(a) Experimental curve. (b) Summed value of the formula (20) from the 1st neighbors to the 7th neighbors, for $\mu=0$. (c) Summed value of the formula (20) from the 1st neighbors to the 13th neighbors for $\mu=0.069\,\mathrm{A}^{-1}$. (d) Summed value of the formula (20) from the 1st neighbors to the 7th neighbors, for $\mu=0.138\,A^{-1}$. (e) Summed value of the formula (20) from the 1st neighbors to the 7th neighbors, for $\mu=0.277\,\mathrm{A}^{-1}$.

Dashed lines.

(c) Calculated value for the second term (17) and the third (18), for $\mu=0.069\,\mathrm{A}^{-1}$. The summation is extended over the values of s,s', 1,1; 1,2; 1,3; 2,2, and of s,t, 1,1; 1,2; 1,3; 2,2; 2,1; 3,1. (d) Calculated value for the second term (17) and the third (18), for $\mu=0.138\,\mathrm{A}^{-1}$. The summation is extended over the same values of s,s' and s,t in (c).

(f) Positions of the anomalies of the absorption ceofficient by Kronig's method for solid.

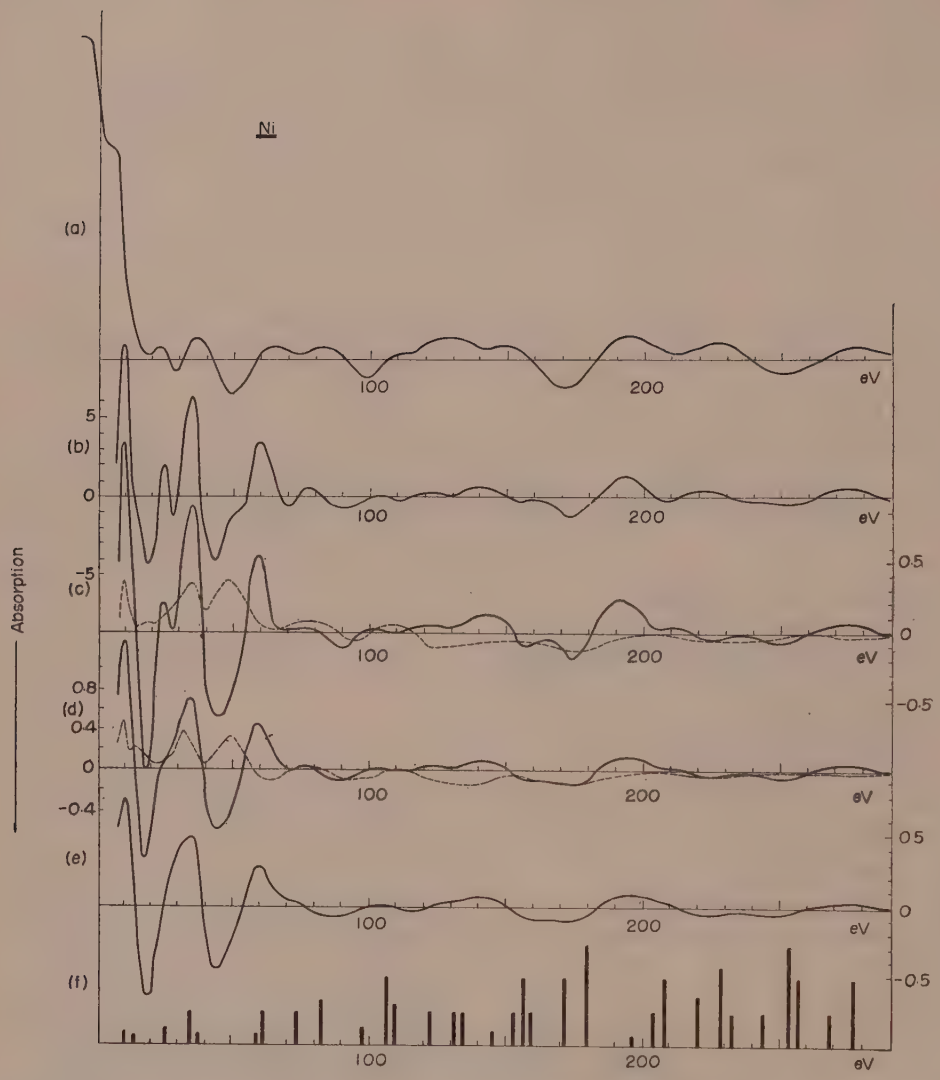

Eig. 3. The fine structure of the X-ray absorption spectrum of Ni at K absorption edge. Solid lines.

(a) Experimental curve. (b) Summed value of the formula (20) from the 1st neighbors to the 7th neighbors, for $\mu=0$. (c) Summed value of the formula (20) from the 1st neighbors to the 13th neighbors, for $\mu=0.071\,\mathrm{A}^{-1}$. (d) Summed value of the formula (20) from the 1st neighbors to the 7th neighbers, for $\mu=0.142\,\mathrm{A}^{-1}$. (e) Summed value of the formula (20) from the 1st neighbors to the 7th neighbors, for $\mu=0.284\,\mathrm{A}^{-1}$.

Dashed lines.

(c) Calculated value for the second term (17) and the third (18), for $\mu=0.071\,\mathrm{A}^{-1}$. The summation is extended over the values of s,s', 1,1; 1,2; 1,3; 2,2, and of s,t, 1,1; 1,2; 1,3; 2,2; 2,1; 3,1. (d) Calculated value for the second term (17) and the third (18), for $\mu=0.142\,\mathrm{A}^{-1}$. The summation is extended over the same values of s,s' and s,t in (c).

(f) Positions of the anomalies of the absorption coefficient by Kronig's method for solid.

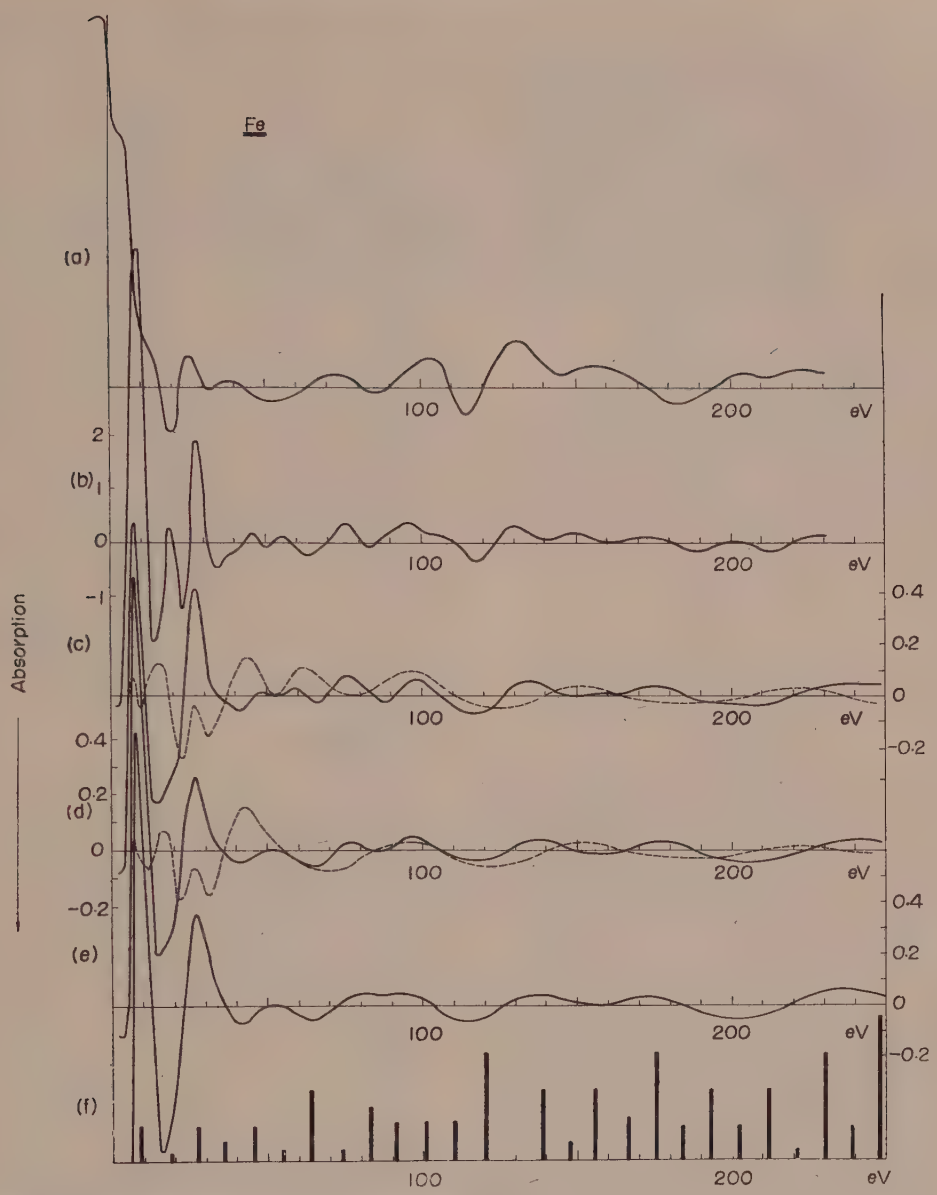

Fig. 4. The fine structure of the X-ray absorption spectrum of Fe at K absorption edge.
Solid lines.

(a) Experimental curve. (b) Summed value of the formula (20) from the 1st neighbors to the 8th neighbors, for $\mu=0$. (c) Summed value of the formula (20) from the 1st neighbors to the 15th neighbors, for $\mu=0.087\ \mathrm{A}^{-1}$. (d) Summed value of the formula (20) from the 1st neighbors to the 15th neighbors, for $\mu=0.174\ \mathrm{A}^{-1}$. (e) Summed value of the formula (20) from the 1st neighbors to the 8th neighbors, for $\mu=0.349\ \mathrm{A}^{-1}$.

Dashed lines.

(c) Calculated value for the second term (17) and the third (18), for $\mu=0.087\ \mathrm{A}^{-1}$. The summation is extended over the values of s,s', 1,1; 1,2; 1,3; 1,4; 2,2; 2,3; 2,4, and of s,t, 1,1; 1,2; 1,3; 1,4; 2,2; 2,3; 2,4; 2,1; 3,1; 4,1; 3,2; 4,2. (d) Calculated value for the second term (17) and the third (18), for $\mu=0.174\ \mathrm{A}^{-1}$. The summation is extended over the same values of s,s' and s,t in (c).

(f) Positions of the anomalies of the absorption coefficient by Kronig's method for solid.

cal line, which shows the position of the anomaly, corresponds to the multiplicity of the corresponding discontinuous plane of energy in the Brillouin zone diagram. In the calculations of (b), (c) and (d), the radius of potential hole a was taken to give the best-fit results with experiments. Considering that its value is the order of one tenth that of the lattice constant, these were found to be

$a=0.42$ A for copper,
$a=0.42$ A for nickel,
$a=0.60$ A for iron.

In order to estimate the above values the following facts were taken into consideration. In Eq. (20), the term modulating the amplitude changes its sign at the value of k which satisfies the

$$\cos 2ka-\frac{\sin 2ka}{2ka}=0\,,$$

hence

$$k=\frac{2\pi}{a}\times 0.355\,.$$

Experimental curves in the same figures are refered to Hayashi[3] for Cu and to our own data for Ni and Fe, photographed with a Johann type spectrograph, 25 cm radius of the Rowland circle and by reflection from the (130) planes of quartz. With this spectrograph the half width of Cu $K\alpha_1$ line is 0.6 x.u., with 7 mm opening of the crystal surface, and it may be assumed that the crystal is bent with a considerably high accuracy. The experimental curve obtained by Hayashi is the density curve itself but ours give the logarithm of the X-ray intensity.

The abscissa in these figures is the value of energy of the free electron corresponding to the wave number $k/2\pi$, and retains, of course, the wave packet uncertainty. The value of $(-2m/\hbar^2\cdot V_0a^3)$ is not necessary in Eq. (20); however, it does become necessary when one considers the terms Eqs. (17) and (18). The ordinate is the value for the case that the cross section for elastic collision is 25% of the total cross section, at 46.5 eV. in copper, 48 eV. in nickel, and 41 eV. in Fe. The relation between $(-2m/\hbar^2\cdot V_0a^3)$ and the cross section of the elastic collision is given by the equation,

$$\sigma_{\rm el}=\left(\frac{2m}{\hbar^2}V_0\,a^3\right)^2\frac{2\pi}{(ka)^2}\left[\frac{1}{4}-\frac{1}{4}\frac{1}{(2ka)^2}+\frac{1}{4}\frac{1}{(2ka)^3}\sin 2ka-\frac{1}{8}\frac{1}{(2ka)^4}(1-\cos 4ka)\right]. \tag{21}$$

In order to make clear the effect of the second term, and the third, these terms were calculated over a few neighboring shells; the results are shown by the dashed curves in the same figures. In iron the ratio of these terms to the first term is large compared with that for f.c.c. crystals. This is due to the b.c.c. structure, that is, to the fact that the value of N_s/r_s^2 for a b.c.c. structure is small compared with that for a f.c.c. crystal and the amplitude of the first term in Eq. (11) becomes correspondingly small. Thus the second and the third terms affect the result, when $\sigma_{\rm el}$ is not small. In the calculation of these terms the main part arises from those pairs of atoms for which $\gamma_{t,ts}$ or $\gamma_{s,s's}$ is small, this result being due to the character of the Born scattering.

§ 4. Discussion

Calculated results shown in Figs. 2, 3 and 4 are in fairly good agreement with experimental curves in the energy region of 50–250 eV.. In the energy region below 50 eV. the magnitudes of the fluctuations in the calculated curves are greater than those of the experiments. Perhaps this is a consequence of the assumption that the total cross section is independent of k, and also that Born's approximation becomes poor in the low energy region. When the second term and the third are taken into consideration better results are obtained for copper and nickel, but it is not so for iron. There are questions about the choice of the parameter a and about the effects of the terms neglected in the present calculation, but it will be meaningless to discuss these points further so long as a well type potential hole is assumed and Born's approximation is used.

The authors have calculated the variation of the transition probability on the assumption that the magnitude of the total cross section of the atom in a crystal is of the order of one square Angstrom and the inelastic part of the cross section is not small, and in this way good results have been obtained, although, to a rough approximation, the simple form of the potential hole and Born's

approximation were adopted. That our results are so good, may be due to the validity of the assumptions. If the assumption for the inelastic cross section is proper, the fine structure of the absorption spectrum will be related only to atoms in the neighborhood of the absorbing atom; consequently the present method allows one to obtain a clearer picture of the relation between the structure of the substance and the spectral fine structure, since one can treat the problem for various substances, from molecules to crystals, with a unified method.

In order to modify the present calculation, it is necessary to consider the following points. One must calculate accurately the scattered amplitude for the actual potential field and consider the additive potential field due to the missing K-electron. This is particularly important for calculations on insulators. Also the departure from the free electron approximation, which is adopted in the present calculation, must be considered. These are important in low energy region. In addition, the variation of the cross section with respect to k should be obtained in the whole energy region. The thermal motion of the atoms has not been considered in the present calculation but its effect can be obtained by averaging the calculated result with respect to the positions of the atoms.

In conclusion, the authors wish to express their sincere thanks to Prof. T. Nagamiya for his kind comment and advice, to Asst. Prof. T. Nishiyama and Asst. Prof. Y. Toyozawa of Kyoto University for useful suggesions, and to Mr. S. Yomosa and Dr. J. Kanamori for valuable discussions. They also express their gratitude to Profs. C. H. Shaw, J. Korringa and E. L. Jossem of Ohio State University for reading the manuscript and giving them kind remarks.

References

1) R. de L. Kronig: Z.S.f. Phys. **70** (1931) 317, **75** (1932) 191.
2) R. de L. Kronig: Z.S.f. Phys. **75** (1932) 468.
H. Petersen: Z.S.f. Phys. **76** (1932) 768, **80** (1933) 258, **98** (1936) 569.
D. R. Hartree, R. de L. Kronig and H. Petersen: Physica **1** (1934) 895.
C. H. Shaw and T. M. Snyder: Phys. Rev. **58** (1940) 600.
E. M. Corson: Phys. Rev. **70** (1946) 645.
3) T. Hayashi: Sci. Repts. Tohoku Univ. Ser. 1 **33** (1949) 123, 183 ibid **34** (1950) 185.
T. Hayashi and S. Okada: Sci. Repts. Tohoku Univ. Ser. 1 **37** (1953) 331.
4) A. I. Kostarev: Zhur. eksptl. teoret. Fiz. S. S.S.R. **11** (1941) 60, **19** (1949) 413, **21** (1951) 917.
5) S. Kiestra: A Conference on the Applications of X-ray Spectroscopy to Solid State Problems. 23–25 Oct., 1950.
M. Sawada, K. Tsutsumi, T. Shiraiwa and M. Obashi: J. Phys. Soc. Japan **10** (1955) 468.
M. Sawada, K. Tsutsumi and A. Hayase: J. Phys. Soc. Japan **12** (1957) 628.
T. Shiraiwa, T. Ishimura and M. Sawada: J. Phys. Soc. Japan **12** (1957) 788.
6) C. Kurylenko: Cahiers de Physique, No. 54, (1955) 1.
7) V. Weisskopf and E. Wigner: Z.S.f. Phys. **63** (1933) 54, **65** (1930) 18.
V. Weisskopf: Physik. Zeits. **34** (1930) 1.
F. Hoyt: Phys. Rev. **35** (1930) 860.
8) F. K. Richtmyer, S. W. Barnes and E. Ramberg: Phys. Rev. **46** (1934) 843.
9) W. W. Beeman and H. Friedman: Phys. Rev. **56** (1939) 392.
10) H. E. Farnsworth: Phys. Rev. **49** (1936) 605.
11) P. M. Morse: Phys. Zeit. **33** (1932) 443.
12) H. Bethe: Ann. d. Phys. **5** (1930) 325.
13) *Landolt-Börnstein Zahlenwerte und Funktionen aus Physik. Chmie. Astronomie. Geophysik. Technik.*, I Band, 1 Teil, 1950 Springer-Verlag Berlin.

JOURNAL OF THE PHYSICAL SOCIETY OF JAPAN Vol. 13, No. 8, AUGUST, 1958

Nuclear Quadrupole Spectra of Boron Trichloride and Tribromide

By Takehiko CHIBA

Department of Chemistry, Faculty of Science
University of Tokyo, Tokyo

(Received March 28, 1958)

The pure quadrupole resonance spectra were observed on Cl^{35} and Cl^{37} in BCl_3 and Br^{79} and B^{31} in BBr_3 at several temperatures. The spectrum of each nucleus consists of characteristic doublet (ν_I and ν_{II}) with the intensity ratio of ca. 3 to 5. The Zeeman study with a single crystal of BBr_3 was also carried out at liquid nitrogen temperature (77°K), to determine the asymmetry parameter η. The results are as follows:

	Cl^{35}	Cl^{37}	Br^{79}	Br^{31}
ν_I	21.582±0.001	17.008±0.002	175.293±0.002	146.434±0.002 Mc,
ν_{II}	21.578±0.001	17.004±0.002	175.264±0.002	146.411±0.002 Mc.
$\nu_I-\nu_{II}$	3.68±0.10 kc	—	26.1±0.5 kc	21.6±0.5 kc
η	—	—	0.45±0.05	—
eQq	42.9 Mc	—	340 Mc	—

The ionic character and the double bond character were estimated to be $i=0.42$ and $f=0.11$, respectively for the B-Br bond from the above results. In BCl_3, $f=0.06$ was obtained by assuming $i=0.50$. The double bond characters of these compounds are fairly smaller than usually assumed.

The doublet separation cannot be explained by direct nuclear dipole-dipole interaction. A reasonable explanation was made by taking into account the effect of the intramolecular vibration: the isotopes of boron B^{10} and B^{11} provide different mean square amplitudes to the bending vibrations of BX_3, which in turn produce a difference of q for $B^{10}X_3$ and $B^{11}X_3$ molecules. The effect was calculated by use of the normal frequencies of BCl_3 and BBr_3. A fair agreement was obtained between the observed separation of the doublet and hte calculated one. The observed intensity is also compatible with the assumption.

§ 1. Introduction

In nuclear quadrupole resonance spectrum the frequency of the absorption line is determined by the coupling of the quadrupole moment of a nucleus with the electric field gradient at the nucleus. In molecular crystals the field gradient is mainly fixed by the distribution of valence shell electrons in bonding and nonbonding orbitals, but a minor contribution of intermolecular field cannot be neglected because of high resolution of this spectroscopy, and, in fact, even a slight nonequivalence of the positions of atoms in the crystal can be detected by a difference of absorption frequencies. Thus the number of absorption lines corresponds to the number of nonequivalent positions of the nuclei in the crystal, though accidental coindidence of the absorption lines often takes place. This expectation has been well established by a number of studies[1] for substances whose structures were determined by the X-ray analysis.

In his early work Livingston[2] reported two line separated by five kilocycles for Cl^{35} nuclear quadrupole resonance spectrum of BCl_3. On the other hand Rollier and Riva[3] found by the X-ray diffraction that all the chlorine atoms are equivalent in BCl_3 crystal. Hence from the relation mentioned above only a single line is expected for Cl^{35} nuclear quadrupole resonance spectrum of BCl_3, and doublet actually observed has to be attributed to another effect. The main purpose of the present study is to make clear the origin of the doublet by the measurement of the resonance lines of BCl_3 and BBr_3, the latter compound being known as isomorphous to the

former[3]. In connection with this, the nature of B-halogen bond will be discussed from the observed coupling constants and the asymmetry parameters obtained from the observation of the Zeeman effect. Two accounts are taken into consideration in the present work: a) dipole-dipole interaction between the neighboring nuclei and b) boron isotope effect on the mean amplitudes of molecular vibration. It is confirmed that the latter is the cause of the doublet.

After this study had been finished, the present author noticed that Douglass[4] also made a study on boron trichloride with similar intention and his conclusion was quite close to the present one, though the effect a) was not definitely excluded because his measurement was carried out only on boron trichloride.

§ 2. Experimental

A. *Preparation of Materials.* Boron trichloride was prepared by passing dried chlorine gas on metallic boron at 400°C. The product obtained was purified twice by vacuum distillation.

Boron tribromide was prepared by heating a mixture of potassium borofluoride and aluminium bromide. As the raw product contained some partially fluorinated compounds, probably $BFBr_2$, it was fractionally distilled to get a fraction boilling at 91°C.

B. *Measurement of Frequency.* Two radio-frequency spectrographs of superregenerative type were used: one for chlorine resonance and the other for bromine. The oscillator-deterctor circuit of the former was similar to that used by Dean[5], and that of the latter was almost the same as that by Kojima[6]. The frequency ranges of the circuits were 15 to 45 Mc/s and 110 to 300 Mc/s respectively. The absorption signals were displayed on an oscilloscope screen or recorded on a pen-recorder through a lock-in amplifier and a phase-sensitive detector. For the accurate measurement of the frequency of an absorption line a signal generator was first adjusted to the absorption signal with the aid of an oscilloscope, then frequency of the signal generator was mixed with harmonics of 1000 kc which was generated by a 1 Mc crystal oscillator calibrated within the order of 10^{-5} by JJY frequency standard. The beat signal in the range of 500 to 1000 kc was picked up and the beat frequency was measured with the precision of 0.3 kc by a frequency-calibrated heterodyne receiver. Small separation between the doublet lines was measured by the comparison with a quenching frequency on a recorder chart.

C. *Observation of Zeeman Effect of a Single Crystal.* The magnetic field used for the Zeeman effect of quadrupole resonance line was furnished by a Helmholtz coil of inner diameter of 16 cm, the field strength being 108 oersted/amp. A single crystal of BBr_3 was prepared by use of the apparatus shown in Fig. 1. An ampule, 1.5 cm in diameter

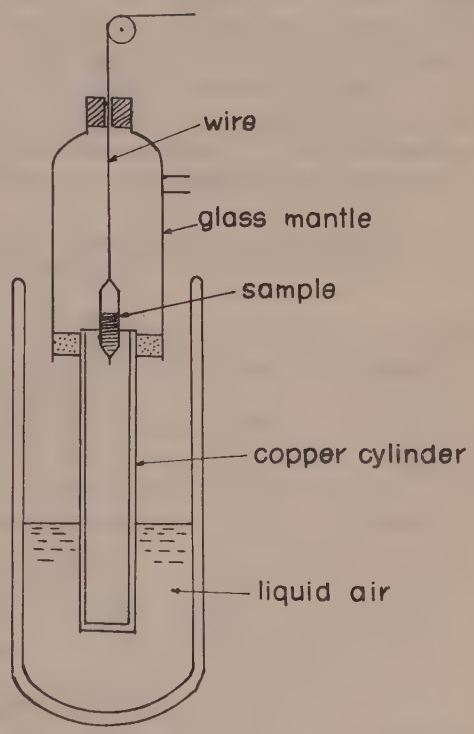

Fig. 1. Apparatus for the preparation of a single crystal.

and 5 cm in length containing ca. 10 g of BBr_3, was lowered slowly (5–6 mm/hr) into a copper tube (3 mm thick, 2.5 cm in diameter, and 13 cm in length) which was cooled by liquid air. The single crystal thus prepared was annealed by storing it for a few days in a Dewar vessel filled with dry ice.

§ 3. Results

A. *Resonance Lines without Magnetic Field.* The measurement of the spectrum was made at the temperatures of liquid nitrogen and

oxygen for BCl_3, and of liquid nitrogen and oxygen and dry ice for BBr_3. Signals of high signal-to-noise ratio were observed both for BCl_3 and BBr_3. In the case of bromide, however, no signal was observed at first. It was found to be attributed to the broadening effect of q by the random neighbor configuration which was caused by the contamination of a small amount of fluorine compounds. A similar broadening effect has been found in the case of solid solutions of p-dihalogenobenzenes[7].

The absorption pattern of the two compounds displayed a similar shape of closely lying doublet lines: the stronger one, ν_I, on the high frequency side and the weaker one, ν_{II}, on the low. The typical recording curve of Br^{81} in BBr_3 is shown in Fig. 2. The frequencies measured at various temperatures are given in Table I. The frequencies of Cl^{35} at the liquid nitrogen temperature are in good agreement with those reported by Livingston[2]. By integrating the differential curve taken on the recorder, the intensity ratio was estimated to be 3 to 5. More accurate value of the ratio was not obtained not only because it depends on the base line assumed somewhat arbitrarily, but also because superregenerative detection is known to be less reliable for the shape of the absorption line. For bromide the absorption was also recorded by autodyne operation. The curve was almost similar to that by superregenerative one. The line widths were fairly large, rough estimate of them being given in Table I. The separation of the lines was measured at the liquid nitrogen temperature. The results are also listed in Table I.

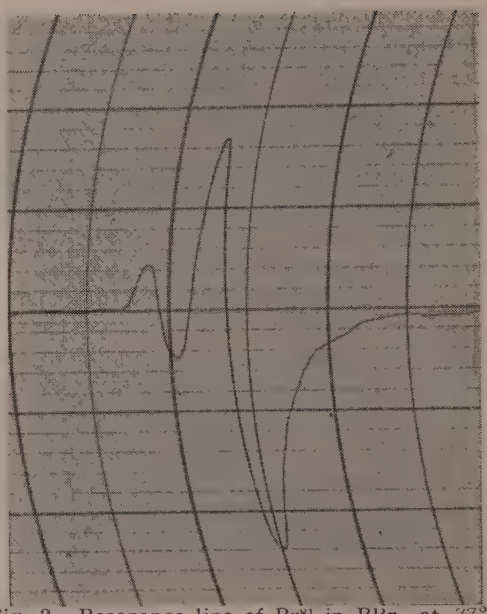

Fig. 2. Resonance line of Br^{81} in BBr_3 at 77°K recorded as a derivative curve.

Table I. Observed frequencies of the pure quadrupole resonance spectra of boron trichloride and tribromide (in Mc).

		77°K	90°K	196°K
BCl_3	ν_I	21.582±0.001 (ca. 3 kc)	21.552±0.001	
Cl^{35}	ν_{II}	21.578±0.001 (ca. 2 kc)	21.549±0.001	
Cl^{37}	ν_I	17.008±0.002	16.986±0.002	
	ν_{II}	17.004±0.002	16.983±0.002	
BBr_3	ν_I	175.293±0.002 (ca. 20 kc)	175.123±0.003	173.084±0.010
Br^{79}	ν_{II}	175.264±0.002 (ca. 15 kc)	175.100±0.003	173.059±0.010
Br^{81}	ν_I	146.434±0.002	146.302±0.003	144.590±0.010
	ν_{II}	146.411±0.002	146.277±0.003	144.570±0.010

Doublet separaration measured at 77°K

BCl_3	Cl^{35}	3.68±0.10 kc	BBr_3	Br^{79}	26.1±0.5 kc
				Br^{81}	21.6±0.5 kc

Values in the parentheses are the band widths.

B. *Zeeman Effect* The main purpose of the observation of Zeeman effect of BBr_3 is to obtain asymmetry parameter of the halogen atoms. On account of the low melting point of the compound (−46°C), a great difficulty

was imposed to study the Zeeman effect of this substance. Furthermore the doublet structure of the original line made it more complicated. Thus the analysis was made to the step which was sufficient to obtain η with the aid of knowledge of crystal structure by the X-ray diffraction.

Now the frequencies of the Zeeman components are given in the case of $I=3/2$ by the following expression which is exact in η and is approximate to the first order in the applied magnetic field $\boldsymbol{H}$

$$\nu=\nu_0\pm\begin{cases}s_1\\ s_2\end{cases} \tag{1}$$

$$\begin{aligned}\left.\begin{matrix}s_1\\ s_2\end{matrix}\right\}=\frac{\mu}{3h\xi}[&\{2(\xi-1)(2\xi+\eta+1)H_x^2\\ &+2(\xi-1)(2\xi-\eta+1)H_y^2+(\xi+2)^2H_z^2\}^{1/2}\\ &\pm\{2(\xi+1)(2\xi-\eta-1)H_x^2\\ &+2(\xi+1)(2\xi+\eta-1)H_y^2+(\xi-2)^2H_z^2\}^{1/2}]\,,\end{aligned} \tag{2}$$

where

$$\xi=\left(1+\frac{1}{3}\eta^2\right)^{1/2}. \tag{3}$$

μ is the magnetic moment of the nucleus, and H_x, H_y and H_z are the components of the applied magnetic field in the direction of three principal axes of the q tensor ($|q_{xx}|<|q_{yy}|<q_{zz}|$). Thus a single line splits in general into four. According to the results of electron diffraction[8], infrared spectrum, and the Raman effect[9], BBr_3 molecule has three B–Br bonds in the directions of 120° with each other, all lying on the same plane. Crystal analysis give the same structure[3),10]. Therefore, a magnetic field will in general give rise to a pattern of twelve-component lines, which may be too complicated to analyse directly. The analysis was made first by determining the direction in which the Zeeman pattern has a component line at its center ($s_2=0$ in Eq. (1)). The relation between the splitting pattern and the direction of the applied field is conveniently understood by a sphere shown in Fig. 3, in which the molecule is put at the center of the sphere and on the equatorial plane with a B–Br bond in the x-direction. A point on the surface of the sphere corresponds to a direction of the magnetic field relative to the molecule. The circles drawn on the surface of the sphere show the directions in which central lines are to be observed. The curve is circle when $\eta=0$, but becomes elongate towards the z-direction as η grows up. In order to get the direction of a bond, first the area is located where two lines BCD and EFG run nearly parallel (actually about twenty degrees apart),

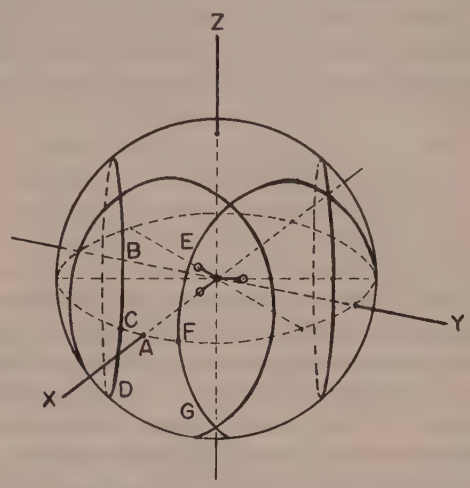

Fig. 3. Sphere showing angular relation of Zeeman patterns.

and then the point A is determined by measuring the split patterns on the bisecting line of the two parallel lines. The arc CAF provides a measure of η. The point C (or F) is the direction making an angle of 60°−CAF/2 with the bond direction. This angle is given from Eq. (2) by letting $s_2=0$ and $H_x=0$:

$$\tan\left(60^\circ-\frac{\mathrm{CAF}}{2}\right)=\frac{H_y}{H_z}=\sqrt{\frac{2}{1+\eta}}\,. \tag{4}$$

From the length of the arc CF, 21±1°, η was calculated to be 0.45±0.05.

C. *Temperature Dependence of Resonance Lines.* The variation of the reasonance lines with temperature was found to be normal in bromide. Since the lattice frequencies of the crystal are not known, exact reasonance frequency free from the effect of the lattice vibration is not obtained. Therefore, the value extrapolated to 0°K, 175.9 Mc/s, is tentatively taken as ν_0 for Br^{79} of BBr_3. This frequency, with the value of η obtained at 77°K, was used to calculate the coupling constant:

$$(eQq)^{79}=2\nu_0\Big/\left(1+\frac{1}{3}\eta^2\right)^{1/2}=340\ \mathrm{Mc/s}\,. \tag{5}$$

For BCl_3, η was not measured and, accordingly, taken $\eta=0.24$ as estimated in the discussion described later, eQq was found to be 42.9 Mc/s.

§ 4. Discussion

A. *Boron-Halogen Bonds in Boron Halide Molecules.* The B–X bond of boron trihalide molecules may be represented by the resonance among the following three structures:

If the scheme is assumed, the amount of unbalanced p-electrons which is directly connected to the field gradient can be calculated by a procedure similar to that used by Kojima[11]. The z-axis is taken to be parallel to a B–Br bond, the x-axis to be perpendicular to the molecular plane, and the y-axis to be in the plane and perpendicular to the bond. The double bond in the configuration II involves a π-orbit in addition to the σ-orbit. The s-hybridization of a p_σ-bond in I or in II is assumed to be 15%[12]. The factor ε, the increase of q by a positive nuclear charge at the halogen nucleus in the configuration II, is assumed to be $+0.15$ as given by Townes[12]. In the configuration I the contribution to the field gradient q at the bromine nucleus comes from $(1-s)q_\sigma$ of the bonding electrons in p_σ plus s orbit, $2sq_\sigma$ of the nonbonding electrons in s plus p_σ orbit, and $2q_x$ and $2q_y$ of the nonbonding electrons in p_π orbits. In the configuration II q comes from $(1-s)q_\sigma(1+\varepsilon)$ of the bonding electrons in p_σ plus s orbit, $2sq_\sigma(1+\varepsilon)$ of the nonbonding electrons in π-orbit, and $q_x(1+\varepsilon)$ of the bonding electrons in π orbit of the double bond. The configuration III contributed nothing to q because in the first approximation X-ion has a spherically symmetric distribution of electrons.

Now if the double bond character of the B–X bond (the fraction of the configuration II in the resonance structure) and its ionic character (that of III) are designated by f and i respectively, then it can be easily shown that the total field gradients in the x-, y- and z-directions are given by

$$q_{xx}=(0.425-0.425i-1.086f)q\ ,$$

$$q_{yy}=(0.425-0.425i+0.639f)q\ ,$$

and

$$q_{zz}=(-0.85+0.85i+0.447f)q\ ,$$

where q denotes the q-value of a pure $4p_\sigma$ orbit electron of a bromine atom in the bond direction, that, is q_{410}. Thus the amount of the unbalanced p electrons of the halogen atom in the bond direction U_p, is

$$U_p==-q_{zz}/q=+0.85-0.85i-0.447f\ , \quad (6)$$

and the asymmetry parameter is

$$\eta=(q_{xx}-q_{yy})/q_{zz}=1.725f/U_p\ . \quad (7)$$

The observed values of $\eta=0.45$ and of $U_p=(eQq)_{\rm obs}/(eQq)_{\rm atom}=340/769.8=0.442$ provide the results of $f=0.12$ and $i=0.42$. The s-curve relation between ionicity and electronegativity proposed by Dailey and Townes[13] gave $i=0.35$ for B–Br. Judging from the fact that in BX_3 three halogen atoms are attached to the same boron atom, the ionicity of the halogen atom should be fairly reduced and the ionicity of 0.42 obtained above seems unreasonable. However, it is hardly attributed to the neglect of the effect of intermolecular partial bond which is seen in some compounds such as iodine[14] and bromine[15]. A recent result of the X-ray reinvestigation by Atoji and Lipscomb[10] shows that the bond length of B–Cl is not quite different from that in the vapor state and the nearest intermolecular Cl···Cl distances have regular Van der Waals' values, which indicates that the bonds are essentially confined in the molecules but not shared between two molecules. The situation must be similar in BBr_3, and it is also consistent with the normal temperature variation of the resonance frequencies in BBr_3.

If U_p of B–Br bonds in other molecules could be explained by taking ionicity of Townes' value 0.35, the large apparent ionicity obtained in BBr_3 might be due to the effect such as intermolecular bonding or large crystalline field. However, U_p of B_2H_5Br is 0.39*, which is consistent with ionicity of at

* The coupling constant of Br^{79} in B_2H_5Br measured in the microwave spectroscopy is 294 Mc/s in the a-axis direction (C. D. Cornwell, J. Phys., **18** (1950) 1118). By transforming the q tensor using the molecular geometry, the coupling constant along the direction of the B–Br bond is estimated to be 298.4 Mc. Unknown asymmetry parameter in this case does not appreciably affect the transformation, since the a-axis is closely parallel to the B–Br bond.

least 50%. The decrease of ionicity from B_2H_5Br to BBr_3 is normal and an ionicity higher than Dailey and Townes' value is necessary to fit to the U_p of both of the two compounds. Therefore, it is hardly probable that large intermolecular effects exist in BBr_3.

Although no asymmetry parameter was measured for BCl_3, the situation must be quite similar. Thus by assuming 50% ionic character for B–Cl bond, $f=0.06$ is obtained from $U_p=42.9/109.7=0.392$. Hence by use of Eq. (6) η is calculated to be 0.24**. Contrary to this result, Gordy[16] estimated $f=0.29$ and $i=0.46$ for B–Cl bond in this compound. These values provide an abnormal result that the maximum q does not lie in the B–Cl bond direction but in the y-axis, and the value of $\eta=0.90$ obtained seems to be unreasonably large. From a relation of bond distance to the bond character Pauling[16] estimated that configuration II is the dominant one, and, accordingly, B–X bond has about 1/3 double bond character and about 2/3 single bond character. Though the present treatment utilizes some simplifying assumptions, it may be noted that the double bond character is found to be appreciably lower than Pauling's estimate in both of the two compounds. A similar situation was also met in the case of p-dichlorobenzene[16),17]: the double bond character derived from quadrupole resonance data was far less than that formerly estimated from the bond distance.

B. *Origin of Doublet Structure.* As described above, the doublet lines are not expected from the crystal structure. It is another evidence of nonstructural origin of the doubling that the two lines showed similar behavior in the temperature dependence of the frequencies and in the Zeeman effect.

The doublet separation of the Cl^{35} resonance line, about 4 kc, is of the order of spin-spin interaction. The largest spin-spin coupling acts between the pair of boron and halogen atoms which form the direct bond, for it is the shortest inter-atomic distance in the boron halide crystal. The B–Cl distance of 1.75A from the X-ray analysis and the spin moment of 2.7 nuclear magnetons of B^{11} (the abundance ratio of B^{11} being 81%) give the splitting of the order of 2.1 kc in case when $\eta=0$. It should be noted that Douglass calculated the splitting due to the same spin-spin interaction for B–Cl in case of $\eta=\pm1$. Change in η gives different patterns but the total splitting is of the same order. Similarly the splitting is found to be 4.5 kc for bromine by assuming B–Br distance to be 1.87A and $\eta=0$. The calculated value for Cl^{35} is almost the same order as the observed one, 4 kc, but for Br^{79} it is too small to explain the observed separation 26 kc. It clearly indicates that the spin-spin interaction is not the main origin of the doublet. Each line of the doublet is remarkably broad, the width being almost 2 kc for BCl_3 and 10 kc for BBr_3, which may be attributed to the spin-spin interaction discussed above.

A reasonable explanation of the doublet structure can be found in the difference of the mean square amplitudes of molecular vibrations in $B^{10}X_3$ and in $B^{11}X_3$ molecules as Douglass pointed out. When a bond with q of axial symmetry oscillates about a space-fixed axis, the q decreases to $q_0\left(1-\frac{2}{3}\langle\theta^2\rangle\right)$, where q_0 is its original value and $\langle\theta^2\rangle$ denotes the mean square amplitude of the angle of oscillation[18]. In crystals the oscillation may be either lattice mode or intramolecular vibration, so that the difference in $\langle\theta^2\rangle$ caused by boron isotopes will reflect on a change in resonance frequency, and thus produces a doublet. Douglass calculated this effect and concluded that, though the agreement between the observed and the calculated is not very good, this is more likely to be the origin of the doubling.

In the present paper a similar calculation is also made for both BCl_3 and BBr_3. The procedure and the values used in the calculation are somewhat different from Douglass' ones a) in the formula of temperature dependence of vibration in the presence of η, and b) in the frequencies of the normal vibrations and force constants.

Wang[19] derived a formula for the effect of molecular torsional motions on the shift of the quadrupole frequency of a nucleus with spin 3/2 in a field gradient without axial

** At the first glance it seems unreasonable for estimating η to use the value 42.9 Mc/s of the eQq which was obtained by assuming $\eta=0.24$. The assumed value of η was used to make a small correction for the asymmetry factor which is often neglected. In fact the correction is only 1%.

symmetry.

His final formula is

$$h\nu = q'\left(1+\frac{1}{3}\eta'^2\right)^{1/2} \tag{8}$$

where

$$q' = q\left[1-\frac{3}{2}(\langle\theta_x^2\rangle+\langle\theta_y^2\rangle)+\frac{1}{2}\eta(\langle\theta_y^2\rangle-\langle\theta_x^2\rangle)+\frac{1}{2}(3-\eta)\langle\theta_x^2\rangle\langle\theta_y^2\rangle\right], \tag{9}$$

and

$$\eta' = (q/q')\left[\eta+\frac{3}{2}(\langle\theta_y^2\rangle-\langle\theta_x^2\rangle)-\frac{1}{2}\eta(\langle\theta_y^2\rangle+\langle\theta_x^2\rangle)+\frac{1}{2}(3-\eta)\langle\theta_x^2\rangle\langle\theta_y^2\rangle\right], \tag{10}$$

and $\langle\theta_x^2\rangle$ and $\langle\theta_y^2\rangle$ are the mean amplitudes of osillations about the x and y axis, q and η are referred to the molecule at rest. Substituting Eqs. (9) and (10) into Eq. (8) and expanding it in the power series of $\langle\theta^2\rangle$,

$$h\nu = h\nu_0(1-\alpha\langle\theta_x^2\rangle-\beta\langle\theta_y^2\rangle), \tag{11}$$

where

$$h\nu_0 = \frac{1}{2}eQq\left(1+\frac{1}{3}\eta^2\right)^{1/2}, \tag{12}$$

and

$$\left.\begin{aligned}\alpha &= \left(3+2\eta+\frac{1}{3}\eta^2\right)\Big/2\left(1+\frac{1}{3}\eta^2\right),\\ \beta &= \left(3-2\eta+\frac{1}{3}\eta^2\right)\Big/2\left(1+\frac{1}{3}\eta^2\right).\end{aligned}\right\} \tag{13}$$

Eq. (13) is more appropriate than that used by Douglass, since the latter is lacking in the terms arising from $(m, m\pm2)$th energy matrix elements which have a significance of the first order.

In this calculation, the procedure of computing the mean square amplitudes about a space-fixed direction by use of a relation of Cartesian displacements to the normal vibrations is applied. This is convenient for treating complicated molecules. The Cartesian displacements $\boldsymbol{X}$ are related to the normal coordinates $\boldsymbol{Q}$ by the well-known matrix expression of $\boldsymbol{X}=\boldsymbol{AQ}$, where $\boldsymbol{A}=\boldsymbol{M}^{-1}\boldsymbol{B}'\boldsymbol{U}'\times(\boldsymbol{L}^{-1})'$ [20]. Therefore θ_j can easily be expressed by the normal coordinates:

$$\theta_j = \sum_i D_{ji}Q_i\,. \quad (j=\text{x, y or z}) \tag{14}$$

Thus by taking time-average,

$$\langle\theta_j^2\rangle = \sum_i D_{ij}^2\langle Q_i^2\rangle\,. \tag{15}$$

and

$$\langle Q_i^2\rangle = \frac{h}{8\pi^2\nu_i}\coth\frac{h\nu_i}{2kT}\,. \tag{16}$$

Normal frequencies used in the present calculation were those determined recently by Lindeman and Wilson[21]. From these normal frequencies generalized force constants, one for out-of-plane and three for in-plane degenerate modes were obtained. Then $\langle\theta^2\rangle$'s were obtained by the method described above. The difference in the mean amplitudes due to boron isotopes gave different values of $B^{10}X_3$ and $B^{11}X_3$. The calculated values of the splitting were compared with the observed ones in the form of a fraction to the resonance frequency, that is,

$$\frac{\Delta\nu}{\nu} = \alpha(\langle\theta_x^2\rangle_{B^{10}}-\langle\theta_x^2\rangle_{B^{11}})+\beta(\langle\theta_y^2\rangle_{B^{10}}-\langle\theta_y^2\rangle_{B^{11}})\,. \tag{17}$$

The results are shown in Tables II and III.

Table II. Calculated difference of mean square amplitudes ($\langle\theta^2\rangle_{B^{10}}-\langle\theta^2\rangle_{B^{11}}$) between $B^{10}X_3$ and $B^{11}X_3$ at 77°K (in 10^{-4}).

vibrational mode	BCl_3	BBr_3
ν_2	0.577	0.577
ν_3	0.329	0.294
ν_4	−0.010	−0.004

Table III. Calculated and observed splitting given in the fraction to the original frequency, $\Delta\nu/\nu\times10^4$.

	$(\Delta\nu/\nu)_{calcd}$			$(\Delta\nu/\nu)_{obsd}$
	out-of-plane	in-plane	total	
BCl_3	0.716	0.549	1.265	1.70
BBr_3	0.586	0.540	1.126	1.49

A fair agreement between the observed and the calculated values is seen in the Table. It is noted that the out-of-plane mode makes larger contribution than the in-plane ones. The mean square amplitude of $B^{11}X_3$ is smaller than that of $B^{10}X_3$ and, therefore, the resonance line due to the former lies on the higher frequency side than that of the latter. As pointed out by Douglass, it is in good accord with the intensity ratio of the two lines; the line of higher frequency is stronger than that of lower frequency, which is expected from the abundance ratio of boron isotopes.

Several accounts will be considered with regards to the small discrepancy between the calculated and the observed values.

1. *The use of force constants obtained in the gaseous state instead of those in the solid state.* Since the normal modes in the solid state are not known, the mean amplitudes were calculated by use of the data in the gaseous state. In the molecular crystal, however, it cannot be considered to be very serious.

2. *The neglect of the stretching effect.* The dependence of q on the stretching coordinate of the bond was neglected in the calculation. Actually for some compounds, a small change of eQq associated with the stretching of a bond was found from the microwave spectroscopy[22]. The change is associated with the increase in the mean bond distance by the anharmonic part of stretching vibration. Unfortunately, there is no way of estimating the effect for the present case.

3. *Bond orbital following effect.* In the above calculation, the direction of the principal axis of the maximum q is considered to lie on the line connecting the boron to the halogen nuclei. However, if the bonding orbital does not follow exactly to the direction, the bending angle of q is not equal to that of B–X. Then, the mean amplitude $\langle\theta^2\rangle$ is likely to be larger than that in the above calculation. Similar effect was found in the case of ICN by the microwave spectroscopy[22], where the change of eQq from the ground vibrational state to an excited state of the bending mode was slightly larger than that calculated from the mean amplitude.

From the above discussion, it is easily understood that the agreement given in Table III is quite good. At any rate it is safe to conclude that the origin of the doubling is the isotope effect of the mean amplitude. In the present study fine structure was not detected both in BCl_3 and in BBr_3. Judging from the close resemblance of the line shape in BCl_3 and BBr_3, the doubling mechanism must be the same for both cases.

A definite evidence which excludes both direct and indirect spin-spin effect* from being the origin of doublet is presented by the following observation. If the spin-coupling is the main origin of the doubling, the ratio of the doublet separation of Br^{79} and Br^{81} must be proportional to $\mu^{79}/\mu^{81}=0.927$, since the spin-coupling is proportional to the product of the magnetic moments of boron and halogen nuclei. On the other hand, if the doublet is due to the isotope effect of molecular vibration, the separation is proportional to $Q^{79}/Q^{81}=1.197$, since the observed separation should be $\frac{1}{2}eQ(\Delta q)$, where Δq is the same for Br^{79} and Br^{81}. The doublet separation was carefully measured both for Br^{79} and Br^{81} lines and the result was $26.1/21.6=1.21$, which agreed with the latter prediction. Therefore, it is sure that the origin of the doubling is the isotope effect of boron on molecular vibration and the spin-spin coupling, thought it is present, may be only effective within each line of the doublet. In fact, ν_{I} line is appreciably broader than ν_{II} in both compounds, which may be associated with the magnetic moment of B^{10} and B^{11} nuclei. In BCl_3 similar consideration cannot provide a conclusive evidence since $Q^{35}/Q^{37}=1.27$ is close to $\mu^{35}/\mu^{37}=1.20$.

The lattice vibration might be effective in the similar sense to the splitting of the resonance line, since the difference of the masses of isotopes of Cl^{35} and Cl^{37} or Br^{79} and Br^{81} cannot be overlooked. If one of the lattice mode, for example, a torsional oscillation about the figure axis, is considered, the splitting due to the isotope effect similar to that described above will occur in BCl_3^{35}, $BCl_2^{35}Cl^{37}$, $BCl^{35}Cl_2^{37}$ and BCl_3^{37}. However, lattice frequencies are considered to be so low that the condition $h\nu<kT$ is fulfilled. As seen in the Appendix, the effect of isotopic mass does not enter so long as the force constant remains unchanged. Thus the vibrations which are effective in the isotope splitting are only those having $h\nu>kT$ and, consequently, it is sufficient to consider only intermolecular vibrations.

Acknowledgment

The author wishes to express his gratitude to Professor Y. Morino for his kind guidance and encouragement throughout the course of this work. The author is also grateful to Professor S. Kojima and Dr. A. Shimauchi,

* The latter effect is referred to in the book by Das and Hahn as being cited from Douglass' conclusion. This is, however, far from the contents of his thesis. The author is grateful to Professor S. Kojima for pointing out this misquotation.

Tokyo University of Education, for their kind advice and discussions. He is also indebted to Mr. H. Shimizu for a help in the preparation of the samples. The expenses of the work were defrayed from the Scientific Research Encouragement Grant of the ministry of Education, to which the author's thanks are also due.

Appendix

Effect of Isotopic Mass on the Mean Amplitude. The magnitude of a change of a mean amplitude caused by mass difference depends on $h\nu/kT$. It is illustrated by a simplified one-dimentional model.

The mean amplitude of a vibration of frequency is given by

$$\langle A^2\rangle=\frac{h}{8\pi^2\nu}\coth\frac{h\nu}{2kT}=\frac{h\nu}{f}\left(\frac{1}{2}+\frac{1}{e^{h\nu/kT}-1}\right), \tag{A.1}$$

where

$$\nu=\frac{1}{2\pi}\sqrt{\frac{f}{m}}, \tag{A.2}$$

and f and m denote respectively a force constant and an effective mass of the vibration. The fractional change of the mean amplitude $\frac{\Delta\langle A^2\rangle}{\langle A^2\rangle}$ caused by a fractional change of the mass $\Delta m/m$ is, therefore, given by

$$\frac{\Delta\langle A^2\rangle}{\langle A^2\rangle}\Big/\frac{\Delta m}{m}=\frac{xe^x}{e^{2x}-1}-\frac{1}{2}, \tag{A.3}$$

where

$$x=h\nu/kT.$$

The value is plotted against x in Fig. 4. From the curve it can be seen that the isotopic mass difference has a negligible effect when $h\nu\lesssim kT$, provided the force constant remains unchanged.

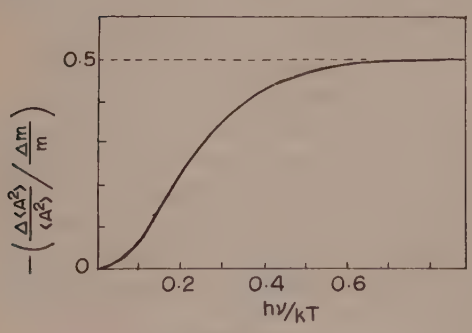

Fig. 4.

Refereuces

1) For instance, Y. Morino, I. Miyagawa, T. Chiba and T. Shimozawa: J. Chem. Phys. **25** (1956) 185.
2) R. Livingston: J. Phys. Chem. **57** (1953) 496.
3) M. A. Rollier and A. Riva: Gazz. chim. Ital. **77** (1947) 361.
4) D. C. Douglass: Thesis of Cornell University (1957).
5) C. Dean: Private communication.
6) S. Kojima, K. Tsukada, A. Shimauchi, and Y. Hinaga: J. Phys. Soc. Japan **9** (1954) 795.
7) C. Dean: J. Chem. Phys. **23** (1955) 1734.
8) H. Levy and L. O. Brockway: J. Am. Chem. Soc. **59** (1947) 2085.
9) T. F. Anderson, E. N. Lassettre and D. M. Yost: J. Chem. Phys. **4** (1946) 703.
10) M. Atoji and W. N. Lipscomb: J. Chem. Phys. **27** (1957) 195.
11) S. Kojima, K. Tsukada and Y. Hinaga: J. Phys. Soc. Japan **10** (1955) 498.
12) C. H. Townes and A. L. Shawlow: Microwave spectroscopy (McGraw Hill Book Co. 1955) p. 237 ff.
13) B. P. Dailey and C. H. Townes: J. Chem. Phys. **23** (1955) 118.
14) C. H. Townes and B. P. Dailey: J. Chem. Phys. **20** (1952) 35.
15) W. Gordy: Discussion Faraday Soc. **19** (1955) 14.
16) L. Pauling: The nature of the chemical bond (Cornell University Press, 1940) p. 237 ff.
17) R. Bersohn: J. Chem. Phys. **22** (1954) 2078.
18) H. Bayer: Zeits. f. Phys. **130** (1951) 227.
19) T. Wang: Phys. Rev. **99** (1955) 566.
20) Y. Morino and E. Hirota: J. Chem. Phys. **23** (1954) 737.
21) L. P. Lindeman and M. K. Wilson: J. Chem. Phys. **24** (1956) 242.
22) T. Oka, H. Hirakawa and A. Miyahara: J. Phys. Soc. Japan **12** (1957) 39.
T. Oka and H. Hirakawa: ibid. **12** (1957) 820.

JOURNAL OF THE PHYSICAL SOCIETY OF JAPAN Vol. 13, No. 8, AUGUST, 1958

Zeeman Effect of Nuclear Quadrupole Resonance Spectrum in Cyanuryl Chloride

By Yonezo MORINO, Takehiko CHIBA, Takashi SHIMOZAWA, and Masaharu TOYAMA

Department of Chemistry, Faculty of Science
University of Tokyo, Tokyo

(Received April 7, 1958)

A study on the Zeeman effect of Cl^{35} nuclear quadrupole resonance spectrum was carried out on a single crystal of cyanuryl chloride. Three distinct q-tensors were found in this crystal, two of them being equivalent. The directions of the principal axes were determined within the accuracy of 1°. It was concluded that in the crystal all molecules are disposed parallel (or antiparallel) to one another and three C–Cl bonds of a molecule are on a plane, making an angle 120° with one another, one of them being not equivalent to the other two. A large asymmetry parameter, 0.26, was obtained. From the coupling constant and the asymmetry parameter, the double bond character and the ionic character of C–Cl bonds were estimated to be 10% and 17%, respectively. The large double bond character was considered to be associated with the large electronegativity of nitrogen atoms in the ring.

§ 1. Introduction

The first study on the Zeeman effect of nuclear quadrupole resonance spectrum in a single crystal was accomplished by Dehmelt[1] for the iodine nuclei in tin tetraiodide. Livingston and Zeldes[2] made a study on the iodine nuclei in iodic acid and showed an evidence of extra Zeeman components resulted from proton interaction. Dean[3] made a study on the chlorine nuclei in p-dichlorobenzene. Meal[4] applied the Zeeman study on the chlorine nuclei in p-chloroaniline to the crystal analysis. Kojima et al.[5),6] made comprehensive studies on the Zeeman splitting of nuclear quadrupole resonance lines of single crystals of bromine and p-dibromobenzene, obtaining accurate values of asymmetry parameters.

Two valuable informations are obtained from the Zeeman studies. One is the spatial orientation of the principal axes of the electric field gradient tensor (q_{ij}) at the nucleus. As the principal axis of the q-tensor is considered to lie on the bond direction at such a nucleus as chlorine in the C–Cl bond, the Zeeman effect is useful for the study of the crystaline structure or of the molecular structure in the solid state. The other information is the asymmetry parameter η of the q-tensor. Although in the case of $I=1$ or $I\geq 2$ it can be obtained from the nuclear quadrupole resonance spectrum in the absence of a magnetic field, in the case of $I=3/2$ as chlorine nucleus it can only be obtained by the Zeeman study. The most important contribution to η in such a case as chlorine in the C–Cl bond is considered to come from the double bond character of the bond, since a single σ-bond provides no asymmetry to the q-tensor. Hence the measurement of the asymmetry parameter gives a unique method for estimating contribution of π-bond. Thus the Zeeman effect is valuable for the study on the nature of a bond.

The molecular structure of cyanuryl chloride was studied by Akimoto[7] by use of the electron diffraction by gaseous molecules, but the crystalline structure is not completely known; only its space group was reported to be C_{2h}^{6} by Hoppe *al* al.[8] The nuclear quadrupole resonance spectrum of the chlorine nuclei in cyanuryl chloride without the applied magnetic field was recently reported by Negita *et al.*[9),10], whose results are in good agreement with those of the present work.

§ 2. Theory

The Zeeman effect of nuclear quadrupole resonance spectrum was first solved by Krüger[11] in the case of axially symmetric q-tensor. Bersohn[12] expanded it to the atoms with asymmetric q-tensors and nuclear spin quantum number of half integers and calcu-

lated the energy levels to the first order in the magnetic field H and to the second order in the asymmetry parameter η.

The principal axes of a q-tensor are defined as the x, y and z-axes, the z-axis representing the direction of the largest component and the x-axis that of the smallest one. Then

$$0 \leqq \eta \leqq 1 ,$$

where

$$\eta = (q_{xx} - q_{yy})/q_{zz} . \qquad (1)$$

In the absence of a magnetic field, the energy levels of $m = \pm 3/2$ or $\pm 1/2$ of quadrupole coupling for a nucleus with a spin quantum number $I = 3/2$ are degenerate, so that only one resonance line is observed corresponding to the transition between the two levels. By applying a magnetic field, each doubly degenerate level splits into two mixed levels and the resonance line splits into four lines corresponding to four transitions as shown in Fig. 1. Although the transition between two mixed levels of $m = \pm 1/2$ is also possible from the selection rule $\Delta m = \pm 1$, its resonance line exists at a region of so low frequency that it is not observed in the usual work, when the applied magnetic field is small.

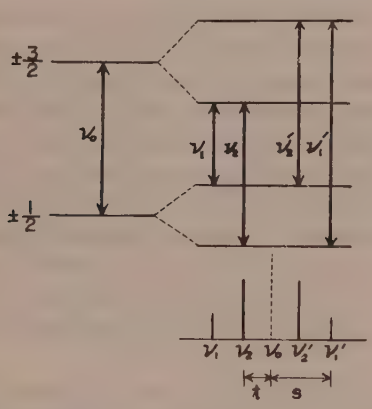

Fig. 1. Splitting of the energy levels for $I = 3/2$ by the Zeeman effect.

By an approximate calculation to the first order in H the frequencies ν_1, ν_1', ν_2 and ν_2' of four splitting lines are given by

$$\left.\begin{aligned} \nu_1, \nu_1' &= \nu_0 \pm s \\ \nu_2, \nu_2' &= \nu_0 \pm t \end{aligned}\right\} \qquad (2)$$

where ν_0 is the unperturbed resonance frequency given by

$$\nu_0 = \frac{eQq_{zz}}{2h}\xi ; \qquad \xi = \left(1 + \frac{1}{3}\eta^2\right)^{1/2} \qquad (3)$$

and s and t are the splittings given by

$$\left.\begin{matrix} s \\ t \end{matrix}\right\} = \frac{\mu}{3h\xi}\{[(4\xi^2 - 2\xi - 2)H^2 - (3\xi^2 - 6\xi - 6)H_z^2 + 2\eta(\xi - 1)(H_x^2 - H_y^2)]^{1/2} \pm [(4\xi^2 + 2\xi - 2)H^2 - (3\xi^2 + 6\xi - 6)H_z^2 - 2\eta(\xi + 1)(H_x^2 - H_y^2)]^{1/2}\} \qquad (4)$$

where μ is the nuclear magnetic moment, H_x, H_y and H_z are the components of the applied magnetic field in the three principal axes of the q-tensor, and h is Planck's constant. Eqs. (2), (3) and (4) hold for any value of η. In the ordinary case where η is small compared to 1, Eq. (4) can be reduced to the following approximate formula of the second order in η*:

$$\left.\begin{matrix} s \\ t \end{matrix}\right\} = \frac{\mu}{3h}\{[9H_z^2 + \eta^2(H^2 - 3H_z^2)]^{1/2} \pm [(4H^2 - 3H_z^2) - 4\eta(H_x^2 - H_y^2) + (1/3)\eta^2(H^2 - 3H_z^2)]^{1/2}\} . \qquad (5)$$

The direction of the principal axes of the q-tensor at the nucleus under consideration can be obtained by comparing the observed splitting curves with the theoretical ones (Fig. 2).

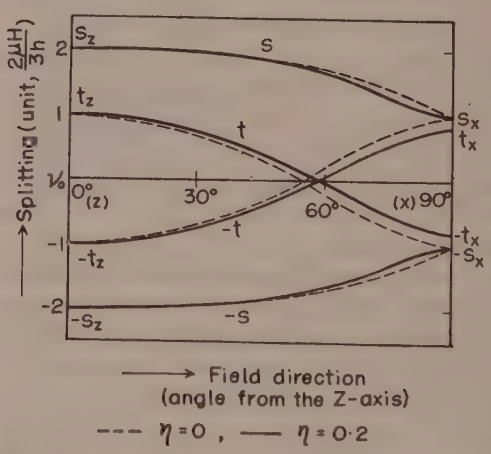

Fig. 2. Angular dependence of the Zeeman effect.

The splitting frequencies, when the magnetic field is applied parallel to the principal axes, are given by

$$\left.\begin{matrix} s_x = s_0 , & s_y = s_0(1+\eta) , & s_z = 2s_0 , \\ t_x = s_0(1-\eta) , & t_y = s_0 , & t_z = s_0 , \end{matrix}\right\} \qquad (6)$$

* The coefficients of the η^2-terms in Eq. (5) slightly differ from those of Bersohn's[12] and Kojima's[5),6)] formula.

where

$$s_0=\frac{2}{3}\cdot\frac{\mu H}{h}\,.$$

It should be noted in the z-direction the outer splitting is twice as large as the inner one, and the latter is equal to the outer splitting in the x-direction as well as to the inner splitting in the y-direction. It provides a good clue for the determination of the principal axes, as shown later. The asymmetry parameter η is calculated from the splitting in the direction of the axis x or y as follows:

$$\eta=\frac{s_x-t_x}{s_x}=\frac{s_y-t_y}{t_y}\,. \qquad (7)$$

The parameter η can also be obtained by measuring the directions in which three-line patterns are observed. The directions of the three-line patterns are given by putting $t=0$ into Eq. (5); it is easily shown that

$$\eta=\{-3(H_x^2-H_y^2)\pm[9(H_x^2-H_y^2)^2+6(H^2-3H_z^2)^2]^{1/2}\}/(H^2-3H_z^2)\,, \qquad (8)$$

where the $\pm$ signs must be taken as $\eta\geq 0$ by the definition.

§ 3. Resonance Spectrum in the Absence of Magnetic Field

The sample was purified by recrystalization of commercial cyanuryl chloride from benzene solution.

Without the applied magnetic field two resonance lines ν_I and ν_{II} with the intensities of $\nu_I:\nu_{II}=2:1$ were observed at room temperature for both nuclei Cl^{35} and Cl^{37}. The signal to noise ratio was very high. The lines were sharp, the line-widths being about 1 kc. Their frequencies are in good agreement with the observation by Negita *et al.*[9),10)]

The resonance frequencies were measured at several temperatures as tabulated in Table I. The frequency changes with temperature are plotted in Fig. 3. It is noted that ν_{II} is higher than ν_I at 294°K (the room temperature), but they are reversed at 197°K (dry ice temperature) and coalesce to one line at 77°K (liquid nitrogen temperature). This anomalous feature in temperature dependence suggests an existence of a transition point between 77°K and 197°K, but in order to comfirm the existence it is necessary to detect abrupt change of the resonance frequencies at a specified temperature.

Table I. Pure quadrupole resonance frequencies in chlorine nuclei of cyanuryl chloride.

Temperature (°K)	Cl^{35} ν_I^{35} (Mc)	ν_{II}^{35} (Mc)	$\nu_I^{35}-\nu_{II}^{35}$ (Mc)	Cl^{37} ν_I^{37} (Mc)	ν_{II}^{37} (Mc)	$\nu_I^{37}-\nu_{II}^{37}$ (Kc)
294	36.2997	36.3172	−17.5	28.6078	28.6202	−12.4
197	36.5502	36.5446	+ 5.6			
77	36.7708	36.7708	0			

$\nu_I^{35}/\nu_I^{37}=1.26891\pm0.00002$, $\nu_{II}^{35}/\nu_{II}^{37}=1.26894\pm0.00002$ (at 294°K)

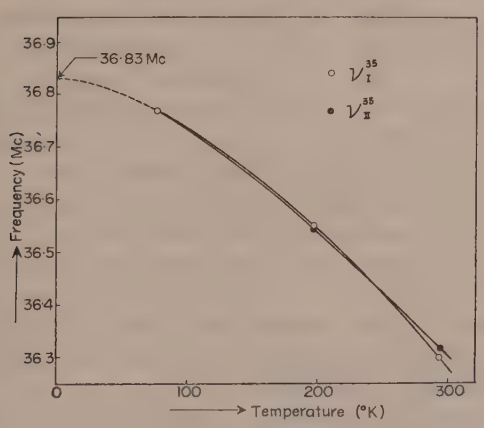

Fig. 3. Temperature dependence of the Cl^{35} resonance frequencies.

The mean frequency of the two lines at 0°K is estimated to be 36.83 Mc by extrapolation. The ratio ν_I^{35}/ν_I^{37} and $\nu_{II}^{35}/\nu_{II}^{37}$ are in good agreement with the ratio Q^{35}/Q^{37} of the quadrupole moments of the two nuclei.

§ 4. Zeeman Effect of the Resonance Lines for Cl^{35}

A). *Preparation of a Single Crystal.* A single crystal of cyanuryl chloride was prepared by the pointed-bottom-crucible method[13)]. The apparatus is schematically illustrated in Fig. 4. A diaphragm was put between the electric furnace and the cooler to keep a suitable temperature gradient. The sample contained in an ampule with a sharp-pointed

bottom was melted in the furnace and then lowered into the cooler to freeze into a single crystal. A good single crystal was obtained at the lowering rate of about 3 mm/hr under such a temperature gradient as shown in Fig. 5.

B). *Apparatus for Observation.* A super-regenerative spectrometer[14] was used. The splitting frequencies were measured by recording the resonance lines as derivative curves of the absorption.

The magnetic field was furnished by Helmholtz coil with a field strength of 108 gauss/ampere at the center (Fig. 6). The field actually used was about 10 gauss. The Helmholtz coil can be rotated in a whole range of angle about the vertical axis, but it cannot be inclined beyond 40° from the vertical axis

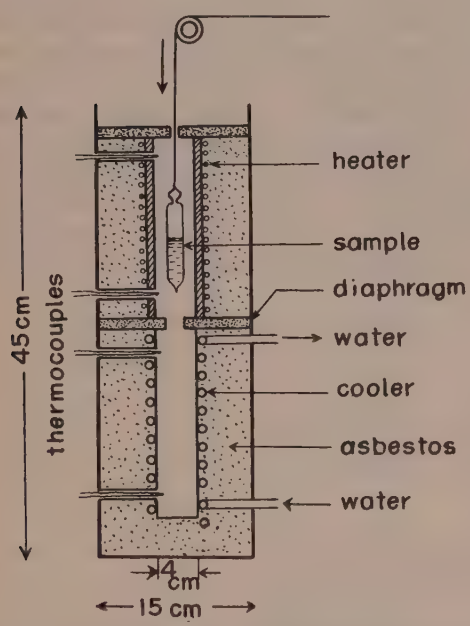

Fig. 4. Apparatus for preparation of single crystals.

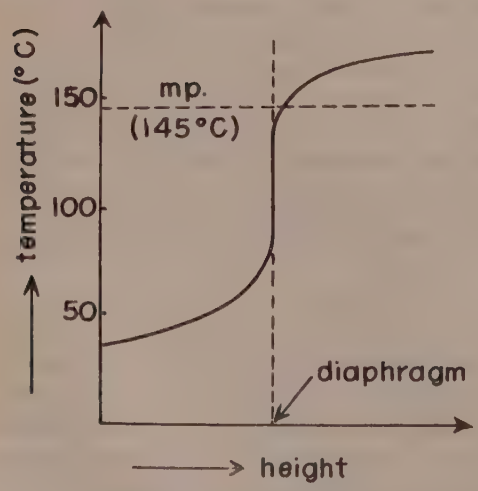

Fig. 5. Temperature distribution in the apparatus shown in Fig. 4.

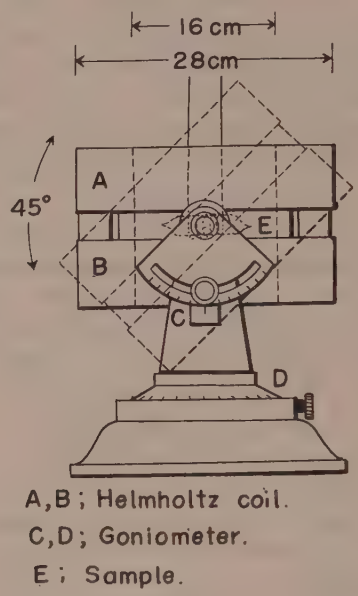

Fig. 6. Magnet for the Zeeman effect.

because of the contact of the lead-wire of the rf-coil with the edge of the Helmholtz coil. All the spherical angles were covered by carrying out several runs at different angular positions of the crystal mounting.

C). *Method of Observation.* The observation with the applied field showed that the line ν_I splits into eight lines in general and ν_{II} into four. Since a resonance line of a q-tensor splits into four lines by a magnetic field, the above result indicates that ν_{II} is due to one kind of q-tensor q_{II}, whereas ν_I due to two kinds of q-tensors q_I and q_I' which are equivalent each other except the direction in the crystal. Any direction on the two planes which bisects the angles between the principal axes z_I and z_I' (the direction of the maximum q components of q_I and q_I') is equivalent for both q_I and q_I'. Hence the fields in these directions yield the same splitting lines for q_I and q_I', so that ν_I splits into four lines. Such planes were first determined by searching the directions where the four-line patterns of ν_I were observed. These planes are called XZ- and YZ-planes. The

Z-axis, the intersection of the two planes XZ and YZ, is perpendicular to both z_I and z_I'. In other words, z_I and z_I' are on the plane XY thus determined. In order to determine the angle between z_I and z_I' on this plane and to locate the direction of the q_{II} referring to the axes X, Y and Z, the splittings by the magnetic field in the directions on the planes XY, YZ and ZX were observed.

The splitting frequencies were measured by referring to the difference between the two resonance lines $\nu_{II}-\nu_I$, and were reduced to the values at a certain field strength by use of the value of electric currents in the Helmholtz coil.

D). *Results.* A good confirmation of the directions of the principal axes of the q-tensor is provided by the consideration of the symmetry property; an axis is determined to be one of the principal axes, if symmetric splitting curves with respect to this axis are obtained in two planes involving it. The observed Zeeman splitting curves are plotted against the direction of the field in Fig. 7. The X, Y and Z axes, therefore, correspond to the three principal axes of the q_{II}-tensor; the X-axis is the principal z-axis, because in the X-direction the outer splitting s_{II} is twice as large as the inner splitting t_{II}, as required by Eq. (6). The Y- and Z-axes are the y- and x-principal axes, respectively, because the inner splitting t_{II} in the Y-direction is equal to the inner splitting t_{II} in the X-direction as well as to the outer splitting s_{II} in

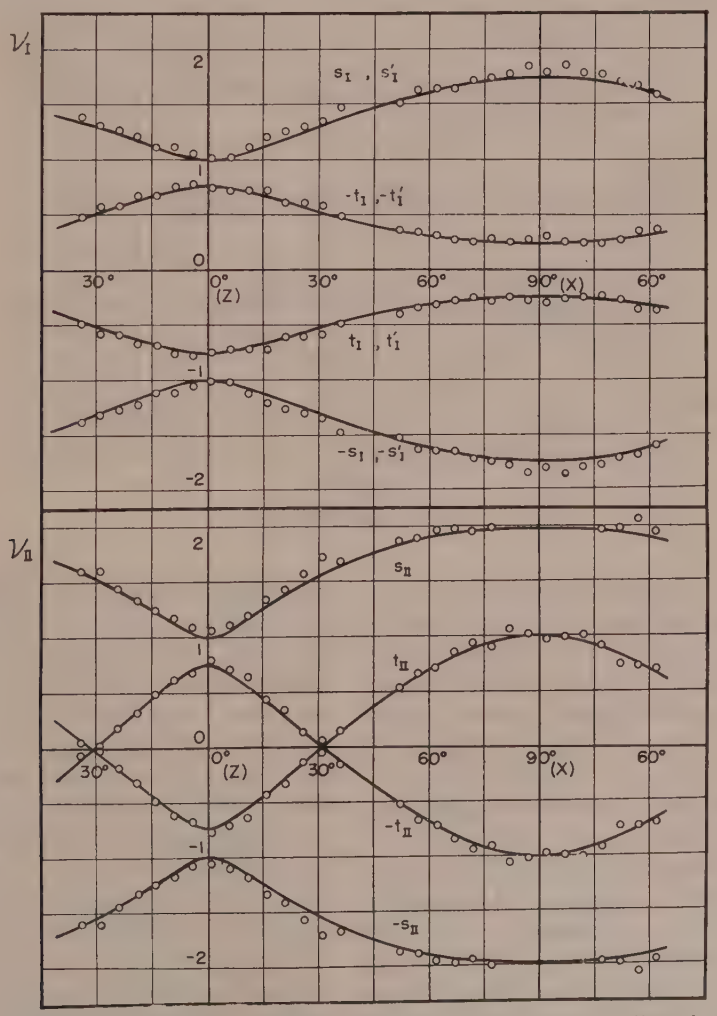

Fig. 7. Angular dependence of the Zeeman effect of Cl^{35} resonance lines in cyanuryl chloride.

a) In the XZ plane

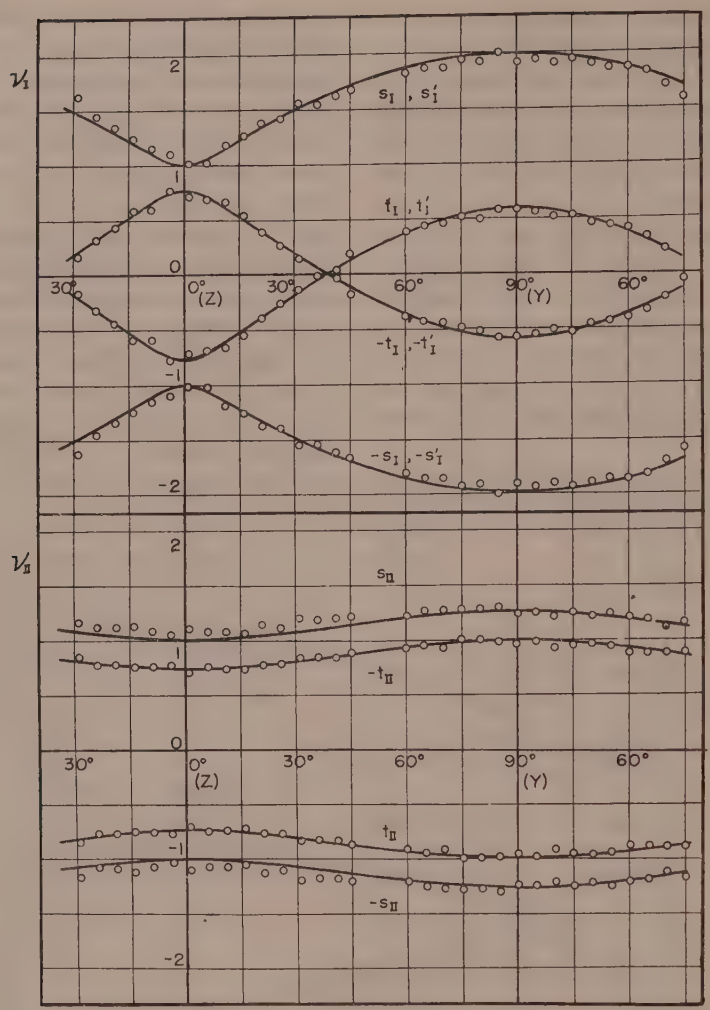

Fig. 7.

b) In the YZ plane

the Z-direction (compare Eq. (6)).

For the q-tensors, q_I and q_I', the X-axis is also concluded to be one of the principal axes from the symmetrical shape of the splitting curves of ν_I in the XZ- and YZ-planes. Eight splitting curves of ν_I in the XY-plane are classified into two groups: one due to the q_I-tensor and the other due to the q_I'-tensor. Two inner splittings t_I and $-t_I$ which are symmetric with respect to ν_I are due to the same q-tensor, for instance, q_I, and similarly t_I' and $-t_I'$ which are symmetric with the formers with respect to the X- and Y-axes are due to the other, q_I'. The splitting curves due to the same q-tensor must have the same symmetrical dependence on the angles whether they are outer or inner. $\pm s_I$ and $\pm t_I$, therefore, compose a group of splitting curves due to q_I, and $\pm s_I'$ and $\pm t_I'$ compose a group due to q_I'. Since the Z-axis is one of the principal axes for both the q_I- and q_I'-tensors, the others must be on the XY-plane; they were found to lie in the directions $(X+30°\,Y)$ and $(X-60°\,Y)$ for the q_I-tensor and $(X-30°\,Y)$ and $(X+60°\,Y)$ for the q_I'-tensor, where $(X+30°\,Y)$ designates the direction 30° far from the X-axis towards the Y-axis on the XY-plane. The principal axes x, y and z are assigned from the splittings in each directions as tabulated in Table II. It is noted that the principal x-axes are along the Z-axis for all q-tensors.

The values of the asymmetry parameters η are determined from the splittings in the

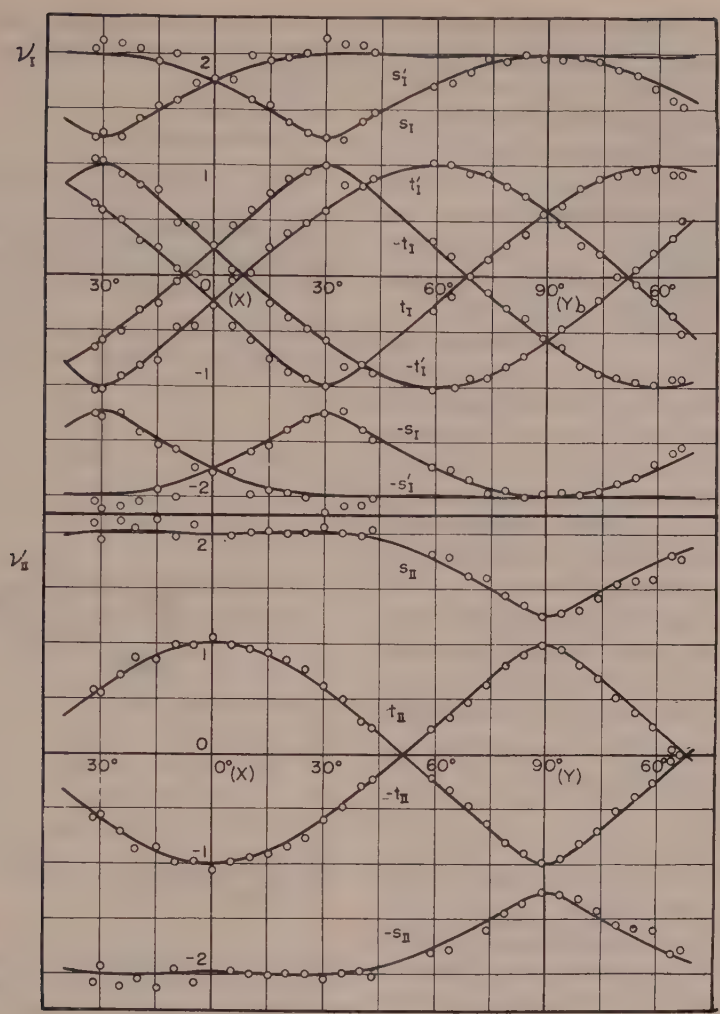

Fig. 7.
c) In the XY plane

Table II. The principal axes of the q-tensors.

	x-axis	y-axis	z-axis
q_I	Z	$X+30°Y$	$X-60°Y$
q_I'	Z	$X-30°Y$	$X+60°Y$
q_{II}	Z	Y	X

(the exp. error; $\pm 1°$)

directions of the principal x- and y-axes by using Eq. (7):

$$\eta_I = 0.23 \pm 0.03 \qquad \text{for } q_I \text{ and } q_I' ,$$

and

$$\eta_{II} = 0.26 \pm 0.03 \qquad \text{for } q_{II} .$$

The directions giving three-line patterns are shown in Table III. The angles between these directions and the principal z-axes in the XY-plane are 51°–52° for the q_I- and q_I'-tensors, and 51.5° for the q_{II}-tensor. From the angle 51·5°, the value of η is also calculated by Eq. (8) to be

$$\eta = 0.26 \pm 0.08 .$$

Table III. The directions giving three-line patterns.

	q_I	q_I'	q_{II}
XY-plane	$X-8°Y$	$X+8°Y$	$X+51.5°Y$
	$X+69°Y$	$X-69°Y$	
YZ-Plane	$Z+37.5°Y$	$Z+37.5°Y$	None
ZX-Plane	None	None	$Z+31°X$

(the exp. error; $\pm 1°$)

This is in good agreement with the results from the splittings in the directions of the principal x- and y-axes.

The observed splitting curves are in good agreement with the theoretical ones which are calculated by putting into Eq. (5) the observed directions of the principal axes and the asymmetry parameters of the q-tensors (see Fig. 7). Slight discrepancies are found in the splitting of ν_{II} near the Z-axis.

The intensities of the outer splitting lines are weaker than those of the inner, and they increase by approaching to the x- and y-axes, whereas they decrease to the z-axis and then become unobservable at the z-axis, just as expected from the theory. But an unexpected feature appeared in a small range close to the x- and y-axes, where the intensities of the outer splitting lines decreased.

The pure quadrupole coupling constant is calculated by Eq. (3) by using the value of η together with that of the resonance frequency $\nu_0=36.83$ Mc which is extrapolated from the observed to 0°K; the result is

$$(eQq)_{Cl^{35}}=73.0 \text{ Mc} .$$

§ 5. Discussion

A). *Directions of the* C–Cl *bonds.* The chlorine atoms corresponding to the electric field gradient tensor q_I, q_I' and q_{II} are denoted by Cl_I, Cl_I' and Cl_{II}, respectively. Since in the C–Cl bond the principal z-axis of the q-tensor at the Cl nucleus is considered to agree with the direction of the bond, the principal z-axes z_I, z_I' and z_{II} of the above q-tensors represent the directions of the bonds C–Cl_I, C–Cl_I' and C–Cl_{II}. Hence there are three kinds of directions of the C–Cl bonds in the crystal. These three directions correspond to those of the three C–Cl bonds in a molecule, because one molecule of cyanuryl chloride contains three Cl atom whose bond directions are different from one another.

From the directions of the z-axes listed in Table II, the angles between the C–Cl bonds are obtained to be either 60° or 120°. Here are two values because of the quadratic nature of q-tensor, but it seems most plausible to prefer the latter such a molecule as cyanuryl chloride. The error of measurement of angles is about 2°. Thus

$$\widehat{Cl_ICl_I'}=\widehat{Cl_ICl_{II}}=\widehat{Cl_I'Cl_{II}}=120°\pm2° ,$$

The angles can also be obtained from the directions in which three-line patterns were observed: that is,

$$\widehat{Cl_ICl_I'}=119° ,$$

$$\widehat{Cl_ICl_{II}} \text{ and } \widehat{Cl_I'Cl_{II}}=119.5-120.5° ,$$

which agree with the value mentioned above within the range of experimental error.

The most probable structure of cyanuryl chloride molecules is thus concluded to be the planar structure as shown in Fig. 8,

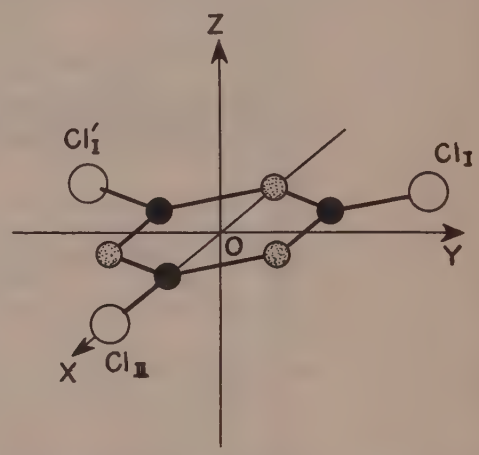

Fig. 8. Disposition of cyanuryl chloride molecules in the crystal.

where all the constituting atoms are arranged on one plane and the angles between the C–Cl bonds are all 120°±2°. Although the Zeeman effect determines the angles between each pair of the three C–Cl bonds, it cannot give the relative positions of the bonds with the triazine ring. Therefore any configuration cannot be discarded in which the triazine ring inclines from the XY-plane, so long as the three bonds remain at the directions described above.

The nuclear quadrupole resonance spectrum obtained above gives informations on the crystalline structure too. As only two lines which corresponded to the three Cl nuclei in a molecule were observed, it is concluded that all the molecules occupy equivalent positions in the crystal with the molecular plane parallel to one another and with all the C–Cl bonds parallel or antiparallel to the corresponding bonds in the other molecules. The atoms Cl_I and Cl_I' are located at equivalent positions in the crystal, but not equivalent

to Cl_{II}. This fact, together with the result of the Zeeman effect that the angle $\widehat{Cl_{II}Cl_I}$ is equal to that of $\widehat{Cl_{II}Cl_I'}$, leads to the conclusion that the crystal has a plane of symmetry through the C–Cl_{II} bond and perpendicular to the XY-plane. The frequency shift between ν_I and ν_{II} must come from a slight difference of the environment of the chlorine nuclei in the crystal.

It was observed that by cooling the crystal cracks run parallel to the XY-plane through the crystal, that is, to the molecular planes in the crystal (see Fig. 8).

B). *Asymmetry parameter.* The asymmetry parameters of Cl atoms in cyanuryl chloride were found to be remarkably large in comparison with those in chlorine derivatives of benzene. It may be attributed to the large double bond character of the C–Cl bonds in cyanuryl chloride.

The ionic character i and the double bond character f of the C–Cl bonds are estimated from the values of η and the coupling constant $(eQq)_{obs}$[15),16)] by the method used by Kojima *et al.* for p-dibromobenzene[6)]. According to them, the number of unbalanced p-electrons contributing to the q_z-component is given by

$$U_p=\tfrac{1}{2}(N_x+N_y)-N_z$$
$$=(1-i-f)(1-s)+\tfrac{1}{2}(1+\varepsilon)(1-2s') \qquad (9)$$

if the resonance scheme shown in Fig. 9 is

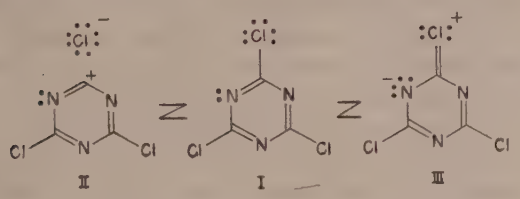

Fig. 9.

assumed for the C–Cl bonds. The π-electrons consisting of the double bond in III are assumed to be supplied from the p_x-orbit of chlorine atom. s and s' denote the s-character of the σ-orbit due to the sp-hybridization in the configurations I and III*, and ε denote the change in the screening effect by a positive formal charge at the chlorine atoms in III. Townes and Dailey[15),16)] estimated $s=s'=0.15$ and $\varepsilon=0.15$ for chlorine atom.

Since $U_p=1$ for a free atom, U_p is calculated by

$$U_p=(eQq)_{obs}/(eQq)_{atom}\,, \qquad (10)$$

where $(eQq)_{atom}$ is the quadrupole coupling constant in a free chlorine atom, that is, 109.7 Mc[17)], and $(eQq)_{obs}$ is the observed in the molecule, that is, 73.0 Mc. Hence $U_p=0.66$ for cyanuryl chloride.

The asymmetry parameter η is given by

$$\eta=\frac{U_x-U_y}{U_z}=\frac{3}{2}\frac{f(1+\varepsilon)}{U_z}\,. \qquad (11)$$

Thus the double bond character f is obtained to be 10% from $\eta=0.26$ and $U_p=0.66$ by use of Eq. (11), and from it the ionic character i is calculated to be 17% by Eq. (9). It should be noted that the double bond structure III is as important as the ionic structure II. This feature has already been pointed out by Negita *et al.*.

The asymmetry parameter η, the double bond character f and ionic character i of the C–Cl bonds in cyanuryl chloride are compared with those of benzene derivatives in Table IV. The C–Cl bonds in cyanuryl chloride have smaller amount of ionic character and considerably larger amount of double bond character than those in p-dichlorobenzene. The C–Br bonds in p-dibromobenzene have an intermediate double bond character between them, and the same order of ionic character as cyanuryl chloride. These features may be explained in terms of electronegativities of the constituting atoms; the electronegativity of nitrogen is 3.0 which is larger than that of carbon, 2.5, and comparable with that of chlorine, 3.0[18)]. In cyanuryl chloride electrons are attracted towards both the chlorine atoms and triazine ring, and then the contributions

Table IV. Comparison of the nature of the carbon-halogen bonds in cyanuryl chloride with those in benzene derivatives.

	η	f	i
p-dichlorobenzene[3)]	0.08	3%	24%
p-dibromobenzene[6)]	0.12	5	15
cyanuryl chloride	0.26	10	17

* In their treatment of p-dibromobenzene, Kojima *et al.* neglected the s character of the σ-bond in the double bond: i.e. they assumed that $s'=0$. It may be reasonable to keep the term s', as in the above argument.

of the configuration III with the double bond should be comparable with that of the ionic configuration II and larger than that of the double bond structure in *p*-dichlorobenzene. The comparison with *p*-dibromobenzene is also established by considering the electronegativity of bromine 2.8 which is smaller than that of chlorine.

It may be interesting to compare the results with 1, 3, 5-trihalogenobenzenes which have the same symmetry as cyanuryl halides. The comparison of the nuclear quadrupole resonance frequencies was carried out by Negita et al., between cyanuryl chloride and 2-chloropyridine and between 1, 3, 5-trihalogenobenzene and monochlorobenzene and similar tendencies were concluded.

The x-directions of C–Cl bonds are concluded to be parallel to the Z-axis, that is, perpendicular to the molecular plane for all the Cl atoms. It is a definite evidence that electrons in the p-orbits which are perpendicular to the plane of the molecule take part in forming the π-bonds.

C). *Temperature Dependence of the Resonance Frequencies.* Both of the resonance frequencies ν_I and ν_{II} decrease with the increase of temperature. This tendency may be explained by the torsional oscillation of molecule as stated by Dehmelt[19], Bayer[20], and Wang[21]. According to Bayer, the temperature coefficient of resonance frequency is expressed as a function of temperature as follows:

$$\frac{1}{\nu_0}\frac{d\nu}{dT}=-\frac{3}{2}\frac{h^2}{4\pi^2kT^2}\sum_m\frac{e^{h\nu_m/kT}}{I_m(e^{h\nu_m/kT}-1)^2} \tag{13}$$

where ν and ν_0 denote the resonance frequencies at T°K and 0°K respectively, and ν_m the torsional frequency corresponding to the moment of inertia I_m. When $h\nu_m/kT<1$,

$$\frac{1}{\nu_0}\frac{d\nu}{dT}=-\frac{3k}{8\pi^2}\sum_m\frac{1}{I_m\nu_m^2}\,. \tag{14}$$

Thus so long as the frequency of torsional oscillation is assumed to be independent of temperature, the temperature dependence is regarded as almost linear as shown by Dehmelt[19].

The temperature coefficient for each resonance line is obtained as follows:

$$\frac{1}{\nu_0}\frac{d\nu_I}{dT}=-0.703\times10^{-4}\,\mathrm{deg}^{-1}\,,$$

$$\frac{1}{\nu_0}\frac{d\nu_{II}}{dT}=-0.637\times10^{-4}\,\mathrm{deg}^{-4}\,,$$

where the extrapolated value 36.8 Mc was put in ν_0. They are almost in the same value as those of ordinary organic compounds; for example, for *p*-dichlorobenzene, Wang[21] obtained $-0.916\times10^{-4}\,\mathrm{deg}^{-1}$ at 16.9°C and Kushida, Benedek, and Bloembergen[22] $-0.60\times10^{-4}\,\mathrm{deg}^{-1}$ by correcting the volume change.

The difference of the temperature coefficients between ν_I and ν_{II} may be explained by the nonequivalence of the positions of Cl_{II} and the other two in the crystal. If the three Cl atoms were all equivalent in a crystal, all the modes of torsional oscillations with the axes in the molecular plane would be degenerate. The degeneracy is, however, removed in cyanuryl chloride by the anisotropy mentioned above, so that the frequency ν_{II} depends on two modes of rotations around Y and Z axes, but ν_I depends on all the modes. ν_I and ν_{II} have, therefore, different temperature coefficients, which are given by

$$\frac{1}{\nu_0}\frac{d\nu_{II}}{dT}=-\frac{3k}{8\pi^2}\left[\frac{1}{I_z\nu_z^2}+\frac{1}{I_y\nu_y^2}\right], \tag{15}$$

and

$$\frac{1}{\nu_0}\frac{d\nu_I}{dT}=-\frac{3k}{8\pi^2}\left[\frac{1}{I_z\nu_z^2}+\frac{1}{I_x\nu_x^2}\cos^2\frac{\pi}{6}+\frac{1}{I_y\nu_y^2}\cos^2\frac{\pi}{3}\right], \tag{16}$$

where I_x, I_y and I_z are the moments of inertia about the axes X, Y and Z, respectively, and ν_x, ν_y and ν_z are the corresponding torsional frequencies which have not yet been measured for cyanuryl chloride.

In the case of *p*-dichlorobenzene[21~23], it was found that the contribution of the Z-mode is twice as large as that of the Y-mode. If the same ratio is assumed for cyanuryl chloride, Eqs. (15) and (16) provide the ratio of

$$I_x\nu_x^2:\,I_y\nu_y^2:\,I_z\nu_z^2=1.4:2:1\,. \tag{17}$$

Since $I\nu^2$ is proportional to the force constant against the rotational motion, Eq. (17) indicates that the molecule can rotate more easily about the X-axis than about the Y-axis. It seems quite reasonable, because the X-axis is a symmetry axis, whereas the Y-axis is not.

§ 6. Conclusion

1). Cyanuryl chloride molecule has a planar

structure in the crystal, the angles between C–Cl bonds being all 120°±2°.

2). At room temperature each molecule occupies an equivalent position in a crystal, the corresponding C–Cl bonds being all parallel (or antiparallel) to one another. One of the C–Cl bonds is nonequivalent to the other two. Thus two resonance lines are observed with the relative intensity of ν_{II}: ν_I=1:2.

3). Large asymmetry parameters in the Cl atoms, η_I=0.23 and η_{II}=0.26, were observed, from which the double bond character and the ionic character are estimated to be 10% and 17%, respectively. The large double bond character was explained as the result of large electronegativity of nitrogen atoms in the triazine ring. The electrons in the *p*-orbits perpendicular to the molecular plane play a role of π-bond in conjugation with the ring.

4). The difference between the temperature coefficients of ν_I and ν_{II} was discussed by the anisotropy of the crystal field.

Acknowledgement

The authors wish to express our indebtedness to Mr. S. Morita, Research Laboratory of Mitsubishi Chemical Industry, Ltd., for the sample used in this research. The expenses of the work were defrayed from the Scientific Research Encouragement Grant of the Ministry of Education, to which the authors' thanks are also due.

References

1) H. G. Dehmelt: Z. Physik **130** (1951) 356.
2) R. Livingston and H. Zeldes: J. Chem. Phys. **26** (1957) 351.
3) C. Dean: Phys. Rev. **86** (1952) 607.
4) H. C. Meal: J. Chem. Phys. **24** (1956) 1011.
5) S. Kojima, K. Tsukada, A. Shimauchi and Y. Hinaga: J. Phys. Soc. Japan **9** (1954) 795.
6) S. Kojima, K. Tsukada and Y. Hinaga: J. Phys. Soc. Japan **10** (1955) 498.
7) Y. Akimoto: Bull. Chem. Soc. Japan **28** (1955) 4.
8) W. Hoppe, H. U. Lenne and G. Morandi: Zeits. f. Krist. **108** (1957) 321.
9) H. Negita and S. Satou: J. Chem. Phys. **27** (1957) 602.
10) H. Negita, S. Satou, T. Yonezawa and K. Fukui: Bull. Chem. Soc. Japan **30** (1957) 721.
11) H. Krüger: Z. Physik **130** (1951) 371.
12) R. Bersohn: J. Chem. Phys. **20** (1952) 1505.
13) F. R. Lipsett: Cand. J. Phys. **35** (1957) 284.
14) R. V. Pound and W. D. Knight: Rev. Sci. Instr. **21** (1950) 152.
15) C. H. Townes and B. P. Dailey: J. Chem. Phys. **17** (1949) 782.
16) C. H. Townes and A. L. Shawlow: "Microwave Spectroscopy," McGraw-Hill, Inc. New York (1955), p. 237ff.
17) B. P. Dailey: J. Phys. Chem. **57** (1953) 490.
18) L. Pauling: "Nature of the Chemical Bond," Cornel Univ. Press, New York, (1940), p. 60.
19) H. G. Dehmelt and H. Krüger: Z. Physik **129** (1950) 401.
20) H. Bayer: Z. Physik **130** (1951) 227.
21) T. Wang: Phys. Rev. **99** (1955) 566.
22) T. Kushida, G. B. Benedek and N. Bloembergen: Phys. Rev. **104** (1956) 1364.
23) B. D. Saksena: J. Chem. Phys. **18** (1950) 1653.

JOURNAL OF THE PHYSICAL SOCIETY OF JAPAN Vol. 13, No. 8, AUGUST, 1958

Absorption Spectra of Cr^{3+} in Al_2O_3

Part A. Theoretical Studies of the Absorption Bands and Lines

By Satoru SUGANO

Department of Physics, Faculty of Science, University of Tokyo, Tokyo

and Yukito TANABE

Department of Applied Physics, Faculty of Engineering, University of Tokyo, Tokyo

(Received, April 5, 1958)

In the frame-work of the crystalline field theory, the excited states of Cr^{3+} in Al_2O_3 and the optical transitions to these states are studied taking into account the effect of trigonal field and spin-orbit interaction. Initial splittings and optical anisotropies of the broad band (transitions to quartet states) and the sharp lines (transitions to doublet states) are examined. For the sharp lines, the Zeeman effect is also examined and the Zeeman patterns are predicted. Comparing these theoretical results with those of the experimental ones given in Part B, the assignments of U, Y bands and R_1, R_2, B_1, B_2 lines have been established. It is shown that the g-shifts of the excited doublets observed in the Zeeman patterns can also be explained under such assignments. It is also shown that the experimental data of the optical absorption can be reasonably connected to those of the paramagnetic resonance absorption.

§ 1. Introduction

In the last several years, it has been believed by many authors that the optical spectra of normal complex ions of the first transition-metal elements are reasonably explained by the crystal-field or the ligand-field theory of d-electrons[1]. It is true that the theory predicted the positions of the absorption bands and lines in agreement with the experiments and gave reasonable order of magnitudes for the intensities and widths. However, we still feel that a more definite evidence than those mentioned above is needed to confirm the theory because the number of the observed absorption bands in the individual complex is rather limited and the detailed analyses of the sharp absorption lines have not yet been made. The main purpose of this series of papers is to give a more sound foundation to the crystal field theory of optical absorption than that previously established by examining, both theoretically and experimentally, the details of the optical spectra of ruby.

The reason why we adopt ruby for this purpose is as follows:

Similarity of the spectra to those of Cr alum: A single crystal of ruby whose colour is, as well known, due to Cr^{3+} impurities in Al_2O_3 crystal shows similar spectra to those of Cr alum; The spectra in the visible region consist of two bands (obs. max. at $\sim 18000\ cm^{-1}$ and $\sim 25000\ cm^{-1}$) and of several groups of lines situated at $\sim 14400\ cm^{-1}$ and $\sim 21000\ cm^{-1}$. From the knowledge of the crystal structure (§ 2), we can see that Cr^{3+} impurities which substitute Al^{3+} ion of Al_2O_3 are surrounded almost octahedrally by six nearest O^{2-} ions and are therefore subject to a strong cubic field just as in the case of Cr^{3+} ion in Cr alum. In addition to this cubic field, there is a relatively strong trigonal field whose axis is the optic axis C_3. Thus we can safely assume that the same treatment will be applicable to both Cr alum and ruby to explain their optical spectra.

Contrast to Cr alum: It has a distinct optic axis and, as will be reported in a later paper, shows a remarkable optical anisotropy which is not observed in the case of Cr alum. It is stable both at high and low temperatures so that we can get much informations on the optical behaviours at these temperatures, while Cr alum is unstable at high temperature and shows phase-transition at low temperature which complicates the interpretation of the line spectra of Cr alum greatly. It shows a

relatively strong luminescence in the red region where the sharp line absorptions are observed. This luminescence is absent in Cr alum.

Thus ruby can provide us with more useful and definite informations than Cr alum that has been regarded as a representative material with its abundance of spectra, the elucidation of which has been the success of the crystal field theory.

Of course, ruby, as a diluted antiferromagnetic substance Cr_2O_3, has many interesting problems in its own and thus the present study may also be interesting from another point of view.

Experimentally, we have a fairly abundant knowledge about ruby. Deutchbein[2] has examined many narrow spectra of both absorption and emission many years ago and Lehmann[3] has performed an elaborate experiment on the Zeeman effect of the characteristic doublet R_1 and R_2 observed at $\sim 14400\ \mathrm{cm}^{-1}$. There remain, however, some doubts with respect to the quantitative aspect of his experiment. In view of the importance of the Zeeman effect in the analysis of the line spectra, measurements of the Zeeman effect were made again under experimentally better conditions both for the line spectra of R_1, R_2 and B_1, B_2. The absorption lines B_1 and B_2 are located at $\sim 21000\ \mathrm{cm}^{-1}$ and their Zeeman effects have not been observed yet. These will be reported in the second paper (Part B).

As for the broad bands, detailed quantitative measurements, especially on splittings and anisotropies, seem absent as far as we know although Thosar[4] has briefly reported the optical anisotropy of the first band (at the longer wave-length side). The results of experimental studies on these bands will be given in a later paper.

The knowledge about the ground state of ruby are provided by the recent experiments of paramagnetic resonance[5].

The present paper is devoted to the theoretical consideration which enables us to analyse the experimental facts already known and those to be reported later. Although details of the newly obtained experimental results will be given in later papers, the results that seem definite and important will be sometimes reffered to, if necessary, in order to confirm the theory.

§ 2. The Crystal Structure

The crystal symmetry of ruby[6] is, as well known, rhombohedral with its unit cell containing two molecules of Al_2O_3. Some of Al^{3+} ions are considered to be substituted by Cr^{3+} ions. Their nearest neighbours are six O^{2-} ions, which form a distorted octahedron around Al^{3+} or Cr^{3+} ion, which has neither inversion nor reflection symmetry (σ_v) as Fig.

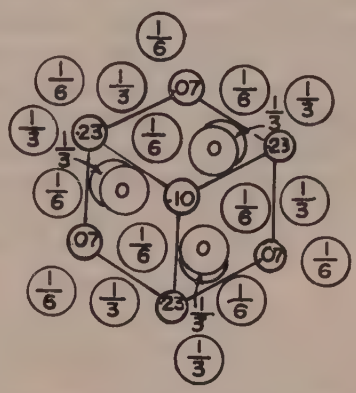

Fig. 1. A portion of the Al_2O_3 arrangement projected upon a plane normal to the 3-fold axis C_3 and passing through the apex of a unit rhombohedron. Fractions give distances below the projection plane measured in terms of the height of the unit rhombohedron. Atoms of Al (or Cr) are small, the oxygens are large circles. (Wyckoff, 1948)

1 shows. The symmetry of this distorted octahedron is C_3 whose principal axis passes through the apexes of the unit rhombohedron. It may be noted that the four positions of Al^{3+} in the unit cell are energetically equivalent, since the four distorted octahedrons are transformed into one another by translation or both by translation and inversion at the central ion.

§ 3. The Hamiltonian for the Cr^{3+} Ion and Wave Functions for *d*-electrons

In our previous pepers[7] on the octahedral complexes, the effect of spin-orbit interaction has been completely neglected. For the analyses of the line spectra of ruby, the spin-orbit interaction plays an essential role together with the trigonal field as we shall see later. Thus the Hamiltonian which we must take for the Cr^{3+} ion in ruby is

$$\left.\begin{aligned} \mathscr{H} &= \mathscr{H}_0 + \mathscr{H}' \\ \mathscr{H}' &= V_{\mathrm{trig}} + V_{so} \end{aligned}\right\}, \qquad (3.1)$$

where $\mathscr{H}_0$ is the Hamiltonian for the cubic case without spin-orbit interaction, V_{trig} the trigonal field and V_{s0} the spin-orbit interaction. Judging from the similarity of the absorption spectra of ruby to those of Cr alum, we may suppose that the cubic part will be larger than the other two terms. $\mathscr{H}'$ will be treated as a small perturbation to the cubic system.

The eigen-functions of $\mathscr{H}_0$ for the chromophoric electrons are already known. They are given in (3.7) of I*, where the z axis was chosen in the direction of the fourfold axis of the octahedron. The principal axis of the trigonal field in ruby is, however, just one of the three fold axis of the octahedron, and it is more convenient to take this axis as the axis of quantization in the present case. The cubic bases, namely, the unperturbed eigenfunctions are accordingly transformed so that they span the irreducible representations of both O_h and C_{3v}**,

$$\varphi(\Gamma M)=\sum_{\gamma}\varphi(\Gamma\gamma)(\Gamma\gamma|\Gamma M)\,, \tag{3.2}$$

where $\varphi(\Gamma\gamma)$ is the previous cubic base belonging to the γ component of the cubic representation Γ and is abbreviated as

$$\left.\begin{aligned}\varphi(E\gamma)&=(u,\,v)\\ \varphi(F_1\gamma)&=(\alpha,\,\beta,\,\gamma)^*\\ \varphi(F_2\gamma)&=(\xi,\,\eta,\,\zeta)^*\end{aligned}\right\}\,, \tag{3.3}$$

while $\varphi(\Gamma M)$ are abbreviated as follows:

$$\left.\begin{array}{lll}\varphi(E\ \pm1)=(u_+,\,u_-) & \text{irreducible representation } E \text{ of } C_{3v} \\ \varphi(F_1\ \pm1)=(a_+,\,a_-) & E \\ \varphi(F_1\ 0)=a_0 & A_2 \\ \varphi(F_2\ \pm1)=(x_+,\,x_-) & E \\ \varphi(F_2\ 0)=x_0 & A_1\end{array}\right\}\,. \tag{3.4}$$

These are at the same time the trigonal bases which belong to the irreducible representation of C_{3v} as shown on the right column of the above table.

The matrix elements of the unitary transformation $(\Gamma\gamma|\Gamma M)$ are given by

$(E\gamma|EM)$

	u_+	u_-
u	$-1/\sqrt{2}$	$1/\sqrt{2}$
v	$-i/\sqrt{2}$	$-i/\sqrt{2}$

$(F_1\gamma|F_1M)$, $(F_2\gamma|F_2M)$

	a_+ (x_+)	a_- (x_-)	a_0 (x_0)
$\alpha(\xi)$	$-\omega/\sqrt{3}$	$\bar{\omega}/\sqrt{3}$	$1/\sqrt{3}$
$\beta(\eta)$	$-\bar{\omega}/\sqrt{3}$	$\omega/\sqrt{3}$	$1/\sqrt{3}$
$\gamma(\zeta)$	$-1/\sqrt{3}$	$1/\sqrt{3}$	$1/\sqrt{3}$

, (3.5)

where $\omega=e^{2\pi i/3}$ and $\bar{\omega}=\omega^2$.

Since almost all of the matrix elements of operators needed in this paper are already given in IV, we now proceed to the discussions of what follows from the theory.

§ 4. Optical Anisotropy and Splitting of the Absorption Bands

As pointed out in § 1, the similarity of the absorption spectra of ruby to those of Cr alum leads us to the expectation that the absorption band at $\sim$18000 cm^{-1}, which we call U band hereafter, corresponds to the transition $(f_2^3)^4A_2 \rightarrow (f_2^2e)^4F_2$ in the cubic case and the band at $\sim$25000 cm^{-1} (called Y band) to the transition $(f_2^3)^4A_2 \rightarrow (f_2^2e)^4F_1$. This expectation will be confirmed if this assignment could explain the experimental facts[8], namely the splitting and the optical anisotropy of these bands.

Let us denote by $U^{\perp}$ and $Y^{\perp}$ the absorptions of U and Y when the electric vector E of the incident light is perpendicular to the optic axis C_3, and by $U^{//}$ and $Y^{//}$ those when E is parallel to C_3. The outline of the observed splittings and anisotropies of the bands

* As to the choice of phase of these bases, see § 2 of IV[10].

** Although actual symmetry of the field which electrons subject to is C_3, it is allowed to treat it as if C_{3v} when we deal with the crystal energy of d-electrons.

to be reported later is as follows: Each absorption peak of $U^{//}$ and $Y^{//}$ is found at the shorter wave-length side of the corresponding peak of $U^{\perp}$ and $Y^{\perp}$. The splitting amounts approximately to 500 cm^{-1} for both U and Y. The absorption intensity of $U^{\perp}$ is much higher than that of $U^{//}$ (the ratio is more than 2), while the absorption intensity of $Y^{\perp}$ is fairly low compared to that of $Y^{//}$ (the ratio is about 1/2). The intensity of $U^{\perp}$ is comparable to that of $Y^{\perp}$.

These experimental facts, especially the marked optical anisotropies of U and Y offer, as we shall see, important evidences in favour of the above assignments. The study of the optical anisotropy in the present case is as powerful as the study of the optical rotatory power. The importance of the study of the rotatory power in making the assignment of $^4F_1$ and $^4F_2$ has been recently emphasized by Moffitt[9].

(a) *The splitting*

Strictly speaking, we must take the spin-orbit interaction into account as well as the trigonal field, in order to discuss the splitting of the bands. Let us, however, neglect the effect of the former for a while. Then group theory shows that $^4F_2$ level splits into two sublevels ^4E and $^4A_1$ of C_{3v} and $^4F_1$ into ^4E and $^4A_2$ under the action of the trigonal field. If we adopt the assumption of strond field limit (i.e. neglect of the configuration interaction among the cubic levels), the positions of these split components measured from the respective unperturbed positions of $^4F_2$ and $^4F_1$ are given by

$$\left.\begin{array}{l} f_2^2e\,{}^4F_2 \begin{cases} {}^4E & ({}^4F_2x_\pm|V_{\text{trig}}|{}^4F_2x_\pm)=K/2 \\ {}^4A_1 & ({}^4F_2x_0|V_{\text{trig}}|{}^4F_2x_0)=-K \end{cases} \\ f_2^2e\,{}^4F_1 \begin{cases} {}^4E & ({}^4F_1a_\pm|V_{\text{trig}}|{}^4F_1a_\pm)=K/2 \\ {}^4A_2 & ({}^4F_1a_0|V_{\text{trig}}|{}^4F_1a_0)=-K \end{cases} \\ f_2e^2\,{}^4F_1 \begin{cases} {}^4E & ({}^4F_1a_\pm|V_{\text{trig}}|{}^4F_1a_\pm)=K \\ {}^4A_2 & ({}^4F_1a_0|V_{\text{trig}}|{}^4F_1a_0)=-2K \end{cases} \end{array}\right\}, \quad (4.1)$$

in terms of a parameter K which measures the strength of the trigonal field and is related to the splitting on one electron level f_2:

$$(f_2x_\pm|v_{\text{trig}}|f_2x_\pm)=K\,, \quad (f_2x_0|v_{\text{trig}}|f_2x_0)=-2K\,. \quad (4.2)$$

(The e level is not split by the action of trigonal field. Note also that the trigonal field as a tensor operator is of type F_2 and $V_{\text{trig}} = V_0(F_2)$ in the notation of IV[10]).

Thus, as far as we neglect the interaction among the sublevels split from different cubic levels, the magnitudes of the splitting of $f_2^2e\,{}^4F_2$ and $f_2^2e\,{}^4F_1$ are both $3K/2$. $^4A_1$ and $^4A_2$ sublevels are on the shorter wave-length side of each ^4E sublevels, in case K is negative, and *vice versa*. As will be seen in the next subsection, the present case seems to be just the former one, and we have

$$K\sim -350\ \text{cm}^{-1} \quad (4.3)$$

from the observed splitting. This value of K in turn justifies the neglect of the effect of spin-orbit interaction in discussing the splitting of $^4F_2$ and $^4F_1$, since the order of magnitude of the relevant matrix elements of V_{so} will be that of the spin orbit coupling parameter $\lambda=\zeta/3$ which will be at most as large as $\sim$90 cm^{-1} (see § 5).

(b) *The optical anisotropy*

In the case of octahedral complex ions, all electric dipole transitions between the multiplets $f_2^ne^{n'}S\Gamma_g$ were forbidden at the equilibrium configuration of nuclei because of the presence of centre of symmetry and the observed intensities of the absorption bands of these ions have been explained by taking the vibrational distortion of the octahedron into account.

In contrast, the environment of Cr^{3+} ion in ruby has no centre of symmetry. The naturally unsymmetrical field (the hemihedral part of the trigonal field V_{hem}) will make the electric dipole transition slightly allowed even in the absence of vibrational distortion. Although the effect of the latter might not be quite negligible, we will discard it in the discussion of the optical anisotropy and concern ourselves only with the effect of the former. This is also somewhat justified by the experimental facts to be reported later that the dependence of the oscillator strength of the absorption bands on temperature is slight at relatively high temperatures and that the band shapes vary with temperature roughly in the same way as that of allowed transitions.

The dipole strength of the transition between the ground state $^4A_2$ and the component M of the excited state $^4\Gamma_g$ is the square of the absolute value of the following matrix element:

$$({}^4A_{2g}|\overline{\boldsymbol{P}}|{}^4\Gamma_gM) = \sum_{\Gamma_{u'}M'} \frac{({}^4A_{2g}|\boldsymbol{P}|{}^4\Gamma_{u'}M')({}^4\Gamma_{u'}M'|V_{\text{hem}}|{}^4\Gamma_gM)}{W({}^4\Gamma_g)-W({}^4\Gamma_{u'})}$$

$$+\sum_{\Gamma_u' M'} \frac{({}^4A_{2g}|V_{\text{hem}}|{}^4\Gamma_u' M')({}^4\Gamma_u' M'|\boldsymbol{P}|{}^4\Gamma_g M)}{W({}^4A_{2g})-W({}^4\Gamma_u')}, \tag{4.4}$$

where ${}^4\Gamma_u'$ is the higher excited state with odd parity and $W({}^4\Gamma_u')$ is the energy of that state. $\boldsymbol{P}$ is the electric dipolement vector $\sum e\boldsymbol{r}_i$ of the system, $\boldsymbol{P}=(P_x, P_y, P_z)$. It is more convenient to use the following linear combination of P_x and P_y corresponding to the present choice of bases,

$$\left.\begin{aligned} P_+&=-\frac{1}{\sqrt{2}}(P_x+iP_y)\,,\\ P_-&=\frac{1}{\sqrt{2}}(P_x-iP_y)\,,\\ P_0&=P_z\,, \end{aligned}\right\} \tag{4.5}$$

so that

$$\left.\begin{aligned} \boldsymbol{P}&=-P_-\boldsymbol{k}^+-P_+\boldsymbol{k}^-+P_0\boldsymbol{k}^0\,,\\ \boldsymbol{k}^+&=-\frac{1}{\sqrt{2}}(\boldsymbol{i}+i\boldsymbol{j})\,,\\ \boldsymbol{k}^-&=\frac{1}{\sqrt{2}}(\boldsymbol{i}-i\boldsymbol{j})\,,\\ \boldsymbol{k}^0&=\boldsymbol{k}\,,\\ |\boldsymbol{k}^+|^2&=|\boldsymbol{k}^-|^2=\frac{1}{2}(\boldsymbol{i}^2+\boldsymbol{j}^2)\,, \end{aligned}\right\} \tag{4.6}$$

where $\boldsymbol{i}$, $\boldsymbol{j}$ and $\boldsymbol{k}$ are the unit vectors in the directions of x, y and z coordinate axes respectively.

V_{hem} must be invariant under the trigonal rotation, and changes sign under the inversion with respect to the origin. If it is expanded in powers of the coordinates of electrons, the first term which will be predominant is of the form $\kappa\sum_i z_i$. This term is of type F_{1u} as an irreducible tensor operator and will be denoted as $V_0(F_{1u})$ in the following. If we assume $V_{\text{hem}}=V_0(F_{1u})$, the excited state ${}^4\Gamma_u'$ in (4.4) is restricted to ${}^4F_{2u}$, since $\boldsymbol{P}$ is also an operator of the type F_{1u}. Then we find

$$\left.\begin{aligned} ({}^4A_2|\overline{\boldsymbol{P}}|{}^4F_2x_\pm)&=\pm\frac{i}{\sqrt{2}}\cdot\boldsymbol{\alpha}({}^4A_2\to{}^4F_2)\cdot\boldsymbol{k}^\pm\,,\\ ({}^4A_2|\overline{\boldsymbol{P}}|{}^4F_2x_0)&=0\,, \end{aligned}\right\} \tag{4.7}$$

$$\left.\begin{aligned} ({}^4A_2|\overline{\boldsymbol{P}}|{}^4F_1a_\pm)&=-\frac{1}{\sqrt{6}}\cdot\boldsymbol{\alpha}({}^4A_2\to{}^4F_1)\cdot\boldsymbol{k}^\pm\,,\\ ({}^4A_2|\overline{\boldsymbol{P}}|{}^4F_1a_0)&=\frac{\sqrt{2}}{\sqrt{3}}\cdot\boldsymbol{\alpha}({}^4A_2\to{}^4F_1)\cdot\boldsymbol{k}^0\,, \end{aligned}\right\} \tag{4.8}$$

where $\boldsymbol{\alpha}$'s are suitable proportionality factors which can be evaluated from (4.4), and the corresponding dipole strengths are

$$\left.\begin{aligned} W({}^4A_2\to{}^4F_2:{}^4E)&=\sum_{M=x_+,x_-}W({}^4A_2\to{}^4F_2M)\\ &\propto\frac{1}{2}|\boldsymbol{\alpha}({}^4A_2\to{}^4F_2)|^2\cdot(\boldsymbol{i}^2+\boldsymbol{j}^2)\,,\\ W({}^4A_2\to{}^4F_2:{}^4A_2)&=W({}^4A_2\to{}^4F_2x_0)=0\,, \end{aligned}\right\} \tag{4.9}$$

$$\left.\begin{aligned} W({}^4A_2\to{}^4F_1:{}^4E)&=\sum_{M=a_+,a_-}W({}^4A_2\to{}^4F_1M)\\ &\propto\frac{1}{6}|\boldsymbol{\alpha}({}^4A_2\to{}^4F_1)|^2\cdot(\boldsymbol{i}^2+\boldsymbol{j}^2)\,,\\ W({}^4A_1\to{}^4F_1:{}^4A_1)&=W({}^4A_2\to{}^4F_1a_0)\\ &\propto\frac{2}{3}|\boldsymbol{\alpha}({}^4A_2\to{}^4F_1)|^2\boldsymbol{k}^2\,. \end{aligned}\right\} \tag{4.10}$$

The transition probabilities for the linearly polarized light $E//C_3$ are given by the coefficients of $\boldsymbol{k}^2$ and those the linearly polarized light $E\perp C_3$ by the coefficients of $\boldsymbol{i}^2$ or $\boldsymbol{j}^2$ in (4.9) and (4.10). Thus with the assignments

$$\left.\begin{aligned} U^{//}&: f_2^3\,{}^4A_{2g}\to(f_2^2e){}^4F_{2g}:{}^4A_1\\ U^{\perp}&:\qquad\to(f_2^2e){}^4F_{2g}:{}^4E\\ Y^{//}&:\qquad\to(f_2^2e){}^4F_{1g}:{}^4A_2\\ Y^{\perp}&:\qquad\to(f_2^2e){}^4F_{1g}:{}^4E \end{aligned}\right\} \tag{4.11}$$

we have the following ratios between the dipole strengths;

$$\left.\begin{aligned} \omega(U^{//}):\omega(U^{\perp})&=0:1\\ \omega(Y^{//}):\omega(Y^{\perp})&=4:1 \end{aligned}\right\}. \tag{4.12}$$

Although the result are not quite satisfactory, the present simple treatment seems to explain the qualitative feature of the observed optical anisotropy in each absorption band under a reasonable assumption. The causes of the discrepancy between the theory and experiment may be as follows; the assumption $V_{\text{hem}}=V_0(F_{1u})$* and the neglect of the vibrational effect. We need, however, more detailed knowledge of the trigonal field and the vibrations excited in the crystal in order to improve the results. These problems will be left for future investigations, together with the unexplained ratio of the absorption intensities of U to that of Y.

§ 5. Splitting and Optical Anisotropy of the Absorption Lines

For the absorption lines R_1 and R_2 of ruby,

* Note that (4.7) and (4.8) holds as long as we assume V_{hem} is of type F_{1u}. They were derived by consideration solely based on the transformation properties of operators and wave functions.

we expect the assignments $f_2^3\,{}^4A_2\rightarrow$ split components of $f_2^3\,{}^2E$ or $f_2^3\,{}^2F_1$, and for B_1 and B_2 $f_2^3\,{}^4A_2\rightarrow$ split components of $f_2^3\,{}^2F_2$, just as in the case of Cr alum. In this section, we will discuss the splitting of f_2^3: ${}^2E$, ${}^2F_2$ and ${}^2F_1$ levels due to the action of the trigonal field and the spin-orbit interaction, and also the optical anisotropy of the absorption lines corresponding to the transition to these split components from the ground state.

(a) *The splitting*

As pointed out in IV, the splitting of ${}^2E$ is described by the effective Hamiltonian

$$\mathscr{H}_{\text{eff}}=\lambda S_z T(A_2)\,, \tag{5.1}$$

where λ is a parameter to be determined empirically and $T(A_2)$ is an orbital operator whose matrix representation is

$$\begin{array}{c} u_+ \\ u_- \end{array}\left\|\begin{array}{cc} 1 & \\ & -1 \end{array}\right\|. \tag{5.2}$$

The eigenvalues of the above Hamiltonian and the corresponding eigenfunctions are

$$W_1=\tfrac{1}{2}\lambda \qquad 2\overline{A}^*\begin{cases}\Psi({}^2E,\ \tfrac{1}{2},\ u_+)^{**}\\ \Psi({}^2E,\ -\tfrac{1}{2},\ u_-)^{**}\end{cases} \tag{5.3}$$

$$W_2=-\tfrac{1}{2}\lambda \quad \overline{E}^*\begin{cases}\Psi({}^2E,\ -\tfrac{1}{2},\ u_+)\\ \Psi({}^2E,\ \tfrac{1}{2},\ u_-)\,.\end{cases} \tag{5.4}$$

It remains to express the parameter λ in terms of known matrix elements. This is easy if we confine ourselves to the second order perturbation in $\mathscr{H}'$. Since ${}^2E$ does not split by the sole action of the trigonal field or of the spin orbit interaction, but split only through the interplay of these two, it follows

$$\begin{aligned}&({}^2EM_sM|\mathscr{H}_{\text{eff}}|{}^2EM_sM)\\ &=\sum_{{}^2\Gamma M_s'M'}\frac{1}{W({}^2E)-W({}^2\Gamma)}\\ &\quad\times\{({}^2EM_sM|V_{\text{trig}}|{}^2\Gamma M_s'M')\\ &\quad\cdot({}^2\Gamma M_s'M'|V_{so}|{}^2EM_sM)\\ &\quad+\text{complex conjugate}\}\,.\end{aligned} \tag{5.5}$$

If the intermediate states ${}^2\Gamma$ are restricted to those in configuration f_2^3 that makes a large contribution in the above summation, the summation reduces to a single term with ${}^2\Gamma={}^2F_2$, since ${}^2E$ does not couple with ${}^2F_1$ either through the trigonal field or the spin-orbit interaction. To make the following discussion clear, the coupling scheme among the doublets in configuration f_2^3 and the quartets in configuration f_2^2e are illustrated in Fig. 2. Evaluating the matrix elements in (5.5) with the aid of the tables given in the Appendix and comparing (5.5) with (5.1), we find

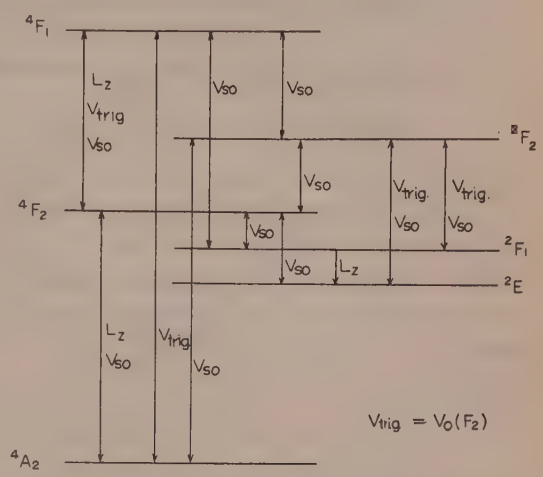

Fig. 2. The coupling scheme among the doublets ${}^2E$, ${}^2F_2$ and ${}^2F_1$ in configuration f_2^3 and the quartets ${}^4A_2(f_2^3)$, ${}^4F_2(f_2^2e)$ and ${}^4F_1(f_2^2e)$.

$$\lambda({}^2E)=4K\zeta/\{W({}^2E)-W({}^2F_2)\} \tag{5.6}$$

where ζ is defined by

$$\zeta=-2(f_2,\ \tfrac{1}{2},\ x_+|v_{so}|f_2,\ \tfrac{1}{2},\ x_+)\,, \tag{5.7}$$

while ζ' which appears in the following discussion is defined by

$$\zeta'=-\sqrt{2}\,(f_2,\ \tfrac{1}{2},\ x_+|v_{so}|e,\ \tfrac{1}{2},\ u_+)\,, \tag{5.8}$$

in which $v_{so}=\zeta\boldsymbol{s}\cdot\boldsymbol{l}$. In this section we assume that ζ and ζ' are isotropic. The second order terms which come from V_{trig}^2 and V_{so}^2 cause only a shift of ${}^2E$ as a whole.

The effective Hamiltonian for ${}^2F_2$ is of the form:

$$\mathscr{H}_{\text{eff}}=FV_0+\lambda(S_xT_x+S_yT_y)+\lambda_0S_zT_z\,, \tag{5.9}$$

where V_0 and T_x, T_y, T_z are the operators whose matrix representations are given respectively by

$$V_0:\ \begin{array}{c|ccc} & x_+ & x_- & x_0 \\ \hline x_+ & -1 & & \\ x_- & & -1 & \\ x_0 & & & 2 \end{array}$$

* These are the two-valued representations of C_3.

** $\frac{1}{2}$ denotes the spin quantum number M_s.

$$T_x:\ \begin{array}{c|ccc} & x_+ & x_- & x_0 \\ \hline x_+ & & & -1/\sqrt{2} \\ x_- & & & -1/\sqrt{2} \\ x_0 & -1/\sqrt{2} & -1/\sqrt{2} & 0 \end{array} \quad T_y:\ \begin{array}{c|ccc} & x & x_- & x_0 \\ \hline x_+ & & & i/\sqrt{2} \\ x_- & & & -i/\sqrt{2} \\ x_0 & -i/\sqrt{2} & i/\sqrt{2} & 0 \end{array} \quad T_z:\ \begin{array}{c|ccc} & x_+ & x_- & x_0 \\ \hline x_+ & -1 & & \\ x_- & & 1 & \\ x_0 & & & 0 \end{array} . \tag{5.10}$$

The eigenvalues of (5.9) and the corresponding eigenfunctions are

$$W_0=-F-\frac{\lambda_0}{2} \qquad 2\overline{A}\begin{cases}\Psi(^2F_2,\ \tfrac{1}{2},\ x_+)\\ \Psi(^2F_2,\ -\tfrac{1}{2},\ x_-)\end{cases} \tag{5.11}$$

$$W_1=-F+\frac{\lambda_0}{2}-\frac{\lambda}{\sqrt{2}}\tan\alpha \qquad \overline{E}_a\begin{cases}\Psi(^2F_2,\ -\tfrac{1}{2},\ x_+)\cos\alpha+\Psi(^2F_2,\ \tfrac{1}{2},\ x_0)\sin\alpha\\ \Psi(^2F_2,\ \tfrac{1}{2},\ x_-)\cos\alpha+\Psi(^2F_2,\ -\tfrac{1}{2},\ x_0)\sin\alpha\end{cases} \tag{5.12}$$

$$W_2=-F+\frac{\lambda_0}{2}+\frac{\lambda}{\sqrt{2}}\cot\alpha \qquad \overline{E}_b\begin{cases}\Psi(^2F_2,\ \tfrac{1}{2},\ x_0)\cos\alpha-\Psi(^2F_2,\ -\tfrac{1}{2},\ x_+)\sin\alpha\\ \Psi(^2F_2,\ -\tfrac{1}{2},\ x_0)\cos\alpha-\Psi(^2F_2,\ \tfrac{1}{2},\ x_-)\sin\alpha\ ,\end{cases} \tag{5.13}$$

where

$$\tan 2\alpha=\sqrt{2}\,\lambda\Big/\left(3F-\frac{\lambda_0}{2}\right), \qquad 0\le\alpha\le\frac{\pi}{2}\ . \tag{5.14}$$

F, λ and λ_0 can also be expressed in terms of K and ζ. Let us first consider F. Since $(f_2{}^3\,{}^2F_2M_sM|V_{\text{trig}}|f_2{}^3\,{}^2F_2M_sM)$ vanishes, trigonal field splits $^2F_2$ through the second order perturbation:

$$\sum_{^2\Gamma M'}\frac{1}{W(^2F_2)-W(^2\Gamma)}(^2F_2M_sM|V_{\text{trig}}|^2\Gamma M_sM')(^2\Gamma M_sM'|V_{\text{trig}}|^2F_2M_sM)\ . \tag{5.15}$$

This, however, causes the shift of $^2F_2$ as a whole as well as the splitting. The magnitude of the shift is equal to the trace of the above expression divided by 6. Subtracting this from (5.15) and comparing suitable matrix element of the resulting expression with the corresponding element of the first term of (5.9), we find under the same assumption as before

$$F(^2F_2)=-2K^2/\{W(^2F_2)-W(^2E)\}-K^2/\{W(^2F_2)-W(^2F_1)\}\ . \tag{5.16}$$

$(f_2{}^3\,{}^2F_2M_sM|V_{s0}|f_2{}^{32}F_2M_s'M')$ also vanishes and the second and the third term in (5.9) come from the second order perturbation:

$$\sum_{^2\Gamma M''}\frac{1}{W(^2F_2)-W(^2\Gamma)}\{(^2F_2M_sM|V_{\text{trig}}|^2\Gamma M_sM'')(^2\Gamma M_sM''|V_{s0}|^2F_2M_s'M')+\text{c.c.}\}\ . \tag{5.17}$$

Proceeding as before we obtain

$$\left.\begin{aligned}\lambda\,(^2F_2)&=2K\zeta/\{W(^2F_2)-W(^2E)\}+K\zeta/\{W(^2F_2)-W(^2F_1)\}\ ,\\ \lambda_0(^2F_2)&=-4K\zeta/\{W(^2F_2)-W(^2E)\}-2K\zeta/\{W(^2F_2)-W(^2F_1)\}\ ,\end{aligned}\right\} \tag{5.18}$$

where the contributions from the second order term V_{s0}^2 are neglected, since they are estimated to be negligible if we use the value of ζ to be determined later.

The effective Hamiltonian for $^2F_1$ is of the same form as that for $^2F_2$. The matrix elements of the operator T for F_1 state is just the opposite sign (negative) of the corresponding elements for F_2 though those of V_0 are same for both F_1 and F_2. The eigen-values and the eigenfunctions for $^2F_1$ is thus written down at once by changing the sign of λ, λ_0 and writting $^2F_1a_+$ etc. for $^2F_2x_+$ etc. in (5.11)~(5.14). F, λ and λ_0 in this case are expressed in terms of K and ζ in the following way:

$$F(^2F_1)=-K^2/\{W(^2F_1)-W(^2F_2)\}\ , \tag{5.19}$$

$$\left.\begin{aligned}\lambda\,(^2F_1)&=-K\zeta/\{W(^2F_1)-W(^2F_2)\}\ ,\\ \lambda_0(^2F_1)&=2K\zeta/\{W(^2F_2)-W(^2F_2)\}\ ,\end{aligned}\right\} \tag{5.20}$$

in which the second order terms V_{sJ}^2 are again neglected.

We will now discuss the splittings of the

doublets in greater detail.

^2E splits into two Kramers doublets $2\overline{A}(^2E)$ and $\overline{E}(^2E)$. Here $2\overline{A}$ lies on the shorter wave-length side if $\lambda(^2E)>0$. This is really the case since it was found in § 4 that K is negative. Further considerations on the anisotropy and the Zeeman effect of the characteristic doublet R_1 and R_2 establish the following assignments in agreement with this prediction:

$$\left.\begin{array}{l} R_1(14418\,\mathrm{cm}^{-1}):\ {}^4A_2\rightarrow\overline{E}(^2E) \\ R_2(14447\,\mathrm{cm}^{-1}):\ {}^4A_2\rightarrow 2\overline{A}(^2E) \end{array}\right\}. \tag{5.21}$$

Using the observed splitting $\lambda(^2E)\sim 30\,\mathrm{cm}^{-1}$ and taking $W(^2E)-W(^2F_2)$ to be $\sim -6500\,\mathrm{cm}^{-1}$, the magnitude of ζ is found to be $\sim 140\,\mathrm{cm}^{-1}$. This is fairly small compared to the free-ion value $\sim 270\,\mathrm{cm}^{-1}$ adopted by Owen[11], but not unreasonably small in view of the fact that the value of ζ generally decreases in crystals.

With this value of ζ, the approximate values of F, λ and λ_0 can now be estimated for $^2F_2$ and $^2F_1$ using (5.16), (5.18) and (5.19), (5.20) respectively:

$$\left.\begin{array}{l} F(^2F_2)\sim -60\,\mathrm{cm}^{-1} \\ \lambda_0(^2F_2)\sim +45\,\mathrm{cm}^{-1} \\ \lambda(^2F_2)\sim -22\,\mathrm{cm}^{-1} \end{array}\right\}, \tag{5.22}$$

$$\left.\begin{array}{l} F(^2F_1)\sim +20\,\mathrm{cm}^{-1} \\ \lambda_0(^2F_1)\sim +15\,\mathrm{cm}^{-1} \\ \lambda(^2F_1)\sim -8\,\mathrm{cm}^{-1} \end{array}\right\}, \tag{5.23}$$

and for these values,

$$\alpha(^2F_2)\sim 0\,,\quad \alpha(^2F_1)\sim 0\,,$$

where it was assumed that $W(^2F_2)-W(^2E)\approx W(^2F_2)-W(^2F_1)$. The predicted arrangements of the split components of $^2F_2$ and $^2F_1$ are given in Fig. 3. The lines that correspond to the transitions to the split components of $^2F_1$ are not yet identified. As to those of $^2F_2$ it is fairly certain, as will be seen in the following, that the following assignments can be made for B_1 and B_2:

$$\left.\begin{array}{l} B_1(20993\,\mathrm{cm}^{-1}):\ {}^4A_2\rightarrow 2\overline{A}(^2F_2) \\ B_2(21068\,\mathrm{cm}^{-1}):\ {}^4A_2\rightarrow \overline{E}_a(^2F_2) \end{array}\right\}. \tag{5.24}$$

If $\alpha(^2F_2)\sim 0$, we have $\lambda_0\sim 75\,\mathrm{cm}^{-1}$ from the observed separation of B_1 and B_2.

As far as we are concerned with the split components $2\overline{A}$ and $\overline{E}_a$ the predicted arrangement is qualitatively good*, but quantitatively not quite satisfactory (compare the experimental value of λ_0 with λ_0 in (5.22)). This disagreement is perhaps partly due to the omission of the interaction between $^2F_2$ and any higher excited doublet which will be larger for $^2F_2$ than for the deeply lying ^2E, and partly due to the assumption $W(^2F_2)-W(^2E)\approx W(^2F_2)-W(^2F_1)$. Though the position of $^2F_1$ has not been known yet, it is highly probable that $^2F_1$ has a higher energy than that of ^2E judging from the sign and the magnitude of the g-shifts of the split components $2\overline{A}(^2E)$ and $\overline{E}(^2E)$ (§ 6 (e)). This will increase the theoretical value of $\lambda_0(^2F_2)$.

(b) *The optical anisotropy*

We assume as in II that the intensities of the line absorption are borrowed from those of the absorption bands through the spin-orbit interaction, that is, the dipole strength for the transition from the component a of the ground state $^4A_2$ to the component b of the doublet $^2\Gamma$ is given by the square of the matrix element

$$\begin{aligned}&(^4A_2a|\overline{\boldsymbol{P}}|^2\Gamma b)\\ &\quad=\sum(^4A_2a|\overline{\boldsymbol{P}}|^4\Gamma' c)(^4\Gamma' c|V_{so}|^2\Gamma b)\\ &\qquad/\{W(^2\Gamma)-W(^4\Gamma')\}\,,\end{aligned} \tag{5.25}$$

where c is the components of the excited quartets $^4F_2$ and $^4F_1$. This means that the contamination of the doublet states to the

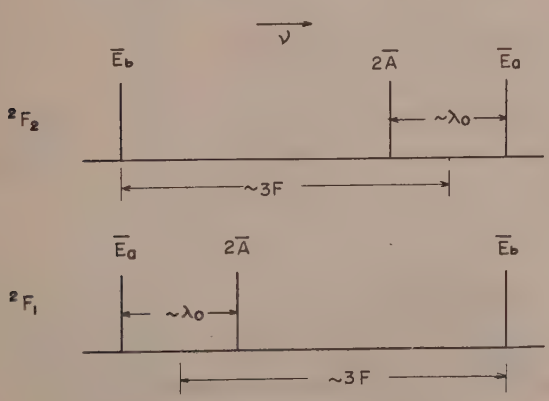

Fig. 3. The splittings of $^2F_2$ and $^2F_1$.

* Though the arrangement of $2\overline{A}(^2F_2)$ and $\overline{E}_a(^2F_2)$ is qualitatively good, we cannot observe any absorption line at the long wave-length side of them. Somewhat broad line can be observed at the shorter wave-length side (21357 cm^{-1} at 78°K)[2]. Thus, our theory might be wrong even qualitatively with respect to the predicted position of $\overline{E}_b(^2F_2)$.

ground quartet is neglected*.

Using the tables of the Appendix, the dipole strengths evaluated by the formula (5.25) are given in Tables I and II, with $\alpha=0$ in (5.12, 5.13). π's and σ's are expressed in terms of ζ' and the dipole strengths of the bands. Using the abbreviations,

$$\left.\begin{aligned} P_\alpha^{0,\pm}(U)&=({}^4A_2|\overline{P}_\alpha|{}^4F_2x_{0,\pm}) \\ P_\alpha^{0,\pm}(Y)&=({}^4A_2|\overline{P}_\alpha|{}^4F_1a_{0,\pm}) \end{aligned}\right\}, \tag{5.26}$$

they are expressed as follows; for the components of ${}^2E$

$$\left.\begin{aligned} \pi_\alpha &= \frac{4}{3}\zeta'^2\left|\frac{P_\alpha^0(U)}{W({}^2E)-W({}^4F_2)}\right|^2, \\ \sigma_{\pm\alpha}&=\frac{4}{3}\zeta'^2\left|\frac{P_\alpha^\pm(U)}{W({}^2E)-W({}^4F_2)}\right|^2, \end{aligned}\right\} \tag{5.27}$$

and for ${}^2F_2$

Table I. The values of $|({}^4A_2M_s|\overline{P}|{}^2EM_s', M')|^2$, in which M_s is quantized with respect to the z axis.

	${}^2E$	$2\overline{A}$		$\overline{E}$	
	M_s', M'	$1/2, u_+$	$-1/2, u_-$	$-1/2, u_+$	$1/2, u_-$
${}^4A_2$ M_s					
$3/2$		$\pi_\alpha/2$			$\sigma_{+\alpha}/2$
$1/2$		$\sigma_{+\alpha}/3$	$\sigma_{+\alpha}/6$	$\pi_\alpha/6$	$\sigma_{-\alpha}/3$
$-1/2$		$\sigma_{-\alpha}/6$	$\sigma_{-\alpha}/3$	$\sigma_{+\alpha}/3$	$\pi_\alpha/6$
$-3/2$			$\pi_\alpha/2$	$\sigma_{-\alpha}/2$	

Table II. The values of $|({}^4A_2M_s|\overline{P}|{}^2F_2M_s', M')|^2$ and $|({}^4A_2M_s|\overline{P}|{}^2F_1M_s', M')|^2$, ih which M_s is quantized with respect to the z axis.

	${}^2F_2({}^2F_1)$	$2\overline{A}$		$\overline{E}_a$		$\overline{E}_b$	
	M_s', M'	$-1/2, x_+(a_+)$	$1/2, x_-(a_-)$	$-1/2, x_+(a_+)$	$1/2, x_-(a_-)$	$1/2, x_0(a_0)$	$-1/2, x_0(a_0)$
${}^4A_2$ M_s							
$3/2$		$\pi_\alpha/2$			$\sigma^0_{+\alpha}/2$	$\sigma'_{+\alpha}/2$	
$1/2$		$\sigma_{+\alpha}/3$	$\sigma^0_{+\alpha}/6$	$\pi_\alpha/6$	$\sigma_{-\alpha}/3$	$\pi_\alpha'/3$	$\sigma'_{-\alpha}/6$
$-1/2$		$\sigma^0_{-\alpha}/6$	$\sigma_{-\alpha}/3$	$\sigma_{+\alpha}/3$	$\pi_\alpha/6$	$\sigma'_{+\alpha}/6$	$\pi_\alpha'/3$
$-3/2$			$\pi_\alpha/2$	$\sigma^0_{-\alpha}/2$			$\sigma'_{+\alpha}/2$

$$\left.\begin{aligned} \pi_\alpha &= \frac{1}{2}\zeta'^2\left\{\left|\frac{P_\alpha^0(U)}{W({}^2F_2)-W({}^4F_2)}\right|^2+\left|\frac{P_\alpha^0(Y)}{W({}^2F_2)-W({}^4F_1)}\right|^2\right\}, \\ \sigma_{\pm\alpha}&=\frac{1}{2}\zeta'^2\left|\frac{P_\alpha^\pm(U)}{W({}^2F_2)-W({}^4F_2)}\pm i\,\frac{P_\alpha^\pm(Y)}{W({}^2F_2)-W({}^4F_1)}\right|^2, \\ \sigma_{\pm}{}^0&=2\zeta'^2\left|\frac{P_\alpha^\pm(Y)}{W({}^2F_2)-W({}^4F_1)}\right|^2, \\ \pi_\alpha'&=2\zeta'^2\left|\frac{P_\alpha^0(Y)}{W({}^2F_2)-W({}^4F_1)}\right|^2, \\ \sigma'_{\pm\alpha}&=\frac{1}{2}\zeta'^2\left|\frac{P_\alpha^\pm(U)}{W({}^2F_2)-W({}^4F_2)}\mp i\,\frac{P_\alpha^\pm(Y)}{W({}^2F_2)-W({}^4F_1)}\right|^2, \end{aligned}\right\} \tag{5.28}$$

and for ${}^2F_1$

$$\left.\begin{aligned} \pi_\alpha &= \frac{1}{6}\zeta'^2\left\{\left|\frac{P_\alpha^0(U)}{W({}^2F_1)-W({}^4F_2)}\right|^2+9\left|\frac{P_\alpha^0(Y)}{W({}^2F_1)-W({}^4F_1)}\right|^2\right\}, \\ \sigma_{\pm\alpha}&=\frac{1}{6}\zeta'^2\left|\frac{P_\alpha^\pm(U)}{W({}^2F_1)-W({}^4F_2)}\mp i\,\frac{3P_\alpha^\pm(Y)}{W({}^2F_1)-W({}^4F_1)}\right|^2, \\ \sigma_{\pm}{}^0&=\frac{2}{3}\zeta'^2\left|\frac{P_\alpha^\pm(U)}{W({}^2F_1)-W({}^4F_2)}\right|^2, \\ \pi_\alpha'&=\frac{2}{3}\zeta'^2\left|\frac{P_\alpha^0(U)}{W({}^2F_1)-W({}^4F_2)}\right|^2, \\ \sigma'_{\pm\alpha}&=\frac{1}{6}\zeta'^2\left|\frac{P_\alpha^\pm(U)}{W({}^2F_1)-W({}^4F_2)}\pm i\,\frac{3P_\alpha^\pm(Y)}{W({}^2F_1)-W({}^4F_1)}\right|^2, \end{aligned}\right\} \tag{5.29}$$

* Note that ${}^4F_2$ and ${}^4F_1$ hybridize with the neighbouring doublets ${}^2E$, ${}^2F_1$ and ${}^2F_2$ to a larger extent than that ${}^2F_2$ does with the ground quartet. Note also that ${}^2F_2$ is the only one among the doublets that couples with the ground state.

where $\alpha=z$ and $\alpha=x$ for $E//C_3$ and $E\perp C_3$ respectively.

Then we observe that, for the sum of the strengths of the split components, $\sum_\alpha$, the following expressions should be given:

$$\sum_\alpha(^2E)=\frac{4}{3}\{\pi_\alpha+(\sigma_{+\alpha}+\sigma_{-\alpha})\}=\frac{16}{9}\zeta'^2\sum_{k=0,+,-}\left|\frac{P_\alpha{}^k(U)}{W(^2E)-W(^4F_2)}\right|^2, \tag{5.30}$$

$$\sum_\alpha(^2F_2)=\frac{2}{3}\{2\pi_\alpha+\pi_\alpha'+(\sigma_{+\alpha}+\sigma_{-\alpha})+(\sigma'_{+\alpha}+\sigma'_{-\alpha})+(\sigma^0_{+\alpha}+\sigma^0_{-\alpha})\}$$

$$=\frac{2}{3}\zeta'^2\sum_{k=0,+,-}\left|\frac{P_\alpha{}^k(U)}{W(^2F_2)-W(^4F_2)}\right|^2+2\zeta'^2\sum_{k=0,+,-}\left|\frac{P_\alpha{}^k(Y)}{W(^2F_2)-W(^4F_1)}\right|^2, \tag{5.31}$$

$$\sum_\alpha(^2F_1)=\frac{2}{3}\{2\pi_\alpha+\pi_\alpha'+(\sigma_{+\alpha}+\sigma_{-\alpha})+(\sigma'_{+\alpha}+\sigma'_{-\alpha})+(\sigma^0_{+\alpha}+\sigma^0_{-\alpha})\}$$

$$=\frac{2}{3}\zeta'^2\sum_{k=0,+,-}\left|\frac{P_\alpha{}^k(U)}{W^2(F_1)-W(^4F_2)}\right|^2+2\zeta'^2\sum_{k=0,+,-}\left|\frac{P_\alpha{}^k(Y)}{W(^2F_1)-W(^4F_1)}\right|^2. \tag{5.32}$$

The relative magnitude of these quantities can thus be estimated from the observed relative strengths of the bands.

If we could neglect the effect of the vibrationally allowed part of transitions, we have

$$\pi_x=\pi_x'=\sigma_{\pm z}=\sigma'_{\pm z}=\sigma^0_{\pm z}=0\,, \tag{5.33}$$

and

$$\left.\begin{aligned}\sigma_{+x}=\sigma_{-x}&\equiv\sigma\,,\\ \sigma'_{+x}=\sigma'_{-x}&\equiv\sigma'\,,\\ \sigma^0_{+x}=\sigma^0_{-x}&\equiv\sigma^0\,,\end{aligned}\right\} \tag{5.34}$$

since for the real trigonal field

$$(P_x{}^\pm)^*=-P_x{}^\mp\,. \tag{5.35}$$

Thus it becomes possible to predict several relations among the intensities of the split components. Using the parameters σ, σ^0, $\pi=\pi_z$ and $\pi'=\pi_z'$, the calculated intensities are given in Table III. Comparing these with

Table III. The calculated absorption intensities of the line spectra corresponding to transitions to the split components of ^2E, $^2F_2$ and $^2F_1$.

		$E\perp C_3$	$E//C_3$
^2E	$2\bar{A}$	σ	π
	$\bar{E}$	$5\sigma/3$	$\pi/3$
$^2F_2$ or $^2F_1$	$2\bar{A}$	$2\sigma/3+\sigma_0/3$	π
	$\bar{E}_a$	$2\sigma/3+\sigma_0$	$\pi/3$
	$\bar{E}_b$	$4\sigma'/3$	$2\pi'/3$

the experimental results given in Fig. 1 of Part B, we shall see that the assignments given in subsection (a) explain nicely the observed intensity ratios between $R_1{}^{\perp,//}$ and $R_2{}^{\perp,//}$ and between $B_1{}^{//}$ and $B_2{}^{//}$ (the superscripts denote the polarization). In order to explain the ratios between $B_1{}^\perp$ and $B_2{}^\perp$, $R_1{}^\perp$ ane $R_1{}^{//}$, and $B_1{}^\perp$ and $B_1{}^{//}$ it is necessary to know the relations among the parameters σ, σ^0, π and π'. It will be shown in Part B that if we assume the relations $\sigma\sim2\pi$ for ^2E and $\sigma^0\sim2\sigma$, $\pi\sim3\sigma$ for $^2F_2$, all the above-mentioned intensity ratios observed are explained.

We notice that for B_1 the absorption is stronger in the case $E//C_3$ than in the case $E\perp C_3$ while for R_2 the relation is reversed. This can be easily understood since $B_1(B_2)$ borrows most of its intensity from Y band which shows a strong absorption for the light $E//C_3$ while $R_1(R_2)$ borrows all of its intensity from U band whose anisotropy is reverse to that of Y band.

If the transitions corresponding to U and Y bands are assumed to be allowed only by the hemihedral part of trigonal field and the relation $\sigma\sim\sigma'$ is assumed to be approximately valid, we can use the observed anisotropy of these bands to get the relations among the parameters σ, σ^0, π and π'. Putting

$$\omega(U^{//}):\omega(U^\perp):\omega(Y^{//}):\omega(Y^\perp)=1:3:3:6$$

to give approximately the observed anisotropy of the bands, we obtain the relations $\sigma\sim1.5\pi$ for ^2E and $\sigma^0\sim4\sigma$, $\pi\sim2\sigma$ for $^2F_2$. This should be compared to the above mentioned empirical relations. The agreement is fair.

We will next see to what extent the relation (5.30) is satisfied. Inserting the observed intensity ratios of R's absorptions, $\omega(R_1{}^\perp)$: $\omega(R_1{}^{//})$: $\omega(R_2{}^\perp)$: $\omega(R_2{}^{//})=10:2:7:4$, we obtain $\sum_z(^2E)/\sum_x(^2E)=6/17\fallingdotseq1/3$ which nicely agrees with the observed anisotropy of U band, $\omega(U^{//})/\omega(U^\perp)=1/3$.

$\bar{E}_b(^2F_2)$ is yet unidentified. The line that will

correspond to this level will show marked anisotropy, because using the observed anisotropy of U and Y bands the relation $\pi' \sim 4\pi$ can be derived and so together with the empirical relation $\pi \sim 3\sigma$ (the approximate relation $\sigma \sim \sigma'$ is also assumed here as before) we suppose that the parallel component will be six times stronger than the perpendicular component. The strength of the parallel component of the line corresponding to $\overline{E}_b(^2F_2)$ thus calculated becomes more than twice that of B_1.

The lines that will correspond to the components of $^2F_1$ borrow their intensities almost equally from both U and Y bands if they are located near R_1 and R_2. The expected anisotropy of these lines (corresponding to $\overline{E}_a(^2F_1)$ and $2\overline{A}(^2F_1)$) are somewhat similar to that of R_1 and R_2 and there is a possibility that R_1 and R_2 correspond respectively to $\overline{E}_a(^2F_1)$ and $2\overline{A}(^2F_1)$. This possibility is, however, excluded by the consideration of the Zeeman effect which will be discussed in the following section.

§ 6. Zeeman Effect of the Absorption Lines

(a) *Zeeman splitting of the excited states*

For the discussion of the Zeeman effect of ^2E, we use the following simplified effective Hamiltonian:

$$\begin{aligned}\mathscr{H}_{\text{eff}} = {} & \lambda S_z T(A_2) + g_{//}\beta H_{0z} S_z \\ & + g_\perp \beta (H_{0x} S_x + H_{0y} S_y) \\ & + (g_{//}'\beta H_{0z} + g_\perp' \beta H_{0x} + g_\perp' \beta H_{0y}) T(A_2)\,, \end{aligned} \tag{6.1}$$

neglecting the term of $\beta \boldsymbol{H}_0 \cdot \boldsymbol{g} \cdot \boldsymbol{S} \cdot \boldsymbol{V}(E)$ in (3.2) of IV, which is negligible in the present case. The splitting factor g^* for $2\overline{A}(^2E)$ and $\overline{E}(^2E)$ when $H_0 // C_3$ is readily found as

$$\left.\begin{aligned} g_{//}(2\overline{A}) &= g_{//} + 2g_{//}'\,, \\ g_{//}(\overline{E}) &= -(g_{//} - 2g_{//}')\,, \end{aligned}\right\} \tag{6.2}$$

When $H_0 \perp C_3$, it is also found that

$$\left.\begin{aligned} g_\perp(2\overline{A}) &= 2g_\perp'\,, \\ g_\perp(\overline{E}) &= 2g_\perp'\,, \end{aligned}\right\} \tag{6.3}$$

and a magnetic field causes the shifts of $2\overline{A}$ and $\overline{E}$ as follows;

$$\left.\begin{aligned} &\text{for } 2\overline{A}(^2E) \quad \beta^2 H^2/\lambda(^2E)\,, \\ &\text{for } \overline{E}(^2E) \quad -\beta^2 H^2/\lambda(^2E)\,, \end{aligned}\right\} \tag{6.4}$$

but this is negligible if $\lambda(^2E)$ is very large compared to the Zeeman energy just as in the present case.

The orbital angular momentum is quenched in ^2E and the first order correction in $g_{//}$, $g_{//}'$ and $g_\perp'$ vanishes, namely

$$\sum_{^2\Gamma} \left\{ \frac{(^2E|L+2S|^2\Gamma)(^2\Gamma|\mathscr{H}'|^2E)}{W(^2E) - W(^2\Gamma)} + \text{c.c.} \right\} = 0\,, \tag{6.5}$$

as long as intermediate doublets are limited to those of f_2^3 (see Fig. 2). We thus expect

$$\left.\begin{aligned} g_{//}(2\overline{A}) &\fallingdotseq 2\,, \qquad g_\perp(2\overline{A}) \fallingdotseq 0\,, \\ g_{//}(\overline{E}) &\fallingdotseq -2\,, \qquad g_\perp(\overline{E}) \fallingdotseq 0\,. \end{aligned}\right\} \tag{6.6}$$

For $^2F_2$ and $^2F_1$, we take the Hamiltonian,

$$\begin{aligned}\mathscr{H}_{\text{eff}} = {} & g_{//}\beta H_{0z} S_z + g_\perp \beta (H_{0x} S_x + H_{0y} S_y) \\ & + g_{//}'\beta H_{0z} T_z + g_\perp' \beta (H_{0x} T_x + H_{0y} T_y)\,. \end{aligned} \tag{6.7}$$

We find then for the components of $^2F_2$

$$\left.\begin{aligned} g_{//}(2\overline{A}) &= g_{//} - 2g_{//}'\,, \\ g_{//}(\overline{E}_a) &= -(g_{//}\cos 2\alpha + 2g_{//}'\cos^2\alpha)\,, \\ g_{//}(\overline{E}_b) &= g_{//}\cos 2\alpha - 2g_{//}'\sin^2\alpha\,, \end{aligned}\right\} \tag{6.8}$$

and of $^2F_1$

$$\left.\begin{aligned} g_{//}(2\overline{A}) &= g_{//} + 2g_{//}'\,, \\ g_{//}(\overline{E}_a) &= -(g_{//}\cos\alpha - 2g_{//}'\cos^2\alpha)\,, \\ g_{//}(\overline{E}_b) &= g_{//}\cos 2\alpha + 2g_{//}'\sin^2\alpha\,. \end{aligned}\right\} \tag{6.9}$$

When $H_0 \perp C_3$, assuming large initial splitting of the components, we find for $^2F_2$

$$\left.\begin{aligned} g_\perp(2\overline{A}) &= 0\,, \\ |g_\perp(\overline{E}_a)| &= |g_\perp \sin^2\alpha - \sqrt{2}\, g_\perp' \sin 2\alpha|\,, \\ |g_\perp(\overline{E}_b)| &= |g_\perp \cos^2\alpha + \sqrt{2}\, g_\perp' \sin 2\alpha|\,, \end{aligned}\right\} \tag{6.10}$$

and for $^2F_1$

* The sign of the $g_{//}$-values of the split components are defined in the following way: The states correspond to the wave functions of the upper (lower) lines of (5.3), (5.4), (5.11), (5.12) and (5.13) have Zeeman energy $\frac{1}{2}g_{//}\beta H_0(-\frac{1}{2}g_{//}\beta H_0)$. The negative sign taken for $g_{//}(\overline{E}_a)$ might be queer at the first sight. It is, however, natural if we notice that, in the present case, $\overline{M} = M_s + M$ is the quantum number for the state $\Psi(^2\Gamma, M_s, M)$ and we take the definition of the $g_{//}$ factor, Zeeman energy $= g_{//}\beta\overline{M}H_0$, just as in the case of the Zeeman effect of free atoms.

Simple consideration based on the selection rule shows that this negative $g_{//}(\overline{E})$ value is the cause of the appearance of the side component of R_1 when $E//C_3$ ($\Delta\overline{M} \equiv 0$, mod 3)$H_0//C_3$ and the strong central component when $E \perp C_3$ ($\Delta\overline{M} \equiv \pm 1$, mod 3).

$$\left.\begin{aligned} &g_\perp(2\overline{A}) = 0\,, \\ &|g_\perp(\overline{E}_a)| = |g_\perp \sin^2\alpha + \sqrt{2}\, g_\perp' \sin 2\alpha|\,, \\ &|g_\perp(\overline{E}_b)| = |g_\perp \cos^2\alpha - \sqrt{2}\, g_\perp' \sin 2\alpha|\,. \end{aligned}\right\} \quad (6.11)$$

The first order correction in $g_{//}$, $g_{//}'$ and $g_\perp'$ vanishes also in this case, and we obtain $g_{//} \fallingdotseq 2$, $g_\perp \fallingdotseq 2$ (spin part) and $g_{//}' \fallingdotseq 1$, $g_\perp' = 1$ (orbital part). Thus we get, assuming $\alpha = 0$, for $^2F_2$

$$\left.\begin{aligned} &g_{//}(2\overline{A}) \fallingdotseq 0\,, && g_\perp(2\overline{A}) \fallingdotseq 0\,, \\ &g_{//}(\overline{E}_a) \fallingdotseq -4\,, && g_\perp(\overline{E}_a) \fallingdotseq 0\,, \\ &g_{//}(\overline{E}_b) \fallingdotseq 2, && |g_\perp(\overline{E}_b)| \fallingdotseq 2\,, \end{aligned}\right\} \quad (6.12)$$

for $^2F_1$

$$\left.\begin{aligned} &g_{//}(2\overline{A}) \fallingdotseq 4\,, && g_\perp(2\overline{A}) \fallingdotseq 0\,, \\ &g_{//}(\overline{E}_a) \fallingdotseq 0\,, && g_\perp(\overline{E}_a) \fallingdotseq 0\,, \\ &|g_{//}(\overline{E}_b)| \fallingdotseq 2\,, && |g_\perp(\overline{E}_b)| \fallingdotseq 2\,. \end{aligned}\right\} \quad (6.13)$$

(b) *The selection rules*

The selection rules or the strengths of the Zeeman components are obtained from Tables I and II given in § 5 in case $H_0 // C_3$. In case $H_0 \perp C_3$, the spin functions of the ground quartet are quantized with respect to the x axis, along which a magnetic field is applied. The ground state wave-functions, in which the quantization axis of spin is x, are expressed as a linear combination of those in which the quantization axis is z as follows;

$$\left.\begin{aligned} \Psi\left(M_s^{(z)} = \pm\frac{3}{2}\right) &= \frac{1}{2\sqrt{2}}\left\{\pm\Psi\left(M_s^{(z)} = \frac{3}{2}\right) + \Psi\left(M_s^{(z)} = -\frac{3}{2}\right)\right\} \\ &\quad + \frac{\sqrt{3}}{2\sqrt{2}}\left\{\Psi\left(M_s^{(z)} = \frac{1}{2}\right) \pm \Psi\left(M_s^{(z)} = -\frac{1}{2}\right)\right\}, \\ \Psi\left(M_s^{(z)} = \pm\frac{1}{2}\right) &= \frac{\sqrt{3}}{2\sqrt{2}}\left\{\mp\Psi\left(M_s^{(z)} = \frac{3}{2}\right) + \Psi\left(M_s^{(z)} = -\frac{3}{2}\right)\right\} \\ &\quad - \frac{1}{2\sqrt{2}}\left\{\Psi\left(M_s^{(z)} = \frac{1}{2}\right) \mp \Psi\left(M_s^{(z)} = -\frac{1}{2}\right)\right\}. \end{aligned}\right\} \quad (6.14)$$

Table IV. The Values of $\sum_{M_s', M'} |(^4A_2 M_s|\overline{P}|^2E M_s', M')|^2$, in which M_s is quantized with respect to the x axis.

$^4A_2$ M_s \ ^2E	$2\overline{A}$	$\overline{E}$
3/2	$\pi_\alpha/8 + 3(\sigma_{+\alpha} + \sigma_{-\alpha})/16$	$\pi_\alpha/8 + 3\,(\sigma_{+\alpha} + \sigma_{-\alpha})/16$
1/2	$3\pi_\alpha/8 + (\sigma_{+\alpha} + \sigma_{-\alpha})/16$	$\pi_\alpha/24 + 11(\sigma_{+\alpha} + \sigma_{-\alpha})/48$
−1/2	$3\pi_\alpha/8 + (\sigma_{+\alpha} + \sigma_{-\alpha})/16$	$\pi_\alpha/24 + 11(\sigma_{+\alpha} + \sigma_{-\alpha})/48$
−3/2	$\pi_\alpha/8 + 3(\sigma_{+\alpha} + \sigma_{-\alpha})/16$	$\pi_\alpha/8 + 3\,(\sigma_{+\alpha} + \sigma_{-\alpha})/16$

Table V. The tables of $\sum_{M_s', M'} |(^4A_2 M_s|\overline{P}|^2F_2 M_s', M')|^2$ and $\sum_{M_s', M'} |(^4A_2 M_s|\overline{P}|^2F_1 M_s', M')|^2$, in which M_s is quantized with respect to the x axis.

$^4A_2$ M_s \ $^2F_2(^2F_1)$	$2\overline{A}$	$\overline{E}_a$
3/2	$\pi_\alpha/8 + (\sigma_{+\alpha} + \sigma_{-\alpha})/8 + (\sigma^0_{+\alpha} + \sigma^0_{-\alpha})/16$	$\pi_\alpha/8 + (\sigma_{+\alpha} + \sigma_{-\alpha})/8 + (\sigma^0_{+\alpha} + \sigma^0_{-\alpha})/16$
1/2	$3\pi_\alpha/8 + (\sigma_{+\alpha} + \sigma_{-\alpha})/24 + (\sigma^0_{+\alpha} + \sigma^0_{-\alpha})/48$	$\pi_\alpha/24 + (\sigma_{+\alpha} + \sigma_{-\alpha})/24 + 3(\sigma^0_{+\alpha} + \sigma^0_{-\alpha})/16$
−1/2	$3\pi_\alpha/8 + (\sigma_{+\alpha} + \sigma_{-\alpha})/24 + (\sigma^0_{+\alpha} + \sigma^0_{-\alpha})/48$	$\pi_\alpha/24 + (\sigma_{+\alpha} + \sigma_{-\alpha})/24 + 3(\sigma^0_{+\alpha} + \sigma^0_{-\alpha})/16$
−3/2	$\pi_\alpha/8 + (\sigma_{+\alpha} + \sigma_{-\alpha})/8 + (\sigma^0_{+\alpha} + \sigma^0_{-\alpha})/16$	$\pi_\alpha/8 + (\sigma_{+\alpha} + \sigma_{-\alpha})/8 + \frac{5}{8}(\sigma^0_{+\alpha} + \sigma^0_{-\alpha})/16$

Using (6.14) the strengths of the Zeeman components in this case can be derived also from Tables I and II, they are given in Tables IV and V. In the predicted Zeeman patterns (Figs. 4, 5), the absence of the vibrational effect is assumed, i.e., $\pi_x = \pi_x' = \sigma_{\pm z} = \sigma^0_{\pm z} = \sigma'_{\pm z} = 0$.

(c) *Zeeman splitting of the ground state*

The Zeeman levels of the ground state have been well examined by paramagnetic resc-

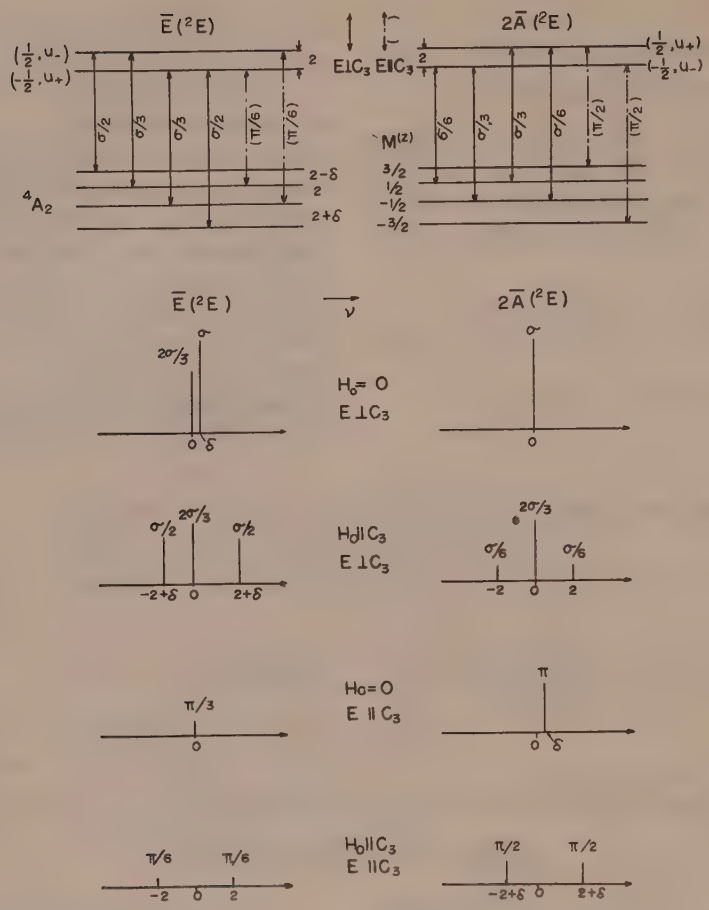

Fig. 4 (a). The predicted Zeeman patterns ($H_0 \| C_3$) for ^2E. Splittings are given in βH_0 unit.

nance. To analyse optical Zeeman patterns, the knowledge about them is also necessary, so that we shall summerize it below: The energies of the split components of the ground quartet are

$$\left.\begin{aligned} W\left(M_s^{(z)}=\pm\frac{3}{2}\right)&=\pm\frac{3}{2}g_{0//}\beta H_0\,,\\ W\left(M_s^{(z)}=\pm\frac{1}{2}\right)&=\pm\frac{1}{2}g_{0//}\beta H_0+\delta\,,\end{aligned}\right\}\quad(6.15)$$

when $H_0 \perp C_3$ and

$$\left.\begin{aligned} W\left(M_s^{(x)}=\pm\frac{3}{2}\right)&=\pm\frac{3}{2}g_{0\perp}\beta H_0+\frac{\delta}{4}\,,\\ W\left(M_s^{(x)}=\pm\frac{1}{2}\right)&=-\frac{1}{2}g_{0\perp}\beta H_0+\frac{3\delta}{4}\,,\end{aligned}\right\}\quad(6.16)$$

when $H_0 \perp C_3$ ($2\beta H_0 \gg \delta$).

The paramagnetic resonance experiment has shown that

$$|\delta|=0.38\ \mathrm{cm}^{-1}\,,\quad g_{0//}\doteqdot g_{0\perp}\doteqdot 2\,.$$

(d) *The Zeeman patterns*

Now we are ready to predict the Zeeman patterns, and they are illustrated in Figs. 4 and 5. From the detailed comparison of these patterns with the experimental ones that will be made in Part B, we may conclude that the assignments (5.21) for R_1 and R_2 and (5.24) for B_1 and B_2 are established.

Moreover, from such comparison, we find that δ is positive and the g-values of the split components of ^2E and $^2F_2$ show fairly large shift from those expected in (6.6) and (6.12).

(e) *g-shifts of the excited states*

The observed $g_{//}$-shifts of the split components of ^2E are

$$\left.\begin{aligned} &g_{//}(2\overline{A})\doteqdot 2-2\Delta\,,\\ &|g_{//}(\overline{E})|\doteqdot 2+2\Delta\,,\\ &\Delta\doteqdot 0.2\,.\end{aligned}\right\}\quad(6.17)$$

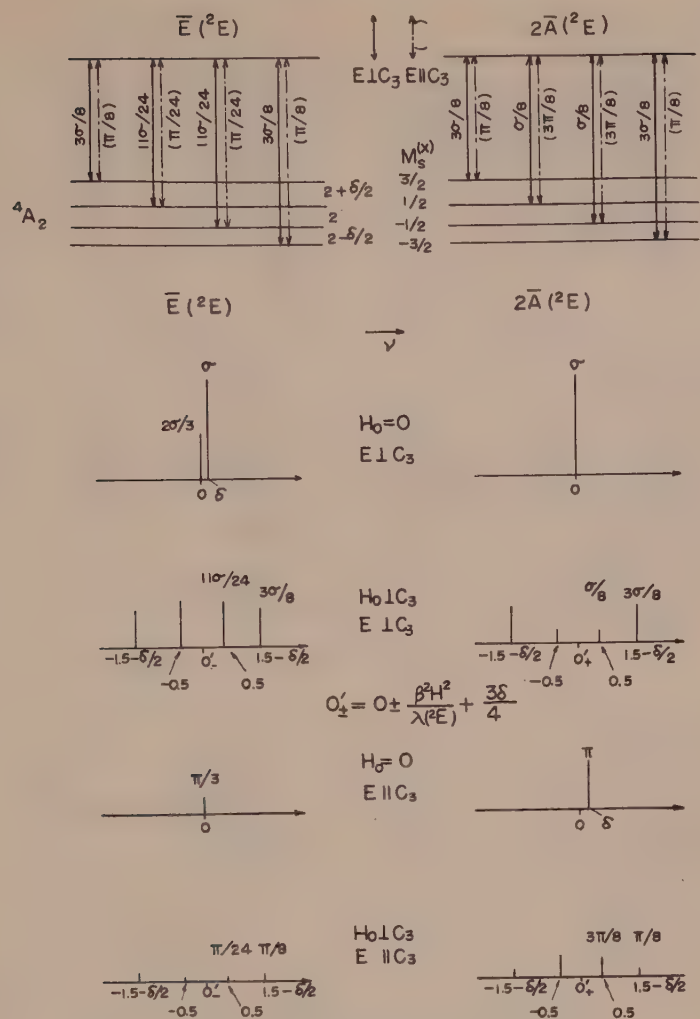

Fig. 4 (b). The predicted Zeeman patterns ($H_0 \perp C_3$).

These relations show that in (6.3) $g_{//}'$ deviates from zero and $g_{//}' = -0.2$. Such a large deviation seems curious at first glance.

In order to explain the cause of such shifts, we must consider the second order effect in $\mathscr{H}'$. Group theoretical consideration shows that the operator of type $T(A_2)$ can be found only in the reduction of the products of operators $L_z \times V_{\text{trig}} \times V_{\text{trig}}$ and $S_z \times V_{\text{trig}} \times V_{s0}$ into their irreducible parts. Hence we have (see Fig. 2)

$$
\begin{aligned}
g_{//}' = {} & \{(^2E, \tfrac{1}{2}, u_+|L_z|^2F_1, \tfrac{1}{2}, a_+)(^2F_1, \tfrac{1}{2}, a_+|V_{\text{trig}}|^2F_2, \tfrac{1}{2}, x_+)(^2F_2, \tfrac{1}{2}, x_+|V_{\text{trig}}|^2E, \tfrac{1}{2}, u_+) + \text{c.c.}\} \\
& \quad /\{W(^2E) - W(^2F_1)\}\{W(^2E) - W(^2F_2)\} \\
& + (^2E, \tfrac{1}{2}, u_+|V_{\text{trig}}|^2F_2, \tfrac{1}{2}, x_+)(^2F_2, \tfrac{1}{2}, x_+|L_z|^2F_2, \tfrac{1}{2}, x_+)(^2F_2, \tfrac{1}{2}, x_+|V_{\text{trig}}|^2E, \tfrac{1}{2}, u_+) \\
& \quad /\{W(^2E) - W(^2F_2)\}^2 \\
& + \{(^2E, \tfrac{1}{2}, u_+|V_{\text{trig}}|^2F_2, \tfrac{1}{2}, x_+)(^2F_2, \tfrac{1}{2}, x_+|2S_z|^2F_2, \tfrac{1}{2}, x_+)(^2F_2, \tfrac{1}{2}, x_+|V_{s0}|^2E, \tfrac{1}{2}, u_+) + \text{c.c.}\} \\
& \quad /\{W(^2E) - W(^2F_2)\}^2 \\
& - \tfrac{1}{2}\{(^2E, \tfrac{1}{2}, u_+|V_{\text{trig}}|^2F_2, \tfrac{1}{2}, x_+)(^2F_2, \tfrac{1}{2}, x_+|V_{s0}|^2E, \tfrac{1}{2}, u_+) + \text{c.c.}\}(^2E, \tfrac{1}{2}, u_+|2S_z|^2E, \tfrac{1}{2}, u_+) \\
& \quad /\{W(^2E) - W(^2F_2)\}^2 \\
& - \tfrac{1}{2}\{(^2E, \tfrac{1}{2}, u_+|2S_z|^2E, \tfrac{1}{2}, u_+)\}\{(^2E, \tfrac{1}{2}, u_+|V_{\text{trig}}|^2F_2, \tfrac{1}{2}, x_+)(^2F_2, \tfrac{1}{2}, x_+|V_{s0}|^2E, \tfrac{1}{2}, u_+) + \text{c.c.}\} \\
& \quad /\{W(^2E) - W(^2F_2)\}^2 \,. \qquad (6.18)
\end{aligned}
$$

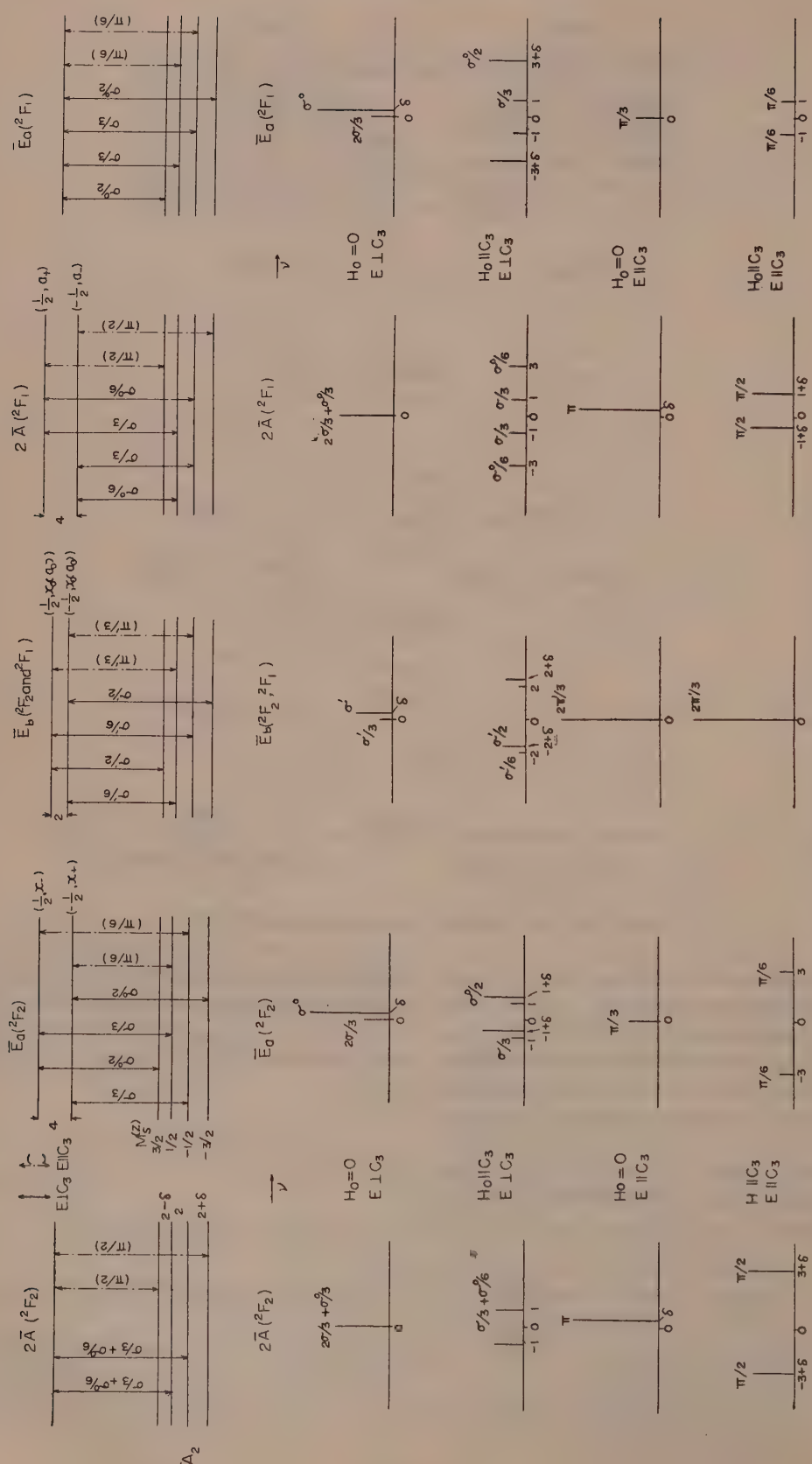

Fig. 5 (a). The predicted Zeeman patterns ($H_0 \| C_3$).

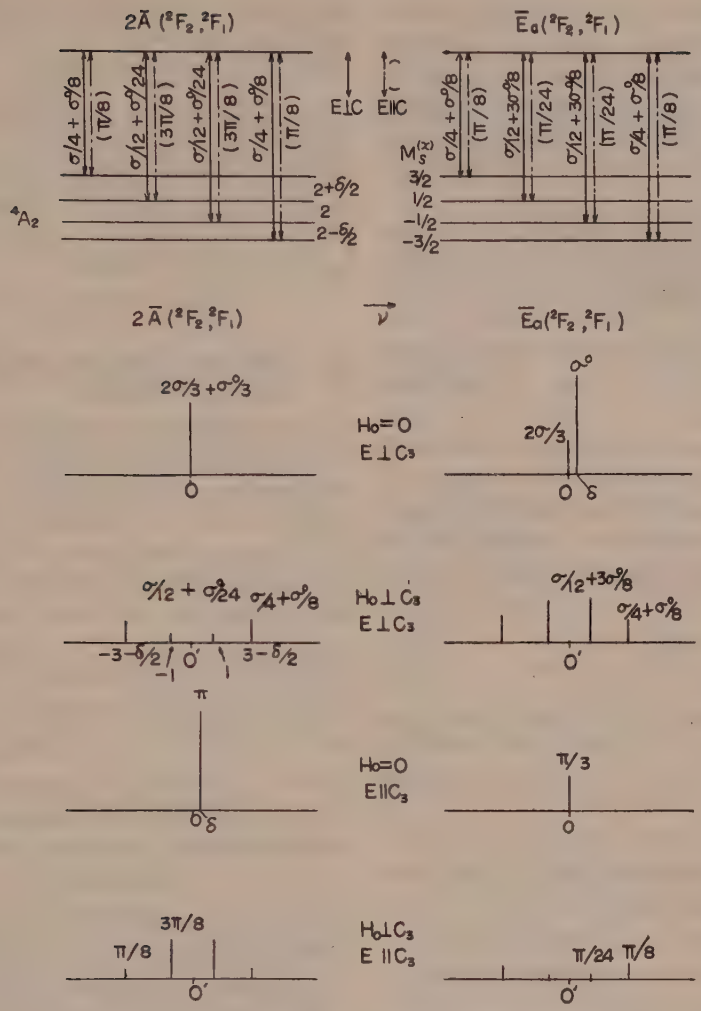

Fig. 5 (b). The predicted Zeeman patterns ($H_0 \perp C_3$).

The terms on the last three lines cancel out, and we have

$$g_{//}'(^2E) = -12K^2/\{W(^2E)-W(^2F_1)\}\{W(^2E)-W(^2F_2)\} - 6K^2/\{W(^2E)-W(^2F_2)\}^2 . \tag{6.19}$$

The second term is fairly small (if $K \sim -350\,\mathrm{cm}^{-1}$, $W(^2E)-W(^2F_2) \sim -6500\,\mathrm{cm}^{-1}$, it becomes ~ -0.02), but the first term will make a large contribution, since $^2F_1$ is supposed to be near ^2E. If we estimate the separation of these levels from the above formula, using the empirical value of $g_{//}'(^2E) \fallingdotseq -0.2$,

$$W(^2E)-W(^2F_1) \fallingdotseq -1200\,\mathrm{cm}^{-1} , \tag{6.20}$$

which is a reasonable value for this separation and we expect from this that the energy of $^2F_1$ is higher than that of ^2E.

Similar consideration shows that the deviation of $g_{//}(^2E)$ from 2, $\Delta g_{//}(^2E)$, also comes mainly from the second order correction (also see Fig. 2);

$$\begin{aligned}\Delta g_{//}(^2E) = {} & 2(^2E, \tfrac{1}{2}, u_+|L_z|^2F_1, \tfrac{1}{2}, a_+)\{(^2F_1, \tfrac{1}{2}, a_+|V_{so}|^2F_2, \tfrac{1}{2}, x_+)(^2F_2, \tfrac{1}{2}, x_+|V_{\mathrm{trig}}|^2E, \tfrac{1}{2}, u_+)+\mathrm{c.c.}\} \\ & /\{W(^2E)-W(^2F_1)\}\{W(^2E)-W(^2F_2)\} \\ & +2\{(^2E, \tfrac{1}{2}, u_+|V_{so}|^2F_2, \tfrac{1}{2}, x_+)(^2F_2, \tfrac{1}{2}, x_+|V_{\mathrm{trig}}|^2F_1, \tfrac{1}{2}, a_+)+\mathrm{c.c.}\} \\ & \cdot(^2F_1, \tfrac{1}{2}, a_+|L_z|^2E, \tfrac{1}{2}, u_+)/\{W(^2E)-W(^2F_1)\}\{W(^2E)-W(^2F_2)\} \\ = {} & -8\zeta K/\{W(^2E)-W(^2F_1)\}\{W(^2E)-W(^2F_2)\} ,\end{aligned} \tag{6.21}$$

which is estimated as ~ 0.05, using the values $\zeta \sim 140\,\mathrm{cm}^{-1}$ and (6.20). Such a small value of $\Delta g_{//}(^2E)$ also justifies the use of the simplified Hamiltonian (6.1), because the neglected terms are found to be of the order of magnitude of this deviation $\Delta g_{//}(^2E)$ multiplied by βH_0.

It must be remarked that a large deviation of $g_{//}'(^2E)$ and a small $g_{//}(^2E)$-shift are due to the special situation, $V_{\mathrm{trig}} > V_{s0}$, in our problem.

By the same reasoning we might expect the deviation of $g_{//}'(^2F_1)$ to be of the same order of magnitude as that for $g_{//}'(^2E)$ while g-values for $^2F_2$ are fairly close to those given in (6.12), since any crystal level cannot be expected to lie near $^2F_2$ as close as $^2F_1$ does to ^2E. Such an expectation, however, is betrayed by the experimental results (Part B § 5),

$$g_{//}(2\overline{A}) \doteqdot 2\Delta' , \quad |g_{//}(\overline{E}_a)| \doteqdot 4-2\Delta' , \quad \Delta' \doteqdot 0.4 , \tag{6.22}$$

where the deviations of $g_{//}$'s from those given in (6.12) are large. Therefore we must examine another cause of such a large deviation for $^2F_2$.

In $^2F_2$, (also in $^2F_1$), orbital angular momentum is not quenched and it gives finite value of $g_{//}'$ in (6.8) and (6.9);

$$\begin{aligned} g_{//}' &= (F_1a_+|L_z|F_1a_+) = -(F_1a_-|L_z|F_1a_-) \\ &= (F_2x_-|L_z|F_2x_-) = -(F_2x_+|L_z|F_2x_+) \\ &= k , \end{aligned} \tag{6.23}$$

where k is defined as

$$k \equiv (f_2x_-|l_z|f_2x_-) = -(f_2x_+|l_z|f_2x_+) . \tag{6.24}$$

If f_2-orbital is constructed from pure d-orbitals, k is equal to 1 and we have (6.12) and (6.13), but if we are allowed to suppose that f_2-orbital is deformed by making a covalent bonding with the surroundings and accordingly is not of pure d-character, k is not necessarily equal to 1. Thus, in place of $g_{//}$'s in (6.12) and (6.13), we have for $^2F_2$

$$\left.\begin{aligned} g_{//}(2\overline{A}) &\doteqdot 2(1-k) , \\ g_{//}(\overline{E}_a) &\doteqdot -2(1+k) , \\ g_{//}(\overline{E}_b) &\doteqdot 2 . \end{aligned}\right\} \tag{6.25}$$

and for $^2F_1$

$$\left.\begin{aligned} g_{//}(2\overline{A}) &\doteqdot 2(1+k) , \\ g_{//}(\overline{E}_a) &\doteqdot -2(1-k) , \\ g_{//}(\overline{E}_b) &\doteqdot 2 . \end{aligned}\right\} \tag{6.26}$$

To satisfy the empirical relations (6.22), we must choose

$$k \doteqdot 0.6 . \tag{6.27}$$

In ^2E the orbital angular momentum is quenched but it contributes to $g_{//}'(^2E)$ and $\Delta g_{//}(^2E)$ through higher order correction of type $L_zV^2_{\mathrm{trig}}$. Thus the right hand side of (6.19) and (6.21) must be multiplied also by k. Then (6.20) becomes

$$W(^2E) - W(^2F_1) \doteqdot 700\,\mathrm{cm}^{-1} . \tag{6.20$'$}$$

§ 7. Connection to the Paramagnetic Resonance Absorption

The analysis of the optical absorption spectra affords important informations not only on the excited electronic states but also on the ground state. For instance, the analyses of the Zeeman effect of the line spectra (Part B § 4) and the polarization-shift (Part B § 3 (d)) show that, of the two Kramers doublets $M_s=\pm 3/2$ and $M_s=\pm 1/2$ of the ground quartet $^4A_2$, $M_s=\pm 3/2$ is the lower, and lead to the following value for the natural splitting

$$\delta = W(\pm 1/2) - W(\pm 3/2) = 0.36 \pm 0.03\,\mathrm{cm}^{-1} . \tag{7.1}$$

This value should be compared with the following precise value determined by the method of paramagnetic resonance absorption

$$|\delta| = 0.38\,\mathrm{cm}^{-1} . \tag{7.2}$$

It should be noted, however, that this method gives us only the absolute value of δ, whereas the optical absorption could determine the sign as well as the approximate value.

Since detailed knowledges of the excited states are now in our hands, we can go a little further and examine whether this value of δ is consistent or not with the other empirical values determined here.

It will then be noticed that the sign of δ is inconsistent with the sign of K if one accepts the usual theory of the natural splitting, which leads to the following formula for δ

$$\delta = \frac{4}{3}\zeta'^2 K \Big/ \{W(^4A_2) - W(^4F_2)\}^2 . \tag{7.3}$$

This formula is, however, derived under the assumption of isotropic spin-orbit interaction, and is not adequate for the present case, because the g-value of the ground quartet obtained by the paramagnetic resonance absorption shows the anisotropy[6], namely

$$\left.\begin{aligned} \Delta g_{0//} &= -g_{0//} + 2.0023 = 0.0183 \pm 0.0006 \\ \Delta g_{0\perp} &= -g_{0\perp} + 2.0023 = 0.0156 \pm 0.0006 \end{aligned}\right\} \tag{7.4}$$

and this should be understood as the indication of the anisotropy in the spin-orbit interaction which has been assumed to be isotropic in the present paper.

The anisotropy of g-value is correlated with the anisotropy of the spin-orbit coupling parameter ζ' in the following way:

$$\left.\begin{aligned}\Delta g_{0//}&=\frac{8}{3}k'\zeta_{//}'\Big/\{W(^4F_2)-W(^4A_2)\}\,,\\ \Delta g_{0\perp}&=\frac{8}{3}k'\zeta_{\perp}'\Big/\{W(^4F_2)-W(^4A_2)\}\,,\end{aligned}\right\}\qquad(7.5)$$

where k' is a parameter to describe the decrease of the angular momentum in crystals;

$$k'=-\frac{1}{\sqrt{2}}(f_2x_+|l_z|eu_+)\,,\qquad(7.6)$$

which is unity for e and f_2 function constructed from pure d functions. (7.5) then gives

$$\left.\begin{aligned}k'\zeta_{//}'&=130\sim120\\ k'\zeta_{\perp}'&=110\sim100\end{aligned}\right\}\qquad(7.7)$$

The formula (7.3) for the expression of δ should be reexamined. The shift of the Kramers doublet due to the perturbation $\mathscr{H}'$ is given by

$$\begin{aligned}W(M_s)=&\sum_{M_s',M'}\frac{(^4A_2M_s|V_{s0}|^4F_2M_s'M')(^4F_2M_s'M'|V_{s0}|^4A_2M_s)}{W(^4A_2)-W(^4F_2)}\\ &+\sum_{M_s',M'}\frac{(^4A_2M_s|V_{s0}|^4F_2M_s'M')(^4F_2M_s'M'|V_{\rm trig}|^4F_2M_s'M')(^4F_2M_s'M'|V_{s0}|^4A_2M_s)}{\{W(^4A_2)-W(^4F_2)\}^2}\\ &+\sum_{M_s',M'}\frac{(^4A_2M_s|V_{\rm trig}|^4F_1M_sa_0)(^4F_1M_sa_0|V_{s0}|^4F_2M_s'M')(^4F_2M_s'M'|V_{s0}|^4A_2M_s)}{\{W(^4A_2)-W(^4F_1)\}\{W(^4A_2)-W(^4F_2)\}}+\text{c.c.}\,.\end{aligned}\qquad(7.8)$$

Taking the difference $W(\pm1/2)-W(\pm3/2)$, we find after evaluating relevant matrix elements

$$\begin{aligned}\delta=&\frac{8}{9}(\zeta_{//}'^2-\zeta_{\perp}'^2)\Big/\{W(^4F_2)-W(^4A_2)\}+\frac{4}{9}(2\zeta_{//}'^2+\zeta_{\perp}'^2)K\Big/\{W(^4F_2)-W(^4A_2)\}^2\\ &-2\sqrt{\frac{2}{3}}K'\times\frac{4}{9}(2\zeta_{//}\zeta_{//}'+\zeta_{\perp}\zeta_{\perp}')\Big/\{W(^4F_2)-W(^4A_2)\}\{W(^4F_1)-W(^4A_2)\}\,,\end{aligned}\qquad(7.9)$$

where $K'=-1\sqrt{2}(f_2x_\pm|v_{\rm trig}|eu_\pm)$. $K'=K$ if f_2 and e are d-functions and $v_{\rm trig}\propto3z^2-r^2$. The second term in the above expression corresponds to (7.3) and gives a negative contribution to δ but we find that this is almost cancelled out by the third term which has been overlooked by Van Vleck[12], if we estimate the third term assuming $K'=K$, $\zeta_{//}=\zeta_{//}'$ and $\zeta_{\perp}=\zeta_{\perp}'$. The first term which is positive ($\zeta_{//}'>\zeta_{\perp}'$) in the present case, gives δ with the positive sign,

$$\delta\approx0.3\sim0.6\,,\qquad(7.10)$$

if we take $k'=k=0.6$, which is a reasonable value. The values of ζ''s are accordingly

$$\left.\begin{aligned}\zeta_{//}'&\sim200\\ \zeta_{\perp}'&\sim170\end{aligned}\right\}.\qquad(7.11)$$

The problem of natural splitting is thus rather delicate one and we will not pursue this problem further, since the inconsistency caused by the formula (7.3) is now removed.

§ 8. Conclusion

Although several problems remain unsolved, the main purpose of the present paper, i.e. the assignments of the absorption bands and lines of ruby $Cr^{3+}:Al_2O_3$, has now been achieved. The results and unsolved problems are summarized below.

(a) For the U and Y bands the assignments (4.11) has been made. The anisotropy shown by these bands is understood qualitatively, but not quantitatively. The parameter K which is a measure of the strength of the trigonal field was determined from the splittings of the bands:

$$K=-350\ \text{cm}^{-1}\,.$$

(b) For R_1 and R_2 the assignments (5.21) has been made. The anisotropies of the lines are closely related to that of the bands, and this problem needs further investigations. The second order perturbation formula (5.6) leads to the following value of the spin-orbit coupling parameter for f_2 electrons:

$$\zeta=140\ \text{cm}^{-1}\,.$$

For B_1 and B_2, the assignments (5.24) has been made. The separation between B_1 and B_2 could not be correctly given by the formulae (5.16) and (5.18) derived under the assumption

of the strong field limit.

(c) For the assignments of these lines, the analyses of the Zeeman effect offer most conclusive evidences.

(d) The large g-shifts of R_1 and R_2 excited states observed in the Zeeman patterns have been explained by taking into account the second order correction of the type $V^2_{\text{trig}}\cdot L_z$. The correction is fairly large if the excited state $^2F_1$ lies near ^2E. From the sign and the magnitude of the observed g-shift, $^2F_1$ is expected to lie at the shorter wave-length side of ^2E separated approximately by $\sim 700\ \text{cm}^{-1}$.

(e) The observed g-values of B_1 and B_2 excited states have also been explained by introducing the reduced expectation value of the orbital angular momentum (for f_2 orbital) in the crystal. As the value of the parameter k which indicates such a reduction (6.23), we have

$$k \sim 0.6\ .$$

(f) The line that corresponds to $\overline{E}_b(^2F_2)$ is yet unidentified. The lines corresponding to the split components of $^2F_1$ are also not identified yet.

(g) It has been shown that experimental data on the excited states (optical absorption) can be reasonably connected to those on the ground state (paramagnetic resonance).

(h) As to the problem of intensity, the present theory is not satisfactory in that it is semi-empirical, and it is hoped to establish a theory that could predict the absolute intensities of bands and lines as well as the widths of the bands and the lines which have not been touched upon in this paper.

Acknowledgements

We should like to express our sincere thanks to Professor M. Kotani for his deep interest in this work and encouragement, and to Professor G. Kuwabara and Mr. A. Misu for their permission to use the experimental data of the absorption bands prior to publication. The authors also wish to express their thanks to the members of Prof. Kotani's laboratory for stimulating discussions.

Appendix

AI) $(f_2^3\,{}^2Eu_\pm|V_{\text{trig}}|f_2^3\,{}^2F_2x_\pm) = -\sqrt{6}\,K$

$(f_2^3\,{}^2F_2x_\pm|V_{\text{trig}}|f_2^2\,{}^2F_1a_\pm) = \mp\sqrt{3}\,iK$

$(f_2^3\,{}^2F_2x_0|V_{\text{trig}}|f_2^3\,{}^2F_1a_0) = 0$

AII) $(f_2^3\,{}^2\Gamma M_sM|V_{s0}|f_2^3\,{}^2\Gamma' M_s'M')$

$$=(-)^{M_s-M_s'}(f_2^3\,{}^2\Gamma\|V_{s0}\|f_2^3\,{}^2\Gamma')/\sqrt{2(\Gamma)}$$
$$(1/2\ M_s|1/2\ M_s'1M_s-M_s')$$
$$\times(\Gamma M|\Gamma' M' F_1M_s'-M_s)\ ,$$

where (Γ) is the dimension of the irreducible representation Γ. $(\Gamma M|\Gamma' M' F_1M_s'-M_s)$ is given in Table VIII of (IV). $(1/2\ M_s|1/2\ M_s'1M_s-M_s')$ is the Wigner coefficient given in TAS.

$(-)^{M_s-M_s'}/\sqrt{2}\,(1/2\ M_s|1/2\ M_s'1\ 1)$

M_s \ M_s'	1/2	−1/2
1/2		$1/\sqrt{3}$
−1/2		

$(-)^{M_s-M_s'}/\sqrt{2}\,(1/2\ M_s|1/2\ M_s'1\ 0)$

M_s \ M_s'	1/2	−1/2
1/2	$1/\sqrt{6}$	
−1/2		$-1/\sqrt{6}$

$(-)^{M_s-M_s'}/\sqrt{2}\,(1/2\ M_s|1/2\ M_s'1\ -1)$

M_s \ M_s'	1/2	−1/2
1/2		
−1/2	$-1/\sqrt{3}$	

$(f_2^3\,{}^2\Gamma\|V_{s0}\|f_2^3\,{}^2\Gamma')$ are evaluated in IV.

$(f_2^3\,{}^2E\|V_{s0}\|f_2^3\,{}^2F_2) = -\sqrt{6}\,i\zeta$

$(f_2^3\,{}^2F_1\|V_{s0}\|f_2^3\,{}^2F_2) = -3i\zeta$

AIII) $(f_2^3\,{}^2\Gamma M_sM|V_{s0}|f_2^2e\,{}^4\Gamma' M_s'M')$

$$=(-)^{M_s-M_s'}(f_2^3\,{}^2\Gamma\|V_{s0}\|f_2^2e\,{}^4\Gamma')/\sqrt{2(\Gamma)}$$
$$(1/2\ M_s|3/2\ M_s'1M_s-M_s')$$
$$\times(\Gamma M|\Gamma' M' F_1M^{s'}-M_s)$$

$(-)^{M_s-M_s'}/\sqrt{2}\,(1/2\ M_s|3/2\ M_s'\ 1\ 1)$

M_s \ M_s'	3/2	1/2	−1/2	−3/2
1/2			$-1/2\sqrt{3}$	
−1/2				−1/2

$(-)^{M_s-M_s'}/\sqrt{2}\,(1/2\ M_s|3/2\ M_s'1\ 0)$

M_s \ M_s'	3/2	1/2	−1/2	−3/2
1/2		$-1/\sqrt{6}$		
−1/2			$-1/\sqrt{6}$	

$(-)^{M_s-M_s'}/\sqrt{2}\,(1/2\ M_s|3/2\ M_s'1\ -1)$

M_s \ M_s'	3/2	1/2	−1/2	−3/2
1/2	−1/2			
−1/2			$-1/2\sqrt{3}$	

$(f_2^3\,{}^2\Gamma \| V_{s0} \| f_2^2 e\,{}^4\Gamma')$ are given below.

$$(f_2^3\,{}^2E \| V_{s0} \| f_2^2 e\,{}^4F_2) = -4i\zeta'$$

$$(f_2^3\,{}^2F_2 \| V_{s0} \| f_2^2 e\,{}^4F_2) = -\sqrt{6}\,i\zeta'$$

$$(f_2^3\,{}^2F_1 \| V_{s0} \| f_2^2 e\,{}^4F_2) = +\sqrt{6}\,i\zeta'$$

$$(f_2^3\,{}^2F_2 \| V_{s0} \| f_2^2 e\,{}^4F_1) = -3\sqrt{2}\,i\zeta'$$

$$(f_2^3\,{}^2F_1 \| V_{s0} \| f_2^2 e\,{}^4F_1) = 3\sqrt{2}\,i\zeta'$$

References

1) W. Moffitt and C. J. Ballhausen: Ann. Rev. Phys. Chem. **7** (1956) 107.
2) O. Deutschbein: Ann. d. Phys. [5] **14** (1932) 712, 729; Ann. d. Phys. [5] **20** (1934) 828.
8) H. Lehmann: Ann. d. Phys. [5] **19** (1934) 99.
4) B. V. Thosar: Phys. Rev. **60** (1941) 616; J. Chem. Phys. **10** (1942) 246.
5) A. A. Manenkov and A. M. Prokhorov: J.E.T.P. **28** (1955) 762.
6) R. W. G. Wyckoff: *Crystal structures*, Interscience Publishers New York, 1948.
7) Y. Tanabe and S. Sugano: J. Phys. Soc. Japan **9** (1954) 753, 766. (cited as I and II respectively).
8) G. Kuwabara, A. Misu and S. Sugano: to be published.
9) W. Moffitt: J. Chem. Phys. **25** (1956) 1889.
10) Y. Tanabe and H. Kamimura: J. Phys. Soc. Japan **13** (1958) 394. (cited as IV).
11) J. Owen: Proc. Roy. Soc. **A227** (1955) 183.
12) J. H. Van Vleck: J. Chem. Phys. **7** (1939) 61.

JOURNAL OF THE PHYSICAL SOCIETY OF JAPAN Vol. 13, No. 8, AUGUST, 1958

Absorption Spectra of Cr^{3+} in Al_2O_3

Part B. Experimental Studies of the Zeeman Effect and Other Properties of the Line Spectra

By Satoru SUGANO

Department of Physics, Faculty of Science
University of Tokyo, Tokyo

and Ikuji TSUJIKAWA

Research Institute for Iron, Steel and Other
Metals, Tohoku University, Sendai

(Received April 5, 1958)

The absorption intensities, widths and wave-numbers of R_1, R_2 and B_1 B_2 lines of Cr^{3+} in ruby for the polarized light $E \perp C_3$ and $E // C_3$ are experimentally studied at 20°K and 4.2°K. Zeeman effect is also studied, using a magnetic field $H_0 = 24{,}000\,\phi$, for both R and B lines. The Zeeman effect has not been observed yet for the B lines, while Lehmann has already observed the Zeeman effect for R lines. In our results of R lines, the quantitative aspects of Lehmann's experiment are improved. The comparison is made with the theoretical results given in Part A and it is shown that nice agreements can be obtained when suitable assignments of the spectra are adopted and when fairly large g-shifts of the excited states are introduced.

§ 1. Introduction

Among the bound transition metal ions which show extremely narrow absorption spectra e.g., Cr^{3+}, Mn^{2+}, Co^{2+} and Ni^{2+} in complex salts or Cr^{3+} impurity in oxide crystals, ruby Cr^{3+}: Al_2O_3 seems to be the most appropriate material, as explained in § 1 of the first paper of this series, to start the studies of these line spectra.

The general behaviour of the many absorption and emission spectra of ruby has been revealed by the original work of Deutschbein.[1] From this we know that, among the numerous observed spectra, R_1, R_2 lines in the red region and B_1, B_2 in the blue region are conspicuously strong and sharp. Especially on R_1, R_2 lines, Lehmann[2] has examined their optical Zeeman effect at 83°K and

has obtained the Zeeman patterns that depend on the directions of the electric vector E of the incident light and of a magnetic field H_0 relative to the crystal axis C_3.

On the other hand, the Zeeman splitting of the ground level of ruby has been recently measured by the paramagnetic resonance method[3] and its splitting factors have been precisely determined. This enables us to expect that the optical Zeeman pattern must contain some Zeeman components of the ground state whose separations are already known, when the optical Zeeman pattern consists of more than two components and the excited state concerned with is considered to be a Kramers doublet. This is because that, in this case, at least two of such Zeeman components must correspond to the transitions from the different Zeeman levels of the ground state to the same Zeeman level of the excited state.

In Lehmann's Zeeman patterns, however, it is impossible to find out the Zeeman components whose separation corresponds to any separation among the Zeeman levels of the ground state. The theoretical investigation given in the first paper also showed that though the qualitative aspects of Lehmann's results could be reasonably explained, the splitting factors he had measured were far from the theoretical expectation. In such a situation, it was felt necessary to repeat the studies of the Zeeman effect of these line spectra at experimentally better condition.*

In this paper the Zeeman effects of R_1, R_2 (§ 4) and B_1, B_2 (§ 5) lines are studied at 20°K and 4.2°K. The Zeeman patterns of B_1, B_2 have not been observed yet. To determine the magnitudes of Zeeman splittings precisely, we have tried to make the spectral widths narrow by using ruby of low Cr^{3+} concentration as well as by performing the experiment at very low temperatures. The concentration dependence of the spectral width and position (§ 3) has been found in the preliminary course of our work.

Besides the Zeeman effect, it will also be useful for the spectral assignments to examine the change of absorption wave-numbers and intensities (anisotropy) of these spectra when we use polarized light of $E \perp C_3$ and $E // C_3$. The results of such examinations at 20°K and 4.2°K (§ 3) will also serve for extending Paetzold's work[4] which has aimed at the problem of the interaction between chromophoric electrons and lattice by examining the temperature dependence of the absorption wave-numbers and the widths of these spectra at temperatures higher than 80°K.

§ 2. The Experimental Methods

The samples used in our experiments are synthetic rubies of 4 mm thickness (sample A) and of 1 mm thickness (sample B). The crystal axes are determined by X-ray and we cut the sample to make the principal axis C_3 (optic axis) to lie in the plain, perpendicularly to which the incident light is passed. The result of chemical analysis shows that samples A and B contain 0.28 and 2.56 weight percent Cr_2O_3 respectively.

In our spectroscopic studies, a grating spectrograph in Eagle mounting with dispersion 2.5 Å/mm in the first order has been used. The light source is a 60–W Zircon-lamp and the diffracted beam is detected by photographic methods. The comparison spectra are supplied by Ne-lamp (6929.468Å, 7032.413 Å lines) or Cd-lamp (4679.156 Å, 4799.-918Å lines) corresponding to the case of determining R_1, R_2 or B_1, B_2 absorption wave-lengths. In the determination of the latter, however, it is sometimes more convenient to utilize the emission lines of the light source (the arc lines of Zr, 4739.478Å, 4772.312Å) as the comparison spectra.

To get the light beams polarized perpendicularly to each other, Wollaston's prism is placed in front of the slit and through the separated parts of the slit both polarized beams are passed simultaneously. Thus in every exposure we can get two kinds of spectral photograph corresponding to the polarized beams $E \perp C_3$ and $E // C_3$. In this case, the astigmatism of the concave grating is eliminated by the cylindrical lens suitably placed in front of the photographic plate.

Further in our absorption measurements of R_1 and R_2, we have inserted, between the light source and the sample, the red filter in order to cut the light of shorter wave-length which lies in the region of the broad absorp-

* Prof. G. H. Dieke of the Johns Hopkins University has kindly informed us that Zeeman experiment on ruby has also been completed in his laboratory but the results are not published yet.

tion bands U and Y located at ~5500Å and ~4000Å; Ruby shows relatively strong emission at the same positions as those of R_1, R_2 when it is excited by visible light in the region of U and Y and so in the absorption measurements we must suppress the undesired emission parts of R_1, R_2 lines by exclusion of such excitation light.

To keep a sample at low temperatures, it is immersed in liquid helium or liquid hydrogen contained in a Dewar vessel. The magnitude of the applied magnetic field to study the Zeeman effects is 24,000 ϕ.

§ 3. Properties of the Line Spectra in Absence of a Magnetic Field

(a) *The optical anisotropies*: Though no quantitative measurement of the absorption intensities has been attempted, the optical anisotropies observed in R_1, R_2 and B_1, B_2 absorption lines are remarkable and so they are schematically described in Fig. 1. The

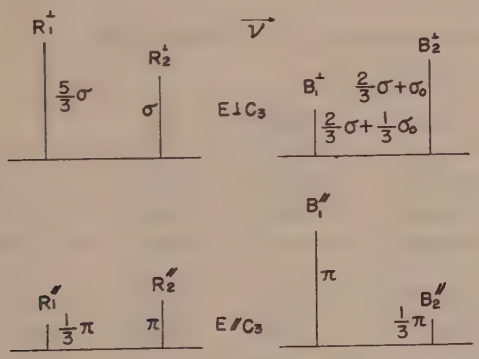

Fig. 1. The optical anisotropies observed in R_1, R_2 and B_1, B_2 absorption lines. Only the relative intensities are schematically represented for R's and B's spectra. The most intense lines $R_1^\perp$ and $B_1^{//}$ in each group are normalized.

relation between the intensities of R_1 and R_2 is inverted when the polarization of the incident light is changed. The same situation also occurs in B_1, B_2, though the relation between the intensities of B_1 and B_2 is just contrary to the case of R_1 and R_2 for each polarization.

The qualitative aspects of these anisotropies are not changed when temperature or concentration of Cr^{3+} is varied.

(b) *The spectral widths*: A tremendously large difference is observed between the spectral widths of the relatively dilute sample A and highly concentrated sample B. In sample A, the spectral widths are very narrow and their approximate values are as follows;*

$R_1^\perp$	$R_2^\perp$	$R_1^{//}$	$R_2^{//}$	
0.7,	0.6,	0.6,	0.6,	(cm^{-1})
$B_1^\perp$	$B_2^\perp$	$B_1^{//}$	$B_2^{//}$	
1.9,	2.6,	1.9,	2.6,	

No noticeable difference is observed among the spectral widths observed at 86°K, 20°K and 4.2°K for R lines and between those measured at 20°K and 4.2°K for B lines. In sample B, the widths of R_1, R_2 are approximately 3 cm^{-1} and those of B_1, B_2 8 cm^{-1} which are about four times larger than those observed in sample A (also see Fig. 2).

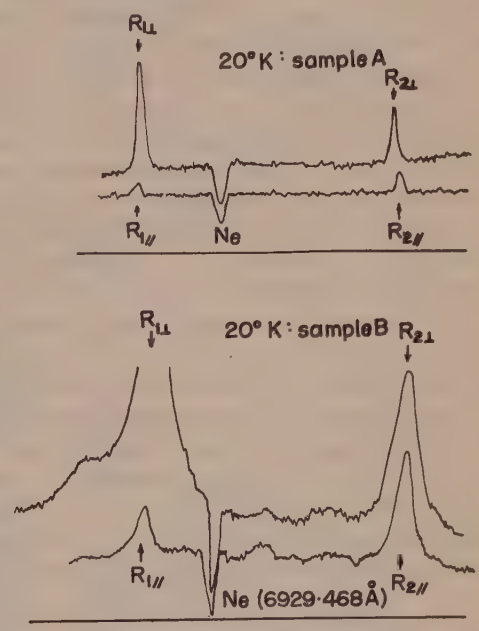

Fig. 2. The microphotometer traces of R_1 and R_2 spectra of samples A and B observed at 20°K.

The spectral widths in sample A are such that in R_1, R_2 lines the widths of $R_1^\perp$ is a little larger than the other components and in B_1, B_2 lines the widths of $B_1^\perp$ and $B_1^{//}$ are clearly smaller than those of $B_2^\perp$, $B_2^{//}$.

(c) *The absorption wave-numbers*: The absorption wave-lengths of R_1, R_2 and B_1, B_2 absorption lines for the polarized lights ($E\perp$

* Throughout this paper, superscripts $\perp$ and // indicate the direction of E and subscripts $\perp$ and // indicate that of H_0 relative to the optic axis C_3.

Table I. R_1, R_2 absorption wave-lengths λ and wave-numbers ν for the polarized light at low temperatures.

Temp.	Polariz.	Spect.	Sample A (dil.)		Sample B (conc.)	
			λ(Å)	ν(cm^{-1})	λ(Å)	ν(cm^{-1})
4.2°K	$E\perp C_3$	R_1	6933.93	14417.87	6933.0	14419.8
		R_2	19.98	46.93	18.8	49.4
	$E//C_3$	R_1	34.03	17.63	33.0	19.8
		R_2	19.83	47.24	18.8	49.4
20°K	$E\perp C_3$	R_1	6933.90	14417.93	6933.0	14419.8
		R_2	19.95	46.99	18.8	49.4
	$E//C_3$	R_1	33.93	17.86	33.0	19.8
		R_2	19.75	47.41	18.8	49.4
86°K	$E\perp C_3$	R_1	6934.01	14417.70	6933.2	14419.4
		R_2	20.06	46.76	19.0	49.0
	$E//C_3$	R_1	34.01	17.70	33.2	19.4
		R_2	19.91	47.08	19.0	49.0
Exp. error			±0.02	±0.04	±0.1	±0.2

Table II. B_1, B_2 absorption wave-lengths λ and wave-numbers ν for the polarized light at low temperatures.

Temp.	Polariz.	Spect.	Sample A (dil.)		Sample B (conc).	
			λ(Å)	ν(cm^{-1})	λ(Å)	ν(cm^{-1})
4.2°K	$E\perp C_3$	B_1	4762.24	20992.7	4762.3	20992
		B_2	45.27	21067.7	45.3	21068
	$E//C_3$	B_1	62.18	20992.9	62.3	20992
		B_2	45.35	21067.4	45.3	21068
20°K	$E\perp C_3$	B_1	4762.26	20992.6	4762.2	20993
		B_2	45.27	21067.7	45.6	21066
	$E//C_3$	B_1	62.18	20992.9	62.2	20993
		B_2	45.37	21067.3	45.6	21066
Exp. error			±0.03	±0.1	±0.2	±1

Table III. The separations of R_1 and R_2 absorption spectra and their polarization-shifts $\nu^{\perp}-\nu^{//}$. (cm^{-1})

	Sample A			Sample B		
	4.2°K	20°K	86°K	4.2°K	20°K	86°K
$\nu(R_2^{\perp})-\nu(R_1^{\perp})$	29.06	29.06	29.06	29.6	29.6	29.6
$\nu(R_2^{//})-\nu(R_1^{//})$	29.61	29.55	20.38			
$\nu(R_1^{\perp})-\nu(R_1^{//})$	0.24	0.07	0.00	—	—	—
$\nu(R_2^{\perp})-\nu(R_2^{//})$	−0.31	−0.42	−0.32	—	—	—

C_3 and $E//C_3$) have been measured precisely as possible and they are given in Tables I and II. The experimental error given in the tables is caused mainly by the difficulty of determining the position of an absorption peak because of the finite spreading of the spectrum.

The most remarkable fact found in such measurements is that the absorption position of the spectrum slightly shifts when the polarization of the incident light is changed (called hereafter polarization-shift). The directions and the magnitudes of these shifts are shown in the last two rows of Tables III and IV, together with the observed separations between R_1 and R_2 and those between B_1 and B_2. These separations and polarization-shifts seem independent of the change of temperature except for the separation $\nu(R_2^{//})-\nu(R_1^{//})$ and the shift $\nu(R_1^{\perp})-\nu(R_1^{//})$.

Table IV. The separations of B_1 and B_2 absorption spectra and their polarization-shifts $\nu^{\perp}-\nu^{//}$. (cm^{-1})

	Sample A		Sample B	
	4.2°K	20°K	4.2°K	20°K
$\nu(B_2^{\perp})-\nu(B_1^{\perp})$	75.0	75.1	76	76
$\nu(B_2^{//})-\nu(B_1^{//})$	74.5	74.4		
$\nu(B_1^{\perp})-\nu(B_1^{//})$	−0.2	−0.3	—	—
$\nu(B_2^{\perp})-\nu(B_2^{//})$	0.3	0.4	—	—

The temperature dependence of the absorption wave-numbers of R_1 and R_2 is illustrated in Fig. 3. When the temperature is increased from 4.2°K to 20°K, these spectra shift towards the shorter wave-length side (blue-shift), while they show a red-shift at high temperatures. The shifts thus found at very low temperatures are, however, so small (the order of these magnitudes is different from that observed at high temperatures) that they cannot be observed in case of B lines, being within the experimental error.

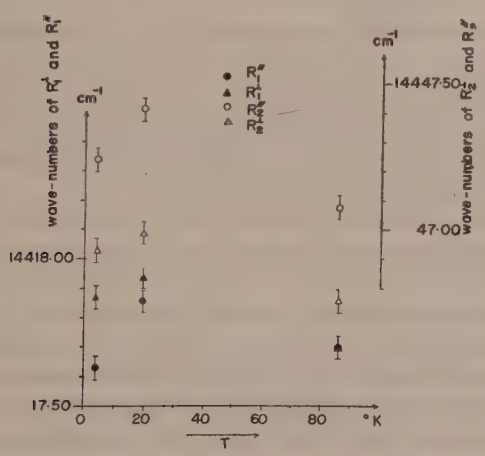

Fig. 3. The temperature dependences of the absorption wave-numbers of $R_1^{\perp}$, $R_1^{//}$, $R_2^{\perp}$ and $R_2^{//}$ (sample A).

In sample B, the absorption positions of R_1 and R_2 lines seem to be shifted towards the shorter wave-length side beyond the experimental error (Table I) in comparison with those measured in sample A, while these concentration-shifts are not clearly observed in B_1, B_2 lines.

(d) *Discussions*: The observation of optical anisotropies provides us with a very useful information for the spectral assignment, especially in case the spectral width is broad and experimental studies of the Zeeman effect are impossible to be made. Theoretically the absorption intensities of the line spectra in our case are supplied from those of the absorption bands by interplay of spin-orbit interaction, i.e., the intensity of R lines is supplied from U band and that of B lines mainly from Y and partly from U. Thus the optical anisotropies of these lines are determined both by the anisotropies of the absorption bands and by the strengths of spin-orbit interactions. In Fig. 1, the results of the theoretical estimates of optical intensities (Part A § 5 (b)) are also given under the presumption that the spectral assignment has been made as follows,*

$$\left.\begin{array}{ll} R_1: & {}^4A_2 \rightarrow \overline{E} \\ B_2: & \quad\quad\;\; \rightarrow 2\overline{A} \end{array}\right\} {}^2E$$

$$\left.\begin{array}{ll} B_1: & {}^4A_2 \rightarrow 2\overline{A} \\ B_2: & \quad\quad\;\; \rightarrow \overline{E}_a \end{array}\right\} {}^2F_2 .$$

We see that the qualitative features of the observed relative intensities for the fixed polarized light are reasonably explained by the theory, though the theory does not explain the intensity ratio between parallel and perpendicular component of a spectrum. Our experimental results recommend the following

* On the meaning of the notations, see Part A. Throughout this paper, we use the notations already used in Part A without explaining their meaning.

approximate relations among the theoretically introduced parameters; $\sigma \sim 2\pi$ (for ^2E), $\sigma_0 \sim 2\sigma$ and $\pi \sim 3\sigma$ (for $^2F_2$).

The problem of the observed separations of R_1 and R_2 and of B_1 and B_2 lines has been already discussed in Part A. The separation is determined mainly by the magnitudes of the trigonal field and the spin-orbit interaction. The remarkable constancy of the observed separations (except $\nu(R_2^{//})-\nu(R_1^{///})$) at low temperatures will indicate that little change of the crystal parameters occurs at these temperatures. The exceptional case $\nu(R_2^{//})-\nu(R_1^{//})$ is brought about by the anomalous temperature dependence of $R_1^{//}$ spectrum. Although $R_1^{//}$ is the faintest spectrum among R's, its observed anomaly seems to be really the case being beyond the experimental error. This anomaly remains unexplained.

The polarization-shifts can be easily understood if attention is paid both to the selection rule and the initial splitting of the ground state (see Figs. 4 and 5 of Part A). Thus the assignments are also confirmed by observing these polarization-shifts. If the sign of δ is defined positive when the Kramers doublet $M_s=\pm 3/2$ is lower than the doublet $M_s=\pm 1/2$, the theoretically predicted polarization-shifts are as follows under the above-mentioned spectral assignments;*

$$\delta/2 < \nu(R_1^{\perp})-\nu(R_1^{//}) < \delta\,,$$
$$\nu(R_2^{\perp})-\nu(R_2^{//}) = -\delta\,,$$
$$\nu(B_1^{\perp})-\nu(B_1^{//}) = -\delta\,,$$
$$\delta/2 < \nu(B_2^{\perp})-\nu(B_2^{//}) \lesssim \delta. \quad (|\delta|=0.38\ \mathrm{cm}^{-1})$$

The experimental results given in Tables III and IV (except $\nu(R_1^{\perp})-\nu(R_1^{//})$) satisfy these relations within the limit of the experimental error when the sign of δ is assumed positive. The exceptional case of $\nu(R_1^{\perp})-\nu(R_1^{//})$ is because of the queer behaviour of $R_1^{//}$ spectrum which has been already pointed out. Since the polarization-shift of R_2 spectrum is measurable with rather high precision, its measurement is one of the ways to determine optically the natural splitting δ. The value of δ thus determined from the polarization-shift of R_2 is $\delta=0.36\pm0.03\ \mathrm{cm}^{-1}$ which agrees well with the result of the paramagnetic resonance experiments, $|\delta|=0.38\ \mathrm{cm}^{-1}$.[3] Such an optical method is superior to the paramagnetic resonance method only in determining the sign of δ.

The problems of the spectral widths and the temperature-shifts will not be discussed in detail in this paper. The slight broadness of $R_1^{\perp}$ compared with the other components of R_1 and R_2 can be understood since theoretically $R_1^{\perp}$ spectrum is the superposition of two lines separated by δ while the others are singlets. To interpret the difference between the widths of B_1 and B_2 lines, however, it is necessary to take other effects into consideration. The curious temperature-shifts of R lines observed at very low temperatures show that Paetzold and Krömer's experimental formula[5] $\nu=\alpha+\beta(T/\Theta)^2$ at $T \ll \Theta$ (Θ: Debye temperature) is not good for R lines at these temperatures.

The observed concentration-broading and concentration-shift seem to offer very interesting problems, but to discuss such problems it will be necessary to make further experiments.

§ 4. Zeeman Effects of R_1 and R_2 Absorption Lines

The Zeeman patterns of R_1, R_2 absorption lines of sample A obtained at 20°K and 4.2°K in the four cases, $H_0//C_3$ $E\perp C_3$, $H_0//C_2$ $E//C_3$, $H_0\perp C_3$ $E\perp C_3$, and $H_0\perp C_3$ $E//C_3$ are illustrated in Figs. 4 and 5 together with the diagrams of transitions.

The observed splitting factors g's and the central wave-numbers ν^0's of these patterns are listed in Table V. Among these Zeeman patterns, those of R_1 ($H_0//C_3$ $E//C_3$) and of R_1, R_2 ($H_0\perp C_3$ $E//C_3$) are too faint to make direct measurements of the original plates precisely. Therefore, suitably reprinted plates with high contrast have been used for the measurements.

In the reprinted plates, it is found that, though the relative positions of absorption

* In the following relations, inequalities occur because $R_1^{\perp}$ and $B_2^{\perp}$ are expected to be unresolved doublets separated by δ (Figs. 4 and 5, Part A) and the observed peak of an unresolved doublet is considered to be located between the middle of the unresolved doublet and the stronger component of the doublet. The observed peak will be just at the middle of the unresolved two components when their intensities are same. In the following discussions, inequalities always appear in such cases.

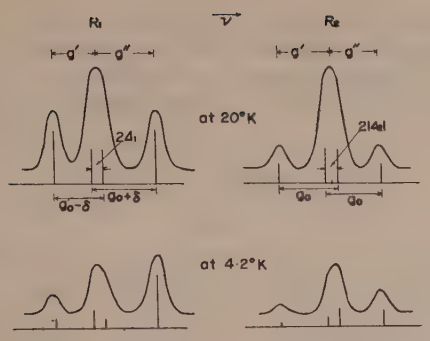

Fig. 4 (a) case I : $H_0 \parallel C_3$, $E \perp C_3$

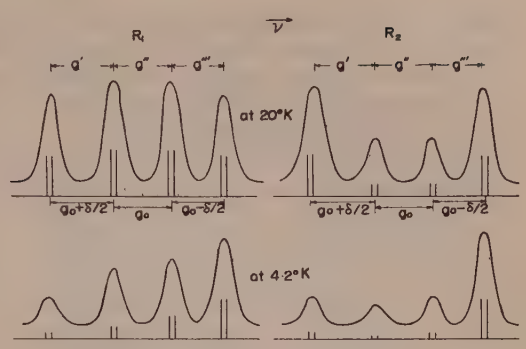

Fig. 5 (a) case III: $H_0 \perp C_3$, $E \perp C_3$

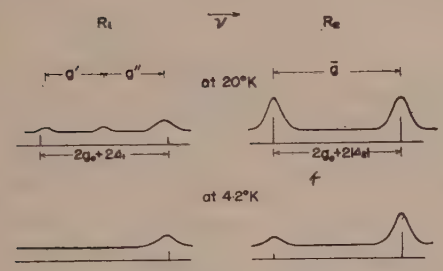

Fig. 4 (b) case II : $H_0 \parallel C_3$, $E \parallel C_3$

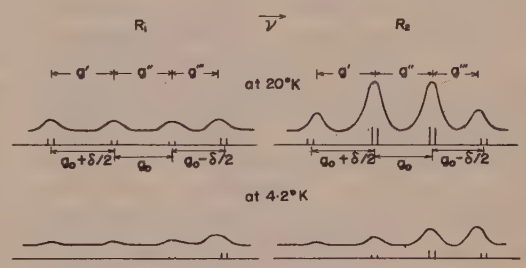

Fig. 5 (b) case IV: $H_0 \perp C_3$, $E \parallel C_3$

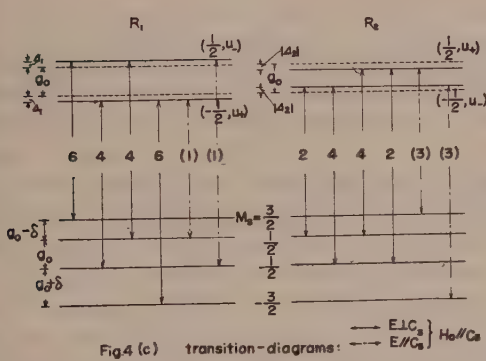

Fig. 4 (c) transition-diagrams:

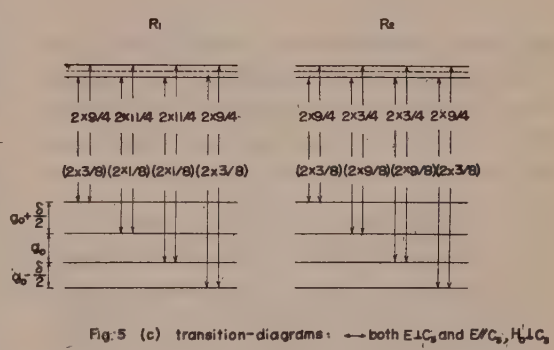

Fig. 5 (c) transition-diagrams: both $E \perp C_3$ and $E \parallel C_3$, $H_0 \perp C_3$

Fig. 4, 5. (a), (b): The observed Zeeman patterns (full curve) and the patterns (vertical lines) derived from the transition-diagrams (c). The intensities and the shapes of the observed patterns are only qualitatively illustrated. In the patterns (vertical lines) of 4.2°K, difference in electron population of the Zeeman levels of the ground state is taken into account. (c): The numbers in brackets indicate the transition probabilities when $E \| C_3$ and the others (without brackets) are those when $E \perp C_3$. In the calculation of the transition probabilities, the empirical relation $\sigma \sim 2\pi$ is used and π is put equal to 1.

lines are represented fairly well, the distance between an emission (comparison spectrum) and an absorption line is sometimes slightly changed from that measured on the original plate. Thus in order to avoid the confusion such unreliable measurements on the absolute positions of the absorption may create, the central wave-numbers ν^0's of these faint patterns are not tabulated. In Table VI the quantities derived from Table V which are useful in the following discussions are also given.

All the qualitative features of the Zeeman patterns obtained at 20°K are in agreement with those obtained by Lehmann at 83°K, but the quantitative features of our patterns

Table V. The observed splitting factors (in βH_0 unit) and the central wave-numbers ν^0(cm^{-1}) of R_1, R_2 Zeeman patterns. The central wave-number ν^0 is defined as the wave-number of the central Zeeman component when three Zeeman components appear, and is defined as the wave-number in the middle of the inner two components when four components appear. On the notation of g's, see Fig. 4.

$H_0=24,000\,\phi$ $\beta H_0=1.12\,\mathrm{cm}^{-1}$			20°K		4.2°K		Exp. error
			R_1	R_2	R_1	R_2	
$H_0//C_3$	$E\perp C_3$	g'	1.46	1.80	1.45	1.92	±0.07
		g''	2.04	1.64	2.12	1.53	
		ν^0	14417.51	14446.85	14417.66	14447.16	±0.04
	$E//C_3$	g'	2.1		—		±0.1
		$\bar{g}$		4.38		4.42	±0.07
		g''	2.0		—		±0.1
		ν^0	—	14447.31	—	14447.29	±0.04
$H_0\perp C_3$	$E\perp C_3$	g'	2.15	2.09	2.13	2.12	±0.07
		g''	1.96	1.92	1.98	2.03	
		g'''	1.80	1.73	1.80	1.79	
		ν^0	14417.89	14417.21	14417.96	14447.31	±0.04
	$E//C_3$	g'	2.2	2.0	2.1	2.1	±0.1
		g''	2.0	2.0	1.9	2.0	
		g'''	1.6	1.6	1.9	1.7	

are entirely different from those of Lehmann's.

To simplify the description, we assume from the beginning the spectral assignments given in § 3 (d) which are established most definitely from the observed Zeeman patterns.

Case I. $H_0//C_3$ and $E\perp C_3$ (Fig. 4 (a)):

The observed splitting factors of the Zeeman patterns in this case are far smaller than those theoretically expected, even though they are increased compared with those of Lehmann's.

The only way to fulfil the previously given proper requirement that the Zeeman pattern in this case must contain some of the Zeeman components of the ground state is to introduce the g-shifts of the excited states assuming the central component to be the unresolved doublet. In fact the central component seems broader than the side components. That this is due to the superposition of two lines can be made clear by observing its apparent shift relative to the side component when the temperature is varied from 20°K to 4.2°K. This is because, if the central component is the superposition of closely located two lines, the decrease of the number of electrons populated in the upper Zeeman levels of the ground states at 4.2°K makes one line of the superposed two central lines weaker than the other. As a result, the apparent peak of the central component shifts to the stronger one while at 20°K it will be almost at the middle of the two.

The quantities $1/2(g_{//}''-g_{//}')$ measured at 20°K and 4.2°K given in the second row of Table VI show such apparent relative shifts of the central component for both R_1 and R_2. Keeping the above-mentioned explanation of the apparent shifts in mind and refering to the theoretically obtained diagram of transitions, we expect the following values for $1/2(g''-g')$;

$$\left.\begin{aligned} 1/2(g_{//}'-g_{//}') &= \delta \text{ for } R_1 \\ &= 0 \text{ for } R_2 \end{aligned}\right\} \text{ at } 20^\circ\mathrm{K}$$

$$\left.\begin{aligned} &> \delta \text{ and } < \delta+|\Delta_1| \text{ for } R_1 \\ &> -|\Delta_2| \text{ and } < 0 \quad \text{for } R_2 \end{aligned}\right\} \text{ at } 4.2^\circ\mathrm{K},$$

where Δ_1 and Δ_2 denote the half g-shifts of the excited states of R_1 and R_2 respectively and their magnitudes will be determined in the following analysis. With the values Δ_1

$=0.22$, $\Delta_2=-0.26$ and $\delta=0.34$ (in βH_0 unit), these relations are held actually in Table VI almost within the limit of experimental error.

The g-shifts of the R_1 and R_2 excited states are determined from

$$1/2(g_{//}'+g_{//}'')=g_0-\Delta_1 \quad \text{for } R_1\,,$$
$$=g_0+\Delta_2 \quad \text{for } R_2\,,$$

where g_0 is the g-value of the ground state and is known as 1.98. The sum of the left hand side is made to eliminate the effect of the natural splitting δ of the ground state. From Table VI, we obtain

$$\Delta_1=0.22\ (\pm0.04),\quad \Delta_2=-0.26\ (\pm0.04)\,,$$
$$g_{e//}(R_1)=g_0+2\Delta_1=2.42\,,$$
$$g_{e//}(R_2)=g_0+2\Delta_2=1.46\,,$$

where $g_{e//}(R_1)$ and $g_{e//}(R_2)$ are the g-values of the R_1 and R_2 excited states respectively. Looking at these results, we notice at once the following simple relation to exist between $g_{e//}$'s,

Table VI. The useful quantities to confirm the assignments. These are derived from Table I and Table V. $g_{//}$ and $g_\perp$ denote the splitting factors in cases of $H_0//C_3$ and $H_0\perp C_3$ respectively. The subscripts of $\nu_{//}^0$ and $\nu_\perp^0$ also indicate the direction of a magnetic field. ν_0 is the absorption wave-number in case of no magnetic field.

$E\perp C_3$		R_1	R_2
$\frac{1}{2}(g_{//}'+g_{//}'')$	20°K	$1.75\,\beta H_0$	$1.72\,\beta H_0$
	4.2°K	1.78	1.72
$\frac{1}{2}(g_{//}''-g_{//}')$	20°K	0.29	−0.08
	4.2°K	0.33	−0.19
$\nu_{//}^0-\nu_0$	20°K	-0.42cm^{-1}	-0.14cm^{-1}
	4.2°K	−0.21	+0.23
$g_\perp''$	20°K	$1.96\,\beta H_0$	$1.92\,\beta H_0$
	4.2°K	1.98	2.03
$\frac{1}{2}(g_\perp'+g_\perp'')$	20°K	1.97	1.91
	4.2°K	1.96	1.95
$g_\perp'-g_\perp'''$	20°K	0.35	0.36
	4.2°K	0.33	0.33
$\nu_{\perp 0}-\nu_0$	20°K	-0.04cm^{-1}	$+0.23\text{cm}^{-1}$
	4.2°K	+0.09	+0.38
$E//C_3$			
$\nu_{//}^0-\nu_0$	20°K	—	-0.10cm^{-1}
	4.2°K		+0.05

$$g_{e//}(R_1)+g_{e//}(R_2)\fallingdotseq 4\,,$$

since

$$\Delta_1\fallingdotseq-\Delta_2\ (\neq 0)\,.$$

The explanation of such an interesting relation between the g-shifts of the R_1 and R_2 excited states is given in the first paper.

Case II. $H_0//C_3$ and $E//C_3$ (Fig. 4 (b)):

The $g_{e//}$ (R_2)-shift is more clearly observed in this case in the Zeeman pattern of R_2 where the separation of the two components $\bar{g}$ must be $2g_0-2\Delta_2=4.52$ (±0.07) if the same $g_{e//}(R_2)$-shift as determined from the pattern of $R_2^\perp$ in the previous case is used. The observed values of $\bar{g}$'s for the both temperatures (Table VI) agree with this within the limit of experimental error.

The observed Zeeman pattern of $R_1^{//}$ which is the faintest among the patterns of R_1 and R_2 we have obtained, however, does not seem to be explained within our scheme even qualitatively. Against our expectation on this pattern that it consists of two weak components separated by $2g_0+2\Delta_1=4.40$ (±0.07), the observed pattern consists of three components and the separation of the side components is 4.1 (±0.1) even if the central component is disregarded. Our previous short report[6] has erroneously described this Zeeman pattern.

Case III $H_0\perp C_3$ and $E\perp C_3$ (Fig. 5 (a)).

In this case, the Zeeman levels of the ground state are directly represented: The paramagnetic resonance experiment has show that the separation of the four Zeeman levels of the ground state are $g_0-\delta/2$, g_0 and $g_0+\delta/2$. If $g_\perp'''$, $g_\perp''$ and $g_\perp'$ are identified to be $g_0-\delta/2$, g_0 and $g_0+\delta/2$ respectively, the relations,

$$g''=g_0=1.98,\quad 1/2(g'+g'')=g_0,$$
$$g_\perp'-g_\perp'''=\delta=0.34$$

must hold among the observed $g_\perp$'s. Table VI shows that the observed $g_\perp$'s actually satisfy these relations within the limit of experimental error. The positive sign of δ is also confirmed in such a comparison. In the Zeeman patterns observed at 4.2°K, the uniformly decreasing inclination of the intensities of the longer wave-length side components which is due to the decrease in electron population of the upper Zeeman levels of the ground state at 4.2°K is consis-

tent with the above-mentioned identification of the observed $g_\perp$'s. In this case, the g-shifts $\Delta g_{e\perp}$'s, i.e., deviations of the g-values of the excited states from zero, will split each of the four Zeeman components into two lines separated by $\Delta g_{e\perp}$, but, if $\Delta g_{e\perp}$'s are smaller than the spectral width, these closely located two lines cannot be resolved and the apparent position of such a superposed component will not be changed from the case of $\Delta g_{e\perp}=0$. In addition to this situation, since the superposed two lines correspond to the transitions from the same Zeeman level of the ground state, the apparent temperature-variations of the splitting factors similar to those previously explained in case of $H_0//C_3$ and $E\perp C_3$ are not expected. In Fig. 5, the finite g-shifts of the both R_1 and R_2 excited states are assumed although they cannot be determined from the observed patterns.

Case IV $H_0\perp C_3$ and $E//C_3$ (Fig. 5 (b)):

An accurate measurement of the splittings is impossible in this case because the intensities are weak. It may be said, however, from Table V that no noticeable difference of the splittings is observed between case III and case IV, which is resonable from the theoretical point of view. The relative intensities of the components, which differ from those observed in case III show a nice agreement between experiment and theory.

A remaining quantity to be discussed is the central wave-number ν^0 of the Zeeman pattern whose definition is given in the footnote of Table V. According to the diagram of transitions, the difference between ν^0 and ν_0 observed in case of no magnetic field, $\Delta\nu=\nu^0-\nu_0$, must satisfy the following relations; when $H_0//C_3$ and $E\perp C_3$

$$0>\Delta\nu(20°\mathrm{K})>\delta\ (=0.38\ \mathrm{cm}^{-1})$$

$$\Delta\nu(20°\mathrm{K})>\Delta\nu(4.2°\mathrm{K})>\Delta\nu(20°\mathrm{K})-|\Delta_1|\quad(|\Delta_1|=0.25\ \mathrm{cm}^{-1})$$

for R_1;

$$\Delta\nu(20°\mathrm{K})=0$$

$$|\Delta_2|>\Delta\nu(4.2°\mathrm{K})>0\quad(|\Delta_2|=0.29\ \mathrm{cm}^{-1})$$

for R_2;

when $H_0//C_3$ and $E//C_3$

$$\Delta\nu(20°\mathrm{K},\ 4.2°\mathrm{K})=0\qquad\text{for } R_2;$$

when $H_0\perp C_3$ and $E\perp C_3$

$$0>\Delta\nu(20°\mathrm{K},\ 4.2°\mathrm{K})>3\delta/4-\delta\quad(=0.10\ \mathrm{cm}^{-1})\ \text{for } R_1;$$

$$\Delta\nu(20°\mathrm{K},\ 4.2°\mathrm{K})=3\delta/4\quad(=0.28\ \mathrm{cm}^{-1})\ \text{for } R_2;$$

The observed $\Delta\nu$'s given in Table VI seem to deviate from these beyond the limit of experimental error. All deviations are systematic in such a way that they are negative at 20°K and positive at 4.2°K.

§ 5. Zeeman Effect of B_1 and B_2 Absorption Lines

The observed Zeeman patterns of B_1, B_2 absorption lines are illustrated in Fig. 6 and Fig. 7 together with the diagram of transitions. The spectral widths of B_1 and B_2 lines are about three times broader than those of R_1 and R_2, but they are still smaller or comparative to the Zeeman energies. Therefore we have obtained the Zeeman patterns, although not so clear as the case of R lines, which depend on the directions of H_0 and E relative to the crystal axis C_3. Thus, together with the theoretical considerations given in the first paper, it is possible to establish definite assignments of B lines by using the observed patterns. For example, a possibility that one of these spectra may be identified to the transition $^4A_2\rightarrow\bar{E}_b(^2F_2)$ can be easily excluded by the fact that the theoretically predicted Zeeman patterns corresponding to it (Fig. 5, Part A) consists of an unsplit component when $H_0//C_3$ and $E//C_3$ (it consists of two components separated by $2\beta H_0$ when $H_0//C_3$ and $E\perp C_3$). We cannot find such a pattern in the observed Zeeman patterns.

In the following discussions, we will assume from the beginning the assignments given in § 3 (d), in the same way as we have done in § 4, and will show to what degree such assignments are convincing.

To observe the faint and diffuse Zeeman patterns, it was necessary to use the suitably reprinted plates instead of using the original ones.

Case I $H_0//C_3$ and $E\perp C_3$ (Fig. 6 (a)):

The Zeeman splitting can be observed rather clearly in $B_1^\perp$ spectrum at 20°K while only vaguely in $B_2^\perp$ at 20°K. In the diagrams of transitions, the finite $g_{e//}$-shift (from zero), Δ_1', of the B_1 excited state and also the finite

$g_{e//}$-shift (from 4), Δ_2', of the B_2 excited state are assumed. Comparing the experimental patterns with those expected from such transition diagrams, a rather good agreement can be obtained if Δ_2' satisfies the relation $g_0-2\Delta_2' \sim g_{obs}(B_2)=2.4+0.5$ (so $\Delta_2' \sim 0.2\pm 0.25$) and if $2\Delta_1'$ is small compared with g_0. Even when Δ_1' differs from zero, $g_{obs}(B_1)=2.1\pm0.2$ is reasonable considering the fact that at 20°K the observed position of the apparent peak will be almost at the middle of the closely located two lines since their intensities become equal when we assume the relation $\sigma_0 \sim 2\sigma$. The necessity that Δ_1' ($\neq 0$) must be introduced will be seen in the analysis of Case II.

Case II $H_0//C_3$ and $E//C_3$ (Fig. 6 (b)):

Among all the observed Zeeman patterns of B_1 and B_2, the Zeeman pattern of $B_1//$ at 20°K in this case is most clear. Thus the most definite conclusion can be derived from

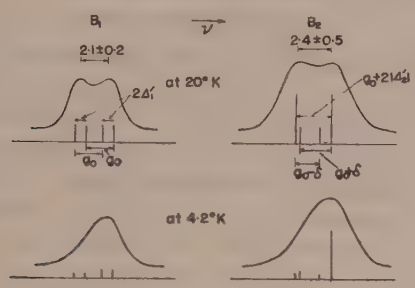

Fig.6 (a) case I: $H_0//C_3$, $E\perp C_3$

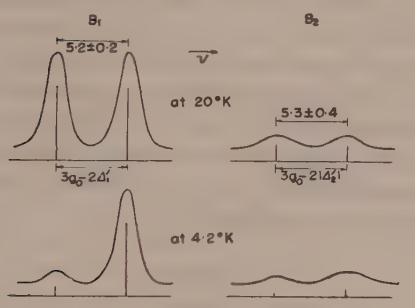

Fig.6 (b) case II: $H_0//C_3$, $E//C_3$

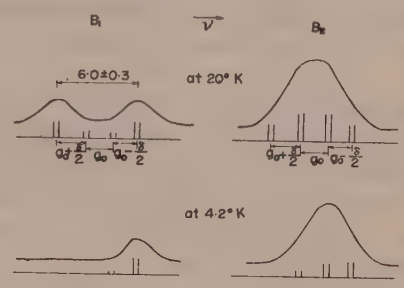

Fig.7 (a) case III: $H_0\perp C_3$, $E\perp C_3$

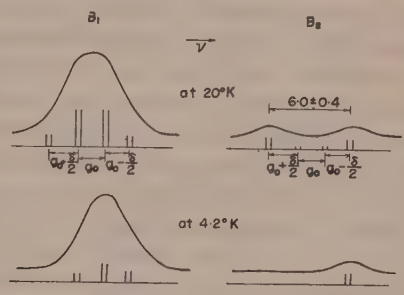

Fig.7 (b) case IV: $H_0\perp C_3$, $E//C_3$

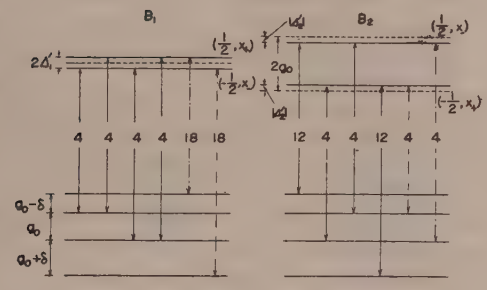

Fig.6 (c) transition-diagrams $\longrightarrow$ $E\perp C_3$, $\leftarrow\rightarrow$ $E//C_3$ } $H_0//C_3$

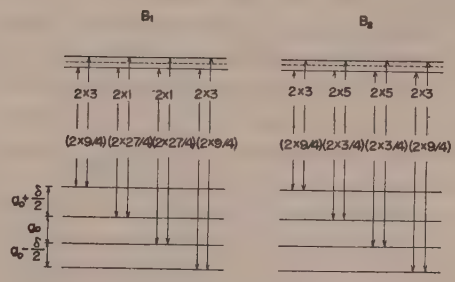

Fig.7 (c) transition-diagrams: $\longleftrightarrow$ both $E\perp C_3$ and $E//C_3$, $H_0\perp C_3$

Figs. 6, 7. (a), (b): The observed Zeeman patterns (full curve) and the patterns (vertical lines) derived from the transition-diagrams (c). The intensities and the shapes of the observed patterns are only qualitatively illustrated. The observed splitting factors are also given in βH_0 unit. In the patterns (vertical) of 4.2°K, difference of the electron population of the Zeeman levels of the ground state is taken into account. (c): The numbers in brackets indicate the transition probabilities when $E||C_3$ and the others (without brackets) are those when $E\perp C_3$. In the calculation of the transition probabilities, the empirical relations $\sigma^\circ \sim 2\sigma$ and $\pi \sim 3\sigma$ are used and σ is put equal to 12.

this pattern. A nice agreement can be obtained between theory and experiment also in this case, when Δ_1' and Δ_2' satisfy the following relations,

$$3g_0-2\Delta_1'=g_{obs}(B_1)=5.2\pm0.2$$
$$3g_0+2\Delta_2'=g_{obs}(B_2)=5.3\pm0.4\,.$$

From these relations we obtain

$$\Delta_1'=0.4\pm0.1$$

and

$$\Delta_2'=-(0.3\pm0.2)$$

the latter of which is consistent with the value of Δ_2' ($\Delta_2'\sim0.2\pm0.25$) obtained in case I.

The g-shifts Δ_1' and Δ_2' seem to satisfy the relation $\Delta_1'+\Delta_2'\fallingdotseq 0$, and the theoretical examination of such g-shifts (§ 6 (e), Part A) shows that they are directly due to the reduction of the orbital angular momentum of f_2-electrons in the crystal.

Case III $H_0\perp C_3$ and $E\perp C_3$ (Fig. 7 (a)):

The observed patterns seem to be the envelopes of the unresolved Zeeman components. The reasonable interpretation of these patterns can be made in such a way that the observed two peaks of B_1 correspond to the stronger two side components and the pattern of B_2 is determined mainly by the inner two components which are stranger than the side components in this spectrum. The reason why none of the split structures is seen in this case (also in case IV) while they are represented in case I even though slightly in B_2, may be due to the relatively large g-shifts (from zero) of the excited states. Thus in the transition-diagram of Fig. 7 the finite g-shifts of the excited states are assumed though their magnitudes cannot be determined from our Zeeman patterns. The reasonable splitting $g_{obs}(B_1)=6.0\pm0.3$ of B_1 will not be affected by introducing such g-shifts.

Slight blue-shift of the apparent peak and narrowing of the apparent width of the unresolved Zeeman pattern $B_2^{\perp}$ at 4.2°K compared to the Zeeman pattern observed at 20°K (the situation is also the same about the Zeeman pattern $B_1^{//}$ in case IV) clearly show that the observed broad pattern is the envelope of the Zeeman components.

Case IV $H_0\perp C_3$ and $E//C_3$ (Fig. 7 (b)):

In the same way as explained in case III, the patterns obtained in this case can also be explained reasonably.

Acknowledgements

We should like to express our sincere thanks to Prof. E. Kanda of Tohoku University, Prof. Z. Koana and Prof. G. Kuwabara of the University of Tokyo for their continual encouragements and advices through the course of this work. We are greatly indebted to Dr. T. Imai and Mr. S. Togashi of Nippon Denkō Laboratories for their kindness of preparing the samples which are well examined chemically, and to Prof. R. Sadanaga and Dr. Y. Iitaka of Mineralogy Department of Tokyo University for their kindness of performing X-ray determination of the crystal axis and cutting. Miss K. Shimada was kind enough to prepare the suitably reprinted plates for the detection of some feeble and diffuse Zeeman patterns.

References

1) O. Deutschbein: Ann. d. Phys. [5] **14** (1932) 712, 729; Ann. d. Phys. [5] **20** (1934) 828.
2) H. Lehmann: Ann. d. Phys. [5] **19** (1934) 99.
3) A. A. Manenkov and A. M. Prokhorov: J.E.T.P. **28** (1955) 762.
M. M. Zaripov and Iu. Ia. Shamonin: J.E.T.P. **30** (1956) 291.
J. E. Geusic: Phys. Rev. **102** (1956) 1252.
4) K. H. Paetzold: Z. Physik **129** (1951) 123.
5) K. H. Paetzold and H. Krömer: Naturwiss. **5** (1953) 163.
6) I. Tsujikawa and S. Sugano: J. Phys. Soc. Japan **13** (1958) 220.

JOURNAL OF THE PHYSICAL SOCIETY OF JAPAN Vol. 13, No. 8, AUGUST, 1958

Measurement of Free Induction Decay Time and Spin-Lattice Relaxation Time of Bromine Nucleus in Sodium Bromate

By Tsuneo HASHI

Department of Physics, Faculty of Science, University of Kyoto

(Received April 5, 1958)

Using transient techniques, the free induction decay time T_2^* and the spin-lattice relaxation time T_1 were measured for Br^{79} and Br^{81} in $NaBrO_3$ at room temperatures. The free induction decay curves were well described by Gaussian curves with $T_2^*=10.2\times10^{-5}$ sec for Br^{79} and 9.8×10^{-5} sec for Br^{81}. Comparison was made with the result of the steady-state measurement. The measured values of T_1 were 2.1×10^{-3} sec for Br^{79} and 3.0×10^{-3} sec for Br^{81}. The agreement of the ratio $T_1(Br^{81})/T_1(Br^{79})=1.4$ with the known ratio $Q^2(Br^{79})/Q^2(Br^{81})=1.44$ indicates that the quadrupole relaxation is principally responsible for spin-lattice relaxation. The apparatus and procedures are also described in some detail.

§ 1. Introduction

The experiments on pure quadrupole resonance were, up to the present, performed mostly by the steady-state method. So, while the measurements of the resonance frequency were reported in abundance, those of the line width and the relaxation time were relatively few. It is due to difficulties in observing the accurate line shape with a frequency modulated superregenerative detector as ordinarily used in such experiments[1], and also due to the existence of the broadening caused by the distribution of electric field gradients resulting from temperature gradient, strain and imperfection in the sample[1]. It is very difficult to differentiate such a broadening from others by merely the measurement of the line width.

In general, three types of mechanisms are considered for loosening precessional coherence in the spin system, namely, (1) different fixed rates of precession caused by static local fields, (2) random fluctuation of precessional frequency and phase, and (3) spin-lattice relaxation. These three contribute simultaneously to the line broadening.

Transient or pulsed techniques[2] offer advantages over the steady-state measurement of line width in obtaining separate informations about these three mechanisms.

In the present paper, the transient pure quadrupole resonance experiment on bromine nuclei is reported. Transient experiments on pure quadrupole resonance were performed by Bloom, Hahn and Herzog[3], Herzog and Hahn[4], Proctor and Tanttila[5], and Woessner and Gutowsky[6], but these authors were chiefly concerned with Cl^{35} nucleus. When bromine compounds are used, the measurements on both Br^{79} and Br^{81} isotopes are easily performed, because of their sufficient natural abundances. The analysis of relaxation is much facilitated by comparison of the measurements on both isotopes.

The present paper includes a brief theory, the description of the apparatus and procedures, and the result of the measurements on the free induction decay time T_2^* and the spin-lattice relaxation time T_1 for Br^{79} and Br^{81} in sodium bromate. The result of experiment on the spin echo will be published in the near future.

§ 2. Theory

Quantum mechanical descriptions of the transient nuclear induction associated with nuclear quadrupole coupling have been given by Bloom, Hahn and Herzog[3], and Das and Saha[7]. These authors treated the case where the electric field gradient had an axial symmetry. For bromine nuclei in sodium bromate, the above analyses are directly applicable.

We consider a nucleus with spin $I=3/2$ in axially symmetric field gradient. The r-f magnetic field:

$$H_x=2H_1\cos\omega t\,,\quad H_y=0\,,\quad H_z=0\,,\qquad (1)$$

is assumed to be applied in form of short pulse of width t_w and begining at $t=0$, where the z-axis is chosen to be the symmetry axis of electric field gradient. The transient response of the nuclear magnetic moment to the driving pulse is described by the expectation values of I_x, I_y and I_z.

If the conditions:

$$|\omega-\omega_0'|\ll 1|t_w\,, \quad \text{and} \quad \omega\gg 1/t_w, \gamma H_1 \tag{2}$$

are satisfied, the expectation values of I_x, I_y and I_z are given by

$$\left.\begin{aligned} &\langle I_x\rangle=\frac{\sqrt{3}\,\omega_0'\hbar}{4kT}\sin(\sqrt{3}\,\gamma H_1 t_w)\sin\omega_0'(t-t_w)\,,\\ &\langle I_y\rangle=0\,,\\ &\langle I_z\rangle=0 \qquad\qquad (t\geqslant t_w)\,, \end{aligned}\right\} \tag{3}$$

where ω_0' is an angular resonance frequency associated with zero field quadrupole splitting of the bromine nucleus.

In order to take into account the static distribution of ω_0' over the sample, we assume:

$$g(\Delta\omega)=\frac{T_2^*}{\sqrt{2\pi}}\exp\left[-\frac{(T_2^*\Delta\omega)^2}{2}\right], \tag{4}$$

where $\Delta\omega=\omega_0-\omega_0'$ and ω_0 is the center frequency of the distribution of ω_0'.

Upon averaging (3) over the distribution (4) and multiplying with $\gamma\hbar N$, the expectation values of the magnetization for the sample are obtained as:

$$\left.\begin{aligned} &M_x=\frac{\sqrt{3}\,N\omega_0\gamma\hbar^2}{4kT}\sin(\sqrt{3}\,\gamma H_1 t_w)\sin\omega_0(t-t_w)\exp\left[-\frac{(t-t_w)^2}{2T_2^{*2}}\right],\\ &M_y=M_z=0 \qquad\qquad (t\geqslant t_w)\,, \end{aligned}\right\} \tag{5}$$

where N is the total number of spins in the sample. Relaxation effects are omitted here.

The free induction voltage induced in a coil placed along the x-direction is proportional to the time derivative of M_x.

If the second pulse of the same form is applied at the time τ after the first pulse, the spin echo is obtained centering at $t=2\tau$ as follows:

$$\left.\begin{aligned} &M_x=-\frac{\sqrt{3}\,N\omega_0\gamma\hbar^2}{4kT}\sin(\sqrt{3}\,\gamma H_1 t_w)\sin^2\frac{\sqrt{3}\,\gamma H_1 t_w}{2}\sin\omega_0(t-2\tau)\exp\left[-\frac{(t-2\tau)^2}{2T_2^{*2}}\right],\\ &M_y=M_z=0 \qquad\qquad (t\geqslant\tau+t_w)\,, \end{aligned}\right\} \tag{6}$$

§ 3. Apparatus and Procedures

The block diagram of the apparatus is shown in Fig. 1. It is divided into four parts: timer, transmitter, receiver, and synchroscope. The timer consists of a basic trigger generator, two delay multivibrators, a one-shot multivibrator, and a mixer. Each component is of usual design[8] and not described here. The output pulse of the basic trigger generator initiates the two delay multivibrators and each produces the output pulse with proper delay time. The delay multivibrators are isolated from each other by the cathode follower stages being utilized at inputs and outputs. The separation of the two pulses is continuously variable from 0 to 30 m sec. After mixing, these two pulses in turn trigger the one-shot multivibrator and produce two successive rectangular pulses, of which the widths are continuously variable from less than 3μ sec to more than 200 μ sec. The repetition period of the pair of rectangular pulses is determined by the frequency of the basic trigger generator, and is chosen to be longer than the spin-lattice relaxation time T_1 in order to ensure thermal equilibrium of the spin system till the next onset of the pair of pulses. The output pulse from the basic trigger generator also trrigger the synchroscope. The time sweep is adjusted so that it covers the time of interest.

When further pulses are required as in the

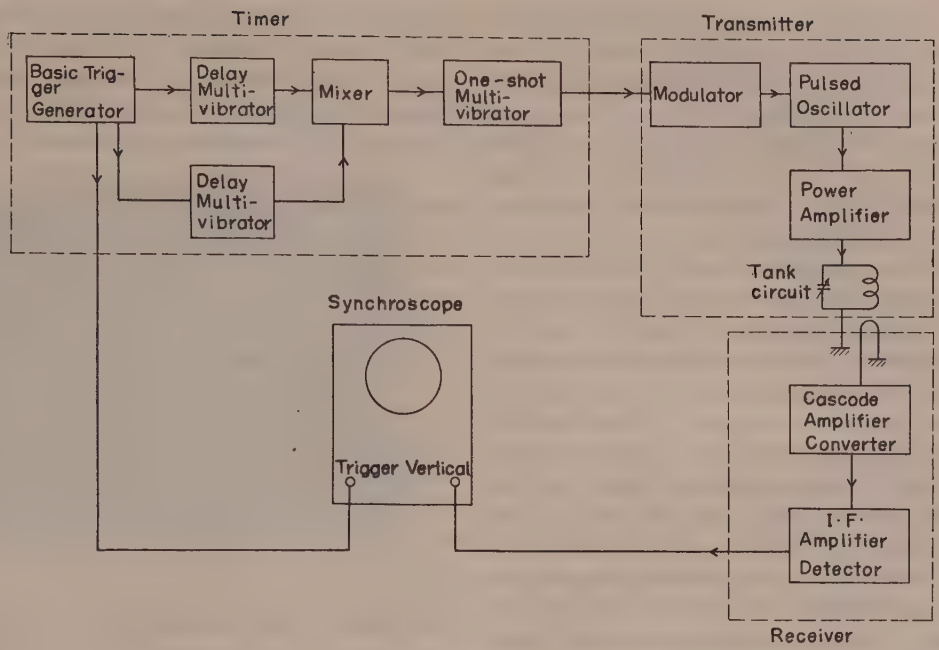

Fig. 1. Block Diagram of the Apparatus.

case of the stimulated echo experiment, they are easily provided by the addition of delay multivibrators of the same kind.

The transmitter consists of a pulsed oscillator, a power amplifier and a tank circuit. For observing free nuclear quadrupole precession signals, much stronger and much shorter r-f pulse is required than for the case of nuclear magnetic resonance in liquid. It is because the characteristic time T_2^* in solid is generally much shorter than in liquid, and the conditions: $T_2^* \gg t_w$ and $\sqrt{3}\gamma H_1 t_w = \pi/2$ must be satisfied for 90° pulse as shown in (2). If these conditions are not satisfied, the free induction decay time depends on H_1 and t_w[9]. For bromine nuclei in sodium bromate ($NaBrO_3$) the r-f pulse with H_1 of more than 10 gauss and t_w of shorter than 10μ sec is required.

The power amplifier is of usual tuned-grid and tuned-plate type and consists of two 4X-150A's connected in push-pull and the available power is sufficient to produce such r-f pulses. Since the tuning circuit with very high "Q" would cause some undesirable transients and make the tuning very critical at such high frequencies (~180 Mc/sec for Br^{79}, ~150 Mc/sec for Br^{81}), the Q's are lowered and thus the amplifier has the bandwidth of about 3 Mc/sec. The broadband character is necessary, on the other hand, for the faithful reproduction of the envelope of the envelope of the oscillator waves. It also permits the fine adjustment of the oscillator frequency without retuning the amplifier, and is very convenient for the present experiment in which the resonance must be achieved by adjusting the frequency of the transmitter. The driving point of the amplifier tubes is chosen below cutoff by supplying a fixed bias, in order to prevent shot noise[11].

The pulsed oscillator is normally held below cutoff and brought into oscillation by the application of rectangular pulses from the timer. The switching action is provided by a tube connected in series with the oscillator tube 2C39A. The author has not used the continuous oscillator and gated power amplifier system because the leakage past the gated amplifier in off-periods would make serious trouble to the receiver, which is extremely sensitive and tuned to the oscillator frequency.

The output power of the power amplifier is led to the tank circuit, which consists of a coil of three windings and about 1 cm diameter and a small tuning condenser. The sample is placed in the coil and subjected to the oscillating magnetic field. Since the quadrupole interaction is temperature-dependent[10,12], air cooling is used to keep the sample at a con-

stant temperature, and further, the tank circuit is situated apart from the power amplifier tubes in order to prevent the sample from heating by them.

In free nuclear quadrupole experiment, the receiver should have the short recovery time of sensitivity from the saturation caused by strong r-f pulses, because the free nuclear quadrupole precession singnal is weak and appears immediately after the strong driving pulse. The receiver consisting of a cascode amplifier and a converter followed by a broadband rather i-f strip[3] has been found to be sufficient for this purpose. The cascode amplifier and converter is a modified television superheterodyne tuner similar to those used by Bloom, Hahn and Herzog[3]. The broadband i-f amplifier is a six-stage 6CB6 stagger tuned radar amplifier with bandwidth of about 4 Mc/sec. Its center frequency is 30 Mc/sec and the maximum gain about 110 db.

Since, as shown in (5) there is no component of the nuclear magnetization perpendicular to the axis of the applied oscillating magnetic field, the crossed coil system can not be used in the present experiment. The input coil of the cascode amplifier is therefore coaxially coupled with the tank coil. Although no special precautions are taken to reduce to reduce the receiver blocking, it has a recovery time of less than 20μ sec, when intense pulse is applied to the input. The amplitude of the detector is limited below one volt to avoid overloading of the video amplifier. Signals are displayed on the synchroscope screen and the measurement of the relaxation time is made by photographic method.

In order to obtain accurate 90° pulses, the adjustment of both frequency and pulse width is necessary. frequency is adjusted so that the amplitude of the free induction is maximized. During the process the pulse width must be held at the minimum possible value because subsidiary maxima exist when the pulse width is longer than 90°[13]. After the adjustment of the frequency, the pulse width is increased until the maximum amplitude of the free induction is obtained. This is a proper 90° setting.

Samples were prepared by the recrystallization from aqueous solution. In order to reduce the strain and imperfection in the crystal, the recrystallization is performed by evaporation at a very slow rate.

§ 4. Results and Discussion

The free induction decay time T_2^* and the spin lattice-relaxation time T_1 have been measured for both Br^{79} and Br^{81} in sodium bromate ($NaBrO_3$) at room temperatures. The measured values of T_2^* and T_1 which were reproducible within the error of $\pm 5\%$ are summarized in Table I, together with the ratios between both isotopes. For samples, two single crystals and a powdered specimen were used. Single crystals were prepared by repeated recrystallization and considered to be fairly perfect, whereas the powdered specimen was not so pure as the single crystals.

The free induction decay curves obtained for these samples were all well described by

Table I. Measured values of T_2^*, T_1 and their ratio.

		$T_2^*(10^{-5}$ sec)	$T_1(10^{-3}$ sec)	$\frac{T_2^*(Br^{81})}{T_2^*(Br^{79})}$	$\frac{T_1(Br^{81})}{T_1(Br^{79})}$
Single crystal No. 1	Br^{79}	10.2	2.1 (8°C)	0.96	1.4
	Br^{81}	9.8	3.0 (8°C)		
Single crystal No. 2	Br^{79}	8.4	2.2 (8°C)	0.98	1.4
	Br^{81}	8.2	3.1 (8°C)		
Powdered specimen	Br^{79}	5.7	2.1 (5°C)	1.1	1.5
	Br^{81}	6.3	3.1 (5°C)		

Gaussian curves of Eq. (5) within experimental errors. In Fig. 2 is shown an oscillographic display of a typical free induction decay curve, which is due to Br^{81} in single crystal No. 2. The experimental free induction decay

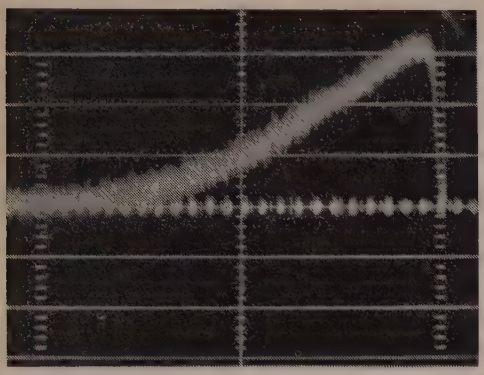

Fig. 2. Oscillographic display of the free induction signal due to Br^{81} in a single $NaBrO_3$ crystal (No. 2) at 150 Mc/sec. Separation between time markers is 10μ sec.

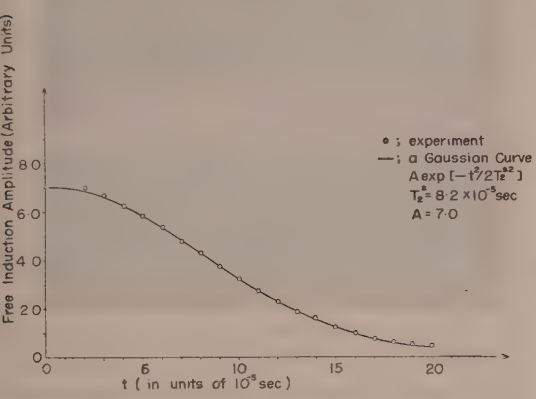

Fig. 3. Free induction decay curve for Br^{81} in a single $NaBrO_3$ crystal (No. 2).

curve was compared with a Gaussian curve as shown in Fig. 3. The values of T_2^* listed in Table I were obtained by adjusting so that the experimental decay curve could be represented by a Gaussian curve. Since the free induction signal could not be observed within the region from $t=t_w$ to about 20μ sec later because of the receiver saturation, there was no way to examine the shape of the free induction decay curve near $t=t_w$. However, if there were any deviations from a Gaussian curve in that region, they would not affect the principal features of the experimental decay curve. The Gussian shape of the free induction decay curve indicates the fact that the local field is essentially static, and the effects of the fluctuation of the local field and the spin-lattice relaxation on the free induction decay is not significant[4]. The insignificance of the spin-lattice relaxation is directly confirmed by the measurements of T_1 as shown latter on. Therefore, the mechanisms mainly responsible for the free induction decay are considered to be the static part of (1) the magnetic dipole-dipole interaction with neighboring nuclei, (2) the distribution of electric field gradients in the crystal due to strain, imperfection and temperature gradient, and (3) Zeeman effect caesed by the earth's magnetic field.

In order to estimate the contribution from (1), the author has calculated classically the root mean square local field parallel to Na–Br axis from both Na and Br neighbors. Such a calculation yielded $T_2^*=19.7\times10^{-5}$ sec for Br^{79} and 18.3×10^{-5} sec for Br^{81}, respectively, which are much longer than the observed values. It is expected that the remaining contribution to the decay is mostly due to the mechanism (2), since the contribution from (3) is small[4]. As shown in Table I, there are some changes in T_2^* with samples, which are considered principally caused by different dontributions by the mechanism (2), since they are the only contributions which are considerably affected by the process of recrystallization. The longest value of T_2^* was obtained for crystal No. 1, which is then the most perfect crystal among the used samples.

The corresponding line shape in the steady state measurement which is given by the Fourier transform of the free induction decay curve[4,16], is Gaussian i.e. $\propto$ exe $[-(\Delta\omega T_2^*)^2/2]$. Using the values of T_2^* for crystal No. 1, the calculated line widths between half maximum points are 3.7 kc/sec and 3.8 kc/sec for Br^{79} and Br^{81}, respectively. These values are consistent with those obtained by Koi for a most perfect crystal[16], using regenerative spectrometer. Koi concluded that the main contribution to the broadening for his most perfect crystal, should come from the mechanism (1), i.e. magnetic dipole-dipole interaction with neighboring nuclei. His argument was based on the circumstance that if the magnetic origin (1) is predominant, the broadening of the line for Br^{81} should be larger than that for Br^{79}, and the converse is true, if the elec-

tric origin (2) is predominant. Though the present measurement for crystal No. 1 is consistent with Koi's conclusion, the experimental accuracy is not sufficient to differentiate between the contribution by (1) and (2) unambiguously from the above reasoning alone. In order to examine the situation more precisely from another point of view, the author is performing a double resonance experiment, in which the changes in the free induction and echo signals for bromine nuclei are examined by the application of the continuous r-f field with resonance frequency of the sodium nuclei. The result will be published in the near future.

The spin echo signal which is like two free induction decay curves placed back-to-back[3], is so broad that the echo envelope decay time cannot be quantitatively measured for crystals whose T_2^*'s are relatively long. In order to make precise measurement on the echo envelope decay time, it is necessary either to apply the magnetic field or to make an artificial temperature gradient. Fig. 4 shows a typical spin echo signal in the presence of an artificial temperature gradient. Observed echo envelope decay time T_2' was relatively unaffected by the temperature gradient. The value of T_2' is of the order of 2×10^{-4} sec and much shorter than T_1. It indicates that the effect of the fluctuation of the local filed on the free induction decay is not completely absent. The measurement on spin echo will be reported more precisely in conjunction with the double resonance.

The measurement of T_1 is made by the application of two r-f pulses[2,6]. As the spacing τ between the two pulses is increased, the initial amplitude $y(\tau)$ of the free induction signal following the second pulse rises exponentially with time constant T_1 towards the initial amplitude y_0 of the free induction signal following the first pulse. Fig. 5 shows the variation of the initial amplitude of the free induction signal following the second pulse with the spacing τ, and Fig. 6 the linear relation between $\log[y_0-y(\tau)]$ and τ. The values of T_1 were estimated from the figure. Since these values were much longer than T_2^*, the effect of the spin-lattice relaxation on the free induction decay was not significant.

It is noted that the measured values of T_1 are almost equal for different samples, even when the T_2^*'s are apparently different. The ratio between both isotopes $T_1(Br^{81})/T_1(Br^{79})$ is

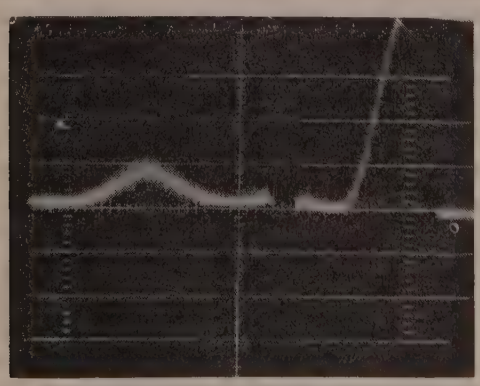

Fig. 4. Spin echo signal due to Br^{79} in a single $NaBrO_3$ crystal in the presence of an artificial temperature gradient. The sweep length is about 1.2 milliseconds.

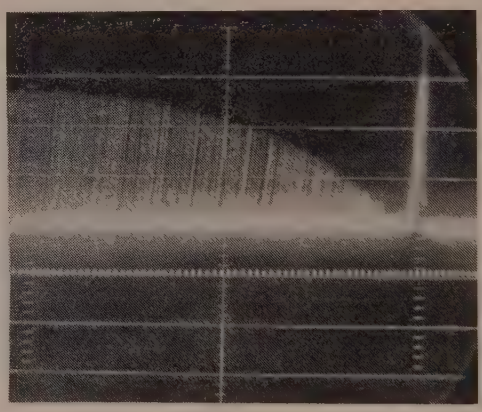

Fig. 5. Variation of the initial amplitude of free induction signal following a second pulse with the spacing from the first pulse. Signals are due to Br^{79} in a single $NaBrO_3$ crystal (No. 1). Separation between makers is 0.1 m/sec.

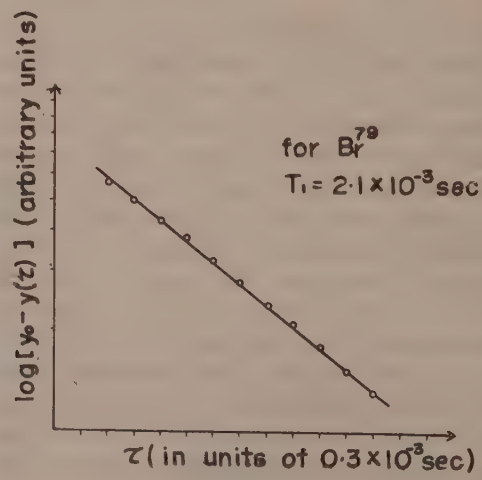

Fig. 6. Relation between $\log[y_0-y(\tau)]$ and τ.

so constant and almost equal to the ratio $^2(Br^{79})/Q^2(Br^{81})=1.44$. These facts show that e spin-lattice relaxation is insensitive to the homogeneity of the electric field gradient nd the principal mechanism for it is the uadrupole relaxation.

Acknowledgment

The author would like to thank Professor Takahashi for his encouragement and dis-ussion, and his thanks are also due to Mr. . Hirai and Mr. M. Sasaki for their assistance performing the experiment, and to Mr. M. abata for his help in numerical calculations.

References

1) See, for example, H. G. Dehmelt: Amer. J. Phys. **22** (1954) 110.
2) E. L. Hahn: Phys. Rev. **80** (1950) 580.
3) M. Boom, E. L. Hahn and B. Herzog: Phys. Rev. **97** (1955) 1699.
4) B. Herzog and E. L. Hahn: Phys. Rev. **103** (1956) 148.
5) W. G. Proctor and W. H. Tanttila: Phys. Rev. **101** (1956) 1757.
6) D. E. Woessner and P. Gutowsky: J. Chem. Phys. **27** (1957) 1072.
7) T. P. Das and H. K. Saha: Phys. Rev. **98** (1955) 516.
8) Waveforms, M. I. T. Radiation Laboratory Series, No. 19 (McGraw-Hill Book Company, Inc., New York, (1949))).
9) A. L. Bloom: Phys. Rev. **98** (1955) 1105.
10) A. L. Schawlow: J. Chem. Phys. **22** (1954) 1211.
11) J. Schwartz: R. S. I., **28** (1957) 780.
12) H. G. Dehmelt and H. Krüger: ZS. f. Phys. **129** (1951) 401.
13) H. Y. Carr: Thesis, Harvard University (1952) (unpublished).
14) Y. Koi, A. Tsujimura and T. Fuke: J. Chem. Phys. **23** (1955) 1346.
15) P. W. Anderson and P. R. Weiss: Rev. Modern Phys. **25** (1953) 269.
P. W. Anderson: J. Phys. Soc. Japan **9** (1954) 316.
R. Kubo and K. Tomita: J. Phys. Soc. Japan **9** (1954) 888.
16) Y. Koi: J. Phys. Soc. Japan **12** (1957) 49.
17) R. V. Pound: Phys. Rev. **79** (1950) 685.

JOURNAL OF THE PHYSICAL SOCIETY OF JAPAN Vol. 13, No. 8, AUGUST 1958

Zeeman Study on Nuclear Quadrupole Resonances* in AsI_3 and $AsI_3 \cdot 3S_8$

By Yoshihito ABE

Department of Physics, Tokyo University of Education
Otsuka, Tokyo

(Received April 14, 1958)

Principal axis systems and asymmetry parameter of the electric field gradient tensors were determined by studying Zeeman effect of nuclear quadrupole resonances of As^{75} and I^{127}. The iodine resonance in AsI_3 showed that there are three principal axis system swhose z axes form a trigonal pyramid having an apex angle of $91.7° \pm 2.5°$. The fact that this angle did not agree with the bond angle of $88°02'$ supports the mechanism of resonance switching of the bond. The arsenic resonance in AsI_3 has only one principal axis system whose z axis is along the trigonal symmetry axis of arsenic tri-iodide molecule. The asymmetry parameter obtained from Zeeman study was nearly zero.

The iodine resonance in $AsI_3 \cdot 3S_8$ also showed that there are three principal axis systems. This fact well agrees with the result from X-rays that the most possible crystal structure of $AsI_3 \cdot 3S_8$ is C_{3v}^1. Three z axes are parallel to the edge of a trigonal pyramid with an apex angle of $101.7° \pm 0.5°$ which is close to the bond angle $100° \pm 2°$ ($\angle$ I–As–I) of AsI_3 molecule in gaseous state. The electric field gradient tensor of arsenic resonance in $AsI_3 \cdot 3S_8$ was nearly axial symmetric about the trigonal symmetry axis of the molecule.

§ 1. Introduction

The pure quadrupole spectrum of arsenic tri-iodide was first studied by Kojima, Tsukada, Ogawa, Shimauchi and myself[1]. The isotope I^{127} has two resonance lines corresponding to the transitions of $m_z = \pm 1/2 \rightleftarrows 3/2$ and $m_z = \pm 3/2 \rightleftarrows \pm 5/2$. The frequencies of the lines were 206 Mc and 401 Mc at room temperature, which yielded the coupling constant of 1345 Mc and the electric field gradient asymmetry parameter of 14.5%[1]. These reseults were explained with the mechanism of resonance switching of the bond[2]. The structure of solid arsenic tri-iodide is that any given iodine atom has two nearest neighbors of arsenic atoms at the same distance of 2.99 A, one being molecular partner and the other belonging to the neighbor molecules and that there are no other neighbor atoms closer than 4.14 A. From this structure Kojima *et al*, proposed the mechanism that the covalent bond of the iodine atom is resonating between these two arsenic atoms with fractional importance of fifty percent. If the mechanism of this resonance switching is correct, the principal z axis of the electric field gradient tensor will be perpendicular to the bond. On the other hand, if it is not applicable, the principal z axis will be along the bond. The orientation of the z axis of the electric field gradient tensor can be determined by Zeeman study on pure quadrupole spectrum[3]. Zeeman study is also useful for the determination of crystal structure and for analysis of nature of the bond between the quadrupolar atom and its neighbors[4)~7)].

Recently, the isotope As^{75} in arsenic tri-iodide was studied by Ogawa[8]. The resonance frequency of it was 32 Mc at room temperature, since the spin number of the isotope is 3/2, the possible transition is $m_z = \pm 1/2 \rightleftarrows \pm 3/2$. Therefore, the asymmetry parameter of the electric field gradient tensor can not be determined without Zeeman study.

In the present experiment Zeeman studies have been carried out on the resonance lines of the isotopes I^{127} and As^{75} in a single crystal of arsenic tri-iodide, whose frequencies are 201 Mc and 32 Mc, respectively.

Similar study has been carried out on sulphur molecular addition compound of arsenic tri-iodide ($AsI_3 \cdot 3S_8$). The two resonance fre-

* A doctorial thesis submitted to Tokyo University of Education.

quencies of the isotope I^{127} in this compound corresponding to the transition $m_z = \pm 1/2 \rightleftarrows \pm 3/2$ and $m_z = \pm 3/2 \rightleftarrows \pm 5/2$ were measured by Robinson, Dehmelt and Gordy[9]. The frequencies were 224 Mc and 448 Mc at room temperature, which yielded that the electric field gradient tensor at the iodine nucleus is axial symmetric.

Arsenic resonance in this compound was also studied by Ogawa[8]. She reported that the isotope As^{75} has a single resonance frequency of 47.5 Mc at room temperature. The asymmetry parameter of the electric field gradient tensor is not yet obtained.

It is known from X-ray analysis that in a crystal of sulphur molecular addition compound of arsenic tri-iodide each arsenic tri-iodide molecules are isolated by neighboring six sulphur molecules, although the precise arrangement of atoms in the unit cell has not been obtained. In this case the direction of the z axis of the electric field gradient tensor will be different from the case of arsenic tri-iodide previously mentioned. The z axis can be determined by the aid of Zeeman effect.

In the present experiment Zeeman study has been applied to the resonance lines of 224 Mc of the isotope I^{127} and that of 47.5 Mc of the isotope As^{75} in a single crystal of sulphur molecular addition compound of arsenic tri-iodide.

§ 2. Experimental Procedure

Arsenic tri-iodide was prepared by the reaction between a solution of arsenic trioxide in concentrated hydrochloric acid and a solution of potassium iodide in water. The precipitation of arsenic tri-iodide was filtered off and dried. Then it was recrystallized from carbon disulphide by evapolating the solvent.

Single crystals of arsenic tri-iodide of about 50 gr. were prepared with the method of pointed bottom crucible[10]. The sample enclosed in a grass envelope, whose inside diameter is 23 mm, is slowly lowered from an oven maintained well above the melting temperature of the sample through a region having steep temperature gradient into a cold room which is cooled with a large water bath.

Sulphur molecular addition compound of arsenic tri-iodide was obtained from a solution of arsenic tri-iodide and sulphur in carbon disulphide. Single crystals of this compound were easily grown from this solution.

Two superregenerative detectors were prepared for the observation of the resonances of two isotopes. One used for the iodine resonance was the transmission line type[11] and the other used for the arsenic resonance was the ordinary type with LC tuned circuit[12]. Frequency modulations were applied for the oscillators with a vibrating condense. The detector out put was amplified and presented on an oscilloscope. In order to remove undesirable amplitude of modulation components, some filters were used.

A magnetic field for Zeeman studies was produced by Helmholz coils[11] which are arranged with mean separation of 7.5 cm. The Helmholz coils were mounted on a goniometer in which azimuthal traverse was available for complete 360°. The axis of Helmholz coils was in a horizontal plane, which contained the axis of the rotation of the sample.

The angle of the azimuthal traverse and of the rotation of crystal was read with a scale having the least count of 0.2°. The magnetic field used for the most experiments was about 100 gauss. Sometimes, however, 300 gauss was applied for the precise studies. The oscillograph display of the resonance of iodine in sulphur molecular addition compounds of arsenic tri-iodide are shown in Fig. 1, as examples. The photograph (a) in Fig. 1 shows the shape of resonance line at zero magnetic field. The photographs (b) and (c) showing the Zeeman patterns were taken when the magnetic field oriented to the direction B which is indicated in Fig. 4 and the strength of the field was 50 gauss and 350 gauss, respectively. In the field of 350 gauss the only central zerosplitting line, which will be mentioned later, remained in the oscillograph. This line changed sensitively by the rotation of the crystal as shown in Fig. 1 (c), (d) and (e). So that the direction of the magnetic field for zerosplitting can be determined accurately.

The directions of the magnetic field for the zerosplitting were measured and the loci of the directions were mapped on a sphere. From these loci the directions of the z axes of the electric field gradient tensor were demined.

After Zeeman studies the used crystal of arsenic tri-iodide was examined by X-rays.

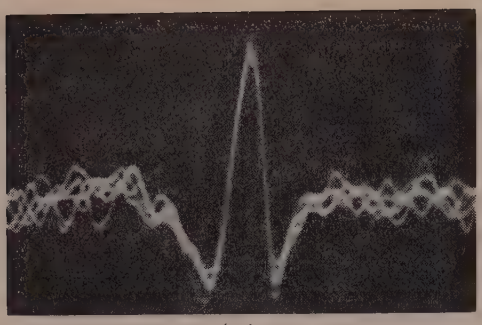

(a)

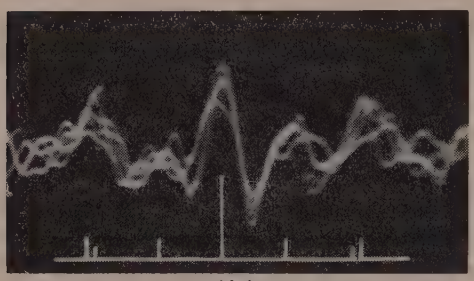

(b)

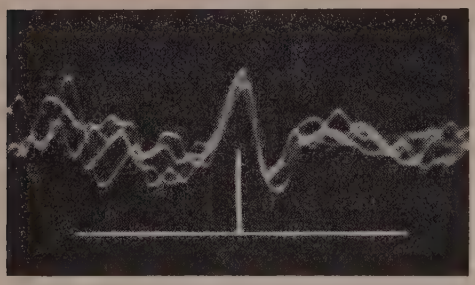

(c)

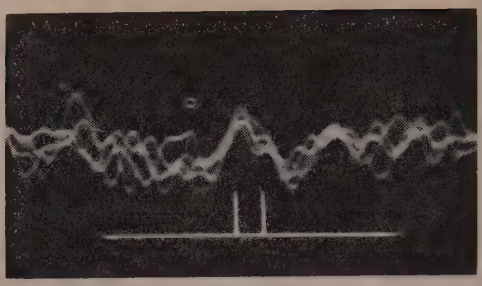

(d)

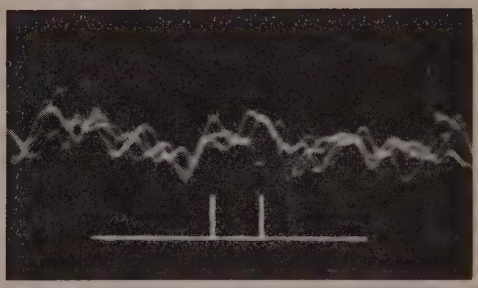

(e)

Fig. 1. Ionine resonance in $AsI_3 \cdot 3S_8$.

(a) Absorption line in the zero field.
(b) The Zeeman pattern in the field of 50 gauss at the orientation B indicated in Fig. 4.
(c) The Zeeman pattern in the field of 350 gauss at the orientation B.
(d) The Zeeman pattern in the field of 350 gauss at the point where Φ is 1° less than the orientation B.
(e) The Zeeman pattern at the point where Φ is 2° less than the orientation B.

§ 3. Method of Analysis

In a static magnetic field the twofold degeneracy of each energy levels of the pure quadrupole interaction is removed by Zeeman effect and a single resonance line, corresponding to the transition $m_z=\pm 1/2 \rightleftarrows \pm 3/2$ splits into four lines. The frequencies of these lines are given by the following equations[11),13),14)]:

$$\nu_{\mathrm{I\,II}}=\nu_0 \pm 1/2 S \qquad (1)$$

$$\nu_{\mathrm{III\,IV}}=\nu_0 \pm 1/2\, s \qquad (2)$$

where ν_0 is the frequency of the unsplit line and S and s are the separation frequencies of outer pair and inner pair, respectively. These values for nuclear spin $I=3/2$ are expressed as follows:

$$\nu_0=\frac{eQq_{zz}}{2h}\left(1+\frac{1}{3}\eta^2\right)^{1/2} \qquad (3)$$

$$\left.\begin{matrix} S \\ s \end{matrix}\right\}=\frac{2\mu}{3h}H\left\{[9\cos^2\theta+\eta^2(\sin^2\theta-2\cos^2\theta)]^{1/2}\right.$$

$$\pm\left[4\sin^2\theta+\cos^2\theta-4\eta\sin^2\theta\cos 2\phi+\frac{\eta^2}{3}(\sin^2\theta-2\cos^2\theta)\right]^{1/2}\Bigg\}. \qquad (4)$$

Those for $I=5/2$ are expressed as follows:

$$\nu_0=\frac{3eQq_{zz}}{20h}\left(1+\frac{59}{54}\eta^2\right) \qquad (5)$$

$$\left.\begin{matrix} S \\ s \end{matrix}\right\}=\frac{4\mu}{5h}H\left\{\left[\frac{9}{4}\cos^2\theta+\eta^2(4\sin^2\theta-3\cos^2\theta)\right]^{1/2}\right.$$

$$\pm\left[\frac{1}{4}\cos^2\theta+\frac{9}{4}\sin^2\theta-6\eta\sin^2\theta\cos 2\phi+\eta^2\left(\frac{22}{9}\sin^2\theta-\frac{76}{81}\cos^2\theta\right)\right]^{1/2}\Bigg\} \qquad (6)$$

The asymmetry parameter η of the electric field gradient tensor is defined by the following equation:

$$\eta=\frac{q_{xx}-q_{yy}}{q_{zz}} \qquad (7)$$

where q_{xx}, q_{yy} and q_{zz} are components of the

electric field gradient tensor which are referred to the principal axis system. These components are in the following relation: $|q_{xx}| \leqslant |q_{yy}| \leqslant |q_{zz}|$. In the equations θ and ϕ designate the orientation of the static magnetic field referred to the principal axis system of the electric field gradient tensor and μ is the magnetic moment of nucleus. The equations for the nuclear spin of $I=5/2$ are calculated using the theory of 1st order Zeeman effect*.

The inner pair coalesces in a single line when the magnetic field orients along some special directions θ, ϕ which are defined by the following equations for nuclear spin $I=3/2$:

$$\sin^2\theta = \frac{2}{3-\eta\cos 2\phi} \tag{8}$$

and for $I=5/2$:

$$\sin^2\theta = \frac{8-(668/81\ \eta^2}{17-24\eta\cos 2\phi-(1172/81)\eta^2}\,. \tag{9}$$

The directions satisfying these relation make an elliptic cone whose axis is the z axis. This cone is called as zerosplitting cone and represented on a sphere by an elliptic locus. Correponding to each principal axis systems, one elliptic locus is obtained. The directions of the z axis can be determined as the center of the locus. When the electric field gradient tensor has the axial symmetry, the direction of the z axis can be simply determined by averaging the maximum and minimum angles of the zerosplitting direction[4]. In the usual cases where the electric field gradient tensor departs from the axial symmetry such simple determination is not available except in some special cases where the $x-z$ plane or the $y-z$ plane of the field gradient tensor contains the rotational axis of crystal. In this case the direction of the z axis can be determined by the method of mapping the zerosplitting loci. The asymmetry parameter η can be also calculated by the following equations: the equation for nuclear spin $I=3/2$ is

$$\eta = \frac{3(\sin^2\theta_{\max}-\sin^2\theta_{\min})}{\sin^2\theta_{\max}+\sin^2\theta_{\min}} \tag{10}$$

and the equation for $I=5/2$ is

$$\eta = \frac{17(\sin^2\theta_{\max}-\sin^2\theta_{\min})}{24(\sin^2\theta_{\max}+\sin^2\theta_{\min})}\,. \tag{11}$$

The equation for the nuclear spin of $I=5/2$ is obtained by neglecting the small terms of the equation (9) which contain the factor of η^2. In the cases where the nuclear spins are greater than 5/2, η can be obtained accurately from the measurement of resonance frequencies.

The angle ξ between two directions Θ_1, Φ_1 and Θ_2, Φ_2 is expressed by the following equation:

$$\cos\xi = \sin\Theta_1\sin\Theta_2\cos(\Phi_1-\Phi_2) + \cos\Theta_1\cos\Theta_2\,. \tag{12}$$

§ 4. Results and Analysis

a) *Arsenic Tri-iodide*

i) *Iodine* By observing the Zeeman patterns on the oscilloscope the zerosplitting loci were obtained. The measured results for the isotope I^{127} are shown in Fig. 2, where closed loci show the zerosplitting loci for each z axes. When it is plotted on a sphere, the zerosplitting cone produces an elliptic locus. Since the loci inF ig. 2 are reproduced on a plane, the loci are deformed from ellipses. These deformed loci, however, clearly correspond to the elliptic contour on a spherical coordinate system. Three directions of the z axes were obtained. The coordinates of the z axes are given in Table I, where the directions in prime system correspond to the negative directions of the z axis. The experimental inaccuracy mainly comes from the measurement of rather weak absorption of iodine resonance, having half maximum width of about 26 kc. From the Zeeman study it was found that the zerosplitting loci show trigonal symmetry and the symmetry axis has the coordinates of ($\Theta=75°\pm1°$, $\Phi=82°\pm1°$) and ($\Theta'=105°\pm1°$, $\Phi'=262°\pm1°$). Using the equation (12) and the values given in Table I, the angles between each z axes in both systems were obtained. The results are listed in Table II with the angles between each z axes and the trigonal symmetry axis. The experimental error is estimated from the inaccuracy of the measurement of the angles Θ and Φ, being $\pm1°$.

ii) *Arsenic* The measured zerosplitting loci of the arsenic resonance are shown in Fig. 3. The coordinates of the z axis are given in Table III with those of the trigonal symmetry axis mentioned before. Since the resonance line of As^{75} was weaker than the resonance

* The paper reported by Bersohn has some misprints. We have recalculated the equations for the cases of spins 3/2 and 5/2.

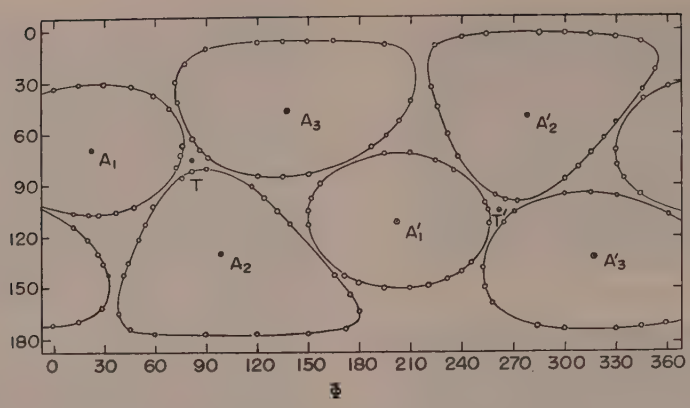

Fig. 2. The zerosplitting loci for I^{127} in AsI_3. Θ and Φ are polar coordinates specifying the direction of magnetic field for the zerosplitting with respect to the laboratory system fixed to the crystal. $A_1, \cdots$ represent the positive direction and $A_1' \cdots$ do the negative direction of the z axes. T and T' represent the direction of trigonal symmetry axis of the loci.

Table I. Coordinates of the z axes.

	Θ	Φ
A_1	$68.2° \pm 1°$	$23.0° \pm 1°$
A_2	$129.7° \pm 1°$	$98.0° \pm 1°$
A^3	$46.0° \pm 1°$	$139.0° \pm 1°$
A_1'	$111.2° \pm 1°$	$204.0° \pm 1°$
A_2'	$50.5° \pm 1°$	$277.0° \pm 1°$
A_3'	$134.0° \pm 1°$	$318.0° \pm 1°$

Table II. Angles between the z axes and between the z axes and the trigonal symmetry axis.

Angles between the z axis		Angles between the z axes and the trigonal symmetry axis	
$A_1 A_2$	$93.2° \pm 2.5°$	$T A_1$	$56.7° \pm 2.5°$
$A_2 A_3$	$91.5° \pm 2.5°$	$T A_2$	$56.7° \pm 2.5°$
$A_3 A_1$	$91.2° \pm 2.5°$	$T A_3$	$56.1° \pm 2.5°$
$A_1' A_2'$	$91.1° \pm 2.5°$	$T' A_1'$	$56.1° \pm 2.5°$
$A_2' A_3'$	$91.2° \pm 2.5°$	$T' A_2'$	$56.3° \pm 2.5°$
$A_3' A_1'$	$91.5° \pm 2.5°$	$T' A_3'$	$56.4° \pm 2.5°$
Average	$91.7° \pm 2.5°$	Average	$56.4° \pm 2.5°$

line of I^{127}, the experimental error was larger than that of the iodine resonance, though it was slightly reduced by the facts that the Zeeman pattern is simple and the locus is almost circular. Only one z axis was obtained in arsenic resonance and the orientation was approximately parallel o the axis of trigonal symmetry of the zerosplitting loci in iodine resonance.

The asymmetry parameter η is probably zero. The upper limit of η was estimated by

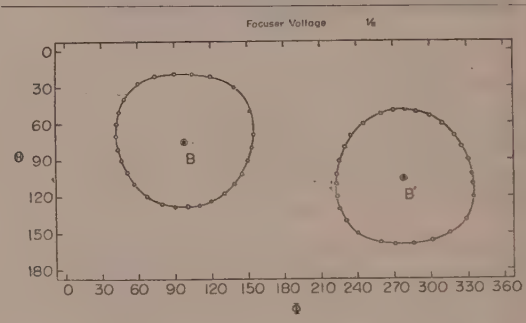

Fig. 3. The zerosplitting loci of arsenic resonance in AsI_3. The coordinates Θ and Φ are same as before.

Table III. Coordinates of trigonal symmetry axis and the z axis of arsenic resonance.

	Θ	Φ
T	$75° \pm 1°$	$82° \pm 1°$
T'	$105° \pm 1°$	$262° \pm 1°$
B	$74° \pm 2°$	$82° \pm 2°$
B'	$105° \pm 2°$	$263° \pm 2°$

the aid of the equation (10) to be less than 0.15. The rather large limits has its origin in the large experimental error.

b) *Sulphur Molecular Addition Compound of Arsenic Tri-iodine*

i) *Iodine* The measured zerosplitting loci of the iodine resonance are shown in Fig. 4. Since the iodine resonance in this compound was rather sharp, Zeeman studies were possible with a small crystal of about 8 gr. Although three different directions of the z axes were obtained similarly to the case in

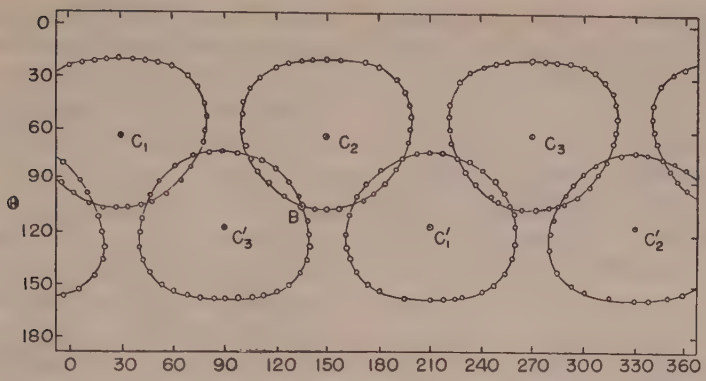

Fig. 4. The zerosplitting loci for I^{127} in $AsI_3 \cdot 3S_8$, Θ and Φ are the polar coordinates fixed to the crystal, as before. Rotational axis was parallel to the growing direction of crystal. $C_1, \cdots, C_1', \cdots$, represent the positive and the negative directions of the z axes.

arsenic tri-iodide, the pattern of zerosplitting loci was different from the pattern of arsenic tri-iodide in that the loci were crossing mutually. This indicates, as shown later, that the angle between the z axes is larger than the angle in the case of arsenic tri-iodide. The measured coordinates of the z axes are listed in Table IV. Since the iodine isotope in this compound has the electric field gradient tensor of axial symmetry, the orientation of the z axes was determined by the simple method, i.e. the coordinates Θ and Φ of the z axis were obtained by averaging the maximum angle and the minimum azimuthal angle of the zerosplitting direction and those of the latitude angles respectively. The rotational axis of the crystal was along the direction of the crystallographic c axis which seemed by inspection to be in accord with the growing direction of the crystal. Angles between the z axes were obtained from the data given in Table IV by using the equation (12). The results are listed in Table V with the angles between the crystallographic c axis and each directions of the z axes. The experimental error estimated from the inaccuracy of the measurement of Θ and Φ was $\pm 0.5°$.

Table IV. Coordinates of the z axes of iodine resonance in $AsI_3 \cdot 3S_8$.

	Θ	Φ
C_1	$63.7° \pm 0.2°$	$29.8° \pm 0.2°$
C_2	$63.6° \pm 0.2°$	$149.8° \pm 0.2°$
C_3	$63.6° \pm 0.2°$	$270.0° \pm 0.2°$
C_1'	$116.4° \pm 0.2°$	$209.8° \pm 0.2°$
C_2'	$116.4° \pm 0.2°$	$329.9° \pm 0.2°$
C_3'	$116.5° \pm 0.2°$	$90.0° \pm 0.2°$

Table V. Obtained angles in $AsI_3 \cdot 3S_8$.

Angles between the z axes		Angles between the crystallographic c axis and the z axes	
$C_1 C_2$	$101.8° \pm 0.5°$	$c\ C_1$	$63.7° \pm 0.2°$
$C_2 C_3$	$101.9° \pm 0.5°$	$c\ C_2$	$63.6° \pm 0.2°$
$C_3 C_1$	$101.7° \pm 0.5°$	$c\ C_3$	$63.6° \pm 0.2°$
$C_1' C_2'$	$101.8° \pm 0.5°$	$c' C_1'$	$63.6° \pm 0.2°$
$C_2' C_3'$	$101.7° \pm 0.5°$	$c' C_2'$	$63.6° \pm 0.2°$
$C_3' C_1'$	$101.5° \pm 0.5°$	$c' C_3'$	$63.5° \pm 0.2°$
Average	$101.7° \pm 0.5°$	Average	$63.6° \pm 0.2°$

ii) *Arsenic* The results of arsenic resonance in this compound are shown in Fig. 5. The accuracy of the measurement was reduced by the weakness of the arsenic resonance. Arsenic had only one z axis, whose coordinates are expressed by $\Theta = 121° \pm 2°$, $\Phi = 62° \pm 2°$ and $\Theta' = 59° \pm 2°$, $\Phi' = 242.5° \pm 2°$. In the present

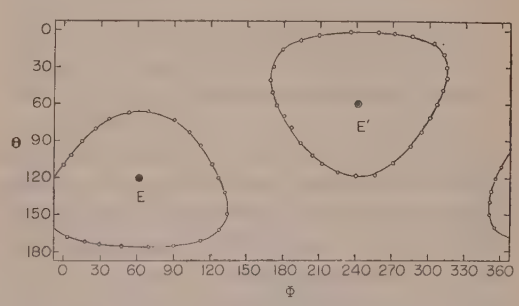

Fig. 5. The zerosplitting loci of the arsenic resonance in $AsI_3 \cdot 3S_8$. In this case the rotational axis was oriented about 60° with respect to the growing direction of crystal. Θ and Φ are same as before.

case the rotational axis of the crystal was different from the axis in the case of iodine resonance and oriented about 60° from the crystallographic c axis for the sake of convenience of experiment. The zerosplitting loci were approximately circular. Owing to the inaccuracy of the measurement of the direction of magnetic field the asymmetry parameter was determined in the limits of ± 0.15.

§ 5. Discussion

A) *Arsenic Tri-iodide*

The crystal structure of arsenic tri-iodide is well known[15]. A typical arrangement of atoms in the crystal is shown in Fig. 6. Any

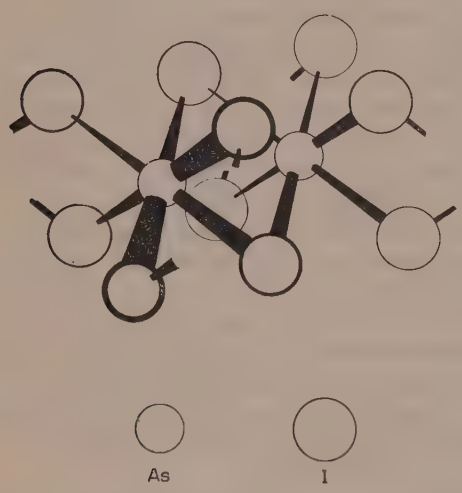

Fig. 6. Typical arrangement of atoms in a crystal of arsenic tri-iodide. Bond angle $\angle$I−As−I $=88°02'$. Bond distance As−I=2.99 A.

given iodine atom has two arsenic atoms as the nearest neighbors and an arsenic atom is neighboring six iodine atoms. Then arsenic tri-iodide forms a layerlike macromolecule. From the crystal structure the bond angle $\angle$I–As–I is estimated as $\gamma=88°02'$ for each of three angles.

To account for the observed values of the pure quadrupole resonance is arsenic tri-iodide two alternative assumptions may be proposed: 1) Simply the solid arsenic tri-iodide csnsist of isolated molecules of AsI_3. 2) The resonance switching of the bond takes place.

According to the assumption 1, the z axis will be along the bond and the angle between the z axes will be 88°02′. On the otherhand, the assumption 2 yields that the covalent bond of the iodine atom resonantes between the two nearest arsenic atoms, so the direction of the principal axis will be different from

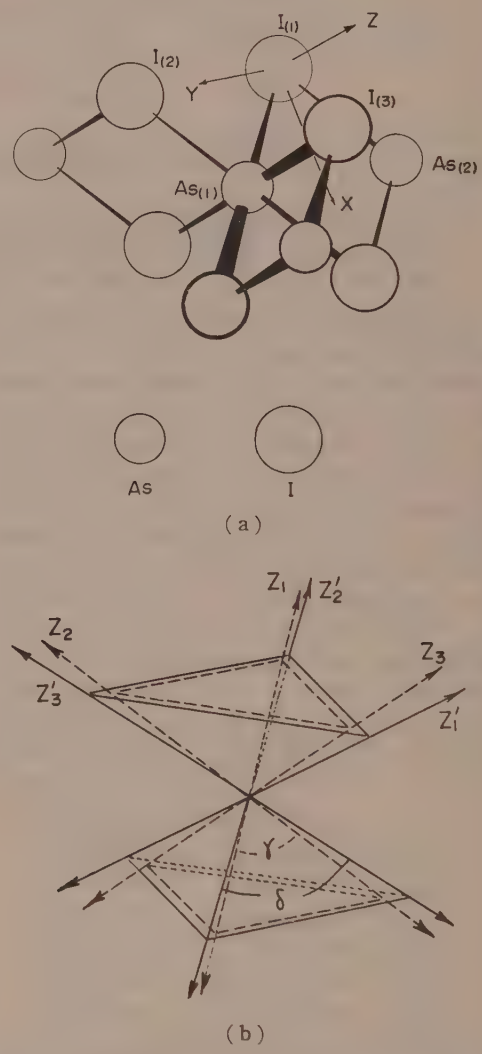

Fig. 7. (a) The direction of the principal axes. If the covalent bond of iodine $I_{(1)}$ resonates between two arsenic atoms $As_{(1)}$ and $As_{(2)}$. the principal axes of the field gradient tensor are as follows:
The x axis is the inner bisector of the angle $\angle As_{(1)}-I_{(1)}-As_{(2)}$ and the z axis is the normal to the plane of $As_{(1)}-I_{(1)}-As_{(2)}$.
(b) Comparison of the principal axis system. Dashed lines show the case according to the assumption 1 and solid lines the case obtained from the assumption 2. $Z_1,\cdots$, $Z_1',\cdots$, indicate the directions of the z axes at nucleus $I_{(1)}$ in in the case of assumption 1 and 2, respectively.

the bonding direction and take such a direction as shown in Fig. 7. Fig. 7 (a) shows that the z axis for the nucleus $I_{(1)}$ is perpendicular to the $As_{(1)}$–$I_{(1)}$ bond. However, its direction is very close to the bonding direction of $As_{(1)}$–$I_{(3)}$. In Fig. 7 (b) it is found that three z axes orient parallel to the edges of a trigonal pyramid. The directions of three bonds are also make another trigonal pyramid. If the apex angles of these two trigonal pyramid are denoted by δ and γ, the relation between these apex angle is expressed by the following equation:

$$\delta = 2\cos^{-1}\frac{1}{2}\sec\frac{\gamma}{2}\,. \qquad (13)$$

Putting 88°02′ for the bond angle γ, δ is obtained as 91°54′. This value well agrees with the average value of 91.7°±2.5° obtained from the experiment.

The difference between the zerosplitting loci based on the alternative assumptions is easily obtained with the help of spherical trigonometry. The obtained difference is shown in Fig. 8, where the trigonal symmetry

Fig. 8. Comparison of the zerosplitting loci based on the alternative assumptions. Dashed curves show the loci according to the assumption 1 and the solid ones the case obtained from the assumption 2. The trigonal symmetry axis of the molecule is taken as the origin of the coordinates. Points represent the measured direction of the magnetic field for the zerosplitting.

axis of the molecule is taken as the origin of the coordinates. Fig. 8 shows that there is no crossing of the loci in the case of the assumption 2, whereas mutually cross takes place in the case of assumption 1. Since the experiment indicated that there are no crossing of the loci near about the trigonal symmetry axis shown in Fig. 2, the assumption 2 is preferable.

The crystal structure indicates that an arsenic tri-iodide molecule has at trigonal symmetry axis parallel to the crystallographic c axis. So it is reasonable to assume that the arsenic has the axial symmetrical tensor of the electric field gradient whose principal z axis orients along the trigonal symmetry axis of arsenic tri-iodide molecule. As mentioned in the last section the arsenic resonance in arsenic tri-iodide showed that there is only one z axis and its direction agreed with the trigonal symmetry axis of the zerosplitting loci which were obtained from the iodine resonance. Although the measured asymmetry parameter has the error of ±0.15, the electric field gradient tensor at the arsenic nucleus in arsenic tri-iodide seems to be axial symmetric.

From the analysis of the Laue pattern the trigonal symmetry axis mentioned before was determined to be parallel to the crystallographic c axis. The growing direction of the crystal* obtained from the same analysis well agreed with the result of the Zeeman study.

B) *Sulphur Molecular Addition Compound of Arsenic Tri-iodide*

The crystal structure of this compound is shown in Fig. 9[16]. Any given arsenic tri-iodide is surrounded by six sulphur molecules in a unit cell and is isolated completely from the other arsenic tri-iodide molecules. The bond angle and the bond distance is not yet given in the literature. The Zeeman study indicated that the iodine resonance has only three different z axes. Then, arsenic tri-iodide molecules in sulphur molecular addition compound of arsenic tri-iodide make same trigonal pyramidal form, which oriented in one direction on a crystallographic c plane. There are no up and down of apexes with respect to the c plane and total arrangement is completed by the simple translation only. Since iodine in this compound has the axial symmetric field gradient, it is resonable to assume that the bond angle equal to the angle

* In the present case the crystal has been grown along the direction $[2\bar{1}0]$ in the term of hexagonal Bravais-Miller indices.

between the z axes of the electric field gradient tensor. Thus the bond angle ∠I–As–I is determined as 101.7°±0.5°.

Fractional importance of ionic bond character β can be obtained from the following equation[17]:

$$U_p=(1-\alpha)(1-\beta) \tag{14}$$

where α is the amount of s-hybridization of the P_σ bond and U_p is the numbers of unbalanced p-electron of the resonance atom which is obtained from the observed frequency and the atomic measurments. Introducing the value $\alpha=0.15$[18], $U_p=1493/2292=0.6514$, β

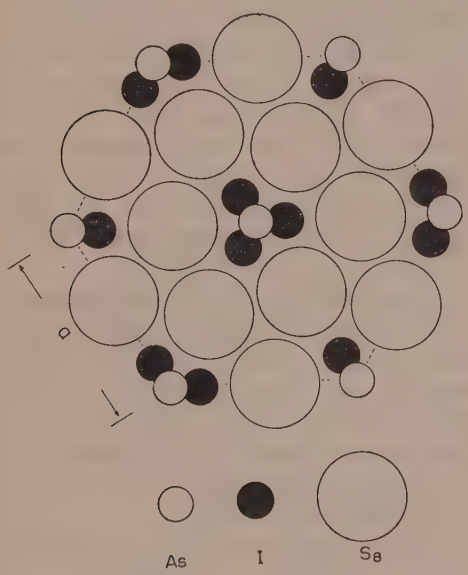

Fig. 9. Arrangement of the atoms in a unit cell of the crystal of $AsI_3 \cdot 3S_8$.
$a=14.2$ A $c=4.48$ A.

is obtained as 23.7%. Then, the bond distance As–I can be determined by the aid of Pauling's formula with Schomaker-Stevenson correction for ionic character[17]. Introducing the single covalent radii for the iodine atom and the arsenic atom, the bond distance of 2.51 A is obtained. The distance between the iodine atom and the nearest sulphur atom, being calculated as 3.28 A, is greater than the sum of the single covalent radii of the iodine atom and the sulphur atom 2.37 A and smaller than the sum of the van der Waal's radii of the atoms, 4.00 A. In this estimation the position of the sulphur atom was so assumed that the distance was minimum taking into account the known structure of sulphur molecular addition compound of arsenic tri-iodide and sulphur molecule[19], which forms puckered rings with $S-S$ distance of 2.12 A and the bond angle of 105°. Therefore, the interaction between iodine atom and sulphur molecule seems to be fairly weak one.

From the consideration of the crystal structure obtained above it can be assumed that the arsenic tri-iodide in sulphur molecular addition compound of arsenic tri-iodide has a trigonal symmetry axis oriented parallel to the crystallographic c axis. Then the similar discussion to the case of arsenic tri-iodide is possible about the arsenic resonance in sulphur molecular addition compound of arsenic tri-iodide. It was obtained from Zeeman study that arsenic has only one z axis oriented parallel to the crystallograpeic c axis and η is less than 0.15. Although η was not determined accurately, it should be zero from the crystallographic consideration.

§ 6. Summary and Conclusion

The structure parameter of molecule of solid arsenic triiodide, sulphur molecular addition compound of arsenic triiodide and free molecule of arsenic triiodide are summarized in Table VI. The angles between z axes in AsI_3 and $AsI_3 \cdot 3S_8$ are those determined by the present Zeeman studies. The bond angle of $AsI_3 \cdot 3S_8$ is assumed to be equal to the angle between the z axes. The bond distance in $AsI_3 \cdot 3S_8$ is estimated from the quadrupole data. The asymmetry parameter are obtained by the present Zeeman studies except those in parentheses which are obtained from the measurement of resonance frequencies. Molecular structure of arsenic tri-iodide in gaseous state was studied by electron diffraction method and found to be a trigonal pyramidal form[20].

In Table VI it must be noticed that the molecular structure of arsenic tri-iodide in solid state is considerably different from the structure in gaseous state, though the structure in sulphur molecular addition compound of arsenic tri-iodide is near to the one in gaseous state. H. Hertel reported that the molecular structure of arsenic tri-iodide in sulphur molecular addition compound seems to be somewhat compressed form[16]. This agrees with the shortening of the distance As–I. The bond angle ∠I–As–I is close to the angle in gaseous state. The bond distance As–I of

Table VI. Constants of molecular structure of arsenic tri-iodide on three states: Solid, $AsI_3 \cdot 3S_8$ and Gaseous State*.

	Solid	$AsI_3 \cdot 3S_8$	Gaseous State
Bond angle ∠I–As–I	88.0°	101.7°±0.5°	100°±2°
Angle between the z axes	91.7°±2.5°	101.7°±0.5°	
Bond distance As–I	2.99 A	2.51 A	2.58 A
Distance between I and the nearest neighbor atom	2.99 A (As)	3.28 A (S)	
η (I^{127})	0.14±0.06 (0.145)	≈0±0.01 (0)	
Distance between As and the nearest neighbor atom	2.99 A (I)	4.05 A (I)	
η (As^{75})	≈0±0.15	≈0±0.15	

* Values in gaseous state is obtained by electron diffraction method[20].

arsenic tri-iodide in solid state is greater than the one in gaseous state. This shows that there are more strong intermolecular interactions among arsenic tri-iodide molecules in solid state than sulphur molecular addition compound of arsenic tri-iodide. These facts support the conclusion that the resonance switching of the bond takes place in AsI_3 and does not in $AsI_3 \cdot 3S_8$.

Acknowledgement

The author wishes to express his hearty thanks to Professor Shoji Kojima for his guidance and encouragement throughout this work. For the study of X-rays, the author wishes to acknowledge the help and encouragement given by Professor Mitsuo Miwa and Dr. Shoichi Annaka. He is also grateful to Dr. Shizuko Ogawa and other members of the laboratory for their valuable discuassions and helps on experiments.

References

1) S. Kojima, K. Tsukada, S. Ogawa, A. Shimauchi and Y. Abe: J. Phys. Soc. Japan **9** (1954) 805.
2) C. H. Townes and B. P. Dailey: J. Chem. Phys. **20** (1952) 35.
3) C. Dean: Phys. Rev. **96** (1954) 1053.
4) K. Shimomura: J. Phys. Soc. Japan **12** (1957) 657.
5) K. Shimomura: J. Phys. Soc. Japan **12** (1957) 1356.
6) Harlan C. Meal: J. Chem. Phys. **24** (1956) 1011.
7) Ralph. Livingston and H. Zeldes: J. Chem. Phys. **26** (1957) 551.
8) S. Ogawa: J. Phys. Soc. Japan **13** (1958) 618.
9) H. Robinson, H. G. Dehmelt and W. Gordy: J. Chem. Phys. **22** (1954) 511.
10) S. Kojima, K. Tsukada and Y. Hinaga: J. Phys. Soc. Japan **10** (1955) 498.
11) S. Kojima, K. Tsukada, A. Shimauchi and Y. Hinaga: J. Phys. Soc. Japan **9** (1954) 795.
12) S. Ogawa: J. Phys. Soc. Japan **12** (1957) 1105.
13) K. Tsukada: J. Phys. Soc. Japan **9** (1957) 956.
14) R. Bersohn: J. Chem. Phys. **20** (1952) 1505.
15) R. W. G. Wyckoff: "*Crystal Structures*" Interscience Publishers Inc., New York (1948).
16) H. Hertel: Z. Physik Chem. **15** (1932) 51.
17) W. Gordy, W. V. Smith and R. F. Trambarulo: "*Microwave Spectroscopy*" John Wiley and Sons Inc., New York (1953).
18) C. H. Townes and A. L. Schawlow: "*Microwave Spectroscopy*" McGraw Hill. Book. Co., New York (1955).
19) B. F. Warren and S. T. Burwell: J. Chem. Phys. **3** (1935) 6.
20) A. H. Gregg, G. C. Hampson, G. I. Jenkins, P. L. F. Jones and L. F. Sutton: Trans. Farad. Soc. **33** (1937) 852, 868.

JOURNAL OF THE PHYSICAL SOCIETY OF JAPAN Vol 13, No. 8, AUGUST, 1958

Elementary Problems on the Configurations of a Linear High Polymer

By Kazuo NAGAI*

Department of Textile Chemistry, Kyoto University Kyoto, Japan

(Received April 28, 1958)

The studies on the configurations of a linear high polymer have based upon the problems of the random flights which have been discussed so far mainly in the form of the Fourier transformation. In this paper these problems being treated by the operational method, the general expressions for the distributions of the end-to-end distance, of the distance between the i-th segment and the centre of gravity and of the segment density around the centre of gravity are obtained. It can be seen that it is rather preferable for the random flights of which each displacement has finite length to use the operational method. This method can be applied to the general random flights problems by adopting the discontinuous integral in the form of the Laplace transformation.

§ 1. Introduction

In order to understand the physical properties of a high polymeric substance, it is very important to have knowledge of the configurations of each polymer chain of which the substance consists. Therefore, as soon as the concept that a high polymer consisted of the linear or branched sequences of the same monomer units was established, this problem began to be investigated by many authors. At present, the solution has been obtained in considerably satisfactory form.

Considering the fact that a linear high polymer consists of a number of the same units and is considerably flexible in the jointing points, the problem is equivalent in the first approximation to the random flights problem which was first studied by Lord Rayleigh[1]. At present, the configurations of a linear high polymer are approximated by the Gaussian distribution which can be obtained from the random flights with fixed bond length under suitable approximations. The more refined treatments tend to the calculations of the correction terms for the Gaussian distribution.

The well-know Gaussian distribution has the following form: the probability that the end-to-end distance of the random flights chain with fixed bond length b_0 has a value in the range r to $r+dr$ is equal to

$$W(r)=(3/2\pi nb_0^2)^{3/2}\exp\{-3r^2/2nb_0^2\}\cdot 4\pi r^2 dr$$

where n is the numbers of the bonds.

In the derivation of the above equation, the two assumptions i.e. (i) $r \ll nb_0$ and (ii) $n \gg 1$ have been made. For usual purposes, the above equation with the effective bond length b instead of b_0 successfully can be applied to the real polymer chain. But, when the chain configurations deviate extremely from its equilibrium one, for example, in the cases of extreme extension of rubber, the deformations under the large shearing stress in solution and crystallization, the above equation ceases to be correct.

In this paper, the problem is solved without any assumption and a useful method for treating the analogous problems is shown. Of course, the several authors have treated the same problem already. First, W. Kuhn, F. Grün[2] and H. M. James, E. Guth[3] obtained the solution containing the inverse Langevin function. Second, L. R. G. Treloar[4] and M. C. Wang and E. Guth[5] obtained the rigorous expression. Following the second method of M. C. Wang and E. Guth[5], the general random flights problem is treated by the operational method, more or less skilfully.

§ 2. End-to-End Distance of a General Random Flights Chain

The problem is set up as follows. The probability that the length of the k-th displacement of the random flights chain with n displacements occurs in the range η to $\eta+d\eta$

* Present address: The Osaka Industrial Research Institute, Daini-Nishi 2-Chome Oyodoku, Osaka, Japan.

is assumed to be $\rho_k(\eta)4\pi\eta^2 d\eta$. Obviously, $\rho_k(\eta)$ is equal to the density distribution of of the one end at the distance η from the other end of the k-th displacement. $\rho_k(\eta)$ is assumed to be normalized as follows:

$$\int_0^\infty \rho_k(\rho)4\pi\eta^2 d\eta = 1 . \qquad (k=1, \cdots, n) \qquad (1)$$

Then the probability that the end-to-end distance of the resultant random flights chain with n displacements occurs in the range r to $r+dr$ is defined by $W_n(r)dr$. As a result of Eq. (1)

$$\int_0^\infty W_n(r)dr = 1 . \qquad (2)$$

We require the relation between $W_n(r)$ and $\rho_k(\eta)$, etc.

In this paper, fixing our eyes upon the fact that the random flight chain with k displacements results from that with $k-1$ displacements after one additional displacement, we derive the recurrence formula relating $W_k(r)$ and $W_{k-1}(r)$ and solve this by means of the operational mothod. The probability that, when (the end-to-end distance of) the random flights chain with $k-1$ displacements occurs in the range ξ to $\xi+d\xi$ and the k-th displacement occurs in the range η to $\eta+d\eta$, the random flights chain with k displacements occurs in the range r to $r+dr$, integrated over all possible values of ξ and η fixing r, must be the probability that the random flights chain with k displacements occurs in the range r to $r+dr$ irrespective of the situations of that with $k-1$ displacements and the k-th displacement i.e. $W_k(r)dr$.

In Fig. 1 A, B and C are assumed to be

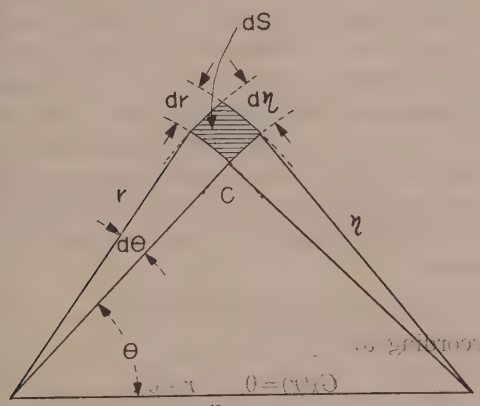

Fig. 1.

the starting point of the first displacement, the end points of the $(k-1)$ and k-th displacements respectively. Then the probability that the end-to-end distance of the random flights chain with $k-1$ displacements being ξ, that with k displacements occurs in the range r to $r+dr$ and the length of the k-th displacement η to $\eta+d\eta$, is equal to the volume enclosed between two spherical shells, the one having its centre at A and the radii r and $r+dr$ and the other having its centre at B and the radii η and $\eta+d\eta$, multiplied by $\rho_k(\eta)d\eta$. The co-volume of two spherical shells is the volume which is produced by rotating the infinitesimal parallelogram dS about the axis $\overline{AB}$.

Let $\angle CAB=\theta$, then

$$\eta^2=\xi^2+r^2-2r\xi\cos\theta .$$

Differentiating the above equation, fixing ξ and r

$$\eta d\eta = \xi r \sin\theta d\theta .$$

Hence

$$\overline{CD} = r\,d\theta = \frac{\eta d\eta}{\xi\sin\theta} .$$

The area of the parallelogram is equal to

$$\frac{\eta\, d\eta\, dr}{\xi\sin\theta} .$$

Consequently, the co-volume is equal to

$$\frac{2\pi\eta r d\eta dr}{\xi} .$$

The above quantity, multiplied by $\rho_k(\eta)$ and integrated over all possible values of η, fixing r and ξ

$$\frac{r\,dr}{\xi}\int_{|r-\xi|}^{r+\xi} 2\pi\eta\cdot\rho_k(\eta)d\eta ,$$

is the probability that the random flights chain occurs in the range r to $r+dr$, fixing ξ. The above quantity, multiplied by $W_{k-1}(\xi)d\xi$ and integrated over all possible values of ξ (from 0 to ∞) must be equal to $W_k(r)dr$:

$$W_k(r)\,dr = r dr\int_0^\infty \frac{W_{k-1}(\xi)}{\xi}d\xi\int_{|r-\xi|}^{r+\xi} 2\pi\eta\cdot\rho_k(\eta)d\eta \qquad (k=2, \cdots, n) . \qquad (3)$$

Employing a function $F_k(r)$ defined by

$$F_k(r) = W_k(r)/r , \qquad (k=1, \cdots, n) \qquad (4)$$

Eq. (3) becomes

$$F_k(r) = \int_0^\infty F_{k-1}(\xi)d\xi\int_{|r-\xi|}^{r+\xi} 2\pi\eta\cdot\rho_k(\eta)d\eta . \qquad (5)$$

For solving Eq. (5), it is inconvenient that the absolute notation is involved in the lower limit of the integration on η in the right hand side of it. To avoid this difficulty, we employ the following device. Although $\rho_k(\eta)$ and $F_k(r)$ are defined only in the positive range of their variables, the definitions are extended to the negative range so that $\rho_k(\eta)$ becomes the even function and $F_k(r)$ the odd function of their variables respectively:

$$\left.\begin{array}{ll} 2\pi\eta\cdot\rho_k(\eta)=\psi_k(\eta) & \eta\geq 0 \\ \psi_k(-\eta)=-\psi_k(\eta) & \end{array}\right\} \qquad (6)$$

$$F_k(-r)=-F_k(r) \qquad (7)$$

After the above procedure, the domain of the integration of Eq. (5) illustrated in Fig. 2 by I turning into $I+II$, Eq. (5) becomes

$$F_k(r)=\int_{-\infty}^{\infty} F_{k-1}(\xi)\,d\xi \int_{r-\xi}^{\infty} \psi_k(\eta)d\eta\,. \qquad (8)$$

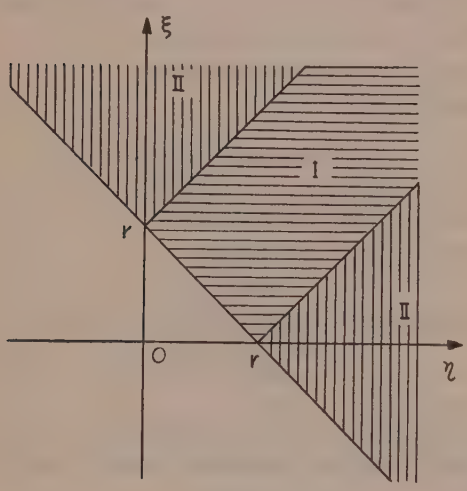

Fig. 2.

Differentiating Eq. (8) with respect to r we obtain

$$F_k'(r)=-\int_{-\infty}^{\infty} F_{k-1}(\xi)\psi_k(r-\xi)d\xi\,. \qquad (9)$$

First we treat tentatively the problem by the Fourier transformation. The right hand side of Eq. (9) is the well-known convolution type in the Fourier transformation. Operating the transformation on both sides of Eq. (9) we obtain

$$f_k(s)=-(\sqrt{2\pi}/is)\varphi_k(s)f_{k-1}(s)\,, \qquad (10)$$

where $f_k(s)$ and $\varphi_k(s)$ are the Fourier-transforms of $F_k(r)$ and $\psi_k(\eta)$ respectively with the parameter s and $i=\sqrt{-1}$. From the definition

$$W_1(r)=4\pi r^2\rho_1(r)\,,$$

$$\psi_1(r)=2\pi r\rho_1(r)=W_1(r)/2r=F_1(r)/2\,.$$

Hence

$$f_1(s)=2\varphi_1(s)\,. \qquad (11)$$

From Eqs. (10) and (11) we obtain

$$f_n(s)=(-1)^{n-1}\frac{2(2\pi)^{(n-1)/2}}{i^{n-1}\,s^{n-1}}\varphi_n(s)\cdots\varphi_1(s)\,. \qquad (12)$$

Operating the inverse transformation on Eq. (12) the required probability is

$$W_n(r)=2(-1)^{n-1}\frac{(2\pi)^{n/2-1}\cdot r}{i^{n-1}}\int_{-\infty}^{\infty}\frac{\varphi_n(s)\cdots\varphi_1(s)}{s^{n-1}}\times\exp(isr)ds\,. \qquad (13)$$

The integration involved in above equation which was obtaind already by Lord Rayleigh and S. Chandrasekhar is difficult to be carried out for the random flights consisting of the displacements with the finite length, as seen in their papers. It seems to the author that the procedure of the integration by M. C. Wang and E. Guth involves a question although their result is correct. But by the Laplace transformation the problem can be solved more easily as follows.

$\rho_k(\eta)$, etc. are assumed to fulfil the conditions

$$\rho_k(\eta)=0 \qquad \eta\geq M_k\,, \qquad (14)$$

where M_k, etc. are the finite positive numbers. Under these conditions the resultant random flights chain also has a finite length:

$$F_k(r)=0 \qquad |r|\geq M\,, \qquad (15)$$

where

$$M>\sum_{k=1}^{n} M_k\,.$$

As is well-known, the Laplace transformation is defined only in the positive range of the variable. Therefore if $F_k(r)$ is transformed directly, the procedure is erroneous in neglecting the negative part of the variable. To avoid this difficulty we define a new function $G_k(r)$ which is produced by shifting $F_k(r)$ toward the positive range of the variable by the amount M and transform this function:

$$G_k(r)=F_k(r-M)\,. \qquad (16)$$

According to Eq. (15)

$$G_k(r)=0 \qquad r\leq 0\,. \qquad (17)$$

Using the relation Eq. (16), Eq. (9) is replaced by

$$G_k'(r)=-\int_{-\infty}^{\infty} G_{k-1}(\xi)\psi_k(r-\xi)d\xi\ ,$$

which reduces to

$$G_k'(r)=-\int_{0}^{\infty} G_{k-1}(\xi)\psi_k(r-\xi)d\xi\ , \qquad (18)$$

according to Eq. (17). From Eq. (14) and (6) the integrand in the right hand side of Eq. (18) is zero for ξ in the range $r-\xi<-M$. Therefore Eq. (18) can be written as

$$G_k'(r)=-\int_{0}^{r+M} G_{k-1}(\xi)\psi_k(r-\xi)d\xi\ . \qquad (19)$$

Again, from $\psi_k(\eta)$ we define the function $U_k(\eta)$ in the analogous way to $G_k(r)$:

$$U_k(\eta)=\psi_k(\eta-M)\ . \qquad (20)$$

Substituting $U_k(\eta)$ for $\psi_k(\eta)$ and replacing r by $r-M$ Eq. (19) becomes

$$G_k'(r-M)=-\int_{0}^{r} G_{k-1}(\xi)U_k(r-\xi)d\xi\ . \qquad (21)$$

The right hand side of Eq. (21) is the well-known convolution type in the Laplace transformation. If $g_k(s)$ and $u_k(s)$ are assumed to be the Laplace-transforms of $G_k(r)$ and $U_k(\eta)$ with the parameter s, after operating the transformation on both sides of Eq. (21) we obtain

$$g_k(s)=-\frac{u_k(s)\exp(Ms)}{s}\cdot g_{k-1}(s)\ . \qquad (22)$$

After the analogous manner to Eq. (11) we obtain

$$g_1(s)=2u_1(s)\ . \qquad (23)$$

From Eqs. (22) and (23) we obtain

$$g_n(s)=(-1)^{n-1}2s\left(\prod_{k=1}^{n} u_k(s)/s\right)\exp\{(n-1)Ms\}\ . \qquad (24)$$

This equation is analogous to Eq. (12) in the process employing the Fourier transformation. Although we can obtain $G_n(r)$ from Eq. (24) by the theorem of the inverse transformation it is very convenient to make use of the tables of the transformations in textbooks, if $g_n(s)$ has a simple form.

§ 3. Random Flights Chain with Fixed Bond Lengths

The random flights chain with fixed bond lengths is the most familiar and important one. In this case we may adopt

$$\rho_k(\eta)=\frac{1}{4\pi b_k^2}\delta(\eta-b_k) \qquad (k=1,\cdots,n)\ , \qquad (25)$$

where $\delta(\eta)$ stands for Dirac's δ function. From Eq. (6) we obtain

$$\psi_k(\eta)=\frac{\eta}{2b_k^2}\delta'(|\eta|-b_k)\ . \qquad (26)$$

By using Eq. (26) for $\psi_k(\eta)$ the Laplace-transform of $U_k(\eta)$ becomes

$$u_k(s)=-\frac{1-\exp(-2b_ks)}{2b_k\exp(-b_ks)}\cdot\exp(-sM)\ . \qquad (27)$$

Using Eq. (27) for $u_k(s)$, Eq. (24) becomes

$$g_n(s)=-\frac{1}{2^{n-1}s^{n-1}}\left(\prod_{k=1}^{n}\frac{1-\exp(-2b_ks)}{b_k\exp(-b_ks)}\right)\exp(-sM)\ , \qquad (28)$$

which is expanded in the form

$$g_n(s)=-\frac{1}{2^{n-1}b_1\cdots b_n}\left[\frac{1}{s^{n-1}}\exp\{-s(M-L)\}-\sum_{i=1}^{n}\frac{1}{s^{n-1}}\exp\{-s(N-L+2b_i)\}\right.$$
$$\left.+\sum_{1\leq i<j\leq n}\sum\frac{1}{s^{n-1}}\exp\{-s(M-L+2b_i+2b_j)\}-\cdots+(-1)^n\frac{1}{s^{n-1}}\exp\{-s(M+L)\}\right]. \qquad (29)$$

To obtain $G_n(r)$ we must know the inverse transformation of $\exp(-as)/s^{n-1}$. After a direct examination we can see that it is equal to

$$[t-a]^{n-2}/(n-2)!$$

where the bracket [ ] has the following meaning

$$[t]=t \qquad t\geq 0$$
$$=0 \qquad t<0\ .$$

Operating the inverse transformation on Eq. (29) by the aid of the above theorem we obtain

$$G_n(r)=-\frac{1}{2^{n-1}(n-2)!\,b_1\cdots b_n}\Big\{[r-M+L]^{n-2}-\sum_{i=1}^{n}[r-M+L-2b_i]^{n-2}$$
$$+\sum_{1\leq i<j\leq n}\sum[r-M+L-2b_i-2b_j]^{n-2}-\cdots+(-1)^n[r-M-L]^{n-2}\Big\}\,, \tag{30}$$

where L is the contour length of the chain:

$$L=\sum_{k=1}^{n}b_k\,.$$

Obtaining $F_n(r)$ from Eqs. (16) and (30), rewriting it by the property that it is the odd function of r and lastly using Eq. (4) we arrived at the required result

$$W_n(r)=\frac{r}{2^{n-1}(n-2)!\,b_1\cdots b_n}\Big\{[L-r]^{n-2}-\sum_{i=1}^{n}[L-2b_i-r]^{n-2}$$
$$+\sum_{1\leq i<j\leq n}\sum[L-2b_i-2b_j-r]^{n-2}-\cdots+(-1)^n[-L-r]^{n-2}\Big\}\,. \tag{31}$$

If we carry out the integration in Eq. (69) in the paper of Chandrasekhar, multiplied by $4\pi r^2$, we shall have the same expression as Eq. (31).

In the special case in which all $b_i's$ are equal to b Eq. (31) becomes

$$W_n(r)=\frac{r}{2^{n-1}b^n(n-2)!}\sum_{k=0}^{n}(-1)^k\,{}_nC_k[nb-2kb-r]^{n-2}\,, \tag{32}$$

which coincides with the expression obtained already by Treloar and Guth and Wang.

§ 4. Reduction of the Problem of End-to-End Distance to That of the Segment Distribution around the Centre of Gravity

The problem discussed in the preceding sections can be summarized as follows

(i) Now, let

$$\boldsymbol{\eta}_k=\begin{pmatrix}x_k\\ y_k\\ z_k\end{pmatrix}\quad(k=1,\cdots,n)\,, \tag{33}$$

be n, three dimensional vectors and distribute symmetrically around the origin of each coordinate system. Assuming the probability that $\eta_k(=|\boldsymbol{\eta}_k|)$ occurs in the range η_k to $\eta_k+d\eta_i$ to be

$$4\pi\eta_k^2\rho_k(\eta_k)d\eta_k\,,$$

we require the probability, $W_n(r)dr$, that the absolute value of the resultant vector

$$\boldsymbol{r}=\boldsymbol{\eta}_1+\boldsymbol{\eta}_2+\cdots\boldsymbol{\eta}_n \tag{34}$$

occurs in the range r to $r+dr$.

The problem which we wish to solve in this section is as follows

(ii) Let us define a new vector derived from the vectors in Eq. (33)

$$\boldsymbol{R}=a_1\boldsymbol{\eta}_1+a_2\boldsymbol{\eta}_2+\cdots a_n\boldsymbol{\eta}_n\,. \tag{35}$$

Then we require the probability, $W_n(R)dR$, that $R(=|\boldsymbol{R}|)$ occurs in the range $R+dR$. The $a_k's$ are arbitrary scalar quantities. If we assign the proper values for $a_k's$, then $\boldsymbol{R}$ can stand for the vector from the centre of gravity to each segment.

To reduce the problem (ii) to (i) we change the variables from $\boldsymbol{\eta}_k$ to $\boldsymbol{\xi}_k$ as follows

$$a_k\boldsymbol{\eta}_k=\boldsymbol{\xi}_k\,, \tag{36}$$

$$\eta_k=\xi_k/|a_k|\,, \tag{37}$$

where $\xi_k=|\boldsymbol{\xi}_k|$. After the above procedure we must solve the problem:

(iii) Let $\boldsymbol{\xi}_k$ be a vector of which the absolute value ξ_k occurs in the range ξ_k to $\xi_k+d\xi_k$ with the probability

$$(4\pi\xi_k^2/|a_k|^3)\rho_k(\xi_k/|a_k|)d\xi_k\,. \tag{38}$$

Then what is the probability that the absolute value R of the resultant vector

$$\boldsymbol{R}=\boldsymbol{\xi}_1+\boldsymbol{\xi}_2+\cdots+\boldsymbol{\xi}_n\,, \tag{39}$$

occurs in the range R to $R+dR$?

If we compare the problem (iii) with (i), we can see there is no difference between them except that $\rho_k(\eta_k)$ is replaced by $\rho_k(\eta_k/|a_k|)/|a_k|^3$.

§ 5. The Distance between the Centre of Gravity and Each Segment and the Segment Density around the Centre of Gravity

We first require the distribution function of the distance between the centre of gravity and each segment of the random flights chain which consists of the bonds $b_1, \cdots, b_n$ in length and has the same weights on both ends and all jointing points. In this case Eq. (35) becomes

$$\boldsymbol{R}=a_{i1}\boldsymbol{\eta}_1+a_{i2}\boldsymbol{\eta}_2+\cdots+a_{in}\boldsymbol{\eta}_n \quad (i=0, 1, \cdots, n) \tag{40}$$

where a_{ik}'s are given by

$$\left.\begin{aligned} a_{ik}&=k/(n+1) && k\leq i \\ &=(n-k+1)|(n+1) && i<k\,. \end{aligned}\right\} \tag{41}$$

The distribution functions of each displacement, when the problem is reduced to that of the end-to-end distance, are obtained by using Eq. (41) for a_k and Eq. (25) for $\rho_k(\eta)$ in Eq. (38)

$$\rho_{ik}(\xi_k)=\frac{1}{4\pi(\beta_{ik})^2}\delta(\xi_k-\beta_{ik})\,, \tag{42}$$

where

$$\left.\begin{aligned} \beta_{ik}&=kb_k/(n+1) && k\leq i \\ &=(n-k+1)b_k/(n+1) && i<k\,. \end{aligned}\right\} \tag{43}$$

In comparison of Eq. (32) with Eq. (25) we see the procedure employed in section 3 can be applied to this case only by replacing b_k β_{ik}. In this case Eq. (28) becomes

$$g_{in}(s)=-\frac{1}{2^{n-1}s^{n-1}}\left\{\prod_{k=1}^{n}\frac{1-\exp(-2\beta_{ik}s)}{\beta_{ik}\exp(-\beta_{ik}s)}\right\} \times\exp(-sM) \tag{44}$$

where i in $g_{in}(s)$ refers to the i-th segment. In the simplest case where

$$b_1=b_2=\cdots=b_n=b \tag{45}$$

Eq. (44) becomes

$$g_{in}(s)=-\frac{(n+1)^n}{2^{n-1}b^n i!\,(n-i)!\,s^{n-1}}\left\{\prod_{k=1}^{i}\frac{1-\exp\{-2kbs/(n+1)\}}{\exp\{-kbs/(n+1)\}}\right\}\left\{\prod_{k=1}^{n-i}\frac{1-\exp\{-2kbs/(n+1)\}}{\exp\{-kbs/(n+1)\}}\right\}\exp(-sM) \quad (i\neq 0, n)\,, \tag{46a}$$

$$g_{0n}(s)=g_{nn}(s)=-\frac{(n+1)^n}{2^{n-1}n!\,b^n s^{n-1}}\left\{\prod_{k=1}^{n}\frac{1-\exp\{-2kbs/(n+1)\}}{\exp\{-kbs/(n+1)\}}\right\}\exp(-sM)\,. \tag{46b}$$

For convenience we define

$$a=\exp\left\{-\frac{2bs}{n+1}\right\}, \tag{47}$$

$$L_i=\frac{b}{n+1}\left\{\sum_{k=0}^{i}k+\sum_{k=0}^{n-i}k\right\} \tag{48}$$

After simple consideration we see L_i is the maximum value of the distance between the centre of gravity and the i-th segment of the chain. We define A_{ik} by

$$\prod_{k=1}^{i}(1-a^k)\prod_{k=1}^{n-i}(1-a^k)=\sum_{k=0}^{(n+1)L_i/b}A_{ik}a^k \qquad (i\neq 0, n)\,, \tag{49a}$$

$$\prod_{k=1}^{n}(1-a^k)=\sum_{k=0}^{(n+1)L_0/b}A_{0k}a^k=\sum_{k=0}^{(n+1)L_n/b}A_{nk}a^k. \tag{49b}$$

Transforming inversely Eqs. (46a) and (46b) by the same method as in section 3, we obtain the required distribution function of the distance between the centre of the gravity and the i-th segment

$$W_{in}(R)=\frac{(n+1)^n R}{2^{n-1}i!\,(n-i)!\,(n-2)!\,b^n}\sum_{k=0}^{(n+1)L_i/b}A_{ik}\left[L_i-\frac{2bk}{n+1}-R\right]^{n-2}. \tag{50}$$

The square bracket in Eq. (50) again has the same meaning as in Eq. (30).

If the mean numbers of the segments found in the volume element dV at a distance R from the centre of gravity is assumed to be $D_n(R)dV$, $D_n(R)$ is simply given by

$$D_n(R)=\frac{1}{4\pi R^2}\sum_{i=0}^{n} W_{in}(R)\,. \tag{5}$$

If we define A_k by

$$\sum_{i=0}^{n} {}_nC_i\, a^{-\{(1/4)n(n+1)-(1/2)i(n-i)\}}\prod_{k=1}^{i}(1-a^k)\prod_{k=1}^{n-i}(1-a^k)=\sum_{k=-n(n+1)/4}^{n(n+1)/4} A_k a^k\,, \tag{5}$$

the required distribution function of the density of the segment becomes

$$D_n(R)=\frac{(n+1)^n}{2^{n+1}n!\,(n-2)!\,\pi b^n R}\sum_{k=-n(n+1)/4}^{n(n+1)/4} A_k\left[-\frac{2bk}{n+1}-R\right]^{n-2}. \tag{5}$$

§ 6. Conclusion

Although the distribution function discussed in this paper has only one variable, that with two variables can be treated by the analogous method[7]. The method employed in this paper may be extended also to the general random flights problem as follows[7]. For this purpose the discontinuous integral of Diricht, employed by S. Chandrasekhar[6] in his paper,

$$\delta_k=\frac{1}{\pi}\int_{-\infty}^{\infty}\frac{\sin(\alpha_k\rho_k)}{\rho_k}\exp(i\rho_k\gamma_k)d\rho_k\,,$$

which has the property

$$\begin{aligned}\delta_k&=1 \quad \text{whenever} \quad -\alpha_k<\gamma_k<\alpha_k\\ &=0 \quad \text{otherwise,}\end{aligned}$$

must be replaced by the integral having the form of the Laplace transformation

$$\delta_k=\frac{1}{\pi i}\int_{\beta-i\infty}^{\beta+i\infty}\frac{\sinh(\alpha_k\rho_k)}{\rho_k}\exp(\gamma_k\rho_k-C_k\rho_l)d\rho_k\,,$$

which has the property that

$$\begin{aligned}\delta_k&=1 \quad \text{whenever} \quad C_k-\alpha_k<\gamma_k<C_k+\alpha_k\\ &=0 \quad \text{otherwise.}\end{aligned}$$

In conclusion we may say that it is convenient to use the former expression for the random flights problem of which the distribution function of each displacement is continuous and the latter expression for that o which the distribution function of each dis placement is discontinuous and limmited i the finite range of the variables.

Acknowledgements

The author would like to express his sincere gratitudes to Professor I. Sakurada and Professor A. Nakajima for their continual discussions and encouragements. He is also grateful to members of the Research Group on Polymer Science of Kyoto University for their useful discussions.

References

1) Lord Rayleigh: Phil. Mag. [6] **37** (1919) 321.
2) W. Kuhn and F. Grün: Kolloid Zeit. **101** (1942) 248.
3) H. M. James and E. Guth: J. Chem. Phys. **11** (1943) 470.
4) L. R. G. Treloar: Trans. Faraday Soc. **42** (1946) 77.
5) M. C. Wang and E. Guth: J. Chem. Phys. **20** (1952) 1144.
6) S. Chandrasekhar: Rev. Mod. Phys. **15** (1943) 1.
7) K. Nagai: Busseiron-Kenkyu (in Japanese) **97** (1956) 171; **99** (1956) 93.

JOURNAL OF THE PHYSICAL SOCIETY OF JAPAN Vol. 13 No. 8, AUGUST, 1958

An Application of the Cellular Method to a Vacancy in Metal

By Hiroshi FUJIWARA

Department of Physics, Minami-Bunko, Hiroshima University, Minami-machi-3, Hiroshima City

(Received May 10, 1956)

The distribution of electrons around a vacancy in metal is studied using a model which was introduced in our previous paper in order to treat the impurity atom.

The arrangement of nuclei of matrix metal at each lattice point, except one where the nucleus is missing, i.e., vacancy, is treated by the cellular method. The deviation of the potential in the cells neighboring to the vacancy, from the periodic one for the pure metal is taken into account. In the first approximation, the lattice distortion due to the vacancy is neglected.

The Thomas-Fermi equation, in which all the electrons, i.e., valence electrons as well as core ones, are taken into account, is solved numerically in each cell and connected smoothly by a suitable set of boundary conditions.

As a result of our calculations for the case of a vacancy in copper, we find that there is the charge of $-1.7e$ inside the atomic sphere for the vacancy.

§ 1. Introduction

In our previous paper[1] (referred to as I hereafter), we have investigated the perturbing potential around a substitutional impurity atom introduced in originally perfect copper crystal by using our newly proposed model (denoted as M_1). According to this model, the positive charges of bare nuclei of foreign and matrix atoms (the atomic number of those foreign and matrix atoms are denoted as Z_i and Z respectively) are put at each lattice point and all the electrons, i.e., valence electrons as well as core ones, are treated with Thomas-Fermi (abbreviated as T. F.) method. Therefore, we need not worry about the proper choice of the number of valence or conduction electrons per atom. And with the use of the cellular method, we have been able to construct the potential which tends to the periodic potential field due to the pure matrix metal as we go far from the impurity atom.

Here in this paper, we shall apply our model M_1 to the case of a vacancy in the lattice of the matrix metal by treating the vacancy as the limit of the impurity with $Z_i=0$. Thus the problem of a vacancy, where $\Delta Z=Z_i-Z$ has very large value in absolute magnitude, can be treated quite similarly to the one of a substitutional impurtiy and it is considered as an extension of Slater and Krutter's treatment for pure metal.[2]

In the treatment of vacancy, most of the authors have hitherto used a simple model in which only the conduction electrons have taken into account in T. F. method and, futhermore, the T. F. equation has been linearized. In that model, first suggested by Dexter[3], the vacancy in monovalent metal has to be treated as a single negative point charge in the uniform charge distribution where the positive charges due to nuclei and negative charges due to core electrons are smeared out. Consequently, according to this scheme, a Ni atom in Cu or a Pt atom in Au should have the same effect as a vacancy.

But in this paper, since we use our refined model M_1, approximation of the smearing out of the charge is not made, and T. F. equation is solved exactly in its non-linear form. After we finished our calculation, a paper by Lee and March[4] came into our notice in which the vacancy was studied in a way quite similar to our present one. However, our treatments are more refined than theirs, because they neglected the deviation of the potential from spherical symmetry.

§ 2. General Considerations about a Vacancy in Metal

We shall now apply the model M_1 in I to the case of a vacancy in metal by simply putting $Z_i=0$. We introduce a vacant lattice

point by removing one of the matrix atoms (hereafter abbreviated as m-atoms) which are arranged in the face-centered cubic crystal. In the first approximation, we assume that the lattice is not distorted due to the removal of this atom and that the concentration of the vacancies is so small that the interaction between the vacancies is negligible.

We take all the electrons in the crystal into our consideration and we assume that the positive charge $+Ze$ corresponding to the bare nuclei of m-atoms are located at each lattice points (denoted by $\boldsymbol{R}_n$) except one (denoted by $\boldsymbol{R}_0$) where no positive charge is present.

Then the crystal potential can be obtained as the solution of the T. F. equation which is appropriate for these arrangements of positive charges and a vacancy.

Now let $u(\boldsymbol{r})$ be the electrostatic potential at the point $\boldsymbol{r}$ valid over the entire crystal containing the vacancies in which every atom is supposed to be at rest at its lattice point. $u(r)$ is given, as usual, by the solution of T. F. equation:

$$\nabla^2 u(r) = \alpha u^{3/2}\,, \tag{1}$$

where

$$\alpha = \frac{32\pi^2 e}{3h^3}(2me)^{3/2}\,. \tag{2}$$

As was the case for the impurity, our problem is treated by cellular method. The polyhedron P_0, belonging to the vacant lattice point and P_n, belonging to the m-atoms are replaced by the spheres S_0 and S_n of equal volume. Hereafter, the potential in S_0 and S_n are denoted by u_0 and u_n respectively. Then u_0 and u_n can be obtained by solving the equation (1) under the following conditions in the vicinity of each lattice point:

$$u_0 = \text{finite}, \qquad \text{near } \boldsymbol{R}_0\,, \tag{3a}$$

$$u_n = \frac{Ze}{|\boldsymbol{r}-\boldsymbol{R}_n|} + \text{finite terms}, \qquad \text{near } \boldsymbol{R}_n \ n \neq 0\,. \tag{3b}$$

Our following formulations can be obtained only with replacing the circumstances concerning the impurity in I with those of vacancy and all of the formulas as to the m-atoms are just the same as those in I. Therefore, we need not give the details of the whole treatments but only its main scheme. Hereafter, the number for the formulas expressed in italic represent those in I.

Hitherto, most of the authors who investigated the problem as to the vacancy as well as the impurity, did not take into account the deviation of the potential from spherical symmetry. But, in I, we introduced this deviation and in the present study of the vacancy, we shall follow the same procedures, i.e., we assume that (i) the potential in the atomic sphere in the distance from the vacancy must tend to that of the pure metal which is taken as spherically symmetric as usual, and that (ii) in the atomic spheres S_n neighboring to S_0, the potential has much lower symmetry and we take into account this lower symmetry by writting:

$$u_n = U(r) + f_n(r,\ \theta,\ \phi); \qquad n \neq 0\,, \tag{4}$$

where $U(r)$ is the potential for perfect crystal and the small term f_n expresses the deviation from the spherical symmetry. Further, (iii) in the atomic sphere S_0 of the vacancy, the potential has the spherical symmetry. Strictly speaking, the potential should have some deviation from spherical symmetry. However, due to the higher symmetry of u_0 in S_0, we assume that the deviation f_n can be neglected in the first approximation as was the case in I.

The potentials u_0 in S_0 and u_n in its neighboring spheres S_n obtained by integrating the T. F. equation under the boundary conditions at the center of each sphere, involve a certain number of parameters which we shall determine by virtue of an appropriate set of boundary conditions at the surface.

§ 3. The Potential u_0 in a Vacancy

The potential u_0, which we have assumed as spherically symmetric, of T. F. equation within the sphere S_0 of the vacancy is to satisfy:

$$\frac{1}{r}\frac{d^2(u_0 r)}{dr^2} = \alpha u_0^{3/2}\,. \tag{5}$$

As r tends to zero, u_0 tends to a finite value c_1. c_1 remains as an adjustable parameter whose value can be determined in such a way that u_0 may be smoothly connected to u_n of its nearest neighbors.

Introducing the usual dimensionless variables $(\phi_0,\ x)$ through the following relations:

$$u_0 = \frac{e}{r}\phi_0 \quad (6a), \qquad r = b\cdot x = 0.885\cdot a_H\cdot x \quad (6b)$$

a_H: Bohr radius

the Poisson equation (5) is transformed into the following dimensionless form:

$$\frac{d^2\phi_0}{dx^2}=\frac{\phi_0^{3/2}}{\sqrt{x}}\,, \tag{7}$$

with the boundary condition:

$$\phi_0=0 \text{ when } x\to 0\,. \tag{8}$$

In the region where x is small, ϕ_0 is assumed to be expanded in the following Taylor series:

$$\phi_0=C_1x+C_2x^2+C_3x^3+\cdots\,. \tag{9}$$

By inserting (9) into (7), we find that ϕ_0 is expanded with an adjustable parameter C_1 as follows:

$$\phi_0=C_1x+\frac{C_1\sqrt{C_1}}{6}x^3+\frac{C_1^2}{80}x^5+\cdots\,. \tag{10}$$

For the interval x which corresponds to the interval $(0, r_c)$ of r, we carry out the numerical integration for different values of C_1. Here, r_c is the atomic radius of matrix atom.

§ 4. The Potentials u_n

As to the calculation of the potentials u_n within the spheres of m-atoms in the neighborhood of the vacancy, we perfom it just in the same way as in I. For the details, the readers should refer to the formulas from (*7*) to (*24*) in I. Fig. 1 (a) and 1 (b) in I express the present circumstances only by replacing the impurity i-atom with a vacancy and for the potential $U(r)$, those values obtained in I are used. (see from (*25*) to (*28*).

Therefore, we describe here only the outlines. We choose one of the twelve nearest neighbor m-atoms to the vacancy, for example, $m_{1,1}$ atom (atomic sphere $S_{1,1}$) in Fig. 1 (a) of I. Then the boundary conditions to be satisfied are constructed between $S_{1,1}$ and each one of its twelve nearest neighbors by assuming that the deviation f_n from the spherical symmetric potential $U(r)$ of pure metal does not vanish only within the spheres of the nearest and the next nearest neighbor m-atoms to the vacancy. Then the deviation $f_n(r, \theta, \phi)$ is expanded in spherical harmonics as follows:

$$\begin{aligned} f_n(r,\theta,\phi) &= a_0\chi_0(r)+a_1\chi_1(r)P_1(\cos\theta)+a_2\chi_2(r)P_2(\cos\theta)+\cdots \\ &\quad +b_2\chi_2(r)P_2^2(\cos\theta)\cos 2\phi \\ &\quad +b_3\chi_3(r)P_3^2(\cos\theta)\cos 2\phi+\cdots\,. \end{aligned} \tag{11}$$

Considering the number of our boundary conditions, i.e., from (*11*) to (*17*), we take into account six coefficients a_0, a_1, a_2, a_3, b_2 and b_3 in this expansion and we can express $a_1\cdots$ and b_3 as multiples of a_0.

Then the remaining parameter c_1 in u_0 is determined by the following implicit equation:

$$A_0=\frac{u_0(r_c, c_1)-U(r_c)}{-(\partial u_0/\partial r)}\,. \tag{12}$$

This is exactly the same equation as (*24*) in I. As to the values A_0 and $U(r_c)$, we use those values obtained in I. With this value of c_1, denoted as c_0, the function u_0 is completely determined and, further, the explicit value of a_0 is also determined from the boundary condition between S_0 and $S_{1,1}$, i.e., from the formula either (*22*) or (*23*).

§ 5. Results and Discussions

According to the above-stated general formulations as to the vacancy in face-centered cubic crystal, we have actually carried out our calculation for the vacancy in copper.

As the value of A_0 in (12) depends only upon the concerning metal, we use likewise the value 0.48 obtained in I. As stated before, the formulas and the values concerning the matrix metal obtained in I are used again and only those concerning the vacancy are calculated here.

Thus we find the following results.

(i) The correct value of C_1 in (10) corresponding to the solution u_0 is found to be 0.215.

(ii) The numerical value of a_0 is $-0.00092e$ from (*22*). Consequently, the coefficients a_1, $\cdots$ and b_2 $\cdots$ in (11) are calculated as the multiples of a_0 as were given in Table I in I.

(iii) The total charge ρ contained in the central sphere S_0 belonging to the vacancy is estimated about $-1.7e$ from (*36*). As was the case in I, it is contributed mainly from the nearest neighbor m-atoms to the vacancy.

(iv) The perturbing potential $V(r)$ caused by the presence of the vacancy might be allowed to define as $V(r)=-e(u_0-U)$. And our obtained curve is shown in Fig. 1. This curve agrees with that of March[5] (Figure 2 in his paper) within the accuracy of graphical representation.

(v) For the sake of explaining our results, especially the potential through S_0 and $S_{1,1}$, the Fig. 2 is shown, in which the potential is shown along the line $\overline{R_0R_{1,1}}$. (The line $\overline{R_0R_{1,1}}$ will be referred in Fig. 1 (a) in I. In Fig. 2, our obtained potential is represented by a solid line. The potential u_0 in the vacancy is finite

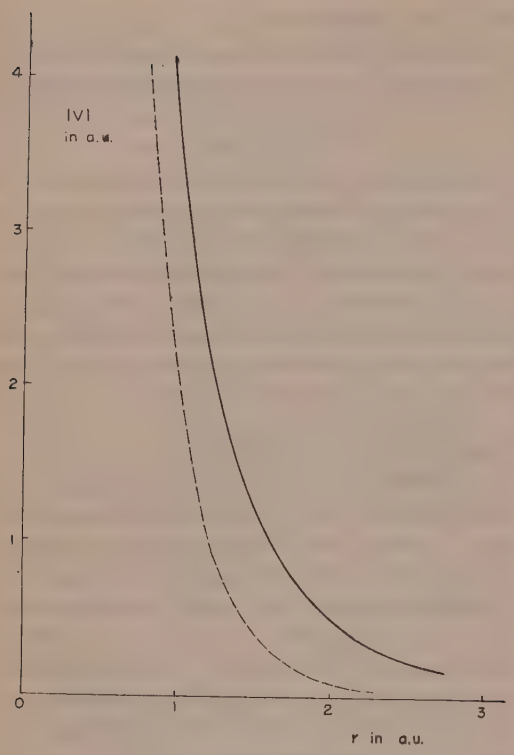

Fig. 1. Perturbing potential as a function of r (atomic units used).
solid line: Our potential
dotted line: Jongenburger's result

at R_0 and monotoniously increases towards the boundary $Q_{1,1}$ and then connected smoothly with the potential u_n, which deviates from U in $S_{1,1}$ at $Q_{1,1}$. In order to compare the present case with the perfect crystal, the potential U in the perfect crystal is also shown by dotted line, which is infinite at each lattice point. The deviation f_n from U in the case of the vacancy is estimated to be about thirty percent.

In order to investigate the vacancy in copper, Jongenburger[6] adopted, as the scattering field due to a vacancy, the negative of the Hartree field of a free Cu^+ ion, supplemented by the potential due to the spherical hole in the free electron gas. He expressed the combined potential approximately in the form $V(r) = 24/r \cdot \exp(-2.5r)$ (in a.u.). In Fig. 1, Jongenburger's potential is shown by dotted line for the sake of comparison. The use of the negative of the Hartree field seems to be reasonable in his treatment in which the periodic variation of the potential in the pure metal is completely ignored, but the shielding due to the free electrons is more or less arbitrarily represented by introducing a spherical hole in the otherwise uniform free electron distribution. In this respect, the models based on

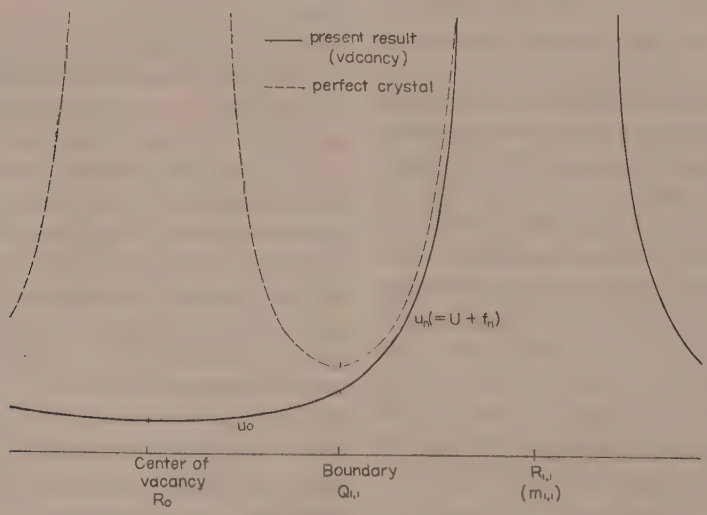

Fig. 2. Graphical representation of the potential through S_0 and $S_{1,1}$ along the line $\overline{R_0R_{1,1}}$.

Thomas-Fermi equation will give in principle more refined discription.

(vi) Furthermore, from the calculated values of $|a_0|$ and $|\rho|$ for the cases of $\Delta Z=-29$ (the present case), and -2 and -1 (the previous ones), it is found that these values are not linearly proportional. The values coresponding to the vacancy are about two times of the linearly extrapolated value from those of $\Delta Z=-2$ and -1.

(vii) March *et al.*[7] pointed out in their first paper concerning the vacancy, that in T. F. method electrons are not allowed to penetrate into the regions of negative kinetic energy. Therefore, they assumed a sphere with suitable radius around the negative point charge in which there is no electrons. Though such artifical technique is certainly necessary for their model, it is not necessary for our model in which all the electrons are taken into account.

(viii) However, as stated in I, we do not believe that our model M_1 is completely satisfactory, since T. F. method can not account for the shell structure of electrons in metal. Therefore, we are developing the method in which the distribution of core electrons is represented by the use of Hartree field and the electrons outside these cores are treated by T. F. method. We hope to be able to report the results in near future.

§ 6. Acknowlegements

The author wishes to express his sincere thanks to Prof. Masao Kotani of University of Tokyo for his continued guidance and encouragements throughout this work and Prof. Frederick Seitz of University of Illinois for his kind interest. The author's appreciations are due to Prof. K. Umeda, Dr. S. Kobayashi who kindly discussed and to Mrs. H. Komuro for her assistance in the numerical calculation.

He is also indebted to the Ministry of Education and the members of Kotani Laboratory of University of Tokyo for their financial aids.

References

1) H. Fujiwara: J. Phys. Soc. Japan **13** (1958) 250.
2) J. C. Slater and H. M. Krutter: Phys. Rev. **47** (1935) 559.
3) D. L. Dexter: Phys. Rev. **87** (1952) 768.
4) P. M. Lee and N. H. March: Phil. Mag. **2** (1957) 1226.
5) P. M. Lee and N. H. March: loc. cit.
6) P. Jongenburger: Appl. Sci. Res. **B3** (1953) 237.
7) L. C. R. Alfred and N. H. March: Phys. Rev. **103** (1956) 877; Phil. Mag. **2** (1957) 985.

JOURNAL OF THE PHYSICAL SOCIETY OF JAPAN Vol. 13, No. 8, AUGUST, 1958

Characteristics of the Beam Type Maser. II

By Koichi SHIMODA

Department of Physics, Faculty of Science, University of Tokyo

(Received April 17, 1958)

Experimental investigation of the characteristics of the ammonia maser is given and compared with theory. Observed saturation characteristics agree fairly well with the theory descibed in the previous paper. The change of oscillation frequency shows the expected increase with focuser voltage which arises from unresolved hyperfine structure of the 3,3 line. Small discrepancies are explained by the velocity distribution and different saturation of each hyperfine component. Frequency pulling due to cavity detuning was measured in detail and compared with theory. Thus the velocity spread of the effective molecules in the cavity can be estimated as roughly $\pm 30\%$. Tentative estimate of the center frequency on $UT2$ is compared with other measurements.

§ 1. Introduction

Theory of the beam type maser which takes the velocity distribution into consideration was described in the previous paper[1], hereafter referred as I. The saturation characteristics and the frequency change of an ammonia maser with focuser voltage were theoretically calculated. In this paper some of the experimental results with the maser on the 3,3 line of ammonia are described. The use of

the 3,2 line which was suggested in I and also by Townes has already been investigated by Bonanomi *et. al.*,[2] hence preliminary work on the 3,2 line is left out of this paper.

§ 2. Experimental Apparatus

A vertical cross-section of the experimental ammonia maser is shown in Fig. 1. In order to pump out the scattered molecules as fast as possible an oil diffusion pump is located near the beam source. A 4-inch oil diffusion pump, TOD-4F (Tokuda Mfg Co.), is connected directly below the flange. The ultimate vacuum without using liquid air trap was measured as 6×10^{-7} mmHg air equivalent.

An eight-pole focuser is surrounded by a cylindrical trap which is cooled by liquid oxygen or liquid nitrogen in a helical copper tube. Because the cold surface is fairly large, the operating tank pressure arround 1×10^{-6} mmHg can be easily obtained with sufficiently

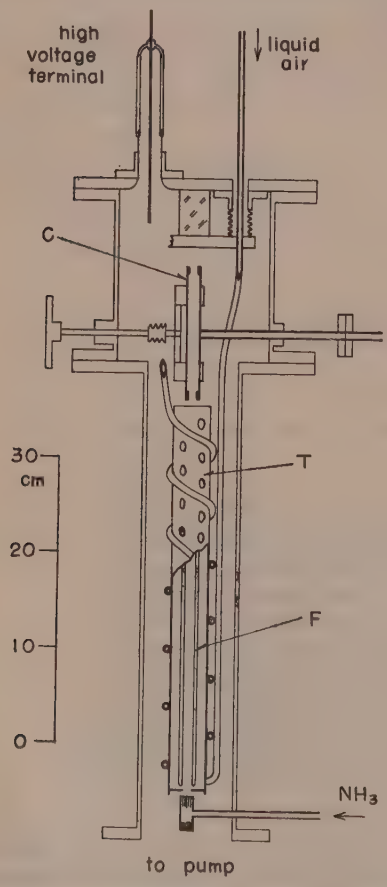

Fig. 1. Cross-sectional view of the experimental ammonia maser. F: focuser, C: cavity resonator, T: trap.

strong beam. The focuser is made of steel rods of 3.5 mm diameter and the crosssection is shown in Fig. 2 (a).

The cavity is a cylindrical TM_{010} mode cavity of 12 cm length and is slotted lengthwise, which allows tuning over 200 Mc/sec range by squeezing the cylinder. The inlet and outlet holes are 8 mm in diameter.

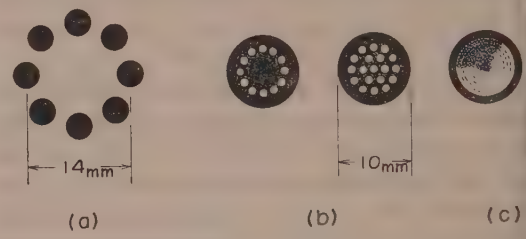

Fig. 2. Cross-sections of the eight-pole focuser (a), and three types of the beam source (b) and (c).

Since several attempts to improve the beam source resulted in poor success, simpler source structures have been used in the following experiments. The typical source is made up of 12 or 19 holes 1 mm in diameter, as shown in Fig. 2 (b). When a cold diaphragm with a 10 mm hole is placed between the source and the focuser, divergent molecules are trapped or reflected to be pumped out, thereby the tank pressure and the threshold focuser voltage decrease.

A typical result of the threshold focuser voltage to start oscillation and the tank pressure as functions of the source pressure behind the 12-hole source is shown in Fig. 3. Without the diaphragm, the threshold voltage was about 4 kV and it was less dependent on the source pressure.

The threshold voltage and the tank pressure with the crinkle foil source, as shown in Fig. 2 (c), is shown in Fig. 4. The crinkle foil source is more transparent, having the transparency of about 0.5, than the 12-hole source for which the transparency is $\frac{1^2}{8^2}\times12=0.19$. The ratio, 0.5: 0.19, is very close to the inverse ratio of the corresponding source pressures in Fig. 3 and Fig. 4. However, this relation does not always hold good for any different type of sources.

The threshold voltage decreases with increasing source pressure at low source pressure, because the beam flux increases with

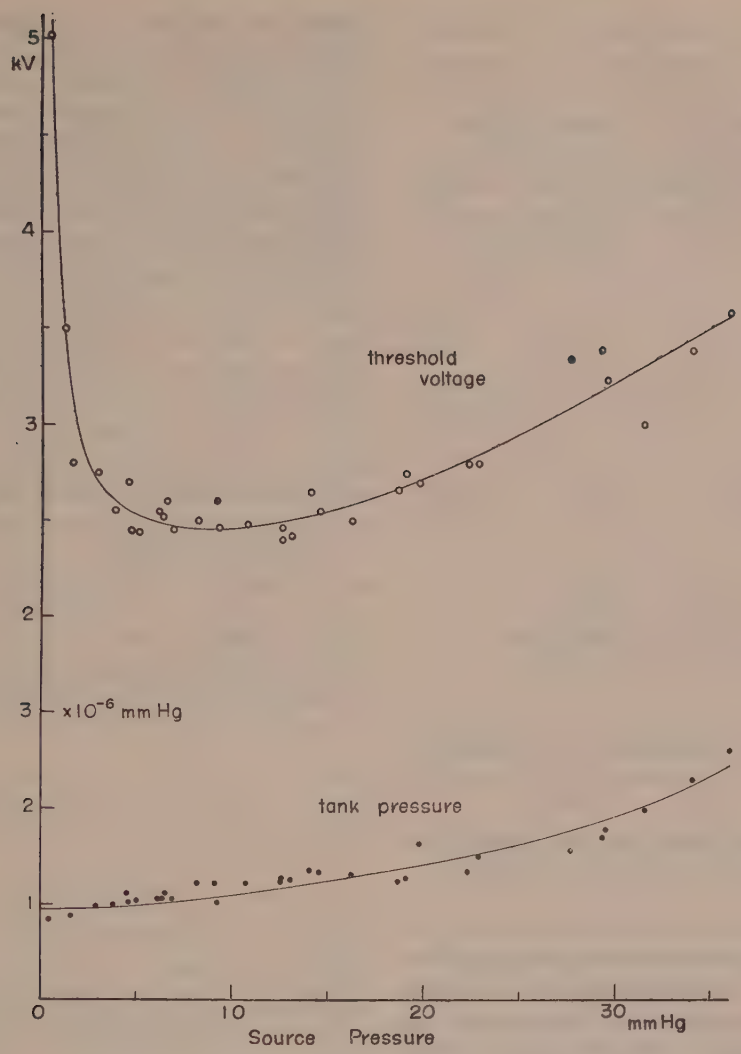

Fig. 3. Threshold voltage and tank pressure with the 12-hole source shown in Fig. 2 (b)

the source pressure. Beyond an optimum pressure, which is about 9 mmHg in Fig. 3 and 4 mmHg in Fig. 4, both the threshold voltage and the tank pressure increase with the source pressure. This evidently seems to be due to the collisions between ammonia molecules inside the focuser. The tank pressure was measured by a Fogel type ionization gauge attached near the cavity, and it does not quantitatively indicate the density of molecules inside the focuser, but does qualitatively.

The reproducible minimum threshold voltage is 2,400 volts and the breakdown focuser voltage is approximately 27 kV. Then the maximum beam intensity is about 100 times stronger than that of the threshold of oscillation (for the 3,3 line of ammonia). Since the focuser is insulated with teflon sheets of 1 mm thickness and the high voltage terminal is insulated with pyrex glass, the leakage current is so small that the maser oscillation continues as long as 25 minutes after the high voltage supply of 8 kV is disconnected. The measured capacitance of the focuser electrode is 102± 6 pF, and the insulation resistance is estimated as about 10^{13} ohms. Thus a nuclear battery might be used as a high voltage source. The breakdown voltage decreases when the ammonia frost has grown on and arround the focuser after several hour's run.

The microwave output from the cavity is taken out through a mica window in a wave-

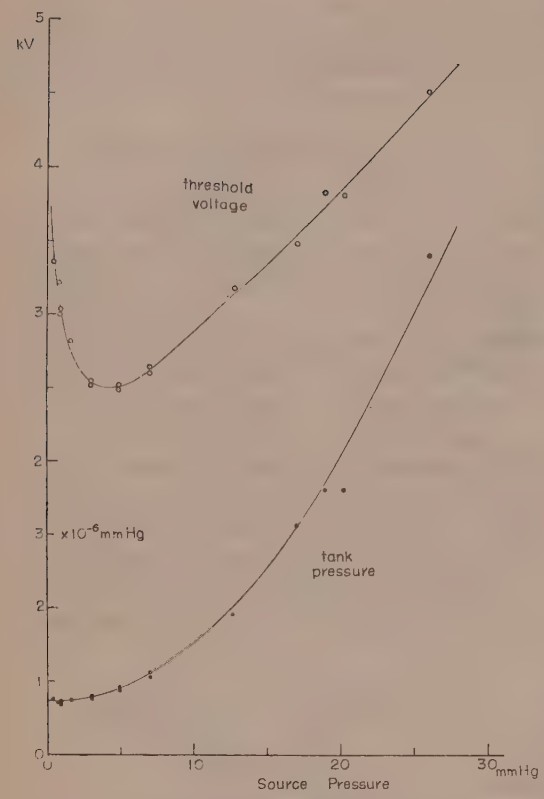

Fig. 4. Threshold voltage and tank pressure with the crinkle foil source as shown in Fig. 2 (c).

guide flange and fed to a crystal mixer. A crystal tripler driven by an X-band klystron, 2K-25, tuned to about 7940 Mc/sec. is used as a local oscillator. With the intermediate frequency of arround 45 Mc/sec. and a 1N26 crystal as mixer, the optimum signal-to-noise ratio was obtained at the rectified current of 30–100μA. The maximum rectified current of the output from the crystals tripler was 303μA, using the best 1N26 among 16 units.

§ 3. Amplitude of Oscillation

The amplitude of oscillation of the ammonia maser was measured and a typical result is shown in Fig. 5. The absolute rf amplitude could not be measured, but the relative amplitude was obtained on the CRO screen. The scale of the ordinate in Fig. 5 has been so adjusted that the amplitude at low focuser voltage may fit the theoretical value of I. The observed amplitude characteristics agrees fairly well with the velocity distribution theory, except that the deviation from approximate calculation with the effective average velocity appears at lower voltage than tha estimated in Fig. 3 of I.

The relative amplitude of oscillation as function of source pressure was reported b Helmer[4]. An example with the 12-hole sourc is shown in Fig. 6 together with the operatin tank pressure. The amplitude shows a max mum at an optimum pressure, as the numbe

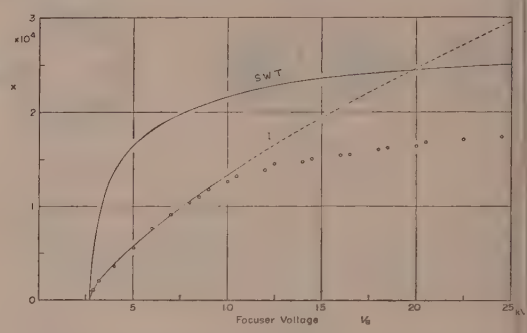

Fig. 5. Observed and theoretical amplitude of oscillation. SWT: uni-velocity theory[3], I: velocity distribution theory[1], circles: observed values.

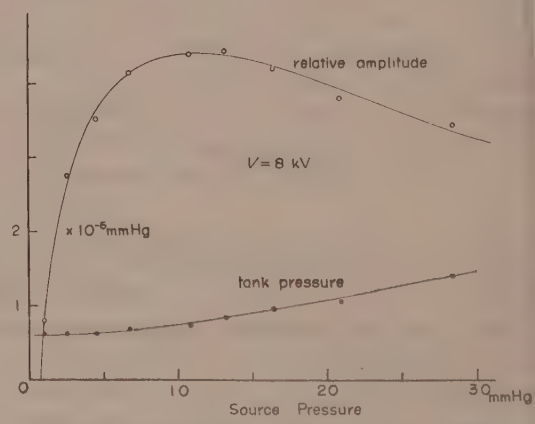

Fig. 6. Ralative amplitude and tank pressure with the 12-hole source.

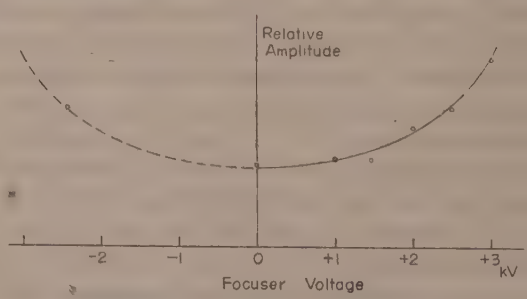

Fig. 7. Change of the relative amplitude of strange oscillation with positive and negative focuser voltage.

of effective molecules at higher source pressure decreases because of the increase of collisions between molecules inside the focuser.

A strange phenomenon was experienced, when the insulator is used arround the hole of the diaphragm which is put close to the end of focuser electrode. After slight discharges by applying overvoltages, the threshold focuser voltage decreased appreciably. Sometimes the maser oscillation could be observed at zero focuser voltage. In this case the amplitude of oscillation increased by applying either positive or negative voltage as illustrated in Fig. 7. Therefore, this cannot be explained by the formation of double layer on the focuser electrode. The amplitude of oscillation at zero focuser voltage increased monotonically with the source pressure as shown in Fig. 8. This

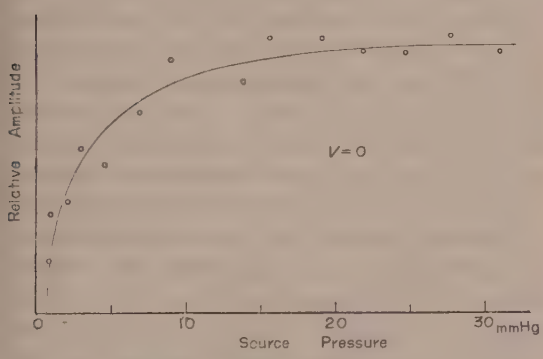

Fig. 8. Relative amplitude of strange oscillation as a function of source pressure.

may be explained from such consideration that the molecules are focused by the electric field arround the diaphragm which is produced by scattered charges on the insulator.

§ 4. Center Frequency of Oscillation

A block diagram of the frequency translator employed in the precise frequency measurement of the maser is shown in Fig. 9. A part of phase lock-in multiplier for an ammonia absorption clock[5] is used for convenience and economy. The 2Mc/sec. crystal oscillator is not very stable, as the Q-value of the quartz crystal is only of the order of 10^4, and the spectrum of the multiplied output is not pure enough to obtain clear beat notes with the maser. This is not due to the random noise but due to the phase modulation produced in the phase lock-in control. Therefore, the beat frequency is divided down by a factor of 24 in order that the maximum frequency deviation becomes much smaller than the value of the phase modulation frequency (2 kc/sec.). Then the 2 Mc/sec. crystal oscillator is controlled so that the divided beat frequency can be phase-locked with respect to the reference signal of 82 kc/sec.

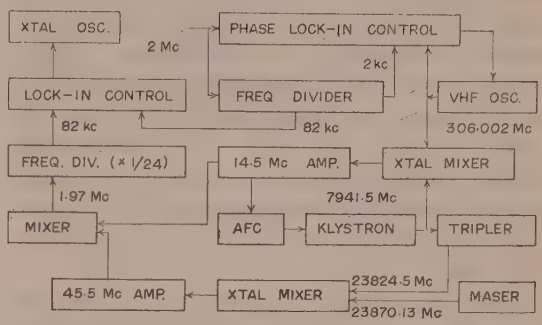

Fig. 9. Block diagram of the frequency translator for the ammonia maser on the 3,3 line.

In this way the frequency of the crystal oscillator, f_x, is controlled by the frequency of the ammonia maser, f_{maser}, with the ratio:

$$\frac{f_x}{f_{\text{maser}}}=\frac{2{,}000}{306{,}002\times 26\times 3+82\times 24}=\frac{2}{23{,}870.124} \qquad (1)$$

The klystron need not be phase-locked in this frequency translator, because it does not affect the beat frequency at the second mixer output written as 1.97 Mc/sec. in Fig. 9. The klystron must only be stabilized so that the beat frequencies with the VHF oscillator and with the maser can be kept within the bandwidth of two i-f amplifiers (14.5 Mc/sec. and 45.5 Mc/sec. amplifiers respectively).

The frequency of the 2 Mc/sec. crystal oscillator, locked to the maser as given in Eq. (1), is compared with the standard frequency broadcast JJY at 5 Mc/sec. and the difference (of the order of 1 cps) is recorded and counted to find the frequency of the maser. The precision of frequency comparison is about 10^{-10}, while the stabitity of the standard frequency broadcast is usually 1 part in 10^9 per day. Sometimes, frequency deviations of several parts in 10^9 which arose from fluctuations in wave propagation were experienced but normally a relative accuracy of about 1 part in 10^9 could be expected since the JJY station

is not far distant. A tentative estimate of the frequency change of JJY has been obtained by the absorption type ammonia clock, and the correction on $UT2$ will be given later.

The frequency of oscillation depends on the cavity design, cavity tuning, focuser voltage, and the source pressure. Relative frequency change with the source pressure has already been reported.[4] Here the absolute frequency shift with the focuser voltage and cavity tuning is reported. In the following experiments the 19-hole source shown in Fig. 2 (b) at the source pressure of about 1 mmHg was used. In order to avoid any complicating effect which might be expected at higher source pressure due to scattering of molecules, lower source pressure than the optimum value was used.

When the cavity is tuned so as to deliver maximum power output or to have minimum threshold voltage, the resonant frequency of the cavity may be assumed to be tuned to the frequency of the line. The observed center frequency of the maser with in-tuned cavity is shown in Fig. 10 as a function of

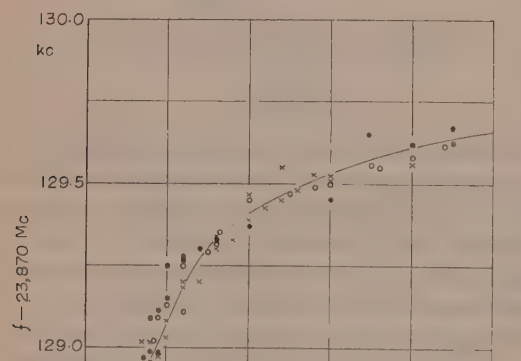

Fig. 10. Center frequency of the ammonia maser on the 3,3 line as a function of the eight-pole focuser voltage.

the focuser voltage, where the frequency is based on the tentative estimate of $UT2$*. The observed frequency increases with the focuser voltage as was theoretically expected in Fig. 7 of I. The experimental results show slower increase at low focuser voltage and do not show independency of focuser voltage even at high voltage, while the magnitude of frequency shift almost agrees with the theoretical result.

The discrepancy can be also explained by the velocity spread of effective molecules flowing into the cavity. Moreover, at higher voltages hyperfine components with $F=3$ and $F=4$ tend to be more divergent and more saturated than the $F=2$ component. Since $F=2$ component lies at a higher frequency, the oscillation frequency still increases at high focuser voltage. Lastly the frequency shift due to the presence of traveling wave in the cavity, which was discussed in SWT[3], must of course be considered. If $V<4.5$ kV in the maser described here, θ is smaller than $\pi/2$ and hence the traveling wave flows in the opposite direction to the beam. At the higher focuser voltage when $V>4.5$ kV, θ is larger than $\pi/2$ and the molecules emit radiation in the former part of the cavity while they absorb in the latter part of the cavity, resulting in the traveling wave in the same direction with the beam. Therefore, as was discussed at the end of page 1315 in ref. (3), the oscillation frequency increases with the focuser voltage by the traveling wave effect. With these considerations which were omitted in I to carry out a simpler calculation, the observed frequency shift can well be explained by the velocity distribution theory. The frequency of oscillation also increases considerably with the cavity length[6], because the longer the cavity, the larger the traveling wave effect and the more important the $F=2$ component which is less divergent becomes.

With these considerations the frequency of ammonia at thermal equilibrium is estimated to be 23,870,129.98±0.15 kc/sec. The uncertainty comes mainly from the tentative estimate of $UT2$ and on the value of the difference of eqQ between the ground and the excited states, which is 3–4 kc/sec. The resettability is of course much better.

On the other hand, the frequency of the ammonia absorption has been measured as 23,870,130.57 kc/sec.** This value seems to

* To obtain revised values of frequencies on $UT2$ Tokyo, Jan. 1958, add +0.07 kc/sec.

** to be published. The values reported before should be corrected by their incorrect estimate of the purity of ammonia and the pressure shift.

include frequency shift due to collision of molecules with the waveguide wall. The frequency of the maser was first measured by Bonanomi et. al. as 23,870,129.42 kc/sec. This was measured with the maser at rather high focuser voltage and extrapolated linearly to zero focuser voltage. Thus it seems to be consistent with more detailed result of Fig. 10, and evidently it includes frequency shift due to quadrupole hyperfine structure. Neither of these two values shows true frequency of a free ammonia molecule.

§ 5. Pulling Effect

The frequency of the maser is pulled by the cavity tuning. A crude theory was given by Gordon *et. al.*[8] and the effect of saturation was calculated by Shimoda *et. al.* based on the uni-velocity theory. However, accurate experimental results have not yet appeared.

The observed frequency of the maser on the 3,3 line of ammonia changes with the cavity tuning and with focuser voltage as shown in Fig. 11. Each curve corresponds to different cavity tuning, which could not be determined quantitatively. These curves show clearly an asymmetrical behavior for the cavity tunings at higher and lower frequencies. This is understood as the superposition of the pulling effect on the center frequency shift due to the unresolved hyperfine structure. Therefore, the frequency pulling can be evaluated by taking the difference with the center frequency shown in Fig. 10.

From Eq. (6) in SWT[3] the pulling is theoretically given by

$$\omega-\omega_0=2Q\frac{v}{L\omega_0}f_2(\theta)\cdot(\omega_c-\omega_0) \qquad (2)$$

$$f_2(\theta)=\frac{1-\cos 2\theta}{1-\sin 2\theta/2\theta} \qquad (3)$$

where ω_0 is the center frequency, ω_c the resonant frequency of the cavity, and $\theta=[(\omega-\omega_0)^2+x^2]^{1/2}L/2v$.

Although ω_c was not measured but the starting voltage for the respective cavity setting, V_{th}, was carefully measured. From Eq. (2.6) of I, the critical radial velocity of molecules, v_c, can be calculated. The value of the critical radial velocity for the tuned cavity which corresponds to the minimum starting focuser voltage is denoted by v_{c0}. Then from Eq. (3.10) of I, one obtains

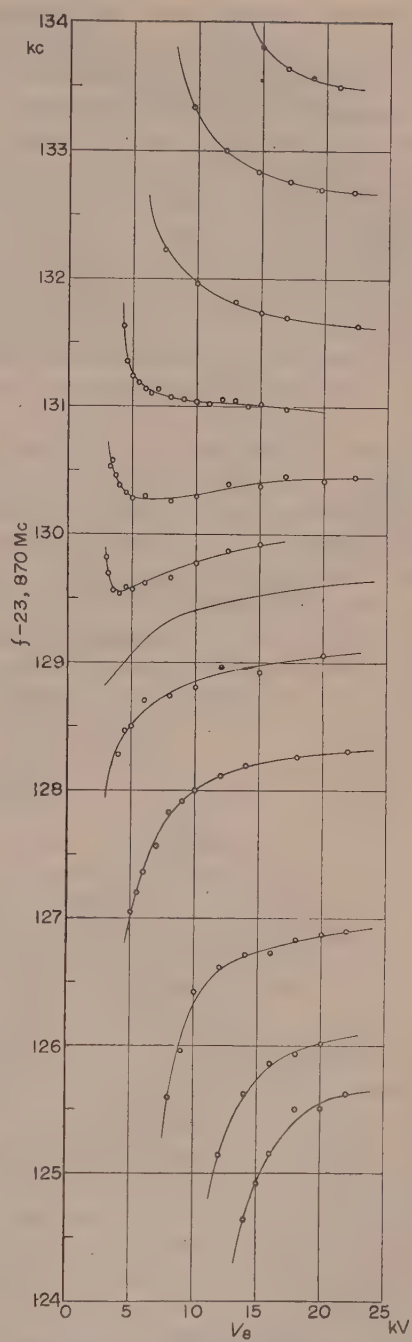

Fig. 11. Frequency change of the ammonia maser. Each curve corresponds to different cavity tuning.

$$\frac{V_{th,\min}}{V_{th}}=\frac{v_{c0}}{v_c}=\frac{\sin(\omega-\omega_0)L/2v}{(\omega-\omega_0)L/2v} \qquad (4)$$

by putting $x=0$ for the starting condition. The magnitude of frequency pulling at the threshold can be calculated from this equation. The value of v may be taken equal to the

most probable velocity from the reasoning described at the end of § 2 in I, since $(\omega-\omega_0)^2 \gg x^2$ in this case. In order to fit it with the extrapolated value of the observed pulling at finite amplitudes, the cavity length, L, must be taken as 8 cm, although the physical length of the cavity is 12 cm. A cavity with large holes at both ends of the cylinder can not produce uniform electric field along the length of the cavity, but the field decreases at both ends in such a way that the cavity might be considered as the open ended TM_{011} mode. Thus the effective length of 8 cm is plausible.

Now, for $x=0$ the magnitude of detuning, $(\omega_c-\omega_0)Qv/L$, can be calculated using Eqs. (2) and (3), since $\omega-\omega_0$ is known from the threshold voltage. The observed change of frequency pulling with the amplitude of oscillation gives the experimental value of the pulling factor, $f_2(\theta)$ in Eq. (2). The value of θ as a function of the focuser voltage is obtained from Eq. (3.10) in I and Fig. 5 in this paper.

The observed pulling factor is plotted in Fig. 12 as a function of θ. Theoretical pulling factor of the uni-velocity beam, Eq. (3), is shown by a solid curve. Although the frequency of the maser could be measured at the focuser voltage only 100 volt above the threshold, frequency pulling for small values of θ could not be obtained, because $\omega-\omega_0$ as well as x must be small for a small value of θ, and the pulling factor for slight detuning was very difficult to measure.

Deviations of the observed points from Eq. (3) are very plausibly explained by the velocity distribution of molecules flowing into the cavity. All molecules in the beam are put in a common oscillating field given by ω and x, but they have different values of θ, when their velocities are different. Therefore, the measured value of the pulling factor must be a kind of average of theoretical value of $f_2(\theta)$. As are shown by broken lines in Fig. 12, it may be estimated that the velocity spread

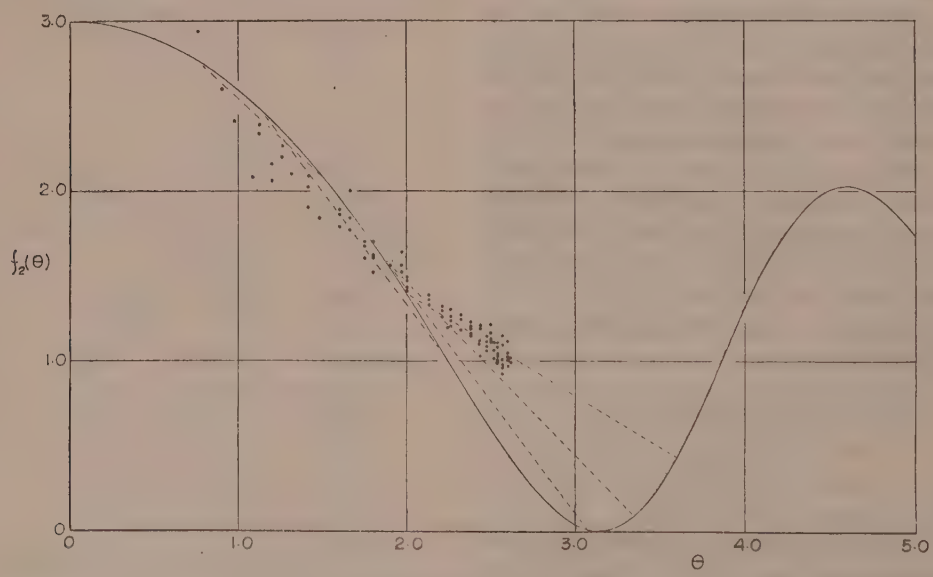

Fig. 12. Observed and theoretical pulling factor as a function of θ.

of effective molecules in the beam is roughly $\pm 30\%$.

In conclusion it appears that the considerations and observations described in these two papers have revealed most of the complicated behavior of beam type masers. Then it has become possible to design a more reliable frequency standard by the beam type maser.

Acknowledgment

The author expresses his thanks for the assistance of Messrs. H. Takuma, Y. Saburi, and N. Kohno. He is also indebted to Dr. J. C. Helmer for the information of his unpublished works.

References

1) K. Shimoda: J. Phys. Soc. Japan, **12** (1957) 1006.
2) J. Bonanomi, J. De Prins, J. Herrmann et P. Kartschoff: Helv. Phys. Acta, **30** (1957) 492.
3) K. Shimoda, T. C. Wang, and C. H. Townes: Phys. Rev., **102** (1956) 1308.
4) J. C. Helmer: J. Appl. Phys., **28** (1957) 212.
5) K. Shimoda: J. Phys. Soc. Japan, **9** (1954) 378, 558, and 567. Further work will be published later.
6) J. Bonanomi, J. De Prins, J. Herrmann et P. Kartschoff: Helv. Phys. Acta, **30** (1957) 288.
7) J. Bonanomi et J. Herrmann: Helv. Phys. Acta, **29** (1956) 451.
8) J. P. Gordon, H. J. Zeiger, and C. H. Townes: Phys. Rev., **99** (1955) 1264.

Errata

Ref. 1), (I), page 1009, line 10 from bottom: $\frac{2\pi L^2}{\sqrt{\pi}\,\alpha^3}v_c^2(\cdot\cdot$ should read $\frac{2NL^2}{\sqrt{\pi}}\frac{A_i}{\alpha^3}v_c^2(\cdot\cdot$

line 8 from bottom: Eq. (2.17) should read Eq. (2.18).

JOURNAL OF THE PHYSICAL SOCIETY OF JAPAN Vol. 13, No. 8, AUGUST, 1958

The Maximum Disturbance Growth Rate for an Unstable Plasma Column

By Shobu KANEKO

Department of Physics, Faculty of Science, University of Tokyo

(Received May 6, 1958)

A dispersion relation for a self-pinched plasma column enclosed by a conducting wall is derived for the case of a model with both surface sheet current and uniform volume current. On the basis of this dispersion relation the maximum disturbance growth rate for the instability is calculated. Both the uniform volume current and longitudinal magnetic flux outside the plasma column decrease the stability and make the growth rate faster, the effect of the magnetic flux being larger.

§ 1. Introduction

In order to make a thermonuclear reactor, it is necessary to confine a hot plasma apart from the vessel for a considerably long time. For this purpose, the application of the "pinch effect" is promissing; but unfortunately a plasma column pinched by a large electric current is unstable. This instability was first investigated theoretically by Kruskal and Schwarzschild[1]; and their work was generalized by Tayler[2]. Shrafranov[3] investigated the influence of a longitudinal magnetic field on this instability. He found that, although a sufficiently strong longitudinal magnetic field within the plasma stabilizes the plasma column against constrictions and short wave-length kinks and also against deformations of higher modes, it does not stablilize the column against long wave-length kinks. Moreover a longitudinal magnetic field outside the plasma has the effect of increasing this instability. So he did not succeed in obtaining the completely stable configuration. Recently, Tayler[4] and Kihara[5] have pointed out independently, by using the sheet current model, that there is a perfectly stable configuration when a longitudinal magnetic field is supplied and the plasma is enclosed by a conducting wall.

In this article we rather investigate unstable regions, and calculate the maximum disturbance growth rate for the instability for the most unstable mode, kink disturbance, by the method of Kruskal and Schwarzschild.

§ 2. Basic Equations, Equilibrium Configuration and Boundary Conditions

In what follows we consider a neutral, ideally conducting plasma column in an equi-

librium state, surrounded by vacuum which is itself enclosed by an ideally conducting cylindrical wall.

Magnetohydrodynamic basic equations for the plasma are

$$\rho\frac{dv}{dt}=\boldsymbol{J}\times\boldsymbol{B}-\mathrm{grad}\,p\,, \tag{2.1}$$

$$\frac{\partial\rho}{\partial t}=-\mathrm{div}\,\rho\boldsymbol{v}\,, \tag{2.1}$$

$$\frac{\partial\boldsymbol{B}}{\partial t}=\mathrm{rot}\,(\boldsymbol{v}\times\boldsymbol{B})\,, \tag{2.3}$$

$$p=\mathrm{const}\,\rho^{\gamma}\,, \tag{2.4}$$

where ρ is the mass density, $\boldsymbol{v}$ the mass velocity, $\boldsymbol{J}$ the electric current density, $\boldsymbol{B}$ magnetic flux, p the pressure and γ the specific heat ratio. In this article the MKS rational system of units is used throughout. As regards these basic equations, Kihara[5] has recently investigated in detail and found that the induction equation (2.3) is valid when the growth rate is smaller than the cyclotron frequency of the ion (i.e. in the quasi-static case).

In the equilibrium configuration, we assume the distribution of the magnetic flux in the cylindrical coordinate system to be

$$(B_r, B_\varphi, B_z)=\begin{cases}(0, B_0\alpha r, B_0) & \text{for } 0\leqq r<a\\ (0, B_1(a/r), B_2) & \text{for } a<r<b\,.\end{cases} \tag{2.5}$$

Here a and b are the radii of the plasma column and the conducting wall respectively; B_0, B_1 and B_2 are constants and αa is assumed to be so small that its square may be neglected. Kihara[5] has pointed out that this model of a self-pinched plasma column will be close to the reality and is appropriate for mathematical treatment. The configuration is in equilibrium provided that

$$\left.\begin{aligned}&J_{ze}=\frac{2}{\mu}B_0\alpha\,,\\&J^*_{\varphi e}=\frac{1}{\mu}(B_0-B_2)\,,\\&J^*_{ze}=\frac{1}{\mu}(B_1-B_0\alpha a)\,,\\&p_e+\frac{B_0^2}{2\mu}=\frac{1}{2\mu}(B_1^2+B_2^2)\,,\end{aligned}\right\} \tag{2.6}$$

where μ is the permeability, the asterisk means the sheet current, and the subscript e stands for the equilibrium state.

Following Kruskal and Schwarzschild, we consider perturbations about the equilibrium state in the form

$$q=q_e+q_p=q_e+q_p(r)\exp\{i(m\varphi+kz)+\omega t\}\,. \tag{2.7}$$

Here the subscript p stands for a perturbed variable, k is a real wave number, m is an integer positive or negative and ω is the disturbance growth rate if ω^2 is positive. Recently Hain, Lüst and Schlüter[6] have proved in general that ω^2 is real for these problems, so there is no overstable solution, that is to say, oscillating solution with increasing amplitude. The dispersion relation, [see the equation (3.12) below], shows that k, B_0/B_1 and B_2/B_1 can be taken as positive if we consider both positive and negative values of m.

Let the gas particles suffer small displacements $\boldsymbol{\xi}(r)\exp\{i(m\varphi+kz)+\omega t\}$, then the surface of the plasma column is displaced by an amount of $\boldsymbol{\xi}(a)\exp\{i(m\varphi+kz)+\omega t\}$. So the unit normal vector $\boldsymbol{n}=(n_r, n_\varphi, n_z)$ to this surface becomes

$$\boldsymbol{n}=(1,0,0)+\left\{0, -\frac{im}{a}\xi_r(a), -ik\xi_r(a)\right\}\times\exp\{i(m\varphi+kz)+\omega t\}\,. \tag{2.8}$$

Boundary condition, sufficient for obtaining the dispersion relation, is as follows

$$\left.\begin{aligned}&p+\frac{1}{2\mu}B^2 && \text{is continuous and}\\&B_n && \text{is continuous}\end{aligned}\right\} \tag{2.9}$$

on the perturbed plasma surface, and

$$B_n \quad \text{vanishes} \tag{2.10}$$

on the rigid conducting wall.

§ 3. Calculation of the Perturbed Variables and the Dispersion Relation

First we consider the inside of the plasma column. In the approximation that only terms linear in perturbations are retained, the perturbation to any quantity is proportional to the displacement.

Equations (2.1) through (2.4) become in this approximation

$$\left.\begin{aligned}&\rho_p=-\rho_e\,\mathrm{div}\,\boldsymbol{\xi}\,,\\&\boldsymbol{B}_p=\mathrm{rot}\,(\boldsymbol{\xi}\times\boldsymbol{B}_e)\,,\\&p_p=-\gamma p_e\,\mathrm{div}\,\boldsymbol{\xi}\,,\end{aligned}\right\} \tag{3.1}$$

and

$$\omega^2\rho_e\boldsymbol{\xi}=\gamma p_e\,\mathrm{grad}\cdot\mathrm{div}\,\boldsymbol{\xi}+\frac{1}{\mu}(\mathrm{rot}\,\boldsymbol{B}_e\times\boldsymbol{B}_p)+\frac{1}{\mu}(\mathrm{rot}\,\boldsymbol{B}_p\times\boldsymbol{B}_e)\,. \tag{3.2}$$

Using equations (3.1) and (3.2) and retaining terms linear in $\boldsymbol{\xi}$ and αr, we obtain simultaneous differential equations for components of the displacement $\boldsymbol{\xi}(r)$:

$$\left.\begin{aligned}
&(c^2+c_H{}^2)\,\mathrm{DD}^+\,\xi_r(r)-(\omega^2+k^2c_H{}^2+2\alpha kmc_H{}^2)\xi_r(r)+im(c^2+c_H{}^2)\,\mathrm{D}\,\frac{\xi_\varphi(r)}{r}\\
&\qquad -i\alpha kc_H{}^2\,\mathrm{D}\,\{r\xi_\varphi(r)\}+i(kc^2-\alpha mc_H{}^2)\,\mathrm{D}\,\xi_z(r)=0\,,\\
&\frac{im}{r}(c^2+c_H{}^2)\,\mathrm{D}^+\,\xi_r(r)-i\alpha kc_H{}^2r^2\,\mathrm{D}\,\frac{\xi_r(r)}{r}-\left\{\omega^2+\frac{m^2}{r}(c^2+c_H{}^2)+k^2c_H{}^2\right\}\xi_\varphi(r)\\
&\qquad -\{kmc^2-\alpha(m^2+k^2r^2)c_H{}^2\}\frac{\xi_z(r)}{r}=0\,,\\
&i(kc^2-\alpha mc_H{}^2)\,\mathrm{D}^+\,\xi_r(r)-\{kmc^2-\alpha(m^2+k^2r^2)c_H{}^2\}\frac{\xi_\varphi(r)}{r}-(\omega^2+k^2c^2)\xi_z(r)=0\,.
\end{aligned}\right\} \tag{3.3}$$

Here we have used the notations

$$\mathrm{D}=\frac{d}{dr}\,,$$

$$\mathrm{D}^+=\frac{d}{dr}+\frac{1}{r}\,,$$

$$c^2=\gamma\frac{p_e}{\rho_e}\qquad\text{square of the sound-wave velocity,}$$

$$c_H{}^2=\frac{B_0{}^2}{\mu\rho_e}\qquad\text{square of the Alfvén-wave velocity.}$$

From this set of equations, we get expressions for $\xi_\varphi(r)$, $\xi_r(r)$ in terms of $\xi_z(r)$:

$$\left.\begin{aligned}
\xi_\varphi(r)=&\frac{1}{k^2c^4(\omega^2+k^2c^2)^2}\Bigg[\frac{km\kappa c^2}{r}(\omega^2+k^2c_H{}^2)+\alpha\kappa c_H{}^2\,\frac{m^2(c^2+c_H{}^2)-k^2r^2c^2}{r}\left(\mathrm{D}^+\mathrm{D}-\frac{m^2}{r^2}\right)\\
&+2\alpha k^2\kappa c^2c_H{}^2\,\mathrm{D}+\frac{\alpha k^2c_H{}^2}{r}\{c^4(m^2+k^2r^2)(\omega^2+k^2c_H{}^2)-m^2\kappa(2c^2+c_H{}^2)\}\Bigg]\xi_z(r)\,,\\
\xi_r(r)=&-\frac{i}{k^2c^4(\omega^2+k^2c_H{}^2)^2}\Bigg[k\kappa c^2(\omega^2+k^2c_H{}^2)\,\mathrm{D}+\alpha m\kappa c_H{}^2(c^2+c_H{}^2)\,\mathrm{D}\left(\mathrm{D}^+\mathrm{D}-\frac{m^2}{r^2}\right)\\
&+\frac{2\alpha k^2m\kappa c^2c_H{}^2}{r}+\alpha k^2mc_H{}^2\{c^4(\omega^2+k^2c_H{}^2)-\kappa(2c^2+c_H{}^2)\}\,\mathrm{D}\Bigg]\xi_z(r)\,,
\end{aligned}\right\} \tag{3.4}$$

where the notation

$$\kappa=\omega^2(c^2+c_H{}^2)+k^2c^2c_H{}^2$$

has been used for simplicity.

Equations (3.3) and (3.4) give a differential equation for $\xi_z(r)$:

$$\mathrm{D}^+\mathrm{D}\,\xi_z(r)-\left[\frac{m^2}{r^2}+\beta^2\right]\xi_z(r)=0\,, \tag{3.5}$$

where

$$\beta^2=\frac{(\omega^2+k^2c^2)(\omega^2+k^2c_H{}^2)}{\omega^2(c^2+c_H{}^2)+k^2c^2c_H{}^2}-\frac{2\alpha km\omega^4c^2c_H{}^2}{\{\omega^2(c^2+c_H{}^2)+k^2c^2c_H{}^2\}^2}\,.$$

This is a modified Bessel equation, whose solution finite at $r=0$ is

$$\xi_z(r)=C^i I_m(\beta r)=C^i\{I_m(\beta_1 r)-\beta_2 r I_m'(\beta_1 r)\}+O(\alpha^2)\ ,$$

$$\beta_1{}^2=\frac{(\omega^2+k^2c^2)(\omega^2+k^2c_H{}^2)}{\omega^2(c^2+c_H{}^2)+k^2c^2c_H{}^2}\ ,\qquad \beta_2=\frac{\alpha k m\omega^4c^2c_H{}^2}{\beta_1\{\omega^2(c^2+c_H{}^2)+k^2c^2c_H{}^2\}^2}\ .$$

Here C^i is an arbitrary constant, the superscript i meaning inside of the plasma; the prime indicates derivative with respect to the argument. Substituting this solution for $\xi_z(r)$ into the equations (3.4) for $\xi_\varphi(r)$ and $\xi_r(r)$, we obtain

$$\left.\begin{aligned}
\xi_z(r)&=C^i\{I_m(\beta_1 r)-\beta_2 r I_m'(\beta_1 r)\}\ ,\\
\xi_\varphi(r)&=\frac{C^i}{k^2c^4(\omega^2+k^2c_H{}^2)^2}\Bigg[\frac{km\kappa c^2}{r}(\omega^2+k^2c_H{}^2)I_m(\beta_1 r)+2\alpha k^2\kappa c^2c_H{}^2\beta_1 I_m'(\beta_1 r)\\
&\quad+\frac{\alpha\omega^2c_H{}^2}{r}\{m^2\omega^2(2c^2+c_H{}^2)-c^2(m^2+k^2r^2)(\omega^2+k^2c_H{}^2)\}I_m(\beta_1 r)\\
&\quad-\beta_2 km\kappa c^2(\omega^2+k^2c_H{}^2)I_m'(\beta_1 r)\Bigg]\ ,\\
\xi_r(r)&=\frac{-iC^i}{k^2c^4(\omega^2+k^2c_H{}^2)^2}\Bigg[k\kappa c^2(\omega^2+k^2c_H{}^2)\beta_1 I_m'(\beta_1 r)+\frac{2\alpha k^2m\kappa c^2c_H{}^2}{r}I_m(\beta_1 r)\\
&\quad+\alpha m\omega^2c_H{}^2\{\omega^2(c^2+c_H{}^2)-k^2c^2c_H{}^2\}\beta_1 I_m'(\beta_1 r)\\
&\quad-k\kappa c^2(\omega^2+k^2c_H{}^2)\left(\beta_1{}^2+\frac{m^2}{r^2}\right)\frac{\beta_2}{\beta_1}rI_m(\beta_1 r)\Bigg]\ .
\end{aligned}\right\}\tag{3.6}$$

Next let us consider the outside which is vacuum. In this part there flows no electric current, so the magnetic flux is irrotational and determined by the scalar potential $\psi(r,\varphi,z)$,

$$\boldsymbol{B}=\mathrm{grad}\,\psi\ ,\qquad \psi=\psi_e{}^o+\psi_p{}^o(r)\exp\{i(m\varphi+kz)+\omega t\}\ ,\tag{3.7}$$

where superscript o stands for the outside of the plasma column. From this equation we obtain perturbations on the magnetic flux as follows:

$$\left.\begin{aligned}
B_{pr}^o(r)&=kC_1{}^oK_m'(kr)+kC_2{}^oI_m'(kr)\ ,\\
B_{p\varphi}^o(r)&=\frac{im}{r}C_1{}^oK_m(kr)+\frac{im}{r}C_2{}^oI_m(kr)\ ,\\
B_{pz}^o(r)&=ikC_1{}^oK_m(kr)+ikC_2{}^oI_m(kr)\ .
\end{aligned}\right\}\tag{3.8}$$

Here $I_m(x)$ and $K_m(x)$ are the modified Bessel functions; and $C_1{}^o$, $C_2{}^o$ are constants to be determined by the boundary conditions (2.9) and (2.10). The results are

$$\left.\begin{aligned}
C_1{}^o&=\frac{i\xi_r(a)}{ka}(mB_1+kaB_2)\frac{I_m'(kb)}{K_m'(ka)I_m'(kb)-I_m'(ka)K_m'(kb)}\ ,\\
C_2{}^o&=-\frac{i\xi_r(a)}{ka}(mB_1+kaB_2)\frac{K_m'(kb)}{K_m'(ka)I_m'(kb)-I_m'(ka)K_m'(kb)}\ .
\end{aligned}\right\}\tag{3.9}$$

Now we can derive the dispersion relation by using these solutions. The boundary condition (2.9) is now expressed in the form

$$2\mu p+B_\varphi{}^{i2}+B_z{}^{i2}=B_\varphi{}^{o2}+B_z{}^{o2}\ .$$

By using relations

$$B_\varphi{}^i(a+\xi_r)=B_{e\varphi}^i(a)+\left(\frac{dB_{e\varphi}^i}{dr}\xi_r\right)_{r=a}+(B_{p\varphi}^i)_{r=a}$$

etc., and equations (3.8) and (3.9), we get

$$\mu\gamma p_e(\mathrm{div}\,\boldsymbol{\xi})_{r=a}=\frac{\xi_r(a)}{a}B_1^2-\frac{\xi_r(a)}{a}(mB_1+kaB_2)^2F(ka,kb)$$
$$+\{ik\xi_z(a)-(\mathrm{div}\,\boldsymbol{\xi})_{r=a}\}B_0^2+i\alpha\{m\xi_z(a)+ka\xi_\varphi(a)\}B_0^2\,,$$

where

$$\mathrm{div}\,\boldsymbol{\xi}=\frac{1}{r}\frac{d}{dr}\{r\xi_r(r)\}+\frac{im}{r}\xi_\varphi(r)+ik\xi_z(r)\,,$$

and

$$F(ka,kb)=\frac{K_m(ka)I_m'(kb)-I_m(ka)K_m'(kb)}{ka[K_m'(ka)I_m'(kb)-I_m'(ka)K_m'(kb)]}\,.$$

Inserting the solution (3.6) for the displacement $\boldsymbol{\xi}(r)$, we finally obtain the dispersion relation

$$\beta_1 a\left[\left(\frac{B_0}{B_1}\right)^2+\frac{\gamma\omega^2}{2(\omega^2+k^2c^2)}\left\{1+\left(\frac{B_2}{B_1}\right)^2-\left(\frac{B_0}{B_1}\right)^2\right\}\right]\frac{I_m(\beta_1 a)}{I_m'(\beta_1 a)}+\alpha aL$$
$$=\left[1+\left\{m+ka\left(\frac{B_2}{B_1}\right)\right\}^2F(ka,kb)\right][1+\alpha aR]\,, \tag{3.10}$$

where

$$L=\frac{m\beta_1}{kc^2(\omega^2+k^2c^2)(\omega^2+k^2c_H^2)}\left[\left(\frac{B_0}{B_1}\right)^2\{\omega^2c_H^2(\omega^2+k^2c^2)+2k^2c^4(\omega^2+k^2c_H^2)\}\right.$$
$$\left.+\frac{\gamma}{2}\left\{1+\left(\frac{B_2}{B_1}\right)^2-\left(\frac{B_0}{B_1}\right)^2\right\}\omega^4c_H^2\right]\frac{I_m(\beta_1 a)}{I_m'(\beta_1 a)}$$
$$-\frac{kma\omega^4c^2c_H^2}{(\omega^2+k^2c^2)\{\omega^2(c^2+c_H^2)+k^2c^2c_H^2\}^2}\left[\left(\frac{B_0}{B_1}\right)^2(\omega^2+k^2c^2)+\frac{\gamma}{2}\left\{1+\left(\frac{B_2}{B_1}\right)^2-\left(\frac{B_0}{B_1}\right)^2\right\}\omega^2\right],$$

$$R=\frac{km\beta_1c_H^2}{a^2(\omega^2+k^2c^2)^2(\omega^2+k^2c_H^2)^2}\left[2(\omega^2+k^2c^2)\{\omega^2(c^2+c_H^2)+k^2c^2c_H^2\}-\omega^4c^2(\beta_1^2a^2+m^2)\right]\frac{I_m(\beta_1 a)}{I_m'(\beta_1 a)}$$
$$+\frac{m\omega^2c_H^2\{\omega^2(c^2+c_H^2)-k^2c^2c_H^2\}}{kac^2(\omega^2+k^2c_H^2)\{\omega^2(c^2+c_H^2)+k^2c^2c_H^2\}}\,.$$

It is convenient for the purpose of calculating the disturbance growth rate for the instability to express this dispersion relation in terms dimensionless variables. Thus we introduce the dimensionless variables:

$$ka=X\,,\quad \beta_1 a=U\,,\quad \alpha a=A\,,\quad \frac{\omega a}{c}=W\,,$$
$$\frac{b}{a}=\Lambda\,,\quad \frac{c}{c_H}=C\,,\quad \frac{B_0}{B_1}=b_i\quad\text{and}\quad \frac{B_2}{B_1}=b_e\,. \tag{3.11}$$

Then equation (3.10) becomes

$$U\left[b_i^2+\frac{\gamma W^2(1+b_e^2-b_i^2)}{2(X^2+W^2)}\right]\frac{I_m(U)}{I_m'(U)}+AL=[1+(m+b_eX)^2F(X,\Lambda X)][1+AR]\,, \tag{3.12}$$

where

$$U=\frac{(X^2+W^2)(X^2+C^2W^2)}{X^2+(C^2+1)W^2}\,,$$

$$F(X,\Lambda X)=\frac{K_m(X)I_m'(\Lambda X)-I_m(X)K_m'(\Lambda X)}{X[K_m'(X)I_m'(\Lambda X)-I_m'(X)K_m'(\Lambda X)]}\,,$$

$$L=\frac{mU}{X(X^2+W^2)(X^2+C^2W^2)}\Big[b_i^2\{W^2(X^2+W^2)+2X^2(X^2+C^2W^2)\}$$
$$+\frac{\gamma}{2}(1+b_e^2-b_i^2)W^4\Big]\frac{I_m(U)}{I_m'(U)}$$
$$-\frac{mC^2XW^4}{(X^2+W^2)\{X^2+(C^2+1)W^2\}^2}\Big[b_i^2(X^2+W^2)+\frac{\gamma}{2}(1+b_e^2-b_i^2)W^2\Big],$$

$$R=\frac{mXU}{(X^2+W^2)^2(X^2+C^2W^2)^2}[2(X^2+W^2)\{X^2+(C^2+1)W^2\}-W^4C^2(m^2+U^2)]\frac{I_m(U)}{I_m'(U)}$$
$$-\frac{mW^2\{X^2-(C^2+1)W^2\}}{X(X^2+C^2W^2)\{X^2+(C^2+1)W^2\}}.$$

This is a generalization of the equation (3.12) of Tayler's paper[4]: he used the sheet current approximation, so we get his equation by putting $A=0$ in our equation.

Further, let W equal zero in our equation, then we get

$$b_i^2=\frac{I_m'(X)}{XI_m(X)}\Big[1-\frac{2mA}{X}\Big\{1-\frac{XI_m(X)}{I_m'(X)}\Big\}\Big][1+(m+b_eX)^2F(X,\Lambda X)]\,. \tag{3.13}$$

This equation was first given by Kihara[5].

Considering the fact that the sings of $1-XI_m(X)/I_m'(X)$ and $F(X,\Lambda X)$ are positive and negative respectively, we can easily show that the modes with negative m are more difficult to stabilize than the modes with positive m. In addition to this, the kink disturbance ($m=\pm1$) is most difficult to stabilize (see References 2), 4)), so we shall consider only the mode with $m=-1$ in the following.

In order to find the completely stable region, Kihara calculated the minimum values of b_i^2 needed for stability as a function of X for various values of Λ using the model $A=0$ and $b_e=0$. Only for this model the mode with $m=-1$ coincides with the mode with $m=1$, and the results are shown graphically in Fig. 4 of his paper[5], which is reproduced in Fig. 1 of the present article.

Then taking b_i^2 as a parameter we calculate the growth rate W, as a function of X in the region of instability and determine the maximum value w of W for each b_i^2. The results are shown in Fig. 2. In this and the following calculations the specific heat ratio γ is assumed to be 5/3. For $b_i^2=1$ the growth rate of an unstable plasma is infinite as it

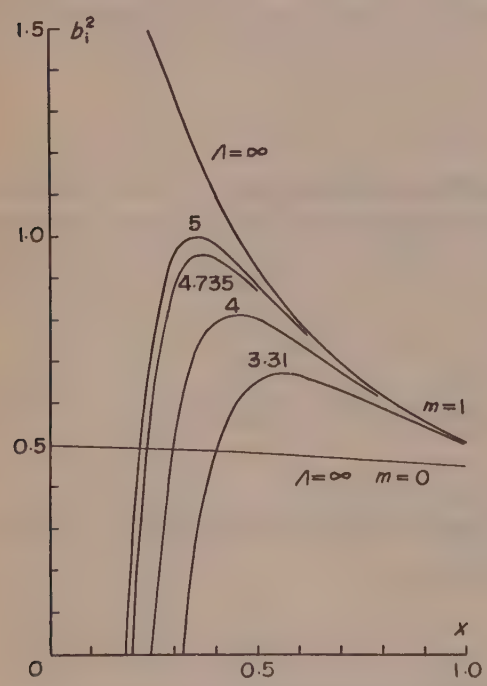

Fig. 1. Stabilizing values of b_i^2 against X for the modes with $m=0$ and $m=1$ of the sheet current model with $b_e=0$.

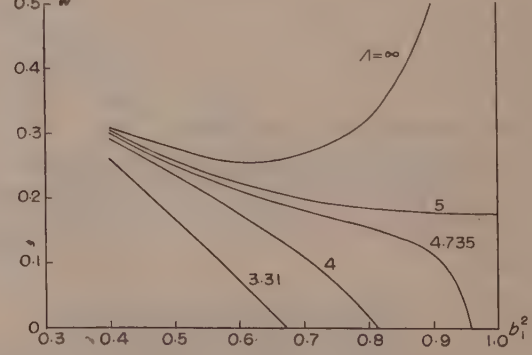

Fig. 2. Curves for maximum growth rate w against b_i^2 for the unstable $m=1$ mode of the sheet current model.

should be since the inertia of the plasma vanishes.

Next we take into account the effects of the uniform volume current within the plasma column and the longitudinal magnetic flux outside the column. Recently Ogasawara[7] has investigated these effects on Kihara's work. We are now interested in the variation of the "critical" value of Λ and the corresponding maximum disturbance growth rate for the instability. For configurations $A=1/4$, $b_e=0$ ane $A=0$, $b_e=1/10$, the critical values of Λ are 4.735 and 3.31 respectively (see Fig. 3). In each case, the maximum disturbance growth rate for the instability is calculated and shown in Figs. 4 and 5.

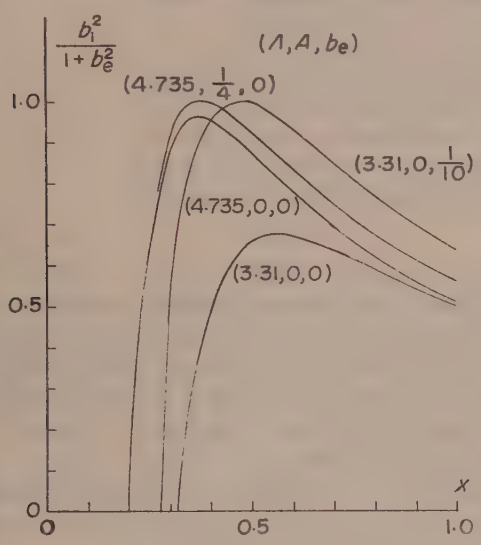

Fig. 3. Stabilizing values of $b_i^2/1+b_e^2$ against X for the unstable $m=-1$ mode of models: $A=1/4$, $b_e=0$ and $A=0$ $b_e=1/10$.

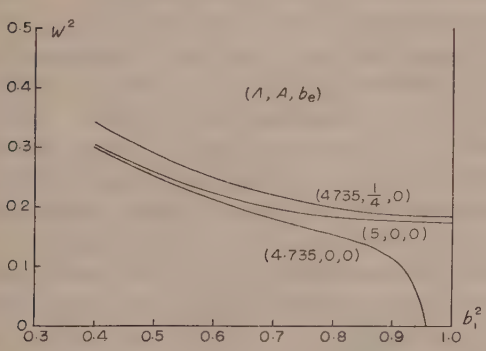

Fig. 4. Curves for maximum growth rate w against b_i^2 for the unstable $m=-1$ mode of the model $A=1/4$, $b_e=0$, $\Lambda=4.735$ and its corresponding sheet current model. For comparison a curve for the sheet current model with $\Lambda=5$ is also drawn.

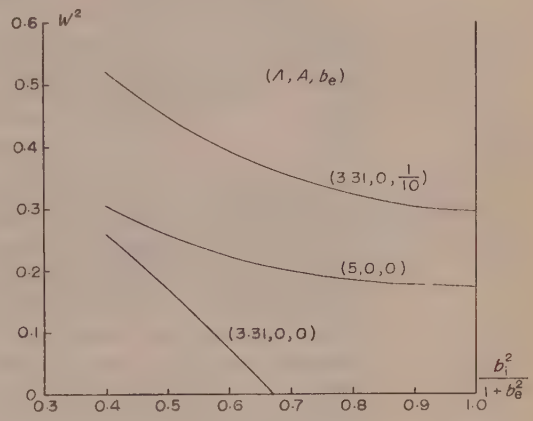

Fig. 5. Curve for maximum growth rate w against $b_i^2/1+b_e^2$ for the unstable $m=-1$ mode of the model $A=0$, $b_e=1/10$, $\Lambda=3.31$ and its corresponding sheet current model with $b_e=0$. For comparison a curve for the sheet current model with $\Lambda=5$ is also drawn.

§ 4. Conclusion

From the above investigation we obtain the following results.

(1) The weak uniform current inside the plasma slightly contracts the stable region and at the same time makes the growth rate a little faster. This is reasonable because the effective radius of the plasma column may decrease on account of the uniform current.

(2) The longitudinal magnetic flux outside the plasma column greatly contracts the stable region and at the same time makes the growth rate much faster.

In conclusion, the author wishes to express his sincere thanks to Prof. T. Kihara for his continual guidance and for his kindness in reading the original manuscript.

References

1) M. D. Kruskal and M. Schwarzschild: Proc. Roy. Soc. (London) A **223** (1954) 348.
2) R. J. Tayler: Proc. Phys. Soc. **B 70** (1957) 31.
3) V. D. Shrafranov: Atomnaya Energia **1** (1956) 38; or Nuclear Energy II **5** (1957) 86.
4) R. J. Tayler: Proc. Phys. Soc. **B 70** (1957) 1049.
5) T. Kihara: J. Phys. Soc. Japan **13** (1958) 473.
6) K. Hain, R. Lüst and A. Schlüter: Z. Naturforschg. **12 a** (1957) 833.
7) M. Ogasawara: Master thesis of the Tokyo University.

JOURNAL OF THE PHYSICAL SOCIETY OF JAPAN Vol. 13, No. 8, AUGUST, 1958

Note on the Forces on an Elliptic Cylinder moving in a Viscous Liquid at Small Reynolds Numbers

By Yorisaburo TAKAISI

Department of Physics, Faculty of Education, Ehime University, Matuyama

(Received April 5, 1958)

The steady flow of a viscous liquid past an elliptic cylinder at an arbitrary angle of attack is discussed on the basis of Reynolds number expansion using conformal transformation of the general solutions of Oseen's equation, which are expressed in integral forms. Thus the expansion formulae for the lift and drag coefficients are obtained to the second approximation, which are in perfect agreement with the results obtained recently by Hasimoto and also by Imai. Although it seems difficult to obtain general expressions for various formulae, such as formulae for the lift and drag, the procedure gives not only a practical method of solving Oseen's equation for the two-dimensional slow steady flow of an unbounded viscous liquid past an arbitray cylindrical body, but also an effective method to study the wall-effect upon a cylinder of arbitrary shape moving in a viscous liquid bounded either by a plane wall or by parallel plane walls, provided the mapping function is known for the cylinder.

§ 1. Introduction

The steady flow of a viscous liquid past an elliptic cylinder has been discussed by several authors on the basis of Oseen's linearized equation of motion, since Harrison's study[1] in 1924. Symmetric flow around an elliptic cylinder whose major axis is parallel or perpendicular to the undisturbed flow has been discussed by Tomotika and Aoi[2], and by Tomotika and Yosinobu[3] by somewhat a different analysis in each case, and thus approximate expansion formulae for the drag experienced by the cylinder have been obtained. The expansion formula of the same kind has also been obtained by Sidrak[4], but his formula is unfortunately incorrect.

On the other hand, asymmetric flow when an elliptic cylinder is set in the uniform flow at an arbitrary angle of incidence ϑ has been studied by Meksyn[5]. But, Lewis[6] has shown that Meksyn's solution is erroneous on account of an infinite circulation, and has given a formal method to give a correct solution on the basis of modified Oseen's approximation due originally to Southwell and Squire[7]. Explicit solution by his method, however, seems to be difficult. Recently Hasimoto[8] studied the same problem and obtained the expansion formulae for the lift and drag in powers of Reynolds number to the second approximation. In the next year, Imai[9] developed a very elegant method applicable to a cylinder of arbitrary shape on the basis of Reynolds number expansion using complex variables, and obtained the expansion formulae for the lift and drag experienced by an inclined elliptic cylinder.

However, it should be mentioned that all these results except Imai's have been derived by the use of Mathieu functions.

In this note, a new approach is proposed to the same problem without recourse to the manipulation of Mathieu functions. The method is based on a kind of Reynolds number expansion using conformal transformation of the general solutions of Oseen's equation, which are expressed in integral forms. Although it seems difficult to obtain general expressions for various formulae, such as formulae for the lift and drag coefficients, the procedure gives a practical method of solving Oseen's equation for the two-dimensional slow steady flow of an unbounded viscous liquid past an arbitrary cylindrical body, provided the mapping function is known for the cylinder. Moreover, the present method is applicable to the study of the steady slow motion of a cylinder of any shape in a viscous liquid bounded by a plane wall or by two parallel plane walls. Thus, in a

quite recent paper[10], the present writer has made investigations on the wall-effect upon the forces experienced by an inclined elliptic cylinder in a viscous liquid.

§ 2. Fundamental Equation and its Solutions

Let us assume that a cylindrical obstacle is placed in a uniform flow of velocity U streaming parallel to the x-axis. Then, Oseen's linearized equation of motion for the two-dimensional steady flow of a viscous liquid can be written in the form

$$\psi=\psi_1+\psi_2\,, \tag{2.1}$$

$$\Delta\psi_1=0\,, \tag{2.2}$$

$$(\Delta-k^2)(e^{-kx}\psi_2)=0\,, \tag{2.3}$$

where ψ is the stream function for the perturbation and is connected with the components of the perturbation velocity as:

$$u=\partial\psi/\partial y\,,\quad v=-\partial\psi/\partial x\,, \tag{2.4}$$

and $k=U/2\nu$, ν is the kinematic viscosity of the liquid and Δ stands for $\partial^2/\partial x^2+\partial^2/\partial y^2$.

The appropriate solutions of (2.2) and (2.3) which satisfy the boundary conditions at infinity are given respectively by

$$\psi_1=A_0\ln r+B_0\theta+\sum_{n=1}^{\infty}r^{-n}(A_n\cos n\theta+B_n\sin n\theta)\,, \tag{2.5}$$

$$\psi_2=a_0\,e^{kx}K_0(kr)+b_0\int_0^{\theta}kr\{K_1(kr)+K_0(kr)\cos\theta\}\,e^{kr\cos\theta}\,d\theta$$
$$+e^{kx}\sum_{n=1}^{\infty}K_n(kr)(a_n\cos n\theta+b_n\sin n\theta)\,, \tag{2.6}$$

where $x=r\cos\theta$, $y=r\sin\theta$, and

$$b_0=-B_0\,, \tag{2.7}$$

$K_n(x)$ is the modified Bessel function of the second kind. The condition (2.7) ensures that the stream function $\Psi=Uy+\psi$ is one-valued and continuous throughout the whole field of flow.

If we confine ourselves to the second order approximation for the lift and drag experienced by an elliptic cylinder, it suffices to take only the first six terms in (2.5) and (2.6) respectively. Then, as shown in our previous paper[11], the conjugate complex velocities can be expressed in integral forms as:

$$w_1=u_1-iv_1=\frac{1}{2}\int_{-\infty}^{\infty}\left(\frac{y}{|y|}+\frac{\alpha}{|\alpha|}\right)\{(A_0-iB_0)+i\alpha(A_1+iB_1)+\alpha^2(A_2+iB_2)\}\,e^{i\alpha x-|\alpha||y|}\,d\alpha\,, \tag{2.8}$$

$$w_2=u_2-iv_2=\frac{1}{2}\int_{-\infty}^{\infty}\left[\left(\frac{y}{|y|}+\frac{\alpha}{\lambda}\right)\left\{-a_0+\frac{i(\alpha+ik)}{k}a_1+\frac{2\lambda^2-k^2}{k^2}a_2\right\}\right.$$
$$\left.+\left(\frac{y}{|y|}+\frac{\lambda}{\alpha}\right)\left\{-ib_0-\frac{\alpha}{k}b_1+\frac{2i\alpha(\alpha+ik)}{k^2}b_2\right\}\right]e^{i\alpha x-\lambda|y|}\,d\alpha\,, \tag{2.9}$$

where $\lambda=\sqrt{\alpha^2+2ik\alpha}$.

In the following analysis, we assume, for the sake of convenience, $y\geq 0$ in (2.8) and (2.9). It is easy to show, however, that the same results are obtained in case when $y<0$.

§ 3. Conformal Transformation of the Solutions of Oseen's Equation

By the transformation function

$$z=x+iy=e^{-i\vartheta}(Z+\sigma^2Z^{-1})\qquad(0\leq\sigma\leq 1)\,, \tag{3.1}*$$

the unit circle $Z=e^{i\omega}$ in the Z-plane is mapped onto an ellipse (Fig. 1), which is inclined at

* In a quite recent paper cited above[10], we have introduced elliptic coordinates ξ, η, related with x, y by the relation $x+iy=2\sigma e^{-i\vartheta}\cosh(\xi+i\eta)$, instead of (3.1). As is well known, however, the two transformations are quite equivalent.

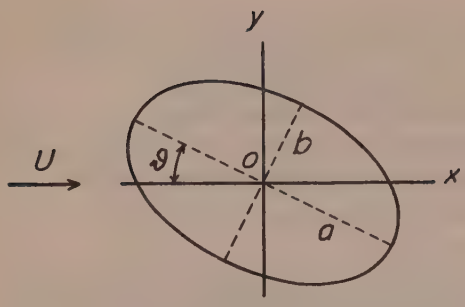

Fig. 1.

an angle ϑ with respect to the x-axis and whose semi-major and minor axes are respectively

$$a=1+\sigma^2\,,\quad b=1-\sigma^2\,. \tag{3.2}$$

Using obvious relations:

$$x=(1/2)(z+\bar{z})\,,\quad y=-(1/2)i(z-\bar{z})\,, \tag{3.3}$$

we have on the profile, that is, for $Z=e^{i\omega}$,

$$\begin{aligned} i\alpha x-\alpha y&=-\alpha\, e^{-i\vartheta}(e^{-i\zeta}-\sigma^2 e^{i\zeta})\,,\\ -i\alpha x-\alpha y&=-\alpha\, e^{i\vartheta}(e^{i\zeta}-\sigma^2 e^{-i\zeta})\,, \end{aligned} \tag{3.4}$$

where

$$\zeta=(1/2)\pi-\omega\,. \tag{3.5}$$

Inserting (3.4) into (2.8), and expanding the function $\exp(\alpha\sigma^2 e^{-i\vartheta+i\zeta})$ or $\exp(\alpha\sigma^2 e^{i\vartheta-i\zeta})$ in the integrands with respect to $e^{i\zeta}$, we obtain, on performing integrations,

$$w_1=e^{i\zeta}(A_0-iB_0)\,e^{i\vartheta}+e^{2i\zeta}(iA_1-B_1)\,e^{2i\vartheta}+e^{3i\zeta}\{(A_0-iB_0)\sigma^2 e^{i\vartheta}+2(A_2+iB_2)\,e^{3i\vartheta}\}+\cdots$$
$$\text{on the profile.} \tag{3.6}$$

On the other hand, inserting (3.3) into (2.9), we have after some appropriate transformations

$$\begin{aligned} w_2=\frac{1}{4}k\Omega[&2(iJ_0-J_1)a_0+2(J_0-iJ_1)b_0+\{(J_1-J_{-1})-i(J_0-J_2)\}a_1\\ &+\{-(J_0+J_2)+i(J_1+J_{-1})\}b_1+\{(J_{-1}+J_3)-i(J_2+J_{-2})\}a_2+\{(J_2-J_{-2})-i(J_{-1}-J_3)\}b_2] \end{aligned}$$
$$\text{on the profile,} \tag{3.7}$$

where

$$\Omega=\exp x \qquad \text{on the profile,} \tag{3.8}$$

and

$$J_m=\int_{-\infty}^{\infty}\exp\{-k\cosh s+k\sigma^2\cosh(s+2i\zeta)+m(s+i\zeta+i\vartheta)\}\,ds \qquad (m=0,\ \pm1,\ \pm2,\ 3). \tag{3.9}$$

Making use of the relations:

$$\exp\{k\sigma^2\cosh(s+2i\zeta)\}=\sum_{n=-\infty}^{\infty}I_n(k\sigma^2)\,e^{n(s+2i\zeta)}\,, \tag{3.10}$$

and

$$\int_{-\infty}^{\infty}e^{-k\cosh s+ns}\,ds=2K_n(k)\,, \tag{3.11}$$

where $I_n(x)$ is the modified Bessel function of the first kind, we obtain from (3.9)

$$J_m=2e^{mi\vartheta}\sum_{n=-\infty}^{\infty}I_n(k\sigma^2)K_{m+n}(k)\,e^{(m+2n)i\zeta} \tag{3.12}$$

Further, after some calculations, we can express (3.8) in terms of $e^{i\zeta}$ as:

$$\Omega=\sum_{n=-\infty}^{\infty}\lambda_n I_n(k\Theta)\,e^{ni\zeta}\,, \tag{3.13}$$

where

$$\lambda_n=(-i)^n\{(e^{i\vartheta}+\sigma^2 e^{-i\vartheta})/(e^{-i\vartheta}+\sigma^2 e^{i\vartheta})\}^{n/2}\,,\qquad \Theta=\{1+\sigma^4+\sigma^2(e^{2i\vartheta}+e^{-2i\vartheta})\}^{1/2}\,. \tag{3.14}$$

If we introduce (3.12) and (3.13) into (3.7) retaining only terms involving $e^{mi\zeta}$ $(m=0,\ \pm1,$

± 2, 3), then we obtain series expressions in powers of k for w_2 on the profile, where k is assumed to be small.

§ 4. Determination of the Constants in the Stream Function

Since the conditions at infinity are already satisfied by (2.8) and (2.9), the integration constants A_n, B_n, a_n and b_n ($n=0$, 1, 2) have to be determined from the boundary condition:

$$w_1+w_2=-U \qquad \text{on the profile.} \tag{4.1}$$

We may expand the constants in powers of k as:**

$$A_0=k^{-1}A_{00}+kA_{01}+O(k^3)\,, \tag{4.2}$$

$$B_0=k^{-1}B_{00}+kB_{01}+O(k^3)\,, \tag{4.3}$$

$$\left.\begin{aligned} A_1&=A_{10}+k^2A_{11}+O(k^4)\,, & B_1&=B_{10}+k^2B_{11}+O(k^4)\,,\\ A_2&=k^{-1}A_{20}+kA_{21}+O(k^3)\,, & B_2&=k^{-1}B_{20}+kB_{21}+O(k^3)\,,\end{aligned}\right\} \tag{4.4}$$

$$a_0=k^{-1}\alpha_{00}+k\alpha_{01}+O(k^3)\,, \tag{4.5}$$

$$b_0=k^{-1}\beta_{00}+k\beta_{01}+O(k^3)\,, \tag{4.6}$$

$$\left.\begin{aligned} a_1&=k\alpha_{10}+k^3\alpha_{11}+O(k^5)\,, & b_1&=k\beta_{10}+k^3\beta_{11}+O(k^5)\,,\\ a_2&=k\alpha_{20}+k^3\alpha_{21}+O(k^5)\,, & b_2&=k\beta_{20}+k^3\beta_{21}+O(k^5)\,.\end{aligned}\right\} \tag{4.7}$$

We insert the expressions for w_1 and w_2 obtained in § 3 together with (4.2) $\sim$ (4.7) into (4.1), and we neglect all terms higher than k^3. Then, on equating to zero the terms of the same powers of k in the coefficients of $e^{mi\zeta}$ ($m=0$, ± 1, ± 2, 3) and separating the real and imaginary parts, we obtain linear algebraic equations for the unknown constants A_{00}, A_{01}, $\cdots$, β_{21}.

Solving these equations successively, we obtain

$$\alpha_{00}=2\sigma^2U\sin 2\vartheta/D_1\,, \tag{4.8}$$

$$\beta_{00}=-2U\{2S-(1+\sigma^2\cos 2\vartheta)\}/D_1\,, \tag{4.9}$$

where

$$\left.\begin{aligned} &D_1=4S^2-(1+\sigma^4+2\sigma^2\cos 2\vartheta)\,,\\ &S=-\gamma-\ln(k/2)\,,\quad \gamma=0.5772\cdots \text{ (Euler's constant).}\end{aligned}\right\} \tag{4.10}$$

$$\begin{aligned}\alpha_{01}=&-(\alpha_{00}/D_1)[2S^3+S^2(2+\sigma^4)+(S/8)(17-14\sigma^4+3\sigma^8)+(1/16)(13+4\sigma^4-7\sigma^8)\\ &+\{4\sigma^2S^3+\sigma^6S^2+(S/6)(\sigma^2-3\sigma^6)+(1/48)(67\sigma^2-21\sigma^6-5\sigma^{10})\}\cos 2\vartheta\\ &-\{(S/12)(6\sigma^4+\sigma^8)-(1/24)(5\sigma^4+2\sigma^8)\}\cos 4\vartheta+(1/16)\sigma^6\cos 6\vartheta]\\ &+(\beta_{00}/D_1)[\{\sigma^2S^2+(1/3)(\sigma^2+3\sigma^6)+(1/48)(11\sigma^2-3\sigma^6-5\sigma^{10})\}\sin 2\vartheta\\ &+\{(S/12)(3\sigma^4-\sigma^8)-(1/12)(\sigma^4-\sigma^8)\}\sin 4\vartheta+(1/16)\sigma^6\sin 6\vartheta]\,,\end{aligned} \tag{4.11}$$

$$\begin{aligned}\beta_{01}=&(\alpha_{00}/D_1)[\{4\sigma^2S^3-S^2(2\sigma^2-\sigma^6)+(S/3)(4\sigma^2-6\sigma^6)+(1/48)(31\sigma^2+21\sigma^6-\sigma^{10})\}\sin 2\vartheta\\ &-\{(S/12)(9\sigma^4+\sigma^8)-(1/6)(2\sigma^4+\sigma^8)\}\sin 4\vartheta+(1/16)\sigma^6\sin 6\vartheta]\\ &-(\beta_{00}/D_1)[2S^3+\sigma^4S^2+(S/8)(1-10\sigma^4-\sigma^8)-(1/16)(5-8\sigma^4-3\sigma^8)\\ &-\{\sigma^2S^2+(S/6)(7\sigma^2+3\sigma^6)-(1/48)(\sigma^2+21\sigma^6+\sigma^{10})\}\cos 2\vartheta\\ &+(1/24)(2\sigma^8S+5\sigma^4-4\sigma^8)\cos 4\vartheta-(1/16)\sigma^6\cos 6\vartheta]\,,\end{aligned} \tag{4.12}$$

** We can obtain the same results even if we use other expansions, for instance $A_n=k^{-1}A_{n0}+A_{n1}+kA_{n2}+k^2A_{n3}+O(k^3)$ etc. ($n=0$, 1, 2).

$$
\left.\begin{aligned}
\alpha_{10}&=-(\alpha_{00}/4)\{4S-1+(8\sigma^2S-4\sigma^2)\cos 2\vartheta-\sigma^4\cos 4\vartheta\}-(\beta_{00}/4)\sigma^4\sin 4\vartheta\,,\\
\beta_{10}&=(\alpha_{00}/4)\{(8\sigma^2S-4\sigma^2)\sin 2\vartheta-\sigma^4\sin 4\vartheta\}-(\beta_{00}/4)(4S+1+\sigma^4\cos 4\vartheta)\,,\\
\alpha_{20}&=(\sigma^2/2)(\alpha_{00}\cos 2\vartheta+\beta_{00}\sin 2\vartheta)\,,\\
\beta_{20}&=-(\sigma^2/2)(\alpha_{00}\sin 2\vartheta-\beta_{00}\cos 2\vartheta)\,,\\
\alpha_{21}&=(\sigma^2/2)(\alpha_{01}\cos 2\vartheta+\beta_{01}\sin 2\vartheta)\\
&\quad+(\alpha_{00}/96)\{(12-24\sigma^4)S-4+6\sigma^4+9\sigma^8-(48\sigma^6S+12\sigma^2-30\sigma^6)\cos 2\vartheta\\
&\qquad+(12\sigma^4S-9\sigma^4+6\sigma^8)\cos 4\vartheta-4\sigma^6\cos 6\vartheta\}\\
&\quad+(\beta_{00}/96)\{(12\sigma^2-6\sigma^6)\sin 2\vartheta+(12\sigma^4S+3\sigma^4-6\sigma^8)\sin 4\vartheta+4\sigma^6\sin 6\vartheta\}\,,\\
\beta_{21}&=-(\sigma^2/2)(\alpha_{01}\sin 2\vartheta-\beta_{01}\cos 2\vartheta)\\
&\quad+(\alpha_{00}/96)\{(48\sigma^6S+12\sigma^2-30\sigma^6)\sin 2\vartheta-(12\sigma^4S-9\sigma^4+6\sigma^8)\sin 4\vartheta+4\sigma^6\sin 6\vartheta\}\\
&\quad+(\beta_{00}/96)[\{(12-24\sigma^4)S+4-6\sigma^4+9\sigma^8\}+(12\sigma^2-6\sigma^6)\cos 2\vartheta\\
&\qquad+(12\sigma^4S+3\sigma^4-6\sigma^8)\cos 4\vartheta+4\sigma^6\cos 6\vartheta]\,,
\end{aligned}\right\}\tag{4.13}
$$

$$
\left.\begin{aligned}
A_{00}&=\alpha_{00}\,,\\
A_{01}&=\alpha_{01}-(\alpha_{00}/4)\{(4+4\sigma^4)S-4\sigma^4+(4\sigma^2S-3\sigma^2-\sigma^6)\cos 2\vartheta\}\\
&\qquad+(\beta_{00}/4)(4\sigma^2S-\sigma^2-\sigma^8)\sin 2\vartheta\,,
\end{aligned}\right\}\tag{4.14}
$$

$$
B_{00}=-\beta_{00}\,,\qquad B_{01}=-\beta_{01}\,,\tag{4.15}
$$

$$
\left.\begin{aligned}
A_{10}&=-\alpha_{10}-(\alpha_{00}/2)(1+\sigma^4+2\sigma^2\cos 2\vartheta)\,,\\
B_{10}&=-\beta_{10}+\sigma^2\alpha_{00}\sin 2\vartheta-(\beta_{00}/2)(1+\sigma^4)\,,\\
A_{11}+\alpha_{11}&=-(\alpha_{01}/2)(1+\sigma^4+2\sigma^2\cos 2\vartheta)\\
&\qquad+(\beta_{00}/48)\{(18\sigma^4+24\sigma^8)S+8-6\sigma^4-24\sigma^8+(48\sigma^6S+16\sigma^2-33\sigma^6-7\sigma^{10})\cos 2\vartheta\\
&\qquad\quad+(2\sigma^4-2\sigma^8)\cos 4\vartheta+2\sigma^6\cos 6\vartheta\}\\
&\qquad-(\beta_{00}/48)\{(12\sigma^6S+2\sigma^2-3\sigma^6-7\sigma^{10})\sin 2\vartheta+(12\sigma^4S+\sigma^4-2\sigma^8)\sin 4\vartheta\}\,,\\
B_{11}+\beta_{11}&=\alpha_{01}\sigma^2\sin 2\vartheta-(\beta_{01}/2)(1+\sigma^4)\\
&\qquad-(\alpha_{00}/48)\{(24\sigma^6S+20\sigma^2-27\sigma^6+\sigma^{10})\sin 2\vartheta+(2\sigma^4-2\sigma^8)\sin 4\vartheta+2\sigma^6\sin 6\vartheta\}\\
&\qquad-(\beta_{00}/48)\{(12-24\sigma^4)S+2+6\sigma^4+3\sigma^8-(24\sigma^6S-22\sigma^2+15\sigma^6-\sigma^{10})\cos 2\vartheta\\
&\qquad\quad+(12\sigma^4S-5\sigma^4+4\sigma^8)\cos 4\vartheta+2\sigma^6\cos 6\vartheta\}\,,\\
A_{20}&=-2\alpha_{20}\,,\\
B_{20}&=-2\beta_{20}\,,\\
A_{21}&=-2\alpha_{21}+(\alpha_{00}/16)[(4-4\sigma^4)S-2-3\sigma^4+4\sigma^8\\
&\qquad+\{(16\sigma^2-8\sigma^6)S-8\sigma^2+2\sigma^6\}\cos 2\vartheta+(4\sigma^4S-5\sigma^4+\sigma^8)\cos 4\vartheta]\\
&\qquad-(\beta_{00}/16)(4\sigma^4S-3\sigma^4+\sigma^8)\sin 4\vartheta\,,\\
B_{21}&=-2\beta_{21}-(\alpha_{00}/16)[\{(16\sigma^2-8\sigma^6)S-8\sigma^2+2\sigma^6\}\sin 2\vartheta+(4\sigma^4S-5\sigma^4+\sigma^8)\sin 4\vartheta]\\
&\qquad+(\beta_{00}/16)\{(4-4\sigma^4)S-5\sigma^4+4\sigma^8-(4\sigma^4S-3\sigma^4+\sigma^8)\cos 4\vartheta\}\,.
\end{aligned}\right\}\tag{4.16}^{***}
$$

From (4.3), (4.6) and (4.15), we obtain the relation $b_0=-B_0$ independently of (2.7), which ensures that the stream function Ψ is one-valued and continuous throughout the field of flow.

§ 5. Formulae for the Lift and Drag Coefficients

As is well known, the lift L and drag D experienced by the cylinder under discussion per its unit length can be expressed as:

$$
L=2\pi\rho UA_0\,,\tag{5.1}
$$

*** To this order of approximation, the constants A_{11} and α_{11}, B_{11} and β_{11} cannot be obtained separately. But, we have no difficulty in discussing the lift and drag experienced by the elliptic cylinder to the second order approximation.

$$D=2\pi\rho UB_0\,, \tag{5.2}$$

where ρ is the density of the liquid concerned.

In order to define the Reynolds number R, let us take the major axis, $2a$, of the elliptic cylinder as the representative length. Thus, remembering (3.2),

$$R=2aU/\nu=4(1+\sigma^2)k\,. \tag{5.3}$$

Making use of (5.1), (5.2) and the integration constants obtained in § 4, we have, after some reductions, for the lift and drag coefficients C_L and C_D correct to the order of R^2 as:

$$\begin{aligned}
C_L&=L/(1/2\cdot\rho U^2\cdot 2a)\\
&=\frac{16\pi}{R}\frac{\sigma^2\sin 2\vartheta}{D_1}\Big\{1-\frac{R^2}{16(1+\sigma^2)^2}\Big[2S^2+\frac{S}{2}(1+\sigma^4+2\sigma^2\cos 2\vartheta)+\frac{1}{6}\{4-(3\sigma^2-\sigma^6)\cos 2\vartheta\}\\
&\quad+\frac{1}{D_1}\Big[\frac{S}{4}(13-4\sigma^4+\sigma^8+8\sigma^2\cos 2\vartheta+2\sigma^4\cos 4\vartheta)\\
&\quad+\frac{1}{6}\{6+9\sigma^4+3\sigma^8+(13\sigma^2+6\sigma^6+\sigma^{10})\cos 2\vartheta+(\sigma^4+\sigma^8)\cos 4\vartheta\}\Big]\Big]\Big\}\,,
\end{aligned} \tag{5.4}$$

$$\begin{aligned}
C_D&=D/(1/2\cdot\rho U^2\cdot 2a)\\
&=\frac{16\pi}{R}\frac{1}{D_1}\Big\{2S-(1+\sigma^2\cos 2\vartheta)-\frac{R^2}{16(1+\sigma^2)^2}\Big[S^2-\frac{S}{2}(1-2\sigma^4+2\sigma^2\cos 2\vartheta+\sigma^4\cos 4\vartheta)\\
&\quad+\frac{1}{48}\{15-36\sigma^4+3\sigma^8+(8\sigma^2-24\sigma^6)\cos 2\vartheta+(18\sigma^4-4\sigma^8)\cos 4\vartheta\}\\
&\quad-\frac{1}{D_1}\Big[\frac{S}{12}\{15-36\sigma^4-9\sigma^8+(11\sigma^2-33\sigma^6-\sigma^{10})\cos 2\vartheta+(14\sigma^4-4\sigma^8)\cos 4\vartheta+3\sigma^6\cos 6\vartheta\}\\
&\quad-\frac{1}{24}\{15-11\sigma^4-33\sigma^8+\sigma^{12}+(26\sigma^2-56\sigma^6-12\sigma^{10})\cos 2\vartheta\\
&\quad-(10\sigma^8+2\sigma^{12})\cos 4\vartheta+(4\sigma^6-2\sigma^{10})\cos 6\vartheta\}\Big]\Big]\Big\}\,,
\end{aligned} \tag{5.5}$$

which are in perfect agreement with the results obtained by Hasimoto and also by Imai.

§ 6. Summary

The steady flow of a viscous liquid past an elliptic cylinder at an arbitrary angle of incidence is discussed on the basis of Reynolds number expansion using conformal transformation of the general solutions of Oseen's equation, which are expressed in integral forms. Thus, the expansion formulae for the lift and drag coefficients are obtained to the second approximation, which are in perfect agreement with the results obtained recently by Hasimoto and also by Imai.

In conclusion, the writer wishes to express his cordial thanks to Professor S. Tomotika for his continual guidance and also for his kind inspection of the manuscript. The writer's thanks are also due to the Ministry of Education for a grant-in-aid for fundamental scientific research.

References

1) W. J. Harrison: Trans. Cambr. Phil. Soc. **23** (1924) 71.
2) S. Tomotika and T. Aoi: Quart. J. Mech. & Appl. Math., **6** (1953) 290.
3) S. Tomotika and H. Yoshinobu: Mem. Coll. Sci. Univ. Kyoto **27** (1953) 11.
4) S. Sidrak: Proc. Roy. Irish Acad. **53** (1950) 65.
5) D. Meksyn: Proc. Roy. Soc. A **162** (1937) 232.
6) T. Lewis: Quart. J. Math. **9** (1938) 21.
7) R. V. Southwell and H. B. Squire: Phil. Trans. A **232** (1934) 27.
8) H. Hasimoto: J. Phys. Soc. Japan **8** (1953) 653.
9) I. Imai: Proc. Roy. Soc. A **224** (1954) 141.
10) Y. Takaisi: J. Phys. Soc. Japan **13** (1958) 496.
11) Y. Takaisi: J. Phys. Soc. Japan **11** (1955) 407.

JOURNAL OF THE PHYSICAL SOCIETY OF JAPAN Vol. 13, No. 8, AUGUST, 1958

Adsorption of Water Vapour on Lead Borosilicate Glass in Vacuum

By Yutaka TUZI and Hiroaki OKAMOTO

Matsuda Research Laboratory, Tokyo Shibaura Electric Co., Ltd. Kawasaki

(Received April 3, 1958)

The adsorption of water vapour on lead borosilicate glass was studied in the pressure region $10^{-5}\sim10^{-6}$ mmHg using the modified flashing technique.

The adsorption is composed of at least two parts, the physical adsorption and the activated adsorption. The amount of the physical adsorption at 1×10^{-6} mmHg, $0\sim50°C$ was $0.1\sim0.4\%$ of a monolayer, and the heat of adsorption was 11 Kcal/mole. The activation energy of adsorption of the activated adsorption was *ca.* 9 Kcal/mole, and the activation energy of desorption was $13\sim40$ Kcal/mole.

§ 1. Introduction

In the preceding paper[1], we tried a preliminary study of adsorption of water vapour on glass, copper, nickel and alumina ceramic *in vacuo* using the time lag method of molecular flow. The results suggested that the adsorption is not a simple physical adsorption. Hence we tried a more quantitative measurement of the adsorption of water vapour on lead borosilicate glass in the pressure region of 10^{-6} mmHg using the modified flashing technique[2),3)].

§ 2. Apparatus and Sample

The essential part of this apparatus is a Beeck's calorimeter type cell[4] (B) shown in Fig. 1. The lower part of the inner glass

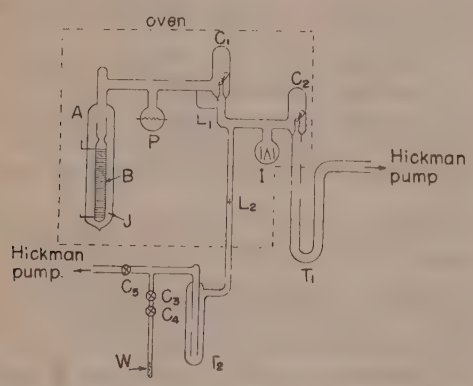

Fig. 1. Schematic diagram of experimental apparatus.

tube of the cell (*ca.* 18 mm$\phi\times$100 mm) was made very thin in order to reduce the heat capacity. The space J between the inner and the outer walls was evacuated for heat insulation. About 4 m (*ca.* 400 ohms) of 0.07 mmϕ tungsten wire was wound over the tube B, which served in two ways, as a resistance thermometer and heating element. The Pirani gauge P, which was read on a 3×10^{-6} V/div. galvanometer, was muffled with a thick copper tube and was immersed in a water bath. A sensitivity of 5×10^{-8} mmHg/div. in the range $10^{-5}\sim10^{-6}$ mmHg could be attained in this way. The calibration of the gauge which we carried out before each experiment against the ion gauge (I) proved that the reading of the former was fairly reproducible. C_1 and C_2 are greaseless stopcocks, and L_1 is a capillary tube of known conductance G (5.4 cc/sec for H_2O vapour at 25°C). The whole apparatus was constructed with lead borosilicate glass.

During the evacuation, the appapatus was baked at 450°C for $2\sim3$ hours while the trap T_1 was immersed in liquid oxygen. The pressure was then reduced to $1\times10^{-8}\sim1\times10^{-9}$ mmHg*.

The adsorbent was a Nonex type lead borosilicate glass powder. The glass, originally in the form of a tube, was first heated to its working temperature by H_2-O_2 flame, annealed in an electric furnace, and then crushed to powder finer than 200 mesh and washed in acetone. The glass powder was spread on the inner wall of B. The real surface area of the adsorbent was measured by the B.E.T. method using ethylene as the adsorbate[6),6)], and was

* Measured by the Bayard-Alpert gauge.

found to be 394 cm^2.

§ 3. Experimental Method

At the biginning of the experiment, B is kept at a high temperature T_1 (*ca.* 200°C) in order to avoid the adsorption, and the pressure of H_2O vapour is kept at a constant value p_0. In order to keep the pressure of H_2O at any desired value down to 10^{-5} mmHg during the experiment, the flow method was used. H_2O vaporized from thoroughly evacuated distilled water W (Fig. 1), was allowed to flow (from reservoir T_2) through a capillary leak L_2 and a cook C_2 to the pumping system.

After the adsorption on the walls of the apparatus reached equilibrium, opening and closing C_1 showed no change in the indication of the Pirani gauge. When this equilibrium state was reached, C_1 was closed, the heating current of B was cut off, and B was cooled down to a temperature T_2 (e.g. 1°C). The pressure slowly reduces to a minimum, and again rises to the initial value as is illustrated in Fig. 6. The amount of adsorption can be estimated from this figure. For brevity, we call this method the "cooling method".

There is another procedure of estimating the amount of adsorption on the sample, which we named the "heating method". If B is suddenly reheated to a high temperature T_3 after a time interval Δt after cutting off the heating current, the pressure will abruptly rise to a maximum as is shown in Fig. 2*.

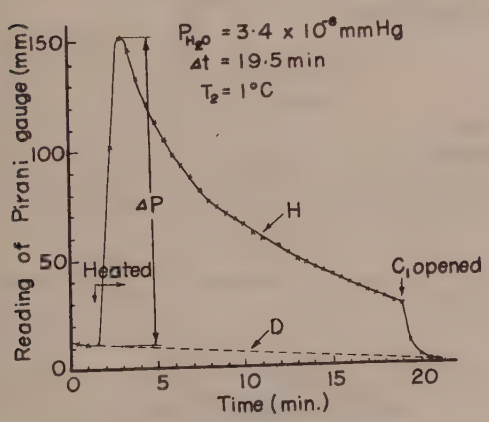

Fig. 2. Pressure variation in heating method.

* Throughout the experiments, the adsorbed H_2O can be regarded to be desorbed as H_2O (cf. ref. (8), (1)).

Theoretically, the amount of adsorption can be obtained from the area enclosed between the curve H and the ground line D of Fig. 2. This is however, impracticable, because for this purpose we have to extrapolate the curve H to $t=\infty$. In order to avoid the ambiguities accompanying this extrapolation, we examined the time constant of the pressure decrease and adopted the method of calculation based on the time constant which is to be given later.

As is described in § 4, the heating method estimates the amount of the physical adsorption exclusively, whereas the cooling method estimates the total adsorption. We tried both, and compared the results.

§ 4. Results

4.1. *Results obtained by the Heating Method*

It was found that Δp, the pressure rise caused by reheating (see Fig. 2), depended not only on p_0 and T_2 but also on some other factors. Experiments proved that

(1) $\Delta p=0$ if $\Delta t < 2$ min.;

(2) Δp increases with Δt in the range 2 min. $< \Delta t <$ 20 min.;

(3) Δp shows no variation with Δt if $\Delta t >$ 20 min.; and

(4) Δp increases with T_3 until it reaches *ca.* 150°C. At higher temperatures Δp seems to be almost constant.

The Δt—dependence ((1), (2), (3)) can be explained by the variation of the temperature of the sample during the cooling period (see Fig. 3). It can be estimated that (1) corres-

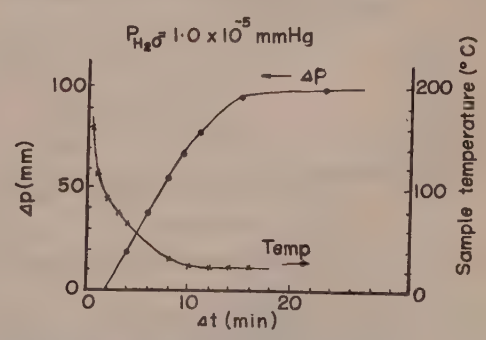

Fig. 3. Δp and sample temperature versus cooling time.

ponds to the fact that practically no adsorption takes place above 50°C.

It was also noticed that the desorption occurred not only when B was reheated but

also when it was evacuated at T_2 for 20~30 minutes. Hence the heating method seems to do with the reversible or physical adsorption.

A typical pressure variation is given in Fig. 2, in which the experimental conditions were as follows: $p_0=3.4\times10^{-6}$ mmHg, $T_2=1°C$ and $\Delta t=19.5$ min.

As is seen in Fig. 2, the reduction of pressure of the desorped H_2O vapour is very slow. The time constant is much greater than the value calculated from the volume V enclosed by C_1 and the conductance of L_1 (32.5 sec). This was supposed to be due to the desorption of the adsorbed H_2O from the walls of the apparatus. In order to check this point, we filled V with H_2O vapour of low pressure (B being kept at T_1), closed C_1, evacuated H_2O through L_1, and measured the pressure decrease. The pressure decrease curves in both cases were quite similar, as is seen in Fig. 4. It seems that the time constant τ is

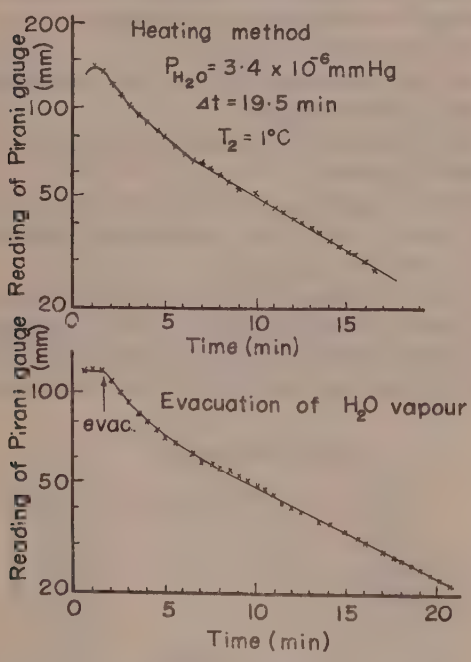

Fig. 4. Comparison of pressure variation in V.

composed of two parts, τ_1, which is of the order of the "calculated" value, and τ_2, which is about ten times as long as τ_1. The latter represents the desorption effect.

Now the amount of adsorption on the sample, or the amount of H_2O evacuated after the "reheating", v_h, could be regarded to be composed of two parts, v_f and v_l. The decrease of pressure of v_f and v_l, p_f and p_l, are characterized by the time constant τ_1 and τ_2 respectively. There are some confusing factors on τ_1. τ_2 represents, however, the desorption effect of H_2O from the walls of the apparatus, and can be calculated in the following way. The amount of H_2O adsorbed on the walls of the apparatus, v_w, depends on p_f and p_l. The reduction of p_f is, however, very rapid, and p_f will become negligibly small against p_l shortly after the reheating. Hence, during the greater part of the pressure reduction process of p_l, H_2O desorbs from the walls of the apparatus, and v_w can be assumed to be proportional to p_l:

$$v_w=ap_l\,, \tag{1}$$

where a is a constant.

As the rate of reduction of p_l is slow, we may assume

$$\frac{dv_w}{dt}=a\frac{dp_l}{dt}\,. \tag{2}$$

From this, it follows that

$$V\frac{dp_l}{dt}=-a\frac{dp_l}{dt}-Gp_l\,. \tag{3}$$

If $p_l=p_{l0}$ at $t=0$,

$$p_l=p_{l0}\exp\left(-\frac{G}{V+a}t\right)=p_{l0}\exp\left(-\frac{t}{\tau_2}\right). \tag{4}$$

Thus

$$\tau_2=\frac{V+a}{G}\,. \tag{5}$$

The amount of v_h can be calculated in the following way (cf. § 3). Assuming $p_f=p_{f0}$ at $t=0$, we obtain

$$p_f=p_{f0}\exp\left(-\frac{t}{\tau_1}\right). \tag{6}$$

Thus

$$v_f=\int_0^\infty Gp_f dt=\int_0^\infty Gp_{f0}\exp\left(-\frac{t}{\tau_1}\right)dt=p_{f0}G\tau_1\,, \tag{7}$$

$$v_l=\int_0^\infty Gp_l dt=\int_0^\infty Gp_{l0}\exp\left(-\frac{t}{\tau_2}\right)dt=p_{l0}G\tau_2\,, \tag{8}$$

and

$$v_h=v_f+v_l=p_{f0}G\tau_1+p_{l0}G\tau_2\,. \tag{9}$$

For the numerical evaluation, p_{f0}, p_{l0}, τ_1 and τ_2 were graphically determined from Fig. 4. The calculated amounts of adsorption under various conditions are shown in Fig. 5. As the number of H_2O molecules necessary to

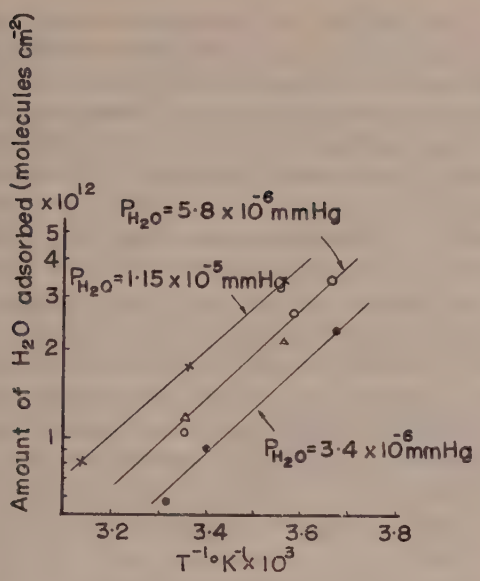

Fig. 5. Amount of H_2O adsorbed versus temperature.

form a monolayer is $9.52\times10^{14}/\text{cm}^2$, the amount of physical adsorption at $p_0=1\times10^{-6}$ mmHg and at 0~50°C is 0.4~0.1% of a monolayer.

4.2. *Results obtained by the Cooling Method*

Before we begin to cool B, we expose the apparatus to a constant H_2O pressure, p_0, so that the adsorbed layer of H_2O on the walls of the apparatus are in equilibrium with p_0. Starting from this condition if we begin to cool B, the pressure in V, p_c, will be reduced, and the H_2O molecules will be supplied from the walls and through L_1. The rate of desorption can be assumed to be similar with Eq. (2), because there is no portion of H_2O corresponding to p_f and the variation of p_c is very slow.

α the rate of adsorption on B, will depend on the amount adsorbed on B. In order to simplify the calculation, it is desirable to obtain the variation of p_c during a short period in which α can be regarded as a constant. This we achieved by opening and closing C_1 intermittently. Hence the experimental curve is composed of many steps. The zero point drift of the Pirani gauge reading can also be checked conveniently by this procedure.

A typical pressure variation in the cooling method is illustrated in Fig. 6. The experimental conditions were; $p_0=8.4\times10^{-6}$ mmHg, $T_1=350°\sim380°$C and $T_2=28.4°$C.

Now that one can assume that α is a constant during a step, the variation of p_c in V during that step will be given by

$$V\frac{dp_c}{dt}=-a\frac{dp_c}{dt}+(p_0-p_c)G-p_c\alpha\,. \qquad (10)$$

Assuming $p_c=p_0$ at $t=0$, we obtain

$$p_c=\frac{1}{G+\alpha}\left\{\alpha p_0\exp\left(-\frac{G+\alpha}{V+a}t\right)+Gp_0\right\}. \qquad (11)$$

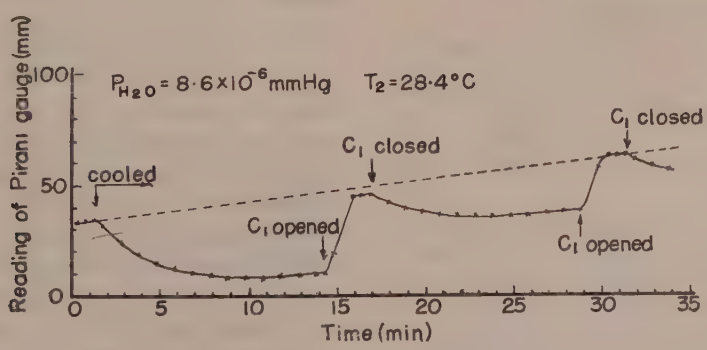

Fig. 6. Pressure variation in cooling method.

Hence, the amount of adsorption v_c becomes

$$v_c=\int_0^t\alpha p_c dt=\frac{1}{G+\alpha}\left[\alpha^2 p_0\left\{-\frac{V+a}{G+\alpha}\times\exp\left(-\frac{G+\alpha}{V+a}t\right)+G\alpha p_0 t\right\}\right]. \qquad (12)$$

In this equation, a can be determined by the heating method. α can be evaluated using Eq. (11), substituting the numerical values for various combinations of p_c, p_0 and t. The results are illustrated in Fig. 7. Thus the amount of adsorption v_c can be determined from Eq. (12).

4.3. *Comparison of the Results obtained by Both Methods*

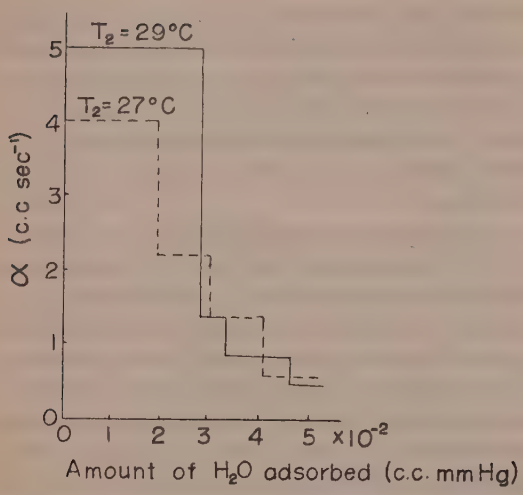

Fig. 7. Rate of activated adsorption vasus amount of H_2O adsorbed.

If we continue the observation in the cooling method for a long time, the adsorption on the specimen as well as on the walls will reach equilibrium with p_0. This happens to be the condition needed for the commencement of the heating method. Thus we can obtain both v_c and v_h in a series of experiments. v_c and the corresponding v_h obtained in this way are given in Table I.

The difference of v_c and v_h suggests the existence of the activated adsorption of H_2O on glass surface. In fact, the activated desorption was observed by heating the sample which had adsorbed H_2O to a high temperature (higher than the heating temperature of the heating method). The rate of desorption thus obtained as a function of temperature is given in Fig. 8.

Table I. Amount of Water Vapour Adsorbed on Lead Borosilicate Glass. Comparison of the Results obtained by Both Methods.

No.	Pressure of water vapour $p_0 \times 10^{-6}$ mmHg	Temperature T_2°C	Cooling time Δt min.	Amount of adsorption $\times 10^{-2}$ cc mmHg (25°C) Cooling method v_c	Heating method v_h
1	8.4	28	64	5.6	2.6
2	6.7	29	93	5.0	1.65
3	7.4	26	65	4.9	1.35

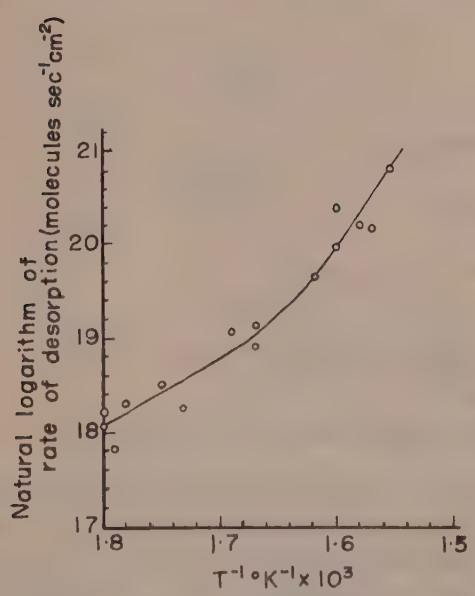

Fig. 8. Rate of desorption versus temperature.

§ 5. Discussion

The heat of adsorption q can be calculated from Fig. 5, using the Clausius-Clapeyron equation

$$q = R\left(\frac{d \ln p_0}{d(1/T_2)}\right)_{v_h}, \tag{13}$$

where R, represents the gas constant. The calculated mean value of the heat of the adsorption was found to be 11 Kcal/mole. It is believed that the adsorption detected by the heating method is a mobile physical adsorption, because the heat of adsorption is nearly equal to the heat of vaporization of water (10.43 Kcal/mole at 30°C)(cf. § 4.1).

In the cooling method, the activation energies of the activated adsorption and desorption can be calculated in the following way[7]. The rate of adsorption per unit area depends on four factors:

(1) The rate of collision of molecules on the surface, which, on unit area at a pressure p is equal to $p/\sqrt{2mkT}$, where m, k and T represent the mass of the gas molecule, the Boltzmann constant and the absolute tempera-

ture respectively.

(2) The condensation factor σ.

(3) The activation energy E.

(4) The probability for a molecule to strike an available site. Since this probability usually depends on the fraction of the surface covered, θ, it is designated by $f(\theta)$.

If A represents the surface area of the sample, the rate of adsorptipn, α/A, is given by

$$\frac{\alpha}{A}=\frac{\sigma p}{\sqrt{2\pi mkT}}f(\theta)\exp\left(-\frac{E}{RT}\right). \qquad (14)$$

Now, in the low pressure region, we may assume with good approximation $\sigma=1$, and $f(\theta)=1$. Hence the activation energy E can be evaluated using Eq. (14), if we assume an appropriate value for α. This was obtained in Fig. 7. There are some confusing factors, however, in the present case. We want the rate of adsorption, α, for the *activated* adsorption, while the values of α in Fig. 7 do not necessarily give what we want. Considering the experimental conditions, it would be most appropriate to assume $\alpha=2$cc/sec for the activated adsorption. Thus we arrive at $E=9$ Kcal/mole.

The rate of desorption similarly depends on three factors:

(1) The number of sites, $f(\theta)'$, from which desorption is possible.

(2) The activation energy of desorption E'.

(3) The rate constant K'.

The rate of desorption, u', is then

$$u'=K'f(\theta)'\exp\left(-\frac{E'}{RT}\right). \qquad (15)$$

Although, K', $f(\theta)'$ and E' vary with θ in general, these factors can be assumed to be constant in our case, because the interaction between the adsorbed molecules are negligible for the density of the adsorbed molecules is very low. We calculated E' from the gradient of the curve in Fig. 8, and obtained $E'=13\sim40$ Kcal/mole. The greater value of E', estimated from the upper part of the curve, is nearly equal to the activation energy of diffusion of H_2O through the Nonex glass[8] (38 Kcal/mole). Therefore, the activated adsorption might have something to do with diffusion.

The experiments were repeated several times in the period of two months. The results were quite reproducible. It is believed consequently that the surface of the sample glass has experienced practically no change by the repeated adsorption and desorption of H_2O in the pressure range $10^{-5}\sim10^{-6}$ mmHg.

§ 6. Conclusion

The following points can be concluded for the adsorption of water vapour on lead borosilicate glass *in vacuo*: (1) The adsorption is composed of at least two parts, the physical adsorption and the activated adsorption. (2) The amount of physical adsorption at $p_0=1\times10^{-6}$ mmHg and $0\sim50$°C is $0.4\sim0.1$% of a monolayer (Fig. 5). (3) The heat of physical adsorption is 11 Kcal/mole. (4) The physically adsorbed molecules are desorbed by heating at $100\sim150$°C or by prolonged evacuation at room temperatures. (5) The activation energy of the activated adsorption is *ca.* 9 Kcal/mole. (6) The activation energy of desorption of the activated adsorption is $13\sim40$ Kcal/mole.

The authors are indepted to Prof. K. Kinosita for his kindness in reading the manuscript and discussions, to Mr. C. Hayashi and Prof. G. Tominaga for their discussions.

References

1) H. Okamoto and Y. Tuzi: J. Phys. Soc. Japan. **13** (1958) 649.
2) J. A. Becker and C. D. Hartman: J. Phys. Chem., **57** (1953) 153
3) J. A. Becker: Advances in Catalysis, **7** (1955) 136.
4) O. Beeck, W. A. Cole and A. Wheeler: Disc. Farad. Soc., **8** (1950) 314.
5) L. A. Wooten and J. R. C. Brown: J. Am. Chem. Soc., **65** (1943) 113.
6) H. Okamoto and Y. Tuzi: Vacuum Techniques (Shinku Gijutsu), **7** (1956) 218 in Japanese.
7) B. M. W. Trapnell: Chemisorption, Chap. 3 (London: Butterworths Scientific Publications, 1955).
8) B. J. Todd: J. Appl. Phys., **26** (1955) 1238.

Short Notes

This section is intended to secure prompt publication of important discoveries in physics. The reports should not exceed 800 words in length. A figure of size 7cm × 7 cm will be counted as 150 words.

J. PHYS. SOC. JAPAN **13** (1958) 966

Variation of the Optical Properties of Iron at Transition Temperature

By Akira KINBARA

Department of Applied Physics University of Tokyo, Tokyo, Japan

(Received May 13, 1958)

The light emitted from a smooth plane surface of a heated metallic plate is polarized, because the emissivities of the component polari ed in parallel with the emitting plane and that polarized perpendicular to it are different from each other. These emissivities are denoted by Ep and Es, respectively.

The degree of polarization Es/Ep depends on the angle of emission.

To study this, the emitted light from metallic surfaces was divided into the parallel and the perpendicular component by a Rochon prism and each component was led separately to two photomultipliers as shown in Fig. 1. The ratio of the

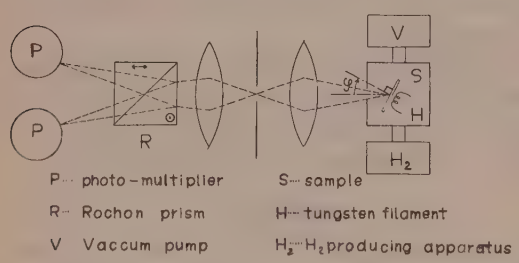

Fig. 1. The schematic illustration of the experimental arrangement.

two photocurrents was measured every 10 degree of the emitting angle φ.

An iron plate was used as the sample as it was expected that the relation $Es/Ep-\varphi$ varies according as the temperature is above or below the transition point, 910°C.

The surface of the sample was polished by emery paper of 500 meshes. The sample plate (2 cm × 4 cm) which could be rotated around a vertical rod was placed in a vacuum vessel and heated by radiation from an incandescent tungsten filament which was located just behind the plate. To avoid oxidation of the surface, the vessel was filled with hydrogen (above 1 mmHg).

The relation between Es/Ep and φ was observed at various temperatures, which were measured by an optical pyrometer. Although optical filters were not used in this experiment, multiplying the spectral sensitivity of the photomultiplier 931 Å by the spectral energy distribution, it was found that only the light in the vicinity of about 6000 Å was detected.

The experimental results (Fig. 2) show that, only when the temperature is near 910°C, $Es/Ep-\varphi$ curve takes a special form, i.e., has a maximum. It means that iron has special bulk or surface properties near the transition temperature.

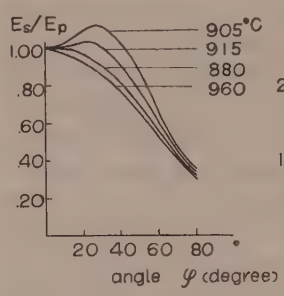

Fig. 2. Es/Ep as a function of φ.

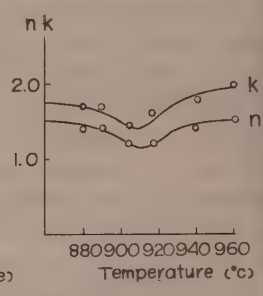

Fig. 3. n and k as a function of temperature.

Now according to the classical theory of electromagnetism, the relation between Es/Ep and φ is given as follows[1],

$$Es/Ep=\cos^2\varphi-\{\sin^2\varphi(-\cos 2\varphi+2n\cos\varphi)/n^2+k^2\}$$

where n is the refractive index and k the extinction coefficient.

At each temperature a pair of n and k was determined so that the equation might fit to corresponding $Es/Ep-\varphi$ curve. n and k thus obtained are given in Fig. 3.

It shows that n and k decrease remarkably only in the vicinity of the transition temperature, while they are approximately constant in both states of b.c.c. and f.c.c..

If the Drude's theory can be applied in this case, this fact corresponds to the decrease of the electric conductivity near the transition point, but as to this point, farther investigations are required.

Reference

1) M. Laue und F. F. Martens: Phys. Z. **32** (1907) 853.

J. PHYS. SOC. JAPAN **13** (1958) 967~968

Electrical Conductivity in N-Type InSb Under Strong Electric Field

By Yasuo KANAI

Electrical Communication Laboratory, Musashinoshi, Tokyo

(Received June 6, 1958)

Under strong electric field, the conducting carriers in solids obtain sufficient energy from field. Hence, even when the field is not so strong as the ionization of carriers sets in, the distribution function for carriers fairly deviates from the form for thermal equilibrium state. In this case the carriers are called as being "hot",[1] and the Ohm's law ceases to valid. This hot electron phenomena were investigated a few years ago; experimental studies were made by Ryder[2] for Ge and Si crystals and theoretical considerations for non-polar semiconductors were made by Shockley[1] and by Yamashita and Watanabe[3]. Following the theoretical calculations, the critical field E_c, where the current-voltage characteristic began to deviate from Ohm's law, was given by the next formula;

$$\mu_0 E_c (\equiv v_{dc}) = 1.51 v_s$$

where μ_0: the drift mobility under weak electric field

v_s: the averaged value of sound velocity in the crystal

v_{dc}: the drift velocity of carriers at E_c.

(The fact was that the experimental values of E_c were 2–5 times larger than the theoretical estimation, and this discrepancy was studied theoretically by Shibuya[4].) Above this critical field, drift velocity, and hence the current density, became proportional to $E^{1/2}$. At higher electric field, they became independent to E, and were followed by the occurrence of carrier ionization.

As is well known, the electron mobility in InSb is rather large. Hence we can expect that, as in the case of Ge and Si, if the interaction with the acoustic modes of lattice vibration is the main process of energy loss for electrons in InSb, E_c will be rather low in this material. For instance, putting the value of v_s and μ_0 as 4×10^5 cm/sec.[5] and 1×10^5 cm^2/volt sec. respectively, we can expect about 6 volts/cm as the value of E_c. (Considering the case of Ge and Si, we can also expect about 10–30 volts/cm as the value of E_c for electrons in InSb.)

The current-voltage characteristics of n-type InSb single crystals were measured under pulsive strong electric field. A typical example of our results at 90°K is shown in Fig. 1. The sample had the following character at 90°K; resistivity $(\rho)=2.41\times10^{-2}$ ohm-cm, and Hall coefficient $(R)=-4.23\times10^3$ cm^3/coul. (Putting the value of the effective mass of electron in InSb as 0.013 m_0,[6] the degenerate temperature of this crystal was about 50°K.) Fig. 1 shows that there is no deviation from Ohm's law near the expected field strength, but at rather high field, about 2×10^2 volts/cm, the deviation sets in. It also shows that the current density increases very rapidly with increasing E above 2×10^2 volts/cm.

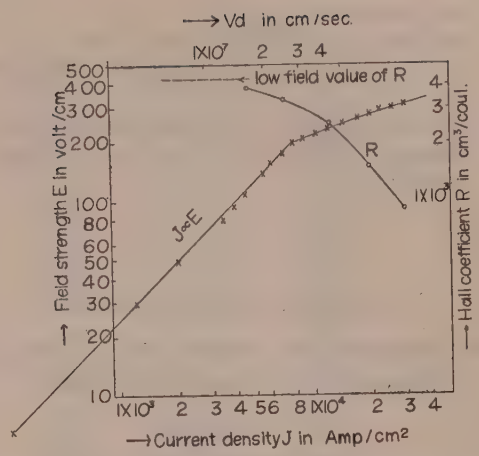

Fig. 1. Current-voltage characteristic and Hall coefficient of a n-type InSb single crystal at 90°K.

To decide whether the deviation from Ohm's law at about 2×10^2 volts/cm was caused by the hot electrons in InSb or caused by the carrier ionization process from the full band, we measured the Hall effect in the same region of electric field. (As the donor impurities in InSb were fully ionized at 90°K, the ionization process from the impurity states would not occur at all). The Hall coefficient of the same sample is also shown in Fig. 1. From the behaviour of R we can believe that the cause of the deviation from Ohm's law is the carrier ionization process from the full band.

From our data shown in Fig. 1, the following results will be drawn.

a) The main process of energy loss of electrons in InSb is not the interaction with the acoustic modes of vibration, but will be the interaction with the optical modes. This result is consistent with the Ehrenreich's calculation[7].

b) When the drift velocity of an electron in InSb reaches the value of about 2×10^7 cm/sec, the carrier ionization process sets in.

Further investigations are now in progress and the results will be published in this Journal.

References

1) Shockley: Bell Syst. Tech. J. **30** (1951) 990.
2) Ryder: Phys. Rev. **90** (1953) 766.
3) Yamashita and Watanabe: Prog. Theor. Phys.

12 (1954) 443.
4) Shibuya: Phys. Rev. **99** (1955) 1189.
5) De Vaux and Pizzarello: Phys. Rev. **102** (1956) 85.
6) Dresselhaus et al: Phys. Rev. **98** (1955) 556.
7) Ehrenreich: Intrn. J. Phys. Chem. Solids **2** (1957) 131.

J. PHYS. SOC. JAPAN **13** (1958) 968

Low Temperature Anomaly in the Proton Resonance of Some Nickel Salts

By Pil Hyon KIM
Department of Physics, Tokyo Metropolitan University, Tokyo
and
Tadashi SUGAWARA
The Research Institute for Iron, Steel and Other Metals, Tohoku University, Sendai

(Received June 2, 1958)

Recently, it has been shown that the deviation from the Curie-Weiss law observed in some nickel salts can be explained as due to the Stark splitting of the ground state of Ni^{2+} [1].

In connection with this, a study was made of the shift and the spin-lattice relaxation time of the proton magnetic resonance in some hydrated and ammoniated salts of nickel.

In single crystals of $NiSiF_6 \cdot 6H_2O$, $NiK_2(SO_4)_2 \cdot 6H_2O$ and $Ni(BrO_3)_2 \cdot 6H_2O$, the proton lines were observable down to 1.4°K, the lowest temperature attainable with our cryostat; while, in powders and single crystals of $Ni(NH_3)_6Cl_2$, $Ni(NH_3)_6(ClO_4)_2$ and $NiCl_2 \cdot 6H_2O$, the lines disappeared at a definite temperature characteristic of each salt. cf. Table I.

Table I. The temperature of line disappearence.

Compound	$Ni(NH_3)_6Cl_2$	$Ni(NH_3)_6(ClO_4)_2$	$NiCl_2 \cdot 6H_2O$
T(dis.) (°K)	1.6	~7	8

The proton line of these salts is expected to show a shift proportional to the mean magnetic moment of Ni^{2+} ion or to the susceptibility of the salt.

This was the case in most of the salts studied. In Fig. 1, as an example, the shift and the susceptibility of $Ni(NH_3)_6Cl_2$ (powder)[2] are plotted against temperature.

However, the circumstances were quite different in $NiCl_2 \cdot 6H_2O$. In powder and single crystal samples of this salt, the shift showed quite different temperature dependency as compared with the susceptibility[1] as shown in Fig. 2.

According to Moriya[3], the spin-lattice relaxation time of protons in a salt of which the spin degeneracy is completely lifted by the crystalline electric field is expected to increase exponentially below the temperature comparable to an interval of the splitting of lowest spin levels. In contradiction to this, the T_1 values of the above salts were shorter than 10^{-3} sec. down to the temperature below which the proton line could not be observed.

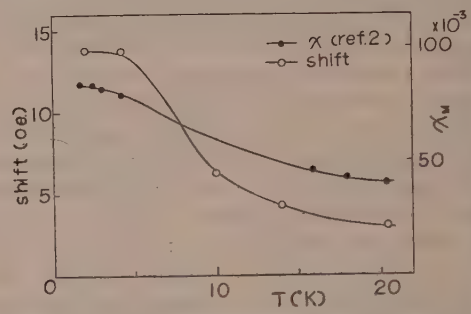

Fig. 1. The shift in 2000 oe. and the susceptibility in powdered $Ni(NH_3)_6Cl_2$.

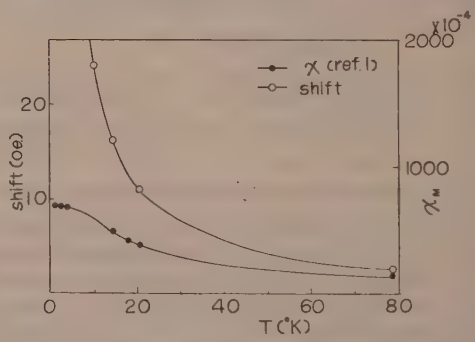

Fig. 2. A comparison of the shift in 2000 oe. and the susceptibility in powdered $NiCl_2 \cdot 6H_2O$.

It is worth noticing that the paramagnetic resonance has not been observed in the salts in which the proton line disappeared at low temperature[4].

It seems interesting to extend this work to the salts of Fe^{2+} and Cr^{2+} having zero field splitting like Ni^{2+}.

In conclusion one (P.H.K.) of the authers wishes to express his thanks to Prof. K. Kido and Prof. E. Kanda for their continued encouragements throughout this work.

References

1) T. Haseda and M. Date: J. Phys. Soc. **13** (1958) 175.
2) T. Watanabe: to be published.
3) M. Moriya: private communication.
4) M. Date: private communication.

J. PHYS. SOC. JAPAN **13** (1958) 969~970

A New Compound in Au-Pb Alloy System

By Yoshibumi FUJIKI, Ryōji SUGANUMA and Toshiho YOSHIDA

Physical Institute, Kyōto Prefectural Medical College

(Received June 9, 1958)

In the course of our electron diffraction study on vacuum evaporated metal films, a new compound in Pb-rich side of Au-Pb alloy system was found and was also confirmed by X-ray diffraction and metallographic investigations with bulk specimens.

In this alloy system, two intermetallic compounds, Au_2Pb and $AuPb_2$, have already been known, and from our electron diffraction study, it is known that the composition of the new phase is between the eutectic (about 15 wt.% Au) and $AuPb_2$ (32.2 wt.% Au). Then for the purpose of accurate determination of the composition, we examined by the ordinary metallographic method the specimens prepared in the range of 15~26 wt.% Au differing by one or two percents, and the results were compared with the X-ray diffraction patterns of the same specimens. The alloy constituents in Terex glass tube were melted in vacuum at about 400°C, quenched in a mixture of ice and NaCl or air-cooled to room temperatures, and annealed for an appropriate time (26.5~53 h.) at about 200°C. After these heat treatments in vacuum, specimens were polished, etched and microscopically investigated.

The air-cooled specimens containing 15 wt.% Au showed the typical eutectic structure. The quenched sample containing 24 wt.% Au indicated the presence of two phases, $AuPb_2$ plus eutectic (Fig. 1 (d)), which were completely transformed by further annealing into 'one phase' by the peritectic reaction (Fig. 1 (b)). It seems that this phase is not a solid solution but a compound like Au_2Pb or $AuPb_2$ (cf. Fig. 1 (a), (b) and (c)). This result should be compared with a theoretical value of 24.08 wt.% Au for the formula unit $AuPb_3$.

Table I.

(hkl)	d (calc.)	d (obs.)	I (obs.)
(110)	8.456Å	(8.46Å)*	w
(200)	5.979	(5.92)*	vw
(101)	5.275	(5.29)*	w
(220)	4.224	(4.22)*	vw
(211)	3.956	(3.96)*	w
(310)	3.781	(3.78)*	vw
(301)	3.299	(3.30)*	vw
(002)	2.939	(2.98)*	vvw
(321)	2.888	2.890	s
(330)	2.818	2.822	vs
(112)	2.776	2.781	m
(420)	2.674	2.672	w
(411)	2.600	2.597	vs
(222)	2.413	2.418	s
(510)	2.345	2.338	m
(312)	2.321	2.314	m
(520)	2.221	2.227	vw
(402)	2.096	2.098	vvw
(521)	2.077	2.075	vw
(611)	1.864	1.863	m
(710)	1.691	1.691	s
(602)	1.650	1.651	w
(711)	1.625	1.628	s
(721)	1.582	1.584	w
(542)	1.576	1.574	vw
(650)	1.531	1.533	vw
(731)	1.517	1.519	vw
(004,523)	1.469	1.470	s
(741,811)	1.438	1.438	m
(660)	1.409	1.408	vvw
(821)	1.408		
(613,224)	1.388	1.388	w
(831)	1.362	1.361	w
(840)	1.337	1.335	vw
(910)	1.321	1.320	vvw
(414)	1.311	1.307	w
(901)	1.296	1.293	m
(921,761)	1.267	1.265	vw
(504,434)	1.252	1.249	vvw
(851)	1.239	1.240	vw
(444,653)	1.206	1.205	w

* These lines are observed by electron diffraction method.

The X-ray diffraction powder pattern of this new compound can be indexed on the basis of a tetragonal unit cell with $a=11.95_8$ Å, $c=5.87_8$ Å (Table I). The measured density was found to be 12.8 g.cm^{-3}.

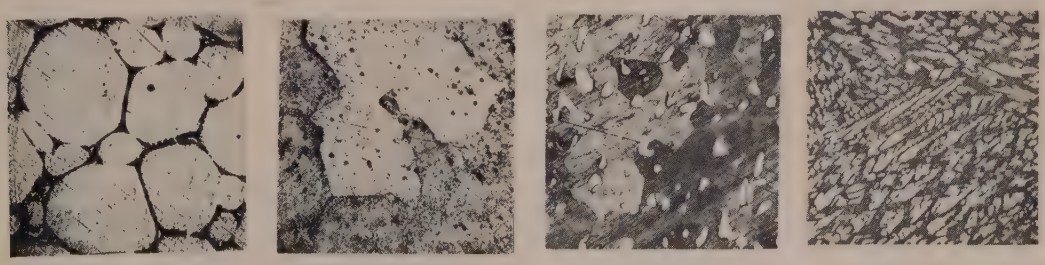

(a) (b) (c) (d)

Fig. 1. ×150 ×1/2.

(a) 23 wt. % Au annealed for 28 hours at 200°C ($AuPb_3$+eutectic)
(b) 24 wt. % Au annealed for 26.5 hours at 200°C ($AuPb_3$)
(c) 25 wt. % Au annealed for 53 hours at 200°C ($AuPb_3$+$AuPb_2$)
(d) 24 wt. % Au quenched ($AuPb_2$+eutectic)

while the density calculated on the basis of 8 molecules per unit cell is 12.93 g.cm.$^{-3}$.

As mentioned above, the quenched specimens containing 24 wt.% Au indicate the presence of only two phases, $AuPb_2$ plus eutectic, but not $AuPb_3$ phase. Similar results were obtained for air-cooled specimens of other compositions between 26 wt.% Au and 17 wt.% Au. These facts seem to suggest that the peritectic point is very close to the eutectic temperature. In fact, our electron diffraction observations on the highest temperature of stability for $AuPb_3$ phase support this suggestion, but the precise determination of the above-mentioned temperature requires further investigations.

The authors wish to thank Prof. K. Iwase and Dr. M. Kyōtani of Kyōto University for their kind advice and discussions.

J. Phys. Soc. Japan **13** (1958) 970~971

Etch Pits in Lead Crystals

By Yosio Hiki

The Government Mechanical Laboratory, Tokyo

(Received June 4, 1958)

The relation of etch pits with dislocations has been often discussed. In some cases one-to-one correspondence was established between the pits and the points where dislocations emerge on crystal surfaces[1]. It was sometimes shown, however, that the association of the dislocations with impurity atoms was necessary to the formation of the etch pits[2]. In the present note, some observations on the etched surfaces of lead single crystals are reported.

Single crystals were prepared by the moving-furnace method from lead of 99.99% purity. The impurities determined by chemical analysis were: C 0.007, Fe 0.0005 and Sn 0.0004 in weight per cent. Good results were obtained to reveal the pits by adopting the electrolytic etching instead of chemical one. The standard procedure of the etching was as follows: First, the specimen was etched chemically with the solution of CH_3COOH and H_2O_2 (1:3) for 15–30 sec, and then washed by alcohol, the surface becoming very flat and bright. Next, it was etched electrolytically using 1 weight per cent aqueous solution of purest sulfamic acid at 18°C for 45 sec with current density of 0.2 Amp./cm^2. When the etching time was increased further, the sizes of the pits were enlarged while the number of the pits per unit area did not increase.

The effect of annealing on the etch figures was mainly studied. The specimen was annealed at

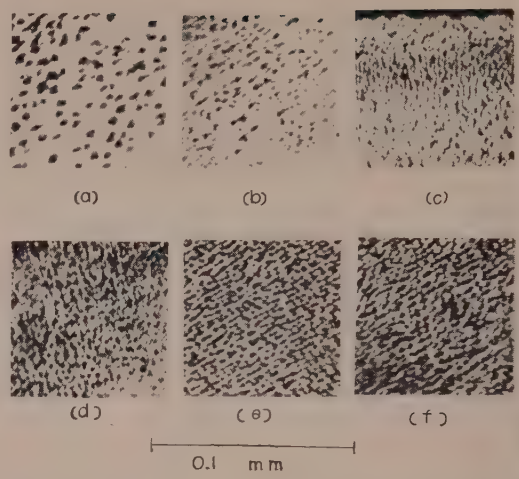

Fig. 1. Etched surface of lead single crystal as grown (a), and annealed at 150 C for 3 hrs. (b), 5 hrs. (c), 15 hrs. (d), 33 hrs. (e) and 60 hrs. (f).

150°C in ethylene glycol and the surface was observed after etching. As the annealing time was prolonged, the shapes of the pits became clear and the number of them increased gradually and approached to a some saturated value, as shown in Fig. 1. In a well annealed specimen, the surface density of the pits was 1.7×10^7/cm^2, and it could not be increased by changing the etching conditions. The shapes of the pits were different if the specimens had different crystallographic orientations.

In the present case, it is likely that dislocations originate etch pits in co-operation with impurity atoms. The stresses due to dislocations may be so locally concentrated that they cannot produce the pits. When the specimen is annealed, the impurity atoms are activated thermally and segregate around the dislocation lines under the influence of the stress field, and thus Cottrell's atmospheres may be created. These atmospheres will then serve as the centers of the etch pits. The migration of the impurities to the dislocations was also verified through the measurements of the internal friction of lead single crystals. The details of this investigation will be published elsewhere.

The number of pits per unit area was about one tenth of the dislocation density in lead powder determined by us using a X-ray technique[3]. This discrepancy may be explained as follows. (1) Only the edge dislocations gather the impurity atoms and contribute to the formation of the etch pits. (2) The line density of the segregated impurities may not be uniform along the dislocations. Only a small portion of the total dislocations which emerge on the crystal surface has enough concentration of atmosphere to form the pits[4]. (3) Specimens prepared in different methods may have different densities of dislocation.

References

1) F. L. Vogel, W. G. Pfann, H. E. Corey and E. E. Thomas: Phys. Rev. **90** (1953) 489.
2) G. Wyon and P. Lacombe: *Report of the Conference on Defects in Crystalline Solids.* (The Phys. Soc. Lond., 1955) p. 187.
J. C. Suits and J. R. Low: Acta Met. **5** (1957) 285.
3) R. Hasiguchi, A. Kawano and Y. Hiki: to be published.
4) A. J. Forty and F. C. Frank: J. Phys. Soc. Japan **10** (1955) 656.

J. PHYS. SOC. JAPAN **13** (1958) 971~972

Paramagnetic Resonance Spectrum of Manganese in Single Crystals of Alkali Halide Grown from the Melt

By Kuniya FUKUDA, Yoichi UCHIDA and Hisamitu YOSHIMURA

Department of Physics, University of Kyoto, Kyoto

(Received June 6, 1958)

The experiments have been carried out at 290°K with a usual field modulation spectrometer, working at 1 cm. The paramagnetic resonance spectrum has been observed in single crystals of LiCl and KCl[1] grown from the melting phase containing 1 mol % manganese.

We took up LiCl and KCl from consideration of the magnitude of ionic radius of Mn^{2+} relative to those of alkali metal ions (the Goudsmidt radii of these ions are $Mn^{2+}=0.80$ Å, $Li^{+}=0.68$ Å, and $K^{+}=1.33$ Å, respectively). Applying Haven's method[2] to the two phase system of alkali halide and $MnCl_2$, the solution energies of Mn in these alkali halide crystals are estimated as 0.8 ev for LiCl and as 1.71 ev for KCl, provided that n in $1/r_n$ of repulsive force in $MnCl_2$ is 8, the value consistent with the experimental value of solution energy of Mn in NaCl given by Haven[3].

The spectrum of KCl/Mn can be classified into three kinds: (a) overlapping lines of about 30 gauss and about 100 gauss (peak to peak) observed after annealing; (b) only one line of about 30 gauss observed after quenching from 300~500°C; (c) hyperfine structure of six lines and a line of about 30 gauss (see Fig. 1), which are observed after quenching from 500°C. The width of hyperfine line is about 20 gauss under the field modulation of 15 gauss amplitude. The g-value is 2.005 ± 0.002. The hyperfine splitting constant is 96 ± 5 gauss. The hyperfine structure in KCl grown from the melt, which has not yet been reported, is very similar to

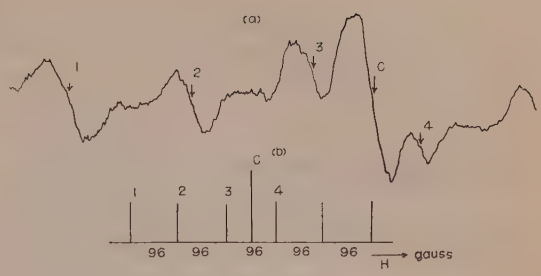

Fig. 1. (a) A part of the observed spectrum of KCl in (100) direction. (b) is the schematic representation of the observed spectrum.

those on KCl grown from solution by Forrester and Schneider and Low[1]. The resonance lines are unstable and bleach at room temperature within a period of 20 hours leaving only the single center peak of 30 gauss width (peak of c in Fig. 1). The appearance of hyperfine structure is somewhat critical as inferred from the calculated value of solution energy so that in heat treatment some cautions must be paid for frozing Mn in a transient state; quenching an annealed specimen after heating at 500°C for about an hour results in the single narrow peak of 30 gauss. Further some heat treatment leads to the decrease of this peak and at the same time to the appearance of hyperfine structure. The period of heating, though it depends on Mn concentration in crystals, is determined by monitoring the resonance lines.

The spectrum of LiCl/Mn consists of strong six hyperfine lines at $g=2.003\pm0.001$ with the mean value of hyperfine splitting constant $A=82\pm5$ gauss and some orientation dependent lines. LiCl crystal was taken out of furnace in the course of crystal growing and quenched to room temperature from the temperature near melting point. The crystals were so hygroscopic that the sample in cavity was coated with polyvinyl film. The hyperfine structure lines are stable and do not bleach so easily as in KCl. The orientation dependent lines are observed in low and high field sides of center six lines; in (100) direction four lines in both low and high field sides, while in (110) direction two lines in each side. The separation of lines is shown in Fig. 2.

Besides these observations, we carried out the measurements on resonance spectrum in LiF/Mn. In the crystal annealed to room temperature from 600°C for 12 hours, two overlapping peaks of about 200 gauss and about 40 gauss were observed. A broad peak of 200 gauss remained after quenching, but no hyperfine splitting appeared by any heat treatment up to 800°C.

The improvement of our spectrometer is now in progress. Experiments are being carried on to obtain finer results on the anisotropy of hyperfine

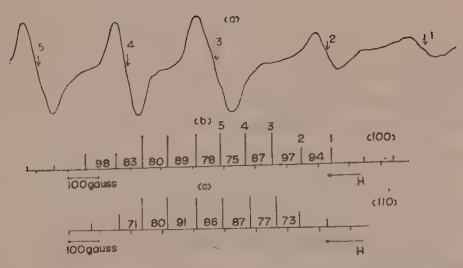

Fig. 2. (a) A part of the observed spectrum of LiCl in (100) direction. (b) and (c) are the schematic representations of the observed spectra corresponding to (100) and (110) directions, respectively. The lengths of lines show rough magnitude of order of relative intensity. The outer two lines in (100) and the outer one line in (110) on both sides of resonance pattern were difficult to confirm their exact positions due to low S/N ratio, but the magnitude of separation between these lines was about 95 gauss.

structure and thereby to examine the model of resonance center from the analysis by spin Hamiltonian.

References

1) H. Abe, H. Nagano, M. Nagusa and E. Osima: J. Chem. Phys. **25** (1956) 378.
P. A. Forrester and E. E. Schneider: Proc. Phys. Soc. B **69** (1956) 833.
W. Low: Proc. Phys. Soc. B **69** (1956) 837.
2) Y. Haven: Rec. Trav. Chim. Pay-Bas 69/2 (1950) 1259.
3) Y. Haven: Defects in Crystalline Solids, Report of 1954 Bristol Conference (London: Physical Society) p. 261.

J. Phys. Soc. Japan **13** (1958) 972~973

Some Electrical and Optical Properties of Tin Monosulphide

By Tadaichi Yabumoto

Institute of Electrical Engineering, Shizuoka University, Hamamatsu, Japan

(Received May 19, 1958)

Among the sulphides of the fourth group elements of periodic table, PbS has only been studied by many investigators.

Recently the author has studied GeS as one example of these sulphides and showed that it has also good characteristics on photoconductivity in visible region[1].

As for tin monosulphide there will be no experiment on its electrical and optical properties.

Metal tin of spectrographically standard grade of Johnson Matthey Co. was distilled in vacuum and excluded other impurities than Cu, Fe.

Sulphur was recrystallised four times by carbon disulphide and distilled in vacuum.

Such metal tin and sulphur was weighed by stoichiometric ratio of SnS and put into silica tube which was evacuated in high vacuum and sealed off.

This silica tube was heated in the electric furnace at 900°C for about 5 hours and 1000°C for about 6 hours respectively and then cooled.

The crystal form of SnS is orthorhombic and its melting point is about 882°C.

Samples were tested by X-ray diffraction and confirmed to be SnS.

Resistivity of tin monosulphide is about 10^6 ohm cm and lower than germanium monosulphide (about 10^{10} ohm cm) at room temperature.

Measurements of optical absorption and photoconductivity were carried out on films which were evaporated to the thickness of about 5 microns and had the resistance in dark of about 10^6 ohm.

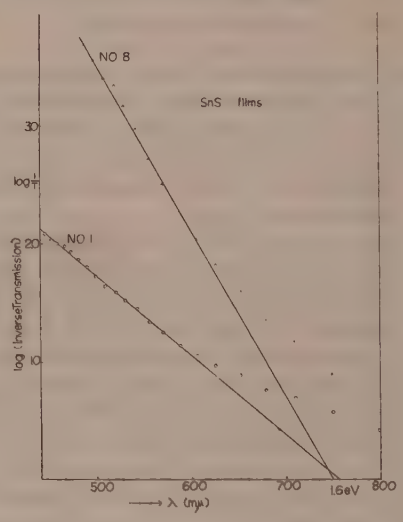

Fig. 1. Optical absorption of SnS films.

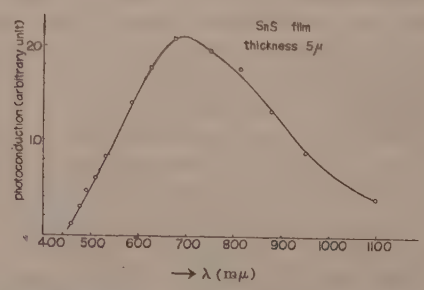

Fig. 2. Spectral photocurrent for equal energy of illumination.

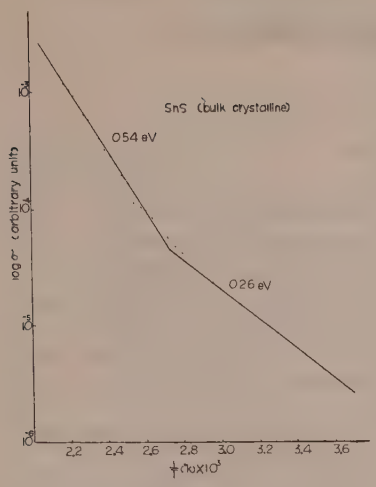

Fig. 3. Temperature depencence of electrical conduction of SnS.

Photoconductivity was measured in high vacuum with Nesa coating as electrodes.

Electrical conductivity was measured on a bulk crystal.

These results are shown in Fig. 1, 2, 3, respectively.

Band gap between the conduction band and the filled band is 1.6 ev from optical absorption, 1.7 ev from maximum value of photoconductivity and is in good agreement.

From the temperature dependency of conductivity activation energy is 0.54 ev at high temperatures and 0.26 ev at lower temperatures.

The true activation energy given from the conductivity at high temperatures subtracted the one at lower temperaturns is 1.1 ev.

It will correspond to thermal activation energy and is somewhat lower than optical value.

In this case activation energy at lower temperature, 0.26 ev will correspond to some impurity level.

Band gaps of GeS, SnS, PbS are about 1.8 ev, 1.6 ev and 0.4 ev respectively and its order of magnitude is reasonable.

The author wishes to express his sincere thanks to Mr. Sakio Suzuki for the helpful assistance to do this experiment.

Reference

1) T. Yabumoto: J. Physical Soc. Japan, **13** (1958) 559.

Errata

The Q-value for the $N^{14}(n, \alpha)B^{11}$ Reaction

By Tadayoshi DOKE, Shoji SUZUKI and Iwao OGAWA

J. Phys. Soc. Japan **13** (1958) 656

Page	Column	Line	Wrong	Corrected
657	left	5	C^{11}	B^{11}
		12	deutrons	deuterons
		17	E_n=2.40 MeV	E_n=2.48 Mev
		21 from the bottom	20°	30°
	right	Caption for Fig. 1.	reactionsinduced	reactions induced

PROGRESS OF THEORETICAL PHYSICS

CONTENTS

Progress of Theoretical Physics Vol. 19, No. 5 May 1958

The Conservation Laws in the Lepton Process and Two Kinds of Neutrinos ..... I. KAWAKAMI..459
Cepheid Vibration .....T. C. ROY..470
The Phenomenological Model of the Interaction of Elementary Particles .... K. FUJII and K. IWATA..475
Phenomenological Analysis of the Decay Processes of the Σ- and Λ-Hyperons ..... Y. YAMAGUCHI..485
On the Collective Mode of Internal Motion of the Nucleus to be coupled with the Irrotational Surface Motion ....S. NAGATA, R. TAMAGAKI, S. AMAI and T. MARUMORI..495
Dispersion Relations in Nucleon-Nucleon Scattering ....S. MATSUYAMA and H. MIYAZAWA..517
Theory of Cohesive Energies and Energy-Band Structures of Diamond-Type Valence Crystals——*The Method of SLCO, II*—— .....A. MORITA..534
A General Theory of Magnetic Resonance Saturation.....K. TOMITA..541
Letters to the Editor:
Note on the Strange Particle Effects in S-Wave Pion-Nucleon Scattering .....K. NAKAYAMA..581
On the Lateral Distribution of the Electron Component in Extensive Air Showers .....A. UEDA and N. OGITA..582
A Possible Size Effect on the Plasma Oscillation of Electrons in Solids.....Y. H. ICHIKAWA..585
Hyperon Decays and Characteristics of Interactions between Elementary Particles.....Y. TAGUCHI and R. KAWABE..586
The Spirality of the Decay Product .....K. FUJII and K. IWATA..589
Reevaluation of the Electric Quadrupole Moment of the Deuteron... ..... H. NARUMI, T. WATANABE and O. NAKAHARA..591
A Covariant Interpretation of the Existence of the Parity Non-Conservation and the New Freedoms for Elementary Particles..K. GOTO..592
Antinucleon Annihilation and Multiplicity of Emitted Pions....Z. KOBA..594
Cluster Expansion of the Ground State of a Bose Particle System... .....F. IWAMOTO..595
Exact Treatment of Bardeen's Theory of Superconductivity in the Strong Coupling Limit .....Y. WADA, F. TAKANO and N. FUKUDA..597

Price $ 1.25 per copy
$ 15.00 per year (postage inclusive)
Annual dues for foreign members (individual subscribers)
$ 12.00 (postage inclusive)
" for foreign members of the Physical Society of Japan
$ 10.00 (postage inclusive)
Application for members, subscriptions and orders for back numbers should be sent, directly or through book-dealers, to

The Publication Office
in
Yukawa Hall, Kyoto University, Kyoto, Japan

. . . . . .

ANNOUNCEMENT

REVISED Price List of Back Numbers (for subscribers abroad)

*Vols. 1–4	$ 6.40 each
*Vols. 5 & 6	$13.00 each (single copy: $2.50)
*Vols. 7 and succeeding ones	$ 8.00 each (single copy: $1.50)

Back number prices are effective for volumes other than last four (4) volumes (the current volume inclusive).

Thus, volumes 1 through 16 will be regarded as back numbers while volume 20 is being published.

The revised prices will be effective on and after August 1, 1958.

. . . . . .

JOURNAL OF THE PHYSICAL SOCIETY OF JAPAN Vol. 13, No. 9, SEPTEMBER, 1958

Dipolar Broadening of the Quadrupole Resonance Line in Crystals $NaClO_3$, $NaBrO_3$

By Kenji KANŌ

Faculty of Liberal Arts and Education, Kagawa University

(Received June 4, 1958)

A few formulae have been derived for the contribution of the dipolar broadening to the second moment of the resonance line in pure quadrupole resonance experiment for crystals in which the following conditions are satisfied:

(1) All nuclear spins involved, both resonant and nonresonant, have spin 3/2.

(2) The electric field gradient tensor at all nuclear sites have axial symmetry. For resonant nuclei the gradient of the electric field has the same magnitude but the symmetry axes of the electric field gradient at several nuclear sites in the unit cell have different directions.

(3) As for the nonresonant unclei no restriction has been set the magnitude of the electric field gradient and its directions.

A comparison is made with the line widths for $NaClO_3$ and $NaBrO_3$ observed by Kōi et al.

§ 1. Introduction

The possible causes of the line broadening in the pure quadrupole resonance experiment are the spin-lattlice relaxation, magnetic dipole interaction and field fluctuation due to the crystal strain. Though in a few compounds the electron-coupled spin-spin interaction was found to contribute to the line broadening, in most compounds the above three are important hence we are interested in their contributions to the observed line width.

Recently, the pure quadrupole resonance line widths in crystals containing bromine and cholrine isotops have been investigated by T. Wang[1], Y. Kôi[2] and T. Fuke[2),5] and T. Hasi[4] and his co-workers[4].

Further Y. Kôi[2,3,5] has shown that the main cause of the line width in $NaClO_3$ or $NaClO_3$ is the magnetic dipole interaction in view of the ratio of the line width of bromine isotopes Br^{79} and Br^{81} or chlorine isotopes of Cl^{35} and Cl^{37}. Therefore it is interesting to confirm his argument theoretically.

A. Abragam and K. Kambe[6] have given the expressions for the second moment of the resonance line in the case of pure quadrupole resonance assuming that the resonant nuclei are identical and experiencing axial electric field gradients of common directions and magnitudes; however, the case in which the gradient of the electric field at the sites of resonant nuclei has the same magnitude but different directions has not yet been considered. The purpose of the present articls is to give theoretical expressions for the second moment of the resonance line investigated by Kôi et al. We here treat the broblem following the method of Van Vleck[7], and A. Abragm and K. Kambe with necessary modification. The calculation in our case is more involved than that of A. Abragam and Kambe but we get rather simple results.

The effects of the relative directions of the electric field gradient at the nuclei will be shown graphically. In the next section, let us consider the interaction between resonant nuclei, and in the last section, the theoretical values of the second moment of the resonance lines for $NaClO_3$ and $NaBrO_3$ are estimated, and they are found to be in fairly good agreement with the experimental data[2,3,5].

§ 2. Interaction between Resonant Nuclei

In this section we consider the case in which the gradient of the electric field at resonant nuclei are the same in magnitude but different in direction.

For the cases in which the symmetry axis of the electric field at different nuclei have three or more different directions, it is easy for us to generalize the following results of two directions. Thus we assume that the directions of the symmetry axes of the electric field gradients at nuclear sites are either along

the z-axis or along z'-axis.

We should designate the nuclear spin operators as I_j ($j=1, 2, 3, \ldots, N$), where I_j is the nuclear spin operator of the j-th nucleus for which the axis of the symmetry is taken as the x-axis, and I_k' is the nuclear spin operator of the k-th nucleus for which the axis of the symmetry is taken as the z'-axis.

Fig. 1 shows the z and z'-axis and the vector $\boldsymbol{r}_{jk}$.

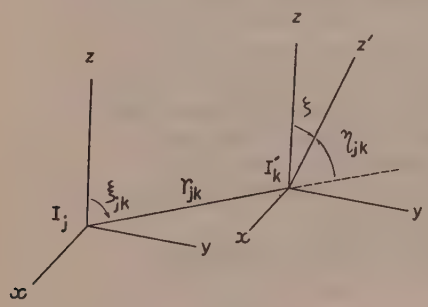

Fig. 1.

The total Hamiltonian $\mathscr{H}$ for the spin system can be written as $\mathscr{H}=\mathscr{H}_0+\mathscr{H}'$ where $\mathscr{H}_0$, is the unperturbed Hamiltonian and $\mathscr{H}'$ is the Hamiltonian representing the magnetic interactions. Here $\mathscr{H}_0$ and $\mathscr{H}'$ can be written as

$$\begin{aligned}
\mathscr{H}_0 &= \mathscr{H}_1+\mathscr{H}_2 \\
\mathscr{H}_1 &= -\delta\textstyle\sum_j I_{zj}^2 \\
\mathscr{H}_2 &= -\delta\textstyle\sum_k I_{z'k}'^2 \\
&= -\delta\textstyle\sum_k \{\alpha\cdot I_{xk}'+\beta\cdot I_{yk}'+\gamma\cdot I_{zk}'\}^2 \\
\mathscr{H}' &= \mathscr{H}_1'+\mathscr{H}_2'+\mathscr{H}_{12}' \\
\mathscr{H}_{12}' &= \textstyle\sum_{jk} \boldsymbol{W}_{jk}=\mu_0^2\sum_{jk}|\boldsymbol{r}_{jk}|^{-3}\cdot \\
&\quad \{(J_j\cdot I_k)-3\boldsymbol{r}_{jk}^{-2}\cdot(I_j\cdot\boldsymbol{r}_{jk})(I_k'\boldsymbol{r}_{jk})\}, \qquad (1)
\end{aligned}$$

where α, β, γ are the direction cosines of the z'-axis with respect to x, y, z-axis, I_{xk}', I_{yk}' and I_{zk}' are x, y and z components of I'_k respectively, and δ is a parameter proportional to the strength of the quadrupole interaction, making the resonance frequency $\nu_0=2\delta/h$ for the spin 3/2. $\mathscr{H}_1'$ is the Hamiltonian of dipolar interaction among the spins I_j, $\mathscr{H}_2'$ is the Hamiltonian among the spins I_k', $\mathscr{H}_{12}'$ is the Hamiltonian between the spins I_j and I_k'.

The matrix representation of $\mathscr{H}_1+\mathscr{H}_2$ is diagonal when the axes of quantization for I_j and I_k' are chosen along the directions of z and z' axes respectively. This means that the axis of quantization varies as going from I_j to I_k'. Thus the calculation of the matrix elements of $\mathscr{H}'$ becames more cumbersome than in the case of A. Abragam and K. Kambe[6].

We performed the calculation by introducing the appropriate transformation matrix S which transforms the axis of quantization from z to z'. First we express the matrix elements of all the Hamiltonian taking the axis of quantization as z axis for I_j as well as I_k', then we transform the quantization for I_k' by means of $\boldsymbol{S}$. Thus the matrices of $\mathscr{H}_1$ and $\mathscr{H}_2$ are diagonalize and the interaction Hamiltonian is expressed in the quantization relevant nucleus is I_j or I_k'.

In order to discard the matrix elements which contribute only to the satellite lines, we have to truncate the interaction Hamiltonian $\mathscr{H}'$ suitably. Thus the truncated Hamiltonian $\overline{\mathscr{H}}$ becames

$$\overline{\mathscr{H}}=\mathscr{H}_0+\overline{\mathscr{H}}'$$

where $\overline{\mathscr{H}}$ is the part of $\mathscr{H}'$ which commute with $\mathscr{H}_0$.

The interaction between the oscillating field and spin system can be expressed of the spin operators, and it should also be truncated appropriately.

We denote this truncated interaction operator as $\bar{R}$. Then we can express the second moment as

$$h^2\langle\Delta\nu^2\rangle=-sp\{\overline{\mathscr{H}}'\bar{R}-\bar{R}\overline{\mathscr{H}}'\}^2/sp\bar{R}^2.$$

The second moments can be divided into three parts as

$$h^2\langle\Delta\nu^2\rangle=h^2\langle\Delta\nu_1^2\rangle+h^2\langle\Delta\nu_2^2\rangle+h\langle\Delta\nu_{12}^2\rangle,$$

where $\langle\Delta\nu_1^2\rangle$, $\langle\Delta\nu_2^2\rangle$ and $\langle\Delta\nu_{12}^2\rangle$ arise from $\mathscr{H}_1'$, $\mathscr{H}_2'$ and $\mathscr{H}_{12}'$ respectively. Since $\langle\Delta\nu_1^2\rangle$ and $\langle\Delta\nu_2^2\rangle$ have already been given by A. Abragam and K. Kambe[6], we will have only to evaluate $\langle\Delta\nu_{12}^2\rangle$. When the sample is an assemblage of small perfect crystal grains which are destributed at random we can calculate the spatial average, so-called the powder mean, for the second moment. Now we denote the spatial average by $\langle\langle\Delta\nu_{12}^2\rangle\rangle$. Then after some lengthy matrix manipulations, we finally obtain

$$\begin{aligned}
h^2\langle\langle\Delta\nu_{21}^2\rangle\rangle &= \mu_0^4\textstyle\sum_j|\boldsymbol{r}_{jk}|^{-6}\cdot U_{jk} \\
U_{jk} &= 6-\frac{9}{16}\{\cos^2\xi_{jk}+\cos^2\eta_{jk}\} \\
&\quad +\frac{15}{16}\cdot\{\cos\zeta-3\cos\xi_{jk}\cdot\cos\eta_{jk}\}^2. \qquad (2)
\end{aligned}$$

Fig. 1 shows ξ_{jk} and η_{jk} and ζ. Fig. 2 and Fig. 3 and Fig. 4 show graphically the effect of the directions of electric field gradient in Eq. (2) for several special nuclear sites.

§ 3. Interaction between Resonant and Non-resonant Nuclei

In this section we shall consider the case where the resonant nuclei interact only with the non-resonant nuclei and both nuclei have spin 3/2 and the non-resonant nuclei have quadrupole splitting. The interaction Hamiltonian $\mathscr{H}''_{12}$ is written below with index j for resonant k' for nonresonant spins,

$$\mathscr{H}''_{12}=\sum_{jk'} W_{jk}=\mu_0^2\cdot\mu'^2_0\sum_{jk'}|\boldsymbol{r}_{jk'}|^{-3}\cdot\{(I_j\cdot I'_{k'})-3|\boldsymbol{r}_{jk'}|^{-2}\cdot(I_j\cdot\boldsymbol{r}_{jk'})\cdot(I'_{k'}\cdot\boldsymbol{r}_{jk'})\}.$$

Following the same procedures described in the foregoing section we get

$$h^2\langle\langle\Delta\nu_{12}^2\rangle\rangle=\mu_0^2\mu'^2_0\sum_{k'}|\boldsymbol{r}_{jk'}|^{-6}\cdot U'_{jk'}$$

$$U'_{jk'}=\frac{15}{4}+\frac{9}{4}\cos^2\eta_{jk'}\,, \qquad (3)$$

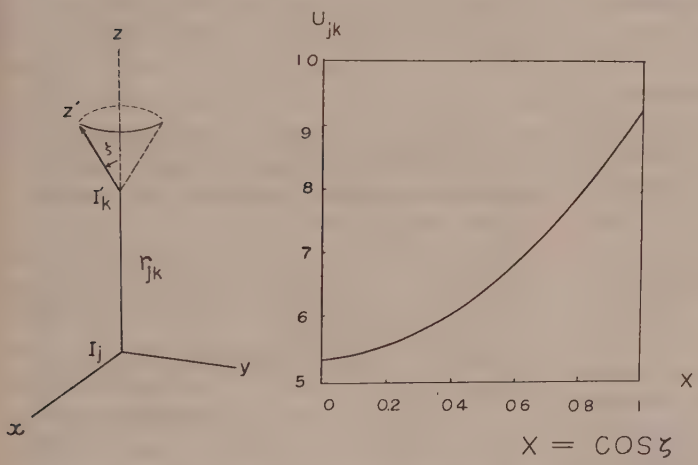

Fig. 2. The case of $\xi_{jk}=0$ and $\eta_{jk}=\zeta$.

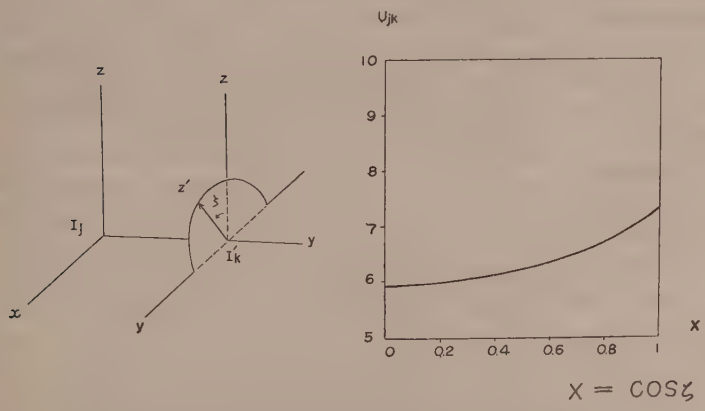

Fig. 3. The case of $\xi_{jk}=\pi/2$ and $\eta_{jk}=\pi/2$.

where $\eta_{jk'}$ have the same meaning as in the previous section. All other things being equal, the non-resonant nuclei having quadrupole splitting are less effective in broadening than that having no quadrupole splitting and we get

$$0.3\leq\frac{U'_{jk'}\ (\text{with quadrupole splitting})}{U'_{jk'}(\text{no quadrupole spliting})}\leq 0.5.$$

§ 4. Line Width of Chlorine in $NaClO_3$ and Bromine in $NaBrO_3$

Y. Kôi[2,3,5] has resently shown that the main cause of the line width in $NaClO_3$ and $NaBrO_3$ is the magnetic dipole interaction in view of the ratio of the widths of lines corresponding to chlorine and bromine isotopes. Therefore, it is interesting to make sure of these results by our theory. The crystals of $NaClO_3$ and $NaBrO_3$ have cubic structure with the lattice constants 6.689 A. and 6.555 A. respectively[8], and unit cell contains four molecules. Their structures are given in Fig. 5.

L. Pauling[9] has shown that the bonds between Na ion and BrO_3 ion or ClO_3 ion in $NaBrO_3$ or $NaClO_3$ are on the whole ionic. The BrO_3 ion or ClO_3 ion are the flat trigonal pyramid having the there oxygen atoms as its base. The binding between O–Br or O–Cl are largely the covalent structures. From the symmetry of the flat triagonal pyramid of oxygens, the symmetrical axes of the gradient of the electric field at the nuclear spins of Br or Cl are the line passing through the Na and Br or Cl nuclei. Fig. 5 shows this axis of symmetry.

As for the Na–Br distances in $NaBrO_3$, the ionic radius of Na ions is 0.95 A, and that of Br ion is 1.95 A., the sum of them is 2.90 A. and this is shorter than the nearest distance of Na–Br, 3.42 A.. This means that the binding between Na–Br is partly covalent and the nuclear spin levels of Na has quadrupole splittings, and the symmetry axis of the field gradient at Na

nucleus is the same as that of Br and this is also true for $NaClO_3$ having the almost same crystal structure as $NaBrO_3$.

The experimental measurements on the full width of the nuclear quadrupole resonances of chlorine and bromine isotopes in these solids have been made to an accuracy of about 0.01 KC. The observed and calculated second moments are given in Table I.

The agreement between our theory and experiment in Table I seems to be on the whole satisfactory as considering the accuracy of the experimental measurements, especially the agreement is good for $NaClO_3$.

Table I. Calculated and observed frequency deviations in $NaClO_3$ and $NaBrO_3$

isotopes	$\langle \Delta\nu^2 \rangle$ (obs.)	$\langle\langle \Delta\nu^2 \rangle\rangle$ (calc.)
Cl^{35} ($NaClO_3$)	0.210 $(KC)^2$*	0.204 $(KC)^2$
Cl^{37} ($NaBlO_3$)	0.149 $(KC)^2$*	0.142 $(KC)^2$
Br^{79} ($NaBrO_3$)	2.68 $(KC)^2$**	0.98 $(KC)^2$
Br^{81} ($NaBrO_3$)	3.02 $(KC)^2$**	2.33 $(KC)^2$

*: Fuke and Kôi[5]

**: Y. Kôi[2] (The observed $\langle \Delta\nu^2 \rangle$ is calculated by the observed full width and Gaussian assumption of the line shape.)

The author wishes to express his sincere thanks to professor K. Kambe for his valuable advice and kind reading of the manuscript. He also wishes to thank professor Y. Kôi for valuable suggestiones and communicating the result of his experiment before publication.

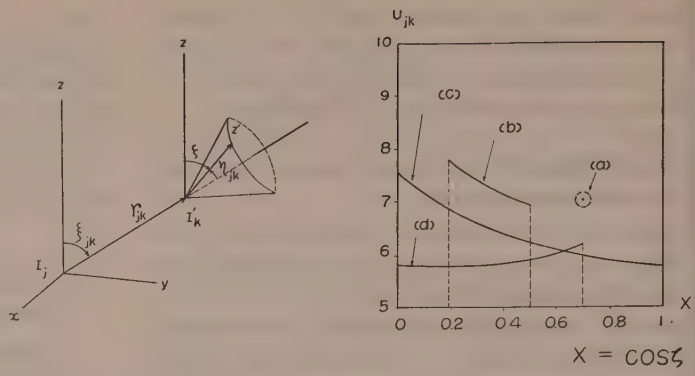

Fig. 4. The case of $\xi_{jk}=\pi/4$ and $\eta_{jk}=$constant.
(a) $\eta_{jk}=0$, (b) $\eta_{jk}=\pi/6$,
(c) $\eta_{jk}=\pi/4$, (d) $\eta_{jk}=\pi/2$.

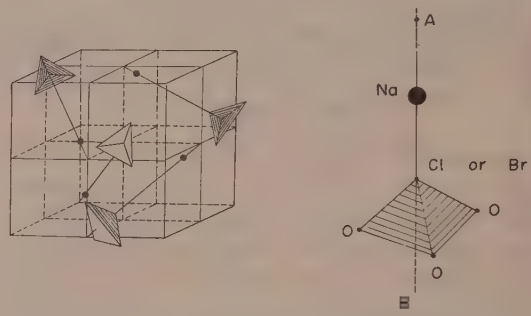

Fig. 5. The crystal structure of $NaClO_3$ type in unit cell. The line passing through A and B is the symmetric axis of the electric field gradient at the sites Na and Cl or Br.

References

1) T. Wang: Phys. Rev. **99** (1955) 566.
2) Y. Koi: J. Phys. Soc. Japan **12** (1957) 49.
3) Y. Koi, A. Tsujimura and T. Fuke: J. Chem. Phys. **23** (1955) 1346.
4) T. Hasi: to be published in J. Phys. Soc. Japan.
5) T. Fuke and Y. Kôi: to be published in J. Chem. Phys.
6) A. Abragam and K. Kambe: Phys. Rev. **91** (1953) 894.
7) Van Vleck: Phys. Rev. **74** (1948) 1168.
8) R. W. G. Wyckoff: Crystal Structures (Interscience Publishers, Inc., New York, 1953).
9) L. Pauling: The Nature of the Chemical Bond. (Oxford Univ. press, London, 1952).

JOURNAL OF THE PHYSICAL SOCIETY OF JAPAN Vol. 13, No. 9, SEPTEMBER, 1958

The Thermoelectric, Galvanomagnetic and Thermomagnetic Effects of Monovalent Metals. III. The Galvanomagnetic and Thermomagnetic Effects for Anisotropic Media.

By Mikio TSUJI

General Education Department, Kyushu University, Fukuoka

(Received June 6, 1958)

A variational principle for the electron transport in a magnetic field is described, and the principle is applied to the calculation of the transverse effects of cubic metals in the transverse magnetic field by using an approximate trial function. Our method gives exact solution for the spherical energy hand model. For the anisotropic energy band, our method gives an approximate solution which coincides with the exact solution if the energy dependent relaxation time exists. Relations between the transverse galvanomagnetic and thermomagnetic coefficients, which hold for arbitrary scattering mechanism, are derived.

§ 1. Introduction

In the part I[1], we have investigated, based on the spherical band model, the thermoelectric effects and transverse galvanomagnetic and thermomagnetic effects in the transverse magnetic field for the case of high temperatures where the time of relaxation exists. At low temperatures, however, the time of relaxation does not exist, and the spherical band model is no longer a good approximation. Therefore in the part II[2], we have investigated the thermoelectric power of monovalent metals at low temperatures based on the anisotropic energy band model. In this part, we shall calculate the galvanomagnetic and thermomagnetic effects for cubic metals by using a variational method.

Kohler[3] has investigated the Hall effect and magnetoresistance of metals based on the two band model by using a variational principle. His method, however, is not easy to generalize for the anisotropic band. Ziman[4] has proposed a different form of the variational principle*. His variational function is not proportional to the entropy production due to the scatterings of the electrons, and so he suggested a modification of the formula for the entropy production in the magnetic field. In § 2 we give a variational method in which the variational function is proportional to the entropy production and, in the connection to the thermodynamical principle, no trouble occurs in the formula of the entropy production. However, the concequence of our variational principle is equivalent to those of Kohler and Ziman.

Using this variational principle, we solve Boltzmann's equation for a cubic metal in the presence of a magnetic field in § 3. In § 4 we show certain relations between the coefficients (Eqs. (47), (48) and (49)), which hold irrespective of the scattering mechanism. Eq. (47) is a well known relation which has been derived by Callen[5] from Onsager's reciprocal relations. Eq. (48) has been derived by Meixner[6] by assuming the existence of the relaxation time, and by Sondheimer[7] by using the free electron model. However, it is a new result of our calculations that (48) holds for any cubic metal irrespective of the scattering mechanism. Eq. (49) is also a new result which is a generalization of Eq. (86) in I. In § 5, we discuss certain special cases, and it is shown that our method of variational principle gives the exact solution, if it is applied to an anisotropic metal in which the energy dependent relaxation time exists. The formulae for the spherical energy band model and those for the pure cubic metals at low temperatures are given also.

§ 2. Variational Principle in the Presence of a Magnetic Field

In this section we consider formally a most general case. We put the distribution func-

* (Added in proof) F. Moliner and S. Simons (Proc. Camb. Phil. Soc. **53** (1957), 848) have extended the variational principle of the form of Ziman to the case including the boundary scatterings.

tion of the electron

$$f_k = f_0 - \Phi_k \frac{\partial f_0}{\partial E}\,, \tag{1}$$

where f_0 is the Fermi distribution. If there are an electric field $\boldsymbol{F}$, a magnetic field $\boldsymbol{H}$ and a temperature gradient ∇T in a metal, Boltzmann's equation is written schematically in the form

$$L(\Phi_k) = X_k - M(\boldsymbol{H})\Phi_k\,, \tag{2}$$

where

$$L(\Phi_k) \equiv -\left(\frac{\partial f_k}{\partial t}\right)_{\text{coll}}\,, \tag{3}$$

$$X_k \equiv \frac{1}{\hbar}\left\{e\boldsymbol{F} - T\,\text{grad}_r \frac{E-\zeta}{T}\right\}\cdot \text{grad}_k\, E \frac{\partial f_0}{\partial E}\,, \tag{4}$$

and

$$M(\boldsymbol{H}) \equiv \frac{e}{\hbar^2 c}\frac{\partial f_0}{\partial E}\,\text{grad}_k\, E\cdot \boldsymbol{H}\times \text{grad}_k\,. \tag{5}$$

If there is no magnetic field, the solution of (2) is obtained[8] by maximizing an integral

$$(\Phi_k, \Phi_k) \equiv \int \Phi_k L(\Phi_k) d\boldsymbol{k}\,, \tag{6}$$

subject to a subsidially condition

$$(\Phi_k, \Phi_k) = \int \Phi_k X_k d\boldsymbol{k}\,. \tag{7}$$

In the presence of a magnetic field, it is shown easily that

$$\int \Phi_k M(\boldsymbol{H}) \Phi_k d\boldsymbol{k} = 0\,, \tag{8}$$

and so, as has been stated by Ziman[4], a simple generalization of (6) and (7) leads to a contradictory solution which is just the solution of the equation without magnetic field. A variational principle which gives the true solution of (2) can be formulated as follows:

Let Φ_k be the solution of (2) and Ψ_k an arbitrary function which satisfies a subsidially condition

$$(\Psi_k, \Psi_k) = \int \Psi_k X_k d\boldsymbol{k} - \int \Psi_k M(\boldsymbol{H}) \Phi_k d\boldsymbol{k}\,. \tag{9}$$

Then the function Φ_k which maximizes the expression (6) is the solution of (2).

(Proof)

Using Lagrange's undetermined multiplier λ, we maximize

$$(1+\lambda)(\Psi_k, \Psi_k) - \lambda \int \Psi_k X_k d\boldsymbol{k} + \lambda \int \Psi_k M(\boldsymbol{H}) \Phi_k d\boldsymbol{k}\,. \tag{10}$$

Eq. (10) must be stationary for any variation $\delta\Psi_k$. From the linearity of the collision operator L and the symmetry relation

$$(\delta\Psi_k, \Psi_k) = (\Psi_k, \delta\Psi_k)\,, \tag{11}$$

we have

$$(2+2\lambda)L(\Psi_k) - \lambda X_k + \lambda M(\boldsymbol{H})\Phi_k = 0\,, \tag{12}$$

and from (9) and (12) we find $\lambda = -2$. Therefore (12) becomes

$$L(\Psi_k) - X_k + M(\boldsymbol{H})\Phi_k = 0\,, \tag{13}$$

which shows that Ψ_k is the solution of (2). This method can be used for any equation of type of Eq. (2) in which the operator M does not have the symmetry charactor, and we have used this method in the calculation of the phonon drift problem[9].

If we use the symmetry charactor of L and the fact that (Ψ_k, Ψ_k) is positive definite and that (9) can be rewritten as

$$(\Psi_k, \Psi_k) = (\Psi_k, \Phi_k)\,, \tag{14}$$

the proof is also straightforward.

Now (Ψ_k, Ψ_k) is proportional to the entropy production due to the collisions, and so our variational principle corresponds to the thermodynamical principle of an irreversible process. There is no trouble such as discussed by Ziman[4]. The electric and magnetic field do not contribute to the entropy production directly. The entropy produced is transfered to the temperature bath in the steady state.

The actual procedure of the application of the variational principle is given in the following section.

§ 3. Application to an Anisotropic Metal

We consider a cubic metal in which a magnetic field $\boldsymbol{H}$ is along z axis and an electric field $\boldsymbol{F}$ and a temperature gradient ∇T are in the $x-y$ plane, and we put as an approximation,

$$\Phi_k = c_x(\eta)\frac{\partial E}{\partial k_x} + c_y(\eta)\frac{\partial E}{\partial k_y}\,, \tag{15}$$

where $\eta = (E-\zeta)/\kappa T$. Eq. (15) is an exact expression for an isotropic metal and may be a fairly good approximation for a cubic metal. The change of the distribution function for the electrons due to the scatterings by the lattice waves or the lattice defects may be written in the form

$$\left(\frac{\partial f}{\partial t}\right)_{\text{coll}}=-L(\Phi)=-\frac{1}{\hbar}\left\{\frac{\partial E}{\partial k_x}\mathscr{L}(c_x)+\frac{\partial E}{\partial k_y}\mathscr{L}(c_y)\right\}\frac{\partial f_0}{\partial E}\,. \tag{16}$$

Then the Boltzmann equation (2) becomes

$$\frac{\partial E}{\partial k_x}\mathscr{L}(c_x)+\frac{\partial E}{\partial k_y}\mathscr{L}(c_y)=\left(eF_x+T\frac{\partial}{\partial x}\frac{\zeta}{T}+\frac{E}{T}\frac{\partial T}{\partial x}\right)\frac{\partial E}{\partial k_x}+\left(eF_y+T\frac{\partial}{\partial y}\frac{\zeta}{T}+\frac{E}{T}\frac{\partial T}{\partial y}\right)\frac{\partial E}{\partial k_y}$$
$$-\frac{eH}{\hbar c}\left\{\left(\frac{\partial^2 E}{\partial k_x^2}\frac{\partial E}{\partial k_y}-\frac{\partial^2 E}{\partial k_x\partial k_y}\frac{\partial E}{\partial k_x}\right)c_x-\left(\frac{\partial^2 E}{\partial k_y^2}\frac{\partial E}{\partial k_x}-\frac{\partial^2 E}{\partial k_x\partial k_y}\frac{\partial E}{\partial k_y}\right)c_y\right\}\,. \tag{17}$$

We put a trial function for (15) as

$$\Psi_k=b_x(\eta)\frac{\partial E}{\partial k_x}+b_y(\eta)\frac{\partial E}{\partial k_y}\,, \tag{18}$$

and then we have (by omitting a constant factor)

$$(\Psi_k,\Psi_k)=\iint\frac{(\partial E/\partial k_x)^2}{|\text{grad}_k E|}b_x\mathscr{L}(b_x)\frac{\partial f_0}{\partial\eta}dSd\eta+\iint\frac{(\partial E/\partial k_y)^2}{|\text{grad}_k E|}b_y\mathscr{L}(b_y)\frac{\partial f_0}{\partial\eta}dSd\eta\,, \tag{19}$$

where the integration with respect to dS is carried out over a constant energy surface. We expand c_x and c_y as

$$\left.\begin{aligned}c_x&=c_{x,0}+c_{x,1}\eta+c_{x,2}\eta^2+\cdots,\\ c_y&=c_{y,0}+c_{y,1}\eta+c_{y,2}\eta^2+\cdots,\end{aligned}\right\} \tag{20}$$

and b_x and b_y as

$$\left.\begin{aligned}b_x&=b_{x,0}+b_{x,1}\eta+b_{x,2}\eta^2+\cdots,\\ b_y&=b_{y,0}+b_{y,1}\eta+b_{y,2}\eta^2+\cdots.\end{aligned}\right\} \tag{21}$$

Then the variational function (19) and the subsidially condition (9) become

$$(\Psi_k,\Psi_k)=\sum_r\sum_s(b_{x,r}b_{x,s}+b_{y,r}b_{y,s})d_{rs} \tag{22}$$

and

$$C\equiv\sum_r\sum_s(b_{x,r}b_{x,s}+b_{y,r}b_{y,s})d_{rs}-\sum_r\sum_s(b_{x,r}c_{y,s}\gamma_{r+s}-b_{y,r}c_{x,s}\gamma_{r+s})$$
$$-\sum_r\left[\left\{\left(eF_x+T\frac{\partial}{\partial x}\frac{\zeta}{T}\right)\alpha_r^{(1)}+\frac{1}{T}\frac{\partial T}{\partial x}\alpha_r^{(2)}\right\}b_{x,r}\right.$$
$$\left.+\left\{\left(eF_y+T\frac{\partial}{\partial y}\frac{\zeta}{T}\right)\alpha_r^{(1)}+\frac{1}{T}\frac{\partial T}{\partial y}\alpha_r^{(2)}\right\}b_{y,r}\right]=0\,, \tag{23}$$

where

$$d_{rs}\equiv\frac{1}{3}\iint|\text{grad}_k E|\eta^r\mathscr{L}(\eta^s)\frac{\partial f_0}{\partial\eta}dSd\eta=d_{sr}\,, \tag{24}$$

$$\gamma_r\equiv\frac{eH}{\hbar c}\int\left\{\frac{\partial^2 E}{\partial k_x^2}\left(\frac{\partial E}{\partial k_x}\right)^2-\frac{\partial^2 E}{\partial k_x\partial k_y}\frac{\partial E}{\partial k_x}\frac{\partial E}{\partial k_y}\right\}\frac{\eta^r}{|\text{grad}_k E|}\frac{\partial f_0}{\partial\eta}dSd\eta\,, \tag{25}$$

$$\alpha_r^{(n)}\equiv\frac{1}{3}\int E^{n-1}|\text{grad}_k E|\eta^r\frac{\partial f_0}{\partial\eta}dSd\eta\,. \tag{26}$$

Integrating the right side of (25) with respect to η, we have

$$\left.\begin{aligned}\gamma_0&=-\frac{eH}{\hbar c}f_5\,,\\ \gamma_1&=-\frac{eH}{\hbar c}\frac{\pi^2\kappa T}{3}\frac{df_5}{dE}\,,\\ \gamma_2&=-\frac{eH}{\hbar c}\frac{\pi^2}{3}f_5\,,\end{aligned}\right\} \tag{27}$$

where

$$f_5(E)=\int\left\{\left(\frac{\partial E}{\partial k_x}\right)^2\frac{\partial^2 E}{\partial k_y^2}-\frac{\partial E}{\partial k_x}\frac{\partial E}{\partial k_y}\frac{\partial^2 E}{\partial k_x\partial k_y}\right\}\frac{1}{|\mathrm{grad}_k E|}dS\,. \tag{28}$$

By using the cubic symmetricity, (28) can be rewritten as

$$f_5=\frac{1}{3}\int\overline{\left(\frac{1}{\rho}\right)}|\mathrm{grad}_k E|^2 dS\,,$$

where $\overline{(1/\rho)}$ is the mean curvature of the constant energy surface at the point $\boldsymbol{k}$ and the sign of the radius of curvature ρ is taken to be positive when the center of curvature is inside (lower energy side) of the surface. The values of $\alpha_r^{(n)}$ have been given in the appendix of II in terms of an integral f_1 and its derivative, where

$$f_1(E)=\frac{1}{3}\int|\mathrm{grad}_k E|dS\,. \tag{29}$$

By putting the partial derivatives of $(\Psi_k, \Psi_k)+\lambda C$ with respect to $b_{x,r}$ and $b_{y,r}$ to be zero, we have $\lambda=-2$. Then, by putting $b_{x,r}=c_{x,r}$ and $b_{y,r}=c_{y,r}$, we obtain a set of equations

$$\left.\begin{aligned}&\sum_s c_{x,s}d_{rs}-\sum_s c_{y,s}\gamma_{r+s}-\left(eF_x+T\frac{\partial}{\partial x}\frac{\zeta}{T}\right)\alpha_r^{(1)}-\frac{1}{T}\frac{\partial T}{\partial x}\alpha_r^{(2)}=0\,,\\&\sum_s c_{y,s}d_{rs}+\sum_s c_{x,s}\gamma_{r+s}-\left(eF_y+T\frac{\partial}{\partial y}\frac{\zeta}{T}\right)\alpha_r^{(1)}-\frac{1}{T}\frac{\partial T}{\partial y}\alpha_r^{(2)}=0\,,\end{aligned}\right\} \tag{30}$$

from which we can determine the expansion coefficients of (20). Actually, for our purpose to obtain the leading terms of the relevant quantities, it suffices to take the first two terms of (20). Then the solutions of (30) can be written in the forms

$$\left.\begin{aligned}c_{x,0}&=\left(eF_x+T\frac{\partial}{\partial x}\frac{\zeta}{T}\right)c_0^{(1)}+\frac{1}{T}\frac{\partial T}{\partial x}c_0^{(2)}+\left(eF_y+T\frac{\partial}{\partial y}\frac{\zeta}{T}\right)\bar{c}_0^{(1)}+\frac{1}{T}\frac{\partial T}{\partial y}\bar{c}_0^{(2)}\,,\\c_{x,1}&=\left(eF_x+T\frac{\partial}{\partial x}\frac{\zeta}{T}\right)c_1^{(1)}+\frac{1}{T}\frac{\partial T}{\partial x}c_1^{(2)}+\left(eF_y+T\frac{\partial}{\partial y}\frac{\zeta}{T}\right)\bar{c}_1^{(1)}+\frac{1}{T}\frac{\partial T}{\partial y}\bar{c}_1^{(2)}\,,\\c_{y,0}&=-\left(cF_x+T\frac{\partial}{\partial x}\frac{\zeta}{T}\right)\bar{c}_0^{(1)}-\frac{1}{T}\frac{\partial T}{\partial x}\bar{c}_0^{(2)}+\left(eF_y+T\frac{\partial}{\partial y}\frac{\zeta}{T}\right)c_0^{(1)}+\frac{1}{T}\frac{\partial T}{\partial y}c_0^{(2)}\,,\\c_{y,1}&=-\left(eF_x+T\frac{\partial}{\partial x}\frac{\zeta}{T}\right)\bar{c}_1^{(1)}-\frac{1}{T}\frac{\partial T}{\partial x}\bar{c}_1^{(2)}+\left(eF_y+T\frac{\partial}{\partial y}\frac{\zeta}{T}\right)c_1^{(1)}+\frac{1}{T}\frac{\partial T}{\partial y}c_1^{(2)}\,,\end{aligned}\right\} \tag{31}$$

where

$$c_0^{(n)}=\frac{1}{|D|}\times\begin{vmatrix}\alpha_0^{(n)} & d_{01} & -\gamma_0 & -\gamma_1\\ \alpha_1^{(n)} & d_{11} & -\gamma_1 & -\gamma_2\\ 0 & \gamma_1 & d_{00} & d_{01}\\ 0 & \gamma_2 & d_{10} & d_{11}\end{vmatrix}\,, \tag{32}$$

$$\bar{c}_0^{(n)}=\frac{1}{|D|}\times\begin{vmatrix}0 & d_{01} & -\gamma_0 & -\gamma_1\\ 0 & d_{11} & -\gamma_1 & -\gamma_2\\ \alpha_0^{(n)} & \gamma_1 & d_{00} & d_{01}\\ \alpha_1^{(n)} & \gamma_2 & d_{10} & d_{11}\end{vmatrix}\,, \tag{33}$$

$$c_1^{(n)}=\frac{1}{|D|}\times\begin{vmatrix}-\alpha_0^{(n)} & d_{00} & -\gamma_0 & -\gamma_1\\ -\alpha_1^{(n)} & d_{10} & -\gamma_1 & -\gamma_2\\ 0 & \gamma_0 & d_{00} & d_{01}\\ 0 & \gamma_1 & d_{10} & d_{11}\end{vmatrix}\,, \tag{34}$$

$$\bar{c}_1^{(n)}=\frac{1}{|D|}\times\begin{vmatrix} 0 & d_{00} & -\gamma_0 & -\gamma_1 \\ 0 & d_{10} & -\gamma_1 & -\gamma_2 \\ -\alpha_0^{(n)} & \gamma_0 & d_{00} & d_{01} \\ -\alpha_1^{(n)} & \gamma_1 & d_{10} & d_{11} \end{vmatrix}, \tag{35}$$

where

$$|D|=\begin{vmatrix} d_{00} & d_{01} & -\gamma_0 & -\gamma_1 \\ d_{10} & d_{11} & -\gamma_1 & -\gamma_2 \\ \gamma_0 & \gamma_1 & d_{00} & d_{01} \\ \gamma_1 & \gamma_2 & d_{10} & d_{11} \end{vmatrix}, \tag{36}$$

From (31), we can calculate the electrical and thermal currents, and the results are

$$\left.\begin{aligned} J_x&=K_{11}e\left(eF_x+T\frac{\partial}{\partial x}\frac{\zeta}{T}\right)+K_{12}\frac{e}{T}\frac{\partial T}{\partial x}-K_{13}e\left(eF_y+T\frac{\partial}{\partial y}\frac{\zeta}{T}\right)-K_{14}\frac{e}{T}\frac{\partial T}{\partial y}, \\ J_y&=K_{13}e\left(eF_x+T\frac{\partial}{\partial x}\frac{\zeta}{T}\right)+K_{14}\frac{e}{T}\frac{\partial T}{\partial x}+K_{11}e\left(eF_y+T\frac{\partial}{\partial y}\frac{\zeta}{T}\right)+K_{12}\frac{e}{T}\frac{\partial T}{\partial y}, \\ w_x&=-K_{21}\left(eF_x+T\frac{\partial}{\partial x}\frac{\zeta}{T}\right)-K_{22}\frac{1}{T}\frac{\partial T}{\partial x}+K_{23}\left(eF_y+T\frac{\partial}{\partial y}\frac{\zeta}{T}\right)+K_{24}\frac{1}{T}\frac{\partial T}{\partial y}, \\ w_y&=-K_{23}\left(eF_x+T\frac{\partial}{\partial x}\frac{\zeta}{T}\right)-K_{24}\frac{1}{T}\frac{\partial T}{\partial x}-K_{21}\left(eF_y+T\frac{\partial}{\partial y}\frac{\zeta}{T}\right)-K_{22}\frac{1}{T}\frac{\partial T}{\partial y}, \end{aligned}\right\} \tag{37}$$

where

$$\left.\begin{aligned} K_{11}&=\frac{1}{4\pi^3\hbar}(c_0^{(1)}\alpha_0^{(1)}+c_1^{(1)}\alpha_1^{(1)}), \\ K_{12}&=\frac{1}{4\pi^3\hbar}(c_0^{(2)}\alpha_0^{(1)}+c_1^{(2)}\alpha_1^{(1)}), \\ K_{13}&=-\frac{1}{4\pi^3\hbar}(\bar{c}_0^{(1)}\alpha_0^{(1)}+\bar{c}_1^{(1)}\alpha_1^{(1)}), \\ K_{14}&=-\frac{1}{4\pi^3\hbar}(\bar{c}_0^{(2)}\alpha_0^{(1)}+\bar{c}_1^{(2)}\alpha_1^{(1)}), \\ K_{21}&=\frac{1}{4\pi^3\hbar}(c_0^{(1)}\alpha_0^{(2)}+c_1^{(1)}\alpha_1^{(2)}), \\ K_{22}&=\frac{1}{4\pi^3\hbar}(c_0^{(2)}\alpha_0^{(2)}+c_1^{(2)}\alpha_1^{(2)}), \\ K_{23}&=-\frac{1}{4\pi^3\hbar}(\bar{c}_0^{(1)}\alpha_0^{(2)}+\bar{c}_1^{(1)}\alpha_1^{(2)}), \\ K_{24}&=-\frac{1}{4\pi^3\hbar}(\bar{c}_0^{(2)}\alpha_0^{(2)}+\bar{c}_1^{(2)}\alpha_1^{(2)}). \end{aligned}\right\} \tag{38}$$

It is easily verified that the reciprocal relations

$$\left.\begin{aligned} K_{21}&=K_{12}, \\ K_{23}&=K_{14}, \end{aligned}\right\} \tag{39}$$

hold. For the calculation of the coefficients of the transverse galvanomagnetic and thermomagnetic effects, we merely need to calculate $K_{m,n}$'s up to the terms of the order of $(\kappa T/\zeta)^2$ and the linear terms of H. The calculations are straightforward (see § 5 of I.), and we have;

(1) Hall constant:

$$R=-\frac{4\pi^3}{ec}\frac{f_5}{f_1^2}\,, \tag{40}$$

(2) Ettingshausen coefficient:

$$A_E=\frac{4\pi^3T}{cf_1^3d_{11}}\left\{\left(f_1\frac{df_5}{dE}-\frac{df_1}{dE}f_5\right)d_{11}-\frac{f_1f_5}{\kappa T}d_{01}+\frac{\pi^2}{3}\frac{df_1}{dE}f_5d_{00}\right\}, \tag{41}$$

(3) Isothermal Ettingshausen-Nernst coefficient:

$$B^i_{EN}=\frac{\pi^4\kappa^2T}{9c\hbar f_1d_{11}^2}\left\{\left(f_1\frac{df_5}{dE}-\frac{df_1}{dE}f_5\right)d_{11}-\frac{f_1f_5}{\kappa T}d_{01}+\frac{\pi^2}{3}\frac{df_1}{dE}f_5d_{00}\right\}, \tag{42}$$

(4) Righi-Leduc coefficient:

$$B_{RL}=-\frac{\pi^2e}{3\hbar c}\frac{f_5}{d_{11}}\,, \tag{43}$$

(5) Electrical conductivity:

$$\sigma=\frac{e^2f_1^2}{4\pi^3\hbar d_{00}}\,, \tag{44}$$

(6) Thermal conductivity:

$$\kappa_T=\frac{\pi\kappa^2Tf_1^2}{36\hbar d_{11}}\,, \tag{45}$$

(7) Absolute thermoelectric power:

$$S=-\frac{\pi^2\kappa^2T}{3ed_{11}}\left\{\frac{1}{f_1}\frac{df_1}{dE}d_{11}-\frac{1}{\kappa T}d_{01}+\frac{\pi^3}{3}\frac{1}{f_1}\frac{df_1}{dE}d_{00}\right\}. \tag{46}$$

§ 4. General Relations between the Coefficients

From the results obtained in § 3, we have the general relations between the coefficients which hold irrespective of the scattering mechanism and the shape of the energy surface (but which must be cubic). They are

$$\frac{B^i_{EN}}{\kappa_T}=\frac{A_E}{T}\,, \tag{47}$$

$$\frac{RB^i_{EN}}{A_EB_{RL}}\left(=\frac{R\kappa_T}{TB_{RL}}\right)=\frac{\pi^2}{3}\left(\frac{\kappa}{e}\right)^2. \tag{48}$$

Callen[5] has shown that Eq. (47) is a general consequence of Onsager's reciprocal relation. From our calculations, it has become clear that (48) is also a most general relation which holds not only for monovalent metals but also for all cubic metals irrespective of the scattering mechanism. It has shown by Meixner[6] that the relation (48) can be derived if we assume the existence of the relaxation time. Sondheimer[7] has also shown that (48) holds for the free electron model at all temperatures.

Further we have a relation which holds irrespective of the scattering mechanism,

$$\frac{1}{T}\left(n_HcA_E+\frac{3e}{\pi^2\kappa^2}S\right)=\frac{1}{f_5}\frac{df_5}{dE}-\frac{2}{f_1}\frac{df_1}{dE}\,. \tag{49}$$

where

$$n_H\equiv-\frac{1}{Rec}\,, \tag{50}$$

and we shall call n_H the Hall number of electrons. For a given metal, the right side of (49) is a constant. Therefore, if S/T increases by a change of the scattering mechanism (for instance, change of temperature or doping of small concentration of impurity atoms) in a metal having a negative Hall constants, A_E/T must decrease. This is a generalization of Eqs. (86) and (92) in I.

§ 5. Special Cases

For the scatterings by lattice waves at high temperatures or by impurity atoms, the time of relaxation τ exists and may be approximated to depend only on the energy of the electronic state[10]. Then, the solution of the

Boltzmann equation (2) is easily obtained by iteration[6),11)] and the coefficients of the effects can be calculated exactly up to the terms of desired order of H. On the other hand, we can derive the results up to the linear terms of H from the general formulae obtained in § 4 by putting

$$\mathscr{L}(c)=-\frac{\hbar}{\tau}c(\eta)\,. \tag{51}$$

The results obtained by the variational method for this case is identical with the exact solutions up to the linear terms. This gives a varification of the validity of our variational procedure. The results are as follows,

$$A_B=\frac{4\pi^3T}{c}\frac{f_5}{f_1^2}\left\{\frac{1}{\tau}\frac{d\tau}{dE}+\frac{1}{f_5}\frac{df_5}{dE}-\frac{1}{f_1}\frac{df_1}{dE}\right\}, \tag{52}$$

$$B^t_{BN}=\frac{\pi^2\kappa^2T\tau}{3\hbar^2c}\frac{f_5}{f_1}\left\{\frac{1}{\tau}\frac{d\tau}{dE}+\frac{1}{f_5}\frac{df_5}{dE}-\frac{1}{f_1}\frac{df_1}{dE}\right\}, \tag{53}$$

$$R_{RL}=-\frac{e\tau}{\hbar^2c}\frac{f_5}{f_1}, \tag{54}$$

$$\sigma=\frac{e^2\tau}{4\pi^3\hbar^2}f_1, \tag{55}$$

$$\kappa_T=\frac{\kappa^2T\tau}{12\pi\hbar^2}f_1, \tag{56}$$

$$S=-\frac{\pi^2\kappa^2T}{3e}\left\{\frac{1}{\tau}\frac{d\tau}{dE}+\frac{1}{f_1}\frac{df_1}{dE}\right\}. \tag{57}$$

In this case, besides Eqs. (47), (48) and (49), a relatian

$$R\sigma=B_{RL} \tag{58}$$

holds, which is a consequence of Eq. (48) and the Wiedemann-Franz law. Meixner[6)] has shown that (58) holds for any metal (not necessarily cubic) when the relaxation time exists.

Now we consider an another special case. If we use the values of d_{rs} given in the appendix of II, the coefficients of pure metals at low temperatures can be derived easily. We write here only the expression of A_B at low temperatures ($T\ll\Theta$),

$$A_B=\frac{4\pi^3T}{cf_1^2f_2}\left\{\left(\frac{1}{f_5}\frac{df_5}{dE}-\frac{1}{f_1}\frac{df_1}{dE}\right)f_2f_5-f_4f_5\right\}, \tag{59}$$

where

$$f_4=\frac{1}{3}\int\frac{\partial^2E/\partial n^2}{|\mathrm{grad}_k E|^2}dS\,. \tag{60}$$

Other coefficients are obtained easily from (47) and (48).

For the spherical band model, (49) reduces to

$$\frac{1}{T}\left(ncA_B+\frac{3e}{\pi^2\kappa^2}S\right)=-\frac{3}{\alpha k_0}\,. \tag{61}$$

In I, we have derived (61) for the case of high temperatures, but in this paper it has become clear that this equation remains valid at all temperatures. If we put Eq. (35) of I into (61), we have

$$A_B=\frac{\kappa T}{nc}\frac{\rho_l\left(\frac{1}{\alpha k_0}+\frac{2\beta}{\alpha^2}-\gamma_1\right)+\rho_0\left\{\left(\frac{1}{\alpha k_0}+\frac{2\beta}{\alpha^2}\right)-\frac{3}{\pi^2}\frac{k_0^2}{q_0^2}\frac{1}{\alpha k_0}\left(\frac{\Theta}{T}\right)^2\right\}}{\rho_l+\rho_0\left\{1+\frac{3}{\pi^2}\frac{k_0^2}{q_0^2}\left(\frac{\Theta}{T}\right)^2\right\}}, \tag{62}$$

where the symbols are identical with those used in I. For the free electron model, (62) reduces to the interpolation formula obtained by Sondheimer[7)]. It is seen from (62) that the Ettingshausen coefficients for pure metals which have spherical energy band are always negative at low temperatures. In the case of the thermoelectric power, the simple representations of the parameters α and β of the spherical band approximation given by (47) and (50) in II have hold. For the galvanomagnetic and thermomagnetic effects, however, there are no simple correspondence such as those in the case of the thermoelectric power.

If the band structure of a metal were known completely, the right side of (59) would be calculated thoroughly, but at present we have no such a complete knowledge about the band structure.

§ 6. Conclusion

Using an approximate distribution function given by (15), we have solved the Boltzmann equation for an cubic metal in the magnetic field by variational method described in § 2. The method gives in principle the exact solution for metals which have the spherical energy band. For cubic metals which have the energy dependent relaxation time, the method also gives exact solution up to the linear terms of the magnetic field. The reason that the

approximate function gives the exact solution in this case is possibly that the coefficients of the effects linear in the magnetic field are the scalar quantities and insensitive comparatively to the anisotropy of the band structure. Therefore the solutions obtained in § 3 for the general case may be valid at least semi-quantitatively. This is also a profitable point of the variational method. (See § 2 in II.) However, for the effects of the second order in the magnetic field such as the magneto-resistance, our approximation (15) fails. Really if we calculate K_{mn}'s up to the second order of H, we easily see that the magneto-reristance disappears. These effects are highly sensitive to the anisotropy of the band structure, and so to investigate these effects in the case where the relaxation time does not exist, we must use more complicated function Φ_k instead of (15).

Acknowledgement

The author wishes to express his hearty thanks to Profs. T. Okada and T. Nakamur for their valuable discussions.

This work has been supported in part b the Scientific Research Fund of the Ministr of Education.

References

1) M. Tsuji: J. Phys. Soc. Japan, **13** (1958) 133
2) M. Tsuji: J. Phys. Soc. Japan, **13** (1958) 818
3) M. Kohler: Ann. d. Phys. (6) **6** (1948) 18.
4) J. M. Ziman: Canad. J. Phys. **34** (1956) 1256
5) H. B. Callen: Phys. Rev. **73** (1948) 1349.
6) J. Meixner: Ann. d. Phys. (5) **35** (1939) 701.
7) E. H. Sondheimer: Proc. Roy. Soc. **A193** (1948) 484.
8) M. Kohler: Z. Phys. **124** (1948) 772.
9) M. Tsuji: Memoirs Fac. Sci. Kyushu Univ. **2** (1958) 119.
10) R. Olson and S. Rodriguez: Phys. Rev. **108** (1957) 1212.
11) H. Jones and C. Zener: Proc. Roy. Soc. **A145** (1934) 268.

JOURNAL OF THE PHYSICAL SOCIETY OF JAPAN Vol. 13, No. 9, SEPTEMBER, 1958

Paramagnetic Resonance in Copper Propionate Monohydrate

By Hidetaro ABE

The Institute for Solid State Physics, University of Tokyo

(Received June 7, 1958)

Paramagnetic resonance absorption was investigated at centimeter wavelength region in single crystals of copper propionate monohydrate $Cu(CH_3CH_2COO)_2 \cdot H_2O$.

The spectrum obtained is not a normal one expected for a ^2D state of Cu^{++} ions in crystals but similar to that observed in copper acetate monohydrate $Cu(CH_3COO)_2 \cdot H_2O$ and more complicated. This spectrum can be explained by an effective spin Hamiltonian with an equivalent spin value $S=1$. This may lead us to a conclusion that each of the magnetic complexes in this crystal consists of a pair of copper ions under a strong interaction and may be created from a bimolecular structure, $Cu_2(CH_3CH_2COO)_4 \cdot 2H_2O$ as in the case of the acetate. The unit cell of this crystal contains six spatially inequivalent pairs, of which three can be derived from the others by a reflection in its ac-plane. Each pair of ions in this crystal is considered to be under a very similar environment, except the direction of the pairs. The rhombicity in its crystalline field is smaller than that of the acetate.

§ 1. Introduction

It was considered to be of interest to examine a series of paramagnetic salts by the method of paramagnetic resonance absorption changing their hydration number or chemical composition systematically.

So we had a plan to study the divalent copper salts derived from the series of monocarboxylic acids: copper formate, copper acetate, copper propionate, copper butylate, and so on. The iron group ions have incomplete 3d-shell which is completed by filling up with 10 electrons. Divalent copper ion has 9 electrons in its 3d-shell, so it can be simply considered as having one electron hole in its 3d-shell, giving $^2D_{5/2}$ as the free ion state. When the copper ion is placed in the crystalline solids, interplay of the spin-orbit coupling and the cubic crystalline electric field splits the orbital quintet, resulting a lower orbital doublet and an orbital triplet lying several thousands cm^{-1} higher.

The crystalline electric field with lower symmetry removes the orbital degeneracy completely, remaining the orbital singlet as the lowest which has the Kramers doublet (spin doublet) and can be lifted only by an externally applied magnetic field. Then the resonance field H is proportional to the measuring frequency ν as

$$h\nu = g\beta H \qquad (1)$$

without any initial splitting, where h is the Planck constant, β the Bohr magneton, and g the spectroscopic splitting factor. By the existence of upper orbital levels, the g-value is affected to deviate from 2.00, the value for the free electron, through the second order perturbation.

In cases of the usual hydrated copper salts, $g_{//}$, the g-value to be observed when the static magnetic field is applied parallel to the axial direction of the crystalline field, ranges from 2.3 to 2.4 according to the sort of salts and $g_{\perp}$, that to be observed when the magnetic field is perpendicular to this axis, ranges from 2.05 to 2.10.

In copper acetate, however, anomalous paramagnetism was found in its static susceptibility,[1),2)] paramagnetic resonance absorption,[3),4)] and optical dichroism.[5)] All of the anomalies can be explained by an interesting atomic configuration in its crystal structure which was afterwards clarified by its x-ray analysis.[6)] Copper acetate monohydrate $Cu(CH_3COO)_2 \cdot H_2O$ has a bimolecular character in its crystalline state which can be throughly expressed as $Cu_2(CH_3COO)_4 \cdot 2H_2O$. As for the paramagnetic resonance spectrum observed in the single crystals of the copper acetate, there appear many lines to be not described by the usual resonance condition, Eq. (1), for the copper ion, but by an energy scheme with an

initial splitting as in the case of Ni^{++} ion.

Copper propionate monohydrate, studied by the method of paramagnetic resonance, also showed many lines in its single crystals, which can not be described by the ordinary resonance condition, equation (1). In powdered sample of this crystal prepared by crashing single crystals, a very broad absorption line was observed. Fig. 1. is a derivative curve observed

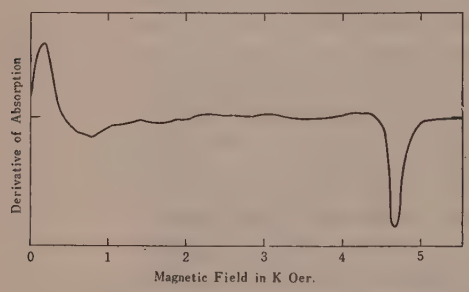

Fig. 1. Derivative curve of the paramagnetic resonance absorption observed at 3.2 cm wavelength in a powdered sample of the copper propionate monohydrate.

at $\lambda=3.2$ cm. Since this curve observed in the powered copper propionate differs from that of usual copper salts and well resembles to that of copper acetate, the circumstances similar to that of copper acetate may be expected in this crystal. In this paper, the results of analysis obtained in the copper propionate monohydrate through paramagnetic resonance will be reported, the preliminary part of which has reported elsewhere.[7]

§ 2. Samples

Single crystals of this substance can be obtained by slow vaporization from aqueous solution of the reagent.

The sample is very stable both in crystalline state and in solution with slightly excess propionic acid. The colour of this solution is dark emerald green. Seed crystals were at first placed at the bottom of a glass vessel containing the solution. More perfect crystals were prepared by hanging a seed crystal with nylon filament in the middle part of a vessel filled with saturated solution of about 500 cc. Some of these vessels were placed in a rough air-thermostat or in a shady room. Single crystals thus obtained have a linear dimension of about 10 mm.

In order to determine the hydration number of these crystals, some of them were crashed and kept in a branched glass tube.[8] Thi vessel was then evacuated, sealed off an warmed moderately at one end of the branc in which the sample was contained. Wate which condensed at the other end was measure showing that this crystal is monohydrate.

The colour of this crystal is dark green Crystallographic data observed by an optica method showed that the well-developed sur faces in our crystals are in good agreemen with those described by Groth.[9] The sym metry is monoclinic with parameters $a:b:c$ $=0.874:1:0.886$ and $\beta=94°22'$. They do no show twinning charactor while in copper acetate all the crystals examined were twins. The {110} plane develops easily to show frequently an external form like a prism as shown in Fig. 2. It is softer and has a more wax-like touch than the copper acetate. Thus it is rather easy to cut and grind large single crystals to obtain suitable specimens of disk-shape.

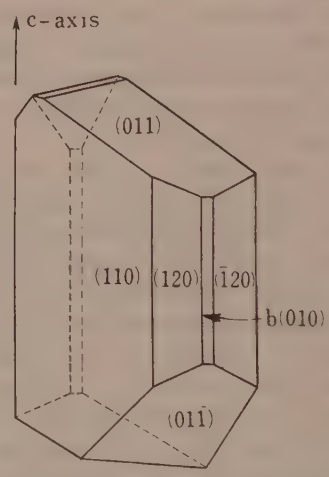

Fig. 2. Typical crystal form of the copper propionate monohydrate.

§ 3. Experimental Apparatus

i) *General arrangement of the measuring apparatus*

Measurements described in this article were performed all at room temperature and mainly at wavelength of about 10.35 mm, although some works were later carried out at the other wavelengths to check the results obtained at this wavelength.

The experimental method at each wavelength is essentially the same which is usually callep the field modulation method with a

transimission-type cavity.

The block diagram of the measuring apparatus is shown in Fig. 3. Microwave power of a constant frequency and at a constant level is fed through attenuators to a loosely coupled cavity containing the sample crystal and tuned at the frequency used. Completeness of this tuning affects the final results and can be easily obtained by the procedure described in the part iii) of this section. Power coming through the cavity is then detected by a crystal detector.

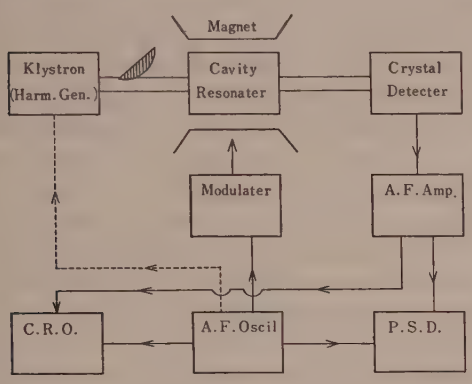

Fig. 3. Block diagram of our spectrometer.

The cavity is placed between pole-pieces of an electromagnet. Modulation field of about 31 cps. is superimposed to the static magnetic field. When the d.c. component of the magnetic field H comes near to that giving a resonance condition, a part of the output voltage across the crystal detector changes with 31 cps by an amount proportional to dA/dH where A means the magnetic absorption. This a.f. out-put voltage is amplified and read by a phase-sensitive detector giving the derivative curve of the absorption lines.

ii) *Components of the apparatus*

a) Microwave source

Microwave powers of $\lambda=16$, 10 and 8 mm were supplied by harmonics multipliers described elsewhere[10] to which the power of fundamental frequency ($\lambda \fallingdotseq 3$ cm) was fed by a 2K25-type klystron.

The electron beam in the klystron is affected by the stray field from the electromagnet and the associated frequency shift makes the measuring cavity slightly detune, bringing some error in the absorption intensity. In our case, distance of 1.5 m between the klystron and the center of electromagnet makes this effect negligiblly small.

The heater voltage for this klystron is supplied by a storage battery and voltages for cavity and repeller electrodes by an electronically stabilized eliminater source which is mainly aimed at the reduction of voltage changes caused by fluctuation in the a.c. line voltage. Since it was constructed for the use of preceeding works on copper acetate using the d.c. galvanometer method, its stability is enough to the present case of the field-modulation method.

b) Cavity resonater

The sample cavity is made of non-magnetic brass. If it is magnetic from impurities or it contains traces of iron, mechanical deformation of the waveguide system caused by a torque acting on the cavity from the applied magnetic field brings the cavity out of tune. This brings a gradual ghost deflection to the output meter reading, perhaps because of a combined effect of mechanical deformation and vibrations of the cavity synchronized with 31 cps modulation.

This ghost deflection also comes from some other reasons, e. g. leakage of modulation voltage or its induction by an improper earth connection.

This ghost may be, in some cases, taken away by inserting soft pieces of insulating dampper in the gaps between cavity and pole-pieces or by rigid setting of the waveguide system accompanied by the appropriate ground at the whole system.

The cavities for measurement are of ordinary rectangular type.[11] They have thin side-walls ($1\sim2$ mm) faced at the pole-pieces in order for the modulation magnetic field to penetrate effectively in it. It is excited either in H_{101} or H_{102} mode and connected to two waveguides through circular coupling windows placed at side-walls other than mentioned above. Adequate coupling is attained by displacement of the plunger with the sample relative to the coupling windows being tuned by adjusting the other (tuning) plunger. Both plunger pistons have quater wave choke sections. The tuning plunger has a moving mechanism of micrometer screw unit, by which the cavity tuning is roughly performed. Precise adjustment is then carried out by changing the movable part of its "vernier section". This vernier section is built in the tuning

plunger at its central axis and has a shape of cylindrical rod whose cross-area is about 1/10～1/20 of that of plunger piston.[12]

c) Electromagnet

The static magnetic field is produced by an electromagnet designed by Prof. Kumagai which has a weight of about one ton. It has pole-pieces of chopped-corn shape inside the frames for the exciting coils.[14] It is excited by a set of storage batteries which is provided only for its use to avoid fluctuations from external origins. As the sample cavity has different dimensions according to its frequency band, gap distance of the electromagnet is varied according to the measuring frequency. By this procedure, the exciting current to observe an absorption at $g=2$ remains 3～4 amp, and only about 150 watt is necessary for all frequencies used.

d) Field Modulater

The frequency of field modulation was settled at about 31 cps in order to avoid the interference between signals and hum components of a.c. line voltage (48～50 cps.) at the phase-sensitive detector. Sinusoidal voltage of about 31 cps is generated by an usual a.f. oscillator with an RC feed back linkage. It is fed to a tuned a.f. power amplifier through one stage of buffer and one stage of driver. Final stage is an 807 push-pull amplifier operating at AB_2-class. Its a.f. power out-put is 120 watts at maximum operation with an out-put transformer tuned in its primary circuit at 31 cps and matched for the modulation coilds with its secondary taps.

The modulation coils (each 400 turns) are wound rigidly on a pair of aluminium spools which are placed at the top of pole-pieces. If the setting of these coils is not rigid, they come to vibrate when the magnet produces a high enough static field. The microwave power modulated directly by the mechanical vibration in microwave circuit makes shift the zero point of detector meter. This is one of the origins of fluctuation which decrease the final effective S/N ratio, though the direct leakage, if any, of the modulation voltage to the input circuit of amplifier prevents severely the measurements.

e) Amplifiers

The a.f. component appeared accross the detecter crystal diode is amplified by a 4-stage amplifier having low-pass characteristics (upper limit of the pass-band is about 100 cps.) and maximum gain of 120 db at 31 cps. Its output voltage is partly introduced to a monitor C.R.O. and, after amplified by one stage of ordinary amplifier, to a phase-sensitive detector (P.S.D.) of Schuster type[13] with a slight modification.

An electronically tuned high-Q circuit named as "selectoject" was also prepared, having band width of order one cycle at 31 cps. In general, a reduced band-width of amplifier is desirable for a higher S/N ratio in the spectrum. In our present case, however, this narrow-band a.f. circuit was not used in the final measurements because of two reasons. (1) It is not a poor S/N ratio of the spectrometer but the finite width of the absorption lines superimposed on each other to prevent the analysis of experimental results in our crystal. (2) The band width of the whole spectrometer can be reduced, providing the cross modulation from the noise voltage is negligible, by the time constant of the P.S.D., so a simple high-cut amplifier is more favorable and a circuit which is too sensitive to phase is rather ineffective to reserve the stability of the whole system against a drift of the modulation frequency.

iii) *Tuning procedure of the measuring cavity*

In order to determine the correct resonance peak of absorption line with a phase-sensitive detector, it is required that the measuring cavity is just in tune. This is easily attained by the following procedures. Very small portion of 31 cps voltage from the master a.f. oscillator is fed to the repeller electrode taking care of giving as minor change as possible in the static operating condition for the klystron. A small 31 cps component then appears in the monitor C.R.O. whose horizontal axis is swept by the modulation voltage after a proper phase adjustment. The cavity resonator is tuned when the 31 cps Lissajous figure becomes symmetric arround the vertical axis. The following procedure is the reduction of the modulation voltage fed to the repeller electrode which may be accompanied by a slight variation in the static operating condition in the klystron bringing a slight change in frequency. The cavity is then retuned to the newly settled frequency by adjusting its vernier piston of

the main plunger of the cavity. The successive retuning procedure can be also attained by changing the repeller voltage by means of a vernier rheostat in the control circuit of the stabilized power supply, which causes a shift in the frequency. By these procedures, the 31 cps. Lissajous in C.R.O. becomes comparable to the noise voltage. The phase-sensitive detector is then used as the monitor to decide the cavity tuning. When these procedures are finished, the part of the circuit branch provided for this 31 cps. source modulation, which is shown by a dotted line in the block diagram, is removed at the begining of each run, in order to avoid undesired source modulation by stray 31 cps. voltage. If the frequency change is considered to be appreciable after these adjustments, a check in the frequency is required which can be replaced by measuring the resonance field of the marker radical (DPPH).

This method of tuning the cavity is more sensitive and easy than the usual method using a *dc* rectified current of detector as an indicater.

§ 4. Experimental Procedures and Result

i) *Preliminary Discussion of Spectra with Copper Acetate as an Example*

One of the single crystals is ground to obtain its *ac*-plane from its external form and attached to the rotatable mount by this ground "*ac*-plane" with polystylene cement. By rotation of the mount, the direction of static magnetic field H may rotate in the "*ac*-plane" of this crystal.

In the first place, let us mention the result of copper acetate as a simpler example. When the static magnetic field H is applied in the *ac*-plane of copper acetate, two absorption peaks are observed at higher values of magnetic field H. Although one more absorption line appears at lower magnetic field which has an apparent g-value of about 4 at shorter wavelengths, it is omitted for the time being from our discussions. When the magnetic field H is rotated in the *ac*-plane, the former two peaks give a pair of lines shown as two thick lines in Fig. 4. which we will call line (a) and (b). They are expressed as functions of angle φ, here φ being the angle between the c-axis and the direction of H. This pair of lines gives a extremum at angle $\varphi=\psi$, where ψ is measured from the c-axis towards the a-axis.

Then a plane is ground out which intersects perpendicularly the *ac*-plane making an angle with the *bc*-plane. This plane is here called as "perpendicular plane". Then the static field is rotated in this perpendicular plane, the direction of which is expressed by an angle ξ measured from the *ac*-plane as in Fig. 5. Each line observed in the *ac*-plane

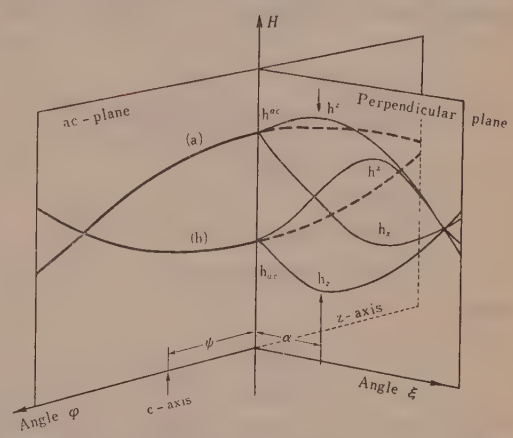

Fig. 4. Schematic expression of peak positions of resonance absorption as a function of direction of static magnetic field in a simplest case of one pair per unit cell, e.g., copper acetate.

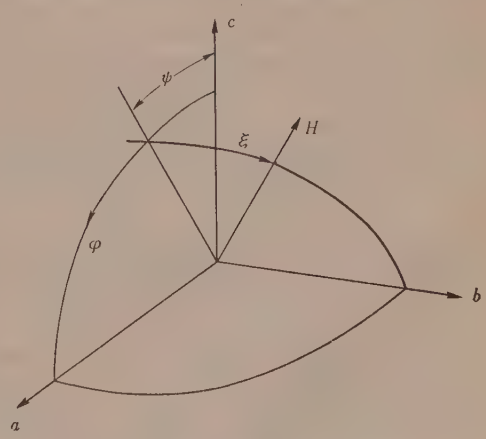

Fig. 5. Definition of the angles.

splits into two lines as shown in Fig. 4. Two of these four lines give their extreme values at the direction of static field, $\xi=\pm\alpha$.

These behaviours of the spectrum are well explained by an effective spin-Hamiltonian[3]

$$\mathscr{H}=[g]\beta\vec{S}\vec{H}+DS_z^2+E(S_x^2-S_y^2) \qquad (2)$$

under the condition of $S=1$. Here x, y and z denote the axes of the crystalline field for

one unit, where z-axis is that of the predominant tetragonal field. Copper acetate contains two inequivalent units. The directions of the z-axes for these units are expressed by $\varphi=\psi$, and $\xi=\pm\alpha$. The y-axis is so chosen that it is within the ac-plane at $\varphi=\psi+90°$.

Assuming the first term in Eq. (2), the Zeeman energy, is sufficiently predominant compared with the other terms, perturbation treatment gives the following resonance fields in the perpendicular plane which contains the z and x axes.

$$\left.\begin{aligned} h\nu &= \Delta w_{(+1\to 0)} \\ &= g\beta H + D/2\cdot(3p^2\cos^2\theta - 1) \\ &\quad + 3E/2\cdot(q^2\sin^2\theta) + \Delta w'' \\ h\nu &= \Delta w_{(0\to -1)} \\ &= g\beta H - D/2\cdot(3p^2\cos^2\theta - 1) \\ &\quad - 3E/2\cdot(q^2\sin^2\theta) + \Delta w'' \end{aligned}\right\} \quad (3)$$

where

$$\left.\begin{aligned} p &= g_{//}/g \\ q &= g_{\perp}/g \end{aligned}\right\} \quad (4)$$

Here θ means an angle between the static field H and the z-axis and $\Delta w''$ means a term from the second order perturbation which may be neglected in our present case, because it is estimated to be 180 oer. at its maximum value which occurs at $\theta\simeq 45°$.

ii) *Results in Copper Propionate*

a) Observation in the ac-plane

A single crystal of copper propionate is ground to have its ac-plane as in the former case and put under observation. An example of the meter reading of phase sensitive detector is shown in Fig. 6, when H is in the

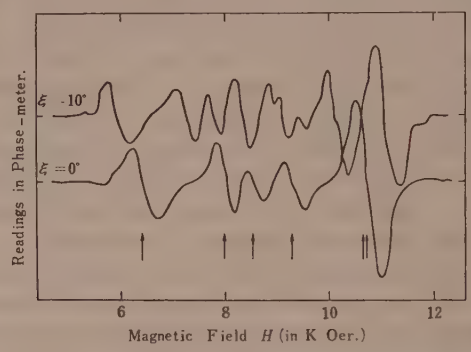

Fig. 6. Results in the perpendicular plane at $\varphi=106°$. The arrows indicate the positions of resonance peaks at $\xi=0°$.

ac-plane and $\varphi=106°$. The wave-length of the measuring microwave is about 10.35 mm. The arrows in the downward part indicate positions of absorption peaks at $\xi=0°$ showing that there are six peaks. One more broad

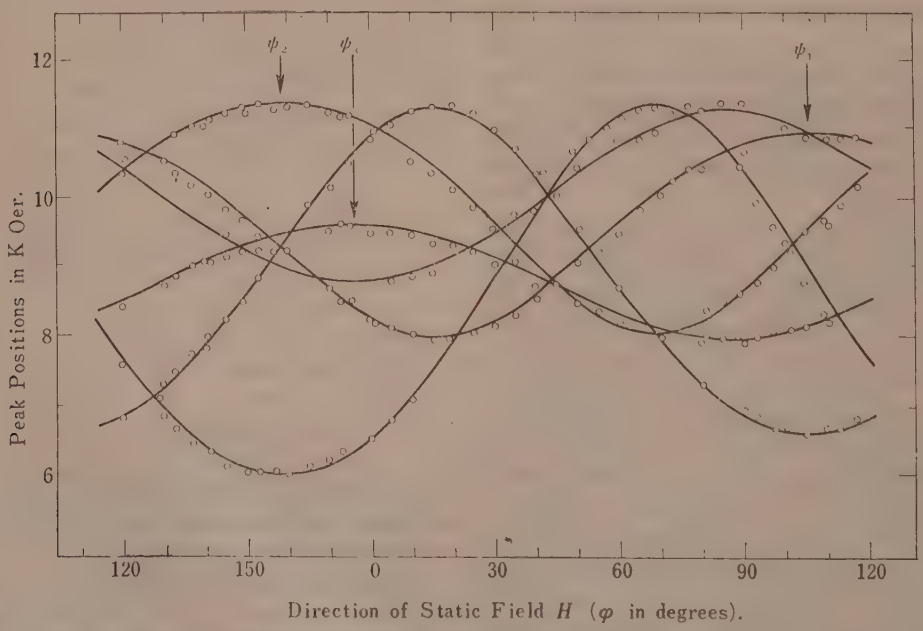

Fig. 7. Peak positions of resonance absorption in the ac-plane of copper propionate as a function of the angle of rotation about the b-axis. The angle φ means direction of the static magnetic field measured from the c-axis towards the a-axis. The solid curves are calculated by equation (2) with the parameters listed in Table I, the circles the experimental points.

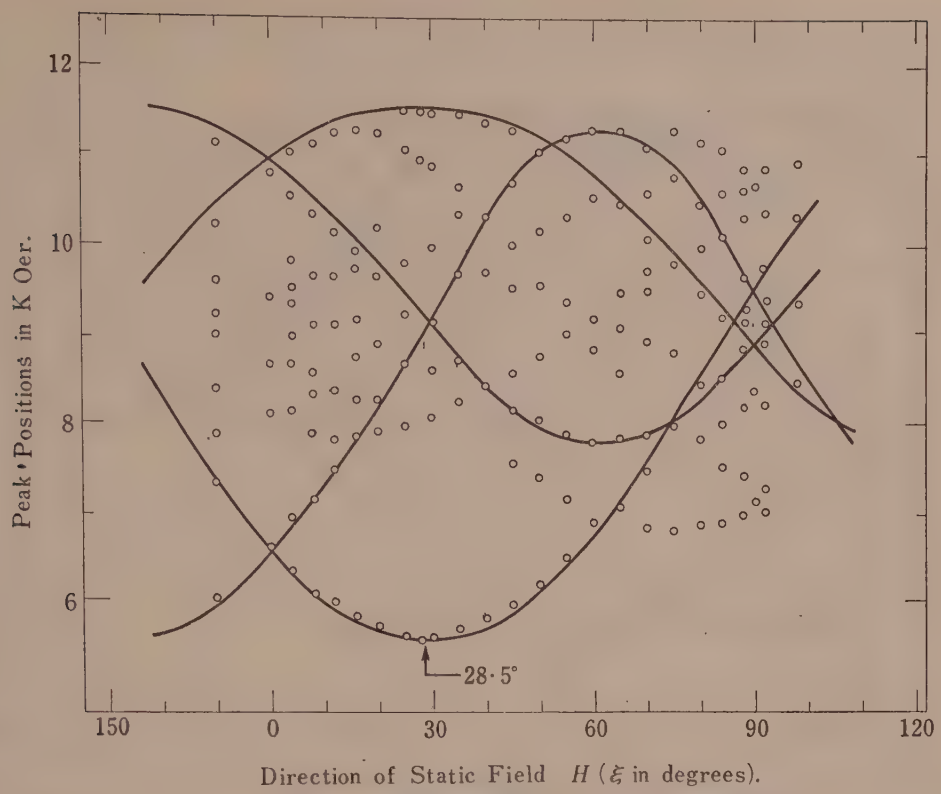

Fig. 8. Positions of resonance peaks in the perpendicular plane (ψ=105.5°) of the copper propionate monohydrate. Circles indicate the observed values and solid curves the calculated ones using the parameters listed in Table I.

absorption peak, however, appears at lower most magnetic field, as in the case of copper acetate, which has an apparent g-value of about 4 and does not depend approximately on the direction of H. It may be omitted from our present discussion.

These six peaks form three pairs of curves when H is rotated in the ac-plane. One of results is shown in Fig. 7 where plots represent the magnetic fields of measured peaks. We shall label three pairs as pair (1), (2) and (3) as shown in the figure. We shall call the angle φ, at which one of the three pairs of curves shows the extreme resonant field, the angle ψ·ψ were observed to be 105.5°, 158.5° and 176° respectively which are indicated by thick arrows in Fig. 7.

b) Observation in the "Perpendicular Planes"

Single crystals are ground to give one of "Perpendicular planes" which are defined in the case of copper acetate: Planes intersect perpendicularly with the ac-plane at angles ψ. At first, H is rotated in one of the perpendicular planes, e.g., in that of pair (1); ψ=105.5°. Each curve belonging to this pair (1) in the ac-plane splits into two lines as shown in Fig. 8 where plots are the measured values and curves are the calculated ones with equation (2) using parameters in Table I. By the same treatments, results on the pairs (2)

Table I. Parameters for the Hamiltonian (2) as giving the best fit to the observed values.

	Copper Propionate			Copper Acetate
	Pair (1)	Pair (2)	Pair (3)	
D (in cm^{-1})	0.344	0.341	0.345	0.345±0.005
E (in cm^{-1})	<0.004	<0.004	<0.002	0.005±0.003
g_z	2.36_8	2.36_0	2.36_8	2.34_4
g_x	2.11_1	2.10_0	2.10_2	2.05_3
g_y	2.09_6	2.08_2	2.10_0	2.09_3
α (degree)	28.5	16.0	54.0	33
ψ (degree)	105.5	158.5	176.0	−34.5±1.5 (145.5±1.5)

Error in the copper propionate is ±0.007 cm^{-1} in D and ±0.015 in g's.

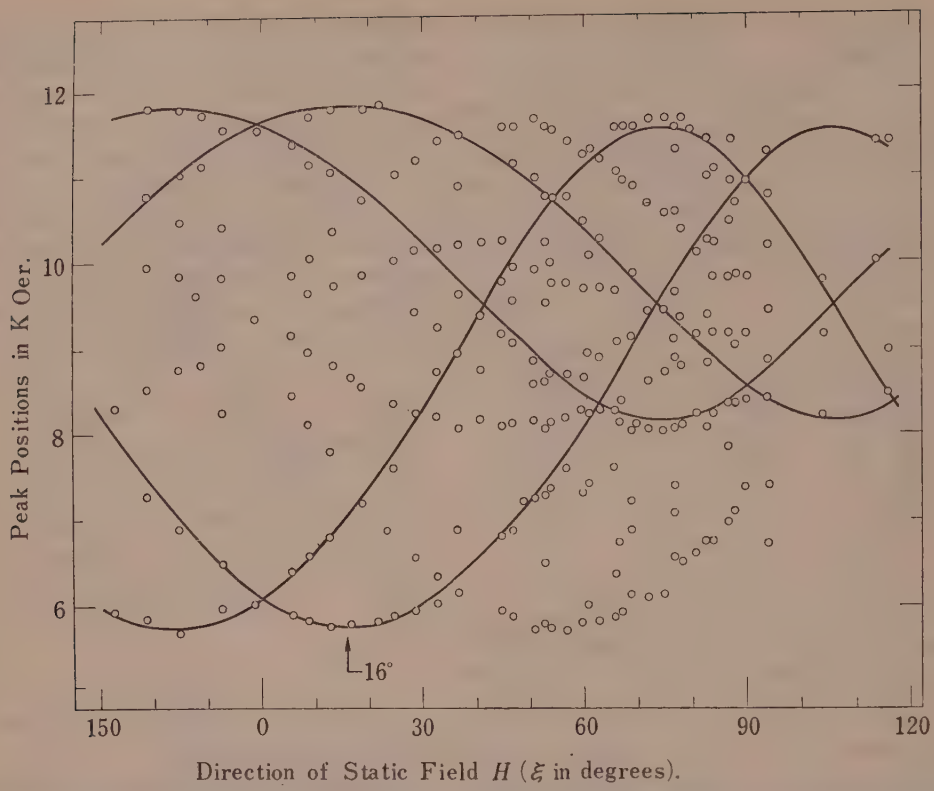

Fig. 9. Positions of resonance peaks in the perpendicular plane ($\psi=158.5°$) of the copper propionate monohydrate. Circles indicate the observed values and solid curves the calculated ones using the parameters listed in Table I.

and (3) are shown in Fig. 9 and Fig. 10. Again the agreements between the calculated curves and the plots of measured values are fairly good. Parameters of the pairs listed in Table I are thus obtained. Using these parameters, resonant fields in the *ac*-plane can be calculated. Curves in Fig. 7 are thus obtained and their agreements with the plots (the measured values) are again satisfactory. Actually, all the parameters, especially the angle α, are adjusted to give the best fit with the results in these four sorts of planes.

As shown in Fig. 4, the higher and the lower resonance fields at directions of z, x and y axes are called as h^z, h_z, h^x, h_x, h^y and h_y, respectively. The two resonance fields observed when H is in the *ac*-plane and $\varphi=\psi$ are called h^{ac} and h_{ac}. The observed values of these quantities are listed in Table II. Differences between the observed values and the calculated ones by Eq. (3) using parameters of Table I are also listed in this Table. Maximum difference at axial directions reaches to 60 oer. As shown in Fig. 8, the two curves belonging to the same "pair" intersect each other at two values of the angle φ in the *ac*-plane. In other words, at two directions of the applied field H in the *ac*-plane, the

Table II. Observed values of the resonance fields characterizing the paramagnetic resonance spectra of the copper propionate monohydrate. Differences between the observed values and those calculated by Eq (3) with parameters of Table I are also listed.

	Pair (1)		Pair (2)		Pair (3)	
	obs.	obs.–calc.	obs.	obs.–calc.	obs.	obs.–calc.
h^z	11780	−50	11790	−60	11820	−30
h_z	5650	+40	5720	+60	5620	+20
h^x	11610	+20	11670	−60	11610	0
h_x	7950	−10	8010	+60	8040	0
h^y	11580	+20	11640	+40	11580	0
h_y	8140	−20	8200	−30	8110	+10
h^{ac}	11170	−30	11630	−20	9770	−40
h_{ac}	6730	+70	6070	+80	8980	+30
$\Delta\varphi$	103.5±2	−2±2	115±2	+1.7±2	55.5±2	+0.2±2

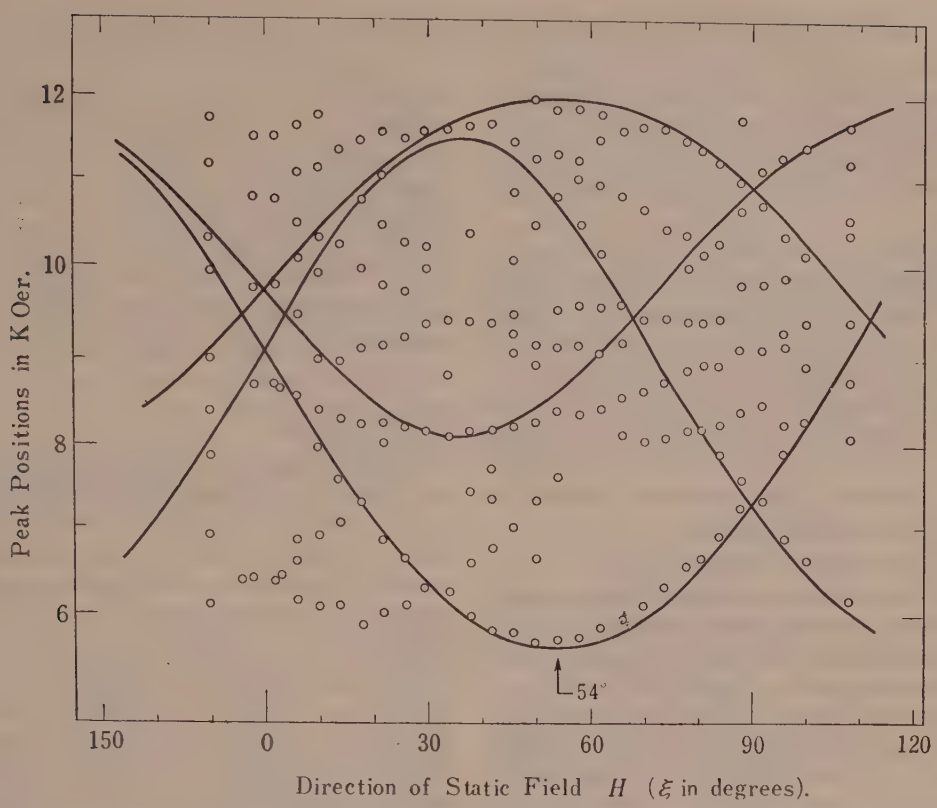

Fig. 10. Positions of resonance peaks in the perpendicular plane ($\psi=176.0°$) of the copper propionate monohydrate. Circles indicate the observed values and solid curves the calculated ones using the parameters listed in Table I.

two resonance fields, $H_{+\to 0}$ and $H_{0\to -}$, coincide, which are demanded by two transitions between three levels of the same "pair". $\Delta\varphi$ in the Table II means the angle between the two directions described above. This angle difference $\Delta\varphi$ is, in some cases, very sensitive to the determination of angle α. In the pair (3), change of one degree in α brings a change of 7° in $\Delta\varphi$, which is only 55.5° in this pair. $\Delta h_{ac}=|h^{ac}-h_{ac}|$ is also severe check for the angle α. One degree in α, in the pair (3), gives a change of 180 oer in $|h^{ac}-h_{ac}|$ which is only 790 oer in this case.

iii) *Experimental Errors*

In determination of resonance field, errors may appear from following origins: (1) Cutting of sample crystal, (2) Tuning of the cavity, (3) Reading of exciting current of the electromagnet and its conversion to the strength of magnetic field, (4) Superposition of undesired peaks from the other pair to the peak in question, and (5) Fluctuations of phase-meter from the noise or unstability.

Errors from these origins can be estimated as follows.

(1) In the axial directions of a magnetic unit, the mis-cutting of crystals does not affect appreciably the determination of resonant fields because they change with *cosine* of the angle, arround the extremum, as shown by Eq. (2). In our case, change in peak position is only about 7 oer. from an error of 2° in θ which may be considered our maximum value of mis-griding. So errors in our cutting process does not affect the final results of g and D, since these values are initially determined through resonance fields observed at the directions of the principal axes of a magnetic unit.

Error in h_y or h_{ac} from this origin may be smaller than the linewidth and included in (4), because h_y, h_{ac} etc. are measured in the ac-plane which is a symmetry plane. Large miscutting in the ac-plane is easily discovered because a peak in the normal ac-plane splits into peaks. The line width of these peaks is

a very sensitive measure, especially in the case of some peaks belonging to the pair (3), of the correctness in which our "*ac*-plane" is ground, because it shows a tendency to become larger even if the direction of H deviates from the *ac*-plane by a fraction of the degree.

(2) If the tuning procedure described in § 3, iii) is adopted, error from the detuned cavity in the field modulation method becomes, in our case, smaller than that of origin (3), so it may be neglected. It is checked by experiments that the detune of cavity from the long time instability brings about 30 oer deviation in peak position with 30 min. Dispersion of the sample does not affect the cavity tuning at the peak position.

(3) The exciting current of the electromagnet is read by a precision type milivoltmeter with a proper shunt resistance. Minimum possible reading is 3 mA at 5A range which corresponds to 9 oer at 10,000 oer. Magnetic field H was calibrated by the proton resonance method as a function of exciting current I. The calibration curve thus obtained is near to a straight line in the range of magnetic field required for the present work for each frequency. The maximum deviation from the linear relation was about 40 oer., in the range of magnetic field used at $\lambda \simeq 10$ mm. The origin of this deviation may be mainly ascribed to the inhomogeneity in meter scaling, which was concluded by a comparison between calibrations for two shunt resistances.

(4) Since the absorption lines are expected to split into twelve peaks at a general direction of magnetic field and they have widths of 350～450 oer, more than one peak may fall on a same magnetic field. Superposition of undesired peaks belonging to the other "pair" makes the determination of either peak position difficult and inaccurate, and in sometimes makes it impossible. In the "perpendicular" planes, this effect brings sometimes severe difficulties in the determination of peak positions. In Fig. 8～10, in fact, some peak positions are omitted which must belong to the pairs other than that in question, in order to avoid conffusions. In all cases, however, of determination of resonance peaks listed in Table II, peaks to be determined are free from this effect of superposition, arround the region giving their extremum values.

Then the sum of experimental errors from above-mentioned origins reaches to 0.3～0.6% of g-values. As for the six resonance fields appeared in the upper part of Table II, the omission of the second order term $\Delta w''$ in the Equation (2) brings no effect, since this term disappears at the axial directions. In determination of D, $\Delta w''$ brings no effect. The observed resonance fields, as shown in Table II, remains in the all cases within the estimated limit of error, 60 oer., from the calculated values.

§ 5. Discussions

The four figures (Figs. 7～10) show that the observed peak positions can be well fitted by three sets of Equation (2) with parameters given by Table I, namely, the paramagnetic resonance spectra observed in the copper propionate monohydrate satisfy eigenvalues of three sets of spin-Hamiltonian of the form of Eq. (2) having parameters shown in Table I.

In the case of copper acetate monohydrate, the results of x-ray analysis[6] show that it is formed by constituents with bimolecular character expressed as $Cu_2(CH_3COO)_4 \cdot 2H_2O$ in which two copper atoms make direct Cu-Cu contact of 2.6 Å apart. Comparison of the result of paramagnetic resonance spectra with that of x-ray analysis has given a knowledge that the axial direction, the z-axis of the tetragonal crystalline field, coincides with the direction joining the two copper atoms in pair.

So we can dare to conclude in the present case of copper propionate monohydrate, without the knowledge of the x-ray analysis, that this crystal consists of bimolecular constituents which can be expressed as $Cu_2(CH_3CH_2COO)_4 \cdot 2H_2O$ from the results of paramagnetic resonance spectra alone. Then, there are six magnetic constituents, from the viewpoint of paramagnetic resonance, in the unit cell of copper propionate which are spatially inequivalent, whereas there are two in the copper acetate. In both cases, the half of them can be derived from the other by reflection in the *ac*-plane. As shown in Table I, the parameters g, D, and E to be used for three pairs well resembles to each other and are similar to those of the copper acetate.

By an analogy to the case of copper acetate, this constituent of magnetic unit in copper propionate may be illustrated as follows;

either of two copper atoms is surrounded by a distorted octahedron of four atoms of oxygen, from four carboxylic acids, one oxygen from molecule of H_2O, and the other copper atom which may be at a distance of order 2.6 Å.

The direction joining the copper ions may be indicated by angles ψ and α in Table I refered to the crystallographic axes, three others being deduced by mirror reflection with the *ac*-plane.

The copper atoms in this crystal are influenced by a tetragonal crystalline field within a good approximation since the g tensor has an axial symmetry and E is nearly zero compared with its D value. It can be, therefore, concluded that the atomic configuration of the constituent has a good tetragonal symmetry.

§ 6. Conclusions

Following a plan taken up in 1951, our group has worked out the study of paramagnetic resonance absorption in single crystals of copper salts derived from the series of monocarboxylic acids; copper formate, copper acetate, copper propionate and so on.

Copper formate has its dihydrate $Cu(HCOO)_2 \cdot 2H_2O$ and its tetrahydrate $Cu(HCOO)_2 \cdot 4H_2O$. In both cases, it was observed[15] that single crystals show a single absorption peak given by Eq (1), as in copper Tutton salt or in copper sulfate, which can be explained by an application of ordinary crystalline field theory to the ^2D state of Cu^{++} ions and of exchange interaction.

In copper acetate, the spectra shows an anomalous behaviour. It can be explained not by an ordinary Cu^{++} ion under an influence of crystalline electric field but by cluster of pairs of copper atoms within a bimolecular constituents $Cu_2(CH_3COO)_4 \cdot 2H_2O$. In a pair, two copper ions have a direct contact in each other located at 2.6 Å apart.

In copper propionate, there are six inequivalent magnetic constituents in unit cell, each of which has a bimolecular character similar to that of copper acetate.

We continued experiments beyonds the copper salts of normal butylate. By our preliminary results, the main resonance line of single crystals of this salt appeared to have a large width which can be ascribed to superposition of many absorption lines. At $\lambda \fallingdotseq 3$ cm, an absorption peak can be clearly resolved at about zero magnetic field. It may be concluded that the crystal of copper normal butylate consists of, at least contains, bimolecular units, each of which obeying spin-Hamiltonians similar to the Equation (2). The number of inequivalent constituents in unit cell may be larger than the case of copper propionate, which causes the difficulty in analysis of the main line. The preliminary results of x-ray analysis shows that unit cell of this crystal contains 32 formula molecules.

Moreover, paramagnetic resonance of copper monochloroacetate shows that this crystal also consists of bimolecular constituents.

§ 7. Acknowledgements

The author wishes to express his sincere thanks to Professor Hiroo Kumagai for his continuous guidance and encouragement. He is grateful to many of his colleagues for helpful discussions, especially to Mr. J. Shimada and to Profs K. Ôno and I. Hayashi. He also wishes to thank Mr. Osafune of the Nihon Electric Co., Ltd. for a part of silicon wafers and Prof. R. D. Myers for the marker radical.

References

1) B. C. Guha: Proc. Roy. Soc. **A206** (1951) 353.
2) G. Foëx, T. Karantassis, and N. Perakis: compt. rend. **237** (1953) 982.
3) B. Bleaney and K. D. Bowers: Proc. Roy. Soc. **A214** (1952) 451.
4) H. Abe and J. Shimada: Jour. Phys. Soc. Japan **12** (1957) 1255.
5) Yamada: Reported at Meeting on Complex Salts, Tokyo.
6) J. N. van Niekerk and F.R.L. Schoening: Acta. Cryst. **6** (1953) 227.
7) H. Abe: Phys. Rev. **92** (1953) 1572.
8) K. Ôno: Jour. Phys. Soc. Japan: **12** (1957) 1231.
9) P. Groth, *Chemische Kristallographie* (Teubner, Leipzig, 1910) **Vol 3**, 202.
10) H. Abe, K. Ôno, I. Hayashi, J. Shimada, and K. Iwanaga: Jour. Phys. Soc. Japan **9** (1954) 814.
11) H. Abe and J. Shimada: Nat. Sci. Rep. O.U. **8** (1957) 80.
12) J. C. Slater: Rev. Mod. Phys. **18** (1946) 482.
13) N. A. Schuster: Rev. Sci. Instr. **22** (1951) 254.
14) H. Kumagai and H. Shôno: Pept of Inst. Sci. Tech., Univ. of Tokyo **6** (1952) 63 (in Japanese).
15) J. Shimada, H. Abe, and K. Ôno; Jour. Phys. Soc. Japan **11** (1956) 137.

JOURNAL OF THE PHYSICAL SOCIETY OF JAPAN Vol. 13, No. 9, SEPTEMBER, 1958

Variation of Hall Coefficient of Some Non-ferromagnetic Superlattice Alloys

By Kiyoshi YONEMITSU and Takao SATO

Department of Physics, Tokyo Metropolitan University

(Received March 22, 1958)

The temperature dependence of Hall coefficient of five superlattice alloys of Cu_3Pd, CuZn, Ni_3Cr, Au_3Cu and Ag_3Mg was measured to find the effect of order-disorder transformation upon it. At the transition temperature, the Hall coefficient of Cu_3Pd and Ag_3Mg showed a discontinuous change, while the change of Hall coefficient of other three alloys (CuZn, Ni_3Cr, Au_3Cu) are very small. Applying Muto's theory, the qualitative discussion was made, and it was found that the general features of the temperature dependence of CuZn and Ni_3Cr are well understood by the theory. For Au_3Cu, the result of the experiment is explained by adopting the assumption of Schubert that each Au atom affords more than one electrons into the conduction band. The assumption also explains why the temperature dependence of Hall coefficient of Au_3Cu differs from that of Cu_3Au.

It remains unknown why Hall coefficient of Cu_3Pd takes strong minimum at transition temperature, while the abrupt increase of the Hall coefficient with the decreasing temperature below T_c can be explained by the existence of a superzone in the ordered state. In addition, the result Ag_3Mg is contrary with that which Nicholas's theory suggested.

§ 1. Introduction

It was suggested by Slater[1] that the electronic energy plays an important role when some kind of superlattice alloys undergoes the order-disorder transformation. According to Salter, the problem is explained by a rather simple band model; i. e. by considering the suppression of Fermi surface and the lowering of electronic energy in the ordered state. The suggestion was applied to a few superlattice alloys by Nicholas[2], who tried to show the effect of suppression of Fermi energy on order-disorder transformation of these alloys. To which extent one can proceed with this rather simple model is not clear, and from this point of view, it will be of some use to know the electrical properties of these alloys.

In 1938, Muto[3] predicted that a drastic change in electrical and magnetic properties of these alloys should be expected at the transformation temperature. The prediction was proved to be true by Komar and Sidrov[4], who had measured Hall coefficient and magnetoresistance coefficient of Cu_3Au. The measurement was held at room temperature, quenching the specimen from high temperatures. The present authors have been measuring Hall coefficient of many superlattice alloys including Cu_3Au. The results for Cu_3Au[5] and alloys of Mg–Cd system[6] were previously printed. In the present paper, we will report on the results of measurements on Cu_3Pd, CuZn, Ni_3Cr, Au_3Cu and Ag_3Mg.

§ 2. Preparation of Specimens and Experimental Procedure

Specimens of Cu_3Pd, Au_3Cu, and Ag_3Mg were presented by Mr. M. Hirabayashi and that of Ni_3Cr by Mr. S. Yoshida. To prepare the specimen of CuZn, 99.98% Cu and 99.98% Zn were melted together in a Tammann tube, and then cast into a small plate 2 mm thick.

Table I. Dimension of Specimens

Specimen	Dimension
Cu_3Pd	$18.0\times5.5\times0.17$ mm
CuZn	$15.0\times6.0\times0.34$ mm
Au_3Cu	$23.0\times6.8\times0.087$ mm
Ni_3Cr	$23.0\times8.0\times0.220$ mm
Ag_3Mg	$22.0\times8.1\times0.16$ mm

After annealed in the argon vapor for 1 hr at 500°C, the specimen was then polished by sand papers. The dimension of every specimen is shown Table I.

The specimen of Au_3Cu was annealed in the argon vapor for 27 days at 180°C, the next

15 days at 150°C, and the following 30 days at 125°C preceding the measurement. The specimen of Ni_3Cr was annealed for one day at 540°C, the next 6 days at 444°C, and the following 10 days at 390°C in argon vapor preceding the measurement.

In measurements of the Hall coefficient and the electrical resistivity, specimens were set in an electric furnace, which was placed between the pole pieces of an electromagnet. 4 pairs of leads were spot-welded to the specimen; 2 pairs for the Hall potential, a pair for the electrical resistivity, and another pair for primary current. Copper wire 0.2 mm in diameter was used as leads. The temperature of the furnace was controlled by controlling the current of the furnace, and was read by a thermo-couple and a potentiometer. The strength of magnetic field was about 6 kOe. and the Hall potential was measured by a D. C. amplifier and galvanometer, the sensitivity of which was 1.1×10^{-8} volt/μA division[7]. The primary current was about 1.5 amp. for Ni_3Cr and about 1 amp. for other alloys.

The measurements of Hall coefficient for Cu_3Pd and Ag_3Mg were carried out while specimens were being cooled from temperature above Curie point, and those for CuZn and Au_3Cu were carried out while they were being heated from room temperature. The measurement of Hall coefficient for Ni_3Cr was held at room temperature for the quenched specimen. This was done so, because on account of high resistivity of Ni_3Cr, Joules heat due to the primary current was apt to disturb the thermal equilibrium of the specimen at high temperature and generate the parasitic thermoelectric potential.

The details of the method of measurements are already described in the preceding paper[6] and will not be repeated here again.

§ 3. Results

The results are shown in Tabs. II~VI, and in Figs. 1~5. From these figures one can see that fluctuations prevail in the temperature ranges just above and below the Curie point because in these temperature ranges just above and below the Curie point because in these temperature ranges, nucleation and growth or extinction of local orders may occur incessantly, which prevent the specimen from the equilibrium temperature distribution.

Table II. (a) Temperature dependence of Hall coefficient of Cu_3Pd

Cooling rate; 520°C~440°C: 7.5°C/hr
440°C~435°C: 8.5°C/hr
435°C~405°C: 3°C/hr
405°C~300°C: 20°C/hr
300°C~R. T. : 50°C/hr

T°C	$-R\times10^4$ e.m.u.	ρ $\mu\Omega$ cm
518	13.34±0.10	
519	13.53±0.10	27.9
509	14.00±0.20	28.1
495	14.47±0.06	28.0
485	15.43±0.16	28.1
476	17.04±0.11	28.2
464	16.43±0.05	28.1
458	15.80±0.10	27.4
452	14.77±0.05	27.0
444	14.37±0.05	25.8
439	13.58±0.14	25.0
432	13.60±0.08	24.4
429	14.00±0.04	24.1
421	13.00±0.07	23.5
419	12.80±0.01	23.4
413	12.40±0.07	23.0
408	11.95±0.92	22.7
405	12.13±0.10	22.5
403	11.20±0.08	22.4
376	10.25±0.03	20.8
354	8.57±0.03	19.7
335	8.52±0.13	18.9
299	8.10±0.01	18.2
244	8.40±0.20	17.5
195	8.00±0.10	16.8
121	7.87±0.06	16.0
149	7.10±0.04	14.9
33	7.23±0.06	14.8

Table II. (b) Hall coefficient of Cu_3Pd after prolonged annealing. The specimen was kept at 388°C for about 27 hrs, and at 276°C about 16 hrs. In other temperature ranges, the cooling rate was same shown in Table 2 (a).

T°C	$-R\times10^4$ e.m.u.	ρ $\mu\Omega$ cm
338	9.40±0.04	20.2
276	7.83±0.04	19.8
32	7.47±0.10	14.9

The Hall coefficient of Cu_3Pd decreases until the temperature decreases to 470°C, the Curie temperature. Below this temperature the Hall coefficient increases with decreasing temperature, and has a sharp mininum at T_c. The electrical resistivity which was measured simultaneously increases slowly above T_c and decreases abruptly below T_c with temperature decreasing, so that the electrical resistivity

Table III. Temperature dependence of Hall coefficient of Au_3Cu. The specimen was annealed at 180°C for 27 days, at 150°C for the next 15 days and at 125°A for the following 30 days. The measurement was done by heating the specimen with the heating rate of 40°/hr for 30°C~110°C, 25°/hr for 110°C~172°C, 4°/hr for 172°C~352°C.

T°C	$-R\times10^4$ e.m.u.	ρ $\mu\Omega$ cm
20	9.97±0.09	11.6
30	10.23±0.08	11.6
44	10.00±0.01	11.7
59	10.10±0.07	11.8
73	9.90±0.07	11.9
92	10.00±0.01	12.0
109	9.80±0.10	12.2
126	9.93±0.10	12.3
140	9.50±0.07	12.3
155	9.73±0.05	12.4
168	8.97±0.02	12.6
175	8.47±0.12	12.6
179	9.35±0.10	12.6
182	9.45±0.17	12.7
186	9.30±0.10	12.7
190	9.50±0.04	12.7
192	9.57±0.10	12.7
194	9.55±0.03	12.7
196	9.65±0.10	12.7
198	9.33±0.10	12.7
201	8.67±0.06	12.7
203	8.95±0.18	12.6
209	9.30±0.01	12.6
210	9.40±0.10	12.5
212	9.23±0.02	12.4
215	9.30±0.01	12.3
222	9.20±0.04	12.2
225	9.20±0.03	12.2
230	9.00±0.07	12.2
234	8.73±0.04	12.2
244	9.13±0.08	12.2
256	8.87±0.05	12.3
272	9.13±0.06	12.4
352	8.10±0.01	
20	9.57±0.09	10.7*

* This was obtained after quenching the specimen from 352°C to room temperature.

has a slight maximum at T_c. In Fig. 1, two curves are shown, each of which represents the variation of Hall coefficient with different cooling rate. It is desirable to measure the value of Hall coefficient at higher temperature than that which are shown in the figure in order to know the data in perfect disordered state, but this was impossible on account of prevailng fluctuations at higher temperature.

Table IV. Temperature dependence of CuZn. The measurement was done while heating the specimen with the heating rate of

R. T.~440°C: 75°C/hr,
440°C~517°C: 20°C/hr.

T°C	$-R\times10^4$ e.m.u.	ρ $\mu\Omega$ cm
25	0.33±0.04	4.95
51	0.77±0.05	5.34
96	0.70±0.14	6.10
149	0.93±0.05	7.11
199	0.77±0.02	7.75
249	0.83±0.08	8.61
293	1.00±0.10	9.51
347	1.00±0.04	10.72
345	1.05±0.03	12.02
424	1.57±0.02	
439	1.23±0.05	13.01
447	1.45±0.08	13.83
455	1.50±0.07	14.17
460	1.73±0.08	14.45
466	1.36±0.13	14.67
474	1.50±0.08	15.18
484	1.88±0.13	15.63
494	1.20±0.01	15.96
507	1.68±0.23	16.18
432	1.80±0.07	13.67*
464	1.60±0.04	14.68
473	1.20±0.01	15.14
486	1.73±0.11	15.74
498	1.50±0.04	16.01
516	1.60±0.12	16.46
26	0.44±0.05	5.00**

* From this point, the measurement was repeated with same heating rate.

** This was obtained after quenching the specimen from 517°C in air.

Table VI. Temperature dependence of Hall coefficient of Ni_3Cr. The data was obtained from the specimen which had been annealed;

at 540°C for 1 day,
at 444°C for 6 days,
and at 390°C for 10 days.

Temperature is the temperature from which the specimen was quenched in air.

T°C	$-R\times10^4$ e.m.u.	ρ $\mu\Omega$ cm
107	3.70±0.10	128.0
224	4.30±0.04	128.0
249	3.70±0.10	126.0
281	3.93±0.07	102.0
313	3.65±0.12	100.0
363	4.20±0.04	99.0

One can find no notable changes in Hall coefficient with well annealed Au_3Cu from room temperature to about 180°C. (Fig. 2)

Table V. Temperature dependence of Hall coefficient of Ag_3Mg.

Cooling rate; 420°C~400°C: 10°C/hr,
400°C~375°C: 5°C/hr
and at 375°C annealed for about 12 hrs, and the rate after that was
375°C~350°C: 5°C/hr,
350°C~130°C: 60°C/hr,
130°C~R. T.: furnace cool.

T°C	$-R\times10^4$ e.m.u.	ρ $\mu\Omega$ cm
420	5.48±0.08	
416		14.12
410	5.52±0.12	
405		14.02
399	5.42±0.12	13.96
397	5.38±0.03	
393	5.40±0.09	
392	5.73±0.05	13.83
390	5.83±0.09	
389	5.76±0.14	13.49
386	5.88±0.15	
585	7.67±0.13	
382	7.26±0.14	
380	7.34±0.13	
377	7.40±0.11	
375		11.43
369		11.20
363	8.67±0.05	
354		10.76
352	8.70±0.14	
344		10.48
328	8.42±0.09	
318		9.83
300	8.53±0.02	
286		9.18
250	8.40±0.08	
213		7.89
200	8.17±0.02	
130	8.20±0.06	
19	7.58±0.11	5.01

At about 180°C, fluctuations increase, and in higher temperature range, Hall coefficient increases toward positive direction with a slight gradient. At room temperature, Hall coefficient of the alloy is -10×10^{-4} e.m.u., and reaches to -8.7×10^{-4} e.m.u. at 350°C. After quenched from 350°C to room temperature, it is nearly equal with that of annealed specimen. However it may be, the variation by temperature of Hall coefficient of Au_3Cu shows a feature much different with that of Cu_3Au; i.e. former shows scarcely any change in transformation, while the latter Hall coefficient is negative in the disordered state and positive in the ordered state.

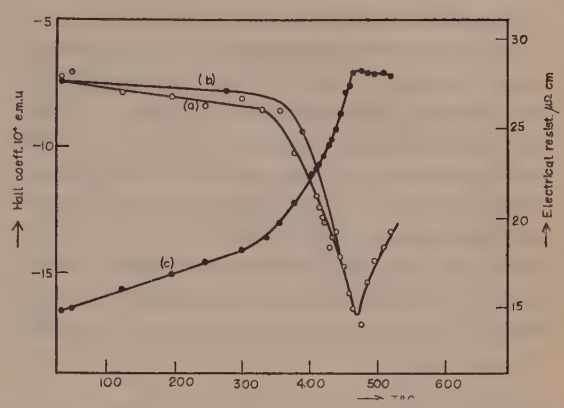

Fig. 1. Temperature variation of Hall coefficient (a), (b) ((b) after prolonged annealing, see Tab. II) and electrical resistivity (c) of Cu_3Pd.
$T_c=470$°C, $\rho_c=28.2$ $\mu\Omega$ cm.

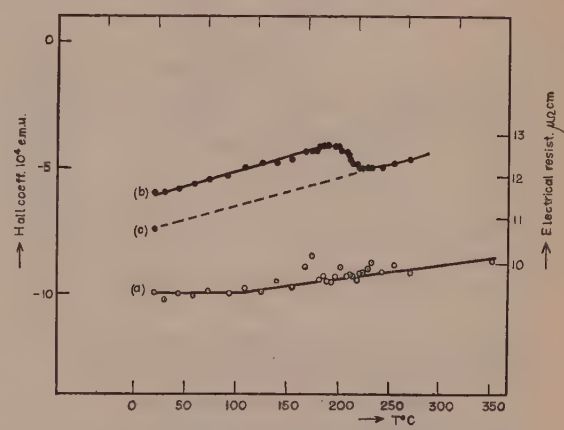

Fig. 2. Temperature variation of Hall coefficient (a) and electrical resistivity (b), (c) ((c) after quenched from 352°C to room temperature) of Au_3Cu.
$T_c=220$°C, $\rho_c=12.2$ $\mu\Omega$ cm.

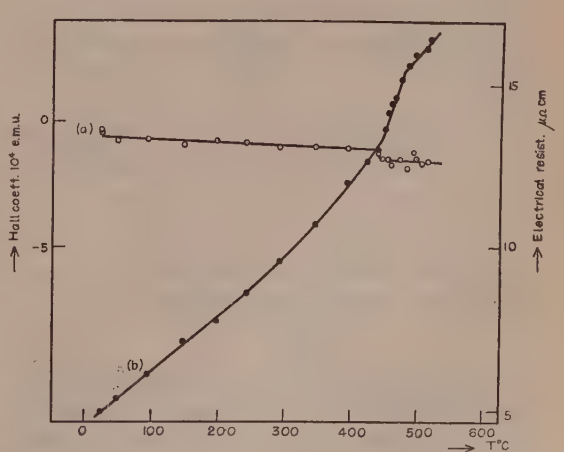

Fig. 3. Temperature variation of Hall coefficient (a) and electrical resistivity (b) of CuZn.
$T_c=476$°C, $\rho_c=15.41$ $\mu\Omega$ cm.

The Hall coefficient of CuZn is -0.5×10^{-4} e.m.u. at room temperature, and its absolute value increases quite slowly with the rising temperature. (Fig. 3) There appears a discontinuous change, though very small, at about 440°C, and the absolute value increases about 0.5×10^{-4} e.m.u.. The temperature at which the change occurs in the Hall coefficient, does not agree with that at which a knick occurs in the electrical resistivity measured simultaneously. This was reproducible in repeated experiments.

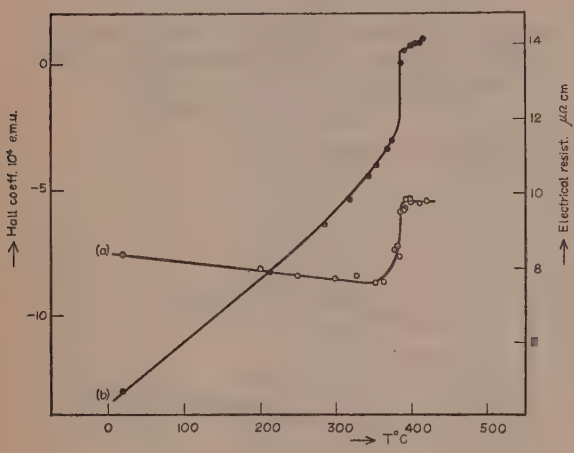

Fig. 4. Temperature variation of Hall coefficient (a) and electrical resistivity (b) of Ag_3Mg. $T_c=386°C$, $\rho_c=13.5\ \mu\Omega$ cm.

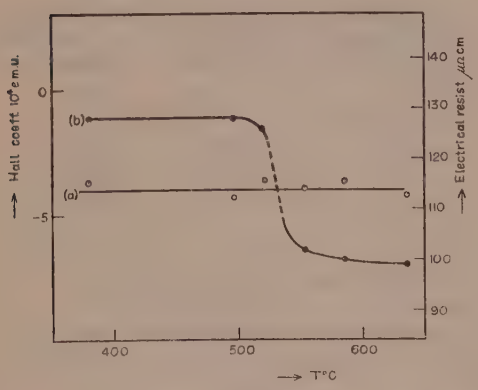

Fig. 5. Hall coefficient (a) and electrical resistivity (b) vs. quenching temperature of Ni_3Cr. $\rho_{336°}=99.0\ \mu\Omega$ cm.

The Curie temperature of Ag_3Mg is 386°C, and just above this, the Hall coefficient is -5.5×10^{-4} e.m.u. (Fig. 4). When the ordering formation begins, the electrical resistivity decreases abruptly, and at the same time, Hall coefficient begins to fall taking a minimum value, -8.5×10^{-4} e.m.u. at 360°C. Below this temperature, Hall coefficient increases again with the decreasing temperature and at room temperature it reaches to -7.5×10^{-4} e.m.u..

As the experiment was carried out with the quenched specimen of Ni_3Cr, it was impossible to determine the transformation temperature accurately. But as it can be seen from Fig. 5 when the specimen is quenched from 520°C or lower the electrical resistivity is larger than that quenched from 550°C or higher. So, it may be reasonable to think that the order-disorder transformation might take place in the temperature range between 520°C and 550°C. From the figure, it can be shown that the electrical resistivity of Ni_3Cr is larger in ordered than in disordered state like in disordered state like in Au_3Cu. The Hall coefficient is nearly constant, and seems scarecely affected by order-disorder transformration.

§ 4. Consideration

Comparing the above described data with those of Mg–Cd superlatice alloys and Cu_3Au, which have been reported in the preceding reports and by Komar and Sidrov, one will note a distinct difference between them. For the latter, Hall coefficient always increases discontinously with the ordering formation, while the former shows various feature of changes above and below the transformation temperature.

For instance, Hall coefficient of Cu_3Pd decreases with decreasing temperature, and takes a minimum at that temperature. Below T_c, the Hall coefficient behaves like that of Cu_3Au or Mg–Cd superlattice alloys, though its sign is always negative. Hall coefficient of Ag_3Mg also has a negative sign, but it decreases with the decreasing temperature just below T_c, and has a minimum at the temperature about 30°C below T_c. Other three superlattice alloys show changes that are not so distinct at T_c as others. These variation seems to be explained to some extent by variation of band structure of these alloys.

As Muto predicted, when superlattice alloys transform from random state to ordered state, Brillouin zone splits to form a superzone. If the boundary of the superzone is near the Fermi level, or cross with it, the Fermi surface will be distorted by the superzone, which

must cause some changes in the electrical property associated with the order-disorder transformation.

The change of Hall coefficient of Cu_3Pd below T_c may be interpreted. Since the crystal structure of Cu_3Pd is f.c.c. above Curie temperature, its 1-st Brillouin zone must be like what is shown by the fine line in Fig. 6. Below T_c, it had tetragonally deformed Cu_3Au

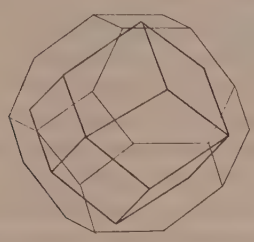

Fig. 6. First Brillouin zone of disordered Cu_3Pd and superzone of ordered Cu_3Pd.

type structure, so that its superzone is a distorted dodecahedron which is shown by gross lines in the figure. Of this alloy, the long range order was found by Ogawa, Watanabe and Hirabayashi[8,9]. The effect of long range order on the superzone is to modify the superzone in a complicated way. It is, however, rather difficult to see the effect of the modification on the electrical property, so that, at present, we will be contented only to examine whether the superzone has any effect on the Fermi surface, and accordingly on the electrical property of the alloy or not.

As palladium is a transition element, it is not clear how many electrons per palladium atom affords into the conduction band. If we assume that it affords 0.6 electrons per atom as nickel, the valency electron concentration (number of conduction electrons per atom) is 0.9. The superzone of the alloy contains electrons nearly equal to one per atom, so that it may be thought that the superzone suppress the Fermi surface, and positive holes must appear in ordered state, thus making Hall coefficient to change in the positive direction. It is not clear why Hall coefficient increases with temperature above T_c. As palladium is a transition element, it is possible that palladium must be contributing to this anomalous behaviour.

The valency electron concentration of CuZn is 1.5, and its 1-st Brillouin zone in random state is a dodechahedron which is surrounded by {110} surfaces and can contain 2 electrons per atom (Fig. 7). The superzone is a cube which is shown in the Fig. 7 by gross lines, and can contain one electron per atom. It is obvious that the superzone has little effect on the Fermi surface, and from this point of view, it is natural that no such drastic change as Cu_3Pd is found at T_c, though there was a small change in Hall coefficient a little below Curie temperature. The reason why such change appears can not yet be explained.

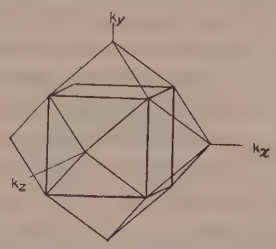

Fig. 7. First Brillouin zone of disordered CuZn and superzone.

It is to be noticed that the temperature dependency of Hall coefficient of Au_3Cu is perfectly different from that of Cu_3Au. If each Au and Cu atom affords one electron into conduction band, it is natural to expect nearly the same behaviour for both alloys, since they have the same crystal structure, though their lattice parameter differ a little. Schubert[10], however, made an interesting assumption that an Au atom affords more than one electrons into conduction band. If we adopt such assumption, the difference between Cu_3Au and Au_3Cu can be easily understood; i.e., if each Au atom affords 1.2 electrons into the conduction band, the valency electron concentration of Au_3Cu is 1.15, while that of Cu_3Au is 1.05. So that, the superzone of Au_3Cu, a dodecahedron that can contain one electron per atom, is nearly filled. The situ-

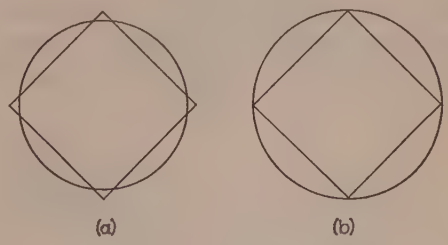

Fig. 8. Schematic representation of superzone and and Fermi surface of ordered Cu_3Au (a) and Au_3Cu (b).

ation for Cu_3Au and Au_3Cu must be such as shown in Fig. 8 schematically. The number of positive holes in Au_3Cu, if they exist in ordered state, may be very small and they give scarecely any effect of the Hall coefficient of Au_3Cu.

The existance of the superlattice structure in Ni_3Cr was ascertained by Taylor and Hinton[11]. It's resistivity is very high in general and higher in ordered state than in disordered state. Since both Ni and Cr transition elements the valence electron concentration of the alloy can not determined. If we assume that each Ni atom affords 0.6 electrons and each Cr atom affords one electron into conduction band, the valency electron concentration is 0.7. Since the structure of Ni_3Cr is Cu_3Au type, the superzone of the alloy can contain one electron per atom and will have little effect on the Fermi surface and accordingly on Hall coefficient. Taylor and Hinton attribute the increasing resistivity in ordered state to the {110} reflection of the electronic wave, which is in this point of view, rather doubtful.

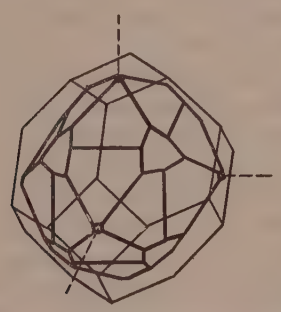

Fig. 9. First Brillouin zone of disordered Ag_3Mg and superzone suggested by Nicholas.

The change of Hall coefficient of Ag_3Mg is of interest, since it is an only alloy that we have studied, which has Hall coefficient more negative in ordered state than disordered state. The band structure of Ag_3Mg is discusssed by Nicholas. According to him, as the alloy has f.c.c. structure in disordered state, it has the 1-st Brillouin zone which is shown by fine lines in Fig. 9. In ordered state the superzone which is shown by gross lines in the figure appears. The superzone is nearly spherical since the ratio of minimum diameter to maximum one is 1 : 1.25. The zone can contain 1.32 electrons per atom and the inscribed sphere 1.09. As the valency electron concentration of the alloy is 1.25, Fermi surface must perfectly lie in the superzone. According to Nicholas, the suppression of Fermi level by the superzone results the lowering of the electronic energy and makes the existence of the superlattice stable in ordered state. If it is so, it is natural to expect Hall coefficient to change in the positive direction when the superlattice is formed. Our result is contrary to the expectation.

Acknowledgements

The authors are indebted to Mr. S. Noguchi for helpful discussion and suggestions. They also express their gratitude to Mr. M. Hirabayashi and Mr. S. Yoshida who have presented specimens to them, and to Mr. H. Nogami for his assistance in measurement.

References

1) J. C. Slater; Phys. Rev. **84** (1951) 179
2) J. F. Nicholas; Proc. Phys. Soc. LXVI, **3A** (1952) 14
3) T. Muto: Sc. Pap. IPCR **34** (1938) 377
4) A. Komar and S. Sidrov: J. Phys. USSR **4** (1941) 552
5) T. Sato and K. Yonemitsu: Kinzoku Butsuri **3** (1957) 153
6) K. Yonemitsu and T. Sato: J. Phys. Soc. Jap. **13** (1958) 15
7) K. Yonemitsu and T. Sato: Oyo Butsuri **26** (1956) 153
8) D. Watanabe and S. Ogawa: J. Phys. Soc. Japan **11** (1956) 226
9) M. Hirabayashi and S. Ogawa: J. Phys. Soc. Japan **12** (1957) 259
10) K. Schubert: Z. Metallkde **43** (1953) 1
11) A. Taylor and K. G. Hinton: J. Inst. Metals 81 (1952) 169

JOURNAL OF THE PHYSICAL SOCIETY OF JAPAN Vol. 13 No. 9, SEPTEMBER, 1958

Study of Metallic Carbides by Electron Diffraction Part II. Crystal Structure Analysis of Nickel Carbide

By Sigemaro NAGAKURA

Tokyo Institute of Technology, Oh-okayama, Meguro-ku, Tokyo

(Received April 15, 1958)

The crystal structure of nickel carbide, Ni_3C, was studied by the electron diffraction method. The observed intensity showed considerable primary extinction and this was corrected, using Wilson's intensity statistics combined with the theory of primary extinction (S. Nagakura, Acta Cryst. **10** (1957) 601). The actual procedure was described in detail and it was concluded that the structure of nickel carbide belongs to the space group $R\bar{3}c$ and nickel atoms occupy 18*e* positions with the parameter $x=1/3$ and carbon atoms 6*b* positions. It was found also that the carbon atoms take a kind of one-dimensionally disordered arrangement in the carbide lattice.

§ 1. Introduction

As a continued work of formation and decomposition of nickel carbide, Ni_3C, reported in Part I[1], the study of crystal structure of the carbide is reported in this paper.

As mentioned in Part I, the electron diffraction method is advantageous in the structure analysis of nickel carbide, since the ratio of the scattering amplitudes of carbon and nickel atoms for electrons is as large as about one-third, while that for X-rays is about one-seventh. However, a serious difficulty in the electron method arises from the effect of dynamical diffraction or primary extinction. The structure proposed in Part I for the carbide seems to be very reasonable from the spacial consideration, but the calculated intensity shows considerable disagreement with the observed intensity, indicating a strong participation of the primary extinction effect. Recently, Honjo and Kitamura[2] gave a method to eliminate the primary extinction effect by extrapolating the observed electron diffraction intensity to zero wave-length. The present author has reported another method to detect and correct the primary extinction effect[3]. This method is based on Wilson's intensity statistics[4] and the current theory of primary extinction[5]. The result of its application to nickel carbide showed the proposed structure in Part I to be correct. In the present paper details of the structure analysis are described.

§ 2. Observed Intensity and Proposed Structure

Polycrystalline nickel carbide films were prepared by the method described in Part I.

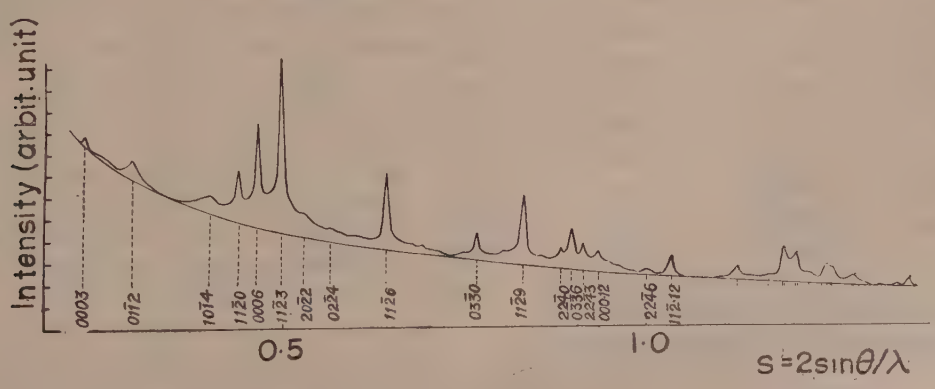

Fig. 1. Intensity curve of Ni_3C.

Table I. Structure data of Ni_3C (λ=0.06 Å, $\bar{\rho}$=240 Å)*

$hkil$	s(Å^{-1})	$\frac{1}{9}\lvert\sqrt{I_0}\rvert$(Å)	x	$f(x)$	$\frac{1}{9}\lvert F_{cor}\rvert$(Å)	$\frac{1}{9}\lvert F_c\rvert$(Å)**
$11\bar{2}0$	0.439	1.3	1.78	0.34	2.2	−3.2
0006	0.465	3.1	3.75	0.15	8.1	−6.7
$11\bar{2}3$	0.497	2.0	3.49	0.13	5.7	±6.3
$11\bar{2}6$	0.639	1.6	1.83	0.32	2.9	+3.3
$03\bar{3}0$	0.761	2.4	2.65	0.19	5.5	+4.8
$11\bar{2}9$	0.824	2.2	1.87	0.32	3.9	∓3.4
$22\bar{4}0$	0.879	1.6	0.79	0.80	1.7	−1.4
$03\bar{3}6$	0.892	1.9	1.74	0.36	3.1	−3.1
$22\bar{4}3$	0.909	1.6	1.61	0.41	2.6	∓2.9
000.12	0.929	2.6	1.98	0.26	5.2	+3.6
$22\bar{4}6$	0.994	1.1	0.97	0.72	1.3	+1.8
$11\bar{2}.12$	1.028	1.5	0.66	0.86	1.6	−1.2
$22\bar{4}9$	1.122	2.0	1.18	0.62	2.5	±2.1
$14\bar{5}0$	1.162	0.9_3	0.53	0.90	0.9_7	−0.96
$14\bar{5}3$	1.185	1.5	1.10	0.66	1.8	±2.0
$03\bar{3}.12$	1.200	2.1	1.36	0.53	2.8	+2.4
$11\bar{2}.15$	1.242	1.7	1.02	0.70	2.0	±1.8
$14\bar{5}6$	1.252	1.1	0.69	0.85	1.2	+1.2
$22\bar{4}.12$	1.279	1.1	0.47	0.92	1.1	−0.84
$33\bar{6}0$	1.318	1.8	1.18	0.62	2.3	+2.1
$14\bar{5}9$	1.355	1.4	0.90	0.75	1.6	∓1.6
$00\bar{0}.18$	1.394	1.4	0.92	0.75	1.6	−1.7
$33\bar{6}6$	1.397	1.4	0.91	0.75	1.6	−1.6
$22\bar{4}.15$	1.456	1.4	0.81	0.80	1.6	∓1.5
$11\bar{2}.18$	1.461	0.9_5	0.54	0.90	1.0	+0.97
$14\bar{5}.12$	1.488	0.9_1	0.38	0.95	0.9_3	−0.68
$06\bar{6}0$	1.522	1.0	0.94	0.74	1.2	+1.7
$25\bar{7}0$	1.584	0.5_6	0.34	0.95	0.5_8	−0.62
$03\bar{3}.18$	1.588	1.3	0.75	0.83	1.4	−1.3
$06\bar{6}6$	1.591	1.3	0.75	0.83	1.4	−1.3
$25\bar{7}3$	1.601	1.1	0.70	0.85	1.2	∓1.3
$03\bar{3}.12$	1.612	1.5	0.85	0.78	1.7	+1.5
$14\bar{5}.15$	1.643	1.3	0.67	0.85	1.4	±1.2
$22\bar{4}.18$	1.647	0.8_5	0.45	0.93	0.8_8	+0.80
$25\bar{7}6$	1.651	0.8_4	0.44	0.93	0.8_7	+0.80
$11\bar{2}.21$	1.684	0.9_3	0.64	0.87	1.0	∓1.2
$25\bar{7}9$	1.731	0.8_2	0.62	0.88	0.8_7	±1.1
$44\bar{8}0$	1.756	0.7_5	0.29	0.96	0.7_7	−0.52
$06\bar{6}.12$	1.783	0.9_6	0.79	0.81	1.1	+1.3
$14\bar{5}.18$	1.815	0.9_1	0.38	0.94	0.9_5	+0.69
$25\bar{7}.12$	1.836	0.5_1	0.27	0.97	0.5_2	−0.48
$22\bar{4}.21$	1.846	0.8_8	0.55	0.90	0.9_2	±1.0

* Only M-reflections are tabulated.

** ± refer to $hkil$ and $hki\bar{l}$, respectively.

Electron diffraction patterns were taken with 40 KV electrons (wave-length $\lambda=0.06$ Å) and the camera length 250 mm. The intensity was measured photometrically up to s $(=2\sin\theta/\lambda)=2.3$ Å^{-1}, utilizing Karle and Karle's method[6]. Fig. 1 shows an example of the intensity curve. The relative intensities of Debye rings were unchanged by inclination of the specimen film against the electron beam, proving that the film had no preferred orientation. The mean particle size of the crystallites, ε, was calculated to be 290 Å from the half-breadth of the rings, β,

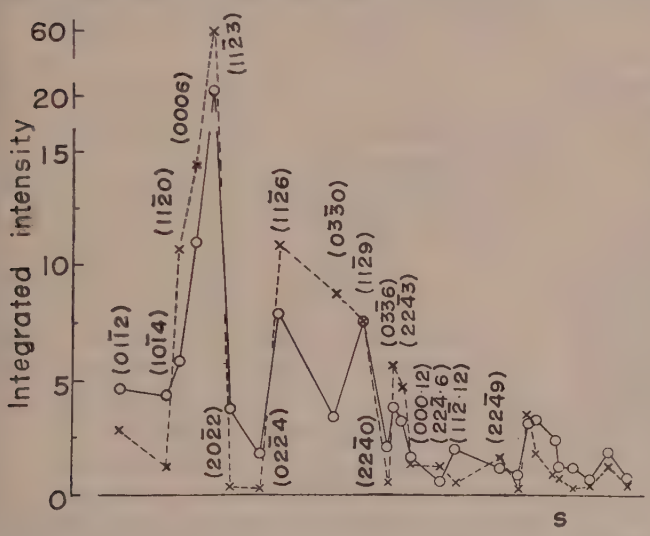

Fig. 2. Comparison of P_0 (open circles) and P_c (crosses), which are normalized at (11$\bar{2}$9) ring.

utilizing the equation $\varepsilon=\lambda/\beta\cos\theta$, where θ is the Bragg angle. Integrated intensities par unit length of the Debye rings, P_0, were evaluated by measuring the peak area of the intensity curve. The overlapping rings were divided into the components assuming the same half-breadth of each component. The intensities of very weak rings were estimated visually. In Fig. 2, P_0 are plotted by open circles. The square roots of the observed intensities, $\sqrt{I_0}$, are tabulated in Table I.

As mentioned in Part I (§ 3.1), the observed reflections are classified in three groups, M-, s- and f-reflections. The M-reflections are sharp and strong and indexed by the c. p. h. lattice proposed by Jacobson and Westgren[7] with the lattice constant

$$a_h=2.628\text{ Å},\quad c_h=4.306\text{ Å and } c_h/a_h=1.638.$$

The s-reflections are weak and broad and can be indexed, together with the M-reflections, by the hexagonal cell

$$a=\sqrt{3}\,a_h=4.553\text{ Å},\quad c=3c_h=12.92\text{ Å}$$

and

$$c/a=2.837\,,$$

which is a super-lattice of Jacobson and Westgren's lattice and contains 18 nickel and 6 carbon atoms. From the observation described in Part I (§ 3.1), the f-reflections are concluded to be the forbidden reflections caused by the multiple reflection and are aside from the following consideration.

Indices of the observed reflections based on the super-lattice satisfy the conditions

$$hkil:\quad -h+k+l=3n,$$
$$\bar{h}kil:\quad l=3n,$$

where n is an integer*. The possible space groups satisfying the above conditions are $R3c$ and $R\bar{3}c$. Here, we assume the space group $R\bar{3}c$ having the centre of symmetry. The appropriate atomic positions are as follows:

(0, 0, 0; 1/3, 2/3, 2/3; 2/3, 1/3, 1/3)+
Ni atoms: 18e, +(x, 0, 1/4; 0, x, 1/4; $\bar{x}$, $\bar{x}$, 1/4; $\bar{x}$, 0, 3/4; 0, $\bar{x}$, 3/4; x, x,3/4),
C atoms: 6b, +(0, 0, 0; 0, 0, 1/2).

If nickel atoms take the c.p.h. arrangement, the parameter x should be 1/3. The structure is illustrated in Fig. 11. The structure amplitudes are given by

(i) $-h+k=3n$, $l=2n'$ (M-reflection)

$$F_{hkil}=6f_{Ni}\left\{\cos\frac{2\pi}{3}h+\cos\frac{2\pi}{3}k+\cos\frac{2\pi}{3}i\right\}\cos\frac{\pi}{2}l+6f_C\,,\qquad(2.1)$$

(ii) $-h+k=3n$, $l=2n'+1$ (M-reflection)

$$F_{hkil}=6f_{Ni}\left\{\sin\frac{2\pi}{3}h+\sin\frac{2\pi}{3}k+\sin\frac{2\pi}{3}i\right\}\sin\frac{\pi}{2}l\,,\qquad(2.2)$$

(iii) $-h+k\neq 3n$, $l=2n'$ (s-reflection)

$$F_{hkil}=6f_C\,,\qquad(2.3)$$

* The first relation is the rhombohedral condition. The lattice constant reffered to the rhombohedral axes are $a_0=5.505$ Å and $\alpha=53°39'$. The unit cell contains 12 nickel and 4 carbon atoms.

(iv) $-h+k \neq 3n,\ l=2n'+1$

$$F_{hkil}=0\,, \tag{2.4}$$

where, f_{Ni} and f_C are the scattering amplitudes of nickel and carbon atom, respectively. It should be noted here that the s-reflections are contributed only from the carbon atoms. From diffraction patterns of single crystalline carbide films (Part I, Photo 4) it can be proved that the broadening of the s-reflections is due to the elongation of the intensity region along the c^*-axis in reciprocal space. This will be discussed in relation to the stacking order of carbon layers in the crystal at the end this paper (§ 7.2).

§ 3. Preliminary Comparison between Observed and Calculated Intensities

The integrated intensities per unit length of Debye rings

$$P_c=\text{const}\cdot j|F_c|^2/s^2,$$

where j is the multiplicity factor and F_c is the calculated structure amplitude, were calculated utilizing the equations (2.1)~(2.4)* and compared with P_0. Fig. 2 shows the comparison, where P_0 and P_c are represented by open circles and crosses, respectively, being normalized at a medium strong ring $(11\bar{2}9)$. The agreement between P_0 and P_c is bad with the reliability factor as large as 45%, though the calculated intensities for some other trial structures showed far larger dispcrepancies.

Fig. 2 reveals that (i) the magnitudes of P_0 and P_c are parallel, (ii) generally speaking, $P_0 < P_c$ for lower order reflections while $P_0 > P_c$ for higher order reflections, and (iii) the discrepancies are especially remarkable for the reflections having high intensities.

As the atomic scattering amplitude for electrons increases rapidly with decreasing scattering angle, the magnitude of structure amplitude is, on the average, larger at lower angles. Since the effect of primary extinction is stronger for the reflections having larger structure amplitudes, the effect should be, on the average, stronger at the lower order reflections. Thus, the observed relations in Fig. 2 between P_c and P_0 are most likely to be due to the primary extinction effect.

* Values of f_{Ni} and f_C were calculated from the equation (4.3) using the values of $f_{X,Ni}$ from James-Brindley's table and $f_{X,C}$ from Mac-Weeny's table.

§ 4. Detection of Primary Extinction by Intensity Statistics

Wilson[4] pointed out that the local average of X-ray diffraction intensities $\langle I\rangle=\langle|F|^2\rangle$ is correlated to the atomic scattering amplitudes by the relation

$$\langle I\rangle=\sum_{i=1}^{n} f^2{}_{X,i}, \tag{4.1}$$

where $f_{X,i}$ represents the atomic scattering amplitude for i-th atom and n the total number of atoms in a unit cell. When the primary extinction effect participates, the relation (4.1) does not hold, and it should be modified in the form

$$\langle I\rangle < \sum_{i=1}^{n} f^2{}_{X,i}. \tag{4.2}$$

This relation can be used to detect the primary extinction.

In the case of electrons, the atomic scattering amplitude is given by

$$f_i=\frac{2me^2}{h^2}\,\frac{(Z-f_X)_i}{s^2}\,, \tag{4.3}$$

where Z is the atomic number and m, e and h have usual meanings. f_i decreases very rapidly with s, while the change of $(Z-f_X)_i$ with s is moderate as is the case of $f_{X,i}$. The intensity statistics is, in principle, appropriate for point scatterers which give the angle-independent scattering amplitudes. Therefore, for the case of electron diffraction, it is reasonable to express the relations corresponding to (4.1) and (4.2) in the form

$$K\langle s^4 I\rangle \leqq \sum_{i=1}^{n}(Z-f_X)_i^2, \tag{4.4}$$

$$K=(h^2/2me^2)^2.$$

The plots $\langle s^4 I\rangle$ for the observed intensities I_0 are shown in Fig. 3 by open circles, where the values of $\langle s^4 I_0\rangle$ are normalized with the curve $\sum_{i=1}^{n}(Z-f_X)_i^2$ at the outermost s-value. It can be seen that the values of $\langle s^4 I_0\rangle$ for the lower angles considerably deviate downward from the curve $\sum_{i=1}^{n}(Z-f_X)_i^2$, showing evidently the effect of primary extinction.

According to the theory of primary extinction[5], the diffraction intensity is given by

$$I=f(x)|F|^2. \tag{4.5}$$

The primary extinction coefficient $f(x)$ for the Laue case of electron diffraction from a parallel plate crystal is given by

$$f(x)=\sum_{n=0}^{\infty} J_{2n+1}(2x)/x, \tag{4.6}$$

$$x=(\bar{\rho}\lambda/v)|F| \tag{4.7}$$

where $J_{2n+1}(x)$ is the Bessel function of the odd order and v the unit cell volume.

$$\bar{\rho}=\frac{H}{\sqrt{|\cos\theta_1\cdot\cos\theta_2|}},$$

where H is the thickness of the parallel plate crystal and θ_1, θ_2 are the angles between the normal of the crystal surface and directions of the primary, secondary wave, respectively. $\bar{\rho}$ can be regarded as the effective thickness of the crystal. The variation of $f(x)$ against x is shown in Fig. 4.

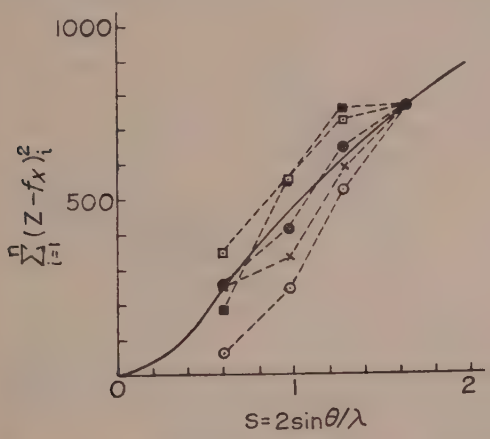

Fig. 3. Local averages of the intensity of Ni_3C. Open circles are the plots of the local averages $\langle s^4 I_0\rangle$ and filled squares are $\langle s^4 I_0^2\rangle$. Other plots are the local averages $\langle s^4 I_{cor}\rangle$: crosses correspond to $\bar{\rho}=190$ Å, filled circles to $\bar{\rho}=240$ Å and open squares to $\bar{\rho}=285$ Å.

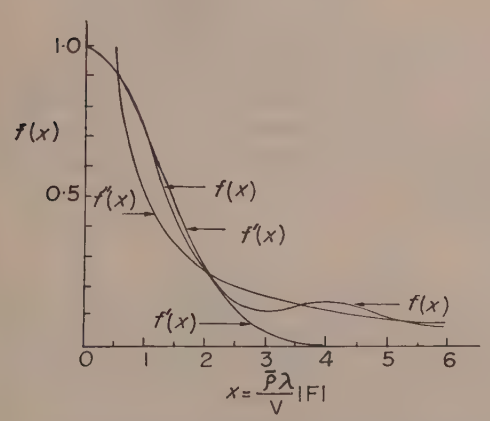

Fig. 4. Variation of the primary extinction coefficient $f(x)$ against x in the Laue case of electron diffraction. $f'(x)$ and $f''(x)$ represent approximate functions of $f(x)$.

The function $f(x)$ can be approximated by

$$f'(x)=\exp(-1/3\cdot x^2), \quad \text{for } x\lesssim 2.5 \tag{4.8}$$

and

$$f''(x)=1/(2x), \quad \text{for } x\gtrsim 2.0 \tag{4.9}$$

as shown in Fig. 4.

When the approximation (4.9) is allowed,

$$I=\frac{v}{2\bar{\rho}\lambda}|F|, \tag{4.10}$$

i.e. the intensity is proportional to $|F|$. If all reflections satisfy this condition, the local averages of the form $\langle s^4 I^2\rangle$ should coincide with the curve $\sum_{i=1}^{n}(Z-f_X)_i^2$. The filled squares in Fig. 3 representing the plots of the local averages $\langle s^4 I_0^2\rangle$ deviate from the curve, showing that the above condition is not satisfied.

§ 5. Modified Patterson Synthesis and Preliminary Fourier Synthesis

In order to obtain the values of the primary extinction coefficient $f(x)$, knowledges of the crystal structure and of the effective thickness of crystallites $\bar{\rho}$ are required at least approximately. In § 2, we proposed that the nickel atoms in Ni_3C take the c.p.h. arrangement. This assumption is verified at least approximately by the methods of modified Patterson synthesis and preliminary Fourier synthesis as follows: The intensity suffering the primary extinction can be expanded into the power series of $|F|^2$

$$I=|F|^2+\left\{-\frac{1}{3}(\bar{\rho}\lambda/v)^2\right\}|F|^4 + \left\{\frac{1}{20}(\bar{\rho}\lambda/v)^4\right\}|F|^6+\cdots. \tag{5.1}$$

Cowley[8] has shown that the peaks of heavy

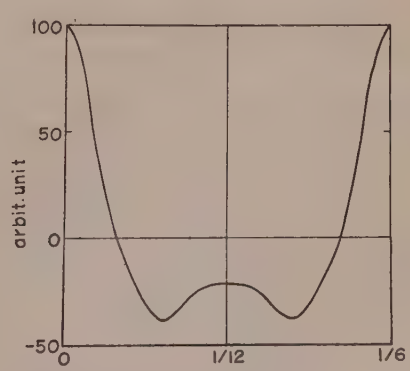

Fig. 5. One-dimensional Patterson function along the c-axis formed from I_0.

atoms in a Patterson diagram are sharpened without any shift in their positions when a power series of $|F|^2$ like (5.1) is used as the coefficient for synthesis. Fig. 5 illustrates the one-dimensional Patterson function along the c-axis obtained from the reflections $(000l)$. The high peaks at 0 and 1/6, and the low peak at 1/12 are considered to be the Patterson peaks corresponding to the layer distances between Ni and Ni, and between Ni and C, respectively. Fig. 6 shows a part of the

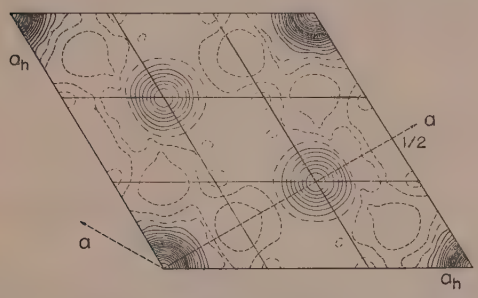

Fig. 6. Two-dimensional Patterson map formed from I_0. The map shows a part of the basal plane projection corresponding to Jacobson and Westgren's unit cell. The contours are drawn at arbitrary unit.

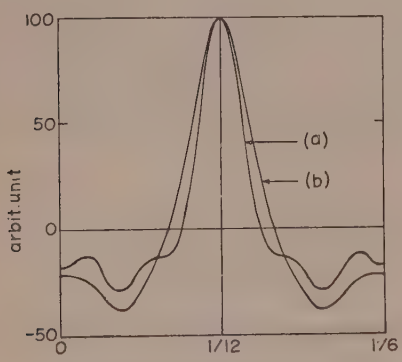

Fig. 7. One-dimensional Fourier series along the c-axis formed from (a) $\sqrt{I_0}$ and (b) I_0.

two-dimensional Patterson function formed by the reflection $(hki0)$ projected on the basal plane. The contours are drawn at arbitrary unit. The high peaks at positions (1/3, 0) and (1/3, 1/3) are considered to represent the interatomic distances between nickel atoms, verifying their c.p.h. arrangement.

Since $f_{Ni} \gg f_C$, signs of the structure amplitudes can be determined without ambiguity. However, magnitude of the structure amplitudes can not be obtained directly from the observed intensities, since the intensities are proportional to neither $|F|^2$ nor $|F|$ by the effect of primary extinction. Therefore, two kinds of preliminary Fourier syntheses, one by using $\sqrt{I_0}$ and the other by using I_0 as the magnitude of amplitudes, were tried. The curve (a) in Fig. 7, showing the one-dimensional Fourier series formed by $\sqrt{I_0(000l)}$, reveals a high peak at 1/12 corresponding to a nickel layer. In Fig. 8, the two-dimensional Fourier map formed by $\sqrt{I_0(hki0)}$, high peaks due to nickel atoms are clearly observed at the c.p.h. positions (1/3, 0) and (1/3, 1/3). However, in this map no peak corresponding to carbon atoms is observed.

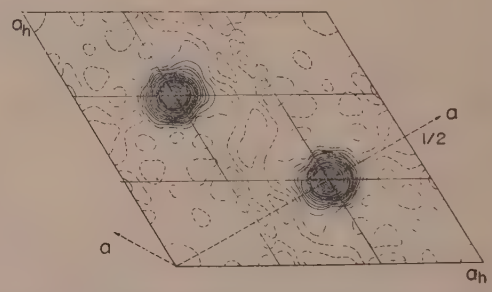

Fig. 8. Two-dimensional Fourier map formed from $\sqrt{I_0}$. The contours are drawn at arbitrary unit.

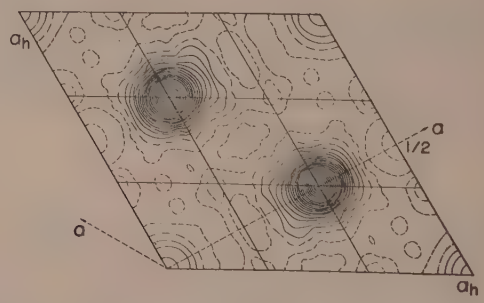

Fig. 9. Two-dimensional Fourier map formed from I_0. The contours are drawn at arbitrary unit.

The curve (b) in Fig. 7, and Fig. 9 are the one- and two-dimensional Fourier maps formed by $I_0(000l)$ and $I_0(hki0)$, respectively. In the former map the low peaks at the positions 0 and 1/6, and in the latter the low peaks at the positions (0, 0), (1/3, 2/3), (2/3, 1/3) and (1/3, 1/3) corresponding to the carbon positions are clearly appearing besides the high peaks due to the nickl atoms.

Although the above Patterson and Fourier syntheses are of a curde nature, the proposed structure of Ni_3C can be confirmed at least approximately by these trials. It is noteworthy that the use of I_0 rather than $\sqrt{I_0}$ as the magnitude of reflection amplitude gives better result in Fourier synthesis. This is due to the primary extinction which is quite strong in the present case.

§ 6. Refinement of Potential Fourier Map

Now, the refinement of Potential Fourier map will be carried out by correcting the primary extinction effect. Though the approximate structure of Ni_3C is already obtained, a difficulty arises concerning the estimation of the value $\bar{\rho}$ necessary for correcting the primary extinction effect. Though $\bar{\rho}$ is considered to be the same order of magnitude as the mean particle size ε[2], there is only little justification in putting $\bar{\rho}$ equal to ε, since the definitions are not identical, and, moreover, the determination of ε from the Debye rings is inaccurate especially when the mean particle size is larger than 100 Å as in the present case. The most appropriate values of $f(x)$ can be obtained by the following method based on the intensity statistics. The values of $f(x)$ are calculated for various values of $\bar{\rho}$ by assuming F for the approximate crystal structure, and the observed intensities are corrected by these values of $f(x)$ to $I_{cor}=f(x)I_0$. By comparing the plots of the local averages of the corrected intensities, $\langle s^4 I_{cor}\rangle$, with the curve $\sum_{i=1}^{n}(Z-f_X)_i^2$, the case showing the best fit is found out. Six trials for $\bar{\rho}=190$, 210, 230, 240, 250 and 285 Å were carried out and some of the plots of the local averages are shown in Fig. 3. The local averages for $\bar{\rho}=240$ Å gave the most satisfactory agreement with the curve $\sum_{i=1}^{n}(Z-f_X)_i^2$. The values of x, $f(x)$ and $\sqrt{I_{cor}}=|F_{cor}|$ for this case are tabulated in Table I. The agreement between $|F_{cor}|$ and $|F_c|$ is satisfactory. The reliability factor $R=\sum(||F_{cor}|-|F_c||)/\sum|F_{cor}|$ was improved to 15%.

Fig. 10 shows the two-dimensional Fourier map calculated from the corrected intensities. The contours are drawn at intervals of 0.5 volt per Å². The mean inner potential $V(0000)$, which is necessary for determining the level of the map was calculated by Tull's method[9]. It was 18.7 volts. The map shows clearly the peaks of carbon atoms at the reasonable positions. The heights of the carbon and nickel peaks are $V_C(0)=2.9$ volt/Å² and $V_{Ni}(0)=18.1$ volt/Å². They give the ratio $V_C(0)/V_{Ni}(0)=0.16$, while the calculated value utilizing Vainstejn's formula[10] is $V_0(0)/V_{Ni}(0)=(2/3)(Z_C/Z_{Ni})^{\alpha_5}=0.19$ taking $\alpha_5=0.75$,

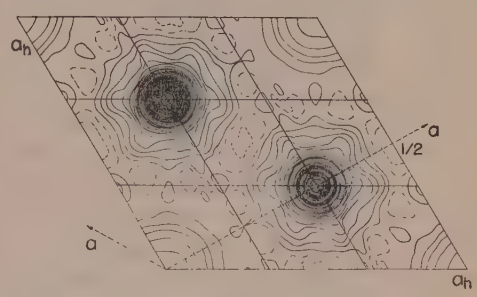

Fig. 10. Two-dimensional Fourier map formed from the final values of $\sqrt{I_{cor}}$. The contours are drawn at intervals of 0.5 VÅ^{-1}. The chain lines indicate zero level and the broken lines negative regions. Peak height: $V_{Ni}(0)=18.1$, $V_C(0)=2.9$.

where 2 and 3 are the numbers of overlapped carbon and nickel atoms on the projected plane, respectively. Both values agree approximately*.

§ 7. Crystal Structure of Ni_3C

1. *Description of the Structure*

The above result shows that the structure proposed in § 2 is appropriate for Ni_3C. Fig. 11 (a) shows the structure schematically, where open circles represent nickel atoms and filled circles, carbon atoms. Fig. 11 (b) shows the basal plane projection of the structure, where A and B represent nickel atoms and (C_1), (C_2) and (C_3), the carbon atoms. Nickel atoms occupy the c.p.h. positions and carbon atoms form a rhombohedral lattice occupying one-third of the octahedral interstices of nickel atoms. The structure can be represented by a structural formula $(C_1)A(C_2)B(C_3)A(C_1)B(C_2)A(C_3)B(C_1)\cdots$, where ABAB$\cdots$ represents hexagonal layers of nickel atoms stacked with the c.p.h. sequence and $(C_1)(C_2((C_3)\cdots$, the hexagonal layers of

* The ratio $V_C(0)/V_{Ni}(0)$ in Fig. 9 of I_0-synthesis is 0.39.

carbon atoms stacked with the rhombohedral sequence. The octahedron formed by nickel atoms is deformed from the regular shape only slightly; six Ni-Ni bond-lengths in the basal plane are 2.628 Å and the other six bond-lengths 2.634 Å. The sequence of the carbon layers forms a rhombohedral lattice with the hexagonal lattice constants $a'=a$ and $c'=(1/2)c$.

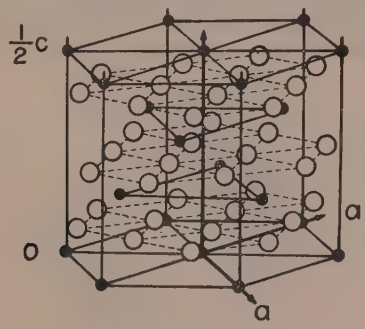

Fig. 11(a).

Fig. 11(b).

Fig. 11. Crystal structure of Ni_3C.
(a) Schematic representation. Figure shows a half of the unit cell. Open circles represent nickel atoms and filled circles, carbon atoms.
(b) Basal plane projection. Large circles represent nickel atoms (A and B) and small circles, carbon atoms (C_1, C_2, C_3). Jacobson and Westgren's unit cell is indicated by dotted lines.

2. *Stacking of Carbon Layers*

As mentioned in § 2 the intensity regions of the *s*-reflections for which $h-k \neq 3n$ elongate along c^*-axis, while those of the *M*-reflections for which $h-k=3n$ are sharp. The observed half-breadths of $(01\bar{1}2)$ and $(10\bar{1}4)$ rings are tabulated in Table II. The calculation of structure amplitudes shows that the *s*-reflections are exclusively due to the carbon atoms and that their breadth depends on the sequence of carbon layers, while that of the *M*-reflections does not. The above observation, therefore, suggests that the $(C_1)(C_2)(C_3)\cdots$ stacking of carbon layers in the matrix of nickl lattice ABAB$\cdots$ has a certain disorder.

According to Wilson's theory[11] the probability $\alpha(\ll 1)$ of the mistakes in the rhombohedral stacking order and the half-width, σ, in l' $(=1/2\cdot l)$ are related by

$$\alpha=2\sigma\,.$$

The observed widths given in Table II correspond to $\alpha \sim 0.5$. This value, however, is inconsistent with the assumption of the theory that α is small. The situation could not be improved even by the more refined theory taking account of longer 'Reichweite'[12].

On the other hand, the elongation of the *s*-reflections can be explained fairly well by a size-effect due to mistakes which take place, on the average, at a regular interval. The observed half-width gives 28 Å (13 carbon layers) for the average value of the interval between the mistakes, δ. It may be worth mentioning that the half-breadth of the *s*-reflections did not change appreciably up to the decomposition temperature of Ni_3C (Part I, Photo. 7).

§ 8. Discussion

In spite of the optimistic view of Pinsker

Table II.

hkil	β (half-breadth of Debye ring)	σ (half-width in $l'=\frac{1}{2}l$)	δ (interval between mistakes (Å))	α (probability of mistakes assuming Wilson's theory)
$01\bar{1}2$	1.1×10^{-3}	0.26	25	0.53
$10\bar{1}4$	1.5×10^{-3}	0.21	31	0.41
mean		0.24	28	0.47

and Jamzin[13] concerning the primary extinction in electron diffraction, the result of the present paper shows that the effect is very significant in practical samples and that the positions of light atoms can not be determined without an appropriate correction of the effect.

Though in the present paper the correction was carried out by assuming an approximate structure, this is not essential. When the approximate structure is unknown, the following procedure can be adopted: By the application of the intensity statistics at a range of larger s-values where the primary extinction is insignificant, we can obtain the absolute scale of intensity. The effective thickness of crystallites are approximately put equal to the mean particle size. These values can be used as starting values of $|F|$ and ρ required for correcting the primary extinction effect. The Fourier map synthesized from the corrected intensities will give the approximate atomic positions. Utilizing this knowledge the values of $f(x)$, therefore, I_0 are recorrected. Then, by the application of intensity statistics for these corrected intensities $\bar{\rho}$ is corrected. Repeating the above procedure the structure analysis can be performed successively until all the plots of the local averages coincide with the curve $\sum_{i=1}^{n}(Z-f_N)_i^2$. By this procedure the atomic positions and, at the same time, the effective thickness of crystallites can be determined. This method can be applied also to X-ray diffraction, in principle.

In the present structure analysis, the temperature effect was not taken into consideration. However, the Debye temperature of nickel carbide is considered to be higher than that of nickel metal. The temperature effect will not give an appreciable influence on the above analysis. It influences the plots of the local averages oppositely to that of the primary extinction.

The merit of applying the intensity statistics to detect the primary extinction and to justify its correction is that they can be done apart from knowledges of a relevant crystal structure. Concerning its application the following comments may be worth mentioning: In the case of nickel carbide, the M-reflections are sharp and strong and are considered as being subjected to a considerable effect of primary extinction, while the s-reflections are weak and broad and are considered as being free from the effect. Therefore, the local averages $\langle s^4 I_0 \rangle$ were taken only over the M-reflections and, since the M-reflections are interpreted by the Jacobson and Westgren's structure, they were compared with the curve $\sum_{i=1}^{n}(Z-f_X)_i^2 = 2(Z-f_X)^2_{Ni} + 2/3\cdot(Z-f_X)^2_C$, where 2 and 2/3 are the numbers of nickel and carbon atoms in the unit cell, respectively. By this procedure the primary extinction was clearly detected. In the intensity statistics to detect the primary extinction, it is preferable to take the local averages only over reflections subjecting to the primary extinction. In the electron diffraction study of crytals containing heavy and light atoms, we often encounter the situation that a super-lattice formed by a particular distribution of light atoms giving only weak super-lattice reflections. The above remarks are appropriate for such cases, in general.

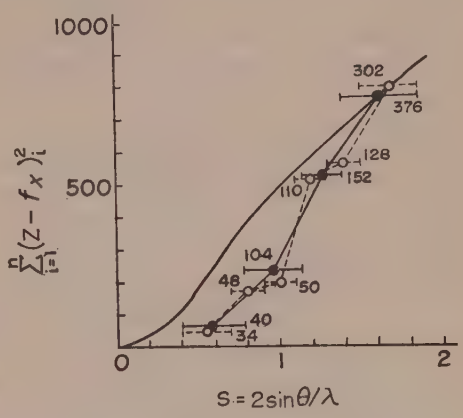

Fig. 12. Change of the local averages $\langle s^4 I_0 \rangle$ by different averaging ranges. Horizontal bars attached to the plots indicate the averaging ranges and numbers represent the numbers of reciprocal-lattice points in the ranges.

Since in the intensity statistics the random distribution of atoms in a unit cell is assumed, an objection might arise against its application to a simple structure such as nickel carbide. However, the essential requirement in the intensity statistics is that the values of the geometrical structure amplitudes are random in an averaging s-range. An important point of the method is

to find out proper ranges of the local averages so that the plots of $\langle s^4 I_0 \rangle$ give a smooth curve. For example, in Fig. 12 the plots of the local averages represented by open circles do not form a smooth curve owing to the inappropriate choice of the averaging ranges. However, when the averaging ranges are changed appropriately, plots of $\langle s^4 I_0 \rangle$ from the same data give a smooth curve as represented by the filled circles in Fig. 12. Refinement of the averaging ranges should be done successively with the correction of I_0.

Acknowledgement

The author wishes to express his hearty thanks to Professors S. Miyake, G. Honjo and S. Oketani for their valuable discussions and helpful advices. This work was supported by a grant in Aid for Fundamental Scientific Research from the Ministry of Education.

References

1) S. Nagakura: J. Phys. Soc. Japan **12** (1957) 482.
2) G. Honjo and N. Kitamura: Acta Cryst. **10** (1957) 533.
3) S. Nagakura: Acta Cryst. 10 (1957) 601.
4) A. J. C. Wilson: Acta Cryst. 2 (1949) 318.
5) M. Blackman: Proc. Roy. Soc. **A 175** (1939) 68; I. Waller: Ann. d. Physik **79** (1926) 261; W. H. Zachariasen; *Theory of X-ray Diffraction in Crystals*, Wiley and Sons, New York. (1945).
6) J. Karle and I. L. Karle: J. Chem. Phys. **17** (1949) 1025; *ibid.* **18** (1950) 963.
7) B. Jacobson and A. Westgren: ZS. f. phys. Chem. **B 20** (1933) 361.
8) J. M. Cowley: Acta Cryst. **9** (1956) 397.
9) V. F. D. Tull: Proc. Roy. Soc. **A 206** (1951) 232.
10) B. K. Vainstejn: *Strukturnaja Elektronografija*, Moscow, Akademii Nauk, SSSR, (1956).
11) A. J. C. Wilson: Proc. Roy. Soc. **A 180** (1942) 277.
12) H. Jagodzinski: Acta Cryst. **2** (1949) 201, J. Kakinoki and Y. Komura: J. Phys. Spc. Japan **7** (1952) 30; M. S. Paterson: J. Appl. Phys. **23** (1952) 805.
13) Z. G. Pinsker: *Diffraktsija Elektronov*, Moscow, Akademii, Nauk, SSSR, (1949); I. I. Jamzin: Trudy Inst. Krist. Akad. Nauk SSSR **5** (1949) 69.

JOURNAL OF THE PHYSICAL SOCIETY OF JAPAN Vol. 13, No. 9, SEPTEMBER, 1958

Electron Diffraction Study of Evaporated Face-centered Cubic Crystallites

By Hidetake MORIMOTO

Physical Institute, Nagoya University, Nagoya, Japan

(Received June 7, 1958)

Germer and White (Phys. Rev. **60** (1941) 447) found that thin evaporated films of face-centered cubic metals produce electron diffraction patterns with anomalous intensities. Kimoto (J. Phys. Soc. Japan **8** (1953) 762) studied the anomaly by a trial method and attributed it to stacking faults in crystallites. By the radial distribution analysis the present author confirmed Kimoto's conclusion.

Intensities of diffraction patterns from evaporated silver were accurately measured by the sector-microphotometer method and they were turned into radial distribution function. These functions reveal anomalous peaks caused by stacking faults. After a specimen is annealed at 350°C for 3.5 hrs., although crystallites do not grow remarkably, these peaks disappear. The amplitude of thermal vibration is found to be 0.15 ± 0.02Å which agrees well with that for massive silver crystal. The narrowing of the first neighbor peak is found and is attributed to the correlative thermal vibration.

Gold shows the same anomaly as is observed for silver, but aluminum shows no anomaly. These facts are in accordance with the value of stacking-fault energy.

§ 1. Introduction

Germer and White[1] reported that thin evaporated films of face-centered cubic metals produce electron diffraction patterns with anomalous intensities. The intensity of (200) reflection is especially weak compared with the normal intensity. They tried to explain the anomaly by attributing it to the small size of crystal, but their explanation was not sufficient.

Kimoto[2] studied the same phenomenon for silver by using an advanced experimental technique. He confirmed the same anomaly as reported by Germer and White and, moreover, found a slight peak shift of (200) reflection. He explained these anomalies by attributing them to stacking faults[3] in crystallites. Since, however, he used a trial method, it is desirable that a direct Fourier analysis be carried out to complete the diffraction study for evaporated crystallites. In this method, the diffracted intensity is accurately measured by the sector-microphotometer[4] method and the measured intensity is turned by Fourier transformation into the radial distribution function (RDF) which directly indicates the atomic arrangement.

Since the stacking faults produce only a slight modification of the atomic arrangement, we carried out the experiment and analysis with great care, estimating errors at every stage. For specimens without annealing, RDFs always showed peaks corresponding to the anomalous neighbors caused by stacking faults. These anomalous peaks became lower as the crystal size increased. When the specimen was treated at 350°C for 3.5 hrs., although crystallites did not grow remarkably, the anomalous peaks disappeared.

From the breadth of peaks in RDF the amplitude of thermal vibration is calculated to be 0.15 ± 0.02Å. This value agrees well with the value for massive silver crystal, 0.16Å[5]. Through a detailed analysis of RDF, we found that the peak corresponding to the nearest neighbor was a little narrower than the other peaks. This narrowing may be attributed to the correlative thermal vibration in crystallites.

While we were carrying out our analysis, much progress was made in the studies of the stacking faults. Paterson[6] formulated the intensity of X-ray diffraction patterns of f.c.c. crystals with stacking faults. The peak shift of (200) reflection found by Kimoto[2] qualititatively agrees with this theory. Following Paterson's theory, Nimura[7] studied the very

slight peak shifts in electron diffraction patterns from evaporated crystallites of gold and silver and found that they were in accordance with the existence of stacking faults, while Rymer[8] found that the peak shifts could be explained also by attributing them to the strain due to sessile dislocations in crystallites. Based on the peak shifts in X-ray diffraction patterns, several authors[9),10),11)] also studied in detail stacking faults in cold-worked f.c.c. metals and concluded that the results agreed well with expected results from the stacking-fault energy.[12),13)]

Table I. Important data of examined specimens.

Specimen	Mean thickness	Base	Annealing	Fault probability	Crystal size	Ratio of breadth
Ag No. 1	3Å	Amorphous carbon	no	28±5%	18Å* (14Å)**	1.6
No. 2	〃	〃	200°C×3.5 hrs.	10	20 (16Å)	1.3
No. 3	〃	〃	350°C×3.5 hrs.	0	22 (18Å)	1.1
No. 4	5	Formvar	no	23	20 (16Å)	1.5
No. 5	10	〃	no	14	22 (18Å)	1.5
Au	10	〃	no		22	1.5
Al	20	〃	no		22	1.1

* Estimated by RDF analysis.
** Estimated by Scherrer formula using (111) breadth.

§ 2. Experimental

Experimental procedure in the present work was similar to that used by Kimoto[2]. By the vacuum evaporation method, silver of mean thickness 3~10Å was deposited on either Formvar or amorphous carbon film of about 100Å thick. The thickness of silver was estimated from the mass of silver before evaporation. The deposited silver does not form a uniform film but it coagulates into minute crystallites. Five silver specimens were prepared: Nos. 1 and 3 were deposited simultaneously. Specimen No. 1 was annealed after the diffraction examination and it was then denoted as No. 2. The diffraction pattern of No. 3 was taken after it had been annealed. The annealing was carried out *in vacuo* at about 1×10^{-3} mmHg. In addition to five silver specimens, one gold and one aluminium specimen were also prepared by vacuum evaporation. Important data of specimens are given in Table I.

Electron diffraction transmission photographs of these specimens were taken by a camera provided with a rotating sector[14]. The sector was of the type $\vartheta=\text{const.}\times\rho$, where ϑ was the angle of aperture, ρ the radius, and the constant was 10 deg/mm. The specimen-to-

Fig. 1. Electron diffraction pattern of evaporated silver (Sp. No. 4) with two intensity scales.

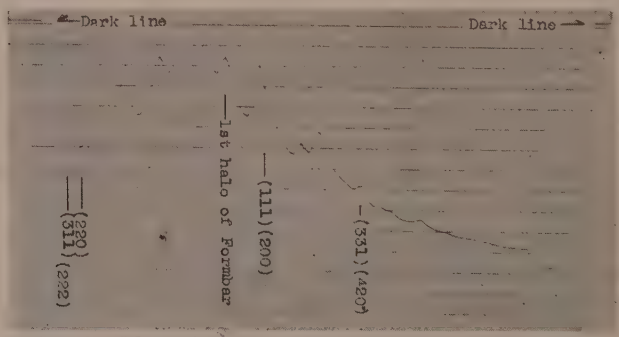

Fig. 2. Microphotometer record of Fig. 1 (Sp. No. 4).

plate distance of the camera was 24 cm for the large angle scattering and 45 cm for the small angle scattering. The accelerating voltage was about 40 kv. An example of diffraction patterns is reproduced in Fig. 1. The darkness of photographic plates was measured by Riken B-type microphotometer improved so that a plate could be rotated about the center of diffraction rings[14]. The rotation is effective to obtain smooth microphotometer records, eliminating noises due to photographic grains. Fig. 2 is an example of photometer records.

In all procedure of photographing and microphotometering, we have taken care to avoid the distortion of line profile. The incident spot of electron beam on the plate was 0.1 mm in diameter which is so small that the spot size can be neglected in the analysis of intensity profiles. The position of the sector was adjusted so that its center was within 0.1 mm of the incident beam. The error of the centering δ introduces only an error of order $(\delta/\rho)^2$ into the diffraction intensity at the position ρ from the incident beam*.

The stray scattering of the incident beam was almost stopped by two slits and by the specimen holder. The residual stray scattering was very small, the value of which was of the same order as the inelastic scattering in Fig. 3a.

In the microphotometry, the area of irradiation on the photographic plate was 0.1 mm in radial direction and 1 mm in tangential direction of Debye rings. The rotating plate was adjusted so that the deviation of the center of rings from the center of rotation was less than 0.1 mm. Thus the broadening and the shift of peaks in the photometer record were avoided. The deflection of electrometer string of the microphotometer was calibrated each time by applying known voltages. The electrometer and its circuits were adjusted so that the time lag was negligibly small.

Photographic density-exposure relationship, i.e. D–E characteristic curve, was determined for every plate by recording the electron intensity scale on the same plate (Fig. 1). The scale was made according to the method previously reported by Cowley[15]. We used Japanese plates "Fuji Process Hard" and developed them by D76d at 20±0.5°C for 10 minutes. The D–E characteristic curves obtained by Cowley's method were in agreement with each other within 3% for $D<0.8$, provided the emulsion number of plates was the same. Sometimes, we also determined D–E curve by Bartell-Brockway's method[16]. In our experiment, this method also showed D–E curves having 3% fluctuations for $D<0.8$. The results obtained by these two methods were in agreement within 3%.

The observed intensity is the sum of elastic scattering (I) from the evaporated metal, inelastic scattering (I_i) from the metal, and scattering (I_b) from the supporting film. We assumed the total intensity I_t to be given by $I_t=I+I_i+I_b$, which implies that the multiple scattering in specimen is negligible. This assumption is adequate because the film is thin. To obtain the intensity I (Fig. 3b), we subtracted I_i+I_b from the total intensity curve I_t (Fig. 3a). Intensity curve I_b (Fig. 3a) was obtained from a supporting film bare of metal and was normalized following Kimoto's pro-

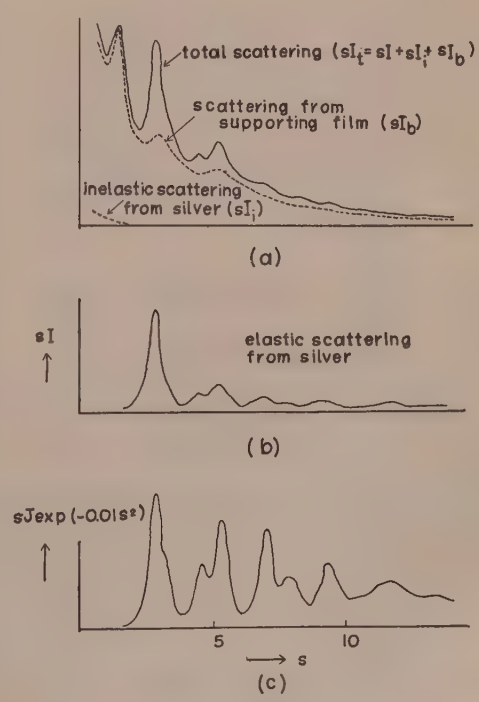

Fig. 3. Intensity profiles (Sp. No. 4).

* When the center of sector deviates from the incident beam by δ, through the sector action the intensity at the position ρ from the incident beam is multiplied by $|\rho-\delta|$, but not $|\rho|=\rho$. In the rotating-plate microphotometering, this error becomes

$$\frac{1}{2\pi}\int_0^{2\pi}\left(\frac{|\rho-\delta|}{|\rho|}-1\right)d\omega \sim O(\delta^2/\rho^2)\,.$$

cedure[2]. Intensity curve I_i (Fig. 3a) was obtained by Bewilogua's formula[17] which gives the ratio of I_i to the atomic part of the elastic scattering. Errors introduced in this procedure are difficult to estimate. Since, however, they have to be a smooth function of scattering angle, they have little influence on the radial distribution analysis (Sec. 6b).

To estimate the accidental error which arose through all procedures, three pairs of diffraction photographs were taken for specimen No. 4. Intensity was measured independently for each pair. The error in the modified intensity (Eq. (2)) was less than 5% of the (111) peak.

§ 3. Intensity Profiles

In Fig. 3 the anomalously diffuse (200) reflection such as observed by Germer-White[1] and Kimoto[2] is seen. In Fig. 4 profiles of combined (111) and (200) reflections are shown for all specimens. By an annealing, (200) reflection becomes normal. Gold also shows the anomaly, but aluminum shows no anomaly.

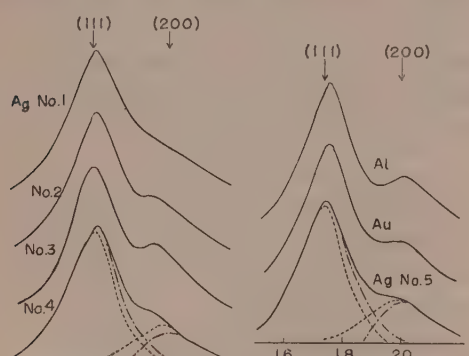

Fig. 4. Intensity profiles of combined (111) and (200) reflections.
Abscissa: $a_0/d=\sqrt{h^2+k^2+l^2}$.

As a measure of anomaly, ratio of (200) half breadth to (111) half breadth is given in Table I.

Germer-White and Kimoto reported that the integrated intensity of (200) reflection was anomalously weak. They separated (200) from (111) by assuming that the peak of the combined (200) and (111) reflection is the peak of (111). According to their method of separation, (200) peak becomes asymmetric as shown by broken curves in Fig. 4. On the other hand, if we assume (111) and (200) are both symmetric, separated (200) reflection is not anomalously weak as shown by dotted curves in Fig. 4. The difference is caused by the different ways of separating two peaks. Based upon his result, Kimoto considered that the anomaly cannot be explained by the external shape effect. According to our result, however, there is a possibility that the anomaly can be explained by the shape effect. Therefore, radial distribution analysis is indispensable to prove the existence of stacking faults in the crystallites.

§ 4. Radial Distribution Analysis

Diffracted intensity from monatomic crystals is given by James[18], taking into account the effect of thermal vibration. If the vibration of each atom is independent, intensity of Debye rings is given by

$$I(s)=|E(s)|^2\left\{N+N\cdot\exp\left(-\frac{\overline{u^2}}{3}s^2\right)\sum_i N_i\frac{\sin sr_i}{sr_i}\right\} \tag{1}$$

where

$$s=4\pi\sin\frac{\theta}{2}\Big/\lambda$$

and $E(s)$ is the atomic scattering factor for electrons, N the total number of atoms, $\overline{u^2}$ the mean-square amplitude of atoms. r_i and N_i indicate, respectively, the interatomic distance and the number of ith neighbors. In Eq. (1) the first term is the atomic scattering and the second is the so-called molecular scattering. We define modified intensity $J(s)$ by

$$J(s)=I(s)/N|E(s)|^2 \tag{2}$$

and multiply it by a proper artificial temperature factor $\exp(-b^2s^2)$. Then RDF is calculated by

$$D_\infty(r)=\frac{4}{\sqrt{\pi}}\int_0^\infty sJ(s)\cdot\exp(-b^2s^2)\cdot\sin sr\cdot ds\,. \tag{3}$$

Substituting Eqs. (1) and (2) into Eq. (3), we obtain

$$D_\infty(r)=D_{1\infty}(r)+D_{2\infty}(r) \tag{4}$$

where

$$D_{1\infty}(r)=\frac{4}{\sqrt{\pi}}\int_0^\infty s\cdot\exp(-b^2s^2)\cdot\sin sr\cdot ds=\frac{r}{b^3}(-r^2/4b^2) \tag{4a}$$

$$D_{2\infty}(r)=\frac{4}{\sqrt{\pi}}\sum_i\frac{N_i}{r_i}\int_0^\infty\exp(-\beta^2s^2)\cdot\sin sr_i\cdot\sin sr\cdot ds$$

$$=\sum_i\frac{N_i}{r_i\beta}\{\exp[-(r-r_i)^2/4\beta^2]-\exp[-(r+r_i)^2/4\beta^2]\} \tag{4b}$$

$$\beta^2=\frac{\overline{u^2}}{3}+b^2\,. \tag{4c}$$

Here, $D_{1\infty}$ gives the peak at the origin corresponding to atoms themselves and $D_{2\infty}$ peaks corresponding to neighbor atoms. Since Eq. (4) holds only for positive values of r, the effect of $\exp[-(r+r_i)^2/4\beta^2]$ is negligible and thus the ith term in the summation of $D_{2\infty}$ represents a Gaussian peak corresponding to the ith neighbor. When $D_{2\infty}$ is separated into peaks, the position and the height of the ith peak give the distance r_i and the number N_i of the ith neighbors, respectively. According to Eq. (4b), the breadth 4β of each peak is equal and gives the amplitude of thermal vibration, $\sqrt{\overline{u^2}}$.

If, however, the correlation is taken into account, the intensity formula (1) is modified as*

$$I(s)=|E(s)|^2\left[N+N\sum_i N_i\frac{\sin sr_i}{sr_i}\exp\left[-\frac{1}{3}\overline{u^2}\{1-\mathcal{E}(r_i)\}\right]\right] \tag{5}$$

where

$$\mathcal{E}(r)=\frac{1}{2\pi\tau_m r}\int_0^{2\pi\tau_m r}\frac{\sin u}{u}du\equiv\frac{\mathrm{Si}\,(2\pi\tau_m r)}{2\pi\tau_m r} \tag{5a}$$

$$2\pi\tau_m r=2\pi(3r^3/4a_0^3)\simeq 3.9r/a_0$$

where a_0 is the lattice constant.

Thus Eqs. (4b) and (4c) are modified as

$$D_{2\infty}=\sum_i\frac{N_i}{r_i\beta_i}\{\exp[-(r-r_i)^2/4\beta_i^2]-\exp[-(r+r_i)^2/4\beta_i^2]\} \tag{4b'}$$

$$\beta_i^2=\frac{\overline{u_i^2}}{3}+b^2 \tag{4c'}$$

where

$$\overline{u_i^2}=\overline{u^2}\{1-\mathcal{E}(r_i)\}\,. \tag{6}$$

Therefore, although each peak is again Gaussian, its breadth $4\beta_i$ should be different for different i. Since $\mathcal{E}(r)$ has a considerable value for small r (Fig. 5), the narrowing may occur for peaks corresponding to near neighbors. The apparent value of the amplitude $\sqrt{\overline{u_i^2}}$ gives $1-\frac{1}{2}\mathcal{E}_i$ times smaller value than the true value, $\sqrt{\overline{u^2}}$.

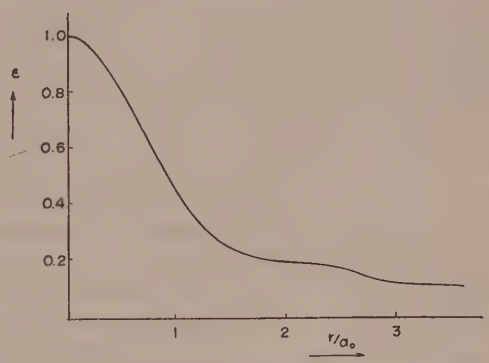

Fig. 5. Correction term $\varepsilon(r/a_0)$ for simple cubic lattice.

* This equation can be driven from Eq. (5.26) of James' book[18] by taking average over whole directions and by assuming the following conditions:

(1) Debye's approximation for specific heat problem.
(2) Longitudinal and transversal waves have the same velocity.
(3) Temperature is higher than Debye temperature.
(4) Simple cubic lattice.

In the practical analysis, RDF is calculated by an integration using relative value of modified intensity $kJ(s)$ within a finite integrating region extending from s_m to s_M and is given by

$$kD(r)=\frac{4}{\sqrt{\pi}}\int_{s_m}^{s_M} s\cdot kJ(s)\cdot\exp(-b^2s^2)\cdot\sin sr\cdot ds\ . \tag{7}$$

Substituting Eqs. (5) and (2) into Eq. (7) and calculating the above finite integral by the use of complex integral, we obtain, instead of Eq. (4), the expression including the finite region effect as follows:

$$kD(r)=kD_1(r)+kD_2(r)+kD_3(r) \tag{8}$$

where

$$D_1(r)=\frac{4}{\sqrt{\pi}}\int_0^{s_M} s\cdot\exp(-b^2s^2)\cdot\sin sr\cdot ds$$

$$=D_{1\infty}\Phi(\gamma_0)+\frac{2r}{\sqrt{\pi}\,b^3}\exp(-\gamma_0^2)\left[\Delta\left(\frac{r}{2b},\ \gamma_0\right)-\frac{b\sin s_M r}{r}\right] \tag{8a}$$

$$D_2(r)=D_{2\infty}\Phi(\gamma_i)+\frac{2}{\sqrt{\pi}}\sum_i\frac{N_i}{r_i\beta_i}\exp(-\gamma_i^2)\left[\Delta\left(\frac{r-r_i}{2\beta_i},\ \gamma_i\right)-\Delta\left(\frac{r+r_i}{2\beta_i},\ \gamma_i\right)\right] \tag{8b}$$

$$D_3(r)=-\frac{4}{\sqrt{\pi}}\int_0^{s_m} sJ(s)\cdot\exp(-b^2s^2)\cdot\sin srds \tag{8c}$$

and where

$$\gamma_0=bs_M\ ,\qquad \gamma_i=\beta_i s_M=s_M\sqrt{\frac{u_i^2}{3}+b^2}$$

$$\Delta(x,\gamma)=\exp(-x^2)\int_0^x\exp(t^2)\cdot\sin 2\gamma t\cdot dt \tag{9}$$

$$\Phi(\gamma)=\frac{2}{\sqrt{\pi}}\int_0^\gamma\exp(-t^2)\,dt\ .$$

Terms D_1 and D_2 in Eq. (9) correspond to $D_{1\infty}$ and $D_{2\infty}$ in Eq. (4), respectively. Term D_3 in Eq. (8) is caused by the neglecting of the small angle scattering and it forms a smooth background in RDF (Sec. 6e). Since $\Phi(\gamma)$ is almost unity under the usual condition (Table II), the first term in D_1 and that in D_2 are almost equal to $D_{1\infty}$ and $D_{2\infty}$, respectively. They represent true peaks. On the other hand, the second term in D_1 and that in D_2 give rippled ghosts caused by the termination error because $\Delta(x,\gamma)$ is a damped oscillating function. As can be seen from the factor $\exp(-\gamma^2)$, ghosts belonging to D_1 are reduced only by the artificial temperature factor while those belonging to D_2 are reduced by both natural and artificial temperature factors.

Table II.

γ	$\exp(-\gamma^2)$	$\Phi(\gamma)$	Δ_m	$\frac{2}{\sqrt{\pi}}\exp(-\gamma^2)\Delta_m$
1.0	0.38	0.84	0.41	0.18
1.5	0.11	0.97	0.39	0.05
1.7	0.06	0.98	0.37	0.025
1.9	0.03	0.993	0.33	0.011
2.0	0.02	0.995	0.32	0.007

For small x, values of function $\Delta(x,\gamma)$ can be calculated by numerical integration, and the first maximum Δ_m is given in Table II. For large x, it can be estimated by the asymptotic formula

$$\Delta(x,\gamma)\sim\frac{1}{2x}\sin 2\gamma x-\frac{\gamma}{2x^2}\cos 2\gamma x+O\left(\frac{1}{x^3}\right)\ . \tag{10}$$

Rippled ghosts belonging to a true Gaussian peak in D_2 are illustrated in Fig. 6. The height of ghost peaks is the order of $\frac{1}{2}\exp(-\gamma^2)$*

* As can be seen by the asymptototic formula Eq. (10), $\Delta\left(\frac{r+r_i}{2\beta_i},\ \gamma_i\right)$ is negligible compared with $\Delta\left(\frac{r-r_i}{2\beta_i},\ \gamma_i\right)$ in the neighborhood of peak r_i. Therefore the first maximum of the ghosts is

$$\frac{2}{\sqrt{\pi}}\Delta_m\exp(-\gamma^2)\ ,$$

where Δ_m is about 0.4 in the usual condition (Table II).

at the first peak and decreases in inverse proportion to $r-r_i$.

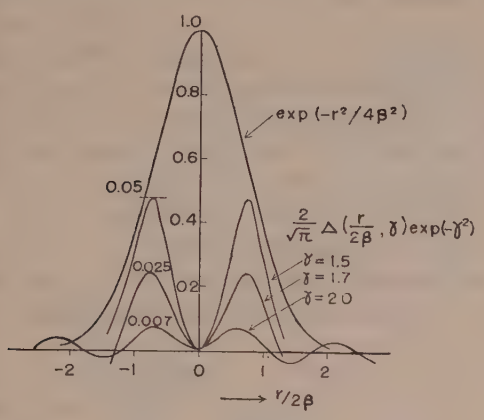

Fig. 6. Rippled ghost belonging to Gaussian peak. Peak height is normalized to unity and ghosts are shown magnified ten times.

§ 5. RDF of Silver Crystallites

(a) *Neighbors in normal and disordered f.c.c. crystals.*

In normal f.c.c. crystal of infinite size, each atom has 12 first neighbors, 6 second neighbors, etc. The interatomic distance r_i for the ith neighbor is given by

$$r_i=\frac{a_0}{\sqrt{2}}\sqrt{i}=d_0\sqrt{i} \tag{11}$$

where a_0 is the lattice constant and d_0 the distance of the nearest neighbor. Interatomic distances in h.c.p. crystal can also be given by Eq. (11). In this case, however, i does not stand for the ith neighbor; it takes fractional values as well as integers. If there are faults in stacking of (111) layers in f.c.c. crystal, i.e. if some stacking sequences of h.c.p. type are mixed in with sequences of f.c.c. type[3], besides the normal neighbors of f.c.c. type the anomalous neighbors with fractional i appear. Interatomic distances r_i for silver (a_0=4.08Å) and the numbers $N_{i\infty}$ for infinite-size f.c.c. and h.c.p. crystals are tabulated in Table III. From these data it can be expected that, even when there are stacking faults, the numbers of the first and the second normal neighbors remain unchanged but that those of higher orders decrease. The decreased numbers are compensated for by those of the anomalous neighbors.

For comparison with experimental RDF, numbers of neighbors N_i are also given for a few models, some of which are normal and some of which are disordered by stacking faults (Table III). These models are denoted as follows:

$[l\cdot m\times k]_n$: Parallelepiped model, normal.

The parallelepiped denoted by $[\ \ ]_n$ is formed by the three edges along [110], [10$\bar{1}$] and [01$\bar{1}$] directions. $l\cdot m$ respresents the number of atoms on the basal (111) net plane and k the number of stacking (111) net planes (Fig. 7a).

$[l\cdot m\times k]_t$: Twinned parallelepiped model, disordered by one twin fault (growth fault) at the middle of stacking.

Model denoted by $[\ \ ]_t$ consists of two parallelepipeds of similar size, one formed by [110], [10$\bar{1}$] and [01$\bar{1}$] directions and the other the mirror image across the twin plane (Fig. 7b).

Ratios N_i/r_i of $[5\cdot5\times8]_n$ and $[5\cdot5\times8]_t$ are shown in Figs. 7a and b. If stacking faults exist in evaporated silver, RDF should show peaks corresponding to the anomalous neigh-

Table III. Interatomic distance and number of neighbors.

i	r_i	$N_{i\infty}$		N_i of models				N_i of specimens				
		f.c.c.	h.c.p.	$[5\cdot5\times8]_n$	$[5\cdot5\times8]_t$	$[8\cdot3\times8]_n$	$[8\cdot3\times8]_t$	No. 1	No. 2	No. 3	No. 4	No. 5
1	2.88 Å	12	12	9.0	9.0	8.7	8.7	10.0	10.5	10.9	9.3	10.0
2	4.08	6	6	3.4	3.4	3.1	3.1	3.7	4.3	4.6	3.6	4.0
$2\frac{2}{3}$	4.71	—	2	—	0.3	—	0.3	1.0	0.4	—	0.8	0.6
3	5.00	24	18	13.1	12.6	11.9	11.4	11.2	15.0	16.8	12.2	13.7
$3\frac{2}{3}$	5.53	—	12	—	1.1	—	1.1	3.0	1.3	—	2.4	2.0
4	5.77	12	6	6.4	5.9	5.8	5.3	4.9	6.8	7.8	5.3	6.6
5	6.45	24	12	9.4	8.6	7.8	7.1	7.0	9.9	13.2	7.0	10.6
$5\frac{2}{3}$	6.86	—	12	—	0.8	—	0.7	2.3	0.7	—	1.9	1.4
6	7.06	8	6	3.0	2.7	2.5	2.2	2.0	3.1	3.8	2.5	3.1
$6\frac{1}{3}$	7.26	—	6	—	1.3	—	1.3	2.1	1.2	—	2.0	1.1
$6\frac{2}{3}$	7.45	—	12	—	0.8	—	0.7	1.6	0.6	—	1.5	0.8
7	7.64	48	24	17.8	15.1	14.3	12.0	13.0	18.4	23.2	14.4	18.4
α				0%	12.5%	0%	12.5%	28%	10%	0%	23%	14%

bors, as indicated by dotted lines in Fig. 7b. It is noteworthy that the peak at $r=5.53$Å corresponding to $i=3\frac{2}{3}$ must be the most conspicuous among anomalous peaks because it is expected to be much larger and easily separated from the normal peaks.

(b) *Calculation of RDF from observed intensity.*

RDFs were calculated for all five silver specimens. The modified intensity was first calculated by dividing the observed $I(s)$ by $|E(s)|^2$. We generally used $E(s)$ calculated by Hoerni and Ibers[19], $E_H(s)$. For the purpose of checking (Sec. 6c), we also used $E(s)$ calculated by Born approximation

$$E_B(s)=c\{Z-f(s)\}/s^2 ,$$

where Z is atomic number, c a numerical constant, and $f(s)$ atomic scattering factor for X-rays[20]. In the following sections, suffix H is usually omitted except when $E_H(s)$ and $E_B(s)$ are confused.

The modified intensity was multiplied by an artificial temperature factor $\exp(-0.01s^2)$ (Fig. 3c) and then, by using punched cards[21], the sine transformation was calculated in integrating region $1.4<s<14$, by approximating the integral in Eq. (7) by the summation

$$kD(r)=\text{const.}\times\sum_n nJ(n\Delta s)\cdot\exp[-b^2(n\Delta s)^2]\cdot\sin(n\Delta s\cdot r) . \quad (12)$$

The interval of the numerical integration was always $(10/\pi)\Delta s=0.2$. To estimate the error due to the finite interval, we carried out the summation by using a smaller interval $(10/\pi)\Delta s=0.1$ for a few specimens. We found that RDFs calculated with 0.1 interval and with 0.2 interval did not differ more than 1% in region $r<10$Å, proving that 0.2 interval was small enough. For example, RDF for specimen No. 4 thus calculated is shown in Fig. 7c. This is RDF calculated from the average of three independently measured intensities (Sec. 2).

(c) *General features of observed RDF.*

The observed RDF (Fig. 7c) shows several large peaks which have physical significance. Their positions are in good agreement with normal interatomic distances r_i. Their forms are nearly Gaussian with almost equal breadth, $4\beta\simeq0.53$Å. Since $b=0.1$Å, we obtain $\sqrt{\overline{u^2}}=0.15$Å; this is in agreement with the value for massive silver crystal[5]. Small anomalous peaks corresponding to stacking faults cannot be recognized at the first sight because normal peaks are broad.

Besides normal peaks, small rippled peaks are conspicuous near the origin. These peaks can be identified with the termination ghosts accompanying the peak at the origin i.e. the second term of Eq. (8a). It must also be noted that the observed RDF has a smooth background, as shown in Fig. 7c.

(d) *Detailed analysis of RDF.*

To detect anomalous peaks due to stacking faults, we analyzed the observed RDF as fol-

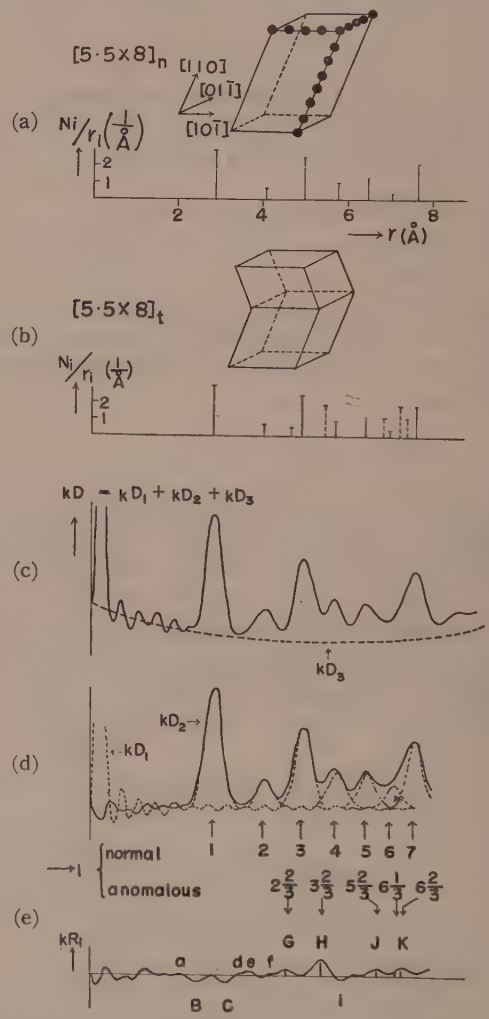

Fig. 7. Analysis of RDF (Sp. No. 4).
(a) and (b): Neighbors in normal and disordered model (Sec. 5a). Height of anomalous neighbors (dotted lines) is magnified ten times. (c), (d) and (e) are explained in Sec. 5c–d. Ordinates of (c), (d) and (e) are in the same scale.

lows. First, we drew an arbitrary smooth background of RDF (Fig. 7c) and subtracted it from the total RDF. Secondary, we further subtracted the peak at the origin including the accompanying ghosts, i.e. kD_1 in Eq. (8) (Fig. 7d). In this procedure, D_1 was calculated by a numerical integration of Eq. (8a) and the normalization factor k was determined so that the residual at the position of peak, $r=0.2$Å, vanished.

After the subtractions, RDF was separated into peaks under the following assumptions:

(i) Normal interatomic distances are given strictly by Eq. (11) with $a_0=4.08$Å;

(ii) All the peaks are Gaussian and have the same breadth $4\beta=0.53$Å;

(iii) The height of each peak is determined so that the residual of RDF vanishes at the position of the peak.

Finally the analyzed normal peaks (Fig. 7d) were subtracted from RDF. Thus we obtained a residual part of RDF, denoted by $kR_1(r)$. The residual for specimen No. 4 (Fig. 7e) shows many peaks and valleys.

For further discussion, we denote peaks and valleys for $r>2$Å by a, B, C, d etc., capital letters showing conspicuous peaks or valleys. The largest peak H coincides well with the expected anomalous neighbor $i=3\frac{2}{3}$. Other large peaks G and J also coincide well with the expected anomalous neighbors, $i=2\frac{2}{3}$ and $5\frac{2}{3}$, respectively; and peak K coincides with the composite of $i=6\frac{1}{3}$ and $6\frac{2}{3}$. On the other hand, large valleys B and C have no correspondence to the expected anomalous peaks. They are on both sides of the first normal peak at $r=2.88$Å and they may be caused by the narrowing of the first normal peak by the correlative thermal vibration (Sec. 4). To prove the results given above, we examine errors in detail in the next section.

§ 6. Examination of Errors

As described in the previous section, the residual was obtained from the observed RDF by subtracting (1) the arbitrarily drawn background, (2) the peak at the origin including accompanying termination ghosts, and (3) the normal peaks. Therefore, the residual may comprise errors of these terms as well as accidental and systematic errors of RDF. In this section we examine all kinds of errors. In Fig. 8 is a collection of errors and residuals calculated under various conditions. In Figs. 8a, b, c, we again show RDF of specimen No. 4 (Fig. 7c), N_i/r_i in $[5\cdot5\times8]_t$ (Fig. 7b), and residual R_1 of specimen No. 4 (Fig. 7e), respectively. In Table IV is tabulated height of peaks and valleys, together with the calculated anomalous peaks for $[5\cdot5\times8]_t$.

(a) *Accidental error of RDF.*

In order to estimate accidental error of RDF, we calculated RDF of specimen No. 4 from each independently measured intensity and from the average intensity. Fig. 7d shows $\Delta_i=D-D^i$ $(i=1, 2, 3)$, where D is the RDF derived from the mean intensity, and D^i is that from each measured intensity. We found that the difference is always smaller than dotted curves in Figs. 8c, h and k. As can be seen in Fig. 8c, peaks G, H, J and K, corresponding to the anomalous neighbors, are considerably larger than the error. Valleys B and C also exceed the margin of the error a little. All of the other peaks, *viz.* a, d, e, f, i and those in $r<2$Å, are below the accidental error and they may be ghosts. The order of the error at the position of each peak

Table IV. Peaks and valleys in residual.

Notation	r	Height							Error	Anomalous peaks for $[5\cdot5\times8]_t$		
		R_1	R_B	R_2	R_3	R_4	R_6	R_7		i	r	$N_i/0.13r_i$
a	2.1Å	0.7	0	0.3	1.6		0.7	0.7	1.5			
B	2.5	−1.7	−1.2	−2.1	−1.1		−0.6	−0.6	1.2			
C	3.2	−2.2	−1.4	−2.8	−1.3		−0.5	−0.5	1.0			
d	3.5	0.7	0.7	−0.3	1.8	R_1	0.9	0.9	0.9			
e	3.8	0.5	0	0	1.2			0.5	0.8			
f	4.2	0.6	0.3	0	0.7			0.6	0.7			
G	4.7	1.5	1.8	0.7	2.8	1.5		1.6	0.7	$2\frac{2}{3}$	4.71 Å	0.5
H	5.5	3.4	3.5	2.5	4.2	1.4	R_1	3.7	0.6	$3\frac{2}{3}$	5.53	1.5
i	5.8	−0.5	−0.6	−0.6	−0.6	−0.6		1.2	0.5			
J	6.8	2.0	1.5	1.5	2.5	2.0		3.1	0.5	$5\frac{2}{3}$	6.86	0.9
K	7.3	2.5	2.2	1.5	2.0	2.5		3.8	0.4	$6\frac{1}{3}$	7.26	1.3
										$6\frac{2}{3}$	7.45	0.8

is given in Table IV.

(b) *Errors of RDF caused by misestimating I_b+I_i and by the stray scattering.*

Observed intensity I may include errors caused by misestimating I_b+I_i and by the stray scattering which was always as smooth as I_i and of the same order as I_i (Sec. 2). Since either of these errors is a smooth function of scattering angle, Fourier transform of either one is considerable only for small r in RDF. If I_b is underestimated by 20%, an error as shown in Fig. 8e appears in RDF. If I_i is misestimated 10 times, an error of the order of 20% I_b-misestimation appears in

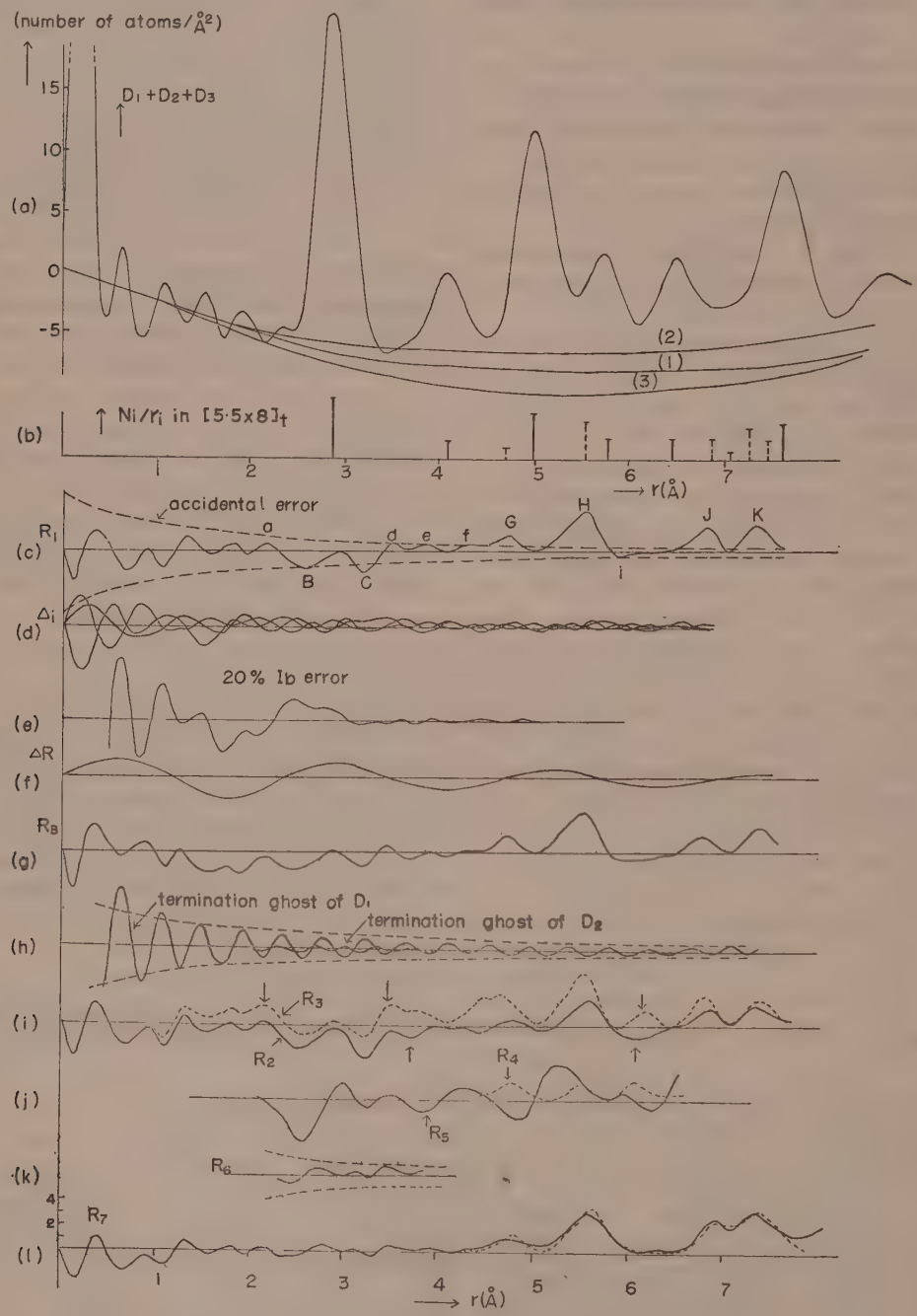

Fig. 8. Residuals and errors (Sp. No. 4).
The scale of the ordinate is the same for (a) and (c)–(1).

$r<2$Å of RDF. Since $I_i(s)$ is a function smoother than $I_b(s)$, in $r>2$Å the error from I_i was smaller than that from I_b. Thus, small peaks near the origin may be ghosts caused by these errors. Valleys B and C, however, may be too large to be attributed to these errors and peaks G, H, J and K cannot be ghosts caused by them. It is also noteworthy that these errors result in a considerable error in the normalization factor k (Table V).

(c) *Influence of different atomic factors on RDF.*

If we use $E_B(s)$ instead of $E_H(s)$ in the calculation of RDF (Sec. 5b), we obtain an RDF, say $(\mathrm{RDF})_B$, slightly different from that obtained before, $(\mathrm{RDF})_H$. As shown in Fig. 8f, the difference, $\Delta R=(\mathrm{RDF})_B-(\mathrm{RDF})_H$, is a damping wave* the amplitude of which is of the same order as the accidental error. When $(\mathrm{RDF})_B$ is analyzed according to the same conditions as those in Sec. 5d, the heights of normal peaks change considerably (Table V). In the obtained risidual R_B, however, large peaks and valleys B, C, H, J and K remain almost unchanged (Fig. 8g). Therefore, even when calculated atomic scattering factors contain an error of the order* (E_B-E_H), it has little bearing on the present discussions on the residual.

(d) *Termination ghosts.*

There are ghosts accompanying D_1 of Eq. (8a) and those accompanying D_2 of Eq. (8b). The latter is made small by the artificial temperature factor** while the former cannot be made small, particularly near the origin (Fig. 8h). For this reason, this ghost was subtracted as described in Sec. 5d. Since the order of magnitude of the former ghost is the same as that of the accidental error for $r>2$Å, the error in estimating this ghost, which mainly arises from the empirical determination of factor k, is negligible.

(e) *Ambiguity of drawing the background of RDF.*

In Sec. 5d, a smooth background was subtracted from RDF. This background can be attributed to the fact that the integral for the region between the origin and s_m was neglected, i.e. D_3 of Eq. (8c). In this region we have only the small angle scattering caused by the external shape of crystallites. The calculation using models proves that the small angle scattering is limited to a very small angle in our experiment and thus curve D_3 gives a smooth background, the periodicity of which is larger than 10Å. For this reason it is certain that the background is not wavy for $r<10$Å. In all other respects, the background is ambiguous. Therefore we tested the effect of different backgrounds. Three different backgrounds, curves (1), (2) and (3) (Fig. 8a), were drawn and the corresponding residuals R_1, R_2 and R_3 were calculated (Fig. 8c and i).

Through the variation in backgrounds, the residual is changed considerably. With the one exception of peak G, however, large peaks and valleys, B, C, H, J and K, are always conspicuous in R_1, R_2 and R_3. Therefore, they cannot be ghosts caused by an arbitrarily drawn background. In addition to these large peaks and valleys, there appear extra valleys in R_2 and extra peaks in R_3 as indicated by arrows in Fig. 8i. Since, however, these extra peaks and valleys appear as being dependent on the background and have no correspondence to any physical origin, they must be ghosts caused by the inadequate background. Therefore, we take background (1) as the most adequate one.

(f) *Three assumptions concerning the normal peaks.*

We further examine how R_1 is reformed by the modification of the three assumptions in Sec. 5d.

Position of normal peaks r_i. We found that if the value of r_4 is taken to be 1% smaller than the normal value, peak H in the residual becomes lower (R_4 in Fig. 8j). However, it

* In Fig. 11, $(E_H/E_B)^2$ of silver atom is nearly constant for $s>5$ and increases for $s<5$. Therefore, except for a constant factor, the main differrence between J_H and J_B, *viz.* modified intensity calculated by using $E_H(s)$ or $E_B(s)$, is that (111) intensity of J_B is larger than that of J_H by about 15%. Thus, the sine transform ΔR of $\Delta J=J_B-J_H$ is a wave with the periodicity $2\pi/s_{(111)}\simeq 2.3$Å having maxima at $r\simeq 0.6$, 2.9, 5.2, 7.5Å etc. and minima at $r\simeq 1.7$, 4.0, 6.3, 8.6Å etc.

** Since in our experiment $\gamma_i=\beta_i s_M\simeq 1.9$,

$$\frac{2}{\sqrt{\pi}}\Delta_m \exp(-\gamma_i^2)\simeq 0.01$$

(Table II). The effect of ghosts belonging to all peaks in D_2 can be estimated by the use of the asymptotic formula Eq. (10).

is impossible to eliminate peak H perfectly by changing the value of r_4. Moreover, it is physically impossible that r_4 decreases without changing other r_i. If all interatomic distances are 1% smaller than normal ones, residual has many large ghosts (R_5 in Fig. 8j). We found no variation in lattice parameter even for crystallite so small as 10Å diameter. This is in agreement with that recently reported by Rymer[22].

Breadth of normal peaks. According to Eqs. (4b′) and (4c′), the breadth of near neighbor peaks should be narrower than that of distant neighbor peaks. By taking a smaller breadth for the first peak $4\beta_1=0.49$Å, valleys B and C can be diminished below the margin of error (R_6 in Fig. 8k). Large peaks in the residual, however, cannot be eliminated by changing the breadth of normal peaks. Therefore, we regard valleys B and C as ghosts caused by the inadequate assumption on breadth. It may be adequate to change assumption (ii) as follows:

(ii′) All peaks except the first have the same breadth $4\beta=0.53$Å. The breadth of the first peak is reduced so that the ghosts in the neighborhood are diminished as small as possible.

Height of normal peaks. We have proved that the large peaks in R_1 cannot be attributed to any other origins than the anomalous neighbors caused by stacking faults. Therefore, we change assumption (iii) as follows:

(iii′) Height of normal peaks is determined so that the residual consists of anomalous peaks at expected positions and of Gaussian form with the same breadth as that of normal peaks.

The solid curve of Fig. 8l (R_7) shows the residual obtained by using the improved assumptions (i), (ii′) and (iii′). The dotted curve in this figure shows Gaussian peaks corresponding to the anomalous neighbors. The difference between the solid and the dotted curve is certainly smaller than the margin of error.

§ 7. Result of RDF Analysis

The refined analysis was carried out for five silver specimens given in Table I. The obtained residuals are shown by solid curves in Fig. 9. In this figure, the calculated anomalous peaks for model $[5\cdot5\times8]_t$ is also shown. Anomalous peaks are always remarkable for specimens before annealing (Nos. 1,

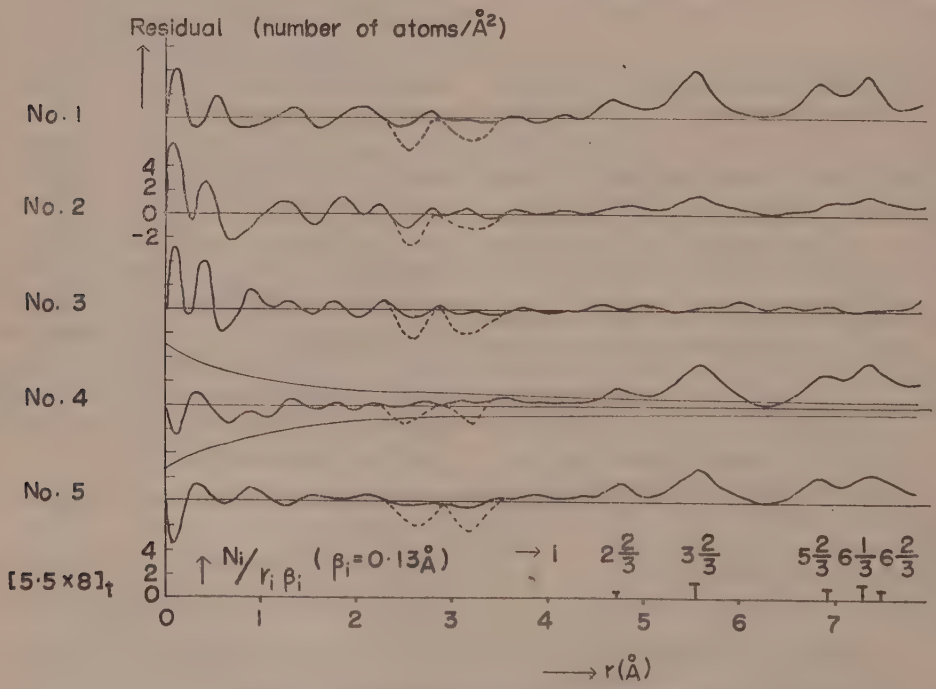

Fig. 9. Residuals for each silver specimen.

Dotted curves indicate residuals when the narrowing of the first normal peak is not taken into account.

4 and 5). After annealings, anomalous peaks become very small (No. 2) or vanish (No. 3). All the anomalous peaks correspond to those in the disordered model, i.e. large peak with index $i=3\frac{2}{3}$, middle size peaks with $i=5\frac{2}{3}$, $6\frac{1}{3}$ and $6\frac{2}{3}$, and small peak with $i=2\frac{2}{3}$. Besides these peaks, there is no ghost for $r>1$Å. Ghosts near the origin may be caused by the error mentioned in Sec. 6b. The dotted curves in Fig. 9 show the residuals calculated according to assumption (ii). They always have valleys on both sides of the first normal peak. It is evident that the first peak is narrower than the other peaks.

Table V. Result of RDF analysis of specimen No. 4.

i	$\sqrt{\overline{u_i^2}}$	$\Delta\sqrt{\overline{u_i^2}}$	Height $N_i/r_i\beta_i$	Error of height: Accidental error	Error of height: 2% I_b or I_i	ΔR
1	0.12Å	0.02Å	26.8	±1.1	0.1	+0.8
2		0.05	6.6	0.8		−0.6
$2\frac{2}{3}$			1.2	0.7		0
3		0.02	18.2	0.6		+0.4
$3\frac{2}{3}$			3.3	0.6		0
4		0.03	6.9	0.5		0
5	0.15	0.03	8.1	0.5	0	−0.4
$5\frac{2}{3}$			2.1	0.5		0
6		0.06	2.6	0.5		+0.2
$6\frac{1}{3}$			2.1	0.4		0
$6\frac{2}{3}$			1.5	0.4		0
7		0.02	14.1	0.4		+0.4
$\Delta k/k$				6%	7%	2%

Apparent value of amplitude of thermal vibration, $\sqrt{\overline{u_i^2}}$, can be calculated by Eq. (4c′) from the observed peak breadth. Apparent amplitudes together with peak heights are summarized in Table V. For all specimens, apparent amplitudes were the same as those for specimen No. 4. The third column of Table V gives the estimated error of the amplitude. Since the effect of changing the peak breadth is small for small peaks, the error of amplitude is large for small peaks, and *vice versa*. It is known that the true value of amplitude is 0.16Å for massive silver crystal[5]. Apparent values, however, are expected to be smaller than the true value by about 20% for the first neighbor, by about 10% for the second and the third neighbor, and by less than 10% for the further neighbors (Eq. (6) and Fig. 5). Therefore, within the experimental error, our result agrees with the theoretical estimation.

Absolute peak height, $N_i/r_i\beta_i$, can be calculated by dividing an observed peak height by the normalization factor k. Calculated values are given in column 4 of Table V. The same table also gives (1) the error of height caused by the accidental error (column 5); (2) the error by 2% misestimation of I_b or 100% of I_i (column 6), and (3) the difference of height determined by $(\mathrm{RDF})_B$ and that determined by $(\mathrm{RDF})_H$ (column 7). The errors of normalization factor k caused by origins (1), (2) and (3) are given in the lowest line of Table V.

Absolute number of neighbors N_i can be calculated from the absolute peak height $N_i/r_i\beta_i$ and the peak breadth $4\beta_i$. Thus obtained N_i as well as those calculated for models are given in Table III. Since both of the two disordered models given in this table have one fault in 8 layers, the fault probability is 1/8= 12.5%. For these models the ratio of $\sum'_{i\leq 7} N_i$ to $\sum_{i\leq 7} N_i$ is 0.073 while the ratio for specimen No. 4 is 0.14, where $\sum$ indicates the summation over all the normal and anomalous neighbors and $\sum'$ that over all the anomalous neighbors. Comparing these values, fault probability of No. 4 is estimated to be 23%. The probabilities estimated in this way for other specimens are given in Tables I and III.

In order to estimate crystal size, we plotted ratio $N_i/N_{i\infty}$ against i in Fig. 10, normalizing $N_1/N_{1\infty}$ to unity because the absolute value includes the error of k. In general, $N_i/N_{i\infty}$ decreases more steeply for smaller crystal. The slope of $N_i/N_{i\infty}$ for every specimen is slower than that for spherical model ($N=180$) and is steeper than that for ($N=54$). This implies that the equivalent diameters of specimens are between 18Å and 12Å. Compared with a crystal without stacking faults, a same size crystal with faults has smaller numbers of distant neighbors (Sec. 5a and Table III) and thus shows steeper $N_i/N_{i\infty}$ (Fig. 10b). If the numbers of anomalous neighbors are included, the effect of faults can be corrected in estimating the crystal size. The correction amounted to about 10% for specimen Nos. 1, 4 and 5. The corrected values are given in the parentheses of column 6 in Table I. Other figures in this column show crystal size estimated from (111) half breadth. For all specimens, the latter estimation gives a value larger than that estimated by the former. If, however, the mean value of breadths of (111)

and (200) reflections is used, both estimations give a similar value.

It is also noteworthy that ratio $N_i/N_{i\infty}$ depends on the crystal shape as shown in Fig. 10b. Since, however, a marked relation between $N_i/N_{i\infty}$ and shape could not be found and since the obtained $N_i/N_{i\infty}$ included a considerable error, it was difficult to obtain information on crystal shape.

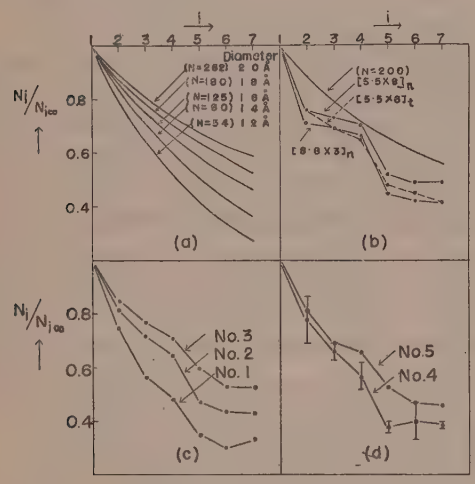

Fig. 10. Ratio $N_i/N_{i\infty}$.
(a) Spherical models.
(b) Models with different shapes and with different parameter values of faults.
(c) Specimens Nos. 1, 2 and 3.
(d) Specimens Nos. 4 and 5.

§ 8. Discussions

(a) *Stacking faults.*

We confirmed Kimoto's conclusion[2] on the existence of stacking faults in evaporated silver crystallites. We found the fault probability of the same order as that found by Kimoto. The faults decrease as crystal size becomes larger and they vanish when the crystallites are annealed.

We estimated fault probability (Table I) by assuming the faults were twin faults. If deformation faults are the case, fault probability turns out to be nearly half because deformation faults cause anomalous neighbors nearly twice those by twin faults. It is impossible to conclude from our RDF which of the faults is actual, because both faults cause a similar type of anomalous neighbors. However, it may be more reasonable to assume that twin faults are dominant in our case.

In the thermal equilibrium state, the probability of stacking faults is given by

$$\alpha=\exp(-F\Delta E/kT) \tag{13}$$

where F is the area of faulted layer and ΔE the energy of stacking fault per unit area. If we assume $\Delta E=20$ erg/cm^2 [12),13)] and $F=15\text{Å}\times15\text{Å}$, α turns out to be less than 0.01% at room temperature. If this were the case, the faults could not have been detected in the present experiment. If, however, we assume that the crystallites are quenched from 1,600°K, the evaporating temperature of silver, to room temperature, α turns out to be 13%. This probability is in agreement with experimental results in the order of magnitude. Since crystallites with high probability of stacking faults are in a meta-stable state at room temperature, faults disappear quickly by an annealing. For aluminum for which ΔE is about 100 erg/cm^2, faults cannot occur even in metastable state. This is in agreement with the experimental result that no anomalous intensity is observed for aluminum. Probability for silver and aluminum are given in Table VI.

Table VI. Fault probability expected from Eq. (13).

Metal	ΔE	F	T	α
Ag	20 (erg/cm^2)	10 Å × 10 Å	1600°K	40%
		15 × 15	300	0.2×10^{-4}
		15 × 15	1600	13%
		20 × 20	1600	3%
Al	100	15 × 15	300	$<10^{-20}$
		15 × 15	1600	0.5×10^{-4}

In Wagner's experiment[11] the crystal size in filings was of the order of 100Å, while in our experiment the crystal size was of the order of 15Å. The difference of annealing temperatures at which stacking faults disappear can be attributed to the difference of crystal sizes. Moreover, in Wagner's experiment the faults were deformation faults. The difference of annealing temperatures may also be due to the difference of energies for deformation and twin faults.

The peak shift such as observed by Nimura[7] and Rymer[8] can be explained by either of the following three: (1) Growth faults with about 20% probability[7], (2) deformation faults with about 2% probability[9], (3) strain caused by sessile dislocations[8]. In the present experiment, growth faults with about 20% was obtained for crystal size of about 15Å. There-

fore, explanation (1) seems to give too high probability because the crystallites used by Nimura and Rymer were a few ten Å in size. We cannot conclude which explanation is the most adequate. To throw light on this problem, analysis of line profile[9] may be useful.

(b) *Thermal vibration and strain in crystallites.*

It is emphasized that the observed amplitude of the thermal vibration for very small crystallites is in agreement with that for massive crystal.

On the other hand, Kimoto[2] had to introduce a frozen heat motion corresponding to 600°K; $\sqrt{\overline{u'^2}}=0.24$Å* in order to make the observed intensity agree with the calculated one. He calculated the intensity profile by using E_B in the region between (111) and (311) reflections, i.e. $s=2.67$ and $s=5.11$. By the introduction of frozen heat motion, the damping between (111) and (311) becomes steeper by

$$\exp\{\tfrac{1}{3}\overline{u'^2}[s^2_{(311)}-s^2_{(111)}]\}=0.70\ .$$

However, if E_H is used instead of E_B, the calculated intensity shows a steeper damping by

$$\left\{\frac{E_H(311)}{E_H(111)}\Big/\frac{E_B(311)}{E_B(111)}\right\}^2=0.85$$

(see Fig. 11). Therefore, the frozen heat motion may be partly due to an inadequate atomic factor. It may also be due to an inadequate background in the intensity curve[23]. In our analysis the same amplitude of thermal vibration was obtained independent of atomic factors. This is due to the fact that the region of s-value in our experiment is so large that $(E_H/E_B)^2$ cannot be expressed by an apparent temperature factor $\exp(-c^2s^2)$ (Fig. 11).

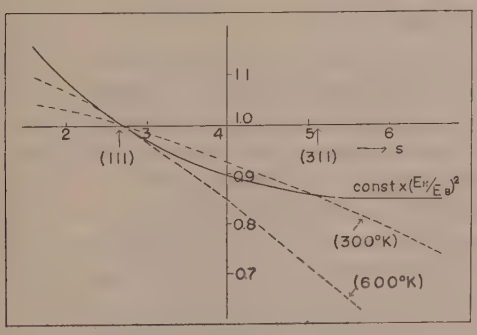

Fig. 11. Ratio $(E_H/E_B)^2$ and temperature factors.
Temperature factor for 300°K
$=\text{const.}\exp(-0.0085s^2)$
Temperature factor for 600°K
$=\text{const.}\exp(-0.0192s^2)$
All curves are normalized to unity at $s_{(111)}=2.76$.

* Kimoto's notation $\langle u^2\rangle_{\mathrm{Av}}$ equal $\frac{1}{3}\overline{u'^2}$.

In discussing the frozen heat motion, E_H seems better than E_B. However, it is difficult to conclude which is actually better, because (111) reflection is much stronger than other reflections and thus the photographic measurement is difficult. It must also be noted that for (111) reflections dynamical effect is not negligible even for fairly small crystallites[24]. The disagreement in data of (111) intensity[24,25,26] may be due to these causes.

It is interesting that the correlative effect of thermal vibrations was detected in RDF. This effect has often been observed in X-ray patterns of a single crystal as temperature diffuse scattering[18], but has not yet been observed in electron diffraction patterns of polycrystals.

We could not find the gradual increase of peak breadth in RDF. Similarly to liquid, highly distorted crystals give peak breadth which increases in proportion to the square root of distance[27]: Δ breadth$\sim\sqrt{r\cdot a_0}\times$strain. Since in our experiment the gradual increase of breadth is smaller than 0.02Å/4Å, we conclude that the strain is smaller than 0.01.

Acknowledgement

The author expresses his sincere appreciation to Professor Ryozi Uyeda and Dr. K. Kimoto for their constant encouragement and kind guidance throughout this work. He is indebted to Professor Y. Morino for his courtesy in loaning punched cards and to Dr. K. Kuchitsu for his immeasurable assistance in the calculation of Fourier transformation by punched cards. This experiment was suggested by Dr. K. Kimoto. The present investigation is supported in part by a Scientific Research Grant from the Ministry of Education.

References

1) L. H. Germer and A. H. White: Phys. Rev. **60** (1941) 447.
2) K. Kimoto: J. Phys. Soc. Japan **8** (1953) 762.
3) W. T. Read: *Dislocations in Crystals* pp. 92–95. McGraw-Hill, New York (1953).
4) I. L. Karle and J. Karle: J. Chem. Phys. **17** (1949) 1052.

J. Karle and I. L. Karle: J. Chem. Phys. **18** (1950) 957.
5) K. Lonsdale: Acta Cryst. **1** (1948) 142.
6) M. S. Paterson: J. Appl. Phys. **23** (1952) 805.
7) H. Nimura: J. Phys. Soc. Japan **10** (1955) 642.
8) T. B. Rymer: Proc. Phys. Soc. **A 235** (1956) 274.
9) B. E. Warren and E. P. Warekois: Acta Met. **3** (1955) 473.
10) F. R. L. Schoening and J. N. van Nierkerk: Acta Met. **3** (1955) 10.
11) C. N. J. Wagner: Acta Met. **5** (1957) 427, 477.
12) R. L. Fullman: J. Appl. Phys. **22** (1951) 448.
13) A. Seeger: *Defects in Crystalline Solids* (Report of the Bristol Conference, 1954) p. 328. Physical Society London (1955).
14) T. Ino: J. Phys. Soc. Japan **8** (1953) 92.
15) J. M. Cowley: Acta Cryst. **6** (1953) 516.
16) L. S. Bartell and L. O. Brockway: J. Appl. Phys. **24** (1953) 656.
17) L. Bewilogua: Physik. Z. **32** (1931) 740.
18) R. W. James: *The Optical Principles of the Diffraction of X-rays* Chap. I and V. G. Bell & Sons Ltd., London (1950).
19) J. A. Ibers and J. A. Hoerni: Acta Cryst. **7** (1954) 405.
20) *International Tables for the Determination of Crystal Structures* Vol. 2 (1939) p. 572.
21) P. A. Shaffer, Jr., V. Schomaker and L. Pauling: J. Chem. Phys. **14** (1946) 648, 659.
Y. Morino and K. Kuchitsu: X-rays **8** (1954) 37 (in Japanese).
22) T. B. Rymer: Nuouo Cimento **6** (1957) Supplemento p. 294.
23) B. E. Warren and B. L. Averbach: *Imperfections in Nearly Perfect Crystals* Chap. V. John Wiley, New York (1952).
24) S. Kuwabara: J. Phys. Soc. Japan **12** (1957) 637.
25) I. I. Yamzin: Trudy Inst. Krist. Akad. Nauk **5** (1949) 69.
26) S. Lennander: Ark. Fys. **8** (1954) 551.
27) J. Frenkel: *Kinetic Theory of Liquids* Chap. III. Oxford, Clarendon Press (1946).

JOURNAL OF THE PHYSICAL SOCIETY OF JAPAN Vol. 13, No. 9, SEPTEMBER, 1958

The Electron Distribution and the Location of the Bonded Hydrogen Atom in Crystals

By Yujiro TOMIIE

Department of Chemistry, Osaka University, Nakanoshima, Osaka, Japan

(Received May 27, 1958)

The electron distribution in a bonded hydrogen in crystals is investigated using mainly the VB method with the Gaussian approximation to the Slater wave functions. This approximation appears to be fairly good if the thermal vibration is considerable. In the present paper is studied the C–H bond as an example. It is concluded that the position of the maximum electron density around the proton is located more or less towards the heavier atom, and hence an apparent bond contraction in the X-ray analysis should occur. This seems to be in accord with experimental results. The apparent bond shortening increases and the peak density decreases with increase in the ionic character of the bond. For a constant value of the ionic character, the magnitude of the apparent bond shortening rapidly reaches a certain constant value when thermal vibration becomes large.

§ 1. Introduction

Since an ordinary atom other than hydrogen has nonbonded K shell electrons whose density is very sharply distributed and very high at the centre of the atom, the position of the maximum electron density in it will coincide with that of the nucleus. In the case of the hydrogen atom, however, the K shell electron is at the same time the valence electron and accordingly the electron distribution should

depend more strongly upon bonding. Recent advances in the technique of x-ray crystal structure analysis have enabled us to locate experimentally hydrogen atoms in crystals. For such purpose is required the so-called (F_o-F_c)-synthesis which means the difference between the observed and calculated distribution of the electron density, the contribution of the hydrogen atoms being omitted in the later. In Table I are given some of the values of the C–H distances determined by X-ray methods. Although the accuracy of the values is not always very high, it is revealed from Table I that many of the distances are more

Table I. The C–H bond distances determined by the X-ray method.

Substance	C–H				Ref.
Adenine. HCl	0.85	1.00			(1)
Salicylic acid	0.78	0.90	0.92	0.94	(2)
Ethylenethiourea*	0.87	0.87	0.87	0.99	(3)
Benzoic acid	0.86 (average)				(4)
Sodium tropolonate	1.03 (average)				(5)
Tropolone. HCl	1.05 (average)				(6)
s-Triazine*	1.00				(7)
α-Pyridone	0.95	0.98	1.02	1.18	(8)
Succinamide*	1.0				(9)
C_2H_2	1.05				(10)
Diformylhydrazine	0.94				(11)

* Three-dimensional investigation.

or less shorter than those spectroscopically accepted. This suggests that the maximum electron density around a proton is located somewhat towards the heavier atom. It is the present purpose to investigate theoretically whether the apparent bond shortening should occur in crystals. Since in general the C–H bond is considered not to be significantly affected by an external field, study on the C–H bond will be adequate for our purpose.

The distribution and the peak density of the electron in an *atomic* hydrogen with thermal vibration have been discussed theoretically by McDonald[12]. The present paper treats the case of a *bonded* hydrogen by using a simple valence bond or molecular orbital method, in which McWeeny's Gaussian approximation[13] to the Slater atomic orbitals is adopted. We may not expect very accurate electron distributions by using McWeeny's two-term Gaussian AO's. It appears, however, that if the influence of thermal vibration is considerable—and this is the case in most molecular crystals—the electron distribution is given fairly well by using such approximate AO's.

In our calculation the C–H bond vibration is not particularly considered. However, the bond vibration is usually not so large as the thermal vibration of the whole molecule in crystals. From the electron gas diffraction data of Morino et all[14], the temperature factor parameter B of the hydrogen atom due to a C–H bond vibration is estimated to be less than 0.5 Å relative to the carbon atom. This value is far smaller than that of the ordinary temperature factor parameter for the molecules in crystals. Therefore, we neglected the bond vibration as a first approximation. Also we consider only the case of the isotropic temperature factor for the molecule as a whole. However, this approximation will be sufficient to be compared with the experimental results as the accuracy of the experiments is not very high at present.

In the present paper are given first the general representations for the electron distribution of a bond by the use of both VB and MO method. Second are derived the mathematical results which give the distribution of the square of an AO, ϕ^2, and of the product of AO's $\phi_a\phi_b$, both of which are required in our procedure. Finally the application of these results to the bonded hydrogen in the C–H bond is given as an example, calculated values being compared with experimental ones.

§ 2. The Electron Density Distribution in a Bond.

Let Ψ be an approximate wave function for the system, built out of atomic orbitals ϕ_a and ϕ_b, using either molecular orbital or valence bond theory. The electron density is then twice that for just one electron, i.e. $2\int\Psi^2 d\tau$, the integral with respect to one electron, and we can write[15],

$$\rho=q_a\phi_a^2+q_b\phi_b^2+q_{ab}(\phi_a\phi_b/S_{ab}) , \qquad (1)$$

where q_a, q_b and q_{ab} are the numbers of electrons distributed according to the normalized density functions ϕ_a^2, ϕ_b^2 and $\phi_a\phi_b/S_{ab}$, S_{ab} being the overlap integral between the orbitals ϕ_a and ϕ_b. The quantities q_a, q_b and q_{ab} may be called atom and bond "charges"[15] or "populations"[16]: their values depend on the approximation used (MO, VB, etc.), but the

density always involves the same orbital and overlap charge distributions, ϕ_a^2, ϕ_b^2 and $\phi_a\phi_b/S_{ab}$.

We have given two approximations: (i) the MO approximation, in which MO's are given as

$$\Psi_j=\sum_r c_{rj}\phi_r\,, \qquad (2)$$

and (ii) the VB approximation, where

$$\Psi=N(\Psi_{\rm cov}+\lambda\Psi_{\rm ion}) \qquad (3)$$

and $\Psi_{\rm ion}$ describes both electrons on atom a, the more electronegative of the two atoms. λ, the degree of ionic character, is estimated in a later section. The populations are easily evaluated in each case, i.e.,

MO:

$$q_a=2\sum_j c_{aj}^2\,, \qquad (4a)$$

$$q_b=2\sum_j c_{bj}^2\,, \qquad (4b)$$

$$q_{ab}=4S_{ab}\sum_j c_{aj}c_{bj}\,, \qquad (4c)$$

$\sum$ being extended over all occuped orbitals,

VB:

$$q_a=2(N_c^2+\lambda^2+2\lambda S_{ab}N_c)/(1+\lambda^2+4\lambda S_{ab}N_c), \qquad (4d)$$

$$q_b=2N_c^2/(1+\lambda^2+4\lambda S_{ab}N_c)\,, \qquad (4e)$$

$$q_{ab}=4N_cS_{ab}(S_{ab}N_c+\lambda)/(1+\lambda^2+4\lambda S_{ab}N_c)\,, \qquad (4f)$$

where $N_c=2(1+S_{ab}^2)^{-1/2}$.

It remains to deal with the basic charge distributions.

§ 3. The ϕ^2 Distribution

McDonald[12] has discussed the influence of the thermal vibration upon the distribution of the electron density in a hydrogen atom three- and two-dimensionally using the square of normalized 1s wave functions. The ϕ^2 distribution with thermal vibration for light atoms could be obtained by applying Fourier transformation numerically to McWeeny's values for Slater type orbital electrons[17]. However, since this Fourier transformation is not an easy matter, we shall adopt in the present paper McWeeny's 2-term Gaussian approximation to the AO[13], which is mathematically more convenient in extending the results to bonded atoms. The general single-term forms of ϕ and ϕ^2 for the 1s, 2s and 2p states are given in Table II.

Following McWeeny's results, terms of the type $r^4\exp(-2ar^2)$ would be expected in $\phi^2(2s)$. However, since the form shown in Table II is more convenient and the numerical values for the parameters are easily derived from those in the 2p function, we shall use terms of the type $r^2\exp(-2ar^2)$ in approximating the $\phi^2(2s)$ function. This will give a more accurate distribution for the 2s electrons than McWeeny's original $\phi^2(2s)$ function, as is clear from the discussion in McWeeny's paper. The resultant ϕ and ϕ^2 for the 1s, 2s and 2p cases are given in Table III, where the atomic unit is chosen as the unit of length.

Table II. Types of terms used in approximating ϕ and ϕ^2.

	ϕ	ϕ^2
(1s)	$\exp(-ar^2)$	$\exp(-2ar^2)$
(2s)	$r^2\exp(-ar^2)$	$r^2\exp(-2a'r^2)$*
(2p)	$\boldsymbol{r}\cdot\boldsymbol{e}\exp(-ar^2)$	$x^2\exp(-2ar^2)$

$\boldsymbol{e}$ is a unit vector along the 2p orbital

* In the present calculation this form is used instead of the form $r^4\exp(-2a'r^2)$.

Table III.

	ϕ (McWeency).
(1s)	$2.426\times10^{-1}\cdot Z^{3/2}\{\exp(-1.330\rho^2)$
	$+0.725\exp(-0.2014\rho^2)\}$
(2s)	$1.493\times10^{-2}\cdot Z^{3/2}\rho^2\{\exp(-0.2037\rho^2)$
	$+0.190\exp(-0.04685\rho^2)\}$
(2p)	$4.109\times10^{-2}\cdot Z^{3/2}\rho\cdot e\{\exp(-0.1512\rho^2)$
	$+0.392\exp(-0.03287\rho^2)\}$
	ϕ^2
(1s)	$5.886\times10^{-2}\cdot Z^3\exp(-2.660\rho^2)$
	$+3.094\times10^{-2}\cdot Z^3\exp(-0.4028\rho^2)$
	$+8.534\times10^{-2}\cdot Z^3\exp(-1.5814\rho^2)$
(2s)	$5.628\times10^{-4}\cdot Z^3\rho^2\exp(-0.3024\rho^2)$
	$+0.8648\times10^{-4}\cdot Z^3\rho^2\exp(-0.06574\rho^2)$
	$+4.412\times10^{-4}\cdot Z^3\rho^2\exp(-0.18407\rho^2)$
(2p)	$16.884\times10^{-4}\cdot Z^3\xi^2\exp(-0.3024\rho^2)$
	$+2.594\times10^{-4}\cdot Z^3\xi^2\exp(-0.06574\rho^2)$
	$+13.236\times10^{-4}\cdot Z^3\xi^2\exp(-0.18407\rho^2)$

Z is the effective nuclear charge same as in the Slater AO's. $\boldsymbol{\rho}=Z\boldsymbol{r}$ and $\boldsymbol{\xi}=Z\boldsymbol{x}$.

The influence of thermal vibration on the density is easily discussed in three-, two-, or one-dimensional case provided the Gaussian approximation to the AO is chosen.

In the first place we consider the three-dimensional case. A function $T(\boldsymbol{r})$ is defined as follows;

$$T(\boldsymbol{r})=\int\exp(-\beta S^2)\exp-(2\pi i\boldsymbol{S}\cdot\boldsymbol{r})d\boldsymbol{S}\,, \qquad (5)$$

where

$$|S|=2\sin\theta/\lambda\,,\quad \beta=2\pi^2\overline{u}^2=\tfrac{1}{4}B\,.$$

β is a constant given as the one fourth of the so-called temperature factor parameter B which will be determined experimentally. $\overline{u}^2$ is related to the mean square displacement of a point from the equilibrium position. Assuming isotropic thermal vibration, we obtain

$$T(\boldsymbol{r})=\left(\frac{\pi}{\beta}\right)^{3/2}\exp(-tr^2)\,, \tag{5a}$$

where

$$t=\pi^2/\beta\,.$$

Since electron density of the system at rest is given as

$$\rho(\boldsymbol{r})=\int f(\boldsymbol{S})\exp(-2\pi i\boldsymbol{S}\cdot\boldsymbol{r})d\boldsymbol{S}\,,$$

where $f(\boldsymbol{S})$ is the scattering factor of the electron distribution, the distribution with thermal vibration becomes,

$$\overline{\rho}(\boldsymbol{r})=\int\rho(\boldsymbol{u})T(\boldsymbol{r}-\boldsymbol{u})d\boldsymbol{u}\,. \tag{6}$$

We are now in a position to obtain the density of the 1s, 2s and 2p electrons by using Gaussian approximation and by Eq. (6). As the three-dimensional $\overline{\rho}(\boldsymbol{r})$ is given in Gaussian form as given below, the two- or one-dimensional projection is easily obtained by suitable integrations. In the derivation of the distribution for each orbital electron with thermal vibration, the following two formulae are necessary,

$$\int\exp(-px^2+2qx)dx=(\pi/p)^{1/2}\exp(q^2/p)\,, \tag{7}$$

and

$$\int x^2\exp(-px^2+2qx)dx$$
$$=1/(2p)\cdot(\pi/p)^{1/2}(1+2q^2/p)\exp(q^2/p)\,. \tag{8}$$

Assuming the general forms of ϕ^2 shown in Table II, the results including the influence of thermal vibration are found to be as follows:

(1s) State.

(3–D) $$\overline{\rho}(r)=K^{3/2}\exp(-2aKr^2)\,, \tag{9}$$

where

$$K=t/(2a+t)\,,\quad t=\pi^2/\beta\,,$$

(2–D) $$\overline{\rho}(r)=(\pi/2a)^{1/2}K\exp(-2aKr^2)\,, \tag{10}$$

(1–D) $$\overline{\rho}(r)=(\pi/2a)K^{1/2}\exp(-2aKr^2)\,. \tag{11}$$

r^2 means $x^2+y^2+z^2$ (3–D), x^2+y^2 (2–D), and x^2 (1–D) respectively.

(2p) State:—The direction of the orbital along the x-axis.

(3–D) $$\overline{\rho}(r)=\tfrac{1}{2}(2a+t)^{-1}\times K^{3/2}(1+2Ktx^2)\exp(-2aKr^2)\,. \tag{12}$$

(2–D) The projection on the xy-plane,

$$\overline{\rho}(r)=\tfrac{1}{2}(\pi/2a)^{1/2}(2a+t)^{-1}\times K(1+2Ktx^2)\exp(-2aKr^2)\,. \tag{13}$$

The projection on the xy-plane,

$$\overline{\rho}(r)=\tfrac{1}{2}(\pi/2a)^{1/2}(1/2a)K\exp(-2aKr^2)\,. \tag{14}$$

(1–D) The projection on the x-axis,

$$\overline{\rho}(r)=\tfrac{1}{2}(\pi/2a)(2a+t)^{-1}\times K^{1/2}(1+2Ktx^2)\exp(-2aKr^2)\,. \tag{15}$$

The projection on the y-axis,

$$\overline{\rho}(r)=\tfrac{1}{2}(\pi/2a)K^{1/2}\exp(-2aKr^2)\,. \tag{16}$$

In Eq. (14) $r^2=y^2+z^2$, and in Eq. (16) $r^2=y^2$.

(2s) State.

(3–D) $$\overline{\rho}(r)=\tfrac{1}{2}(2a+t)^{-1}\times K^{3/2}(3+2Ktr^2)\exp(-2aKr^2)\,, \tag{17}$$

(2–D) $$\overline{\rho}(r)=\tfrac{1}{2}(\pi/2a)^{1/2}(2a+t)^{-1}\times K(3+t/2a+2Ktr^2)\exp(-2aKr^2)\,, \tag{18}$$

(1–D) $$\overline{\rho}(r)=\tfrac{1}{2}(\pi/2a)(2a+t)^{-1}\times K^{1/2}(3+t/a+2Ktr^2)\exp(-2aKr^2)\,, \tag{19}$$

§ 4. $\phi_a\phi_b$ Distribution

Assuming the Gaussian approximation shown in Table II, the vibrational modification of the overlap distribution, $\phi_a\phi_b$, can be obtained. For the sake of convenience, $\exp(-ar_a^2)\times\exp(-br_b^2)$, for instance, is defined as $(1s)_a(1s)_b$. The notation for the coordinates is shown in Fig. 1.

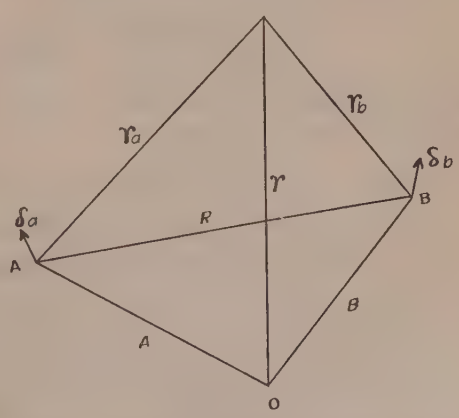

Fig. 1 Vector notation of coordinates.

$(1s)_a(1s)_b$ Distribution.

Considering the following relations, which are obvious from Fig. 1,

$$r_a^2=r^2-2r\cdot A+A^2\,,\qquad r_b^2=r^2-2r\cdot B+B^2\,,$$

and using Eqs. (7) and (8), the $(1s)_a(1s)_b$ distribution is given as follows,

$$\text{(3–D)}\qquad \bar{\rho}(r)=K'^{3/2}\exp\{-abR^2/(a+b+t)\}\exp\{-K'(ar_a^2+br_b^2)\} \tag{20}$$

where $K'=t(a+b+t)$, $\boldsymbol{R}=\boldsymbol{B}-\boldsymbol{A}$ (see Fig. 1),

$$\text{(2–D)}\qquad \bar{\rho}(r)=\{\pi/(2+b)\}^{1/2}\exp\{-K'abR_z^2/(a+b)\}$$
$$\times K'\exp\{-abR^2/(a+b+t)\}\exp\{-K'(ar_a^2+br_b^2)\}\,, \tag{21}$$

$$\text{(1–D)}\qquad \bar{\rho}(r)=\pi/(a+b)\cdot\exp\{-K'ab(R_z^2+R_y^2)/(a+b)\}$$
$$\times K'^{1/2}\exp\{-abR^2/(a+b+t)\}\exp\{-K'(ar_a^2+br_b^2)\}\,, \tag{22}$$

It is clear that r_a^2 is $x_a^2+y_a^2+z_a^2$ (3–D), $x_a^2+y_a^2$ (2–D) or x_a^2 (1–D), and also $R_z=B_z-A_z$, etc.

$(2s)_a(1s)_b$ Distribution.

If we denote the expressions (20), (21) and (22) by I_3, I_2 and I_1 respectively, it follows that $-(\partial I_3/\partial a)$, $-(\partial I_2/\partial a)$ and $-(\partial I_1/\partial a)$ give the expressions of the three-, two- and one-dimensional $(2s)_a(1s)_b$ distribution. This is analogous to McWeeny's procedure in obtaining the bond structure factor[13]. The results are as follows:

$$\text{(3–D)}\qquad \bar{\rho}(r)=(a+b+t)^{-2}K'^{3/2}\{\tfrac{3}{2}(a+b+t)+(b\boldsymbol{R}+t\boldsymbol{r}_a)^2\}$$
$$\times\exp\{-abR^2/(a+b+t)\}\exp\{-K'(ar_a^2+br_b^2)\}\,, \tag{23}$$

$$\text{(2–D)}\qquad \bar{\rho}(r)=\{\pi/(a+b)\}^{1/2}(a+b+t)^{-2}K'\{(a+b+t)+\tfrac{1}{2}(a+b+t)^2/(a+b)$$
$$+bt(b^2-a^2+bt)R_z^2/(a+b)^2+(bR+tr_a)^2\}\exp\{-abR^2/(a+b+t)\}$$
$$\times\exp\{-abtR_z^2/(a+b+t)(a+b)\}\exp\{-K'(ar_a^2+br_b^2)\}\,, \tag{24}$$

$$\text{(1–D)}\qquad \bar{\rho}(r)=\pi(a+b)\cdot(a+b+t)^{-2}K'^{1/2}\{\tfrac{1}{2}(a+b+t)+(a+b+t)^2(a+b)$$
$$+bt(b^2-a^2+bt)(R_z^2+R_y^2)/(a+b)^2+(b\boldsymbol{R}+t\boldsymbol{r}_a)^2\}\exp\{-abR^2/(a+b+t)\}$$
$$\times\exp\{-abt(R_z^2+R_y^2)/(a+b+t)(a+b)\}\exp\{-K'(ar_a^2+br_b^2)\}\,. \tag{25}$$

$(2p)_a(1s)_b$ Distribution.

In order to deal with the $(2p)_a(1s)_b$ distribution it is convenient to introduce vectors $\boldsymbol{A}'=\boldsymbol{A}+\boldsymbol{\delta}_a$, etc., where $\boldsymbol{\delta}_a=\delta_a\boldsymbol{e}_a$ ($\boldsymbol{e}_a$ being a unit vector) is the vector pointing along the directed $(2p)$ orbitals at A (Fig. 1), and to denote the expressions (20), (21) and (22) by I_3', I_2' and I_1' in which $\boldsymbol{A}$ and $\boldsymbol{B}$ are replaced by $\boldsymbol{A}'$ and $\boldsymbol{B}'$ respectively. It then follows easily that,

$$\frac{1}{2a}(\partial I_3'/\partial\delta_a)\,,\qquad \frac{1}{2a}(\partial I_2''\partial\delta_a)\,,\quad\text{and}\quad \frac{1}{2a}(\partial I_1'/\delta\partial_a)$$

give the expressions of the three-, two- and one-dimensional $(2p)_a(1s)_b$ distributions. The results are given as follows,

$$\text{(3–D)}\quad \bar{\rho}(r)=(a+b+t)^{-1}K'^{3/2}(b\boldsymbol{R}\cdot\boldsymbol{e}_a+t\boldsymbol{r}_a\cdot\boldsymbol{e}_a)\exp\{-abR^2/(a+b+t)\}\exp -K'(ar_a^2+br_b^2)\,, \tag{26}$$

$$\text{(2–D)}\quad \bar{\rho}(r)=\{\pi/(a+b)\}^{1/2}(a+b+t)^{-1}K'\{b\boldsymbol{R}\cdot\boldsymbol{e}_a+bt\boldsymbol{R}_z\cdot\boldsymbol{e}_a/(a+b)+t\boldsymbol{r}_a\cdot\boldsymbol{e}_a\}$$
$$\times\exp\{-abR^2/(a+b+t)\}\exp\{-abtR_z^2/(a+b+t)(a+b)\}\exp\{K'(ar_a^2+br_b^2)\}\,, \tag{27}$$

$$\text{(1–D)}\quad \bar{\rho}(r)=\pi/(a+b)\cdot(a+b+t)^{-1}K'^{1/2}\{b\boldsymbol{R}\cdot\boldsymbol{e}_a+bt(\boldsymbol{R}_z+\boldsymbol{R}_y)\cdot\boldsymbol{e}_a/(a+b)+t\boldsymbol{r}_a\cdot\boldsymbol{e}_a\}$$
$$\times\exp\{-abR^2/(a+b+t)\}\exp\{-abt(R_z^2+R_r^2)/(a+b+t)(a+b)\}\exp\{-K'(ar_a^2+br_b^2)\}\,. \tag{28}$$

Eqs. (21), (22), (24), (25), (27) and (28) become much simpler if the bond lies in a projection

plane or projection line.

§ 5. Applications

In the preceding sections are derived the analytical expressions for ϕ^2 and $\phi_a\phi_b$ with thermal vibration which are useful in obtaining the electron distribution of a bond in which a hydrogen atom is participating. The distribution thus calculated is almost the same as that derived by using Slater AO's in particular cases. For example, in Fig. 2 are shown the curves which give the ratios between the values of the peak density for a hydrogen atom calculated by the Gaussian approximation and the Slater AO as the functions of temperature factor parameter B (in Å^2 unit). Slater 1s function gives a sharp electron distribution at the centre when the atom is at rest. However, from this figure, it is clear that the Gaussian approximation (two-terms) is fairly good especially in the two-dimensional projection if the thermal vibration is considerable.

Next we shall discuss the distribution of the electron density of a C–H bond. We assume that (a) the distance between carbon nucleus and proton is 2 atomic units (1.058 Å), (b) $\beta=2.0$ in atomic unit which corresponds to $B=2.332$ Å, a value usually found in actual crystals, (c) the valence AO of the carbon atom is sp^2-hybridized since we have found that the peak position is practically unaffected by the change of carbon hybridization among sp, sp^2 and sp^3. (Peak height is, however, slightly affected.) From the VB point of view, the electron distribution in the C–H bond is given by Eqs. (1) and (4d, e, f) and the numerical values of the distribution can be obtained if λ is suitably chosen.

Coulson[18] has estimated the value of λ as 0.95 from the theoretical discussion of the C–H

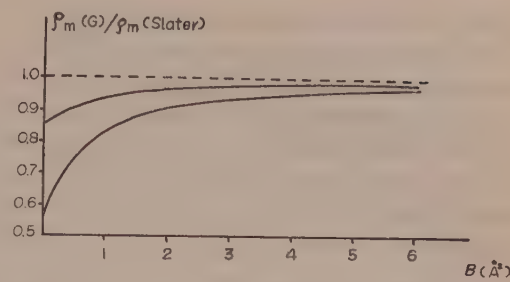

Fig. 2. Ratios of the peak density of 1s electron distribution as the function of temperature factor B. ρ_m(G) and ρ_m(Slater) represent the value of peak density given by Gaussian and Slater respectively.

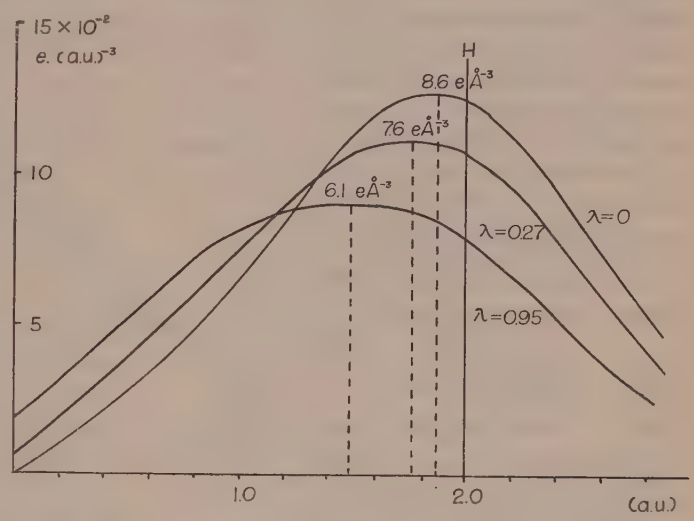

(a)

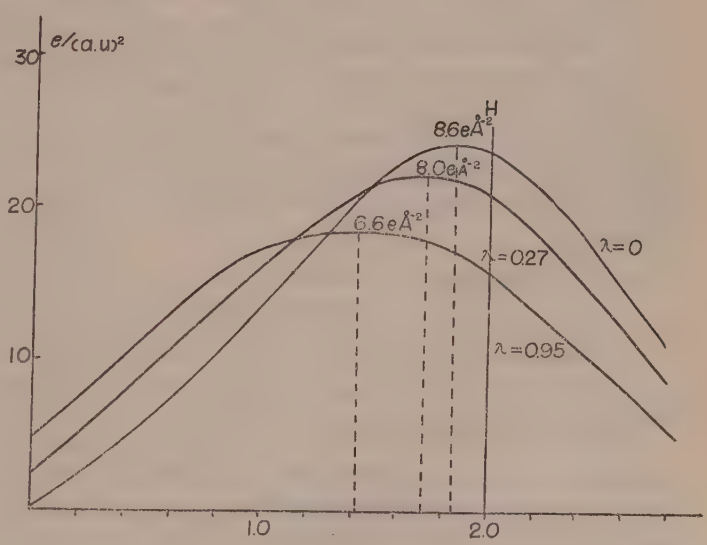

(b)

Fig. 3. The electron distribution in a bonded hydrogen combined with the carbon atom whose valence state is sp^2. λ is the degree of ionic character. (a) Three-dimensional case. (b) Two-dimensional case. The temperature factor $B=2.232$ Å^2 ($\beta=2.0$ a.u.).

dipole moment. On the other hand, Hannay and Smyth have proposed a formula[19] relating the percentage ionic character of a bond, i.e., $100\lambda^2/(1+\lambda^2)$, to the Pauling electronegativities of atoms a and b: namely,

$$\text{Percentage ionic character} = 16|x_a - x_b| + 3.5|x_a - x_b|^2 . \quad (29)$$

This leads to a much lower value, $\lambda=0.27$. The disagreement is probably associated with hybridization effects[18]. We shall consider three cases corresponding to the three values of λ, 0.00, 0.27 and 0.95. The C–H electron distributions corresponding to the three cases are given as follows,

$$0.658\phi_C^2+0.658\phi_H^2+0.949\phi_C\phi_H , \quad \text{for } \lambda=0.00 , \quad (30a)$$

$$0.823\phi_C^2+0.433\phi_H^2+1.032\phi_C\phi_H , \quad \text{for } \lambda=0.27 , \quad (30b)$$

$$1.161\phi_C^2+0.189\phi_H^2+0.901\phi_C\phi_H , \quad \text{for } \lambda=0.95 , \quad (30c)$$

The information about the position and the electron distribution of a bonded hydrogen is usually obtained from the map of the (F_o-F_c)-synthesis, which corresponds, in the present case, to the distribution obtained by substracting ϕ_C^2 from the above distribution. Thus the electron distribution around a hydrogen atom attached to a carbon atom is given as,

$$-0.342\phi_C^2+0.658\phi_H^2+0.949\phi_C\phi_H , \quad \text{for } \lambda=0.00 , \quad (31a)$$

$$-0.177\phi_C^2+0.433\phi_H^2+1.032\phi_C\phi_H , \quad \text{for } \lambda=0.27 , \quad (31b)$$

$$0.161\phi_C^2+0.189\phi_H^2+0.901\phi_C\phi_H , \quad \text{for } \lambda=0.95 , \quad (31c)$$

In Figs. 3a and 3b are shown the three- and two-dimensional electron distributions along the C–H line when β is 2.0 (B=2.232 Å). Similarly in Figs. 4a and 4b are shown the distributions when β is 7 (B=7.81 Å), and in Fig. 5 are shown those when β is zero. From these figures, we conclude the following points.

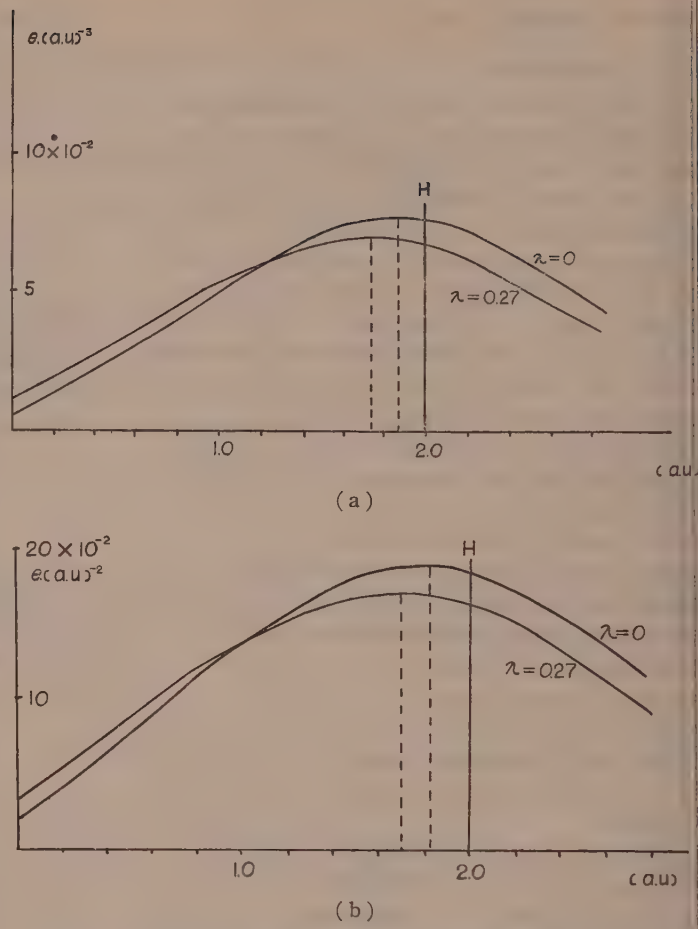

Fig. 4. The electron distribution in a bonded hydrogen combined with the carbon atom whose valence state is sp^2. (a) Three-dimensional case. (b) Two-dimensional case. The temperature factor B=7.81 Å² (β=7.0 a.u.).

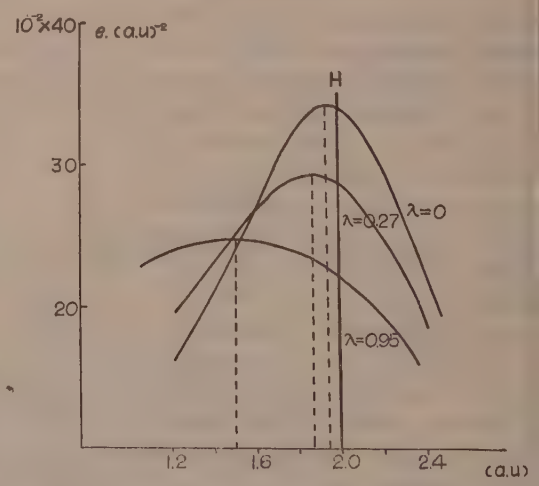

Fig. 5. The electron distribution in a bonded hydrogen combined with the carbon atom whose valence state is sp^2. Two-dimensional case. The temperature factor B=0.

(a) The position of the maximum electron density is located more or less towards the carbon atom and hence the apparent bond shortening should occur. (b) This apparent shortening is greater as the λ value increases. (c) Also the peak density decreases when the λ value increases. (d) The magnitude of the apparent bond shortening, at a constant value of λ, reaches rapidly a certain constant value when the thermal vibration becomes large. (e) Even if the temperature factor parameter is zero (this does not occur owing to the zero point vibration), the two-dimensional distribution shows more or less an apparent bond shortening, while it can be seen that the three-dimensional distribution does not give such contraction. In these cases, we adopt the ϕ_H^2 curves obtained by McDonald[12], at the Gaussian approximation is not good.

It seems likely, from Figs. 3, 4 and 5, that the value of λ is too large if we choose $\lambda=0.95$, because, for instance in Fig. 3, this gives the peak densities 0.61 e. Å^{-3} and 0.66 e. Å^{-2}, which seem to be somewhat too small in comparison with the experimental results, and also the apparent bond distance 0.76 Å (in average) derived from these figures gives a minimum value of the experimental results. On the other hand, it seems unlikely that λ is zero because of the difference between the electronegativities of carbon and hydrogen. When λ is 0.27, the peak densities are 0.76 e. Å^{-3} and 0.80 e. Å^{-2} and the apparent bond distance is 0.92 Å (in average). These values seem to be more reasonable as compared with the experimental ones. However, it is to be remarked that, as is seen from Table I, the reported values for the C–H distance are rather diverse. Therefore, it will be safe to say that the actual λ for the C–H bond may have a value between 0.25 and 0.9, and probably closer to the former. McDonald[12] has pointed out that the experimental electron distribution curve around a bonded hydrogen atom is similar to that obtained using the atomic hydrogen wave function, though the peak is displaced more or less towards the heavy atom. The electron distribution curves shown in Fig. 3 are quite similar to those given by McDonald if peaks are adjusted (private communication).

In the two-dimensional projection, it is found that the inclination of a bond direction to the projection plane gives no practical change upon the above conclusion about the apparent C–H bond contraction if the angle of inclination is not large.

I wish to express my thanks to Professor I. Nitta for his interest and helpful advice, to Dr. R. McWeeny for his kind discussion, and to Mr. K. Sakurai and Mr. T. Yamaguchi for their continued interest and for checking the mathematical derivations. My thanks are also due to Professor C. A. Coulson for reading the manuscript. This research was supported by a grant of the Ministry of Education.

References

1) W. Cochran: Acta Cryst. **4** (1951) 81.
2) W. Cochran: Acta Cryst. **6** (1953) 260.
3) P. J. Weatley: Acta Cryst. **6** (1953) 369.
4) G. A. Sim, J. M. Robertson and T. H. Goodwin: Acta Cryst. **8** (1955) 157.
5) S. Sasada and I. Nitta: Acta Cryst. **9** (1956) 205.
6) Y. Sasada and I. Nitta: Bull. Chem. Soc. Japan **30** (1957) 62.
7) P. J. Weatley: Acta Cryst. **8** (1955) 224.
8) B. R. Penfold: Acta Cryst. **6** (1953) 591.
9) D. R. Davis and R. A. Pasternak: Acta Cryst. **9** (1956) 334.
10) C. Sugawara: X-sen **8** (1954) 21 (in Japanese).
11) Y. Tomiie, C. H. Koo and I. Nitta: to be published.
12) T. R. R. McDonald: Acta Cryst. **9** (1956) 162.
13) R. McWeeny: Acta Cryst. **6** (1953) 631.
14) Y. Morino, K. Kuchitsu, A. Takahashi and K. Maeda: J. Chem. Phys. **21** (1953) 1927.
15) R. McWeeny: J. Chem. Phys. **19** (1951) 1614. ibid **20** (1952) 920; Proc. Roy. Soc. (London) **A223** (1954) 63.
16) R. S. Mulliken: J. Chem. Phys. **23** (1955) 1833.
17) R. McWeency: Acta Cryst. **4** (1951) 513.
18) C. A. Coulson: Trans Faraday Soc. **38** (1942) 433.
19) N. B. Hannay and C. P. Smyth: J. Am. Chem. Soc. **68** (1946) 171.

JOURNAL OF THE PHYSICAL SOCIETY OF JAPAN Vol. 13, No. 9, SEPTEMBER, 1958

Luminescence and Dichroism of F and M Centers in Potassium Chloride

By Goro KUWABARA and Akira MISU

Department of Physics, Faculty of Science, University of Tokyo, Tokyo

(Received May 6, 1958)

In order to determine the model of the M center, the luminescence and dichroism of additively colored KCl were studied in detail. The polarization factor of luminescence due to M centers excited with polarized light in the F band are $P(\pi/4)=-0.37$ and $P(0)=-0.17$. The F band as well as the M band becomes dichroic by irradiating with polarized light in the M band at room temperature or in the F band at low temperature, and the same quantitative relation exists between the amounts of dichroism in the F and M band for both cases.

Above results do not contradict the hypothesis that the second M band overlaps with the F band, and if this assumption is granted, it is concluded from the experiment that the symmetry type of the M center is not C_{2v} but D_{2h}. The oscillator strengths were found to be 0.65 and 0.53 of that of the F band.

If the emission due to M centers excited with light in the F band is assumed to be caused by the resonance transfer from F to M centers, in order to explain the experimental value of transfer probability, the distance between both centers must be less than the order of 10 Å.

§ 1. Introduction

The color centers of alkali halides and their mutual transformation have been investigated by many authors, and the model of the F center is almost conclusively confirmed by the optical and electron spin resonance experiments. However, the models of other centers, proposed chiefly by Seitz[1], are not so sure.

As to the M center, Ueta[2] concluded from experiments on the anisotropic bleaching at room temperature that the M center has the symmetry type of C_{2v} or D_{2h}, whose axis is oriented along a face diagonal.

Inui, Uemura and Toyozawa[3] calculated the energy levels of the M center by assuming the model proposed by Seitz, and showed that another absorption band (the second M band) due to the M center might exist on the shorter wavelength side of the ordinary M band (the first M band). Van Doorn[4] found that, when the crystal containing both F and M centers was irradiated with polarized light in the F band at liquid nitrogen temperature, the F and M bands became dichroic, whose directions of maximum absorption were perpendicular with each other.

It has been found recently that not only F centers but also M and R centers luminesce under suitable conditions, and the measurement of the polarization of luminescence provides powerful means for determining the symmetry of centers. In order to explain the dichroism induced by light in the F band and the polarized luminescence of M centers, van Doorn[5] proposed a hypothesis that the second M band overlaps with the F band, and assigned D_{2h} symmetry to the M center. However, his experiment on the polarization of the luminescence by M centers excited with light in the F band was in contradiction with his model. On the other hand, from experiments on the luminescence of crystals colored by β-ray bombardment, Lambe et al[6] showed that the model of the M center proposed by Seitz can explain the experimental facts and suggested that the luminescence of the M center excited with light in the F band is not caused by direct absorption but by transportation of energy from F to M centers through the crystal.

In order to clarify these points it seems necessary to obtain a quantitative knowledge on the amount of dichroism caused by irradiation with light in the F and M band, polarization, quantum efficiency, and temperature dependence of luminescence.

§ 2. Experimental Procedures

The optical arrangement for measuring the absorption and emission spectra is shown in Fig. 1. For excitation and inducing dicoroism with light in the F band, the polarized light of λ 546 mμ from a high pressure mercury lamp of 500 watts isolated by suitable filbers and a polaroid was used. The luminescence was focused through a Nicol prism and a infrared filter on a detector or on a slit of a monochromator for measurement of spectral distributions. Aperture of the monochromator was F: 1.9 and the focal length of a collimator lens was 20 cm. The width of slits were 0.08 mm, which corresponded to the band width of 9 mμ at 1000 mμ. The polarization characteristic of luminescence was measured by fixing the Nicol relative to the crystal and rotating the polaroid. For absorption measurements and inducing dichroism with light in the M band, the light from a quartz double monochromator passed through a Nicol prism was used.

A Ag-Cs phototube with a D. C. amplifier, a photomultiplier or a PbS cell was used as a detector. In the latter, the light was chopped with the frequency of 800 c/s, and the signal was amplified by a tuned amplifier with the gain of 156 db.

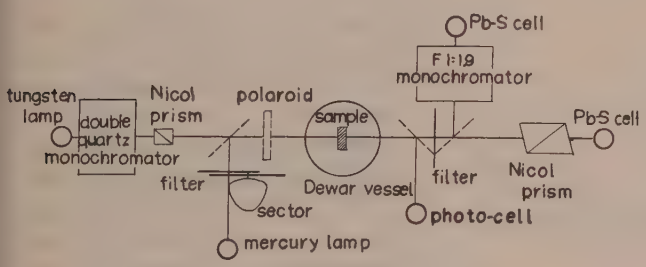

Fig. 1. Optical arrangement.

Crystals of potassium chloride grown by Kyropoulos method was additively colored at about 650°C for about 2 hours. Before experiments, a specimen of about 1 mm in thickness cleaved from a crystal was again heated up to 700°C for a few minutes and quenched in the liquid air. The crystals thus obtained contained almost only F centers and remained free from M centers at least for a few days even at room temperature in the dark. The density of F centers was the order of $10^{17} \sim 10^{16}/\text{cm}^3$.

The sample was clamped to a holder in the liquid air and attached to a dewar vessel shown in Fig. 2.

In order to grow M centers, the crystal was warmed up to above room temperature and irradiated in the F band.

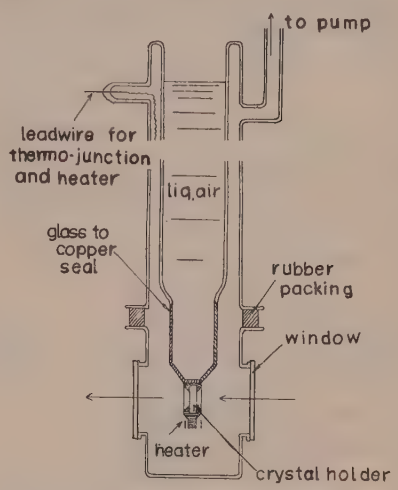

Fig. 2. Dewar vessel.

§ 3. The Luminescence of the F and M Centers Excited with Light in the F Band.

Absorption and emission spectra of luminescence excited with light in the F band for crystals containing various amounts of F, M and R centers are shown Fig. 3, in which the ordinates for luminescent intensity is in an arbitrary unit common for four cases.

Three emission peaks observed at liquid air temperature, which were situated at about 1.19, 1.12 and 1.02 ev might be attributed to the luminescence of F, M and R centers, respectively. The luminescence due to the F center was perceived even for crystals containing large amount of M centers. However, in this case the ratio of the emission and absorption intensities of the F center for a crystal containing M centers appears to be less than that for a crystal containing only F centers.

As shown in Fig. 3, luminescent intensities descreased with the rise of temperature for all cases, and the temperature dependence was the largest for F emission and the smallest for M emission, which remained even at room temperature.

The temperature dependence of the total

emission excited with light in the F band is shown in Fig. 4. A freshly quenched crystal containing only F centers luminesce below $-50°C$, and the intensity, increasing with the derease of temperature, became saturated below $-180°C$. The intensity of luminescence η was linear to that of the exciting light. Between $-210°C$ and $-50°C$, the variation of the intensity with temperature was reversible, and the saturated quantum efficiency at low temperature was about 9 per cent.

Temperature dependence was analysed to the following formula,

$$\eta/\eta_{sat}=1/[1+B\exp(-E/kT)]\,, \qquad (1)$$

with $B=2.5\times10^4$ and $E=0.11$ ev.

Except for the low quantum efficiency, the above values seem to be reasonable, if the luminescence is regarded as a competing process with thermal ionization of excited F centers. However, in order to ascertain this point, the measurement of photoconductivity on a luminescent crystal is desirable.

When the crystal containing only the F center was irradiated with light in the F band at room temperature, the M band gradually increased at the cost of the F band, and with prolonged irradiation R_1 and R_2 bands also grew up, while the M band decreased after passing through the maximum value. The rate of growth was sensitive to the temperature as well as the intensity of illuminating light. During the growth of the M band, the R bands were hardly perceptible.

The luminescent behaviour of the crystal containing large amounts of F centers, more than $10^{18}/cm^3$ seemed rather peculiar compared with crystals of low concentration. In the latter, the intensity of F emission was almost proportional to the absorption intensity of the F band, while in the former, the decrease of the intensity of F emission was more rapid than the decrease of the absorption intensity of the F band, and in some crystals, during the excitation with intense light, the luminescent intensity dereased to one-tenth of the initial value. This fact seems to show the mutual interaction

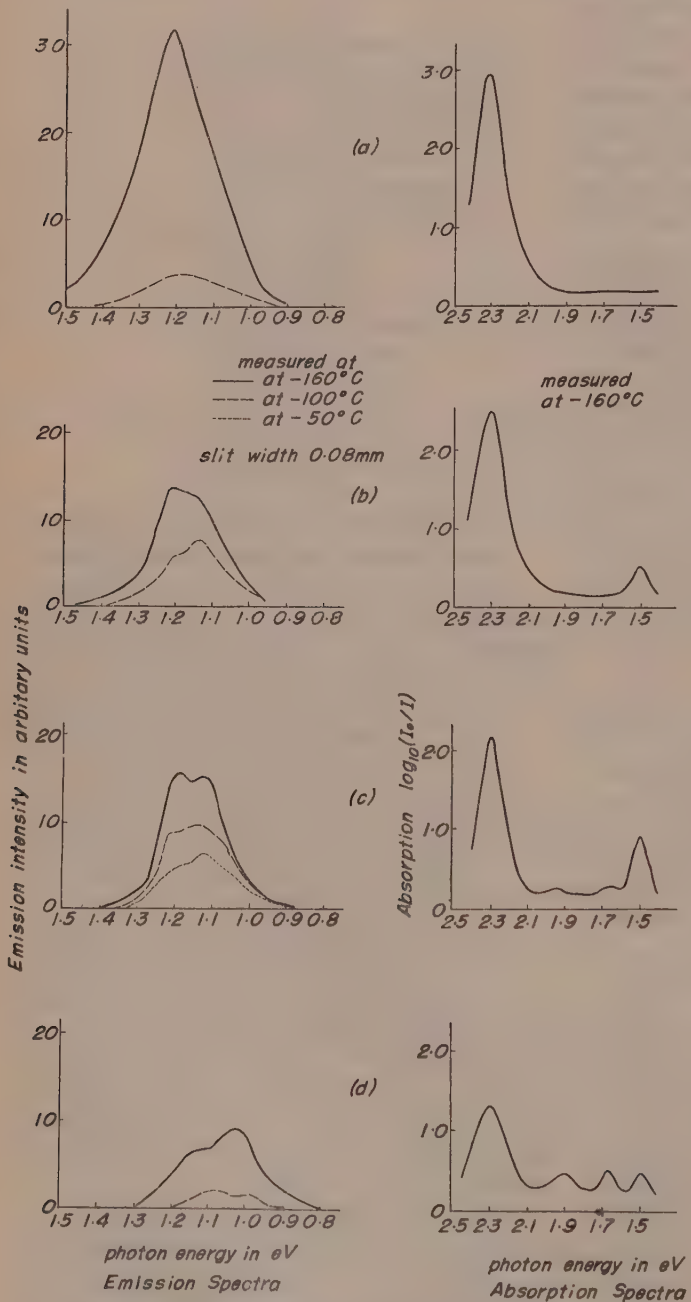

Fig. 3. Emission and absorption spectra of a crystal in various states. Absorption spectra were measured at $-160°C$. Full lines, broken lines and dotted lines show the emission spectra measured at $-160°C$, $-100°C$ and $-50°C$, respectively.

between F centers.

If the exciting light is polarized along the direction of [011], the luminescence of the M center is remarkably polarized. The degree of polarization is expressed by P factor defined as

$$P(\alpha)=(I_{//}-I_{\perp})/(I_{//}+I_{\perp}) , \qquad (2)$$

where the exciting light travelling along the [100] direction, α is the angle between (010) plane and the polarization plane of an analyzer. $I_{//}$ and $I_{\perp}$ are the intensities of luminescence when a polarizer is set parallel and perpendicular to that of the analyzer, respectively.

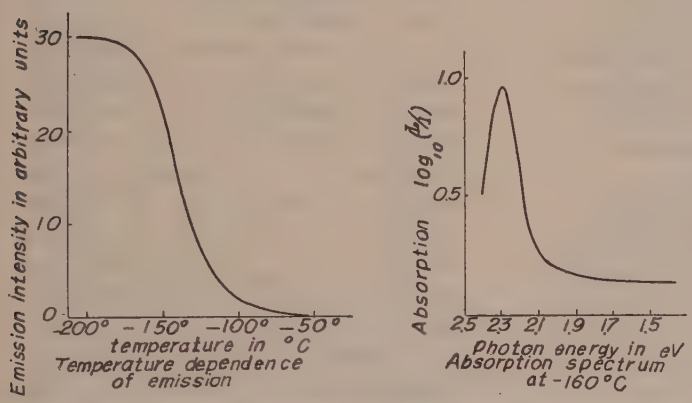

Fig. 4. Temperature dependence of luminescent intensity due to F centers.

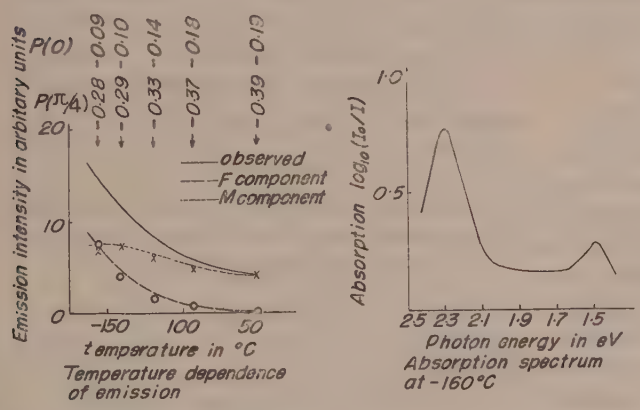

Fig. 5. Temperature dependence of luminescent intensity and P factor due to F and M centers.

The luminescence of a freshly quenched crystal containing only F centers was entirely unpolarized, i.e. $P=0$ for all angles as well as its absorption. (cf. Fig. 6a)

The temperature dependence of the intensity and P factors of the total emission for a crystal containing both F and M centers excited with light in the F band is shown in Fig. 5. The maximum quantum efficiency of M emission at room temperature was about one fourth of the saturated value, which was obtained for the same crystal when it contained only F centers.

At room temperature, where only M centers might luminesce, the mean values of P for the emission excited with light in the F band were found to be

$$P(\pi/4)=-0.37\pm0.05 , \quad P(0)=-0.17\pm0.07 .$$

Above values were different from those reported by Lambe et al[6] ($P(\pi/4)=-0.30$) and van Doorn[5] ($P(\pi/4)=+0.24$). Taking the amount of experimental errors and the theoretical values (cf. Tab. I) into consideration, in the following analysis we used $P(\pi/4)=-0.4$ and $P(0)=-0.2$ as the polarization characteristic of M emission.

The absolute value of P factor of the total emission decreased with the decrease of temperature, and at low temperature it increased with the increase of M center concentration. These facts can be explained as due to the superposition of F and M emissions, and the intensity of the total emission was decomposed into components due to F and M centers as shown in the figure. The encircled and cross points are the mean values obtained by using $P(\pi/4)$ and $P(0)$. The broken line is the temperature dependence of F emission fitted at -150°C. The temperature dependence of luminescence due to F centers was found to be not influenced by the presence of M centers.

In Fig. 6, the spectral distribution of P factor at liquid air temperature is shown. The observed emission spectrum in (b) was also the superposition of F, M and a small amount of R emissions. By using P values the spectrum was decomposed into its components, which seemed reasonable as shown in the figure.

If it is assumed, in addition to the uniform

orientation of M centers along six equivalent directions, that the absorption band corresponding to the transition from the ground to the second excited states of the M center overlaps with the F band, and that M centers excited to this state by F-light absorption make radiationless transition to the first excited state

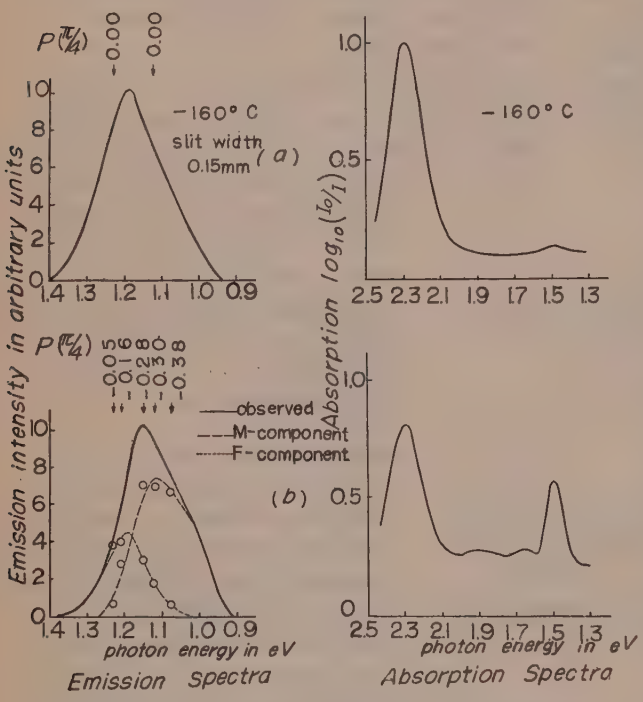

Fig. 6. Spectral distribution of P factor. (a) emission due to F centers (b) due to F and M centers.

and then luminesce, the symmetry type of the M center can be determined from the polarization characteristic of luminescence. polarization of luminescence excited with light in the M band—the emission spectrum is quite the same as that in case of F-light excitation— has been reported by Lambe et al[6] as $+0.60$ and $+0.33$ for $\alpha=\pi/4$ and $\alpha=0$, respectively. This can be explained by assuming C_{2v} or D_{2h} for the symmetry type of the M center, and agrees with the results obtained by Ueta. For the C_{2v} symmetry, the polarization of luminescence due to the M center excited with polarized light in the F band should be -0.66 and $+0.33$ for $\alpha=\pi/4$ and $\alpha=0$, and for the D_{2h} symmetry, they might be -0.40 and -0.20. These theoretical values are given by the following formulas, which can be easily derived by considering the angles between directions of the polarizer or analyzer and the dipoles corresponding to the transitions to the first and second excited states of M centers[7].

$$P(\alpha)=-(3-\cos 4\alpha)/10 \quad \text{for the } D_{2h} \text{ symmetry.}$$

$$P(\alpha)=-(1-3\cos 4\alpha)/6 \quad \text{for the } C_{2v} \text{ symmetry.}$$

In the above argument and throughout this paper, it is assumed that in the case of C_{2v} the transitions from the ground to the first and to the second excited states are active to the light polarized along face diagonals perpendicular to each other, and that in the case of D_{2h} two higher excited states are nearly degenerate. Because the model of the M center cosisted of two negative ion vacancies along a face diagonal is similar to a homonuclear diatomic molecule ($D_{\infty h}$), and the transition which corresponds to the band over lapping with the F band is active to the polarized light, whose electric vector lies in the plane normal to the symmetry axis. The transition to the first excited state is active to the light polarized along the axis. The P factor for various cases are listed in Table I. The present result, especially the negative value of $P(0)$ indicates that the symmetry type of the M center is D_{2h}, under the above assumption, that is, the overlapping of the M with the F band, and the degeneracy of the second and the third excited states.

Table I. The polarization characteristic (P factor) of liminescence due to the M center excited with the polarized light in the F band.

	$P(\pi/4)$	$P(0)$
Calculated for C_{2v}	-0.66	$+0.33$
for C_{2h}	-0.40	-0.20
van Doorn et al	$+0.235$	$+0.17$
Lambe et al	-0.30 ± 0.04	-0.10 ± 0.04
Present authors	-0.37 ± 0.05	-0.17 ± 0.07

The amounts of components of luminescent intensity excited with light in the F band are expected to be proportional to the amount of absorption for both F and M centers. For F centers the relation appears to be a little unsatisfactory as described before. The intensity

of the total emission excited with light in the F band, which might be taken as the intensity of luminescence due to M centers at temperature above $-50°C$, was measured as a function of the concentration of the M center. As seen in Fig. 7, the luminescent intensity at room temperature increased almost linearly with the concentration until the R bands appeared remarkably. The initial concentration of F centers was $1.2\times10^{17}/cm^3$, and the concentrations of M centers were calculated from absorption coefficients assuming the oscillator strength of the M band to be unity.

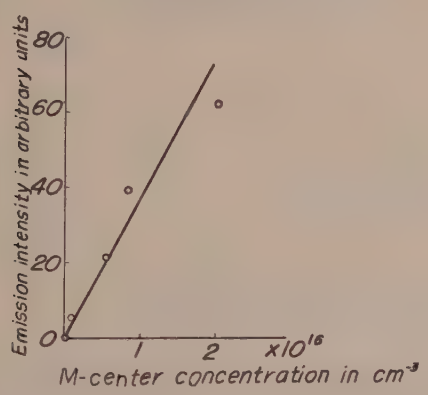

Fig. 7. Concentration dependence of luminescent intensity due to M centers at room temperature.

If it is assumed that the luminescence of M centers by exciting with light in the F band is caused by the transportation of energy from F to M centers through the crystal, the probability of dipole-dipole transfer can be given as follows by putting the experimental values into the formula (Equ. (17)) derived by Dexter[8],

$$P_{FM}=(12.2/R)^6/\tau_F\ , \qquad (3)$$

where R is the distance between F and M centers in Å, and $1/\tau_F$ is the transition probability of the F band. In this calculation, the shapes of the emission and absorption spectra due to F and M centers were assumed to be Gaussian with the observed half widths and the thermal ionization of excited F centers was neglected. Overlap of emission and absorption spectra due to the F and M centers was calculated to be 5.9×10^{-5} ev. In order to have an appreciable transfer probability competing with emission in F centers, the condition $P_{FM}\cdot\tau_F\approx1$ must exist at low temperature.

Let C be the concentration of M centers in unit of $10^{16}/cm^3$, which are assumed to be uniformly dispersed throughout the crystal. If we neglect the radiationless transition at M centers, the quantum efficiency of the luminscence due to the M center excited with light in the F band is given by

$$\eta_{FM}=\{6.3C-2\times10^{-5}(C)^2\}\times10^{-4}\ . \qquad (4)$$

The maximum value of η_{FM}/η_{sat} determined experimentally amounts to 0.3 at room temperature. η_{sat} is the saturated quantum efficiency of luminescence due to F centers, when the same specimen contained only F centers. However, even in the case of neglecting the thermal ionization of excited F centers, whose probability far exceeds $1/\tau_F$ at room temperature, the calculated value for $C=2$ attains at most 1.3×10^{-3}. Therefore, as long as the luminescence of M centers is regarded as the result of resonance transfer between F and M centers, it must be assumed that both centers distribute not at random but near with each other within a small distance about 10 Å forming a pair.

If the F and M centers lie within a small distance, the shape of the F band might be influenced with the growth of the M band. The complicated shift of the F and M bands during the growth of the M band was reported by Kanzaki[9]. However, the definite conclusion has not been obtained concerning the interaction of both centers.

§ 4. Dichroism of the F and M Bands Induced by Polarized Light

If the second M band is assumed to overlap with the F band, the F band as well as the M band should become dichroic, when the M centers in certain orientations are preferentially bleached by polarized light in the M band at room temperature, and moreover, it is expected that some quantitative relations exist between the amount of dichroism of the F band and that of the M band irrespective of the amount or the methods of inducing dichroism, that is, by irradiating with polarized light in the F band at liquid air temperature or with polarized light in the M band at room temperature.

In order to test the above assumption, the crystals containing almost only F and M centers were irradiated with light in the F band polarized along [011] direction at low temperature or light in the M band polarized along [$\bar{0}$11] direction at room temperature, and the

absorptions for the light polarized along [011] and [0$\bar{1}$1] directions were measured at −160°C for both cases. As shown in Fig. 8b, the F band became also dichroic by preferential bleaching of M centers, and the maximum absorption for the F and M bands occurred along [0$\bar{1}$1] and [011] direction, respectively. As shown in Fig. 8a, the dichroism of the F and the M band induced by irradiation in the F band at low temperature was also observed as stated by van Doorn[4], however, in contrast with his result, the dichroism remained stable even at room temperature for several days just as in the case induced by bleaching of M centers in the dark.

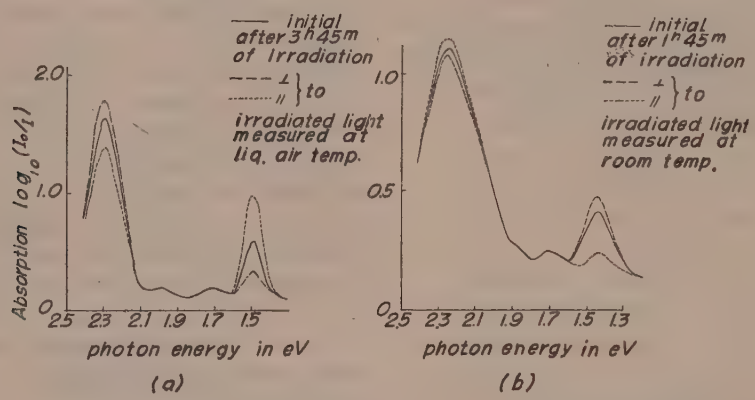

Fig. 8. Dichroism induced by polarized light. (a) irradiated in the F band at liquid air temperature (b) in the M band at room temperature.

Under the above mentioned assumption, the ratio of the difference between the absorptions in the F band for both directions to that in the M band is expected to be constant for all dichroic crystals, i.e.

$$K=\frac{[h_{F[0\bar{1}1]}-h_{F[011]}]}{[h_{M[011]}-h_{M[0\bar{1}1]}]}=\frac{f_{M2}\cdot\nu_{M1}}{f_{M1}\cdot\nu_{M2}}, \qquad (5)$$

where h is the absorption coefficient at the peak of a band, and suffixes show the band and the direction of polarization of measuring light. The mean value of K measured for several crystals and for various degree of dichroism induced by light in the M band at room temperature was 0.50±0.05, and that by light in the F band at low temperature was 0.55±0.09. The values of K for both cases can be regarded to agree within the accuracy of our experiment. The measured value scattered considerably. This might be partly due to the effect of measuring light.

The ratio of the oscillator strength of the second M band to that of the first M band was calculated by the equation (5) as

$$f_{M2}/f_{M2}=0.82\ .$$

In the equation (5), ν_{M1} and ν_{M2} are the half widths of the first and the second M bands, respectively, and ν_{M2} was estimated as 0.15 ev at −160°C by plotting the differences between absorption intensities in the F band for the light polarized along [011] and [0$\bar{1}$1] directions. The peark of the difference shifted somewhat to longer wavelength side than that of the original F band.

There is some remarkable difference between the dichroism caused by irradiation with light in the F band at low temperature and that with light in the M band at room temperature polarized along [011] and [0$\bar{1}$1] directions, respectively. In the latter case, the dichroism was mainly due to the decrease of absorption coefficients for light polarized along [0$\bar{1}$1] in the M band, and for light along [011] in the F band. On the other hand in the former case, the absorption coefficients remarkably increased for light along [011] in the M band and for light along [0$\bar{1}$1] in the F band.

The irradiation in the M band at room temperature is considered to cause ionization and consequently, decrease of M centers in certain directions. In this case, the absorption intensity of the M band for the light polarized along [011] remained almost constant

or a little increased, while that for [0$\bar{1}$1] decreased remarkably. This result does not accord with that obtained by Ueta[2], which showed that the absorption intensity of the M band for both directions decreased. Our result may be explained that some electrons ejected from M centers in one direction, e.g. [0$\bar{1}$1] were trapped by vacancies oriented along another direction, e.g. [011]. The experimental results were obtained, which would show the existence of the M center-like vacancies for a while after ejection of electrons by light in the M band. These results will be reported in another paper.

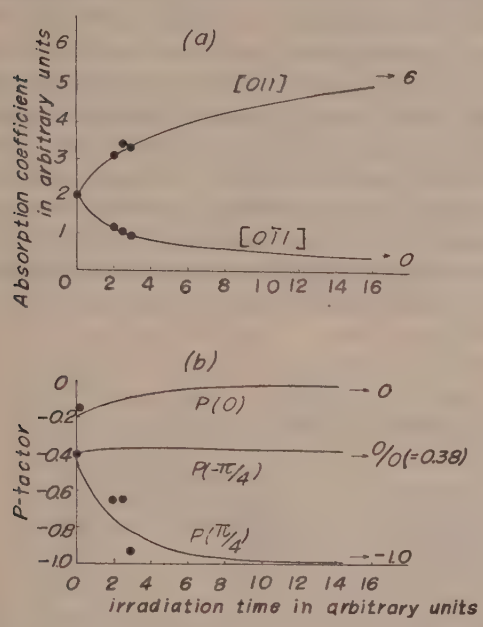

Fig. 9. Calculated curves showing the change of dichroism in the M band (a), and P factor of M emission (b) as a function of irradiation time. Irradiated at low temperature with light in the F band polarized along [011]. Points in the figure show the experimental values.

The irradiation in the F band at low temperature, on the other hand, may cause reorientation of the symmetry axis of the M center, and the total number of the centers is expected to remain constant.

We assume that by absorbing light in the F band, the M centers whose axes point to a direction, e.g. [011], change their orientation to [101], [10$\bar{1}$], [110] or [$\bar{1}$10] with equal probability, and that numbers of F and M centers remain constant. Then, the amount of dichroism and the polarization character of M emission can be obtained as a function of the irradiation time by solving the simultaneous differential equations for the numbers of M centers lying in each of six direction along face diagonals. The F light polarized along [011] direction and travelling along [100] was used for producing dichroism, and the symmetry of the M center was assumed to be D_{2h}.

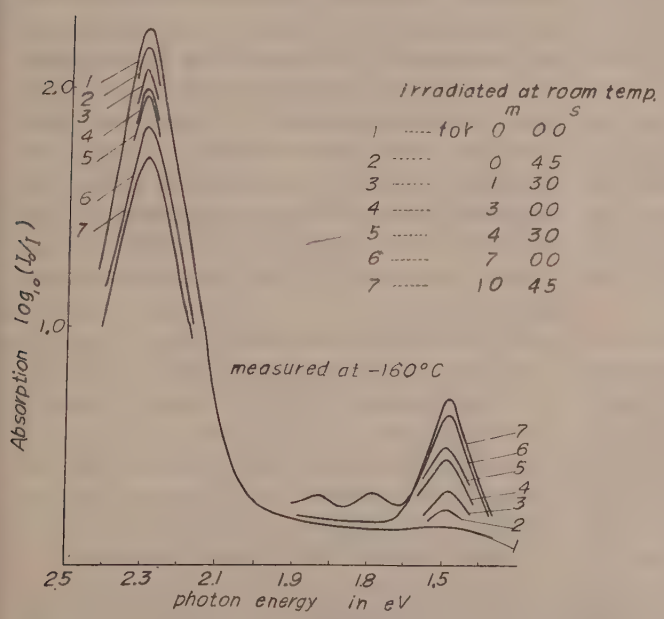

Fig. 10. Variation of absorption spectra by irradiation in the F band at room temperature.

In Fig. 9, the calculated results on the dichroism in the M band and P factor are compared with experimental values. The second assumption that the numbers of F and M centers remain constant could be checked by the experiment and proved valid in some cases. When the dichroic crystal was excited with the light polarized along the direction perpendicular to that of the light used for inducing dichroism, the dichroism was unstable and easily decreased even at low temperature. Moreover, at low temperature the experimental values of P factor of M emission were determined by assuming the amount of contribution from luminescence due to F centers. Taking the above uncertainties into consideration, the agreement between

experimental and calculated results would be regarded satisfactory.

When the crystal containing F centers was irradiated in the F band at room temperature, the intensity of the F band decreased and that of the M band increased as shown in Fig. 10. If the overlapping of F and the second M absorption band is assumed, the apparent absorption intensity of the F band is the sum of contributions from both centers, and the following relation was expected to exist between the amount of decrease of the intensity in the F band, $\Delta h'$, and the amount of increase in the M band, Δh,

$$L=\frac{3\Delta h}{3K\Delta h-\Delta h'}=\frac{f_{M1}\cdot\nu_F}{f_F\cdot\nu_{M1}}. \qquad (6)$$

Accordingly, the oscillator strength of the first M band (f_{M1}) refered to that of the F band (f_F) can obtained. ν_{M1} and ν_F are the half widths of the M and F bands, respectively. In the above consideration, it is assumed that the symmetry of the M center is D_{2h}, and that one M center is produced at the cost of one F center. The latter assumption seemed valid until the R bands appeared remarkably. The value L, which is expected to be constant, was 1.66 ± 0.11, and the oscillator strength obtained from Fig. 10 and the half widths used for it were listed in Table II. The oscillator strength of the M band has been also measured by Okura[10], but analysed in a different way.

Table II. The oscillator strengths of the first and the second M bond.

	Absorption (−160°C)			Emission (−160°C)	
	peak position (ev)	half width (ev)	oscillator strength	peak position (ev)	half width (ev)
F band	2.28	0.24	f	1.19	0.20
first M band	1.52	0.10	$0.65f$	1.12	0.19
second M band	2.26	0.15	$0.53f$	—	—

§ 5. Discussion and Summaries

The analysis of the temperature dependence of luminescence emitted by the crystal containing only F centers shows that the emission may be regarded as the competing process of thermal ionization of the excited F centers. However, to confirm this, it would be necessary to determine whether luminescence, which is found only for specially treated crystals, is the inherent or the accidental character of color centers, and also to know the quantum yield of photoconductivity or of $F-F'$ transformation for a luminescent crystal.

The high quantum efficiency of luminescence due to M centers excited with light in the F band, its polarization characteristic and quantitative relation on the amounts of dichroism in the F and M bands seem to be in favour of the model proposed by van Doorn, that is, the M center having a symmetry type of D_{2h}, whose symmetry axis lies along face diagonals, the ordinary M band corresponds to the transition from the ground state to the first excited state, which is active to the polarized along the symmetry axis, and the absorption band, which corresponds to the transition to the upper excited state and active to the light polarized perpendicular to the symmetry axis overlaps with the F band. The emission due to the M center corresponds to the transition from the first excited to the ground state. The oscillator strengths for these two bands due to the M center are $f_{M1}=0.65f_F$, $f_{M2}=0.53f_F$, respectively. However, as far as our results concern, the most serious weak point for the above assumption is that, in some cases, the amount of the decrease of luminescence due to the F center was large compared with that of the absorption in the F band. In the above assumption, the quantum efficiency of luminescence in the M center must be large, and that of the F center must be constant irrespective of the presence or the amount of M centers. About this point, more detailed experiments are desirable. In our results obtained for crystals containing M centers, the ratios of the intensity of luminescence of F centers to that of M centers at low temperature, which was determined

by using the difference of temperature dependence and P factor, is not so reliable; they should be precisely determined by measuring the spectral distributions of luminescence, however, owing to the overlap of the emission bands, it might be difficult.

The second difficulty is the mechanism of luminescence due to R centers excited with light in the F band. The overlap of three absorption bands, i.e. the F band, the second M band and the second or third R band for various crystals investigated[5),6)] is hardly to be conceived. The experiment on LiF, in which the lattice constant differs remarkably from those of other alkali halides, may give a clue for this problem.

On the contrary, if the luminescence of M centers is regarded as due to the resonance transfer of energy from F to M centers, in order to explain its probability, which must be large compared with that for luminescence or thermal ionization of F centers in the excited state, i.e. $1/\tau_F=10^8$/sec or 10^{12}/sec, we must assume that the distance between F and M centers is less than 10 Å, and in order to explain the dichroism and the polarization characteristic of the luminescence, there must be also assumed a strong interaction between both centers or another new center which has absorption band overlapping with the F band and interacts strongly with the M center. They may be explained by the asymmetry of crystalline field at the F center caused by the presence of the M center. It seems, however, difficult to testify this model from the present results. The measurement of temperature dependence of photoconductivity due to light in the F band for crystals with and without the M band and the detailed measurement of the absorption during the growth of the M band may gave clues for this problem.

As a conclusion, it can not be decided conclusively at present which of the two assumptions is correct, the overlapping of the second M band with the F band or the resonance transfer between both centers. However, if the former is assumed, we conclue from our experiment that the M center has a symmetry type of D_{2h}, and the dipole for the first M band lies along a face diagonal, and that for the second M band lies in the plane normal to it.

In conclusion the authors wish to express their thanks to Professor Koana for his kindness to offer us facility to using optical instruments, and also to Professor Uemura for his valuable suggestions. The present work was supported partly by the research expenditure of the Ministry of Education.

References

1) F. Seitz: Revs. Mod. Physics **26** (1954) 7.
2) M. Ueta: Journ. Phys. Soc. Japan **7** (1952) 107.
3) T. Inui, Y. Uemura and Y. Toyozawa: Progr. Ther. Phys. **8** (1952) 355.
4) C. D. van Doorn and Y. Haven: Phys. Rev. **100** (1955) 753.
5) Th. P. J. Botden, C. Z. van Doorn and Y. Haven: Philips Res. Rep. **9** (1954) 469.
C. Z. van Doorn and Y. Haven: ibid **11** (1956) 479.
C. Z. van Doorn: ibid **12** (1957) 309.
6) J. Lambe and W. D. Compton: Phys. Rev. **106** (157) 684.
7) P. P. Feofilov: Journ. Exp. Theor. Phys., Moscow **26** (1954) 609.
8) D. L. Dexter: Journ. Chem. Phys. **21** (1953) 836.
9) H. Kanzaki: Lecture at the meeting of the Phys. Soc. Japan. Mar. 1958.
10) H. Okura: Journ. Phys. Soc. Japan. **12** (1957) 1313.

JOURNAL OF THE PHYSICAL SOCIETY OF JAPAN Vol. 13, No. 9, SEPTEMBER, 1958

The Flow with Wake past an Oblique Plate

By Yōichi MIMURA

Department of Physics, Faculty of Science, Hiroshima University

(Received May 20, 1958)

In the case of two-dimensional flow with wake of a perfect fluid past an oblique plate, the pressure distributions on the front surface of the plate as well as on the free streamlines are calculated, together with the shapes of the latter, by applying the method of notched hodograph devised by Roshko. The calculated values are compared with the experimental ones obtained by Fage and Johansen. It is thus found that the calculated and the observed values of the pressure distribution along the front surface of the plate coincide fairly well with each other so far as the observed base pressure is constant, but discrepancies between them increase as the angle of attack decreases.

§ 1. Introduction

Roshko[1] treated the two-dimensional flow of a perfect fluid past bluff bodies by the method of notched hodograph which was devised by himself and obtained excellent results especially for a normal plate. In the present investigation, the writer applies his method to the case of flow with wake past an oblique plate placed at various angles of attack, and the pressure distributions on the front (wetted) surface of the plate as well as on the free streamlines, together with the shapes of the latter, are calculated. The calculated values are compared with the experimental ones obtained by Fage and Johansen[2].

In the following lines, we shall use, for the sake of convenience, such scales of length and time that make both the breadth of the plate, d, and the velocity of undisturbed flow, U, equal to unity.

§ 2. Method of Notched Hodograph

In the method of notched hodograph devised by Roshko, the following assumptions are made concerning free streamlines, namely:

(1) The direction of the free streamline at the point of separation is in the tangent plane of the body at that point;

(2) The fluid velocity q on the free streamline remains equal to that at the point of separation, which will be denoted by q_s, until the direction of the free streamline becomes parallel to the undisturbed flow;

(3) Further downstream the free streamline remains parallel to the undisturbed flow.

Adopting these assumptions we shall here deal with the two-dimensional flow with wake of a perfect fluid past an oblique plate. Then

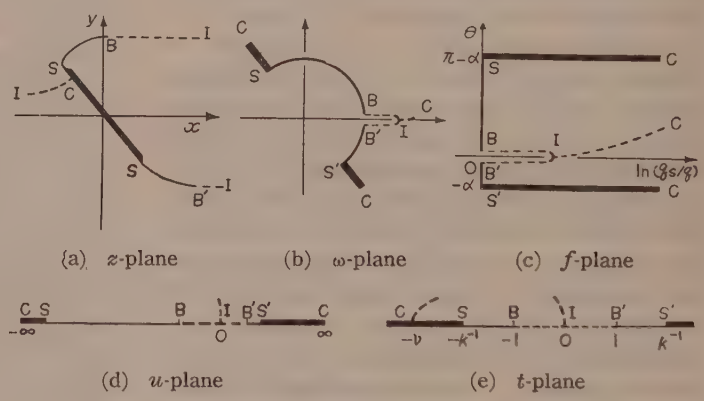

Fig. 1.

the notched hodograph becomes as shown in Fig. 1 (b), where ω is defined by

$$\omega = dz/dw = q^{-1}e^{i\theta}. \tag{2.1}$$

Here $z=x+iy$ is the complex coordinate, the x-axis being taken parallel to the undisturbed flow, and w is the complex potential, while θ is the direction of flow. The flow in the physical plane (z-plane) is shown schematically in Fig. 1 (a), where C is the stagnation point, S and S′ are the points of separation, B and B′ are the points where the free streamlines become parallel to the undisturbed flow at infinity I.

Next, we map the ω-plane onto an f-plane by the relation:

$$f=\ln(q_s\omega)=\ln(q_s/q)+i\theta\,. \tag{2.2}$$

The f-plane is shown in Fig. 1 (c).

The polygon CSBIB′S′C in the f-plane is then mapped onto the upper half of a u-plane by applying the theorem of Schwarz-Christoffel. The transformation function is easily seen to be

$$f(u)=a'\int_{b'}^{u}\frac{(u-I)du}{\{(u-B)(u-B')(u-S)(u-S')\}^{1/2}}+c', \tag{2.3}$$

where B, B′, S, S′ and I are the values of u at the corresponding points, and a', b' and c' are certain constants. We choose these constants so as to make I in (2.3) equal to zero (Fig. 1 (d)).

Further, we map the upper half of the u-plane onto the upper half of a t-plane by the relation:

$$u=\nu_0-\nu_1(t+\nu)^{-1}, \tag{2.4}$$

where ν_0, ν_1 and ν are certain (positive) constants, and if we choose suitable values for these constants, we can make the lengths of two sections SB and B′S′ in the t-plane equal to each other. Then, values of t corresponding to the points S, B, I, B′ and S′ become $-k^{-1}$, -1, $-r$, 1 and k^{-1} respectively, where k and r are constants (Fig. 1 (e)).

Thus, taking account of the values of $\ln(q_s/q)$ and θ at the points S, B, I, B′ and S′, we easily find that the values of f, as a function of t, at these points are given by

$$f(-k^{-1})=(\pi-\alpha)i\,, \tag{2.5}$$

$$f(-1)=0\,, \tag{2.6}$$

$$f(-r)=\ln q_s\,, \tag{2.7}$$

$$f(1)=0\,, \tag{2.8}$$

$$f(k^{-1})=-\alpha i\,. \tag{2.9}$$

Combining (2.3) and (2.4), the value of f, as a function of t, now becomes

$$f(t)=aF(\sin^{-1}t,\ k)-b\sigma_{-1}(\sin^{-1}t,\ \nu,\ k)+c\,, \tag{2.10}$$

where we have put

$$F(\sin^{-1}t,\ k)=\int_0^t\frac{dt}{\{(1-t^2)(1-k^2t^2)\}^{1/2}}\,, \tag{2.11}$$

$$\sigma_{-1}(\sin^{-1}t,\ \nu,\ k)=\int_0^t\frac{dt}{(t+\nu)\{(1-t^2)(1-k^2t^2)\}^{1/2}}\,, \tag{2.12}$$

and

$$\left.\begin{aligned}a&=a'\nu_0\nu_1^{-1}\sqrt{(\nu^2-1)(k^2\nu^2-1)}\,,\\ b&=a'\sqrt{(\nu^2-1)(k^2\nu^2-1)}\,.\end{aligned}\right\} \tag{2.13}$$

§ 3. The Function f

In order to determine the function $f(t)$ it is first necessary to know the value of the two-valued function $\{(1-t^2)(1-k^2t^2)\}^{1/2}$ in $f(t)$. This can be easily attained by comparing it with the one in the case of a normal plate where $\alpha=\pi/2$. In this case, after some simple calculations Eq. (2.3) is transformed to

$$f(u)=-\int_0^u\frac{k_0udu}{\{(1-u^2)(1-k_0^2u^2)\}^{1/2}}+\ln q_s\,, \tag{3.1}$$

with

$$k_0=(q_s^2-1)/(q_s^2+1)\,.$$

Hence in this case Eq. (2.4) becomes $u=t$ so that $\nu_1=\nu^2$, $\nu_0=\nu$ and $\nu\to\infty$ and therefore $a'=1$. (3.1) can be easily integrated and therefore, by virtue of Eqs. (2.5) ~ (2.9), the value of $\{(1-u^2)(1-k_0^2u^2)\}^{1/2}$ in (3.1) can be determined as shown in (3.2) below, with k_0 in place of k. Thus, by virtue of continuity, the value of $\{(1-t^2)(1-k^2t^2)\}^{1/2}$ in our case can be determined as:

$$\{(1-t^2)(1-k^2t^2)\}^{1/2}=\left\{\begin{array}{ll}\sqrt{(1-t^2)(1-k^2t^2)}, & (0\le|t|\le 1)\\ \mp i\sqrt{(t^2-1)(1-k^2t^2)}, & \begin{cases}(1\le t\le k^{-1})\\(-k^{-1}\le t\le -1)\end{cases}\\ -\sqrt{(t^2-1)(k^2t^2-1)}, & (k^{-1}\le|t|\le\infty)\,.\end{array}\right\} \tag{3.2}$$

(2.11) is the elliptic integral of the first kind. For the evaluation of the integral (2.12), we have used convenient formulae in Byrd and Friedman's handbook*[3]. Thus, for the calculation of (2.12) we have applied (B. 330.50) which involves the function

$$\Pi(\sin^{-1}t,\ \nu^{-2},\ k).$$

This function can be evaluated as follows under the conditions given in the respective brackets:

(B. 435.01) in $0\le|t|\le 1$, $(k^2\nu^2>1)$,

(B. 436.01) in $k^{-1}\le|t|\le\infty$, $(k^2\nu^2>1)$,

(B. 434.01) in $1\le|t|\le k^{-1}$,

$$(k'^2\le k'^2\nu^2(\nu^2-1)^{-1}<k')\,, \tag{3.3}$$

(B. 433.01) in $1\le|t|\le k^{-1}$,

$$(k'<k'^2\nu^2(\nu^2-1)^{-1})\,. \tag{3.4}$$

* Here as well as in what follows the formulae in this book will be quoted as (B.⋯). Thus, for example, (B. 330.50) means the formula (330.50) in the book.

As will be seen from (3.12) below, the condition $k^2\nu^2>1$ is satisfied in general. Both the formulae (3.3) and (3.4) are used in practical cases (cf. Table I). Using (3.2) and the above formulae we can evaluate $f(t)$ for all ranges of t.

On the other hand, since the point at infinity I corresponds to $u=0$ in the u-plane and to $t=-r$ in the t-plane, we have from (2.4) $r=-\nu_1\nu_0^{-1}+\nu$ and therefore by (2.13) we have ultimately

$$r=-ba^{-1}+\nu\,. \tag{3.5}$$

Hence the undetermined (positive) constants involved in $f(t)$ are k (<1), ν (>1), a, b and c, which can be determined by the five equations (2.5)$\sim$(2.9) when the values of α and q_s are prescribed. The calculation is laborious but straightforward, so that we shall give here the results only.

First, the constants a, b and c can be expressed in terms of k and ν as follows:

$$a=b\nu^{-1}+Z(\beta,\ k)\,, \tag{3.6}$$

$$b=\sqrt{(\nu^2-1)(k^2\nu^2-1)}\,, \tag{3.7}$$

$$c=(1/2)\ln\{D(1)/D(0)\}\,, \tag{3.8}$$

where Z is the Jacobian zeta function, and β and $D(t)$ are defined by (3.12) and (3.19) below, respectively.

Secondly, k and ν are decided by the use of λ ($=\pi/2-\alpha$) and q_s as follows:

$$2\lambda/\pi=K^{-1}F(\beta,\ k)\,, \tag{3.9}$$

$$q_s=\sqrt{D(1)/D(r)}\exp\Omega_3(r)\,, \tag{3.10}$$

where

$$K=F(\pi/2,\ k)\,, \tag{3.11}$$

$$\beta=\sin^{-1}(1/k\nu)\,, \tag{3.12}$$

$$r=\nu Z(\beta,\ k)\{b\nu^{-1}+Z(\beta,\ k)\}^{-1}\,, \tag{3.13}$$

and $\Omega_3(t)$ will be defined by (3.20) below.

Inserting the values of a, b and c as given by (3.6) $\sim$ (3.8) into (2.10), $f(t)$ can be expressed for each range of t as follows:

On the plate ($k^{-1}\leq|t|\leq\infty$), using a variable defined by

$$\xi=(kt)^{-1},\qquad (-1\leq\xi\leq 1)\,, \tag{3.14}$$

we have*

$$f(\xi)=i(\pm\pi/2+\lambda)+\frac{1}{2}\ln\left[\frac{G(\xi)\sin\{\lambda-(\pi/2)K^{-1}F(\sin^{-1}\xi,\ k)\}}{G(1)\sin\{\lambda+(\pi/2)K^{-1}F(\sin^{-1}\xi,\ k)\}}\right]-\overline{\Omega}_4(\xi)\,, \tag{3.15}$$

* The symbol f is still used irrespective of the change of variables.

the plus and minus signs corresponding to $k^{-1}\leq t\leq\infty$ and $-\infty\leq t\leq -k^{-1}$ respectively, where

$$G(\xi)=(1-k^2\nu^2\xi^2)^{-1}\{2b^2+(\nu^2+\nu^2k^2-2)(1-k^2\nu^2\xi^2)+2k\nu^2b\sqrt{(1-\xi^2)(1-k^2\xi^2)}\}\,,$$

$$\overline{\Omega}_4(\xi)=\sum_{m=1}^{\infty}\frac{q^m\sin 2mw\sin 2mv(\xi)}{m\sinh 2mp}\,,$$

$$v(\xi)=(\pi/2)K^{-1}F(\sin^{-1}\xi,\ k),\quad w=\lambda,$$

$$p=(\pi/2)K'K^{-1},\quad q=\exp(-2p),$$

$$K'=F(\pi/2,\ k'),\quad k'^2=1-k^2.$$

On the free streamlines of constant pressure ($1\leq|t|\leq k^{-1}$), we use a variable μ defined by

$$\mu=\sqrt{t^2-1}(k't)^{-1},\quad (-1\leq\mu\leq 1). \tag{3.16}$$

There are two cases in which (3.3) or (3.4) is to be used. In the first case we have

$$f(\mu)=-i\tan^{-1}E(\mu)\pm i\lambda K'^{-1}F(\sin^{-1}\mu,\ k')\pm i\overline{\Omega}_6(\mu)\,, \tag{3.17}$$

according as $1\leq t\leq k^{-1}$ or $-1\geq t\geq -k^{-1}$, where

$$E(\mu)=\sqrt{(k^2\nu^2-1)/(\nu^2-1)}\cdot\mu/\sqrt{1-\mu^2},$$

$$\overline{\Omega}_6(\mu)=\tan^{-1}\left\{\left(2\sum_{m=1}^{\infty}q'^{m^2}\sinh 2mw'\sin 2mv'(\mu)\right)\div\left(1+2\sum_{m=1}^{\infty}q'^{m^2}\cosh 2mw'\cos 2mv'(\mu)\right)\right\},$$

$$v'(\mu)=(\pi/2)K'^{-1}F(\sin^{-1}\mu,\ k'),\quad w'=\lambda K'K^{-1},$$

$$p'=(\pi/2)KK'^{-1},\quad q'=\exp(-2p')\,,$$

while, in the second case, $\overline{\Omega}_6(\mu)$ in the above formula should be replaced by $\overline{\Omega}_2(\mu)$, which is defined by

$$\overline{\Omega}_2(\mu)=\tan^{-1}\left\{\left(2\sum_{m=1}^{\infty}q'^{m^2}\sinh 2m(p'-w'')\sin 2mv'(\mu)\right)\div\left(1+2\sum_{m=1}^{\infty}q'^{m^2}\cosh 2m(p'-w'')\cos 2mv'(\mu)\right)\right\},$$

with

$$w''=(\pi/2)K'^{-1}F(\theta,\ k),$$

$$\theta=\sin^{-1}\sqrt{(\nu^2-k^{-2})/(\nu^2-1)}\,,$$

the other symbols in $\overline{\Omega}_2(\mu)$ being the same as those in $\overline{\Omega}_6(\mu)$.

On the free streamlines parallel to the undisturbed flow ($0\leq|t|\leq 1$), we have

$$f(t)=-(1/2)\ln\{D(t)/D(1)\}-\Omega_3(t), \tag{3.18}$$

where

$$D(t)=(\nu^2-t^2)^{-1}\{2b^2+(1+k^2-2k^2\nu^2)(\nu^2-t^2)+2b\sqrt{(1-t^2)(1-k^2t^2)}\}\,, \tag{3.19}$$

$$\Omega_3(t)=\sum_{m=1}^{\infty}\frac{\sin 2mw\sin 2mv(t)}{m\sinh 2mp}, \tag{3.20}$$

symbols used in $\Omega_3(t)$ being the same as in $\overline{\Omega}_4(\xi)$.

§ 4. Solution in the Physical Plane

It was found in the previous paragraph that f and hence q and θ are represented as the functions of t. To determine the flow in the physical plane it is necessary to express the coordinates of this plane as functions of t. For this purpose we map the t-plane onto a g-plane by the relation:

$$g=N_1(t+\nu)(t+r)^{-1}, \tag{4.1}$$

where N_1 is a constant, and the point C is mapped to the origin in the g-plane, while the point I is mapped to the point at infinity. Furthermore the g-plane is mapped onto the w-plane by

$$w=g^2. \tag{4.2}$$

Then the streamlines past the front surface of the body are mapped onto the real axis in the w-plane. Hence the w-plane is the potential plane. Therefore, z is represented by t by the use of (2.1), (4.2) and (4.1) as:

$$z=\int q^{-1}e^{i\theta}\frac{dw}{dg}\frac{dg}{dt}dt. \tag{4.3}$$

Applying this equation to the plate, the length s from the leading edge to any point on the plate is, using ξ in (3.14), given by

$$s(\xi)=\frac{1}{q_s}\int_{-1}^{\xi}\frac{q_s}{q(\xi)}\frac{dw}{dg}\frac{dg}{dt}\frac{dt}{d\xi}d\xi$$
$$=N\int_{-1}^{\xi}\frac{q_s}{q(\xi)}\frac{1+k\nu\xi}{(1+kr\xi)^3}d\xi, \tag{4.4}$$

where

$$N=N_1{}^2 2k(\nu-r)/q_s.$$

N is to be determined so as to make $s(1)$ equal to unity, i.e.

$$N=\left\{\int_{-1}^{1}\frac{q_s}{q(\xi)}\frac{1+k\nu\xi}{(1+kr\xi)^3}d\xi\right\}^{-1}. \tag{4.5}$$

We next apply (4.3) to the free streamline. The origin of the coordinates $z=x+iy$ is taken as S or S′ according as we deal with the upper or the lower free streamline. Then, on the free streamlines of constant pressure, x and y are given as the functions of μ in (3.16) by

$$\left.\begin{matrix}x(\mu)\\ y(\mu)\end{matrix}\right\}=-N\frac{k'^2}{k}\int_{\mp 1}^{\mu}\left.\begin{matrix}\cos\mu\\ \sin\mu\end{matrix}\right\}$$
$$\times\frac{q_s}{q(\mu)}\frac{1+\nu\sqrt{1-k'^2\mu^2}}{(1+r\sqrt{1-k'^2\mu^2})^3}\frac{\mu}{\sqrt{1-k'^2\mu^2}}d\mu. \tag{4.6}$$

On the free streamlines parallel to the undisturbed flow, x as determined by (4.3) takes the simple form:

$$x(t)=-\frac{N}{k}\int_{\mp 1}^{t}\frac{q_s}{q(t)}\frac{t+\nu}{(t+r)^3}dt. \tag{4.7}$$

§ 5. Results

Calculations have been carried out for the cases in which the angle of attack α of the plate is equal to 70°, 50°, 30° and 15° respectively. The values of q_s used have been determined in such a manner that the values of $1-q_s{}^2$ become the same as the observed mean base pressure coefficients obtained by Fage and Johansen[3] except the case when $\alpha=15°$. In this exceptional case q_s has been determined from the observed pressure coefficient at the trailing or the leading edge, and these two cases are distinguished by denoting them as 15°A and 15°B respectively.

The results are shown in Tables I and II and also in Figs. 2 ~ 4. In case when $\alpha=90°$, the results obtained by Roshko by using $q_s=1.54$ are also shown for comparison.

In Table I, the first and second columns show the values of α and q_s used in the calculations. The third and fourth columns show the values of k and ν which have been determined from the given values of α and q_s by

Table I. Calculated results for the oblique plate.

α	q_s	k	ν	Formula	s_{stag} (cal.)	s_{stag} (obs.)	C_N (cal.)	C_N (obs.)
90°	1.545	0.4095	∞	—	0.500	0.500	2.130	2.130
70°	1.540	0.4294	6.512	(3.3)	0.277	0.257	2.072	2.070
50°	1.490	0.4791	3.131	(3.3)	0.106	0.178	1.776	1.800
30°	1.385	0.5680	1.987	(3.4)	0.019	0.032	1.269	1.290
15°A	1.237	0.6924	1.481	(3.4)	0.002	0.000	(0.163)	0.950
15°B	1.257	0.6982	1.468	(3.4)	0.002	0.000	(0.147)	(0.218)

Table II. Data concerning the shapes of the free streamlines for the oblique plate.

α	x_S	y_S	x_B	y_B	$x_{B'}$	$y_{B'}$	d'	d'/d''	h
90°	0	0.500	0.565	0.773	0.565	−0.773	1.546	1.546	1.475
70°	−0.171	0.470	0.312	0.760	0.713	−0.712	1.468	1.562	1.365
50°	−0.321	0.383	0.051	0.644	0.786	−0.547	1.191	1.555	1.248
30°	−0.433	0.250	−0.194	0.436	0.770	−0.303	0.739	1.408	1.146
15°A	−0.483	0.129	−0.338	0.206	0.665	−0.149	0.355	1.371	0.776

the method mentioned in § 3. The fifth column shows which formula of (3.3) and (3.4) has been used.

The distributions of the pressure coefficient on the front surface, $C_{pw}(s(\xi))[=1-q^2(s(\xi))]$, can be obtained by (3.15) and (4.4) and are shown in Figs. 2 (a)~(d). The black circles in

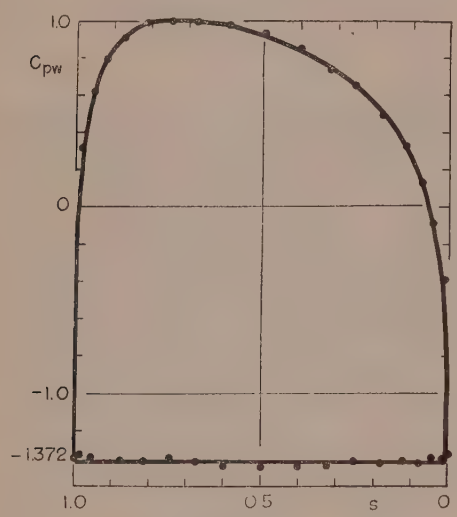

(a) $\alpha=70°$

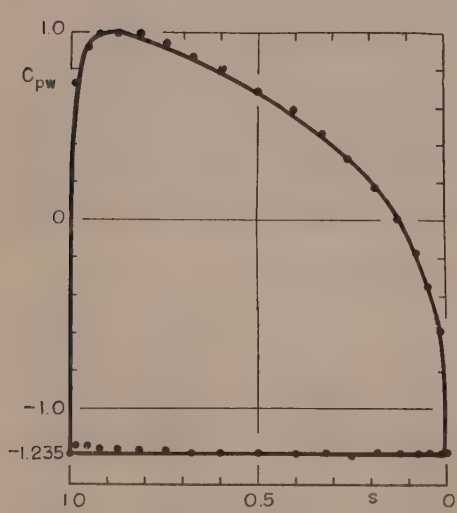

(b) $\alpha=50°$

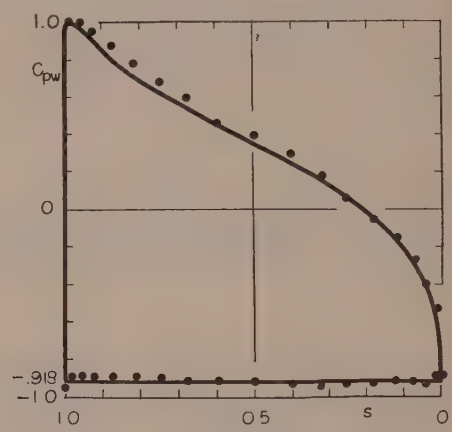

(c) $\alpha=30°$

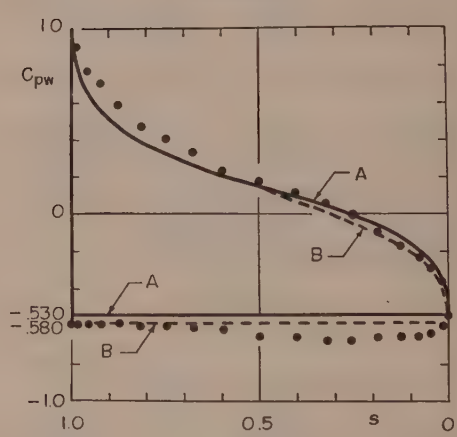

(d) $\alpha=15°$

Fig. 2. Pressure distributions on the front surface of the oblique plate.

these figures show the experimental results of $C_{pw}(s(\xi))$ in the cases in which $\alpha=69°.85$, 49°.85, 29°.85 and 14°.85 respectively. These observed results were obtained by Fage and Johansen[3], but no correction due to the tunnel interference effect was made.

The sixth column in Table I gives the values of $s(\xi)$ at the stagnation point, where $\xi=-(k\nu)^{-1}$ by (3.15), while the seventh column shows the corresponding observed

values read from Fig. 2. Also, the eighth column shows the calculated values of the drag coefficient C_N which is given theoretically by

$$C_N = C_{N\mathrm{w}} - (1 - q_s^2)\,, \tag{5.1}$$

where

$$C_{N\mathrm{w}} = \int_0^1 C_{p\mathrm{w}}(s)ds\,. \tag{5.2}$$

The ninth column gives the observed values of C_N due to Fage and Johansen. In case when $\alpha = 15°$, the base pressure is not uniform as shown in Fig. 2 (d) so that $C_{N\mathrm{w}}$ has been calculated in place of C_N and the value is shown in the brackets in the eighth column. $C_{N\mathrm{w}}$ has also been estimated from the observed distribution of $C_{p\mathrm{w}}$ in Fig. 2 (d) and is shown in the brackets in the ninth column.

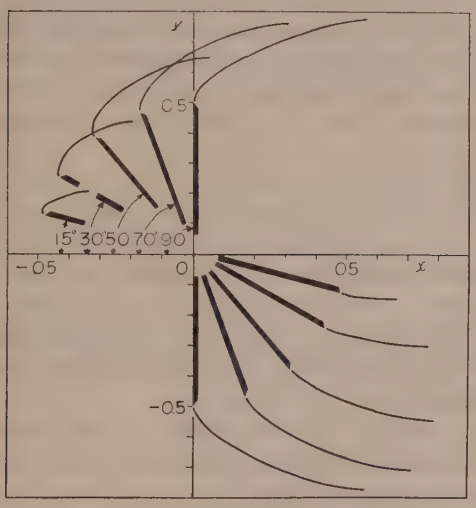

Fig. 3. Shapes of the free streamlines for the oblique plate.

The shapes of the free streamlines until they become parallel to the undisturbed flow can be obtained by (4.6) and are shown in Fig. 3. The pressure coefficients along the free streamlines parallel to the undisturbed flow can be obtained by (4.7) and (3.18), and are shown in Fig. 4.

Table II shows various data concerning the shapes of the free streamlines. Thus, in the columns from the second to the seventh are given the values of the coordinates x, y of the points S, B and B′ with the origin at the centre of the plate. The eighth column shows the values of $d' = y_{\mathrm{B}} - y_{\mathrm{B}'}$, while the ninth column gives the values of the ratio d'/d'', where d'' is equal to $2y_{\mathrm{S}}$. This ratio d'/d'' gives the rate of spreading towards downstream of the distance between the free streamlines. For comparison the longitudinal spacing of Kármán vortex street h is shown in the tenth column, which has been determined from the observed value of the lateral vortex spacing a due to Fage and Johansen, using the well-known Kármán's relation $h = 0.281\,a$.

The principal results of our calculations are summarized below:

[1] The calculated values of the normal force acting on the plate become smaller and smaller than the observed ones as α decreases, but they coincide fairly well with each other in cases when $\alpha = 90°$, 70°, 50° and 30°. In this range of values of α the observed base pressure of the plate is almost uniform.

[2] The calculated position of the stagnation point on the oblique plate is nearer to the leading edge than the observed one in cases when $\alpha = 50°$ and 30° (Table I). From Fig. 2 it is found that the main discrepancy between the calculated and the observed values of $C_{p\mathrm{w}}$ appears beyond the observed stagnation point and it becomes

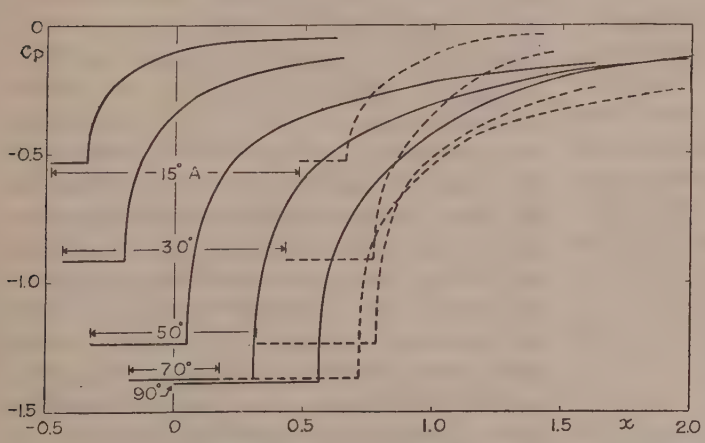

Fig. 4. Pressure distributions on the free streamlines for the oblique plate.

——— Pressure coefficient on the upper free streamline, C_{p+}.

- - - - - Pressure coefficient on the lower free streamline, C_{p-}.

← a^0 → Length of the oblique plate projected in the x-axis.

larger as the angle of attack becomes smaller. This discrepancy disappears near the trailing edge.

[3] Discrepancy of C_{pw} between the cases 15°A and 15°B exists only near the trailing edge (Fig. 2 (d)).

[4] The smaller the angle of attack becomes, the shorter becomes the portion of the constant pressure on the free streamline (Figs. 3 and 4).

[5] The value of C_p recovers rapidly to zero as it passes the range of constant pressure (Fig. 3). By Eqs. (3.18) and (4.7) it is clear that the behaviour of $C_p(x)$-curve near the points B and B′ is given by $(\delta C_p)^2 \propto \delta x$.

[6] The value of C_p recovers almost to zero at a point whose distance from the leading edge is nearly the same as the breadth of the plate (Fig. 3). When $x \gg 1$, $q-1 \propto x^{-1}$. It can be proved by the fact that $q(t)$ at infinity $(t=-r)$ takes the minimum value of unity so that $q(-r\pm\varepsilon)=1+O(\varepsilon^2)$ for small value ε and $x(-r\pm\varepsilon)=O(\varepsilon^{-2})$ by (4.7).

§ 6. Discussion

[1] In actual flow, a circulation exists around the plate, so the free streamlines cannot remain parallel to the undisturbed flow as is indicated by the notched hodograph. But the effect of the upper and the lower vortex layers on the front surface of the body may be treated as the crowd of doublets when they are situated far from the body, so that as their distance from the body becomes larger, their effect becomes smaller. The situation is the same when vortex layers change to Kármán vortex street*. Therefore the value of C_{pw} may be almost determined by the values of C_p near the body and the effect of the circulation on the far downstream free streamline may be irrelevant. This conclusion can be ascertained by the fact that the present treatment by the notched hodograph gives a fairly good result.

From the result [6] in § 5 C_{pw} may be determined by the observed data of C_p on the free streamlines in a range from the separation point to a certain point whose length is of the order of the breadth of the plate. This will be verified in the case when $\alpha=90°$ in a subsequent paper.

* This phenomenological interpretation is due to Prof. T. Maekawa.

[2] As is well known, by the form of Eq. (2.2) θ and $\ln(q_s/q)$ can be interpreted by analogy, e.g. as the displacement and the gradient of a membrane (cf. Woods[4]). Therefore, in the ω-plane in Fig. 1, if $\ln(q_s/q)$ on SB is decreased near S, it affects predominantly only the flow near S, and hence $\ln(q_s/q)$ on SS′ decreases predominantly near S. (This relation will be discussed in detail in a later paper). For this reason, in order to make the calculated C_{pw} coincide with the observed one, taking into account the discrepancies discussed in [2] and [3] in § 5, we can deduce the following conclusion about the values, C_{p+} and C_{p-}, of C_p on the upper and the lower free streamlines, namely near the leading edge C_{p+} must recover to zero more rapidly than that given by the notched hodograph, but C_{p-} may have the same character as the calculated one.

[3] When the shape of the free streamlines given in Fig. 3 is modified by this result, it may be stated that the nearer the upper free streamline flows to the back surface of the body, the more rapidly C_{p+} may recover to zero. The recovery of C_{p-} near the trailing edge may result from the strong effect of the already recovered C_{p+}.

In general, the magnitude of the vortex flux $\tilde{\omega}$ passing through the vortex layer in a unit time is given by

$$\tilde{\omega}=\int \zeta \boldsymbol{v}\cdot d\boldsymbol{s}=(q_1^2-q_2^2)/2\,, \tag{6.1}$$

where $\boldsymbol{v}$ (u, v) is the mean velocity vector and ζ $(=\partial v/\partial x-\partial u/\partial y)$ is the vorticity. The integration is taken along a path with line element $d\boldsymbol{s}$ which crosses the streamlines perpendicularly. q_1 and q_2 are respectively the magnitudes of velocities at the outer and the inner end points of the vortex layer along the path. Where C_p keeps the constant value C_{ps} along the free streamline as is the case in the notched hodograph, it must be $q_1=q_s$ and $q_2=0$ by (6.1) when $\tilde{\omega}$ remains constant. Where C_p decreases, the vorticity in the vortex layer must dissipate or diffuse. The more strongly these occur, the nearer the separated flow approaches the back of the body.

[4] When C_{p+} is modified by the above result [2], the distance between the two free streamlines may be widened. This may explain to some extent why h in Table II diminishes more slowly than d' does when α

decreases.

[5] When α decreases, d' also decreases (cf. Table II). Moreover C_{p-} may recover more rapidly than the calculated one when α is small. Therefore, even if it is taken into account that the modified distance between the two streamlines is larger than the calculated one, the non-equilibrium of the pressure between the upper and the lower free streamlines becomes more and more violent. Therefore, the condition of the constant base pressure may be destroyed gradually as α decreases. When α decreases further, the non-equlibrium of the pressure near the trailing edge cannot be supported after all and the upper free streamline may be reattached to the back surface of the plate (cf. e.g. Crabtree[5]). This phenomenon will be treated in later papers.

Acknowledgements

The author expresses his sincere thanks to Professor S. Tomotika for his valuable advice and kind inspection of the manuscript. The author's thanks are also due to Professor T. Maekawa for his helpful advice and to Mr. H. Yamaoka for his help in numerical calculation.

References

1) A. Roshko: NACA TN 3168 (1954).
2) A. Fage and F. C. Johansen: Proc. Roy. Soc. A **116** (1927) 170.
3) P. F. Byrd and M. D. Friedman: Handbook of Elliptic Integrals for Engineers and Physicists (Springer Verlag, 1954).
4) L. C. Woods: Quart. J. Mech. & Appl. Math. **7** (1954) 263.
5) L. F. Crabtree: J. Aero. Sci. **24** (1957) 597.

JOURNAL OF THE PHYSICAL SOCIETY OF JAPAN Vol. 13, No. 9, SEPTEMBER, 1958

Flow past a Bent Flat Plate with an Unsymmetric Dead Air at Mach Number 1

By Takeo SAKURAI*

Department of Aeronautics, Faculty of Engineering, Kyoto University

(Received May 27, 1958)

The ideal case of the flow past a bent flat plate with an unsymmetric dead air region at Mach number 1, in which a streamline comes tangentially to the plate at its leading edge, is discussed by means of the simple procedure of Imai's WKB method. Numerical results are given for several values of the form parameter.

§ 1. Introduction

Since von Kármán's pioneer work[7], the transonic flow problem has been studied by many authors. The mathematical difficulty of the problem, however, still prevents us from arriving at thorough understanding of the flow features. A few typical cases that have hitherto been attacked with success are mostly concerned with wedge profiles symmetric with respect to the chord lines. When the angle of attack is zero, it suffices to discuss the upper half of the plane of flow. Such a case has been treated by Cole[1], Trilling[8], Trilling and Walker[9], and Yoshihara[12] for the high subsonic case, by Guderley and Yoshihara[2] for the sonic case and by Vincenti and Wagoner[10] for the low supersonic case. In the case of the wedge with an angle of attack, we have to deal with the difficult boundary conditions which correspond to the unsymmetric flow pattern. The sonic flow investigated by Guderley seems to be the only case that has been dealt with analytically. He studied with Yoshihara the sonic flow past a wedge profile at an angle of attack[3] which

* This work was done at the Department of Physics, Faculty of Science, University of Tokyo. This was presented in partial fulfillment of the requirements for the degree of Doctor of Science at the University of Tokyo.

is small compared with the apex angle. He also discussed the flow past a flat plate with a small angle of attack[4], which can be regarded as the limiting case in which the apex angle of the wedge becomes small in comparison with the angle of attack.

As already mentioned, the above problems are all concerned with the wedge profiles that are symmetric with respect to the chord lines. The unsymmetry of the flow condition is wholly due to the presence of the angle of attack. In view of the fact that practical profiles are usually unsymmetric, it seems to be desirable to investigate the transonic flow past an unsymmetric profile.

As one of the simplest cases, we shall discuss the ideal case of the flow past a bent flat plate with an unsymmetric dead air region at Mach number 1, in which the zero streamline comes tangentially to the plate at its leading edge.

§ 2. Basic Equations

According to Imai's WKB method[5], the exact equation for the two-dimensional steady irrotational flow of an inviscid compressible fluid can be approximated as follows:

$$(\partial^2/\partial\tilde{\tau}^2+\partial^2/\partial\tilde{\theta}^2)\psi=0 \tag{2.1}$$

where

$$\tilde{\tau}=-\int_1^{\tilde{q}}(\mu/\tilde{q})d\tilde{q} \tag{2.2}$$

$$\mu=(1-M^2)^{1/2} \tag{2.3}$$

$$\Psi=K^{-1/4}\psi \tag{2.4}$$

$$K=(\mu\rho_0/\rho)^2 \tag{2.5}$$

and $(\tilde{q}, \tilde{\theta})$ are the magnitude and the direction of the velocity vector, M is the local Mach number, Ψ is the stream function, ρ is the density and ρ_0 is the stagnation density.

The correspondence between the physical and the hodograph planes is expressed as follows:

$$dx+idy=\tilde{q}-1e^{i\tilde{\theta}}[d\Phi+i(\rho_0/\rho)d\Psi] \tag{2.6}$$

$$\partial\Phi/\partial\tilde{\tau}=K^{1/2}\partial\Psi/\partial\tilde{\theta},\ \partial\Phi/\partial\tilde{\theta}=-K^{-1/2}\partial\Psi/\partial\tilde{\tau} \tag{2.7}$$

where (x, y) are the Cartesian coordinates and Φ is the velocity potential.

For the adiabatic gas, we have

$$\mu=\{(1-\tilde{q}^2)/(1-a^2\tilde{q}^2)\}^{1/2} \tag{2.8}$$

$$\tilde{\tau}=\tanh^{-1}\mu-a^{-1}\tanh^{-1}a\mu \tag{2.9}$$

$$K=(1-\tilde{q}^2)/(1-a^2\tilde{q}^2)^{1/a^2} \tag{2.10}$$

$$a^2=(\gamma-1)/(\gamma+1) \tag{2.11}$$

where γ is the ratio of the specific heats, and the unit of the magnitude of the velocity is taken to be the critical velocity c_*, at which the fluid velocity is equal to the local velocity of sound.

§ 3. The Boundary-Value Problem in the Hodograph Plane

Before discussing the boundary conditions in the hodograph plane, let us introduce the modified hodograph variables (τ, θ) by the following equations,

$$\theta=\tilde{\theta}/\theta_0,\ \tau=\tilde{\tau}/\theta_0 \tag{3.1}$$

where θ_0 is defined in Fig. 1. Then the basic equation (2.1) remains unchanged:

$$(\partial^2/\partial\tau^2+\partial^2/\partial\theta^2)\psi=0 \tag{3.2}$$

In the following, the $\sigma=\tau+i\theta$ plane will be called the hodograph plane.

The corresponding points in the physical and the hodograph planes are denoted by the same letters. The correspondence will be best understood if we consider the streamline (OCDO or OCBAO) on which the boundary condition $\psi=0$ is prescribed. (This streamline may be denoted as the zero streamline.) The streamline starts at negative infinity O of the physical plane horizontally with the free stream Mach number 1, which corresponds to the singular point O in the hodograph plane $\sigma=\tau+i\theta$. As we proceed along the zero

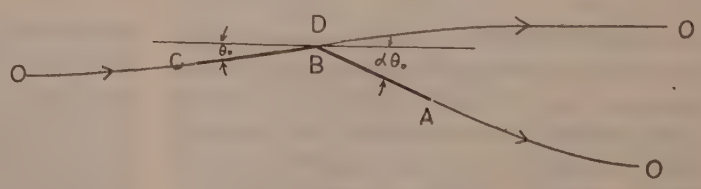

Fig. 1.

streamline towards the profile the magnitude of the velocity decreases and its inclination increases. The streamline comes in contact with the surfaces of the profile CD and CB. Tangentially at the leading edge C, where the streamline bifurcates into two branches. One of them flows along the upper side of the profile towards the point D where the sonic

velocity is reached and the streamline separates from the profile to form the free streamline DO. The other flows along the lower side of the profile towards the point B where the magnitude of the velocity vanishes and its inclination θ changes from $+1$ to $-\alpha$. Then, it proceeds along the profile towards the trailing edge A, where it separates from the profile to form the free streamline AO, with sonic velocity.

§ 4. The Method of Solution

Our task in this section is to solve the boundary value problem described in the last section for a given parameter α. The basic equation (3.2) governs the incompressible flow in the σ-plane (Fig. 2), so that the problem can

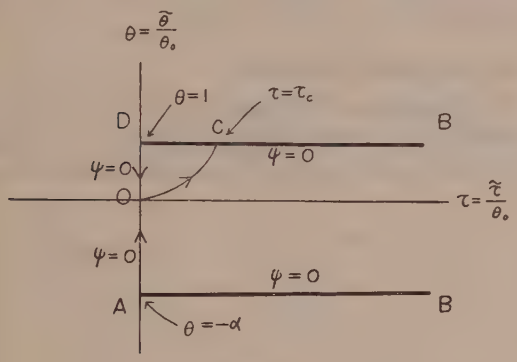

Fig. 2.

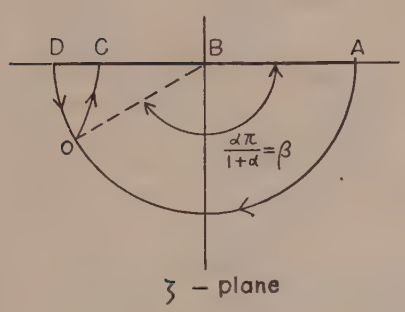

Fig. 3.

be solved easily by the usual method of conformal mapping, superposing the dipole and the quadrupole solutions. To determine the ratio of the strengths of these poles we make use of the condition that the lengths of the upper and the lower sides of the profile (CD and CB in Fig. 1) should be equal. Then the ratio of the lengths of the front and the rear parts of the profile (CB and BA in Fig. 1) is determined *a posteriori* for a given parameter α. Therefore, we can regard α as the form parameter of the profile.

By the mapping function

$$\zeta=\exp\left[-\frac{\pi}{1+\alpha}(\sigma+i\alpha)\right] \tag{4.1}$$

the flow field in the σ-plane is mapped onto the flow field in the ζ-plane. (Fig. 3) The complex velocity potential in the ζ-plane is easily found by superposing the dipole and the quadrupole solutions, as follows,

$$\begin{aligned} w=&A[\zeta\{e^{-i\beta}(\zeta-e^{-i\beta})^{-2}+e^{i\beta}(\zeta-e^{i\beta})^{-2}\} \\ &-iB\{e^{-i\beta}(\zeta-e^{-i\beta})^{-1}-e^{i\beta}(\zeta-e^{i\beta})^{-1}\}] \\ =&2A\sum_{n=0}^{\infty}\zeta^n\{n\cos(n\beta)-B\sin(n\beta)\} \end{aligned} \tag{4.2}$$

where

$$\beta=\frac{\alpha\pi}{1+\alpha} \tag{4.3}$$

Substituting Eq. (4.1) into Eq. (4.2) and taking its imaginary part, we obtain the stream function.

$$\begin{aligned} \psi=&-2A\sum_{n=0}^{\infty}\exp\left(-\frac{n\tau\beta}{\alpha}\right)\sin\left\{\beta n\left(1+\frac{\theta}{\alpha}\right)\right\}\cdot \\ &\{n\cos(n\beta)-B\sin(n\beta)\} \end{aligned} \tag{4.4}$$

The flow field in the physical plane is easily found, if we substitute Eq. (4.4) into Eqs. (2.6) and (2.7). Now, we are interested only in the pressure distribution over the profile where the boundary conditions $\theta=1$ or $-\alpha$ and $\psi=0$ are prescribed. Then Eqs. (2.6) and (2.7) can be simplified, yielding,

$$dl=(K^{1/4}/\tilde{q})(\partial\psi/\partial\theta)_{\theta=\text{const}}\,d\tau \tag{4.5}$$

where l is the length measured along the profile from some fixed point on it (e.g. the leading edge C). Thus, the correspondence over the front and the rear part of the profile is described as follows,

$$dl_{\theta=1}=-A_1[\{dl^{(1)}_{\theta=1}+dl^{(2)}_{\theta=1}\}+B_1\{dl^{(3)}_{\theta=1}+dl^{(4)}_{\theta=1}\}] \tag{4.6}$$

$$dl_{\theta=-\alpha}=-A_1[dl^{(1)}_{\theta=1}+B_1dl^{(3)}_{\theta=1}] \tag{4.7}$$

where

$$\begin{aligned} dl^{(1)}_{\theta=1}=&-\frac{1}{2}\sinh\xi\left\{\frac{\cos\beta}{(\cosh\xi-\cos\beta)^2}\right. \\ &\left.-\frac{2\sin^2\beta}{(\cosh\xi-\cos\beta)^3}\right\}\frac{K^{1/4}}{\tilde{q}}d\tau \end{aligned} \tag{4.8}$$

$$\begin{aligned} dl^{(2)}_{\theta=1}=&2\sinh(2\xi)\left\{\frac{2\cos2\beta}{(\cosh2\xi-\cos2\beta)^2}\right. \\ &\left.-\frac{4\sin^2 2\beta}{(\cosh2\xi-\cos2\beta)^3}\right\}\frac{K^{1/4}}{\tilde{q}}d\tau \end{aligned} \tag{4.9}$$

$$\begin{aligned} dl^{(3)}_{\theta=0}=&-\tfrac{1}{2}\sinh\xi\sin\beta\cdot \\ &(\cosh\xi-\cos\beta)^{-2}(K^{1/4}/\tilde{q})d\tau \end{aligned} \tag{4.10}$$

$$dl^{(4)}_{\theta=1}=2\sinh(2\xi)\sin(2\beta)\cdot$$
$$(\cosh 2\xi-\cos 2\beta)^{-2}(K^{1/4}/\tilde{q})d\tau \tag{4.11}$$

$$A_1=-\frac{2\pi A}{1+\alpha},\quad B_1=-B \tag{4.12}$$

and

$$\xi=\frac{\pi\tau}{1+\alpha} \tag{4.13}$$

Here use has been made of the formula[11)]

$$\sum_{n=1}^{\infty} e^{-nt}\sin nx=\frac{1}{2}\frac{\sin x}{\cosh t-\cos x} \tag{4.14}$$

In the above formulae, the factor A_1 represents the length scale in the physical plane and it can be chosen arbitrarily; thus we obtain similar flow with various length scales for various values of A_1. On the other hand, the factor B_1 is uniquely determined for a given parameter α, by the condition that the lengths of the upper and the lower side of the profile (CD and CB in Fig. 1) should be equal. Using Eq. (4.6), the above condition can be expressed as follows,

$$\int_{\tau_c}^{0} dl_{\theta=1}=\int_{\tau_c}^{\infty} dl_{\theta=1}\rightarrow\int_{0}^{\infty} dl_{\theta=1}=0 \tag{4.15}$$

Hence the value of B_1 can be determined as

$$B_1=-\left\{\int_0^{\infty}(dl^{(1)}_{\theta=1}+dl^{(2)}_{\theta=1})\right\}\Big/\left\{\int_0^{\infty}(dl^{(3)}_{\theta=1}+dl^{(4)}_{\theta=1})\right\} \tag{4.16}$$

The correspondence between the physical and the hodograph planes are given by the integrals:

$$l_u(\tau)=\frac{1}{L}\int_{\tau_c}^{\tau} dl_{\theta=1}\qquad (0<\tau<\tau_c) \tag{4.17}$$

$$l_{lf}(\tau)=\frac{1}{L}\int_{\tau_c}^{\tau} dl_{\theta=1}\qquad (\tau_c<\tau<\infty) \tag{4.18}$$

$$l_{lr}(\tau)=\frac{1}{L}\left\{\int_{\tau_c}^{\infty} dl_{\theta=1}+\int_{\infty}^{\tau} dl_{\theta=-\alpha}\right\}\qquad (0<\tau<\infty) \tag{4.19}$$

Here the suffixes u, lf and lr signify the upper surface, the front part of the lower surface, and the rear part of the lower surface, respectively. Also, L is the chord of the profile defined as

$$L=\int_{\tau_c}^{\infty} dl_{\theta=1}+\int_{\infty}^{0} dl_{\theta=-\alpha} \tag{4.20}$$

Once the factor B_1 is determined by Eq. (4.16), the ratio of the lengths of the front and the rear parts is determined by the above formulae.

Since the pressure is a known function of τ, the pressure distribution over the profile can be obtained by the use of these τ-l relations.

The modified lift coefficient $\tilde{C}_L$ is

$$\tilde{C}_L=\frac{1}{L}\left\{\int_0^{\infty}\tilde{C}_p dl_{\theta=1}+\int_{\infty}^{0}\tilde{C}_p dl_{\theta=-\alpha}\right\} \tag{4.21}$$

where $\tilde{C}_p$ is the modified pressure coefficient;

$$\tilde{C}_p=(\gamma+1)^{1/3}\theta_0^{-2/3}C_p$$
$$=(\gamma+1)^{1/3}\theta_0^{-2/3}\frac{p-p_\infty}{\frac{1}{2}\rho_\infty q_\infty^2} \tag{4.22}$$

If the velocity is close to sonic, we can make further approximations[6)] for $K^{1/4}/\tilde{q}$ and $\tilde{C}_p$

$$K^{1/4}/\tilde{q}\doteqdot\{\tfrac{3}{2}(\gamma+1)\}^{1/6}(\rho_0/\rho_*)^{1/2}\theta_0^{1/6}\tau^{1/6} \tag{4.23}$$

$$\tilde{C}_p\doteqdot 2^{1/3}3^{2/3}\tau^{2/3} \tag{4.24}$$

where ρ_0 is the stagnation density, and ρ_* is the density at the sonic state.

§ 5. Numerical Results

We performed the integrations (4.16)–(4.21) numerically, using Simpson's rule, for the cases $\alpha=1, 2, 3, 4, 5$. The results are shown

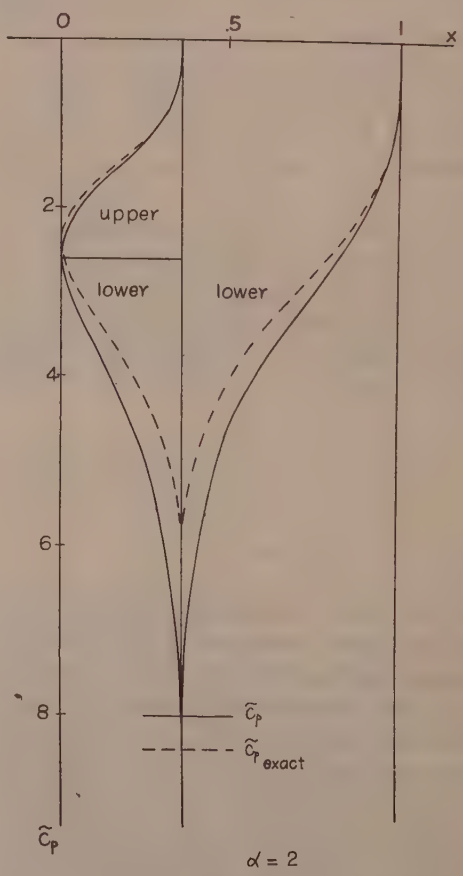

Fig. 4.

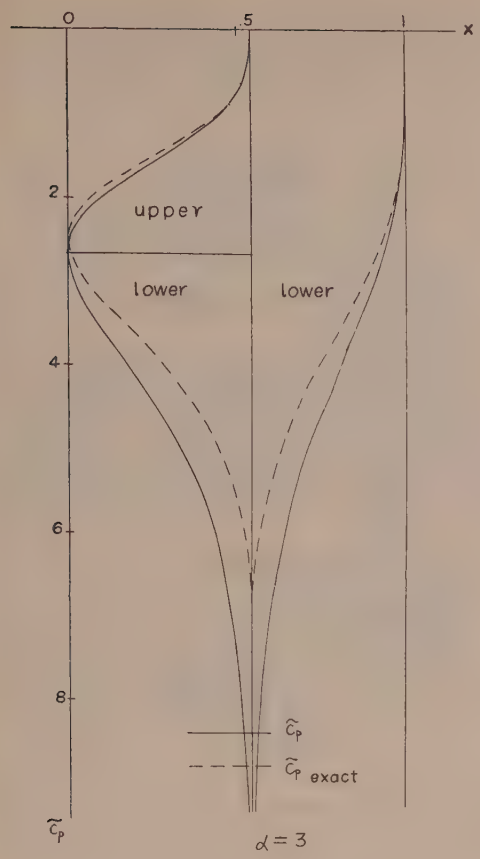

Fig. 5.

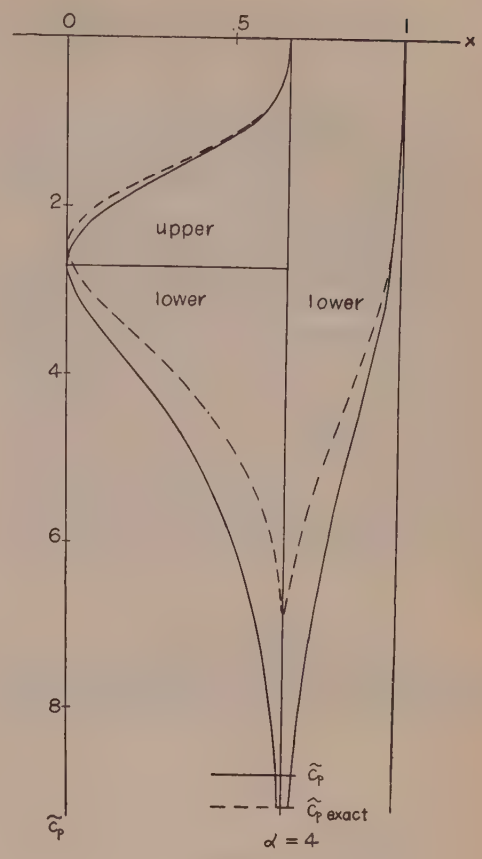

Fig. 6.

Table I

α	$\frac{\vartheta}{\theta_0}$	$\frac{\kappa}{\theta_0}$	$\frac{L_2}{L_1}$	$\tilde{C}_L$	$\tilde{C}_{L\,\mathrm{exact}}$
1	0.76	0.21	7.5	2.32	2.12
2	0.92	0.69	1.8	3.36	2.87
3	0.84	0.99	0.84	3.91	3.17
4	0.70	1.12	0.51	4.17	3.26
5	0.56	1.15	0.35	4.36	3.31

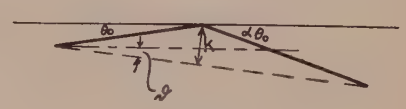

Fig. 7.

in Figs. 4–6 and in Table I.

ϑ and κ in Table I are the attack angle and the camber of the profile, respectively, as shown in Fig. 7.

If $\theta_0 \ll 1$, κ and ϑ are represented by θ_0, α, L_1 and L_2 as follows,

$$\left.\begin{aligned}\kappa&=\{1+(\alpha L_2-L_1)/(L_1+L_2)\}L_1\theta_0\\ \vartheta&=\{(\alpha L_2-L_1)/(L_1+L_2)\}\theta_0\end{aligned}\right\} \tag{5.1}$$

In Table I $\tilde{C}_{L\,\mathrm{exact}}$ are calculated by means of (4.21) using the exact value of $\tilde{C}_p$, while $\tilde{C}_L$ are estimated using the approximated value given by (4.24). The applicability of the transonic approximation becomes questionable

Fig. 8.1.

Fig. 8.2.

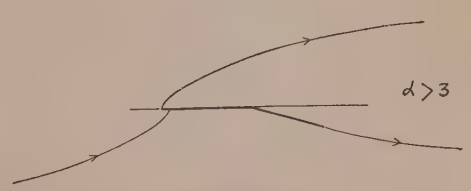

Fig. 8.3.

in the neighbourhood of the stagnation point at middle part of lower side of the profile. The comparison of $\tilde{C}_{L\,\mathrm{exact}}$ and $\tilde{C}_L$ shows that the approximation is comparatively good for the small value of α but becomes worse as α increases. Since α corresponds to the deflection angle of the rear half of the profile, these results seem to be plausible.

As was mentioned already, our solutions deal with a family of the ideal cases where the zero streamline touches the profile tangentially at its leading edge and ϑ may be considered as a kind of critical angle of attack. Thus, for example, the flow past a bent flat plate corresponding to $\alpha=3$ will change its type in the manner as shown in Fig. 8 as the angle of attack is smaller than, equal to, or greater than the critical value $0.84\,\theta_0$, respectively.

Aknowledgement

The writer wishes to express his cordial thanks to Professor Isao Imai for his hearty guidance and continual encouragement. The writer is also indebted to Professor Hidenori Hasimoto for his invaluable advice and discussions in the course of this study.

References

1) J. D. Cole: J. Math. Phys. **30** (1951) 79
2) G. Guderley and H. Yoshihara: J. Aeron. Sci. **17** (1950) 723
3) G. Guderley and H. Yoshihara: J. Aeron. Sci. **20** (1953) 757
4) G. Guderley: J. Aeron. Sci. **21** (1954) 261
5) I. Imai: J. Math. Phys. **28** (1949) 173
6) I. Imai: J. Aeron. Sci. **19** (1952) 496
7) Th. v. Kármán: J. Math. Phys. **29** (1947) 182
8) L. Trilling: Z. a. Math. Phys. **4** (1953) 358
9) L. Trilling and K. Walker: J. Math. Phys. **32** (1953) 72
10) W. G. Vincenti and C. B. Wagoner: N. A. C. A. T. R. **1095** (1952)
11) Magnus and F. Oberhettinger: Formeln und Sätze für die Speziellen Funktionen der Mathematischen Physik (1948) 213
12) H. Yoshihara: J. Aeron. Sci. **24** (1957) 661

Short Notes

This section is intended to secure prompt publication of important discoveries in physics. The reports should not exceed 800 words in length. A figure of size 7cm × 7 cm will be counted as 150 words.

J. PHYS. SOC. JAPAN **13** (1958) 1061

Observation of the Lateral Photovoltage by Surface Field Effect

By Makoto KIKUCHI

Electrotechnical Laboratory, Tokyo, Japan

(Received June 18, 1958)

It was expected that the lateral photovoltage[1,2] could be observed by the surface field effect. In our experiment, apparatus was constructed as shown in Fig. 1. A chopped light is focused on the germanium specimen whose back surface is facing to a metal electrode separated by a mylar spacer.

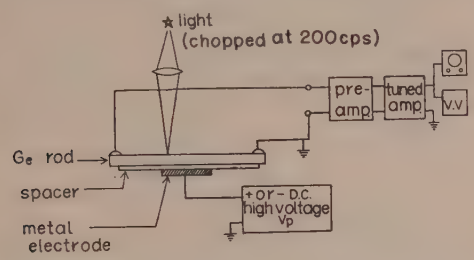

Fig. 1. Experimental apparatus for the measurment of lateral photovoltage.

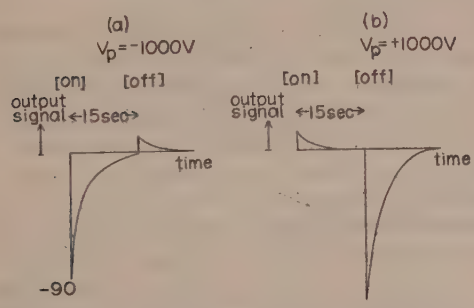

Fig. 2. Time dependence of the lateral photovoltage. (n-type 25 ohm-cm, thickness 150 microns) The light spot is at the position of 1.0 mm in Fig. 3.

When no high voltage is applied to the metal electrode, no output signal is observed. If, however, high voltage is applied, either plus or minus output signal can be observed depending on the position of the small light spot along on the germanium specimen. The sign of the signal is detected from the pattern on the oscilloscope.

Fig. 2 shows the time dependence of the output signal measured on an n-type 25 ohm-cm specimen (150 microns in thickness). The decay of the signal after "on" and "off" of the high voltage is, as expected, quite similar to the one observed in the ordinary surface field effect. Fig. 3 and 4 show the results of the dependence of the signal (at the instant of the high voltage "on") on the position of the light spot along on the specimen. As shown in the figures, the sign of the signal for the same electrode voltage are opposite for p-type and n-type samples.

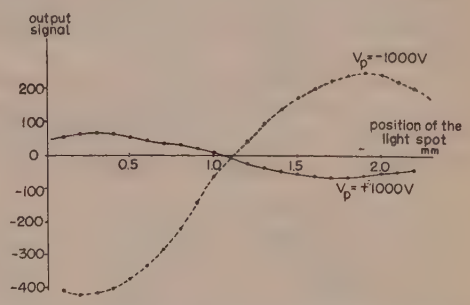

Fig. 3. Dependence of the lateral photovoltage on the position of the light spot. n-type 25 ohm-cm.

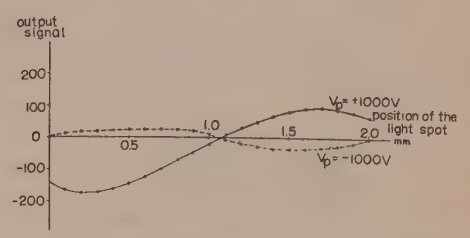

Fig. 4. Dependence of the lateral photovoltage on the position of the light spot. p-type 1 ohm-cm.

The variation of the surface conductance and the surface recombination velocity with the surface field was measured in parallel to determine the surface potential. The results will be presented in the near future.

References

1) Moore and Webster: Proc. I. R. E. **43** (1955) 427.
2) Wallmark: Proc. I.R.E. **45** (1957) 474.

J. PHYS. SOC. JAPAN **13** (1958) 1062

Study on Annealing of Radiation Induced 1/*f* Noise in Ge *p*—*n* Junction

By Ki-ichi KOMASTUBARA
Kobe Kogyo Corporation
and Utaka HASHIMOTO
Miyakozima Techinical High School

(Received June 28, 1958)

The 1/*f* noise of Ge *p*—*n* junction is strongly enhanced by pre-irradiation of γ ray as was reported by Inuishi[1]. We have investigated its annealing process in more detail.

The annealing of the short circuit current noise of the *p*—*n* junction with reverse bias voltage after 5×10^6 röntgen preirradiation of γ ray from Co^{60} is shown in Fig. 1 and 3. It is interesting to

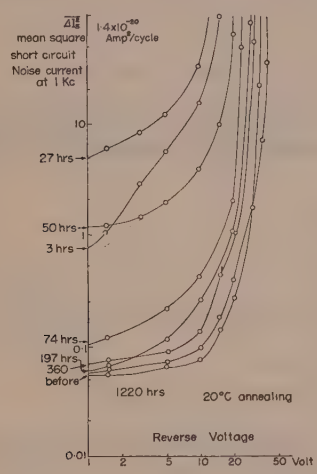

Fig. 1. Noise is reverse voltage at different time.

note that the short circuit current noise increases immediately after irradiation and then decrease to the level of before irradiation value. The frequency spectrum reveals that thise noise is mainly 1/*f* type. This annealing speed increases with increasing annealing temperature, but the tendency of the noise variation was similar, as shown in Fig. 3. The variation of grounded emitter current gain, α_{cb}, when operated as a transister, is also shown in Fig. 3, and Fig. 2 shows the changes of the reverse current after γ irradiation during annealing process.

The sample used for this study was the collector junction of *p*—*n*—*p* fused transistor which were sealed in vacuum of 10^{-4} mm Hg in order to keep the surface free from the troubles by unknown factors caused by γ ray irradiation. There may be two types of recovery process of defect. One is the rapid variation of noise level, and of α_{cb}, and the other is a very slow variation of Is and the

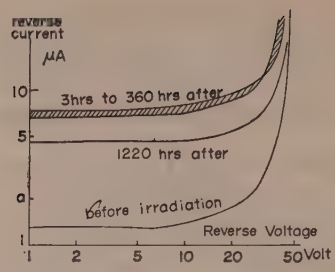

Fig. 2. Reverse current with different times of annealing.

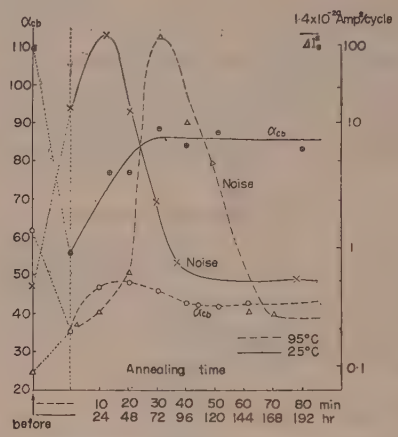

Fig. 3. Annealing curves of noise at 1 kc, 5 V, and α_{cb} of 1 mA, 5 Vc.

long time variation of α_{cb} and noise.

The mechanism of the above mentioned annealing process is not clear at present, however, one possible speculation may be as follows. Since interstitual atoms introduced by γ irradiation have larger diffusion constant in comparison with vacancies, the former would diffuse more rapidly and stays at surfaces or dislocations. The Vacancies, on the other hand, remains persistently, and may constitute slow annealing process. So perhaps interstitial diffusion causes some noise and the noise may increass at first step of annealing. The increase of 1/*f* type noise may be mainly caused from increase of surface inversion layer and increased defect under γ ray irradiation. It should be emphasized that the annealing speed of α_{cb}, and reverse current were small in comparison with that of 1/*f* noise, but if we assume the recovery of conductivity of bulk wafer is rapid and surface recombination velocity *S* is hard to recover from above speculation, we may have some clues. We can estimate 0.59 eV for numerical value of the activation energy for rapid decay of noise curves in Fig. 3.

Reference

1) Y. Inuishi: J. Phys. Soc. Japan **2** (1957) 439.

J. PHYS. SOC. JAPAN **13** (1958) 1063~1064

A Remark on the Chemical Kinetics in Polymers during Irradiation

By Tsutomu WATANABE

Department of Applied Physics, Faculty of Engineering, University of Tokyo, Tokyo

(Received June 20, 1958)

In studying the chemical mechanism of radiation effects of polymers, it has usually been regarded that the radical concentration is stationary constant[1]. But it is very questionable on the stand point of the paramagnetic resonance data of irradiated polymers[2].

Let us set v the concentration of radical produced by the radiation, r the radiation dose, I the dose rate of irradiation, γI the radical production rate per unit volume per unit time, α', β' radical reaction constant of unimolecular and bimolecular type respectively, then the equation for v is expressed as follows:

$$\gamma I-\alpha' v-\beta' v^2=\frac{dv}{dt}=I\frac{dv}{dr}\,. \qquad (1)$$

The solution of (1) with $v(r)=0$ at $r=0$ becomes

$$v=\frac{ab[1-\exp(-\sqrt{\alpha^2+4\beta\gamma}\cdot r)]}{b-a\cdot\exp(-\sqrt{\alpha^2+4\beta\gamma}\cdot r)}\,, \qquad (2)$$

where

$$a=(-\alpha+\sqrt{\alpha^2+4\beta\gamma})/2\beta\,,\quad b=(-\alpha-\sqrt{\alpha^2+4\beta\gamma})/2\beta$$

$$\alpha'=\alpha I\,,\qquad \beta'=\beta I\,.$$

And after irradiation, the tendency of decay of v is

$$v=\frac{\alpha v_0\exp(-\alpha It)}{\beta v_0[1-\exp(-\alpha It)]+\alpha} \qquad (3)$$

where v_0 is the concentration at $t=0$. Consequently, the value of v at the irradiation dose r and after a time t, is expressed in the case of $\alpha\ll\beta v$,

$$v=\frac{\sqrt{\gamma/\beta}\tanh(\sqrt{\gamma\beta}\cdot r)}{It\sqrt{\gamma\beta}\tanh(\sqrt{\gamma\beta}\cdot r)+1}\,, \qquad (4)$$

and in the case of $\alpha\gg\beta v$

$$v=\frac{\gamma}{\alpha}e^{-\alpha It}(1-e^{-\alpha r})\,. \qquad (5)$$

Calculating γ from G value and in comparison with teflon and polymethylmethacrylate data the measured v agrees roughly with the equation (5) as shown in Fig. 1. α' is estimated to be about 2.8×10^{-3} in teflon and of the order of $10^{-4}\,\mathrm{sec}^{-1}$ in PMMA. In the case of other polymers the data

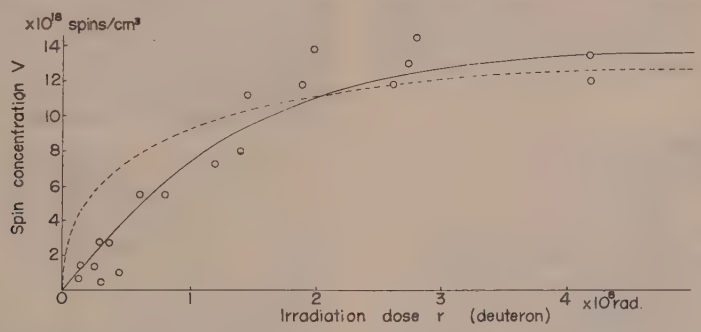

Fig. 1. Spin concentration dependence on irradiation dose in teflon (after Abe). - - - - - curve of Eq. (4), ——— of Eq. (5).

is not enough to decide the value of α' and β', but by assuming (4), or (5), α' or β' is estimated from v, resulting

$$\alpha'=10^{-2}\sim10^{-4}\,\mathrm{sec}^{-1}\ \text{or}\ \beta'=10^{-18}\sim10^{-20}\,\mathrm{cm}^3\,\mathrm{sec}^{-1}$$

in the cases of polyethylene and polystyrene.

In the case of $\alpha\gg\beta v$, the reaction of radical disappearance can be considered that the reaction like

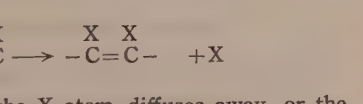

takes place and the X atom diffuses away, or the cage effect such as

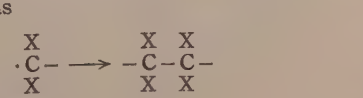

is often occurred.

From these results it may well be said that the life-time of radical is pretty long ($10^2\sim10^4$ sec) in solid polymers, and it is not good to assume the stationary state. The long life-time is also expected by the facts of graft copolymerization of gas phase monomers to the solid polymer after irradiation. As it has been measured that at 30 minutes after the cease of irradiation the graft copolymerization can take place in polyethylene, nylon and polyvinyl alcohol,[3] it is properly said that the above conclusion is reasonable.

The author wishes to express his thanks to Prof. H. Abe for his kind offering of experimental data and giving discussions.

References

1) R. W. Pearson: J. Polym. Sci. **25** (1957) 189;

R. Simha and L. A. Well: J. Phys. Chem. **61** (1957) 425, etc.
2) H. Abe: private communication; E. E. Shneider: Diss. Faraday Soc. No. 12 (1955) 158.
3) Y. Shinohara et al; T. Ohnishi: The Second Isotope Congress of Japan, Feb. 4–6, 1958 Tokyo.

J. PHYS. SOC. JAPAN **13** (1958) 1064~1065

Effects of Impurities and Temperature on the Spectra of Electroluminescence

By Ryoichiro HUZIMURA
Department of Applied Physics, Kyoto University, Kyoto

and Tunahiko SIDEI
Department of Nuclear Science, Kyoto University, Kyoto

(Received April 8, 1958)

The dependence of the electroluminescence spectrum of ZnS on impurity concentration and temperature has been observed. The prepared samples are ZnS; Cu, Pb of powder type imbeded in polystyrene and they were excited by high alternating voltage of 60 c.p.s.. The emitted light was recorded by a combination of a spectrometer of constant deviation type and an E.M.I. type 6262 photomultiplier.

Fig. 1 shows the normalized intensity spectra of five specimens with different impurity concentrations measured at room temperature. The composition of each sample in the figure is tabulated in Table I. They can be resolved into three Gaussian components which are centred at 4600, 5200, 5800 A. As the shape of the most intense component at 5200 A, we assumed $C \exp\{-(E_0-E)^2/0.04\}$, where $E_0=2.4$ ev. The relative intensities of the other components were determined as shown in table I. The relative total emission intensities of several samples with different impurity concentrations are also tabulated in Table I where the intensities of sample No. 1 is chosen as the standard.

From the behavior of Pb impurity in these phosphors it may be concluded that Pb intensifies the total emission intensity in proportion to its concentration without affecting the relative intensities of three components in the spectrum in a certain range of concentration. Comparing the intensities of sample No. 1, No. 4 and No. 5 in the table, we see that, with the fixed concentration of Pb, the peak at 4600 A tends to vanish at lower and higher concentration of Cu, and the peak at 5800 A tends to grow with decreasing concentration of Cu. Then, the variation of spectrum with Cu concentration is similar to the well known behavior of ordinary photoluminescence. However, when a sample of hexagonal symmetry (No. 6), which has the same initial composition as the sample No. 1, is examined, the peak at 4600A is most intense.

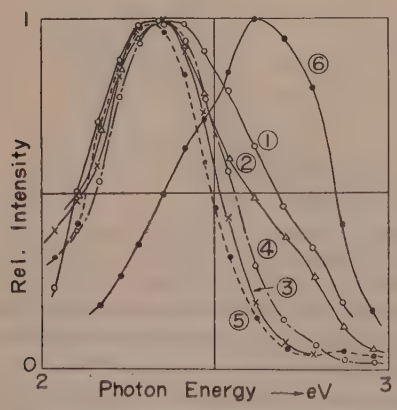

Fig. 1. Effects of composition on $E\ L$ spectra. Resolution ~ 20 A

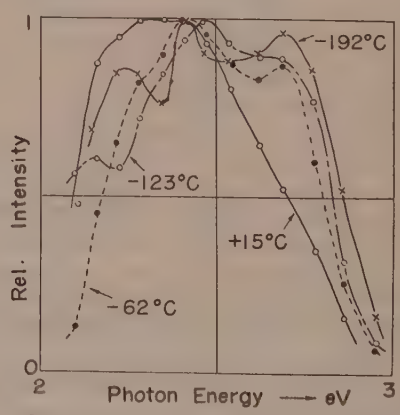

Fig. 2. Effects of temperature on $E\ L$ spectra.

Table I. Compositions and Relative Emission Intensities of $E\ L$ Spectra.

Sample No.	Added Impurity (mole ratio) Cu	Pb	Firing Temp.	Relative Emission Intensity 4600 A	5200 A	5800 A	Total
1	0.001	0.001	1000°C	0.35	1	0.45	100
2	0.001	0.0001	〃	0.33	1	0.5	10
3	0.001	0.00002	〃	—	1	0.5	3.2
4	0.003	0.001	〃	—	1	0.3	52
5	0.0004	0.001	〃	—	1	0.9	34
6	0.001	0.001	1100°C	2	1	—	14

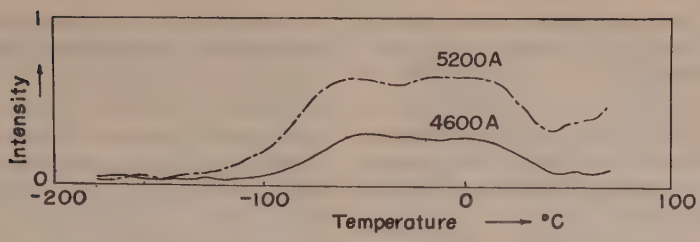

Fig. 3. Temperature variation of electroluminescence at two emission bands, 4600 A and 5200 A.

The emission color of sample No. 1 was blue at low temperature but changed to green at higher temperature. The normalized temperature variation of electroluminescent spectrum is shown in Fig. 2. The ratio of the actual peak height of 5200 A at −196°C to that at room temperature was 1/10. When the temperature was lowered, each component became sharper and the increase of the relative intensity of the 4600 A component was remarkable. These tendencies, too, are similar to the well known behavior of ordinary photoluminescence.

From these three similarities mentioned above, we may speculate that the energy scheme of luminescence center in the electroluminecence process of cub. −ZnS type is not so much different from that of the ordinary photoluminescence process, and that the high external electric field has little effect on the emission process, but has an important influence on the excitation process as discussed in many literatures.[1)]

Furthermore, the temperature variation of electroluminescence[2)] has been examined with sample No. 1 at 4600 A and 5200 A simultaneously to see the difference of the phenomena between different emission bands. Peaks of the two curves in Fig. 3 show a similar change as the function of temperature, so it may be suggested that the contribution of traps to electroluminescence is not so much different with these two emission bands.

References

1) z. B., W. W. Piper and F. E. Williams: Brit. J. App. Phys., Supplement **4** ('54) 39; G. E. Alfrey and J. B. Taylor: Proc. Phys. Soc. **68** B ('55) 775.
2) The experimental method was similar to that done by Alfrey-Taylor.

J. Phys. Soc. Japan **13** (1958) 1065~1066

Electrical Conductivity in *p*-Type InSb Under Strong Electric Field

By Yasuo Kanai

Electrical Communication Laboratory, Musashinoshi, Tokyo

(Received June 3, 1958)

Recently we measured the current-voltage characteristics and Hall effects of *n*-type InSb under strong pulsive electric field (up to about 3×10^2 volts/cm) at 90°K, and found that the carrier ionization from full band began to occur at about 2×10^2 volts/cm $v_d\simeq3\times10^7$ cm/sec.)[1)] In this note we will report the similar experimental results about *p*-type InSb.

Fig. 1 shows a typical example of the current-voltage characteristics and Hall coefficients of *p*-

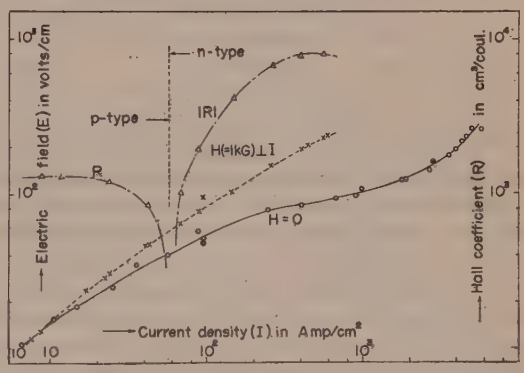

Fig. 1. The current-voltage characteristics with and without magnetic field, and Hall effect of a *p*-type InSb single crystal at 78°K. The absolute values of Hall coefficient are rather erroneous.

type InSb single crystals at 78°K. This sample had the following character at this temperature; resistivity (ρ)=2.18 ohm-cm and Hall coefficient (R) $=+2.32\times10^3$ cm³/coul.. As is shown in the figure we observed an interesting current-voltage characteristic of *p*-type InSb; i.e. at rather low electric field strength (about 15–20 volts/cm) the Ohm's law ceased to be valid and the current increased very rapidly with increasing electric field. Moreover the Hall coefficient of the crystal changed its sign from *p*-type to *n*-type and the current increase in this region was rather suppressed by the magnetic field of about 1 kG. As the characters mentioned above were independent of the conditions of lead wires-InSb contacts, we could believe that the current increase at low electric field was caused not by the electron-injection but by the ionization process from full band due to the energetic holes in *p*-type InSb. Comparing our results with those

of n-type InSb, in which the similar process occured at about 2×10^2 volts/cm, we would expect that there were very light holes in p-type InSb and the mobility of them was about ten times larger than that of electrons. These holes probably correspond to the light holes which have been theoretically predicted by several investigators[2)-5)] but not yet verified experimentally.

References

1) Kanai: J. Phys. Soc. Japan **13** (1958).
2) Kane: J. Phys. Chem. Solids **1** (1957) 247.
3) Dresselhaus: Phys. Rev. **100** (1955) 580.
4) Parmenter: Phys. Rev. **100** (1955) 573.
5) Herman: J. Elec. **1** (1955) 103.

J. Phys. Soc. Japan **13** (1958) 1066

Piezo-Effect of Selenium Rectifiers

Tadasi Numata
Nagasaki University, Ohashi-Machi, Nagasaki

(Received July 21, 1958)

Two lead wires were soldered one each on the counter electrode and on the base metal plate of a commercial selenium rectifier disk by using a small piece of Wood's metal, and the other ends of the wires were connected to a cathode ray oscilloscope.

Oscillating the rectifier disk by applying a mechanical impulse perpendicularly to the surface of the disk, such an oscillating electromotive force as illustrated in Fig. 1 was observed on the oscilloscope. When a mechanical impulse was applied in the direction parallel to the surface of the disk, the electromotive force was fairly smaller than that in the case of the perpendicular impulse.

⟶ time

Fig. 1. Piezo-effect of a commercial selenium rectifier. The large white line in the central part of the photograph is a sweep line.

The frequency of the oscillating electromotive force is equal to the frequency of the mechanical oscillation of the disk, and the amplitude of the electromotive force damps rapidly with damping of the oscillation of the disk. The magnitude of the electromotive force in Fig. 1 is about 10 milli-volts.

Rectifier disks having an evaporated nickel film as a counter electrode instead of Wood's metal used in commercial rectifiers had poor rectification and showed very small oscillating electromotive forces as illustrated in Fig. 2. Also for selenium rectifiers showing poor rectifying characteristics, the above-mentioned effects were in general small.

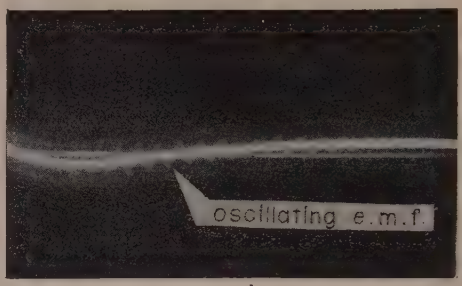

⟶ time

Fig. 2. Piezo-effect of a disk having an evaporated nickel film as a counter electrode.

The same effect was observed for selenium photocells. But in this case, the electromotive forces were considerably smaller than those of the commercial selenium rectifiers, and decreased fairly by an illumination of light.

All the above experiments had been done in a quasi-dark room.

Since bulk metallic selenium consists of microcrystalls whose orientations are at random, and since the piezo-effect is very small for the disks having an evaporated nickel film as a counter electrode as shown above, this effect may not be considered a usual piezo-effect of crystals, but to be a barrier piezo-effect caused by oscillating deformation potential of selenium associated with the oscillation of the rectifier disk.

Finally, the author expresses his sincere thanks to Professor A. Okazaki of Kyushu University for his useful discussions and encouragement.

J. Phys. Soc. Japan **13** (1958) 1066~1067

Structure of the F Band in Potassium Chloride

By Goro Kuwabara and Akira Misu
Department of Physics, Faculty of Science, University of Tokyo, Tokyo

(Received August 2, 1958)

Recent experiments[1),2),3)] on the luminescence and dichroism of the color centers suggest that between various absorption bands there may exist more intimate relations than expected before.

If the absorption band associated with the M or R band is hidden under the F band, it is expected

that some changes might occur in the F band, according to the various states of the crystal or the degree of development of the R and M bands. In this note, the distinct structure in the F band of additively colored potassium chloride observed in the excitation spectrum of luminescence and also in inducing dichroism in the R and M bands is reported.

Curve (a) in Fig. 1 is the excitation spectrum at

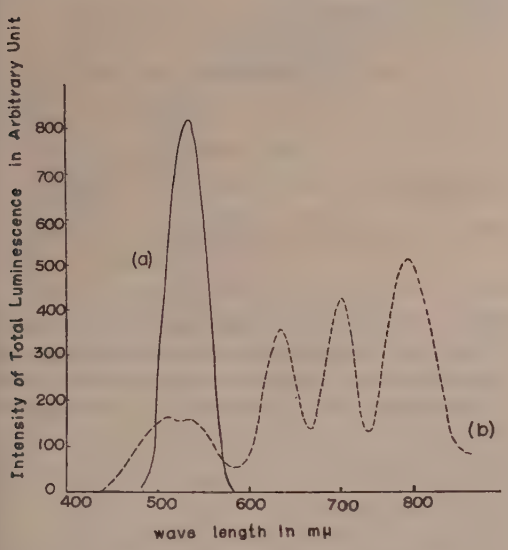

Fig. 1. The excitation spectra of additively colored KCl.
(a) Crystal containing only F centers (measured with VR-1 filter). (b) Crystal containing large amounts of M and R centers (with Si filter) measured at −170°C, (slit width 2 mμ at 546 mμ).

low temperature when a crystal contained only F centers, and the curve (b) shows the spectrum when the large amounts of R centers were developed in the same crystal by irradiating with light in the F band. For excitation the light from a Xenon-arc-lamp passed through a quartz double monochromator was used, and the luminescence in the near infrared region was measured with a PbS cell. To cut off the exciting light, VR-1 filter or a slice of Si crystal was used. In curve (a) the shape of the excitation spectrum near the F band almost coincides with that of the absorption spectrum. However, in curve (b), in which the peaks correspond to the F, R_1, R_2, and M bands, two peaks were observed in the F band, one of which nearly coincided with that of the absorption and another was displaced towards shorter wavelength side by about 20 mμ.

Fig. 2 shows the absorption spectra of the crystal irradiated at room temperature with two monochromatic lights in the F band polarized along [011] direction, one of which lies in the shorter (curve (a), 510 mμ) and another in the longer wave

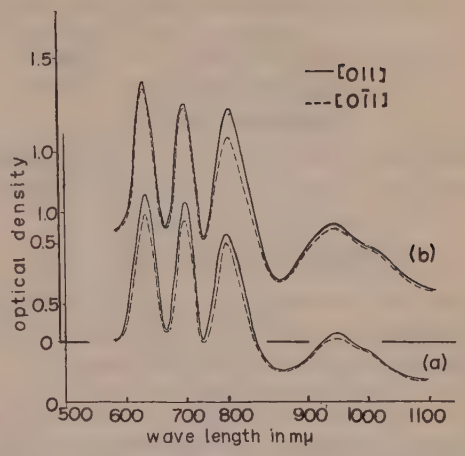

Fig. 2. Absorption spectra of the crystals irradiated at room temperature with the lights of the wavelength (a) 510 mμ and (b) 565 mμ (slit width 4 mμ at 546 mμ) polarized along [011] direction.

length side (curve (b), 565 mμ) of the absorption peak. The former produced the dichroism mainly in the R band (probably, together with the N band), and the latter mainly in the M band, respectively. If the crystal was irradiated with the polarized light in the R (R_1 and R_2) or M band, the dichroism appeared also in the F band as well as in the irradiated band. The direction of the maximum absorption in the F band lay along [011] direction in both cases, and the maximum amount of dichroism was developed at about 505 mμ or 545 mμ corresponding to the R or the M band. The R_1 and R_2 bands behaved almost similarly, that is, the dichroism in the same sense and of nearly the same amount appeared, but the M band behaved differently.

From the results above mentioned, it might be concluded that the shorter and the longer wave length parts of the F band slightly different from the peak are associated with the R and the M band, respectively. However, the role of impurities in these phenomena, especially that of divalent ions, should be checked more carefully. The detailes of the experiments on the variation of emission spectra with the exciting light, polarization of luminescence and dichroism in the N band will appear in this journal.

References

1) C. Z. van Doorn and Y. Haven: Phillips Res. Rep. **11** (1956) 479.
C. Z. van Doorn: ibid. **12** (1957) 309.
2) J. Lambe and W. D. Compton: Phys. Rev. **106** (1957) 684.
3) G. Kuwabara and A. Misu: Journ. Phys. Soc. Japan **13** (1958) 1066.

J. PHYS. SOC. JAPAN **13** (1958) 1068~1069

Small Angle Scattering of X-rays by Deuteron-irradiated Germanium Crystal

By Francisco Eiichi FUJITA* and Ulrich GONSER**

Department of Physics, University of Illinois, Urbana, Illinois, U.S.A.

(Received May 31, 1958)

Some recent investigations seem to give evidence for existence of thermal spikes produced by high energy particle bombardment in some materials. For instance, it was thought that the observed volume contraction of the GaSb crystal irradiated by 12 Mev deuterons at liquid nitrogen temperature is due to temperature spike regions in which the crystal is locally melted with about 9 % contraction and the liquid lattice configuration is then frozen in at such low temperature.[1,2,3,4] According to the theory of thermal spike,[5] their size will be 10–1000 Å in diameter.

J. S. Koehler suggested the application of small angle scattering of x-rays to this problem. Guinier gives a formula for the intensity distribution of the scattering of x-rays at small angles ϕ from N identical spherical particles with random distribution,

$$I = I_e n^2 N \exp(-4\pi^2 R^2 \phi^2 / 3\lambda^2) \qquad (1)$$

where n is the number of excess or deficit electrons in one particle, I_e the intensity scattered by one electron, λ the wave length of the incident x-rays, and R the radius of gyration of a particle regarding the electron density.

Single crystalline specimens of germanium (5 × 15 mm) were cut, polished and etched with CP–4 to a final thickness of 0.1 mm. The specimens were kept at about −180°C in a liquid nitrogen cryostat during the deuteron irradiation and the x-ray measurement. 8 Mev deuteron beam from the cyclotron irradiated the specimens perpendicularly, then they were turned to the direction perdendicular to the Cu $K\alpha$ x-ray beam from a bent crystal monochromater. A non-screen Kodack film was placed at the focus of the x-rays, 44 mm distant from the specimen, to record the scattered intensity of x-rays.

In Fig. 1 the angular intensity distribution of scattering from one irradiated crystal and that after annealing at room temperature are plotted in log I vs ϕ^2. According to Eq. 1, the size of the

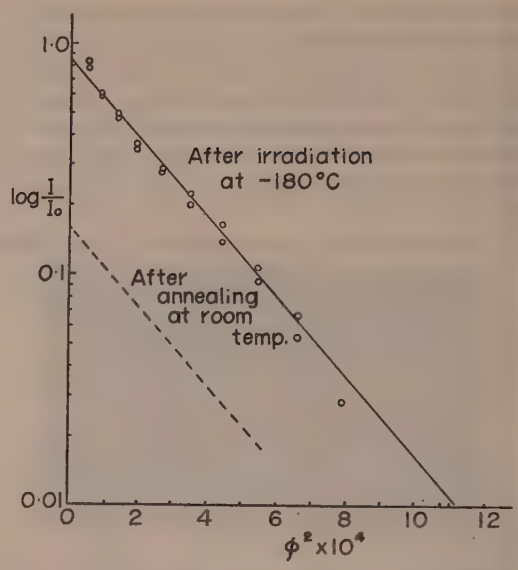

Fig. 1. The angular intensity distribution of scattering of X-rays from an irradiated germanium crystal plotted in log I vs φ^2. The dotted line is estimated from the scattered experimental values.

small particles which are supposed to be the spiked regions is found to be 35 Å in radius, R being 27 Å. Therefore, one region may contain about 9×10^3 atoms, since the atomic volume in germanium is 22.5 Å^3. From the comparison between the intensity of the incident x-ray beam and the scattered intensity, the number of particles N was estimated to be 2×10^{17}/cm^3 in a specimen irradiated by deuterons of about 5×10^{16}/cm^2 by assuming the density increase of several % in spike regions like that in melting. These results are in good agreement with the theory.[5,6,7]

Between the liquid nitrogen and room temperatures, the scattered intensity decreased to about 1/5 of the original value in spite of little change in the radius. This would suggest that the frozen lattice configuration with higher density was transformed to the normal lattice structure apart from the crystal orientation in this temperature range, retaining a considerable amount of imperfections which can still produce some scattering effect.

We want to express our gratitude to Prof. J. S. Koehler and Prof. F. Seitz for many valuable discussions and Prof. J S. Allen of the Illinois Cyclotron for his kind cooperation.

References

1) U. Gonser and B. Okkerse: Phys. Rev. **105** (1957) 757.
2) J. W. Marx, H. G. Cooper and J. W. Henderson: Phys. Rev. **88** (1952) 106.
3) L. G. Cook and R. L. Cushing: Acta Met. **1**

* Present address; Japan Atomic Energy Research Institute, Tokai-mura, Ibaragi, Japan.

** Institut für allgemeine Metallkunde und Metallphysik, Technische Hochschule Aachen, Rhein-Westf., West Germany.

(1953) 539.
4) L. R. Aronin: J. Appl. Physics **25** (1954) 344.
5) F. Seitz and J. S. Koehler: Solid State Physics **2** (Editors, F. Seitz and D. Turnbull, Academic Press INc., New York, 1956) 305.
6) F. Seitz, Manhattan District Rep., CP-1598.
7) J. A. Brinkman: J. Appl. Physics, **25** (1954) 961.

J. PHYS. SOC. JAPAN **13** (1958) 1069~1070

A Note on Numerical Evaluation of Integral Square Error

By Sitiro MINAGAWA
Faculty of Engineering, Nagoya University, Nagoya, Japan

(Received July 5, 1958)

The integral square error (or quadratic control area) is often used for determining the optimum parameters of an automatic control system. Those who are interested in inquiring into practical systems, however, find it difficult to get this value by using any one of the methods hitherto proposed[1),2)], because there is no theoretical transfer function available to them.

The author introduces here a new method of estimating the integral square error *numerically* from an indicial response. In this method, the integral square error is expressed by the product of error and time integrated with respect to error. By using this expression, we can evaluate this value more rapidly with less computational error than by performing immediate numerical integration of the square of indicial response.

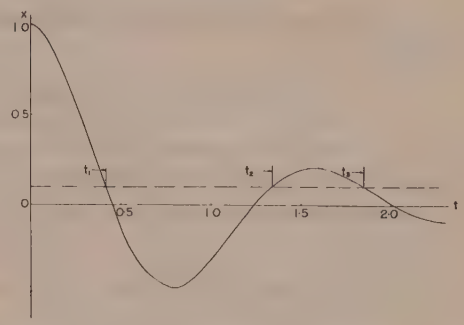

Fig. 1.

The integral square error is defined as follows:

$$\int_0^\infty \{x(t)\}^2\,dt\,, \tag{1}$$

where $x(t)$ is the deviation of controlled variable from its final value and t is the time.

By using the integration variable x instead of t, the expression (1) is easily transformed as follows:

$$\oint_{x_0}^{0} x^2\left(\frac{dt}{dx}\right)dx=[tx^2]_{x_0}^{0}-2\oint_{x_0}^{0} tx\,dx\,,$$

where x_0 is the initial value of x and the integral on the right hand side, i.e. $\oint dx$, means the integral taken along the demeanour of the system. Therefore, we get the following new form of the integral square error:

$$2\oint_0^{x_0} tx\,dx \tag{2}$$

Table.

	x / sgn (dx/dt)	1.0	0.8	0.6	0.4	0.2	0	−0.2	−0.4
t_1	−	0.0	0.16	0.24	0.31	0.38	0.45	0.53	0.67
t_2	+					1.50	1.24	1.09	0.91
t_3	−					1.65	2.03		
t_4	+						2.80		
$\sum t$		0.0	0.16	0.24	0.31	0.53	−1.56	−0.56	−0.24
$x\sum t$		0.0	0.128	0.144	0.124	0.106	0.0	0.112	0.096
Coefficients for Integration		1	3	3	1 1	4	2	4	1
		0.0	0.384	0.432	0.124	0.424	0.0	0.448	0.096
Total		0.940				1.092			
		$3/8\times0.2\times0.940=0.071$				$1/3\times0.2\times1.092=0.073$			
I.S.E.		$2\times(0.071+0.073)=0.288$							

for stable system such that

$$\lim_{t\to\infty}[tx^2]=0\ .$$

In a non-oscillatory performance, the expression (2) becomes

$$2\int_0^{x_0} tx\,dx \qquad (3)$$

by ordinary integral expression, but in an oscillatory performance, because there are several values of t corresponding to one value of x, we have to express as follows:

$$2\int_{x_{\min}}^{x_{\max}} \sum \left\{\mathrm{sgn}\left(-\frac{dx}{dt}\right)t\right\}x\,dx\ , \qquad (4)$$

where $\sum$ indicates the sum of all t's corresponding to one value of x and sgn stands for the sign of.

Formulae (3) and (4) are suitable for numerical integration for the reason that the calculation of square of experimental value is not required and, accordingly, this computation is much less complicated than direct numerical integration of expression (1).

We have calculated the value of the integral square error of the indicial response shown by the figure. The procedure of calculation is tabulated, where Newton-Cotes numerical integration formula[3] is used.

The main computational error arises from experimental data ambiguously read from the experimental figure. Such kind of error appearing in the calculation of the integral square error by the method stated here is about one-half that appearing in the direct numerical integration of the expression (1) in which the square of experimental data is included.

The author expects this method to be a new step for the application of Lebesgues integral to the theory of automatic control.

References

1) P. Hazebroek: Trans. A.S.M.E. **73** (1950) 39.
2) J. Dorr: Regelungstechnik **4** (1957) 114.
3) W. E. Milne: Numerical Analysis. (1949) 122.

Errata

A Note on the Normal Cathode Fall in the Glow Discharges in Inert Gases

By Yoshiyuki TAKEISHI

J. Phys. Soc. Japan 13 (1958) 767

Place	Wrong	Corrected
line 4 in section 3	clusty	crusty
line 4 in section 5	〃	〃
column 3 in Table I	〃	〃

JOURNAL OF THE PHYSICAL SOCIETY OF JAPAN Vol. 13, No. 10, OCTOBER, 1958

Excited States of Pt^{192}

By Mitsuhiro KAWAMURA, Atsushi AOKI and Takeo HAYASHI
Department of Physics, Saikyo University, Kyoto

(Received June 6, 1958)

The directional correlations of the 300 KeV–300 KeV, 468 KeV–316 KeV and 300 KeV–600 KeV gamma-gamma cascades in Pt^{192} have been measured by using the coincidence spectrometer reported previously. It is found that the spins of the 784 KeV and 920 KeV levels are 4 and 3, respectively.

§ 1. Introduction

Iridium–192 decays by electron emission to Pt^{192} and by orbital electron capture to Os^{192}. Extensive studies[1–6] have been made for the gamma radiations following the decay. The decay scheme[5] of Pt^{192} proposed recently is shown in Fig. 1. Spins and parities of the excited states of this nucleus have been investigated by the measurement of the internal conversion coefficients and the angular correlation functions.[5),7–11] However, there still remain some uncertainties on the spin values assigned to the third and the fourth excited states. Especially, for the fourth excited state, its spin seems to be even contradictory: $J_E=4$[9),12)]; $J_E=3$ or 4[5)]; $J_E=2$ or 3 or 4 or 5[11)]; $J_E=3$[10)]. The present investigation was intended to remove the above uncertainties by further measurements of the gamma-gamma angular correlations corrected more precisely for the interference effect caused by the higher energy gamma rays.

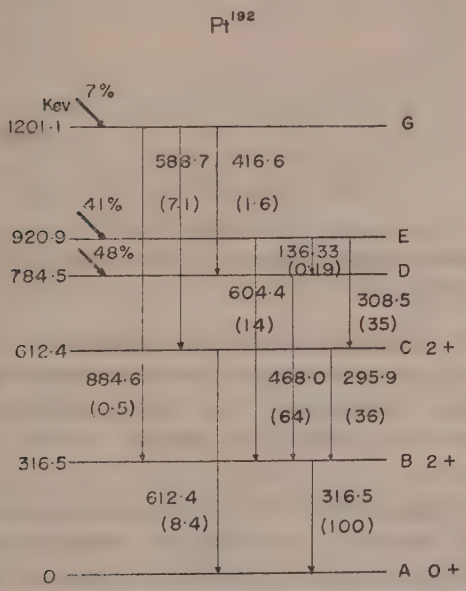

Fig. 1. Decay scheme for Pt^{192} based on Baggerly *et al.* Relative intensities of gamma rays are given in parentheses. Unambiguous spin assignments are indicated.

§ 2. Experimental Procedure

The detectors were NaI(Tl) crystals, 1½ in. diameter and 1 in. thick, obtained from Harshaw Chemical Corporation, and were coupled to the photo-cathodes of the RCA–5819 photomultiplier tubes. The coincidence spectrometer was the same one as reported in the previous paper[13)], operating at a resolving time of 6×10^{-8} sec. The source material (Na_2IrCl_6 in HCl solution) was produced at Oak Ridge National Laboratory whose radiochemical purity was more than 98 %. For the measurements of the single and coincidence spectra, as well as for the 300 KeV–300 KeV and 468 KeV–316 KeV angular correlation experiments, the source was prepared by enclosing the solution in a thin glass sphere having about 1 mm inner diameter. While, in the case of the 300 KeV–600 KeV angular correlation experiment, linear source, placed symmetrically on the axis of the rotation of the counter system, was used in order to increase the source intensity. The extranuclear interaction was minimized by using the sources in liquid form. Following procedures were taken to get the true correlation function from the measured one. When the measurements were performed with the linear sources, the experimental data were fitted firstly with the theoretical correlation function corrected for both the finite source size and the detector size. This corrected function[14)] can be written as

$$\overline{W}(\theta)=1+A_2\left[G_2P_2(\cos\theta)+\frac{1}{4}\left(\frac{L}{D}\right)^2(1-P_1(\cos\theta))P_1(\cos\theta)\right]$$
$$+A_4\left[G_4P_4(\cos\theta)+\frac{1}{4}\left(\frac{L}{D}\right)^2(1-P_1(\cos\theta))\left(P_1(\cos\theta)+\frac{7}{3}P_3(\cos\theta)\right)\right], \qquad (1)$$

where L, D, and G's denote the length of the linear source, the distance between the source and the front surface of the crystal and the attenuation factors due to the finite detector size, respectively. Then, by using A's in Eq. (1) thus obtained, the true correlation function is expressed as

$$W(\theta)=1+A_2P_2(\cos\theta)+A_4P_4(\cos\theta)\,. \quad (2)$$

To get the corrected function for the point source, it is enough to insert $L=0$ in Eq. (1).

§ 3. Measurements and Results

1) *Single and coincidence spectra*

The result of the gamma ray spectrum measurement is shown in Fig. 2. The 300 KeV and 600 KeV peaks in Fig. 2 correspond to the composite peak of the 296 KeV, 308 KeV and 316 KeV gamma rays, and that of the 589 KeV, 604 KeV and 612 KeV gamma rays, respectively. The peak area ratios of the measured 300 KeV, 468 KeV and 600 KeV gamma rays were consistent with those calculated from the gamma ray intensities reported by Baggerly *et al.*[5] The spectra of the gamma rays in coincidence with the 300 KeV and 468 KeV gamma rays are also given in Figs. 3–4. In measuring the coincidence spectra, the window of the pulse height analyzer in the fixed channel was set on the shaded portion as shown in Fig. 2, while the sweeping channel had the same window width as in the case of the single spectrum measurement.

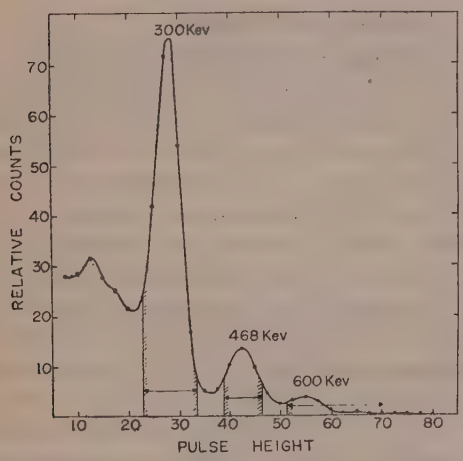

Fig. 2. Gamma ray spectrum of Ir^{192}. The shaded portions represent the windows of the pulse height analyzers in the measurement of the coincidence spectra and the angular correlations.

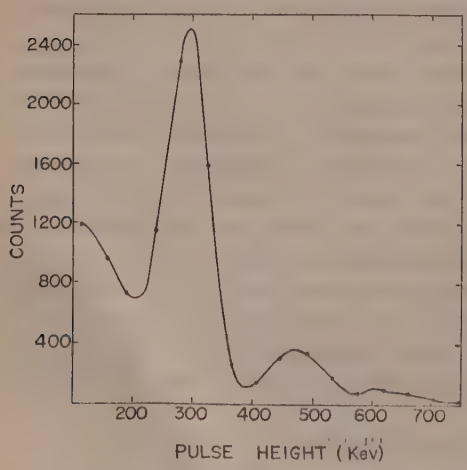

Fig. 3. Coincidence spectrum of the 300 KeV gamma rays.

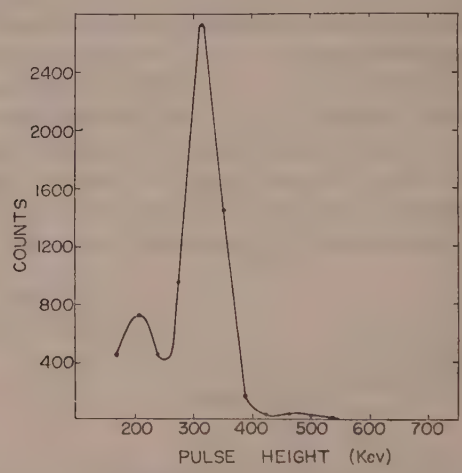

Fig. 4. Coincidence spectrum of the 468 KeV gamma ray.

2) *Angular correlation measurements*

In all cases of angular correlation measurements, the windows of the pulse height analyzers were set on the shaded portions in Fig. 2.

a) The 300 KeV–600 KeV angular correlation

In this case, the distances between the source and the crystal surfaces connected to the photomultiplier tubes for the 300 KeV and the 600 KeV gamma rays were 10 cm and 7 cm, respectively. Further, the lead absorber of 5 mm thick was placed in front of the detector for the 600 KeV gamma ray in order to reduce unnecessary background caused by the 300 KeV gamma ray entering this detector. The measurements were made at angles of 90°,

112.5°, 135°, 157.5° and 180°, and the true coincidence counting rate was about 200/min. The measured results and the most fitted curve for them are shown in Fig. 5. The most fitted A's were obtained, as described in Sec. 2, by Eq. (1) using the geometrical mean of 10 cm and 7 cm for D, $L=7$ mm, $G_2=0.937$

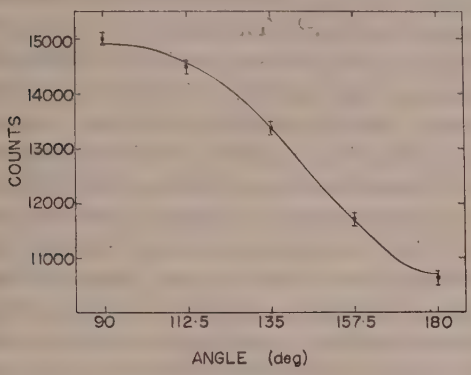

Fig. 5. Directional correlation of the 300 KeV–600 KeV gamma rays. The solid curve represents the least-squares fit of the experimental data.

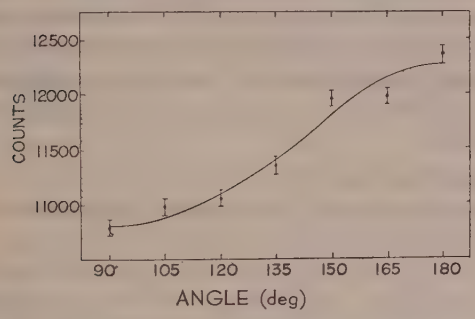

Fig. 6. Directional correlation of the 468 KeV–316 KeV gamma rays. The solid curve represents the least-squares fit of the experimental data.

and $G_4=0.802$. With these A's, the true correlation function is written as

$$W(\theta)=1-(0.200\pm0.010)P_2(\cos\theta)-(0.047\pm0.015)P_4(\cos\theta)\,. \quad (3)$$

b) The 468 KeV–316 KeV angular correlation

The distance between the point source and the front face of each crystal was 7 cm. The measurements were made at angles of 90°, 105°, 120°, 135, 150°, 165° and 180° and the true coincidence counting rate amounted to about 600/min. The experimental results and the most fitted curve for them are shown in Fig. 6. The most fitted correlation function can be expressed as

$$W'(\theta)=1+(0.080\pm0.006)P_2(\cos\theta)+(0.011\pm0.007)P_4(\cos\theta)\,. \quad (4)$$

This function is expected to contain the desired 468 KeV–316 KeV angular correlation and some contribution from the 600 KeV–300 KeV angular correlation, because, the 600 KeV gamma rays have its Compton component of about 468 keV energy. Hence, we should subtract from Eq. (4) this contribution which has been estimated by using the single spectrum of the 660 KeV gamma ray in Cs^{137} and the coincidence spectrum of the 300 KeV gamma rays. The subtracted correlation function can be represented as

$$W''(\theta)=1+(0.094\pm0.006)P_2(\cos\theta)+(0.014\pm0.007)P_4(\cos\theta)\,. \quad (5)$$

Since the attenuation factors are $G_2=0.918$ and $G_4=0.747$ for the detector geometry in this case, the true correlation function is given as

$$W(\theta)=1+(0.103\pm0.006)P_2(\cos\theta)+(0.018\pm0.010)P_4(\cos\theta)\,. \quad (6)$$

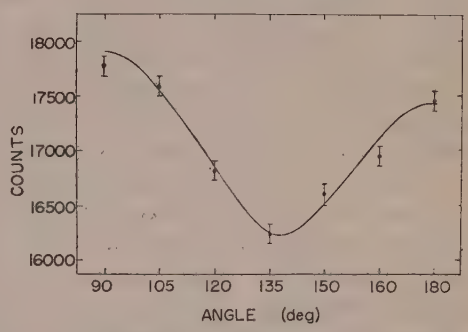

Fig. 7. Directional correlation of the 300 KeV–300 KeV-gamma rays. The solid curve represents the least-squares fit of the experimental data.

c) The 300 KeV–300 KeV angular correlation

The distance between the point source and the front face of each crystal was 7 cm. The measurements were made at angles of 90°, 105°, 120°, 135°, 150°, 165° and 180°. The true coincidence counting rate was about 1800/min. The experimental results and the most fitted curve for them are shown in Fig. 7. The most fitted correlation function can be written as

$$W'(\theta)=1-(0.051\pm0.004)P_2(\cos\theta)+(0.076\pm0.005)P_4(\cos\theta)\,. \quad (7)$$

In this case, it is also necessary to subtract the effects of the interference caused by the 300 KeV–600 KeV and 468 KeV–316 KeV gamma ray cascades. These interference effects were estimated from the spectral shapes of the

660 KeV gamma ray of Cs^{137} for the 600 KeV gamma rays and the 510 KeV annihilation gamma ray of Na^{22} for the 468 KeV gamma ray respectively, by the same procedure described in the case of 468 KeV–316 KeV angular correlation. The subtracted correlation function is

$$W''(\theta)=1-(0.053\pm0.005)P_2(\cos\theta)+(0.086\pm0.006)P_4(\cos\theta)\,. \quad (8)$$

Thus, the true correlation function, applying $G_2=0.917$ and $G_4=0.744$ for Eq. (8), can be written as

$$W(\theta)=1-(0.058\pm0.005)P_2(\cos\theta)+(0.116\pm0.008)P_4(\cos\theta) \quad (9)$$

§ 4. Analysis and Discussion

The correlation function of the 468 KeV–316 KeV cascade represented by Eq. (6) agrees very well with the theoretical function for the 4(Q)2(Q)O sequence. Taylor and Pringle[9], though obtaining the experimental result similar to us, explained their data by the 3(94.2 %D 5.8 %Q)2(Q)O sequence in which δ had negative sign.* They insisted the spin assignment of 3 to the 786 KeV level because of the existence of the crossover transition to the ground level. But according to the internal conversion measurements as reported by Baggerly *et al*[5], and Kelman *et al*[7], the 468 KeV gamma ray must be pure electric quadrupole radiation. Therefore it seems better to assign the 4(Q)2(Q)O sequence for this cascade.

Next, the results of the 300 KeV–300 KeV and 300 keV–600 KeV angular correlations were used to determine the spin of the 920 KeV level. Both correlation functions given by Eqs. (9) and (3) are expected to be composed of several elementary angular correlation functions: for instance, as easily seen in Fig. 1, the 300 KeV–300 KeV correlation function is the superposition of the 308 KeV–295 KeV, 295 KeV–316 KeV and 308 KeV–316 KeV correlation functions. Accordingly, the information about the relative weights of these elementary processes are required for the analysis of Eqs. (9) and (3). This information can be obtained from the relative intensities of the gamma rays concerned. Among several propositions on this subject, we prefer the result reported by Baggerly *et al*[5], as the peak area ratios observed in our single spectrum measurement are consistent with those calculated from their gamma ray intensities. By use of the relative intensities* shown in Fig. 1, in the case of the 300 KeV–300 KeV measurement, the contribution of each cascade to the coincidence rate was found to be: 38.8% (316 KeV–296 KeV), 30.6% (316 KeV–308 KeV), and 30.6% (308 KeV–296 KeV). For the 300 KeV–600 KeV case, we obtained 20.5 % (308 KeV–612 KeV), 43.5 % (316 KeV–604 KeV), 18.0 % (296 KeV–589 KeV) and 18.0 % (316 KeV–589 KeV). Now as the error of the intensity measurements by Baggerly *et al* is estimated to be ±20 %, the mixing ratios of the gamma rays obtained from our experiment, have corresponding errors. However, the determination of the spin value for the 920 KeV level may be possible even in such a situation, as the correlation function shows notable changes for various spin assignments to the 920 KeV level. Assuming $J_c=2$ for the 612 KeV level supported by the internal conversion measurement, several possibilities for the spin assignment of the 920 KeV level, J_E, can be examined as follows.

(Case 1) $J_E=4$

As shown in Fig. 8, the experimental curves

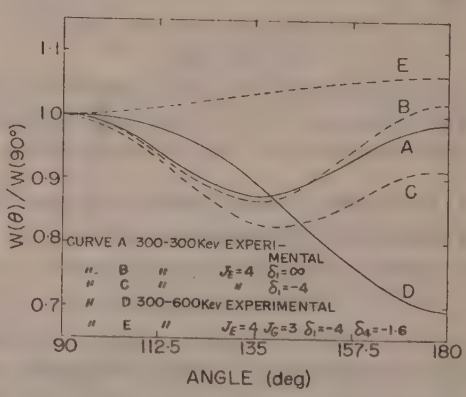

Fig. 8. Comparison of the theoretical angular correlation curves for the 300 KeV–300 KeV and the 300 KeV–600 KeV gamma ray cascades with the experimental curves represented by Eq. (9) and Eq. (3), in the case of $J_E=4$. δ_1, δ_4 denote the mixing ratios in the 296 KeV and the 589 KeV gamma rays, respectively.

* δ is the ratio of the reduced matrix element of the quadrupole transition to that of the dipole transition.

* The relative intensities of gamma rays reported recently by O. I. Sumbaev[6] agree very well with Baggerly's data.

for the 300 keV–300 keV correlation given by Eq. (9) could be fitted within statistical error with the theoretical curve corresponding to the pure electric quadrupole for the 296 KeV gamma ray. Next, we examined the 300 KeV–600 KeV result. To discuss this result, two cases of spin assignments for the 1200 KeV level should be taken into consideration; namely, $J_G=3$ and 4. In the case of $J_G=3$, all possible combinations of the multipole mixtures from $\delta_1=\pm\infty$ to $\delta_1=\pm 4$ for the 296 KeV gamma ray and from $\delta_4=\pm\infty$ to $\delta_4=\pm 1.6$ for the 589 KeV gamma ray, were examined to fit the measured data with the theoretical curve. Here, $\delta_1=\pm 4$ and $\delta_4=\pm 1.6$ correspond to the maximum and to the value far beyond the maximum of the dipole admixture reported up to the present, respectively. The theoretical curve for the case of $\delta_1=-4$ and $\delta_4=-1.6$ is given in Fig. 8. This curve shows gross disagreement with the experimental one. For all the other combinations, the theoretical curves deviated more markedly. In the case of $J_G=4$, the fit became much worse. Accordingly, we should reject $J_E=4$ to the 920 KeV level.

(Case 2) $J_E=3$

In the analysis of the 300 KeV–300 KeV angular correlation, we could fit, as shown in Fig. 9, our data with the theoretical curve corresponding to the mixing ratios given by Kelman *et al*[7] ($\delta_2=-4$ and $\delta_1=\pm\infty$ for the 308 KeV and 296 KeV gamma rays, respectively).

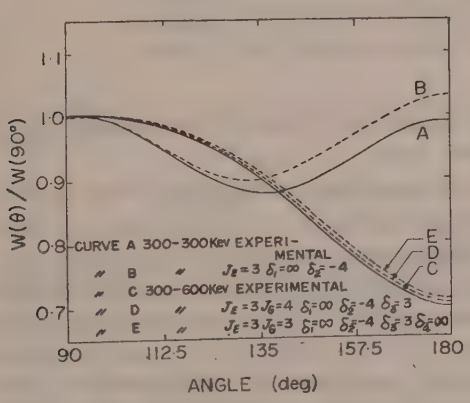

Fig. 9. Comparison of the theoretical angular correlation curves for the 300 KeV–300 KeV and the 300 KeV–600 KeV gamma ray cascades with the experimental curves represented by Eq. (9) and Eq. (3), in the case of $J_E=3$. δ_1, δ_2, δ_3, δ_4 denote the mixing ratios in the 296 KeV, 308 KeV, 604 KeV, and 589 KeV gamma rays, respectively.

Their mixing ratios obtained from the measurement of the internal conversion coefficient by their prism beta ray spectrometer seem to be reliable. For the 300 KeV–600 KeV correlation, two cases of spin assignments to the 1200 KeV level, namely $J_G=4$ and 3, were examined. For $J_G=4$, the experimental curve agreed well with the theoretical curve which was expected from the mixing ratios supported by Kelman *et al* for the gamma rays concerned ($\delta_3=3$, $\delta_2=-4$ and $\delta_1=\pm\infty$ for the 604 KeV, 308 KeV and 296 KeV gamma rays, respectively). For $J_G=3$, we could also reproduce the experimental 300 KeV–600 KeV correlation curve, assuming $\delta_4=\pm\infty$ for the 589 KeV gamma ray in addition to the above-mentioned assumption for the other gamma rays.

(Case 3) $J_E=2$ or 5

For the case of $J_E=2$, the counting rate at 135° expected from the theoretical 300 KeV–600 KeV angular correlation should be smaller than the counting rate at 180°, as the theoretical correlation curve is mainly contributed from 2(Q, D)2(Q)O sequence where the admixture of the dipole radiation is limited to the one permitted by the internal conversion data. This tendency is incompatible with our experimental data. Furthermore, $J_E=2$ seems unlikely from the information on the beta transitions. The case of $J_E=5$ should also be set aside, since the 308 KeV and 604 KeV gamma rays are predominantly electric quadrupole.

§ 5. Conclusion

Judging from the arguments in the preceding sections, it seems that the spin assignment $J_D=4$ is very reasonable, while it is concluded that the spin assignment for the 920 KeV level must be $J_E=3$, notwithstanding that $J_G=3$ or 4 can not be confirmed without ambiguity. Here, we note that Baggerly *et al* reported the same result for J_D and, for J_E, the present work agreed with Shiel's result but is not consistent with the assignment $J_E=4$ reported by Mráz.

Acknowledgement

The authors express their hearty gratitude to Professor K. Kimura and Professor S. Shimizu of Kyoto University for their sustained interest and encouragement throughout the present work. This work was partly supported by a grant-in-aid for scientific research

of the Ministry of Education.

References

1) J. M. Cork, J. H. LeBlanc, A. E. Stoddard, W. J. Childs, C. E. Branyan and W. Martin: Phys. Rev. **82** (1951) 258.
2) D. E. Müller, H. C. Hoyt, D. J. Klein and J. W. M. Dumond: Phys. Rev. **88** (1952) 775.
3) R. W. Pringle, W. Turchenetz and H. W. Taylor: Phys. Rev. **95** (1954) 115.
4) H. W. Johns and S. V. Nablo: Phys. Rev. **96** (1954) 1599.
5) L. L. Baggerly, P. Marmier, F. Boehm and J. W. M. Dumond: Phys. Rev. **100** (1955) 1364.
6) O. I. Sumbaev: Soviet Physics JETP **5** (1957) 170.
7) V. M. Kelman, R. Ya. Metskhvarishrill, V. A. Romanov and V. V. Tuchkevich: Nucl. Phys. **4** (1957) 240.
8) Bashilov, Anton'eva and Bzhelepov: Izvest. Akad. Nauk. Ser. Fiz. SSSR **16** (1952) 264, as cited in Nuclear Science Abstracts **7** No. 24B (1953) 53.
9) H. W. Taylor and R. W. Pringle: Phys. Rev. **99** (1955) 1345.
10) V. Shiel, L. D. Wyly and C. H. Braden: Phys. Rev. **105** (1957) 1521.
11) W. H. Kelly and M. L. Wiedenbeck: Phys. Rev. **102** (1956) 1130.
12) J. Mráz: Nucl. Phys. **4** (1957) 457.
13) T. Hayashi: Journ. Phys. Soc. Japan **13** (1958) 117.
14) L. S. Lawson, Jr., and H. Frauenfelder: Phys. Rev. **91** (1953) 649.

JOURNAL OF THE PHYSICAL SOCIETY OF JAPAN Vol. 13, No. 10, OCTOBER 1958

Sector Type Double Focusing Beta Ray Spectrometer
Part I General properties

Mitsuo SAKAI and Hidetsugu IKEGAMI
Institute for Nuclear Study, University of Tokyo

(Received June 28, 1958)

A small scale beta ray spectrometer was built, making use of the double focusing principle applied to sector-field. The fringing field was found to be easily corrected and not to be serious for conventional purposes. The gathering power of 0.3% was obtained for the resolving power of 0.7%. Since the source can be placed outside of the magnetic field, this type of spectrometer might serve as a powerful tool for coincidence and correlation measurements.

§ 1. Introduction

The beta ray spectrometers have been greatly developed during the last decade. The magnetic spectrometer is divided into two types, namely, prismatic beta ray spectrometer and lens type spectrometer. The electrons in the former type are deflected in the right direction to the magnetic field and in the latter type the trajectory makes only a small angle with the axis of symmetry of the magnetic field. It is a well known fact that the inhomogenious magnetic field produces the best focusing character in both type of spectrometers. The typical spectrometers with inhomogenious magnetic field are the double focusing spectrometer[1] in the former case and the intermediate image spectrometer[2] in the latter case.

Corresponding to progress of the theory of nuclear structure, it was intended to develop a spectrometer especially suitable for coincidence experiments and for angular correlation measurements which give important informations on the nuclear level. In selecting a type among many types of spectrometers, the lens type spectrometer was first excluded because a diverging electron beam should be used in this type of spectrometer, making it difficult to do the measurements of angular correlation. On the other hand in the double focusing spectrometer the source and the detector should be put in the magnetic field, making

inconvinient for coincidence measurements and especially for correlation measurements.

Under the circumstances, we were led to adopt the sector type double focusing spectrometer. This type of spectrometer is not unusual and it was built in many laboratories for analysing particles produced in nuclear reaction.[3] But in this case the solid angle was in general an order of 10^{-3} steradian and the effect of fringing field in the entrance and in the exit region has a little influence on the focusing properties. Since the beta ray spectrometer should have a large solid angle of order of 10^{-1} steradian, the fringing field above mentioned might have a large effect on the focusing properties as in the case for Kofoed-Hansen's spectrometer.[4] This fact was considered as a grave disadvantage for this type of spectrometer. However, as is seen in the proceeding section, this effect was found to be not so serious if a suitable correction was made.

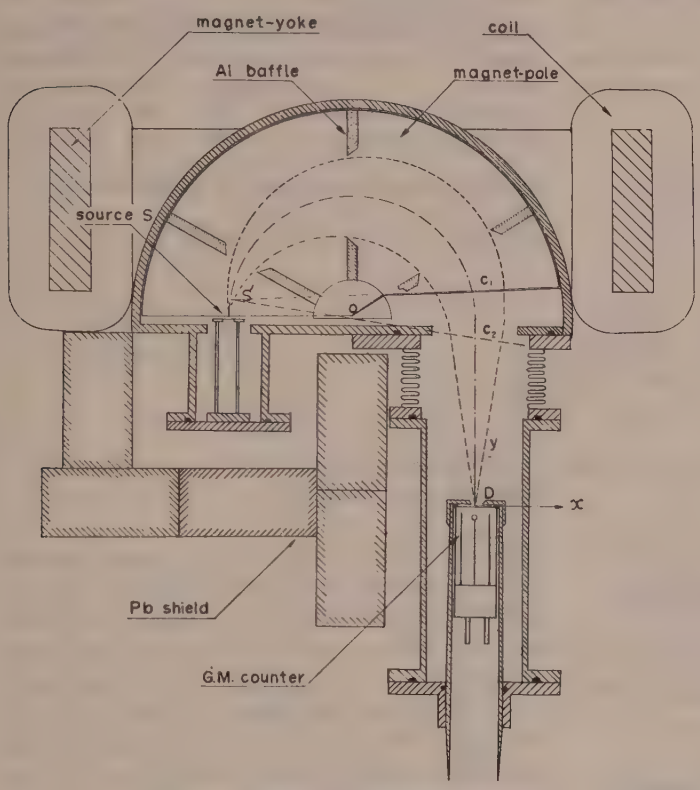

Fig. 1. Top view of sector typs double focusing beta ray spectrometer.

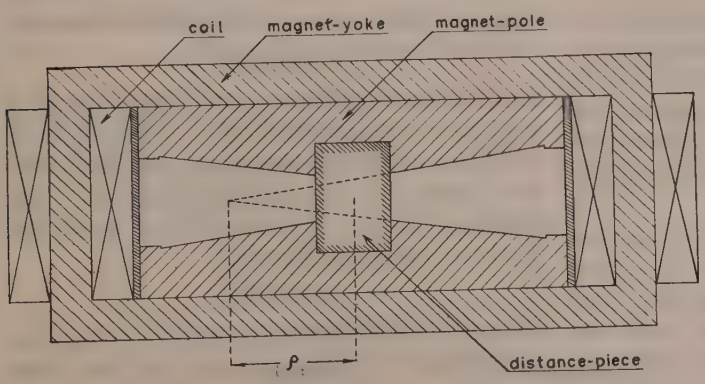

Fig. 2. Side view of sector type double focusing beta ray spectrometer.

§ 2. Design

In order to study the general properties of this type of spectrometer a small scale spectrometer with the mean radius of curvature of 9 cm was built. As is presented schematically in Fig. 1, the electrons were deflected in 180°. This angle was chosen for the practical reason that the pair of pole tips can be made at a time by cutting an iron disk machined by lathe. The inhomogeneous magnetic field between the pole tips chosen in the present apparatus has the following character;

$$B(r)=B(\rho)\left\{1-\frac{1}{2}\frac{(\rho-r)}{\rho}+\frac{1}{4}\frac{(\rho-r)^2}{\rho^2}+\cdots\right\}$$

This field distribution was easily obtained by a cone type pole tip[5] of which the extension of surface intersects on the median plane at ρ as shown in Fig. 2. The periphery of pole tips was empirically modified for keeping the field shape near the end of pole gap. The field distribution actually measured was presented in Fig. 3. After a small adjustment of ρ-value, agreement of the actual field with the theoretical one was satisfactory. The source (or the detector) was placed at S on the pole boundary. The other pole boundary

was cut as shown in Fig. 1 by taking account of the fringing field. In view of getting the virtual boundary[6] of the magnetic field at the line $\overline{C_2O}$, the cutting line of exit pole boundary was determined in the first approximation to intersect at S' and $\overline{C_1C_2}$ was chosen to 0.7 pole gap. In the present apparatus the pole gap was taken to be $1/2\rho$.

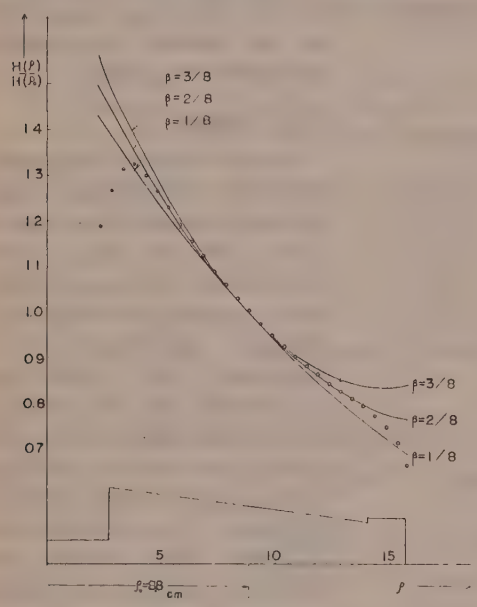

Fig. 3. Radial distribution of magnetic field.

The first order theory of this type of spectrometer[7] gives the following characters;

focusing distance: $\overline{C_2D}=1.87$
maximum solid angle:
$=A/2$; for the source at pole boundary
$=A/5.4$; for the source at the point D in Fig. 1.

where $A\ \rho^2$ is the available cross-sectional area of the electron beam in the spectrometer. In the present apparatus the maximum $A\ \rho^2$ is limited by $\rho\times\frac{1}{2}\rho$. The electron beam was defined by a baffle system which was designed on the basis of conventional second order calculation.

The focal point was first determined by varying the position of the detector in x and y directions by means of O-ring seal. (see Fig. 1.) and by measuring at each point the conversion spectra of Cs^{137}. This spectrum served as a measure of the focusing properties. The focal point of which the coordinates were denoted as x_{op} and y_{op} was presented in Table I. The counting rate and resolving power measured at each point were also tabulated. As can be noticed in this figure, the electrons were focused on a rather large focal line with about a same quality of focusing. This fact was already pointed out in the particle analyser[8] and it suggests one of the advantages for this type of spectrometer. A typical spectrum was presented in Fig. 4.

Table I Optimum point in the image area

x_{op} (cm)	+0.5	0.0	−0.5	−1.0
y_{op} (cm)	11.5	10.0	9.5	7.0
Counting rate (Arbitrary)	170	180	170	180
Resolving power (%)	0.62	0.66	0.65	0.71

The sense of x coordinate is shown in Fig. 1.

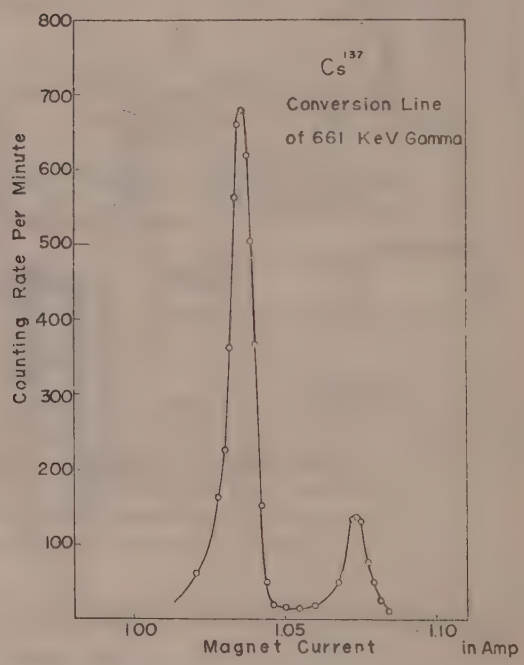

Fig. 4. Line spectrum of conversion electrons of 661 KeV gamma ray from Cs^{137}.

The fraction of electrons collected at the peak of line spectrum referred to the total electrons belonging to this line emitted from the source was defined as the gathering power. The gathering power can be obtained practically from the following formula.

$$L=n/n_0\xi$$

where n is the counting rate at the peak point, n_0 the total electrons counted by the same detector and ξ the ratio of the area of the line spectrum to the total area taken by the

spectrometer. By using a source of about 3 mm diameter, a gathering power of 0.3% was obtained for a resolving power of 0.7%.

§ 3. Concluding Remark

This type of spectrometer has the versatile characters because 1) the accessibility to the source or to the detector is very good and 2) the electron beam in pensil form can be used and 3) the good relation of gathering power to resolving power can be obtained easily without any serious consideration for the fringing field. Fig. 5 shows some examples for use of this type of spectrometer.

Fig. 5 (a) shows the coincidence and the angular correlation measurements between gamma and conversion or beta radiations. Coupling two spectrometers as in Fig. 5 (b), we are able to do the coincidence measurements for the genetic relation and the correlation function between conversion electrons and conversion electrons or beta radiations. It is worth noting that the long arm reduces largely the effect of magnetic field resulting from the other spectrometer. Fig. 5 (c) illustrates other possibility of this type of spectrometer. Two spectrometers are coupled as in the case of (b). A slit S' is set at the

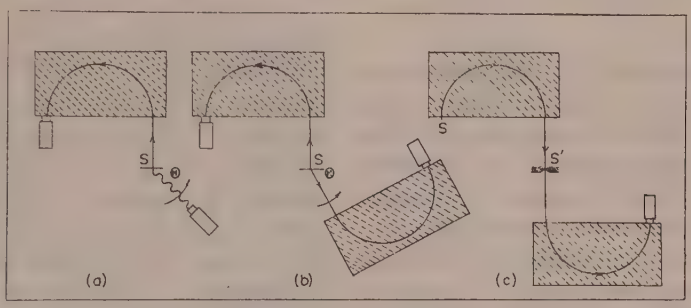

Fig. 5. Some typical setting configuration for use of sector type double focusing spectrometer.

detector point in the first spectrometer and this slit serves as the virtual source for the second spectrometer. By this setting one can easily get rid of the false counts resulting from the scattering electrons at the wall or from the electrons having the trochoidal trajectory.[9] This twin setting is especialy suitable for the measurement of the higher weak beta component in the presence of the lower strong beta component as is the case of Cs^{137}, Co^{60} and $Sc.^{64}$ This point will be verified in the succeeding report.[10]

References

1) N. Svartholm and K. Siegbahn: Ark. Mat. Astr. Fys. A. 33. (1946) No. 21.
2) H. Slätis and K. Siegbahn: Ark. f. Fysik **1**. No. 17. (1949) 339.
3) C. Snyder, S. Rubin, W. Fowler and C. Lauritsen: Rev. Sci. Inst. **21** (1950) 852 C. Mileiikowsky Ark. f. Fysik **7** No. 3, (1953) 33.
4) O. Kofoed-Hansen, J. Lindhard and O. Nielsen: Kgl. Danske Vid Selsk Med. **25** (1950) No. 16.
5) C. Mileiikowsky: Ark. f. Fysik **7** No. 3. (1953) 33.
E. Arbman and N. Svartholm: Ark. f. Fysik **10** No. 1 (1955).
6) N. D. Coggeshall: J. Appl. Phys. **18** (1947) 855.
7) D. L. Judd: Rev. of Sci. Instr. **21** (1950) 213.
8) C. Mileiikowsky: Ark. f. Fysik. **7** No. 3 (1953) 33.
9) E. Arbman and N. Svartholm: Ark. f. Fysik. **10** No. 1 (1955).
10) T. Yamazaki, H. Ikegami and M. Sakai: J. Phys. Soc. Japan, to be published.

JOURNAL OF THE PHYSICAL SOCIETY OF JAPAN Vol. 13, No. 10, OCTOBER, 1958

Sector Type Double Focusing Beta Ray Spectrometer Part II. Twin Setting Measurement of the Weak Higher Component of Cs^{137}

Toshimitsu YAMAZAKI, Hidetsugu IKEGAMI and Mitsuo SAKAI

Institute for Nuclear Study, University of Tokyo

(Received June 28, 1958)

A twin setting of two sector type double focusing beta ray spectrometers was used for measurement of the weak higher component of Cs^{137} in order to remove completely the contributions resulting from the secondary causes. The measured spectrum agreed well with those of the previous results, which were therefore confirmed to provide a reliable basis for the analysis of the coupling constants in beta decay.

§ 1. Introduction

Two sets of small scale ($\rho=9$ cm) sector-type double focusing beta ray spectrometers were constructed as models for larger ones. This type of beta ray spectrometers, as described in detail in the preceeding paper[1], is suitable for $\beta-\gamma$, $e^--\gamma$, $\beta-e^-$ and e^--e^- angular correlation experiments. In addition to these a special use for the measurements of beta ray spectra was pointed out, which consists in making use of the other spectrometer connected with one spectrometer. Since the second spectrometer selects electron momentum once more, this twin spectrometer setting is especially suitable for getting rid of the secondary effects caused in the measurements of weak higher components.

The usual measurements of the weak higher components of Cs^{137}, Co^{60}, Sc^{46} etc, which may need use of strong sources (perhaps of several milli-curies), necessarily involve the following disturbing effects resulting from the coexistence of other strong beta and gamma radiations: false counting of 1) multiply scattered electrons from the low energy beta components, 2) Compton electrons from various points of apparatus by the strong gamma rays, and 3) low energy electrons with trochoidal trajectories[2]. These effects, though they can be much reduced by using good baffle system, may still be possible to make disturbance more or less on the observed spectra. By adopting this twin spectrometer method, however, we can expect to get spectra free from these effects. Since the shapes of the higher-forbidden spectra, such as weak higher components of Cs^{137}, Co^{60}, Sc^{46}, etc., provide important informations about the coupling constants of beta decay, it seems worthwhile to measure these spectra once again by means of this

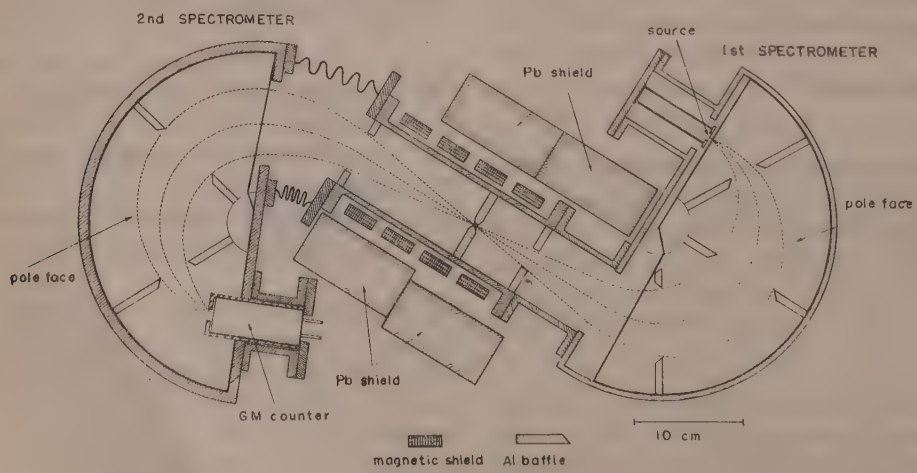

Fig. 1. Experimental arrangement.

twin setting. The present paper concerns the measurement of the weak higher component of Cs^{137}.

§ 2. Experimental Method

The arrangement of experimental apparatus is shown in Fig. 1. The source was put at the point S in the first spectrometer. Then the electrons were focused at F. If one sets the second spectrometer in such a manner that F serves as a virtual source for the second spectrometer, the electron beam passing through a slit placed at F can be refocused at D under a suitable field of the second spectrometer. Of course, the direction of electron trajectory at F is limited by the first.

When the field of the first spectrometer is fixed at $(B\rho)_1=p$, then the ideal momentum distribution of electrons passing through the slit F (i.e., of the virtual source) may be as the solid line in Fig. 2 a), with a width corresponding to the resolution of the first spectrometer. But the actual distribution may involve moreover low energy part (broken line). This part, resulting from the disturbing electrons in question, corresponds to the false counts in usual single setting. This momentum distribution is observed at D as a sweeping curve in Fig. 2 b), by sweeping the current of the second spectrometer I_2. If I_2 is fixed on peak, then the true momentum distribution of electrons incident on the detector may be as in Fig. 2 c). Being analysed by the second spectrometer, the low energy disturbing electrons are completely removed here, so far as secondary electrons produced in the second spectrometer can be regarded as negligible. The area of the peak divided by p is the value of the beta spectrum $n(p)$. In practice, to make measurements easier, we adopted so-called flat-topped method making the detector slit large enough to cover the peak. Then the sweeping curve may be flat and broad as in Fig. 2 d). In this case the over-all resolution is equal to the resolution of the first spectrometer, and we get the momentum spectrum $n(p)=N_p/p$, where N_p is the counting rates on the flat peak at $(B\rho)_1=p$.

In the present measurement the detector slit of 10 mm was used. Observed sweeping curves are shown in Fig. 3. It has a flat part of 2%. The shape of this curve was found to be independent whether $(B\rho)_1$ was set on or off a conversion line. No detectable amount of low energy electrons were found by sweeping I_2.

The present twin spectrometer method can

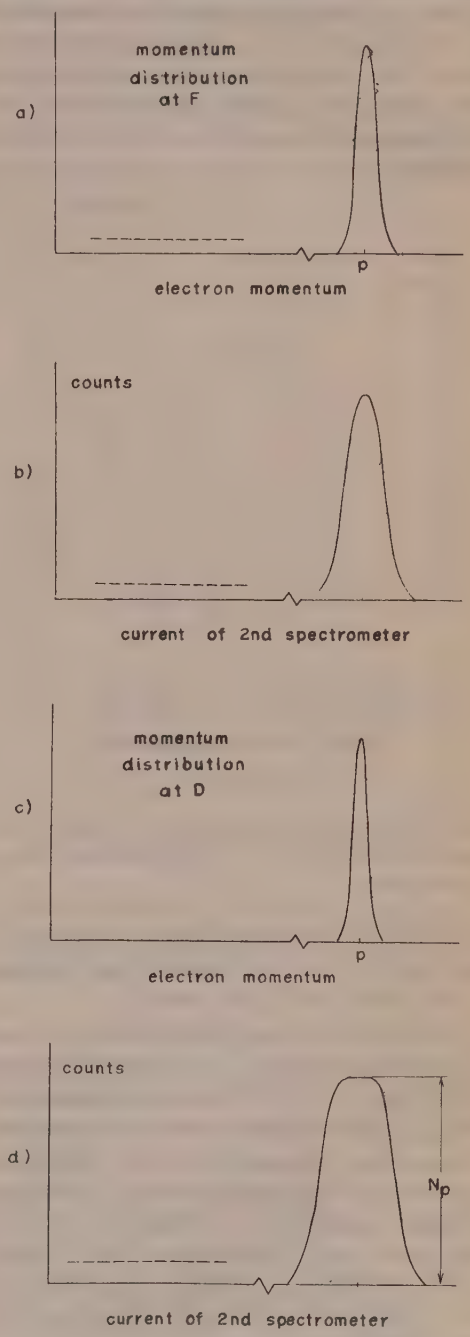

Fig. 2. Illustration of the principle of twin spectrometer method. a) momentum distribution of electrons passing through F. b) sweeping curve with a detector slit. c) momentum distribution of electrons incident on D. d) sweeping curved without a detector slit.

be compared with the case where in usual single spectrometers measurements the scintillation counter is employed as a detector for discriminating the scattered electrons by making use of the energy sensitive character of this type of detector[3]. The latter method is simpler than ours, but may be inferior because of the incomplete energy discrimination especially due to back scattering on the surface of scintillator.

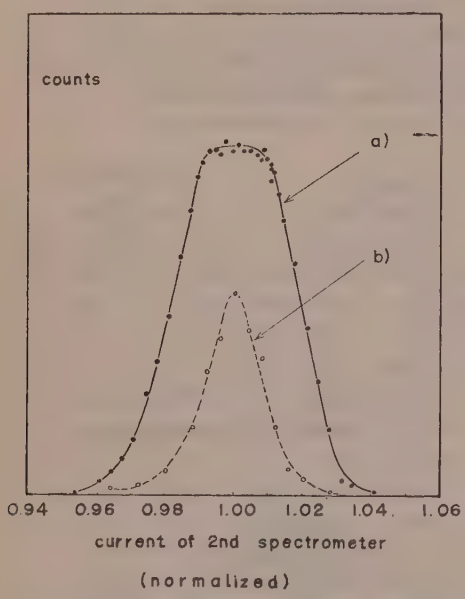

Fig. 3. Observed sweeping curves. a) with a detector slit of 10 mm b) with a detector slit of 2 mm width.

7 mm thick aluminum baffles were set as shown in Fig. 1. The slit at F was rectangle of 2 mm width and 5 mm length.

A mica end-window Geiger-Müller counter with window thickness of 3 mg/cm² was used as the detector. No influence of counter efficiency by the magnetic field was recognized.

The source contained about 2 milli-curies of Cs^{137} with high specific activity, which was uniformly spread over a rectangular area of 3 mm width and 7 mm length. The counting rates at energies just above the conversion lines of 662 Kev gamma ray were about 600 counts per minute.

The interference effect of the fringing fields of each spectrometer was first studied. Setting a source of Cs^{137} at F and a detector at S, we measured the internal conversion peak by the first spectrometer by varying the exciting current of the second spectrometer. A few percent shift of the peak was observed in case of high current. A simple magnetic shielding in the straight arm section reduced this shift to within one percent. In usual correlation experiments, where each field should vary independently, such an interference effect may be serious, but for the present purpose, where each field varies proportionally, it makes no disturbance.

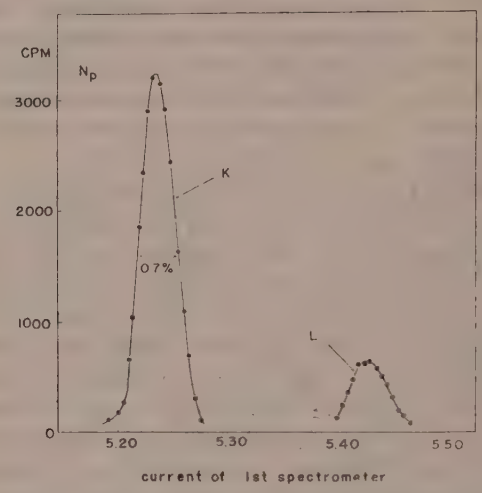

Fig. 4. Observed spectrum of the internal conversion lines of Cs^{137}.

The overall resolution and gathering power were found to be 0.7% and 0.3%, from measurement of the internal conversion line of Cs^{137}.

The spectrometer field was measured indirectly from the exciting current. Calibration was made by Cs^{137} K-internal conversion line ($B\rho=3381.3$), Cs^{137} L-internal conversion line ($B\rho=3498.2$) and Co^{60} 1.17 Mev K-internal conversion line ($B\rho=5322.5$). The currents were stabilysed within 0.1%.

§ 3. Result and Discussion

In the present experiment the efforts were focused on the measurement of the higher component of Cs^{137} above the internal conversion lines ($\gtrsim 0.65$ Mev). For each $(B\rho)_1=p$, we measured the sweeping curves as in Fig. 3 and got N_p. This procedure was rather tedious, especially near the end point of the spectrum, because of difficulty in finding peaks.

Usual Kurie plot $\sqrt{n(q)/f}$ of the observed spectrum is shown in Fig. 5 and experimental

correction factor $C=n(p)/(E_0-E)^2f$, which indicates the deviation from allowed type, is plotted in Fig. 6 as a function of electron energy E. The broken curve is the best fitted function: $C=q^2+0.003p^2$. The results are in good agreement with the previous investigators[4),5)]. This means that in their experiments such disturbing effects, so far as the shape of Kurie plot was concerned, are regarded as negligible.

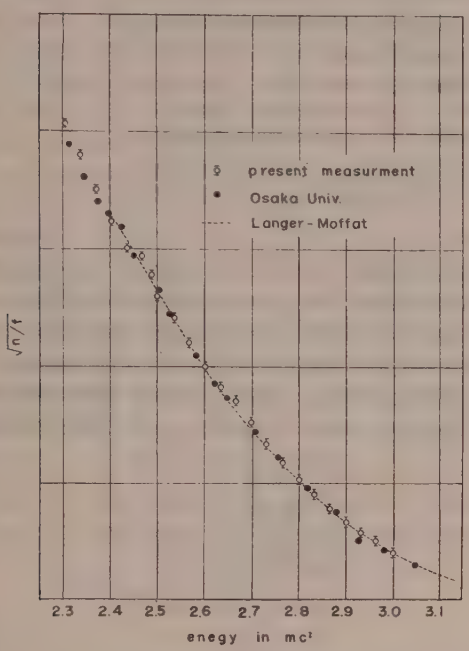

Fig. 5. Kurie plot of the higher component of Cs^{137}. The previous results are also plotted. These are normalized at $E=2.6$.

It is well known that the weak beta transition from $g_{7/2}$ ground state of Cs^{137} to the $d_{3/2}$ ground state of Ba^{137} exists with branching ratio of 8% and that its spectrum indicates twice-forbidden shape involving no change of parity and a spin change of two. L. M. Langer and R. J. D. Moffat, who studied in detail this beta ray component with a magnetic spectrometer, showed the shape of the spectrum could be adequately described by a twice-forbidden factor, C_{2T}, resulting from the tensor form of interaction. Recently the same experimental results were reported by T. Katoh, M. Nozawa, Y. Yoshizawa and Y. Koh, who made analysis of the shape of the spectrum assuming only a linear combination of the ordinary scalar and tensor interactions and concluded the sign of G_S/G_T was negative. Although these analyses will perhaps have to be corrected in near future from the today's viewpoint[6)], the present experiment confirmed that their experimental data are reliable and can be a good basis for analysis.

The present authors express their sincere thanks to Prof. S. Kikuchi, director of this institute, for his constant encouragement during this research.

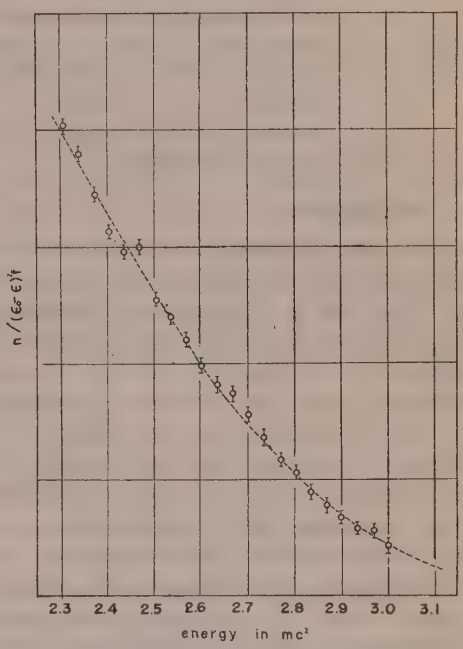

Fig. 6. Plot of the experimental correction fractor $C=n(p)/(E_0-E)^2f$. Broken line is the best fitted curve: $C=q^2+0.003p^2$.

References

1) M. Sakai and H. Ikegami: J. Phys. Soc. Japan, to be published.
2) E. Arbman and N. Svartholm: Ark. f. Fysik **10** No. 1 (1955).
3) M. Sakai: J. Phys. Soc. Japan **9** (1954) 437 (L).
4) L. M. Langer and R. J. D. Moffat: Phys. Rev. **82** (1951) 635.
5) T. Katoh, M. Nozawa, Y. Yoshizawa and Y. Koh: J. Phys. Soc. Japan **12** (1957). 728.
Y. Yoshizawa: Nucl. Phys. **5** (1958) 122.
6) S. Nakamura, J. Fujita and J. Matsumoto: Soryushiron Kenkyu (in Japanese) **16** (1958) 605.

JOURNAL OF THE PHYSICAL SOCIETY OF JAPAN Vol. 13, No. 10, OCTOBER, 1958

Temperature Distribution during the Martensite Plate Formation*

By Zenji NISHIYAMA, Akira TSUBAKI
Institute of Scientific and Industrial Research, Osaka University
Hideo SUZUKI and Yasusada YAMADA
Department of Physics, Faculty of Science, Osaka University

(Received January 16, 1958)

With the object of obtaining some basis for the thermodynamical consideration of the martensite formation, the temperature distribution during the transformation has been calculated using Bunshah and Mehl's data for the speed of propagation of the transformation front. From the results of calculation it is concluded that (1) the nucleation may be treated as isothermal and that (2) the growth may also be treated in the same way if the propagation of the transformation is steady, but the treatment must be nearly adiabatic if the propagation is intermittent and its unit is large.

§ 1. Introduction

It has been reported that the martensite transformation** in iron alloys occurs very fast. This fact is of importance, because the speed of the transformation has influence upon the resulting configuration in the alloy, and consequently upon its mechanical properties, etc. Notwithstanding the fast speed of the martensite formation some metallurgists have often tried to interprete several phenomena on the assumption that the martensite is produced isothermally. More than ten years ago, Nishiyama and Shimomura[3] proposed the idea*** that the isothermal treatments is not applicable to the thermodynamics of the martensite transformation. As for the temperature distribution during the propagation of the transformation front, they supposed a model as shown in Fig. 1. This model, however, was not on the experimental basis, because any quantitative facts concerning the speed of propagation had not yet been reported in those days.

In 1953, Bunshah and Mehl[5] found that the period of formation of a martensite plate is of the order of 10^{-7} sec. From the parallelism between the period and the size of a martensite plate, they could estimate the speed of propagation to be 1.1×10^{6} cm/sec.

In the present paper further discussion is to be given using Bunshah and Mehl's data.

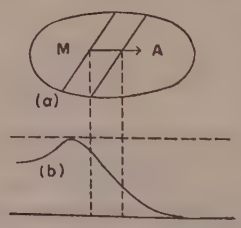

Fig. 1. Propagation of transformation (a) and distribution of temperature (b) in a martensite needle, assumed formerly.[3]

But as it is not yet clear whether nucleation start at the mid-rib or at the end of the plate, and also in what crystallographic direction the plate grows, we adopt a simple model without considering any of these matters. Adopting such a model and assuming the steadiness of the propagation of transformation in a martensite plate, numerical calculations of the temperature distribution and its variation with time are to be carried out. And also some discussions on the result are to be described in connection with the thermodynamical meaning of the martensite formation, extending to the case of the intermittent propagation.

§ 2. The Equation of Heat Conduction

As is well known, the martensite phase

* This paper was read before the annual meeting (1957) of the Phys. Soc. Japan.

** According to Förster-Scheil[1] and Suzuki-Homma[2] there are two modes, fast (Umklapp) and slow (Schiebung), in the martensite transformation. Only the former mode is the subject of discussion in this paper.

*** Crussard[4] noticed the dynamical nature of the martensite transformation.

grows with incessant evolution of heat in the austenite phase. The temperature is, therefore, not uniform in the vicinity of the transformation front.

To simplify the problem, we assume that (1) density ρ, specific heat c, and thermal conductivity κ of the two phases are equal, and that (2) in a very large material the martensite plate nucleates at $x=0$ in the form of a plane, which is a plane of symmetry in the course of growth, so that one dimentional treatment may be permissible. These assumptions do not injure the essential nature of the phenomenon and will be allowable for the estimation of the general aspect of the temperature distribution.

Let v denote the velocity of propagation with which the martensite phase grows in the austenite, and Q_0 the heat of transformation, then the heat evolution during an infinitesimal time, Δt, per unit area is given by $Q_0\rho(v\Delta t)$. Since this heat is generated only in the vicinity of the position $x=vt$, the heat of formation per unit area during Δt may be expressed as follows:

$$Q_0\rho(v\Delta t)\delta(x-vt)\,, \qquad (1)$$

where x is the coordinate and $\delta(x)$ is Dirac's δ-function satisfying the following relations:

$$\delta(x)\begin{cases} =0 & \text{if} \quad x\neq 0 \\ \neq 0 & \text{if} \quad x=0 \end{cases}$$

and

$$\int_{-\varepsilon}^{\varepsilon}\delta(x)dx=1 \qquad (1\geqslant\varepsilon>0)\,. \qquad (2)$$

Then we have the equation of heat conduction

$$\frac{\partial\theta}{\partial t}=a^2\frac{\partial^2\theta}{\partial x^2}+b\delta(x-vt)\,, \qquad (3)$$

where θ is the temperature, $a^2=\dfrac{\kappa}{c\rho}$, and $b=\dfrac{Q_0 v}{c}$.

§ 3. The Solution of Conduction Equation

In order to solve Eq. (3), we use the method of the Laplace transformation. If $\Theta(x,p)$ is the Laplace transformation of $\theta(x,t)$ such that

$$\int_0^\infty e^{-pt}\theta(x,t)dt=\Theta(x,p)\,, \qquad (4)$$

then

$$\int_0^\infty e^{-pt}\frac{\partial\theta(x,t)}{\partial t}dt=p\Theta(x,p)-\theta(x,0)\,. \qquad (5)$$

With (4) and (5), (3) becomes

$$p\Theta(x,p)-\theta(x,0)-a^2\frac{\partial^2\Theta(x,p)}{\partial x^2}-\frac{b}{v}e^{-px/v}=0\,. \qquad (6)$$

Let us assume that, before the nucleation of the martensite, the temperature is zero throughout the parent austenite, i.e.

$$\theta(x,t)=0 \qquad \text{for} \quad t\leqq 0\,. \qquad (7)$$

And as we are considering a case in which a martensite plate nucleates at $x=0$ and then grows in the same manner on both side of $x=0$,

$$\left(\frac{\partial\theta(x,t)}{\partial x}\right)_{x=0}=0\,, \qquad \theta(\infty,t)=\text{finite}. \qquad (8)$$

Substituting (7) into Eq. (6), we have

$$\frac{\partial^2\Theta}{\partial x^2}-\frac{p}{a^2}\Theta=-\frac{b}{a^2v}e^{-px/v}\,. \qquad (6)'$$

The general solution of this equation is

$$\Theta=-\frac{b}{a^2v}\frac{e^{-px/v}}{p^2/v^2-p/a^2}+c_1e^{\sqrt{p}x/a}+c_2e^{-\sqrt{p}x/a}\,.$$

And the condition (8) leads to

$$\Theta=-\frac{b}{a^2v}\frac{e^{-px/v}}{p^2/v^2-p/a^2}+\frac{b}{av^2}\frac{e^{-\sqrt{p}x/a}}{(p/v^2-1/a^2)\sqrt{p}}\,. \qquad (9)$$

Table I.

$F(x,p)$	$f(x,t)$
$e^{-xp/v}/p$	$u\left(t-\dfrac{x}{v}\right)\equiv\begin{cases}0 & \text{for } t<\dfrac{x}{v}\\ 1 & \text{for } t>\dfrac{x}{v}\end{cases}$
$e^{-xp/v}\Big/\left(p-\dfrac{v^2}{a^2}\right)$	$\exp\left[\dfrac{v^2}{a^2}\left(t-\dfrac{x}{v}\right)\right]u\left(t-\dfrac{x}{v}\right)$
$e^{-x\sqrt{p}/a}\Big/\left(\sqrt{p}\pm\dfrac{v}{a}\right)$	$\exp\left(\pm\dfrac{vx}{a^2}\right)\Big/(4\sqrt{\pi}\,t^{3/2})\displaystyle\int_{x/a}^{\infty}\mu\exp\left(-\frac{\mu^2}{4t}\mp\frac{v}{a}\mu\right)d\mu$
$e^{-x\sqrt{p}/a}/\sqrt{p}$	$\dfrac{1}{\sqrt{\pi t}}\exp\left(-\dfrac{x^2}{4a^2t}\right)$

Rewriting this for the benefit of inverse transformation, we have

$$\Theta=-\frac{b}{v}e^{-px/v}\left\{-\frac{1}{p}+\frac{1/v^2}{p/v^2-1/a^2}\right\}$$
$$+\frac{ab}{2v^2}\left\{\frac{1}{\sqrt{p}+v/a}-\frac{1}{\sqrt{p}-v/a}-\frac{2}{\sqrt{p}}\right\}e^{-\sqrt{p}x/a}. \tag{9}'$$

Inverting this equation, we can obtain the temperatue distribution θ. Table I shows the relations available for the inversion, which are in the text by Morse and Feshbach[6] except the one on the second row.*

The results of the inversion are as follows:

(i) In the transformed region, $vt>x$,

$$\theta=\frac{b}{v}\left\{1-\exp\left[\frac{v^2}{a^2}\left(t-\frac{x}{v}\right)\right]\right\}$$
$$-\frac{b}{\sqrt{\pi}v}\left\{\exp\left[\frac{v^2}{a^2}\left(t+\frac{x}{v}\right)\right]\int_{\frac{x+2vt}{2a\sqrt{t}}}^{\infty}e^{-w^2}dw\right.$$
$$\left.+\exp\left[\frac{v^2}{a^2}\left(t-\frac{x}{v}\right)\right]\int_{\frac{x-2vt}{2a\sqrt{t}}}^{\infty}e^{-w^2}dw\right\}. \tag{10}$$

For simplicity we use a function $E(x)$ defined by

$$E(x)=\int_{-\infty}^{x}\frac{1}{\sqrt{2\pi}}e^{-u^2/2}dw\,, \tag{11}$$

then (10) become

$$\theta=\frac{b}{v}\left\{1-\exp\left[\frac{v^2}{a^2}\left(t-\frac{x}{v}\right)\right]\right\}$$
$$+\frac{b}{v}\left\{\exp\left[\frac{v^2}{a^2}\left(t-\frac{x}{v}\right)\right]E\left(\frac{2vt-x}{\sqrt{2ta}}\right)\right.$$
$$\left.-\exp\left[\frac{v^2}{a^2}\left(t+\frac{x}{v}\right)\right]\left[1-E\left(\frac{2vt+x}{\sqrt{2ta}}\right)\right]\right. . \tag{10}'$$

(ii) In the austenite region, $vt<x$, those corresponding to (10) and (10)′ are

$$\theta=-\frac{b}{v}\frac{1}{\sqrt{\pi}}\left\{\exp\left[\frac{v^2}{a^2}\left(t-\frac{x}{v}\right)\right]\int_{\frac{x+2vt}{2a\sqrt{t}}}^{\infty}e^{-w^2}dw\right.$$
$$\left.-\exp\left[\frac{v^2}{a^2}\left(t+\frac{x}{v}\right)\right]\int_{\frac{x-2vt}{2a\sqrt{t}}}^{\infty}e^{-w^2}dw\,, \right. \tag{12}$$

and

$$\theta=\frac{b}{v}\left\{\exp\left[\frac{v^2}{a^2}\left(t+\frac{x}{v}\right)\right]E\left(\frac{2vt-x}{\sqrt{2ta}}\right)\right.$$
$$\left.-\exp\left[\frac{v^2}{a^2}\left(t-\frac{x}{v}\right)\right]\left[1-E\left(\frac{x+2vt}{\sqrt{2ta}}\right)\right]\right\} \tag{12}'$$

respectively.

§ 4. Numerical Calculations

Now let us estimate the temperature distribution introducing numerical values of physical constants into (10)′ and (12)′. For iron

thermal conductivity $\kappa=0.11$ cal/cm. sec. deg,
specific heat $c=0.11$ cal/gr. deg,
density $\rho=7.9$.

Then we have

$$a^2=\kappa/c\rho\simeq0.1\ \mathrm{cm^2/sec}.$$

And since the values

$$Q_0=10\ \mathrm{cal/gr}\,,\qquad v=1.1\times10^5\ \mathrm{cm/sec}$$

are given from the result of experiment[5],

$$b=Q_0v/c\simeq1.1\times10^7\ \mathrm{deg.\ cm/sec}.$$

(a) The temperature variation at the plane of nucleus $x=0$. The result is shown in Fig. 2. In this figure the rise of temperature near

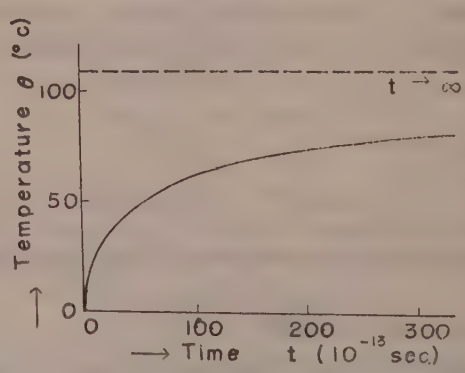

Fig. 2. Temperature variation at the centre of a martensite plate.

$t=0$ appears to be steep, but this has resulted from δ-function in (1). Actually it must be remembered that the generated heat at the earliest stage is almost absorbed by the surrounding matrix, and $\partial\theta/\partial t$ may be nearly zero at $x=0$ and $t=0$. That is to say, at the nucleation period the temperature of martensite may be not yet raised.

(b) The temperature distribution at the time when half the thickness of a martensite plate has grown to be (1) 10 Å ($t=10^{-12}$ sec), (2) 100 Å ($t=10^{-11}$ sec), or (3) 1000 Å ($t=10^{-10}$ sec).

---

* This is obtained in the following way; according to the table of Morse and Feshbach[6] the Laplace transform of $\begin{cases}f(x,t-\alpha) & \text{for } t>\alpha\\ 0 & \text{for } t<\alpha\end{cases}$ is $e^{-\alpha p}F(x,p)$, where $F(x,p)$ is the Laplace transform of $f(x,t)$. Putting $F(x,p)=\dfrac{1}{p-\beta}$, we obtain that the inverse transformation of $e^{-\alpha p}\dfrac{1}{p-\beta}$ is $\begin{cases}e^{\beta(t-\alpha)} & \text{for } t>\alpha\\ 0 & \text{for } t<\alpha\end{cases}$.

Fig. 3 shows that the temperature falls steeply in the vicinity of the transformation front, and becomes nearly zero at a distance about 100 Å away from the front. Such a sharp gradient of temperature suggests important problems to be discussed. If the propagation of the transformation is steady, these curves will show the true distribution of temperature. But if it is intermittent, the result of calculation must be regarded to show merely the values smoothed out, because the value of propagation speed adopted here is only the average one.

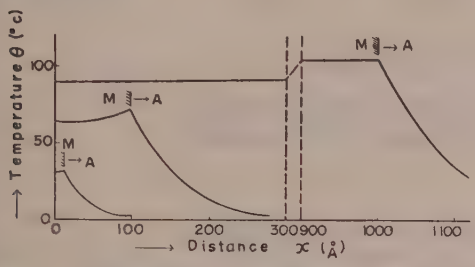

Fig. 3. Temperature distributions at the time when half the size of a martensite plate becomes, (1) 10Å, 10×10^{-13} sec. (2) 100Å, 100×10^{-13} sec. (3) 1000Å, 1000×10^{-13} sec.

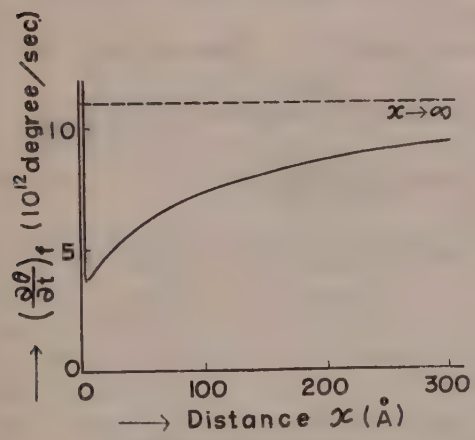

Fig. 4. $\left(\frac{\partial\theta}{\partial t}\right)_f - x$ curve.

(c) $\partial\theta/\partial t$ at the time when the transformation front has travelled a certain distance x. Differentiating (12)′ with respect to t, and putting $vt=x$, we have

$$\left(\frac{\partial\theta}{\partial t}\right)_f=\frac{b}{a}\sqrt{\frac{v}{\pi x}}\exp\left(-\frac{vx}{4a^2}\right)+\frac{vb}{a^2}\left\{E\left(\sqrt{\frac{vx}{2a^2}}\right)-\exp\left(\frac{2vx}{a^2}\right)\left[1-E\left(\sqrt{\frac{9vx}{2a^2}}\right)\right]\right\}, \quad (13)$$

where suffix f denotes the transformation front in the austenite side. This relation is shown in Fig. 4. $(\partial\theta/\partial t)_f$ is infinity at $x=0$, which again has come from the characteristic of δ-function and therefore this does not necessarily mean the adiabatic change.

(d) $\partial\theta/\partial x$ at the time when the transformation front has travelled a certain distance x. Differentiating (12)′ with respect to x, and putting $vt=x$, we have

$$\left(\frac{\partial\theta}{\partial x}\right)_f=\frac{b}{a^2}\left\{E\left(\sqrt{\frac{9vx}{2a^2}}\right)\exp\left(\frac{2vx}{a^2}\right)-E\left(\sqrt{\frac{vx}{2a^2}}\right)-\exp\left(\frac{2vx}{a^2}\right)\right\}. \quad (14)$$

Fig. 5 shows this relation. At $x=0$, $(\partial\theta/\partial x)_f$ has a finite value -1.1 degree/Å.

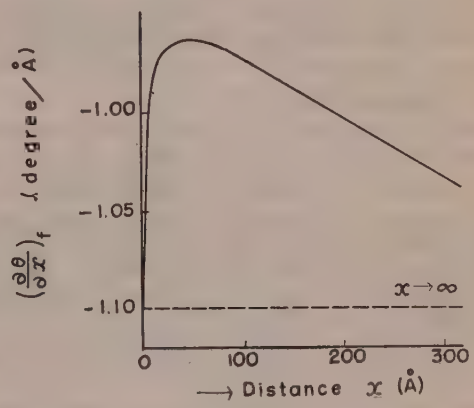

Fig. 5. $\left(\frac{\partial\theta}{\partial x}\right)_f - x$ curve.

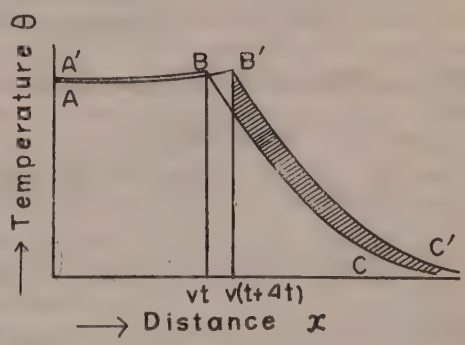

Fig. 6.

§ 5. The Degree of Heat Removal (γ) at the Transformation Front

In Fig. 6, ABC is the temperature distribution at time t, and A′B′C′ at $t+\Delta t$. The forward heat conduction during the transformation of the region between $x=vt$ and $v(t+\Delta t)$ can be measured by the area (S) of the shaded region.

$$S=\int_{v(t+\Delta t)}^{\infty}\{\theta(x,t+\Delta t)-\theta(x,t)\}dx\,, \tag{15}$$

where $\theta(x,t)$ is given by (12)′

Now we define a parameter γ by

$$\gamma=S/b\Delta t\,, \tag{16}$$

where $b\Delta t$ is the heat evolution during Δt divided by $c\rho$. Regarding the proportion of the backward (toward the already transformed region) heat conduction, we have

$$\begin{aligned}\frac{S'}{b\Delta t}&=\int_0^{vt}\{\theta(x,t+\Delta t)-\theta(x,t)\}dx/b\Delta t\\ &=-\frac{a^2}{v^2\Delta t}\left\{\left(1-\exp\left[\frac{v^2}{a^2}t\right]\right)+\exp\left[\frac{v^2}{a^2}t\right]E\left(\frac{2vt}{\sqrt{2}ta}\right)-3E\left(\frac{vt}{\sqrt{2}ta}\right)\right.\\ &\quad+\left(1-\exp\left[-\frac{v^2}{a^2}t\right]\right)\exp\left[\frac{v^2}{a^2}(t+\Delta t)\right]+2E\left(\frac{vt}{\sqrt{2(t+\Delta t)}a}\right)\\ &\quad\left.-\exp\left[\frac{v^2}{a^2}(t+\Delta t)\right]\left[E\left(\frac{2v(t+\Delta t)}{\sqrt{2(t+\Delta t)}a}\right)-\exp\left[-\frac{v^2}{a^2}t\right]E\left(\frac{vt+2v\Delta t}{\sqrt{2(t+\Delta t)}a}\right)\right]\right\}.\end{aligned} \tag{17}$$

For $t\to$large

$$\frac{S'}{b\Delta t}\longrightarrow-\frac{3a^3}{v^3\Delta t}\cdot\frac{1}{\sqrt{\pi t}}\left\{\frac{1}{2}\exp\left[-\frac{v^2}{a^2}t\right]-\exp\left[-\frac{v^2}{4a^2}t\right]\right\}. \tag{18}$$

this value is very small, and also the temperature gradient is very small in the backward direction. Therefore the parameter γ may be taken as a quantity to measure approximately the proportion of the transformation heat removed by the surrounding regions. If $\gamma=0$, the transformation is adiabatic, and if $\gamma=1$, it is isothermal.

To calculate the area S, substitute (12)′ into (15) and integrate it. Then we have

$$\begin{aligned}S=\frac{a^2b}{v^2}&\left[3E\left(\frac{v(t+\Delta t)}{\sqrt{2(t+\Delta t)}a}\right)-2E\left(\frac{v(t+\Delta t)}{\sqrt{2}ta}\right)+\exp\left(\frac{2v^2}{a^2}\right)\left\{\exp\left(\frac{2v^2}{a^2}\Delta t\right)\left[1-E\left(\frac{3v(t+\Delta t)}{\sqrt{2(t+\Delta t)}a}\right)\right]\right.\right.\\ &\left.\left.-\exp\left(\frac{v^2}{a^2}\Delta t\right)\left[1-E\left(\frac{v(3t+\Delta t)}{\sqrt{2(t+\Delta t)}a}\right)\right]-\exp\left(-\frac{v^2}{a^2}\Delta t\right)E\left(\frac{v(t-\Delta t)}{\sqrt{2(t+\Delta t)}a}\right)\right]\end{aligned} \tag{19}$$

Substituting this in (16) and expanding the formula in the power series of Δt, we have

$$\begin{aligned}&\gamma=\gamma^{(0)}+\gamma^{(1)}\Delta t+\gamma^{(2)}(\Delta t)^2+\cdots;\\ &\gamma^{(0)}=E\left(\frac{v}{\sqrt{2}a}\sqrt{t}\right)+\exp\left(\frac{2v^2}{a^2}t\right)\left[1-E\left(\frac{3v\sqrt{t}}{\sqrt{2}a}\right)\right],\\ &\gamma^{(1)}=\frac{3v^2}{2a^2}\left[1-E\left(\frac{3v\sqrt{t}}{\sqrt{2}a}\right)\right]-\frac{v^2}{2a^2}E\left(\frac{v\sqrt{t}}{\sqrt{2}a}\right)+\frac{1}{\sqrt{2\pi}}\exp\left(-\frac{v^2t}{4a^2}\right)\left(\frac{a}{8\sqrt{2}t^3v}-\frac{7v}{2\sqrt{2}ta}\right).\end{aligned} \tag{20}$$

The relation between $\gamma^{(0)}$ and t is plotted in Fig. 7. This curve shows that, if the propagation of the transformation is steady ($\Delta t=0$), the process may be considered nearly isothermal. The deviation of γ from 1.0 is about 10 % in the extreme case where the thickness of martensite is thinner than 100 Å.

The ratio γ defined by (16) comes to have a special significance if the small region $v\Delta t$ which is here called the "transformation unit" may be regarded as a physical unit of the intermittent transformation. The attempt to consider such a transformation unit is suggested from the fact that the martensite has fine lamellar structures, which has been made clear through the electron-microscopic observation.[7] On this point we will advance some discussions later.

Putting $t\to\infty$ in (19), we have

$$\gamma_{t\to\infty}=\left[1-\exp\left(-\frac{v^2}{a^2}\Delta t\right)\right]\Big/\frac{v^2}{a^2}\Delta t\,. \tag{21}$$

The relations $\gamma_{t\to\infty}$ and the transformation

unit $v\Delta t$ for $a^2/v \simeq 9.0$, 0.9 and 0.09 Å are shown in Fig. 8. From these curves it is noted that the transformation goes more adiabatically as the transformation unit becomes large. In the state where the martensite has not yet grown large, $t \ll \infty$, the transformation process must be more adiabatic, because those curves lie below the corresponding ones in Fig. 8.

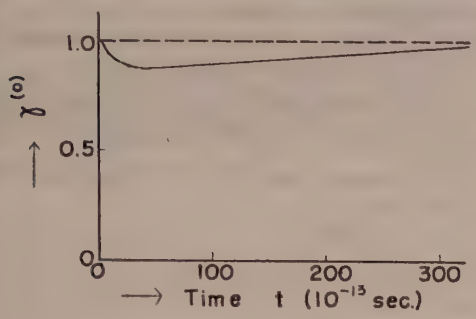

Fig. 7. $\gamma^{(0)}-t$ curve.

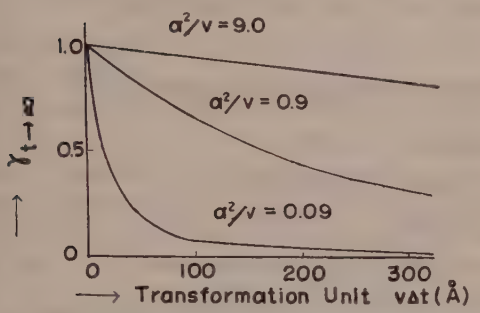

Fig. 8. Relation between the degree of heat removal ($\gamma_{t\to\infty}$) and transformation unit ($v\Delta t$).

For Fe-30 % Ni alloy the value of κ is 0.028 cal/cm. sec. deg[8] which is about 1/5 of that of pure iron. And so is the value of a^2. Therefore the behaviour of $\gamma_{t\to\infty}$ in this case must be similar to that in the case where $a^2=0.01$. Fig. 8 makes it clear that if the value of a^2/v is of the order of 0.9 Å, the transformation process is isothermal for $v\Delta t \simeq 10$ Å or less, and less isothermal for 100 Å or more, and that if the value of a^2/v is of the order of 0.09 Å, it is isothermal only for a few Å or less, but it is nearly adiabatic for 40 Å or more.

It must be noticed here that the more rapid the transition in the transformation unit is, the more adiabatic it is.

§ 6. Discussion

In the above treatment we considered the change of γ in terms of the transformation unit $v\Delta t$. If the transformation goes on intermittently, the unit $v\Delta t$ described above becomes to play an important role in the thermodynamics of the martensite transformation. Strictly speaking it is an open question from the characteristics of the equation of the heat conduction (3) whether such a quantity defined here may have any significance, and it is desirable to solve the equation including the correct term of the heat source. To carry out this evaluation we must know in detail the facts concerning the existence of the discontinuous phenomena. For this transformation, however, we have had no data experimentally ascertained. There will be no objection, however, to the introduction of such a transformation unit $v\Delta t$, so long as it is small, because the solution in the case of steady propagation may be the good approximation to the case where transformation propagates intermittently. Though in the latter case v may vary with time, a good agreement may be expected, provided that the transforming region during Δt is written in the form of $v\Delta t$. The larger $v\Delta t$, the worse this approximation. And it may be a great deal to assume that the treatment in this paper is valid qualitatively at least.

From the results described above an approval may be given to the idea that the martensite nucleates isothermally. But the matter is not so simple for the process of the growth, which is an important question about the martensite formation that we must answer. If the transformation proceeds continuously, e.g., it occurs by every atomic layer, or the thickness of the unit is smaller than a certain magnitude which depends on the value of a^2/v, the isothermal treatment is allowable, provided that an account is taken of the fact that the temperature at the transformation front has already been raised. If the thickness of the transformation unit is large, the process comes to be more adiabatic with the size. In this case the size of the unit would play a very important role, but it is very difficult for the present to give a concrete physical meaning to it, because the present discussion is nothing but a speculative one in view of scanty of experimental data. Recently Nishiyama, Shimizu and Sato[6] found a lamellar structure of the spacing 200 Å in the martensite plate of iron-nickel alloy. If this spacing has some

relation to the transformation unit in question, the existence of the lamellar structre is important for discussing the thermodynamic and the mechanism of the martensite formation. As a consequence of this consideration we feel keenly the need of furthur study to find supermicroscopical details.

The authors express their sincere thanks to Prof. T. Nagamiya with whom the authors have enjoyed the discussion.

References

1) F. Förster and E. Scheil: Zeits. f. Metallk., **28** (1936) 245.
2) H. Suzuki and T. Homma: J. Metals, **4** (1952) 519.
3) Z. Nishiyama and Y. Shimomura: J. Japan Inst. Metals, **12** (1948) No. 2–3, 9, No. 5, 1.
4) C. Crussard and O. Krisement: Intern. Union Cryst., 3rd Congress, Symposium on the transition mechanism in martensitic type transitions, 2°, 2 (1954).
5) R. F. Bunshah and R. F. Mehl: J. Metals, **5** (1953) 1250.
6) P. M. Morse and H. Feshbach: Method of Theoretical Physics II (1953) p. 1579.
7) Z. Nishiyama, K. Shimizu and S. Sato: Mem. Inst. Sci. Ind. Res., Osaka University, **13** (1956) 1.
8) L. R. Ingersoll and et. al.: Phys. Rev., **16** (1920) 126.

JOURNAL OF THE PHYSICAL SOCIETY OF JAPAN Vol. 13, No. 10, OCTOBER, 1958

Theory of Thermoelectric Power of Ionic Crystals (I)

By Eijiro HAGA

Department of Physics, Faculty of Science, Niigata University

(Received May 7, 1958)

A theory of the thermoelectric power in AgBr is developed, in which the experimental conditions are properly considered. The gradient of the electrochemical potential of silver ions is calculated, since it is related to the quantity measured by the potentiometer, that is, the difference between the Fermi levels at two free ends of lead wires. An expression for the thermoelectric power is derived, which is applicable to AgBr mixed with $CdBr_2$ at arbitrary temperatures.

The Peltier and Thomson coefficients in the steady state are independently calculated for this special case, and the result shows that the Kelvin relations are really statisfied in the steady state.

Finally, the theory is compared with the experiments of Patrick and Lawson.

§ 1. Introduction and Conclusions

The thermoelectric power together with the electrical conductivity gives us useful informations for comprehension of the ionic crystals. As for AgBr the electrical conductivity has been measured in detail on pure and Cd doped samples and several important parameters have been estimated by making use of the theory.[1),2)] The thermoelectromotive force of this substance has been also measured on a sample of AgBr+0.25 % $CdBr_2$ besides the pure one,[3)] and explained on the basis of the old theory.[4)] According to that theory the value obtained by subtracting the thermoelectromotive force in the lead wires from the observed one is equal to the difference of the electrostatic potential between two silver electrodes at different temperatures. This, however, is not correct, unless the variation of the band levels of metal with temperatures is negligibly small. In addition, the estimation of the so-called heterogeneous effect is not correct. Considering these points we shall develop a theory which takes into account the experimental conditions in the measurements of the thermoelectromotive force. Here

we restrict the meaning "complex" to a combination of a Cd^{++} ion and an Ag^{+} vacancy. In the present case there may be other kinds of complex, for example, a pair of Ag^{+} interstitial ion and Ag^{+} vacancy, but they will have no effect on the present arguments.

Now, it is known from the measurements of the electrical conductivity of AgBr that the Schottky type disorder can be neglected, except near its melting point.[2),5)] Hence we shall develope a theory with an assumption that the defects in the pure AgBr are completely the Frenkel type.

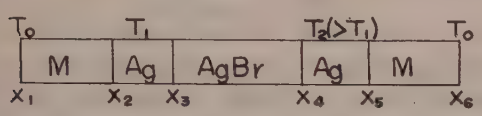

Fig. 1. Schematic diagram for measurements of thermoelectromotive forces.

Before developing the theory of the thermoelectromotive force, let us consider an experimental arrangement for its measurement. As shown in Fig. 1, the two silver metals are put in contact with the respective ends of an AgBr sample so as to keep AgBr in the state of thermal equilibrium with Ag at junctions, and the two lead wires of the same substance M are jointed with the respective silver electrodes. Keeping two electrode at different temperatures T_1 and T_2 the potential difference $\Theta(T_1, T_2)$ between two free ends of lead wires x_6 and x_1 are measured by the potentiometer method. Denoting the magnitude of electronic charge as e, $e\Theta(T_1, T_2)$ is the difference of the Fermi level between the position x_1 and that at x_6. Let us denote absolute thermoelectromotive force of the lead wire M as $\Theta^M(T_1, T_2)$. The quantity $e\Theta(T_1, T_2) - e\Theta^M(T_1, T_2)$ represents the difference of the Fermi level rather than that of the electrostatic potential between the silver electrode at T_1 and that at T_2, and it will be shown in Section 2 that the quantity is related to the difference of the electrochemical potential of a silver ion between two ends of the sample. Then the problem is merely to calculate the gradient of the electrochemical potential of a silver ion in AgBr in the presence of temperature gradient rather than to calculate both the homogeneous and heterogeneous effects.

In Section 3 the thermodynamic relations of Kelvin will be derived, taking the experimental arrangement shown in Fig. 1 into consideration. Also, the Peltier and Thomson coefficients in the steady state will be derived independently and it will be shown that the Kelvin relations are really satisfied in the steady state. In Section 4 we shall compare our theoretical expressions with the experiment by Patrick and Lawson.

§ 2. Thermoelectric Power

Under the experimental arrangement described in Section 1, the electrochemical potentials of a silver ion and of an electron are continuous at the Ag−AgBr and Ag−M junctions respectively. Taking as positive when the potential at x_6 is higher than that at x_1, $\Theta(T_1, T_2)$ mentioned in Section I is given by

$$e\Theta(T_1, T_2) = \zeta_{e^-}^{M}(x_1) - \zeta_{e^-}^{M}(x^6)\,, \qquad (1)$$

where $\zeta_{e^-}^{M}$ is the electrochemical potential of an electron in the lead wire M. We can connect $\Theta(T_1, T_2)$ with the difference of the electrochemical potential between two ends of AgBr sample, x_3 and x_4, by tracing the electrochemical potential of a silver ion or an electron from x_1 to x_6:

$$e\Theta(T_1, T_2) = [{}_{Ag^+}^{AgBr}(x_4) - \zeta_{Ag^+}^{AgBr}(x_3)] + [\mu_{Ag}^{Ag}(T_1) - \mu_{Ag}^{Ag}(T_2)] + e\Theta^M(T_1, T_2)\,, \qquad (2)$$

where μ_{Ag}^{Ag} is the chemical potential of a silver atom in the silver metal. If we denote the thermoelectric power corresponding to Θ as Q Eq. (2) gives

$$eQ = eQ_{Ag^+}^{AgBr} + s_{Ag}^{Ag} + eQ^M\,. \qquad (3)$$

Here, $eQ_{Ag^+}^{AgBr}$ is the value obtained by subtracting the electrochemical potential of a silver ion at the point at lower temperature from that at higher temperature in the case where two points in AgBr are kept at different temperatures by unity, s_{Ag}^{Ag} is the entropy of a silver atom in the silver metal. Hence we need obtain only the gradient of the electrochemical potential of a silver ion in AgBr.

Now the chemical potential of an Ag^{+} vacancy, μ_v, is defined as the Gibbs free energy required to take out a silver ion at a normal site into the outside, and the chemical potential of an Ag^{+} interstitial ion, μ_i, is defined as the Gibbs free energy required to bring a silver ion from the outside vacuum into an interstitial position in AgBr. We shall

assume, in the present paper, that the concentrations of Ag^+ interstitial ions and vacancies, n_i and n_v, are distributed at random. Then μ_d is given by

$$\mu_v = \mu_v^0 + kT \ln (n_v/N_0) , \qquad (4)$$

where N_0 is the concentration of the Ag^+ lattice sites. A similar equation is valid for μ_i. The chemical potential of an Ag^+ ion in AgBr, μ_{Ag+}^{AgBr}, is given by

$$\mu_{Ag+}^{AgBr} = -\mu_v = \mu_i . \qquad (5)$$

According to the theory of transport phenomena, the electrical current densities in the x-direction owing to the Ag^+ interstitial ions and vacancies, j_i and j_v, are written as[4),6),7)]

$$j_i = eD_i\left(-\frac{dn_i}{dx} + \frac{en_iE}{kT} - \frac{n_iQ_i^*}{kT^2}\frac{dT}{dx}\right)$$

$$j_v = -eD_v\left(-\frac{dn_v}{dx} - \frac{en_vE}{kT} - \frac{n_vQ_v^*}{kT^2}\frac{dT}{dx}\right), \qquad (6)$$

where $D_{i,v}$ and $Q_{i,v}^*$ are the ordinary diffusion coefficient and the heat of transport of the two kind of defects respectively.

From above we can obtain $d\zeta_{Ag+}^{AgBr}/dx$ making use of

$$\frac{d\zeta_{Ag+}^{AgBr}}{dx} = -eE + \frac{d\mu_{Ag+}^{AgBr}}{dx} . \qquad (7)$$

The electric field E is obtained from the condition that the total electrical current densities, $j_i + j_v$, should vanish everywhere, and $d\mu_{Ag+}^{AgBr}/dx$ is obtained making use of Eqs. (4) and (5). In the result we have

$$\frac{d\zeta_{Ag+}^{AgBr}}{dx} = -\left[\frac{1}{T}\frac{c_i\varphi(h_F+Q_i^*)-c_vQ_v^*}{c_i\varphi+c_v} + \frac{d\mu_v^0}{dT} + k\ln c_v\right]\frac{dT}{dx} , \qquad (8)$$

where c_i and c_v are the mol fractions of Ag^+ interstitial ions and vacancies, h_F is the enthalpy of formation of one pair of Frenkel defect, and φ is the ratio of the mobility of Ag^+ interstitial ions to that of vacancies.

The free energy required to take out a silver ion from a normal lattice site in a perfect crystal of AgBr to the vacuum in the outside of the crystal, μ_v^0, is estimated by dividing this process into the following two steps. (i) A silver ion occupying a normal lattice site at the surface of the crystal is taken out of the crystal. The Gibbs free energy required for this step is, on the average, $-\mu_P$, where μ_P means the Gibbs free energy of a silver ion in the interior of a perfect crystal of AgBr. (ii) A silver ion on the lattice site in a perfect crystal of AgBr is brought to a lattice site at the surface of the crystal. The temperature-dependent term of the Gibbs free energy required for this step is $-kT\Sigma \ln (\nu_P/\nu_v)$, where ν_P and ν_v are the frequency of a normal mode of lattice oscillations in a perfect crystal of AgBr and that in a crystal including only an Ag^+ vacancy as defect respectively, and Σ means the summation over all normal modes.[8)] Hence, $d\mu_v^0/dT$ in Eq. (8) becomes, from (i) and (ii),

$$\frac{d\mu_v^0}{dT} = s_P - k\Sigma \ln \frac{\nu_P}{\nu_v} \qquad (9)$$

where s_P is the entropy of a silver ion in a perfect crystal of AgBr. Using Eqs. (3), (8) and (9) we find a theoretical expression for the thermoelectric power Q:

$$eQ = -\frac{1}{T}\frac{c_i\varphi(h_F+Q_i^*)-c_vQ_v^*}{c_i\varphi+c_v} - k\ln c_v + \alpha + eQ^M , \qquad (10)$$

where

$$\alpha = s_{Ag}^{Ag} - s_P + k\Sigma \ln \frac{\nu_P}{\nu_v} . \qquad (11)$$

As seen above, the theoretical expression (10) is obtained on the conditions that the ionic current should vanish and that the Ag^+ interstitial ions and vacancies are in thermal equilibrium, and so it is valid whether the current of complexes exist or not. Let us consider the process approaching the steady state when a certain temperature gradient is set up in the sample. The concentration distributions of Ag^+ interstitial ions and vacancies will vary with time since the associations of complexes take place at each place in the sample owing to these current. The electric field in the sample depends on dn_i/dx or dn_v/dx as seen from Eqs. (6) and (5), and so varies with time. The gradient of electrochemical potential of silver ions in the sample is, however, independent of dn_i/dx or dn_v/dx and so does not vary with time. Hence, the thermoelectric power does not vary with time.

§ 3. Kelvin Relations

We shall derive the Kelvin relations on the basis of the experimental arrangement shown in Fig. 1, and then the Peltier and Thomson coefficients independently and show that the Kelvin relations are really satisfied.

Let us assume that unit charge is let flow quasi-statically across $x_1x_2x_3x_4x_5x_6$ and back to x_1 through an outside imaginary path in Fig. 1. In such a process, silver ions in the silver electrode enter AgBr at x_3 by unit charge and flow through AgBr and reach x_4. On the other hand, electrons left at x_3 flow across, x_2x_1, imaginary pass, x_6x_5 and reach x_4 and recombine with silver ions above mentioned, forming $1/e$ silver atoms at x_4. Hence, in order to complete the cycle, we must carry $1/e$ silver atoms from the silver electrode at temperature T_2 to that at T_1, and, in this case, the heat given out to the outside is $1/e\cdot\int_{T_2}^{T_1} c_{\mathrm{Ag}}^{\mathrm{Ag}}dT$, where $c_{\mathrm{Ag}}^{\mathrm{Ag}}$ means the specific heat of a silver atom in the silver metal. We shall denote the Pelter coefficient, that is to say, the heat emitted at the junction when unit current flows from the lead wire M to the silver electrode as $\pi_{M\to\mathrm{Ag}}$ and the Thomson coefficient in the lead wire M as σ^M. Making use of the first and second laws of thermodynamics we can find the Kelvin relations on the basis of the experimental arrangement shown in Fig. 1:

$$Q=(\pi_{M\to\mathrm{Ag}}+\pi_{\mathrm{Ag}\to\mathrm{AgBr}})/T\,, \tag{12}$$

and

$$\frac{dQ}{dT}=(\sigma^M-\sigma^{\mathrm{AgBr}})/T+c_{\mathrm{Ag}}^{\mathrm{Ag}}/eT\,. \tag{13}$$

Now we shall calculate the Peltier heat, $J\pi_{\mathrm{Ag}\to\mathrm{AgBr}}$, when a constant current J flows through a junction of Ag and AgBr in the direction Ag→AgBr. For convenience, let us denote the contacting area in Ag and in AgBr as x_{Ag} and x_{AgBr} respectively. The theoretical expression for this Peltier heat can be obtained by dividing it into following three factors.

(i) J/e electrons per second flow from x_{Ag} to the interior of Ag. The contribution of this factor to the Peltier heat is

$$-J/e\cdot Q_{e^-}^{*\mathrm{Ag}}\,, \tag{14}$$

where $Q_{e^-}^{*\mathrm{Ag}}$ means the heat of transport of an electron in Ag.

(ii) Let the transport numbers of Ag^+ interstitial ions and vacancies in AgBr be t_i and t_v respectively. Then t_iJ/e Ag^+ interstitial ions per second flow from x_{AgBr} to the interior of AgBr and t_vJ/e Ag^+ vacancies per second flow from the interior of AgBr to x_{AgBr}. The contribution of this second factor is

$$J/e\cdot(-t_iQ_i^*+t_vQ_v^*)\,. \tag{15}$$

(iii) J/e silver ions per second flow from x_{Ag} to x_{AgBr}. Of these silver ions, t_iJ/e enter the interstitial sites in AgBr and t_vJ/e recombine with Ag^+ vacancies which come from the interior of AgBr to x_{AgBr}. The contribution of this third factor is given by

$$JT/e\cdot\left[t_i\left(\frac{\partial\mu_i}{\partial T}\right)_{c_i,p}-t_v\left(\frac{\partial\mu_v}{\partial T}\right)_{c_v,p}-\left(\frac{\partial\mu_{\mathrm{Ag}^+}^{\mathrm{Ag}}}{\partial T}\right)_p\right], \tag{16}$$

where p is the pressure.

The Peltier heat is obtained by summing up these factors (14), (15) and (16):

$$\begin{aligned}e\pi_{\mathrm{Ag}\to\mathrm{AgBr}}=&-\frac{c_i\varphi(h_F+Q_i^*)-c_vQ_v^*}{c_i\varphi+c_v}\\&+T\left(s_{\mathrm{Ag}}^{\mathrm{Ag}}-\frac{d\mu_v^0}{dT}-k\ln c_v\right)\\&+T\left(\frac{\partial\mu_{e^-}^{\mathrm{Ag}}}{\partial T}\right)_p-Q_{e^-}^{*\mathrm{Ag}}\end{aligned} \tag{17}$$

We can see easily that the sum of the last two terms in Eq. (17) is the absolute thermoelectric power of Ag multiplied by eT, which is equal to $e(TQ^M-\pi_{M\to\mathrm{Ag}})$ from the Kelvin relation for metals. Thus Eq. (17) gives the Kelvin relation (12).

Next, we shall calculate the Thomson heat when an infinitesimal steady current J flows in the x-direction through a crystal of AgBr in the presence of temperature gradient. We shall consider a portion A in AgBr lying between the position x at the temperature T and the position $x+dx$ at the temperature $T+dT$. For convenience, we shall denote two ends in A as x_A and $(x+dx)_A$. Now J/e silver ions per second leave x_A and the same amount of silver ions comes to $(x+dx)_A$. Then the Thomson coefficient σ_{AgBr} will be calculated by using the thermodynamic law that the sum ΔW of the work done and the heat given from the outside of A to A is equal to the increase of internal energy ΔU of A.

First we consider the current of Ag^+ interstitial ions in A. The $t_i(T)J/e$ Ag^+ interstitial ions leave x_A per second. The heat given and the work done from the outside to A owing to this current are $t_i(T)Q_i^*(T)J/e$ and $t_i(T)v_i(T)pJ/e$ per second respectively, where v_i is the increase of volume for forming an Ag^+ interstitial ion. On the other hand the $t_i(T+dT)J/e$ Ag^+ interstitial ions come to the

position $(x+dx)_A$ per second. The heat given and the work done from the outside to A owing to this are $-t_i(T+dT)Q_i^*(T+dT)J/e$ and $-t_i(T+dT)v_i(T+dT)pJ/e$ per second respectively. Next, we shall consider the current of Ag^+ vacancies in A. The $t_v(T+dT)J/e$ Ag^+ vacancies leave $(x+dx)_A$ per second and the $t_v(T)J/e$ Ag^+ vacancies come to x_A per second. The heat given and the work done from the outside of A to A owing to this is obtained similarly. Furthermore, the Thomson heat $\sigma^{AgBr}JdT$ is given from the outside to A as the current flows in A in the presence of temperature gradient. The transport numbers, t_i and t_v, depend, in general, on the temperature, and so the each current of Ag^+ interstitial ions and vacancies varies with the position though the sum of the two is constant. Hence, the recombination (or generation) between Ag^+ interstitial ions and vacancies takes place at each position. The heat given by this from the outside to A should be included in the Thomson heat. Thus we have

$$\Delta W = J/e\cdot dT\frac{d}{dT}(t_vQ_v^*-t_iQ_i^*+t_vv_vp-t_iv_ip) + \sigma^{AgBr}JdT\,. \tag{18}$$

Next, we shall calculate ΔU. If we denote the internal energy of an Ag^+ interstitial ion and an Ag^+ vacancy as u_i and u_v respectively, we have

$$\Delta U = J/e\cdot dT\frac{d}{dT}(t_iu_i-t_vu_v)\,, \tag{19}$$

where

$$\left.\begin{aligned} u_i &= -pv_i+\mu_i+e\Phi-T\partial\mu_i/\partial T\,,\\ u_v &= -pv_v+\mu_v-e\Phi-T\partial\mu_v/\partial T\,,\end{aligned}\right\} \tag{20}$$

Φ being the electrostatic potential of the vacuum. When (20) and (4) are used Eq. (19) becomes

$$\Delta U = J/edT\frac{d}{dT}[t_vv_vp-t_iv_ip+Tt_v(\partial\mu_v/\partial T)_{c_v} -Tt_i(\partial\mu_i/\partial T)_{c_i}]+J/e\cdot dx(d\mu_{Ag^+}^{AgBr}/dx-eE) \tag{21}$$

$d\mu_{Ag^+}^{AgBr}/dx-eE$ in Eq. (21) is the gradient of electrochemical potential of a silver ion when the current J is present. This now is equal to the gradient of electrochemical potential of a silver ion when the current is not present, since J is infinitesimal. Hence we can obtain the Thomson coefficient σ^{AgBr} from the thermodynamic law $\Delta W=\Delta U$:

$$\sigma^{AgBr} = \frac{T}{e}\frac{d}{dT}\left[\frac{1}{T}\frac{c_i\varphi(h_F+Q_i^*)-c_vQ_v^*}{c_i\varphi+c_v} +k\ln c_v+\frac{d\mu_v^0}{dT}\right]. \tag{22}$$

We can see that the Kelvin relation (13) is really satisfied from Eqs. (10) and (22).

The Kelvin relations apply only to the steady state, where irreversible currents of complexes are not present, as seen from these derivations. We calculated in this Section the Peltier and Thomson coefficients in the steady state, while the expression for the thermoelectric power is valid whether the currents of complexes may exist or not. We now have seen that the thermoelectric power, the Peltier and Thomson coefficients independently derived obey the Kelvin relations in the steady state.

§ 4. Comparisons with Experiments

Thermoelectric power in the experimental arrangement shown in Fig. 1 was measured by Patrick and Lawson for the samples of pure AgBr and AgBr+0.25 Mol−% $CdBr_2$. The Chromel wires was used as leads and its absolute thermoelectric power Q^M was taken as 20 $\mu v/°C$.

We shall compare Eq. (10) with the experimental data of Patrick and Lawson. We obtained the carrier concentration in the pure

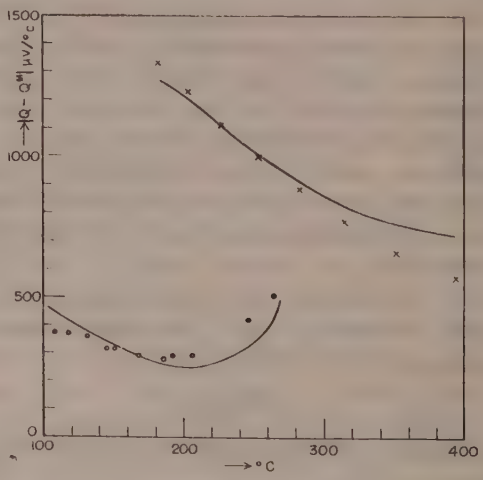

Fig. 2. The thermoelectric power of pure and doped $AgBr$ as a function of temperature.
—— Theoretical curve with $Q_v^*=-0.52$ ev, $Q_i^*+h_F=1.20$ ev and $\alpha=320$ $\mu v/°C$.
× Experimental value for pure $AgBr$.
○ Experimental value for $AgBr$+0.25% $CdBr_2$.

sample by using the interpolation formula of Teltow, and also those in the impure sample by using the interpolation formula and taking the activation energy of complexes as 0.16 ev. Three parameters $Q_i^*+h_F$, Q_v^* and α are assumed to be independent of temperature and their valus are taken as 1.20 ev, -0.52 ev and 320 $\mu v/°C$ respectively so that we may obtain a best fit between Eq. (10) and the experimental data on the pure and impure samples. $Q_i^*+h_F$ is nearly equal to that of h_F and consequently the value of Q_i^* is very small. If we take the value of $s_F-s_{Ag}^{Ag}$ as 130 $\mu v/°C$ then $k\ln(\nu_F/\nu_v)$ becomes 450 $\mu v/°C$. The full lines of Fig. 2 show Eq. (10) with these values.

The dependence of the thermoelectric power on the concentration of added Cd over wide temperature range is interesting to the author. Measurements of the thermoelectric power on samples of AgCl doped with $CdCl_2$ of various concentrations are being carried out at our department of physics, and the theory explains fairly well the behaviors of experimental data. The result will be reported in near future.

The writer wishes to express his cordial thanks to Mr. S. Miyatani and Mr. I. Yokota for their useful discussions and kind advices.

The present work was supported by the Scientific Research Fund of the Ministry of Education.

In preparing the manuscript of this paper the writer has been informed of the work of R. E. Howard and A. B. Lidiard (Discussions Faraday Soc. **23** (1957) 113, Phil. Mag. **2** (1957) 1462). The expression derived by the writer is different from that derived by them by the term $(\partial\mu_e^{Ag}/\partial T)_p$. This is expected to be of the order of 100 $\mu v/°C$ from thermionic emission experiments.

References

1) J. Teltow: Phys. Lpz. **5** (1949) 63, 71.
2) S. W. Kurnick: J. Chem. Phys. **20** (1952) 218.
3) L. Patrick and A. W. Lawson: J. Chem. Phys. **22** (1954) 1492.
4) C. Wagner: Ann. Phys. Ppz. **3** (1929) 629.
5) C. R. Berry: Phys. Rev. **82** (1951) 422.
6) For example, S. R. de Groot: Thermodynamics of Irreversible Processes
7) A. B. Lidiard: Handbuch der Physik Vol. 20 p. 339 (1957).
8) G. H. Vineyard and G. J. Dienes: Phys. Rev. **93** (1954) 265.
9) H. Reinhold and A. Blachny: Z. Electrochem. **39** (1933) 290.

JOURNAL OF THE PHYSICAL SOCIETY OF JAPAN Vol 13, No. 10, OCTOBER, 1958

A Theory of Impurity Conduction I

Tadao KASUYA

Faculty of Science, University of Nagoya

(Received May 19, 1958)

The phenomena of impurity conduction of semiconductors such as G_e and S_i are treated theoretically by deviding into the following three ranges of impurity concentration: (i) The concentration of impurity atom is fairly large and the impurity levels are merged into the conduction bands. Then the impurity atoms play a role of scatterers. (ii) The concentration of impurity atom becomes fairly small and the impurity levels split from the conduction bands. The energy width of this impurity band is, however, determined mainly by the translational energy of electron in this band. (iii) The concentration of impurity atom becomes very small and the width of the impurity band is determined mainly by the fluctuation of the local potential energy. In this paper we treat the first two cases. For this purpose, the general theory of transport phenomena is developped and the condition that the ordinary Boltzman—Bloch equation is applicable is given on this general theory. The result of impurity conduction given by E. M. Conwell is obtained as a limiting case of our formula. However the condition that the Conwell's formula is applicable is not satisfied in actual cases.

§ 1. Introduction

The electron mobility in S_i and G_e is determined by the scattering of electrons by phonons at higher temperatures. At low temperatures, however, the mobility is determined mostly by the presence of impurity atoms. Concerning the mobility at higher temperatures, some peculiarities are observed experimentally. These problems are also interesting from the theoretical point of view, and will be discussed in another paper. In this paper, however, we restrict ourselves only to phenomena at lower temperatures where the mobility is determined by impurity atoms.

It may be possible to classify the concentration of impurity atoms into the following three ranges:

(1) When the concentration of impurity atoms is fairly large and the overlapping between atomic wave founctions localizing in each impurity atom is large, impurity levels become very broad and we can not distinguish the impurity band from the conduction band. In this case, only one conduction band exists (the structure of this conduction band may be complicated in general), and impurity atoms play a role of scatterers. Scattering potential of each impurity atom is, however, neither of a short range force nor of a weak force compared with the translational energy of the electron, because in general the number of conduction electrons is nearly equal to that of impurity atoms and the screening effect of Coulomb field of impurity atoms by conduction electrons is not so large. As well-known, the transport equation of Boltzmann-Bloch is applicable only in the case where the effective range of scattering potential is fairly small compared with the whole space and the energy of thermal fluctuation κT (where κ is the Boltzmann constant and T is the absolute temperature) is larger than the energy uncertainty due to scattering processes h/τ (where h is Planck's constant and τ is the relaxation time appearing in the definition of conductivity). The above mentioned conditions for the applicability of Boltzmann-Bloch's transport equation are not fulfilled when the temperature becomes lower and mean translational energy of electrons becomes smaller. In this case, we can not use the Boltzmann-Bloch's equation to calculate the conductivity and must consider the transport phenomena from a more general stand point. In § 2, we discuss about this general transport equation first proposed by F. Nakano[1], and in § 3 we calculate the mobility in this range practically.

(2) When the concentration of impurity

atoms becomes smaller, a new band composed mainly by the atomic wave functions localized in each impurity atom splits from the conduction band. We call this band as an impurity band. Main factors to determine the mobility in this impurity band are such that: (i) Correlation energy between electrons induced by Coulomb interaction between them. (ii) Resonance energy induced by overlapping between atomic wave functions localized in different impurity atoms. This energy corresponds to the translational energy of electron in the impurity band. (iii) Fluctuation of potential energy at each impurity atom induced mainly by Coulomb potential of minority impurity atoms with plus or minus charge. Amongst these effects, correlation energy is, in general, largest, and thus we can consider in fairly good approximation that only one electron is possible to occupy the state of atomic wave function localized at a particular impurity atom. In this approximation, the existence of minority impurity atoms is essentially important, because if there is no minority impurity atom the number of free electron equals just that of majority impurity atom and only one configuration that one electron is localized at each impurity atom is possible, and thus electrical conductivity does not occur. Further we can divide this range into two cases such that: (i) resonance energy is much larger than fluctuation of potential energy. (ii) fluctuation of potential energy is much larger than resonance energy. When the concentration of majority impurity atoms is not so small, the condition of first case is fulfilled. In this case, the energy width of the impurity band is determined mainly by the resonance-energy, and electron can walk about over the whole space. In § 4 we calculate the mobility in this range.

(3) When the concentration of impurity atoms becoms very small, the fluctuation of potential energy becomes much larger than the resonance energy. In this case, the ennergy width of impurity band is mainly determined by the fluction of potential energy at each majority impurity atom, and the localized state belonging to a particular impurity atom becomes stable, and transport phenomenon does not occur if we consider only the freedom of electron system. In this range, the interaction of electron with the other freedom, for example phonon system, is essentially important for transport phenomena. Electron is possible to walk about by hopping from one localized state to the other exchanging the difference of local potential energy for phonon system. Mobility in this range is calculable on this hopping model. This calculation is, however, given in the following paper, and in this paper we restrict ourselves only to the first two cases, namely (1) and (2), in which it is sufficient to consider only the freedom of electron system.

§ 2. General Discussion to Calculate Transport Coefficients

To treat transport phenomena of electrons, Boltzmann-Bloch equation is the most familiar technique. This equation bases on the classical gas transport theory and is obtained by straight extension to quantum particle. The logic of Boltzmann-Bloch equation is as follows: We consider that the Hamiltonian of the system is written by $H=H_0+H_1$, where H_0 is unperturbed and H_1 is perturbing Hamiltonian. H_0 is chosen as simple form and in general the eigen-state of electron of unperturbed Hamiltonian is given by Bloch function ψ_{lk} where l represents the class of band and $\boldsymbol{k}$ wave vector. H_1 represents the remaining Hamiltonian and includes the scattering matrix of electron represented by Bloch function. When there is no external field or internal strain, the system is in thermal equilibrium subjected by total Hamiltonian H. When the external field is applied in the system, the state of above mentioned thermal equibrium is no more equilibrium state, and the system begins to move into a new equilibrium state. When there is the internal strain initially, the state is not in thermal equilibrium and the system also moves into the state of thermal equilibrium. If the structure of the system is complicated and includes some kind of randomness, in the process of this motion, the state of the system reaches to the quasi equilibrium state with steady flows. We call this state as steady state. The time to reach to the steady state is of the order of relaxation time τ determined by the definition of conductivity, and the time to reach to the final equilibrium

state is the order of macroscopic scale and becomes infinity when the scale of the system becomes infinity, and thus the steady state is obtained if the scale of the system is fairly large. At a arbitrary time t, when the system is in steady state, we observed the system and diagonalize the state regarding to the unperturbed Hamiltonian H_0. Thus we obtain the distribution function of unperturbed state at time t. After this observation, we pursue the change of the state dividing into two mechanisms, that is the change by drift effect (free accelleration by external force and restoring effect from internal strain when the perturbation H_1 does not exist) and the change by collision effect (the motion of state by H_1). The steady state is defined by the condition that the change of the diagonal element of the state induced by the above two mechanisms cancels out each other, namely the change of the distribution function by drift and collision effect is zero. This equation is well known Boltzmann's transport equation, and from this equation we can obtain the distribution function in steady state.

As seen from the above consideration, this process to obtain Boltzmann-Bloch equation is very complicated and the justification of this equation from the fundamental stand point is very difficult problem although remarkable proceeding has been done recently by works of van Hove and so on[2]. Even apart from the fundamental problem, application of this equation is limited in the case mentioned already in § 1, that is the effective range of scattering potential is small and the condition

$$\kappa T > h/\tau \tag{1}$$

is satisfied. In general, these conditions are not satisfied in phenomena of impurity conduction, especially in the range (2) in § 1. Thus we must consider the transport phenomena on a more general stand point.

In quantum mechanics, when the state ψ_0 of the system with Hamiltonian $\mathscr{H}$ is given at a time $t=0$, expectation value of arbitrary physical quantity A is given by $\langle\psi_0 A\psi_0\rangle$ at time $t=0$. Wave function ψ moves by well known Schrödinger equation, and in arbitrary time $t>0$, the initial state becomes $\exp[-i\mathscr{H}t/h]\psi_0$* and the expectation value of A becomes as

$$\langle A(t)\rangle=\langle\psi_0 \exp[i\mathscr{H}t/h]\, A \exp[-\mathscr{H}i/h]\psi_0\rangle\,. \tag{2}$$

When the Hamiltonian of the system is given by $\mathscr{H}_0$ in time $t<0$, and the system is in thermal equilibrium by this Hamiltonian $\mathscr{H}_0$, we should take a statistical average, and the expectation value of A at time $t>0$ is given by

$$\langle A(t)\rangle=T_r \exp[-\beta\mathscr{H}_0] \times \exp[i\mathscr{H}t/h]A \exp[-i\mathscr{H}t/h]\,, \tag{3}$$

where β represents $(\kappa T)^{-1}$. This formula is one of the most fundamental one in quantum mechanics, and also the starting formula to obtain the transport coefficient.

For example we consider the case that the Hamiltonian of the system is given by H, and in time $t<0$, the system is in thermal equilibrium, and in time $t=0$ constant electric field $\boldsymbol{F}$ is applied suddenly. In this case, we can substitute in Eq. (3) $\mathscr{H}_0$ by $H-e\boldsymbol{F}\sum_i \boldsymbol{r}_i$. When we want to know the current $\boldsymbol{J}$ in time $t>0$, we may substitute A by $\boldsymbol{J}=e\sum_i \boldsymbol{v}_i$, and to know the energy flow $\boldsymbol{W}$, substitute A by $\boldsymbol{W}$, (general formula of $\boldsymbol{W}$ is not simple but depends on the formula of interaction Hamiltonian. If the interaction Hamiltonian is negligibly small, we obtain the usual formula of energy flow density.)

If we restrict ourselves to the linear theory concerning to the external field, we can expand the Eq. (3) into a power series of $\boldsymbol{F}$ and take the first second terms of this series. From the usual expansion formula (see Appendix I) we obtain as

$$\langle A(t)\rangle=\mathrm{T}_r\, e^{-\beta H}\left\{A-\frac{i}{h}eF\int_0^t dt_1\left[e^{-iHt_1/h}\sum_i \boldsymbol{r}_1 e^{iHt_1/h},\ A\right]\right\}, \tag{4}$$

or we can rewrite into the following formula (see Appendix II)

$$\langle A(t)\rangle=\mathrm{T}_r\, e^{-\beta H}\left\{A-\frac{i}{h}eF\left[\sum_i \boldsymbol{r}_i,\ A\right]+\frac{i}{h}F\int_0^t dt_1(t-t_1)[e^{-iHt_1/h}\boldsymbol{J}\, e^{iHt_1/h},\ A]\right\} \tag{5}$$

* Hereafter h means the Plancks constant divided by 2π.

$$=\mathrm{T}_r\, e^{-\beta H}\left\{A+\boldsymbol{F}\int_0^t dt_1\int_0^\beta d\lambda\, e^{-iH(t_1+i\hbar\lambda)/\hbar}\boldsymbol{J}\, e^{iH(t_1+i\hbar\lambda)/\hbar}A\right\}. \tag{6}$$

The same treatment is possible when the motion of the state is derived by internal strain. When the potential of internal strain is written as $\boldsymbol{\alpha}V$ and in time $t<0$ the system is in thermal equilibrium under the Hamiltonian $H+\boldsymbol{\alpha}V$ including the potential of strain, we can replace in Eq. (3) $\mathscr{H}_0$ by $H+\boldsymbol{\alpha}V$. In time $t>0$, we consider that the potential of internal strain is removed. Then the motion of the system is subjected by the Hamiltonian H, and the system begins the motion to remove the internal strain. Thus we can replace $\mathscr{H}$ in Eq. (3) by H. Using the linear theory with respect to $\boldsymbol{\alpha}V$, the following formula resembling to Eq. (6) is obtained easily (see Appendix I, II)

$$\langle A(t)\rangle=\mathrm{T}_r\left[e^{-\beta(H+\boldsymbol{\alpha}V)}A+e^{-\beta H}\boldsymbol{\alpha}\int_0^\beta d\lambda\int_0^t dt_1 e^{-iH(t_1+i\hbar\lambda)/\hbar}\dot{V}e^{iH(t_1+i\hbar\lambda)/\hbar}A\right], \tag{7}$$

where

$$\dot{V}=\frac{i}{\hbar}[H,\ V]. \tag{8}$$

In the case that internal strain means the constant gradient of electron density, we may take $\boldsymbol{\alpha}$ as $-\kappa T\nabla(\zeta/\kappa T)$ and $\dot{V}$ as $\boldsymbol{J}/e=\sum_i \boldsymbol{v}_i$, and when constant gradient of temperature exists, we may take $\boldsymbol{\alpha}$ as $\kappa T\nabla(\kappa T)^{-1}$ and V' as energy flow operator $\boldsymbol{W}$.

Even in the case that external field or internal strain is not uniform but changes in time and in space, and thus the resultant flows also change in time and in space, the same treatment is possible. For example, when the motion is derived by the external field, we can substitute in Eq. (3) $\mathscr{H}_0$ by H, and $\mathscr{H}$ by $H+eV$, where V is given by

$$V=\int\varphi(\boldsymbol{r},\ t)n(\boldsymbol{r})d\boldsymbol{r}, \tag{9}$$

where $\varphi(\boldsymbol{r},\ t)$ is the potential of external field varying in time and in space, and $n(\boldsymbol{r})$ is the operator of density of electron. The continuous equation exists between $n(\boldsymbol{r})$ and the operator of current density $\boldsymbol{J}(\boldsymbol{r})/e$ as follows

$$dn(\boldsymbol{r})/dt+\mathrm{div}\,\boldsymbol{J}(\boldsymbol{r})/e=0 \tag{10}$$

where

$$n(\boldsymbol{r})=\sum_i \delta(\boldsymbol{r}-\boldsymbol{r}_i)$$

$$\boldsymbol{J}(\boldsymbol{r})\Big/e=\frac{1}{2}\sum_i\{\boldsymbol{v}_i\delta(\boldsymbol{r}-\boldsymbol{r}_i)+\delta(\boldsymbol{r}-\boldsymbol{r}_i)\boldsymbol{v}_i\} \tag{11}$$

The resembling equation as Eq. (6) is given by the same method as that used to induce the Eq. (6), considering the condition that the normal component of the flow $\boldsymbol{J}(\boldsymbol{r})$ is zero at the surface of the boundary,

$$\langle A(\boldsymbol{r},\ t)\rangle=\mathrm{T}_r\, e^{-\beta H}\left\{A(\boldsymbol{r})+\int_0^t dt_1\int_0^\beta d\lambda\int d\boldsymbol{r}'\boldsymbol{F}(\boldsymbol{r}',\ t_1)e^{iH(t_1+i\hbar\lambda)/\hbar}\boldsymbol{J}(\boldsymbol{r}')\, e^{-iH(t_1+i\hbar\lambda)/\hbar}A(\boldsymbol{r})\right\}, \tag{12}$$

or we can write by using Fourier transformation

$$\langle A_{\boldsymbol{k}}(t)\rangle=\mathrm{T}_r\, e^{-\beta H}\left\{A_{\boldsymbol{k}}+\sum_{\boldsymbol{k}'}\int_0^t dt_1\int_0^\beta d\lambda\boldsymbol{F}_{\boldsymbol{k}'}(t_1)\, e^{iH(t_1+i\hbar\lambda)/\hbar}\boldsymbol{J}_{-\boldsymbol{k}'}\, e^{-iH(t_1+i\hbar\lambda)/\hbar}A_{\boldsymbol{k}}\right\}, \tag{13}$$

where

$$\boldsymbol{J}_{\boldsymbol{k}}=\int d\boldsymbol{r}\, e^{i\boldsymbol{kr}}\boldsymbol{J}(\boldsymbol{r})=\frac{e}{2}\sum_i(\boldsymbol{v}_i e^{\boldsymbol{kr}_i}+e^{i\boldsymbol{kr}_i}\boldsymbol{v}_i),\quad A_{\boldsymbol{k}}=\int d\boldsymbol{r}\, e^{i\boldsymbol{kr}}A(\boldsymbol{r}),$$

and $A(\boldsymbol{r})$ is the operator of a given flow density to be required.

Also in the case that internal strain is exist, the same treatment is possible. When we write the potential of internal strain as V

$$V=\int \alpha(\boldsymbol{r},\ t)w(\boldsymbol{r})\,d\boldsymbol{r} \tag{14}$$

we obtain the following relation

$$\langle A(\boldsymbol{r},\ t)\rangle=\mathrm{T}_r\Big[e^{-\beta(H+V)}A(\boldsymbol{r})+e^{-\beta H}\int_0^t dt_1\int_0^\beta d\lambda\int d\boldsymbol{r}'$$
$$\nabla'\alpha(\boldsymbol{r}',\ t_1)\,e^{-iH(t_1+i\hbar\lambda)/\hbar}\boldsymbol{W}(\boldsymbol{r}')\,e^{iH(t_1+i\hbar\lambda)/\hbar}A(\boldsymbol{r})\Big\}\ , \tag{15}$$

where $\boldsymbol{W}(\boldsymbol{r})$ is the operator of the flow density given by the following continuous equation

$$dw(\boldsymbol{r})/dt+\mathrm{div}\ \boldsymbol{W}(\boldsymbol{r})=0 \tag{16}$$

For example, when the internal strain means the density fluctuation of electron, we may substitute $\boldsymbol{\alpha}$ by $\beta^{-1}\nabla(\beta(\boldsymbol{r})\zeta(\boldsymbol{r}))$, $w(\boldsymbol{r})$ by the operator of electron density $n(\boldsymbol{r})$ and $\boldsymbol{W}(\boldsymbol{r})$ by the operator of electron current density $\boldsymbol{J}(\boldsymbol{r})$, and when temperature gradient exists, $\boldsymbol{\alpha}$ by $\beta^{-1}\nabla\beta(\boldsymbol{r})$, $w(\boldsymbol{r})$ by the operator of energy density, and $\boldsymbol{W}(\boldsymbol{r})$ by the operator of energy flow density.

These like formulas of transport coefficients are first considered by F. Nakano[1] in the case of electric conductivity and later obtained by R. Kubo, etc., in general case. Our stand point to obtain these formulas differs somewhat from that of R. Kubo etc. which bases on Onsager's fluctuation-dissipation theory and is its direct expansion to quantum mechanics. On this stand point, in both the cases that the motion of the state is derived by external field, or by internal strain, R. Kubo etc. obtained the same formulas of transport coefficients. On the other hand, we obtained the different formulas respectively in two cases as seen from Eqs. (6) and (7) or Eqs. (12) and (15) which differs each other in the first term. This difference is essential in the case to discuss the antisymmetric part of conductivity tensor. For example we consider the simple case that the system consists of only free electrons and the constant magnetic field is applied in Z-axis. When the constant electric field is applied in X-axis, the constant electric current is induced in the direction both perpendicular to magnetic and electric field, namely Y-axis as well known. On the other hand, when the density gradient is given in X-axis and there is no electric field, electric current does not occur because in this case we can construct the eigen state with arbitrary density fluctuation in X-direction. The above situations are included in our formulation, as easily seen, and not in Kubo's formulation. This difference is owing to the fact that the electric current induced in the above case is polarization current and is reversible phenomena which is not described perfectly well in Onsager's theory. The more detailed discussion may be given in another paper[4].

To apply the above results on phenomena of impurity conduction classified by (1) and (2) in § 1, we can use the one electron approximation, and the formula to obtain the electric current becomes simpler. The Hamiltonian of the system is given by

$$H=\sum_i H_i\ , \tag{17}$$

$$H_i=\frac{\boldsymbol{p}_i^2}{2m}+V_0(\boldsymbol{r}_i)+V_1(\boldsymbol{r}_i)\ , \tag{18}$$

where V_0 is a periodic potential by atoms constructing regular lattice points, and V_1 is non periodic potential by impurity atoms locating at random. Using the second quantization method basing the eigen function ψ_s of the total Hamiltonian of one electron H_i, we can write

$$H=\sum_s E_s a_s^* a_s \tag{19}$$

$$e^{-iHt/\hbar}\sum_i \boldsymbol{v}_i\,e^{iHt/\hbar}=\sum_s\sum_{s'}\langle s|\boldsymbol{v}|s'\rangle\exp\left[i(E_{s'}-E_s)t/h\right]a_s^* a_{s'}\ , \tag{20}$$

where a_s^* and a_s represent respectively the creation and annihilation operator of the state ψ_s. Substituting these formulas to Eq. (5), and taking A as current operator $\boldsymbol{J}$,

$$\boldsymbol{J}=e\sum_i \boldsymbol{v}_i=e\sum_s\sum_{s'}\langle s|\boldsymbol{v}|s'\rangle a_s^* a_{s'}\,, \tag{21}$$

and further performing the time integration and trace, we obtain the expectation value of current in time t as

$$\langle \boldsymbol{J}(t)\rangle=\boldsymbol{F}e^2\left\{\frac{n}{m}t+\sum_{s'\neq s}\sum\langle s|\boldsymbol{v}|s'\rangle\wedge\langle s'|\boldsymbol{v}|s\rangle\frac{f_s-f_{s'}}{E_s-E_{s'}}\left(t-h\frac{\sin(E_s-E_{s'})t/h}{E_s-E_{s'}}+ih\frac{1-\cos(E_s-E_{s'})t/h}{E_s-E_{s'}}\right)\right\}, \tag{22}$$

where n is the number density of electron, $\boldsymbol{A}\wedge\boldsymbol{B}$ means the tensor of second rank, namely $(\boldsymbol{A}\wedge\boldsymbol{B})_{ij}=A_iB_j$, and f_s is the Fermi distribution function

$$f_s=\left[\exp\left(\frac{E_s-\zeta}{\kappa T}\right)+1\right]^{-1}. \tag{23}$$

In this paper we treat only the case that there is no magnetic field and further we assume that the system is isotropic. Then the induced electric current is parallel to the electric field, and Eq. (22) becomes

$$\langle \boldsymbol{J}(t)\rangle=\boldsymbol{F}e^2\left\{\frac{n}{m}t-\sum_{s'\neq s}\sum 2f_s\frac{|\langle s|v_x|s'\rangle|^2}{E_{s'}-E_s}t\right.$$
$$\left.-h\sum_{s'\neq s}\sum(f_{s'}-f_s)\frac{|\langle s|v_x|s'\rangle|^2}{(E_s-E_{s'})^2}\sin\frac{E_{s'}-E_s}{h}t\right\}. \tag{24}$$

When there is no impurity potential, eigen state ψ_s is represented by Bloch function ψ_{lk}. Then wave vector $\boldsymbol{k}$ commutes with velocity operator $\boldsymbol{V}$, and matrix element of $\boldsymbol{V}$ is not zero only in the elements of interband transition except diagonal element. Therefore the third term of Eq. (24) oscillates rapidly with time and becomes zero in time average. From the relation of f-sum rule, namely

$$\sum_{l'\neq l}2\frac{|\langle l\boldsymbol{k}|v_x|l'\boldsymbol{k}\rangle|^2}{E_{l'\boldsymbol{k}}-E_{l\boldsymbol{k}}}=\frac{1}{m}-(\mathrm{M}_{l\boldsymbol{k}}^{-1})_{xx} \tag{25}$$

$$(\mathrm{M}_{l\boldsymbol{k}}^{-1})_{ij}=\frac{1}{h^2}(\partial^2E_{l\boldsymbol{k}}/\partial k_i\partial k_j)\,, \tag{26}$$

the remaining terms of Eq. (24) becomes as

$$\langle J(t)\rangle=Fe^2t\sum_{l,\boldsymbol{k}}f_{l\boldsymbol{k}}(\mathrm{M}_{l\boldsymbol{k}}^{-1})_{xx}\,, \tag{27}$$

where $\mathrm{M}_{l\boldsymbol{k}}$ is effective mass tensor in l-band and this equation represents a well known accelleration equation of electron in a periodic potential.

When impurity potential exists, Bloch function is no more a eigen function of total Hamiltonian and the true eigen function ψ_s is represented by complicated linear combination of Bloch function. Then we may rewrite the second term of Eq. (24) using the relation

$$\langle s|v_x|s'\rangle=\frac{i}{h}\langle s|[H,\ X]|s'\rangle=\frac{i}{h}(E_s-E_{s'})\langle s|X|s'\rangle\,, \tag{28}$$

as follows,

$$\sum_{s'\neq s}2\frac{|\langle s|v_x|s'\rangle|^2}{E_{s'}-E_s}=\frac{i}{h}\sum_{s'\neq s}\{\langle s|v_x|s'\rangle\langle s'|X|s\rangle-\langle s|X|s'\rangle\langle s'|v_x|s\rangle\}\,. \tag{29}$$

In the above summation over s', we must omit the case $s'=s$. However, if there is no singularity in the point $s'=s$, we may add the point $s'=s$ in the above summation. This is not allowed always as seen in the above case that there is no impurity potential. Even in

the system with impurity atoms, for example, Bose gas in degenerate state and perphaps the state in superconductivity, the ground state is a singular point and the above treatment may not be applicable. However, if we confine the system in a closed box, the above treatment is always possible because in this case the diagonal element of X has always finite value and the contribution from the point $s'=s$ is exactly zero. In this case, the boundary condition of wave functions becomes complicated and the singurarity is removed into the third term. Therefore, we may say that the above treatment may be applicable for the system in which the state is not affected essentially by the existence of boundary condition. In this paper, we consider the case that the above treatment is applicable, and then Eq. (29) becomes as

$$\frac{i}{h}\langle s|[v_X,\ X]|s\rangle=\frac{1}{m}\ , \tag{30}$$

and using the fact that $\sum_s f_s=n$, the first and the second term of Eq. (24) cancels out exactly each other.

In the third term of Eq. (24), we can expand $f_{s'}-f_s$ as

$$f_{s'}-f_s=f_1(\mathcal{E})\frac{E_s-E_{s'}}{\kappa T} \tag{31}$$

$$f_1(\mathcal{E})=[(e^{\mathcal{E}}+1)(1+e^{-\mathcal{E}})]^{-1},\qquad \mathcal{E}=\frac{E_s-\zeta}{\kappa T}\ , \tag{32}$$

when time t is sufficiently large, because in summation over $E_{s'}$ only the range that $E_{s'}$ equals nearly to E_s is important by the well known relation

$$\lim_{t\to\infty}\frac{\sin(E_{s'}-E_s)t/h_s}{E_{s'}-E_s}=\pi\delta(E_s-E_{s'})\ . \tag{33}$$

Thus Eq. (17) becomes

$$\langle J(t)\rangle=Fe^2\frac{\pi h}{\kappa T}\sum_{s\neq s'}\sum f_1(\mathcal{E})|\langle s|v_X|s'\rangle|^2\delta(E_s-E_s')\ , \tag{34}$$

or replacing the summation by integration and performing the integration over s', we obtain

$$\frac{\langle J(t)\rangle}{F}\equiv\sigma=\frac{\pi e^2h}{nT}\int_0^\infty dES^2(E)f_1(\mathcal{E})\eta(E,\ E)\ , \tag{35}$$

where $S(E)$ is the state density, that is, $S(E)dE$ represents number of states included in the energy range $E\sim E+dE$, and $\eta(E,\ E')$ is the mean value of $|\langle s|v_X|s'\rangle|^2$ over the constant energy surface E about s and E' about s' respectively, namely

$$\eta(E,\ E')=\sum_s\sum_{s'}|\langle s|v_X|s'\rangle|^2\delta(E_s-E)\delta(E_{s'}-E')/S(E)S(E')\ . \tag{36}$$

In the above treatment, we assumed that time t is sufficiently large. The more detail condition is as follows: if we define Δ_0 as that, when the energy E' changes near by Δ_0, one of $f_1(\mathcal{E}')$, $\eta(E,\ E')$ and $S(E')$ changes apparently, time t should satisfy the condition

$$t\gg 2\pi h/\Delta_0 \tag{37}$$

When time t is not so large and the above condition is not satisfied, we may expand $\sin(E_{s'}-E_s)t/h$ in Eq. (24) as $(E_{s'}-E_s)t/h$. Then we obtain once more the accelleration equation (28). Thus we may say that when time t is much smaller than $2\pi h/\Delta_0$, the system suffer accelleration and current $J(t)$ increases with time, and when t becomes much larger than $2\pi h/\Delta_0$, the system reaches to quasi-equilibrium state and $J(t)$ becomes to steady current. We determine the conductivity σ in this steady state as in Eq. (35), and the time defined by $2\pi h/\Delta_0$ means the relaxation time to reach to the steady state.

Eq. (35) is our fundamental equation to calculate the conductivity of impurity conduction. When the state density $S(E)$ is given, our main problem to obtain σ is how to calculate the value $\eta(E, E)$.

§ 3. Conductivity in the Range of Impurity Scattering

In this section we treat the conductivity of case (1) in § 1, that is, the concentration of impurity atoms is fairly large and there is only one conduction band and impurity atom plays a role of scatterer.

At first, we consider the system of a following simplified model: (i) The system is isotropic. (ii) The structure of conduction band is represented only by one band. (iii) The Hamiltonian of the system does not include the spin freedom, and thus we do not need to consider the freedom of spin to calculate the conductivity when we multiply factor two to the final result. (iv) The magnitude of interaction Hamiltonian is much smaller than both the energy width of conduction band and the energy gaps between conduction band and the other bands, and thus the effect of interband transition is negligible. Thus it is sufficient to consider only one conduction band. (v) Impurity potential V_1 can be considered as the sum of the potential of each impurity atom, that is

$$V_1=\sum_n V_n \tag{38}$$

and V_n can be considered as δ-function type, that is, $|\langle \boldsymbol{k}|V_n|\boldsymbol{k}'\rangle|$ is constant and the scattering is isotropic.

As mentioned in § 2, our main problem is how to calculate $\eta(E, E)$ in Eq. (35). For this purpose, we expand ψ_s by Bloch function ψ_k as

$$\psi_s=\sum_k C_k{}^s\psi_k \tag{39}$$

The phase factor of the expansion parameter $C_k{}^s$ may be regarded as at random in a fairly good approximation corresponding to the randomness of positions of impurity atoms and the δ-function type character of impurity potential. Absolute value of $C_k{}^s$ is, however, calculable by some assumption. For example, we may write $|C_k{}^s|^2$ as

$$|C_k{}^s|^2=\frac{\xi(E_s,\ E_k)}{(E_s-E_k)^2+\Delta_s{}^2}\ , \tag{40}$$

where $\xi(E_s,\ E_k)$ may depend on E_k fairly weak, and, corresponding to perturbation theory, becomes $|\langle \boldsymbol{k}_s|V_1|\boldsymbol{k}\rangle|^2=\text{constant}\equiv|V_1|^2$ when E_k differs from E_s fairly larger than Δ_s. In the range that E_k does not differ so largely from E_s, mixing of states occurs in nearly equal weight, and Δ_s means the measure of the energy range where the mixing occurs. From the normalization of the wave function ψ_s, the relation

$$\sum_k |C_k{}^s|^2=\int_0^\infty S_0(E)\,dE\,\frac{\xi(E_s,\ E)}{(E_s-E)^2+\Delta_s{}^2}=1. \tag{41}$$

should be satisfied, where $S_0(E)$ means the state density of unperturbed system. When we assume simply as that, iv) $\xi(E_s,\ E)$ is given by $|V_1|^2$, we can determine Δ_s by the above relation, and thus $|C_k{}^s|^2$ is also determined.

When the absolute value of expansion coefficient $|C_k{}^s|$ is obtained, $|\langle s|v_X|s'\rangle|^2$ is given by

$$|\langle s|v_X|s'\rangle|^2=|\sum_k \langle \boldsymbol{k}|v_X|\boldsymbol{k}\rangle C_k{}^s C_k{}^{s'}|^2. \tag{42}$$

Due to the fact that the phase factor of $C_k{}^s$ is at random, cross terms such as $C_k{}^s C_{k'}{}^{s'}$, etc. cancel out each other in the average process respecting to s or s', and only autocorrelation termsre main. Thus $\eta(E, E)$ is obtained as follows,

$$\begin{aligned}\eta(E,\ E)&=\sum_k (|C_k{}^E|^2)^2|\langle \boldsymbol{k}|v_X|\boldsymbol{k}\rangle|^2\\ &=\frac{1}{3}\int\left(\frac{1}{h}\frac{\partial E_k}{\partial k}\right)_{E'}\left(\frac{\xi(E,\ E')}{(E-E')^2+\Delta_E{}^2}\right)^2\\ &\quad\cdot S_0(E')dE'\ .\end{aligned} \tag{43}$$

From the above process, we can calculate the conductivity σ irrespective of the strength of impurity potential $|V_1|^2$. In following, we calculate σ more qualitatively in some extreme cases.

(1) Δ_E is sufficiently smaller than E_s and $S(E)$, $S_0(E)$ and $v(E)$ do not change markedly when E changes about the order of Δ_E.

In this case, we can obtain Δ_E from Eq. (41), by using the following approximation

$$\int_0^\infty S_0(E')\,dE'\frac{|V_1|^2}{(E-E')^2+\Delta_E{}^2}=S_0(E)\,|V_1|^2\,\frac{\pi}{\Delta_E} \tag{44}$$

such as

$$\Delta_E=\pi|V_1|^2S_0(E)\ , \tag{45}$$

$\eta(E,\ E)$ is also obtained by the same approximation,

$$\eta(E,\ E)=\frac{\pi}{6}v^2S_0(E)|V_1|^2/\Delta_E{}^3\ , \tag{46}$$

or using Eq. (45)

$$=\frac{1}{6\pi^2}\overline{\frac{v^2}{S_0^2(E)|V_1|^2}}\,. \tag{47}$$

Thus, the conductivity σ is written by

$$\sigma=\frac{e^2}{3\pi}\frac{h}{\kappa T}\int_0^\infty dEf_1(\varepsilon)\frac{S^2(E)}{S_0^2(E)}\overline{\frac{v^2}{|V_1|^2}}. \tag{48}$$

This result is just same as that obtained by using Boltzmann-Bloch equation, when we take $S(E)=S_0(E)$. For example, when the energy spectrum of unperturbed system is given by effective mass formular, that is $E_k=h^2k^2/2m$, we can get the following results in some extreme cases.

(a) $\zeta\gg\kappa T$ in Fermi degeneracy

Conductivity σ becomes

$$\sigma=\frac{e^2}{3\pi}\frac{hv_\zeta^2}{|V_1|^2}\frac{S^2(\zeta)}{S_0^2(\zeta)}=\frac{2e^2}{3\pi}\frac{h\zeta_0}{m|V_1|^2}\equiv\sigma_0, \tag{49}$$

where ζ_0 is Fermi energy when the system is in perfect Fermi degeneracy, namely

$$\zeta_0=\frac{h^2}{2m}(3\pi^2n)^{2/3}. \tag{50}$$

(b) $\zeta\ll\kappa T$

In this case, distribution function $f(\varepsilon)$ is written by Maxwell's distribution function,

$$f(\varepsilon)=2^{1/2}\pi^{3/2}n\frac{h^3}{(m\kappa T)^{3/2}}e^{-E/\kappa T}, \tag{51}$$

$$E=\frac{1}{2}mv^2,\ S(E)=S_0(E)=\frac{3}{4}n\frac{E^{1/2}}{\zeta_0^{3/2}} \tag{52}$$

and thus

$$\sigma=\frac{2^{3/2}\pi^{1/2}}{3}ne^2\frac{h^4}{m^{5/2}|V_1|^2(\kappa T)^{1/2}}$$
$$=\frac{4}{3\pi^{1/2}}\sigma_0\left(\frac{\zeta_0}{\kappa T}\right)^{1/2}. \tag{53}$$

As is well known, Boltzmann-Bloch equation is applicable when the condition

$$\kappa T>\frac{2\pi h}{\tau} \tag{54}$$

is satisfied. In our theory, however, the criterion to obtain the Eq. (48) is such as given in (1), or roughly

$$\overline{E}>\overline{\Delta_E}\,, \tag{55}$$

where $\overline{A}$ means the averaged value of A. When the system is non-Fermi degeneracy, $\overline{E}$ is nearly same as κT, and Δ_s is neary same as h/τ as easily seen from Eqs. (45) and (52), and the conditions (54) and (55) are nearly equal. When the system is in Fermi degeneracy, however, we can put E as ζ_0 and $\overline{\Delta_E}$ as $h/2\tau$, and thus the condition (55) is further applicable than that of (54). In actual, if we adopt the former condition (54), Boltzmann-Bloch equation is not applicable for neary almost systems in Fermi degeneracy at sufficiently low temperatures. From the above treatment, we may say that when the condition (55) is satisfied, Boltzmann-Bloch equation may be applicable by adopting the real state density $S(E)$ instead of that of unperturbed system, $S_0(E)$.

(2) Δ_E is sufficiently larger than E.

In this case, we should determine the formula of $S(E)$ to proceed the calculation. For simplicity, we assume that $S_0(E)=S(E)=(3/4)nE^{1/2}/\zeta_0^{3/2}$ and $\xi(E,E)=|V_1|^2$ as in Eq. (52) and assumption (iv). Then using a approximation that

$$\int_0^\infty S_0(E')dE'\frac{\xi(E,E')}{(E-E')^2+\Delta_E^2}=\frac{3}{4}\frac{n|V_1|^2}{\zeta_0^{3/2}}\int_0^\infty dE'\frac{E'^{1/2}}{E'^2+\Delta_E^2}=\frac{3\pi}{4\sqrt{2}}\frac{n|V_1|^2}{\zeta_0^{3/2}}\frac{1}{\Delta_E^{1/2}}\,, \tag{56}$$

we can obtain Δ_E from the Eq. (41) as

$$\Delta_E\equiv\Delta=\frac{9\pi^2}{32}\frac{n^2|V_1|^4}{\zeta_0^3}\,, \tag{57}$$

and $\eta(E,E)$ becomes as follows

$$\eta(E,E)=\frac{1}{2}\frac{n|V_1|^4}{m\zeta_0^{3/2}}\int_0^\infty\frac{E^{3/2}}{(E^2+\Delta^2)^2}dE=\frac{\pi}{8\sqrt{2}}\frac{n|V_1|^4}{m\zeta_0^{3/2}\Delta^{3/2}}\,, \tag{58}$$

or using Eq. (57)

$$=\frac{16}{27\pi^2}\frac{\zeta_0^3}{mn^2|V_1|^2}\,. \tag{59}$$

Thus, the conductivity σ becomes

$$\sigma=\frac{e^2}{3\pi}\frac{h}{\kappa T}\frac{1}{m}\int_0^\infty dE f_1(\mathcal{E})\frac{E}{|V_1|^2}\,. \tag{60}$$

This result is just half of Eq. (48). Thus, in the case that impurity potential is approximated by δ-function type, the conductivity becomes just half of that obtained by using Boltzmann-Bloch equation when potential energy $\sqrt{n}\,|V_1|$ becomes much larger than Fermi energy ζ_0.

When impurity potential is not represented by δ-function type, but is more general formula, we must consider the following effects that: (i) Born approximation is not applicable, (ii) there appears localized state, (iii) there exists some correlation amongst $C_k{}^s$ in Eq. (39). By these effects, $\xi(E, E')$ and state density $S(E)$ become in general very complicated forms and it becomes fairly difficult problem to obtain $\xi(E, E')$ and $S(E)$ rigorously. Mathematically, however, we can obtain conductivity σ by assuming the energy dependence of $\xi(E, E')$, $S_0(E)$ and $S(E)$ respectively such as, $\xi(E, E')=\xi_0(E'-E)^\alpha/n\zeta_0{}^{\alpha-2}$, $S_0(E)=(\beta+1)nE^\beta/2\zeta_0{}^{\beta+1}$, and $S(E)=(\gamma+1)nE^\gamma/2\zeta_0{}^{\gamma+1}$. Then using the same approximation as in Eq. (56) etc. we obtain (see Appendix III)

$$\Delta_B=\Delta=\zeta_0\left\{4\Big/(\beta+1)\xi_0 B\left(1-\frac{\alpha+\beta+1}{2},\ \frac{\alpha+\beta+1}{2}\right)\right\}^{1/(\alpha+\beta-1)}, \tag{61}$$

and

$$\eta(E,\ E)=\eta=\frac{3\xi_0{}^2}{4(\beta+1)}\frac{1}{n}\frac{\Delta^{2\alpha+\beta/3-5/3}}{h^2k_0{}^2\zeta^{2\alpha+\beta/3-11/3}}B\left(2-\frac{2\alpha+\beta/3+7/3}{2},\ \frac{2\alpha+\beta/3+7/3}{2}\right), \tag{62}$$

or using Eq. (61)

$$=\frac{3}{4}\frac{\xi_0{}^2}{(\beta+1)}\left\{4\Big/(\beta+1)\,\xi_0 B\left(1-\frac{\alpha+\beta+1}{2},\ \frac{\alpha+\beta+1}{2}\right)\right\}^{(2\alpha+\beta/3-5/3)/(\alpha+\beta-1)}$$

$$\times B\left(2-\left(\alpha+\frac{\beta}{6}+\frac{7}{6}\right),\ \alpha+\frac{\beta}{6}+\frac{7}{6}\right)\frac{\zeta_0{}^2}{nh^2k_0{}^2}\,, \tag{63}$$

where $B(a, b)$ means β-function and we assumed that $-1<\alpha+\beta<1$ and $-7/6<\alpha+1/6\cdot\beta<5/6$ to replace the limit of integration by E' from zero to infinity.

Conductivity σ is obtained as

$$\sigma=\frac{\pi(\gamma+1)^2}{4}e^2\frac{n^2}{\zeta_0{}^{2\gamma+2}}\frac{h}{\kappa T}\eta\int_0^\infty dE\,E^{2\gamma}f_1(\mathcal{E})\,. \tag{64}$$

If we put $\alpha=0$, $\beta=\gamma=1/2$, and $\xi_0=n|V_1|^2/\zeta_0{}^2$, we obtain the Eq. (60). Temperature dependence of σ is determined only by the energy dependence of the state density, namely γ. We show in following some extreme cases more quantitatively.

(i) $\zeta\gg\kappa T$

$$\sigma=\frac{\pi(\gamma+1)^2}{4}e^2\frac{n^2h\eta}{\zeta_0{}^2}=\sigma_0\,. \tag{65}$$

(ii) $\zeta\ll\kappa T$

$$f_1(\mathcal{E})=\frac{1}{(\gamma+1)\Gamma(\gamma+1)}\left(\frac{\zeta_0}{\kappa T}\right)^{\gamma+1}e^{-\mathcal{E}/\kappa T}, \tag{66}$$

$$\sigma=\frac{\pi(\gamma+1)}{4}\frac{\Gamma(2\gamma+1)}{\Gamma(\gamma+1)}e^2\frac{n^2}{\zeta_0{}^2}h\eta\left(\frac{\kappa T}{\zeta_0}\right)^{\gamma-1} \tag{67}$$

$$=\frac{1}{\gamma+1}\frac{\Gamma(2\gamma+1)}{\Gamma(\gamma+1)}\sigma_0\left(\frac{\kappa T}{\zeta^0}\right)^{\gamma-1}, \tag{68}$$

where $\Gamma(x)$ means Γ-function.

§ 4. Impurity Band Conduction

When the concentration of impurity atoms becomes smaller, and overlapping of atomic wave functions localized at different impurity atoms becomes not so large, impurity levels split from the ordinary conduction band. Our problem in this section is how to treat the conduction phenomena in these impurity bands.

As mentioned in § 1, we adopt in this section the following model: (i) Impurity band is composed only by the 1S wave function localized at each impurity atom, and only one electron is possible to occupy a state of atomic wave function localized in a particular impurity atom. This assumption is applicable when the width of impurity band is fairly smaller than the energy gap between impurity band and conduction band. When this condition is not satisfied, we must add the wave functions of higher energy states to compose the impurity bands, and further consider the correlation energy to include the states in which more than two electrons occupy atomic wave functions localized at a particular impurity atom. In this case, the situation is fairly complicated and does not study in this paper.

Wave function ψ_s of the impurity band may be written from the above assumption such as,

$$\psi_s=\sum_n C_n{}^s\psi_n \tag{69}$$

where ψ_n means the atomic 1S wave function localized in the impurity atom of position $\boldsymbol{R}_n$.

Concerning to the expansion coefficient $C_n{}^s$, we obtain the following relation from the normalization of the wave function ψ^s

$$\sum_n |C_n{}^s|^2=1 \tag{70}$$

neglecting the overlapping of atomic wave functions localizing at different impurity atoms, and further we assume that the phase factor of $C_n{}^s$ is at random resulting from the randomness of the position of impurity atom. From the above consideration, we can obtain $\eta(E,\ E)$ easily as

$$\eta(E,\ E)=\sum_n\sum_m |C_n{}^s|^2|C_m{}^s|^2|\langle\psi_n|v_x|\psi_m\rangle|^2. \tag{71}$$

Further we can use the model already mentioned in § 1, that is: (ii) the resonance energy induced by the overlapping of atomic wave functions localized at different impurity atoms is much larger than the fluctuation energy of local potential induced mainly by the Coulomb potential of minority impurity atoms, and thus the energy width of impurity band is determined mainly by the resonance energy. From the above condition, we can put $|C_n{}^s|^2$ roughly as constant, that is, the inverse of the number of majority impurity atoms, $N_{\mathrm{maj}}{}^{-1}$. Then, $\eta(E,\ E)$ becomes simply

$$\eta(E,\ E)=\frac{1}{N_{\mathrm{maj}}}\sum_m \overline{|\langle\psi_n|v_x|\psi_m\rangle|^2}^{R_n}\equiv\frac{1}{3}\frac{v^2}{N_{\mathrm{maj}}}, \tag{72}$$

and the conductivity σ becomes

$$\sigma=\frac{\pi e^2h}{3\kappa T}\frac{v^2}{N_{\mathrm{maj}}}\int_0^\infty dE\,S^2(E)f_1(E). \tag{73}$$

For the further calculation, we assume, for example, the formula of $S(E)$ such as

$$\left.\begin{aligned} S(E)&=\frac{8}{\pi}\frac{N_{\mathrm{maj}}}{E_0{}^2}\sqrt{E(E_0-E)}\,,\\ &\qquad\text{when } 0<E<E_0\\ &=0\,,\\ &\qquad\text{when } E<0 \text{ or } E_0<E \end{aligned}\right\} \tag{74}$$

where E_0 means the width of impurity band and nearly equals to the resonance energy. $S(E)$ is normalized such as

$$\int_0^{E_0} S(E)dE=N_{\mathrm{maj}}\,. \tag{75}$$

In some extreme cases, we can write σ more definitely as follows.

(a) ζ and $E_0-\zeta\gg\kappa T$

$$\sigma=(\pi/3)e^2hv^2S^2(\zeta)/N_{\mathrm{maj}} \tag{76}$$

$$=\frac{64}{3\pi}e^2N_{\mathrm{maj}}\frac{hv^2\zeta(E_0-\zeta)}{E_0{}^4}\,. \tag{77}$$

Using the following relation

$$v^2=3\sum_m \overline{|\langle\psi_n|v_x|\psi_m\rangle|^2}^{R_n}$$

$$=\frac{3}{h^2}\sum_m \overline{|X_{nm}\langle\psi_n|H|\psi_m\rangle|^2}^{R_n}=\frac{a_0{}^2}{h^2}V^2, \tag{78}$$

we can write σ in a following form

$$\sigma=\frac{64}{3\pi}\frac{e^2a_0{}^2}{h}N_{\mathrm{maj}}\frac{V^2\zeta(E_0-\zeta)}{E_0{}^4}\,, \tag{79}$$

where V means the resonance energy

$$V^2=\sum_m \overline{|\langle\psi_n|H|\psi_m\rangle|^2}^{R_n}, \tag{80}$$

and a_0 means the effective distance between the nearest two impurity atoms. When $N_{\min}$

is much smaller than N_{maj}, that is $E_0 \gg E_0 - \zeta$, we can use the following approximation

$$N_{\min} = \int_{E_0-\zeta}^{E_0} S(E)\,dE \doteqdot \frac{16}{3\pi} N_{\mathrm{maj}} \left(1 - \frac{\zeta}{E_0}\right)^{3/2}, \tag{81}$$

and we can

$$\sigma = 8\left(\frac{2}{3\pi}\right)^{1/3} \frac{e^2 a_0^2}{h} (N_{\mathrm{maj}} N_{\min}^2)^{1/3} \frac{V^2}{E_0^2}. \tag{82}$$

(b) $\kappa T \gg E_0$

In this case, some part of electron may occupy conduction band and conductivity may be written as a sum of two part,

$$\sigma = \sigma_c + \sigma_i, \tag{83}$$

where σ_c comes from the electron of conduction band and σ_i from the impurity band. When we write the number of electron occupying the impurity band as N, we can replace

$$f_1(E) \equiv f(E)(1-f(E)) \doteqdot \frac{N(N_{\mathrm{maj}}-N)}{N_{\mathrm{maj}}^2}, \tag{84}$$

and thus

$$\sigma_i = \frac{32}{9\pi} e^2 \frac{N(N_{\mathrm{maj}}-N)}{N_{\mathrm{maj}}} \frac{hv^2}{\kappa T E_0} \tag{85}$$

$$= \frac{32}{9\pi} \frac{e^2 a_0^2}{h} \frac{N(N_{\mathrm{maj}}-N)}{N_{\mathrm{maj}}} \frac{V^2}{\kappa T E_0}. \tag{86}$$

When the number of electrons occupying the conduction band is negligible small, we can replace N by $(N_{\mathrm{maj}} - N_{\min})$, in the above equations.

This like result was obtained at first by Conwell-Weiskof.[3] Their result is obtainable by the following consideration. We consider the case that κT is much larger than the resonance energy V_{nm}, and the probability that the atomic state localizing at each impurity atom is constant. When the external field F is applied, the transition probability to translate from state ψ_n to ψ_m differs from that to translate from ψ_m to ψ_n. This difference may be written as

$$FeX_{nm}/\kappa T \tau_{nm}, \tag{87}$$

where τ_{nm} means the resonance frequency and may be written by the resonance energy V_{nm} such as

$$\frac{h}{\tau_{nm}} = V_{nm} = |\langle \psi_n | H | \psi_m \rangle|. \tag{88}$$

The conductivity due to this process is obtained roughly

$$\sigma = e^2 \frac{N(N_{\mathrm{maj}}-N)}{N_{\mathrm{maj}}^2} \sum_n \sum_m \frac{X_{nm}^2}{\kappa T \tau_{nm}}$$

$$= \frac{e^2}{h} \frac{N(N_{\mathrm{maj}}-N)}{N_{\mathrm{maj}}} \frac{\overline{\sum_m |X_{nm}^2 V_{nm}|}^{R_n}}{\kappa T} \tag{89}$$

Considering that E_0 nearly equals to V, Eq. (89) has the same form as Eq. (86) except merely a numerical factor, and thus may say that Conwell's result corresponds to the extreme case (b) of our formula.

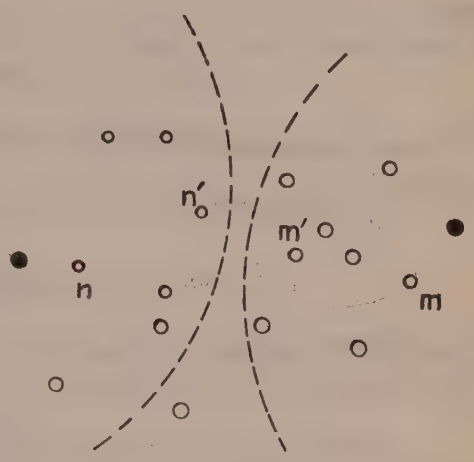

Fig. 1.
●: minority impurity atom.
○: majority impurity atom.

When the energy fluctuation of local potential is much larger than the resonance energy, we can not regard the expansion coefficient C_n^s as nearly constant. In this case, it may be more convenient to devide impurity atoms into molecules as shown in Fig. 1, where potential energy at $\boldsymbol{R}_n$ and $\boldsymbol{R}_m$ nearly equal to E_s, and $\boldsymbol{R}_{n'}$ and $\boldsymbol{R}_{m'}$ differ apparently from E_s, and thus dotted closed line mean each molecule. Overlapping integral between these molecules becomes very small, and thus conductivity becomes also very small. In this situation, however, the new mechanism mentioned in (3) of §1 becomes important. We shall discuss this mechanism in the forth-coming paper, and the comparison with experimental results would be also given in that paper.

§5. Conclusion

The author wishes to express his cordial thanks to Prof. S. Nakajima, Prof. F. Nakano and the members of our laboratory for their valuable discussions.

Appendix I

We consider the system with the Hamiltonian $H+\alpha(t)V$, where $\alpha(t)$ is the expansion parameter and depends on time t. The motion of an arbitrary operator A is given by

$$\frac{dA(t)}{dt}=\frac{i}{h}[H+\alpha(t)V,\ A(t)]\,, \tag{A1}$$

and the solution of this equation is given by

$$A(t)=e^{i(Ht+a(t)V)/h}Ae^{-i(Ht-a(t)V)/h}\,, \tag{A2}$$

where,

$$a(t)=\int_0^t \alpha(t)dt\,. \tag{A3}$$

To obtain the expansion formula of (A2), we use the following relation

$$\frac{d}{dt_1}\{e^{-iHt_1/h}e^{i(Ht_1+a(t_1)V)/h}Ae^{-i(Ht_1+a(t_1)V)/h}e^{iHt_1/h}\}$$
$$=\frac{i}{h}e^{-iHt_1/h}[\alpha(t_1)V,\ e^{i(Ht_1+a(t_1)V)/h}Ae^{-i(Ht_1+a(t_1)V)/h}]e^{iHt_1/h}\,. \tag{A4}$$

Integrating with respect to t_1 from 0 to t, and multiplying $e^{iHt/h}$ and $e^{-iHt/h}$ respectively from each side, we obtain the relation

$$e^{i(Ht+a(t)V)/h}Ae^{-i(Ht+a(t)V)/h}=e^{iHt/h}\Big\{A+\frac{i}{h}\int_0^t dt_1$$
$$\times e^{-iHt_1/h}[\alpha(t_1)V,\ e^{i(Ht_1+a(t_1)V)/h}Ae^{-i(Ht_1+a(t_1)V)/h}]\,e^{iHt_1/h}\Big\}e^{-iHt/h}\,. \tag{A5}$$

Using the method of iteration, we obtain the required result.

$$A(t)=e^{iHt/h}\Big\{A+\sum_{n=1}^{\infty}\Big(\frac{i}{h}\Big)^n\int_0^t dt_1\int_0^{t_1}dt_2\cdots\int_0^{t_{n-1}}dt_n$$
$$\times[e^{-iHt_1/h}\alpha(t_1)Ve^{iHt_1/h}[\cdots[e^{-iHt_n/h}\alpha(t_n)Ve^{iHt_n/h},\ A]\cdots]]\Big\}e^{-iHt/h}\,. \tag{A6}$$

The expansion formula of $e^{-\beta(H+V)}$ with respect to V is also obtained easily by the same method as the above. We start with the relation

$$\frac{d}{d\lambda}(e^{\lambda H}e^{-\lambda(H+V)})=-e^{\lambda H}Ve^{-\lambda(H+V)}\,. \tag{A7}$$

Integrating with respect to λ from 0 to β, and performing some transformation, we obtain the following relation

$$e^{-\beta(H+V)}=e^{-\beta H}\Big\{1-\int_0^\beta d\lambda e^{\lambda H}Ve^{-\lambda(H+V)}\Big\}\,. \tag{A8}$$

Using the method of iteration, we obtain

$$e^{-\beta(H+V)}=e^{-\beta H}+\sum_{n=1}^{\infty}(-1)^n\int_0^\beta d\lambda_1\int_0^{\lambda_1}d\lambda_2\cdots\int_0^{\lambda_{n-1}}d\lambda_n$$
$$\times e^{(\lambda_1-\beta)H}Ve^{(\lambda_2-\lambda_1)H}V\cdots e^{(\lambda_n-\lambda_{n-1})H}Ve^{-\lambda_n H}\,. \tag{A9}$$

Appendix II

To obtain the Eqs. (5) and (6), we used the following relations.

$$\text{(i)}\quad e^{-iHt/\hbar}Ae^{iHt/\hbar}=\int_0^t dt_1\frac{d}{dt_1}(e^{-iHt_1/\hbar}Ae^{iHt_1/\hbar})+A=A-\int_0^t dt_1 e^{-iHt_1/\hbar}\frac{i}{\hbar}(HA-AH)e^{iHt_1/\hbar}. \tag{A10}$$

$$\text{(ii)}\quad \mathrm{T}_r e^{-\beta H}[B,\ A]\to \mathrm{T}_r[e^{-\beta H},\ B]A=-\mathrm{T}_r e^{-\beta H}\int_0^\beta d\lambda\frac{d}{d\lambda}(e^{\lambda H}Be^{-\lambda H}A)$$

$$=-\mathrm{T}_r e^{-\beta H}\int_0^\beta d\lambda\, e^{\lambda H}(HB-BH)\,e^{-\lambda H}A\,. \tag{A11}$$

To obtain the second relation (A9), it is necessary to exist the first equation. The first equation does not exist in arbitrary operator B and A, because this equation exists only when we can exchange the order of the following double summation

$$\sum_s\sum_{s'}\sum_{s''}(e^{-\beta H})_{ss'}A_{s's''}B_{s''s}=\sum_{s''}\sum_s\sum_{s'}(e^{-\beta H})_{ss'}A_{s's''}B_{s''s}\,, \tag{A12}$$

in a suitable representation $\{s\}$. For example, in the case that $B=p_x$ and $A=x$, Eq. (A12) is not applicable.

Appendix III

We consider the case that there is no impurity atom, and the energy spectrum of the system is written as

$$E=\zeta_0(k/k_0)^p\,, \tag{A13}$$

where k_0 mean the wave vector of Fermi surface at absolute zero temperature. Expectation value of velocity is written as

$$v_k=\frac{1}{\hbar}\frac{\partial E}{\partial k}=\frac{\zeta_0 p}{\hbar k_0}\left(\frac{k}{k_0}\right)^{p-1}=\frac{p\zeta_0}{\hbar k_0}\left(\frac{E}{\zeta_0}\right)^{1-1/p}, \tag{A14}$$

and the state density $S_0(E)$ is written as

$$S_0(E)=\left(\frac{1}{2\pi}\right)^3 4\pi k^2\frac{dk}{dE}=\frac{1}{2\pi^2}\frac{k_0^3}{p\zeta_0}\left(\frac{k_0}{k}\right)^{p-3}=\frac{1}{2\pi^2}\frac{k_0^3}{p\zeta_0}\left(\frac{\zeta_0}{E}\right)^{(p-3)/p}, \tag{A15}$$

or, using the relation

$$n=\frac{k_0^3}{3\pi^2} \tag{A16}$$

$S_0(E)$ is written as

$$S_0(E)=\frac{3}{2}\frac{n}{p\zeta_0}\left(\frac{\zeta_0}{E}\right)^{1-3/p}. \tag{A17}$$

β in main paper is obtained by

$$\beta=\frac{3}{p}-1\,, \tag{A18}$$

and thus v is written by using the parameter β as

$$v=\frac{3}{\beta+1}\frac{\zeta_0}{\hbar k_0}\left(\frac{E}{\zeta_0}\right)^{(2-\beta)/3}. \tag{A19}$$

References

1) F. Nakano, Prog. Theor. Phys. **15** (1956) 1029.
R. Kubo, M. Yokota and S. Nakajima, J. Phys. Soc. Japan. **12** (1957) 1203.
2) van Hove, Physica **21** (1955) 517.
W. Kohn and J. H. Luttinger, Phys. Rev. **108** (1957) 509.
3) E. M. Conwell, Phys. Rev. **103** (1956) 51.
4) To be published in Jour. Phys. Soc. Japan.

JOURNAL OF THE PHYSICAL SOCIETY OF JAPAN Vol. 13, No. 10, OCTOBER, 1958

Magnetic Property and Crystal Chemistry of Ilmenite ($MeTiO_3$) and Hematite (αFe_2O_3) System
I. Crystal Chemistry

By Yoshikazu ISHIKAWA*
Institute for Solid State Physics, University of Tokyo, Tokyo
and Syun-iti AKIMOTO
Geophysical Institute, University of Tokyo, Tokyo

(Received June 18, 1958)

Solid solutions of ilmenite ($MgTiO_3$, $MnTiO_3$, $FeTiO_3$, $CoTiO_3$ and $NiTiO_3$) and hematite (αFe_2O_3) were prepared and their crystal structure was investigated by an X-ray analysis. It was confirmed that the solid solutions could be classified into three groups: 1) The specimens of ilmenite side and hematite side in the solid solution have the different crystal symmetries; $R\bar{3}$ and $R\bar{3}c$ respectively and there exists a miscibility gap between them ($MnTiO_3$, $MgTiO_3$ and $CoTiO_3$ series). 2) Ilmenite and hematite make the solid solution in the whole range of composition and the crystal symmetry changes from $R\bar{3}$ to $R\bar{3}c$ continuously ($NiTiO_3$ series). 3) The ranges of the crystal symmetries $R\bar{3}$ and $R\bar{3}c$ of the solid solution are overlapped with each other and a transformation from $R\bar{3}$ to $R\bar{3}c$ is observed in one specimen of the overlapped range ($FeTiO_3$ series). Such differences among different ilmenite and hematite systems may be attributed to the following three factors; differences in ionic radii, in electronic conductivity and in stability of other two solid solution series with spinel and pseudobrookite structures which exist in a ternary system of MeO-Fe_2O_3-TiO_2.

§ 1. Introduction

Since the discovery of strong ferrimagnetic substances in the solid solution series of $FeTiO_3$ and αFe_2O_3[1], detailed investigations of this series have been carried out by ourselves[2),3),4),5)], and others[6),7),8)]. Outstanding features of this series are the appearance of the ferrimagnetism only in a limited range of composition in the solid solution and a peculiar mode of thermomagnetic curve of all ferrimagnetic specimens. Such features have also been found in the solid solution of $NiTiO_3$ and Fe_2O_3[9)] and it was expected that these properties are common to solid solutions having the same crystal structure. It must be mentioned, however, that there exist some differences between magnetic properties of these two solid solution series in detailed points.

Nowadays five titanates: $FeTiO_3$, $NiTiO_3$, $CoTiO_3$, $MnTiO_3$ and $MgTiO_3$ are reported to be of the ilmenite structure[10)]. Hence it is worthwhile to prepare the solid solutions of these titanates and hematite and to examine

* Present address: Department of Applied Physics, Faculty of Engineering, University of Tokyo, Tokyo.

whether such magnetic properties as were found for $FeTiO_3$ and $NiTiO_3$ systems are also observed for other ilmenite-hematite systems or not. In this paper we shall report magnetic properties and crystal structures of the solid solutions of hematite and substance having the ilmenite structure in general and discuss in detail the differences among them. By making such comparisons we could understand better the peculiarity of the $FeTiO_3$ system only in which a cation stays in two different valence states.

Ilmenite ($MeTiO_3$) and hematite (αFe_2O_3); the end members of the solid solution, both being of the rhombohedral structure, have slightly different crystal symmetries $R\bar{3}$ and $R\bar{3}c$ with each other. In ilmenite and hematite, oxygen ions construct a slightly distorted hexagonal close-packed structure and cations occupy two thirds of octahedral interstices of oxygen layers, forming a honey comb structure. The cation lattice in the structure is shown in Fig. 1, where a rhombohedral unit cell is also drawn. As this figure shows, the cation lattice can be divided into four sublattices; A_1, A_2, B_1, and B_2. The $R\bar{3}$ symmetry corresponds to a case where A and B sublattices are occupied by different cations, while in $R\bar{3}c$ all sublattices are equivalent.

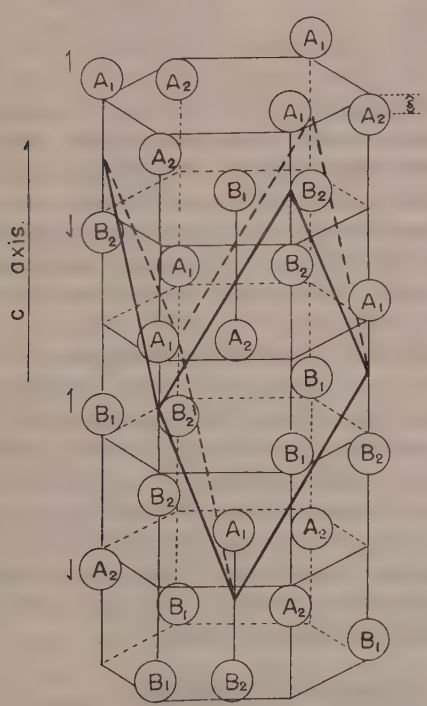

Fig. 1. Cation lattice in a rhombohedral sesquioxide. The cations deviate from the hexagonal site towards the direction of arrows. Rhombohedral unit cell is drawn by the thick line.

In the solid solution of ilmenite and hematite, Me and Ti ions occupy only A and B sublattices respectively in $R\bar{3}$ symmetry. The ferrimagnetism is expected to appear in the solid solution with this crystal symmetry, while the antiferromagnetism is attributed to the symmetry $R\bar{3}c$ as we stated in the previous paper.[3] It is, therefore, necessary for understanding the magnetic properties to investigate the crystal symmetry of the solid solution first of all, which we shall treat in this paper. Magnetic properties will be discussed in the next paper with particular reference to the crystal symmetry.

In the present stage, very few magnetic oxides are of the rhombohedral structure and magnetic couplings in this structure are not so well understood compared with those in the cubic structure to which many magnetic oxides belong. Hence it may have a considerable significance to establish a new magnetic oxide system of the rhombohedral structure and to discuss its magnetic properties in general.

§ 2. Ternary System of MeO-Fe_2O_3-TiO_2

Hitherto an investigation of the ternary system of FeO-Fe_2O_3-TiO_2 has been carried out by one of the authors and it has been reported that there exist three kinds of solid solution series in this system[11]. We have found this results can be generalized to the ternary system of MeO-Fe_2O_3-TiO_2 with $Me=Mg^{+2}$, Mn^{+2}, Fe^{+2}, Ni^{+2}, and Co^{+2} and the solid solution of $MeTiO_3$ and Fe_2O_3 is better understood when

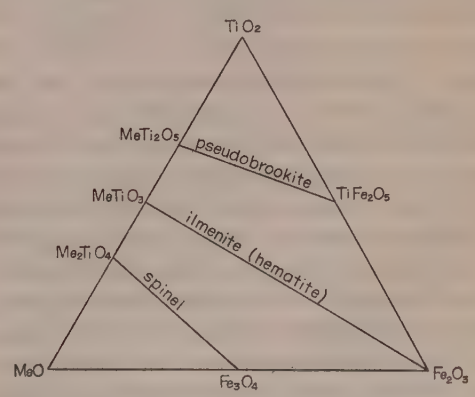

Fig. 2. Generalized phase diagram of MeO-Fe_2O_3-TiO_2 system.

we consider it as one of the solid solution series which exist in the ternary system of MeO-Fe_2O_3-TiO_2. This generalized phase diagram is shown in Fig. 2. Through an X-ray analysis, it was confirmed that there exist three kinds of solid solution series in every ternary system of MeO-Fe_2O_3-TiO_2 with Me= Mg,$^{+2}$ Mn^{+2}, Fe^{+2}, Co^{+2} and Ni^{+2}. They are:

1) $xMe_2TiO_4-(1-x)MeFe_2O_4$ with spinel structure,
2) $xMeTiO_3-(1-x)Fe_2O_3$ with ilmenite (hematite) structure,
3) $xMeTi_2O_5-(1-x)Fe_2TiO_5$ with pseudobrookite structure.

As to the end members of these solid solution series, it has been known that $MeTiO_3$ and $MeFe_2O_4$ exist for all these cations, while as to Me_2TiO_4 all but Ni_2TiO_4 have been reported to exist[12]. No data could have been obtained about $MeTi_2O_5$ except $FeTi_2O_5$ and $MgTi_2O_5$[13), 14)]. The solid solutions of the first series (spinel) have been investigated for Me= Ni and Fe and either have been reported to be ferrimagnetic[11)15)]. As to the solid solution of the third series (pseudobrookite), $FeTi_2O_5$ and Fe_2TiO_5 have been reported to make the solid solution in the whole range of the composition and they are paramagnetic at room temperature[13)]. It is out of our investigation whether there exist miscibility gaps in the solid solutions of the first and third series for other cations systems. In Table I, we show the ratio of the numbers of cations to oxygen ions in a molecule of the compounds of these three series. The ratio of cations to oxygen ions is the smallest for the third series, which means when the mixture of MeO, TiO_2 and Fe_2O_3 is sintered under a high oxygen pressure, the third series is the most stable, while in a reducing atmosphere, the spinel structure becomes more favourable. Hence we can understand that the second series can be prepared only in a restricted oxygen atomosphere.

Table. I. Three kinds of solid solution series.

No.	Solid solution series	Cations/Oxygens	Magnetic ions/Total ions, y
1	$xMe_2TiO_4\cdot(1-x)MeFe_2O_4$	0.75	$0.43 \geqq y \geqq 0.29$
2	$xMeTiO_3\cdot(1-x)Fe_2O_3$	0.67	$0.40 \geqq y \geqq 0.20$
3	$xMeTi_2O_5\cdot(1-x)Fe_2TiO_5$	0.60	$0.25 \geqq y \geqq 0.125$

When the mixture of $MeTiO_3$ and Fe_2O_3 is sintered in a slightly reducing atmosphere than is required for the ilmenite phase, the spinel phase begins to precipitate. At the same time, the pseudobrookite phase must precipitate in order to keep the ratio of Me, Ti and Fe constant. Then, in general, we found diffraction patterns corresponding to three phases on a "Norelco" chart when the sintering atmosphere was not controlled properly. This situation is not hold in the case of $FeTiO_3$ series in which Fe^{+2} can change into Fe^{+3} by the addition of oxygen ions, only two phases being sufficient to keep the ratio of cations constant in this solid solution series. In fact, we could not observe the coexistence of three phases in this solid solution series when the solid state reaction was completed. From these considerations, if we find the spinel and pseudobrookite phases only coexisted in the specimen which was prepared by sintering the mixture of $MeTiO_3$ and Fe_2O_3 in a desired proportion under a certain oxygen pressure, we may suppose that there is no adequate oxygen pressure under which the ilmenite-hematite phase of this composition is stable.

In the second column of Table I, we also indicate the ratio y of the numbers of magnetic ions to the total ions which give approximately the degree of dilution of the magnetic coupling in the compound. From these values we understand the situation that the first and third series are ferrimagnetic and paramagnetic respectively. Furthermore we can expect that the magnetic coupling in the second series is not so strong particularly in the compound near the ilmenite side. We shall show in the next paper that all characteristics of the ferrimagnetic properties of the solid solution of ilmenite and hematite can be interpreted by this diluted magnetic coupling.

§ 3. Preparation of Specimens

Following the considerations above mentioned, we have tried to prepare the solid solution between $MeTiO_3$ and Fe_2O_3 with Me= Mg, Mn, Fe, Co and Ni by usual ceramic

method. Most of the specimens were prepared by sintering the mixture of Fe_2O_3 and $MeTiO_3$ in the desired proportion at high temperatures, but some were prepared from the mixture of MeO, TiO_2 and Fe_2O_3. $MeTiO_3$ used was also prepared in advance in our laboratory. In any case, the sintering atmosphere was controlled appropriately. Since the magnetic properties of all solid solution series except $FeTiO_3$ series were found not to be sensitive to the heat treatments, they were cooled naturally in the furnace. In the case of $FeTiO_3$ series, however, magnetic properties are greatly affected by the heat treatment, details having already been reported in the previous papers.[3),5)]

Chemical analysis was carried out by T. Katsura of Tokyo Institute of Technology for the prepared specimens of $MnTiO_3$ and $FeTiO_3$ series. It was confirmed that the mol. ratios of $MeTiO_3$ and Fe_2O_3 determined by this analysis are not so much deviated from those originally adopted in mixing, but some of the specimens in $MnTiO_3$ series were found to contain traces of Mn^{+3} and Fe^{+2}. It is not clear how magnetic property and crystal structure of this solid solution series are affected by these impurities. For the specimens of other series no chemical analysis has yet been practised, so that we must consider that the specimens keep their original composition unchanged during sintering. It is, therefore, expected that the real composition is deviated from the original one when other phases coexist, which may result in a scattering of the results as are found for $MgTiO_3$ and $CoTiO_3$ series.

§ 4. Crystallographic Study of the Solid Solution

An X-ray analysis of the solid solution was conducted by a "*Norelco*" diffractometer with Fe *K* radiation. Practically we determined the crystal parameters of $FeTiO_3$, $MnTiO_3$, $CoTiO_3$ and $MgTiO_3$ series by least square method in making use of eight diffraction peaks, i.e. (300), (214), (116), (204), (113), (110), (104) and (102) planes in hexagonal indices. On the other hand, since $NiTiO_3$ has the nearly same crystal parameters as those of Fe_2O_3, five higher angle diffraction peaks, i.e. (226), (2 0 10), (1 0 10), (300) and (214) planes were taken for this series. The results of the X-ray analysis of $FeTiO_3$-Fe_2O_3 solid solution series have already been reported in the previous paper[2)]. They are reproduced in this paper to be compared with the results of other series. A characteristic of this series is the linear change of the volume of unit cell with composition as Fig. 3 shows.

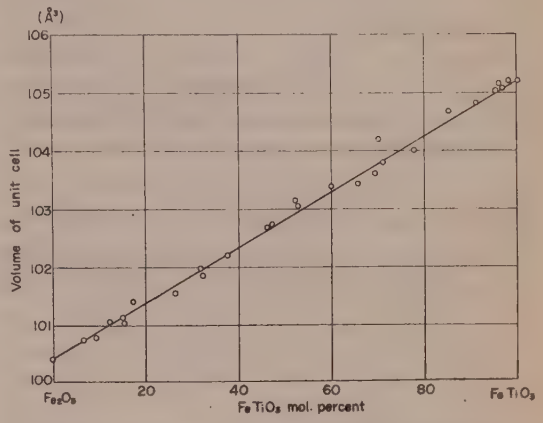

Fig. 3 (a). Volume of unit cell of $FeTiO_3$-Fe_2O_3 solid solution series.

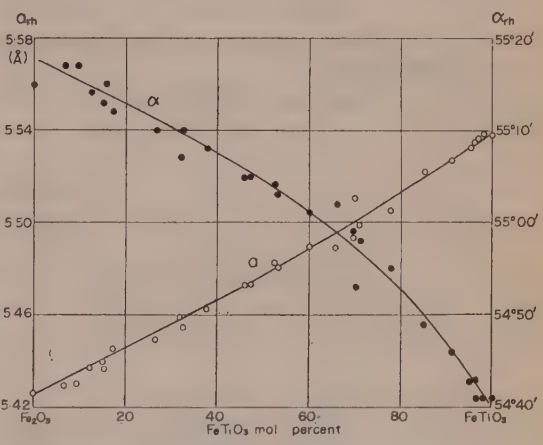

Fig. 3 (b). Crystal parameters of $FeTiO_3$-Fe_2O_3 solid solution series.

In Figs. 4~7, we show the change of the crystal parameters a_{rh}, α_{rh} and the volume of unit cell with composition for $MnTiO_3$, $MgTiO_3$, $CoTiO_3$ and $NiTiO_3$ series. First of all, it must be noticed in these figures that the linear change of the volume of unit cell with composition, which was the case for $FeTiO_3$ series, could not be observed for any other ilmenite system. In Fig. 4 (a) the results for $MnTiO_3$ series are shown, where we find that the volume of unit cell does not change continuously from that of ilmenite to that of hematite but there exists a miscibility gap in the middle

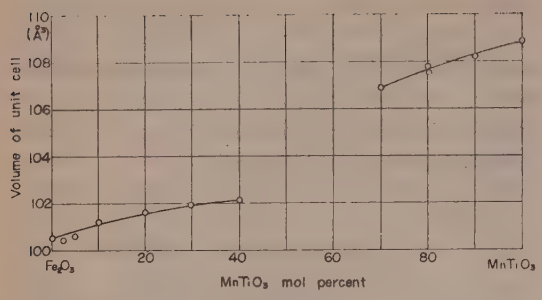

Fig. 4 (a). Volume of unit cell of $MnTiO_3$-Fe_2O_3 solid solution series.

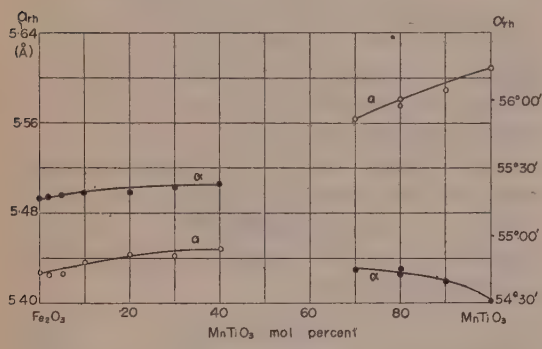

Fig. 4 (b). Crystal parameters of $MnTiO_3$-Fe_2O_3 solid solution series.

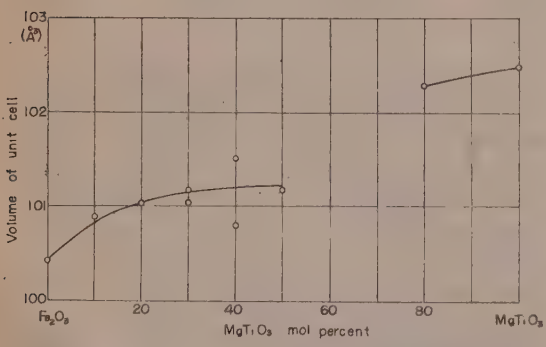

Fig. 5 (b). Volume of unit cell of $MgTiO_3$-Fe_2O_3 solid solution series.

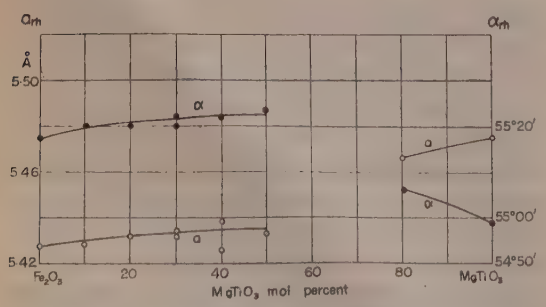

Fig. 5 (b). Crystal parameters of $MgTiO_3$-Fe_2O_3 solid solution series.

range of composition. In this range we obtained only mixtures of two phases with spinel and pseudobrookite structures. This situation can be more clearly seen in Fig. 4 (b) where the change in the crystal parameters with composition are shown. These figures suggest that the solid solution on the ilmenite side has a different crystal symmetry from that on the hematite side, which must be a chief reason why there exists a miscibility gap between $MnTiO_3$ and Fe_2O_3.

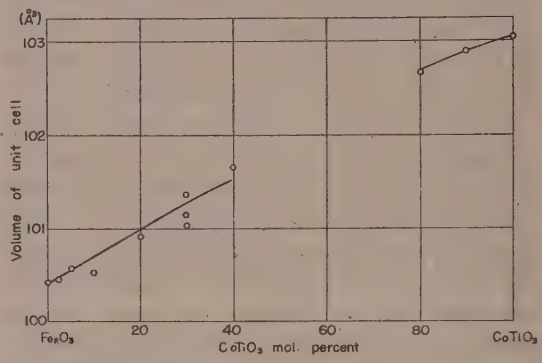

Fig. 6 (a). Volume of unit cell of $CoTiO_3$-Fe_2O_3 solid solution series.

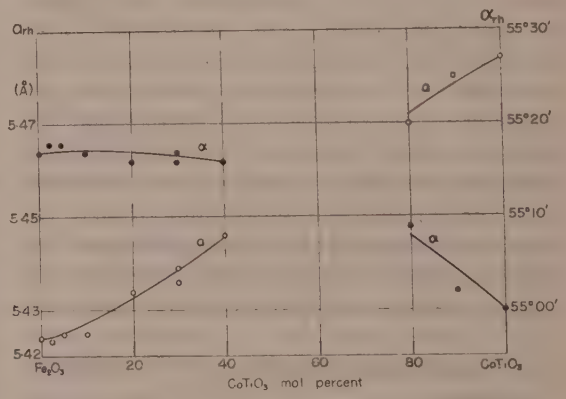

Fig. 6 (b). Crystal parameters of $CoTiO_3$-Fe_2O_3 solid solution series.

In Figs. 5 and 6 the cases for $MgTiO_3$ and $CoTiO_3$ series are shown, where we find that the feature of the former series is very similar to that of $MnTiO_3$ series, but for the latter series, the volume of unit cell and crystal parameters seem to vary rather continuously. It is worthwhile to note, however, that in both cases miscibility gaps between ilmenite and hematite are found.

On the other hand, in the case of $NiTiO_3$ series, it was found that the ilmenite and the hematite make a complete solid solution in the

whole range of composition as is shown in Fig. 7. It must also be noticed in the figure that a slight discontinuous change of the volume and the crystal parameters can be observed between the composition range of $0.5NiTiO_3$-$0.5Fe_2O_3$ and $0.55NiTiO_3$-$0.45Fe_2O_3$. This discontinuous change is, however, very small and nearly within an experimental error,

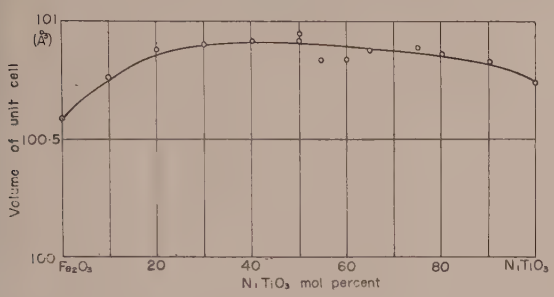

Fig. 7 (a). Volume of unit cell of $NiTiO_3$-Fe_2O_3 solid solution series.

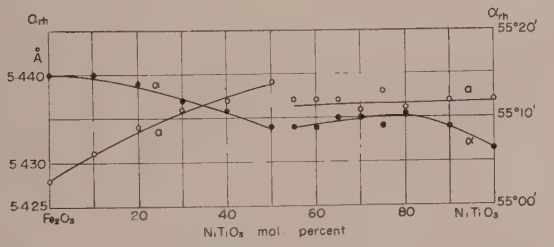

Fig. 7 (b). Crystal parameters of $NiTiO_3$-Fe_2O_3 solid solution series.

hence we can not decide whether such a change really exists in this series or not. If such a change really existed, the change of the crystal symmetry would be considered as occuring at this point, the specimen of $0.6NiTiO_3$-$0.4Fe_2O_3$ being expected to be of the crystal symmetry $R\bar{3}$ as we have done in other ilmenite systems. On the other hand, we presumed from the magnetic study that it, being feebly ferromagnetic, belongs to the symmetry $R\bar{3}c$ and the crystal symmetry changes gradually from $R\bar{3}c$ to $R\bar{3}$ near this composition. These conflicting situations may suggest that it is very difficult to determine accurately the crystal symmetry of the middle part of $NiTiO_3$ series from such X-ray and magnetic analyses. The more detailed analyses are required for this series.

We have thus expected that for the solid solution series having the miscibility gap the solid solution take crystal symmetry of either $R\bar{3}$ or $R\bar{3}c$: those of the end members. It is, therefore, necessary to determine this symmetry directly by the X-ray analysis. In the crystal structure of ilmenite and hematite, intensities of diffraction lines $I(h\,\bar{h}\,0\,l)$ for $l=2n+1$, are very weak and they completely disappear for the compounds with the crystal symmetry $R\bar{3}c$. In the actual cases the lines indexed by (0 0 0 3) and (1 $\bar{1}$ 0 1) are the strongest of the lines for $l=2n+1$ and the presence of these lines which we call superlines is the best indication of the symmetry $R\bar{3}$. Unfortunately Me^{+2} and Ti^{+4} ions have very closed atomic scattering factors and the superlines are very weak even for pure $MeTiO_3$ except $MgTiO_3$ and they become weaker with

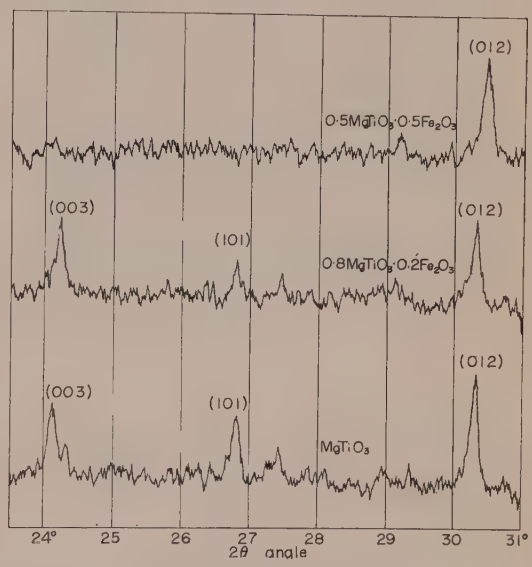

Fig. 8. X-ray diffraction chart showing super lines peculiar to $R\bar{3}$ crystal symmetry.
Specimen: $MgTiO_3$-Fe_2O_3 solid solution series.
Radiation: Fe K.
Superline: (003), (101) in hexagonal indices.

the increase of the content of Fe_2O_3 in the solid solution. In Fig. 8 we showed the superlines which are observed in the solid solution of $MgTiO_3$ and Fe_2O_3. As this figure shows superlines disappear in the specimen of $0.5MgTiO_3$-$0.5Fe_2O_3$, which is consistent with those inferred from Fig. 4. We also detected the superline (0003) in the specimens of the ilmenite side of $MnTiO_3$ and $NiTiO_3$ series though they are very weak. In the case of $FeTiO_3$ series it was confirmed by the X-ray analysis of a single crystal[16] and the neutron

Table. II. Solid solution of ilmenite and hematite: $x\mathrm{MeTiO_3}\cdot(1-x)\mathrm{Fe_2O_3}$.

$\mathrm{MeTiO_3}$	Ionic radius, r_{Me}[18] (Å)	Crystal symmetry $R\bar{3}$	$R\bar{3}c$
$\mathrm{MgTiO_3}$	0.65	$1 \geqq x \geqq 0.8$	$0.5 \geqq x \geqq 0$
$\mathrm{MnTiO_3}$	0.80	$1 \geqq x \geqq 0.7$	$0.4 \geqq x \geqq 0$
$\mathrm{FeTiO_3}$	0.75	$1 \geqq x \geqq 0.45$	$0.6 \geqq x \geqq 0$
$\mathrm{CoTiO_3}$	0.72	$1 \geqq x \geqq 0.8$	$0.4 \geqq x \geqq 0$
$\mathrm{NiTiO_3}$	0.70	$1 \geqq x > 0.6$ (?)	$0.6 \geqq x \geqq 0$

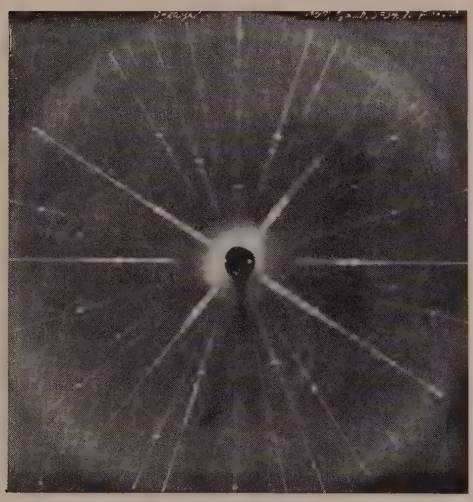

Fig. 9 (a).

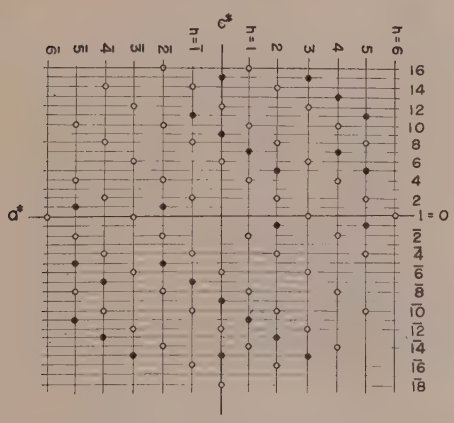

Fig. 9 (b). Precession photograph of ferromagnetic $\mathrm{FeTiO_3}$-$\mathrm{Fe_2O_3}$ series minerals, using unfiltered Mo K radiation.

Specimen: Notoro ferrimagnetic ilmenite (0.70 $\mathrm{FeTiO_3}\cdot$0.30 $\mathrm{Fe_2O_3}$)

Precession axis: $[h\,0,\,l]$, 0−layer

○: normal spot of $R\bar{3}c$

●: super structure spot peculiar to $R\bar{3}$ symmetry.

analysis[17] that the ilmenite side of the solid solution belongs to the symmetry $R\bar{3}$. The result of the X-ray analysis of a single crystal is illustrated by photograph in Fig. 9, where we can clearly find many spots peculiar to the $R\bar{3}$ crystal symmetry. Accordingly we can conclude in general that the ilmenite side of the solid solution between ilmenite and hematite retains the same crystal symmetry as that of pure ilmenite. The results thus obtained are summarized in Table II. Here we used also the knowledge obtained from the magnetic study. The symmetry $R\bar{3}$ corresponds to the case where Ti and Me ions are arranged in order as we stated in introduction and we shall denote this state as the ordered one, while the symmetry $R\bar{3}c$ corresponds to the case where all ions are arranged at random. In this table, it must be noticed that, in the case of $\mathrm{FeTiO_3}$ series the ranges of $R\bar{3}$ and $R\bar{3}c$ are overlapping. This means that in this overlapped range of the composition the transformation from $R\bar{3}$ to $R\bar{3}c$ or from the ordered state to the disordered state is observed in a specimen. Such a transformation phenomenon has been discussed in detail in another paper[5].

§ 5. Discussion

We have found in the preceding section that the solid solution of ilmenite and hematite can be classified into following three groups:

(1) The solid solutions of ilmenite side and hematite side have the different crystal symmetries and there exists miscibility gap between them ($\mathrm{MnTiO_3}$, $\mathrm{CoTiO_3}$ and $\mathrm{MgTiO_3}$ series).

(2) Ilmenite and hematite make a complete solid solution in the whole range of the composition and the crystal symmetry changes from $R\bar{3}$ to $R\bar{3}c$ continuously ($\mathrm{NiTiO_3}$ series).

(3) The ranges of the crystal symmetry $R\bar{3}$ and $R\bar{3}c$ are overlapped and the transformation from $R\bar{3}$ to $R\bar{3}c$ is observed in the specimen of this range ($\mathrm{FeTiO_3}$ series).

As this classification and Table II show, the miscibility of ilmenite and hematite varies with different ilmenite system. We may suppose that such differences in the miscibility are attributed to following three factors which will be discussed separately.

i) *Difference in the ionic radius*

Generally speaking the existence of a solid solution between two compounds can be explained thermodynamically as follows. It is well known that any reactions proceed so as to minimize the free energy $F=U-TS$ of the system, where U and S are the internal energy and entropy respectively. The internal energy, that is the electrostatic energy in our case, of the microscopic mixture of two kinds of compounds is larger than that of a macroscopic mixture of them. The entropy, is also increased considerably by making the solid solution. Hence at high temperatures the second term of the free energy predominates over the first one and it becomes to be possible that the solid solution is more stable than the mixture of two compounds.

When, therefore, we make the solid solution of two compounds having much different lattice parameters or crystal symmetries, the increase of the internal energy is too great to be compensated by the entropy term. Hence the solid solution of these compounds has often a miscibility gap. For example, there exists a miscibility gap in the solid solution between a cubic spinel and one with a slightly elongated unit cell ($CuFe_2O_4$)[19], in contrast with the situation that many cubic oxides make solid solution with each other in the whole range of the composition. The miscibility gap in the solid solution of ilmenite and hematite may be explained chiefly by this factor and the width of such a miscibility gap is expected to be proportional to the difference among the ionic radii of the cations relevant to our case.

We have found that $NiTiO_3$ and Fe_2O_3 make the solid solution in the whole range of the composition. This situation can be explained when we consider that Ni^{+2} and Ti^{+4} have nearly equal ionic radii (0.70Å and 0.68Å respectively) and they are not so large compared with that of Fe^{+3} (0.60Å). The range of miscibility of $MnTiO_3$ and $MgTiO_3$ series can be interpreted in the same manner: that is, as the difference between the ionic radii of Me^{+2} and Fe^{+3} is greater for Mn^{+2} (0.80Å) than for Mg^{+2} (0.65Å), the miscible range is narrower for $MnTiO_3$ series than for $MgTiO_3$ series.

On the other hand, the fact that $FeTiO_3$ and Fe_2O_3 make the solid solution in the whole range of the composition or the miscibility gap of $CoTiO_3$ series is the widest of all series can not be explained by the difference in the ionic radii, because the ionic radius of Fe^{+2} ion is relatively large (0.75Å) and that of Co^{+2} ion (0.72Å) is not greater than that of Mn^{+2} ion (0.80Å). The miscibility gaps of these solid solution series must be controlled by other factors.

ii) *Migration of cations*

It seems rather peculiar that $FeTiO_3$ and Fe_2O_3 make the solid solution in the whole range of composition and the volume of unit cell changes linearly with the composition in spite of the facts that the ionic radius of Fe^{+2} ion is fairly larger than those of Ti^{+4} and Fe^{+3} and the crystal symmetry of the solid solution changes from $R\bar{3}$ to $R\bar{3}c$ at a certain value of the composition. Such a peculiarity of this series is undoubtedly correlated with the situation that only in this series a cation stays in two valence states and the electronic conductivity is very high. We can expect that the free energies of the states with crystal symmetries $R\bar{3}$ and $R\bar{3}c$ are extraordinally close in this system compared with other systems, but it is not clear why such a situation exists in this system. It may be supposed that in this system the activation energy required for migration of Ti ions which may be very high in other ilmenite-hematite system is reduced by the situation that Fe^{+2} and Fe^{+3} ions can easily change their arrangement through the electron transfer so as to reduce the repulsive force between Ti and Fe ions when they migrate to other lattice points. The increase in the electrostatic energy due to the rearrangement of Ti ions may also be reduced by the same mechanism. We may suppose by such a mechanism that the free energies of the states with $R\bar{3}$ and $R\bar{3}c$ are close to each other and ilmenite and hematite can make the solid solution over the whole range of composition for $FeTiO_3$ series. The situation that the order-disorder transformation between $R\bar{3}$ and $R\bar{3}c$ takes place only in this series may also be explained by the same manner.

iii) *Stability of other phases*

There seems to exist another factor which restricts the miscibility of two compounds, and this may be a chief factor which determines the range of miscibility of $CoTiO_3$ series.

We have discussed in section 2 that there exist three kinds of solid solution series in the ternary system of MeO-Fe_2O_3-TiO_2, and showed that the series with the spinel structure is stable in the reducing atmosphere and the series with the pseudobrookite structure is stable under high oxygen pressure. Then, if the ranges of the oxygen pressure under which spinel phase is stable overlap with those for pseudobrookite phase, it comes to be possible that the free energy of these two phases are lower than that of ilmenite-hematite phase under any oxygen pressures. In this case only the first (spinel) and the third (pseudobrookite) series can be prepared when they are left in thermal equilibrium. In reality we have often observed that for the specimen in the inmiscible range, when the sintering time was very short and the reaction did not proceed fully, three phases coexisted, but the ilmenite-hematite phase disappeared on more prolonged heating. This means though the ilmenite-hematite phase was stable it decomposed intc other more stable two phases in thermal equilibrium.

The fact that the miscibility gap of $CoTiO_3$ series is the widest of all may be due to this factor. We inferred it from the following situation. It is found that $FeTiO_3$ and $MnTiO_3$ series are not stable in an open air at high temperatures, as Fe^{+2} and Mn^{+2} are unstable. This means that the range of oxygen pressure where the first series of Mn and Fe systems are stable are relatively narrow compared with that of the third series. On the other hand, in Ni system the first series is stable even in the oxygen flow at high temperature. It is, therefore, expected that in case of Co^{+2} system both the first and third series are stable in a wide range of oxygen pressure because Co^{+2} is more stable than Mn^{+2} and Fe^{+2} ions but less than Ni^{+2} ions.

In concluding the present paper the authors express their sincere thanks to Prof. Shozo Sawada and Prof. Takesi Nagata for their encouragements and advice. Their thanks are also due to Dr. T. Katsura for his chemical analysis and to Dr. R. Sadanaga and Mr. M. Korekawa for their help in the X-ray analysis of single crystal.

References

1) T. Nagata, S. Akimoto and S. Uyeda: J. Geomag. Geoelec. **5** (1953) 168.
2) T. Nagata and S. Akimoto: Geofisica Pura e Applic. Milano **34** (1956) 36.
3) Y. Ishikawa and S. Akimoto: J. Phys. Soc. Japan **12** (1957) 1083.
4) Y. Ishikawa: J. Phys. Soc. Japan **13** (1958) 37.
5) Y. Ishikawa: J. Phys. Soc. Japan **13** (1958) 828.
6) S. Uyeda: J. Geomag. Geoelec. **9** (1957) 61.
7) R. Chevallier, J. Bolfa and S. Mathieu: Bull. Soc. France Min. Crist. **78** (1955) 365.
8) R. M. Bozorth, D. E. Walsh and A. J. Williams: Phys. Rev. **108** (1957) 157.
9) Y. Ishikawa: J. Phys. Soc. Japan **12** (1957) 1165.
10) F. W. Posnjak and F. W. Barth: Zeit. fur Krist. **88** (1934) 271.
11) S. Akimoto: Advances in Phys. **6** (1957) 288.
12) E. W. Gorter: Advances in Phys. **6** (1957) 336.
13) S. Akimoto, T. Nagata and T. Katsura: Nature **179** (1957) 37.
14) C. H. Moore and H. Sigurdson: J. Metals. **1** (1949) 914.
15) E. W. Gorter: Philips Res. Rep. **6** (1955) 412.
16) S. Akimoto: Thesis, Tokyo University (1957).
17) G. Shirane, S. J. Pickert, R. Nathan and Y. Ishikawa: to be published.
18) L. Pauling: The Nature of Chemical Bond. (1940).
19) E. W. Gorter: Proc. I. R. E. **43** (1955) 1945.

JOURNAL OF THE PHYSICAL SOCIETY OF JAPAN, Vol. 13, No. 10, OCTOBER, 1958

Lattice Defects in Zincblende
Part I. Phenomenological Expressions of Interionic Potentials*

By Sumitada ASANO and Yasuo TOMISHIMA

Department of Physics, Faculty of Science, Okayama University

(Received July 3, 1958)

As the basis of the calculation on formation energies of lattice defects, phenomenological expressions of interionic potentials are derived. In zincblende crystal which is partly ionic and partly covalent, the effective charge on the constituent ions is reduced to a certain amount Ze ($Z=1.66$, e: magnitude of the electronic charge), whereas covalent attraction between two ions adjacent to each other is generated, which is assumed to be exponential form $-b_C \exp(-r/\rho_C)$ such as the usual expression of exchange repulsion. As a preliminary calculation to Part II, the lattice energy variation when one anion or cation is displaced from its regular position in a perfect crystal is calculated on taking account of the Madelung, Van der Waals, exchange repulsion, covalency attraction energies and the polarization energies of the displaced ion and all other surrounding ions. All the physical constants already known in references and derived in our calculation are tabulated in Table III.

§ 1. Introduction

The luminescence and photoconductivity of ionic crystals, for the most part, are infered to originate from the crystal imperfections such as vacancies, substitutional and interstitial impurity atoms. In general, the ions surrounding the vacancy or the impurity atom deviate from their regular sites. In order to explain the behaviors of the phosphors and photoconductors known hitherto and further to devise new ones, it is desirable to clarify the aspects of the local distorsions caused by the crystal imperfections and the states of the electrons trapped in the vacancies and impurity atoms. For this purpose, in the first place, it is necessary to derive the phenomenological expressions of the interionic potentials.

In this paper, we will seek these expressions for cubic ZnS (zincblende) which is one of the most useful crystal among luminescent materials. It is well known that zincblende is not purely ionic crystal but partly covalent one, and the electrons of S^{2-} ion are partly transfered to the neighbouring Zn^{2+} ion. Therefore, the effective charges of Zn and S ions are reduced to the amounts Ze and $-Ze$ respectively (e: magnitude of the electronic charge). According to our previous calculation on the cohesive energy of zincblende, $Z=2\times 0.83$ [1]. As a result of this reduction in effective charges of constituent ions, Coulomb interaction energy (Madelung energy) decreases, so that we have to introduce another interaction which may be called covalent interaction.

As the interactions between constituent ions, we may point out the following five kinds:

Short range interactions which act between nearest neighbours only.

(1) Repulsive energy E_R
(2) Coulomb overlap energy** E_O
(3) Covalent energy E_C

Long range interactions.

(4) Madelung energy E_M
(5) Van der Waals energy E_V

The necessity of the introduction of a new and fairly strong interaction such as covalency for zincblende is indicated also by the following fact. The usual Born-Mayer's method, which takes into account the Madelung, exchange and Van der Waals interactions between constituent ions, and in which the force constants are determined by using the observ-

* The results in this paper were partly reported at the Autumn Meeting of the Society of Applied Physics (Japan), held at Okayama in October 1957.

** Coulomb overlap energy means the correction to the Madelung energy for overlap of the electron clouds of ions adjacent to one another.

ed values of lattice constant and compressibility, gives a fairly low value of cohesive energy in comparison with the observed value (cf. Table V), in contrast with the typical ionic crystal such as alkali halide. On the contrary, if we determine force constants in the Born-Mayer's equation by using the observed values of lattice energy and lattice constant, the compressibility obtained becomes much smaller than the observed one.

Madelung energy has usual expression except that the effective ionic charge is reduced to $\pm Ze$. In § 2, we will determine the form of Van der Waalf interaction using the empirical values of polarizabilities and ionization potentials of the constituent ions, and the form of Coulomb overlap energy by using the wave functions of both ions. In § 3, the forms of potentials of exchange repulsion and covalent interaction are determined from the empirical values of lattice constant, compressibility and cohesive energy. Further in § 4, in order to examine the reliability of the potential forms obtained above, the lattice energy variation due to the virtual displacement of one cation or anion in (111) direction (cf. Fig. 1) are calculated, taking into account

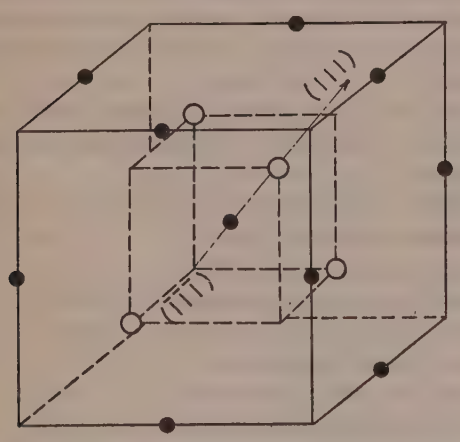

Fig. 1. Atomic arrangement in a unit cell of zincblende.

the polarization energy of the displaced ion and all the ions surrounding it. For this purpose, it is necessary to calculate the Madelung constant, the constants in Van der Waals energy expression, the electric field originating from the surrounding ionic charges and some constants associated with the polarization energy of surrounding medium at various positions of the displaced ion. These values are tabulated in Appendix.

§ 2. Determination of the Van der Waals Energy and Coulomb Overlap Energy

(1) *Van der Waals energy*

Van der Waals energy between two ions is given by[2)]

$$\varepsilon_{ij}=-C_{ij}/r_{ij}^6\,, \tag{2.1}$$

where r_{ij} is the interionic distance and

$$C_{ij}=\frac{3}{2}\frac{\varepsilon_i\varepsilon_j}{\varepsilon_i+\varepsilon_j}\alpha_i\alpha_j\,. \tag{2.2}$$

In (2.2), ε_i and ε_j may be assumed to be approximately equal to the series limits of the discrete spectra of the two ions, i.e. their ionization energies[3)], and α_i and α_j are their polarizabilities.

The first ionization energy of free Zn^{2+} ion, ε_{Zn}, is 39.5 eV[4)] and that of S^{2-} ion in zincblende, ε_S, is estimated to be 5 eV*.

J. R. Tessman et al[7)] have given an approximate measure of the electronic polarizabilities of various ions in crystals, rather than as "free" ions. According to their estimation, in zincblende the polarizabilities of Zn ion and S ion are 0.8 Å^3 and 4.9 Å^3 respectively.

By inserting the numerical values of ε_{Zn}, ε_S, α_{Zn} and α_S in (2.2), we may compute C_{++}, C_{--} and C_{+-} as follows.

$$C_{++}=30.36\times10^{-60}\,,\quad C_{--}=144.2\times10^{-60}\,,$$
$$C_{+-}=41.81\times10^{-60}\,(\mathrm{erg\,cm^6})\,. \tag{2.3}$$

(2) *Coulomb overlap energy*

The Coulomb overlap energy ε_0 between two ions[8)] is computed by numerical calculations by using the radial charge densities of S^{Z-} and Zn^{Z+} ions evaluated from their wave functions on the assumption of spherical charge distribution.

In zincblende, the actual state of the crystal

* The ionization energy for $S^{2-}\rightarrow S^-$ in free state is estimated to be about -5 eV[5)]. For S^{2-} ion in the crystal, however, the energy required to remove one valence electron of S^{2-} ion and to place it on a Zn^{2+} ion in the vicinity or at infinity should be used as ε_S, since this transition evidently corresponds to ionization. The latter energy ε is estimated to be about 10.5 eV and the former ε' is identified with that of the first excitation band 6 eV[5)]. On the other hand, if the absorption edge is identified with the latter energy, ε is equal to about 3.5 eV[6)]. Taking into consideration these numerical values, we assume $\varepsilon_S\approx5$ eV.

may be assumed to be intermediate between the totally ionic state consisting of S^{2-} ($3s^2$, $3p^6$: $^1S_0$) and Zn^{2+} ($3d^{10}$: $^1S_0$), and the totally covalent one consisting of S^{2+} ($3s$, $3p^3$: ^5S) and Zn^{2-} ($4s$, $4p^3$: ^5S)[9]. Since the effective charge of each of the constituent ions of zincblende is estimated to be $\pm 2\times 0.83\,e$[1], on the orbitals $4s$, $4p^3$ of Zn ion there are 0.34 electrons on the average. These wave functions of S^{2-} and Zn^{2-} ions may be computed by interpolation[1] from those of Cl^- ion[10] and As^+ ion[11].

Table I. Coulomb overlap energy (eV) versus interionic distance a (AU).

a	ε_O
2.202	−33.4287
3.303	−13.8986
4.405	−3.1428
5.506	−0.5560
6.607	-0.0988_6

The computed values of ε_O between Zn^{Z+} $-S^{Z-}$ ion pair are tabulated in Table I and plotted in Fig. 2 against interionic distance a.

As shown in Fig. 2, these values fall on a straight line in semi-log plotting, except for small values of a. Therefore, in the straight part ε_O may be expressed in the form $\varepsilon_O = -b_O \exp(-a/\rho_O)$, and the values of ρ_O and b_O are 0.336 Å and 5.259×10^{-9} erg respectively. Then

$$\begin{aligned}\varepsilon_O(a) &= -b_O \exp(-a/\rho_O)\\ &= -5.259\cdot\exp(-a/0.336\times 10^{-8})\times 10^{-9}\ \text{erg}\\ &\qquad (a \text{ in cm}) . \qquad (2.4)\end{aligned}$$

Since the computed values of ε_O deviate from the straight line at small values of a, we obtain its actual values for that range of a by multiplying a correction factor (<1) which is determined from Fig. 2, to the values obtained by the formula (2.4).

§ 3. The Determination of Exchange Repulsion and Covalency Attraction Energies

The customary form of repulsive energy ε_R for two interacting ions separated by a distance a is

$$\varepsilon_R(a) = b_R \exp(-a/\rho_R) . \qquad (3.1)$$

Furthermore, we will assume the form of the covalent binding energy in an analogous form

$$\varepsilon_C(a) = -b_C \exp(-a/\rho_C) . \qquad (3.2)$$

Then we have to determine the four unknown parameters b_R, ρ_R, b_C and ρ_C.

At first, ρ_R may be evaluated by using Williams' method[8]. According to his notation, the repulsive energy is expressed approximately by

$$\varepsilon_R(a) = K' S^2/a , \qquad (3.3)$$

where K' is a constant and S is the overlap integral defined by

$$S = \int \varphi_A \varphi_B \, dV , \qquad (3.4)$$

φ_A and φ_B are $\sqrt{4\pi}$ times the square roots of the total charge densities of the unperturbed A and B ions interacting with each other respectively. In computing (3.4), Williams has used an approximate expression based on the fact that the overlap of the charge distribution only occurs near the segment connecting the nuclei of both ions in KCl.

In ZnS, however, the overlap stated above occurs appreciabley even at the position apart from the segment connecting both nuclei. Therefore we will evaluate S using the following exact expression derived from (3.4) by a simple transformation

$$\frac{S}{2\pi} = S' = \frac{1}{a}\int_0^a r\varphi_A(r)\,dr \int_{|a-r|}^{a+r} \varphi_B(y)\,dy . \qquad (3.5)$$

Table II. Overlap integrals versus interionic distance.

a(AU)	S'	S'^2/a
2.202	7.371	24.260
3.303	4.260	5.494
4.405	2.246	1.145
5.506	1.153	0.241_5
6.607	0.592	0.053_1
$\rho_R = 0.391$ Å		

The calculated values of S'^2/a as a function of a using the wave function of S^{Z-} and Zn^{Z+} ions stated in § 2 are tabulated in Table II and plotted in Fig. 2. Since the curve of S'^2/a in semi-log plotting may be regarded as nearly straight, we can conclude that the repulsive energy ε_R is expressed pretty well in an exponential form as (3.1). From Fig. 2, the value of ρ_R may be estimated to be 0.391 Å.

In order to determine the other three unknown parameters b_R, ρ_σ and b_σ, we may employ the experimental data concerning the cohesive energy, lattice distance and compressibility of zincblende.

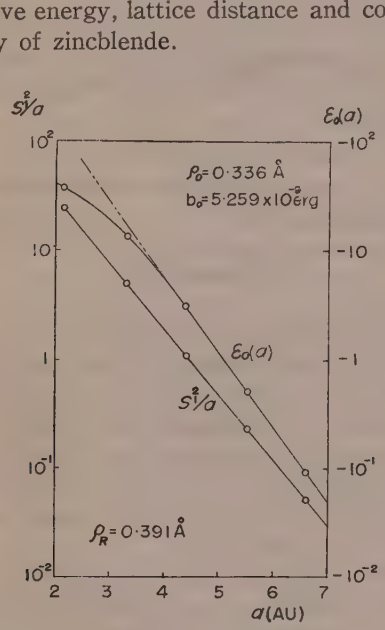

Fig. 2. Dependences of overlap integral S' and Coulomb overlap energy $\varepsilon_\sigma(a)$ on interatomic distance a.

The cohesive energy per ion pair in the present approximation is expressed as

$$E_{pa}(a)=-A_M\frac{(Ze)^2}{a}$$
$$-\frac{1}{a^6}\left[C_{+-}S_{V0}+\frac{C_{++}+C_{--}}{2}S_{V0}'\right]$$
$$+4b_R\exp(-a/\rho_R)-4b_\sigma\exp(-a/\rho_\sigma)$$
$$-4b_\sigma\exp(-a/\rho_\sigma)\,, \qquad (3.6)$$

where a is the nearest neighbour distance, A_M Madelung constant, S_{V0} and S_{V0}' well-known constants characteristic of the lattice structure[2]. Ze is the magnitude of the effective charge of the constituent ions, $2\times 0.83\,e$. In (3.6), the values of all constants except b_R, ρ_σ and b_σ are already known.

On the other hand, we have the well-known relations

$$(dE_{pa}/da)_{a=a_0}=0\,, \qquad (3.7)$$

$$\frac{1}{a_0}\left(\frac{d^2E_{pa}}{da^2}\right)_{a=a_0}=\frac{48}{\sqrt{3}\,\beta}\,, \qquad (3.8)$$

where a_0 is the observed value of a, and β is the compressibility. If we use the experimental values for a_0 (=2.34 Å[12]), β (=1.306 $\times 10^{-12}$ barye^{-1} [13]) and E_{pa} ($E_L{}^*=N_AE_{pa}=851$ Kcal/mol, N_A: Avogadro's number[14]). Three equations (3.6), (3.7) and (3.8) can determine the unknown parameters b_R, b_σ and ρ_σ as 4.092×10^{-9} erg, 4.148×10^{-11} erg and 1.489 Å respectively. Then (3.1) and (3.2) become

$$\varepsilon_R(a)=4.092\cdot\exp(-a/0.391\times 10^{-8})\times 10^{-9}\ \text{erg}\,, \qquad (3.9)$$

$$\varepsilon_\sigma(a)=-4.148\cdot\exp(-a/1.489\times 10^{-8})\times 10^{-11}\ \text{erg}\,. \quad (a\ \text{in cm}) \qquad (3.10)$$

All the constants known already in references and computed in the present paper (in italic) are listed in Table III for convenience.

Table III. Numerical values of parameters* in Zincblende.

A_M	1.6381
S_{V0}	4.354 [2]
S_{V0}'	0.762 [2]
α_+ (Å^3)	0.8 [7]
α_- (Å^3)	4·9 [7]
C_{++} (erg·cm^6)	*30.36×10^{-60}*
C_{--} (erg·cm^6)	*144.2×10^{-60}*
C_{+-} (erg·cm^6)	*41.81×10^{-60}*
$E_L{}^*$ (Kcal/mol)	851 [14]
β (barye^{-1})	1.306×10^{-12} [13]
b_0 (erg)	*5.259×10^{-9}*
ρ_0 (Å)	*0.336*
b_R (erg)	*4.092×10^{-9}*
ρ_R (Å)	*0.391*
b_σ (erg)	*4.148×10^{-11}*
ρ_σ (Å)	*1.480*

* The numerical values in italic are computed in the present paper.

§ 4. Lattice Energy Variation due to Virtual Displacement of One Ion

As a first step of the calculation of the formation energy of lattice defects in zincblende, treated in Part II, we will here estimate the lattice energy variation due to the displacement of one anion or one cation in (111) direction indicated in Fig. 1 preserving all the other ions at their respective regular sites, by using the phenomenological expressions of interionic interactions derived in § 2 and § 3. This estimation may also give a criterion as to the accuracy of the results obtained in preceding sections by the following reason. Referring to Fig. 1, we notice that when the reference ion is displaced in positive (111) direction, the potential is steeply

increased by the repulsion originating from the unlike ion sitted in front of the displacement, whereas when the reference ion is displaced in negative (111) direction, the potential will slowly increase and then decrease through a maximum point owing to the lack of the unlike ion in front of the displacement. If the hight of the potential barrier is too low, the crystal will not be stable at high temperatures. Of course, the surrounding ions of the reference ion are also displaced, therefore the barrier height obtained fixing all the other ions is not exact, but will give a measure of the crystal stability.

In performing the calculations, other than short-range and long-range interactions, stated in § 1, between the displaced ion and all the other ions of the crystal, polarization energies of all ions due to the displacement of the reference ion from its regular site, have to be taken into account.

(1) *Short-range interactions*

Exchange repulsion, covalency attraction and Coulomb overlap energies, so far as they are considered to act only between nearest neighbouring ions, need be taken only between the displaced ion and its four nearest neighbours. Therefore, the energy variation due to these interactions are easily calculated by using the formulae (2.4), (3.9) and (3.10).

(2) *Long-range interactions*

As regards Madelung and Van der Waals energies, we have to take into considerations those from sufficiently distant ions.

Madelung energy E_M is given by

$$E_M=(Ze)^2\sum\frac{\delta_i}{a_i} \tag{4.1}$$

where a_i is the distance from the displaced ion to the ith ion in the crystal and δ_i is 1 or -1 according as the ith ion is like or unlike the reference ion. The summation $\sum\delta_i/a_i$ is carried out for several positions of the reference ion by the Ewald's method[15] and the results are tabulated in Appendix.

Van der Waals energy of a reference cation or anion $E_V(+)$ or $E_V(-)$ is given by

$$E_V(\pm)=-[C_{+-}S_V+C_{\pm\pm}S_V']\frac{1}{a_0^6}\,, \tag{4.2}$$

where

$$S_V=a_0^6\sum_i^{(u)}\frac{1}{a_i^6}\quad\text{and}\quad S_V'=a_0^6\sum_i^{(l)}\frac{1}{a_i^6}\,.$$

$\sum_i^{(u)}$ and $\sum_i^{(l)}$ means the summations only with respect to unlike ions and like ions as the reference ion respectively. When the reference ion is at its regular site, S_V and S_V' coincide with S_{V0} and S_{V0}' respectively. The numerical results S_V and S_V' at several positions of the reference ion are also listed in Appendix.

(3) *Polarization energies*

If one ion in the crystal is displaced from its regular site, it is acted on by the electric field from the other ions in the crystal. This field intensity in (111) direction on the reference ion is given by

$$E=\sum e_i\bar{a}_i/a_i^3=\pm(Ze)\sum\bar{a}_i\delta_i/a_i^3\,, \tag{4.3}$$

where $\bar{a}_i$ is the component in (111) direction of the vector $\boldsymbol{a}_i$ pointing from the ith ion with charge e_i to the displaced reference ion. + and − signs in (4.3) correspond to the cases of positive and negative reference ion respectively. The summation is carried out by means of Ewald's method and the numerical results are also given in Appendix. Then the polarization energy of the reference ion with polarizability α becomes

$$E_P=-\frac{1}{2}\alpha E^2\,. \tag{4.4}$$

On the other hand, all the other ions in the crystal are also polarized by the displacement of the reference ion stated above. These polarization energies may be estimated as follows:

If the vector drawn from the ith ion to the regular site of the reference ion with charge Ze is denoted by $\boldsymbol{a}_{i0}$, the electric field $\boldsymbol{D}_i$ exerted on the ith ion by two point free charges $-Ze$ and Ze as the results of the displacement of the reference ion in the direction (111) is given by

$$\boldsymbol{D}_i=\frac{Ze}{a_i^3}\boldsymbol{a}_i-\frac{Ze}{a_{i0}^3}\boldsymbol{a}_{i0}\,. \tag{4.5}$$

The dipole moment $\boldsymbol{\mu}_i$ on the ith ion is then written as[16]

$$\boldsymbol{\mu}_i=M_{0i}a_0^3\boldsymbol{D}_i\,, \tag{4.6}$$

where

$$M_{0i}=M_{0\pm}=\frac{2\alpha_\pm}{\alpha_++\alpha_-}\frac{1}{4\pi}\left(1-\frac{1}{\kappa_0}\right), \tag{4.7}$$

according as the ith ion being cation or anion, and κ_0 is the optical dielectric constant of the

crystal (=5.07[13]). In (4.7) the atomic polarization of the ions is not taken into account, since we have assumed all but the reference ion to be fixed at their respective regular sites.

Then the polarization energy E_{PL} of the ions except the reference ion is given by

$$E_{PL}=-\frac{1}{2}\sum_i (\boldsymbol{D}_i\boldsymbol{\mu}_i)\,. \tag{4.8}$$

From (4.4), (4.6) and (4.8), we obtain

$$E_{PL}=-\frac{1}{2}(Ze)^2a_0^3\sum_i M_{0i}\left(\frac{1}{a_i^4}+\frac{1}{a_{i0}^4}-2\frac{\cos\theta_i}{a_i^2a_{i0}^2}\right), \tag{4.9}$$

where θ_i is the angle between the vectors $\boldsymbol{a}_i$ and $\boldsymbol{a}_{i0}$. $(\cos\theta_i=(\boldsymbol{a}_i\boldsymbol{a}_{i0})/a_ia_{i0})$.

If we put

$$\left.\begin{aligned} C&=a_0^4\sum_i^{(\alpha)}\frac{1}{a_i^4}, & C'&=a_0^4\sum_i^{(l)}\frac{1}{a_i^4},\\ G&=a_0^4\sum_i^{(u)}\frac{\cos\theta_i}{a_{i0}^2a_i^2}, & G'&=a_0^4\sum_i^{(l)}\frac{\cos\theta_i}{a_{i0}^2a_i^2}, \end{aligned}\right\} \tag{4.10}$$

E_{PL} is written as

$$E_{PL}(\pm)=-\frac{1}{2}\frac{(Ze)^2}{a_0}\{(C_0+C-2G)M_\mp+(C_0'+C'-2G')M_\pm\}\,, \tag{4.11}$$

where the upper signs correspond to a positive reference ion and the lower signs to a negative one, and C_0 and C_0' are the values of C and C' at $\Delta a=|\boldsymbol{a}_i-\boldsymbol{a}_{i0}|=0$. When $\Delta a=0$, $G=C_0$ and $G'=C_0'$. Then $E_{PL}(\pm)=0$. The values of C_0 and C_0' is well known as[17]

$$C_0=6.6697\,,\qquad C_0'=3.5633\,.$$

The values of C, C' and G, G' for various values of Δa are computed and shown in Appendix.

Summing all the energy terms stated above, we obtain the total energy changes $\Delta E(+)$ or $\Delta E(-)$ due to one cation or anion displacement Δa.* The results are plotted in Fig. 3.

Referring to Fig. 3, we may point out that the potential barrier is fairly high, so the crystal will be stable even at about 1000°C. $(\exp(-\Delta E/kT)\approx 10^{-4})$ Therefore, the potential forms derived in preceding sections may be considered as reasonable.

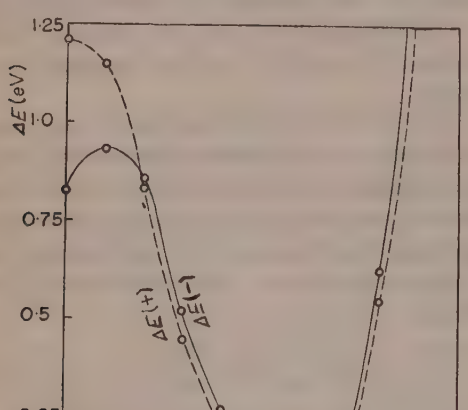

Fig. 3. Lattice energy variation $\Delta E(+)$ and $\Delta E(-)$ due to one cation or anion displacement along (111) direction.

§ 5. Conclusions

Covalency corrections introduced in our model are summarized as follows:

(1) The effective charges of Zn and S ions are assumed to be $2\times0.83\,e$ and $-2\times0.83\,e$ respectively.

(2) The attractive energy originating from covalency binding is introduced in the exponential form $-b\sigma\exp(-a/\rho c)$.

However, this model contains some departures from the actual aspects in the case of zincblende, since the degree of covalency will be a function of the interionic distance. Accordingly, the effective charge and the polarizability of a constituent ion may also change with the interionic distance. But it will be practically impossible to take account of these detailed behaviours thoroughly. Because it is not known nowadays in what manner the covalency degree changes with interionic distance, if we want to take account of this fact it is necessary to introduce some unknown parameters to be determined phenomenologically in addition to those occurring in (3.6). However, our model would be applicable to actual zincblende crystal approximately, so far as the displacement of a ion is not very large.

Lastly, the cohesive energy per mol, E_L*, obtained in our model is classified in Table IV,

* The displacement in positive and negative (111) directions, Δa, are taken as positive and negative respectively.

Table IV. Classification of lattice energy in Kcal/mol.

	Present Model	Born-Mayer
Madelung	639.2	927.9
Covalency	495.0	
Repulsion	−588.4	−167.2
Coulomb Overlap	283.6	
Van der Waals	21.6	21.6
E_L^*	851.0	782.3

where the classified values of the energy obtained by using usual Born-Mayer equation (ionic model) are also tabulated for comparison. In ionic model, Madelung, overlap repulsion and Van der Waals interactions are taken into account. For the calculation of Madelung energy, the effective charges of Zn and S ions are taken to be $\pm 2e$, and for the repulsive potential the form $b_R' \exp(-a/\rho_R')$ are used, in which b_R' and ρ_R' are determined by the conditions (3.7) and (3.8);

$$b_R' = 1.625 \times 10^{-9}\ \text{erg}\ , \quad \rho_R' = 0.370\ \text{Å}\ . \tag{5.1}$$

In ionic model, the repulsive energy derived in this way, includes the Coulomb overlap energy in the present model[18].

With regards Table IV, it may be pointed out that the covalency attractive energy nearly amends the decrease in Madelung energy, which is caused by the decrease in effective charge of the ions.

Appendix

a_i is the magnitude of a vector $\boldsymbol{a}_i$ pointing from the ith ion in the crystal sitting at its normal position to the reference ion, displaced in (111) direction in Fig. 1 by an amount Δa from its regular lattice site. δ_i is 1 or −1 according as the ith ion being like or unlike as the reference ion. $\bar{a}_i$ is the component of the vector $\boldsymbol{a}_i$ in (111) direction.

Table V.

			S_V'	S_V	C'	C	G'	G
$\Delta a/a_0$	$-a_0 \sum_i \delta_i/a_i$	$a_0^2 \sum_i \bar{a}_i\delta_i/a_i^3$	$a_0^6 \sum^{(l)} 1/a_i^6$	$a_0^6 \sum^{(u)} 1/a_i^6$	$a_0^4 \sum^{(l)} 1/a_i^4$	$a_0^4 \sum^{(u)} 1/a_i^4$	$a_0^4 \sum^{(l)} \frac{\cos\theta_i}{a_{i0}^2 a_i^2}$	$a_0^4 \sum^{(u)} \frac{\cos\theta_i}{a_{i0}^2 a_i^2}$
0.3	1.71804	0.64199	0.9047	10.2660	3.7038	8.6842	3.5621	6.9585
0.2	1.67622	0.23909	0.8296	6.0374	3.6206	7.3085	3.5604	6.7385
0.15	1.66722	0.11828	0.8049	5.1267	3.5908	6.9641	3.5603	6.6962
0.1	1.66331	0.04250_6	0.7914	4.6422	3.5747	6.7829	3.5604	6.6760
0.05	1.66237	0.00445_0	0.7799	4.4198	3.5672	6.6935	3.5617	6.6711
0	1.66216	0	0.7622	4.3544	3.5633	6.6697	3.5633	6.6697
−0.05	1.66185	0.02279_1	0.7799	4.3868	3.5672	6.6805	3.5617	6.6682
−0.1	1.65973	0.07226_1	0.7914	4.4864	3.5747	6.7218	3.5604	6.6549
−0.15	1.65393	0.14804	0.8049	4.6192	3.5908	6.7797	3.5603	6.6413
−0.2	1.64022	0.24319	0.8296	4.7357	3.6206	6.8295	3.5604	6.6048
−0.3	1.60873	0.47035	0.9047	4.8653	3.7038	6.8819	3.5621	6.4813

Madelung constant in the 1st column and the coefficient of electric field in (111) direction, in the 2nd column, originating from all the ions (regarded as point charge) except the reference ion (cf. (4.3)) are calculated anew by Ewald's method, with the precision of five decimals. It should be noticed that for $\Delta a = 0$ the values 1.66216 is obtained instead of 1.6381 given first by Ewald. However, the difference in energy due to this correction is very small, so that we will use the traditional value of Madelung constant throughout the present work.

In the 3rd, 5th and 7th columns, summations are carried out only with respect to like ions as the reference ion and in the 4th 6th and 8th columns with respect to unlike ions only. These summations are actually performed in 57 unit cells around the reference ion, where about 450 ions are contained. The small contributions from the residual outer region of the crystal are obtained by expanding the summands in terms of power series of Δa and integrating them to infinity. The lower limits of the integrations are ef-

fectually determined by comparing the sums obtained in the 57 unit cells stated above for $\Delta a=0$ with the corresponding values published in references.[2),17)] Since the convergences of these summations are so fairly good, in particular for S_V and S_V', that the simple method stated above may be allowed.

References

1) S. Asano and Y. Tomishima: J. Phys. Soc. Japan **11** (1956) 644.
2) F. Seitz: *Modern Theory of Solid* (McGraw-Hill Co. N. Y. 1940) p. 84.
3) F. Seitz: *ibid.* p. 267.
4) Landolt-Börnstein: *Physikalishe Chemishe Tabellen* (J. Springer, Berlin 1931) Erg.-Bd. II p. 567.
5) F. Seitz: Reference 2) p. 448-449.
6) H. W. Leverentz: *Introduction to Luminescence of Solids* (John Wiley & Sons Co. N. Y. 1950) p. 122, 161.
7) J. R. Tessman, A. H. Kahn and W. Shockley: Phys. Rev. **92** (1953) 890.
8) F. D. Williams: J. Chem. Phys. **19** (1951) 457.
9) B. D. Saksena: Phys. Rev. **81** (1951) 1012.
10) D. R. Hartree and W. Hartree: Proc. Roy. Soc. A **156** (1936) 45.
11) D. R. Hartree, W. Hartree and M. F. Manning: Phys. Rev. **59** (1941) 211.
12) J. D. H. Donay and W. Nowacki: *Crystal Data* (Geological Society of America N. Y. 1954) p. 501.
13) B. Szigeti: Trans. Faraday Soc. **45** (1949) 155.
14) F. Seitz: Reference 2) p. 83.
15) P. P. Ewald: Ann. d. Phys. **64** (1921) 253.
16) N. F. Mott and R. W. Gurney: *Electronic Processes in Ionic Crystals* (Oxford 1940) p. 59.
17) J. E. Johnes and A. E. Ingham: Proc. Roy. Soc. **A 107** (1924) 636.
18) R. S. Knox and D. L. Dexter: Phys. Rev. **104** (1956) 1245.

JOURNAL OF THE PHYSICAL SOCIETY OF JAPAN Vol. 13, No. 10, OCTOBER, 1958

Lattice Defects in Zincblende
Part II. Formation Energy of Lattice Defects.*

By Sumitada ASANO and Yasuo TOMISHIMA

Department of Physics, Faculty of Science, Okayama University

(Received July 3, 1958)

The formation energies of various types of lattice defects in zincblende are calculated by means of Mott-Littleton's method. A phenomenological expression of interionic potential which contains the covalency binding energy is used in the calculation. In addition, the total energy when the lattice around a defect is not in equilibrium is computed at several positions of the surrounding ions of the defect near the equilibrium point. The results of calculation show that the formation energies of Schottky defect, double hole and Frenkel defect by zinc ion are estimated to be 4~6 eV. The result that the formation energy of Schottky defect is nearly equal to that of double hole is qualitatively in agreement with the experimental results which have been obtained with pure host crystal of ZnS phosphor.

§ 1. Introduction

The formation energies of Schottky defects in alkali halides and alkali-earth oxides have been computed by using the ionic model by several authors.[1),2)] This model, however, is not suited for the case of zincblende, since the binding energy due to covalency has fairly large proportion in the total lattice energy. We have showed this fact actually by quantum mechanical calculation.[3)] According to the results of this calculation, the lattice energy of zincblende is lowered by about 60 % when

* The results in this paper were partly reported at the Hiroshima Meeting of the Chugoku-Shikoku Branch of the Physical Society of Japan, in February 1958.

the covalency correction is taken into account, and the effective charges on constituent ions are estimated to be $\pm Ze = \pm 2 \times 0.83e$ (e: absolute value of electronic charge).

By using these results, we determined, in Part I[4], the phenomenological expression of the interionic potential in zincblende, which is analogous to the Born-Mayer's one in purely ionic crystals. In this paper, the formation energy of lattice defect in zincblende is computed by using the results obtained in Part I.

First, we will calculate, in § 2 and § 3, the energy required to remove an ion in a regular site and that required to interpose an ion to an interstitial site, then in § 4 we derive the formation energies of Schottky and Frenkel defects by combining these energies. In addition, we will estimate in § 5 the dissociation energies of double hole and double interstitial ion. Table I shows the physical constants of zincblende, which are used in this calculation.

Table I. Physical constants of zincblende.

A_M	1.6381	M_+	0.0370
a_0 (Å)	2.34[5]	M_-	0.1785
κ	8.3[6]	C_{++} (erg cm^6)	30.36×10^{-60}
κ_0	5.07[6]	C_{+-} (〃)	41.81×10^{-60}
α_- (Å^3)	0.8[7]	C_{--} (〃)	144.22×10^{-60}
α_+ (Å^3)	4.9[7]	E_L (eV/ion pair)	36.9212 (=851 Kcal/mol)[8]

The numerical values of C_{++}, C_{+-} and C_{--} have been calculated in § 2 of Part 1.

§ 2. Energy Required to Remove an Regular Ion

In this section we will calculate $W(+)$ or $W(-)$ required to remove a cation or an anion in a regular site to an infinitely distant position respectively. First, the positions of the four ions adjacent to the vacancy are considered to be fixed at their respective original sites. (cf. Fig. 1) The work necessary for the removal consists of the following terms.

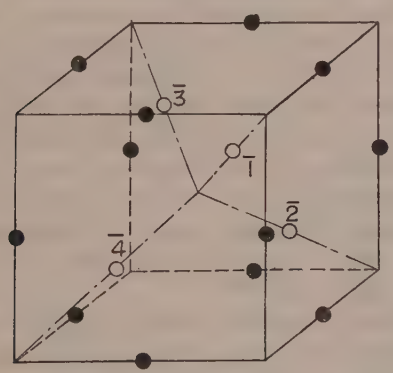

Fig. 1. Atomic arrangement around a vacancy in zincblende. An ion represented by dot is located at the center of the cube in perfect lattice. In double hole the ion $\bar{1}$ is missed also.

(1) *Madelung and Van der Waals energies* Since the ions removed from the crystal must have the effective charges $\pm Z_0 e (Z_0 = 2)$, the electron cloud having charge $-(Z_0 - Z)e/4$ on the cation, which is transfered from the adjacent anion owing to the covalency bonding the two ions, will return to the parent anion after the bond has been cut off. Then the electronic polarizability of the anions around the cation vacancy will be slightly increased owing to the increase in magnitude of effective electronic charge. On the other hand, that of the cations around the anion vacancy will be decreased.

We assume that the electronic polarizability varies between $\alpha_\pm$ and $\alpha_\pm^0$ linearly with effective charge of the ion, where $\alpha_\pm$ are the electronic polarizabilities of the ordinary ions with effective charges $\pm Ze$ and $\alpha_\pm^0$ are those of the ions with effective charges $\pm Z_0 e$. $\alpha_\pm$ are 0.8×10^{-24} cm^3 and 4.9×10^{-24} cm^3 as stated in Part I. In order to estimate $\alpha_\pm^0$, we will use the Kirkwood's formula,[9]

$$\alpha = K \left[\sum_i \int_0^\infty r^2 P_i^2 dr \right]^2 \Big/ N, \qquad (2.1)$$

where K is a constant, P_i^2 the radial density of the ith electron and N is the total number of electrons of the ion. By using the wave functions of S and Zn ion stated in Part I, we may estimate the ratios of $\alpha_\pm^0$ to $\alpha_\pm$ to be $\alpha_+^0/\alpha_+ = 0.7314$ and $\alpha_-^0/\alpha_- = 1.059$. Therefore we have $\alpha_+^0 = 0.585 \times 10^{-24}$ cm^3 and α_-^0

$5.19\times10^{-24}\,\mathrm{cm}^3$. Then the values of the electronic polarizabilities $\alpha^{+\prime}$ and $\alpha_-{}'$ of the cation and anion with effective charge

$$\pm(Z+(Z_0-Z)/4)e=1.75e$$

become $0.747\times10^{-24}\,\mathrm{cm}^3$ and $4.958\times10^{-24}\,\mathrm{cm}^3$ respectively.

Then the contributions from Madelung and Van der Waals energies are given by

$$E_M=A_M\frac{Z^2e^2}{a_0}+6\frac{Z^2e^2}{a_0}\left(\frac{a_0}{a_1}\right)\left[\left(\frac{Z'}{Z}\right)^2-1\right]-4\left[A_M-1+\frac{3a_0}{a_1}\right]\left(\frac{Z'}{Z}-1\right)\frac{Z^2e^2}{a_0} \quad (2.2)$$

and

$$E_V(\pm)=\frac{1}{a_0{}^6}[C_{+-}S_{V_0}+C_{\pm\pm}S'_{V_0}]-\frac{1}{a_0{}^6}\left\{(S_{V_0}-1)(C'_{\mp\pm}-C_{+-})+\left[S'_{V_0}-3\left(\frac{a_0}{a_1}\right)^6\right](C'_{\mp\pm}-C_{\mp\mp})\right\}\times4-\frac{6}{a_0{}^6}(C''_{\mp\mp}-C_{\mp\mp}), \quad (2.3)^*$$

where

$$Z'=Z+(Z_0-Z)/4=1.75, \quad \frac{a_0}{a_1}=\frac{1}{2}\sqrt{\frac{3}{2}},$$

$$S_{V_0}=4.354,^{10)} \qquad S'_{V_0}=0.762,^{10)}$$

$$C'_{\mp\pm}=C_{+-}\alpha_\mp{}'/\alpha_\mp, \qquad C'_{\mp\mp}=C_{\mp\mp}\alpha_\mp{}'/\alpha_\mp,$$

$$C''_{\mp\mp}=C_{\mp\mp}(\alpha_\mp{}'/\alpha_\mp)^2. \quad (2.4)$$

a_0 is the nearest neighbour distance and a_1 the next-nearest neighbour distance.

(2) *Polarization energy.*

The polarization energy E_P of the medium is given by

$$E_P=-\frac{1}{2}\sum_i(\boldsymbol{\mu}_i\boldsymbol{D}_i). \quad (2.5)$$

$\boldsymbol{\mu}_i$ is the dipole moment on the ith ion, including both electronic and atomic polarization, and $\boldsymbol{D}_i$ is electric field acting on it from the free charge $\mp Z_0e$, $\mp Ze$ of which is located at the centre of the vacancy and the residual charge $\mp(Z_0-Z)e$ is equally shared on the four nearest-neighbouring ions.

In the first order approximation, we may write the polarization energies $E_P(\pm)$ as

$$E_P(\pm)=E_P{}^*(\pm)+E_{P1}(\pm). \quad (2.6)$$

The first term of the above equation is the polarization energy of all the ions in the crystal other than the four around the vacancy, calculated on the continuum model following Mott and Littleton,[1)] and is given by

$$E_P{}^*(\pm)=-\frac{1}{2}\frac{(Z_0e)^2}{a_0}[(C_0-4)M_\mp+C_0{}'M_\pm], \quad (2.6a)^{**}$$

where C_0 and $C_0{}'$ are the numerical constants 6.697[11)] and $3.563\left(=6.3346\times\left(\frac{\sqrt{3}}{2}\right)^4\right)$[11)] respectively. $M_\pm$ are given by

$$M_\pm=\frac{4}{3\sqrt{3}\pi}\left(1-\frac{1}{\kappa_0}\right)\left[\frac{\alpha_\pm}{\alpha_++\alpha_-}+\frac{1}{2}\frac{\kappa-\kappa_0}{\kappa(\kappa_0-1)}\right], \quad (2.7)$$

where κ and κ_0 are the static and optical dielectric constants respectively. (cf. App. I) The numerical values of M_+ and M_- are 0.0370 and 0.1785.

The second term in (2.6) is the contribution from four ions (ions, $\bar{1}$, $\bar{2}$, $\bar{3}$ and $\bar{4}$ in Fig. 1) adjacent to the vacancy and is given by

$$E_{P1}(\pm)=-\frac{1}{2}\left(\frac{Ze}{a_0{}^2}\right)\mu_1(\mp)\times4, \quad (2.8)$$

$$\mu_1(\mp)=\frac{D+(Z_0/Z)(SM_\pm+S'M_\mp)}{1+5\mathcal{E}\alpha_\mp{}'/a_1{}^3}\left(\frac{Ze}{a_0{}^2}\right)\mathcal{E}\alpha_\mp{}', \quad (2.9)$$

where $\mu_1(\mp)$ means the dipole moment on one of the four ions adjacent to the vacancy, which is derived by the same procedures as in the case of rock salt.[12)] $(Ze/a_0{}^2)D$ is the electric field at one of these four ions due to the free charges at the vacancy and the other three ions adjacent to the vacancy and $(Z_0e/a_0{}^2)(SM_\pm+S'M_\mp)$ is that due to dipoles on all the ions outside these four ions. The numerical values of D, S and S' are 1.0441, 0.577 and 0.266 respectively.***

The electronic polarization of an anion neighbouring to the cation vacancy is hindered to some extent by the overlap repulsive force

* The upper of the double sign in the energy expressions corresponds to the case of the removal or interposal of a cation, and the under to the case of the removal or interposal of an anion, hereafter.

** In (2.6a), the calculations of electric field and dipole moment on a ion outside the four nearest neighbours around the vacancy are simplified by regarding the dispersed free charges as a point charge Z_0e at the center of the vacancy.

*** In calculating S and S', the summations are taken over 21 rings around the vacancy. The contributions from rings outside them are estimated to be less than 0.005.

between this anion and the three cations adjacent to it.[2] This situation is taken into account in (2.9) by using $\varepsilon\alpha_-'$ $(0<\varepsilon\leq 1)$ insteads of α_-'. However, for $\mu_1(+)$ in (2.9), ε should be taken as unity, since the ionic radius and electronic polarizability of a cation are very small in comparison with those of an anion.

(3) *Short-Range Force.*

For the sake of simplicity, it is assumed that the three remaining covalency bonds of each ions adjacent to the vacancy is not affected by the removal of the central ion. Then the energy for removal of a central ion due to short range forces is given by

$$E_S=4F_S(a_0)=4[b_0\exp(-a_0/\rho_0)+b_c\exp(-a_0/\rho_c)-b_R\exp(-a_0/\rho_R)]\,. \tag{2.10}$$

The numerical values of the force constants b's and ρ's are given in Table III in Part I.

(4) *Energy depression by atomic relaxation.*

Next we will consider the reduction of lattice energy $\Delta E(\pm)$, due to atomic polarization of the four ions adjacent to the vacancy. It is evident that these four ions are symmetrically displaced in the radial directions joining the center of the vacancy to their respective regular sites. Let us pick up only those parts of the lattice energy, which vary with the displacement of these four ions neighbouring to the vacancy.

Table II. Numerical values (eV) of energy terms constituting $W(\pm)$

	$W(+)$				$W(-)$
ε	1.0	0.9	0.8	0.7	1.0
E_M		25.6783			25.6783
E_V		0.6459			1.2507
E_S		8.2501			8.2501
E_p E_p^*		− 7.5234			− 9.0869
E_p E_{p1}	−8.8600	−8.2214	−7.5469	−6.8221	− 2.2941
ΔE_m	−0.6530	−0.4472	−0.2571	−0.1039	− 0.8451
W	17.5370	18.3823	19.2469	20.1249	22.9527
$E_p^{(0)}$		−16.3524			−12.0107
s_m	−0.06370	−0.05528	−0.04280	−0.02774	0.0883

s_m is the value of s corresponding to the minimum energy and $E_p^{(0)}$ is the polarization energy in zero-order approximation.

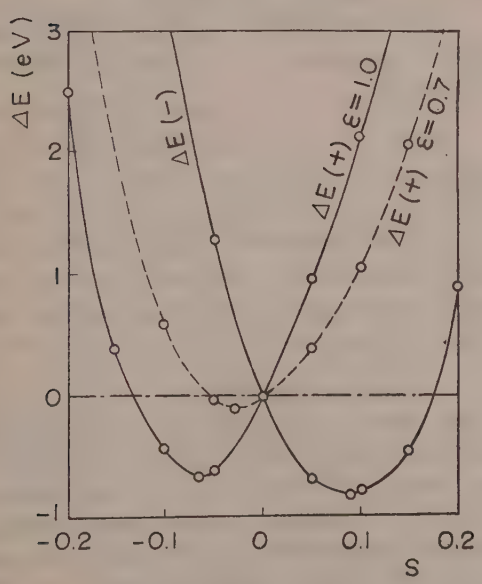

Fig. 2. Total energy change $\Delta E(\pm)$ with atomic relaxation around vacancy.

The changes of Madelung and Van der Waals energies may be immediately computed from the results in Appendix of Part I. Here it should be noted that, for these four ions the effective charges $\mp Z'e$ and electronic polarizabilities $\alpha'_\mp$ have to be used unlike those of the other regular ions in the crystal.

The part of the polarization energy which changes with the displacement of the four ions consists of both $E_{p1}(\pm)$ given by (2.8 and 9), in which D, S, S' and a_1 vary with displacement sa_0* of the four ions**, and

* Outward displacement of the ions around the vacancy is taken as positive.

** The changes of S and S' are computed with five rings around the vacancy and the small contribution from outer rings are neglected.

$E_{PL}(\pm)$, the polarization energy of all the ions other than the four, given by

$$E_{PL}(\pm)=-\frac{Z_0Z'}{a_0}e^2[M_\pm Q+M_\mp Q']\times 4\,, \quad (2.11)$$

where Q and Q' are numericals depending on s. The derivation of (2.11) is stated in Appendix II.

The varying part of the short range energy is given by

$$E_s(s)=3F_s(r_2)\times 4\,, \quad (2.12)$$

where $r_2\left(=\frac{a_0}{\sqrt{3}}\sqrt{3s^2-4s+4}\right)$ is the distance from an ion adjacent to the vacancy to one of the unlike ions neighbouring to it.

Fig. 2 shows the change of the total energy due to the displacement of the four ions for various cases. The maximum depressions $\Delta E_m(\pm)$ for the cation and anion vacancies are determined by expressing each energy contour in a quadratic form of the displacement s which are determined by the method of least mean square from several computed points near the origin $s=0$. These values are shown in Table II.

Thus $W(\pm)$ are given by

$$W(\pm)=E_M+E_V(\pm)+E_P(\pm)+E_S+\Delta E_m(\pm)\,. \quad (2.13)$$

The results of the numerical calculation are given in Table II.

§ 3. Work Required to Interpose an Interstitial Ion.

In this section we will calculate the work $W'(+)$ or $W'(-)$ necessary to bring a cation or an anion to an interstitial site. In zincblende, there are two types of interstitial sites, one is adjacent to four anions and the other to four cations. (cf. Fig. 3) A cation would preferably occupy the former, whereas an anion the latter, since the electrostatic energy becomes somewhat higher in the inverse cases. In particular, when a sulphur ion is interposed to the former, the overlap repulsive energy between the interposed sulphur ion and the four sulphur ions surrounding it will be conspicuously high because of large ionic radius of sulphur ion. Therefore, we will consider only an interstitial cation adjacent to four anions and an interstitial anion adjacent to four cations.

Furthermore, we assume that the interstitial ion has no covalency bonds but only ionic interactions with the neighbouring ions and that it does not affect the covalency bonds between these ions and their neighbours in normal sites. First, we assume that the four ions adjacent to an interstitial ion are fixed to their respective regular sites. Then the energy required for the interposition consists of the following parts.

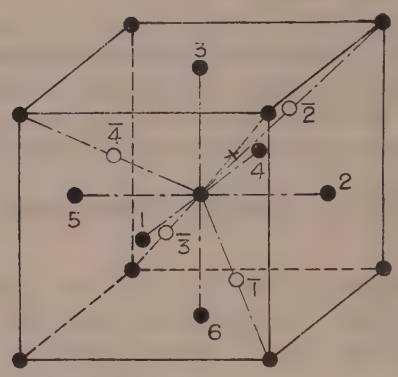

Fig. 3. Atomic arrangement around an interstitial site in zincblende. The dot at the center of the cube represents an interstitial ion. In double interstitial ion the ion represented by circle is also interposed at the point marked by cross.

(1) *Madelung and Van der Waals energies* are expressed as follows:

$$E_M'=-A_M'\frac{Z_0Ze^2}{a_0}\,, \quad (3.1)$$

where

$$A_M'=A_M-1.7476\times\sqrt{3}/2=0.1246\,.$$

1.7476 is the Madelung constant of rock salt type crystal.

$$E_V'(\pm)=-\frac{1}{a_0^6}[C^0_{\pm\mp}S_{V0}+C^0_{\pm\pm}S''_{V0}]\,, \quad (3.2)$$

where

$$S''_{V0}=6.5952\times(\sqrt{3}/2)^6=2.7824$$

$$C^0_{\pm\mp}=C_{+-}(\alpha_\pm{}^0/\alpha_\pm)\,,\quad C^0_{\pm\pm}=C_{\pm\pm}(\alpha_\pm{}^0/\alpha_\pm)\,.$$

6.5952 is the corresponding constant of rock salt type crystal.[10]

(2) *Polarization energy.*

The distance between the interstitial ion and its second nearest-neighbours is $(2/\sqrt{3})a_0$ $(=1.1547a_0)$. Therefore, it is necessary to treat, even in the first order approximation, six second nearest-neighbours (ions 1, 2, $\cdots$ 6 in Fig. 3) together with the four first ones (ions $\bar{1}$, $\bar{2}$, $\bar{3}$ and $\bar{4}$ in Fig. 3) from the atomistic standpoint. Then

$$E_P'(\pm)=E_P^{*\prime}(\pm)+[E_{P1}'(\pm)]_{s=0}\,. \quad (3.3)$$

The first term in (3.3) is the polarization energy of all the ions except the first and the second nearest-neighbours on the continuum model, and is given by

$$E_P^{*\prime}(\pm)=-\frac{1}{2}\frac{(Z_0e)^2}{a_0}[(C_0-4)M_\mp +(C_0''-3.3750)M_\pm]\,, \quad (3.3a)$$

where $C_0''=5.7362(=10.1977\times(\sqrt{3}/2)^4)$[11]

The second term E_{P1}' is the contribution from these ten ions to be added to the first term. (cf. App. III) $[E_{P1}'(\pm)]_{s=0}$ is the value of $E_{P1}'(\pm)$ at $s=0$.

(3) *Short range energy.*

In totally ionic state the short range forces between an interstitial ion and a nearest regular ion in the crystal will be nearly similar to those between two adjacent regular ions in the crystal. However, actually, the latter should be considered as the short range forces between S^{Z-} and Zn^{2+} or Zn^{Z+} and S^{2-}, binded with one another by predominantly ionic interaction. Since we cannot find any appropriate way to determine the force constants of these short-range forces, the short range interaction between S and Zn ions in zincblende in the case, where the interaction between them is considered as totally ionic, is used instead of the short range interactions between S^{Z-} and Zn^{2+} or Zn^{Z+} and S^{2-}.

Then the short-range interaction energy may be expressed as

$$E_S'=4b_R'\exp(-a_0/\rho_R')=4F_S'(a_0)\,. \quad (3.4)$$

The numerical values of b_R' and ρ_R' are shown by (5.1) in Part I.

(4) *Energy Depression by Atomic Relaxation.*

Next, we will consider the energy depression $\Delta E'(+)$ or $\Delta E'(-)$ resulting from atomic polarization of four anions or actions adjacent to an interstitial cation or anion respectively. Let us pick up only the parts of lattice energy varying with the displacements of the four ions adjacent to an interstitial ion.

The change of Madelung and Van der Waals energies may be easily computed from the results shown in Appendix of Part I, considering that the interposed ion has effective charge $\pm Z_0e=\pm 2e$ and electronic polarizability $\alpha_\pm{}^0$.

The varying parts of the polarization energy are given by the sum of $E_{P1}'(\pm)$ and

$$E_{PL}'(\pm)=\frac{Z_0Z}{a_0}e^2[M_\pm Q''+M_\mp Q']\times 4\,, \quad (3.5)$$

where Q'' is a numerical depending on the displacement s and may be easily obtained from the value of $\overline{Q}''$ in Appendix IV. $E_{PL}'(\pm)$ is the polarization energy of all the ions other than four nearest neighbours and six next nearest neighbours of the interstitial ion. Eq. (3.5) may be derived in a similar manner as stated in App. II.

Short range energy is given by

$$E_S'(s)=[3F_S(r_2)+F_S(a_0+a_0s)+F_S'(a_0-a_0s)]\times 4\,, \quad (3.6)$$

where

$$r_2=a_0\sqrt{3s^2-4s+4}/\sqrt{3}\,.$$

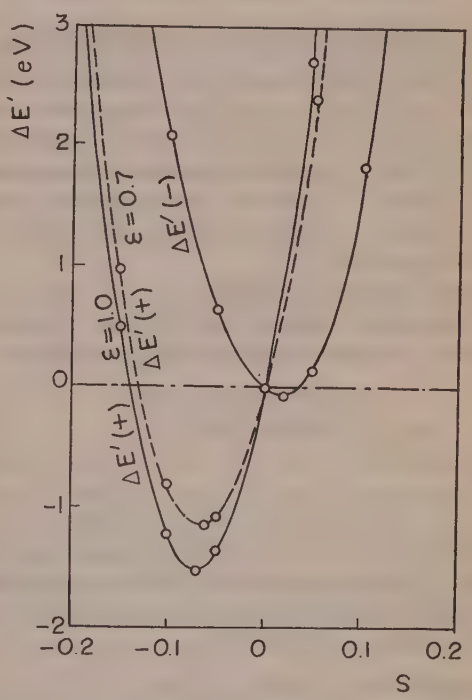

Fig. 4. Total energy change $\Delta E'(\pm)$ with atomic relaxation around interstitial ion.

Fig. 4 shows the change $\Delta E'(\pm)$ of the total energy for various cases. The maximum energy depressions $\Delta E_m'(+)$ and $\Delta E_m'(-)$ for the interstitial cation and anion may be determined in the same manner as in § 2. These values are shown in Table III.

Then $W'(\pm)$ are given by

$$W'(\pm)=E_M'+E_V'(\pm)+E_P'(\pm) +E_S'+\Delta E_m'(\pm)\,. \quad (3.7)$$

Table III. Numerical values (eV) of energy terms constituting $W'(\pm)$.

	$W'(+)$				$W'(-)$
ε	1.0	0.9	0.8	0.7	1.0
E_M'			-2.5476		-2.5476
E_S'			7.2544		7.2544
E_V'			-0.7353		-2.3622
E_p' $E_p^{*\prime}$			-6.9733		-6.4335
E_p' E_{p1}'	-9.7517	-9.3480	-8.9227	-8.4722	-8.4267
$\Delta E_m'$	-1.5180	-1.4130	-1.2279	-1.1533	-0.0374
W'	-14.2715	-13.7628	-13.1524	-12.6273	-12.5354
$E_p^{(0)\prime}$			-17.3468		-15.7136
s_m	-0.07116	-0.07012	-0.06994	-0.06427	-0.01496

The results obtained are shown also in Table III.

§ 4. Formation Energy of Lattice Defects

As lattice defects, we will consider, in addition to Schottky and Frenkel defects, the defect such that a cation and an anion on the surface of crystal are releazed into crystal and located at interstitial sites distant from one another, which may be called "inverse Schottky defect."

The formation energies W_S, W_F and W_S' of Schottky, Frenkel and inverse Schottky defects are written in the following forms.

$$W_S = W(+) + W(-) - E_L\,, \tag{4.1}$$

$$W_F(\pm) = W(\pm) + W'(\pm)\,, \tag{4.2}$$

and

$$W_S' = W'(+) + W'(-) + E_L\,, \tag{4.3}$$

where $E_L(>0)$ is the lattice energy per ion-pair. The numerical values of these formation energies obtained from the results of § 2 and § 3 are shown in Table IV.

Table IV. Numerical values (eV) of W_S, $W_F(\pm)$ and W_S'.

ε	1.0	0.9	0.8	0.7
W_S	3.5729	4.4182	5.2828	6.1608
$W_F(+)$	3.2655	4.6195	6.0945	7.4976
$W_F(-)$		10.4173		
W_S'	10.1099	10.6186	11.2290	11.7541

§ 5. Estimation of Dissociation Energies of Double Defects

As double defects, the pair of a cation vacancy and an anion vacancy adjacent to one another and the pair of an interstitial cation and an interstitial anion adjacent to one another are considered here. We call the former a double hole and the latter a double interstitial ion. (cf. Figs. 1 and 3)

First the polarization energy of medium which appears in forming a double defect is put aside. Then the formation energy $\overline{W}(+-)$ of a double hole is simply given by

$$\begin{aligned}\overline{W}(+-) &= \overline{W}_1(+) + \overline{W}_2(-) + E_L \\ &= \overline{W}_1(-) + \overline{W}_2(+) + E_L\,,\end{aligned} \tag{5.1}$$

where

$$\overline{W}_1(\pm) = E_M + E_V(\pm) + E_S \tag{5.1a}$$

$$\overline{W}_2(\pm) = E_{M2} + E_{V2}(\pm) + E_{S2} \tag{5.1b}$$

$\overline{W}_1(\pm)$ is the energy to remove an ion in the crystal to an infinitly distant point (cf. (2.13)), and $\overline{W}_2(\pm)$ is the similar energy for an ion adjacent to the vacancy formed by the removal of the first ion. The right-hand side of (5.1a) is already known in § 2. E_{M2}, $E_{V2}(\pm)$ and E_{S2} are given in the forms:

$$\left.\begin{aligned} E_{M2} &= (A_M - 1)\frac{Z'Ze^2}{a_0} + \delta E_{M2} \\ E_{V2}(\pm) &= \frac{1}{a_0^6}[C'_{\pm\mp}(S_{V0} - 1) + C'_{\pm\pm}S'_{V0}] + \delta E_{V2}(\pm) \\ E_{S2} &= 3F_S(a_0) = \tfrac{3}{4}E_S\,. \end{aligned}\right\} \tag{5.2}$$

δE_{M2} and $\delta E_{V2}(\pm)$ are the changes of Madelung and Van der Waals energies associated with the charge transfer stated in § 2.

In the smilar manner, the formation energy $\overline{W}'(+-)$ of a double interstitial ion is given by

$$\overline{W}'(+-)=\overline{W}_1'(+)+\overline{W}_2'(-)-E_L$$
$$=\overline{W}_1'(-)+\overline{W}_2'(+)-E_L \qquad (5.3)$$

where

$$\overline{W}_1'(\pm)=E_M'+E_V(\pm)+E_S' \qquad (5.3a)$$
(cf. 3.7))

$$\overline{W}_2'(\pm)=E_{M2}'+E_{V2}'(\pm)+E_{S2}' \qquad (5.3b)$$

and

$$\left.\begin{aligned} E_{M2}' &= -A_M'\frac{Z_0Z'}{a_0}e^2-\frac{Z_0^2e^2}{a_0} \\ E_{V2}'(\pm) &= -\frac{1}{a_0^6}[C^0_{\pm\mp}S_{V0}+C^0_{\pm\pm}S_{V0}'']-\frac{C^{00}_{+-}}{a_0^6} \\ E_{S2}' &= 5F_S'(a_0)=\frac{5}{4}E_S' \\ C^{00}_{+-} &= C_{+-}(\alpha_+{}^0\alpha_-{}^0/\alpha_+\alpha_-)\,. \end{aligned}\right\} \qquad (5.4)^*$$

Next we consider the polarization energy of the medium except the atomic polarization of the six nearest-neighbours of a double hole (ions $\bar{2}$, $\bar{3}$, $\bar{4}$ and 1, 2, 3 in Fig. 1) and that except the eight nearest-neighbours (ions $\bar{1}$, $\bar{2}$, $\bar{3}$, $\bar{4}$ and 1, 2, 3, 1′ in Fig. 3) and the two interstitial ions of a double interstitial ion. Then the polarization energy $E_P(+-)$ for a double hole is given by

$$E_P(+-)=E_P{}^*(+-)+E_{P1}(+-)\,, \qquad (5.5)$$

$$E_P{}^*(+-)=-\frac{1}{2}\frac{(Z_0e)^2}{a_0}\Big\{[(C_0-4)+(C_0'-0.4219)](M_++M_-)\Big\}+\frac{(Z_0e)^2}{a_0}[(Q_0-0.9192)(M_++M_-)]\,, \qquad (5.5a)$$

where $\overline{Q}_0$ is a numerical constant. (cf. App. IV.) In the similar manner the polarization energy $E_P'(+-)$ for a double interstitial ion is given by

$$E_P'(+-)=E_P{}^{*\prime}(+-)+E_{P1}'(+-)\,, \qquad (5.6)$$

$$E_P{}^{*\prime}(+-)=-\frac{1}{2}\frac{(Z_0e)^2}{a_0}\{[(C_0-4)+(C_0''-1.7500)](M_++M_-)\}+\frac{(Z_0e)^2}{a_0}[(\overline{Q}_0''-1.5485)(M_++M_-)]\,, \qquad (5.6a)$$

* The short range forces between two interstitial ions of double interstitial ion is assumed to be the same as those between an interstitial ion and the four regular ions adjacent to it. (cf. § 3. (3))

where $\overline{Q}_0''$ is a numerical constant. (cf. App. IV.)

$E_{P1}(+-)$ and $E_{P1}'(+-)$ in (5.5) and (5.6) are the electronic polarization energy of the six neighbours of a double hole and that of the eight neighbours and the two interstitial ions of a double interstitial ion respectively. $E_{P1}(+-)$ and $E_{P1}'(+-)$ may be computed in the similar manner as in the calculation of $E_{P1}'(\pm)$ in (3.3). (cf. App. II.) $E_P{}^*(+-)$ and $E_P{}^{*\prime}(+-)$ in (5.5) and (5.6) are the polarization energies of all the ions other than these ions on the continuum model. The numerical subtrahends 4, 0.4219 and 0.9192 in (5.5a) and 4, 1.7500 and 1.5485 in (5.6a) originate from the lack of ion at the vacancy and from the exception of the neighbours.

It would be very difficult to calculate the atomic polarization energy of these ions, since the electric field around the double defect has lower symmetry than that around a single defect. Therefore, we roughly assess the atomic polarization energy of these ions by using the values of their electronic polarization energy as follows:

$$\left.\begin{aligned} \Delta E_m(+-) &= (\Delta E_m(+)+\Delta E_m(-)) \times\frac{E_{P1}(+-)}{E_{P1}(+)+E_{P1}(-)}\,, \\ \Delta E_m'(+-) &= (\Delta E_m'(+)+\Delta E_m'(-)) \times\frac{E_{P1}'(+-)}{E_{P1}'(+)+E_{P1}'(-)}\,, \end{aligned}\right\} \qquad (5.7)$$

where $\Delta E_m(+-)$ and $\Delta E_m'(+-)$ are the total energy changes due to atomic polarization, at equilibrium configuration, of the six neighbours of a double hole and that of the eight neighbours and the two interstitial ions of a double interstitial ion respectively. Then the total formation energies $W(+-)$ and $W'(+-)$ of a double hole and a double interstitial ion are given by

$$\left.\begin{aligned} W(+-) &= \overline{W}(+-)+E_P(+-)+\Delta E_m(+-), \\ W'(+-) &= \overline{W}'(+-)+E_P'(+-)+\Delta E_m'(+-). \end{aligned}\right\} \qquad (5.8)$$

Then dissociation energies V_D and V_D' of a double hole and a double interstitial ion into two single holes and two single interstitial ions are written respectively as

$$\left.\begin{aligned} V_D &= W_S-W(+-) \\ V_D' &= W_S'-W'(+-)\,. \end{aligned}\right\} \qquad (5.9)$$

The results of numerical calculation are shown

Table V. Numerical values (eV) of energy terms constituting $W(+-)$.

ε	1.0	0.9	0.8	0.7
$\overline{W}_1$, $\overline{W}_2$		48.1214		
$E_p(+-)$ $E_p^*(+-)$		−1.7916		
$E_p(+-)$ $E_{p1}(+-)$	−5.0635	−4.7118	−4.3491	−3.9755
$\Delta E_m(+-)$	−0.6804	−0.5793	−0.4873	−0.4142
$W(+-)$	3.6691	4.1219	4.5766	5.0233
V_D	−0.0962	0.2963	0.7062	1.1375
$E^{(0)}(+-)$		−6.0118		

Table VI. Numerical values (eV) of energy terms constituting $W'(+-)$.

ε	1.0	0.9	0.8	0.7
$\overline{W}_1'$, $\overline{W}_2'$		−16.7068		
$E_p'(+-)$ $E_p^{*\prime}(+-)$		− 3.0437		
$E_p'(+-)$ $E_{p1}'(+-)$	−11.2807	−10.5437	−9.7811	−8.9884
$\Delta E_m'(+-)$	− 0.9653	− 0.8604	−0.7134	−0.6331
$W'(+-)$	4.9203	5.7622	6.6718	7.5448
V_D'	5.1896	4.8564	4.5572	4.2093
$E_p^{(0)\prime}(+-)$		−12.7790		

in Tables V and VI. In the calculation of V_D and V_D', the difference is taken between the values of W_S and $W(+-)$, and those of W_S' and $W'(+-)$ with the same ε value, by assuming that the effective reduction in polarizability of anions is nearly equal for single defect and double defect.

§ 6. Conclusion

Referring to Table IV, we may point out that Frenkel defect caused by sulphur ion and inverse Schottky defect will be hardly formed at ordinary high temperatures (<1020°C)*, which are realized in synthesis of luminescent materials. In particular, $W_F(-)$ will be somewhat more larger than the value in Table IV, since the overlap between the interposed sulphur ion and the six sulphur ions located at next-nearest sites, will be fairly large, although this overlap is not taken into account in the calculation. If inverse Schottky defects and double interstitial ions were formed in zincblende at a high temperature, there might be a dissociative equilibrium between these two kinds of defects. However, the relation $(1/2)W_S' > V_D'$ holds except for the case $\varepsilon=1$. Then most of the interstitial ions will be dissociated.[13] (cf. Tables IV and VI)

As easily understood from Table IV and V, most probable defects in zincblende are Shottky defects, double holes and Frenkel defects by zinc ion. Since the dissociation energy of double hole into two isolated holes in negative for the case $\varepsilon=1$, ε would be somewhat smaller than unity. Recalling the fact that zincblende shows no ionic conductivity even at high temperatures, we may estimate ε to be 0.9~0.8, namely $W_S=4\sim5$ eV, and V_D to be less than 1 eV. The fact that V_D is considerably small compared with W_S suggests that nearly random distribution of vacancies will be realized in zincblende. If this is the case, the number of double holes in zincblende is proportional to the square of the number of single holes[14] and this fact has been to some extent experimentally evidenced by R. H. Bube.[15] The activation energy for Shottky defects and double holes are assessed to be $(1/2)W_S=2\sim3$ eV and $W(+-)=4\sim6$ eV respectively. These values may be compared with the activation energies of shallow and

* 1020°C is the transition temperature between zincblende and wurzite structures.

deep traps in zincblende 4.5 eV and 7.4 eV obtained experimentally by Bube.

Referring to Table IV, the formation energy of Frenkel defect by zinc ion, $W_F(+)$, is estimated to be 4.5~6 eV. Smallness of $W_F(+)$ in comparison with $W_F(-)$ is attributed to the large electronic polarizability of sulphur ions surrounding the zinc ion to be removed and interposed. This tendency will be much more exaggerated, when the overlap repulsion between the interposed sulphur ion and six sulphur ions located at next-nearest sites is taken into account. According to current views, neutral atoms of some foreign metals may be located at interstitial sites in zincblende, and form efficient luminescence centers. If we assume that these foreign atoms are located at interstitial sites surrounded by four sulphur ions and that repulsive force between these foreign atoms and sulphur ions is nearly equal to that between interstitial zinc ion and sulphur ion, we may estimate the energy required to interpose the foreign atoms into the crystal from the exterior. Then the polarization energy of the medium, E_P' in Table III, will be negligibly small, and the energy for the interposal may be assessed to be 2~3 eV. Thus atoms of some foreign metals with atomic radii of appropriate magnitude will be located easily at interstitial sites during the heating procedure of phosphor preparation.

The calculation in this paper is also applicable to the other sphalerite-type crystals such as ZnSe, provided that Hartree solutions of constituent ions and effective charges on them are known.

Appendix I

When an additional free charge Ze is put into the crystal, the polarization $P(R)$ at the distance R from the free charge is given by

$$P(R)=\left(1-\frac{1}{\kappa}\right)\frac{Ze}{R^2} \qquad \text{(AI-1)}$$

in continuum model, where κ is the static dielectric constant. Further, the macroscopic polarization caused by electronic polarization of individual ions is given by

$$P_e(R)=\left(1-\frac{1}{\kappa_0}\right)\frac{Ze}{R_2}\,, \qquad \text{(AI-2)}$$

where κ_0 is the optical dielectric constant.

If we denote electronic dipole moments on a cation and an anion in the crystal by μ_+ and μ_- respectively, and the atomic dipole moment by μ_a, we may write, for sphalerite-type crystals,

$$\left.\begin{aligned} P(R)&=(\mu_++\mu_-+2\mu_a)/2\left(\frac{2}{\sqrt{3}}\right)^3 a_0^3\,,\\ P_e(R)&=(\mu_++\mu_-)/2\left(\frac{2}{\sqrt{3}}\right)^3 a_0^3\,,\\ \mu_+/\mu_-&=\alpha_+/\alpha_-\,,\end{aligned}\right\} \qquad \text{(AI-3)}$$

where a_0 is the nearest-neighbour distance, and α_+ and α_- are the electronic polarizabilities of the cation and anion. By using (AI-1, 2 and 3), ratio of electronic polarization to atomic one is given by

$$(\mu_++\mu_-)/2\mu_a=\frac{\kappa(\kappa_0-1)}{\kappa-\kappa_0}\,. \qquad \text{(AI-4)}$$

Furthermore, if we introduce the dimensionless quantities M_+ and M_- which are defined by

$$M_\pm\frac{a_0^3Ze}{R^3}=\mu_\pm+\mu_a\,, \qquad \text{(AI-5)}$$

we may obtain

$$M_\pm=\frac{4}{3\sqrt{3}\,\pi}\left(1-\frac{1}{\kappa_0}\right)\left\{\frac{\alpha_\pm}{\alpha_++\alpha_-}+\frac{1}{2}\,\frac{\kappa-\kappa_0}{\kappa(\kappa_0-1)}\right\}. \qquad \text{(AI-6)}$$

The numerical values of M_+ and M_- for zincblende are shown in Table I.

Appendix II

Polarization energy of the medium except four ions adjacent to the vacancy is given by (2.5), where $\sum_i$ should be taken over all ions except these four ions. When the four ions adjacent to the vacancy are displaced on the tetrahedral directions, the field $\boldsymbol{D}_i$ from the free charges acting on the ith ion in the crystal and the dipole μ_i on it are given by (cf. Fig. 5)

$$\boldsymbol{D}_i=\mp\frac{Z_0e}{R_i^3}\boldsymbol{R}_i\pm\sum_{j=1}^{4}\left[\frac{Z'e}{r_{ij}^3}\boldsymbol{r}_{ij}-\frac{Z'e}{r_{ij}'^3}\boldsymbol{r}_{ij}'\right], \qquad \text{(AII-1)*}$$

$$\mu_i=M_ia_0^3\boldsymbol{D}_i \quad (M_i=M_+ \text{ or } M_-)\,. \qquad \text{(AII-2)}$$

$\sum_j$ should be taken over the four ions surrounding the vacancy. When the displacements sa_0 of the four ions are not so large, the second term in the brackets of (AII-1) is very small, comparing with the first term. If

* cf. foot-note concerning (2.6a) in § 2.

we neglect the square of this small term, then we obtain the following form by inserting (AII-1 and 2) into (2.5)

$$E_P=-\frac{1}{2}\frac{(Z_0e)^2}{a_0}\sum_i M_i\frac{a_0^4}{R_i^4}+\frac{Z_0Z'e^2}{a_0}\sum_i\sum_j M_i\frac{a_0^4\cos\theta_{ij}}{R_i^2r_{ij}^2}-\frac{Z_0Z'e^2}{a_0}\sum_i\sum_j M_i\frac{a_0^4\cos\theta_{ij}'}{R_i^2r_{ij}'^2}\,. \quad \text{(AII-3)}$$

When $s=0$, $r_{ij}=r_{ij}'$ and $\theta_{ij}=\theta_{ij}'$. Then E_p coinside with the first term in (3.5). Only the last term in (AII-3) varies with displacements sa_0. It may be written as

$$E_{PL}=-\frac{Z_0Z'e^2}{a_0}[M_\pm Q+M_\mp Q']\times 4\,, \quad \text{(AII-4)}$$

where

$$Q=a_0^4\sum_i^{(u)}\frac{\cos\theta_{ij}'}{R_i^2r_{ij}'^2}\,,\qquad Q'=a_0^4\sum_i^{(l)}\frac{\cos\theta_{ij}'}{R_i^2r_{ij}'^2}\,.$$

$\sum_i^{(l)}$ and $\sum_i^{(u)}$ mean the summations over the like and unlike ions respectively referring to the jth ion, to which one of the nearest neighbour unlike ions is absent. The numerical values of Q and Q' for various values of s are easily computed from those of $\overline{Q}$ and $\overline{Q}'$ in Appendix IV, where the summations are taken over all the cations or anions in perfect crystal except the reference ion (jth ion).

Appendix III

If the local electrostatic field excerted on an ion in the crystal is denoted by $\boldsymbol{E}$ and the dipole moment induced on it by $\boldsymbol{\mu}$,

$$\boldsymbol{\mu}=\alpha\boldsymbol{E}=\alpha(\boldsymbol{D}+\boldsymbol{E}')\,, \quad \text{(AIII-1)}$$

where α is the polarizability of the ion, $\boldsymbol{D}$ the electric field from free charges, $\boldsymbol{E}'$ that due to dipoles induced on all the other ions. If we write down this equation with respect to the ions 1 and $\bar{1}$ in Fig. 3,

$$\mu_s=\varepsilon\alpha_\mp\left[D_s(s)-\frac{15}{16}\sqrt{\frac{3}{2}}\frac{1}{(1+s)^3}\frac{\mu_s}{a_0^3}-\left(\Gamma_1(s)\frac{9}{f_1(s)^3}+\Gamma_2(s)\frac{9}{f_2(s)^3}\right)\frac{\mu_x}{a_0^3}+(S''M_\pm-S'M_\mp)\frac{Z_0e}{a_0^2}\right] \quad \text{(AIII-2)}$$

$$\mu_x=\alpha_\pm^*\left[D_x(s)-\left(\Gamma_1(s)\frac{6}{f_1(s)^3}+\Gamma_2(s)\frac{6}{f_2(s)^3}\right)\frac{\mu_s}{a_0^3}-\left(\frac{3\sqrt{3}}{32}+\frac{9}{8}\sqrt{\frac{3}{2}}\right)\frac{\mu_x}{a_0^3}-(0.016M_\mp+0.170M_\pm)\frac{Z_0e}{a_0^2}\right], \quad \text{(AIII-3)}$$

where

$$f_1(s)\equiv\sqrt{(1-s)^2+2(1+s)^2}\,,\qquad f_2(s)\equiv\sqrt{(3+s)^2+2(1+s)^2}$$

$$\Gamma_1(s)\equiv 1+3\frac{(1+3s)(1-s)}{f_1(s)^2}\qquad \Gamma_2(s)\equiv -1+3\frac{(5+3s)(3+s)}{f_2(s)^2}$$

$$D_x(s)\equiv\frac{3}{4}\frac{Z_0e}{a_0^2}+\frac{Ze}{a_0^2}\left[\frac{2}{\sqrt{3}}+\frac{18}{11\sqrt{11}}-\frac{6(1-s)}{f_1(s)^3}-\frac{6(3+s)}{f_2(s)^3}\right].$$

sa_0 is the radial displacement of the four ions adjacent to the interstitial ion, μ_s and μ_x the dipole moments pointed to (111) and (100) on the ions $\bar{1}$ and 1 in Fig. 3 respectively. $\alpha_\pm^*$ are the total polarizabilities of cation and anion, containing atomic and electronic polarizabilities, and are given by

$$\alpha_\pm^*=\alpha_\pm\frac{\mu_\pm+\mu_a}{\mu_\pm}=\alpha_\pm+\frac{(\alpha_++\alpha_-)(\kappa-\kappa_0)}{2\kappa(\kappa_0-1)}\,.$$

$D_s(s)$ and $D_x(s)$ is the electric fields acting on the ions $\bar{1}$ and 1, from the free charges. When $s=0$, $D_s(s)=Z_0e/a_0^2$ and $D_x(s)=(3/4)Z_0e/a_0^2$. The last terms in (AIII-2) and (AIII-3) are the electric field due to the dipoles on the ions $\bar{1}$ and 1 from all the ions outside the ion 1. (cf. Fig. 3) The change of $D_s(s)$ with s is easily obtained from the results in Appendix of Part I. S' is the same quantity as in (2.9). The value of S'' at $s=0$ is 0.372. This value and the numericals 0.016 and 0.170 occurring in (AIII-3) are obtained in the same manner as in calculation of S and S' in (2.9). The change of S'' with s is computed with five rings around the interstitial ion, as in the case of S and S' in (2.9).

By solving (AIII–2) and (AIII–3) simultaneously we may obtain μ_s and μ_x at a given s value. Then electronic polarization energy $E'_{P1}(\pm)$ of the four nearest-neighbours ($\bar{1}$, $\bar{2}$, $\bar{3}$ and $\bar{4}$ in Fig. 3) and the six next nearest neighbours (1, 2, $\cdots$6 in Fig. 3) given by

$$E'_{P1}(\pm)=\frac{1}{2}[4D_s(s)\mu_s+6D_x(s)\mu_x]\,. \qquad \text{(AIII–4)}$$

$\varepsilon(\leq 1)$ has the same meaning as stated in § 2. Accordingly, in the case of an interstitial anion ε in (AIII–2) should be taken as 1.

Appendix IV

$\overline{Q}''$ is defined by

$$\overline{Q}''=a_0^4\sum_i^{(u)}\frac{\cos\theta_{ij}'}{R_i^2 r_{ij}'^2}\,, \qquad \text{(AIV–1)}$$

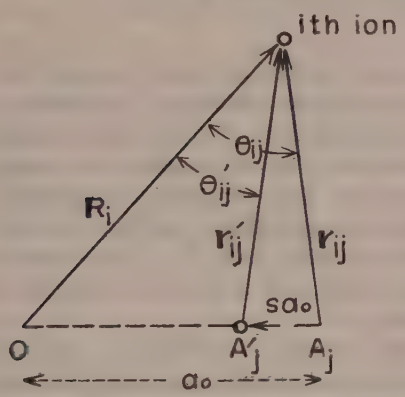

Fig. 5. Diagram illustrating the relation among vectors $\boldsymbol{R}_i$, $\boldsymbol{r}_{ij}$ and $\boldsymbol{r}_{ij}'$.
O: Center of vacancy.
A_j: Regular site of the jth ion adjacent to vacancy (j=1, 2, 3, 4).
sa_0: Displacement of the jth ion.

Table VII.

s	$\overline{Q}$	$\overline{Q}'$	$\overline{Q}''$
−0.3	3.5618	3.8488	5.1684
−0.2	3.5534	3.7192	4.8915
−0.15	3.5440	3.6584	4.7472
−0.1	3.5305	3.5995	4.5946
−0.05	3.5141	3.5403	4.4504
0	3.4876	3.4876	4.3054
0.05	3.4588	3.4235	4.1657
0.1	3.4174	3.3828	4.0392
0.15	3.3670	3.3307	3.9233
0.2	3.3161	3.2858	3.8334
0.3	3.1910	3.1934	3.6944

$\overline{Q}_0$ and $\overline{Q}_0''$ in (5.5) and (5.6) are the values of $\overline{Q}$ and $\overline{Q}''$ at s=0, respectively.

where the summation should be taken over all ions but the reference ion (jth ion). The meaning of the notations in (AIV–1) is to be refered in Fig. 5, where the point O is regarded as an interstitial site for this case. The summation for like ions, $a_0^4\sum_i^{(l)}\frac{\cos\theta_{ij}'}{R_i^2 r_{ij}'^2}$ equals to $\overline{Q}'$ stated in App. II and given in Table VII. Q'' in (3.5) may be obtained by excluding from $\overline{Q}''$ the summation with respect to the other three ions equivalent to the jth ion and the six next-nearest ions of the interstitial site.

In calculating $\overline{Q}$, $\overline{Q}'$ and $\overline{Q}''$ the summations are taken over the ions within 57 cells around vacancy or the interstitial site, and the residual parts are computed by integrating the summands which are expanded in terms of power series of the displacement s. As the lower limits of integrations, those for the calculations of $a_0^4\sum_i^{(u)}\frac{1}{R_i^4}$ and $a_0^4\sum_i^{(l)}\frac{1}{R_i^4}$ are used. (cf. Part I Appendix)

References

1) N. F. Mott and K. J. Littleton: Trans. Faraday Soc. **34** (1938) 485.
2) J. Yamashita and T. Kurosawa: J. Phys. Soc. Japan **9** (1954) 944.
T. Kurosawa: J. Phys. Soc. Japan **13** (1958) 153.
3) S. Asano and Y. Tomishima: J. Phys. Soc. Japan **11** (1956) 644.
4) S. Asano and Y. Tomishima: J. Phys. Soc. Japan **13** (1958).
5) J. D. H. Donay and W. Nowacki: *Crystal Data* (Geological Society of America N. Y. 1954) p. 501.
6) K. Hφjendahl: K. Danske Vidensk. Selskab, **16**, No. 2 (1938).
7) J. R. Tessman, A. H. Kahn and W. Shockley: Phys. Rev. **92** (1953) 890.
8) F. Seitz: *Modern Theory of Solids* (McGraw-Hill Co. N. Y. 1940) p. 83.
9) J. G. Kirkwood: Physik. Z. **33** (1932) 57.
10) F. Seitz: reference 8) p. 85.
11) J. E. Ingham and A. E. Jones: Proc. Roy. Soc. **A107** (1927) 636.
12) N. F. Mott and R. W. Gurney: *Electronic Process in Ionic Crystals* (Oxford 1940) p. 59.
13) N. F. Mott and R. W. Gurney: *ibid.* p. 42.
14) H. W. Leverentz: *Introduction to Luminescence of Solids* (John Wiley & Sons. Co. N. Y. 1950) p. 478.
15) R. H. Bube: J. Chem. Phys. **20** (1952) 708.

JOURNAL OF THE PHYSICAL SOCIETY OF JAPAN Vol. 13, No. 10, OCTOBER, 1958

Internal Friction of Lead. I

By Yosio HIKI

The Government Mechanical Laboratory, Suginami-ku, Tokyo, Japan

(Received July 5, 1958)

Internal friction of single crystal of lead (99.99% pure) was measured with longitudinal vibration in kilocycle range using the composite piezo-electric quartz oscillator. The dependences of the internal friction on the strain amplitude ($0.5-12\times10^{-6}$), on the frequency (64, 192 kc/sec) of vibration, and on temperature (140—340°K) were mainly studied. The internal friction is of the order of 10^{-3} at low temperatures, and increases slightly as the temperature is raised, and increases also with increasing strain amplitude. Near the room temperature, the value of the internal friction rises steeply. A peculiar temperature (about 300°K) has been found above which the internal friction decreases with increasing amplitude. The amplitude-dependent internal friction does not depend on the frequency of vibration and the amplitude-independent one seems to be proportional to the frequency.

§ 1. Introduction

Internal friction, which is the ratio of the mechanical energy dissipated per cycle to twice the total vibrational energy, is one of the most structure-sensitive quantities of the crystalline solids[1]. There are several kinds of origins of internal friction according as the frequency of the vibration is different. In general, the internal friction also depends on other parameters such as strain amplitude of the vibration, temperature, purity, crystallographic orientation and mechanical or heat treatment of the specimens.

There have been some investigations about the internal friction of lead. In the audio-frequency range, the internal friction was measured as a function of frequency, and several resonance-type peaks were found[2]. Some of these peaks seem to have relations with the crystal dislocation. A peak was also found which might be due to the thermal current in the specimen vibrating transversely[3]. In the kilocycle range, the pronounced dependence on the strain amplitude of the internal friction was observed[4]. This phenomenon may be explained by assuming the dislocation damping. Measurements at very large vibrational strain, which was in the range of plastic fatigue, were also carried out[5]. The effect of impurity on the internal friction of lead was investigated, and it was found that impurity atoms decrease the value of the internal friction and alter the feature of the amplitude dependence[6]. At low temperature, the Bordoni's peak was observed in lead as in other metals[7]. The behavior of the internal friction at high temperatures was also studied[8]. In the megacycle range, the difference of the ultrasonic attenuation in normal and superconducting states was firstly detected in lead metal[9]. This phenomenon is considered to be originated from conduction electrons.

In the present investigation, the internal friction of lead single crystals in the kilocycle range has been measured as a function of strain amplitude, temperature and frequency.

§ 2. Experimental Procedures

The composite piezo-electric oscillator was used to measure the internal friction[10]. Two identical 18.5° X-cut quartz bars, 40 mm × 2 mm × 2 mm, were cemented together in their end faces with Araldite 101. Gold electrodes were plated through vacuum deposition on the faces perpendicular to their electrical axes. Their fundamental frequencies of longitudinal vibration were about 64 kc/sec, being matched within 0.01 per cent. The composite quartz oscillator was supported upright with four fine phosphor-bronze wires welded to the vibrational nodes on each electrodes and these wires also served as electrical leads. Such supporting device made the oscillation stable and the reproducibility of the measured values of the internal friction was improved markedly. The energy loss of this oscillator system was about 10^{-5} *in vacuo* and could be neg-

lected in comparison with the internal friction of lead which was larger than 10^{-3}.

A cylindrical specimen was cemented to the quartz oscillator. The diameter of the specimen was 2 mm, and its length was adjusted so as to make its frequency of vibration coincide with that of quartz. This matching need not be very strict when the internal friction of the specimen is not small. Phenyl salicylate was used as the adhesive between the specimen and the quartz for room temperature measurements. Silicone compound DC–40C was used for the case of low or high temperature. These joints are always located at the stress nodes of vibration and generally have little effects on the measurement.

When the frequency of the input alternating voltage on the electrodes of one quartz oscillator coincides with its fundamental or one of the odd overtone frequencies, the composite system oscillates longitudinally, and the output voltage occurs on the electrodes of the other quartz. The input and output voltages were measured by vacuum tube voltmeters. The ratio of the input voltage to the output voltage is proportional to the internal friction of this system, while the maximum strain amplitude of the specimen is proportional to the output voltage. After the resonance curve of the quartz system is measured without specimen, these proportionality constants can be determined using the known elastic and electrical constants of quartz. The accuracy of the internal friction measurement was estimated to be better than 5 per cent. Young's modulus of the specimen is also obtained by measuring the resonant frequency of the oscillator system.

The total assembly was enclosed in a evacuated brass tube in order to eliminate the air damping. Temperatures were measured by means of a copper-constantan thermocouple mounted very close by but not in contact with the specimen.

Specimens were made from 99.99% lead. The impurities were determined by chemical analysis and the results were as shown in Table I. Single crystals were prepared in the following way. The lead was melted and sucked up into a glass tube. It was re-melted by a horizontally moving furnace and then solidified as a single crystal. The glass tube was dissolved away with hydrofluoric acid. The crystal was deeply etched electrolytically by sulfamic acid. For cutting the crystals, the electrolytical method was also applied to avoid the cold-working by mechanical cutting. When the specimens were to be annealed, they were heated in ethylene glycol to protect themselves from oxidization.

Table I. Impurities in lead used. (in weight per cent)

C	Si	S	Cr	Fe	Ni	Cu
0.007	0.0004	0.0003	none	0.0005	none	0.0003
Zn	As	Ag	Cd	Sn	Sb	Bi
0.0003	0.0003	0.0002	none	0.0004	0.0003	0.0002

§ 3. Experimental Results

3.1. *Time dependence*

When the measurements were started as soon as the specimen was mounted to the quartz oscillator at room temperature, the internal friction, δ, varied with time, t, as shown in Fig. 1. These curves were composed of three portions: (i) $t=0-10^2$ min. In slowly cooled specimen, δ decreased with time. In quenched specimen, there appeared a small peak. (ii) $t\sim 3\times 10^2$ min. There existed irregular peaks which were so large that their maximum values could not be measured. (iii) $t>3\times 10^2$ min. δ decreased monotonously and approached to a constant value although the change could be detected

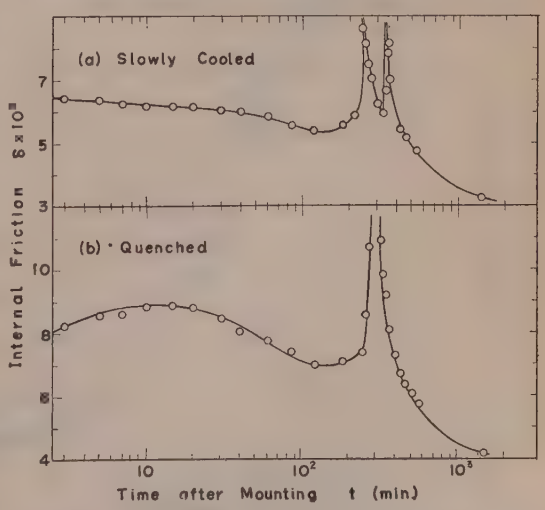

Fig. 1. Variation of internal friction with time lapse after mounting a specimen (a) slowly cooled and (b) quenched into ethylene glycol from 150°C.

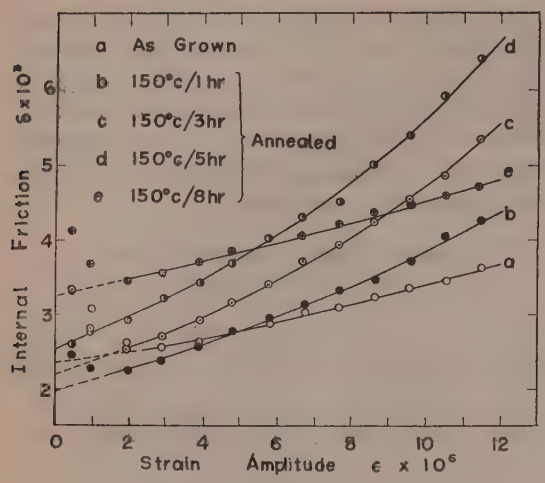

Fig. 2. Internal friction *vs* strain amplitude curves for a specimen annealed successively.

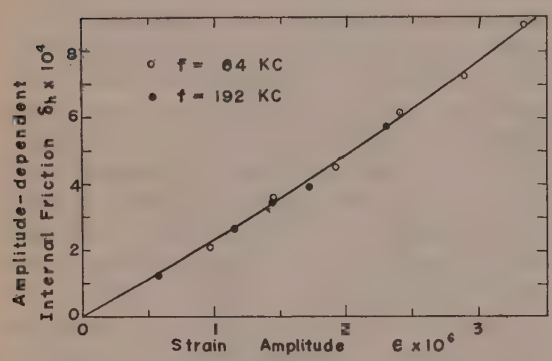

Fig. 3. Amplitude-dependent internal friction of a specimen measured at two frequencies.

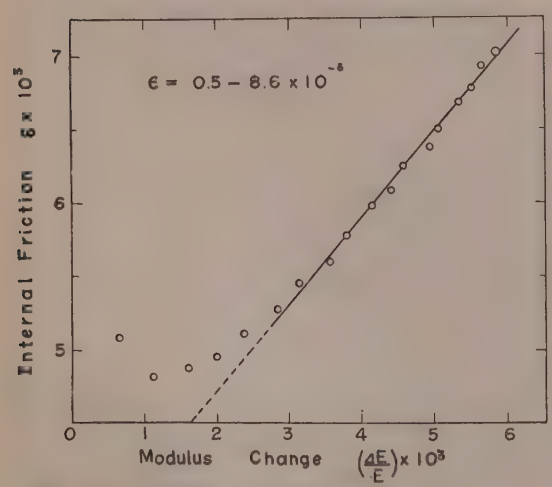

Fig. 4. Relation between internal friction and fractional change of Young's modulus at various strain amplitudes.

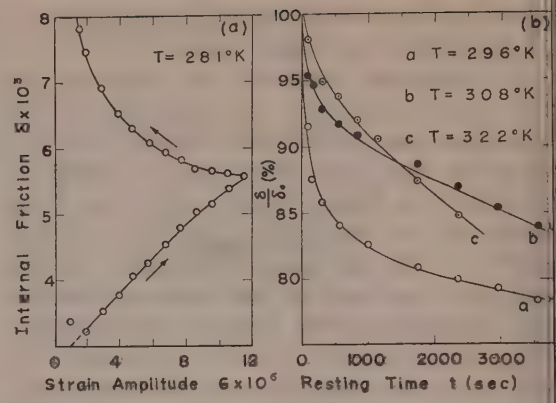

Fig. 5 (a). Internal friction *vs* strain amplitude curve showing a hysteresis. (b) Decrease of internal friction with resting time.

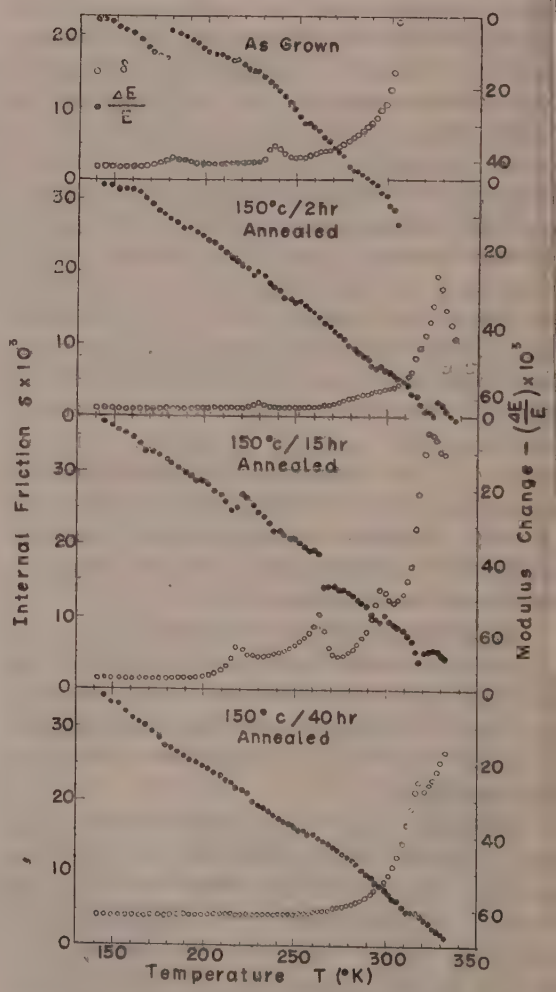

Fig. 6. Temperature dependences of internal friction and fractional change of Young's modulus of the specimen B_2–6–C.

after several ten days after mounting.

For the measurement of the internal friction of lead, attention should be given to the time lapse after mounting the specimen.

3.2. *Amplitude dependence*

Internal friction of lead, δ, depends on the strain amplitude of vibration, ε, markedly. Following measurements were always carried out 18 hours after the mounting and at constant temperature, 8°C.

δ *vs* ε curves of a specimen as grown, and annealed at 150°C for 1, 3, 5 and 8 hours are shown in Fig. 2. The same specimen was also annealed at 135°C for 1, 3 and 5 hours; 120°C for 1, 3 and 5 hours; 105°C for 2, 4 and 7 hours, successively, and similar sets of curves were obtained. As a general feature, δ increased monotonously with increasing amplitude. When the amplitude was very small, however, δ decreased as the amplitude was increased. This extraordinary part in small amplitude region disappeared as temperature was lowered.

To analyze the data, the amplitude-dependent part of the internal friction $\delta_h=\delta-\delta_i$ was considered, where δ_i was obtained by extrapolating the value of δ to $\varepsilon=0$, disregarding the extraordinary part at small amplitude. In well annealed specimens, δ_h did not depend on frequency of vibration, f, as illustrated in Fig. 3.

Young's modulus E varied with ε and its fractional change, $\Delta E/E$, was proportional to δ except the small amplitude part [Fig. 4].

When ε is increased to a large value and then decreased, δ *vs* ε curve always shows an apparent hysteresis loop as can be seen in Fig. 5 (a). The value of δ corresponding to the decreasing amplitude part diminishes gradually when the vibration is stopped, as the following manner. After the specimen was vibrated with $\varepsilon=12\times10^{-6}$ for 5 min, internal friction was measured with small amplitude of about 2.9×10^{-6}. As soon as δ was measured, the vibration was stopped and the specimen was rested. The changes of the ratio δ/δ_0 with the resting time, at different temperatures, are shown in Fig. 5 (b), where δ_0 is the initial value of δ.

3.3. *Temperature dependence*

The variation of δ and $\Delta E/E$ with temperature, T, were measured from 140°K to 340°K. Fig. 6 shows the results for a specimen as grown, and annealed at 150°C for 2, 15 and 40 hours. These measurements were always carried out exactly at the constant vibrational strain amplitude $\varepsilon=2.86\times10^{-6}$. This fixed condition is important because of the strain

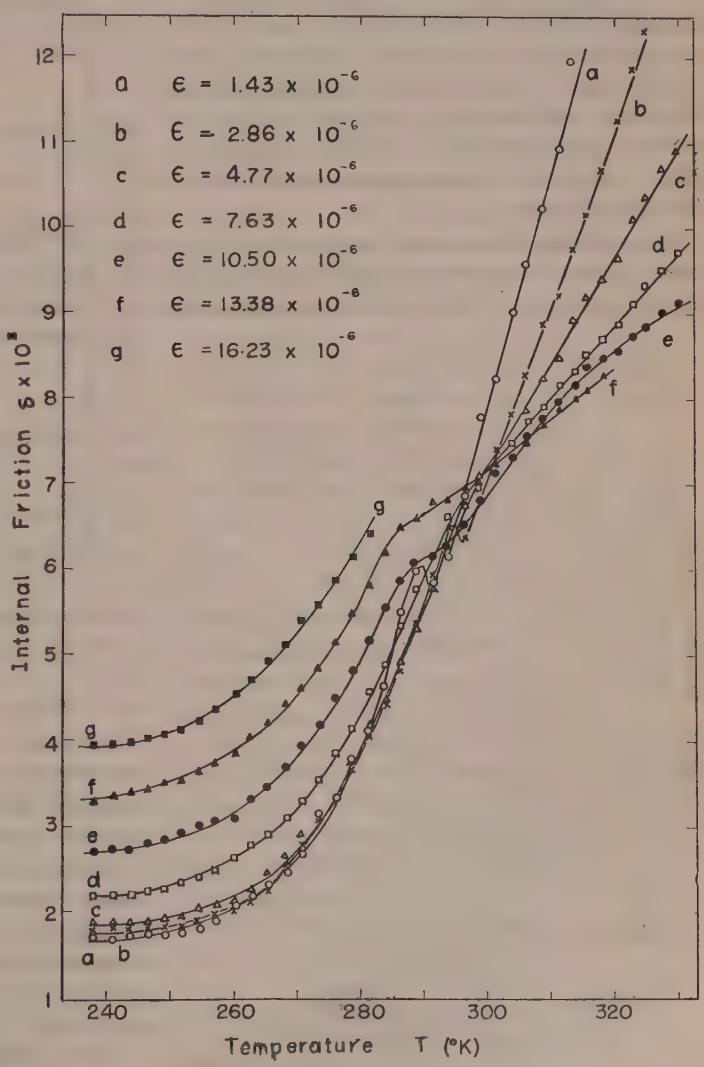

Fig. 7. Internal friction *vs* temperature curves for the specimen B_1–5–B, annealed at 150°C for 60 hours, at various strain amplitudes.

amplitude hysteresis mentioned above, particularly at low temperatures. If ε is once increased and then decreased, δ does not return to its initial value so rapidly. This may be one origin of "false peak" which is sometimes observed in δ *vs* T curve.

It seems that δ *vs* T curves can be divided into three regions. (i) In the low temperature region ($T<270°K$), δ increases slightly with increasing T. There also exist small peaks which disappear when the specimen is well annealed. These peaks are sometimes not reproducible, but it cannot be considered that they come from experimental failure because $\Delta E/E$ also shows anomalies at the same temperatures. (ii) In the intermediate region near room temperature, δ increases steeply. An anomalous point T_0 (290—330°K) exists which sometimes appears to be an inflection point rather than a maximum of a peak. (iii) In the high temperature region ($T>T_0$), δ increases with increasing T, but the increasing rate is lowered in comparison with that of the second region.

In another well annealed specimen, δ was measured as a function of temperature, taking ε as a parameter. The results are summarized in Fig. 7. When δ is replotted against ε under the condition that T is constant, Fig. 8 is obtained. The amplitude dependence of the internal friction in high temperature region is entirely different from that in low temperature region. Namely, δ increases or decreases with increasing amplitude according as T is lower of higher than T_0. At temperatures lower than but not far from T_0, the high-temperature type curve is partly superposed upon the usual low-temperature type curve in the region of small amplitude (e.g. curve e in Fig. 8), which has been already noticed in section 3.2.

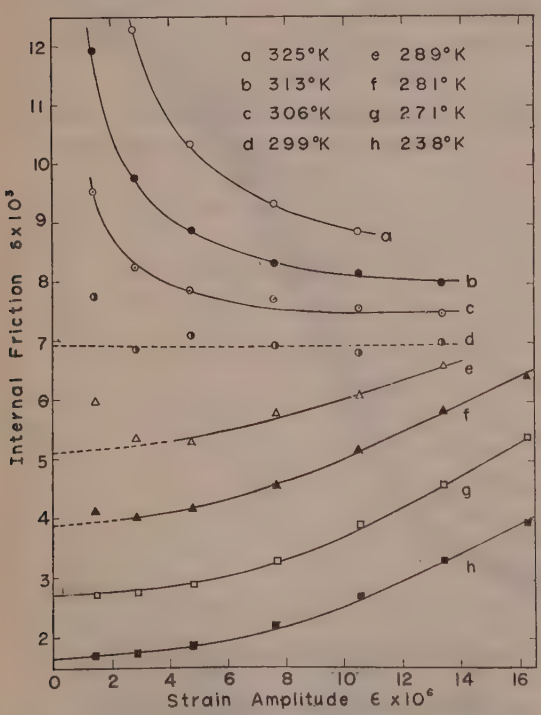

Fig. 8. Internal friction *vs* strain amplitude curves at various temperatures.

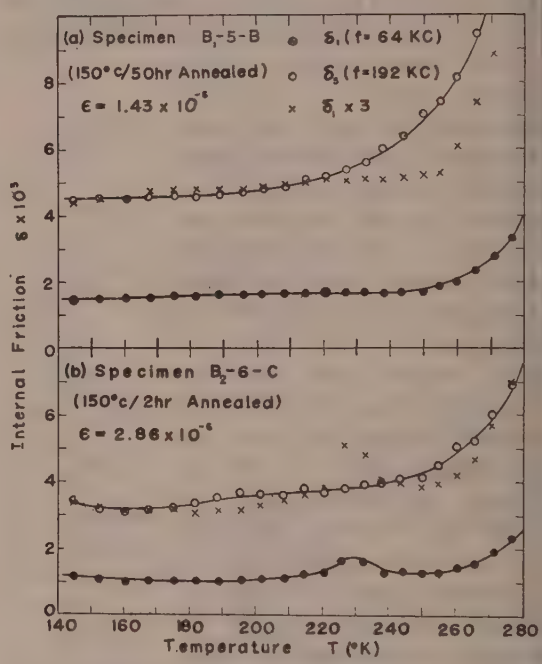

Fig. 9. Internal friction *vs* temperature curves for two specimens measured at two frequencies.

3.4. *Frequency dependence*

In Fig. 9, δ *vs* T curves for two specimens are shown. Two frequencies were used by exciting the fundamental and third harmonic oscillation of the quartz. Higher harmonics of sufficient intensity applicable for measurement could not be obtained. These measurements were carried out about two or three hundred hours after mounting the specimen and no appreciable change of δ with time was observed.

The strain amplitude used was so small that the measured value of δ might be regarded as the amplitude-independent internal

friction δ_i. At low temperatures, δ_i seems to be proportional to the vibrational frequency, f. The same specimen vibrating in its second overtone was measured by other quartz oscillator. Low temperature δ was more than twice as large as the value of fundamental vibration. Probably, the specimen was cold-worked through handling.

§ 4. Discussion

Various mechanisms were proposed to account for the internal friction of crystalline solids. When the internal friction is measured with a high frequency vibration at low temperatures, it may not be attributed to the "relaxation by diffusion"[11]. The only possible diffusion-like mechanism which may contribute to the internal friction of single crystals under longitudinal vibration of high frequency is the thermoelastic heat flow in the crystal[12]. It can be estimated, however, that the magnitude of the internal friction of lead from this origin is less than 10^{-4} at 64 kc/sec. Moreover, the remarkable amplitude dependence of the internal friction cannot be explained only by assuming the damping with the nature of dynamic hysteresis including the "anelasticity." Some notions of static hysteresis are required.

Since Read[13] suggested the possibility of dislocation damping as a source of internal friction, this idea was applied to interpret some of the experimental facts. There are now two types of models to treat the dislocation damping theoretically: "pinned-down" dislocation model by Koehler[14] and Granato-Lücke[15], and "unpinned" model as that of Weertman[16]. The former assumes pinned-down or fixed state of dislocations by point imperfections such as impurity atoms. This model may be valid to the case of rather pure crystals at low temperatures. On the contrary, the latter, using the solution hardening theory of Mott-Nabarro, may be suitable to treat the internal friction of impure metals.

It seems that the amplitude and frequency dependences of the internal friction of lead single crystals at low temperatures can be understood satisfactorily by adopting the treatment of Granato and Lücke. This can be summarized as follows.

A thoroughly annealed single crystal contains a stable three-dimensional network of dislocations and their intersections are usually immovable. If there exist enough impurity atoms which exert forces on the dislocation lines, the network loops of dislocations may be further pinned down here and there by impurities. When the external alternating stress is applied to the crystal, the dislocation lines between pinning points bow out in their slip planes like streched strings. With increasing stress, at the instance when some part of the dislocation line is torn away from an impurity atom, the other impurity-pinning points in that network loop are also broken down as a catastrophe, while the network-pinning points are fixed. During the decreasing part of the stress cycle, the loop collapses elastically until it is again pinned down by impurities. Using this picture, it can be shown that the internal friction of single crystal is expressed as a sum of two losses. The first is the dynamic one originated from the damping force to the dislocation motion. This force is assumed to be proportional to the velocity of the dislocation. The second loss is the one of the static hysteresis type which originates necessarily from the break-away process mentioned above. The former loss is proportional to the frequency and independent on the strain amplitude, while the latter increases with increasing amplitude and does not depend on the frequency.

The temperature dependence of the internal friction of lead, however, cannot be fully explained by this theory only. The steep increase of the internal friction near room temperature may be due to the break-away of pinning points through thermal agitation. The reverse of the amplitude dependence at high temperatures is particularly noticeable and some expositions are wanted for it.

It is supposed that there also exist some unstable dislocations or other imperfections in crystals. These may be the origins of the transient phenomena such as the variation of the internal friction with time after mounting the specimen.

Detailed analysis of the present experimental results will be published later.

Acknowledgements

The author wishes to express his sincere gratitudes to Dr. T. Kawada for the continual encouragement during the course of this work.

He is also greatly indebted to Professor Y. Tomono and Professor R. Hasiguti for kind advices. Thanks are also due to Mr. A. Hikata for his valuable discussions.

References

1) A. S. Nowick: *Progress in Metal Physics* (Interscience Publishers, Inc., New York, 1953) Vol. 4, p. 1.
2) E. R. Fitzgerald: Phys. Rev. **108** (1957) 690.
3) R. Kamel: Phys. Rev. **75** (1949) 1606.
4) J. Marx and J. S. Koehler: *Pittsburgh Symposium on the Plastic Deformation of Crystalline Solids* (O.N.R., Washington, 1950) p. 171.
5) W. P. Mason: J. Acoust. Soc. Am. **28** (1956) 1197.
6) J. Weertman and E. I. Salkovitz: Acta Met. **3** (1955) 1.
7) P. G. Bordoni: Ricerca Sci. **23** (1953) 1193.
8) P. G. Bordoni and M. Nuovo: Nuovo Cimento **11** (1954) 127.
9) H. E. Bömmel: Phys. Rev. **96** (1954) 220.
10) J. Marx: Rev. Sci. Instr. **22** (1951) 503.
11) C. Zener: *Elasticity and Anelasticity of Metals* (University of Chicago Press, 1948)
12) K. Lücke: J. App. Phys. **27** (1956) 1433.
13) T. A. Read: Phys. Rev. **58** (1940) 371.
14) J. S. Koehler: *Imperfections in Nearly Perfect Crystals* (John Wiley and Sons, Inc., New York, 1952) p. 197.
15) A. Granato and K. Lücke: J. App. Phys. **27** (1956) 583, 789.
K. Lücke and A. Granato: *Dislocations and Mechanical Properties of Crystals* (John Wiley and Sons, Inc., New York, 1957) p. 425.
16) J. Weertman: J. App. Phys. **26** (1955) 202.

JOURNAL OF THE PHYSICAL SOCIETY OF JAPAN Vol. 13, No. 10, OCTOBER, 1958

Scattering of Electrons by Carbon Films

By Yoshihiro KAMIYA

Physical Institute, Nagoya University, Nagoya, Japan

(Received April 2, 1958)

Intensity distribution of electrons scattered by carbon films was measured by the photographic method using a sector camera. The absolute intensity was obtained by the use of an intensity scale. The angular range of the measurement was $1.0\times10^{-2}\sim1.2\times10^{-1}$ rad., the thickness of films 350~4,400Å and the accelerating voltage 47 kv. Results of the measurement were in fair agreement with the theory of Lenz (Z. Naturforschg. 9a (1954), 185). For the detailed agreement, however, we must take a smaller atomic radius than that of Lenz and we must take into account the inter-atomic interference effect.

§ 1. Introduction

The contrast of electron microscope images is determined mainly by scattering of electrons in the specimen. Intensity distributions of scattered electrons were extensively studied in the field of the electron diffraction. This field, however, is mainly concerned with the single scattering for large angles. For an interpretation of electron microscope images, a knowledge of multiple scattering as well as of single scattering is required, particularly for small angles.

v. Borries[1] and Lenz[2] treated this problem theoretically. Lenz[2] calculated the intensity distribution for carbon, chromium and gold films of various thickness. Their theory assumes amorphous substances, *viz*, perfectly random arrangement of atom. The assumption is not satisfied for thin films of chromium and gold prepared by vacuum evaporation because they produce Debye-Scherrer rings.

Biberman *et al.*[3] measured the intensity distribution for a very thin chromium film. A more extensive experimental investigation of gold and collodion films was carried out by Leisegang[4]. To prove Lenz's theory by experiment, the use of carbon films are more appropriate than metal films because they are

amorphous. Carbon films also are convenient because they do not show charging-up like collodion films. Kempf and Lenz[5] measured the *relative* value of intensity distribution for thin carbon films, while the measurements of contrast for carbon films were carried out by Lippert[6] and Komoda[7]. In the present paper we describe our measurement of *absolute* value of scattering distribution for carbon films. The thickness was 350~4,400 Å and scattering angle $1.0\times10^{-2}\sim1.2\times10^{-1}$ rad.

§ 2. Experimentals

Carbon films were prepared by the method of vacuum evaporation developed by Bradley. A film was evaporated on glass, floated on water and scooped up on a copper plate having a hole 0.5~1.0 mmϕ. The thickness of films was estimated using the proportional relation between thickness and darkness[9]: darkness 1.0 corresponds to thickness 1,000Å. The mass-thickness was derived from the thickness using the density of graphite. Specimens used in the experiment are listed in Table I. The thickness measurement becomes inaccurate for films thicker than 1,500Å. Therefore for specimen No. 4, the evaporation was carried out in two successive stages. By measuring the thickness for each stage, we determined the thickness of specimen No. 4. Specimen No. 5 was made by overlapping two films, each having the same thickness as that of specimen No. 4.

Table I. Thickness of specimens; p mass-thickness in unit "Aufhellungsdicke": 1.4×10^{-5}g/cm².

No. of specimen	Thickness	p
1	350 Å	0.55
2	700	1.1
3	1400	2.1
4	2200	3.5
5	4400	7.0

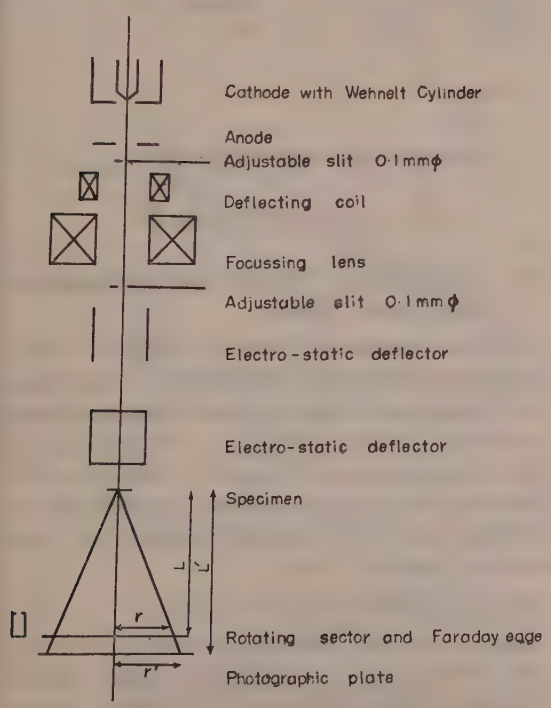

Fig. 1. Schematic drawing of sector camera.

The apparatus used for the intensity measurement was the electron diffraction camera provided with a rotating sector[10], designed specially for the intensity measurement[11] (Fig. 1). In our arrangement, the opening of the sector ϕ is $2\pi r/3.6$ rad., where r is the radius on the plane of the sector, the unit of r being cm. Scattering angle θ is given by $\theta=r/L=r'/L'$ where L is the speminen-to-sector distance, r' the radius on the photographic plate and L' the specimen-to-plate distance. By rotating the sector in front of the photographic plate during an exposure, the effective exposure time is made proportional to the scattering angle, resulting in a flat blackening of the photograph allowing an accurate intensity measurement.

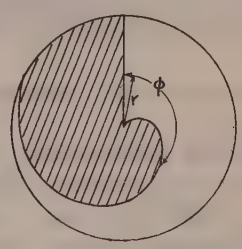

Fig. 2. Sector $\phi=2\pi r/3.6$ sad, radius in cm

The incident beam has a cross section of about 0.1 mmϕ at the specimen and an aperture angle of less than 2.0×10^{-4} rad. The whole beam passes through a specimen which is larger than 0.5 mmϕ. Under this condition, no charging-up effect was detectable for carbon films, while for Formvar films it was detected. Before and after exposure, the incident beam was received by a Faraday cage 10mm in length and 1.8 mm in diameter and the beam current was measured by a small current amplifier with sensitivity of 5×10^{-12}A.

The loss of the received charge by the secondary emission[12] was less than the experimental error. The exposure time was measured by counting the number of 50 cycle pulses which were produced by oscillating an electromagnetic tuning-fork. We discarded photographs when the current varied more than 10% during the exposure.

One of the most important factor in photographic intensity measurement is the characteristic of the used plate. The characteristic can be determined by two methods, *i.e.* by the successive method[11),13] and by the intensity scale method[14]. The former gives only the relative characteristic while the latter

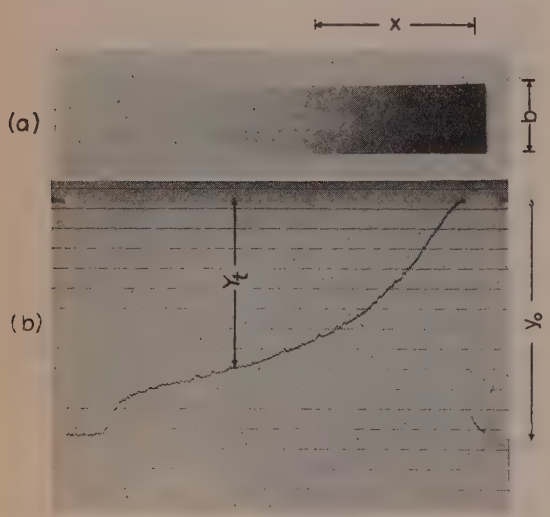

Fig. 3. (a) Intensity scale. (b) Microphotometry curve of (a).

gives the absolute characteristic which is indispensable for our purpose. Two pairs of electro-static deflectors were set in the camera perpendicular to each other (Fig. 1). On one of the pair, 15 kc saw-toothed voltage was applied and on the other the voltage damping exponentially with time constant 0.023 sec. was applied. Thus by the deflected beam, the intensity scale is made on the photographic plate (Fig. 3). The exposure on the intensity scale was estimated from the geometrical relation

$$Exp.=I_0\tau/bx \qquad (1)$$

where I_0 is the incident current, τ the time constant of damping voltage, b the width of intensity scale and x is indicated in Fig. 3. By means of micrometer, we measured darkness defined by

$$D=\log(Y_0/Y_t) \qquad (2)$$

where Y_0 is the intensity of incident light and Y_t the intensity of transmitted light. Fig. 4 is a typical example of the characteristic. Circles in the figure were obtained by the successive method. The circle at $D=0.43$ was normalized to the absolute measurement. Absolute characteristics agree with each other within the experimental error of 10% provided the emulsion number and the developing conditions are the same. Relative characteristics agree within 5% error when they are properly normalized. Scattered intensity scale were taken on the same plate. The plate used was "Fuji, Process Hard" and it was developed with D 76 d for 10 min. at 18°C and fixed with F-5 for 10 min. During the microphotometering, the plate was rotated around the incident spot so that the grain effect of the plate was eliminated.

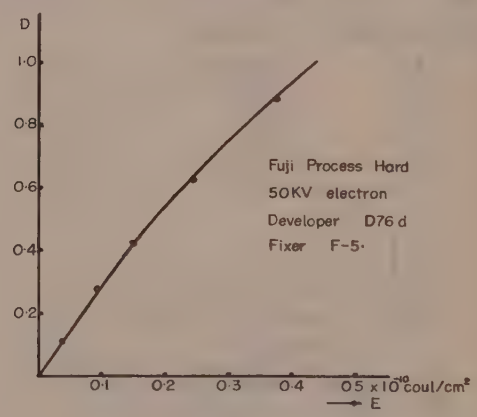

Fig. 4. Characteristic curve.

§ 3. Experimental Result and Comparison with Lenz's Theory

For each specimen given in Table I, photographs of scattering were taken. Darkness $D(r')$ obtained by the microphotometory was converted into exposure $E(r')$, making use of the characteristic of the plate. Intensity distribution $f(\theta)$, which is the probability of electrons scattered between θ and $\theta+d\theta$, was derived from $E(r')$ by

$$\theta f(\theta)=2\pi cE(r')L'/I_0t \qquad (3)$$

where I_0 is the incident current, t the exposure time and c a numerical factor which depends on the opening of the sector: $c=4.0$ for the sector used. The experiment was

carried out at 47 kv. Each result, however, was rewritten for 50 kv by $\theta_{50\text{kv}}=\theta_{47\text{kv}}\times(47/50)^{1/2}$ so that it can be compared with Lenz's theory. Rewritten results are given in Figs. 5a~e.

For the differental cross section of an atom Lenz assumed an analytical function

$$\frac{d\sigma}{d\Omega}=\frac{4Z}{q_H^2}\left[\frac{ZR^4}{(1+q^2R^2)^2}+\frac{1}{q^4}\left(1-\frac{1}{(1+q^2R^2)^2}\right)\right] \tag{4}$$

where Z is the atomic number, a_H Bohr radius, $q=4\pi\sin(\theta/2)/\lambda$ and R the atomic radius derived from the diamagnetic susceptibility. This formula includes inelastic scattering as well as elastic scattering. By applying the theory of multiple scattering[15] to Eq. (4), Lenz derived the formula for the intensity of scattering by a film:

$$f(\theta)=\int_0^\infty e^{2\pi N_L\gamma l\bar{\phi}(\chi)}J_0(\chi\theta)\chi\,d\chi \tag{5}$$

$$\bar{\phi}(\chi)=\int_0^\infty\frac{d\sigma}{d\Omega}[J_0(\chi\theta)-1]\theta\,d\theta \tag{5a}$$

where J_0 is Bessel function of zero order, N_L Loschmidt number and γl the mass-thickness of the film. He carried out numerical calculation at 50 kv for various thickness,

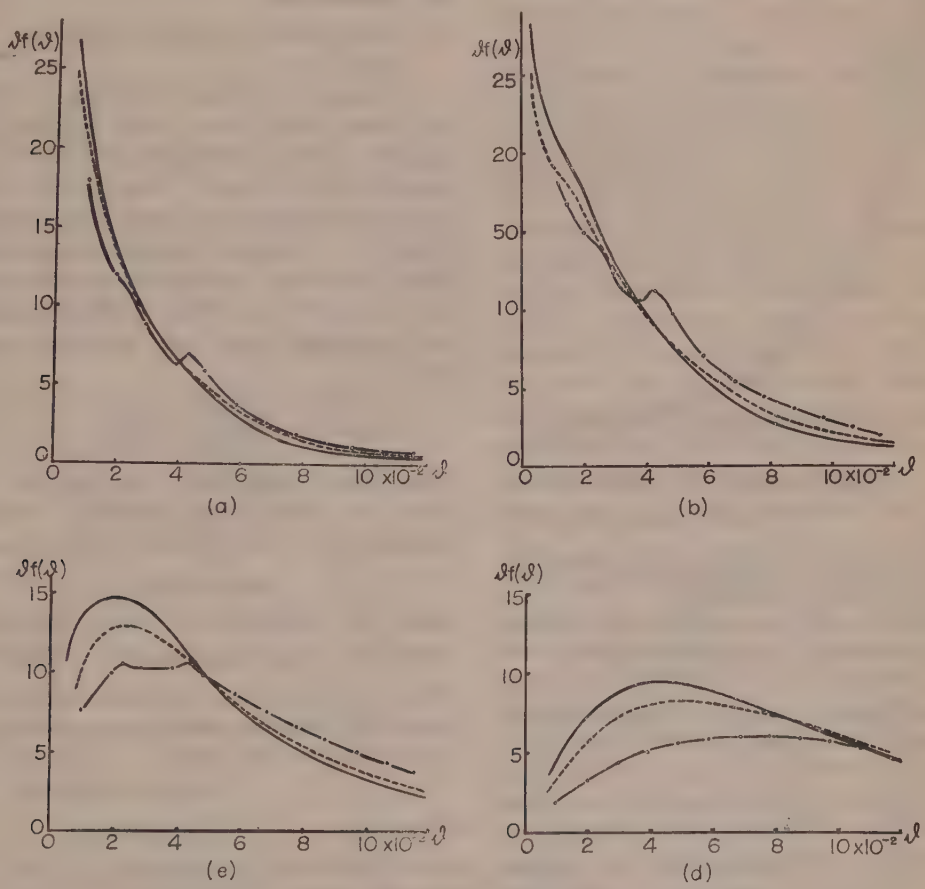

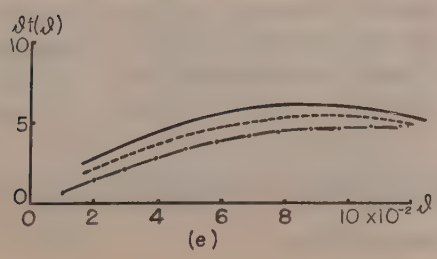

Fig. 5. Scattering intensity curves

—o— Experimental result.

——— Lenz theory with atomic radius 0.35 Å.

Lenz theory with atomic radius 0.30 Å.

Experiment	Theory
a) specimen No. 1	p=0.5
b) specimen No. 2	p=1.0
c) specimen No. 3	p=2.0
d) specimen No. 4	p=4.0
e) specimen No. 5	p=8.0

assuming the radius of carbon atom to be $R=0.35$Å. He gave his result in "Abb. 14" of his paper, taking the thickness as a parameter p which is given in the unit of "Aufhellungsdicke $\gamma l'$"

$$P=\frac{\gamma l}{\gamma l'} \qquad (6)$$
$$\gamma l'=\frac{M}{N_L \sigma_{el}{}^t}$$

where M is the atomic weight and $\sigma_{el}{}^t$ is the total cross section for the elastic scattering. Fig. 6 illustrates the effect of multiple scattering to be considerable even for film with thickness of only 320Å. Lenz's results are given by solid line curves in Figs. 5a~e. It must be emphasized that a fair agreement has been obtained for absolute values. At small angles, however, experimental curves are lower than theoretical ones. This trend is observed for all specimens. Small peaks which are observed at 2.5×10^{-2} and 4.5×10^{-2} rad. in Fig. 5 are attributed to diffraction halos. (Sec. 4 c).

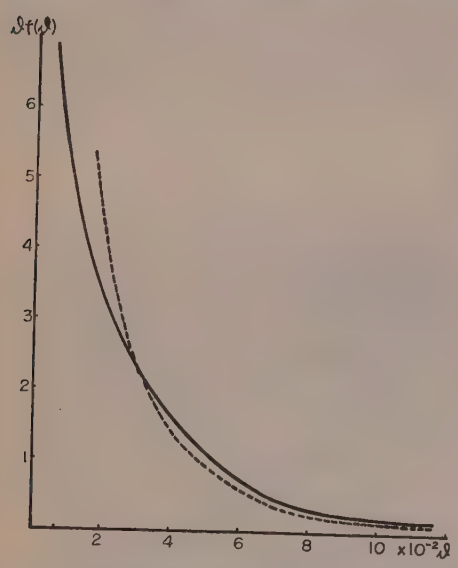

Fig. 6. Calculated intensity of scattering from carbon film Thickness: 320Å i.e. 7×10^{-6} g/cm² or p=0.5
Solid line curve: Direct calculation by Eq. (5), neglecting multiple scattering
Broken line curve: Calculated by Eq. (6) where multiple scattering is taken into account.

§ 4. Discussions

a) *Comparison with the result of Kempf and Lenz*

To compare our result with that of Kempf and Lenz[5], Figs. 5a~e were replotted taking $\log(f(\theta))$ as the ordinate and $\log\theta$ as the abscissa (Figs. 7a~e). We found that for small scattering angles, tangent $\eta=d(\log(f(\theta)))/d(\log\theta)$ is a constant independent of θ, which agrees with their findings for angles smaller than 1.0×10^{-3} rad. They plotted η against p and confirmed that the following relation holds:

$$\eta=\frac{4Z}{p}-2 \qquad (7)$$

Since their experiment was carried out at 70 Kv, our value of p obtained at 47 Kv was rewritten for 70 Kv through the relation

$$p_{70\mathrm{kv}}=0.8\,p_{47\mathrm{kv}} \qquad (8)$$

where the coefficient 0.8 was derived from "Abb. 2" of Lenz's paper[2]. Their result

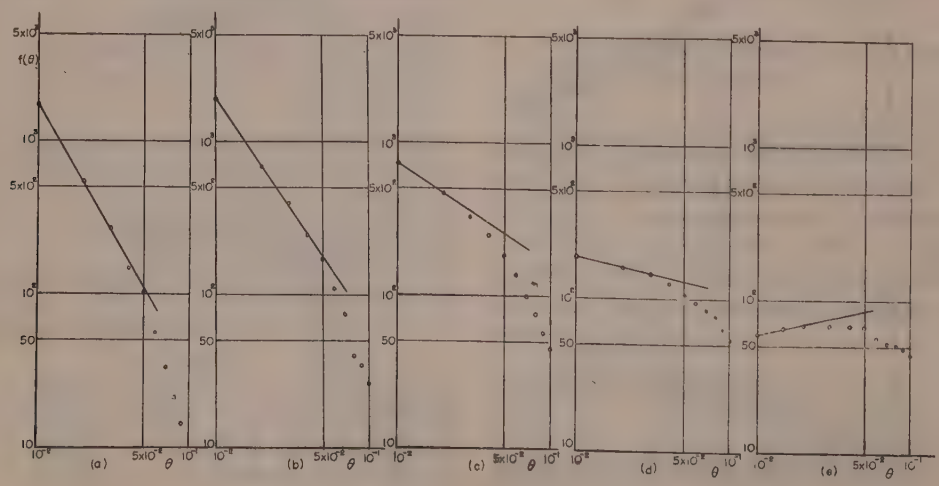

Fig. 7. Scattering intensity curves.

and ours are plotted in Fig. 8. Our result is also in agreement with relation (7) (Fig. 8).

In our experiment the absolute value of $f(\theta)$ was measured in the angular range which did not cover such small angles as those in the experiment of Kempf and Lenz. Since the values of η obtained in both experiments are in agreement, the relative value of $f(\theta)$ in their experiment can be normalized to our absolute value.

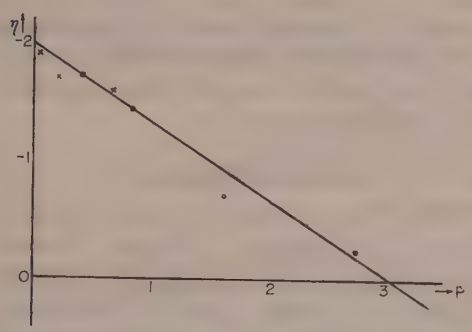

Fig. 8. Relation between gradient η and mass-thickness p.
× Kempf and Lenz
○ Present experiment

Table II. Scattering absorption coefficients.

Obj. Aperture (rad.)	Absorption coefficients (1/Å)		
	Komoda	Lenz	Present exp.
1.6×10^{-3}	2.2×10^{-3}	4.1×10^{-3}	
2.0	1.9	3.9	
5.5	1.6	2.8	
9.3	1.3	2.2	1.4×10^{-3}
24.0	0.74	1.0	0.9
49.0	0.36	0.36	0.36

b) *Comparison with the result of Komoda*

At various objective apertures, Komoda[7] measured the contrast of carbon films having a thickness 180 ~ 1,800 Å. Contrast is given by the empirical formula[16]

$$Contrast = 1 - e^{-\mu l} \qquad (9)$$

where l is the thickness of film and μ is the scattering absorption coefficient which depends on the objective aperture. In Table II, values of μ calculated from both Komoda's data and ours are given as well as those derived from Lenz's theory. Our experimental value is normalized to Komoda's value at objective aperture 4.9×10^{-2} rad.* A discrepancy is observed between Komoda's result and Lenz's theory at small objective apertures. This fact indicates that experimental intensity curves are lower than theoretical ones at small angles. This trend is also found in our experimental result. Although the discrepancy is not conspicuous in plots such as Fig. 7, it appears markedly in Fig. 5.

c) *Value of atomic radius*

Lenz adopted 0.35Å as the atomic radius of carbon. Since, however, there is variety in data of diamagnetic susceptibility, the corresponding atomic radius turns out to be between 0.29 and 0.40Å. For the diamond structure, the atomic radius turns out to be only 0.11Å. According to Kakinoki et al.,[17] the structure of evaporated carbon film is a combination of diamond-like structure and graphite-like structure. Thus we expect an atomic radius much smaller than Lenz's value. If we adopt a smaller atomic radius, agreement between theory and experiment is improved. In Figs. 5a~e broken line curves represent the calculated intensity assuming $R=0.3$Å. Agreement might be improved by assuming R smaller than 0.3Å. We did not carry out the calculation under such an assumption because the interference effect described in the next subsection may be larger than the effect of atomic radius.

d) *Interference effect*

Although evaporated carbon film is amorphous, atomic arrangement in the film is not perfectly at random. Thus the diffraction halos appear (Fig. 5). The effect of halos on image contrast is not considerable and may be neglected in the present discussion. We cannot, however, neglect the interference effect which is caused by non-overlapping of atoms; two atoms cannot overlap even though the atomic arrangement is otherwise at random. In Lenz's theory the effect of non-overlapping is neglected. By this effect the intensity of the elastic scattering at small angles is much reduced and vanishes at zero of the scattering angle[18]. Fig. 9 illustrates the effect. Since inelastic and multiple scatterings are neglected, Fig. 9 cannot be directly compared with experimental results. At any rate, the trend of the effect is in accordance with the experimental results in Figs. 5a~e, *i.e.* at small angles, experimental

* The numerical agreement between Komoda and Lenz's values at objective aperture 4.9×10^{-2} rad. is accidental.

curves are lower than Lenz's theory. Since this effect takes place for any sample, it must always be taken into account in calculating image contrast.

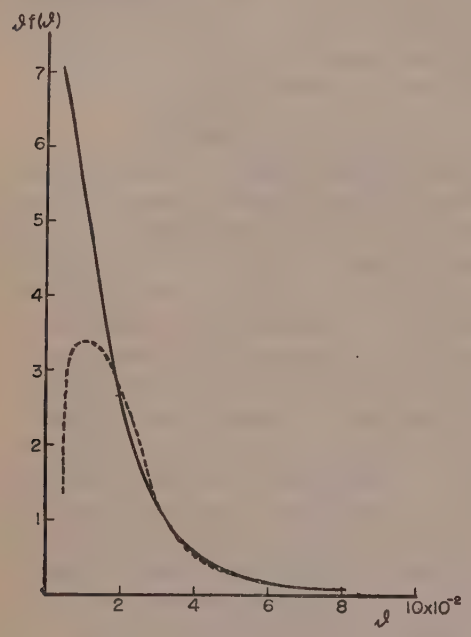

Fig. 9. Relative intensity distribution of elastic scattering by a thin film. (theory)
——— Interference effect, neglected.
Interference effect, taken into account.

e) *Inelastic scattering*

In the theory of scattering, atoms in solid films are usually assumed to be free. The theory, therefore, is a good approximation for inner shells which are effective for large angles. The bonding effect changes the state of outer shells. In Lenz's theory this effect is taken into account by using the atomic radius derived from diamagnetic susceptibility. However, for scattering at such small angles as 10^{-4} rad., the assumption of free atoms is not adequate. Broadly speaking, the scattering at the scattering angle θ is caused mainly by electrons which are spread in dimension $d=\lambda/\theta$. For $\theta=10^{-4}$ rad., d has the order of magnitude 400Å. Thus it is more reasonable to consider that the inelastic scattering at such small angles is caused by a free electron.

Recent investigations on energy losses from electrons revealed that in solids the important part of the inelastic scattering is caused by the excitation of plasma oscillations[19)-20)]. For this type of inelastic scattering we must have a mental picture of the scattering taking place within the whole electron system existing in the film. The inelastic scattering due to band-band transition is also caused by electrons extended in solid material. It should be noted that at small angles, the scattering distribution depends not alone on the substance but also on the shape which is well known in X-ray optics as "small angle scattering". In order to know the intensity distribution of scattered electron more exactly, it is necessary to measure the intensity of elastic and inelastic scatterings separately at small scattering angles.

Acknowledgement

The author expresses his deep appreciation to Prof. Ryozi Uyeda of Nagoya University for his advice and encouragement throughout this work and thanks to Mr. H. Morimoto for his kind guidance and indispensable help. Thanks are also due to Prof. K. Kinosita and Dr. Y. Doi for measuring the thickness of films and to Mr. T. Komoda for prepublication information on his results.

References

1) B. v. Borries: Z. Naturforschg. 4a (1949) 51.
2) F. Lenz: Z. Naturforschg. 9a (1954) 185.
3) L. M. Biberman, E. N. Wtorow, I. A. Knowner, N. G. Ssuschkin and B. M. Jaworskij: C. R. Akad. Sci. USSR **69** (1949) 519.
4) S. Leisegang: Z. f. Phys. **132** (1952) 183.
5) G. Kempf and F. Lenz: Electron Microscopy. Proceedings of the Stockholm Conference (1956) p. 67.
6) W. Lippert: Electron Microscopy. Proceedings of the Stockholm Conference (1956) p. 73.
7) T. Komoda: Electron-Microscopy **6** (1957) 10 (in Japanese)
8) D. E. Bradley: Brit. J. Appl. Phys. **5** (1954) 65.
9) E. Sugata: Electron-Microscopy **6** (1957) 653 (in Japanese).
10) P. P. Debye: Phys. Z. **40** (1939) 66.
11) T. Ino: J. Phys. Soc. Japan **8** (1953) 92.
12) M. E. Haine and P. A. Einstein: Brit. J. Appl. Phys. **3** (1952) 40.
13) J. Karle and I. L. Karle: J. Chem. Phys. **18** (1950) 963.
14) J. M. Cowley: Acta Cryst. **6** (1953) 516.
15) W. Bothe: Handbuch der Physik, Band XXII /2 (1933).
16) C. E. Hall: Introduction to Electron Microscopy Chapter 9.

17) J. Kakinoki, T. Ino, K. Katada and T. Hanawa: Acta Cryst. **10** (1957) 829.
18) R. W. James: The Optical Principles of the Diffraction of X-rays Chapter 9.
19) G. Möllenstedt: Optik **9** (1952) 473.
20) F. Leonhard: Z. Naturforschg. 9a (1954) 1019.
21) H. Watanabe: J. Phys. Soc. Japan **10** (1455) 321.
22) L. Marton: Rev. Mod. Phys. **28** (1956) 172.
23) D. Pines: Rev. Mod. Phys. **28** (1956) 184.

JOURNAL OF THE PHYSICAL SOCIETY OF JAPAN Vol. 13, No. 10, OCTOBER, 1958

The Crystal Structure of Germanium Selenide GeSe

By Atsushi OKAZAKI

Department of Physics, Faculty of Science, Kyusyu University, Fukuoka, Japan

(Received May 12, 1958)

The crystal structure of germanium selenide has been analysed by X-ray method. The structure is orthorhombic with the space group D_{2h}^{16}-*Pcmn*. The dimensions of the unit cell containing four chemical units, GeSe, are $a=4.38$, $b=3.82$ and $c=10.79$ Å. It follows from the positions of all atoms determined by means of the electron-density projection that the structure is of a distorted NaCl type isomorphous with SnS and SnSe. The distances Ge–Se are 2.54, 2.58, 3.30 and 3.39 Å.

§ 1. Introduction

The semiconducting properties and the crystal structures of some intermetallic compounds composed of elements of IV b and VI b groups in the periodic table have been studied in our laboratory. In connection with the investigation of the semiconducting properties of germanium selenide GeSe[1], the structure analysis of this compound was performed by X-ray method to determine the accurate atomic coordinates.

The result was compared with the structural data for the crystals of germanium sulphide GeS[2], stannous sulphide SnS[3] and stannous selenide SnSe[4]. The structure of GeS reported by Zachariasen, giving atomic coordinates inconsistent with those in the other isomorphous compounds, was criticized.

§ 2. Crystallographic and X-ray Data

Single crystals of GeSe were prepared by the following method: germanium (resistivity =a few Ω cm) and selenium (99.997%) in stoichiometric proportions were sealed in an evacuated silica tube. The mixture was heated up to about 1000°C and kept at the temperature for 50 hours (M.P. of GeSe is about 780°C). Then it was cooled gradually down to room temperature taking 50 hours, containing 12 hours for annealing at 600°C. Throughout these procedures temperature was controlled automatically.

The crystals have metallic lustre and are gray and fairly soft. They cleave along the (001) planes very remarkably.

X-ray diffraction data were obtained mainly from rotation and oscillation photographs taken with nickel-filtered Cu K radiation. Laue photographs and oscillation photographs taken with zirconium-filtered Mo K radiation were used auxiliarily. The preliminary results are shown in Table I.

Table I. Elementary X-ray data.

Laue symmetry	orthorhombic
Lattice constants	$a=4.38$, $b=3.82$, $c=10.79$ Å
Compositions	4 units of GeSe

The $hk0$ reflexions with $h+k$ odd and the $0kl$ with l odd are systematically absent. This extinction rule is satisfied in the orthorhombic system only in the cases of the space groups D_{2h}^{16}-*Pcmn* and C_{2v}^{9}-$Pc2_1n$, in which there are possible fourfold positions as follows:

for D_{2h}^{16}-$Pcmn$: $x, \frac{1}{4}, z;\ \bar{x}, \frac{3}{4}, \bar{z};$
$\frac{1}{2}+x, \frac{3}{4}, \frac{1}{2}-z;\ \frac{1}{2}-x, \frac{1}{4}, \frac{1}{2}+z$,

for C_{2v}^{9}-$Pc2_1n$: $x, y, z;\ \bar{x}, \frac{1}{2}+y, \bar{z};$
$\frac{1}{2}+x, \frac{1}{2}+y, \frac{1}{2}-z;\ \frac{1}{2}-x, y, \frac{1}{2}+z$.

It is evident that these are centro- and noncentro-symmetrical, respectively, and that if all the y parameters of the two kinds of atoms in C_{2v}^{9}-$Pc2_1n$ are equal to $\pm\frac{1}{4}$, these two space groups give the same results.

§ 3. Intensities

The integrated intensities of the $0kl$ and $h0l$ reflexions were recorded on oscillation multiple-film photographs. The integration was carried out only in the rotational direction by means of manual control. All the intensities were determined visually. The intensity ratio of the strongest reflexion to the weakest one was about 2000.

A few pieces of crystals cut from a large block of single crystal were used to get X-ray data. It was necessary to take care of the shape of the specimen since the linear absorption coefficient μ is 4.1×10^2 and $3.7\times10^2\,\mathrm{cm}^{-1}$ for Cu $K\alpha$ and Mo $K\alpha$ radiations, respectively. Due to the softness of the crystals, attempts to obtain specimens of thin cylindrical shape by grinding were unsuccessful. Therefore use had to be made of specimens having rectangular cross-section (about 0.01×0.1 mm) and length of about 1 mm parallel to the rotation axis prepared as follows. A slice with thickness of about 0.01 mm were carefully cleaved off along the (001) planes at liquid air temperature. After the determination of the crystallographic axes by Laue photographs, the slice was carefully cut along the a or b axis again at liquid air temperature.

Because the absorption effect is not significant except for several reflexions for which the paths of the X-ray beam are nearly parallel to the rectangular edge with length of about 0.1 mm, no corrections were made at the first stage of analysis.

The corrections for polarization and Lozentz factors were made in the usual way. The secondary extinction was not taken into account.

§ 4. Structure Determination

(i) *x and z parameters*

There is no difference between the atomic positions $4c$ of D_{2h}^{16} and $4a$ of C_{2v}^{9} in the (010) projection and both have centres of symmetry.

The Patterson synthesis on the (010), evaluated making use of Beevers and Lipson strips at 6° intervals, is shown in Fig. 1. The cross-section of the broad maximum at $x=a/2$ is shown in Fig. 2 and is resolved into two peaks A and B by the following way. The left half of the peak B indicated by a broken line is drawn symmetrically to the right half.

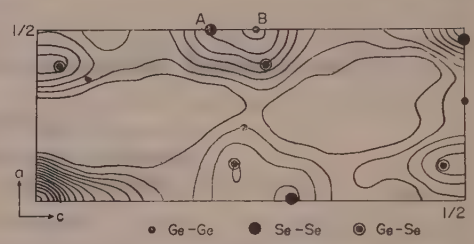

Fig. 1. Patterson projection on (010). Position of maxima obtained from the final atomic coordinates are indicated by the three kinds of marks

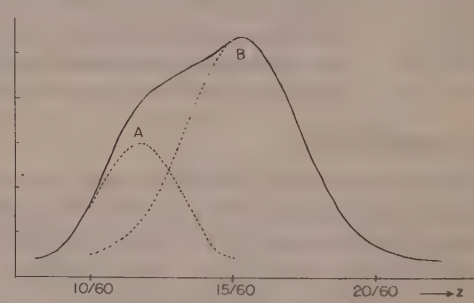

Fig. 2. Cross-section of the broad peak in Fig. 1 at $x=a/2$, which is resolved into two peaks A and B.

Table II. Preliminary atomic coordinates.

	x	z
Ge	0.092	0.151
Se	0.492	0.879

The peak A is obtained by subtracting the peak B from the broad peak. The maxima A and B were considered to be due to the Ge–Ge and Se–Se vectors, respectively. From these figures preliminary atomic coordinates are determined as shown in Table II.

With the help of the above coordinates the signs of the observed structure factors $F(h0l)$ were determined and the two-dimensional electron-density map on (010) was computed. From this map it was found that the z parameters of Ge and Se atoms had to be inter-

changed. This did not influence the signs of $F(h0l)$. After computing the second electron-density map the absorption correction was applied in a simple way. That is, the ratio of the observed unitary structure factors to

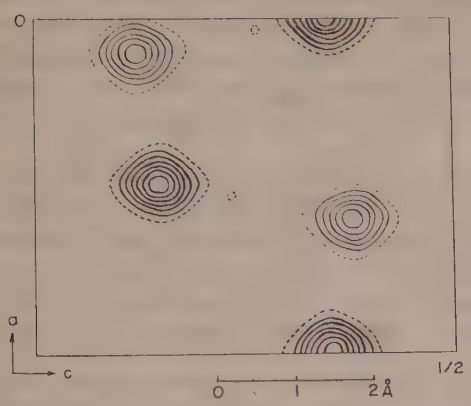

Fig. 3. The final (010) Fourier synthesis. Fine and bold contours indicate Ge and Se contours, respectively, and both are drawn at intervals of 10e. Å^{-2}. The zero contour is indicated by broken curves.

Table III. Final atomic coordinates.

	x	z
Ge	0.106 (0.104)	0.879 (0.878)
Se	0.503 (0.502)	0.148 (0.149)

Values in the brackets show the corresponding values obtained from the second electron-density map, that is, before the absorption correction.

the calculated ones was first evaluated as the function of the path length of X-ray beam in the specimen. Then the correction was made by dividing the observed $F(h0l)$ by the above ratios. Thereafter the computation of the electron-density map was repeated. In Fig. 3 the fourth electron-density map is shown, from which the final atomic coordinates were determined as shown in Table III.

In Table IV the observed structure factor F_o is compared with the calculated one F_c. F_c was calculated using atomic scattering factors of Ge and Se atoms given by Thomas and Umeda[5] with an isotropic temperature

Table IV. Observed and calculated structure factors.

$h0l$	$\|F_o\|/4$	$F_c/4$	$h0l$	$\|F_o\|/4$	$F_c/4$	$h0l$	$\|F_o\|/4$	$F_c/4$
002	8.0	− 7.4	200	38.9	28.3	307	14.6	−14.6
004	44.6	−45.6	201	18.3	13.6	308	0	− 1.3
006	9.9	12.9	202	8.3	− 6.1	309	0	1.6
008	17.6	21.3	203	9.9	14.1	3010	5.0	7.4
0010	8.0	− 9.6	204	17.4	−21.0	3011	6.0	7.0
0012	4.8	− 6.3	205	7.9	− 9.4	400	3.8	2.2
101	4.2	− 2.0	206	13.7	12.1	401	3.2	2.9
102	16.6	16.8	207	11.6	−11.4	402	6.0	− 3.1
103	11.2	12.0	208	9.0	8.4	403	1.8	3.6
104	0	1.2	209	5.3	5.4	404	0	− 0.1
105	9.8	−11.1	2010	10.3	−10.0	405	0	− 2.1
106	12.4	−11.3	2011	4.0	7.7	406	8.4	7.8
107	10.5	− 9.7	2012	0	0.3	407	3.4	− 3.5
108	0	− 1.5	301	20.3	−15.3	408	1.4	− 3.4
109	11.4	15.3	302	16.2	15.2	501	17.9	−11.4
1010	5.3	6.7	303	19.0	19.3	502	0	− 0.7
1011	4.4	3.6	304	0	0.8	503	14.0	13.2
1012	0	1.4	305	5.8	5.3	504	0	− 0.6
1013	11.8	−12.3	306	8.6	−11.7	505	3.4	6.2

factor $\exp[-B(\sin\theta/\lambda)^2]$ for $B=1.6$ Å^2. The observed structure factors were placed on an absolute scale by being multiplied by a scale factor. The temperature and scale factors were determined by plotting $\log(F_o/F_c)$ against $(\sin\theta/\lambda)^2$.

The reliability index $R=\Sigma||F_o|-|F_c||/\Sigma|F_o|$ is 20%. If the nonobservable reflexions are omitted, R becomes 18%. The total electron numbers at Ge and Se peaks in Fig. 3 were about 30 and 36, respectively, and the ratio of the heights of these peaks were also equal to the ratio 30:36. This suggests that about 2 electrons might be transferred from a neutral Ge atom to a neutral Se atom. The accuracy of this analysis, however, was not sufficient to discuss the electron transfer in detail, because the value of R was not sensitive to the slight change of atomic scattering factor due to the slight change of the total

electron numbers*.

(ii) *y parameters*

The intensity data of the $(0kl)$ reflexions were obtained using a specimen of shape similar to that of the $(h0l)$ specimen. Measurements and transformation to $F(0kl)$ of the $(0kl)$ intensities were carried out in the manners similar to those in the case of the $(h0l)$ reflexions. The observed values of $F(0kl)$ up to $(07l)$ reflexions are in good agreement with the calculated one, with y parameters of $\pm\frac{1}{4}$.

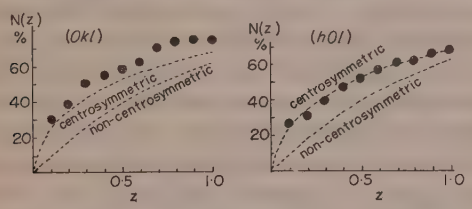

Fig. 4. Intensity distributions for the $(0kl)$ and the $(h0l)$ reflexions. The broken lines give the theoretical distributions.

Three statistical tests were applied to distinguish whether a symmetry centre was present or not. The results of the $N(z)$ test[6] are illustrated in Fig. 4. The observed distribution is raised due to a few extremely strong reflexions. Furthermore there are only 28 independent $(0kl)$ reflexions so that the results of the Wilson ratio test[7] and the variance test[8] deviated from the theoretical values. But the comparison with the results of these tests for 57 independent $(h0l)$ reflexions shows that the space group D_{2h}^{16}-*Pcmn* is more probable.

Thus the space group for GeSe was concluded to be D_{2h}^{16}-*Pcmn*.

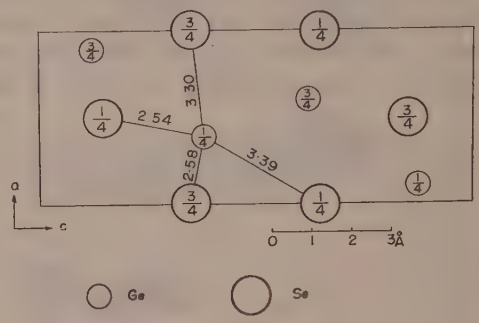

Fig. 5. Schematic (010) projection of GeSe. Fraction on each atom indicates its height along b from the level plane. Ge-Se distances are given in Å.

§ 5. Discussion

In Fig. 5 the schematic projection of the unit cell on (010) and the Ge–Se distances are shown. This structure is of a distorted NaCl type, isomorphous with SnS and SnSe. The Ge–Se distances (Å) are as follows:

2.54 (1), 2.58 (2), 3.30 (2), 3.39 (1).

Figures in the brackets show the number of the Ge–Se bonds. These six bonds correspond to those between the nearest neighbours in NaCl.

Table V. Lattice constants and atomic coordinates of GeS, GeSe, SnS and SnSe.

GeS	GeSe	SnS	SnSe
a=4.29 kX	a=4.38 Å	a=4.33 kX	a=4.46 Å
b=3.64	b=3.82	b=3.98	b=4.19
c=10.42	c=10.79	c=11.18	c=11.57
x z	x z	x z	x z
Ge 0.167* 0.875	Ge 0.106 0.879	Sn 0.115 0.882	Sn 0.103 0.882
S 0.111* 0.111	Se 0.503 0.148	S 0.478 0.150	Se 0.479 0.145

* These values obtained by Zachariasen seem to be not correct as described in § 5.

In Table V the results of the structure analyses of GeS[2], GeSe, SnS[3] and SnSe[4] are compared. In the table some of the crystallographic axes in the original papers are interchanged and the origins are displaced from those in the original papers. The atomic coordinates in the crystals of GeSe, SnS and SnSe correspond to each other. The coordinates in the crystal of GeS, however, are not consistent with them. Wyckoff[9] remarked the fact that very different parameters had been assigned to the atoms in GeS and SnS crystals in spite of the similarity of their cell size. The strangeness becomes more conspicuous by the above comparison of the four

* The change of the value of R was estimated to be less than 2% for a particular case where Ge and Se atoms were substituted by Zn and Kr atoms, respectively, in the calculation of F_c.

compounds. Thus the analysis of GeS[2] performed by Zachariasen was reexamined and a mistake was found in the determination of the x parameters. The calculated structure factors for GeS assuming the same parameters as GeSe are in better agreement with the intensity data. Consequently it seems that the atomic coordinates in GeS are similar to those in the other three compounds and all the four compounds belong to the $B29$ type.

The author wishes to express his hearty thanks to Prof. T. Okada for his kind guidance and also to Mr. S. Asanabe for preparation of GeSe single crystals. This investigation was partly supported by the Scientific Research Expenditure of the Ministry of Education.

References

1) S. Asanabe and A. Okazaki: Reported at the branch meeting of the Physical Society of Japan in 1957.
2) W. H. Zachariasen: Phys. Rev. **40** (1932) 917.
3) W. Hofmann: Z. Kristallogr. **92** (1935) 161.
4) A. Okazaki and I. Ueda: J. Phys. Soc. Japan **11** (1956) 470.
5) L. H. Thomas and K. Umeda: J. Chem. Phys. **26** (1957) 293.
6) E. R. Howells, D. C. Phillips and D. Rogers: Acta Cryst. **3** (1950) 210.
7) A. J. C. Wilson: Acta Cryst. **2** (1949) 318.
8) A. J. C. Wilson: Research, Lond. **4** (1951) 141.
9) R. W. G. Wyckoff: *Crystal Structures* (New York, 1948) Section 1.

JOURNAL OF THE PHYSICAL SOCIETY OF JAPAN Vol. 13, No. 10, OOTOBER, 1958

Anisotropy of Nuclear Magnetic Resonance due to Crystal Dislocations

By Eizo OTSUKA

Institute of Polytechnics, Osaka City University, Osaka

(Received June 9, 1958)

Using plastically deformed crystals of KI, the nuclear magnetic resonance of I^{127} has been observed. The broadened signals of I^{127} show distinct anisotropy as regards the direction of the external magnetic field. This anisotropy is interpreted to arise from the definite orientation of a crystal dislocation. The experimental results are analyzed in terms of the gradient-elastic tensor which has been introduced by Shulman-Wyluda-Anderson. It is concluded that densities of edge and screw dislocations are fairly well balanced and increase for a certain range almost linearly with degree of cold-working, in agreement with the previously reported result for KBr. Assuming the total dislocation density to be $10^9\,\mathrm{cm}^{-2}$ for ten percent deformation, we get $|C_{44}|\sim 8\times 10^4$ statvolts/dyne and its one-third for $|C_{11}|$. Comparison with the result for KBr shows that the amplification factor of eQq is greater than 50 for I^{127} in KI.

§ 1. Introduction

Nuclear magnetic resonance technique has proved to be an immensely convenient means to lay open the characteristics of the internal defects of solids. Of all these internal defects, a most interesting one is the crystal dislocation, which has a close relation with the plasticity of a solid. So far many both theoretical and experimental approaches have been made on this subject[1] and now nobody doubts the dislocation concept. There remain, however, still many unsolved problems and the need of more experimental works is strongly emphasized. This paper aims to offer a new material from the side of nuclear resonance studies.

In a previous investigation of KBr[2], we made a plain assumption that the electric field

gradients caused by the dislocations are simply proportional to the strains around them, and using the amplification factor of eQq, obtained from a different source of experiment, we estimated the order of magnitude densities of dislocations, and along with this described the unsuccessful attempt of getting directional effects of dislocation lines, in other words, the anisotropy of nuclear magnetic resonance due to dislocations. If such anisotropy is caught on the resonance line, it will provide a direct way to study the crystalline field around the dislocation. With this point in view, a further investigation has been made with single crystals of KI, taking the resonance lines of I^{127}, which has a larger eQq than Br^{79} or Br^{81} and hence a greater effect is expected.

Although the dislocation concept was first developed in the theory of plasticity, which deals with an ideal continuum, the direction of a dislocation line in an actual solid is restricted by the crystallographic configuration. In the case of alkali halides, the slip plane is always (110) with the slip direction being along [110]. Hence an edge dislocation line lies parallel to [100], while a screw dislocation has its axis along [110]. This definiteness of the crystallographic orientations of dislocations should reflect itself upon the curve shape of a nuclear resonance line, if the field gradients due to the dislocation have an appreciable interaction with the nuclear quadrupole moment of the nucleus in question.

A pioneer work was done by Watkins[3] about the effect of dislocations on the nuclear magnetic resonance. He considered merely the stress field of an edge dislocation and further simplified that the field gradients arise only from the shear strain σ_{xy}/G, which we also followed in the previous paper[2] in dealing with an edge dislocation, in view of the small shear modulus of KBr[4]. Watkins then calculates the angular distribution of dislocation lines and deduces the net frequency shift toward the lower frequency side in the case of the second order broadening, which conforms well with the experiment. This calculation, however, is based upon the assumption that the crystal is an ideal continuum and a dislocation line may have its axis in an arbitrary direction, which fundamentally differs from the actual situation. On account of this randomness of directions of dislocation lines, such a continuum model can predict no anisotropy of nuclear magnetic resonance line, and the net frequency shift is not affected by the direction of the applied magnetic field. If the crystallographic orientation of the dislocation line is taken into account, the net frequency shift goes in the opposite direction for $H_0//[100]$, so far as the shear strain of the edge dislocation is concerned. In order to explain the experimental result, we had therefore to introduce the effect of the screw dislocations, which, if invested with nearly equal density to that of edge dislocations, could well account for the observed frequency shift[2].

Further, the definite orientation of a dislocation line will evidently give rise to some kind of anisotropy of the resonance line, if the quadrupolar interaction is sufficiently strong. In the previous attempt with KBr[2], we wanted to get many unidirectional edge dislocations through the bending technique. The reason why this attempt ended in failure was ascribed to the insufficiency of the density of the produced edge dislocations. It is indeed a rather difficult task to produce so many pure edge dislocations free from the screw dislocation group. Moreover, the electric field around an edge dislocation is not so simple in reality, if a proper account is paid also on the stress components other than shear. The calculation would not go beyond a qualitative stage. And as long as we are satisfied with a qualitative result, the presence of screw dislocations would not fatally spoil our treatment, since the stress field and hence electric field around a screw dislocation is much simpler than that of an edge dislocation.

Recently Shulman, Wyluda and Anderson[5] performed an interesting NMR experiment on single crystals of InSb which were subject to axial elastic deformation and measured the eQq with In^{115} caused by this artificial distortion of the originally cubic lattice. In the course of analysis, they introduced the so-called gradient-elastic tensor which, under the assumption of linear response as usual, converts stress or strain to field gradient. With this new tensor concept, formal treatment of field gradients has got much easier and hence a more extensive study of crystal dislocations has become possible. Accordingly, much of this successful gradient-elastic tensor

concept has been utilized in the present work.

§ 2. Field Gradients of Dislocations

In a cubic crystal as alkali halide, there is originally no electric field gradient at the site of a given nucleus. If some imperfection is created within the crystal, however, there arises a deviation from the cubic symmetry and we have a finite field gradient. If the quadrupole moment of the nucleus is sufficiently large, the quadrupolar interaction cannot be treated by a simple first order perturbation and higher order perturbation should be taken into account. Plastically deformed KBr or KI belongs to the category which needs this higher order approximation, since the eQq at Br or I is so great. So far the electric field due to a dislocation line has been approximated to be an axially symmetric one and simply replaced by the elastic shear strain. In order to make an order of magnitude argument, such as dislocation density, it would be still useful to employ such a simplified model. Yet in dealing with a little more delicate problem like anisotropy of the resonance line, it is quite doubtful how such a rough treatment is lucky enough. Hence we shall follow a more orthodox way of approach. Thus the hypothesis of an axially symmetric field will no longer be retained and the stress field around a dislocation will be converted to the electric field according to the Shulman-Wyluda-Anderson's gradient-elastic tensor[6].

The energy eigenvalues of the nuclear Hamiltonian

$$\mathscr{H}=-\gamma\hbar\boldsymbol{I}\cdot\boldsymbol{H}+\boldsymbol{Q}\cdot\nabla\boldsymbol{E} \tag{1}$$

have been calculated by the method of perturbation to the third order and the result is as follows[6]:

$$\begin{aligned}
E_m=&-m\gamma\hbar H+A[3m^2-I(I+1)](\nabla E)_0\\
&-3A^2\frac{(\nabla E)_1(\nabla E)_{-1}}{\gamma\hbar H}m[4I(I+1)-1-8m^2]\\
&-3A^2\frac{(\nabla E)_2(\nabla E)_{-2}}{\gamma\hbar H}m[2I(I+1)-1-2m^2]\\
&-9A^3\frac{(\nabla E)_0(\nabla E)_1(\nabla E)_{-1}}{\gamma^2\hbar^2H^2}[I(I+1)+m^2\{12I(I+1)-7\}-20m^4]\\
&-9A^3\frac{(\nabla E)_0(\nabla E)_2(\nabla E)_{-2}}{\gamma^2\hbar^2H^2}[I^2(I+1)^2-2I(I+1)+m^2\{-6I(I+1)+7\}+5m^4]\\
&+\frac{3\sqrt{6}}{2}A^3\frac{(\nabla E)_1^2(\nabla E)_{-2}+(\nabla E)_{-1}^2(\nabla E)_2}{\gamma^2\hbar^2H^2}[2I^2(I+1)^2-3I(I+1)+m^2\{-24I(I+1)+15\}+30m^4]
\end{aligned} \tag{2}$$

where

$$\begin{aligned}
(\nabla E)_0&=\frac{1}{4}eq(3\cos^2\theta-1)+\frac{1}{4}\eta eq\sin^2\theta\cos 2\psi\\
(\nabla E)_{\pm1}&=\mp\frac{\sqrt{6}}{4}eq\sin\theta\cos\theta\, e^{\pm i\varphi}+\frac{1}{4\sqrt{6}}\eta eq\sin\theta\{(1\pm\cos\theta)e^{\pm i\varphi+2i\psi}-(1\mp\cos\theta)e^{\pm i\varphi+2i\psi}\}\\
(\nabla E)_{\pm2}&=\frac{\sqrt{6}}{8}eq\sin^2\theta e^{\pm 2i\varphi}+\frac{1}{8\sqrt{6}}\eta eq\{(1\pm\cos\theta)^2e^{\pm 2i\varphi+2i\psi}+(1\mp\cos\theta)^2e^{\pm 2i\varphi-2i\psi}\}
\end{aligned} \tag{3}$$

and

$$A=eQ/2I(2I-1)\,.$$

These are the results of the general treatment by Bersohn[7], and the asymmetry parameter η, which is defined by

$$\eta=\left(\frac{\partial E_x^*}{\partial x^*}-\frac{\partial E_y^*}{\partial y^*}\right)\Big/\frac{\partial E_z^*}{\partial z^*} \tag{4}$$

has been included. In (4) x^*, y^* and z^* are the principal axes of the field gradient tensor,

the largest component being along $0z^*$. θ, φ and ψ are the Eulerian angles of the principal axis system with respect to the coordinate system, the z-axis of which is the direction of the magnetic field.

Although the full expression (2) is rather lengthy, the first and third order terms contain only even powers of the magnetic quantum number m; hence these have no contribution to the broadening of the resonance line which arises from the transition $m=1/2$ to $m=-1/2$. Thus the energy difference between these two states becomes

$$E_{1/2\to-1/2}=h\nu_0+\frac{3}{\gamma\hbar H}\frac{2I+3}{4I^2(2I-1)}\left[(\nabla E)_1(\nabla E)_{-1}+\frac{1}{2}(\nabla E)_2(\nabla E)_{-2}\right], \tag{5}$$

where ν_0 is the Zeeman frequency. Taking the full expressions (3) for ∇E components into (5), we obtain

$$\begin{aligned}E_{1/2\to-1/2}=&h\nu_0+\frac{3}{\gamma\hbar H}\frac{2I+3}{4I^2(2I-1)}e^2q^2Q^2\\&\times\frac{1}{16}\Big[\sin^2\theta\Big\{-6\cos^2\theta+4\eta\cos 2\psi\cos^2\theta+\frac{\eta^2}{6}(2\sin^2\theta\cos 4\psi-2\cos^2\theta-2)\\&+\frac{1}{8}(6\sin^2\theta+4\eta\cos 2\psi(1+\cos^2\theta))\Big\}+\frac{\eta^2}{24}(\sin^4\theta\cos 4\psi+1+6\cos^2\theta+\cos^4\theta)\Big].\end{aligned} \tag{6}$$

Since we have taken the z-axis to be the direction of the applied magnetic field, the Eulerian angles are defined as follows: $\theta=\angle z0z^*$, φ the angle between the y-axis and the intersecting line of the xy-plane with the x^*y^*-plane and ψ between the y^*-axis and the same intersecting line. φ has disappeared in (6) merely because the choice of the x and y-axes are quite arbitrary within the plane normal to the magnetic field. For simplicity, we shall denote (6) in the following simplified form:

$$h(\nu-\nu_0)\propto q^2f(\theta,\psi)\,. \tag{7}$$

Our next step is to determine q, η, θ and ψ around a dislocation line. At present, a dislocation line is thought to be a closed loop and consists of edge and screw types being mixed-up. Then, there should be a certain amount of iodine nuclei, which undergo the composite stress field due to both type dislocations. Those iodines, if treated properly, would yield a complicated cross term in the expression of the net frequency shift. This dislocation loop, however, is expected to be nearly rectlinear rather than curvilinear and the two types of the dislocation are considered to be well separated. Hence the stress field around a given iodine nucleus may be approximated to be either screw or edge type one and the small portion of iodines which see the composite stress field will be neglected.

Shulman-Wyluda-Anderson's gradient-elastic tensor is composed of 36 components C_{ij}'s with properties very similar to the ordinary elastic constants in the stress-strain relation. The C_{ij}'s are not necessarily symmetric, but the requirement that the trace of the field gradient tensor sould vanish on account of the Laplace equation reduces the number of independent components. In particular, the case of a cubic crystal becomes exceedingly simple and we have only two independent components C_{11} and C_{44}, which appear in the stress-field gradient conversion formulae in the following manner:

$$\left.\begin{aligned}q_{XX}&=C_{11}[\sigma_{XX}-\tfrac{1}{2}(\sigma_{YY}+\sigma_{ZZ})]\,,\\q_{XY}&=C_{44}\sigma_{XY}\,.\end{aligned}\right\} \tag{8}$$

Here the q's are the field gradient tensor components and σ's are the stress tensor ones. The suffixes X, Y, Z refer to the cubic axes and the relations (8) are cyclic. Starting from (8), we shall investigate the field gradients resulting from the dislocations.

1) *Screw Dislocation*

On account of the simplicity of the stress field, this one is taken first. The only non-vanishing stress components of the screw dislocation are

$$\left.\begin{aligned}\sigma_{zx}&=-\frac{Gb}{2\pi}\frac{y}{x^2+y^2}\\\sigma_{yz}&=\frac{Gb}{2\pi}\frac{x}{x^2+y^2}\end{aligned}\right\} \tag{9}$$

where b is the magnitude of the Burgurs

vector and G is the shear modulus. The z-axis is taken along the dislocation line and we shall take the x-axis to be [100] direction, which is perpendicular to the dislocation line. Then, the xyz system is obtained by rotating the XYZ system by 45° around the X-axis. With this relation, the transformation of the tensor is carried out in quite an elementary manner and the field gradient tensor is represented in the xyz system as follows:

$$q_{xyz}=\begin{pmatrix} 0 & 0 & q_{zx} \\ 0 & 0 & q_{yz} \\ q_{zx} & q_{yz} & 0 \end{pmatrix} \tag{10}$$

where

$$\left.\begin{aligned} q_{zx}&=C_{44}\sigma_{zx}\,, \\ q_{yz}&=\tfrac{3}{2}C_{11}\sigma_{yz}\,. \end{aligned}\right\} \tag{11}$$

Next solving the usual eigenvalue equation given in the Appendix, we obtain the q tensor with respect to the $x^*y^*z^*$ system:

$$q_{x^*y^*z^*}=\begin{pmatrix} -\sqrt{q_{yz}^2+q_{zx}^2} & 0 & 0 \\ 0 & 0 & 0 \\ 0 & 0 & \sqrt{q_{yz}^2+q_{zx}^2} \end{pmatrix}. \tag{12}$$

It is seen from (12) that the asymmetry parameter defined by (4) is constant and has the value -1. The directions of the principal axes $x^*y^*z^*$ are derived in the Appendix and it is found that one of them always lies in the xy-plane, while the other two have the slope of 45° to this plane. We have chosen the first one to be the y^*-axis and the latters to be the z^* and x^*-axes, respectively. It is immaterial whether we choose the first one to be x^* or y^*; the former choice will give $\eta=1$ instead of $\eta=-1$, but the coefficient of η in (6) also changes its sign and the result is quite identical.

From (12) it is evident that q is given by the relation

$$q^2=q_{yz}^2+q_{zx}^2 \tag{13}$$

$$=C_{44}^2\sigma_{zx}^2+\frac{9}{4}C_{44}^2\sigma_{yz}^2 \tag{13a}$$

$$=\left(\frac{Gb}{2\pi}\right)^2\frac{1}{r^2}\left[C_{44}^2\sin^2\alpha+\frac{9}{4}C_{11}^2\cos^2\alpha\right] \tag{13b}$$

$$=\left(\frac{Gb}{2\pi}\right)^2\frac{C_{44}^2}{r^2}[1+\delta\cos^2\alpha] \tag{13c}$$

where

$$\delta=\frac{\frac{9}{4}C_{11}^2-C_{44}^2}{C_{44}^2} \tag{14}$$

and

$$\alpha=\tan^{-1}\frac{y}{x}\,. \tag{15}$$

δ defined by (14) is a measure of elastic anisotropy, the isotropic condition being $\delta=0$, or $9C_{11}^2-4C_{44}^2=0$, in which case q has no angular dependence. One of our task is to determine the value of δ.

$f(\theta,\psi)$ defined by (7) depends on the direction of the magnetic field. In the course of experiment, we have chosen three different directions of the magnetic field: With [001] being the direction of linear compression, *a*) H_0//[100], *b*) H_0//[010] and *c*) H_0//[110]. The difference between *a*) and *b*) is that in the former the field direction is parallel to the slip plane, while in the latter it makes an angle of 45° with it. Such descrimination requires that only a single pair of slip systems which are perpendicular to each other go into action upon the linear compression. As will be described in the next section, it was indeed possible to produce a slip of such fashion. Anyway, the Eulerian angles in each case are given as follows:

a) H_0//[100]

$$\left.\begin{aligned} \sin^2\theta&=\frac{1}{2}+\frac{1}{2}\frac{q_{yz}^2}{q_{yz}^2+q_{zx}^2}\,, \\ \sin^2\theta\cos 2\psi&=\frac{1}{2}-\frac{3}{2}\frac{q_{yz}^2}{q_{yz}^2+q_{zx}^2}\,, \end{aligned}\right\} \tag{16}$$

b) H_0//[010]

$$\left.\begin{aligned} \sin^2\theta&=\frac{3}{4}-\frac{1}{2}\frac{q_{yz}}{\sqrt{q_{xy}^2+q_{zx}^2}}-\frac{1}{4}\frac{q_{yz}^2}{q_{yz}^2+q_{zx}^2}\,, \\ \sin^2\theta\cos 2\psi&=-\frac{1}{4}-\frac{1}{2}\frac{q_{yz}}{\sqrt{q_{yz}^2+q_{zx}^2}}+\frac{3}{4}\frac{q_{yz}^2}{q_{yz}^2+q_{zx}^2}\,, \end{aligned}\right\} \tag{17}$$

c) $H_0//[110]$

$$\left.\begin{aligned}
\sin^2\theta &= \frac{5}{8}+\frac{1}{\sqrt{q_{yz}^2+q_{zx}^2}}\left(\frac{1}{2\sqrt{2}}q_{zx}-\frac{1}{2}q_{yz}\right)+\frac{1}{q_{yz}^2+q_{zx}^2}\left(\frac{1}{8}q_{yz}^2+\frac{1}{2\sqrt{2}}q_{yz}q_{zx}\right),\\
\sin^2\theta\cos 2\phi &= -\frac{3}{8}+\frac{1}{\sqrt{q_{yz}^2+q_{zx}^2}}\left(\frac{1}{4}q_{yz}-\frac{1}{2\sqrt{2}}q_{zx}\right)\\
&\quad+\frac{1}{q_{yz}^2+q_{zx}^2}\left(\frac{1}{8}q_{yz}^2-\frac{3}{2\sqrt{2}}q_{yz}q_{zx}+\frac{1}{2}q_{zx}^2\right)\\
&\quad+\frac{1}{(q_{yz}^2+q_{zx}^2)^{3/2}}\left(-\frac{1}{2}q_{yz}^3+\frac{1}{\sqrt{2}}q_{yz}^2q_{zx}-\frac{1}{2}q_{yz}q_{zx}^2+\frac{1}{\sqrt{2}}q_{zx}^3\right).
\end{aligned}\right\}\tag{18}$$

2) *Edge Dislocation*

The treatment is quite similar to the case of a screw dislocation. The stress field of an edge dislocation, however, is much more complicated than that of a screw dislocation; hence some approximation becomes unavoidable. The q tensor in the representation with respect to the dislocation axes is found to be

$$q_{xyz}=\begin{pmatrix} q_{xx} & q_{xy} & 0\\ q_{xy} & q_{yy} & 0\\ 0 & 0 & q_{zz}\end{pmatrix}\tag{19}$$

with

$$\left.\begin{aligned}
q_{xx}&=\frac{C_{11}}{2}\left(\frac{1}{2}-\nu\right)(\sigma_{xx}+\sigma_{yy})-\frac{C_{44}}{2}(\sigma_{yy}-\sigma_{xx}),\\
q_{yy}&=\frac{C_{11}}{2}\left(\frac{1}{2}-\nu\right)(\sigma_{xx}+\sigma_{yy})+\frac{C_{44}}{2}(\sigma_{yy}-\sigma_{xx}),\\
q_{xy}&=\frac{3}{2}C_{11}\sigma_{xy}, \qquad q_{zz}=C_{11}\left(\nu-\frac{1}{2}\right)(\sigma_{xx}+\sigma_{yy}),
\end{aligned}\right\}\tag{20}$$

and

$$\left.\begin{aligned}
\sigma_{xx}&=-D\frac{y(3x^2+y^2)}{(x^2+y^2)}, \qquad \sigma_{yy}=D\frac{y(x^2-y^2)}{(x^2+y^2)^2},\\
\sigma_{xy}&=D\frac{x(x^2-y^2)}{(x^2+y^2)^2}; \qquad D=Gb/2\pi(1-\nu)
\end{aligned}\right\}\tag{21}$$

ν being the Poisson ratio.

After the transformation to the $x^*y^*z^*$ system we have

$$q_{x^*y^*z^*}=\begin{pmatrix} -\frac{q_{zz}}{2}-\frac{1}{2}\sqrt{(q_{xx}-q_{yy})^2+4q_{xy}^2} & 0 & 0\\ 0 & q_{zz} & 0\\ 0 & 0 & -\frac{q_{zz}}{2}+\frac{1}{2}\sqrt{(q_{xx}-q_{yy})^2+4q_{xy}^2}\end{pmatrix}.\tag{22}$$

It is seen that on account of the presence of q_{zz}, the tensor is rather involved compared with that of a screw dislocation. One is relieved, however, if he observes that the mean square of q_{zz} is only $\frac{6}{7}C_{11}^2/(9C_{11}^2+4C_{44}^2)$ times that of $\sqrt{(q_{xx}-q_{yy})^2+4q_{xy}^2}$, that is, the former is less than a tenth of the latter. Hence we shall neglect q_{zz} in the subsequent treatment. If this is allowed, the tensor reduces to

$$q_{x^*y^*z^*} \sim \begin{pmatrix} -\frac{1}{2}\sqrt{(q_{xx}-q_{yy})^2+4q_{xy}^2} & 0 & 0 \\ 0 & 0 & 0 \\ 0 & 0 & \frac{1}{2}\sqrt{(q_{xx}-q_{yy})^2+4q_{xy}^2} \end{pmatrix}. \tag{23}$$

As shown in the Appendix, the two nonvanishing axes of the field gradient tensor in this approximation always lie in the xy-plane of the dislocation line and rotate as the angle $\alpha = \tan^{-1} y/x$ changes. The q value and the necessary Eulerian angles are found to be

$$q^2 = \frac{1}{4}[(q_{xx}-q_{yy})^2+4q_{xy}^2] \tag{24}$$

$$= \frac{D^2}{r^2}\left[C_{44}^2 \sin^2 2\alpha + \frac{9}{4}C_{11}^2 \cos^2 2\alpha\right]\cos^2\alpha \tag{24a}$$

$$= \frac{D^2}{r^2} C_{44}^2(1+\delta\cos^2 2\alpha)\cos^2\alpha \tag{24b}$$

and

a) $H_0//[100]$

$$\left.\begin{aligned} \sin^2\theta &= 1\,. \\ \sin^2\theta\cos 2\psi &= -1\,; \end{aligned}\right\} \tag{25}$$

b) $H_0//[010]$

$$\left.\begin{aligned} \sin^2\theta &= \frac{1}{2} - \frac{q_{xy}(q_{yy}-\lambda)}{q_{xy}^2+(q_{yy}-\lambda)^2}\,, \\ \sin^2\theta\cos 2\psi &= \frac{1}{2} - \frac{q_{xy}(q_{yy}-\lambda)}{q_{xy}^2+(q_{yy}-\lambda)^2}\,; \end{aligned}\right\} \tag{26}$$

c) $H_0//[110]$

$$\left.\begin{aligned} \sin^2\theta &= \frac{3}{4} - \frac{1}{2}\,\frac{q_{xy}(q_{yy}-\lambda)}{q_{xy}^2+(q_{yy}-\lambda)^2}\,, \\ \sin^2\theta\cos 2\psi &= -\frac{1}{2} - \frac{q_{xy}(q_{yy}-\lambda)}{q_{xy}^2+(q_{yy}-\lambda)^2}\,. \end{aligned}\right\} \tag{27}$$

where λ is the root of the eigenvalue equation given in the Appendix. The final step to get the net frequency shift is to take the average and add together the effects due to both type dislocations. This procedure, of course, assumes the insignificance of the composite stress field as mentioned before. The result in each case is

a) $H_0//[100]$

$$\langle\nu-\nu_0\rangle = B\left[\left(-\frac{2}{3}+\frac{2}{3}\delta\right)\pi a^2 c_s \ln\frac{1}{9\pi a^2 c_s} + \left(\frac{2}{3}+\frac{1}{3}\delta\right)\pi a^2 c_e \ln\frac{1}{9\pi a^2 c_e}\right], \tag{28}$$

b) $H_0//[010]$

$$\langle\nu-\nu_0\rangle = B\left[\left(-\frac{1}{6}+\frac{1}{6}\delta\right)\pi a^2 c_s \ln\frac{1}{9\pi a^2 c_s} + \left(-\frac{7}{12}+\frac{1}{12}\right)\pi a^2 c_e \ln\frac{1}{9\pi a^2 c_e}\right], \tag{29}$$

c) $H_0//[110]$

$$\langle\nu-\nu_0\rangle = B\left[\left(-\frac{1}{24}+\frac{1}{24}\delta\right)\pi a^2 c_s \ln\frac{1}{9\pi a^2 c_s} + \left(\frac{179}{768}+\frac{101}{384}\delta\right)\pi a^2 c_e \ln\frac{1}{9\pi a^2 c_e}\right]; \tag{30}$$

where

$$B = \frac{3}{400}\,\frac{1}{\pi^2}\,\frac{e^2Q^2}{h^2\nu_0}\,C_{44}^2 G^2\,. \tag{31}$$

As in the last paper[2], the radial integration has been carried out from $3a$ to $(\pi c)^{-1/2}$, where a is the lattice spacing. c_s and c_e are the densities of screw and edge dislocations, respectively. In view of the approximation made in dealing with edge dislocations, the Poisson ratio which has the value of $\sim 1/7$ has been neglected compared with unity. These expressions for three different angles of the applied magnetic field clearly indicate the possibility of the anisotropy of the nuclear magnetic resonance, which is to be demonstrated in the fourth section.

§ 3. Experimental Procedures

The measuring equipments for the resonance experiment are almost the same as reported in the previous papers,[2),7)] except for the use of a Sumitomo-made permanent magnet. This magnet has poles of 13 cm in diameter and 4 cm in gap. The produced magnetic field is 4150 gauss at the center of the gap. The sweep of the magnetic field was made by changing the current through the auxilliary coils with a motor-driven slide rheostat.

The specimens of KI were produced by the Kyropoulos method from the melt of commercial reagent branded as "of special degree." Using the platinum crucible, crystallization was twice repeated in order to raise purity of the produced crystals. These grown crystals were then annealed at 30°C below the melting point for 24 to 48 hours by means of a potentiometric temperature-adjusting programmer and then cooled down to room temperature by the rate of 5°C per hour.

The method of plastic deformation was limited to a linear compression along one of the cubic axes. The oil-compressing weight-tester of the Civil Engineering Department was used in order to produce the deformed crystals of any desired degree of deformation, ranging from ten to twenty percent, which are most suitable for the present purpose.

Some of the crystals were so deformed that only a single pair of slip systems which are perpendicular to each other went into motion upon the compression. This queer way of slip was recognized by examining the resultant shape of the deformed crystal. In general the rectangular cleaved crystal is swollen to its all four side directions upon deformation. By a method with some knack, however, only a pair of opposite side planes get swollen, indicating that the slip has occurred only two-fold. This situation is schematically shown in Fig. 1, in which it is assumed that the direction of linear compression is along [001]. Such a slip is easily achieved when the cross-sectional edge lengths of the cleaved crystal are different by a factor of more than two. Yet in the case of a crystal having a square cross section, the achievement of such slipping is rather fortuitous and critically depends on the initial conditions of the stress application.

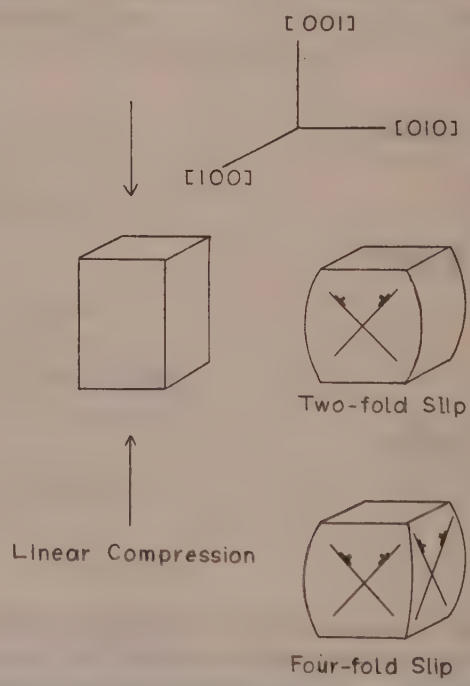

Fig. 1. The ways of slip after linear compression along one of the cubic axes. Two- and four-fold slips are indicated in the figures of the resultant deformed crystals.

In order to study the anisotropy of the resonance line, we prepared two such specimens with two-fold slip, one having a square cross section and the other consisting of six small pieces with rectangular cross sections. The degree of deformation for these crystals were around fourteen percent.

Except for some test experiment in the liquid air temperature, every measurement was carried out in the room temperature at the sacrifice of signal-to-noise ratio, since the specimens, especially heavily cold-worked ones,

got easily cracked upon soaking into the liquid air, however carefully we did it.

§ 4. Experimental Results and Analyses

Owing to the large eQq, the resonance line promptly broadens upon plastic deformation. Under the usage of a relatively low magnetic field, this effect is more pronounced, since the frequency shift and hence the broadening is inversely proportional to the applied field strength in the case of the second order perturbation. Even the resonance line of an undeformed crystal has a slight asymmetry, indicating that the defects have not completely been removed. This slight asymmetry, however, is next to independent of the direction of the magnetic field and hence is expected to arise partly from point defects such as impurities or vacancies or their clusters. If the magnetic field were somewhat raised, say to 6,000 gauss, this asymmetry would almost completely escape one's notice.

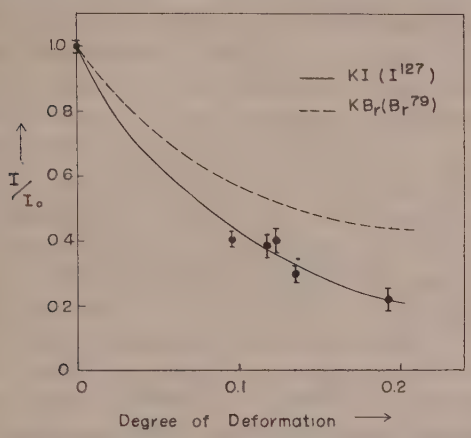

Fig. 2. Reduction of peak intensity of the resonance absorption curves upon ths linear compression. A similar result with KBr under a lower magnetic field of 3,600 gauss is indicated by the dotted line.

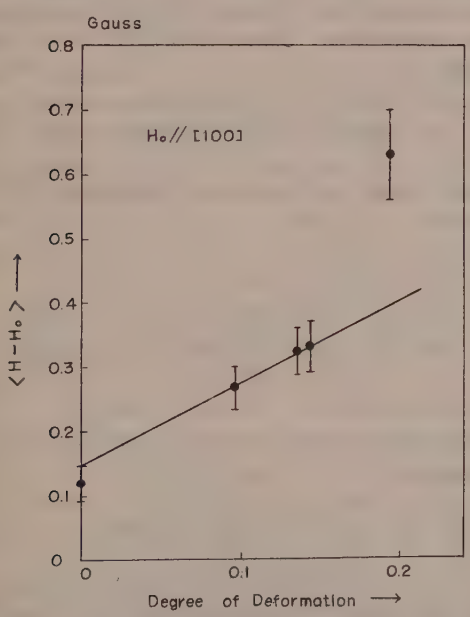

Fig. 3. The first moments of the resonance absorption curves in the case of H_0// [100]. Those crystals used were with four-fold slips as indicated in Fig. 1.

The intensity reduction of the resonance line against the degree of deformation is shown in Fig. 2, and in Fig. 3 are plotted the observed first moments (asymmetry) of the resonance lines for H_0//[100] with the crystals which underwent the ordinary four-fold slip. Since the latter is a linear function of the dislocation density,* the straight line

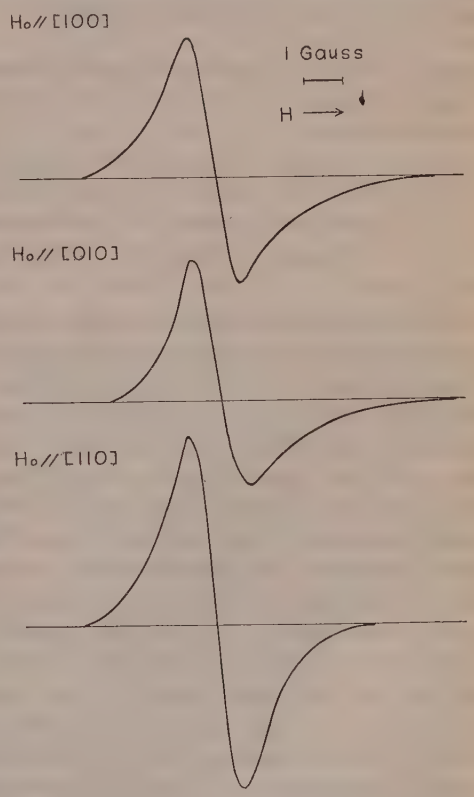

Fig. 4. Anisotropy of the resonance lines for a deformed crystal which underwent a two-fold slip. The directions of the magnetic field are as specified in Fig. 1.

* The logarithmic factors are considered to be constant.

drawn in the figure indicates that the dislocation density increases linearly with the degree of plastic deformation in the range of 10 to 15 percent. This is in esssential agreement with the conclusion of the previous paper[2]. The datum on the heaviest deformed specimen may not be looked upon with much weight, since the smaller sample size and poor signal-to-noise ratio owing to a large broadening considerably obscured the evaluation of the first moment.

By the specimens with two-fold slip, we see a conspicuous anisotropy characteristic of the reasonance line shape as shown in Fig. 4. If we specify the directions of the magnetic field as defined in § 2, the degree of asymmetry is greatest for $H_0//[010]$ and smallest for $H_0//[110]$. The results of the first moment evaluations for the two specimens are listed in the Table I. The sample I is that with square cross section and the other is a glued pack of six small rectangular slices.

Table I. The first moments of the resonance lines for the deformed crystals with two-fold slip (in units of gauss).

Sample	$H_0//[100]$	$H_0//[010]$	$H_0//[110]$
I	0.30 ± 0.02	0.38 ± 0.04	0.11 ± 0.04
II	0.31 ± 0.02	0.41 ± 0.03	0.13 ± 0.03

If we handle these figures with the formulae (28), (29) and (30), we shall get the values of δ and the ratio of the dislocation densities of two types. We should, however, not take the figures in Table I at their face values, since the specimens already had a slight initial asymmetry before plastic deformation. This initial asymmetry was sensibly constant for each undeformed crystal and within experimental error equal for $H_0//[100]$ and $H_0//[110]$, having the value of (0.12 ± 0.03) gauss. If we subtract this from the figures in Table I, we get the pure effect caused by the plastic deformation. Owing to the relatively large errors, which are inherent in the measurement of the first moment, such subtraction is rather arbitrary and might be regarded with some doubt. Especially, with $H_0//[110]$ the result of such subtraction will be quite meaningless. We should be more sensible by stating that for $H_0//[110]$ the resonance line has no asymmentry so long as the effect of the plastic deformation is concerned. This situation was scanned also for other deformed crystals which rather underwent the four-fold slip and the result is given in Fig. 5. In contrast with $H_0//[100]$, in which asymmetry increases with increasing degree of deformation, any heavy amount of cold-working seems not to affect the asymmetry characteristic of the resonance line more than its initial stage for $H_0//[110]$.

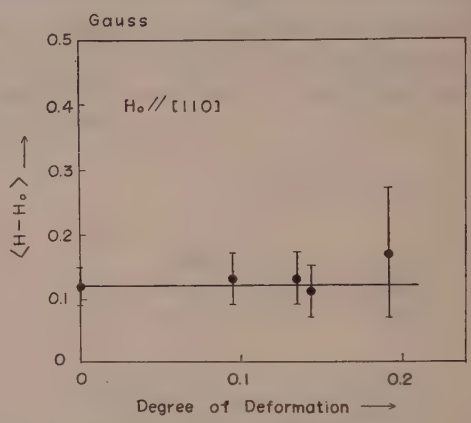

Fig. 5. The first moments of the resonance absorption curves in the case of $H_0//[110]$. The crystals are the same as in Fig. 3.

Hence we may in a rough sense equate (30) to zero. For the other two directions, the above-mentioned subtraction should be allowed with some ease. When it is done, the ratios of the first moments of the resonance lines for $H_0//[100]$ to $H_0//[010]$ become 0.69 and 0.65 for samples I and II, respectively. For brevity, we substitude 0.67, their mean, to both. Then, by connecting (28) with (29), we have

$$\left(-\frac{2}{3}+\frac{2}{3}\delta\right)p+\frac{2}{3}+\frac{1}{3}\delta$$
$$=0.67\left[\left(-\frac{1}{6}+\frac{1}{6}\delta\right)p+\left(-\frac{7}{12}+\frac{1}{12}\delta\right)\right], \tag{32}$$

while equating (30) to zero, we have another equation

$$\left(-\frac{1}{24}+\frac{1}{24}\delta\right)p+\frac{179}{768}+\frac{101}{364}\delta=0\,. \tag{33}$$

Here $p=c_s/c_e$, and the logarithmic factors have been removed out being regarded as constants. Solving these simultaneous equations, we obtain $p=0.88\sim0.9$ and $\delta=-0.76$. It is seen that the densities of the two dislocation types are essentially of the same order of magnitude

and the above value of δ yields $|C_{44}/C_{11}|\sim 3$.

§ 5. Discussion

It is reasonable that the dislocation density is divided nearly equally to screw and edge types. If the edge dislocations were predominant, (28) predicts that the sign of the first moment would be contrary to the experimental result for $H_0//[100]$. Inversely, one observes that neither screw dislocations can be overwhelming, since (29) should give one-fourth the first moment of (28) for screw dislocations, which again is contradictory to the experimental result. Thus, the dislocation densities are found to be quite well balanced.

The absolute values of C_{11} and C_{44} cannot be determined directly from the present experiment. They are, however, obtained if we give the densities of dislocations. In the previous paper we determined the dislocation densities of plastically deformed KBr[2]. The way of analysis used there is less precise and hence no such delicate analysis as obtaining anisotropy of the resonance line should be extracted from it; nevertheless we expect that a rather rough talk like an order of magnitude density estimation of dislocations would not be so far from the real one. If all the four slip systems have acted, the total asymmetry is given by

$$\langle\nu-\nu_0\rangle_{\text{total}} = \frac{-9+15\delta}{6400}\frac{1}{\pi^2}\frac{e^2Q^2}{h^2\nu_0}C_{44}^2G^2\pi a^2c\ln\frac{1}{9\pi a^2c} \tag{36}$$

where it is assumed $c_s=c_e=c/2$. Take a value from Fig. 2 for $\langle\nu-\nu_0\rangle_{\text{total}}$ and give a proper corresponding value of c; then we shall get C_{44}. For ten percent deformation $\langle\nu-\nu_0\rangle_{\text{total}}$ is -130 cps, while the corresponding dislocation density for KBr was $\sim 10^9\,\text{cm}^{-2}$ as reported in the last paper, which would be nearly the same for KI. We thus obtain $C_{44}=\pm(8.3\times 10^4)$ statvolts/dyne with $C_{11}=\pm(2.7\times 10^4)$ statvolts/dyne. If we put $c=10^8\,\text{cm}^{-2}$, they are multiplied by a factor of ~ 3, and for $c=10^{10}\,\text{cm}^{-2}$ reduced by the same factor. Those values given above are somewhat larger than those for In^{115} in InSb, which have been found to be $C_{11}=\pm(2.4\times 10^4)$ statvolts/dyne and $C_{44}=\mp(2.4\times 10^4)$ statvolts/dyne.

Shulman et al. conclude from their analysis that C_{11} and C_{44} should have opposite signs for InSb. Since our case is concerned only with the second order effect, these tensor components always appear as square and hence their signs cannot be determined. The derivation of C tensor does not predict that C_{11} and C_{44} should have opposite signs. Hence in our analyses both C values have been given a simple double sign.

Finally some comments should be made on the intensity reduction of the deformed crystals. Since we formerly performed a similar experiment on KBr, it is of interest to compare the effects on Br^{79} and I^{127}. In Fig. 2 is plotted also the result for Br^{79} with a dotted line. It seems that the effect is nearly 1.3 times greater with KI. The nuclear spin values for them, however, are different; i.e., $I=3/2$ for Br^{79} and $I=5/2$ for I^{127}. Furthermore, the experiment on KBr was performed under a lower magnetic field of 3,600 gauss. If these differences are taken into account, we see that the amplification factor of eQq of I^{127} is nearly twenty percent larger than that of Br^{79}. Therefore, if we take $\lambda\sim 40$ for the latter, as derived in the last paper, the amplification factor of I^{127} in KI should become $\lambda\sim 50$. It should further be noted, however, that in the case of KI, the intensity standard itself is not actually 1.0 as given in Fig. 2, but is already reduced a bit, and hence we should consider the actual effect must be somewhat larger with KI. Then, $\lambda\sim 50$ should be regarded only as the lower limit of the real value of λ. In the previous paper, determination of λ for KBr was achieved by the mixed crystal technique; namely, the studies of eQq due to the minority component NaBr, which was introduced into the mother crystal KBr, enabled us to estimate λ. Such a procedure might be followed also for KI, by growing another kind of mixed crystal, say KI–NaI, and studying a similar effect. For the intensity standard, we should, of course, require a more perfect crystal than that used in the present work. Or, at least we require a higher magnetic field. Using the value of λ thus determined, we might as well go along the line as described in the former paper in order to do a simplified dislocation analysis. The present treatment requires two parameters C_{11} and C_{44} and hence is rather complicated compared with the former one.

§ 6. Conclusion

The anisotropy of nuclear magnetic resonance due to crystal dislocations can be well accounted for, if we assume nearly equal densities for edge and screw dislocations and $\delta=-0.76$. Since $\delta=0$ is the isotropic condition, this values indicates that KI is highly anisotropic in elastic properties. This is supported by the fact that the anisotropy factor defined by $2c_{44}/(c_{11}-c_{12})$ is 0.37 and much smaller than unity which is the condition for elastic isotropy. Assuming the total dislocation density to be $\sim 10^9\,\mathrm{cm}^{-2}$ for a ten percent deformed crystal, we get $|C_{44}|\sim 8\times 10^4$ statvolts/dyne and its one-third for $|C_{11}|$.

§ 7. Acknowledgement

The author wishes to express his sincere thanks to Prof. H. Kawamura, under whose guidance this work has been completed. Comments and discussions on this subject made by Prof. T. Nagamiya and his laboratory members are highly appreciated. Particular thanks go to Mr. H. Okura in our laboratory for his kind cooperation in preparing single crystals of KI, which were most essential in the present work. The author also thanks Mr. Y. Fukui for his technical assistance in some parts of experiment. This work has partially been supported by the Scientific Research Grant of the Ministry of Education.

Appendix

The principal axes of the field gradient tensor around a screw dislocation are found by solving the determinantal equation

$$\begin{vmatrix} -\lambda & 0 & q_{zx} \\ 0 & -\lambda & q_{yz} \\ q_{zx} & q_{yz} & -\lambda \end{vmatrix}=0 \tag{A1}$$

for λ, and we get

$$\left.\begin{aligned} \lambda_1&=0\,, \\ \lambda_2&=+\sqrt{q_{yz}^2+q_{zx}^2}\,, \\ \lambda_3&=-\sqrt{q_{yz}^2+q_{zx}^2}\,. \end{aligned}\right\} \tag{A2}$$

Their direction cosines with respect to the axes of the dislocation, l_p, m_p, n_p, where p is the suffix of λ, are obtained through the linear relations:

$$\left.\begin{aligned} q_{zx}n_p&=\lambda_p l_p\,, \\ q_{yz}n_p&=\lambda_p m_p\,, \\ q_{zx}l_p+q_{yz}m_p&=\lambda_p n_p\,. \end{aligned}\right\} \tag{A3}$$

For $p=2$ and 3, we get

$$\left.\begin{aligned} l_p^2&=\frac{1}{2}\frac{q_{zx}^2}{q_{yz}^2+q_{zx}^2}\,, \\ m_p^2&=\frac{1}{2}\frac{q_{yz}^2}{q_{yz}^2+q_{zx}^2}\,, \\ n_p^2&=\frac{1}{2}\,. \end{aligned}\right\} \tag{A4}$$

and for $p=1$

$$\left.\begin{aligned} l_1^2&=\frac{q_{yz}^2}{q_{yz}^2+q_{zx}^2}\,, \\ m_1^2&=\frac{q_{zx}^2}{q_{yz}^2+q_{zx}^2}\,, \\ n_1^2&=0\,. \end{aligned}\right\} \tag{A5}$$

In the text we have allotted λ_2 to the z^*-axis, λ_3 to the x^*-axis and λ_1 to the y^*-axis.

A similar treatment is applied to the field gradient tensor around an edge dislocation. In this case we must solve the determinantal equation

$$\begin{vmatrix} q_{xx}-\lambda & q_{xy} & 0 \\ q_{xy} & q_{yy}-\lambda & 0 \\ 0 & 0 & q_{zz}-\lambda \end{vmatrix}=0\,. \tag{A6}$$

The homogeneous equations determining the direction cosines of the principal axes become

$$\left.\begin{aligned} q_{xx}l_p+q_{xy}m_p&=\lambda_p l_p\,, \\ q_{xy}l_p+q_{yy}m_p&=\lambda_p m_p\,, \\ q_{zz}n_p&=\lambda_p n_p\,; \end{aligned}\right\} \tag{A7}$$

where $p=1, 2, 3$ and

$$\left.\begin{aligned} \lambda_1&=q_{zz}\,, \\ \lambda_2&=-\frac{q_{zz}}{2}+\frac{1}{2}\sqrt{(q_{xx}-q_{yy})^2+4q_{xy}^2}\,, \\ \lambda_3&=-\frac{q_{zz}}{2}-\frac{1}{2}\sqrt{(q_{xx}-q_{yy})^2+4q_{xy}^2}\,. \end{aligned}\right\} \tag{A8}$$

The allocation of λ_p's to the $x^*y^*z^*$ axes is likewise to a screw dislocation.

From the third equation of (A7), we get

$$n_{2,3}=0\,; \tag{A9}$$

then we have for $p=2$ and 3:

$$\left.\begin{aligned} l_p^2&=\frac{q_{xy}^2}{(q_{xx}-\lambda_p)^2+q_{xy}^2}=\frac{(q_{yy}-\lambda_p)^2}{q_{xy}^2+(q_{yy}-\lambda_p)^2}\,, \\ m_p^2&=\frac{(q_{xx}-\lambda_p)^2}{(q_{xx}-\lambda_p)^2+q_{xy}^2}=\frac{q_{xy}^2}{q_{xy}^2+(q_{yy}-\lambda_p)^2}\,. \end{aligned}\right\} \tag{A10}$$

It should be emphasized that although we have neglected q_{zz} compared with $\sqrt{(q_{xx}-q_{yy})^2+4q_{xy}^2}$ in the course of analysis described in the text,

we must use exact λ_p values in (A10) in order to evaluate the direction consines. Only with this care being taken, we may calculate the average of $q^2 f(\theta, \psi)$.

References

1) A. H. Cottrell: *Dislocations and Plastic Flow in Crystals*, 1953 (Oxford: University Press).
2) E. Otsuka and H. Kawamura: Jour. Phys. Soc. Japan **12** (1957) 1071.
3) G. D. Watkins: Thesis, Harvard University 1952 (unpublished).
4) C. Kittel: *Introduction to Solid State Physics*; Second Edition, 1956, p. 93 (New York: John Wiley and Sons).
5) R. G. Shulman, B. J. Wyluda and P. W. Anderson: Phys. Rev. **107** (1957) 953.
6) R. Bersohn: Jour. Chem. Phys. **20** (1952) 1505.
7) H. Kawamura, E. Otsuka and K. Ishiwatari: Jour. Phys. Soc. Japan **11** (1956) 1064.

JOURNAL OF THE PHYSICAL SOCIETY OF JAPAN Vol. 13, No. 10, OCTOBER, 1958

Effect of Velocity Gradient on the Radial Distribution of Polymer Molecules in Dilute Solution

By Ryuzo KOYAMA

Electrical Communication Laboratory, Musashino-shi, Tokyo.

(Received June 11, 1958)

A differential equation which determines the time dependence of the radial distribution function of polymer molecules in dilute solution is derived. The equation is represented in a form of a diffusion equation.

For a case in which the solution is flowing with the constant velocity gradient, and the system is at a steady state, a calculation is carried out, adopting a Gaussian intermolecular potential between free draining chain polymer molecules. The result shows that the velocity gradient in solution causes the radial distribution function to be deformed into a non-spherical symmetry, and this deformation is increased with the increase of the velocity gradient and the molecular weight of polymer.

§ 1. Introduction

In the recent articles[1-3] we considered the interaction properties of polymer molecules in solution, and derived theoretical expressions for the mean intermolecular potential and the radial distribution function between two centers of gravity of two polymer molecules in dilute solutions. In these treatment the solutions were considered to be in thermodynamical equilibrium, and the mean intermolecular potential function and the radial distribution function obtained are spherically symmetric and of course do not depend on time. In the present article, such problems are considered from a more detailed situation, and the methods are extended to a more general case where the solutions are not always in thermodynamical equilibrium.

§ 2. Distribution of Molecular Pairs in Solution

In the following treatment we shall assume that the every point in our polymer solution is in the same external condition at the same moment. However, it is considered that if this assumption is not satisfied in a solution, the same discussion can be applied separately for each individual domain of different external condition of the solution.

For the simplicity of discussion, we shall neglect the internal configurations of the polymer molecules, and shall notice only the coordinates and the velocity of the center of gravity of each polymer melecule in the solution.

We denote the coordinates of the center of gravity of the i-th polymer molecule existing

in our polymer solution by $\boldsymbol{r}_i$, and define the pair vector $\boldsymbol{r}_{ij}$ which represents the relative coordinates of two polymer molecules i and j, as follows:

$$\boldsymbol{r}_{ij}=\boldsymbol{r}_j-\boldsymbol{r}_i\,, \qquad i\neq j \tag{2.1}$$

If n polymer molecules exist in a unit volume of the solution, the total number z of the possible pair vectors which can be taken from this unit volume is given by $z=n(n-1)$.

We also define a density distribution function of these pair vectors $g(\boldsymbol{r}, t)$ and represent the number of the pair vectors which fall in a small volume element $d\boldsymbol{r}$ situated at the position $\boldsymbol{r}$ at the time t by $zg(\boldsymbol{r}, t)d\boldsymbol{r}$. If all the possible pair vectors in this unit volume of solution are represented in a common space $(\boldsymbol{r})$ of three dimensions, we can consider an assembly of the representative points of the pair vectors in this space, and the number density of these points at the position $\boldsymbol{r}$ at the time t is given by $zg(\boldsymbol{r}, t)$.

As in our case every point in the solution is at the same external condition, the distribution function $g(\boldsymbol{r}, t)$ defined here is equivalent to the radial distribution function of polymer molecules in the solution at the same external condition. Therefore, as we stated in the previous section, when the polymer solution is in the thermodynamical equilibrium, and any external field does not exist, the distribution function $g(\boldsymbol{r}, t)$ is spherically symmetric about the origin and does not depend on the time. But, in more general case where the solution is not in equilibrium, the function $g(\boldsymbol{r}, t)$ would be supposed to have a more complicated feature and generally to depend on the time. We shall consider such a problem in this work.

A solute polymer molecule in solution is moving under complex exertion of the various intermolecular forces of the solvent and the other solute molecules surrounding it, and its instantaneous acceleration or velocity is generally determined by all the coordinates of these molecules. However, in our treatment, following an ordinary theoretical method for dilute polymer solution, we shall suppose that our polymer solution is composed of a continuous medium of solvent and of the solute polymer molecules dispersed in this solvent medium.

Assuming such a theoretical model, we can decompose generally the molecular velocity of a solute polymer molecule into the following several components:

i) The component for the random thermal motion, which is considered to represent the random Brownian motion of an isolated solute molecule in the pure solvent of the same external conditions.

ii) The component caused by the intermolecular effects exerted by the other solute molecules and by other external forces. (In the present work, for the simplicity of discussion, we shall not consider any effects of external forces).

iii) The component due to the velocity of solvent medium.

When a single solute molecule is isolated in a pure solvent, the motion of this molecule is considered to be a certain isotropic random Brownian motions. But it is supposed that if another solute molecule is introduced into the system, the random motion of the former molecule is affected by the presence of the latter molecule, and certain components of velocity which depends on the relative coordinates of two molecules are added. Such components can be described as the effects of intermolecular interaction.

Generally the solute molecules interact according to the intermolecular force acting between them. As shown in the general statistical mechanics of solution, the possible microscopic configurations of the solution yield the average intermolecular force between the solute molecules in the solution, which is dependent on the relative coordinates of the two molecules. Besides this, we can consider another kind of intermolecular effect of solute molecules, which we may call the hydrodynamic interaction. Since the solvent medium is regarded as a viscous liquid, the relative motion of the solute molecule to the solvent causes the viscous motion in the surrounding solvent, and affects the motion of the other solute molecules. This intermolecular effect is dependent on the relative coordinates of two molecules and also on their velocities in the solvent. Therefore we may consider that even if the intermolecular force does not exist between the solute molecules, their thermal motions are usually affected by this effect.

However, according to ordinary discussions, these intermolecular effects are usually not

conspicuous excepting the case where the molecular separating is so small that the distance between the centers of gravity of two polymer molecules is comparable with the dimension of the molecules, and that the segments of the other molecule can contact with each other. As the solution becomes dilute, the mean intermolecular distance between neighbouring solute molecules becomes large, and so the average number of molecules which exert the conspicuous interaction effects on one solute molecule is decreased.

We shall here assume that our polymer solution is sufficiently diluted and that the whole intermolecular effects exerted on one polymer molecule from the surrounding molecules can be neglected except that exerted from its nearest neighbouring molecule, and also that if a solute molecule has not any neighbouring molecules in a certain distance, such a molecule can be described to be isolated.

Thus, more quantitatively, it is assumed that we can choose a certain distance, l, in our solution, which satisfies the following conditions:

i) The total intermolecular effects exerted on one solute molecule from the whole part of the solution which is at a distance of more than l from this molecule can be neglected or at least can be left out of account in our discussion.

ii) If a spherical surface having radius of l is supposed in our solution, the probability of finding more than three solute molecules in the interior of this spherical surface is negligibly small compared with that of finding two solute molecules in it.

On this assumption, we suppose a spherical surface, S, whose center is at the origin of the space $(\boldsymbol{r})$, and radius is l, then we can conclude that every point of the molecular pair involved in the interior of this surface is moving independently with each other. For the two molecules i and j corresponding to a vector $\boldsymbol{r}_{ij}$ in this domain are interacting with each other, but there is considered not to exist any other molecules exerting the conspicuous interactions on them, and so the motion of the vector $\boldsymbol{r}_{ij}$ is determined by itself and does not depend on the other vectors in the interiors of S, except on the inverse $\boldsymbol{r}_{ji}$. Thus, from this conclusions we can obtain the change of the distribution function $g(\boldsymbol{r}, t)$ in space $(\boldsymbol{r})$.

We shall consider the motion of a point of pair vector $\boldsymbol{r}_{ij}$ in the interior of the spherical surface S. We denote the friction constants of two molecules i and j by ζ_i and ζ_j respectively, and define the diffusion constants D_i and D_j of the respective molecules by the well known relations:

$$D_i\zeta_i = kT\,, \quad D_j\zeta_j = kT\,, \tag{2.2}$$

where T is the absolute temperature, and k is Boltzmann's constant. Since the two molecules i and j are interacting hydrodynamically, the constants ζ_i, ζ_j; D_j and D_j depend on the coordinates $\boldsymbol{r}_{ij}$ and are generally to be represented in the tensor forms, whose elements are functions of $\boldsymbol{r}_{ij} = \boldsymbol{r}$.

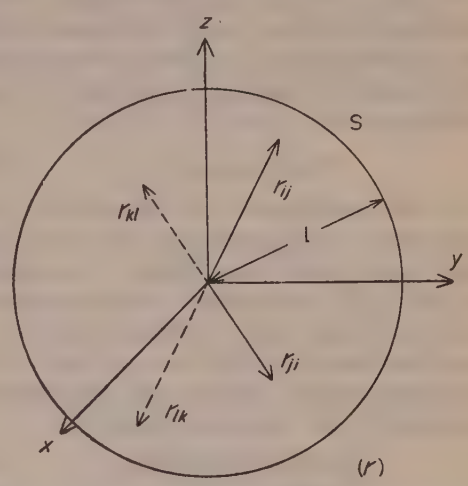

Fig. 1. Pair vector and spherical surface S in the space $(\boldsymbol{r})$.

The velocity of the point $\boldsymbol{r}_{ij}$ in space $(\boldsymbol{r})$ is given by the difference of those of two molecules i and j in the solution. So we can decompose the velocity of the point into several components in a similar manner as that in case of the solute molecule in the solution.

i) The components for the random thermal motion of two solute molecules i and j in solution induce a similar component of motion for the point $\boldsymbol{r}_{ij}$ in space $(\boldsymbol{r})$, which is given by the resultant of those of two molecules in the solution. Therefore the diffusion constant D_{ij} associated with the induced thermal motion of point $\boldsymbol{r}_{ij}$ in space $(\boldsymbol{r})$ is clearly given by the sum of those of two molecules,

$$D_{ij} = D_i + D_j\,. \tag{2.3}$$

From the conception of the diffusion constant and from the symmetry property of the configuration of two molecules, we can conclude that

$$\left.\begin{aligned} D_i = D_j = D_0(\boldsymbol{r}_{ij}) = D_0(\boldsymbol{r}), \\ D_{ij} = 2D_0(\boldsymbol{r}) \end{aligned}\right\} \tag{2.4}$$

where $\boldsymbol{r}$ denotes the coordinates of the point of pair vector in space $(\boldsymbol{r})$.

As has been often indicated[4], the Brownian motion of a solute particle in the solution can be replaced by a stochastic random flight motions, in which the element of the diffusion tensor is represented as proportional to the number of flights in unit time. This consideration leads us to the relations of Eq. (2.3) and (2.4), with the aid of a hydrodynamic consideration.

The points of pair vectors in space $(\boldsymbol{r})$ are distributed according to the distribution function $g(\boldsymbol{r}, t)$, and hence the flow of the density of points due to the thermal motion in space $(\boldsymbol{r})$ is given by

$$-2D_0(\boldsymbol{r}) \operatorname{grad} g(\boldsymbol{r}, t) . \tag{2.5}$$

ii) The components of velocities of two molecules i and j caused by their intermolecular force $f(\boldsymbol{r}_{ij})$ also induce a component of velocity for the motion of the point $\boldsymbol{r}_{ij}$, which is equal to the difference of those of two molecules. Similarly as in case of the diffusion constants, we can get the following relations for the friction constants,

$$\zeta_i = \zeta_j = \zeta_0(\boldsymbol{r}_{ij}) = \zeta_0(\boldsymbol{r}) \tag{2.6}$$

So employing the friction tensor $\zeta_0(\boldsymbol{r})$, the flow of the density of points in space $(\boldsymbol{r})$ caused by the intermolecular force $f(\boldsymbol{r})$ is written as

$$2\zeta_0(\boldsymbol{r})^{-1} f(\boldsymbol{r}) g(\boldsymbol{r}, t) . \tag{2.7}$$

iii) Also, the velocity gradient in the solvent medium causes a hydrodynamic relative velocity $v(\boldsymbol{r}, t)$ between two solute molecules which are separated by the distance $\boldsymbol{r}$. As in our case every point in the solution is at the same external condition at the same time, the velocity $v(\boldsymbol{r}, t)$ is a function of only the relative corrdinates of two molecules and of the time. The corresponding flow of the density of points in space $(\boldsymbol{r})$ due to the velocity gradient of solution can be written as

$$v(\boldsymbol{r}, t) g(\boldsymbol{r}, t) . \tag{2.8}$$

Thus the total flow of the density of the points, $u(\boldsymbol{r}, t)$ is represented by

$$\begin{aligned} v(\boldsymbol{r}, t) = & -2D_0(r) \operatorname{grad} g(\boldsymbol{r}, t) \\ & + 2\zeta_0(r)^{-1} f(r) g(\boldsymbol{r}, t) + v(\boldsymbol{r}, t) g(\boldsymbol{r}, t) \end{aligned} \tag{2.9}$$

and we obtain a differential equation for the distribution function $g(\boldsymbol{r}, t)$, in the form of the equation of continuity, as follows:

$$\begin{aligned} \operatorname{div} [& D_0(\boldsymbol{r}) \operatorname{grad} g(\boldsymbol{r}, t) - \zeta_0(\boldsymbol{r})^{-1} f(\boldsymbol{r}) g(\boldsymbol{r}, t) \\ & - 2^{-1} v(\boldsymbol{r}, t) g(\boldsymbol{r}, t)] = 2^{-1} \partial g(\boldsymbol{r}, t)/\partial t . \end{aligned} \tag{2.10}$$

In case that the intermolecular force $f(\boldsymbol{r})$ is derived from a potential function $W(\boldsymbol{r})$, that is

$$f(\boldsymbol{r}) = -\operatorname{grad} W(\boldsymbol{r}) , \tag{2.11}$$

Eq. (2.10) can be written in the form,

$$\begin{aligned} \operatorname{div} [& D_0(\boldsymbol{r}) \operatorname{grad} g(\boldsymbol{r}, t) + \zeta_0(r)^{-1} \operatorname{grad} W(\boldsymbol{r}) g(\boldsymbol{r}, t) \\ & - 2^{-1} v(\boldsymbol{r}, t) g(\boldsymbol{r}, t)] = 2^{-1} \partial g(\boldsymbol{r}, t)/\partial t . \end{aligned} \tag{2.12}$$

When the velocity gradient does not exist through the solution, and the system is at the equilibrium, we have

$$v(\boldsymbol{r}, t) = 0; \ \partial g(\boldsymbol{r}, t)/\partial t = 0 , \tag{2.13}$$

and also the total flow $u(\boldsymbol{r}, t)$ should vanish, i.e.

$$u(\boldsymbol{r}, t) = 0 \tag{2.14}$$

so from Eq. (2.9) or Eq. (2.12) we obtain the relation:

$$D_0(\boldsymbol{r}) \operatorname{grad} g(\boldsymbol{r}) + \zeta_0(\boldsymbol{r})^{-1} \operatorname{grad} W(\boldsymbol{r}) g(\boldsymbol{r}) = 0 \tag{2.15}$$

Employing the relation, $D_0(\boldsymbol{r})\zeta_0(\boldsymbol{r}) = kT$, of Eq. (2.2), we have a natural solution for this case,

$$g_0(\boldsymbol{r}) = \exp\{-W(\boldsymbol{r})/kT\} . \tag{2.16}$$

§ 3. A Simple Calculation for Free Draining Macromolecules

There can be considered various examples or applications of Eq. (2.10)[8]. We shall here treat a simple example, in which the solution is flowing with the constant velocity gradient, and the system is at the steady state. In this case the distribution function $g(\boldsymbol{r}, t)$ and the velocity function $v(\boldsymbol{r}, t)$ do not depend on the time, and Eq. (2.12) can be written as follows:

$$\begin{aligned} \operatorname{div} [& D_0(\boldsymbol{r}) \operatorname{grad} g(\boldsymbol{r}) + \zeta_0(\boldsymbol{r})^{-1} \operatorname{grad} W(\boldsymbol{r}) g(\boldsymbol{r}) \\ & - 2^{-1} v(\boldsymbol{r}) g(\boldsymbol{r})] = 0 . \end{aligned} \tag{3.1}$$

As previously stated, there exist generally two kinds of interaction effects between solute polymer molecules in solution, and it is considered that the properties of such molecular interaction effects are different for the individual solute-solvent system, and also they de-

pend on the physical states of the solution. Therefore it is convenient to discuss the various examples according to their individual characterized properties of the system.

In our present problem we shall assume that the effects of the hydrodynamic interaction of the solute molecules is very small compared with that of the static intermolecular potential, and shall examine the effect of the velocity gradient on the radial distribution of the polymer molecules in solution.

According to this assumption we shall put the molecular diffusion tensor $D_0(\boldsymbol{r})$ and the friction tensor $\zeta_0(\boldsymbol{r})$ to be constants which are independent of the coordinates $\boldsymbol{r}$.

The velocity function $v(\boldsymbol{r})$ is generally to be determined by the pure hydrodynamical calculation for the system of two molecules. But, as in our calculation we are not considering the hydrodynamic molecular interaction, here we also assume a so-called free draining molecule, which has been often adopted in the various theoretical treatment[5], that is, in which the streaming line of the solvent is assumed not to be disturbed by the presence of the solute molecules. Thus, denoting the velocity gradient by q, we put

$$\left.\begin{aligned} &v(\boldsymbol{r})=(qy,\ 0,\ 0); \\ &v_x=qy\ ,\quad v_y=v_z=0\ , \end{aligned}\right\} \tag{3.2}$$

where the coordinate axes are so chosen that the streaming line is parallel to the x-axis and the velocity gradient is in y-direction as shown in Fig. 2. This assumption directly gives us the relation:

$$\operatorname{div} v(\boldsymbol{r})=0 \tag{3.3}$$

We have also necessity of the knowledge of the intermolecular potential function $W(\boldsymbol{r})$ in our calculation. In the recent paper[2], we derived an expression of the mean intermolecular potential between chain polymer molecules, which is written in the form:

$$W(r)=kTXe^{-\alpha^{-2}r^2} \tag{3.4}$$

where X and α are constants depending upon the molecular weight of polymer and on the temperature. We shall adopt this form of the potential function $W(r)$ in the following calculation.

Next, we shall consider the equipotentital surface in space $(\boldsymbol{r})$, which is defined by the equation:

$$g(\boldsymbol{r})=\text{constant}\ . \tag{3.5}$$

This equation means that the distribution function $g(\boldsymbol{r})$ or the apparent intermolecular potential $-kT\log g(\boldsymbol{r})$ should assume a constant value on the equipotential surface. As is often repeated, when the solution has not the velocity gradient, and the system is at the thermodynamical equilibrium, the distribution function $g(\boldsymbol{r})$ depends only on the magnitude of the coordinates $\boldsymbol{r}$ as shown in Eq. (2.16), and hence the equipotential surface is clearly given as the spherical surface. Therefore, it is generally considered that when the velocity gradient exist in the solution, the equipotential surface would be deformed into the non-spherical symmetry, corresponding to the magnitude of the velocity gradient. If the differential equation (3.1) is integrated, the equipotential surface can be determined from the definition in Eq. (3.5). But, in the following discussions we shall not integrate the equation directly, but employing a suitable assumption for the equipotential surface, an approximate calculation shall be shown.

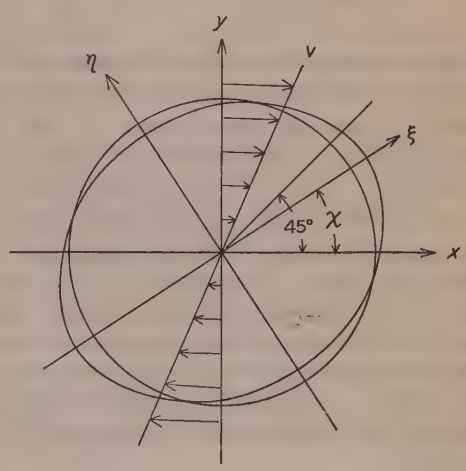

Fig. 2. Deformation of the equipotential surface by the velocity gradient.

From the symmetric property of our physical state of solution and a simple geometrical consideration, we shall here assume that the equipotential surface can be approximately represented by the ellipsoidal surface, and we write tne equation of tne equipotential surface as the following form:

$$(1-\lambda)\xi^2+(1-\mu)\eta^2+(1-\nu)\zeta^2=\text{constant}\ . \tag{3.6}$$

where the coordinate axes ξ, η and ζ are so chosen as to coincide with the principal axes of the ellipsoid. The parameters λ, μ and ν

are considered to be functions of the velocity gradient, and when the velocity gradient vanishes they should assume an equal value. Then, according to this assumption, and Eqs. (2.41) and (3.4), the distribution function $g(\boldsymbol{r})$ should be put as follows:

$$\left.\begin{aligned} g(\boldsymbol{r})&=\exp\{-Xe^{-\alpha^{-2}(r^2-\psi(r,q))}\}\,,\\ \psi(\boldsymbol{r},q)&=\lambda\xi^2+\mu\eta^2+\nu\zeta^2\,.\end{aligned}\right\}\qquad(3.7)$$

From the symmetricity of the physical condition of our solution we can conclude that one of the principal axis, ζ is coincident with the z axis of the original coordinate system. Thus, substituting Eq. (3.7) into Eq. (3.1), and comparing the terms of the constants and those of each second power of ξ, η and ζ respectively, the following relations are obtained.

$$\left.\begin{aligned} &4\lambda(7-2\lambda)-8X\lambda(1-\lambda)\\ &\quad-(1-\lambda)\alpha^2D_0^{-1}q\sin 2\chi=0\,,\\ &\mu=-\lambda\,,\\ &\nu=0\,,\\ &\tan^2\chi=\frac{1-\lambda}{1+\lambda}\,,\end{aligned}\right\}\qquad(3.8)$$

where χ denotes the angle between the flow direction x and the principal axis of the ellipsoid ξ, or between the direction of the velocity gradient y and another principal axis η as shown in Fig. 2. Thus, knowing the value of the quantity $\alpha^2D_0^{-1}q$, the parameters λ, μ and ν and the angle χ can be calculated from these equations. As is shown in Eq. (3.8), in case that the velocity gradient q is very small, and the deviation of the equipotential surface from the spherical surface is also very small, the angle χ is nearly equal to $\pi/4=45°$, and λ and μ are approximately represented by the formula:

$$\lambda=-\mu=\frac{\alpha^2D_0^{-1}q}{4(7-2X)}\,,\qquad(3.9)$$

As the velocity gradient q increases, λ and $-\mu$ are increased, and the angle χ is decreased from a value 45°.

From the above results the equipotential surface can be again written as the form:

$$(1-\lambda)\xi^2+(1+\lambda)\eta^2+\zeta^2=\text{constant}\,.\qquad(3.10)$$

The eccentricity of the ellipsoidal surface, e, is given by the next formula,

$$e=(\lambda/1+\lambda)^{1/2}\approx\lambda^{1/2}(1-\tfrac{1}{2}\lambda+\cdots)\,,\qquad(3.11)$$

and when $\lambda(=-\mu)$ is very small, this is written approximately as

$$e\approx 2^{-1}(7-2X)^{-1/2}\alpha D_0^{-1/2}q^{1/2}\,.\qquad(3.12)$$

According to our recent discussions[2,3] the quantity, kTX, represents the maximum or minimum value of the mean intermolecular potential, and for some polymer solutions[4] X assumes the values less than at most the order of unity, and also α^2 is proportional to the mean square end to end distance L of the polymer chain in the solution, as given by the relation:

$$\alpha^2=0.81\cdot 2/9\cdot L^2\approx(0.42L)^2\qquad(3.13)$$

From this Eq. (3.12) can be also written as

$$\begin{aligned} e&\approx 2^{-1}\cdot 0.42\cdot(7-2X)^{-1/2}LD_0^{-1/2}q^{1/2}\,,\\ &\approx 10^{-1}LD_0^{-1/2}q^{1/2}\,.\end{aligned}\qquad(3.12')$$

Several experimental results in ordinary polymer solutions show that L has the order of about 10^{-5} cm, and D_0^{-1} has the order of about 10^{-7} cm^2 sec^{-1}. So, according to Eq. (3.12′), in order that the eccentricity e attains to a value of the order of 10^{-1}, the velocity gradient q should have a value of the order of about 10^3, which is rather a high value as the velocity gradient. Therefore in ordinary order of the velocity gradient the non-spherical symmetricity of the radial distribution function should be small. But, usually L and D_0^{-1} increase with the molecular weight of polymer in the same solvent, and D_0^{-1} is considered to have larger value for more viscous solvent. Consequently it is considered that the non-spherical character of the radial distribution function increases with the molecular weight of polymer and with the viscosity of solvent, and moreover it may become more appreciable for greater value of the velocity gradient.

§ 4. Discussions

In our present discussions the internal freedom or configuration of polymer molecule is not taken into consideration, and we adopt the spherically symmetric intermolecular force between two polymer molecules, which depends only on the molecular distance and so acts along the line connecting the two molecular centers of gravity. However, it is considered that the polymer molecule consists usually of large number of molecular segments, and can take various configurations in the solution, and so in more detailed discussions their interaction property should be described by their total internal coordinates.

Also, when the solution has the velocity gradient, the solute polymer molecule performs a rotational motion as a whole about the axis perpendicular to the flow direction and the velocity gradient, in addition to its translational motion following the flow of solvent. This rotational motion may produce another component of intermolecular force which acts in the tangential direction of two molecules, as it were a rotational friction between two molecules.

Besides these, as we can see in the several theoretical treatments[6] for the flow birefringence or the viscosity of polymer solutions, the velocity gradient causes the statistical orientation for the solute particle having the non-spherically symmetric configuration, and moreover it may deform the internal configuration for the chain polymer molecule owing to the frictional force exerting on the molecular segments from the solvent. Consequently we can consider that such molecular orientation and the deformation effects also affect the intermolecular interaction between two polymer molecules, and deform the intermolecular potential function into the non-spherical symmetry.

However, such rotational or intramolecular effects are considerably small compared with the intramolecular effect, and they can be appreciable for very large velocity gradient, for it is supposed that the order of the intermolecular binding force is far greater than that of the intermolecular interaction, and also the internal diffusion of a polymer molecule is more rapid than that of the translation of the whole molecule. On such considerations the rotational and intramolecular effects are neglected in our calculation. But, it is considered that these effects may become more greater in case of the very large velocity gradient.

Moreover, in the calculation in section 3, we did not consider the hydrodynamic interaction between polymer molecules, and also adopted a model of the free-draining polymer molecule. In the recent various theoretical calculations[6,7], the hydrodynamic intermolecular interaction is often considered between molecular segments in a chain polymer molecule, and in order to explain the observed relations between molecular weight of polymer and the intrinsic viscosity of the solution, this effect has been utilized by some authors[7]. The hydrodynamic intramolecular interaction in a polymer molecule, as shown in these treatment, would perturb or deform the streaming lines of the solvent near the polymer molecules as well as in the inside of them, and thus the velocity function $v(\boldsymbol{r})$ would have more complicated form than that of Eq. (3.2). But, in our present calculations, taking account of the intermolecular potential of chain polymer molecules, the property of the effect of the velocity gradient on the radial distribution of the polymer molecules was considered in a simple calculation.

References

1) A. Isihara and R. Koyama: J. Chem. Phys. **25** (1956) 712.
2) R. Koyama: J. Chem. Phys. **27** (1957) 234.
3) R. Koyama: J. Polymer Sci. to be published.
4) S. Chandrasekhar: Rev. Mod. Phys. **15** (1943) 1, etc.
5) P. Debye: J. Chem. Phys. **14** (1946) 636, etc.
A. Peterlin: J. Polymer Sci. **23** (1957) 187;
A. Peterlin, W. Heller and M. Nakagaki: J. Chem. Phys. **28** (1958) 470.
6) J. M. Burgers: Second Report on Viscosity and Plasticity, Chapter 3, North Holland, Amsterdam, (1938);
Ch. Sadron and J. J. Hermans: in Flow Properties of Disperse System, Hermans ed. North Holland, Amsterdam, (1953);
W. Kuhn and H. Kuhn: Helv. Chim. Acta. **26** (1934) 1934;
J. G. Kirkwood and P. C. Auer, J. Chem. Phys. **19** (1951) 281;
O. Nakada: J. Phys. Soc. Japan **10** (1955) 804;
B. H. Zimm: J. Chem. Phys. **24** (1956) 127;
R. Cerf: J. Polymer Sci. **23** (1957) 125 etc.
7) J. G. Kirkwood and J. Riseman: J. Chem. Phys. **16** (1948) 565;
P. Debye and A. M. Bueche: J. Chem. Phys. **16** (1948) 673.
8) R. Koyama: Reports on Progress in Polymer Physics in Japan p. 17 (1958).

JOURNAL OF THE PHYSICAL SOCIETY OF JAPAN Vol. 13, No. 10, OCTOBER 1958

Paramagnetic Resonance Spectrum of Mn^{++} in NaCl Single Crystal

By Kazuo MORIGAKI, Minoru FUJIMOTO and Junkichi ITOH

Department of Physics, Osaka University, Osaka

(Received June 10, 1958)

The paramagnetic resonance spectrum of Mn^{++} ions contained in NaCl single crystal with concentrations of $1\sim3\times10^{-4}$ in mole fraction has been investigated. From the analysis of the spectrum the existence of $Mn^{++}-Na^{+}$ vacancy complex, in which a Na^{+} vacancy is at one of the nearest neighbor positions with respect to the Mn^{++} ion, has been verified at room temperature in crystals quenched from high temperatures. However, this state of Mn^{++} ion is unstable at room temperature, and such complexes diffuse through the lattice to form aggregates of Mn^{++} ions. The ground level splitting parameters of a Mn^{++} ion accompanying a Na^{+} vacancy at one of its nearest neighbor positions have been obtained as follows: $D=137.9\pm1$ gauss, $E=51.4\pm0.4$ gauss, where D and E represent the parameters in the spin Hamiltonian, $D[S_z^2-1/3\cdot S(S+1)]+E(S_x^2-S_y^2)$, in which z axis is in the direction of $Mn^{++}-Na^{+}$ vacancy and y axis along the cubic axis perpendicular to it.

§ 1. Introduction

By investigating the paramagnetic resonance spectra of paramagnetic impurities in diamagnetic crystals, certain informations about their electronic states in crystals will be derived. Since the electronic states strongly depend upon the crystalline field, the state of the environment around the paramagnetic ions may be informed by analyzing the structure of their resonance lines. When the valency of the impurity ions is different from that of the ions in the base crystal, additional vacancies would be produced by the principle of charge compensation. For example, if Mn^{++} ions are added to a monovalent ionic crystal, a positive ion vacancy is produced for each Mn^{++} ion. In this case, relative positions between these divalent ions and positive ion vacancies will be known by paramagnetic resonance studies, and a basic knowledge may be obtained concerning complex formation between them.

From this point of view, the paramagnetic resonance of added paramagnetic impurities in alkali-halide crystals has been investigated by several workers.[1)-9)] Schneider and Caffyn[1)] first investigated the paramagnetic resonance spectrum of a NaCl-Mn^{++} single crystal, and observed fine structures in Mn^{++} resonance when the crystal was quenched from a high temperature while only broad single line was observed before quenching. This shows that, when the crystal is quenched from high temperature, some $Mn^{++}-Na^{+}$ ion vacancy pairs, "complexes", are formed and then a crystalline field of a lower symmetry is produced at each Mn^{++} ion by a Na^{+} ion vacancy associated with it. However, detailed analysis of the fine structure has not yet been published.* The change of the line shape and line width with heat treatment of the crystals has been reported also by Oshima et al,[2)] who did not observe any fine structure of the resonance line. On the other hand, Low[5)] observed weak h.f.s. lines superposed on a strong bell-shaped line even without heat treatment. He concluded that these h.f.s. lines originated from isolated Mn^{++} ions still remaining in the crystal, so that only cubic crystalline field acted upon them.

Later, Watkins and Walker[6)] have made an experiment at high temperatures, and found that when the temperature was raised to about 200°C, fine structures of the resonance lines which originated from two different states of Mn^{++} in the crystal were observed (one being in axial symmetric, another in orthorhombic crystalline field). They interpreted these crystalline fields as those originating from Na^{+} ion vacancies in the next nearest neighbor position and in the nearest neighbor position to Mn^{++} ions respectively. Also

* A brief report of the analysis of the fine structure was given by Schneider at the Conference on the Radio & Microwave Spectroscopy, Duke University, November 1957.

they observed only six h.f.s. lines at 450°C, which meant that at this temperature Mn^{++} ions did not accompany any vacancies, so that the crystalline field at them was of cubic symmetry. They also made an experiment with quenched crystals.[10]

In this paper the results of the paramagnetic resonance of Mn^{++} in NaCl single crystals grown from aqueous solutions are reported. When the crystals were quenched from high temperatures, fine structures were observed at room temperature in accordance with Schneider and Caffyn's result. Analyzing the fine structure, it was found to be explainable as the effect of a Na^{+} ion vacancy associated with a Mn^{++} ion. So the existence of $Mn^{++}-Na^{+}$ vacancy complex is verified in the crystal quenched from high temperatures. The crystals before quenching showed no such structure. It is interesting to compare these results with that of the existence of two kinds of $Mn^{++}-Na^{++}$ vacancy complexes at high temperatures observed by Watkins and Walker. Analysis of the fine structure together with the discussion is given in section 3.

§ 2. Experimental Method

Measurements were made at a wavelength of 3.17 cm and at room temperature, using a TE_{114} circular reflection cavity. The signal detected by a standing wave detector was amplified with a pre-amplifier and then with a narrow band amplifier, and finally detected by a phase sensitive detector and recorded as the first derivative of the absorption line. The frequency of the magnetic field modulation was 60 c/s or 315 c/s. The magnetic field measurement was made with proton resonance. The g-factor was determined by comparison with the absorption line of $\alpha-\alpha$ diphenyl β-picryl hydrazyl ($g=2.0036$).

NaCl-Mn^{++} single crystals were obtained by slow vaporization of aqueous solutions of NaCl containing small amounts of $MnCl_2$ at 60°C. By spectroscopic analysis the concentration of Mn^{++} was found to be $1\sim3\times10^{-4}$ in mole fraction. With the base NaCl crystal alone, no resonance lines were observed.

The procedure of the quenching was as follows. The specimen kept at a high temperature for about three hours was dropped into dry ice as rapidly as possible. It took about five seconds. In this procedure the specimens cracked into several parts occasionally, but some parts of the crystal remained uncracked. They were used in the measurement with the static magnetic field parallel to [100] or [110]. The specimen used in the measurement with the magnetic field parallel to [111] was the crystal cut along a (110) plane before the quenching, and for this specimen many cracks appeared after the quenching, probably due to strains produced by the cutting. Therefore, the results of the experiments in this case may include some ambiguities in the line shape, the line width, the intensity, and others. The resonance measurements were started about thirty minutes after the quenching. Since the fine structures decayed with time, as will be shown in section 3, the quenching of the crystal was repeated before each resonance measurement. The fine structures observed were quite reproducible.

§ 3. Experimental Results and Discussions

Experiments are divided into two parts. One is the measurements of the resonance line with the crystals without heat treatment. The other is the measurements of many lines with the single crystals quenched from high temperatures.

1) *A single line*

In the case without heat treatment, an orientation-independent single line was observed with a half-width of 205±20 gauss, the g-factor of 2.020±0.005 and a shape of approximately Lorentzian. This results agree with those of Oshima et al[2] and Low.[5] But in our case, any resolved h.f.s. lines superposed on the broad line could not be observed, which Low observed with weak intensities. The origin of the line width has been discussed by Schneider and Caffyn,[1] and Oshima et al.[2]

2) *Fine structure*

With the single crystals quenched from high temperatures (350°C to 785°C) to dry ice temperature, many strongly orientation-dependent lines were observed at room temperature, which were similar to those obtained by Schneider and Caffyn[1]. By the following analysis, it will be shown that they correspond to the fine structure of a Mn^{++} ion accompanying a Na^{+} ion vacancy in the nearest neighbor site. This fine structure

disappeared in several days and a single broad line appeared, which was just the same as the line observed without heat treatment*. This result agrees with the observation of Schneider and Caffyn.[1]

The observed spectra of resonance lines in crystals quenched from about 410°C, are shown in Fig. 1. Fig. 2 shows partially resolved structures superposed on a broad line at sixty eight hours after the quenching.

Now we discuss the results of the above measurements. From the consideration on the line width and the line shape of the single broad line, Mn^{++} ions are probably in aggregate states prior to the heat treatment, so that line width originating from dipole-dipole interaction is narrowed and h.f.s. are smeared out by the exchange interaction among them, resulting in Lorentzian line shape. This situation has been already discussed by several workers.[1)-3)]

According to the experiment of Watkins and Walker[6)], Mn^{++} ions will exist freely in the lattice above 410°C. When the crystal

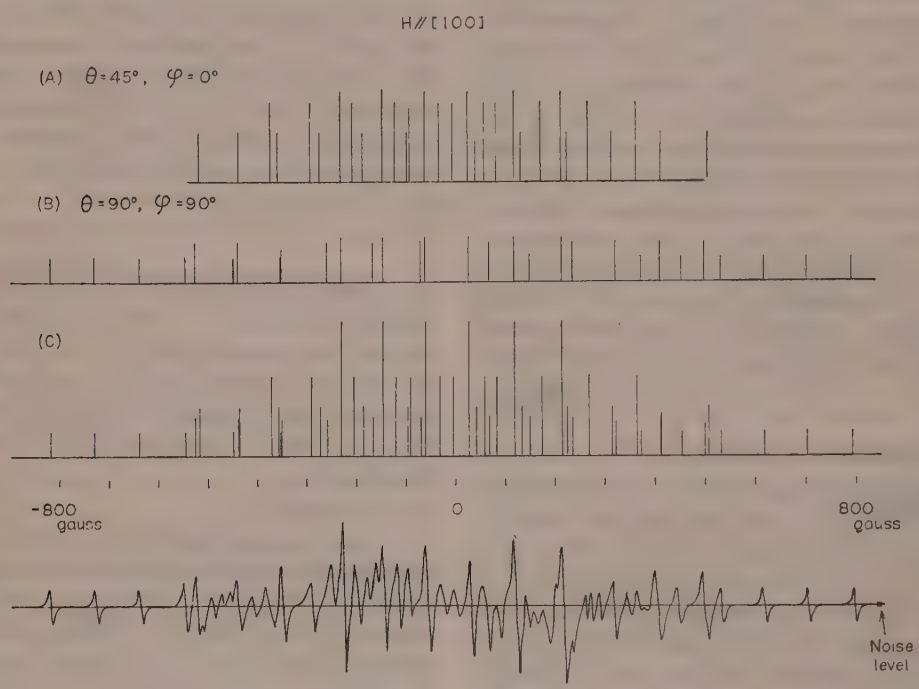

Fig. 1 (a).

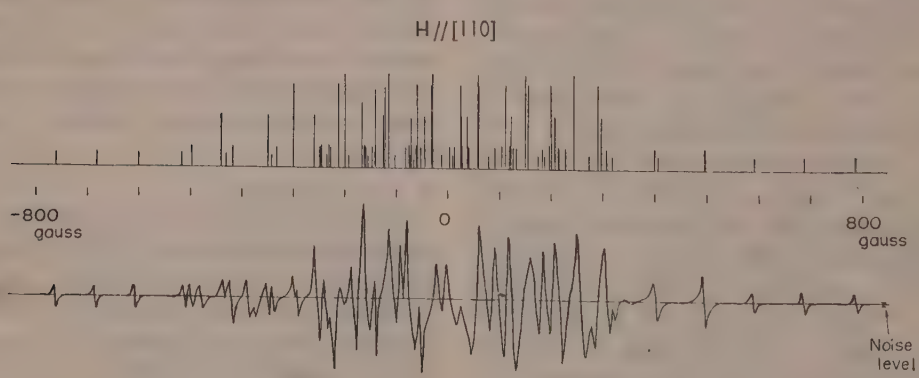

Fig. 1 (b).

* In the first investigation using the powder specimen, partially resolved six h.f.s. lines were observed immediately after quenching, which disappeared in several days and became a single broad line in the same way as in the case of single crystals.[11)]

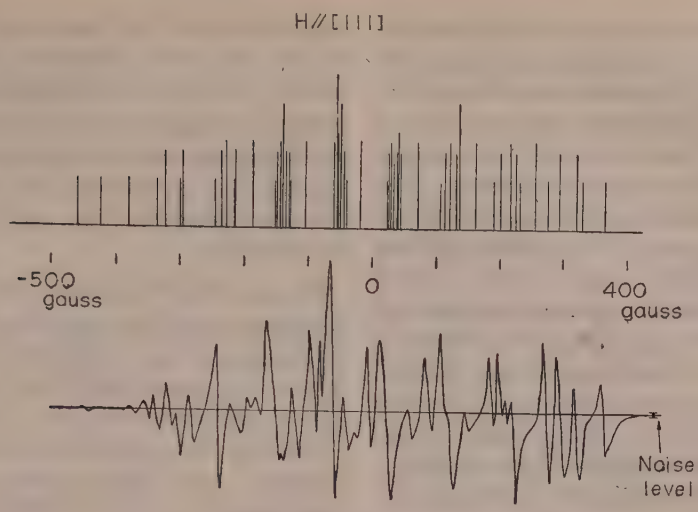

Fig. 1 (c).

Fig. 1 (a), (b), (c). The paramagnetic resonance spectrum of Mn^{++} in quenched NaCl single crystal. The observed spectrum is shown in the lower part of each figure and the calculated one in the upper part. The static magnetic field is along the [100] direction in Fig. 1 (a), the [110] direction in Fig. 1 (b), and the [111] direction in Fig. 1 (c). In Fig. (a), the calculated spectrum, (C), is shown to be composed of two spectra (A) and (B), corresponding to two orientations of $Mn^{++}-Na^{+}$ vacancy complexes in the static magnetic field. In Fig. 1 (b) and (c), a composed spectrum alone is shown. In the observed spectrum, noises and a slight drift of the zero line which eventually occurred are omitted. Noise levels are shown in each figure. The zero point in the field scale indicates the position of the magnetic field corresponding to the g-value of Mn^{++} in NaCl crystal (g=2.0012).

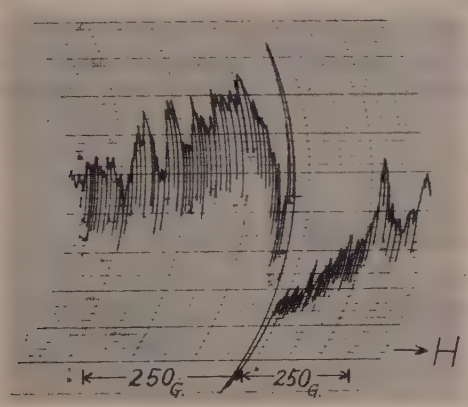

Fig. 2. Experimental record for Mn^{++} in quenched NaCl single crystal with H parallel to [100] obtained sixty eight hours later after quenching. Partially resolved structures can be seen. The center strong signal is that due to DPPH. Many marks drawn on the resonance curve are the dc current marks.

is quenched from this temperature, it might be considered that Mn^{++} ions occupying positive ion sites in the lattice are frozen without accompanying Na^{+} vacancies. Then, six h.f.s. lines alone would be expected. However, complex spectra which are composed of the mixture of fine structure and h.f.s. are always observed instead of six h.f.s. lines alone, even in the case of the crystal quenched from 785°C, at thirty minutes after the quenching. This means that during the process of the quenching or the time to set crystals into cavity, a Na^{+} ion vacancy diffuses through the lattice to form some kind of a complex with a Mn^{++} ion. This supposition may be reasonable by the following discussion. If the diffusion of free Na^{+} ion vacancies is assumed to be isotropic, for simplicity, the time, t, required for a Na^{+} ion vacancy to diffuse on the distance l is estimated by the following relations,

$$t=\frac{\pi}{16D_{\mathrm{vac}}}l^2\,,\quad D_{\mathrm{vac}}\cong\frac{\nu a^2}{6}\,,$$

where D_{vac} and ν are the diffusion coefficient and the jump frequency of Na^{+} vacancies and a is the spacing between neighboring Na^{+} ions. The jump frequency ν at room temperature is of the order of 1 c/s.[12] If the distance l is taken to be about 80Å (the average distance between Mn^{++} ions if they are assumed to distribute uniformly in the NaCl crystal containing Mn^{++} ions of 10^{-4}

mole fraction), the time, t, is estimated to be of the order of several minutes by the above relations*. So during the time of the preparation of our resonance measurement, a Na^+ ion vacancy will certainly diffuse to a site around a Mn^{++} to form a complex. Also it may be considered that during the process of the quenching Na^+ ion vacancies diffuse through the lattice to form some sort of the complexes since the jump frequency of a Na^+ ion vacancy at high temperatures is larger than that at room temperature. Indeed, in NaCl containing small amount of divalent impurities, Ca^{++}, Cd^{++}, Mn^{++}, such complexes are suggested to exist from dielectric loss measurements[13] and also, in the case of NaCl–Cd^{++}, from ionic conductivity measurements[12),14)]. In these cases, it has been suggested that the complex consists of a divalent impurity and a Na^+ ion vacancy occupying one of the Na^+ sites nearest to the divalent impurity. In our case, this position of a Na^+ ion vacancy associated with a Mn^{++} ion is also assumed. Then, the crystalline field at a Mn^{++} ion will no longer be cubic and fine structure will appear in Mn^{++} resonance lines.

Now, there are twelve equivalent positions for the vacancy around a Mn^{++} ion. If the orientation of the vacancy referring to a Mn^{++} ion is taken as the z-axis, which is assumed to be the [110] direction, for example, as shown in Fig. 3, orthorhombic crystalline field is produced with the x-axis in $[\bar{1}10]$ and the y-axis in cubic axis [001]. Then, the effect of the crystalline field on a Mn^{++} ion can be described by the following spin Hamiltonian

$$\mathscr{H}_{\text{crys}}=D[S_z^2+1/3\cdot S(S+1)]+E(S_x^2-S_y^2). \quad (1)$$

Considering twelve equivalent Na^+ ion vacancy positions, the z-axis must be taken as one of the six equivalent [110] orientations with appropriate choices of the x- and y-axes.

With Zeeman energy and the hyperfine interaction with ^{55}Mn nucleus, the total spin Hamiltonian of a Mn^{++} ion is given by

$$\mathscr{H}=g\beta\boldsymbol{H}\cdot\boldsymbol{S}+\mathscr{H}_{\text{crys}}+A\boldsymbol{I}\cdot\boldsymbol{S}, \quad (2)$$

where the first term gives Zeeman energy and the last term represents the hyperfine interaction. Here fourth order terms in components of S and the anisotropic part of the hyperfine interaction are omitted because experimental data can be explained without them.

Let the magnetic field H be in the (θ, φ) direction in the (x, y, z)-coordinate system. In the second order perturbation calculation, the field strength of resonance lines for the electronic $(M\leftrightarrow M+1)$ transition is given by

$$\begin{aligned}H=H_0&-\frac{2M+1}{2}[D(3\cos^2\theta-1)+3E\cos 2\varphi\cdot\sin^2\theta]\\&-\frac{1}{2H_0}[(D-E\cos 2\varphi)^2\cdot\sin^2\theta\cdot\cos^2\theta+E^2\sin^2\theta\cdot\sin^2 2\varphi][24M(M+1)-4S(S+1)+9]\\&-\frac{1}{8H_0}\{[D\sin^2\theta+E\cos 2\varphi(1+\cos^2\theta)]^2+4E^2\cos^2\theta\cdot\sin^2 2\varphi\}\cdot[2S(S+1)-6M(M+1)-3]\\&-Am-\frac{A^2}{2H_0}[I(I+1)-m^2+m(2M+1)], \quad (3)\end{aligned}$$

where M and m are the components of the electronic and nuclear spins in the applied magnetic field, H_0 is $h\nu/g\beta$ and the values of D, E, and A are reduced by a factor of $g\beta$ from those in Eq. (2).

In the present case, resonance spectrum consists, in general, of 180 lines because the z-axis of the crystalline field must be taken as each one of the six orientations and the fine structure consists of 30 lines for each direction of the z-axis. But, if the magnetic field H lies along some symmetry axis, the number of resonance lines is reduced. For example, if H is parallel to the cubic axis, resonance lines consist of two sets, one being given by Eq. (3) with $\theta=45°$, $\varphi=0°$ and the other with $\theta=90°$, $\varphi=90°$ (See Fig. 1 (a)). Similarly, for the cases in which H lies in

* According to Haven (Report of Bristol Conference in the reference (13)), the jump frequency of free Na^+ vacancies at 20°C in the NaCl crystal is estimated to be 17 c/s. If this value is used, it takes about 28 sec for Na^+ vacancies to diffuse on the same distance.

[110] and [111] the numbers of the equivalent sets can be easily obtained. Table I shows the equivalent values of θ and φ for these sets, together with the numbers of the equivalent orientations of z-axes for each set.

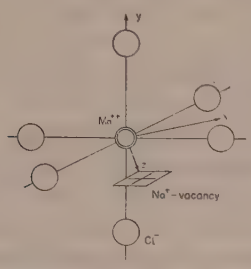

Fig. 3. A coordinate system with the origin at the position of Mn^{++} on a Na^{+} site. The crystalline field about a Mn^{++} ion accompanying a Na^{+} vacancy at one of the nearest neighbor Na^{+} sites has orthorhombic symmetry, and for the analysis of the fine structures, x, y, z-axes were taken as shown in this figure (see text).

Table I. Classification of the orientations of equivalent crystalline field z-axes at Mn^{++} in the static magnetic field.

Direction of H	θ	φ	Abundance
[100]	45°	0°	4
	90°	90°	2
[110]	0°		1
	90°	0°	1
	60°	$\frac{1}{2}\cos^{-1}\left(-\frac{1}{3}\right)$	4
[111]	$\cos^{-1}\sqrt{\frac{2}{3}}$	90°	3
	90°	$\frac{1}{2}\cos^{-1}\left(\frac{1}{3}\right)$	3

By fitting the observed spectra for the orientations of H in [100] and [110] with the calculated ones as shown in Fig. 1 (a), (b), we find the following values for the parameters, g, A, D, and E.

$$\begin{aligned} g&=2.0012\pm0.0008 \\ A&=-88.8\pm0.8 \text{ gauss} \\ D&=137.9\pm1 \text{ gauss} \\ E&=51.4\pm0.4 \text{ gauss} \end{aligned} \tag{4}$$

The signs of D and E in the above asignments were determined from the consideration of the variation of the spacings of h.f.s. multiplets assuming that A is negative.

We now compare the experimental results for H parallel to [111] with the spectrum calculated by Eq. (3) using the parameters given by Eq. (4). As shown in Fig. 1 (c), the agreement of the observed spectrum with the calculated one is not satisfactory. This may partially be due to the difficulty of setting the crystal with the desired orientation because the crystal used was cut along a (110) plane. Moreover, in the observed spectrum, some of the lines expected at the lowest field side are so weak that their existence can not be confirmed by the masking effect of noise. Theoretically, it is expected that these lines have equal intensities with those of the corresponding lines at the highest field side. We have no appropriate interpretation as to this intensity anomaly even if a slight distribution of the orientation of the crystal axes due to cracks is taken into consideration. Wertz and Auzins[15] also reported similar anomaly in intensity in the case of Cr^{+++} resonance in MgO–Cr^{+++} crystal.

The width of h.f.s. components at the highest and lowest field sides in the spectra with H parallel to [100] and [110] is $10\sim12$ gauss, and the width between maximum slopes of the main h.f.s. components ($M=1/2 \leftrightarrow -1/2$ transition) observed with H parallel to [100] is about 8 gauss. The orign of these widths may be attributed mainly to the unresolved h.f.s. due to neighboring six Cl nuclei and a small distribution in the parameters D and E due to strains in the crystal. Also the dipolar interactions with neighboring Cl nuclei and Na nuclei contribute to the width by 2.7 gauss for H parallel to [100] and by 2.2 gauss for H parallel to [110].

Watkins and Walker observed complex structures when the crystal was heated to 200°C. By analyzing them, they concluded that two types of Mn^{++}–Na^{+} vacancy complexes existed in the crystal, one with the vacancy in the nearest neighbor position with respect to a Mn^{++} ion and the other in the next nearest neighbor position, and they obtained the values of the parameters for each case. In order to compare the value of of the parameters which they obtained for the former case with our values given by Eq. (4), a new coordinate system is taken,

in which the z-axis is along the cubic axis and the x-axis in the direction of Mn^{++} to Na^{+} vacancy. In this new coordinate system the following values of the parameters are obtained:

$$D=-146.0\pm1 \text{ gauss},$$
$$E=43.3\pm0.3 \text{ gauss}.$$

These values agree very well with those obtained by Watkins[7].

In our measurements, the fine structure of the resonance lines of Mn^{++} ions which accompany Na^{+} ion vacancies occupying the next nearest neighbor Na^{+} sites could not be observed. This indicates that the complex with the vacancy in the nearest neighbor Na^{+} site is more stable than that with the vacancy in the next nearest neighbor Na^{+} site, so that the former prevails at room temperature when the specimens were quenched from high temperature. According to Watkins[7], the binding energy of the former type of complex is larger than that of the latter by 0.03 eV. This difference in the binding energy may be the reason why the resonance lines of one type of complexes could not be observed in our measurement.

The change of the relative intensity of the resonance line with time after quenching was investigated with the lowest h.f.s. line in $M=1/2\leftrightarrow-1/2$ transition when H is parallel to [100], using the specimen quenched from 410°C. The results are shown in Fig. 4. These two decay curves correspond to two different times of the duration of heating at 410°C which are about fourty minutes and about three hours respectively. The reason for the disappearance of the fine structure of the resonance line will be that the Mn^{++}—Na^{+} vacancy complexes diffuse through the lattice and eventually form aggregates of Mn^{++} ions. As already stated, Mn^{++} ions in aggregate state in the crystal should not yield fine structure of the resonance lines, but they should yield a single broad line.[15,5] Fig. 4 shows that in the case of the fourty minutes' heating the initial decrease of the intensity of the resonance line is rapid. This may be explained as follows: As the time of heating is not long enough to separate Mn^{++} ions completely, the initial recovery of the aggregate state of Mn^{++} ions is attained quickly. In the case of three hours' heating the decay is slow, meaning that the Mn^{++}—Na^{+} vacancy complexes are distributed more uniformly throughout the lattice, so that it takes a longer time to diffuse and aggregate together. It may be considered that aggregation of Mn^{++} ions may occur at a sort of internal boundary or may form an ordered state with Na^{+} ion vacancies as found in the NaCl–Ca^{++} crystal by Miyake and Suzuki[16]. Then, when the crystal is heated, Mn^{++}—Na^{+} complexes may first diffuse easily on this boundary plane, and after a prolonged heating, they may diffuse slowly to the inside of the host crystal itself. After quenching, Mn^{++}—Na^{+} complexes may diffuse back to the aggregate state just in the reversed way, and this might be the origin of the different rate of the intensity decay for the both cases in Fig. 4.

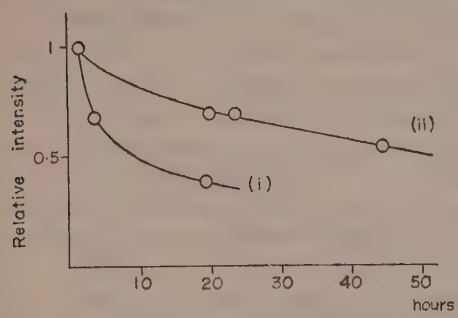

Fig. 4. The change of the intensity of the lowest h.f.s. line ($m=-5/2$) in $M=1/2\leftrightarrow-1/2$ transition when the static magnetic field is parallel to [100] in NaCl single crystal quenched from 410°C. Two decay curves correspond to the cases of two different times of the duration of heating at 410°C, which is about fourty minutes for the lower curve, (i), and is about three hours for the upper curve, (ii). For each case the intensity of the resonance line was compared with the intensity of the resonance line of DPPH. The relative intensities are so normalized that they have the same value at the starting time of the measurement which is an hour and a half after the quenching.

It seems to us that the quantitative analysis of the decay curve might supply some valuable informations about the divalent impurity diffusion. Though a quantitative treatment of the decay curve on the base of the theory of the impurity diffusion by vacancy mechanism[17] has been tried, any conclusive explanation could not be obtained at the present stage because no reliable information about the aggregate state of Mn^{++}

ions is available.*

§ 4. Concluding Remarks

In this paper there have been presented the experimental results of the resonance spectrum of Mn^{++} contained as impurity ions in NaCl crystals, and the fine structure of the resonance lines observed in the crystals quenched from high temperature has been analyzed on the base of a spin Hamiltonian containing an orthorhombic crystalline field term. From the analysis of the fine structure the existence of $Mn^{++}-Na^{+}$ vacancy pairs, "complexes", was confirmed. At room temperature these free complexes are unstable and diffuse slowly through the lattice to form aggregates of Mn^{++} ions.

The authors wish to thank Dr. T. Kojima for his valuable suggestions about the complex formation from Mn^{++} and positive ion vacancies. One of the authors (J.I.) would like to thank Dr. G. D. Watkins for his valuable discussions which were given to him at Duke University on the occasion of the Conference on the Radio and Microwave Spectroscopy, November 1957.

References

1) E. E. Schneider and J. E. Caffyn: Defects in Crystalline Solids, Report of 1954 Bristol Conference (London: Physical Society) 1955, 74.
2) K. Oshima, H. Abe, H. Nagano and M. Nagusa: J. Chem. Phys. **23** (1955) 1721.
3) H. Abe, H. Nagano, M. Nagusa and K. Oshima: J. Chem. Phys. **25** (1956) 378.
4) P. A. Forrestor and E. E. Schneider: Proc. Phys. Soc. **B 69** (1956) 833.
5) W. Low: Proc. Phys. Soc. **B 69** (1956) 837.
6) G. D. Watkins and R. M. Walker: Bull. Am. Phys. Soc. Ser. **II**, 1, (1956) 324.
7) G. D. Watkins: Private communication to Dr. H. Abe.
We would like to thank Dr. H. Abe for informing us Watkins' results.
8) B. Bleaney and W. Hayes: Proc. Phys. Soc. **B 70** (1957) 626.
W. Hayes and D. A. Jones: Proc. Phys. Soc. **71** (1958) 503.
9) Z. Miduno, O. Matumura, K. Hukuda and K. Horai: Presented at the annual meeting of Phys. Soc. Japan, July 1956.
K. Fukuda, Y. Uchida and H. Yoshimura: Presented at the meeting of Phys. Soc. Japan, March 1958.
10) G. D. Watkins: Private conversation with one of the authors (J.I.).
11) J. Itoh, M. Fujimoto and K. Morigaki: Presented at the annual meeting of Phys. Soc. Japan, October 1955.
12) F. Seitz: Rev. Mod. Phys. **26** (1954) 7.
13) Y. Haven: J. Chem. Phys. **21** (1953) 171. Defects in Crystalline Solids, Report of 1954 Bristol Conference (London: Physical Society) 1955, 261.
O. Matumura and K. Shiraishi: Memoirs of the Faculty of Science, Kyushu University Ser. **B, 2** (1957) 107.
14) H. W. Etzel and R. J. Maurer: J. Chem. Phys. **18** (1950) 1003.
A. B. Lidiard: Phys. Rev. **94** (1954) 29.
15) J. E. Wertz and P. Auzins: Phys. Rev. **106** (1957) 484.
16) S. Miyake and K. Suzuki: Acta. Cryst. **7** (1954) 514. J. Phys. Soc. Japan **9** (1954) 702.
K. Suzuki: J. Phys. Soc. Japan **10** (1955) 794.
17) A. B. Lidiard: Phil. Mag. **46** (1955) 1218.

---

* In order to obtain some informations about the aggregate state of Mn^{++} ions, we made some observation on the NaCl-Mn^{++} single crystal used in the resonance experiments by means of a electron microscope. Because of ambiguity in etching, we could not obtain any reliable information about this problem by the electron microscope studies.

JOURNAL OF THE PHYSICAL SOCIETY OF JAPAN Vol. 13, No. 10, OCTOBER, 1958

Nuclear Magnetic Resonance Studies of Iodine Ions in Aqueous Solution

By Junkichi ITOH and Yukio YAMAGATA

Department of Physics, Osaka, University, Osaka, Japan

(Received June 19, 1958)

Chemical shift and line width were measured for the nuclear magnetic resonance of iodine nuclei in aqueous solutions of alkali iodides. The chemical shift was independent of temperature, but was dependent on the concentration of the solution. The spin lattice relaxation time calculated from the line width varied with temperature as well as concentration. General trend of the variation of the spin lattice relaxation time agrees with that of viscosity. By analysing the data of the chemical shift and spin lattice relaxation time, it is suggested that even in very dilute solution there exists chemical shift of the order of 6×10^{-4} as compared to the case of 'pure ion'.

§ 1. Introduction

When strong electrolytes such as alkali halides are desolved in water, each molecule separates into positive and negative ions. Often the nuclear magnetic resonance frequency for these ions was taken as a standard, to express the chemical shift for other compounds containing the same nucleus. To discuss the chemical shifts in solid metal halides, it is necessary to know the shift of resonance frequency for solids from that of pure ion[1], and in some previous works, the shift of resonance frequency of the solids from that of ions in aqueous solution was taken as the true shift from 'pure ion', without detailed considerations[2),3)]. However, ions in aqueous solution are usually surrounded by several water molecules of hydration[4] and, as pointed out already by Saika and Slichter[5], there seems to exist considerable effect on resonance frequency by the hydration. Moreover, in the case of Tl nuclei, Gutowsky and McGarvey[6] observed that the resonance frequency for Tl ions in aqueous solution showed marked concentration dependency in some cases. Also, they pointed out that a similar concentration dependence of the resonance frequency was found in the case of Cs ions, suggesting some other effects than the hydration.

During the investigation of the chemical shifts for solid alkali halides, which will be published in near future, we noticed that it is necessary to know the true resonance frequency for nuclei in pure alkali or halogen ions. However, it is very difficult, almost impossible, to measure the resonance frequency for pure ions, so we aimed to investigate the effect of hydration for ions in aqueous solution. If the hydration has some effect on the chemical shift, it seems probable that also it has some effect on the electric quadrupole interaction, when the nucleus has spin larger than 1 and momentary configuration of water molecules of hydration is not highly symmetrical, and by this electric quadrupole interaction spin lattice relaxation time, T_1, of the nucleus in ion may be considerably shortened. Therefore, we measured the concentration and temperature dependence of the shift and spin lattice relaxation time for various metal and halogen ions in aqueous solution. In this report, we shall describe the results of our experiments on iodine ions. As will be discussed in section III, it is very difficult to analyse clearly our experimental results to obtain the resonance frequency for 'pure ion', though it may be suggested that there exists considerable chemical shift for iodine ion even in very dilute solution as compared to 'pure iodine ion', and further experiments of different kinds should be made to determine accurately true resonance frequency for 'pure ion'.

§ 2. Experimental Results

(a) *The chemical shift.*

The resonance field for iodine ions in aqueous solution was compared with that for solid sodium iodide. First, we desolved potassium iodide in water and noticed that there existed

considerable concentration dependency of the resonance field. Since the spin lattice relaxation time of iodine nuclei is rather short in aqueous solution which will be described in (b), it might be the case that the shift in resonance field is not a true chemical shift, but is caused by some other origins such as second order quadrupole effect[7]. If the shift is a true chemical shift, $\Delta H/H$ where ΔH is the shift of the resonance field from a standard (in this case the resonance field for solid sodium iodide) and H is the applied field, will be constant for all values of H[8], while if the shift originated from quadrupole effect, $\Delta H/H$ will depend strongly upon H. We checked that the resonance field for the standard solid sodium iodide was exactly proportional to the frequency, by measuring the ratio of the resonance frequency for sodium ions in aqueous solution of sodium bromide and that for iodine nuclei in solid sodium iodide at various fields. In the case of sodium nuclei in aqueous solution, the line width is very narrow, being almost equal to the width corresponding to field inhomogeneity, and no effect of second order quadrupole term will exist.

The measured values of $\Delta H/H$ are constant within experimental errors at three frequencies, 3.4, 4.5 and 6.0 Mc/sec, indicating that there exists a true chemical shift between the resonance field for iodine ions in aqueous solution and that in solid sodium iodide. The results of the measurements are shown in Fig. 1, in which the relative shifts of the resonance field for aqueous solution from that for solid sodium iodide are plotted against the concentration of the solution. The resonance for solution lies always in diamagnetic side with respect to that for solid. In this figure, the results of the measurements for other alkali iodides, NaI and LiI, are also included. The concentration dependence of the shift is almost linear, and the shift is independent of the nature of positive ions.

Next, we measured the temperature dependence of the chemical shift. In this case, we used only an aqueous solution of potassium iodide with the concentration of 1 gr of KI in 1 gr of water. Keeping the reference sample of solid sodium iodide at room temperature, the temperature of the solution was changed from room temperature upto about 80°C. No

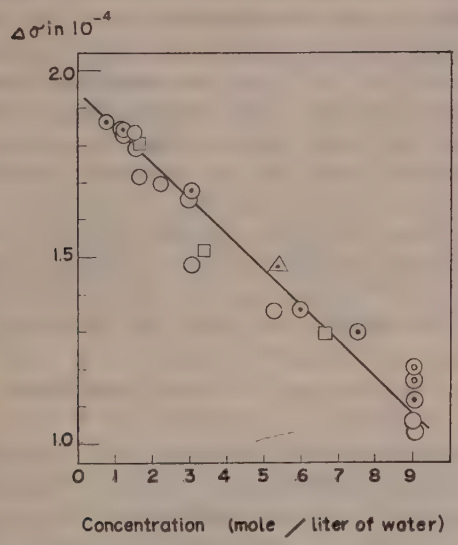

Fig. 1. Concentration dependence of the chemical shift for iodine ions in aqueous solutions.
$\triangle\sigma$ is relative shift of the resonance for aqueous solutions from that for solid sodium iodide. Different marks show the experimental results for KI aq., NaI aq. and LiI aq. at three frequencies: ○ KI aq. at 3.4 Mc/sec, ◎ KI aq. at 4.5 Mc/sec, ⊙ KI aq. at 6.0 Md/sec, □ NaI aq. at 3.4 Mc/sec, and △ LiI aq. at 6.0 Mc/sec. Solid line was drawn to fit best with the experimental plots.

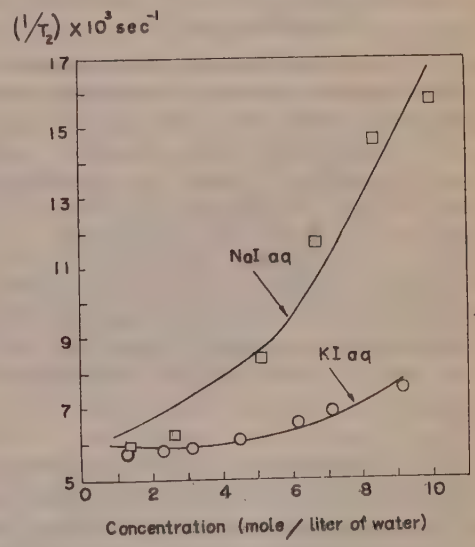

Fig. 2. Concentration dependence of the inverse of T_2 for aqueous solutions of potassium iodide and sodium iodide.
Circular marks are the experimental points for KI aq., while square marks are those for NaI aq.. Solid curves show the concentration dependence of η, normalized to fit best with the experimental plots of $1/T_2$ for KI aq.

change in $\Delta H/H$ was observed within the experimental errors which were about $\pm 0.5\times 10^{-5}$.

(b) *The width of the resonance line; The spin lattice relaxation time.*

Since the nuclear magnetic resonance line width is rather broad for iodine ions in aqueous solution and also the line shape is Lorentzian, it will be safe to assume that $T_1=T_2$ in this case. Therefore, to determine the value of T_1, we only measured the line width, δH, (full width between maximum and minimum deflections in the derivative of the absorption curve), and $T_1(=T_2)$ is calculated by the relation $T_1=2/\sqrt{3}\gamma\delta H$.

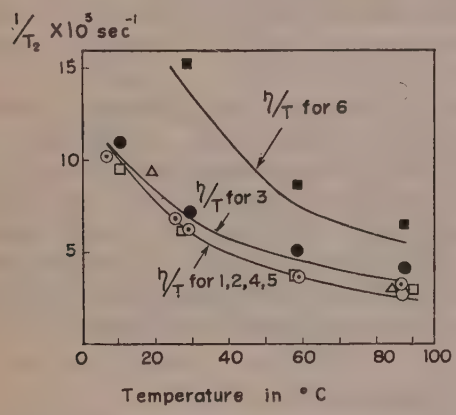

Fig. 3. Temperature variation of the inverse of T_2 for aqueous solutions of potassium, sodium and lithium iodides, with various concentrations. 1: ⊙ KI aq. 1.10 mole/liter of water, 2: ○ KI aq. 0.27 mole/liter, 3: ● KI aq. 7.5 mole/liter, 4: ▣ NaI aq. 1.21 mole/liter, 5: □ NaI aq. 0.30 mole/liter, 6: ■ NaI aq. 8.3 mole/liter, 7: △ LiI aq. 1.30 mole/liter. Solid curves show the temperature dependence of the values of η/T for corresponding concentrations, normalized to fit best with the experimental plots of $1/T_2$ for KI aq. with the concentration of 1.10 mole/liter of water.

δH was measured for aqueous solutions of potassium, sodium and lithium iodides with various concentrations and at different temperatures. Typical values of $1/T_1$ calculated from the line width are shown in Fig. 2 and Fig. 3. T_1 depends upon the concentration in the case of NaI aq., while T_1 is almost constant in the case of KI aq. The viscosity of the solution of sodium and potassium iodides changes with the concentration by similar ways as those of $1/T_1$. Also for the temperature dependency of $1/T_1$, similar parallelity with the change of viscosity exists. The absolute values of T_1 are much shorter than those expected from the dipolar interaction with surrounding water molecules which is time dependent by the Brownian motion of water molecules. Therefore it is suggested that the origin of the relaxation is time varying electric quadrupole interaction which is produced by the motion of water molecules of hydration.

The extrapolated value of T_1 for infinitely dilute solution which is, of course, equal for KI aq. and NaI aq., is rather short even at higher temperatures.

§ 3. Discussion

Though the concentration of the solution by which nuclear magnetic resonance measurement of iodine nuclei is possible is not so dilute as is considered 'dilute in electrochemical sence', the interaction between positive and negative ions may be neglected in the discussion of nuclear magnetic relaxation for dilute solutions used in our experiment, because the width of the resonance line is almost independent of the concentration when the concentration of the solution is made less than 3 mole/liter for KI aq. and less than 2 mole/liter for NaI aq.. This means that in these cases the spin lattice relaxation time is determined solely by the interaction between the ion and water molecules of hydration. If, as a first order approximation, we neglect the interaction between ions at all concentrations, $1/T_1$ may be assumed to be proportional to η/T according to the theory of Bloembergen, Purcell and Pound[9], where η is the viscosity of the solution and T is the temperature. In Fig. 2 and Fig. 3, values of η/T[10] are also shown, normalizing the curves of η/T to fit best with the experimental $1/T_1$-curve for dilute solution of KI. General tendencies of the curves of $1/T_1$ and η/T agree with each other, suggesting that the main origin of the relaxation is time dependent electric quadrupole interaction of iodine nuclei which is produced by the water molecules of hydration. It is not clear, however, whether the electric quadrupole energy is produced by the asymmetric configuration of water molecules around the iodine ion which is made time dependent by the rotational motion of the system of iodine ion plus water molecules of hydration among

free water, or the configuration of the water molecules of hydration changes from time to time by Brownian motion, or both.

Next, we shall discuss the chemical shift. The chemical shift shows considerable concentration dependency. Therefore, contrary to the discussion given above, some effect from positive ions should exist. The fact that the shift is independent of the kind of positive ions suggests that the perturbing effect of positive ions is not the association to form neutral molecule. On the other hand, according to the theory of strong electrolyte[11], a sheath of positive charge is formed around each negative ion on an average, the mean radius of which is determined by the concentration, and this positive sheath may polarize the water molecules of hydration around the negative ion. This polarization, in turn, may perturb the charge distribution of the negative ion and change the chemical shift.

If this picture is the actual case, there must exist concentration dependence of momentary electric quadrupole energy which is the origin of the spin lattice relaxation. In fact, strictly speaking, the measured values of $1/T_1$ are not exactly proportional to η/T.

Now, we shall assume that root mean square of momentary electric quadrupole energy and the shift come from the same origin. Then, $\overline{E}_Q$, root mean square of quadrupole energy, can be assumed to be proportional to $(1/T_1\eta)^{1/2}$, and also to the net shift, σ, from purely ionic state. Then the following relation is easily derived:

$$\frac{(1/T_1\eta)_1{}^{1/2}-(1/T_1\eta)_0{}^{1/2}}{(1/T_1\eta)_0{}^{1/2}}=\frac{\sigma_1-\sigma_0}{\sigma_0} \qquad (1)$$

where 1 and 0 means two solutions of concentration 1 and 0, provided that all these quantities are measured at one temperature. Taking the concentration 0 as very dilute one (or the extrapolated one to zero concentration), σ_0, that is the chemical shift of iodine nuclei in very dilute solution as compared to that of 'pure ion', can be calculated. The estimated value of σ_0 from the experimental values of $(1/T_1)_1$, $(1/T_1)_0$, and $\sigma_1-\sigma_0$, is $\sim 6\times 10^{-4}$, both for aqueous solutions of potassium and sodium iodides. Of course, equation (1) might be very crude one, since the origin of σ and $1/T_1$ is not known exactly. So, the estimated value of σ_0 might be only tentative, but, to explain the concentration dependence of the shift and also rather short relaxation time in very dilute solution, we must assume considerable chemical shift from 'pure ion' even at very small concentration.

The main force between an ion and surrounding water molecules of hydration is probably electrostatic one, but there might exist some kind of bonding by which small part of electron charge of the ion may transfer to water molecules. Then by p-electron hole produced by electron transfer, chemical shift and also electric quadrupole interaction for iodine nuclei will be produced. In this case, theoretical treatment given by Saika and Slichter[4] or Yoshida and Moriya[1] will be applicable. If we assume the number of water molecules attached to one iodine ion is four, the estimated fraction of p-electron hole per one pair of iodine ion and water molecule becomes about 4 percent to interpret the chemical shift in very dilute solution from that for 'pure ion'. Then electric quadrupole energy of about 80 Mc/sec is expected for a pair of iodine ion and water molecule. If we assume further that electric quadrupole interaction of this order of magnitude fluctuates with time by a correlation time corresponding to the viscosity of the solution, we get spin lattice relaxation time of right order of magnitude as compared with the experimental values. Concentration dependency of the chemical shift can be well interpreted by the change of electron tranfer caused by the polarization effect due to positive ions around the hydrated iodine ion. The analysis of the experimental data given above has been done, taking these considerations on the chemical shift and spin lattice relaxation in mind.

Interactions between ions and water molecules of hydration can also be investigated by measurements of the chemical shift and spin lattice relaxation time of proton. Broersma[12] and Shoolery and Alder[13] investigated proton magnetic resonance, but direct correlation between proton and metal or halogen nuclear magnetic resonances was not clearly shown in the present stage.

Hitherto, the chemical shift in metal halides was referred to that of ions in aqueous solution, and also often the nuclear magnetic moments have been calculated from the reso-

nance condition for ions in aqueous solution with diamagnetic shielding correction for 'pure ion'[13,14]. Therefore, these values should be considerably revised by the chemical shifts of the ions in aqueous solution as compared to the pure ion.

Similar concentration dependency of the shift was observed in other alkali metal and halogen ions, too. The results of these measurements for other ions will be reported in near future.

References

1) K. Yoshida and T. Moriya: J. Phys. Soc. Japan **11** (1956) 33.
2) T. Kanda: J. Phys. Soc. Japan **10** (1955) 85.
3) P. P. Sorokin: Thesis, Harvard (unpublished) (1957).
N. Bloembergen and P. P. Shrokin: Phys. Rev. **110** (1958) 865.
4) For example, G. W. Brady: J. Chem. Phys. **28** (1958) 464.
5) A. Saika and C. P. Slichter: J. Chem. Phys. **22** (1954) 26.
6) H. S. Gutowsky and B. R. McGarvey: Phys. Rev. **91** (1953) 81.
7) R. V. Pound: Phys. Rev. **79** (1950) 685, R. Bersohn: J. Chem. Phys. **20** (1952) 1505.
8) N. F. Ramsay: Phys. Rev. **77** (1950) 567, **78** (1950) 699.
9) N. Bloembergen, E. M. Purcell and R. V. Pound: Phys. Rev. **73** (1948) 679.
10) International Critical Tables vol. **V**, Randolt Bernstein: Physikalische-Chemische Tabellen, **IV** Teil 1.
11) For example, see Harned, Owen: Physical Chemistry of Electrolytic Solutions (Reinhold Publishing Corporation, 1950).
12) S. Broersma: J. Chem. Phys. **24** (1956) 153, **27** (1957) 481.
13) J. N. Shoolery and B. J. Alder: J. Chem. Phys. **23** (1955) 805.
14) For example, see N. F. Ramsay: Nuclear moments (Wiley, New York, 1953).

JOURNAL OF THE PHYSICAL SOCIETY OF JAPAN Vol. 13, No. 10, OCTOBER, 1958

The Lower Excited States and the Phosphorescent State of Diphenyl II. Scheme of Modification of MO

Kaoru IGUCHI

Electrical Communication Laboratory, Musashino-shi, Tokyo

(Received June 24, 1958)

To treat the problem of phosphorescence of alternant hydrocarbon we propose a new method to take account of the mixing of higher order AO's.

We give here a theoretical scheme of the modification of $2p\pi$ MO with the addition of $3d$ AO's for diphenyl molecule. With the modified MO's thus obtained, the singlet triplet intercombination matrix is given in the concrete form.

§ 1. MO Expansion

The $2p\pi$ MO method with two center integrals is unable to approximate the observed value of the singlet-triplet intercombination intensity in the phosphorescence of alternant hydrocarbon. Some authors have yet published works concerning this problem.[1-3]

But, in the preceeding paper[4] we have proposed a new method modifying MO's consisted simply of $2p\pi$ AO's with higher order AO's.

A generalized MO ϕ^s can be written in the following form;

$$\phi^s=\sum_A \sum_{pqr} c_A{}^{pqr} x_a{}^p y_a{}^q z_a{}^r e^{-\delta_A r_a}. \qquad (1)$$

Note. A. atom. x_a, y_a, z_a. coordinates measured from the atom A. δ_A depends on (pqr). $r_a{}^2=x_a{}^2+y_a{}^2+z_a{}^2$.

When the antisymmetric property of MO by the reflection to the xy plane is taken into account, the Eq. (1) can be transformed as;

$$\phi^s=\sum_A \{c_A{}^0\chi_A+(c_A'x_a+c_A{}^2y_a)\chi_A'+\cdots\}=\sum_l \alpha_l'S_l+\beta_l'U_l+\gamma_l'V_l+\cdots \tag{2}$$

Here S_l, U_l, and V_l are the simple symmetry MO's defined for an irreducible representation Γ as follows;

$$\left.\begin{aligned}
&S_l=\sum_A \sigma_A{}^l(\Gamma')\chi_A\,; && \Gamma'=\Gamma\times B_{1u}\\
&U_l=\sum_A \sigma_A{}^l(\Gamma'')\sqrt{\frac{2\delta'^2}{3}}x_a\chi_A'=\sum_A \sigma_A{}^l(\Gamma'')\xi_A\,, && \Gamma''=\Gamma\times B_{2g}\\
&V_l=\sum_A \sigma_A{}^l(\Gamma''')\sqrt{\frac{2\delta'^2}{3}}y_a\chi_A'=\sum_A \sigma_A{}^l(\Gamma''')\eta_A\,, && \Gamma'''=\Gamma\times B_{3g}\\
&\chi_A=\sqrt{\frac{\delta^5}{\pi}}\,e^{-\delta r_a}z_a\cdots 2p\pi\ \mathrm{AO}\,, && \xi_A=\sqrt{\frac{2\delta'^7}{3\pi}}\,e^{-\delta' r_a}x_az_a\cdots 3d_{zz}\ \mathrm{AO}\,.\\
&\eta_A=\sqrt{\frac{2\delta'^7}{3\pi}}\,e^{-\delta' r_a}y_az_a\cdots 3d_{yz}\ \mathrm{AO}\,.
\end{aligned}\right\} \tag{3}$$

$\sigma_A{}^l(\Gamma')$ is already known in the construction of $2p\pi$ symmetry MO, and from this we can easily find out $\sigma_A{}^l(\Gamma'')$ and $\sigma_A{}^l(\Gamma''')$.

On the other hand, the Hueckel orbitals are found in the form;

$$\left.\begin{aligned}
&2p\pi\ \mathrm{MO}\ \phi_f=\sum_l \alpha_{fl}S_l=\sum_A \alpha_A{}^f\chi_A\,, && f=1\to n \text{ occupied, } n'\to 1'(n+1\to 2n) \text{ unoccupied}\\
&3d_{zz}\mathrm{MO}\ \psi_f=\sum_l \beta_{fl}U_l=\sum_A \beta_A{}^f\zeta_A\,, && f=1\to 1'\\
&3d_{yz}\mathrm{MO}\ \omega_f=\sum_l \gamma_{fl}V_l=\sum_A \gamma_A{}^f\eta_A\,. && f=1\to 1'
\end{aligned}\right\} \tag{4}$$

Here $\alpha_A{}^f$, $\beta_A{}^f$, $\gamma_A{}^f$ are the Hueckel coefficients.[5]

One might consider the necessity to include $3p\pi$ MO's in the Eq. (2) because they lie lower than $3d$ MO's. But even if they were included, it can be shown that they disappear in the course of evaluation of S–T intercombination integral because of the symmetry property.

§ 2. Determination of Expansion Coefficients

Substituting Eq. (4) into Eq. (2) we have the following form for the modified MO's;

$$\left.\begin{aligned}
&\phi_i{}^s=\phi_i+\sum_k a_{ik}\phi_k+\sum_f b_{if}\psi_f+\sum_f c_{if}\omega_f\,, && \phi_k{}^s=\phi_k-\sum_i a_{ik}\phi_i+\sum_f b_{kf}\psi_f+\sum_f c_{kf}\omega_f\,,\\
&\psi_f{}^s=\psi_f-\sum_i b_{if}\phi_i-\sum_k b_{kf}\phi_k\,, && \omega_f{}^s=\omega_f-\sum_i c_{if}\phi_i-\sum_k c_{kf}\phi_k\,.
\end{aligned}\right\} \tag{5}$$

$$i,\ j=1\to n \text{ occupied.}\quad k,\ l=n'\to 1' \text{ unoccupied.}\quad f,\ g=1\to 1'.$$

With these MO's, the orthonormality can be proved to hold if one retains untill the first order terms.[6]

The energy diagonalization conditions also can be shown to be satisfied by the following choice of the coefficients a_{ik}, b_{if}, c_{if} etc.;

$$\left.\begin{aligned}
&a_{ik}=\frac{(\phi_kH'\phi_i)}{E_i-E_k}\,,\quad b_{if}=\frac{(\psi_fH'\phi_i)}{E_i-E_{\psi_f}}\,,\quad c_{if}=\frac{(\omega_fH'\phi_i)}{E_i-E_{\omega_f}}\,,\\
&\text{with}\\
&H'=G^s-G=\sum_j 2(J_j{}^s-J_j)-(K_j{}^s-K_j)\,,
\end{aligned}\right\} \tag{6}$$

and E_i=energy of ϕ_i etc.

J_j and K_j and Coulomb and exchange operators respectively. Here the Hueckel MO ϕ_is

are assumed to be sufficiently approximate to SCF orbitals.

When expanded in MO integrals.

$$\left.\begin{aligned}(\varphi H'\phi_i)&=(\varphi|\sum_j 2(J_j^s-J_j)-(K_j^s-K_j)|\phi_i)\\&=\sum_{kj}4a_{jk}[\varphi\phi_i|\phi_j\phi_k]+\sum_{fj}4b_{jf}[\varphi\phi_i|\phi_j\psi_f]+\sum_{fj}4c_{jf}[\varphi\phi_i|\phi_j\omega_f]\\&\quad-\sum_{kj}a_{jk}\{[\varphi\phi_k|\phi_i\phi_j]+[\varphi\phi_j|\phi_i\phi_k]\}-\sum_{fj}b_{jf}\{[\varphi\psi_f|\phi_i\phi_j]+[\varphi\phi_j|\phi_i\psi_f]\}\\&\quad-\sum_{fj}c_{jf}\{[\varphi\omega_f|\phi_i\phi_j]+[\varphi\phi_j|\phi_i\omega_f]\}\,,\end{aligned}\right\}\qquad(7)$$

φ=either of ϕ_l, ψ_g, ω_g.

$$i,\ j=1\to n.\quad k,\ l=n'\to 1'\ (n+1\to 2n).\quad f,\ g=1\to 1'\ (1\to 2n).$$

These MO integrals can be expanded in terms of AO integrals as follows;

$$\left.\begin{aligned}[\phi_i\phi_j|\varphi\varphi']&=\sum_{ABCD}a_A{}^i a_B{}^j\varepsilon_C\varepsilon_D'(\chi_A\chi_B|\zeta_C\zeta_D')\\&\cong\sum_{AC}a_A{}^i a_A{}^j\varepsilon_C\varepsilon_C'(\chi_A\chi_A|\zeta_C\zeta_C')\qquad\text{in Pariser approximation}\\[phi_i\varphi|\phi_j\varphi']&=\sum_{ABCD}a_A{}^i\varepsilon_B a_C{}^j\varepsilon_D'(\chi_A\zeta_B|\chi_C\zeta_D')\cong\sum_{AC}a_A{}^i\varepsilon_A a_C{}^j\varepsilon_C'(\chi_A\zeta_A|\chi_C\zeta_C')\,,\\\varepsilon_A&=\text{either of } a_A{}^f,\ b_A{}^f,\ c_A{}^f\,,\qquad\zeta=\text{either of }\chi,\ \xi,\ \eta\,.\end{aligned}\right\}\qquad(8)$$

Thus we have two types of AO Coulomb integrals to be evaluated: $(\chi_A\chi_A|\zeta_C\zeta_C')$ and $(\chi_A\zeta_A|\chi_C\zeta_C')$ which contain $3d_{xz}$ and $3d_{yz}$ AO's.

When the AO integrals are evaluated, we substitute them into Eq. (8) and obtain the numerical values of MO Integrals. With these values put into Eq. (7) and (6) we get numerical values of a_{ik}, b_{if}, c_{if} etc. We may better utilize the interation method to solve the complexity of simultaneous equations.

§ 3. *S–T* Intercombination Integral

After the modified MO's are obtained, we proceed to compute the *S–T* intercombination integral. It is given as[4];

$$\langle\Psi_T H_{LS}\Psi_S\rangle=i\left(\frac{\hbar}{2mc}\right)^2\int V\left\{\frac{\partial\phi_i{}^s}{\partial x}\frac{\partial\phi_j{}^s}{\partial y}-\frac{\partial\phi_i{}^s}{\partial y}\frac{\partial\phi_j{}^s}{\partial x}\right\}dv\,,\qquad(9)$$

where $\phi_i{}^s$ and $\phi_j{}^s$ are the combining MO's belonging to the singlet and triplet states respectively. They are illustrated in Fig. 4 and Table IV of the reference 4.

Putting the AO expansion of ϕ^s as given by Eqs. (3), (4) and (5) into Eq. (9), we have, retaining only the first order terms,

$$\begin{aligned}I&=\int V\left\{\frac{\partial\phi_i{}^s}{\partial x}\frac{\partial\phi_i{}^s}{\partial y}-\frac{\partial\phi_i{}^s}{\partial y}\frac{\partial\phi_j{}^s}{\partial x}\right\}dv\\&=\sqrt{\frac{\delta^5}{\pi}}\sqrt{\frac{2\delta'^7}{3\pi}}\,\delta\sum_{AB}\int\frac{z_a z_b}{r_a}e^{-\delta r_a-\delta' r_b}V dv\sum_f\beta_B{}^f\{y_a(\alpha_A{}^i b_{jf}-\alpha_A{}^j b_{if})-x_a(\alpha_A{}^i c_{jf}-\alpha_A{}^j c_{if})\}\,.\end{aligned}\qquad(10)$$

One may remark that the coefficients a_{ik} do not come in Eq. (10). This is quite natural because they represent the mixing of $2p\pi$ MO of higher levels. In other words, this indicates that the adoption of SCF MO instead of Hueckel MO makes no matter to obtain far better computation value of *S–T* intercombination intensity.

As for the form of potential V, we may assume the ordinary electrostatic potential composed of the nuclear attraction and electronic repulsion.[7]

Numerical computation must be made now on the evaluation of AO Coulomb integrals involving $3d$ orbitals and then the determination of the expansion coefficients a_{ik}, b_{if}, c_{if} by the iteration method, and finally the intercombination integral.

Unfortunately publications concerning the evaluation of integrals containging $3d$ AO are very rare at present and we can find neither formula nor table utilizable directly for our calculation. Only in the table of Kotani *et al.*,[8] some formulae are given in the unresolved form, but they are not enough for our purpose.

Now we are studying to extend the formulae given by Kotani *et al.* to serve for our calculation. The result of numerical computation shall be published later.

In the succeeding paper, we shall discuss the emission spectra of the triplet states and the lifetime of phosphorescence of diphenyl. The method can be extended directly to other compounds and we may compare the result of our method with those of other workers.

Acknowledgement

The author wishes to express his sincere thanks to Prof. R. Daudel, Dr. R. Lefebvre of Centre de Chimie Théorique de France and equally to Prof. M. Kotani of the University of Tokyo for their very kind advice and encouragement.

References

1) M. Mizushima and S. Koide: J. Chem. Phys. **20** (1952) 765.
2) D. S. McClure: J. Chem. Phys. **20** (1952) 682.
3) M. Moodie and C. Reid: J. Chem. Phys. **22** (1954) 252.
4) K. Iguchi: J. Phys. Soc. Japan **12** (1957) 1250.
5) Numerical values for many molecules are given in; C. A. Coulson, R. Daudel: Dictionary of values of molecular constants. Vol. II. (1955).
6) R. Lefebvre and C. Moser: J. Chem. Soc. (1956) 1557.
7) R. G. Parr, and B. L. Crawford: J. Chem. Phys. **16** (1948) 1049.
8) M. Kotani, A. Amemiya, R. Ishiguro and T. Kimura: Table of Molecular Integrals. Maruzen Co. Ltd. Tokyo (1955).

JOURNAL OF THE PHYSICAL SOCIETY OF JAPAN Vol. 13, No. 10, OCTOBER, 1958

Methods of Approximation of Molecular Integrals. I.

By Sigeru HUZINAGA

General Education Department, Kyushu University, Otsubo-machi, Fukuoka

(Received June 26, 1958)

The Mulliken and the Sklar approximations for difficult molecular integrals have for some years been the subject of several investigations. So far, however, we are not provided with clear insight into these approximate methods and, accordingly, with sufficiently reliable criteria for the choice between them for each individual case.

In this paper a possible answer to the problem is presented by examining carefully the accuracies of these two methods. In addition, a new approximate method is proposed, which is useful when both the Mulliken and the Sklar approximations break down seriously.

§ 1. Introduction

Among various approximations for difficult molecular integrals the Mulliken[1] and the Sklar[2] approximations are most widely used. Close examinations of these approximations have been the subject of several papers[3)–10)]. In spite of those rather extensive studies, it seems that we have still no clear insight into the natures of these approximations and, accordingly, we have no sufficiently reliable criteria for the choice between them in actual molecular calculations. In the treatment of

the electronic levels of the benzene Parr, Craig and Ross[3] estimated three- and four-center integrals by the Sklar approximation. They examined the accuracies of the Sklar and the Mulliken approximations in reference to several two-center integrals and they stated "In these, and other similar cases, the success of the approximations perhaps varies too much to justify a choice between them; Sklar's method was therefore adopted to secure continuity with previous work." Eyring et al[8] arrived at a similar conclusion after their long effort to clarify the point of the present subject: "The tables for the individual integral values indicate that generalizations as to the direction or magnitude of errors caused by the approximations examined are dubious if not dangerous." Shull and Ellison[4),9] have made a distinct contribution by suggesting a qualitative criterion for the choice between the Mulliken and the Sklar approximations. Their suggestion, based on the experience of actual molecular calculations, is that "in future computations using these approximations, one should use that approximation for each integral which gives the lower value to that integral."

In this paper we present a possible answer to the present problem. We hope it is clear enough to justify a choice between the approximations for each individual case. In addition we shall see that a new approximate formula suggests itself in the course of examinations of the Mulliken and the Sklar approximations, which works well where both of these two approximations break down seriously.

§ 2. On Rüdenberg's Argument

Mulliken[1] gives a general approximate formula for multicenter repulsion integrals in terms of two-center overlap and Coulomb integrals. His expression may be written,

$$[\chi_a\chi_b|\chi_c\chi_d]=\int\chi_a(1)\chi_b(1)(1/r_{12})\chi_c(2)\chi_d(2)d\tau_1 d\tau_2$$
$$\simeq\tfrac{1}{4}(\chi_a|\chi_b)(\chi_c|\chi_d)\{[\chi_a\chi_a|\chi_c\chi_c]+[\chi_a\chi_a|\chi_d\chi_d]$$
$$+[\chi_b\chi_b|\chi_c\chi_c]+[\chi_b\chi_b|\chi_d\chi_d]\}\,, \qquad (2.1)$$

where

$$(\chi_a|\chi_b)=\int\chi_a(1)\chi_b(1)d\tau_1 \quad \text{(overlap integral)},$$

$$[\chi_a\chi_a|\chi_c\chi_c]=\int\chi_a(1)\chi_a(1)(1/r_{12})\chi_c(2)\chi_c(2)d\tau_1 d\tau_2$$

(Coulomb integral),

χ_a, χ_b, χ_c, χ_d=atomic orbitals centered on nuclei a, b, c and d. It is easily seen that if we use the following approximate expression for the product $\chi_a(1)\chi_b(1)$,

$$\chi_a(1)\chi_b(1)\simeq\tfrac{1}{2}(\chi_a|\chi_b)\{\chi_a(1)\chi_a(1)+\chi_b(1)\chi_b(1)\}\,, \qquad (2.2)$$

we obtain the expression (2.1). This is the core of the Mulliken approximation. Mulliken suggested his formula on an intuitive basis and, subsequently, Rüdenberg[11] succeeded in showing that this approximation corresponds to the leading term in an infinite series development. We shall recapitulate here Rüdenberg's argument in a simple case of two homonuclear centers a and b. Let

$$\chi_{a1},\ \chi_{a2},\ \cdots,\ \chi_{ak},\ \cdots$$

be a complete set of orthogonalized real orbitals on center a and analogously

$$\chi_{b1},\ \chi_{b2},\ \cdots,\ \chi_{bk},\ \cdots$$

on center b. Then we may have the expansions, for example,

$$\left.\begin{aligned}\chi_{a1}(1)&=\sum_{k=1}^{\infty}(\chi_{a1}|\chi_{bk})\chi_{bk}(1)\,,\\ \chi_{b1}(1)&=\sum_{k=1}^{\infty}(\chi_{b1}|\chi_{ak})\chi_{ak}(1)\,,\end{aligned}\right\} \qquad (2.3)$$

whence:

$$\begin{aligned}&\chi_{a1}(1)\chi_{b1}(1)\\ &=\tfrac{1}{2}\sum_{k=1}^{\infty}(\chi_{a1}|\chi_{bk})\{\chi_{a1}(1)\chi_{ak}(1)+\chi_{b1}(1)\chi_{bk}(1)\}\\ &=\tfrac{1}{2}(\chi_{a1}|\chi_{b1})\{\chi_{a1}(1)\chi_{a1}(1)+\chi_{b1}(1)\chi_{b1}(1)\}\\ &\quad+\tfrac{1}{2}(\chi_{a1}|\chi_{b2})\{\chi_{a1}(1)\chi_{a2}(1)+\chi_{b1}(1)\chi_{b2}(1)\}\\ &\quad+\cdots\,. \qquad (2.4)\end{aligned}$$

The first term is nothing but the Mulliken approximation (2.2). This justification of the Mulliken approximation seems quite lucid mathematically but it does not provide us practical criteria of the approximation useful for each individual case encountered in actual molecular calculations. Concerning this point, one might suggest an "improvement" of the Mulliken approximation by including the second term of the expansion (2.4). This "improvement" has an apparent disadvantage. To fix the idea, let us suppost our χ_{a1} be a $1s$ orbital. Then it is natural to take a $2p\sigma$ orbital for χ_{a2}. Thus we have to estimate additional overlap and Coulomb integrals involving $2p\sigma$. Actually, it turns out that such a straightforward inclusion of a second term does not constitute an "improvement" at all.

One can see this, for example, by evaluating the following two-center integrals using first two terms in (2.4);

$$[a|\chi_a\chi_b]=\int(1/r_{a1})\chi_a(1)\chi_b(1)d\tau_1$$

(nuclear attraction integral),

$$[\chi_a(1)\chi_b(1)|\chi_a(2)\chi_b(2)]$$
$$=\int\chi_a(1)\chi_b(1)(1/r_{12})\chi_a(2)\chi_b(2)d\tau_1 d\tau_2$$

(exchange integral).

For these cases the Mulliken approximation yields too large values in large nuclear separation R_{ab} as shown in Table I and Table II, and it is easily seen that the inclusion of the second term makes them still larger. Barker and Eyring[7] have revealed another example showing that the mathematically elegant discussion of Rüdenberg does not necessarily lead us to practically useful approximations. This situation seems to indicate that it would be rather difficult to proceed purely mathematically to reach our desired clear-cut answer to the present problem. Probably we should recede a little and start again from more or less intuitive bases after the manner of Mulliken's original reasoning.

§ 3. Types of Approximation

In the present treatment, we shall start by recalling Ellison's important observation[9] that "in general, good approximations of AO interaction integrals can be obtained only by securing good approximate representations of the actual charge distributions involved."

Now let the atomic orbitals χ's be simply 1s hydrogen-like functions such as

$$\chi_a(1)=s_a(1)=(Z^3/\pi)^{1/2}\exp(-Zr_{a1}), \quad (3.1)$$

where Z is the effective nuclear charge. Then the "charge distribution" $\chi_a(1)\chi_b(1)$ is explicitly written

$$s_a(1)s_b(1)\sim\exp[-Z(r_{a1}+r_{b1})]. \quad (3.2)$$

Here, it is important to recognize that this function is "flat" on the line connecting two centers a and b, as pictured in Fig. 1(a). With this in mind, we shall try to examine the natures of the Mulliken and the Sklar approximations:

$$\text{(M)}\quad s_a(1)s_b(1)\simeq\tfrac{1}{2}(s_a|s_b)\{s_a(1)s_a(1)+s_b(1)s_b(1)\}, \quad (3.3)$$

$$\text{(S)}\quad s_a(1)s_b(1)\simeq(s_a|s_b)s_m(1)s_m(1), \quad (3.4)$$

where m is the middle point between a anb b. Corresponding charge distributions are pictured in Fig. 1(b) and (c), respectively. It is clearly observed that the resemblances between these two approximate charge distributions and the actual one are rather poor, especially at large internuclear separation (right-hand side of Fig. 1). Looking at these three figures, (a), (b), (c), we naturally arrive at an idea of increasing the resemblance by

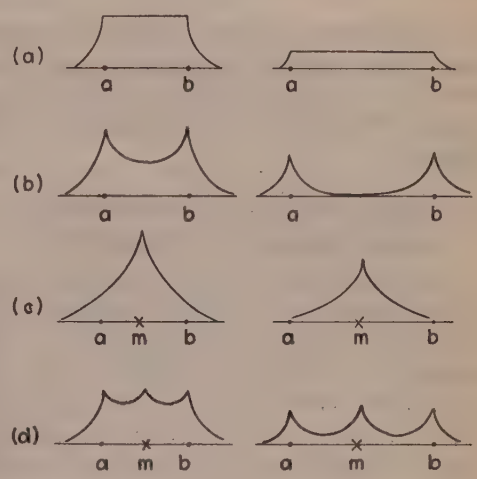

Fig. 1.

superposing (b) to (c) with the resulting figure (d). More precisely, this means to take

$$\text{(MS)}\quad s_a(1)s_b(1)\simeq\tfrac{1}{3}(s_a|s_b)\{s_a(1)s_a(1)+s_m(1)s_m(1)+s_b(1)s_b(1)\}. \quad (3.5)$$

This formula may be regarded as one of possible hybrids of the Mulliken and the Sklar approximations and we shall call this here the MS approximation tentatively.

At first sight, it is expected that the use of the approximate formula (3.5) yields the results always better than those of the Mulliken and the Sklar approximations because the figure (d) seems to have the best resemblance to the actual distribution (a) in Fig. 1. Actually, however, this is not the case. A nuclear attraction integral $[a|s_as_b]$ presents a notable example: we observe in Table I that the Sklar approximation is consistently superior to other two approximations for this integral. What is the reason for this rather perplexing situation? The reason lies in the fact that the molecular integrals interested here are not integrals over simple products of certain charge distributions, as is the case

Table I. $[a|s_a s_b]/Z$ (in au)

$q=ZR$	Actual value	M	S	MS
2.0	0.4060	0.4318	0.4277	0.4304
3.0	0.1991	0.2318	0.2034	0.2223
4.0	0.09158	0.1182	0.08943	0.1086
5.0	0.04043	0.05794	0.03772	0.05120
6.0	0.01735	0.02747	0.01554	0.02350
8.0	0.003019	0.005724	0.002540	0.004662
10.0	0.0004994	0.001107	0.0004024	0.0007547
12.0	0.00007987	0.0002030	0.00006246	0.0001562

for overlap integrals, but contain the "weight factor" such as $(1/r_{a1})$ or $(1/r_{12})$ in the integrands. In the next section we shall try to explain more clearly the implication of this statement.

§ 4. Approximate and Actual Values of Various Molecular Integrals (Part I)

In this section we compare values calculated using the three types of approximation, (M), (S) and (MS), with actual values of two- and three-center 1*s* orbital integrals, where the centers are located linearly with equal distances. Fig. 2 is prepared for the purpose of easy identification of the definition of each integral.

Group I. Nuclear attraction integrals.

(I-α) $\quad [a|s_a s_b]=\int(1/r_{a1})s_a(1)s_b(1)d\tau_1$.

(I-α-M): $\quad \frac{1}{2}(s_a|s_b)\{[a|s_a s_a]+[a|s_b s_b]\}$,

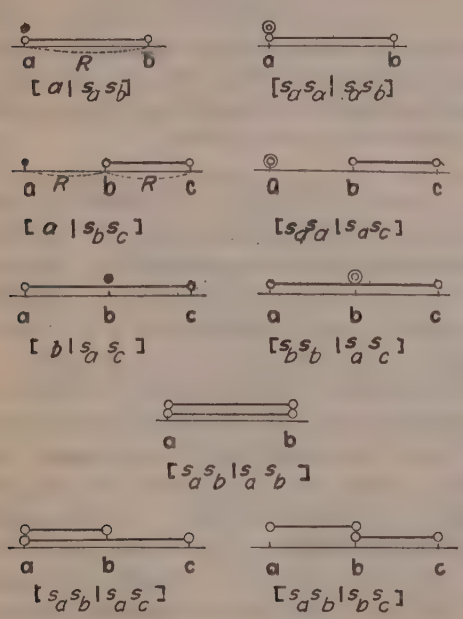

Fig. 2.

(I-α-S): $\quad (s_a|s_b)[a|s_m s_m]$,

(I-α-MS): $\quad \frac{1}{3}(s_a|s_b)\{[a|s_a s_a]+[a|s_m s_m]+[a|s_b s_b]\}$
$\quad =\frac{1}{3}\{2(\mathrm{M})+(\mathrm{S})\}$.

$[a|s_a s_b]$ is a simple two-center integral which can be evaluated exactly. Table I shows that the Mulliken approximation gives always higher values and the departure from actual values grows seriously for larger values of $q=ZR$. At those large distances the first term $(s_a|s_b)[a|s_a s_a]$ of (I-α-M) makes dominant contribution. Since $[a|s_a s_a]$ is a constant, the above mentioned tendency of the Mulliken approximation means that the decay of the factor $(s_a|s_b)$ is too slow as compared with that of the actual values of $[a|s_a s_b]$. Let us try to speak a little more pictorically. As may be seen from (3.2) and Fig. 1(a), the actual shape of $s_a(1)s_b(1)$ is something like an elongated spindle. In the Mulliken approximation the half of the charge distribution is gathered to a spherical distribution $s_a(1)s_a(1)$ centered at a and another half to $s_b(1)s_b(1)$. Then the charge distribution $s_a(1)s_a(1)$ at a tends to exaggerate the effect of the "weight" $(1/r_{a1})$ centered also at a. Thus, the effect of $[a|s_a s_a]$ becomes predominant more and more for larger distances because of insufficient suppressive effect of $(s_a|s_b)$ which is a simple integral over $s_a(1)s_b(1)$ lacking any damped weight factor and decaying too slowly.

In the Sklar approximation the actual charge distribution is replaced simply by a single charge cloud $s_m(1)s_m(1)$ at the middle point m between a and b, and there exists finite distance between the center of Coulomb potential $(1/r_{a1})$ and that of the interacting charge cloud. According to Table I, this situation works rather faborably at least for intermediate values of q. It should be noted, however, that (I-α-S) yields consistently smaller values (except for $q=2$ and 3) and the discrepancies

seem to become larger with increasing distance. This may be understood again by considering the effect of the weight $(1/r_{a1})$: in the actual distribution $s_a(1)s_b(1)$ there survives finite portion of the distribution in the deep "hole" of $(-)(1/r_{a1})$ but in the Sklar approximation there lies only rapidly vanishing tail of $s_m(1)s_m(1)$.

Finally, as for the MS approximation, it may easily be inferred that this approximation should yield too large values because the fatal defect of the Mulliken approximation mentioned above is remedied only insufficiently here.

(I–β) $\quad [a|s_bs_c]=\int(1/r_{a1})s_b(1)s_c(1)d\tau_1$.

(I–β–M): $\quad \frac{1}{2}(s_b|s_c)\{[a|s_bs_b]+[a|s_cs_c]\}$,

(I–β–S): $\quad (s_b|s_c)[a|s_ms_m]$,

(I–β–MS) $\quad \frac{1}{3}\{2(\mathrm{M})+(\mathrm{S})\}$.

In this case the center a of the troublesome weight factor $(1/r_{a1})$ lies outside of main portion of the charge distribution s_bs_c as contrasted to the case of $[a|s_as_b]$. Nevertheless, it is probable that the charge concentration $s_b(1)s_b(1)$ in the Mulliken and the MS approximations is still prone to exaggerate the effect of $(1/r_{a1})$. Thus, in view of the detailed discussion in the case of $[a|s_as_b]$, it is quite natural to expect that the general tendency that the Mulliken approximation gives larger values and the Sklar approximation yields smaller values will still be observed but the degree of diversity of the actual and approximate values will become less conspicuous in this case of $[a|s_bs_c]$ as compared with the case of $[a|s_as_b]$. These expectations are completely comfirmed in Table II.

(I–γ) $\quad [b|s_as_c]=\int(1/r_{b1})s_a(1)s_c(1)d\tau_1$.

(I–γ–M): $\quad (s_a|s_c)[b|s_as_a]$,

(I–γ–S): $\quad (s_a|s_c)[b|s_bs_b]$,

(I–γ–MS): $\quad \frac{1}{3}\{2(\mathrm{M})+(\mathrm{S})\}$.

This integral seems to deserve careful considerations because both (I–γ–M) and (I–γ–S) provide only very poor approximate values. Let us try to "predict" characteristic features of the Mulliken and the Sklar approximations for this case. Imagine that we dig a deep hole of the Coulomb potential $(-)(1/r_1)$ at the middle point between a and b in each diagram of Fig. 1. Comparison of the diagrams thus obtained immediately render us to predict that the Mulliken approximation shoud give smaller values and, on the contrary, the Sklar approximation should give badly exaggerated values. Our reasoning in this case is quite similar to that used in (I–α) and (I–β) and it would be unnecessary to describe it in detail. Table III tells us that our predictions are quite right. It should be remarked that both the Mulliken and the Sklar approximation break down seriously especially for large

Table II. $[a|s_bs_c]/Z$ (in au)

$q=ZR$	Actual value	M	S	MS
1.0	0.501	0.516	0.501	0.511
1.5	0.313	0.331	0.311	0.324
2.0	0.197	0.212	0.194	0.206
2.5	0.124	0.135	0.122	0.131
3.0	0.0791	0.0866	0.0774	0.0835
4.0	0.0323	0.0354	0.0315	0.0341
6.0	0.00536	0.00589	0.00523	0.00567

Table III. $[b|s_as_c]/Z$ (in au)

$q=ZR$	Actual value	M	S	MS
1.0	0.465	0.428	0.586	0.481
1.5	0.242	0.203	0.349	0.252
2.0	0.117	0.0894	0.189	0.123
2.5	0.0539	0.0377	0.0966	0.0573
3.0	0.0240	0.0155	0.0471	0.0260
4.0	0.00443	0.00254	0.0102	0.00509
6.0	0.000128	0.000062	0.000375	0.000166

values of q and the MS approximation yields consistently rather good results.

Group II. Hybrid integrals.

(II-α) $[s_a s_a | s_a s_b]$

$$= \int s_a(1) s_a(1) (1/r_{12}) s_a(2) s_b(2) d\tau_1 d\tau_2 ,$$

(II-β) $[s_a s_a | s_b s_c]$

$$= \int s_a(1) s_a(1) (1/r_{12}) s_b(2) s_c(2) d\tau_1 d\tau_2 ,$$

(II-γ) $[s_b s_b | s_a s_c]$

$$= \int s_b(1) s_b(1) (1/r_{12}) s_a(2) s_c(2) d\tau_1 d\tau_2 ,$$

There are obvious relationships between the integrals of Group I and Group II. It is clear that, if $s_a(1)s_a(1)$ or $s_b(1)s_b(1)$ is contracted to a δ-function-like distribution in (II-α), (II-β), (II-γ), we immediately obtain (I-α), (I-β), (I-γ), respectively. Conversely, we may say that the integrals of Group II can be obtained by smearing the point charge in Group I to form a spherical distribution $s_a(1)s_a(1)$ or $s_b(1)s_b(1)$. These observations serve to clarify the behaviors of our three approximations for the hybrid integrals in question. Thus, it is expected that the general situation would remain essentially unchanged but several distinct features remarked for the nuclear attraction integrals (Group I) would be moderated here because the troublesome "singularity" of $(1/r_{a1})$ or $(1/r_{b1})$ in Group I is somewhat blurred in Group II. In fact, we can easily notice close correspondences and resemblances between the results exhibited in Tables I, II, III and Tables IV, V, VI.

Table IV. $[s_a s_a | s_a s_b]/Z$ (in au)

$q=ZR$	Actual value	M	S	MS
2.0	0.3080	0.3082	0.3252	0.3138
3.0	0.1607	0.1646	0.1709	0.1667
4.0	0.07698	0.08257	0.08062	0.08192
6.0	0.01531	0.01864	0.01506	0.01745
8.0	0.002739	0.003816	0.002519	0.003384
10.0	0.0004611	0.0007296	0.0004017	0.0006203

Table V. $[s_a s_a | s_b s_c]/Z$ (in au)

$q=ZR$	Actual value	M	S	MS
1.0	0.4171	0.4208	0.4209	0.4208
2.0	0.1884	0.1975	0.1875	0.1942
4.0	0.03222	0.03525	0.0315	0.0340
6.0	0.005355	0.005885	0.005233	0.005668

Table VI. $[s_b s_b | s_a s_c]/Z$ (in au)

$q=ZR$	Actual value	M	S	MS
1.0	0.3358	0.3252	0.3665	0.3390
2.0	0.09421	0.08062	0.1183	0.09318
4.0	0.003923	0.002519	0.006360	0.003799
6.0	0.001178	0.00006244	0.0002342	0.0001197

Table VII. $[s_a s_b | s_a s_b]/Z$ (in au)

$q=ZR$	Actual value	M	S	MS
2.0	0.1842	0.1807	0.2150	0.1890
3.0	0.05851	0.05738	0.07591	0.06040
4.0	0.01563	0.01563	0.02239	0.01621
5.0	0.003717	0.003845	0.005829	0.003884
6.0	0.0008140	0.0008779	0.001386	0.0008595
8.0	0.00003290	0.00003883	0.00006472	0.00003584
10.0	1.138×10^{-6}	1.469×10^{-6}	2.532×10^{-6}	1.293×10^{-6}
12.0	3.548×10^{-8}	4.975×10^{-8}	8.780×10^{-8}	4.227×10^{-8}

Group III. Exchange integrals.

(III-α) $[s_a s_b | s_a s_b]$

$$=\int s_a(1)s_b(1)(1/r_{12})s_a(2)s_b(2)d\tau_1 d\tau_2 .$$

(III-α-M): $\frac{1}{2}(s_a|s_b)^2\{[s_a s_a|s_a s_a]+[s_a s_a|s_b s_b]\}$,

(III-α-S): $(s_a|s_b)^2[s_m s_m|s_m s_m]$,

(III-α-MS): $\frac{1}{9}(s_a|s_b)^2\{3[s_a s_a|s_a s_a]$
$+4[s_a s_a|s_m s_m]+2[s_a s_a|s_b s_b]\}$.

This integral brings about a new feature. Let us first examine the results of Table VII. The most interesting point is that both (III-α-M) and (III-α-S) yield higher values for larger q. So far, this is never the case. Mathematically, this is a direct consequence of the fact that both approximate formulas contain a constant term, $[s_a s_a|s_a s_a] \equiv [s_m s_m|s_m s_m]$. In this respect, (III-$\alpha$-M) is quite similar to (I-α-M) and (III-α-S) to (I-γ-S). Some reflections on the shapes of the actual and the approximate charge distributions seem to be useful again for the present case. $[s_a s_b|s_a s_b]$ describes the Coulomb interaction between two overlapping charge distributions, $s_a(1)s_b(1)$ and $s_a(2)s_b(2)$, of an elongated shape. In the Sklar approximation this is approximated by the interaction between two identical spherical charge distributions centered always at the middle point m between a and b. Just as in $[b|s_a s_c]$ (I-γ) and $[s_b s_b|s_a s_c]$ (II-γ), we are bound to overestimate the "weight" $(1/r_{12})$ under such a condition, especially for large q. Thus, the Sklar approximation gives consistently higher values in the present case. Also in the Mulliken approximation the term $[s_a s_a|s_a s_a]$, representing the interaction between two identically overlapping spherical charges, gives rise to the same kind of departure from actual values but the existence of another term $[s_a s_a|s_b s_b]$ which represents the interaction between two distant charge distributions prevents to some extent serious breakdown of the approximation as compared with the Sklar approximation. Inferring in this way, we may understand that the MS approximation yields always values of tolerable accuracy. It is of interest to note that for $q>6$ (III-α-MS) gives lower values than either those of (III-α-M) and of (III-α-S).

(III-β) $[s_a s_b|s_a s_c]$

$$=\int s_a(1)s_b(1)(1/r_{12})s_a(2)s_c(2)d\tau_1 d\tau_2 .$$

We may obtain this type of integral from $[s_a s_b|s_a s_b]$ (III-α) by making one of the two $s_a s_b$'s longer than the other, or from $[s_a s_a|s_a s_c]$ (II-α) by elongating the spherical charge distribution $s_a s_a$ to $s_a s_b$. From such view-points, we may expect the following features. (I) In the Mulliken approximation the tendency of departure from the actual values will be more or less similar to the cases of $[s_a s_b|s_a s_b]$ and $[s_a s_a|s_a s_b]$, namely the approximate values will be smaller at the beginning and eventually surpass the actual values because of the overlapping of two spherical charge distributions at a. (2) In the Sklar approximation, a serious overestimation exhibited in the case of $[s_a s_b|s_a s_b]$ will be avoided because there now exists finite separation between centers of the two approximate spherical charge distributions, but this very separation might bring about a tendency of giving smaller values in the long run in analogous manner encountered in the case of $[a|s_a s_b]$ and $[s_a s_a|s_a s_b]$. Unfortunately, these expectations are not fully confirmed in Table VIII, because comparisons are performed for only three values of q, 2, 4, 6. Nevertheless, the present author believes that

Table VIII. $[s_a s_b|s_a s_c]/Z$ (in au)

$q=ZR$	Actual value	M	S	MS
2.0	0.05121	0.04785	0.06155	0.05185
4.0	0.0006539	0.0005995	0.0008204	0.0006711
6.0	4.769×10^{-6}	4.596×10^{-6}	5.645×10^{-6}	5.068×10^{-6}

Table IX. $[s_a s_b|s_b s_c]/Z$ (in au)

$q=ZR$	Actual value	M	S	MS
2.0	0.1412	0.1483	0.1465	0.1490
4.0	0.009128	0.01115	0.0008867	0.01066
6.0	0.0004364	0.0005775	0.0003695	0.0005101

the above expectations should turn out essentially correct, if comparisons are made for larger values of q. It is of interest to note that the MS approximation yields rather excellent values.

(III–γ) $[s_a s_b | s_b s_c]$

$$=\int s_a(1)s_b(1)(1/r_{12})s_b(2)s_c(2)d\tau_1 d\tau_2 \ .$$

This integral represents the interaction of two elongated charge distributions, $s_a(1)s_b(1)$ and $s_b(2)s_c(2)$, with their end tails overlapped. The Mulliken approximation will exaggerate this overlapping by placing two spherical charge distributions at b. On the contrary, the Sklar approximation will tend to yield smaller values because two spherical charge distributions are put separately here. Table IX seems to confirm these expectations.

§ 5. Rules of Choice

Anyone who is patient enough to follow rather tiresome discussions in the preceding section may recognize that the line of reasoning is very simple and almost trivial but, none the less, seems to be useful in some cases. It is based upon intuitive comparisons of the forms of the actual and approximate charge distributions with accompanied consideration of the effect of the "weight" factor such as $(1/r_{a1})$ or $(1/r_{12})$ in each individual integral. It may be possible, if we wish, to write down the "rules" explicity in fixed sentences but we will not do so here. The reason is that we believe we had better keep the manner of reasoning in mind as a working principle to be applied flexibly to individual cases.

Here, let us try to find a possible explanation of a rule of choice between the Mulliken and the Sklar methods for interactions involving symmetrical charge distributions proposed empirically by Ellison[9]: "Here, the best procedure is to utilize the lower value as given by the two methods for each integral." In the preceding section it is observed that we obtain exaggerated values when approximate charge distributions are placed in such a way that the Coulomb interaction, $(1/r_{a1})$ or $(1/r_{12})$, is apt to be overestimated under insufficient suppression due to the factor, $(s_a|s_b)$ or $(s_a|s_b)^2$. In many cases we can identify terms mainly responsible for such troubles in approximate formulas and it seems almost always certain that the higher of two approximate values from the two methods comes directly from such troublesome terms in respective approximate formula. Because of this distinct cause, it seems that deviations take place more seriously to larger value side than to the opposite side. Presumably here lies one of possible explanations of the rule of Ellison and Shull. The most typical examples are the Sklar approximations for $[b|s_a s_c]$ (I–γ), $[s_b s_b|s_a s_c]$ (III–γ) and $[s_a s_b|s_a s_b]$ (III–α). (See Tables III, VI, VII). Another example is found in the Mulliken approximation for $[a|s_a s_b]$ (I–α) or $[s_a s_a|s_a s_b]$ (II–α). (See Tables I, IV). Here the "lower value" rule favors the Sklar approximation.

In the present paper, we have three approximate methods. In addition to the Mulliken and the Sklar methods, we have proposed a new approximation which is properly regarded as one of possible hybrids of the Mulliken and the Sklar approximations. This third method works rather well where both parent methods break down seriously. As will be shown in the following sections, we can be definite about the choice among these three methods in some cases, but in some other cases we are not quite sure about the matter. In such cases we may rely upon the "lower value" rule explained above or upon the MS approximation.

§ 6. Approximate and Actual Values of Various Molecular Integrals (Part II)

Taylor[12] in his treatment of the linear H_4 system calculated accurately various multicenter integrals. We shall make use of them to check the accuracies of our three approximation methods. The accurate values of integrals are listed in Table X together with the approximate values given by our three methods. Before we begin to examine Table X, les us try to choose the best method for each integral. Diagrams similar to those in Fig. 2 may easily be drawn for the integrals in the table. The nuclei a, b, c, d are spaced linearly at equal intervals (R=1.4au), the equilibrium internuclear separation H_2. Looking at those diagrams, we may foresee the following features. (1) The Sklar approximation will be successful for $[a|s_b s_c]$, $[a|s_b s_d]$, $[a|s_c s_d]$; $[s_a s_a|s_b s_c]$, $[s_a s_a|s_b s_d]$, $[s_a s_a|s_c s_d]$; $[s_a s_b|s_c s_d]$, be-

cause these integrals belong essentially to the same type as $[a|s_b s_c]$ (I–β) and $[s_a s_a|s_b s_c]$ (II–β) in § 4. (2) For $[b|s_a s_c]$, $[b|s_a s_d]$; $[s_b s_b|s_a s_c]$, $[s_a s_d|s_b s_c]$, the Mulliken approximation will yield lower values and the Sklar approximation will give too high values. Probably the MS approximation will give the best approximate values. (3) As for the remaining integrals, we cannot be quite certain about selection of a single method for each integral. The interval between nuclei, $R=1.4$ au, is not large enough to permit us to say something definite about the behaviors of the three approximate methods. Here we may use the "lower value" rule between the Mulliken and the Sklar approximations or rely upon the MS approximation.

Table X. Taylor's integrals. (in eV)

	Actual value	M	S	MS
$[a\|s_b s_c]$	9.321	9.807	9.256	9.623
$[a\|s_b s_d]$	3.840	4.476	3.718	4.223
$[a\|s_c s_d]$	5.839	6.013	5.800	5.942
$[b\|s_a s_c]$	7.523	6.441	10.56	7.814
$[b\|s_a s_d]$	2.655	2.164	3.732	2.687
$[s_a s_a\|s_b s_c]$	8.376	8.579	8.435	8.531
$[s_a s_a\|s_b s_d]$	3.589	3.906	3.570	3.794
$[s_a s_a\|s_c s_d]$	5.583	5.856	5.706	5.806
$[s_b s_b\|s_a s_c]$	5.722	5.316	6.599	5.744
$[s_b s_b\|s_a s_d]$	2.113	1.893	2.643	2.143
$[s_a s_b\|s_a s_c]$	4.050	3.916	4.671	4.141
$[s_a s_b\|s_a s_d]$	1.481	1.442	1.705	1.534
$[s_a s_c\|s_a s_d]$	0.776	0.747	1.031	0.806
$[s_a s_b\|s_b s_c]$	7.475	7.560	7.728	7.634
$[s_a s_b\|s_b s_d]$	3.207	3.385	3.290	3.380
$[s_a s_b\|s_c s_d]$	5.033	5.434	5.190	5.358
$[s_a s_c\|s_b s_d]$	1.903	1.798	2.073	1.803
$[s_a s_d\|s_b s_c]$	1.776	1.425	2.117	1.622

Table XI. $[a|\pi_a\pi_b]/\delta$ (in au)

$q=\delta R$	Actual value	M	S
2.0	0.2932	0.2977	0.3108
3.0	0.1743	0.1829	0.1881
4.0	0.09463	0.1043	0.1025
5.0	0.04829	0.05640	0.05192
6.0	0.02355	0.02927	0.02499
7.0	0.01109	0.01469	0.01160
8.0	0.005088	0.007172	0.005233
9.0	0.002283	0.003420	0.002312
10.5	0.001006	0.001599	0.001005
11.0	0.0004370	0.0007345	0.0004305

In Table X we find just what we expect. As for the integrals mentioned in (3), the Mulliken and the MS approximations reveal almost the same degree of accuracy.

Table XII. $[\pi_a\pi_a|\pi_a\pi_b]/\delta$ (in au)

$q=\delta R$	Actual value	M	S
4.0	0.08599	0.08713	0.09087
5.0	0.04480	0.04694	0.04728
6.0	0.02217	0.02425	0.02321
7.0	0.01056	0.01212	0.01092
8.0	0.004881	0.005893	0.004978

Table XIV. Integrals for the benzene molecule*. (in eV)

Integrals	S	M	MS
(1:23)	0.039	0.113	**0.0883**
(1:24)	0.006	0.0167	**0.0131**
(1:25)	0.015	0.0077	**0.0101**
(1:26)	0.318	0.0333	**0.128**
(1:34)	0.002	0.00208	**0.00205**
(1:35)	0.002	0.000505	**0.00100**
(11|23)	1.870	**1.780**	
(11|24)	0.280	**0.272**	
(11|25)	0.160	0.130	**0.140**
(11|26)	0.524	0.351	**0.409**
(11|34)	1.421	1.382	**1.395**
(11|35)	0.251	0.220	**0.231**
(12|13)	0.136	**0.103**	
(12|14)	0.046	**0.042**	
(12|15)	**0.091**	0.092	
(12|16)	**0.677**	0.687	
(12|34)	0.436	**0.428**	
(12|35)	0.073	0.064	**0.0661**
(12|36)	0.046	0.0338	**0.0368**
(12|45)	0.383	**0.359**	
(13|14)	0.009	**0.0063**	
(13|15)	0.015	**0.0128**	
(13|24)	0.020	0.0121	**0.0145**
(13|25)	0.009	0.0051	**0.0062**
(13|46)	0.014	0.0106	**0.0111**
(14|25)	0.005	0.0023	**0.0029**

* This table includes the three- and four-center integrals listed in Table II of Parr, Craing and Ross[3]. They used the approximate valves given by the Sklar method. Values due to the Mulliken and the MS approximations can easily be calculated by using numerical values in their Table II. $(pq|rs)$ is the Coulomb-exchange integral $\int \pi_p^*(1)\pi_r^*(2)(e^2/r_{12})\pi_q(1)\pi_s(2)d\tau_1 d\tau_2$, where π_p is the $2p\pi$ orbital on the pth carbon atom, and the carbon atom are numbered consecutively around the ring as is shown in Fig. 3.

§ 7. Approximate and Actual Values of Various Molecular Integrals (Part III)

So far, we have concerned exclusively with 1s orbitals. Practically, however, it would be more important to examine the approximate methods in the case of difficult integrals involving $2p\pi$ orbitals such as

$$(2p\pi)_a = \pi_a(1)$$
$$= (\delta^5/\pi)^{1/2} r_{a1} \sin\theta_{a1} \cos\varphi_{a1} \exp(-\delta r_{a1}) .$$

Unfortunately, there have been found no accurate values of the multicenter integrals available to the present author. We believe, however, that examinations of the approximate methods with reference to available two-center integrals are useful enough to draw some general conculsions at least for homonuclear systems. Comparisons are made between the actual[13] and the approximate values in Table XI ($[a|\pi_a\pi_b]$), Table XII ($[\pi_a\pi_a|\pi_a\pi_b]$) and Table XIII ($[\pi_a\pi_b|\pi_a\pi_b]$). These are to be examined in relation to Table I ($[a|s_as_b]$), Table IV ($[s_as_a|s_as_b]$) and Table VII ($[s_as_b|s_as_b]$) respectively. It is immediately noticed that, except for smaller values of $q=\delta R$ devoid of practical importance, the parallelisms between the two corresponding tables are very close. This suggests strongly that the line of reasoning successful for 1s orbitals could be applied also to $2p\pi$ orbitals without suffering any essential modification.

Parr, Craig and Ross[3] in their famous treatment of the benzene molecule calculated three- and four-center integrals by using the Sklar approximation. It would be of interest to try to check the accuracies of adopted approximate values because it is shown by them that the inclusion of those multicenter integrals affects the final result quite appreciably. Table XIV contains the relevant numerical values and Fig. 3 will be helpful for the inspections of the results displayed in the table. In view of the discussion of § 5 we may expect that the "lower value" criterion of Ellison and Shull should work well for the present case. This criterion favors the Mulliken approximation overwhelmingly here as is seen in Table XIV. Values due to the MS approximation are given for the integrals for which the MS method is expected to be the best. We may easily pick up those integrals

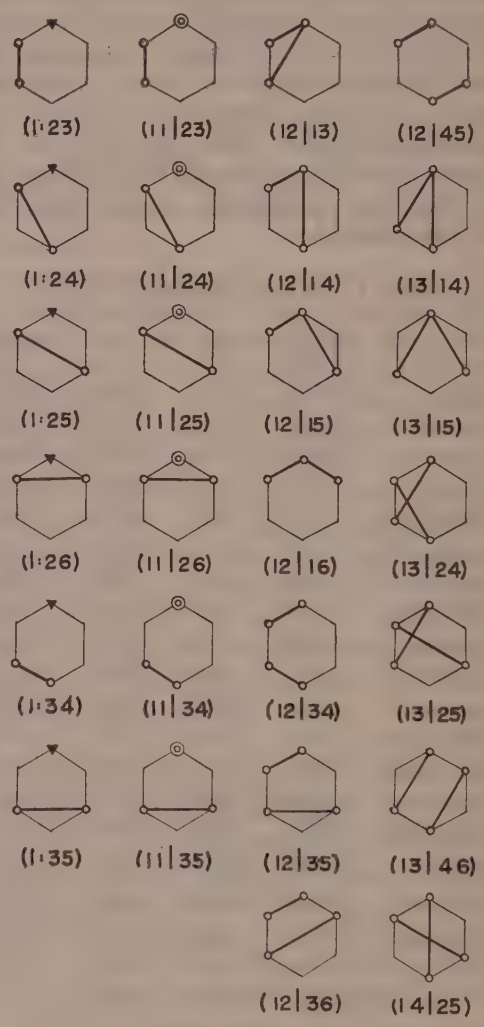

Fig. 3.

Table XIII. $[\pi_a\pi_b|\pi_a\pi_b]/\delta$ (in au)

$q=\delta R$	Actual value	M	S	MS
2.0	0.1760	0.1709	0.1889	
3.0	0.07507	0.07151	0.08573	
4.0	0.02644	0.02500	0.03223	0.02628
5.0	0.008096	0.007696	0.01052	0.008035
6.0	0.002231	0.002152	0.003082	0.002214
7.0	0.0005660	0.0005577	0.0008289	0.0005633
8.0	0.0001345	0.0001359	0.0002081	0.0001345

by inspecting the corresponding diagrams in Fig. 3 a little carefully. For example, the type of (11|26) is already familiar to us. The integrals such as (13|24), (13|25), (14|25) present new features. In those integrals the two interacting charge distributions are crossing each other as indicated in Fig. 3. It is easily imagined that the Sklar approximation should give too exaggerated values and the Mulliken approximation too lower values for those cases. In this connection, especially striking is the way in which values as given by the Mulliken and the Sklar approximations differ each other for the so-called penetration integrals. The most conspicuous case is (1:26), where the value due to the Sklar approximation is almost ten times larger than that of the Mulliken approximation. It seems necessary to pay special attentions to these integrals. The definition of the penetration integrals is

$$(p:rs) = -\int U_p(1)\pi_r^*(1)\pi_s(1)d\tau_1 ,$$

where $U_p(1)$ is the potential on electron 1 caused by a neutral pth carbon atom. We may obtain this type of integrals by replacing the Coulomb potential $(1/r_p)$ with $U_p(r)$ in the usual nuclear attraction integral. It is quite important to notice that the new "weight" function $U_p(r)$ decays much faster than $(1/r)$. Then, it follows that approximate values are bound to be quite sensitive to the location of the concentrated charge distributions in individual approximations. Let us consider the integral (1:23) as an example. The actual distribution of the electron feeling the potential $U_1(r)$ is extending over the region between the points 2 and 3 (See Fig. 3, (1:23)). In view of the steep dependence of $U(r)$ on r, the "tail" of the charge distribution around the point 2 would essentially determine the actual value of the penetration integral (1:23). In the Mulliken method the half of the distribution is concentrated at 2 and this is bound to exaggerate the value of the integral. On the other hand, the whole charge is gathered on the middle point between 2 and 3 in the Sklar method and this procedure may give too lower value. These reasonings seem to be justified if we note that the discrepancy between the results as given by the two methods is diminished appreciably for (1:24) and still lesser for (1:25), where the Sklar method gives larger value probably because the distances are equal here between 1 and 2 and between 1 and the middle point of 2 and 4. Now let us return to (1:26). In this case the middle point between 2 and 6 (the charge center of the Sklar method) locates very closely to the potential origin 1, while the points 2 and 6 are equally far apart from 1. Then, the numerical result mentioned above and shown in Table XIV is now accepted as quite natural one. Situation in the remaining two integrals, (1:34), (1:35) may also be understood analogously.

In Table XIV the presumably best values are printed in boldface. As a whole, the modifications of approximate values proposed here are not insignificant and it is hoped to repeat tne calculation of the electronic levels of the benzene molecule with these new values of integrals.

Concluding Remark

In this paper the discussions are limited within homonuclear systems involving $1s$ or $2p\pi$ orbitals only, not because we are not capable of treating other cases but because we wish to expose the essential features of our way of reasoning about the present subject as clearly as possible. In the subsequent papers we shall treat several other cases of practical importance.

References

1) R. S. Mulliken: J. chim. phys. **46** (1949) 500 and 521.
2) A. L. Sklar: J. Chem. Phys. **7** (1939) 990.
3) R. G. Parr, D. P. Craig and I. G. Ross: J. Chem. Phys. **18** (1950) 1561.
4) H. Shull and F. O. Ellison: J. Chem. Phys. **19** (1951) 1215.
5) R. S. Barker, H. Eyring, C. J. Thorne and D. A. Baker: J. Chem. Phys. **22** (1954) 699.
6) R. S. Barker and H. Eyring: J. Chem. Phys. **22** (1954) 1182.
7) R. S. Barker and H. Eyring: J. Chem. Phys. **22** (1954) 2072.
8) R. S. Barker, H. Eyring, D. A. Baker and C. J. Thorne: J. Chem. Phys. **23** (1955) 1381.
9) F. O. Ellison: J. Chem. Phys. **23** (1955) 2358.
10) E. A. Mason and J. O. Hirschfelder: J. Chem. Phys. **26** (1957) 173.
11) K. S. Rüdenberg: J. Chem. Phys. **19** (1951) 1433.
12) R. Taylor: Proc. Phys. Soc. **A64** (1951) 249.
13) M. Kotani, A. Amemiya, E. Ishiguro and T. Kimura: *Table of Molecular Integrals*, Maruzen Co., Ltd., Tokyo, Japan (1955).

JOURNAL OF THE PHYSICAL SOCIETY OF JAPAN Vol. 13, No. 10, OCTOBER, 1958

The Visco-elastic Properties of Network Structure III. Normal Stress Effect (Weissenberg Effect)

Misazo YAMAMOTO

Department of Chemistry, Faculty of Science, Kyoto University

(Received July 2, 1958)

A statistical mechanical theory of the so-called Weissenberg effect (or, normal stress effect) is presented. We adopt the weakly coupled rubber-like network model which we have formulated and applied to investigate the shearing and the tensile viscosity of concentrated solutions of linear high polymers. When the elastico-viscous liquid is compelled to stationary shearing flow, our theory shows that an additional normal tension arises in the direction of flow owing to the orientation of the network structure in addition to the usual shearing stress. Furthermore if the fluid is in a concentric circular motion with the angular velocity gradient in the radial or the axial direction, each doughnut-shaped piece along a flow line behaves as a streched rubber loop due to the said additional tension. As the result the inner bulk of the liquid is squeezed. The pressure increases as one approaches to the rotational axis. Such pressure distribution is calculated for the instruments of three types, i.e., the coaxial cylinder, the parallel plate and cone and plate instrument. The results are at least qualitatively in good agreement with various experimental results reported by Roberts, Philippoff, Rivlin, Kurata, Kotaka and Tamura and others.

§ 1. Introduction

In the previous papers[1),2)] of this series we have developed a molecular theory on visco-elastic properties of amorphous polymeric substances as well as concentrated polymer solutions making use of the weakly coupled rubber-like network model. A genral formulation was given in the first paper, and in the next paper we treated the shearing and the tensile viscosity. In the present paper, we shall consider the application of our theory to the so-called normal stress effect (Weissenberg effect).

Let us consider a liquid put into the gap between coaxial cylinders and subjected to a continuous shear. If the liquid is purely viscous and inelastic, a concave surface may be observed because of the centrifugal force. On the contrary, in the case of elastico-viscous liquids, the liquid often climbs up around the inner cylinder. The phenomena of this type which are commonly termed "Weissenberg effects" have been investigated with increasing interest from rheological point of view since 1946.[3)]

On the other hand, it has long been remarked that when a cylindrical piece of certain elastic materials such as steel, lead or vulcanized rubber are subjected to a torsional couple, the cylinder shows an anomalous effect termed "Poynting effect" or an elongation proportional to the square of the amount of torsion.[4)] These two effects, however, are essentially the same in nature and are characterized by the non-uniformity and anisotropy in the normal components of the stress tensor. Hence we will use in this paper the term "normal stress effects".

A quantitative measurement of normal stresses in steady flow has first been carried out by Roberts by using a cone-plate instrument with a narrow gap (the Weissenberg rheogoniometer)[5)], in which the rate of shear, λ, remains constant throughout the gap. He has determined separately the normal pressures (i.e. the negative sign of normal stresses), P_r, P_θ and P_φ, in three directions of the polar coordinate system, and found the following relations between them:

$$P_r = P_\theta\,, \tag{1}$$

$$P_\varphi - P_r = P_\varphi - P_\theta \tag{2}$$

$$= \frac{\partial P_i}{\partial \log r} = -C\,, \qquad (i = r,\ \theta,\ \varphi) \tag{3}$$

where C is a positive constant and depends only on the rate of shear, λ, in the manner

shown in Fig. 1. He has also noted that the relation (1) was favorably in agreement with the *cross elasticity* theories,[6] but not with the *cross viscosity* theories.[7] After that, the normal stress measurements have been conducted by many investigators:[8)–13)] i.e. by Markovitz, Philippoff and their coworkers with the same type of instrument as above; by Padden and DeWitt with a coaxial cylinder instrument; and Greensmith and Rivlin, and Kurata, Kotaka and Tamura with parallel plate instruments. As a result of these experiments, a considerable amount of the normal stress data are now accumulated for concentrated solutions of high polymeric substances.

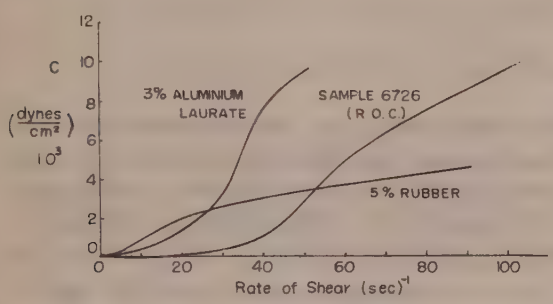

Fig. 1. Rate of shear dependence of the Weissenberg effect. (Roberts)

There are number of phenomenological theories of the effect,[6),7),14–18)] but the treatments for molecular point of view are still scarce. In the paper of Zimm,[20)] it was noted that the elastic stress tensor for an isolated polymer coil in solutions also involves normal stress components, but they appear so small that we can not detect them by the present accuracy of experiment. Thus in this paper, we will develop a molecular theory of the normal stress effect in concentrated polymer solutions and/or in amorphous polymers following the weakly coupled network model proposed in the previous papers of this series,[1),2)] and make an interpretation of some existing data. We start with the stress tensor for a simple shearing flow. Resides the shearing stress component it has an additional tensile stress component in the flow-direction which is proportional to the square of the velocity gradient (§ 2). This additional tension results in non-uniformity and anisotropy in the distribution of the pressure for simple circular motions of the said three types (§ 3 and § 4). This gives a satisfactory interpretation of the Weissenberg effect. Although Lodge presented recently a theory[21)] similar in nature to ours, the overlap between his theory and ours seems only slight.

§ 2. General Consideration

We begin with general remarks on the stress tensor in steady flow. For the flowing pattern of fluids, we assume that:

i) Motion of the liquid is irrotational, laminar steady flow.

ii) Velocity of the liquid has no components in the radial and vertical directions, and therefore flow lines are simply concentric circles around an axis.

In what follows, the cylindrical coordinates, (r, φ, z), are adopted in the cases of coaxial cylinder and parallel plate instruments, and the polar coordinates, (r, θ, φ), in the case of cone-plate instrument. As is easily seen from the above assumptions, the motion of the liquid can be described as a steady, simple shearing flow in the φ-direction and the velocity gradient is generated in the r-, z- and θ-directions in the coaxal cylinder, parallel plate and cone-plate instruments, respectively.

For this simple shearing flow, let us define the steady stress tensor, $\boldsymbol{s}(\lambda)=(\sigma_{ij}(\lambda))$, as a function of the velocity gradient, λ. The explicit form of the function $\boldsymbol{s}(\lambda)$ corresponding to our weakly coupled network model will be given at the end of this section. The distribution of the velocity gradient, λ, and inner hydrostatic pressure, P, which is considered to be a function of coordinates, may be determined by Euler balancing equations.

The Euler equations for steady flow are written down in the cylindrical coordinates

$$\frac{\partial\sigma_{rr}}{\partial r}+\frac{1}{r}\frac{\partial\sigma_{\varphi r}}{\partial\varphi}+\frac{\partial\sigma_{zr}}{\partial z}+\frac{\sigma_{rr}-\sigma_{\varphi\varphi}}{r}+R=0\,, \tag{4a}$$

$$\frac{\partial\sigma_{r\varphi}}{\partial r}+\frac{1}{r}\frac{\partial\sigma_{\varphi\varphi}}{\partial\varphi}+\frac{\partial\sigma_{z\varphi}}{\partial z}+2\frac{\sigma_{r\varphi}}{r}+\Phi=0\,, \tag{4b}$$

$$\frac{\partial\sigma_{rz}}{\partial r}+\frac{1}{r}\frac{\partial\sigma_{\varphi z}}{\partial\varphi}+\frac{\partial\sigma_{zz}}{\partial z}+\frac{\sigma_{rz}}{r}+Z=0\,, \tag{4c}$$

and in the polar coordinates,

$$r\frac{\partial\sigma_{rr}}{\partial r}+\frac{\partial\sigma_{\theta r}}{\partial\theta}+\frac{1}{\sin\theta}\frac{\partial\sigma_{\varphi r}}{\partial\varphi}+2\sigma_{rr}-\sigma_{\theta\theta}-\sigma_{\varphi\varphi}-\cot\theta\cdot\sigma_{\theta r}+Rr=0\,, \tag{5a}$$

$$r\frac{\partial\sigma_{r\theta}}{\partial r}+\frac{\partial\sigma_{\theta\theta}}{\partial\theta}+\frac{1}{\sin\theta}\frac{\partial\sigma_{\varphi\theta}}{\partial\varphi}+3\sigma_{r\theta}+\cot\theta\cdot(\sigma_{\theta\theta}-\sigma_{\varphi\varphi})+\Theta r=0\,, \tag{5b}$$

$$r\frac{\partial\sigma_{r\varphi}}{\partial r}+\frac{\partial\sigma_{\theta\varphi}}{\partial\theta}+\frac{1}{\sin\theta}\frac{\partial\sigma_{\varphi\varphi}}{\partial\varphi}+3\sigma_{r\varphi}+2\cot\theta\cdot\sigma_{\varphi\theta}+\Phi r=0\,, \tag{5c}$$

where $(R,\ \Phi,\ Z)$ and $(R,\ \Theta,\ \Phi)$ are the external body forces acting on the bulk of liquid.

Let the liquid be constrained to the simple shearing flow in the x-direction with a constant velocity gradient, λ, in the y-direction. The deformation tensor, $\boldsymbol{e}(t)$, is written as

$$\boldsymbol{e}(t)=\begin{pmatrix}1 & \lambda t & 0\\ 0 & 1 & 0\\ 0 & 0 & 1\end{pmatrix}. \tag{6}$$

We shall employ the weakly coupled network model, which has been treated in the two previous papers, in the determination of the stress tensor for this deformation. For the time being, we assume that the network is constructed of so-called Gaussian chains and breaks with a constant rate $\beta(r,\ N)=\beta$. (The definition of the "chain-breakage coefficient" $\beta(r,\ N)$ was given in § 4 of Part 1.[1]) More general case will be treated afterward. The stress tensor,

$$\boldsymbol{s}=\boldsymbol{s}_n+P\mathbf{1}\,, \tag{7}$$

satisfies the equation of motion

$$\frac{d\boldsymbol{s}_n}{dt}=\frac{d\boldsymbol{e}}{dt}\cdot\boldsymbol{e}^{-1}\cdot\boldsymbol{s}_n+\boldsymbol{s}_n\cdot\boldsymbol{e}^{\dagger-1}\cdot\frac{d\boldsymbol{e}^{\dagger}}{dt}+\left(\frac{d\boldsymbol{s}_n}{dt}\right)^{b,r}, \tag{8}$$

with the isotropic inner hydrostatic pressure, P. $(d\boldsymbol{s}_n/dt)^{b,r}$ expresses the creation of stress due to breakage and reformation of the junctions. Here if we assume that the instantaneous distribution of the reformed chains is isotropic, the term $(d\boldsymbol{s}_n/dt)^{b,r}$ in the right-hand side of Eq. (8) may be written as

$$(d\boldsymbol{s}_n/dt)^{b,r}=\beta(\sigma_0\mathbf{1}-\boldsymbol{s}_n)\,. \tag{9}$$

Substitution of Eqs. (6) and (9) into Eq. (8) yields the steady stress tensor

$$\boldsymbol{s}_n=\sigma_0\begin{pmatrix}1+2(\lambda/\beta)^2 & \lambda/\beta & 0\\ \lambda/\beta & 1 & 0\\ 0 & 0 & 1\end{pmatrix}. \tag{10}$$

The xy- and yz-components give the shearing stresses constraining the simple shearing flow Eq. (6), and μ defined by

$$\mu=\sigma_{xy}/\lambda=\sigma_0/\beta \tag{11}$$

represents the Newtonian viscosity coefficient. σ_0 is the instantaneous elastic modulus (rigidity) of our network, and

$$\tau=1/\beta \tag{12}$$

has the meaning of the so-called relaxation time.

Purely viscous liquids may have no normal components of stress but only the isotropic hydrostatic pressure in simple shearing flow. In our system, however, there exists an additional normal component of stress, $2\sigma_0(\lambda/\beta)^2$, in the flow-direction. This quantity which is

of second order with respect to the flow parameter, λ, is one of the cross effects in the stress-strain relation, and is always neglected in the classical linear theory of (visco-) elasticity. But it is this term which plays an important role in the normal stress effect, as will be shown in the following sections.

Through an analogous procedure to that of the previous paper[2] we can easily get an expression of the stress tensor without appealing to the assuming of Gaussian chain and of the constant chain-breakage coefficient. In the case of small values of λ, the stress tensor may expanded in powers of λ as

$$\sigma_{tt}=\sum_{n=0}^{\infty}\sigma_{tt}^{(2n)}\lambda^{2n}\,,\quad (t=x,\ y,\ z),\tag{13a}$$

$$\sigma_{xy}=\sigma_{yx}=\sum_{n=0}^{\infty}\sigma_{xy}^{(2n+1)}\lambda^{2n+1}\,,\tag{13b}$$

$$\sigma_{zs}=\sigma_{sz}=0\,,\qquad (s=x,\ y).\tag{13c}$$

The details of calculation and the final expression of $\sigma_{tt}^{(m)}$ for $m=0\sim3$ are given in Appendix. σ_{yy} is generally not equal to σ_{zz}. σ_{xy} may have the terms of higher powers of λ than the first, which correspond to the so-called non-Newtonian (or, structural) viscosity:

$$\mu=\sigma_{xy}/\lambda=\sum_{n=0}^{\infty}\mu^{(2n)}\lambda^{2n}\,,\tag{14}$$

$$\mu^{(2n)}=\sigma_{xy}^{(2n+1)}\,.\tag{15}$$

Eq. (13c) hold for any value of λ in our model.

If the higher derivatives of $\beta(r,\ N)$ and $\phi(r,\ N)$ with respect to r are sufficiently small, the following relation is obtained (cf. Appendix):

$$\frac{|\sigma_{yy}^{(2)}-\sigma_{zz}^{(2)}|}{\sigma_{yy}^{(0)}}\lesssim\frac{1}{5}\,\frac{|\mu^{(2)}|}{\mu^{(0)}}\,.\tag{16}$$

This means that the "order" of the anisotropy of normal stress components should be smaller than the "order" of the structural viscosity.

§ 3. Pressure Distribution in Circular Motion of Liquid. (I)

By application of the expressions for the stress tensor obtained in the last section and of Euler equations (4) or (5) we can calculate the pressure distribution in the circular motion of liquid. In this section the simplest stress tensor, Eq. (10), is adopted for three types of instruments. The more general stress tensor, Eq. (14), will be treated only for the cone-plate instrument in the next section.

A. *Coaxial cylinder instrument*

Consider the motion of liquid put into the gap between two coaxial cylindrical surfaces (their radii are a and b ($a>b$), respectively), both of which rotate around their common axis with angular velocities Ω_A and Ω_B ($\Delta\Omega=\Omega_A-\Omega_B$), respectively. Using cylindrical coordinates (r, φ, z), let us consider a steady flow in φ-direction with angular velocity $\omega=\omega(r)$ and neglect the end effect for simplicity's sake. The velocity gradient,

$$\lambda=r(d\omega/dr)\tag{17}$$

is in the r-direction. In this system the gravitational and the centrifugal force act on the bulk of the liquid, and since we assume that the z-axis is in the vertical direction, the body force is written as

$$(R,\ \Phi,\ Z)=(\rho r\omega^2,\ 0,\ -\rho g)\tag{18}$$

where ρ is the density of the liquid.

P and λ are obtained as the functions of coordinates by solving the Euler equations with Eq. (17) and the stress tensor which is analogous to Eq. (10). That is,

$$\lambda=2A/r^2\,,\tag{19}$$

$$P=P'-2A^2(\sigma_0/\beta^2)(1/r^4)\,.\tag{20}$$

Where P' is a part of the hydrostatic pressure arising from the body force,

$$P'=\rho\left\{\frac{A^2}{2}\frac{1}{r^2}+AB\log r-\frac{B^2}{2}r^2\right\}+\rho gz+P_0\,,\tag{21}$$

and constants A and B are given in the forms

$$A=(\Omega_A-\Omega_B)\frac{a^2b^2}{a^2-b^2}\tag{22}$$

and

$$B=\frac{a^2\Omega_A-b^2\Omega_B}{a^2-b^2}\,.\tag{23}$$

In Eq. (20), the second term $2A^2\sigma_0/\beta^2r^4$ gives the contribution from the additional normal stress component. If the network formation is remarkable, P' may be neglected in the expression of P.

Substitution of P into Eq. (7) gives the distribution of stress in the velocity field. As the actually measurable pressures are the minus signes of the stresses, we obtain

$$P_z = P_r = P_0 + 2A^2(\sigma_0/\beta^2)(1/r^4) \quad (24)$$

and

$$P_\varphi = P_0 - 6A^2(\sigma_0/\beta^2)(1/r^4) \,. \quad (25)$$

Eq. (24) suggest that the vertical cross-section of the free surface of the liquid passing through the rotational axis is expressed as $z=c/r^4$. This is just the tendencies of the experimental results.

Eqs. (24) and (25) show that the nearer is the location of the bluk of the liquid to the rotational axis, the larger are the pressures in the r- and z-directions, and the smaller in the φ-direction. Let us consider a doughnut-shaped section of the liquid along a flow line. Eqs. (7) and (10) imply that there exists a tension along the circular axis of this doughnut-shaped section. Then this bulk may squeeze the inner part of the liquid as the circularly streched rubber loop. This effect results in the pressure distributions, Eqs. (24) and (25), and then, in the normal stress effect.

B. *Parallel plate instrument.*

The similar procedure determines the pressure distribution in the parallel plate instrument. The velocity gradient

$$\lambda = r(d\omega/dz) = r(\Delta\Omega/h) \quad (26)$$

is in the z-direction, where h is the distance between two horizontal circular plates which rotate around the vertical axis with angular velocities, Ω and $\Omega+\Delta\Omega$, respectively. If the gravitational and the centrifugal forces are neglected, we arrive at the pressure distribution

$$P_r = P_z = P_0 - (\sigma_0/\beta^2)(\Delta\Omega/h)^2 r^2 \,, \quad (27)$$

$$P_\varphi = P_0 - 3(\sigma_0/\beta^2)(\Delta\Omega/h)^2 r^2 \,. \quad (28)$$

Eq. (27) suggests that the vertical component of pressure, which can be measured by capillary tube, decreases parabolically with increasing distance from the rotating axis. This tendency is not strictly the one observed by the experiments. Greensmith and Rivlin's data of 6% decalin solution of polyisobutylene,[11] and Kotaka, Tamura and Kurata's data for aqueous solutions Na-carboxylmethylcellulose (Na-CMC) with several amounts of NaOH[12] show clearly the departures from parabolic pressure-distribution. This may be due to "non-linearity" of visco-elastic proparties of these systems, that is, due to the velocity gradient dependences of the elastic modulus, σ_0, and of the relaxation time, τ.

C. *Cone and plate instrument (Involved cone-cone arrangement).*

It is convenient to make use of the polar coordinate, (r, θ, φ), for the conical surface (cone-plate and cone-cone) instruments. Two conical surfaces are characterized by $\theta=\alpha$ and $\theta=\beta$ $(\alpha-\beta=\delta>0)$ and rotate with angular velocities, $\Omega+\Delta\Omega$ and Ω, respectively. With sufficiently small value of δ, the liquid flows laminarly in the φ-direction with the velocity gradient

$$\lambda = d\omega(\theta)/d\theta \quad (29)$$

in the θ-direction. Eq. (5c) leads to

$$\lambda = A/\sin^2\theta \,, \quad (30)$$

where

$$A = -\Delta\Omega/(\cot\alpha - \cot\beta) \,. \quad (31)$$

In what follows, for the convenience of calculation, we assume that both α and β are nearly equal to 90°. The velocity gradient in this situation

$$\begin{aligned}\lambda &= \frac{A}{\sin^2\alpha}[1-2\cot\alpha\cdot(\theta-\alpha) \\ &\quad +(1+3\cot^2\alpha)(\theta-\alpha)^2+\cdots] \\ &\simeq A/\sin^2\alpha = \Delta\Omega/\delta \end{aligned} \quad (32)$$

is independent of location of the point being considered. The cone-plate instrument with a narrow gap satisfies this condition. The pressure distribution may be obtained as

$$P_r = P_\theta = P_0 - 2(\sigma_0/\beta^2)(\Delta\Omega/\delta)^2 \log r \,, \quad (33)$$

$$P_\varphi = P_0 - 2(\sigma_0/\beta^2)(\Delta\Omega/\delta)^2 \log r - 2(\sigma_0/\beta^2)(\Delta\Omega/\delta)^2 \,. \quad (34)$$

with the neglection of body forces. The θ-component of the pressure has the logarithmic dependence on distance from the axis. This is consistent with the experimental results carried out by several authors. However, λ vs. $(-\partial P_\theta/\partial \log r)$ relations obtained by experiments show more or less departure from the parabolic dependence. In the next section, we shall consider this point in more detail.

§ 4. Pressure Distribution in Circular Motion of Liquid. (II)

A part of this section is concerned with the more general liquids inserted into the cone-plate instrument. The stress tensor for laminar rotating motion in this instrument

may have such a form in the polar coordinate that (cf. Eq. (13))

$$\boldsymbol{s}=\begin{pmatrix} \sigma_{rr}'(\lambda) & 0 & 0 \\ 0 & \sigma_{\theta\theta}'(\lambda) & \sigma_{\theta\varphi}'(\lambda) \\ 0 & \sigma_{\varphi\theta}'(\lambda) & \sigma_{\varphi\varphi}'(\lambda) \end{pmatrix}+P\mathbf{1}, \quad (35)$$

with

$$\sigma_{\theta\varphi}'(\lambda)=\sigma_{\varphi\theta}'(\lambda)\,. \quad (36)$$

Substitution of Eq. (35) into Eq. (5c) gives the equation

$$(\partial\sigma_{\theta\varphi}/\partial\lambda)(d\lambda/d\theta)=-2\cot\theta\cdot\sigma_{\varphi\theta}\,. \quad (37)$$

This implies the constancy of λ in the cone-plate instrument in which $\theta\simeq 90°$, $\cot\theta\simeq 0$:

$$\lambda=\Delta\Omega/\delta=\text{const.} \quad (38)$$

Eqs. (5a), (5b) and (38) determine the hydrostatic pressure, P. With neglection of the body forces, normal components of the pressure,

$$P_t=-\sigma_{tt},\ (t=r,\ \theta,\ \varphi)$$

may be written as

$$P_t=P_0(\theta)+(2\sigma_{rr}'-\sigma_{\theta\theta}'-\sigma_{\varphi\varphi}')\log r-\sigma_{tt}'\,,$$
$$(t=r,\ \theta,\ \varphi)\,. \quad (39)$$

Then, we have

$$(\partial P_t/\partial\log r)=2\sigma_{rr}'-\sigma_{\theta\theta}'-\sigma_{\varphi\varphi}'$$
$$=-C=\text{const.}, \quad (40)$$

$$P_r-P_\theta=\sigma_{\theta\theta}'-\sigma_{rr}'\,, \quad (41)$$

$$P_r-P_\varphi=\sigma_{\varphi\varphi}'-\sigma_{rr}'\,. \quad (42)$$

Eq. (40) suggests the logarithmic r-dependence of the normal components of the pressure, which has just been observed by Roberts, Rhilippoff, and others. Eqs. (1) and (2), the results of Robert's experiment,[5] are considered to be the special case of $\sigma_{\theta\theta}'=\sigma_{rr}'$.

Eq. (16) may be expected for the network model in which $\beta(r,\ N)$ and $\phi(r,\ N)$ are not so singular function of r. This implies that the difference $|P_r-P_\theta|$ may be comparatively small even if the non-Newtonian flow is observed, at least in the range of small λ-value. What may happen for large λ-value? With Gaussian chains and constant chain-breakage coefficient, there exists only the additional tension $(2\sigma_0/\beta^2)\lambda^2$ in the normal stress component of the flow-direction. If $\beta(r,\ N)$ increases with r, i.e., the probability of breakage of junctions increases with stretching of chains, the effective number and the average tension of chains may be smaller than those in the case of constant β for the same of stress. Especially, $\sigma_{\theta\theta}-\sigma_{rr}$, which is zero at $\lambda=0$, may remain in the vicinity of zero although σ_{tt} itself apparently deviates from those of the ideal case. Similarly, an effect of non-Gaussian behavior of constituent chains may arise. Denoting the effective instantaneous elastic modulus by $\kappa_e(\lambda)=\langle\sigma_0\rangle$ and the effective relaxation time by $\tau_e(\lambda)=1/\langle\beta\rangle$, we may write approximately the stress tensor for simple shearing flow, Eq. (16), in the form

$$\boldsymbol{s}=\kappa_e\begin{pmatrix} 1+2\tau_e^2\lambda^2 & \tau_e\lambda & 0 \\ \tau_e\lambda & 1 & 0 \\ 0 & 0 & 1 \end{pmatrix}+P\mathbf{1}\,. \quad (43)$$

This stress tensor gives an explanation of Robert's experimental results,[3] Eqs. (1)~(3).

λ-dependence of the additional normal tension, $\Delta\sigma=2\kappa_e\tau_e^2\lambda^2$, can be obtained directly from the measurement of the normal stress effect in any instrument. On the other hand, measurement of the structural viscosity gives the $\mu=\kappa_e\tau_e$ vs. λ relation. Then, we can separately obtain the λ-dependence of the effective elastic modulus $\kappa_e(\lambda)$ and of the effective relaxation time $\tau_e(\lambda)$. This is an important feature of the observation of the normal stress effect in the rheological considerations of elastico-viscous liquids.

In a suitable range of λ-value, it has been seen experimentally that $\Delta\sigma$ and μ depend on λ in the power forms

$$\Delta\sigma=A\lambda^\alpha\,, \quad (44)$$

$$\mu=B\lambda^{-\beta}\,. \quad (45)$$

This implies in this range of λ-value the tendencies

$$\kappa_e(\lambda)=\kappa_0\lambda^\delta\,, \quad (46)$$

$$\tau_e(\lambda)=\tau_0\lambda^{-\varepsilon}\,. \quad (47)$$

In Fig. 2 is shown the relation between $[\alpha,\ \beta]$ and $[\delta,\ \varepsilon]$. τ_e should decrease with λ, and the degree of the orientation of the internal mechanism, which is expressed by $\xi=\tau_e\lambda$, should increase with λ. Then, it is necessary that $0<\varepsilon<1$. In our network model δ expresses the departure from the Gaussian nature of chains, and because of the nature of real chains, it is supposed that $\delta>0$. Observable set of $[\alpha,\ \beta]$ would be in the domain MABN in Fig. 2. In this figure, the full circles represent the experimental results for aqueous solutions of Na-carboxylmethyl-

cellulose (Na-CMC), the deltas for aqueous solutions of methylcellulose (MC) and the crosses for decalin solutions of polystyrene by Kurata, Kotaka and Tamura.[12]* The open circle corresponds to the decalin solution of polyisobutylene by Garner, Nissan and Wood,[13] and Mooney.[16] These plots suggest that in the case of random coiled linear molecules such as polystyrene and polyisobutylene in decalin, polymer chains are fairly approximately represented by the Gaussian chains, and non-Newtonian flow of these system is chiefly due to the λ-dependence of the relaxation time. On the contrary, chains of cellulose derivatives and polyelectrolytes show remarkable departure from the Gaussian character. This is an expected result.

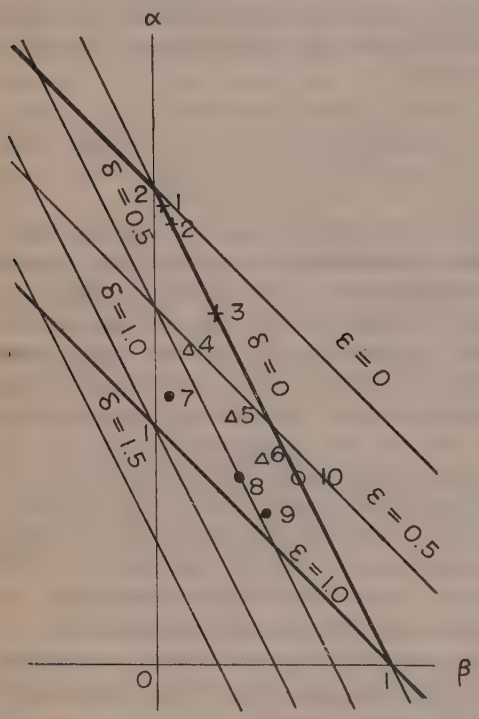

Fig. 2. Weissenberg effect and structural viscosity.

+ Polystyrene in decalin
  1. 23.6 wt.% Pst.
  2. 24.5 wt.% Pst.
  3. 30.8 wt.% Pst.

△ Methylcellulose in water
  4. 1.72 wt.% MC.
  5. 2.60 wt.% MC.
  6. 3.54 wt.% MC.

● 2 gr. Na-Carboxylmethylcellulose in 100 ml. water.
  7. With 0.1 N-NaOH (preheating at 80°C 48 hr.).
  8. with 0.1 N-NaOH.
  9. with no Salt.

○ Polyisobutylene in decalin.
  (1.~9. by Kurata, Kotaka & Tamura.
  10. by Garner, Nissan & Wood and Mooney).

* The author is indebted to Professor M. Tamura, Professor M. Kurata and Mr. T. Kotaka for their kind permission to cite their unpublished data (MC and PS) in this publication.

§ 5. General Remarks

A. *Assumption of simple circular motion.*

Pressure distributions in elastico-viscous liquids were treated for simple circular motions of three types. In our calculations it was assumed that the flow lines of liquid-motion were concentric circles around the rotational axis. This assumption is actually not the case for the parallel plate instrument and the conical surface instrument, when we take the effect of body forces into consideration. For example, let us consider the parallel plate instrument. The body force in this case, too, is given by Eq. (18). The angular velocity is the function of z given by

$$\omega(z)=\Omega_0+(\Delta\Omega/h)z \qquad (48)$$

with the velocity gradient, Eq. (26), in the z-direction. With Eqs. (18), (26) and (48) and suitable expression of stress tensor, Euler equations (4) can not be solved with respect to P; P is not a total differential of r and z. This implies that the assumption of the simple circular motion conflicts with the actual flow pattern under the influence of the body force, Eq. (18). Consider a vertical cylindrical section of the liquid in this instrument. The gravitational force homogeneously acts in parallel to the cylindrical axis and gives no moment of force. On the other hand, the centrifugal force is in the r-direction orthogonal to the cylindrical axis, and its magnitude is a function of z, because of non-uniformity of the angular velocity, Eq. (48). Then there exists a moment of force in the φ-direction. This moment leads to an additional convection of the liquid in the $r\theta$-plane. Hence a bluk of the liquid will make a complex helical motion. The neglection of body forces, then, amounts to the assumption of the simple circular motion at least for the parallel plate instrument.

For the cone-cone instrument, furthermore, this assumption does not hold even if body

forces are neglected. Substituting the expression of the velocity gradient, Eq. (30), Euler equations (5) may not lead to the consistent solution of P. In this case, the balancing of the stress as a whole is impossible, and then, a convective motion of the liquid may happen. However, in the case of the cone-plate instrument, in which $\theta \simeq 90°$, the dependence of λ on θ may be neglected, and the liquid is in the simple circular motion under the condition of no body force. Our calculation has a meaning only in this case.

B. *Symmetry and asymmetry of deformation.*

The essential point of the normal stress effects, either Poynting or Weissenberg effects, lies in the existence of the additional normal tension which is of the second order with respect to the magnitude of the deformation or velocity gradient in the deformation- or flow-direction. An unequality of the normal stress components of such direction and the gradient-direction is important in the interpretations of several results on the anisotropy of the normal pressure. This property of the stress tensor is clearly due to the asymmetry of the deformation tensor, Eq. (6).

In the explanation of the normal stress effect, Rivlin has symmetrized the deformation tensor, as has been done in the classical theory of elasticity.* His symmetrized tensor

$$\boldsymbol{e}_s = \begin{pmatrix} 1 & \lambda t/2 & 0 \\ \lambda t/2 & 1 & 0 \\ 0 & 0 & 1 \end{pmatrix} \tag{49}$$

leads to the stress tensor such as

$$\boldsymbol{s}_s = \begin{pmatrix} \Psi\lambda^2/2 & \Theta\lambda & 0 \\ \Theta\lambda & \Psi\lambda^2/2 & 0 \\ 0 & 0 & 0 \end{pmatrix} + P\mathbf{1}, \tag{50}$$

which has the discrepancy from that experimentally obtained, Eqs. (1) and (2).

The symmetrization of deformation is accompanied with the neglection of second order quantities of deformation. This procedure is permitted in the classical linear theories of elasticity and visco-elasticity in which only small deformations are treated. However, this symmetrization may, of cause, be impossible in the treatment of second order effects such as the normal stress effects.

The symmetric deformation, Eq. (49), has the strain ellipsoid one of whose principal axes bisects the first quarter of the xy-plane. On the other hand, in the case of asymmetric stress tensor, Eq. (6), the x-axis has an acute angle with a principal axis of the strain ellipsoid in the first quarter of the xy-plane. This implies that the extinction angle, χ, is less than 45° in the experiment of flow birefringence. χ is dependent on the velocity gradient such as

$$2\cot 2\chi = \lambda\tau_e(\lambda) \tag{51}$$

for our network model. $\lambda\tau_e(\lambda)$ may be obtained for any λ-value by measurement of the normal stress effect and of the viscosity coefficient, as was shown in the last section. Philippoff showed a good agreement between the extinction angle obtained by a direct measurement of the flow birefringence and that obtained by measuring the mechanical properties using Eq. (51).[9] This fact suggests that the asymmetry of deformation is important in our system.

§ 6. Summary

The normal stress effect of elastico-viscous liquids (Weissenberg effect) was treated adopting the weakly coupled rubber-like network model. It was shown that the normal stress of these systems is no longer isotropic for a stationary simple shearing flow. Although normal components of the stress are in general different from each other in magnitude, those along the directions orthogonal to the flow-direction are almost isotropic. A remarkable additional tension must be applied in the flow-direction in order to compel the system to the said flow. This tension leads to the non-uniform distribution of the normal pressure in some concentric circular motion of the liquid. These distributions were obtained for three types of experimental arrangements with coaxial cylinders, parallel plates and cone-plate, respectively. The results of our theory are at least qualitatively consistent with that obtained by ex-

* In the recent paper,[16] Rivlin has developed the phenomenological theory of elasticity in which the general asymmetrical deformation is correctly treated. He has obtained the stress tensor which is essentially equivalent to Eq. (10) for the simple shearing deformation with the displacement gradient, λ, instead of the velocity gradient.

periments, although the treatment is limited in the rather simple case, that is, in the simple concentric circular motions. By the observations of the normal stress effect and the viscosity coefficient, we can determine the effective elastic modulus (rigidity) and the effective relaxation time at any value of velocity gradient. This may have an important role in the study of the rheological behavior of such systems. For example, it can be possible to separate the non-linearity of visco-elastic properties into that of conservative elastic part and that of dissipative relaxational part. The similar separation may be made for the well-known molecular weight dependence of visco-elastic parameters. Especially, it will be expected that in the analysis of the law of 3.4th power for molecular weight dependence of the bulk viscosity of amorphous polymers, the normal stress effect will give an important contribution.*

Acknowledgement

The author wishes to express his sincere thanks to Professor T. Yamamoto and Professor M. Kurata for the continual encouragement and the guidance throughout the course of the present study. They have kindly inspected and revised the manuscript, too. He is also obliged to Professor T. Nakagawa of Tokyo University who suggested the problem, Professor H. Fujita and Dr. Y. Ikeda for their kindly lending of reference papers, and Dr. E. Teramoto and the members of our laboratory (Quantum Chemistry Lab., Dept. of Chemistry, Kyoto Univ.), of Research Group of High Polymer in Kyoto and of Kobayasi Institute of Physical Research, Tokyo, for their fruitful discussions. His thanks are also due to Miss M. Matsuda for the preparation of the manuscript. The present investigation was supported partly by the Scientific Research Grant of the Ministry of Education.

Appendix

In the first paper[1] of this series, we have derived the stress tensor, $\boldsymbol{s}$, of the weakly coupled network structure for any strain tensor, $\boldsymbol{e}$. In the case of incompressible substances, the stress tensor is given by

$$\boldsymbol{s}=\Sigma_N\iiint(\boldsymbol{hh})\left(\frac{1}{r}\frac{d\phi}{dr}\right)_{r=|\boldsymbol{h}|}F(\boldsymbol{h},\ N,\ t)d\boldsymbol{h}+P\boldsymbol{1}\ , \tag{A.1}$$

where $\phi(r,\ N)$ is the free energy of a chain having the end-to-end distance, r. The chain-distribution function, $F(\boldsymbol{h},\ N,\ t)$, satisfies the equation

$$F(\boldsymbol{h},\ N,\ t)=F_0(\boldsymbol{e}^{-1}(t)\cdot\boldsymbol{h},\ N)\exp\left[-\int_0^t\beta(\boldsymbol{e}(t')\cdot\boldsymbol{e}^{-1}(t)\cdot\boldsymbol{h},\ N)\,dt'\right]$$
$$+\int_0^t G(\boldsymbol{e}(t')\cdot\boldsymbol{e}^{-1}(t)\cdot\boldsymbol{h},\ N,\ t')\exp\left[-\int_{t'}^t\beta(\boldsymbol{e}(t'')\cdot\boldsymbol{e}^{-1}(t)\cdot\boldsymbol{h},\ N)dt''\right]dt'\ , \tag{A.2}$$

where $G(\boldsymbol{h},\ N,\ t)$ is the chain-reformation function and $\beta(\boldsymbol{h},\ N)$ is the chain-breakage coefficient.

In our case the strain tensor $\boldsymbol{e}(t)$ has the form

$$\boldsymbol{e}(t)=\begin{pmatrix}1 & \lambda t & 0\\ 0 & 1 & 0\\ 0 & 0 & 1\end{pmatrix}. \tag{A.3}$$

Substitution of Eq. (A.3) into Eq. (A.2) gives the following stational chain-distribution function

$$F(\xi,\ \eta>0,\ \zeta;\ N)=\frac{1}{\lambda\eta}\int_{-\infty}^{\xi}G(\xi',\ \eta,\ \zeta;\ N)\exp\left[-\frac{1}{\lambda\eta}\int_{-\xi}^{\xi}\beta(\xi'',\ \eta,\ \zeta;\ N)\,d\xi''\right]d\xi'\ , \tag{A.4a}$$

* Such measurement of the molecular weight dependence of normal stresses are now in progress by Kotaka, Kurata, Sakamoto and Tamura for polystyrene solutions as an example.

$$F(\xi,\ \eta<0,\ \zeta;\ N)=\frac{1}{\lambda|\eta|}\int_{-\infty}^{-\xi}G(\xi',\ |\eta|,\ \zeta;\ N)\exp\left[-\frac{1}{\lambda|\eta|}\int_{\xi'}^{-\xi}\beta(\xi'',\ |\eta|,\ \zeta;\ N)\,d\xi''\right]d\xi'\,. \tag{A4b}$$

Making use of the similar procedure to that of the second paper[2] of this series, we can obtain the stress components, that is,

$$\sigma_{xx}=2\Sigma_N\iiint_{\Omega''}\xi^2G(|\boldsymbol{h}|,\ N)[K_2^{+}+K_2^{-}]\,d\boldsymbol{h}+P\,, \tag{A.5a}$$

$$\sigma_{xt}=\sigma_{tx}=2\Sigma_N\iiint_{\Omega''}\xi\tau G(|\boldsymbol{h}|,\ N)[K_1^{+}+K_1^{-}]\,d\boldsymbol{h} \tag{A.5b}$$

and

$$\sigma_{st}=\sigma_{ts}=2\Sigma_N\iiint_{\Omega''}\sigma\tau G(|\boldsymbol{h}|,\ N)[K_0^{+}+K_0^{-}]\,d\boldsymbol{h}+P\delta_{st}\,, \tag{A.5c}$$

$$(s,\ t=y,\ z;\ \sigma,\ \tau=\eta,\ \zeta)\,.$$

In this derivation, it is assumed that $\beta(\boldsymbol{h},\ N)$ and $G(\boldsymbol{h},\ N,\ t)$ are spherically symmetric. Ω'' denotes the quartered space, $\xi>0$ and $\eta>0$. $K_n^{\pm}$ is defined such as

$$K_n^{\pm}=\frac{\xi}{\lambda\eta}\int_{\pm1}^{\infty}\theta^n\left(\frac{1}{r}\frac{d\phi}{dr}\right)_{(\theta)}\exp\left[-\frac{\xi}{\lambda\eta}\int_{\pm1}^{\infty}\beta(\xi\theta',\ \eta,\ \zeta;\ N)\,d\theta'\right]d\theta\,. \tag{A.6}$$

where $(1/r)(d\phi/dr)_{(\theta)}$ is the abbreviation

$$\left(\frac{1}{r}\frac{d\phi}{dr}\right)_{(\theta)}=\left(\frac{1}{r}\frac{d\phi}{dr}\right)_{r=\sqrt{\theta^2\xi^2+\eta^2+\zeta^2}}\,. \tag{A.7}$$

Because of the spherical symmetry of $G(\boldsymbol{h},\ N)$, $\beta(\boldsymbol{h},\ N)$ and $\phi(\boldsymbol{h},\ N)$, $K_n^{\pm}$ has planar symmetry with respect to the xy-plane. Hence we have

$$\sigma_{xz}=\sigma_{zx}=\sigma_{yz}=\sigma_{zy}=0\,. \tag{A.8}$$

No more reduction of these equations can be made for general functional forms of $\beta(r,\ N)$ and $\phi(r,\ N)$.

If the chains are Gaussian and $\beta(r,\ N)$ is independent of r and N, i.e.,

$$\phi(r,\ N)=(3kT/2)(r^2/Na^2) \tag{A.9}$$

and

$$\beta(r,\ N)=\beta=\text{const.}\,, \tag{A.10}$$

$K_n^{\pm}$ may be read

$$K_0^{\pm}=\frac{3kT}{Na^2}\frac{1}{\beta}\,, \tag{A.11}$$

$$K_1^{\pm}=\frac{3kT}{Na^2}\frac{1}{\beta}\left(\frac{\lambda}{\beta}\frac{\eta}{\xi}\right)\left[1\pm\frac{\beta}{\lambda}\frac{\xi}{\eta}\right], \tag{A.12}$$

$$K_2^{\pm}=\frac{3kT}{Na^2}\frac{1}{\beta}\left[1\pm2\frac{\lambda}{\beta}\frac{\eta}{\xi}+2\left(\frac{\lambda}{\beta}\frac{\eta}{\xi}\right)^2\right]. \tag{A.13}$$

Introducing of the instantaneous elastic modulus, σ_0,

$$\sigma_0=\frac{kT}{a^2}\frac{1}{\beta}\Sigma_N\frac{1}{N}\iiint\boldsymbol{h}^2G(\boldsymbol{h},\ N)d\boldsymbol{h}\,, \tag{A.12}$$

we can reduce the stress tensor, Eq. (A.5), to the form described in Eq. (10).

For sufficiently small λ-value, the stress tensor is expanded in powers of λ, as has been done in the calculation of the viscosity coefficients in the previous paper[2]:

$$\sigma_{tt}=\sum_{n=0}^{\infty}\sigma_{tt}^{(2n)}\lambda^{2n}\,, \tag{A.13}$$

$$\sigma_{xy}=\sigma_{yx}=\sum_{n=0}^{\infty}\sigma_{xy}^{(2n+1)}\lambda^{2n+1}\,. \tag{A.14}$$

Simple but lengthy calculation determines the expansion coefficients as follows:

Define the differential operator

$$D^n=\left(\frac{1}{r}\frac{d}{dr}\right)^n, \tag{A.15}$$

to give

$$\sigma_{xx}^{(0)}=\sigma_{yy}^{(0)}=\sigma_{zz}^{(0)}=\frac{4}{3}\pi\,\Sigma_N\int r^4\frac{G(r,\ N)}{\beta(r,\ N)}D^1\phi\,dr, \tag{A.16}$$

$$\begin{aligned}\sigma_{xx}^{(2)}=&\frac{8}{3}\pi\,\Sigma_N\int r^6\frac{G(r,\ N)}{\beta^3(r,\ N)}D^1\phi\,dr+\frac{4}{15}\pi\,\Sigma_N\int r^6\frac{G(r,\ N)}{\beta^3(r,\ N)}\left[6D^2\phi-7D^1\phi\left(\frac{D^1\beta}{\beta}\right)\right]dr\\&+\frac{4}{35}\pi\,\Sigma_N\int r^8\frac{G(r,\ N)}{\beta^3(r,\ N)}\left[2D^3\phi-3D^2\phi\left(\frac{D^1\beta}{\beta}\right)-D^1\phi\left\{\left(\frac{D^2\beta}{\beta}\right)-\left(\frac{D^1\beta}{\beta}\right)^2\right\}\right]dr\,,\end{aligned} \tag{A.17a}$$

$$\begin{aligned}\sigma_{yy}^{(2)}=&\frac{4}{5}\pi\,\Sigma_N\int r^6\frac{G(r,\ N)}{\beta^3(r,\ N)}\left[2D^2\phi-D^1\phi\left(\frac{D^1\beta}{\beta}\right)\right]dr\\&+\frac{4}{35}\pi\,\Sigma_N\int r^8\frac{G(r,\ N)}{\beta^3(r,\ N)}\left[2D^3\phi-3D^2\phi\left(\frac{D^1\beta}{\beta}\right)-D^1\phi\left\{\left(\frac{D^2\beta}{\beta}\right)-\left(\frac{D^1\beta}{\beta}\right)^2\right\}\right]dr\,,\end{aligned} \tag{A.17b}$$

$$\sigma_{zz}^{(2)}=\frac{1}{3}\sigma_{yy}^{(2)}\,, \tag{A.17c}$$

$$\sigma_{xy}^{(1)}=\frac{4}{3}\pi\,\Sigma_N\int r^4\frac{G(r,\ N)}{\beta^2(r,N)}D^1\phi dr+\frac{4}{15}\pi\,\Sigma_N\int r^6\frac{G(r,\ N)}{\beta^2(r,N)}\left[D^2\phi-D^1\phi\left(\frac{D^1\beta}{\beta}\right)\right]dr\,, \tag{A.18}$$

$$\begin{aligned}\sigma_{xy}^{(3)}=&\frac{8}{5}\pi\,\Sigma_N\int r^6\frac{G(r,\ N)}{\beta^4(r,N)}\left[3D^2\phi-2D^1\phi\left(\frac{D^1\beta}{\beta}\right)\right]dr\\&+\frac{4}{35}\pi\,\Sigma_N\int r^8\frac{G(r,\ N)}{\beta^4(r,N)}\left[24D^3\phi-28D^2\phi\left(\frac{D^1\beta}{\beta}\right)-D^1\phi\left\{7\left(\frac{D^2\beta}{\beta}\right)-25\left(\frac{D^1\beta}{\beta}\right)^2\right\}\right]dr\\&+\frac{4}{105}\pi\,\Sigma_N\int r^{10}\frac{G(r,\ N)}{\beta^4(r,N)}\left[6D^4\phi-12D^3\phi\left(\frac{D^1\beta}{\beta}\right)-D^2\phi\left\{\left(\frac{D^2\beta}{\beta}\right)-15\left(\frac{D^1\beta}{\beta}\right)^2\right\}\right.\\&\left.-D^1\phi\left\{\left(\frac{D^3\beta}{\beta}\right)-10\left(\frac{D^2\beta}{\beta}\right)\left(\frac{D^1\beta}{\beta}\right)+15\left(\frac{D^1\beta}{\beta}\right)^3\right\}\right]dr\,,\end{aligned} \tag{A.19}$$

Consider the difference $\sigma_{yy}-\sigma_{zz}$:

$$\sigma_{yy}^{(0)}-\sigma_{zz}^{(0)}=0\,, \tag{A.20}$$

$$\begin{aligned}\sigma_{yy}^{(2)}-\sigma_{zz}^{(2)}=&\frac{8}{15}\pi\,\Sigma_N\int r^6\frac{G(r,\ N)}{\beta^3(r,N)}\left[2D^2\phi-D^1\phi\left(\frac{D^1\beta}{\beta}\right)\right]dr\\&+\frac{8}{105}\pi\,\Sigma_N\int r^8\frac{G(r,\ N)}{\beta^3(r,N)}\left[2D^3\phi-3D^2\phi\left(\frac{D^1\beta}{\beta}\right)-D^1\phi\left\{\left(\frac{D^2\beta}{\beta}\right)-\left(\frac{D^1\beta}{\beta}\right)^2\right\}\right]dr\,,\end{aligned} \tag{A.21}$$

The viscosity coefficient, μ, is given by

$$\mu=\sigma_{xy}/\lambda=\sum_{n=0}^{\infty}\mu^{(2n)}\lambda^{2n} \tag{A.22}$$

where the expansion coefficients are

$$\mu^{(2n)}=\sigma_{xy}{}^{(2n+1)}\,. \tag{A.23}$$

If $\beta'r, N)$ and $\phi(r, N)$ do not so sharply change with r, comparison of Eqs. (A.18), (A.19) and (A.20), (A.21) leads to the relation

$$\frac{|\sigma_{yy}{}^{(2)}-\sigma_{zz}{}^{(2)}|}{\sigma_{yy}{}^{(0)}}\lesssim\frac{1}{5}\frac{|\mu^{(2)}|}{\mu^{(0)}}\,. \tag{A.24}$$

References

1) M. Yamamoto: J. Phys. Soc. Japan **11** (1956) 413.
2) M. Yamamoto: J. Phys. Soc. Japan **12** (1957) 1148.
3) K. Weissenberg: Nature **159** (1947) 310.
4) J. H. Poynting: Proc. Roy. Soc. **A82** (1909) 546; **A86** (1912) 534; Note in India-Rubber J. Oct. 4 (1913) p. 6.
5) J. E. Roberts: Ministry of Supply Report ADE 13/153 (England) (1952); Proc. 2nd Intern. Congr. Rheology, New York, 1953 (1954) 91.
6) M. Mooney: J. Colloid Sci. **6** (1951) 96.
7) R. S. Rivlin: Proc. Roy. Soc. (London) **A193** (1948) 260; **A200** (1950) 68; Trans. Faraday Soc. **45** (1949) 739.
8) H. Markovits and R. B. Williamson: Trans. Soc. Rheology **1** (1957) 25.
9) W. Philippoff: J. Applied Phys. **27** (1956) 984; Nature **178** (1956) 811: J. G. Brodnyan, F. H. Gaskins and W. Philippoff: Trans. Soc. Rheology **1** (1957) 109; W. Philippoff, J. G. Brodnyan and F. H. Gaskins: J. Applied Phys. **28** (1957) 1118.
10) F. J. Padden and T. W. De Witt: J. Applied Phys. **24** (1953) 675; **25** (1954) 1086.
11) H. W. Greensmith and R. S. Rivlin: Phil. Trans. **245** (1953) 399.
12) M. Kurata, T. Kotaka and M. Tamura: Busseiron-Kenkyu **98** (1956) 141, 153; **101** (1956) 69 (in Japanese); Zairyo-Shiken (J. Japan Soc. Testing Materials) **6** (1956) 227 (in Japanese); J. Applied Phys. (to be published).
13) F. H. Garner, A. H. Nissan and G. F. Wood: Phil. Trans. Roy. Soc. **A241** (1950) 379.
14) K. Weissenberg: Proc. 1st Intern. Congr. Rheology, Amsterdam, 1948 (1949) 36.
15) R. S. Rivlin: "Large Elastic Deformations" Rheology, ed. by Eirich, Ch. X N. Y. 1956.
16) M. Mooney: J. Applied phys. **24** (1953) 675.
17) R. S. Rivlin: J. Rational Mech. Anal. **5** (1956) 179.
18) H. Markovitz: Trans. Soc. Rheology **1** (1957) 37.
19) W. Philippoff: Trans. Soc. Rheology **1** (1957) 95.
20) B. H. Zimm: J. Chem. Phys. **24** (1956) 269.
21) A. S. Lodge: Trans. Faraday Soc. **52** (1956) 120.

JOURNAL OF THE PHYSICAL SOCIETY OF JAPAN Vol. 13, No. 10, OCTOBER, 1958

Disturbance Phenomena in Probe Measurement of Ionized Gases

By Takayoshi OKUDA and Kenzo YAMAMOTO

Faculty of Engineering, University of Nagoya, Nagoya

(Received June 20, 1958)

This paper is concerned with disturbance phenomena occuring when a probe is immersed in plasma.

There are two types of disturbance, i.e., one independent of probe potential and one which depends upon it. The former (inherent) disturbance has three effects which are classified: Asymmetrical effect, formation effect of transition region, and the scattering effect. The latter (incidental) depends on either the negative probe or the positive probe. In the negative probe, penetration of ion sheath into surrounding plasma is characteristic. In the positive probe, there is an unexpected change of electron current, as a result of drainage of electron, which is observed with rise of positive probe voltage.

The mechanism of collection of ion and electron on probe is also explained in terms of these disturbance effects.

§ 1. Introduction

A complicated situation arises when, as is usually encountered in the laboratory work, a probe of finite dimension is immersed in a plasma having a finite extent and density, resulting in disturbance. In reality, the disturbance has a marked influence on determination of plasma density made by ordinary probe method, as already described in a previous paper[1].

Here, for the purpose of insuring accuracy of measurement, it is necessary to have complete knowledge of the conditions resulting from insertion of probe in laboratory plasma.

Since disturbance may be responsible for formation of a disturbed region spreading extensively into plasma and controlling density of charged particle near the probe[2], the purpose of this paper is to clarify disturbance phenomena and to explain how it affects collection of charged particle.

Finally, we elucidate causes of error and improve reliability of measurement. Also, the conclusions obtained in this study offer helpful information on interesting problems in practical use of the third electrode, viz., grid electrode in discharge tube or extracting electrode in various ion sources.

§ 2. Experimental Procedures

All experimental discharge tubes used in this work are sealed-off tubes, made of hard glass, having an oxide coated cathode, a Ni disc anode and Mo probes. Gases of Ne and Ar are used. Since commercial Ne and Ar are both only 99.9% pure, they are purified by means of Ca getter.

Ultimate pressure of vacuum system is of the order of 10^{-7} mm Hg and gas pressure used ranges from 10^{-3} to 10 mm Hg. The discharge currents are below 1.0 A and tube voltages are several tens volts. Structures, dimensions and materials of pecular probes are described in detail in Section 3.

§ 3. Experimental Results and its Consideration

A. *General view of disturbance*

(1) Visual observation of disturbance near a probe

When a probe with floating potential is immersed in a plasma, the outline of an ion sheath forming around the probe is indistinct and in the space surrounding the ion sheath a faintly luminous "disturbed region" appears. Extent of the disturbed region in the direction toward the anode is found to be less than that in the direction toward the cathode, and at the boundary of the disturbed region on the anode side, there is clearly observed a dense plasma having more intense luminosity than that of undisturbed plasma.

At low pressure (below 10^{-3} mm Hg) the local dense plasma is too diffusive to be observed and the distance between probe and the center of the local dense plasma is of the order of several cm. As pressure is raised, such anisotropic appearance becomes more

remarkable and moves nearer the probe.

Fig. 1 shows the disturbed region appearing around a probe held at the floating potential. As shown by the dotted line, the cathode side of the disturbed region expands owing to increase of negative voltage, while the local dense plasma formed on the anode side grows progressively without changing its relative position to the probe.

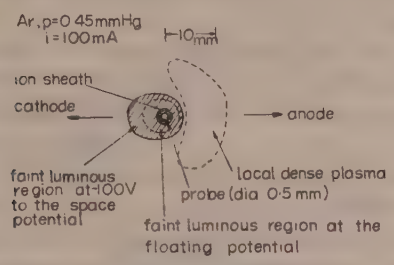

Fig. 1. Illustrating disturbed region asymmetrically developed around a probe.

As discharge current is reduced, the distance from the probe to the center of local dense plasma decreases slightly, while the extent of the disturbed region on the cathode side increases. Of course, the larger the dimension of probe employed, the greater such an effect.

On the other hand, if the probe potential approaches the plasma potentials by application of probe potential relative to the cathode, ion sheath becomes thinner and at the same time the disturbed region becomes unobservable. Here a somewhat anomalous circumstance is found where the luminosity of the disturbed region on the anode side rather far from probe, as well as that of the local dense plasma, become slightly weaker in comparison with luminosity when the probe potential is negative to plasma. Meanwhile, on the contrary, luminosity of the rigion close to probe increases. Also, no matter how probe potential is with respect to plasma, the relative position of the local dense plasma is unchanged.

Whenever probe potential is raised until the potential difference between plasma and probe reaches a magnitude corresponding to the first excitation potential of the gas, the layer just covering the probe has a faint glow which is followed by gradual development of a glow similar to the anode glow, indicating occurence of ionization in electron sheath. As a result, currents flowing into the probe quickly increase, limited by the resistance of probe circuit. At high pressure, the faint glow can not be distinctly observed, abruptly changing into a glow mode.

(2) Distribution of potential and plasma density in disturbed region.

A movable probe construction is more convenient for measuring potential and plasma density in the disturbed region. In the tube shown in Fig. 2, a disturbing-thick probe can be inserted into or removed from the discharge column normal to the discharge axis, while a measuring-thin probe moves parallel along the discharge axis. In every case, interaction between the thick probe and the thin probe can be regarded as negligible, because the mersuring-thin probe is made of small dimension and is always far from the thick probe by several mm.

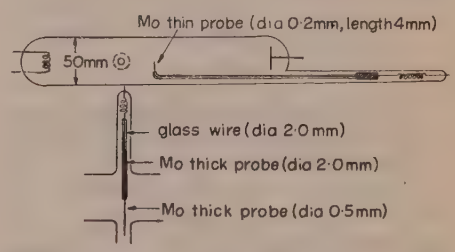

Fig. 2. Experimental discharge tube with movable probes.

From measurements of potential and plasma density using the thin probe, it is found that the disturbance may exist to a considerable extent even if the pressure is below 10^{-3} mm Hg, where the depletion due to elastic scatterihg seems to be small compared with that at high pressure, as already mentioned in a previous paper[1].

Consistent with visual observation, the local dense plasma is observed as a maximum of potential and plasma density on anode side of disturbed region. The potential and the plasma density on cathode side of disturbed region change monotonously toward the undisturbed plasma.

By taking the deviation of ion current Δi_p measured at -30 V with respect to the space potential, and taking the deviation of potential ΔV from the undisturbed condition realized by removing the thick probe from the discharge column, we obtain Fig. 3.

Fig. 3 shows distribution of the potential and the ion current as a measure of plasma

density in cases where the thick probe is held at the floating potential.

The way in which the disturbance is connected with discharge current, pressure and probe dimension is obvious from this. As discharge current increases, the local dense plasma develops with increasing distance from the probe, while the extent of cathode side of disturbed region decreases. Those effects, of course, become more remarkable as the probe radius is enlarged.

To examine how the meterial of the thick probe affects such disturbance, the same procedure as for Mo probe is carried out with a glass cylinder having the same dimension as Mo probe. The results are identical for both the glass cylinder and the Mo probe.

As potential of probe approaches the space potential, a remarkable change takes place in

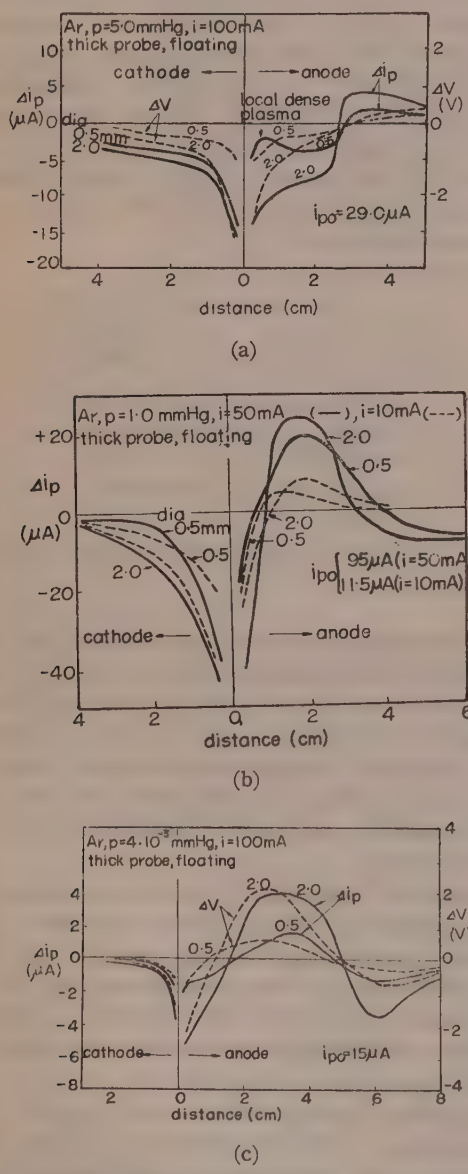

Fig. 3. Deviation of ion current and potential from those of the undisturbed case, where the thick probe is absent. The ion current i_{po} of the undisturbed casd is written in figure.
(a) 5 mm Hg, (b) 1 mm Hg, (c) $4 \cdot 10^{-3}$ mm Hg of Ar.

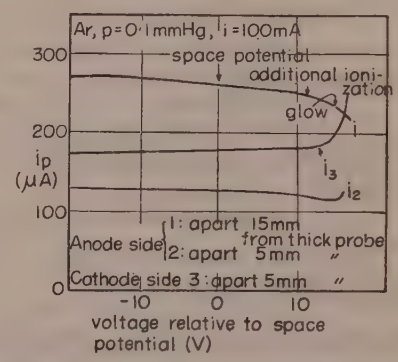

Fig. 4. Ion current flowing into thin probes near a thick probe and potential of the thick probe.

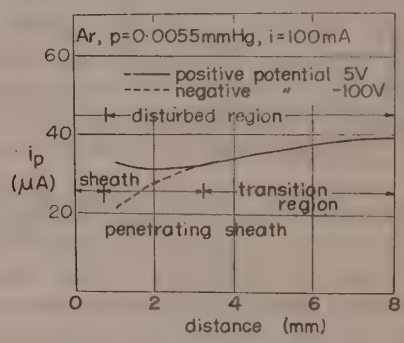

Fig. 5. Disturbed region.

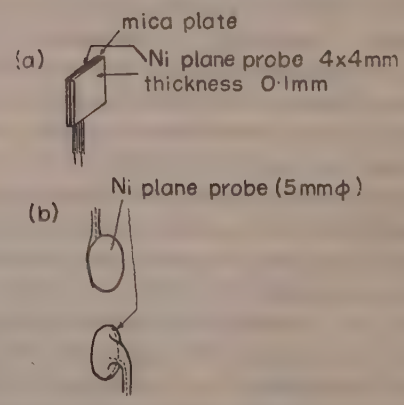

Fig. 6. Probe structure for measuring directional collection.
(a) Back-to-back probe, (b) Unidirectional probe.

the space around the thick probe. In Fig. 4 the ion current measured by the thin probe is plotted against the potential of the thick probe, showing that the plasma density on anode side of disturbed region decreases, as we observed under visual observation of disturbance near probe.

As shown in Fig. 5, the disturbed region distant from the probe is formed independent of the probe potential. Such a distant disturbed region is called a "transition region". Of course, the disturbed region close to probe is different depending upon whether the potential of probe is negative or positive with respect to plasma.

(3) Directional distribution of ion collection

Here, we investigate how the asymmetrical disturbance is connected with collection of ion on the probe. For this purpose, we prepare the back-to-back plane probes shown in Fig. 6 (a) and a pair of plane probes facing only in the direction, as shown in Fig. 6 (b).

From experiments, it is seen that at extremely low pressures (below 10^{-3} mm Hg) the ion collection on the probe facing the cathode is larger than that on the probe facing the anode, while at high pressure inversed results are obtained. The data obtained by using the tube shown in Figs. 6 (a) and (b), are given in Figs. 7 (a) and (b) respectively.

To obtain the distribution of collection over the whole orientation around probe, we use a parent-daughter probe structure, as shown in Fig. 8, consisting of a (parent) cylindrical probe made of Ni and a plane (daughter) probe made of Mo mounted in an aperture on the surface of the parent probe. This apparatus can be rotated with the help of a magnet.

Measurement of the ion current flowing into the daugnter probe at an appropriate negative potential, yields the orientational distribution of the ion collection, provided the parent probe is held at a fixed negative posential. From experiments, we see that asymmetry of distribution of ion collection becomes appreciable as discharge current is raised, as shown in Fig. 9.

We may conclude, therefore, that the asymmetry is closely related to the development of local dense plasma on anode side of disturbed region.

Fig. 10 shows the effect of potential of the parent probe. As the potential of parent probe

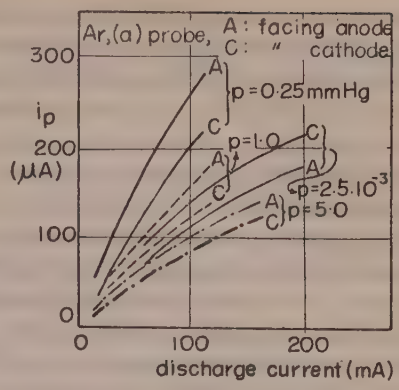

(a)

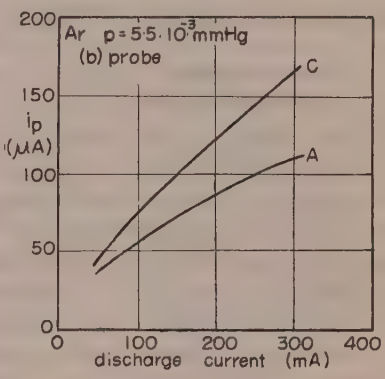

(b)

Fig. 7. Comparison of ion current flowing into a facing-anode probe with that flowing into a facing-cathode probe. Symbol A and C indicates facing-anode and facing-cathode, respectively. (a) Back-to-babk probe is used at 5, 0.25 and 2.5×10^{-3} mm Hg of Ar.
(b) Unidirectional probe is used at 5.5×10^{-3} mm Hg of Ar.

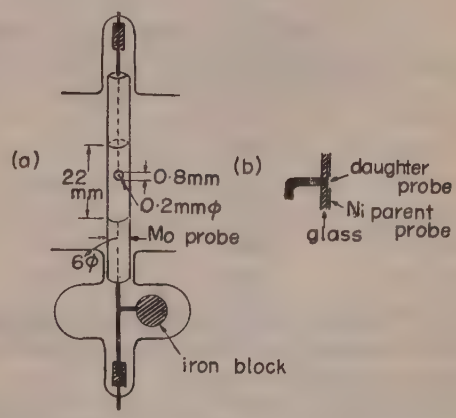

Fig. 8. Parent-daughter probe for measurement of directional collection around probe. (a) Scheme of parent-daughter probe, (b) structure of daughter probe.

approaches the space potential, the ion current flowing into the daughter probe increases owing to the increase of plasma density caused by drainage of electron, which we shall discuss later.

The results of experiments may be summarized as follows:

(a) However a probe is held, whether at a negative or positive potential with respect to the plasma, the space surrounding the probe is forced to be disturbed asymmetrically along the direction of discharge axis.

(b) The circumstances of disturbance formed on cathode side of probe and those on anode side are not identical, and their dependencies upon such parameters as pressure and discharge current are opposite. A feature of the disturbance appearing on cathode side corresponds to a mechanism of loss of electron by probe acting as an absorbant, while that appearing on anode side corresponds to a mechanism of compensation against loss of electron.

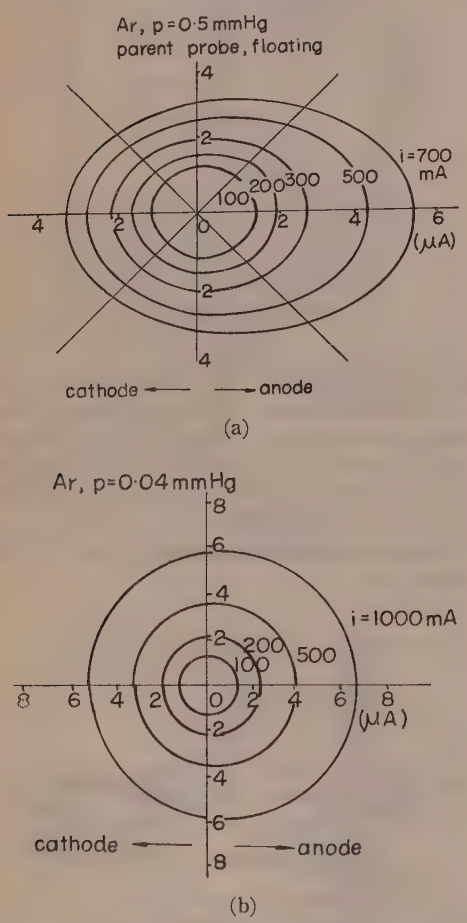

Fig. 9. Directional distribution of ion collection to the daughter probe, when the parent probe is held at the floating potential.
(a) Potential of daughter probe is −65 V with respect to the space. Pressure is 0.5 mm Hg of Ar.
(b) Potential of daughter probe is −45 V with respect to the space. Pressure is 0.04 mm Hg.

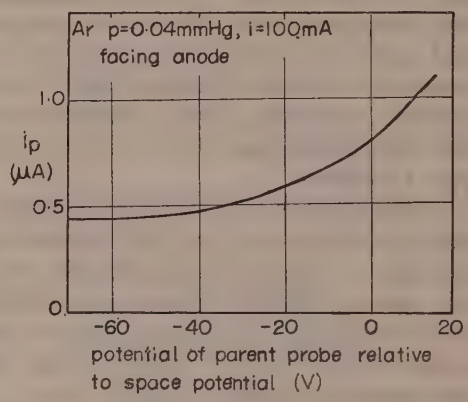

Fig. 10 Ion current flowing into a daughter probe measured at −45 V with respect to the space and the potential of the parent probe.

(c) Distant disturbance is not noticeable affected by the material and potential of probe, except that, at positive potential, the plasma density on anode side decreases slightly without changing the relative spatial distribution of density. On the other hand, a close disturbance may be affected by the potential of probe. At negative potential, the penetration of ion sheath occurs, while at positive potential, the increase of density occurs close to electron sheath by virtue of the drainage.

B. *Collection of electron and disturbance*

Positive probe characteristics are likely to be influenced from some source. It has been seen that in positive column, the electron drift velocity is only a few percent of random velocity of electron[3]. As a result, if the sheath area is a few percent of the cross section of positive column, the probe current may become comparable to discharge current and, consequently, a distorted characteristic may be obtained, from which one can not estimate plasma quantities of undisturbed plasma.

In addition to this type of disturbance, another one called "drainage" occurs even in conditions in which such distorted character-

istics are not observable.

Now from this standpoint, we examine the behavior of positive probe.

(1) Voltage-current characteristic

Here, we are concerned with slope s in the plot of electron current *vs.* positive probe voltage in log-log scale.

Provided that the collection of electron is limited by sheath area, the value of s depends on plasma density, probe radius and space charge equation applied under that condition. Computation of theoretical value of s can be derived from the assumption that electron current related to sheath area be set equal to electron current based upon space charge equation, as already described in a previous note[4].

We prepare a concentric cylinder-type tube, as shown in Fig. 11, for the purpose of eliminating asymmetrical disturbance.

Using this tube, we may expect the ratio of cross-section for electrons drifting towards anode to the sheath area to be greater than that when the ordinary long cylindrical tube is used, and consequently we can expect asymmetrical disturbance to be less than for the long tube.

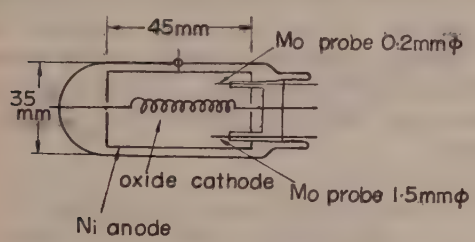

Fig. 11. Concentric-cylinder type tube.

Experimental results are tabulated in Table I, showing that there is a discrepancy between the measured and the theoretical values. According to our experiment, such discrepancy becomes large as pressure and plasma density are raised.

As a reasonable explanation of the discrepancy, a change in potential of the surrounding plasma relating to probe potential is considered.

To examine this relation, it is better to measure the potential difference ΔV between the space potential deduced from the inflection point of semi-log plot of probe characteristic and a potential where an additional ionization takes place, which means that the sheath voltage reaches a voltage corresponding to the first excitation potential for the gas used. Even under a condition that there is a large discrepancy of slope s, the difference between the first excitation potential and the potential difference ΔV is seen to be quite small. This confirms the fact that the change of plasma potential of the space surrounding probe with change of probe potential, can not be the reason for the discrepancy.

Furthermore, it has already been pointed out in a previous note that there is no ob-

Table. I. Comparison of measured slope of log-log plot of electron current *vs.* positive voltage with theoretically expected slope. Gas is Ar.

Pressure (mm Hg)	Discharge current (mA)	Probe radius (cm)	Random electron current density (mA/cm²)	Slope s	
				Measured	Theoretical
0.0055	50	0.01	10	0.67	0.51 (L)
〃	100	〃	33	0.57	0.45 (L)
0.12	25	〃	2.5	0.95	0.72 (L)
〃	〃	0.075	6.5	1.12	0.33 (L)
〃	100	0.01	5.0	0.85	0.55 (L)
〃	〃	0.075	2.0	1.00	0.44 (L)
5.0	10	〃	0.34	0.16	0.40 (b)
〃	50	0.01	13.6	0.92	0.38 (b)
〃	〃	0.075	1.7	0.46	0.35 (b)
〃	200	0.01	180	1.12	0.28 (b)
〃	〃	0.075	3.2	0.52	0.27 (b)

In computation of s, end effect is taken into account, where probe length is 3.3 mm.
Simbols L and b indicate Langmuir's and b's law, respectively.

servable relation between collection of electron and sheath radius[4].

Consequently, as a possible source of such discrepancy, we may consider an anomalous dependency of density of the surrounding space upon positive voltage, which is caused by a drainage of electrons. The drainage appears as a result of penetration of electrons accumulated in electron sheath. Thus, the drainage becomes more pronounced as accumulated charge is increased or as diffusion flow outgoing from the neighboring space of probe is decreased. Consequently it can be seen that as plasma density and gas pressure are increased, slope s must be increased due to the drainage.

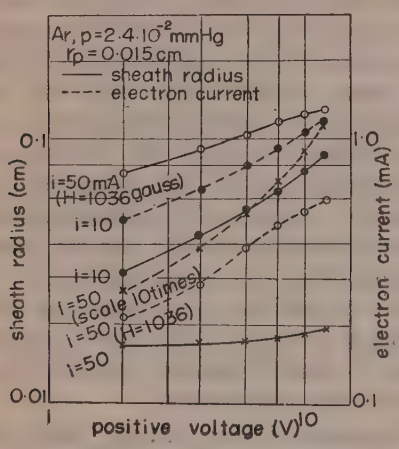

Fig. 12. Electron current and sheath radius plotted against positive probe voltage.

Next, we consider the mechanism of collection of electrons on positive probe. When the discharge current is lowered, there is less discrepancy between the measured sheath radius and the theoretical radius. Also, as the discharge current is decreased, there is a closer correspondency between the plot of sheath radius *vs.* positive voltage and the plot of electron current *vs.* positive voltage, as shown in Fig. 12.

Since the drainage decreases as the discharge current or collecting electron current is decreased, a close correspondency between electron current and sheath radius is obtained at low density plasma.

Discrepancy between measured sheath radius and theoretically expected sheath radius can be explained by formation of a penetrating sheath, as in negative probe. Therefore the measured sheath radius corresponds to a positive voltage which is less than the applied positive voltage. Since the penetrating sheath develops as positive voltage is increased, the slope of the plot of sheath *vs.* positive voltage is always less than the expected slope, as reported in previous note[4]. This is the reason that at large discharge current the measured sheath radius has only slight dependence on positive voltage.

At high pressure where the drainage is prominent, there is not the same close relation between the drainage and the penetration as at low pressure. The departure of measured sheath radius from theoretical radius is less than that at low pressure. This is due to the fact that at high pressure the penetrating sheath posseses a characteristic more plasma-like than sheath-like.

Next, we are concerned with collection of electron at low pressure where electron collection is determined by orbital motion. Under such condition, an effective collecting radius of probe determines the degree of collection of electron. Using the same procedure as that used in measuring sheath radius under condition that the collection is limited by the sheath area, we can measure the collecting radius.

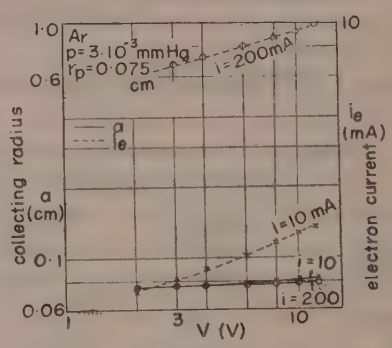

Fig. 13. Collecting radius and electron current plotted against positive probe voltage under the condition of orbital motion.

Fig. 13 shows typical data obtained for Ar. The measured collecting radius is fairly constant with positive voltage V, independent of plasma density. This would indicate that Langmuir's orbital motion theory of collection[5] in which collecting radius is roughly proportional to $V^{1/2}$ is not valid, and that Bohm's theory in which collecting radius is independent of V is valid[6].

In spite of the constancy of collecting radius, a considerable increase in electron collection is obtained with increasing positive voltage, as shown in Fig. 13. This increase is due to the drainage.

(2) Electron collection in magnetic field

Here we deal with the subject of electron collection in magnetic field in order to acquire information on the relation between drainage and voltage-current characteristic.

Since magnetic field used in this measurement is below 1,500 gauss, the ion is hardly affected by magnetic field, while the electron is so affected that the probe characteristic of positive probe is strongly influenced by magnetic field.

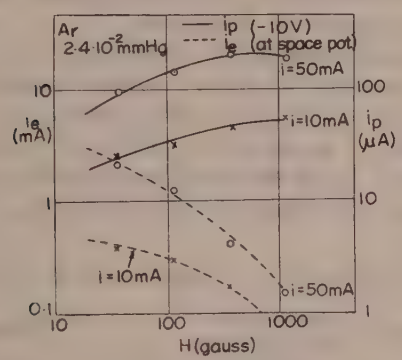

Fig. 14. Electron and ion currents as a function of magnetic field applied to the direction of the probe axis.

Such magnetic effect on electron colleciton can be understood from the fact that the electron current flowing into probe held at the same potential as the plasma potential decreases with increasing magnetic field, while the ion current flowing into probe at an appropriate negative potential with respect to the plasma potential, increases with increasing magnetic field, as shown in Fig. 14. Since there is no doubt that ion collection is not affected by magnetic field, it can be considered as an approximate measure of plasma density.

We may postulate, therefore, that the decrease of electron collection is caused by the magnetic effect. The reason considered for this effect is a decrease of diffusion coefficient[5].

Next, we consider collection of elctron at positive potential. With increasing magnetic field the slope of log-log plot of positive probe characteristics decreases almost independent of probe orientation. Since from the standpoint of drainage decrease of the slope corresponds to decrease of plasma density, it is concluded that the drainage becomes less pronounced by virtue of decrease of plasma density near probe with increasing magnetic field.

As shown in Fig. 12, the correlation of the plot of electron current *vs.* positive voltage with the plot of the measured sheath radius *vs.* positive voltage in magnetic field is distinct as compared with that in the condition when magnetic field is absent.

A saturation of electron current appearing in high positive voltage range when magnetic field is applied, is the result of a backward flow of electron caused by magnetic field. Also, decrease of sheath radius when magnetic field is applied, can be explained by decrease of effective sheath voltage through circulating motion of electron, while the lowering of plasma density by applying magnetic field should result in large sheath radius.

C. *Ion collection affected by disturbance*

The probe theory proposed by Langmuir is based upon the assumption that ion sheath is completely screened by the surrounding plasma[5]. In laboratory plasma, however, such screening is not complete.

To study this type of disturbance, it is necessary to obtain knowledge of dependency of the disturbance upon plasma density, probe voltage, dimension of probe and gas pressure.

(1) Voltage-current characteristics

Numerical value of $s = d\log i_p / d\log V$ decreases with rising pressure and with increasing probe radius and plasma density when the rate of expansion of ion sheath accompanied by negative voltage is lowered.

Using a similar procedure for electron, we examine the way in which measured value of s differs from the theoretical value.

Experimental results are tabulated in Table II. At all except intermediate pressures, the measured value of s is less than the theoretical value based upon the theory that collection is limited by sheath area: as discharge current is lowered, the difference between these values becomes greater.

To see whether or not the value of s is affected by the asymmetrical disturbance above mentioned, the measurements are carried out in various tubes, that is, in the ordinary long tube (Fig. 2), the concentric cylinder tube

(Fig. 11) and a large spherical tube with diameter of 15 cm. These results are all consistent in their general dependence upon various parameters.

As a possible cause responsible for discrepancy between measured and theoretical values of s, we may consider that real sheath voltage is less than the applied negative voltage and that the discrepancy between them increases with increasing negative potential. By measuring the real sheath radius by applying a variable-length probe method already proposed by us, an answer may be given.

(2) Penetration of ion sheath

We have already described in a previous paper that in all cases of sheath area limited condition, the sheath radius measured by using the variable-length probe method agreed with or was less than the sheath radius evaluated by using an appropriate space charge equation, and that the discrepancy between them increased with decreasing discharge current or plasma density.

A most acceptable reason for such discrepancy is that the sheath voltage V is less than the applied negative voltage deduced from probe characteristic.

The expected value V' of the sheath voltage corresponding to the measured radius is always less than the applied voltage and the discrepancy between them becomes large as the applied voltage increases and as the discharge current is reduced.

Now we consider how the disturbance affects the collection of ion on probe. The two important effects are the penetration effect and the scattering effect. The penetration effect results in the sheath voltage being less than the applied voltage, as we described above. Also, it may arise that the penetration effect leads to a decrease of plasma density at the outer boundary of ion sheath.

This is checked by examining how ion current density j at the boundary, estimated from the measured sheath radius and ion current, is changed by increase of negative voltage. Table. III gives some results of this examination, showing that the value of j

Table. II. Measured and theoretical slope of log-log plot of ion current *vs.* negative voltage in Ar.

Tube type	Pressure (mm Hg)	Discharge current (mA)	Probe radius (cm)	Random ion current density (μA/cm^2)	Slope s Measured	Slope s Theoretical
a	0.0055	100	0.01	40	0.55	0.63 (L)
〃	〃	〃	0.075	〃	0.55	0.63 (L)
〃	0.02	〃	〃	350	0.40	0.55 (L)
〃	0.1	〃	〃	490	0.28	0.28 (μ)
〃	1.0	〃	0.025	570	0.22	0.30 (μ)
〃	〃	〃	0.075	290	0.18	0.20 (μ)
〃	5.0	〃	0.025	380	0.17	0.38 (b)
b	0.15	〃	0.01	170	0.49	0.44 (μ)
〃	〃	〃	0.075	240	0.27	0.29 (μ)
〃	1.0	〃	0.01	360	0.38	0.41 (μ)
〃	5.0	200	〃	1900	0.31	0.44 (b)
c	0.004	50	0.075	30	0.36	0.40 (L)
〃	0.02	200	0.015	270	0.36	0.45 (L)
〃	〃	25	〃	60	0.46	0.50 (L)
〃	0.35	5	0.075	105	0.50	0.37 (μ)
〃	〃	25	0.015	75	0.43	0.40 (μ)
〃	5.0	200	〃	51	0027	0.43 (b)
〃	〃	50	〃	17	0.32	0.44 (b)

Symbols a, b and c in the first column represent the ordinary long cylindrical, concentric cylinder and large spherical tube, respectively. In computation of s in cases when a and b tubes are used, the end effect is taken into account (probe length is 3.3 mm), while in tube c, the end effect is not taken into account, because this effect is eliminated by using variable-length probe method. Symbols L, μ and b in the last column indicate Langmuir's, μ's and b's law, respectively.

Table. III. Ion current density outside ion sheath.

Gas	Pressure (mA)	Discharge current (mA)	Probe radius (cm)	Probe voltage (V)	Ion current density (μA/cm^2)
Ar	0.004	25	0.015	30	9.2
	〃	〃	〃	60	8.7
	〃	100	0.075	30	30.0
	〃	〃	〃	60	28.1
	0.026	25	〃	30	12.8
	〃	〃	〃	90	12.8
	0.15	50	0.075	30	30.5
	〃	〃	〃	90	31.8
	〃	〃	0.015	30	76.2
	〃	〃	〃	60	77.4
	1.0	〃	0.075	30	34.2
	〃	〃	〃	90	35.6
	5.0	〃	0.015	30	39.0
	〃	〃	〃	90	34.8
Ne	0.02	50	〃	30	105.0
	〃	〃	〃	60	93.0
	〃	〃	0.075	30	61.2
	〃	〃	〃	60	57.3
	0.35	200	〃	30	75.5
	〃	〃	〃	60	84.6
	5.0	25	0.015	30	20.6
	〃	〃	〃	60	20.1

decreases slightly with increasing negative voltage, except when the pressure is intermediate. This fact serves to explain the reason why the decrease of density by penetration effect can be neglected by us when we determine plasma density of undisturbed plasma.

A proof for such picture is also given by following the way which shows how the slope s obtained by employing the sheath voltage V' instead of the applied voltage agrees with the theoretical slope.

Results obtained at low pressure are plotted in Fig. 15 (a). In this case the slope s is 0.63 independent of the radius of probe, which is consistent with the theoretical value of Schultz and Brown[7] based on their assumption that the sheath area limited collection and Langmuir's

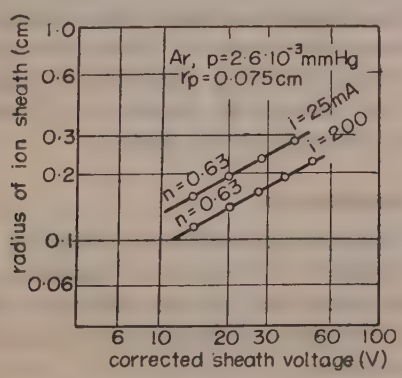

(a)

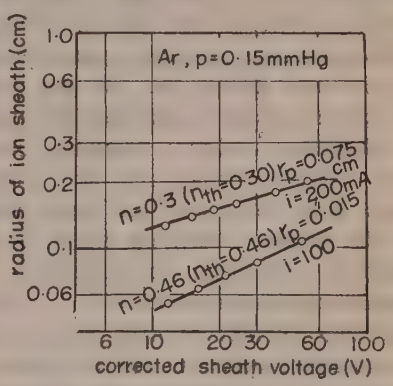

(b)

Fig. 15. Radius of ion sheath plotted against the corrected sheath voltage.
(a) At 2.6×10 mm Hg of Ar, (b) At 0.15 mm Hg of Ar.

law of space charge equation are valid. At high pressure, as shown in Fig. 15 (b), the slope s agrees with the theoretical value obtained by assuming the sheath area limited collection and μ's law of space charge equation to be applicable. Those results show that the ion current density outside ion sheath is constant. This fact may be interpreted from the point of view of Boyd's sheath criterion[8].

Finally, we deal with the anomality observed in intermediate pressure in which the measured slope of log-log plot of ion current *vs.* negative voltage exceeds the theoretically expected slope. This would indicate that in such a pressure the depletion due to elastic scattering affects ion collection, because the extent of a range in which spatial distribution of plasma density changes appreciably because of elastic scattering, becomes comparable to sheath radius.

The fact that at intermediate pressure, value of j estimated by measured sheath radius increases with increasing negative voltage, as seen in results of pressure of 0.35 mm Hg for Ne in Table. III, is successfully explained by such scattering effect.

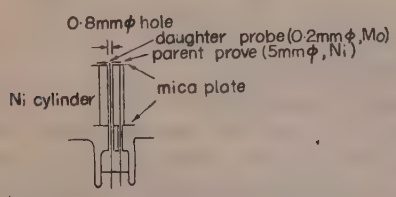

Fig. 16. A parent-daughter probe.

Furthermore, to prove the existence of a discrepancy between the sheath voltage and applied voltage, we prepare a parent-daughter probe as shown in Fig. 16. As the potential of the parent probe is lowered, the potential of the daughter probe is lowered, but they are not always equal and the difference becomes large especially at high pressure. After the relation between those potentials is checked, we obtain a characteristic of the daughter probe as shown in Fig. 17, in which the electron current at each space potential of the daughter probe is plotted against the negative voltage of the daughter probe. The broken lines in Fig. 17 represent the expected characteristics estimated from the electron temperature by the ordinary technique, that is to say, from the slope of the semi-log plot of the probe characteristic of the daughter probe when the parent probe is held at the plasma potential.

From this figure, it is found that the electron current at high negative voltage greatly exceeds the expected value. Therefore, it is reasonable to suppose that the sheath voltage is always less than the applied voltage. A comparison of the magnitude of discrepancy observed in the variable-length method with that in this experiment, shows that both are identical numerically.

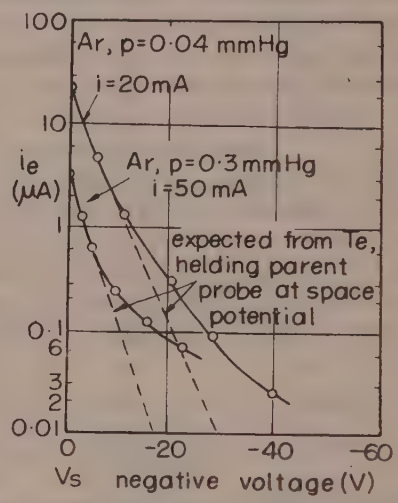

Fig. 17. Plot of electron current flowing into the daughter probe *vs.* its negative potential with respect to plasma potential. Broken line represents an expected curve which is derived from the measured electron temperature.

Now we may interpret the discrepancy as being the result of a penetration of ion sheath. As in electron collection, the penetrating effect is a result of electrostatic repulsion of accumulated charge. The penetrating sheath thus formed is an intermediate region between plasma and sheath, so that a high voltage drop can be applied across it. This takes place in front of an extracting electrode of discharge type ion source and results in a broadened energy spectrum of ion beam.

§ 4. Conclusions

(1) Inherent disturbance. When a probe is immersed in a plasma, a transition region appears, extending for a considerable distance around the probe, independent of the potential of the probe.

Transition region posseses less density and

has lower potential when compared with density and potential of the undisturbed plasma. The transition region is characterized by a loss of charged particles toward the probe acting as an obstacle.

Especially in d.c discharge plasma, there is an asymmetrical effect which is caused by drift of electron toward anode. As a result, the transition region posseses an asymmetrical configuration along the drift direction, that is to say, behavior of anode side of the transition region is altered by development of a local dense plasma as compensating for the loss of electron near the probe.

Besides the formation of transition, there is another important effect. It is the scattering effect which leads to depletion of charged particle density near probe, and depends upon the mean free path as well as on the geometrical dimension of the probe. At high pressure, this scattering effect plays a suprisingly important role and results in a remarkable error in estimation of plasma density unless it is taken into account.

The transition region is observed over a fairly large area, while the elastic scattering effect is restricted closely around the probe. Consequently we can not observe the scattering effect by means of a thin probe placed close to a large probe, because the thin probe itself posseses an ion sheath of finite thickness.

(2) Disturbance at negative potential. In Langmuir's probe theory it is assumed that the applied probe voltage is impressed across the ion sheath and do not penetrate into the surrounding plasma. However, we observe that at low density plasma, a penetration of probe voltage takes place and becomes prominent with increasing negative probe voltage. Owing to the penetration, a penetrating sheath is formed outside the ion sheath, and as a consequence, the applied voltage is not only imposed across the ion sheath, but across the penetrating sheath.

This conclusion is confirmed by our probe method using variable-length structure and other examinations using unique probe technique.

(3) Disturbance at positive potential. In positive probe, change of plasma density near probe called "drainage effect" is an important process. This is experimentally verified by the fact that the slope of log-log plot of electron current *vs.* positive probe voltage is startlingly different from the theoretical value.

Also the fact that measured sheath radius is always less than the theoretically expected one, can be identified with the formation of a penetrating sheath just outside the electron sheath, in a way similar to that in the negative probe.

Thus we reveal that collection of electron is determined by the drainage and that ion sheath is influenced by the penetration effect.

References

1) T. Okuda and K. Yamamoto: J. Phys. Soc. Japan **13** (1958) 411.
2) T. Okuda and K. Yamamoto: J. Phys. Soc. Japan **11** (1956) 177.
3) A. von Engel: "Ionized Gases", Clarendon Press, Oxford, 1955.
4) T. Okuda and K. Yamamoto: J. Phys. Soc. Japan **13** (1958) 112.
5) H. Moot-Smith and I. Langmuir: Phys. Rev. **28** (1926) 729.
6) D. Bohm; in "A. Guthrie and R. K. Wakerling, The Characteristics of Electrical Discharges in Magnetic Fields, McGraw-Hill, New York, 1949.
7) G. J. Schultz and S. C. Brown: Phys. Rev. **98** (1955) 1642.
8) R. L. F. Boyd: Proc. Roy. Soc. **201 A** (1950) 329.

JOURNAL OF THE PHYSICAL SOCIETY OF JAPAN Vol. 13, No. 10, OCTOBER, 1958

Magneto-hydrodynamic Oscillations of a Perfectly Conducting Fluid Sphere Placed in a Uniform Magnetic Field

By Tsuneji RIKITAKE

Earthquake Research Institute, Tokyo University

(Received July 1, 1958)

An attempt to improve theories of magneto-hydrodynamic oscillations of a conducting fluid sphere in a uniform magnetic field is made. Unlike the previous theories which have been developed by M. Schwarzschild and T. Rikitake, analytical expressions for zonal oscillations are obtained rigorously in this paper. It turns out that no eigen-periods are determined accurately. However, they are approximately obtained with drastic simplifications. Two fundamental normal modes of oscillation are also approximately obtained and illustrated.

§ 1. Introduction

Magneto-hydrodynamic oscillations in stars, the sun and the earth's core have been investigated by M. Schwarzschild[1], V. C. A. Ferraro[2], T. Rikitake[3] and others. All through the studies, it has turned out that magneto-hydrodynamic oscillations of a fluid sphere placed in a uniform magnetic field are quite different from electromagnetic, hydrodynamic or elastic oscillations which have been hitherto examined. In those oscillations, normal modes are usually given as spherical harmonics. However, normal modes for magneto-hydrodynamic oscillations are given as certain combinations of various spherical harmonics.

Schwarzschild[1] has succeeded in obtaining normal modes approximately, though his solutions did not completely satisfy the boundary conditions at the surface of the sphere. Meanwhile, Rikitake[3] tried to examine the couplings between poloidal and toroidal magnetic fields of different types. Although he could obtain a set of simultaneous differential equations, which govern the oscillations, in a general form, no accurate solutions of the equations have been obtained, because the equations contained harmonic constituents of successive degree and consequently it was apparently required to solve a set of simultaneous differential equations of infinite numbers with infinite unknowns.

From the theoretical stand-point, however, it is highly desirable to obtain exact normal modes of magneto-hydrodynamic oscillations as well as their eigen-periods as has been done in theories of electromagnetic, hydrodynamic and elastic oscillations related to a spherical body. The purpose of this paper is to obtain normal modes for a perfectly conducting sphere in an analytical form, though it seems impossible to determine exact eigen-periods.

§ 2. Fundamental Equations

Since we assume that there are no fluid motion and no electric current in the equilibrium state, the fundamental equations can be written as

$$\vec{e}+\vec{v}\wedge\vec{H}_0=0\,, \tag{2-1}$$

$$\mathrm{curl}\,\vec{e}=-\partial\vec{h}/\partial t\,, \tag{2-2}$$

$$\mathrm{curl}\,\vec{h}=4\pi\vec{i}\,, \tag{2-3}$$

$$\rho\partial\vec{v}/\partial t=\vec{i}\wedge\vec{H}_0-\mathrm{grad}\,p\,, \tag{2-4}$$

where $\vec{i}$, $\vec{e}$, $\vec{h}$, $\vec{H}_0$, ρ, p and $\vec{v}$ denote respectively electric current density, electric field, magnetic field, steady magnetic field applied from outside, density, pressure and velocity. It is also assumed (1) that the magnetic permeability is unity, (2) that there is no non-electromagnetic force that depends on time, and (3) that the inertia term of fluid motion can be ignored. The fluid is also assumed to be incompressible, so that

$$\mathrm{div}\,\vec{v}=0\,. \tag{2-5}$$

Following Schwarzschild, let us introduce a vector potential $\vec{A}$ which is defined by

$$\vec{v}=\mathrm{curl}\,\vec{A}\,. \tag{2-6}$$

In that case, by taking the curl of both sides of (2-4) and applying the formulas of vector analysis, we obtain

$$-\rho D\nabla^2\vec{A}=H\partial\vec{i}/\partial z\ , \tag{2-7}$$

where $\theta=0$ axis is taken as the z-axis. The external magnetic field is parallel to the z-axis, its intensity being denoted by H. D stands for the operator $\partial/\partial t$.

By taking curl of (2-1) and eliminating $\vec{e}$ with the aid of (2-2), we obtain

$$D\vec{h}=H\partial(\mathrm{curl}\,\vec{A})/\partial z\ , \tag{2-8}$$

from which it follows, by taking the curl of (2-8), that

$$4\pi D\vec{i}=-H\partial(\nabla^2\vec{A})/\partial z\ . \tag{2-9}$$

On eliminating $\vec{i}$ from (2-7) and (2-9), we obtain

$$K^2\nabla^2\vec{A}=\partial^2(\nabla^2\vec{A})/\partial z^2\ , \tag{2-10}$$

where

$$K^2=4\pi\rho D^2H^{-2}\ . \tag{2-11}$$

§ 3. Solutions for Zonal Magnetic Fields

(2-10) has been already obtained by Schwarzschild. He considered solutions only for meridional motions. He described the solutions in terms of power series of radial distance and the periods of free oscillations were estimated from the boundary conditions. In this solutions, however, the boundary conditions were fulfilled only at a few points on the surface of the sphere.

It is intended here to solve (2-10) in a more rigorous way. As has been done by Schwarzschild, it is also assumed that the fluid motion occurs entirely in meridional planes. In that case, the r and θ components of $\vec{A}$ do not exist, so that (2-10) can be written for the ϕ component as

$$K^2(\nabla^2A_\phi-A_\phi/(r^2\sin^2\theta))=(\cos\theta\partial/\partial r-\sin\theta\partial/(r\partial\theta))^2(\nabla^2A_\phi-A_\phi/(r^2\sin^2\theta))\ . \tag{3-1}$$

It is suggested that the solutions will be of the form such as $\sum_n R_n(r)P_n^1(\cos\theta)$ where P_n^1 is the associated Legendre function of degree n and order 1. If we put

$$A_\phi=\sum_n R_n(r)P_n^1(\cos\theta)\ , \tag{3-2}$$

the lefthand-side of (3-1) is easily reduced to $K^2\sum_n S_n(r)P_n^1$, where

$$S_n(r)=r^{-2}\frac{d}{dr}\left(r^2\frac{dR_n}{dr}\right)-n(n+1)r^{-2}R_n\ . \tag{3-3}$$

Meanwhile, the righthand-side of (3-1) can be rewritten by recurrence formulas as follows;

Righthand-side of (3-1)

$$=(\cos\theta\partial/\partial r-\sin\theta\partial/r\partial\theta)\sum_n\left[\frac{dS_n}{dr}P_n^1\cos\theta-\frac{S_n}{r}\frac{dP_n^1}{d\theta}\sin\theta\right]$$

$$=(\cos\theta\partial/\partial r-\sin\theta\partial/r\partial\theta)\sum_n\left[\frac{n}{2n+1}\left\{\frac{dS_n}{dr}-n\frac{S_n}{r}\right\}P_{n+1}^1+\frac{n+1}{2n+1}\left\{\frac{dS_n}{dr}+(n+1)\frac{S_n}{r}\right\}P_{n-1}^1\right]$$

$$=(\cos\theta\partial/\partial r-\sin\theta\partial/r\partial\theta)\sum_n T_n(r)P_n^1\ ,$$

where

$$T_n(r)=\frac{n-1}{2n-1}\left\{\frac{dS_{n-1}}{dr}-(n-1)\frac{S_{n-1}}{r}\right\}+\frac{n+2}{2n+3}\left\{\frac{dS_{n+1}}{dr}+(n+2)\frac{S_{n+1}}{r}\right\}\ , \tag{3-4}$$

and repeating the similar reduction, we obtain

$$\text{Righthand-side of (3-1)}=\sum_n U_n(r)P_n^1\ ,$$

where

$$U_n(r)=\frac{n-1}{2n-1}\left\{\frac{dT_{n-1}}{dr}-(n-1)\frac{T_{n-1}}{r}\right\}+\frac{n+2}{2n+3}\left\{\frac{dS_{n+1}}{dr}+(n+2)\frac{S_{n+1}}{r}\right\}\ . \tag{3-5}$$

On comparing both sides of (3-1) thus reduced, we see that S_n should satisfy the differential equation

$$K^2 S_n(r) = U_n(r) , \tag{3-6}$$

where S_n and U_n are defined respectively by (3-3) and (3-5).

A solution of (3-6), which does not become infinite at $r=0$, is to be of the form

$$S_n(r) = (2n+1)(Kr)^{-1/2} I_{n+(1/2)}(Kr) , \tag{3-7}$$

where $I_{n+(1/2)}$ is the modified Bessel function of degree $n+\frac{1}{2}$. When we consider recurrence formulas for modified Bessel functions, it is easily shown that

$$\frac{dS_{n-1}}{dr} - (n-1)\frac{S_{n-1}}{r} = K(2n-1)(Kr)^{-1/2} I_{n+(1/2)}(Kr) ,$$

$$\frac{dS_{n+1}}{dr} + (n+2)\frac{S_{n+1}}{r} = K(2n+3)(Kr)^{-1/2} I_{n+(1/2)}(Kr) ,$$

so that (3-4) gives

$$T_n = KS_n ,$$

and consequently we have

$$U_n = KT_n = K^2 S_n$$

from (3-5). We thus see that S_n as given in (3-7) is the solution of (3-6).

Introducing such a function to S_n of (3-3), the differential equation for R_n is obtained as

$$r^{-2}\frac{d}{dr}\left(r^2\frac{dR_n}{dr}\right) - n(n+1)r^{-2}R_n = C(2n+1)(Kr)^{-1/2} I_{n+(1/2)}(Kr) , \tag{3-8}$$

where C denotes a free constant which determines the amplitude of oscillation. It is easily seen that the particular solution of (3-8) is given by $K^{-2}C(2n+1)(Kr)^{-1/2} I_{n+(1/2)}(Kr)$, so that the general solution, which does not become infinite at $r=0$, can be written as

$$R_n(r) = \lambda_n r^n + K^{-2}C(2n+1)(Kr)^{-1/2} I_{n+(1/2)}(Kr) , \tag{3-9}$$

in which λ_n is a constant which will be determined later. In the above process, it is obvious that $\sum_n$ should be read $\sum_{n=1}^{\infty}$.

Since A_ϕ is given by (3-2) together with (3-9), the typical term of r, θ and ϕ components of $\vec{v}$ is calculated as

$$\vec{v} = \sum_{n=1}^{\infty} \begin{cases} \dfrac{R_n}{r}\dfrac{1}{\sin\theta}\dfrac{d}{d\theta}(\sin\theta P_n^1) \\ -\dfrac{d(rR_n)}{rdr}P_n^1 \\ 0 \end{cases} = \sum_{n=1}^{\infty} \begin{cases} n(n+1)\dfrac{R_n}{r}P_n \\ \dfrac{d(rR_n)}{rdr}\dfrac{dP_n}{d\theta} \\ 0 \end{cases} \tag{3-10}$$

with the aid of (2-6). From (2-8), the corresponding magnetic field inside the sphere is obtained as

$$\vec{h} = D^{-1}H\sum_{n=1}^{\infty} \begin{cases} n(n+1)\dfrac{V_n(r)}{r}P_n \\ \dfrac{d(rV_n)}{rdr}\dfrac{dP_n}{d\theta} \\ 0 \end{cases} , \tag{3-11}$$

where

$$V_n(r)=\frac{n-1}{2n-1}\left\{\frac{dR_{n+1}}{dr}-(n-1)\frac{R_{n-1}}{r}\right\}+\frac{n+2}{2n+3}\left\{\frac{dR_{n+1}}{dr}+(n+2)\frac{R_{n+1}}{r}\right\}, \tag{3-12}$$

which can be also transformed to

$$V_n(r)=(n+2)\lambda_{n+1}r^n+K^{-1}C(2n+1)(Kr)^{-1/2}I_{n+(1/2)}(Kr)\,. \tag{3-13}$$

§ 4. Boundary Conditions for Fluid Motion

1) *Rigid boundary*

If the sphere is surrounded by a rigid surface, the normal component of velocity should vanish at $r=a$, whence, from (3-9) and (3-10), we have

$$\lambda_n=-a^{-n}(2n+1)K^{-2}C(Ka)^{-1/2}I_{n+(1/2)}(Ka)\,. \tag{4-1}$$

Putting (4-1) into (3-13), we obtain

$$V_n(r)=CK^{-1}[(2n+1)(Kr)^{-1/2}I_{n+(1/2)}(Kr)-(n+2)(2n+3)(Ka)^{-3/2}I_{n+(3/2)}(Ka)(r/a)^n]\,. \tag{4-2}$$

2) *Free boundary*

In this case, the condition which should be satisfied at the boundary is

$$p=0\,. \tag{4-3}$$

We can calculate grad p and subsequently p from (2-4). After some calculations, p is found to be

$$p=-K^2\sum_n[(n+1)\lambda_n r^n+2K^{-2}C(2n+1)(Kr)^{-1/2}I_{n+(1/2)}(Kr)]P_n\,, \tag{4-4}$$

hence (4-3) implies

$$\lambda_n=-2K^{-2}C\frac{2n+1}{n+1}a^{-n}(Ka)^{-1/2}I_{n+(1/2)}(Ka)\,. \tag{4-5}$$

Putting (4-5) into (3-13), we obtain

$$V_n(r)=CK^{-1}[(2n+1)(Kr)^{-1/2}I_{n+(1/2)}(Kr)-2(2n+3)(Ka)^{-3/2}I_{n+(3/2)}(Ka)(r/a)^n]\,. \tag{4-6}$$

No detailed discussion about cases of free boundary, however, will be made in this paper because we are mainly interested in oscillations of a sphere surrounded by a rigid boundary such as the earth's core.

§ 5. Eigen-values

The eigen-values of K should be determined by the boundary conditions that electric and magnetic fields are continuous at $r=a$. However, unlike usual hydrodynamic, elastic or electromagnetic oscillations of a sphere, no rigorous eigen-equation is likely to be obtained because the components of magnetic field inside the sphere are given by infinite series such as that shown in (3-11). In the following, a method for obtaining approximate eigen-values will be described.

In the case of a rigid boundary, from (3-11) and (4-2), the magnetic field at $r=a$ should be written as

$$\vec{h}_{r=a}=\begin{cases} D^{-1}HCf(\theta;Ka) \\ D^{-1}HCg(\theta;Ka) \\ 0 \end{cases}, \tag{5-1}$$

where

$$\left.\begin{aligned} &f(\theta;Ka)\\ &\quad=\sum_n n(n+1)(Ka)^{-1}[(2n+1)(Ka)^{-1/2}I_{n+(1/2)}(Ka)-(n+2)(2n+3)(Ka)^{-3/2}I_{n+(3/2)}(Ka)]P_n(\cos\theta)\,,\\ &g(\theta;Ka)\\ &\quad=(Ka)^{-1/2}\sum_n[(2n+1)I_{n-(1/2)}(Ka)-n(2n+1)(Ka)^{-1}I_{n+(1/2)}(Ka)-(n+1)(n+2)(2n+3)(Ka)^{-2}\\ &\qquad\times I_{n+(3/2)}(Ka)]\frac{dP_n(\cos\theta)}{d\theta}\,. \end{aligned}\right\} \tag{5-2}$$

Since the magnetic field has a magnetic potential outside the sphere, we have

$$\vec{h}=\sum_s\begin{cases}(s+1)r^{-s-2}h_sP_s(\cos\theta)\\ -r^{s-2}h_s\dfrac{dP_s(\cos\theta)}{d\theta} & \text{for } r>a\\ 0\end{cases}\,. \tag{5-3}$$

The continuity of the magnetic field at the surface of the sphere implies

$$\left.\begin{aligned}&\sum_s(s+1)a^{-s-2}h_sP_s(\cos\theta)=D^{-1}HCf(\theta;Ka)\\ &-\sum_s a^{-s-2}h_s\frac{dP_s(\cos\theta)}{d\theta}=D^{-1}HCg(\theta;Ka)\end{aligned}\right\}\,. \tag{5-4}$$

When C is eliminated from these equations, we obtain

$$\sum_s k_s\Phi_s(\theta;Ka)=0\,, \tag{5-5}$$

where

$$\Phi_s(\theta;Ka)=(s+1)g(\theta;Ka)P_s(\cos\theta)+f(\theta;Ka)\frac{dP_s(\cos\theta)}{d\theta} \tag{5-6}$$

and

$$k_s=a^{-s-2}h_s\,. \tag{5-7}$$

In order to obtain approximate eigen-values, we may assume that (5-5) holds good at $\theta=\theta_1,\ \theta_2,\ \cdots,\ \theta_N$. By taking terms for $s=1,\ 2,\ \cdots,\ N$, we obtain a set of simultaneous equations such as

$$\left.\begin{aligned}&\Phi_1(\theta_1;Ka)k_1+\Phi_2(\theta_1;Ka)k_2+\cdots+\Phi_N(\theta_1;Ka)k_N=0\,,\\ &\Phi_1(\theta_2;Ka)k_1+\Phi_2(\theta_2;Ka)k_2+\cdots+\Phi_N(\theta_2;Ka)k_N=0\,,\\ &\cdots\cdots\cdots\cdots\\ &\Phi_1(\theta_N;Ka)k_1+\Phi_2(\theta_N;Ka)k_2+\cdots+\Phi_N(\theta_N;Ka)k_N=0\,.\end{aligned}\right\} \tag{5-8}$$

In order to have non-vanishing solutions for $k_1,\ k_2,\ \cdots,\ k_N$, we should have

$$\begin{vmatrix}\Phi_1(\theta_1;Ka) & \Phi_2(\theta_1;Ka) & \cdots\Phi_N(\theta_1;Ka)\\ \Phi_1(\theta_2;Ka) & \Phi_2(\theta_2;Ka) & \cdots\Phi_N(\theta_2;Ka)\\ \cdots & \cdots & \cdots\\ \Phi_1(\theta_N;Ka) & \Phi_2(\theta_N;Ka) & \cdots\Phi_N(\theta_N;Ka)\end{vmatrix}=0\,, \tag{5-9}$$

which may be regarded as the approximate eigen-equation.

It is no easy matter to solve such a complicated eigen-equation as (5-9) in a general

way. Some crude approximations of eigen-values will be obtained in the following with drastic simplifications.

From what we have been dealing with in Section 3, we see that there are no couplings between harmonic constituents of even and odd modes separately. This fact has been also pointed out in the writer's previous paper[3].

1) *Odd mode*

If we disregard terms for $s>1$ and $n>1$ in (5-9), (5-9) is reduced to

$$(Ka)^2 I_{1/2}(Ka)=15 I_{5/2}(Ka)\,, \tag{5-10}$$

which may be regarded as the crude approximation of the eigen-equation for the lowest odd mode. In that case, the eigen-values become

$$Ka=0.76i,\ 5.77i,\ \cdots\,, \tag{5-11}$$

hence the largest period of this oscillation mode is given by

$$T=5.2\pi^{3/2}\rho^{1/2}aH^{-1}\,. \tag{5-12}$$

2) *Even mode*

In this case, we take into account only the term for $s=2$ and $n=2$, ignoring higher degree terms. We therefore have, from (5-9),

$$(Ka)^2 I_{3/2}(Ka)=28 I_{7/2}(Ka)\,, \tag{5-13}$$

which gives

$$Ka=2.08i,\ 7.49i,\ \cdots\,, \tag{5-14}$$

and the largest period becomes

$$T=1.9\pi^{3/2}\rho^{1/2}aH^{-1}\,. \tag{5-15}$$

§ 6. Oscillation Modes

Since $\operatorname{div}\vec{v}=0$ and $\operatorname{div}\vec{h}=0$, we may express $\vec{v}$ and $\vec{h}$ in terms of appropriate Stokes' "stream functions", ψ and u respectively. The curves for $\psi=$constant will then be the stream-lines of the motion, while the curves for $u=$constant give the equations of the lines of force of the magnetic field. As has been shown by Ferraro[2], there are relations such as

$$\vec{v}=\begin{cases} -\dfrac{1}{r^2\sin\theta}\dfrac{\partial\psi}{\partial\theta} \\ \dfrac{1}{r\sin\theta}\dfrac{\partial\psi}{\partial r} \\ 0 \end{cases}, \tag{6-1}$$

$$\vec{h}=\begin{cases} -\dfrac{1}{r^2\sin\theta}\dfrac{\partial u}{\partial\theta} \\ \dfrac{1}{r\sin\theta}\dfrac{\partial u}{\partial r} \\ 0 \end{cases}. \tag{6-2}$$

From (3-10), (3-11) and (5-3), we see that the stream functions become

$$\psi=-r\sum_n R_n\sin\theta P_n^1\,, \tag{6-3}$$

$$u=-D^{-1}Hr\sum_n V_n\sin\theta P_n^1 \quad \text{for } r<a\,, \tag{6-4}$$

$$u=-\sum_s \frac{h_s}{s}r^{-s}\sin\theta P_s^1 \quad \text{for } r>a\,. \tag{6-5}$$

Corresponding to the even mode discussed in the last section, we obtain

$$u=-D^{-1}HrV_2(r)\sin\theta P_2^1 \quad \text{for } r<a\,, \tag{6-6}$$

$$u=-\frac{h_2}{2}r^{-2}\sin\theta P_2^1 \quad \text{for } r>a\,, \tag{6-7}$$

where only the terms for $n=2$ and $s=2$ are taken into account as before. h_2 is determined

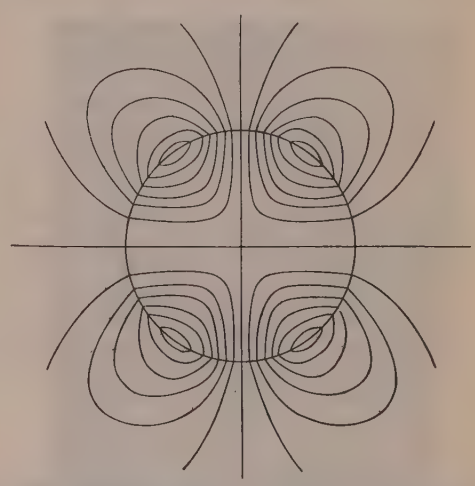

Fig. 1. Magnetic lines of force for the lowest even mode. External magnetic field is directed upwards.

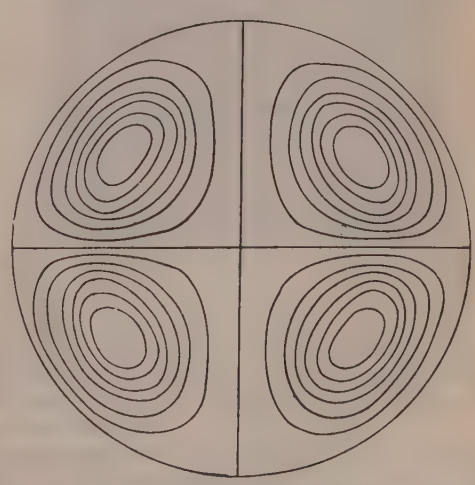

Fig. 2. Stream-lines of motion for the lowest even mode. External magnetic field is directed upwards.

by (5–4) or by the continuity of u at $r=a$, we therefore have

$$h_2=2D^{-1}Ha^3V_2(a)\ . \qquad (6\text{–}8)$$

The magnetic lines of force can be calculated from (6–6) and (6–7) as shown in Fig. 1.

It is obvious from (3–12) that the stream function of the motion is described, to the degree of the present approximation, as

$$\psi=-rR_1\sin\theta P_1^1 \qquad (6\text{–}9)$$

from which the stream-lines are calculated as shown in Fig. 2. All through the calculations in the above, the lowest eigen-value given in (5–14) is to be taken. In that case, it is easily seen that higher degree terms for u and ψ become fairly small, so that the above procedure, in which only the spherical harmonic of lowest degree is taken, would be justified.

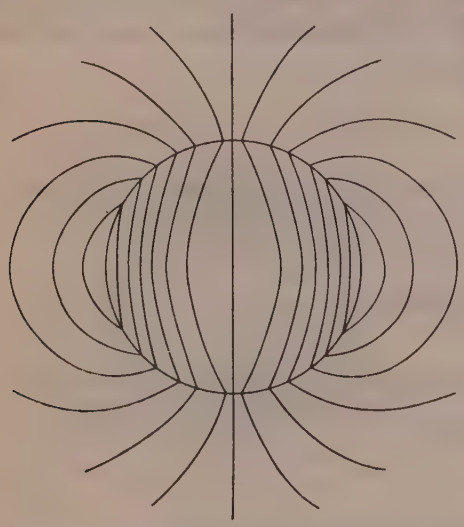

Fig. 3. Magnetic lines of force for the lowest odd mode. External magnetic field is directed upwards.

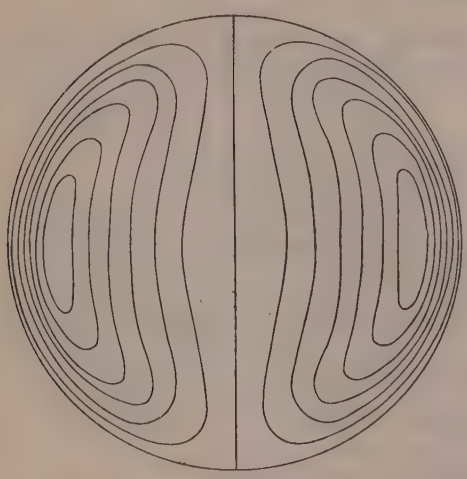

Fig. 4. Stream-lines of motion for the lowest odd mode. External magnetic field is directed upwards.

As for the odd mode, we obtain

$$u=-D^{-1}HrV_1(r)\sin\theta P_1^1 \quad \text{for } r<a\ , \qquad (6\text{–}10)$$

$$u=-h_1r^{-1}\sin\theta P_1^1 \quad \text{for } r>a\ , \qquad (6\text{–}11)$$

where

$$h_1=D^{-1}Ha^2V_1(a)\ , \qquad (6\text{–}12)$$

and

$$\psi=-rR_2\sin\theta P_2^1\ . \qquad (6\text{–}13)$$

With these expressions, the magnetic lines of force and stream-lines of motion for this mode are obtained as shown in Figs. 3 and 4 respectively, while the lowest eigen-value given in (5–11) are adopted.

§ 7. Discussion and Concluding Remark

It is interesting that the analytical expression of normal oscillation modes are given by (3–10) and (3–11). However, it is not possible to determine accurate eigen-periods of free oscillations. A crude estimate with some simplification suggests that the eigen-periods for oscillations of the lowest mode are nearly the same as those obtained in the previous paper. If we imagine a perfectly conducting liquid sphere, of which the density and the radius are assumed to be 10 g/cm^3 and 10 cm respectively, placed in a magnetic field of 10 gauss, the period for the lowest odd mode is estimated as 110 sec., while that for the lowest even mode as 33 sec. However, it is not possible to make such an experiment because of low conductivity of existing fluid.

If we consider problems of astronomical and geophysical scale, the present study has some bearing. But since the results in this paper are more or less similar to those obtained in references mentioned in the introduction, no detailed discussion in this line will be tried here.

References

1) M. Schwarzschild: Ann. d' Astrophys. **12** (1949) 148.
2) V. C. A. Ferraro and D. J. Memory: Mon. Not. Roy. Astro. Soc. **112** (1952) 361.
3) T. Rikitake: Bull. Earthquake Res. Inst. Tokyo Univ. **33** (1955) 175.

Short Notes

This section is intended to secure prompt publication of important discoveries in physics. The reports should not exceed 800 words in length. A figure of size 7cm × 7 cm will be counted as 150 words.

J. PHYS. SOC. JAPAN **13** (1958) 1231~1232

Chemical and Thermal Polish of KCl Crystals

By Masayoshi SAKAMOTO and Shunsuke KOBAYASHI

Physics Department, Tokyo College of Science Shinjuku-ku, Tokyo, Japan

(Received July 31, 1958)

KCl crystals are so soft that its surfaces are likely to have many dislocations by any slight mechanical shocks from outside[1]. In other words, they are apt to be contaminated in the meaning of dislocation theory. In order to remove these contaminations effectively, we have some methods of chemical and thermal polish[2].

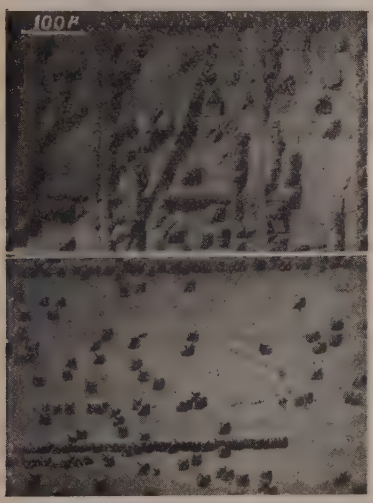

(a)

(b)

Fig. 1. An example of a chemically polished surface.

Fig. 1 is an example of a deep chemical polish with H_2O only. In the field of Fig. 1(a) there are one oblique cleavage step and two glide bands running in the [100] direction, which have existed since before the generation of other stripes of dislocation groups. Besides these we can see about four stripes of dislocation groups in the [010] direction, which have a large density of dislocation respectively. These stripes resulted from the rubbing of KCl crystal surface with a sheet of paper by about 3 cm in distance under the loading of 20 gr/cm² in weight. A picture after the chemical polish of about 5 seconds in time and about 100 μ in depth with H_2O is Fig. 1(b) and it is well recognized that the stripes of dislocation groups in high density and also the oblique step vanished completely.

Adequate heat treatment can give us an effect of polish which never cause so much volumal change as chemical polish. Fig. 2(b) shows the stripes of dislocation groups generated on a cleaved surface by rubbing under the same load as in Fig. 1. In this picture two glide bands and one boundary can be seen clearly the same as the picture before the rubbing [Fig. 2(a)]. After the heat treatment of 600°C in temperature, one hour in duration and 40°C/hour in its cooling rate, we got a result of Fig. 2(c). Contrary to the facts that the characteristic stripes of dislocation groups and glide hands vanished undoubtedly, it is notable that the boundary and most of cleavage steps did not vanish through treatment.

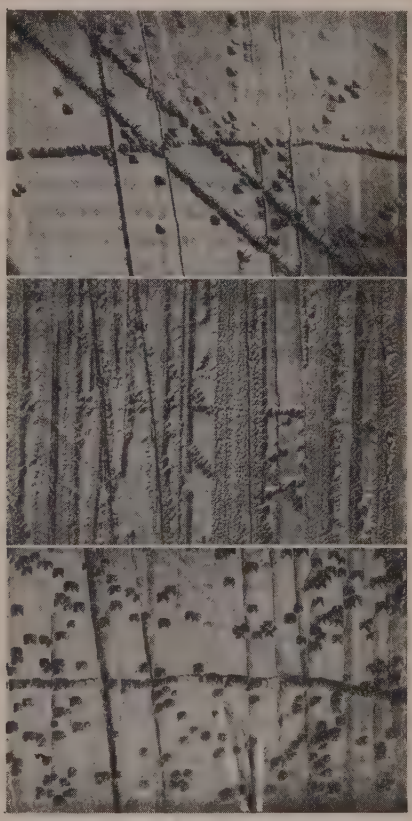

(a)

(b)

(c)

Fig. 2. An example of a thermally polished surface

Contamination in the meaning of dislocation theory and also geometrical roughness in usual meaning on KCl crystal surfaces will be removed by using together both methods of chemical and thermal polish described above. Both are usable

for the removing of surface contaminations, but especially chemical polish is effective for the removing of cleavage steps and thermal polish for the removing of glide bands.

References

1) M. Sakamoto and S. Kobayashi: Journ. Phys. Soc. Japan **13** (1958) 800.
2) On chemical polish in LiF, see the following Book "Dislocations and Mechanical Properties of Crystals" (John Wiley, 1957), p. 116.

J. PHYS. SOC. JAPAN **13** (1958) 1232~1233

Nuclear Magnetic Resonance Experiments of I^{127} in KI

By Junkichi ITOH and Yukio YAMAGATA
Department of Physics, Faculty of Science, Osaka University

(Received July 7, 1958)

We have made a series of experimental studies on nuclear magnetic resonance of alkali halides. In this note, the temperature dependence of the spin-lattice relaxation time and chemical shift of iodine nuclear magnetic resonance in KI crystal will be reported.

Fig. 1 shows the results of T_1 measurements, in which $\sqrt{1/T_1}$ is plotted against temperature, T. Now, time dependent nuclear electric quadrupole

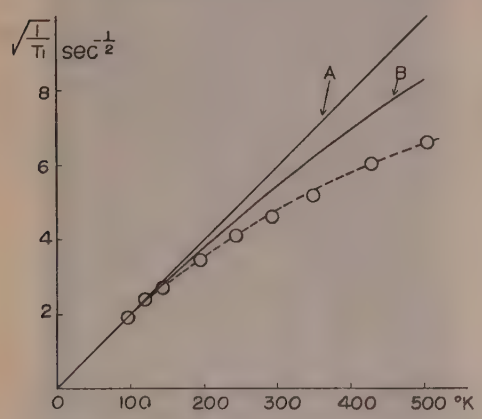

Fig. 1.

interaction caused by lattice vibration probably contributes mainly to the spin-lattice relaxation in alkali halides. Kranendonk[1] calculated T_1 theoretically by assuming the electric quadrupole interaction arises from electrostatic field gradient due to relative displacement of ions by lattice vibration, while later Yosida and Moriya[2] extended the theory to the case in which a small degree of covalency exists in the bond between positive and negative ions. According to these both theories, $\sqrt{1/T_1}$ is nearly proportional to T, in the temperature range of our measurements (line A in Fig. 1). The experimental plots deviate from this straight line at higher temperatures. As for this deviation, higher order terms in T in the theoretical calculation and effects due to the temperature variation of Debye temperature and sound velocity in the crystal are negligibly small, and the implicit temperature dependence due to thermal expansion of the lattice seems to be most important. Using known value of the thermal expansion coefficient and assuming a relation $\lambda(\text{covalency}) \propto \exp(-R/0.345)$ (R is the interionic distance in Å), which Yosida and Moriya assumed in their calculation, a numerical calculation was done (curve B in Fig. 1). The result of the calculation explains the experimental data in some extent, but, to interprete the experiments perfectly, much stronger dependence of λ upon R should be assumed, which seems to be inadequate. Kranendonk's theory gives much less improvement than Yosida and Moriya's one does.

The experimental results of the temperature dependence of the chemical shift are shown in Fig. 2. Here relative shifts of the resonance frequency from that at room temperature are plotted against T. A numerical calculation of the temperature dependence of the shift was made along the line of Yosida and Moriya's theory (curve A in Fig. 2).

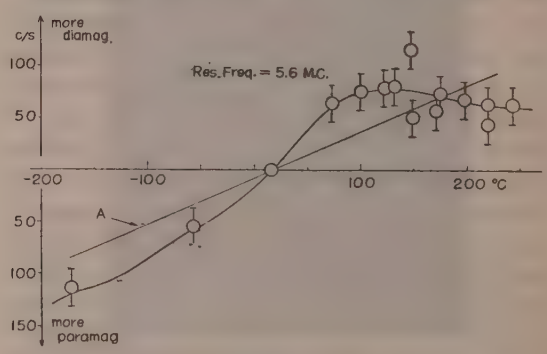

Fig. 2.

In this calculation, it is needed to use the absolute shift of solid resonance from pure iodine ion resonance. Solid KI shows a chemical shift of -1.7×10^{-4} relative to dilute KI aq., while by the measurement of concentration dependence of the shift of KI aq., a shift of the order of -6×10^{-4} was found for the resonance in dilute KI aq. from that of free iodine ion[3]. Therefore, we took the sum of these two shifts (-7.7×10^{-4}) as the true chemical shift of solid KI from pure iodine ion at room temperature. Though general feature of the theoretical temperature dependence agrees with the experiments, there appears an abnormal behavior of the measured shifts at higher temperatures. These descrepancies at higher temperatures are still opened to question

both for T_1 and the shift.

The absolute values of T_1 and the shifts can be interpreted by Yosida and Moriya's theory, at least in their orders of magnitude, if a covalent degree of about 5 percent is assumed in each bond between K^+ and I^-, though this value of covalency seems to be too large. Kranendonk's theory, with appropriate value of Sternheimer antishielding coefficient gives also right order of magnitude for T_1, but Sternheimer's ion core deformation may not give a shift of the order of magnitude mentioned above.

References

1) J. van Kranendonk: Physica **20** (1954) 781.
2) K. Yosida and T. Moriya: J. Phys. Soc. Japan **11** (1956) 33.
3) J. Itoh and Y. Yamagata: to be published in J. Phys. Soc. Japan (this issue).

J. PHYS. SOC. JAPAN **13** (1958) 1233~1234

A Proposed Explanation of Irradiation Growth of Uranium

By Ryukiti R. HASIGUTI, Hideo SAKAIRI* and Tetuya SUGAI

Department of Metallurgy, University of Tokyo

(Received July 8, 1958)

The problem of irradiation growth of uranium is far from being fully understood at present. It is observed that an α uranium crystal elongates in [010] direction, and contracts in [100] direction under the neutron irradiation. No dimensional change is observed in [001] direction. To explain this phenomenon, two concurrent theories, i.e. anisotropic diffusion theory[1] and slip and twin theory[2], were proposed and are still being examined by many investigators. We have taken another step forward along the line of twin theory, and then combined it with the precipitation scheme of interstitials and vacancies produced by irradiation. This proposed theory will be discussed here briefly.

Pugh[2] proposes a theory, in which he states that local elongations in [010] direction and local contractions in [100] direction are effected by successive twinnings caused by stresses of thermal spikes. However his statement is only qualitative in nature, and he does not designate any specific twinning system.

We propose (130) $[3\bar{1}0]$ twinning caused by thermal stresses due to local heating by thermal spikes. This kind of twinning is most frequent in α uranium, and is actually observed in large quantity in thermal cycled uranium. As is shown in Fig. 1, average deformation of various {130} $\langle 3\bar{1}0\rangle$ type twins results precisely in [010] elongation and [100] contraction.

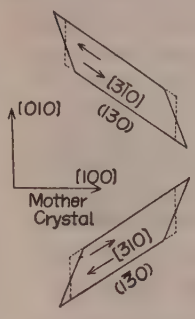

Fig. 1.

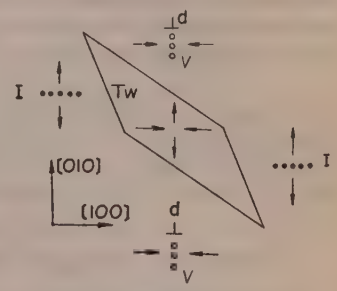

Fig. 2.

The most important requirement for the mechanism of uni-directional elongation is the irreversibility of deformation. The slip mechanism is *a priori* reversible. But the twinning is considered to be irreversible according to the circumstances, although the conditions for a twin not to make detwinning are not yet known.

The internal stress produced by small local twinning, mentioned above, must be released in some ways in order that the growth process is continued without an appreciable hardening. We consider that the stress release is achieved by means of precipitation of vacancies and interstitials which were produced by irradiation.

Precipitation of vacancies means here the absorption of vacancies by [100] edge dislocations, which climb in [010] direction, resulting in a contraction in [100] direction. Interstitials tend to precipitate in (010) plane, because the atomic bond is considered to have covalent nature in (010) plane, and metallic nature between these planes. The precipitation of interstitials in (010) plane results in an elongation in [010] direction.

Fig. 2 shows a schematic representation of the proposed mechanism of precipitation. Tw is a small twinned region, where there exist [010] elongation and [100] contraction in average. The internal stress will be released, if the surrounding medium deforms in the same way as in Tw. Thus the precipitation of interstitials (I) in (010) planes and the climbing of dislocations (d) will bring about the deformations indicated by the arrows in the figure.

We did not hitherto mention about slips at all. But we think that slips do actually take place. They may probably release the internal stresses partly.

Seigle and Opinsky[1] discussed the anisotropic diffusion of interstitials and vacancies. This may also help the growth phenomenon to occur in addition to the mechanism described here.

The irradiation growth does not occur both at

* Graduate Course in Physics

low temperatures (say at liquid air temperature) and at high temperatures (for example at 500°C). This is explained by the facts that diffusion and precipitation become very slow at low temperatures, and that twinning becomes very difficult to take place at high temperatures.

References

1) L. L. Seigle and A. J. Opinsky: USAEC Report SEP-160, 1954.
2) S. F. Pugh: Genave Conf. P/443, 1955.

J. PHYS. SOC. JAPAN **13** (1958) 1234~1235

On the Conduction Mechanism of Oxide Coated Cathode

By Hiroyuki MIZUNO

Matsushita Electronics Corporation, Takatsuki

(Received July 15, 1958)

According to Loosjes-Vink[1] the conduction of matrix of oxide coated cathode was explained by dual mechanisms. One mechanism is the electron conduction through the oxide coating particle which is seen in the so called low temperature region. The other mechanism is the conduction through the electron cloud emitted from the grains which is seen in the high temperature region. The experimental tube used in their work consists of two symmetrical cathodes which pressed against each other by springs. The essential feature of the experimental tube is the dimensional symmetry about the center of (BaSr)O matrix.

We have measured the potentital distribution in oxide coated cathode for low and high temperatures by means of potentiometer flowing the current to one direction. The design of tested cathode is similar to Loosjes-Vink's which is shown in Fig. 1. The obtained results are given in Fig. 2 which were contradicted to Loosjes-Vink's theory. From those results one can see that nearly all applied voltage falls across the contact layer of so called reverse direction between (BaSr)O and metal sleeve in low temperature region where-as that is monotonous in high temperature region*. When the current direction is changed, the same phenomenon appeared in the opposite contact layer.

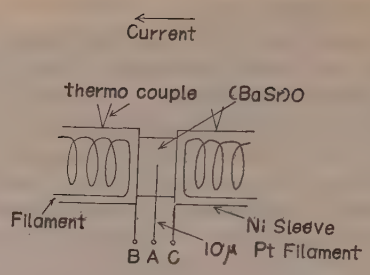

Fig. 1. Test tube for potential measurement.

It seems reasonable to conclude that the barrier layer across the contact between matrix and sleeve has main role in the usual measurement of conductivity of oxide coated cathode in low temperature region. It is pointed out by Mott-Schottky[3] that there is the rectification property at contact boundary between metal and semiconductor. Accordingly, it is supposed that there should be the rectification in the contact layer between (BaSr)O and metal sleeve. Therefore the conduction of oxide coated cathode should be explained in view point of rectification theory. Wright[4] had tried for the first time to explain the conduction in high temperature region by assuming that the electrons have to pass through the barrier layer between (BaSr)O and sleeve. However his explanation is also contra-

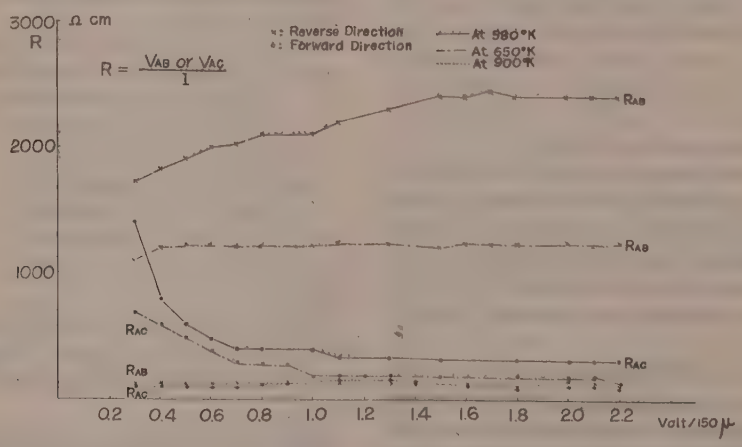

Fig. 2. Resistance of the contact layer in either reverse or forward direction writh various applied voltages.

* Note: Metson[2] carried out the potential measurement only in high temperature region with outaware of low temperature.

dicted to our results.

According to our opinion one has to do essentially with newly proposed mechanism as shown below:

In low temperature region, the conduction current is mainly determined by the resistance of barrier layer of reverse direction produced between (BaSr)O and sleeve which is represented by the rectification formula proposed by Mott-Schottky whereas in high temperature region, as almost all electrons emitted from grains have sufficient energy to pass through the barrier thermally the conduction depends almost upon the properties of electron gas present in the pores.

Details of our consideration on our explanation and some experiments which are carried out for further confirmation of that will be published later.

References

1) R. Loosjes and H. J. Vink: Philips Res. Rept. **4** (1949) 449.
2) G. H. Metson: P.I.E.E. **104** part C, **6** (1957), 316.
3) N. F. Mott and R. W. Gurney: Electronic Processes in Ionic Crystals (1940) 168.
4) D. A. Wright: Proc. Roy. Soc. **A190** (1947) 394.

J. Phys. Soc. Japan **13** (1958) 1235~1236

The Far Infrared Absorption of Sulfides, Selenides and Tellurides of Zinc and Cadmium

By Akiyoshi Mitsuishi, Hiroshi Yoshinaga and Shigeru Fujita

Department of Applied Physics, Faculty of Engineering, Osaka University, Osaka, Japan

(Received July 31, 1958)

The far infrared absorption due to the lattice vibration of ZnS, ZnSe, ZnTe, CdS, CdSe and CdTe was measured. These materials have the simple crystal structure such as zincblende or wurtzite and no measurement of the far infrared absorption has been reported previously except ZnS.

The absorption spectra were recorded by the far infrared spectrograph which was constructed in this laboratory and reported by Yoshinaga et al[1].

As the single crystals of these materials which were thin enough to produce the appropriate transmission and at the same time large enough to cover the relatively large slit of the spectrograph could not be obtained and only a small amount of the materials was supplied except ZnS and CdS, recource was made to the polyethylene suspension technique which was proposed by Yoshinaga and Oetjen[2]. A small amount of the finely powdered material was mixed with small pieces of polyethylene by the heated roll to produce the uniform suspension of the material in polyethylene film. The thickness of a polyethylene film was about 0.3 mm and the concentration ranged from 1 to 2.5 mg/cm^2. The evaporated layers of ZnS and CdS on polyethylene films were also measured.

For each material investigated only one strong absorption band was observed. The wave number of the absorption band is given in Tab. I together with the crystal structure. As is clear from Tab. I, the material with smaller reduced mass has the larger wave number as in the case of alkali halides[3].

Table I.

Material	Structure*	Freq. (cm^{-1})
ZnS	Z	310
ZnS	W	300
ZnSe	Z	215
ZnTe	Z	190
CdS	Z	270
CdS	W	260
CdSe	W	185
CdTe	Z	150

* Z: zincblende, W: wurtzite.

The zincblende type lattice has one molecule in its unit cell and in the harmonic approximation only one optically active mode is expected. This agrees with the present experimental result.

For the wurtzite type lattice which contains two molecules in the unit cell two optically active modes are expected and two bands or the indication of the splitting of the band was reported for BeO and ZnO[4]. In our case hexagonal ZnS and CdS gave only one strong absorption band which shifted to a little smaller wave number than the cubic one and showed no indication of the splitting nor the broadening compared with the cubic one. Also this was true for the hexagonal CdSe.

In the case of the evaporated layer, the absorption band was observed at 275 cm^{-1} for ZnS and 245 cm^{-1} for CdS. The same result has been reported for ZnS[5]. The slight differences of these values from those of the powdered materials would be due to the effect suggested by Fröhlich and Mott[6].

Kröger and Meyer[7] deduced the infrared lattice frequency of CdS to be 227 cm^{-1} from the spacing of the line series in the edge emission. The present investigation gives the experimental value of 245 cm^{-1}. The difference is somewhat large compared with the case of ZnS which showed the good agreement[7].

The authors wish to thank Mr. H. Suzuki of

Kyushu University for providing ZnSe, ZnTe, CdSe and CdTe and Mr. S. Ibuki of Mitsubishi Electric Manf. Co. for ZnS and CdS.

References

1) H. Yoshinaga et al: J. Opt. Soc. Am. **48** (1958) 315.
2) H. Yoshinaga and R. A. Oetjen: J. Chem. Phys. **45** (1955) 1085.
3) R. B. Barnes: Z. Phys. **75** (1932) 723.
4) Cl. Schaefer and F. Matossi: Das ultrarote Spectrum (1930) 310, M. Parodi: Compt. Rend. **204** (1937) 1111.
5) C. Haas and J. P. Mathieu: J. Phys. Rad. **15** (1954) 492.
6) H. Fröhlich and N. F. Mott: Proc. Roy. Soc. **171** A (1939) 496, also C. Hass: Srectrochim. Acta **8** (1954) 19.
7) F. A. Kröger and H. J. G. Meyer: Physica **20** (1954) 1149.

J. PHYS. SOC. JAPAN **13** (1958) 1236~1237

The Far Infrared Absorption of Ferrites

By Akiyoshi MITSUISHI, Hiroshi YOSHINAGA and Shigeru FUJITA

Department of Applied Physics, Faculty of Engineering, Osaka University, Osaka, Japan

(Received July 24, 1958)

Recently Waldron[1], using the KBr pellet technique, has measured the infrared absorption of several ferrites in the spectral region from 4000 to 280 cm^{-1}. In this spectral region he found two strong absorption bands due to the lattice vibration of ferrite.

Assuming the ions in the primitive unit cell to be subdivided into two MO_4 groups (M stands for a divalent ion) and one Fe_4 group with tetrahedral symmetry, he obtained theoretically four optically active modes of lattice vibrations. The frequencies of these vibrations were labeled ν_1, ν_2, ν_3 and ν_4 in the order of decreasing wave number. Among these, ν_3 and ν_4 have low values and absorption bands due to these vibrations are to be observed beyond 280 cm^{-1}, the lowest limit of the spectral region of his spectrograph.

It is the purpose of this note to report the experimental results on ferrites obtained with our far infrared spectrograph.

The ferrites investigated were $ZnFe_2O_4$, $NiFe_2O_4$, $CoFe_2O_4$ and $MgFe_2O_4$ in powdered form. A suitable amount of the powder was suspended uniformly in polyethylene film by a heated roll.

The far infrared spectrograph was constructed in our laboratory and has been reported by Yoshinaga et al[2]. The spectral region covered in this investigation was from 500 to about 10 cm^{-1}.

Fig. 1 shows the transmission curves obtained. The absorption band at about 400 cm^{-1} for all the ferrites examined is the same as ν_2 band obtained by Waldron. Another fairly strong band which is only observed for $ZnFe_2O_4$ at 330 cm^{-1} has also been reported by him. The slight difference in the wave number of these bands is due to the different matrix used. Furthermore, a weak shoulder band was observed at 425 cm^{-1} for $ZnFe_2O_4$ in our investigation. These bands were obtained with the

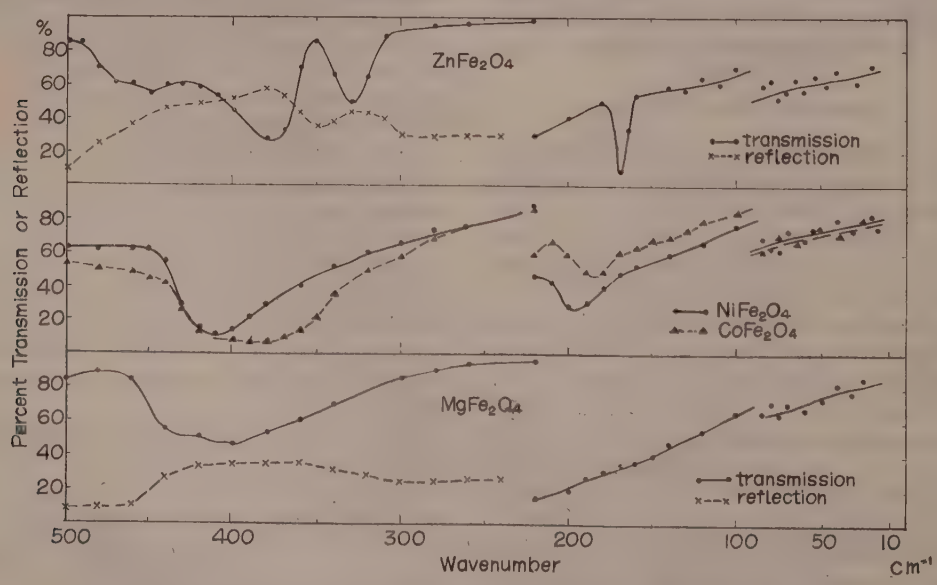

Fig. 1. Far infrared absorption and reflection spectra of ferrites. (Fluctuations of points in the lower wavenumber region are due to the interference effect of the polyethylene film.)

concentration of about 1 mg/cm^2.

Increasing the concentration to about 7 mg/cm^2 another band which might correspond to ν_3 band was observed except $MgFe_2O_4$. The absorption band of $ZnFe_2O_4$ was very sharp and located at 169 cm^{-1}. The absorption bands of $NiFe_2O_4$ and $CoFe_2O_4$ were rather broad as in the case of ν_2 band and observed at 196 cm^{-1} and 181 cm^{-1} respectively. We could not find any definite absorption band of $MgFe_2O_4$ in the corresponding spectral region.

The observation was extended up to about 1 mm region and the concentration increased to 25 mg/cm^2 to find the ν_4 band, but no absorption band could be obtained for all the ferrites examind.

The reflectivity of the sintered plates of $ZnFe_2O_4$ and $MgFe_2O_4$ is also measured and given in Fig. 1. The reflectivity maxima which correspond to ν_2 band of both materials and to 330 cm^{-1} band of $ZnFe_2O_4$ are clearly shown.

The authors wish to thank Mr. B. Kubota of Matsushita Electric Industrial Co. for providing the ferrites examined.

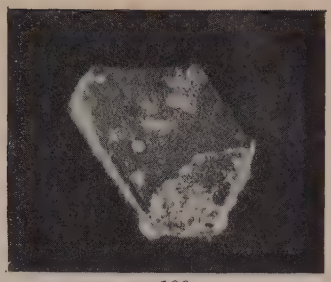

×100

Fig. 1.

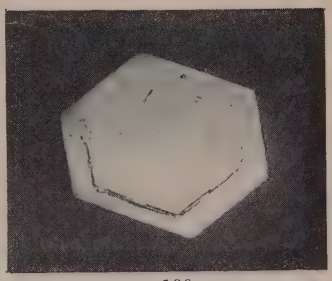

×100

Fig. 2.

References

1) R. D. Waldron: Phys. Rev. **99** (1955) 1727, P. A. Milles, W. B. Westphal and A. von Hippel: Rev. Mod. Phys. **29** (1957) 289.
2) H. Yoshinaga et al: J. Opt. Soc. Am. **48** (1958) 315.

J. Phys. Soc. Japan **13** (1958) 1237~1238

Growth and Extinction of Guanidine Aluminum Sulfate Hexahydrate Crystals

By Atsuo Nishioka and Kyozo Sekikawa

Electrical Communication Laboratory, Musashino, Tokyo, Japan

(Received December 17, 1957)

Forroelectricity of Guanidine aluminum sulfate hexahydrate (GASH) has been found by Holden et al[1], but detailed studies are yet to be done. We have observed the growth of single crystals under crossed nicols and have observed several curious facts. Fig. 1 shows one of the crystals which seemed to be so called *c*-plate, but most of them did not show any extinction around *c* axis (Fig. 2). Viewing from *a*-axis, straight extinction was observed in *a* or *c* direction (Fig. 3 and 4). From X-ray analysis of these crystals, *c*-axis is found to be perpendicular to hexagonal plane.

Next, we observed the growing process of seed crystals from saturated solution under polarizing microscope at room temperature (Fig. 5 and 6 under parallel nicols). At the stage in Fig. 6, the nicols

×100

Fig. 3.

×100

Fig. 4.

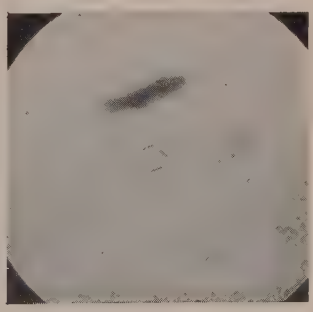

×100

Fig. 5.

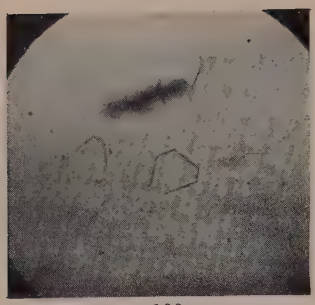

×100

Fig. 6.

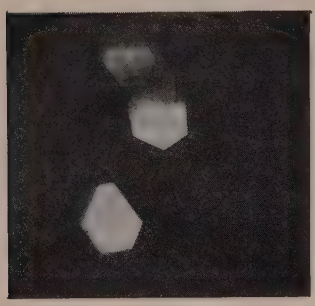

×100

Fig. 7.

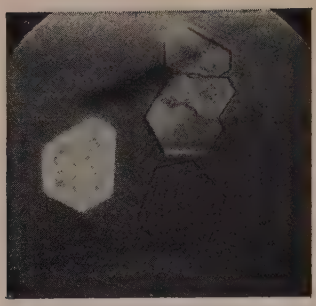

×100

Fig. 8.

×100

Fig. 9.

were crossed and the viewing field was rotated. As shown in Fig. 7, 8 and 9, the crystal A is always dark around the c-axis, showing that this is a c-plate crystal. But the crystal B has extinction in a special direction, and so appears to be a kind of a-plate. The crystal C seems to be mixed in a and c-plate. These anomalous behaviors of B and C crystals, which is not expected from the results of X-ray analysis of the crystals shown in Fig. 3 and 4, would probably be related with crystal habits of GASH. Further study is now going on.

Reference

1) A. N. Holden, B. T. Matthias, W. J. Merz and J. P. Pemeika: Phys. Rev. **98** (1955) 546.

Errata

The Electron Distribution and the Location of Bonded Hydrogen Atom in Crystals

By Yujiro TOMIIE

J. Phys. Soc. Japan **13** (1958) 1030

Page

1032 Last line of Eq. (4), $2(1+S_{ab}^2)^{-1/2}$ should be $\{2(1+S_{ab}^2)\}^{-1/2}$.

1033 Line 8 in right column, xy should be yz.

1033 Eq. (16), $(1/2a)$ should be inserted after $(\pi/2a)$.

1034 Line 3, $2r\cdot A$ and $2r\cdot B$ should be $2\boldsymbol{r}\cdot A$ and $2\boldsymbol{r}\cdot B$ respectively.

1034 Line 6, $K'=t(a+b+t)$ should be $K'=t/(a+b+t)$.

1034 Eq. (21), the denominator of the first term should be $(a+b)$ instead of $(2+b)$.

1034 Line 30, $(\partial I_2''/\partial\delta_a)$ should be $(\partial I_2'/\partial\delta_a)$.

1034 Eq. (27), $\exp\{K'(ar_a^2+br_b^2)\}$ should be $\exp\{-K'(ar_a^2+br_b^2)\}$.

1035 Line 34, 2.332 Å should be 2.232 Å.

1035 Fig. 2, in legend, following sentence should be added: Upper curve is for 2-D and lower curve for 3-D.

1035 Fig. 3, the figures for maximum electron densities should be (a) 0.86, 0.76, 0.61 instead of 8.6, 7.6, 6.1, and (b) 0.86, 0.80, 0.66 instead of 8.6, 8.0, 6.6.

1036 Lines 5 and 3 from the bottom, Å should be Å^2.

1037 Line 18 in left column, at should be as.

1037 References 3) and 7), Weatley should be Wheatley.

1037 Reference 5), S. Sasada should be Y. Sasada.

Piezo-Effect of Selenium Rectifiers

Tadasi NUMATA

J. Phys. Soc. Japan **13** (1958) 1066

The following line should be inserted after 'connected to' on line 5: 'a voltage amplifier whose output terminals were connected to'.

Diffusion of Cobalt into Single Crystals of Copper

By Masanobu SAKAMOTO

J. Phys. Soc. Japan **13** (1958) 845

Page 846. Fig. 2.

Wrong

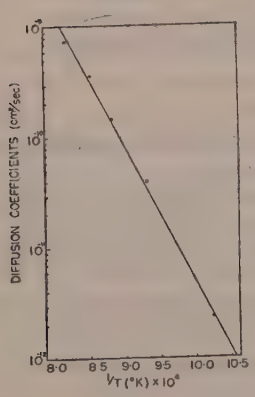

Corrected

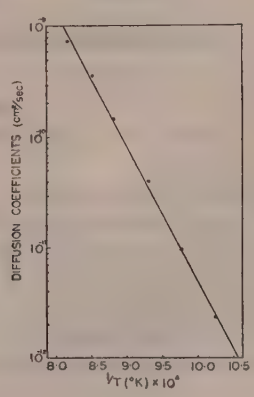

PROGRESS OF THEORETICAL PHYSICS

CONTENTS

Progress of Theoretical Physics Vol. 19, No. 6 June 1958

Single Particle Transition in Neutron Inelastic Scattering by Deformed Nuclei ..... H. MATSUNOBU and S. YOSHIDA..599
A Theory of Clothed Uustable Particles.....N. NADANISHI..607
The Possible Existence of a Neutral Meson with Isotopic Spin 0..Y. YAMAGUCHI..622
Isotopic Spin and Strange Particles .....G. TAKEDA..631
Long-Range Spin Interaction and the Meissner-Ochsenfeld Effect.....646
Cluster Theory of Condensing Systems .....K. IKEDA..653
Quantum-Mechanical Many-Body Problem with Hard-Sphere Interaction..R. ABE..699
Quantum Mechanics of Strongly Interacting Particles with an Application to Lennard-Jones Potential .....R. ABE..713
General Solution of the Bethe-Salpeter Equation in Instantaneous Interaction Approximation.....S. N. Biswas..725
Letters to the Editor:
A Theory of Lepton which is Invariant under Space Inversion .... K. SEKINE..740
On the Hydrodynamical Theory in Multiple Particle Production ....M. HAMAGUCHI..741
Note on Heavy Ion Induced Nuclear Reaction .....R. NAKASIMA..743
Elastic Scattering in High Energy and Impulse Approximation .... Y. SAKAMOTO and T. SASAKAWA..745
On the $|\Delta I|=1/2$ Rule for the Decay of Σ .....K. ITABASHI..747
An Example of Isentropic Steady Flow in the Magnetohydrodynamics .....T. TANIUCHI..749
Contents of Journ. Phys. Soc. of Japan, Vol. 13, Nos. 4 & 5 751
Contents and Authors Index to Volume 19 .....i–x

Price $ 1.25 per copy
$ 15.00 per year (postage inclusive)
Annual dues for foreign members (individual subscribers)
$ 12.00 (postage inclusive)
" for foreign members of the Physical Society of Japan
$ 10.00 (postage inclusive)

Application for members, subscriptions and orders for back numbers should be sent, directly or through book-dealers, to

The Publication Office
in
Yukawa Hall, Kyoto University, Kyoto, Japan

. . . . . .

ANNOUNCEMENT

REVISED Price List of Back Numbers (for subscribers abroad)

*Vols. 1–4	$ 6.40 each
*Vols. 5 & 6	$13.00 each (single copy: $2.50)
*Vols. 7 and succeeding ones	$ 8.00 each (single copy: $1.50)

Back number prices are effective for volumes other than last four (4) volumes (the current volume inclusive).

Thus, volumes 1 through 16 will be regarded as back numbers while volume 20 is being published.

The revised prices will be effective on and after August 1, 1958.

. . . . . .

JOURNAL OF THE PHYSICAL SOCIETY OF JAPAN Vol. 13, No. 11, NOVEMBER, 1958

The Reaction $F^{19}(d, n)Ne^{20}$ and the Energy Levels of Ne^{20}

By Susumu MORITA and Kenji TAKESHITA

Department of Physics, Faculty of Science, Kyushu University, Fukuoka, Japan

(Received, July 7, 1958)

The energy spectra of neutrons emitted in the reaction $F^{19}(d, n)Ne^{20}$, produced by the 2.17 MeV deuteron, were measured with nuclear plates disposed at angles of 0 to 165 degrees, with respect to the incident deuteron, at intervals of 15 degrees. The general features of the spectra were consistent with the evaporation model. From these spectra, the energy levels of Ne^{20} were found at excitation energies of 1.74 ± 0.03, 4.20 ± 0.04, 4.96 ± 0.05, 5.62 ± 0.04, 6.80 ± 0.01, 7.16 ± 0.09, 7.41 ± 0.05, 7.90 ± 0.04, 9.15 ± 0.04 and 10.01 ± 0.03 MeV. Some evidences for the existence of new levels at 0.65 ± 0.04, 2.53 ± 0.07, 8.32 ± 0.03, 8.71 ± 0.01 and 9.50 ± 0.04 MeV were also obtained. The Q-value for the ground state transition was determined to be 10.81 ± 0.03 MeV. The angular distributions of the neutrons leading to the ground state and the lowest four excited states, with exception of the uncertain states, were obtained and compared with the stripping theory. The agreement is not very good. The relative values of total cross sections for each neutron group were estimated.

§ 1. Introduction

It has been proved that the shell model is successful for the interpretation of properties of low-lying levels of light nuclei and the configuration mixing is very probable in the states of nuclei of mass number near 20. On the other hand, the energy levels of C^{12} and O^{16} have been well fitted with the predictions of alpha particle model. From these point of view, it seems interesting to investigate the level structure of $4n$-self conjugate nucleus Ne^{20}. The characteristics of the 4.97 MeV level in Ne^{20} is of special interest for thermonuclear reaction in stars.

The energy level scheme of Ne^{20} has been studied mainly by the reaction $Na^{23}(d, \alpha)Ne^{20}$ [1),2)] and the elastic and inelastic scattering of protons by Ne^{20} [3),4)], and the consistent results have been obtained. However, the spins and parities have been determined only for the ground state and the 1.63 MeV state.

As for the reaction $F^{19}(d, n)Ne^{20}$, Bonner, in 1940[5)], measured the energy spectrum of neutrons, produced with deuteron beam of 0.9 MeV, at an angle of 90 degrees with respect to the incident deuteron by means of cloud chamber. Powell, in 1943[6)], measured the same spectrum at an angle of 100 degrees with nuclear plate. In 1955, Calvert et al.[7)] measured the angular distributions of neutrons, produced with the 9.06 MeV deuterons, in the angular range of 0 to 60 degrees by means of fast neutron spectrometer and obtained the results consistent with the stripping theory. But in their work, the three levels in the range of 4 to 6 MeV of excitation energy, which had been well established by the study of the reactions emitting charged particles, were not observed.

The aim of the present experiment is to measure the energy spectra of neutrons, at the deuteron energy of 2.17 MeV, at various angles in the whole angular range and to determine the energy levels of Ne^{20}, with the reaction $F^{19}(d, n)Ne^{20}$ as accurately as possible. Moreover, we intended to obtain the angular distributions of neutrons, which will be useful for the interpretation of the mechanism of the (d, n) reaction at rather lower energy of deuteron.

§ 2. Experimental Arrangements and Procedures

The experimental arrangement is shown in Fig. 1. The deuterons were accelerated to 2.22 MeV by the Van de Graaff generator at Kyushu University, whose voltage was calibrated with the resonances in the reaction $F^{19}(p, \alpha)O^{16*}(\gamma)O^{16}$ and the accuracy of deuteron energy was about 0.5 percent. The thickness

of the target of CaF_2, which were evaporated onto a silver plate, was determined to be 100 KeV for proton of 1.3 MeV by measuring the apparent width of the resonance peak of the reaction $F^{19}(p, \alpha)$. The target could be rotated with a small magnet and removed from the deuteron beam in the background runs. The beam duct in front of the target chamber, shown in Fig. 1, was made of thin brass tube

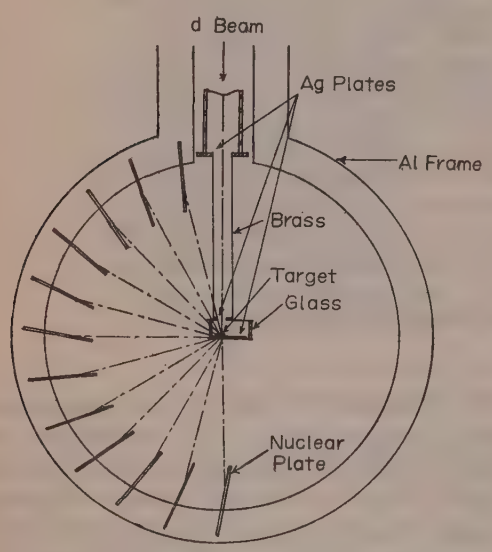

Fig. 1. Arrangements of the target and photographic plates.

of wall thickness of 0.5 mm to minimize the absorption and scattering of neutrons emitted backwards. The attenuation of neutron intensity in the materials which were present between the target and plates was estimated by considering their total neutron cross section. The correction was found to reach maximum at the direction of 75 degrees and amounted to 14 percent. The inner surface of beam duct hit by the deuteron beam were all covered with silver plates to avoid the neutron production.

The bombardment was carried out with beam current of 1 to 2 microamperes for about nine hours. The neutrons were detected with Fuji ET-2E emulsion of 250 microns thickness and these plates were arranged in the angular range of 0 to 165 degrees in laboratory system, with respect to the direction of the incident deuteron beam, at intervals of 15 degrees. The glancing angle of neutron to the emulsion surface was chosen to be 10 degrees and the distance between the target and the centers of scanned area of each plate was 19 cm. Those tracks of recoil protons were recorded which had horizontal angles to the direction of incident neutrons of less than or equal to 10 degrees and dip angles of less than or equal to 10 degrees in the unprocessed emulsion[8]. The energy spectra of neutrons were obtained by applying the corrections due to the different probabilities with which recoil protons with different energies escape from the emulsion surface and due to the variation of $n-p$ scattering cross section with neutron energy.

As the range-energy relation of the Fuji ET-2E emulsion for protons had not been known yet, it was obtained by measuring the recoil-proton ranges in the emulsion exposed to the neutrons of known energies from the reactions $D^2(d, n)He^3$ and $T^3(d, n)He^4$. The result is shown in Fig. 2. In this figure, the

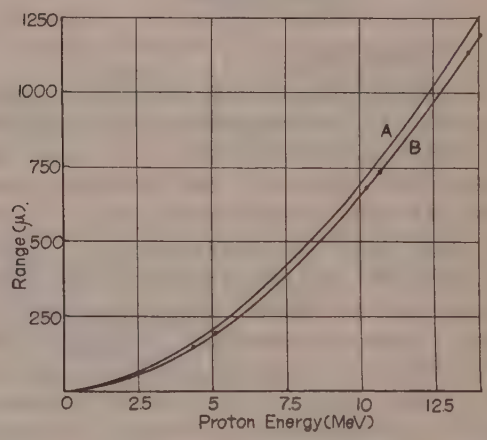

Fig. 2. Range-energy relation of the emulsion Fuji ET-2E for protons. Curve A is the calculated one and curve B was determined by experiment.

curve A is the calculated one from the stopping powers of the chemical components of the dried emulsion and the curve B is determined by the experiments. The abscissa shows the energies of protons E_p, which were determined from the known energy of neutron E_n by the relation $E_p=0.961E_n$[8]. The three points on curve B at lower proton energies were determined based on the neutrons emitted in the directions of 0, 45 and 120 degrees in the reaction $D^2(d, n)He^3$, produced by deuterons of 2.04 MeV and the point of the higher energy was determined by the neutron

emitted in the direction of 90 degrees in the reaction $T^3(d,n)He^4$, produced by deuterons of 170 KeV.*) The energy spectra of these standard neutrons are shown in Fig. 3. The two

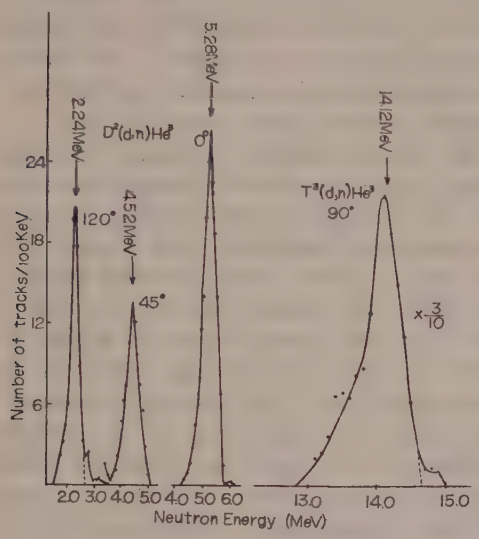

Fig. 3. Energy spectra of neutrons emitted from the reactions $D^2(d, n)He^3$ and $T^3(d, n)He^4$.

points on the curve B of Fig. 2 in the middle energy range of protons correspond to the neutrons emitted in the directions of 0 and 75 degrees in the reaction $F^{19}(d, n)Ne^{20}$ leading to the first excited state at 1.63 MeV of Ne^{20}. As is shown in Fig. 2, this range-energy relation gives an energy value three percent larger than that given by the calculated curve A.

§ 3. Results and Discussions

The examples of energy spectra of neutrons from the reaction $F^{19}(d, n)Ne^{20}$, thus obtained, are shown in Fig. 4. The energy spectra of neutrons greater than 2 MeV were investigated on the three plates placed at 15, 90 and 165 degrees, and one of these, obtained at 165 degrees, is shown in Fig. 4 (a). From these spectra, in the range of excitation energy higher than 6 MeV, the states of Ne^{20} were found at 8.32±0.03, 8.71±0.01, and 9.50 ±0.04 MeV, besides the 6.80±0.01, 7.16± 0.09, 7.41±0.05, 7.90±0.04, 9.15±0.04, and 10.01±0.03 MeV states, which were obtained previously in the reactions $Ne^{20}(p, p')Ne^{20}$ [4]

*) This bombardment was carried out in the nuclear laboratory of Kōnan University. The authors wish to express their cordial thanks to the staff of that laboratory for their kind assistance.

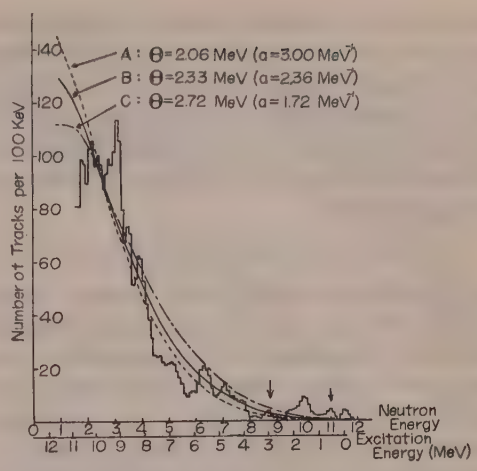

Fig. 4 (a). Energy spectrum of neutrons from the reaction $F^{19}(d, n)Ne^{20}$. The histogram shows the spectrum of neutrons of energy higher than 2 MeV, obtained at the direction of 165 degrees. The smooth curves show the calculated spectra based on the evaporation model. The curves A, B and C correspond to the nuclear temperature Θ=2.06, 2.33, and 2.72 MeV, respectively.

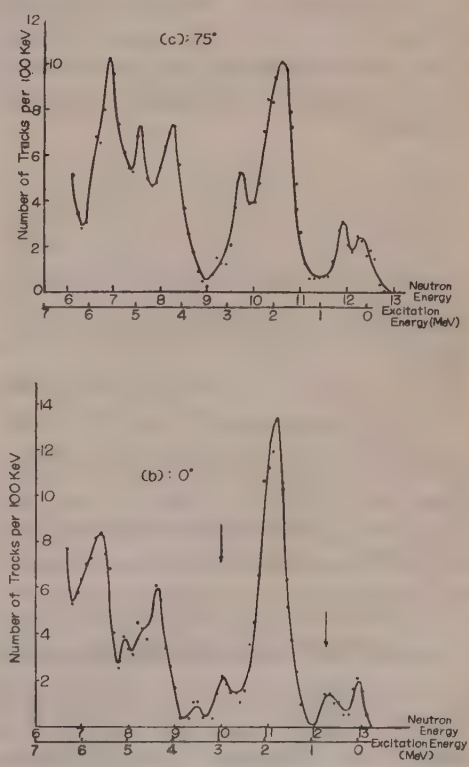

Fig. 4 (b) and (c). Energy spectra of neutrons from the reaction $F^{19}(d, n)Ne^{20}$. The curves show the detailed features of neutrons of energy higher than 6 MeV, obtained at the directions of 0 and 75 degrees.

and $Ne^{20}(\alpha, \alpha')Ne^{20}$ [9]. The 7.16 MeV state will be the unresolved overlapping of the 7.18 and 7.22 MeV states found in the reaction $Ne^{20}(\alpha, \alpha')Ne^{20}$. The smooth curves in Fig. 4 (a) were calculated by the following equation[10], based on the statistical theory of compound nucleus formation.

$$I(\mathcal{E})d\mathcal{E}=\text{const}\ \mathcal{E}\sigma_c(\mathcal{E})\omega_{Ne}(E_d+Q-\mathcal{E})d\mathcal{E}$$

in which $Q=10.81$ MeV is the energy release of this reaction, E_d the energy of incident deuteron in the center of mass system, $\mathcal{E}$ the energy of emitted neutron, $\sigma_c(\mathcal{E})$ the cross section for the formation of a compound nucleus by an incident neutron of energy $\mathcal{E}$ and ω_{Ne} the level density of the residual nucleus Ne^{20} as a function of excitation energy. The values of $\sigma_c(\mathcal{E})$ were referred to the table given by Blatt and Weisskopf and the level density used are based on Fermi gas model and is given by

$$\omega(E)=C\exp(2\sqrt{aE})$$

in which E is the excitation energy and a and C are constants. The calculations were carried out for $a=1.73$, 2.36, and 3.00 MeV^{-1}, and best fit was obtained for $a=2.36\ MeV^{-1}$, which corresponds to the nuclear temperature $\Theta=2.33$ MeV.

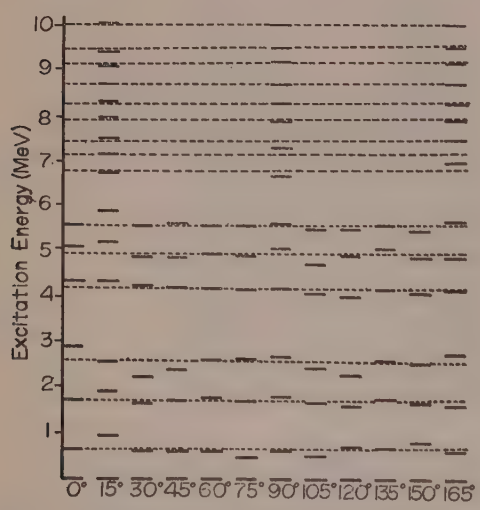

Fig. 5. The level schemes of Ne^{20}, determined from the energy spectra of neutrons. The abscissa shows the angles at which the nuclear plates were disposed. The dotted lines show the mean values of the energy states. The range of excitation energy higher than 6 MeV were studied only on the plates placed at 15, 90 and 165 degrees.

It will be seen in this figure that the theoretical curve is in fair but not good agreement with the experimental result, and it will be probable that the compound nucleus formation is predominant in this reaction, although some contribution from the stripping reaction may not be excluded. This result is consistent with the angular distributions of neutrons, which will be described later.

The energy spectra of neutrons of energy higher than about 5 MeV, where the spectra can be decomposed into discrete groups of neutrons, were studied in more details on all the twelve plates. The smoothed curves in Fig. 4 (b) and (c) show the spectra, thus obtained on the plates disposed at angles of 0, and 75 degrees. The energy levels of Ne^{20} determined from these spectra are shown in Fig. 5 and the mean values of the excitation energies of these states are shown in Table I, together with the results previously obtained by other investigators. The Q-value for the ground state transition was estimated to be 10.81 ± 0.03 MeV, which is to be compared with the values of 10.645 MeV given by Ajzenberg and Lauritzen[11] and 10.80 ± 0.2 MeV given by Segre[12]. The three levels at 4.20, 4.96, and 5.62 MeV, which were completely missing in the results obtained by Calvert et al.[7], were distinctly observed and in good agreement with the results obtained by the reactions emitting charged particles. The second and the fourth peaks in Fig. 4, shown with arrows, might correspond to the level of Ne^{20} at 0.65 and 2.53 MeV. As these peaks are so small that the existence of levels corresponding to them is not certain. But these two small peaks were observed in almost all of the energy spectra and the variation of the position of these peaks with the angles of observation were consistent with the reaction $F^{19}(d, n)Ne^{20}$. Moreover, the possible contaminants responsible for these higher energy neutron groups are B^{11}, Na^{23}, and Al^{27}, and the result of the chemical analysis*) of the sample of CaF_2 used for the target indicated that the abundances of these impurities were less than 0.01 percent.

For the estimation of the intensities of

*) This chemical analysis was performed by Prof. Yoshimura and Mr. Takashima of Dept. of Chemistry of Kyushu University. The authors wish to express cordial thanks to them.

Table I. Excited states of Ne^{20} observed by several investigators. (The two levels in the brackets in the last column are not certain)

Investigator	Powell (1940)	Cameron (1953)	Freemantle et al. (1954)	Calvert et al. (1955)	Shrank et al. (1956)	Buechner et al. (1954)	Present Experiment
Reaction	$F^{19}(d, n)Ne^{20}$	$Ne^{20}(\alpha, \alpha')Ne^{20}$	$Ne^{20}(p, p')Ne^{20}$	$F^{19}(d, n)Ne^{20}$	$Ne^{20}(p, p')Ne^{20}$	$Na^{23}(p, \alpha)Ne^{20}$	$F^{19}(d, n)Ne^{20}$
							(0.65)
	1.5		1.58	1.63	1.63	1.635	1.74
	2.2						(2.53)
	4.2		4.20		4.26	4.248	4.20
			4.95		4.97	4.969	4.96
	5.4		5.62		5.81	5.631	5.62
		6.74					6.80
	7.1	7.18					7.16
		7.22		7.3			
		7.45			7.45		7.41
	7.8	7.85			7.85		7.90
							8.32
							8.71
	9.0	9.2		9.2	9.2		9.15
							9.50
	10.1	10.1			10.0		10.01

neutron groups overlapping each other, the upper and lower limits of the energy of each group were estimated as follows. The highest end was obtained by merely extrapolating the slope of the higher energy side of each spectral peak, and the lowest end was assumed to be lower by eight percent than the neutron energy of the peak. These assumptions were made because the shapes of the well separated peaks are consistent with them, as shown in Figs. 3 and 4. The uncertainties caused by such decomposing procedures are included in the following angular distributions as well as the statistical one. The theoretical curves, shown in the following figures, were calculated by the Born approximation theory[13] of stripping for $l_p=0$ and 2, using a nuclear radius $r=(2.7+1.22A^{1/3})\times 10^{-13}$ cm for F^{19}. As the ground state of F^{19} has spin 1/2 and even parity and is supposed to be $(1d_{5/2})^2\ s_{1/2}$ configuration, the angular distributions corresponding to the excited levels of Ne^{20} in the same shell as the ground state, that is $(d_{5/2})(s_{1/2})(d_{3/2})$, would fit the theoretical curves of $l_p=0$ or 2.

The ground State

The angular distribution of neutron leading to the ground state, including the neutrons leading to the 0.65 MeV state, is shown in Fig. 6 (a). The ground state of Ne^{20}, which is even-even nucleus, has spin 0 and even parity and has been supposed to have the configuration $(1d_{5/2})^2(2s_{1/2})^2$. The angular distribution in the forward direction obtained by Calvert et al.[7], was in good agreement with the theoretical curve of $l_p=0$. As is shown in Fig. 5 (a), the present result is not consistent with the theoretical curve of $l_p=0$ and is rather near to that of $l_p=2$. This disagreement may be due to the effect of Coulomb barrier, which was not taken into account in

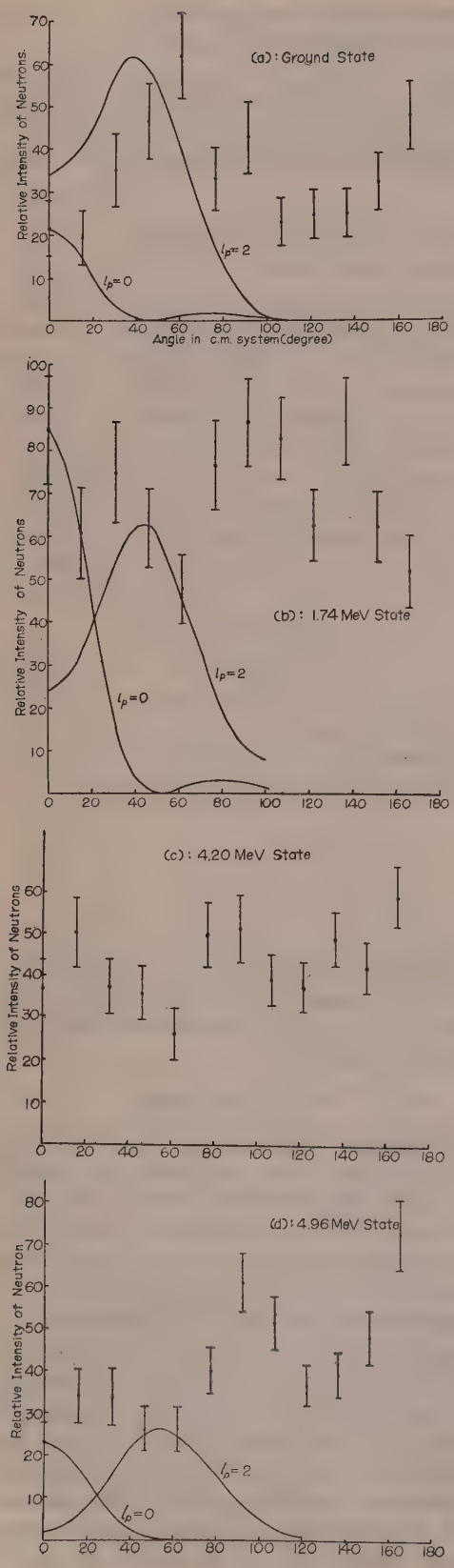

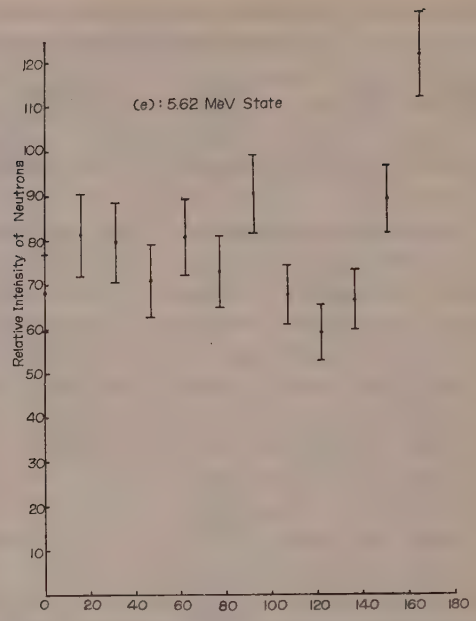

Fig. 6. The angular distributions of neutrons from the reaction $F^{19}(d, n)Ne^{20}$, leading to the various states of Ne^{20}. The smooth curves were compted with the stripping theory for $l_p=0$ and 2, using a nuclear radius $R=6\times10^{-13}$ cm.

the theoretical calculation, or may be due to the configuration mixing and the interference with the compound nucleus formation. The effect of configuration mixing will be excluded because of the fact that the Calvert's result was obtained with a considerably higher energy of deuteron and it is not likely that the higher angular momentum transfer becomes more probable in lower bombarding energy.

1.74 MeV State

This level coincides well with the 1.63 MeV state, obtained by the reactions emitting charged particle, within the accuracy of the determination of the neutron energy. It has been proved that this level has spin 2 and even parity by the measurement of angular correlation in the reaction $Na^{23}(p, \alpha)Ne^{20}$ [14]. The angular distribution in the forward direction, obtained by Calvert et al.[7], well fitted the theoretical stripping curve of $l_p=2$. The present angular distribution, shown in Fig. 5 (b), is not much consistent with the theoretical curve.

2.53 MeV State

In the early experiments on the beta decay of F^{20}, the 2.2 MeV state has been reported[15),16] and some indication for the existence of this

state was found in the reaction $F^{19}(d, n)Ne^{20}$ also by Powell[6]. But this state has been missing in the charged particle measurements. Jelley, in 1950[27], found the 2.45 MeV state in the measurements of beta- and gamma-rays from F^{20}. This value is consistent with the present result. The existence of this state is probable but not certain yet.

4.20, 4.96 and 5.62 MeV States

The angular distributions of neutrons leading to the 4.20, 4.96 and 5.62 MeV states are shown in Fig. 6 (c), (d) and (e), respectively. The angular distributions in Fig. 6 (c) and (e) are rather isotropic compared with the others. As is usual in the second excited state of even-even nucleus, the 4.20 MeV state may have spin 4 and even parity. The reason why these levels were missing in the Calvert's experiment and appeared distinctly in the present experiment is not clear but it seems to be probable that the stripping process is predominant in this reaction at higher energy of deuteron and in our case, the compound nucleus formation becomes predominant.

The 4.96 MeV state is just above the sum of the masses of O^{16} and He^4, which is 4.476 MeV higher than the ground state of Ne^{20} and the characteristics of this state has much effect on the abundance of neon in stars. It will be seen in Fig. 5 (d) that the transition to the 4.96 MeV state may be interpreted by the stripping reaction of $l_p=0$. Accordingly, this state might have spin 0, or 1, and even parity.

The relative values of total cross sections corresponding to each neutron group are shown in Table II. These values are normalised to the largest one for the 5.62 MeV state transition. The values, obtained by Calvert et al.[7], for the relative values of cross sections at their peaks, are shown in the third column.

Table II. Relative values of total cross sections for each neutron groups.

Excitation energy of Ne^{20} corresponding to each neutron groups	Relative values of total cross sections. (Present experiment)	Relative values of cross sections at peaks. (Calvert's results)
0	0.43	0.16
1.74	0.89	1.00
2.53	0.37	0
4.20	0.54	0
4.96	0.52	0
5.62	1.0	0

The authors wish to express their cordial thanks to Prof. I. Nonaka and all other staff of the nuclear laboratory of Kyushu University for their support and discussion throughout this work. Thanks are also due to Mr. Y. Kozeki of Research Laboratory of Fuji Photographic Film Industry for his kind preparation of nuclear plates and to Miss Y. Kajiwara, Miss M. Hirakura and Miss R. Hanada for their skilful scanning of the nuclear plates. This work has been supported by the Scientific Expenditure of the Ministry of Education.

References

1) D. J. Donahue, K. W. Jones, M. T. Mc Ellistrem and H. T. Richards: Phys. Rev. **89** (1953) 824.
2) W. W. Buechner and A. Sperduto: Phys. Rev. **106** (1957) 1008.
3) R. G. Freemantle, D. J. Prowse, A. Hossian and J. Rotblat: Phys. Rev. **96** (1954) 1270.
4) G. Schrank and G. K. O'Neill: Bull. Am. Phys. Soci. Ser. **1** (1956) 29.
5) T. W. Bonner: Proc. Roy. Soc. **A 174** (1940) 339.
6) C. F. Powell: Proc. Roy. Soc. **A 181** (1943) 344.
7) J. M. Calvert, A. A. Jaffe and E. E. Maslin: Proc. Phys. Soc. **A 68** (1955) 1017.
8) L. Rosen: Nucleonics **11** (1953) 38.
9) J. R. Cameron: Phys. Rev. **90** (1953) 839.
10) J. M. Blatt and V. F. Weisskopf: Theoretical Nuclear Physics (1952).
11) F. Ajzenberg and T. Lauritzen: Rev. Mod. Phys. **27** (1955) 77.
12) E. Segre: Experimental Nuclear Physics Vol. **1** (1956).
13) A. B. Bhatia, K. Huang, R. Huby and H. O. Newns: Phil. Mag. **43** (1952) 485.
14) J. Seed: Phil. Mag. **44** (1953) 921.
15) J. C. Bonner and W. E. Burcham: Proc. Soc. **A 173** (1939) 379.
16) S. C. Curran and J. E. Strothers: Proc. Camb. Phil. Soc. **36** (1940) 252.
17) J. V. Jelly: Proc. Phys. Soc. **A 63** (1950) 538.

JOURNAL OF THE PHYSICAL SOCIETY OF JAPAN Vol. 13, No. 11, NOVEMBER, 1958

Differential Elastic Scattering of 14 MeV Neutrons in Aluminum, Iron, Lead and Bismuth for Large Angles

By Kazunori YUASA

Department of Physics, Faculty of Science, Konan University, Kobe

(Received July 5, 1958)

The absolute differential cross sections for the elastic scattering of 14 MeV neutrons in Al, Fe, Pb and Bi have been measured for large angles up to 170°. The neutrons generated by $^3T(d, n)^4He$ reactions were scattered by the disk-shaped scatterer, and counted by the $n-\alpha$ coincidence circuit with the resolving time of 4 ns. An anticoincidence method was used to reduce the accidental coincidences between the α-particles and the neutrons which run directly to the detector from the target.

Except for the lighter nucleus, the angular distributions obtained fit fairly well with distributions based on the optical model theory employing a surface imaginary part and a real spin-orbit coupling term.

§ 1. Introduction

Experimental data on the differential cross sections for elastic scattering of neutrons have been reported by many authors[1] for the energy region 1~5 MeV, and have been compared with the optical model theory developed by Feshbach, Portor and Weisskopf[2]. Recently some experimenters[3-11] have extended the energy region up to 14 MeV. The use of high energy neutrons has the following advantage. By the optical model theory, the elastic cross section is divided into the "compound elastic" cross section and "shape elastic" cross section. The shape elastic scattering occurs without the formation of a compound nucleus, while the compound elastic scattering comes from the formation of a compound nucleus and the subsequent emission of the incident particle through the entrance channel. Since the observed differential elastic cross section is an unknown mixture of these two cross sections, it cannot be compared directly with the calculated cross section. The compound elastic scattering, however, is appreciable only at the neutron energy below several MeV. If the neutrons of higher energy were used, the possibility of compound elastic scattering would become very small, more nuclear levels being available for inelastic scattering. In consequence, the theory can be tested more rigidly by comparing directly with the calculated results. The theoretical angular distribution depends upon the detailed assumptions made about the potential used in the calculations especially at large angles. The data for 14 MeV neutrons published so far have, however, been confined to the relatively small angular range. Therefore, the experiments at larger angles are desirable but are very difficult owing to the extremely small cross section.

Quite recently, a combination of the ring geometry and the time-of-flight technique by a pulsed neutron source has been adopted by Wong, Anderson, Gardner and Nakada[12,13]. This technique seems very promising for the measurements of large angle scattering, but there are two limitations in the ring geometry: (1) There is difficulty for many elements in constructing large ring-shaped scatterers for their high prices. (2) The energy spread becomes considerably large except when the ring-shaped sample is placed symmetrically with respect to the direction of the deuteron beam.

The present experimental method is of course quite suitable for measuring expensive elements, but the author tentatively performed the measurements on such commoner elements as aluminum, iron, lead and bismuth, because the theoretical calculations for these nuclei were available in detail for the whole angular range[14].

§ 2. Experimental Method

The 14 MeV neutrons were generated by the $^3T(d, n)^4He$ reaction. A target of T-Zr or

T–Ti was bombarded with a magnetically analyzed beam of 150 keV deuterons from a Cockcroft-Walton accelerator[15].

The deuteron beam was deflected by 60° in a double focusing electromagnet and focused on a target about 65 cm apart from the magnet. The beam was defined by a slit of elliptical shape to give a round spot of diameter 5 mm on a target which was inclined by 45° to the beam. The current density of the beam was made to be less than 10 μA/cm^2 to avoid the local heating of the target plate.

Precautions were taken to diminish the scattering and absorption of neutrons by the target chamber. The chamber was made of an iron cylinder of 2 mm thickness with two acrylite windows for alpha-particle counters and a window of copper foil of 0.15 mm thickness through which the neutron beam passed out to the scatterer. The T–Zr or T–Ti target was 1 cm in diameter and was fixed on a copper slab 2 mm thick and it was maintained at a fixed temperature by circulating hot water. The back of the target was holed to avoid the absorption and scattering of neutrons.

The number of neutrons emitted was monitored by a plastic scintillator at a fixed position and a counting-rate meter connected to the alpha-particle detector. The neutron intensity was kept as constant as possible during the measurements.

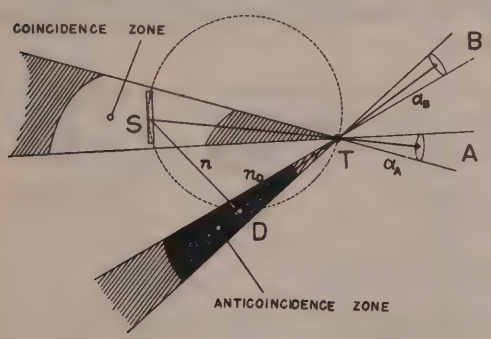

Fig. 1. Experimental arrangements.

n: neutrons scattered by S,
n_D: neutrons which go directly to the detector from the target,
α_A, α_B: alpha-particles corresponding to n and n_D respectively,
A: alpha-particle detector (for coincidence),
B: alpha-particle detector (for anticoincidence),
D: neutron detector,
S: scatterer,
T: target. (The deuteron beam injects perpendicularly to the figure at T.)

Fig. 1 shows the experimental arrangements. The scattering experiments were performed at 90° in the direction of the deuteron beam. The alpha-particles from the reaction ^{3}T(d, n)^{4}He were detected in the counter A, and only the neutrons emitted in coincidence with those alpha-particles were recorded.

The background coincidence rate, taken without scatterer, consisted mainly of accidental coincidences between the alpha-particles and the neutrons which wet directly from the source to the neutron counter. To avoid these accidental coincidences, the alpha-particles corresponding to those neutrons were detected by another alpha-counter B, the pulses of which were used to cancel the pulse of the corresponding neutrons.

In this way, the accidental rate was reduced without using an absorber between the source and the neutron counter so that the counter was allowed to come nearer to the target without causing much increase of background rate, and thus the scattering measurements at large angle were made possible.

Disk-shaped scatterers of diameter of 10 cm, 15 cm and 20 cm respectively were used, the thicknesses of which were such that 10 to 15 per cent of the incident neutrons were scattered elastically. The larger and thicker scatterers among these were used only for measurements at larger angles.

The scatterer was placed roughly tangent to the locus of point for which the scattering angle was constant, and the angular resolution could be limited in a range from ±2° to ±4° in spite of the comparatively large diameter of the scatterer.

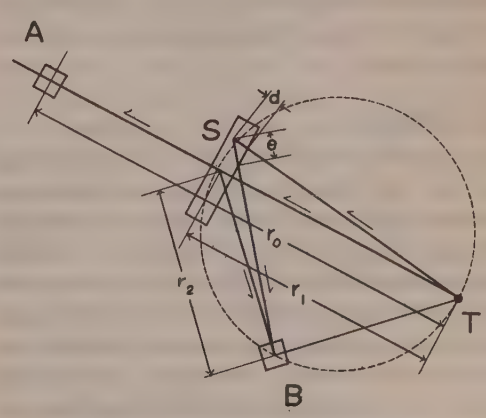

Fig. 2. Position of neutron detector.

The differential elastic cross section was deduced from the results of the following three runs (Fig. 2). (1) The scatter was removed, the neutron detector was placed at A and the coincidence rate N_0 between neutron- and alpha-counter was measured. (2) The detector was transferred to the point B, the scatterer was placed at S and the coincidence rate N_S was measured. (3) The scatterer was removed, the detector was placed at B, and the background N_B was counted. N_0, N_S and N_B were all normalized for a given number of monitor counts.

The absolute differential cross section can be calculated from the scattering ratio defined as:

$$g(\theta_0)=\frac{N_S-N_B}{N_0}\,, \qquad (2.1)$$

where θ_0 is the scattering angle at the center of the scatterer. It is not necessary to determine the value of the absolute neutron flux in this case.

To make the coincidence efficiency the same for the three measurements (1), (2) and (3) it was necessary that

$$r_0 \simeq r_1+r_2\,. \qquad (2.2)$$

Since the neutrons were measured in coincidence with the alpha-particles of the reaction, the background counting rate at the N_0 measurement was negligibly small.

The angle θ_0 may be varied either by changing the distance between the source and the neutron detector, or by changing that between the source and the scatterer, or by changing both distances. For some value of θ_0, several different geometries were used to confirm the results. $g(\theta_0)$ was measured over the angular range from 70° to 170° for aluminum, iron and bismuth, and from 90° to 170° for lead.

§ 3. Detectors

A cylindrical stilben of 3/4″ in diameter and 3/4″ in length was used as the neutron detector. The crystal was connected optically through an acrylite light guide to an RCA 6810 photomultiplier. The discriminator bias was set to count only the pulses corresponding to recoil protons of energies greater than 10~11 MeV. Such a criterion can eliminate almost all inelastically scattered neutrons, for a great majority of these neutrons have considerably lower energies[16]. The gamma rays were also rejected by this bias setting and further by means of the flight time. The pulse height spectrum of the neutron detector for 14 MeV neutrons and gamma-rays from radium is shown in Fig. 3.

The alpha-particle detectors were both the sheet of plastic scintillator of 5 cm in diameter and 0.12 mm in thickness, which was prepared by pressing a small disk-shaped plastic scintillator* with two glass plates in an oven heated at 160°C[17].

The pulse height distribution for alpha-particles from polonium is shown in Fig. 4. This curve was taken by coupling the scintil-

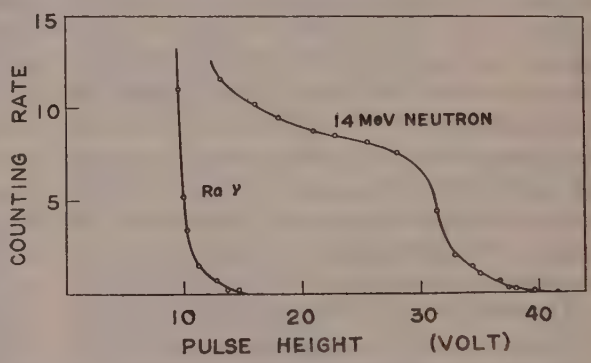

Fig. 3. Differential pulse height distribution of neutron counter. The curve for the gama-ray was taken only to show its maximum pulse height, and there was no definite relation between the intensity of the gamma-ray and the neutron.

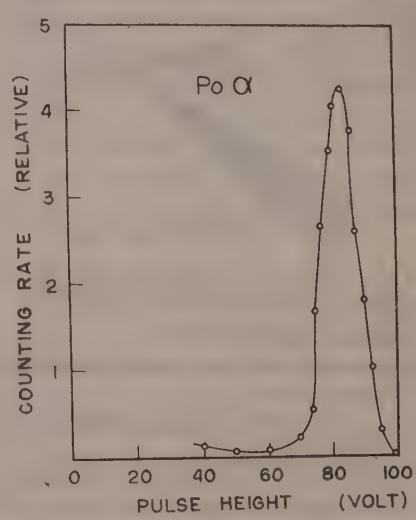

Fig. 4. Pulse height distribution of plastic scintillator for alpha-particles from polonium.

* Plastifluor, Larco Nuclear Instrument Company, Palisades Park, New Jersey, U.S.A.

lator sheet directly to the face of a photomultiplier EMI 5311 with some silicone oil. During the scattering experiments, however, each sheet was attached to the inner surface of the respective acrylite window of the target chamber. The scintillator was covered by 0.39 mg/cm² aluminum foil to stop the scattered deuteron and the light from the deuteron beam. To each outer surface of the acrylite window, the head of RCA 6810 photomultiplier was optically connected.

All the three photomultipliers were operated at 2000~2300 volts with their anodes at the grounded potential. The dynode voltage dividing ratio was taken as specified by the manufacturer[18]. The magnetic shield of 0.9 mm permalloy sheet* was provided to each photomultiplier. This sheet was also used as an electrostatic shield by being maintained at the same potential as that of the photocathode. The electrostatic shield was necessary to suppress the noise due to internal discharge of the surface charge in the tube. The high potential was supplied from a common source developed by K. Sugiyama[19] in this laboratory. It was very stable against the primary voltage change and the drift was less than 0.05 per cent for many hours.

§ 4. Electronic Circuits

The block diagram of the overall electronic circuit is shown in Fig. 5.

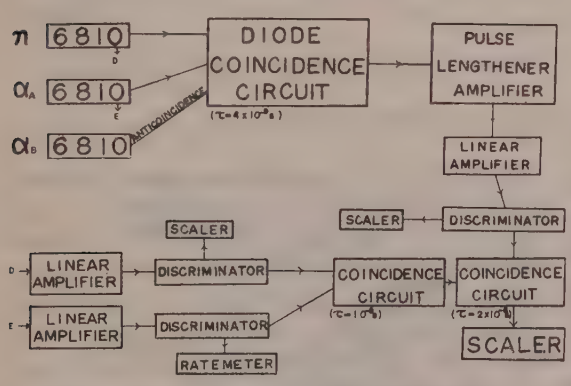

Fig. 5. Block diagram of electronic circuits.

The fast rising pulses from the anode of each photomultiplier were directly fed to a coaxial cable RG 63/U** or C44T***. Each cable was grounded at the end near the photomultiplier anode through a resistance equal to the characteristic impedance of the cable. To the other end, the diode coincidence circuit and another coaxial cable of L cm in length were connected. This cable was short-circuited at the farther end and clipped to the width of $2Lt$ seconds, where t means the time delay of the cable per cm. The value of $2Lt$ was chosen usually at about 4 ns (1 nano second $=10^{-9}$ second) for coincidence pulses, and about 10 ns for anticoincidence pulses.

The coaxial cables were also used to give suitable delays to the pulses from the photomultipliers. Fig. 6 shows the relation between

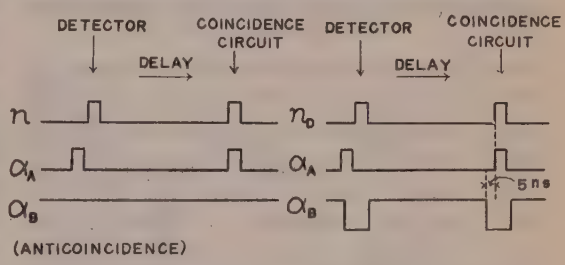

(a) coincidence (b) accidental coincidence

Fig. 6. Time delay of each pulse.

the time delays for the pulses from each counter. In the figure, n is the pulse due to the neutron elastically scattered and n_D is that due to the neutron which goes directly to the detector from the target. α_A and α_B are the alpha-pulses from the counter A and B respectively (Fig. 1). These pulses are produced at different time instants depending on the flight time of the neutrons or alpha-particles between the target and the detector. In Fig. 6 (a), the neutron pulse n and the pulse α_A are produced by the identical neutron production. These pulses were made to arrive at the same time to the coincidence circuit by suitable delay lines. In Fig. 6(b), the neutron pulse n_D is caused by the identical nuclear reaction as the pulse α_B. The n_D- and α_A-pulses have reached to the coincidence circuit simultaneously only by chance, though they are independent of each other. This chance coincidence is avoided by the anticoincidence of the α_A- and α_B-pulses as described before. The latter pulse is made to arrive at the coincidence circuit about 5 ns earlier and end slightly later than the neutron pulse to make sure of the anticoincidence.

The diode coincidence circuit is shown in

* Permalloy P. C., Sumitomo Metal Industries, LTD., Osaka, Japan.

** Fujikura Densen LTD., Tokyo, Japan.

*** Transradio LTD., London SW 7 England.

Fig. 7. It is, in principle, the circuit of R. Madey[20], though we have made some modifications. The most essential point of the modifications was the attachment of an anticoincidence circuit, which was specially designed to work satisfactorily when the time rate of the anticoincidence pulses is very large. E180F tube at the input was used as an amplitude limiter. The anticoincidence circuit requires the pulses of the same polarity and height as those of the pulses for coincidence, but the pulse height and the duration were made somewhat larger than those of the pulses for coincidence to provide against possible fluctuations not only in the pulse height but also in the time when pulse arrives at the coincidence circuit due to uncertainty in the transit time in the photomultiplier.

The pulse lengthener circuit was just the same as that used by Madey. The linear amplifier and discriminator were of the types described by Jordan and Bell[21].

The positive dynode pulses from the neutron counter and the alpha counter A were used for amplitude discrimination for selection of neutron energy and to avoid spurious count from alpha-counter. These pulses were amplified by the respective amplifier with low gain and discriminated. They were clipped by shorted delay line to 100 ns at the input of the linear amplifier. The linear amplifier was of conventional ring-of-three unit, the rise time of

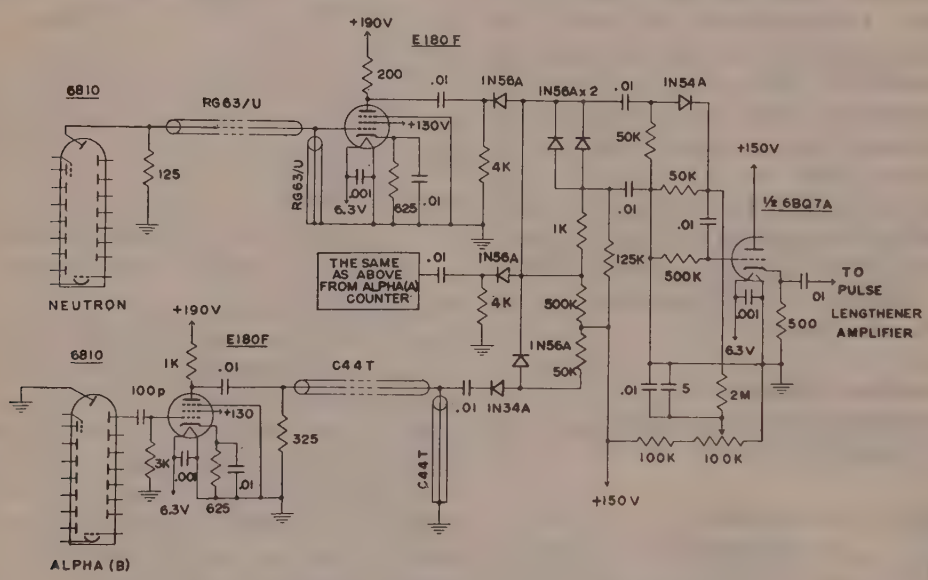

Fig. 7. Schematic diagram of fast coincidence circuit.

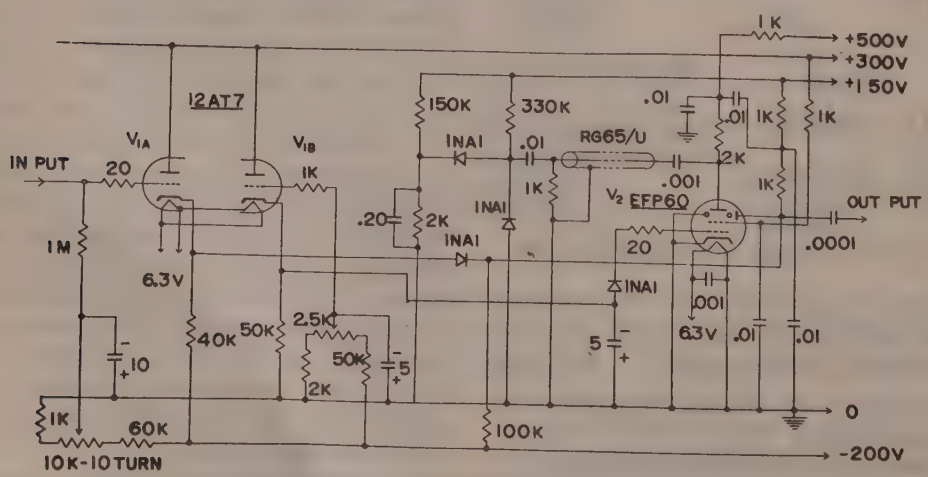

Fig. 8. Schematic diagram of EFP60 trigger discriminator circuit.

which was about 100 ns. Fig. 8 shows the amplitude discriminator of EFP60 trigger type[22,23] which generates output pulses of 100 ns in duration. The trigger level of this circuit was determined by changing the bias voltage of the cathode follower V_{1A} by a 10 turn helicalohm*. The duration of the output pulse was determined by the delay line between the anode and grid of EFP60 tube. In the present circuit, RG65/U of 80 cm length was used. The output pulses from the two EFP60 discriminators were fed to the two grids of 6BN6 tube in a coincidence circuit. The time resolution of this circuit was about 100 ns. The number of alpha-particles was so large that a coincidence circuit with such relatively short resolving time was required.

The output of this 6BN6 tube was coupled to the output of the fast coincidence circuit by a slow coincidence circuit. The resolving time of this circuit was about 2 μs, and its output was led to the scaler through a univibrator and a gate tube. The scaler was of scale-of-100 type modified from a Higinbotham circuit[24]. The spurious counts and natural background counts were not observed for several hours.

§ 5. Calculation of the Cross Section

The relation between the scattering ratio $g(\theta_0)$ defined by (2.1) and the differential cross section $\sigma(\theta)$ is expressed by the following equation:

$$g(\theta_0)=\frac{N_S-N_B}{N_0}=\int_V r_0^2 r_1^{-2} r_2^{-2} S(E) f(\theta)\sigma(\theta) \times\{\exp[-\mu(d+e)]\} n dV\,, \tag{5.1}$$

where θ is the scattering angle in the laboratory system, $S(E)$ is the sensitivity of the detector for scattered neutrons, $f(\theta)$ is the correction factor for the variation of the detector sensitivity due to the incident angle of the neutrons, μ is the total absorption coefficient, n is the number of atoms per unit volume in the scatterer and what are represented by the remaining symbols are seen in Fig. 2.

The integration has to be performed over the entire volume V of the scatterer. The factor $S(E)$ is derived from the energy E of the scattered neutron. E is given approximately as follows:

$$E=\frac{A-1+\cos\theta}{A+1-\cos\theta}E_0\,, \tag{5.2}$$

where E_0 is the energy of the incident neutron and A is the mass number of scattering nucleus.

The factor $f(\theta)$ was determined by a test measurement, but it was almost unity, the angular sensitivity of the detector being nearly constant.

Since r_0^2 and n are constant and $\sigma(\theta)$, $S(E)$ and $f(\theta)$ are nearly constant in the formula (5.1), $g(\theta)$ can be rewritten approximately as follows:

$$g(\theta_0)=\sigma(\theta_0) r_0^2 S(E) f(\theta) n\int_V r_1^{-2} r_2^{-2} \times\{\exp[-\mu(d+e)]\} dV\,, \tag{5.3}$$

where $\sigma(\theta_0)$ is the differential elastic cross section at the center of the scatterer. This integration was performed numerically by dividing the scatterer into several zones. Thus the curve of differential elastic cross section was obtained to a first approximation. The correction for the angular spread due to the finite dimensions of the scatterer and the detector was carried out by integrating the formula (5.1) using the value of $\sigma(\theta)$ from the above curve. This process was continued until the shape of the curve did not appreciably change any more, but this correction itself was very small in the present angular range where the dip and rise of the curves were not so distinct and the iteration was not necessary adequate in most cases.

Since the thickness of the scattering samples was so chosen that they scatter only about 10 to 15 per cent of the incident neutrons elastically, the correction for the multiple scattering was not so large compared to experimental errors in our data and only the correction for the double scattering was performed. In calculating the correction, it was noticed that the angular distributions were strongly peaked in the forward direction. The details are given in Appendix.

§ 6. Results and Discussions

The experimental results are represented in Figs. 9~12, and the numerical data are shown in Table I. The errors indicated in the curves and table are the statistical ones, and they do not include the other experimental errors which are usually much smaller than

* Sakae Tsushin Kogyo Co. LTD. Tokyo, Japan.

this. Only the error due to the normalization of the neutron intensity amounts to about 6 per cent. The errors of the corrections for multiple scattering and angular resolution were far smaller because the corrections themselves were small.

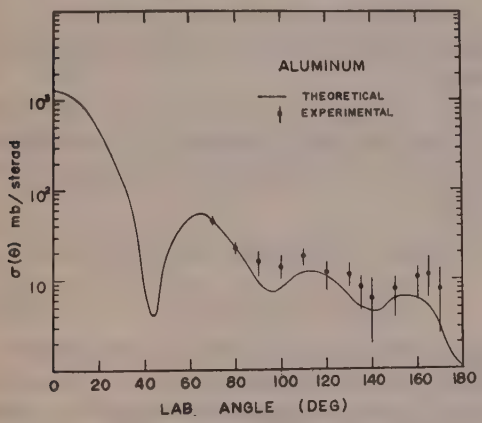

Fig. 9. Differential elastic cross section of alminum.

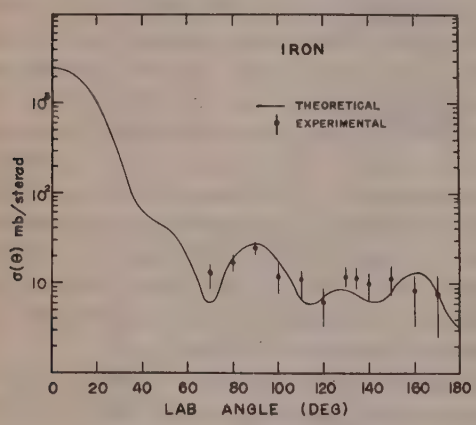

Fig. 10. Differential elastic cross section of iron.

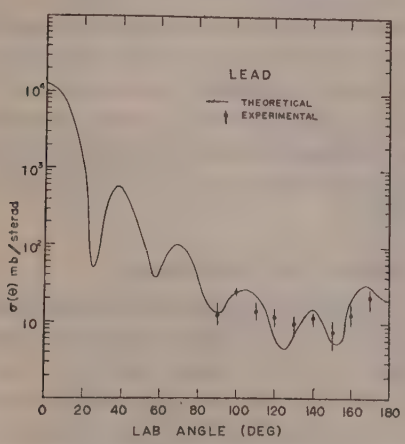

Fig. 11. Differential elastic cross section of lead.

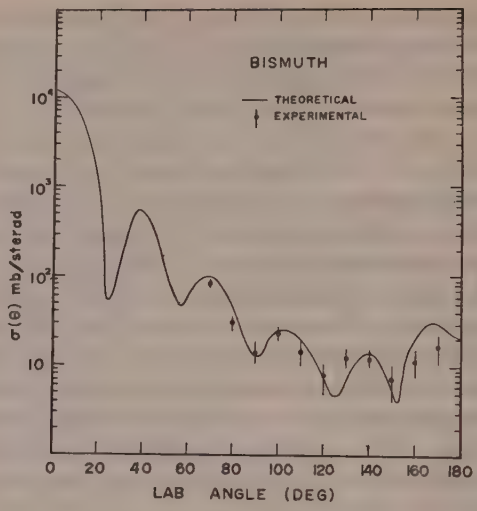

Fig. 12. Differential elastic cross section of bismuth.

In the angular range below 60°, the experimental results[3-11] closely fitted into the theoretical calculations based on the optical model theory when simple square-well potential was used. At angles larger than 60°, however, it was difficult to fit by such a simple well potential. Culler, Fernbach and Sherman[25] used the tailed-well including the spin-orbit potential, but there appeared some pronounced dips which were not observed experimentally. Bjorklund, Fernbach and Sherman[26] used a tailed-well as the real part, and a Gaussian type potential for the imaginary part, namely:

$$\left.\begin{array}{ll}\text{real part:} & U=U_0/[1+\exp(R-R_0)/a]\,,\\ \text{imaginary part:} & V=V_0\exp[-(R-R_0)/b^2]\,,\end{array}\right\} \tag{6.1}$$

where $U_0=40.3$ MeV, $V_0=8$ MeV, $R_0=(1.2A^{1/3}+0.64)$ Fermi, $a=0.6$ Fermi, $b=0.977$ Fermi.

Their results still show too large dips at large angles. Recently they have extended their calculations so as to include the spin-orbit potential as well as the central potential[14]. The potential used in their calculation was of the form:

$$V=V_{CR}\rho(r)+iV_{CI}q(r)+V_{SR}\left(\frac{h}{\mu c}\right)^2\frac{1}{r}\frac{d\rho(r)}{dr}\boldsymbol{\sigma l}\,,$$

where

$$\left.\begin{array}{l}\rho(r)=1/[1+\exp(r-R_0)/a]\,,\\ q(r)=\exp[-(r-R)^2/b^2]\,,\\ \text{and}\\ R_0=r_0A^{1/3}.\end{array}\right\} \tag{6.2}$$

Table I. Elastic scattering of 14 MeV neutrons.

	Differential cross section, millibarns per steradian							
	Aluminum		Iron		Lead		Bismuth	
Lab angle	$\sigma(\theta)$	error	$\sigma(\theta)$	error	$\sigma(\theta)$	error	$\sigma(\theta)$	error
70°	46.2	4.5	12.8	4.3			83.2	9.8
80°	22.6	4.2	17.1	3.2			30.5	5.7
90°	16.0	5.0	24.7	4.5	13.1	4.2	14.7	3.9
100°	14.1	4.0	12.4	4.7	24.9	4.1	23.6	4.1
110°	18.5	3.8	10.3	3.8	14.0	3.8	14.9	4.0
120°	11.7	4.1	6.1	2.8	11.8	3.5	8.0	3.2
130°	11.8	3.8	12.6	3.5	9.9	3.2	12.8	3.0
135°	8.2	3.6	12.2	3.4				
140°	6.1	4.2	10.0	3.6	11.9	3.0	12.5	2.8
150°	7.9	4.0	11.9	4.5	7.7	3.3	7.1	3.1
160°	10.3	4.3	8.3	4.8	13.8	4.7	11.8	4.0
165°	12.0	5.8						
170°	7.8	5.3	7.9	5.3	21.6	6.8	16.7	5.6

(The notation is the same as that used by Riesenfeld and Watson[27].) The numerical values in the formula are as follows: $V_{CR}=44$ MeV, $V_{CI}=11$ MeV, $V_{SR}=8.3$ MeV, $a=0.65$ Fermi, $b=0.98$ Fermi and $r_0=1.25$ Fermi. Their results are shown by solid-line curves in the figures.

Our results for medium weight and heavy nuclei are in good agreement with the theoretical curves. They also agree with the data of Coon and Davis[3], Gardner *et al.*[13] and the normalized results by Berko, Whitehead and Groseclose[28]. Whereas, the data of Mehlhorn[6] and Rhein[4] up to the scattering angle of 150° seems to be inconsistent with ours.

In aluminum, our experimental values are appreciably larger than the theoretical ones for the backward scattering. The optical model theory may not be applied satisfactorily for a lighter nucleus such as aluminum.* Fujimoto and Hossain[29] and Burge *et al.*[30] have shown, however, that the optical model with a simple square-well is able to explain fairly well the experimental data of the angular distribution up to 160° for a nucleus of much smaller mass number such as nitrogen or oxygen. The discrepancy between theory and experiments still remains unexplained. The experiments for other light nuclei and the reexamination of theory will be necessary.

* Note added in proof: Recently it was shown by M.P. Nakada et al. (Phys. Rev. 110 (1958) 1439) for C and Be and by J. H. Coon et al. (Phys. Rev. 111 (958) 250) for C that the observed differential cross section differ considerably from the results af optical model calculations.

Acknowledgements

The author wishes to express his sincere gratitude to Professor M. Sonoda of Kyusyu University for his constant guidance. He is grateful to Professor B. Arakatsu, President of Konan University, and Professor K. Kimura of University of Kyoto for their interest and advice. Thanks are also due to Mr. K. Sugiyama and Mr. B. Saeki for their contributions throughout the course of this investigation.

This work was supported by the Scientific Research Fund of the Ministry of Education.

Appendix

The Correction for the Multiple Scattering

The calculations for multiple scattering have been performed by several authors, but little of them was found to be applicable to the present case. Langsdrof *et al.*[1] derived an exact solution of the multiple scattering by expanding the differential cross section in Legendre's polynomical, but their calculation was very complicated. In the present measurements, very simple assumptions can be used, because the scattering of neutrons is strongly predominant in the forward direction. It is to be noticed, however, that this approximation is only applicable to large angle scat-

tering in which the rise and dip of the cross section are not appreciable.

Since the thicknesses of the scatterers are so chosen that only 10 to 15 per cent of the incident neutrons are elastically scattered, it is always sufficient to consider only the correction for the double scattering as stated before.

Suppose the sample to be a infinite slab of thickness t. Moreover, we assume, for the sake of simplicity, that the incident and scattered neutrons are collimated and are in the same plane perpendicular to the slab. Then, the flux Φ_1 of the neutrons which are scattered once in the slab, is given as:

$$\Phi_1=\Phi_0\cos\theta_1\int_0^t n\sigma(\phi_0)$$
$$\times\exp\{-(\sec\theta_1+\sec\theta_2)\mu x\}\frac{dx}{\cos\theta_1}$$
$$=\Phi_0\sigma(\phi_0)\frac{n}{b}\{1-\exp(1-bt)\}\,, \qquad \text{(A.1)}$$

where

$$b=(\sec\theta_1+\sec\theta_2)\mu\,.$$

In this formula, Φ_0 is the flux of the incident neutrons, n is the number of nuclei in the scatterer and $\sigma(\phi_0)$ is the differential cross section of elastic scattering. The meaning of other notations can readily be seen from Fig. 13.

Next, we consider the neutrons which suffer the double scattering in the slab. Since the scattering is strongly peaked in the forward direction, only the two extreme cases shown in Fig. 14 (a) and (b) will occur in practice when the over-all scattering angle is large. Since the probability for occurrence is nearly equal in the two cases, we can consider only one of the cases (e.g. the case (a)) and mul-

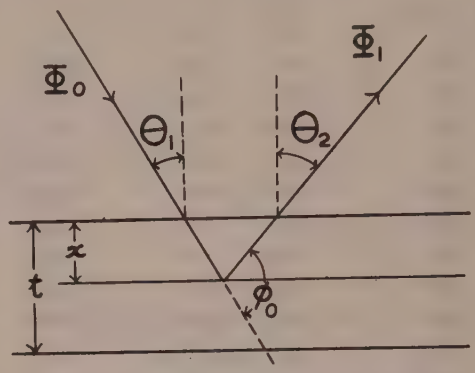

Fig. 13. Diagram of single scattering.

tiply the result by two. The flux $d\Phi_2$ of the neutrons which make the first scattering at a point of depth x and then the second scattering at a point of depth $x+u$, as shown in Fig. 14 (a), is given as:

$$d\Phi_2=\Phi_0\sigma(\phi_1)ndx\frac{rdrd\varphi}{R^2}\sigma(\phi_2)n$$
$$\times\exp[-\{x\sec\theta_1+R+\sec\theta_2(x+u)\}\mu]du. \quad \text{(A.2)}$$

where R is the distance between the two points. Thus, the total flux Φ_2 of the neutrons which suffer the double scattering in the slab and emerge at the angle θ_2 is expressed in the form:

$$\Phi_2=2\Phi_0n^2\sigma(\phi_2)\int_0^t dx\int_0^{t-x}du\int_0^{2\pi}d\varphi\int_0^\infty\sigma(\phi_1)\frac{rdr}{R^2}$$
$$\times\exp[-\{x\sec\theta_1+R+\sec\theta_2(x+u)\}\mu]\,. \quad \text{(A.3)}$$

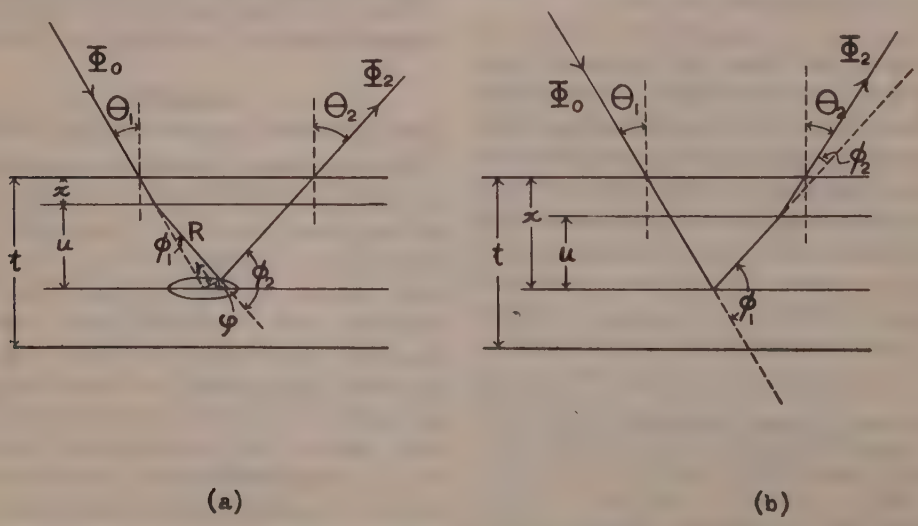

Fig. 14. Diagram of double scattering.

Since the scattering is strongly peaked in the forward direction, we can assume

$$\sigma(\phi_1) \simeq \sigma_0 \exp\{-A(1-\cos\phi_1)\} ,$$
$$\sigma(\phi_2) \simeq \sigma(\phi_0) ,$$

and

$$R \simeq u \sec\theta_1 ,$$

where σ_0 is the differential cross section for $\phi_1=0$ and A is a constant to be so chosen as to fit the experimental angular distribution of the scattered neutrons[31]. Substituting the above approximate equations into the right-hand side of (A.3), we obtain:

$$\Phi_2 = 2\frac{\Phi_0\sigma(\phi_0)n^2}{b^2}\frac{2\pi\sigma_0}{A}\{1-(1+bt)\exp(-bt)\} . \tag{A.4}$$

Since the measured intensity of the scattered neutrons is proportional to $\Phi_1+\Phi_2$, the correction factor for the double scattering which should be multiplied to the observed data, is given by:

$$\frac{\Phi_1}{\Phi_1+\Phi_2} = \frac{1-\exp(-bt)}{\{1-\exp(-bt)\}+4\pi\sigma_0 n\{1-(1+bt)\exp(-bt)\}/Ab} \tag{A.5}$$

An example of the numerical data is shown in Fig. 15.

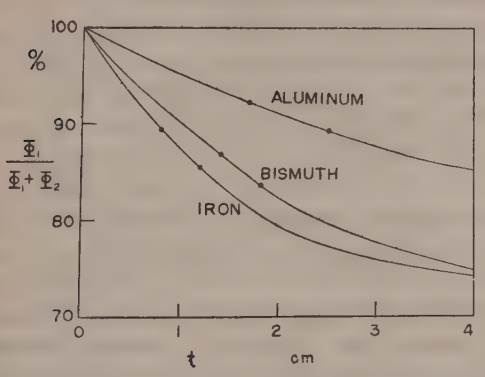

Fig. 15. Example of correction for double scattering ($\theta_1=0°$, $\theta_2=10°$, $\phi_0=170°$). The values for the scatterers used in this measurement are represented by black circles.

References

1) For example:
W. D. Whitehead and S. C. Snowdon: Phys. Rev. **92** (1953) 114.
M. Walt and H. H. Barshall: Phys. Rev. **93** (1954) 1062.
S. C. Snowdon and W. D. Whitehead: Phys. Rev. **94** (1954) 1267.
R. N. Little, Jr., B. P. Leonard, Jr., J. T. Prud'homme and L. D. Vincent: Phys. Rev. **98** (1955) 634.
M. Walt and J. R. Beyster: Phys. Rev. **98** (1955) 677.
R. L. Allen, R. B. Walton, R. B. Perkins, R. A. Olson and R. F. Taschek: Phys. Rev. **104** (1956) 731.
J. R. Beyster, M. Walt and E. W. Salmi: Phys. Rev. **104** (1956) 1319.
A. Langsdorf, Jr., R. O. Lane and J. E. Monaham: Phys. Rev. **107** (1957) 1077.
2) H. Feshbach, C. E. Portor and V. Weisskopf: Phys. Rev. **96** (1954) 448.
3) J. H. Coon and R. W. Davis: Phys. Rev. **94** (1954) 785 (A) and private communication.
4) W. J. Rhein: Phys. Rev. **98** (1955) 1300.
5) W. G. Cross and R. G. Javis: Phys. Rev. **99** (1955) 621 (A) and prevate communication.
6) H. A. Mehlhorn: Bull. American Phys. Soc. Ser. II **1** (1956) 56.
7) P. J. Dolan, H. A. Fincher, P. J. Kenny, S. Berco and W. D. Whitehead: Bull. American Phys. Soc. Ser. II **1** (1956) 339.
9) J. O. Elliot: Phys. Rev. **101** (1956) 684.
9) H. Nauta: Nuclear Physics **2** (1956/57) 124.
10) J. H. Coon, R. W. Davis, Felthauser and D. B. Nicodemus: Bull. American Phys. Soc. Ser. II **2** (1957) 233.
11) L. A. Rayburn: Bull. American Phys. Soc. Ser. II **2** (1957) 233.
12) J. D. Anderson, C. C. Gardner, M. P. Nakada and C. Wong: Bull. American Phys. Soc. Ser. II **2** (1957) 233; Phys. Rev. **110** (1958) 160.
13) C. C. Gardner, J. D. Anderson, M. P. Nakada and C. Wong: Bull.American Phys. Soc. Ser. II **2** (1967) 233.
14) F. Bjorklund and S. Fernbach: private communication and Phys. Rev. **109** (1958) 1295.
15) S. Yasumi, K. Yuasa, M. Sakisaka, Y. Oyama and M. Sonoda: Abstract of the 1955 Annual Meeting of the Phys. Soc. of Japan **1** (1955) 15 (in Japanese).
16) E. R. Graves and L. Rosen: Phys. Rev. **89** (1953) 343.
17) K. Sugiyama and K. Yuasa: J. Appl. Phys. Japan **27** (1958) 59 (in Japanese).
18) *RCA Tentative Data for 6810*, 6810-12-55.
19) K. Sugiyama: Electronics (Japan) **2** (1957) 1049 (in Japanese).
20) R. Madey: Rev. Sci. Instr. **26** (1955) 971.
21) W. H. Jordan and P. R. Bell: Rev. Sci. Instr. **18** (1947) 703.
22) I. A. D. Lewis and F. H. Wells: *Millimicrosecond Pulse Techniques*. (Pergamon Press, London, 1954) p. 232.

23) B. Collinge, A. W. Merrison and D. Eccleshall: J. S. I. **33** (1956) 72.
24) R. Ishiwari and K. Yuasa: Mem. Coll. Sci. Univ. of Kyoto, Ser. A. **25** (1949) 155.
25) G. Culler, S. Fernbach and N. Sherman: Phys. Rev. **101** (1956) 1047.
26) F. E. Bjorklund, S. Fernbach and N. Sherman: Phys. Rev. **101** (1956) 1832.
27) W. B. Riesenfeld and K. M. Watson: Phys. Rev. **102** (1956) 1157.
28) S. Berko, W. D. Whitehead and B. C. Groseclose: Nuclear Physics **6** (1958) 210.
29) Y. Fujimoto and A. Hossain: Phil. Mag. **46** (1955) 542.
30) E. J. Burge, Y. Fujimoto and A. Hossain: Phil. Mag. **1** (1956) 19.
31) D. J. Hughes and R. S. Carter: *Neutron Cross Sections, Angular Distributions, BNL 400.* (Associated Universities, Inc. 1956).

JOURNAL OF THE PHYSICAL SOCIETY OF JAPAN VOL. 13 No. 11 NOVEMBER 1958

The Multiplicity of Mesons Produced in the Nuclear Interaction of High Energy Nucleons and α-Particles in Cosmic Radiation

By Shin-ichi KANEKO*

Institute of Polytechnics, Osaka City University

(Received July 14, 1958)

It was proposed in a previous paper[1] that the multiplicity $n_\pm$ of charged mesons produced in the high energy nucleon-nucleon interaction can be empirically expressed as a function of the inelasticity K and the Lorentz factor γ_c in the center-of-mass system: $n_\pm \simeq 3.5\ K(\gamma_c-1)$ for $\gamma_c \lesssim 7$, $n_\pm \simeq 9\ K(\gamma_c-1)^{1/2}$ for $\gamma_c \gtrsim 7$. It it shown here that further experimental results published in recent years are also consistent with this dependence. It is also suggested, with the support of experimental material, that the peripheral collision of high energy α-particles with nuclei can be explained in terms of a superposition of a few nucleon-nucleon collisions so that the meson multiplicity in the interaction can also be represented by the above equations. The results of observation of a jet $(3+33_\alpha)$ initiated by a high energy α-particle ($\sim 1.2\times 10^{13}$ eV/nucleon) are described.

§ 1. Introduction and Summary

It is well known from observations with photographic emulsions that the multiplicity of charged mesons produced in the high energy nucleon-nucleon interactions shows wide fluctuation even for a given primary energy. However, it was shown in our previous paper[1] that the multiplicity normalized at the completely inelastic interaction for individual events seems to be a rather smooth function of primary energy; i.e., the multiplicity is empirically given by

$$n_\pm \cong 3.5\ K(\gamma_c-1) \qquad \text{for } 2 \lesssim \gamma_c \lesssim 7, \qquad (1)$$

$$n_\pm \cong 9\ K(\gamma_c-1)^{1/2} \qquad \text{for } 7 \lesssim \gamma_c\,, \qquad (2)$$

where $n_\pm$, K and γ_c are the number of charged mesons, the inelasticity, and the Lorentz factor of the incident nucleon in the center-of-mass (C-) system measured for each event, respectively.

Recent observations made at different laboratories seem also to support this dependence as will be shown in § 2. Some possible evidence for this view is discussed in § 3 in regard to an apparent discrepancy between the conclusion given by the Bristol group and ours. In this connection, the validity of the assumption that the transverse momenta of

* Now at the Physics Department, University of Washington, Seattle, Washington, U.S.A. on leave of absence from the Osaka City University.

shower particles have a fairly constant value is also discussed.

The interaction of high energy α-particles (or heavier particles) with nuclei in photographic emulsions has so far been analysed by many authors under the assumption that the event was produced by a single nucleon-nucleon (N–N) interaction. The assumption may be inadequate for analysing the nucleus-nucleus collision, especially the head-on collision, since some of nucleons in both of the nuclei may as a whole interact with each other. In § 4, it is pointed out that at least the peripheral collision of high energy α-particles with nuclei should be explained in terms of a simple superposition of the N–N interactions. The experimental results now available are shown to be in agreement with this prediction. Therefore, it results that the multiplicity of mesons produced in the peripheral collision of α-particles can also be approximately represented by Eqs. (1) and (2) within the present experimental limitations.

The results of observation of a jet $(3+33_\alpha)$*, which gives a support to the argument in § 4, initiated by a high energy α-particle ($\sim 1.2\times 10^{13}$ eV/nucleon) are described in detail in § 5.

§ 2. Nucleon-Nucleon Interactions

We reproduce in Fig. 1 the relation of $n_\pm/K$ *versus* γ_c-1 (Fig. 1 in reference 1). In drawing this figure, we have supposed that the process of antiproton-nucleon annihilation is equivalent to the N–N collision of $\gamma_c=2$ and $K=1$ as far as we are concerned with the meson multiplicity. This assumption has not yet been proved to be correct on experimental and theoretical grounds. Afterwards, Iizuka *et al.*[2] have shown that a simple relation between $n_\pm/K$ and γ_c-1 holds still at the energy region of Cosmotron. They have calculated average values of $n_\pm/K$ from the average energies of pions produced in the proton-proton collisions at the Cosmotron energies and have shown that the straight line fitted to these experimental values passes through the antiproton annihilation point (□ in Fig. 1) with slope 0.78 as shown in Fig. 1. This probably shows that the average energy in the C-system of pions produced in the proton-proton collisions at 6 GeV ($\gamma_c=2$) should be approximately the same as that in the antiproton-nucleon annihilation and hence the above assumtion should be correct**.

At extremely high energies, on the other hand, some observations have been done at various laboratories in recent years. The experimental data[3–5] of these showers selected under the similar criteria to reference 1 are shown in Fig. 1 and Table I. It seems to require explanation for the individual events especially for estimates of inelasticity.

Event A–1[3]: This shower $(1+7_p)$ was detected by the tracing back method[6] and is not a pure proton-proton collision, since a proton ejected backwards with $\sim$100 MeV was accompanied. Multiple scattering was satisfactorily measured for five shower particles ejected at large angles with respect to the primary direction. The energy of a neutral pion ejected into the forward cone was determined by measuring energies and angles of two electron pairs. Assuming all the shower particles to be pions, we found that $\gamma_c=13_{-4}^{+5}$ and $K\cong 0.18$.

Event A–2[4]: The average energy of two neutral pions in the C-system of this event was found to be $\sim$4.2 GeV. Assuming that the charged mesons were emitted with the same average energy, we can estimate the value of $n_\pm/K$.

Events observed by the Bristol group[5]: Edwards *et al.* have carried out a systematic observation on the transverse momenta, p_T, of secondary particles arising from the energetic nuclear interactions, and have shown that p_T of secondary pions has a rather narrow distribution around 0.5 GeV/c. (The same conclusion, but with a somewhat lower value of the average $\langle p_T\rangle$, has also been

* This is the conventional nomenclature of the type of shower. The first and the second numbers refer to those of heavily ionizing prongs and secondary relativistic charged particles, respectively. The subscript α (or p) means that the primary particle of the shower is an α-particle (or a singly charged particle).

** *Note added in proof*: By making use of nuclear plates, Kalbach, Lord and Tsao have recently observed that in the proton-proton interaction at 6.2 Gev the average charged pion multiplicity and the average degree of inelasticity are 1.9 ± 0.3 and 0.49 ± 0.05, respectively. This observation appears to support the above prediction. We are indebted io Prof. J. J. Lord for informing us of their results before publication.

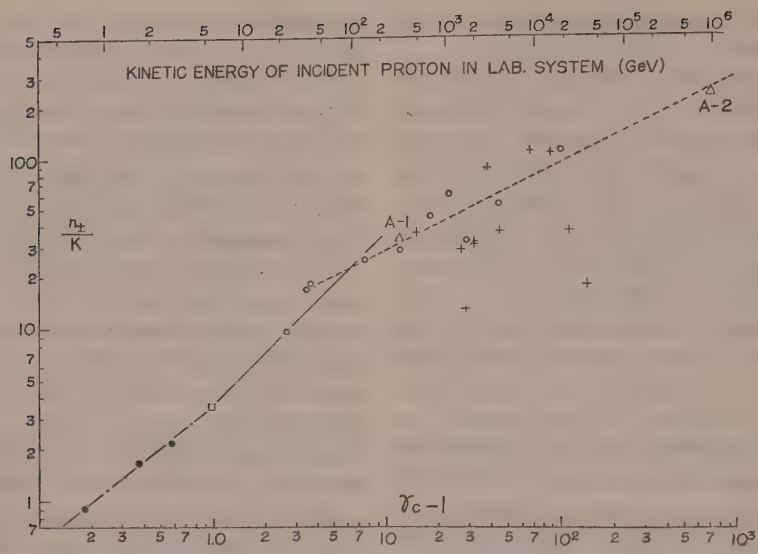

Fig. 1. The normalized multiplicity, the multiplicity divided by the inelasticity, of charged mesons plotted against the kinetic energy (in units of the nucleon rest energy) of the incident nucleon in the center-of-mass system. The chain line is the one given by Iizuka *et al.*[2], which has been fitted to three experimental points (marked with dotts) and has slope 0.78. The square and the circles are the experimental points already described in the previous paper[1]. The solid and the dotted lines represent Eqs. (1) and (2), respectively. The triangles show the experimental results of the proton-induced showers: A-1($1+7_p$) observed by Kaneko *et al.*[3] and A-2($1+6_p$) observed by Fowler[4]. The crosses are those observed by the Bristol group[5].

Table I. Experimental data of high energy showers plotted in Figs. 1 and 2.

Shower number	Type of shower	Lorentz factor in the C-system γ_c	Normalized multiplicity of charged mesons, $n_\pm/K$	Remarks
A-1	$1+7_p$	13	33	Kaneko *et al.*[3]
A-2	$1+6_p$	730	230	Fowler[4]
(P-17)	$2+11_p$	16	36	Edwards *et al.*[6] (The shower numbers in parentheses are those given by these authors. The normalized multiplicity has been taken as $0.8\,n_s/K''$.)
(P-7)	$2+13_p$	28	29	
(P-19)	$0+3_p$	30	13	
(P-13)	$0+8_p$	33	31	
(P-10)	$0+16_p$	33	32	
(P-9)	$0+18_p$	39	85	
(P-16)	$1+11_p$	46	37	
(P-5)	$0+32_p$	68	107	
(P-2)	$0+22_p$	88	104	
(P-24)	$0+11_p$	112	37	
(P-20)	$0+4_p$	143	18	
B-1	$3+33_\alpha$	76	64	The present paper
B-2	$1+37_\alpha$	200	120	Gramenitzkij *et al.*[12]
12	$0+14_\alpha$	420	160	Ciok *et al.*[13]

obtained by the Japanese group using emulsion cloud chambers[7].) Assuming that 80 per cent of secondary particles are pions with $p_T=0.5$ GeV/c, they have estimated the inelasticity for 13 jets induced by high energy protons*:

$$K''=\frac{1.5p_T\sum \cos\overline{\theta}}{2\gamma_c}, \qquad (3)$$

* We are very much indebted to Drs. D. H. Perkins and J. Iwadare for informing us of the detailed data of these jets.

where $\overline{\theta}$ is the angle of a secondary particle in the C-system. The values of $0.8\,n_s/K''$ of eleven jets with $N_h<4$ among them are plotted in Fig. 1, where n_s and N_h are the numbers of shower particles and of heavily ionizing particles, respectively.

§ 3. Discussion of Nucleon-Nucleon Interactions

It can be seen from Fig. 1 that the dotted curve (Eq. (2)) is in excellent agreement with events A–1 and A–2. The Bristol events are also consistent with the curve within factor two expect for two events (P–19 and P–20). It should be noted, however, that they indicate the general trend that the events with low multiplicity lie below the curve, whereas those with high multiplicity lie above. It was also shown that the jet with low multiplicity shows a strong angular anisotropy rather than that with high multiplicity. These facts have led the Bristol group to the conclusion that the inelasticity does not appear to be dependent strongly on the multiplicity at a fixed energy. This conclusion contradicts to the dependence given by Eq. (2) that the multiplicity is proportional to the inelasticity at a given energy.

The estimate of K for the events described in our previous paper and events A–1 and A–2 is based upon the direct measurement of energies of secondary particles in the laboratory system and upon the determination of the average energy in the C-system. We have then noticed that all of these data can be well approximated by Eq. (2) in spite of the fact that they were obtained by many different observers. Whereas, the Bristol result relies on the assumtion that the average value of transverse momenta is constant for each event. It is to be noted, however, that the assumption $p_T=\text{const.}$ should be valid only in the statistical meaning. Moreover, due to their selection of particles on which the energy measurements were made, a strong bias should be given to the events with high multiplicity. It may therefore be possible that $\langle p_T\rangle$ for individual events depends to some extent upon n_s or it shows fairly large fluctuation from event to event. For example, $\langle p_T\rangle$ computed for the showers analysed in detail by Debenedetti *et al.*[8] $(3+39_p)$ and Glasser *et al.*[9] $(2+15_p)$ was 0.34 and 0.07 GeV/c, respectively. As was explained in the previous paper, these showers are in a good agreement with the dotted line in Fig. 1. However, by computing K'' for these showers by Eq. (3) with $p_T=0.5$ GeV/c, one can see that the resulting value of $n_\pm/K''$ for the second shower would then be far from the dotted line, while the first shower would be still consistent with the line. It seems therefore that Eq. (3) with $p_T=0.5$ GeV/c gives a reliable estimate of the inelasticity only for events with high multiplicity.* These considerations show that it is necessary to accumulate further data of $\langle p_T\rangle$ for individual events especially for those with low multiplicity, in order to prove the statement given by the Bristol group that K does not depend strongly upon n_s at a given energy. At present, it seems more reasonable to suppose that almost all jets analysed in detail are in fact consistent with Eq. (2) so that $n_\pm$ is proportional to K at a given energy.

§ 4. Interaction of High Energy α-Particle with a Nucleon or the Peripheral Nucleons

We restrict ourselves to the interaction of high energy α-particle with either a nucleon or peripheral nucleons in a target nucleus. This should probably correspond to an α-particle induced shower with $N_h\lesssim 4$ observed in photographic emulsion. The interaction is assumed to be explained by a simple superposition of single N–N interactions. (This assumtion has already been employed by some authors[10] for analysing the interaction of α-particles or heavier nuclei.) A support for the assumption seems to be given by the fact observed by Appa Rao *et al.*[11] that the nuclear interactions initiated by cosmic-ray α-particles (median energy $\sim$10 GeV/nucleon) can be classified into those in which 0, 1, or 2 protons inside the α-articles have taken part, by observing the number of shower particles ejected within a definite cut-off

* It may be more reasonable to interpret this view in terms of the degree of anisotropy rather than the multiplicity. As stated already, the Bristol result suggests that the multiplicity depends strongly upon the angular anisotropy. If we assume that $\langle p_T\rangle$ for events showing the strong anisotropy is comparatively small, we could obtain not only a satisfactory explanation of the data of the above two showers but also a justification of the dependence given by Eq. (2) (see Eq. (5)).

angle. Furthermore, fragmentation products consisting of nucleons, α-particles, and heavier fragments emerge quite often from collisions of heavy primary particles with emulsion nuclei. These observations show that many nucleons within the incident nucleus do not experience any significant effect from the collision and are simply emitted by a process such as the evaporation from the nucleus in its own system of reference. It is apparent therefore that some of nucleons in an α-particle play a significant role in the collision, but the remaining ones are not concerned with the interaction so that the whole process may be considered as a simple sum of a few N–N collisions. This simple view might, however, seem to be invalid for the central collision of an extremely energetic α-particle with a heavy nucleus, since several nucleons existing behind the first target nucleon in the heavy nucleus come to participate in the interaction, resulting in that only a collision between the incident α-particle and the target particle heavier than a nucleon is responsible for the meson production, and hence the interaction would no longer be a simple superposition of the elementary processes.

It has been shown in the previous section that the normalized multiplicity in the N–N collisions is satisfactorily expressed by Eqs. (1) and (2) with the support of experimental material. If we assume that the peripheral collision of α-particle can be explained in terms of a simple superposition of N–N collisions, then it results in that $n_\pm/K$ observed for α-induced showers should also be represented by Eqs. (1) and (2). This is simply due to the proportionality between $n_\pm$ and K at a given energy. If we estimate γ_c and K for an α-induced shower under the assumption that the shower has been produced by a single N–N collision, the resulting values of $n_\pm$ and K are of course the sums of those in the elementary processes involved in the interaction so that they are usually greater than those in an N–N collision (The value of K thus estimated can amount to 4 in the upper limit.), but the ratio $n_\pm/K$ remains to be the same as that in the latter at the same value of γ_c.

The normalized multiplicities of three α-induced jets are shown in Fig. 2 and Table I. Shower B–1 is the one observed by us and is described in detail in § 5. The inelasticity of shower B–2 has not been explicitly given by Gramenitzkij *et al.*[12] but can be roughly estimated from the angular distribution of shower particles given in their paper by assuming p_T to be constant (see §§ 3 and 5). Shower 12 is the one[13] used already for the analysis in the previous paper.

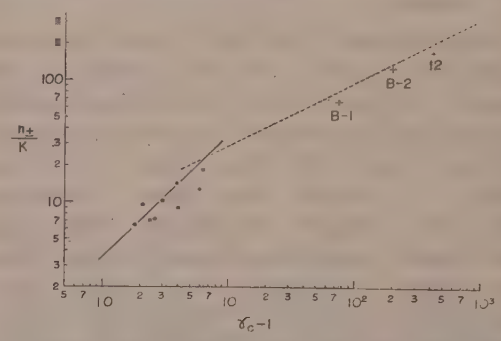

Fig. 2. The normalized multiplicity of showers initiated by high energy α-particles plotted against the kinetic energy per nucleon (in units of the nucleon rest energy) of the incident α-particle in the center-of-mass system. The solid and the dotted lines represent Eqs. (1) and (2), respectively. The crosses show the experimental results of the α-particle induced jets: B–1 ($3+33_\alpha$) described in § 5; B–2 ($1+37_\alpha$) observed by Gramenitzkij *et al.*[12]; 12($0+14_\alpha$) observed by Ciok *et al.*[13] The quantity $9(\gamma_c-1)/(\gamma_c \sin\theta_m) = n_\pm/K$ computed for 9 α-induced showers observed by Winkler[10] is shown with dotts.

In the lower energy region, the inelasticity in interactions initiated by α-particles was not estimated so far by plausible method; it seems therefore that there are no experimental data to be plotted in Fig. 2. However, we could obtain some knowledge from angular distribution observed in α-particle induced showers. Winkler[10], for example, has presented the maximum angle, θ_m, of shower particles together with the primary energy for 26 α-induced showers. We can estimate, as was explained in the previous paper, the normalized multiplicity as

$$\frac{n_\pm}{K} = \frac{9(\gamma_c-1)}{\gamma_c \sin\theta_m},$$

assuming that pions have been emitted with a single energy in the C-system. The quantity on the right-hand side in the above formula has been computed for 9 showers having $N_h < 4$ and plotted in Fig. 2. (The values of γ_c estimated by the method of Castagnoli *et al.*[14]

for these showers have been employed in this computation.) It is to be noted that the uncertainty in the position of the individual point should be quite large due to possible fluctuations in γ_c and θ_m and to incorrectness of the assumption of the single energy.

It seems that the dotted and the solid lines (Eqs. (2) and (1)) are consistent with experimental points in the higher and the lower energy regions, respectively*. This probably suggests that the peripheral collision of α-particles with nuclei can be explained in terms of a simultaneous occcurrence of a few N–N collisions of the same energy. The experimental and statistical precisions for α-induced showers are quite insufficient at present in order to draw any decisive conclusions. But if we confirm the above view to be correct, it turns out that the investigation of α-induced showers is very helpful for studying the single N–N interactions. This is due to the fact that an α-induced jet should in general be subject to a smaller fluctuation in the normalized multiplicity than a proton jet, because the former itself is already a superposition of the latter. It is to be noted, in this connection, that α-induced showers can perhaps be observed with a frequency comparable with proton-induced showers in the stacks exposed at an altitude higher than 30 km, and also that much more peripheral collisions should occur for incident α-particles rather than for protons[15].

Furthermore, it seems possible to give some indication of the number of interacting nucleons in the incident α-particle. Edwards *et al.*[5] have observed three α-induced jets and six proton-jets with $N_h<3$ in the energy interval 2,000~5,000 GeV/nucleon (Fig. 1 in their paper). The average multiplicity for these proton-jets is found to be ~10 (which gives the average inelasticity in the N–N collision in this energy region to be ~1/5 with the aid of Fig. 1), whereas it amounts to ~30 for the α-jets. This seems to suggest, although the statistical precision is quite low, that on the average three nucleons in the incident α-particle come to interact during the peripheral collision. At the lower energies (~100 GeV/nucleon), on the other hand, the ratio of average multiplicity between α- and proton-induced showers (irrespective of N_h) was found to be about 1.3 by Engler *et al.*[16] and Winkler[10]. It seems that this value gives a lower estimate, since in this energy region proton-showers with low N_h and n_s are likely to escape from observation and the correction made for their frequency seriously affects the result. Indeed, the average number of nucleons taking part in collisions (including central collisions) has been estimated to be 2.4 by Appa Rao *et al.*[11] in a quite different but more reasonable manner**. This should be compared with the above value at the higher energies allowing for the fact that the former refers to all values of N_h but the latter to $N_h<3$.

§ 5. Observation of Jet B–1 ($3+33_\alpha$)

Event B–1, as well as A–1, was detected in a large stack (108 sheets of 6″×9″ size) of 600 microns thick G5 stripped emulsions exposed at 29 km altitude during six hours in Japan. Shower particles consist of 14 and 19 tracks in the inner and the outer cones, respectively. The shower axis has length 6.5 mm per plate and passes through 13 plates. Except for three, all the secondary shower tracks have been carefully traced from plate to plate (total length ~240 cm), and only one nuclear interaction ($2+13_p$) could be found. This observation corresponds to an extreme case improbable to occur, if we assume the mean free path for interaction of shower particles to be geometrical (~35 cm) and also take into account some neutral particles involved in the inner cone.

The target diagram of the shower particles in the laboratory system is shown in Fig. 3. The primary energy of the incident α-particle is estimated by the method of Edwards *et al.*[5] assuming that the jet has been initiated by a single N–N collision:

$$-2\log\gamma_c=\langle\log\tan\theta\rangle_f+\langle\log\tan\theta\rangle_b\,, \quad (4)$$

where θ is the laboratory angle of a shower particle with respect to the primary direction and both of the terms on the right-hand side are the averages taken for the forward and the backward cones respectively. Thus, we

* *Note added in proof*: In addition, the Bristol event $\alpha-5(0+11_\alpha,\ \gamma_c=108,\ K''=0.105)$ agrees fairly well with the dotted line.

** By using a simple model for the nuclear interaction of α-particles, Ceccarelli *et al.*[15] have shown that the average number of interacting nucleons is calculated to be 2.8.

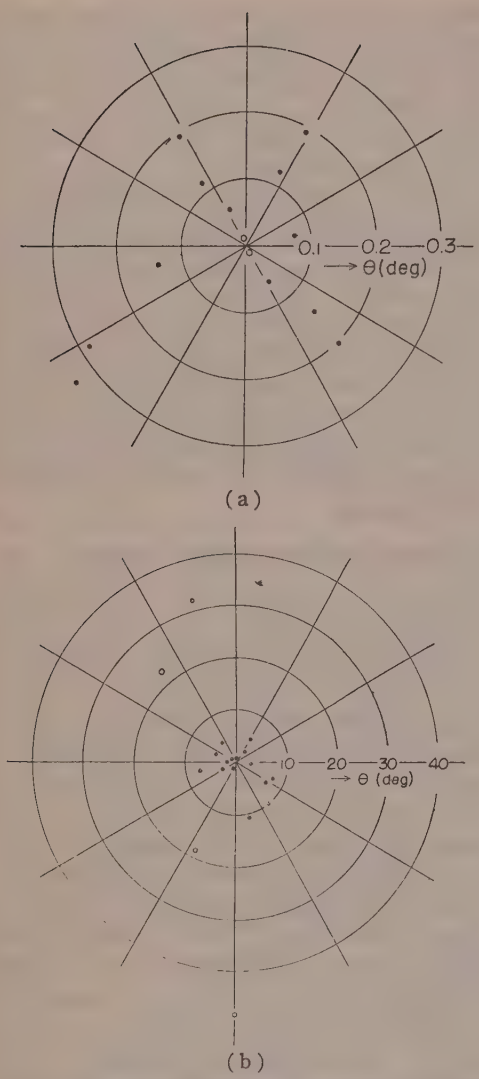

Fig. 3. The target diagram of the shower particles in the laboratory system of jet B-1 ($3+33_\alpha$): (a) the inner cone, (b) the outer cone. The six white circles correspond to the particlesexcluded for estimating the inelasticity (see the text).

obtain $\gamma_c=76_{-23}^{+33}$; i.e., the primary energy of the incident α-particle is estimated to be $(1.2_{-0.6}^{+1.2})\times 10^{13}$ eV/nucleon.

An estimate of the inelasticity of the interaction will be most easily given by making the assumption of $p_T=\text{const}$. The high multiplicity of the shower particles in this event should justify to make this assumption (see § 3). Using Eq. (3) with $p_T=0.5$ GeV/c, the normalized multiplicity is then written as

$$\frac{n_\pm}{K}=\frac{2\gamma_c}{1.5\,p_T\langle\operatorname{cosec}\bar{\theta}\rangle}=\frac{2.7\,\gamma_c}{\langle\operatorname{cosec}\bar{\theta}\rangle}\,. \qquad (5)$$

In Fig. 4 is shown the distribution in $\operatorname{cosec}\bar{\theta}$ of the shower particles which have been transformed by the relation usually employed:

$$\operatorname{cosec}\bar{\theta}=\frac{1+\gamma_c^2\tan^2\theta}{2\gamma_c\tan\theta}\,.$$

In addition to those shown in Fig. 4, there are four particles having very large values of $\operatorname{cosec}\bar{\theta}$. If we assume that these particles are pions with $p_T=0.5$ GeV/c, their values of Lorentz factor in the C-system would be too high as compared with the value of γ_c; this is inconsistent with the fact that none of the shower particles was ejected into the backward direction in the laboratory system. They should therefore be either the pions having $p_T\ll 0.5$ GeV/c or the particles heavier than the pion.

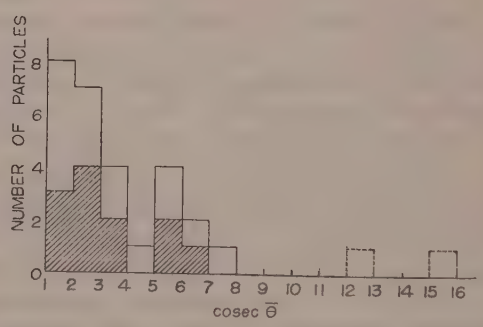

Fig. 4. The distribution in $\operatorname{cosec}\bar{\theta}$ of 29 shower particles of jet B-1, where $\bar{\theta}$ is the angle of a shower particle in the center-of-mass system with respect to the primary direction. The shaded histogram shows the particles ejected into the forward cone. Two particles represented by the dotted squares, together with four particles having the values of $\operatorname{cosec}\bar{\theta}$ too high to be shown in the figure, are discarded for estimating the inelasticity.

Two particles among those shown in Fig. 4 have also the values of $\operatorname{cosec}\bar{\theta}$ much higher than the others. They appear to be similar to the four particles mentioned above. Of these six particles showing the higher values of $\operatorname{cosec}\bar{\theta}$, two being in the forward cone may be two protons initially involved in the incident α-particle. It is remembered, in this connection, that at the lower energies a non-interacting proton in an incident α-particle emerges within an extremely small angle relative to the primary direction[11]. In the present event, however, either of the two tracks may be such a non-interacting proton,

but the other cannot be, since the relative momentum between them in the transverse direction would be computed to be too high (~5 GeV/c) assuming that their energy is the same as that at incidence. Whereas, the remaining four out of the six particles are in the backward cone and may consist of the colliding partners and the shower particles produced in the secondary interaction inside the target nucleus. (The existence of three heavy prongs accompanied by the jet suggests that some of the shower particles in the outer cone might have been originated from the secondary interaction.)

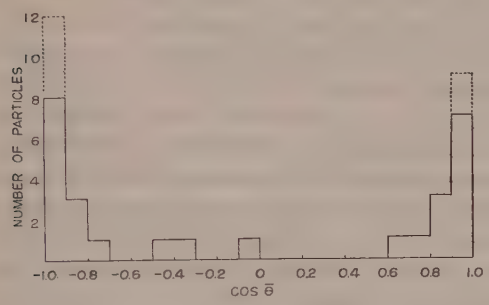

Fig. 5. The angular distribution of the shower particles in the center-of-mass system of jet B-1. The dotted area corresponds to the six shower particles discarded for computing the inelasticity.

With the exception of these six particles, it results in that the average values $\langle \mathrm{cosec}\,\bar{\theta} \rangle$ for the forward and the backward cones agree quite well with each other. The normalized multiplicity is therefore estimated to be 64 using Eq. (5).

The angular distribution of the shower particles in the C-system is strongly peaked at the forward and the backward directions as shown in Fig. 5.

Acknowledgments

The author wishes to express his sincere thanks to Prof. Y. Watase for his interest and kind encouragement. Thanks are due to Mr. S. Matsumoto for helpful discussion and criticism during the course of the work. He is also indebted to Prof. M. Okazaki and Mr. O. Kusumoto for valuable advice, and to Prof. S. Hayakawa for reading the manuscript.

The emulsion stack used in the work has been provided, exposed, and processed with the cooperative efforts of the members of the Japanese emulsion group under the auspices of the Institute for Nuclear Study, University of Tokyo. The author should like to take this opportunity of thanking the members of the group and the staff of the Institute, especially Profs. S. Kikuchi, O. Minakawa, and J. Nishimura.

The work has been supported in part by a Grant-in-Aid for Fundamental Scientific Research from the Ministry of Education.

References

1) S. Kaneko and M. Okazaki: Nuovo Cimento **8** (1958) 521.
2) Z. Iizuka, D. Ito, S. Minami and Y. Tanaka: Soryushiron Kenkyu (in Japanese), **17** (1958) 19 (to be published in Nuovo Cimento).
3) S. Kaneko, O. Kusumoto and S. Matsumoto: to be published.
4) P. H. Fowler: *Proceedings of the 7th Rochester Conference*, p. XI-18. Interscience Publishers, Inc., New York, 1958.
5) B. Edwards, J. Losty, D. H. Perkins, K. Pinkau and J. Reynolds: Phil. Mag. **3** (1958) 237.
6) S. Kaneko, O. Kusumoto and S. Matsumoto: J. Phys. Soc. Japan **11** (1956) 1129.
7) O. Minakawa, Y. Nishimura, M. Tsuzuki, H. Aizu, H. Hasegawa, Y. Ishii, S. Tokunaga, Y. Fujimoto, S. Hasegawa, J. Nishimura, K. Niu, K. Nishikawa, K. Imaeda and M. Kazuno: Preprint (1958).
8) A. Debenedetti, C. M. Garelli, L. Tallone and M. Vigone: Nuovo Cimento **4** (1956) 1142.
9) R. G. Glasser, D. M. Haskin, M. Schein and J. J. Lord; Phys. Rev. **99** (1955) 1555.
10) For example, W. Winkler: Helv. Phys. Acta **29** (1956) 267; S. Tokunaga: J. Phys. Soc. Japan **12** (1957) 454.
11) M. V. K. Appa Rao, R. R. Daniel and K. A. Neelakantan: Proc. Ind. Acad. Sci. **43** (1956) 181.
12) I. M. Gramenitzkij, G. B. Judanov, E. A. Zamchalova and M. N. Shcherbakova: Zh. eksper. teor. Fiz. SSSR **32** (1957) 936.
13) P. Ciok, M. Danysz, J. Gierula, A. Jurak, M. Miesowicz, J. Pernegr, J. Vrana and W. Wolter: Nuovo Cimento **6** (1957) 1409.
14) C. Castagnoli, G. Cortini, C. Franzinetti, A. Manfredini and D. Moreno: Nuovo Cimento **10** (1953) 1539.
15) M. Ceccarelli, C. Quareni and G. T. Zorn: Nuovo Cimento **1** (1955) 669.
16) A. Engler, U. Haber-Schaim and W. Winkler: Nuovo Cimento **12** (1954) 930.

JOURNAL OF THE PHYSICAL SOCIETY OF JAPAN Vol. 13, No. 11, NOVEMBER, 1958

On the Theory of the Brownian Motion

By Morikazu TODA

Department of Physics, Tokyo University of Education, Tokyo, Japan

(Received August 1, 1958)

The Brownian motion of an oscillator in a thermostat is considered assuming simple forms of interaction between them. No further assumption is made except that the thermostat is always in thermal equilibrium in itself. Solving the Liouville equation or its counterpart in quantum mechanics the long time evolution of the system is clarified. Thus the theory connects automatically the irreversible and the equilibrium behaviors of the system without any ad hoc assumption as in conventional theories. The results include, as a special case, the equation derived by Kramers and Chandrasekhar using the theory of stochastic processes. It is shown that the oscillating part of the distribution function or the density matrix plays an important role to which the peculiar way of damping of the oscillator is to be attributed.

§ 1. Introduction

The purpose of this paper is to treat the problem of the Brownian motion in the framework of the general statistical mechanics of irreversible processes developed quite recently. While the latter deals with a large system in which irreversible processes themselves take place, the former pays special attention to a small system or a particle embedded under the supposition that the rest of the system stays always is thermal equilibrium playing the role of a thermostat. With the thermostat included, the problem of the Brownian motion reduces to a very special case in the general statistical mechanics of irreversible processes in which the initial condition is that only a small number of freedoms is out of equilibrium. The interaction within the thermostat will guarantee the state of equilibrium for it.

Though there exists a number of theories of the Brownian motion, most of them are based on the theory of random flights or of stochastic processes[1] and are rather phenomenological in nature. The coefficients in the Fokker-Planck equation, for instance, are left unknown, though certain relations among them are found by other considerations such as the requirement of the state of equilibrium to which the whole system has to approach. The same can be said with respect to the Langevin equation, in which one assumes the friction constant and the correlation constant of the fluctuating part of the force acting on the particle under consideration. The relation between these two constants is left unknown till one demands that the asymptotic solution ought to be the Maxwell-Boltzmann distribution law. Thus the theory is usually supplemented artificially to meet the request of the statistical mechanics of the equilibrium state.

From the microscopic point of view the friction constant and correlation constant are to be derived from the interaction between the particle and the thermostat. Moreover one has to show the force due to the thermostat can be split out in two parts, the friction and the random forces, as is done in the Langevin equation. An attempt in this direction is seen in one of the papers by Kirkwood[2], in which the friction force is attributed to the plateau value of a certain quantity. Actually he intended to formulate the equation which had been derived by Kramers and Chardrasekhar[1] using the theory of stochastic processes. The validity of the time-smoothing procedure employed in the theory of Kirkwood, together with the existence of the plateau value, however, remain to be justified.

There is another kind of microscopic theories in which one calculates the transition probability from a state to another, and thus formulates the so-called Pauli's equation in quantum mechanical terminology. If one is concerned only with the diagonal elements in the representation in which the unperturbed state is diagonal, it is clear that one gets some

equation different from that of Chandrasekhar and quite different evolution to equilibrium.[3),4)] As we shall see later we can formulate this kind of theory including the off-diagonal elements and clarify that it is still insufficient to describe the detailed behavior of the system.

Recently we have developed the general statistical mechanics of irreversible processes[6)] which is quite transparent in mathematical manipulations and affords direct application to concrete problems. In this paper we shall use this method to provide us with a consistent theory of the Brownian motion.

As the essential feature of the problem of the Brownian motion is to ask the behavior of a small system under the influence of the thermostat, we treat an oscillator which interacts by a certain simple interaction with the thermostat, which we assume to consist of a large number of harmonic oscillators. In § 2 we shall derive equations which are purely mechanical and are applied in the following sections. In § 3 we shall use the solution of the Liouville equation obtained from the general theory[6)]. Assuming a simple from of interaction we get the Kramers equation, a kind of diffusion equation in phase space. Other kinds of interaction are examined. It is shown that if the interaction is proportional to the displacement of the oscillator one gets the Langevin friction and that if it is proportional to the momentum one gets the Lozentz friction. The latter is what we meet in the problem of a charged particle in a radiation field, that is the problem of radiation damping. In § 4 analogous treatments for quantum mechanical case are performed.

In § 5 we derive the average equation of motion with friction in one step. In § 6 an extension to forced oscillation with application to the problem of stopping power is given. § 7 is devoted to clarify the origin of the discrepancy between the result of Chandrasekhar and that of Zwanzig[4)]. It is shown that the exact interpretation of the latter has to be expressed in terms of the so-called systematic part of the density matrix or the distribution function. The important role of the remaining terms, oscillating terms, is stressed in this connection.

In this paper we do not make explicit use of the so-called diagonal singularity condition stated by van Hove[5)] and used in our general statistical mechanics, because this condition is to do with large systems, the thermostat in our present case. The state of thermal equilibrium of the thermostat is maintained by this condition.

§ 2. Mechanical Equations in Classical Case

To treat the problem rigorously we have to define a system, simple as possible but relevant of real situations. Most of the systems we can treat with rigour can be regarded as composed of harmonic oscillators. Therefore we shall consider a system of harmonic oscillators to clarify the fundamental nature of the Brownian motion. In so doing little of the general feature of the problem will be lost. Our model is then as follows: a harmonic oscillator, the motion of which is under consideration, is interacting with a large system composed of a great number of harmonic oscillators. The latter is afterwards assumed to be in thermal equilibrium and serves as a thermostat. We can also extend our treatment to the case where there is an external force depending on time; but we shall omit it for a while.

We denote by x, p and m the coordinate, the momentum and the mass of the oscillator under Brownian motion, and by x', p' and m' the coordinates, the momenta and the masses of oscillators of the thermostat. The energy of the total system is then

$$\mathscr{H}=H^0(x,p)+H'(x',p')+\lambda V(x,p;x'p') \tag{2.1}$$

with

$$H^0(x,p)=\frac{1}{2m}p^2+\frac{1}{2}m\omega^2x^2\,, \tag{2.1'}$$

$$H'(x',p')=\sum_j\left(\frac{1}{2m'}p_j'^2+\frac{1}{2}m'\omega_j'^2x_j'^2\right) \tag{2.1''}$$

where H^0 represents the energy of the central oscillator with the frequency ω, and H' that

of the thermostat, and λV the interaction between them, λ being the coupling constant assumed to be small.

The Liouville equation for the distribution function $\rho(x, p; x', p')$ of the total system is

$$\frac{\partial \rho}{\partial t} = [\mathscr{H}, \rho] , \tag{2.2}$$

where we have used the notation for the Poisson bracket. We may use the Liouville operators defined as

$$L^0\rho = [H^0 + H', \rho] , \tag{2.2'}$$

$$L^1\rho = [V, \rho] . \tag{2.2''}$$

We make use of a suitable transformation and rewrite (2.2) in the form:

$$\frac{\partial \rho_t}{\partial t} = \lambda [V_t, \rho_t] . \tag{2.3}$$

As we will make use of the explicit forms of the transformed quantities in the next section, we shall write down some of them. The transformation which brings (2.2) into (2.3) is

$$\rho \to \rho_t = e^{-tL^0}\rho , \qquad L \to L_t = L(x_t, p_t) , \qquad \text{etc.}$$

Any quantity F which does not depend on time explicitly is transformed at the same time into F_t, where

$$\partial F_t / \partial t = -L_t{}^0 F_t . \tag{2.4}$$

Especially

$$\begin{aligned} dx_t/dt = -L_t{}^0 x_t &= -\left(\frac{\partial H^0(x_t, p_t)}{\partial x_t} \frac{\partial}{\partial p_t} - \frac{\partial H^0(x_t, p_t)}{\partial p_t} \frac{\partial}{\partial x_t} \right) x_t \\ &= p_t/m . \end{aligned} \tag{2.5}$$

Further

$$dp_t/dt = -L_t{}^0 p_t = -m\omega^2 x_t . \tag{2.6}$$

Thus x_t satisfies the differential equation

$$d^2x_t/dt^2 + \omega^2 x_t = 0 . \tag{2.7}$$

Solving the last equation with the initial condition that

$$t=0 : \qquad x_t = x , \qquad p_t = p ,$$

we get

$$x_t = x \cos \omega t + (p/m\omega) \sin \omega t . \tag{2.8}$$

Similarly

$$p_t = p \cos \omega t - m\omega x \sin \omega t . \tag{2.8'}$$

It must be noted that the oscillating nature of these quantities comes from the fact that the eigen-values of the operator L^0 are purely imaginary. The operator $\exp -tL^0$ gives thus oscillating behavior to the quantities transformed. At the same time one notes that the transformation is merely a rotation of the coordinate axes; the angle of rotation being a function of time.

It is convenient to introduce an arbitrary function $F(x, p)$ which is a function of the coordinate and the momentum of the oscillator and does not depend on time explicitly. Its average is

$$\langle F\rangle=\iint F\rho\, d\tau\, d\tau' \tag{2.9}$$

where

$$d\tau=dx\,dp\,, \qquad d\tau'=dx'dp'=\prod_j dx_j'dp_j'\,.$$

We may write it referring to the coordinate system (x_t, p_t) in such a way that

$$\langle F\rangle=\iint F_t\rho_t\, d\tau_t\, d\tau^{t\prime}\,, \qquad d\tau_t=dx_t\,dp_t\,, \quad \text{etc.}$$

We multiply F to the both sides of (2.2) to get

$$\iint F\frac{\partial\rho}{\partial t}d\tau\, d\tau'-\iint FL^0\rho\, d\tau\, d\tau'=\lambda\iint FL^1\rho\, d\tau\, d\tau'\,. \tag{2.10}$$

The right hand side of this equation can be written as

$$\mathscr{F}\equiv\lambda\iint FL^1\rho\, d\tau\, d\tau'=\lambda\iint F_tL_t^1\rho_t\, d\tau_t\, d\tau_t'\,. \tag{2.10'}$$

§ 3. Statistical Behavior of the System

We shall solve the equation

$$d\rho_t/dt=\lambda[V_t, \rho_t] \tag{3.1}$$

assuming that λ is sufficiently small. We have to know the long-time evolution of the system, and this requires some special technique. We first observe that if $\lambda=0$, then ρ_t remains constant all the time. Whereas when λ does not vanish, but is small, ρ_t will approach slowly to equilibrium value, although there is fluctuation always. So we may split ρ_t in two parts: the one is the systematic part $\bar{\rho}$, which is to approach to equilibrium value, being governed by some sort of master equation. The other is the fluctuating part, which is zero if $\lambda=0$, and can be expanded in powers of λ. It is then convenient to look the fluctuating part as a function of $\bar{\rho}$ and t. That is, we assume the form

$$\rho_t=\bar{\rho}+\lambda P(\bar{\rho}, t)+\lambda^2Q(\bar{\rho}, t)+\cdots\,. \tag{3.2}$$

If $\lambda=0$, it is again evident that $d\bar{\rho}/dt$ vanishes, indicating the expansion

$$d\bar{\rho}/dt=\lambda\varphi(\bar{\rho})+\lambda^2\psi(\bar{\rho})+\cdots\,, \tag{3.3}$$

in which we have used the fact that we can define the systematic part in such a way that the rate of change in $\bar{\rho}$ is determined by the value of $\bar{\rho}$ at that time. This implies that $d\bar{\rho}/dt$ and $\varphi, \psi, \cdots$ are independent of time and are functions of $\bar{\rho}$ itself. We can decide φ, $P, \psi, Q, \cdots$ in the following manner. We insert (3.2) and (3.3) into (3.1), and get, as the first power of λ,

$$\varphi+\partial P/\partial t=[V_t, \bar{\rho}]\,. \tag{3.4}$$

For the derivative $\partial P/\partial t$ in (3.4) $\bar{\rho}$ is regarded as if it were a constant. The term $(\partial P/\partial\bar{\rho})d\bar{\rho}/dt$ is of higher order.

To determine φ and P from this single equation we assert, as mentioned above, that φ is a function of $\bar{\rho}$ and does not depend on time explicitly. This kind of requirement on $\bar{\rho}$ is sufficient to determine the systematic part and the master equation for this. Consequently

it may be said that $F, Q, \cdots$ represent oscillating behavior of the system around the smooth path $\bar{\rho}(t)$. The role of the oscillating part will be elucidated in the following calculation.

We have noticed that in general V_t oscillates with time. If the time average of V_t does not vanish and depends on the energy of the oscillator, it gives small shift of the frequency or the energy of the oscillator. In principle we can get rid of this term by a small shift of the origin of the energy and a small shift of the potential of the oscillator.* We may safely assume that $\varphi=0$.**

We make use of a converging factor, and obtain

$$P(\bar{\rho}, t)=\lim_{\varepsilon\to 0}\left[\int_{-\infty}^{t} e^{\varepsilon t_1} V_{t_1} dt_1, \bar{\rho}\right]. \tag{3.5}$$

Inserting the expansion (3.2) into the right side of (2.10), we get

$$\mathscr{F}=\lambda\iint F_t L_t^1 \bar{\rho}\, d\tau_t d\tau_t' + \lambda^2 \iint F_t L_t^1 P(\bar{\rho}, t)\, d\tau_t d\tau_t' . \tag{3.6}$$

We assume that the thermostat is in equilibrium. This implies that the coordinates and the momenta of the oscillators in the thermostat are distributed randomly obeying the Maxwell-Boltzmann distribution law. The integral

$$\int L_t^1 \bar{\rho}\, d\tau_t' = \int [V_t, \bar{\rho}]\, d\tau_t'$$

represents the shift of the potential of the central oscillator as mentioned above. We can omit, therefore, the first term in (3.6). We have

$$\begin{aligned}\mathscr{F} &= \lambda^2 \iint F_t L_t^1 P d\tau_t d\tau' \\ &= \lambda^2 \iint F(x_t, p_t)\left\{\left(\frac{\partial V_t}{\partial x_t}\frac{\partial P}{\partial p_t} - \frac{\partial V_t}{\partial p_t}\frac{\partial P}{\partial x_t}\right) + \sum_j \left(\frac{\partial V_t}{\partial x_{tj}'}\frac{\partial P}{\partial p_{tj}'} - \frac{\partial V_t}{\partial p_{tj}'}\frac{\partial P}{\partial x_{tj}'}\right)\right\} d\tau_t d\tau_t' .\end{aligned}$$

The second term including the Poisson bracket with respect to the thermostat vanishes after partial integration. Thus

$$\begin{aligned}\mathscr{F} &= +\lambda^2 \iint F(x_t, p_t)\left(\frac{\partial V_t}{\partial x_t}\frac{\partial P}{\partial p_t} - \frac{\partial V_t}{\partial p_t}\frac{\partial P}{\partial x_t}\right) d\tau_t d\tau_t' \\ &= -\lambda^2 \iint \left(\frac{\partial F_t}{\partial p_t}\frac{\partial V_t}{\partial x_t} P - \frac{\partial F_t}{\partial x_t}\frac{\partial V_t}{\partial p_t} P\right) d\tau_t d\tau_t' .\end{aligned} \tag{3.7}$$

To carry out further calculation we shall first assume the case:

$$V = x \sum_j x_j' , \tag{3.8}$$

where we have omitted the interaction within the thermostat, which does not seem to be quadratic. Because if it were quadratic the total system would afford many constants of motion, which are in contradiction with the requirement on the irreversibility. In our case this is out of question: the thermostat is playing the role of the source of the random force on the oscillator in question, and that is all. In the special case expressed by (3.8) we get (using invariant property of the Poisson bracket) from (3.7) and (3.5)

* The energy shift corresponds to the first order perturbation due to the interaction λV, which is $\lambda V_0(J)$ in terms of the expansion coefficient in (7.12) below. See also the detailed analysis by I. Prigogine & F. Henin[10], and, for the quantum mechanical case, I. Prigogine & M. Toda[6].

** ψ does not vanish (diagonal singularity condition), yielding (7.9) or (7.22) below.[6),8),10)]

$$\mathscr{F}=-\lambda^2\lim_{s\to 0}\int_{-\infty}^{t} e^{s(t_1-t)}\,dt_1\iint\frac{\partial F_t}{\partial p_t}\left\{\left(\frac{\partial V_{t_1}}{\partial x_t}\frac{\partial\bar\rho}{\partial p_t}-\frac{\partial\bar\rho}{\partial x_t}\frac{\partial V_{t_1}}{\partial p_t}\right)\right.$$
$$\left.+\sum_j\left(\frac{\partial V_{t_1}}{\partial x_{tj}'}\frac{\partial\bar\rho}{\partial p_{tj}'}-\frac{\partial\bar\rho}{\partial x_{tj}'}\frac{\partial V_{t_1}}{\partial p_{tj}'}\right)\right\}\sum x_{tk}'\,d\tau_t\,d\tau_t'\,. \tag{3.9}$$

We note that (see Eq. (2.5))

$$\left.\begin{aligned} x_{t_1}&=x_t\cos\omega(t_1-t)+(p_t/m\omega)\sin\omega(t_1-t)\,,\\ x_{t_1j}'&=x_{tj}'\cos\omega_j'(t_1-t)+(p_{tj}'/m'\omega_j')\sin\omega_j'(t_1-t)\,.\end{aligned}\right\} \tag{3.10}$$

Integrating partially we get thus

$$\mathscr{F}=\lambda^2\lim_{s\to 0}\int_{-\infty}^{0}e^{s\theta}\,d\theta\left\{\iint\bar\rho\,\frac{\partial F_t}{\partial p_t^2}\cos\omega\theta\sum_j(x_{tj}'\cos\omega_j'\,\theta+(p_{tj}'/m'\omega_j')\sin\omega_j'\theta)\sum_j x_k'\right.$$
$$-\iint\bar\rho\,\frac{\partial^2F_t}{\partial x_t\partial p_t}\,\frac{\sin\omega\theta}{m\omega}\sum(x_{tj}'\cos\omega_j'\theta+(p_{tj}'/m\omega_j')\sin\omega_j'\theta)\sum x_k'$$
$$\left.-\iint\bar\rho\,\frac{\partial F_t}{\partial p_t}(x_t\cos\omega\theta+(p_t/m\omega)\sin\omega\theta)\sum\frac{1}{m'\omega_j'}\sin\omega_j'\theta\right\}.$$

Integrals with respect to $\theta=t_1-t$ yield terms like

$$\left.\begin{aligned}\lim_{s\to 0}\int_{-\infty}^{0}e^{s\theta}d\theta\cos\omega\theta\cos\omega'\theta&=\frac{\pi}{2}\{\delta(\omega+\omega')+\delta(\omega-\omega')\}\,,\\ \lim_{s\to 0}\int_{-\infty}^{0}e^{s\theta}\,d\theta\sin\omega\theta\cos\omega'\theta&=\frac{\pi}{2}\{-\delta(\omega+\omega')+\delta(\omega-\omega')\}\,.\end{aligned}\right\} \tag{3.11}$$

The integral of $\sin\omega\theta\cos\omega'\theta$ will never give rise to large contribution compared to the above integrals. Consequently ($(x_j'x_k')_t=x_{tj}'x_{tk}'$ etc.)

$$\mathscr{F}=\lambda^2\sum_j\frac{\pi}{2}\delta(\omega-\omega_j')\iint\left(\frac{\partial^2F_t}{\partial p_t^2}\sum(x_j'x_k')_t+\frac{\partial^2F_t}{\partial p_t\partial x_t}\sum\frac{(p_j'x_k')_t}{mm'\omega^2}-\frac{\partial F_t/\partial p_t}{mm'\omega^2}\,p_t\right)\bar\rho\,d\tau_t\,d\tau_t'\,. \tag{3.12}$$

The assumption that the thermostat is in equilibrium implies that $\bar\rho$ factorizes:

$$\bar\rho=\bar f(x,p)\bar\rho_{th}(x',p')\,, \tag{3.13}$$

and

$$\int(x_j'x_k')_t\bar\rho_{th}\,d\tau_t'=(kT/m'\omega_j'^2)\delta_{j,k}\,, \tag{3.14}$$

$$\int(x_j'p_k')_t\bar\rho_{th}\,d\tau_t'=0\,. \tag{3.14'}$$

We assume that there are

$$D\omega'^2d\omega'/(2\pi)^3 \tag{3.15}$$

oscillators in the thermostat which have the frequency between ω' and $\omega'+d\omega'$, where D is a constant. Finally we come back to the original representation (x,p), and define

$$f(x,p)=\int\rho(x,p;\,x',p')\,d\tau'\,, \tag{3.16}$$

where we have to notice the fact that while $\bar\rho$ factorizes, ρ does not. This is a situation which have never been stated clearly. The difference between ρ and $\bar\rho$ is λP. Neglecting higher powers of λ we get the final equation for $\mathscr{F}$.

$$\mathscr{I}=\lambda^2\frac{\pi}{2}\frac{D}{(2\pi)^3}\frac{1}{mm'}\iint\left(mkT\frac{\partial^2 F}{\partial p^2}-\frac{\partial F}{\partial p}p\right)f\,dx\,dp$$
$$=\zeta\iint F\frac{\partial}{\partial p}\left(mkT\frac{\partial f}{\partial p}+pf\right)dx\,dp\ , \tag{3.17}$$

where

$$\zeta=\lambda^2\frac{\pi}{2}\frac{D}{(2\pi)^3}\frac{1}{mm'}\ . \tag{3.18}$$

Thus (2.10) takes the form

$$\iint F(\partial f/\partial t)\,dx\,dp+\iint F\left(\frac{p}{m}\frac{\partial f}{\partial x}-m\omega^2 x\frac{\partial f}{\partial p}\right)dx\,dp$$
$$=\zeta\iint F\frac{\partial}{\partial p}\left(mkT\frac{\partial f}{\partial p}+pf\right)dx\,dp+\mathrm{O}(\lambda^3)\ . \tag{3.19}$$

As the function F is quite arbitrary we get the following differential equation for the distribution function f for the oscillator.

$$\frac{\partial f}{\partial t}+\frac{p}{m}\frac{\partial f}{\partial x}-m\omega^2 x\frac{\partial f}{\partial p}=\zeta\frac{\partial}{\partial p}\left(mkT\frac{\partial f}{\partial p}+pf\right). \tag{3.20}$$

This is nothing but the Kramers-Chandrasekhar equation. It is easy to see that the same equation can be obtained for the case in which the interaction between the oscillator and the thermostat is $V=x\sum b_j'/m'\omega_j'$. Thus the Kramers equation is verified from the first principle.

We shall close this section with a comment that if the interaction is of the form either $V=p\sum x_j'$ or $V=p\sum p_j'/m'\omega_j'$ we get, instead of (3.20), the equation

$$\frac{\partial f}{\partial t}+\frac{p}{m}\frac{\partial f}{\partial x}-m\omega^2 x\frac{\partial f}{\partial p}=\zeta'\frac{\partial}{\partial x}\left(\frac{kT}{m}\frac{\partial f}{\partial x}+\omega^2 xf\right), \tag{3.21}$$

with

$$\zeta'=\lambda^2\frac{\pi}{2}\frac{D}{(2\pi)^3}\frac{m^2}{m'}\ . \tag{3.22}$$

This equation can be obtained immediately from (3.20) by rotating the (x, p) coordinate system $-\pi/2$, that is, by changing the variables from $x\sqrt{m\omega/2}$ and $p/\sqrt{2m\omega}$ to $-p/\sqrt{2m\omega}$ and $x\sqrt{m\omega/2}$.

For a charged oscillator interacting with a radiation field

$$\lambda^2=\frac{4\pi}{3}\left(\frac{e}{m}\right)^2,\qquad D=8\pi/c^3\ ,\qquad m'=1\ . \tag{3.23}$$

So that $\zeta'=2e^2/3c^3$.

§ 4. Quantum Mechanical Case

Calculation in the quantum mechanical case goes nearly in parallel to those of § 2 and § 3. One gets formulas in which the Poisson brackets are replaced by the corpesponding commutators. We shall show briefly what happens here.

The Liouville equation for the density matrix ρ is

$$d\rho/dt=[\mathscr{H},\rho]\ , \tag{4.1}$$

with

$$[\mathscr{H},\rho]=(i/\hbar)(\mathscr{H}\rho-\rho\mathscr{H})\ .$$

By the transformation matrix U, which satisfies the equation

$$-i\hbar\,\partial U/\partial t=(H^0+H')U\,, \tag{4.2}$$

quantities are transformed in such a way that

$$\rho\to\rho_t=U\rho U^{-1}\,,\qquad V\to V_t=UVU^{-1}\,. \tag{4.3}$$

And the Liouville equation takes the form

$$d\rho_t/dt=\lambda[V_t,\rho_t]\,. \tag{4.4}$$

One sees readily that the operators x_t and p_t satisfy the same forms of operator equations as (2.8) to (2.8′).

The average of an arbitrary quantity F is now

$$\langle F\rangle=\mathrm{T}_r(F\rho)\,. \tag{4.5}$$

The time-rate of change of $\langle F\rangle$ is given by the equation

$$\frac{d}{dt}\mathrm{T}_r(F\rho)-\mathrm{T}_r(F[H^0+H',\rho])=\lambda\,\mathrm{T}_r(F[V,\rho])\equiv\mathscr{F}. \tag{4.6}$$

We write as before $\rho_t=\bar{\rho}+\lambda P(\bar{\rho},t)+\cdots$, and get the same expression for $P(\bar{\rho},t)$ as (3.5). Inserting $\rho_t=\bar{\rho}+\lambda P(\bar{\rho},t)$ into the right hand side of (4.6) and dropping the term proportional to λ as we have done in § 3, we get

$$\mathscr{F}=\frac{\lambda^2}{i\hbar}\mathrm{T}_r\{(F_tV_t-V_tF_t)P\}\,. \tag{4.7}$$

We treat the case, as before, in which the interaction between the oscillator and the thermostat is $V=xX(x',p')$ omitting the interaction within the thermostat. In virtue of the relation

$$Fx-xF=(\hbar/i)\partial F/\partial p\,, \tag{4.8}$$

we get

$$\begin{aligned}\mathscr{F}&=-\lambda^2\,\mathrm{T}_r\left(\frac{\partial F_t}{\partial p_t}X_tP\right)\\&=-\lambda^2\,\mathrm{T}_r\left(\frac{\partial F_t}{\partial p_t}X_t\int^t[V_{t_1},\bar{\rho}]\,dt_1\right)\\&=\frac{\lambda^2}{i\hbar}\int^t dt_1\,\mathrm{T}_r\left\{\left(\frac{\partial F_t}{\partial p_t}x_{t_1}X_tX_{t_1}-x_{t_1}\frac{\partial F_t}{\partial p_t}X_{t_1}X_t\right)\bar{\rho}\right\}.\end{aligned} \tag{4.9}$$

In the representation in which the unperturbed energy ($\lambda=0$) is diagonal, we denote by n and N the eigen-states of the oscillator and the thermostat, and write (N stands for $N(\omega_j')$)

$$\left(\frac{\partial F_t}{\partial p_t}x_{t_1}\right)_{n,l}=\left(\frac{\partial F_t}{\partial p_t}\right)_{n,l+1}x_{l+1,l}\,e^{i\omega(t_1-t)}+\left(\frac{\partial F_t}{\partial p_t}\right)_{n,l-1}x_{l-1,l}\,e^{-i\omega(t_1-t)}\,, \tag{4.10}$$

$$(X_tX_{t_1})_{N,N}=|X_{N,N+1}|^2e^{i\omega(t_1-t)}+|X_{N,N-1}|^2e^{-i\omega(t_1-t)}\,. \tag{4.11}$$

We have also the corresponding equations for $x_{t_1}\partial F_t/\partial p_t$ and $X_{t_1}X_t$. We have assume that the only elements which do not vanish are $X_{N,N\pm1}$ or $X_{N\pm1,N}$. We have taken the diagonal elements with respect to the thermostat, because we are dealing with the case in which the thermostat is in equilibrium, and the systematic part of the density matrix factorizes as (3.4), in which $\bar{\rho}_{th}$, the density matrix for the thermostat, is diagonal.

We perform the integration with respect to t_1, obtaining

$$\mathscr{F}=\frac{i}{\hbar}\sum\left\{\frac{(\partial F_t/\partial p_t)_{n,l+1}x_{t;l+1,l}|X_{N,N+1}|^2-x_{t;n,n-1}(\partial F_t/\partial p_t)_{n-1,l}|X_{N,N-1}|^2}{s+i(\omega+\omega')}\right.$$
$$+\frac{(\partial F_t/\partial p_t)_{n,l-1}x_{t;l-1,l}|X_{N,N+1}|^2-x_{t;n,n+1}(\partial F_t/\partial p_t)_{n+1,l}|X_{N,N-1}|^2}{s-i(\omega-\omega')}$$
$$+\frac{(\partial F_t/\partial p_t)_{n,l+1}x_{t;l+1,l}|X_{N,N-1}|^2-x_{t;n,n-1}(\partial F_t/\partial p_t)_{n-1,l}|X_{N,N+1}|^2}{s+i(\omega-\omega')}$$
$$\left.+\frac{(\partial F_t/\partial p_t)_{n,l-1}x_{t;l-1,l}|X_{N,N-1}|^2-x_{t;n,n+1}(\partial F_t/\partial p_t)_{n+1,l}|X_{N,N+1}|^2}{s-i(\omega+\omega')}\right\}\bar{\rho}_{l,n;N,N}\,.$$

We make use of the relation

$$\frac{1}{s+ix}=\pi\delta(x)-i(1/x)_{\mathrm{P}}\,. \tag{4.12}$$

The second term gives rise to the energy shift which corresponds to the second order perturbation. We may ignore it as before. We assume

$$|X_{N,N-1}|^2=CN\,,\qquad |X_{N,N+1}|^2=C(N+1)\,, \tag{4.13}$$

which is correct for the case treated before, that is, when $X=\sum x_j'$ or $X=\sum p_j'$. In such a case we have

$$\mathscr{F}=\frac{iC}{\hbar}\sum\pi\delta(\omega-\omega')\left\{\left(\frac{\partial F_t}{\partial p_t}\right)_{n,l-1}x_{t;l-1,l}(N+1)-x_{t;n,n+1}\left(\frac{\partial F_t}{\partial p_t}\right)_{n+1,l}N\right.$$
$$\left.+\left(\frac{\partial F_t}{\partial p_t}\right)_{n,l+1}x_{t;l+1,l}N-x_{t;n,n-1}\left(\frac{\partial F_t}{\partial p_t}\right)_{n-1,l}(N+1)\right\}\bar{\rho}_{l,n;N,N}$$
$$=\frac{iC}{\hbar}\sum\pi\delta(\omega-\omega')\left\{\left(\frac{\partial F_t}{\partial p_t}x_t-x_t\frac{\partial F_t}{\partial p_t}\right)_{n,l}\left(\overline{N}+\frac{1}{2}\right)+\frac{1}{2}\left(\left(\frac{\partial F_t}{\partial p_t}\right)_{n,l-1}x_{t;l-1,l}\right.\right.$$
$$\left.\left.+x_{t;n,n+1}\left(\frac{\partial F_t}{\partial p_t}\right)_{n+1,l}-\left(\frac{\partial F_t}{\partial p_t}\right)_{n,l+1}x_{t;l+1,l}-x_{t;n,n+1}\left(\frac{\partial F_t}{\partial p_t}\right)_{n-1,l}\right\}\bar{\rho}_{l,n;N,N}\,. \tag{4.14}$$

We take the trace as to the thermostat and write

$$\overline{f}_{l,n}=\sum_N\bar{\rho}_{l,n;N,N}\,,\qquad \overline{N}=\sum_N N\bar{\rho}_{l,n;N,N}/\overline{f}_{l,n}\,, \tag{4.15}$$

Making use of the relation

$$ix_{n,n-1}=p_{n,n-1}/m\omega\,,\qquad ix_{n,n+1}=-p_{n,n+1}/m\omega\,, \tag{4.16}$$

we get

$$\mathscr{F}=\frac{C}{m\omega\hbar}\sum\pi\delta(\omega-\omega')\left\{\left(\frac{\partial^2F_t}{\partial p_t^2}\right)_{n,l}\left(\overline{N}+\frac{1}{2}\right)\hbar\omega m-\frac{1}{2}\left(\frac{\partial F_t}{\partial p_t}p_t+p_t\frac{\partial F_t}{\partial p_t}\right)_{n,l}\right\}\overline{f}_{l,n}\,. \tag{4.17}$$

For the case $X=\sum x_j'$ or $X=\sum p_j'/m'\omega_j'$ we have $C=\hbar/2m'\omega'$, and the coefficient in (4.14) gives ζ defined as (3.18), provided there are $D\omega'^2d\omega'/(2\pi)^3$ oscillators within the frequency range from ω' to $\omega'+d\omega'$. In such a case we obtain (now $\overline{N}$ is the value for $\omega'=\omega$)

$$\frac{d}{dt}\mathrm{T}_r(Ff)-\mathrm{T}_r(F[H^0,f])=\zeta\,\mathrm{T}_r\left\{\left(\frac{\partial^2F}{\partial p^2}\left(\overline{N}+\frac{1}{2}\right)\hbar\omega m-\frac{1}{2}\left(\frac{\partial F}{\partial p}p+p\frac{\partial F}{\partial p}\right)\right)f\right\}\,. \tag{4.18}$$

The right hand side of the last equation can be modified using the identity

$$\mathrm{T}_r\left(\frac{\partial A}{\partial p}f\right)=\frac{i}{\hbar}\mathrm{T}_r\{(Ax-xA)f\}=-\mathrm{T}_r\left(A\frac{\partial f}{\partial p}\right)\,. \tag{4.19}$$

Thus we get

$$\mathrm{T}_r\left(F\frac{\partial f}{\partial t}\right)-\mathrm{T}_r(F[H^0, f])=\zeta\,\mathrm{T}_r\left\{F\frac{\partial}{\partial p}\left(\left(\overline{N}+\frac{1}{2}\right)\hbar\omega m+\frac{1}{2}(pf+fp)\right)\right\} \tag{4.20}$$

which is quite analogous to (3.19). Further as the function F is arbitrary we almost recover (3.20) formally:

$$\frac{\partial f}{\partial t}-[H^0, f]=\zeta\frac{\partial}{\partial p}\left\{\left(\overline{N}+\frac{1}{2}\right)\hbar\omega m+\frac{1}{2}(pf+fp)\right\}. \tag{4.21}$$

This equation goes over to (2.20) in classical limit because for $\hbar\to 0$,

$$\overline{N}+\frac{1}{2}\to kT/\hbar\omega\,, \qquad [H^0, f]\to L^0 f\,.$$

§ 5. Friction Constant

Observation of (2.20) shows that the friction force acting on the particle is the Langevin force $-\zeta\, dx/dt$. Actually if one multiplies x and p to the both sides of (3.20) and integrates, one gets the average equations,

$$d\langle x\rangle/dt=\langle p\rangle/m\,, \tag{5.1}$$

$$d\langle p\rangle/dt=-m\omega^2\langle x\rangle-\zeta\, d\langle x\rangle/dt\,. \tag{5.1'}$$

Consequently one gets

$$d^2\langle x\rangle/dt^2+\zeta\, d\langle x\rangle/dt+\omega^2\langle x\rangle=0\,. \tag{5.2}$$

This is the well-known damping equation, or the "average" of the so-called Langevin equation.

We have pointed out that (5.2) can be derived directly from the Liouville equation[6]. We shall show a simplified way of doing so. First we consider the classical case. We have

$$\langle x\rangle=\iint x\rho(x, p;\, x', p')\, d\tau\, d\tau'\,. \tag{5.3}$$

It is easy to see from (2.2) that

$$\frac{d\langle x\rangle}{dt}=\frac{\langle p\rangle}{m}+\lambda\iint\frac{\partial V}{\partial p}\rho\, d\tau\, d\tau'\,. \tag{5.4}$$

And further differentiation gives

$$\frac{d^2\langle x\rangle}{dt}+\omega^2\langle x\rangle=Y\,, \tag{5.5}$$

where Y stands for the friction term, given by

$$\begin{aligned} Y&=-\frac{\lambda}{m}\iint\frac{\partial V}{\partial x}\rho\, d\tau\, d\tau'+\lambda\frac{d}{dt}\iint\frac{\partial V}{\partial p}\rho\, d\tau\, d\tau' \\ &=-\frac{\lambda}{m}\iint\frac{\partial V_t}{\partial x_t}\rho_t\, d\tau_t\, d\tau_t'+\lambda\frac{d}{dt}\iint\frac{\partial V_t}{\partial p_t}\rho_t\, d\tau_t\, d\tau_t'\,. \end{aligned} \tag{5.6}$$

We insert the expression $\rho_t=\overline{\rho}+\lambda P(\overline{\rho}, t)+O(\lambda^2)$ into the right hand side of the last equation. As mentioned before we can drop the term proportional to the first power of λ, obtaining

$$Y=-\frac{\lambda^2}{m}\iint\frac{\partial V_t}{\partial x_t}P(\overline{\rho}, t)\, d\tau_t\, d\tau_t'+\lambda^2\frac{d}{dt}\iint\frac{dV_t}{\partial p_t}P(\overline{\rho}, t)\, d\tau_t\, d\tau_t'\,. \tag{5.7}$$

For the special case $V=x\sum x_j'$ the above equation yields

$$Y=-\frac{\lambda^2}{m}\iint\sum_j x_{tj}'P(\bar{\rho},t)\,d\tau_t\,d\tau_t'$$
$$=-\frac{\lambda^2}{m}\int_{-\infty}^{t}dt_1\iint d\tau_t\,d\tau_t'\sum_j x_{tj}'\left\{\left(\frac{\partial V_{t_1}}{\partial x_t}\frac{\partial\bar{\rho}}{\partial p_t}-\frac{\partial V_{t_1}}{\partial p_t}\frac{\partial\bar{\rho}}{\partial x_t}\right)+\cdots\right\}. \tag{5.8}$$

We can perform the integration, as before, with respect to t_1, which gives δ-function given by (3.11). We get finally

$$Y=-\zeta\frac{d\langle x\rangle}{dt} \tag{5.9}$$

with ζ given by (3.18).

Quantum mechanically

$$Y=-\frac{\lambda^2}{m}\mathrm{T}_r\left(\frac{\partial V_t}{\partial x_t}P\right)+\lambda^2\frac{d}{dt}\mathrm{T}_r\left(\frac{\partial V_t}{\partial p_t}P\right) \tag{5.10}$$

corresponds to (5.7).

For the case $V=x\sum x_j'$, we get

$$Y=-\frac{\lambda^2}{m}\mathrm{T}_r\left(\frac{i}{\hbar}\int_{-\infty}^{t}dt_1\,x_{t_1}\{\sum x_{t_1j}'\sum x_{tk}'-\sum x_{tj}'\sum x_{t_1k}'\}\bar{\rho}\right)$$
$$=-\frac{\lambda^2}{m}\mathrm{T}_r\left\{\left(\frac{i}{\hbar}\int_{-\infty}^{t}dt_1\{x_t\cos\omega(t_1-t)+(p_t/m\omega)\sin(t_1-t)\}\right.\right. \tag{5.11}$$
$$\left.\left.\times\sum\sum\left(\{x_{tj}'\cos\omega_j'(t_1-t)+(p_{tj}/m'\omega_j')\sin\omega_j'(t_1-t)\}x_{tk}'-x_{tk}'\{\cdots\ \cdots\}\right)\bar{\rho}\right)\right\}.$$

Using the relation $p_j'x_k'-x_k'p_j'=(\hbar/i)\delta_{jk}$ and (3.11), we get the same equation as (5.9) for the quantum mechanical case.

That analogous results are obtainable for other types of interaction is quite obvious. One gets, for instance, the Lozentz type of friction if the interaction is proportional to the momentum of the oscillator.

§ 6. Forced Oscillation and Energy Absorption

When an external force acts on the oscillator, it is clear that the only change in the treatment of the foregoing sections is to add a term to the hamiltonian H^0 of the oscillator. That is, we have

$$H^0(x,p)=\frac{p^2}{2m}+\frac{1}{2}m\omega^2x^2-xK(t)\,. \tag{6.1}$$

This way of introducing the external force has the advantage that we can treat it however large it may be. Using the transformation of the type (2.4) or (4.2), the effect of the external force can be treated without relying on perturbation methods. For example the transformed x is now

$$x_t=x\cos\omega t+\frac{p}{m\omega}\sin\omega t+\frac{1}{m\omega}\int_0^t K(t')\sin\omega(t-t')\,dt'\,. \tag{6.2}$$

The equations (3.20) and (5.2) are changed respectively into

$$\frac{\partial f}{\partial t}+\frac{p}{m}\frac{\partial f}{\partial x}-\{m\omega^2x-K(t)\}\frac{\partial f}{\partial p}=\zeta\frac{\partial}{\partial p}\left(mkT\frac{\partial f}{\partial p}+pf\right), \tag{6.3}$$

$$d^2\langle x\rangle/xt^2+\zeta\,d\langle x\rangle/dt+\omega^2\langle x\rangle=K(t)/m\,. \tag{6.4}$$

We shall calculate the energy absorbed by the oscillator. This is equal to the amount of work done by the oscillator against the external force. Thus the energy transferred from the external system to the oscillator is

$$\Delta H = -\left\langle \int K(t)\, dx \right\rangle = -\int K(t)(d\langle x\rangle/dt)\, dt \tag{6.5}$$

where $\langle x\rangle$ is the solution of (6.4). If $K(-\infty)=K(\infty)=0$ the increment in the total energy of the oscillator is

$$\Delta H = \frac{1}{m\omega_1}\int_{-\infty}^{\infty} dt\, e^{-\zeta t/2}\frac{dK}{dt}\int_{-\infty}^{t} dt'\, e^{\zeta t'/2}K(t')\sin\omega_1(t'-t) \tag{6.6}$$

with $\omega_1=\sqrt{\omega^2-\zeta^2/4}$.

When $K(t)$ is the force due to an incident particle, which interact with the oscillator by coulomb interaction, the above formula (6.6) gives the stopping power against the incident particle modified by the interaction with the surrounding. If the oscillator is isolated, that is if ζ vanishes, (6.6) reduces to the well-known formula:

$$\Delta H = \frac{1}{2m}\left|\int_{-\infty}^{\infty} e^{i\omega t}K(t)\, dt\right|^2 .$$

§ 7. Discussion

We have seen that in a special case the problem we have considered so far is identical to that treated by Chandrasekhar using the thery of stochastic processes. Now, we note the fact that the solution of the Kramers equation (3.20) shows quite peculiar character as was pointed out by Wang and Unlenbeck[7]. This behavior can be illustrated by the following example: Consider the energy of the oscillator given by

$$\langle E\rangle = \iint\left(\frac{p^2}{2m}+\frac{1}{2}m\omega^2x^2\right)f\, dx\, dp\,. \tag{7.1}$$

The rate of change of $\langle E\rangle$ is obtained from (3.20). That is

$$\frac{d}{dt}\langle E\rangle = 2\zeta\left(\frac{kT}{2}-\left\langle\frac{p^2}{2m}\right\rangle\right). \tag{7.2}$$

This means that the rate of change of the total energy of the oscillator is governed by its kinetic energy. This is very peculiar since, for instance, if the oscillator starts with a large displacement but zero momentum, having larger energy than kT, the total energy goes up first and then decreases. It approaches to kT of cource, but every time the oscillator comes to largest displacement, the energy goes up a little. Thus the total energy of the oscillator shows oscillatory damping behavior, which is in sharp contrast to the following argument.

One considers the probability x_n, the diagonal element of the density matrix, that the oscillator is in the n-th quantum state. x_n will satisfy the Pauli equation of the form:

$$dx_n/dt = \frac{\gamma}{(1-e^{-\theta})}\{n e^{-\theta}x_{n-1}-[n+(n+1)e^{-\theta}]x_n+(n+1)x_{n+1}\} \tag{7.3}$$

where γ is a constant proportional to the transition probability and $\theta=\hbar\omega/kT$. (7.3) can be obtained in many ways[3]. But we shall only point out that (7.3) gives

$$d\overline{E}/dt = \gamma(\overline{E}_{eq}-\overline{E})\,, \qquad \overline{E}=\sum x_n(n+\tfrac{1}{2})\hbar\omega\,. \tag{7.4}$$

This is a smooth approach to equilibrium in contrast to (7.2).

Recently Zwanzig[4] derived a phase-space respresentation from (7.3). His result, including small off-diagonal elements, can be written as

$$\frac{\partial \bar{f}}{\partial t}+\frac{p}{m}\frac{\partial \bar{f}}{\partial x}-m\omega^2 x\frac{\partial \bar{f}}{\partial p}=\frac{\gamma}{2}\left\{\frac{\partial p\bar{f}}{\partial p}+mkT\frac{\partial^2 \bar{f}}{\partial p^2}+\frac{\partial x\bar{f}}{\partial x}+\frac{kT}{m\omega^2}\frac{\partial^2 \bar{f}}{\partial x^2}\right\} \tag{7.5}$$

in the classical limit. In (7.5) we write $\bar{f}$ instead of $\bar{f}$ because of the fact that this equation is concerned with the systematic part of the distribution function as will be seen below. It is easy to see that (7.5) shows smooth damping given by (5.4).

The very drastic difference between (3.20) and (7.3) (or (7.1) and (7.4)) can be explained in the following manner. As will be seen immediately below, (7.3), (7.4) and (7.5) are concerned with the systematic part, or the smooth part of the irreversible change. This situation will be made clear if one observes that the solution of (3.20) given by Wang and Unlekbeck[7] is of the form:

$$\langle E\rangle=kT+(\langle E\rangle_{t=0}-kT)e^{-\zeta t}+\zeta e^{-\zeta t}\times\left(\text{a function of } \begin{matrix}\sin\\ \cos\end{matrix}\ \omega t\right)+O(\zeta^2)\,. \tag{7.6}$$

One sees that $d\langle E\rangle/dt$ is oscillating as is given by (7.2), but also that $\Delta\langle E\rangle/\Delta t$ can be approximated by an equation of the form (7.4) with $\gamma=\zeta$ if Δt is taken sufficiently large. We shall examine this point of view more systematically.

In classical mechanics it is more convenient to use, instead of x and p, the conjugate variables α and J, where α is the angle and J the action variable defined by

$$\alpha=-\mathrm{tg}^{-1}\,p/xm\omega\,,\qquad J=\frac{1}{\omega}\left(\frac{p^2}{2m}+\frac{1}{2}m\omega^2x^2\right). \tag{7.7}$$

Using these, for an assembly of harmonic oscillators,

$$L^0=-\sum\omega_k\frac{\partial}{\partial\alpha_k}\,. \tag{7.7'}$$

The transformation from ρ to ρ_t can be expressed, for the systematic part, as the transformation from $\bar{\rho}$ to the Fourier coefficients $\bar{\rho}_k$ defined by

$$\bar{\rho}=\sum\bar{\rho}_n(J,t)\exp i\sum n_k(\alpha_k-\omega_k t)\,. \tag{7.8}$$

The master equation for the systematic part is [6),8)]

$$\partial\bar{\rho}_n/\partial t=\lambda^2\Omega\bar{\rho}_n-\lambda^2M_n{}^2\bar{\rho}_n\,, \tag{7.9}$$

where

$$\Omega=\pi\sum_\mu\left(\sum_k\mu_k\frac{\partial}{\partial J_k}\right)V_{-\mu}V_\mu\delta(\mu\omega)\left(\sum_k\mu_k\frac{\partial}{\partial J_k}\right), \tag{7.10}$$

$$M_n{}^2=\pi\sum_\mu\left(\sum_k n_k\frac{\partial V_{-\mu}}{\partial J_k}\right)\left(\sum_k n_k\frac{\partial V_\mu}{\partial J_k}\right)\delta(\mu\omega) \tag{7.11}$$

in which we have used the expansion:

$$V=\sum V_\mu(J)\exp i\sum n_k\alpha_k\,. \tag{7.12}$$

We shall treat the case where the interaction is of the form

$$\begin{aligned}V=\sum x_ix_j&=\sum\sqrt{\frac{2J_i}{m_i\omega_i}}\cos\alpha_i\sqrt{\frac{2J_j}{m_j\omega_j}}\cos\alpha_j\\&=\frac{1}{2}\sum\sqrt{\frac{J_iJ_j}{m_im_j\omega_i\omega_j}}(e^{\alpha_i+\alpha_j}+e^{\alpha_i-\alpha_j}+e^{-\alpha_i+\alpha_j}+e^{-\alpha_i-\alpha_j})\,.\end{aligned} \tag{7.13}$$

These four terms on the right hand side correspond to $V_{1,1}$, $V_{1,-1}$, $V_{-1,1}$ and $V_{-1,-1}$ respectively. When the thermostat is in equilibrium the distribution function $\bar{\rho}$ factorizes as

$$\bar{\rho}=\bar{f}(\alpha, J)\bar{\rho}_{th}(J') \tag{7.14}$$

where $\bar{\rho}_{th}$ is given by the Boltzmann law, i.e. $\bar{\rho}_{th}\sim\exp(-\sum\omega_j'J_j'/kT)$.

Integration with respect to the coordinates of the thermostat can be carried out, we shall denote the results by the bracket $\langle\ \rangle$. For instance we have

$$\langle\Omega\rho\rangle=2\pi\frac{\partial}{\partial J}\left\{\langle\sum_j|V_{1,-1(j)}|^2\bar{\rho}_{th}\rangle\frac{\partial}{\partial J}+\left\langle\sum_j\left(\frac{\partial}{\partial J_j'}|V_{1,-1(j)}|^2\right)\bar{\rho}_{th}\right\rangle\right\}\bar{f}\,,\quad(\omega_j'=\omega) \tag{7.15}$$

where

$$|V_{1,-1(j)}|^2=\frac{1}{4}\frac{JJ_j'}{mm'\omega\omega'}\,. \tag{7.16}$$

We get for $\omega'=\omega$

$$\langle|V_{1,-1(j)}|^2\bar{\rho}_{th}\rangle=\frac{J}{4mm'}\frac{kT}{\omega^3}\,,$$

$$\left\langle\frac{\partial|V_{1,-1(j)}|^2}{\partial J_j'}\bar{\rho}_{th}\right\rangle=\frac{J}{4mm'\omega^2}\,, \tag{7.17}$$

where $E=\omega J$ is the energy of the oscillator. Since we assume that there are $D\omega'^2d\omega/(2\pi)^3$ oscillators in the thermostat within the frequency interval $\omega'<\omega_j'<\omega'+d\omega'$, using ζ defined by (3.18) we get

$$\lambda^2\langle\Omega\bar{\rho}\rangle=\zeta\frac{\partial}{\partial E}E\left(kT\frac{\partial}{\partial E}+1\right)\bar{f}(\alpha, E)\,. \tag{7.18}$$

Further we can rewrite M_n^2 as

$$M_n^2=\frac{\pi}{8}\sum_j\left(\sum_i n_i\frac{1}{\sqrt{m_im_j\omega_i\omega_j}}\sqrt{\frac{J_j}{J_i}}\right)^2, \tag{7.19}$$

so that

$$\langle\sum e^{i\Sigma n(\alpha-\eta t)}\lambda^2M_n^2\bar{\rho}\rangle=-\zeta\frac{kT}{4E}\frac{\partial^2}{\partial\alpha^2}\bar{f}\,, \tag{7.20}$$

Writing $E=r^2$ we get finally

$$\frac{\partial\bar{f}}{\partial t}+\omega\frac{\partial\bar{f}}{\partial\alpha}=\zeta\left\{\frac{r}{2}\frac{\partial}{\partial r}+1+\frac{kT}{4}\left(\frac{\partial^2}{\partial r^2}+\frac{1}{r}\frac{\partial}{\partial r}+\frac{1}{r^2}\frac{\partial^2}{\partial\alpha^2}\right)\right\}\bar{f}\,, \tag{7.21}$$

which is written in porlar coordinates, the last bracket on the right being the Laplacian operator. If we go back to the coordinates $x\sqrt{m\omega/2}$ and $p/\sqrt{2m\omega}$, (7.21) yields (7.5), $\gamma=\zeta$. This equation is valid even if ρ_n $(n\neq 0)$ is not small. Thus the Zwanzig's equation has wider validity than he would have thought. But it is concerned with the systematic part only.

The quantum analogue of (7.7) is[6]

$$\frac{d\bar{\rho}_{\alpha\alpha'}}{dt}=\frac{\pi\lambda^2}{\hbar^2}\int d\alpha''\left\{-|V_{\alpha\alpha''}|^2\delta\left(\frac{E_{\alpha''}-E_\alpha}{\hbar}\right)-|V_{\alpha'\alpha''}|^2\delta\left(\frac{E_{\alpha''}-E_{\alpha'}}{\hbar}\right)\right\}\bar{\rho}_{\alpha\alpha'}$$
$$+2\frac{\pi\lambda^2}{\hbar^2}\int d\mu V_{\alpha,\alpha+\mu}\bar{\rho}_{\alpha+\mu,\alpha'+\mu}V_{\alpha'+\mu}\delta\left(\frac{E_\mu}{\hbar}\right). \tag{7.22}$$

The equation for the oscillator in the thermostat is obtained from (7.22):

$$\frac{1}{\zeta}\frac{\partial \overline{f}_{nn'}}{\partial t} = -\frac{1}{2}\{(n+1)\overline{N}+n(\overline{N}+1)+(n'+1)\overline{N}+n'(\overline{N}+1)\}\overline{f}_{nn'}$$
$$+\sqrt{nn'}\,\overline{N}\overline{f}_{n-1,n'-1}+\sqrt{(n+1)(n'+1)}\,(\overline{N}+1)\overline{f}_{n+1,n'+1}\,. \tag{7.23}$$

The corresponding density matrix in coordinate representation is

$$\overline{\rho}(q, q', t)=\sum \psi_n(q)\overline{f}_{nn'}\psi_{n'}^*(q')\,, \tag{7.24}$$

where ψ_n is the n-th eigen-function of the unperturbed oscillator. The equation of motion of the Wigner function

$$\overline{f}(x, p, t)=\frac{1}{\pi\hbar}\int_{-\infty}^{\infty} \exp(2ipy/\hbar)\overline{\rho}(x-y, x+y, t)\,dy \tag{7.25}$$

can be derived after some calculations which are quite similar to those of Zwanzig[4]. Finally we get the equation of the form (7.5). The only difference is that kT is replaced by $(2\hbar\omega)\,\mathrm{tgh}\,(kT/2\hbar\omega)$.

§ 8. Concluding Remarks

The fundamental role of the oscillating part of the distribution function or of the density matrix is clarified. And a straight way of treating the problem of the Brownian motion has been given. In our formalism we split the distribution function into two parts: the systematic part and the oscillating part. The former obeys the master equation given by Philippot and Prigogine[8], and the equation derived by Zwanzig is equivalent to this. On including the oscillating part one gets another type of equation. As a special case one gets the Kramers equation. Without referring to the equilibrium state we get the friction constant and the correlation constant (or the diffusion constant in the momentum space). Thus our theory covers automatically the irreversible change and the equilibrium state.

The irreversible change towards equilibrium is attributed to the nature of the thermostat. To maintain the state of equilibrium the thermostat has to fulfill certain conditions such as the diagonal singularity condition of van Hove. The systematic part of the distribution function can be written as a product of the terms; one is for the oscillator and the other is for the thermostat. This does not imply that the distribution function factorizes. Actually the Liouville equation is not satisfied by a factorized distribution function. The factorization is true only for the systematic part.

It seems worth-while to stress that most of current theories in this field might lead to incorrect results if they were used without caution. Because most of them are concerned only with the systematic part. Interference between the oscillating part and physical quantity to be considered may give rise to important contribution.

The system we have considered in this paper is of the same type to that of Callen and Welton[9] in treating the generalized Nyquist theorem. The author wishes to return to this subject in the near future.

The author wishes to express his thank to Prof. I. Prigogine of the Brussels University for illuminating discussions and communications. The resent study was partially financiated by the Scientific Research Fund of the Ministry of Education.

References

1) S. Chandrasekhar: Revs. Mod. Phys. **15** (1943) 2.
2) J. G. Kirkwood: J. Chem. Phys. **14** (1946) 180.
3) E. W. Montroll and K. E. Shuler: J. Chem. Phys. **26** (1957) 454.
4) R. Zwanzig: J. Chem. Phys. **28** (1958) 365.
5) L. van Hove: Physica **21** (1957) 517.
6) I. Prigogine and M. Toda: Molecular Physics **1** (1958) 48.
7) M. C. Wang and G. E. Uhlenbeck: Revs. Mod. Phys. **17** (1945) 323.
8) I. Prigogine and J. Philippot: Physica **23** (1957) 569.
9) H. B. Callen and T. A. Welton: Phys. Rev. **83** (1951) 134.
10) I. prigogine and F. Henin: Physica **23** (1957) 585.

JOURNAL OF THE PHYSICAL SOCIETY OF JAPAN, Vol. 13, No. 11, NOVEMBER, 1958

Excess Noise in Narrow Germanium *p-n* Junctions

By Tatsuo YAJIMA*

Technical Research Laboratory, Broadcasting Corporation of Japan, Tokyo.

and Leo ESAKI

Sony Corporation, Tokyo.

(Received June 3, 1958)

Excess noise has been studied on narrow alloyed *p-n* junctions fabricated on heavily doped *p*-type and *n*-type germanium with less than 200 Å junction width, which exhibit inverted rectification and negative resistance in the forward direction. Considerable $1/f$ noise has been observed in a forward range, the character of which is stable and surface insensitive. Moreover, the noise was found to be mainly associated with the excess forward current that is peculiar to narrow *p-n* junctions. Measurements were made also at low temperatures down to 77°k on both noise and static characteristics. The origins of the excess forward current and the associated excess noise were discussed in connection with the crystal imperfection.

§ 1. Introduction

In the recent experiment by one of the authors,[1),2)] it was found that extremely narrow *p-n* junctions fabricated on heavily doped degenerate germanium exhibit much different current-voltage characteristics from those of the usual *p-n* junctions. The main features encountered are the inversion of rectification direction** and the existence of negative resistance in the forward direction. Both features are fairly well explained by considering Zener current, or internal field emission, across the energy gap at the junction. Moreover, various new effects will be expected associated with the properties of the material having high impurity concentrations. Therefore, the noise properties have been studied here as an inherent character of the device.

It has been well known that $1/f$ noise, or excess noise, appears commonly in almost all semiconductor devices and crystals accompanied with flowing current while it is absent in metals. In semiconductor crystals, however, an experimental tendency that the magnitude of $1/f$ noise becomes lower with the decrease in resistivity might be probably accepted. Actually, it is usually difficult to observe $1/f$ noise in germanium single crystal filaments with the resistivity below about 1 ohm-cm. On the one hand, $1/f$ noise is belived to be predominantly a surface effect, because of its large dependence on surface conditions especially for reverse biased usual diode. Accordingly, most of the existing $1/f$ noise theories[3)] include the surface as a part of the model, though exact picture has not yet been established.

Considering above facts, it was simply expected at first that the narrow *p-n* junction will have very low or no detectable $1/f$ noise, since the device is composed of metal-like semiconductor with extremely low resistivity of the order of 10^{-3} ohm-cm and its static characteristics are quite stable to surface conditions in the whole bias range. Practically we observed considerable $1/f$ noise in a certain bias range, and its properties were found to be somewhat different from those of the usuall *p-n* junctions in several points. This is a subject of interest as a particular example of $1/f$ noise. It is the purpose of the present paper to describe the experimental results about this $1/f$ noise and to discuss the underlying physical processes.

§ 2. Samples and Noise Measurement

The samples are fabricated by alloying technique on heavily doped *p*-type and *n*-type

* Present address: Department of Physics, Faculty of Science, University of Tokyo, Tokyo.

** In this paper, we defined the *forward* direction of any *p-n* junction as the case where *p*-side is positively biased relative to *n*-side, regardless of the relative easiness of the current flow.

Table I.

Sample	Base Crystal				Alloying Dot
	conductivity type	doping agent	impurity content (cm^{-3})	resistivity (ohm-cm)	component
5-12	p	pure Ga	1.6×10^{19}	0.0021	0.5–1% P–In
IID-3	n	intermetallic In–P	1.2×10^{19}	0.0015	0.5% Ga–In

germanium of $10^{18}\sim3\times10^{19}\,cm^{-3}$ impurity concentration. The main features of the typical units used are listed in Table I.

Fig. 1 shows typical current-voltage characteristics of the narrow p-n junction. Large current in the reverse direction and current peak in the low voltage forward region can be attributed predominantly to Zener current corresponding to the electron transition between valence band and conduction band at the junction.[1),2)] The current peak appears for the units having above about $2\times10^{18}\,cm^{-3}$ impurity concentration, and the higher the concentration the higher the height of the peak. In the large forward voltage range, the observed characteristics were found to obey the usual diode current voltage relation

$$I=I_s[\exp(qV/kT)-1]$$

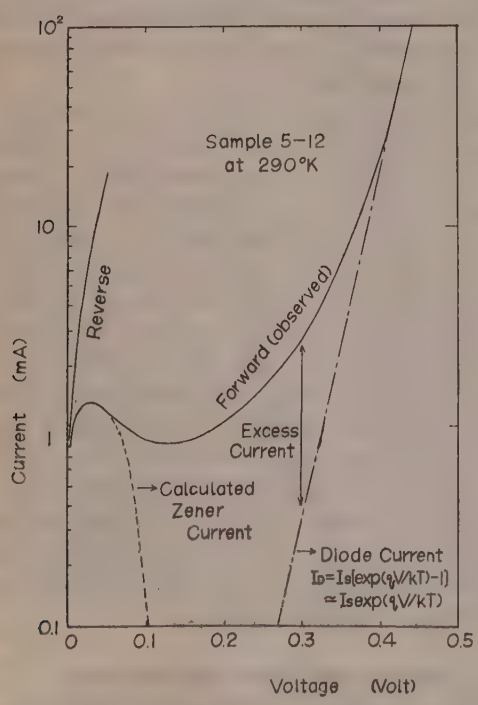

Fig. 1. Current—voltage characteristics of narrow p–n junction.

where q is the electronic charge, k is Boltzmann constant, T is the absolute temperature, and I_s is a constant. The whole static characteristics are quite stable both for ambient variation and light illumination unlike usual p-n junctions.

There still remains, however, an excess current component dominantly observable in the range from 0.2 volt to 0.4 volt at room temperature. Though the nature of this current component has not yet been completely explained, it was found to be related closely with the observed excess noise. This is the principal subject of this paper, and the more details will be described in the later sections.

Noise measurements were performed in the usual manner according to the circuit diagram as shown in Fig. 2. For the sample with

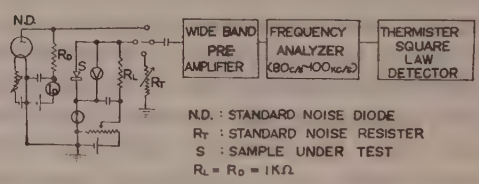

Fig. 2. Circuit diagram of noise measuring sistem.

large nonlinearity as in this case, it is necessary to determine the mean square short-circuit noise current $\overline{i_{ns}^2}$ and/or the mean square open-circuit noise voltage $\overline{v_{no}^2}$ correctly in order to know the intrinsic noise behavior of the units, because load resistance affects the observed noise characteristics considerably. ($\overline{i_{ns}^2}$ and $\overline{v_{no}^2}$ are simply related as $\overline{v_{no}^2}=r^2\overline{i_{ns}^2}$, where r is the dynamic resistance of the sample). In the present case, they are determined through the simple circuit relations, using the measured values of the output noise voltage across a given load resistance and the sample dynamic resistance. Actual measurements were made approximately

under the open-circuit conditions due to the low sample resistance.

§ 3. Experimental Results

In the whole reverse region and in the forward region up to the current peak, we observed no detectable excess noise even for the open-circuit conditions. The situatisn is the same for negative resistance range. In this range, however, we were obliged to use very low load resistance below 10 ohm to set a stable bias, which results in great undesirable decrease of sensitivity of noise measurement. Although these results might be partly due to the low dynamic resistance of the sample, it seems to show that Zener current dominant in these range does not accompany particular excess noise. This seems to be in accordance with the previous results by other workers for less narrow *p-n* junctions.[4]

On the other hand, considerably excess noise was observed beyond the current minimum in the forward direction. The frequency spectrum was found to show typical $1/f$ character and to be much higher above thermal and shot noise with white spectrum as indicated in Fig. 3. Also, this noise is fairly stable without pulsive character, and relatively surface insensitive. Even for the heavy ambient conditions, that is, dipping in water and some organic liquids such as benzene, carbontetrachloride, ethylalcohol, or, for the re-etching of the samples, no appreciable changes of both noise and static characteristics were found. This is in contrast with the behavior usually associated with the $1/f$ noise.

The variation of the noise with the forward

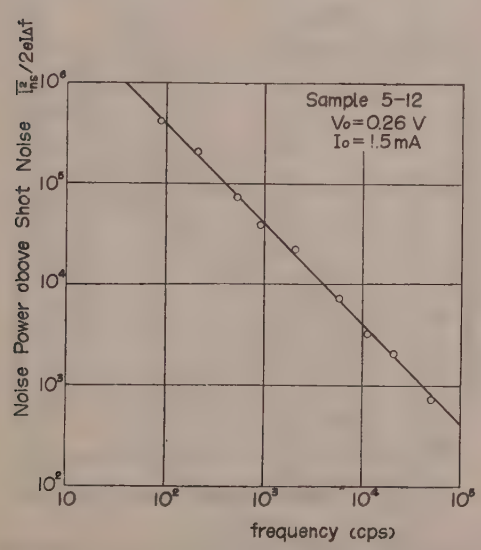

Fig. 3. Noise frequency spectrum of narrow *p–n* junction.

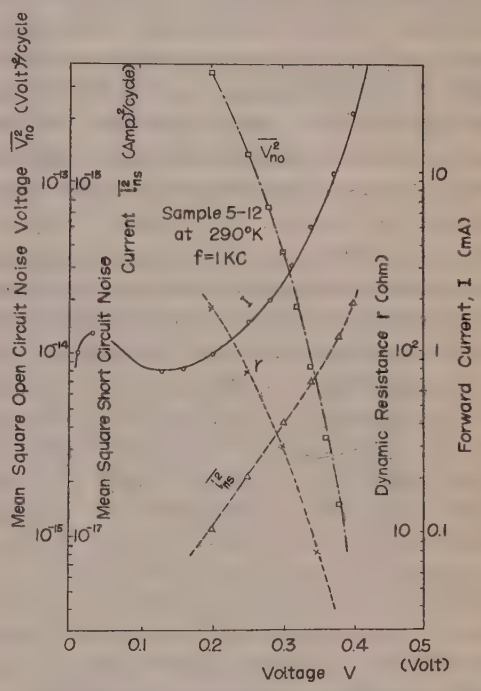

Fig. 4. Noise and current-voltage characteristics of narrow *p–n* junction.

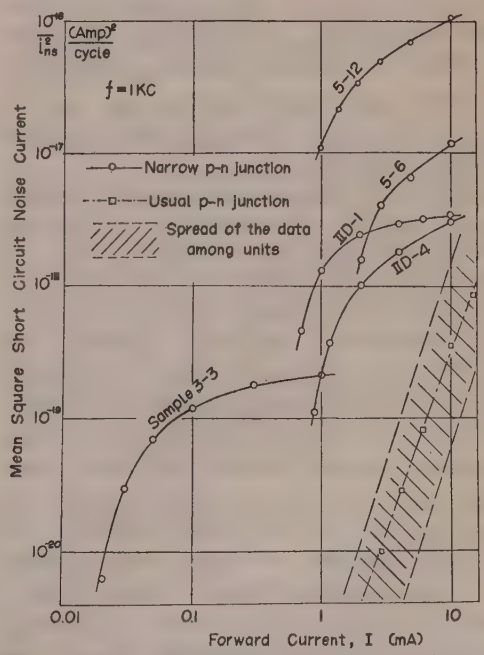

Fig. 5. Mean square noise current as a function of forward current for narrow and usual *p–n* junctions.

voltage is shown in Fig. 4. The outstanding feature is that the mean square open circuit noise voltage $\overline{v_{no}^2}$ decreases rapidly with the bias voltage, while mean square short circuit noise current $\overline{i_{ns}^2}$ increases. From a simple equivalent circuit consideration, this can be interpreted as that the noise source is concentrated at the junction as a form of current generator which is nearly identical with i_{ns}, and that the decrease in $\overline{v_{no}^2}$ with the bias voltage is due to the change of barrier resistance of the junction. It is noted, however, that no such decrease in $\overline{v_{no}^2}$ has been found in the forward range of usual *p-n* junctions. Series or bulk resistance seems to contribute to the excess noise in direct or indirect way in the latter case. In Fig. 5, $\overline{i_{ns}^2}$ of several units are plotted as a function of the forward current, simultaneously compared with that of the usual forward biased alloyed *p-n* junctions. The latter represents an average characteristics of the excess noise of randomly selected 20 units, and the spread of the data among units is indicated by the hatched section. Two points should be noticed about the difference between narrow junctions and usual junctions. First, the noise level of narrow junction is much higher than that of the usual junction in the forward direction. Second, the current dependence of the noise for narrow *p-n* junction deviate greatly from the normal square-law relation, i.e., $\overline{i_{ns}^2} \propto I^2$, for the $1/f$ noise, while it is nearly normal for usual junctions.

Above results can be interpreted phenomenologically in the following way. In the case of usual germanium *p-n* junction diode, the observed forward current is known to consist almost only of the theoretical diode current, though modified by the series resistance, and hence the fact of normal current dependence for the excess noise may naturally be accepted. On the other hand, the forward current of narrow junction consists of three components, i.e., Zener current, diode current, and excess current, as described previously. In the voltage region of interest, the contribution of the theoretical Zener current will be negligible, and hence the last two components are sufficient to be considered. Since these two components can be thought to have different origins, it will be natural to consider different $1/f$ noise sources for each component. Then, the spectral density of the observed noise current may be the sum of two independent mean square noise current generators accompanied by the diode current and the excess current, respectively, and is expressed by

$$\overline{i_{ns}^2} = K_1 \frac{I_d^2}{f} + K_2 \frac{I_{ex}^2}{f}$$

where I_d is the diode current, I_{ex} is the excess current and K_1, K_2 are the proportionality constants of different values. It is easily shown that in this case $\overline{i_{ns}^2}$ cannot be proportional to the square of the total current, $(I_d + I_{ex})^2$, unless I_d is always proportional to I_{ex}. This might explain the departure from the square-law current dependence. Furthermore, suppose that the excess current is much noisier than the diode current, i.e., $K_1 \ll K_2$, as is guessed from the results in Fig. 5. Then, the square-law relation between the noise and the excess current, instead of the total current, will be expected. By the method indicated in Fig. 1, we can always obtain the excess current as a monotonic increasing function of the voltage, except in the small region where normal diode current dominate extremely over the excess current and so the estimation of the latter becomes uncertain. Thus

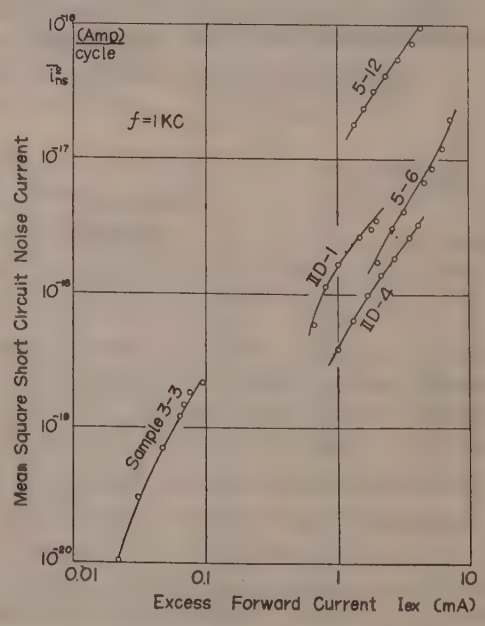

Fig. 6. Mean square noise current as a function of excess forward current for narrow *p–n* junctions.

we can plot the noise as a function of the excess current as shown in Fig. 6. The results yield the relation fairly close to square-law for most of the measured samples as expected. This seems to be a strong indication that the excess noise in narrow *p-n* junction is mainly accompanied with the excess forward current. This is quite analogous to the situation that the excess noise in usual reverse-biased *p-n* junction arises mainly from the leakage or excess reverse current,[5] although physical origins of these two excess currents might be quite different.

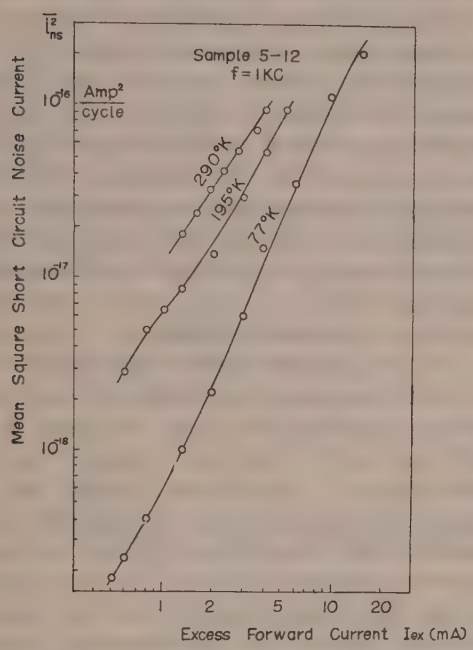

Fig. 8. Mean square noise current as a function of excess forward current for narrow *p–n* junction at low temperature.

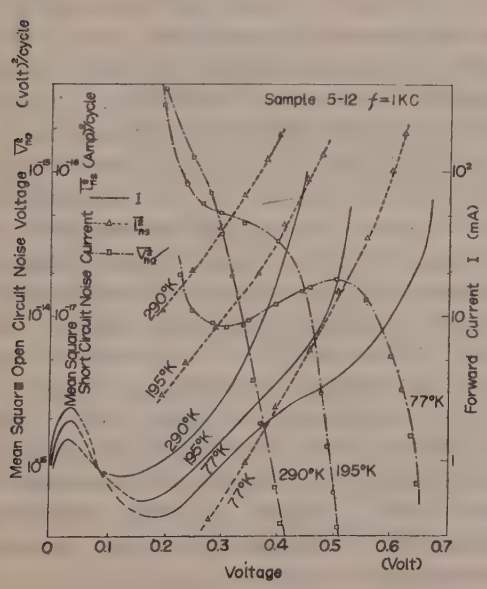

Fig. 7. Noise and current-voltage characteristics for narrow *p–n* junction at low temperature.

To understand the phenomena more clearly, measurements were made at lower temperatures of 195°k and 77°k. The results are shown in Fig. 7 and Fig. 8. Following features were found concerning to the excess current;

(1) The excess current is relatively independent on temperature both in its magnitude and voltage dependence, and hence it becomes dominant at low temperature because of the rapid decrease of the diode current.

(2) The excess current varies nearly exponentially with voltage.

(3) The excess current vs. voltage curve has a gradual hump which appears more clearly for lower temperatures, but still keeping to be a monotonic increasing function.

Similarly, the results of noise measurements are summarized as follows;

(1) At low temperatures $\overline{v_{no}^2}$ varies in a complicated manner with the forward voltage, while $\overline{i_{ns}^2}$ increases monotonically. This again seems to indicate that $\overline{i_{ns}^2}$ represents more direct physical nature of the excess noise.

(2) $\overline{i_{ns}^2}$ shows nearly normal current dependence as a function of the excess current even at low temperatures, which might be a further support for the relation between the excess noise and the excess current.

(3) The magnitude of the noise always decreases with decreasing temperature but not so strongly. This is in contrast with the situation that in the usual *p-n* junction transistors, the excess noise associated with the emitter current shows considerable increase at low temperatures.[6]

§ 4. Discussion of the Results

Summarizing all the results mentioned above, it may be believed that the observed $1/f$ noise is a pure junction effect associated with the remarkable excess forward current, and the understanding of the latter will afford a key to the understanding of the former.

Since we have not yet get a satisfactory explanation, only a brief qualitative discussion will be given below. The nature of the excess forward noise in usual *p-n* junction, which is the problem to be solved at the sametime, will not be concerned here.

First, it might be quite natural to suppose that the excess current is caused by some kinds of crystal imperfections, such as the dislocations or the impurity aggregate, due to the heavy doping. In fact, etch pit observation showed many characteristic pit clusters when the impurity amount becomes as high as $10^{20}\,cm^{-3}$. However, the possibility of any current mechanism, arised from the thermal process governed by the activation energy or the potential barrier, may be excluded because of the relatively weak temperature dependence of the excess current. The current through local ohmic contacts is a possible cause with the desired temperature dependence. But it may be improbable because observed characteristics are non-ohmic, and noisy ohmic contact is unlikely. Another possibility is some non-ohmic leakage current through the imperfection at the junction, which can be large because of the small effective leakage path length due to narrow junction width. Surface leakage will also come to mind from the analogy of usual junction, but this must not be predominant, if present, since any heavy surface conditions do not greatly affect the characteristics as described previously. Now, one might question whether the excess current is peculiar to narrow *p-n* junctions or not. According to our measurements, we could not find such distinct excess current in the usual forward biased *p-n* junctions even at the liquid nitrogen temperature. This result seems to suggest that the excess forward current is governed not only by the degree of imperfection, even if it were so, but also by some another properties directly associated with the narrow junction width.

At this stage, an idea of another type of internal field emission will be proposed as a cause of the excess current. This can be considered to be present *in addition to* the internal field emission, previously introduced to explain the negative resistance, by the following reason. Since the internal field emission of the type described previously is the one produced by the direct interband electronic transition at the junction, it must go to zero above the critical forward voltage where the bottom of the conduction band in the *n*-side coincide with the top of the valence band in the *p*-side.[1),2)] This voltage is derived from the position of the Fermi level, and is estimated theoretically as ranging about 0.1~0.2 volt depending on the impurity concentration and temperature. Then, if any internal field emission mechanism is to be considered above this value, it must occur through the additional energy levels in the forbidden gap. Since there are many experimental evidences for the existence of such levels associated with the impurities and the dislocations, it will not be impossible that this new type of internal field emission causes the excess forward current with the temperature-insensitive character. Although we will not proceed further because of the lack of the necessary knowledge to treat the problem quantitatively, one following fact might be worth noticing. Namely, as is shown in Fig. 7, the excess current has a gradual but clear hump at low temperature centered in the range about 0.3~0.4 volt corresponding to about the half of the energy gap, and sometimes noise current also showed similar hump in the corresponding range. Since some impurity or dislocation levels are known to lie near the midgap in germanium, this would seem to suggest a correlation between these levels and the excess current.

If this is true, the associated excess noise will be understood naturally according to the following modulation mechanism. Appart from the explicit details, it is evident that the current produced by this cause will strongly depend on the situation of the imperfections and the associated field distributions near the junction. Since there would be the statistical fluctuations of the trapping and recombination processes through these levels such as suggested by Morrison[7)] or of the impurity state itself, the resultant fluctuation of the population or the number of levels and of the neighbouring field distributions will strongly modulate the field emission current associated these levels. Further, if these modulation sources have $1/f$ type fluctuation, $1/f$ noise must arise.

Of course, above explanation is only a possibility, and it is hoped to seek more reason-

able point of view in future. There will be also a question whether the $1/f$ noise described here is actually different from the usual surface-sensitive $1/f$ noise in its intrinsic nature. Regarded from the general appearance of $1/f$ noise, it seems to be desirable to consider unified model for all the units exhibiting $1/f$ noise. However, it may be possible or even natual to suppose that the different physical causes of $1/f$ noise dominate for different types of device, as far as the underlying statistical elementary processes satisfy the mathematical requirement for the derivation of $1/f$ type spectrum.

In conclusion the authors wish to express their thanks to Miss Y. Kurose for her assistance in the experiment and the calculations.

References

1) L. Esaki: Phys. Rev., **109** (1958) 603.
2) L. Esaki: Presented at the International Conference on Solid State Physics in Brussels, June 1958.
3) H. C. Montgomery: B. S. T. J. **31** (1952) 950.
L. Bess: Phys. Rev. **103** (1956) 72.
S. R. Morrison: Phys. Rev. **99** (1955) 1904; **102** (1956) 1297.
A. L. Mc Whorter: in "Semiconductor Surface Physics", p. 207 Univ. Pennsylvania Press., 1956.
4) A. G. Chynoweth & K. G. McKay: Phps. Rev. **106** (1957) 418.
5) For instance.
F. J. Hyde: Proc. Phys. Soc. **69B** (1956) 231.
W. H. Fonger: in "Transistors I", RCA Lab. p. 239.
J. W. Englund: ibid. p. 309.
6) K. Amakasu & M. Asano: J. Appl. Phys. **27** (1956) 1249.
K. Komatsubara: J. Appl. Phys. Japan **26** (1957) 72. (in Japanese)
7) S. R. Morrison: Phys. Rev. **104** (1956) 619.

Journal of the Physical Society of Japan Vol. 13, No. 11, November, 1958

A Theory of Impurity Conduction. II

By Tadao Kasuya and Sigenao Koide

Physical Institute, Nagoya University

(Received June 25, 1958)

The impurity band conduction was treated where the resonance energy (or the translational energy) is much smaller than the fluctuation of local potential energy. By the interaction with phonon, electron can hop from one localized state to another, exchanging the difference of the local potential energies for a phonon. The agreement between theoretical and experimental results is fairly satisfactory.

§ 1. Introduction

In the previous paper[1] (hereafter referred to [1]), one of us discussed impurity conduction of semiconductor, and classified it as follows.

(1) High impurity concentration: In this range, impurity levels are merged into conduction band, and we can treat the problem as a single band conduction. Then, impurity atoms play a role of scatterers.

(2) Low impurity concentration: When the concentration of impurity atoms becomes smaller, impurity levels are separated from the conduction band. Our problem is how to treat the transport phenomena in this impurity level. In the range (2), we treat the case that the energy width of impurity band is determined mainly by the resonance energy between atomic wave functions localized in different impurity atoms.

We treated these cases in [1], and here we treat the third case, that is:

(3) Very low impurity concentration: When the concentration of impurity atoms becomes very small, the fluctuation of local potential energy becomes much larger than the resonance energy which corresponds to the translational energy. Thus the localized state be-

longing to a particular impurity atom becomes stable, and transport phenomena hardly occur if we consider only the freedom of electron system. In this situation, the interaction of eelctron with phonon system becomes important because electron is possible to walk about the whole crystal by hopping from one localized state to the other, exchanging the difference of the local potential energy for phonon system.

To perform the calculation practically in Ge and Si, we must consider the complex effects of band structures in both n-and p-type. In n-type Ge and Si, the conduction band has many valley structure and as many degenerate states as a number of valleys exist. In p-type, the valence hand is constructed by three degenerated bands. By the effects of spin-orbital interaction, these degeneracy are released partly and the band structure becomes such that: two bands with different effective masses are degenerated at $\boldsymbol{k}=0$, and the other one band has lower energy than these two bands at $\boldsymbol{k}=0$ in order of spin-orbital interaction energy. Localized states composed by these bands are fairly complicated and considered in § 2. In § 3, we treat the effect of electron-phonon interaction. In § 4 the mechanism of conduction is discussed, and in § 5 the comparison with experimental results is done.

§ 2. Localized State of Ge and Si

At first, we treat electronic states trapped by a particular impurity atom when the effects of the other impurity atoms are negligibly small.

We begin with n-type. When there is no impurity atom, wave functions of electron can be expressed by Bloch function

$$\psi_{\boldsymbol{k}}(\boldsymbol{r})=e^{i\boldsymbol{k}\boldsymbol{r}}u_{\boldsymbol{k}}(\boldsymbol{r}) \tag{1}$$

We can rewrite it as a following form

$$\psi_{\boldsymbol{k}_i}(\boldsymbol{r})=e^{i\boldsymbol{k}_i\boldsymbol{r}}u_{\boldsymbol{k}_i}(\boldsymbol{r}) \tag{2}$$

$$u_{\boldsymbol{k}_i}(\boldsymbol{r})=e^{i\boldsymbol{K}_i\boldsymbol{r}}u_{\boldsymbol{K}_i+\boldsymbol{k}_i}(\boldsymbol{r}) \tag{3}$$

where $\boldsymbol{K}_i$ is the wave vector of the state corresponding to the bottom of i-th valley, and $\boldsymbol{k}_i$ means the wave vector measured from the bottom of i-th valley.

The potential of impurity atom may be written in a form

$$V(r)=-\frac{e^2}{\varepsilon_0 r} \tag{4}$$

where $\boldsymbol{r}$ is measured from the center of the impurity atom, and ε_0 is dielectric constant. Then, if $\boldsymbol{k}_i$ dependence of $U_{\boldsymbol{k}_i+\boldsymbol{k}_i}$ is negligible, 1s state composed by the i-th valley may be approximated by the following form as shown by Kittel-Mitchell[2].

$$\varphi_{1s,i}(\boldsymbol{r}) =\left(\frac{ab^2}{\pi r_0^3}\right)^{1/2}\exp\left[-\{a^2x^2+b^2(y^2+z^2)\}^{1/2}/r_0\right] \times e^{i\boldsymbol{K}_i\boldsymbol{r}}u_{\boldsymbol{k}_i}(\boldsymbol{r}), \tag{5}$$

where

$$r_0=\frac{\varepsilon_0\hbar^2}{me^2}, \tag{6}$$

and parameters are given in Ge and Si as follows

	Ge	Si	
$\varepsilon_0=$	16	12	
$a^2=$	0.135	0.216	(7)
$b^2=$	0.017	0.073	

In rigorous sense, however, $\varphi_{1s,i}$ is not orthogonal to $\varphi_{1s,j}$ when i and j represent different valleys. In Ge and Si, however, as shown by Kittel-Mitchell, $\boldsymbol{K}_{ij}r_0/a$ or b (where $\boldsymbol{K}_{ij}=\boldsymbol{K}_i-\boldsymbol{K}_j$) is sufficiently larger than 1, and we can consider in fairly good approximation that $\{\varphi_{1s,i}\}$ are nearly orthogonalized each other. On the other hand, $V_{ij}=\langle\varphi_{1s,i}|V|\varphi_{1s,j}\rangle$ remains in lower order than $\langle\varphi_{1s,i}|\varphi_{1s,j}\rangle$ with respect to $a/\boldsymbol{K}_{ij}r_0$ and we can not neglect this effect. From this effect, wave functions of 1s states may be approximated by the linear combinations of $\varphi_{1s,i}$ with same weight, that is,

$$\psi_{1s,l}=\frac{1}{\sqrt{n_0}}\sum_j C_j^l\varphi_{1s,j}, \tag{8}$$

where $|C_j^l|$ is constant, and n_0 is the number of valleys. The degeneracy of energy spectrum is also released. Energy splitting by this effect may be of the order of V_{ij}. To estimate the order of V_{ij}, we use the isotropic effective mass $m^*=(m_l m_t^2)^{1/3}$, where m_l and m_t are respectively longitudinal and transversal effective masses, and further assume that $\int_{\Omega_0} u^*_{\boldsymbol{K}_i}(\boldsymbol{r})u_{\boldsymbol{K}_j}(\boldsymbol{r})d\boldsymbol{r}=1$. Then a and b are replaced by m^*/m and V_{ij} becomes

$$V_{ij}=-\frac{e^2}{\varepsilon_0 r_0^*[1+(K_{ij}r_0^*/2)^2]}, \tag{9}$$

where

$$r_0^* = \frac{m}{m^*} r_0 \,. \tag{10}$$

For example, in Ge, if we take K_{ij} as the principal wave vector in the direction of [1, 1, 1], V_{ij} becomes 0.2κ, and nearly the same order in Si, too. Fluctuations of local potential energy are more than 10κ in Fritzsche's samples[3] as shown in Table I, and thus we may neglect, in the following consideration, the effect of energy splitting of 1s states compared with the local fluctuation energy.

When the overlapping of 1s wave functions locating at the nearest nighbour impurity atoms becomes large, the wave function which makes the overlapping most effective becomes stable. In this case, Eq. (8) are not applicable.

In p-type Ge and Si, it is very difficult to calculate 1s state theoretically due to the degenerated band structure. Experimentary, however, ionization energys of electron in impurity level were observed, that is, 0.01 e.v. in p-type Ge and 0.05 e.v. in p-type Si. If we assume that in this case, too, a hydrogen like wave function is applicable and effective mass is considered as isotropic, m^*/m becomes 0.19 in Ge and 0.53 in Si. In § 5, we compace these values with that obtained as to satisfy the experimental results of mobility of p-type Ge and Si.

§ 3. Electron-Phonon Interaction

In the preceding section, we considered 1s states where only one impurity atom exists. When there exist more than one impurity atoms, mixing of 1s wave functions localizing at different impurity atoms occurs even if we do not consider the effect of electron-phonon interaction, because these 1s wave functions are not orthogonalized. At first, we consider this mixing effect by choosing only two nearest neighbours impurity atoms, because in this paper we treat only the case that in average the difference of local potential energy at two impurity atoms is much larger than the resonance energy between 1s wave functions localized in these impurity atoms induced by non-orthogonality of these wave functions, and thus the ratio of the mixing is small and we can regard each electron to be trapped approximately in each impurity atom.

When there are two impurity atoms locating in position $\boldsymbol{R}_1$ and $\boldsymbol{R}_2$, the real wave function Ψ may be approximated by the linear combination of 1s wave functions ψ_1 and ψ_2 localized respectively in impurity atoms of position $\boldsymbol{R}_1$ and $\boldsymbol{R}_2$

$$\Psi = c_1\psi_1 + c_2\psi_2 \,. \tag{11}$$

Hamiltonian of this system is written as

$$H = H_0 + V_1(|\boldsymbol{r}-\boldsymbol{R}_1|) + V_2(|\boldsymbol{r}-\boldsymbol{R}_2|) + v(r) \,, \tag{12}$$

where H_0 is the Hamiltonian with periodic potential, V_1 and V_2 mean respectively the potentials of impurity atoms at positions $\boldsymbol{R}_1$ and $\boldsymbol{R}_2$, and $v(r)$ is potential energy changing very slowly in space mainly induced by minority impurity atoms. c_1 and c_2 are determined by variation principle, and we obtain the wave functions of ground state Ψ_1 and excited state Ψ_2 as

$$\Psi_1 = x_1\psi_1 + \psi_2/(1+2x_1J+x_1^2)^{1/2} \tag{13}$$

$$\Psi_2 = x_2\psi_1 + \psi_2/(1+2x_2J+x_2^2)^{1/2} \tag{14}$$

where

$$x_{1,2} = [v_1 - v_2 \pm \{(v_1-v_2)^2 + 4(v_1-v_2)JL + 4L^2\}^{1/2}]/2L \,, \tag{15}$$

$$L = \langle\psi_1|V_2+v|\psi_2\rangle - \langle\psi_1|V_2+v|\psi_1\rangle J \,, \tag{16}$$

$$J = \langle\psi_1|\psi_2\rangle \,, \tag{17}$$

$$v_i = \langle\psi_i|v|\psi_i\rangle \,, \qquad i=1,\ 2 \,, \tag{18}$$

and we took that $v_1 < v_2$.

When a perturbation H' is added, the transition matrix element $\langle\Psi_1|H'|\Psi_2\rangle$ is given from Eqs. (13) and (14) by

$$\langle\Psi_1|H'|\Psi_2\rangle = \frac{x_1x_2H_1' + H_2' + (x_1+x_2)H_{12}'}{(1+2Jx_1+x_1^2)^{1/2}(1+2Jx_2+x_2^2)^{1/2}} \,, \tag{19}$$

where

$$H_i' = \langle\psi_i|H'|\psi_i\rangle \,, \qquad i=1,\ 2 \,, \tag{20}$$

$$H_{12}'=\langle\psi_1|H'|\psi_2\rangle\,, \tag{21}$$

and further using the assumption that $v_2>v_1$, $|x_1|\gg 1\gg|x_2|$ which corresponds to the assumption that the local fluctuation energy $|v_2-v_1|$ is much larger than the resonance energy L, Eq. (19) is approximated by

$$\langle\Psi_1|H'|\Psi_2\rangle\doteqdot\frac{1}{2}(H_1'+H_2')J-H_{12}'$$
$$+\frac{H_2'-H_1'}{v_2-v_1}\left\{\langle\psi_1|V_2|\psi_2\rangle-\langle\psi_1|V_2|\psi_1\rangle J+\langle\psi_1|v|\psi_2\rangle-\frac{v_1+v_2}{2}J\right\}. \tag{22}$$

As to replace H' for usual electron-phonon interaction, however, it remains a complicated problem. In usual electron-phonon interaction, the motion of electron is more rapid than that of ion, and thus we can use adiabatic approximation for the motion of electron. In our hopping model of impurity conduction, however, the time of hopping becomes rather larger than the periodic time of the motion of lattice, and the hopping of electron from one localized state to the other accompanies the motion of the deformation of lattice. This effect is interesting problem in itself and may be important also in other phenomena. In this paper, however, we adopt the zeroth approximation to neglect the effect of deformation of lattice, and discussion about this problem should be given in an other paper.

As to H', we use here the form of deformation potential proposed by Bardeen-Shockley[4].

$$H'\equiv H_{ep}=\sum_q Dqe^{iqr}\xi_q\,, \tag{23}$$

where D is the coupling constant of electron-phonon interaction and ξ_q means the coordinate of accoustical phonon of longitudinal mode with wave vector $\boldsymbol{q}$, and the matrix element of ξ_q is

$$\langle N_q|\xi_q^*|N_q-1\rangle=\langle N_q-1|\xi_q|N_q\rangle=\left(\frac{\hbar N_q}{2M\omega_q N}\right)^{1/2}, \tag{24}$$

where M is the mass of each lattice point, N is the number density of lattice point, and ω_q is the angular velocity of phonon with wave vector $\boldsymbol{q}$. Optical mode is not important in region of impurity conduction. In Eq. (22), the third term may, in general, be considered as smaller than the first term, and the second term is also smaller than the first term due to the oscillation term e^{iqr} of Eq. (23). From the above consideration, we adopt only the first term hereafter, and the square of the matrix element becomes

$$|\langle\Psi_1|H_{ep}|\Psi_2\rangle|^2\equiv|W_{12}(\Delta)|^2=\frac{1}{4}\frac{D^2\Delta_{12}}{NMs^2}J_{12}^2(1-\cos\boldsymbol{qR}_{12}) \tag{25}$$

where Δ_{12} is the energy difference between two states, Ψ_1 and Ψ_2, and nearly equals to $|v_2-v_1|$, S is the velocity of the longitudinal phonon and the wave vector $\boldsymbol{q}$ is determined by the condition of energy balance

$$\hbar qu=\Delta_{12} \tag{26}$$

In samples we refer, Δ_{12} is nearly the order of 10ε and then $\boldsymbol{qR}_{12}$ becomes the order of 10 and thus the term $\cos\boldsymbol{qR}_{12}$ cancels out each other in average. J_{12} is the overlapping integral, $|\langle\psi_1|\psi_2\rangle|$, and written in p-type Ge and Si as

$$J_{12}=\left|\exp\left(-\frac{R_{12}}{r_0^*}\right)\left\{1+\frac{R_{12}}{r_0^*}+\frac{1}{3}\left(\frac{R_{12}}{r_0^*}\right)^2\right\}\right|, \tag{27}$$

when the ground state wave function of p-type impurity level is represented by the hydrogen like 1s function with isotropic effective mass m^*. In n-type Ge and Si, if we write the ground

state wave function by the type of Eq. (8), we obtain the following form using the approximation that wave functions of different valleys are nearly orthogonal, and the energy splitting of states $\{\psi_{1s,i}\}$ is negligible,

$$J_{12}^2=\frac{1}{n_0^2}\sum_i|\sum_i c_i^l c_i^{l'}\langle\varphi_{1s,i}(R_1)|\varphi_{1s,i}(R_2)\rangle|^2=\frac{1}{n_0}\sum_i|\langle\varphi_{1s,i}(R_1)|\varphi_{1s,i}(R_2)\rangle|^2\,, \tag{28}$$

by the relation between the coefficients c_i^l

$$\sum_l c_i^l c_j^l=n_0\delta_{ij}\,. \tag{29}$$

Eq. (28) is also applicable when 1s state is not written by Eq. (8) but single valley wave function (5). Using Eq. (5)

$$J_{12}^2=\frac{1}{n_0}\sum_i\left|\exp\left(-\frac{R_{12}^{i*}}{r_0}\right)\left\{1+\frac{R_{12}^{i*}}{r_0}+\frac{1}{3}\left(\frac{R_{12}^{i*}}{r_0}\right)^2\right\}\right|^2, \tag{30}$$

where

$$R_{12}^{i*}=[(aR_{12,x}^i)^2+(bR_{12,y}^i)^2+(bR_{12,z}^i)^2]^{1/2} \tag{31}$$

and $R_{12,x}^i$ etc. are measured by the coordinate of i-th valley. Or, we may replace summation by valley, $\sum_i$, in Eq. (30) by integration by the direction of $\boldsymbol{R}_{12}$. Then J_{12} becomes

$$J_{12}^2=\int_0^1 dx\exp\{-2bd(1+(t^2-1)x^2)\}\left[1+bd(1+(t^2-1)x^2)^{1/2}+\frac{b^2d^2}{3}(1+(t^2-1)x^2)\right]^2, \tag{32}$$

where $d=R_{12}/r_0$, and $t=a/b$, and when d is fairly larger than unity, J_{12} is approximated by

$$J_{12}^2=\frac{\sqrt{\pi}}{2}\sqrt{\frac{br_0}{(a^2-b^2)R_{12}}}\left|\exp\left(-\frac{bR_{12}}{r_0}\right)\left\{1+\frac{bR_{12}}{r_0}+\frac{1}{3}\left(\frac{bR_{12}}{r_0}\right)^2\right\}\right|^2. \tag{33}$$

We neglected here the second order effects (see Appendix I).

§ 4. Mechanisms of Conduction

In this section, we consider the mechanisms of conduction. Our model adopted in this section is such that: Fluctuation of local potential energy is much larger than resonance energy and localized state of electron trapped by a particular impurity atom is nearly stable if we do not consider electron-phonon interaction. By electron-phonon interaction, electron can hop from one localized state to the other emitting or absorping a phonon. We consider that initially there is no external electric field and then the system is in thermal equilibrium. Then the distribution function f_n, which means the probability to find a electron in the localized state belonging to the impurity atom locating at R_n, is represented approximately by Fermi distribution function $f(\varepsilon_n)$,

$$f(\varepsilon_n)=[\exp\varepsilon_n+1]^{-1}\,,\quad \varepsilon_n=\frac{E_n-\zeta}{\kappa T}\,, \tag{34}$$

where E_n is the energy of the state Ψ_n and we may approximate it by the local potential energy v_n as in Eq. (18). ζ is the chemical potential and given by

$$\sum_n f(\varepsilon_n)=N_{\mathrm{maj}}-N_{\mathrm{min}} \tag{34}$$

When external electric field $\boldsymbol{F}$ is applied on the system, the probability of hopping to the direction of electric field increases, and the electric current begins to flow in the direction of electric field. In steady state, the distribution function f_n should satisfy the following condition

$$\left(\frac{\partial f_n}{\partial t}\right)_{\text{coll}}=\frac{2\pi}{\hbar}\sum_n\sum_q|W_{nm}(q)|^2\left\{f_n(1-f_n)\begin{bmatrix}N(\boldsymbol{q})+1\\N(\boldsymbol{q})\end{bmatrix}-f_n(1-f_m)\begin{bmatrix}N(\boldsymbol{q})\\N(\boldsymbol{q})+1\end{bmatrix}\right\}$$
$$\times\delta(E_n-E_m-eFX_{nm}\pm\hbar\omega_q)=0 \tag{35}$$

where $|W_{nm}(q)|^2$ is the constant of transition probability and given by Eq. (25). $N(\boldsymbol{q})$ is the distribution function of phonon with wave vector $\boldsymbol{q}$ given by Eq. (26) and upper or lower part is taken corresponding to $E_n \gtrless E_m$. Here we assume that the phonon system is always in thermal equilibrium, and thus $N(\boldsymbol{q})$ is given by

$$N(\boldsymbol{q})=\left[\exp\frac{\hbar\omega_q}{\kappa T}-1\right]^{-1}. \tag{36}$$

When the distribution function in steady state is obtained by Eq. (35), the electric current J_x in steady state is given by

$$J_x=e\frac{2\pi}{\hbar}\sum_{(n,m)}\sum_q|W_{nm}(q)|^2X_{nm}\left\{f_n(1-f_m)\begin{bmatrix}N(\boldsymbol{q})\\N(\boldsymbol{q})+1\end{bmatrix}-f_m(1-f_n)\begin{bmatrix}N(\boldsymbol{q})+1\\N(\boldsymbol{q})\end{bmatrix}\right\}$$
$$\times\delta(E_m-E_n+eFX_{nm}\pm\hbar\omega_q)\,. \tag{38}$$

It is very difficult to solve the Eq. (35) rigorously due to the random distribution of impurity atom. For this reason, we use in following some simplified model and calculate it in some extreme cases.

At first, we consider the case that f_n is replaced approximately by $f(\mathcal{E}_n)$. To examine this assumption, we replace f_n in Eq. (35) by $f(\mathcal{E}_n)$. Then, using the linear theory with respect to external field,

$$\left(\frac{\partial f_n}{\partial t}\right)_{\text{coll}}=\frac{2\pi}{\hbar}\sum_n\sum_q|W_{nm}(q)|^2f(\mathcal{E}_n)f(\mathcal{E}_m)N(q)\frac{eFX_{nm}}{\kappa T}\begin{bmatrix}e^{\varepsilon_m}\\e^{\varepsilon_n}\end{bmatrix}\delta(E_n-E_m\pm\hbar\omega_q)$$
$$=6\pi\frac{eFN}{\hbar\kappa T(\kappa\Theta)^3}\sum_n\frac{|W_{nm}(q)|^2\Delta_{nm}{}^2X_{nm}}{(e^{\varepsilon_n}+1)(e^{-\varepsilon_m}+1)|e^{\varepsilon_m-\varepsilon_n}-1|}\,. \tag{39}$$

As is easily seen from Eq. (39), if the distribution of impurity atoms and the local potential energy are symmetric with respect to the point $\boldsymbol{R}_n$, $(\partial f/\partial t)_{\text{coll}}$ becomes zero, namely, $f(\mathcal{E}_n)$ represents the distribution function of steady state. In case (I) of Fig. 1, that is, when N_{maj} is not so larger than N_{min}, the situation of the surrounding of any point $\boldsymbol{R}_n$ may be regarded as nearly at random, and in average the distribution of impurity atoms and the local potential may be considered as symmetrical distribution in not a so bad approximation. Therefore, we may replace f_n by $f(\mathcal{E}_n)$ in case (I).

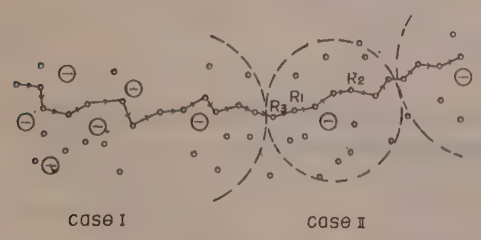

Fig. 1.

⊖ means the position of minority impurity atom
∘ means the position of majority impurity atom
→ means the direction of current flow

In case (II) of Fig. 1, that is, when N_{maj} is much larger than N_{min}, the approximation to replace f_n by $f(\mathcal{E}_n)$ becomes not so good. In this case, it may be more convenient to consider the impurity atoms by deviding into the molecules as is represented by dotted line in Fig. 1. Each molecule has one minority impurity atom, in the center, and in average contains one hole which suffers atractive Coulomb force to the direction of the minority impurity atom at center (hereafter, we consider the case of n-type. In p-type, too, the situation is just same as that of n-type when we exchange the role of electron for hole.). At first, let us look at the points $\boldsymbol{R}_1$ and $\boldsymbol{R}_2$ near by the centered minority impurity atom as in Fig. 1. In the point $\boldsymbol{R}_1$, we may say that $E_1 \gtrless E_n$ corresponding to $X_1 \lessgtr X_n$ comparing to the point $\boldsymbol{R}_n$ near by $\boldsymbol{R}_1$. If the space distribution of majority impurity atoms

is considered as nearly symmetrical with respect to $\boldsymbol{R}_1$, $(\partial f_{R_1}/\partial t)_{\text{coll}}$ becomes negative, that is, the probability to find a electron in the localized state belonging to the impurity atom at $\boldsymbol{R}_1$ decreases. In the position $\boldsymbol{R}_2$, the situation is reversible and $(\partial f_{R_2}/\partial t)_{\text{coll}}$ becomes positive. The above situation becomes weak at point $\boldsymbol{R}_3$ near by the surface of the molecule, and here the distribution function f_{R_3} may be replaced by $f(\mathcal{E}_n)$ in a fairly good approximation. Thus, we may say that each molecule suffers polarization by the existence of the external field in near neighbours of the minority impurity atom, and the electrical current occurs by transition of hole from one molecule to the other. Therefore we calculate the electrical conductivity in the case (II) by using a following model: The electrical current in steady state is determined mainly by the transition of hole from a state localized at a majority impurity atom locating near by surface of a certain molecule to that of another molecule, and the distribution function f_{R_n} near neighbour of the surface of the molecule is replaced by $f(\mathcal{E}_n)$.

In the following, we calculate the electrical conductivity in case (I) and (II) more qualitatively.

Case (I). N_{maj} is not so larger than N_{min}, and f_n is replaced by $f(\mathcal{E}_n)$.

Eq. (38) becomes

$$J_x=e^2F\frac{6\pi N}{\hbar(\kappa\Theta)^3\kappa T}\times\sum_{(nm)}\sum\frac{|W_{nm}(q)|^2\Delta_{nm}{}^2X_{nm}{}^2}{(e^{\varepsilon_n}+1)(1+e^{-\varepsilon_m})|e^{\varepsilon_m-\varepsilon_n}-1|}\,. \tag{40}$$

To calculate Eq. (40) more qualitatively, we use further the following approximation. As is seen from Eq. (25), $W_{nm}(q)$ decreases rapidly when R_{nm} becomes larger, because it contains the overlapping integral J_{nm}. Therefore, it is sufficient to consider only the terms with small value of R_{nm} in the summation with respect to R_{nm}. However, it may be given a non sense result to consider only nearest neighbour impurity atom, because this current gives

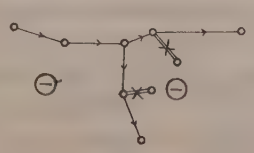

Fig. 2.

= means the polarization current

merely a polarization current as is seen from Fig. 2, and should vanish in the true distribution function of steady state. Therefore we must consider at least until next nearest neighbours impurity atom in the summation with respect to R_{nm}. Further, we define d as a mean distance between these next nearest neighbours impurity atoms, and replace R_{nm} by d. Here, we determine the value of d by

$$d=\left(\frac{2\pi}{3}N_{\text{maj}}\right)^{-1/2}, \tag{41}$$

which corresponds to the condition that when each impurity atom has average volume N_{maj}^{-1}, we can find two other impurity atoms when we draw a sphere of radius d with the center on the given impurity atom (see Appendix II). Then we can rewrite Eq. (40) as

$$J_x=e^2F\frac{2\pi Nd^2}{\hbar(\kappa\Theta)^3\kappa T}\int_{-\infty}^{\infty}F(E)dE\times\int_{-\infty}^{\infty}G(E,\Delta)d\Delta\frac{|W_d(\Delta)|^2\Delta^2}{(e^x+1)(1+e^{-\varepsilon-x})|e^x-1|}, \tag{42}$$

where

$$x=\Delta/\kappa T\,, \tag{43}$$

and $F(E)dE$ is the number of majority impurity atom with local potential energy of value between E and $E+dE$, and $G(E,\Delta)d\Delta$ means the probability that when the impurity atom with the potential energy E is given, the other impurity atom with distance d from the given impurity atom and the potential energy of value between $E+\Delta$ and $E+\Delta+d\Delta$ is observed. Tnese quantities are normalized such as

$$\int_{-\infty}^{\infty}F(E)dE=N_{\text{maj}} \tag{44}$$

$$\int_{-\infty}^{\infty}G(E,\Delta)d\Delta=1 \tag{45}$$

Next, we calculate $F(E)$ and $G(E,\Delta)$, using the following simplified model.

[Calculation of $F(E)$]. Now we consider a sphere of volume Ω_0 with center on a given minority impurity atom. Average volume of Ω_0 is N_{min}^{-1} and it is assumed that in each sphere, there is one hole in average and the potential energy within this sphere is determined by Coulomb field of the minority impurity atom at the center and effects from the other spheres are canceled out in average because they are neutral in average. As the distribution of majority impurity atoms is as-

sumed as uniform, the probability to find majority impurity atom in the distance between r and $r+dr$ from the centered minority impurity atom is proportional to r^2dr. As Coulomb field is proportional to $-1/r$, $F(E)dE$ is proportional to dE/E^4. On the other hand, from the normalization condition, the relation

$$\int_{-\infty}^{-5} F(E)dE = N_{\min} \tag{46}$$

exists, and thus $F(E)$ becomes

$$F(E) = N_{\min}\frac{3\zeta^3}{E^3} \tag{47}$$

where ζ is determined by

$$\zeta = \frac{e^2}{\varepsilon_0}\left(\frac{4\pi}{3}N_{\text{maj}}\right)^{1/3} \equiv \frac{e^2}{\varepsilon_0 d_{\text{maj}}} \tag{48}$$

The upper limit E_0 of impurity band is determined by the normalization condition (44) and E_0 becomes

$$E_0 = \frac{e^2}{\varepsilon_0}\left(\frac{4\pi}{3}N_{\min}\right)^{1/3} \equiv \frac{e^2}{\varepsilon_0 d_{\min}} \tag{49}$$

In the temperature range where impurity conduction is important, ζ is much larger than κT for almost samples we consider. In this case, we can write

$$F(E) \doteqdot F(\zeta) = \frac{3N_{\min}}{\zeta} \tag{50}$$

[Calculation of $G(E, \Delta)$]. Calculation of $G(E, \Delta)$ is more difficult than that of $F(E)$, because in former calculation inter molecular transition is important. In a rough approximation, E may be replaced by ζ as mentioned above, and when Δ becomes negative $G(E, \Delta)$ may be small and thus replaced zero in this range. When Δ is positive, however, we may say approximately that $G(\zeta, \Delta)$ does not depend on Δ, corresponding to the assumption to replace f_n by $f(\varepsilon_n)$. Thus from the normalization condition (45) we can write that

$$\begin{aligned} G(\zeta, \Delta) &= (\zeta - E_0)^{-1} \quad \text{when} \quad 0 < \Delta < \zeta - E_0 \\ &= 0 \qquad\qquad \text{otherwise} \end{aligned} \tag{51}$$

Using Eqs. (50) and (51), we can obtain J_x as

$$J_x = e^2 F \frac{3\pi}{2} N_{\min} \frac{d^2 D^2 \kappa \Theta}{\hbar M u^2 \zeta(\zeta - E_0)} \times \left(\frac{T}{\Theta}\right)^4 J_d^2 \phi_4\left(\frac{\zeta - E_0}{\kappa T}\right), \tag{52}$$

where

$$\phi_n(x) = \int_0^x \frac{y^n dy}{(e^y - 1)(1 - e^{-y})}. \tag{53}$$

As a condition of applicability of Eq. (52), we may say roughly such that; electron can transfer from one atomic state with energy ζ localizing at an majority impurity atom belonging to a certain sphere to another atomic state with energy ζ localizing at an majority

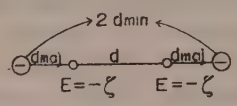

Fig. 3.

impurity atom belonging to another sphere. As seen from Fig. 3, the above condition is written by

$$\frac{N_{\text{maj}}}{N_{\min}} < (1 + 2^{-2/3})^3 \doteqdot 5 \tag{54}$$

Case (II). N_{maj} is much larger than $N_{\min}$, and it is convenient to devide the impurity atoms into molecules.

From the above consideration, we calculate the conductivity by the model that the steady current is determined by the inter-molecular transitions, and in this process, the majority impurity atoms locating within distance d from the surface of each molecule is important.

Concerning to $F(E)$, we can use Eq. (47) also in this case. Further, if the condition, ζ, $E_0 \gg \kappa T$, is satisfied, we can replace E by E_0, and thus $F(E)$ becomes as

$$F(E) \doteqdot F(E_0) = \frac{3\zeta^3}{E_0^4} N_{\min} \tag{55}$$

The range of the integration by E is defined by, $-\dfrac{E' E_0}{E' - E_0} \leq E \leq -E_0$, where E' is defined by

$$E' = e^2/\varepsilon_0 d. \tag{56}$$

On the other hand, the determination of $G(E, \Delta)$ is fairly complicated. However, here, we assume it as constant for simplicity. Then $G(E, \Delta)$ becomes

$$G(E, \Delta) = \frac{E' - E_0}{E_0^2}, \tag{57}$$

and the range of the integration by Δ is defined by $0 \leq \Delta \leq E_0/E - E_0$.

From the above consideration, J_x is written by

$$J_x = e^2 F \frac{3\pi}{2} N_{\min} \eta \frac{d^2 D^2 \kappa \Theta \zeta^3 (E' - E_0)}{\hbar M u^2 E_0^6} \left(\frac{T}{\Theta}\right)^4 J_d^2 \times \exp\left(\frac{E_0 E'/(E' - E_0) - \zeta}{\kappa T}\right) \varphi_3\left(\frac{E_0^2}{\kappa T (E' - E_0)}\right) \tag{58}$$

where

$$\varphi_n(x)=\int_0^x \frac{y^n dy}{e^y-1} \tag{59}$$

$$\eta^{-1}=1-\left(1-\frac{d}{d_{\min}}\right)^3 \tag{60}$$

The facror η is multiplied to extend the surface current to the total current.

The range where Eq. (58) is applicable may be determined by the condition that the potential energy of the surface range considered

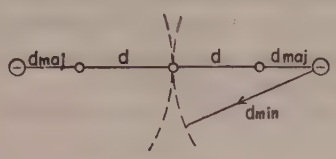

Fig. 4.

in the above calculation is larger than the Fermi energy $-\zeta$, as is shown in Fig. 4. This condition is written by

$$N_{\mathrm{maj}}/N_{\min} > (1+2^{1/3})^3 \fallingdotseq 11.5 \tag{61}$$

The range $5 < N_{\mathrm{maj}}/N_{\min} < 11.5$ is not covered by the above cases. However, we can obtain a knowledge of this range by the extrapolation from the both sides.

§ 5. Comparison with Experimental Results

In this section, our results obtained in the preceding section are compared with the experimental results made by Fritze[3] for several samples of n- and p-type Germanium. The results are shown in Table I.

The first three samples are Sb-doped n-type Ge, and the next three are In-doped and the last three are Ga-doped p-type Ge. These three samples of each kind of impurity atom are chosen to contain the minority impurity atom of the concentration about 10^{14}, 10^{15} and 10^{16} cc^{-1}, or the majority impurity atom of the concentration about 10^{15}, 10^{16} and 10^{17} cc^{-1}. The ratio of N_{maj} and $N_{\min}$ runs from 2 to 44. As mentioned in § 2, the effective mass m^* of p-type Ge or Si is not determined in the localized impurity level state, and in Table I we take m^*/m as 0.1 in order to get a good agreement with the experimental results. This value of m^*/m may be not so unreasonable.

Table I. Theoretical and experimental results of both n- and p-type Germanium.

Samples	Sb–15–1	Sb–19–1	Sb–19–3	In–1	In–2	In–5	Ga–3	Ga–4–1	Ga–4–4
$N_{\min}$ cc^{-1}	4.7×10^{14}	2.8×10^{15}	2.6×10^{16}	3.1×10^{14}	1.4×10^{15}	3.3×10^{16}	1.4×10^{14}	1.5×10^{15}	7.0×10^{15}
N_{maj} cc^{-1}	6.9×10^{15}	3.4×10^{16}	1.2×10^{17}	9.3×10^{14}	3.0×10^{15}	1.3×10^{17}	4.4×10^{15}	2.1×10^{16}	7.3×10^{16}
$N_{\mathrm{maj}}/N_{\min}$	15	12	4.6	3	2	4	44	14	10
d cm	4.1×10^{-6}	2.4×10^{-6}	1.6×10^{-6}	8.0×10^{-6}	5.4×10^{-6}	1.54×10^{-6}	4.8×10^{-6}	2.8×10^{-6}	1.9×10^{-6}
J_d^2	3.4×10^{-4}	1.65×10^{-2}	8.6×10^{-2}	1×10^{-5}	1.26×10^{-3}	4.1×10^{-1}	3.6×10^{-3}	8.4×10^{-2}	2.8×10^{-1}
ζ °K	32	54.5	83	16.4	24.3	85.5	27.5	46.7	70.5
E_0 °K	13	23.7	50	11.4	18.8	54	7.7	19.2	32.2
$\rho_4^{\exp}$ Ω	2×10^5	8×10^2	2×10^{-1}	1.3×10^7	3×10^4	3	3×10^5	1.5×10^4	3.5
$\rho_2^{\exp}/\rho_4^{\exp}$	50	25	1.5	4	6	5	57	30	16
ρ_4^{theo} Ω	4.5×10^4	5×10^2	2.5×10^2	1.4×10^7	3×10^4	8.5	1.2×10^5	3.3×10^2	3×10^1
$\rho_2^{\mathrm{theo}}/\rho_4^{\mathrm{theo}}$	30	28	14.5	2.5	3	14.4	139	65	16
ρ_4^{theo}*			0.8×10^{-2}			0.7×10^{-2}			1×10^{-2}

* To evaluate the value of Eq. (79) in [I], we assume that $V=E_0$ and $a_0=d$.

Not with standing of our rough approximation, both in the absolute value and the temperature dependence of resistivity, we get a fairly good agreement with the experimental results except the samples of highest impurity concentration. Especially, we must consider the fact that the overlapping integral depends sensitively on the values of m^* and d, and thus if d varies with the change of temperatures, the temperature dependence of the resistivity changes fairly markedly.

In samples of highest impurity concentration, that is Sb–19–3 and In–5, the overlapping integrals are nearly the order of unity, and thus the model adoped in this paper is not applicable. These samples are considered rather to belong to the range 2) in § 1 already considered in the preceding paper [I]. In fact, as seen from [I], if the conduction mechanism of the range 2) is dominant, the re-

sistivity does not depend on temperature in the temperature range of impurity conduction, and it is rather satisfactory with the experimental results as shown in Table I. In the absolute values of the resistivity, too, the theoretical values calculated using the Eq. (79) of [I] is rather satisfactory with experimental results as shown in the last line of Table I.

In the sample Ga-4-4, too, the overlapping integral is nearly the same ordes as that of Sb-19-5. Nevertheless, the experimental results show that in Ga-4-4 our model adopted in this paper is applicable in fairly good approximation rather than that of the range 2). This situation seems to cause from the fact that the ratio $N_{\mathrm{maj}}/N_{\mathrm{min}}$ is fairly large in Ga-4-4, because the larger the ratio $N_{\mathrm{maj}}/N_{\mathrm{min}}$ becomes, the more stable our model of molecular system becomes. Thus, our model is applicable until higher concentration of impurity atom in order that the fluctuation of the local potential energy, that is $\zeta-E_0$, becomes larger.

In Si and the other substances, for example InSb, too, the theoretical calculations are performable. However, in these substances, the detailed experimental results such as Fritzsch's in Ge are not performed, and further the some parameters are lacking. Therefore, the detailed comparison with experimental results are not given in this paper.

Appendix I

We assume here that the Hamiltonian of electron-phonon interaction is written as

$$H_{ep}=D\left(\frac{\hbar}{2MNu}\right)^{1/2}\sum_q\sum_k\sum_n q^{1/2}C_{k+q}\{e^{-i(k+q)R_n}a_k^*a_n(A_q+A_{-q}^*)+e^{i(k+q)R_n}a_n^*a_k(A_{-q}+A_q^*)\} \quad \text{(AI.1)}$$

where D means the coupling constant, a_k^*, a_k and a_n^*, a_n mean respectively criation and anihilation operators of the electronic state ψ_k of the conduction band and the localized state $\psi_{1s,n}$ and A_q^*, A_q mean respectively criation and anihilation operators of phonon with wave vector $\boldsymbol{q}$ of longitudinal mode. C_k is the Fourie component of the state ψ_{1s}, that is

$$C_{\boldsymbol{k}}=\int\psi_{1s}^*(\boldsymbol{r})e^{i\boldsymbol{kr}}u_{\boldsymbol{k}}(\boldsymbol{r})d\boldsymbol{r}\,. \quad \text{(AI.1)}$$

$\{\psi_k,\ \psi_{1s,n}\}$ compose a orthogonal set and ψ_k is nearly represented by the Bloch function.

Electron can make a hopping from a localized state $\psi_{1s,n}$ to $\psi_{1s,m}$ by using the conduction state ψ_k as the intermediate state. This process is represented by the second order perturbation of H_{ep} such as

$$\begin{aligned}H_{ep}^{(2)}=(D^2\hbar/2MNu)&\sum_{q_1}\sum_{q_2}\sum_k\sum_n\sum_m(q_1q_2)^{1/2}C_{k+q_1}C_{k+q_2}e^{i(k+q_2)R_m-i(k+q_1)R_n}a_m^*a_n\\&\times\{a_ka_k^*(A_{-q_2}+A_{q_2}^*)(A_{q_1}/(E_k-E_n-\hbar\omega_1)+A_{-q_1}/(E_k-E_n+\hbar\omega_1))\\&+a_k^*a_k(A_{q_1}+A_{-q_1}^*)(A_{-q_2}/(E_k-E_m+\hbar\omega_2)+A_{q_2}^*/(E_k-E_m-\hbar\omega_2))\}\,.\end{aligned} \quad \text{(AI.3)}$$

This mechanism represents essentially a Raman Process, and not important in very low temperatures where the impurity conduction is important. The only important term amongst this process comes from the term $\boldsymbol{q}_1=\boldsymbol{q}_2$. We consider for simplicity the absolute zero temperature, then this term becomes

$$\frac{D^2\hbar}{2MNu}\sum_n\sum_m a_m^*a_n\left\{\sum_k\sum_q\frac{q|C_{k+q}|^2\exp i(\boldsymbol{k}+\boldsymbol{q})\boldsymbol{R}_{nm}}{E_k-E_n+\hbar\omega_q}\right\}. \quad \text{(AI.4)}$$

In the denominator, we can neglect $\hbar\omega_q$ because it is always finitely positive. Further we can replace $\boldsymbol{q}$ approximately by $\boldsymbol{k}$ because in the summation of $\boldsymbol{q}$, the main contribution comes from the terms in which $\boldsymbol{k}+\boldsymbol{q}$ is nearly zero. Then the summation by $\boldsymbol{q}$ is performed easily and gives the overlapping integral between the localized states $\psi_{1s,n}$ and $\psi_{1s,m}$ that is J_{nm}. The summation by $\boldsymbol{k}$ is also performable and the above term is written approximately by

$$\frac{3}{8}\frac{D^2\hbar q_0}{E_0 Mu}J_{nm} \qquad \text{(AI.5)}$$

where E_0 means the energy width of the considering band, and q_0 is the Debye cut off wave vector. This term gives the correction of the overlapping integral J_{nm} and the correcting factor is nearly given by

$$\frac{3D^2\hbar q_0}{8E_0\Delta Mu}, \qquad \text{(AI.6)}$$

where Δ is the ionization energy of the impurity state $\psi_{1s,n}$. In Ge, this correction factor is the order of 10^{-1}.

Appendix II

We consider the system where the identical particles of N numbers are contained per unit volume, and the probability to find a particle in a volume v is proportional to v. Then the probability to find n-particles in a fixed volume v is given by

$$W_n=\binom{N}{n}v^n(1-v)^{N-n} \qquad \text{(AII.1)}$$

As easily seen, W_n satisfies the condition

$$\sum_{n=0}^{N} W_n=1 \qquad \text{(AII.2)}$$

When the conditions, $v \ll 1$, $n \ll N$ and $vn \ll 1$ are satisfied, W_n is approximated by

$$W_n=\frac{N^n}{n!}v^n e^{-v(N-n)}=\frac{1}{n!}x^n e^{-x} \qquad \text{(AII.3)}$$

where

$$x=Nv \qquad \text{(AII.4)}$$

Therefore, the probability to find more than two particles in a fixed volume v is given by

$$W_2=1-W_0-W_1=1-(1+x)e^{-x} \qquad \text{(AII.5)}$$

For example, if we put $x=2$, W_2 becomes 0.61.

Next, we obtain the other probability, that is, the probability to find n particles in volume v and δn particles in a different volume δv, where δv is a arbitrary small volume. It is written by

$$W_n^{\delta n}=\binom{N}{n}v^n\binom{N-n}{\delta n}\delta v^{\delta n}(1-v-\delta v)^{N-n-\delta n} \qquad \text{(AII.6)}$$

or using the above mentioned conditions, and in limit of $\delta v \to 0$,

$$=W_n\frac{N^{\delta n}}{\delta n!}\delta v^{\delta n} \qquad \text{(AII.7)}$$

For example, if we put $\delta n=1$, and replace v and δv respectively by $(4\pi/3)r^3$ and $4\pi r^2 dr$ as shown in Fig. A1, the probability to find

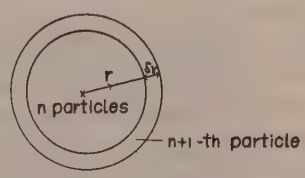

Fig. 5.

$(n+1)$-th neighbours particle in distance $r \sim r+dr$ from a given center is written by

$$W_n^r=4\pi N r^2\frac{x^n e^{-x}}{n!}dr, \qquad \text{(AII.8)}$$

and the average of r^t of $(n+1)$-th neighbour's particle is

$$\langle r_{n+1}^t\rangle=4\pi N\int_0^\infty r^{2+t}\frac{x^n e^{-x}}{n!}dr \qquad \text{(AII.9)}$$

$$=a_0^t\Gamma\left(n+\frac{t}{3}+1\right)\Big/n! \qquad \text{(AII.10)}$$

where

$$\frac{4\pi}{3}a_0^3=N^{-1}, \qquad \text{(AII.11)}$$

and $\Gamma(x)$ is ordinary Γ-function. If we put $n=1$ and $t=3$, r^3 average of next nearest neighbour becomes $\langle r_2^3\rangle=2a_0^3$ or $x=2$.

References

1) T. Kasuya: Jour. Phys. Soc. Japan **13** (1958) 1096.
2) C. Kittel and A. M. Mitchell: Phys. Rev. **96** (1954) 1488.
3) H. Fritzsch: Phys. Rev. **99** (1955) 406.
4) J. Bardeen and W. Shockley: Phys. Rev. **80** (1950) 72.

JOURNAL OF THE PHYSICAL SOCIETY OF JAPAN Vol. 13, No. 11, NOVEMBER, 1958

Magnetic Property and Crystal Chemistry of Ilmenite ($MeTiO_3$) and Hematite (αFe_2O_3) System
II. Magnetic Property

By Yoshikazu ISHIKAWA*
Institute for Solid State Physics, University of Tokyo, Tokyo
and Syun-iti AKIMOTO
Geophysical Institute, University of Tokyo, Tokyo

(Received July 11, 1958)

Magnetic properties of synthesized solid solutions of ilmenite ($MgTiO_3$, $MnTiO_3$, $FeTiO_3$, $CoTiO_3$ and $NiTiO_3$) and hematite (αFe_2O_3) are investigated and it was confirmed that those of any ilmenite-hematite series can be divided into three parts: i) pure ilmenite, ii) solid solutions with $R\bar{3}$ crystal symmetry and iii) those with $R\bar{3}c$ crystal symmetry. Pure ilmenites are antiferromagnetics having their Néel temperature below 80°K except $MgTiO_3$, the Néel temperature of $MnTiO_3$ being determined to be 41°K. The solid solutions with $R\bar{3}$ symmetry are ferrimagnetic except $MgTiO_3$ series which is paramagnetic. Ferrimagnetism in $FeTiO_3$, $CoTiO_3$ and $NiTiO_3$ series is due to the same mechanism, while that in $MnTiO_3$ series to the different one. The solid solutions with $R\bar{3}c$ symmetry are again antiferromagnetics on which feeble ferromagnetism is superimposed.

Through the analysis of magnetic properties of ferrimagnetic specimens, the sign of superexchange interaction with the coupling angle ($\angle$Me–O–Me) of 90° in the rhombohedral structure was determined.

§ 1. Introduction

In the previous paper[1] we have discussed the crystallographic problem in the solid solution of ilmenite ($MeTiO_3$) and hematite (αFe_2O_3) and showed that the miscibility of ilmenite and hematite in the solid solution varies with different ilmenite-hematite systems. That is, $FeTiO_3$ and $NiTiO_3$ make the solid solution with Fe_2O_3 in the whole range of composition, while in the solid solution of hematite and $MgTiO_3$, $MnTiO_3$ or $CoTiO_3$, there exists inmiscible range of composition. It has also been established that, in any cases, the solid solutions on the ilmenite side and hematite side have different crystal symmetries, i.e. $R\bar{3}$ and $R\bar{3}c$ respectively.

In this paper we shall discuss the magnetic properties of these solid solution systems. As we reported in previous paper of the solid solution of $FeTiO_3$ and Fe_2O_3[2] magnetic properties of the solid solutions are greatly correlated with their crystal symmetry and can be divided into three parts; i) antiferromagnetism of pure ilmenite, ii) ferrimagnetism of specimens with $R\bar{3}$ symmetry and iii) antiferromagnetism for specimens with $R\bar{3}c$ symmetry on which parasitic ferromagnetism is superimposed.

The investigations of magnetic properties in the solid solution have different significances for these three parts, which are discussed separately in the following.

i) Pure ilmenite, which we shall use as a generalized name of substances with the ilmenite structure such as $FeTiO_3$, $NiTiO_3$, $MnTiO_3$, $CoTiO_3$ and $MgTiO_3$ in this paper is found to be antiferromagnetics with their Néel temperature below 80°K except $MgTiO_3$. Antiferromagnetism of $FeTiO_3$ was first found by Bizette and Tsai[3] and its antiferromagnetic structure was determined by Shirane et al. by a neutron diffraction analysis[4]. According to their results, magnetic structure of $FeTiO_3$ is constructed by two kinds of superexchange interactions between magnetic ions. One is that in a hexagonal layer of which coupling angle ($\angle Me^{2+}$–O^{2-}–Me^{2+}) is

* Department of Applied Physics, Faculty of Engineering, University of Tokyo.

nearly 90° and the other is that between magnetic ions on different layers which are separated by two oxygen layers. Such interactions have formerly been neglected as weak ones, but recently much attention has come to be paid on. For example, it has been reported that in chlorides of transition metals[5] or in a zinc ferrite[6] such interactions as stated now play an important role in constructing the magnetic structure. Through the investigation of magnetic properties of ilmenites, we can obtain some knowledge about these interactions in the rhombohedral structure.

ii) The solid solutions with the crystal symmetry $R\bar{3}$ are found to be ferrimagnetic except $MgTiO_3$ series. These ferrimagnetic substances are of the rhombohedral structure and do not belong to any groups of the ferrimagnetic oxides hitherto investigated. This ferrimagnetism was first found in the solid solution of $FeTiO_3$ and Fe_2O_3 by Nagata et al. in nature[7]. Since then, detailed investigations have been carried out on this solid solution series and results are reported in the previous papers.[2),8),9] Although we have showed in these papers that the ferrimagnetism is interpreted qualitatively by the theory proposed by Néel if the proper arrangement of cations is assumed, several points are left unexplained. Furthermore it has been expected that in $FeTiO_3$ series the situation that Fe^{2+} ions are unstable at high temperature and their orbital moments are left unquenched may complicate the magnetic properties of this series. It is, therefore, necessary for the purpose of understanding the ferrimagnetism newly discovered to extend our investigation to isomorphic compounds such as the solid solution series of $CoTiO_3$–Fe_2O_3, $MnTiO_3$–Fe_2O_3 and $NiTiO_3$–Fe_2O_3 and to distinguish the properties common to all the solid solution series from those peculiar to each series.

iii) The solid solutions with the crystal symmetry $R\bar{3}c$ are antiferromagnetics on which a feeble ferromagnetism is superimposed. It is confirmed that the antiferromagnetism and the feeble ferromagnetism in the solid solutions are due to the same origin with those in hematite. Although the antiferromagnetism in hematite is easily understood by its cations arrangement and the superexchange interactions between them[10),11] no decisive interpretation has yet been done on the feeble ferromagnetism. Besides, the change of anisotropy below 260°K in hematite[12] is also left unexplained. We have showed in the previous paper[1] that the solid solutions with $R\bar{3}c$ symmetry have entirely the same crystal structure as hematite. Hence we can substitute Fe^{3+} ions in hematite by other cations such as Mg^{2+}, Mn^{2+}, Co^{2+}, Fe^{2+}, Ni^{2+} and Ti^{4+} for the wide range of composition without changing its crystal symmetry by preparing the solid solutions of hematite and ilmenite with these cations. Such a substitution produces a change in the magnetic couplings in hematite continuously and may throw some light on the above-mentioned magnetic properties of hematite.

A. Experimental Results

In the following sections magnetic properties of the ilmenite and hematite system are studied in conformity with the three classifications mentioned in the introduction. All specimens used were prepared in the ceramic forms. The methods for preparing them are described in the previous paper.[1]

§ 2. Magnetic Properties of Ilmenite

The magnetic susceptibilities of ilmenites ($FeTiO_3$, $MnTiO_3$, $CoTiO_3$ and $NiTiO_3$) are measured with the aid of a magnetic balance. It was confirmed that they are paramagnetic above 80°K and their magnetic susceptibilities obey the Curie-Weiss law $\chi_M = C_M/(T-\Theta)$ above room temperature. The values of Θ and μ_{eff} calculated from C_M are presented in Table I. The magnetic susceptibilities below 80°K was measured for $FeTiO_3$ and $MnTiO_3$ at the Research Institute for Iron, Steel and other Metals, Tôhoku University* and both are found to become antiferromagnetic at low temperature. The result for $FeTiO_3$ has already been reported[2] and that for $MnTiO_3$ is shown in Fig. 1. From this figure the Néel point of this substance is determined to be 41°K. Although measurements have not yet been extended below 80°K for other ilmenites, we can expect, with sufficient plausibility, that other two ilmenites may also

* The authors are entirely indebted to Dr. Tsubokawa for the measurements.

Table I. Magnetic properties of ilmenite.

Substance	$T_n(K)$	C_{Mol}	Θ (°K)	μ_{eff}	$\sqrt{4S(S+1)}$	$\sqrt{L(L+1)+4S(S+1)}$
$FeTiO_3$	55°	3.92	17	5.62	4.90	5.50
$NiTiO_3$		1.30	− 55	3.24	2.87	4.49
$CoTiO_3$		3.30	− 15	5.17	3.87	5.21
$MnTiO_3$	41°	4.15	−210	5.80	5.92	5.92

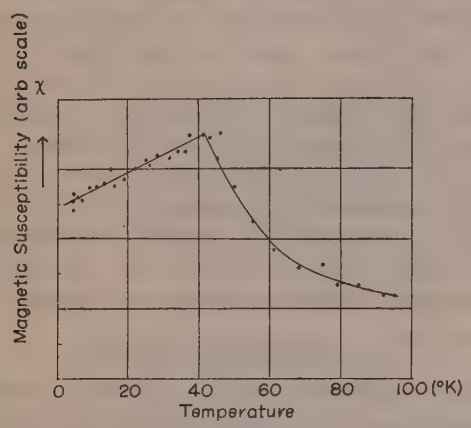

Fig. 1. Magnetic susceptibility *vs.* temperature for $MnTiO_3$.

become antiferromagnetic below 80°K. In Table I, it must be noticed that $FeTiO_3$ has a positive value of Θ, while that of $MnTiO_3$ is negative and very large compared with those of other ilmenites. In the table we also show the values of μ_{eff} calculated from the formulae $\mu_{eff}=\sqrt{4S(S+1)}$ and $\mu_{eff}=\sqrt{L(L+1)+4S(S+1)}$ where L and S are the orbital and spin angular momentum quantum number respectively. From these values we expect that in $MnTiO_3$ the orbital moment is completely quenched and in $NiTiO_3$ and $CoTiO_3$ it is left slightly unquenched, while in $FeTiO_3$ it is left highly unquenched. The effective g factor of $NiTiO_3$ obtained from a measurement of paramagnetic resonance absorption is 2.22_5 which accords well with the above situation.*

§ 3. Magnetic Properties of Solid Solutions with $R\bar{3}$ Symmetry

It has already been reported that the solid solutions of $FeTiO_3$ and $NiTiO_3$ series are ferrimagnetic in this range.[2),13)] In this section we show the results for $MnTiO_3$ and $CoTiO_3$ series.

3.1. *Intensity of magnetization*

The intensity of magnetization was measured by the same method as that previously reported. In Figs. 2 and 3, thermomagnetic curves of several specimens $MnTiO_3$ and

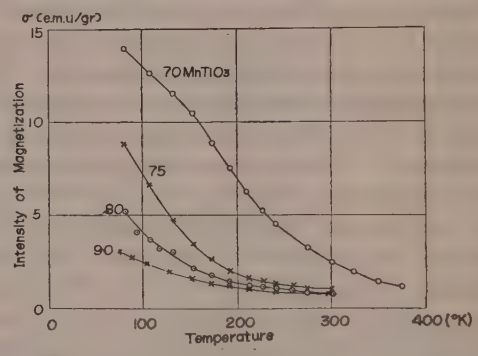

Fig. 2. Intesity of magnetization in a field strength of 8500 Oe. vs. temperature for the specimens with $R\bar{3}$ symmetry of $MnTiO_3$–Fe_2O_3 system.

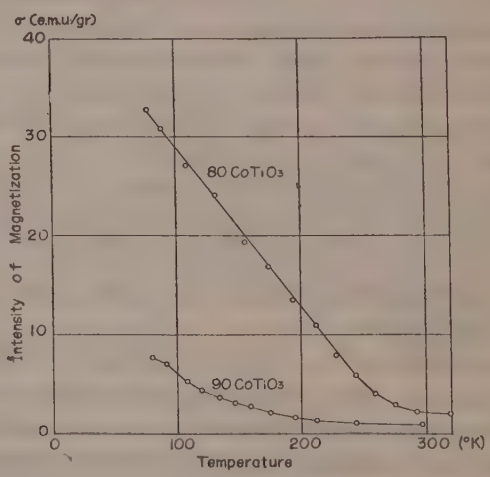

Fig. 3. Intensity of magnetization in a field strength of 8500 Oe. *vs.* temperature for the specimens with $R\bar{3}$ symmetry of $CoTiO_3$–Fe_2O_3 system.

* The measurement was carried out by Mr. Shimada in Institute for Solid State Physics, University of Tokyo.

$CoTiO_3$ series measured down to liquid nitrogen temperature in a field strength of 8500 Oe. are shown. The specimens of both series are found to be ferrimagnetic at low temperature and the intensity of magnetization increases linearly with decrease of temperature. These situations are quite similar to those for $NiTiO_3$ and $FeTiO_3$ series.[2),13)] By making the detailed comparison, however, we can find the magnetic properties of $MnTiO_3$ series are considerably different from those of other series. This situation can be better understood by comparing Figs. 4 and 5, where the field dependence of magnetization at 80°K of specimens in the various series is given. As these figures show, the characteristics of the field dependence of $MnTiO_3$ series are quite different from those of other series, that is, the magnetizations of all specimens in $MnTiO_3$ series are far from saturation under the field strength of 8500 Oe., while for other series they are nearly saturated by this field strength when the content of ilmenite in the solid solution is less than 80 mol. per cent. It seems to be more reasonable to suppose that such a characteristics of the field dependence of $MnTiO_3$ series may indicate that a weak ferromagnetism is superimposed on the paramagnetism. In Fig. 6, estimated satu-

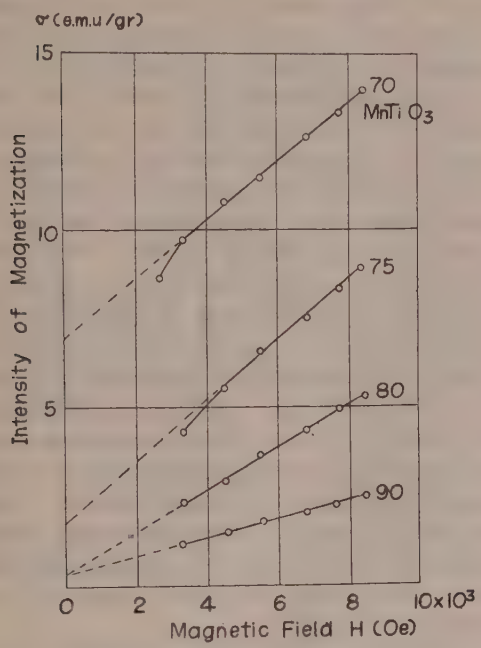

Fig. 4. Field dependence of magnetization at 80°K of the specimens with $R\bar{3}$ symmetry of $MnTiO_3$–Fe_2O_3 system.

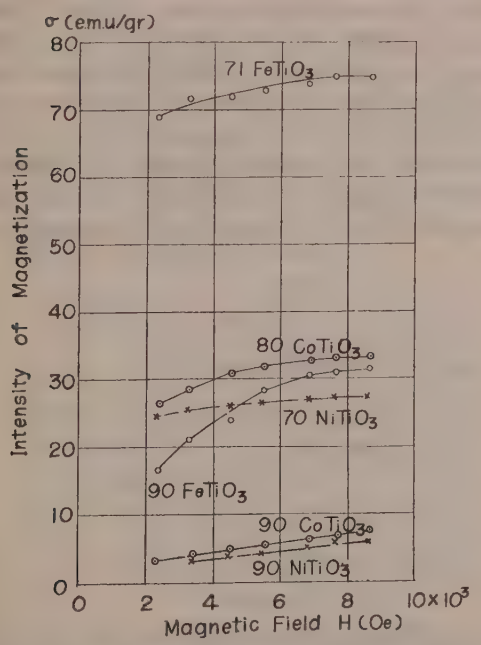

Fig. 5. Field dependence of magnetization at 80°K of the specimens with $R\bar{3}$ symmetry of $FeTiO_3$–, $NiTiO_3$– and $CoTiO_3$–Fe_2O_3 systems.

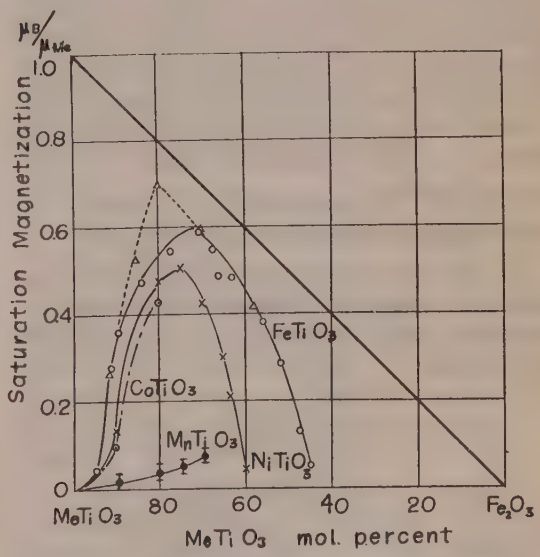

Fig. 6. Estimated saturation magnetization at 0°K *vs.* composition for $MeTiO_3$–Fe_2O_3 system. The solid straight line indicates the theoretical value, $J=x\mu_{Me^{2+}}$. (see text)

○——○ $FeTiO_3$–Fe_2O_3 system (annealed)
×——× $NiTiO_3$– ,,
⊙— - ⊙ $CoTiO_3$– ,,
●——● $MnTiO_3$– ,,
△- - -△ $FeTiO_3$– ,,
(after Bozorth et al.[14)])

ration values of magnetization at 0°K of all ilmenite-hematite system with $R\bar{3}$ symmetry are drawn against the composition, which are expressed in the unit of the reduced Bohr magneton number (μ_B/μ_{Me}, where $\mu_{Mn^{+2}}=5$, $\mu_{Fe^{+2}}=4$, $\mu_{Co^{+2}}=3$ and $\mu_{Ni^{2+}}=2$ respectively) for the convenience of comparison. These values are obtained by extrapolating the values at 80°K to 0°K by the method previously reported.[2] In the case of $FeTiO_3$ series only the results for annealed specimens are shown. In the figure, the results of Bozorth et al. for $FeTiO_3$ series which were obtained by the measurements at 1.3°K in the field strength of 11000 Oe. are also plotted.[14] Their results accord fairly well with ours except that of 0.8 $FeTiO_3 \cdot 0.2$ Fe_2O_3, for such a composition range our method of extrapolation is expected to include a considerable error. Although our results are only approximate ones and only a few data could be obtained for $CoTiO_3$ series because of the narrowness of the $R\bar{3}$ region in $CoTiO_3$ series, we may safely suppose from the figure that the ferrimagnetism in $NiTiO_3$ and $CoTiO_3$ is nearly the same as that in $FeTiO_3$ series, while that in $MnTiO_3$ series is greatly different. We shall show in the later section that such a difference may be attributed to the situation that $MnTiO_3$ has a different antiferromagnetic structure from other ilmenites.

3.2. *Magnetic susceptibility*

In the previous papers we have reported that the magnetic susceptibilities of $NiTiO_3$ series at high temperatures obey of Curie-Weiss law

$$\chi_M = \frac{C_M}{T+\Theta}$$

and C_M and Θ change continuously from those of Fe_2O_3 to those of $NiTiO_3$,[13] while in the case of $FeTiO_3$ series the anomalous change was observed.[2] In Fig. 7 the reciprocal of the magnetic susceptibilities of $0.8MnTiO_3$–$0.2Fe_2O_3$ and $0.8\,CoTiO_3$–$0.2Fe_2O_3$ is shown. In both cases their modes are similar to those of ordinary ferrimagnetics and the Curie constant C_M obtained from the straight line part in the figure by the least mean square method is turned out to be 5.90 for $MnTiO_3$ series and 3.30 for $CoTiO_3$ series respectively. It must be noticed that in the case of $0.8CoTiO_3$–0.2 Fe_2O_3 the value of C_M calculated by assuming the orbital moment is completely quenched is 3.16, which may indicate, in reference to the result in Table I, that the orbital moment which is left unquenched in pure $CoTiO_3$ is more quenched in the solid solution. The same situation may be expected in the solid solution of $FeTiO_3$ and the decrease in C_M in this series may, to some extent, be attributed to this effect.

§ 4. Magnetic Properties of Ilmenite-Hematite System with $R\bar{3}c$ Symmetry

All specimens investigated are found to be feebly ferromagnetic in this range. The thermomagnetic curves measured in a field strength of 8500 Oe. of $MnTiO_3$ series and $MgTiO_3$ series are shown in Figs. 8 and 9, and the intensity of magnetization at room temperature in the field strength of 8500 Oe. is plotted against the composition in Fig. 10. From this figure, we can find the intensity of

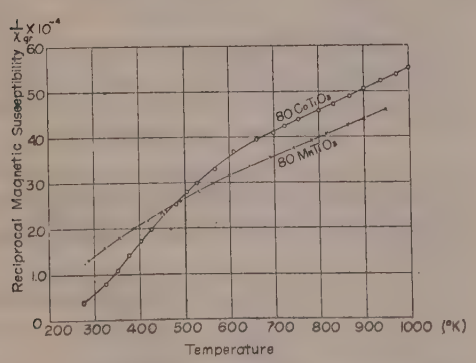

Fig. 7. Reciprocal magnetic susceptibility *vs.* temperature for the specimens of $0.8MnTiO_3 \cdot 0.2Fe_2O_3$ and $0.8CoTiO_3 \cdot 0.2Fe_2O_3$.

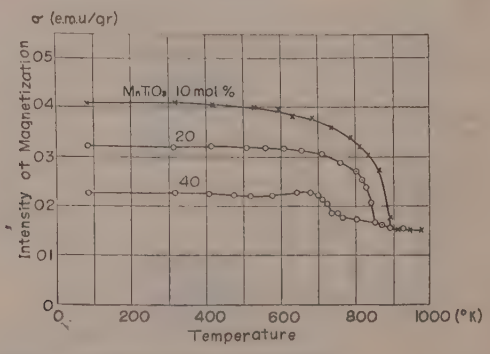

Fig. 8. Intensity of magnetization in a field strength of 8500 Oe. *vs.* temperature for the specimens with $R\bar{3}c$ symmetry of $MnTiO_3$–Fe_2O_3 system.

magnetization of the feeble ferromagnetism decreases linearly with increase in the content of $MnTiO_3$ from that of the parasitic ferromagnetism in Fe_2O_3. As the parasitic ferromagnetism is greatly affected by the atmosphere under which the specimen is prepared, all specimens are prepared in the same atmosphere. It must also be noticed in the figure that the rate of decrease is the same for both $MnTiO_3$ and $MgTiO_3$ series, which indicate that Mn^{2+}, Mg^{2+} and Ti^{4+} do not contribute at all on the feeble ferromagnetism and the parasitic ferromagnetism of hematite are only diluted by these ions. In Fig. 11, we show the intensity of magnetization at low temperature of the specimens in $MgTiO_3$ series, whose composition deviates slightly from Fe_2O_3. Here we pay an attention to the low temperature transition of the parasitic ferromagnetism found by Morin.[15] As we found in the figure this transition temperature which is confirmed to exist in pure hematite is shifted by about 50°C to the low temperature side when only two mol per cent of $MgTiO_3$ is added to Fe_2O_3. Furthermore such a transition almost disappears when the content of $MgTiO_3$ exceeds 5 mol per cent. The entirely similar phenomenon is observed for $MnTiO_3$ series. In the case of $FeTiO_3$ series the situation is expected to be the same, for which we found as was reported in the previous paper[2] that the specimen of $0.93Fe_2O_3$–$0.07FeTiO_3$ does not show any low temperature transition above 80°K.

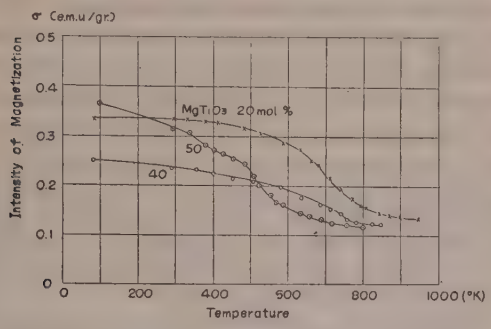

Fig. 9. Intensity of magnetization in a field strength of 8500 Oe. *vs.* temperature for the specimens with $R\bar{3}c$ symmetry of $MgTiO_3$–Fe_2O_3 system.

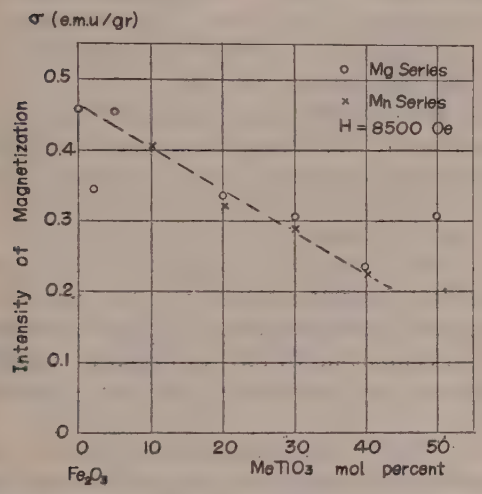

Fig. 10. Intensity of magnetization in a field strength of 8500 Oe. at room temperature *vs.* composition for the specimens with $R\bar{3}c$ symmetry of $MeTiO_3$–Fe_2O_3 system.

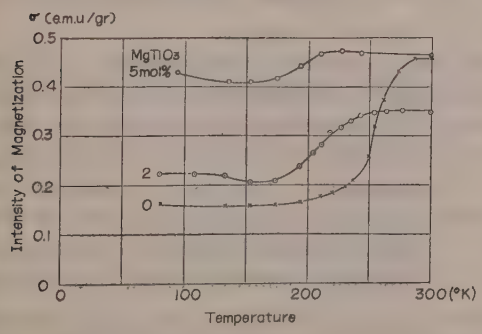

Fig. 11. Thermomagnetic curve at low temperatures of the specimens of $MgTiO_3$–Fe_2O_3 system of which composition deviates slightly from αFe_2O_3.

§ 5. Summary of Experimental Results on Magnetic Properties of Ilmenite-Hematite System

In the above sections we have described the magnetic properties of the $MnTiO_3$, $CoTiO_3$ and $MgTiO_3$ series. These results, together with those of $FeTiO_3$ and $NiTiO_3$ series reported previously, are summarized as follows.

1) All ilmenites except $MgTiO_3$ are expected to be antiferromagnetics having the Néel temperature below 80°K. The magnetic structures of $CoTiO_3$ and $NiTiO_3$ are expected to be the same as that of $FeTiO_3$ which has been determined by the neutron analysis, while $MnTiO_3$ may have a different structure from those of other ilmenites.

2) The solid solutions of any $MeTiO_3$ and Fe_2O_3, $xMeTiO_3$–$(1-x)Fe_2O_3$ have a remarkable characteristic that the magnetic properties of the specimens on the ilmenite side

are considerably different from those on the hematite side. The former is ferrimagnetic at low temperature except in the case of $MgTiO_3$ series which is paramagnetic in this region, while the latter is antiferromagnetic on which the feeble ferromagnetism is superimposed. These characteristics are correlated with the situation that the crystal symmetries of both sides in the solid solutions are different with each other. The ferrimagnetism occurs only in the specimen having the crystal symmetry $R\bar{3}$, that is only in the specimen where Me^{2+} and Ti^{4+} ions are arranged in order, while the antiferromagnetism in the specimen with the crystal symmetry $R\bar{3}c$ where all cations are distributed at random among the lattice sites.

3) All ferrimagnetic specimens have a common characteristic that the magnetization increases almost linearly down to the liquid nitrogen temperature with decrease of temperature, indicating that molecular fields acting on the magnetic ions in these compounds are relatively weak.

4) The mechanism of occurrence of the ferrimagnetism is expected to be the same for $FeTiO_3$, $CoTiO_3$ and $NiTiO_3$ series. By analyzing the results of $FeTiO_3$ series for which the most reliable data have been obtained, we can find the mechanism of ferrimagnetism of this group is different in the following four regions of composition.

i) The region where the magnetization is very weak and the magnetic structure is expected to be antiferromagnetic as a whole on which the feeble ferromagnetism is superimposed, which is $1>x\geqq0.95$ for $FeTiO_3$ series, $1>x\geqq0.9$ for $NiTiO_3$ and $CoTiO_3$ series.

ii) The region where the magnetization at 8500 Oe. increases abruptly with the increase of the content of hematite in the solid solution. The maximum value of magnetization in this region is most close to the value calculated by assuming that all magnetic moments on each layer in the compound are aligned in the same direction, coupling antiferromagnetically with those on the adjacent layer. This region is $0.95>x\geqq0.8$ for $FeTiO_3$ series, $0.9>x\geqq0.8$ for $NiTiO_3$ and $CoTiO_3$ series.

iii) The region where the saturation value of magnetization takes the value lower than the one calculated by adopting the above assumption, which is $0.8>x>0.5$ for $FeTiO_3$ series and $0.8>x\geqq0.7$ for $NiTiO_3$ series.

iv) The region where the saturation value of magnetization decreases sharply to zero with the further increase of the content of hematite in the solid solution, corresponding to the situation that the crystal symmetry $R\bar{3}$ in which Me^{2+} and Ti^{4+} ions are orderly arranged is changed into the symmetry $R\bar{3}c$ in which all ions are arranged at random, which is $0.5\geqq x\geqq0.45$ for $FeTiO_3$ series and $0.7\geqq x>0.6$ for $NiTiO_3$ series.

5) On the contrary to the above situation the ferrimagnetism in $MnTiO_3$ series is caused by an origin common to whole composition range, which may be classified into i) of the above group. That is, the magnetization of all specimens of this solid solution series is very weak and it is far from saturation in the field strength of 8500 Oe.

6) The magnetization of the ferrimagnetic specimen in $FeTiO_3$ series is much affected by the heat treatment, while those of other solid solution series are not affected at all by the heat treatment.

7) The intensity of magnetization of the parasitic ferromagnetism in the antiferromagnetic specimen decreases with the increase of the content of $MeTiO_3$ in hematite, usually attaining to a minimum value for x around 0.4.

8) The low temperature transition of the parasitic ferromagnetism which is observed at 260°K for pure hematite is considerably shifted to the lower temperature side by addition of a small amount of $MeTiO_3$ in hematite. This transition disappears when the content of $MeTiO_3$ is increased more than five mol percent in the solid solution.

9) The magnetic susceptibility of the ferrimagnetic specimens in $FeTiO_3$ series shows a peculiar behavior, that is the value of C_M decreases and the value of Θ in $\chi=C_M/T-\Theta$ increases in keeping its positive sign as the composition changes from $x=1$ to $x=0.5$. Such a situation could not be observed for other solid solution series, that is the value of C_M obtained for these solid solution series can be interpreted by assuming that only spins contribute to the magnetic moment and the values of Θ are negative for the whole range of composition.

B. Discussions

As we have described in detail in the previous papers[1),2)] cation sites in the rhombohedral sesquioxide can be divided into four sublattices A_1, A_2, B_1 and B_2 and three types of superexchange interaction, Γ_a, Γ_b and Γ_c between magnetic ions on these sites have been expected to predominate in the structure. The former two are between magnetic ions on adjacent layers and the latter between ions on the same layer. The coupling angle ∠Me–O–Me is greater for the former than the latter. In order to describe the magnetic structure of pure ilmenite, it is more appropriate to divide the sublattices A_1 and A_2 into four sublattices A_1, A_2, A_1' and A_2' as is shown in Fig. 12. In the following sections

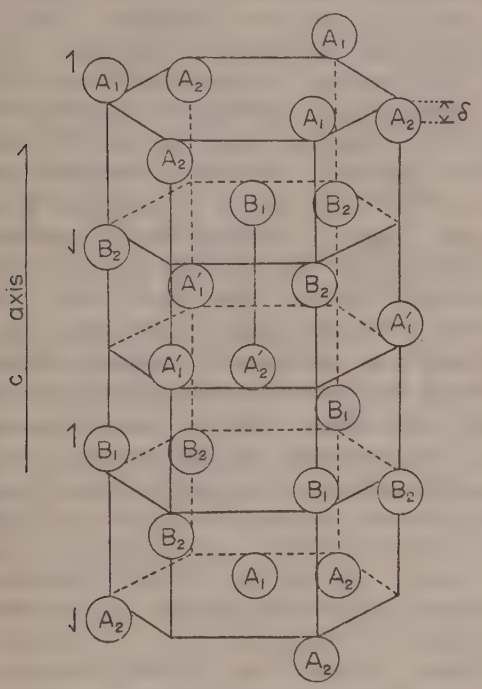

Fig. 12. Cation lattice in a rhombohedral sesquioxide. A- sublattice must be further divided into two sublattices, A and A′ in order to describe the antiferromagnetic structure in ilmenite.

magnetic properties of ilmenite and hematite system will be discussed by using these sublattices and superexchange interactions.

§ 6. Antiferromagnetism in Ilmenite

In ilmenite ($MeTiO_3$) Me^{2+} and Ti^{4+} ions occupy A and B sublattice selectively. As Ti^{4+} ions have no magnetic moments, the antiferromagnetic arrangement of Me^{2+} ions is constructed by two kinds of superexchange interactions. One is that between A_1 and A_2 or A_1' and A_2'; (Γ_c) and the other is that between A_1 or A_2 and A_1' or A_2'. We can easily find that three kinds of antiferromagnetic structure are possible in ilmenite, which are as follows;

(a) A_1+, A_2+, $A_1'-$, $A_2'-$
(b) A_1+, A_2-, $A_1'+$, $A_2'-$
(c) A_1+, A_2-, $A_1'-$, $A_2'+$

where + and − indicate the directions of spins on the lattice site. Through the neutron analysis carried out by Shirane et al. the antiferromagnetic structure of $FeTiO_3$ was determined to be the case (a).[4)] The spins are directed along *c*-axis in it. Hence we may decide that the sign of the superexchange interaction within the layer (Γ_c) is positive in $FeTiO_3$. Although nothing is known about the antiferromagnetism in other ilmenites we can suppose their configurations through the magnetic studies of the solid solution. Because, as we state in detail in the next section, the structures (a), (b) and (c) grant different situations for the magnetic property of the solid solutions. We expect that $NiTiO_3$ and $CoTiO_3$ belong to the case (a), while $MnTiO_3$ to (b). If such an expectation is correct, we may obtain a knowledge about the sign of the superexchange interaction with the coupling angle 90°, the results being indicated in Table II.

§ 7. Ferrimagnetism in the Solid Solution

(a)	$1>x\geqq0.45$	for $FeTiO_3$ series
	$1>x>0.6$	for $NiTiO_3$ series
	$1>x\geqq0.8$	for $CoTiO_3$ series
(b)	$1>x\geqq0.7$	for $MnTiO_3$ series

In this region the ordering of Me^{2+} and Ti^{4+} established in pure ilmenite is retained. Hence Me^{2+} and Ti^{4+} ions are expected to occupy the A and B sublattices respectively, while Fe^{3+} ions distribute at random among all sublattices. If, then, we assume that the intractions Γ_a and Γ_b are negative and their strength is fairly large compared with Γ_c, the magnetic momets on each layer are orientated in the same direction, coupling antiferromagnetically between those on the adjacent layers. Consequently the saturation magnetization of the solid solution, $x MeTiO_3$–$(1-x)$·

Fe_2O_3 at 0°K is given by

$$J_s = J_A - J_B = x\mu_{Me^{2+}}$$

where J and μ_{Me} are the magnetization per one molecule of the solid solution and that of Me^{2+} ions respectively expressed by the number of Bohr magnetons. In Fig. 6 of the sec tion 3, this value is drawn by a straight solid line. As is seen in the figure the estimated saturation values of the magnetization of the solid solutions deviate considerably from this line. As the ferrimagnetism of ilmenite and hematite system is divided into two groups, (a) $FeTiO_3$, $CoTiO_3$ and $NiTiO_3$ series and (b) $MnTiO_3$ series, the deviation from this line is discussed separately for these two groups.

(a) *Ferrimagnetism in $FeTiO_3$, $CoTiO_3$ and $NiTiO_3$ series*

As the magnetic properties of this group is represented by those of $FeTiO_3$ series which had been discussed in detail in the previous paper[2], the ferrimagnetism in four regions of this group is discussed only qualitatively in this section.

i) When the amount of Fe^{3+} ions which enter into the B sublattice is very small and the interaction between cations on the A and B sublattices are too weak to destroy the antiferromagnetic coupling between those on A and A′ sublattices, the spin orientations of cations which enter into the B_1 sublattice are opposite to those of cations on the B_2 sublattice by the reason stated in (b) of this section. Consequently if Fe^{3+} ions are distributed at random among these two sublattices, the resultant spin configurations become antiferromagnetic and the difference in the occupation number between B_1 and B_2 sublattice produces a feeble ferromagnetism. As the interaction between the cations on the A and A′ sublattices is very weak compared with that between the cations on the A and B sublattices, the region i) is expected to be very narrow if the interaction within the A or A′ sublattices, that is Γ_o, is ferromagnetic.

ii) When the amount of magnetic ions on the B sublattice is increased, the antiferromagnetic coupling between the A and A′ sublattice is destroyed by the strong interactions between A and B or B and A′ sublattices and the magnetic moments on both A and A′ sublattices began to align in the same direction,* which results in the sharp increase in the resultant magnetizations with increase in Fe_2O_3 in the solid solution as is seen in Fig. 6. The magnetization of the specimen of $0.8FeTiO_3$–$0.2Fe_2O_3$ attains nearly to the value which is expected when the magnetic moments on A and B sublattices are aligned in the same direction, coupling antiferromagnetically with one another.

iii) When the content of Fe^{3+} ions in the solid solution is further increased the resultant magnetization comes to deviate from the value expressed by $J = x\mu_{Me}$ in spite of the fact that the interaction between A and B sublattices is more increased than that in the region ii). This situation can be interpreted if we put an assumption that the sign of the superexcange interaction with 90° angle Γ_c between Fe^{2+} and Fe^{3+} is negative. This assumption does not seem unacceptable, since we have expected in the above section that the superexchange interaction Γ_c between Fe^{2+} and Fe^{2+} is positive while between Fe^{3+} and Fe^{3+} is negative. Accordingly when the content of Fe^{3+} ions on the A sublattice is increased, negative superexchange interaction is predominant over positive one on the A sublattice. On the other hand, more than half of B sublattice sites are occupied by nonmagnetic ions and then the magnetic coupling between the A and B sublattices is expected to be fairly weak. Such a situation results in a non-saturation of magnetization or a magnetic coupling at an angle on the A sublattice as was theoretically treated by Néel[16] and Yafet and Kittel[17] and found by Prince in $CuCr_2O_4$ through the neutron diffraction analysis[18]. Hence the resultant magnetization deviates from the line $J = x\mu_{Me}$. It has been confirmed through the neutron diffraction analysis that magnetic moments are aligned in the planes perpendicular to c-axis in the solid solution of $FeTiO_3$ and Fe_2O_3[19]. As the anisotropy energy within the layer is expected to be very weak in the rhombohedral oxide,[20),21] the magnetic moments may easily rotate in the plane. Such a situation is very favourable for the coupling of magnetic moments at an angle.

iv) With the further increase of Fe_2O_3 content, the magnetization decreases rather sharply, attaining to zero in both $FeTiO_3$ and $NiTiO_3$ series. This corresponds to the situa-

* see note added.

tion that the perfect ordering of Me^{2+} and Ti^{4+} ions which we assumed in the above consideration is difficult to be maintained even in an annealed specimen[9] and the crystal symmetry changes from $R\bar{3}$ to $R\bar{3}c$ gradually in this region. As the range of $R\bar{3}$ is narrower for $NiTiO_3$ series than for $FeTiO_3$ series, the magnetization at 0°K begins to decrease at the lower content of Fe_2O_3 for $NiTiO_3$ series.

(b) *Ferrimagnetism in $MnTiO_3$ series*

The ferrimagnetism of the $MnTiO_3$–Fe_2O_3 series is greatly different from that of other series. As we can find in Fig. 6 the deviation of the saturation magnetization of $MnTiO_3$ series from the value $J=5x$ is so great that we can not attribute the mechanism of the ferrimagnetism in this series to the same one as that of (a) group.

We have found that such a magnetic property of $MnTiO_3$ series can be interpreted successfully if we assume that the superexchange interaction between Mn ions within a layer is negative. Such an assumption was expected from the fact that $MnTiO_3$ has large negative value of Θ.

In order to explain the magnetic properties of this series, we consider the molecular field $\vec{h}_{B_1}$ or $\vec{h}_{B_2}$ which act on a magnetic ion on B_1 or B_2 sublattice sites. The A sublattice must be divided into four sublattices A_1, A_2, A_1' and A_2' as we show in Fig. 12. Then $\vec{h}_{B_1}$ and $\vec{h}_{B_2}$ are expressed as follows by using the same notation as we used in the previous paper.[2]

$$\vec{h}_{B_1}=2/(Ng^2\mu_B^2)[3\Gamma_a\vec{J}_{a_1}+3\Gamma_b\vec{J}_{a_2}+3\Gamma_a\vec{J}_{a_1'}+\Gamma_a\vec{J}_{a_2'}]$$

$$\vec{h}_{B_2}=2/(Ng^2\mu_B^2)[3\Gamma_a\vec{J}_{a_2}+3\Gamma_a\vec{J}_{a_2'}+3\Gamma_b\vec{J}_{a_1'}+\Gamma_a\vec{J}_{a_1}] \qquad (1)$$

where $\vec{J}_{a_1}$, $\vec{J}_{a_2}$, $\vec{J}_{a_1'}$ and $\vec{J}_{a_2'}$ are the magnetic moments on the A_1, A_2, A_1' and A_2' sublattices respectively. The last term may be neglected as we stated in that paper.[2] The interaction between the B_1 and B_2 sublattices is also neglected because the number of magnetic ions on the B sublattice is small and probability that these magnetic ions form pairs is expected to be very small. We next put another assumption that the configuration of the magnetic moments on the A and A′ sublattices is not altered by the interaction between the A and B sublattices. In the cases of $FeTiO_3$, $CoTiO_3$ and $NiTiO_3$ series, such an assumption was permitted only when the content of magnetic ions on the B sublattice is very small. On the other hand, in the case of $MnTiO_3$ series, such an assumption is permissible for a considerably wide range of content of the magnetic ions on the B sublattice. This is inferred from the situation that as the magnetic moments on the A and A′ sublattice align antiferromagnetically within each sublattice, the magnetic ions on the B sublattice need not destroy the magnetic structure within the A and A′ sublattices, because they tend to align the magnetic moments on both A and A′ sublattices in the same direction through the negative interaction between B and A or A′ sublattices. In the following we discuss the molecular field $\vec{h}_{B_1}$ and $\vec{h}_{B_2}$ in the three possible cases.

i) $\vec{J}_{a_1}=\vec{J}_{a_2}=-\vec{J}_{a_1'}=-\vec{J}_{a_2'}$

This is the case where the magnetic moments are coupled ferromagnetically within each A and A′ sublattice, corresponding to the group (a). In this case the Eq. (1) is reduced to

$$\vec{h}_{B_1}=2/(Ng^2\mu_B^2)\cdot 3\Gamma_b\vec{J}_{a_2}$$

$$\vec{h}_{B_2}=2/(Ng^2\mu_B^2)\cdot 3\Gamma_b\vec{J}_{a_1'}=-\vec{h}_{B_1}. \qquad (2)$$

As this equation shows the direction of the magnetic moment on the B_1 sublattice is opposite to that on the B_2 sublattice. Hence if these two sublattices are occupied by the magnetic ions with an equal probability, the structure is antiferromagnetic as a whole, and a slight difference in the probability produces a weak ferromagnetism. Such a situation may be realized when a very small amount of Fe^{3+} ions is added to $FeTiO_3$, $NiTiO_3$ or $CoTiO_3$. This may correspond to the region i) of the group (a) in the section 5.

ii) $\vec{J}_{a_1}=-\vec{J}_{a_2}=\vec{J}_{a_1'}=-\vec{J}_{a_2'}$.

This is the case where the magnetic moments on the A_1 and A_2 or A_1' and A_2' sublattices are coupled antiferromagnetically, while those on the A_1 and A_1' or A_2 and A_2' sublattices ferromagnetically. In this case the Eq. (1) is reduced to

$$\vec{h}_{B_1}=2/(Ng^2\mu_B^2)(6\Gamma_a-3\Gamma_b)\vec{J}_{a_1}$$

$$\vec{h}_{B_2}=2/(Ng^2\mu_B^2)(6\Gamma_a-3\Gamma_b)\vec{J}_{a_2}=-\vec{h}_{B_1}. \qquad (3)$$

Again in this case the molecular fields on the B_1 and B_2 sublattices are opposite. Hence the situation becomes similar to the case i).

iii) $\vec{J}_{a_1}=-\vec{J}_{a_2}=-\vec{J}_{a_1'}=\vec{J}_{a_2'}$.

In this case the Eq. (1) is reduced to

$$\vec{h}_{B_1}=2/(Ng^2\mu_B^2)\cdot 3\Gamma_b\vec{J}_{a_2}$$

$$\vec{h}_{B_2}=2/(Ng^2\mu_B^2)\cdot 3\Gamma_b\vec{J}_{a_1'}=\vec{h}_{B_1}\,. \qquad (4)$$

From this equation we can find that all magnetic moments which enter into the B sublattice align to the same direction. Then, a strong ferromagnetism is expected to appear and the resultant magnetization J_s of the solid solution $x\mathrm{MeTiO_3}\cdot(1-x)\mathrm{Fe_2O_3}$ is given by

$$J_s=(1-x)J_B=5(1-x)\,. \qquad (5)$$

We can find from these considerations that the solid solution of $MnTiO_3$ and Fe_2O_3 must exclusively belong to the case ii) and therefore find that the only permissible spin configuration in $MnTiO_3$ is (b) of the section 6, that is

$$A_1+,\ A_2-,\ A_1'+,\ A_2'-$$

where + and − means the spin directions on the sublattices. It may be possible to suppose that a tendency that Fe^{3+} ions occupy selectively one of two sublattices is increased when the content of Fe^{3+} ions in the B sublattice is increased. Accordingly the uncompensated magnetic moments are increased with increase in the content of Fe_2O_3 in the solid sulution. Thus we can explain the magnetic properties of $MnTiO_3$ series. We hope that the situation we have expected is examined by the neutron diffraction analysis in near future.

§ 8. Superexchange Interaction with 90° Angle (Γ_o) in the Rhombohedral Oxide

In the above considerations we have shown that the superexchange coupling with 90° angle plays a very important role on the magnetic properties of the solid solution of ilmenite and hematite. In this section we summarize the results obtained from above considerations about the superexchange interaction, which are presented in Table II.

It has been reported that in the chloride of the transition metals the magnetic structure is chiefly determined by the superexchange interaction with 90° angle as in ilmenite. The sign of its interaction is found by the neutron diffraction analysis to be positive in $FeCl_2$, $CoCl_2$ and $NiCl_2$,[22] while in $MnCl_2$ and $FeCl_3$ it is expected to be negative

Table II. The sign of the superexchange interaction with 90° angle in the rhombohedral oxides.

Configuration	Magnetic ions	sign
$(3d)^5$–$(3d)^5$	Fe^{+3}–O–Fe^{+3}	−
	Mn^{+2}–O–Mn^{+2}	−
$(3d)^6$–$(3d)^6$	Fe^{+2}–O–Fe^{+2}	+
$(3d)^7$–$(3d)^7$	Co^{+2}–O–Co^{+2}	+
$(3d)^8$–$(3d)^8$	Ni^{+2}–O–Ni^{+2}	+
$(3d)^5$–$(3d)^6$	Fe^{+3}–O–Fe^{+2}	−
$(3d)^5$–$(3d)^7$	Fe^{+3}–O–Co^{+2}	?
$(3d)^5$–$(3d)^8$	Fe^{+3}–O–Ni^{+2}	−(?)

in taking the sign of Θ of the paramagnetic susceptibility into consideration.[23] These results are very consistent with ours. Furthermore, Kanamori predicted in his theory of superexchange interaction that the interaction with 90° angle between $(3d)^5$ ions is negative, while positive for $(3d)^8$ under a cubic crystalline field.[24] It has been reported that the sign of superexchange interaction is dependent not only on the numbers of electrons in the 3d shell but also on many other factors such as the orbital state of electrons which is determined by the symmetry of crystalline field.[24] Although the crystal symmetry of the chlorides is slightly different from that of ilmenite, the orbital state of cations in ilmenite is expected to be not so different from that of chlorides. Hence our results which are obtained by an indirect method seems to be very reasonable.

§ 9. Magnetic Properties in the Solid Solution with R$\bar{3}$c Symmetry

$0.5\geqq x\geqq 0$ for $FeTiO_3$ series
$0.6\geqq x\geqq 0$ for $NiTiO_3$ series
$0.4\geqq x\geqq 0$ for $MnTiO_3$ series
$0.4\geqq x\geqq 0$ for $CoTiO_3$ series
$0.5\geqq x\geqq 0$ for $MgTiO_3$ series.

All specimens with R$\bar{3}$c symmetry show the antiferromagnetism on which feeble ferromagnetism is superimposed. The antiferromagnetism in the specimen is easily under-

stood by their crystal structure, but as to the origin of the feeble ferromagnetism we can not deduce any decisive conclusion through our experiments. It is, however, expected that its origin must be the same as that in hematite, hence careful investigations of our series may be very profitable for understanding the parasitic ferromagnetism in hematite.

Among many hypotheses proposed to explain the feeble ferromagnetism in hematite, those by Li[25] and Finch and Sinha[26] seem to be the most plausible in the present stage. The one attribute the parasitic ferromagnetism to the uncompensated magnetization in the antiferromagnetic domain walls which is stabilized by some imperfections, while the latter suggest through their electron diffraction analysis that it is a ferrimagnetic deformation of Fe_2O_3 (βFe_2O_3) precipitated in the form of the basal intergrowth with hematite (αFe_2O_3). In any cases, it may be safely said that the parasitic ferromagnetism owes its origin to some imperfections in the crystal.

We have found, as shown in Fig. 10, that the intensity of magnetization of the feeble ferromagnetism in the solid solution is decreased with increase of the content of ilmenite ($FeTiO_3$, $MnTiO_3$ or $MgTiO_3$). This experimental results imply that the parasitic ferromagnetism is entirely inherent to Fe_2O_3 and does not related to such a crystalline defect as dislocations because the addition of $MeTiO_3$ is not expected to decrease systematically such a defect. Accordingly the suggestion of Finch and Sinha is very attractive to explain our experimental results. Detailed investigations are now going on along this line.

In Fig. 11 we showed that the low temperature transition in hematite is lowered with the addition of $MeTiO_3$ in it and disappears when the content of $MeTiO_3$ exceeds 5 mol. per cent. This result is nearly consistent with that of Haigh who measured the effect of addition of Al_2O_3 and TiO_2 in Fe_2O_3.[27] As the low temperature transition is closely related to the change of anisotropy, we may suppose that the addition of small amount of any impurities such as Ti^{4+}, Al^{3+}, Fe^{2+}, Mg^{2+} and Mn^{2+} is sufficient to suppress such a change.

In concluding the present paper the authors wish to express their hearty thanks to Prof. Shozo Sawada and Prof. Takesi Nagata under whose guidance and encouragement the work of this series has been accomplished. Their thanks are also due to Dr. I. Tsubokawa for their magnetic measurement at liquid helium temperature, to Dr. G. Shirane for his neutron analysis and to Mr. Kondho for his illuminating discussions.

Note added

According to a recent communication from Dr. Shirane, it was confirmed through a neutron analysis that the long range magnetic order vanishes in a specimen of $0.9FeTiO_3$ $-0.1Fe_2O_3$ even at 4°K, while broadly diffused scattering lines indicate the presence of short range order. The magnetic moment observed in a field strength of 8500 Oe. for this specimen must be due to that of the cluster.

It seems to be plausible that A–B or A′–B interactions, which are strong enough to destroy the antiferromagnetic A–A′ interaction, are still insufficient to construct a long range magnetic order over the whole crystal in the specimen with this composition.

References

1) Y. Ishikawa and S. Akimoto: J. Phys. Soc. Japan **13** (1958) **13** (1958) 1110.
2) Y. Ishikawa and S. Akimoto: J. Phys. Soc. Japan **12** (1957) 1083.
3) H. Bizette and B. Tsai: C. R. Acad. Sci. **234** (1956) 2124.
4) G. Shirane, S. J. Pickert, R. Nathans: Pittsburgh Diffraction Conference Nov. **7** (1957).
5) H. Bizette, C. Terrier et B. Tsai: C. R. Acad. Sci. **234** (1956) 895. ibid. **234** (1956) 1295.
6) J. M. Hastings and L. M. Corliss: Phys. Rev. **102** (1956) 1460.
7) T. Nagata, S. Akimoto and S. Uyeda: J. Geomag. Geoelec. **5** (1953) 168.
8) Y. Ishikawa: J. Phys. Soc. Japan **13** (1958) 37.
9) Y. Ishikawa: J. Phys. Soc. Japan **13** (1958) 828.
10) Y. Y. Li: Phys. Rev. **102** (1956) 1015.
11) S. Iida: J. Phys. Soc. Japan **11** (1956) 1300.
12) C. G. Shull, W. A. Strauser and E. O. Wollan: Phys. Rev. **83** (1951) 333.
13) Y. Ishikawa: J. Phys. Soc. Japan **12** (1957) 1165.
14) R. M. Bozorth, D. E. Walsh and A. J. Williams: Phys. Rev. **108** (1957) 157.
15) E. T. Morin: Phys. Rev. **78** (1950) 819.
16) L. Néel: Ann. de Phys. **4** (1949) 249.

17) Y. Yafet and C. Kittel: Phys. Rev. **87** (1952) 290.
18) E. Prince: Acta Cryst. **10** (1957) 554.
19) G. Shirane, S. J. Pickert, R. Nathans and Y. Ishikawa: J. Phys. Chem. Solid. to be published.
20) P. W. Anderson, F. R. Merritt, J. P. Remeika and W. A. Yager: Phys. Rev. **93** (1954) 717.
21) H. M. A. Urquhart and J. E. Goldman: Phys. Rev. **101** (1956) 1443.
22) M. L. Wilkinson and J. W. Cable: Bull. Amer. Phys. Soc. **1** (1956) 190.
23) C. Starr, F. Bitter and A. R. Kaumann: Phys. Rev. **58** (1940) 977.
24) J. Kanamori: Busseiron-Kenkyu **105** (1957) 80.
25) Y. Y. Li.: Phys. Rev. **101** (1956) 1450.
26) G. I. Finch and K. P. Shinha: Proc. Roy. Soc. (Lond) A **241** (1957) 1.
27) G. Haigh: Phil. Mag. **2** (1957) 505.

JOURNAL OF THE PHYSICAL SOCIETY OF JAPAN Vol. 13, No. 11, NOVEMBER, 1958

The Temperature Dependence of Forced Magnetostriction

By Toshiro TSUJI*

Department of Chemistry, Faculty of Science, Kyoto University

(Received July 31, 1951)

The forced magnetostriction above technical saturation was measured on some ferromagnetic materials at various temperatures, from the boiling point of oxygen to about 250°C. As expected theoretically, large forced magnetostrictions were observed either as the temperature approached up to the Curie point, or in the sample which has a considerable anomaly of thermal dilatation, such as alloys of invar system. The results obtained were discussed from the standpoint of thermodynamics. We also observed the magnetostriction at the temperature above the Curie point.

§ 1. Introduction

Small deformations of a ferromagnetic crystal in the presence of magnetic field are made up of three parts. The first depends merely on the sharp of the sample, while the second is caused by the anisotropy of the spontaneous distortion. These two effects are observed at low and intermediate field strengths as the sample is magnetized through domain wall motion and by the rotation of magnetization vectors within domains. Beyond the technical saturation there is a different process of magnetization corresponding to the increase in saturation magnetization by external field. In the region of the apparent saturation the sample still changes its dimensions linearly with external field. This deformation is called the forced magnetostriction, or the volume magnetostriction because of its nearly isotropic nature. The forced magnetostriction is closely connected with the anomaly in thermal dilatation. Both effects arise from the volume dependence of spontaneous magnetization.

Ferromagnetic expansion (or contraction) takes place with the appearance of the spontaneous magnetization. The magnitude of the distortion may be estimated by assuming a non-magnetic state below the Curie point. This state is not realized, but its dilatation curve is drawn by extrapolating the real curve in paramagnetic region into the lower temperature range. The difference of these two curves gives the spontaneous distortion. Thus estimated values attain the order of $10^{-3}\sim10^{-4}$ in the relative change of length for ferromagnetic metals. The spontaneous distortion is

This paper was submitted to the Faculty of Science, University of Kyoto, in partial fulfillment of the requirements of the degree of Doctor of Science, July, 1958.

* Present address; Nippon Electric Company Ltd., Tokyo.

almost isotropic. Though the spontaneous distortion itself cannot be measured, its change with magnetic field is observable as the forced magnetostriction. This effect, so small as it is, has an importance in providing us a direct information on the nature of ferromagnetic coupling.

For this reason we have investigated the temperature dependence of the forced magnetostriction of some ferromagnetic materials. The experimental results are discussed from the standpoint of thermodynamics. It has been considered difficult to measure the small magnetostriction at various temperatures, but the difficulty is reduced by the use of strain gauge. At the same time we extended our measurements of the magnetostriction into the region above the Curie point.

§ 2. Theory of the Forced Magnetostriction

The fundamental relation of thermodynamics concerning magnetostriction at constant temperature is given as follows,

$$\left(\frac{\partial\omega}{\partial H}\right)_P = -\frac{1}{V_0}\left(\frac{\partial(VI)}{\partial P}\right)_H, \qquad (1)$$

where V_0 and ω are the unit volume and its its relative change. Using bulk modulus K,

$$\left(\frac{\partial\omega}{\partial H}\right)_P = \frac{1}{KV_0}\left(\frac{\partial(VI)}{\partial\omega}\right)_H. \qquad (2)$$

Let us consider the forced magnetostriction which is proportional to an increase in spontaneous magnetization with field. According to the molecular field approximation we can derive an expression for the volume effect,

$$\left(\frac{\partial\omega}{\partial H}\right) = \frac{1}{K}\frac{dW}{d\omega}\cdot I\left(\frac{\partial I}{\partial H}\right), \qquad (3)$$

where W is the molecular field constant and $dW/d\omega$ means the variation of the exchange interaction with interatomic distance. If the forced magnetostriction is isotropic and sufficiently small, the relative change in volume can simply be obtained from the linear change.

In the equation (3) $d\omega/dH$ is proportional to $I(\partial I/\partial H)$, provided that both $dW/d\omega$ and K are considered to be constant. According to the molecular field theory $I(\partial I/\partial H)$ increases as the temperature approaches to the Curie point from below. Consequently we can observe large forced magnetostriction near the Curie point.

The experimental works on the temperature dependence were made by Kornetzki[1] and Döring[2]. Their results have the same tendency consonant with the above argument, though the measurements were not carried out in wide temperature range. But in this simple theory a difficulty arises in determining the value of $dW/d\omega$. Néel[3] and other authors[4] tried to find this value. It was assumed that the small change in interatomic distance would merely give rise to the variation of exchange interaction without affecting the electronic structure of atom. Nevertheless the results obtained are unsatisfactory in that they contradict with each other; as shown in Fig. 1,

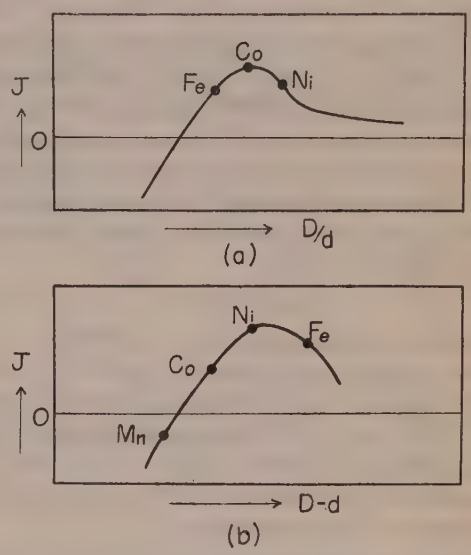

Fig. 1. Interaction curves relating the exchange energy to the distance D between atom centers, with fixed diameter d of $3d$ shell. (a) Bethe-Slater curve. (b) Néel's curve.

$dW/d\omega$ is negative for iron in Néel's interaction curve, but positive in Bethe-Slater's[5].

Using the molecular field approximation Néel gave the relation of the anomaly in thermal dilatation. This result reads as follows;

$$\lambda = \lambda_0(I/I_0)^2, \qquad (4)$$

where λ and λ_0 are the relative change in length of spontaneous distortion at an arbitrary temperature and at 0°K, respectively. The analogous equation can be derived by integrating the equation (3) with regard to I, from 0 to I.

To visualize how the change in dimensions takes place with spontaneous magnetization, we employ the Ising ferromagnet which has

a magnetic moment of spin 1/2 at each lattice point. Two different interatomic distances are assumed for parallel and antiparallel configurations of nearest neighbour spins. Therefore the ordering process of spin gives rise to the change in dimensions. The anomaly in thermal dilatation is due to the spontaneous ordering below the Curie point. The forced magnetostriction corresponds to the field-induced-increase in the degree of order. The strong external field produces the spin ordering in the paramagnetic region. As far as the exchange interaction remains the magnetostriction can be observed even above the Curie point.

On this basis we calculated the mean relative change in length as a function of magnetization. The same equation as (4) was obtained when the Bragg-Williams approximation was used for spin arrangement (See Appendix I). The magnetostriction in the paramagnetic region can be expressed by simply replacing I by (χH), as follows,

$$\lambda = \lambda_0 (\chi H / I_0)^2 , \qquad (5)$$

χ being the paramagnetic susceptibility.

In a rough estimation λ turns out to be more than 10^{-6} for a sample, $\chi = 2 \times 10^{-3}$ emu, $\lambda_0 = 5 \times 10^{-3}$ and $I_0 = 1000$ gausses, placed in the magnetic field of 10,000 oersteds. The relative change of the order of 10^{-6} can be easily detected in our experiments.

§ 3. Experimental Method

To investigate the temperature dependence of the forced magnetostriction the measurements were carried out at various temperatures from the boiling point of oxygen to 250°C. The upper limit means that of using the strain gauge, but it is sufficiently higher than the Curie points of some ferromagnetic materials.

In order to obtain a constant temperature higher than the room temperature we used an oil bath with a heater. The measurement at lower temperatures was made in the Dewar bottle containing cooling agents. These heat controllers have so large heat capacities that the measuring system is not sensible to slight thermal disturbances. A small sample and its holder were set, together with the heat controller, between the pole pieces of De Little type electromagnet. The distance between these pole pieces and their diameters are 3 cm and 5 cm, respectively. A schematical diagram of the apparatus is shown in Fig. 2. With this arrangement we observed the magnetostriction up to the field strength of 23,000 oersteds.

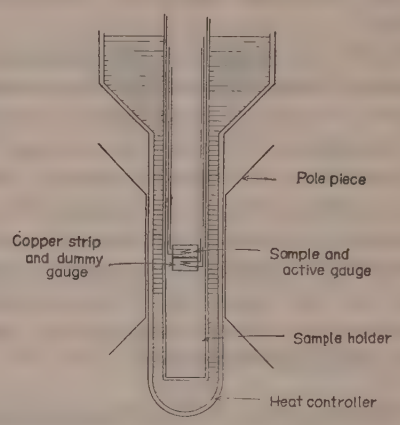

Fig. 2. Schematical diagram of measuring apparatus.

In measuring the magnetostriction the strain gauge technique[6] has been used; the change in length was directly detected by the deflection of galvanometer composing an element of the Wheatstone Bridge circuit. The strain sensitivity of the order of 5×10^{-7} per mm scale can be obtained. Unfortunately the usual strain gauge coated by paper is not available at temperatures higher than 50°C. But the bakelite coated gauge enables us to employ it to 250°C. When we use the strain gauge at much higher temperatures special coating such as ceramic one is necessary.

The usual strain gauge made of the constantan alloy (Ni 44.5%, Cu 55.5%) has large magnetoresistance effect especially at lower temperatures. On the other hand we observed the negligible magnetoresistance effect for the strain gauge of the alloy containing 57% nickel, 16.5% chromium, 24% manganese and 2.5% molybdenum. This gauge was used in the measurement at lower temperatures.

§ 4. Results and Discussions

The anisotropy of the spontaneous distortion or magnetostriction constants can be determined by rotating a crystal in the strong magnetic field. In this state the forced magnetostriction superposes upon the spontaneous distortion. If the forced magnetostriction is

anisotropic the magnetostriction constants would be dependent on the field strength.

Sato[7] pointed out that the anisotropic term was important especially at lower temperatures. The large anisotropy was observed by Vautier[8] for iron single crystal. On the contrary we saw the small anisotropy in forced magnetostriction of 2.6% and 3.2% silicon steel[9]. The similar results were previously obtained by Carr and Calhoun[10].

The magnetostriction in cubic crystal is described analytically by the following equation,

$$\lambda=h_0+h_1\sum_i \alpha_i^2\beta_i^2+h_2\sum_{i>j}\alpha_i\alpha_j\beta_i\beta_j+\cdots, \quad (6)$$

where the α_i's and β_i's are the direction cosines of magnetization and those of measured change in length with respect to the crystal axes. Assuming that λ varies linearly with the external field, we can write all h_i's as follows,

$$h_i=h_i^0+h_i'H. \quad (7)$$

According to our previous data the anisotropic linear coefficients were extremely small for 2.6% and 3.2% silicon-steel. h_1' and h_2' were only a few percent of h_0' in our experiment. In consequence the volume change of the forced magnetostrictions is approximately equal to three times h_0'. Our previous results are cited again in Table I.

The forced magnetostriction is nearly isotropic, especially in the samples having cubic symmetry. Accordingly we used polycrystalline samples in the study of the temperature dependence. We can also estimate the order of magnitude of the forced magnetostriction from the differential form of equation (4),

$$\left(\frac{\partial\lambda}{\partial H}\right)=2\lambda_0\left(\frac{I}{I_0^2}\right)\left(\frac{\partial I}{\partial H}\right). \quad (8)$$

Table I.

Sample	$(\partial\lambda/\partial H)_{obs}$	$(\partial\lambda/\partial H)_{cal}$	λ_0	Is (gauss)	θ (°C)
Ni	-0.31×10^{-10}	-0.5×10^{-10}	-1×10^{-4}*	510	358
Fe	1.7	2	4**	1730	770
2.6% Si-Fe	4.4			1670	746
3.2% Si-Fe	4.7			1560	742
32% Ni-Fe	24.0	40	40**	830	130
37% Ni-Fe	38.6	60	57**	1050	220
10% Cu-Ni	−0.3			415	280
20% Cu-Ni	−0.4			330	180
30% Cu-Ni	−0.6			250	70
Mn-Zn-Ferrite	−3.2			360	220

* Williams[12] ** Chevenard[13]

$(\partial I/\partial H)$ calculated from the molecular field theory is too small as compared with the observed value; for example, this is less than 10^{-5} for nickel, the observed one being 1.3×10^{-4}. Consequently, using the experimental values of λ_0, I and $(\partial I/\partial H)$, we calculated the forced magnetostriction for nickel and iron, as indicated in Table I. These are in good agreement with our experiment.

Kornetzki[1] observed the forced magnetostriction for iron between 0°C and 100°C while Döring[2] studied it for nickel near the Curie point. According to their results the forced magnetostriction increases as the temperature approaches to the Curie point from below, but they did not study it at temperatures below 0°C and above the Curie point. In order to further the study of the temperature dependence in detaie, we measured the forced magnetostriction of the materials having comparatively low Curie temperatures.

It is well known that the invar alloys containing about 30~40% nickel have large anomaly in thermal dilatation. We selected as samples some of these alloys having comparatively low Curie temperatures such as 37% Ni-Fe (θ=220°C) and 32% Ni-Fe (θ=130°C). The samples were prepared by melting the mixed powder. Prior to melting the mixture was reduced in hydrogen gas atmosphere at 600°C for 1 hour. The small ingot was cold rolled

and cut into strips of size $1\times5\times10$ mm. The forced magnetostriction of these samples was measured at various temperatures as shown in Fig. 3. As expected theoretically large forced magnetostriction was observed.

We estimated the values of $(\partial\lambda/\partial H)$ at the room temperature from the anomalies in thermal dilatation. The calculated values are cited in Table I. The values of $(\partial\lambda/\partial H)$ at various temperatures are plotted against the reduced temperature T/θ in Fig. 4. Although the relation (3) predicts a sharp increase of $(\partial\lambda/\partial H)$ near the Curie point, observed $(\partial\lambda/\partial H)$ varies linearly with temperature. The curves have a maximum a little below the Curie temperatures. Such a tendency is consistent with the observed temperature dependence of $I(\partial I/\partial H)$.

Recently Belov[11] measured the change of spontaneous magnetization with linear stress σ for 36% Ni–Fe alloy. The temperature dependence of this change is shown in Fig. 5. It is in fair agreement with the temperature dependence of $(\partial\lambda/\partial H)$ in our experiment, as

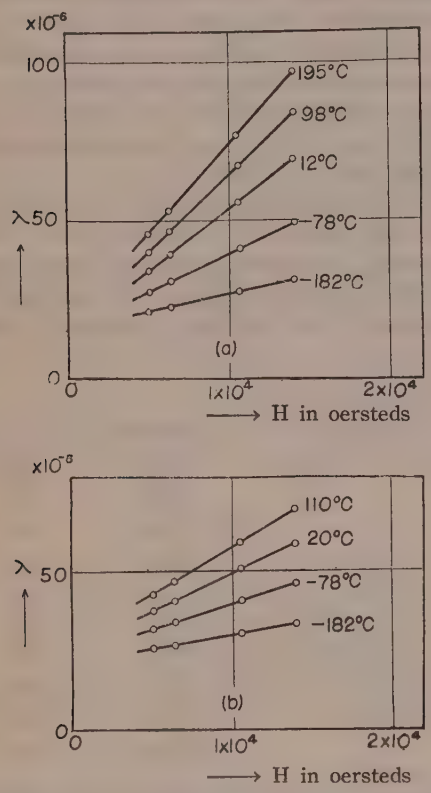

Fig. 3. Linear forced magnetostriction at various temperatures.
(a) 37% Ni–Fe. (b) 32% Ni–Fe.

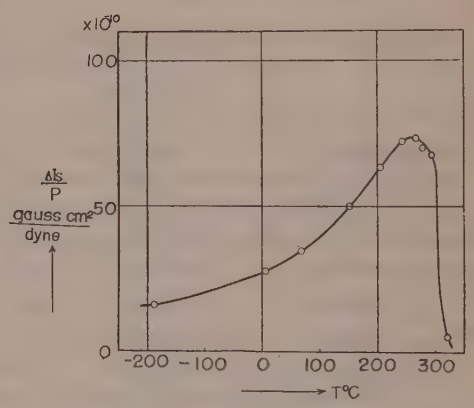

Fig. 5. Temperature dependence of the change of spontaneous magnetization with linear stress for 36% Ni–Fe. (After Belov)

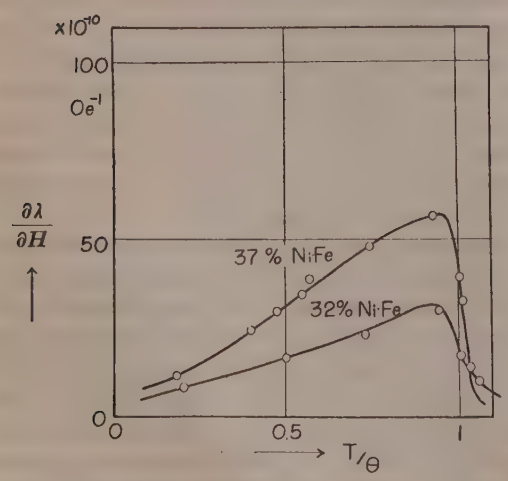

Fig. 4. Temperature dependence of forced magnetostriction.

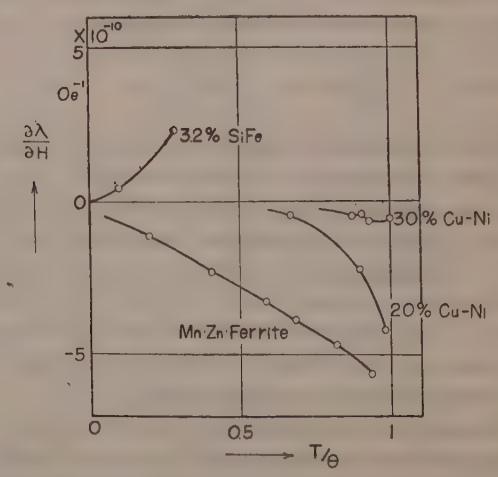

Fig. 6. Temperature dependence of forced magnetostriction.

well expected from the thermodynamical relation,

$$\left(\frac{\partial\lambda}{\partial H}\right)_{T,\sigma}=\left(\frac{\partial I}{\partial\sigma}\right)_{T,H}. \qquad (9)$$

Further we measured the forced magnetostriction of other ferromagnetic materials. Their temperature dependences are shown in Fig. 6. In cases of copper-nickel alloys and a Mn–Zn-ferrite, $(\partial\lambda/\partial H)$ is negative and its absolute value increases with temperature. From the data of the forced magnetostriction we can estimate the ferromagnetic contraction for Mn–Zn-ferrite to be of the order of 10^{-3} in relative change of length.

The magnetostriction in the region above the Curie point has scarcely been investigated up to the present. Using the samples of 32% and 37% nickel-iron alloys we measured the magnetostriction above their Curie points. The results obtained are shown in Fig. 7. At a

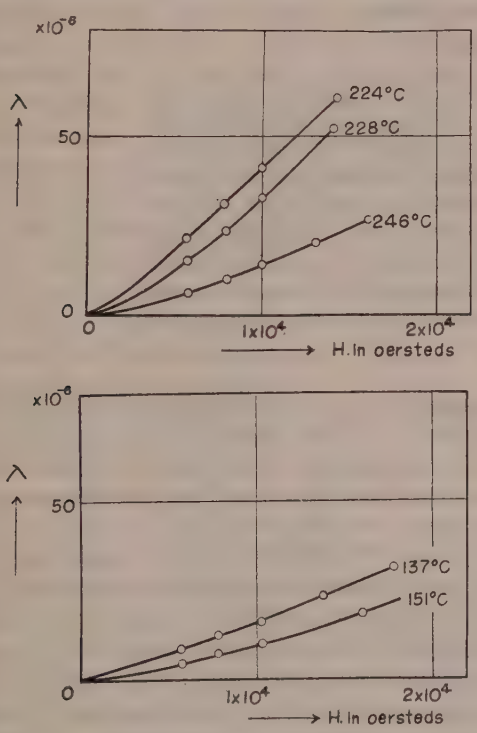

Fig. 7. Magnetostriction at temperatures above the Curie point.
(a) 37% Ni–Fe. (b) 32% Ni–Fe.

sufficiently higher temperature than the Curie point, the change in length is predicted by the equation (5) to be proportional to H^2. But in our case the measurements were carried out a little above the Curie point so that χ is not constant but decreases with the external field. It is natural to consider that the magnetostriction is proportional to the square of the field-induced-magnetization, χH.

From the equation (3) and the experimental data of the forced magnetostriction we get an information on the variation of the exchange interaction with interatomic distance. According to the molecular field theory it is easily seen that the signs of $(\partial\lambda/\partial H)$ and $(\partial W/d\omega)$ are the same. And the larger the forced magnetostriction the greater the variation of the exchange interaction. $dW/d\omega$ thus calculated is consistent with the prediction by Bethe-Slater interaction curve for nickel and iron.

In conclusion the author acknowledges Professor H. Takaki for his kind guidance and encouragement thoroughout the work. The author also thanks Mr. Y. Nakamura and Mr. J. Hayashi for their instructive discussions. The expense involved in this research has been partly defrayed by the Scientific Research Expenditure of the Ministry of Education.

Appendix I

Let us consider a simple cubic crystal composed of N atoms. As mentioned in § 2, a length of the crystal containing $N_{\uparrow\uparrow}$ parallel and $N_{\uparrow\downarrow}$ antiparallel spin pairs is assumed to be proportional to

$$aN_{\uparrow\uparrow}+bN_{\uparrow\downarrow}$$

a and b being the lattice parameters corresponding to the two different spin configurations. According to the Bragg-Williams approximation,

$$\overline{N}_{\uparrow\uparrow}=\frac{zN}{4}\left\{1+\left(\frac{I}{I_0}\right)^2\right\}, \qquad (A1)$$

and

$$\overline{N}_{\uparrow\downarrow}=\frac{zN}{4}\left\{1-\left(\frac{I}{I_0}\right)^2\right\}, \qquad (A2)$$

where z is the number of nearest neighbour atoms and I_0 is the magnetization at 0°K. The magnetic expansion referred to the non-magnetic state is given by

$$\left(\frac{\delta l}{l}\right)_{\text{magnetic}}=\left(\frac{a-b}{a+b}\right)\left(\frac{I}{I_0}\right)^2. \qquad (A3)$$

It is the same relation as Néel's, (4).

References

1) M. Kornetzki: Z. Physik **98** (1935) 289.

2) W. Döring: Z. Physik **103** (1936) 560.
3) L. Néel: Ann. de physique **8** (1937) 227.
4) K. Azumi and J. E. Goldman: Phys. Rev. **93** (1954) 630.
5) J. C. Slater: Phys. Rev. **36** (1930) 57.
6) H. Takaki and T. Tsuji: J. Phys. Soc. Japan **11** (1956) 1153.
7) H. Sato: Phys. Rev. **109** (1958) 802.
8) R. Vautier: Ann. de physique **9** (1954) 322.
9) H. Takaki and T. Tsuji: Metal Phys. **3** (1957) 111, (in Japanese).
10) B. A. Calhoun and W. J. Carr, Jr.: Conference on Magnetism and Magnetic Materials, (1955) 107.
11) K. P. Belov: J.E.T.P. **19** (1949) 346.
12) C. Williams: Phys. Rev. **46** (1934) 1011.
13) P. Chevenard: C.R.A.S. **172** (1921) 594.

JOURNAL OF THE PHYSICAL SOCIETY OF JAPAN Vol. 13, No. 11, NOVEMBER, 1958

Diffusion Processes in Polymers under Irradiation; Polyvinyl Alcohol and CCl_4 System

By Tsutomu WATANABE

Department of Applied Physics, Faculty of Engineering, University of Tokyo, Tokyo

(Received June 20, 1958)

When the PVA film is irradiated in CCl_4, PVA is swollen and crosslinked. A Phenomenological theory is proposed for this experiment. The processes are considered that with the change of diffusion constant CCl_4 enters into PVA as the radiation dose increases, and the radicals from CCl_4 react upon PVA and cause crosslinking. The results of calculation agree reasonably with experiments, that is, the weight changes of swollen polymers against the total dose, the gel fraction changes and the viscosity average molecular weight changes in sol fractions against the total dose. Other various mechanisms that can be considered are discussed.

§ 1. Introduction

On the irradiation effects on polymers, the diffusion processes of radicals or of gas molecules in polymers play sometime an important role, in many relations, such as does rate, temperature, sample thickness dependence of oxidation effect, of gas evolution effect, and of paramagnetic resonance absorption effect, etc. These phenomena have not been researched quantitatively from the standpoint of diffusion mechanism, but only discussed in qualitative views.

It has been known that the gel formation takes place in the aqueous solution of polyvinyl alcohol by irradiation[1], but the similar experiment has not been carried out in the case of PVA-insoluble liquid systems. Recently Yoshitake[2] has discovered new experimental results that the gel of polyvinyl alcohol is obtained by irradiation in carbon tetrachloride, or in dichlorbenzen. With 12.5 rad. sec^{-1} of ^{60}Co gamma-ray dose rate, at room temperature, the polyvinyl alcohol film was irradiated in CCl_4 or in dichlorbenzen to the extent of $10^6 \sim 3\times10^7$ rad. Before irradiation, the PVA film was not swollen at all, but with increase of dose, the liquid molecules entered into PVA and the weight of film was increased. The weight change is so large ($\sim$30% of the initial weight) that the entered molecule may be CCl_4 or dichlorbenzen. When this film was dried in vacuum in order that the entered molecules were made to get out of it, its weight came back to the value of unirradiated and the gel formation was detected from the results of gel fraction and viscosity measurements of its aqueous solution. And the relation between gel fraction and irradiation dose had not the tendency of Charlesby's curve[3]. The detailed report of

these experimental methods and results, involving the measurements of other properties such as infra-red spectra, chemical analysis, etc. is to be published by Yoshitake before long.

These results are also concerned with the diffusion processes of liquid molecules being caused by irradiation. In this paper, the author proposed a phenomenological theory of this mechanism in PVA–CCl_4 system, obtained the results of calculation with some assumptions, and compared them with experimental data, and discussed other mechanisms that can be considered.

§ 2. Theoreticals of Swelling and Gel Fraction

A model of reaction mechanism is proposed as follows. When the PVA film is irradiated in insoluble liquid CCl_4, this film increases the affinity of CCl_4 with certain reason, the liquid molecules enter into polymer and cause the swelling of polymer. The reason of their entrance has not yet been evident from the experimental data that has been given. It may, however, be said that some changes are occured in PVA by irradiation and the value of diffusion constant of CCl_4 in PVA is increased, causing CCl_4 entrance. Then radicals are mainly produced of CCl_4 by radiation, for CCl_4 has the larger G value (70.0)[4] than that of PVA. This radical reacts upon the PVA molecules, maks intermolecular linkings, and network structure of them.

The diffusion equation for CCl_4 entrance is as follows:

$$\nabla[D(r)\nabla u]=\frac{\partial u}{\partial t}\,, \qquad \frac{dr}{dt}=I\,, \tag{1}$$

where $D(r)$; the diffusion constant of CCl_4 in PVA polymer, which is the function of total exposed dose of irradiation, r: the total exposed dose of irradiation, I: the dose rate of irradiation, t: the time, $u(x, y, z, t)$: the concentration of CCl_4 in a place (x, y, z) at a time (t).

The specimens used in Yoshitake's experiments were of 1/100 mm and 3/100 mm films in thickness, and thus equation (1) now becomes one dimentional problem, in which we take x as variable, with the boundary condition of $u(0, r)=u(l, r)=1$ and the initial condition $u(x, 0)=0$ for $0<x<l$ and $u(0, 0)=u(l, 0)=1$. Here we take the variable r instead of t and u is normalize to 1 which is the CCl_4 concentration of corresponding to the maximum swelling, and l is the thickness of specimen.

Equation (1) is solved easily with the resulting formula:

$$u=1-\sum_{n=0}^{\infty}\frac{4}{(2n+1)\pi}\sin\left(\frac{2n+1}{l}\pi x\right)\times\exp\left[-\left(\frac{2n+1}{l}\pi\right)^2\int_0^r\frac{D(r')}{I}dr'\right]. \tag{2}$$

Now we define $U=\int_0^l u dx \Big/ \int_0^l dx$, then

$$U=1-\sum_{n=0}^{\infty}\frac{8}{\pi^2(2n+1)^2}\times\exp\left[-\left(\frac{2n+1}{l}\pi\right)^2\int_0^r\frac{D(r')}{I}dr'\right]. \tag{3}$$

Next, let us consider $D(r)$, $D(r)$ must be zero when $r=0$ because CCl_4 scarcely enters into polymer initially, and $D(r)$ may increase linearly with r when r is small, and be constant when r is infinite. Thus we assume the following formula for $D(r)$:

$$D(r)=D_\infty(1-e^{-\alpha r})\,. \tag{4}$$

We substitute equation (4) to (3), then we aquire the equation:

$$U=1-\frac{8}{\pi^2}\sum_{n=0}^{\infty}\frac{1}{(2n+1)^2}\times\exp\left[-\left(\frac{2\pi+1}{l}\pi\right)^2\frac{D_\infty}{I}\left(r+\frac{1}{\alpha}e^{-\alpha r}-\frac{1}{\alpha}\right)\right]. \tag{5}$$

As U is the average concentration ratio of liquid molecules in PVA per unit volume to the maximum one, we can compare this value with the data of the increased weight ratio of swollen film to the initial one, that is, $\Delta W/W$. U equals to $\Delta W/\Delta W_m$, where ΔW_m is the maximum of ΔW.

In order to determine the value of D_∞ and α experimentally from (3) we can obtain the relation:

$$\frac{l(\partial/\partial l)U}{2(\partial/\partial r)U}=\frac{D(r)}{\int_0^r D(r')dr'}\,, \tag{6}$$

and with (4) we can transform (6) into the following:

$$\frac{l(\partial/\partial l)U}{2(\partial/\partial r)U}=\frac{r}{1-e^{-\alpha r}}-\frac{1}{\alpha}\,. \tag{7}$$

The curves of equation (7) are shown Fig. 1. The intercept of the asymptote is to be $1/\alpha$, and the slope for $r=0$ is to be $\alpha/2$, and we

can get α from these relations. This α is substituted to (5) and we can get the unknown parameter D_∞.

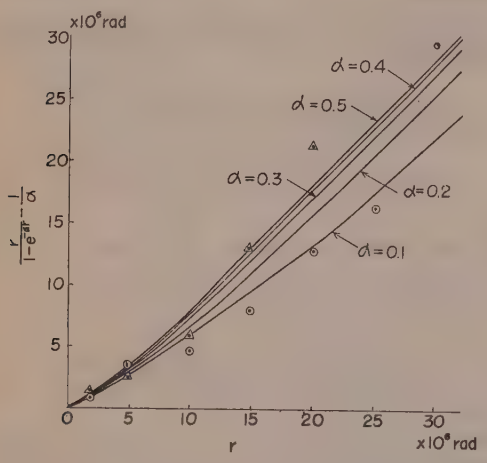

Fig. 1. Relation between $l\frac{\partial U}{\partial l}\Big/2\frac{\partial U}{\partial r}$ and r.

⊙ The values which are derived from the data in the neighbourhood of $l=1/100$ mm.

△ The values in the neighbourfood of $l=3/100$ mm.

Next, we consider the relation between irradiation dose and crosslinking number or gel fraction. Let v be the concentration of radicals produced from CCl_4 by radiation such as Cl, CCl_3 etc., δ be the radiation-induced reaction constant of radical production, that is, the yield of radicals per unit dose rate per unit CCl_4 concentration, β be the reaction constant of radical recombination, then the equation for radicals is

$$\nabla(D_v\nabla v)+\delta Iu-\beta v^2=\frac{\partial v}{\partial t}=I\frac{\partial v}{\partial r}\,. \qquad (8)$$

Taking into account of $\partial v/\partial t\geq 0$ and $v>0$, equation (8) becomes

$$0<v\leq\frac{D_v\nabla^2+\sqrt{D_v^2\nabla^4+4\beta\delta Iu}}{2\beta}\,.$$

One may suppose that D_v is not different so far from D_∞, which is, as described later, of the order of $10^{-11}\,cm^2\,sec$. $D_v\nabla^2$ is of the order of $I(\partial/\partial r)$ in equation (1), from experimental data it is of the order of $10^{-6}\,sec^{-1}$, and δIu is of the order of $10^{-9}\sim10^{-8}\,sec^{-1}$ which is obtained from the G value of CCl_4 and its concentration and PVA density. It is very difficult to estimate the order of β, because β concerns the various process, such as the mobility of radical in PVA, the transmission coefficient of reaction, the activation energy, etc., and can not be measured directly in this case. The smallest β may be obtained from the case of solid polymer phase. We can get the smallest β from the data of paramagnetic resonance[5], and it seems to be of the order of $10^3\sim10^{-1}\,sec^{-1}$ [6]. On account of the swollen polymer system in our case, β is supposed to have the larger value than that of solid polymer. And if (8) is stationary in the region of $r=10^6\sim10^7$ rad., β is the order of $<10^{10}\,sec^{-1}$. We consider, therefore, three cases when β is of the order of 10^{-1}, 10^8, and $10^{10}\,sec^{-1}$, which correspond to 10^{-18}, 10^{-13}, $10^{-11}\,cm^3\,sec^{-1}$ in CGS units respectively. For $\beta=10^{-1}\,sec^{-1}$, we get $0<v\leq10^{-4}$ which correspond to the value smaller than 10^{17} radicals cc^{-1}.

The first term of equation (8) is of the order of $10^{-10}\,sec^{-1}$, the second one is of the order of $10^{-9}\sim10^{-8}\,sec^{-1}$ and the third one is less than the second. Then we ignore the diffusion term in (8) in treating v. In stationary state,

$$v=\sqrt{\frac{\partial Iu}{\beta}} \qquad (9)$$

and in the other two cases with the numerical calculation by the method of perturbation which is shown in appendix, we obtain v as a function of u and x, namely,

$$v=f(u,\ x)\,. \qquad (9')$$

The crosslinking process is considered in the case of unimolecular, or bimolecular reaction mechanism such as

$$\left.\begin{aligned}\frac{\partial r}{\partial t}&=kv\\ \frac{\partial\gamma}{\partial t}&=kv^2\end{aligned}\right\}, \qquad (10)$$

where γ is the crosslinking index to the initial molecule of PVA in a place x, k is a constant. But it is said that PVA in the solid state degrade by irradiation[7] and the gel formation of PVA aqueous solution by irradiation is well explained with a mechanism of endlinking process[1]. It is the reason why we must take the bond rupture process of main-chain of PVA into account. Now let γ'' be the true crosslinking index which is the average number of crosslinked monomers per molecule, taking the main-chain rupture into account[3], then

$$\gamma''=\frac{r}{1+P_0\varepsilon r}\,, \qquad (11)$$

where P_0 is the number average of number of monomer units for the initial PVA molecules, and ε is the probability of the main-chain rupture per monomer per unit dose, equals to $8.7\times10^{-11}\,\mathrm{rad}^{-1}$ from the data of G value of PVA main-chain rupture, namely, 1.8[7]. The viscosity average of the degree of polimerization, where exponential factor is 0.62, is 1740 in our case, and so the number average P_0 is 855 with assuming the Poisson distribution for the degree of polimerization.

The measured gel fraction G are related with γ'' by the following equation, that is,

$$G=\langle g\rangle_x=\frac{1}{l}\int_0^l g\,dx \tag{12}$$

where g is the local gel fraction in a place x at a time t, $\langle g\rangle_x$ means x average of g. And

$$\left.\begin{aligned} g&=\frac{1}{2}-\frac{1}{\gamma''}+\sqrt{\frac{1}{4}+\frac{1}{\gamma''}} && \text{for } \gamma''\geq\frac{1}{2}\\ g&=0 && \text{for } 0\leq\gamma''<\frac{1}{2}\end{aligned}\right\} \tag{13}$$

which is derived from the equation[3]

$$s(1+\gamma''-\gamma''s)^2=1$$
$$s=1-g$$

where s is the sol fraction.

Equations (9) and (9′) do not involve an unknown parameter, but in (10) k is not known from other data. In order to decide k from the measured gel fraction, one point, that is, the value of r from $G=50\%$ in the specimen of $l=1/100$ mm, is used.

With such known parameters, we can calculate G. The line shape of G against r for $l=1/100$, $l=3/100$ mm, and the separating space of two curves can be compared with experiments.

§ 3. Comparison with the Experimental Data of Swelling and Gel Fraction

We get α, $1.0\times10^{-5}\sim5.0\times10^{-5}\,\mathrm{rad}^{-1}$ from Fig. 1, where $\partial u/\partial l$ has been obtained by way of interpolation. Now we take the value of α $2.0\times10^{-5}\,\mathrm{rad}^{-1}$. Then from the data U and r in Fig. 2, when $l=1/100$ mm, we take the value of $D_\infty/I=1/4\times10^{-12}\,\mathrm{cm}^2\,\mathrm{rad}^{-1}$. In Fig. 3 we can show U as a function of ρ only, where

$$\rho=D_\infty\left(r+\frac{1}{\alpha}e^{-\alpha r}-\frac{1}{\alpha}\right)\Big/Il^2 \tag{14}$$

and the shape of U against ρ agree with each other in the general character. We may, therefore, conclude that U is a formula as shown in (5), and the diffusion process of CCl_4 is regarded to obey generally the equation (1). $D_\infty=3.13\times10^{-11}\,\mathrm{cm}^2\,\mathrm{sec}^{-1}$ can be compared with the diffusion constant of gas in rubber which is of the order of $10^{-9}\,\mathrm{cm}^2\,\mathrm{sec}^{-1}$, and so be regarded plausible, considering that PVA can permeate gas much less than rubber.

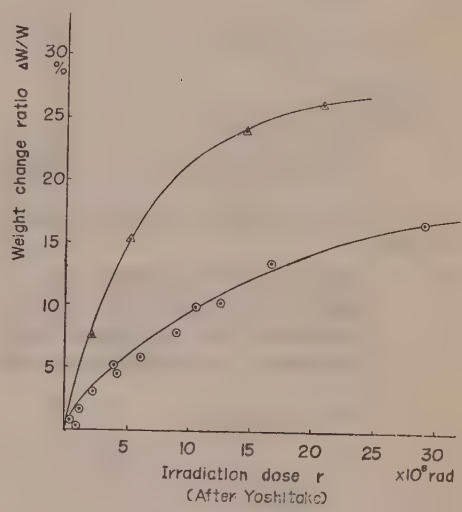

Fig. 2. Relation between weight change ratio and irradiation dose.

⊙ 1/100 mm specimen.
△ 3/100 mm ,, .

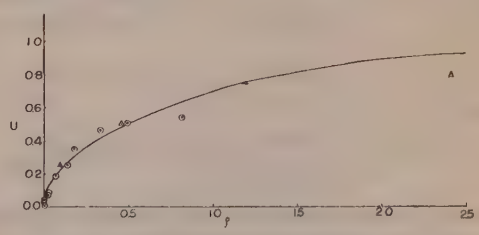

Fig. 3. Relation between U and ρ.

⊙ 1/100 mm.
△ 3/100 mm.

Numerical solutions of (8) with $\beta=1$ and $10^8\,\mathrm{sec}^{-1}$ are performed. We see that, when $\beta=10^8\,\mathrm{sec}^{-1}$, v equals almost to that of the stationary state. And that little difference is obtained among four cases, that is, stationary-unimolecular, -bimolecular, nonstationary-unimolecular, and -bimolecular, as shown in Fig. 4, so it is impossible to decide which process is the most proper one to explain. But the

line shapes and the separation of two lines agree well with the experimental data in four cases. While, among these processes in (9), (9′), and (10) the stationary-unimolecular reaction type may be proper. Because, in liquid CCl_4, β may not be so small, and from G

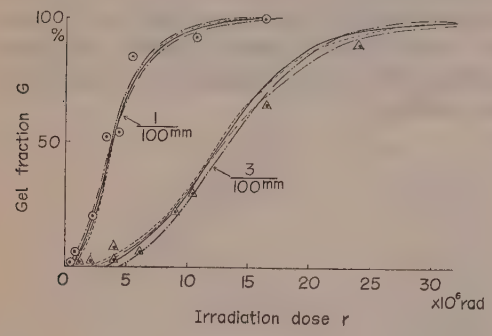

Fig. 4. Relation between gel fraction and irradiation dose.

——— stationary and bimolecular type.
—··—·· stationary and unimolecular type.
- - - - - unstationary and bimolecular type.
—·—·— unstationary and unimolecular type.

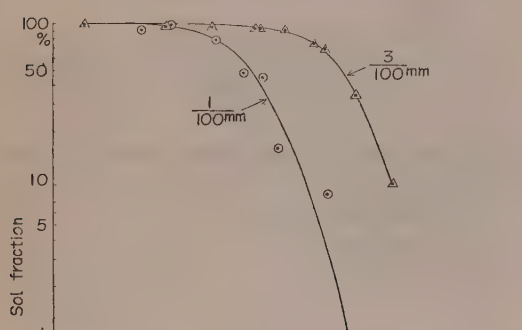

Fig. 5. The log-log plot of sol fraction against total dose. (After Yoshitake)

value of CCl_4 and the measured G about 3.2 radicals may produce one crosslink, so crosslinking reaction seems to be of so high efficiency that it is supposed unimolecular. But for deciding the reaction mechanism of crosslinking it is necessary to observe the dose rate dependency of viscosity and gel fraction, and the swelling ratio which is effective when γ'' is large. The relation between $\log(1-G)$ and $\log\gamma$ is shown in Fig. 5 and these curves do not resemble to the Charlesby's ones. The reason is evident, because in (11) γ is not a linear function of r, and that the crosslinking reaction does not occure homogeneously in every place, so γ'' increases rapidly with r in the neighbourhood of $x\sim 0$, $x\sim l$, and the gel formation takes place early, but late in the neighbourhood of $x\sim l/2$. Consequently it is only the case when l is small ($\sim$1/1000 mm) and r is large, to be able to compare $\log(1-G)$ with the Charlesby's curve.

§ 4. Changes of the Molecular Weight before Gel Formation

In the above description, we consider the both processes of crosslinking and degration, and that the ratio of probability $\gamma/\varepsilon p_0$ of crosslinking to that of degradation are not constant as illustlated in Fig. 6. So it is of importance

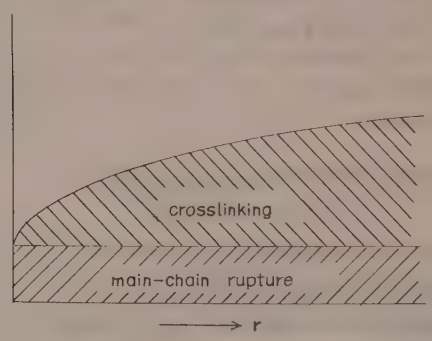

Fig. 6. The ratio of crosslinking to main-chain rupture is a function of r.

to investigate the behavior of molecular weight before gel formation.

From Saito's equation[8], we can obtain

$$\frac{\partial m(p,r)}{\partial t}+2pm(p,r)\dot{c}(r)$$
$$=\dot{c}(r)\int_0^p p'(p-p')m(p',r)m(p-p',r)dp' \tag{15}$$

and

$$m(p,r)=n(p,r)/N$$

where $n(p,r)$: the number of molecules which have the degree of polimerization p and are exposed to radiation r, $\dot{c}$: the probability of a monomer to form the active centre for crosslinking by unit radiation, which is not a constant but a function of r in our case. In the same manner in reference (8), we can obtain the number average of molecular weight M_n and the weight average of molecular

weight M_w as follows:

$$M_n = M_{n,0} \cdot f_{0,0} \Big/ \left(f_{0,0} - \int_0^r \dot{c}(r')dr' \right) \qquad (16)$$

where $f_{0,0} = \int_0^\infty m(p, 0)dp$, $M_{n,0}$ is the initial number average of molecular weight, and

$$M_w = M_{w,0} \Big/ \left(1 - 2\int_0^r \dot{c}(r')dr' \cdot f_{2,0} \right) \qquad (17)$$

where $f_{2,0} = \int_0^\infty p^2 m(p, 0)dp$, $M_{w,0}$ is the initial weight average of molecular weight.

In order to take the degradation effect into account, we can as well take m involving the effect of degradation for the initial $m(p, 0)$ in calculating $f_{0,0}$ and $f_{2,0}$. By assuming Poisson distribution initially, M_n and M_w become

$$\left.\begin{aligned} M_n &= \frac{M_{n,0}}{1+\varepsilon p_0 r - p_0 \int_0^r \dot{c}(r')dr'} \\ M_w &= \frac{M_{w,0}}{1+\varepsilon p_0 r - 4p_0 \int_0^r \dot{c}(r')dr'} \end{aligned}\right\} \qquad (18)$$

here

$$2p_0\dot{c}(r) = \frac{\partial \gamma}{\partial r} \quad \text{and} \quad \gamma = 2p_0 \int_0^r \dot{c}(r')dr'$$

with (9), (9′) and (10), we can calculate numerically M_n and M_w against r.

As in every case mentioned in (9), (9′) and (10), γ is scarcely different from one another when $\gamma \lesssim 3$, we take the simplest case, namely

$$\begin{aligned} r &= 2p_0 \int_0^r \dot{c}(r')dr' = \frac{k\delta I}{\beta} \int_0^r u(r')dr' \\ &= \frac{k\delta I}{\beta} \int_0^r \Bigg\{ 1 - \sum_{n=0}^{\infty} \frac{1}{(2n+1)\pi} \sin\left(\frac{2n+1}{l}\pi x\right) \\ &\quad \times \exp\left[-\left(\frac{2n+1}{l}\pi\right)^2 \right. \\ &\quad \left. \times D_\infty \left(r' + \frac{1}{\alpha} e^{-\alpha r'} - \frac{1}{\alpha} \right) \right] \Bigg\} dr' . \end{aligned} \qquad (19)$$

For small r, $\int_0^r p_0\dot{c}(r')dr'$ changes like something in proportion to r^3 in the above case and also in proportion to $r^n (n > 1)$ in the other three cases. For large r changes as $\gamma = A - Br$ (A, B are constants) in all cases. Accordingly, when r is small,

$$4p_0 \int_0^r \dot{c}(r')dr' < \varepsilon p_0 r$$

and we obtain

$$\frac{\partial M_n}{\partial r} < 0 , \qquad \frac{\partial M_w}{\partial r} < 0 .$$

When the gel formation occurs, γ'' must be 1/2 in (11), so

$$1 + \varepsilon p_0 r - 4p_0 \int_0^r \dot{c}(r')dr' = 0 .$$

Then, M_w must have a minimum as shown in Fig. 7, but M_n has not always a minimum.

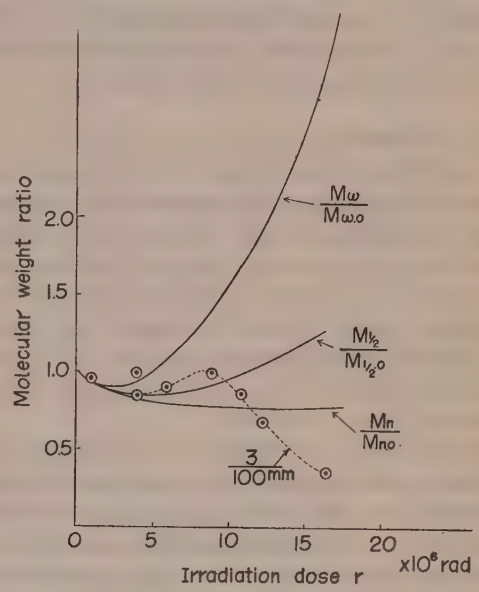

Fig. 7. Relation between molecular weight dependence and irradiation dose.

Numerical calculations of $\langle M_n \rangle_x$ and $\langle M_w \rangle_x$ are carried out by the equation:

$$\left.\begin{aligned} \langle M_n \rangle_x &= \frac{1}{l} \int_0^l \frac{M_{n,0}dx}{1+\varepsilon p_0 r - \frac{1}{2}\gamma(r, x)} \\ \langle M_w \rangle_x &= \frac{1}{l} \int_0^l \frac{M_{w,0}dx}{1+\varepsilon p_0 r - 2\gamma(r, x)} \end{aligned}\right\} \qquad (20)$$

but the averages are not taken into account for M_n and M_w of the following value, that is; $M_n > 4M_{n,0}$ and $M_w > 4M_{w,0}$ respectively, because the measured viscosity is not considered to be detected with these conditions.

It is very difficult to calculate the viscosity average of molecular weight M_v against r (the exponent of viscosity against molecular weight is 0.62 for PVA–H_2O system). But Saito has gotten the viscosity average molecular weight in the analytical form with the constant ratio of crosslinking and degradation. From his formula one can get $M_{1/2}$ with the previous method, that is,

$$M_{1/2}=M_{1/2,0}(1+p_0\mathcal{E}r)^{1/2}\int_0^1\frac{y^{3/2}dy}{(1-y)^{1/2}\left[1-2y(y+1)\int_0^r c(r')dr'\Big/(1+p_0\mathcal{E}r)\right]^{1/2}}.$$

The calculation of $M_{1/2}$ can be easily made by using the table of elliptic integrals[10] and was performed, averaging out with x only for $M_{1/2}\leq 4M_{1/2,0}$. Since the viscosity average of molecular weight M_v is a value between M_w and $M_{1/2}$, the results of calculation agree plausibly with experiments as shown in Fig. 7 which are measured from the aqueous solutions of soluble part of these films.

§ 5. Discussion

The diffusion mechanism in the microscopic sense which causes CCl_4 entrance has not yet been clear, but we may suppose three cases. The first of these is the process that is shown in equation (1), that is, PVA is made by irradiation some chemical changes that occur to increase the diffusion constant of CCl_4. The chemical changes may be something like bond-rupture or decrystalization.

Second, the permeation of molecule into polymer is regarded to be decided by the solubility for its molecule and the diffusion constant, that is, the permeability constant is represented by the product of the solubility and the diffusion constant. It is also supposed that the entrance of CCl_4 into PVA caused by the change of overall solubility of PVA for CCl_4. If so, the equation that determine $u(x, r)$ is the following form, i.e.

$$D\nabla^2 u=I\frac{\partial u}{\partial r} \tag{22}$$

with the initial and the boundary conditions:

$$u(x, 0)=0$$
$$u(0, r)=u(l, r)=1-e^{-ar}$$

where the boundary condition $1-e^{-ar}$ is the overall solubility that changes in this case with r and D is constant.

We can solve equation (22) by the method of Duhamel[11], with the resulting formula

$$\left.\begin{aligned} u&=\sum_{n=0}^{\infty}\frac{4}{(2n+1)\pi}\sin\left(\frac{2n+1}{l}\pi x\right)\\ &\quad\times\left\{1-e^{-Br}-\frac{B}{B-a}(e^{-ar}-e^{-Br})\right\}\\ B&=\frac{D}{I}\left(\frac{2n+1}{l}\pi\right)^2 \end{aligned}\right\} \tag{23}$$

and

$$U=\sum_{n=0}^{\infty}\frac{8}{(2n+1)^2\pi^2}\left\{1-e^{-Br}-\frac{B}{B-a}(e^{-ar}-e^{-Br})\right\}, \tag{24}$$

on the other hand equation (2) becomes

$$u=\sum_{n=0}^{\infty}\frac{4}{(2n+1)\pi}\sin\left(\frac{2n+1}{l}\pi x\right)\times\{1-e^{-Br}-(\exp(-(2n+1)^2\rho)-e^{-Br})\}. \tag{25}$$

Comparing (23) with (25), we can see that both equations resemble to each other in x and r dependency, and choosing the favourable values of D and a, we can make u in (23) agree with experiment. In fact, u in (23) agrees with experiment in every case of $l=1/100$ and $l=3/100$ mm with the values of $D=D_\infty$ and $a\cong(1/3)\cdot D_\infty/I(\pi/l)^2$.

Third, HCl or PVA chloride, for instance, are produced in PVA by irradiation after reacting CCl_4 or Cl_2 to PVA molecule, and more CCl_4 enters into the solid polymer as the results of inducing of HCl or PVA chloride. The presence of HCl or PVA chloride may determine the local solubility of PVA for CCl_4, and so u is a function of HCl concentration or chride contents in PVA molecule. According to this view, the diffusion equation is as follows:

$$\nabla[D\nabla u+\mathrm{grad}\ V(u)]=\frac{\partial u}{\partial r} \tag{26}$$

where $V(u)$ is a potential for CCl_4 in PVA. Equation (26) becomes

$$\nabla\left[\left(D+\frac{\partial V(u)}{\partial u}\right)\nabla u\right]=I\frac{\partial u}{\partial r}. \tag{27}$$

In general character, V must be infinite or very large value for $u=0$, because none of CCl_4 entered into PVA, and must have minimum for $u=1$, because when $u=1$ and force is not act on CCl_4 in PVA. $D(r)$ in (1) may regard as corresponding to $\langle D+\partial V/\partial u\rangle_x$ in (27), here $\langle D+\partial V/\partial u\rangle_x$ means the x average of $D+\partial V/\partial u$. More generally we may consider the equation such as

$$\nabla^2 u+\nabla^2 V(x, y, z, r)=I\frac{\partial u}{\partial r}.$$

And in the case of one dimensional problem by means of Laplace transformation of r, we

can obtain the potential form of $V(x, r)$ from the data of l and r dependency of experimental U. In order to study this process more completely, one expects the measuring data of more various shapes and thickness of specimens and of its temperature dependency.

One may anxious to use (11) and to take m involving the effect of degradation, for the initial $m(p, 0)$ in calculating $f_{0,0}$ and $f_{2,0}$ in (16) and (17) in spite of non-constant ratio of crosslinking and main-chain rupture. Nevertheless, it is proper, because in Charlesby's or Saito's theory, nothing like the velocity of crosslinking or degradation, or the sexuences of these processes is taken into account, and the matter is treated as it is static.

In above we have considered crosslinking only to explain the forming of gel, but it is possible to suppose to cause the gel formation as a result of endlinking process. And it is difficult to conclude which process, crosslinking or endlinking, is more proper without other experimental results. Anyway, it is known that, no sooner the chain rupture has occured by 2/3 per initial molecule, than the gel formation has begun to appear when the radicals of ruptured end is most effectively used[12]. Only 0.5 bond per number average molecule is ruptured directly for 3×10^6 rad which correspond to the dose of 50% gel fraction of 1/100 mm specimen. According to the high efficiency of gel formation and to the effect of specimen's thickness, the bond rupture for endlinking must be caused by the influence of radicals from CCl_4 or HCl, if the endlinking process be the main process. But it does not seem natural to suppose the process of the main-chain rupture by the external radicals, for its reaction must be complicated one.

Acknowledgement

The author is much indebted to Mr. T. Yoshitake for his kind offer of experimental data. And he wishes to express his gratefull thanks to Prof. A. Amemiya and Dr. K. Shinohara for their helpful advice from mathematical and experimental aspects, and to Prof. O. Saito and Mr. M. Inokuti for their valuable remarks and suggestions. He also thanks to other members of the Group for the Study of Irradiated Polymers in Tokyo, who gave the usefull discussions.

Appendix

In order to solve equation (8) neglecting the diffusion term, with non-stationary state, the method of perturbation is used as follows. As u is a slowly varing function of r, u can be expanded with r's power series, that is,

$$u=u_0+u_1(r-r_i)+u_2(r-r_i)^2+\cdots . \qquad \text{(A1)}$$

And we set

$$v=v_0+v_1+v_2+\cdots$$

that is, the solution of zeroth order, first order and second order approximation, etc.

One can easily obtain v_0, namely,

$$v_0=\sqrt{\frac{I\delta u_0}{\beta}}\tanh\left\{\sqrt{\frac{\beta}{I}}[(r-r_i)+r_i']\right\}, \qquad \text{(A2)}$$

where r_i' is determined with the condition $v_0=v(r_i')$ for $r=r_i'$. And v_1 becomes

$$v_1=\exp\left(-2\int_{r_i}^{r}\frac{\beta}{I}v_0dr'\right)\times\left[\int_{r_i}^{r}\delta u_1(r'-r_i)\cdot\exp\left(2\int_{r_i}^{r'}\frac{\beta}{I}v_0dr''\right)dr'\right] \qquad \text{(A3)}$$

with assuming $v_1v_0 \gg v_1^2$.

But when $r_0=0$ the expanded form of u do involve zeroth power of r, then we must solve (8) by some different method. In this case, in (A1) $u_0=0$ and $v_0=0$, equation for v_1 is

$$\delta Iu_1r-\beta v_1^2=I\frac{dv_1}{dr} . \qquad \text{(A4)}$$

When we set

$$\frac{\beta}{I}v_1=\frac{1}{\eta}\frac{d\eta}{dr}$$

and

$$r=\frac{3}{2}\xi^{2/3} \qquad \eta=\xi^{1/3}\omega . \qquad \text{(A5)}$$

Equation (A4) becomes

$$\frac{d^2\omega}{d\xi^2}+\frac{1}{\xi}\cdot\frac{d\omega}{d\xi}-\frac{1}{9}\frac{\omega}{\xi^2}-\delta u_1\frac{\beta}{I}\omega=0 .$$

And we can solve easily with the resulting formula,

$$\omega=AJ_{1/3}\left\{\sqrt{-\delta u_1\frac{\beta}{I}}\xi\right\}+BJ_{-1/3}\left\{\sqrt{-\delta u_1\frac{\beta}{I}}\xi\right\} \qquad \text{(A6)}$$

where A and B are constant.

Considering that r is small, and

$$v_1=\frac{\delta Iu_1}{4\beta}r^2 . \qquad \text{(A7)}$$

Next, we divide r axis into n parts, and

denote r and u as follows

$$r_0,\ r_1,\ r_2,\ \cdots r_i,\ \cdots r_n$$

$$r_{i+1}-r_i=\Delta r$$

$$u(r_0)=u(0)=0$$

$$u(r_1)=u(1),\ u(r_2)=u(2),\ \cdots u(r_i)=u(i),\ \text{etc.}$$

and

$$u_1(i)=\frac{u(i+1)-u(i)}{\Delta r}\ .$$

Considering that $(r-r_i)$ is small and $v\ll 1$ with above expression we can obtain $v(i)$ from the value of $v(i-1)$ using the succesive approximation, namely,

$$\left.\begin{aligned} v(i)=v(i-1)&+\left[2\sqrt{\delta u(i-1)}\left(1+\frac{\beta v(i-1)^2}{I\delta u(i-1)}\right)\right.\\ &\left.+\frac{\delta}{2}(u(i)-u(i-1))\right]\Delta r\\ &-4\frac{\beta}{I}\left[\left(1+\frac{\beta v(i-1)^2}{I\delta u(i-1)}\right)v(i-1)\right]\Delta r^2\\ &\qquad\qquad\qquad\qquad \text{for}\quad i\neq 1\\ \text{and}\quad v(1)=&\frac{\delta I u(1)}{4\beta}\cdot\Delta r \qquad\qquad \text{for}\quad i=1 \end{aligned}\right\}. \tag{A8}$$

References

1) A. Danno: J. Phys. Soc. Japan **13** (1958) 722. J. Berkowitch, A. Charlesby and V. Desreux: J. Polymer Sci. **25** (1957) 490.
2) T. Yoshitake: Private communication; The Second Simposium of Atomic Energy of Japan, Feb. 2-4, 1958, Tokyo.
3) A. Charlesby: J. Polymer Sci. **11** (1953) 513; Proc. Roy. Soc. (London) **A222** (1954) 542.
4) A. Prevost-Bernas, A. Dhapiro, C. Gousin, Y. Landler and M. Magat: Disc. Faraday Soc. **12** (1952) 98.
5) E. E. Shneider: Disc. Farady Soc. **19** (1955) 158.
6) T. Watanabe: J. Phys. Soc. Japan **13** (1958) 1063.
7) A. Danno: J. Phys. Soc. Japan **13** (1958) 609.
8) O. Saito: J. Phys. Soc. Japan **13** (1958) 198.
9) O. Saito: to be published in this Journal.
10) P. F. Byrd and M. D. Friedman: "*Hondbook of Elliptic Integrals for Engineers and Physicists*" Springer (1954).
11) R. Courant und D. Hilbert: "*Methoden der Mathematischen Physik II*" Springer (1937) 184.
12) A. Charlesby: Proc. Roy. Soc. (London) **A232** (1955) 521.

JOURNAL OF THE PHYSICAL SOCIETY OF JAPAN Vol. 13, No. 11, NOVEMBER, 1958

The Study of the Transition Phenomena of Chain Polymers by the Photoelastic Method

By Motozo KANEKO

Department of Physics, Faculty of Science, Hokkaido University

(Received July 5, 1958)

In the present work, it is reported that the glass transition phenomena of chain polymers can be studied by observing the temperature dependency of the photoelasticity of the materials, and the transition temperature determined using this method agrees with the second order transition point by the specific volume method for P.V.C., but for polystyrene it is a little higher and rather near to the softening point by the dynamical elastic method.

§ 1. Introduction

The glass transition phenomena of chain polymers have been studied by a few methods of measurement. These phenomena are also studied by means of the temperature dependency of photoelasticity.[1),2)] This photoelastic method appears to be a kind of elastic method, but it is applicable to the measurement in a softening state as it is not so strongly interrupted by the plastic flow as an ordinary

elastic method. And also it is profitable in observing of the existence of a rubber-like state. In the present work the transition point of chain polymers, especially of polystyrene, and the existence of a rubber-like state above that point are investigated by this method.

§ 2. Experimental Method

To maintain the plastic flow of specimens as small as possible, it is desirable that the tension applied to specimens is small. For that reason Szivessy-Dierksmann's compensation method[3] which is applicable to the measurement of weak birefringence was used. The compensation plates were made of mica and the birefringences of the plates were 0.148 (Na_D) for the weak birefringence and 1.45 (Na_D) for usual one. As the birefringence as weak as about 0.001 radian could be observed by this method, the measurement could be done under small tension whose order is about 100 g/cm².

The films of commercial polystyrene ($\overline{M}_v$= 270,000) and polyvinyl chloride (P.V.C.) ($\overline{M}_v$= 47,000) were used as specimens. These films were cast from solutions of the materials, chlorobenzene solution for polystyrene and nitrobenzene solution for P.V.C. Then they were carefully dried. From a part with uniform thickness of these films, strips were cut out, each with a size of 1.5 cm in width and 2.3 cm in length. Their thickness was 0.05~0.07 mm for polystyrene and 0.25 mm for P.V.C.

These strips were hung perpendicularly in the center of a little furnace with two windows through which the birefringence was observed. The lower end of the strip was tied by the wire, a part of which was put out of the furnace. The weight was applied on the lower end of this wire for the purpose of changing the tensile load at the outside of the furnace. And at the same time the elongation of the specimens was observed by measuring the displacement of the end of this wire by a microscope. The temperature of the furnace was raised at the rate of about 0.5°C/min during observation by controlling the electric current. The temperature of strips was read by the thermometer which was inserted in the center of the furnace. In all measurement, Na_D was used as the source of light. In order to put the strips under the uniform tension, the both ends of the strip were clipped by the two small metal plates.

§ 3. Results and Discussion

The results for polystyrene are shown Fig. 1. Below about 80°C the birefringence is seldom observed. Passing though about 80°C, the birefringence begins to appear slightly, but the value is still very small. At tempera-

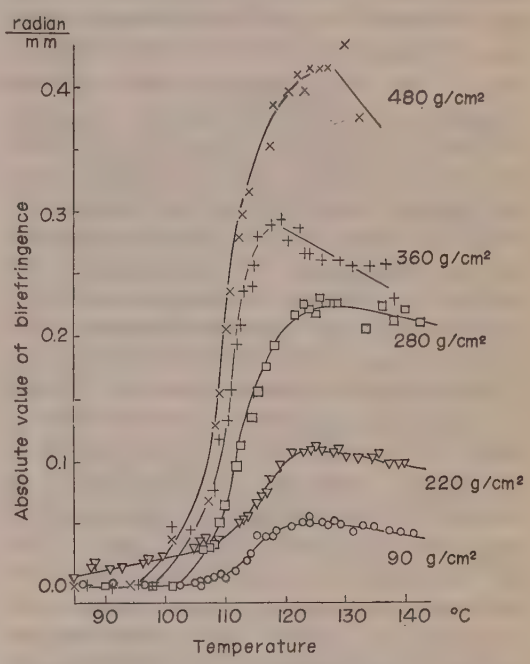

Fig. 1. The temperature dependency of the birefringence of Polystyrene. (The sign of the birefringence is negative)

tures from 100°C to 120°C the absolute value of the birefringence suddenly increases. Above 120°C it appears that the value slightly decreases with increasing temperature. The first region in which the birefringence does not appear may be in an amorphous solid state. The birefringence in this region is believed to be too weak to be observed under such small tension as applied in this experiment. It is likely that the second region where the birefringence begins to appear and shows a sudden increase is in a transition state. Also recognized in this region is the elongation of the specimens which does not appear in the first region. For example, in case of the curve for the tension of 90 g/cm² in Fig. 1, the elongation of a specimen at

about 120°C becomes about 1%; above this temperature the elongation increases and the absolute value of the birefringence decreases with increasing the temperature; and the elongation at about 140°C is about 2% against the length at 120°C. If compensation is made for the value of the birefringence on the assumption that the volume is kept constant, as is the case with the rubber-like material, the absolute value of the birefringence should increase about 1% with the increase in tension of about 2% and the decrease in thickness of about 1%. However, the observed value of the birefringence at 140°C indicates a decrease of about 20% against the value measured at 120°C. Therefore, it seems reasonable to assume that in the region where the absolute value of the birefringence decreases the specimen is in a rubber-like state and its birefringence is proportional to the reciprocal of absolute temperature, as known from a theory for the birefringence of the rubber-like material[4]. Likewise it applies to all the curves for different tensions. Though the elongation becomes larger with the increase in tension, such a large decrease in the absolute value of the birefringence as measured is unexplainable by considering the compensation for the elongation alone. It is also interesting to note that the rate of the decrease in that value becomes larger with the increase in tention. This can likewise be expected from the theory for the birefringence of the rubber-like material[4]. If these facts are considered, it is likely that the third region where the absolute value of the birefringence decreases as shown in Fig. 1 is in a rubber-like state. As the temperature is raised higher, other regions appear where the elongation increases rapidly and the absolute value of the birefringence shows again a tendency for increase,[1),2)] although in this figure the regions showing the increase in that value are not plotted.

When the tension is decreased at 140°C, both the elongation and the absolute value of the birefringence are slowly decreasing. But the former never returns to the latter. This indicates that the plastic flow is included in this elongation.

If the first region were in a solid-like state and the third region were in a rubber-like state, according to the above discussion, the second region, that is the transition region, would be the one where the materials change to a rubber like state from a solid like state. In the first place of this region the materials may rapidly change to a rubber like stage and the observed value of the birefringence becomes larger but in the final state the rate of the increase of that value may be lowered by the opposite effect of the part changed to the rubber like stage. Then here it is assumed that the glass transition point is the inflexion point of the second region of the curve in Fig. 1. The transition point obtained by the above assumption are plotted against tensions in Fig. 2. From this figure it is revealed that the transition point shifts slightly to the lower temperature side with the increase in tension, as the case of Nielsen et al[5] and that, when tension is extrapolated to zero, the transition temperature approximates 115°C. This value is fairly higher than the second order transition point estimated by means of specific volume[6),7),8)] or specific heat[9]. However, this one nearly agrees with the so-called softening point obtained by the dynamical elastic measurement[10].

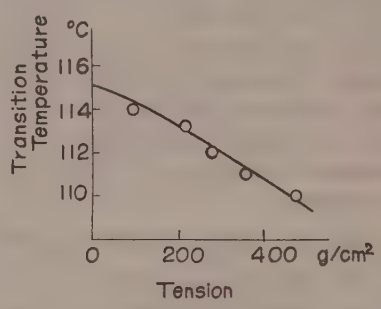

Fig. 2. The relationship between the transition points and the tensions.

The temperature at which the birefringence begins to appear was not discussed because of the accuracy of the present work, but it is likely that this temperature also slightly depended on the tensile load.

Fig. 3 shows the results for P.V.C. In this case the shape of the curve is also the same as that for polystyrene. In this figure the region of plastic flow is also shown. In the case for P.V.C. the transition point has likewise the tendency of decreasing with increasing tension. The transition points estimated from Fig. 2 are 74°C for 100 g/cm² tension

and 70°C for 200 g/cm² tension. This value is near the so-called second order transition point obtained by means of specific volume[6].

It has been reported that the rubber-like stage does not appear for polystyrene[11], but the foregoing results obtained by our experiment suggest the existence of a rubber-like

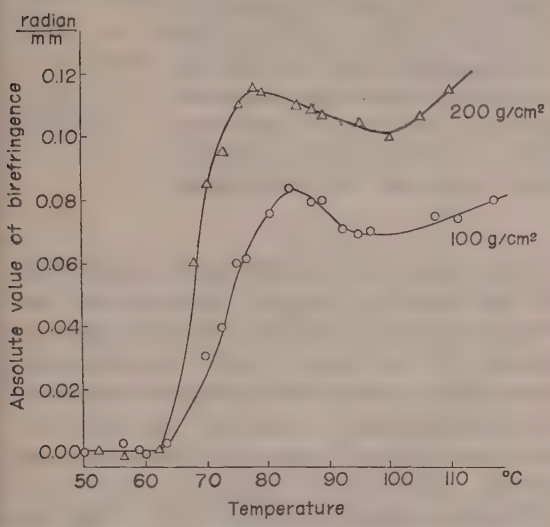

Fig. 3. The temperature dependency of the birefringence of P.V.C. (The sign of the birefringence is positive)

stage for polystyrene. This may be attributable to the fact that, as the amount of tension was not sufficiently large in our experiment, effects by the secondary cross-linkage due to entanglement, and so forth, were working. It is likely that the effectiveness of the secondary cross-linkage was a cause of the lowering of the transition point with the increasing tension.

The value of the transition point for polystyrene reported in the past work is a little lower than in the present work[1]. It is believed that the difference was caused by the insufficient drying of samples in the past measurement which permitted solvent remaining in the samples to act as plasticizer[2].

Acknowledgement

The author has to acknowledge his hearty thanks to Professor J. Furuichi of Hokkaido University for his kind advice and encouragement, and to Mr. Y. Miyake for his assistance in determining of the molecular weight.

References

1) M. Kaneko, R. Murai, K. Kishi and D. Mori: J. Phys. Soc. Japan **10** (1955), 78.
2) M. Kaneko, R. Murai, K. Kishi and D. Mori: J. Faculty Science, Hokkaido University Series II. **4** (1954) 305.
3) G. Szivessy and A. Dierksmann: Ann. der Phys. **11** (1931) 949.
G. Szivessy, A. Dierksmann and Cl. Münster: Zs. f. Phys. **82** (1933) 279.
4) R. Kubo: J. Phys. Soc. Japan **2** (1947) 84; **3** (1948) 119.
5) L. Nielsen and K. Buchdahl: J. Appl. Phys. **21** (1950) 488.
6) R. F. Boyer and R. S. Spencer: Advances in Colloid Science **2** (1946) 1.
7) R. S. Spencer and R. F. Boyer: J. Appl. Phys. **17** (1946) 398.
8) T. G. Fox Jr. and P. L. Flory: J. Appl. Phys. **21** (1950) 581.
9) R. F. Boyer and R. S. Spencer: J. Appl. Phys. **15** (1944) 398.
10) von K. Schmieder and K. Wolf: Kolloid. Zeit. **134** (1953) 149.
11) R. Klein and E. Jenkel: Z. Naturforschung **7a** (1952) 800.

JOURNAL OF THE PHYSICAL SOCIETY OF JAPAN Vol. 13, No. 11, NOVEMBER, 1958

Paramagnetic Relaxation of Copper Tutton Salt

Yosuke NAGAOKA

Department of Physics, University of Tokyo, Tokyo

(Received July 17, 1958)

The spin-lattice relaxation time of Cu-Tutton salt is calculated basing on the Van Vleck theory. At liquid helium temperatures, calculated relaxation time shows a remarkable anisotropy, which arises from the nature of orbital states of Cu^{2+} in the crystalline field. Its order of magnitude is too large compared with the value 2×10^{-4} sec. measured by Townes et al.. At liquid air temperatures, however, it is in fairly good agreement with experimental data if a reasonable value is assumed for the separation of the first excited orbital state from the ground state.

§ 1. Introduction

The spin-lattice relaxation time of paramagnetic salts was calculated by Van Vleck[1)-3)] for Cr- and Ti-alum. He considered the mechanism that the lattice vibrations modulate the spin-orbit coupling and reverse spins through it. The results of his calculation were in fairly good agreement with experimental data at liquid air temperatures in the order of magnitude of the relaxation time and its dependence on magnetic field and temperature. At liquid helium temperatures, however, there remains a big discrepancy between theory and experiments.[4)]

At present this discrepancy is attributed to the fact that the bottleneck of the relaxation is not the energy transfer between the spin system and the lattice but between the lattice and the helium bath, and that the relaxation time observed in usual experiments is the lattice-bath (not spin-lattice) one. Townes and co-workers[5)] have presented experimental evidence indicating this. They have observed also the time constant which they think is the true spin-lattice relaxation time. It is about 2×10^{-4} sec. for Cu-Tutton salt.

However Bloembergen[6)] has recently pointed out that such a strong coupling between the spins and the lattice is incompatible with the successful operation of three-level steady-state masers in some salts. If his objection is right, the relaxation time of Cu-Tutton salt may also be longer than that measured by Townes et al..

In the present paper we shall calculate the spin-lattice relaxation time of Cu-Tutton salt on the basis of the Van Vleck theory. In Tutton salts each divalent cation is surrounded by a slightly distorted octahedron of six water molecules just like a trivalent cation in alums. In the case of Cu^{2+} ions, however, the orbital states in the crystalline field have a different property from Ti^{3+} and Cr^{3+}; i.e. the lower states Γ_3 separated from the upper by the cubic field are degenerate (see Fig. 1) but are non-magnetic unlike Ti^{3+}. Then we should take into account also the upper states Γ_5 in the perturbational calculation. Because of this the relaxation time of Cu-Tutton salt shows a new property which is not seen in the cases of Ti^{3+} and Cr^{3+}; i.e. a remarkable anisotropy as to the direction of an external magnetic field.

The calculation is rather straightforward and is done nearly in a parallel way to the

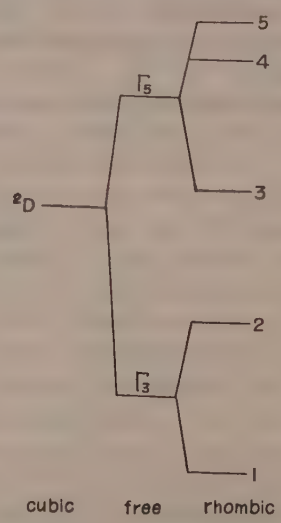

Fig. 1. Splitting of the orbital states of Cu^{+2} by the crystalline field.

cases of Ti- and Cr-alum. In the following sections we show only essential points of the calculation and the main results.

§ 2. Orbital States in the Crystalline Field

The ground state of the free Cu^{2+} ion is $3d^9\ {}^2D$. In the crystalline field of Tutton salts, which has a rhombic symmetry, it splits as shown in Fig. 1. If we label the split states as 1, 2, 3, 4 and 5 from the bottom, their wave functions are given as follows:

$$\left.\begin{aligned}
\psi_1&=\frac{1}{\sqrt{2}}(\varphi_2+\varphi_{-2})+c\varphi_0\\
\psi_2&=\varphi_0-c\frac{1}{\sqrt{2}}(\varphi_2+\varphi_{-2})\\
\psi_3&=\frac{1}{\sqrt{2}\,i}(\varphi_2-\varphi_{-2})\\
\psi_4&=\frac{1}{\sqrt{2}\,i}(\varphi_1+\varphi_{-1})\\
\psi_5&=\frac{1}{\sqrt{2}}(\varphi_1-\varphi_{-1})\,.
\end{aligned}\right\}\qquad(1)$$

Here φ_M's are the eigenfunctions of the component of the orbital angular momentum along the approximate tetragonal axis, and c is a constant determined by the ratio of rhombic component to tetragonal one of the crystalline field. We assume $|c|\ll 1$.

The values of g-factor of Cu-K-Tutton salt measured at 90°K are[7]

$$g_x=2.14,\quad g_y=2.04,\quad g_z=2.36.\qquad(2)$$

Making use of these values, we can estimate magnitudes of level separations and c. If we neglect the separation among the states 3, 4 and 5 of Γ_5, the separation Δ between 1 and Γ_5 and c are obtained as

$$\Delta=15500\ \mathrm{cm}^{-1},\quad c=0.15,\qquad(3)$$

taking the spin-orbit interaction constant $\lambda=-710\ \mathrm{cm}^{-1}$.[8] The separation Δ' between 1 and 2 is not known because it has no effect on g-factor.

§ 3. Calculation of Direct Processes

The original Hamiltonian is given as follows:

$$\mathscr{H}=\mathscr{H}_o+\mathscr{H}_l+\mathscr{H}_{Zs}+\mathscr{H}_{Zo}+\mathscr{H}_{so}+\mathscr{H}_{ol}\,.\qquad(4)$$

Here $\mathscr{H}_o$ is the Hamiltonian for the orbital motion of d-electrons of Cu^{2+}, $\mathscr{H}_l$ that for the lattice vibrations, $\mathscr{H}_{Zs}=2\mu_B\boldsymbol{H}\cdot\boldsymbol{S}$ and $\mathscr{H}_{Zo}=\mu_B\boldsymbol{H}\cdot\boldsymbol{L}$ (μ_B=the Bohr magneton) respectively the spin and orbital part of the Zeeman energy, $\mathscr{H}_{so}$ the spin-orbit interaction and $\mathscr{H}_{ol}$ the orbit-lattice interaction. The spin-spin interaction is neglected assuming that the sample is magnetically dilute. Now we take $\mathscr{H}_o+\mathscr{H}_l+\mathscr{H}_{Zs}$ as the unperturbed Hamiltonian and $\mathscr{H}_{Zo}+\mathscr{H}_{so}+\mathscr{H}_{ol}$ as the perturbation, and carry out a perturbational calculation of higher order. By eliminating the orbital motion we obtain the effective Hamiltonian $\mathscr{H}_{sl}$ which represents the spin-lattice interaction. Then (4) is effectively reduced to

$$\mathscr{H}_{eff}=\mathscr{H}_{Zs}+\mathscr{H}_l+\mathscr{H}_{sl}\,.\qquad(5)$$

In connection with $\mathscr{H}_{ol}$, we have only to consider the vibrational modes of the complex $Cu^{2+}\cdot 6H_2O$ which are even with respect to inversion when we calculate direct processes, as Van Vleck has pointed out. Neglecting the distortion of $6H_2O$ from an octahedron, even modes are Q_1 (totally symmetric vibration, representation: Γ_{1g}): Q_2, Q_3 (Γ_{3g}): Q_4, Q_5, Q_6 (Γ_{5g}): Q_{19}, Q_{20}, Q_{21} (rotational motion, Γ_{4g})[1]. Now we should take into account not only $Q_2\sim Q_6$ as in the cases of Ti^{3+} and Cr^{3+}, but also Q_1 and Q_{19}, Q_{20}, Q_{21}, for the orbital states have the translational properties of Γ_3 and Γ_5 and their products are

$$\begin{aligned}
[\Gamma_3{}^2]^*&=\Gamma_{1g}+\Gamma_{3g}\\
[\Gamma_5{}^2]&=\Gamma_{1g}+\Gamma_{3g}+\Gamma_{5g}\\
\Gamma_3\times\Gamma_5&=\Gamma_{4g}+\Gamma_{5g}\,.
\end{aligned}\qquad(6)$$

Then each mode has non-vanishing matrix elements only between the following orbital states.

Q_1 : $\Gamma_3-\Gamma_3$, $\Gamma_5-\Gamma_5$. (diagonal)
Q_2, Q_3 : $\Gamma_3-\Gamma_3$, $\Gamma_5-\Gamma_5$.
Q_4, Q_5, Q_6 : $\Gamma_5-\Gamma_5$, $\Gamma_3-\Gamma_5$.
Q_{19}, Q_{20}, Q_{21}: $\Gamma_3-\Gamma_5$.

Taking a point dipole model for the crystalline field, we explicitly obtain $\mathscr{H}_{ol}$ linear in these Q's.

In $\mathscr{H}_{sl}$ appear two kinds of terms, *adiabatic* and *non-adiabatic* terms.

(1) Adiabatic terms.

These terms are obtained by the so-called adiabatic approximation, i.e. by carrying out the perturbational calculation leaving $\boldsymbol{S}$ and Q as operators. So in order to reverse spin,

* $[\Gamma^2]$ denotes the representation of the symmetric product of Γ with itself.

according to Kramers' theorem, it requires the magnetic field and hence the third order perturbation including $\mathscr{H}_{Zo}$ as well as $\mathscr{H}_{so}$ and $\mathscr{H}_{ol}$. In other words these are the effect of the lattice vibrations on g-factor in the spin Hamiltonian.

We remark here that there are two kinds of terms different in the order of magnitude.

(a) Terms, the denominator of which is Δ^2: e.g.

$$(1|\mathscr{H}_{ol}|3)(3|\mathscr{H}_{so}|5)(5|\mathscr{H}_{Zo}|1)/\Delta^2 .$$

(b) Terms, the denominator of which is $\Delta\Delta'$: e.g.

$$(1|\mathscr{H}_{ol}|2)(2|\mathscr{H}_{so}|5)(5|\mathscr{H}_{Zo}|1)/\Delta\Delta'.^*$$

Terms (b) are larger than (a) by the factor Δ/Δ'. Because 1 and 2 are connected neither by $\mathscr{H}_{so}$ nor $\mathscr{H}_{Zo}$, in terms (b) $\mathscr{H}_{so}$ and $\mathscr{H}_{Zo}$ appear always in such a form as

$$(2|\mathscr{H}_{so}|\Gamma_5)(\Gamma_5|\mathscr{H}_{Zo}|1) = \lambda\mu_B \boldsymbol{S}\cdot(2|\boldsymbol{L}|\Gamma_5)(\Gamma_5|\boldsymbol{L}|1)\cdot\boldsymbol{H} . \qquad (7)$$

As one can see easily, the factor $(2|\boldsymbol{L}|\Gamma_5)(\Gamma_5|\boldsymbol{L}|1)$ does not vanish only when $\boldsymbol{LL}$ is equal to L_xL_x, L_yL_y or L_zL_z, where x, y and z correspond to the axes of the crystalline field. As a result terms (b) are always proportional to either S_xH_x, S_yH_y or S_zH_z.

(2) Non-adiabatic terms.

When we calculate adiabatic terms, contributions of $\mathscr{H}_l$ and $\mathscr{H}_{Zs}$ to the energy difference appearing in the denominator is neglected, so we obtain none from the second order perturbation. If we do not neglect them, however, we get the spin-lattice interaction from the second order perturbation of $\mathscr{H}_{so}$ and $\mathscr{H}_{ol}$ too. These terms are of the same order as (a) of adiabatic terms.

In order to proceed to the numerical evaluation of the relaxation time of direct processes, it is necessary to know the values of a few constants. We use (2) and the following values:

$$e\mu\langle r^4\rangle R^{-6}=1900\ \mathrm{cm}^{-1}$$
$$e\mu\langle r^2\rangle R^{-4}=5200\ \mathrm{cm}^{-1}$$
$$\text{density:}\quad d=2\ \mathrm{g/cm}^3 \qquad (8)$$
$$\text{sound velocity:}\quad v=2.3\times10^5\ \mathrm{cm/sec}$$
$$\Delta/\Delta'\simeq2\sim10 .$$

Here $-e$ is the electron charge, μ the dipole moment of a water molecule, R the distance between Cu^{2+} and H_2O, $\langle r^2\rangle$ and $\langle r^4\rangle$ respectively the mean square and mean forth power radius of the d-electron orbit. The value of $e\mu\langle r^4\rangle R^{-6}$ can be evaluated directly from that of Δ under the assumption of a point dipole model of the crystalline field. $e\mu\langle r^2\rangle R^{-4}$ is obtained from $e\mu\langle r^4\rangle R^{-6}$ assuming that the wave function of d-electrons is hydrogen-like and further $\langle r^2\rangle=0.9\times10^{-16}\ \mathrm{cm}^{-1}$ (R=2 A). Unfortunately no specific heat data of the lattice vibration of Tutton salts can be found, so we take the value of sound velocity used by Van Vleck for alums. We cannot estimate Δ' from experimental data but the above value of Δ/Δ' may be plausible.

Finally the relaxation time τ_{sl} of direct processes is as follows:

if $kT\gg\mu_BH$,

$$\tau_{sl}=0.78\times10^{16}F^{-1}\cdot H^{-4}T^{-1}, \qquad (9)$$

and if $kT\ll\mu_BH$,

$$\tau_{sl}=1.1\times10^{20}F^{-1}\cdot H^{-5}. \qquad (9')$$

$$F=\alpha_1+\alpha_2n^2+\alpha_3n^2(n^2-1)+\alpha_4(1-l^4-m^4-n^4) +\beta_1(m^2-l^2)+\beta_2n^2(m^2-l^2). \qquad (10)$$

Here H is the applied magnetic field in oersteds, T the temperature in °K, (l, m, n) the directional cosine of H and

$$\left.\begin{aligned}
&\alpha_1=0.015\\
&\alpha_2=1.3\\
&\alpha_3=2.8\left(\frac{\Delta}{\Delta'}\right)^2+0.5\left(\frac{\Delta}{\Delta'}\right)+0.4\\
&\alpha_4=1.9\left(\frac{\Delta}{\Delta'}\right)^2+0.3\left(\frac{\Delta}{\Delta'}\right)\\
&\beta_1=0.013\\
&\beta_2=0.28\left(\frac{\Delta}{\Delta'}\right)^2+0.10\left(\frac{\Delta}{\Delta'}\right).
\end{aligned}\right\} \qquad (11)$$

In Fig. 2 we show the dependence of F (proportional to τ_{sl}^{-1}) on the direction of the magnetic field in a few planes. An interesting fact is that τ_{sl} becomes extremely long when the magnetic field is parallel to a principal axis of the crystalline field. It is much shorter in other cases. This anisotropy is the more emphasized, the larger Δ/Δ' is.

Such a remarkable anisotropy arises from the fact that in $\mathscr{H}_{sl}$ there are terms (b) larger than others by a factor Δ/Δ'. These terms are proportional to H_xS_x, H_yS_y or H_zS_z, and therefore unable to reverse spins and to have any effect on the relaxation time if the magnetic field is parallel to a crystalline field axis. It should be noticed here that

* The modes Q_2 and Q_3 connect 1 with 2.

Table I. τ_{sl} of direct processes (sec.)

$H(\phi)$	T (°K)	Direction of H (100)	(010)	(001)	(110)	
3000	4	1.2×10^4	8.6×10^2	1.9×10	5.9*	2.5×10^{-1}**
	1	4.8×10^4	3.4×10^3	7.4×10	2.3×10	1.0
10000	4	9.8×10	7.0	1.5×10^{-1}	4.8×10^{-1}	2.1×10^{-3}
	1	3.9×10^3	2.8×10	6.0×10^{-1}	1.9×10^{-1}	8.2×10^{-3}

* $\Delta/\Delta'=2$, ** $\Delta/\Delta'=10$.
Values at $H=10000\,\phi$, $T=1$°K are obtained by means of (9), although $kT\simeq\mu_B H$ in this case.

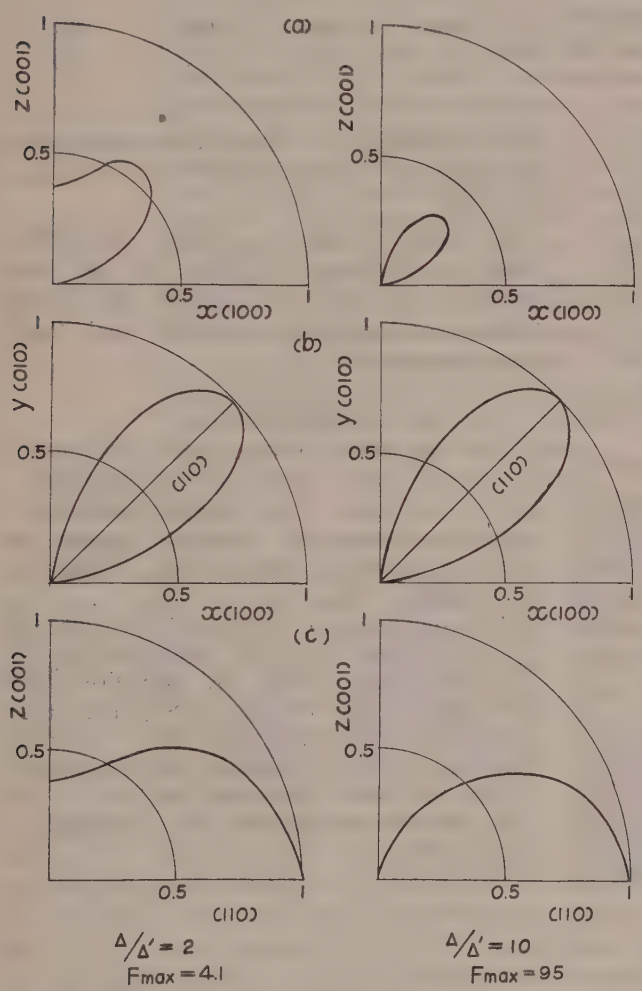

Fig. 2. Dependence of the value of $F/F_{\max}$ ($\simeq F/F_{(110)}$) on the magnetic field direction.
(a) x-z plane.
(b) x-y plane.
(c) z-(110) plane.

such anisotropy is, at least qualitatively, independent of approximations taken in the Van Vleck theory; i.e. the crystalline field approximation, its point dipole model, the Debye approximation of the lattice vibrations and so on.

We show numerical results in Table I. The value of the spin-lattice relaxation time of Cu-NH_4-Tutton salt measured by Townes et al.[5] is of the order 2×10^{-4} sec. at the frequency 9000 Mc ($H\simeq3000\,\phi$) and the temperature 1.3~4°K. The values calculated here and too large compared with this experimental result. Townes et al.[5] have also found the anisotropy of the relaxa tion time in connection with the phenomenon of the asymmetry of the cross saturation. But as the direction of the magnetic field is not shown in the paper, it is not clear whether their observation can be explained by our result.

§ 4. Calculation of Raman Processes

We now proceed to the calculation of Raman processes. The most important contributions are from non-adiabatic terms obtained by means of the third order perturbation $\mathscr{H}_{ol}{}^2\mathscr{H}_{so}$ ($\mathscr{H}_{ol}$: linear in Q's) in which one of the intermediate state is 2; e.g.

$$\frac{(1,\ n_k|\mathscr{H}_{ol}|2,\ n_k+1)(2+|\mathscr{H}_{so}|4-)\times(4,\ n_{k'}|\mathscr{H}_{ol}|1,\ n_{k'}-1)}{(-\Delta'-\hbar\omega_k)(-\Delta-\hbar\omega_{k'})}$$

Here n_k represents the number of phonons with wave number k and frequency ω_k. We calculate only such terms.

Neglecting effects of the rhombic component of the crystalline field ($c=0$) for simplicity, final results are as follows:

$$\tau_{sl}=\tau_0\frac{b+CH^2}{b+pCH^2} \qquad p=0.5 \qquad (12)$$

$$\tau_0=\rho(1+0.23\,n^2)^{-1}, \qquad (13)$$

where ρ is a constant dependent on temperature and n is the cosine of the angle between the magnetic field and the tetragonal axis. We do not neglect the spin-spin interaction here. As Eq. (13) shows, τ_{sl} of Raman processes has not so remarkable anisotropy as that of direct processes. The numerical values of ρ are shown in Table II. In the calculation of ρ at liquid air temperatures the Debye temperature was assumed to be 330°K.[3]

Table II. ρ of (13). (sec.)

Δ/Δ' \ T(°K)	1	4	77	90
2	1.0×10^7	3.8×10	1.9×10^{-6}	1.0×10^{-6}
3	2.6×10^6	9.9	4.7×10^{-7}	2.6×10^{-7}
10	3.7×10^4	1.4×10^{-1}	6.8×10^{-9}	3.7×10^{-9}

Comparing these values of Raman processes with those of direct processes calculated in § 3, we see that even at $T=4$°K Raman processes are more effective than direct processes if the magnetic field is not so strong and is parallel to a crystalline field axis. As a result the anisotropy at helium temperatures will be smaller than expected from the calculation of direct processes.

In the liquid air region the calculated values are in good agreement with experimental results if we take $\Delta/\Delta'=3$. We show in Table III the values averaged over the direction of the magnetic field with experimental results of Cu-NH_4-Tutton salt.[9] Our calculations are so rough that we cannot regard this agreement as a proof that $\Delta'=\Delta/3=5000\,\mathrm{cm}^{-1}$. However it may well be said at least that the Van Vleck theory agrees with experiments at liquid air temperatures for Cu-Tutton salts too.

Table III. τ_{sl} at liquid air temperatures. (sec.) Experimental results are for Cu-NH_4-Tutton salt.

T		$\tau_0\cdot10^6$	$\tau_\infty\cdot10^6$	p
77°K	calc.	0.43	0.87	0.5
	exp.	0.35	0.7	0.5
90°K	calc.	0.24	0.48	0.5
	exp.	0.24	0.4	0.6

The author wishes to express his sincere thanks to Professor R. Kubo for his kind guidance, and to Dr. T. Moriya and to the members of Kubo Laboratory for their helpful discussions.

References

1) J. H. Van Vleck: J. Chem. Phys. **7** (1937) 73.
2) J. H. Van Vleck: Phys. Rev. **57** (1940) 426.
3) J. H. Van Vleck: Phys. Rev. **57** (1940) 1052.
4) See for instance, C. J. Gorter: Progress in Now Temperature Physics Vol. 2 Chap. 9 (Amsterdam 1957).
5) J. A. Giordmaine, L. E. Aloop, F. R. Nash and C. H. Townes: Phys. Rev. **109** (1958) 302.
6) N. Bloembergen: Phys. Rev. **109** (1958) 2209.
7) B. Bleaney, R. P. Penrose and B. J. Plumpton: Proc. Roy. Soc. **A 198** (1949) 406.
8) B. Bleaney, K. D. Bowers and M. H. L. Pryce: Proc. Roy. Soc. **A 228** (1955) 166.
9) C. J. Gorter: Paramagnetic Relaxation (Amsterdam 1947).

JOURNAL OF THE PHYSICAL SOCIETY OF JAPAN Vol. 13, No. 11, NOVEMBER, 1958

Spin Quenching and Magnetic Resonance

By Tôru MORIYA
Department of Physics, Tokyo Metropolitan University
and Yukio OBATA
Department of Physics, University of Tokyo

(Received August 2, 1958)

The effect of the magnetic ions of those paramagnetic salts whose spin degeneracy is completely lifted by the combined action of the spin-orbit coupling and the crystalline electric field, on the magnetic resonance of nuclear spins and electronic spins of other kind of ions such as Cu^{2+}, Co^{2+}, Mn^{2+} substituted for the host ions are studied theoretically. General formulas for the resonance field shift, line width and the thermal relaxation time in nuclear (or electron) spin resonance in magnetic substances are given. T_1 and T_2 are here related to the difference between isothermal and isolated susceptibilities. Temperature dependence of T_1 and T_2 as well as magnetic field dependence of them are studied. At low temperatures they become longer rapidly (exponentially) as temperature is lowered while at high temperatures they are independent of temperature. Field dependence of the line width is of the type of $H_0^2+H_i^2$ when the line is narrowed by spin-spin interaction among the host ion spins, or $\sqrt{H_0^2+H_i^2}$ when the line is not narrowed, where H_i denotes the local magnetic field. Field dependence of $1/T_1$ is always like $H_0^2+H_i^2$. The theoretical results are compared with some available experimental data on electron spin resonance. The agreement between theory and experiment seems to be not unreasonable as far as order of magnitude and qualitative characters of the line width are concerned, though experimental data are now rather scanty.

§ 1. Introduction

A certain amount of studies on the nuclear magnetic resonance in magnetic compounds have been done in recent years. These could reveal us many important informations on the properties of several para and antiferromagnetic compounds. Among them are some problems concerned with those paramagnetic salts whose magnetic ion has even number of unpaired electrons and then has no Kramers' degeneracy. As examples there are Cr^{2+}, Mn^{3+}, Fe^{2+} and Ni^{2+} ions. Under the crystalline electric field in solid their spin degeneracies are generally lifted. In an orthorhombic field all the degeneracies in the spin states are completely lifted so that the spin operator has no diagonal components in the absence of the external magnetic field. This situation may be said that the spin is quenched by the combined action of the spin-orbit coupling and the crystalline electric field. The spins have in this case only high frequency components because of the absence of the diagonal elements and won't have effect on the magnetic resonance of nuclear spins or other kinds of electron spins substituted for host magnetic ions in the crystal. However, when the external field is set in, magnetic moments are induced on the ions owing to the polarization effect. These moments interact with nuclear spins as well as other kinds of electron spins, but to the extent much smaller than usual magnetic ions whose spins are not quenched. Some experimental studies have been carried out on this type of salts. Paramagnetic resonance of Mn^{2+}, Co^{2+} and Cu^{2+} ions placed instead of Fe^{2+} and Ni^{2+} respectively in $Fe(NH_4)_2(SO_4)_2 6H_2O$ and $Ni(NH_4)_2(SO_4)_2 6H_2O$ were reported first by Ôno and Hayashi[1] and recently by Otsuka, Abe and Kanda[2]. The latter authors measured also the susceptibility of $Fe(NH_4)_2(SO_4)_2 6H_2O$ and deduced from it the initial splittings of the spin levels. Non-resonant dispersion and absorption measurements on (Co–Ni) $(NH_4)_2(SO_4)_2 6H_2O$ and (Co–Fe) $(NH_4)_2(SO_4)_2 6H_2O$ have been studied by Haseda[3]. Nuclear resonance experiments have been studied recently by Sugawara and

Kim[4] though the results are not yet conclusive.

As for the theoretical side, the idea of diminution of the resonance line width due to spin quenching was first put forth by P. W. Anderson and worked out in the case of high temperatures by one of the authors (Y. O.)[5]. In the present article we shall treat the problem in more detail and from more general point of view especially taking notice of the temperature and field dependences of the line width and the relaxation time.

At first we shall give in § 1 general formulas for the resonance field shift, the line width or T_2 and the thermal relaxation time T_1 due to the paramagnetic ion related with the nuclear resonance (or electron spin resonance of a different kind of ion). The problem of calculating T_1 and T_2 are then reduced to the calculation of the frequency distribution or time correlation functions of the paramagnetic spin fluctuation. The frequency distribution of the spin fluctuation for our case where the degeneracy of the spin levels are completely lifted by the crystalline electric field is studied in § 3 and their low frequency components are shown to be related to the difference between the isothermal and the isolated susceptibilities, χ_T and χ_{is}. Isolated susceptibility is an adiabatic one in Ehrenfest's sense. In another word, χ_{is} appears when the populations of the energy levels are kept constant during the change of the measuring field. In § 4 $(\chi_T-\chi_{is})$ is calculated for Ni^{2+} $(S=1)$ and Fe^{2+} $(S=2)$ salts. Numerical values are given for $Ni(NH_4)_2(SO_4)_2 6H_2O$ and $Fe(NH_4)_2(SO_4)_2 6H_2O$. The relaxation times T_1 and T_2 of nuclear spins as well as electron spins of different kinds of ions are discussed respectively in § 5 and in § 6. For the latter case the theoretical results are compared with some available experimental data. The agreement proves to be not unreasonable in the order of magnitude and in the qualitative characters of the temperature and field dependences of the relaxation times. In the last section, § 7, some remarks on this problem are made.

§ 2. General Formulas

We shall here consider a system consisting of two kinds of spins, electronic spins of a kind of magnetic ions and nuclear spins. The latter can, as occasion demands, be replaced by spins of different kind of magnetic ions. The reasonance frequency, the line width and the relaxation time T_1 of the latter will in general be strongly affected by the former. In this section this effect is treated. For brevity we shall consider one resonating spin (hereafter called the nuclear spin) and neglect the interaction among the resonating spins. This can not only be justified when the concentration of the resonating spins is low but also be useful when the all sorts of contributions to the line width and to the relaxation time work additively. The formulas for the line width, the frequency shift and T_1 in this case have already been derived for a special case[6]. We shall reproduce them in more general forms.

The Hamiltonian of the system is written as

$$\mathscr{H}=\mathscr{H}_N+\mathscr{H}_e+\mathscr{H}_{Ne}\,, \tag{2.1}$$

$$\mathscr{H}_N=-\gamma_N\hbar\boldsymbol{I}\cdot\boldsymbol{H}_0\,, \tag{2.2}$$

$$\mathscr{H}_{Ne}=\gamma_N\gamma_e\hbar^2\sum_{\nu=1}^{3}I_\nu\sum_j\sum_{\mu=1}^{3}\Phi_j^{\nu\mu}S_{j\mu}\,, \tag{2.3}$$

where $\mathscr{H}_e$ is the Hamiltonian of the electron spin system which can, as circumstances require, include the lattice vibrations, $\mathscr{H}_N$ that of the nuclear spin, and $\mathscr{H}_{Ne}$ that of the interaction between the nuclear spin and the electron spins. $\boldsymbol{I}$ denotes the nuclear spin, $\boldsymbol{S}_j$ the j-th electron spin, γ_N and γ_e the gyromagnetic ratios of the nuclear and the electronic spins, $\boldsymbol{H}_0$ the external magnetic field. The suffixes $\mu, \nu=1, 2, 3$, represent respectively the x, y, z components of vectors and tensors. $\Phi_j^{\mu\nu}$ is the coupling constant of the nuclear spin to the j-th electron spin which is written in the case of pure dipole-dipole interaction as

$$\Phi_j^{\mu\nu}=\sum_{\nu'}\tfrac{1}{2}g_{\nu'\nu}r_j^{-3}(\delta_{\mu\nu'}-3t_j^{\mu}t_j^{\nu'}) \tag{2.4}$$

where $g_{\nu\nu'}$ is a component of the g-tensor, $\boldsymbol{r}_j(r_j=|\boldsymbol{r}_j|)$ the position vector of the j-th magnetic ion, assuming the nuclear spin is located at the origin, $t_j^{\nu}=r_j^{\nu}/r_j$ its direction cosine.

Dividing an electron spin into two parts, i.e. the thermal equilibrium value and the deviation from it:

$$S_{j\nu}=\langle S_{j\nu}\rangle+\delta S_{j\nu}\,, \tag{2.5}$$

(2.1) (2.3) can be rewritten as

$$\mathscr{H}=\mathscr{H}_0+\mathscr{H}'+\mathscr{H}_e\,, \tag{2.6}$$

$$\mathscr{H}_0=-\gamma_N\hbar\boldsymbol{I}\cdot\boldsymbol{H}\,, \tag{2.7}$$

$$\mathscr{H}'=-\gamma_N\hbar\boldsymbol{I}\cdot\delta\boldsymbol{H}\,, \tag{2.8}$$

where $\boldsymbol{H}$ is the thermal average of the total magnetic field at the nucleus and $\delta\boldsymbol{H}$ the fluctuating part of the local magnetic field. They are written

$$H_\nu=H\alpha_\nu=H_{0\nu}-\gamma_e\hbar\sum_j\sum_{\mu=1}^{3}\Phi_j{}^{\nu\mu}\langle S_{j\mu}\rangle\,, \tag{2.9}$$

$$\delta H_\nu=-\gamma_e\hbar\sum_j\sum_{\mu=1}^{3}\Phi_j{}^{\nu\mu}\delta S_{j\mu}\,, \tag{2.10}$$

α_1, α_2, α_3 being the direction cosines of $\boldsymbol{H}$. The second term of (2.9) represents the shift of the resonance field. By a orthogonal coordinate-transformation $\{\alpha_{\mu\nu}\}$ we take the direction of $\boldsymbol{H}$ as the new third axis, the quantization axis for the nuclear spin. The components of $\boldsymbol{I}$ and $\delta\boldsymbol{H}$ in the new coordinate system are written as J_ν and K_ν. They satisfy

$$\left.\begin{aligned} I_\mu&=\sum_\nu J_\nu\alpha_{\nu\mu}\,,\\ \delta H_\mu&=\sum_\nu K_\nu\alpha_{\nu\mu}\,,\end{aligned}\right\} \tag{2.11}$$

where $\alpha_{3\nu}=\alpha_\nu$. In the new coordinate system, the Hamiltonians are expressed as follows:

$$\mathscr{H}_0=-\gamma_N\hbar J_3H\equiv-\hbar\omega_0J_3\,, \tag{2.7'}$$

$$\begin{aligned}\mathscr{H}&=-\gamma_N\hbar\sum_{\nu=1}^{3}J_\nu K_\nu\\ &=-\gamma_N\hbar[J_3K_3+\tfrac{1}{2}(J_+K_-+J_-K_+)]\,,\end{aligned} \tag{2.8'}$$

where $J_\pm=J_1\pm iJ_2$ and $K_\pm=K_1\pm iK_2$.

The shape of the resonance absorption line is obtained as follows[7]:

$$I(\omega)=\int_{-\infty}^{\infty}\exp\,[i\omega t-\psi(t)]\,dt\,, \tag{2.12}$$

$$\psi(t)=\gamma_N{}^2\int_0^t d\tau(t-\tau)\{F_0(\tau)+e^{i\omega_0\tau}F_1(\tau)\}\,, \tag{2.13}$$

$$\begin{aligned}F_0(t)&=\langle\{K_3(t)K_3\}\rangle\\ &=\sum_\nu\sum_{\nu'}\alpha_\nu\alpha_{\nu'}\langle\{\delta H_\nu(t)\delta H_{\nu'}\}\rangle\,,\end{aligned} \tag{2.14}$$

$$\begin{aligned}F_1(t)&=\langle\{K_+(t)K_-\}\rangle/2\\ &=\sum\sum\tfrac{1}{2}(\delta_{\nu\nu'}-\alpha_\nu\alpha_{\nu'})\langle\{\delta H_\nu(t)\delta H_{\nu'}\}\rangle\end{aligned} \tag{2.15}$$

where

$$\delta\boldsymbol{H}(t)=\exp\,(it\mathscr{H}_e/\hbar)\delta\boldsymbol{H}\exp\,(-it\mathscr{H}_e/\hbar)\,. \tag{2.16}$$

The relaxation time T_1 becomes

$$\begin{aligned}1/T_1&=(\gamma_N/2)^2\int_{-\infty}^{\infty}dt\cos\omega_0t[\langle K_+(t)K_-\rangle+\langle K_-(t)K_+\rangle]\\ &=\gamma_N{}^2\int_{-\infty}^{\infty}dt\cos\omega_0tF_1(t)\,.\end{aligned} \tag{2.17}$$

$\langle\{\delta H_\nu(t)\delta H_{\nu'}\}\rangle$ are expressed as follows neglecting the small effect of the modulation of the coordinate by lattice vibrations:

$$\langle\{\delta H_\nu(t)\delta H_{\nu'}\}\rangle=(\gamma_e\hbar)^2\sum_{j,k}\sum_{\mu,\mu'}\Phi_j{}^{\nu\mu}\Phi_k{}^{\nu'\mu'}\langle\{\delta S_{j\mu}(t)\delta S_{k\mu'}\}\rangle\,, \tag{2.18}$$

When the correlations between two different spin fluctuations are neglected, which is actually the case in the usual paramagnetic state, (2.18) reduces itself simply to

$$\langle\{\delta H_\nu(t)\delta H_{\nu'}\}\rangle=(\gamma_e\hbar)^2\sum_j\sum_{\mu,\mu'}\Phi_j{}^{\nu\mu}\Phi_j{}^{\nu'\mu'}\langle\{\delta S_{j\mu}(t)\delta S_{j\mu'}\}\rangle\,. \tag{2.19}$$

§ 3. Fluctuations of the Electron Spins

We shall deal with the time correlation functions of the spin fluctuations in the case where the degeneracy of the electron spin states are completely lifted by the combined influence of the spin-orbit coupling and the crystalline electric field. The Hamiltonian of the electron spin system is expressed as follows:

$$\mathscr{H}_e=\mathscr{H}_{e0}+\mathscr{H}_e'\,, \tag{3.1}$$

$$\mathscr{H}_{e0}=\sum_j\mathscr{H}_j=\sum_j[\boldsymbol{S}_j\cdot\Lambda_j\cdot\boldsymbol{S}_j+\mu_B\boldsymbol{S}_j\cdot\boldsymbol{g}_j\cdot\boldsymbol{H}_0]\,, \tag{3.2}$$

$$\mathscr{H}_e'=\sum_{j>k}\mathscr{H}_{jk}\,. \tag{3.3}$$

$\mathscr{H}_{e0}$ is the one-spin energy and $\mathscr{H}_e'$ is the interaction energy. Λ_j denotes the tensor expressing the fine structure coupling under the crystalline electric field, $\boldsymbol{g}_j$ the g-tensor.

When $\mathscr{H}_e'$ is smaller than $\mathscr{H}_{e0}$, we can use the perturbation method to calculate the motion of the spin fluctuations and then their correlation functions[7]. We get

$$\langle\{\delta S_{j\mu}(t)\delta S_{j\nu}\}\rangle=G_{\mu\nu}{}^j(t)=\sum_{n=0}^{\infty}G_{\mu\nu}{}^{j(n)}(t)\,, \tag{3.4}$$

$$\begin{aligned}G_{\mu\nu}{}^{j(n)}(t)&=(i\hbar)^{-n}\int_0^t dt_1\int_0^{t_1}dt_2\cdots\int_0^{t_{n-1}}dt_n\langle\{[S_{j\mu}(t);\\ &\quad\mathscr{H}_e(t_1),'\mathscr{H}_e'(t_2),\cdots,\mathscr{H}_e'(t_n)]S_{j\nu}\}\rangle\\ &\quad-\delta_{n0}\langle S_{j\mu}\rangle\langle S_{j\nu}\rangle\,,\end{aligned} \tag{3.5}$$

$$S_{j\mu}{}^0(t)=\exp\,(it\mathscr{H}_{e0}/\hbar)S_{j\mu}\exp\,(-it\mathscr{H}_{e0}/\hbar)\,, \tag{3.6}$$

$$\mathscr{H}_e'(t)=\exp\,(it\mathscr{H}_{e0}/\hbar)\mathscr{H}_e'\exp\,(-it\mathscr{H}_{e0}/\hbar)\,, \tag{3.7}$$

where

$$[A;B,C,\cdots,K]=[[\cdots[A,B],C]\cdots],K]\,.$$

The suffix j specifying the j-th spin will

hereafter be neglected.

We shall take such a representation as to diagonalize $\mathscr{H}_{e0}$:

$$\mathscr{H}_{e0}=\begin{pmatrix} E_1 & & & & & 0 \\ & E_2 & & & & \\ & & \ddots & & & \\ 0 & & & E_m & & \\ & & & & \ddots & \\ & & & & & E_{2s+1} \end{pmatrix}, \tag{3.8}$$

where it is assumed that there is no degeneracy of the energy levels. $\langle S\rangle$ and $G_{\mu\nu}^{(0)}(t)$ are then expressed as follows:

$$\langle S_\mu\rangle=\sum_m f_m(S_\mu)_{mm}\,, \tag{3.9}$$

$$f_m=\exp(-E_m/kT)/\sum_n \exp(-E_n/kT)\,, \tag{3.10}$$

$$\begin{aligned} G_{\mu\nu}^{(0)}(t)=&\sum_m f_m(S_\mu)_{mm}(S_\nu)_{mm} \\ &-\sum_{n,m} f_n f_m(S_\mu)_{nn}(S_\nu)_{mm} \\ &+\sum_{n\neq m}\frac{f_n+f_m}{2}\exp(i\omega_{nm}t)(S_\mu)_{nm}(S_\nu)_{mn}\,, \end{aligned} \tag{3.11}$$

$$\hbar\omega_{nm}=E_n-E_m\,. \tag{3.12}$$

To get $G_{\mu\nu}(t)$ we have in principle to extend the calculation to the higher order terms of the perturbation series. However, $G_{\mu\nu}(t)$ may be considered as to have a form (3.11) multiplied, term by term, by such functions as to satisfy the following condition:

$$f(t)=\begin{cases} 1 & \text{for} \quad t=0\,, \\ 0 & \text{for} \quad t\to\infty\,. \end{cases} \tag{3.13}$$

In many cases we anticipate by physical insight the form of $f(t)$ and then determine the parameters from lower order terms of the perturbation series. The possible form of $f(t)$ may be $\exp(-\frac{1}{2}\omega_e^2t^2)$, $\exp(-|t|/\tau_e)$ and their intermediary, etc., where $\hbar\omega_e$ and $\hbar/\tau_e$ are of the order of magnitude of the effective spin-spin interaction. In our case the former form may be taken when the concentration of magnetic ions is not low, and the latter when the concentration of magnetic ions is low or when the spin-lattice relaxation gives the dominating mechanism of the fluctuating motions of spins[8]. When the former type, the Gaussian function, is taken, we need only to know the second moment which is expected to depend scarcely on temperature. Actually we calculated it in the special case where $S=1$ (Ni^{2+}) and $H_0//z$-axis, and confirmed that the temperature dependence of ω_e is very weak and its order of magnitude does not appreciably change in all the temperature range.

We shall here simply make an approximating assumption:

$$G_{\mu\nu}(t)=G_{\mu\nu}^{(0)}(t)f(t)\,, \tag{3.14}$$

where $f(t)$ satisfies the condition (3.13) and its decay time is of the order of magnitude of $\hbar$ divided by the effective spin-spin interaction and does not depend on temperature. The shape of $f(t)$ will be assumed properly according to the case. This assumption, though simple, is sufficient for the qualitative discussions and is useful even for the quantitative order estimation.

We shall here remark on the correction terms to $G_{\mu\nu}^{(0)}(t)$ arising from the higher order terms of the perturbation series. This correction to zero frequency component is not always negligible as compared to the first and the second terms of (3.11), which are small themselves. The ratio of the zero-frequency component of this higher order correction to that of $G_{\mu\nu}^{(0)}$ may be given by (spin-spin interaction energy/Zeeman energy)^2. Therefore, the results of this and the following sections are applicable not only to the case where the Zeeman energy is much larger than the spin-spin interaction energy but also to the case where they are of comparable order of magnitude provided we replace H_0^2 by $H_0^2+H_i^2$, H_i being the effective internal magnetic field.*

* We have calculated this correction for the simple case where there is only one kind of magnetic ion site in the unit cell, and the static field is applied along one of the magnetic principal axes. The results are as follows:

$$G_{\mu\mu}(0)=\frac{g^2\mu_B^2}{X_\mu^2+(g\mu_BH_0)^2}\left[H_0^2F_{\mu\mu}+\frac{X_\mu^2}{X_\mu^2+(g\mu_BH_0)^2}H_{i\mu}^2F_{\mu\mu}'\right],$$

in which $F_{\mu\mu}$ and X_μ are given by (4.6), (4.7), and $H_{i\mu}^2$ and $F_{\mu\mu}'$ are given it the following table.

	$H_0//x$	$H_0//y$	$H_0//z$
$H_{i\mu}^2$	$\frac{3}{2}\sum_k \frac{(g\mu_B)^2y_{jk}^2z_{jk}^2}{r_{jk}^{10}}$	$\frac{3}{2}\sum_k \frac{(g\mu_B)^2z_{jk}^2x_{jk}^2}{r_{jk}^{10}}$	$\frac{3}{2}\sum_k \frac{(g\mu_B)^2x_{jk}^2y_{jk}^2}{r_{jk}^{10}}$
$F_{\mu\mu}'$	$3(f_1+f_2)f_3$	$3(f_2+f_3)f_1$	$3(f_1+f_3)f_2$

↗

We shall now further study the properties of $G_{\mu\nu}^{(0)}(t)$. The first and the second terms of (3.11) are secular terms and the third is a non-secular term. One can easily see from (2.13), (2.14), (2.15) and (2.17) that the contribution of the non-secular term to the line width and $1/T_1$ is far smaller than that of the secular terms provided $|\omega_{nm}|$ and $|\omega_0+\omega_{nm}|$ are sufficiently larger than ω_e whose order of magnitude is that of the inverse of the decay time of $f(t)$. This condition is satisfied in many cases; when all the energy level separations are larger than the spin-spin interaction, it is satisfied in almost all the cases of nuclear resonance and in the case of the electron spin resonance of different ions except when the resonance frequency is near to one of the resonance frequencies of the host ion spins. In the following treatment we shall confine ourselves to the case where this condition is satisfied. Neglecting then the third term of (3.11) we can write

$$G_{\nu\nu}^{(0)}(t)=\langle(S_\mu)_d(S_\nu)_d\rangle-\langle S_\mu\rangle\langle S_\nu\rangle\,, \quad (3.15)$$

where $(\ )_d$ means the diagonal component. This can further be related to the isothermal and the isolated susceptibility tensors as follows:

$$\begin{aligned} g_\mu g_\nu \mu_B{}^2 G_{\mu\nu}^{(0)}(t) &= \sum_m f_m \frac{\partial E_m}{\partial H_\mu}\frac{\partial E_m}{\partial H_\nu} \\ &\quad - \sum_m f_m \frac{\partial E_m}{\partial H_\mu}\sum_n f_n \frac{\partial E_n}{\partial H_\nu} \\ &= \left\langle \frac{\partial E}{\partial H_\mu}\frac{\partial E}{\partial H_\nu}\right\rangle - \left\langle \frac{\partial E}{\partial H_\mu}\right\rangle\left\langle \frac{\partial E}{\partial H_\nu}\right\rangle \\ &= kT(\chi_T-\chi_{is})_{\mu\nu}\,. \end{aligned} \quad (3.16)$$

From the properties of $(\chi_T-\chi_{is})$ qualitative discussions on the general properties of T_1 and T_2 can be given.

(1) At low temperatures where $kT<\Delta E$, ΔE being the energy separation between the lowest two levels, T_1 and T_2 increase very rapidly (exponentially) as temperature is lowered, since $(\chi_T-\chi_{is})$ is proportional to $e^{-\Delta E/kT}$ at these temperatures.

(2) At high temperatures where kT is larger than the overall separation of the spin levels, T_1 and T_2 are independent of temperature since $kT(\chi_T-\chi_{is})$ is there independent of temperature.

(3) When the Zeeman energy is smaller than the initial splitting, $(S)_d\propto H_0$ and $G_{\mu\nu}(t)\propto H_0{}^2$ so that we have

$$1/T_2\propto H_0\,, \quad (3.17)$$

provided there is no narrowing effect, i.e. $\{|\gamma_N{}^2F_0|\}^{1/2}>\omega_e$. With the narrowing effect we have stronger field dependence of T_2. In the case of extreme narrowing, i.e. $\{|\gamma_N{}^2F_0|\}^{1/2}\ll\omega_e$, we have

$$1/T_2\propto H_0{}^2\,. \quad (3.18)$$

As for the field dependence of T_1 we expect

$$1/T_1\propto H_0{}^2\,, \quad (3.19)$$

except for the factor arising from the field dependence of ω_0. In the case of nuclear resonance (3.19) will represent the correct field dependence of T_1, while for electron spin resonance the factor coming from the field dependence of ω_0 will be important.

Before concluding this section, we shall transform (3.16) into the form convenient for later use. When the Zeeman energy is smaller than the initial splitting the energy eigenvalues given by (3.8) are written as follows taking up to the second order terms with respect to the external magnetic field:

$$E_m=E_m{}^0-\tfrac{1}{2}\sum_{\nu=1}^{3}A_{\nu m}H_\nu{}^2\,. \quad (3.20)$$

From (3.16) we get

$$kT(\chi_T-\chi_{is})_{\mu\nu}=(\langle A_\mu A_\nu\rangle-\langle A_\mu\rangle\langle A_\nu\rangle)H_\mu H_\nu\,. \quad (3.21)$$

§ 4. $(\chi_T-\chi_{is})$ for $Ni^{2+}(S=1)$ and $Fe^{2+}(S=2)$

The spin Hamiltonian of a magnetic ion in an orthorhombic crystalline field can be written in a usual form:

$$\begin{aligned}\mathscr{H} &= -DS_z{}^2-E(S_x{}^2-S_y{}^2) \\ &\quad +\mu_B(g_xH_xS_x+g_yH_yS_y+g_zH_zS_z)\,, \end{aligned} \quad (4.1)$$

where x, y, and z axes are the principal axes of the crystalline electric field. We shall calculate $kT(\chi_T-\chi_{is})$ by using (3.16) and (3.21).

(I) $Ni^{2+}(S=1)$

The expressions for χ_T and χ_{is} as well as χ_s (adiabatic susceptibility in a thermodynami-

If we assume that the crystal has symmetry higher than cubic the magnitude of $H_i{}^2$ is one-twelfth of the square of what is usually called an internal field. [See, for instance, Eq. (14) of Van Vleck's paper; Phys. Rev. **74** (1948) 1168.]

$$H_i{}^2=\frac{1}{10}g^2\mu_B{}^2\sum_k r_{jk}{}^{-6}=\frac{1}{12}\times\left[\frac{3}{5}S(S+1)g^2\mu_B{}^2\sum_k r_{jk}{}^{-6}\right]_{S=1}\,.$$

cal sense) have already been obtained for this case[9]. Some numerical calculations for the case of $Ni(NH_4)_2(SO_4)_2 6H_2O$ have also been carried out[9]. Here we reproduce some of the results in which the terms up to the second order with respect to the external magnetic field H_0 are taken into account.

The energy eigenvalues are expressed in the form of (3.20) of which the values of the constants are given in the following table:

m	E_m^0	A_{xm}	A_{ym}	A_{zm}
1	$-D-E$	$\frac{2g_x^2\mu_B^2}{D+E}$	0	$\frac{g_z^2\mu_B^2}{E}$
2	0	$-\frac{2g_x^2\mu_B^2}{D+E}$	$-\frac{2g_y^2\mu_B^2}{D-E}$	0
3	$-D+E$	0	$\frac{2g_y^2\mu_B^2}{D-E}$	$-\frac{g_z^2\mu_B^2}{E}$

(4.2)

From this we get

$$\langle S_\nu\rangle=\frac{g_\nu^2\mu_B^2}{X_\nu}h_\nu H\,, \tag{4.3}$$

$$h_1=f_1-f_2\,,\quad h_2=f_3-f_2\,,\quad h_3=f_1-f_3\,. \tag{4.4}$$

$$kT(\chi_T-\chi_{is})_{\mu\nu}=\frac{g_\mu^2g_\nu^2\mu_B^4H_\mu H_\nu}{X_\mu X_\nu}F_{\mu\nu}\,, \tag{4.5}$$

$$\left.\begin{aligned}
F_{11}&=f_1+f_2-(f_1-f_2)^2\,,\\
F_{12}&=f_2-(f_2-f_1)(f_2-f_3)\,,\\
F_{22}&=f_2+f_3-(f_2-f_3)^2\,,\\
F_{23}&=-f_3+(f_3-f_2)(f_3-f_1)\,,\\
F_{33}&=f_3+f_1-(f_3-f_1)^2\,,\\
F_{31}&=f_1-(f_1-f_3)(f_1-f_2)\,,
\end{aligned}\right\} \tag{4.6}$$

$$X_1=(D+E)/2\,,\quad X_2=(D-E)/2\,,\quad X_3=E\,. \tag{4.7}$$

The numerical results for $Ni(NH_4)_2(SO_4)_2 6H_2O$ are shown in Fig. 1. For the values of D, E and g we used the experimental values at 90°K:[10]

$$D=1.99\,\mathrm{cm}^{-1}\,,\quad E=0.486\,\mathrm{cm}^{-1}\,,\quad g=2.25\,. \tag{4.8}$$

The contribution of Zeeman energy to the Boltzmann factors are neglected in calculating numerical values in Fig. 1.

(II) $Fe^{2+}(S=2)$

The energy eigenvalues are expressed by (3.20) up to the second order with respect to the external magnetic field H_0. The values of the constants are shown in the following table:

m	E_m^0	A_{xm}	A_{ym}	A_{zm}
1	$-2D(1+\sqrt{1+\eta^2})$	$\frac{g_x^2\mu_B^2(c+\sqrt{3}s)^2}{D\left(\frac{1}{2}+\sqrt{1+\eta^2}-\frac{\sqrt{3}}{2}\eta\right)}$	$\frac{g_y^2\mu_B^2(c-\sqrt{3}s)^2}{D\left(\frac{1}{2}+\sqrt{1+\eta^2}+\frac{\sqrt{3}}{2}\eta\right)}$	$\frac{4g_z^2\mu_B^2c^2}{D(\sqrt{1+\eta^2}-1)}$
2	$-4D$	$\frac{2g_x^2\mu_B^2}{D(3+\sqrt{3}\eta)}$	$\frac{2g_y^2\mu_B^2}{D(3-\sqrt{3}\eta)}$	$\frac{4g_z^2\mu^2}{D}\left\{\frac{s^2}{\sqrt{1+\eta^2}+1}-\frac{c^2}{\sqrt{1+\eta^2}-1}\right\}$
3	$-D(1+\sqrt{3}\eta)$	$\frac{g_x^2\mu_B^2}{D}\left\{\frac{(s-\sqrt{3}c)^2}{\sqrt{1+\eta^2}+\frac{\sqrt{3}}{2}\eta-\frac{1}{2}}-\frac{(c+\sqrt{3}s)^2}{\sqrt{1+\eta^2}-\frac{\sqrt{3}}{2}\eta+\frac{1}{2}}\right\}$	$-\frac{2g_y^2\mu_B^2}{D(3-\sqrt{3}\eta)}$	$\frac{g_z^2\mu_B^2}{D\sqrt{3}\eta}$
4	$-D(1-\sqrt{3}\eta)$	$-\frac{2g_x^2\mu_B^2}{D(3+\sqrt{3}\eta)}$	$\frac{g_y^2\mu_B^2}{D}\left\{\frac{(s+\sqrt{3}c)^2}{\sqrt{1+\mu^2}-\frac{\sqrt{3}}{2}\eta+\frac{1}{2}}-\frac{(c-\sqrt{3}s)^2}{\sqrt{1+\eta^2}+\frac{\sqrt{3}}{2}\eta+\frac{1}{2}}\right\}$	$-\frac{g_z^2\mu_B^2}{D\sqrt{3}\eta}$
5	$2D(\sqrt{1+\eta^2}-1)$	$-\frac{g_x^2\mu_B^2(s-\sqrt{3}c)^2}{D\left(\sqrt{1+\eta^2}+\frac{\sqrt{3}}{2}\eta-\frac{1}{2}\right)}$	$-\frac{g_y^2\mu_B^2(s+\sqrt{3}c)^2}{D\left(\sqrt{1+\eta^2}-\frac{\sqrt{3}}{2}\eta-\frac{1}{2}\right)}$	$-\frac{4g_z^2\mu_B^2s^2}{D(\sqrt{1+\eta^2}+1)}$

(4.9)

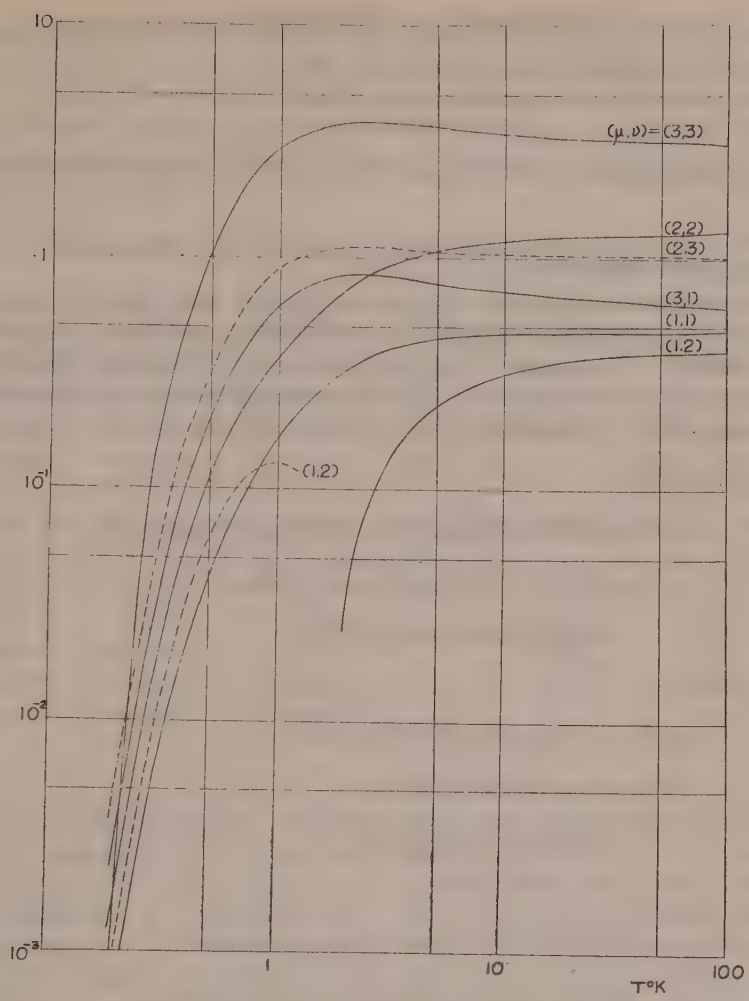

Fig. 1. $[kT(\chi_T-\chi_{is})_{\nu\mu}/H_\mu H_\nu g^2\mu_B{}^2]\times 10^8$ for $Ni(NH_4)_2(SO_4)_2 6H_2O$. The two figures in the braces specify tensor components. The dotted lines are used where negative values are taken.

Table I. $[kT(\chi_T-\chi_{is})_{\mu\nu}/H_\mu H_\nu g^2\mu_B{}^2]\times 10^{-8}$ for $Fe(NH_4)_2(SO_4)_2 6H_2O$.

T°K \ μ,ν	1,1	2,2	3,3	1,2	2,3	3,1
1	1.0×10^{-6}	5.1×10^{-7}	5.1×10^{-4}	-7.3×10^{-7}	-1.6×10^{-5}	2.3×10^{-5}
2	1.0×10^{-4}	5.0×10^{-5}	5.0×10^{-2}	-7.1×10^{-5}	-1.6×10^{-3}	2.3×10^{-3}
3	4.4×10^{-4}	2.2×10^{-4}	2.2×10^{-1}	-3.1×10^{-4}	-6.9×10^{-3}	9.8×10^{-3}
4	8.6×10^{-4}	4.2×10^{-4}	0.42	-6.0×10^{-4}	-1.3×10^{-2}	1.9×10^{-2}
20	3.4×10^{-3}	4.4×10^{-2}	1.1	-5.5×10^{-4}	-5.4×10^{-2}	5.3×10^{-2}
300	6.5×10^{-3}	1.8	0.59	-2.5×10^{-2}	-3.7×10^{-2}	2.7×10^{-2}
∞	6.2×10^{-3}	2.1	0.51	-3.0×10^{-2}	-3.8×10^{-2}	2.3×10^{-2}

where

$$\eta=\sqrt{3}\,E/D\,,\qquad c=\cos\theta\,,\qquad s=\sin\theta\,,\qquad \tan 2\theta=\eta\,. \tag{4.10}$$

The values of $kT(\chi_T-\chi_{is})$ are calculated by using (3.21). The numerical results for $Fe(NH_4)_2(SO_4)_2 6H_2O$ are shown in Table I. The values of D and E are taken from Ohtsuka, Abe and Kanda's result[2]:

$$D=14.5\ \mathrm{cm}^{-1}\,, \qquad E=5.86\ \mathrm{cm}^{-1}\,. \tag{4.11}$$

The anisotropy of g is neglected and the average value,

$$g_{\mathrm{av}}=2.14\,, \tag{4.12}$$

are taken. The contribution of the Zeeman energy to the Boltzmann factors are here also neglected.

§ 5. Nuclear Magnetic Resonance

The motion of the electron spins are usually much faster than that of nuclear spins in the local field, so that the narrowing condition for the nuclear resonance line stated in § 3 is almost always satisfied. The neglect of the non-secular perturbation (nondiagonal components of the electron spins) are also justified. The line shape therefore is Lorentzian and T_1 and T_2 are of the same order of magnitude. By using the formulas in § 2 we get

(a) for $f(t)=\exp(-\frac{1}{2}\omega_e^2t^2)$,

$$1/T_2=(\pi/2)^{1/2}(\gamma_N^2/\omega_e)[F_0'(0)+F_1'(0)\exp(-\tfrac{1}{2}\omega_0^2/\omega_e^2)]\,, \tag{5.1}$$

$$1/T_1=(2\pi)^{1/2}\gamma_N^2F_1'(0)\exp(-\tfrac{1}{2}\omega_0^2/\omega_e^2)/\omega_e\,, \tag{5.2}$$

$$(\text{usually } \exp(-\tfrac{1}{2}\omega_0^2/\omega_e^2)\sim 1)$$

(b) for $f(t)=\exp(-|t|/\tau_e)$,

$$1/T_2=\gamma_N^2\tau_e[F_0'(0)+F_1'(0)/(1+\omega_0^2\tau_e^2)]\,, \tag{5.3}$$

$$1/T_1=2\gamma_N^2\tau_eF_1'(0)/(1+\omega_0^2\tau_e^2)\,. \tag{5.4}$$

$$(\text{usually } (1+\omega_0^2\tau_e^2)\sim 1)$$

where

$$F_0'(0)=\sum_j\sum_{\nu,\nu'}P_{0j}^{\nu\nu'}kT(\chi_T-\chi_{is})_{\nu\nu'}/g_\nu g_{\nu'}\mu_B^2\,, \tag{5.5}$$

$$F_0'(0)=\sum_j\sum_{\nu,\nu'}P_{1j}^{\nu\nu'}kT(\chi_T-\chi_{is})_{\nu\nu'}/g_\nu g_{\nu'}\mu_B^2\,, \tag{5.6}$$

$$P_{0j}^{\nu\nu'}=(\gamma_e\hbar)^2\sum_{\mu,\mu'}\alpha_\mu\alpha_{\mu'}\Phi_j^{\mu\nu}\Phi_j^{\mu'\nu'}\,, \tag{5.7}$$

$$P_{1j}^{\nu\nu'}=\tfrac{1}{2}(\gamma_e\hbar)^2\sum_{\mu,\mu'}(\delta_{\mu\mu'}-\alpha_\mu\alpha_{\mu'})\Phi_j^{\mu\nu}\Phi_j^{\mu'\nu'}\,. \tag{5.8}$$

$P_{0j}^{\nu\nu'}$ and $P_{1j}^{\nu\nu'}$ depend in a complicated way on the direction of the magnetic field and on the arrangements of the magnetic ions. When the interaction between the nuclear spin and the electron spins are of purely dipolar character, we may estimate

$$P_{0j}^{\nu\nu'}\sim P_{1j}^{\nu\nu'}\sim g^2\mu_B^2/r_j^6\,,$$

except for the angular dependent factor whose order of magnitude is 1.

We shall make, for example, an order estimation of T_1 and T_2 of protons of the water molecules in $Ni(NH_4)_2(SO_4)_2 6N_2O$ and $Fe(NH_4)_2(SO_4)_2 6H_2O$. In this case one magnetic ion nearest to the considering proton makes a dominant contribution. Estimating $P_{0j}^{\nu\nu'}\sim P_{1j}^{\nu\nu'}\sim 10^6$, we get

$$1/T_1\sim 1/T_2\sim(10^{15}/\omega_e)\sum_{\nu,\nu'}kT(\chi_T-\chi_{is})_{\nu\nu'}/g^2\mu_B^2\,. \tag{5.9}$$

For $Ni(NH_4)_2(SO_4)_2 6H_2O$ we estimate $\omega_e\sim 5\times 10^9$ from the paramagnetic resonance line width[10]. For $Fe(NH_4)_2(SO_4)_2 6H_2O$ we shall here assume $\omega_e\sim 10^{10}$ since no data is available, though it

will be estimated from a measurement of the nuclear relaxation time stated here. In Tables II and III the relaxation time in the case where the external field is applied along the x, y, and z axes are given. The numerical values in the Tables II and III are only of order of magnitude significance, though the temperature dependence is reliable. We can of course make more precise calculations taking account of the exact arrangement of the ions in the crystals by using (5.1)~(5.6).

Table II. $T_1 \sim T_2$ (in sec.) for protons in H_2O in $Ni(NH_4)_2(SO_4)_2 6H_2O$ at $H_0=3000$ gauss. ($\omega_e \simeq 5\times 10^9$)

T°K	$H_0//x$	$H_0//y$	$H_0//z$	T°K	$H_0//x$	$H_0//y$	$H_0//z$
∞	1.1×10^{-4}	4.3×10^{-5}	1.8×10^{-5}	0.4	2.7×10^{-3}	1.0×10^{-3}	1.0×10^{-4}
4	1.3×10^{-4}	5.6×10^{-5}	1.5×10^{-5}	0.3	8.3×10^{-3}	3.1×10^{-3}	3.2×10^{-4}
2	1.7×10^{-4}	7.8×10^{-5}	1.5×10^{-5}	0.2	8.4×10^{-2}	3.1×10^{-2}	3.3×10^{-3}
1	3.3×10^{-4}	1.5×10^{-4}	1.9×10^{-5}	0.1	91	34	3.5

Table III. $T_1 \sim T_2$ (in sec.) for protons in H_2O in $Fe(NH_4)_2(SO_4)_2 6H_2O$ at $H_0=3000$ gauss. ($\omega_e \simeq 10^{10}$)

T°K	$H_0//x$	$H_0//y$	$H_0//z$	T°K	$H_0//x$	$H_0//y$	$H_0//z$
∞	1.8×10^{-2}	5.3×10^{-5}	2.2×10^{-4}	4	0.13	0.26	2.6×10^{-4}
300	1.7×10^{-2}	6.3×10^{-5}	1.9×10^{-4}	3	0.25	0.51	5.1×10^{-4}
20	3.2×10^{-2}	2.5×10^{-3}	9.8×10^{-5}	2	1.1	2.2	2.2×10^{-3}
				1	110	220	0.22

As one sees in Tables II and III the temperature and the magnetic field dependences and the anisotropies of T_1 and T_2 seem especially to be interesting. A remarkable temperature dependence of T_1 and T_2 is expected at liquid helium temperatures for $Fe(NH_4)_2(SO_4)_2 6H_2O$, though it is expected below 1°K for $Ni(NH_4)_2(SO_4)_2 6H_2O$.

§ 6. Paramagnetic Resonance and Relaxation

In this section we shall chiefly be concerned with the paramagnetic resonance and relaxation of ions like Mn^{2+}, Co^{2+}, Cu^{2+}, etc., which are diluted in the salts of Fe^{2+} or Ni^{2+}. Let Mn^{2+} and Fe^{2+} be the representatives of the resonating and the host ion spins, respectively. If all the resonance frequency differences of Mn^{2+} and Fe^{2+} are much greater than the interaction energy (dipolar or exchange) divided by $\hbar$, the effect of nondiagonal elements (high frequency components) of Fe^{2+} spin on the resonance spectrum of Mn^{2+} can be neglected, i.e., (3.15) and (3.16) are satisfied. Further, if the condition, $\langle(\delta S)_d^2\rangle \ll S(S+1)$, is satisfied for Fe^{2+} spins, their contribution to the Mn^{2+} resonance line width is narrowed by the interaction (dipolar or exchange) among Fe^{2+} spins. Tre above inequality expresses that the *effective* $Fe^{2+}-Mn^{2+}$ interaction is smaller than the $Fe^{2+}-Fe^{2+}$ interaction. This is valid when the initial splittings of Fe^{2+} spin levels are much larger than the Zeeman energy. In this case the line shape becomes Lorentzian, and the expressions for T_1 and T_2 are the same as Eq. (5.3) and (5.4) except that the γ_N there should be replaced by γ_e. One should be careful, however, that the neglect of high frequency components of Fe^{2+} spins in the expression of T_1 is not so good an approximation as in the NMR case. In the case where $\omega_0 \gg \omega_e$, the second term in the right-hand side of the equations of T_2 (Eq. (5.1) and (5.3)) can be neglected.

Let us first make simple order estimations and qualitative discussions. When the Mn^{+} resonance line width is not narrowed by the $Fe^{2+}-Fe^{2+}$ interaction, the width is of the order,

$$\gamma_e \sqrt{|F_0'(0)|}\ , \tag{6.1}$$

which, as compared to the value when the Fe^{2+} spins are assumed free, is reduced by a factor of $(\delta S)_d/S$. When $(\delta S)_d/S \ll 1$ is satisfied, the line width is necessarily narrowed since ω_e is of the same order of magnitude

as in the case where Fe^{2+} spins are free*, and we obtain the following expression for T_2:

$$\frac{1}{T_2} \simeq \left(\frac{(\delta S)_d}{S}\right)^2 (1/T_2)_{\text{free spin}}$$
$$= \frac{kT(\chi_T - \chi_{ts})}{g^2 \mu_B{}^2 S^2} (1/T_2)_{\text{free spin}}, \qquad (6.2)$$

where $(1/T_2)_{\text{free spin}}$ in a measure for line width of Mn^{2+} resonance when the Fe^{2+} spins are assumed free. The exchange interaction between Mn^{2+} and Fe^{2+} spins also contributes to $(1/T_2)_{\text{free spin}}$. The line width will show strong temperature dependence (at low temperatures) and field dependence like $H_0{}^2+H_i{}^2$ as in the NMR case.

T_1 shows different behaviors in cases (a) and (b) in § 5. Its temperature dependence is the same as that of T_2, but the field dependence is as follows:

in case (a),

$$1/T_1 \propto (H_0{}^2+H_i{}^2) \exp(-\tfrac{1}{2}\gamma_e{}^2 H_0{}^2/\omega_e{}^2), \qquad (6.3)$$

which has a minimum near $H_0 \sim H_i$, and

in case (b),

$$1/T_1 \propto (H_0{}^2+H_i{}^2)\tau_e/(1+\gamma_e{}^2 H_0{}^2 \tau_e{}^2), \qquad (6.4)$$

and when τ_e depends weakly on H_0, so is T_1. When the spin-lattice mechanism determines τ_e, the decay time of $f(t)$, its field dependence plays an important role. It should also be noticed that the contribution of high frequency components of Fe^{2+} spins to $(1/T_1)$ can not necessarily be neglected.

In the following we shall discuss, as some examples, the line width and the relaxation time of Mn^{2+} which are substituted for Fe^{2+} or Ni^{2+} in the salts of $Fe(NH_4)_2(SO_4)_2 6H_2O$, $Ni(NH_4)_2(SO_4)_2 6H_2O$ and $NiSO_4 7H_2O$. However, there are 2, 2 and 4 non-equivalent magnetic ion sites respectively in these salts, which makes the exact calculation of the line width and the relaxation time very much complicated though possible. So we here discuss about their order of magnitudes and qualitative characters of temperature and field dependences.

(i) $Fe(NH_4)_2(SO_4)_2 6H_2O$.

Details of the crystal structure, the orientation of the magnetic principal axes etc, are found in ref. 2). If we take the external magnetic field to be 3000 gauss, we obtain from Eq. (6.2) and Table I the following:

for $H_0 \perp K_2$,

$$1/T_2 \lesssim 10^{-2}(1/T_2)_{\text{free spin}} \quad \text{at } 4°\text{K},$$
$$1/T_2 \lesssim 10^{-3}(1/T_2)_{\text{free spin}} \quad \text{at } 2°\text{K},$$

and for $H_0 \| K_2$,

$$1/T_2 \sim 10^{-5}(1/T_2)_{\text{free spin}} \quad \text{at } 4°\text{K},$$
$$1/T_2 \sim 10^{-6}(1/T_2)_{\text{free spin}} \quad \text{at } 2°\text{K}.$$

As one can readily see from the Table I (§ 4), the line width at room temperature is, when $H_0 \perp K_2$, the same order of magnitude as (or a little greater than) the value at 4°K, while it becomes about 10 times greater than the value at 4°K when $H_0 \| K_2$.

If we take the line width of free Fe^{2+} spins, $(\Delta H)_{\text{free spin}}$, to be 700 gauss, the line width of Mn^{2+} in this salt is always less than 7 gauss at liquid helium temperatures, decreasing rapidly when the temperature is further lowered. Its field dependence is like $H_0{}^2+H_i{}^2$. (H_i being several hundred gauss).

One can, if necessary, calculate the line width, taking into account the effect of anisotropy arising from the arrangement of Fe^{2+} around Mn^{2+}. However, it is clear from above rough estimations that, $Mn^{2+}-Fe^{2+}$ interaction mechanism is insufficient to explain the whole line width obtained in Ohtsuka et al's experiment, so long as the initial splittings of the spin levels they obtained are used. It is certain that this mechanism contributes to the line width, but very weak magnetic field dependence and the very weak temperature dependence of the observed line width may suggest that the main contribution comes from another mechanism. However, the qualitative characters of the temperature and field dependences of the field dependent part of the line width seem to favor our theory**.

* We should notice here that ω_e is of order of magnitude of the mean frequency of spin diffusion which decreases when one applies the magnetic field of a certain magnitude provided that there are some different sites of magnetic ions in a unit cell as is usually the case. It is because the ions in the different sites have usually different energy levels under the magnetic field, which causes to prevent the spin diffusion. In the following statement this effect is not taken into account.

Though Eq. (6.2) is valid, strictly speaking, when all the ions are equivalent, it may be allowed to use it for order estimations.

** Ohtsuka et al as well as Hayashi, refered to below, obtained the field dependence of the line width by measuring the widths of several resolved fine and hyperfine components of Mn^{2+} resonance lines, varying the static magnetic field and keeping the resonance frequency constant, while our theory deals with the field dependence of the line width of free spins. However, the correction owing to this different situations turned out to be of minor importance after careful examination.

(ii) $Ni(NH_4)_2(SO_4)_2 6H_2O$.

Concerning this salt all the necessary data are at hand[10]. From Eq. (6.2) and Fig. 1 in § 4, the line width for $H_0=3000$ gauss has been calculated. We obtain the following:

for $H_0 \| K_1$,

$$1/T_2 \sim 0.3(1/T_2)_{\text{free spin}}$$

for room temp. ~ liq. He temp.,

$$\sim 0.05(1/T_2)_{\text{free spin}} \quad \text{at } 0.4°\text{K}.$$

The calculated line width is not strictly constant from room temperature to liquid He temperature, but shows a maximum near 2~3°K.

For $H_0 \| K_2$ or K_3,

$$1/T_2 \sim 0.1(1/T_2)_{\text{free spin}}$$

for room temp. ~ liq. He temp.,

$$\sim 0.003(1/T_2)_{\text{free spin}} \quad \text{at } 0.4°\text{K}.$$

The line width decreases only slightly as we go from room temperature down to liquid helium temperatures. If we take $(\Delta H)_{\text{free}} \sim$ 400 gauss for Ni^{2+} in this salt, the width of Mn^{2+} becomes of the order of 100 ~ 40 gauss for this temperature range. This result is consistent with experiment so long as the order of magnitude is concerned. Its temperature dependence should become remarkable only below 1°K. As the narrowing condition, $(\delta S)_d \ll S$, is not so well satisfied for Ni^{2+} as for Fe^{2+} spins, the value of the line width may become a little larger than the above estimation. The magnetic field dependence may be somewhat between $\sqrt{H_0^2+H_1^2}$ (no narrowing) and $H_0^2+H_i^2$ (extreme narrowing). There is no available data of the field dependence of the line width.

If we assume $f(t)=\exp(-\frac{1}{2}\omega_e^2 t^2)$, we shall be justified to estimate the relaxation time T_1 from

$$T_1 \sim T_2 \exp(\tfrac{1}{2}\omega_0^2/\omega_e^2) .$$

Since this quantity depends strongly on ω_e, accurate value of ω_e is necessary in order to obtain a reliable result. T_1 reaches its minimum (same order of magnitude as T_2) when $\omega_0 \sim \omega_e$, and it becomes longer very rapidly when H_0 is further increased. If we take, for the time being, $H_0=3000$ gauss, $\omega_0/\omega_e \sim 6$, the following results are obtained:

for Mn^{2+} in $Fe(NH_4)_2(SO_4)_2 6H_2O$,

$H_0 \perp K_2$ $\quad T_1 \gtrsim 1$ sec. at 4°K,

$\gtrsim 10$ sec. at 2°K,

$H_0 \| K_2$ $\quad T_1 \sim 10^3$ sec. at 4°K,

$\sim 10^4$ sec. at 2°K.

for Mn^{2+} in $Ni(NH_4)_2(SO_4) 6H_2O$,

$H_0 \| K_1$ $\quad T_1 \sim 0.03$ sec.

for room temp. ~ liq. He temp.

$H_0 \perp K_1$ $\quad T_1 \sim 0.1$ sec.

for room temp. ~ liq. He temp.

These are only rough order estimations, but it is certain that this mechanism is more important in Ni^{2+} salts than in Fe^{2+} salts.

(iii) $NiSO_4 7H_2O$.

Magnetic field dependence of the line width at room temperature was measured by I. Hayashi*. According to it the line width increases as the magnetic field increases and the magnitude of the field dependent part of the line width is much larger than in $Fe(NH_4)_2(SO_4)_2 6H_2O$ and is of the same order of magnitude as in $Ni(NH_4)_2(SO_4)_2 6H_2O$, in qualitative agreement with the expectation from our theory.

The fine structure constants of this salt were determined by Ôno from paramagnetic resonance experiment[11]. They are

$$D=3.56\ \text{cm}^{-1}, \quad E=1.50\ \text{cm}^{-1}. \tag{6.5}$$

The crystal structure is found in reference 11).

The whole considerations on T_1 in this section are valid when the heat capacity of Fe^{2+} (or Ni^{2+}) spin system is much larger than that of Mn^{2+} spins. Even if this condition is not so well satisfied, our considerations remain at least qualitatively valid when the heat contact of Fe^{2+} spin system with the lattice is very good. Some results of paramagnetic relaxation experiments by Haseda[3] may be interpreted in connection with the above-mentioned mechanism. Relaxation rate due to this is additive to that due to the spin-orbit coupling (Van Vleck mechanism).

§ 7. Concluding Remarks

Our study presented above is of almost purely theoretical character based on a spin Hamiltonian. Though some experimental results of electron spin resonances seem to support our theory, more experimental studies are needed to confirm it.

Disappearance of the proton resonance line

* I. Hayashi, unpublished data. We should like to thank Dr. I. Hayashi for allowing us to quote his data prior to publication.

in some Ni salts at low temperatures reported by Kim and Sugawara[4] is not understood from our theory, though the very rapid increase of T_1 at low temperatures may have some relation to those phenomena.

We expect further experimental studies on both nuclear and electron spin resonances.

In conclusion the writers would like to thank Dr. T. Sugawara and Mr. P. H. Kim for providing them with a stimulus to the problem. They thank also Prof. R. Kubo and Dr. M. Shimizu for their kind interest and discussions.

References

1) K. Ôno and I. Hayashi: J. Phys. Soc. Japan **8** (1953) 561.
H. Kumagai: Proc. International. Conf. on Theoret. Phys. Kyoto, Sept. (1953) 791.
2) T. Ohtsuka, H. Abe and E. Kanda: Sci. Rep. RITU, A **9** (1957) 476.
3) T. Haseda: Physica **24** (1958) 93; and private communication.
4) P. H. Kim and T. Sugawara: J. Phys. Soc. Japan **13** (1958) 968.
5) Y. Obata: spoken at the Annual Meeting of the Physical Society of Japan at Sendai July 1954.
6) T. Moriya: Prog. Theor. Phys. **16** (1957) 23, 641.
7) R. Kubo and K. Tomita: J. Phys. Soc. Japan **9** (1954) 888.
8) P. W. Anderson: Phys. Rev. **82** (1951) 342.
C. Kittel and E. Abrahams: Phys. Rev. **90** (1953) 238.
9) T. Moriya: Busseiron Kenkyu II **3** (1958) 332 (in Japanese).
10) J. H. E. Griffiths and J. Owen: Proc. Roy. Soc. A **213** (1952) 459.
11) K. Ôno: J. Phys. Soc. Japan **8** (1953) 802.

JOURNAL OF THE PHYSICAL SOCIETY OF JAPAN Vol. 13, No. 11, NOVEMBER, 1958

Nuclear Magnetic Resonance of Transition Elements in Paramagnetic Salts

By Tôru MORIYA

Department of Physics, Tokyo Metropolitan University

(Received August 2, 1958)

Nuclear magnetic resonance of transition elements in paramagnetic salts under two situations is studied theoretically. One is the case where the magnetic ions have no Kramers degeneracy and their spin degeneracy is completely lifted by the combined action of the spin-orbit coupling and the crystalline electric field. Another is the case of the ideal paramagnetic substances under a strong magnetic field and at low temperatures. The resonance field (or frequency) shift, the relaxation times T_1 and T_2 due to hyperfine interaction and the indirect nuclear spin coupling via electron spins are calculated. The results show that the nuclear resonance of transition elements in paramagnetic salts is expected to be observable under favorable conditions.

§ 1. Introduction

Nuclear magnetic resonance of transition elements has never been observed except when the ions are diamagnetic such as cobalt in complex salts. The reason for this is in paramagnetic substances considered to be due to very large fluctuating magnetic field at the nucleus produced by the electron spin through hyperfine interaction, which makes the nuclear resonance line width so large and T_1 so short as to prevent the observation of the resonance[1]. In antiferromagnetic state this fluctuating magnetic field decreases rapidly as temperature is lowered[1], while there grow very large indirect couplings among the nuclei via spin waves[2),3)] which again make the observation of the nuclear resonance difficult.

In the present article we shall give a theore-

tical treatment of the nuclear magnetic resonance of transition elements in paramagnetic salts for two cases. One is the case which was our concern in the preceding article[4)]*, i.e., the case where the magnetic ions have no Kramers degeneracy and their spin degeneracy is completely lifted by a crystalline electric field. Another is the case where the paramagnetic ordering occurs in a usual Zeeman system under strong magnetic field at low temperatures.

In both of these cases nuclear resonance is expected to be observable provided the energy level separation between the ground state and the lowest excited state is large compared with the spin-spin interaction energy as well as kT, though the frequency will be shifted quite remarkably. These conditions mean that there is a considerable amount of spin ordering and thus a decrease of the fluctuating magnetic field at the nucleus produced by the electron spins. There are, however, a competing effect of indirect nuclear spin coupling via electron spins which becomes larger as temperature is lowered and is unfavorable for the observation of nuclear resonance. If the above stated conditions are satisfied this indirect nuclear spin coupling also will not be very large as will be shown in the following sections.

We shall here treat the problems of nuclear resonance field shift, relaxation rate by hyperfine interaction, and indirect coupling between nuclear spins in two cases stated above.

§ 2. The Case where a Crystalline Field removes the Spin Degeneracy Completely

(I) *Resonance field shift*

The general formulas for the shift, T_1 and T_2 in § 2 of I are of course applicable here. The coupling constant between the nuclear spin and the electron spins are taken as

$$\Phi_{ij}=(\gamma_e\gamma_N\hbar^2)^{-1}[A_i\delta_{ij}+B_{ij}(1-\delta_{ij})]\,, \qquad (2.1)$$

where A_i is the hyperfine coupling tensor for the i-th ion, B_{ij} comes from the dipole-dipole interaction between the i-th nuclear spin and the j-th electron spin. Inserting (2.1) into (2.9) of I, we get the following expression for the total magnetic field at the i-th nucleus:

$$\boldsymbol{H}_i=(1+\boldsymbol{\sigma}_i)\cdot\boldsymbol{H}_0\,, \qquad (2.2)$$

$$\boldsymbol{\sigma}_i=(1/\gamma_N\hbar\mu_B)[\boldsymbol{A}_i\cdot\boldsymbol{g}_i^{-1}\cdot\bar{\boldsymbol{\chi}}_i+\sum_{j\,(\neq i)}\boldsymbol{B}_{ij}\cdot\boldsymbol{g}_j^{-1}\cdot\bar{\boldsymbol{\chi}}_j]\,, \qquad (2.3)$$

where $\bar{\boldsymbol{\chi}}_i$ denotes the magnetic susceptibility tensor (per ion) for the i-th ion defined by $\mu_B\boldsymbol{g}_i\langle\boldsymbol{S}_i\rangle=\bar{\boldsymbol{\chi}}_i\cdot\boldsymbol{H}_0$**.

Usually $\boldsymbol{A}$ is much larger than $\boldsymbol{B}$ and the shift of the resonance field is principally determined by the hyperfine coupling. Its order of magnitude is estimated as follows: we have $A/(\gamma_N\times10^{-4})\sim10^{-2}\,\mathrm{cm}^{-1}\sim2\times10^{-18}$ cgs for V^{2+}, Cr^{3+} and Mn^{2+}[5)], so that

$$\sigma=10^{25}\bar{\chi}\sim20\bar{\chi}_M\ (\text{per mole})\,. \qquad (2.4)$$

χ takes a constant value at low temperatures whose order of magnitude is $\chi\sim2g^2\mu_B^2/\Delta\sim4\times10^{-24}/\Delta$ (in cm^{-1}) for $S=1$, Δ being the initial splitting. For example, if we take $\Delta\sim2\,\mathrm{cm}^{-1}$ we get $\sigma\sim20$. Usually we expect very large shift.

R. J. Elliott considered a similar problem for a rare earth ion Eu^{3+}[6)]. In this case σ becomes negative i.e. the shift is diamagnetic.

(II) *Relaxation times*

The nuclear relaxation times T_1 and T_2 due to the hyperfine coupling are calculated with the use of the formulas in §§ 2, 3, and 5 of I. The results are

$$1/T_1=\frac{(\pi/2)^{1/2}}{\hbar^2\omega_e}\sum_{\nu,\nu'}(\delta_{\nu\nu'}A_\nu^2-\alpha_\nu\alpha_{\nu'}A_\nu A_{\nu'})\times kT(\chi_T-\chi_{is})_{\nu\nu'}/g_\nu g_{\nu'}\mu_\beta^2\,, \qquad (2.5)$$

$$1/T_2=\frac{(\pi/2)^{1/2}}{2\hbar^2\omega_e}\sum_{\nu,\nu'}(\delta_{\nu\nu'}A_\nu^2+\alpha_\nu\alpha_{\nu'}A_\nu A_{\nu'})\times kT(\chi_T-\chi_{is})_{\nu\nu'}/g_\nu g_{\nu'}\mu_\beta^2\,, \qquad (2.6)$$

Where we took the principal axes of the hyperfine coupling tensor as x, y and z axes. α_1, α_2, α_3 are the direction cosines of the total magnetic field, $\boldsymbol{H}=(1+\boldsymbol{\sigma})\cdot\boldsymbol{H}_0$, at the nucleus, χ_T, χ_{is} the isothermal and isolated susceptibilities per ion. Calculations of χ_T and χ_{is} for $S=1$, 2 are found in I. We assumed a Gaussian shape for the frequency distribution of the electron spin fluctuations, i.e. we took

* Referred to below as I. In that article we presented a theory of magnetic resonance of nuclear spins and electron spins of impurity ions in those paramagnetic salts where the spin degeneracy of an ion is completely lifted by the combined action of the spin-orbit coupling and the crystalline electric field.

** The susceptibility defined here is not always a usual one. When H_0 is large $\bar{\chi}$ differs from the differential susceptibility, $\chi=-(\partial^2F/\partial H^2)$, F being the free energy.

the form $f(t)=e^{-(1/2)\omega_e^2 t^2}$ for the decay of the time correlation functions of the electron spin fluctuations. $\hbar\omega_e$ is of the order of magnitude of electronic spin-spin interaction. As was seen in I, T_1 and T_2 increase rapidly (exponentially) as temperature is lowered at low temperatures.

(III) *Indirect coupling*

Indirect couplings among the nuclear spins are derived by the second order perturbation calculation taking $\mathscr{H}_e$, the Hamiltonian of the electron spin system, as an unperturbed Hamiltonian and $\mathscr{H}_{Ne}$, the interaction between the nuclear spins and the electron spins, as a perturbing Hamiltonian. It is, however, usually very difficult to obtain the eigenstates of the electron spin system, the eigenstates of $\mathscr{H}_e$. In ferro and antiferromagnetic substances spin waves represent the eigen states in good approximation at low temperatures. In the present case the perturbation method is applicable to calculate the approximate eigenstates of the electron spin system when the energy level separations of the spin levels are large compared to the spin-spin interaction energy. The couplings arising from the lower order approximation to the electron spin system are concerned only with a few electron spins.

The indirect coupling between the nuclear spin of a magnetic ion and that of a nonmagnetic ion is principally due to magnetic antishielding effect, where the electron spin of only one ion takes part in. On the other hand, the indirect coupling between two nuclear spins of magnetic ions comes mainly by way of the hyperfine couplings in the fwo ions; the electron spins of the two ions take part in this mechanism. We shall below deal with these two mechanisms.

We want now to obtain an expression for the indirect nuclear spin coupling at an arbitrary temperature. Our approximate eigenstates are localized ones concerned with only one or two electron spins. In calculating the indirect coupling between two nuclear spins it will be justified to take an average over all the electron spin states, since the transitions among the localized spin states due to the spin-spin interactions are so rapid as to satisfy

$$\hbar^{-1}A\omega_0\tau^2 \ll 1\,, \tag{2.7}$$

where A is the hyperfine coupling constant, ω_0 the nuclear Larmor frequency and τ the electron spin relaxation time due to spin-spin interactions. This condition mean that the motion of the electron spins is so rapid that they show their average values at any instant of the nuclear spin motion. Denoting the eigenfunctions and the eigenvalues of the electron spin system by ψ_α and E_α etc., we may write

$$\mathscr{H}^{\text{eff}}=\sum_{\alpha>\beta}\frac{f_\alpha-f_\beta}{E_\alpha-E_\beta}(\alpha|\mathscr{H}'|\beta)(\beta|\mathscr{H}'|\alpha) \tag{2.8}$$

as the effective Hamiltonian for the indirect nuclear spin coupling, where

$$f_\alpha=\exp(-E_\alpha/kT)/\sum_\beta \exp(-E_\beta/kT)\,,$$

$\mathscr{H}'$ represents the interaction between the electron spins and the nuclear spins including hyperfine as well as the dipole-dipole interactions.

It is of interest to remark here that the above expression is not accurate when the spin-lattice relaxation time τ_1 of the electron spins is rapid. When τ_1 satisfies

$$\hbar^{-1}A\omega_0\tau_1^2 \ll 1\,, \tag{2.9}$$

we have rather to calculate the free energy of the system regarding the nuclear spin operators as parameters. From the second order terms of the perturbation calculation of the free energy the effective Hamiltonian for the indirect nuclear spin coupling results. This may be formulated as follows:

$$F=F_0+\langle\mathscr{H}'\rangle+\frac{1}{2}\left\{\langle\mathscr{H}'\rangle^2/kT-\int_0^{1/kT}d\lambda\langle\mathscr{H}'(\lambda)\mathscr{H}'\rangle\right\}+\cdots\,, \tag{2.10}$$

where

$$\mathscr{H}'(\lambda)=\exp(-\lambda\mathscr{H}_e)\mathscr{H}'\exp(\lambda\mathscr{H}_e)\,.$$

F is the free energy, F_0 that of the electron spin system neglecting the nuclear spin system, i.e.

$$\exp(-F_0/kT)=\mathrm{Tr}\exp(-\mathscr{H}_e/kT)$$

where $\mathscr{H}_e$ is the Hamiltonian of the electron spin system including the spin-spin interactions, $\langle\ \rangle$ means to take thermal average,

$$\langle Q\rangle=\mathrm{Tr}\,Q\exp(-\mathscr{H}_e/kT)/\mathrm{Tr}\exp(-\mathscr{H}_e/kT)\,,$$

and $\mathscr{H}'$ denotes the Hamiltonian of the interaction between the nuclear spins and the electron spins. The third term is to be used as the effective Hamiltotian of the indirect nuclear spin coupling.

These two formulas are in general different though it is equivalent when $\mathscr{H}'$ has no diagonal element. It is to be determined according to the case which of these two formulas should be used. In both cases, as one sees easily, the antishielding effect arises from those terms bilinear with respect to the hyperfine and the dipole-dipole interactions (and those quadratic in the dipole-dipole interaction) though we derive it below in an instinctive but equivalent way.

(*a*) *Antishielding effect*

In a magnetic ion the nuclear spin polarizes the electron spin by the hyperfine coupling between them. The polarized moment of the electron spin follows the nuclear spin as it processes, i.e. the induced moment may be written as

$$\boldsymbol{\chi}_i \cdot \boldsymbol{g}_i^{-1} \cdot \boldsymbol{A}_i \cdot \boldsymbol{I}_i / \mu_B \,, \tag{2.11}$$

where $\boldsymbol{\chi}_i$ is the susceptibility tensor of the i-th ion. When the spin-lattice relaxation time is not short and does not satisfy (2.9) $\boldsymbol{\chi}_i$ should be an isolated susceptibility, while when (2.9) is satisfied the state of affairs becomes much difficult though to take isothermal susceptibility for $\boldsymbol{\chi}_i$ may represent an extreme approximation. The latter approximation will be justified when the spin-lattice relaxation time is shorter than the spin-spin relaxation time. However, the above two alternatives are not much different when the Zeeman energy is not too large; isothermal and isolated susceptibilities agree when the external field is neglibible compared to the initial splittings of the spin levels.

The induced magnetic moment given by (2.11) interacts with the nuclear spins of the surrounding ions, resulting in an effective coupling between the nuclear spins. The effective couplings among tne nuclear spins thus produced can be written as follows:

$$\mathscr{H}^{\text{eff}} = \hbar^2 \sum_{i>j} \gamma_i \gamma_j r_{ij}^{-3} [\boldsymbol{I}_i \cdot (1 - 3\boldsymbol{t}_{ij}\boldsymbol{t}_{ij}) \cdot \boldsymbol{\sigma}_j \boldsymbol{I}_j + \boldsymbol{I}_j \cdot (1 - 3\boldsymbol{t}_{ij}\boldsymbol{t}_{ij}) \cdot \boldsymbol{\sigma}_i \cdot \boldsymbol{I}_i] \,, \tag{2.12}$$

where

$$\boldsymbol{\sigma}_i = \boldsymbol{A}_i \cdot \boldsymbol{g}_i^{-1} \cdot \boldsymbol{\chi}_i / \gamma_i \hbar \mu_B \,, \tag{2.13}*$$

γ_i and γ_j being the gyromagnetic ratios of the i-th and the j-th nuclear spins.

This coupling is σ-times as large as the direct spin-spin interaction. From the estimation of (I), one sees that this coupling can, in some cases at low temperatures, be more than ten times as large as the direct dipole-dipole interaction.

We shall remark here that this effect may be regarded as a magnetic counterpart of Sternheimer's antishielding correction to the nuclear quadrupole interaction[7].

(*b*) *Indirect coupling between two nuclei of magnetic ions through hyperfine couplings*

The approximate eigenstates of the electron spin system are obtained by perturbation calculation. If we terminate the series at the first order term of the eigenfunction, we get the indirect coupling concerned with two electron. The convergence of the perturbation series will be good for the coupling between neighboring spins and when the electron spin-spin interaction is of short range character. The calculation is usually rather troublesome though straightforward. We shall here pick up a representative term in which a kind of configuration mixing is taken into account.

In the representation in which $\mathscr{H}_{e0}$ is diagonal, $\mathscr{H}_e'$ can be divided into two part, i.e. secular or energy-diagonal terms and non-secular terms. Here we take into account only the secular terms in which, as is seen below, those representing the simultaneous flippings of two spins are important. The contribution of the non-secular terms of the indirect nuclear spin coupling is of the same order of magnitude as that of the secular terms.

Let us consider the coupling between the i-th and the j-th nuclear spins. We may take the electron spin eigenfunctions concerned with the i-th and the j-th ions. They are

$$\left.\begin{aligned} \Psi_{mm} &= \varphi_m(i)\varphi_m(j) \,, \\ \Psi^{\alpha}_{mm'} &= \frac{1}{\sqrt{2}}\{\varphi_m(i)\varphi_{m'}(j) - (-1)^{\alpha}\varphi_{m'}(i)\varphi_m(j)\} \,. \end{aligned}\right\} \tag{2.14}$$

α takes 1 and 2 and $\varphi_m(i)$ denotes the eigenfunction of one spin Hamiltonian $\mathscr{H}_i$ belonging to the eigenvalue E_m. The energy eigenvalues corresponding to the eigenfunctions given by

* It should be noticed that this expression is, in general, different from (2-3).

(2.4) are

$$\left.\begin{aligned} &E_{mm}=2E_m+U_{ij}(mm)\,, \\ &E^{\alpha}_{mm'}=E_m+E_{m'}+U_{ij}(mm')-(-1)^{\alpha}W_{ij}(mm')\,, \qquad (m\neq m') \end{aligned}\right\} \tag{2.15}$$

where

$$\left.\begin{aligned} &U_{ij}(m,\,m')=(\varphi_m(i)\varphi_{m'}(j)|\mathscr{H}_{ij}|\varphi_m(i)\varphi_{m'}(j))\,, \\ &W_{ij}(m,\,m')=(\varphi_m(i)\varphi_{m'}(j)|\mathscr{H}_{ij}|\varphi_{m'}(i)\varphi_m(j))\,. \end{aligned}\right\} \tag{2.16}$$

Taking the hyperfine coupling,

$$\mathscr{H}'=\sum_{\nu} A_{i\nu}I_{i\nu}S_{i\nu}+\sum_{\nu} A_{j\nu}I_{j\nu}S_{j\nu}\,, \tag{2.17}$$

as a perturbing Hamiltonian, we get the effective Hamiltonian for the indirect coupling between the i-th and the j-th nuclear spins. The result is

$$\left.\begin{aligned} &\mathscr{H}_{ij}^{\mathrm{eff}}=\boldsymbol{I}_i\cdot\mathfrak{A}_{ij}\cdot\boldsymbol{I}_j\,, \\ &\mathfrak{A}_{ij}=\sum_{m>n}\frac{W_{ij}(m,\,n)}{(E_m-E_n)^2}(f_m-f_n)^2\cdot\boldsymbol{A}_i\cdot\{(m|S|n)(n|S|m)+(n|S|m)(m|S|n)\}\cdot\boldsymbol{A}_j\,, \end{aligned}\right\} \tag{2.18}$$

where

$$f_m=\exp(-E_m/kT)/\sum_n \exp(-E_n/kT)\,.$$

This coupling has a nearly constant value at very low temperatures where $kT\ll E_1-E_g$, E_g and E_1 being the energies of the ground and the excited states and decreases as temperature rises. At high temperatures it vanishes like $1/T^2$.

The magnitude of this coupling at low temperatures is estimated as

$$\sim\left(\frac{A}{\Delta E}\right)^2\cdot\left(\frac{\gamma_e}{\gamma_N}\right)^2\cdot\mathscr{H}_d\,, \tag{2.19}$$

where $\mathscr{H}_d$ denotes the direct dipole-dipole interaction between the nuclear spins. Estimating $(A/\gamma_N)\sim10^{-6}\,\mathrm{cm}^{-1}$, $\gamma_e=1.76\times10^7$, we see that the indirect coupling is about $\sim3\times10/\Delta E^2$ (in cm^{-1}) times as large as direct dipole-dipole interaction. This coupling will be more important than the effect of antishielding as regards the indirect coupling between two magnetic ions. When the concentration of magnetic ion is high the effect of this coupling is of major importance. On the other hand when this concentration is low such as in hydrated salts the antishielding effect may predominate.

§ 3. Paramagnetic Ordering and Nuclear Resonance

The problems treated in the preceding sections were rather special ones because the absence of the Kramers degeneracy and comparatively large initital splittings of the spin levels were the essential conditions. In this section our consideration will be extended to the ideal paramagnetic substances under a strong external magnetic field and at low temperatures. When the Zeeman energy is large compared to the spin-spin interaction as well as kT, the fluctuation of spins decreases rapidly as temperature is lowered and as the external field becomes stronger. The observation of the nuclear resonance will become easier since T_1 and T_2 will become longer as H/T increases. However, there is again an unfavorable effect of indirect coupling as in the case treated in the preceding section. There is of course a large shift of the nuclear resonance frequeucy. We shall calculate below the shift, the relaxation time due to the hyperfine coupling and the indirect nuclear spin coupling. The Zeeman energy is assumed to be much larger than the spin-spin interaction energy.

(I) *Resonance field shift*

The direction of the external magnetic field is taken as z-axis. Then the total magnetic field at the i-th nuclear spins is written as

$$H_{i\nu}=H\alpha_\nu=H_{0\nu}+g\mu_B\sum_j \Phi_{ij}^{\nu 3}\langle S_{jz}\rangle\,, \tag{3.1}$$

$$\langle S_{jz}\rangle=-SB_S(g\mu_B H_0 S/kT) \tag{3.2}$$

where $B_S(x)$ denotes a Brillouin function:

$$B_S(x)=\frac{2S+1}{2S}\coth\left(\frac{2S+1}{2S}x\right)-\frac{1}{2S}\coth(x/2S)\,.$$

At low temperatures the shift amounts to the same order of magnitude as in ferro and antiferromagnetic substances.

(II) *Relaxation time due to hyperfine coupling*

The skeleton of the frequency spectrum of the spin fluctuation is as follows:

$$\left.\begin{aligned}
&\langle\{\delta S_z^0(t)\delta S_z\}\rangle=\langle S_z^2\rangle=\langle S_z\rangle^2\,,\\
&\langle\{\delta S_x^0(t)\delta S_x\}\rangle=\langle\{\delta S_y^0(t)\delta S_y\}\rangle=-\tfrac{1}{2}\coth(z/2)\langle S_z\rangle\cos(\omega_z t)\,.\\
&\langle\{\delta S_x^0(t)\delta S_y\}\rangle=-\langle\{\delta S_y^0(t)\delta S_x\}\rangle=\tfrac{1}{2}\coth(z/2)\langle S_z\rangle\sin(\omega_z t)\,,\\
&\langle\{\delta S_x^0(t)\delta S_z\}\rangle=\langle\{\delta S_y^0(t)\delta S_z\}\rangle=\langle\{\delta S_z^0(t)\delta S_x\}\rangle=\langle\{\delta S_z^0(t)\delta S_y\}\rangle=0\,.
\end{aligned}\right\} \tag{3.3}$$

where $S^0(t)$ is defined by $S^0(t)=\exp(it\mathscr{H}_{e0}/\hbar)S\exp(-it\mathscr{H}_{e0}/\hbar)$, $\mathscr{H}_{e0}$ denoting the Zeeman energy, $\langle S_z\rangle$ is given by (3.2) and $\langle S_z^2\rangle$ is given as follows:

$$\langle\delta S_z^2\rangle=\langle S_z^2\rangle-\langle S_z\rangle^2=-(\partial/\partial z)\langle S_z\rangle=\tfrac{1}{4}\operatorname{cosech}^2(z/2)-(S+\tfrac{1}{2})\operatorname{cosech}^2(S+\tfrac{1}{2})z\,, \tag{3.4}$$

where

$$z=g\mu_B H_0/kT\,,\qquad \omega_z=g\mu_B H_0/\hbar\,. \tag{3.5}$$

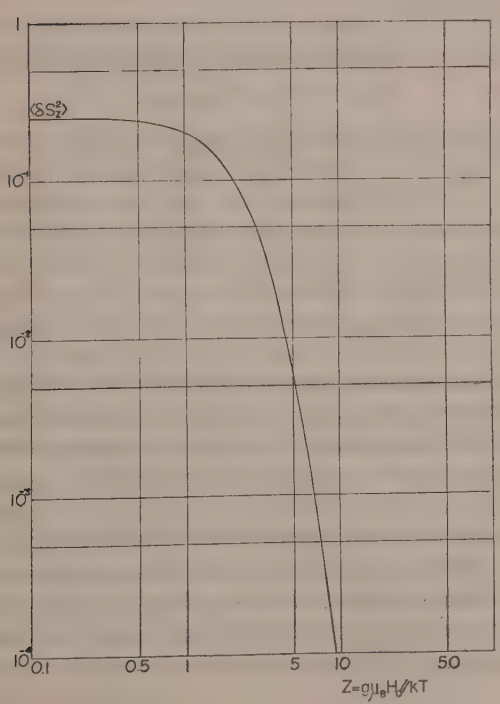

Fig. 1. $\langle\delta S^2{}_z\rangle$ as a function of $z=g\mu_B H_0/kT$ calculated from (3.4).

As one sees easily, when the Zeeman energy is much larger than the spin-spin interaction energy, only the z-component of the spin fluctuations is effective to the nuclear relaxation because the x and y components are mainly of high frequency: their low frequency components are negligible. Finally we get the following expressions for the nuclear relaxation times:

$$1/T_2=(\pi/2)^{1/2}(\gamma_N{}^2g^2\mu_B{}^2/\omega_e)\sum_j\sum_{\nu,\nu'}[\alpha_\nu\alpha_{\nu'}+\tfrac{1}{2}(\delta_{\nu\nu'}-\alpha_\nu\alpha_{\nu'})\,e^{-\omega_0{}^2/2\omega_e{}^2}]\Phi_{ij}{}^{\nu 3}\Phi_{ij}{}^{\nu' 3}\langle\delta S_{iz}{}^2\rangle\,, \tag{3.6}$$

$$1/T_1=(\pi/2)^{1/2}(\gamma_N{}^2g^2\mu_B{}^2/\omega_e)\sum_j\sum_{\nu,\nu'}(\delta_{\nu\nu'}-\alpha_\nu\alpha_{\nu'})\times e^{-\omega_0{}^2/2\omega_e{}^2}\Phi_{ij}{}^{\nu 3}\Phi_{ij}{}^{\nu' 3}\langle\delta S_{jz}{}^2\rangle\,, \tag{3.7}$$

where $\langle\delta S_z{}^2\rangle$ is given by (3.4) and is shown in Fig. 1 as a function of H_0/T.

(III) *Isothermal and isolated (adiabatic) susceptibilities*

Before entering the discussion on the indirect couplings we shall calculate the magnetic susceptibilities. As was stated in I, isolated and adiabatic susceptibilities mean the

adiabatic susceptibilities in the Ehrenfest sense and in the thermodynamical sense respectively. Isothermal one is the usual one measured keeping thermal equilibrium of the spin system with the heat reservoir. In another words the isolated susceptibility comes only from the effect of magnetic polarization of the system while the isothermal one comes not only from the polarization effect but also from the effect of redistribution of the populations in the spin levels. As is easily seen the external field along the z-axis cannot polarize the system except due to the small effect of dipole-dipole interaction. Therefore we have

$$\left.\begin{aligned}
&(\chi_{is})_z=\left\langle\frac{\partial^2 E}{\partial H_z^2}\right\rangle=0\,,\\
&(\chi_T)_z=(\chi_{is})_z+\frac{1}{kT}\left(\left\langle\left(\frac{\partial E}{\partial H_z}\right)^2\right\rangle-\left\langle\frac{\partial E}{\partial H_z}\right\rangle^2\right)=g^2\mu_B{}^2(\langle S_z{}^2\rangle-\langle S_z\rangle^2)/kT\,,\\
&(\chi_s)_z=(\chi_T)_z-\left(\left\langle E\frac{\partial E}{\partial H_z}\right\rangle-\langle E\rangle\left\langle\frac{\partial E}{\partial H_z}\right\rangle\right)^2\Big/kT(\langle E^2\rangle-\langle E\rangle^2)=0\,.
\end{aligned}\right\}\tag{3.8}$$

Similarly

$$(\chi_{is})_x=(\chi_s)_x=(\chi_T)_x=-g\mu_B\langle S_z\rangle/H_0\,.\tag{3.9}$$

(IV) *Indirect coupling*

The indirect coupling in this case can be treated in the same way as in the preceding section. We shall here give more precise expressions than in the preceding section, because the result is simpler in this case.

(*a*) *Antishielding effect*

When the spin-lattice relaxation time of the electron spin is not too short, the electronic moments induced by nuclear spins are coming only from the polarization effect. We should then use the isolated susceptibility in the expression (2.13). As was seen in the preceding paragraph, the only nonvanishing components of the isolated susceptibility are

$$(\chi_{is})_{xx}=(\chi_{is})_{yy}=-g\mu_B\langle S_z\rangle/H_0\,.$$

The nuclear spin coupling by antishielding effect can be written as follows assuming the isotropic hyperfine interactions:

$$\begin{aligned}
\mathscr{H}^{\text{eff}}=-(\hbar A\langle S_z\rangle/H_0)[&\sum_{i>j}\gamma_N r_{ij}{}^{-3}\{(1-\tfrac{3}{2}t_{ij}{}^+t_{ij}{}^-)(I_{i+}I_{j-}+I_{i-}I_{j+})-\tfrac{3}{2}t_{ij}{}^zt_{ij}{}^-(I_{iz}I_{j+}+I_{jz}I_{i+})\\
&-\tfrac{3}{2}t_{ij}{}^zt_{ij}{}^+(I_{iz}I_{j-}+I_{jz}I_{i-})+\tfrac{3}{2}(t_{ij}{}^-)^2I_{i+}I_{j+}-\tfrac{3}{2}(t_{ij}{}^+)^2I_{i-}I_{j-}\}\\
&+\sum_{i,l}\gamma_l r_{il}{}^{-3}\{\tfrac{1}{2}(1-\tfrac{3}{2}t_{il}{}^+t_{il}{}^-)(I_{l+}I_{i-}+I_{l-}I_{i+})-\tfrac{3}{2}t_{il}{}^zt_{il}{}^-I_{lz}I_{i+}\\
&-\tfrac{3}{2}t_{il}{}^zt_{il}{}^+I_{lz}I_{i-}-\tfrac{3}{4}(t_{il}{}^-)^2I_{l+}I_{i+}-\tfrac{3}{4}(t_{il}{}^+)^2I_{l-}I_{i-}\}]\,,
\end{aligned}\tag{3.10}$$

where i and j specify the magnetic ions and l the nonmagnetic ions. A denotes the isotropic hyperfine coupling constant, γ_l the gyromagnetic ratio of the l-th nuclear spin and $\boldsymbol{t}_{ij}=\boldsymbol{r}_{ij}/r_{ij}$.

In the expression (3.10) the first term is the only secular term. The coupling between different kinds of nuclear spins has in general no secular terms because of their different gyromagnetic ratios. Therefore, the indirect nuclear spin coupling between the magnetic ion and the different kind of ions such as protons in the water molecules will not make any contribution to the line width of the nuclear resonance of the magnetic ions, in contrast with the preceding section. On the other hand this type of indirect nuclear spin coupling between the same kind of magnetic ions proves to contribute to the line width but to the smaller extent than the contribution stated in the following paragraph. This was also the case in the preceding section.

(*b*) *Indirect coupling between two nuclei of magnetic ions through hyperfine interactions*

Hamiltonian of the electron spin system is expressed as follows:

$$\left.\begin{aligned}&\mathscr{H}_e=\sum_i \mathscr{H}_i^{(e)}+\sum_{i>j}\mathscr{H}_{ij}^{(e)}\,, \qquad \mathscr{H}_i^{(e)}=g\mu_B H_0 S_{iz}\,,\\ &\mathscr{H}_{ij}^{(e)}=4A_{ij}S_{iz}S_{jz}+B_{ij}(S_{i+}S_{j-}+S_{i-}S_{j+})+C_{ij}(S_{iz}S_{j+}+S_{i+}S_{jz})\\ &\qquad +D_{ij}(S_{iz}S_{j-}+S_{i-}S_{jz})+E_{ij}S_{i+}S_{j+}+F_{ij}S_{i-}S_{j-}\,,\end{aligned}\right\} \tag{3.11}$$

where A_{ij}, B_{ij}, $\cdots$ are given by

$$\left.\begin{aligned}&A_{ij}=\tfrac{1}{4}\{J_{ij}+K_{ij}[1-3(t_{ij}^z)^2]\}\,, \qquad B_{ij}=\tfrac{1}{2}\{J_{ij}K_{ij}(1-3t_{ij}^+t_{ij}^-/2)\}\,,\\ &C_{ij}=-3K_{ij}t_{ij}^z t_{ij}^-/2\,, \qquad D_{ij}=-3K_{ij}t_{ij}^z t_{ij}^+/2\,,\\ &E_{ij}=-3K_{ij}(t_{ij}^-)^2/4\,, \qquad F_{ij}=-3K_{ij}(t_{ij}^+)^2/4\,,\end{aligned}\right\} \tag{3.12}$$

J_{ij} being -2 times the exchange integral between i-th and j-th ions and $K_{ij}=g^2\mu_B^2/r_{ij}^3$. The interaction between the electron and the nuclear spins are expressed as

$$\mathscr{H}_{Ne}=\sum_i (A_1 I_{ix}S_{ix}+A_2 I_{iy}S_{iy}+A_3 I_{iz}S_{iz})\,. \tag{3.13}$$

The calculation of the indirect coupling is carried out in the same way as in the preceding section. We shall give here only the result:

$$\begin{aligned}\mathscr{H}_{ij}^{\text{eff}}=&\tanh^2(g\mu_B H_0/kT)/(4g\mu_B H_0)^2[\{(A_+^2+A_-^2)B_{ij}+A_+A_-(E_{ij}+E_{ij})\}(I_{i+}I_{i-}+I_{i-}I_{j+})\\ &+\{2A_+A_-B_{ij}+A_+^2E_{ij}+A_-^2F_{ij}\}I_{i+}I_{j+}+\{2A_+A_-B_{ij}+A_-^2E_{ij}+A_+^2F_{ij}\}I_{i-}I_{j-}\\ &-(A_+C_{ij}+A_-D_{ij})A_3(I_{iz}I_{j+}+I_{jz}I_{i+})-(A_-C_{ij}+A_+D_{ij})A_3(I_{iz}I_{j-}+I_{jz}I_{i-})]\,,\end{aligned} \tag{3.14}$$

where $A_\pm=A_1\pm A_2$. When the hyperfine coupling is isotropic this reduces itself simply to

$$\begin{aligned}\mathscr{H}_{ij}^{\text{eff}}=&A^2\tanh^2(g\mu_B H_0/kT)/(2g\mu_B H_0)^2[B_{ij}(I_{i+}I_{j-}+I_{i-}I_{j+})\\ &-\tfrac{1}{2}C_{ij}(I_{iz}I_{j+}+I_{jz}I_{i+})-\tfrac{1}{2}D_{ij}(I_{iz}I_{j-}+I_{jz}I_{i-})+E_{ij}I_{i+}I_{j+}+F_{ij}I_{i-}I_{j-}]\,.\end{aligned} \tag{3.15}$$

In the above expression only the first term can contribute to the line width. Its order of magnitude at low temperatures is

$$A^2B_{ij}/(2g\mu_B H_0)^2\sim 10^{10}\mathscr{H}_d/H_0^2\,, \tag{3.16}$$

where $\mathscr{H}_d$ denotes the direct dipole-dipole interaction between nuclear spins. When $H_0 \simeq 10000$ gauss, the indirect coupling is about 100 times as large as the direct dipole-dipole interaction. However, this does not necessarly mean that the observation of the nuclear resonance is difficult. In the usual hydrated salts, the magnetic ions are located keeping rather long distances with each other and the actual magnitude of their indirect coupling is not necessarily so large as to prevent the observation of nuclear resonance.

§ 4. Concluding Remarks

From the results of the preceding sections we see that it seems to be possible to observe nuclear magnetic resonance of transition elements in some paramagnetic salts under favorable conditions.

The first case treated in § 2 is a rather special one. When the initial splitting is sufficiently large (far larger than spin-spin interaction as well as kT) we expect that the relaxation times T_1 and T_2 by hyperfine interaction are not very short and at the same time the indirect nnclear spin couplings will not be large, thus favoring the observation of the nuclear resonance of transition elements. We expect these situations in some salts of Mn^{3+}, Cr^{2+} and V^{3+}.

In § 3 we dealt with the case of ideal paramagnetic substances, where the nuclear resonance of transition elements is expected to be observable under sufficiently strong magnetic field and at sufficiently low temperatures. The treatment will easily be extended to more general cases where the magnetic ions have Kramers doublets under no external magnetic field and show magnetic anisotropy.

When the resonance is observed we shall be able to add some interesting information to the magnetic properties of paramagnetic ions such as fine and hyperfine structures under the influence of the crystalline electric field, and then some characters of the wavefunctions of the magnetic ions, some informa-

tion on spin-spin interaction in paramagnetic salts, etc.

The writer wishes to thank Prof. R. Kubo and Dr. M. Shimizu for their valuable discussions.

References

1) T. Moriya: Prog. Theor. Phys. **16** (1956) 641.
2) T. Nakamura: Prog. Theor. Phys. **20** (1958) 542.
3) H. Suhl: Phys. Rev. **109** (1958) 606.
4) T. Moriya and Y. Obata: J. Phys. Soc. Japan **13** (1958) 1333.
5) K. D. Bowers and J. Owen: Rep. Prog. Phys. **18** (1955) 304.
6) R. J. Elliott: Proc. Phys. Soc. **B70** (1957) 119.
7) R. Sternheimer: Phys. Rev. **80** (1950) 102; **84** (1951) 244; and the papers succeeding to them.

JOURNAL OF THE PHYSICAL SOCIETY OF JAPAN Vol. 13, No. 11, NOVEMBER, 1958

Electroluminescence of Insulated Particles

By Keiji MAEDA

Matsuda Research Laboratory, Tokyo Shibaura Electric Co., Kawasaki

(Received July 25, 1958)

The origin of the local high electric field in the electroluminescence of insulated phosphor particles is considered and attributed to the disturbance of the applied field due to the conductive substance in the insulative phosphor. The distributions of local field are calculated and the dependence of brightness on the applied voltage is discussed. However, the comparison with experiments is impossible because of the complicated structure of the phosphor. Finally, the luminous efficiency of electroluminescent cell is estimated and an agreement is obtained with the observed value.

§ 1. Introduction

The phenomenon that phosphors emit light by the direct action of electric field alone is generally called electroluminescence. The electroluminescence was already found in 1936[1] and an idea of utilizing this as light source appeared about at the beginning of this decade. Although the luminous efficiency of electroluminescence was very low at first, it has been improved to be approximately 10 lm/W up to the present. Therefore, it is not only theoretically but also practically important to understand the mechanisms and characteristics of electroluminescence.

In some experiments of electroluminescence electrodes are in contact with a phosphor layer or with a single crystal while in other experiments there are no electrode contacts. In these two cases the constitution of sample and the method of application of electric field are different. Therefore, these two cases must be discussed separately, although many investigators do not distinguish them. It is the latter case when electroluminescence is utilized as light source; an insulating dielectric layer, in which phosphor particles are dispersed, is sandwiched between two parallel electrodes and an alternating voltage is applied. As we can suppose from the structure of electroluminescent phosphor, electroluminescence is very complicated phenomenon and we have not a little uncertainties about it, although many investigations have been carried out.[2] In this paper, we shall discuss the electroluminescence of insulated particles under the action of alternating electric field.

§ 2. Local High Field

Up to the present, only the small group of ZnS type phosphor is known as efficient powder phosphor for the electroluminescence.

The ordinary phosphor even in this group which is suitable for ultraviolet or cathode-ray excitation does not emit light when it is subjected to an electric field. It becomes electroluminescent if (a) it is covered with metal by evaporation, (b) copper sulfide is deposited on it by washing it with solution of copper salt or (c) the surface is slightly oxidized.[2),3)] For the preparation of electroluminescent phosphor the copper content in the raw materials is much higher than that for the ordinary phosphor. By removing the surface of the finished phosphor particle chemically, it is known that the copper is concentrated near the surface and the remainder is weakly electroluminescent.[4)] The copper is usually considered to be present as Cu_2S segregated from the ZnS crystal. As Cu_2S and ZnO are known to have good electrical conductivity, the common feature among the above observations is that the presence of conductive substance is essential to make the phosphor electroluminescent.

Further the following facts are important for the discussion of electroluminescence:

(a) The microscopic observation of electroluminescent particle shows that the light is emitted from small spots.[5)]

(b) By applying a strong enough magnetic field to quench electroluminescence simultaneously with an electric field, it becomes clear that the electric field strengh at the luminous spot is at least ten times larger than the average field in the electroluminescent cell.[6)]

(c) The brightness wave of the cell has two peaks and that of each luminous spot has only a single peak in an alternating cycle.[5)]

From these results, many workers considered that the field concentration is due to the presence of rectifying barrier between the conductive substance and ZnS. The reality of this model is investigated below.

(1) There is no limitation on the nature of conductive substance. For instance, metals (Cu, Ag), *p*-type semiconductor (Cu_2S) and *n*-type semiconductor (ZnO) are used as conductive substance. While, it is reported that various metals including Cu and Ag evaporated on ZnS single crystal do not show noticeable rectifying properties.[7)] Therefore, careful examinations are necessary to assume preferable rectifying barrier in other cases.

(2) The potential distribution in the electroluminescent phosphor particle is drawn schematically in Fig. 1 (a) in the same manner as in the theory of rectification. Differentiating this, we get the field distribution shown in Fig. 1 (b) and, by further differentiation, we get the charge distribution shown in Fig. 1 (c). It should be noted that net charge in the conducting substance is indispensable for the field localization. If the the conductor is neutral, i.e., $\rho_A = -\rho_B$ in Fig. 1 (c), the field strength at the surface of ZnS is the same as that in the dielectric. Probably dipole layer is present at the boundary of two kinds of materials when no electric field

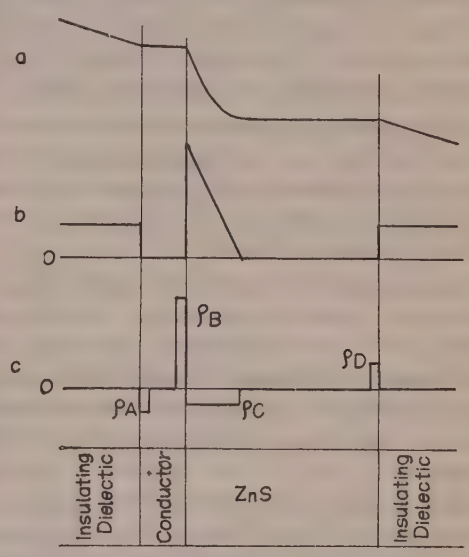

Fig. 1. Local high field due to the rectifying barrier in the insulated phosphor particle.
(a) potential distribution, (b) field distribution, (c) charge distribution.

is applied and the conductor may be charged to some degree due to this dipole layer. When an electric field is applied, provided the conductor is negatively charged, i.e., $|\rho_A| < |\rho_B|$, the field is localized due to the dipole consisting of the charge $\rho_A + \rho_B$ in the conductor and the charge of equal magnitude and opposite sign, ρ_C, in ZnS. The excess charge in ρ_C more than the above decreases the field strength in a part of ZnS distant from the boundary to smaller value than that in the dielectric but has no correlation with the field concentration at the surface of ZnS. In order to increase the local high field proportional to the applied field, the net negative

charge in the conductor $\rho_A+\rho_B$ should be increased in the same proportion. As there is no external charge supply to the conductor and the neutrality of the phosphor particle is maintained, such an increase of space charge cannot but result from a current within the phosphor particle in the opposite direction to the applied field. It is unreasonable. This situation is in contrast to the ordinary rectifying barrier, where electrodes are in contact with semiconductor and the charge in electrodes is supplied externally. Consequently, even if considerable field is present at the boundary between the conductor and ZnS when no electric field is applied, the local field is only the sum of the initial field and the average applied field when an electric field is applied. The observed characteristics cannot be explained by such a local field.

It is concluded, therefore, that the rectifying barrier does not contribute essentially to the electroluminescence of insulated particles. Of course, a possibility that it plays a secondary role cannot be denied.

Zalm presented a model in which the surface dipole varies proportionally with the applied field.[3] In his calculation, however, the polarization is neglected. When the polalization is evaluated according to his model, it becomes clear that his model is not self-consistent.

When a uniform electric field is applied on a dielectric, in which conductive material is dispersed, the electric field is disturbed and a very high field is possibly produced. Lehmann observed that the normally nonelectroluminescent phosphors become electroluminescent when they are mechanically mixed with powder of good conductivity, and called this phenomenon contact electroluminescence.[8] He concluded from the similarity between the ordinary and contact electroluminescence that the former is also due to substances of relatively high conductivity incorporated as small segregations within the insulating phosphor particles. His conclusion is supported by the consideration of electric properties of the constituent materials in the phosphor. Although the resitivities of semiconductors depend greatly on the impurity concentrations and the histories, ZnS is usually a poor conductor[9] in contrast to ZnO[10] and Cu_2S.[11] The reciprocal of the relaxation time of electric field of ZnS is much smaller and that of ZnO and Cu_2S is much larger than the applied frequencies in the usual experiments of electroluminescence. Therefore, the former can be regarded as insulator and the latter as conductors in the discussion of a.c. electroluminescence. Further, he showed qualitatively that the electric field near the sharp edge of the contact substance is considerably higher than the average electric field across the phosphor crystal. His conclusion is quite reasonable. In the following, the field distribution around the conductive substance will be investigated.

Considering the conditions of preparation of electroluminescent phosphor, the conductive substance is probably a thin layer on the surface of the phosphor particle in many cases. Sometimes it may be a grain incorporated inside the particle. Although the shape of individual conductive substance is quite irregular, we shall assume simple models, i.e., oblate spheroids and prolate spheroids. Probably the edge of conductive substance has a form which is intermediate between the two simple spheroids assumed here. These spheroids are assumed to be embedded in an ideal insulative medium. The boundary between the conductive substance and ZnS may not be a clear cut and, moreover, there may be a dipole layer as discussed above. Hence, the above assumptions must be regarded as a first approximation. Since both ZnS and the dielectric have nearly equal dielectric constant, they are not distinguished in our calculations.

When the conductive spheroid is placed in a uniform electric field E_0 with its major axis parallel to the field, i.e., in the x direction, the potential φ around it is given with ellipsoidal coordinate u

$$\varphi=-E_0x\left\{1-\int_u^\infty\frac{du}{(a^2+u)R(u)}\Big/\int_0^\infty\frac{du}{(a^2+u)R(u)}\right\}, \tag{1}$$

where

$$R(u)=\{(a^2+u)(b^2+u)(c^2+u)\}^{1/2}$$

and a, b and c are the axes of spheroid.[12]. For the conductive spheroid around which high field is produced, the major axis is much larger than the minor axis; i.e.,

$$a=b\gg c \quad \text{for oblate spheroid}$$

and

$$a\gg b=c \quad \text{for prolate spheroid.}$$

The field distribution along the extension of the major axis is calculated from Eq. (1) in a first approximation for the oblate spheroid

$$E=\frac{4E_0}{\pi}\left\{\frac{a}{\sqrt{c^2+2ax}}+\frac{x}{c}\right\} \quad \text{for } x\lesssim c \quad (2)$$

and similary for the prolate spheroid

$$E=\frac{E_0}{\{\log(2a/b)-1\}}\left\{\frac{a^2}{b^2+2ax}+\frac{1}{2}\log\left(1+\frac{2ax}{b^2}\right)\right\} \quad \text{for } x\lesssim a/2, \quad (3)$$

where x measures the distance from the surface of the spheroid. From these equations, we see that the ratio of the maximum field at the surface to the average field is nearly equal to the ratio of major axis to minor axis for the oblate spheroid and to the square of the axis ratio for the prolate spheroid. Therefore, the local high field exceeding the average by two or more orders of magnitude is conceivable near an edge of actual conductive substance.

For theoc currence of electroluminescence, however, an extension of high field over some distance as well as the high field itself is necessary; i.e., the potential drop in the high field region must be larger than a certain value. For the local high field expressed by Eq. (2) or (3), the extent of the high field cannot be defined unambiguously. We shall compare the field strength at the position, where the first and the second term are equal in Eqs. (2) and (3) respectively, with the maximum field at the surface. Denoting this position by $x=\delta$, we have for the oblate spheroid

$$\delta=\left(\frac{ac^2}{2}\right)^{1/2} \quad \text{and} \quad \frac{E(\delta)}{E(0)}=\left(\frac{2c}{a}\right)^{2/3} \quad (4)$$

and for the prolate spheroid

$$\delta=\frac{a}{n} \quad \text{and} \quad \frac{E(\delta)}{E(0)}=\frac{1}{n}\left(\frac{b}{a}\right)^2, \quad (5)$$

where n is defined by $(a/b)^2=ne^n/2$. It is seen that the field decreases considerably at δ for the spheroid with large axis ratio. Therefore, δ gives a rough estimate of the dimension of luminous spot. The average electric field which is necessary to produce electroluminescence E_{th} is roughly estimated by equating the potential difference in the high field region between the surface and δ when E_0 is equal to E_{th} with the energy of forbidden gap I_G eV. Thus we have for the oblate spheroid

$$E_{th}=\frac{\pi}{4}\frac{I_G}{\{(2a^2c)^{1/3}-c\}} \quad (6)$$

and for the prolate spheroid

$$E_{th}=\frac{2I_G}{an}\left\{\log\left(\frac{2a}{b}\right)-1\right\} \quad (7)$$

Of course, other considerations concerning the behaviour of free electrons in high field must be added to an accurate estimation of E_{th}. Accordingly the above equations give the order of the average field intensity necessary for electroluminescence.

As examples, the ratio of the maximum field to the average, the average field strength necessary for electroluminescence and the length of luminous spot for an oblate spheroid with $a=b=1\,\mu$ and $c=0.1\,\mu$ and for a prolate spheroid with $a=1\,\mu$ and $b=c=0.1\,\mu$ are tabulated respectively in Table 1. The above

Table I. Examples of local high field around conductive spheroid.

	oblate spheroid	prolate spheroid
axes	$a=b=1\mu$ $c=0.1\mu$	$a=1\mu$ $b=c=0.1\mu$
$E(0)/E_0$	13	50
Eth	6.0×10^4 V/cm	3.7×10^4 V/cm
δ	0.17μ	0.25μ

dimensions of the conductive spheroids are chosen since the actual phosphor particles are of the order of $10\,\mu$ in length. Here the energy of forbidden gap for ZnS is taken to be 3.7 eV. The calculated values are reasonable in comparison with usual experimental results.[2] As the shape and size of the conductive substance are quite random, the local field varies from spot to spot. Accordingly, we cannot observe the minimum applied voltage for the electroluminescence when we measure the light output from a cell as a whole. This consideration is also in agreement with experiment.[2),5] The observation that the electroluminescent sensitivity of the phosphor containing much copper increases by washing in cyanide solution[2),13] is explained as follows; the conductive substance, which covers too much the phosphor surface and shields the phosphor from the applied field, is partly resolved and becomes suitable in size for the electroluminescence excitation.

§ 3. Dependence of Brightness on Applied Voltage

Since the location of the high field has been

made clear in the preceding section, the dependence of electroluminescent brightness on the applied voltage will be considered in this section. Although we measure the applied voltage directly in experiments, we shall use the local field intensity in this section, as the latter is proportional to the former and is suitable for theoretical treatments. Several possible mechanisms has been considered for the electroluminescence.[14] Among them, the impact excitation theory is supported by many workers.[2] We shall also consider along this theory. The electrons introduced in the high field region are accelerated and some of them aquire sufficient energy to excite an electron from the valence band to the conduction band. The secondary electrons are also accelerated and a repetition of such electron multiplication process leads to an avalanche well known in the dielectric breakdown of solid. The holes generated in the valence band are trapped by the luminescence centers and then recombine radiatively with electrons which return to the ionized region when the direction of field is reversed. The sequence of the application of field and the emission of light is unambiguously demonstrated in the experiments by Zalm.[3] The luminescence center may be ionized or excited directly by a collision of accelerated electron, but the probability of such transitions would be small due to the small concentration of luminescence centers.

It is difficult to obtain the probatility that an electron in the conduction band is accelerated in a uniform field to an energy sufficient to excite an electron from the valence band to the conduction band, since the interaction of electron with the lattice is not known accurately. Seitz gave the probability that an electron is accelerated to ionization energy without a collision with the lattice due to statistical fluctuation

$$P=\exp\left(-\frac{C}{E}\right), \tag{8}$$

where C is a constant.[5] The situation in electroluminescence is more complicated, as the local field is not uniform but varies considerably in a short distance; i.e., the field strength where the electron is generated differs from that where that electron makes a collision excitation. Since the average velocity of electron in the direction of field is μE, where μ is the mobility, and $1/\tau$ is the collision frequency of electron with the lattice, the electron makes $(dx/\mu E\tau)$ collisions with the lattice while it moves dx in the field direction. Therefore, the number of secondary electrons produced while n electrons move dx is given by

$$dn=\frac{n}{\mu E\tau}\exp\left(-\frac{C}{E}\right)dx\,. \tag{9}$$

Exactly speaking, the interaction of electron with the lattice is a function of the energy of electron and above μ and τ are the average values of all electrons at the position where the field strength is E. Further, the probability given above is not a good approximation when the field strength increases to be comparable to C. In spite of these drawbacks, Eq. (9) will be used in the following calculations with μ and τ independent of field strength, as there is no other suitable expression for the present situation.

The variation of the local high field with position depends on the shape and size of the conductive substance. When the field at the surface of the conductive substance is E_s, the local field distribution is given generally by

$$E=\frac{E_s}{(1+\alpha x)^m}\,. \tag{10}$$

Here, α and m are constants depending on the conductive substance. Using the results of the simple models in the preceding section, they are from Eq. (2)

$$\alpha=\frac{2a}{c^2} \quad \text{and} \quad m=\frac{1}{2}$$

for the field due to conductive oblate sphroid and from Eq. (3)

$$\alpha=\frac{2a}{b^2} \quad \text{and} \quad m=1$$

for the field due to conductive prolate spheroid. From Eqs. (9) and (10), the differential equation for the electron multiplication is obtained;

$$\frac{dn}{dx}=\frac{n}{\mu E_s\tau}(1+\alpha x)^m\exp\left\{-\frac{C(1+\alpha x)^m}{E_s}\right\}. \tag{11}$$

The total number of electrons resulting from a primary electron, which is generated at x_0, is given by the integration of Eq. (11) from x_0 to infinity

$$n(E_s,\ x_0)=\exp\left\{\frac{1}{\alpha m\mu E_s\tau}\int_{y_0}^{\infty}y^{1/m}\cdot\exp\left(-\frac{Cy}{E_s}\right)dy\right\},\qquad(12)$$

where $y=(1+\alpha x)^m$ and $y_0=(1+\alpha x_0)^m$. The primary electron is considered to be generated by the ionization of electron in traps or donors due to the action of the high field alone or the simultaneous action of the field and temperature.[2] Since various positions and energy levels are considered to exist for these traps or donors, the distribution of the supply of primary electron should be taken into account. Denoting the number of primary electrons generated per unit volume at x when the surface field is E_s by $\rho(E_s,\ x)$, and the maximum value of E_s in an alternating cycle by $E_{\max}$, the total number of secondary electrons produced in a luminous spot during a half cycle is given by integrating over field strength and volume

$$N=\iint_0^{E_{\max}}\rho(E_s,\ x)\{n(E_s,\ x)-1\}dE_s\,dv.\qquad(13)$$

Here ρ is not known and further detailed discussions cannot be made. However, provided that ρ is a slowly varying function of x and E_s, the values of ρ and n at $x=0$ and $E_s=E_{\max}$ contribute predominantly to the total number of secondary electrons because of the strong dependency of $n(E_s,\ x)$ on these variables. Therefore, for simplicity, the integrations in Eq. (13) are replaced by the substitutions of the values at $x=0$ and $E_s=E_{\max}$ and ρ is assumed constant. By performing the integration involved in Eq. (12) and putting $x_0=0$, it becomes for the field due to the conductive oblate spheroid

$$n(E_s)=\exp\left[\frac{2}{\alpha\mu\tau C}\left\{1+2\frac{E_s}{C}+2\left(\frac{E_s}{C}\right)^2\right\}\cdot\exp\left(-\frac{C}{E_s}\right)\right]\qquad(14)$$

and for the field due to the conductive prolate sphroid

$$n(E_s)=\exp\left[\frac{1}{\alpha\mu\tau C}\left(1+\frac{E_s}{C}\right)\exp\left(-\frac{C}{E_s}\right)\right].\qquad(15)$$

Since the magnitude of $\alpha\mu\tau C$ is an order of unity (see later section), the total number of secondary electrons is expressed in the same form irrespective of the shape of conductive spheroid if $E_{\max}$ is smaller than C

$$N=\text{const}\times\{n(E_{\max})-1\}=\text{const}\times\exp\left(-\frac{C}{E_{\max}}\right).\qquad(16)$$

However, if $E_{\max}$ is larger than C, the total number of secondary electrons is expressed by

$$N=\text{const}\times\exp(AE_{\max}^{p}),\qquad(17)$$

where $p=1$ for the field due to the oblate spheroid, $p=2$ for the field due to the prolate spheroid and A is a constant depending on the size and shape of spheroid. Therefore, for the actual high field p would take a value between one and two. It should be noted that Eq. (9), from which Eq. (17) is derived, is no more a good approximation for an electric field intensity comparable to or stronger than C.

For the discussion of the dependence of brightness on the applied field, the relation between the probability of radiative recombinations and the total number of secondary electrons, i.e., the relation between the brightness and the excitation intensity, must be known. Generally the brightness of phosphor varies linearly with the excitation intensity when the excitation is weak but sublinearly when the excitation is intense. In order words, the efficiency of phosphor is constant up to a certain excitation intensity but lowers for more intense excitation. This is well known

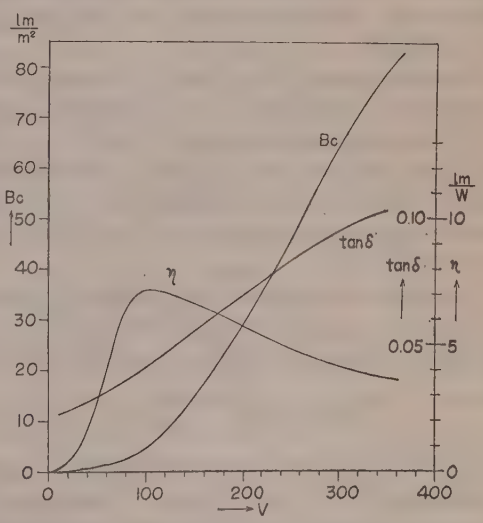

Fig. 2. Power factor $\tan\delta$, emission intensity $B_c(lm/m^2)$ and efficiency $\eta(lm/W)$ as function of applied voltage V. The frequency is constant at 120 c/s. These are obtained from measurements on electroluminescent cell giving green light[15].

as the saturation of brightness under the cathode-ray excitation. Similarly for the electroluminescence, when the applied voltage is not so high, the excitation is weak and the brightness is proportional to the number of secondary electrons. Accordingly, the brightness of luminous spot is from Eq. (16)

$$B_S=\alpha_S \exp\left(-\frac{\beta_S}{V}\right) \tag{18}$$

for low applied voltages, where α_S and β_S are particular constants for the spot.

Since the luminous efficiency of the electroluminescent cell decreases with increasing applied voltage as shown in Fig. 2,[16] the brightness cannot be discussed from the excitation intensity alone for this voltage range. Following reasons for the saturation of brightness may be considered:

(a) When the density of impact ionization during a cycle becomes locally comparable to the density of luminescence center, the probability of nonradiative recombination rapidly increases,

(b) when the space charge in the surface region of ZnS becomes comparable to the surface charge of conductive substance, the high field intensity decreases and the probability of impact ionization diminishes and

(c) due to the high current density in the high field region, the phosphor is locally heated and the luminescence may be thermally quenched.

Experimentally it is difficult to measure the dependence of brightness of a luminous spot on the applied voltage, as the spot is very small in size and the emission intensity is weak. Several measurements have been reported but an agreement is not yet obtained among them.[3),5)]

The observed brightness of electroluminescent cell as a whole can be expressed over the range of several orders of magnitude by

$$B_G=\alpha_G \exp\left(-\frac{\beta_G}{\sqrt{V}}\right) \tag{19}$$

where α_G and β_G are constants and α_G is proportional to the applied frequency.[3)] There are several other expressions similar to Eq. (19).[2)] The emission intensity of the cell is the sum of the emission intensity of individual spot. As stated before, the conductive substance, around which local high field is produced, is quite irregular in size and shape. Therefore, even in the voltage range where Eq. (18) is satisfied, the values of α_S and β_S are different for each luminous spot. The situation is more complicated when Eq. (18) is not satisfied as discussed above. Consequently, we can hardly discuss the quantitative dependence of brightness of electroluminescent cell on the applied voltage.

However, the explanation for the dependence of brightness on the applied frequency can be made similarly as given by previous workers[2),3)] irrespective of the origin of high field. As stated before, the primary electrons in the excitation process are considered to be generated by the ionization of electrons in traps or donors due to the action of electric field alone or the simultaneous action of electric field and temperature. The probability of field ionization of electrons in a certain depth from the conduction band is nearly zero under an electric field below a critical value, and rapidly increases under a field above the critical value.[17)] Therefore, the ionization of primary electron is almost determined by the maximum applied field intensity but not by the duration while the maximum field is applied. Nearly equal excitation occurs in a cycle irrespective of the applied frequency and the average brightness is proportional to the applied frequency.

§ 4. Efficiency of Electroluminescent Cell

In this section the luminous efficiency of the electroluminescent cell will be roughly estimated. The whole phenomenon occuring in the cell under operation can be separated into several processes and the energy loss is involved in each of them. They are considered in the order of occurrence.

(1) *Energy loss in ZnS*

Let us consider the high field region of the phosphor particle first. When an electron moves the distance dx in the direction of field, it aquires an energy $eEdx$ and the probability of impact ionization that the electron makes during this time is given by Eq. (9). The energy necessary for the ionization is the band gap energy and this is utilized in the later process. Therefore, the energy efficiency in this acceleration and ionization proceses is given by

$$\eta=\frac{I_G}{\mu\tau E^2}\exp\left(-\frac{C}{E}\right). \tag{20}$$

Assuming μ and τ are independent of the field strength, the optimum field strength is given by the condition

$$\frac{d\eta}{dE}=0 .$$

Hence, the optimum field strength is

$$E=\frac{C}{2} . \tag{21}$$

The maximum efficiency is obtained by substituting Eq. (21) into Eq. (20).

$$\eta=\frac{4I_G}{\mu\tau C^2}\exp(-2) . \tag{22}$$

It is not reasonable that the efficiency of impact ionization decreases for the field strength larger than $C/2$. This is due to poor approximity of Eq. (9) for strong field strengh comparable to or greater than C. Actually the efficiency would tend to unity when E approaches infinity. For the estimation of the average efficiency over the local high field region, however, the contribution from the relatively low field, where the number of electrons is much larger than that in the relatively high field, is more important. For ZnS the various constants in Eq. (22) are determined as follows: $I_G=3.7$ eV, $\mu=100$ cm²/volt·sec,[9] $\tau=5.7\times10^{-14}$ (m^*/m) sec by the relation $\tau=\mu m^*/e$, where m^* is the effective mass of electron, and $C=3.8E_H$, where E_H is the breakdown field strength by von Hippels' low energy criterion.[15] E_H is calculated by Callen[18]; it is at 0°K

$$E_H=\frac{2^{3/2}\pi^2 m^* e}{h^2}\hbar\omega_t\frac{\varepsilon_s-\varepsilon_0}{(\varepsilon_s\varepsilon_0^3)^{1/2}} . \tag{23}$$

For ZnS, the constants involved are; ε_s=static dielectric constant=8.3, ε_0=optical dieletric constant=5.07, and $\hbar\omega_t$=energy of reststrahl frequency=0.035 eV. Substituting these values, it becomes $E_H=4.46\times10^5\,(m^*/m)$ V/cm. At room temperature, correction is made and we have $C=2.1\times10^6\,(m^*/m)$ V/cm. With these values the efficiency expressed by Eq. (22) becomes

$$\eta=0.081\times\left(\frac{m}{m^*}\right)^3. \tag{24}$$

We see that the efficiency varies considerably with the value of the effective mass, which is not known for ZnS and may vary with the energy of electron. Although Kröger assumed $m^*=0.4$ m in comparison with that of CdS,[9] the substitution of his value in Eq. (24) results an efficiency larger than unity. It is quite unreasonable to set $\eta=1$ which means that all the electrons are accelerated to the ionization energy without dissipating energy by collisions with the lattice. However, when we consider the similarity between ZnS and CdS, it is not plausible to assume a large value of m^*. Accordingly we shall assume the efficiency of the acceleration and collision process to be approximately 2/3.

The electrons generated in the high field region drift in the average field region and reach the end of the crystal or are trapped on their way. They are drawn back to the ionized region when the applied field direction is reversed. The high field region is confined to the small spot in the phosphor particle and the number of electrons which enter into the average field region is nearly equal to that of impact ionization for high applied voltages. Therefore, it is not probably quite in an error to estimate that the energy loss in the average field region in ZnS is twice of that in the high field region at the optimum applied voltage.

(2) *Energy loss in dielectric*

The energy loss discussed above is due to the resistance, which is dependent on the applied field. There is another energy loss in the electroluminescent cell due to the resistance which is independent of the applied field. We know this from the value of $\tan\delta$ of the electroluminescent cell when low voltage is applied. Such an energy dissipation occurs in the dielectric and ZnS but not in the conductive substance as there is no electric field in the latter. The dissipation in the dielectric is probably larger than that in ZnS. This estimation is based on the reason that the observed value of $\tan\delta$ of the cell is nearly equal to that of dielectric although simple calculation taking into account the resitivities and volume ratio expects a greater energy loss in ZnS than that in the dielectric. The small energy loss in ZnS is considered due to the limited carried injection from the surroundings into it.

The relative magnitudes of the energy losses stated in (1) and (2) are evaluated by comparing the value of $\tan\delta$ at low applied voltages and that at the optimum voltage for the electroluminescence efficiency. In Fig. 2

the value of tan δ at the optimum voltage is twice that at the low voltages. Hence, these two energy losses are equal in magnitude at the optimum applied voltage.

The results obtained above are shown in the diagram below. The figure in each term is the relative magnitude of energy dissipation at the optimum applied voltage.

- Work done by electric field 6
  - Energy loss in ZnS 3
    - Energy loss in local high field 1
      - Energy utilized for ionization 2/3
      - Energy transfered to lattice as heat 1/3
    - Energy loss in average field 2
  - Energy loss in dielectric 3

Therefore, the energy efficiency for all these processes is 1/9.

(3) *Efficiency of radiative recombination*

The energy efficiency of the radiative recombination of electrons and holes, which are produced by the collision ionization, is the product of the probability of the radiative recombination and the ratio of luminescence energy to the excitation energy. The latter factor represents the energy efficiency in the luminescence center. These processes are compared with those in the cathodoluminescence. Under the cathode-ray excitation, electron-hole pairs are produced on the pass of incident and secondary high speed electrons and the light is emitted when the recombination occurs at the luminescence center. In the electroluminescence, one more process is added, i.e., the secondary electrons are swept away in the field direction and then drawn back to the ionized region. Hence, the probability of radiative recombination in the electroluminescence is not larger but possibly smaller than that in the cathodoluminescence. The energy efficiency in the luminescence center is the same for both excitation methods. According to the measurement by Bril and Klasens, the energy efficiency of green luminescence of ZnS:Cu, Al phosphor is 25% under 20 kV cathode-ray excitation.[19] In the cathode-ray excitation, the total incident energy is not utilized for the excitation and the average energy dissipated to produce an electron-hole pair is arbitrarily estimated to be 1.5 I_G, as an electron with energy more than I_G can produce another pair. We are here concerned with the efficiency of radiative recombination of already produced electrons. Accordingly, the energy efficiency in these processes is $0.25\times1.5=0.38$.

(4) *Absorption of luminescence*

It is practically impossible to take out the whole luminescence emitted in the phosphor from the front surface of the electroluminescent cell. For example, the luminescence emitted backward suffers a considerable loss, even in the presence of the reflection plate, and the transparent electrode absorbs the luminescence to some extent. Therefore, the luminescence energy taken out from the front surface is probably 2/3 of the total. This estimation is made by an analogy with the light output from the glass side of cathode-ray tube screen.[19]

The luminous efficiency of the electroluminescent cell is estimated from the considerations given above. The spectrum of green luminescence of ZnS:Cu phosphor has a lumen equivalent of about 450 lm/W. Taking the product of efficiencies for each process, we have for the luminous efficiency of the cell emitting green light

$$450\times\frac{1}{9}\times0.38\times\frac{2}{3}=13\ \mathrm{lm/W}\ .$$

Although the above estimation is quite rough and gives an order of the maximum luminous efficiency, the result is approximately equal to the maximum efficiency observed up to the present[16]. The efficiency lower than this is easily understood. For the applied voltage lower than the optimum, the efficiency of the acceleration and ionization process diminishes and further the ratio of energy loss in the high field region to that in the dielectric decreases. For the applied voltage higher than the optimum, the decrease in efficiency can be explained by the several reasons stated in the preceding section. It would be unnecessary to mention the low efficiency of phosphor which is not suitable for electroluminescence excitation.

The author expresses his sincere thanks to

Dr. Y. Uehara for his valuable discussions and kind reading of the manuscript and to Dr. H. Miyazawa for his helpful discussions.

References

1) G. Destriau: J. Chim. Phys. **33** (1936) 620, **34** (1937) 117.
2) General review was given by G. Destriau and H. F. Ivey: Proc. IRE **43** (1955) 1911.
3) P. Zalm: Philips Res. Repts. **11** (1956) 353, 415.
4) G. Destriau: cited in reference (2).
5) J. F. Waymouth and F. Bitter: Phys. Rev. **95** (1954) 941.
6) A. N. Ince: Proc. Phys. Soc. B **67** (1954) 870.
7) Y. Tanabe, T. Matsumura and H. Fujisaki: Meeting of Appl. Phys. Soc. Japan (April 1, 1958, Tokyo).
8) W. Lehmann: J. Electrochem. Soc. **104** (1957) 45.
9) F. A. Kröger: Physica **22** (1956) 637.
10) G. Heiland: Z. Physik **138** (1954) 459.
11) E. Hirahara: J. Phys. Soc. Japan **6** (1951) 422.
12) J. A. Stratton: *Electromagnetic Theory* (McGraw-Hill Book Co., New York, 1951) p. 209.
13) S. Kawashima: Meeting of Appl. Phys. Soc. Japan. (Appril 1, 1958, Tokyo).
14) W. W. Piper and F. E. Williams: Phys. Rev. **98** (1955) 1809.
15) F. Seitz: Phys. Rev. **76** (1949) 1376.
16) G. Diemer, H. A. Klasens and P. Zalm: Philips Tech. Rev. **19** (1957/58) 1.
17) W. Franz: Ann. Phys. **11** (1952) 17.
18) H. Callen: Phys. Rev. **76** (1946) 1394.
19) A. Bril and H. A. Klasens: Philips Res. Repts. **7** (1952) 401.

JOURNAL OF THE PHYSICAL SOCIETY OF JAPAN Vol. 13, No. 11, NOVEMBER, 1958

Phenomenological Free Streamline Theory, Part I. Flow past a Normal Plate

By Yōichi MIMURA

Faculty of Science, Hiroshima University, Hiroshima

(Received June 23, 1958)

The flow past a normal plate is discussed phenomenologically by the free streamline theory. The pressure distribution on the normal plate is determined by the pressure distribution on a free streamline which is obtained as a function of the distance from the separation point. In case when the latter is obtained only in the "free streamline range" (e.g., the range from the separation point to a distance equal to about one and a half of the breadth of the plate), the pressure distribution and other quantities on the normal plate are estimated with their probable deviations. The shape of the free streamline is also examined.

§ 1. Introduction

It is well known* that the free streamline theory of the Kirchhoff type gives satisfactory results for the free jet problem and related ones. By the use of the theory, Kirchhoff himself calculated the resistance of a plane lamina with wake, thus dissolving the d'Alembert paradox, but no satisfactory result in good agreement with observations has yet been obtained. Recently Roshko[1] and Woods[2] improved the theory by assuming the pressure distributions on the free streamlines to be variable, and good results have been obtained by Roshko in the case of flow past a normal plate and also by Woods in the case of flow past a circular cylinder. However, they postulated data on the free streamlines intuitively.

We shall now consider the problem to dis-

* The historical review of the free streamline theory has been given by several writers. See, for instance, Birkhoff's book: "*Hydrodynamics. A Study in Logic, Fact, and Similitude*" (Princeton Univ. Press, 1950).

cuss phenomenologically the observed distribution of pressure coefficient C_{pw} on the front surface of a body with wake by the free streamline theory*. Here the front (wetted) surface is referred to as a part of the surface of the body ranging from the stagnation point to two separation points. We assume that the observed pressure coefficient C_{pw} is equal to that as calculated by the theory of perfect fluid flow with free streamlines. The pressure coefficient on the free streameline thus assumed, expressed as a function of streamwise distance x from the separation point, is denoted by $C_{pR}(x)$.

It is known experimentally that the shear layer is thin and approximately steady in a certain range of distance downstream the separation point, which is of the order of the length of the body. We call provisionally such a range the "free streamline range", and we assume for simplicity that the pressure distribution in this range can be obtained definitely by the observation in the shear layer. We denote it by $C_{pE}(x)$. It is expected that this $C_{pE}(x)$ is closely related to $C_{pR}(x)$ (cf. § 7 (4)).

In the further downstream range, however, the shear layer becomes broader and broader and at the same time non-uniformity of the pressure distribution across the layer increases and finally the layer rolls up into Kármán vortex street or becomes directly the region of turbulent mixing. In such a range, which we call here provisionally the "mixing range", the shape of the free streamline as well as the pressure coefficient $C_p(x)$ cannot be determined definitely, so that it is insignificant to treat them either phenomenologically or theoretically (cf., e.g. the introduction of ref. 1)). The boundary of the above two ranges is of course altered according to the treatment of the problem.

Thus, in the phenomenological free streamline theory it is desirable to discuss the flow by the use of $C_{pE}(x)$ alone and also to study the determination of $C_{pE}(x)$ from the observation in the wake. The standpoint that the drag of a body is determined by the use of data near the body is in contrast to the theories in which, like the theory of Kármán vortex street, the drag is determined by the use of data at a great distance from the body.

Thus, the problems to be discussed in the phenomenological free streamline theory may be summarised as follows:

Problem I. When the pressure distributions on the free streamlines, $C_{pE}(x)$, are known only in the finite "free streamline ranges", to what extent the pressure distribution, C_{pw}, and other quantities on the wetted surface of the body as well as the shape of the free streamlines can be determined?

Problem II. When C_{pw} is known within experimental error, to what extent $C_{pR}(x)$ as well as the shape of the free streamlines can be determined?

Problem III. How the mechanism of the wake near the body should be approximated experimentally or theoretically by the free streamlines and what should be the general law which may be determined from this ap-approximation?

In the present paper we shall discuss Problem I in the case of a normal plate. A study of uncertainty of $C_{pE}(x)$ in the real shear layer and its effect upon C_{pw} and other quantities is a further advanced problem relating to Problem I. The discussion on other cases in Problem I than the case of a normal plate as well as on Problems II and III will be postponed to later papers.

§ 2. Method of Woods

We shall now discuss the above-mentioned Problem I by the method of Woods[2], an outline of which may be given in this section.

With the origin of coordinate-axes (x, y) at a certain point on the body, we take the x- and y-axes parallel and perpendicular to the undisturbed flow respectively, and we denote, as usual, the complex coordinate by $z=x+iy$. Then, if we denote the complex potential by w and the magnitude and the direction of the fluid velocity at any point in the flow field by q and θ respectively, we have

$$\frac{dz}{dw}=\frac{1}{q}e^{i\theta}. \tag{2.1}$$

Following Woods, we map the w-plane onto a $\zeta(=\eta+i\gamma)$-plane by the relation:

$$w=4\alpha(i\sinh\tfrac{1}{2}\zeta+\sin\tfrac{1}{2}\lambda)^2, \tag{2.2}$$

where α and λ are constants to be chosen

* Throughout the present paper the physical quantities with the suffix w refer to the wetted surface, while those without it refer to the free streamlines only.

adequately so that the wetted surface of the body is mapped onto the line-segment $\eta=0$, $-\pi\leq\gamma\leq\pi$ and the free streamlines are mapped onto two parallel semi-infinite straight lines $\eta\leq 0$, $\gamma=\pm\pi$. According to Woods, the function $f=\ln(e^{i\theta}/q)$ in the ζ-plane is given by

$$f(\zeta)=i\theta_{\mathrm{w}}(-\pi)-\frac{1}{\pi}\int_{\gamma^*=-\pi}^{\pi}\ln\frac{\sin\frac{1}{4}(\gamma^*+i\zeta)}{\cos\frac{1}{4}(\gamma^*-i\zeta)}d\theta_{\mathrm{w}}(\gamma^*)-\frac{\cosh\frac{1}{2}\zeta}{2\pi}\int_0^{-\infty}\left\{\frac{\Omega_+(\eta^*)}{\cosh\frac{1}{2}\eta^*+i\sinh\frac{1}{2}\zeta}+\frac{\Omega_-(\eta^*)}{\cosh\frac{1}{2}\eta^*-i\sinh\frac{1}{2}\zeta}\right\}d\eta^*, \tag{2.3}$$

where

$$f=-\Omega+i\theta, \tag{2.4}$$

$$\Omega=\ln q, \tag{2.5}$$

$\theta_{\mathrm{w}}(\gamma)$ being the value of θ on the wetted surface, and $\Omega_+(\eta)$, $\Omega_-(\eta)$ being respectively the values of Ω on the upper and the lower free streamlines, while γ^* and η^* being integration variables.

When the shape of the wetted surface of the body and $\Omega_+(\eta)$, $\Omega_-(\eta)$ on the free streamlines are prescribed, implying that the angle of attack, the positions of the two separation points and the separation velocities q_s are known, the flow can be determined by (2.3). In the case of symmetric flow where we always concern only with the upper free streamline and denote Ω_+ simply by Ω, Woods proposed a convenient form for Ω as:

$$\Omega=\frac{\ln q_s}{1+b^2\sinh^2\frac{1}{2}\eta}, \tag{2.6}$$

(b: a constant),

which was deduced by assuming that far downstream on the free streamline, i.e. when $x\gg 1$,

$$q-1\approx\beta x^{-1}, \qquad (x\gg 1) \tag{2.7}$$

β being a constant. Such an assumption is quite legitimate, e.g. in the cases of the free streamlines which are deduced by Roshko using the method of the elliptic hodograph[1] and of the notched hodograph[1].

The condition that the upper and the lower free streamlines do not cross each other is given by:

$$\int_{-\pi}^{\pi}\theta_{\mathrm{w}}(\gamma^*)\sin\tfrac{1}{2}\gamma^*d\gamma^*+\int_0^{-\infty}\{\Omega_+(\eta^*)+\Omega_-(\eta^*)\}\cosh\tfrac{1}{2}\eta^*d\eta^*\geq 0, \tag{2.8}$$

which is referred to as the "condition of physical reality". The equality in (2.8) holds when the width of the two free streamlines at infinity is finite. We shall call Ω given by (2.6) the "Woods type" when it satisfies such a condition of finite width.

§ 3. Application to the Case of a Normal Plate

(1) We now consider the flow past a normal plate placed in a uniform flow. We adopt such units of length and time that both the breadth of the plate and the magnitude of the undisturbed velocity become unity.

In the present case $\theta_{\mathrm{w}}(\gamma)$ is given by

$$\left.\begin{aligned}\theta_{\mathrm{w}}(\gamma)&=-\pi/2, \quad (-\pi\leq\gamma\leq 0),\\ \theta_{\mathrm{w}}(\gamma)&=\pi/2, \quad (0\leq\gamma\leq\pi),\end{aligned}\right\} \tag{3.1}$$

and λ in (2.2) is equal to zero.

In order to express physical quantities conveniently, we use, on the free streamlines,

$$X=-\sinh(\eta/2), \quad (0\leq X\leq\infty), \tag{3.2}$$

while, on the wetted surface of the body,

$$W=\cos(\gamma/2), \qquad (0\leq W\leq 1). \tag{3.3}$$

Then, using (2.1)~(2.5), the physical quantities are written as follows. Namely, on the wetted surface ($\zeta=i\gamma$), where $W=0$ at the separation points and $W=1$ at the stagnation point, we have

$$q_{\mathrm{w}}(W)=q_s\sqrt{\frac{1-W}{1+W}}e^{-WG(W)}, \tag{3.4}$$

with

$$G(W)=\frac{2}{\pi}\int_0^{\infty}\{\Omega(0)-\Omega(X^*)\}\frac{dX^*}{W^2+X^{*2}}, \tag{3.5}$$

$$y_{\mathrm{w}}(W)=N\int_0^{W}q_{\mathrm{w}}^{-1}(W^*)W^*dW^*, \tag{3.6}$$

where

$$N^{-1}=2\int_0^1 q_{\mathrm{w}}^{-1}(W^*)W^*dW^*, \tag{3.7}$$

the coordinate y_{w} having been measured from the lower separation point.

On the other hand, we have, on the upper free streamline ($\zeta=\eta+i\pi$) where $X=0$ at the separation point and $X=\infty$ at the point at infinity,

$$q(X)=\exp\Omega(X), \tag{3.8}$$

$$\theta(X)=\cot^{-1}X-H(X), \tag{3.9}$$

with

$$H(X)=\frac{2}{\pi}X\,\mathrm{Re}\left\{\int_0^{\infty}\Omega(X^*)\frac{dX^*}{X^2-X^{*2}}\right\}, \tag{3.10}$$

where Re means "the real part of", and

$$x(X)=N\int_0^X q^{-1}(X^*)\cos\theta(X^*)X^*dX^*\,, \quad (3.11)$$

$$y(X)=N\int_0^X q^{-1}(X^*)\sin\theta(X^*)X^*dX^*\,, \quad (3.12)$$

x and y having been measured from the upper separation point. By (2.8) the condition of physical reality now turns out to be

$$\int_0^\infty \Omega(X^*)dX^* < \pi/2\,, \quad (3.13)$$

and the condition of finite width becomes

$$\int_0^\infty \Omega(X^*)dX^* = \pi/2\,. \quad (3.14)$$

(2) By the use of the above formulae we shall discuss briefly the manner in which $\Omega(X^*)$ in the range $X^* \gg 1$ affects quantities on the wetted surface of the plate as well as on the free streamlines in the vicinity of the body where $X \lesssim 1$. It is readily found that since the function $G(W)$ in (3.5) has the damping factor $(W^2+X^{*2})^{-1}$, the range of X^* in which $\Omega(X^*)$ affects remarkably the quantities on the wetted surface is short. Also we see that the range of X^* in which $\Omega(X^*)$ affects remarkably the quantities on the free streamline in the vicinity of the seperation point is short too, because the function $H(X)$ in (3.10) has the damping factor $(X^2-X^{*2})^{-1}$. But the latter damping factor becomes infinite at $X^*=X$, implying that the shape of the free streamline is much more affected by $\Omega(X^*)$ than the quantities on the wetted surface. The detailed discussions on these points will be given in §§ 6~8.

Similarly to the above case, the effect of $\Omega_\pm(X)$ can also be discussed by (2.3) for the case of asymmetric flow past an arbitrary body by resolving $\Omega_\pm(X)$ into symmetric and antisymmetric parts. The interpretation of these damping effects which behave approximately as X^{*-2} has been given phenomenologically by Prof. T. Maekawa (cf. § 7 in ref. 3).

(3) When $\Omega(X)$ is given by (2.6), i.e. when

$$\Omega(X)=\frac{\ln q_s}{1+b^2X^2}\,, \quad (0\le X\le\infty)\,, \quad (3.15)$$

the integrals involving $\Omega(X^*)$ in (3.5), (3.10), (3.13) and (3.14) can be easily evaluated. Thus we have

$$G(W)=\ln q_s\cdot b(1+bW)^{-1}, \quad (3.16)$$

$$H(X)=\ln q_s\cdot bX(1+b^2X^2)^{-1}, \quad (3.17)$$

and the condition of physical reality becomes

$$b\ge \ln q_s\,. \quad (3.18)$$

Since $\Omega(X^*)$ for large X^* has only small effects upon $G(W)$ and $H(X)$, the functions $G(W)$ and $H(X)$ for $X\gg 1$ may be approximated by (3.16) and (3.17) respectively in which the value of b is so determined as to approximate $\Omega(X)$ by (3.15) near $X=0$.

If we denote $\Omega(X)$ of the Woods type by $\Omega_{\mathrm{W}}(X)$, we have, by (3.15) and (3.18),

$$\Omega_{\mathrm{W}}(X)=\frac{\ln q_s}{1+(\ln q_s)^2X^2}\,, \quad (0\le X\le\infty). \quad (3.19)$$

If, in this case, we determine $C_p(X)$ by (3.8) and $x(X)$ by (3.11), (3.9) and (3.17), the behaviour of $C_p(x)$ near the separation point is represented by $\{C_p(x)-C_p(0)\}^{3/2}\propto x$. This behaviour should be compared with that of $C_p(x)$ as treated by the notched hodograph (cf. § 6 in ref. 3)). The calculated results by the use of the Woods type, together with the results for other cases, will be given in § 5. It will be seen from Table I there that the value of $C_{N\mathrm{W}}$, i.e., the sum of $C_{p\mathrm{W}}$ over the wetted surface, as obtained by the use of the Woods type is too large.

§ 4. Procedure of Determining the Flow by the Use of Observed Pressure Distribution on the Free Streamline

Taking the case of normal plate we shall explain the procedure of determining the flow when the value of C_p is obtained experimentally as a function of x. The procedure can however be extended to the case of a body of arbitrary shape. In accordance with the discussion in § 1, we assume that $C_p=C_{p\mathrm{E}}(x)$ is obtained definitely in the free streamline range.

To begin with, we calculate $\Omega\equiv\Omega_{\mathrm{E}}(x)$ corresponding to $C_p=C_{p\mathrm{E}}(x)$ by the relation $C_p=1-q^2=1-\exp(2\Omega)$. To a first approximation, we first take an approximate value for $\Omega(X)$ in $0\le X\le\infty$ which will be denoted as $\Omega^{\widetilde{I}}(X)$, and then, by aid of (3.7) we determine N^I on the wetted surface.* In the next place, we determine, by (3.11), the value of x on the free streamline, which will be denoted as $x^I(X)$, and if we insert this value of x into $\Omega_{\mathrm{E}}(x)$, we obtain the second appro-

* Indices I, II, $\cdots$ will be used to denote the order of successive approximations.

ximation of $\Omega(X)$, i.e. $\Omega^{II}(X)=\Omega_{\mathrm{E}}(x^{I}(X))$. In like manner, further approximations $\Omega^{III}(X)$, $\Omega^{IV}(X)$, $\cdots$ can be obtained. As will be proved in § 8 (2a), the successive approximations converge rapidly.

When $C_{p\mathrm{E}}(x)$ is obtained experimentally in the finite free streamline range $x\leq x_{\mathrm{M}}$, we must, in addition, supply $C_p(x)$ in the mixing range $x\geq x_{\mathrm{M}}$. Alternatively, we may appropriately choose $\Omega(X)$ in $X\geq D$ in each order of successive approximations, where D is so chosen that $x(D)$ corresponds to x_{M}. The value of D can easily be determined approximately since $x(X)$ is insensitive to $\Omega(X)$, especially $x(X)$ in $X\leq D$ is almost insensitive to the choice of $\Omega(X)$ in $X\geq D$ as will be shown in § 8 (1c) and (2b).

The practical method of determining $\Omega^{N}(X)$ $(N\geq 2)$ is as follows. First, $\Omega^{N}(X)$ in $X\leq D$ can be determined when $\Omega^{N-1}(X)$ is determined for $0\leq X\leq\infty$. Next, as $\Omega^{N}(X)$ in $X\geq D$ we choose the form

$$\Omega_{\mathrm{a}}(X)=\Omega(D)D^{2}X^{-2}\,,\quad (X\geq D)\,,\qquad (4.1)$$

and put D^{N} and $\Omega^{N}(D^{N})$ in place of D and $\Omega(D)$ respectively, D^{N} being the value of D in the nth approximation. We denote $\Omega_{\mathrm{a}}(X)$ thus determined as $\Omega_{\mathrm{a}}{}^{N}(X)$. As will be explained in detail in § 7, by virtue of the simple form of $\Omega_{\mathrm{a}}{}^{N}(X)$, we can easily estimate the probable errors involved in the calculation of $C_{N\mathrm{w}}$ and other quantities arising from this choice. Hence we can estimate the value of D^{N} in order to determine $C_{N\mathrm{w}}$ within experimental error (see § 7 (3)).

§ 5. The Solution for the Case of a Normal Plate

As an example we shall here deal with the flow past a normal plate by applying the method described in the preceding section. As for $C_{p\mathrm{E}}(x)$ we first adopt the one which is determined by the elliptic hodograph used by Roshko[1], and also we use the value of 1.545 for q_s which was observed by Fage and Johansen.[4] In the present case $D=\infty$. For the first approximation of $\Omega(X)$ we have used the Woods type (3.19). As mentioned in § 3 the convergency of successive approximations is rapid, and the second and third approximations of $\Omega(X)$, i.e. $\Omega_{\mathrm{ellip}}{}^{II}(X)$ and $\Omega_{\mathrm{ellip}}{}^{III}(X)$, nearly coincide with each other (Fig. 1). We may therefore consider $\Omega_{\mathrm{ellip}}{}^{III}(X)$ as the final form of $\Omega(X)$, which may be approximated by the form (3.15), namely:

$$\Omega_{\mathrm{L}}(X)=\frac{\ln q_s}{1+b^{2}X^{2}}\,,\quad (\text{with } b=1.2),\qquad (5.1)$$

(cf. Fig. 1).

We have determined the flow by making use of (5.1) in place of the elliptic hodograph obtaining the results as shown below.

Next we have adopted for $C_{p\mathrm{E}}(x)$ the experimental curve obtained by Roshko[1], modyfying it in the vicinity of the separation point in such a manner that q_s takes the value of 1.545 (see Fig. 3), and we denote the resulting modified curve by $C_{p\,\mathrm{exp}}(x)$ and the quantities in this case by attaching the suffix "exp". The adequacy of such a modified curve will be discussed in § 7 (4).

In order to determine the flow we have used, as in the above case, the formula (3.19) for the first approximation, and for higher approximations we have followed the treatment of the case where $\Omega_{\mathrm{E}}(x)$ is obtained only in a finite range. Here we have determined D^{N} without the use of the method described in the last paragraph. For the second approximation D^{II} has been determined by $x^{I}(D^{II})\approx 1$ under the consideration that the free streamline range may be of about this length. For the third approximation we have chosen $D^{III}=3.12$ so that (3.14) is satisfied by $\Omega_{\mathrm{exp}}{}^{III}(X)$. Concerning these choices of D^{II} and D^{III} we will discuss in § 7 (3) and (4) respectively.

The calculated results are shown in Tables I, II and Figs. 1∼5,* together with the results as obtained by using Woods type (3.19) and the elliptic hodograph (5.1). For comparison the calculated results for the Kirchhoff flow, in which $\Omega_{\mathrm{K}}(X)=0$ in $0\leq X\leq\infty$, and for the notched hodograph devised by Roshko, as well as the experimental results obtained by Fage and Johansen are also shown in these tables and figures.

Table I shows $C_{N\mathrm{w}}$ for various cases, while Table II gives the values of D, $\Omega(D)$, $x(D)$, N and d' where $d'=1+2y(\infty)$ is the distance between the two free streamlines at infinity. Figs. 1∼5 show $\Omega(X)$, $x(X)$, $y(X)$, $C_p(x)$, $C_{p\mathrm{w}}(y_{\mathrm{w}})$ and the shape of the upper free streamline.

The calculations have been performed correct to four significant figures, using the

* We use abbreviated symbols such as K, L, W, N, exp^{N} and ellip^{N} which are explained in Table I and Fig. 1.

Table I. The total value, $C_{N\mathrm{w}}$, of the pressure coefficient $C_{p\mathrm{w}}(y_{\mathrm{w}})$ over the wetted surface for various cases of Ω (X) $(q_s=1.545)$.
K: Kirchhoff flow, L: modified elliptic hodograph, W: Woods type (3.19), N: notched hodograph, $\exp^N$: nth approximation of the case of the modified experimental curve $C_{p\,\exp}(x)$.

K	L	W	$\exp^{II}$	$\exp^{III}$	N	Obs.*
0.8798	0.8019	0.7633	0.7479	0.7472	0.7424	0.743

* The observed value of $C_{N\mathrm{w}}$ is obtained by the relation $C_{N\mathrm{w}}=C_D+(1-q_s^2)$ using the observed drag coefficient C_D and putting the base pressure to be uniform.

Table II. Numerical data for various cases of $\Omega(X)$.

	D	$\Omega(D)$	$x(D)$	N	d'
K	∞	0	∞	0.2806	∞
L	∞	0	∞	0.3508	∞
W	∞	0	∞	0.3868	2.55
$\exp^{II}$	2.90	0.1532	1.085	0.4005	–
$\exp^{III}$	3.12	0.1220	1.299	0.4103	1.51

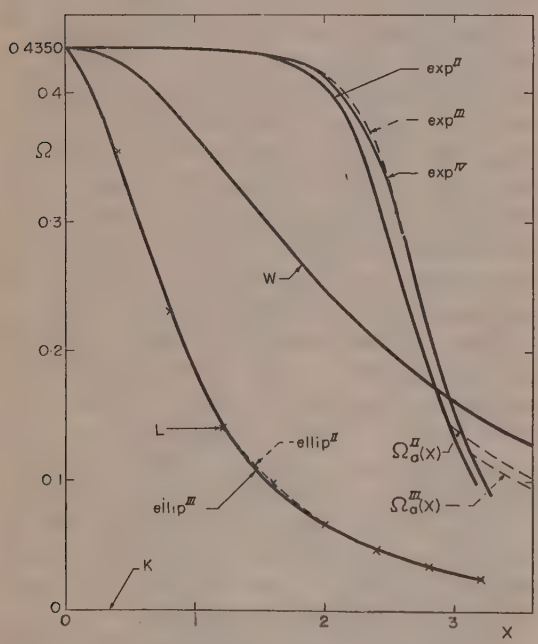

Fig. 1. Ω(X) for various cases.
ellip^N: the nth approximation in the case of the elliptic hodograph.
Other symbols used in Figs. 1~5 are explained in Table I.

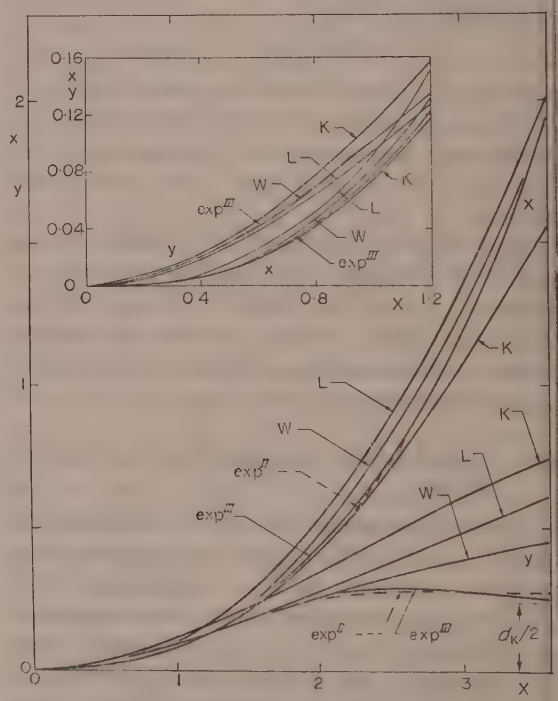

Fig. 2. $x(X)$ and $y(X)$ on the upper free streamlines for various cases (the breadth of a normal plate is taken as unity). d_K is the lateral spacing of Kármán vortex street.

once determined data of $\Omega_{\exp}(x)$, in order to discuss the convergency of successive approximations and the errors of approximate formulae in the succeeding paragraphs.

The convergency of successive approximations in the case of $\Omega_{\exp}(x)$ is somewhat worse than that in the case of $\Omega_{\mathrm{ellip}}(X)$ owing to arbitrary choice of D and $\Omega(X)$ in $X\geq D$.

In case when we use the result of experiment, however, the final form of $\Omega(X)$, i.e.

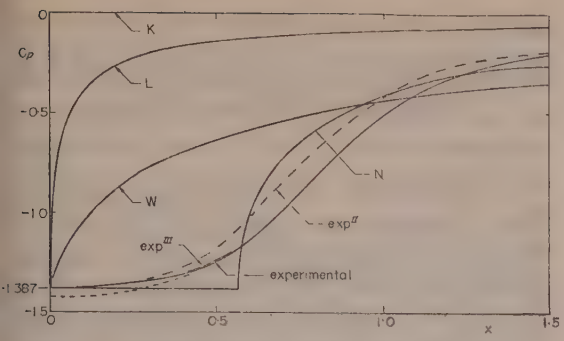

Fig. 3. Pressure distributions on the free streamlines $C_p(x)$ for various cases.

Original experimental curve taken from Fig. 2 in ref. 1.

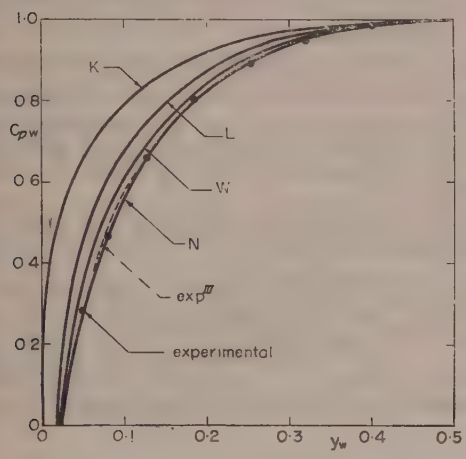

Fig. 4. The pressure distributions on the normal plate $C_{pw}(y_w)$ for various cases.

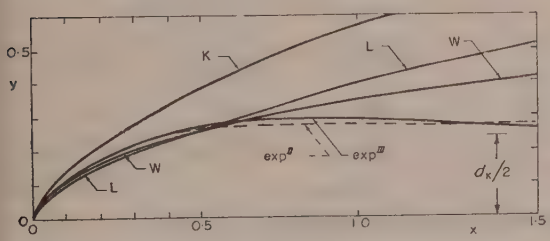

Fig. 5. The shapes of the upper free streamlines for various cases.

$\Omega_{\exp}(X)$, can be determined only when $\Omega_{\exp}(x)$ is determined in $0\leq x\leq\infty$, but, as will be shown in § 8 (2b), it is nearly equal to $\Omega_{\exp}{}^{III}(X)$ in $X\lesssim D$. Other calculated results will be discussed in §§ 6~8.

§ 6. Approximate Formulae for Quantities on the Front Surface of the Normal Plate, as determined by $\Omega(X)$

From Fig. 1 it is seen that there are three typical types of $\Omega(X)$, namely: $\Omega_L(X)$, $\Omega_w(X)$ and $\Omega_{\exp}{}^{III}(X)$. However, $\Omega(X)$ may take also various forms experimentally. Thus, the two-dimensional flow past a body whose wetted surface forms a normal plate can be treated by the free streamline theory as the flow past the normal plate irrespectively of the shape of the back surface as well as the Reynolds number. In this paragraph we give approximate formulae for quantities on the front surface of the normal plate as determined by various $\Omega(X)$.

(1) *General formulae.* Following the discussion in § 3 (3), we may approximate $G(W)$ by (3.16), so that, choosing b properly, we have

$$WG(W)\approx WG(1)+\frac{bW(1-W)}{1+bW}G(1)\,. \tag{6.1}$$

Neglecting the second term and noting that the first term is small, we put

$$\exp\{WG(W)\}\cdot(1+\mathcal{E}(W))=1+rW, \tag{6.2}$$

with

$$r=\exp G(1)-1. \tag{6.3}$$

The value of r is shown in Table IV. Since, as will be shown in Appendix 1, the value of $\mathcal{E}(W)$ is fairly small, we shall put $\mathcal{E}(W)=0$ in the following lines.

Using (6.2) and (3.4) $q_w(W)$ is approximated by

$$q_w(W)=q_s\sqrt{\frac{1-W}{1+W}}\,\frac{1}{1+rW}\,. \tag{6.4}$$

Then approximate formulae for various quantities on the front surface of the normal plate can be easily obtained. Namely, putting

$$\left.\begin{aligned} A_n&=\int_0^1\sqrt{\frac{1-W}{1+W}}\,W^n dW\,,\\ B_n&=\int_0^1\sqrt{\frac{1+W}{1-W}}\,W^n dW\,,\\ &(n=1,\,2,\,\cdots)\end{aligned}\right\} \tag{6.5}$$

thus, e.g. $A_1=1-\pi/4$, $A_2=\pi/4-2/3$, $A_3=2/3-3\pi/16$, $A_4=3\pi/16-8/15$, $B_1=1+\pi/4$, $B_2=\pi/4+2/3$ and $B_3=2/3+3\pi/16$, we obtain by (3.7)

$$N=q_s/2(B_1+B_2r). \tag{6.6}$$

Using its definition as well as (3.6), C_{Nw} can be expressed as

$$\begin{aligned} C_{Nw}&=\int_{-1}^1 C_{pw}(y_w)d(y_w)\\ &=1-2N\int_0^1 q_w(W^*)W^*dW^*. \end{aligned} \tag{6.7}$$

Thus, expanding $(1+rW)^{-1}$ and neglecting terms of $O(r^3)$ we obtain

$$C_{N\mathrm{w}}=1-q_s^2(A_1-A_2r+A_3r^2)/(B_1+B_2r). \quad (6.8)$$

The accuracy of the above two approximate formulae (6.6) and (6.8) will be examined in Appendix 1.

Next we shall estimate the deviations of the quantities on the front surface of the normal plate due to Δr, which denotes the deviation of r caused by $\Delta\Omega(X)$, by neglecting terms of the order $O(r^3)$ and $O(\Delta r)^2$. The maximum deviation including sign (i.e., one of the maximum and minimum of the deviation which has a larger absolute value) of $C_{p\mathrm{w}}(=1-q_{\mathrm{w}}^2)$ is given by

$$(\Delta C_{p\mathrm{w}})_{\max}=2q_s^2\frac{1-W}{1+W}\frac{W}{(1+rW)^3}\Delta r\,, \quad (6.9)$$

where

$$W=W_p=\sqrt{2}-1+0.5(10-7\sqrt{2})r+O(r^2)\,.$$

The calculated value of $y_{\mathrm{w}}(W)$ at $W=W_p$ in the cases in Fig. 4 is about 0.03.

Using (6.6) and (6.8) the deviations of N and $C_{N\mathrm{w}}$ are found to be given respectively by

$$\Delta N=-2N(N/q_s)B_2\Delta r=-2.904N(N/q_s)\Delta r\,, \quad (6.10)$$

and

$$\Delta C_{N\mathrm{w}}=4N^2(A_1B_2+A_2B_1-2A_3B_1r-2A_3B_2r^2)\Delta r$$
$$=(2\pi/3)N^2(1-0.5293r-0.431r^2)\Delta r\,. \quad (6.11)$$

(2) *Application.* We shall next apply the above formulae to various $\Omega(X)$ in Fig. 1. When $C_p(x)$ is pushed down, $\Omega(x)$ is pushed up and hence $\Omega(X)$ is also pushed up (noting that $\Delta x(X)$ caused by $\Delta\Omega(X)$ is always small (cf. § 8 (1c)), so that r is decreased by (3.5) and (6.3) (cf. Table IV). Hence $(C_{p\mathrm{w}})_{\max}$ and $C_{N\mathrm{w}}$ decrease by (6.9) and (6.11) respectively, but N increases by (6.10). This is found to be the case in Figs. 3 and 4 and Table I (cf. the membrane analogy: § 7 [2] in ref. 4). ($C_{p\mathrm{w}}(y_{\mathrm{w}})$ and $C_{N\mathrm{w}}$ coincide well with each other in the cases of the notched hodograph and of the experiment and it is explained by the fact that r may be almost equal for both cases.)

Table III shows the accuracy of the approximate equations (6.9)~(6.11). The first column of the numerical data gives the approximate values of the deviations, Δ_{appr}, of the quantities in the case of $\Omega_{\exp}{}^{I}(X)$ from those in the case of $\Omega_{\exp}{}^{III}(X)$ and the second column gives the exact values of these deviations, Δ_{e},

Table III. The approximate and the exact deviations for various quantities of the first and the second approximations in the case of $\Omega_{\exp}(x)$.

	$\exp^{I}-\exp^{III}$			$\exp^{II}-\exp^{III}$		
	Δ_{appr} $(\times10^{-2})$	Δ_{e} $(\times10^{-2})$	$\frac{\Delta_{\mathrm{appr}}}{\Delta_{\mathrm{e}}}-1$	Δ_{appr} $(\times10^{-4})$	Δ_{e} $(\times10^{-4})$	$\frac{\Delta_{\mathrm{appr}}}{\Delta_{\mathrm{e}}}-1$
$(\Delta C_{p\mathrm{w}})_{\max}$	3.29	4.86	−0.32	12	29	(−0.6)*
ΔN	−1.37	−1.45	−0.055	− 5	− 8	(−0.4)
$\Delta C_{N\mathrm{w}}$	1.38	1.61	−0.14	5	7	(−0.3)

* The values of the last column are shown in brackets as they are rough.

while the third column gives the values of $(\Delta_{\mathrm{appr}}/\Delta_{\mathrm{e}})-1$. The remaining columns give the corresponding values in the case of $\Omega_{\exp}{}^{II}(X)$ as compared with $\Omega_{\exp}{}^{III}(X)$. It will readily be seen from this table that the convergence of approximate values of various quantities is rapid.

(3) Owing to the rapid convergence of the values of $C_{N\mathrm{w}}{}^{N}$ we have

$$(\Delta_{\mathrm{e}}C_{N\mathrm{w}})^{N,\infty}\approx(\Delta_{\mathrm{e}}C_{N\mathrm{w}})^{N,N+1}\,, \quad (6.12)$$

where, for example, $(\Delta_{\mathrm{e}}C_{N\mathrm{w}})^{N,\infty}$ means the exact deviation of the nth approximate value of $C_{N\mathrm{w}}$ from its final value. Hence from Table III we have $(\Delta_{\mathrm{e}}C_{N\mathrm{w}})^{I,\infty}\approx2\times10^{-2}$, $(\Delta_{\mathrm{e}}C_{N\mathrm{w}})^{II,\infty}\approx1\times10^{-3}$. Furthermore, in the calculation of $C_{N\mathrm{w}}{}^{IV}$ we choose D^{IV} equal to D^{III} and we have $(\Delta_{\mathrm{e}}C_{N\mathrm{w}})^{III,\infty}\approx1\times10^{-4}$. For rough estimation we may use (6.11) and put $(\Delta_{\mathrm{e}}C_{N\mathrm{w}})^{N,\infty}\approx(\Delta_{\mathrm{appr}}C_{N\mathrm{w}})^{N,N+1}$.

§ 7. Effect of the Deviation of $\Omega(X)$ in the Mixing Range

Next, we shall estimate deviations of the quantities on the front surface of the normal

plate caused by uncertainty of $\Omega(X)$ in the mixing range $X \geq D$. Such deviations will be denoted by δ, distinguishing them from the deviations, denoted by Δ, caused by the general deviation of $\Omega(X)$. In this paragraph, $\Omega(X)$ in $X \leq D$, i.e. $\Omega_E(X)$, is supposed to be given definitely.

(1) *General formulae.* First, we derive convenient formulae to estimate the deviations $\delta C_{N\mathrm{w}}$ of $C_{N\mathrm{w}}$ and δN of N. Let $G_M(W)$ denote the contribution of $\Omega(X)$ in $X \geq D$ to $G(W)$. Then we have, by (3.5),

$$G_M(W) = -\frac{2}{\pi}\int_D^\infty \Omega(X^*)\frac{dX^*}{W^2+X^{*2}} . \quad (7.1)$$

Simplifying the approximate expression (6.2), we put

$$\exp\{WG_M(W)\}\cdot(1+\varepsilon_M(W)) = 1+WG_M(1) , \quad (7.2)$$

and use the approximation: $\varepsilon_M(W)=0$. The ratio of error of this approximation, $\varepsilon_M(W)$, and the errors in the calculations using this approximation will be examined in Appendix 2.

The deviation of $G(W)$ which arises from $\delta\Omega(X)$ is denoted by $\delta G_M(W)$. Following the approximate method in (7.2) we put

$$\exp\{W\delta G_M(W)\}\cdot(1+\delta\varepsilon_M(W)) = 1+W\delta G_M(1) , \quad (7.3)$$

and neglect $\delta\varepsilon_M(W)$. Further we put

$$\left.\begin{aligned} A_n' &= \int_0^1 \sqrt{\frac{1-W}{1+W}}\, e^{-WG(W)} W^n dW , \\ B_n' &= \int_0^1 \sqrt{\frac{1+W}{1-W}}\, e^{WG(W)} W^n dW . \\ &\qquad (n=1,\ 2,\ \cdots) \end{aligned}\right\} \quad (7.4)$$

Then, by (6.7) and (3.4), neglecting $O(\delta G_M(1))^2$, we have

$$\delta C_{N\mathrm{w}} = q_s^2(A_1'B_2'+A_2'B_1')B_1'^{-2}\delta G_M(1) , \quad (7.5)$$

which, by using (6.2) and (6.5) and neglecting terms of $O(r^3)$, is further simplified to

$$\begin{aligned} \delta C_{N\mathrm{w}} &= 4N^2\{A_1B_2+A_2B_1 \\ &\qquad -(A_2B_3-A_4B_1)r^2\}\delta G_M(1) \\ &= (2\pi/3)N^2(1-0.095r^2)\delta G_M(1) . \end{aligned} \quad (7.6)$$

Here, by (3.7) and (3.4), $N=q_s/2B_1'$.

Similarly, by (3.7), δN becomes

$$\begin{aligned} \delta N &= -2N(N/q_s)(B_2+B_3r)\delta G_M(1) \\ &= -2N(N/q_s)(1.4521+1.2557r)\delta G_M(1) . \end{aligned} \quad (7.7)$$

(2) *Formulae to estimate* $|\delta C_{N\mathrm{w}}|_{\max}$. To find $\delta C_{N\mathrm{w}}$ by (7.6) it is necessary to estimate $\delta G_M(1)$. In the mixing range there may exist the most adequate $\Omega(X)$ which is denoted by $\Omega_t(X)$. ($\Omega_t(X)$ may have different form for each order of approximations corresponding to, e.g. different $\Omega^N(D^N)$.) We here postulate a probable and most simple limitation to $\Omega_t(X)$ as: $0 \leq \Omega_t(X) \leq \Omega_E(D)$ in $X \geq D$.

We use three forms of $\Omega(X)$ in $X \geq D$ and discriminate those by suffices a, b and c. The form (a) is represented by (4.1) and the other two forms are defined respectively by

$$\text{form (b):}\quad \Omega_b(X)=\Omega(D) , \quad (X \geq D) , \quad (7.8)$$

$$\text{form (c):}\quad \Omega_c(X)=0 , \quad (X \geq D) . \quad (7.9)$$

These forms are shown in Fig. 6.

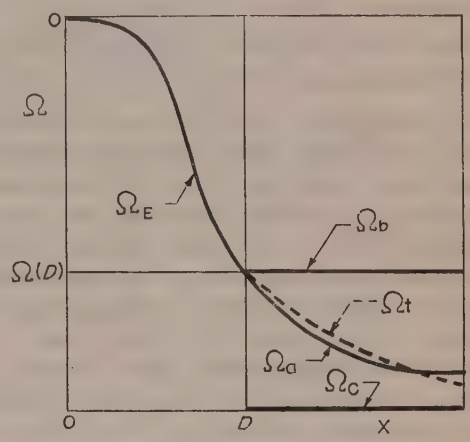

Fig. 6. Sketch of various forms of $\Omega(X)$ in $X \geq D$.

By the use of (7.1) we have calculated $WG_M(W)$ in each of the forms (a), (b) and (c), obtaining

$$WG_{Ma}(W) = -\frac{2}{\pi}\Omega(D)\left\{\frac{D}{W}-\left(\frac{D}{W}\right)^2\tan^{-1}\frac{W}{D}\right\} , \quad (7.10)$$

$$WG_{Mb}(W) = -\frac{2}{\pi}\Omega(D)\tan^{-1}\frac{W}{D} , \quad (7.11)$$

$$WG_{Mc}(W) = 0 . \quad (7.12)$$

We shall estimate the upper limit of $|(\delta G_M(1))_{at}|$, where, for example, we denote $G_{Ma}(1)-G_{Mt}(1)$ by $(\delta G_M(1))_{at}$. When $|(\delta G_M(1))_{at}|$ becomes maximum, $\Omega_a(X)-\Omega_t(X)$ should have the definite sign by (7.1), so that using (7.10) and (7.11), we have

$$\begin{aligned} |(\delta G_M(1))_{at}| &\leq \max\{(\delta G_M(1))_{ab},\ -(\delta G_W(1))_{ac}\} \\ &= (\delta G_M(1))_{ab} \\ &= (2/\pi)\Omega(D)\{(1+D^2)\tan^{-1}(1/D)-D\} . \end{aligned} \quad (7.13)$$

Here "max" means "the larger term of".

In case when we use the form (a) in $X \geq D$,

the maximum estimation of $(\delta C_{N\mathrm{w}})_{\mathrm{at}}$ is calculated by (7.6) and (7.13) taking $\Omega_{\mathrm{b}}(X)$ in place of $\Omega_{\mathrm{t}}(X)$. If we denote this by $|(\delta C_{N\mathrm{w}})_{\mathrm{at}}|_{\max}$, we have

$$\begin{aligned}|(\delta C_{N\mathrm{w}})_{\mathrm{at}}|_{\max} &= (\delta C_{N\mathrm{w}})_{\mathrm{ab}} \\ &= (4/3)N^2\Omega(D)(1-0.095r^2) \\ &\qquad \times\{(1+D^2)\tan^{-1}(1/D)-D\} \\ &= \frac{8}{9}N^2\frac{\Omega(D)}{D}(1-0.095r^2)\left(1-\frac{1}{5}\frac{1}{D^2}+\cdots\right).\end{aligned} \tag{7.14}$$

The last expansion holds provided $D>1$.

In case when the form (c) is used in $X\geq D$, we have, by (7.11), (7.12), (7.6) and (7.13),

$$\begin{aligned}&|(\delta C_{N\mathrm{w}})_{\mathrm{ct}}|_{\max} \\ &= \tan^{-1}(1/D)\{(1+D^2)\tan^{-1}(1/D)-D\}^{-1}(\delta C_{N\mathrm{w}})_{\mathrm{ab}} \\ &\approx 1.5|(\delta C_{N\mathrm{w}})_{\mathrm{at}}|_{\max}\,.\end{aligned} \tag{7.15}$$

(3) *Application.* We shall examine the results in § 5 by the above formulae, treating three cases where $\Omega_{\mathrm{E}}(X)$ in the free streamline range, $X\leq D$, is given by the elliptic hodograph $\Omega_{\mathrm{L}}(X)$, the Woods type $\Omega_{\mathrm{W}}(X)$ and the experimental curve $\Omega_{\exp}(X)$, respectively. We cut off the data given by the above examples in the range $X\geq D$ and treat this range as the mixing range, where we use the form (a) in place of $\Omega_{\mathrm{t}}(X)$, so that the maximum deviation of $C_{N\mathrm{w}}$, i.e. $|(\delta C_{N\mathrm{w}})_{\mathrm{at}}|_{\max}$, is

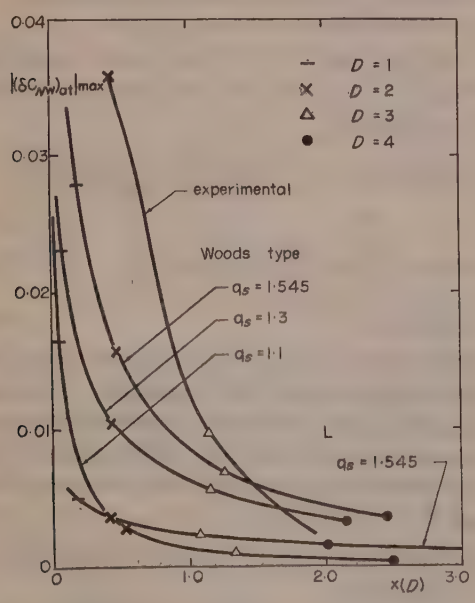

Fig. 7. $|(\delta C_{N\mathrm{w}})_{\mathrm{at}}|_{\max}$ *vs.* $(x)D$. The marks on the curve show the relation $x(D)$ for $D=1$, 2, 3 and 4. The symbols used in the figure are explaned in Table I.

given by (7.14). Fig. 7 shows the relation of $|(\delta C_{N\mathrm{w}})_{\mathrm{at}}|_{\max}$ *versus* $x(D)$, from which it will be seen that $|(\delta C_{N\mathrm{w}})_{\mathrm{at}}|_{\max}$ is mainly affected by $\Omega(D)/D$.

For example, we shall estimate the total error involved in the calculation of $\Omega_{\exp}{}^{II}(X)$. We have $x^{II}(D^{II})=1.085$ as shown in Table II so that $|(\delta C_{N\mathrm{w}})_{\mathrm{at}}|_{\max}\approx 1.1\times10^{-2}$ by Fig. 7. Furthermore, by the result of § 6 (3), $(\Delta_{\mathrm{e}}C_{N\mathrm{w}})^{II,\infty}\approx 1\times10^{-3}$. The total error can be approximately estimated to be the sum of these two, namely 1.2×10^{-2}.

The range $0\leq x\leq x_{\mathrm{nec}}(D)$ of the free streamline is referred to as the "necessary free streamline range" on which $C_p(x)$ must be obtained to determine $C_{N\mathrm{w}}$ within permissible experimental error. In case when $C_{p\,\exp}(x)$ is used in $x\leq x(D)$ and $\Omega_{\mathrm{a}}(X)$ is used in $X\geq D$, the value $x_{\mathrm{nec}}(D)$ is determined by the use of Fig. 7. For example, when the experimental error of $C_{N\mathrm{w}}$ is 1×10^{-2} or 1×10^{-3}, $x_{\mathrm{nec}}(D)$ is given by 1.2 or 2.3. It is of interest to examine experimentally whether the so-estimated necessary free streamline range may be regarded as a free streamline range or not.

So far we have postulated the simplest limitation to $\Omega_{\mathrm{t}}(X)$: $0\leq\Omega_{\mathrm{t}}(X)\leq\Omega_{\mathrm{E}}(D)$. If $\Omega_{\mathrm{t}}(X)$ in $X\geq D$ combined with $\Omega_{\mathrm{E}}(X)$ in $X\leq D$ is considered to satisfy the condition of finite width (3.14), the choice of $\Omega(X)$ in $X\geq D$ can be severely limited, so that x_{nec} may be shortened appreciably. It is clear that even the rough knowledge of the damping behaviour of $\Omega(X)$ less than about $0.3\Omega(0)$ or that of $C_p(x)$ in $x=1\sim3$ is very useful to estimate $C_{N\mathrm{w}}$.

In general, if we use the Woods type $\Omega_{\mathrm{W}}(X)$ for the first approximation of $\Omega(X)$ and choose adequately D and $\Omega(X)$ in $X\geq D$ ($x_{\mathrm{nec}}(D)$ being able to be estimated by the use of $\Omega^{II}(X)$ and $x^{II}(X)$), it may not be necessary in many cases to carry out the third approximation for practical purpose to determine $C_{N\mathrm{w}}$ from the observed data of $C_{p\mathrm{E}}(x)$.

(4) *Examination of the experimental curve* $\Omega_{\exp}(x)$ *used in* § 5. We see from Table I that the calculated value of $C_{N\mathrm{w}}$ is larger by 4×10^{-3} than the experimental value. We examine the errors involved in the calculation of $C_{N\mathrm{w}}{}^{III}$. First, when we use $x(D)=2.3$, $|(\delta C_{N\mathrm{w}})_{\mathrm{at}}|_{\max}$ decreases to 1×10^{-3} as explained above. Taking $D^{(III)}$, which has been determined by $x^{III}(D^{(III)})\approx2.3$ in place of D^{III},

the new $\Omega_{\exp}^{III}(X)$, i.e. $\Omega_{\exp}^{(III)}(X)$, becomes smaller than $\Omega_{\exp}^{III}(X)$ in $X \geq D^{III}$ (cf. Fig. 1). Hence $C_{N\mathrm{w}}$ increases by the result of § 6 (2). Secondly, by the result of § 6 (3) $(\Delta_e C_{N\mathrm{w}})^{III,\infty} \approx 1\times 10^{-4}$. Therefore the theoretical value of $C_{N\mathrm{w}}$ determined by the tentatively adopted $\Omega_{\exp}(x)$ is larger than the experimental value of $C_{N\mathrm{w}}$. Their difference may be larger than permissible experimental error of $C_{N\mathrm{w}}$.

Thus the experimental value of $C_{N\mathrm{w}}$ will be given correctly by pushing up $\Omega_{\exp}(x)$ in the free streamline range by the result of § 6 (2). Referring to § 1 we denote this correct $\Omega(x)$ by $\Omega_{\mathrm{ER}}(x)$. Hence $\Omega_{\mathrm{ER}}(x)$ may recover more rapidly to zero at $X \approx D$ than does $\Omega_{\exp}(x)$ when it should satisfy (3.14), so that its behaviour approaches that given by the notched hodograph (cf. Fig. 3).

This improvement is appropriate concerning the condition (3.14): We try to choose, in place of $\Omega_{\mathrm{a}}^{III}(X)$, the form:

$$\Omega(X)=\Omega_{\mathrm{E}}(D)\{1-(\Omega_{\mathrm{E}}'(D)/\Omega_{\mathrm{E}}(D))(X-D) +b^2(X-D)^2\}^{-1}\,, \qquad (7.16)$$

where $\Omega'(X)=d\Omega(X)/dX$, as the form of $\Omega(X)$ in $X \geq D$ to continue to $\Omega_{\mathrm{E}}(X)$ in $X \leq D$ smoothly at $X=D$, and determine the constant b so as to satisfy (3.14). Then it can be shown that b is unreasonably small in the case of $\Omega_{\exp}^{III}(X)$ because of the too small value of $\int_0^{D^{III}} \Omega_{\exp}^{III}(X^*)dX^*$. But, in the case of $\Omega_{\mathrm{ER}}(x)$, b may take a reasonable value and we may treat $\Omega_{\mathrm{ER}}(x)$ to satisfy (3.14).

We examine the width of the free streamlines at about $x=1.5\sim 2$ which we denote by d'' (cf. § 8 (2c)). From the comparison of various $\Omega(X)$ in Fig. 1 and the corresponding values of d'' we may expect that d'' determined by $\Omega_{\mathrm{ER}}(x)$ (in this case $d''\approx d'$) approaches the width of Kármán vortex street which has been observed as 1.475 by Fage and Johansen[4] (cf. Table II in ref. 3).

§ 8. Effect of the Deviation of $\Omega(X)$ on the Free Streamline

(1) *General formulae.* (1a) In order to examine the effect of the deviation of $\Omega(X)$ on the free streamline, we first examine the behaviour of $H(X)$ in the regions $X \ll 1$, $X \approx 1$ and $X \gg 1$. In $X \ll 1$ we may approximate $H(X)$ by (3.17) as stated in § 3 (3) so that

$$H(X)\approx \ln q_s\cdot bX\,, \qquad (X \ll 1). \qquad (8.1)$$

We illustrate this relation: In the cases of $\Omega_{\mathrm{L}}(X)$, $\Omega_{\mathrm{W}}(X)$, $\Omega_{\exp}^{III}(X)$ and $\Omega_{\mathrm{K}}(X)$ [$\equiv 0$] the values of $H'(0)$, i.e. $dH(X)/dX$ at $X=0$ are $b\ln q_s=0.52$, $(\ln q_s)^2=0.18$ (both by (3.19)), 0.10 (by numerical calculation) and 0 respectively.

From (3.10), putting $X^*=X(1-t)$ in $0 \leq X^* \leq X$ and $X^*=X(1-t)^{-1}$ in $X \leq X^* \leq \infty$, we have

$$H(X)=(2/\pi)\int_0^1 \{\Omega(X(1-t))-\Omega(X(1-t)^{-1})\}\cdot \times(2t-t^2)^{-1}dt\,.$$

If $\Omega(X^*)$ is analytic in $|X^*-X| \leq k$, k being a constant, $\Omega(X(1-t))-\Omega(X(1-t)^{-1})$ can be expanded in power series of t in the range of $t \leq t_0$ where we choose t_0 less than both kX^{-1} and $k(1+X)^{-1}$, so that

$$H(X)=\frac{2}{\pi}\left\{\int_0^{t_0}\frac{-2\Omega'(X)X-\Omega'(X)Xt+\mathrm{O}(t^2)}{2-t}dt +\int_0^{t_0}\frac{\Omega(Xu)-\Omega(Xu^{-1})}{1-u^2}du\right\},$$

where we have put $t=1-u$ in $t_0 \leq t \leq 1$. By rough estimation of this equation we have

$$H(X)\approx\frac{2}{\pi}\left\{-\left(4\ln\frac{2}{2-t_0}-t_0\right)\Omega'(X)X +\Omega(0)(1-t_0)\right\}\,. \qquad (8.2)$$

Hence $H(X)$ is large when $\Omega'(X)$ and X are large. This formula may be useful for moderate X.

The maximum value of $H(X)$ and the corresponding value, X_h, of X in the case of $\Omega_{\mathrm{L}}(X)$ and $\Omega_{\mathrm{W}}(X)$ are found, by (3.17), to be $H(X_h)=(\ln q_s)/2=0.218$, $X_h=b^{-1}=0.83$ and $H(X_h)=0.218$, $X_h=2.30$ respectively, while in the cases of $\Omega_{\exp}^{II}(X)$ and $\Omega_{\exp}^{III}(X)$ we find, by numerical calculations, that $H(X_h)=0.365$, $X_h=2.68$ and $H(X_h)=0.388$, $X_h=2.79$ respectively. The large discrepancies between these values are due to the large deviation of $\Omega'(X)$ near $X\approx 2.5$ (Fig. 1).

Using (3.9), we have, for large X,

$$\theta(X)=-H(X)+X^{-1}-(1/3)X^{-3}+\cdots\,,$$

so that, using (3.12), the condition of finite width (3.14) can be replaced by

$$H(X)=X^{-1}+\mathrm{O}(X^{-n})\,, \quad (n>2,\ X\gg 1)\,. \qquad (8.3)$$

When (3.13) is satisfied, the coefficient of X^{-1} in (8.3) is less than unity or $H(X) \leq \mathrm{O}(X^{-2})$.

For example, using (3.17), we have $H(X)\approx \ln q_s \times b^{-1}X^{-1}$ in $X\gg 1$ in the case (3.15) and using (3.18), we find that $\ln q_s\cdot b^{-1}<1$ when (3.13) is

satisfied. In the Kirchhoff flow $H(X)=0$.

(1b) When $X \ll 1$, we have, by (3.9) and (8.1), $\sin\theta \approx 1$ and $\cos\theta \approx (1+H'(0))X$, so that

$$x(X) \approx N q_s^{-1}(1+H'(0))X^3/3\,, \tag{8.4}$$

$$y(X) \approx N q_s^{-1} X^2/2\,, \tag{8.5}$$

and therefore

$$y(x) \approx (N/q_s)^{1/3} 2^{-1} 3^{2/3} (1+H'(0))^{-2/3} x^{2/3}\,. \tag{8.6}$$

Hence we have $y \propto x^{2/3}$ irrespective of $\Omega(X)$, and the rise of $y(x)$ near the separation point ($x=0$) is smaller, the larger is $H'(0)$. ($(N/q_s)^{1/3}$ is less sensitive to $\Delta\Omega(X)$ than $H'(0)$.)

(1c) We next estimate $\Delta x(X)$. Using (3.11) we have

$$d(\Delta x(X)) = \{-\Delta\Omega(X) + \Delta N/N + \Delta H(X)\tan\theta\} \times dx(X)\,. \tag{8.7}$$

In the range $X \ll 1$, we have, using (3.9), $\Delta H(X)\tan\theta \approx H'(0)(1+H'(0))$ and it can be verified that $\Delta H(X)\tan\theta$ is the main term in the brackets of (8.7) when $X \ll 1$. But, by (8.7), $\Delta x(X)$ is small in $X \ll 1$ for $dx(X) \propto X^2 dX$.

Let X_A be the value of X at a point where $|\Delta\Omega(X)|$ becomes maximum. Then, in the range $X \approx X_A$ we can verify that $\Delta\Omega(X)$ becomes the main term in (8.7) when q_s is unchanged. Therefore

$$\Delta x(X) \approx -x\overline{\Delta\Omega}(X)\,, \qquad (X \approx X_A)\,, \tag{8.8}$$

where $\overline{\Delta\Omega}(X)$ is a weighted mean:

$$\overline{\Delta\Omega}(X) = \left\{\int_0^X \Delta\Omega(X)dx(X)\right\} \Big/ x(X)\,. \tag{8.9}$$

Hence for positive $\Delta\Omega(X)$ at $X \approx X_A$, $\Delta x(X)$ is negative there, $\Delta x(X)$ for moderate X ($X=1 \sim 4$ or $x=0.2 \sim 2$) may be at most of the order of $\Delta\Omega(X_A)$ when q_s is unchanged so that it is small in general.

In the range where $\Delta\Omega(X)$ becomes small, $\Delta N/N$ predominates in (8.7). For positive $\Delta\Omega(X)$ at $X \approx X_A$, ΔN is positive (cf. § 6 (2)) so that negative $\Delta x(X)$ which appeared at $X \approx X_A$ begins to decrease in the range where $\Delta\Omega(X)$ becomes small.

(1d) Lastly, we shall estimate $\Delta y(X)$ for moderate X. Using (3.12) we have

$$d(\Delta y(X)) = \{-\Delta\Omega(X) + \Delta N/N + \Delta H(X)\cot\theta\} \times dy(X)\,. \tag{8.10}$$

$\Delta H(X)\cot\theta$ is negligible for $X \ll 1$, but it can be large at moderate X (cf. (1a)), so that $\Delta y(X)$ can be large at moderate X (cf. Fig. 2). For further discussion on $\Delta y(X)$, see (2c).

(2) *General results.* (2a) First we prove roughly the rapid convergency of successive approximations prescribed in § 4. By its definition together with (8.10), $(\Delta\Omega(X))^{N,N+1}$ is estimated to be

$$\begin{aligned}(\Delta\Omega(X))^{N,N+1} &= \Omega_{\mathrm{E}}(x^{N-1}(X)) - \Omega_{\mathrm{E}}(x^N(X)) \\ &\approx \frac{d\Omega_{\mathrm{E}}(x^{N-1}(X))}{dx^{N-1}(X)}(\Delta x)^{N-1,N} \\ &\approx \frac{d\Omega^N(X)}{dX}\frac{dX}{dx^{N-1}(X)}x^{N-1}(X)(\overline{\Delta\Omega}(X))^{N-1,N}\,.\end{aligned} \tag{8.11}$$

Hence $(\Delta\Omega(X))^{N,N+1}$ decreases appreciably in $x \approx 0$. For moderate x, we estimate this equation at $x=1$ by taking $\Omega_{\exp}(X)$ as $\Omega_{\mathrm{E}}(X)$. From Figs. 1 and 2, we find $-d\Omega_{\exp}(X)/dX \approx 0.3$ and $dX/dx \approx 1.4$, so that

$$(\Delta\Omega(X))^{N,N+1} \approx 0.4(\overline{\Delta\Omega}(x))^{N-1,N}\,. \tag{8.12}$$

Therefore, when q_s is unchanged, $(\Delta\Omega(X))^{N,N+1}$ at $x \approx 1$ becomes much smaller than $(\Delta\Omega(X))^{N-1,N}$. By (8.12) we can explain the fact in § 6 (3) that $(\Delta C_{N\mathrm{w}})^{N,N+1}$ is about $0.1 \times (\Delta C_{N\mathrm{w}})^{N-1,N}$.

(2b) In case when $\Omega(X)$ has a deviation, $\delta\Omega(X)$, only in $X \geq D$, the deviation $\delta x(X)$ of $x(X)$ is especially small in $X < D$, since $\overline{\Delta\Omega}(X)=0$ in $X \leq D$. By (7.6) and (7.7) $\delta N/N \approx 0.4N^{-2}\delta C_{N\mathrm{w}}$ so that $\delta N/N$ is small when D and $\delta\Omega(X)$ are so chosen that $\delta C_{N\mathrm{w}}$ is small. Therefore in $X < D$ a small $\delta x(X)$ may appear, if possible, only in the neighbourhood of $X=D$ by (8.7).

(2c) Lastly we consider the width between the free streamlines. We take $\Omega(X)$ which satisfies the condition of finite width (3.14). If we push down (or up) $\Omega(X)$, the left-hand side of (3.14) becomes smaller (or greater) than $\pi/2$, so that the width between the free streamlines at infinity, $1+2y(\infty)$, becomes $+\infty$ (or $-\infty$). Therefore, if we combine properly these modifications of $\Omega(X)$ and keep $\Omega(X)$ to satisfy (3.14), we can make $1+2y(\infty)$ to take an arbitrary value, e.g. zero or the width of Kármán vortex street. Moreover, since, as will be seen from (7.6) and (7.1) (cf. Fig. 7), $\delta\Omega(X)$ in $X \geq D$ has little effect upon $C_{N\mathrm{w}}$, the effect of these modifications of $\Omega(X)$ upon $C_{N\mathrm{w}}$ can easily be made within experimental error. Hence, instead of $1+2y(\infty)$, only d'' in § 7 (4) is significant in the experimental relation to $C_{N\mathrm{w}}$.

(3) *Application.* We shall apply the above results in (1) to the results in § 5. (3a) At

$x \approx 0$, the rise of the curve $y(x)$ of the free streamline is in the order of the cases of $\Omega_L(X)$, $\Omega_W(X)$, $\Omega_{exp}{}^{III}(X)$ and $\Omega_K(X)$ (the last case being the largest) (see Fig. 5). This can be explained from the value of $H'(0)$ in (1a).

(3b) We see that $X_A=1\sim2$ in each case of Fig. 1. Corresponding to this, remarkable but small $\Delta x(X)$ of the order of $\Delta\Omega(X_A)$ appears at $X\approx X_A$ in Fig. 2. As will be seen in Fig. 2, $\Delta x(X)$ at $X\approx3$ tends to decrease by the effect of ΔN.

(3c) In the examples in (1a), $\Delta H(X)\cot\theta$ is large in $X=2.5\sim3$ so that it makes a large contribution to $\Delta y(X)$ there (Fig. 2). Thus, in order to determine the shape of the free streamline in the free streamline range it is desirable to choose $\Omega(X)$ in $X\geq D$ in such a manner that the gradient at $X=D$ is continuously connected, e.g. like the form (7.16). In this way the shape in this range may be determined within experimental error. To know the damping behaviour of $C_p(x)$ in $X\approx D$ (e.g. $x=1\sim3$), even if it is rough, is very useful not only to determine C_{Nw} but also to find the shape of the free streamline.

§ 9. Effect of the Separation Velocity and the Condition of Finite Width upon δC_{Nw}

Using the formulae in §§ 6∼8, it is easy to estimate quantitatively the change of Δr, $\Delta x(X)$, etc. when $\Omega_E(X)$ in $X\leq D$ is changed by the decrease of q_s ($q_s=1.545$ may be extremely large value observed in experiment, cf. the data of Roshko[5]). But we only illustrate here the effect of the decrease of q_s upon $|(\delta C_{Nw})_{at}|_{max}$ in Fig. 7 in which $\Omega_E(X)$ in $X\leq D$ is given by the Woods type (3.19) and q_s takes 1.3 and 1.1 other than 1.545.

$|(\delta C_{Nw})_{at}|_{max}$ in the case where the condition of finite width (3.14) is not satisfied is illustrated in Fig. 7 where $\Omega_E(X)$ in $X\leq D$ is given by the case of the elliptic hodograph (5.1). In the Kirchhoff flow ($q_s=1$), $\delta C_{Nw}=0$. In general, it may be easily verified, using the formulae in §§ 6∼8, that in case when (3.13) is satisfied the necessary free streamline range becomes longer when it is pushed up to satisfy (3.14).

Appendix I

In Table IV the accuracy of the approximate formulae (6.6) and (6.8) is examined for the cases of $\Omega_L(X)$, $\Omega_W(X)$, $\Omega_{exp}{}^{II}(X)$ and $\Omega_{exp}{}^{III}(X)$. The first column shows the value of r defined by (6.3). The second column shows ε_{max} which denotes the value of $\varepsilon(W)$ corresponding to maximum $|\varepsilon(W)|$ (hence, when ε_{max} is negative, it means the minimum value of $\varepsilon(W)$). It is found that the slower $\Omega(X)$ recovers to zero, the smaller become r and $|\varepsilon_{max}|$. This tendency can be seen by the use of (6.1). The third and the fourth columns show the ratios of the approximate values of N and $1-C_{Nw}$ respectively, which are obtained by (6.6) and (6.8). The values in the third and the fourth columns should be compared to $(1+\varepsilon_{max})^{-1}-1$ and $(1+\varepsilon_{max})^{-2}-1$ respectively. It may be said that the accuracy of the approximate formulae (6.6) and (6.8) is sufficient.

Table IV. The accuracy of the approximate formulae (6.6) and (6.8).

	r	ε_{max}	$\frac{N_{appr}}{N}-1$	$\frac{1-C_{Nw\,appr}}{1-C_{Nw}}-1$
L	0.26780	-3.9×10^{-2}	1.3×10^{-2}	4.4×10^{-2}
W	0.14096	-1.1×10^{-2}	3.5×10^{-3}	1.0×10^{-2}
exp^{II}	0.09748	-5.0×10^{-4}	9.7×10^{-4}	1.3×10^{-3}
exp^{III}	0.09581	-5.7×10^{-4}	2.4×10^{-4}	5.1×10^{-4}

Appendix II

We estimate the value of $\varepsilon_M(W)$ in (7.2) when $|\varepsilon_M(W)|$ becomes maximum. We denote this by $\varepsilon_{M\,max}$ (the negative $\varepsilon_{M\,max}$ is the minimum value of $\varepsilon_M(W)$). To estimate the order of $\varepsilon_{M\,max}$, we put, e.g. $\Omega(D)=0.15$ and $D=2$. Then $\varepsilon_{M\,max}$ becomes 1.0×10^{-3} and 6.7×10^{-4} in the cases of the forms (a) and (b) respectively. Therefore the approximation $\varepsilon_M(W)=0$ in (7.2) is a good one.

In a practical problem, noting the order of the quantities r, $|\varepsilon_{max}|$ and $|\delta\varepsilon_{M\,max}|$, the last one being of the order of $|\varepsilon_{M\,max}|$, the maximum error ratio for the approximate formulae (7.6) and (7.7) may not exceed 5×10^{-2} even in the worst condition. For the purpose to estimate the necessary free streamline range x_{nec} by the use of Fig. 7 this rough error estimation is sufficiently enough.

Acknowledgements

The author wishes to express his sincere thanks to Professor S. Tomotika for valuable advices and kind inspection of the manuscript. The author's thanks are also due to Professor T. Maekawa for helpful advices.

References

1) A. Roshko: NACA TN 3168 (1954).
2) L. C. Woods: Proc. Roy. Soc. A **227** (1955) 367.
3) Y. Mimura: J. Phys. Soc. Japan **13** (1958) 1048.
4) A. Fage and F. C. Johansen: Proc. Roy. Soc. A **116** (1927) 170.
5) A. Roshko: NACA TN 3169 (1954).

JOURNAL OF THE PHYSICAL SOCIETY OF JAPAN Vol. 13, No. 11, NOVEMBER, 1958

On the Acoustic Field by a Vibrating Source Arbitrarily Distributed on a Ribbon Plate. I

By Norio KAWAI

Department of Physics, Tôkyo Institute of Technology

(Received June 25, 1958)

Two-dimensional rigorous solutions are presented for the acoustic field in the air caused by the vibrating source arbitrarily distributed on an infinitely thin and infinitely long ribbon. Using rectangular coordinates, the unique solution satisfying the boundary condition is obtained by the method of expansion in the hypergeometric polynomials. The expression of the velocity potential at large distance, pressure on the ribbon plate and power of radiation are obtained as a function of $k=2\pi a/\lambda$, where a is the half-breadth of the plate and λ is the wave length.

§ 1. Introduction

The calculation of the acoustic field caused by an emitter with a baffle of infinite dimensions can be carried out by the Rayleigh formula, and various problems for such emitters have been solved. So far as we are aware, however, there have been rather few treatises on the acoustical radiation of an emitter vibrating freely or with a baffle of finite dimensions; only the general theories[7),8),9)] with respect to such problems and the calculations of examples for a circular plate source are treated, but no example for a ribbon source.

Our method of calculation is applicable to the case of an emitter with a finite or an infinite baffle, and also to the calculation of the diffracted waves by a ribbon plane which is fixed or vibrating.

As a rule, the elliptic cylindrical coordinates are used for problems concerning the domain outside an infinitely thin and infinitely long ribbon plate, the method of integral equation or other methods[9)] are used, but those are still far from convenient for numerical computation. In the present paper we use the rectangular cartesian coordinates for the same problem. That is, we express the wave equation in the rectangular coordinates and express the solution of the wave equation in terms of modified Weber-Schafheitlin integrals.

The arbitrary constants in the expression of the velocity potential are determined by the method of expansion in hypergeometric polynomials.

In the forgoing papers[1)], we applied this method to the calculation of the field caused by a vibrating source arbitrarily distributed on a circular plate, and discussed as an example the radiation of sound wave from a vibrating plane circular plate with a fixed circular baffle[2)]. The expression of the field for a ribbon plate has the factors $G_{n\nu}{}^{1/2}$ and $G_{n\nu}{}^{-1/2}$, whereas the former calculation for a circular plate have the factor $G_{n\nu}{}^{m}$, where m is an integer. $G_{n\nu}{}^{m}$ with integer m are tabulated in the paper, " Acoustic field by a vibrating source arbitrarily distributed on a plane circular disc "[1)] which is referred to as A in the present paper. Tables of $G_{n\nu}{}^{1/2}$ and $G_{n\nu}{}^{-1/2}$ are to be published in the next report II.

We refer to the paper, "Diffraction of electromagnetic waves by ribbon and slit"[5] as B.

§ 2. General Solution

Taking X and y axes on the ribbon plate and Z axis normal to the plate, we use X, y, Z as the rectangular coordinates of a point. Further we set $x=X/a$, $\rho=y/a$ and $z=Z/a$, where a is the half-breadth of the plate.

When the velocity potential of the acoustic field is expressed by $\Phi \exp(i\omega t)$, Φ must satisfy the following wave equation

$$\frac{\partial^2\Phi}{\partial\rho^2}+\frac{\partial^2\Phi}{\partial z^2}+k^2\Phi=0\,, \qquad (1)$$

where $k=(\omega/c)a=(2\pi/\lambda)a$, c is the propagation velocity and λ is the wave length of sound.

Since the field is antisymmetric with respect to the plane $z=0$, the condition

$$\Phi=0 \qquad (2)$$

must hold for $z=0$ and $|\rho|>1$*.

We can use the following expression, as a solution of (1) satisfying the condition (2),

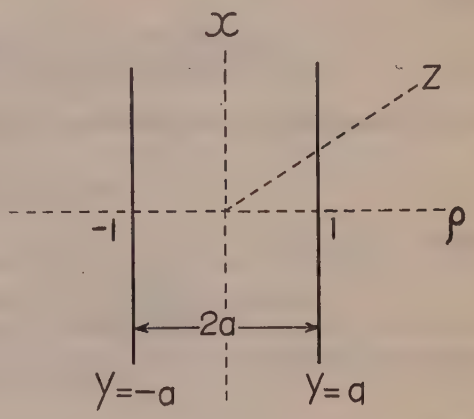

Fig. 1.

$$\Phi=\mp\sqrt{\rho}\sum_{n=0}^{\infty}\left\{A_n^{1/2}\int_0^\infty\frac{J_{1/2}(\rho\xi)J_{(1/2)+2n+(3/2)}(\xi)}{\sqrt{\xi}}\exp(\mp\sqrt{\xi^2-k^2}\,z)d\xi\right.$$
$$\left.+A_n^{-1/2}\int_0^\infty\frac{J_{-1/2}(\rho\xi)J_{-(1/2)+2n+(3/2)}(\xi)}{\sqrt{\xi}}\exp(\mp\sqrt{\xi^2-k^2}\,z)d\xi\right\}, \qquad (3)$$

taking the upper sign for $z>0$ and the lower sign for $z<0$.

The integrals in the bracket are modified Weber-Schafheitlin integrals, and have the property to become zero for $|\rho|\geqq 1$ or $|y|\geqq a$ when $z=0$[6], and the formula (3) means that $\partial\Phi/\partial z$ is continuous at $z=0$. The first integral having subscript 1/2 is an odd solution and the second integral having subscript $-1/2$ is an even solution of ρ respectively.

The coefficients $A^{1/2}$ and $A^{-1/2}$ are to be determined by the velocity distribution on the ribbon plate,

$$-\frac{1}{a}\left(\frac{\partial\Phi}{\partial z}\right)_{z=0}=v \text{ (Vibration velocity of each point on the plate)}$$
$$\equiv\frac{1}{a}f(\rho) \qquad \text{for } |\rho|<1\,, \qquad (4)$$

and $f(\rho)$ can be expressed as the sum of an even function $f_e(\rho)$ and odd function $f_0(\rho)$; that is $f(\rho)=f_e(\rho)+f_0(\rho)$,

Using the hypergeometric polynomials

$$v_n^m(x)=x^{-m/2}\int_0^\infty\sqrt{\xi}\,J_m(\sqrt{x}\,\xi)J_{m+2n+(3/2)}(\xi)d\xi$$
$$=\frac{\sqrt{2}\,\Gamma(m+n+\frac{3}{2})}{n!\,\Gamma(m+1)}F\left(m+n+\frac{3}{2},\ -n,\ m+1,\ x\right)$$
$$=\frac{\sqrt{2}\,\Gamma(m+n+\frac{3}{2})}{m!\,\Gamma(m+n+1)}x^{-m}(1-x)^{-1/2}\frac{d^n}{dx^n}\{x^{m+n}(1-x)^{n+(1/2)}\}^{**}\,, \qquad (0\leqq x\leqq 1) \qquad (5)$$

* This condition means that the pressure is zero or unchanged from an undisturbed state. Or this condition is derived from the consideration that the velocity potential due to a linearly vibrating point source has the value zero on the plane through that source and perpendicular to the vibration of source, and that the vibrating source on the plane is an ensemble of such point sources.

** $v_n^{-1/2}(x)$ are used for the expansion of even functions and $v_n^{1/2}(x)$ are used for odd functions.

an arbitrary function $f(x)$ can be expanded into the following series

$$f(x)=\sum_{n=0}^{\infty} B^{(n)} v_n^m(x)\,, \tag{6}$$

where

$$B^{(n)} \frac{m+2n+\frac{3}{2}}{\sqrt{2}\,\Gamma(n+\frac{3}{2})}\int_0^1 f(x)\,\frac{d^n}{dx^n}\{x^{m+n}(1-x)^{n+(1/2)}\}dx^*\,. \tag{7}$$

By the above theorem, the following relations are obtained,

$$f_e(\sqrt{x})=\sum_{n=0}^{\infty} a_n^{-1/2} v_n^{-1/2}(x)\,,$$

where

$$a_n^{-1/2}\frac{2n+1}{\sqrt{2}\,\Gamma(n+\frac{3}{2})}\int_0^1 f_e(\sqrt{x})\,\frac{d^n}{dx^n}\{x^{n-(1/2)}(1-x)^{n+(1/2)}\}dx;$$

$$f_0(\sqrt{x})=\sqrt{x}\sum_{n=0}^{\infty} a_n^{1/2} v_n^{1/2}(x)\,,$$

where

$$a_n^{1/2}=\frac{2n+2}{\sqrt{2}\,\Gamma(n+\frac{3}{2})}\int_0^1 f_0(\sqrt{x})x^{-1/2}\,\frac{d^n}{dx^n}\{x^{n+(1/2)}(1-x)^{n+(1/2)}\}dx\,. \tag{8}$$

Writing $\rho=\sqrt{x}$, we have

$$\begin{aligned}\left(\frac{\partial\Phi}{\partial z}\right)_{z=0} &= \sqrt{\rho}\sum_{n=0}^{\infty}\left\{A_n^{1/2}\int_0^\infty \frac{J_{1/2}(\rho\xi)J_{(1/2)+2n+(3/2)}(\xi)\sqrt{\xi^2-k^2}}{\sqrt{\xi}}d\xi\right.\\ &\quad\left.+A_n^{-1/2}\int_0^\infty \frac{J_{-1/2}(\rho\xi)J_{-(1/2)+2n+(3/2)}(\xi)\sqrt{\xi^2-k^2}}{\sqrt{\xi}}d\xi\right\}\\ &= x^{1/4}\sum_{n=0}^{\infty}\left\{A_n^{1/2}\int_0^\infty \frac{J_{1/2}(\sqrt{x}\,\xi)J_{(1/2)+2n+(3/2)}(\xi)\sqrt{\xi^2-k^2}}{\sqrt{\xi}}d\xi\right.\\ &\quad\left.+A_n^{-1/2}\int_0^\infty \frac{J_{-1/2}(\sqrt{x}\,\xi)J_{-(1/2)+2n+(3/2)}(\xi)\sqrt{\xi^2-k^2}}{\sqrt{\xi}}d\xi\right\}\end{aligned} \tag{9}$$

By the aid of the expansion formula

$$x^{-m/2}J_m(p\sqrt{x})=\left(\frac{p}{2}\right)^m\sum_{s=0}^{\infty}\frac{(-1)^s(p\sqrt{x}/2)^{2s}}{s!\,\Gamma(m+s+1)}$$

and the equations (6) and (7), we get

$$J_m(p\sqrt{x})=x^{m/2}\sum_{n=0}^{\infty}(2m+4n+3)\frac{J_{m+2n+(3/2)}(p)}{p^{3/2}}v_n^m(x)^{**}\,. \tag{10}$$

Using (10)

$$x^{1/4}\int_0^\infty \frac{J_m(\sqrt{x}\,\xi)J_{m+2n+(3/2)}(\xi)\sqrt{\xi^2-k^2}}{\sqrt{\xi}}d\xi=x^{(2m+1)/4}\sum_{\nu=0}^{\infty}(2m+4\nu+3)G_{n\nu}^m v_\nu^m(x)\,, \tag{11}$$

where

$$G_{n\nu}^m=\int_0^\infty \frac{(\xi^2-k^2)^{1/2}J_{m+2n+(3/2)}(\xi)J_{m+2\nu+(3/2)}(\xi)}{\xi^2}d\xi\,. \tag{12}$$

* Reference (6), P. 203 and P. 209, 210.

** See the paper B, P. 193, (2.14), and reference (4) P. 301.

Then, by (11)

$$x^{1/4}\int_0^\infty \frac{J_{1/2}(\sqrt{x}\,\xi)J_{(1/2)+2n+(3/2)}(\xi)\sqrt{\xi^2-k^2}}{\sqrt{\xi}}d\xi = x^{1/2}\sum_{\nu=0}^{\infty}(4\nu+4)G_{n\nu}{}^{1/2}v_\nu{}^{1/2}(x) \tag{13}$$

for $m=1/2$ (odd), and

$$x^{1/4}\int_0^\infty \frac{J_{-1/2}(\sqrt{x}\,\xi)J_{-(1/2)+2n+(3/2)}(\xi)\sqrt{\xi^2-k^2}}{\sqrt{\xi}}d\xi = \sum_{\nu=0}^{\infty}(4\nu+2)G_{n\nu}{}^{-1/2}v_\nu{}^{-1/2}(x) \tag{14}$$

for $m=-1/2$ (even).

Therefore

$$\left(\frac{\partial\Phi}{\partial z}\right)_{z=0} = \sum_{n=0}^{\infty}\left\{A_n{}^{1/2}x^{1/2}\sum_{\nu=0}^{\infty}(4\nu+4)G_{n\nu}{}^{1/2}v_\nu{}^{1/2}(x)+A_n{}^{-1/2}\sum_{\nu=0}^{\infty}(4\nu+2)G_{n\nu}{}^{-1/2}v_\nu{}^{-1/2}(x)\right\}. \tag{15}$$

Substituting (8) and (15) into the equation (4), and equating the even term in the left-hand side to the even term in the right-hand side and the odd term to the odd term respectively, we obtain

$$-\sum_{n=0}^{\infty}A_n{}^{1/2}x^{1/2}\sum_{\nu=0}^{\infty}(4\nu+4)G_{n\nu}{}^{1/2}v_\nu{}^{1/2}(x)=\sqrt{x}\sum_{\nu=0}^{\infty}a_\nu{}^{1/2}v_\nu{}^{1/2}(x)$$

$$-\sum_{n=0}^{\infty}A_n{}^{-1/2}\sum_{\nu=0}^{\infty}(4\nu+2)G_{n\nu}{}^{-1/2}v_\nu{}^{-1/2}(x)=\sum_{\nu=0}^{\infty}a_\nu{}^{-1/2}v_\nu{}^{-1/2}(x)\,.$$

Then we can set

$$\sum_{s=0}^{\infty}A_s{}^{1/2}G_{sn}{}^{1/2}=-a_n{}^{1/2}/(4n+4)\,,\qquad \sum_{s=0}^{\infty}A_s{}^{-1/2}G_{sn}{}^{-1/2}=-a_n{}^{-1/2}/(4n+2)$$
$$(n=0,\ 1,\ 2,\ 3,\ \cdots)\,. \tag{16}$$

Introducting $X_{s\nu}{}^m$ by the follows relations

$$\sum_{s=0}^{\infty}G_{sn}{}^mX_{s\nu}{}^m=-\delta_{n\nu}\qquad\left(m=\frac{1}{2}\ \text{ or }\ -\frac{1}{2}\right), \tag{17}$$

where $\delta_{n\nu}=1$ as $\nu=n$ and $\delta_{n\nu}=0$ as $\nu\neq n$, we can set that

$$A_n{}^{1/2}=\sum_{\nu=0}^{\infty}\frac{a_\nu{}^{1/2}}{4\nu+4}X_{n\nu}{}^{1/2}\,,\qquad A_n{}^{-1/2}=\sum_{\nu=0}^{\infty}\frac{a_\nu{}^{-1/2}}{4\nu+2}\,. \tag{18}$$

The arbitrary coefficients $A_n{}^{1/2}$ and $A_n{}^{-1/2}$ in the expansion formula (3) are thus determined.

§ 3. Calculation of $G_{n\nu}{}^m$ and $X_{n\nu}{}^m$ ($m=1/2,\ -1/2$)

For the calculation we express $G_{n\nu}{}^m$ as follows

$$G_{n\nu}{}^m=g_1(\alpha,\ \beta)+ig_2(\alpha,\ \beta)\,, \tag{19}$$

where

$$\left.\begin{aligned} &g_1(\alpha,\ \beta)=\int_k^\infty\frac{\sqrt{\xi^2-k^2}\,J_\alpha(\xi)\,J_\beta(\xi)d\xi}{\xi^2}\,,\qquad g_2(\alpha,\ \beta)=\int_0^k\frac{\sqrt{\xi^2-k^2}\,J_\alpha(\xi)\,J_\beta(\xi)d\xi}{\xi^2}\\ &\text{and}\\ &\alpha=m+2n+\frac{3}{2}\,,\qquad \beta=m+2\nu+\frac{3}{2}\,.\end{aligned}\right\} \tag{20}$$

By the paper *B*,

$$g_1(\alpha,\beta)=\frac{\sqrt{\pi}}{4}\sum_{\mu=0}^{((\alpha+\beta)/2)-1}\frac{(-1)^\mu}{\mu!}\frac{\Gamma\left(\frac{\alpha+\beta}{2}-\mu\right)\Gamma(2\mu+1)\left(\frac{k}{2}\right)^{2\mu}}{\Gamma\left(\mu+1+\frac{\alpha-\beta}{2}\right)\Gamma\left(\mu+1+\frac{\beta-\alpha}{2}\right)\Gamma\left(\mu+1+\frac{\alpha+\beta}{2}\right)\Gamma\left(-\mu+\frac{3}{2}\right)}$$

$$+(-1)^{((\alpha+\beta)/2)+1}\frac{\sqrt{\pi}}{4}\sum_{\mu=0}^{\infty}$$

$$\cdot\frac{\Gamma(\alpha+\beta+2\mu+1)\left(\frac{k}{2}\right)^{\alpha+\beta+2\mu}}{\Gamma(\mu+1)\Gamma\left(\frac{\alpha+\beta}{2}+\mu+1\right)\Gamma(\alpha+\mu+1)\Gamma(\beta+\mu+1)\Gamma(\alpha+\beta+\mu+1)\Gamma\left(-\frac{\alpha+\beta}{2}-\mu+\frac{3}{2}\right)}$$

$$\cdot\left\{2\log\frac{k}{2}+2\psi(\alpha+\beta+2\mu+1)-\psi(\mu+1)-\psi\left(\frac{\alpha+\beta}{2}+\mu+1\right)-\psi(\alpha+\beta+1)\right.$$

$$\left.-\psi(\beta+\mu+1)-\psi(\alpha+\beta+\mu+1)+\psi\left(-\frac{\alpha+\beta}{2}-\mu+\frac{3}{2}\right)\right\}, \tag{21}$$

where $\psi(z)=(d/dz)\log\Gamma(z)=\Gamma'(z)/\Gamma(z)$, and by the paper A,

$$g_2(\alpha,\beta)=\frac{\sqrt{\pi}}{4}\sum_{\mu=0}^{\infty}\frac{(-1)^\mu\left(\frac{k}{2}\right)^{\alpha+\beta+2\mu}(\alpha+\beta+2\mu)!\,\Gamma\left(\frac{\alpha+\beta-1}{2}+\mu\right)}{\mu!\,(\alpha+\beta+\mu)!\,\Gamma(\alpha+\mu+1)\Gamma(\beta+\mu+1)\Gamma\left(\frac{\alpha+\beta}{2}+\mu+1\right)}. \tag{22}$$

Using the two formulae (21) and (22), we obtain the following results,

$$G_{00}{}^{1/2}=\frac{1}{4}-\frac{1}{12}\left(\frac{k}{2}\right)^2+\left(\frac{1}{32}\log\frac{k}{2}+\frac{b_1}{64}\right)\left(\frac{k}{2}\right)^4+O(k^6\cdot\log k)+i\left\{\frac{\pi}{64}\left(\frac{k}{2}\right)^4+O(k^6)\right\}$$

$$G_{01}{}^{1/2}=-\frac{1}{96}\left(\frac{k}{2}\right)^2-\frac{1}{480}\left(\frac{k}{2}\right)^4+O(k^6\cdot\log k)+iO(k^6)$$

$$G_{11}{}^{1/2}=\frac{1}{8}-\frac{1}{120}\left(\frac{k}{2}\right)^2-\frac{1}{1920}\left(\frac{k}{4}\right)^4+O(k^6\cdot\log k)+iO(k^6)$$

$$G_{02}{}^{1/2}=-\frac{1}{16\cdot 6!}\left(\frac{k}{2}\right)^4+O(k^6)+iO(k^6)$$

$$G_{12}{}^{1/2}=-\frac{1}{480}\left(\frac{k}{2}\right)^2-\frac{1}{2\cdot 7!}\left(\frac{k}{2}\right)^4+O(k^6)+iO(k^{10})$$

$$G_{22}{}^{1/2}=\frac{1}{12}-\frac{12}{7!}\left(\frac{k}{2}\right)^2-\frac{36}{16\cdot 8!}\left(\frac{k}{2}\right)^4+O(k^6)+iO(k^{12}),$$

and

$$G_{00}{}^{-1/2}=\frac{1}{2}+\left(\frac{1}{2}\log\frac{k}{2}+\frac{a_2}{4}\right)\left(\frac{k}{2}\right)^2-\left(\frac{1}{8}\log\frac{k}{2}+\frac{a_3}{16}\right)\left(\frac{k}{2}\right)^4+O(k^6\cdot\log k)$$
$$+i\left\{\frac{\pi}{4}\left(\frac{k}{2}\right)^2-\frac{\pi}{16}\left(\frac{k}{2}\right)^4+O(k^6)\right\}^*$$

$$G_{01}{}^{-1/2}=-\frac{1}{24}\left(\frac{k}{2}\right)^2+\left(\frac{1}{48}\log\frac{k}{2}+\frac{a_4}{96}\right)\left(\frac{k}{2}\right)^4+O(k^6\cdot\log k)+i\left\{\frac{\pi}{96}\left(\frac{k}{2}\right)^4+O(k^6)\right\}$$

$$G_{11}{}^{-1/2}=\frac{1}{6}-\frac{1}{48}\left(\frac{k}{2}\right)^2-\frac{1}{320}\left(\frac{k}{2}\right)^4+O(k^6\cdot\log k)+iO(k^6)$$

* $G_{n\nu}{}^{-1/2}$ is denoted by $G_{n\nu}{}^{*-1/2}$, and k by γ in the paper B. $\pi/48(\gamma/2)^4$ in the expression of $G_{00}{}^{*-1/2}$ (B. p. 196) is incorrect, and to be replaced $\pi/16(k/2)^4$.

$$G_{02}^{-1/2}=-\frac{1}{1920}\left(\frac{k}{2}\right)^4+O(k^6\cdot\log k)+iO(k^6)$$

$$G_{12}^{-1/2}=-\frac{1}{240}\left(\frac{k}{2}\right)^2-\frac{1}{2880}\left(\frac{k}{2}\right)^4+O(k^6)+iO(k^8)$$

$$G_{22}^{-1/2}=\frac{1}{10}-\frac{1}{240}\left(\frac{k}{2}\right)^2-\frac{1}{6720}\left(\frac{k}{2}\right)^4+O(k^6)+iO(k^{10}),$$

where

$$b_1=-\psi(1)-3\psi(3)+\psi(5)+\psi(-\tfrac{1}{2})=-0.6484$$

$$a_2=-\psi(1)-3\psi(2)+\psi(3)+\psi(\tfrac{1}{2})=-1.7317$$

$$a_3=-\psi(2)-3\psi(3)-\psi(4)+2\psi(5)+\psi(-\tfrac{1}{2})=-1.3983$$

$$a_4=-\psi(1)-\psi(2)-\psi(3)-\psi(4)+\psi(5)+\psi(-\tfrac{1}{2})=-0.4817\,.$$

The method of calculation of $X_{n\nu}{}^m$ from $G_{n\nu}{}^m$ is as follows*. We have

$$X_{n\nu}{}^m=\sum_{p=0}^{\infty}X_{n\nu}{}^{m(p)}\,,$$

where

$$X_{nn}{}^{m(0)}=-\frac{1}{G_{nn}{}^m}\,,\qquad X_{n'n}{}^{m(0)}=\frac{-G_{nn'}{}^m}{G_{n'n'}{}^m}X_{nn}{}^{m(0)}\qquad(n'\neq n)$$

and

$$X_{nn}{}^{m(p)}=-\frac{1}{G_{nn}{}^m}\sum_{s=0}^{\infty}{}'\,X_{ns}{}^{m(p-1)}G_{sn}{}^m\,,$$

$$X_{n'n}{}^{m(p)}=-\frac{G_{nn'}{}^m}{G_{n'n'}{}^m}X_{nn}{}^{m(p)}-\frac{1}{G_{n'n'}{}^m}\sum_{s=0}^{\infty}{}'\,X_{sn}{}^{m(p-1)}G_{sn'}{}^m\,,\qquad(p=1,\ 2,\ 3,\ \cdots)$$

Σ' denoting the omission of the terms $s=n$ and $s=n'$.

By the above mentioned method we obtain $X_{n\nu}{}^m$ as follows,

$$-X_{00}{}^{1/2}=4+\frac{4}{3}\left(\frac{k}{2}\right)^2+\left(\frac{33}{72}-\frac{1}{2}\log\frac{k}{2}-\frac{b_1}{4}\right)\left(\frac{k}{2}\right)^4+O(k^6\cdot\log k)+i\left\{-\frac{\pi}{4}\left(\frac{k}{2}\right)^4+O(k^6)\right\}$$

$$-X_{01}{}^{1/2}=-\frac{1}{3}\left(\frac{k}{2}\right)^2-\frac{1}{5}\left(\frac{k}{2}\right)^4+O(k^6\cdot\log k)+iO(k^6)$$

$$-X_{11}{}^{1/2}=8+\frac{8}{15}\left(\frac{k}{2}\right)^2+\frac{1}{10}\left(\frac{k}{2}\right)^4+O(k^6\cdot\log k)+iO(k^6)$$

$$-X_{00}{}^{-1/2}=2-\left(2\log\frac{k}{2}+a_2\right)\left(\frac{k}{2}\right)^2+\left\{\frac{1^{**}}{24}-\frac{\pi^2}{2}+\frac{1}{2}\log\frac{k}{2}+\frac{a_3}{4}+\frac{1}{2}\left(2\log\frac{k}{2}+a_2\right)^2\right\}\left(\frac{k}{2}\right)^4$$

---

* See paper *A*, S. 201.

** $-X_{n\nu}{}^{-1/2}$ in the present paper corresponds to $X_{n\nu}{}^*$ in the paper *B*, because $\sum_{\nu=0}^{\infty}G_{n\nu}{}^{-1/2}X_{\nu s}{}^{-1/2}=-\delta_{sn}$ is used instead of $\sum_{\nu=0}^{\infty}G_{n\nu}{}^{*-1/2}X_{\nu s}{}^*=\delta_{sn}$. $19/240+\pi^2/2$ in the expression of $X_{00}{}^*$ in *B* is incorrect, and to be replaced by $1/2-\pi^2/2$.

$$+i\left\{-\pi\left(\frac{k}{2}\right)^2+\left(\frac{\pi}{4}+2\pi\log\frac{k}{2}+\pi a_2\right)\left(\frac{k}{2}\right)^4\right\}+O(k^6\cdot\log k)+iO(k^6)$$

$$-X_{01}^{-1/2}=-\frac{1}{2}\left(\frac{k}{2}\right)^2+\left(-\frac{1}{16}+\frac{3}{4}\log\frac{k}{2}+\frac{a_2}{4}+\frac{a_4}{8}\right)\left(\frac{k}{2}\right)^4+O(k^6\cdot\log k)+i\left\{\frac{3\pi}{8}\left(\frac{k}{2}\right)^4+O(k^6)\right\}^*$$

$$-X_{11}^{-1/2}=6+\frac{3}{4}\left(\frac{k}{2}\right)^2+\frac{27}{80}\left(\frac{k}{2}\right)^4+O(k^6\cdot\log k)+iO(k^6)\,.$$

§ 4. Acoustic Field at Large Distance from the Source

It is shown in paper A, p. 202, that

$$\int_0^\infty \frac{J_m(\rho\xi)J_{m+2n+(3/2)}(\xi)}{\sqrt{\xi}}\exp(-\sqrt{\xi^2-k^2}\,z)d\xi$$
$$=-\sqrt{\frac{2}{\pi}}\sum_{s=0}^{\infty}\frac{(-1)^s}{s!\,2^{m+2n-(3/2)+2s}\Gamma(m+2n+s+\frac{5}{2})}\frac{1}{\rho^m}\left(\frac{1}{\rho}\frac{\partial}{\partial\rho}\right)^{n+1}\rho^{2(m+n+s)}$$
$$\cdot\frac{\partial}{\partial z}e^{i(\pi/2)(m+n+s+(1/2))}\left(\frac{k}{r}\right)^{m+n+s+(1/2)}K_{-(m+n+s+(1/2))}(ikr)\,, \tag{23}$$

where $r=\sqrt{z^2+\rho^2}$.

For large distance r, using

$$H_\nu^{(1)}(z)\doteqdot\left(\frac{2}{\pi z}\right)^{1/2}\exp\left\{i\left(z-\frac{1}{2}\nu\pi-\frac{1}{4}\pi\right)\right\}$$

and

$$K_\nu(z)=\frac{\pi i}{2}l^{(1/2)\nu\pi i}H_\nu^{(1)}(iz)\doteqdot\sqrt{\frac{\pi}{2z}}e^{-z}\,,$$

we obtain

$$K_{-(m+n+s+(1/2))}(ih\nu)\doteqdot\sqrt{\frac{\pi}{2ikr}}e^{-ikr}\,.$$

Then we have

$$\int_0^\infty \frac{J_m(\rho\xi)J_{(m+2n+(3/2))}(\xi)}{\sqrt{\xi}}\exp(-\sqrt{\xi^2-k^2}\,z)d\xi$$
$$\doteqdot(i)^{m+1}k\cos\theta\,\frac{e^{-ikr}}{r}\sum_{s=0}^{\infty}\frac{(-1)^s k^{m+2n+2s}(\sin\theta)^{m+2n+2s}}{s!\,2^{m+2n+(3/2)+2s}\Gamma(m+2n+s+\frac{5}{2})}$$
$$\cdot\sum_{\nu=0}^{n+s}\frac{1}{\nu!}\frac{(n+s)!}{(n+s-\nu)!}\cdot\frac{(m+n+s)!}{(m+n+s-\nu)!}\left(-\frac{ik}{2}\right)^{-\nu}\frac{1}{r^\nu(\sin\theta)^{2\nu}}\,, \tag{24}$$

where $\rho/r=\sin\theta$, and θ denotes the angle between the normal to the ribbon plate and the vector from the middle line of plate to any point in the field.

For the point where r is large, taking only the term $\nu=0$ from the above formula, we have

$$\int_0^\infty \frac{J_m(\rho\xi)J_{m+2n+(3/2)}(\xi)}{\sqrt{\xi}}\exp(-\sqrt{\xi^2-k^2}\,z)d\xi\doteqdot(i)^{m+1}k\cos\theta\,\frac{e^{-ikr}}{r}\,\frac{J_{m+2n+(3/2)}(k\sin\theta)}{(k\sin\theta)^{3/2}}\,. \tag{25}$$

Using (25) and (3), we have

---

* $X_{01}^*=\frac{1}{2}\left(\frac{\gamma}{2}\right)^2-\left(-\frac{1}{16}+\frac{3}{8}\log\frac{\gamma}{2}+\frac{a_2}{4}+\frac{a_4}{8}\right)\left(\frac{\gamma}{2}\right)^4+O(\gamma^6\cdot\log\gamma)-i\left\{\frac{3\pi}{8}\left(\frac{\gamma}{2}\right)^4+O(\gamma^6)\right\}$

in B is incorrect, and to be replaced by the expression for $-X_{01}^{-1/2}$.

$$\Phi=\mp\sqrt{\rho}\,k\cos\theta\cdot\frac{e^{-ikr}}{r}i^{1/2}\sum_{n=0}^{\infty}\left\{A_n^{1/2}i\frac{J_{(1/2)+2n+(3/2)}(k\sin\theta)}{(k\sin\theta)^{3/2}}+A_n^{-1/2}\frac{J_{-(1/2)+2n+(3/2)}(k\sin\theta)}{(k\sin\theta)^{3/2}}\right\}.$$

Then the velocity potential at large distance from the middle line of the ribbon plate is given by the equation

$$\Phi=\mp i^{1/2}k\cos\theta\cdot\sin^{1/2}\theta\,\frac{e^{-ikr}}{\sqrt{r}}\sum_{n=0}^{\infty}\left\{iA_n^{1/2}\frac{J_{2n+2}(k\sin\theta)}{(k\sin\theta)^{3/2}}+A_n^{-1/2}\frac{J_{2n+1}(k\sin\theta)}{(k\sin\theta)^{3/2}}\right\}. \tag{26}$$

Obviously the sound wave becomes a cylindrical wave and its amplitude depends on the two-dimensional distribution of the source of vibration.

§ 5. Pressure on the Ribbon Plate

Denoting by σ the density of air, we can calculate the intensity of pressure $pe^{i\omega t}$ on the ribbon plate by the following formula:

$$p=i\omega\sigma(\Phi)_{z=0}=\mp i\omega\sigma\sqrt{\rho}\sum_{n=0}^{\infty}\left\{A_n^{1/2}\int_0^{\infty}\frac{J_{1/2}(\rho\xi)J_{(1/2)+2n+(3/2)}(\xi)}{\sqrt{\xi}}d\xi\right.$$
$$\left.+A_n^{-1/2}\int_0^{\infty}\frac{J_{-1/2}(\rho\xi)J_{-(1/2)+2n+(3/2)}(\xi)}{\sqrt{\xi}}d\xi\right\}. \tag{27}$$

It is shown in reference (6), p. 199, that

$$\int_0^{\infty}\frac{J_\mu(\rho\xi)J_\nu(\xi)}{\xi^\lambda}d\xi=\rho^\mu\frac{\Gamma\{(\mu+\nu+1-\lambda)/2\}}{2^\lambda\Gamma(\mu+1)\Gamma\{(\lambda+\nu+1-\mu)/2\}}F\left\{\frac{\mu+\nu+1-\lambda}{2},\ \frac{\mu+1-\lambda-\nu}{2},\ \mu+1,\ \rho^2\right\}.$$
$$\left(x=\rho^2\leqq 1,\ \ \rho=\frac{y}{a}\right).$$

Setting

$$S_n^m(y,0)=\sqrt{\frac{y}{a}}\int_0^{\infty}\frac{J_m(y/a\cdot\xi)J_{m+2n+(3/2)}(\xi)}{\sqrt{\xi}}d\xi,$$

we have

$$S_n^{-1/2}(y,0)=\sqrt{\frac{2}{\pi}}\frac{1}{(2n+1)}(1-\rho^2)F\left(-n,\ n+1,\ \frac{1}{2},\ \rho^2\right)$$
$$=\frac{\sqrt{2}}{\Gamma(n+\frac{1}{2})}\frac{1}{2n+1}x^{1/2}\frac{d^n}{dx^n}\{x^{n-(1/2)}(1-x)^{n+(1/2)}\}=\frac{1}{2n+1}(1-x)^{1/2}v_n^{-1/2}(x),$$

$$S_n^{1/2}(y,0)=\sqrt{\frac{2}{\pi}}\rho(1-\rho^2)^{1/2}F\left(-n,\ n+2,\ \frac{3}{2},\ \rho^2\right)$$
$$=\frac{1}{\sqrt{2}}\frac{1}{\Gamma(n+\frac{3}{2})}\frac{d^n}{dx^n}\{x^{n+(1/2)}(1-x)^{n+(1/2)}\}=\frac{1}{2(n+1)}\sqrt{x}(1-x)^{1/2}v_n^{1/2}(x).$$

Therefore by the equation (27) we obtain, as the pressure on the ribbon plate,

$$p=\mp i\omega\sigma\sum_{n=0}^{\infty}\left\{A_n^{1/2}\frac{1}{2(n+1)}\sqrt{x}(1-x)^{1/2}v_n^{1/2}(x)+A_n^{-1/2}\frac{1}{2n+1}(1-x)^{1/2}v_n^{-1/2}(x)\right\}$$
$$=\mp i\omega\sigma\sum_{n=0}^{\infty}\left\{A_n^{1/2}\frac{1}{2(n+1)}\rho(1-\rho^2)^{1/2}v_n^{1/2}(\rho^2)+A_n^{-1/2}\frac{1}{2n+1}(1-\rho^2)^{1/2}v_n^{-1/2}(\rho^2)\right\}, \tag{28}$$

or we can express p in another form,

$$p=\mp i\omega\sigma\sum_{n=0}^{\infty}\left[A_n^{-1/2}\frac{\sqrt{2}}{\Gamma(n+\frac{1}{2})}\frac{1}{2n+1}x^{1/2}\frac{d^n}{dx^n}\{x^{n-(1/2)}(1-x)^{n+(1/2)}\}\right.$$
$$\left.+A_n^{1/2}\frac{1}{\sqrt{2}}\frac{1}{\Gamma(n+\frac{3}{2})}\frac{d^n}{dx^n}\{x^{n+(1/2)}(1-x)^{n+(1/2)}\}\right]. \tag{29}$$

The total pressure are unit length, P, on the ribbon plate is expressed as follows,

$$P=\int_{-a}^{a}(p_{z=+0}-p_{z=-0})dy=a\int_{-1}^{1}(p_{z=+0}-p_{z=-0})d\rho\,. \tag{30}$$

Owing to the formula (29), we have

$$P=-2i\omega\sigma a\sum_{n=0}^{\infty}\left[A_n^{-1/2}\frac{\sqrt{2}}{\Gamma(n+\frac{1}{2})}\frac{1}{2n+1}\int_{-1}^{1}x^{1/2}\frac{d^n}{dx^n}\{x^{n-(1/2)}(1-x)^{n+(1/2)}\}d\rho\right.$$
$$\left.+A_n^{1/2}\frac{1}{\sqrt{2}}\frac{1}{\Gamma(n+\frac{3}{2})}\int_{-1}^{1}\frac{d^n}{dx^n}\{x^{n+(1/2)}(1-x)^{n+(1/2)}\}d\rho\right].$$

In the above formula the first series corresponds to an integration of even terms, and the second series corresponds to odd terms, so that the value of second vanishes; accordingly we obtain the following expression

$$P=-2i\omega\sigma a\sum_{n=0}^{\infty}A_n^{-1/2}\frac{\sqrt{2}}{\Gamma(n+\frac{1}{2})}\frac{1}{2n+1}\int_{-1}^{1}x^{1/2}\frac{d^n}{dx^n}\{x^{n-(1/2)}(1-x)^{n+(1/2)}\}d\rho\,.$$

The integral for $n=0$ has the value $\pi/2$ and has the value zero for $n=1, 2, 3, \cdots$, so that we have

$$P=-i\omega\sigma a\sqrt{\frac{\pi}{2}}A_0^{-1/2}\,. \tag{31}$$

§ 6. Power of Radiation

The total power radiated per unit length is given by the real part of the quantity,

$$W=2a\int_{-1}^{1}\frac{p\tilde{v}}{2}d\rho\,. \tag{32}$$

Here $\sim$ means conjugate complex.

The velocity of the air on the ribbon plate, v is given by the following formula

$$v=\frac{1}{a}\{f_e(\rho)+f_0(\rho)\}=\frac{1}{a}\left\{\sum_{m=0}^{\infty}a_m^{-1/2}v_m^{-1/2}(x)+\sqrt{x}\sum_{m=0}^{\infty}a_m^{1/2}v_m^{1/2}(x)\right\},$$

but at substitution of the expressions of p and $\tilde{v}$ in (32), we may only use the even term of $p\cdot\tilde{v}$. The even term takes the form,

$$\left(\frac{p\cdot\tilde{v}}{2}\right)_{\text{even}}=-\frac{1}{2a}i\omega\sigma\left\{\left(\sum_{m=0}^{\infty}\tilde{a}_m^{-1/2}v_m^{-1/2}(x)\right)\left(\sum_{n=0}^{\infty}A_n^{-1/2}\frac{1}{2n+1}(1-x)^{1/2}v_n^{-1/2}(x)\right)\right.$$
$$\left.+\left(\sqrt{x}\sum_{m=0}^{\infty}\tilde{a}_m^{1/2}v_m^{1/2}(x)\right)\left(\sum_{m=0}^{\infty}A_n^{1/2}\frac{1}{2(n+1)}\sqrt{x}(1-x)^{1/2}v_n^{1/2}(x)\right)\right\}.$$

Using (see Appendix)

$$2\int_0^1(1-x)^{1/2}v_m^{-1/2}(x)v_n^{-1/2}(x)d\rho=\delta_{mn}$$

$$2\int_0^1 x(1-x)^{1/2}v_m^{1/2}(x)v_n^{1/2}(x)d\rho=\delta_{mn}\,,$$

we have

$$W=4a\int_0^1\left(\frac{p\tilde{v}}{2}\right)_{\text{even}}d\rho=-i\omega\sigma\sum_{m=0}^{\infty}\left\{\tilde{a}_m^{-1/2}A_m^{-1/2}\frac{1}{2m+1}+\tilde{a}_m^{1/2}A_m^{1/2}\frac{1}{2(m+1)}\right\}. \tag{33}$$

§ 7. Conclusion

The unknown coefficients $A_n^{1/2}$ and $A_n^{-1/2}$ in the formula (3) giving the velocity potential are determined from the equation (16) in terms of the coefficients $a_n^{1/2}$ and $a_n^{-1/2}$ in the expansion of the velocity distribution (4) in a series of hypergeometric polynomials. The solution of equation (16) is obtained from (18) using the tables for $X_{n\nu}^{1/2}$ and $X_{n\nu}^{-1/2}$ which is a solution of equation (17). Therefore, if we determine the coefficients $a_n^{1/2}$ and $a_n^{-1/2}$ by the formula (8) from the velocity distribution on the ribbon plate, we obtain a solution of the problem.

But these tables are given in the present paper only for small values of k. We intend to publish the tables of $X_{n\nu}^m$ in the next report II.

At large distance, the velocity potential is given by the formula (26) and it expresses a cylindrical wave. The deviation of the amplitude from the $\cos\theta$-distribution depenes upon the wave length and the distribution of the vibrating sources. For the direction $\theta=0$, the odd part of the velocity distribution function does not contribute to the velocity potential at large distance.

In the end we indicated a method of calculation for the power of radiation from the vibrating plate.

Appendix

We have (see reference (6), p. 201)

$$v_n^m(x)=\frac{\sqrt{2}\,\Gamma(m+n+\frac{3}{2})}{n!\,\Gamma(m+n+1)}x^{-m}(1-x)^{-1/2}\frac{d^n}{dx^n}\{x^{m+n}(1-x)^{n+(1/2)}\}$$

$$\cdot\int_0^1 x^m(1-x)^{1/2}v_n^m(x)v_{n'}^m(x)dx=0 \qquad n'\neq n$$

$$=\frac{2\Gamma(n+\frac{3}{2})\Gamma(m+n+\frac{3}{2})}{(m+2n+\frac{3}{2})n!\,\Gamma(m+n+1)} \qquad n'=n$$

Using above formulas, and taking $m=(-1)/2$, $+1/2$ and $x=\rho^2$,

$$2\int_0^1(1-x)^{1/2}v_n^{-1/2}(x)v_n^{-1/2}(x)d\rho=\int_0^1 x^{-1/2}(1-x)^{1/2}v_n^{-1/2}(x)v_n^{-1/2}(x)dx$$

$$=\frac{2\Gamma(n+\frac{3}{2})\Gamma(-\frac{1}{2}+n+\frac{3}{2})}{(-\frac{1}{2}+2n+\frac{3}{2})n!\,\Gamma(-\frac{1}{2}+n+1)}=1\,,$$

$$2\int_0^1 x(1-x)^{1/2}v_n^{1/2}(x)v_n^{1/2}(x)d\rho=\int_0^1 x^{1/2}(1-x)^{1/2}v_n^{1/2}(x)v_n^{1/2}(x)dx$$

$$=\frac{2\Gamma(n+\frac{3}{2})\Gamma(\frac{1}{2}+n+\frac{3}{2})}{(\frac{1}{2}+2n+\frac{3}{2})\cdot n!\cdot\Gamma(\frac{1}{2}+n+1)}=1\,.$$

References

1) Y. Nomura and N. Kawai: Sci. Rep. Tôhoku Univ. (I) **33** (1949) 197. On the acoustic field by a vibrating source arbitrarily distributed on a plane circular plate. [which is denoted by paper *A* in the present paper].
2) Y. Nomura and N. Kawai: ibid. (I) **33** (1949) 208. On the radiation of sound wave from a vibrating plane circular plate with a fixed circular baffle.
3) N. Kawai: ibid. (I) **35** (1952) 210. On the theory of Rayleigh disc.
4) Y. Nomura and S. Katsura: Jour. Phys. Soc. Japan **10** (1955) 285. Diffraction of electromagnetic waves by circular plate and circular hole.
5) Y. Nomura and S. Katsura: ibid. **12** (1957) 190. Diffraction of electromagnetic waves by

ribbon and slit I. [which is denoted by paper *B* in the present paper].
6) I. Kobayashi: Sci. Rep. Tôhoku Imp. Univ. (I) **20** (1931) 197. Darstellung eines Potentials in zylindrischen Koordinaten, das sich auf einer Ebene innerhalb und ausserhalb einer gewissen Kreisbegrenzung verschiedener Grenzbedingung unterwirft.
7) M. Lax and H. Feshbach: J. Acoust. Soc. Amer. **19** (1947) 682. On the radiation problem at high frequency.
8) J. Pachner: ibid. **23** (1951) 198. On the acoustical radiation of an emitter vibrating freely or in a wall of finite dimensions.
9) H. L. Oestreicher: ibid. **29** (1957) 1219. Representation of the field of an acoustic source as a series of multipole fields.

JOURNAL OF THE PHYSICAL SOCIETY OF JAPAN Vol. 13, No. 11, NOVEMBER, 1958

A New Approach to the Theory of Slender Body in Compressible Flow

By Haruo MORIGUCHI

Department of Physics, Faculty of Liberal Arts, Shizuoka University, Shizuoka

(Received July 26, 1958)

It is shown that the equation of perturbation given to a known two-dimensional or axisymmetric flow of compressible fluid can be written in a simple form by choosing appropriate coordinates.

From an approximate solution of this equation in the case of a slender body, we can deduce a velocity transformation formula

$$\int_U^q \frac{\sqrt{1-q^2/c^2}}{q}\,dq=\log\left(\frac{q}{U}\right)_i,$$

where q, c and U are the velocity of fluid at an arbitrary point on the surface of the body, the local velocity of sound and the velocity of free stream (the critical speed of sound being taken as the unit of velocity), and $(q/U)_i$ is the velocity of incompressible flow at the same point taking the velocity of free stream as unit.

Though this result has been given earlier by Imai in two-dimensional case and by Kusukawa in axisymmetric case, our deduction gives it as a first approximate solution which could be refined by a procedure of successive approximations. It is also expected that the perturbation equation will play some important role in mathematical discussion on mixed flow problems.

§ 1. Introduction

For treating subsonic flow of a compressible fluid past a slender body, methods of successive approximations, starting from the Prandtl-Glauert rule as a first approximation, are often used, and especially in the two-dimensional case some examples, e.g. elliptic cylinders[1] and circular arc aerofoils[2], have been worked out to higher-order approximations. These methods, however, are believed to be unsuitable for treating such flows as involving nearly sonic speeds.

Imai[3),4),5)] offered a new procedure to treat the two-dimensional flow and deduced a transformation formula which gives the velocity of compressible flow directly from the velocity of the corresponding incompressible flow, and Kusukawa[6),7)] extended the formula to the case of axisymmetric flow. Though these methods seem to represent the flow pattern more precisely than the usual slender body theory, the prescribed boundary conditions cannot always be satisfied exactly, and it is not clear how to proceed to higher-order ap-

proximations.

In this paper, we first give a simple representation of the perturbations for a flow of compressible fluid and then, in the case of a slender body, we find approximate solutions which satisfy the exact boundary conditions and show that our result leads immediately to Imai's formula.

Our perturbation equation is essentially the same as the usual one which, for example, has been used by Bers[8] in the discussion of mixed flow problems, but is expressed in a more simplified form by a suitable choice of independent variables. Therefore we may expect that our equation can play some important role in the mathematical discussion on transonic flow.

The higher-order approximations for our equation may be found by the usual method of iteration. But it seems difficult to find an analytical formula which covers a wide range of Mach number.

We shall treat the two-dimensional case in §§2~5 and axisymmetric case in §6, and show the slide rule technique for the calculation of velocity in §7.

§2. Fundamental Equations in Two-dimensional Case

The two-dimensional irrotational flow of a compressible fluid is governed by the equations:

$$u=\frac{\partial\Phi}{\partial x}=\frac{1}{\mathrm{P}}\frac{\partial\Psi}{\partial y}, \tag{2.1}$$

$$v=\frac{\partial\Phi}{\partial y}=-\frac{1}{\mathrm{P}}\frac{\partial\Psi}{\partial x}, \tag{2.2}$$

$$\mathrm{P}=\left(\frac{\gamma+1}{2}-\frac{\gamma-1}{2}Q^2\right)^{1/(\gamma-1)}, \tag{2.3}$$

$$Q^2=u^2+v^2, \tag{2.4}$$

where (u, v) are the component velocities in the x- and y-directions, Q is the magnitude of velocity, P is the density, Φ is the velocity potential, Ψ is the stream function, and γ is the ratio of specific heats. In these as well as in the following expressions we take as units the values at the critical state where the local velocity of sound C is equal to flow velocity Q. For the local velocity of sound we have

$$C^2=\frac{\gamma+1}{2}-\frac{\gamma-1}{2}Q^2. \tag{2.5}$$

Let us suppose that the solution for a uniform flow of free stream velocity U past a given obstacle is already known:

$$u_0=\frac{\partial\varphi}{\partial x}=\frac{1}{\rho}\frac{\partial\psi}{\partial y}, \tag{2.6}$$

$$v_0=\frac{\partial\varphi}{\partial y}=-\frac{1}{\rho}\frac{\partial\psi}{\partial x}, \tag{2.7}$$

$$\rho=\left(\frac{\gamma+1}{2}-\frac{\gamma-1}{2}q^2\right)^{1/(\gamma-1)}, \tag{2.8}$$

$$q^2=u_0^2+v_0^2, \tag{2.9}$$

and choose φ and ψ as independent variables. Then the fundamental equations can be written as

$$\frac{\partial\Phi}{\partial\varphi}=\frac{\rho}{\mathrm{P}}\frac{\partial\Psi}{\partial\psi}, \tag{2.10}$$

$$\frac{\partial\Phi}{\partial\psi}=-\frac{1}{\rho\mathrm{P}}\frac{\partial\Psi}{\partial\varphi}. \tag{2.11}$$

The relations between (x, y) and (φ, ψ) are given by (2.6), (2.7) and the inverse relations:

$$\frac{\partial x}{\partial\varphi}=\frac{u_0}{q^2}, \tag{2.12}$$

$$\frac{\partial y}{\partial\varphi}=\frac{v_0}{q^2}, \tag{2.13}$$

$$\frac{\partial x}{\partial\psi}=-\frac{v_0}{\rho q^2}, \tag{2.14}$$

$$\frac{\partial y}{\partial\psi}=\frac{u_0}{\rho q^2}. \tag{2.15}$$

When we consider the flow of a different free stream velocity $U+\Delta U$ about the same obstacle, the boundary conditions for (2.10) and (2.11) are given by

$$\Psi=\text{const.}\quad\text{on the surface of the obstacle,} \tag{2.16}$$

and

$$\left.\begin{aligned}
&\frac{\partial\Psi}{\partial\psi}\to\frac{\mathrm{P}_\infty}{\rho_\infty}\frac{U+\Delta U}{U}, && (2.17)\\
&\frac{\partial\Phi}{\partial\varphi}\to\frac{U+\Delta U}{U}, && (2.18)\\
&\frac{\partial\Psi}{\partial\varphi}\to 0, && (2.19)\\
&\frac{\partial\Phi}{\partial\psi}\to 0, && (2.20)
\end{aligned}\right\}\ \text{at infinity,}$$

where P_∞ and ρ_∞ are the free stream density of the unknown and known flow respectively. We can put

$$\Psi=\psi=0 \tag{2.21}$$

on the surface of obstacle.

§ 3. Perturbation Equations

Now let us consider the case in which the difference ΔU is so small that Φ and Ψ are very close to φ and ψ respectively. Then we can put

$$\Phi=\varphi+\varphi' , \tag{3.1}$$
$$\Psi=\psi+\psi' , \tag{3.2}$$
$$P=p+p' , \tag{3.3}$$
$$Q=q+q' , \tag{3.4}$$

and neglect the second and higher order terms in primed quantities. Thus we have, from (1.3),

$$p'=-\frac{q\rho}{c^2}q' \tag{3.5}$$

and, from (2.1), (2.2) and (2.4),

$$q'=q\frac{\partial\varphi'}{\partial\varphi} , \tag{3.6}$$

or, making use of (2.10),

$$q'=\frac{q}{\mu^2}\frac{\partial\psi'}{\partial\psi} , \tag{3.7}$$

where

$$\mu^2=1-q^2/c^2 , \tag{3.8}$$

and c is the local velocity of sound corresponding to q. Substituting these expressions in (2.10) and (2.11) we have for φ' and ψ'

$$\mu^2\frac{\partial\varphi'}{\partial\varphi}=\frac{\partial\psi'}{\partial\psi} , \tag{3.9}$$

$$\rho^2\frac{\partial\varphi'}{\partial\psi}=-\frac{\partial\psi'}{\partial\varphi} , \tag{3.10}$$

or eliminating ψ' or φ'

$$\frac{\partial}{\partial\varphi}\left(\mu^2\frac{\partial\varphi'}{\partial\varphi}\right)+\frac{\partial}{\partial\psi}\left(\rho^2\frac{\partial\varphi'}{\partial\psi}\right)=0 , \tag{3.11}$$

$$\frac{\partial}{\partial\varphi}\left(\frac{1}{\rho^2}\frac{\partial\psi'}{\partial\varphi}\right)+\frac{\partial}{\partial\psi}\left(\frac{1}{\mu^2}\frac{\partial\psi'}{\partial\psi}\right)=0 . \tag{3.12}$$

These are the basic equations for our discussions.

As is seen from our deduction, when the boundary conditions for φ' and ψ' are given by

$$\left.\begin{aligned}\frac{\partial\varphi'}{\partial\psi}&=0 , &(3.13)\\ \psi'&=0 , &(3.14)\end{aligned}\right\}\ \text{on the surface}$$

and

$$\left.\begin{aligned}\frac{\partial\varphi'}{\partial\varphi}&\to\frac{1}{U} , &(3.15)\\ \frac{\partial\varphi'}{\partial\psi}&\to 0 , &(3.16)\\ \frac{\partial\psi'}{\partial\psi}&\to\frac{\mu_\infty^2}{U} , &(3.17)\\ \frac{\partial\psi'}{\partial\varphi}&\to 0 , &(3.18)\end{aligned}\right\}\ \text{at infinity,}$$

where the suffix ∞ means the value at infinity, then φ' and ψ' denote respectively

$$\varphi'=\frac{\partial\varphi(x, y, U)}{\partial U} , \tag{3.19}$$

and

$$\psi'=\frac{\partial\psi(x, y, U)}{\partial U} , \tag{3.20}$$

where $\varphi(x, y, U)$ and $\psi(x, y, U)$ are the velocity potential and stream function for the flow about the given obstable with the free stream velocity U. This fact will be used in the following sections.

If we take x and y as independent variables in (3.11), then we have

$$(c^2-u_0^2)\frac{\partial^2\varphi'}{\partial x^2}-2u_0v_0\frac{\partial^2\varphi'}{\partial x\partial y}+(c^2-v_0^2)\frac{\partial^2\varphi'}{\partial y^2}$$
$$+A\frac{\partial\varphi'}{\partial x}+B\frac{\partial\varphi'}{\partial y}=0 , \tag{3.21}$$

where A and B are certain functions of x and y. This is the form which has been employed, for example, by Bers[8].

§ 4. Simple Approximate Solutions for Thin Aerofoil

In the case of a thin aerofoil where the disturbance due to the presence of the aerofoil is small, we can deduce simple approximate solutions of our equation (3.11) or (3.12).

For this purpose, let us put

$$\psi'=\mu\psi^* \tag{4.1}$$

in (3.12). Then we have

$$\frac{\partial}{\partial\varphi}\left(\frac{\mu^2}{\rho^2}\frac{\partial\psi^*}{\partial\varphi}\right)+\frac{\partial^2\psi^*}{\partial\psi^2}+J\psi^*=0 , \tag{4.2}$$

where

$$J=\mu\frac{\partial}{\partial\varphi}\left(\frac{1}{\rho^2}\frac{\partial\mu}{\partial\varphi}\right)+\mu\frac{\partial}{\partial\psi}\left(\frac{1}{\mu^2}\frac{\partial\mu}{\partial\psi}\right) . \tag{4.3}$$

The boundary conditions for ψ^* are the same as those for ψ' given by (3.14) and (3.18).

Since μ and ρ are functions of q, (4.3) can be written as

$$J=\mu\left\{\frac{\partial}{\partial\varphi}\left(\frac{\mu'}{\rho^2}\frac{\partial q}{\partial\varphi}\right)+\frac{\partial}{\partial\psi}\left(\frac{\mu'}{\mu^2}\frac{\partial q}{\partial\psi}\right)\right\} , \tag{4.4}$$

where

$$\mu'=d\mu/dq . \tag{4.5}$$

Now we have, by means of (2.12)~(2.15), the relations

$$\frac{\partial q}{\partial\varphi}=-\frac{\rho q}{\mu^2}\frac{\partial\theta}{\partial\psi} , \tag{4.6}$$

$$\frac{\partial q}{\partial \psi}=\frac{q}{\rho}\frac{\partial \theta}{\partial \psi}, \tag{4.7}$$

where

$$\theta=\tan^{-1}(v_0/u_0). \tag{4.8}$$

Eliminating θ from (4.6) and (4.7), we have

$$\frac{\partial}{\partial \varphi}\left(\frac{\mu^2}{\rho q}\frac{\partial q}{\partial \varphi}\right)+\frac{\partial}{\partial \psi}\left(\frac{\rho}{q}\frac{\partial q}{\partial \psi}\right)=0. \tag{4.9}$$

Substituting (4.9) into (4.4) we have

$$J=\left\{\frac{\mu^2}{\rho^2}\left(\frac{\partial q}{\partial \varphi}\right)^2+\left(\frac{\partial q}{\partial \psi}\right)^2\right\}j(q), \tag{4.10}$$

where

$$j(q)=\left(\frac{\mu}{\rho^2}\frac{d\rho^2}{dq}-\frac{\mu^3}{q}\right)\frac{d}{dq}\left(\frac{1}{\mu}\right)-\mu\frac{d^2}{dq^2}\left(\frac{1}{\mu}\right). \tag{4.11}$$

If the deviation from the uniform flow is small, the bracketed factor in (4.10) can be regarded as small quantity of the second order, as is obvious when we write

$$q=U+\varepsilon q_1, \tag{4.12}$$

where ε is a small parameter. Therefore in this case we can neglect J in (4.2) except the case in which there appears sonic speed which makes $j(q)$ singular, and we have an approximate solution

$$\psi^*=\text{const.}\ \psi=c_1\psi, \tag{4.13}$$

which satisfies the boundary conditions (3.14) and (3.18).

From this solution, we have, by means of (3.7) and (2.21),

$$q_s'=c_1\frac{q_s}{\mu_s} \tag{4.14}$$

for the perturbation surface velocity, where the suffix s denotes the value on the surface of the obstacle.

According to the remark given in § 3, when we put

$$c_1=\frac{\mu_\infty}{U}, \tag{4.15}$$

q_s' can be regarded as the approximate value of the partial derivative of q_s with respect to U:

$$\frac{\partial q_s}{\partial U}=\frac{\mu_\infty}{U}\frac{q_s}{\mu_s}, \tag{4.16}$$

or

$$\frac{\partial q_s}{\partial U}=\frac{\sqrt{1-U^2/c_\infty^2}}{U}\frac{q_s}{\sqrt{1-q_s^2/c_s^2}}. \tag{4.17}$$

On integration we have

$$\int_{q_s}^{1}\frac{\sqrt{1-q_s^2/c_s^2}}{q_s}dq_s=\int_U^1\frac{\sqrt{1-U^2/c_\infty^2}}{U}dU+\text{const.}, \tag{4.18}$$

where const. means a function of coordinates only.

If U tends to zero, then q_s must also tend to zero; therefore for small values of U we have

$$-\log q_s=-\log U+\text{const}. \tag{4.19}$$

This means that the constant should be equal to

$$\lim_{U\to 0}\left(-\log\frac{q_s}{U}\right)=-\log\left(\frac{q_s}{U}\right)_i, \tag{4.20}$$

where the suffix i denotes the incompressible flow. Thus we have finally

$$\int_{q_s}^{1}\frac{\sqrt{1-q_s^2/c_s^2}}{q_s}dq_s=\int_U^1\frac{\sqrt{1-U^2/c_\infty^2}}{U}dU-\log\left(\frac{q_s}{U}\right)_i, \tag{4.21}$$

which is the transformation formula given by Imai[3),4),5)].

It is to be noticed that in our deduction the boundary conditions are satisfied completely in contrast to Imai's deduction.

Further, since the functional relation between c_s and q_s is the same as that between c_∞ and U, we can rewrite (4.21) as

$$\int_U^{q_s}\frac{\sqrt{1-q^2/c^2}}{q}dq=\log\left(\frac{q_s}{U}\right)_i. \tag{4.22}$$

Similar procedure gives another approximate solution. Let us consider Eq. (3.11), and put

$$\varphi'=\frac{\varphi^*}{\mu}. \tag{4.23}$$

Then we have

$$\frac{\partial^2\varphi^*}{\partial\varphi^2}+\frac{\partial}{\partial\psi}\left(\frac{\rho^2}{\mu^2}\frac{\partial\varphi^*}{\partial\psi}\right)+K\varphi^*=0, \tag{4.24}$$

where K is a small factor of the second order as can be seen from consideration similar to that given in the preceding case. Neglecting $K\varphi^*$ we have an approximate solution:

$$\varphi^*=C_2\varphi \tag{4.25}$$

which satisfies the boundary conditions at infinity.

In this case, however, the boundary condition on the surface of the obstacle is not satisfied. The velocity potential corresponding to (4.25) may be regarded as one which represents a flow with a slightly different boundary. But when we neglect the term which contains $(\partial/\partial\psi)(1/\mu)$, (4.25) satisfies the boundary conditions and give the perturbation surface velocity in the form:

$$q_s' = C_2 \frac{q_s}{\mu_s} + C_2 \varphi_s \frac{\partial}{\partial s}\left(\frac{1}{\mu_s}\right), \tag{4.26}$$

where s means length along the surface. The first term is in accord with (4.14).

The difference between (4.14) and (4.26) can be interpreted to be due to the fact that in the velocity potential procedure the boundary conditions are only approximately satisfied while in the stream function procedure the conditions are exactly fulfilled, so that (4.14) should be regarded as superior to (4.26).

Finally a comment is added here. When we put

$$C_2 = \frac{\mu_\infty}{U}, \tag{4.27}$$

we have an approximate relation

$$\frac{\partial \varphi_s}{\partial U} = \frac{\mu(U)}{\mu(q_s)} \frac{\varphi_s}{U}, \tag{4.28}$$

where

$$\mu(q) = 1 - q^2/c^2, \tag{4.29}$$

as is seen from the remark in § 3. Since

$$q_s = \frac{\partial \varphi_s}{\partial s}, \tag{4.30}$$

we can regard (4.28) as a partial differential equation for φ_s with independent variables s and U.

§ 5. Complex Formulation of the Preceding Procedure and the Possibility of Higher-Order Approximations

We can write the procedure in a more compact form as follows.

Let us put

$$\varphi = \xi, \tag{5.1}$$

$$\psi = \frac{\rho_\infty}{\mu_\infty}\eta, \tag{5.2}$$

and use φ^* and ψ^* given by (4.1) and (4.23). Then (3.9) and (3.10) become

$$\frac{\partial \varphi^*}{\partial \eta} + \frac{\partial \psi^*}{\partial \xi} = \varphi^* \frac{\partial \alpha}{\partial \eta} - (1+\delta)\psi^* \frac{\partial \alpha}{\partial \xi} - \delta \frac{\partial \psi^*}{\partial \xi}, \tag{5.3}$$

$$\frac{\partial \varphi^*}{\partial \xi} - \frac{\partial \psi^*}{\partial \eta} = \varphi^* \frac{\partial \alpha}{\partial \xi} + \psi^* \frac{\partial \alpha}{\partial \eta}, \tag{5.4}$$

where

$$\alpha = \log \mu, \tag{5.5}$$

$$\delta = \frac{\mu^2}{\rho^2} \frac{\rho_\infty^2}{\mu_\infty^2} - 1. \tag{5.6}$$

It is to be noted that for Kármán-Tsien's gas

$$\delta = 0. \tag{5.7}$$

Further let us put

$$\varphi^* + i\psi^* = F, \tag{5.8}$$

$$\varphi^* - i\psi^* = \overline{F}, \tag{5.9}$$

$$\xi + i\eta = \zeta, \tag{5.10}$$

$$\xi - i\eta = \overline{\zeta}, \tag{5.11}$$

then (5.3) and (5.4) can be combined into

$$2\frac{\partial F}{\partial \overline{\zeta}} = 2\overline{F}\frac{\partial \alpha}{\partial \overline{\zeta}} - \frac{\delta}{2}(F - \overline{F})\left(\frac{\partial \alpha}{\partial \zeta} + \frac{\partial \alpha}{\partial \overline{\zeta}}\right) - \frac{\delta}{2}\left(\frac{\partial F}{\partial \zeta} - \frac{\partial \overline{F}}{\partial \zeta} + \frac{\partial F}{\partial \overline{\zeta}} - \frac{\partial \overline{F}}{\partial \overline{\zeta}}\right), \tag{5.12}$$

and the approximate solutions given in the preceding section are the imaginary and real parts of

$$F_0 = C_0 \zeta, \tag{5.13}$$

which is a solution of approximate equation obtainable when we neglect the right-hand side of (5.12).

At first sight F_0 would seem to be an approximation neglecting the small quantities of the first order, but as we have shown in the preceding section, (5.13) gives a higher approximate solution.

Now we can see the possibility of successive approximations starting from (5.13), although the procedure of calculation is a problem left to future.

§ 6. The Case of Axisymmetric Flow

The fundamental equations for axisymmetric flow are

$$u = \frac{\partial \Phi}{\partial x} = \frac{1}{\mathrm{P}y}\frac{\partial \Psi}{\partial y}, \tag{6.1}$$

$$v = \frac{\partial \Phi}{\partial y} = -\frac{1}{\mathrm{P}y}\frac{\partial \Psi}{\partial x}, \tag{6.2}$$

where x and y are the coordinates parallel and perpendicular to the axis of symmetry, u and v are the component velocities in the x- and y-directions, Φ is the velocity potential, Ψ is Stokes' stream function and other quantities are the same as those in the two-dimensional case.

If we know a flow represented by φ and ψ, we can write the fundamental equations as

$$\frac{\partial \Phi}{\partial \varphi} = \frac{\rho}{\mathrm{P}}\frac{\partial \Psi}{\partial \psi}, \tag{6.3}$$

$$\frac{\partial \Phi}{\partial \psi} = -\frac{1}{\rho \mathrm{P}}\frac{1}{y^2}\frac{\partial \Psi}{\partial \varphi}, \tag{6.4}$$

and the perturbation equations for

$$\varphi' = \Phi - \varphi\,, \tag{6.5}$$

$$\psi' = \Psi - \psi \tag{6.6}$$

can be deduced in a similar way to that in § 4:

$$\frac{\partial}{\partial\varphi}\left(\mu^2\frac{\partial\varphi'}{\partial\varphi}\right)+\frac{\partial}{\partial\psi}\left(\rho^2y^2\frac{\partial\varphi'}{\partial\psi}\right)=0\,, \tag{6.7}$$

$$\frac{\partial}{\partial\varphi}\left(\frac{1}{\rho^2y^2}\frac{\partial\psi'}{\partial\varphi}\right)+\frac{\partial}{\partial\psi}\left(\frac{1}{\mu^2}\frac{\partial\psi'}{\partial\psi}\right)=0\,, \tag{6.8}$$

which coorrespond respectively (3.11) and (3.12).

These equations are of the same forms as (3.11) and (3.12) except that (6.7) and (6.8) have ρ^2y^2 in place of ρ^2 in (3.11) and (3.12).

Accordingly we get the same approximate solutions and velocity transformation formula as in § 4.

The velocity transformation formula for the case of axisymmetric flow has been derived by Kusukawa[6),7)] in a different way. As he has also pointed out, in this case the neglected term corresponding to J in (4.2) or K in (4.24) is a small quantity of the first order, whereas it was of the second order in the two-dimensional case.

§ 7. Slide Rule for the Calculation of Velocity

As is seen from the form of (4.22), our formula permits slide rule calculations, when we know the velocity distribution at a certain Mach number, for example, at zero Mach number. In this section such a slide rule is considered.

Fig. 1 shows the slide rule for the flow of adiabatic gas with $\gamma=1.4$. On the A-rule the value of q is marked at the point where the distance from the mark q_0 is

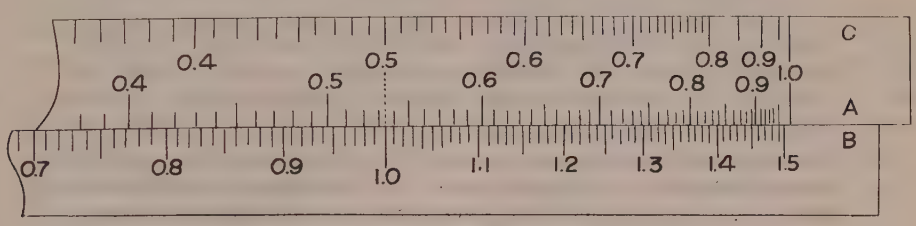

Fig. 1. Slide rule for calculation of velocity.

$$\int_{q_0}^{q}\frac{\sqrt{1-q^2/c^2}}{q}dq\,,$$

where q_0 is a proper standard value. On the B-rule the value of $(q/U)_i$ is marked at the point where the distance from the mark 1 is

$$\log\,(q/U)_i\,.$$

The graduation C denotes the Mach number corresponding to the free stream velocity graduated on the A-rule.

Now let us find the velocity at a point on the aerofoil, where the velocity for incompressible flow is $(q/U)_i$. We should make the mark 1 on the B-rule in line with the mark U or mark M on the A or C-graduation, where U or M means the velocity of free stream or Mach number of the flow required.

Then the mark on A-rule, which is in line with $(q/U)_i$ on B-rule is the velocity required. Of course the critical speed is taken as the unit of velocity.

Fig. 1 shows the corresponding relations between the incompressible flow and the flow of Mach number 0.5; if, for example, $(q/U)_i$ is 1.1, then at such a point q is 0.598 when the Mach number is 0.5.

Acknowledgements

The author wishes to express his sincere thanks to Professor I. Imai of the University of Tokyo who kindly read the manuscript and gave him much valuable advice after continued encouragement, and to the members of Professor Imai's seminar for their useful discussions.

The author is indebted to the Ministry of Education for a grant.

References

1) Y. Matsunobu: J. Phys. Soc. Japan **12** (1957) 72.
2) S. Asaka: J. Phys. Soc. Japan **10** (1955) 482.
3) I. Imai: J. Phys. Soc. Japan **3** (1948) 352.
4) I. Imai: J. Math. Phys. **28** (1949) 173.
5) I. Imai and H. Hasimoto: J. Math. Phys. **28** (1950) 205.

6) K. Kusukawa: J. Phys. Soc. Japan **9** (1954) 605.
7) K. Kusukawa: J. Phys. Soc. Japan **10** (1955) 1093.
8) L. Bers: Comm. Pure and Appl. Math. **7** (1954) 79.

JOURNAL OF THE PHYSICAL SOCIETY OF JAPAN Vol. 13, No. 11, NOVEMBER, 1958

Attenuation of Ultrasonic Waves in Suspensions of Viscoelastic Spheres

By Yasaku WADA

Department of Applied Physics, Faculty of Engineering, University of Tokyo, Bunkyo-ku, Tokyo

(Received July 7, 1958)

The attenuation of ultrasonic waves for suspensions of polymethyl methacrylate particles (mean radius a=ca. 40μ) in ethyl alcohol, carbon tetrachloride and their mixtures are measured in the range of frequency 1−6 Mc/s. For $ka>0.5$ ($k=2\pi$/wave length) the scattering and reflection losses are found to be predominant origins of the attenuation. But when ka approaches unity, the observed attenuation lies markedly below the prediction from Rayleigh's formula which is established under the condition of $ka\ll 1$. For $ka<0.5$, the viscous loss predicted by Lamb and Urick and the loss due to the internal viscosity of suspended particles become appreciable. A simple theory for the latter loss is developed under some assumptions. The sum of the theoretical values of these three kinds of losses is in satisfactory agreement with the experimental one. In the frequency range where the internal loss predominates, the method employed in this research can be used to measure the volume viscosity of a solid material.

§ 1. Introduction

The attenuation of sound in suspensions or hydrosols is of great importance in underwater sound transmission, in the study of colloidal systems and in many other applications. While the attenuation properties of homogeneous liquids and solids have been widely studied and are now well known, the amount of study in suspensions has been rather limited. The first calculation of the attenuation of sound due to the scattering by a single sphere suspended in a non-viscous liquid was made by Rayleigh.[1] Lamb[2] calculated the velocity potential of waves scattered from a mobile sphere in a viscous liquid. Urick[3] cast Lamb's theory in a more convenient form and obtained the attenuation due to the relative motion of a sphere in a viscous liquid.

Since most of the previous experiments[3,4,5] in this relation have been made for aqueous suspensions of natural powders, for example, kaolin, quartz sand, lycopodium etc. which are not perfectly spherical in shape and mechanical properties of which are not well determined, the results could not be quantitatively compared with theory. Busby and Richardson[6] recently investigated the attenuation of sound in aqueous suspensions of glass spheres and the result was accurately explained in terms of scattering and viscous loss. In this case, however, since the density and elastic modulus are much higher in glass than in water and as the internal loss in glass is negligibly small, the behavior of particles in the sound field can be expected to be rather simple.

It is actually often the case, especially for organic suspensions, that the density and compressibility of a suspended particle lie near

those of a suspending liquid and the translational oscillation and deformation of the particle in the sound field must be taken into consideration. It is this more general case which was investigated by us. In the present investigation, the attenuation was measured for suspensions of polymethyl methacrylate powder. Since this material is perfectly spherical in shape and, moreover, its physical properties can be well examined in bulk phase, it satisfies reasonably well the requirement for the test of the theory. This material seems very appropriate also for the study of the effect of internal loss of suspended particles on the attenuation, which has never been discussed in the existing reports.

§ 2. Nomenclature

α: Total amplitude attenuation coefficient in suspension

α_1: Attenuation coefficient in suspending liquid

α_p: Attenuation coefficient for suspended particles $\alpha_p \equiv \alpha - \alpha_1$

α_s: Attenuation coefficient due to scattering of sound

α_v: Attenuation coefficient due to viscous drag at surface of particles

α_i: Attenuation coefficient due to internal loss of particles

c: Volume fraction of particles in suspension

a: Radius of particles

ρ_1, ρ_2: Density of suspending liquid and suspended particle respectively,

$$\sigma \equiv \rho_2/\rho_1$$

K_1, K_2: Adiabatic compressibility of liquid and particle respectively,

$$\tau \equiv K_2/K_1$$

η_1, η_2: Shear viscosity of liquid and particle respectively

κ_1, κ_2: Volume viscosity of liquid and particle respectively

V_1, V: Sound velocity in liquid and suspension respectively

k: Propagation constant of sound (compressional wave) in suspension

$$k \equiv 2\pi f/V$$

β: Propagation constant of transverse wave in liquid

$$\beta \equiv (\pi f \rho_1/\eta_1)^{1/2}$$

f: Frequency of sound

V_l, V_t: Velocity of longitudinal and transverse waves in particle respectively

α_l, α_t: Absorption coefficient of longitudinal and transverse waves in particle respectively.

§ 3. Experimental

The attenuations were measured in this research by a pulse technique (see block diagram, Fig. 1). A barium titanate transmitter of 3 cm diameter was excited by a high frequency pulse for the duration of several microseconds, the repetition rate of pulses being about one kilocycle. Acoustic energy passes through the suspension to a receiver, which is also a barium titanate transducer of the same size as the transmitter. The transmitter and receiver were fixed at a distance of 10 cm, their faces being set accurately parallel by a block gauge.

The received signal was attenuated by a variable attenuator (0–50 db in steps of 0.2 db), amplified by a fixed amount and displayed on an oscilloscope. The increase in the attenuation due to the addition of the particles was compensated by the variable attenator so as to regain the original pulse height. The value of α_p was then obtained from the reading of the attenuator. Adding the particles to the liquid in approximately equal quantities and taking a series of measurements after each addition, α_p could be determined as a function of concentration.

It should be noticed here that the density and sound velocity of the suspensation depend on particle concentration,[7] so that the efficiency as well as the directional characteristics of both the transmitter and receiver might vary in the course of one run of experiment. In the present experiment, however, the transmitter used was of sufficient cross section to insure a well collimated wave through the medium and the receiver was placed in the Fresnel region of sound field, hence the variation of directional characteristics could be safely neglected. The correction for the variation of efficiency of the transducers was estimated from the theory of transducers[8] as less than one percent of the observed attenuation and also ignored.

A glass tank of $11 \times 8\,\mathrm{cm}^2$ base and 10 cm depth was used as a container. In order to

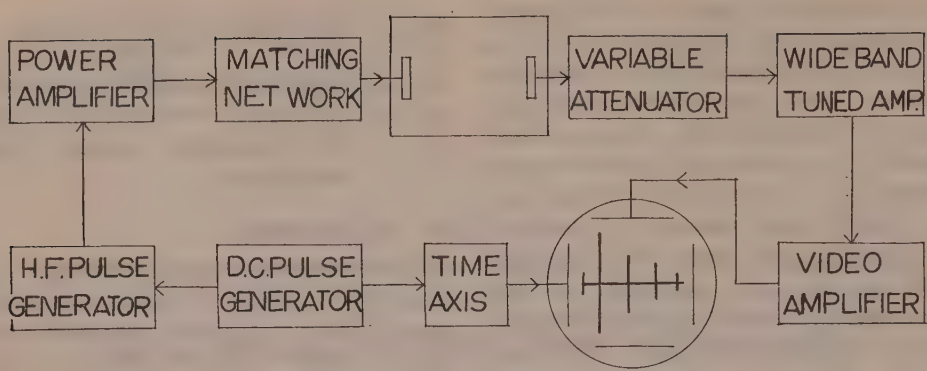

Fig. 1. Block diagram of electronic apparatus.

obtain a uniform concentration of particles throughout the medium, the suspension was continuously stirred at an optimum speed. When the speed was too high, air bubbles were dragged into the suspension. When too low, on the other hand, sedimentation or floatation of particles occurred. Measurements in ethyl alcohol medium showed that the turbulence caused by stirring had no effect on the attenuation at the optimum stirring. All the measurements were carried out at room temperatures from 15° to 20°C. The temperature dependence of the attenuation coefficient was found within the experimental accuracy in this temperature range.

§ 4. Suspension

Commercially produced powders of polymethyl methacrylate (PMMA) were used as suspended particles. The particles were perfectly spherical in shape under microscopic examination. The distribution of radius was determined from microphotographs of about one thousand individual particles. There was a wide range of particle size, as is indicated by Fig. 2, where the number percent of particle in each radius interval of 5 microns is plotted. For the purpose of studying the particle size dependence of attenuation, some of the particles were fractionated into five fractions from the difference of sedimentation rate in ethyl alcohol, the fraction of the smallest size being not used because of extremely small amount. Except in the study in § 8, however, unfractionated particles were employed throughout this investigation.

In Table I, two sorts of average radius, $\langle a\rangle_s$ and $\langle a\rangle_v$, which are necessary to the numerical evaluation of the theories, are com-

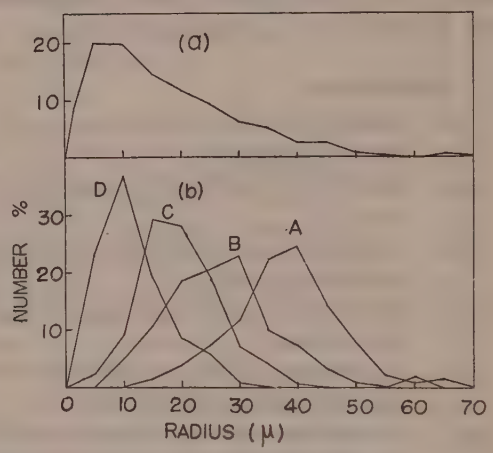

Fig. 2. Particle radius distribution of polymethyl methacrylate powder: (a) unfractionated, (b) fractionated samples.

Table I. Average radius of particle (micron).

	Unfractionated	Fractionated			
		A	B	C	D
$\langle a\rangle_s$	40.3	47.0	39.6	28.2	21.3
$\langle a\rangle_v$	31.7	42.7	33.2	24.6	17.4

puted from the distribution curve by the following definitions respectively:

$$\langle a\rangle_s=(\sum c_i a_i^3/\sum c_i)^{1/3}=(\sum n_i a_i^6/\sum n_i a_i^3)^{1/3} \quad (1)$$

and

$$\langle a\rangle_v=(\sum c_i a_i^{-1}/\sum c_i)^{-1}=(\sum n_i a_i^2/\sum n_i a_i^3)^{-1}, \quad (2)$$

where c_i is the volume fraction of particles of radius a_i, n_i the number fraction.

The values of density, adiabatic compressibility and volume viscosity* of PMMA are

* The term "viscosity" in a solid is here used as the imaginary part of complex modulus divided by $2\pi f$. "Compressibility" expresses here the reciprocal of the real part of complex bulk modulus.

also to be estimated for evaluation of the theoretical formulae. These were determined by use of a PMMA plate. PMMA plate and powder probably have different polymerization degree, since the method of polymerization differs in them. But, as is well known, mechanical behaviors of a polymer in the glassy state is very nearly independent of polymerization degree.

The density was determined by the floatation method. The result obtained is $\rho_2=1.19$ g/cm^3.

For the purpose of estimation of adiabatic compressibility, velocities of longitudinal and transverse waves were measured at 1.08 Mc/s by the total reflection method[9] using a PMMA plate immersed in carbon tetrachloride. The results are $V_l=2650$ m/s and $V_t=1240$ m/s. From these data adiabatic compressibility can be calculated by eliminating shear modulus G_2 from the following relations:

$$\rho_2 V_l^2=\frac{1}{K_2}+\frac{4}{3}G_2, \quad \rho_2 V_t^2=G_2 . \qquad (3)$$

The present data yield a value of $K_2=1.70$ 10^{-11} cm^2/dyne.

In order to obtain a value of volume viscosity in PMMA, the absorbtion coefficients of longitudinal and transverse waves in a PMMA plate was measured, inserting the plate into the sound path in a water tank. At the normal incidence of sound beam from water into the plate, only longitudinal wave is excited in the latter, and from the insertation loss corrected for the reflection loss at the interfaces one can easily obtain the absorption coefficient of longitudinal wave. On the other hand, when the incident angle is larger than the total reflection angle of longitudinal wave, transverse wave alone is transmitted in the plate. For the case at hand, i.e. PMMA plate in water, the reflection at the interfaces is reduced to nearly zero at an incident angle of ca. 50°,[10] hence the absorption coefficient of transverse wave can directly be obtained. From the absorption coefficients, volume viscosity is calculated by the following relations:

$$\alpha_l=\frac{2\pi^2 f^2}{\rho_2 V_l^3}\left(\kappa_2+\frac{4}{3}\eta_2\right), \quad \alpha_t=\frac{2\pi^2 f^2}{\rho_2 V_t^3}\eta_2 . \qquad (4)$$

Since the absorption coefficients markedly vary with frequency, ultrasonic waves of the same frequency must be used in measurements in the plate and the suspension in order to make a reasonable comparison. In the present case, it was observed at 1.08 Mc/s that $\alpha_l=0.115$ cm^{-1} and $\alpha_t=0.613$ cm^{-1}, hence $\kappa_2=50$ poise. In the above experiments one must use a plate of thickness more than a half pulse length in order to avoid a possible error from multiple reflection of sound in the plate. A plate of 2.2 cm thickness was employed in our case.

As suspending liquids, methyl alcohol and carbon tetrachloride were employed. PMMA particles, when added, immediately disperse in these liquids and no swelling was observed at least for the period of one run. Since the density of PMMA lies between those of the two liquids, their mixture in a proper ratio, about 50 to 50 in volume, has the density equal to PMMA. In this case an appreciable swelling of particles was observed in one hour or so, hence the experiment was performed within this time.

The numerical values of density, sound velocity and adiabatic compressibility in these liquids were compiled from Sacher's paper[11] and the International Critical Tables.

§ 5. Concentration Dependence of Attenuation

The values of α_p for suspensions in ethyl alcohol, carbon tetrachloride and their mixtures were obtained at six frequencies, 1.08, 1.61, 2.20, 3.24, 4.12 and 5.40 Mc/s, as a function of concentration. An example of concentration dependence of α_p is shown in Fig. 3.

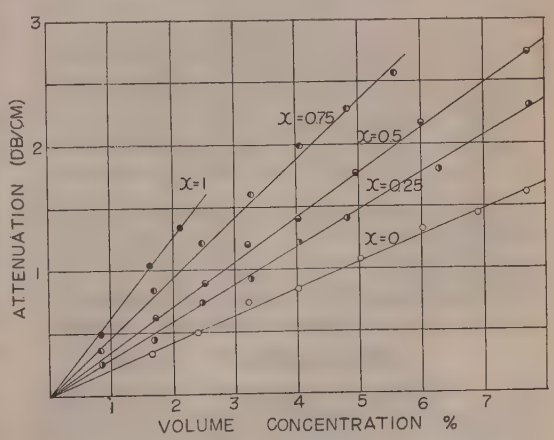

Fig. 3. Concentration dependence of attenuation at 3.24 Mc/s. x denotes volume fraction of carbon tetrachloride in ethyl alcohol.

The general behavior is the same at other frequencies. Since in most cases α_p varies linearly with particle concentration over the range observed, it is to be expected that the scattering of sound from particles is single, not multiple in this range at least and the attenuation is additive with respect to the number of particles. Sometimes, especially at high frequencies, there is some indication that the curves level off at high concentration, probably due to the multiple scattering and other interactions among particles. In the following sections the value of α_p/c obtained from the linear portion of the α_p *vs.* concentration plot is indicated and compared with theories.

§ 6. Frequency Dependence of Attenuation and Scattering Loss

The frequency dependence of α_p/c for unfractionated particles in two liquids is indicated in Fig. 4.

The origin of the sound attenuation in a suspension has been ascribed, among others, to the scattering of sound beams from particles. The attenuation coefficient due to the scattering from elastic spheres free to move in a non-viscous liquid has been theoretically derived by Rayleigh[1] and Epstein[12] as

$$\alpha_s=\frac{k^4a^3}{8}\left\{\frac{4}{3}(1-\tau)^2+\left(\frac{\sigma-1}{\sigma+1/2}\right)^2\right\}c \qquad (5)$$

under the condition $ka\ll 1$. For a polydisperse system, it is theoretically required to replace a by the average radius $\langle a\rangle_s$ defined by the formula (1). In Fig. 4, theoretical values of α_s/c are given in broken lines evaluated using the numerical values obtained in § 4. For both liquids the experimental curve is in very good agreement with the theoretical one near the frequency of 2 Mc/s, corresponding to about $ka=0.5$, i.e. the radius being of the order of one tenth of the wave length. But at higher frequencies the experimental curve lies fairly below the theoretical one and at lower frequencies the former is far above the latter.

Since Eq. (5) is valid only under the assumption $ka\ll 1$, the discrepancy between the theory and experiment at high frequencies may be ascribed to the failure of this assumption. In fact, when the radius of a particle approaches the wave length, the interference of the scattered waves from different parts of the particle may considerably diminish the scattered energy. From the above reasons it may be concluded that the scattering loss is a predominant factor of the attenuation in suspensions at frequencies above 2 Mc/s in this experiment. Additional confirmations of this conclusion will be provided in the following two sections.

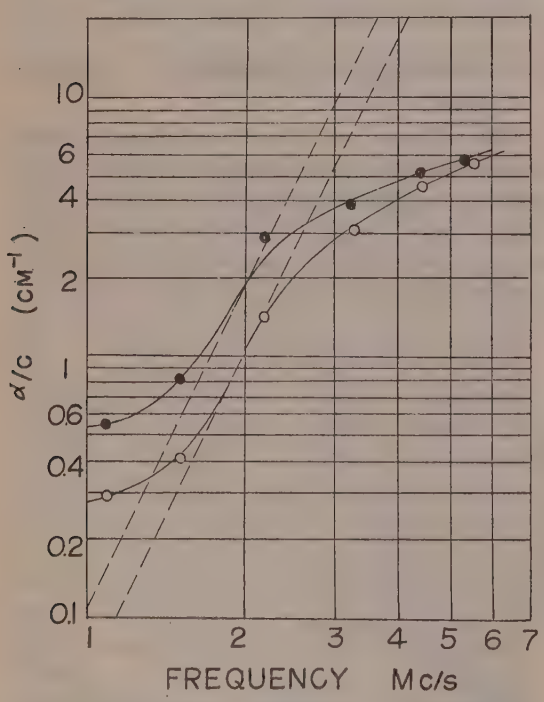

Fig. 4. Frequency dependence of attenuation: experimental values of α_p/c in ethyl alcohol (○) and carbon tetrachloride (●). Broken lines indicate theoretical valus of α_s/c in ethyl alcohol (below) and carbon tetrachloride (above).

§ 7. Effect of Suspending Liquid on Attenuation

The effect of a suspending liquid on α_p/c was measured at the frequency of 3.24 Mc/s, where the scattering loss is expected to be predominant. The results are illustrated in Fig. 5, together with the theoretical curves calculated from Eq. (5).

In the case of ethyl alcohol—carbon tetrachloride system, both liquids having good affinity to PMMA, the experimental curve has a quite similar behavior to the theoretical one, disregarding that the latter is always about twice larger than the former, probably due to the reason described in the last section.

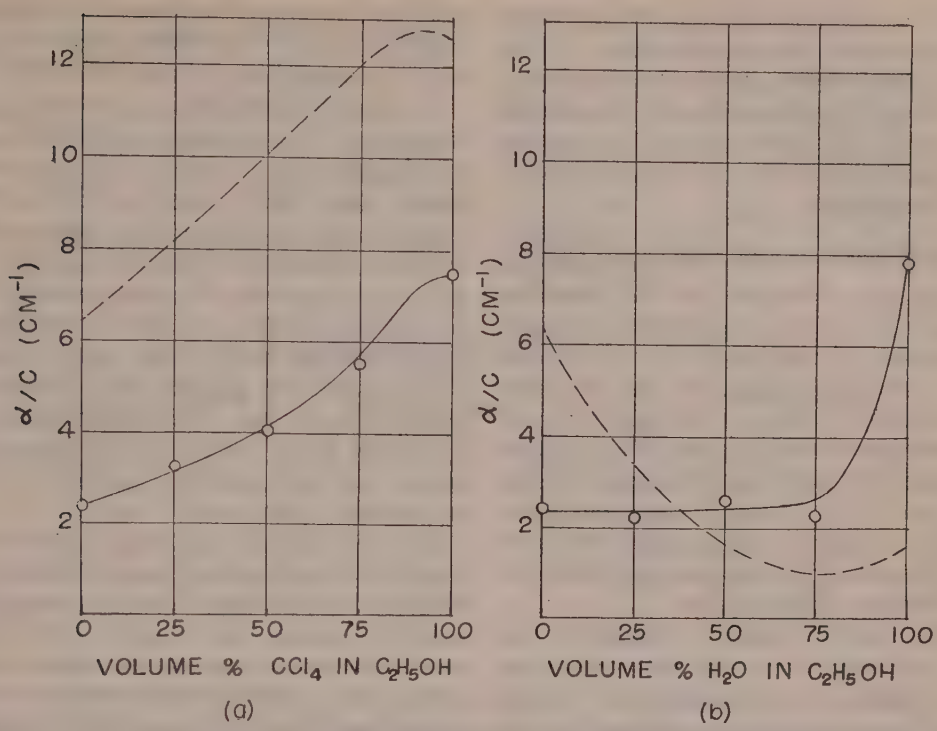

Fig. 5. Effect of suspending liquid on attenuation at 3.24 Mc/s: (a) ethyl alcohol-carbon tetrachloride system, (b) ethyl alcohol-water system. Solid line indicates experimental value of α_p/c, broken line theoretical value of α_s/c.

On the other hand, in the case of ethyl alcohol—water system, the latter having only poor affinity to PMMA, the experimental value very rapidly increases with volume fraction of water. This may be due to the incomplete deflocculation of particles in the liquid. The association of particles should increase the effective radius, so make rise to the attenuation, as is readily known from Eq. (5). In fact, the association of PMMA particles in water was observed by a microscope and an appreciable decrease in the attenuation was found for the aqueous suspension of PMMA particles after violent stirring for an hour.

§ 8. Dependence of Attenuation on Particle Radius

Fig. 6 shows the attenuation for ethyl alcohol suspensions of fractionated and unfractionated particles at the frequency of 3.24 Mc/s, together with the theoretical curve calculated from Eq. (5). The accuracy of the data presented here is somewhat less than the others because the available amount of the fractionated particles were rather limited.

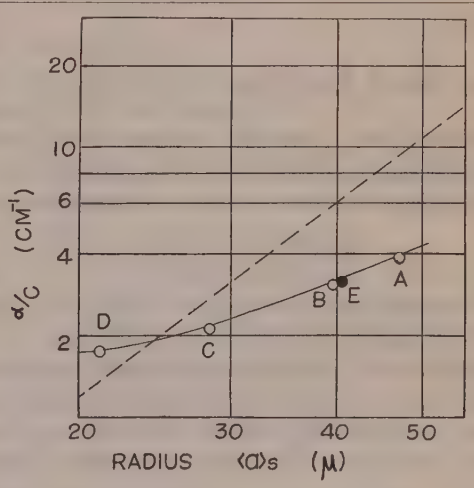

Fig. 6. Dependence of attenuation on particle radius at 3.24 Mc/s: ethyl alcohol suspensions of (A, B, C, D) fractionated and (E) unfractionated particles. Solid line indicates experimental value of α_p/c, broken line theoretical value of α_s/c.

As is easily seen, the experimental curve is nearly of the same form as that of the frequency dependence given in Fig. 4. It is apparent from Eq. (5) that increasing the fre-

quency has the same effect on the scattering loss as increasing the particle radius. In Fig. 6, the accord between experiment and theory is encountered for the radius of 25 microns, corresponding to a value of $ka=0.5$, which is in good agreement with the case of the frequency dependence.

§ 9. Attenuation in Low Frequency Range

As has been described in the preceding sections, the scattering of sound from suspended particles is considered as a dominant origin of the attenuation for the frequency range of $ka>0.5$. Below this frequency, however, the observed attenuation is appreciably larger than that predicted from the scattering theory (see Fig. 4), hence there must exist some other origins of attenuation, which, at high frequencies, may become negligible compared with the scattering loss.

In this relation, Lamb,[2] Epstein[12] and Urick[3] calculated the energy loss due to the viscous friction at the surface of a sphere, socalled "viscous loss", and obtained for the attenuation the formula

$$\alpha_v=\frac{k}{2}(\sigma-1)^2\frac{S}{S^2+(\sigma+T)^2}c\,, \qquad (6)$$

where

$$S\equiv\frac{9}{4\beta a}\left(1+\frac{1}{\beta a}\right),\quad T\equiv\frac{1}{2}+\frac{9}{4\beta a}\,.$$

When $\beta a\gg 1$, that is, viscous shear wave in the liquid damps out very rapidly as is our case, the above equation is simplified as

$$\alpha_v=\frac{9k}{8\beta a}\left(\frac{\sigma-1}{\sigma+1/2}\right)^2 c\,. \qquad (7)$$

For a polydisperse system a in Eq. (7) must be replaced by $\langle a\rangle_v$ defined by Eq. (2).

Recently, Lane[13] calculated another type of viscous loss caused by the acoustic streaming from an oscillating sphere. But this type of viscous loss was found to be extremely small in our case, so will no more be referred to in this paper.

Busby and Richardson[5] in aqueous suspensions of glass spheres found good agreement between experiment and theory, considering the scattering and viscous loss. In the present study, however, the situation is more complicated. Since PMMA has much higher internal viscosity than the suspending liquids, the absorption of sound due to the internal viscosity becomes of great significance. In fact, the absorption coefficient of longitudinal wave is 0.11 cm^{-1} in PMMA, but only 0.005 cm^{-1} in carbon tetrachloride at 1 Mc/s.

No theory for the sound attenuation in a suspension of viscoelastic particles has been developed as yet. Here we assume for simplicity that, firstly, the particle radius is much smaller than the wave length, i.e. $ka\ll 1$, and secondly, the particle oscillates perfectly in phase with the surrounding liquid, so that there exists no relative translational motion between them. The first assumption is of course valid in such low frequencies as in the present case. The second assumption is fulfilled if the density is the same for the particle and the liquid,[3] a condition also nearly satisfied in our case.

As is well known, generally a material in the field of longitudinal wave undergoes dilatation as well as shear. But in a suspension, since a particle has rigidity and a liquid none, the former undergoes no shear, but dilation alone. Under these conditions a suspended particle in the sound field is expected to be applied by uniform pressure equal to a surrounding liquid and from a simple calculation[7] the compressibility of a suspension K is found to have an additive character in volume:

$$K=K_1(1-c)+K_2c\,.$$

For a viscoelastic medium, compressibility becomes a complex quantity, so its imaginary part, and therefore the voluminal part of absorption coefficient per unit wave length, should also have an additivity.

From the above considerations the absorption coefficient per wave lengh in a suspension is approximated by

$$\frac{\alpha V}{f}=\frac{\alpha_1 V_1}{f}(1-c)+\left(\text{voluminal part of }\frac{\alpha_l V_l}{f}\right)c\,. \qquad (8)$$

It should be noted that, since there may exist additional shear motion of liquid at the surface of particle due to the discontinuity of rigidity, the shear viscosity term in $(\alpha_1 V_1/f)$ must somewhat be modified from the case of homogeneous liquid. This effect, however, is neglected here because the particle radius is much smaller than the wave length. Anyway, the first term in the righthand side of Eq. (8) plays a rather limited role in the fol-

lowing deduction.

The absorption coefficient per unit length therefore becomes

$$\alpha=\alpha_1\frac{V_1}{V}(1-c)+\frac{2\pi^2f^2\kappa_2K_2}{V}c$$

$$\fallingdotseq\alpha_1+\left(\frac{2\pi^2f^2\kappa_2K_2}{V_1}-\alpha_1\right)c\,.$$

Hence the contribution of suspended particle is obtained as

$$\alpha_i=\alpha-\alpha_1\fallingdotseq\frac{2\pi^2f^2\kappa_2K_2}{V_1}c\,. \qquad (9)$$

In the above derivation, the approximations were employed that $\alpha_1\ll$(voluminal part of absorption coefficient in particle) and $V\fallingdotseq V_1$. V was computed by use of Urick's equation[7] as a function of concentration and the approximation was found to be reasonable in the present case.

Table II. Attenuation coefficient (cm^{-1}) at 1.08 Mc/s.

Suspending liquid: volume fraction of CCl_4 in C_2H_5OH (%)	Observed value of α_p/c	Calculated value			
		α_s/c	α_v/c	α_i/c	Total
0	0.30	0.11	0.08	0.18	0.37
25	0.31	0.15	0.02	0.19	0.36
50	0.36	0.18	0.00	0.20	0.38
75	0.41	0.22	0.01	0.22	0.45
100	0.48	0.22	0.04	0.22	0.48

In Table II the experimental values of attenuation coefficient at 1.08 Mc/s are listed, together with the theoretical ones calculated from Eqs. (5), (7) and (9) respectively. The sum of the three theoretical values is in satisfactory agreement with the experimental ones within the limits of accuracy of the experiment and of the approximations of the theories.

The frequency dependence of the viscous loss and internal loss is not so strong as the the scattering loss. The viscous loss is proportional only to half-power of the frequency and the frequency dependence of the internal loss is smaller than proportional to square of the frequency since the viscosity of a high-polymeric solid is a decreasing function of frequency due to the relaxational effect. At high frequencies, therefore, the loss in these fashions may be well covered by the scattering loss, so the conclusion that the attenuation at high frequencies can be explained in terms of scattering alone may little be influenced by taking into consideration the viscous and internal loss.

In the study of viscoelastic behavior or high polymers, measurements of dynamic bulk modulus and volume viscosity have a great significance.[14] The bulk modulus can be obtained, as described by Urick,[7] from the measurement of sound velocity in suspensions of the material to be studied. The method used in this research can be employed to measure the volume viscosity, if spherical particles of the material can be obtained in an appropriate radius.

§ 10. Conclusion

Specific conclusions to be drawn from this research are the following:

(1) The attenuation coefficient of sound in suspensions depends linearly on the concentration of suspended particles in the range of concentration up to several percents.

(2) At high frequencies ($ka>0.5$), the scattering and reflection of sound from suspended particles are the major causes of attenuation. At these frequencies, however, the experimental value of attenuation lies markedly below the theoretical one predicted from Rayleigh's equation, which is established for $ka\ll1$.

(3) At low frequencies ($ka<0.5$), the scattering plays a role of relatively decreasing importance and the viscous absorption term as well as the loss due to the internal viscosity of particles must be considered. The sum of these three effects gives satisfactory agreement with the experiment.

(4) In the low frequency range where the internal loss predominates, the method employed in this research can be used to measure

the volume viscosity of a solid material.

§ 11. Acknowledgements

The author is very much indebted to Mr. Motokuni Gotō (now at Asahi Glass Co. Ltd.), Mr. Shinya Yoshimura (now at Bridgestone Tire Co. Ltd.), Mr. Takehiko Haga (now at Kawasaki Iron and Steel Co. Ltd.) and Mr. Masabumi Yoshizawa (now at Fuji Iron and Steel Co. Ltd.) for their performance of the experiment. The author is also indebted to Mr. Akihiro Mizuno (now at Maruzen Oil Co. Ltd.) and Mr. Tetsu Yoshizaki (now at Fuji Photo Film Co. Ltd.) for their preliminary investigation.

References

1) Lord Rayleigh: Theory of Sound Vol. 2 (1879) p. 272.
2) H. Lamb: Hydrodynamics 6th ed. (1932) p. 659.
3) R. J. Urick: J. Acous. Soc. Am. **20** (1948) 283.
4) C. R. Hartmann & A. B. Focke: Phys. Rev. **57** (1940) 221.
5) V. J. Stakutis, R. W. Morse, M. Dill & R. T. Beyer: J. Acous. Soc. Am. **27** (1955) 539.
6) J. Busby & E. G. Richardson: Proc. Phys. Soc. Lon. **69B** (1956) 193.
7) R. J. Urick: J. Appl. Phys. **18** (1947) 983
8) T. F. Hueter & R. H. Bolt: Sonics (1955) p. 99, p. 126.
9) W. C. Schneider & C. J. Burton: J. Appl. Phys. **20** (1949) 48.
10) Y. Torikai & F. Fujimori: Rep. Inst. Ind. Sci. Univ. Tokyo **3** (1954) 268.
11) K. Sacher: Phys. Zeits. **41** (1940) 360.
12) P. S. Epstein: Theodore von Karman Aniversary Volume (California Institute of Technology, Pasadena, California, 1941).
13) C. A. Lane: J. Acous. Soc. Am. **28** (1956) 1194.
14) R. S. Marvin, R. Aldrich & H. S. Sack: J. Appl. Phys. **25** (1954) 1213.

JOURNAL OF THE PHYSICAL SOCIETY OF JAPAN Vol. 13, No. 11, NOVEMBER, 1958

On the Limit of Superheat

By Hiromu WAKESHIMA and Kazuo TAKATA

Kobe University of Mercantile Marine, Kobe

(Received July 9, 1958)

A new method of observing the limit of superheat was devised, in which small drops of a sample liquid are heated as they rise up in the non-soluble heating liquid with a suitable temperature gradient upward. Using the method, the limit of superheat was determined, mainly for some saturated hydrocarbons and polymethylenes. The result was compared with Döring's theory of spontaneous bubble formation in superheated liquids. The agreement between the theory and experiment was satisfactory, which seems to throw some light upon the problem of surface free energy on the nuclear bubble.

§ 1. Introduction

The limit of superheat is interesting from the standpoint of research on nucleation, because the rate of homogeneous nucleation for bubble formation can be evaluated theoretically in the case of superheat[1] as in the case of condensation in supersaturated vapors, so far as we assume macroscopic values for the surface free energy on the boundaries of nuclei. As for reliable experimental facts which can be compared with the theoretical conclusion, however, only observations by K. L. Wismer and his collaborators[2] have been available up to the present. This situation may probably be due to the difficulty of obtaining reproducible results, owing to gas cavities on the wall of the container of the liquid in question, which are liable to act as sources of heterogeneous nucleation. Recently L. Trefethen[3] has shown that liquids can

easily be superheated when they are surrounded by other liquids. (i.e. they are not in contact with solids) But he failed to observe the limit of superheat of the liquids he investigated, because of his experimental conditions. Encouraged by his observation, we devised a new method of observing the limit, by which rather a definite limit of superheat has been obtained for some liquids. Here will be given the experimental procedure, the results obtained and their comparison with the expectation from the theory of homogeneous nucleation for bubble formation in superheated liquids and some discussion on this problem will be made.

§ 2. Experimental Procedure

The principle of our method is as follows: The vertical tube containing the suitable liquid which practically does not dissolve a sample liquid and which has a larger density and sufficiently higher boiling point than that of the liquid in question, is heated at the upper end and a stable, vertical temperature gradient is maintained in the column of the heating liquid. Through a small hole on the container of the liquid at the lower end of the column, small drops of the specimen is suitably introduced and the height, at which the drops, in rising up the column, reaches the the limit of superheat for the liquid and explode, is measured.

Fig. 1 shows the general scheme of the equipment used. The container of the heating liquid, made with a glass tube of about 35 cm in length, 2 cm in outer diameter, is surrounded by a brass pipe, 20 cm long, 1 mm thick and of about 2.5 cm in outer diameter, which is fixed coaxially to the container. The pipe has blackened inside and its outside is polished. Two vertical slits were suitably cut along the pipe, one for illumination of the central part of the heating column and the other for observation of this part from outside. The upper part of the brass pipe can be kept at various constant temperatures, using the electric heater wound up on the pipe and supplied by a stabilized power source. The heating column with the brass pipe outside, is enclosed air tight in another coaxial glass tube, of about 3.5 cm in diameter, the lower end of which is closed with a metallic hollow stopper, and the space between the two glass tubes is evacuated, in order to prevent heat conduction radial to the heating column. Water at constant temperature from a big reservoir flows inside the stopper at constant speed, controlled by the overflow device. The heating liquid is sucked up by a suction pump, from the beaker through a small hole, of about 1 mm in diameter, into the container until its surface is raised somewhat above the heater. To keep the height of the surface constant, the air leak is effectively used, together with the large flask and the narrow capillary tube, inserted between the container and the suction pump. When the current through the heater and the height of the heating liquid column remain unchanged, we can maintain in the heating column a stable temperature slope, e.g. from about 250°C down to room temperature, as we confirmed it using a thermo-couple. The guide tube, made of glass, is to guide the sample droplets below the hole of the container. To produce small drops of a sample liquid, the latter was poured into the guide tube about one centimetre thick over the heating liquid and then a small quantity of either the heating liquid or the specimen was injected, with a syringe having a glass nozzle, against the interface between the sample and the heating liquids. After a little preliminary exercise, we could manage to let drops of suitable sizes (usually about 20 μ to 200 μ in diameter) leak out of the nozzle of the guide tube, to such a degree that some of the drops occasionally passed through the hole into the container of the heating liquid. The drops, in rising up the heating column, are illuminated against dark back-ground by a lamp and a cylindrical lens and are observed directly with naked eyes or through a cathetometer when it is needed. In order to know the size of droplets, the time required by droplets to ascend a definite distance was measured with a stop-watch and the radii of the droplets were calculated, using Stoke's law of resistance for a liquid sphere moving uniformly in stagnant fluid. When the droplet reaches the superheat limit and vaporize in an instant, it suddenly lights up brighter with a small cracking sound and begins to ascend faster than before. So we can easily locate the point of explosion.

The materials, of which we investigated the

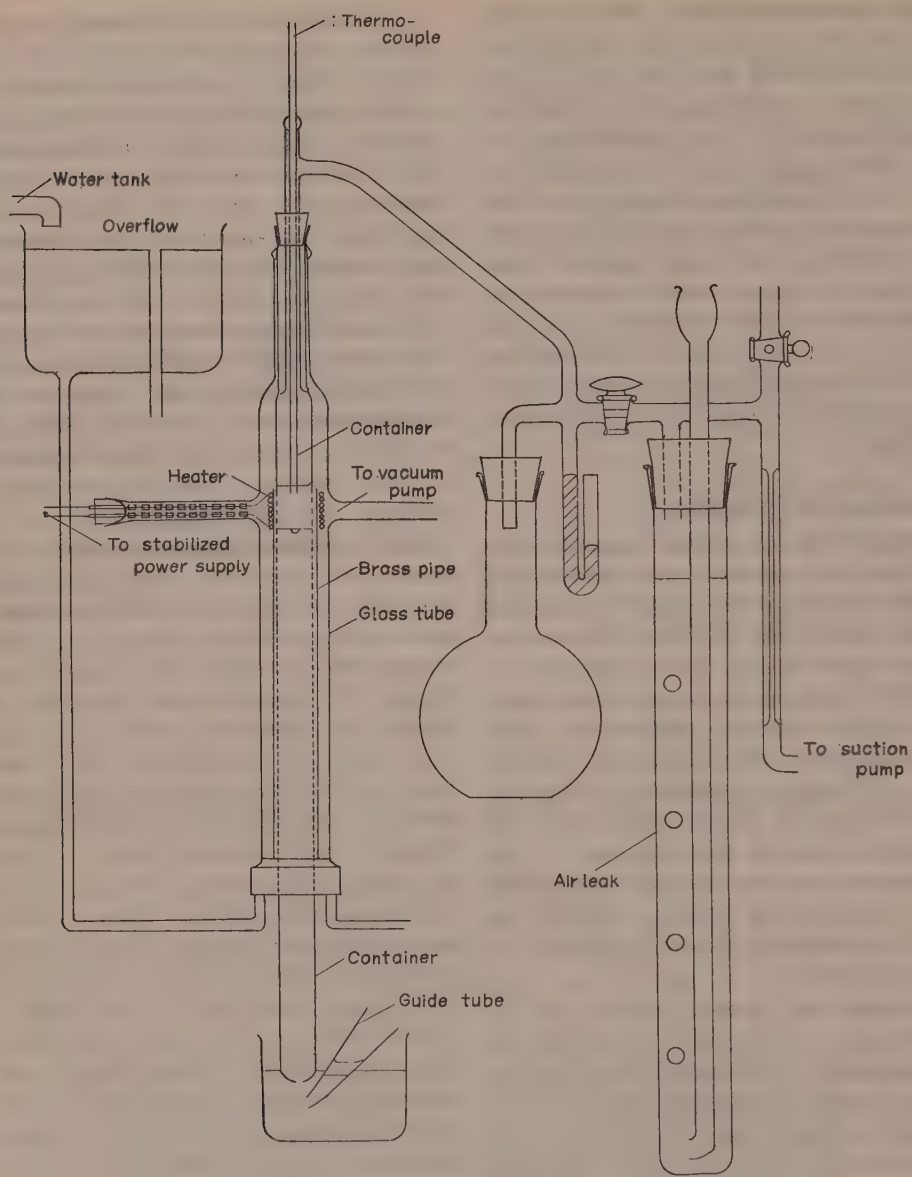

Fig. 1.

limit of superheat, were mostly saturated hydrocarbons and polymethylenes of the highest quality, purified by Phillip Petrolium Company or Maruzen Petrolium Company. Namely the purity of n-pentane, n-hexane, isopentane, cyclopentane and methylcyclopentane supplied by Phillip Petrolium Company was between 99.99 to 99.67 in mol-percent, while n-heptane and cyclohexane specimens were distilled by Research Institute of Maruzen Company, within the temperature range less than 0.1°C. The corresponding heating liquid was pure sulfuric acid. We also made investigation on ethyl ether of extra pure grade obtainable on the market. As for the heating liquid in this case, glycerin and ethylene glycol were used.

§ 3. Experimental Results and Comparison with Theory

The most remarkable fact observed thus far was that the limit of superheat was pretty definite. Especially in cases of saturated hydrocarbons and polymethylenes in sulfuric acid, almost all of about fifty observed droplets in each case exploded within narrow ranges of about 1 mm width, irrespective of

the size of drops. (in most cases the largest was almost hundred times the smallest in volume) In the cases of ethyl ether in glycerin and ethylene glycol, though the majority of droplets exploded at first within a rather narrow range of few millimetres, there were undoubtedly some which exploded prematurely without any apparent reason. And, possibly because of the slight solubility of ether in these heating liquids, the condition in the column seemed to change as the specimen drops were sent into the heated container for some time; by and by there appeared droplets which did not show any sign of superheating. Larger viscosity of, and the solubility in, the heating liquids compelled us to work with larger drops in these cases (~0.6 mm in diameter), which fact caused difficulties and might have led to various errors.

In the following Table I, will be listed boiling points, explosion temperatures and the

Table I.

Material	boil. p.	expl. temp.	limit of superheat exper.	theoret.
n-pentane	36.1°	146°	110°	110.4°
n-hexane	68.7°	182°	113°	111.6°
n-heptane	98.4°	211°	113°	114.4°
isopentane	27.8°	138°	110°(107°)	109.3°
cyclopentane	49.3°	180°	131°	128.7°
methylcyclo-pentaine	71.8°	200°	128°	125.2°
cyclohexane	81.1°	216°	135°	138.2°
ethyl ether	34.6°	147°	112°(108°)	109.4°

corresponding limits of superheat obtained in this experiment, together with the theoretical conclusion according to Döring's formula which will be explained afterwards. Values observed by Wismer are also given in bracket for comparison.

In calculating superheat limits theoretically, the formula given by W. Döring

$$J=Z_1e^{-\lambda/kT}\{6\sigma/(3-b)\pi m\}^{1/2} \times\exp\{-16\pi\sigma^3/3kT(p_k-p_1)^2\} \qquad (1)$$

was used, where J denotes the time rate of homogeneous nucleation in a droplet containing Z_1 molecules. As for the size of droplet, we adopted in this calculation the value 0.1 mm for the diameter. λ means the heat of vaporization per molecule, σ the surface tension and m the molecular mass of the liquid in question. b stands for $(p_k-p_1)/p_k$, in which p_k and p_1 represent the pressure inside the nuclear bubble and that acting upon the bubble from outside respectively. k and T have the usual meaning. The limit of superheat is supposed to be corresponding to the temperature at which $J=1$; this assumption will be permissible in view of the extremely great dependence of J-value on the temperature, as will be seen from Table II which shows an example of such a relation. (n-pentane)

Table II.

Temperature	J-value
140°C	6.37×10^{-25}
145°C	2.39×10^{-4}
150°C	5.89×10^{7}

Values of physical constants necessary for the calculation refer to those given in "International Critical Table", "Timmerman's Physico-Chemical Constant of Pure Organic Compounds" and others[4]. Specifically, values of surface tension for the liquids in the temperature range near the explosion temperatures, which are most relevant to the limit as will be discussed later, and yet which are not given in any literature, were calculated using Katayama's formula for the temperature dependence of surface tension[5], from the values at lower temperatures.

§ 4. Discussions

In estimating the experimental errors for the determination of superheat limits, we have to take into account various factors. Though the spots at which droplets explode can be located within the error of a few tenth millimetres, assigning a temperature to each exploding droplet is open to some sources of errors.

First, the explosion of a droplet and the rapid rise of the bubble thereafter might be suspected, inevitably to disturb the temperature distribution of the surroundings which would influence the next explosion. Nevertheless, for the tiny droplets used in our experiment where one explosion took place after the interval of at least thirty to forty seconds from the preceding one, this kind of influence is neglisible. That the location of explosion did not disperse for a given condition shows this facts.

Second, in the preliminary measurement of

the temperature distribution in the heating column, we had to insert the thermo-couple along the axis of the column from above, i.e. along the slope of temperature, because of the structure of our apparatus. We noticed that this condition possibly brings about a serious error in the determination of temperature at the spot of thermo-junction, unless a thin couple with a larger joint than a usual one is not used. We used a thermo-couple consisting of a constantan wire of 0.3 mm in width and a copper wire 0.15 mm wide covered with a glass capillary, and having at the junction a copper ball, about 1 mm in diameter. When this couple, enclosed in a thin glass tube, was put in reverse directions in the heating column (in a similar column as the one used in the main experiment, but which was made to permit the couple to be inserted from the bottom as well as from the top), it showed temperature differences of 2°~3°C, according to the magnitude of temperature gradient in the surrounding liquid column. From these differences we evaluated the necessary correction to the temperature measured.

Third, the temperature of rising drops might be somewhat lower than that of the surroundings. It would be difficult to calculate the lag of temperature rise vigorously. In a rough estimation of its order of magnitude, we neglected the heat conduction inside the droplet and assumed a stationary heat flow outside of, and spherically symmetric to, the droplet, corresponding to the temperature difference between the droplet and the point distant from it. Then it is easy to derive a formula $\Delta\theta = (r^2/3\kappa)\alpha v$ where r, κ, α and v denote the radius of the droplet, the thermal diffusivity, the temperature gradient and the rising speed of droplet respectively. For the condition in this experiment, $\Delta\theta$ came out to be of the order of magnitude a few tenth degrees centigrade. (except for the case of ethyl ether)

In short, considering various factors mentioned above, we have estimated the error for the cases of saturated hydrocarbons and polymethylenes to be about 1°C and that for the case of ethyl ether not much larger than 5°C.

As for the theoretical values, we cannot estimate the limit of error for sure. Particulary we are not certain how accurate Katayama's formula is in predicting surface tension at higher temperatures in question here. Judging from the dispersion of extrapolated values when reference surface tensions at different sets of temperatures were used, we are not likely to be free from errors less than a few percent in the values of surface tension. Then our theoretical values might have errors of one or two degrees at least.

Now the question might be raised whether the limits of superheat we observed actually correspond to the spontaneous formation of bubbles in the liquid themselves, i.e. to the homogeneous nucleation, or the bubble formation took place on the boundary of droplets, namely it corresponds to the heterogeneous nucleation. In this connection it is interesting to notice the agreement of our result for isopentane with that given by Wismer. The fact that these two cases were in good accordance, in spite of very different nature of the boundaries of the specimen, seems to indicate clearly that the explosion of droplets was due to bubble formation by homogeneous nucleation. In evitable existence in this experiment, of motes and dissolved molecules of ambient liquid in the droplets was not likely to have conspicuous influence upon the superheat limit, as such a conclusion was already drawn by Wismer.

If all the limits of superheat observed in this experiment actually correspond to the homogeneous nucleation, then the remarkable agreement between the observed limits and the calculated, shown in Table I, gives another strong evidence that Döring's theory is applicable to the spontaneous bubble formation in superheated liquids, in spite of the difficulty of a bubble model of nucleus from statistical mechanical point of view. (for bubbles of the order of magnitude 10^{-7} cm in diameter) Moreover, it means, at least for the liquids investigated here, surface free energy on the boundaries of nuclear bubbles does not differ much from that of the macroscopic vapor-liquid boundaries. Because, according to the calculation mentioned above, the change of five percent of surface tension corresponds to the change of one to two degrees centigrade of the superheat limit, i.e. to the limit of error for observation as well as calculation.

Acknowledgement

The authors wish to express their sincere

thanks to Professor Itsuro Uhara of Kobe University for his valuable discussions on this problem, and to Mr. Tsunehide Kôzuma of Maruzen Petrolium Company for his kind donation of saturated hydrocarbon and polymethylene specimens of high purity. Their thanks are also due to Miss Hiroko Yamamoto for her help in calculating the superheat limits for various liquids.

References

1) W. Döring: Z. Phys. Chem. **36** (1937) 371.
W. Döring: Ibid. **38** (1938) 292.
2) K. L. Wismer: J. Phys. Chem. **26** (1922) 301.
F. B. Kenrick, C. S. Gilbert and K. L. Wismer: Ibid. **28** (1924) 1297.
3) L. Trefethen: J. App. Phys. **28** (1957) 923.
4) "Selected Values of Physical and Thermal Properties of Hydrocarbons and Related Compounds", Carnegie Press, 1953.
Weissberger: "Organic Solvents", Technique of Organic Chemistry, Vol. VII, Interscience Publisher, Inc., New York.
K. A. Kobe and R. E. Lynn Jr.: Chem. Rev. **52** (1953) 117.
5) M. Katayama: Sci. Rep. Tohoku Univ. **4** (1916) 373.

Short Notes

This section is intended to secure prompt publication of important discoveries in physics. The reports should not exceed 800 words in length. A figure of size 7cm × 7 cm will be counted as 150 words.

J. PHYS. SOC. JAPAN **13** (1958) 1404

Etch Pits of Sb Single Crystals

By Jiro SHIGETA and Makoto HIRAMATSU

Department of Physics, Okayama University, Okayama

(Received July 25, 1958)

Chemical as well as thermal etch pits of Sb single crystals prepared by zone-melting were studied in connection with dislocations. The Sb ingot used is analysed as 99.42 wt. % Sb, 0.225 S, 0.025 Cu, 0.006 Bi, 0.022 As, 0.192 Fe and only a trace of Zn. Cleavage faces of Sb single crystals were etched by etching reagent (consisted of 10 g $FeCl_3$, 30 cc HCl and 120 cc H_2O) at temperatures from 25 to 45°C for one to several minutes. The density of etch pits ranges from ca. 1×10^6 to ca. $2\times10^7/cm^2$, the latter of which corresponds to heavily strained crystals.

At the initial stage of etching the shape of each pit is a shallow regular-trigonal-pyramid and the progress of etching causes the following peculiar changes in each pit: the eccentricity of the pit-core, the formation of irregular pit contours and the growth of steps on pit sides. In an electron micrograph the shape of each pit-core is a simply conical dimple without any particular structure.

#1. When a cleavage face of a single crystal is etched progressively, the site of each pit is almost fixed throughout the whole etching period. Further, when the originally etched cleavage face is cleaved off by the thickness of about 20μ and the renewed cleavage face is etched afresh, etch pits on both cleavage faces correspond to one another.

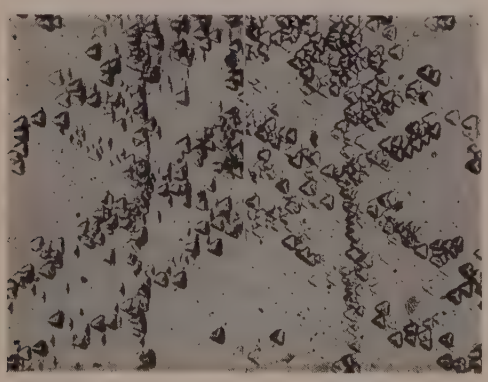

(a) (b)

Fig. 1. Etch pits closely matched on opposite sides of a cleft Sb single crystal (both normal printing). ×125.

These facts indicate that through each etch pit a line singularity particularly sensitive to etching continues into the crystal.

#2. The etch pits can be closely matched on the pair of separated faces of a cleft crystal as shown in Fig. 1.

#3. A single crystal, annealed at 520°C for several to several tens hours, reveals regular etch-pit arrays on sub-boundaries.

#4. The etching of a cleavage face previously scratched quickly and finely by a steel needle reveals, besides incidental pits, etch-pit arrays lined up on many straight lines parallel to $\langle 1\bar{1}0\rangle$ directions. The similar etch-pit arrays can be observed frequently on cleavage faces of Sb single crystals bended or pressed.

#5. When a cleavage face of a single crystal is thermally etched at ca. 400°C in vacuum of 10^{-2} to 10^{-4} mm Hg for several minutes, fairly well defined etch pit or etch-pit arrays can be observed as well. Etch-pit arrays thus revealed on sub-boundaries by thermal and chemical etching correspond qualitatively to one another, while quantitatively the etch pit density of the former is far lower than that of the latter.

These experimental results #1~4 suggest that chemical etch pits thus developed on cleavage faces of Sb single crystals are due to dislocations emerging from the grains and one to one correspondence between dislocations and etch pits may be expected. Thus, by means of chemical etch pits it is possible to observe the distribution of dislocations in Sb single crystals. On the other hand, the result of thermal etching #5 seems to show that thermal etch technique such as reported by Hendrickson and Machlin[1] cannot be applied successfully to Sb single crystals because of its high vapour pressure at high temperature[2]. Details of this investigation will be published later elsewhere.

The authors wish to express their gratitude to Professor Sho Yoshida for his valuable discussions.

References

1) A. A. Hendrickson and E. S. Machlin: Acta Met. 3 (1955) 64.

2) H. Suzuki: Proc. Int. Conf. of Dislocations and Mechanical Properties of Crystals held at Lakè Placid (John Wiley & Sons, Inc., New York 1957) p. 172.

J. PHYS. SOC. JAPAN **13** (1958) 1405

Molecular Collisions in the Two-Dimensional Gases

By Kazuo TAKAYANAGI

Department of Physics, Saitama University, Urawa

(Received September 29, 1958)

Gases adsorbed on the surface of liquid or solid are often treated as two-dimensional gases. Especially for the van der Waals adsorption, this simplified treatment has been found fruitful[1]. Thus it may be worth studying the collision processes in the two-dimensional space.

The probability of scattering in the central force potential $V(r)$ can be calculated just as in the three-dimensional case. The Schrödinger equation in terms of the polar coordinates is (in the centre-of-gravity system)

$$\{-(\hbar^2/2\mu r^2)(r^2\cdot\partial^2/\partial r^2+r\cdot\partial/\partial r+\partial^2/\partial\theta^2)+V(r)\}\phi=E\phi\ , \tag{1}$$

where $E=\hbar^2k^2/2\mu$ is the energy of the system, μ the reduced mass. For the adsorbed gas, it may be necessary to use *effective* molecular masses*. We can obtain the solution of (1) in the form $R(r)\Theta(\theta)$, where $\Theta(\theta)$ is $\sin m\theta$ or $\cos m\theta$, $m=0, \pm1, \pm2, \cdots$. $R(r)$ is obtained by solving

$$\{r^2\cdot d^2/dr^2+r\cdot d/dr+(k^2r^2-m^2)\}R(r)=2\mu\hbar^{-2}r^2V(r)R(r)\ . \tag{2}$$

For $V=0$, the proper solution is given by the Bessel function $J_m(kr)$.

Now we must obtain the solution of (1) with the asymptotic form

$$\phi\sim\exp(ikr\cos\theta)+f(\theta)\exp(ikr)/\sqrt{r}\ . \tag{3}$$

$dQ\equiv|f(\theta)|^2d\theta$ is of dimension of the length and is the differential cross section in the two-dimensional collision. By making use of the well known expansion

$$\exp(ikr\cos\theta)=\sum_{m=0}^{\infty} i^m\,\varepsilon_m J_m(kr)\cos m\theta\ ,$$

$$\varepsilon_m=2-\delta_{m0}\ ,$$

we can easily obtain

$$\phi=\sum_{m=0}^{\infty} i^m\varepsilon_m\sqrt{2/\pi}\exp(i\delta_m)R_m(r)\cos m\theta\ , \tag{4}$$

where $R_m(r)$ is the proper solution of (2) with the asymptotic form

$$\cos(kr-m\pi/2-\pi/4+\delta_m)/\sqrt{kr}\ .$$

The amplitude of the scattered wave is given by

$$f(\theta)=\sqrt{2/\pi k}\exp(i\pi/4)\sum_m \varepsilon_m\exp(i\delta_m)\sin\delta_m\cos m\theta\ , \tag{5}$$

so that the total scattering cross section is

$$Q_t=\int_{-\pi}^{\pi}|f(\theta)|^2d\theta=(4/k)\sum_m \varepsilon_m\sin^2\delta_m\ . \tag{6}$$

The phase shifts δ_m is easily calculated for the uniform potential hole as well as for the uniform potential barrier. For the rigid spheres with radius a, the phases are simply given by $\tan\delta_m=J_m(ka)/N_m(ka)$, where $N_m(z)$ is the Neumann function.

The Virial coefficients for the two-dimensional gas have been studied by Kihara[2] using a simplified intermolecular potential function.

Kinetic theory of the two-dimensional gases is developed along the same line as in the three-dimensional case. Maxwellian distribution in the two-dimensional case is of the form

$$(nM/2\pi\kappa T)\exp(-Mv^2/2\kappa T)dv\ ,$$

where κ is the Boltzmann constant, M the molecular mass, and other notations as usual. Transport coefficients are also obtained without difficulty. Among others the diffusion coefficient of the binary mixture is given by

$$D_{ij}=(\kappa T/2n\mu_{ij})/A_{ij}\ , \tag{7}$$

where n is the total number density, μ_{ij} is the reduced mass of the colliding pair and

$$A_{ij}=\sqrt{2\kappa T/\mu_{ij}}\int_0^{\infty}\gamma^4\exp(-\gamma^2)Q_D(\gamma)d\gamma\ .$$

In the integral

$$\gamma^2=\mu_{ij}g_{ij}^2/2\kappa T\ ,\quad Q_D=\int_{-\pi}^{\pi}(1-\cos\theta)|f(\theta)|^2d\theta\ ,$$

and g_{ij} is the relative incident velocity. Substitution of (5) into the last expression gives

$$Q_D=(4/k)\sum_{m=0}^{\infty}\sin^2(\delta_m-\delta_{m+1})\ .$$

References

1) J. H. de Boer: *The Dynamical Character of Adsorption.* Oxford Univ. Press (1953).

2) T. Kihara: Nihon Sugaku Buturi Gakkaisi **17** (1943) 11.

---

* This was pointed out by Prof. T. Kihara (University of Tokyo), whom the author wishes to thank for discussions.

J. PHYS. SOC. JAPAN **13** (1958) 1406

A Note on the Magnetoresistance Effect of Strain Gauge Wire

By Hideo TAKAKI and Toshiro TSUJI*

Department of Chemistry Faculty of Science, Kyoto University

(Received July 31, 1958)

As previously described[1] the strain gauge of constantan (Ni 45%, Cu 55%) has a notable magnetoresistance effect. The electrical conductivity increases in the presence of magnetic field, while that of non-magnetic metals decreases with magnetic field. The temperature dependence of the magnetoresistance effect of the strain gauge wire is reported in this short note.

The method of measurement of the electrical resistance was the same as in the case of magnetostriction. The strain gauge bonded on copper strip was placed in magnetic fields. Copper has no magnetostriction so that only the change in electrical resistance of the gauge can be measured. To measure the magnetorsistance the method of using such a fine wire is very effective because of its high electrical resistivity.

The results obtained are shown in Fig. 1. At a

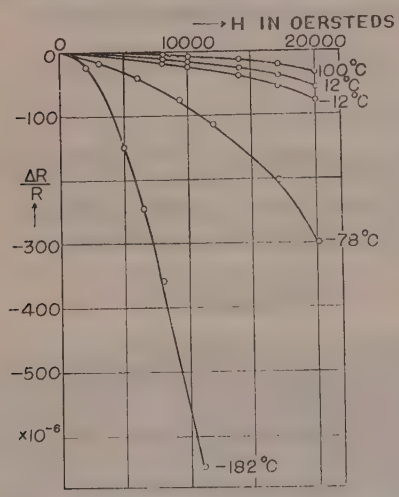

Fig. 1. Magnetoresistance effect of Constantan strain gauge at various temperatures.

constant temperature all the measured point fall on the parabolla described by

$$\frac{\Delta R}{R} = -kH^2 , \qquad (1)$$

k being a constant. The material used is ferromagnetic below 60°K. The tendency that the conductivity increases with magnetic field can therefore be considered to be the magnetoresistance effect of ferromagnetic metal above the Curie point.

We may assume that the above relation (1) can be analytically described by the following equation,

$$\frac{\Delta R}{R} = -k'I^2 = -k'\left(\frac{C}{T-\theta}\right)^2 H^2 , \qquad (2)$$

where k' is a constant and I is equal to the effective magnetization above the Curie point. In Fig. 2 the inverse square root of $-(\Delta R/R)/H^2$ versus absolute temperature was plotted. The plotted points composed a straight line. The Curie point is determined from the intersecting point of the straight line and the abscissa. We see a close agreement between the value thus obtained and that found by other methods.

Gerlach and Schneiderhan[2] measured the magnetoresistance of nickel near the Curie point and concluded that the decrease of electrical resistance with external field was proportional to the square of effective magnetization. Our results coincide

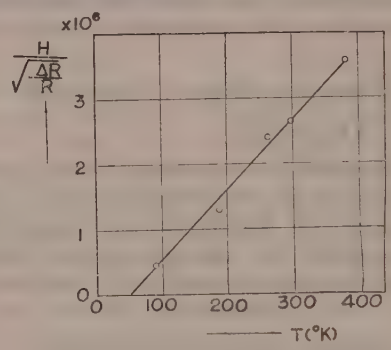

Fig. 2. Temperature dependence of magnetoresistance effect.

$H/\sqrt{-\Delta R/R}$ varies linearly with $(T-\theta)$.

well with their conclusion.

Large magnetoresistance effect causes the error in the measurement of magnetostriction. At room temperature the magnetoresistance effect of the active gauge on ferromagnetic sample is cancelled out by that of the dummy gauge. At the temperature of the boiling point of oxygen magnetoresistance effect of both gauges is too large to be compensated. The error is due to the difference of magnetic fields which act on two gauges. Actually the difference is inevitable because of the demagnetizing field on the sample. The difference between active and dummy gauges in these effects is described as follows,

$$\left(\frac{\Delta R}{R}\right)_{\text{active}} - \left(\frac{\Delta R}{R}\right)_{\text{dummy}} = -k\{(H-NI)^2 - H^2\} , \qquad (3)$$

where $-NI$ denotes the demagnetizing field. This difference is positive in higher fields. Consequently the positive error is expected to intermix in the value of forced magnetostriction.

References

1) H. Takaki and T. Tsuji: Metal Phys. **3** (1957) 111, (in Japanese).
2) W. Gerlach and K. Schneiderhan: Ann. Physik, **6** (1930) 772.

* Present address; Nippon Electric Company Ltd., Tokyo.

J. PHYS. SOC. JAPAN **13** (1958) 1407

A Certain Anomalous Behavior of Iron Sulfides

By Miyuki MURAKAMI and Eiji HIRAHARA

Department of Physics, Faculty of Science, Tōhoku University, Sendai, Japan

(Received September 4, 1958)

We have experimentally studied the anisotropies of magnetic and electrical properties of iron sulfide single crystal[1]. We have recently found an anomalous behavior of susceptibility at a temperature somewhat lower than T_α (the temperature of α-transformation) on a cooling process.

The temperature dependences of susceptibility of single crystal on heating are shown by solid lines in Fig. 1. The curves 1 and 2 are those of the

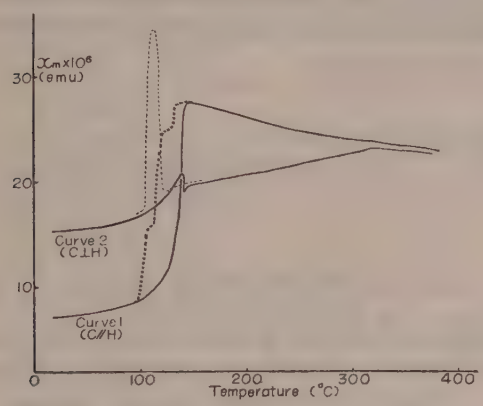

Fig. 1. The temperature dependence of susceptibility of the single crystalline sample. The solid lines are heating curves, and the dotted lines cooling curves.

cases the external magnetic field is applied in parallel and in perpendicular to the c-axis of crystal, respectively. The sample being cooled along curve 2 from a temperature above T_α, a large peak of susceptibility has been observed at 110°C with a temperature width of about 15°C as shown by dotted lines in Fig. 1. On the other hand, the sample being cooled along curve 1, the susceptibility starts to fall at a temperature rather lower than T_α, and exhibits two steps before it settles down to the normal value. The temperature at which the anomaly occurs seems to shift lower with the rate of cooling. The results using of a polycrystalline sample have been observed as shown in Fig. 2, which should be anticipated from the results of single crystal sample.

However, so far no clear explanation of the anomalous behavior have been obtained, it may be provisionally understood as follows. According to

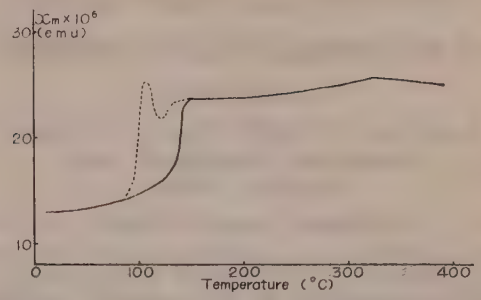

Fig. 2. The temperature dependence of susceptibility of the polycrystalline sample. The solid line is heating curve, and the dotted line cooling curve.

the X-ray measurements[2], the stoichiometric iron sulfide contracts abruptly along c-axis on heating. We have been also observed the same results by using of a interferential dilatometer, and observed a hysteresis phenomenon on cooling. Connecting with the hysteresis phenomenon of lattice, we assume a change of exchange energy on the cooling process take place at a temperature lower than T_α, but a change of anisotropy energy just at T_α. According to our previous works[1], the preferred direction of spins is on c-plane at the temperatures above T_α, and is along c-axis below T_α. When the sample is cooled along curve 2, the susceptibility abruptly increases with the change of anisotropy energy at T_α, and after that it decreased to the normal value because of the increase of exchange energy. When the sample is cooled along curve 1, although the change of anisotropy energy takes place at T_α the susceptibility would keep a considerable value because of the small value of exchange energy, and then, it starts to decrease after the increase of exchange energy.

The studies of these anomalous behavior seem to give a light to an elucidation for the nature of α-transformation, and so they have been required the more detailed measurements, which will be soon reported on another paper by the one of authors.

References

1) T. Kamigaichi, T. Hihara, H. Tasaki and E. Hirahara: J. Phys. Soc. Japan **11** (1956) 606, **11** (1956) 1123.
T. Hihara, M. Murakami and E. Hirahara: J. Phys. Soc. Japan **12** (1957) 743.

2) R. Ueda, T. Ichinokawa and T. Mitsui: Busseiron Kenkyu **33** (1950) 55.

J. PHYS. SOC. JAPAN **13** (1958) 1408~1409

On the Mechanical Loss of Polyethylene

By Yasaku WADA

Department of Applied Physics, Faculty of Engineering, University of Tokyo, Bunkyo-ku, Tokyo

(Received August 14, 1958)

During the past several years many reports[1-14] have been published on the temperature variation of dynamic mechanical loss factor of polyethylene and it has been quite firmly established that for branched polyethylene there exist three loss peaks below the melting point. It is customary to label these peaks as α, β and γ descending from higher temperatures. For unbranched polyethylene, i.e. polyethylene of high crystallinity, it has been observed[8,9,11] that the α peak shifts to high temperatures, the β disappears and the γ remains unchanged. The whole set of these investigations covers the frequency range from 10^{-1} to 10^{7} cps and makes it possible to illustrate the "transition map", which is presented in this short note.

Fig. 1 represents this transition map, giving the frequency used in the measurement in logarithmic scale against the reciprocal of absolute temperature of observed loss maxima. In Fig. 1, numbers beside each point refer to the reference at the end of this note.

While each observed point in Fig. 1 has been obtained by use of different specimens and different modes of vibration, almost all the points lie near a straight line for each transition respectively. A large deviation from the line is found only in the data of Schmieder-Wolf and Butta. Neglecting these exceptions, the gradient of the lines gives apparent activation energy of 40, 30 and 9 kcal/mol for α, β and γ transitions respectively. For the α transition the data are still too scanty for the precise evaluation of activation energy.

The discussion about the molecular mechanism associated with these loss peaks is beyond the scope of this short note.

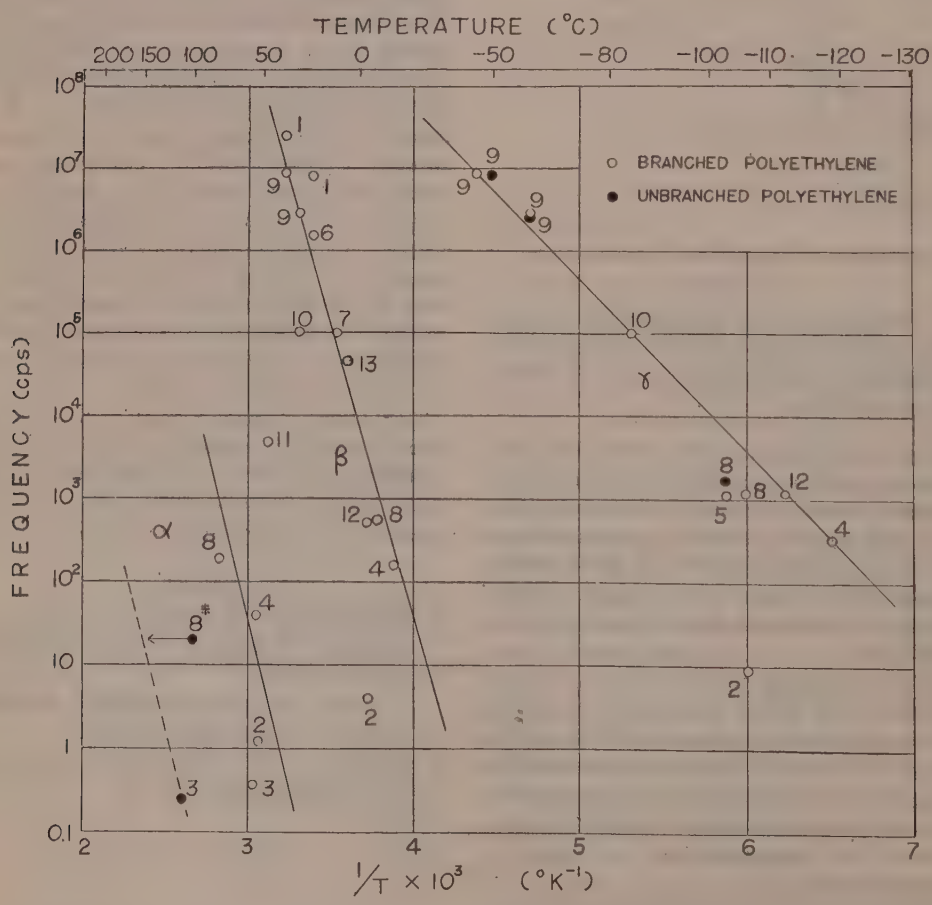

Fig. 1. Relation between temperature of mechanical loss maxima and frequency of measurement for branched and unbranched polyethylene. (* above this temperature)

References

1) W. P. Mason and H. J. McSkimin: Bell Sys. Tech. J. **21** (1952) 112.
2) K. Schmieder and K. Wolf: Kolloid-Z. **134** (1953) 149.
3) L. Nielsen: J. Appl. Phys. **25** (1954) 1207.
4) W. G. Oakes and D. W. Robinson: J. Polym. Sci. **14** (1954) 505.
5) J. A. Sauer and D. E. Kline: ibid. **18** (1955) 491.
6) Y. Wada: J. Appl. Phys. Japan **24** (1955) 287.
7) Y. Wada and K. Yamamoto: J. Phys. Soc. Japan **11** (1956) 887.
8) D. E. Kline, J. A. Sauer and A. E. Woodward: J. Polym. Sci. **22** (1956) 455.
9) Y. Maeda: J. Polym. Chem. Japan **14** (1957) 442.
10) I. G. Michailov and V. A. Soloview: Akust. Zh. **3** (1957) 65.
11) E. Butta: J. Polym. Sci. **25** (1957) 239.
12) N. Fuschillo and J. A. Sauer: J. Appl. Phys. **28** (1957) 1073.
13) Y. Wada and H. Hirose: J. Appl. Phys. Japan **27** (1958) No. 11.
14) S. P. Kabin: Zhur. Tekh. Fiz. **26** (1956) 2628, J. Tech. Phys. **1** (1957) 2542.

J. PHYS. SOC. JAPAN **13** (1958) 1409~1410

Study on the Correlation between the Noise by Hole Generation and Surface Recombination Velocity at Ge Fused Junction

By Kiichi KOMATSUBARA

Semiconductor Dep. Kobe Kogyo Corporation

(Received September 8, 1958)

The effects of surrounding atmospheres upon the saturation current, I_s, and the mean square short circuit noise current of collector junction of Ge fused $p-n-p$ transistor were measured, and the correlation between surface recombination velocity and the $G-R$ noise was studied. The junction was biased at 1V reversely when its noise was measured, and was put in vaccum or some ambient gases, O_2, N_2, H_2. The values of surface recombination velocity, S, were calculated from the Websters equation of saturation current[1],

$$I_s=\pi q p_0 S\{2(a+\lambda_p)^2+(a^2+c^2)\} . \qquad (1)$$

By differentiation, it gives[2]

$$\frac{I_s}{dI_s}\frac{dS}{S}=-\frac{(a^2-c^2)+4a\lambda_p+2\lambda_p}{(a^2-c^2)+2a\lambda_p} , \qquad (2)$$

In the present case, collector dia. $2a$ was 1.25 mm, emitter dia. $2c$ was 0.8 mm, and base width w was 0.145 mm, respectively, and the value of diffusion length λ_p was assumed to be 0.025 mm (s=522 cm/sec).

Then, above equations become

$$I_s=3.3\ \mu A ,$$

and

$$\frac{dS}{S}=1.6\frac{dI}{I} . \qquad (4)$$

The shape of alloy junction cross section of the used transistor was observed after measurements. This junction was nearly perfect, and the surface condition of the junction seemed sufficiently good since the value of I_s at the voltage between 0.5 to 10 volt was similar to calculated value from equation (3). This suggests that the surface leakage current can be neglected, so the reverse current at 1V is only diffusion current of holes generated near the junction, and this means the noise generated in this case is originated by hole generation, i.e., $G-R$ noise, (N_r). The noise spectrum measured at 1V reversely biased voltage is shown in Fig. 1. This spectrum has no indication of $1/f$

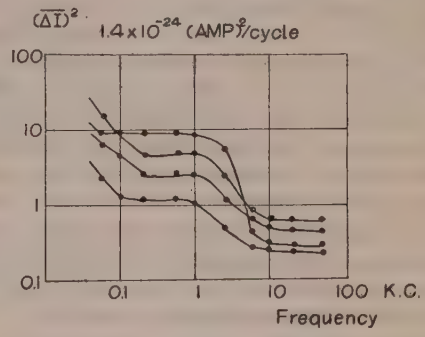

Fig. 1. Noise spectrums of fused p–n junction with various atmospheres at IV reverse bias.

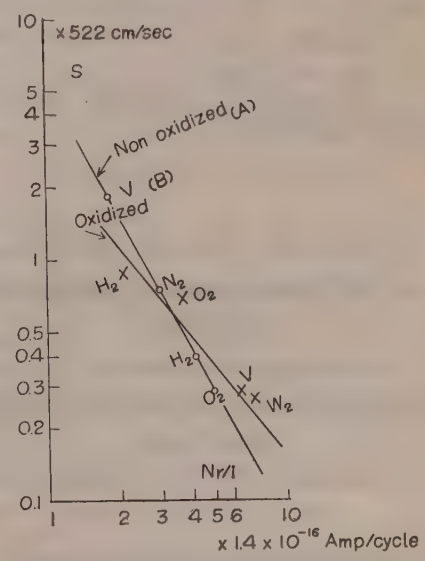

Fig. 2. Correlations between sand Nr/Is.

Table I. The measured value of I_s, N_r with reverse bias of 1 V and center frequency of 1. K.C. and 20°C, S is estimated value from I_s. A: with thin oxide layer. B: with thick oxide layer.

	A				B			
	H_2	O_2	Vac.	N_2	Vac.	N_2	O_2	H_2
$I_s \times 10^{-6}$ ampere	3.0	2.3	1.8	1.7	5.0	2.8	1.8	2.0
$S \times 522$ cm/sec.	0.88	0.66	0.27	0.26	1.82	0.71	0.27	0.38
$N_r \times 1.4 \times 10^{-24}$ (ampere)$_2$/cycle	3.1	6.0	9.5	1.5	3.0	5.0	9.0	8.0
$N_r/I_s \times 1.4 \times 10^{-20}$ ampere/cycle	1.0	2.3	5.6	6.0	0.6	1.8	5.0	4.0

noise component at 1 KC. In Table I there are presented the data of I_s and N_r measured in various atomspheres as 1V reverse voltage and center frequency of 1 K.C. and S estimated from Eq. (4). A and B are obtained from the same sample with different surface treatment to give the appreciable thickness of oxide layer before each measurement. Fig. 3 is the correlation between S and N_r/I_s and is represented by

$$N_r = CI_s S^{-L}, \qquad (5)$$

where C and L are constants, and the value of L in Fig. 2 are 1~1.5. The $G-R$ noise in germanium bar is a function of square of current flowing througn crystal[3], but equation (5) may be able to be explained, in the case of alloy type germanium $P-N$ junction with small value of reverse bias voltage, as it is assumed that the noise may be caused by the fluctuation of the minority carriers generated on effective area for generation, and the fluctuation by the conductivity modulation by the variation of surface potential may not be contributed to the $G-R$ noise (at this case, $w\tau_h \ll 1$).

References

1) W. M. Webster: Prc. Inst. Radio Engrs. **42** (1954) 914.
2) J. E. Rhomas Jr and R. H. Rediker: Phys. Rev. **101** (1956) 984.
3) J. E. Hill and K. M. Van Vlet: J. of App. Phys. **29** (1958) 177.

J. Phys. Soc. Japan **13** (1958) 1410

On RF Electrodeless Discharges in a Capillary

By Shigeo Takemoto
Department of Physics, Tohoku University
Mineo Kasai
Tohoku Electric Power Company

(Received August 18, 1958)

Electrodeless discharges in high-frequency fields, from 30 Mc to 100 Mc, have been investigated. The experimental configurations are shown in Fig. 1(a) and (b). The dumb-bell shaped discharge tubes made of hard glass and of fused silica were prepared, the spheres of about 50 mm in diameter were connected by a capillary, which is 0.1~1 mm in diameter and about 15 mm in length. The following phenomena were found at the pressure of about 10^{-2}~10^{-4} mm Hg.

(1) When discharge tube was placed parallel to the electric field of the condenser, discharge through the capillary, with bright luminescence, was found, as shown in Phot. 1(a). If the capillary was smaller than 0.1 mm in diameter, the long slender beems from the capillary extended to the ends of both spheres, and plasma density was so high that the inside of the capillary made of hard glass was damaged with many cracks in a few tenth of second. And we were able to get long term discharge only by a tube made of fused silica.

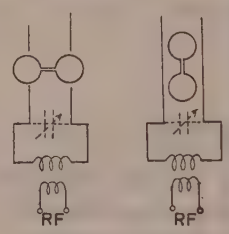

(a) (b)

Fig. 1.

(a) (b)

Phot. 1.

(2) When the tubes were placed parallel to the magnetic field of the condenser, only faint luminescence in the spheres and no discharge in the capillary were found, as shown in Phot. 1(b).

We believe the former type of discharge to be quite useful for light source and ion source. We are going to study the deutron ion source of this type.

J. Phys. Soc. Japan **13** (1958) 1411~1412

Dichroism of Color Centers in KCl Crystal

By Takehiko Ishii, Tetsuhiko Tomiki and Masayasu Ueta

Department of Physics, The Faculty of Science, Tohoku University, Sendai, Japan

(Received September 5, 1958)

Many authors[1] have studied the dichroic properties of color centers in alkali halide crystals by means of both absorption and emission spectra. Recently, Kuwabara and Misu[2] observed that the absorption coefficient of the M band measured with light polarized along the [011] direction (denoted as $A^{M}_{[011]}$ for brevity) decreased but $A^{M}_{[0\bar{1}1]}$ remained constant, when the M band was bleached with light polarized along the [011] direction, and pointed out the discrepancy with the earlier results by one of the present authors. We considered that this difference may have been caused by the dependence on the crystal temperature, and studied the thermal effects on the bleaching processes of M centers with polarized light. The dichroic properties of other centers were also measured.

F centers were formed as usual by heating KCl crystal with potassium metal (M absorption was detected slightly). The crystal was irradiated with monochromatic light (λ=560 mμ, slit width=5 mμ) polarized along [011] at room temperature in such a way as to produce only M centers. In this case, the dichroism in the F and M bands were negligible. Observations were made at the temperatures 0°C, 27°C, 63°C, 83°C and 100°C for the dichroic behaviors in the F, M and R bands in the course of irradiation with M light (λ=820 mμ, slit width =40 mμ) polarized along the [011] direction. Unless otherwise stated, M centers were bleached with this polarized light throughout these experiments.

The results are summarized as follows:

i) 27°C: For brevity, we define the degree of dichroism as $D=(A_{[0\bar{1}1]}-A_{[011]})/(A_{[0\bar{1}1]}+A_{[011]})$. As the bleaching of M centers proceeded, $A^{M}_{[011]}$ decreased, while $A^{M}_{[0\bar{1}1]}$ did not change as shown in Fig. 1a, and the dichroism appeared in the F and R bands. This dichroic behavior of M centers corresponds to the results by Kuwabara et. al[2]. In this case, $D_F<0$, $D_R>0$ and $D_M>0$ were obtained. Subsequent irradiation with light (λ= 560 mμ, slit width=5 mμ) polarized along the [011] direction made D_F tend to zero from its negative value and made D_M and D_R tend to zero from their positive values, and then changed their signs respectively. In the case of irradiation with F light polarized along [$0\bar{1}1$], these reversals of signs did not occur. During the course of this F-bleach, a shoulder band appeared at the shorter wavelength side ($\lambda \leq 550$ mμ) of the F-peak. This shoulder was also observed when the crystal containing only F centers was bleached with F light polarized along the [011] (or [$0\bar{1}1$]) direction. This fine structure of the F band may correspond to the luminescence excitation doublet in the F band found independently by Kuwabara and Misu[3].

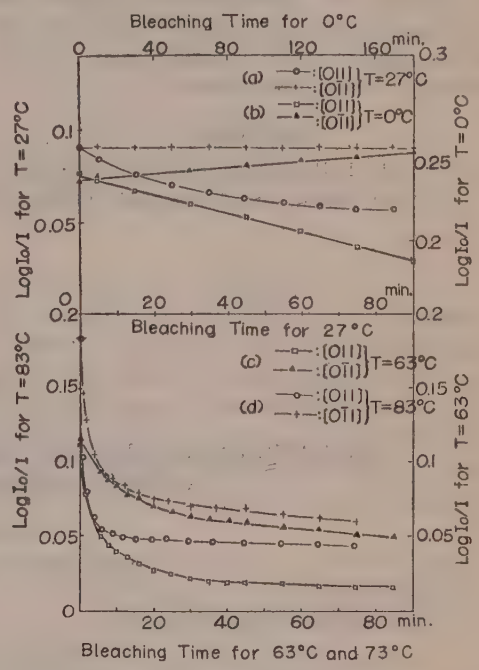

Fig. 1. Variation of absorption coefficients of the M-band for light polarized in the [011] and [$0\bar{1}1$] directions when the M-band was bleached with light polarized in [011] direction at different temperatures of 0°, 27°, 63°, and 83°C.

ii) 0°C: It was more difficult to bleach the M band at this temperature than at room temperature. When the crystal was illuminated with polarized M light, $A^{M}_{[011]}$ decreased and $A^{M}_{[0\bar{1}1]}$ increased. (cf. Fig. 1b).

iii) 63°C and 83°C: Both $A^{M}_{[011]}$ and $A^{M}_{[0\bar{1}1]}$ decreased on irradiation with polarized M light as shown in Figs. 1c and 1d. These results will correspond to our early report[1]. The degree of dichroism either remained nearly constant or decreased slightly when the crystal was kept in the dark for several hours at these temperatures. The absorption did not change in the wavelength region of the R band during these experiments and the shoulder just described could not be detected in the F band.

iv) 100°C: In the similar bleaching experiment, the dichroism of the M band could not be found after the bleaching time of 5 minutes. Though it

could be produced by bleaching the F band with polarized light, it was very small and unstable thermally. The critical temperature, at which it vanishes thermally, lies probably in the vicinity of 100°C.

These facts may probably be the evidence that the dichroic behaviors of the M band are severely affected thermally and that the dichroism is related not only with the reorientation of symmetry axes of M centers in their excited states, but also with the ionic motions. The experiment is now being extended to lower temperatures.

References

1) M. Ueta: J. Phys. Soc. Japan **7** (1952) 107.
C. Z. van Doorn and Y. Haven: Phys. Rev. **100** (1955) 753.
C. Z. van Doorn: Phil. Res. Repts. **12** (1957) 309.
J. Lambe and W. D. Compton: Phys. Rev. **106** (1957) 684.
H. Kanzaki: Phys. Rev. **110** (1958) 1063.
2) G. Kuwabara and A. Misu: J. Phys. Soc. Japan **13** (1958) 1038.
3) G. Kuwabara and A. Misu: J. Phys. Soc. Japan **13** (1958) 1067.

Errata

Crystal Structure and Phase Transition of Some Metallic Halides (IV) On the Anomalous Structure of α-AgI

By Sadao HOSHINO

J. Phys. Soc. Japan **12** (1957) 315

P. 319 left column, line 4 to 5

0 1/8 1/8 Ω, 0 7/8 7/8 Ω ;
0 1/8 7/8 Ω, 0 7/8 1/8 Ω .

should be read

1/2 1/8 1/8 Ω, 1/2 7/8 7/8 Ω ;
1/2 1/8 7/8 Ω, 1/2 7/8 1/8 Ω .

P. 321 left column, in the equation (4), $\Delta f_s \cdot \Delta f_{s'}$
should be read $\langle \Delta f_s \cdot \Delta f_{s'} \rangle$

in the equation (6), $(\Delta f_s)^2$ and $\Delta f_s \cdot \Delta f_{s'}$
should be read $\langle (\Delta f_s)^2 \rangle$ and $\langle \Delta f_s \cdot \Delta f_{s'} \rangle$

Adsorption of Water Vapour on Glass and Other Materials in Vacuum

By Hiroaki OKAMOTO and Yutaka TUZI

J. Phys. Soc. Japan **13** (1958) 649

Eq. (11), page 652, $\int_0^t \frac{Nax}{Kc_1} dx$ should read $\int_0^t \frac{Nax}{Kc_1} dx$.

Adsorption of Water Vapour on Lead Borosilicate Glass in Vacuum

By Yutaka TUZI and Hiroaki OKAMOTO

J. Hhys. Soc. Japan **13** (1958) 960

Caption of Fig. 7, page 964, should read: "Rate of adsoption versus amount of H_2O adsorbed."

JOURNAL OF THE PHYSICAL SOCIETY OF JAPAN Vol. 13, No. 12, DECEMBER, 1958

On the Observation of Magnetic Poles

By Eiichi GOTO

Department of Physics, University of Tokyo

(Received August 8, 1958)

Expected behaviours of magnetic poles, especially their interaction with magnetic matters are considered. The magnetic pole is supposed to be an elementary particle having magnetic true charge satisfying Dirac's quantum condition, namely 68.5 times as large as the electron charge. Magnetic poles would be attracted and trapped in ferromagnetic and paramagnetic matters. The magnetic minerals are the most promising source of magnetic poles and an efficient method for detecting the presence of even one magnetic pole among thousands of tons of magnetic minerals is proposed. This method is sensitive enough to detect such a small amount of magnetic pole as has escaped from the whole cosmic ray observations so far conducted.

§ 1. Introduction

Studies conducted so far over centuries on electromagnetism have bequeathed us the empirical law that denies the existence of magnetic true charge or magnetic poles in the nature. From the viewpoint of general theory, however, it is one of the prominent characteristics of classical electromagnetics that electricity and magnetism are perfectly symmetric with each other. The classical theories hold good without any modification even if magnetic true charge should exist. Therefore, it is a universal question anyone may raise "why only a special case where magnetic true charge does not exist actually appear in the nature, while there regions the all-embracing law applicable to more general cases where it does exist". Nevertheless, only few studies seem to have been made relating to this question and, within my knowledge, there are only those reports listed at the end of this paper.

Among them, Dirac[1),2)] discovered the following very important fact. He gave methods for generalizing quantum electrodynamics so as to be applied to cases where a "magnetic pole" i.e. an elementary particle having magnetic true charge, exists. As a result of this generalized quantum theory, he showed that the smallest electric charge quantum, e and the smallest magnetic charge quantum, g_0 must satisfy the following quantum condition:

$$e/g_0=4\pi e^2/hc=2/137 \qquad (1)$$

The right side is the fine structure constant multiplied by 2 and the numerical value of g_0 (in e.m.u.) is 68.5 times greater than that of e (in e.s.u.).

He says that an enormous energy is needed to separate magnetic poles of opposite sign, and this fact can very well explain why such particles have never been observed yet. Furthermore, formula (1) may give the only theoretical explanation so far known of the quantization of electric charge to integral multiples of e.

In regard to his theory of magnetic poles, Dirac[1)] himself states, "One would be surprised if Nature had made no use of it", and I also think his theory is of exceeding elegance.

In this paper, assuming the existence of magnetic poles that satisfy Dirac's quantum condition (1), behaviour of magnetic poles especially their interaction with magnetic matters will be treated. It will be shown that magnetic poles are attracted and trapped in magnetic matters. A method, utilizing this property, for detecting the existence of a magnetic pole and some other possible experiments will be discussed.

Although there are some experimental reports[4)-6)] asserting the existence of magnetic poles, no one has yet received general acceptance. This seems to imply that the magnetic pole, even if it existed, might not be found much in amount. Hence, special stress will be lain on methods which will most efficiently collect magnetic poles. Possible sources of magnetic poles and experimental facts such as those obtained from cosmic ray observations will also be discussed. The most possible source of magnetic poles seems to be magnetic minerals on the earth and an effici-

ent method capable of detecting even one magnetic pole among thousands of tons of magnetic ores will be proposed.

§ 2. Behaviour of a Magnetic Pole in Magnetic Field due to various Sources

The magnetic pole treated here is assumed to be an elementary particle with magnetic charge g_0, without electric charge and unaffected by special forces such as nuclear force, etc. The motion of such a magnetic pole will be determined by magnetic field and Lorentz force due to electric field. In regard to the sources of magnetic field, the following four kinds will be considered:

f1) Electric Current
f2) Permanent Magnet
f3) Magnetic Image
f4) Other Magnetic Poles

The magnetic field produced by electric current has potential which is multi-valued and has neither minimum point nor maximum point. Therefore, this magnetic field will be suitable for giving acceleration to a magnetic pole and will also be useful in transporting it from one place to another, but will not be suitable to confine a magnetic pole into a definite small space.

Next, the potential of magnetic field produced by a permanent magnet has maximum and minimum points in the neighbourhood of its "poles" (of the magnet). Hence, a permanent magnet will be capable to trap magnetic poles at these points. An explanation of this fundamental difference between these two kinds of magnetic fields may be given as follows. When a magnetic pole g_0 turns n times around electric current I, it obtains energy $4\pi nIg_0$ and this energy after all is supplied from the battery which supplies the current I.

On the other hand, such a phenomenon can never take place in a permanent magnet, since the magnetized state of a permanent magnet i.e. a ferromagnetic body in the state of spontaneous magnetization, corresponds to the lowest quantum energy state, and such a energy source as in the former case does not exist in the permanent magnet.

The magnetic image above mentioned means the magnetic analogy of electric field induced when an electron is in the neighbourhood of a dielectric body or a conductor. In order to pull out an electron from a conductor, an energy called work function is needed. Similarly, a certain amount of energy will be necessary to pull out a magnetic pole from paramagnetics of ferromagnetics and it will be called the trapping energy W_m.

Now, we shall calculate the trapping energy. For the sake of simplicity, let us suppose that magnetics here is isotropic and has such a magnetizing character that the magnetisation M changes linearly from 0 to saturation value M_s when the applied field H changes from 0 to a certain value H_s. The trapping energy W_m in this case may be considered as the energy difference between two cases: one in which a magnetic pole g_0 is placed in vacuum (suffix v) and the other in which it is placed in infinitely vast magnetics (suffix f). Namely:

$$W_m=\int_{\text{volum}} dv\,\frac{1}{4\pi}\int_B (H_v dB_v - H_f dB_f) \quad (2.1)$$

By using polar coordinates and considering the following relations;

$$B_v=H_v=B_f=g_0/r^2 \quad (2.2)$$

$$H_f=B_f-4\pi M_s\,, \quad \text{for} \quad r<R=\sqrt{\frac{g_0}{H_s+4\pi M_s}} \quad (2.3)$$

$$H_f=\frac{B_f H_s}{H_s+4\pi M_s}\,, \quad \text{for} \quad r>R \quad (2.4)$$

(2.1) gives the following value:

$$\begin{aligned} W_m &= \int_0^\infty r^2 dr \int_B 4\pi M dB_f = \int_R^\infty \frac{4\pi M_s B_f^2 r^2 d}{2(H_s+4\pi M_s)} \\ &\quad + \int_0^R r^2 dr \left(\int_0^{H_s+4\pi M_s} 4\pi M dB_f \right. \\ &\quad \left. + \int_{H_s+4\pi M_s}^{B_f} 4\pi M_s dB_f \right) \\ &= \frac{4}{3} g_0^{3/2} (4\pi M_s)^{1/2} (1+H_s/4\pi M_s)^{-1/2} \end{aligned} \quad (2.5)$$

Considering that the magnitude of $4\pi M_s$ is much greater than H_s for ordinary ferromagnetics, we may neglect H_s in (2.5) and obtain the following numerical value:

$$W_m=4.966\sqrt{4\pi M_s}\ \text{eV}\ (4\pi M_s \text{ in gauss}) \quad (2.6)$$

Futher, considering that the magnitude of $4\pi M_s$ for ordinary ferromagnetics is from 1000 to 20000 gauss, (2.6) gives the value from 160 to 700 eV.

Next, we shall consider paramagnetics, of which the relation between the magnetization M and applied field H is given in terms of

Langevin function $L(x)$ as follows:

$$M=M_sL(H\beta/kT)\,,\ L(x)=\coth x-1/x\,,\ M_s=N\beta\,, \tag{2.7}$$

where β is the magnetic dipole of a molecule, N the number of dipoles per unit volum and M_s the saturating magnetization. As the susceptibility of ordinary paramagnetics is much smaller than unity, we may replace H in (2.7) by B and (2.5) becomes

$$\begin{aligned} W_m&=\int_0^\infty r^2dr\int^B 4\pi M_sL(B\beta/kT)dB \\ &=\int_0^\infty r^2dr\int_0^{g_0} 4\pi M_sL(g\beta/r^2kT)g/r^2dg \\ &=\frac{2}{3}L4\pi M_sg_0^{3/2}\sqrt{\beta/kT}\,, \end{aligned} \tag{2.8}$$

where

$$L=\int_0^\infty L(1/x^2)dx\,. \tag{2.9*}$$

Using the values $T=300°\mathrm{K}$ and $\beta=1$ Bohr magneton, we obtain:

$$W_m=1.28\times 4\pi M_s\times 10^{-3}\,\mathrm{eV}\,. \tag{2.10}$$

Further, considering that the magnitude of $4\pi M_s$ for ordinary paramagnetics is from 1000 to 10000 gauss, (2.10) gives the value from 1.28 to 12.8 eV.

As this value of trapping enegry and that given by (2.6) for ferromagnetics are both much greater than the thermal energy of normal temperature (about 1/40 eV), *magnetic poles will be attracted and trapped in ferromagnetics or paramagnetics and would not escape from it by thermal motion.*

As may be observed from formula (2.5), the trapping energy depends on the material constant $H_s/4\pi M_s$ only through its square root: therefore, it will be not so difficult to calculate the trapping energy for actually existing magnetic materials with fairly good accuracy.

From the fore-going studies we have learnt that any one of the magnetic matters, permanent magnet, ferromagnetics and paramagnetics has the property of attracting and trapping magnetic poles. When a magnetic body in which magnetic poles are trapped is brought in an external field which exceeds a certain critical value, the magnetic poles will be pulled out from the magnetic body. For the sake of simplicity, we shall assume that the external field is uniform, and shall call the critical value above mentioned the critical stripping field H_{st}.

In case there is no external field, a fairly accurate value of the trapping energy was calculatable by a phenomenological treatment. On the other hand, the calculation of the critical stripping field H_{st} will be sensitive to molecular structure of the surface, so atomistic treatment will be necessary and it will be extremely difficult to calculate the accurate value of H_{st} without carrying out any experiments at all. Consequently, only rough estimations of the upper and lower bounds can be given here.

Nevertheless, it will be good enough to give quantitative basis for experiments discussed in later sections. The image field H_i attracting a magnetic pole g_0 placed at a distance R from a plane boundary of soft ferromagnetics is given, if the distance is not so small as to cause saturation, by an image $-g_0$ placed at a distance $2R$. Assuming that the permeability is much greater than unity, we obtain

$$H_i=g_0/(2R)^2\,,\quad \text{if}\quad R^2>\frac{2g_0}{4\pi M_s}\,. \tag{2.11}$$

Further by considering the concentrating effect of magnetic flux, we may obtain the following lower bound of H_{st} for a sphere made of soft ferromagnetics:

$$H_{st}>\frac{4\pi M_s}{16}\,. \tag{2.12}$$

From this formula and the facts that saturation $4\pi M_s$ of magnetite is 6000 Gauss and the value of terrestrial field is about 0.5 Gauss, we may come to the following conclusion. *Magnetic poles trapped in magnetite will not part with it by terrestrial magnetic field.*

In order to obtain an upper bound for H_{st}, the following has to be taken into consideration. An atom is trapped inside ordinary matters with trapping energy which is generally less than and at most equal to the chemical binding energy E_c. Especially, in crystals an atom is trapped by a periodic potential, E_c in depth. Assuming that the form of the periodic potential is sinusoidal, an external force f acting on an atom greated than $\pi E_c/l$, where l is the lattice constant, will surely separate the atom from the substance.

* The numerical value of definite integral (2.9) has been calculated by an electronic computer PC-1 and the result is: $L=1.08778316$.

A magnetic pole trapped in a magnetic substance will also be separated if a large force as above acts on it, because even in the extreme case the magnetic pole would be separated accompanying an ordinary atom.

Here, by using the values, $E_0=2$ eV, $l=1$Å and $g_0H=\pi E_0/l$, we obtain $H=30000$ oersted. This field may differ from the external field because of demagnetizing field but not much since the saturation value of any existing magnetics is less than 30000 oersted.

Unless a more accurate information on the critical stripping field H_{st} is obtained, the word, "a magnetic field greater than H_{st}", in the later discussions must be understood as "a magnetic field as strong as possible and at least stronger than 30000 oersted".

So far, we have neglected possibility of interactions of other than electromagnetic origin. As for the behaviour of magnetic poles in ferromagnetics, however, this is not essential. As the range of such interactions is expected to be very short, if it were of repulsive nature, it would not cause any significant change in the results obtained. If it were of attractive nature, the trapping energy and other results might be affected by a small amount, since even in a extreme case in which the interaction is so strong as to form a compound particle the trapping energy (which is more than 100 eV) would only change by amount of chemical binding energy of atoms (which is about 2 eV or less).

On s4), the influence of magnetic field caused by other magnetic poles will be worth considering only if magnetic poles should be obtained in large amount. Therefore, it will not be treated here.

§ 3. Possible Sources of Magnetic Poles

The fact that no evidence of the existence of magnetic poles has yet been obtained seems to imply that even though it should exist, it would not amount to much. Possibly the reason will be sought, as Dirac says in that the magnetic charge quantum, g_0 is much greater than electric charge quantum, e. Although there is no reliable theory relating to the mass of a magnetic pole, if we assume that it has the same classical radius as an electron i.e. $r_0=e^2/mc^2=2.818\times10^{-13}$ cm, the mass will be $(137/2)^2=4692.25$ times greater than the mass of an electron, and at least energy of 4.7×10^9 eV will be necessary to separate magnetic poles of opposite sign, or in other words to give rise to pair creation.

If it should be possible for us to find magnetic poles on the earth, they would be from one of the following four sources:

s1) Those existed since the formation of the earth.

s2) Those contained in the primary cosmic ray and trapped in the earth.

s3) Those created by the interaction between primary cosmic ray (nucleons) and the substance of the earth.

s4) Those created by artificial accelerators.

The first three relate to possible natural sources. Through the studies in § 2, magnetic poles should be attracted and trapped in paramagnetic of ferromagnetic matters, and it is also known that such magnetic matters are very widely distributed among earth crust. Hence, natural magnetic poles should be concentrated on magnetic minerals in earth crust. Specially, if a state near thermal equilibrium is realized, magnetic poles will be concentrated in the largest rate on ferromagnetic minerals such as magnetite and magnetite sand.

In regard to s1), as the inside of the earth is of exceedingly high temperature, ferromagnetics will not be present and thermal agitation will be fairly large; therefore, the magnetic poles will move by force of terrestrial magnetism and will finally be attracted and trapped in magnetic minerals distributed among earth crust.

As for magnetic poles, s2) and s3), originated from cosmic ray, the large ionization loss of magnetic poles, referred to later, must be taken into consideration. The energy of magnetic poles will be lost at high altitude because of ionization loss and other losses in the air, and those which receive downward force from terrestrial field will reach the surface of the earth and will finally be trapped in magnetic minerals. In the northern and southern hemisphere, the polarity of these magnetic poles will be opposite with each other.

On s2) and s3), the integration effect on time i.e. time elapse of at least 10^8 years since the formation of earth crust, will be a very important factor.

If we think of the cosmic ray as a source for magnetic poles, a question may arise as

to its relation to the fact that no trace of a magnetic pole has yet been found in any of the cosmic ray observations so far conducted. The total integration of the cosmic ray observations will surely not exceed the value: a detector of 100 m^2 being operated for 100 years. Though this value seems to be an extreme over-estimation, if it is taken into consideration that magnetic poles have never been searched purposely, the value is equal to that which came into only 1 cm^2 in 10^8 years. In other words, the total sum of the cosmic ray observations so far conducted corresponds at most only to the examination of magnetic minerals under 1 cm^2 of the surface of the earth. Consequently, the failure of direct observations made on cosmic ray to find magnetic poles would be no deterrent of starting the examination of magnetic minerals.

Next, as to the accelerator, the largest ones at present are the Phasotron and the Bevatron and generally these produce 10^{10} eV protons at the rate 10^9 particles/sec. Consequently, by operating these continuously for 1 year, we may obtain 3×10^{16} particles. As the intensity of primary cosmic ray having energy greater than 10^{10} eV is about 10^{-1} particles $sec^{-1}\,cm^{-2}\,sterad^{-1}$, the above value corresponds to the cosmic ray which came into only 15 cm^2 in 10^8 years. Besides, energy of 10^{10} eV does not seem enough to cause pair creation of magnetic poles. If this is the case, we will come to the following conclusion. *In order to find a magnetic pole, the only way possible at present to do is to examine magnetic minerals in the earth crust.*

§ 4. A Method for Collecting and Detecting Magnetic Poles

Magnetic poles will be separated from magnetic minerals by applying a external magnetic field much stronger than the critical stripping field H_{st} discussed in § 2. The recollection of the magnetic poles separated in this way will be accomplished by placing a ferromagnetic plate (this will be called the "target") at a position where the magnetic field becomes weaker than H_{st}. In this operation, magnetic poles of opposite polarity will fly out to opposite directions so that it will be possible to collect them on separate targets.

By this method, it will be possible to transfer even one magnetic pole among thousands of tons of magnetic minerals to a target of relatively small size, say 1 kg in weight. By repeating similar operations in each of which the magnetic pole is separated from a target and re-collected into another smaller target, it will be possible to transfer the magnetic pole into a magnetic body of very small size.

One method of detecting the existence of a magnetic poles is to observe the movement of a small magnetic particle which is supposed to have trapped a magnetic pole. In an external magnetic field less than the critical stripping field H_{st}, the particle will show behaviour as if it were only possible to be explained by the fact that the particle has magnetic true charge. For example, if an iron sphere, in which a magnetic pole g_0 is trapped and having diameter less than 2/100 mm, is placed in a uniform vertical magnetic field of 1000 oersted strong, the sphere will move upwords conteracting gravity. Considering (2.12), the field of 1000 oersted will be less than H_{st} and the observation of the motion of a sphere, 2/100 mm in size, will be made very easily.

It seems that Ehrenhaft[4)-6)] and others might have observed such a phenomenon as above.

In order to transfer a magnetic pole trapped in a target to such a particle as used in the above experiment, iron powder, i.e. ensamble of such particles, may well be used as the final target. The particular one particle having trapped a magnetic pole, may be separated from other particles by means of a magnetic field.

It will also be possible to measure the value of the magnetic charge quantum, g_0 by observing the motion of the above mentioned particle in viscous fluid and this will be almost the same as Millikan's oil drop experiment.

§ 5. Discussion and Remarks

The experiments in regard to the detection of magnetic poles discussed in § 4 were static. These static experiments seem to be the most effective and unfailing method of collecting and detecting magnetic poles existing only in very small numbers. If once the existence of a magnetic pole has been confirmed in this way, it will be quite easy to carry out various kinds of dynamic experiments by accelerating the magnetic pole. It is easy to ac-

celerate magnetic poles up to high energy. For 1 e.s.u. of electric field is 300 volt/cm and magnetic charge quantum is 68.5 times as large as the electron charge, 1 orsted cm of magnetic field will accelerate a magnetic pole, g_0 up to $300\times68.5=2.055\times10^4$ eV. Here, take a magnetic field, 10000 orsted strong and 100 cm long; it will provide an accelerator of 2×10^{10} eV, and further, it will be not very difficult to obtain accelerators 100 or even 1000 times stronger. In order to inject magnetic poles into such accelerators, it is only to apply a impulsive field sufficiently greater than the critical stripping field H_{st} on the magnetic body in which it has been confirmed by static experiments that magnetic poles have been trapped. The great value of ionizing power of magnetic poles has been already pointed out and calculated by Dirac[2], Yazaki and Miyatake[7]. Especially, Dirac states, "they would appear as heavily ionizing particles and would be distinguishable from ordinary charged particle by the property that the ionization they produce would not increase towards the end of their range, but remain roughly constant". Therefore, it would be quite easy to observe the traces of magnetic poles by cloud chambers and the like. From these dynamic experiments, we shall be able to study interactions between magnetic poles and other elementary particles.

Particulary, the charge to mass ratio, g_0/m will be measured through the speed of magnetic poles of which the energy is known.

As a magnetic pole never vanishes unless it should meet another magnetic pole of opposite polarity, the magnetic pole used in a dynamic experiment can always be trapped inside a ferromagnetic shield surrounding the whole apparatus of the experiment, and afterwards it may be re-collected by the method discribed in § 4. Therefore, even one magnetic pole should be found in the whole world, then the one could be used repeatedly for almost all kinds of experiments except those relatihg to annihilation.

In order to study the interaction between two magnetic poles of opposite polarity, unless we could obtain magnetic poles in large quantity, there will be no other way but the static method. When two small magnetic bodies (spheres of diameter 1/100 mm, for example) which have each trapped a magnetic pole of opposite polarity are put together, reaction will occur between magnetic poles attracting each other. From the energy of γ ray produced in this reaction, we shall be able to know whether these two have caused annihilation as between an electron and a positron or produced an atom as between an electron and a proton.

§ 6. Conclusion

We have found out that if a magnetic pole should exist it should be attracted and trapped by magnetic matters. From this property, it is presumed that natural magnetic poles, which have either been existing since the formation of the earth or originated from cosmic ray, are concentrated on magnetic minerals in the earth crust and also it has become known that there is an efficent and unfailing method of collecting and detecting such natural magnetic poles. Besides, we have reached the conclusion that even though direct observations of cosmic ray or experiments relating to artificial accelerators may fail to find magnetic poles, there is fairly large probability of discovering them among magnetic minerals because of integration effect lasting at least for 10^8 years. Under these circumstances, *I* believe it is at least worth while to try experiments with regard to magnetic minerals and hope that they will be started at an earliest opportunity.

On closing the author wishes to express his sincere thanks to professor H. Takahasi for his encouragement and discussion.

References

1) P. A. M. Dirac: Proc. Roy. Soc. **133** (1931) 60.
2) P. A. M. Dirac: Phys. Rev. **74** (1948) 817.
3) I. Tamm: Z. f. Phys. **71** (1931) 141.
4) F. Ehrenhaft: Comptes Rendus **227** (1948) 626.
5) F. Ehrenhaft: Phys. Rev. **67** (1945) 63, 626.
6) C. B. Reynolds: Phys. Rev. **67** (1955) 202.
7) T. Yazaki and O. Miyatake: Preprint for the sectional meeting on elementary particles of the Phys. Soc. of Japan (may 17, 1957).

JOURNAL OF THE PHYSICAL SOCIETY OF JAPAN Vol. 13, No. 12, DECEMBER, 1958

Gamma Ray Spectroscopy of Mn^{54}

By Toshio KATOH, Masao NOZAWA, Yasukazu YOSHIZAWA
Department of Physics, Faculty of Science, Osaka University, Osaka
and Yujiro KOH
Faculty of Science and Engineering, Osaka City University, Osaka

(Received August 20, 1958)

Internal conversion electrons of 0.84 Mev gamma ray were measured by a two-directional focusing beta-ray spectrometer, and it was determined that $E_\gamma=837.9\pm0.3$ kev and $K/L+M=8.5\pm0.7$. Weak gamma rays were searched, using scintillation counters, but no gamma ray was observed.

§ 1. Introduction

It has been well known that Mn^{54}, 290 days, dacays to the first excited state of Cr^{54}, through the electron capture. Neither positive nor negative beta ray was found[1]. The 0.84 Mev gamma transition from the first excited state is E2 transition and the spin and parity of this level are $2+$[2),3)]. The internal conversion coefficient or K/L has not been reported.

The internal conversion electrons of this gamma ray were measured using the two-directional focusing beta-ray spectrometer with the mean radius, $\rho=40$ cm[4], and the gamma ray energy and $K/L+M$ were determined. As the gamma ray of Mn^{54} was precisely measured and moreover it is single gamma ray, Mn^{54} should be used as a good standard gamma emitter, especially, for the calibration of the scintillation spectrometer.

In general the second excited state of even-even nucleus is expected to be about twice higher than the first excited state. It was measured that the energy 0.528 Mev[5] is emitted in the electron capture. Hence the decay energy between the ground states of Mn^{54} and Cr^{54} is 1.37 Mev, which is expected to be lower than the second excited state. Nevertheless in order to investigate whether the second excited state is lower than the ground state of Mn^{54} or not, weak gamma rays were searched for.

§ 2. Sourse Preparation

Mn^{54} was produced by bombarding the internal target of Cr with deutron beam accelerated by the Osaka 11.4 Mev cyclotron. Cr was electroplated on copper sheet. After bombarding Mn was oxidezed by Br_2 and separated by the radiocolloid method[6]. The carrier free source for spectrometer was deposited on 0.8 mg/cm² myler film covered with thin aluminum layer.

§ 3. Gamma Ray Energy and $K/L+M$

The internal conversion lines of the 0.84 Mev gamma ray were measured. In the case of the precise energy measurement, the gamma ray of Co^{60} and Cs^{137} were used for the standard gamma rays and the gamma rays of Mn^{52} were also used for the substandards[7]. The results are shown in Table I. The resolution of the spectrometer was 0.7 percent in this measurement.

Table I. The energy of gamma ray of Mn^{54}

E_γ (kev)	Method	Reference
833 ±15	Lens spectrometer	a)
825 ±20		b)
840 ± 7	Scintillation Spectrometer	c)
837.9± 0.3	Double focusing spectrometer	Present

a) M. Deutsch and L. G. Elliott, Phys. Rev. **65** (1954) 211.
b) G. H. Stafford and L. H. Stein, Nature **172** (1954) 1103.
c) Maeder, Wapstra, Nijh and Ornstein, Physica **20** (1954) 521.

In our spectrometer L and M conversion lines cannot be separated, but K and $L+M$ lines are slightly splitted, though the resolution of 0.7 percent is larger than usual. $K/L+M$ was determined to be 8.5 ± 0.7. This value is larger than the theoretical value[8] for $E2$ transition beyond the experimental error, as shown in Table II. The screening effect are neglected in Rose's theoretical values for

M-shell. This effect can decrease the M-shell value by a factor 0.6[9], and the theoretical value becomes in agreement with experimental one.

Table II. Theoretical and experimental Values of $K/L+M$

Experimental	Theoretical			
	$E1$	$E2$	$M1$	$M2$
8.5±0.7	8.1	7.7	8.0	7.8

§ 4. Search of Weak Gamma Ray

Only 0.84 Mev gamma ray has been reported in Mn^{54} decay. If the second excited state of Cr^{54} is lower than the ground state of Mn^{54} and has the spin and parity of 2+, a weak high energy gamma ray may be observed. If the spin and parity of such a state are 2+ or 4+, the coincidence measurement with the 0.84 Mev gamma ray can show the existence of a weak cascade gamma ray. In order to research such unknown weak gamma rays, two scintillation counters of 1½ inch NaI and 20 channel pulse height analyzer were used for the single as well as the coincidence counting method. Sources were $MnCl_2$ solution of about 100, 10 and 1 μC.

However, no gamma ray was observed, and upper limit of gamma rays were determined to be about 10^{-4} per one decay for the high energy gamma ray in the single count measurement and to be about 10^{-3} for low energy gamma ray in the coincidence measurement.

§ 5. Acknowledgement

The authors wish to express their thanks to Prof. S. Kikuchi, Prof. T. Wakatuki, Prof. J. Itoh and the cyclotron group for their interest and many helps. They are indebted to Prof. K. Otozai, Mr. S. Kume, Mr. S. Iwata, Mr. Y. Yamamoto and Mr. I. Fujisawa for the chemical separation, and also to Dr. M. E. Rose for the internal conversion coefficients.

References

1) K. Way, R. W. King, C. L. McGinnis and R. van Lieshout: Nuclear Level Schemes. (Nuclear Data Project, Washington D. C., June 1955).
2) M. A. Grace, C. E. Johnson, N. Kurti, H. R. Lemmer and F. N. H. Robinson: Phil. Mag. **45** (1954) 1192.
3) G. R. Bishop, J. M. Daniels, H. Durand, C. E. Johnson and J. Perez: Phil. Mag. **45** (1954) 1197.
4) Y. Yoshizawa: Nuc. Phys. **5** (1958) 122.
5) P. G. Jung and M. L. Pool: Bull. Am. Phys. Soc. **1** (1956) 172.
6) K. Otozai, S. Kume, S. Iwata, Y. Yamamoto and I. Fujisawa: Isotopes and Radiation (Tokyo) **1** (1958) 39.
7) T. Katoh, M. Nozawa, Y. Yoshizawa and Y. Koh: to be published.
8) M. E. Rose: privately circulated tables.
9) M. E. Rose: private communication.

JOURNAL OF THE PHYSICAL SOCIETY OF JAPAN Vol. 13, No. 12, DECEMBER, 1958

Grain Boundary-Hardening due to Piled-up Dislocations

By Jin-ichi TAKAMURA and Sei MIURA

Department of Metallurgy, Kyoto University, Kyoto

(Received August 28, 1958)

The grain boundary in deformed bicrystals of α-brass has the hardening layer of 50~100 microns in thickness. Evidences for the assumption that the hardening is attributable to the dislocations piled up against the grain boundary were provided by the fact that the amount of hardening could be reduced by the application of reversed stress, and also by the analysis of the hardness distribution which showed the amount of hardening to be approximately proportional to the density of piled-up dislocations.

§ 1. Introduction

A linear array of like dislocations piled up against a barrier has been treated in detail by Eshelby, Frank and Nabarro[1]. And it has been suggested by Mott[2] that the strains around piled-up groups of dislocations are responsible for the intense work-hardening of metals. Such a barrier may be, for instance, a grain boundary; it would be expected to be more hardened at the grain boundary than in the grain of deformed polycrystals.

Evidences for piled-up dislocations have been obtained by producing etch pits at the sites of dislocations in α-brass by Jacquet[3], Bilby and Entwisle[4], and Sun and Wilsdorf[5], and also in zinc crystals by Gilman[6]. The present work was undertaken for the purpose of providing a clearer picture of the grain boundary-hardening caused by the piling-up of dislocations. α-brass was chosen for the specimen and the hardening was measured by a microhardness tester.

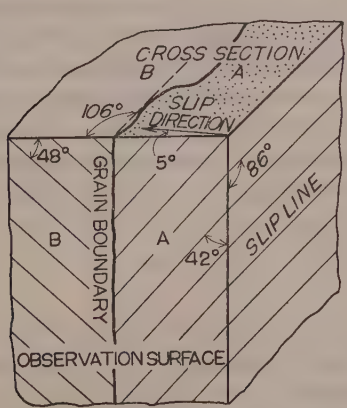

Fig. 1. Relative position of the grain boundary with respect to the slip direction in bicrystal specimen No. 2.

§ 2. Experimental Details

Bicrystal specimens of 70–30 brass, 8 mm square in cross section, were grown by the Bridgman method in split molds of graphite. Test specimens, originally polished mechanically, were electropolished in a solution of phosphoric acid. Specimens were next fully annealed in Ar at 800°C. After the deformation by Amsler testing machine, specimens were again carefully abraded through emery paper to flatten the surface and then electropolished in order to eliminate completely the abrasion effect. This technique was necessary for minimizing the amount of dispersion of microhardness measurements. The microhardness testing was carried out with a load of 25 gr.

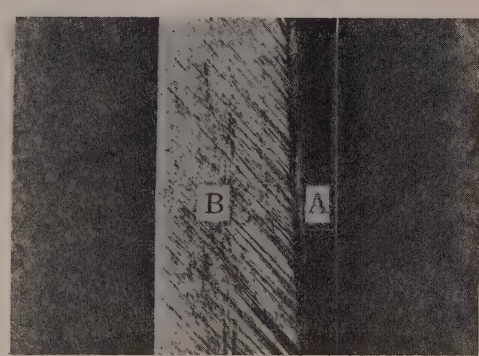

↑
Grain Boundary

Fig. 2. The observation surface of bicrystal specimen No. 2 as extended by 9.3%. ×3

Fig. 1 shows the relative orientation of a bicrystal specimen No. 2. This can be seen also in Fig. 2. The vertical direction in the figures is the specimen axis and it is illustrated in the stereographic projection of Fig. 3.

Let φ be the relative angle of the mean direction of the curved grain boundary with respect to the slip direction on the active slip plane of crystal A, then $\varphi \simeq 80°$ as understood from Fig. 1. This means that dislocations held up against the grain boundary have almost pure edge component. Microhardness measurements were made on crystal A as shown in Fig. 4.

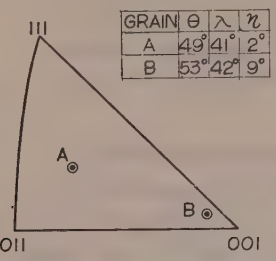

GRAIN	θ	λ	η
A	49°	41°	2°
B	53°	42°	9°

Fig. 3. Specimen axes of bicrystals A and B illustrated in Fig. 1. Here, θ is the angle between the specimen axis and the normal to the slip plane, λ the angle between the axis and the slip direction, η the angle between the slip direction and the direction of maximum slope on the slip plane.

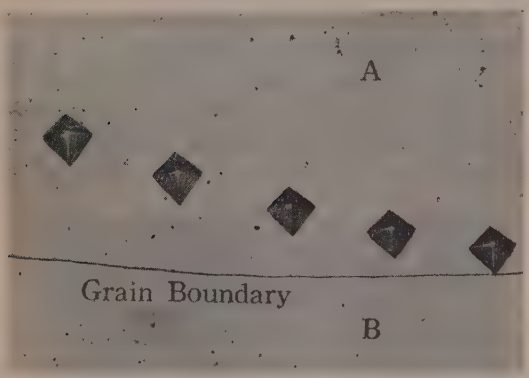

Fig. 4. The measurement of microhardness in the grain boundary region of specimen No. 2 extended by 9.3%. ×290

§ 3. Results

It can be seen in Figs. 4 and 5 (a) that the grain boundary region of deformed specimens is much hardened; the thickness of the hardening layer in most specimens used in this experiment ranges from 50 to 100 microns.

The application of reversed stress, for instance, the compression subsequent to the extension alters the distribution of hardness; the amount of hardening at the grain boundary much decreased and the hardness in the center of grain, on the other hand, showed slight increase, as clearly shown in Fig. 5 (b) and also in the composite diagram of Fig. (c).

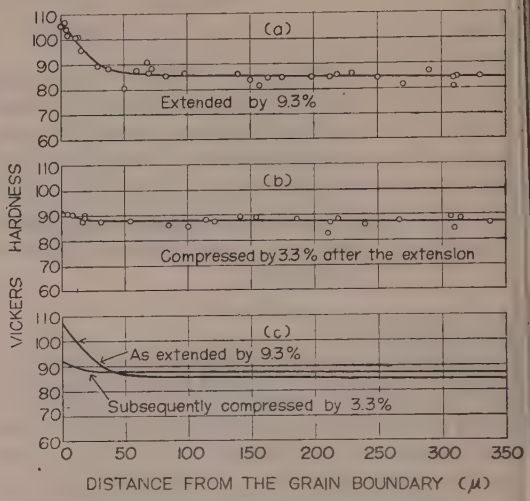

Fig. 5. The distribution of hardness in crystal A of specimen No. 2. The lowest diagram shows the difference in the distribution between diagrams (a) and (b).

§ 4. Discussion of Results

It is first necessary to examine whether the hardening at a grain boundary is attributable to the piling-up of dislocations. Evidence in favor of it was provided by the fact that the application of reversed stress had changed the distribution of hardness in the grain boundary region, as indicated in Fig. 5 (c). This observation strongly supports the supposition that the dislocations piled up against the grain boundary have jumped back towards the center of grain and dispersed there rather uniformly. It should be noticed that the observation is closely connected with the Bauschinger effect.

Now we shall consider the distribution curve of hardness given in Fig. 5 (a). Assuming that the amount of increase in hardness, ΔH, is proportional to the density of piled-up dislocations, we have

$$\Delta H = k\frac{dn}{dx} . \qquad (1)$$

Here k is the constant and n is the number of piled-up dislocations lying between the grain boundary and a point at the distance x from it, which is given under the acting stress σ by the following equation[1)]

$$n = cx^{1/2} , \qquad (2)$$

where

$$c=(2/\pi)(2N\sigma/A)^{1/2}\,,$$

$$A=\mu b(1-\nu\cos^2\varphi)/2\pi(1-\nu)\,,$$

and N is the total number of piled-up dislocations, μ the shear modulus, ν the Poisson's ratio and b the strength of dislocation. Eliminating n between (1) and (2), we obtain

$$H=(kc/2)x^{-1/2}+H_0\,, \qquad (3)$$

where H_0 is the hardness at a position far away from the grain boundary. Thus if, as in Fig. 6, we plot H against $x^{-1/2}$, we should

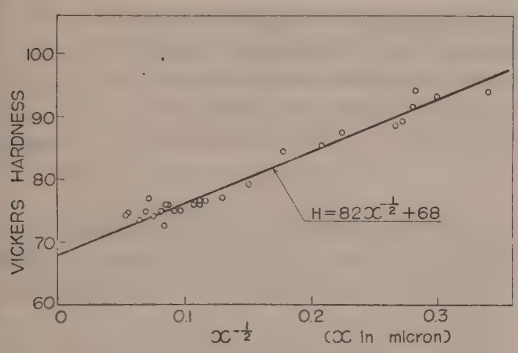

Fig. 6. Microhardness data plotted as a function of $x^{-1/2}$. Here x is the distance from the grain boundary.

get points which cluster around a line of slope $kc/2$ with an intercept H_0 on the hardness axis. The figure shows that this is the case, although some rearrangement of the piled-up dislocations should have taken place during the relaxation of the load after straining; it can be said that the amount of hardening at the grain boundary region is approximately proportional to the density of dislocations and hence a large part of the grain boundary-hardening is ascribed to the piled-up dislocations.

§ 5. Summary

A study on the grain boundary-hardening in deformed bicrystals of α-brass was carried out by microhardness testing. The results obtained are as follows. The grain boundary of deformed bicrystals has the hardening layer of 50~100 microns in thickness. A large part of the grain boundary-hardening is ascribed to the piling-up of dislocations.

Evidence in favor of this conclusion was provided by the observation that the application of reversed stress had altered the distribution of hardness as shown in Fig. 5. It should be noticed that the observation is closely connected with the Bauschinger effect. Another proof was given by the analysis of the hardness distribution, which showed the amount of hardening to be approximately proportional to the density of the dislocations piled-up against the grain boundary.

References

1) J. D. Eshelby, F. C. Frank and F. R. N. Nabarro: Phil. Mag. **42** (1951) 351.
2) N. F. Mott: Phil. Mag. **43** (1952) 1151.
3) P. A. Jacquet: Acta Met. **2** (1954) 752, 770; Compt. Rend. **237** (1953) 1248.
4) B. A. Bilby and A. R. Entwisle: Acta Met. **4** (1956) 257.
5) R. Sun and H. Wilsdorf: J. Franklin Inst. **265** (1958) 413.
6) J. J. Gilman: Trans. AIME, J. Metals **8** (1956) 998.

JOURNAL OF THE PHYSICAL SOCIETY OF JAPAN Vol. 13, No. 12, DECEMBER, 1958

On the V-centers in KBr Crystals

By Yoshio NAKAI

Yoshida College, University of Kyoto

(Received September 11, 1958)

The natures of V bands in the additively colored crystals of KBr has been investigated. Mollwo's results were confirmed and extended. A new technique of additive coloring was devised to produce a high concentration of V centers in the crystal of KBr. By using this method, the degree of coloration could be increased by about ten times of that reported by Mollwo. Besides the well-known V_2 and V_3 bands, another band of V-type was observed below 210 mμ.

It was found to be possible to color electrolytically the crystal of KBr revealing the same absorption spectrum as that of additively colored crystals. Evidently, this confirms that these absorption bands are produced as the result of the combination of positive holes and positive ion vacancies. Discussions were made in comparison with the results obtained for KBr colored with X-rays.

§ 1. Introduction

It is possible to color certain of the alkali halides by heating them in the proper halogen vapor. This was done by Mollwo for KI[1),2)] and KBr[2)]. Absorption was produced in the ultraviolet region of the spectrum. The absorption band did not have a simple bell-shaped form as seen in the F-band but seemed to consist of two or more overlapping bands. This group of bands has been named the V-band by Seitz[3)].

Similar absorption is produced in the ultraviolet region when crystals of KCl and KBr are exposed to X-rays. Recently, various experiments on the V-bands have been carried out mainly on the crystals colored with X-rays.

The V center problems are reviewed systematically and discussed in great detail by Seitz[4)]. He proposed various models for V centers, V_1, V_2, V_3, V_4 etc., which show definite absorption bands in the optical spectrum of the colored crystals under a certain condition specified for each case. Mollwo's result[2)] plays an important role in his discussions about V_2 and V_3 centers. The main band, 365 mμ in KI and 265 mμ in KBr, was named V_2 band and the shoulder, 275 mμ in KI and 240 mμ in KBr, on the shorter wavelength side of the main band was named V_3 band. Considering the natures of these bands with various informations obtained from the studies on the crystals colored with X-rays, he proposed that the V_2 center consists of two positive ion vacancies and two positive holes trapped by them, while the V_3 center consists of two positive ion vacancies and one positive hole.

Unfortunately, however, the correspondence is rather poor between the spectra of V-band obtained by the above-mentioned two methods of coloration for certain kind of salt. This state of affairs is quite different from the case of F-band and seems to prevent more or less the development of studies on the V-center problems. In KCl and NaCl, the V-bands produced by X-ray coloring have been studied in detail[5),6)] but, so far as the writer is aware of, the additive coloration has not been found to be possible for these crystals. On the other hand, the additive coloration is possible for KI[2),7)] but no definite correspondence seems to exist between the results of additive coloration and the results of the study carried out by Hersh[8)] on this crystal exposed to X-rays. The state of things is not so hopeless for KBr, because both additive[2)] and X-ray[5),6),8),9)] coloration have been found to produce the similar absorption at least in the short wavelength region of the spectra. However, informations about the V-bands in the additively colored crystals are available only from the Mollwo's work which was carried out about twenty years ago.

Hence it seems important to investigate in the light of recent informations the natures of V-band in additively colored crystals. The present study is concerned with some proper-

ties of the V-bands in the additively colored crystals of KBr.

§ 2. Experimental Methods

i) *General*

Crystals of KBr were grown in our laboratory by using the Kyropoulos method. Greater part of the experiments was repeated also on the crystal which was available through the kindness of Professor Maurer of the University of Illinois. No significant difference was found between the experimental results obtained for both crystals.

The optical measurements were made using a Beckman-DU or Shimazu-QB spectrometer both at room and liquid air temperatures, the optical absorption of the crystal having been obtained in terms of log (I_0/I), where I and I_0 are the intensities of light with and without the crystal sample in the light path respectively. Hence it is necessary to subtract the absorption of uncolored crystal having the same thickness as that of colored specimen in order to obtain the absorption constant. A mercury arc lamp of AH-6 type with a quartz envelope was used to illuminate the crystal. Since this mercury lamp is of super high-pressure type, the relative intensity in the ultraviolet region is rather low. However the very high total brightness of this lamp overcomes sufficiently such a drawback.

ii) *Technique of additive coloring*

Fig. 1 shows the cross-sectional view of the vessel used in the additive coloration. The crystals of KBr were sealed in the evacuated quartz tube with a certain amount of bromine. This tube was inserted into the stainless steel container with an adequate quantity of water, and this container was then packed tightly using a copper ring as a gasket material.

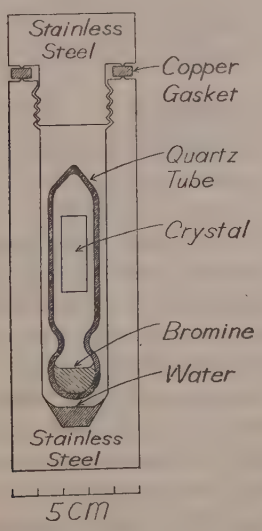

Fig. 1. Cross-sectional view of the vessel used in the additive coloration of KBr.

Use of water keeps the quartz tube from breaking due to a rise of bromine pressure at high temperature. Since the vapor pressure of water increases with temperature very much alike that of bromine, both inside and outside of quartz tube suffer nearly the same pressure in raising the temperature. Van der Waals' equation was used to determine the adequate quantity of water producing the best fit of pressure for the quantity of bromine sealed in the quartz tube.

The whole vessel was heated at 600°C for about three hours, and then quenched to room temperature within ten minutes by dropping it into a water-tank. It was necessary to store colored crystals below −40°C in order to prevent its thermal bleaching.

Usually, colorations were made under 50∼100 atmospheric pressure of bromine. This method makes it possible to color the crystal about ten times as much as that reported previously[2].

Unfortunately, degree of coloration was never reproducible; in other words, absorption constants of the colored crystals varied from case to case in spite of great care taken for the crystal temperature and the density of bromine surrounding the crystal. Therefore, no definite relation could be found between the solubility of Br_2 in KBr and the concentration of Br_2 in the vapor.

§ 3. Absorption Spectra

The typical absorption spectrum of the additively colored crystal of KBr is shown in Fig. 2, curve a. Coloration was made at 630°C in the bromine gas of 50 atmospheric pressure. For comparison, Mollwo's result is also shown by curve b for which the ordinate scale is given on the right-hand side of the figure. Curve c shows the absorption of uncolored crystal used in the present experiment using air as blank. All measurements were made at room temperature.

The main band having its maximum at 265 mμ coincides exactly with the peak obtained by Mollwo, and, as described above, this is

named the V_2 band in recent literatures. A sharp rise occurs below 210 mμ in curve a, but not in curve b. Since this region is located near the short wavelength limit of the spectrometer used, the precise determination of peak wavelength was impossible. The hump occurring at 410 mμ in curve b does not appear at all in curve a, and the shoulder at 240 mμ in curve b, named recently the V_3 band, is not so well defined in curve a. As will be described later, part of these differences can be ascribed to the thermal instability of the main band (V_2 band).

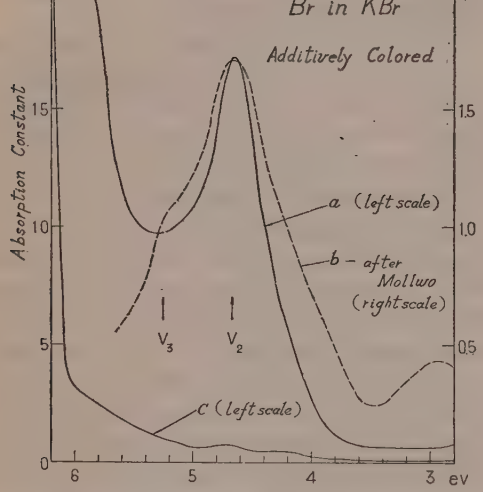

Fig. 2. Absorption spectra of additively colored crystal of KBr measured at room temperature. Curve a: colored at 630° Cin Br_2 of 50 atm. pressure (left-hand scale); curbe b: after Mollwo (right-hand scale); curve c: uncolored crystal used in the present study (left-hand scale. Absorption is plotted *versus* air.).

It is worth mentioning that the exactly same spectrum as that shown by curve a in Fig. 2 was obtained in the crystal colored electrolytically by using a pointed anode. As reported previously[7], when a certain amount of current is passed in the blank crystal of KI from a sharp anode at high temperature, the crystal is colored* and shows the same absorption spectrum as that of additively colored crystal of KI. Similar facts were confirmed also for KBr as shown in Fig. 3. The measurements were made both at room and liquid air temperatures.

By lowering the measuring temperature the width of the main band decreased as expected. However the temperature shift of the peak wavelength was not so large as that of the F band. Indications of some component bands are seen near 240 mμ and 300 mμ in the low temperature spectrum. Therefore, the main band observed at room temperature can never be recognized as a purely single band.

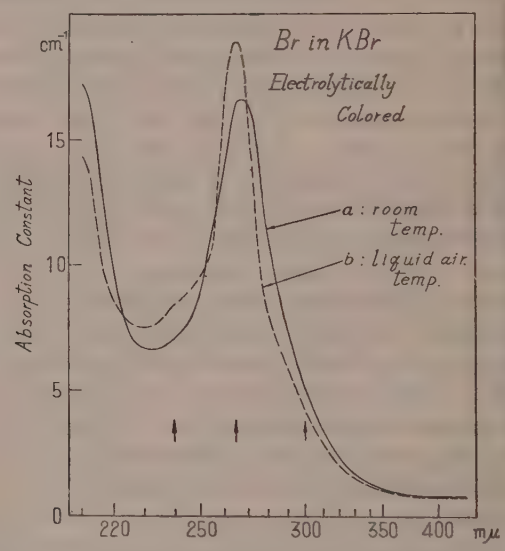

Fig. 3. Absorption spectra of the electrolytically colored crystals of KBr. Curve a: measured at room temperature; curve b: measured at liquid air temperature.

§ 4. Thermal Behavior

It was found that the V_2 band is stable only when the colored crystal is stored below −40°C. At room temperature, the V_2 band decreases gradually and the enhancement of absorption occurs near 240 mμ and 300 mμ. Fig. 4 shows the effects of aging the colored crystal at room temperature. Curve a shows the absorption immediately after the additive coloration. As long as the temperature of the colored crystal is kept below −40°C by using dry ice as coolant, absorption curve does not change at all. However aging for 24 hours at room temperature produces a slight change as shown by curve b. Curves c and d show the spectra after aging for 18 days and 60

* Attempt to measure the drift mobility of V-centers was made by Mollwo by applying a uniform static field at high temperature to the additively colored crystal of KI, but he did not try to *color* the crystal by using a sharp anode.

days at room temperature, respectively. Needless to say, the crystals were kept in dark to exclude the effect of light.

The rate of this process is considerably increased by heating the colored crystal at higher temperatures instead of aging it at room temperature. For example, by heating at 200°C, the final state was established in three hours having nearly the same absorption as in the case of bleaching at room temperature.

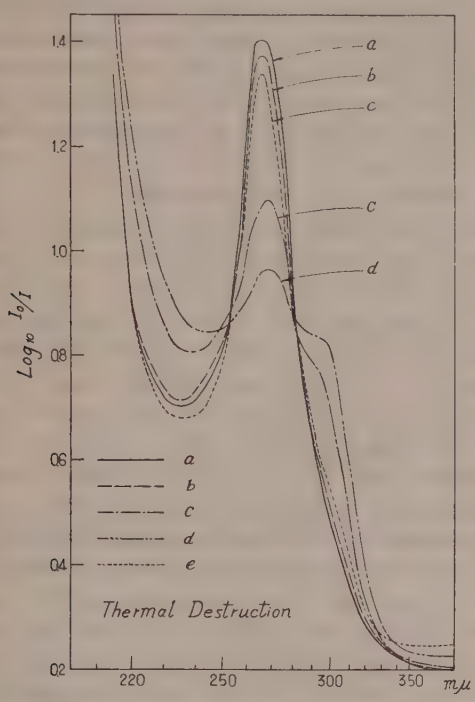

Fig. 4. Thermal destruction of V band in KBr at room temperature. Absorption was measured at room temperature. Curve a: initial state, immediately after the additive coloration; curve b: after aging for 24 hours; curve c: after 18 days; curve d: after two months; curve e: restoration of the original bands after heating at 550°C for 30 minutes.

It is interesting enough to note that, as shown in Fig. 4 curve e, the original bands are nearly reproduced by heating these crystals above 550°C for 30 minutes and quenching from that temperature. In addition, no difference was found between the properties of the recovered crystals and the freshly colored crystals. This means that the bleached crystal can always be restored by this method, that is, storing the colored crystal below −40°C is not required for the most part of the present study.

§ 5. Optical Bleaching

It is possible to bleach the V_2 band by illuminating the colored crystal at room temperature with light absorbed in this band. Fig. 5 shows the light bleaching of V band irradiated at room temperature. A light from AH-6 mercury lamp with the appropriate filter was used to illuminate the crystal. Main band at 265 mμ was bleached considerably and the enhancement of absorption occurred near 240 and 300 mμ. General view of the spectrum was similar to that of thermal bleaching.

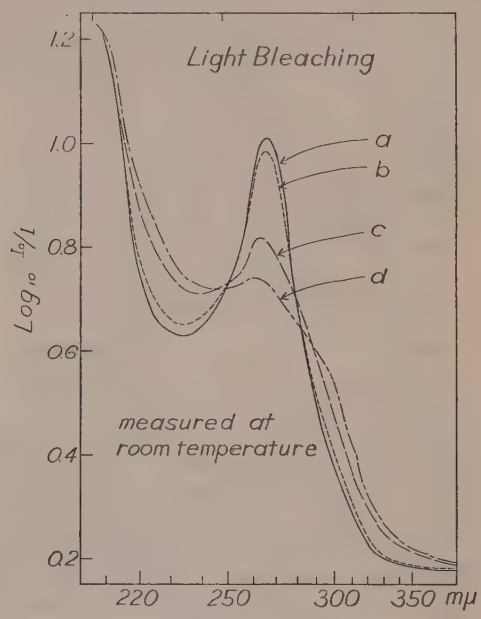

Fig. 5. Light bleaching of V_2 band in KBr by illuminating with the mercury lamp at room temperature. Absorption was measured at room temperature. Curve a: initial state, additively colored; curve b: after having irradiated for 1/2 hours; curve c: after having irradiated for further 12 hours; curve d: after having irradiated for further 12 hours.

However, enhancement in the short wavelength side of the main band seems relatively larger than in the case of thermal destruction. This difference makes its appearance in Fig. 5 (curves c and d) as a gradual shift of the main peak toward the short wavelength side in the course of the optical bleaching.

Fig. 6 shows the absorption after irradiating for four hours both at liquid air and at room temperature, all absorption measurements having been made at liquid air temperature. Irradiation at liquid air temperature

was made because it was expected that, at low temperatures, the V_1 band might be formed as the result of dissociation of the V_2 centers by illuminating them with the light in the V_2 band. However, no significant change was produced by irradiating at liquid air temperature (from curve a to curve b) in comparison with the case of irradiation at room temperature (from curve b to curves c and d).

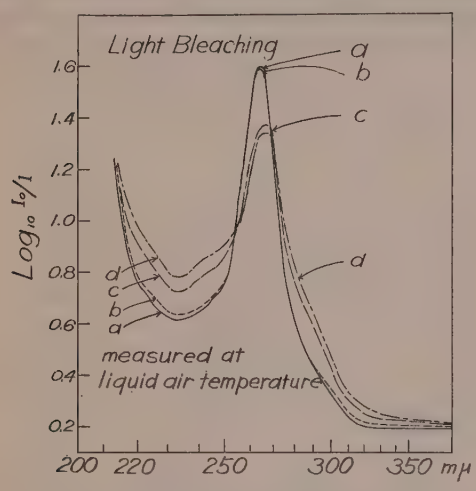

Fig. 6. Light bleaching of V_2 band in KBr by illuminating with the mercury lamp. Absorption was measured at liquid air temperature. Curve a: initial state, electrolytically colored; curve b: after having irradiated at liquid air temperature for 4 hours; curve c: after having irradiated at room temperature for 4 hours; curve d: after having irradiated at room temperature for further 4 hours.

Similar experiment was made by using a monochromatic light (Hg 265 mμ line) to bleach the V_2 band in order to obtain the efficiency of this optical bleaching processes measured in terms of the number of V_2-centers destroyed per absorbed quantum of light. This quantity will be called the quantum yield for optical bleaching, and will be designated by η.

In practice, the number of V_2-centers destroyed was obtained from the change of absorption constant at 265 mμ using the formura derived by Smakula[10] in which the oscillator strength of this band was taken as unity. The calibrated thermocouple was used to know the number of light quanta absorbed, the readings of which were made when the height of the V_2-band has decreased to about 95 per cent of its initial value.

Thus it was found that the value of η at room temperature is 0.042, and η at liquid air temperature is less than one hundredth of this value. Qualitatively, it is obvious from Fig. 5 that η will decrease with increasing time, thus reaching nearly zero after the prolonged period of irradiation. Therefore the value of η obtained in this experiment is the one averaged over the initial period of illumination.

If the optical bleaching of the V_2-band is due to the release of holes from their traps, the bleaching process should be accompanied by a photocurrent. Then the yield for the production of free hole, η', may be assumed as being equal to the value of η obtained in the experiment of light bleaching.

A current larger than 10^{-12} amperes could be expected by using a usual formula for the photocurrent, if we assume that η' is equal to the quantum yield for optical bleaching at room temperature, 0.042, and that the mean range of free hole, ω_0, is equal to the value obtained by Dutton and Maurer[11] in the crystal of KBr irradiated with X-rays at low temperatures*. But, contrary to these expectations, such a magnitude of photocurrent was never observed; it was not possible to obtain any signal which exceeds the noise level (0.7×10^{-14} amperes) of the amplifier used in the present experiment. This means that the assumptions made above are not adequate. In practice, it seems unlikely that the magnitude of ω_0 in this case is far less than that of Dutton and Maurer, even if we take into consideration that the temperature and the density of traps in colored crystals are appreciably different for both cases. Accordingly, it will be supposed that η' must be much smaller than

* Photocurrent is given by the expression:

$$I = N\eta' e\omega_0 E/d\ ,$$

were N is the number of light quanta absorbed per second, η' the fraction of these which actually release holes, ω_0 the mean range of free hole in unit field strength, E the electric field, and d the distance between electrodes.

N was larger than 10^{15} quanta/sec when the filtered light from AH-6 lamp was focused with a usual quartz lens. It was assumed, as described above, that $\eta' = \eta = 0.042$ and $\omega_0 = 3 \times 10^{-11}$ cm²/volt. Electric field of 2000 volt/cm was used and d was 0.3 cm. Then we have

$$I \geqslant 1.3 \times 10^{-12} \text{ amperes.}$$

η. This means that either the tunneling of holes from the excited state of the V_2 center or the photo-dissociation processes will be rather predominant in bleaching the V_2 band. Further details will be discussed later.

§ 6. Electrolytic Bleaching

It was found by Mollwo[2] that when an electrostatic field is applied to the colored crystal at high temperature, the flow of currents is observed in excess of the purely ionic current which will be obtained in uncolored crystal at the same temperature. The magnitude of this current decreases with time, reaching finally a steady ionic current. Mollwo used this method to determine the number of V centers contained in the crystals of KI and of KBr colored additively.

In the present study, attention was paid on the variation of absorption spectrum in the course of these processes. The results obtained are shown in Figs. 7–9. In Fig. 7 is shown the decrease of the excess currents with increasing time, and in Fig. 8 the absorption spectra before and after the application of the electric field to the colored crystal at 570°C. It should be noted that 265 mμ and <210 mμ bands have disappeared in this case and the resultant spectrum differs little from that of the original blank crystal.

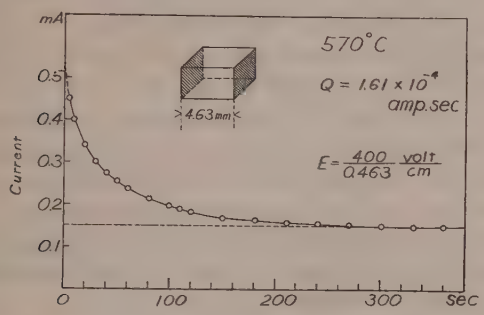

Fig. 7. Current *versus* time curve. A potential of 400 volts was applied at 570°C for an electrolytically colored crystal of KBr.

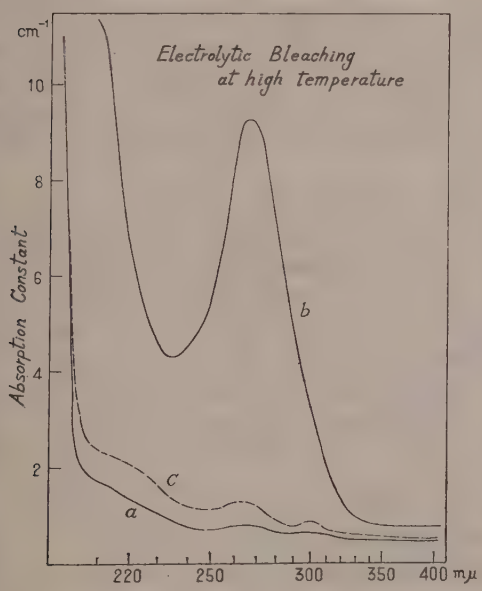

Fig. 8. Electrolytical bleaching of V bands in KBr at 570°C. Absorption was measured at room temperature. Curve a: original uncolored crystal; curve b: after colored electrolytically; curve c: after bleached electrolytically.

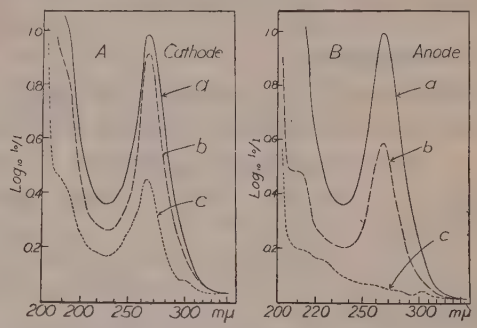

Fig. 9. Variation of V bands in KBr with increasing time of current flow. Absorption measurements were made for the narrow portions of the crystal sample near cathode (Fig. 9A), and near anode (Fig. 9B). In both figures, curve a: initial state, colored electrolytically; curve b: after a flow of currents by applying 135 volts for 90 seconds at 593°C; curve c: after a further flow of currents by applying 135 volts for 120 seconds at 610°C.

Further, it was found that the destruction of V band begins in the portion of the colored crystal near anode as shown in Fig. 9A and B. This experiment was done by comparing the spectra obtained from two narrow parts of the same specimen, the one near cathode and the other near anode, at various early stages of current flow. Fig. 9A shows the spectra of the part near cathode, and Fig. 9B those near anode. In both figures, curve a shows the spectrum before the application of the electric field and curves b and c show those after the flow of current produced by applying 135 volt for 90 sec at 593°C and for 120 sec at 610°C, respectively. Despite of curves a and b being of nearly equal height in the part near cathode (Fig. 9A), the height

of curve b is about one half of that of curve a in the part near anode (Fig. 9B). In addition, comparison of curves c in both parts shows that when the absorption in the cathode side decreases to about one half of its initial value, the absorption is no longer seen in the anode side.

Finally, it is to be noted that the degree of destruction is nearly equal for both 265 mμ and 210 mμ bands, namelly, the relative intensity of these bands is not altered in the course of these processes. This fact suggests that color centers responsible for these two bands can drift toward the cathode, so that positive holes play an important role in the species giving rise to these bands.

§ 7. Discussions

The results of the present experimental investigations are summarized in the following:

1. The same absorption spectrum was obtained for the KBr crystals colored either additively or electrolytically.
2. Two strong bands were produced at 265 mμ and below 210 mμ immediately after the coloration was made (Fig. 2).
3. Indications of two subsidiary bands appeared at about 240 mμ and 300 mμ when measured at low temperature (Fig. 3).
4. When the colored crystal of KBr is kept or irradiated with a light absorbed in the 265 mμ band at room temperature, this band is lowered and the 240 mμ and 300 mμ bands are enhanced without significant change in the range below 210 mμ (Figs. 4–6).
5. Release of free holes was not observed upon irradiating the colored crystal of KBr with light absorbed in the 265 mμ band (§ 5).
6. All these bands disappear after the electrolytic bleaching, leaving the same absorption spectrum as in the original uncolored crystal (§ 6).

First of all, it is of interest to note that similar absorption spectrum was observed by Dorendorf[6] for the crystal of KBr irradiated with X-rays. He obtained seven absorption bands of V-type as a result of X-raying at various temperatures. Wavelengths of these bands are given in Table I. Of these, V_2, V_3, V_5, and V_7 bands were produced upon irradiating with X-rays at 20°C. Fig. 10 shows the absorption curve obtained by him. The similarity is rather striking in comparing this

Table I. Peak wavelengths of V band in KBr (in mμ).

	V_1	V_2	V_3	V_4	V_5	V_6	V_7
Dorendorf (X-raying)	410	265	231	275	<202	362	30[illegible]
The present study (additive coloring)	—	265	240	?	<210	—	30[illegible]

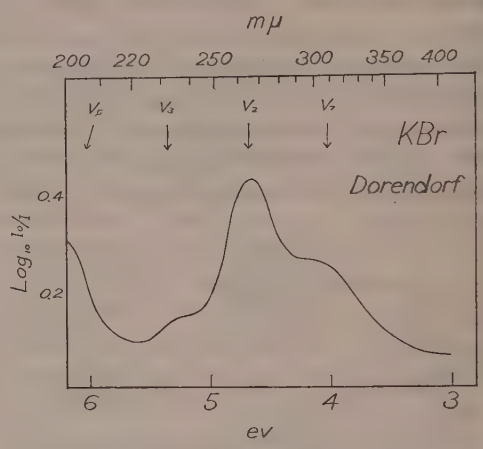

Fig. 10. Absorption spectrum of KBr X-rayed at 20°C and measured at −180°C. After Dorendorf (Fig. 2e in reference 6).

curve with the curve d in Fig. 6, which shows the effect of light bleaching at room temperature for the crystal colored electrolytically with a sharp anode. Further, it is worth mentioning that the similar absorption has been observed also by Teegarden[12] for a thin film which was prepared by evaporating simultaneously both KBr and Br_2 on a quartz plate.

There is some evidence as described in § 6, that the strong absorption appearing in the region below 210 mμ will be of V-type, and it seems therefore reasonable to designate this absorption as the V_5 band. It has been suggested by Seitz that the V_5 band would be associated with the α and β bands in KBr[4]. This suggestion is reasonable in view of the fact that the V_5 band has been observed by Dorendorf under X-ray irradiation by which the F centers and negative-ion vacancies are produced in the crystal. However, it seems unlikely that these (α- and β-) bands appear also in the case of the (halogen-) additive coloration in which neither the F center nor the negative-ion vacancy can be formed. Thus the species giving rise to the V_5 band may be supposed to have some of V character rather

than that of "Greek" band, though further details of its nature are not known at present.

The 265 mμ band can be assigned undoubtedly as the V_2 band, and the 240 mμ and 300 mμ bands, which are enhanced as the result of the thermal or optical bleaching of the V_2 band, are located near the V_3 and the V_7 band respectively. There was no definite indication of absorption which might be correlated to the V_4 band. In Table I are also shown these correspondences.

From the results of the present experiments, the V_3 and V_7 bands were found to be produced as the result of bleaching of the V_2 band, the absorption spectrum being similar whether bleached thermally or optically. In order to understand the mechanism of the optical bleaching, it is necessary to assume either the tunneling of holes from, or the photo-dissociation of, the V_2 center, as remarked in § 5. However the first alternative seems unlikely because the quantum yield for optical bleaching is strongly dependent upon the temperature at which the irradiation has been made. Thus it might be possible to suppose that most of V_2 centers are destroyed through the process of either thermal or optical dissociation. In this way, the following is offered tentatively as an explanation for these processes.

According to Seitz model, two V_1 centers might be produced through the dissociation of V_2 center. However, at room temperature, these V_1 centers must be combined rapidly with the lattice defects such as the positive-ion vacancy or the pair vacancies, both of which are sufficiently mobile even at room temperature. The former will associate with the V_1 center to form the V_3 center, and the latter to form the V_4 center which is the antimorph of the M center. On the other hand, a V_4 center may be formed also if one V_3 center is combined with pair vacancies and then one positive-ion vacancy is ejected from this aggregate.

Hence the following two processes are supposed to be most probable to occur through the destruction of V_2 centers at room temperature:

(A) $V_2 \longrightarrow 2V_1$ (virtual) $\longrightarrow V_3$ or V_4,

(B) V_3+(pair vacancies) $\longrightarrow$ V_4+(one positive-ion vacancy ejected).

In the process (A), dissociation of the V_2 center will take place either thermally or optically. The process (B) may occur only through the thermal reactions. According to the results of bleaching experiments, the rate of optical process is much higher than that of the thermal process at room temperature. As described in § 5, enhancement of the V_3 band is more evident in the optical bleaching than in the thermal bleaching at room temperature. This may be explained by supposing that, in the case of thermal bleaching, part of the V_3 centers produced through the process (A) will be changed gradually to the V_4 centers through the process (B).

In view of these speculations, the writer would like to identify the species giving rise to the 300 mμ band as V_4 centers. In other words, it seems more reasonable to designate this band as the V_4 band in KBr.

Acknowledgements

The writer wishes to express his sincere thanks to Prof. Y. Uchida of University of Kyoto for his continued guidance and encouragements throughout this work, and to Dr. K. Fukuda and Mr. H. Yoshimura for their kind interests and discussions.

He further appreciates the valuable and kind assistance of Mr. Y. Nishida, who is now working in the Electrical Communication Laboratory, Tokyo, in carrying out this work.

References

1) E. Mollwo: Nachr. Akad. Wiss. Göttingen, (1935) 215.
2) E. Mollwo: Ann. Phys. **29** (1937) 394.
3) F. Seitz: Rev. Mod. Phys. **18** (1946) 384.
4) F. Seitz: Rev. Mod. Phys. **26** (1954) 7.
5) R. Casler, P. Pringsheim and P. Yuster: J. Chem. Phys. **18** (1950) 1564.
6) H. Dorendorf: ZS. f. Phys. **129** (1951) 317.
7) Y. Uchida and Y. Nakai: J. Phys. Soc. Japan **8** (1953) 795; **9** (1954) 928.
Y. Uchida, Y. Nakai and T. Tomotika: J. Opt. Soc. America **47** (1957) 246.
8) H. N. Hersh: Phys. Rev. **105** (1957) 1158; J. Chem. Phys. **27** (1957) 1330.
9) H. Rüchardt: Phys. Rev. **103** (1956) 873.
10) A. Smakula: ZS. f. Phys. **59** (1930) 603.
11) D. Dutton and R. Maurer: Phys. Rev. **90** (1953) 126.
12) K. J. Teegarden: J. Chem. Phys. **24** (1956) 161.

JOURNAL OF THE PHYSICAL SOCIETY OF JAPAN Vol. 13, No. 12, DECEMBER, 1958

On the Magnetic Properties of Nickel Sulfide*

By Ichiro TSUBOKAWA

The Research Institute for Iron, Steel and Other Metals, Tohoku University, Sendai

(Received July 14, 1958)

Magnetic measurements were performed on the specimens of powdered and single crystals of nickel sulfide having the structure of nickel arsenide type. From the results of measurements of the susceptibility, specific heat and other data, it was found that nickel sulfide is antiferromagnetic with the Néel point at 150°K. However, below 120°K, the susceptibility of the powder specimen increased with the fall of temperature and also showed a dependence of magnetic field. Such a rise in susceptibility at lower temperatures is here interpreted as due to the influence of paramagnetic islands. Correction for the atom core diamagnetism was applied to the observed susceptibilities, and from the inverse susceptibility *vs* temperature relation, the Curie constant per mol, C_M, the spin quantum number, S, and the asymptotic Curie temperature, θ, were obtained as 0.89, 1.9/2 and *ca* 3000° respectively. From the torque measurement of a single crystal of this compound, it was seen that the antiferromagnetic easy direction lies in (0001) plane of the crystal.

§ 1. Introduction

Magnetic properties of a number of chalcogenides of the transition elements with the structure of nickel arsenide type have hitherto been investigated mostly with polycrystalline specimens. Recently preparation of single crystals of such compounds has been undertaken with success and with such crystals some interesting knowledge about magnetocrystalline properties of the compounds of this type, for example, FeS[1], Fe_7S_8[2] and Fe_3Se_4[3], were found. In the present investigation, we fixed our eyes on the single crystal of nickel sulfide with nickel arsenide structure and studied the antiferromagnetic behavior of this crystal which showed a peculiar behavior of parasitic susceptibility in the antiferromagnetic temperature range. The results obtained and a short discussion thereon are given in the following lines.

§ 2. Metallographic Survey and Preparation of the Specimens

Metallographic study of the binary system of nickel and sulfur was once made by Bornemenn, Alsen and Willems[4]. However only a few description were hitherto presented, on the behaviors of the sulfur rich side of this system including the stoichiometric composition (fifty atomic percent of sulfur). It was reported[5] that a compound with the stoichiometric composition, NiS was able to be prepared, which was found to have three different kinds of modifications. Natural nickel sulfide and that obtained from nickel sulfate added with sulfuric acid have a rhombohedral structure (γ-NiS or millerit), while those obtained by direct synthetic method and from the acetate added with acetic acid have nickel arsenide type structure (β-NiS). The third form (α-NiS) is amorphous.

In order to obtain sufficient metallographic information on the compound of nickel sulfide with the structure of nickel arsenide type, we prepared several specimens of NiS_x including the stoichiometric composition ($x=1$). The adopted method of the preparation of the polycrystalline specimen was as follows; powders of electrolytic nickel (99.9%) and sulfur (99.9%) were mixed with the desired proportions, the mixtures were sealed in evacuated silica tubes and then heated at about 900°C for 24 hours, promoting the reaction of sulfur and nickel. During the heating process the specimen was kept at about 380°C for one week. By means of such a heat treatment the reaction tubes could be protected

* This investigation was supported in part by the Grant-in-Aid of Fundamental Scientific Research of Ministry of Education.

perfectly from the explosion due to the evaporation of sulfur. The reaction products were then cooled down in the furnace. The appearance of them showed evidence of melting at high temperatures and except for the cases of $x \leq 1.0$ the products were made up of two parts having clear boundary distinguishable by their colors. One part was of metallic gloss and the other of black color with tinged red.

Table I. X-ray analysis of NiS. (Cu-K$_\alpha$).

Index	$\sin^2\theta$		Intensity	
hkl	obs.	cal.	obs.	cal.
100	0.068	0.069	vs	297
002		0.084		3
101	0.090	0.090	vs	115
102	0.153	0.153	vvs	593
110	0.204	0.206	vs	465
103	0.258	0.258	w	115
200	0.273	0.274	w	139
112		0.290		31
201	0.294	0.295	w	115
004	0.338	0.336	m	155
202	0.356	0.358	s	588
104	0.406	0.405	w	137
203	0.460	0.463	vvw	115
120	0.475	0.479	vvw	669
121	0.496	0.500	m	115
114	0.540	0.542	s	929
122	0.557	0.564	s	588
204	0.591	0.611	vvw	139
300	0.605	0.617	m	465
123	0.661	0.669	vw	115
302		0.701		31
006		0.757		5
205	0.792	0.800	vw	115
124	0.810	0.816	m	139
220	0.819	0.823	m	465
106	0.824	0.826	m	593
116		0.963		31

The diffraction lines, whose indices satisfy the following relation, viz. h=k+3m, l=2m+l, where m and n are zero, positive or negative integers, should be missed in the case of a nickel aresenide type crystal. As the above table shows, such lines were not observable in the present case.

Table II. X-ray analysis of Ni_6S_5. (Cu-K$_\alpha$).

$\sin^2\theta$	Intensity	$\sin^2\theta$	Intensity
0.0014	vvw	0.025	s
0.0026	s	0.027	w
0.0036	vw	0.029	w
0.0049	vvw	0.030	w
0.0052	vvw	0.031	w
0.0062	m	0.033	vvw
0.0078	vs	0.035	m
0.0082	vs	0.038	w
0.0094	s	0.040	vvw
0.0101	s	0.041	w
0.0110	vw	0.043	w
0.0120	s	0.044	vw
0.0138	s	0.045	w
0.0144	vvw	0.047	vw
0.0154	vw	0.048	s
0.0166	vvw	0.052	vvw
0.0173	vvs	0.059	m
0.0181	vs	0.061	w
0.0194	vw	0.062	m
0.0198	s	0.066	vw
0.021	vw	0.069	s
0.022	vvw	0.071	m
0.023	vs	0.072	m
0.024	s	0.074	w

Now we studied at first the crystal structure of the specimens with x=1.0, 0.9, 0.833 add then the separated parts with metallic gloss and those with tinged red colour with compositions x=1.1, 1.2, 1.3, all these results of X-ray analysis are shown in Tables I, II and III. As seen from the Table I all the diffraction lines for the compound with the composition x=1.0 can be indexed as those

Table III. X-ray analysis of $Ni_{6.8}$. (Cu-K$_\alpha$).

obs.		NiS	NiS_2	NiS_2		Ni_3S_4	
$\sin^2\theta$	I.	hkl	hkl	$\sin^2\theta$	I.	nkl	$\sin^2\theta$
0.056	m		111	0.057	80	111	0.01
0.068	s	100				220	0.05
0.075	vs		200	0.074	257	311	0.07
0.089	s	101				222	0.08
0.094	s		210	0.093	74	400	0.10
0.112	s		211	0.112	47	331	0.121
0.151	vs		220	0.148	127	422	0.153
0.153	vs	102				333,511	0.172
0.167	m		221,300	0.167	5	440	0.203
0.203	vvs	110	311	0.204	387	531	0.223
0.222	m		322	0.223	147	620	0.255
0.240	s		320	0.242	32	533	0.274
0.259	vs	103	321	0.259	113	622	0.280
0.271	vw	200				444	0.306
0.292	w	201				551,711	0.325
0.335	w	004				642	0.357
0.349	m		331	0.353	61	553,731	0.376
0.355	m	202				800	0.408
0.365	m		420	0.371	68	733	0.427
0.404	vw		421	0.389	67	660,822	0.459
0.441	m		423	0.445	92	555,751	0.478
0.460	vvw	203				662	0.484
0.476	vvw	120				840	0.510
0.497	vs		333,511	0.501	473		
0.554	m		432,520	0.539	3		
0.588	s	114	440	0.594	461		
0.605	w	300	441	0.613	14		
0.642	vw		431	0.650	15		
0.659	s		442,600	0.668	251		
0.679	vvw		610	0.686	51		
0.696	s		611,532	0.704	187		
0.733	vvw		620	0.740	63		
0.753	vw		443,621	0.760	66		
0.790	w		533	0.797	159		
0.808	w	220	622	0.815	122		
0.817	vw						

All observed lines are indexed either as those of NiS or NiS_2. The calculated $\sin^2\theta$ and intensity for NiS_2 are shown in the fifth column respectively. The last two columns give indices and calculated $\sin^2\theta$ of Ni_3S_4.

of the nickel arsenide structure with lattice constants $a=3.39$ Å, $c=5.30$ Å and with the axial ratio $c/a=1.56$, and it was also found that the compound showed the same structure at the temperature of liquid nitrogen. The diffraction lines for $x=0.833$ given in Table II could not easily be indexed by the present author, but based on the results of thermal analysis mentioned below, it will be supposed that these diffraction lines will be due to the compound Ni_6S_5, as proposed by previous authors[4]. For $x=0.9$, diffraction lines of NiS were recognizable, however, other lines were seen to be identified as those of Ni_6S_5 mentioned above. The separated part with metallic gloss from the specimen with x greater than unity was also found to show only the diffraction lines of NiS. Some of the lines of the tinged red part were those of NiS while the rest of the lines could be indexed as those of a cubic lattice with the parameter 5.65 Å. As shown in Table III all these lines can be indexed by assuming the pyrite structure which is to be identified with NiS_2 found previously by Jong and Willems[6]. It was once reported by Menzer and Jong[7] that natural leucite, whose composition is represented by Ni_3S_4, has spinel structure with parameter 9.65 Å, but for the present specimens, and diffraction lines of such type were not found: In the last two columns, the indices and calculated $\sin^2\theta$ for Ni_3S_4 based on the reported spinel structure are shown, which do not coincide with the observed diffraction angles.

Now the thermal analyses for all the prepared reaction products were undertaken. The specific heat *vs* temperature curves are shown in Fig. 1. From these results we can recognize that for $x=0.833$, there appears an anomaly at 585°C, which coincides with the peritectoid point of Ni_6S_5 proposed formerly by Borneman and others[4]. In some cases, a a peak was also found at 400°C. This peak, however, would be considered as due to the heat absorption by the evaporation of free sulfur, since the quantity of the anomalous heat absorption changed or vanished with various heat treatments of specimen. For the specimen $x=1.0$, there appeared no anomaly up to 750°C.

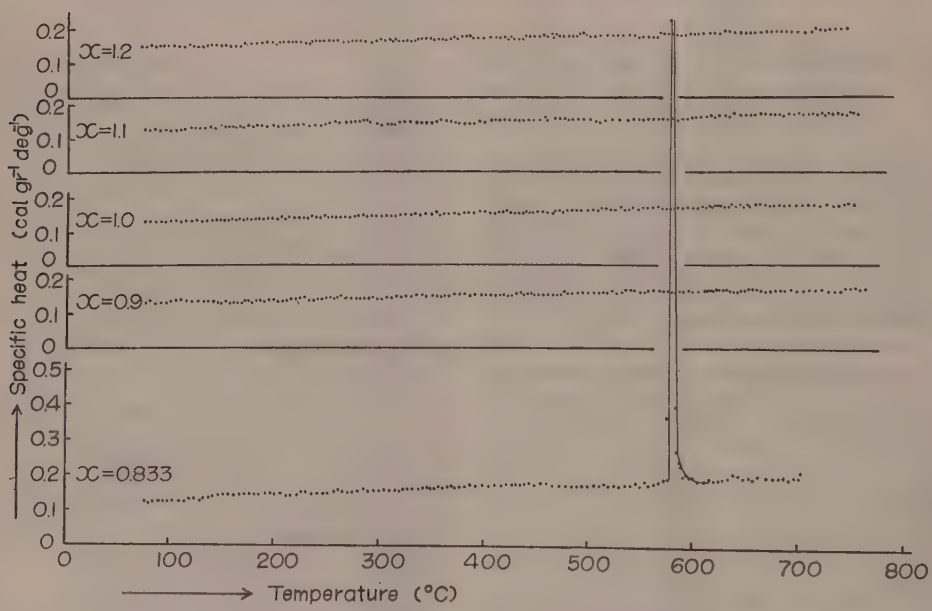

Fig. 1. The specific heat *vs* temperature curves for the specimens $x=0.833$. 0.9, 1.0, 1.1, 1.2.

From these findings it can be concluded that the compound NiS with nickel arsenide structure coexist with the compound Ni_6S_5 or with NiS_2 for excess of nickel or sulfur content respectively. Also it is to be considered that the range of compositions of nickel sulfide with nickel arsenide structure is very narrow in the phase diagram.

In order to prepare the single crystal of

NiS, the powdered specimen of NiS sealed in an evacuated silica tube was cooled down in furnace from about 900°C at the rate of half a degree per minute. In this way, single crystals larger than $15\times6\times6\,mm^3$ were obtained.

§ 3. Experimental Results

(i) *Magnetic susceptibility of the powder specimens*

The temperature dependence of the magnetic susceptibility of nickel sulfide ($x=1$) in powder form was at first determined in the temperature range from the boiling point of liquid helium to 500°C with a magnetic balance of an automatically recording type[8]. The specimens containing NiS_2 and Ni_6S_5 were also examined. These results are shown in Fig. 2.

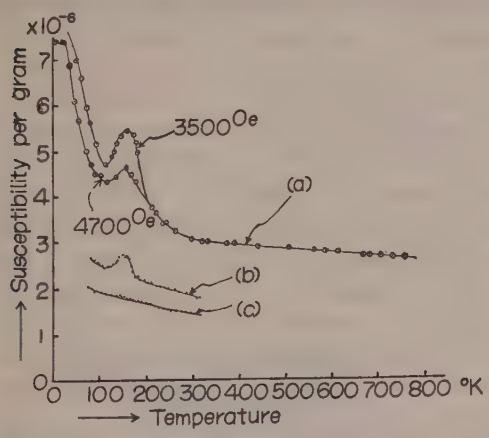

Fig. 2. The relation between magnetic susceptibilities and temperature. Curves (a), (b) and (c) show for NiS, $NiS_{1.1}$ (containg NiS_2) and Ni_6S_5 respectively. Diamagnetic correction were performed for curve (a).

The observed value of susceptibility was so small that it is desirable to take into account the correction coming from diamagnetism of atom cores. Such a correction was made in the following way: Diamagnetic susceptibility of several numbers of atom cores of the first transition group of ions (Sc^{+3}, Ti^{+4}, V^{+5}, Cr^{+6}, Mn^{+7}) due to Pauling's result[9] was plotted in the order of atomic number as in Fig. 3a. Then diamagnetic susceptibility, χ_d for Ni^{+10} which is considered to be the core of a nickel atom excluding the outer-shell electrons is obtained to be -3.2×10^{-6} (per mol) by means of the extraporation of this curve. On the other hand, the susceptibility for cuprous ion also been known to be -13.2×10^{-6} (per mol), and this value may not differ greatly from that of a hypothetical nickel ion with perfectly filled 3-d shell. If we assume that the χ_d of a nickel ion with a desired number of 3-d-electrons changes linearly from Ni^{+10} to Cu^{+1}, then the value for Ni^{+2} is determined by the interpolation to be $-11\times10^{-1}\,mol^{-1}$ (confer Fig. 3b). On the other hand, the diamagnetic correction term from S^{-2} is 40×10^{-6} per mol and is much greater than the value for Ni^{+2}. From these values we obtained the term of diamagnetic correction for the susceptibility of NiS as $0.72\times10^{-6}\,gr^{-1}$. The curve for NiS shown in Fig. 2 was obtained by applying the diamagnetic correction mentioned above.

As the curve shows, the susceptibility has

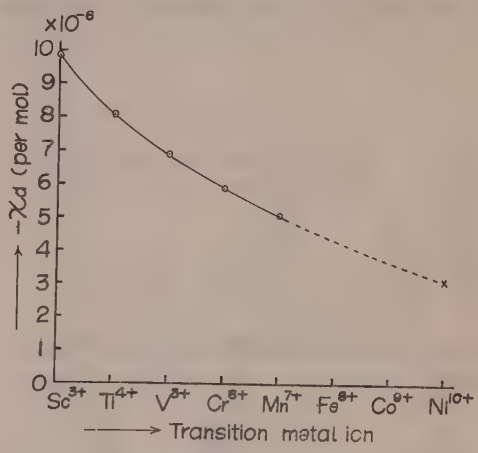

Fig. 3a. Diamagnetic susceptibilities for transition metal ions.

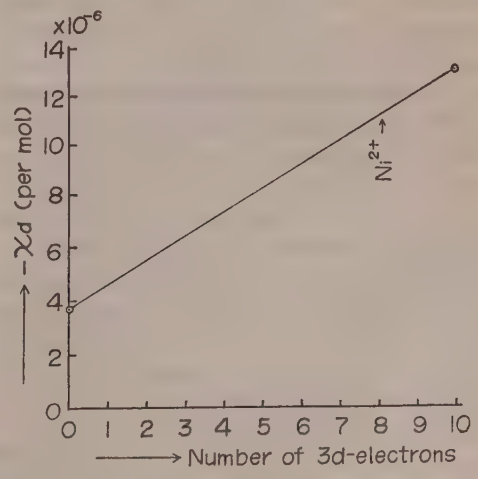

Fig. 3b. The relation between the diamagnetic susceptibility and the number of 3-d electrons.

a maximum at 150°K, then decreases during the fall of temperature but at 120°K, it reaches a minimum and again increases rapidly with the further cooling of the specimen.

(ii) *Torque measurement of the single crystal*

A magnetic torsion balance was used for the measurement of torque exerted on a single crystal specimen by the application of the magnetic field. The dimension of the single crystal used was 10 mm in length and 5×4 mm² in section. The crystal was mounted on the torsion balance with its c-axis normal to the suspension fiber. The changes of torque with the field direction at several temperatures are shown in Fig. 4. As is shown in the figure, the torque changes with field direction nearly proportionally to sin 2θ, θ being the angle between the c-axis of the crystal and the direction of the applied field. The maximum of torque occurs at $\theta=\pi/4$ at every temperature. It was also found that the maximum torque changes proportionally to the square of the applied magnetic field. As an example, the torque value at −190°C is shown in Fig. 5.

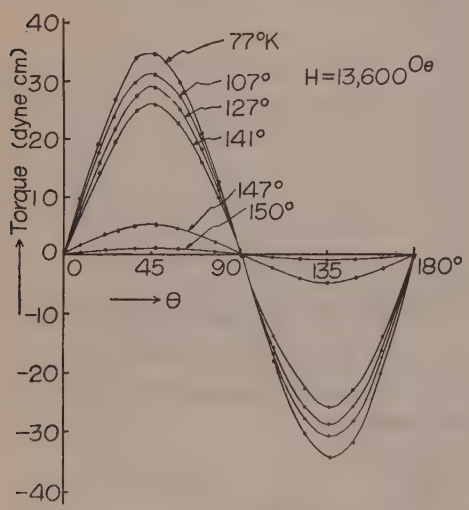

Fig. 4. Torque curves of NiS in the a-c plane. $\theta=0°$ refers to the c-axis and $\theta=90°$ to the a-axis.

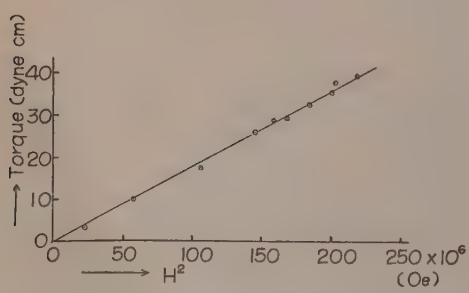

Fig. 5. H² dependence of the maximum torque, where H is the applied magnetic field.

(iii) *Specific heat at low temperatures*

The apparatus for the measurement of specific heat in the temperature range below room temperature was of an automatically recording type[10]. About 15 grams of the specimen was used for the measurement. The heating rate during the measurement was about 6 deg./min. The relation between the specific heat, C_p, and the temperature is shown in Fig. 6. A flat hump was seen in the vicinity of about 148°K, corresponding to the maximum of susceptibility mentioned in the preceeding paragraph. The amount of the heat absorption due to this hump was estimated to be about 0.13 cal/gr or 12 cal/mol.

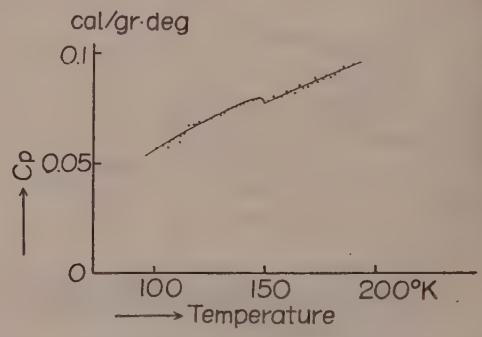

Fig. 6. The relation between specific heat and temperature for NiS.

§ 4. Discussion of the Experimental Results

It is to be noticed at first that any inconsistency will hardly occur among the present results if we assume that the maximum at 150°K in the susceptibility temperature curve of the compound NiS is due to the magnetic transition from antiferro. to paramagnetism. Firstly, an anomalous heat absorption due to this transformation can also be seen as a hump at 148°K in the curve of specific that *vs* temperature mentioned above. Néel and Smart et all[11] have proposed the expressions of the anomalous heat capacity ΔQ and jump of specific heat ΔC_p at the Néel point as follows,

$$\Delta Q=\frac{3}{10}\frac{S^2+(1+S)^2}{(1+S)^2}T_N\Delta C_p$$

$$\Delta C_p=\frac{5S(S+1)}{S^2+(1+S)^2}R$$

where S, T_N and R are the spin quantum number, the Néel temperature and the gas constant respectively. Introducing the experimental values 1.9/2 for S, which will be mentioned later, and 150°K for T_N, we can obtain $\Delta Q=225$ cal/mol and $\Delta C_p=4$ cal/mol deg, so that the experimental value of $\Delta Q=12$ cal/mol is about one twentyth smaller in magnitude than that expected theoretically. But we encounter frequently that experimental values are found to be far smaller than those expected from the expression above mentioned. For example, for FeO and NiO, antiferromagnetic spin orderning was confirmed by aid of neutron diffraction experiments[12] and the anomalous heat absorptions at their Néel points were found to be 60[13] and 110[14] cal/mol respectively, which are far smaller than the expected values from the above expressions.

Now it will be expected that the powder susceptibility of the antiferromagnetic substances decreases with the fall of temperature and at absolute zero of temperature, reaching two thirds of the values at the Néel point. Nevertheless in the present case the susceptibility begins to increase again at 120°K during the fall of temperature. Moreover there appears a magnetic field dependence of the susceptibility in the temperature range lower than the Néel point. It might seem possible at first sight to explain this fact by assuming that the specimen contains a little amount of ferromagnetic impurities, the Curie point of which lies at about 150°K. From the phase diagram above mentioned, indeed, it will be possible that the present specimen of NiS will contain a small quantity of NiS_2 or Ni_6S_5 for the excess of sulfur or nickel content. However, the $\chi-T$ curves of these compounds are of the antiferromagnetic and paramagnetic types as illustrated in Fig. 2. Therefore, the contribution from the impurities occurring from such neighboring phases can not introduce any effect of the above mentioned type on the susceptibility of nickel sulfide with the stoichiometric composition. The possibility of other kinds of ferromagnetic impurities can not be excluded so simply if the impurity distribution be in a homogeneous form in the crystal or the impurities have no magnetic anisotropy. However, such an estimation is improbable since several kinds of specimens were prepared with nickel and sulfur of different origins and it was found that all these specimens had the same $\chi-T$ relationship. Now it will become more improbable to attribute the increase of susceptibility at low temperature to any kind of parasitic ferromagnetism, if the magnetic anisotropy mentioned above in the case of the single crystal is considered. In such a case the observed anisotropy will be of an uniaxial nature and the torque will reach asymptotically a constant value for a strong field, while in the range of weak magnetic field it will increase linearly with the field. As shown in Fig. 5, the torque is proportional to the square of the magnetic field at every temperature, so above mentioned possibility will be excluded.

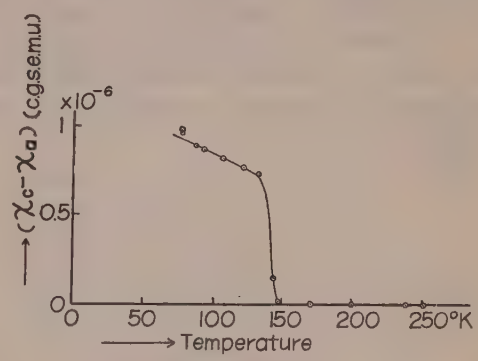

Fig. 7. Temperature dependence of the difference between parallel and perpendicular susceptibilities.

From the result of the torque measurement (Fig. 4), and based on the formula for torque τ, $\tau=m/2\cdot(\chi_c-\chi_a)H^2\sin 2\theta$, we obtained the temperature dependence of the difference between the susceptibility in the direction of c-axis and that in the c-plane, $\chi_c-\chi_a$, as in Fig. 7. The difference decreases from the boiling point of liquid nitrogen at first gradually but it is to be noticed here that no marked discontinuity appears at the temperature 120°K of the minimum of susceptibility. On the other hand at the temperature 150°K the said difference disappears suddenly. This fact will easily be understood that the latter is the Néel point of the compound and such a rise in susceptibility in the temperature range lower than 120°K will be attributable to the existence of a kind of paramagnetic islands as in the case of CoO, which will make small contribution to the anisotropy of sus-

ceptibility. In this case the field dependence of the powder susceptibility will be caused by the antiferromagnetic part of the compound.

In the case of the nickel arsenide structure each cation is surrounded octahedrally by six neighboring anions. The crystal field due to such anion shells is pseudo-cubic type added with small trigonal symmetry, the latter greatly depending upon the axial ratio c/a and it is expected that the change of sign in the magneto-crystalline property will occur $c/a=1.63$. For NiS, the axial ratio is less than 1.63, and from the results of calculation of $L-S$ coupling energy in Ni^{2+} ion in NiS[15], it is concluded that the spin direction falls in c-plane. Such a conclusion coincides perfectly with the result of the torque measurement above mentioned.

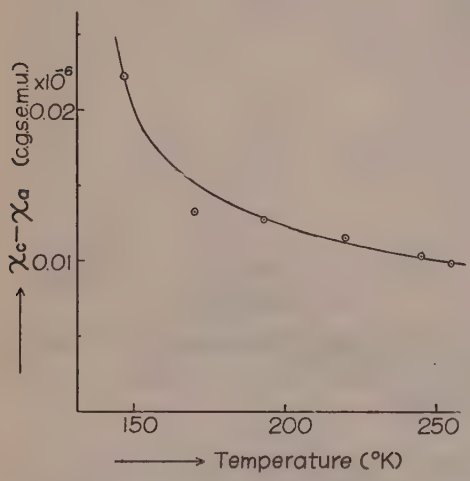

Fig. 8. Temperature dependence of the difference between parallel and perpendicular susceptibilitise. (above the Néel point)

From the measurement of the powder susceptibility above the Néel temperature, we can obtain the relation between the inverse susceptibility and temperature, and from this relation various constants were determined as follows. The number of effective Bohr magnetons is 2.66, the spin quantum numbers S is 1.9/2 assuming the Landé factor equal to two and the asymptotic Curie point, $-\theta$ is about 3000°K. If the compound NiS is an ideally ionic one, a nickel ion has eight electrons in outer d-shell, and S would be considered as unity. The experimental value agrees very well with the theoretical one.

K. Yoshida[16] discussed on the difference $(\chi_c-\chi_a)$ above the Néel temperature, and reduced the following relation,

$$\chi_c-\chi_a=\frac{D}{kT}\left\{\frac{3}{2}S(S+1)-\frac{3}{10}\right\}$$

where D is anisotropy constant in effective Hamiltonian. Using the experimental data (Fig. 7), we estimate $D\fallingdotseq 2.4\,\mathrm{cm}^{-1}$. This is a reasonable value since, in this case, there exists $l-s$ coupling in addition to the spin-spin interaction.

Acknowledgements

The author wishes to express his cordial thanks to Professor T. Hirone for his encouragement and useful discussions. Also he wishes to express his hearty thanks to Doctors S. Maeda and N. Tsuya for their valuable discussions.

References

1) T. Kamigaichi, T. Hihara, H. Tagaki and E. Hirahara: J. Phys. Soc. Japan **11** (1956) 1123.
2) I. Mikami et al: to be published.
3) K. Hirakawa: J. Phys. Soc. Japan **12** (1957) 929.
4) N. Alsen: Foel. Fören Stockholm Foch **47** (1925) 19.
N. W. V. Willems: Physica **7** (1927) 203.
K. Bornemann: Metallurgie **5** (1908) 13.
5) G. R. Levi and A. Baroni: Zeit. f. Krist. **92** (1935) 210.
6) W. F. Jong and H. W. V. Willems: Zeit. anorg. allg. Chem. **160** (1927) 185.
7) G. Menzer: Zeit. Kristallogr. **64** (1926) 506.
W. F. Jong: Zeit. anorg. allg. Chem. **160** (1927) 185.
8) T. Hirone, S. Maeda and N. Tsuya: Rev. Sci. Instr. **25** (1954) 516.
9) Refered to in "*Theory of Electric and Magnetic Susceptibilities*" by J. H. Van Vleck, (1936) 225, Oxford.
10) T. Hirone, S. Maeda, I. Tsubokawa and N. Tsuya: Sci. Rep. RITU **A 5** (1953) 513.
11) L. Néel: Ann. Phys. **3** (1948) 137.
L. N. Howard and J. S. Smart: Phys. Rev. **90** (1953) 374; Phys. Rev. **91** (1953) 17.
12) W. A. Strauser and E. O. Wollan: Phys. Rev. **83** (1951) 333.
13) R. W. Millar: J. Amer. Chem. Soc. **51** (1929) 215.
14) Y. Shimomura and I. Tsubokawa: J. Phys. Soc. Japan **9** (1954) 19.
15) To be published in this journal.
16) T. Nagamiya, K. Yoshida and R. Kubo: Advances in Physics **4** (1955) No. 13.

JOURNAL OF THE PHYSICAL SOCIETY OF JAPAN Vol. 13, No. 12, DECEMBER, 1958

Relaxation Spectrum of Chain High Polymeric Substances

By Tsuyoshi ONISHI* and Misazo YAMAMOTO

Department of Chemistry, Faculty of Science, Kyoto University, Kyoto, Japan

(Received August 14, 1958)

The wedge type relaxation spectrum of amorphous chain substances having next-nearest neighbor interaction is derived. The interaction is taken in the form of special square type potential against a distance. The potential indicates that the chain has stiffness. The equation of motion is solved by normal coordinate method for Bueche's vibrating string model.

The slope of the relaxation spectrum of our model is steeper than that of ideal elastic chain model for which the slope of $-1/2$ in the log-log plot is proved, and quite coincides with the experimental data.

§ 1. Introduction

It is well known that there are generally two distinct types[1] in the Relaxation Spectrum of amorphous polymers. One is the box type spectrum located in the long relaxation time region; the other is the wedge type spectrum in the short relaxation time region. From the stand point of molecular structure, the former originates from inter-chain entanglement; the latter from intra-chain relaxation, i.e., its source is in micro-Brownian motion of a chain. Theories of inter-chain relaxation have been developed by several authors[2] based on a model of weak rubber-like network structure. These theories however are rather qualitative in nature, and have not yet succeeded in explaining the character of the box type spectrum.

For theoretical treatment of the micro-Brownian motion following Kirkwood's theory, a Pearl Necklace model immerse in viscous liquid has been proposed[3]. Nakada suggested that the wedge type spectrum can be explained by the Rouse model. His spectrum has a slope of $-1/2$ in the log-log plot, as has been observed for typical flexible chain substances such as amorphous polyisobutylene.

But experimental data for the slopes of many polymeric substances differ somewhat from $-1/2$. Many textile fibers have flat spectrum in the comparatively wide range of relaxation time, whereas for some flexible chain substances, the slope of the spectrum is generally a little steeper than $-1/2$ especially in short relaxation time region (Fig. 1).

For the flat spectrum, Chikahisa proposed a model and obtained less steep spectrum[4], it is still not satisfactory. The purpose of this paper is to discuss the tendency for the spectrum to become steeper. For simplicity, we adopt Bueche's vibrating string model,

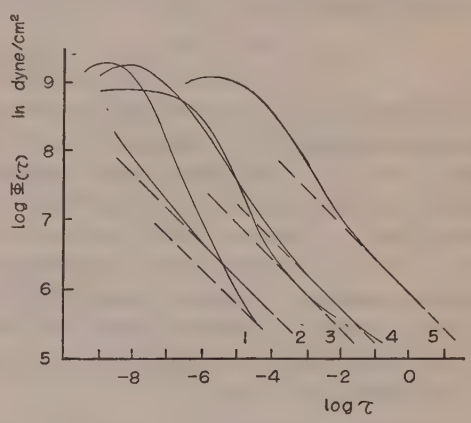

Fig. 1. Wedge type relaxation spectrum of several different polymer systems at 25°C (Ferry[6]). 1, 10% Polyvinylchloride in dimethyl thianthrene; 2, 20% cellulose tributyrate in dimethyl phthalate; 3, 50% polyvinyl acetate in tricresyl phosphate; 4, polyisobutylene; 5, 40% polyvinyl chloride in dimethyl thianthrene. Dashed lines are drawn with slope of $-1/2$.

instead of Rouse model which would necessitate solving the diffusion equation. Although there may be some ambiguity in Bueche's model, these two models should give the same results as far as the relaxation spectrum is concerned.

§ 2. Vibration String Model

Let $(N+1)$ spherical segments be connected by N Gaussian springs and be immersed into

* Present address: Department of Physics, Faculty of Science, Nagoya University, Nagoya, Japan.

viscous liquid in which the frictional constant is f. The equation of motion of jth segment is

$$m\ddot{x}_j=-f\dot{x}_j+\Phi(j,\ t)-\frac{\partial V(\{x_j\})}{\partial x_j},\quad \begin{pmatrix} j=0,\ 1,\ 2,\cdots,\ N \\ x,\ y,\ z \end{pmatrix}, \tag{1}$$

where m is the mass of a segment, $\Phi\ (j,\ t)$ external force acting on j^{th} segment at time t, and $V(\{x_j\})$ elastic potential of the chain springs, and $(x,\ y,\ z)$ indicates that this form of the equation is satisfied by the three components x, y and z of the coordinate.

In Bueche's ideal model, V comes only from the nearest neighbor interaction, i.e.,

$$V(\{x_j\})=(\alpha/2)\textstyle\sum_j(x_j-x_{j-1})^2. \tag{2}$$

In this paper, to express the stiffness of a chain, we take into consideration the next-nearest neighbor interaction and put in the following form:

$$V(\{x_j\})=(\alpha/2)\textstyle\sum_j(x_j-x_{j-1})^2 +\lambda\sum_j\left(\frac{x_{j+1}+x_{j-1}}{2}-x_j\right)^2. \tag{3}$$

The meaning of the additional potential is easy to understand in transversal vibrational mode. For the ideal chain with potential energy (2), no difference is found in the potential energy between mode (a) and (b) in Fig. 2. But in a chain with the next-nearest neighbor interaction, potential energy becomes higher in mode (b) than in mode (a). Here λ is a constant which could give the measure of the stiffness of a chain.

Fig. 2. The meaning of our potential, Eq. (3), is easy to understand in transversal vibrational mode.

Our problem, then, is to solve Eq. (1) using internal potential (3) in the sinusoidally oscillating external force field, and to obtain the complex compliance $J^*(\omega)$ and finally to derive the relaxation spectrum.

§ 3. Normal Coordinate

Equation of motion (1) with intra-chain interaction potential (3) can be solved by the method of normal coordinate. Consider the equation of motion for the "free" chain, viz.,

$$m\ddot{x}_j=\alpha(x_{j-1}-2x_j+x_{j+1}) -\lambda(\tfrac{1}{2}x_{j-2}-2x_{j-1}+3x_j-2x_{j+1}+\tfrac{1}{2}x_{j+2}). \tag{4}$$

with the periodical boundary condition

$$x_j=\pm x_{j+N}. \tag{5}$$

The solution of Eq. (4) under the condition (5) may be written in the form

$$x_j=\sum_{n=0}^{N}A_n\cos(jk_n)\exp(i\omega_n t), \tag{6}$$

where

$$k_n=(n/N)\pi, \tag{7}$$

$$\omega_n{}^2=(2\kappa/m)\{(1-\cos k_n)-(\varepsilon/2)(1-\cos 2k_n)\} \tag{8}$$

and

$$\kappa=\alpha+2\lambda, \tag{9}$$

$$\varepsilon=\lambda/\kappa. \tag{10}$$

Here κ has a meaning of apparent elastic modulus of the chain, and ε may be called a "stiffness parameter" restricted in the range

$$0\leq\varepsilon\leq 1/2. \tag{11}$$

Obviously $\varepsilon=0$ correspond to an ideal chain.

Eq. (1) with Eq. (3) can be solved by normal coordinate q_n:

$$x_j=\sum_{n=0}^{N}\sqrt{(2/mN)}\ q_n\cos(jk_n). \tag{12}$$

Then q_n must satisfy the equation

$$\ddot{q}_n+(f/m)\dot{q}_n+\omega_n q_n=F_n, \tag{13}$$

where F_n is a Fourier transform of the external force:

$$F_n=\textstyle\sum_j\sqrt{2/mN}\ \Phi(j,\ t)\cos(jk_n). \tag{14}$$

Eq. (13) is an ordinary linear differential equation, and knowing $\Phi(j,\ t)$ it may be solved easily.

§ 4. Relaxation Spectrum

It is assumed that the system has a temporary rubber-like network structure in which the motion of the junction points follow the theorem of proportionality. Consequently external force is exerted only at the junctions, i.e., at the chain ends. Then $\Phi(j,\ t)$ can be taken in the form

$$\Phi(j,\ t)=\begin{cases} \mathscr{F}e^{i\omega t}; & j=0\ , \\ -\mathscr{F}e^{i\omega t}; & j=N\ , \\ 0\ ; & \text{otherwise.} \end{cases} \tag{15}$$

According to Eq. (14), F_n is

$$F_n=\begin{cases} (4\mathscr{F}/\sqrt{2mN})e^{i\omega t}; & n\text{: odd}\ , \\ 0\ ; & n\text{: even.} \end{cases} \tag{16}$$

Eq. (13) gives the solution

$$q_n=\begin{cases}\dfrac{4\mathscr{F}}{\sqrt{2mN}}\dfrac{e^{i\omega t}}{\omega_n^2-\omega^2+i\omega f/m}; & n\text{: odd},\\ 0 \quad ; & n\text{: even}.\end{cases} \tag{17}$$

Complex compliance J^* can be written

$$J^*=\frac{\Delta x/R}{\nu\mathscr{F}e^{i\omega t}}=\frac{8}{\nu RmN}\sum_{n:\,\mathrm{odd}}\frac{1}{\omega_n^2-\omega^2+i\omega f/m}, \tag{18}$$

where ν is the effective number of chains crossing the unit area of any cross section in in the sample, and $\Delta x=x_0-x_N$ denotes relative displacement of end-to-end vector of the chain, which has a length R in equilibrium state.

Eq. (1) and Eq. (18) contain the effect of inertia term $m\ddot{x}$ and ω^2 respectively. However, we may neglect these terms in the phenomenological theory of viscoelasticity. By neglecting ω^2 in the denominator of Eq. (18), we are led to complex compliance

$$J^*=\frac{8}{\nu RNf}\sum_{n:\,\mathrm{odd}}\frac{\tau_n}{1+i\omega\tau_n} \tag{19}$$

which is in agreement phenomenological expressions. Here τ_n denotes the retardation time

$$\tau_n=f/(m\omega_n^2)$$
$$=\frac{f}{2\kappa}\frac{2}{(1-\cos k_n)-(\varepsilon/2)(1-\cos 2k_n)}. \tag{20}$$

With large value of N, summation of Eq. (19) may be approximated by the integration

$$J^*=-\frac{4}{\pi\nu Rf}\int_{\tau_\alpha}^{\tau_\beta}\frac{\tau}{1+i\omega\tau}\frac{dx}{d\tau}d\tau, \tag{21}$$

where

$$\tau=\frac{f}{2k}\frac{1}{(1-\cos x)-(\varepsilon/2)(1-\cos 2x)} \tag{22}$$

and

$$\tau_\alpha=f/4\kappa,\quad \tau_\beta=(N/\pi)^2(f/\alpha). \tag{23}$$

When the distribution function of retardation time $G(\tau)$ is introduced by the relation

$$J^*=-\int_0^\infty\frac{G(\tau)}{1+i\omega\tau}d\tau, \tag{24}$$

we are led directly to the $G(\tau)$ in our system, i.e., to

$$G(\tau)=\begin{cases}\dfrac{1}{\pi\nu\kappa R}\dfrac{1}{\tau}\dfrac{1}{\sin x-\varepsilon\sin 2x}; & \tau_\alpha\leq\tau\leq\tau_\beta,\\ 0 \quad ; & \text{otherwise}.\end{cases} \tag{25}$$

Relaxation time spectrorum $\Phi(\tau)$ is obtained from Eq. (25) by using the the method described in Gross' text[5]:

$$\Phi(\tau)=\frac{1}{\pi\tau}\frac{\pi G(\tau)}{[K(\tau)]^2+[\pi G(\tau)]^2}, \tag{26}$$

where

$$K(\tau)=\int_0^\infty G(u)/(\tau-u)du. \tag{27}$$

Using the reduced quantities τ^* and $\Phi^*(\tau^*)$, i.e.,

$$\Phi(\tau)=\nu\kappa R\Phi^*(\tau^*), \tag{28}$$
$$\tau=(f/4\pi)\tau^*, \tag{29}$$

the final expression of relaxation spectrum is

$$\Phi^*(\tau^*)=\begin{cases}\dfrac{4}{\pi}\dfrac{1}{\tau^*}\dfrac{\pi G^*(\tau^*)}{[K^*(\tau^*)]^2+[\pi G^*(\tau^*)]^2}; & 1\leq\tau^*\leq\tau_\beta/\tau_\alpha,\\ 0 \quad ; & \text{otherwise},\end{cases} \tag{30}$$

where

$$G^*(\tau^*)=\frac{1}{2\pi}\frac{1}{\tau^*}\frac{1}{\sin x-\varepsilon\sin 2x}, \tag{31}$$

$$K^*(\tau^*)=\frac{8}{\pi}\frac{1}{(\tau^*-1)(a_+^2+a_-^2)}\times$$
$$\times\left[\frac{1+a_-^2}{2a_-}\ln\frac{a_-+\pi/2N}{|a_--\pi/2N|}-\frac{1-a_+^2}{a_+}\left\{\frac{\pi}{2}-\tan^{-1}\frac{\pi}{2Na_+}\right\}\right]. \tag{32}$$

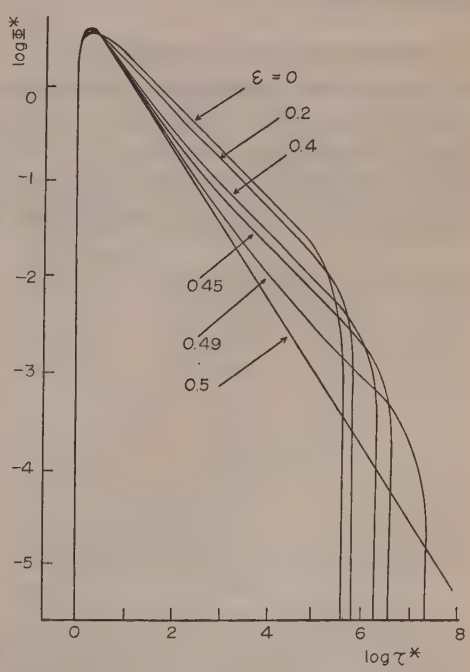

Fig. 3. Reduced relaxation spectrum $\Phi^*(\tau^*)$ for $N=10^3$ for various ε.

Here x is the function of τ^*,

$$\tau^*=1/\{(1-\cos x)-(\varepsilon/2)(1-\cos 2x)\}, \quad (33)$$

and $a_\pm$ is given by

$$a_\pm=\frac{\sqrt{(1-2\varepsilon)^2\tau^{*2}+8\varepsilon\tau^*}\pm\{(1-2\varepsilon)\tau^*-2\}}{2(\tau^*-1)}. \quad (34)$$

As can be easily seen from Eqs. (28) and (29), shape of the spectrum is independent of κ and f, as long as N and ε are kept constant. In other words when κ and f change with temperature, spectrum would shift as a whole without changing its shape. This fact suggests thermorheological simplicity in the viscoelastic behavior of high polymer systems.

Fig. 3 shows curves of $\Phi^*(\tau^*)$ for $N=10^3$ for various values of parameter ε. In the limit of $\varepsilon=0$, our spectrum reduces to that of Bueche which has the $-1/2$ slope. With increasing ε, the slope in the short time region increases, leaving the slope in the longer range unchanged. This tendency may be better understood when we consider that the second term of our potential has a considerale effect on vibrational mode at high frequency, i.e. on the spectrum in short relaxation time region.

Degree of polymerization N has little influence on the shape of spectrum for finite ε: the higher the degree, the more linear the shape becomes.

§ 5. Comparison with Experiment

As stated under introduction, our model is useful for rubber-like substance. Fig. 4(a) shows the experimental relaxation spectrum for polyisobutylene[6], a typical rubber-like substance, and (b) the theoretical spectrum with $\varepsilon=0.47$. Good agreement is observed between these two spectra.

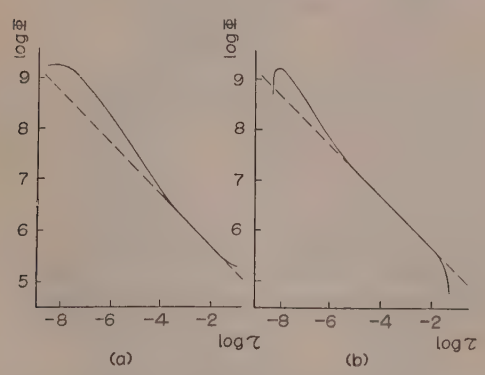

Fig. 4. Wedge type relaxation spectrum of polyisobutylene. (a) Experimental data[6]. (b) Theoretical curve ($N=10^3$, $\varepsilon=0.47$). Dashed lines are drawn with slope of $-1/2$.

The values of parameters are determined by Nakada's method. By considering that, on an average, 1/3 of the chain lies in the x direction, the effective number ν is given

$$\nu=A\rho R/3M, \quad (35)$$

where ρ: density, M: molecular weight ($M=m'N$; m': molecular weight of a segment), R: root mean square end-to-end distance ($R=\sqrt{N}l$; l: distance between segments), and A: Avogadro's number.

For elastic modulus of the chain κ, the theory of rubber easticity gives

$$\kappa=3kT/l^2 \quad (36)$$

which may be used here for an approximation. For polyisobutylene $m'\sim 50$, $l\sim 3\times 10^{-8}$ cm, $l\sim$ 1Å, $N\sim 10^3$, we finally get

$$\nu\kappa R\sim 10^8 \text{ dyne/cm}^2,$$

which makes the value of the spectrum reasonable.

Apparent frictional constant f can not be deduced by the known constant, but by adjusting τ_α to the maximum point of wedge spectrum, f becomes

$$f\sim 10^{-5} \text{ dyne/cm/sec}.$$

Assuming that Stokes' law is valid, viscosity coefficient η is

$$\eta\approx 10^2\sim 10^3 \text{ poise},$$

and this value is satisfactory, as suggested by Nakada.

§ 6. Discussion and Conclusion

The relaxation spectrum of elastic chain substance having the next-nearest neighbor interaction is derived. We have used the special potential from Eq. (3). There are two advantages of our potential, viz., the stiffness of the chain can be introduced intuitively and the eigen value problem of vibration can be solved with no approximation except periodic boundary condition.

Our model gives relaxation spectra with slopes between -0.5 and -0.8. There are

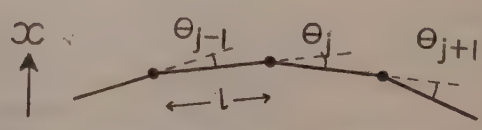

Fig. 5. Special case of $\varepsilon=1/2$ corresponds to the bending vibration of rods.

substances which have spectra steeper than our model, and although there may be some ambiguity in our model, our results suggest that the origin of the spectrum slope steeper than $-1/2$ is generally attributable to the existence of the stiffness of the chain.

The limit of $\mathcal{E}=1/2$ is interpreted as follows: Suppose the segments are all connected by rigid rods (see Fig. 5) and have an internal potential which is proportional to the square of the relative angle

$$V=\lambda'\sum_j\theta_j^2. \tag{37}$$

For small vibration, θ_j becomes

$$\begin{aligned}\theta_j&=\{(x_j-x_{j+1})+(x_j-x_{j-1})\}/l\\&=(2/l)\{x_j-(x_{j+1}+x_{j-1})/2\},\end{aligned} \tag{38}$$

and taking $\lambda=4\lambda'/l^2$, Eq. (37) becomes equal to the special case of Eq. (3), as $\alpha=0$ when $\mathcal{E}=1/2$.

Accordingly, this special case corresponds to the bending vibration of rods, and the spectrum becomes linear, as shown in Fig. 2. Formally, τ_β is infinite, but as the summation of Eq. (19) can not, in this case, be approximated by the integration, continuous spectrum terminates at finite τ, and discrete relaxation time spectrum appears.

It is likely that this special case of $\mathcal{E}=1/2$ offer a good model for any fibrous substance composed of rigid polymeric chains. However, real fibrous substances have almost flat spectra in wide range of relaxation time, and show behavior quite contrary to our model.

Then, for the spectrum of the amorphous polymer, where does this flat spectrum belong? The box type is not suitable, because of its very long relaxation time. It may rather be assumed that it belongs in the glass state region which is situated to the left of glass transition point where wedge type spectrum has a maximum value. If so, general schematic spectrum of amorphous chain-polymeric substances is composed of three types, viz., one wedge spectrum between two box type spectra. Some experimental data endorse this idea.

The authors express their sincere appreciation to Prof. T. Yamamoto for his constant encouragement and advice throughout this research, and thanks the members of Quantum Chemistry Laboratory of Chemistry Department of Kyoto University, and Profs. S. Onogi and H. Kawai and others in the High Holymer Research Group of Kyoto for their valuable discussions.

References

1) A. V. Tobolsky and J. R. McLouglin: J. Polymer Sci. **8** (1952) 543;
A. V. Tobolsky: J. Amer. Chem. Soc. **74** (1952) 3786.
2) M. S. Green and A. V. Tobolsky: J. Chem. Phys. **14** (1946) 80.
K. W. Scott and R. S. Stein: ibid. **21** (1953) 1281.
J. Furukawa: J. Polymer Sci. **15** (1955) 193.
M. Yamamoto: J. Phys. Soc. Japan **11** (1956) 413.
3) J. G. Kirkwood: Rec. Trav. Chim., **68** (1949) 649.
P. E. Rouse: J. Chem. Phys. **21** (1953) 1272.
F. Bueche: ibid, **22** (1954) 603.
O. Nakada: J. Phys. Soc. Japan **10** (1955) 804.
B. H. Zimm: J. Chem. Phys. **24** (1956) 269.
4) Y. Chikahisa: Busseiron-Kenkyu **2** (1957) 707.
5) B. Gross: "Mathematical Structure of The Theories of Viscoelasticity" Hermann and Cie, Paris (1953).
6) J. D. Ferry: Record Chem. Prog. **16** (1955) 85.

JOURNAL OF THE PHYSICAL SOCIETY OF JAPAN Vol. 13, No. 12, DECEMBER, 1958

On the Ferromagnetic Phase in Manganese-Aluminum System

By Hiroshi KŌNO

The Research Institute for Iron, Steel and Other Metals, Tōhoku University, Sendai

(Received August 15, 1958)

A metallographical investigation of manganess-aluminum system was made in the compositional range of 47% to 60% of manganese, with the results of a new hexagonal close-packed phase and a metastable tetragonal ferromagnetic phase derived therefrom. The conditions necessary for formation, structure, stability and thermal and magnetic properties of the latter phase have been studied. A discussion was also given on its magnetic properties.

§ 1. Introduction

The existence of a ferromagnetic phase in manganese-aluminum system was pointed out by Hindricks[1] in 1908; Ishiwara[2] and later Köster[3] et al. made further metallographical investigations on the nature of this phase, but they failed to find its well-defined positions in the phase diagram of this binary system. Also the structure and thermal and magnetic properties of this phase have not yet been studied in detail. Moreover, there are some inconsistencies between the reported those diagrams and magnetic properties found by these authors: According to Ishiwara's phase diagram, the composition corresponding to the maximum magnetization in the ferromagnetic range lies in the two-phase region of α and δ. For the purpose of clarifying the metallographical nature of this phase, the present writer studied this system with specimens in the compositional range from 47% to 60% Mn, and with various heat treatments; basing on the results obtained, the phase diagram of this region was studied. Then the stability, the structure and thermal, magnetic and electrical properties of the ferromagnetic phase were then investigated.

§ 2. Specimens and Experimental Method

Electrolytic manganese (purity 99.9%) and aluminum pieces (99.99%) were put together in Tammann tubes in desired proportions, the inside of which was coated with alumina, and melted in an induction furnace in air; in this way mother alloys of 40 and 70 atomic per cent manganese at charge were prepared. (Chemical analysis gave 40.9% and 72.5% Mn respectively.) They were crushed, mixed in proper proportions and melted in the same way as mentioned above and cast into bars 5 mm in diameter. The specimens thus obtained were named A_{47}, A_{48}, etc., the suffices indicating the atomic percentage of charged manganese content. During the course of melting the actual composition may be changed slightly from the initially charged one, but the shift of composition on the whole, is considered to occur regularly, so that no serious error may be introduced into a description of their physical properties in terms of charged compositions. For reference, the result of chemical analysis is given in Table I.

Table I. Chemical analysis of the specimens.

	A_{49}	A_{50}	A_{51}	A_{53}	A_{54}	A_{56}	A_{58}	A_{60}
Atomic per cent of manganese	49.1	50.1	52.2	53.8	55.1	57.1	57.9	62.5

The magnetic measurement was carried out by a ballistic method or with a magnetic balance described elsewhere[4], the X-ray structure analysis by the Debye-Scherrer method with Fe–K_α radiation and the thermal analysis by an adiabatic method, the detailed description of which was given by Nagasaki[5] and Takagi as well as Maeda[6]. This method is considered to be good for the magnitude estimation of the latent heat for the first order transformations. For the purpose of keeping adiabatic condition at high temperatures in the present experiment, a specimen container of nickel, 5 mm in thickness, was used, and the container was further shielded by a hollow steel cylinder of 1 mm in thickness. In this way the temperature distribution in the nickel-container was homogenized. Moreover, in the present case a specimen vessel of nickel was

used, which was filled by the bar-formed specimens of proper length.

§ 3. Results of Metallographical Study

First the results of metallographical study will be described. Since the existence of a eutectoid reaction was expected above 800°C in the compositional range mentioned above, the specimens were subjected to an annealing for 1 hour at 950°C to remove the segregation, then slowly cooled to 700°C, annealed again for about 5 hours at this temperature and then cooled slowly down to room temperature in vacuum. From the fact that the specific heat *vs* temperature curves of the specimens annealed for 30 minutes and those for 3~4 hours at 700°C did not differ from each other, it may be considered that the equilibrium at 700°C has almost been reached by the heat treatment mentioned above.

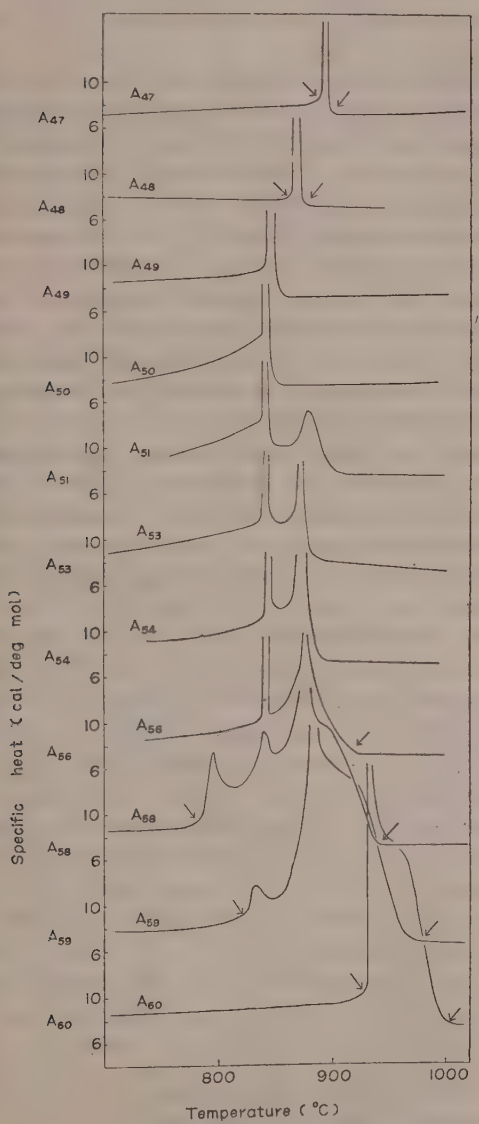

Fig. 1. Specific heat *vs* temperature curves

First of all the specific heats of these specimens were measured at the heating rate of about 2 deg./min. As shown in Fig. 1, the absorptions of heat with the latent heat type could be observed both at the temperatures 840°C and 870°C. Such measurements were repeated several times and it was found that the result here mentioned was quite reproducible. Moreover, it must be noted that the absorbed heat quantities as well as the temperatures of the heat absorption were hardly affected by the lowering of the heating rate to a value one-third of the above mentioned one during the measurement. From the results of the specific heat measurements, each absorbed heat quantity at 840°C was plotted against the composition from A_{49} to A_{57} in

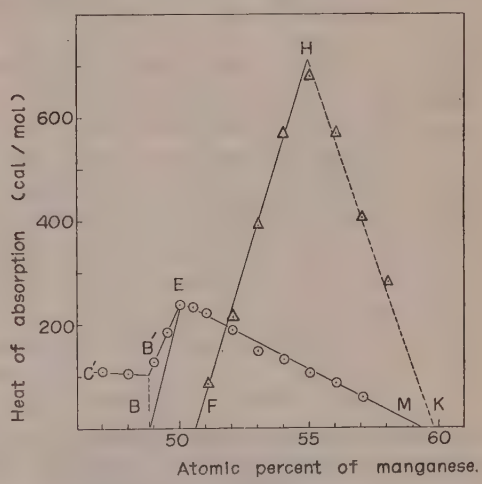

Fig. 2. Heat of absorption at 840°C, 870°C and $\zeta \rightarrow \zeta'$ reaction. For the points ○ and △, the accuracy of the measurement is not sufficient.

Fig. 2; As can be seen from the result in Fig. 2, the absorbed heat quantity of the latent heat type is greatest at 50% and decreases linearly with the change of composition on both sides. Thus the triangle $B'EM$ was obtained. Moreover, the absorbed heat quantity for peaks A_{47} and A_{48} were also plotted, and a line $B'C'$ was obtained. Based on these results as well as on the results of X-ray analysis described in the next paragraph, it is to be proposed that the latent heat ob-

served at 840°C is due to a eutectoid reaction. The eutectoid product was named ζ'-phase. However, it is to be considered here that the two phase region $\zeta'+\zeta$, ζ being one of the reactants of the eutectoid reaction, is very narrow, so the mutual mixing of ζ and ζ', which follows the eutectoid reaction, takes place at very narrow temperature range, and the heats of both reactions cannot be separated by the present specific heat measurement. Hence, it follows that heat quantities plotted in the compositional range between B and E in Fig. 2 represent the total evolved heats due to these two reactions. In this case the bracking point B' is the end point of the eutectoid line. Consequently the line EB represents the heat of the eutectoid reaction in the compositional range from B to E, and the range in which the eutectoid reaction occurs

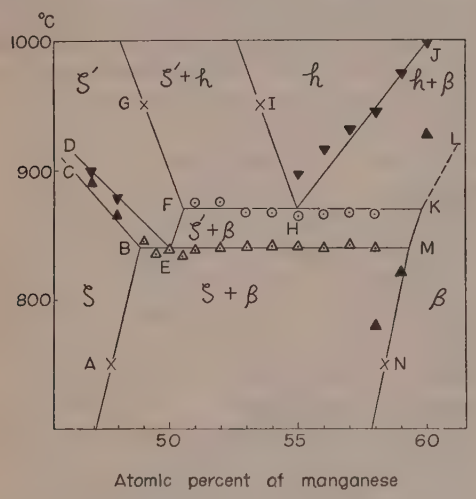

Fig. 3. Phase diagram in the vicinity of MnAl. The upright and inverted black triangles ▲ and ▼ in this figure correspond to the temperatures of appearance and disappearance of excess specific heat respectively. These points are shown by signs ↘ and ↙ in Fig. 1.

extends from point B of about 49% Mn to point M of about 59.5%, and the composition of the eutectoid point E is 50% Mn. The temperatures at which such heat absorption occurs are indicated by △ for various compositions in Fig. 3 and thus the eutectoid line BEM is obtained.

Now another supplementary fact for the above mentioned reasoning can be seen from Fig. 1 at temperatures just below 840°C. Specific heats per mol*. C_p of the alloy A_{47}, A_{48} and A_{60} do not differ so remarkably from the value expected from the Dulong-Petit law, while those of the other specimens, the compositions of which lie in the range of the eutectoid line, show excess specific heat over the Dulong-Petit value, which is supposed to be due to the solubility change of both phases in the two-phase region $\zeta+\beta$ under BEM line in Fig. 3. It may be confirmed from such behaviors of the specific heats of the alloys that the two-phase region extends over the compositional range from about 49% Mn to about 59% Mn at temperatures just below 840°C. The peaks of A_{47} and A_{48} correspond to the heat absorption which is caused by the intersection of the two-phase region $\zeta+\zeta'$ (see Fig. 3).

Now, the absorbed heat quantities at 870°C are also plotted against composition in Fig 2. As can be seen from this figure, the quantity of the latent heat absorbed at 870°C is greatest at 55% Mn and decreases linearly with change of composition on both sides of the maximum point, as is shown in Fig. 2. As can be seen from Fig. 1, the excess specific heat over the Dulong-Petit value is also seen in the specimens from A_{51} to A_{59} between 840°C and 870°C, and corresponds to the solubility change of both phases in the two phase region $\zeta'+\beta$. Based on these results, it may be supposed that the latent heat observed at 870°C is due to another eutectoid reaction. As can be estimated from Fig. 2, the range in which the eutectoid reaction mentioned here occurs extends from point F at about 50.5% Mn to point K at abont 60% Mn in Fig. 3, and the eutectoid point H lies at 50% Mn. The temperatures at which such heat absorption occurs are also indicated against composition by ⊙ in Fig. 3 and thus the eutectoid line FHK is obtained in the same was as in the case of the line BEM. The eutectoid product is named h-phase. The excess specific heat of the specimens from A_{55} to A_{60} above 870°C will be due to the solubility change of the both phases in the two-phase region $h+\beta$. The excess specific heat observed over the Dulong-Petit value in A_{51}, A_{52} and A_{53} was relatively small, which can be accounted for by assuming that

* Mol number in this case was calculated by the expression $54.93x+26.98\{(100-x)/100\}x$ being the atomic percent of manganese.

the phase boundaries between the two-phase region $\zeta'+h$ and the single phase region ζ'- or h-phase are nearly perpendicular to the composition axis. Based on these results as well as on the results of X-ray analysis described in the following paragraph, the eutectoid reaction at 870°C was confirmed.

There are peaks in the neighbourhood of 790°C, 830°C and 930°C on the specific heat v.s. temperature curves of A_{58}, A_{59} and A_{60} respectively. The values of C_p on the lower temperature side than these peaks are somewhat larger than those expected from the Dulong-Petit law, but as will be described later, X-ray analysis suggests that these specimens are in the single phase region β. From these facts, these peaks may be accounted for by assuming that the superheated β-phase suddenly decomposes into β- and ζ- or h-phases, and the specific heat v.s. temperature curves show the transformation of latent heat type.

The results of the X-ray analysis will now be described. All the specimens were annealed at 950°C for 20 minutes or at 750°C for 1 hour and then quenched into water, smashed into powder, and the Debye photographs were taken. No significant differences was found between diffraction patterns of the specimens quenched from 950°C in ζ'region and those from 750°C in ζ-region. It was difficult to make structure analysis from the diffraction lines of these two phases.

Observed intensities and Bragg angles of the Debye-Scherrer lines of quenched specimen A_{54} from the region of h-phase are shown in Table II. As the table shows all the lines can be indexed, by assuming a hexagonal close-packed form. ($c/a=1.63$, $c=4.38$Å, $a=2.69$Å) The β-phase is of the β–Mn type structure[7].

Table II. X-ray analysis of h-phase (quenched state).

Observed $\sin\theta$	Observed line intensity (Fe–K_α)	Line inde	Calculated $\sin\theta$ with the lattice parameters $a=2.69$Å $c=4.38$Å
0.416	s.	$(10\bar{1}0)$	0.416
0.445	s.	(0002)	0.445
0.472	v.s.	$(10\bar{1}1)$	0.471
0.608	m.	$(10\bar{1}2)$	0.609
0.720	m.	$(11\bar{2}0)$	0.720
0.786	m.	$(10\bar{1}3)$	0.786
0.846	m.	$(11\bar{2}2)$	0.846
0.858	f.	$(20\bar{2}1)$	0.861
0.886	m.	(0004)	0.889

v: very, f: faint, m: medium, s: strong.

To determine phase boundaries, the Bragg angles θ of some strong lines of the Debye-Scherrer photographs taken with Fe–K_α radiation were plotted against composition. The phase boundaries were determined from the breaking points of the Bragg angle v.s. composition curve, the angle being independent of composition in the two phase region. The points N, A, G and I in Fig. 3 were obtained by this method.

From X-ray analysis of the specimens quenched from 750°C it was confirmed that Al-rich ζ-phase and M-rich β-phase coexist at 750°C in the compositional range from about 48 to 58% Mn, and the phase boundary line MN was determined by connecting M and N determined as mentions above, and the line AB was determined in the same way. The phase boundary line HJ was also determined from H and points ▼ of A_{55}, A_{56}, $\cdots$, A_{60} the CB line from point B and points ▲ of A_{47}, A_{48}, and the DE line from point E and points ▼ of A_{47}, A_{48}. The lines FG and HI were determined by connecting F and G, and H and I respectively, but the location of G and I from which the lattice parameters of ζ'-phase and h-phase respectively begin to change was rather poor in accuracy. The line KL could not be determined accurately, and the determination of its correct position will be a future problem.

§ 4. Physical Properties of the Ferromagnetic Phase and its Relation to Phase Diagram

From the magnetic measurements, both ζ- and β-phase as well as the quenched phase h were found to be non-ferromagnetic at room temperature, while the bar-formed specimens e.g. A_{54}, of the Al-rich side of h-phase which were cooled in air from 950°C were found to show ferromagnetism. The cooling rate was found to have some influence of the magnetic properties of the products. For an example, the cooling curves of A_{54} from 950°C are shown in Fig. 4 together with the room temperature values of the magnetization at $H_{\text{eff}}=1500$ Oe. From this figure the heat evolution due to the transformation h-phase → ferromag-

netic phase can be observed at about 750°C. Therefore, the rate of cooling shown by B or C for A_{54} in Fig. 4 is considered to be appropriate for hindering the decomposition of the specimen into β- and ζ-phase and permitting the formation of the ferromagnetic phase. It was also found that the magnetization of the air-cooled specimens from 950°C increases linearly with composition in the range from 50.5% to 54% Mn. In this compositional range, the relative line intensities of ζ'- and the ferromagnetic phase varied monotonously with composition, which was seen from the X-ray analysis of the air-cooled specimens.

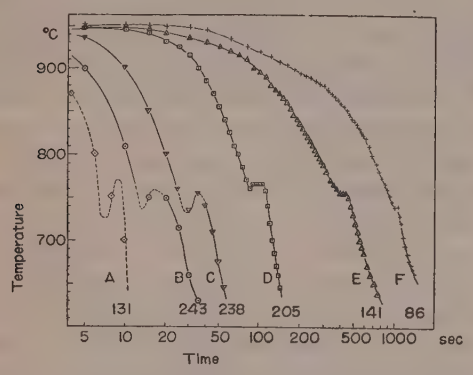

Fig. 4. Cooling curves of A_{54} measured from 950°C. The curves for air cooling are shown by B or C. The figures under the curves are the magnetization in gauss at room temperature. (H_{eff}=1,500 Oe.)

The observed Bragg angles θ and intensities of the diffraction lines in the Debye-Scherrer photograph of the ferromagnetic A_{54} specimen are shown in Table III. As shown in this table, all lines could be indexed by assuming the lattice to be tetragonal. (see the 3rd column. c/a=0.908, a=3.94Å, c=3.58) Moreover, no diffraction lines due to the β or ζ-phase were not be able to be found in the same photograph, while in the case of the Al-rich specimens the diffraction lines due to ζ'-phase were contained besides the original lines of the ferromagnetic phase and the intensity of the former increased with decreasing manganese content, while that of the latter decreases, disappearing at the composition of 50% Mn. In the Mn-rich case those due to the β-phase appeared. Hence, it is to be concluded that the specimen that could be regarded as a single phase was only A_{54} and the others contained β and ζ'-phase. Moreover, the line intensities are calculated* by assuming the CuAu type superstructure, in which Mn and Al atoms occupy alternately successive layers perpendicular to the c-axis. In this case, the manganese content is a little richer than that of aluminum, so that some of Al-atoms are substituted by excess Mn-atoms. The results of calculation are shown in Table III. In this case it can easily be

Table III. X-ray analysis of the ferromagnetic A_{54}.

Observed (Fe-K_α) sin θ	Observed line intensity	Line index	Calculated sin θ with a=3.94Å c=3.58Å	Calculated line intensity
0.271	v.f.	001	0.271	14
0.347	v.f.	110	0.348	15
0.442	v.v.s.	111	0.441	249
0.492	s.	200	0.492	92
0.540	f.	002	0.542	36
0.562	v.v.f.	201	0.562	7.3
		112	0.644	5.2
0.695	m.	220	0.696	42.5
0.731	s.	202	0.732	81.4
		221	0.746	4.3
		310	0.778	4.7
		003	0.813	1.2
0.824	v.s.	131	0.824	171
0.882 } dif-		222	0.882	102 } 210
0.882 } fuse	v.s.	113	0.884	105 }

v: very, f: faint, m: medium, s: strong.

shown that the structure factors of the reflections, for which the sum of h and k in the Miller index (h, k, l) is odd, vanish. As the table shows, the observed relative line intensity is seen to be consistent with the result of calculation. Hence, it is probable that the structure of the forromagnetic phase is of the superstructure of CuAu type.

Now for the purpose of testing the stability of the ferromagnetic A_{54} the variation of the magnetization of the specimens due to annealing was studied in the field of $H_{\rm eff}$=1750 Oe. It was found that the intensity of the magnetization was reduced to one half of its ori-

* In the calculation, the absorption due to the specimen and the decrease of the atomic scattering factor of Mn atoms due to the K-absorption edge were taken into consideration[8].

ginal value after annealing for ten hours at 910°C and almost disappeared after 50-hours annealing. At 650°C, it decreased to one half in one hour and disappeared after 7 hours, while at 700°C it decreased to one-half in a few minutes and disappeared after 30 minutes. By 500°C annealing, however, the magnetization was found to remain constant even after 162 hours.

The specific heat of the ferromagnetic A_{54} specimen prepared by air cooling from 950°C was measured in the temperature range from 100°C to 500°C at the heating rate of about 1.5 deg/min. and then this specimen was slowly cooled to room temperature in the apparatus. The measurement was repeated quite in the same way. As can be seen from Fig. 5, curve I, which was obtained in the first run, shows a broad minimum in the neighbourhood of 300°C, while curve II, corresponding to the second run, does not show such a minimum.

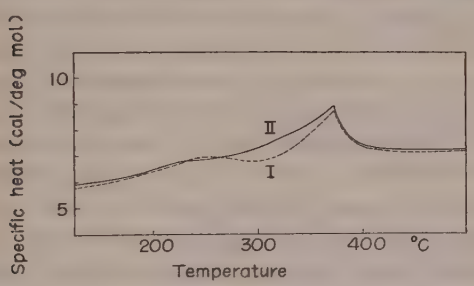

Fig. 5. Specific heat *vs.* temperature curves of the ferromagnetic A_{54}.

Measurements in subsequent runs reproduced exactly the result of the second run. However, for the specimen which was annealed for 18 hours at 400°C, the specific heat v.s. temperature curves did not show such a minimum and the results were quite reproducible within error of experiment at temperatures below 500°C. Therefore, the ferromagnetic A_{54} subjected to the low temperature annealing can be regarded as a stable phase with the superstructure of CuAu type in this temperature range, so we performed such a heat treatment for all of the specimens hereafter. From the thermomagnetic curve shown later, the peak at 373°C in Fig. 5 may be considered to be due to the magnetic transformation. When the measurement of the specific heat of the ferromagnetic A_{54} was extended to higher temperatures, a significant minimum of the specific heat appeared at about 700°C. It is considered to be due to the decomposition of the ferromagnetic A_{54} into ζ- and β-phases, the accompanying evolution producing the minimum mentioned above.

The magnetization curve for powdered ferromagnetic A_{54} was taken by the ballistic method. The H^{-2} plot of specific magnetization σ is given in Fig. 6. Thus, the extraporated saturation values at the room temperature and the boiling point of liquid nitrogen are found to be $\sigma_\infty=95.4$ and 99.6 respectively. Based on these two values, the extraporated saturation value at absolute zero $\sigma_\infty(O)$ by the formula $\sigma_\infty(T)=\sigma_\infty(O)\ (1-aT^2)$ was found to be $\sigma_\infty(O)=100$. The thermomagnetic curve at $H_{ex.}=4500$ Oe. and the sus-

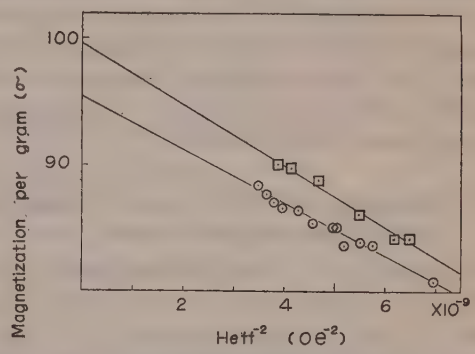

Fig. 6. The extraporated saturation values at the room temperature (⊙) and the boiling point of liquid nitrogen (⊡).

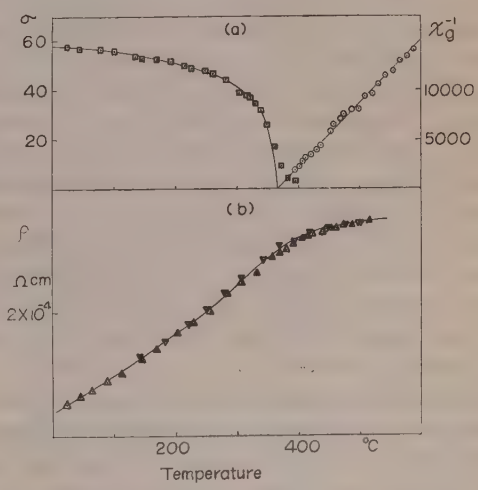

Fig. 7. Magnetization and electric resistance of the ferromagnetic A_{54}.

⊡ magnetization per gram (H_{ex} =4500 Oe.) } heating
⊙ inverse of susceptibility per gram } heating
△ specific resistance } heating
△ specific resistance ..... cooling

ceptibilities above the Curie temperature are shown in Fig. 7(a). In the ferromagnetic region the magnetization decreases with rising temperature, following a Weiss type curve, and disappears at the Curie point of about 370°C. On the heating curve of the susceptibility measurement, the Curie-Weiss law is seen to hold below 550°C, while at higher temperatures susceptibility decrease rapidly due to decomposition. The high temperature phase h shows weak paramagnetism in its stable range. It was seen from the cooling curve at the rate of about 3 deg/min. that h-phase remained unchanged until about 800°C and then decomposed. From these results, it is considered that the formation of the ferromagnetic phase is influenced by the cooling rate at about 800°C. The variation of specific resistance with temperature is shown in Fig. 7(b). The curve in the figure show a behavior usually observed in ordinary ferromagnetic metals below the Curie point.

§ 5. Discussions of the Magnetic Properties of the Ferromagnetic Phase

As stated above, the ferromagnetic phase discussed in the present investigation is supposed to be of the superstructure of CuAu type, which has a layer structure: Each (011) net plane contains mainly Mn or Al atoms respectively, stacking alternately in [001] direction of the crystal. Now we shall make a brief remark on the interatomic distance between two Mn atoms in the nearest neighbouring pair in a layer or in two adjacent layers. There are a few Mn atoms in an Al layer. The nearest neighbouring pair of Mn atoms in two adjacent layers has the distance 2.66Å, while that in a Mn layer has the distance 2.79Å. Now, according to the Bethe-Slater curve representing the relation between the exchange energy of magnetization and the interatomic distance, the exchange coupling between $3d$-electrons of adjacent Mn atoms changes from antiferromagnetic to ferromagnetic at the interatomic distance of about 2.57Å. The distances between Mn atoms in our crystal are greater than this critical value, and so the occurrance of ferromagnetism in this alloy is compatible with this prediction.

The Curie temperature T_c, the absolute saturation value $\sigma_\infty(O)$, the heat of absorption per gram atom of manganese in the alloy, ΔE due to the magnetic transformation, the spin S_χ estimated from the $1/\chi$ v.s. T curve above the Curie point and the spin S_σ estimated from the saturation magnetization at $T=0$ are summarized in Table IV; these figures are obtained by assuming that all the Mn atoms are equivalent. Moreover, though not shown in Table IV, both T_c and ΔE increase with Mn content; there is an evidence that the Curie point increases by 14°C with the increase of manganese content from 54 to 55%.

Table IV.

T_c	$\sigma_\infty(0)$	ΔE	S_χ	S_σ
373°C	100	320 cal	1.16	0.70

The discrepancy between the magneton number estimated from the magnetic saturation at low temperatures and that from the Curie-Weiss representation of the susceptibilities above the Curie point may be caused partly by the difficulty in saturating the magnetization, but since the latter magneton number is significantly greater than the former, there must be another reason for this, probably related to some intrinsic nature of this material. Since the $1/\chi$ v.s. T curve follows the Curie-Weiss law, we have no strong reason to consider the material to be ferrimagnetic*.

§ 6. Summary

The ferromagnetic phase in the manganese-aluminum system was investigated together with the related phase diagram. It was found that the ferromagnetic phase is formed by cooling down the h-phase (hexagonal lose-packed form) with about 54 atomic percent of manganese at charge to the room temperature at the cooling rate of about 10 deg./sec at 800°C. The ferromagnetic phase is metastable and has the CuAu type superstructure; the shortest distance between a pair of manganese atoms within the lattice is 2.66Å. The Curie point of this phase is about 380°C, and

* One may consider that the magnetization of this substance is smaller than that predicted from the total spin alignment because of the effective smallness of the exchange energy as is often considered in the theory of collective electron ferromagnetism.

values of the mean magnetic moment per manganese atom estimated from the low temperature saturation magnetization and the Curie-Weiss representation of the susceptibilities are 1.40 and 2.31 μ_B respectively.

Acknowledgements

The present writer would like to express his sincere thanks to Profs. T. Hirone, H. Watanabe, S. Nagasaki and S. Maeda for their kind guidance during his studies of the present project in the Graduate Course of the Faculty of Science, Tōhoku University.

References

1) G. Hindricks: Z. Anorg. Chem. **59** (1908) 444.
2) T. Ishiwara: Kinzoku no Kenkyu **3** (1926) 13 (in Japanese).
3) W. Koster and W. Beckthold: Z. Metallk. **30** (1938) 294.
4) T. Hirone, S. Maeda and N. Tsuya: Rev. Sci. Instr. **25** (1954) 516.
5) S. Nagasaki and Y. Takagi: J. Appl. Phys. Japan (in Japanese) **17** (1948) 104.
6) S. Maeda: Sci. Rep. RITU. **A9** (1957) 347.
7) A. J. Bradley and P. Jones: Phil. Mag. **12** (1931) 1137.
8) A. J. Bradley and J. W. Rodgers: Proc. Roy. Soc. London **A144** (1936) 340.

JOURNAL OF THE PHYSICAL SOCIETY OF JAPAN Vol. 13, No. 12, DECEMBER 1958

Effects of High Energy Radiation on Polymers II. End-linking and Gel Fraction

By Osamu SAITO

Faculty of Engineering, Chuo University, Tokyo

(Received September 5, 1958)

The effect of end-linking induced in polymers by high energy radiation is discussed. When cyclization does not occur, the same results are obtained as those derived by A. Charlesby, and moreover it is known that for any initial distribution the gel formation does not occur when σ is smaller than 1/4, where σ represents the probability that an end produced by a molecular scission links with a monomer unit of another molecule. The theory also gives the average molecular weights and the average end numbers. For the initial uniform distribution the weight average molecular weight has a maximum in case $1/12<\sigma<1/4$, while for the initial Poisson distribution it has no maximum. The weight average end number becomes infinite at the gel point, but the number average end number does not. It is shown that the retardation of incipient gel formation is negligible when cyclization occurs. Beyond the gel point the gel part grows rapidly. The feature is studied in the cases of cross-linking and end-linking with or without cyclization, and it is shown that the gel fraction is smaller by several per cent in the case with cyclization than in the case without cyclization.

§ 1. Introduction

The effects of high energy radiation on long chain polymers are classified into cross-linking, degradation and end-linking. The first two effects were already discussed in the previous paper.[1] End-linking will be studied in the first part of this paper. When the number of links produced by radiation in polymers are increased, the average molecular weight increases resulting in the formation of insoluble part, that is, the gel. It will also be discussed how the gel fraction increases with the number of links or the radiation dose. The linkage between two monomer units belonging to the same molecule is called cyclization. It does not contribute to the increment of the molecular weight and the gel fraction. Therefore, the radiation dose

for gelation with cyclization will be larger than that without cyclization. We know from the result of the previous paper[1] that the retardation of the gel formation due to the cyclization in cross-linking was negligible. However, the effect of cyclization in increasing the gel fraction beyond gel point will not be neglected. The details will be discussed later.

§ 2. End-linking without Cyclization

When some polymers are irradiated by high energy radiation, the molecular scissions will occur. A fraction of the ends newly produced will be stable, but the other fraction may combine with other monomer units at their side bonds. This type of linking is called end-linking. We will now consider how the molecular weight distribution may be affected by the end-linking induced by the radiation.

Basic assumptions made are as follows: (1) the number of scissions is proportional to the radiation dose, (2) the end-linkages take place at random and their number is proportional to the number of scission, (3) the number of end-linkages is small compared with the total number of monomer units, (4) the cyclization does not occur, and (5) the degree of polymerization can be treated as being continuous (from zero to infinity).

Let a polymer substance be exposed to a radiation with total dose R and the number of monomer units be N, then the number of scissions induced by the radiation is expresed by $N\dot{r}R$, where $\dot{r}$ represents the probability that a monomer unit is ruptured by the radiation of unit dose. The number of ends newly produced by the scissions is $2N\dot{r}R$, while the number of end-linkages is given by $2N\sigma\dot{r}R$, where σ represents the probability that an end newly produced by the scission end-links with a monomer unit of another molecule.

It was shown in the previous paper[1] that the statistical results remained unaltered even if the order of the cross-linking and the degradation was exchanged with each other. It will also be deduced from the same reasoning that the molecular weight distribution will not be altered by the exchange of the order of end-linking and scission. Therefore, we will consider that scissions occur first and then linkings follow.

When the initial molecules are linear, the new distribution function induced by the degradation is given by Eq. (29) of **I**[1] as follows:

$$n_2(p,\ 0)=\left\{n(p,\ 0)+2\tau\int_p^\infty n(p,\ 0)dp+\tau^2\int_p^\infty dp\int_p^\infty n(p,\ 0)dp\right\}e^{-p\tau}, \qquad (1)$$

where p is the degree of polymerization, $\tau=\dot{r}R$ and $n(p,\ 0)$ represents the initial distribution. Particularly when the initial distribution is Poisson-like, i.e. $n(p,\ 0)=(N/u^2)\cdot\exp(-p/u)$, we obtain

$$n_2(p,\ 0)=N\left(\frac{1}{u}+\dot{r}R\right)e^{-p(1/u+\dot{r}R)} \qquad (2)$$

Next we consider that this distribution is altered by the existence of the end-linkings. We suppose the virtual radiation dose t, which varies from zero to R, and when it increases from t to $t+dt$, $2N\sigma\dot{r}dt$ of the ends produced by the scissions link to the monomer units of other molecules. Since the number of active ends having already been end-linked at $t=t$ is $2N\sigma\dot{r}t$, the probability that an end get linked in the interval of t to $t+dt$ is

$$\frac{2N\sigma\dot{r}dt}{2N/u+2N(R-\sigma\dot{r}t)}=\frac{\sigma\dot{r}dt}{1/u+R\dot{r}-\sigma\dot{r}t}=\omega(t)dt\,, \qquad (3)$$

where u is the initial number average degree of polymerization. If we use $n_k(p,\ t)$ to express the number of the molecules which have the degree of polymerization p and the number of ends k at $t=t$, the equation representing the variation of $n_k(p,\ t)$ is given by

$$\frac{\partial n_k(p,\ t)}{\partial t}+kn_k(p,\ t)\omega(t)+\frac{pn_k(p,\ t)}{N}\int_0^\infty\sum_{i=2}^{\infty}in_i(l,\ t)\omega(t)dl$$
$$=\sum_{i=2}^{k-1}\int_0^p in_i(l,\ t)\omega(t)\frac{(p-l)n_{k-i+1}(p-l,\ t)}{N}dl\,.$$

Using the new notations $m_k(p,\ t)=n_k(p,\ t)/N$,

$$\frac{dx}{dt}=\omega(t), \quad \text{and} \quad x=0 \quad \text{at} \quad t=0, \tag{4}$$

we obtain

$$\frac{\partial m_k(p,\ x)}{\partial x}+km_k(p,\ x)+pm_k(p,\ x)\psi(x)=\sum_{i=2}^{k-1}\int_0^p im_i(l,\ x)(p-l)m_{k-i+1}(p-l,\ x)dl\ , \tag{5}$$

where

$$\psi(x)=\int_0^\infty \sum_{i=2}^{\infty} im_i(l,\ x)dl$$

means the total number of end-points. And it is expressed by the following formula because the number of end-points is increased from $2/u$ to $2(1/u+\dot{r}R)$ by molecular scissions and is decreased to $2\{1/u+\dot{r}(R-\sigma t)\}$ by end-linking,

$$\psi(x)=2\left\{\frac{1}{u}+\dot{r}(R-\sigma t)\right\}=2\left(\frac{1}{u}+\dot{r}R\right)e^{-x}\ . \tag{6}$$

If we apply the Laplace transformation

$$F(\xi,\ \eta,\ x)=\sum_{k=2}^{\infty}e^{-k\eta}\int_0^\infty m_k(p,\ x)e^{-p\xi}dp \tag{7}$$

to Eq. (5), we obtain

$$\frac{\partial F}{\partial x}=\frac{\partial F}{\partial \eta}+\psi(x)\frac{\partial F}{\partial \xi}+e^{\eta}\frac{\partial F}{\partial \xi}\frac{\partial F}{\partial \eta}\ . \tag{8}$$

The solution is given

$$\left.\begin{aligned} &F(\xi,\ \eta,\ x)=G(\xi_0,\ \eta_0)+\left(\xi-\xi_0+\int_0^x\psi dx\right)\frac{\partial G}{\partial \xi_0}\ ,\\ &\xi-\xi_0+\int_0^x\psi dx=e^{\eta_0}(e^{-x}-1)\frac{\partial G}{\partial \eta_0}\ ,\\ &e^{-\eta}=e^{x-\eta_0}+(e^{-x}-1)\frac{\partial G}{\partial \xi_0}\ , \end{aligned}\right\} \tag{9}$$

where $G(\xi_0,\ \eta_0)=F(\xi_0,\ \eta_0,\ 0)$.

Now we use the notation

$$f_{ij}(x)=\sum_{k=2}^{\infty}\int_0^\infty p^ik^jm_k(p,\ x)\,dp=(-1)^{i+j}\frac{\partial^{i+j}F(0,\ 0,\ x)}{\partial \xi^i\,\partial \eta^j}\ . \tag{10}$$

Then for $i=1$ and $j=0$, we obtain

$$f_{10}(x)=-\frac{\partial F(0,\ 0,\ x)}{\partial \xi}=-\left[\frac{\partial G}{\partial \xi_0}\right]_{\substack{\xi=0\\ \eta=0}}. \tag{11}$$

As $f_{10}(x)$ is the ratio of the total monomer units and N, it must be unity. Therefore

$$\left[\frac{\partial G}{\partial \xi_0}\right]_{\substack{\xi=0\\ \eta=0}}=-1\ . \tag{12}$$

Inserting Eq. (12) in the last equation of Eq. (9), we get for $\xi=\eta=0$,

$$\eta_0=0\ . \tag{13}$$

For this value of η_0 the following equation holds

$$\left[\frac{\partial G}{\partial \xi_0}\right]_{\eta_0=0} = -\sum_{k=2}^{\infty}\int_0^{\infty} pm_k(p,\ 0)e^{-p\xi_0}dp = -1\ ,$$

which gives, with the equation $f_{10}(0)=-1$,

$$\sum_{k=2}^{\infty}\int_0^{\infty} pm_k(p,\ 0)(1-e^{-p\xi_0})dp=0\ .$$

Since the integrant can not be negative, we obtain

$$\xi_0=0\ . \tag{14}$$

Therefore, it is concluded that when the total number of monomer units is constant, $\xi_0=\eta_0=0$ at $\xi=\eta=0$.

For $i=j=0$, we have

$$f_{00}(x)=G(0,\ 0)-\int_0^x \psi dx=\left(\frac{1}{u}+\dot{r}R\right)\{1-2(1-e^{-x})\}\ .$$

Using the notation x_m, which represents the value of x at $t=R$, we get

$$f_{00}(x_m)=\frac{1}{u}+(1-2\sigma)\dot{r}R\ , \tag{15}$$

and also the number average molecular weight

$$M_n(R)=M_n(0)/\{1+(1-2\sigma)u\dot{r}R\}\ . \tag{16}$$

This equation shows that the number average molecular weight does not depend on the shape of the initial distribution.

For $i=2$ and $j=0$, we get

$$f_{20}(x_m)=f_{20}(0)(1+\gamma)^2/[\{1+(1-2\sigma)\gamma\}^2-2\sigma^2\gamma^2(1+\gamma)f_{20}(0)/u]\ , \tag{17}$$

where $\gamma=u\dot{r}R$ and

$$f_{20}(0)=\frac{2}{\tau}-\frac{2}{\tau^2}\int_0^{\infty} m_2(p,\ 0)(1-e^{-p\tau})dp\ . \tag{18}$$

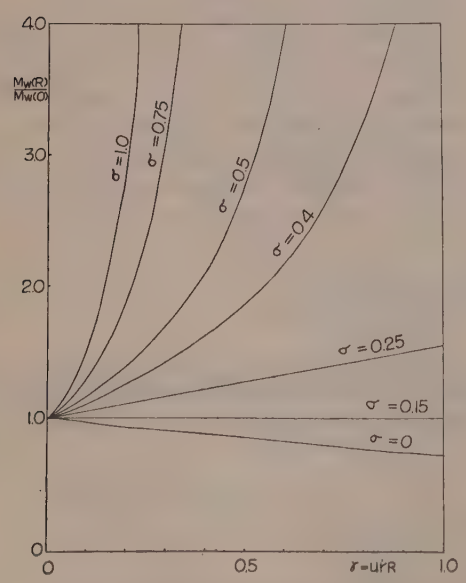

Fig. 1 (a). The weight average molecular weights for initial uniform distribution.

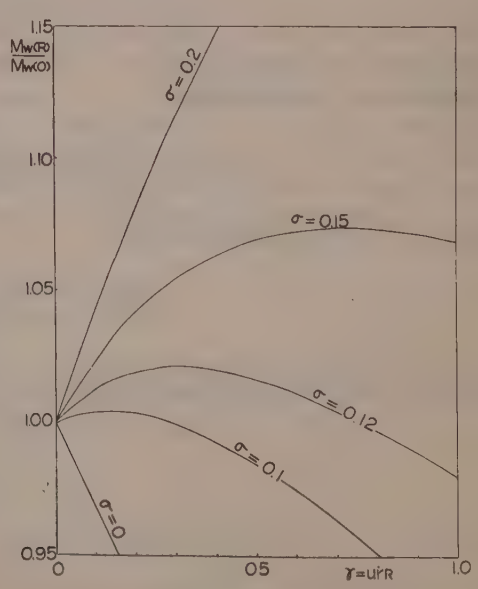

Fig. 1 (b). The weight average molecular weights for initial uniform distribution.

we can easily obtain from Eq. (17) the weight average molecular weight

$$M_w(R)=M_w(0)\frac{(1+\gamma)^2 f_{20}(0)}{2u}\Bigg/\left[\{1+(1-2\sigma)\gamma\}^2-\frac{2(1+\gamma)f_{20}(0)}{u}\sigma^2\gamma^2\right]. \tag{19}$$

When the initial distribution is uniform, we have

$$f_{20}(0)=4u(e^{-\gamma}-1+\gamma)/\gamma^2. \tag{20}$$

And when the initial distribution is Poisson-like, we have

$$f_{20}(0)=2u/(1+\gamma)\,, \tag{21}$$

and then

$$M_w(R)=M_w(0)/\{1+(1-4\sigma)\gamma\}\,. \tag{22}$$

These results are represented in Figs. 1 and 2. In Fig. 1 (a) the weight average molecular weight M_w for the case of initial uniform distribution is shown for various values of σ. It is easily derived from the preceding formulas that when σ is larger than 1/12, the initial slope of M_w is positive, and it will also be shown from the following deduction that, when σ is smaller than 1/4, the gel formation will not occur for any dose of irradiation. Therefore we may expect that, when σ has a value which lies between 1/12 and 1/4, the M_w curve will have a maximum, which is shown in Fig. 1 (b). This maximum does not occur for the initial Poisson distribution shown in Fig. 2.

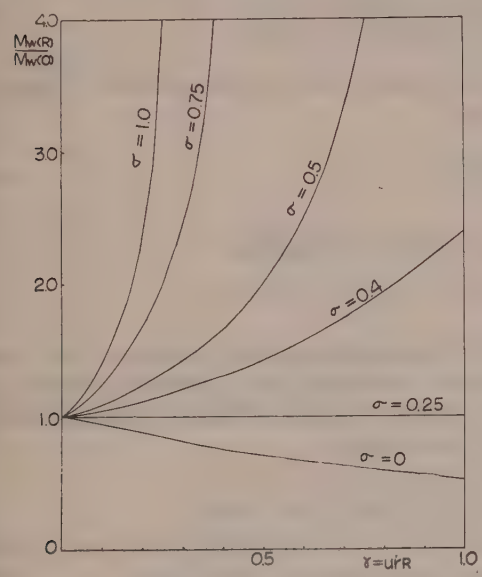

Fig. 2. The weight average molecular weights for initial Poisson distribution.

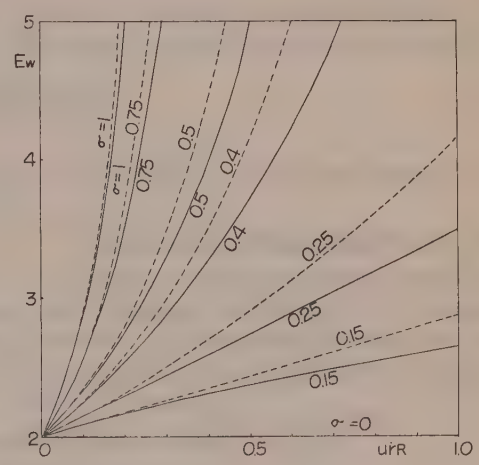

Fig. 3. Weight average end number, ——— for initial Poisson distribution and - - - for initial uniform distribution.

The value of γ at the gel point is given from the relation

$$1+\gamma-\left\{2+\sqrt{\frac{2(1+\gamma)f_{20}(0)}{u}}\right\}\sigma\gamma=0\,. \tag{23}$$

When the initial distribution is Poisson-like, it follows

$$\gamma_{gel}=1/(4\sigma-1)\,. \tag{24}$$

This shows that the gel formation occurs when σ is larger than 1/4. This is the result which A. Charlesby[2)] has already obtained. It is verified that this restriction for gel formation

holds for an arbitrary initial distribution. From Eq. (18) we know that for large γ it becomes

$$f_{20}(0)=\frac{2u}{\gamma}+O\left(\frac{1}{\gamma^2}\right).$$

Substituting this formula into Eq. (23), we obtain

$$\lim_{\gamma\to\infty}\sigma=\frac{1}{4}.$$

It is easily shown from Eq. (23) that σ is a decreasing function of γ. Then we know that for any initial distribution the gel formation does not occur when σ is smaller than 1/4.

For $i=0$ and $j=1$, we get

$$f_{01}(x_m)=\frac{2\{1+(1-\sigma)\gamma\}}{u}.$$

This gives the number average end number

$$E_n=\frac{f_{01}}{f_{00}}=\frac{2\{1+(1-\sigma)\gamma\}}{1+(1-2\sigma)\gamma}. \tag{25}$$

This result is independent of the shape of the initial distribution.

For $i=1$ and $j=1$, we get $f_{11}(x_m)$ and then the weight average end number

$$E_w=\frac{f_{11}}{f_{10}}=\frac{1+(1-\sigma)\gamma}{\sigma\gamma}\left[\frac{(1+\gamma)\{1+(1-2\sigma)\gamma\}}{\{1+(1-2\sigma)\gamma\}^2-(2/u)\sigma^2\gamma^2(1+\gamma)f_{20}(0)}-1\right]. \tag{26}$$

This value depends on the shape of the initial distribution and diverges at the gel point. When the initial distribution is Poisson-like, it gives

$$E_w=\frac{2\{1+(1-\sigma)\gamma\}}{1+(1-4\sigma)\gamma}. \tag{27}$$

Fig. 3 shows the curves of E_w for the Poisson and uniform distribution.

§ 3. End-linking with Cyclization

We consider in this section the effect of end-linking accompanied by cyclization. We now express by $\varphi(p, N)$ the propability that an active end, belonging to a molecule which has the degree of polymerization p, links to a monomer unit of another molecule. Then the distribution function $m_k(p, x)$ should satisfy the following equation

$$\frac{\partial m_k(p, x)}{\partial x}+km_k(p, x)\varphi(p, N)+pm_k(p, x)\int_0^\infty\sum_{i=2}^\infty im_1(l, x)\varphi(l, N)dl$$
$$=\sum_{i=2}^{k-1}\int_0^p im_i(l, x)\varphi(l, N)(p-l)m_{k-i+1}(p-l, x)dl. \tag{28}$$

For the sake of simplicity we may assume

$$\varphi(p, N)=1-p/N$$

Then Eq. (28) becomes

For $p\leqq N$,

$$\frac{\partial m_k(p, x)}{\partial x}+k(1-\varepsilon p)m_k(p, x)+pm_k(p, x)\int_0^N\sum_{i=2}^\infty i(1-\varepsilon l)m_i(l, x)dl$$
$$=\sum_{i=2}^{k-1}\int_0^p i(1-\varepsilon l)(p-l)m_i(l, x)m_{k-i+1}(p-l, x)dl, \tag{29}$$

and for $p>N$,

$$m_k(p,\ x)=0$$

where $\varepsilon=1/N$.

If we now apply the Laplace transformation (7) to Eq. (29), we obtain

$$\frac{\partial F}{\partial x}=\frac{\partial F}{\partial \eta}+\varepsilon\frac{\partial^2 F}{\partial\xi\partial\eta}+\frac{\partial F}{\partial\xi}\{\psi(x)-\varepsilon f_{11}(x)\}+e^{\eta}\left(\frac{\partial F}{\partial\xi}\frac{\partial F}{\partial\eta}+\varepsilon\frac{\partial F}{\partial\xi}\frac{\partial^2 F}{\partial\xi\partial\eta}\right). \tag{30}$$

Now assume

$$\left.\begin{aligned} F(\xi,\ \eta,\ x)&=F_0(\xi,\ \eta,\ \zeta)+\varepsilon F_1(\xi,\ \eta,\ \zeta)+\cdots,\\ x&=\zeta+\varepsilon v_1(\xi,\ \eta,\ \zeta)+\cdots\cdots\cdots\cdots.\end{aligned}\right\} \tag{31}$$

Substituting these into Eq. (30), and determining v_1 so that F_1 is identically equal to zero, we obtain

$$\frac{\partial F_0}{\partial\zeta}=\frac{\partial F_0}{\partial\eta}+\frac{\partial F_0}{\partial\xi}\psi(\zeta)+e^{\eta}\frac{\partial F_0}{\partial\xi}\frac{\partial F_0}{\partial\eta}, \tag{32}$$

$$\frac{\partial F_0}{\partial\zeta}\frac{\partial v_1}{\partial\zeta}+\frac{\partial F_0}{\partial\xi}\psi'(\zeta)v_1=f_{11}(\zeta)\frac{\partial F_0}{\partial\xi}-\left(1+e^{\eta}\frac{\partial F_0}{\partial\xi}\right)\frac{\partial^2 F_0}{\partial\xi\partial\eta}. \tag{33}$$

The solution of Eq. (32) is given by Eq. (9). For $\xi=\eta=0$ Eq. (33) becomes

$$\psi(\zeta)\frac{\partial v_1}{\partial\zeta}+\psi'(\zeta)v_1=f_{11}(\zeta). \tag{34}$$

It gives

$$v_1(0,\ 0,\ \zeta)=\frac{1}{\psi(\zeta)}\int_0^{\zeta}f_{11}(\zeta)d\zeta. \tag{35}$$

From Eqs. (31) and (32) we get

$$\left.\begin{aligned} f_{20}(x)&=f_{20}(0)\Big/\left[\{1-2(1-e^{-\zeta})\}^2-\frac{2(1+\gamma)}{u}f_{20}(0)(1-e^{-\zeta})^2\right],\\ x&=\zeta+\varepsilon v_1(0,\ 0,\ \zeta).\end{aligned}\right\} \tag{36}$$

From Eq. (34) we obtain

$$v_1(0,\ 0,\ \zeta)=-\frac{1}{2\psi(\zeta)}\log\left\{(2e^{-\zeta}-1)^2-\frac{2(1+\gamma)}{u}f_{20}(0)(e^{-\zeta}-1)^2\right\}. \tag{37}$$

When the initial distribution is Poisson-like, we get

$$f_{20}(x)=\frac{2u}{(1+\gamma)(4e^{-\zeta}-\zeta)},\qquad x=\zeta-\varepsilon\frac{ue^{\zeta}\log(4e^{-\zeta}-\zeta)}{4(1+\gamma)}. \tag{38}$$

If we assume that the largest degree of polymerization at the gel point is kN, then

$$f_{20}(x_{gel})\doteqdot k^2N$$

and

$$-x_{gel}=\log\frac{3+\varepsilon'}{4}+\frac{k^2\varepsilon'\log\varepsilon'}{2(3+\varepsilon')}, \tag{39}$$

where

$$\varepsilon'=\frac{2u\varepsilon}{(1+\gamma)k^2}.$$

As $\mathcal{E}$ and $\mathcal{E}'$ are very small, the right hand side of Eq. (39) is approximately equal to log (3/4), which is the value of the case where the cyclization does not occur. This result shows that the retardation of the gel formation owing to the cyclization is negligible. Comparing this result with that in the case of cross-linking, we know that the effect of cyclization on the incipient gel formation in the end-linking is smaller than that in the cross-linking.

§ 4. Gel Fraction in Cross-Linking without Cyclization

We considered in I[1] the effect of the cross-linking without cyclization and obtained the equation

$$\frac{\partial m(p,\ t)}{\partial t}+2pm(p,\ t)$$
$$=\int_0^p l(p-l)m(l,\ t)m(p-l,\ t)dl\,, \qquad (40)$$

where $t=\dot{c}R$ and $\dot{c}$ represents the probability that a monomer unit irradiated by unit dose cross-links with a unit of another molecule, and $m(p,\ t)$ indicates the fraction of the molecules which have the degree of polymerization p.

In I we solved Eq. (40) under the condition that the total number of monomer units was constant. If we put

$$f_i(t)=\int_0^\infty p^i m(p,\ t)\,dp\,,$$

then $f_2(t)$ is an increasing function and diverges at a certain value of t, which is called the gel point. If we assume that the total number of monomer units is constant in the region beyond the gel point, then $f_2(t)$ must be negative. Therefore, we must consider that the total number of monomer units varies beyond the gel point. Then let us assume

$$f_1(x)=1-g(t)\,, \qquad (41)$$

where g expresses the gel fraction. Even if the gel part exists, the distribution function $m(p,\ t)$ of the degree of polymerization p in the sol fraction still satisfies Eq. (40).

If we apply the Laplace transformation

$$F(s,\ t)=\int_0^\infty m(p,\ t)e^{-ps}dp\,, \qquad (42)$$

to Eq. (40), we obtain

$$\frac{\partial F}{\partial t}=2\frac{\partial F}{\partial s}+\left(\frac{\partial F}{\partial s}\right)^2. \qquad (43)$$

The general solution is given by

$$\left.\begin{aligned} F(s,\ t)&=G(s_0)-\{G'(s_0)\}^2t\,,\\ s&=s_0-2\{1+G'(s_0)\}t\,,\end{aligned}\right\} \qquad (44)$$

where $G(s_0)$ is given by the initial distribution as follows

$$G(s_0)=\int_0^\infty m(p,\ 0)e^{-ps_0}dp\,. \qquad (45)$$

If we put

$$f_i(t)=(-1)^i\frac{\partial^i F(0,\ t)}{\partial s^i}\,, \qquad (46)$$

we get

$$f_1(t)=1-\frac{s_0}{2t}\,. \qquad (47)$$

Comparing Eqs. (41) and (47) with each other, it follows

$$s_0=2tg\,. \qquad (48)$$

Inserting this formula in the last equation of (44), we obtain

$$g=1+G'(2tg)\,, \qquad (49)$$

from which g is given as a function of t.

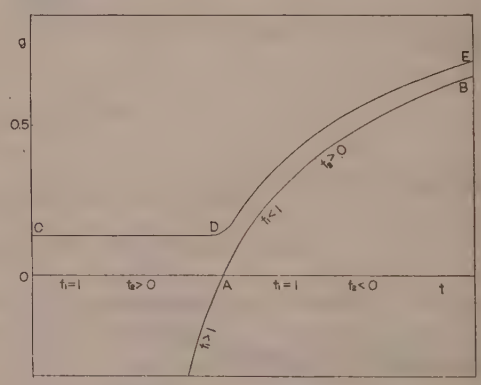

Fig. 4. Gel fraction.

When the initial value of g is zero, g keeps the value zero until the gel point A (Fig. 4) and lies on the branch OA where $f_1=1$. When f_1 maintains the value unity, f_2 is an increasing function of t. f_2 has a positive value on the branch OA and diverges at the gel point A. Therefore, g cannot remain to be zero beyond the point A and must turn on another branch AB, where f_1 is smaller than unity and f_2 is positive. Thus we know that the gel part appears at the gel point and grows as t increases.

When g has a certain value larger than zero at $t=0$, the curve of g starts at C, runs parallel to OA until point D is reached which

corresponds to the gel point A. From the point D on g increases rather rapidly.

When the initial distribution is, for instance, Poisson-like, we obtain

$$G(s_0)=1/u(1+us_0)\,,$$

and Eq. (47) becomes

$$g=1-\frac{1}{(1+2utg)^2}\,, \tag{50}$$

which is the same as that given by A. Charlesby.[4]

§ 5. Gel Fraction in Cross-Linking with Cyclization

In the case of cross-linking with cyclization, the integro-differential equation indicating the variation of the distribution function $m(p,\ t)$ was given by Eq. (1) of the previous paper.[1] And we knew that, if the total number of monomer units assumed to be constant, f_2 increased with t and became infinite at a certain point where the incipient gel was formed. Beyond the point, f_1 could not keep the value unity.

If we assume, as in the last section, that the number of monomer units is not constant, that is

$$f_1(t)=1-g(t)\,,$$

then we obtain,

$$\left.\begin{aligned}&\text{for } p\leqq N:\\ &\frac{\partial m(p,\ t)}{\partial t}+pm(p,\ t)\left\{\int_0^N(1-\varepsilon l)lm(l,\ t)dt+(1-g)g\right\}\\ &\qquad+(1-\varepsilon p)m(p,\ t)=\int_0^p(1-\varepsilon l)l(p-l)m(l,\ t)m(p-l,\ t)dl\,,\\ &\text{for } p>N:\qquad m(p,\ t)=0\,.\end{aligned}\right\} \tag{51}$$

The expression in the brackets of the second term of the left hand side is reduced to the following form

$$\int_0^N(1-\varepsilon l)lm(l,\ t)dl+(1-g)g=\int_0^\infty lm(l,\ t)dl+g-g^2-\varepsilon\int_0^\infty l^2m(l,\ t)dl=1-g^2-\varepsilon f_2(t)\,.$$

We know from the result of I[1] that $f_2(t)$ has the greatest value k^2N at the gel point and beyond that point $f_2(t)$ decreased because the larger the molecule is the easier it is for the molecule to link to the gel part. Therefore for all the value of t, we have

$$\varepsilon f_2(t)\leqq\varepsilon k^2N=k^2\,.$$

Since the order of k is equal to or smaller than 10^{-2}, we may neglect the term $\varepsilon f_2(t)$, and Eq. (51) becomes,

$$\frac{\partial m(p,\ t)}{\partial t}+pm(p,\ t)(1-g^2)+pm(p,\ t)=\int_0^p l(p-l)m(l,\ t)m(p-l,\ t)dl\,. \tag{52}$$

If we apply the Laplace transformation (42) to this equation, we get

$$\frac{\partial F}{\partial t}=(2-g^2)\frac{\partial F}{\partial s}+\left(\frac{\partial F}{\partial s}\right)^2. \tag{53}$$

The solution is

$$F(s,\ t)=G(s_0)-\{G'(s_0)\}^2t\,,\qquad s=s_0+\int_0^t g^2dt-2\{1+G'(s_0)\}t\,, \tag{54}$$

where $G(s_0)$ is the same as Eq. (45). We obtain easily

$$f_1(t)=-\frac{\partial F(0,\ t)}{\partial s}=1-\left(s_0+\int_0^t g^2\,dt\right)\Big/2t\,, \tag{55}$$

and then

$$s_0=2gt-\int_0^t g^2dt\ . \tag{56}$$

From Eqs. (54) and (56), we get

$$g=1+G'\left(2gt-\int_0^t g^2\,dt\right). \tag{57}$$

This corresponds to Eq. (49) for cross-linking without cyclization. Both expressions are the same until the gel point is reached. However, beyond the gel point they differ from each other.

For the initial Poisson distribution, Eq. (57) gives

$$1+u\left(2gt-\int_0^t g^2dt\right)=1\Big/\sqrt{1-g}\ . \tag{58}$$

Differentiating the equation with respect to g, we obtain

$$\frac{dt}{dg}+\frac{2}{g(2-g)}t=\frac{1}{2ug(2-g)(1-g)^{3/2}}\ . \tag{59}$$

The solution is

$$t=\frac{2-g}{2ug}\left\{\frac{2}{\sqrt{1-g}}+3\tan^{-1}\sqrt{1-g}+\frac{\sqrt{1-g}}{2-g}-\frac{10+3\pi}{4}\right\}. \tag{60}$$

The corresponding expression for the case of cross-linking without cyclization is

$$t=\frac{1}{2ug}\left(\frac{1}{\sqrt{1-g}}-1\right). \tag{61}$$

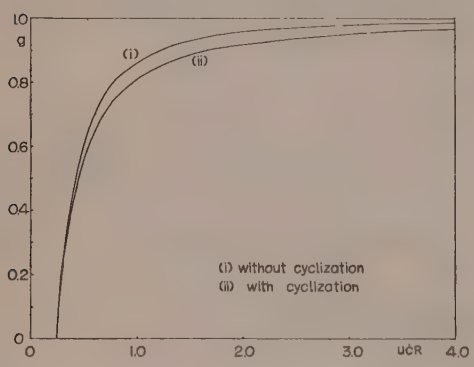

Fig. 5. Gel fractions in cross-linking for initial Poisson distribution.

These two expressions are shown in Fig. 5, by which we know that the cyclization retards the growth of gel fraction.

§ 6. Gel Fraction in Cross-Linking with Degradation

When cross-linking and degradation coexist, it is shown in paper I[1] that the correct statistical results are obtained by considering that all the degradations occur first and then the cross-linkings follow. If the initial distribution $m(p,\ 0)$ is given, the new distribution $m(p,\ \tau)$ due to the degradation is derived from Eq. (1). We then obtain

$$G(s_0)=\int_0^\infty m(p,\ \tau)e^{-ps_0}dp\ . \tag{62}$$

If we substitute this expression into Eq. (49), we get the gel fraction without cyclization. On the contrary, if we insert Eq. (62) in Eq. (57) we obtain the gel fraction with cyclization.

For the initial Poisson distribution $m(p,\ 0)=(l/u^2)\exp(-p/u)$, it gives

$$m(p,\ \tau)=\left(\frac{1}{u}+\tau\right)^2 e^{-(1/u+\tau)p}\ , \tag{63}$$

from which it follows

$$G(s_0)=\frac{(1+u\tau)^2}{u\{1+u(s_0+\tau)\}}\ . \tag{64}$$

Substituting this expression into Eq. (49), we get

$$g=1-\frac{(1+u\tau)^2}{\{1+u(2tg+\tau)\}^2}\ . \tag{65}$$

Using $\tau=\dot{r}R$ and $t=\dot{c}R$, it follows

$$g=1-1\Big/\left\{1+\frac{2u\dot{c}R}{1+u\dot{r}R}g\right\}^2. \tag{66}$$

Comparing this expression to that for no degradation:

$$g=1-1/\{1+2u\dot{c}Rg\}^2\ , \tag{67}$$

we know that if we use the formula

$$\gamma' = \frac{u\dot{c}R}{1+u\dot{r}R} = \frac{\gamma}{1+(\dot{r}/\dot{c})\gamma} \tag{68}$$

in place of $u\dot{c}R$ of Eq. (67), we obtain Eq. (66). This feature was indicated by A. Charlesby.[3]

In the case of cyclization, we obtain, by inserting Eq. (64) in Eq. (57),

$$g = 1 - 1 \Big/ \left\{ 1 + \frac{u}{1+u\dot{r}R} \left(2gt - \int_0^t g^2\, dt \right) \right\}^2 . \tag{69}$$

Fig. 6 shows the g *vs* R curves for the several values of $\dot{r}/\dot{c}$.

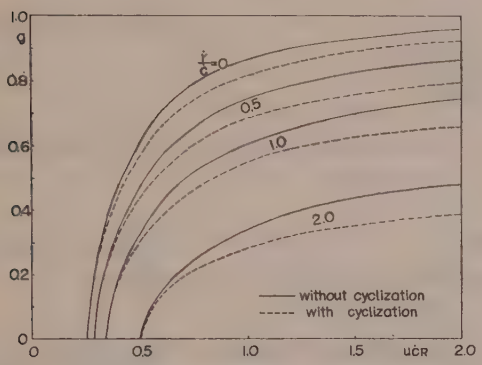

Fig. 6. Gel fractions in cross-linking with degradation for initial Poisson distribution.

§ 7. Gel Fraction in End-Linking without Cyclization

We considered in § 2 the effect of end-linking in the case where all the polymer molecules are soluble, and we know that when the total number of monomer units is constant the gel formation occurs at a certain radiation dose. After the gel is formed, we must consider sol and gel, at the same time.

Now we assume that both sol and gel part coexist and that $m_k(p, t)$ is the distribution function in the sol. A consideration analogous to that in § 2 gives the following equation

$$\frac{\partial m_k(p,t)}{\partial t} + k m_k(p,t)\omega(t) + p m_k(p,t)\left\{ \int_0^\infty \sum_{i=2}^\infty i m_i(l,t)\,dl + E_g \right\}\omega(t)$$
$$= \sum_{i=2}^{k-1} \int_0^p i m_i(l,t)\omega(t)(p-l) m_{k-i+1}(p-l,t)\,dl\,, \tag{70}$$

where E_g represents the total number of ends of the gel part. The expression

$$\int_0^\infty \sum_{i=2}^\infty i m_i(l,t)\,dl + E_g$$

is equal to the total number of ends in the sol as well as in the gel part, which is expressed by $\psi(x)$ in § 2. If we use x defined by Eq. (4) in place of t, we obtain

$$\frac{\partial m_k(p,x)}{\partial x} + k m_k(p,x) + p m_k(p,x)\psi(x) = \sum_{i=2}^{k-1} \int_0^p i m_i(l,x)(p-l) m_{k-i+1}(p-l,x)\,dl\,, \tag{71}$$

which is the same as Eq. (5). Now let us solve Eq. (71) under the condition

$$\sum_{k=2}^\infty \int_0^\infty p m_k(p,x)\,dp = 1 - g(x)\,. \tag{72}$$

The solution of Eq. (71) is given by Eq. (9). The solution together with Eq. (72) gives

$$\xi_0 - (1-e^{-x})e^{\eta_0} G_{\eta_0}(\xi_0, \eta_0) = \int_0^x \psi\, dx\,, \qquad e^{-\eta_0} = 1 - g(1-e^{-x})\,, \qquad 1 - g + G_{\xi_0}(\xi_0, \eta_0) = 0\,. \tag{73}$$

Eliminating ξ_0 and η_0 from Eq. (73), we get a relation between g and x. Since there exists the relation

$$e^{-x} = \frac{1+(1-\sigma)u\dot{r}R}{1+u\dot{r}R}\,, \tag{74}$$

we can, after all, obtain a relation between g and R.

For instance, when the initial distribution is Poisson-like, it follows

$$G(\xi_0,\ \eta_0)=\frac{(1+u\dot{r}R)^2}{u\{1+u(\xi_0+\dot{r}R)\}}e^{-2\eta_0}\ , \tag{75}$$

and the relation between g and R becomes

$$u\dot{r}R\{(1+2\sigma)\sqrt{1-g}-(2-3g)\sigma-1\}=1-\sqrt{1-g}\ . \tag{76}$$

For $\sigma=1$, it gives

$$g=1-\left(\frac{1}{3u\dot{r}R}\right)^2,\qquad \text{for}\quad u\dot{r}R>\frac{1}{3}\ . \tag{77}$$

This is the same as that given by A. Charlesby.[2] The curves of Eq. (76) for the several values of σ are given by full lines in Fig. 7.

§ 8. Gel Fraction in End-Linking with Cyclization

When cyclization takes place, the equation corresponding to Eq. (70) is as follows:

$$\frac{\partial m_k(p,\ t)}{\partial t}+km_k(p,\ t)\omega(t)\varphi(p,\ N)+pm_k(p,\ t)\left\{\int_0^\infty\sum_{i=2}^{\infty}im_i(l,\ t)\varphi(l,\ N)dl+(1-g)E_g\right\}\omega(t)$$
$$=\sum_{i=2}^{k-1}\int_0^p im_i(l,\ t)\omega(t)\varphi(l,\ N)(p-l)m_{k-i+1}(p-l,\ t)dl\ . \tag{78}$$

Using x in place of t and assuming $\varphi(p,\ N)=1-\varepsilon p$, we have

$$\int_0^\infty\sum_{i=2}^{\infty}im_i(l,\ x)\varphi(l,\ N)dl+(1-g)E_g=\psi(x)-gE_g-\varepsilon\int_0^\infty\sum_{i=2}^{\infty}ilm_i(l,\ x)dl\ . \tag{79}$$

The integral on the righ-hand side attains its maximum value at the gel point. If we express by kN the degree of polymerization of the largest molecule at the gel point, the number of the end points of that molecule is not greater than $kN+1$. Therefore, we have, to a good approximation,

$$\int_0^\infty\sum_{i=2}^{\infty}ilm_i(l,\ x)dl\doteqdot\frac{kN(kN+1)}{N}\doteqdot k^2N\ .$$

Accordingly, the last term of Eq. (79) has the value of the order k^2, which is negligible. Then Eq. (78) becomes

$$\frac{\partial m_k(p,\ x)}{\partial x}+km_k(p,\ x)+pm_k(p,\ x)\{\psi(x)-gE_g\}=\sum_{i=2}^{k-1}\int_0^p im_i(l,\ x)(p-l)m_{k-i+1}(p-l,\ x)dl\ . \tag{80}$$

As E_g is the total number of end points of the gel part, it is given as follows:

$$E_g=\psi(x)-(\text{the number of end points of sol part})=\psi(x)+\frac{\partial F(0,\ 0,\ x)}{\partial\eta}\ ,$$

where $F(\xi,\ \eta,\ x)$ is defined by

$$F(\xi,\ \eta,\ x)=\sum_{k=2}^{\infty}\int_0^\infty m_k(p,\ x)e^{-p\xi-k\eta}dp\ . \tag{81}$$

If we assume now

$$\psi(x)-gE_g=\theta(x)\ , \tag{82}$$

Eq. (80) becomes to be of the same type as Eq. (5) and the solution is given by

$$\left.\begin{aligned} &F(\xi,\ \eta,\ x)=G(\xi_0,\ \eta_0)+\left(\xi-\xi_0+\int_0^x\theta(x)dx\right)\frac{\partial G}{\partial\xi_0}\ ,\\ &\xi-\xi_0+\int_0^x\theta(x)dx=e^{\eta_0}(e^{-x}-1)\frac{\partial G}{\partial\eta_0}\ ,\\ &e^{-\eta}=e^{x-\eta_0}+(e^x-1)\frac{\partial G}{\partial\xi_0}\ . \end{aligned}\right\} \tag{83}$$

Therefore, we have

$$\frac{\partial F(0,\ 0,\ x)}{\partial\eta}=e^{\eta_0-x}\frac{\partial G}{\partial\eta_0}\ ,$$

and

$$\theta(x)=(1-g)\psi(x)-ge^{\eta_0-x}\frac{\partial G}{\partial\eta_0}\ . \tag{84}$$

Considering that

$$\sum_{k=0}^{\infty}\int_0^{\infty}pm_k(p,\ x)dx=1-g(x)\ , \tag{85}$$

we finally obtain

$$\left.\begin{aligned} &\xi_0+e^{\eta_0}(e^{-x}-1)G_{\eta_0}(\xi_0,\ \eta_0)-\int_0^x\theta(x)dx=0\ ,\\ &e^{-\eta_0}=1-g(1-e^{-x})\ ,\qquad 1-g+G_{\xi_0}(\xi_0,\ \eta_0)=0\ . \end{aligned}\right\} \tag{86}$$

Elimination of ξ_0 and η_0 from these equations will give the relation between g and x.

When the initial distribution is, for instance, Poisson-like, we get from Eq. (86)

$$\frac{1+u\dot{r}R}{u}\left\{3\sqrt{1-g}-1+\frac{3g-2}{\sqrt{1-g}}e^{-x}\right\}-\int_0^x\theta(x)dx=0\ , \tag{87}$$

and also from Eq. (84)

$$\theta(x)=\frac{2(1+u\dot{r}R)}{u}\sqrt{1-g}(\sqrt{1-g}+g)e^{-x}\ . \tag{88}$$

If we assume $\sqrt{1-g}=y$ and $e^{-x}=z$, we obtain from Eqs. (87) and (88)

$$3y-1+\frac{1-3y^2}{y}z+2\int_1^z y(1+y-y^2)dz=0\ , \tag{89}$$

which gives

$$y(1-y)(1+y+2y^3)\frac{dz}{dy}-(1+3y^2)z=-3y^2\ . \tag{90}$$

The solution is

$$z=\frac{3y}{1-y}(y+a)^A\{(y+\alpha)^2+\beta^2\}^Be^{2C\tan^{-1}((y+\alpha)/\beta)}\int_y^1\frac{(y+a)^{-A}}{1+y+2y^3}\{(y+\alpha)^2+\beta^2\}^{-B}e^{-2C\tan^{-1}((y+\alpha)/\beta)}dy\ , \tag{91}$$

where

$$A=-\frac{1+3a^2}{a(1+a)(1+6a^2)}\ ,\qquad B+iC=-\frac{\{1+3(\alpha+i\beta)^2\}}{(\alpha+i\beta)(1+\alpha+i\beta)\{1+6(\alpha+i\beta)^2\}}\ ,$$

$$a=\sqrt[3]{\frac{\sqrt{87}+9}{36}}-\sqrt[3]{\frac{\sqrt{87}-9}{36}}\ ,\qquad \alpha=-\frac{a}{2}\ ,\qquad \beta=-\frac{\sqrt{3}}{2}\left\{\sqrt[3]{\frac{\sqrt{87}+9}{36}}+\sqrt[3]{\frac{\sqrt{87}-9}{36}}\right\}\ .$$

The broken lines in Fig. 7 are those given by Eq. (91). These indicate that the reduction of gel fraction due to cyclization amounts to more than ten per cent.

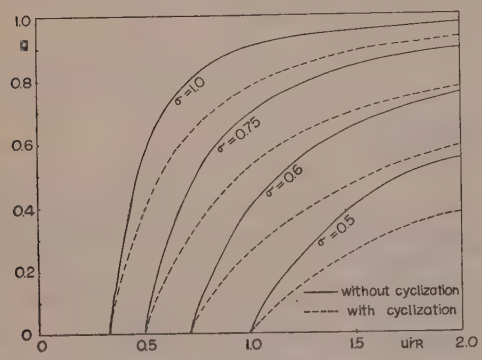

Fig. 7. Gel fractions in end-linking for initial Poisson distribution.

§ 9. Summary

The effects of high energy radiation on long chain polymers are classified into cross-linking, degradation and end-linking. The first two effects were discussed in a previous paper. The effect of end-linking without cyclization is studied in § 2 of this paper. The number and the weight averge molecular weight are given in Eqs. (16) and (19) respectively. It is known that the latter diverges at the gel point, while the former does not. The radiation at the gel point is given by Eq. (23), and especially when the initial distribution is Poisson-like it reduces to Eq. (24). When the initial distribution is uniform, the weight average molecular weight has a maximum if $1/12<\sigma<1/4$. It is also clarified that for any initial distribution the gel formation does not occur when the value of σ is smaller than 1/4. The number and the weight average end number are given by Eqs. (25) and (26) respectively, showing that the weight average end number diverges at the gel point, while the number average end number does not. In § 3 the effect of end-linking with cyclization is discussed and it is shown that the retardation of the incipient gel formation is negligible. In §§ 4 and 5 the variation of the gel fraction in cross-linking is discussed. For the case where there is no cyclization, the same result as that of A. Charlesby is obtained. The effect of cyclization to gel fraction is given by Eq. (57) and Fig. 5, and the reduction of gel fraction due to cyclization amounts to several per cent. It is concluded that, in general, the radiation dose necessary to induce the same gel fraction is larger in cyclization than in no cyclization. In § 6 the gel formation by cross-linking with degradation is studied. It is again found that when there is no cyclization the same result as that of A. Charlesby is obtained. And when cyclization occurs Eqs. (66) and (69), and Fig. 6 are derived. In §§ 7 and 8 the gel fraction in end-linking is studied, giving the results indicated by Eqs. (73) and (86), and also by Fig. 7. We know from these results that the effect of cyclization on gel fraction is never neglected in the period beyond gel point. Therefore, the radiation effects determined from gel fraction or solubility will not be correct.

Acknowledgements

It is a pleasure to express my gratitude to Dr. A. Amemiya. His continued interest and support in all phases of this research are gratefully appreciated. I wish to express my gratitude to Dr. A. Harasima who reviewed the manuscript critically, and to Dr. K. Shinohara and others who are the members of the Group for the Study of Irradiated Polymers in Tokyo.

References

1) O. Saito: J. Phys. Soc. Japan **13** (1958) 198.
2) A. Charlesby: Proc. Roy. Soc. **A231** (1955) 521.
3) A. Charlesby: Proc. Roy. Soc. **A222** (1954) 60.
4) A. Charlesby: Proc. Roy. Soc. **A222** (1954) 542.

JOURNAL OF THE PHYSICAL SOCIETY OF JAPAN Vol 13, No. 12, DECEMBER, 1958

Effects of High Energy Radiation on Polymers III. Viscosity

By Osamu SAITO

Faculty of Engineering, Chuo University, Tokyo

(Received September 5, 1958)

It was known that solubility of irradiated polymers was not free from the effect of cyclization. On the contrary, viscosity before gel point is not affected by it and it is utilized in order to investigate the effects of high energy radiation on polymers. Intrinsic viscosity is discussed first for the case where cross-linking and degradation occur. In certain cases intrinsic viscosity decreases in the initial period of irradiation, but increases in larger radiation doses, so that it has a minimum and becomes infinite at a certain radiation dose which corresponds to gel point. It is also derived that G-value of cross-linking and degradation are calculated from the intrinsic viscosity in the initial period of irradiation. An example of polyvinylchloride gives G-values whose orders of magnitude are not unreasonable. The more accurate is the measurement, the more correct values will be obtained. Intrinsic viscosity for the case where end-linking occurs is likewise discussed, and the same properties as those in cross-linking are derived. Finally we know that the gel point determined from an asymptotic behaviour of intrinsic viscosity will be more correct than that determined from an extrapolation of solubility curve.

§ 1. Introduction

It was known from the results deduced in the paper II[2] that the effect of cyclization induced by irradiation was negligible before gel point, while a reduction of gel fraction due to cyclization amounted to more than several per cent. Therefore, we can not neglect the effect of cyclization beyond gel point. However, if we take the effect in consideration, the theoretical treatment becomes much more complicated. Accordingly, if we analyze some properties of irradiated polymers from experimental curves of gel fraction or solubility, we can not avoid errors amounting to or more than several per cent. On the contrary, if we use experimental results before gel point, we are free from the effect of cyclization. Among many physical quantities in this stage, viscosity may be one of the best for our purpose. We will now consider the effect of high energy radiation on viscosity of polymers.

It is well known that the intrinsic viscosity $[\eta]$ of the solution of polymer, of which degree of polymerization is p, is given by

$$[\eta] \propto p^{\alpha}$$

where α is a constant and it has in general a value between 1 and 1/2. For the solution of polymer, whose degree of polymerization is not uniform, the intrinsic viscosity is given by an average as follows:

$$[\eta] \propto \int_0^\infty p^{\alpha+1} m(p)\, dp\,, \qquad (1)$$

where $m(p)$ denotes the normalized distribution function of molecules with respect to degree of polymerization p. When a polymer is irradiated, the occurance of linkages between molecules and molecular scissions may vary the distribution function $m(p)$ and then the value of $[\eta]$. The value of α may not be greatly affected by irradiation, because it depends on the shape of polymer molecules in solution. Accordingly, we may assume that α has a constant value during irradiation. Especially for the initial period of irradiation, α may well be considered to be a constant. When the value of α varies greatly with radiation dose, we can easily modify the theory so that it may take in the unconstancy.

§ 2. Intrinsic Viscosity in Cross-linking

From the paper I[1] and II[2], we know that when cyclization is neglected for cross-linking the distribution function $m(p, t)$ satisfies the

following equation

$$\frac{\partial m(p,t)}{\partial t}+2pm(p,t)$$
$$=\int_0^p l(p-l)m(l,t)m(p-l,t)\,dl\,, \qquad (2)$$

where $t=\dot{c}R$, R is radiation dose and $\dot{c}$ represents the probability that a monomer unit irradiated by unit dose cross-links with a unit of another molecule. If we apply the Laplace transformation

$$f(z,t)=\int_0^\infty m(p,t)\,e^{-zp}\,dp \qquad (3)$$

to Eq. (2), we obtain

$$\frac{\partial f}{\partial t}=2\frac{\partial f}{\partial z}+\left(\frac{\partial f}{\partial z}\right)^2. \qquad (4)$$

The general solution of this differential equation is given by

$$\left.\begin{aligned} &f(z,t)=G(z_0)-\{G'(z_0)\}^2t\,,\\ &z=z_0-2\{1+G'(z_0)\}t\,,\end{aligned}\right\} \qquad (5)$$

where

$$G(z_0)=\int_0^\infty m(p,0)\,e^{-z_0p}\,dp\,. \qquad (6)$$

On the other hand, the numerator of the right hand side of Eq. (1) is expressed by the following complex integral (*cf.* Appendix I)

$$J=\int_0^\infty p^{\alpha+1}m(p,t)\,dp$$
$$=e^{\alpha\pi i}\frac{\Gamma(\alpha+2)}{2\pi i}\int_C\frac{dz}{z^{\alpha+2}}\int_0^\infty m(p,t)\,e^{-zp}\,dp\,. \qquad (7)$$

Substituting Eq. (5) into Eq. (7), we get (*cf.* Appendix II)

$$J=\frac{1}{\Gamma(1-\alpha)}\int_0^\infty G''(\rho)[\rho-2\{1+G'(\rho)\}t]^{-\alpha}\,d\rho\,. \qquad (8)$$

If the initial distribution is assumed to be Poisson-like, Eq. (8) gives (*cf.* Appendix II)

$$J=\frac{2u^\alpha}{\Gamma(1-\alpha)}\int_0^1\frac{y^{\alpha+1}\,dy}{(1-y)^\alpha\{1-2uty(y+1)\}^\alpha}\,, \qquad (9)$$

where u denotes the initial number average degree of polymerization. Intrinsic viscosity is expressed by the following formula

$$[\eta]/[\eta]_0=J\Big/\left\{\frac{\alpha(\alpha+1)\pi u^\alpha}{\sin\alpha\pi\cdot\Gamma(1-\alpha)}\right\}, \qquad (10)$$

where $[\eta]_0$ is the initial value of $[\eta]$.

Especially when $\alpha=1/2$, Eq. (9) is written by complete elliptic integrals as follows:

$$J=2\sqrt{\frac{2u}{\pi}}\{4K(k)$$
$$-(3+h)E(k)\}/(1-h)\sqrt{(1+h)(3+h)}\,, \qquad (11)$$

where

$$k^2=\frac{(1-h)(3-h)}{(1+h)(3+h)}\,,\qquad h=\sqrt{1-4ut}\,. \qquad (12)$$

If we replace all u's in Eq. (11) with

$$u/(1+u\dot{r}R)\,, \qquad (13)$$

we obtain the intrinsic viscosity in cross-linking with degradation, where $\dot{r}$ represents the probability that a monomer unit is ruptured by unit radiation dose. Fig. 1 shows the curves of intrinsic viscosity for several values of $\lambda=\dot{r}/\dot{c}$. In Fig. 2 those curves are given

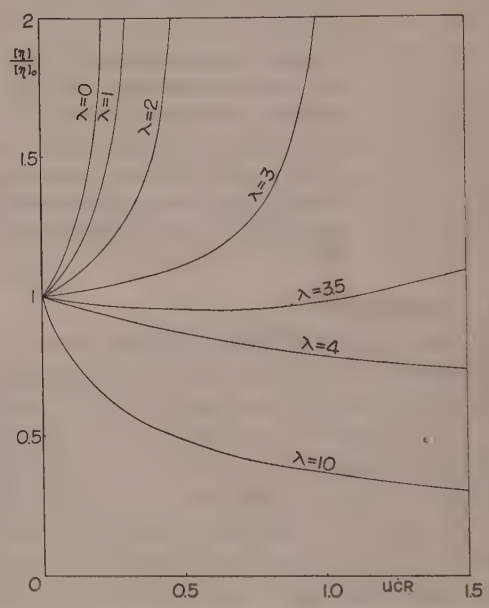

Fig. 1. Intrinsic viscosity in cross-linking with degradation.

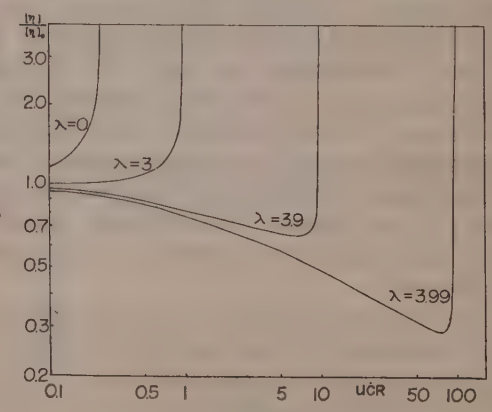

Fig. 2. Intrinsic viscosity in cross-linking with degradation.

in log-log scale. Particularly when the value of λ is smaller than and nearly equal to 4, intrinsic viscosity decreases considerably first and then it increases very rapidly.

It is easily known by expanding Eq. (9) in power series of t that when λ satisfies the following relation

$$\lambda > \frac{(\alpha+2)(\alpha+7)}{6}, \tag{14}$$

the initial slope of intrinsic viscosity curve is negative. On the other hand we know from Appendix of paper I[1] that gel formation occurs when λ satisfies the relation

$$\lambda < 4 . \tag{15}$$

Therefore, for λ satisfying the relation

$$4 > \lambda > (\alpha+2)(\alpha+7)/6 , \tag{16}$$

intrinsic viscosity decreases first and then increases, and at a certain value of t it becomes infinite. Thus we know that intrinsic viscosity curve has a minimum when λ satisfies Eq. (16) and that even if intrinsic viscosity decreases at the initial period of irradiation, gel formation may occur. The reason is that intrinsic viscosity is dropped first by molecular scissions, at the same time, however the distribution of molecular sizes is varied gradually by cross-linking and in the later period of irradiation the effect of the latter overcomes that of the former, resulting in the gel formation. Therefore, we must measure accurately the value of λ in order that we may decide whether a certain polymer will cross-link or not.

If we expand intrinsic viscosity in a power series of t, we obtain

$$[\eta]/[\eta]_0 = 1 + a_1 ut + a_2 (ut)^2 + \cdots , \tag{17}$$

where

$$a_1 = \alpha\left\{\frac{(\alpha+2)(\alpha+7)}{6} - \lambda\right\} ,$$

$$a_2 = \frac{\alpha(\alpha+1)}{2}\left\{\frac{(\alpha+2)(\alpha+3)(\alpha+7)(\alpha+14)}{90} - \frac{(\alpha+2)(\alpha+7)}{3}\lambda + \lambda^2\right\} .$$

When we approximate the initial portion of experimental curve of intrinsic viscosity with a parabola

$$[\eta]/[\eta]_0 = 1 + A_1 uR + A_2 (uR)^2 , \tag{18}$$

and determine the value of A_1 and A_2, we obtain the relations

$$a_1 \dot{c} = A_1 \quad \text{and} \quad a_2 \dot{c}^2 = A_2 . \tag{19}$$

If we know the value of α, we get the value of $\dot{c}$ and λ by solving these simultaneous equations. In the paper I[1] the value of radiation dose at gel point R_g was given by

$$R_g = 1/u\dot{c}(4-\lambda) . \tag{20}$$

Then we know that when the value of α is not given, we get $\dot{c}$, λ and α by measuring R_g, determining A_1 and A_2 and solving simultaneous equations (19) and (20). When the value of u instead of α is not known, we can likewise obtain it.

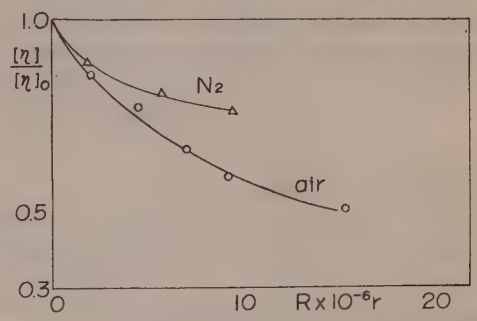

Fig. 3. Intrinsic viscosity of polyvinylchloride.

For example, the intrinsic viscosity curves of polyvinylchloride measured by H. Hozo[3] are given in Fig. 3. A sample of polyvinylchloride was irradiated in air by γ-ray of Co-60 and the other sample was irradiated in nitrogen gas. The value of u for both samples is 882 and the value of α is 0.85. The analysis gives for the first sample

$$\dot{c} = 1.6 \times 10^{-10} r^{-1} , \qquad \lambda = 4.5$$

which give $\dot{r} = 7.2 \times 10^{-10} r^{-1}$ and G-value of cross-linking G_c and degradation G_r as follows:

$$G_c = 2.6 , \qquad G_r = 12 .$$

Those values for the other sample are

$$\dot{c} = 1.7 \times 10^{-10} r^{-1} , \quad \lambda = 4.4 , \quad \dot{r} = 7.4 \times 10^{-10} r^{-1} ,$$
$$G_c = 2.8 , \quad G_r = 12 .$$

The orders of those G-values are not unreasonable. If the experiments were performed carefully in the initial period of irradiation, G-values would be given accurately.

§ 3. Intrinsic Viscosity in End-linking

Let us now consider the case where end-linking occurs in an irradiated polymer. We know from the results of paper II[2] that the effect of cyclization is negligible before gel point and the normalized distribution function $m_k(p, x)$, which denotes the fraction of mole-

cules having degree of polymerization p and number of end points k, satisfies following equation

$$\frac{\partial m_k(p, x)}{\partial x}+km_k(p, x)+pm_k(p, x)\psi(x)=\sum_{i=2}^{k-1}\int_0^p im_i(l, x)(p-l)m_{k-i+1}(p-l, x)\,dl\,, \tag{21}$$

where

$$e^{-x}=\{1+u\dot{r}(R-\sigma t)\}/(1+u\dot{r}R)\,, \tag{22}$$

$$\psi(x)=\frac{2}{u}+2\dot{r}(R-\sigma t)\,, \tag{23}$$

t is a variable varying from 0 to R, and σ is the probability that an end produced by a molecular scission end-links with a monomer unit.

If we apply the Laplace transformation

$$F(\xi, \eta, x)=\sum_{k=2}^{\infty}e^{-k\eta}\int_0^{\infty}m_k(p, x)e^{-\xi p}\,dp \tag{24}$$

to Eq. (21), we obtain

$$\frac{\partial F}{\partial x}=\frac{\partial F}{\partial \eta}+\psi(x)\frac{\partial F}{\partial \xi}+e^{\eta}\frac{\partial F}{\partial \xi}\frac{\partial F}{\partial \eta}\,. \tag{25}$$

The general solution is given by

$$\left.\begin{aligned} &F(\xi, \eta, x)=G(\xi_0, \eta_0)+\left\{\xi-\xi_0+\int_0^x\psi(x)\,dx\right\}\frac{\partial G}{\partial \xi_0}\,,\\ &\xi-\xi_0+\int_0^x\psi(x)\,dx=e^{\eta_0}(e^{-x}-1)\frac{\partial G}{\partial \eta_0}\,,\\ &e^{-\eta}=e^{x-\eta_0}+(e^x-1)\frac{\partial G}{\partial \xi_0}\,, \end{aligned}\right\} \tag{26}$$

where

$$G(\xi_0, \eta_0)=F(\xi_0, \eta_0, 0)\,.$$

Intrinsic viscosity in end-linking is given by

$$\frac{[\eta]}{[\eta]_0}=\frac{\sum_{k=2}^{\infty}\int_0^{\infty}p^{\alpha+1}m_k(p, x)\,dp}{\sum_{k=2}^{\infty}\int_0^{\infty}p^{\alpha+1}m_k(p, 0)\,dp}\,, \tag{27}$$

The numerator of right hand side is transformed to the following form (*cf.* Appendix III)

$$\begin{aligned} J&=\sum_{k=2}^{\infty}\int_0^{\infty}p^{\alpha+1}m_k(p, x)\,dp\\ &=e^{\alpha\pi i}\frac{\Gamma(\alpha+2)}{2\pi i}\int_C\frac{F(z, 0, x)}{z^{\alpha+2}}dz\\ &=\frac{1}{\Gamma(1-\alpha)(1-e^{-x})}\int_0^{\infty}\frac{e^{-\eta_0}}{\xi^{\alpha}}\frac{(e^x-1)G_{\xi_0\xi_0}}{e^{x-\eta_0}-(e^x-1)G_{\xi_0\eta_0}}\,d\xi_0\,. \end{aligned} \tag{28}$$

For the initial Poisson distribution, we get

$$G(\xi_0, \eta_0)=\frac{\gamma^2}{\gamma+\xi_0}e^{-2\eta_0}\,,$$

where $\gamma=1/u+\dot{r}R$. Substituting this expression into Eq. (28), we obtain

$$J=\frac{2e^{\alpha x}}{\Gamma(1-\alpha)\gamma^{\alpha}}\int_0^1\frac{y^{\alpha+1}dy}{(1-y)^{\alpha}\{1-3(e^x-1)y\}^{\alpha}}\,.$$

when $\alpha=1/2$, J is expressed by complete elliptic integrals:

$$J=\frac{2e^{x/2}}{\Gamma(1/2)\sqrt{\gamma}}\int_0^1\frac{y^{3/2}}{\sqrt{(1-y)(1-k^2y)}}dy$$

$$=\sqrt{\frac{u}{\pi}}\frac{2}{3k^4\sqrt{1+(1-\sigma)u\dot{r}R}}\{(k^2+2)K(k)-2(k^2+1)E(k)\}\,, \tag{30}$$

where

$$k^2=3(e^x-1)=3\sigma u\dot{r}R/\{1+(1-\sigma)u\dot{r}R\}\,.$$

And for $R=0$, we get

$$J=\frac{3}{8}\sqrt{\pi u}\,.$$

Fig. 4 shows the curves of intrinsic viscosity with respect to $u\dot{r}R$. For the value of σ satisfying the following relation

$$\frac{1}{4}<\sigma<\frac{2}{7}\,,$$

intrinsic viscosity has a minimum. The behaviour of intrinsic viscosity, particularly when the value of σ is about 1/4, is represented in Fig. 5. These curves have the same behaviour as those in Fig. 2.

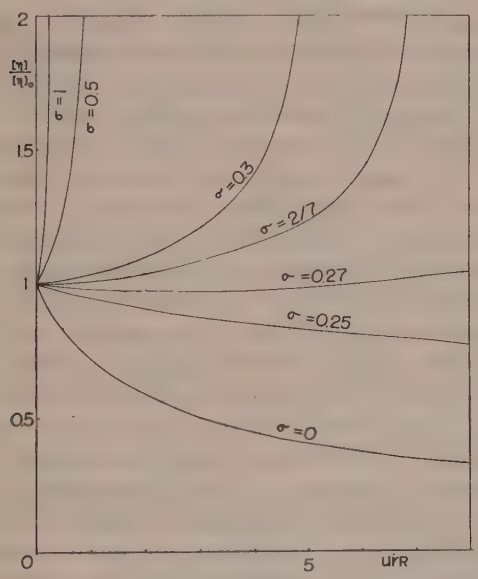

Fig. 4. Intrinsic viscosity in end-linking.

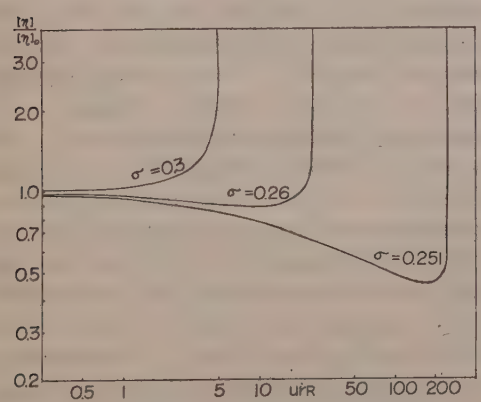

Fig. 5. Intrinsic viscosity in end-linking.

In order to determine accurately the value of σ for an arbitrary value of α, we expand the expression (29) in a power series of R, namely

$$[\eta]/[\eta]_0=1+b_1u\dot{r}R+b_2(u\dot{r}R)^2+\cdots\,, \tag{32}$$

where

$$b_1=\alpha\{\sigma(\alpha+3)-1\}\,,$$

$$b_2=\frac{\alpha(\alpha+1)}{2}\left\{\frac{3}{4}\sigma^2(\alpha+2)(\alpha+3)-2\sigma(1-\sigma)(\alpha+2)+(1-\sigma)^2\right\}\,.$$

If we approximate the experimental values of intrinsic viscosity in the initial period of irradiation by a parabora

$$[\eta]/[\eta]_0=1+B_1uR+B_2(uR)^2\,,$$

we obtain simultaneous equations

$$b_1\dot{r}=B_1 \quad\text{and}\quad b_2\dot{r}^2=B_2\,. \tag{33}$$

From these equations $\dot{r}$ and σ will be determined, when the value of α is known. If the value of α is not known, we need one more equation, which is given by[2)]

$$R_g=1/u\dot{r}(4\sigma-1)\,. \tag{34}$$

The last Eq. (34) may also be used in order to test the validity of our theory.

If we put $\sigma=1/\lambda$ or $\sigma\dot{r}=\dot{c}$, Eq. (34) coincides with Eq. (20). And when $\alpha=1$, Eq. (17) is equal to Eq. (32). We can not distinguish

between cross-linking and end-linking by measuring intrinsic viscosity in this case. When α satisfies the relation $1/2 \leqq \alpha < 1$, Eqs. (17) and (32) would not coincide with each other, even if put the relation $\sigma\dot{r}=\dot{c}$. However, the discrepancy being less than ten per cent, it is difficult to distinguish between them. For the radiation dose which is not small, the value of intrinsic viscosity for cross- and end-linking may differ considerably from each other. In such cases we must perform numerical integration of Eqs. (9) and (29). The results will be reported later.

§ 4. Determination of Gel Point

The dose of gel point is usually determined by extrapolating the solubility curve. It is, however, very difficult to measure accurately the solubility of polymer. The sol part closed in gel part by linkages and cyclizations may not be neglected. Therefore, the gel point determined from solubility measurement will not be correct. The dose of gel point R_g is necessary, in order to calculate G-values or to distinguish between cross- and end-linking. It must, therefore, be given accurately. For this purpose we may use the method to determine the dose R_g by intrinsic viscosity.

We know that intrinsic viscosity becomes infinite when the radiation dose R is equal to R_g. Eqs. (9) and (29) indicate us that intrinsic viscosity has the following asymptotic formula, which has the same form for both cross-linking and end-linking. For $\alpha \neq 1/2$, it is

$$[\eta]/[\eta]_0 \propto (R_g-R)^{-(2\alpha-1)}, \quad \text{for} \quad R \fallingdotseq R_g \tag{35}$$

and for $\alpha=1/2$, it is

$$[\eta]/[\eta]_0 \propto -\log(R_g-R), \quad \text{for} \quad R \fallingdotseq R_g. \tag{36}$$

If we, for $\alpha \neq 1/2$, choose $\{[\eta]_0/[\eta]\}^{1/(2\alpha-1)}$ as ordinate and R as abscissa, measured values will be plotted on a straight line. We can easily obtain the dose of gel point R_g from the intersection of this line and abscissa. We must take care of the fact that the value of α in Eq. (35) may differ from that before irradiation. We may use as the value of α in Eqs. (19) and (33) the value before irradiation, but we can not always use it for α in Eq. (35). The value of α of the latter case must be determined so that $\{[\eta]_0/[\eta]\}^{1/(2\alpha-1)}$ lies on a straight line. For $\alpha=1/2$, we must choose $e^{-[\eta]/[\eta]_0}$ as ordinate. In this case, the plotted line will not be a straight line, but a curve crosses abscissa vertically. The intersection gives the dose R_g.

§ 5. Summary

It was known from the results deduced in the paper II[2] that the effect of cyclization was not neglected in the period beyond gel point. On the contrary, we can neglect the effect on viscosity before gel point, so that we can utilize intrinsic viscosity in order to investigate the effect of high energy radiation on polymers. In § 2 intrinsic viscosity is discussed for the case where cross-linking and degradation occur. When the initial distribution is Poisson-like, it is given by Eqs. (9), (10) and (13). Especially when the value of α is equal to 1/2, intrinsic viscosity is expressed by complete elliptic integrals and shown in Figs. 1 and 2. When λ satisfies the relation (16), intrinsic viscosity has a minimum and becomes infinite at a certain dose of irradiation which gives gel point. If the value of λ is larger than 4, gel formation never occurs. We can obtained G-value of cross-linking and of degradation from measuring the intrinsic viscosity in the initial period of irradiation, that is, by solving simultaneous equations (19) and (20). An example of irradiated polyvinylchloride gives G-values, of which orders of magnitude are not unreasonable. This fact shows that our theory is applicable for cross-linking and degradation of irradiated polymers. The more accurate is the measurement of intrinsic viscosity in the initial period of irradiation, the more correct G-values will be obtained. In § 3 intrinsic viscosity for end-linking is deduced, and the expressions (27) and (28) are obtained. For the initial Poisson distribution they are expressed by Eq. (29). If we consider the case where $\alpha=1/2$ holds, intrinsic viscosity is represented by complete elliptic integrals. The behaviour of intrinsic viscosity for end-linking represented in Figs. 4 and 5 is like that for cross-linking and degradation shown in Figs. 1 and 2. By the same method as illustrated in the case of cross-linking and degradation, we can calculate the value of $\dot{r}$ and σ, from which we can obtain G-value of degredation and end-linking. However, it is very difficult to distinguish between cross-linking and end-

linking by measuring the intrinsic viscosity in the initial period of irradiation. The behaviour of intrinsic viscosity for larger radiation doses will be useful for this purpoes, but we must then perform numerical integration of Eqs. (9) and (29). The result will be reported later. We must obtain the value of radiation dose at gel point R_g in order to use Eqs. (20) and (34). The value of R_g determined from the measurement of solubility may not be accurate. For this purpose we can also utilize the measurement of intrinsic viscosity. If we choose $\{[\eta]_0/[\eta]\}^{1/(2\alpha-1)}$ as ordinate and R as abscissa, measured values will be plotted on a straight line. The intersection of the line and abscissa will give the value of R_g.

We know from the discussion mentioned above that the effects of high energy radiation on polymers are determined faily accurately from the measurement of intrinsic viscosity.

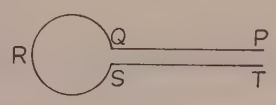

Fig. 6. Path of integration.

Appendix I

We will here verify Eq. (7). If the path of integration C is chosen as indicated in Fig. 6, it follows

$$\int_C \frac{dz}{z^{\alpha+2}}\int_0^\infty m(p,t)e^{-zp}\,dp=\int_0^\infty m(p,t)\,dp\int_C \frac{e^{-pz}}{z^{\alpha+2}}\,dz\ . \tag{37}$$

If we put the radius of circle QRS to be equal to r, we obtain

$$\int_{PQ}\frac{e^{-pz}}{z^{\alpha+2}}\,dz=\left[-\frac{e^{-pz}}{(\alpha+1)z^{\alpha+1}}+\frac{p}{\alpha(\alpha+1)}\frac{e^{-pz}}{z^{\alpha}}\right]_P^Q+\frac{p}{\alpha(\alpha+1)}\int_{PQ}\frac{e^{-pz}}{z^{\alpha}}\,dz$$

$$=-\frac{\alpha-pr}{\alpha(\alpha+1)r^{\alpha+1}}e^{-pr}-\frac{p^2}{\alpha(\alpha+1)}\int_r^\infty\frac{e^{-p\rho}}{\rho^{\alpha}}\,d\rho\ ,$$

$$\int_{ST}\frac{e^{-pz}}{z^{\alpha+2}}\,dz=-\frac{\alpha-pr}{\alpha(\alpha+1)r^{\alpha+1}}e^{-pr-2\pi\alpha i}+\frac{p^2}{\alpha(\alpha+1)}e^{-2\pi\alpha i}\int_r^\infty\frac{e^{-p\rho}}{\rho^{\alpha}}\,d\rho\ ,$$

$$\int_{QRS}\frac{e^{-pz}}{z^{\alpha+2}}\,dz=-\frac{\alpha-pr}{\alpha(\alpha+1)r^{\alpha+1}}e^{-pr}(e^{-2\pi\alpha i}-1)$$

$$+\frac{ip^2}{\alpha(\alpha+1)r^{\alpha-1}}\int_0^{2\pi}\exp\{-pre^{i\theta}+i(1-\alpha)\theta\}\,d\theta\ .$$

Since the relation $1/2\leqq\alpha<1$ holds, we obtain, for the limit $r\to 0$, the following equation

$$\int_{PQRST}=\frac{p^2}{\alpha(\alpha+1)}(e^{-2\pi\alpha i}-1)\int_0^\infty\rho^{-\alpha}e^{-p\rho}\,d\rho=\frac{p^{\alpha+1}}{\alpha(\alpha+1)}(e^{-2\pi\alpha i}-1)\Gamma(1-\alpha)$$

$$=\frac{2ip^{\alpha+1}e^{-\alpha\pi i}\sin\alpha\pi}{\alpha(\alpha+1)}\Gamma(1-\alpha)\ .$$

Therefore

$$e^{\alpha\pi i}\frac{\Gamma(\alpha+2)}{2\pi i}\int_C\frac{dz}{z^{\alpha+2}}\int_0^\infty m(p,t)e^{-zp}\,dp=\frac{\sin\alpha\pi\cdot\Gamma(\alpha+2)\Gamma(1-\alpha)}{\alpha(\alpha+1)\pi}\int_0^\infty p^{\alpha+1}m(p,t)\,dp$$

$$=\int_0^\infty p^{\alpha+1}m(p,t)\,dp\ .$$

Thus Eq. (7) is verified.

Appendix II

We will here deduce Eqs. (8) and (9). We get from the second equation of Eq. (5) the following equation

$$\frac{dz_0}{dz}=1/\{1-2G''(z_0)t\}\,. \tag{38}$$

Since the relation

$$\int_0^\infty pm(p,t)\,dp=1$$

always holds, we obtain for $z=z_0=0$

$$G'(0)=-1\,. \tag{39}$$

When the absolute value of z is very small, we get from Eq. (38) that

$$z_0=\frac{z}{1-2G''(0)t}+O(z^2)\,. \tag{40}$$

Accordingly, the following relations are derived

$$\left.\begin{aligned} G(z_0)&=G(0)-\frac{z}{1-2G''(0)t}+O(z^2)\,,\\ G'(z_0)&=-1+\frac{G''(0)z}{1-2G''(0)t}+O(z^2)\,,\\ G''(z_0)&=G''(0)+\frac{G'''(0)z}{1-2G''(0)t}+O(z^2)\,. \end{aligned}\right\} \tag{41}$$

If we substitute these relations into Eq. (7), we obtain the following formulas

$$J_{PQ}=e^{\alpha\pi i}\frac{\Gamma(\alpha+2)}{2\pi i}\int_{PQ}\frac{dz}{z^{\alpha+2}}f(z,t)=-e^{\alpha\pi i}\frac{\Gamma(\alpha+2)}{2\pi i}H\,,$$

$$J_{ST}=e^{\alpha\pi i}\frac{\Gamma(\alpha+2)}{2\pi i}e^{-2\pi\alpha i}H\,,$$

where

$$H=\int_r^\infty\frac{d\rho}{\rho^{\alpha+2}}\{G(\rho_0)-G'(\rho_0)^2t\}\,.$$

Then

$$\begin{aligned} J_{PQ}+J_{ST}&=-\frac{\Gamma(\alpha+2)\sin\alpha\pi}{\pi}H\\ &=-\frac{\Gamma(\alpha+2)\sin\alpha\pi}{\pi}\left\{\left|-\frac{1}{(\alpha+1)\rho^{\alpha+1}}[G(\rho_0)-G'(\rho_0)^2t]\right.\right.\\ &\quad+\frac{1}{\alpha(\alpha+1)\rho^\alpha}G(\rho_0)\Big|_r^\infty+\frac{1}{\alpha(\alpha+1)}\int_r^\infty\frac{G''(\rho_0)}{\rho^\alpha}\,d\rho_0\,. \end{aligned} \tag{42}$$

Likewise we obtain

$$\begin{aligned} J_{QRS}&=e^{\alpha\pi i}\frac{\Gamma(\alpha+2)}{2\pi i}\int_{QRS}\frac{dz}{z^{\alpha+2}}f(z,t)\\ &=-\frac{e^{\alpha\pi i}\Gamma(\alpha+2)}{2\pi r^{\alpha+1}}\int_0^{2\pi}e^{-i\alpha\theta}\{G(\rho_0)-G'(\rho_0)^2t\}\,d\theta\,. \end{aligned} \tag{43}$$

Substituting Eq. (41) into Eqs. (42) and (43) and making r tend to zero, we get

$$\lim_{r\to0}(J_{PQ}+J_{QRS}+J_{ST})=\frac{1}{\Gamma(1-\alpha)}\int_{\rho=0}^{\rho=\infty}\frac{G''(\rho_0)}{\rho^\alpha}\,d\rho_0\,,$$

therefore

$$J=\frac{1}{\Gamma(1-\alpha)}\int_{\rho=0}^{\rho=\infty} G''(\rho_0)\{\rho_0-2[1+G'(\rho_0)]t\}^{-\alpha}\,d\rho_0\,. \tag{44}$$

We know from § 2 of the paper I[1] that $\rho_0=0$ holds for $\rho=0$. On the other hand the following relation is derived from Eq. (5)

$$\frac{\partial f(\rho,t)}{\partial\rho}=-\int_0^\infty pm(p,t)e^{-\rho p}\,dp=G'(\rho_0)\,.$$

If p_0 be an arbitrary positive number, we obtain the following relation

$$\begin{aligned}\int_{p_0}^\infty pme^{-\rho p}\,dp&<\int_{p_0}^\infty pm\,e^{-\rho p_0}\,dp<\int_0^{p_0} pm\,e^{-\rho p}\,dp+e^{-\rho p_0}\left(1-\int_0^{p_0} pm\,dp\right)\\&=\int_0^{p_0} pm(e^{-\rho p}-e^{-\rho p_0})\,dp+e^{-\rho p_0}\\&=p_0\xi m(\xi,t)(e^{-\rho\xi}-e^{-\rho p_0})+e^{-\rho p_0}\,,\qquad 0<\xi<\rho_0\\&\leqq p_0^2 m(\xi,t)\,e^{-\rho p_0}\{e^{\rho(p_0-\xi)}-1\}+e^{-\rho p_0}\,.\end{aligned}$$

Since the last expression converges to 0 as $\rho\to\infty$, we get

$$\lim_{\rho\to\infty} G'(\rho_0)=0\,.$$

Considering Eq. (5), we derive the following equation

$$\lim_{\rho\to 0}\rho_0=\infty\,. \tag{45}$$

Therefore Eq. (44) becomes

$$J=\frac{1}{\Gamma(1-\alpha)}\int_0^\infty G''(\rho_0)\{\rho_0-2[1+G'(\rho_0)]t\}^{-\alpha}\,d\rho_0\,.$$

When the initial distribution is Poisson-like, we have

$$G(\rho_0)=1/u(1+u\rho_0)\,,$$

where u denotes the initial number average degree of polymerization. If we put $1+u\rho_0=1/y$, we obtain finally

$$J=\frac{2u^\alpha}{\Gamma(1-\alpha)}\int_0^1\frac{y^{\alpha+1}\,dy}{(1-y)^\alpha\{1-2uty(y+1\}^\alpha}\,.$$

Appendix III

We will here derive Eq. (28). If we apply the relation (7), we get the following equation

$$\begin{aligned}J&=\sum_{k=2}^\infty\int_0^\infty p^{\alpha+1}m_k(p,x)\,dp\\&=e^{\alpha\pi i}\frac{\Gamma(\alpha+2)}{2\pi i}\int_C\frac{dz}{z^{\alpha+2}}\sum_{k=2}^\infty m_k(p,x)e^{-zp}\,dp\,.\end{aligned}$$

The last expression is transformed into the following formula

$$\begin{aligned}&=e^{\alpha\pi i}\frac{\Gamma(\alpha+2)}{2\pi i}\int_C\frac{F(z,0,x)}{z^{\alpha+2}}\,dz\\&=e^{\alpha\pi i}\frac{\Gamma(\alpha+2)}{2\pi i}\int_C\frac{dz}{z^{\alpha+2}}\left\{\left(z-z_0+\int_0^x\psi\,dx\right)G_{z_0}(z_0,\eta_0)+G(z_0,\eta_0)\right\}\,.\end{aligned}$$

Therefore

$$J_{PQ}+J_{ST}=-\frac{\Gamma(\alpha+2)}{\pi}\sin\alpha\pi\int_r^\infty\frac{d\rho}{\rho^{\alpha+2}}\left\{\left(\rho-\rho_0+\int_0^x\psi\,dx\right)G_{\rho_0}(\rho_0,\eta_0)+G(\rho_0,\eta_0)\right\}$$

$$=-\frac{\Gamma(\alpha+2)}{\pi}\sin\alpha\pi\left\{\left|-\frac{1}{(\alpha+1)\rho^{\alpha+1}}\left[\left(\rho-\rho_0+\int_0^x\psi\,dx\right)G_{\rho_0}(\rho_0,\eta_0)+G(\rho_0,\eta_0)\right]\right|_{\rho=r}^{\rho=\infty}\right.$$

$$\left.+\frac{1}{\alpha}\int_r^\infty\frac{1}{\rho^{\alpha+1}}\left[G_{\rho_0}(\rho_0,\eta_0)+\left(\rho-\rho_0+\int_0^x\psi\,dx\right)G_{\rho_0\rho_0}(\rho_0,\eta_0)\right]\frac{d\rho_0}{d\rho}d\rho\right\}$$

$$=-\frac{\Gamma(\alpha+2)}{\pi}\sin\alpha\pi\left\{\left|-\frac{1}{(\alpha+1)\rho^{\alpha+1}}\left[\left(\rho-\rho_0+\int_0^x\psi\,dx\right)G_{\rho_0}(\rho_0,\eta_0)+G(\rho_0,\eta_0)\right]\right.\right.$$

$$\left.-\frac{1}{\alpha(\alpha+1)}\frac{G_{\rho_0}(\rho_0,\eta_0)}{\rho^\alpha}\right|_{\rho=r}^{\rho=\infty}-\frac{1}{\alpha}\int_{\rho=r}^{\rho=\infty}\frac{G_{\rho_0\eta_0}(\rho_0,\eta_0)}{\rho^\alpha}d\eta_0\Bigg\}.$$

By differentiating Eq. (26), we obtain

$$\frac{\partial F}{\partial\xi}=\frac{\partial G}{\partial\xi_0}=-\sum_{k=2}^\infty\int_0^\infty pm_ke^{-\xi p}\,dp\,.$$

The right hand side converges to 0, where ξ is real and tends to infinity. Therefore, from Eq. (26) we obtain

$$\lim_{\xi\to\infty}\frac{\partial G}{\partial\xi_0}=\lim_{\xi\to\infty}\frac{e^{-x}-e^{-\eta_0}}{1-e^{-x}}=0\,, \tag{46}$$

hence

$$\lim_{\xi\to\infty}\eta_0=x\,. \tag{47}$$

From Eq. (26) the following relation holds

$$-\sum_{k=2}^\infty k\int_0^\infty m_ke^{-\xi p}\,dp=\frac{\partial F(\xi,0,x)}{\partial\eta}=\left(\xi-\xi_0+\int_0^x\psi\,dx\right)\frac{1}{1-e^x}\,.$$

Making ξ tend to infinity, we obtain

$$0=\left(\xi-\xi_0+\int_0^x\psi\,dx\right)\frac{1}{1-e^x}\,,$$

therefore the following equation is derived

$$\lim_{\xi\to\infty}\xi_0=\infty\,. \tag{48}$$

From these results we get

$$\lim_{\xi\to\infty}G(\xi_0,\eta_0)=\lim_{\substack{\xi_0\to\infty\\ \eta_0\to x}}\sum_{k=2}^\infty\int_0^\infty m(p,0)e^{-\xi_0p-k\eta_0}\,dp=0\,, \tag{49}$$

and then

$$J_{PQ}+J_{ST}=-\frac{\Gamma(\alpha+2)}{\pi}\sin\alpha\pi\left\{\frac{1}{(\alpha+1)r^{\alpha+1}}\left[\left(r-\rho_0+\int_0^x\psi\,dx\right)G_{\rho_0}(\rho_0,\eta_0)\right.\right.$$

$$\left.\left.+G(\rho_0,\eta_0)\right]+\frac{1}{\alpha(\alpha+1)}\frac{G_{\rho_0}(\rho_0,\eta_0)}{r^\alpha}-\frac{1}{\alpha}\int_{\rho=r}^{\rho=\infty}\frac{1}{\rho^\alpha}G_{\rho_0\eta_0}(\rho_0,\eta_0)\,d\eta_0\right\}. \tag{50}$$

As we already know from the results of § 2 of the paper II[2)] that $\rho_0=\eta_0=0$ holds for $\rho=\eta=0$, we can put for the case where $\eta=0$ the following relations

$$\left.\begin{aligned}\rho_0&=a\rho+O(\rho^2)\,,\\ \eta_0&=b\rho+O(\rho^2)\,,\end{aligned}\right\}\tag{51}$$

where a and b are independent with ρ. If we substitute these expressions into the second and the third equation of Eq. (26), we get

$$\{B(1-e^{-x})-1\}a+(C+D)(1-e^{-x})b=-1\,,$$

$$A(1-e^{-x})a+\{B(1-e^{-x})-1\}=0\,.$$

From these simultaneous equations a and b are solved,

$$a=\frac{1-B(1-e^{-x})}{\{B(1-e^{-x})-1\}^2-A(C+D)(1-e^{-x})^2}\,.\tag{52}$$

$$b=\frac{A(1-e^{-x})}{\{B(1-e^{-x})-1\}^2-A(C+D)(1-e^{-x})^2}\,.\tag{53}$$

where $A=G_{\rho_0\rho_0}(0,0)$, $B=G_{\rho_0\eta_0}(0,0)$, $C=G_{\eta_0\eta_0}(0,0)$ and $D=G_{\eta_0}(0,0)$. If we insert Eq. (51) in Eq. (50), we get

$$\begin{aligned}J_{PQ}+J_{ST}=&-\frac{\Gamma(\alpha+2)}{\pi}\sin\alpha\pi\left\{\frac{r^{-\alpha-1}}{\alpha+1}[V+D(1-e^{-x})-r+O(r^2)]\right.\\&\left.+\frac{r^{-\alpha}}{\alpha(\alpha+1)}[-1+O(r)]-\frac{1}{\alpha}\int_{\rho=r}^{\rho=\infty}\rho^{-\alpha}G_{\rho_0\eta_0}(\rho_0,\eta_0)\,d\eta_0\right\}\,,\end{aligned}\tag{54}$$

where $V=G(0,0)$. On the other hand, we obtain likewise

$$\begin{aligned}J_{QRS}&=e^{\alpha\pi i}\frac{\Gamma(\alpha+2)}{2\pi r^{\alpha+1}}\int_0^{2\pi}e^{-i(\alpha+1)\theta}\{V+D(1-e^{-x})-re^{i\theta}+O(r^2)\}\,d\theta\\&=\frac{\Gamma(\alpha+2)}{\pi r^{\alpha+1}}\sin\alpha\pi\left\{\frac{V+D(1-e^{-x})}{\alpha+1}-\frac{r}{\alpha}+O(r^2)\right\}\,.\end{aligned}\tag{55}$$

Ultimately J is given by

$$J=J_{PQ}+J_{QRS}+J_{ST}=\frac{\Gamma(\alpha+2)}{\alpha\pi}\sin\alpha\pi\int_{\rho=r}^{\rho=\infty}\rho^{-\alpha}G_{\rho_0\eta_0}(\rho_0,\eta_0)\,d\eta_0+O(r^{1-\alpha})\,.$$

When r tends to zero, J becomes

$$\begin{aligned}J&=\frac{\Gamma(\alpha+2)}{\alpha\pi}\sin\alpha\pi\int_{\rho=0}^{\rho=\infty}\rho^{-\alpha}G_{\rho_0\eta_0}(\rho_0,\eta_0)\,d\eta_0=\frac{1}{\Gamma(1-\alpha)(1-e^{-x})}\int_0^x\frac{e^{-\eta_0}}{\rho^\alpha}\,d\eta_0\\&=\frac{1}{\Gamma(1-\alpha)(1-e^{-x})}\int_0^\infty\frac{e^{-\eta_0}(e^x-1)G_{\rho_0\rho_0}(\rho_0,\eta_0)}{\rho^\alpha\{e^{x-\eta_0}-(e^x-1)G_{\rho_0\eta_0}(\rho_0,\eta_0)\}}\,d\rho_0\,.\end{aligned}\tag{56}$$

When the initial distribution is Poisson-like, the function G is expressed by

$$G(\rho_0,\eta_0)=\frac{\gamma^2}{\gamma+\rho_0}e^{-2\eta_0}\,,$$

where $\gamma=1/u+\dot{r}R$. If we put

$$y=\sqrt{\frac{e^{x-\eta_0}-1}{e^x-1}}\,,$$

we obtain finally

$$J=\frac{2e^{\alpha x}}{\Gamma(1-x)}\int_0^1\frac{y^{\alpha+1}\,dy}{(1-y)^\alpha\{1-3(e^x-1)y\}^\alpha}\,.\tag{57}$$

Acknowledgements

It is a pleasure to express my gratitude to Dr. A. Amemiya. His continued interest and support in all phases of this research are gratefully appreciated. I wish to thank Dr. A. Harasima and Dr. K. Shinohara for their direction and guidance of this problem, and also to thank the members of the Group for the Study of Irradiated Polymers in Tokyo.

References

1) O. Saito: J. Phys. Soc. Japan **13** (1958) 198.
2) O. Saito: J. Phys. Soc. Japan **13** (1958) 1451.
3) H. Hozo: First Symposium on Atomic Energy, Japan Feb. 1957.

JOURNAL OF THE PHYSICAL SOCIETY OF JAPAN Vol. 13, No. 12, DECEMBER, 1958

Theory of Excited Plasma Waves

By Masao SUMI

Electrical Communication Laboratory, Tokyo

(Received August 20, 1958)

The excitation of oscillations in a uniform plasma by an injected electron beam is considered. The dispersion relation for this system is derived by means of Fourier-Laplace transform method. The solutions of the dispersion relation are obtained which yield the characteristics of excited waves; the frequency, the phase velocity and the time-rate of wave-growth as functions of the wave number. It is demonstrated that the wave characteristics are varied by the influence of thermal velocity of electrons in the main plasma and by taking the ratio of electron density in the beam to that in the main plasma over a wide range of values. It is then examined that both the velocity spread in the beam and collisions in the medium have the decaying effect on the growing wave. By the use of the above results the case is also discussed where the main plasma is bounded by ideally thin sheaths.

§ 1. Introduction

We shall deal with in this work the longitudinal oscillations in a uniform main plasma excited by an electron beam injected from an external source. In the region where the electron beam passes through, the total charge is assumed to be cancelled out on the average on account of positive ions created in the medium by electron impacts. The main plasma may be supposed either unbounded or bounded by ideally thin sheaths.

The beam excitation of plasma oscillations has since been discussed by many authors. Some of them treated the waves generated by multi-stream interactions[1]. The problem of the beam excitation in a thermal plasma was also considered in several papers; Bohm and Gross studied in a series of their works the instability of beams of well-defined velocity and the excitation due to fast beams emitted from an electrode[2]. They have derived the dispersion relation and discussed about solutions only for a weak beam. The results obtained as for instabilities are qualitatively valid, but unsatisfactory from a quantitative point of view, and besides the stationary solutions discussed there are open to criticism, because they have used the substitution analysis to get the dispersion relation. Akhiezer and Feinberg have also led the dispersion relation, but have not studied the detailed features on oscillations[3]. The more quantitative treatment has been carried out by Lampert[4], who obtained the rate of growth-in-time for the case of thermal velocity negligible in the main plasma and also the amplification factor for traveling plasma waves. It is found, however, that the results attained were restricted only in the weak beam limit and the whole characteristics of excited waves were not examined.

Lately the author has also tried to get the characteristics of excited waves[5]. But the approximate procedure then employed was unsatisfactory and therefore the more accurate and detailed study will be developed in this paper.

In the study of plasma waves has been widely used the method of substitution analysis. But it has been pointed out that this method leads to difficulties in some respects[6)-9)]. The way which overcomes the difficulties is to employ the more favorable methods, that is, the Laplace transform method first applied by Landau[6] or the stationary-wave method recently completed by Van Kampen[9]. However the latter one applies only for a stationary or a decaying wave and does not for an excited wave which is growing exponentially with time. Therefore we shall adopt here the Laplace transform method by which we can without ambiguity get the dispersion relation for the problem considered.

In sections 2 and 3 will be preliminarily reviewed the fundamental equations and their solutions obtained by means of the usual technique of Laplace transform method. With a specified velocity distribution function which consists of one part for electrons in the main plasma and the other part for those in the beam, the dispersion relation in our case will be derived in section 4. Next will be discussed the excitation of plasma waves which build up exponentially in time. The characteristics of the plasma waves such as the frequency, the phase velocity and the time-rate of growth will be given as the wave number is varied. It will then be examined how much the wave characteristics change by taking into consideration of the thermal motion of electrons in the main plasma and by varying the ratio of the electron density in the beam to that in the main plasma. The effects of the velocity spread in the beam and the collisional damping will be discussed in sections 6 and 7. Finally in section 8 we shall consider the oscillations excited in a plasma layer bounded by ideally thin sheaths, which correspond more closely to practical cases.

§ 2. Fundamental Equations

The behaviors of electons in a plasma can be described by the distribution function of their velocities $f(\boldsymbol{v}, \boldsymbol{x}, t)$ satisfying an integro-differential equation of Boltzmann type. Positive ions are simply assumed to be a uniform and continuous background of positive charges neutralizing the medium as a whole. In the absence of external fields, the Boltzmann equation can be written as*

$$\frac{\partial f}{\partial t}+\boldsymbol{v}\frac{\partial f}{\partial \boldsymbol{x}}-\frac{e\boldsymbol{E}}{m}\frac{\partial f}{\partial \boldsymbol{v}}=\left.\frac{\delta f}{\delta t}\right|_{coll}. \tag{2.1}$$

The term $\delta f/\delta t|_{coll}$ represents the instantaneous change of the distribution function arising from the binary close collisions. The electric field $\boldsymbol{E}$ is connected with the fluctuating charge concentrations of electrons by the Poisson equation. This field acts on an electron as a long-range force arising from the other electrons, as assumed by Vlasov[10]. Then

$$\frac{\partial \boldsymbol{E}}{\partial \boldsymbol{x}}=\frac{e}{\varepsilon_0}\left(n_0-\int f d\boldsymbol{v}\right), \tag{2.2}$$

where n_0 is the density of the uniform positive background or the average density of electrons. Diving the distribution function into a stationary part $f_0(\boldsymbol{v})$ and a fluctuating part $f_1(\boldsymbol{v}, \boldsymbol{x}, t)$, then

$$f(\boldsymbol{v}, \boldsymbol{x}, t)=f_0(\boldsymbol{v})+f_1(\boldsymbol{v}, \boldsymbol{x}, t). \tag{2.3}$$

The linearized equation for f_1 is obtained from Eq. (2.1) for small fluctuating components as usual,

$$\frac{\partial f_1}{\partial t}+\boldsymbol{v}\frac{\partial f_1}{\partial \boldsymbol{x}}-\frac{e\boldsymbol{E}}{m}\frac{\partial f_0}{\partial \boldsymbol{v}}=\left.\frac{\delta f_1}{\delta t}\right|_{coll}. \tag{2.4}$$

While the Poisson equation (2.2) becomes

$$\frac{\partial \boldsymbol{E}}{\partial \boldsymbol{x}}=-\frac{e}{\varepsilon_0}\int f_1 d\boldsymbol{v}, \tag{2.5}$$

since $\int f_0(\boldsymbol{v})d\boldsymbol{v}=n_0$. In a low-pressure region, short-range collisions play so little an important role that at present we neglect the collisional effect and in a later section we shall be back to this point.

We consider first the case where the plasma is extended to infinity and a spatial disturbance is given at an initial instance. Hence the fluctuating parts of the distribution function and the field intensity is conveniently represented by Fourier-analysis in space. Thus we can write

* We use the MKS rationalized unit throughout this paper.

$$\left.\begin{aligned} f_1(\boldsymbol{v},\ \boldsymbol{x},\ t)&=\iiint_{-\infty}^{\infty} f_k(\boldsymbol{v},\ t)e^{i\boldsymbol{kx}}d\boldsymbol{k}\ ,\\ \boldsymbol{E}(\boldsymbol{x},\ t)&=\iiint_{-\infty}^{\infty}\boldsymbol{E}_k(t)e^{i\boldsymbol{kx}}d\boldsymbol{k}\ . \end{aligned}\right\} \tag{2.6}$$

Then fundamental equations (2.4) and (2.5) become for each component,

$$\left.\begin{aligned} &\frac{\partial f_k}{\partial t}+ikvf_k-\frac{e}{m}\boldsymbol{E}_k\frac{\partial f_0}{\partial v}=0\ .\\ &ik\boldsymbol{E}_k=-\frac{e}{\varepsilon_0}\int f_k(\boldsymbol{v},\ t)d\boldsymbol{v}\ . \end{aligned}\right\} \tag{2.7}$$

These equations can be solved by means of Laplace transform method for a given initial condition. Each Fourier component and its time derivative are transformed by the following relations

$$\left.\begin{aligned} &\int_0^\infty f_k(\boldsymbol{v},\ t)e^{i\omega t}dt=F(\boldsymbol{v},\ \boldsymbol{k},\ \omega)\ ,\\ &\int_0^\infty \boldsymbol{E}_k(t)e^{i\omega t}dt=\mathcal{E}(\boldsymbol{k},\ \omega), \end{aligned}\right\} \tag{2.8}$$

and

$$\int_0^\infty \frac{\partial f_k}{\partial t}e^{i\omega t}dt=-i\omega F(\boldsymbol{v},\ \boldsymbol{k},\ \omega)-f_k(\boldsymbol{v},\ 0)\ . \tag{2.9}$$

While the inverse transformations are written as

$$\left.\begin{aligned} f_k(\boldsymbol{v},\ t)&=\frac{1}{2\pi}\int_{-\infty+i\gamma}^{\infty+i\gamma}F(\boldsymbol{v},\ \boldsymbol{k},\ \omega)e^{-i\omega t}d\omega\ ,\\ \boldsymbol{E}_k(t)&=\frac{1}{2\pi}\int_{-\infty+i\gamma}^{\infty+i\gamma}\mathcal{E}(\boldsymbol{k},\ \omega)e^{-i\omega t}d\omega\ . \end{aligned}\right\} \tag{2.10}$$

where the integration is carried out along a straight line parallel to the real ω-axis and lying onto the above of all the singularities of the integrands, $F(\boldsymbol{v},\ \boldsymbol{k},\ \omega)$ and $\mathcal{E}(\boldsymbol{k},\ \omega)$, so that γ is larger than some positive value of γ_a for which both

$$\int_0^\infty e^{-\gamma_a t}|f_k|\,dt$$

and

$$\int_0^\infty e^{-\gamma_a t}|\boldsymbol{E}_k|\,dt$$

are bounded.

Then we obtain from Eq. (2.7)

$$\left.\begin{aligned} &i(\omega-\boldsymbol{kv})F(\boldsymbol{v},\ \boldsymbol{k},\ w)+f_k(\boldsymbol{v},\ 0)\\ &\quad+\frac{e}{m}\mathcal{E}(\boldsymbol{k},\omega)\frac{\partial f_0}{\partial \boldsymbol{v}}=0\ .\\ &ik\mathcal{E}(\boldsymbol{k},\ \omega)=-\frac{e}{\varepsilon_0}\int F(\boldsymbol{v},\ \boldsymbol{k},\ \omega)d\boldsymbol{v}\ . \end{aligned}\right\} \tag{2.11}$$

Here we take the wave vector of propagation $\boldsymbol{k}$ directed to the z-axis and assume the uniform distribution function f_0 to be an even function with respect to the velocity components perpendicular to z. These correspond essentially to the one-dimensional treatment, considering only the longitudinal fluctuations in the plasma. Putting $k_z=k$, $v_z=u$ and $\mathcal{E}_z=\mathcal{E}$, and integrating with respect to v_x and v_y in Eq. (2.11), we get

$$i(\omega-ku)G(u,\ k,\ \omega)+g(u,\ k,\ 0)+\frac{e}{m}\mathcal{E}(k,\ \omega)\frac{dg_0}{du}=0\ , \tag{2.12}$$

$$ik\mathcal{E}(k,\ \omega)=-\frac{e}{\varepsilon_0}\int_{-\infty}^{\infty}G(u,\ k,\ \omega)du\ , \tag{2.13}$$

where

$$\left.\begin{aligned} G(u,\ k,\ \omega)&=\iint_{-\infty}^{\infty}F(\boldsymbol{v},\ \boldsymbol{k},\ \omega)dv_xdv_y\ ,\\ g(u,\ k,\ 0)&=\iint_{-\infty}^{\infty}f_k(\boldsymbol{v},\ 0)dv_xdv_y\ ,\\ g_0(u)&=\iint_{-\infty}^{\infty}f_0(\boldsymbol{v})dv_xdv_y\ . \end{aligned}\right\} \tag{2.14}$$

§ 3. Solution by Laplace Transform Method

We shall solve the combined equations (2.12) and (2.13). Since both k and u are real and $Im(\omega)>0$, $\omega-ku\neq 0$. Then Eq. (2.12) gives

$$G(u,\ k,\ \omega)=\frac{i}{(\omega-ku)}\times\left[\frac{e}{m}\mathcal{E}(k,\ \omega)\frac{dg_0}{du}+g(u,\ k,\ 0)\right]. \tag{3.1}$$

Inserting it into Eq. (2.13), we find for the Fourier-Laplace transform of the electric field component

$$\mathcal{E}(k,\ \omega)=\frac{e}{\varepsilon_0k^2}\ \frac{\displaystyle\int_{-\infty}^{\infty}\frac{g(u,\ k,\ 0)}{(u-\omega/k)}du}{\left[1-\dfrac{e^2}{m\varepsilon_0k^2}\displaystyle\int_{-\infty}^{\infty}\frac{dg_0/du}{u-\omega/k}du\right]}\ . \tag{3.2}$$

Note that the above relation holds only in the region of $Im(\omega)>\gamma_a>0$, where $E(k,\ \omega)$ is an analytic function of ω. However, to find $E(z,\ t)$ explicitly it is necessary to define $E(k,\ \omega)$ on the whole complex ω-plane, by means of an analytic continuation of the function. For a positive value of k, $Im(\omega/k)$ is

also positive. In this case, following Landau[6], the path of integration along the real axis in Eq. (3.2) with respect to velocity u can be modified on the complex u-plane to a path C in the lower half-plane such that we have no singularity of $g(u, k, 0)$ or dg_0/du either on C or between C and the real axis (Fig. 1(a)).

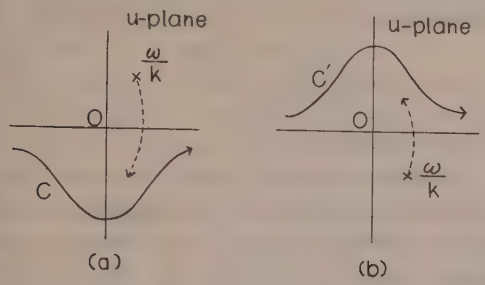

Fig. 1 (a) represents the contour of integration C on the complex u-plane for $k>0$; (b) C' for $k<0$.

It is easily shown that the integration thus defined with the contour C is always single-valued and analytic as the point ω/k crosses the real axis from the upper half u-plane and then moves into the lower half plane. Hence the integration defined above gives the analytic continuation over the whole region of ω-plane. Thus we can get, for $k>0$,

$$\mathcal{E}(k, \omega)=\frac{e}{\varepsilon_0 k^2}\frac{\int_C \frac{g(u, k, 0)}{u-w/k}du}{\left[1-\frac{e^2}{m_0\varepsilon_0 k^2}\int_C \frac{dg_0/du}{u-\omega/k}du\right]}. \tag{3.3}$$

For a negative value of k, $Im(\omega/k)$ becomes negative. Therefore the integrand in the integration on the u-plane has a singularity $u=\omega/k$ in the lower half plane. Hence according to the similar argument we must take a countour of integration C' deformed to the upper half plane as in Fig. 1(b) instead of the the contour C for the positive k. Then the analytical continuation over the whole plane yield the result for $k<0$:

$$\mathcal{E}(k, \omega)=\frac{e}{\varepsilon_0 k^2}\frac{\int_{C'} \frac{g(u, k, 0)}{u-\omega/k}du}{\left[1-\frac{e^2}{m\varepsilon_0 k^2}\int_{C'} \frac{dg_0/du}{u-\omega/k}du\right]}. \tag{3.4}$$

The electric field component $E(z, t)$ is obtained by means of the following inverse Laplace transformation

$$E(z, t)=\frac{1}{(2\pi)^2}\int_{-\infty}^{\infty}\int_{-\infty+i\gamma}^{\infty+i\gamma} E(k, \omega)e^{i(kz-\omega t)}dkd\omega. \tag{3.5}$$

Substituting the expressions (3.3) and (3.4) into the above relation, and integrating on the ω-plane, we get finally

$$E(z, t)=\frac{1}{2\pi}\int_{-\infty}^{\infty} dk[\sum_j C_j(k)e^{i(kz-ku_j t)} + \sum_l D_l(k)e^{i(kz-\omega_l t)}], \tag{3.6}$$

where u_j are the singular points of $g(\omega/k, k, 0)$, if any, in the lower half ω-plane, providing the decaying feature to the first term, while ω_l are the roots of the denominator of $E(k, \omega)$ and are determined by the dispersion relation as follows

$$D(k, \omega)=1-\frac{e^2}{m\varepsilon_0 k^2}\int_{C \text{ or } C'} \frac{dg_0/du}{u-\omega/k}du=0. \tag{3.7}$$

The contour of integration C or C' corresponds to the positive or negative value of k, respectively.

§ 4. Dispersion Relation with Specified Distribution Functions

The dispersion relation $D(k, \omega)=0$ gives the connection between ω and k for plasma waves; in our case ω is in general complex such as $\omega=\omega_0+i\gamma$. Solving ω as a function of k, we have the frequency of the plasma wave $\omega_0(k)$ and the time rate of wave-growth or wave-decay $\gamma(k)$.

In this section we shall treat a case when an electron beam is injected into a uniform thermal plasma. The one-dimensional treatment allows us to regard the injected beam as the uniform flow parallel to the z direction in the region through which the beam really passes. Then the distribution function $g_0(u)$ is divided into two parts: $g_p(u)$ for the uniform plasma and $g_b(u)$ for the injected beam. Here $g_p(u)$ is considered as the Maxwellian form as below

$$g_p(u)=n_p\left(\frac{m}{2\pi\kappa T}\right)^{1/2}e^{-mu^2/2\kappa T} = \frac{n_p}{\sqrt{\pi}u_T}e^{-(u/u_T)^2}, \tag{4.1}$$

where n_p is the electron density in the plasma $u_T=(2\kappa T/m)^{1/2}$ and κ the Boltzmann constant. For the present $g_b(u)$ is simply specified with the extremely sharp velocity distribution of δ-functional form

$$g_b(u)=n_b\delta(u-u_b)\ , \tag{4.2}$$

where n_b is the electron density in the beam and u_b the velocity of it. Here it is to be noted that in the derivation of dispersion relation in the last section, the distribution function $g_0(u)$ is assumed to be an analytic function over the whole complex u-plane. Therefore, if we take this form of $g_b(u)$, we have to return to Eq. (3.2), the denominator of which gives in the present case

$$1-\frac{e^2}{m\varepsilon_0k^2}\left[\int_{-\infty}^{\infty}\frac{dg_p/du}{u-\omega/k}du+\frac{n_b}{(u_b-\omega/k)^2}\right].$$

Then the analytical continuation can be carried out in the same way as before. The contour of integration along the real u axis can be replaced by the contour C or C'. Thus we get the following dispersion relation instead of Eq. (3.7)

$$D(k,\omega)=1-\frac{e^2}{m\varepsilon_0k^2}\left[\int_{C\text{ or }C'}\frac{dg_p/du}{u-\omega/k}du+\frac{n_b}{(u_b-\omega/k)^2}\right]=0\ . \tag{4.3}$$

The integration with the contour C has been obtained by several authors for the Maxwellian distribution[11]. The result is

$$\int_C\frac{dg_p/du}{u-\omega/k}du=-\frac{2n_p}{u_T^2}\times\left[1+i\sqrt{\pi}\beta e^{-\beta^2}\{1+\Phi(i\beta)\}\right]. \tag{4.4}$$

where $\beta=\omega/ku_T$ and $\Phi(x)$ is the error function of the form

$$\Phi(x)=\frac{2}{\sqrt{\pi}}\int_0^x e^{-t^2}dt\ .$$

While the integration with the contour C' is obtained by reversing the direction of imaginary axis, as seen in Figs. 1(a) and 1(b). Thus one finds immediately

$$\int_{C'}\frac{dg_p/du}{u-\omega/k}du=-\frac{2n_p}{u_T^2}\times[1-i\sqrt{\pi}\beta e^{-\beta^2}\{1-\Phi(i\beta)\}]\ . \tag{4.5}$$

Taking Eqs. (4.4) and (4.5), we can write Eq. (4.3) as

$$D(k,\omega)=1+\left[2\left(\frac{\omega_p}{ku_T}\right)^2\{1\pm i\sqrt{\pi}\beta e^{-\beta^2}[1\pm\Phi(i\beta)]\}-\left(\frac{\omega_b}{ku_T}\right)^2\frac{1}{(\xi-\beta)^2}\right]=0\ , \tag{4.6}$$

(+sign for $k>0$, −sign for $k<0$)

where $\xi=u_b/u_T$, $\omega_p^2=n_pe^2/m\varepsilon_0$ and $\omega_b^2=n_be^2/m\varepsilon_0$. Since the wave for $k<0$ runs backward in the direction of electron beam, the disperison relation for $k<0$ is seen to be identical with that for $k>0$ with the electron beam running backward. Actually the relation (4.6) may be written as follows

$$D(k,\omega)=1+\left[2\beta_p^2\{1+i\sqrt{\pi}\beta e^{-\beta^2}[1+\Phi(i\beta)]\}-\frac{\beta_b^2}{(\xi\mp\beta)^2}\right]=0\ , \tag{4.7}$$

with the abbreviation of

$$\beta_p=\omega_p/ku_T \text{ and } \beta_b=\omega_b/ku_T\ , \tag{4.8}$$

where the value of k is always positive and the minus or the plus sign of the last term corresponds respectively to the wave which travels forward or backward in the beam direction. Thus Eq. (4.7) represents the dispersion relation for growing, stationary or decaying waves according to $Im(\omega)\gtreqless 0$ respectively.

§ 5. Excitation of Plasma Waves

As an electron beam passes through a stationary plasma, the interaction between the beam and the plasma may be considered as rather strong in the range that the phase velocity of plasma wave is very near the beam velocity. When the electrons in the beam are slightly faster than the wave phase velocity, they will deliver their energy to the plasma wave. Hence the growing-up of the wave will occur. On the contrary if the wave phase velocity is too small, the coupling with the beam will become very weak or negligible and the plasma waves will not grow up. Thus it might be reasonable that we consider only the case for forward waves, since backward waves are easily shown not to give any growing wave. Furthermore, when there exists only the thermal plasma with a Maxwellian distribution in the limit of the vanishing electron beam, it will be also shown that we have no growing wave.

To discuss the behaviors of excited plasma wave we shall now solve the dispersion relation for $Im(\omega)>0$. Then we write the relation (4.7) for a forward wave as

$$D(k,\omega)=1+\beta_s^2[A(\beta)-B(\beta)]=0\ , \tag{5.1}$$

where $\beta_s^2=\beta_p^2+\beta_b^2$ and

$$A(\beta)=2\sigma_p\{1+i\sqrt{\pi}\beta e^{-\beta^2}[1+\Phi(i\beta)]\}\ , \tag{5.2}$$

$$B(\beta)=\sigma_b/(\xi-\beta)^2\ , \tag{5.3}$$

with $\sigma_p=\beta_p^2/\beta_s^2=n_p/(n_p+n_b)$ and $\sigma_b=\beta_b^2/\beta_s^2=n_b/(n_p+n_b)$. Dividing the real and imaginary part of $A(\beta)$ and $B(\beta)$, we find

$$1+\beta_s^2(A_r-B_r)=0\,, \tag{5.4}$$

$$A_i-B_i=0\,. \tag{5.5}$$

Two equations (5.4) and (5.5) thus obtained may be solved to determine a pair of unkown parameters; the real and imaginary parts of β, β_r and β_i, or $\omega_0(k)$ and $\gamma(k)$.

In Eq. (5.2) A_i is always positive for $Im(\omega)>0$, and hence in the absence of beam we have no solution of Eq. (5.5). On the contrary, in the presence of beam B_i is also positive for forward waves and therefore we can get some solutions in Eq. (5.5), while for backward waves B_i becomes negative which implies that there is no solution. These are just what mentioned at the beginning of this section.

For $|\beta|\gg 1$, the usual asymptotic expansion of $\Phi(i\beta)$ can be used which results

$$A(\beta)=-\frac{\sigma_p}{\beta^2}\left(1+\frac{3}{2\beta^2}+\frac{15}{4\beta^4}+\cdots\right). \tag{5.6}$$

Hence we find from Eq. (5.1)

$$\frac{\beta^2}{\beta_s^2}=\sigma_p\left(1+\frac{3}{2\beta^2}+\frac{15}{4\beta^4}+\cdots\right)+\sigma_b\frac{\beta^2}{(\xi-\beta)^2}\,. \tag{5.7}$$

It seems rather complicated to solve the above relation directly as functions of a variable k. Accordingly for the sake of convenience we may express the real and imaginary part of Eq. (5.7) in terms of variables $\chi=(\xi/\beta_r)-1$ and $\mathcal{E}=(\beta_i/\beta_r)^2$. Then the real part can be written as follows

$$\left(\frac{\omega_0}{\omega_s}\right)=\sigma_p\frac{(1-\mathcal{E})}{(1+\mathcal{E})^2}[1+S(\chi,\ \mathcal{E};\ \xi)]+\sigma_b\frac{(\chi^2-\mathcal{E})}{(\chi^2+\mathcal{E})^2}\,, \tag{5.8}$$

where

$$S(\chi,\ \mathcal{E};\ \xi)=\frac{3(\chi+1)^2}{\xi^2}\left[\frac{1}{(1+\mathcal{E})}\left\{2\left(\frac{1-\mathcal{E}}{1+\mathcal{E}}\right)-\left(\frac{1+\mathcal{E}}{1-\mathcal{E}}\right)\right\}+\frac{5(\chi+1)^2}{4\xi^2(1+\mathcal{E})^2}\left\{4\left(\frac{1-\mathcal{E}}{1+\mathcal{E}}\right)^2-3\right\}\right] \tag{5.9}$$

and $\omega_s=(\omega_p^2+\omega_b^2)^{1/2}$ represents the plasma frequency corresponding to the total electron density (n_p+n_b). While the imaginary part becomes for $\mathcal{E}>0$,

$$\left(\frac{\chi^2+\mathcal{E}}{1+\mathcal{E}}\right)^2[1+T(\chi,\ \mathcal{E};\ \xi)]=\sigma\chi\,, \tag{5.10}$$

where

$$T(\chi,\ \mathcal{E};\ \xi)=\frac{3(\chi+1)^2}{\xi^2}\left[\frac{(1-\mathcal{E})}{(1+\mathcal{E})^2}+\frac{5(\chi+1)^2}{4\xi^2(1+\mathcal{E})^2}\left\{3-\frac{16\mathcal{E}}{(1+\mathcal{E})^2}\right\}\right], \tag{5.11}$$

and $\sigma=\sigma_b/\sigma_p=n_b/n_p$. The functions $S(\chi,\ \mathcal{E};\ \xi)$ and $T(\chi,\ \mathcal{E};\ \xi)$ represent the effect due to the thermal motion of electrons in the main plasma.

To see the range that γ becomes positive, we look for the points for $\gamma\to 0$; that is, $\mathcal{E}\to 0$ or $(\omega_0/\omega_s)\to 0$, since $\gamma/\omega_s=\mathcal{E}^{1/2}(\omega_0/\omega_s)$. The case with negligible thermal effects can be simply treated. For $\mathcal{E}\to 0$, Eq. (5.10) yields real roots of χ; $\chi\to 0$ and $\chi\to\sigma^{1/3}$. The root $\chi\to 0$ is excluded since it makes the right hand side of Eq. (5.8) negative. For $\chi\to\sigma^{1/3}$, we get $(\omega_0/\omega_s)\to[(1+\sigma^{1/3})/(1+\sigma)]^{1/2}$, $ku_b/\omega_s\to[(1+\sigma^{1/3})^3/(1+\sigma)]^{1/2}$ and $u_w/u_b\to(1+\sigma^{1/3})^{-1}$. From $(\omega_0/\omega_s)\to 0$ we find $\chi=\mathcal{E}\to\sigma$ and at this limiting point $k\to 0$ and $u_w/u_b\to(1+\sigma)^{-1}$. The maximum value of γ/ω_s lies in an intermediary region between these two limits. In the case with a finite thermal temperature, the limiting value will be more or less corrected. The circumstances described above will be shown in Figs. 2–4.

In Eq. (5.10) we can obtain numerically $\chi(\mathcal{E};\ \xi,\ \sigma)$ with parameters ξ and σ, which, inserted into the right hand side of Eq. (5.8) yields ω_0/ω_s as a function of $\mathcal{E}$. From these the time rate of wave-growth γ/ω_s and the phase velocity of the wave $u_w/u_b=1/(1+\chi)$ is obtained against a variable $\mathcal{E}$. Then we can

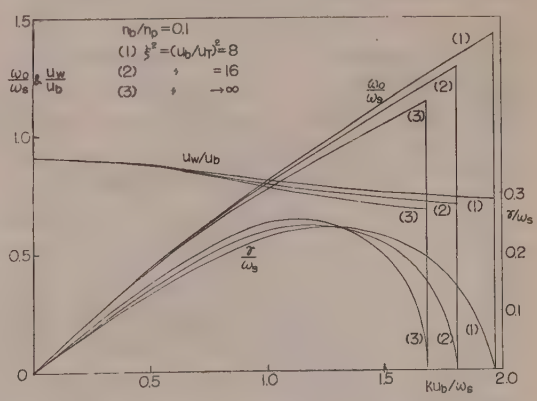

Fig. 2. Effect of mean thermal velocity of electrons in the main plasma on wave characteristics; say, normalized frequency ω_0/ω_s, time-rate of wave-growth γ/ω_s and phase velocity u_w/u_b of excited plasma waves for $n_b/n_p=0.1$.

represent all the quantities as a function of ku_b/ω_s instead of $\mathcal{E}$. Thus we get finally Figs. 2–4.

In Fig. 2 the ratio of the electron density in the beam to that in the plasma is fixed, typically at 0.1. Then it can be regarded as representing the effect due to, on the one hand, the increase of the beam velocity u_b for a definite thermal velocity u_T and, on the other hand, the decrease of the thermal velocity in the main plasma for a definite beam velocity. The figure represents the wave characteristics in detail which for the fixed beam velocity u_b the time rate of wave-growth γ becomes positive in the range of wave number k between zero and some critical value and reaches its maximum in an intermediate value of k, as

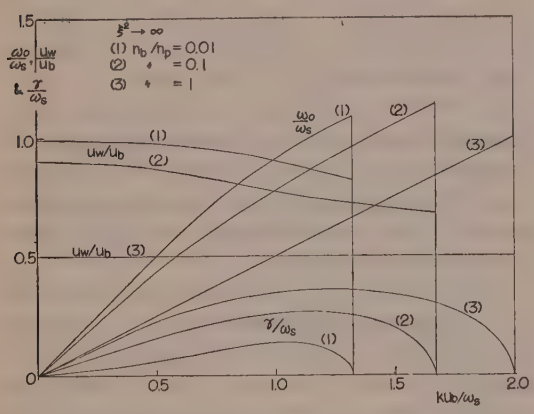

Fig. 3. Wave characteristics for negligible thermal effects with values of ratio n_b/n_p equal to and less than one.

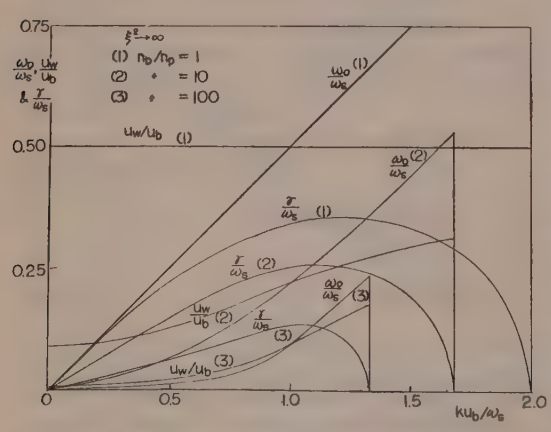

Fig. 4. Wave characteristics for negligible thermal effect with values of ratio n_b/n_p larger than one.

excited wave has a value a little below the beam velocity and decreases gradually from the maximum at $k=0$ to that at the critical mentioned previously. The phase velocity of value of k. Accordingly the frequency of oscillation increases almost linearly with k. For small value of ku_b/ω_s we have oscillations far below the main plasma frequency ω_p or the total plasma frequency ω_s, while for $ku_b/\omega_s \sim 1$ the coupling between the beam and the main plasma is greatest and γ has a maximum in this region. For $ku_b/\omega_s \gg 1$, there can be no growing wave; there remains only stationary or attenuating waves. These are just what has been discussed by Bohm and Gross qualitatively[2].

Fig. 3 shows the variations with the increase of the density in the beam from a small value to the value equal to the density in the main plasma with a negligible thermal velocity. As the beam density approaches to the plasma density, the phase velocity becomes slower until it takes a constant value independent of k or a half velocity of the beam for $n_b/n_p=1$. In the latter case the wave frequency is exactly proportional to k from zero to ω_s; for a maximum γ, however, the frequency ω_0 is rather below the total plasma frequency ω_s and is very near the main plasma frequency ω_p. In Fig. 4 are shown, in a way similar to Fig. 3, the characteristics of growing waves for the case where the beam density is further increased beyond the plasma density. The characteristics in this region of density can be readily obtained from those for lower densities as seen in Fig. 3 in a following way.

In the case when the ratio of density σ has a value σ_1 less than one, as in Fig. 3, the dense main plasma is at rest and the beam running through it. Then we get for this system ω_0/ω_s, γ/ω_s and u_w/u_b as before. Next consider a system having the value of the ratio n_b/n_p equal to $1/\sigma_1$, larger than one. If we slide with the same velocity as that of the beam in this system, the electrons in the beam may be seen at rest and the electrons in the main plasma running to the reverse direction. Then we find the same system as before with the value of ratio σ_1 except the beam velocity reversed, so that the phase velocity becomes negative without change of ω_0 and γ. Hence, back to the original system, we can express the phase velocity and the wave frequency of

the system with the value of density ratio $1/\sigma_1$ as $1-(u_w/u_b)$ and $(\omega_0/\omega_s)(u_b-u_w)/u_w$, by the use of the value of (u_w/u_b) in the system with the value of ratio σ_1. The characteristics for $\sigma=10$ and 100 in Fig. 4 are thus readily obtained from those for $\sigma=0.1$ and 0.01 in Fig. 3, respectively. From both Figs. 3 and 4 we see the following features by the variation of n_b/n_p; the time rate of building-up in excited waves (normalized by ω_s) is greatest at $n_b/n_p=1$ and becomes smaller as the value of n_b/n_p deviates from 1, and its maximum for each case lies near the region of $ku_b/\omega_s\sim 1$. The phase velocity and the normalized oscillating frequency of waves still more decrease with the increase of the ratio n_b/n_p.

§ 6. Effects by Velocity Spread of Electron Beam

Thus far we have not taken into account of the velocity spread in the electron beam. An actual beam will have a velocity spread due to an initial distribution of electron and due to collisions or scatterings of electrons in the medium. Here we shall simply assume the approximate velocity distribution function of the form

$$g_b(u)=\begin{cases} n_b/2\delta & \text{for} \quad u_b-\delta<u<u_b+\delta\,, \\ 0 & \text{otherwise.} \end{cases} \tag{6.1}$$

Then we get, instead of the term $B(\beta)$ in Eq. (5.1)

$$B_\delta(\beta)=\sigma_b/[(\xi-\beta)^2-\eta^2] \tag{6.2}$$

with $\eta=\delta/u_T$. Thus Eqs. (5.8) and (5.10) are modified, resulting finally in the limit of negligible thermal effects in the main plasma

$$\left(\frac{\omega_0}{\omega_s}\right)^2=\frac{1}{1+\sigma}\left[\frac{1-\mathcal{E}}{(1+\mathcal{E})^2}+\sigma\frac{\chi^2-(\mathcal{E}+\varphi)}{(\chi^2+\mathcal{E})^2-2(\chi^2-\mathcal{E})\varphi+\varphi^2}\right] \tag{6.3}$$

and

$$\frac{1}{(1+\mathcal{E})^2}[(\chi^2+\mathcal{E})^2-2(\chi^2-\mathcal{E})\varphi+\varphi^2]=\sigma\chi\,, \tag{6.4}$$

where

$$\varphi=\eta^2/\beta_r^2=(\delta/u_b)^2(1+\chi)^2=\mu(1+\chi)^2 \tag{6.5}$$

with $\mu=(\delta/u_b)^2$. Hence we have

$$\left(\frac{\omega_0}{\omega_s}\right)^2=\frac{(1+\chi)}{(1+\sigma)(1+\mathcal{E})^2}\left[\left(1-\frac{\mathcal{E}}{\chi}\right)-\mu\frac{(1+\chi)}{\chi}\right]. \tag{6.6}$$

and

$$\frac{1}{(1+\mathcal{E})^2}[(\chi^2+\mathcal{E})^2-2(\chi^2-\mathcal{E})\mu(1+\chi)^3+\mu^2(1+\chi)^4]=\sigma\chi\,. \tag{6.7}$$

Fig. 5 represents the effect by the velocity spread obtained from Eqs. (6.6) and (6.7). It is seen that the height of γ/ω_s becomes lower with the increase of the beam spread and that the waves with lower frequency are cut off.

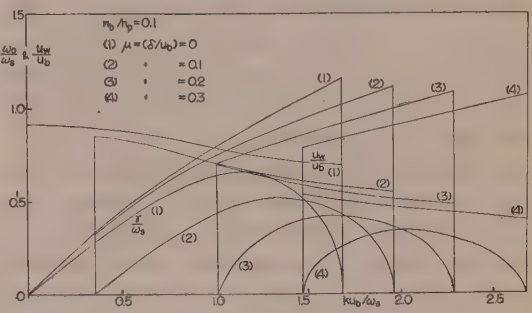

Fig. 5. Effect of velocity spread in the beam on wave characteristics for $n_b/n_p=0.1$.

§ 7. Effects of Collisional Damping

We have neglected the collisional term in the Boltzmann equation in section 2. This may be justified as a good approximation in the low pressure region where the mean free path of electrons is longer than or comparable with the dimension concerned. However, as the mean free path becomes comparatively shorter, the effect of collisions will not be disregarded. Now we shall be contented ourselves with a most simple treatment that $\delta f_1/\delta t|_{coll}$ is replaced by $-\gamma_c f_1$, since the more satisfactory treatment of this term would lead us to a rather complex formula. γ_c is the damping rate by collision and the inverse of the collisional relaxation time τ_c. Setting like this and putting $f_1=\bar{f}_1(t)\,e^{-\gamma_c t}$ in Eq. (2.4), we then find that the function $\bar{f}_1(\boldsymbol{v}, \boldsymbol{x}, t)$ satisfies the same form of equation as Eq. (2.4) in the absence of the collisional term. Consequently using this form of $\bar{f}_1$, we can discuss the wave characteristics as before and obtain the time rate of wave increase $\gamma(k)$, which is just represented in Figs. 2–5. Thus all the oscillatory quantities have such a factor of $\exp[(\gamma-\gamma_c)t]$ that γ must be greater than γ_c in order to give rise to the building-up of oscillations. Therefore the collisional damping becomes more effective when there are some causes that suppress the height of γ. For

instance, the suppression of oscillations due to the velocity spread in the beam will be more considerable, when combined with the collisional effect.

§ 8. Oscillations in a Uniform Plasma Layer

Consider the case when the medium is bounded by sharply defined sheaths and hence the main plasma is contained within a uniform layer having a finite thickness. The boundary sheaths are ideally assumed to have an infinitecimal thickness, so that the thermal electrons in the plasma are all reflected without any loss of energy.

If we excite a growing wave by an electron beam traversing in this layer, we shall have a standing wave with nodes at both ends. A standing wave is decomposed into a forward wave, which propagates to the same direction as that of beam velocity, and a backward wave. According to the arguments in the previous section, the former will interact strongly with the electron beam when almost synchronized, while the latter will not. The forward component of the wave will be delivered the energy from the beam and the backward component will play a regenerative role by which the wave energy will return to the forward component.

In a layer with the thickness of D is contained an integer times a half wavelength of the standing wave, i.e., $D=n\lambda/2$ where n is an integer and λ the wavelength. Hence k has discrete values: $k=2\pi/\lambda=n\pi/D$. These cases are also covered by Figs. 2–5. with the fixed values of k given above. Figs. 3–5 indicate that, as the beam velocity increases, γ starts from a small value, passing through a maximum and then decreases to zero, beyond which the beam is so faster than the wave that the net exchange of energy between them vanishes. It is interesting to note that, for a suitable value of D, there may be several oscillations with different values of k corresponding to the fundamental ($n=1$) and the harmonics ($n\leq 2$); but in frequency they are not exactly the harmonics.

§ 9. Discussions

In seeking the solutions of the dispersion relation we have employed an approximation such as $|\beta|\gg 1$, which means that the phase velocity of the plasma wave u_w is much greater than the thermal velocity u_T in the main plasma. As seen in Figs. 2 and 3, the value of u_w/u_b is very near or at least of the same order of magnitude with one. In consequence, if $\xi=u_b/u_T$ is much larger than 1, so is the case for β, resulting a good approximation. In Fig. 2 the errors introduced are really small for $\xi^2\geq 16$, but it will probably become a little larger for $\xi^2=8$, although we have not evaluated it. For a still lower value of ξ, the approximate expansion used does not give the reasonable result. Then the evaluation will have to be made by the use of a numerical table.

Since the whole treatment is based on the linearized theory, the range of validity of this work is restricted to an initial stage in which the plasma waves build up from the ground level. To find the intensity of excited plasma waves we must obtain the stationary amplitude of enhanced plasma waves, taking into account of the non-linear terms.

We have neglected the decceleration of electrons in the beam which is caused by the energy transfer to the plasma wave or by collisions with the particles in the main plasma It corresponds to the circumstance that such an energy exchange is very small in the linearized theory.

In section 6 we considered the phenomenological spread of the beam velocity, which is due partly to the collisions in the medium and partly to the interaction with the growing plasma wave. It seems probable, in particular, that the latter interaction will be responsible for an abnormal scattering of the beam which has been pointed out by Langmuir[12] and others[2]. This will also be related to the non-linear plasma wave.

We have not examined here the amplification of an traveling plasma wave, in the case of which the fundamental equations are Fourier-analysed in time and Laplace-transformed in space. The dispersion relation thus obtained by similar procedures as before is turned out to have the same expression as Eq. (4.7), where, on the contrary, ω is real and k is complex. Recently a corresponding experiment has successfully performed[13]. In near future we shall present the results for this case in another place.

Acknowledgements

The author would like to thank Professor T. Kihara for his helpful remarks concerning this manuscript. He is also indebted to Professor S. Kojima and Dr. K. Takayama for their interest and valuable discussions.

References

1) A. V. Haeff: Phys. Rev. **74** (1948) 1532; Proc. I. R. E. **37** (1949) 4.
L. S. Nergaard: RCA Rev. **9** (1948) 585.
J. R. Pierce: J. Appl. Phys. **20** (1949) 1060.
J. Feinstein and H. K. Sen: Phys. Rev. **83** (1951) 405.
2) D. Bohm and E. P. Gross: Phys. Rev. **75** (1949) 1851, 1864; ibid. **79** (1950) 992.
3) A. I. Akhiezer and I. B. Feinberg: Ж.Э.Т.Ф. (1951) 1262.
4) M. A. Lampert: J. Appl. Phys. **27** (1956) 5.
5) M. Sumi: J. Phys. Soc. Japan **9** (1954) 88.
6) L. Landau: J. Phys. USSR. **10** (1946) 25.
7) R. W. Twiss: Phys. Rev. **88** (1952) 1392.
8) F. Berz: Proc. Phys Soc. **B68** (1956) 939.
9) N. G. Van Kampen: Physica **21** (1955) 949; ibid. **23** (1957) 641.
10) A. Vlasov: J. Phys. USSR. **9** (1945) 25, 130.
11) B. A. Fock: Diffractive Radiowaves (Book) 1946 (in Russian).
P. L. Bhatnagar, E. P. Gross and M. Krook: Phys. Rev. **94** (1954) 511.
F. Berz: Thesis, University of London (1955).
12) I. Langmuir: Phys. Rev. **26** (1925) 585.
13) G. D. Boyd, L. M. Field and R. W. Gould: Phys. Rev. **109** (1958) 1393.

JOURNAL OF THE PHYSICAL SOCIETY OF JAPAN Vol. 13, No. 12, DECEMBER, 1958

Half-Shade Device for the Precise Measurement of the Principal Angle of Incidence

By Koreo KINOSITA and Sadao NOMURA

Department of Physics and Chemistry, Gakushuin University, Mejiro, Tokyo

(Received September 6, 1958)

Pfund's half-shade analyzer, which originally was devised for the measurement of the Brewsterian angle, φ_B, can be applied to the measurement of the principal angle of incidence, φ_p. Its sensitivity, h, and possible sources of systematic errors are discussed. It is shown that, in the measurement of φ_B, h can be made to approach ∞, but in the measurement of φ_p, h is finite and sometimes very small. A superior half-shade device for the precise determination of φ_p is proposed, which consists of a $\lambda/4$-plate, a half-shade plate of the type of Bravais bi-plate, and an analyzer (polarizing plate). Its sensitivity is fully discussed and the systematic errors are analyzed. Experimental test of the new device is briefly described.

§ 1. Introduction

One of us pointed out several years ago[1] that Pfund's half-shade method[2] for the accurate measurement of the Brewsterian angle can be applied to the measurement of the principal angle of incidence. The angle determined by Pfund's method, φ_P, will be equal to the *Brewsterian angle* of the sample φ_B if the surface of the sample is ideally well-defined. If there is a surface layer on the sample, as would be the case in most experiments, φ_P will be equal to the *principal angle of incidence* φ_p, i.e. the angle of incidence at which one of the principal axes of the vibration ellipse of the reflected beam lies in the plane of incidence. We found[1] that the Pfund angle φ_P of a clean glass surface did change when the humidity of the ambient atmosphere was varied, showing that φ_P, or φ_p, was influenced by the presence of an extremely thin layer of adsorbed water on the sample.

A systematic experiment was started to in-

vestigate the thickness d and the refractive index n of this adsorbed water film as a function of the relative humidity. The specimen is illuminated with a parallel beam of linearly polarized light, and the reflected beam which is elliptically polarized is examined. The principal angle of incidence φ_p is determined by Pfund's method. According to Sissingh and Groosmuller's theory[3] the difference between φ_p and φ_B (the Brewsterian angle of the substrate), $\varphi'=\varphi_p-\varphi_B$, will, in combination with the ellipticity ρ of the reflected beam measured at the angle of incidence equal to φ_B, allow us to calculate both d and n. It was soon noticed, however, that the sensitivity of Pfund's method was unsatisfactory for this purpose.

It is true that measurement of any parameter* of the elliptical vibration other than φ_p may also serve for the evaluation of d and n; but difficulties arising from the fact that the adsorbed film was extremely thin suggested that the above method was the most promising. So we entered into the investigation of a more sensitive half-shade method for the measurement of the principal angle of incidence.

Few workers have been engaged in this problem. Sissingh[3] seems to have succeeded in determining φ_p with a probable error of the order of 1′ or less, but no detailed description of his method of measurement could be found in the literatures available to us. Pfund[2] also claimed a sensitivity of the same order in his measurement of the "Brewsterian angle."** In some of our measurements, however, we were unable to attain this sensitivity.

In § 2 of this paper, the characteristics, including the sensitivity, of Pfund's method will be fully discussed, and an explanation of the discrepancy between Pfund's claim and our experience will be given. In § 3, a new half-shade device suitable for the measurement of the principal angle of incidence will be described with a discussion on its sensitivity and systematic errors. In §§ 2 and 3, $(\partial\delta/\partial\varphi)_p$, i.e. the derivative at φ_p of the phase lag of the s-component behind the p-component, δ, with respect to the angle of incidence, φ, which appears in the expressions of sensitivity and systematic errors, is left as an unknown parameter. This will be evaluated in § 4. Experimentals will be described in § 5.

§ 2. Pfund's Method as a Method of Measurement of the Principal Angle of Incidence

a) *Pfund's Method*

If a parallel beam of linearly polarized light of azimuth α_0 is allowed to fall on the plane, quite well-defined surface (without any surface layer) of a transparent, isotropic medium, the reflected light restores linear polarization, but its azimuth α varies as a function of the angle of incidence φ:

$$\tan\alpha=\tan\alpha_0\cdot\frac{r_s}{r_p}=-\tan\alpha_0\frac{\cos(\varphi-\chi)}{\cos(\varphi+\chi)} \qquad (1)$$

Here r_p and r_s denote the amplitude reflectivities of the two components vibrating parallel and perpendicular to the plane of incidence respectively, and χ the angle of refraction. All azimuths are measured from the plane of incidence (throughout this paper). If φ is increased passing through φ_B, the Brewsterian angle of the sample, α will change from an obtuse into an acute angle coinciding with $\pi/2$ at $\varphi=\varphi_B$ (Fig. 1). As is illustrated in Fig. 1, the change of α in the neighbour-

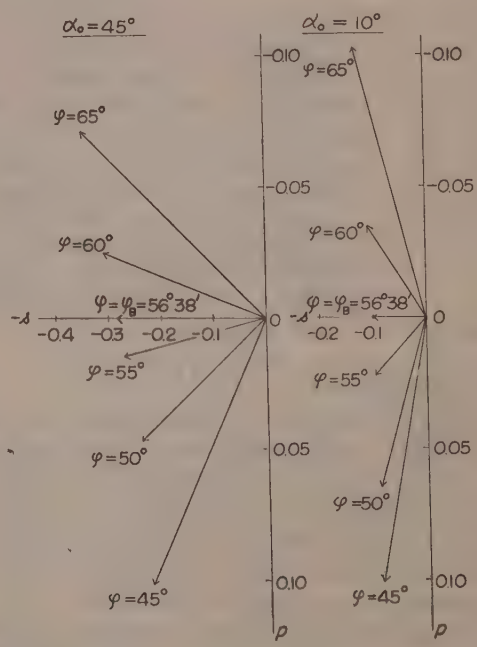

Fig. 1. Change of α as given by Eq. (1) *vs.* the angle of incidence φ. $\varphi_B=56°38'$ ($n_2=1.5183$).

* This of course has to be independent of ρ.

** It is believed that at least some, not to say all, of his measurements gave φ_p instead of φ_B.

hood of $\pi/2$ can be much enhanced if α_0 is made small.

Pfund's method consists in exaggerating the change of α in this way and detecting its coincidence with $\pi/2$ very sensitively by the use of his half-shade analyzer. *Pfund's half-shade analyzer*, illustrated in Fig. 2, is similar in principle to the one employed by Chauvin[4] in improving the sensitivity of the Sénarmont compensator. A half-wave plate* is cut and cemented on the right half of a polarizing plate (Polaroid) so that the fast axis of the

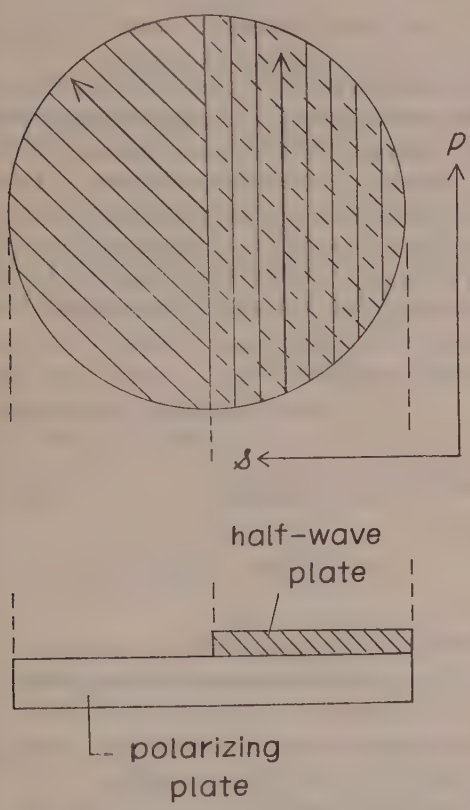

Fig. 2. Pfund's half-shade analyzer.

former is parallel, and the transmission axis of the latter makes an angle of $\pi/4$, with respect to the line of demarcation. This analyzer is used with the half-wave plate away from the observer. The line of demarcation, or the fast axis of the half-wave plate, should be set exactly parallel to the plane of incidence. Now, if the light reflected from the sample be allowed to fall on the analyzer, it will be found, as a rule, that the "half-shade" reveals a large contrast. When $\varphi=\varphi_B$, or when $\alpha=\pi/2$, however, the two halves of the analyzer will appear the same in brightness. Thus Pfund's method gives an accurate means of determining the Brewsterian angle.

This matching of brightness happens, as was remarked before[1], not only when the light reflected from the sample is linearly polarized light of azimuth $\pi/2$, but also when it is elliptically polarized with one of its axes in the plane of incidence (See §2–c). Hence Pfund's method can also be applied to the measurement of the principal angle of incidence.

b) *The Brightness of the Two Halves of the Field*

Now we shall proceed to quantitative discussions of Pfund's method outlined above, with the aim of examining its ability as a method of measuremet of the principal angle of incidence. For this, we shall adopt the Poincaré sphere representation[5].

In Pfund's original treatment, he assumed that

I. The light reflected from the sample is linearly polarized.

II. The birefringent plate is an exact half-wave plate with its axis exactly parallel to the plane of incidence.

and

III. The transmission axis of the polarizing plate makes an angle exactly equal to $\pi/4$ with the plane of incidence.

In place of these, our calculation will be based on the following generalized postulates.

I′. The reflected beam is elliptically polarized light represented by

$$\boldsymbol{E}_p=A\exp i(\omega t+\delta) \quad \text{and} \quad \boldsymbol{E}_s=B\exp i\omega t \qquad (2)$$

where ω stands for the circular frequency of light. For the convenience of the discussion

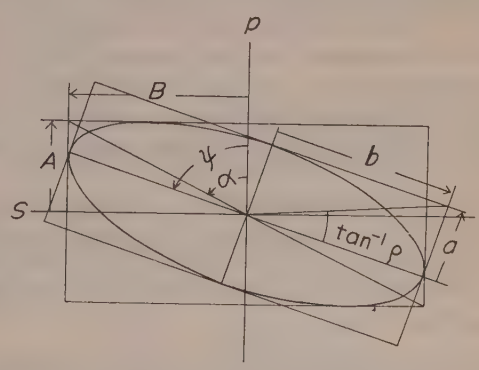

Fig. 3. Parameters of the elliptical orbit of the reflected beam. $\rho=b/a$: ellipticity. ψ: azimuth of the ellipse.

* Pfund used a sheet of Cellophane.

to be given below, we define α by

$$\tan\alpha = B/A = \tan\alpha_0 \cdot |r_s/r_p| \ . \quad (0 \leq \alpha \leq \pi/2) \tag{3}$$

Here r_p and r_s denote tne complex amplitude reflectivities of the p- and s-component respectively. A, B and α are illustrated in Fig. 3 together with the other parameters ρ, the ellipticity, and ψ, the azimuth, of the elliptical orbit of the reflected beam.

II′. The azimuth of the fast axis and the phase lead of the birefringent plate are assumed to be ξ_1 and δ_1 respectively.

III′. The azimuth of the transmission axis of the polarizing plate is assumed to be σ.

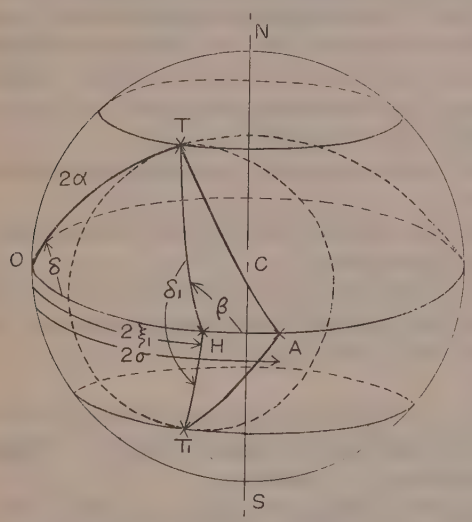

Fig. 4. Poincaré sphere representation. T: light to be examined. H: birefringent plate. A: analyzer (polarizing plate).

The incident light, the birefringent plate and the polarizing plate are represented by points T, H and A on the Poincaré sphere respectively (Fig. 4). If we assume the intensity of light reflected from the sample to be unity and neglect the loss due to reflection and absorption by the half-shade analyzer, the intensities transmitted by the left half (polarizer) and the right half (birefringent plate +polarizing plate), J_1 and J_2 respectively, are calculated as follows.

It can be shown in general that when elliptically polarized light, represented by point T on the Poincaré sphere, is incident on a polarizer represented by point A, the transmitted intensity is equal to the square of cosine of one half the geodesic distance between T and A. Thus

$$\begin{aligned} J_1 &= \cos^2 \tfrac{1}{2}\mathrm{AT} = \tfrac{1}{2}(1+\cos \mathrm{AT}) \\ &= \tfrac{1}{2}(1+\cos 2\sigma \cos 2\alpha + \sin 2\sigma \sin 2\alpha \cos\delta) \end{aligned} \tag{4}$$

The last transformation is deduced from the cosine rule for spherical triangles.

In order to obtain J_2, we have, in the first place, to find the point T_1 on the sphere which represents the polarization of light after passing through the birefringent plate. This is obtained by simply rotating the sphere by δ_1 about the axis HC (C is the center of the sphere). Thus T moves to T_1 in Fig. 4. Calculations using spherical trigonometry show that

$$\begin{aligned} \cos \mathrm{HT}_1 &= \cos \mathrm{HT} \\ &= \cos 2\alpha \cos 2\xi_1 + \sin 2\alpha \sin 2\xi_1 \cos\delta \ , \end{aligned} \tag{5}$$

$$\sin \mathrm{HT}_1 = \sin 2\alpha \sin\delta / \sin\beta \tag{6}$$

where

$$\beta = \angle\mathrm{THA} = \pi - \angle\mathrm{THO} \ , \tag{7}$$

and

$$\begin{aligned} \cos \mathrm{AT}_1 &= \cos 2(\sigma-\xi_1) \cos \mathrm{HT}_1 \\ &\quad + \sin 2(\sigma-\xi_1) \sin \mathrm{HT}_1 \cos(\beta+\delta_1) \ , \end{aligned} \tag{8}$$

Substituting for $\cos \mathrm{HT}_1$ and $\sin \mathrm{HT}_1$ from Eqs. (5) and (6), and using the relation

$$\begin{aligned} \cot\beta &= -\cot\angle\mathrm{THO} \\ &= (\cos 2\xi_1 \cos\delta - \cot 2\alpha \sin 2\xi_1)/\sin\delta \end{aligned} \tag{9}$$

which can be obtained by applying the cotangent rule to the spherical triangle THO, we get

$$\begin{aligned} J_2 = \tfrac{1}{2}(1+\cos \mathrm{AT}_1) &= \tfrac{1}{2}\{1+\cos 2(\sigma-\xi_1)(\cos 2\alpha \cos 2\xi_1 + \sin 2\alpha \sin 2\xi_1 \cos\delta)\} \\ &\quad + \sin 2(\sigma-\xi_1) \sin 2\alpha \{(\cos 2\xi_1 \cos\delta - \cot 2\alpha \sin 2\xi_1) \cos\delta_1 - \sin\delta_1 \sin\delta\} \ . \end{aligned} \tag{10}$$

The difference in brightness of the two halves, I, can be obtained by subtracting Eq. (10) from Eq. (4).

$$\begin{aligned} I = J_1 - J_2 = \tfrac{1}{2}[&\cos 2\sigma \cos 2\alpha + \sin 2\sigma \sin 2\alpha \cos\delta \\ &- \cos 2(\sigma-\xi_1)(\cos 2\alpha \cos 2\xi_1 + \sin 2\alpha \sin 2\xi_1 \cos\delta) \\ &- \sin 2(\sigma-\xi_1) \sin 2\alpha \{(\cos 2\xi_1 \cos\delta - \cot 2\alpha \sin 2\xi_1) \cos\delta_1 - \sin\delta_1 \sin\delta\}] \ . \end{aligned} \tag{11}$$

c) *Conditions for the Matching of Brightness*

Pfund assumed that $\xi_1=0$, $\delta_1=\pi$ and $\sigma=\pi/4$, and that the light incident on the half-shade analyzer is linearly polarized ($\delta=0$). But in the following discussion inevitable errors in ξ_1 and δ_1 will be taken into account and an arbitrary value for σ assumed. If

$$\xi_1=\Delta\xi_1 \quad \text{and} \quad \delta_1=\pi+\Delta\delta_1 \tag{12}$$

where $\Delta\xi_1$ and $\Delta\delta_1$ are small quantities, the difference in brightness of the two halves will be

$$I=\sin 2\sigma \sin 2\alpha \cos\delta-2\Delta\xi_1(\sin 2\sigma \cos 2\alpha+\cos 2\sigma \sin 2\alpha \cos\delta) -\tfrac{1}{2}\Delta\delta_1 \sin 2\sigma \sin 2\alpha \sin\delta\ . \tag{13}$$

Case 1. $\delta=0$: When light reflected from the sample is linearly polarized ($\delta=0$), Eq. (13) becomes

$$I=\sin 2\sigma \sin 2\alpha-2\Delta\xi_1 \sin 2(\sigma+\alpha) \tag{14}$$

showing that, if $\Delta\xi_1=0$, the two halves of the field will appear the same in brightness when

$$\alpha=0\ , \quad \pm\pi/2\ , \quad \text{or} \quad \pi\ . \tag{15}$$

$\alpha=(\pm)\ \pi/2$ is realized when $\varphi=\varphi_B$. It is clear that, for the half-shade analyzer to be useful, σ may be given any value other than 0 and π. The best result is obtained when $\sigma=\pm\pi/4$, however, in which case $|\sin 2\sigma|$, and accordingly the contrast of the half-shade, reaches a maximum (See also § 2–d).

If there is a small error $\Delta\xi_1$ in the azimuth of the fast axis of the half-wave plate, the matching at $\alpha=\pi/2$ will be shifted to

$$\alpha=(\pi/2)+\Delta\alpha\ . \tag{16}$$

It can easily be shown that

$$\Delta\alpha=\Delta\xi_1\ , \tag{17}$$

if the second and the higher power terms in $\Delta\xi_1$ and $\Delta\alpha$ are neglected. But it would be preferable to represent the shift in terms of the angle of incidence. For this purpose, we calculate the derivative at $\varphi=\varphi_B$ of α, which is given by Eq. (1), with respect to φ. This is represented in terms of the refractive index n_2 of the sample (the substrate) as follows:

$$\left(\frac{\partial\alpha}{\partial\varphi}\right)_B=-\cot\alpha_0\cdot\frac{(n_2^2+1)^2}{2n_2^3}\ . \tag{18}$$

Accordingly, the shift from φ_B of the angle of incidence at which the matching is observed is given by

$$\Delta\varphi=-\tan\alpha_0\cdot\frac{2n_2^3}{(n_2^2+1)^2}\cdot\Delta\xi_1\ . \tag{19}$$

A small error in the phase lead of the half-wave plate, $\Delta\delta_1$, causes no error in the determination of φ_B.

Case 2. $\delta\neq 0$: If the light reflected from the sample is elliptically polarized ($\delta\neq 0$), and $\Delta\xi_1=\Delta\delta_1=0$, Eq. (13) becomes

$$I=\sin 2\sigma \sin 2\alpha \cos\delta\ , \tag{20}$$

showing that the difference in brightness of the two halves disappears when one of the following conditions is satisfied:

$$\delta=\pm\pi/2\ , \tag{21}$$

$$\alpha=0\ , \quad \pm\pi/2\ , \quad \text{or} \quad \pi\ . \tag{22}$$

But Eq. (22) is to be discarded, because it is contradictory to the assumption that $\delta\neq 0$. Eq. (21) proves that the principal angle of incidence φ_p can be determinded by Pfund's method. The sensitivity depends on σ and α.

If there are small errors in ξ_1 and δ_1, the matching at $\delta=\pi/2$ will be shifted to

$$\delta=(\pi/2)+\Delta\delta\ . \tag{23}$$

Calculation neglecting the higher order terms shows that

$$\Delta\delta=-(2\Delta\xi_1 \cot 2\alpha+\tfrac{1}{2}\Delta\delta_1)\ . \tag{24}$$

It is again preferable to represent the shift in terms of the angle of incidence. This can be written as

$$\Delta\varphi=\Delta\delta/(\partial\delta/\partial\varphi)_p\ , \tag{25}$$

but evaluation of $(\partial\delta/\partial\varphi)_p$, the derivative of δ with respect to φ at $\varphi=\varphi_p$, is accompanied by some complications. This will be discussed later (§ 4).

d) *Sensitivity*

In discussing the sensitivity, the errors $\Delta\xi_1$ and $\Delta\delta_1$ are insignificant and will be neglected.

Case 1. $\delta=0$: In this case, the matching in brightness is observed when $\alpha=\pi/2$, or when $\varphi=\varphi_B$. The intensity transmitted by the half-shade analyzer in this case is given by

$$J_1=J_2=\tfrac{1}{2}(1-\cos 2\sigma)=J_B\ . \tag{26}$$

Now, if the angle of incidence is changed by a small amount, say $\Delta\varphi$, a contrast in brightness will arise, which is represented by

$$H=\left|\frac{J_1(\varphi_B+\Delta\varphi)-J_2(\varphi_B+\Delta\varphi)}{2J_B}\right|=\left|\frac{(\partial I/\partial\varphi)_B}{2J_B}\cdot\Delta\varphi\right| . \tag{27}$$

Substituting from Eqs. (14) into Eq. (27) and making use of the relations $\Delta\xi_1=0$ and $\partial I/\partial\varphi=\partial I/\partial\alpha\cdot\partial\alpha/\partial\varphi$, we get

$$H=\left|\frac{2\sin 2\sigma}{1-\cos 2\sigma}\cdot\left(\frac{\partial\alpha}{\partial\varphi}\right)_B\cdot\Delta\varphi\right|=h|\Delta\varphi| . \tag{28}$$

The coefficient

$$h=\left|\frac{2\sin 2\sigma}{1-\cos 2\sigma}\right|\cdot\left|\left(\frac{\partial\alpha}{\partial\varphi}\right)_B\right| \tag{29}$$

shall be called the *sensitivity* of the half-shade analyzer. In this expression, $(\partial\alpha/\partial\varphi)_B$ is independent of the characteristics of the analyzer and has been calculated in Eq. (18). $|2\sin 2\sigma/(1-\cos 2\sigma)|$ reaches a maximum when $\sigma=\pm\pi/4$ or $\pm 3\pi/4$, which is equal to 2. Hence the maximum sensitivity attainable is given by

$$h_{\max}=2\left|\left(\frac{\partial\alpha}{\partial\varphi}\right)_B\right|=2|\cot\alpha_0|\,\frac{(n_2^2+1)^2}{2n_2^3} . \tag{30}$$

Case 2. $\delta\neq 0$: If $\delta\neq 0$, the matching is observed when $\delta=\pi/2$, or when $\varphi=\varphi_p$. The intensity of light transmitted by the half-shade analyzer in this case is given by

$$J_1=J_2=\tfrac{1}{2}(1+\cos 2\sigma\cos 2\alpha)=J_p . \tag{31}$$

The contrast in brightness which is revealed when $\varphi=\varphi_p+\Delta\varphi$ will be

$$H=\left|\frac{J_1(\varphi_p+\Delta\varphi)-J_2(\varphi_p+\Delta\varphi)}{2J_p}\right|$$
$$=\left|\frac{\left(\frac{\partial I}{\partial\alpha}\right)_p\left(\frac{\partial\alpha}{\partial\varphi}\right)_p+\left(\frac{\partial I}{\partial\delta}\right)_p\left(\frac{\partial\delta}{\partial\varphi}\right)_p}{2J_p}\cdot\Delta\varphi\right| . \tag{32}$$

Substituting from Eq. (20) and Eq. (31) into Eq. (32), and making use of the relation that $\delta=\pi/2$ at φ_p, we get

$$H=h|\Delta\varphi| , \tag{33}$$

where

$$h=\left|\frac{\sin 2\sigma\sin 2\alpha}{1+\cos 2\sigma\cos 2\alpha}\cdot\left(\frac{\partial\delta}{\partial\varphi}\right)_p\right| \tag{34}$$

represents the sensitivity. In this expression, α and $(\partial\delta/\partial\varphi)_p$ are independent of the characteristics of the half-shade analyzer. The maximum sensitivity is obtained when $\sigma=\pm\pi/4$ or $\pm 3\pi/4$ and* $\alpha=\pm\pi/4$ or $\pm 3\pi/4$, and is represented by

$$h_{\max}=|(\partial\delta/\partial\varphi)_p| . \tag{35}$$

* α can be varied through α_0. See Eq. (3).

e) *Discussion*

Pfund's half-shade analyzer is an excellent device for the accurate determination of the Brewsterian angle φ_B. If the azimuth of the linearly polarized light incident on the sample, α_0, is made small enough, the sensitivity will approach infinity (Eqs. (29), (30)), and, at the same time, the systematic error in the determination of φ_B due to the error in the azimuth of the half-wave plate will become negligibly small (Eq. (19)). There is a practical limit for the sensitivity, of course, because the intensity of light reflected from the sample approaches zero as α_0 approaches zero, but this is a character common to all sensitive half-shade devices.

In contrast, Pfund's analyzer is not very adequate for the determination of the principal angle of incidence φ_p. Firstly, a systematic error is hardly avoidable. The shift due to $\Delta\xi_1$ (Eq. (24)) can be cancelled by making α equal to $\pi/4$, which happens to be the condition for the maximum sensitivity; but there is no avoiding the shift due to $\Delta\delta_1$ but using an absolutely correct half-wave plate. Secondly, the sensitivity is rather poor. As was shown above, the maximum attainable sensitivity is equal to $|(\partial\delta/\partial\varphi)_p|$. If the sample be a piece of metal whose surface is ideally well-defined, $|(\partial\delta/\partial\varphi)_p|$ will be finite, as is shown by Fresnel's formulae. In case the sample be a transparent medium coated with a thin transparent film, this quantity will approach infinity only when nd, the optical thickness of the film, is *extremely* small; otherwise it will be finite and often rather small (See § 4).

Thus the discrepancy between Pfund's experience and our own is explained.

One of the conclusions of the discussions given above is that if one intends to measure the Brewsterian angle of a dielectric sample by Pfund's analyzer one should be extremely careful to avoid an alien film on its surface. Indeed, if the sample is kept in the unconditioned atmosphere, the water vapour will be adsorbed on it, and the measurement will give φ_p which is determined by the *composite surface* (the surface of the sample + the adsorbed film of water). The difference between φ_p and φ_B is small and could be neglected for most practical purposes, but the lowering of sensitivity might be serious.

§ 3. New Half-Shade Device

a) *Description of the device*

A new half-shade apparatus useful for the accurate determination of the principal angle of incidence was devised on the basis of the discussions given in § 2. It consists of a quarter-wave plate Q, a half-shade plate of the type of Bravais bi-plate H, and an analyzer (polarizing plate) A arranged in line as is illustrated in Fig. 5.

The fast axis of Q is set parallel to the plane of incidence.

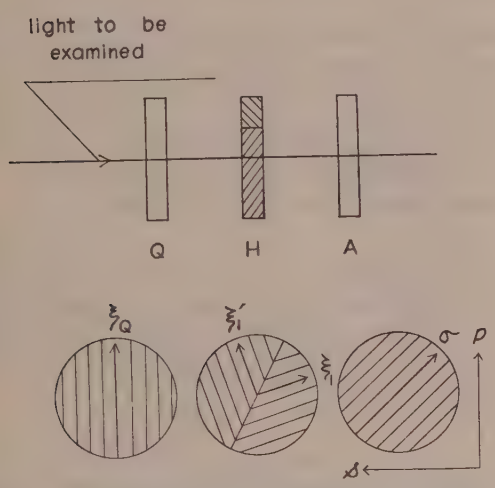

Fig. 5. New half-shade device for the determination of the principal angle of incidence. Q: quarter-wave plate. H: half-shade plate. A: analyzer (polarizing plate).

The half-shade plate H is prepared by cutting a uniform sheet of mica along a line which forms an angle of $\pi/4$ with the fast axis and cementing the two halves on to a sheet of glass, one half being turned over before it is cemented. Thus, if the azimuth of the fast axis of the right half is ξ_1, that of the left half ξ_1' is equal to $\xi_1+(\pi/2)$. As is evident from the method of preparation, the absolute values of the phase lead caused by passage through the two halves are identical. We shall denote it by δ_1.

The transmission axis of A is set in an azimuth of σ. σ, as well as ξ_1, is adjustable.

b) *Principle*

Let the beam reflected from the sample be elliptically polarized light as given by Eq. (2). The p- and s-component of the beam after passage through Q are given by

$$\boldsymbol{E}_p = A \exp i\left(\omega t+\delta+\frac{\pi}{2}\right)$$

and

$$\boldsymbol{E}_s = B \exp i\omega t$$

respectively. Hence, the intensity transmitted by the right half of the half-shade device, J_1, can be obtained by substituting $\delta+(\pi/2)$ for δ in Eq. (10). If we substitute $\xi_1'=\xi_1+(\pi/2)$ for ξ_1 in the expression of J_1 thus obtained, it will represent J_2, the intensity transmitted by the left half. It can easily be shown that

$$\left.\begin{matrix} J_1 \\ J_2 \end{matrix}\right\} = \tfrac{1}{2}[1+\cos 2(\sigma-\xi_1)(\cos 2\alpha \cos 2\xi_1 - \sin 2\alpha \sin 2\xi_1 \sin \delta)$$
$$-\sin 2(\sigma-\xi_1) \sin 2\alpha\{(\cos 2\xi_1 \sin \delta + \cot 2\alpha \sin 2\xi_1) \cos \delta_1 \pm \cos \delta \sin \delta_1\}] \ . \qquad (36)$$

In the last term the positive sign is for J_1 and the negative for J_2 respectively.

The difference in brightness of the two halves I is given by

$$I = J_1 - J_2 = -\sin 2(\sigma-\xi_1) \sin 2\alpha \sin \delta_1 \cos \delta \qquad (37)$$

Eq. (37) implies that the both halves will appear the same in brightness if $\delta=\pi/2$, or $\varphi=\varphi_p$, irrespective of the values of σ, α and ξ_1.

Needless to say, the measurement will give the Brewsterian angle φ_B if $\delta=0$, or if the beam reflected from the sample be linearly polarized

c) *Sensitivity*

The contrast in brightness of the two halves of the field, H, which is to be observed when $\varphi=\varphi_p+\Delta\varphi$, where $\Delta\varphi$ is small, is given by Eq. (32). J_p, the transmitted intensity at $\varphi=\varphi_p$, is obtained by substituting $\pi/2$ for δ in Eq. (36):

$$J_p = \tfrac{1}{2}\{1+\cos 2(\sigma-\xi_1) \cos 2(\alpha+\xi_1)$$
$$-\sin 2(\sigma-\xi_1) \sin 2(\alpha+\xi_1) \cos \delta_1\} \ . \qquad (38)$$

Substitution from Eqs. (37) and (38) into Eq. (32) gives

$$H = h|\Delta\varphi| \ , \qquad (39)$$

where

$$h = |\sin 2(\sigma-\xi_1) \sin 2\alpha \sin \delta_1$$
$$\times\{1+\cos 2(\sigma-\xi_1) \cos 2(\alpha+\xi_1)$$
$$-\sin 2(\sigma-\xi_1) \sin 2(\alpha+\xi_1) \cos \delta_1\}^{-1}$$
$$\times(\partial\delta/\partial\varphi)_p| \qquad (40)$$

represents the sensitivity of the half-shade device.

Here we have a free choice in the value of δ_1; σ and ξ_1 are adjustable parameters of the half-shade device; α also is adjustable through α_0 (See Eq. (3)). The most useful combination of the values of these parameters is found to be the following:

$$\delta_1 \approx \pi/2\,, \quad \sigma-\xi_1 \approx \pi/2 \quad \text{and} \quad \alpha+\sigma \approx \pi/2$$

Let us assume

$$\left.\begin{aligned} \delta_1 &= (\pi/2)+\Delta\delta_1\,, \\ \sigma-\xi_1 &= (\pi/2)+\varepsilon\,, \\ \alpha+\sigma &= (\pi/2)+\eta\,. \end{aligned}\right\} \tag{41}$$

Substitution into Eq. (40) yields

$$h=\left|\frac{\varepsilon \sin 2\alpha}{2\varepsilon^2-2\varepsilon\eta+\eta^2}\cdot\left(\frac{\partial\delta}{\partial\varphi}\right)_p\right|, \tag{42}$$

if we neglect the third powers of the small quantities $\Delta\delta_1$, ε and η. Eq. (42) implies that h tends to infinity if the half-shade plate is made of (approximate) quarter-wave plates, σ is set equal to $(\pi/2)-\alpha$, and ξ_1 is allowed to approach $(\sigma-\pi/2)$, or $-\alpha$. It is evident that the best value for α is $\pm\pi/4$.

In practice there is a limit for sensitivity, of course, because if $(\sigma-\xi_1)$ is exactly equal to $\pi/2$ the transmitted intensity J_p will be zero and the observation will be impossible. This point, together with the experimental procedures for realizing the conditions given above, will be discussed later (§ 5).

d) *Error analysis*

Possible sources of a shift $\Delta\varphi$ in the value of φ_p determined by means of this new half-shade device are:

an error in the azimuth of Q: $\Delta\xi_Q$,

an error in the phase lead of Q: $\Delta\delta_Q$,

and

an error in the orthogonality of the fast axes of the two halves of H: $\Delta\xi_1'$.

1°. *Shift due to* $\Delta\xi_Q$. If the azimuth of the quarter-wave plate be $\Delta\xi_Q$ instead of zero, the quarter-wave plate will be represented by point Q′ on the equator of the Poincaré sphere distant by $2\Delta\xi_Q$ from the Greenwich meridian (Fig. 6). If we regard the vertical great circle crossing the equator at Q′ as new zero longitude, α, δ, ξ_1 and σ will be α', δ', ξ_1' and σ' respectively, where*

$$\sin 2\alpha' = \sin 2\alpha \sin\delta/\sin\delta'\,, \tag{43}$$

$$\cot\delta' = \frac{(\cos\delta\cos 2\Delta\xi_Q - \cot 2\alpha \sin 2\Delta\xi_Q)}{\sin\delta}\,, \tag{44}$$

$$2\xi' = 2(\xi-\Delta\xi_Q)\,, \tag{45}$$

and

$$2\sigma' = 2(\sigma-\Delta\xi_Q)\,. \tag{46}$$

Substitution from the above equations into Eq. (37) gives

$$I = -\sin 2(\sigma-\xi_1)\sin 2\alpha \sin\delta_1 \times(\cos\delta\cos 2\Delta\xi_Q - \cot 2\alpha \sin 2\Delta\xi_Q)\,. \tag{47}$$

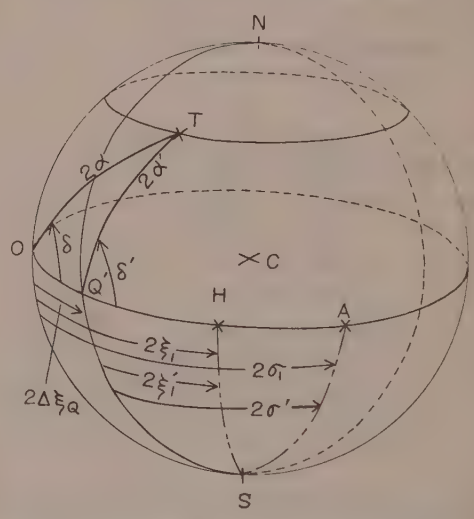

Fig. 6. Illustrating the transformations Eq. (43)—Eq. (46).

Accordingly, if $\Delta\xi_Q$ is small enough, the matching in brightness of the two halves of the field will be observed when $\delta=(\pi/2)+\Delta\delta$ where

$$\Delta\delta = -2\cot 2\alpha\cdot\Delta\xi_Q\,. \tag{48}$$

In terms of the angle of incidence, the matching will be observed at $\varphi_p+\Delta\varphi$ instead of φ_p, where

$$\Delta\varphi = \Delta\delta\Big/\left(\frac{\partial\delta}{\partial\varphi}\right)_p = \left\{-2\cot 2\alpha\Big/\left(\frac{\partial\delta}{\partial\varphi}\right)_p\right\}\Delta\xi_Q\,. \tag{49}$$

At $\alpha=\pm\pi/4$ (the best values for obtaining high sensitivity), $\cot 2\alpha=0$, and $\Delta\xi_Q$ will cause no shift in the determination of φ_p in so far as $(\partial\delta/\partial\varphi)_p \neq 0$.

2°. *Shift due to* $\Delta\delta_Q$. If the phase lead of the quarter-wave plate be $(\pi/2)+\Delta\delta_Q$, the difference in brightness of the two halves, I, will become

$$I = -\sin 2(\sigma-\xi_1)\sin 2\alpha \sin\delta_1(\cos\delta - \Delta\delta_Q \sin\delta)\,. \tag{50}$$

* As for the derivation of Eq. (44), refer to Eq. (9).

Hence the matching will be observed when $\delta=(\pi/2)+\Delta\delta$, or $\varphi=\varphi_p+\Delta\varphi$, where

$$\Delta\delta=\Delta\delta_Q\,,\quad \Delta\varphi=\Delta\delta_Q\Big/\left(\frac{\partial\delta}{\partial\varphi}\right)_p\,. \tag{51}$$

This systematic error can be eliminated by rotating the quarter-wave plate Q by $\pi/2$ and making the measurement over again. In the latter case,

$$I=\sin 2(\sigma-\xi_1)\sin 2\alpha\sin\delta_1(\cos\delta+\Delta\delta_Q\sin\delta)\,, \tag{52}$$

and the matching will be observed when $\delta=(\pi/2)+\Delta\delta'$, or $\varphi=\varphi_p+\Delta\varphi'$, where

$$\Delta\delta'=-\Delta\delta_Q\,,\quad \Delta\varphi'=-\Delta\delta_Q\Big/\left(\frac{\partial\delta}{\partial\varphi}\right)_p\,. \tag{53}$$

Thus the arithmetic mean of the two readings of the angle of incidence at which the matching is observed before and after rotating Q will give the correct value of the principal angle of incidence.

3°. *Shift due to* $\Delta\xi_1'$. Another systematic error will arise if the fast axes of the both halves of the half-wave plate are not exactly perpendicular to each other. If we let

$$\xi_1'=\xi_1+(\pi/2)+\Delta\xi_1'\,, \tag{54}$$

the difference in brightness of the two halves, I, will be given by the following equation.

$$\begin{aligned}I=J_1-J_2=&-\sin 2(\sigma-\xi_1)\sin 2\alpha\sin\delta_1\cos\delta\\&-\Delta\xi_1'[(1-\cos\delta_1)\{\sin 2(\sigma-\xi_1)(\cos 2\alpha\cos 2\xi_1-\sin 2\alpha\sin 2\xi_1\sin\delta)\\&-\cos 2(\sigma-\xi_1)(\cos 2\alpha\sin 2\xi_1+\sin 2\alpha\cos 2\xi_1\sin\delta)\}-\cos 2(\sigma-\xi_1)\sin 2\alpha\sin\delta_1\cos\delta]\,.\end{aligned} \tag{55}$$

Thus the matching will be observed when $\delta=(\pi/2)+\Delta\delta$, or $\varphi=\varphi_p+\Delta\varphi$, where

$$\left.\begin{aligned}\Delta\delta&=\frac{\sin 2(\sigma-\alpha-2\xi_1)(1-\cos\delta_1)}{\sin 2(\sigma-\xi_1)\sin 2\alpha\sin\delta_1}\Delta\xi_1'\,,\\ \Delta\varphi&=\Delta\delta\Big/\left(\frac{\partial\delta}{\partial\varphi}\right)_p\,.\end{aligned}\right\} \tag{56}$$

But this systematic error can be eliminated again by rotating the half-shade plate by $\pi/2$, making another measurement, and taking the arithmetic mean of the angles of incidence at which the matching is observed before and after the rotation.

§ 4. On $(\partial\delta/\partial\varphi)_p$

We have left $(\partial\delta/\partial\varphi)_p$ as an unknown parameter in Eqs. (25), (34), (42), (49), (51), (53) and (56). As is evident from these equations, the numerical value of this derivative may have an important influence on sensitivity and possible systematic errors of the half-shade device concerned.

It is well-known that if the reflecting surface is a perfectly well-defined surface of a transparent medium, $(\partial\delta/\partial\varphi)_p$, or $(\partial\delta/\partial\varphi)_B$, is equal to infinity; and if it is a perfectly well-defined metallic surface, $(\partial\delta/\partial\varphi)_p$ is equal to a finite value determined by the refractive index and the absorption coefficient of the metal. But as for the surface of a transparent medium covered with a thin transparent film, the investigation of which aroused our interest in the present study, hardly any quantitative informations on $(\partial\delta/\partial\varphi)_p$ have been available. Detailed examination of the dependence of δ on φ in the last case implies some interesting problems*, but here we shall confine ourselves to an approximate evaluation of $(\partial\delta/\partial\varphi)_p$ for a number of typical cases, which is immediately needed. The calculation will be based on Drude's theory[7].

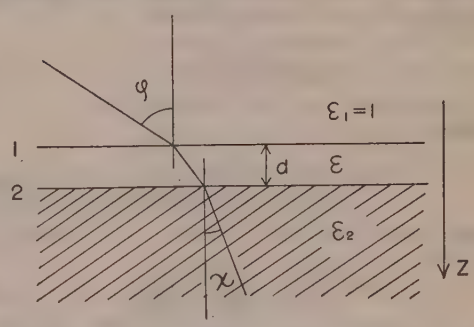

Fig. 7. Illustration for Eq. (57).

Let a parallel beam of linearly polarized light of azimuth α_0 fall on the composite surface as illustrated in Fig. 7. The dielectric constants of the ambient medium, the film (of thickness $d\ll\lambda$), and the substrate are assumed to be 1, ε $(=n^2)$, and ε_2 $(=n_2^2)$ respectively. The inward normal of the surface shall be taken as the z-axis. If we neglect the second and the higher order terms in d/λ, the ratio in amplitude of the p-component to the

* These will be fully discussed in another paper to be published in the near future.

s-component of the reflected beam is given by[7]

$$\frac{R_p}{R_s}=\frac{E_p r_p}{E_s r_s}=-\cot\alpha_0\frac{\cos(\varphi+\chi)}{\cos(\varphi-\chi)}\times\left(1+i\frac{4\pi}{\lambda}\cdot\frac{\varepsilon_2}{1-\varepsilon_2}\cdot\frac{\cos\varphi\sin^2\varphi}{\sin^2\varphi-\varepsilon_2\cos^2\varphi}\cdot\eta\right). \tag{57}$$

Here φ and χ denote the angle of incidence and the angle of refraction respectively, and

$$\eta=p-d(1+\varepsilon_2)+q\varepsilon_2\,, \tag{58}$$

where

$$p=\int_1^2\varepsilon dz \quad\text{and}\quad q=\int_1^2\frac{1}{\varepsilon}dz\,. \tag{59}$$

The limits of the integrals are the upper (1) and the lower (2) boundaries of the film (See Fig. 7).

Now, if the angle of incidence is in the neighbourhood of φ_p, we can put

$$\varphi=\varphi_p+\Delta=\varphi_B+\Delta\,. \quad (\Delta\ll 1) \tag{60}$$

The last transformation is allowed because the difference between φ_p and φ_B is neglected in the Drude approximation. Substituting from Eq. (60) into Eq. (57), and using the relations that $\tan\varphi_B$ is equal to $\sqrt{\varepsilon_2}$ and that the ratio of the imaginary part to the real part of r_p/r_s is equal to $\tan\delta$, we obtain the following equation:

$$\tan\delta=\frac{a+b\Delta}{\Delta}\cdot\eta\,. \tag{61}$$

Here

$$a=\frac{2\pi}{\lambda}\frac{\varepsilon_2\sqrt{\varepsilon_2}}{(1-\varepsilon_2^2)\sqrt{1+\varepsilon_2}}\,, \tag{62}$$

and

$$b=\frac{2\pi}{\lambda}\frac{\varepsilon_2(2-\varepsilon_2)}{(1-\varepsilon_2^2)\sqrt{1+\varepsilon_2}}\,. \tag{63}$$

Differentiation of Eq. (61) with respect to φ, or Δ (it is evident that $\partial/\partial\varphi=\partial/\partial\Delta$), gives

$$\frac{\partial\delta}{\partial\varphi}=-\frac{1}{a+2b\Delta}\cdot\frac{1}{\eta}\,. \tag{64}$$

Thus the approximate value of $(\partial\delta/\partial\varphi)_p$ is given by

$$\left(\frac{\partial\delta}{\partial\varphi}\right)_p=-\frac{1}{a\eta}\,. \tag{65}$$

If we apply the mean value theorem* to Eqs. (58) and (59), and put

$$\eta=(\bar{\varepsilon}-\varepsilon_2)(\bar{\varepsilon}-1)d/\bar{\varepsilon}\,, \tag{66}$$

Eq. (65) is rewritten as

$$\left(\frac{\partial\delta}{\partial\varphi}\right)_p=-\frac{A}{d} \tag{67}$$

where

$$A=\frac{\lambda}{2\pi}\frac{(1-\varepsilon_2^2)\sqrt{1+\varepsilon_2}}{\varepsilon_2\sqrt{\varepsilon_2}}\frac{\bar{\varepsilon}}{(\bar{\varepsilon}-\varepsilon_2)(\bar{\varepsilon}-1)}\,. \tag{68}$$

If $\bar{\varepsilon}=1$, $\bar{\varepsilon}=\varepsilon_2$, or $d=0$, i.e. if there is no film on the surface,

$$(\partial\delta/\partial\varphi)_p=\infty\,.$$

In this case, φ_p is reduced to φ_B, and this equation represents the well-known phase jump of the p-component at the Brewsterian angle.

Table I. Evaluation of $(\partial\delta/\partial\varphi)_p$. For λ5461 Å.

$n_1=\sqrt{\varepsilon_1}$	$\bar{n}=\sqrt{\bar{\varepsilon}}$	$n_2=\sqrt{\varepsilon_2}$	A
1.00	1.33	1.70	5.24×10^3 Å
1.00	1.46	1.70	6.27×10^3
1.00	1.33	1.50	9.10×10^3
1.00	1.46	1.50	33.4×10^3

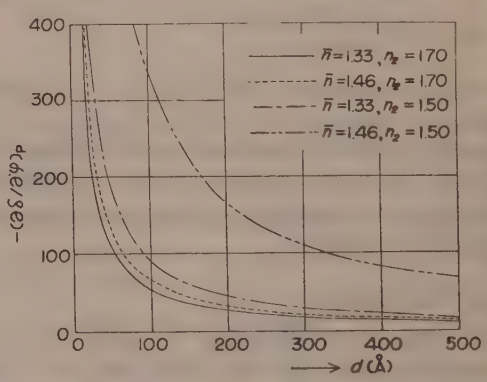

Fig. 8. $-(\partial\delta/\partial\varphi)_p$ *vs.* film thickness d. $\bar{n}$: mean refractive index of the film. n_2: refractive index of the substrate.

The numerical evaluation of $(\partial\delta/\partial\varphi)_p$ given in Table I and Fig. 8 is based on Eqs. (67) and (68). It will be seen that $|(\partial\delta/\partial\varphi)_p|$ approaches infinity if nd ($\bar{n}=\sqrt{\bar{\varepsilon}}$) draws toward zero, but it decreases monotonously as nd increases. In case $|(\partial\delta/\partial\varphi)_p|$ is small, the sensitivity of Pfund's method as a method of measurement of φ_p is inevitably poor (Eq. (35)). In contrast, the sensitivity of the new method can be made to approach infinity by means of the procedures described in § 3–c, even when $|(\partial\delta/\partial\varphi)_p|$ is very small.

* The mean values of ε as defined by $p=\bar{\varepsilon}d$ and $q=d/\bar{\varepsilon}$ are not necessarily identical. But we equate them, just as Drude[7] *et al.* did.

§ 5. Experimentals

A half-shade device of the type described in § 3 was mounted on a polarizing spectrometer* recently constructed in this laboratory, and was put to a series of experimental tests.

The optical system is schematically illustrated in Fig. 9. P: the polarizer (Polaroid), Q: the quarter-wave plate** of mica, H: the half-shade plate prepared according to the description given in § 3, and A: the analyzer (Polaroid), are so arranged that each can be independently rotated about the optical axis.

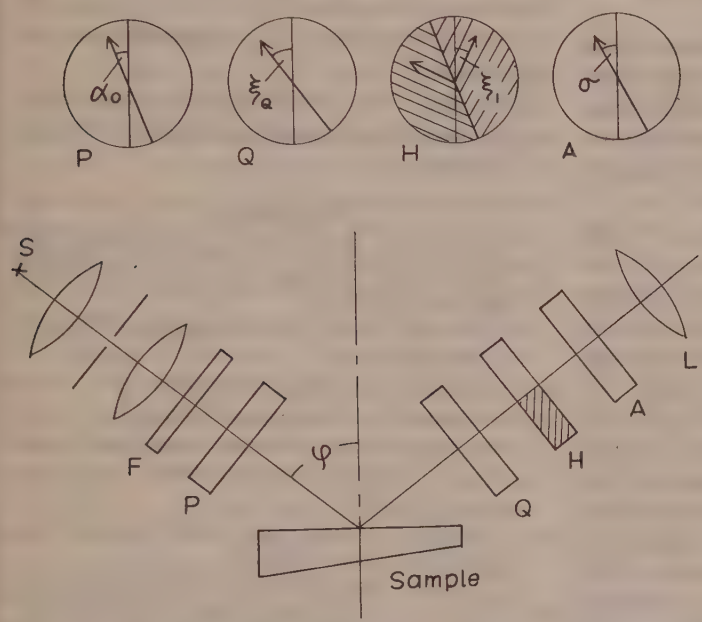

Fig. 9. Polarization spectrometer. S: light source (ultra-high pressure Hg-lamp). F: interference filter for monochromatization. P: polarizer. Q: quarter-wave plate. A: analyzer. L: viewing lens.

The errors of the quarter-wave plate and the half-shade plate we employed, as expressed in terms of $\Delta\delta_Q$, $\Delta\delta_1$ and $\Delta\xi_1'$, were as follows:

$$\Delta\delta_Q = +2°53' \pm 10' ,$$
$$\Delta\delta_1 = +2°10' \pm 10' ,$$
$$\Delta\xi_1' = \pm(1°02' \pm 1') .$$

These values, in combination with the numerical value of $(\partial\delta/\partial\varphi)_p$ which can be read from Fig. 8, will allow us to estimate the order of magnitude of the shift (or the systematic error) $\Delta\varphi$ inevitably introduced in a single measurement of φ_p. It will be seen that $\Delta\varphi$ may sometimes amount to several minutes of arc or more, but this is by no means serious because we can eliminate it easily by an appropriate combination of measurements, as was described in § 3–d.

The following arrangements are to be made prior to the measurement of the principal angle of incidence.

1°. The reflecting surface of the sample is set exactly horizontal (perpendicular to the plane of incidence).

2°. The fast axis of Q is set parallel to the plane of incidence as exactly as possible ($\xi_Q=0$).

3°. The transmission axis of A is carefully set so that it makes an angle of $\pi/4$ with the plane of incidence ($\sigma=\pi/4$).

4°. The fast axis of the right half of H is so set that it makes an angle approximately (but not exactly) equal to $-\pi/4$ with the plane of incidence ($\xi_1 \approx -\pi/4$).

5°. The azimuth of the transmission axis of P is temporarily fixed at an arbitrary value between zero and $\pi/4$ ($0 < \alpha_0 < \pi/4$).

Now, if the half-shade device is viewed through L (Fig. 9), the both halves of the field will in general reveal a remarkable contrast; on changing the angle of incidence, however, one will be able to find out an angle of incidence where the both halves appear the same in brightness—the principal angle of incidence φ_p. In this stage, however, one could determine φ_p only with an allowance of say scores of minutes or more. Thereupon one turns P, the polarizer, in order to let α approach toward $\pi/4$. The residual, invisible contrast will be enhanced by this operation, and when it is most exaggerated, α ($=\tan^{-1} B/A$. See Eq. (3)) will be equal to $\pi/4$. This is the condition for maximizing the sensitivity on the one hand and minimizing

* This is equipped with an air-tight sample chamber convenient for the study of adsorption. The sample is held horizontally, and the collimator as well as the telescope-arm can be rotated in a vertical plane by means of a pantagraph mechanism. Details of this instrument will be described elsewhere.

** For λ 5461Å.

the systematic error due to $\Delta\xi_Q$ on the other. If this is accomplished, the half-shade device will work pretty satisfactorily, but the sensitivity can be improved still further by rotating H, the half-shade plate, so that ξ_1 approaches toward $-\pi/4$. As was pointed out before, this operation is accompanied by darkening of the field, and if ξ_1 is exactly equal to $-\pi/4$ the entire field will appear completely dark, but the sensitivity of the half-shade device will be sufficiently increased before the field becomes too dark. Thus the principal angle of incidence φ_p can be determined with a probable error less than 1′.

We have to repeat the measurement over again after rotating the quarter-wave plate, and the half-shade plate, in order to eliminate the systematic errors due to $\Delta\delta_Q$ and $\Delta\xi_1'$ respectively, but no further details will have to be described here.

The excellent sensitivity of the new device was confirmed in our measurements of φ_p on newly polished surfaces of optical glasses kept in extremely desiccated atmosphere. But in these measurements Pfund's half-shade analyzer was found to work equally well. In either case, the measurements carried out independently by two observers agreed within 1′. This is only natural if one considers that in these measurements the surface layers must have been extremely thin, because in that case $|(\partial\delta/\partial\varphi)_p|$ approaches infinity (Fig. 8), and accordingly the sensitivity of Pfund's method will be very great (Eq. (35)).

In the measurements on *aged* polished surfaces of optical glasses, the new device proved to work as well as before, while Pfund's analyzer failed to determine φ_p within 1°.

These data will be published, in the near future, in a paper on some optical investigations of the adsorption of water vapour on polished glass surfaces, in which this new method is being employed.

Acknowledgements

The authors derived valuable suggestions from the works[8] of Mr. Y. Doi, the Government Mechanical Laboratory, Tokyo, to whom they wish to express their cordial gratitude. Thanks are also due to Mr. M. Takasima for his useful discussions and cooperation in experiments.

This work was partly supported by the Scientific Research Expenditure of the Ministry of Education.

References

1) K. Kinosita: J. Opt. Soc. Amer. **43** (1953) 924.
2) A. H. Pfund: J. Opt. Soc. Amer. **26** (1936) 453; **31** (1941) 679.
3) R. Sissingh und J. Th. Groosmuller: Physik. Z. **27** (1926) 518.
4) Chauvin: J. de phys. (2) **9** (1890) 21.
5) H. Poincaré: *Théorie mathématique de la lumière*, Gauthiers-Villars, Paris (1892), tom. **2**, p. 12. *See also* H. G. Jerrard: J. Opt. Soc. Amer. **44** (1954) 634.
6) A. Bravais: Comt. rend. **32** (1851) 112; Ann. Chim. Phys. **43** (1855) 131.
7) P. Drude: *Lehrbuch der Optik*, Leipzig (1912).
8) Y. Doi: J. Appl. Phys. Japan. **25** (1956) 85; 133.
Y. Doi and Y. Ishida: J. Mech. Lab. **8** (1954) 122; 178.

JOURNAL OF THE PHYSICAL SOCIETY OF JAPAN Vol. 13, No. 12, DECEMBER, 1958

On the Theory of Fluids

By Kazuo HIROIKE

Department of Physics, Tokyo Institute of Technology, Oh-Okayama, Meguro, Tokyo

(Received August 7, 1958)

The "netted ring approximation" is proposed. Several thermodynamic properties are derived by means of this approximation. The radial distribution function is also derived, the expression of which is similar to one based on the netted chain approximation of Rushbrooke and Scoins. The possibility of a phase change in the gas of hard spheres is pointed out.

§ 1. Introduction

In a paper with the same title as ours, Rushbrooke and Scoins[1] have related the theory of fluids based on the radial distribution function to the direct correlation function of scattering theory. They have shown that the second approximation to the direct correlation function is related to the netted chain approximation to the radial distribution function. The netted chain approximation is as follows: The radial distribution function can be expressed as a power series in density. In order to obtain an approximate radial distribution function, Montroll and Mayer[2] have collected particular terms from the series and arranged in a closed form. The approximation adopted by them has been called the simple chain approximation by Rushbrooke[3], which has been shown to give the same result as Green's linear theory.[4),5] Rushbrooke and and Scoins[1] have taken account of some terms omitted by Montroll and Mayer. This is called the netted chain approximation.

Rushbrooke and Scoins[1] have argued that their theory effects a considerable improvement on earlier theories. It has been, however, pointed out by us[6] that their theory fails to derive the Helmholtz free energy in a consistent way. In the present paper we shall eliminate this failing without changing the essential feature of their theory. Our method, which will be presented in the following section, is similar to one of Montroll and Mayer or Rushbrooke and Scoins, but is different from it in starting with the density expansion of the Helmholtz free energy instead of the radial distribution function.* Our approximation will be called the "netted ring approximation."

Although in the present paper we are concerned with the equilibrium theory of classical fluids, the mathematical process similar to ours, that is, the process of collecting particular terms from a series, has been adopted by several authors in other fields of research. Among them Montroll and Ward[7] have generalized the simple chain approximation to the case of quantum statistics and have shown that in the case of the electron gas the classical limit of the approximation leads to the Debye-Hückel theory** while the low temperature limit leads to the Gell-Mann-Brueckner equation for the correlation energy of the ground state. The netted ring approximation adopted by us may be able to find its quantum statistical counterpart in the formulation of Montroll and Ward, though such an attempt will not be made in the present paper.

§ 2. Netted Ring Approximation

We shall consider a classical fluid of volume V and temperature T composed of N interacting molecules. The interaction energy will be assumed to be written as a sum of terms, each depending only on the distance apart r_{ij} of two molecules i and j, namely

$$\sum_{N\geq i>j\geq 1}\sum \phi(r_{ij}) .$$

In such a case, the Helmholtz free energy A can be given by the well known expression[9]

$$\frac{A}{NkT}=\log\left(\frac{h^2}{2\pi mkT}\right)^{3/2}\frac{\rho}{e}-\sum_{n=1}^{\infty}\frac{1}{n+1}\beta_n\rho^n , \tag{1}$$

* A general theory on this line is being constructed by Abe and Morita.

** Ono[8] has also shown that in the case of electrolytes Green's linear theory, which is equivalent to the classical simple chain theory, leads to the Debye-Hückel theory.

where ρ is the number density N/V, k the Boltzmann constant and h the Planck constant. The irreducible integrals β_n's are defined by

$$\beta_n=\frac{1}{n!\,V}\iint\cdots\int\sum_{n+1\geq i>j\geq 1}\prod_{\substack{\text{All products which are more}\\ \text{than singly connected.}}}\alpha_{ij}\,d\boldsymbol{r}_1 d\boldsymbol{r}_2\cdots d\boldsymbol{r}_{n+1}\,, \tag{2}$$

where

$$\alpha_{ij}=\alpha(r_{ij})=\exp(-\phi(r_{ij})/kT)-1 \tag{3}$$

The integral β_n is a sum of integrals of various types as can be seen from Eq. (2).

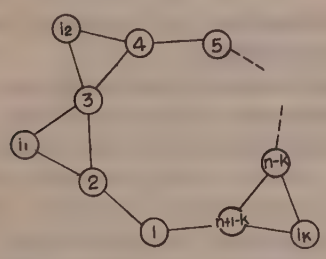

Fig. 1.

By the "netted ring approximation" we will mean that we consider only the netted ring integrals, the integrands of which are illustrated by Fig. 1. In Fig. 1 $n+1$ molecules are represented by numbered circles and a factor α_{ij} occurring in the integrand under consideration is represented by a line drawn between two circles i and j. For brevity the function α_{ij} will be called the interaction between molecules i and j. The integral illustrated by Fig. 1 can be transformed as follows. Firstly we shall integrate over molecule i_1. Because of the fact

$$\int\alpha(r_{2,i_1})\alpha(r_{i_1,3})d\boldsymbol{r}_{i_1}$$
$$=\int\beta^2(u)\exp(i\boldsymbol{u}\boldsymbol{r}_{23})\,d\boldsymbol{u}\equiv a(r_{23})\,,^* \tag{4}$$

where

$$\beta(u)=\frac{1}{(2\pi)^{3/2}}\int\alpha(r)\exp(-i\boldsymbol{u}\boldsymbol{r})\,d\boldsymbol{r}\,,^* \tag{5}$$

the integration over molecule i_1 leads to the effect that the interaction between molecules 2 and 3 is changed from $\alpha(r_{23})$ into $\alpha(r_{23})a(r_{23})$. The integration over molecules i_2 leads to the similar effect, and so forth. Thus the integration over molecules $i_1, i_2, \cdots$, and i_k changes Fig. 1 into Fig. 2, where a double line shows that the interaction between two molecules is given by $\alpha(r)a(r)$ and a single line means $\alpha(r)$ as in Fig. 1. In Fig. 2 there are $(n+1-2k)$ single lines and k double lines. The integration over molecules $1, 2, \cdots$, and $n+1-k$ can be carried out with the help of Fourier transform. Lastly the netted ring integral illustrated by Fig. 1 is written as

$$V(2\pi)^{3/2\cdot(n-1)}\int\{\beta(u)\}^{n+1-2k}\{\gamma(u)\}^k\,d\boldsymbol{u}\,, \tag{6}$$

where

$$\gamma(u)=\frac{1}{(2\pi)^3}\int\alpha(r)a(r)\exp(-i\boldsymbol{u}\boldsymbol{r})\,d\boldsymbol{r}\,.^* \tag{7}$$

Let $N_n^{(k)}$ be the number of netted ring integrals considered above in β_n. The number of different ways in which k molecules may be selected from $n+1$ molecules, irrespective of the order of choice, is $(n+1)!/k!(n+1-k)!$.

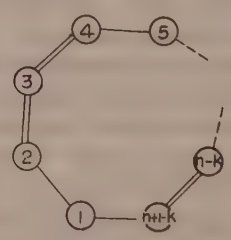

Fig. 2.

The number of different ways in which $n+1-k$ molecules may be placed in a ring is $(n-k)!/2$. The number of different ways in which k molecules may be placed in $n+1-k$ positions is $(n+1-k)!/(n+1-2k)!$. Hence

$$N_n^{(k)}=\frac{(n+1)!}{k!(n+1-k)!}\times\frac{(n-k)!}{2}\times\frac{(n+1-k)!}{(n+1-2k)!}$$
$$=\frac{(n+1)!}{2}\,\frac{{}_{n+1-k}C_k}{n+1-k}\,, \tag{8}$$

where ${}_nC_k$ is the number of combinations in which k objects may be selected from n distinguishable objects, namely

$${}_nC_k=\frac{n!}{k!(n-k)!}\,.$$

The integer k cannot be larger than $n+1-k$, that is,

$$k\leq\frac{n+1}{2}\,.$$

* The definition of $a(r)$, $\beta(u)$ and $\gamma(u)$, denoted by Eqs. (4), (5) and (7) respectively, is equivalent to one given in reference 6. It is also equivalent to the definition given in reference 1 except for $\gamma(u)$, where the function $\gamma(u)$ differs from ours by a factor $(2\pi)^{3/2}$.

Putting Eqs. (6) and (8) together, we shall obtain as a contribution $\beta_n^{(n.r)}$ of the netted ring integrals to β_n

$$\beta_n^{(n.r)}=\int du(2\pi)^{3/2\cdot(n-1)}\sum_{k=0}^{k\leq(n+1)/2}\frac{1}{2}\frac{n+1}{n-k+1}{}_{n-k+1}C_k\ \{\beta(u)\}^{n+1-2k}\{\gamma(u)\}^k \quad \text{for} \quad n\geq 4\,. \tag{9}$$

The above consideration cannot be applied for $n\leq 3$. And so we shall put for $n\leq 3$

$$\left.\begin{aligned}
&\beta_3^{(n.r)}=\int du\left[\frac{1}{2}(2\pi)^4\{\beta(u)\}^4+(2\pi)^4\gamma(u)\{\beta(u)\}^2\right],\\
&\beta_2^{(n.r)}=\beta_2=\int du\left[\frac{1}{2}(2\pi)^{3/2}\{\beta(u)\}^3\right],\\
\text{and}\quad &\beta_1^{(n.r)}=\beta_1=(2\pi)^{3/2}\beta(0)\,.
\end{aligned}\right\} \tag{9'}$$

A straightforward calculation leads to

$$\begin{aligned}\sum_{n=1}^{\infty}\beta_n^{(n.r)}\rho^n=\bar{\rho}\beta(0)+\frac{1}{(2\pi)^{3/2}}\frac{1}{\bar{\rho}}\int du\Bigg[&\frac{1}{2}\frac{\bar{\rho}\beta(u)+2\bar{\rho}^2\gamma(u)}{1-\bar{\rho}\beta(u)-\bar{\rho}^2\gamma(u)}-\frac{1}{2}\bar{\rho}\beta(u)\\
&-\frac{1}{2}\bar{\rho}^2\beta^2(u)-\bar{\rho}^2\gamma(u)-\frac{3}{2}\bar{\rho}^3\beta(u)\gamma(u)-\bar{\rho}^4\beta^2(u)\gamma(u)-\bar{\rho}^4\gamma^2(u)\Bigg],\end{aligned} \tag{10}$$

where

$$\bar{\rho}=(2\pi)^{3/2}\rho\,. \tag{11}$$

With the help of

$$\sum_{n=1}^{\infty}\frac{1}{n+1}\beta_n^{(n.r)}\rho^n=\frac{1}{\bar{\rho}}\int_0^{\bar{\rho}}\left[\sum_{n=1}^{\infty}\beta_n^{(n.r)}\rho^n\right]d\bar{\rho}\,,$$

the Helmholtz free energy $A^{(n.r)}$ in the netted ring approximation is obtained as follows:

$$\begin{aligned}\frac{A^{(n.r)}}{NkT}=\log\left(\frac{h^2}{2\pi mkT}\right)^{3/2}\frac{\rho}{e}-\frac{1}{2}\bar{\rho}\beta(0)+\frac{1}{(2\pi)^{3/2}}\frac{1}{\bar{\rho}}\int du\Bigg[&\frac{1}{2}\log\{1-\bar{\rho}\beta(u)-\bar{\rho}^2\gamma(u)\}\\
&+\frac{1}{2}\bar{\rho}\beta(u)+\frac{1}{4}\bar{\rho}^2\beta^2(u)+\frac{1}{2}\bar{\rho}^2\gamma(u)+\frac{1}{2}\bar{\rho}^3\beta(u)\gamma(u)+\frac{1}{4}\bar{\rho}^4\beta^2(u)\gamma(u)+\frac{1}{4}\bar{\rho}^4\gamma^2(u)\Bigg].\end{aligned} \tag{12}$$

§ 3. Several Thermodynamic Quantities and Radial Distribution Function

From Eq. (12), by means of the usual thermodynamic relations, all the other thermodynamic properties of the system may be derived. We shall give the expressions for the pressure p, the internal energy E and the chemical potential μ in the following. Hereafter we shall drop the superscript letter $(n.r)$ which means the netted ring approximation.

$$\begin{aligned}\frac{p}{\rho kT}=1-\frac{1}{2}\bar{\rho}\beta(0)+\frac{1}{(2\pi)^{3/2}}\frac{1}{\bar{\rho}}\int du\Bigg[&-\frac{1}{2}\log\{1-\bar{\rho}\beta(u)-\bar{\rho}^2\gamma(u)\}-\frac{1}{2}\frac{\bar{\rho}\beta(u)+2\bar{\rho}^2\gamma(u)}{1-\bar{\rho}\beta(u)-\bar{\rho}^2\gamma(u)}\\
&+\frac{1}{4}\bar{\rho}^2\beta^2(u)+\frac{1}{2}\bar{\rho}^2\gamma(u)+\bar{\rho}^3\beta(u)\gamma(u)+\frac{3}{4}\bar{\rho}^4\beta^2(u)\gamma(u)+\frac{3}{4}\bar{\rho}^4\gamma^2(u)\Bigg].\end{aligned} \tag{13}$$

$$\begin{aligned}\frac{E}{NkT}=\frac{3}{2}+\frac{1}{2}\bar{\rho}T\frac{\partial\beta(0)}{\partial T}+\frac{1}{2}\frac{1}{(2\pi)^{3/2}}\frac{1}{\bar{\rho}}\int du\frac{\{\bar{\rho}\beta(u)+\bar{\rho}^2\gamma(u)\}^2}{1-\bar{\rho}\beta(u)-\bar{\rho}^2\gamma(u)}T\frac{\partial}{\partial T}\{\bar{\rho}\beta(u)+\bar{\rho}^2\gamma(u)\}\\
-\frac{1}{4}\frac{1}{(2\pi)^{3/2}}\frac{1}{\bar{\rho}}\int duT\frac{\partial}{\partial T}\{\bar{\rho}^4\beta^2(u)\gamma(u)\}\,.\end{aligned} \tag{14}$$

$$\frac{\mu}{kT}=\log\left(\frac{h^2}{2\pi mkT}\right)^{3/2}\rho-\bar{\rho}\beta(0)+\frac{1}{(2\pi)^{3/2}}\frac{1}{\bar{\rho}}\int du\Big[-\frac{1}{2}\frac{\bar{\rho}\beta(u)+2\bar{\rho}^2\gamma(u)}{1-\bar{\rho}\beta(u)-\bar{\rho}^2\gamma(u)}$$
$$+\frac{1}{2}\bar{\rho}\beta(u)+\frac{1}{2}\bar{\rho}^2\beta^2(u)+\bar{\rho}^2\gamma(u)+\frac{3}{2}\bar{\rho}^3\beta(u)\gamma(u)+\bar{\rho}^4\beta^2(u)\gamma(u)+\bar{\rho}^4\gamma^2(u)\Big]. \tag{15}$$

It has been proved[10] that the radial distribution function $g(r)$ is related to the Helmholtz free energy A by

$$g(r)=\frac{2V}{N^2}\left(\frac{\delta A}{\delta\phi}\right)_r, \tag{16}$$

where $(\delta A/\delta\phi)_r$ is defined as follows. When the interaction potential ϕ is varied by $\Delta\phi$, the corresponding first order variation, with respect to $\Delta\phi$, of A is denoted by $F[\Delta\phi(r')]$, which is a linear functional of $\Delta\phi$. Then

$$\left(\frac{\delta A}{\delta\phi}\right)_r\equiv F[\delta(\boldsymbol{r}-\boldsymbol{r}')].$$

The above definition is generalized to quantities other than the Helmholtz free energy. Relation (16) will be used for the calculation of $g(r)$ from Eq. (12), which gives the following expression for $g(r)$

$$g(r)=\frac{kT}{\rho}\Big[-\bar{\rho}\left(\frac{\delta\beta(0)}{\delta\phi}\right)_r-\frac{1}{(2\pi)^{3/2}}\frac{1}{\bar{\rho}}\int du\frac{\{\bar{\rho}\beta(u)+\bar{\rho}^2\gamma(u)\}^2}{1-\bar{\rho}\beta(u)-\bar{\rho}^2\gamma(u)}\left\{\bar{\rho}\left(\frac{\delta\beta(u)}{\delta\phi}\right)_r+\bar{\rho}^2\left(\frac{\delta\gamma(u)}{\delta\phi}\right)_r\right\}$$
$$+\frac{1}{2}\frac{1}{(2\pi)^{3/2}}\frac{1}{\bar{\rho}}\int du\left\{2\bar{\rho}^4\beta(u)\gamma(u)\left(\frac{\delta\beta(u)}{\delta\phi}\right)_r+\bar{\rho}^4\beta^2(u)\left(\frac{\delta\gamma(u)}{\delta\phi}\right)_r\right\}\Big]. \tag{17}$$

By the definition of $(\delta/\delta\phi)_r$-operation we shall obtain

$$\left(\frac{\delta\alpha(r')}{\delta\phi}\right)_r=-\frac{1}{kT}\exp(-\phi(r)/kT)\,\delta(\boldsymbol{r}-\boldsymbol{r}')$$

and hence

$$\left(\frac{\delta\beta(u)}{\delta\phi}\right)_r=\frac{1}{(2\pi)^{3/2}}\int d\boldsymbol{r}'\left(\frac{\delta\alpha(r')}{\delta\phi}\right)_r\exp(-i\boldsymbol{u}\boldsymbol{r}')=-\frac{1}{(2\pi)^{3/2}}\frac{\exp(-\phi(r)/kT)}{kT}\exp(-i\boldsymbol{u}\boldsymbol{r}),$$

$$\left(\frac{\delta a(r')}{\delta\phi}\right)_r=2\int du\,\beta(u)\left(\frac{\delta\beta(u)}{\delta\phi}\right)_r\exp(i\boldsymbol{u}\boldsymbol{r}')=-\frac{2}{(2\pi)^{3/2}}\frac{\exp(-\phi(r)/kT)}{kT}\int du\,\beta(u)\exp(i\boldsymbol{u}(\boldsymbol{r}'-\boldsymbol{r})),$$

$$\left(\frac{\delta\gamma(u)}{\delta\phi}\right)_r=\frac{1}{(2\pi)^3}\int d\boldsymbol{r}'\left[\left(\frac{\delta\alpha(r')}{\delta\phi}\right)_r a(r')+\alpha(r')\left(\frac{\delta a(r')}{\delta\phi}\right)_r\right]\exp(-i\boldsymbol{u}\boldsymbol{r}')$$
$$=-\frac{1}{(2\pi)^{3/2}}\frac{\exp(-\phi(r)/kT)}{kT}\Big[\frac{1}{(2\pi)^{3/2}}a(r)\exp(-i\boldsymbol{u}\boldsymbol{r})$$
$$+\frac{2}{(2\pi)^3}\iint du'\,d\boldsymbol{r}'\,\beta(u')\alpha(r')\exp(i\boldsymbol{u}'\boldsymbol{r}'-i\boldsymbol{u}'\boldsymbol{r}-i\boldsymbol{u}\boldsymbol{r}')\Big].$$

The use of the above equations in Eq. (17) gives

$$g(r)=\exp(-\phi(r)/kT)\Big[1+\{1+\rho a(r)\}f_0(r)+2\rho\int f_0(r')\alpha(r')\alpha(\boldsymbol{r}'-\boldsymbol{r})\,d\boldsymbol{r}'$$
$$-\frac{1}{2}\rho^2a^2(r)-2\rho^2\int a(r')\alpha(r')\alpha(\boldsymbol{r}'-\boldsymbol{r})\,d\boldsymbol{r}'\Big], \tag{18}$$

where

$$f_0(r)=\frac{1}{(2\pi)^{3/2}}\frac{1}{\bar{\rho}}\int du\,\frac{\{\bar{\rho}\beta(u)+\bar{\rho}^2\gamma(u)\}^2}{1-\bar{\rho}\beta(u)-\bar{\rho}^2\gamma(u)}\exp(-i\boldsymbol{ur})\,, \tag{19}$$

or

$$\begin{aligned} g(r)=\exp(-\phi(r)/kT)\Big[&1+\{1+\rho a(r)\}\overline{f_0}(r)+2\rho\int\overline{f_0}(r')\alpha(r')\alpha(\boldsymbol{r}'-\boldsymbol{r})\,d\boldsymbol{r}' \\ &-\{1+\rho a(r)\}^2\alpha(r)-\frac{1}{2}\rho^2a^2(r) \\ &-\int\{2\rho\alpha^2(r')+2\rho^2\alpha(r')a(r')+2\rho^2\alpha^2(r')a(r')\}\,\alpha(\boldsymbol{r}'-\boldsymbol{r})\,d\boldsymbol{r}'\Big]\,, \end{aligned} \tag{18'}$$

where

$$\overline{f_0}(r)=\frac{1}{(2\pi)^{3/2}}\frac{1}{\bar{\rho}}\int du\,\frac{\bar{\rho}\beta(u)+\bar{\rho}^2\gamma(u)}{1-\bar{\rho}\beta(u)-\bar{\rho}^2\gamma(u)}\exp(-i\boldsymbol{ur})\,. \tag{19'}$$

It should be noted that the number density ρ, instead of $\bar{\rho}$, is used in Eqs. (18) and (18′).

As is well known, the pressure p and the internal energy E can be expressed in terms of $g(r)$ as[11]

$$\frac{p}{\rho kT}=1-\frac{\rho}{6kT}\int r\frac{d\phi(r)}{dr}g(r)\,d\boldsymbol{r} \tag{20}$$

and

$$\frac{E}{NkT}=\frac{3}{2}+\frac{\rho}{2kT}\int\phi(r)g(r)\,d\boldsymbol{r}\,. \tag{21}$$

We have proved in the previous paper[10] that relation (16) is consistent with Eqs. (20) and (21). In our present case we can verify directly that the use of Eq. (18) in Eqs. (20) and (21) gives Eqs. (13) and (14) respectively.

We shall define the function $S(k)$, which is closely related with the intensity of X-rays scattered by the fluid, by

$$S(k)=1+\rho\int[g(r)-1]\exp(i\boldsymbol{kr})\,d\boldsymbol{r}\,. \tag{22}$$

Using Eq. (18) in Eq. (22) we obtain

$$S(k)=1+\bar{\rho}\beta(k)+S_0(k)+\frac{1}{(2\pi)^{3/2}}\int du\,\beta(\boldsymbol{u}-\boldsymbol{k})S_0(u)\,, \tag{23}$$

where

$$\begin{aligned} S_0(k)=&\frac{\{\bar{\rho}\beta(k)+\bar{\rho}^2\gamma(k)\}^2}{1-\bar{\rho}\beta(k)-\bar{\rho}^2\gamma(k)}-2\bar{\rho}^3\beta(k)\gamma(k)-\frac{1}{2}\frac{\bar{\rho}^3}{(2\pi)^{3/2}}\int du\,\beta^2(u)\beta^2(\boldsymbol{u}-\boldsymbol{k}) \\ &+\frac{\bar{\rho}}{(2\pi)^{3/2}}\int du\frac{\{\bar{\rho}\beta(u)+\bar{\rho}^2\gamma(u)\}^2}{1-\bar{\rho}\beta(u)-\bar{\rho}^2\gamma(u)}\{\beta^2(\boldsymbol{u}-\boldsymbol{k})+2\beta(k)\beta(\boldsymbol{u}-\boldsymbol{k})\}\,. \end{aligned}$$

We obtain, in particular,

$$S(0)=1+\bar{\rho}\beta(0)+S_0(0)+\frac{1}{(2\pi)^{3/2}}\int du\,\beta(u)S_0(u)\,. \tag{24}$$

From Eq. (13) we obtain

$$\begin{aligned} \frac{1}{kT}\left(\frac{\partial p}{\partial\rho}\right)_T=1-\bar{\rho}\beta(0)+\frac{1}{(2\pi)^{3/2}}\frac{1}{\bar{\rho}}\int du\Big[&-\frac{1}{2}\frac{\{\bar{\rho}\beta(u)+2\bar{\rho}^2\gamma(u)\}^2}{\{1-\bar{\rho}\beta(u)-\bar{\rho}^2\gamma(u)\}^2}-\frac{\bar{\rho}^2\gamma(u)}{1-\bar{\rho}\beta(u)-\bar{\rho}^2\gamma(u)} \\ &+\frac{1}{2}\bar{\rho}^2\beta^2(u)+\bar{\rho}^2\gamma(u)+3\bar{\rho}^3\beta(u)\gamma(u)+3\bar{\rho}^4\beta^2(u)\gamma(u)+3\bar{\rho}^4\gamma^2(u)\Big]\,. \end{aligned} \tag{25}$$

In an exact theory there should be the relation

$$kT\left(\frac{\partial\rho}{\partial p}\right)_T=S(0) \tag{26}$$

or

$$kT\left(\frac{\partial\rho}{\partial p}\right)_T=1+\rho\int[g(r)-1]\,d\boldsymbol{r}\,. \tag{26'}$$

It can be seen that relation (26) is not satisfied by Eqs. (24) and (25), that is, the netted ring approximation is not consistent with Eq. (26).

§ 4. Discussion

The radial distribution function $g^{(n.c)}(r)$ based on the netted chain approximation of Rushbrooke and Scoins[1] is

$$g^{n.c}(r)=\exp(-\phi(r)/kT)[1+f_0(r)]\,, \tag{27}$$

where $f_0(r)$ is defined by Eq. (19). Rushbrooke and Scoins have related a critical point to a singularity of $f_0(r)$ and obtained $p/\rho kT=1/3$ at a critical point. Since our expression (18) also has the function $f_0(r)$, our theory ought to lead to the same result as above if the conjecture of Rushbrooke and Scoins is well-founded.

It is an open question whether the singularity of $f_0(r)$ is related to a phase change of fluids or not. If, however, we assume that the singularity of $f_0(r)$ is related to a phase change, we shall find an interesting fact that, even in the case of the gas of hard spheres, there will be a phase change. In fact we obtain[1),6)] for hard spheres of diameter a

$$\beta(u)=\sqrt{\frac{2}{\pi}}\frac{1}{u^3}[ua\cos ua-\sin ua]$$

and

$$\gamma(u)=\frac{1}{24\pi}\frac{1}{u^6}[-24-24(ua)^2 +\{24+12(ua)^2+5(ua)^4\}\cos ua +\{24ua+4(ua)^3\}\sin ua]\,.$$

The singularity of $f_0(r)$ occurs when the equation

$$1-\bar{\rho}\beta(u)-\bar{\rho}^2\gamma(u)=0 \tag{28}$$

possesses real roots. As the number density ρ is increased, it can be shown that Eq. (28) begins to possess real roots at a value

$$\rho=0.86\rho_{\max} \quad\text{or}\quad v=1.16v_{\min}$$

where $\rho_{\max}=\sqrt{2}/a^3$ is the maximum density of the gas of hard spheres, and $v=1/\rho$ and $v_{\min}=1/\rho_{\max}$. It should be compared with $v/v_{\min}\approx 1.55\sim 1.60$ obtained by the use of Monte Carlo method[12)] or detailed molecular dynamics[13)] and also compared with $v/v_{\min}=1.48$ obtained by the superposition theory[14)]. It ought to be noted that the simple chain theory does not give such a singularity in the case of hard spheres, because the equation

$$1-\bar{\rho}\beta(u)=0$$

possesses no real root for the value of ρ smaller than $\rho_{\max}$.

As has been stated in the preceding section, our netted ring approximation is not consistent with Eq. (26). For quantitative investigation of this point we shall again consider the gas of hard spheres. When a radial distribution function is given, the pressure can be calculated either by Eq. (20) or by Eq. (26′). It is needless to say that both equations lead to the same expression for the pressure if the exact distribution function is used. Our expression (18) gives

$$D_p=0.4453b^3 \quad\text{and}\quad D_c=0.2092b^3\,,$$

where D_p and D_c are the fourth virial coefficients of the pressure obtained by the use of Eqs. (20) and (26′) respectively and $b=2\pi a^3/3$. These values should be compared with the exact value $D=0.2869b^3$.[15)] They should be also compared with the values based on several theories:

Born-Green non-linear integral equation:[16),17)]

$$D_p=0.2252b^3,\quad D_c=0.3424b^3$$

netted chain approximation:[1)]

$$D_p=0.2500b^3,\quad D_c=0.2969b^3$$

Rodriguez (1957):[18)]

$$D_p=D_c=0.2773b^3.$$

As can be seen above, our theory does not give any better result than earlier theories so far as the fourth virial coefficient in the case of hard spheres is concerned. However it may be not the case for more general

forms of interaction potential. Further our theory will be more suitable than other theories for the investigation of thermodynamic properties of fluids, since the thermodynamic quantities can be given the explicit expressions such as Eqs. (13), (14) and (15). A generalization of our theory to fluid mixtures and a numerical analysis for the case of definite interaction potential will be attempted in later papers.

The author is much indebted to Professor H. Ichimura, Mr. R. Abe and Mr. T. Morita for their fruitful discussions. A part of this work was supported by the Scientific Research Expenditure of the Ministry of Education.

References

1) G. S. Rushbrooke and H. I. Scoins: Proc. Roy. Soc. **A 216** (1953) 203.
2) E. W. Montroll and J. E. Mayer: J. Chem. Phys. **9** (1941) 626.
3) G. S. Rushbrooke: Phil. Mag. **43** (1952) 1276.
4) H. S. Green: Proc. Roy. Soc. **A 189** (1947) 103.
5) A. E. Rodriguez: Proc. Roy. Soc. **A 196** (1949) 73.
6) K. Hiroike: J. Phys. Soc. Japan **12** (1957) 326.
7) E. W. Montroll and J. C. Ward: Phys. of Fluids **1** (1958) 55.
8) S. Ono: Prog. Theor. Phys. **6** (1951) 447.
9) See, for example, J. E. Mayer and M. G. Mayer: "Statistical Mechanics" (Wiley, New York, 1940) Chapter 13.
10) K. Hiroike: J. Phys. Soc. Japan **12** (1957) 864.
11) See, for example, T. L. Hill: "Statistical Mechanics" (McGraw-Hill, New York, 1956), pp. 189 and 190.
12) W. W. Wood and J. D. Jacobson: J. Chem. Phys. **27** (1957) 1207.
13) B. J. Alder and T. E. Wainwright: J. Chem. Phys. **27** (1957) 1208.
14) J. G. Kirkwood, E. K. Maun and B. J. Alder: J. Chem. Phys. **18** (1950) 1040.
15) R. H. Fowler and A. E. Guggenheim: "Statistical Thermodynamics" (Cambridge, London, 1939) § 717.
16) B. R. A. Nijboer and L. van Hove: Phys. Rev. **85** (1952) 777.
17) G. S. Rushbrooke and H. I. Scoins: Phil. Mag. **42** (1951) 582.
18) A. E. Rodriguez: Proc. Roy. Soc. **A 239** (1957) 373.

JOURNAL OF THE PHYSICAL SOCIETY OF JAPAN Vol. 13, No. 12, DECEMBER, 1958

Effect of Transverse Magnetic Field on the Flow due to an Oscillating Flat Plate

By Tsunehiko KAKUTANI

Department of Physics, Faculty of Science, University of Kyoto

(Received August 14, 1958)

Under the well-known assumption in magnetohydrodynamics, the distributions of velocity, magnetic field, and related quantities such as pressure, electric field and current density are obtained for the flow of an incompressible, viscous and electrically conducting fluid due to an infinite oscillating flat plate in the presence of transverse magnetic field.

General solutions are first derived and then some special cases are discussed corresponding to limiting values of parameters such as magnetic pressure number S and magnetic Reynolds number R_m.

It is found that each of the velocity distribution and other related quantities consists of two different oscillations whose decaying factors differ from the corresponding wave numbers, which contrasts to the well-known velocity distribution in classical hydrodynamics.

§ 1. Introduction

In recent years, the subject of magnetohydrodynamics has attracted many authors in view not only of its own interest but also of the applications to the geophysical and astronomical problems.

The general equations of unified velocity and magnetic fields for the flow of an incompressible, viscous and electrically conducting fluid subject to a magnetic field have been derived by Batchelor[1]. More recently, Cowling[2] published a monograph which contains important reviews and references on this subject so far reported.

In this paper, we discuss the effect of transverse magnetic field on the flow due to an oscillating plate, which is one of the most familiar problems in the classical hydrodynamics in the absence of magnetic field, and an exact solution is obtained for the modified Navier-Stokes and Maxwell's equations under usual assumption in magnetohydrodynamics.

§ 2. Fundamental Equations

The fundamental equations of magnetohydrodynamics are:

(1) Maxwell's equations:

$$\operatorname{div} \boldsymbol{E}=4\pi c^2 q/\varepsilon\,, \tag{2.1}$$

$$\operatorname{div} \boldsymbol{H}=0\,, \tag{2.2}$$

$$\operatorname{curl} \boldsymbol{E}=-\mu\frac{\partial \boldsymbol{H}}{\partial t}\,, \tag{2.3}$$

$$\operatorname{curl} \boldsymbol{H}=4\pi \boldsymbol{j}+\frac{\varepsilon}{c^2}\frac{\partial \boldsymbol{E}}{\partial t}\,; \tag{2.4}$$

(2) Ohm's law:

$$\boldsymbol{j}=\sigma(\boldsymbol{E}+\mu \boldsymbol{v}\times \boldsymbol{H})+q\boldsymbol{v}\,; \tag{2.5}$$

(3) The equation of continuity:

$$\operatorname{div} \boldsymbol{v}=0\,; \tag{2.6}$$

(4) The modified Navier-Stokes equation:

$$\frac{\partial \boldsymbol{v}}{\partial t}+(\boldsymbol{v}\cdot\operatorname{grad})\boldsymbol{v} =-\frac{1}{\rho}\operatorname{grad} p+\nu\nabla^2\boldsymbol{v}+\frac{\mu}{\rho}\boldsymbol{j}\times\boldsymbol{H}+\frac{q}{\rho}\boldsymbol{E}\,. \tag{2.7}$$

Here, $\boldsymbol{E}$ is the electric field, $\boldsymbol{H}$ the magnetic field, $\boldsymbol{j}$ the current density, q the excess charge density, ε the dielectric constant, μ the magnetic permeability, σ the electrical conductivity, c the speed of light, $\boldsymbol{v}$ the velocity of the fluid p the pressure, and ρ and ν are respectively the density and the kinematic coefficient of viscosity of the fluid. All electromagnetic quantities are measured in electromagnetic unit. ε and μ are assumed to be uniform throughout the whole field, and the fluid is assumed to be non-magnetic.

As in most analysis in magnetohydrodynamics, the displacement current in (2.4) may be neglected, since no oscillations of very high frequency occur and the magnitude of the fluid velocity $|\boldsymbol{v}|$ is much smaller than the speed of light c. In consistence with the above assumption, the convection current in (2.5) and the electric force due to excess charges in (2.7) are also ignored. In the following analysis, Eqs. (2.4), (2.5) and (2.7) should be understood to have been simplified

by the above assumptions.

Eliminating electric field $\boldsymbol{E}$ between (2.3) and (2.5) with the help of (2.2) and (2.4), we have the magnetic equation as follows:

$$\frac{\partial \boldsymbol{H}}{\partial t}=\mathrm{curl}\,(\boldsymbol{v}\times\boldsymbol{H})+\eta\nabla^2\boldsymbol{H}\,, \tag{2.8}$$

where $\eta=1/(4\pi\mu\sigma)$ which is interpreted as a magnetic diffusivity or a magnetic viscosity. On the other hand, elimination of $\boldsymbol{j}$ between (2.4) and (2.7) leads to the dynamical equation containing no electromagnetic variables other than $\boldsymbol{H}$:

$$\frac{\partial \boldsymbol{v}}{\partial t}+(\boldsymbol{v}\cdot\mathrm{grad})\boldsymbol{v}$$
$$=-\frac{1}{\rho}\mathrm{grad}\,p+\nu\nabla^2\boldsymbol{v}+\frac{\mu}{4\pi\rho}(\mathrm{curl}\,\boldsymbol{H}\times\boldsymbol{H})\,. \tag{2.9}$$

Equations (2.8) and (2.9), together with (2.2) and (2.6), are the fundamental equations of magnetohydrodynamics.

In the present problem, we take the coordinate origin O at an arbitrary point on the oscillating plate, which is assumed to be non-conducting and non-magnetic, and use Cartesian coordinates x, y and z, with the axis Ox in the direction of oscillation and Oy perpendicular to the plate. It is then plausible to assume that

(1) The flow is parallel to the plate, that is, $\boldsymbol{v}=\boldsymbol{v}(u,\ 0,\ 0)$;

(2) The magnetic field imposed is uniform and perpendicular to the plate. Thus in the region considered, $\boldsymbol{H}=\boldsymbol{H}(H_x,\ H_y,\ 0)$;

(3) All quantities are functions of the space coordinate y and time t only.

The fundamental equations of our problem now become

$$\frac{\partial u}{\partial t}=\nu\frac{\partial^2 u}{\partial y^2}+\frac{\mu}{4\pi\rho}H_y\frac{\partial H_x}{\partial y}\,, \tag{2.10}$$

$$\frac{\partial}{\partial y}\left(\frac{p}{\rho}+\frac{\mu}{8\pi\rho}H_x^2\right)=0\,, \tag{2.11}$$

$$\frac{\partial H_x}{\partial t}=H_y\frac{\partial u}{\partial y}+\eta\frac{\partial^2 H_x}{\partial y^2}\,, \tag{2.12}$$

$$\frac{\partial H_y}{\partial t}=\eta\frac{\partial^2 H_y}{\partial y^2}\,, \tag{2.13}$$

while the equation of continuity (2.6) is automatically satisfied by the above assumptions.

The boundary conditions for the velocity field are exactly the same as those in ordinary hydrodynamics, namely, on the oscillating plate the velocity of the fluid coincides with that of the plate, and at a great distance from the plate u tends to zero. Thus we have

$$y=0:\ u=Ue^{i\omega t};\quad y\to\infty:\ u\to 0\,, \tag{2.14a}$$

where U and ω denote respectively the velocity amplitude and angular frequency of the oscillating plate.

The boundary conditions for the magnetic field are that both the tangential component of the magnetic field and the normal component of the magnetic induction are continuous at the plate. Since, however, both the fluid and the plate are assumed to be non-magnetic in the present problem, the continuity condition for the magnetic induction may be replaced by that for the magnetic field itself. The total magnetic field at the plate is the vector sum of the imposed and induced fields, the latter resulting from the induced current distribution in the fluid. This distribution depends on the solution and is therefore unknown. The induced field at the plate, however, is secondarily important and may be neglected as compared with the imposed field. On the other hand, since the velocity tends to zero asymptotically at far distance from the plate, no interactions exist there. Hence the magnetic field tends to the imposed field H_0 as $y\to\infty$. Since the imposed magnetic field H_0 is uniform and perpendicular to the oscillating plate which is non-conducting and non-magnetic, the boundary conditions for the magnetic field may be

$$y=0:\ H_y=H_0\,;\quad y\to\infty:\ H_y\to H_0\,, \tag{2.14b}$$

and

$$y=0:\ H_x=0\,;\quad y\to\infty:\ H_x\to 0\,. \tag{2.14c}$$

The latter conditions (2.14c) imply that the total flux of current in the direction Oy is taken to be zero, because $\boldsymbol{j}=(1/4\pi)\,\mathrm{curl}\,\boldsymbol{H}$.

Our problem is to determine the four unknowns u, H_x, H_y and p from Eqs. (2.10)~(2.13) together with the boundary conditions (2.14 a, b, c).

3. Analysis and General Solutions

If the pressure at infinity is p_∞, it follows immediately from (2.11) that

$$p+\frac{\mu}{8\pi}H_x^2=p_\infty\,, \tag{3.1}$$

which shows the balance between the fluid pressure and 'magnetic pressure' in the flow

field, because H_y is uniform throughout the whole flow field as will be shown below. Remembering the boundary conditions for H_y, we can easily solve Eq. (2.13) and obtain

$$H_y \equiv H_0 \,. \tag{3.2}$$

Introducing (3.2) into (2.10) and (2.12) and eliminating H_x between them we have

$$\left[\left(\nu\frac{\partial^2}{\partial y^2}-\frac{\partial}{\partial t}\right)\left(\eta\frac{\partial^2}{\partial y^2}-\frac{\partial}{\partial t}\right)-k\frac{\partial^2}{\partial y^2}\right]u=0\,, \tag{3.3}$$

where $k=\mu H_0^2/(4\pi\rho)$. If we eliminate u instead of H_x we have a similar equation for H_x to (3.3). In the limiting case of $\nu\to 0$, $\eta\to 0$, (3.3) and the similar equation for H_x reduce to Alfvén's[3] equation for 'magnetohydrodynamic waves'.

Assuming $u\propto e^{\kappa t+\lambda y}$ and inserting it into (3.3), we have

$$(\nu\lambda^2-\kappa)(\eta\lambda^2-\kappa)-k\lambda^2=0\,,$$

which gives

$$\lambda=\pm\lambda_1\,,\ \pm\lambda_2\,,$$

where

$$\lambda_{1,2}=\left[\frac{(k+\kappa\nu+\kappa\eta)\pm\{(k+\kappa\nu+\kappa\eta)^2-4\nu\eta\kappa^2\}^{1/2}}{2\nu\eta}\right]^{1/2},$$

$$\mathrm{Re}\,(\lambda_{1,2})>0\,,$$

signs + and − in the square bracket corresponding to λ_1 and λ_2 respectively*. Thus we have the following formal expression for u:

$$u=\mathop{\mathbf{S}}_{\kappa} e^{\kappa t}[Ae^{\lambda_1 y}+Be^{-\lambda_1 y}+Ce^{\lambda_2 y}+De^{-\lambda_2 y}]\,,$$

where A, B, C and D are constants of integration which depend on the parameter κ, and symbol $\mathbf{S}$ denotes the summation or integration over all possible values of κ.

It is easily seen that we have to put $A=C=0$ by virtue of the boundary condition at infinity for u. On the other hand, from the boundary condition on the plate it is required that

$$\kappa=i\omega \quad\text{and}\quad B+D=U\,. \tag{3.4}$$

Thus we have a formal solution for u as follows:

$$u(y,t)=e^{i\omega t}[Be^{-\lambda_1 y}+De^{-\lambda_2 y}]\,, \tag{3.5}$$

with

$$\lambda_{1,2}=\left[\frac{(k+i\omega(\nu+\eta))\pm\{(k+i\omega(\nu+\eta))^2+4\nu\eta\omega^2\}^{1/2}}{2\nu\eta}\right]^{1/2}. \tag{3.6}$$

Insertion of (3.5) into (2.10) leads to

$$\frac{\partial H_x}{\partial y}=\frac{H_0}{k}e^{i\omega t}[(i\omega-\nu\lambda_1^2)Be^{-\lambda_1 y}+(i\omega-\nu\lambda_2^2)De^{-\lambda_2 y}]\,. \tag{3.7}$$

Integrating (3.7) with respect to y and remembering that $H_x\to 0$ when $y\to\infty$, we have

$$H_x(y,t)=-\frac{H_0}{k}e^{i\omega t}\left[\left(\frac{i\omega}{\lambda_1}-\nu\lambda_1\right)Be^{-\lambda_1 y}+\left(\frac{i\omega}{\lambda_2}-\nu\lambda_2\right)De^{-\lambda_2 y}\right]. \tag{3.8}$$

The boundary condition on the plate requires that

$$\left(\frac{i\omega}{\lambda_1}-\nu\lambda_1\right)B+\left(\frac{i\omega}{\lambda_2}-\nu\lambda_2\right)D=0\,. \tag{3.9}$$

Solving (3.4) and (3.9) for B and D, we have

$$B=-\frac{\lambda_1(\nu\lambda_2^2-i\omega)}{(\lambda_1-\lambda_2)(\lambda_1\lambda_2\nu+i\omega)}U\,,\qquad D=\frac{\lambda_2(\nu\lambda_1^2-i\omega)}{(\lambda_1-\lambda_2)(\lambda_1\lambda_2\nu+i\omega)}U\,. \tag{3.10}$$

Insertion of B and D thus determined into (3.5) and (3.8) yields

$$u(y,t)=-\frac{(\nu\lambda_1^2-i\omega)(\nu\lambda_2^2-i\omega)}{(\lambda_1-\lambda_2)(\lambda_1\lambda_2\nu+i\omega)}Ue^{i\omega t}\left[\frac{\lambda_1}{\nu\lambda_1^2-i\omega}e^{-\lambda_1 y}-\frac{\lambda_2}{\nu\lambda_2^2-i\omega}e^{-\lambda_2 y}\right], \tag{3.11}$$

and

* This convention will also be used hereafter.

$$H_x(y,t)=-\frac{(\nu\lambda_1^2-i\omega)(\nu\lambda_2^2-i\omega)}{k(\lambda_1-\lambda_2)(\lambda_1\lambda_2\nu+i\omega)}H_0Ue^{i\omega t}[e^{-\lambda_1 y}-e^{-\lambda_2 y}] \tag{3.12}$$

Putting (3.12) into (2.4), we have

$$\left.\begin{aligned} &j_x=0\,,\quad j_y=0\,,\\ &j_z(y,t)=-\frac{(\nu\lambda_1^2-i\omega)(\nu\lambda_2^2-i\omega)}{4\pi k(\lambda_1-\lambda_2)(\lambda_1\lambda_2\nu+i\omega)}H_0Ue^{i\omega t}[\lambda_1 e^{-\lambda_1 y}-\lambda_2 e^{-\lambda_2 y}]\,. \end{aligned}\right\} \tag{3.13}$$

Also, putting (3.11), (3.12) and (3.13) into (2.5) we have

$$\left.\begin{aligned} &E_x=0\,,\qquad E_y=0\,,\\ &E_z(y,t)=-\frac{i\omega(\nu\lambda_1^2-i\omega)(\nu\lambda_2^2-i\omega)}{k(\lambda_1-\lambda_2)(\lambda_1\lambda_2\nu+i\omega)}\mu H_0Ue^{i\omega t}\left[\frac{1}{\lambda_1}e^{-\lambda_1 y}-\frac{1}{\lambda_2}e^{-\lambda_2 y}\right]. \end{aligned}\right\} \tag{3.14}$$

The above (3.11)~(3.14), together with (3.1) and (3.2), give the general solutions of the present problem. It will be seen that all quantities consist of two different oscillations whose complex decaying factors are $\lambda_{1,2}$, $\mathrm{Re}(\lambda_{1,2})$ and $\mathrm{Im}(\lambda_{1,2})$ representing the decaying factors and the wave numbers respectively. The above result should be compared with that of the well-known classical hydrodynamics: $u=Ue^{i\omega t-\sqrt{i\omega/\nu}\cdot y}$. Since $H_y=H_0$, the fundamental equations (2.10), (2.11), (2.12) and (2.13) are all linear. Hence we can make up more general solutions by superposing several oscillations of different frequencies and amplitudes so long as the angular frequencies ω and amplitudes U are not so extremely large as to make displacement current important.

The skin friction τ can be easily obtained from the formula·

$$\tau=\left(\rho\nu\frac{\partial u}{\partial y}\right)_{y=0},$$

which yields

$$\tau=\mathrm{Re}\left[-\rho\nu Ue^{i\omega t}\left\{\frac{i\omega(\lambda_1+\lambda_2)}{\lambda_1\lambda_2\nu+i\omega}\right\}\right].$$

On the other hand, the drag on the plate due to the direct magnetic effect is zero, because

$$\int_0^\infty\frac{\mu}{4\pi\rho}H_0\frac{\partial H_x}{\partial y}dy=0\,.$$

In order to clarify the magnetic effect, we shall consider, in the next section, the behaviours of the solutions in some special cases corresponding to the limiting values of parameters such as magnetic pressure number S and magnetic Reynolds number R_m.

§ 4. Behaviours of the Solutions in Some Special Cases

For proceeding further, it is convenient to define some non-dimensional parameters such as

$$\left.\begin{aligned} &\text{Reynolds number:}\quad R=\frac{U^2}{\nu\omega}\,,\\ &\text{Magnetic Reynolds number:}\quad R_m=\frac{U^2}{\eta\omega}\,,\\ &\text{Magnetic pressure number:}\quad S=\frac{\mu H_0^2}{4\pi\rho U^2}\,, \end{aligned}\right\} \tag{4.1}$$

and to introduce non-dimensional quantities with asterisk as follows:

$$\left.\begin{aligned} u&=Uu^*, & p&=\frac{1}{2}\rho U^2 p^*, \\ y&=\frac{U}{\omega}y^*, & \boldsymbol{H}&=H_0\boldsymbol{H}^*, \\ t&=\frac{1}{\omega}t^*, & \boldsymbol{E}&=\mu H_0 U\boldsymbol{E}^*, \\ \lambda_{1,2}&=\frac{\omega}{U}\lambda_{1,2}^*, & \boldsymbol{j}&=\sigma\mu H_0 U\boldsymbol{j}^*. \end{aligned}\right\} \tag{4.2}$$

It is to be noted here that the Hartmann number M frequently used in the analysis of problems in magnetohydrodynamics is equal to $\sqrt{SRR_m}$ in our notation.

Then the solutions expressed in non-dimensional forms are:

$$u^*=-\frac{(\lambda_1^{*2}-iR)(\lambda_2^{*2}-iR)}{(\lambda_1^*-\lambda_2^*)(\lambda_1^*\lambda_2^*+iR)}e^{it^*}\left[\frac{\lambda_1^*}{\lambda_1^{*2}-iR}e^{-\lambda_1^*y^*}-\frac{\lambda_2^*}{\lambda_2^{*2}-iR}e^{-\lambda_2^*y^*}\right], \tag{4.3}$$

$$H_x^*=-\frac{(\lambda_1^{*2}-iR)(\lambda_2^{*2}-iR)}{SR(\lambda_1^*-\lambda_2^*)(\lambda_1^*\lambda_2^*+iR)}e^{it^*}[e^{-\lambda_1^*y^*}-e^{-\lambda_2^*y^*}], \tag{4.4}$$

$$E_z^*=-\frac{i(\lambda_1^{*2}-iR)(\lambda_2^{*2}-iR)}{SR(\lambda_1^*-\lambda_2^*)(\lambda_1^*\lambda_2^*+iR)}e^{it^*}\left[\frac{1}{\lambda_1^*}e^{-\lambda_1^*y^*}-\frac{1}{\lambda_2^*}e^{-\lambda_2^*y^*}\right], \tag{4.5}$$

$$j_z^*=-\frac{(\lambda_1^{*2}-iR)(\lambda_2^{*2}-iR)}{SRR_m(\lambda_1^*-\lambda_2^*)(\lambda_1^*\lambda_2^*+iR)}e^{it^*}[\lambda_1^*e^{-\lambda_1^*y^*}-\lambda_2^*e^{-\lambda_2^*y^*}], \tag{4.6}$$

$$p^*+SH_x^{*2}=p_\infty^*, \tag{4.7}$$

with

$$\lambda_{1,2}^*=\left[\frac{SRR_m+i(R+R_m)\pm\{(SRR_m+i(R+R_m))^2+4RR_m\}^{1/2}}{2}\right]^{1/2}. \tag{4.8}$$

There are the three characteristic parameters S, R and R_m in this problem. Since, however, R and R_m are contained symmetrically in $\lambda_{1,2}^*$, we have only to discuss the cases of the limiting values of S and R_m instead of those of S, R and R_m.

In the following discussions, only the first dominant terms are retained in each case.

(1) $S\ll 1$.

In this case, if $R>R_m$

$$\lambda_1^*\sim\sqrt{iR}\left(1-\frac{SRR_m}{2(R-R_m)}i\right), \qquad \lambda_2^*\sim\sqrt{iR_m}\left(1+\frac{SRR_m}{2(R-R_m)}i\right). \tag{4.9}$$

Hence, $\dfrac{(\lambda_1^{*2}-iR)(\lambda_2^{*2}-iR)}{(\lambda_1^*-\lambda_2^*)(\lambda_1^*\lambda_2^*+iR)}\sim-\dfrac{SR^2R_m}{\sqrt{iR}(R-R_m)}$, so that

$$\left.\begin{aligned} u^*&\sim\frac{SR^2R_m}{\sqrt{iR}(R-R_m)}e^{it^*}\left[\frac{\sqrt{iR}(R-R_m)}{SR^2R_m}e^{-\sqrt{iR}y^*}-\frac{i\sqrt{iR_m}}{R-R_m}e^{-\sqrt{iR_m}y^*}\right], \\ H_x^*&\sim\frac{RR_m}{\sqrt{iR}(R-R_m)}e^{it^*}[e^{-\sqrt{iR}y^*}-e^{-\sqrt{iR_m}y^*}], \\ E_z^*&\sim\frac{iRR_m}{\sqrt{iR}(R-R_m)}e^{it^*}\left[\frac{1}{\sqrt{iR}}e^{-\sqrt{iR}y^*}-\frac{1}{\sqrt{iR_m}}e^{-\sqrt{iR_m}y^*}\right], \\ j_z&\sim\frac{R}{\sqrt{iR}(R-R_m)}e^{it^*}[\sqrt{iR}e^{-\sqrt{iR}y^*}-\sqrt{iR_m}e^{-\sqrt{iR_m}y^*}]. \end{aligned}\right\} \tag{4.10}$$

In the limit of $S\to 0$, u^* tends to the solution of the classical hydrodynamics as expected. If $R<R_m$, λ_1^* takes the place of λ_2^* in (4.9) and *vice versa*. Since, however, λ_1^* and λ_2^* are contained symmetrically in u^*, H_x^*, E_z^* and j_z^*, the final expressions (4.10) remain unaltered.

(2) $S\gg 1$.

In this case, $\lambda_1^* \sim \sqrt{SRR_m}\left(1+\frac{R+R_m}{2SRR_m}i\right)$ and $\lambda_2^* \sim \frac{i}{\sqrt{S}}\left(1-\frac{R+R_m}{2SRR_m}i\right)$. Hence, $\frac{(\lambda_1^{*2}-iR)(\lambda_2^{*2}-iR)}{(\lambda_1^*-\lambda_2^*)(\lambda_1^*\lambda_2^*+iR)} \sim -\frac{R\sqrt{SR_m}}{\sqrt{R}+\sqrt{R_m}}$, and therefore

$$\left.\begin{aligned}
u^* &\sim \frac{R\sqrt{SR_m}}{\sqrt{R}+\sqrt{R_m}} e^{it^*}\left[\frac{1}{\sqrt{SRR_m}} e^{-\sqrt{SRR_m}y^*} + \frac{1}{R\sqrt{S}} e^{-i/\sqrt{S}\cdot y^*}\right], \\
H_x^* &\sim \frac{\sqrt{R_m}}{\sqrt{S}(\sqrt{R}+\sqrt{R_m})} e^{it^*}\left[e^{-\sqrt{SRR_m}y^*} - e^{-i/\sqrt{S}\cdot y^*}\right], \\
E_z^* &\sim \frac{i\sqrt{R_m}}{\sqrt{S}(\sqrt{R}+\sqrt{R_m})} e^{it^*}\left[\frac{1}{\sqrt{SRR_m}} e^{-\sqrt{SRR_m}y^*} + i\sqrt{S}\, e^{-i/\sqrt{S}\cdot y^*}\right], \\
j_z^* &\sim \frac{1}{\sqrt{SR_m}(\sqrt{R}+\sqrt{R_m})} e^{it^*}\left[\sqrt{SRR_m}\, e^{-\sqrt{SRR_m}y^*} - \frac{i}{\sqrt{S}} e^{-i/\sqrt{S}\cdot y^*}\right].
\end{aligned}\right\} \tag{4.11}$$

Thus the first terms of each quantity decay rapidly with increasing y and are vanishingly small except for the vicinity of the plate, and the second terms become dominant which represent the oscillations whose phase velocity is the same as that of the magnetohydrodynamic waves of Alfvén. Because the decaying factors of the second terms of each quantity are of higher order in $(1/S)$ than the wave number terms, the second terms decay very slowly.

(3) $R_m \ll 1$.

Since $\lambda_1^* \sim \sqrt{iR}(1-\frac{1}{2}SR_m i)$ and $\lambda_2^* \sim \sqrt{iR_m}(1+\frac{1}{2}SR_m i)$, $\frac{(\lambda_1^{*2}-iR)(\lambda_2^{*2}-iR)}{(\lambda_1^*-\lambda_2^*)(\lambda_1^*\lambda_2^*+iR)} \sim -\frac{SRR_m}{\sqrt{iR}}$. Hence, the general character of the solutions is similar to that in the case (1).

(4) $R_m \gg 1$.

In this case $\lambda_1^* \sim \sqrt{R_m(SR+i)}\left(1+\frac{SR^2}{2R_m(SR+i)^2}i\right)$ and $\lambda_2^* \sim \sqrt{\frac{R}{SR+i}}\, i\left(1-\frac{SR^2}{2R_m(SR+i)^2}i\right)$. Hence, $\frac{(\lambda_1^{*2}-iR)(\lambda_2^{*2}-iR)}{(\lambda_1^*-\lambda_2^*)(\lambda_1^*\lambda_2^*+iR)} \sim -\frac{SR^2}{\sqrt{R(SR+i)}}$, so that

$$\left.\begin{aligned}
u^* &\sim \frac{SR^2}{\sqrt{R(SR+i)}} e^{it^*}\left[\frac{1}{\sqrt{R_m(SR+i)}} e^{-\sqrt{R_m(SR+i)}\,y^*} + \frac{\sqrt{R(SR+i)}}{SR^2} e^{-\sqrt{R/(SR+i)}\,iy^*}\right], \\
H_x^* &\sim \frac{R}{\sqrt{R(SR+i)}} e^{it^*}\left[e^{-\sqrt{R_m(SR+i)}y^*} - e^{-\sqrt{R/(SR+i)}\,iy^*}\right], \\
E_z^* &\sim \frac{iR}{\sqrt{R(SR+i)}} e^{it^*}\left[\frac{1}{\sqrt{R_m(SR+i)}} e^{-\sqrt{R_m(SR+i)}\,y^*} + \sqrt{\frac{SR+i}{R}}\, ie^{-\sqrt{R/(SR+i)}\,iy^*}\right], \\
j_z^* &\sim \frac{R}{R_m\sqrt{R(SR+i)}} e^{it^*}\left[\sqrt{R_m(SR+i)}\, e^{-\sqrt{R_m(SR+i)}y^*} - \sqrt{\frac{R}{SR+i}}\, ie^{-\sqrt{R/(SR+i)}\,iy^*}\right].
\end{aligned}\right\} \tag{4.12}$$

Hence, the general character is similar to that in the case (2) except that the decaying factors of the second terms in this case are of the same order as the wave number terms. Therefore, even the second terms which are of course dominant over the first terms decrease normally as the distance from the plate increases.

Acknowledgement

The writer wishes to express his cordial thanks to Professor S. Tomotika for his continual guidance and encouragement throughout the present study, and especially for his kind inspection of the manuscript. The writer's thanks are also due to Professor K. Tamada, Dr. H. Hasimoto, Messrs. H. Yosinobu and K. Gotoh for their invaluable advices and helpful discussions at every stage.

References

1) G. K. Batchelor: Proc. Roy. Soc. A, **201** (1950) 405.
2) T. G. Cowling: '*Magnetohydrodynamics*' (Interscience Tract on Physics and Astronomy, No. 4) (Interscience Publishers, Inc., New York, 1957).
3) H. Alfvén: '*Cosmical Electrodynamics*' (Clarendon Press, Oxford, 1950).

JOURNAL OF THE PHYSICAL SOCIETY OF JAPAN Vol. 13, No. 12, DECEMBER, 1958

Some Nonlinear Effect in Compressible Flow

By Haruo MORIGUCHI

Department of Physics, Faculty of Liberal Arts, Shizuoka University, Shizuoka, Japan

(Received August 30, 1958)

The two-dimensional potential flow of a compressible fluid past a family of cylindrical obstacles with two parameters which includes elliptic cylinder and Kaplan bump is investigated by use of Imai's method.

An very interesting example has been found such that the surface velocity distribution changes its character with increasing Mach number, namely, it has two maxima for $M=0$, which tend to coalesce into one as the Mach number increases. Such an effect, however, is very small within the approximation used.

§ 1. The Shape of Cylinder and Incompressible Flow

In this paper we shall consider a family of symmetrical profiles in the complex z-plane which are obtained by means of the transformation

$$z=\zeta+\frac{a^2}{\zeta}-\frac{c^4}{3\zeta^3}$$

from the unit circle $\zeta=e^{i\theta}$ in the complex ζ-plane.

For $c=0$ our obstacle reduces to an elliptic cylinder, for $c^4=a^2-1$ a Kaplan bump with thickness ratio $t=-4c^4/(6+2c^2)$ is obtained and for $c=1$ a profile with four cusps and similar to an asteroid. An obstacle which is similar to Cherry's profile[1] is also included in this family. Some examples are shown in Fig. 1.

Taking the undisturbed flow velocity as unit, the incompressible flow past our profile

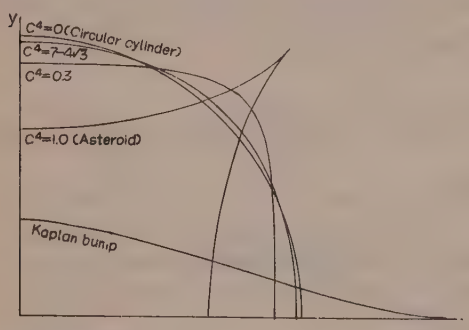

a: Profiles for $a=0$ and Kaplan bump with thickness ratio 2/9.

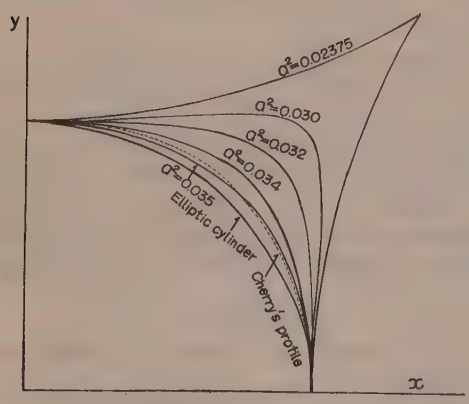

b: Profiles with the same thickness ratio 0.9312 as Cherry's profile.

Fig. 1. Examples of profiles.
(Because of symmetry, only the parts in the first quadrant are shown).

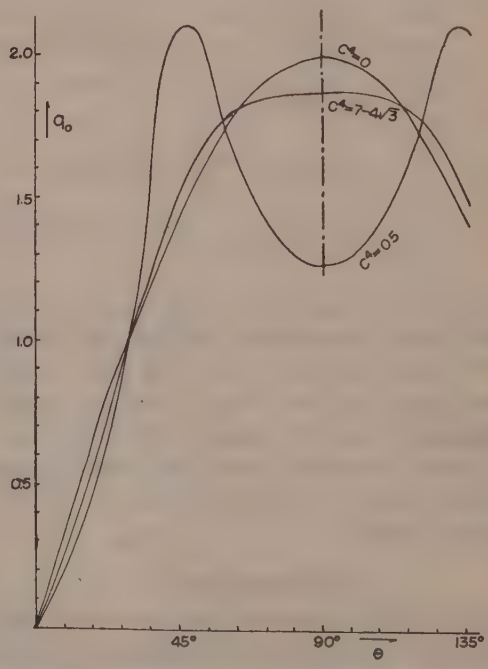

Fig. 2. Examples of incompressible flows for profiles with $a=0$.

is given by the complex velocity potential

$$F_0=\zeta+\frac{1}{\zeta} \tag{1.1}$$

and the surface velocity q_0 is given by

$$q_0^2=\left|\left(\frac{dF_0}{dz}\right)_p\right|^2$$
$$=2\frac{1-\cos 2\theta}{1-2a^2(1+c^4)\cos 2\theta+2c^4\cos 4\theta+a^4+c^8} \tag{1.2}$$

where the suffix p denotes the value on the profile. In this flow the velocity distribution has two maxima when

$$c^4>7+a^2-4\sqrt{3+a^2}\ , \tag{1.3}$$

and one maximum when

$$c^4\leq 7+a^2-4\sqrt{3+a^2}\ , \tag{1.4}$$

here as well as in what follows we suppose $0\leq a<1$. Fig. 2 shows some examples.

§ 2. The Compressibility Effect

We shall calculate the compressibility effect for the flow given in the preceding section up to the order of M^2 by use of Imai's method[2], where M is the free stream Mach number.

When the velocity potential on the surface of the obstacles expanded as

$$\varphi(\theta)=\varphi_0(\theta)+M^2\varphi_1(\theta)+O(M^4) \tag{2.1}$$

$$\varphi_0(\theta)=2\cos\theta\ , \tag{2.2}$$

then, according to Imai's formulas, we have

$$\varphi_1(\theta)=P_1(\theta)-Q_1^*(\theta) \tag{2.3}$$

$$P_1(\theta)+iQ_1(\theta)=\frac{1}{4}\frac{d\varphi_0}{d\theta}\frac{d\theta}{ds}e^{-i\omega}\int_0^\theta\left(\frac{d\varphi_0}{d\theta}\right)^2\frac{d\theta}{ds}e^{i\omega}d\theta-\frac{1}{4}(e^{i\theta}+e^{-i\theta}) \tag{2.4}$$

$$\frac{ds}{d\theta}e^{-i\omega}=\frac{dz_p}{d\theta}\ , \tag{2.5}$$

where s denotes the length along the surface of the obstacle and $Q_1^*(\theta)$ is the conjugate Fourier series associated with $Q_1(\theta)$. In the case when we can write

$$P_1(\theta)+iQ_1(\theta)=f(e^{i\theta})\ , \tag{2.6}$$

where $f(u)$ is an analytic function of u, the right-hand side of (2.3) can be expressed as

$$P_1(\theta)-Q_1^*(\theta)=2Re\left[\frac{1}{2\pi i}\oint\frac{f(u)}{u-e^{i\theta}}du\right], \tag{2.7}$$

where the pass of integration is the unit circle with centre at the origin and with a semi-circular indentation around $u=e^{i\theta}$.

According to § 1,

$$z_p=e^{i\theta}+a^2e^{-i\theta}-\frac{c^4}{3}e^{-3i\theta}\ , \tag{2.8}$$

and substituting this expression into (2.4) we have

$$P_1(\theta)+iQ_1(\theta)=\frac{1}{4}\frac{e^{4i\theta}-e^{2i\theta}}{e^{4i\theta}-a^2e^{2i\theta}+c^4}\left[e^{-i\theta}+C_1+\frac{1}{\sqrt{a^4-4c^4}}\left\{s_1\log\frac{1-u_1e^{i\theta}}{1+u_1e^{i\theta}}-s_2\log\frac{1-u_2e^{i\theta}}{1+u_2e^{i\theta}}\right\}\right]$$
$$-\frac{1}{4}(e^{i\theta}+e^{-i\theta})\ , \tag{2.9}$$

where

$$s_1=\frac{1-c^4}{2u_1}-\frac{2-a^2}{2}u_1 \tag{2.10}$$

$$s_2=\frac{1-c^4}{2u_2}-\frac{2-a^2}{2}u_2 \tag{2.11}$$

$$u_1^2=\frac{a^2+\sqrt{a^4-4c^4}}{2} \tag{2.12}$$

$$u_2^2=\frac{a^2-\sqrt{a^4-4c^4}}{2} \tag{2.13}$$

and C_1 is a constant.

The integral in (2.7) can be calculated as the sum of the residues at six poles included in the contour, and the result is

$$2\varphi_1(\theta)=Re\left[\frac{1}{e^{4i\theta}-a^2e^{2i\theta}+c^4}\{(e^{4i\theta}-e^{2i\theta})F(\theta)+Pe^{i\theta}+Qe^{3i\theta}\}-e^{i\theta}\right], \tag{2.14}$$

where

$$F(\theta)=\left(\frac{1-c^4}{4c^2}-\frac{2-a^2}{4}\right)\frac{1}{\sqrt{a^2-2c^2}}\log\frac{1-\sqrt{a^2-2c^2}e^{i\theta}-c^2e^{2i\theta}}{1+\sqrt{a^2-2c^2}e^{i\theta}-c^2e^{2i\theta}}$$
$$-\left(\frac{1-c^4}{4c^2}+\frac{2-a^2}{4}\right)\frac{1}{\sqrt{a^2+2c^2}}\log\frac{1-\sqrt{a^2+2c^2}\,e^{i\theta}+c^2e^{2i\theta}}{1+\sqrt{a^2+2c^2}\,e^{i\theta}+c^2e^{2i\theta}} \tag{2.15}$$

$$P=\frac{1}{a^4-4c^4}\left\{p_1\log\frac{1-c^2}{1+c^2}+p_2\log\frac{1-a^2+c^4}{1+a^2+c^4}+p_3\sqrt{a^4-4c^4}\log\frac{1-c^4-\sqrt{a^4-4c^4}}{1-c^4+\sqrt{a^4-4c^4}}\right\} \tag{2.16}$$

$$Q=\frac{1}{a^4-4c^4}\left\{q_1\log\frac{1-c^2}{1+c^2}+q_2\log\frac{1-a^2+c^4}{1+a^2+c^4}+q_3\sqrt{a^4-4c^4}\log\frac{1-c^4-\sqrt{a^4-4c^4}}{1-c^4+\sqrt{a^4-4c^4}}\right\} \tag{2.17}$$

$$p_1=\frac{c^2}{2}(2-3a^2+a^4+2c^4-a^2c^4) \tag{2.18}$$

$$p_2=\frac{1}{4}(-a^2+6c^4-3a^2c^4+a^4c^4-2c^8) \tag{2.19}$$

$$p_3=\frac{1}{4}(1-3c^4+a^2c^4) \tag{2.20}$$

$$q_1=\frac{1}{2c^2}(-a^2+a^4+2c^4-3a^2c^4+2c^8) \tag{2.21}$$

$$q_2=\frac{1}{4}(2-3a^2+3a^4-a^6-6c^4+3a^2c^4) \tag{2.22}$$

$$q_3=\frac{1}{4}(-3+3a^2-a^4+c^4)\ . \tag{2.23}$$

In these expressions we should write

$$\sqrt{a^4-4c^4}\log\frac{1-c^4-\sqrt{a^4-4c^4}}{1-c^4+\sqrt{a^4-4c^4}}=2\sqrt{4c^4-a^4}\tan^{-1}\frac{\sqrt{4c^4-a^4}}{1-c^4} \tag{2.24}$$

when

$$4c^4>a^4\ .$$

Simple special cases of (2.14) are given as follows:

i) Elliptic cylinder $c\to 0$:

$$2\varphi_1(\theta)=Re\left[\frac{1}{e^{2i\theta}-a^2}\left\{(e^{2i\theta}-1)\left(\frac{1-2a^2+a^4}{2a^3}\right)\log\frac{1-ae^{i\theta}}{1+ae^{i\theta}}+\frac{e^{3i\theta}}{a^2}+\left(\frac{(1-a^2)^3}{2a^4}\log\frac{1-a^2}{1+a^2}-1\right)e^{i\theta}\right\}-e^{i\theta}\right] \tag{2.25}$$

ii) Circular cylinder $a=c\to 0$:

$$2\varphi_1(\theta)=Re\left[\frac{4}{3}e^{i\theta}-\frac{1}{3}e^{3i\theta}\right] \tag{2.26}$$

iii) Kaplan bump $c^4=a^2-1$:

$$2\varphi_1(\theta)=Re\left[\frac{e^{2i\theta}}{e^{2i\theta}-c^4}\frac{1-c^4}{2c^2}\log\frac{1+c^2e^{i\theta}}{1-c^2e^{i\theta}}-e^{i\theta}\right]. \tag{2.27}$$

The surface velocity distribution is given by differentiation of (2.12) and the final result is

$$q_1=\frac{d\varphi_1(\theta)}{ds}\frac{d\theta}{ds} \tag{2.28}$$

where

$$\frac{d\varphi_1}{d\theta}=\frac{1}{K_2(\theta)}\{C_R(\theta)ReF(\theta)+C_I(\theta)ImF(\theta)+G(\theta)\}+\frac{H(\theta)}{K(\theta)}+\sin\theta \tag{2.29}$$

$$C_R(\theta)=\alpha_2\sin 2\theta+\alpha_4\sin 4\theta+\alpha_6\sin 6\theta \tag{2.30}$$

$$C_I(\theta)=\beta_0+\beta_2\cos 2\theta+\beta_4\cos 4\theta+\beta_6\cos 6\theta \tag{2.31}$$

$$G(\theta)=\gamma_1\sin\theta+\gamma_3\sin 3\theta+\gamma_5\sin 5\theta+\gamma_7\sin 7\theta \tag{2.32}$$

$$\gamma_n=\gamma_{n1}P+\gamma_{n2}Q\ \ (n=1,\ 3,\ 5,\ 7) \tag{2.33}$$

$$H(\theta)=\delta_1\sin\theta+\delta_3\sin 3\theta \tag{2.34}$$

$$\alpha_2=2-2a^2-2a^4+2a^6+c^4(-4-2a^2+6a^4)+c^8(-4+8a^2)+2c^{12} \tag{2.35}$$

$$\alpha_4=c^4(4+8a^2-12a^4)+2c^8a^2-4c^{12} \tag{2.36}$$

$$\alpha_6=-2c^4-2c^8 \tag{2.37}$$

$$\beta_0=4a^2-4a^4+c^4(-2a^2-2a^4)+c^8(-8-4a^2) \tag{2.38}$$

$$\beta_2=-2+2a^2-2a^4+2a^6+c^4(-4+14a^2+10a^4)+c^8(4+8a^2+2c^{12}) \tag{2.39}$$

$$\beta_4=c^4(-4-12a^4)+c^8(2a^2-4c^{12}) \tag{2.40}$$

$$\beta_6=2c^4-2c^8 \tag{2.41}$$

$$\gamma_{11}=6a^2+3a^4+a^6+c^4(6-6a^4)-2c^8a^2-c^{12} \tag{2.42}$$

$$\gamma_{31}=-3-2a^4+c^4(2-6a^2)+2c^8 \tag{2.43}$$

$$\gamma_{51}=a^2-2a^2c^4+3c^8 \tag{2.44}$$

$$\gamma_{71}=c^4 \tag{2.45}$$

$$\gamma_{12}=-1-2a^2+2a^4+a^6+c^4(4a^2+3a^4)+c^8(6+6a^2) \tag{2.46}$$

$$\gamma_{32}=-a^2+a^4+c^4(2-6a^2-10a^4) \tag{2.47}$$

$$\gamma_{52}=c^4(3-2a^2)-c^8a^2 \tag{2.48}$$

$$\gamma_{72}=c^8 \tag{2.49}$$

$$\delta_1=-5+2a^2+c^4 \tag{2.50}$$

$$\delta_3=1-c^4 \tag{2.51}$$

$$ReF(\theta)=-\mu\frac{1}{2}\log\frac{1+(a^2+2c^2)+c^4+2c^2\cos 2\theta-2\sqrt{a^2+2c^2}(1+c^2)\cos\theta}{1+(a^2+2c^2)+c^4+2c^2\cos 2\theta+2\sqrt{a^2+2c^2}(1+c^2)\cos\theta}$$

$$+\nu\begin{cases}\dfrac{1}{\sqrt{a^2-2c^2}}\dfrac{1}{2}\log\dfrac{1+(a^2-2c^2)+c^4-2c^2\cos 2\theta-2\sqrt{a^2-2c^2}(1-c^2)\cos\theta}{1+(a^2-2c^2)+c^4-2c^2\cos 2\theta+2\sqrt{a^2-2c^2}(1-c^2)\cos\theta} & (a^2>2c^2)\\[2ex] \dfrac{-1}{\sqrt{2c^2-a^2}}\tan^{-1}\dfrac{2\sqrt{2c^2-a^2}(1-c^2)\cos\theta}{1-(2c^2-a^2)+c^4-2c^2\cos 2\theta} & (a^2<2c^2)\end{cases} \tag{2.52}$$

$$ImF(\theta)=\mu\tan^{-1}\frac{2\sqrt{a^2+2c^2}(1-c^2)\sin\theta}{1+c^4-(a^2+2c^2)+2c^2\cos 2\theta}$$

$$-\nu\begin{cases}\dfrac{1}{\sqrt{a^2-2c^2}}\tan^{-1}\dfrac{2\sqrt{a^2-2c^2}(1+c^2)\sin\theta}{1+c^4+(2c^2-a^2)-2c^2\cos 2\theta} & (a^2>2c^2)\\[2ex] \dfrac{1}{\sqrt{2c^2-a^2}}\dfrac{1}{2}\log\dfrac{1+(2c^2-a^2)+c^4-2c^2\cos 2\theta+2\sqrt{2c^2-a^2}(1+c^2)\sin\theta}{1+(2c^2-a^2)+c^4-2c^2\cos 2\theta-2\sqrt{2c^2-a^2}(1+c^2)\sin\theta} & (a^2<2c^2)\end{cases} \tag{2.53}$$

$$\mu=\left(\frac{1-c^4}{4c^2}+\frac{2-a^2}{4}\right)\frac{1}{\sqrt{a^2+2c^2}} \tag{2.54}$$

$$\nu=\frac{1-c^4}{4c^2}-\frac{2-a^2}{4} \tag{2.55}$$

$$K(\theta)=1+a^4+c^8-2a^2(1+c^4)\cos 2\theta+2c^4\cos 4\theta \tag{2.56}$$

$$\frac{d\theta}{ds}=-\frac{1}{\sqrt{K(\theta)}}\,. \tag{2.57}$$

§ 3. The Variation of Curvature of the Velocity Distribution Curve

A few years ago, Takami[3] calculated the velocity distribution, both for incompressible and purely subsonic flow, over the surface of a special obstacle for which Cherry[1] had shown the existence of continuous mixed flow, and showed that the velocity distribution curve has two maxima, in contrast to the fact that the velocity distribution in the transonic case given by Cherry has only one maximum. Thus it seems to be of some interest to study the manner in which the character of the velocity distribution curve is affected by the free stream Mach number. Our family of profiles seems to be particularly suited for this purpose, since it covers both cases of velocity distribution, one-peak as well as two-peak distribution, for the incompressible flow.

For a qualitative discussion it would be sufficient to study the sign of $d^2q/d\theta^2$. Further, because of symmetry only the value at $\theta=\pi/2$ is necessary. When $d^2q/d\theta^2$ is positive, the flow has two maximum velocities on the surface, and when it is negative, the flow has only one maximum.

To see the possibility of transition between these types of flow we have calculated $d^2q_1/d\theta^2$ in the case of

$$c^4=7+a^2-4\sqrt{3+a^2} \tag{3.1}$$

for which the incompressible flow velocity distribution has one flat maximum with zero curvature. The result is shown in Fig. 3, which indicates that the sign is always negative, that is, q_1 has one maximum with finite curvature. In Fig. 4, q_1 is shown for the

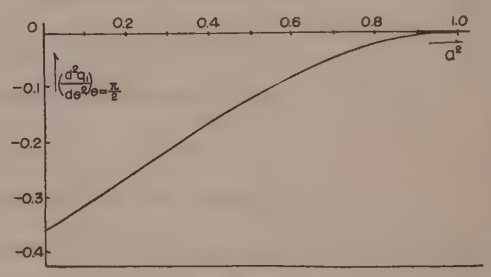

Fig. 3. $\left(\dfrac{d^2q_1}{d\theta^2}\right)_{\theta=\pi/2}$ for $c^4=7+a^2-4\sqrt{3+a^2}$.

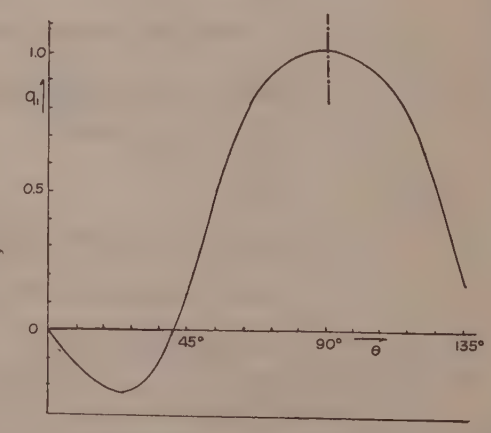

Fig. 4. The first approximation for the profile with $a=0$, $c^4=7-4\sqrt{3}$.

simplest case $a=0$, $c^4=7-4\sqrt{3}$. For sufficiently small values of M the M^2-expansion series is convergent, and the curvature of the velocity distribution curve should have the same sign as $d^2q_1/d\theta^2$ provided that the velocity distribution curve for the incompressible flow has zero curvature.

Now let us consider the case where the value of c^4 exceeds $7+a^2-4\sqrt{3+a^2}$ a little. Then the curvature of q_0 remains unchanged and negative, but the curvature of q_1 becomes positive, that is, q_0 has two maxima and q_1 has only one. Therefore, when the free stream Mach number increases, the velocity distribution has a tendency to assume one-peak distribution instead of two-peak distribution. If c^4 is sufficiently close to $7+a^2-4\sqrt{3+a^2}$ this transition will take place really.

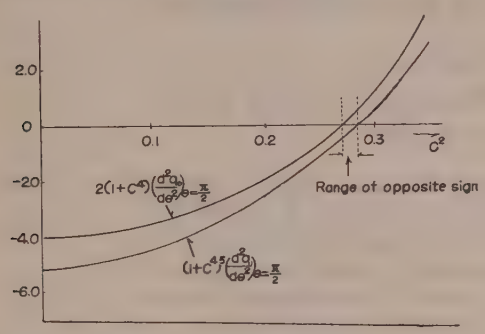

Fig. 5. $\left(\frac{d^2q_0}{d\theta^2}\right)_{\theta=\pi/2}$ and $\left(\frac{d^2q_1}{d\theta^2}\right)_{\theta=2/\pi}$ for $a=0$.

The next problem is to study whether the transition is observable. For this purpose we need some numerical work. For $a^2=0$ $d^2q_0/d\theta^2$ and $d^2q_1/d\theta^2$ are shown in Fig. 5, which shows that the transition can take place in a very narrow range of c. For such values of c the curvature of q_0 is very small, so that we cannot expect an observable effect. For example, let us consider the incompressible flow for $c=0.729$. In this case the difference between the maximum velocity and minimum velocity at $\theta=\pi/2$ is only about 1/300 percent of the minimum velocity. Outside of the narrow range in the neighborhood of $c^2=2-\sqrt{3}=0.268$ the curvatures of q_0 and q_1 have the same sign, so that the transition cannot take place.

Similar circumstances occur also for other values of a. Therefore such an effect should be regarded as merely mathematical, at least within the first approximation.

§ 4. Comparison with the Case of Cherry's Profile

In this section we shall study the cases in which our profiles have the same thickness ratio 0.9312 as Cherry's profile for which flow of mixed type with Mach number 0.5098 take place. For our family of profiles with thickness ratio 0.9312, the boundary case between one-peak and two-peak distribution in incompressible flow is that corresponding to $a^2=0.0348$, $c^4=0.0665$. As is seen in Fig. 1 Cherry's profile is very similar to the profile for which we have shown the possibility of the transition from two-peak to one-peak velocity distribution. But Takami's result reproduced in Fig. 6 as well as some of our

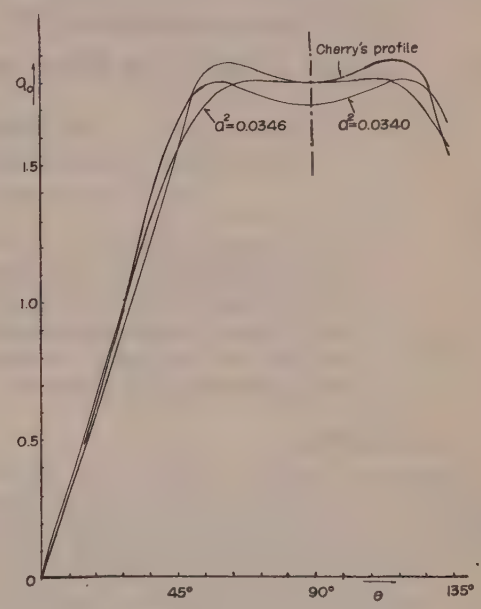

Fig. 6. Incompressible flows for Cherry's profile[3] and our profiles with the same thickness ratio.

family shows that the difference between the maximum and the minimum velocity is quite large. For our family of the same thickness ratio such a sharp two-peak distribution can appear for $a^2=0.0340$ and $c^4=0.133$. Since for $a^2=0.0340$ the value of c^4 corresponding to the boundary case is about 0.0666, the value 0.133 of c^4 is too large to expect the transition phenomenon. We may say that even if the higher order approximations are taken in account, we could not expect the transition. Therefore in spite of the fact that mathematically the transition phenomenon is not ruled out, Takami's conjec ture that the

character of the surface velocity distribution for Cherry's profile will be unchanged up to the critical Mach number will probably remain unaffected.

Acknowledgement

In conclusion the writer wishes to express his sincere thanks to Professor I. Imai for his guidance throughout this work and to Mr. H. Takami for private communication of his numerical data. He is also indebted to the Ministry of Education for a grant.

References

1) T. M. Cherry: Proc. Roy. Soc. **A196** (1949) 32.
2) I. Imai: Rep. Aeron. Res. Inst., Tokyo Imp. Univ. No. 275 (1943).
3) H. Takami: J. Phys. Soc. Japan **11** (1956) 145.

JOURNAL OF THE PHYSICAL SOCIETY OF JAPAN Vol. 13, No. 12, DECEMBER, 1958

The Forces experienced by a Lattice of Equal Flat Plates in a Uniform Flow at Small Reynolds Numbers

By Shinji KUWABARA

Department of Physics, Faculty of Science, University of Tokyo

(Received September 1, 1958)

Two-dimensional incompressible viscous flow past a lattice of equal parallel and equidistant flat plates without stagger placed parallel to a uniform flow is studied on the basis of Stokes' approximation by use of the Fourier transformation method. Asymptotic solutions are explicitly obtained for two cases $h\to\infty$ and $h\to 0$, where h is the distance between the neighbouring two flat plates.

§ 1. Introduction

Tamada and Fujikawa studied the viscous flow past a lattice of equal parallel circular cylinders on the basis of Oseen's approximation[1] and Miyagi also attacked the same problem on the basis of Stokes' approximation[2]. Recently, Hasimoto discussed the flow past a thin screen having a series of parallel equal and equidistant slits[3]. In this parer, we shall study the flow past a lattice of parallel equal and equidistant flat plates without stagger placed parallel equal and equidistant flat plates without stagger placed parallel to a uniform flow. It should be added that Tamada has quite recently discussed the same problem in the general case of arbitrary angle of attack and stagger[4].

Our studies are based on Stokes' equations of motion and make use of the method of Fourier-transformation which has been successfully applied by Hasimoto to the Rayleigh problem for a plate of finite breadth[5].

In §§ 3 and 4, we investigate the asymptotic solutions of the integral equation when $h\to\infty$ and $h\to 0$, where h is the distance between the neighbouring two flat plates.

§ 2. Deduction of the Integral Equation for the Vorticity Distribution on the Flat Plate

Stokes' approximate equations of motion and the equation of continuity for the two-dimensional steady flow of an incompressible viscous fluid are

$$\frac{\partial p}{\partial x}=\mu\Delta u\ , \tag{2.1}$$

$$\frac{\partial p}{\partial y}=\mu\Delta v\ , \tag{2.2}$$

and

$$\frac{\partial u}{\partial x}+\frac{\partial v}{\partial y}=0\ , \tag{2.3}$$

where $\Delta=\partial^2/\partial x^2+\partial^2/\partial y^2$, (x, y) are the cartesian co-ordinates, (u, v) are the velocity components, p is the pressure and μ is the coefficient of viscosity.

Eliminating p from (2.1) and (2.2), we have

$$\Delta\omega=0\,, \tag{2.4}$$

where ω is the vorticity defined by

$$\omega=\frac{\partial v}{\partial x}-\frac{\partial u}{\partial y}\,. \tag{2.5}$$

Introducing the stream function Ψ defined as

$$u=\frac{\partial\Psi}{\partial y}\,,\qquad v=-\frac{\partial\Psi}{\partial x}\,, \tag{2.6}$$

we can rewrite (2.5) in the form

$$\Delta\Psi=-\omega\,. \tag{2.7}$$

We consider the flow past a lattice of parallel equal and equidistant flat plates without stagger placed parallel to the uniform flow (Fig. 1). Then, the boundary conditions for ω and Ψ are as follows:

$$\omega=0 \qquad \text{for } y=0,\ |x|>1, \tag{2.8a}$$

$$\omega=g(x) \qquad \text{for } y=0,\ |x|\leq 1, \tag{2.8b}$$

$$\omega=0 \qquad \text{for } y=h/2, \tag{2.8c}$$

$$\psi=0 \qquad \text{for } y=0,\ h/2, \tag{2.8d}$$

$$\partial\psi/\partial y=-U \qquad \text{for } y=0,\ |x|<1, \tag{2.8e}$$

where $g(x)$ is an unknown function, ψ is a perturbation stream function defined as $\Psi=Uy+\psi$, and U is the undisturbed flow velocity.

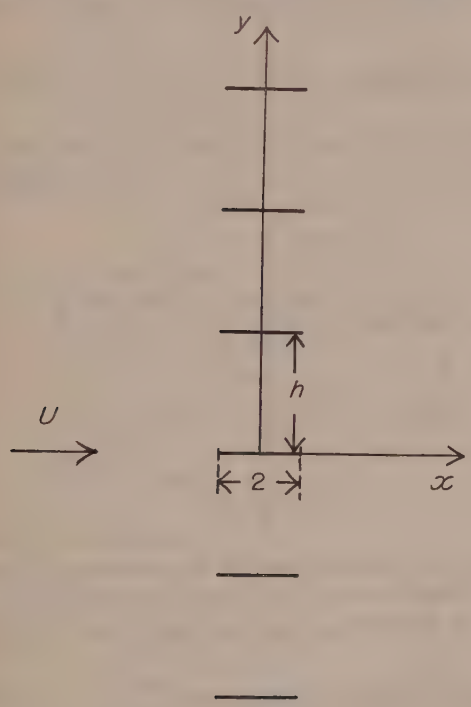

Fig. 1. Configuration of a lattice of flat plates in a uniform flow.

We define the Fourier transform and the inverse Fourier transform of $f(x, y)$ as

$$f^*(\alpha, y)=\int_{-\infty}^{\infty} f(x, y)e^{-i\alpha x}dx\,, \tag{2.9a}$$

$$f(x, y)=\frac{1}{2\pi}\int_{-\infty}^{\infty} f^*(x, y)e^{i\alpha x}d\alpha\,. \tag{2.9b}$$

Then, we can transform (2.4) and (2.7) as follows;

$$\frac{d^2\omega^*}{dy^2}-\alpha^2\omega^*=0\,, \tag{2.10}$$

$$\frac{d^2\psi^*}{dy^2}-\alpha^2\psi^*=-\omega^*\,. \tag{2.11}$$

Also, the boundary conditions (2.8) become

$$\omega^*=g^*(\alpha)\equiv\int_{-1}^{1} g(x)e^{-i\alpha x}dx \quad \text{for } y=0, \tag{2.12a}$$

$$\omega^*=0 \qquad \text{for } y=h/2 \tag{2.12b}$$

$$\psi^*=0 \qquad \text{for } y=0,\ h/2 \tag{2.12c}$$

Solving (2.10) subject to the boundary conditions (2.12a) and (2.12b), we obtain

$$\omega^*(\alpha, y)=\frac{\sinh\alpha(h-y)}{\sinh(\alpha h/2)}g^*(\alpha)\,. \tag{2.13}$$

Substituting (2.13) into (2.11) and solving (2.11) subject to the condition (2.12c), we have

$$\psi^*(\alpha, y)=\frac{g^*(\alpha)}{4\alpha\cdot\sinh^2(\alpha h/2)}\{y\sinh\alpha(h-y)-(h-y)\sinh\alpha y)\}\,. \tag{2.14}$$

In order to obtain $\psi(x, y)$ from (2.14), we make use of the convolution theorem, that is,

$$\frac{1}{2\pi}\int_{-\infty}^{\infty} f^*(\alpha)h^*(\alpha)e^{i\alpha x}d\alpha=\int_{-\infty}^{\infty} f(p)h(x-p)dp\,. \tag{2.15}$$

Thus, we have

$$\psi(x, y)=\frac{1}{2\pi}\int_{-\infty}^{\infty} g^*(\alpha)K^*(\alpha, y)e^{i\alpha x}d\alpha=\int_{-\infty}^{\infty} g(p)K(x-p, y)dp\,, \tag{2.16}$$

where

$$K^*(\alpha, y)=\frac{1}{4\alpha\cdot\sinh^2(\alpha h/2)}\{y\sinh\alpha(h-y)-(h-y)\sinh\alpha y\}\,, \tag{2.17}$$

and

$$K(x, y)=\frac{1}{2\pi}\int_{-\infty}^{\infty}K^*(\alpha, y)e^{i\alpha x}\,d\alpha\,. \tag{2.18}$$

By use of the method of contour integral, we can evaluate the integral of (2.18). The contours are such as shown in Fig. 2. Residues of $K^*(\alpha)e^{i\alpha x}$ are

$$R_n=\frac{ie^{-(2\pi n/h)x}}{2\pi nh}\cdot\left(\frac{h}{2\pi n}+x\right)$$
$$\times\left\{y\sinh\frac{2\pi n}{h}(h-y)-(h-y)\sinh\left(\frac{2\pi n}{h}y\right)\right\},$$
$$\text{at}\quad \alpha=i\,\frac{2\pi n}{h}\quad (n=\cdots-2,\,-1,\,1,\,2,\,\cdots)\,. \tag{2.19}$$

It is to be noted that the singularity at $\alpha=0$ is a removable one.

Now, $K(x)$ expressed as the contour integral consists of the sum of residues corresponding to the singularities enclosed in the contour and a contribution from the integral over the semi-circle, whose radius R is to be taken as infinite. It can be easily verified that the latter contribution vanishes by making $R\to\infty$. Then, we can express the contour integral as follows:

$$K(x)=\begin{cases} i\sum_{n=1}^{\infty}R_n & \text{for } x\geq 0\,,\\ -i\sum_{n=1}^{\infty}R_{-n} & \text{for } x\leq 0\,,\end{cases} \tag{2.20}$$

which becomes, by (2.19),

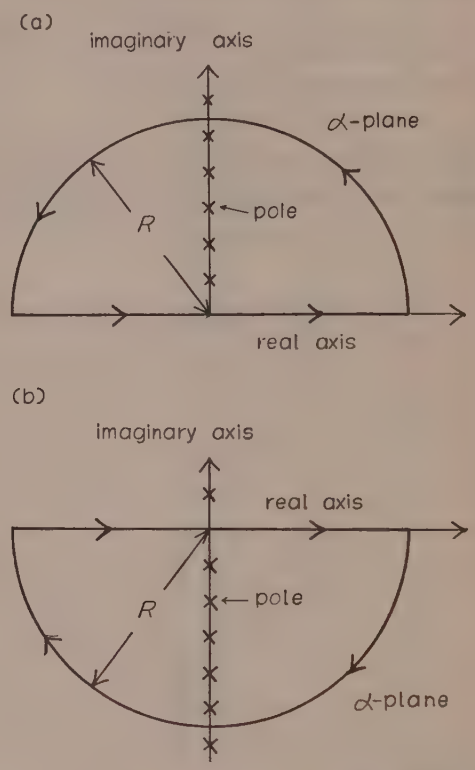

Fig. 2. Contours used for the evaluation of the integral (2.18). (a) is used in case of $x\geq 0$ and (b) in case of $x\leq 0$.

$$K(x)=-\frac{1}{2\pi h}\sum_{n-1}^{\infty}\frac{1}{n}\left(\frac{h}{2\pi n}+|x|\right)e^{-(2\pi n/h)|x|}\left\{y\sinh\frac{2\pi n}{h}(h-y)-(h-y)\sinh\frac{2\pi n}{h}y\right\}. \tag{2.21}$$

Hence (2.16) becomes

$$\psi(x, y)=-\frac{1}{2\pi h}\int_{-1}^{1}g(p)\sum_{n=1}^{\infty}\frac{1}{n}\left(\frac{h}{2\pi n}+|x-p|\right)e^{-(2\pi n/h)|x-p|}$$
$$\times\left\{y\sinh\frac{2\pi n}{h}(h-y)-(h-y)\sinh\frac{2\pi n}{h}y\right\}dp\,. \tag{2.22}$$

Now, we have

$$\left.\frac{\partial\psi}{\partial y}\right|_{y=0}=\frac{1}{h}\int_{-1}^{1}g(p)\left\{-\frac{h}{2\pi}\ln(1-e^{-(2\pi/h)|x-p|})+|x-p|\frac{e^{-(2\pi/h)|x-p|}}{1-e^{-(2\pi/h)|x-p|}}\right\}dp\,. \tag{2.23}$$

Thus, the boundary condition (2.8e) gives

$$2\pi U=\int_{-1}^{1}g(p)\left\{\ln(1-e^{-(2\pi/h)|x-p|})+\frac{2\pi}{h}|x-p|\frac{e^{-(2\pi/h)|x-p|}}{1-e^{-(2\pi/h)|x-p|}}\right\}dp\quad\text{for } |x|<1\,, \tag{2.24}$$

which is the Fredholm integral equation of the first kind with respect to the vorticity $g(x)$ on the flat plate. This forms the basic equation for the subsequent treatment of our problem.

§ 3. Asymptotic Solution when $2\pi/h \to 0$

In case when $2\pi/h \ll 1$, we can expand the kernel of the integral equation (2.24) as follows:

$$\ln(1-e^{-(2\pi/h)|x-p|})-\frac{2\pi}{h}|x-p|\frac{e^{-(2\pi/h)|x-p|}}{1-e^{-(2\pi/h)|x-p|}}=\ln\frac{2\pi}{h}-1+\ln|\cos\alpha-\cos\beta|$$
$$-\frac{1}{24}\left(\frac{2\pi}{h}\right)^2(\cos\alpha-\cos\beta)^2+\frac{1}{960}\left(\frac{2\pi}{h}\right)^4(\cos\alpha-\cos\beta)^4+\cdots, \tag{3.1}$$

where we have put

$$x=\cos\alpha, \quad p=-\cos\beta, \tag{3.2}$$

In view of the form of (3.1), let us write

$$g(\cos\beta)\sin\beta=\sum_{n=0}^{\infty}\left(\frac{2\pi}{h}\right)^{2n}\varphi_n(\beta). \tag{3.3}$$

Substituting (3.1) and (3.3) into (2.24) and equating terms of the order $(2\pi/h)^{2n}$ on both sides (where $n=0, 1, 2, \cdots$), we have series of integral equations

$$\int_0^\pi \varphi_0(\beta)\left(-P-\sum_{m=1}^{\infty}\frac{2}{m}\cos m\alpha\cos m\beta\right)d\beta=2\pi U, \tag{3.4}$$

$$\int_0^\pi\left\{\varphi_1(\beta)\left(-P-\sum_{m=1}^{\infty}\frac{2}{m}\cos m\alpha\cos m\beta\right)-\frac{1}{24}\varphi_0(\beta)(\cos\alpha-\cos\beta)^2\right\}d\beta=0, \tag{3.5}$$

$$\int_0^\pi\left\{\varphi_2(\beta)\left(-P-\sum_{m=1}^{\infty}\frac{2}{m}\cos m\alpha\cos m\beta\right)-\frac{1}{24}\varphi_1(\beta)(\cos\alpha-\cos\beta)^2\right.$$
$$\left.+\frac{1}{960}\varphi_0(\beta)(\cos\alpha-\cos\beta)^4\right\}d\beta=0, \tag{3.6}$$

and so on, where

$$P=1-\ln(\pi/h), \tag{3.7}$$

and we have used the formula

$$\ln|\cos\alpha-\cos\beta|=-\sum_{m=1}^{\infty}\frac{2}{m}\cos m\alpha\cos m\beta-\ln 2.$$

Let us assume

$$\varphi_n(\alpha)=\sum_{m=0}^{\infty}c_{nm}\cos 2m\alpha. \tag{3.8}$$

Then, substituting (3.8) into (3.4), we can determine c_{0m}:

$$c_{00}=-2U/P, \quad c_{01}=c_{01}=c_{02}=c_{03}=\cdots=0, \tag{3.9}$$

so that we have

$$\varphi_0(\alpha)=-2U/P. \tag{3.10}$$

In quite a similar manner, we can obtain

$$\varphi_1(\alpha)=\frac{1}{12}\frac{U}{P^2}(1+P\cos 2\alpha), \tag{3.11}$$

$$\varphi_2(\alpha)=-\frac{1}{288}\frac{U}{P^2}\left\{1+\frac{8}{5}+P\left(1+\frac{12}{5}P\right)\cos 2\alpha-\frac{3}{10}\cos 4\alpha\right\}, \tag{3.12}$$

and so on.

The drag D of the flat plate is determined by

$$D=-2\mu\int_{-1}^{1}g(x)dx=-2\mu\int_0^{\pi}\sum_{n=0}^{\infty}\left(\frac{2\pi}{h}\right)^{2n}\varphi_n(\alpha)d\alpha$$

$$=4\pi\mu\frac{U}{P}\left\{1-\frac{1}{24}\left(\frac{2\pi}{h}\right)^2\frac{1}{P}+\frac{1}{576}\left(\frac{2\pi}{h}\right)^4\frac{1}{P}\left(1+\frac{8}{5}P\right)+\cdots\right\}, \tag{3.13}$$

and the drag coefficient C_D by

$$C_D\equiv\frac{D}{\frac{1}{2}\rho U^2\cdot 2}=\frac{8\pi}{R}\frac{1}{P}\left\{1-\frac{1}{24}\left(\frac{2\pi}{h}\right)^2\frac{1}{P}+\frac{1}{576}\left(\frac{2\pi}{h}\right)^2\frac{1}{P}\left(1+\frac{8}{5}P\right)+\cdots\right. \tag{3.14}$$

where

$$R=\frac{2U\rho}{\mu} \tag{3.15}$$

is the Reynolds number based on the breadth of the flat plate. It should be noted that the formulae (3.13) and (3.14) are valid only for the case $P>0$, and hence by (3.7), for $h>\pi/e=1.1557\cdots$.

§ 4. Asymptotic Solution when $2\pi/h\to\infty$

In order to solve (2.24) when $2\pi/h\gg 1$, we put

$$\xi=bx,\qquad \eta=bp\qquad (b=2\pi/h). \tag{4.1}$$

Substituting (4.1) into (2.24), we have

$$2\pi bU=\int_{-b}^{b}g(\eta)\left\{\ln(1-e^{-|\xi-\eta|})-|\xi-\eta|\frac{e^{-|\xi-\eta|}}{1-e^{|\xi-\eta|}}\right\}d\eta. \tag{4.2}$$

Taking into account the fact that $b\gg 1$ and that the kernel is singular at $\xi=\eta$, we may write (4.2) approximately in the form

$$2\pi bU=2g(\xi)\int_0^{\infty}\left\{\ln(1-e^{-\eta})-\eta\frac{e^{-\eta}}{1-e^{-\eta}}\right\}d\eta=-\frac{2\pi^2}{3}g(\xi). \tag{4.3}$$

Then we have

$$g(x)=-\frac{6U}{h} \tag{4.4}$$

so that the tangential stress τ on the flat plate is

$$\tau=-\mu g(x)=\frac{6\mu U}{h}. \tag{4.5}$$

We can obtain the drag and the drag coefficient of the flat plate in the same way as (3.13) and (3.14)

$$D_0=\frac{24\mu U}{h}, \tag{4.6}$$

$$C_D=\frac{48}{R}\frac{1}{h}. \tag{4.7}$$

Let us now consider the plane Poiseuille flow in a channel of breadth h with total flux Uh. In this case the vorticity ω and the stress τ on the walls of the channel can be readily calculated as

$$\omega=-\frac{6U}{h} \quad \text{and} \quad \tau=\frac{6\mu U}{h}. \tag{4.8}$$

These coincide with (4.4) and (4.5). This should naturally be expected, in view of the fact that the flow between the flat plates approaches the plane Poiseuille flow when h becomes small, except in the immediate neighbourhood of the leading and the trailing edges.

Next, we shall investigate the edge effect on the vorticity distribution $g(x)$. To this end, we put

$$\xi=b(x+1), \qquad \eta=b(x+1), \qquad (b=2\pi/h). \tag{4.9}$$

Then, we can transform (2.24) as

$$2\pi bU=\int_0^\infty g(\eta)\left\{\ln(1-e^{-|\xi-\eta|})-|\xi-\eta|\frac{e^{-|\xi-\eta|}}{1-e^{-|\xi-\eta|}}\right\}, \tag{4.10}$$

by considering that $b\gg 1$. (4.10) is an integral equation of the Wiener-Hopf type.

In order to solve (4.10), we put

$$\frac{1}{2\pi}\int_0^\infty g(\eta)\left\{\ln(1-e^{-|\xi-\eta|})-|\xi-\eta|\frac{e^{-|\xi-\eta|}}{1-e^{-|\xi-\eta|}}\right\}d\eta=\begin{cases} bUe^{-\alpha\xi} & \text{for } \xi>0, \\ h(\xi) & \text{for } \xi<0, \end{cases} \tag{4.11}$$

where α is a small positive parameter to be made 0 in the limit. We apply the Fourier transformation to (4.11) as shown in (2.9). Then, (4.11) becomes

$$\frac{1}{2}g^*(\zeta)\frac{1}{\zeta}\frac{\sinh 2\pi\zeta-2\pi\zeta}{\cosh 2\pi\zeta-1}=h^*(\zeta)+\frac{bU}{\alpha+i\zeta}, \tag{4.12}$$

by using

$$\int_{-\infty}^\infty\left\{\ln(1-e^{-|\eta|})-|\eta|\frac{e^{-|\eta|}}{1-e^{-|\eta|}}\right\}e^{-i\zeta\eta}d\eta=\frac{\pi}{\zeta}\frac{\sinh 2\pi\zeta-2\pi\zeta}{\cosh 2\pi\zeta-1}. \tag{4.13}$$

We shall consider the region where ξ is large. This corresponds to the small value of $|\zeta|$, and hence we can expand (4.13) as follows:

$$\frac{\sinh 2\pi\zeta-2\pi\zeta}{\cosh 2\pi\zeta-1}=\frac{2\pi}{\zeta}\frac{1+(1/20)(2\pi\zeta)^2+(1/840)(2\pi\zeta)^4+\cdots}{1+(1/12)(2\pi\zeta)^2+(1/360)(2\pi\zeta)^4+\cdots}. \tag{4.14}$$

As a first approximation, we retain only the first two terms in the denominator and the numerator in (4.14), so that (4.11) becomes

$$\frac{\pi}{5}g^*(\zeta)\frac{\zeta^2+5/\pi^2}{\zeta^2+3/\pi^2}=h^*(\alpha)-\frac{ibU}{\zeta-i\alpha}. \tag{4.15}$$

Noting that $g^*(\zeta)$ is regular in the lower half of the complex ζ-plane and $h^*(\zeta)$ is regular in the upper half plane, we may rewrite (4.15) as

$$\begin{aligned}\frac{\pi}{2}g^*(\zeta)\frac{\zeta-i\sqrt{5}/\pi}{\zeta-i\sqrt{3}/\pi}+\frac{ibU}{\zeta-i\alpha}\frac{\alpha+\sqrt{3}/\pi}{\alpha+\sqrt{5}/\pi}& \\ =\frac{\zeta+i\sqrt{3}/\pi}{\zeta+i\sqrt{5}/\pi}h^*(\zeta)-\frac{ibU}{\zeta-i\alpha}\left(\frac{\zeta+i\sqrt{3}/\pi}{\zeta+i\sqrt{5}/\pi}-\frac{\alpha+\sqrt{3}/\pi}{\alpha+\sqrt{5}/\pi}\right).&\end{aligned} \tag{4.16}$$

The left-hand side is regular in the lower half plane and the right-hand side is regular in

the upper half plane. Therefore, both sides should be regular in the whole ζ-plane, and hence, equal to a constant. It can be readily shown that the constant is zero. $g^*(\zeta)$ being thus found, we can determine $g(\xi)$:

$$g(\xi)=\frac{1}{2\pi}\int_{-\infty}^{\infty} g^*(\zeta)e^{i\xi\zeta}d\zeta=-\frac{2\sqrt{15}U}{h}\frac{1}{2\pi i}\int_{-i\infty}^{i\infty}\frac{p+\sqrt{3}/\pi}{p(p+\sqrt{5}/\pi)}e^{\xi p}dp$$

$$=-\frac{6U}{h}\left(1+\frac{\sqrt{5}-\sqrt{3}}{\sqrt{3}}e^{-(2\sqrt{5}/h)(x+1)}\right), \tag{4.17}$$

where we have used the formula

$$\frac{1}{2\pi i}\int_{-i\infty}^{i\infty}\frac{\lambda p+\mu}{p(p+\beta)}e^{\xi p}dp=\frac{\mu}{\beta}+\frac{\beta\lambda-\mu}{\beta}e^{-\beta\xi}. \tag{4.18}$$

If we let x tend to infinity, (4.17) agrees with (4.4) which corresponds to the case of the plane Poiseuille flow. The second term in the bracket is a correction term due to the edge effect, which we shall write in the form:

$$g_1(x)=-\frac{6U}{h}\frac{\sqrt{5}-\sqrt{3}}{\sqrt{3}}e^{-(2\sqrt{5}/h)(x+1)}. \tag{4.19}$$

The correction D_1 to the drag is obtained as follows:

$$D_1=-4\mu\int_{-1}^{\infty}g_1dx=\frac{24\mu U}{h}\frac{\sqrt{5}-\sqrt{3}}{2\sqrt{15}}. \tag{4.20}$$

The drag coefficient becomes

$$C_D=\frac{D_0+D_1}{\frac{1}{2}\rho U^2\cdot 2}=\frac{48}{R}\frac{1}{h}\left(1+\frac{\sqrt{5}-\sqrt{3}}{2\sqrt{15}}h\right). \tag{4.21}$$

In the second approximation, we retain the first three terms in (4.14). In quite a similar manner to the first approximation, we obtain the correction terms g_2 and D_2 for the vorticity $g(x)$ and the drag as

$$g_2(x)=-\frac{6U}{h}\{A\cos a_1(x+1)+B\sin a_1(x+1)\}e^{-a_2(x+1)}, \tag{4.22}$$

Table I. Calculated values of RC_D for various values of h.

1) The case $h\to\infty$.

h	2	3	4	5	7	10	20	50	70	100
I_∞	45.83	26.35	20.24	17.13	13.95	11.65	8.815	6.671	6.124	5.635
II_∞	11.46	21.30	18.57	16.36	13.69	11.56	8.803	6.670	6.124	5.634
III_∞	46.26	24.57	19.31	16.61	13.74	11.57	8.803	—	—	—

I_∞, II_∞, III_∞ are the values calculated by (3.14) retaining only the first terms, the first two terms and the first three terms, respectively.

2) The case $h\to 0$.

h	0.01	0.02	0.05	0.07	0.1	0.2	0.5	0.7	1	2	5	7	10
I_0	4800	2400	960.0	685.7	480.0	240.0	96.00	68.57	48.00	24.00	9.600	6.857	4.800
II_0	4803	2403	963.1	688.8	483.1	243.1	99.12	71.69	51.12	27.12	12.72	9.980	7.923
III_0	4804	2404	964.4	690.2	484.4	244.4	100.44	73.01	52.44	28.44	14.04	11.298	9.240

I_0 is calculated by (4.7), II_0 by (4.21) and III_0 by (4.26).

$$D_2=\frac{24\mu U}{h}\frac{h}{\sqrt{180}}\{(\sqrt{840}-21)^{1/2}-(\sqrt{360}-15)^{1/2}\}\,, \tag{4.23}$$

where

$$A=\sqrt{7/3}-1,\ B=(\sqrt{840}-21)^{-1/2}\{(\sqrt{7/3}-1)(\sqrt{840}+21)^{1/2}-2\sqrt{7/3}(\sqrt{360}+15)^{1/2}\}\,, \tag{4.24}$$

$$a_1=\frac{1}{\sqrt{2}\,h}(\sqrt{840}-21)^{1/2}\,,\quad a_2=\frac{1}{\sqrt{2}\,h}(\sqrt{840}+21)^{1/2}\,, \tag{4.25}$$

and the drag coefficient becomes

$$C_D=\frac{D_0+D_2}{\frac{1}{2}\rho U^2\cdot 2}=\frac{48}{R}\frac{1}{h}\left[1+\frac{h}{\sqrt{180}}\{(\sqrt{840}+21)^{1/2}-(\sqrt{360}+15)^{1/2}\}\right]. \tag{4.26}$$

§ 5. Numerical Discussions

The drag coefficient is inversely proportional to the Reynolds number as is natural in the Stokes approximation. Thus, RC_D is a function of h only. Fig. 3 and Table I show the numerical values of RC_D for the various values of h.

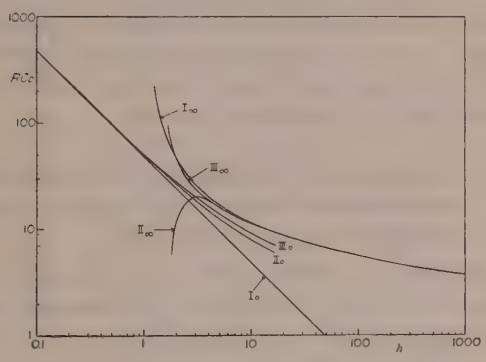

Fig. 3.

The asymptotic solution (3.14) corresponding to $h\to\infty$ can be used only for $h<\pi/e=1.1557\cdots$. However, it seems that RC_D obtained from this asymptotic solution is correct within several per cent in the range $h=5\sim\infty$ in the third approximation in which $O(h^{-4})$ is retained. It appears that the asymptotic solution corresponding to $h\to 0$ would give under-estimated value of RC_D. But the matching of both asymptotic solution seems to be satisfactory.

Acknowledgement

The author wishes to express his sincere thanks to Professor Isao Imai for his suggestion of this problem and continual guidance throughout this study. He is also indebted to Professor Hidenori Hasimoto for his advice and discussions and Dr. Mitutosi Kawaguti and Mr. Hideo Takami for their invaluable discussions.

References

1) T. Tamada and H. Fujikawa: Quart. J. Mech. and Appl. Math. **10** (1957) 423.
2) T. Miyagi: J. Phys. Soc. Japan **13** (1958) 493.
3) H. Hashimoto: J. Phys. Soc. Japan **13** (1958) 633.
4) K. Tamada: Read at the Joint Meeting on Appl. Math. and Mech. of the Phys. Soc. Japan and Japan Soc. Aeron. Engg. held at Tokyo Metropolitan Univ., May 1958.
5) H. Hasimoto: Proc. 1st Japan Nat. Congr. Appl. Mech. 1951 (1952) 447.
5) A. Erdélyi: *Tables of Integral Transforms*, vol. I (McGraw-Hill Book Co., Inc., 1954).

JOURNAL OF THE PHYSICAL SOCIETY OF JAPAN Vol. 13, No. 12, DECEMBER, 1958

Deviation from Linearity of the Concentration Dependence of the Molecular Sound Velocity in Liquid Mixtures

By Otohiko NOMOTO

Kobayasi Institute of Physical Research, Kokubunzi, Tokyo

(Received August 18, 1958)

Accuracy of the linear dependence of the molecular sound velocity on the molar fractions of the component liquids was investigated in about 100 binary mixtures, employing existing ultrasonic data. The linearity proved to hold true within an accuracy of 0.3% for mixtures of two hydrocarbons or two monovalent alcohols, among others, while the deviation from linearity was larger (0.3%–4%) for the following mixtures: the aqueous solutions, mixtures containing one heavy component such as carbon tetrachloride or chloroform with light partners, mixtures containing glycerine, glycol, aniline, acetone, nitrobenzene, etc. The molecular compressibility (of Wada) showed a similar tendency, though the deviation from linearity was somewhat smaller than that of the molecular sound velocity, especially in case of the mixtures consisting of two component liquids of widely different densities.

§ 1. Introduction

It has been pointed out in a previous paper[1] that Rao's molecular sound velocity[2] in liquid mixture

$$R=\frac{M}{\rho}V^{1/3}=vV^{1/3} \qquad (1.1)$$

is approximately a linear function of the molar fraction n_A, n_B of the component liquids:

$$R=n_AR_A+n_BR_B=R_A+n_B(R_B-R_A)\,, \qquad (1.2)$$

where V means the sound velocity, ρ the density, v the molar volume, and

$$M=n_AM_A+n_BM_B \qquad (1.3)$$

means the average molecular weight of the mixture. The quantities with suffixes A, B, refer to the component liquids A and B, respectively.

About 40 liquid mixtures were examined previously, and the linear relation was found to hold true except for the aqueous solutions and the mixtures consisting of one heavy component liquid such as carbon tetrachloride or chloroform with a light partner.

The linear relationship holds true also for aqueous sugar solutions and aqueous polyalcohol solutions[3], within the range of the concentrations investigated.

Although the relation (1.2) has not found any theoretical explanation as yet, it seems rather striking that such a simple relationship exists between v and V (or ρ and V), considering the rather complicated dependence of V (or ρ) on concentration in some mixtures, even exhibiting maximum or minimum in some cases. So it seems worth while to investigate the deviation from linearity of the molecular sound velocity in detail.

§ 2. Deviation from Linearity of the Molecular Sound Velocity *vs.* Molar fraction in Binary Liquid Mixtures

Molecular sound velocity was computed for about 60 liquid mixtures in dependence on concentration by employing the existing ultrasonic data[4)–11)] and compared with the value computed from the linear formula (1.2). The result is summarized in Table I, together with the results on about 40 liquid mixtures, for which the molecular sound velocity was investigated in the previous paper[1]. For example, the mixture numbered as I–20 refers to the No. 20 mixture in the previous paper. (cf. the references in the previous paper for the sources of ultrasonic data for these first group of mixtures). Some of the mixtures reported in the previous paper were reinvestigated employing new ultrasonic data.[4),6),7)]

In this table, ΔR means

$$\Delta R=R_{\rm cal}-R_{\rm exp}\,, \qquad (2.1)$$

where $R_{\rm cal}$ is the value computed by (1.2) and $R_{\rm exp}$ the value computed by employing the sound velocity and density of the mixture.

In many of the cases, the molecular compressibility introduced by Wada[12]

Table I. Deviations from linearity of the molecular sound velocity R and the molecular compressibility W in some liquid mixtures (Range of concentration=0~100% unless otherwise stated).

No.	Liquid mixtures	Range of concentration n_B %	$\Delta R/R$ %	$\Delta W/W$ %	Author of the sound velocity data
I-1	water-formic acid	0-93.85	−0.9	−0.8	Mikhailov
I-2	water-acetic acid		−0.61	−0.6	Mikhailov
				∓1.22	Prosorow[6]
I-3	water-acetone		±1.6	±1.5	Ramachandra Rao
				−1.66	Jacobson[7]
I-4	water-methanol	0-85.50	−2.3		Parshad
		0-100	−2.3	−2.0	Pesce-Giacomini
			−2.7		Jacobson[7]
I-5	water-ethanol		∓1.6	∓1.4	Parshad
				−2.77	Jacobson[7]
I-6	water-propanol	0-19.39	−2.05		Parshad
		0-100	−2.23	−1.88	Jacobson[7]
I-7	nitrobenzene-ethanol		0.9	0.6	Gabrielli-Poiani
I-8	nitrobenzene-methanol		2.2	1.8	〃
I-9	ethanol-aniline		0.75		〃
I-10	benzene-acetone		∓0.13		Tuomikoski-Nurmi
I-11	benzene-ethanol		±0.38	±0.29	〃
I-12	benzene-ethyl ether		±0.47	±0.24	Parshad
I-13	tetraline-carbon tetrachloride		2.3	±1.2	Parthasarathy
I-14	nitrobenzene-toluene		0.25	±0.8	Gabrielli-Poiani
I-15	benzene-dichloromethane		0.5	0.3	Tuomikoski-Nurmi
I-16	chloroform-benzene		1.0	0.3	Gabrielli-Poiani
I-17	benzene-carbon tetrachloride		1.2	±0.5	Tuomikoski-Nurmi
I-18	benzene-chlorobenzene		±0.47	±0.37	〃
I-19	benzene-carbon disulphide		0.5	0.1	〃
I-20	benzene-toluene		±0.14	±0.1	Gabrielli-Poiani
I-21	heptane-benzene		−0.07		Tuomikoski-Nurmi
			∓0.06		Danusso[4]
I-22	heptane-chlorobenzene		∓0.7		Tuomikoski-Nurmi
I-23	heptane-n. butanol		0.32	0.27	Wilson-Richards
I-24	heptane-carbon tetrachloride		1.45	0.4	Tuomikoski-Nurmi
I-25	ethyl acetate-carbon tetrachloride		−1.24		Parthasarathy
I-26	carbon disulphide-carbon tetrachloride		∓0.66	−0.66	〃
I-27	carbon tetrachloride-chloroform		±0.2	±0.2	Gabrielli-Poiani
I-28	chloroform-acetone		1.5	0.6	Parthasarathy
I-29	ethanol-ether		0.5	0.4	Gabrielli-Poiani
I-30	methanol-ether		0.75	0.64	〃
I-31	ethanol-cyclohexane		0.6	0.5	〃
I-32	nitrobenzene-aniline		−0.34	−0.30	〃
I-33	heptane-ethanol		0.9	0.8	Tuomikoski-Nurmi
I-34	heptane-dichloromethane		0.6	0.6	〃
I-35	acetone-cyclohexane		−0.9	−0.4	Gabrielli-Poiani
I-36	carbon tetrachloride-ethanol		1.5	0.5	Sacher
I-37	chloroform-ether		2.8	1.7	Parshad
1	hexane-paraffin oil (Mixtures) (Molecular weight=268)		±1.3		Danusso[4]
2	cyclohexane-benzene		−0.3		〃
3	cyclohexane-decalin		0.12		〃
4	n. heptane-cyclohexane		−0.2		〃
5	n. heptane-decalin		0.24	0.19	〃
6	n. heptane-cetane		∓0.15		〃
7	isoosctane-benzene		−0.3		〃
8	isooctane-cyclohexane		−0.4		〃
9	isooctane-n. heptane		∓0.07		〃

Table I. continued

No.	Liquid mixtures	Range of concentration n_B %	$\Delta R/R$ %	$\Delta W/W$ %	Author of the sound velocity data
10	isooctane-decalin		±0.2		Danusso[4]
11	isooctane-cetane		∓0.2		〃
12	decalin-benzene		0.14		〃
13	cetane-cyclohexane		±0.05	±0.04	〃
14	cetane-decalin		0.05	±0.02	〃
15	nitrobenzene-benzene		±0.4		Gabrielli-Poiani[5]
16	aniline-benzene		0.3		〃
17	aniline-toluene		0.44		〃
18	aniline-acetone		±0.6		〃
19	nitrobenzene-chloroform		±0.3		〃
20	methanol-n. butanol		0.14	0.11	Danusso[4]
21	methanol-isoamyl alcohol		0.2	0.2	〃
22	methanol-cyclohexanol		0.24		〃
23	methanol-octyl alcohol		±0.1	0.1	〃
24	methanol-dodecyl alcohol		0.4		〃
25	isopropanol-n. butanol		0.18		〃
26	n-propanol-cyclohexanol		0.01		〃
27	isopropanol-cyclohexanol		0.3		〃
28	n. butanol-cyclohexanol		±0.12	±0.08	〃
29	glycerine-glycol		0.3		Danusso[4]
30	methanol-glycol		∓1.5	∓1.6	〃
31	ethanol-glycol		0.95	0.76	〃
32	n. propanol-glycol		0.87	0.70	〃
33	isopropanol-glycol		1.0	0.8	〃
34	n. butanol-glycol		0.87	0.94	〃
35	isobutanol-glycol		0.9	0.7	〃
36	isoamyl alcohol-glycol		0.7	0.5	〃
37	octylalcohol-glycol		1.2		〃
38	cyclohexanol-glycol		0.43	0.36	〃
39	methanol-glycerine		2.3	1.8	Danusso[4]
40	n. propanol-glycerine		2.3		〃
41	isopropanol-glycerine		2.2	±1.7	〃
42	n. butanol-glycerine		2.5	3.1	〃
43	isobutanol-glycerine		2.7		〃
44	cyclohexanol-glycerine		2.7	2.2	〃
45	water-glycerine		∓2.1	±0.4	Danusso[4]
46	water-glycol		−1.2	−1.2	〃
47	water-sulfuric acid	0-65	3.7	2.7	Prosorow[6]
48	water-nitric acid	0-30	1.5	(1.1)	〃
49	water-isopropanol		∓2.8	∓2.4	Jacobson[7]
50	nitrobenzene-acetone		∓1.7		Gabrielli-Poiani[5]
51	aniline-chloroform		1.4		〃
52	aniline-ether		1.3	0.63	〃
53	nitrobenzene-ether		1.3		〃
54	cetane-benzene		0.1		Danusso[4]
55	pentane-heptane		∓0.35	∓0.30	Jacobson[7]
56	methanol-ethanol		0.12	0.1	〃
57	nitrobenzene-isoamylalcohol		0.5		Melkonjan[9]
58	carbontetrachloride-toluene		1.0		Dmitrieva[10]
59	hexane-pyridine		±0.1		Jacobson[8]
60	hexane-diphenyl methane		2.1		〃
61	pyridine-acetic acid		±1.9		Balachandran[11]

$$W = v\beta^{-1/7} \tag{2.2}$$

was also computed and the deviation

$$\Delta W = W_{\text{cal}} - W_{\text{exp}} \tag{2.3}$$

was obtained. Here W_{exp} is the value computed by employing the velocity and density data of the mixture and W_{cal} is the value corresponding to the linear formula:

$$W_{\text{cal}} = n_A W_A + n_B W_B \,. \tag{2.4}$$

The table indicates the maximum percentage deviations of R and W as the concentration is varied. For example, $\Delta R/R = 0.1\%$ means that the deviation is always positive, and that the maximum deviation is 0.1%, while $\Delta R/R = -0.1\%$ means that the deviation is always negative, the maximum deviation being -0.1%. On the other hand, $\Delta R/R = \pm 0.1\%$ means that the deviation assumes both positive and negative values, though the positive deviation is the greater, the maximum being 0.1%. $\Delta R/R = \mp 0.1\%$ means, on the contrary, that the negative deviation is the greater, the maximum being -0.1%.

The percentage deviation of R and W indicated in the table contain, naturally, also the experimental errors of V, ρ and n_B, so that the actual deviations may be some what smaller or larger than the tabular values.

§ 3. Result

We see that the deviation is comparatively large in the following mixtures;

(a) *Aqueous solutions*
(I–1∼I–6, 45∼49)
$\Delta R/R$ max. 3.7% (water-sulfuric acid)
max. −2.7% (water-ethanol)
min. −0.9% (water-formic acid).

(b) *Mixtures containing one heavy component with a light partner*
CCl_4-mixtures (I–13, I–17, I–24, I–25, I–26, I–36, 58)
max. $\Delta R/R = 2.3\%$, $\Delta W/W = 1.2\%$ (tetralin-carbon tetrachloride)
$CHCl_3$-mixtures (I–16, I–28, I–37, 19, 51)
max. $\Delta R/R = 2.8\%$, $\Delta W/W = 1.7\%$ (chloroform-ether)
min. $\Delta R/R = \pm 0.3\%$ (nitrobenzene-chloroform)
CH_2Cl_2-mixtures (I–15, I–34)
max. $\Delta R/R = 0.6\%$, $\Delta W/W = 0.6\%$ (heptane-dichloromethane)
min. $\Delta R/R = 0.5\%$, $\Delta W/W = 0.3\%$ (benzene-dichloromethane)

(c) *Mixtures containing glycerine, aniline, nitrobenzene, glycol*
glycerine mixtures (39∼45)
$\Delta R/R = 2.2 \sim 2.7\%$
aniline mixtures (I–9, I–32, 16, 17, 18, 51, 52)
max. $\Delta R/R = 1.4\%$ (chloroform-aniline)
mix. $\Delta R/R = 1.3\%$, $\Delta W/W = 0.63\%$ (aniline-ether)
nitrobenzene mixtures (I–7, I–8, I–14, I–32, 19, 53, 57)
max. $\Delta R/R = 2.2\%$, $\Delta W/W = 1.8\%$ (nitrobenzene-methanol)
min. $\Delta R/R = \pm 0.3\%$ (nitrobenzene-chloroform)
$\Delta R/R = \pm 0.25\%$, $\Delta W/W = \pm 0.8\%$ (nitrobenzene-toluene)
glycol mixtures (29∼38)
max. $\Delta R/R = \mp 1.5\%$, $\Delta W/W = \mp 1.6\%$ (methanol-glycol)
min. $\Delta R/R = 0.3\%$ (glycerine-glycol)

On the other hand, the deviation is small in the mixtures:

(d) *Mixtures of two hydrocarbons* (I–20, I–21, 1∼14, 54, 55, 60), *for which*
$\Delta R/R$ is usually smaller than 0.3%, except hexane-paraffin oil (±1.3%), isooctane-cyclohexane (−0.4%), pentane-heptane (∓0.35%) and hexane-diphenyl methane (2.1%).

(e) *Mixtures of two monovalent alcohols* (20∼28, 56), *for which*
$\Delta R/R \leqq 0.3\%$, except methanol-dodecyl alcohol mixture (0.4%).

Although there is no theoretical explanation for the approximate linearity of the molecular sound velocity *vs.* molar fractions in binary mixtures, the fact that the linearity is most satisfactory in the mixtures consisting of two hydrocarbons and those of two monovalent alcohols seems to indicate that the deviation from linearity in other mixtures are due to the change in association of the liquids, at least to some extent. The effect of association is presumably great in case of aqueous solutions (cf. Nomoto[13]). On the other hand, the cause of deviation from linearity in class (b) mixtures (one heavy component and a light partner) is mainly due to the density effect, as pointed out in a previous paper[1]. In this case the linearity of Wada's molecular compressibility is far better than that of the molecular sound velocity.

We may conclude, that the molecular sound

velocity in binary liquid mixtures is a linearly dependent quantity on the molar fractions of the component liquids in case there is no association, or in case the degree of association does not change with concentration, as long as the density of the component liquids are not so widely different each other.

References

1) O. Nomoto: J. Phys. Soc. Japan **8** (1953) 553, J. Chem. Phys. **21** (1953) 950, Bull. Kobayasi Inst. Phys. Res. **2** (1952) 137.
2) Rama Rao: Indian J. Phys. **14** (1940) 109.
3) O. Nomoto: J. Phys. Soc. Japan **12** (1957) 311, J. Acous. Soc. Japan **13** (1957) 129, Bull. Kobayasi Inst. Phys. Res. **7** (1957) 136.
4) F. Danusso: Atti Accad. Naz. Lincei **13** (1952) 131, **17** (1954) 109, 114, 234, 370.
5) I. Gabrielli e G. Poiani: Ricerca Scientifica **24** (1954) 424.
6) P. Prosorow: Zh. Fiz. Khim. **14** (1940) 384. B. B. Kudrjawzew: "Anwendung von Ultraschallverfahren bei physikalisch-chemischen Untersuchungen." (1955) 228.
7) B. Jacobson: Arkiv för Kemi **2** (1950) 177.
8) B. Jacobson: Acta Chemica Scandinaviaca **6** (1952) 1485.
9) L. G. Melkonjan: Primenenie ultraakustiki k issledovanijo veshchestva **3** (1956) 31.
10) N. A. Dmitrieva: Dissertatschia MOPI (1953).
11) Balachandran: J. Indian Inst. Sci. **36** (1954) 10.
12) Y. Wada: J. Phys. Soc. Japan **4** (1949) 280.
13) O. Nomoto: J. Phys. Soc. Japan **11** (1956) 1146, Bull. Kobayasi Inst. Phys. Res. **6** (1956) 23.

JOURNAL OF THE PHYSICAL SOCIETY OF JAPAN VOL. 13 No. 12 DECEMBER 1958

Empirical Formula for Sound Velocity in Liquid Mixtures

By Otohiko NOMOTO

Kobayasi Institute of Physical Research, Kokubunzi, Tokyo

(Received August 18, 1958)

An empirical formula $V=(R/v)^3=\{(n_AR_A+n_BR_B)/(n_Av_A+n_Bv_B)\}^3$, was derived for the sound velocity in binary liquid mixtures consisting of two component liquids A and B, on the assumption of the linear dependence of the molecular sound velocity $R=vV^{1/3}$ (v=molar volume and V=sound velocity) on concentration (molar fractions n_A, n_B) and the additivity of the molar volume. The suffixed quantities correspond to the component liquids. This formula holds true for such mixtures for which the linearity of the molecular sound velocity and the additivity of the molar volume is comparatively good, the mixtures of two hydrocarbons and those of two monovalent alcohols being the examples. The values of the empirical sound velocity were compared with those calculated by this formula for 38 mixtures with comparatively small values of the percentage deviation from linearity of R, and 28 of them showed deviations not larger than 1% in V. Of the 31 liquid mixtures with $\Delta R/R \leqq 0.3\%$, 5 showed deviations of V larger than 1%, 4 of them being the mixtures consisting of two component liquids of widely different molar volumes.

§ 1. Introduction

As the sound velocity in liquid mixtures is known to be a quantity which depends on concentration in a variety of manners according to the nature of each component liquids, it becomes of considerable interest and importance if we can establish a formula to predict the sound velocity in liquid mixtures. This, however, is not an easy task considering of the various manners of the concentration dependency, even exhibiting maximum or minimum at certain concentrations in some cases. So it will become necessary to employ one formula for some mixtures and other

formulas for other mixtures, even if we succeed to obtain some approximate formulas to represent the sound velocity.

Some formulas have been proposed[1),2),3)] for the sound velocity in liquid mixtures. Schaaffs[1)] considered the sound velocity in ideal solutions to be a linear function of the weight percentages of the mixtures. Natta and Baccaredda[2)] showed that a better agreement with experiment is attained by the formula

$$V=\frac{1}{\left(\frac{1-p}{\rho_A V_A}+\frac{p}{\rho_B V_B}\right)\rho} \tag{1.1}$$

where ρ means the density and p the weight fraction of the liquid B. This formula is based on the assumption that the sound velocity is the same as in the case when the two component liquids are separated in two layers and the direction of propagation of the sound is perpendicular to the interface. The formula proposed by Danusso[3)] for ideal mixtures

$$V=\frac{1}{\rho}\left(\frac{1-p}{\rho_A{}^2 V_A{}^2}+\frac{p}{\rho_B{}^2 V_B{}^2}\right)^{-1/2}$$
$$=\frac{1}{\rho}\left[\frac{1}{M}\left(\frac{n_A M_A}{\rho_A{}^2 V_A{}^2}+\frac{n_B M_B}{\rho_B{}^2 V_B{}^2}\right)\right]^{-1/2} \tag{1.2}$$

has been found to hold true for some mixtures, but not necessarily in others. Here

$$M=n_A M_A+n_B M_B \tag{1.3}$$

means the mean molecular weight of the mixture. The quantities with suffixes A and B mean the corresponding quantities for the component liquid A and B, respectively, and n_A and n_B are the molar fractions of the component liquids. The ideal mixture is defined here as the mixture without volume change. So we have additivity of the molar volume

$$v=n_A v_A+n_B v_B\ , \tag{1.4}$$

and the density becomes

$$\rho=\frac{M}{v}=\frac{n_A M_A+n_B M_B}{n_A v_A+n_B v_B}\ . \tag{1.5}$$

For non-ideal liquids, however, the formula (1.2) does not hold true no longer. Danusso[4)] has investigated the deviation from ideal velocity formula of the sound velocity in many mixtures and obtained some results of interest, especially the approximate proportionality amongst the percentage deviations of the quantities V (sound velocity), v (molar volume) and B (=Danusso's molecular compressibility), defined as

$$B=v\beta\ , \tag{1.6}$$

where β means the adiabatic compressibility.

Poupko[5)] has performed a theoretical analysis of the sound velocity based on Prigogine et al.'s theory of liquid mixtures[6),7)] and derived the result

$$\Delta v/v=k(\Delta\beta/\beta) \tag{1.7}$$

where k is a constant for each mixture. This, however, furnishes only an order of magnitude explanation for the deviation from ideality of the molar volume and the adiabatic compressibility (or sound velocity).

§ 2. Additivity of the Molar Volume and Proposal of an Empirical Formula for Sound Velocity

The formula proposed here is based on the assumption of the linearity of the molecular sound velocity *vs.* molar fractions and the additivity of the molar volume in liquid mixtures. The deviation from linearity of the molecular sound velocity has been investigated in a previous paper[8)] and it has been reported that some mixtures, especially the mixtures of two hydrocarbons and those of two monovalent alcohols, exhibit the linear dependency on concentration with an accuracy usually not exceeding 0.3%.

Now we investigated the additivity of the molar volume in those mixtures for which the deviation from linearity of the molecular sound velocity is small, and it was revealed that a great part of these mixtures has also a good additivity relationship of the molar volume. So we can establish an emprical formula for the sound velocity in liquid mixtures based on the assumption of the linearity of the molecular sound velocity

$$R=n_A R_A+n_B R_B \tag{2.1}$$

where

$$R=\frac{M}{\rho}V^{1/3}=vV^{1/3} \tag{2.2}$$

and the additivity of the molar volume (1.3), namely

$$V=\left(\frac{R}{v}\right)^3=\left(\frac{n_A R_A+n_B R_B}{n_A v_A+n_B v_B}\right). \tag{2.3}$$

Table I summarizes the result on the percentage deviation of the sound velocity computed by this formula ($\Delta V/V$) together with the percentage deviations of R and the molar volume v, for those mixtures with compara-

Table I. Maximum percentage deviations of the molecular sound velocity (R), and the molar volume (v) from linearity in some liquid mixtures and the maximum percentage deviation of the sound velocity (V) from the empirical formula (2.3).

No.*	Liquid mixtures	Deviations: Sound velocity $\Delta V/V\%$	molar volume $\Delta R/R$	molecular s.v. $\Delta v/v\%$	Ratio of the molar volumes**
I-20	benzene-toluene	0.3	±0.15	−0.13	1.196
1	hexane-paraffine oil (mixtures) (M=268)	±0.6	±1.3	±1.0	2.5021
2	cyclohexane-benzene	1.0	−0.3	−0.7	1.215
3	cyclohexane-decalin	0.4	0.12	−0.08	1.4401
I-21	n. heptane-benzene	1.6	±0.06	−0.5	1.646
4	n. heptane-cyclohexane	−0.25	−0.2	−0.25	1.3562
5	n. heptane-decalin	−0.4	0.25	0.34	1.0623
6	n. heptane-cetane	−0.8	∓0.15	±0.3	1.9883
7	isooctane-benzene	0.9	−0.3	−0.4	1.855
8	isooctane-cyclohexane	−1.2	−0.4	−0.04	1.5264
9	isooctane-n. heptane	∓0.3	∓0.07	0.03	1.1257
10	isooctane-decalin	−1.6	±0.2	0.6	1.0620
11	isooctane-cetane	−1.1	−0.2	0.3	1.765
12	decalin-benzene	1.0	−0.3	−0.7	1.749
13	cetane-cyclohexane	1.1	−0.05	−0.4	2.695
14	cetane-decalin	0.3	0.05	−0.05	1.8717
15	nitrobenzene-benzene	0.6	±0.4	∓0.34	1.1466
16	aniline-benzene	0.3	0.3	0.23	1.0222
I-14	nitrobenzene-toluene	−0.4	±0.25	1.2	1.0431
17	aniline-toluene	±0.4	0.4	0.4	1.170
18	aniline-nitrobenzene	0.9	−0.35	−0.6	1.1216
I-23	heptane-butanol	1.4	0.32	−0.20	1.604
I-11	benzene-ethanol	1.36	0.38	±0.11	1.526
I-29	ethanol-ether	−1.3	0.5	0.9	1.779
18	aniline-acetone	0.8	±0.6	∓0.6	1.239
I-18	benzene-chlorobenzene	±0.52	±.47	∓0.42	1.139
I-27	carbon tetrachloride-chloroform	0.6	±0.2	∓0.2	1.192
19	nitrobenzene-chloroform	0.4	±0.3	±0.26	1.270
20	methanol-n. butanol	0.8	0.14	−0.2	2.257
21	methanol-isoamyl alcohol	0.2	−0.14	0.8	2.671
22	methanol-cyclohexanol	0.9	0.25	−0.07	2.601
23	methanol octyl alcohol	1.4	±0.04	−0.4	3.926
24	methanol-dodecyl alcohol	2.1	0.4	−0.3	5.506
25	isopropanol-n. butanol	0.3	0.2	0.1	1.194
26	n. propanol-cyclohexanol	0.3	0.2	0.1	1.411
27	isopropanol-cyclohexanol	−1.0	0.08	0.25	1.377
28	n. butanol-cyclohexanol	±0.3	±0.12	±0.03	1.1527
29	glycerine-glycol	−0.8	0.3	0.3	1.306

* The number of mixtures correspond to that of the previous paper[8].

** The molar volume of the more bulky component divided by that of the less voluminous component.

tively small values of $\Delta R/R$. All the values in the table indicate the maximum deviations as the concentration is varied. A detailed result for one mixture (aniline-acetone) is reproduced in Table II. The deviations mean

$$\left.\begin{aligned} \Delta R &= R_{\text{cal}} - R_{\text{exp}}\,, \\ \Delta V &= V_{\text{cal}} - V_{\text{exp}}\,, \\ \Delta v &= v_{\text{cal}} - v_{\text{exp}}\,. \end{aligned}\right\} \tag{2.4}$$

Of the 38 mixtures investigated, 9 showed

Table II. Comparison of the sound velocities computed by two empirical formulas with the experimental values.

		No. 18 Aniline-Acetone		25°C		(Gabrielli-Poiani (1954))			
	n_B %	0	10.1	20.0	40.1	60.0	74.9	89.9	100
	M	93.06	89.52	86.06	79.02	72.05	66.84	61.59	58.05
	ρ g/cm³	1.017	0.995	0.974	0.931	0.884	0.853	0.818	0.786
Formula (2.3)	V m/sec	1635	1587	1543	1448	1354	1289	1213	1167
	V cal m/sec	——	1591	1550	1459	1365	1293	1219	——
	ΔV m/sec	——	4	7	11	11	4	6	——
	$\Delta V/V$ %					0.8%			
Formula (3.4)	V cal m/sec	——	1593	1549	1459	1366	1293	1218	——
	ΔV m/sec	——	6	6	11	8	4	5	——
Molecular sound velocity	R exp.	1078.0	1049.4	1021.0	960.2	901.6	852.8	803.0	777.5
	R cal	——	1047.6	1017.9	957.5	897.7	852.9	807.9	——
	ΔR	——	−1.8	−3.1	−2.7	−3.9	0.1	4.9	——
	$\Delta R/R$ %	——	−0.2	−0.3	−0.3	−0.4	0.01	0.6	——
	N^* exp	1081.0	1046.8	1016.5	948.8	883.3	830.5	776.6	746.9
	N cal	——	1047.3	1014.2	947.0	880.5	830.8	780.6	——
	ΔN	——	0.5	1.7	−1.8	−2.8	0.3	4.0	——
	$\Delta N/N$ %	——	0.05	0.2	−0.2	−0.3	0.4	0.5	——
Molar volume	v cm³	91.50	89.97	83.36	84.88	81.50	78.36	75.29	73.85
	v_0 cm³	——	89.73	87.97	84.42	80.91	78.28	75.63	——
	Δv cm³	——	−0.25	−0.39	−0.46	−0.59	−0.08	0.34	——
	$\Delta v/v$ %	——				−0.6 %			

* In conventional unit, where the sound velocity is measured in m/sec, and the density in g/cm³.

deviations of V exceeding 1%. Of the 31 liquid mixtures with percentage deviation of the molecular sound velocity not exceeding 0.3%, only 5 showed deviations of V exceeding 1%, 4 of these being the mixtures consisting of two constituent liquids of widely different molar volume. (I–21, n-heptane-benzene (ratio of the molar volumes=1.646), 11. isooctane-cetane (1.765), 13. cetane-cyclohexane (2.695), 22. methanol-octyl alcohol (3.926)). A more striking example is the mixture cetane-benzene, which is not included in Table I. This mixture exhibits a minimum of sound velocity at an intermediate concentration, which cannot be derived from the empirical formula (2.3). The ratio of the molar volumes being 3.253, $\Delta R/R=0.2\%$, and $\Delta v/v=-0.5\%$, and the deviation of the sound velocity attains $\Delta V/V=3\%$, or $\Delta V=40$ m/sec.

These are the exceptional examples, and as the accuracy of good ultrasonic measurements are of the order of 0.1%, while that of rough measurements are of the order of 0.5—1%, an approximate formula of this order of accuracy may be of practical use in some cases.

Fig. 3–5 illustrate for three mixtures the

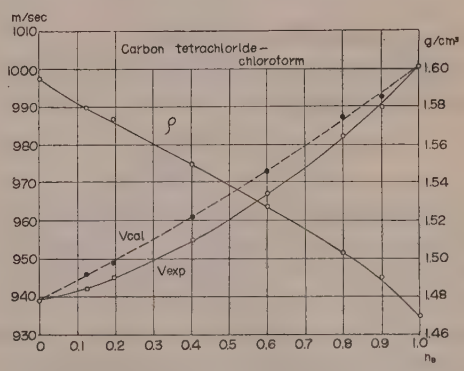

Fig. 1. Sound velocity and density of carbon tetrachloride-chloroform mixtures in dependence on concentration.

computed and the empirical sound velocities as functions of the concentration. By the way, it was remarked that most of the liquid mixtures satisfying the empirical formula (2.3) show a rather similar dependence of V and ρ on concentration, Fig. 2 (methanol-dodecyl alcohol mixture) and Fig. 3 (cetane-decalin) being such examples.

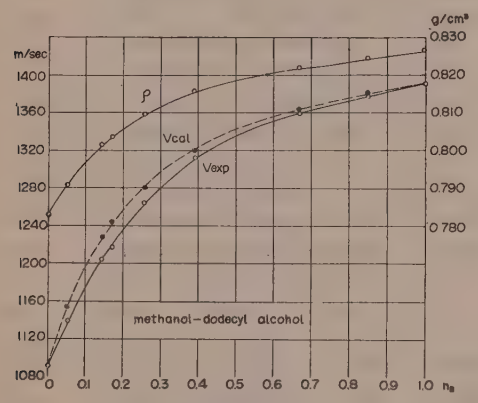

Fig. 2. Sound velocity and density of methanol-dodecyl alcohol mixtures in dependence on concentration.

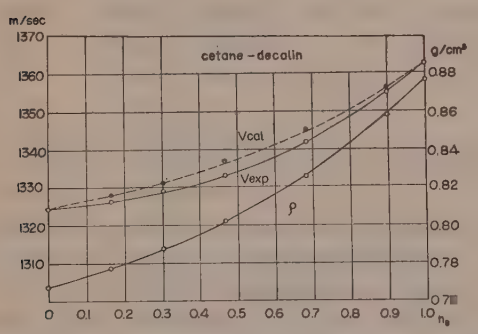

Fig. 3. Sound velocity and density of cetane-decalin mixtures in dependence on concentration.

§ 3. An Alternative Formula

As the linearity of the molecular compressibility (of Wada[9])

$$W=\frac{M}{\rho}\beta^{-1/7}=\frac{M}{\rho^{6/7}}V^{2/7} \tag{3.1}$$

is somewhat better than the linearity of the molecular sound velocity, it is possible to make an empirical formula using this relation and assuming the additivity of the molar volume. The formula, however, becomes somewhat complicated, and numerical computation of some examples revealed that the practical result is not so improved because of the increased stages of the numerical computation involved.

A convenient alternative method consists in employing the linearity of the quantity

$$N=\frac{M}{\rho^{5/6}}V^{1/3}=R\rho^{1/6} \tag{3.2}$$

which shows as good a linearity of cencentration dependence as the molecular compressibility (of Wada) (cf. Nomoto[10]), namely

$$N=n_AN_A+n_BN_B\,. \tag{3.3}$$

This gives, together with the additivity of the molar volume (1.4), the velocity formula:

$$V=\frac{N^3}{M^{1/2}v^{5/2}}$$
$$=\frac{(n_AN_A+n_BN_B)^3}{(n_AM_A+n_BM_B)^{1/2}(n_Av_A+n_Bv_B)^{5/2}}\,. \tag{3.4}$$

This formula, though somewhat better than the formula (2.3), is of the same order of accuracy with (2.3), and, therefore, not to be recommended because of the complexity.

Table II gives the sound velocity computed by this formula together with those computed by (2.3) and the empirical velocity data for the aniline-acetone mixture.

References

1) W. Schaaffs: Zeits. Phys. **105** (1937) 658.
2) G. Natta e M. Baccaredda: Atti Accad. Nazionale di Lincei **4** (1948) 360.
3) F. Danusso: Atti Accad. Naz. Lincei **10** (1951) 235.
4) F. Danusso e E. Fadigati: Atti Accad. Naz. Lincei **14** (1953) 81.
F. Danusso: Atti. Accad. Naz. Lincei **13** (1952) 131, **17** (1954) 109, 114, 234, 370.
5) J. -P. Poupko: Bull. Acad. roy. Belgique **41** (1955) 1009.
6) I. Prigogine and V. Mathot: J. Chem. Phys. **20** (1952) 49.
I. Prigogine and A. Bellemans: Faraday Soc. Discuss. **15** (1953) 80.
7) I. Prigogine, A. Bellemans and A. Englert-Chwoles: J. Chem. Phys. **24** (1956) 518.
8) O. Nomoto: J. Phys. Soc. Japan, in Printing.
9) Y. Wada: J. Phys. Soc. Japan **4** (1949) 280.
10) O. Nomoto: J. Phys. Soc. Japan **8** (1953) 553, J. Chem. Phys. **21** (1953) 950, Bull. Kobayasi Inst. Phys. Res. **2** (1952) 137.

JOURNAL OF THE PHYSICAL SOCIETY OF JAPAN Vol. 13, No. 12, DECEMBER, 1958

Condenser Microphones with Plastic Diaphragms for Airborne Ultrasonics, I

By Kiichiro MATSUZAWA

Department of Physics, Faculty of Science and Literature, Ehime University

(Received August 30, 1958)

A study is made on various condenser microphones, each of which consists of a metallic back plate and a thin plastic film stretched over the back plate, being in direct touch with it at a number of points. The surface of the back plate has been roughened or provided with grooves, hollows or holes, while the external surface of the plastic film has been made conductive by metallizing it.

The microphones are calibrated in the frequency range 1.5~150 kc/s. A fair agreement is found between the classifications of the back plates according to the mechanical roughnesses of the surfaces and the classifications based upon the frequency responses of the microphones. It is shown that the microphones with the back plates having finely roughened surfaces can be considered as single resonance systems.

Detailed data are given, with which a microphone having a flat frequency response up to a desired high frequency below 150 kc/s can be easily constructed.

§ 1. Introduction

Microphones for airborne ultrasonics are mainly used in two fields of research, namely: small model experiment in architectural acoustics in which n times of audible frequencies must be used in one nth model, and the study of ultrasonic cry and hearing of insects and small animals in biology.

For a long time workers in the fields of airborne ultrasonics had been handicapped by the lack of suitable microphones. In 1948, I. Rudnick and M. N. Stein[1] calibrated two Western Electric 640-AA condenser microphones up to 100 kc/s, and found the drop-off of the frequency responses at a rate of about 12 dB per octave above 15 kc/s. In 1950, D. R. Griffin[2] used a W. E. 640-AA microphone in conjunction with electric filters. To make the resultant frequency response flat against the drop-off of the frequency response of the microphone, he had to use the electric filters whose frequency response increased at the same rate as that of the microphone. The resultant frequency response thus obtained was roughly flat for 20~100 kc/s, but the response had some peaks and dips[1] and the absolute sensitivity was low.

In 1954, W. Kuhl, G. R. Schodder and F. K. Schröder constructed microphones and transmitters of the condenser type with plastic diaphragms for airborne ultrasonics and named them "transducers with solid dielectric"[3]. Each of the transducers consisted of a metallic back plate and a thin plastic film stretched over the back plate, being in direct touch with it at a number of points.

Although the investigation of Kuhl *et al.* is very extensive with both microphones and

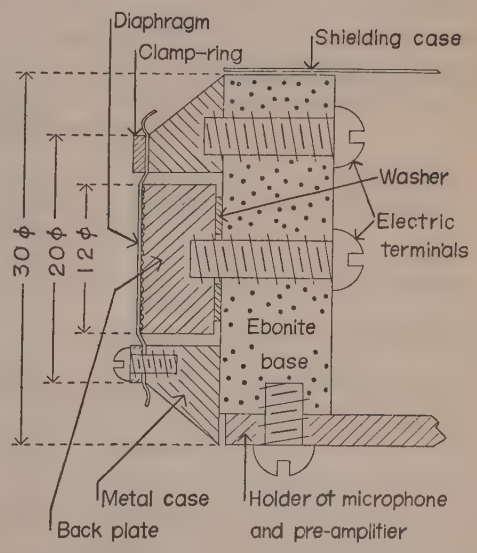

Fig. 1. Cross-section of the microphone (unit mm).

transmitters, yet their study is not sufficient with regard to both the roughnesses of various back plates and the mechanical pre-strains of the diaphragms. In this paper, a study is made on the microphones with back plates of different roughnesses and with various diaphragms under different pre-strains. Thus, detailed data are given, with which a microphone having a flat frequency response up to a desired high frequency below 150 kc/s can be easily constructed.

§ 2. Construction of Microphones

The construction of our microphones is shown schematically in Fig. 1. After having cleaned up a plastic film by ethyl alcohol, its periphery was glued to the front surface of a metal case, the external surface of the film was painted by Du Pont Silver Paste No. 4817 diluted by benzene to make conductive, and then, the film was clamped by a clamp-ring. A copper back plate was screwed to an ebonite base, inserting a washer between them. By fixing the metal case to the ebonite base, the surface of the back plate was pushed out beyond the front surface of the metal case through a distance δ, which was adjusted from 0.2 to 0.7 mm by using a washer of moderate thickness. So that the diaphragm was stretched tightly and was in direct touch with the back plate at a number of points as

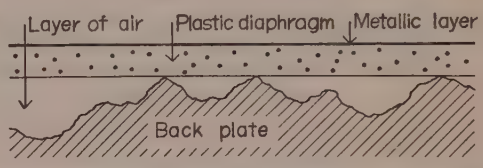

Fig. 2. Principle of the condenser microphone.

Table I. List of back plates.

Classification based upon roughnesses of the surfaces			Symbols of back plates	Details of the roughnesses of the surfaces of the back plates
Group	Sub-group			
I	IA		IA–1	The mechanically flattened surface is given small roughness with a sand paper.
			IA–2	The mechanically flattened surface is finely scribed with a scriber and is smoothly polished with a sand paper.
			IA–3	The surface is provided with a shallow spiral groove of about 0.5 mm in width.
			IA–4	The mechanically flattened surface is lightly prickpunched with a distance of about 1 mm to make small dips with ring margines on the surface.
	IB	IBa	IBa–5	The mechanically flattened surface is provided with about 500 small hollows of about 0.25 mm in diameter and 0.1 mm in depth.
			IBa–6 IBa–7	The mechanically flattened surface is provided with about 300 small hollows of about 0.4 mm in diameter and 0.25 mm in depth.
		IBb	IBb–8	The mechanically flattened surface is provided with about 110 hollows of about 0.9 mm in diameter and 0.4 mm in depth.
II	IIA		IIA–9	The surface is provided with a spiral groove of about 0.1 mm in depth and 1.5 mm in width.
	IIB		IIB–10	The mechanically flattened surface is provided with four holes of 2 mm in diameter and 2 mm in depth.
			IIB–11	The surface of IIB–10 is prickpunched in the similar manner to IA–4.
			IIB–12	The holes of IIB–11 are drilled through and are packed with cotton wool.

shown in Fig. 2. Thus, the dielectric of the condenser consists not only of one solid material but of two layers, namely the plastic diaphragm and a layer of air. Under a sound pressure, a displacement of the diaphragm occurs, in consequence of which the electrostatic capacitance formed by the back plate and the metallic layer of the diaphragm is altered.

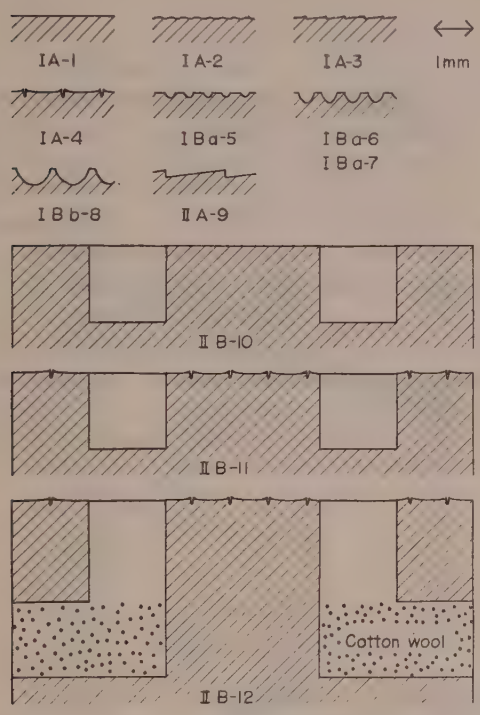

Fig. 3. Schematic cross-sections of back plates.

The 12 back plates used in our experiments are listed in Table I, and the schematic cross-sections of the back plates are also sketched in Fig. 3. As seen in Table I, the back plates may be divided into two groups based upon the mechanical roughnesses of the surfaces, namely: the back plates of group I having finely roughened surfaces and those of group II having ruggedly roughened surfaces. Each group is able to be classified into some sub-groups. The back plates of group I are classified into two sub-groups, namely: the back plates of group IA having uniformly roughened surfaces and those of group IB having surfaces composed of planes and many hollows. Further, the back plates of group IB are classified into two sub-groups, namely: the back plates of group IBa having surfaces with smaller hollows and the back plate of group IBb having a surface with somewhat larger hollows. In Table I, the back plates of group IA and those of group IBa are arranged respectively in order of the mechanical fineness of the surfaces. On the other hand, the back plates of group II are classified into two sub-groups, namely: the back plate of group IIA having a uniformly roughened surface and those of group IIB having surfaces with large holes.

As diaphragms, films of polyethylene and polyester are used. The thickness of the film of polyethylene is about 20 μ. For the films of polyester, Du Pont gauge 100, 50 and 25 Mylar and gauge 50 Metallized Mylar are used, the thicknesses being about 25, 13, 6 and 13 μ respectively.

§ 3. Free-field Correction and Free-field Calibration

The free-field correction for normal incidence sound is defined as the difference between the free-field calibration for normal incidence and the pressure calibration.

An MR-103 condenser microphone, which is frequently used in our country in the audible frequency range, is provided with a metallic capsule so as to give the similar figure to our microphones. The effect of the capsule on the sensitivity in a free field is found to be merely about ± 1 dB even for 3~12 kc/s. On the other hand, the free-field correction of MR-103 condenser microphone may be estimated to be equal to that of a W. E. 640-AA microphone, which has been measured up to 100 kc/s[1], even for ultrasonics because of the identical dimensions.

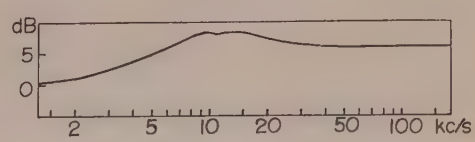

Fig. 4. Free-field correction vs. frequency.

Based on the facts above mentioned, the free-field correction of our microphones is obtained as shown in Fig. 4.

Any two of our microphones are placed face to face at a certain distance and the one is used as a source and the other as a receiver. With this arrangement, linearity, spherical sound field and the reciprocity are examined

as follows.

i) *Linearity* The perfectness of linearity of our microphones is ascertained by the proportionality between the current flowing through the source and the output voltage of the receiver.

ii) *Spherical sound field* Spherical sound field is ascertained by the fact that the output voltage of the receiver is proportional to the reciprocal of the distance between the source and the receiver.

iii) *Reciprocity* Two microphones are named A and B respectively, and both the ratio of the current through the microphone A operating as a source to the output voltage of B as a receiver and the ratio of the current through

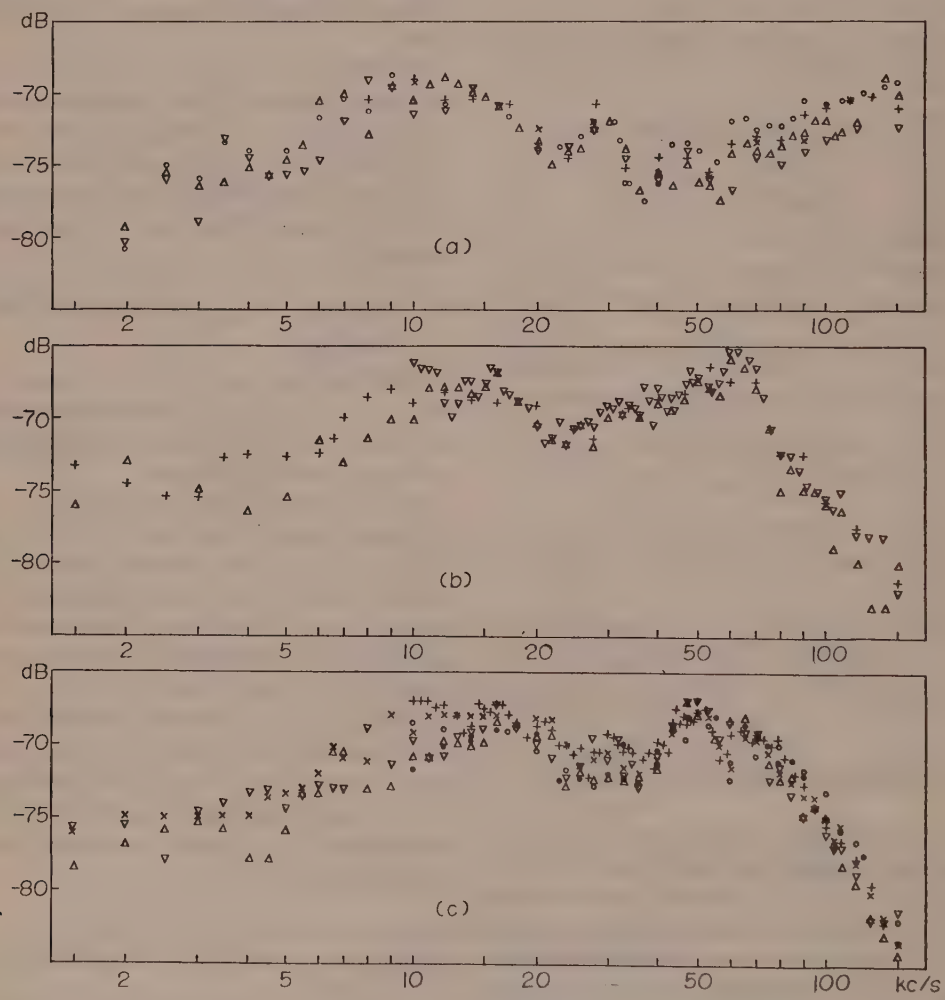

Fig. 5. Long-time constancy of frequency responses. Sensitivity in dB rel. 1V/μbar vs. frequency.

	(a)	(b)	(c)
Back plate	IBa-5	IBa-6	IBa-7
δ	0.36 mm	0.45 mm	0.35 mm
Diaphragm	13μ Polyester	20μ Polyethylene	20μ Polyethylene
Date of calibration (Room temp.)	△ Apr. 28, 1957 (20°C) ▽ Aug. 19, 1957 (33°C) + Sept. 12, 1957 (24°C) × Oct. 1, 1957 (22°C) ○ Dec. 24, 1957 (10°C)	△ Oct. 2, 1956 (20°C) ▽ Apr. 18, 1957 (13°C) + Aug. 19, 1957 (33°C)	△ Feb. 13, 1957 (8°C) ▽ Mar. 20, 1957 (12°C) + Apr. 18, 1957 (13°C) × Apr. 28, 1957 (20°C) ○ Jul. 19, 1957 (33°C) ● Dec. 26, 1957 (10°C)

the microphone B operating as a source to the output voltage of A as a receiver are measured. Thus, it is found that in any case these two ratios are equal to each other, and accordingly it is concluded that our microphones obey the reciprocity theorem.

Based on the three points above mentioned, our microphones can be calibrated according to the reciprocity method in a free field[1]. Thus, for the calibration of our microphones, the reciprocity method has been used for 10 ~150 kc/s, whereas in the frequency range 1.5~10 kc/s the method of comparison with the known sensitivity of the MR-103 microphone has been used. The straying of the sensitivities with the different calibrations are almost within ±1.5 dB, and the difference in the sensitivities at 10 kc/s by the two methods is also within the errors of measurements. As an addendum, some of our microphones are calibrated up to 190 kc/s.

The sound absorption in air is not taken into account, because even at high frequencies the error in the sensitivity due to the absorption is less than 1 dB[1),4)], which is of the same order as the errors of measurements.

The polarizing voltage applied to our microphones is 200 volts in any case.

The self-noise of our microphones is less than that of a pre-amplifier.

§ 4. Stability

i) *Microphones with back plates of group I*

The stability of the frequency responses of our microphones with the back plates of group I are examined with regard to the following five points. And then the frequency responses are found to be stable.

1) *Temporal constancy* A temporal inconstancy of the sensitivity by the application of the polarizing voltage is inappreciable. Accordingly, the drop of the sensitivities due to the charging effect reported by Kuhl *et al.*[3] is small enough for our microphones.

2) *Long-time constancy* Three examples of the long-time variations in the sensitivities of our microphones are shown in Fig. 5. The straying of the sensitivities are within about 3 dB excepting the straying of 4~5 dB at 6, 8 and 60 kc/s in Fig. 5(a); at 4, 10, 130 and

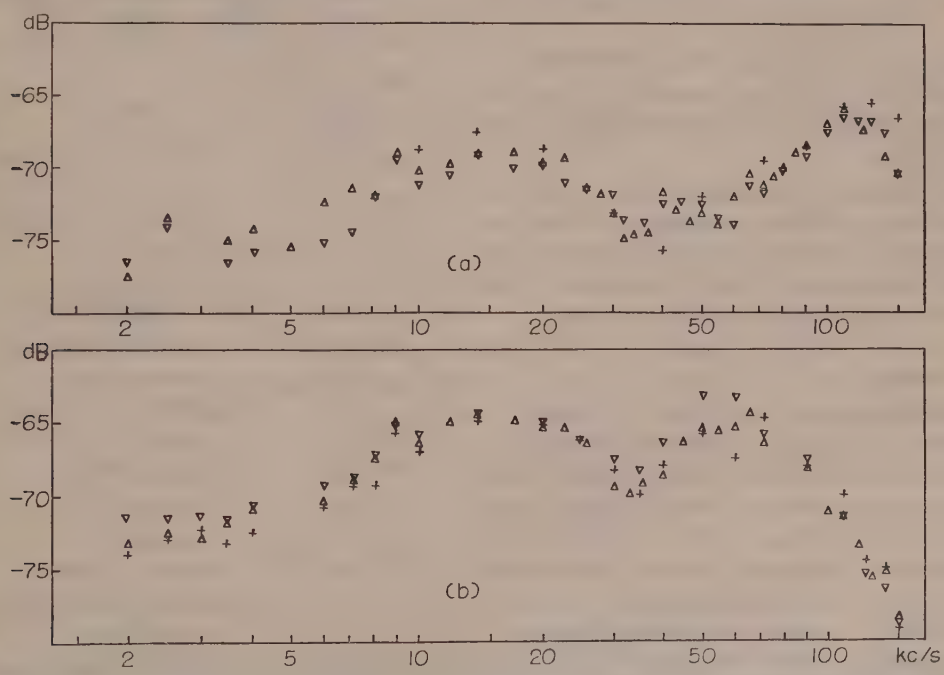

Fig. 6. Frequency responses of microphones obtained by renewing the diaphragms of same microphones. Sensitivity in dB rel. 1V/μbar vs. frequency.

	Back plate	δ	Diaphragm
(a)	IA-2	0.3 mm	13μ Polyester (Metallized Mylar)
(b)	IBb-8	0.63 mm	

140 kc/s in Fig. 5(b); and at 4, 4.5, 8, 9, 10, 11 and 60 kc/s in Fig. 5(c). The straying is, on the whole, only a little larger than the errors of measurements.

3) *Uniformity* The frequency responses in Fig. 5(b) and those in Fig. 5(c) show that the identical construction data (see the back plate IBa–6 and the back plate IBa–7 in Table I) give the similar responses.

4) *Reproducibility* To check the reproducibility of the frequency responses, some of our microphones are decomposed and are composed again by using new films of the same sorts as before. Two examples are shown in Fig. 6, the straying of the sensitivities by renewing 3 times the diaphragms is within 3 dB excepting the straying of about 4 dB at 40 and 150 kc/s in Fig. 6(a) and at 60 kc/s in Fig. 6(b). The straying is, on the whole, only a little larger than the errors or measurements. Accordingly the reproducibility is good. When the films other than the Metallized Mylar are used, as a matter of course, the reproducibility is not always good as shown in Fig. 6 because of the different surface densities of the metallic layers on the films painted by hand.

5) *Effect of humidity* Throughout our experiments, the effect of humidity upon the frequency responses of our microphones is inappreciable.

ii) *Microphones with back plates of group II*

The stabilily of the microphones with the back plates of group II is not examined because of uselessness of the microphones. The details will be mentioned in § 6.

§ 5. Effect of δ

i) *Microphones with back plates of group I*

The relation between the frequency responses and the amount δ, which has an effect on the mechanical pre-strains of the diaphragm, has been examined. When δ is less than 0.4 mm, the frequency responses of some microphones of group I are almost independent of δ. However, those of some others depend upon it, the sensitivities of the flat parts of the frequency responses decreasing with increasing δ and the cut-off frequencies increasing with increase of δ. Moreover, the dependences of the frequency responses on δ are altered by varying strains with which the films are initially glued to the metal cases.

Table II. Effect of δ upon frequency responses.

	Diaphragm	
	Polyethylene	Polyester
$(Q)_{\delta=0.55}/(Q)_{\delta=0.4}$	1~1.1	0.8~1.2
$(f)_{\delta=0.55}/(f)_{\delta=0.4}$	1	1~1.08
$(S)_{\delta=0.55}-(S)_{\delta=0.4}$	0 dB	−2~0 dB (rarely −3 dB)

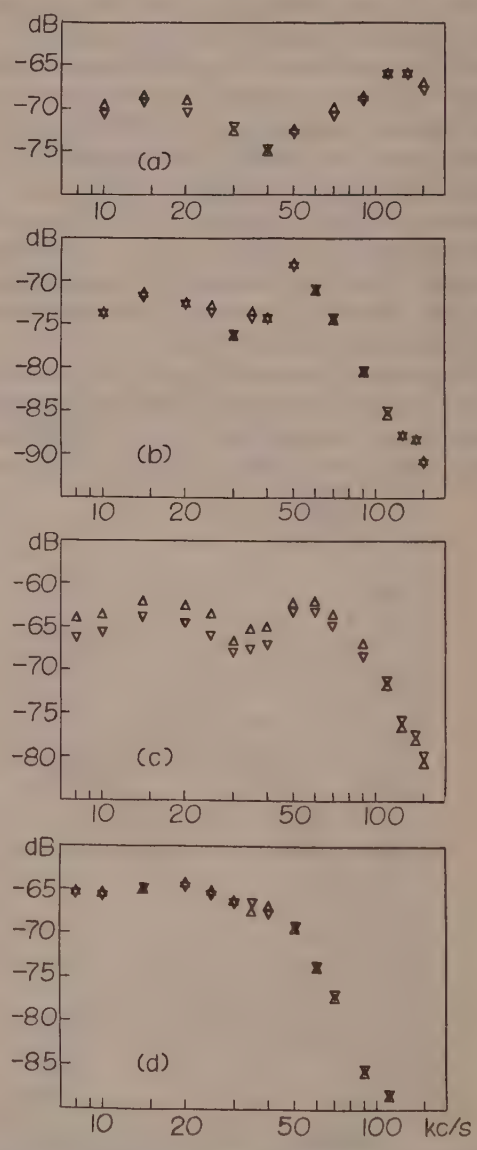

Fig. 7. Effect of δ upon frequency responses. Sensitivity in dB rel. 1V/μbar vs. frequency.

	Back plate	Diaphragm	
(a)	IA-2	13μ Polyester	△ δ=0.4 mm
(b)	IA-4	20μ Polyethylene	
(c)	IBb-8	13μ Polyester	▽ δ=0.55 mm
(d)	IBb-8	20μ Polyethylene	

Next, the Q-factor, the resonance frequency f, and the low frequency sensitivity S for our microphones at $\delta=0.55$ mm and those for the same microphones at $\delta=0.4$ mm have been examined. The results of the measurements are given in Table II, and some examples of the effects of δ upon the frequency responses are shown in Fig. 7. The method of determination of Q, f and S for our microphones may be explained in § 6. As seen in Table II and Fig. 7, when δ is larger than 0.4 mm, the effects of δ for the microphones with the diaphragms of polyethylene are almost inappreciable and those of polyester are very little. Therefore, for each of our microphones, only the mean of the two frequency responses at $\delta=0.55$ mm and at $\delta=0.4$ mm may be given in § 6, i).

ii) *Microphones with back plates of group II*

The dependence upon δ of the frequency responses of our microphones of group II has not been examined because of their uselessness (§ 6).

§ 6. Dependence of Frequency Responses upon Back Plates and Diaphragms

i) *Microphones with back plates of group I*

The details of 20 microphones with the back plates of group I used in our experiments are shown in Table III. In the first, second and third columns there are shown the symbol of the back plate, the material of the diaphragm and the surface density M of the diaphragm with the metallic layer, respectively. In the fourth column there is shown the effective thickness d_e of the diaphragm, obtained by the measurement of the electrostatic capacitance of the film. In the fifth column there is shown the electrostatic capacitance of the microphone. For the shortness sake, the frequency responses of the microphones (a)~(g) denoted in the ninth column are shown representatively in Fig. 8.

Each of the theoretical frequency responses in Fig. 8 is obtained as follows. A theoretical pressure response of an ideal microphone, which is a single resonance system, is deter-

Table III. Details of microphones with back plates of group I.

Construction of microphone				Capacitance of microphone ($\mu\mu$F)	Frequency response of microphone			
	Diaphragm							
Back plate	Material	Surface density M (mg/cm²)	Effective thickness d_e (μ)		Q-factor	Resonance frequency f (kc/s)	Low frequency sensitivity S (dB rel. 1V/μbar)	
IA-1	25 μ Polyester	4.6	7.4	86	2.9	120	−86.0	(a)
IA-2	20 μ Polyethylene	2.7	8.2	65	2.1	110	−83.0	
	20 μ Polyethylene	3.2	9.4	52.5	3.0	95	−83.5	
	25 μ Polyester	4.8	8.2	52.5	3.3	80	−82.0	
	13 μ Polyester	1.9	3.9	90	2.5	130	−79.5	(b)
	6 μ Polyester	2.0	2.2	102	2.3	130	−77.5	
IA-3	20 μ Polyethylene	2.7	9.1	55	2.3	98	−80.5	
	13 μ Polyester	2.2	4.3	74	2.9	108	−78.0	(c)
IA-4	20 μ Polyethylene	3.8	9.0	38.5	2.4	58	−83.0	(d)
	13 μ Polyester	1.8	4.4	51	2.0	84.5	−80.5	
	6 μ Polyester	1.8	2.3	69	2.0	86	−79.0	
IBa-5	20 μ Polyethylene	3.0	9.0	70	1.2	125	−83.5	
	20 μ Polyethylene	3.7	7.8	73	1.1	110	−83.0	(e)
	13 μ Polyester	2.1	4.3	113	1.1	150	−79.5	
IBa-7	20 μ Polyethylene	3.0	9.8	55	1.1	80	−80.5	
	13 μ Polyester	1.8	3.9	107	1.1	106	−76.5	(f)
	13 μ Polyester	1.8	4.6	104	0.9	112	−77.0	
IBb-8	20 μ Polyethylene	3.5	10.5	37	1.2	40	−74.5	(g)
	25 μ Polyester	4.9	7.8	42	1.4	39	−72.5	
	13 μ Polyester	1.8	4.4	59	1.4	69	−72.5	

mined by three factors, namely: the Q-factor, the resonance frequency f and the low frequency sensitivity S. The theoretical free-field response of the ideal microphone is obtained by superposing the theoretical pressure response of the ideal microphone on the free-field correction shown in Fig. 4. Then, the three factors of the single resonance system are provided with suitable numerical values

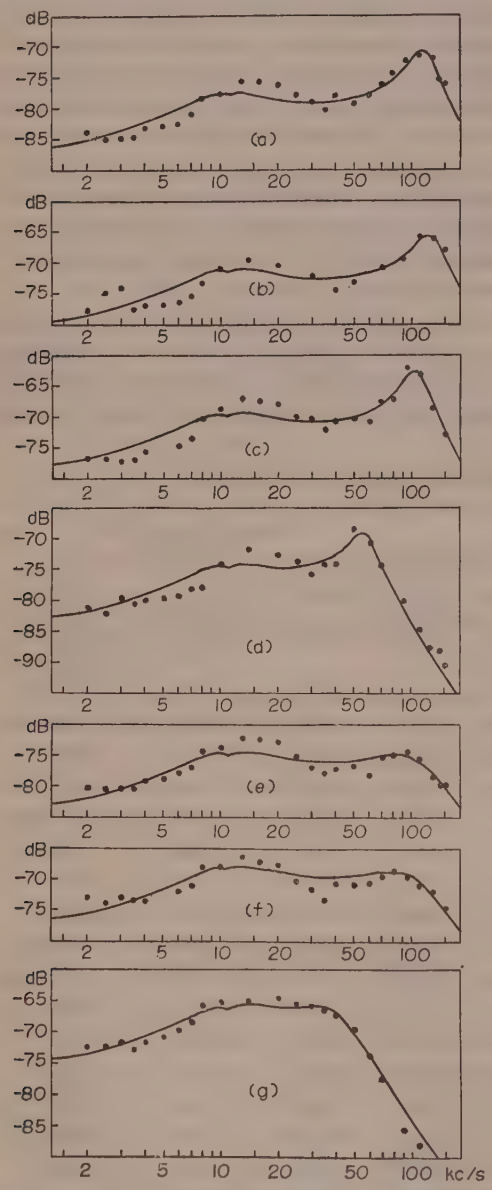

Fig. 8. Frequency responses of microphones with back plates of group I, and theoretical responses corresponding to them. Sensitivity in dB rel. 1V/μbar vs. frequency.

● measurement

—— theory

so that the theoretical frequency response of the ideal microphone in a free field is in accord with the experimental frequency response. The suitable numerical values of the three factors are shown in the sixth, seventh and eighth columns of Table III. As shown in Fig. 8, the theoretical responses are in good agreement with the experiments excepting the small deviations for 4~7 kc/s and 13~20 kc/s, which might be caused by the systematic errors of measurements. The agreements between the theoretical responses and the experimental responses show that our microphones can be considered as the single resonance systems. The dependence of the three factors, namely, the Q-factor, the resonance frequency f and the low frequency sensitivity S, upon the back plates and the diaphragms are discussed in the following:

1) Q-factor

As shown in the first and sixth columns of Table III, the values of Q-factor for the microphones with the back plates of group IA are 2.0~3.3, while those for the microphones of group IB are 0.9~1.4. Accordingly, the sub-classification of the back plates of group I into IA and IB based upon the mechanical roughnesses of the surfaces is in accord with the classification based upon the values of Q.

2) *Resonance frequency f*

Values of the resonance frequency f and the surface density M as tabulated in Table III are shown graphically in Fig. 9(a), (b) and (c), on logarithmic scale.

From these figures it will be seen that for each of our microphones with the back plates IA-2, IA-3, IA-4, IBa-5 and IBa-7, there holds, within experimental error, a linear relationship given by $\ln f = \ln k - \frac{1}{2} \ln M$ where k is a constant. As will be explained in our subsequent paper[5], a similar relationship holds also for the back plate IA-1.

The existence of the relation $f = kM^{-1/2}$ for each of the above 6 back plates shows that, among various properties of the diaphragms, only the surface density M affects the resonance frequency f, thus showing that the diaphragm acts dynamically as a mass.

On the contrary, no such relationship holds for the back plate IBb-8, as can be seen from Fig. 9(c).

Thus, it is found that the sub-classification of the back plates of group IB into IBa and

IBb based upon the mechanical roughnesses of the surfaces is in accord with the classification due to whether the relation $f=kM^{-1/2}$ holds good or not.

The order of the arrangement of the back plates of group IA in Table I, being the order of the mechanical fineness of the surfaces, is in accord with the order of the straight lines from right to left in Fig. 9(a). Namely, the order agrees with the order of the values of k. Similar relations hold also for the back plates of group IBa.

3) *Low frequency sensitivity S*

Curves of the low frequency sensitivity S plotted against the effective thickness d_e in Table III are shown in Fig. 10. The values of S decrease with increasing values of d_e. A

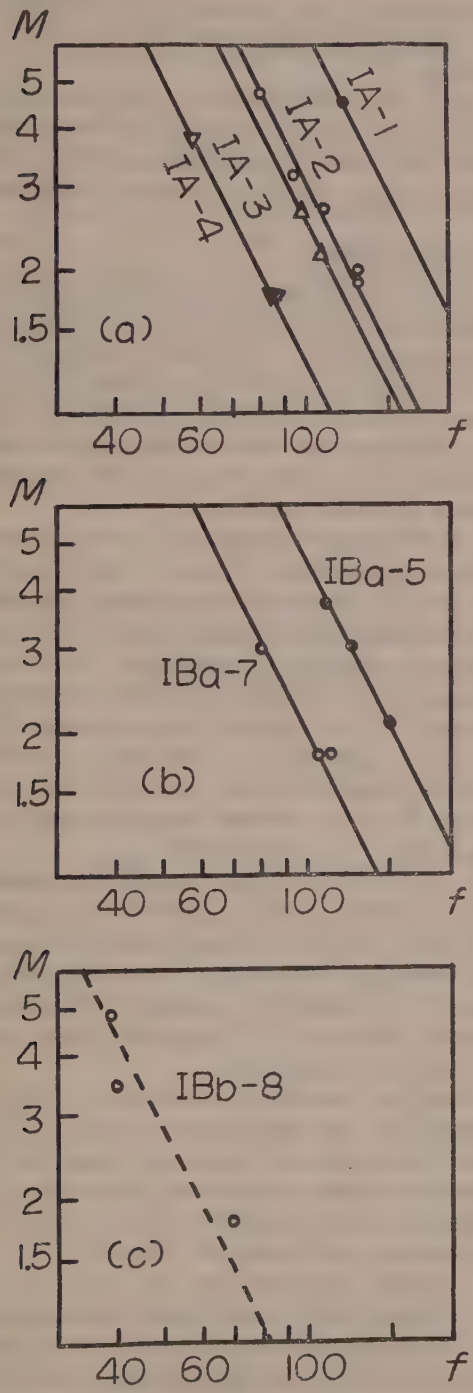

Fig. 9. Surface density M in mg/cm² of diaphragm vs. resonance frequency f in kc/s.

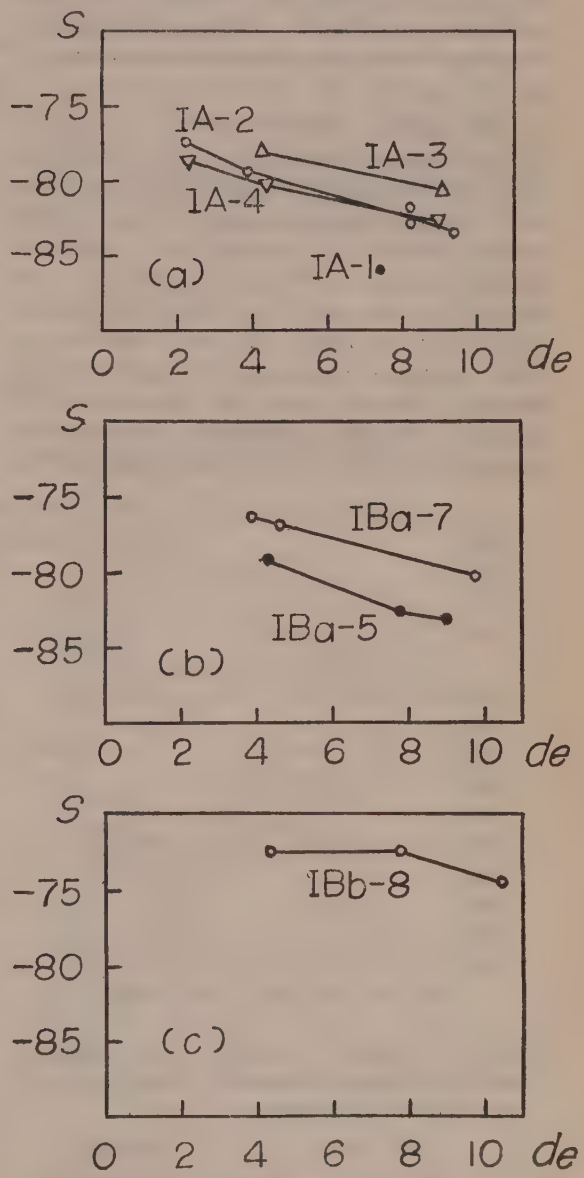

Fig. 10. Low frequency sensitivity S in dB rel. 1V/μbar vs. effective thickness d_e in μ of diaphragm.

similar relation holds between S and d_e for the back plate IA–1, as will be explained in our subsequent paper[5].

As shown in Fig. 10(a), except for the back plate IA–4, the order of the arrangement of the back plates of group IA in Table I is in accord with the increasing values of S for the same values of d_e. Similar relations hold also for the back plates of group IBa.

A microphone having a flat frequency response up to a desired high frequency below 150 kc/s can be easily constructed if we refer to Table I and Fig. 9. The sensitivity of the microphone can be estimated beforehand if we refer to Fig. 10.

ii) *Microphones with back plates of group II*

The frequency response of our microphone with the back plate of group IIA and those with the back plates of group IIB are shown in Fig. 11(a) and (b) respectively. The frequency response in Fig. 11(a) is similar to the theoretical response of the ideal microphone except for the large dips at 3 and 60 kc/s. The frequency responses in Fig. 11(b) are evidently different from the theoretical response of the ideal microphone because of the sharp dip at 50 kc/s for the back plate IIB–10, also of the sharp dip at 40.5 kc/s for the back plate IIB–11 and of the large peak at about 3 kc/s as well as the large dip for 33~60 kc/s for the back plate IIB–12. Therefore the subclassification of the back plates of group II into IIA and IIB based upon the mechanical roughnesses of the surfaces is in accord with the classification based upon the frequency responses.

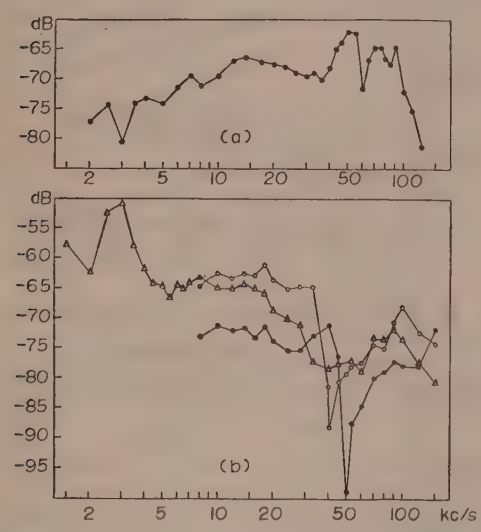

Fig. 11. Frequency responses of microphones with back plates of group II. Sensitivity in dB rel. 1V/μbar vs. frequency.

		Back plate	δ	Diaphragm
(a)	●	IIIA-9	0.4 mm	13μ Polyester
(b)	●	IIB-10	〃	〃
	○	IIB-11	〃	〃
	△	IIB-12	〃	〃

Thus, the classifications of the back plates based upon the roughnesses of the surfaces shown in Table I are in accord with the classifications based upon the frequency responses.

§ 7. Conclusion

In the present paper, properties of condenser microphones with various back plates are studied in detail. The back plates used in the present experiment are divided into two groups I and II on the basis of the mechanical roughnesses of the surfaces and each of these two groups is further classified into some subgroups as shown in Table I.

The frequency responses of our microphones with the back plates of group I are found to be equal to the theoretical frequency responses of the ideal microphones which are single resonance system. Accordingly, our microphones can be supposed to be single resonance systems. The Q-factor, the resonance frequency f and the low frequency sensitivity S of the single resonance system are then obtained for each of the measured frequency responses of our microphones.

It is found that for each of our microphones with the back plates of group IA and group IBa there exists a relation $f=kM^{-1/2}$ between the resonance frequency f and the surface density M, where k is a constant. This shows that the diaphragm of the microphone acts dynamically as a mass.

Next, the frequency responses of our microphones with the back plates of group II are found to be different from the theoretical frequency response of the ideal microphone because of some peaks and dips, so that those microphones are practically useless.

It is thus concluded that the classifications of the back plates based upon the mechanical roughnesses of the surfaces shown in Table I are in accord with the classifications based upon the frequency responses of the microphones with the back plates.

The stability of the frequency responses of our microphones with the back plates of group I is studied on the five points: the temporal constancy, the long-time constancy, the uniformity, the reproducibility and the effect of humidity, and it is found that the frequency responses are stable.

The dependence of the frequency responses of our microphones with the back plates of group I upon δ, the push-out of the back plates, is examined, and it is found that they are almost independent of δ in case when $\delta \geqq 0.4$ mm.

Summarising it may be concluded that a microphone having a flat frequency response up to a desired high frequency below 150 kc/s can be easily constructed if we refer to Table I and Fig. 9, and that the sensitivity of the microphone can be estimated beforehand if we refer to Fig. 10.

In conclusion, the writer wishes to express his cordial thanks to Professor S. Tomotika for his continual guidance and also for his kind inspection of the manuscript. The waiter's thanks are also due to Dr. O. Nomoto of the Kobayasi Institute of Physical Research for useful advice and discussions.

References

1) I. Rudnick and M. N. Stein: J. Acous. Soc. America **20** (1948) 818.
2) D. R. Griffin: J. Acous. Soc. America **22** (1950) 247.
3) W. Kuhl, G. R. Schodder and F. K. Schröder: Acustica **4** (1954) 519.
4) L. J. Sivian: J. Acous. Soc. America **19** (1947) 914.
5) K. Matsuzawa: Condenser Microphones with Plastic Diaphragms for Airborne Ultrasonics, II. (To be published in this Journal.)

Erratum

Temperature Distribution during the Martensite Plate Formation

By Zenji NISHIYAMA, Akira TSUBAKI, Hideo SUZUKI and Yasusada YAMADA

J. Phys. Soc. Japan **13** (1958) 1084

Page	Column	Line	Wrong	Corrected
1084	left	14	treatments	treatment
1086	left	13	$-\frac{1}{\sqrt{\pi}v}\{\cdots$	$+\frac{1}{\sqrt{\pi}v}\{\cdots$
		14	$+\exp\left[\cdots\right]$	$-\exp\left[\cdots\right]$
		18	become	becomes
	right	2	$\left(t+\frac{x}{v}\right)$	$\left(t-\frac{x}{v}\right)$
		3	$\left(t-\frac{x}{v}\right)$	$\left(t+\frac{x}{v}\right)$
1087	left	Fig. 3	Mark the number (1), (2) or (3) to each curve from left to right.	

Short Notes

This section is intended to secure prompt publication of important discoveries in physics. The reports should not exceed 800 words in length. A figure of size 7cm×7cm will be counted as 150 words.

J. PHYS. SOC. JAPAN **13** (1958) 1544~1546

A Possible Mechanism of the Potential Variation of the Joshi Effect

By M. Venugopalan

Department of Chemistry, Banaras Hindu University, Banaras, India

(Received February 17, 1958)

The Joshi effect 1–6, an instantaneous and reversible photovariation of the discharge current i ($+\Delta i$, enhancement and $-\Delta i$, diminution) has been studied in a number of gases and vapours, elemental and compound[3,7], excited in Siemens' tube, G. M. Counter like semiozoniser[3,8,9,], Geissler or Crooke's tube with internal metallic electrodes or (as in the so called electrodeless discharge) with external metallic sleeves[10]. The potential dependence[11] of $\pm\Delta i$, at constant intensity I and frequency ϑ of irradiation and for medium gas pressures p, is shown graphically in Fig. 1. The positive effect $+\Delta i$, the photoincrease of i, is small at low applied potentials V and increases initially with V to a maximum at $V+\Delta i$ max, identical with V_m, the threshold potential[1]. Above this last, $+\Delta i$ decreases rapidly and changes to the negative effect $-\Delta i$, the photosuppression of i, at an inversion[12] potential V_i^I. Beyond V_i^I, $-\Delta i$ first increases rapidly, and diminishes slowly thereafter. A second inversion, $-\Delta i$ to $+\Delta i$, obtains, in certain systems[13], at V_j^{II} in the region of high V; this part of the curve is shown discontinuous in Fig. 1.

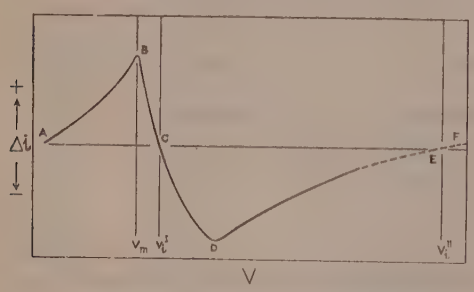

Fig. 1. Potential variation of the Joshi effect.

Various theories[2,9,10,14–22] have been postulated from time to time to explain the above phenomenon on the assumption that $\pm\Delta i$ is either a volume effect or a surface phenomenon; however, the evidence for its surface origin is overwhelming. Of these Joshi's theory[2,9,14], which accounts for many of the observations as compared to others, contemplates (a) formation under discharge of an adsorption-like electrode layer consisting of excited particles and ions and (b) characterised by a low work function ϕ; (c) light releases electrons from this layer; (d) they are captured by the particles, whose electron affinity is enhanced by excitation under discharge to form negative ions (e) determined by the probability factor p/X (where p is the gas pressure and X, the applied electrical field): (f) the current decrease $-\Delta i$ is a space charge effect due to the formation of slow moving negative ions and also their much smaller ionizing efficiency compared with free electrons; (g) uncaptured photoelectrons and others, produced by their impact ionization under X, cause the positive effect $+\Delta i$ observed at low (and less often at large) V, which disfavour electron capture.

Based on the above theory, a possible explanation has been now offered by the author for the potential variation of $\pm\Delta i$, by considering in detail the nature of the adsorbed layer and specifying the conditions for the formation and stability of negative ions. It is as follows:

1. Ordinarily when a gas or vapour is enclosed in a reaction vessel (in the present case, the discharge space), there is an instantaneous uptake of the gas molecules on the interior surface of the reaction vessel. This is characterised by features of physical adsorption[23,24] involving van der Waals' forces with very low heats of adsorption (1–5 kilocalories) and is always in dynamic equilibrium with the gas phase.

2. When a low electrical field is applied ($V \leqslant V_m$), the surface equilibrium is disturbed and when the activation energy (electrical) exceeds the heat of adsorption[24,25], electrical desorption of the layer occurs, resulting in a decrease in the surface work function ϕ and therefore, increased photoelectron emission causing $+\Delta i$, as shown by AB in Fig. 1. Evidence for this has been adduced from measurements of activation energies E and heats of activation $\Delta E^{\neq}$, for the adsorption[26] process responsible for $+\Delta i$. Such measurements showed that the magnitudes of E and $\Delta E^{\neq}$ are of the order of 5–6 and 4–5 kilocalories. The fact that this energy while excluding that resulting from electrical activation is not of the order of magnitude of activation energies in chemical reactions substantiates that the type of adsorption responsible for $+\Delta i$ is physical in nature.

3. (i). When the applied electrical field is enhanced progressively ($V \geqslant V_m$) activation energy (5–10 kilocalories) is available for the formation of a chemisorbed layer[24,27], and as this layer develops, ϕ increases resulting in a decreased photoelectron emission and hence $+\Delta i$ decreases, as shown by

BC in Fig. 1. (ii) This decrease in $+\Delta i$ becomes precipitous due to the cooccurrence of $-\Delta i$ at this stage, as a result of negative ion formation[28], determined by the probability factor p/X. Evidence for (i) has been obtained from measurements[26] of E and $\Delta E\neq$ which are of the order of 12–13 and 11–12 kilocalories. This last is of the order of those of chemical reactions and hence the type of adsorption involved herein, is chemisorption[27]. Evidence for (ii) has been obtained from the observation[29] that the effect of light investigated in various visible spectral regions is to cause two simultaneous changes, both itstantaneous and light reversible: (a) a decrease in the amplitude of some of the h.f. pulses but (b) increase in their total number. An examination of a number of oscillograms[29] undertaken to obtain more information about (a) has revealed that the amplitude reduction on irradiation is apparently linked with alternate h.f. pulses, which is suggestive of the occurrence of $-\Delta i$. Now $-\Delta i$ would be reduced (numerically) due to the cooccurrence of (b), which *per se* should cause $+\Delta i$. The net influence of light under any given circumstances would therefore, depend on the resultant of (a) and (b) which alone is shown by the current detector.

4. When the applied electrical energy ($V > V_i^I$) exceeds the sum of the activation energy and heat of chemisorption, desorption[27] of the chemisorbed layer sets in, and as the electrical field is further increased, desorption increases. This decreases ϕ and hence photoelectron emission increases; applied field being very favourable for negative ion formation[30] ($X/p \not\equiv 50$), $-\Delta i$ increases as shown by CD in Fig. 1. Evidence for this has been adduced from measurements[26] of E and $\Delta E\neq$, for the adsorption process responsible for $-\Delta i$, which are of the order of 19–20 and 17–18 kilocalories. This is of the order of the sum E and $\Delta E\neq$ for chemisorption[27], indicating thereby that desorption by the applied field of the chemisorbed layer is responsible for enhancement in $-\Delta i$ with V.

5. At very high applied electrical fields, negative ion formation decreases[30] ($X/p > 50 < 90$) and therefore $-\Delta i$ decreases as shown by DE in Fig. 1. At $X/p \geqslant 90$, $-\Delta i$, reverses to $+\Delta i$, due to detachment of electrons from negative ions[30], as has been observed at $V > V_i^{II}$ or $\gg V_m$ (EF in Fig. 1.)

6. It is further contemplated that the threshold potential V_m is characterised by the setting in of chemisorption; at this last, desorption of van der Waals' layer is maximum. Similarly at the inversion potentials V_i, the potential at which the observed $+\Delta i$ changes over to $-\Delta i$, desorption of the chemisorbed layer commences as also the formation of the chemisorbed layer is a maximum. It is therefore, likely that at constant mass conditions, there are two equilibrium processes (i) between the formation and desorption of a chemisorbed layer and (ii) between a van der Waals' layer and a partially chemisorbed layer; variation in the energy (any form) supplied to the surface disturbs the equilibrium conditions.

It is instructive to note that the present mechanism attempts at an explanation on the basis of interaction between an adsorbed phase on an electrically excited surface and external radiation and is supported by the results on the activation energy measurements of such systems and was called for, to explain theoretical deficiencies in substantiating the potential variation of $\pm\Delta i$ and certain other experimental observations, which could not be explained otherwise. Work pertaining to a theoretical explanation of the results observed hitherto in the field of Joshi effect in the light of the above theory is being published elsewhere.

Grateful thanks of the author are due to Prof. S. S. Joshi for his valuable suggestions.

References

1) Joshi, S. S.: Journal of the Banaras Hindu University (1943).
2) Joshi, S. S.: Curr. Sci., **8** (1939) 548; Proc. Ind. Acad. Sci **14** (1945) 317; Curr. Sci., **15**, 281 (1946).
3) Joshi, S. S.: Presi. Addr., Proc. Ind. Sci. Cong., Chem. Sec., (1943).
4) Joshi, S. S: Nature, (1944) 154, 147; Curr. Sci, **14** (1945) 67; Proc. Ind. Acad. Sci., **22** (1945) 225.
5) Joshi, S. S.: Curr. sci., **13** (1944) 253; **14** (1945) 35, 175.
6) Joshi, S. S: Unpublished results., *Cf.* Marathe and Bommannawar: Nature, **165** (1950) 890.
7) Deshmukh, G. S.: J. Ind. Chem. Soc., **24** (1947) 211.
8) Arnikar, H. J.: Proc. Ind. Sci. Cong., Phy. Sec., **A 20** (1951).
9) Ramana Rao & Sharma: J. Phys. & Colloid Chem., **53** (1949) 753.
10) Jatar, D. P.: Proc. Ind. Sci. Cong., Phys. Sec., **A 22** (1951).
11) Mohanty *et al*: J. Phys. Soc. of Japan, **9** (1954) 576.
12. Mohanty: J. Sci. Res., Banaras Hindu University, Vol: VI (i) (1955–56) 56.
13) Shukla: J. Phys. & Colloid Chem., **53** (1949) 1239.
14) Joshi, S. S.: Proc. Ind. Sci. Cong., Phys. Sec., **A 26** (1946), **A 27** (1947); Curr. Sci., **16** (1947) 19.
15) Deb an Ghosh: Sci. & Cult., **12** (1946) 17; J. Ind. Chem. Soc., **25** (1948) 449; J. Chem. Phys., **21** (1953) 1486; Proc. Phys. Soc. (London), **65 B** (1952) 304.
16) Ramanamoorthy & Shamim Ahmed: Curr.

Sci., **18** (1949) 416; **19** (1950) 350.
17) Parshad: Nature, **155** (1945) 362.
18) Sahay: Curr. Sci., **14** (1945) 122.
19) Garg: ibid., **19** (1950) 115.
20) Rais Ahmed & Gill: ibid., **19** (1950) 206.
21) Ramaiah: J. Sci. Ind. Res., **10 A** (1951) 182.
22) Harris & von Engel: Proc. Phys. Soc. (London), **64 B** (1951) 916.
23) Rideal, Frankenburg, Komarewsky, Emmett & Taylor: "Advances in Catalysis and Related Subjects" Vol. I (1948) and Vol. II (1950), Academic Press Inc., N. Y.
24) Stephen Brunauer: "The Adsorption of Gases and Vapours", Vols. I & II, Oxford Univ. Press, (1943).
25) Roberts: "Some Problems in Adsorption" Camb. Phys. Tracts (1939).
26) Madhavan: M. Sc. Thesis, Banaras Hindu University (India) (1957).
27) Trapnell: "Chemisorption" Butterworths' Scientific Publications, London (1955)
28) Massey: "Negative Ions", Camb. Univ. Press (1950).
29) Jatar, D. P.: J. Sci. & Ind. Res., **9 B** (1950) 283.
30) Cravath: Phys. Rev. **33** (1929) 603.
31) Glasstone, Laidler and Eyring: "The Theory of Rate Processes", Mc Graw Hill Book Co., N. Y. (1041).

J. PHYS. SOC. JAPAN **13** (1958) 1546~1547

NMR Study of γ Ray Induced Polymerisation of Ethyl Acrylate

Toshikazu SHIBATA, Itsuro KIMURA and Tokuo SUITA

Department of Nuclear Engineering, College of Engineering, Osaka University, Osaka

(Received September 15, 1958)

Some experimental results of proton magnetic resonance absorption of ethyl acrylate etc. during polymerisation are reported here.

The samples were prepared with sufficient purification and evacuation. The radiation source for γ ray irradiation was 100 curies of ^{60}Co and the dose rate was about 2×10^6 r/hr. The irradiation was carried out continuously except the occasional interruptions for observation of NMR. The Pound-Watkins circuit, lock-in amplifier and ordinary *rf* spectrometer techniques were used to observe the proton magnetic resonance. The magnetic field used was about 4500 gauss and its uniformity was some 10^{-2} gauss over the samples. Line width observed at lower doses was limited by the inhomogeneity of the magnetic field.

The resonance patterns varied with increasing γ ray doses. In the actual procedure, the second moment was taken for the line width, but the resonance curves in our case, were generally very narrow and submerged in the noises at the wings where the contribution to the second moment is large. Therefore, the line width obtained may have appreciable errors especially in lower dose region. In Fig. 1 the line width is plotted against

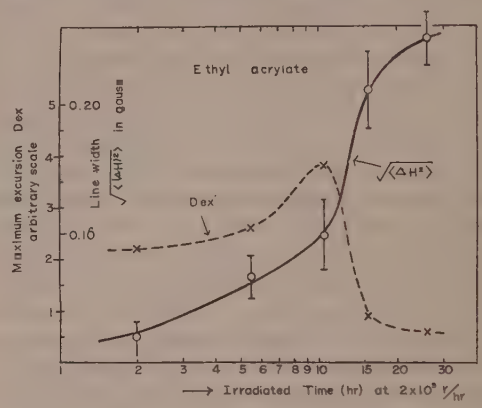

Fig. 1. Line width and maximum excursion curve against γ irradiated dose.

the γ irradiation dose in the case of ethyl acrylate.

In the same figure, the line intensity or conveniently the maximum excursion in its derivative curve is also shown as the dotted line.

The line intensity curve has a peak at a certain dose. Similar results were obtained on other monomers such as acrylonitryl, methylmethacrylate etc., but their peaks occured at different values of γ doses. It is interesting that the peaks of the line intensity curves occur at about the maximum slopes of the line width curves.

Following considerations may be given to the present result. The viscosity of samples increased with γ dose, because polymerisation occured. The increase of viscosity shortens the spin lattice relaxation time T_1 as $T_1 \propto T/\eta$, where T is the temperature and η the viscosity of the samples.[1] Hence the saturation effects are avoided at higher viscosity, and the line intensity or maximum excursion increases. The viscosity rises very rapidly even in the region before the D_{ex} peak, and the sample becomes apparently solid after only a few hours of irradiation. At the stage when the sample begun to solidify some hindered motions may still be possible. However, when the polymerisation is accomplished any internal motion characteristic to the liquid state may not be possible and accordingly D_{ex} decreases. Thus the peak occurs and simultaneously line width becomes larger.

More detailed experiments with other cooperative procedures on many other samples are now in progress.

The authors wish to thank Mr. H. Sumitomo for his help in the preparation of the samples.

Reference

1) N. Bloembergen, E. M. Purcell & R. V. Pound, Phys. Rev. **73**, 679 (1948).

J. Phys. Soc. Japan **13** (1958) 1547

Field Effect on Molybdenite

By Ichiro Nakada

Kobayashi Institute of Physical Research, Kokubunji, Tokyo

(Received September 10, 1958)

Previously the existence of the surface space charge layer on molybdenite was qualitatively assured by the measurement of surface conduction and surface photovoltaic effect[1)2)]. Further quantitative investigation by the method of "field effect"[3)] is reported.

The measurement is made on two kinds of surfaces; the one is prepared by the cleavage of a natural crystal and the other is the surface soaked in HCl or HNO_3 for a few seconds after cleaving. All the specimens measured are n-type with carrier density of about $10^{16}/cm^3$. As the carrier density is a little too high for the performance of such experiments, the surface field up to 10^6V/cm is applied using a mica sheet as a separator. The highest field strength is limited by the electric breakdown of the mica sheet.

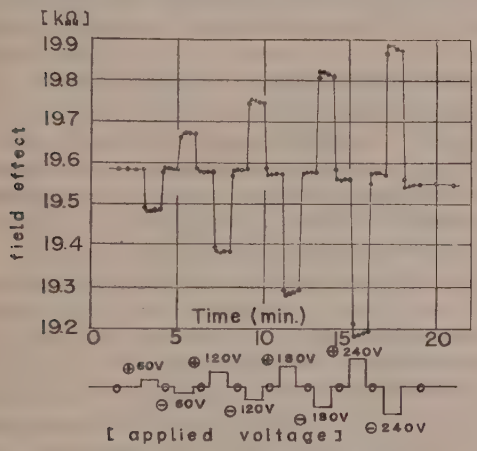

Fig. 1. Field effect of the freshly cleaved surface measured at 6.0°C.

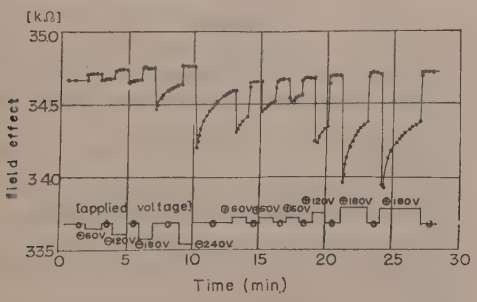

Fig. 2. Field effect of the surface treated by HCl and measured at 3.8~3.9°C.

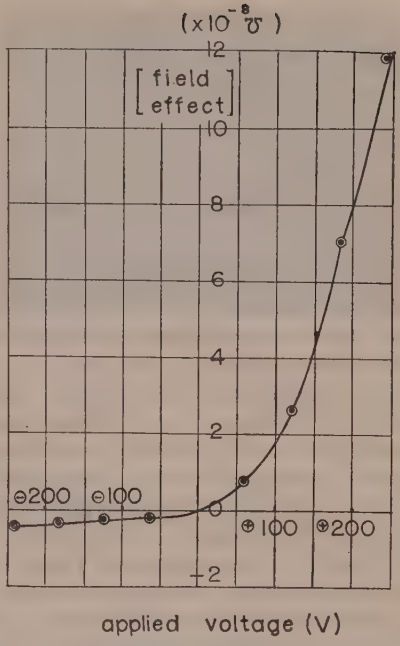

Fig. 3. The relation between the applied voltage and field effect obtained from the result of Fig. 2.

On the surface without any chemical treatment the field effect is as shown in Fig. 1. The relation between the applied field and the conductivity change is linear. From this linear relation only the level of the trapping state cannot be deduced anyway. Fig. 2 is the result on the chemically treated surface which would probably be covered with the electronegative gas layer of HCl. The relation between the applied voltage and the conductance change is shown in Fig. 3. In this case the notable trapping effect appears and from the nonlinearity of the field effect the behavior of the inversion layer can be analysed. With the assumption that the mobility of holes induced by the high negative field is reduced because of the narrow conducting path in the inversion layer[4)], the result on the chemically treated surface is analysed as follows: the trapping level situates 1.4 eV below the conduction band and the state density is 4×10^{12} /cm² volt. The detail would be reported later.

References

1) I. Nakada: J. Phys. Soc. Japan **11** (1956) 1122.
2) I. Nakada: Oyo Butsuri **26** (1957) 571.
3) W. L. Brown: Phys. Rev. **100** (1955) 590.
4) J. R. Schrieffer: Phys. Rev. **97** (1955) 641.

J. PHYS. SOC. JAPAN **13** (1958) 1548

Quadrupole Moment of the Second Excited State of ^{19}F

By Kenzo SUGIMOTO*, Akira MIZOBUCHI and Hisasi YAMAMOTO

Department of Physics, Faculty of Science, Osaka University, Osaka

(Received October 9, 1958)

Angular distributions of the 200-keV gamma-radiations by the reaction ^{19}F$(p, p')^{19}$F* have been measured by bombarding a CaF_2 target and also a polytetrafluoroethylene ($(C_2F_4)_n$) target of each about 200-keV thickness for 1.4-MeV protons. Each distribution was fitted to the form $W(\theta)=1+A_2G_2P_2(\cos\theta)$, where A_2 is the coefficient of the distribution in the Legendre polynominal $P_2(\cos\theta)$, and predicted theoretically $0.40>A_2>0.143$ by Christy[1], and G_2 is the attenuation factor caused by the effect of nuclear environment during the life $T_{1/2}=85$-mμ sec of the emitting state. $A_2G_2=0.242\pm0.010$ and $A_2G_2=0.071\pm0.010$ for the CaF_2 target and the polytetrafluoroethylene target were obtained respectively by 1.4-MeV incident protons. The result obtained by the CaF_2 target was in good agreement with the result obtained by Peterson, *et al.*[2], and if one assumes $0.6<G_2<0.8$ for this case following the discussion by Christy[1], then one gets $G_2\sim0.2$ for the polytetrafluoroethylene target, which is just the hard core value of G_2 by the static quadrupole coupling of polycrystalline case[3].

The attenuation factor of the delayed correlation, $G_2(t)$, by the static quadrupole coupling of polycrystalline state was calculated by Abragam and Pound[3] as follows;

$$G_2(t)=\frac{1}{5}\left(1+\frac{13}{7}\cos\omega_0 t+\frac{10}{7}\cos 2\omega_0 t+\frac{5}{7}\cos 3\omega_0 t\right), \tag{1}$$

for nuclear spin $I=5/2$, where

$$\omega_0=\frac{3}{2I(2I-1)}\frac{eQ(\partial^2V/\partial Z^2)}{\hbar} \tag{2}$$

is the angular frequency equivalent to the smallest nonvanishing energy difference by the pure quadrupole coupling with the field $\partial^2V/\partial Z^2$ of nuclear environment.

Delayed angular distribution were measured by using a chopped proton beam of 2-mμ sec duration and 100-mμ sec repetition rate, and employing a fast coincidence detector with NaI(Tl) scintillation spectrometer, whose resolving time was better than 10-mμ sec for 200-keV gamma-rays. Intensities of the radiations with various delayed times were measured for 0° and 90° with respect to the incident protons. The result of this delayed correlation is shown in Fig. 1. The curves drawn in this figure were calculated with the formula (1) by considering the nuclear life time and geometrical factor of the experimental set-up, and assuming $A_2=0.35$. The result was only a preliminary one, but the delayed charactor was clearly seen, and the best fit with the case of the frequency $f_e^0=\omega^0/2\pi=7$ MC of quadrupole coupling was obtained.

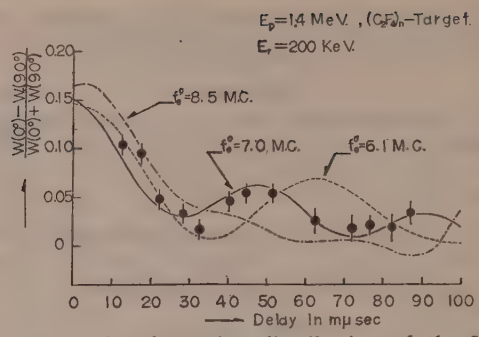

Fig. 1. Delayed angular distribution of the 200-keV radiations. The curves drawn in this figure were calculated theoretically for the respective frequency of the quadrupole coupling f_e^0. The errors indicated are only statistical ones.

The C–F bonding energy of polytetrafluoroethylene is very high (120-kcal) and the examination under irradiation have shown that the main event caused by the radiation is a puncture of C–C bond[4]. The recoil fluorine atom will travel many molecular layers loosing its kinetic energy with ionization and in a relatively short period ($<10^{-10}$ sec) reach an energy comparable to the energy of C–F bond. One can assume that the recoil fluorine atom is trapped by the C–F bond of a polytetrafluoroethylene and the quadrupole field caused by the C–F bond effect to the excited nucleus.

Under this assumption, $\partial^2V/\partial Z^2$ can be calculated as $4.8\cdot10^{15}$ e.s.u. using the value q_{210} for the $2p$ electron by Barnes and Smith[5] and assuming the s-hybridization of 15% and the ionic charactor of 64% following the estimation by Towns[6]. Inserting each values to the formula (2), the quadrupole-moment of the excited state was obtained as

$$Q\left(^{19}\mathrm{F}, \frac{5^+}{2}\right)\sim0.1_3\cdot10^{-24}\ \mathrm{cm}^2 .$$

References

1) R. F. Christy: Phys. Rev. **94** (1954) 1077 L.
2) R. W. Peterson, C. A. Barnes, W. A. Fowler and C. C. Lauritsen: Phys. Rev. **94** (1954) 1075 L.
3) A. Abragam and R. V. Pound: Phys. Rev. **92** (1953) 943.
4) Conference on Effects of Radiation on Dielectric Materials, ONR Symposium Report ACR–2 (1954).
5) R. G. Barnes and W. V. Smith: Phys. Rev. **93** (1954) 95.
6) C. H. Towns and A. L. Schawlow: Microwave Spectroscopy, McGraw-Hill Book Co., New York (1955).

* Now at the Laboratory for Nuclear Science, M.I.T., U.S.A.

J. PHYS. SOC. JAPAN **13** (1958) 1549

Ferroelectricity in the Phase III of KNO_3

By Shozo SAWADA, Shoichiro NOMURA and Shin'ichi FUJII

Institute for Solid State Physics, University of Tokyo

(Received September 30, 1958)

Potassium nitrate (KNO_3) has the aragonite structure (D_{2h}^{16}) at room temperature (phase II). On heating, the crystal structure changes from orthorhombic to trigonal at about 130°C and the high temperature phase (phase I) is said to have the calcite structure (D_{3d}^{6})[1]. On cooling, on the other hand, the phase I changes first to the phase III at about 124°C and next III to II at about 110°C[2),3)]. It has been reported that the temperature range corresponding to the phase III is broadened and III appears also on heating, by an application of high pressure[4),3)] and that III belongs to the space group C_{3v}^{6}.[5)]

We have found that the phase III is ferroelectric. Many of dielectric measurements have hitherto been made for fused samples, since the fact that crystals of KNO_3 are successively cracked by repeatedly passing through the 130°C transition[6),7)] has let us hesitate to perform our measurements using only single crystals.

A disc electrode was suspended inside a cylindrical crucible which was used as another electrode and the diameter of disc electrode and the gap between two electrodes were 4 mm and 0.5 mm respectively. After being charged into the crucible, KNO_3 powder which had beforehand been dried in 10^{-3} mmHg vacuum at about 120°C for several days was melted in a furnace and slowly cooled down. Fig. 1 shows the $D\sim E$ hysteresis loop (max. field 17 kV/cm, 50 C/sec) at 121°C for a fused sample, from which the coersive field and the spontaneous polarization at this temperature turn out to be 4.5 kV/cm and 6.3 μC/cm^2, respectively. The fact that the typical hysteresis loop is observed and the value of spontaneous polarization is large, even for the fused sample, would be noticeable.

Fig. 2 shows the permittivity *vs* temperature relation (1043 kC/sec) measured on heating and cooling for a twinned crystal (area 0.55 cm^2, thickness 0.05 cm) using air-drying silver paste electrodes. In the phase I, the Curie-Weiss law holds with the Curie-Weiss temperature of 293°K and the Curie constant of 4.3×10^3°K.

The pyroelectricity was unambiguously observed in the phase III for fused samples. An effect of biasing field upon the permittivity-temperature relation was not clearly observed. The ferroelectricity in the phase III is considered to be due to a shift of the NO_3 group in the *c*-direction from

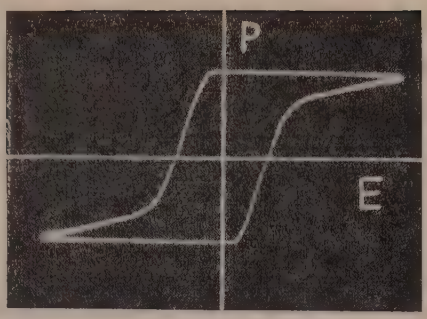

Fig. 1. Hysteresis loop at 121°C.

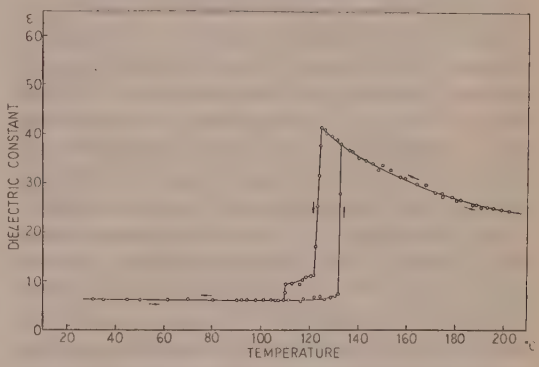

Fig. 2. Permittivity (1043 kC/sec) *vs* temperature for a twinned crystal.

the center of a rhombohedral unit cell whose corners are occupied by K ions. The result that the phase III is ferroelectric may lead us to imagine that the phase II is antiferroelectric in the *b*-direction, since the aragonite structure is antipolar in this direction, but no double hysteresis loop was observed just below the III→II transition at least for fused samples. The fact that no bias effect and no double hysteresis loop were observed might partly be due to large amounts of latent heat at I→III and III→II transitions[3),8)].

Although the change of twin structure of crystals at each transition could be observed under a polarized light microscope, these twins would not be ferroelectric domains. More thorough studies on single crystals will be shortly reported.

References

1) D. A. Edwards: Zeit. Krist. **80** (1931) 159.
2) E. Cohen and H. L. Bredée: Zeit. Phys. Chem. **A 140** (1929) 391.
3) F. C. Kracek: Journ. Phys. Chem. **34** (1930) 225.
4) P. W. Bridgman: Proc. Amer. Acad. **51** (1916) 579.
5) F. W. Barth: Zeit. Phys. Chem. **B 43** (1939) 448.
6) W. Borchert: Zeit. Krist. **95** (1936) 28.
7) S. W· Kennedy, A. R. Ubbelohde and I. Woodward: Proc. Roy. Soc. **A 219** (1953) 303.
8) H. Miekk-Oja: Ann. Acad. Sci. Fennicae, Series **A, 1** (1946) 7.

J. PHYS. SOC. JAPAN **13** (1958) 1550~1551

Thermal Conductivity of $BaTiO_3$ Ceramics

By Ikushi YOSHIDA, Shoichiro NOMURA and Shozo SAWADA

Institute for Solid State Physics, University of Tokyo

(Received September 30, 1958)

A great deal of investigations of the thermal conductivity of insulators, performed by many workers[1], have made it clear that the temperature dependence of the thermal conductivity of simple, insulating crystals can be explained, at least qualitatively, by the phonon theory[2]. The status of understanding in cases of more complex crystals, however, remains very unsatisfactory. The behavior of thermal conductivity of crystals with phase transformations has been thought to be beyond our grasp, although some contributions have been reported concerning molecular crystals[3].

Many properties of ferroelectric and antiferroelectric substances have been investigated, but the measurement of thermal conductivity has scarecely been made[4], although by this measurement there seems a reasonable promise for shedding some light on the understanding of the above problems.

We have planned to investigate the temperature dependence of thermal conductivity of a series of substances including ferroelectrics, antiferroelectrics and their solid solutions, with hopes to get some knowledge on, how the phonons are scattered by ferroelectric domain boundaries, or how they are coupled together in the ferroelectric and antiferroelectric state, or what the situation is, compared with molecular crystals reported formerly.

The specimens used were sintered from $BaCO_3$ and TiO_2 powders of the special reagent grade by the usual method. The thermal conductivity of the specimen was compared with that of pure iron by a so-called "divided bar method".

Fig. 1 shows the temperature dependence of the thermal conductivity of $BaTiO_3$ ceramics. Its absolute value at 100°C is about 28 mW/cm.deg., which is rather high for such a ceramic substance. The temperature coefficient is negative, but it does not obey the $1/T$ law required by the phonon theory. Most noticeable is the small hump at about 120°C, which is the ferro-para transition temperature. For comparison, the thermal conductivity of $SrTiO_3$ ceramics measured in the same temperature range is shown in Fig. 2. This substance belongs, as is well known, to the perovskite group as $BaTiO_3$ does, but is not ferroelectric. In this case, the temperature coefficient was also negative but no anomaly was observed. The absolute value at 100°C is about 52 mW/cm.deg., nearly twice that of $BaTiO_3$. A preliminary measurement for ferroelectric $PbTiO_3$, which has also the same crystal

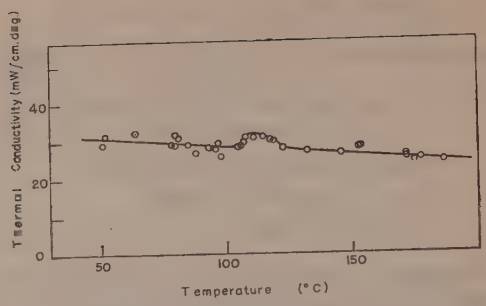

Fig. 1. Thermal conductivity of $BaTiO_3$ ceramics.

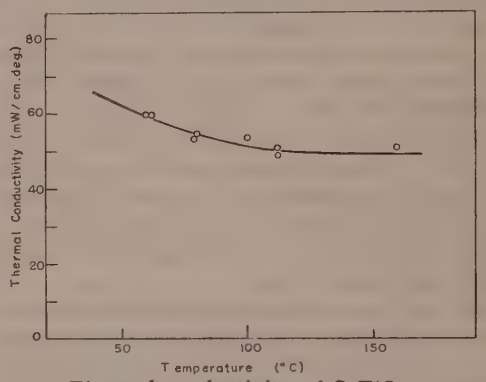

Fig. 2. Thermal conductivity of $SrTiO_3$ ceramics.

structure, has been performed. As far as the present stage of the measurement tells us, a similar tendency as in the case of $BaTiO_3$ is observed. The value at 100°C is about 29 mW/cm.deg., which is also comparable to that of $BaTiO_3$.

Of the three specimens that we have measured, only $SrTiO_3$ showed the conspicuously high value of thermal conductivity. Porosity of these ceramic specimens might prohibit such a direct comparison of the absolute values, but all of our specimens have nearly equal porosity slightly larger than 10%, and, as has been reported[5], the effect of not extremely large porosity would safely be eliminated by using a simple formula. After all, the fact that $SrTiO_3$ is thermally much more conductive than $BaTiO_3$ or $PbTiO_3$ would not be a mere result of the difference of porosities. Then, we infer, this fact seems to suggest an intimate relation of the thermal conductivity with the ferroelectricity, resulting from a singular behavior of the thermal vibration of ions shifted to cause the ferroelectricity.

Investigations of other perovskite crystals, their solid solutions and other classes of ferroelectric substances in a wider temperature range are now in progress.

References

1) R. Berman: Phil. Mag. Suppl. **2** (1953) 103.
2) R. E. Peierls: Ann. Physik **3** (1929) 1055.
3) A. Eucken and Schroeder: Ann. Physik **36** (1939) 609.
A. N. Gerritsen and P. van der Star: Physica **9** (1942) 503.
Cl. v. Simon: Naturwiss. **38** (1951) 559.

4) S. Nomura: Rep. Inst. Sci. and Tech., Univ. Tokyo **6** (1952) 117.
5) J. Francl and W. D. Kingery: Jour. Amer. Cer. Soc. **37** (1954) 99.

J. PHYS. SOC. JAPAN **13** (1958) 1551

Difference between Dynamic and Static Surface Tensions*

By Sohei KONDO

National Institute of Genetics, Misima, Japan

(Received January 21, 1958)

We consider a plane non-equilibrium interface between phases α and β. Following Defay[1], we consider the system as composed of many thin, substantially homogeneous layers $-u, \cdots, 0, 1, \cdots, w$, with thickness d, each being parallel to the interface. Let $p_T{}^t$ denote the tangential pressure of the t-th layer; p^α and p^β the pressures of bulk phases α and β. The mechanical definition of surface tension γ, which is applicable to non-equilibrium interfaces as well, gives[2]

$$\gamma = d\sum_{t=-u}^{w} (p^{\alpha\beta} - p_T{}^t)\,, \qquad (1)$$

$$p^\alpha = p^\alpha(1-A(t)) + p^\beta A(t);\ A(t) = \begin{cases} 0, & t<0 \\ 1, & t \geqslant 0 \end{cases} \qquad (2)$$

where Gibbs' dividing surface is placed between the layers 0 and 1. We can get a non-equilibrium interface called the "completely fresh surface", where the concentration is the same as in the interior of the bulk liquid phase, by bringing rapidly an amount of the interior part to an equilibrium interface, keeping the composition unaltered[3,4]. The completely fresh surface, when left in a natural aging process, will tend to equilibrium passing through various, intermediately fresh states. Surface tension of such a fresh surface is calld "dynamic surface tension" and that of an equilibrium interface "static surface tension"[3,4]. For simplicity, we assume in the following treatment that liquid phase α is confined below the layer 0 while vapor phase β can be treated as a vacuum.

We suppose an alternative way to obtain a fresh surface of a pure liquid, whose density is larger than that of the corresponding equilibrium interface. We can change the equilibrium interface into the desired fresh interface by giving rapidly some proper amounts of tangential isothermal contraction to layers 1, 2, $\cdots$, respectively. This will cause *increases* of $p_T{}^1$, $p_T{}^2$, etc., if eace layer obeys a relation similar to the equation of state of liquids**. Thus, the fresh interface has tangential pressures higher than those of the equilibrium interface. Then, from (1) we may conclude that dynamic surface tension of a pure liquid is smaller than static one. According to Harasima's[5] calculation based on Kirkwood and Buff's[6] statistical-mechanical treatment of surface tension of liquid argon at 90°K, $p_T{}^t$ becomes highly *positive* in the completely fresh interface. This means from (1) that the pure dynamic surface tension (surface tension of a completely fresh surface) of liquid argon is highly negative and much less than the static surface tension of 11.9 dyne/cm[6]. We find in a similar manner that surface tension of a non-equilibrium interface, where the density transition from liquid to vapor is less sharp than in the equilibrium interface, is larger than the static surface tension.

Now we consider a dilute solution with a plane interface, in which the solvent is in equilibrium while the solutes are out of equilibrium. If the adsorption is *positive*, a fresh surface must have a *lower* concentration than that of the equilibrium interface. The fresh surface can be brought about by diluting rapidly at constant temperature the solution in the equilibrium interface until the latter gains the same concentration as the desired fresh surface. To carry out this dilution procedure, we assume that one of the walls of the container is composed of stripped semi-permeable membranes of width d, which are permeable only to the solvent and in contact with a pure liquid in an osmotic equilibrium with the above solution. Then, we can change the concentration of any layer into the desired one by pushing outward rapidly the strip membrane of the layer. This procedure will decrease $p_T{}^1$, $p_T{}^2$, etc. We then find from (1) that for the case of positive adsorption, dynamic surface tension must be larger than static one. This agrees with experimental results[7]. Similarly, we find that for negative adsorption, dynamic surface tension will be smaller than static one. This is expected to be observed in the case of ionic solutions. The details of the present treatment based on quasi-thermodynamics[2] and statistical mechanics will be presented elsewhere. This work is partly supported by grant-in-aid for scientific research from the Ministry of Education.

References

1) R. Defay: J. Chim. Phys. **46** (1949) 375.
2) S. Kondo: Busseiron Kenkyû, Series II, **2** (1957) 926. See also Reference 6.
3) O. K. Rice: J. Phys. Chem. **31** (1927) 207.
4) R. Defay: J. Chim. Phys. **51** (1954) 299.
5) A. Harasima: Proc. Intern. Confer. Theoret. Phys., Kyoto and Tokyo (1953) 435.
6) J. G. Kirkwood and F. P. Buff: J. Chem. Phys. **17** (1949) 338.
7) R. Defay et J. Roba-Thilly: J. Colloid Science, Supplement **1** (1954) 36.
D. Rycker et R. Defay: Bull. Soc. Chim. Belgique, **65** (1956) 794.

* Contribution No. 234 fron National Institute of Genetids.

** This is a quasi-thermodynamic assumption and not offhand exact due to non-autonomy of layers[1,2].

Contents

(Vol. 13)

No. 1 Page

Angular Distribution of Photo-neutrons Produced by 17 Mev X-rays..... Tsunesaburo ASADA, Masayoshi MASUDA, Masayuki OKUMURA and Juro OKUMA 1

The Phase Transformation of Solid Normal Hexadecanamide. ..... Tosio SAKURAI and Masaya YABE 5

Variation of the Hall Coefficient of Mg–Cd Superlattice Alloys with Degree of Order. ..... Kiyoshi YONEMITSU and Takao SATO 15

Surface Photoconductivity of Cadmium Sulphide with Magnetic Field. ..... Shōji TANAKA and Taizō MASUMI 22

Electron Spin Resonance of *M*-centers in Potassium Chloride. ..... Hazimu KAWAMURA and Keiko ISHIWATARI 33

Electrical Properties of $FeTiO_3$-Fe_2O_3 Solid Solution Series. .....Yoshikazu ISHIKAWA 37

Absorption Coefficients of Fine Structures of X-ray Absorption Spectra at Various Absorber Thickness. ..... Kenjiro TSUTSUMI, Masayoshi OBASHI and Masao SAWADA 43

Studies on the Radial Distribution Analysis is Diffraction Methods. II–Effect of Non-nuclear Scattering and Analysis of the Radial Distribution Curve. ....Kinya KATADA 51

Uniaxial Anisotropy in Iron-Cobalt Ferrites..... ..... Shūichi IIDA, Hisashi SEKIZAWA and Yoshimichi AIYAMA 58

Narrowing Effect in Nuclear Magnetic Double Resonance in Solids ....Yushiro SAITO 72

Theory of Dilute Polymer Solutions (I) Chain Configuration and Light Scattering. ..... Hiromi YAMAKAWA and Michio KURATA 78

Theory of Dilute Polymer Solutions (II) Osmotic Pressure.....Hiromi YAMAKAWA 87

Theory of Dilute Polymer Solutions (III) Intrinsic Viscosity. .... Hiromi YAMAKAWA and Michio KURATA 94

Quadrupole Moment of Nb^{93} and Test of the Hyperfine Structure Formulas. .... Kiyoshi MURAKAWA 101

Note on the Information Capacity of a Coloured Picture. .....Hiroshi SATŌ 108

SHORT NOTES

Electron Collection and Electron Sheath. ....Takayoshi OKUDA and Kenzo YAMAMOTO 112

Afterglow of Pure and Mixed Gases.....Susumu TAKEDA 113

Dielectric Properties of Lead Titanate and Its Solid Solutions at Low Temperature under Strong Electric Field. .....Shoichiro NOMURA and Jinzo KOBAYASHI 114

Errata

Molecular Sound Velocity of Aqueous Sugar Solutions..... .....Otohiko NOMOTO and Tadashi KISHIMOTO 115

Application of the Thin-Wing-Expansion Method to the Flow of a Compressible Fluid past a Symmetrical Circular Arc Aerofoil. .....Saburo ASAKA 115

No. 2

Directional Correlations of Gamma Rays in Te^{124}. .....Takeo HAYASHI 117

Excitation Curves of the $N^{14}(d, n)O^{15}$ Reaction.....Susumu MORITA 126

$Co^{59}(n, \alpha)Mn^{56}$ and $Mn^{55}(n, \alpha)V^{52}$ Reactions Induced by 14.8-Mev Neutrons..... ..... Isao KUMABE, Eiko TAKEKOSHI, Hiroshi OGATA, Yoshikazu TSUNEOKA and Shinpei ŌKI 129

The Thermoelectric, Galvanomagnetic and Thermomagnetic Effects of Monovalent Metals. .....Mikio TSUJI 133

Thomas-Fermi Function for Impurity Atom Dissolved in a Matrix Metal. .... Kwai UMEDA and Shigehiro KOBAYASHI 148

Defects in Ionic Crystals. I. Improvement of the Method of Mott and Littleton and its Applications to Simple Defects. .....Tatsumi KUROSAWA 153

On Solvent Effects in Dipole Moment Determinations. .....Kisaburo SHOGENJI 160
Study on the Ordered Alloy Ag_3Mg.....
Kunio FUJIWARA, Makoto HIRABAYASHI, Denjiro WATANABE and Shiro OGAWA 167
The Paramagnetic Susceptibility of Some Nickel Salts. .....
.....Taiichiro HASEDA and Muneyuki DATE 175
X-ray Studies on the Structures of Solid Solutions $NaCl$-$CaCl_2$. III. Influence of Heat Treatments on the Diffuse Reflexions of X-rays due to {111} and {310} Plate-Zones. .....Kazuo SUZUKI 179
Collective Electron Ferromagnetism, III. Relative Magnetization of Ferromagnetic Alloys. .....Hiroshi WATANABE 187
On the Effects of High Energy Radiation to Polymers. I. Cross-linking and Degradation. .....Osamu SAITO 198
Paramagnetic Resonance Absorption in Two Copper Salts at Wavelengths of 5.4 mm and 6.6 mm. .....Kazuo ÔNO and Mieko OHTSUKA 206
A Hydrodynamical Model for the Sedimentation.....Mitutosi KAWAGUTI 209
On a Theorem for Estimating Eigenvalues. .....Hiroshi FUJITA and Tosio KATO 215

SHORT NOTES

Anomalous g-shifts of Excited States of Cr^{3+} in Ruby.....
.....Ikuji TSUJIKAWA and Satoru SUGANO 220
Theoretical Considerations on Radiation-Induced Reactions of Saturated Long-Chain Hydrocarbons. .....Mitio INOKUTI and Tsutomu WATANABE 221
Liquid-Like Layers in the Adsorbed Film of H_2O on Glass.....
.....Koji KAWASAKI, Kyoichi KANOU and Yoshiyasu SEKITA 222
Current Amplification by Electron Bombardment in the Semiconductor Barrier Layer.
..... Kenichi TAKEYA and Keiichi NAKAMURA 223
Fading of Coloration of Irradiated Glass. .....Sohei KONDO 224
Surface Area Variation of Evaporated Barium Film by Oxidation. .....
..... Yutaka TUJI and Hiroaki OKAMOTO 225
Crystal Growth of CdS by the Vacuum Sealed Method. .....
..... Hirosuke YAMASHITA and Sumiaki IBUKI 226
Asymmetry of Proton Resonance Signals in Some Hydrates of Iron Group Salts. ..
..... Syukuro YANO, Sōji SASAKI and Tunahiko SIDEI 227
Magnetostriction Constants of Nickel-Copper and Nickel-Cobalt Alloys.....
..... Mikio YAMAMOTO and Takurô NAKAMICHI 228

Errata

Studies on the Radial Distribution Analysis in Diffraction Methods. II. Effect of Non-nuclear Scattering and Analysis of the Radial Distribution Curve. ....
.....Kinya KATADA 229

No. 3

Elastic Scattering of 5.7 Mev Protons from Fe, Cr and Ti.....Michiya KONDO, Takashi YAMAZAKI, Atsutomo TOI, Ryuzo NAKASIMA and Shotaro YAMABE 231
Excited States of ^{40}Ca...Yasuo HIRAO, Eiji OKADA, Iwao MIURA and Tetsuo WAKATSUKI 233
Angular Distribution of Protons Inelastically Scattered from Mg^{24}. ..Shotaro YAMABE 237
Magnetic Moment of the First Excited State of $_{62}Sm^{152}$. .....Kenzo SUGIMOTO 240
Optical Study on the Resultant Movement of Many Walls in Rochelle Salt.....
.....Ryuji ABE 244
On the Screened Field around an Impurity Atom in Metal. .....Hiroshi FUJIWARA 250
Calculation of the Energy Band Structure of the β-SiC Crystal by the Orthogonalized Plane Wave Method. .....Syoiti KOBAYASI 261
The Crystallographic Aspect of the Mechanical Twinning in Ti and α-U...Hiroshi KIHO 269
Ferroelectricity of $NaNH_4$-Tartrate.....Yutaka TAKAGI and Yasuharu MAKITA 272
On the Temperature Diffuse Scattering of Electrons — I. Derivation of General Formulae..... Satio TAKAGI 278

On the Temperature Diffuse Scattering of Electrons—II. Applications to Practical Problems.....Satio TAKAGI 287
Optical and Electrical Properties of Tin Oxide Films. ..... Kozo ISHIGURO, Taizo SASAKI, Toshihiro ARAI and Isamu IMAI 296
Statistical Aspect in Accelerating Creep and Creep Fracture of OFHC Copper. ..... Takeo YOKOBORI and Hideharu OHARA 305

SHORT NOTES

A Method for Measuring the Dynamic Viscosity and Dynamic Rigidity of Visco-elastic Liquids I. .....Ali Abdel Kerim IBRAHIM 313
Magneto-resistance Effect in Cadmium Sulphide. ....Shōji TANAKA and Taizō MASUMI 314
Absorption Lines in the Antiferromagnetic States of $MnCl_2 \cdot 4H_2O$ and $MnBr_2 \cdot 4H_2O$. .....Ikuji TSUJIKAWA 315
Magnetic After-Effect Due to Quenched-in Vacancies in Nickel. ..... Yoji NAKAMURA and Jin-ichi TAKAMURA 316
Electrical properties of Ag_2Se. .....Shin-ya MIYATANI 317
The Effect of G-P (1) and G-P (2) Aggregates on the Plastic Deformation of an Age-Hardenable Al-Cu 4% Alloy. ..... Keisuke MATSUURA, Sôichi IZUMI and Shigeyasu KODA 318
Some Observations on Germanium Bi-crystals. ....Makoto KIKUCHI and Sigeru IIZIMA 319
The Consecutive Observations on the Twin Intersections. ..... Hiroshi KIHO and Saiyu MARUYAMA 320
Microwave Spectrum of Hydrazine ..... Takeshi KOJIMA, Hiromasa HIRAKAWA and Takeshi OKA 321

No. 4

On the Low Lying Levels of Mn^{55}. .....Sadaaki YANAGAWA 323
Alpha Particles from the Interaction of 14.8-Mev Neutrons with Medium Weight Nuclei. .....Isao KUMABE 325
Some Studies on the Ternary System $(Ba\text{–}Pb\text{–}Ca)TiO_3$. .....Takuro IKEDA 335
Electrical Properties of Ag_2Te. .....Shin-ya MIYATANI 341
On the Backward Leakage Current in the Alloyed Germanium *p–n* Junction. ....Makoto KIKUCHI 350
Effect of External Stress on the Domain Structure of WO_3. .....Sigetosi TANISAKI 363
Ferroelectric and Optical Properties of $Na(K\text{–}NH_4)$-tartrate Mixed Crystals. .... Yasuharu MAKITA and Yutaka TAKAGI 367
The Change of Carrier Concentration in the Simple Semiconductor with Static Magnetic Field.....Yasutada UEMURA and Masaharu INOUE 377
The Change of Carrier Concentration in the Graphite with Static Magnetic Field ..... Yasutada UEMURA and Masaharu INOUE 382
Effect of the Basic Strength of Attached Groups on Light Absorption Spectra—III. Dissociations in the Excited States of Naphthalene Derivatives—. .... Reikichi ITOH 389
On the Absorption Spectra of Complex Ions.—IV. The Effect of the Spin-orbit Interaction and the Field of Lower Symmetry on *d* electrons in Cubic Field —. .....Yukito TANABE and Hiroshi KAMIMURA 394
A New Probe Method for Measuring Ionized Gases ....Takayoshi OKUDA and Kenzo YAMAMOTO 411
Oscillation of the Wake behind a Flat Plate parallel to the Flow..... ..... Sadatoshi TANEDA 418

SHORT NOTES

Transport Phenomena in Monovalent Metals. .....Mikio TSUJI 426
Observation of a Beryllium Hyperfragment. .....Shigeo MATSUMOTO 427
Asymptotic Expansions of Weber's Functions. .....Ryozo YAMADA 428

Errata

Thomas-Fermi Function for Impurity Atom Dissolved in a Matrix Metal. ..... Kwai UMEDA and Shigehiro KOBAYASHI 429

No. 5

Excitation Curve for the Reaction $P^{31}(n, p)Si^{31}$. ..... Susumu MORITA 431
Electronic Structure of Bismuth Type Crystals. ..... Shoichi MASE 434
Effects of Impurities on Nuclear Quadrupole Resonance in *p*-Dichlorobenzene. .... Shoji KOJIMA, Shizuko OGAWA, Midori MINEMATSU and Makoto TANAKA 446
Origin of the Magnetic Anisotropy Energy of Antiferromagnetic Cr_2O_3. .... Masashi TACHIKI and Takeo NAGAMIYA 452
Anisotropy of Hot Electrons in *n*-type Germanium. .... Wataru SASAKI, Motoichi SHIBUYA and Kanji MIZUGUCHI 456
Magnification Calibration of Electron Microscopes by Crystal Lattice Spacings... Ryozi UYEDA, Tatsunosuke MASUDA, Hiroshi TOCHIGI, Kazuo ITO and Haruo YOTSUMOTO 461
An Application of the Thomas-Fermi Method to Complex Ions. ....Hiroshi KAMIMURA, Shoichiro KOIDE, Satoru SUGANO and Yukito TANABE 464
Macroscopic Foundation of Plasma Dynamics. ..... Taro KIHARA 473
Externally Pinched Plasma..... Tihiro OHKAWA and Taro KIHARA 482
The Arc Spectrum of Iodine and the Quadrupole Moment of I^{127}... Kiyoshi MURAKAWA 484
Viscous Flow at Low Reynolds Numbers past an Infinite Row of Equal Circular Cylinders. ..... Tosio MIYAGI 493
The Wall-effect upon the Forces Experienced by an Elliptic Cylinder in a Viscous Liquid..... Yorisaburo TAKAISI 496
The Forces Experienced by Two Elliptic Cylinders in a Uniform Flow at Small Reynolds Numbers. ..... Shinji KUWABARA 506
Experimental Studies on the Initiation of Electric Arcs..... Tasaburô YAMAGUTI 520
The Thermoluminescence of Glasses. ..... Takeo KIKUCHI 526

SHORT NOTES

Orientation Dependence of the Uniaxial Ferromagnetic Anisotropy Induced by Magnetic Annealing in 20% Co-Ni Single Crystals..... ..... Keizô AOYAGI, Satoshi TANIGUCHI and Mikio YAMAMOTO 532
Pits on Germanium Surface Formed by Molten Indium. ..... Sei-ichi DENDA 533
Stepped Structure in Moiré Fringe. ..... Hatsujiro HASHIMOTO 534
On the Superstructure of the Alloy Au_3Mn. ..... Denjiro WATANABE 535
Ultrasonic Velocity and Adiabatic Compressibility of Mixture of Sulfuric Acid and Water..... Yoshio ISHIDA 536
Excitation of π-Electrons in Benzene by Fast Electron According to FE Model..... ..... Mitio INOKUTI 537
Contact Behavior of Metals to CdSe, CdTe, ZnSe and ZnTe..... ..... Hiroshi TUBOTA and Hiromichi SUZUKI 538

Errata

On the Temperature Diffuse Scattering of Electrons. I. Derivation of General Formulae. ..... Satio TAKAGI 539
On the Temperature Diffuse Scattering of Electrons. II. Applications of Practical Problems..... Satio TAKAGI 539
On the Absorption Spectra of Complex Ions IV..... ..... Yukito TANABE and Hiroshi KAMIMURA 539

No. 6

Gamma Rays from the Proton Bombardment of Silicon. .... Eiji OKADA, Iwao MIURA, Tetsuo WAKATSUKI and Yasuo HIRAO 541
Magnetic Spectrometer having Inclined Plane Pole-Faces for Low-energy Electrons. ..... Susumu KATO 544

On the Magnetic Annealing Effect in 2% Cobalt-Copper Alloy-I. Induced Ferromagnetic Anisotropy.....Tadayasu MITUI 549
Electrical and Optical Properties of GeS. .....Tadaichi YABUMOTO 559
Electronic Structure and Diamagnetism of Graphite.....Shoichi MASE 563
Electron Spin Resonance of Z_1-centers in Potassium Chloride. .....Hazimu KAWAMURA and Keiko ISHIWATARI 574
Magnetic Anisotropy Measurements of NiO Single Crystal.....Hisamoto KONDOH, Enji UCHIDA, Yoshihide NAKAZUMI and Takeo NAGAMIYA 579
Fine Structures of X-ray K Absorption Spectra of Nickel in Oxides of Nickel.....Kenjirō TSUTSUMI 586
Fine Structures of the X-ray Absorption by the Single Crystals of Germanium.....Kenjirō TSUTSUMI and Masayoshi OBASHI 591
Nuclear Magnetic Resonance Experiment on Metal Cadmium. II.....Yoshika MASUDA 597
Effects of Ionizing Radiations on Polyethylene.....Kenichi SHINOHARA, Ayao AMEMIYA and Akibumi DANNO 604
Effects of Ionizing Radiations on Polyvinyl Alcohol-I. Breakdown of Main-chain and Formation of Carbonyl Groups. .....Akibumi DANNO 609
Effects of Ionizing Radiation on Polyvinyl Alcohol II. Changes of Physical Properties of the Irradiated Specimen Caused by Heat Treatment. .....Akibumi DANNO 614
Nuclear Quadrupole Resonances in Arsenic and Antimony Trihalides and Sulphur Molecular Addition Compounds.....Shizuko OGAWA 618
A Torsion Magnetometer for Determining Free Radicals in Some Organic Solutions .....Hideo TAKAKI, Naoto KAWAI, Chie MIYAKE and Tadasuke MORITA 629
On the Flow of a Viscous Fluid past a thin Screen at Small Reynolds Numbers.....Hidenori HASHIMOTO 633
Asymptotic Behaviour of the Response Function of an Optical System with the Primary Spherical Aberration. .....Hirosi ITÔ 639
Adsorption of Water Vapour on Glass and Other Materials in Vaccum. .....Hiroaki OKAMOTO and Yutaka TUZI 649

SHORT NOTES

Specific Heats of Copper Ferrite.....Thoru INOUE and Shuichi IIDA 656
The Q-value for the $N^{14}(n, a)B^{11}$ Reaction. .....Tadayoshi DOKE, Shoji SUZUKI and Iwao OGAWA 656
A Richter Type Magnetic Loss in Yttrium-Iron Garnet. .....Hisashi SEKIZAWA, Shūichi IIDA and Tomonao MIYADAI 658
On the Measurement of Isotope Abundance of Lithium with Mass Spectrometer.....Itiro OMURA and Nozomu MORITA 659
Higher Order Transitions in Double Nuclear Resonance Experiments in Solids.....N. BLOEMBERGEN 660
Polarization Reversal in Triglycine Sulphate Crystal. .....Kiyasu ZENITI, Kazuo HUSHIMI and Keisuke KATAOKA 661

Errata

The Thermoelectric, Galvanomagnetic and Thermomagnetic Effects of Monovalent Metals.....Mikio TSUJI 655
Structural Investigation by Means of Nuclear Quadrupole Resonance II. .....Kenji SHIMOMURA 655

No. 7

Isotope Shift in the Spectrum of WI.....John A. VREELAND and Kiyoshi MURAKAWA 663
On the Electrical Properties of Polycrystalline Boron.....Ryosei UNO 667
Change of Oxygen Concentration with Temperaure of the Nickel and Cobalt Oxide Solid Solutions.....Tamio SAKATA and Kimiko SAKATA 675
Paramagnetic Effect in Superconductors. Part I. Quasi-Paramagnetism and Resistance of Indium at the Superconducting Transition.....Yoshio SHIBUYA 684
Paramagnetic Effect in Superconductors. Part II. Quasi-Paramagnetism in Non-Circular Cylindrical Tin Specimens. .....Yoshio SHIBUYA 695

The Effect of Tension on the Magnetostriction of Iron Single Crystals. ..... Hideo TAKAKI and Jun-ichi HAYASHI 703
Electronmicroscopic Observation of Coloured and Bleached Alkali- Halide Crystals. ..... Tadatosi HIBI and Kazuo ISHIKAWA 709
A Note on Thermodynamics of the Harmonic Oscillator with Radiation Damping. ..... Nobuhiko SAITÔ and Jun-ichi HORI 717
Gel Formation of Aqueous Solution of Polyvinyl Alcohol Irradiated by Gamma Rays from Cobalt-60.....Akibumi DANNO 722
The Paramagnetic Resonance Absorption of Some Free Radicals in Sulfuric Acid Solution. ..... Yasaburo YOKOZAWA 727
Moving Striations in Arc Discharge..... .....Hirosi YOSIMOTO, Mituo SATO and Yasuhiro NAKAO 734
Moving Striations due to Space Charge Waves..... .....Hirosi YOSIMOTO, Mituo SATO and Yasuhiro NAKAO 741
Flow Formation with Suction or Injection.....R. S. NANDA 748

SHORT NOTES

The Magnetic Field at the Nucleus of Sm^{+++} induced by Paramagnetism of 4*f*-Electrons. .....Junjiro KANAMORI and Kenzo SUGIMOTO 754
Plasma Oscillation in the Electrically Conductive Tin Oxide Film. .... Kozo ISHIGURO, Taizo SASAKI, Toshihiro ARAI and Isamu IMAI 755
Magnetic annealing of Fe_3Al Single Crystal. .....Kenzō SUZUKI 756
Magnetic Properties of Nickel and Cobalt Ferrite-Chromite Series .... Syohei MIYAHARA and Tachiro TSUSHIMA 758
On Magneto-Acoustic Resonance in Metals. .....Nobuo MIKOSHIBA 759
Space Charge Phenomena in Nitrobenzene under High Electric Field..... ..... Pyong-un CHONG, Chiyoe YAMANAKA and Tokuo SUITA 760
Electric Breakdown and Conduction in $BaTiO_3$ Single Crystals..... ..... Yoshio INUISHI and Shigeyuki UEMATSU 761
Diffusion of Iron in Single Crystals of Copper.....Yuzo TOMONO and Akira IKUSHIMA 762
Beta and Gamma Ray Spectroscopy of Co^{60}..... ..... Kazumasa KAMADA, Tomoyuki TERANISHI and Yasukazu YOSHIZAWA 763
A Note on Direct Observation of Dislocations by Electron Microscopy..... ..... Hatsujiro HASHIMOTO and Toshio NAIKI 764
On the Auger Ejection of Electrons from Nickel by Inert Gas Ions. .... Yoshiyuki TAKEISHI 766
A Note on the Normal Cathode Fall in the Glow Discharges in Inert Gases. .... Yoshiyuki TAKEISHI 767
Electron Spin Resonance of Eu^{++} in Natural CaF_2. .... On MATUMURA, Kazumi HÔRAI and Zen'emon MIDUNO 768
Measurement of the Thermal Conductivity in Semiconductors. .....Riro NII 769

No. 8

Elastic and Inelastic Scattering of Protons from Neon .... Michiya KONDO and Takashi YAMAZAKI 771
Angular Distribution of Protons Inelastically Scattered from Si^{28} and Mg^{24}..... .... Shotaro YAMABE, Michiya KONDO, Takashi YAMAZAKI and Atsutomo TOI 777
An Experimental Study of Extensive Air Showers. ..... Saburo MIYAKE, Kensaku HINOTANI, Tatsunosuke KANEKO and Itsuo KATSUMATA 782
Recombination Centers in Germanium.....Jun'ichi OKADA 793
One to One Correspondence between Etch Pits and Dislocations in KCl Crystals. .. .. Masayoshi SAKAMOTO and Shunsuke KOBAYASHI 800
The Internal Friction of Barium Titanate Ceramics. .....Takuro IKEDA 809
The Thermoelectric, Galvanomagnetic and Thermomagnètic Effects of Monovalent Metals. II. The Thermoelectric Power for Anisotropic Media...Mikio TSUJI 818
An Order-Disorder Transformation Phenomenon in the $FeTiO_3$–Fe_2O_3 Solid Solution Series.....Yoshikazu ISHIKAWA 828

Diffusion of Cadmium into Single Crystals of Copper. .....
Tokutaro HIRONE, Nobuhiko KUNITOMI, Masanobu SAKAMOTO and Hideo YAMAKI 838
Diffusion of Cobalt into Iron-Cobalt Alloy.....
.....Tokutaro HIRONE, Nobuhiko KUNITOMI and Masanobu SAKAMOTO 840
Diffusion of Cobalt into Single Crystals of Copper.....Masanobu SAKAMOTO 845
The Theory of the Fine Structure of the X-ray Absorption Spectrum. .....
....., Toshio SHIRAIWA, Tsutomu ISHIMURA and Masao SAWADA 847
Nuclear Quadrupole Spectra of Boron Trichloride and Tribromide.....Takehiko CHIBA 860
Zeeman Effect of Nuclear Quadrupole Resonance Spectrum in Cyanuryl Chloride...
..Yonezo MORINO, Takehiko CHIBA, Takashi SHIMOZAWA and Masaharu TOYAMA 869
Absorption Spectra of Cr^{3+} in Al_2O_3. Part A. Theoretical Studies of the Absorption Bands and Lines.....Satoru SUGANO and Yukito TANABE 880
Absorption Spectra of Cr^{3+} in Al_2O_3. Part B. Experimental Studies of the Zeeman Effect and other Properties of the Line Spectra.....
.....Satoru SUGANO and Ikuji TSUJIKAWA 899
Measurements of Free Induction Decay Time and Spin-Lattice Relaxation Time of Bromine Nucleus in Sodium Bromate .....Tsuneo HASHI 911
Zeeman Study on Nuclear Quadrupole Resonances in AsI_3 and $AsI_3 \cdot 3S_8$...Yoshihito ABE 918
Elementary Problems on the Configurations of a Linear High Polymer...Kazuo NAGAI 928
An Application of the Cellular Method to a Vacancy in Metal. ....Hiroshi FUJIWARA 935
Characteristics of the Beam Type Maser. II. .....Koichi SHIMODA 939
The Maximum Disturbance Growth Rate for an Unstable Plasma Column. .....
..... Shobu KANEKO 947
Note on the Forces on an Elliptic Cylinder moving in a Viscous Liquid at Small Reynolds Numbers.....Yorisaburo TAKAISI 954
Adsorption of Water Vapour on Lead Borosilicate Glass in Vacuum.....
..... Yutaka TUZI and Hiroaki OKAMOTO 960

SHORT NOTES

Variation of the Optical Properties of Iron at Transition Temperature...Akira KINBARA 966
Electrical Conductivity in N-type InSb under Strong Electric Field. ....Yasuo KANAI 967
Low Temperature Anomaly in the Proton Resonance of Some Nickel Salts.....
..... Pil Hyon KIM and Tadashi SUGAWARA 968
A New Compound in Au–Pb Alloy System. .....
..... Yoshibumi FUJIKI, Ryōji SUGANUMA and Toshiho YOSHIDA 969
Etch Pits in Lead Crystals. .....Yosio HIKI 970
Paramagnetic Resonance Spectrum of Manganese in Single Crystals of Alkali Halide Grown from the Melt. .....
..... Kuniya FUKUDA, Yoichi UCHIDA and Hisamitu YOSHIMURA 971
Some Electrical and Optical Properties of Tin Monosulphide. ....Tadaichi YABUMOTO 972

Errata

The Q-value for the $N^{14}(n, \alpha)B^{11}$ Reaction. .....
..... Tadayoshi DOKE, Shoji SUZUKI and Iwao OGAWA 973

No. 9

Dipolar Broadening of the Quadrupole Resonance Lines in Crystals $NaClO_3$, $NaBrO_3$
..... Kenji KANŌ 975
The Thermoelectric, Galvanomagnetic and Thermomagnetic Effects of Monovalent Metals. III. The Galvanomagnetic and Thermomagnetic Effects for Anisotropic Media.....Mikio TSUJI 979
Paramagnetic Resonance in Copper Propionate Monohydrate.....Hidetaro ABE 987
Variation of Hall Coefficient of Some Non-ferromagnetic Superlattice Alloys. .....
.....Kiyoshi YONEMITSU and Takao SATO 998
Study of Metallic Carbides by Electron Diffraction. Part II. Crystal Structure Analysis of Nickel Carbide. .....Sigemaro NAGAKURA 1005

Electron Diffraction Study of Evaporated Face-centered Cubic Crystallites. .... Hidetake MORIMOTO 1015
The Electron Distribution and the Location of the Bonded Hydrogen Atom in Crystals..... Yujiro TOMIIE 1030
Luminescence and Dichroism of *F* and *M* Centers in Potassium Chloride..... ..... Goro KUWABARA and Akira MISU 1038
The Flow with Wake past an Oblique Plate .....Yōichi MIMURA 1048
Flow past a Bent Flat Plate with an Unsymmetric Dead Air at Mach Number 1... ..... Takeo SAKURAI 1055

SHORT NOTES

Observation of the Lateral Photovoltage by Surface Field Effect. ....Makoto KIKUCHI 1061
Study on Annealing of Radiation Induced $1/f$ Noise in Ge p–n Junction. ....Ki-ichi KOMATSUBARA and Utaka HASHIMOTO 1062
A Remark on the Chemical Kinetics in Polymers during Irradiation. ....Tsutomu WATANABE 1063
Effects of Impurities and Temperature on the Spectra of Electroluminescence. ....Ryoichiro HUZIMURA and Tunahiko SIDEI 1064
Electrical Conductivity in p-Type InSb Under Strong Electric Field. ....Yasuo KANAI 1065
Piezo-Effect of Selenium Rectifiers. .....Tadasi NUMATA 1066
Structure of the *F* Band in Potassium Chloride. ....Goro KUWABARA and Akira MISU 1066
Small Angle Scattering of X-rays by Deuteron-irradiated Germanium Crystal. .... Francisco Eiichi FUJITA and Ulrich GONSER 1068
A Note on Numerical Evaluation of Integral Square Error.....Sitiro MINAGAWA 1069

Errata

A Note on the Normal Cathode Fall in the Glow Discharges in Inert Gases. .... Yoshiyuki TAKEISHI 1070

No. 10

Excited States of Pt^{192}. ....Mitsuhiro KAWAMURA, Atsushi AOKI and Takeo HAYASHI 1071
Sector Type Double Focusing Beta Ray Spectrometer. Part I. General Properties ..... Mitsuo SAKAI and Hidetsugu IKEGAMI 1076
Sector Type Double Focusing Beta Ray Spectrometer. Part II. Twin Setting Measurement of the Weak Higher Component of Cs^{137}. .... Toshimitsu YAMAZAKI, Hidetsugu IKEGAMI and Mitsuo SAKAI 1080
Temperature Distribution during the Martensite Plate Formation. .... Zenji NISHIYAMA, Akira TSUBAKI, Hideo SUZUKI and Yasusada YAMADA 1084
Theory of Thermoelectric Power of Ionic Crystals (I).....Eijirō HAGA 1090
A Theory of Impurity Conduction. I. .....Tadao KASUYA 1096
Magnetic Property and Crystal Chemistry of Ilmenite ($MeTiO_3$) and Hematite (αFe_2O_3) System. I. Crystal Chemistry. ....Yoshikazu ISHIKAWA and Syun-iti AKIMOTO 1110
Lattice Defects in Zincblende. Part I. Phenomenological Expressions of Interionic Potentials..... Sumitada ASANO and Yasuo TOMISHIMA 1119
Lattice Defects in Zincblende. Part II.. Formation Energy of Lattice Defects. .... Sumitada ASANO and Yasuo TOMISHIMA 1126
Internal Friction of Lead. I. .....Yosio HIKI 1138
Scattering of Electrons by Carbon Films. .....Yoshihiro KAMIYA 1144
The Crystal Structure of Germanium Selenide GeSe. .....Atsushi OKAZAKI 1151
Anisotropy of Nuclear Magnetic Resonance due to Crystal Dislocations...Eizo OTSUKA 1155
Effect of Velocity Gradient on the Radial Distribution of Polymer Molecules in Dilute Solution. .....Ryuzo KOYAMA 1167
Paramagneic Resonance Spectrum of Mn^{++} in NaCl Single Crystal. .... Kazuo MORIGAKI, Minoru FUJIMOTO and Junkichi ITOH 1174
Nuclear Magnetic Resonance Studies of Iodine Ions in Aqueous Solution..... ..... Junkichi ITOH and Yukio YAMAGATA 1182

The Lower Excited States and the Phosphorescent State of Diphenyl. II. Scheme of Modification of MO. ..... Kaoru IGUCHI 1186
Methods of Approximation of Molecular Integrals. I. ..... Sigeru HUZINAGA 1189
The Visco-elastic Properties of Network Structure. III. Normal Stress Effect (Weissenberg Effect). ..... Misazo YAMAMOTO 1200
Disturbance Phenomena in Probe Measurement of Ionized Gases. ..... Takayoshi OKUDA and Kenzo YAMAMOTO 1212
Magneto-hydrodynamic Oscillations of a Perfectly Conducting Fluid Sphere Placed in a Uniform Magnetic Field. ..... Tsuneji RIKITAKE 1224

SHORT NOTES

Chemical and Thermal Polish of KCl Crystals. ..... Masayoshi SAKAMOTO and Shunsuke KOBAYASHI 1231
Nuclear Magnetic Resonance Experiments of I^{127} in KI. ..... Junkichi ITOH and Yukio YAMAGATA 1232
A Proposed Explanation of Irradiation Growth of Uranium. ..... Ryukiti R. HASIGUTI, Hideo SAKAIRI and Tetuya SUGAI 1233
On the Conduction Mechanism of Oxide Coated Cathode. ..... Hiroyuki MIZUNO 1234
The Far Infrared Absorption of Sulfides, Selenides and Tellurides of Zinc and Cadmium. ..... Akiyoshi MITSUISHI, Hiroshi YOSHINAGA and Shigeru FUJITA 1235
The Far Infrared Absorption of Ferrites. ..... Akiyoshi MITSUISHI, Hiroshi YOSHINAGA and Shigeru FUJITA 1236
Growth and Extinction of Guanidine Aluminum Sulfate Hexahydrate Crystals. ..... Atsuo NISHIOKA and Kyozo SEKIKAWA 1237

Errata

The Electron Distribution and the Location of Bonded Hydrogen Atom in Crystals ..... Yujiro TOMIIE 1239
Diffusion of Cobalt into Single Crystals of Copper. ..... Masanobu SAKAMOTO 1239
Piezo-Effect of Selenium Rectifiers. ..... Tadasi NUMATA 1239

No. 11

The Reaction $F^{19}(d, n)Ne^{20}$ and the Energy Levels of Ne^{20}. ..... Susumu MORITA and Kenji TAKESHITA 1241
Differential Elastic Scattering of 14 MeV Neutrons in Aluminum, Iron, Lead and Bismuth for Large Angles. ..... Kazunori YUASA 1248
The Multiplicity of Mesons Produced in the Nuclear Interaction of High Energy Nucleons and α-Particles in Cosmic Radiation. ..... Shin-ichi KANEKO 1258
On the Theory of the Brownian Motion. ..... Morikazu TODA 1266
Excess Noise in Narrow Germanium p–n Junctions. ..... Tatsuo YAJIMA and Leo ESAKI 1281
A Theory of Impurity Conduction. II. ..... Tadao KASUYA and Sigenao KOIDE 1287
Magnetic Property and Crystal Chemistry of Ilmenite ($MeTiO_3$) and Hematite (αFe_2O_3) System II. Magnetic Property. ..... Yoshikazu ISHIKAWA and Syun-iti AKIMOTO 1298
The Temperature Dependence of Forced Magnetostriction. ..... Toshiro TSUJI 1310
Diffusion Processes in Polymers under Irradiation; Polyvinyl Alcohol and CCl_4 System. ..... Tsutomu WATANABE 1316
The Study of the Transition Phenomena of Chain Polymers by the Photoelastic Method. ..... Motozo KANEKO 1324
Paramagnetic Relaxation of Copper Tutton Salt. ..... Yosuke NAGAOKA 1328
Spin Quenching and Magnetic Resonance. ..... Tôru MORIYA and Yukio OBATA 1333
Nuclear Magnetic Resonance of Transition Elements in Paramagnetic Salts. ..... Tôru MORIYA 1344
Electroluminescence of Insulated Particles. ..... Keiji MAEDA 1352
Phenomenological Free Streamline Theory, Part 1. Flow past a Normal Plate. ..... Yôichi MIMURA 1361
On the Acoustic Field by a Vibrating Source Arbitrarily Distributed on a Ribbon Plate. I. ..... Norio KAWAI 1374

A New Approach to the Theory of Slender Body in Compressible Flow. ..... Haruo MORIGUCHI 1384
Attenuation of Ultrasonic Waves in Suspensions of Viscoelastic Spheres. ..... Yasaku WADA 1390
On the Limit of Superheat. ..... Hiromu WAKESHIMA and Kazuo TAKATA 1398

SHORT NOTES

Etch Pits of Sb Single Crystals. ..... Jiro SHIGETA and Makoto HIRAMATSU 1404
Molecular Collisions in the Two-Dimensional Gases. ..... Kazuo TAKAYANAGI 1405
A Note on the Magnetoresistance Effect of Strain Gauge Wire. ..... Hideo TAKAKI and Toshiro TSUJI 1406
A Certain Anomalous Behavior of Iron Sulfides. ..... Miyuki MURAKAMI and Eiji HIRAHARA 1407
On the Mechanical Loss of Polyethylene. ..... Yasaku WADA 1408
Study on the Correlation between the Noise by Hole Generation and Surface Recombination Velocity at Ge Fused Junction. ..... Kiichi KOMATSUBARA 1409
On RF Electrodeless Discharges in a Capillary. .. Shigeo TAKEMOTO and Mineo KASAI 1410
Dichroism of Color Centers in KCl Crystal. ..... Takehiko ISHII, Tetsuhiko TOMIKI and Masayasu UETA 1411

Errata

Crystal Structure and Phase Transition of Some Metallic Halides (IV). On the Anomalous Structure of α-Ag I. ..... Sadao HOSHINO 1412
Adsorption of Water Vapour on Glass and Other Materials in Vacuum. ..... Hiroaki OKAMOTO and Yutaka TUZI 1412
Adsorption of Water Vapour on Lead Borosilicate Glass in Vacuum. ..... Yutaka TUZI and Hiroaki OKAMOTO 1412

No. 12

On the Observation of Magnetic Poles. ..... Eiichi GOTO 1413
Gamma Ray Spectroscopy of Mn^{54}. ..... Tosio KATO, Masao NOZAWA, Yasukazu YOSHIZAWA and Yujiro KOH 1419
Grain Boundary-Hardening due to Piled-up Dislocations. ..... Jin-ichi TAKAMURA and Sei MIURA 1421
On the V-centers in KBr Crystals. ..... Yoshio NAKAI 1424
On the Magnetic Properties of Nickel Sulfide. ..... Ichiro TSUBOKAWA 1432
Relaxation Spectrum of Chain High Polymeric Substances. ..... Tsuyoshi ONISHI and Misazo YAMAMOTO 1439
On the Forromagnetic Phase in Manganese-Aluminum System. ..... Hiroshi KŌNO 1444
Effects of High Energy Radiation on Polymers II. End-linking and Gel Fraction. ..... Osamu SAITO 1451
Effects of High Energy Radiation on Polymers III. Viscosity. ..... Osamu SAITO 1465
Theory of Excited Plasma Waves. ..... Masao SUMI 1476
Half-Shade Device for the Precise Measurement of the Principle Angle of Incidence. ..... Koreo KINOSITA and Sadao NOMURA 1485
On the Theory of Fluids. ..... Kazuo HIROIKE 1497
Effect of Transverse Magnetic Field on the Flow due to an Oscillating Flat Plate. ..... Tsunehiko KAKUTANI 1504
Some Nonlinear Effect in Compressible Flow. ..... Haruo MORIGUCHI 1510
The Forces Experienced by a Lattice of Equal Flat Plates in a Uniform Flow at Small Reynolds Numbers. ..... Shinji KUWABARA 1516
Deviation from Linearity of the Concentration Dependence of the Molecular Sound Velocity in Liquid Mixtures. ..... Otohiko NOMOTO 1524
Empirical Formula for Sound Velocity in Liquid Mixtures. ..... Otohiko NOMOTO 1528
Condenser Microphones with Plastic Diaphragms for Airborne Ultrasonics, I. ..... Kiichiro MATSUZAWA 1533

SHORT NOTES

A Possible Mechanism of the Potential Variation of Joshi Effect. ....M. VENUGOPALAN 1544
NMR Study of γ Ray Induced Polymerisation of Ethyl Acrylate..... Toshikazu SHIBATA, Itsuro KIMURA and Tokuo SUITA 1546
Field Effect on Molybdenite.....Ichiro NAKADA 1547
Quadrupole Moment of the Second Excited State of ^{19}F..... Kenzo SUGIMOTO, Akira MIZOBUCHI and Hisasi YAMAMOTO 1548
Ferroelectricity in the Phase III of KNO_3..... Shozo SAWADA, Shoichiro NOMURA and Shin'ichi FUJII 1549
Thermal Conductivity of $BaTiO_3$ Ceramics. .....Ikushi YOSHIDA, Shoichiro NOMURA and Shozo SAWADA 1550
Difference between Dynamic and Static Surface Tensions. .....Sohei KONDO 1551

Erratum

Temperature Distribution during the Martensite Plate Formation..... .... Zenji NISHIYAMA, Akira TSUBAKI, Hideo SUZUKI and Yasusada YAMADA 1543

AUTHOR INDEX TO Vol. 13

ABE Hidetaro: Paramagnetic Resonance in Copper Propionate Monohydrate 987

ABE Ryuji: Optical Study on the Resultant Movement of Many Walls in Rochelle Salt 244

ABE Yoshihito: Zeeman Study on Nuclear Quadrupole Resonances in AsI_3 and $AsI_3 \cdot 3S_8$ 918

AIYAMA Yoshimichi;

S. IIDA, H. SEKIZAWA and ———: Uniaxial Anisotropy in Iron-Cobalt Ferrites 58

AKIMOTO Syun-iti;

Y. ISHIKAWA and ———: Magnetic Property and Crystal Chemistry of Ilmenite ($MeTiO_3$) and Hematite (αFe_2O_3) System. I. Crystal Chemistry.... 1110

Y. ISHIKAWA and ———: Magnetic Property and Crystal Chemistry of Ilmenite($MeTiO_3$) and Hematite (αFe_2O_3) System. II. Magnetic Property.... 1298

AMEMIYA Ayao;

K. SHINOHARA, ——— and A. DANNO: Effects of Ionizing Radiations on Polyethylene 604

AOKI Atsushi;

M. KAWAMURA, ——— and T. HAYASHI: Excited States of Pt^{192} 1071

AOYAGI Keizô;

———, S. TANIGUCHI and M. YAMAMOTO: Orientation Dependence of the Uniaxial Ferromagnetic Anisotropy Induced by Magnetic Annealing in 20% Co-Ni Single Crystals (S. N.) 532

ARAI Toshihiro;

K. ISHIGURO, T. SASAKI, ——— and I. IMAI: Optical and Electrical Properties of Tin Oxide Films 296

K. ISHIGURO, T. SASAKI, ——— and I. IMAI: Plasma Oscillation in the Electrically Conductive Tin Oxide Film (S. N.) 755

ASADA Tsunesaburo;

———, M. MASUDA, M. OKUMURA and J. OKUMA: Angular Distribution of Photo-neutrons Produced by 17 Mev X-rays 1

ASAKA Saburo: (Errata) Application of the Thin-Wing-Expansion Method to the Flow of a Compressible Fluid past a Symmetrical Circular Arc Aerofoil.... 115

ASANO Sumitada;

——— and Y. TOMISHIMA: Lattice Defects in Zincblende. Part I. Phenomenological Expressions of Interionic Potentials 1119

———, and Y. TOMISHIMA: Lattice Defects in Zincblende. Part II. Formation Energy of Lattice Defects 1126

BLOEMBERGEN, N.: Higher Order Transitions in Double Nuclear Resonance Experiments in Solids (S. N.) 660

CHIBA Takehiko;

———: Nuclear Quadrupole Spectra of Boron Trichloride and Tribromide.... 860

Y. MORINO, ———, T. SHIMOZAWA and M. TOYAMA: Zeeman Effect of Nuclear Quadrupole Resonance Spectrum in Cyanuryl Chloride 869

CHONG, Pyong-un;

———, C. YAMANAKA and T. SUITA: Space Charge Phenomena in Nitrobenzene under High Electric Field (S. N.) 760

DANNO Akibumi;

K. SHINOHARA, A. AMEMIYA and ———: Effects of Ionizing Radiations on Polyethylene 604

———: Effects of Ionizing Radiations on Polyvinyl Alcohol–I. Breakdown of Main-chain and Formation of Carbonyl Groups 609

———: Effects of Ionizing Radiation on Polyvinyl Alcohol II. Changes of Physical Properties of the Irradiated Specimen Caused by Heat Treatment.. 614

———: Gel Formation of Aqueous Solution of Polyvinyl Alcohol Irradiated Gamma Rays from Cobalt-60 722

DATE Muneyuki;
T. HASEDA and ———: The Paramagnetic Susceptibility of Some Nickel Salts .. 175
DENDA Sei-ichi: Pits on Germanium Surface Formed by Molten Indium (S. N.) 533
DOKE Tadayoshi;
———, S. SUZUKI and I. OGAWA: The Q-value for the $N^{14}(n, \alpha)B^{11}$ Reaction (S. N.) 656
———, S. SUZUKI and I. OGAWA: (Errata) The Q-value for the $N^{14}(n, \alpha)B^{11}$ Reaction (S. N.) 973
ESAKI Leo;
T. YAJIMA and ———: Excess Noise in Narrow Germanium p–n Junctions.. 1281
FUJII Shin'ichi;
S. SAWADA, S. NOMURA and ———: Ferroelectricity in the Phase III of KNO_3 (S. N.) 1549
FUJIKI Yoshibumi;
———, R. SUGANUMA, and T. YOSHIDA: A New Compound in Au–Pb Alloy System (S. N.) 969
FUJIMOTO Minoru;
K. MORIGAKI, ——— and J. ITOH: Paramagnetic Resonance Spectrum of Mn^{++} in NaCl Single Crystal 1174
FUJITA, Francisco Eiichi;
——— and U. GONSER: Small Angle Scattering of X-rays by Deuteron-irradiated Germanium Crystal (S. N.) 1068
FUJITA Hiroshi;
——— and T. KATO: On a Theorem for Estimating Eigenvalues 215
FUJITA Shigeru;
A. MITSUISHI, H. YOSHINAGA and ———: The Far Infrared Absorption of Sulfides, Selenides and Tellurides of Zinc and Cadmium (S. N.) 1235
A. MITSUISHI, H. YOSHINAGA and ———: The Far Infrared Absorption of Ferrites (S. N.) 1236
FUJIWARA Hiroshi;
———: On the Screened Field around an Impurity Atom in Metal 250
———: An Application of the Cellular Method to a Vacancy in Metal 935
FUJIWARA Kunio;
———, M. HIRABAYASHI, D. WATANABE and S. OGAWA: Study on the Ordered Alloy Ag_3Mg 167
FUKUDA Kuniya;
———, Y. UCHIDA and H. YOSHIMURA: Paramagnetic Resonance Spectrum of Manganese in Single Crystals of Alkali Halide Grown from the Melt. (S. N.) 971
GONSER, Ulrich;
F. E. FUJITA and ———: Small Angle Scattering of X-rays by Deuteron-irradiated Germanium Crystal (S. N.) 1068
GOTO Eiichi: On the observation of Magnetic Poles ....
HAGA Eijirō: Theory of Thermoelectric Power of Ionic Crystals (I) 1090
HASEDA Taiichiro;
——— and M. DATE: The paramagnetic Susceptibility of Some Nickel Salts.. 175
HASHI Tsuneo: Measurements of Free Induction Decay Time and Spin-Lattice Relaxation Time of Bromine Nucleus in Sodium Bromate 911
HASHIMOTO Hatsujiro;
———: Stepped Structure in Moiré Fringe (S. N.) 534
——— and T. NAIKI: A Note on Direct Observation of Dislocations by Electron Microscopy (S. N.) 764
HASHIMOTO Hidenori: On the Flow of a Viscous Fluid past a thin Screen at Small Reynolds Numbers 633
HASHIMOTO Utaka;
K. KOMATSUBARA and ———: Study on Annealing of Radiation Induced $1/f$ Noise in Ge p–n Junction (S. N.) 1062

HASIGUTI, Ryukiti R.;
———, H. SAKAIRI and T. SUGAI: A Proposed Explanation of Irradiation Growth of Uranium (S. N.) 1233
HAYASHI Jun-ichi;
H. TAKAKI and ———: The Effect of Tension on the Magnetostriction of Iron Single Crystals 703
HAYASHI Takeo;
———, Directional Correlations of Gamma Rays in Te^{124} 117
M. KAWAMURA, A. AOKI and ———: Excited States of Pt^{192} 1071
HIBI Tadatosi;
——— and K. ISHIKAWA: Electronmicroscopic Observation of Coloured and Bleached Alkali-Halide Crystals 709
HIKI Yosio;
———: Etch Pits in Lead Crystals (S. N.) 970
———: Internal Friction of Lead. I 1138
HINOTANI Kensaku;
S. MIYAKE, ———, T. KANEKO and I. KATSUMATA: An Experimental Study of Extensive Air Showers 782
HIRABAYASHI Makoto;
K. FUJIWARA, ———, D. WATANABE and S. OGAWA: Study on the Ordered Alloy Ag_3Mg 167
HIRAHARA Eiji;
M. MURAKAMI and ———: A Certain Anomalous Behavior of Iron Sulfides (S. N.) 1407
HIRAKAWA Hiromasa;
T. KOJIMA, ——— and T. OKA: Microwave Spectrum of Hydrazine (S.N) .. 321
HIRAMATSU Makoto;
J. SHIGETA and ———: Etch Pits of Sb Single Crystals (S. N.) 1404
HIRAO Yasuo;
———, E. OKADA, I. MIURA and T. WAKATSUKI: Excited States of ^{40}Ca.... 233
E. OKADA, I. MIURA, T. WAKATSUKI and ———: Gamma Rays from the Proton Bombardment of Silicon 541
HIROIKE Kazuo: On the Theory of Fluids .....
HIRONE Tokutaro;
———, N. KUNITOMI, M. SAKAMOTO and H. YAMAKI: Diffusion of Cadmium into Single Crystals of Copper 838
———, N. KUNITOMI and M. SAKAMOTO: Diffusion of Cobalt into Iron-Cobalt Alloy 840
HÔRAI Kazumi;
O. MATUMURA, ——— and Z. MIDUNO: Electron Spin Resonance of Eu^{++} in Natural CaF_2 (S. N.) 768
HORI Jun-ichi;
N. SAITÔ and ———: A Note on Thermodynamics of the Harmonic Oscillator with Radiation Damping 717
HOSHINO Sadao: (Errata) Crystal Structure and Phase Transition of Some Metallic Halides (IV). On the Anomalous Structure of 2-Ag I 1412
HUSHIMI Kazuo;
K. ZENITI, ——— and K. KATAOKA: Polarization Reversal in Triglycine Sulphate Crystal (S. N.) 661
HUZIMURA Ryoichiro;
——— and T. SIDEI: Effects of Impurities and Temperature on the Spectra of Electroluminescence (S. N.) 1064
HUZINAGA Sigeru: Methods of Approximation of Molecular Integrals. I 1189
IBRAHIM, Ali Abdel Kerim: A Method for Measuring the Dynamic Viscosity and Dynamic Rigidity of Viscoelastic Liquids I (S. N.) 313
IBUKI SUMIAKI;
H. YAMASHITA and ———: Crystal Growth of CdS by the Vacuum Sealed Method (S. N.) 226

IGUCHI Kaoru: The Lower Excited States and the Phosphorescent State of Diphenyl. II. Scheme of Modification of MO 1186
IIDA Shūichi;
———, H. SEKIZAWA and Y. AIYAMA: Uniaxial Anisotropy in Iron-Cobalt Ferrites 58
T. INOUE and ———: Specific Heats of Copper Ferrite (S. N.) 656
H. SEKIZAWA, ——— and T. MIYADAI: A Richter Type Magnetic Loss in Yttrium-Iron Garnet (S. N.) 658
IIZIMA Sigeru;
M. KIKUCHI and ———: Some Observations on Germanium Bi-crystals (S. N.) .. 319
IKEDA Takuro;
———: Some Studies on the Ternary System (Ba–Pb–Ca)TiO_3 335
———: The Internal Friction of Barium Titanate Ceramics 809
IKEGAMI Hidetsugu;
M. SAKAI and ———: Sector Type Double Focusing Beta Ray Spectrometer. Part I. General Properties 1076
T. YAMAZAKI, ——— and M. SAKAI: Sector Type Double Focusing Beta Ray Spectrometer. Part II. Twin Setting Measurement of the Weak Higher Component of Cs^{137} 1080
IKUSHIMA Akira;
Y. TOMONO and ———: Diffusion of Iron in Single Crystals of Copper (S. N.) 762
IMAI Isamu;
K. ISHIGURO, T. SASAKI, T. ARAI and ———: Optical and Electrical Properties of Tin Oxide Films 296
K. ISHIGURO, T. SASAKI, T. ARAI and ———: Plasma Oscillation in the Electrically Conductive Tin Oxide Film (S. N.) 755
INOKUTI Mitio;
——— and T. WATANABE: Theoretical Considerations on Radiation-Induced Reactions of Satulated Long-Chain Hydrocarbons (S. N.) 221
———: Excitation of π-Electrons in Benzene by Fast Electron According to FE Model (S. N.) 537
INOUE Masaharu;
Y. UEMURA and ———: The Change of Carrier Concentration in the Simple Semiconductor with Static Magnetic Field 377
Y. UEMURA and ———: The Change of Carrier Concentration in the Graphite with Static Magnetic Field 382
INOUE Tohru;
——— and S. IIDA: Specific Heats of Copper Ferrite (S. N.) 656
INUISHI Yoshio;
——— and S. UEMATSU: Electric Breakdown and Conduction in $BaTiO_3$ Single Crystals (S. N.) 761
ISHIDA Yoshio: Ultrasonic Velocity and Adiabatic Compressibility of Mixture of Sulfuric Acid and Water (S. N.) 536
ISHIGURO Kozo;
———, T. SASAKI, T. ARAI and I. IMAI: Optical and Electrical Properties of Tin Oxide Films 296
———, T. SASAKI, T. ARAI and I. IMAI: Plasma Oscillation in the Electrically Conductive Tin Oxide Film (S. N.) 755
ISHII Takehiko;
———, T. TOMIKI and M. UETA: Dichroism of Color Centers in KCl Crystal (S. N.) 1411
ISHIKAWA Kazuo;
T. HIBI and ———: Electronmicroscopic Observation of Coloured and Bleached Alkali-Halide Crystals 709
ISHIKAWA Yoshikazu;
———: Electrical Properties of $FeTiO_3$-Fe_2O_3 Solid Solution Series 37

———: An Order-Disorder Transformation Phenomenon in the $FeTiO_3$–Fe_2O_3 Solid Solution Series 828
——— and S. AKIMOTO: Magnetic Property and Crystal Chemistry of Ilmenite ($MeTiO_3$) and Hematite (αFe_2O_3) System. I. Crystal Chemistry 1110
——— and S. AKIMOTO: Magnetic Property and Crystal Chemistry of Ilmenite ($MeTiO_3$) and Hematite (αFe_2O_3) System II. Magnetic Property 1298
ISHIMURA Tsutomu;
T. SHIRAIWA, ——— and M. SAWADA: The Theory of the Fine Structure of the X-ray Absorption Spectrum 847
ISHIWATARI Keiko;
H. KAWAMURA and ———: Electron Spin Resonance of *M*-centers in Potassium Chloride 33
H. KAWAMURA and ———: Electron Spin Resonance of Z_1-centers in Potassium Chloride 574
ITÔ Hirosi: Asymptotic Behaviour of the Response Function of an Optical System with the Primary Spherical Aberration 639
ITO Kazuo;
R. UYEDA, T. MASUDA, H. TOCHIGI, ——— and H. YOTSUMOTO: Magnification Calibration of Electron Microscopes by Crystal Lattice Spacings 461
ITOH Junkichi;
K. MORIGAKI, M. FUJIMOTO and ———: Paramagnetic Resonance Spectrum of Mn^{++} in NaCl Single Crystal 1174
——— and Y. YAMAGATA: Nuclear Magnetic Resonance Studies of Iodine Ions in Aqueous Solution 1182
——— and Y. YAMAGATA: Nuclear Magnetic Resonance Experiments of I^{127} in KI (S. N.) 1232
ITOH Reikichi: Effect of the Basic Strength of Attached Groups on Light Absorption Spectra—III. Dissociations in the Excited States of Naphthalene Derivatives— 389
IZUMI Sôichi;
K. MATSUURA, ——— and S. KODA: The Effect of G-P (1) and G-P (2) Aggregates on the Plastic Deformation of an Age-Hardenable Al-Cu 4% Alloy (S. N.) 318
KAKUTANI Tsunehiko: Effect of Transverse Magnetic Field on the Flow due to an Oscillating Flat Plate 1504
KAMADA Kazumasa;
———, T. TERANISHI and Y. YOSHIZAWA: Beta and Gamma Ray Spectroscopy of Co^{60} (S. N.) 763
KAMIMURA Hiroshi;
Y. TANABE and ———: On the Absorption Spectra of Complex Ions.—IV. The Effect of the Spin-orbit Interaction and the Field of Lower Symmetry on *d* electrons in Cubic Field— 394
———, S. KOIDE, S. SUGANO and Y. TANABE: An Application of the Thomas-Fermi Method to Complex Ions 464
Y. TANABE and ———: (Errata) On the Absorption Spectra of Complex Ions IV 539
KAMIYA Yoshihiro: Scattering of Electrons by Carbon Films 1144
KANAI Yasuo;
———: Electrical Conductivity in N-type InSb under Strong Electric Field (S. N.) 967
———: Electrical Conductivity in *p*-Type InSb Under Strong Electric Field (S. N.) 1065
KANAMORI Junjiro;
——— and K. SUGIMOTO: The Magnetic Field at the Nucleus of Sm^{+++} Induced by Paramagnetism of 4*f*-Electrons (S. N.) 754
KANEKO Motozo: The Study of the Transition Phenomena of Chain Polymers by the Photoelastic Method 1324

KANEKO Shin-ichi: The Multiplicity of Mesons Produced in the Nuclear Interaction of High Energy Nucleons and α-Particles in Cosmic Radiation 1258
KANEKO Shobu: The Maximum Disturbance Growth Rate for an Unstable Plasma Column 947
KANEKO Tatsunosuke;
S. MIYAKE, K. HINOTANI, ——— and I. KATSUMATA: An Experimental Study of Extensive Air Showers 782
KANŌ Kenji: Dipolar Broadening of the Quadrupole Resonance Lines in Crystals $NaClO_3$, $NaBrO_3$ 975
KANOU Kyoichi;
K. KAWASAKI, ——— and Y. SEKITA: Liquid-Like Layers in the Adsorbed Film of H_2O on Glass (S. N.) 222
KASAI Mineo;
S. TAKEMOTO and ———: On RF Electrodeless Discharges in a Capillary (S. N.) 1410
KASUYA Tadao;
———: A Theory of Impurity Conduction. I 1096
——— and S. KOIDE: A Theory of Impurity Conduction. II 1287
KATADA Kinya;
———: Studies on the Radial Distribution Analysis in Diffraction Methods. II–Effect of Non-nuclear Scattering and Analysis of the Radial Distribution Curve 51
———: (Errata) Studies on the Radial Distribution Analysis in Diffraction Methods. II. Effect of Non-nuclear Scattering and Analysis of the Radial Distribution Curve 229
KATAOKA Keisuke;
K. ZENITI, K. HUSHIMI and ———: Polarization Reversal in Triglycine Sulphate Crystal (S. N.) 661
KATO Susumu: Magnetic Spectrometer having Inclined Plane Pole-Faces for Low-energy Electrons 544
KATO Tosio;
H. FUJITA and ———: On a Theorem for Estimating Eigenvalues 215
———, M. NOZAWA, Y. YOSHIZAWA and Y. KOH: Gamma Ray Spectroscopy of Mn^{54} 1419
KATSUMATA Itsuo;
S. MIYAKE, K. HINOTANI, T. KANEKO and ———: An Experimental Study of Extensive Air Showers 782
KAWAGUTI Mitutosi: A Hydrodynamical Model for the Sedimentation 209
KAWAI Naoto;
H. TAKAKI, ———, C. MIYAKE and T. MORITA: A Torsion Magnetometer for Determining Free Radicals in Some Organic Solutions 629
KAWAI Norio: On the Acoustic Field by a Vibrating Source Arbitrarily Distributed on a Ribbon Plate. I. 1374
KAWAMURA Hazimu;
——— and K. ISHIWATARI: Electron Spin Resonance of M-centers in Potassium Chloride 33
——— and K. ISHIWATARI: Electron Spin Resonance of Z_1-centers in Potassium Chloride 574
KAWAMURA Mitsuhiro;
———, A. AOKI and T. HAYASHI: Excited States of Pt^{192} 1071
KAWASAKI Koji;
———, K. KANOU and Y. SEKITA: Liquid-Like Layers in the Adsorbed Film of H_2O on Glass (S. N.) 222
KIHARA Taro;
———: Macroscopic Foundation of Plasma Dynamics 473
T. OHKAWA and ———: Externally Pinched Plasma 482
KIHO Hiroshi;
———: The Crystallographic Aspect of the Mechanical Twinning in Ti

and α-U 269
——— and S. MARUYAMA: The Consecutive Observations on the Twin Intersections (S. N.) 320
KIKUCHI Makoto;
——— and S. IIZIMA: Some Observations on Germanium Bi-crystals (S. N.).. 319
———: On the Backward Leakage Current in the Alloyed Germanium p–n Junction 350
———: Observation of the Lateral Photovoltage by Surface Field Effect (S. N) 1061
KIKUCHI Takeo: The Thermoluminescence of Glasses 526
KIM, Pil Hyon;
——— and T. SUGAWARA: Low Temperature Anomaly in the Proton Resonance of Some Nickel Salts (S. N.) 968
KIMURA Itsuro;
T. SHIBATA, ——— and T. SUITA: NMR Study of γ Ray Induced Polymerisation of Ethyl Acrylate (S. N.) 1546
KINBARA Akira: Variation of the Optical Properties of Iron at Transition Temperature (S. N.) 966
KINOSHITA Koreo;
——— and S. NOMURA: Half-Shade Device for the Precise Measurement of the Principle Angle of Incidence 1485
KISHIMOTO Tadashi;
O. NOMOTO and ———: (Errata) Molecular Sound Velocity of Aqueous Sugar Solutions 115
KOBAYASHI Jinzo;
S. NOMURA and ———: Dielectric Properties of Lead Titanate and Its Solid Solutions at Low Temperature under Strong Electric Field (S. N.).... 114
KOBAYASHI Shigehiro;
K. UMEDA and ———: Thomas-Fermi Function for Impurity Atom Dissolved in a Matrix Metal 148
K. UMEDA and ———: (Errata) Thomas-Fermi Function for Impurity Atom Dissolved in a Matrix Metal 429
KOBAYASHI Shunsuke;
M. SAKAMOTO and ———: One to One Correspondence between Etch Pits and Dislocations in KCl Crystals 800
M. SAKAMOTO and ———: Chemical and Thermal Polish of KCl Crystals (S. N.) 1231
KOBAYASI Syoiti: Calculation of the Energy Band Structure of the β-SiC Crystal by the Orthogonalized Plane Wave Method 261
KODA Shigeyasu;
K. MATSUURA, S. IZUMI and ———: The Effect of G-P (1) and G-P (2) Aggregates on the Plastic Deformation of an Age-Hardenable Al-Cu 4% Alloy (S. N.) 318
KOH Yujiro;
T. KATO, M. NOZAWA, Y. YOSHIZAWA and ———: Gamma Ray Spectroscopy of Mn^{54} 1419
KOIDE Shoichiro;
H. KAMIMURA, ———, S. SUGANO and Y. TANABE: An Application of the Thomas-Fermi Method to Complex Ions 464
KOIDE Sigenao;
T. KASUYA and ———: A Theory of Impurity Conduction. II..... 1287
KOJIMA Shoji;
———, S. OGAWA, M. MINEMATSU and M. TANAKA: Effects of Impurities on Nuclear Quadrupole Resonance in p-Dichlorobenzene 446
KOJIMA Takeshi;
———, H. HIRAKAWA and T. OKA: Microwave Spectrum of Hydrazine (S. N.).. 321
KOMATSUBARA Ki-ichi;

——— and U. HASHIMOTO: Study on Annealing of Radiation Induced $1/f$ Noise in Ge p–n Junction (S. N.) 1062
———: Study on the Correlation between the Noise by Hole Generation and Surface Recombination Velocity at Ge Fused Junction (S. N.) 1409
KONDO Michiya;
——— T. YAMAZAKI, A. TOI, R. NAKASIMA and S. YAMABE: Elastic Scattering of 5.7 Mev Protons from Fe, Cr and Ti 231
——— ane T. YAMAZAKI: Elastic and Inelastic Scattering of Protons from Neon 771
S. YAMABE, ———, T. YAMAZAKI and A. TOI: Angular Distribution of Protons Inelastically Scattered from Si^{28} and Mg^{24} 777
KONDO Sohei;
———: Fading of Coloration of Irradiated Glass (S. N.) 224
———: Difference between Dynamic and Static Surface Tensions (S. N.) 1551
KONDOH Hisamoto;
———, E. UCHIDA, Y. NAKAZUMI and T. NAGAMIYA: Magnetic Anisotropy Measurements of NiO Single Crystal 579
KONO Hiroshi:
On the Ferromagnetic Phase in Manganese Aluminum System 1444
KOYAMA Ryuzo: Effect of Velocity Gradient on the Radial Distribution of Polymer Molecules in Dilute Solution 1167
KUMABE Isao;
———, E. TAKEKOSHI, H. OGATA, Y. TSUNEOKA and S. ŌKI: $Co^{59}(n, \alpha)$ and $Mn^{55}(n, \alpha)V^{52}$ Reactions Induced by 14.8-Mev Neutrons 129
———: Alpha Particles from the Interaction of 14.8-Mev Neutrons with Medium Weight Nuclei 325
KUNITOMI Nobuhiko;
T. HIRONE, ———, M. SAKAMOTO and H. YAMAKI: Diffusion of Cadmium into Single Crystals of Copper 838
T. HIRONE, ——— and M. SAKAMOTO: Diffusion of Cobalt into Iron-Cobalt Alloy 840
KURATA Michio;
H. YAMAKAWA and ———: Theory of Dilute Polymer Solutions (I) Chain Configuration and Light Scattering 78
H. YAMAKAWA and ———: Theory of Dilute Polymer Solutions (III) Intrinsic Viscosity 94
KUROSAWA Tatsumi: Defects in Ionic Crystals. I. Improvement of the Method of Mott and Littleton and its Applications to Simple Defects 153
KUWABARA Goro;
——— and A. MISU: Luminescence and Dichloism of F and M Centers in Potassium Chloride 1038
——— and A. MISU: Structure of the F Band in Potassium Chloride (S. N.) 1066
KUWABARA Shinji;
———: The Forces Experienced by Two Elliptic Cylinders in a Uniform Flow at Small Reynolds Numbers 506
———: The Forces Experienced by a Lattice of Equal Flat Plates in a Uniform Flow at Small Reynolds Numbers 1516
MAEDA Keiji: Electroluminescence of Insulated Particles 1352
MAKITA Yasuharu;
Y. TAKAGI and ———: Ferroelectricity of $NaNH_4$-Tartrate 272
——— and Y. TAKAGI: Ferroelectric and Optical Properties of $Na(K–NH_4)$-tartrate Mixed Crystals 367
MARUYAMA Saiyu;
H. KIHO and ———: The Consecutive Observations on the Twin Intersections (S. N.) 320
MASE Shoichi;

———: Electronic Structure of Bismuth Type Crystals 434
———: Electronic Structure and Diamagnetism of Graphite 563
MASUDA Masayoshi;
T. ASADA, ———, M. OKUMURA and J. OKUMA: Angular Distribution of Photo-neutrons Produced by 17 Mev X-rays 1
MASUDA Tatsunosuke;
R. UYEDA, ———, H. TOCHIGI, K. ITO and H. YOTSUMOTO: Magnification Calibration of Electron Microscopes by Crystal Lattice Spacings..... 461
MASUDA Yoshika: Nuclear Magnetic Resonance Experiment on Metal Cadmium. II .. 597
MASUMI Taizō;
S. TANAKA and ———: Surface Photoconductivity of Cadmium Sulphide modified with Magnetic Field 22
S. TANAKA and ———: Magneto-resistance Effect in Cadmium Sulphide (S. N.)..... 314
MATSUMOTO Shigeo: Observation of a Beryllium Hyperfragment (S. N.) 427
MATSUURA Keisuke;
———, S. IZUMI and S. KODA: The Effect of G-P (1) and G-P (2) Aggregates on the Plastic Deformation of an Age-Hardenable Al-Cu 4% Alloy (S. N.) 318
MATUZAWA Kiichiro: Condenser Microphones with Plastic Diaphragms for Airborne Ultrasonics, I 1533
MATUMURA On;
———, K. HÔRAI and Z. MIDUNO: Electron Spin Resonance of Eu^{++} in Natural CaF_2 (S. N.)..... 768
MIDUNO Zen'emon;
O. MATUMURA, K. HÔRAI and ———: Electron Spin Resonance of Eu^{++} in Natural CaF_2 (S. N.) 768
MIKOSHIBA Nobuo: On Magneto-Acoustic Resonance in Metals (S. N.) 759
MIMURA Yōichi;
———: The Flow with Wake past an Oblique Plate..... 1048
———: Phenomenological Free Streamline Theory, Part 1. Flow past a Normal Plate 1361
MINAGAWA Sitiro: A Note on Numerical Evaluation of Integral Square Error (S. N.).. 1069
MINEMATSU Midori;
S. KOJIMA, S. OGAWA, ——— and M. TANAKA: Effects of Impurities on Nuclear Quadrupole Resonance in *p*-Dichlobenzene 446
MISU Akira;
G. KUWABARA and ———: Luminescence and Dichroism of *F* and *M* Centers in Potassium Chloride 1038
———: Piezo-Effect of Selenium Rectifiers (S. N.)..... 1066
MITSUISHI Akiyoshi;
———, H. YOSHINAGA and S. FUJITA: The Far Infrared Absorption of Sulfides, Selenides and Tellurides of Zinc and Cadmium (S. N.)..... 1235
———, H. YOSHINAGA and S. FUJITA: The Far Infrared Absorption of Ferrites (S. N.) 1236
MITUI Tadayasu: On the Magnetic Annealing Effect in 2% Cobalt-Copper Alloy–I. Induced Ferromagnetic Anisotropy 549
MIURA Iwao;
Y. HIRAO, E. OKADA, ——— and T. WAKATSUKI: Excited States of ^{40}Ca.... 233
E. OKADA, ———, T. WAKATSUKI and Y. HIRAO: Gamma Rays from the Proton Bombardment of Silicon 541
MIURA Sei;
J. TAKAMURA and ———: Grain Boundary-Hardening due to Piled-up Dislocations..... 1421
MIYADAI Tomonao;
H. SEKIZAWA, S. IIDA and ———: A Richter Type Magnetic Loss in Yttrium-Iron Garnet (S. N.) 658

MIYAGI Tosio: Viscous Flow at Low Reynolds Numbers past an Infinite Row of Equal Circular Cylinders 493
MIYAHARA Syohei;
——— and T. TSUSHIMA: Magnetic Properties of Nickel and Cobalt Ferrite- Chromite Series (S. N.) 758
MIYAKE Chie;
H. TAKAKI, N. KAWAI, ——— and T. MORITA: A Torsion Magnetometer for Determining Free Radicals in Some Organic Solutions 629
MIYAKE Saburo;
———, K. HINOTANI, T. KANEKO and I. KATSUMATA: An Experimental Study of Extensive Air Showers 782
MIYATANI Shin-ya;
———: Electrical Properties of Ag_2Se (S. N.) 317
———: Electrical Properties of Ag_2Te 341
MIZOBUCHI Akira;
K. SUGIMOTO, ——— and H. YAMAMOTO: Quadrupole Moment of the Second Excited State of ^{19}F (S. N.) 1548
MIZUGUCHI Kanji;
W. SASAKI, M. SHIBUYA and ———: Anisotropy of Hot Electrons in *n*-type Germanium 456
MIZUNO Hiroyuki On the Conduction Mechanism of Oxide Coated Cathode (S. N.) .. 1234
MORIGAKI Kazuo;
———, M. FUJIMOTO and J. ITOH: Paramagnetic Resonance Spectrum of Mn^{++} in NaCl Single Crystal 1174
MORIGUCHI Haruo;
———: A New Approach to the Theory of Slender Body in Compressible Flow 1384
———: Some Nonlinear Effect in Compressible Flow 1510
MORIMOTO Hidetake: Electron Diffraction Study of Evaporated Face-centered Cubic Crystallites 1015
MORINO Yonezo;
———, T. CHIBA, T. SHIMOZAWA and M. TOYAMA: Zeeman Effect of Nuclear Quadrupole Resonance Spectrum in Cyanuryl Chloride 869
MORITA Nozomu;
I. OMURA and ———: On the Measurement of Isotope Abundance of Lithium with Mass Spectrometer (S. N.) 659
MORITA Susumu;
———: Excitation Curves of the $N^{14}(d, n)O^{15}$ Reaction 126
———: Excitation Curve for the Reaction $P^{31}(n, p)Si^{31}$ 431
——— and K. TAKESHITA: The Reaction $F^{19}(d, n)Ne^{20}$ and the Energy Levels of N^{20} 1241
MORITA Tadasuke;
H. TAKAKI, N. KAWAI, C. MIYAKE and ———: A Torsion Magnetometer for Determining Free Radicals in Some Organic Solutions 629
MORIYA Tôru;
——— and Y. OBATA: Spin Quenching and Magnetic Resonance 1333
———: Nuclear Magnetic Resonance of Transition Elements in Paramagnetic Salts 1344
MURAKAMI Miyuki;
——— and E. HIRAHARA: A Certain Anomalous Behavior of Iron Sulfides (S. N.) 1407
MURAKAWA Kiyoshi;
———: Quadrupole Moment of Nb^{93} and Test of the Hyperfine Structure Formulas 101
———: The Arc Spectrum of Iodine and the Quadrupole Moment of I^{127} 484
J. A. VREELAND and ———: Isotope Shift in the Spectrum of WI 663
NAGAI Kazuo: Elementary Problems on the Configurations of a Linear High Polymer .. 928

NAGAKURA Sigemaro: Study of Metallic Carbides by Electron Diffraction. Part II. Crystal Structure Analysis of Nickel Carbide 1005
NAGAMIYA Takeo;
M. TACHIKI and ———: Origin of the Magnetic Anisotropy Energy of Antiferromagnetic Cr_2O_3 452
H. KONDOH, E. UCHIDA, Y. NAKAZUMI and ———: Magnetic Anisotropy Measurements of NiO Single Crystal 579
NAGAOKA Yosuke: Paramagnetic Relaxation of Copper Tutton Salt 1328
NAIKI Toshio;
H. HASHIMOTO and ———: A Note on Direct Observation of Dislocations by Electron Microscopy (S. N.) 764
NAKADA Ichiro: Field Effect on Molybdenite (S. N.) 1547
NAKAI Yoshio: On the V-centers in KBr Crystals 1424
NAKAMICHI Takurô;
M. YAMAMOTO and ———: Magnetostriction Constants of Nickel-Copper and Nickel-Cobalt Alloys (S. N.) 228
NAKAMURA Keiichi;
K. TAKEYA and ———: Current Amplification by Electron Bombardment in the Semiconductor Barrier Layer (S. N.) 223
NAKAMURA Yoji;
——— and J. TAKAMURA: Magnetic After-Effect due to Quenched-in Vacancies in Nickel (S. N.) 316
NAKAO Yasuhiro;
H. YOSHIMOTO, M. SATO and ———: Moving Striations in Arc Discharge .. 734
H. YOSHIMOTO, M. SATO and ———: Moving Striations due to Space Charge Waves 741
NAKASIMA Ryuzo
M. KONDO, T. YAMAZAKI, A. TOI, ——— and S. YAMABE: Elastic Scattering of 5.7 Mev Protons from Fe, Cr and Ti 231
NAKAZUMI Yoshihide;
H. KONDOH, E. UCHIDA, ——— and T. NAGAMIYA: Magnetic Anisotropy Measurements of NiO Single Crystal 579
NANDA, R. S.: Flow Formation with Suction or Injection 748
NII Riro: Measurement of the Thermal Conductivity in Semiconductors (S. N.) 769
NISHIOKA Atsuo;
——— and K. SEKIKAWA: Growth and Extinction of Guanidine Aluminum Sulfate Hexahydrate Crystals (S. N.) 1237
NISHIYAMA Zenji;
———, A. TSUBAKI, H. SUZUKI and Y. YAMADA: Temperature Distribution during the Martensite Plate Formation 1084
NOMOTO Otohiko;
———: Deviation from Linearity of the concentration Dependence of the Molecular Sound Velocity in Liquid Mixtures 1524
———: Empirical formula for Sound Velocity in Liquid Mixtures 1528
——— and T. KISHIMOTO: (Errata) Molecular Sound Velocity of Aqueous Sugar Solutions 115
NOMURA Sadao;
K. KINOSITA and ———: Half-Shade Device for the Precise Measurement of the principle Angle of Incidence 1485
NOMURA Shoichiro;
——— and J. KOBAYASHI: Dielectric Properties of Lead Titanate and Its Solid Solutions at Low Temperature under Strong Electric Field (S. N.) .. 114
I. YOSHIDA, ——— and S. SAWADA: Thermal Conductivity of $BaTiO_3$ Ceramics (S. N.) 1550
S. SAWADA, ——— and S. FUJII: Ferroelectricity in the Phase III of KNO_3 (S. N.) 1549
NOZAWA Masao;
T. KATO, ———, Y. YOSHIZAWA and Y. KOH: Gamma Ray Spectroscopy

of Mn^{54} 1419
NUMATA Tadasi;
———: Piezo-Effect of Selenium Rectifiers (S. N.) 1066
———: (Errata) Piezo-Effect of Selenium Rectifiers 1239
OBASHI Masayoshi;
K. TSUTSUMI, ——— and M. SAWADA: Absorption Coefficients of Fine Structures of X-ray Absorption Spectra at Various Absorber Thickness.... 43
K. TSUTSUMI and ———: Fine Structures of the X-ray Absorption by the Single Crystal of Germanium..... 591
OBATA Yukio;
T. MORIYA and ———: Spin Quenching and Magnetic Resonance 1333
OGATA Hiroshi;
I. KUMABE, E. TAKEKOSHI, ———, Y. TSUNEOKA and S. ŌKI: $Co^{59}(n, \alpha)Mn^{56}$ and $Mn^{55}(n, \alpha)V^{52}$ Reactions Induced by 14.8-Mev Neutrons 129
OGAWA Iwao;
T. DOKE, S. SUZUKI and ———: The Q-value for the $N^{14}(n, \alpha)B^{11}$ Reaction (S. N.) 656
T. DOKE, S. SUZUKI and ———: (Errata) The Q-value for the $N^{14}(n, \alpha)B^{11}$ Reaction..... 973
OGAWA Shiro;
K. FUJIWARA, M. HIRABAYASHI, D. WATANABE and ———: Study on the Ordered Alloy Ag_3Mg 167
OGAWA Shizuko;
S. KOJIMA, ———, M. MINEMATSU and M. TANAKA: Effects of Impurities on Nuclear Quadrupole Resonance in p-Dichlorobenzene 446
———: Nuclear Quadrupole Resonances in Arsenic and Antimony Trihalides and Sulphur Molecular Addition Compounds 618
OHARA Hideharu;
T. YOKOBORI and ———: Statistical Aspect in Accelerating Creep and Creep Fracture of OFHC Copper..... 305
OHKAWA Tihiro;
——— and T. KIHARA: Externally Pinched Plasma 482
OHTSUKA Mieko;
K. ÔNO and ———: Paramagnetic Resonance Absorption in Two Copper Salts at Wavelengths of 5.4 mm and 6.6 mm 206
OKA Takeshi;
T. KOJIMA, H. HIRAKAWA and ———: Microwave Spectrum of Hydrazine (S. N.) 321
OKADA Eiji;
Y. HIRAO, ———, I. MIURA and T. WAKATSUKI: Excited States of ^{40}Ca 233
———, I. MIURA, T. WAKATSUKI and Y. HIRAO: Gamma Rays from the Proton Bombardment of Silicon 541
OKADA Jun'ichi: Recombination Centers in Germanium 793
OKAMOTO Hiroaki;
Y. TUZI and ———: Surface Area Variation of Evaporated Barium Film by Oxidation (S. N.)..... 225
——— and Y. TUZI: Adsorption of Water Vapour on Glass and Other Materials in Vacuum 649
Y. TUZI and ———: Adsorption of Water Vapour on Lead Borosilicate Glass in Vacuum..... 960
——— and Y. TUZI: (Errata) Adsorption of Water Vapour on Glass and Other Materials in Vacuum 1412
——— and Y. TUZI: (Errata) Adsorption of Water Vapour on Lead Borosilicate Glass in Vacuum..... 1412
OKAZAKI Atsushi: The Crystal Structure of Germanium Selenide GeSe..... 1151
ŌKI Shinpei;
I. KUMABE, E. TAKEKOSHI, H. OGATA, Y. TSUNEOKA and ———: Co^{59}

(n, α)Mn^{56} and Mn^{55}(n, α)V^{52} Reactions Induced by 14.8-Mev Neutrons..... 129
OKUDA Takayoshi;
——— and K. YAMAMOTO: Electron Collection and Electron Sheath. (S. N.).. 112
——— and K. YAMAMOTO: A New Probe Method for Measuring Ionized Gases 411
——— and K. YAMAMOTO: Disturbance Phenomena in Probe Measurement of Ionized Gases 1212
OKUMA Juzo;
T. ASADA, M. MASUDA, M. OKUMURA and ———; Angular Distribution of Photo-neutrons Produced by 17 Mev X-rays 1
OKUMURA Masayuki;
T. ASADA, M. MASUDA, ——— and J. OKUMA: Angular Distribution of Photo-neutrons Produced by 17 Mev X-rays 1
OMURA Itiro;
——— and N. MORITA: On the Measurement of Isotope Abundance of Lithium with Mass Spectrometer (S. N.) 659
ONISHI Tsuyoshi;
——— and M. YAMAMOTO: Relaxation Spectrum of Chain High Polymeric Substances 1439
ÔNO Kazuo;
——— and M. OHTSUKA: Paramagnetic Resonance Absorption in Two Copper Salts at Wavelengths of 5.4 mm and 6.6 mm 206
OTSUKA Eizo: Anisotropy of Nuclear Magnetic Resonance due to Crystal Dislocations..... 1155
RIKITAKE Tsuneji: Magneto-hydrodynamic Oscillations of a Perfectly Conducting Fluid Sphere Placed in a Uniform Magnetic Field 1224
SAITÔ Nobuhiko;
——— and J. HORI: A Note on Thermodynamics of the Harmonic Oscillator with Radiation Damping 717
SAITO Osamu;
———: On the Effects of High Energy Radiation to Polymers. I. Cross-linking and Degradation 198
———: Effects of High Energy Radiation on Polymers II End-linking and Gel Fraction 1451
———: Effects of High Energy Radiation on Polymers III Viscosity 1465
SAITO Yushiro: Narrowing Effect in Nuclear Magnetic Double Resonance in Solids .. 72
SAKAI Mitsuo;
——— and H. IKEGAMI: Sector Type Double Focusing Beta Ray Spectrometer. Part I. General Properties 1076
T. YAMAZAKI, H. IKEGAMI and ———: Sector Type Double Focusing Beta Ray Spectrometer. Part II. Twin Setting Measurement of the Weak Higher Component of Cs^{137} 1080
SAKAIRI Hideo;
R. R. HASIGUTI, ——— and T. SUGAI: A Proposed Explanation of Irradiation Growth of Uranium (S. N.) 1233
SAKAMOTO Masanobu;
T. HIRONE, N. KUNITOMI, ——— and H. YAMAKI: Diffusion of Cadmium into Single Crystals of Copper 838
T. HIRONE, N. KUNITOMI and ———: Diffusion of Cobalt into Iron-Cobalt Alloy 840
———: Diffusion of Cobalt into Single Crystals of Copper 845
———: (Errata) Diffusion of Cobalt into Single Crystals of Copper 1239
SAKAMOTO Masayoshi;
——— and S. KOBAYASHI: One to One Correspondence between Etch Pits and Dislocations in KCl Crystals 800
——— and S. KOBAYASHI: Chemical and Thermal Polish of KCl Crystals (S. N.) 1231
SAKATA Kimiko;

T. SAKATA and ———: Change of Oxygen Concentration with Temperature of the Nickel and Cobalt Oxide Solid Solutions 675
SAKATA Tamio;
——— and K. SAKATA: Change of Oxygen Concentration with Temperature of the Nickel and Cobalt Oxide Solid Solutions 675
SAKURAI Takeo: Flow past a Bent Flat Plate with an Unsymmetric Dead Air at Mach Number 1 1055
SAKURAI Tosio;
——— and M. YABE: The Phase Transformation of Solid Normal Hexadecanamide 5
SASAKI Sōji;
S. YANO ——— and T. SIDEI: Asymmetry of Proton Resonance Signals in Some Hydrates of Iron Group Salts (S. N.) 227
SASAKI Taizo;
K. ISHIGURO, ———, T. ARAI and I. IMAI: Optical and Electrical Properties of Tin Oxide Films 296
K. ISHIGURO, ———, T. ARAI and I. IMAI: Plasma Oscillation in the Electrically Conductive Tin Oxide Film (S. N.) 755
SASAKI Wataru;
———, M. SHIBUYA and K. MIZUGUCHI: Anisotropy of Hot Electrons in n-type Germanium 456
SATŌ Hiroshi: Note on the Information Capacity of a Coloured Picture 108
SATO Mituo;
H. YOSHIMOTO, ——— and Y. NAKAO: Moving Striations in Arc Discharge .. 734
H. YOSHIMOTO, ——— and Y. NAKAO: Moving Striations due to Space Charge Waves 741
SATO Takao;
K. YONEMITSU and ———: Variation of the Hall Coefficient of Mg–Cd Superlattice Alloys with Degree of Order 15
K. YONEMITSU and ———: Variation of Hall Coefficient of Some Non-ferromagnetic Superlattice Alloys 998
SAWADA Masao;
K. TSUTSUMI, M. OBASHI and ———: Absorption Coefficients of Fine Structures of X-ray Absorption Spectra at Various Absorber Thickness 43
T. SHIRAIWA, T. ISHIMURA and ———: The Theory of the Fine Structure of the X-ray Absorption Spectrum 847
SAWADA Shozo;
I. YOSHIDA, S. NOMURA and ———: Thermal Conductivity of $BaTiO_3$ Ceramics (S. N.) 1550
———, S. NOMURA and S. FUJII: Ferroelectricity in the Phase III of KNO_3 (S. N.) 1549
SEKIKAWA Kyozo;
A. NISHIOKA and ———: Growth and Extinction of Guanidine Aluminum Sulfate Hexahydrate Crystals (S. N.) 1237
SEKITA Yoshiyasu;
K. KAWASAKI, K. KANOU and ———: Liquid-Like Layers in the Adsorbed Film of H_2O on Glass (S. N.) 222
SEKIZAWA Hisashi;
S. IIDA, ——— and Y. AIYAMA: Uniaxial Anisotropy in Iron-Cobalt Ferrites .. 58
———, S. IIDA and T. MIYADAI: A Richter Type Magnetic Loss in Yttrium-Iron Garnet (S. N.) 658
SHIBATA Toshikazu;
—, I. KIMURA and T. SUITA: NMR Study of γ Ray Induced Polymerisation of Ethyl Acrylate (S. N.) 1546
SHIBUYA Motoichi;
W. SASAKI, ——— and K. MIZUGUCHI: Anisotropy of Hot Electrons in n-type Germanium 456

SHIBUYA Yoshio;
———: Paramagnetic Effect in Superconductors. Part I. Quasi-Paramagnetism and Resistance of Indium at the Superconducting Transition 684
———: Paramagnetic Effect in Superconductors. Part II. Quasi-Paramagnetism in Non-Circular Cylindrical Tin Specimens 695
SHIGETA Jiro;
——— and M. HIRAMATSU: Etch Pits of Sb Single Crystals (S. N.) 1404
SHIMODA Koichi: Characteristics of the Beam Type Maser. II 939
SHIMOMURA Kenji: (Errata) Structural Investigation by Means of Nuclear Quadrupole Resonance II 655
SHIMOZAWA Takashi;
Y. MORINO, T. CHIBA, ——— and M. TOYAMA: Zeeman Effect of Nuclear Quadrupole Resonance Spectrum in Cyanuryl Chloride 869
SHINOHARA Kenichi;
———, A. AMEMIYA and A. DANNO: Effects of Ionizing Radiations on Polyethylene 604
SHIRAIWA Toshio;
———, T. ISHIMURA and M. SAWADA: The Theory of the Fine Structure of the X-ray Absorption Spectrum 847
SHOGENJI Kisaburo: On Solvent Effects in Dipole Moment Determinations 160
SIDEI Tunahiko;
S. YANO, S. SASAKI and ———: Asymmetry of Proton Resonance Signals in Some Hydrates of Iron Group Salts (S. N.) 227
R. HUZIMURA and ———: Effects of Impurities and Temperature on the Spectra of Electroluminescence (S. N.) 1064
SUGAI Tetuya;
R. R. HASIGUTI, H. SAKAIRI and ———: A Proposed Explanation of Irradiation Growth of Uranium (S. N.)..... 1233
SUGANO Satoru;
I. TSUJIKAWA and ———: Anomalous g-shifts of Excited States of Cr^{3+} in Ruby (S. N.) 220
H. KAMIMURA, S. KOIDE, ——— and Y. TANABE: An Application of the Thomas-Fermi Method to Complex Ions 464
——— and Y. TANABE: Absorption Spectra of Cr^{3+} in Al_2O_3. Part A. Theoretical Studies of the Absorption Bands and Lines 880
——— and I.TSUJIKAWA: Absorption Spectra of Cr^{3+} in Al_2O_3. Part B. Experimental Studies of the Zeeman Effect and other Properties of the Line Spectra..... 899
SUGANUMA Ryōji;
Y. FUJIKI, ——— and T. YOSHIDA: A New Compound in Au–Pb Alloy System (S. N.)..... 969
SUGAWARA Tadashi;
P. H. KIM and ———: Low Temperature Anomaly in the Proton Resonance of Some Nickel Salts (S. N.)..... 968
SUGIMOTO Kenzo;
———: Magnetic Moment of the First Excited State of $_{62}Sm^{152}$ 240
J. KANAMORI and ———: The Magnetic Field at the Nucleus of Sm^{+++} induced by Paramagnetism of $4f$-Electrons (S. N.) 754
———, A. MIZOBUCHI and H. YAMAMOTO: Quadrupole Moment of the Second Excited State of ^{19}F (S. N.)..... 1548
SUITA Tokuo;
P. CHONG, C. YAMANAKA and ———: Space Charge Phenomena in Nitrobenzene under High Electric Field (S. N.) 760
T. SHIBATA, I. KIMURA and ———: NMR Study of γ Ray Induced Polymerisation of Ethyl Acrylate (S. N.) 1546
SUMI Masao: Theory of Excited Plasma Waves 1476
SUZUKI Hideo;

Z. NISHIYAMA, A. TSUBAKI, ——— and Y. YAMADA: Temperature Distribution during the Martensite Plate Formation 1084
SUZUKI Hiromichi;
H. TUBOTA and ———: Contact Behavior of Metals to CdSe, CdTe, ZnSe and ZnTe (S. N.) 538
SUZUKI Kazuo: X-ray Studies on the Structures of Solid Solutions NaCl-$CaCl_2$. III. Influence of Heat Treatments on the Diffuse Reflexions of X-rays due to {111} and {310} Plate-Zones 179
SUZUKI Kenzō: Magnetic Annealing of Fe_3Al Single Crystal (S. N.) 756
SUZUKI Shoji;
T. DOKE, ——— and I. OGAWA: The Q-value for the $N^{14}(n, \alpha)B^{11}$ Reaction (S. N.) 656
T. DOKE, ——— and I. OGAWA: (Errata) The Q-value for the $N^{14}(n, \alpha)B^{11}$ Reaction 973
TACHIKI Masashi;
——— and T. NAGAMIYA: Origin of the Magnetic Anisotropy Energy of Antiferromagnetic Cr_2O_3 452
TAKAGI Satio;
———: On the Temperature Diffuse Scattering of Electrons—I. Derivation of General Formulae 278
———: On the Temperature Diffuse Scattering of Electrons—II. Applications to Practical Problems 287
———: (Errata) On the Temperature Diffuse Scattering of Electrons. I. Derivation of General Formulae 539
———: (Errata) On the Temperature Diffuse Scattering of Electrons. II. Applications of Plactical Problems 539
TAKAGI Yutaka;
——— and Y. MAKITA: Ferroelectricity of $NaNH_4$-Tartrate 272
Y. MAKITA and ———: Ferroelectric and Optical Properties of Na(K–NH_4)-tartrate Mixed Crystals 367
TAKAISI Yorisaburo;
———: The Wall-effect upon the Forces experienced by an Elliptic Cylinder in a Viscous Liquid 496
———: Note on the Forces on an Elliptic Cylinder moving in a Viscous Liquid at Small Reynolds Numbers 954
TAKAKI Hideo;
———, N. KAWAI, C. MIYAKE and T. MORITA: A Torsion Magnetometer for Determining Free Radicals in Some Organic Solutions 629
——— and J. HAYASHI: The Effect of Tension on the Magnetostriction of Iron Single Crystals 703
——— and T. TSUJI: A Note on the Magnetoresistance Effect of Strain Gauge Wire (S. N.) 1406
TAKAMURA Jin-ichi;
Y. NAKAMURA and ———: Magnetic After-Effect Due to Quenched-in Vacancies in Nickel (S. N.) 316
——— and S. MIURA: Grain Boundary-Hardening Due to Piled-up Dislocations 1421
TAKATA Kazuo;
H. WAKESHIMA and ———: On the Limit of Superheat 1398
TAKAYANAGI Kazuo: Molecular Collisions in the Two-Dimensional Gases (S. N.) 1405
TAKEDA Susumu: Afterglow of Pure and Mixed Gases (S. N.) 113
TAKEISHI Yoshiyuki;
—: On the Auger Ejection of Electrons from Nickel by Inert Gas Ions (S. N.) 766
———: A Note on the Normal Cathode Fall in the Glow Discharges in Inert Gases (S. N.) 767
———: (Errata) A Note on the Normal Cathode Fall in the Glow Discharges in Inert Gases 1070

TAKEKOSHI Eiko;
I. KUMABE, ———, H. OGATA, Y. TSUNEOKA and S. ŌKI: $Co^{59}(n, \alpha)Mn^{56}$ and $Mn^{55}(n, \alpha)V^{52}$ Reactions Induced by 14.8-Mev Neutrons 129
TAKEMOTO Shigeo;
——— and M. KASAI: On RF Electrodeless Discharges in a Capillary (S. N.).. 1410
TAKESHITA Kenji;
S. MORITA and ———: The Reaction $F^{19}(d, n)Ne^{20}$ and the Energy Levels of Ne^{20} 1241
TAKEYA Kenichi;
——— and K. NAKAMURA: Current Amplification by Electron Bombardment in the Semiconductor Barrier Layer (S. N.) 223
TANABE Yukito;
——— and H. KAMIMURA: On the Absorption Spectra of Complex Ions.—IV. The Effect of the Spin-orbit Interaction and the Field of Lower Symmetry on *d* electrons in Cubic Field 394
H. KAMIMURA, S. KOIDE, S. SUGANO and ———: An Application of the Thomas-Fermi Method to Complex Ions 464
S. SUGANO and ———: Absorption Spectra of Cr^{3+} in Al_2O_3. Part A. Theoretical Studies of the Absorption Bands and Lines 880
——— and H. KAMIMURA: (Errata) On the Absorption Spectra of Complex Ions IV 539
TANAKA Makoto;
S. KOJIMA, S. OGAWA, M. MINEMATSU and ———: Effects of Impurities on Nuclear Quadrupole Resonance in *p*-Dichlorobenzene 446
TANAKA Shōji;
——— and T. MASUMI: Surface Photoconductivity of Cadmium Sulphide modified with Magnetic Field 22
——— and T. MASUMI: Magneto-resistance Effect in Cadmium Sulphide (S. N.) 314
TANEDA Sadatoshi: Oscillation of the Wake behind a Flat Plate parallel to the Flow 418
TANIGUCHI Satoshi;
K. AOYAGI, ——— and M. YAMAMOTO: Orientation Dependence of the Uniaxial Ferromagnetic Anisotropy Induced by Magnetic Annealing in 20% Co-Ni Single Crystals (S. N.) 532
TANISAKI Sigetosi: Effect of External Stress on the Domain Structure of WO_3 363
TERANISHI Tomoyuki;
K. KAMADA, ——— and Y. YOSHIZAWA: Beta and Gamma Ray Spectroscopy of Co^{60} (S. N.) 763
TOCHIGI Hiroshi;
R. UYEDA, T. MASUDA, ———, K. ITO and H. YOTSUMOTO: Magnification Calibration of Electron Microscopes by Crystal Lattice Spacings 461
TODA Morikazu: On the Theory of the Brownian Motion 1266
TOI Atsutomo;
M. KONDO, T. YAMAZAKI, ———, R. NAKASIMA and S. YAMABE: Elastic Scattering of 5.7 Mev Protons from Fe, Cr and Ti 231
S. YAMABE, M. KONDO, T. YAMAZAKI and ———: Angular Distribution of Protons Inelastically Scattered from Si^{28} and Mg^{24} 777
TOMIIE Yujiro;
———: The Electron Distribution and the Location of the Bonded Hydrogen Atom in Crystals 1030
———: (Errata) The Electron Distribution and the Location of Bonded Hydrogen Atom in Crystals 1239
TOMIKI Tetsuhiko;
T. ISHII, ——— and M. UETA: Dichroism of Color Centers in KCl Crystal (S. N.) 1411
TOMISHIMA Yasuo;

S. ASANO and ———: Lattice Defects in Zincblende. Part I. Phenomenological Expressions of Interionic Potentials 1119
S. ASANO and ———: Lattice Defects in Zincblende. Part II. Formation Energy of Lattice Defects 1126
TOMONO Yuzo;
——— and A. IKUSHIMA: Diffusion of Iron in Single Crystals of Copper (S. N.) 762
TOYAMA Masaharu;
Y. MORINO, T. CHIBA, T. SHIMOZAWA and ———: Zeeman Effect of Nuclear Quadrupole Resonance Spectrum in Cyanuryl Chloride 869
TSUBAKI Akira;
Z. NISHIYAMA, ———, H. SUZUKI and Y. YAMADA: Temperature Distribution during the Martensite Plate Formation 1084
TSUBOKAWA Ichiro: On the Magnetic Properties of Nickel Sulfide 1432
TSUJI Mikio;
———: The Thermoelectric, Galvanomagnetic and Thermomagnetic Effects of Monovalent Metals 133
———: Transport Phenomena in Monovalent Metals (S. N.) 426
———: The Thermoelectric, Galvanomagnetic and Thermomagnetic Effects of Monovalent Metals. II. The Thermoelectric Power for Anisotropic Media 818
———: The Thermoelectric, Galvanomagnetic and Thermomagnetic Effects of Monovalent Metals. III. The Galvanomagnetic and Thermomagnetic Effects for Anisotropic Media 979
———: (Errata) The Thermoelectric, Galvanomagnetic and Thermomagnetic Effects of Monovalent Metals. III. The Galvanomagnetic and Thermomagnetic Effects for Anisotropic Media 979
———: (Errata) The Thermoelectric, Galvanomagnetic and Thermomagnetic Effects of Monovalent Metals 655
TSUJI Toshiro;
———: The Temperature Dependence of Forced Magnetostriction 1310
H. TAKAKI and ———: A Note on the Magnetoresistance Effect of Strain Gauge Wire (S. N.) 1406
TSUJIKAWA Ikuji;
——— and S. SUGANO: Anomalous g-shifts of Excited States of Cr^{3+} in Ruby (S. N.) 220
———: Absorption Lines in the Antiferromagnetic States of $MnCl_2 \cdot 4H_2O$ and $MnBr_2 \cdot 4H_2O$ (S. N.) 315
S. SUGANO and ———: Absorption Spectra of Cr^{3+} in Al_2O_3. Part B. Experimental Studies of the Zeeman Effect and other Properties of the Line Spectra 899
TSUNEOKA Yoshikazu;
I. KUMABE, E. TAKEKOSHI, H. OGATA, ——— and S. ŌKI: $Co^{59}(n, \alpha)Mn^{56}$ and $Mn^{55}(n, \alpha)V^{52}$ Reactions Induced by 14.8-Mev Neutrons 129
TSUSHIMA Tachiro;
S. MIYAHARA and ———: Magnetic Properties of Nickel and Cobalt Ferrite-Chromite Series (S. N.) 758
TSUTSUMI Kenjiro;
—, M. OBASHI and M. SAWADA: Absorption Coefficients of Fine Structures of X-ray Absorption Spectra at Various Absorber Thickness.... 43
: Fine Structures of X-ray K Absorption Spectra of Nickel in Oxides of Nickel 586
– and M. OBASHI: Fine Structures of the X-ray Absorption by the Single Crystal of Germanium 591
TUBOTA Hirosi;
——— and H. SUZUKI: Contact Behavior of Metals to CdSe, CdTe, ZnSe and ZnTe (S. N.) 538

TUZI Yutaka;
——— and H. OKAMOTO: Surface Area Variation of Evaporated Barium Film by Oxidation (S. N.) 225
H. OKAMOTO and ———: Adsorption of Water Vapour on Glass and Other Materials in Vaccum..... 649
——— and H. OKAMOTO: Adsorption of Water Vapour on Lead Borosilicate Glass in Vaccum..... 960
H. OKAMOTO and ———: (Errata) Adsorption of Water Vapour on Glass and Other Materials in Vacuum 1412
H. OKAMOTO and ———: (Errata) Adsorption of Water Vapour on Lead Borosilicate Glass in Vacuum 1412
UCHIDA Enji;
H. KONDOH, ———, Y. NAKAZUMI and T. NAGAMIYA: Magnetic Anisotropy Measurements of NiO Single Crystal 579
UCHIDA Yoichi;
K. FUKUDA, ——— and H. YOSHIMURA: Paramagnetic Resonance Spectrum of Manganese in Single Crystals of Alkali Halide Grown from the Melt (S. N.)..... 971
UEMATSU Shigeyuki;
Y. INUISHI and ———: Electric Breakdown and Conduction in $BaTiO_3$ Single Crystals (S. N.) 761
UEMURA Yasutada;
——— and M INOUE: The Change of Carrier Concentration in the Simple Semiconductor with Static Magnetic Field 377
——— and M. INOUE: The Change of Carrier Concentration in the Graphite with Static Magnetic Field 382
UETA Masayasu;
T. ISHII, T. TOMIKI and ———: Dichroism of Color Centers in KCl Crystal (S. N.) 1411
UMEDA Kwai;
——— and S. KOBAYASHI: Thomas-Fermi Function for Iimpulity Atom Dissolved in a Matrix Metal 148
——— and S. KOBAYASHI: (Errata) Thomas-Fermi Function for Impurity Atom Dissolved in a Matrix Metal 429
UNO Ryosei: On the Electrical Properties of Polycrystalline Boron 667
UYEDA Ryozi;
———, T MASUDA, H. TOCHIGI, K. ITO and H. YOTSUMOTO: Magnification Calibration of Electron Microscopes by Crystal Lattice Spacings 461
VENUGOPALAN, M.: A Possible Mechanism of the Potential Variation of Josh Effect (S. N.) 1544
VREELAND, John A.;
——— and K. MURAKAWA: Isotope Shift in the Spectrum of WI..... 663
WADA Yasaku;
———: Attenuation of Ultrasonic Waves in Suspensions of Viscoelastic Spheres 1390
———: On the Mechanical Loss of Polyethylene (S. N.) 1408
WAKATSUKI Tetsuo
Y. HIRAO, E. OKADA, I. MIURA and ———: Excited States of ^{40}Ca 233
E. OKADA, I. MIURA, ——— and Y. HIRAO: Gamma Rays from the Proton Bombardment of Silicon 541
WAKESHIMA Hiromu;
——— and K. TAKATA: On the Limit of Superheat 1398
WATANABE Denjiro;
K. FUJIWARA, M. HIRABAYASHI, ——— and S. OGAWA: Study on the Ordered Alloy Ag_3Mg 167
———: On the Superstructure of the Alloy Au_3Mn (S. N.) 535
WATANABE Hiroshi: Collective Electron Ferromagnetism, III. Relative Magneti-

zation of Ferromagnetic Alloys 187
WATANABE Tsutomu;
M. INOKUTI and ———: Theoretical Considerations on Radiation-Induced Reactions of Saturated Long-Chain Hydrocarbons (S. N.) 221
———: A Remark on the Chemical Kinetics in Polymers during Irradiation (S. N.) 1063
———: Diffusion Processes in Polymers under Irradiation; Polyvinyl Alcohol and CCl_4 System 1316
YABE Masaya;
T. SAKURAI and ———: The Phase Transformation of Solid Normal Hexadecanamide 5
YABUMOTO Tadaichi;
———: Electrical and Optical Properties of GeS 559
———: Some Electrical and Optical Properties of Tin Monosulphide (S. N.) .. 972
YAJIMA Tatsuo;
——— and L. ESAKI: Excess Noise in Narrow Germanium *p–n* Junctions .. 1281
YAMABE Shotaro;
M. KONDO, T. YAMAZAKI, A. TOI, R. NAKASIMA and ———: Elastic Scattering of 5.7 Mev Protons from Fe, Cr and Ti 231
———: Angular Distribution of Protons Inelastically Scattered from Mg^{24} .. 237
———, M. KONDO, T. YAMAZAKI and A. TOI: Angular Distribution of Protons Inelatistically Scattered from Si^{28} and Mg^{24} 777
YAMADA Ryozo: Asymptotic Expansions of Weber's Functions (S. N) 428
YAMADA Yasusada;
Z. NISHIYAMA, A. TSUBAKI, H. SUZUKI and ———: Temperature Distribution during the Martensite Plate Formation 1084
YAMAGATA Yukio;
J. ITOH and ———: Nuclear Magnetic Resonance Studies of Iodine Ions in Aqueous Solution 1182
J. ITOH and ———: Nnclear Magnetic Resonance Experiments of I^{127} in KI (S. N.) 1232
YAMAGUTI Tasaburô: Experimental Studies on the Initiation of Electric Arcs 520
YAMAKAWA Hiromi;
——— and M. KURATA: Theory of Dilute Polymer Solutions (I) Chain Configuration and Light Scattering 78
———: Theory of Dilute Polymer Solutions (II) Osmotic Pressure 87
——— and M. KURATA: Theory of Dilute Polymer Solutions (III) Intrinsic Viscosity 94
YAMAKI Hideo;
T. HIRONE, N. KUNITOMI, M. SAKAMOTO and ———: Diffusion of Cadmium into Single Crystals of Copper 838
YAMAMOTO Hisashi;
K. SUGIMOTO, A. MIZOBUCHI and ———: Quadrupole Moment of the Second Excited State of ^{19}F (S. N.) 1548
YAMAMOTO Kenzo;
T. OKUDA and ———: Electron Collection and Electron Sheath (S. N.) 112
T. OKUDA and ———: A New Probe Method for Measuring Ionized Gases .. 411
T. OKUDA and ———: Disturbance Phenomena in Probe Measurement of Ionized Gases 1212
YAMAMOTO Mikio
——— and T. NAKAMICHI: Magnetostriction Constants of Nickel-Copper and Nickel-Cobalt Alloys (S. N.) 228
K. AOYAGI, S. TANIGUCHI and ———: Orientation Dependence of the Uniaxial Ferromagnetic Anisotropy Induced by Magnetic Annealing in 20% Co-Ni Single Crystals (S. N.) 532
YAMAMOTO Masazo;
———: The Visco-elastic Properties of Network Structure. III. Normal

Stress Effect (Weissenberg Effect) 1200
T. ONISHI and ———: Relaxation Spectrum of Chain High Polymeric Substances..... 1439
YAMANAKA Chiyoe;
P. CHONG, ——— and T. SUITA: Space Charge Phenomena in Nitrobenzene under High Electric Field (S. N.) 760
YAMASHITA Hirosuke;
——— and S. IBUKI: Crystal Growth of CdS by the Vacuum Sealed Method (S. N.)..... 226
YAMAZAKI Takashi;
M. KONDO, ———, A. TOI, R. NAKASIMA and S. YAMABE: Elastic Scattering of 5.7 Mev Protons from Fe, Cr and Ti 231
M. KONDO and ———: Elastic and Inelastic Scattering of Protons from Neon 771
S. YAMABE, M. KONDO, ——— and A. TOI: Angular Distribution of Protons Inelastically Scattered from Si^{28} and Mg^{24} 777
YAMAZAKI Toshimitsu;
———, H. IKEGAMI and M. SAKAI: Sector Type Double Focusing Beta Ray Spectrometer. Part II. Twin Setting Measurement of the Weak Higher Component of Cs^{137}..... 1080
YANAGAWA Sadaaki: On the Fow Lying Levels of Mn^{55} 323
YANO Syukuro;
———, S. SASAKI and T. SIDEI: Asymmetry of Proton Resonance Signals in Some Hydrates of Iron Group Salts (S. N.) 227
YOKOBORI Takeo;
——— and H. OHARA: Statistical Aspect in Accelerating Creep and Creep Fracture of OFHC Copper 305
YOKOZAWA Yasaburo: The Paramagnetic Resonance Absorption of Some Free Radicals in Sulfuric Acid Solution 727
YONEMITSU Kiyoshi;
——— and T. SATO: Variation of the Hall Coefficient of Mg–Cd Superlattice Alloys with Degree of Order 15
——— and T. SATO: Variation of Hall Coefficient of Some Non-ferromagnetic Superlattice Alloys..... 998
YOSHIDA Ikushi;
———, S. NOMURA and S. SAWADA: Thermal Conductivity of $BaTiO_3$ Ceramics (S. N.)..... 1550
YOSHIDA Toshiho;
Y. FUJIKI, R. SUGANUMA and ———: A New Compound in Au–Pb Alloy System (S. N.)..... 969
YOSHIMOTO Hirosi;
———, M. SATO and Y. NAKAO: Moving Striations in Arc Discharge 734
———, M. SATO and Y. NAKAO: Moving Striations due to Space Charge Waves..... 741
YOSHIMURA Hisamitu;
K. FUKUDA, Y. UCHIDA and ———: Paramagnetic Resonance Spectrum of Manganese in Single Crystals of Alkali Halide Grown from the Melt. (S. N.)..... 971
YOSHINAGA Hiroshi;
A. MITSUISHI, ——— and S. FUJITA: The Far Infrared Absorption of Sulfides, Selenides and Tellurides of Zinc and Cadmium (S. N.) 1235
A. MITSUISHI, ——— and S. FUJITA: The Far Infrared Absorption of Ferrites (S. N.) 1236
YOSHIZAWA Yasukazu;
K. KAMADA, T. TERANISHI and ———: Beta and Gamma Ray Spectroscopy of Co^{60} (S. N.)..... 763
T. KATO, M. NOZAWA, ——— and Y. KOH: Gamma Ray Spectroscopy of

Mn^{54} 1419
YOTSUMOTO Haruo;
R. UYEDA, T. MASUDA, H. TOCHIGI, K. ITO and ———: Magnification Calibration of Electron Microscopes by Crystal Lattice Spacings 461
YUASA Kazunori: Differential Elastic Scattering of MeV Neutrons in Aluminum, Iron, Lead and Bismuth for Large Angles 1248
ZENITI Kiyasu;
———, K. HUSHIMI and K. KATAOKA: Polarization Reversal in Triglycine Sulphate Crystal (S. N.) 661